1998 Hoffmann La Roche Award Lecture Understanding and exploiting glycosidases[1]

Stephen G. Withers

Abstract: Glycosidases fall into two major mechanistic classes; those that hydrolyse the glycosidic bond with retention of anomeric configuration and those that do so with inversion. Retaining glycosidases employ a mechanism involving a covalent glycosyl–enzyme intermediate formed and hydrolysed with acid–base catalytic assistance via oxocarbenium ion-like transition states. This intermediate has been trapped in two distinct ways, either by modification of the substrate through fluorination, or of the enzyme through mutation of key residues. This allows the amino acid residue to which this sugar is attached to be identified through LC/MS–MS analysis of peptic digests. Three-dimensional structures of several of these glycosyl–enzyme complexes, along with those of Michaelis complexes, have been determined through X-ray crystallographic analysis, revealing the identities of important amino acid residues involved in catalysis, particularly the involvement of the catalytic nucleophile in strong hydrogen bonding to the sugar 2-hydroxyl. They have also revealed evidence of substantial substrate distortion upon binding. Insight into the function of the acid–base catalyst Glu172 in *Bacillus circulans* xylanase has been obtained through NMR titration of side chain ^{13}C-labelled glutamic acid enzyme both free and in the 2-fluoroxylobiosyl–enzyme complex. The pK_a of Glu172 is relatively high in the free enzyme, consistent with its role as an acid catalyst, but drops 2.5 units upon formation of the intermediate, consistent with its new role as a base catalyst. This "cycling" of the pK_a is shown to be a direct consequence of the change in charge of the nucleophile, Glu78. Finally, an efficient catalyst for synthesis, but not hydrolysis, of glycosidic bonds has been generated by mutation of the glutamic acid catalytic nucleophile of a β-glucosidase to an alanine. When used with α-glucosyl fluoride as a glycosyl donor, along with a suitable acceptor, oligosaccharides up to five sugars in length have been made with yields of up to 90% on individual steps. These new enzymes have been named glycosynthases.

Key words: enzymatic mechanism, glycoside hydrolysis, inhibitors.

Résumé : Les glycosidases appartiennent à deux grandes classes de mécanismes : celles qui hydrolysent la liaison glycosidique avec rétention de la configuration anomérique et celles qui le font avec inversion. Les glycosidases qui conduisent à une rétention font appel à un mécanisme avec formation d'un intermédiaire covalent glycosyl–enzyme et une hydrolyse assistée par une catalyse acide–base comportant un état de transition qui ressemble à un ion oxocarbénium. On a piégé cet intermédiaire de deux façons distinctes en procédant à une modification du substrat par fluoration ou de l'enzyme par mutation de résidus clés. Une analyse par chromatographie liquide/spectrométrie de masse – spectrométrie de masse (CL/SM–SM) sur les produits de digestion peptique permet alors d'identifier l'acide aminé auquel le sucre est attaché. Faisant appel aux méthodes d'analyse cristallographiques par diffraction des rayons X, on a déterminé les structures tridimensionnelles de plusieurs de ces complexes glycosyl–enzymes avec ceux de complexes de Michaelis; elles permettent d'identifier les résidus d'acides aminés importants dans la catalyse et, en particulier, elles permettent de démontrer l'implication du nucléophile catalytique dans la forte liaison hydrogène avec l'hydroxyle en position 2 du sucre. Elles ont aussi permis de mettre en évidence la présence d'une distorsion importante du substrat lors de sa fixation. On a effectué des titrages RMN sur des enzymes, autant libre que formant un complexe 2-fluorooxylobiosyl–enzyme, comportant de l'acide glutamique marqué au ^{13}C dans la chaîne latérale; ces données ont permis d'obtenir des informations sur la fonction de l'acide du Glu172 de la xylanase du *Bacillus circulans* comme catalyseur acide–base. Le pK_a du Glu172 est relativement élevé dans l'enzyme libre et cette valeur est en accord avec son rôle comme catalyseur acide; il diminue toutefois de 2,5 unités lors de la formation de l'intermédiaire et ceci est en accord avec son nouveau rôle comme catalyseur basique. On a montré que cette « variation » du pK_a est une conséquence directe du changement de charge du nucléophile, le Glu78. Enfin, on a effectué le remplacement de l'acide glutamique, qui agit comme nucléophile d'une β-glucosidase, par une alanine; cette opération a permis de générer un catalyseur efficace pour la synthèse, mais pas pour l'hydrolyse, des liaisons glycosidiques. Lorsqu'on l'a utilisé avec un fluorure d'α-glucosyle, agissant comme donneur, avec un accepteur

Received October 15, 1998.

S.G. Withers.[2] Protein Engineering Network of Centres of Excellence of Canada, and Departments of Chemistry and Biochemistry, The University of British Columbia, Vancouver, BC V6T 1Z1, Canada.

[1]The 1998 Hoffman-La Roche Award Lecture was presented by Professor Withers at the 81st Conference of the Canadian Society for Chemistry, Whistler, British Columbia, June 1998.

[2]Telephone: (604) 822-3403. Fax: (604) 822-2847. e-mail: withers@chem.ubc.ca

 © 1999 NRC Canada

approprié, on a réalisé la synthèse d'oligosaccharides comportant jusqu'à cinq sucres avec des rendements allant jusqu'à 90% pour les étapes individuelles. Ces nouveaux enzymes ont été nommés glycosynthases.

Mots clés : mécanisme enzymatique, hydrolyse de glycosides, inhibiteurs.

[Traduit par la Rédaction]

Introduction

Glycosidic bonds occur in a wide range of contexts. These include polysaccharides, which function as storage, structural, or recognition components; oligosaccharides, which function in energy storage or also as recognition elements; and a wide variety of other glycoconjugates such as glycolipids, glycoproteins, or saponins. In large part reflecting this wide variety in substrate structure, there also exists a wide range of different enzymes, glycosidases, whose function is the cleavage of these bonds. Amino acid sequences of well over 1000 different glycoside hydrolases are now available, primarily deduced from their gene sequences, and these have been arranged into over 60 different families on the basis of sequence similarities (1). At the time this article is being written an excellent web site is available that gives updated listings of these family members, plus some other information on the identities of important amino acid residues (http://afmb.cnrs-mrs.fr/~pedro/CAZY/db.html). This categorization has proved to be extremely useful in understanding structural and mechanistic relationships, and has been reviewed recently (2, 3). Three-dimensional structures are now available as representatives of at least 27 of these families, revealing their incredible diversity. Monomer sizes range from approximately 14 000 to 170 000 Da, and compositions range from essentially completely α-helical to almost exclusively β-sheet. The reasons for this diversity are likely twofold: the diverse nature of the substrates themselves, and different evolutionary pathways.

Enzymatic hydrolysis of glycosidic bonds is carried out with one of two stereochemical outcomes, net retention or net inversion of anomeric configuration; thus glycosidases are classified as either retaining or inverting. Elementary mechanisms for these two classes of glycosidase were proposed by Koshland some 45 years ago (4), and these mechanisms (Fig. 1) have largely passed the test of time, having been supported by structural, mechanistic, and kinetic analyses since that time. The inverting glycosidases use a direct displacement mechanism in which two carboxylic acids at the active site are suitably positioned such that one provides base catalytic assistance to the attack of water while the other provides acid catalytic assistance to cleavage of the glycosidic bond. Reaction proceeds through an oxocarbenium ion-like transition state.

Catalysis by retaining glycosidases proceeds via a double-displacement mechanism in which a covalent glycosyl–enzyme intermediate is formed and hydrolysed via oxocarbenium ion-like transition states. Again the reaction is acid–base catalysed, though in this case all such catalysis is provided by a single group at the active site that acts as an acid catalyst for the first (glycosylation) step and as a base catalyst for the second (deglycosylation) step. The active sites of the two classes of enzymes are similar in that they provide an array of amino acid side chains suitable for stabilizing an oxocarbenium ion-like transition state. One significant difference, however, is that the two carboxylic acid side chains are much closer together (5.5 Å apart) in the retaining enzymes than in the inverters (11 Å apart) (5–7). This greater separation in the inverters allows the inclusion of a water molecule in the active site at the same time as the leaving group. Background information on these mechanisms, and references to the original publications, can be found in the following reviews: refs. 2, and 7–9.

Trapping the intermediate

Research within our group, in close collaboration with that of Dr. Tony Warren (Department of Microbiology, University of British Columbia), has focussed on mechanistic studies of retaining glycosidases, and in particular on developing methods to trap the covalent intermediate formed during catalysis. Attempts initially focussed upon methods involving modification of the substrate. The basic strategy involved slowing *both* the glycosylation and deglycosylation steps by destabilization of the oxocarbenium ion-like transition states. This was achieved by replacement of the 2-hydroxyl of the substrate with a fluorine, thereby inductively destabilizing the positively charged transition states. In addition, this substitution removed a key hydrogen-bonding substituent, interactions with the 2-position hydroxyl having been shown to contribute up to 10 kcal/mol to transition state stabilization (10–12). Having slowed both steps it was then necessary to reaccelerate the glycosylation step in order to render the intermediate kinetically accessible. This was achieved by incorporation of a reactive leaving group such as dinitrophenolate or fluoride into the substrate. Such a group would accelerate the glycosylation step, but could have no effect upon deglycosylation.

Compounds such as 2,4-dinitrophenyl 2-deoxy-2-fluoro-β-D-glucopyranoside were therefore synthesized and shown to be effective mechanism-based inactivators, functioning via the accumulation of a covalent 2-deoxy-2-fluoroglycosyl–enzyme intermediate, as shown in Fig. 2. Evidence for the accumulation of this intermediate was obtained from the inactivation itself, from ^{19}F NMR studies of the inactivated enzyme, from the stoichiometric burst of dinitrophenolate released upon inactivation of the enzyme, and from the mass increase of the enzyme. The intermediate so formed was surprisingly stable, with half-lives for turnover in the order of hundreds of hours. However, turnover could be considerably accelerated by inclusion of a sugar in the reactivation mixture, the reactivation in this case occurring by a more efficient transglycosylation reaction (Fig. 2). For leading references see the following publications and reviews: refs. 13–17.

An interesting feature of these 2-fluoro inactivators is that, while they are successful with all β-glycosidases thus far studied, they are relatively ineffective as inactivators of α-glycosidases, serving rather as slow substrates. Alternative approaches have therefore been evolved for α-glycosidases.

© 1999 NRC Canada

Fig. 1. Mechanisms of retaining and inverting glycosidases.

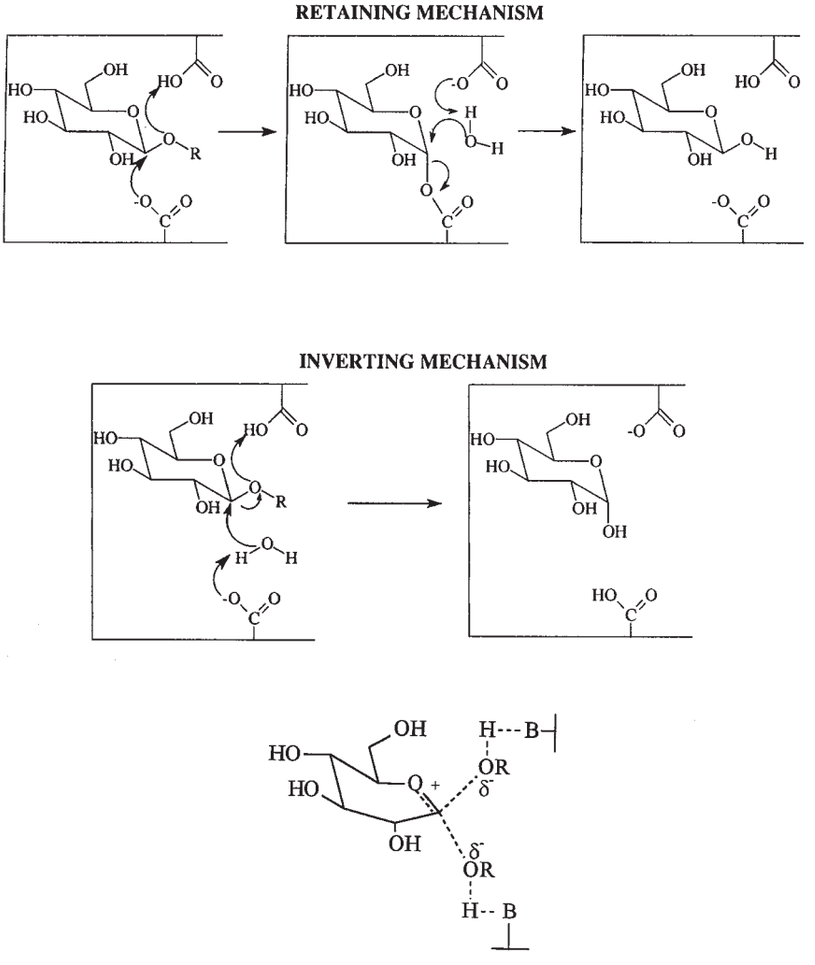

Fig. 2. Inactivation and reactivation with 2-fluoroglycosides.

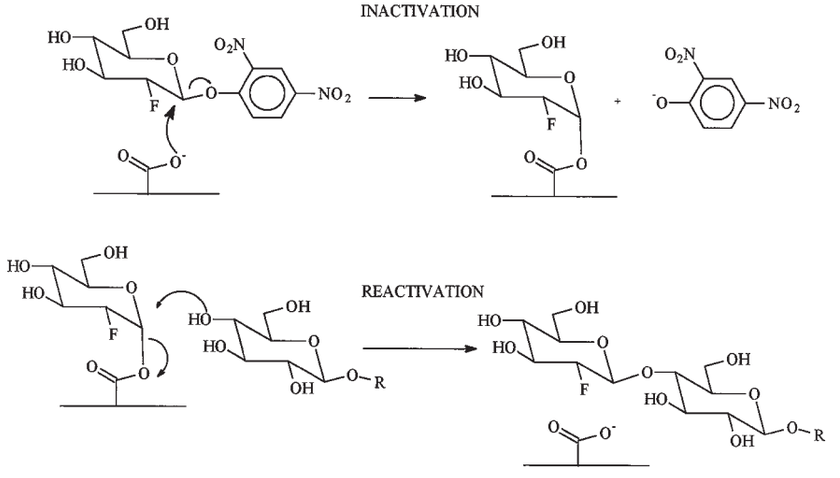

One has involved the use of a 2-deoxy-2,2-difluoro glycoside, the idea being that the presence of a second fluorine would ensure that turnover would occur only *much* more slowly. Such compounds require even more reactive leaving

© 1999 NRC Canada

Fig. 3. Structures of inactivators.

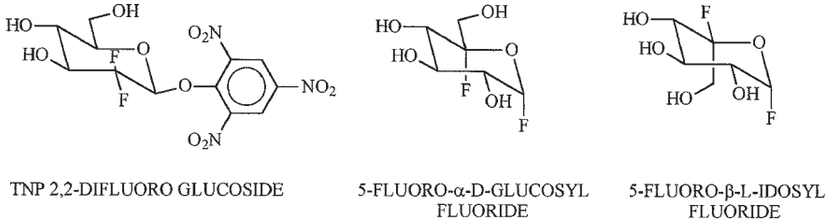

Fig. 4. Schematic of the active site of 2-fluorocellobiosyl-Cex. Adapted from ref. 22.

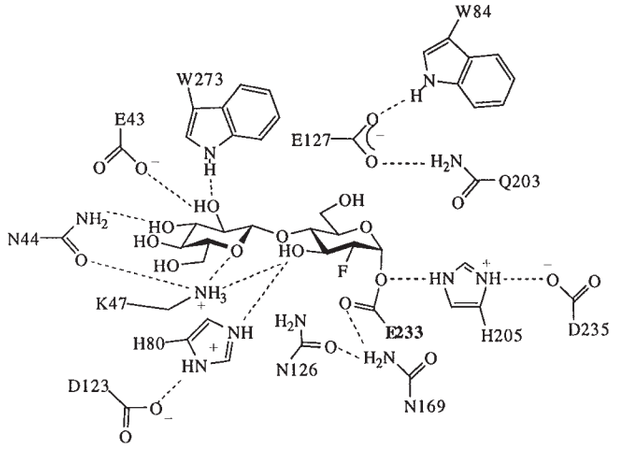

groups to allow accumulation of the intermediate; thus trinitrophenyl derivatives such as that shown in Fig. 3 were synthesized and shown to be effective in trapping intermediates on an α-glucosidase as well as on human pancreatic α-amylase (18). A more subtle approach was taken in moving the fluorine from the 2-position to the 5-position, the idea being that this substituent is close to the endocyclic oxygen, where most of the charge accumulation at the transition state is taking place. This resulted in compounds such as 5-fluoro-α-D-glucosyl fluoride and 5-fluoro-β-L-idosyl fluoride, both of which can be used to trap an intermediate on yeast α-glucosidase (Fig. 3). The compounds of opposite anomeric stereochemistry were shown to be equally effective at trapping intermediates on β-glycosidases (19, 20).

Both the 2-fluoro and 5-fluoro glycosyl fluorides have been used to derivatize and thereby ultimately identify the catalytic nucleophiles of a large number of glycosidases. This work was originally devised in collaboration with Dr. Ruedi Aebersold, now in the Department of Molecular Biotechnology, University of Washington. The identification was achieved by labelling the enzyme, cutting it into a peptide mixture using pepsin, then separating the peptides by HPLC. Use of on-line MS–MS analysis has allowed localization of the glycosylated peptide within such mixtures by means of a neutral loss experiment in which a specific fragmentation event of the glycosylated peptide within the collision cell of the mass spectrometer is identified. Having localized the peptide, its sequence is determined by subsequent tandem mass spectrometric analysis in the daughter ion mode. In this way the identities of the catalytic nucleophiles in a large number of the families of retaining glycosidases have now been determined (13, 15, 17, 21).

Structural studies on the intermediate

Further insight into catalysis has come from the determination of the three-dimensional structures of several covalent glycosyl–enzyme intermediates. The first of these to be resolved was that of the 2-deoxy-2-fluorocellobiosyl–enzyme intermediate formed on the *exo*-xylanase/cellulase Cex from *Cellulomonas fimi* in collaboration with Dr. David Rose (Ontario Cancer Institute, Toronto) (22). This structure revealed that no significant structural change occurs within the protein upon formation of the glycosyl–enzyme. It also revealed the identities of the amino acid side chains involved in binding and catalysis, including those interacting with the 6-hydroxyl and therefore likely responsible for determining the cellulose/xylan specificity (Fig. 4). This was supported by the subsequent determination of the structure of the 2-deoxy-2-fluoroxylobiosyl–enzyme in which two of the residues that had moved position slightly in the fluorocellobiosyl–enzyme complex no longer moved, consistent with the higher specificity for xylan (23). Surprisingly, when mutations at one of these positions were made there was no significant effect upon the cellulose/xylan specificity.

The structures also provided clues concerning the nature of the very strong interactions (>10 kcal/mol) formed with the 2-position of the natural substrate at the transition state. Residues close to the fluorine of the substrate moiety were the highly conserved Asn126 and the carbonyl oxygen of the nucleophile itself. While the interaction with the amide moiety of Asn126 is undoubtedly important (and mutants are currently under construction to test this hypothesis), the transition state interaction with the charged nucleophile itself seems the most likely source of the majority of this stabilization at the transition state. However, the fact that the actual substituent present at the 2-position in this structure is a fluorine, which of course does not interact positively, detracts from the value of this structure. A structure with a hydroxyl at this position would be preferred. To achieve the trapping of a 2-hydroxy-intermediate without significant turnover of substrate, the glycosyl–enzyme was trapped by mutating the enzyme instead of modifying the substrate.

The first attempt to do this involved mutation of the acid–base catalyst Glu127 to Ala. This mutant was active, but with a k_{cat} value some 300-fold lower than the wild-type enzyme (24). By use of a substrate with an excellent leaving group, such as 2,4-dinitrophenolate, it was possible to accumulate the intermediate. However, turnover was still too fast for crystallographic analysis. A second mutant was therefore constructed in which the histidine residue (His 205) that

© 1999 NRC Canada

hydrogen bonds to the catalytic nucleophile, Glu233, was mutated to Asn and Ala. Again these mutants were found to have substantially decreased activities (8500-fold and 4800-fold, respectively), and they also accumulated intermediates when activated substrates were employed. However, again the turnover of this intermediate was too fast for crystallographic analysis. The final solution to this problem involved creation of a double mutant in which both mutations were present. When His205Asn/Glu233Ala Cex was reacted with 2,4-dinitrophenyl cellobioside it relatively rapidly formed a cellobiosyl–enzyme complex that turned over only on a time scale of weeks. The catalytic domain of Cex so trapped was then crystallized and its three-dimensional structure solved to 1.8 Å (25). Apart from some small changes in the positioning of the nucleophile itself and rearrangement of hydrogen-bonding patterns as a consequence of the mutations, the overall structure was very similar to that of the wild-type enzyme in its 2-deoxy-2-fluorocellobiosyl–enzyme form. Most importantly, however, the carbonyl oxygen of the nucleophile was now found to be hydrogen bonded to the sugar 2-hydroxyl with an O—O distance of 2.35 Å. This is a rather short interaction, reminiscent of those proposed to be low-barrier hydrogen bonds (26, 27). This short distance, and the fact that very strong interactions (>10 kcal/mol) are known to be formed with the 2-hydroxyl at the transition state, suggests that the hydrogen bond formed at this position is a major contributor to transition state stabilization. The interaction seen in this structure is, of course, that present in an intermediate complex, not that at the transition state. The suggestion is that this interaction is optimized at the transition state both geometrically, as the ring flattens, and electronically, as the positive charge develops at the anomeric centre, acidifying the 2-hydroxyl and thereby increasing its hydrogen bond donor capability.

Other insights have been obtained through structural studies, in collaboration with Dr. Gideon Davies (Department of Chemistry, University of York, U.K.), on the endoglucanase Cel5A from *Humicola insolens*. These studies have provided "snapshots" of the enzyme at every stable state along the reaction coordinate diagram: free enzyme, Michaelis complex, covalent intermediate, and product complex (Fig. 5) (28). These structures were achieved as follows. Excellent crystals of the native enzyme, whose pH optimum is around 7.0, were obtained at a pH of 4.5, and the structure was solved to 0.95 Å resolution. Even though the enzyme has only very low activity at this pH, substrates diffused into crystals, with their extremely high enzyme concentration, were nonetheless cleaved before data could be collected. However, by use of 2,4-dinitrophenyl 2-deoxy-2-fluoro-β-cellobioside as substrate, the structure of the Michaelis complex could be solved. The interesting feature of this structure was the substantial distortion of the substrate sugar bound in the –1 site to a $^{1}S_{3}$ skew boat, thereby placing the leaving group dinitrophenyl moiety in a pseudo-axial orientation. Such distortion should serve to facilitate the formation of the planar transition state structure. It also removes the barrier to attack of the nucleophile at the anomeric centre arising from 1,3-diaxial interactions present in the $^{4}C_{1}$ conformation.

The structure of the covalent intermediate was solved by reacting the enzyme with 2,4-dinitrophenyl 2-deoxy-2-fluoro β-cellobioside (and also the cellotrioside) at pH 7, then lowering the pH to 4.5 and crystallizing the enzyme in that form. As with *C. fimi* Cex, the intermediate was clearly seen in an undistorted $^{4}C_{1}$ conformation. Finally, simply soaking the enzyme with cellotriose and collecting data solved the structure of the product complex. This structure was unremarkable in that no significant distortion was observed, although the reducing end of the oligosaccharide was somewhat disordered, suggesting the presence of some destabilizing interactions. These structures have therefore provided useful insights into catalysis and the roles of specific residues, and of distortion, therein.

Acid–base catalysis

While the structural picture for these enzymes at least would seem now to be fairly clear, a remaining mechanistic concern was how the acid–base catalyst could efficiently function both as a good acid catalyst in the glycosylation step and then as a good base catalyst in the deglycosylation step. To probe this, ^{13}C NMR measurements of the pK_a values of the two key active site carboxylic acids of the *Bacillus circulans* xylanase (Bcx) were undertaken in collaboration with Dr. Lawrence McIntosh (Departments of Biochemistry and Chemistry, University of British Columbia) (29). Bcx was chosen for this study because it is small (20 kDa), its X-ray structure has been determined (30), and it has the enviable property of containing only two glutamic acid residues, these being the nucleophile, Glu78, and the acid–base catalyst, Glu172. The gene encoding Bcx was therefore moved into a strain of *Escherichia coli* that is auxotrophic for glutamic acid, the organism grown in the presence of side chain ^{13}C-labelled glutamic acid, and the labelled protein isolated. Because this strain will still interconvert glutamic acid and glutamine, all five glutamines were also labelled, giving a total of seven resonances in the ^{13}C NMR spectrum.

The two resonances arising from Glu78 and Glu172 were initially assigned on the basis of parallel studies with mutants in which Glu78 and Glu172 had been individually replaced; these assignments were later confirmed from the complete assignment of the ^{13}C and ^{15}N NMR spectra of this protein (31). In this way the five glutamine resonances were also assigned. ^{13}C NMR spectra were measured at a series of pH values, as shown in Fig. 6, and, from the changes in chemical shift with pH, pK_a values for the two glutamic acid residues were determined. Interestingly, several of the glutamine resonances shifted with pH also, their chemical shifts changing in response to the lower pK_a ionization. Particularly surprising in this regard was the fact that the largest such shift was observed for Gln7, a residue some 10 Å away from either active site carboxylic acid. Since Gln7 sits in close proximity to Tyr166, which hydrogen bonds through Tyr69 to Glu78, it seems likely that the large shift observed is a consequence of changing aromatic ring current effects on the chemical shift of Gln7 arising from small changes in conformation. In any case, pK_a values for Glu78 and Glu 172 of 4.2 and 6.7, respectively, were determined (Fig. 7). These values are completely consistent with the optimal pH of this enzyme (5.5) since at this pH the nucleophile will be largely deprotonated and the acid catalyst protonated,

© 1999 NRC Canada

Fig. 5. Snapshots along the reaction coordinate of Cel5A. Structures of the Michaelis complex, the glycosyl–enzyme complex, and the product complex. Adapted from ref. 28.

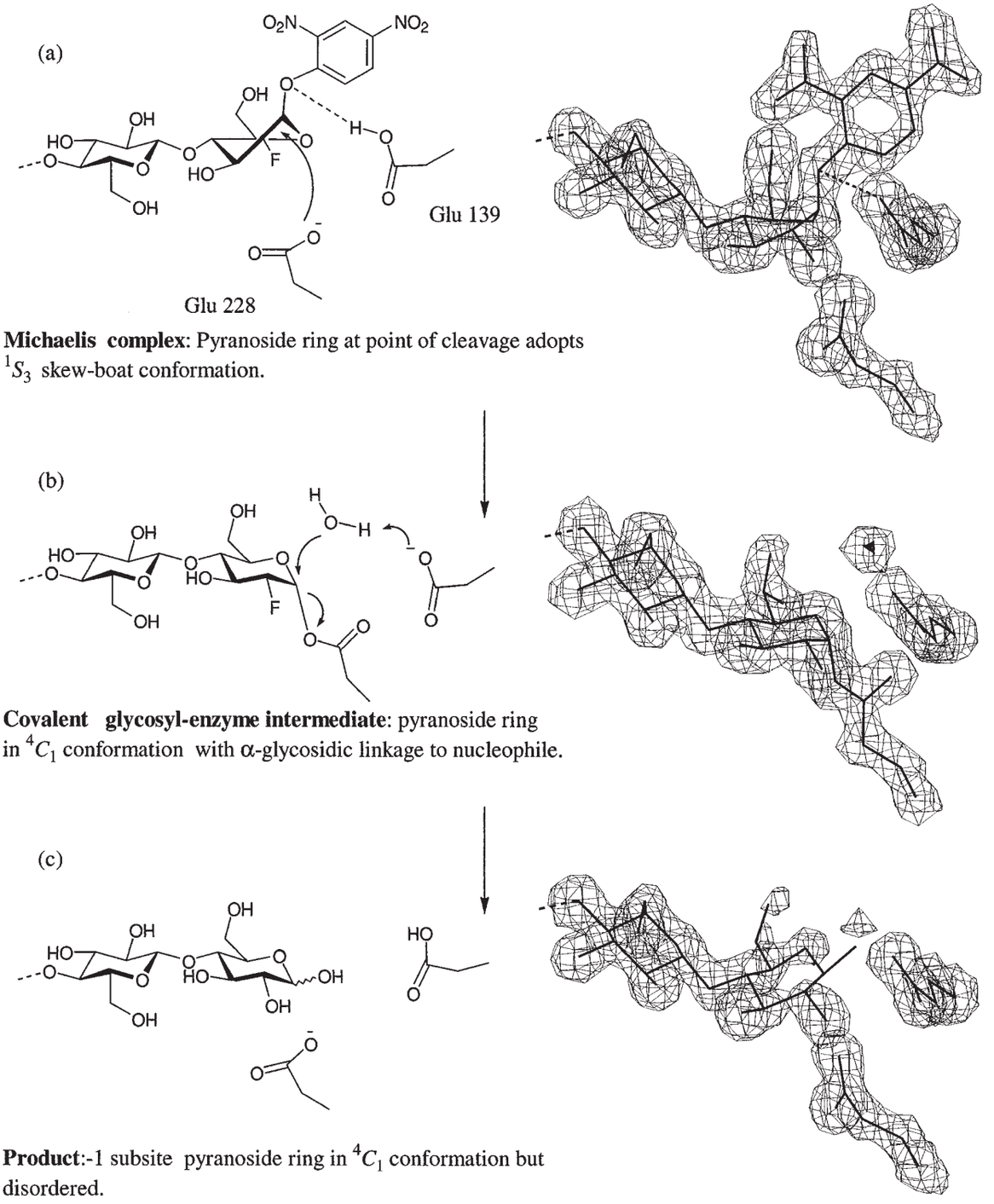

as required for the first step. Indeed, the two pK_a values measured agree exactly with those determined from the dependence of k_{cat}/K_m upon pH, as would be expected.

The pK_a of Glu172 for the second step was measured by trapping the ^{13}C-labelled Bcx as its 2-deoxy-2-fluoroxylobiosyl–enzyme intermediate and then once again titrating the sample and measuring ^{13}C NMR spectra. To our delight the pK_a was found to have dropped to 4.2 in this intermediate, a decrease of 2.5 pH units. This lower pK_a therefore sets Glu172 up to function as the base catalyst for the second

© 1999 NRC Canada

Fig. 6. Titration of ^{13}C resonances in side chain Glu labelled xylanase. Taken from ref. 29.

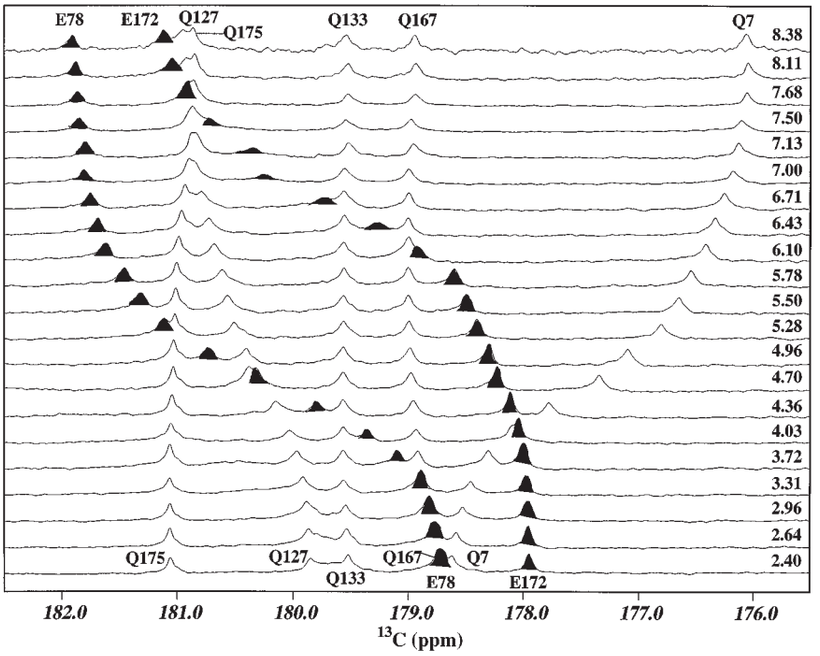

Fig. 7. pK_a values of the active site carboxyl groups in *B. circulans* xylanase. Taken from ref. 29.

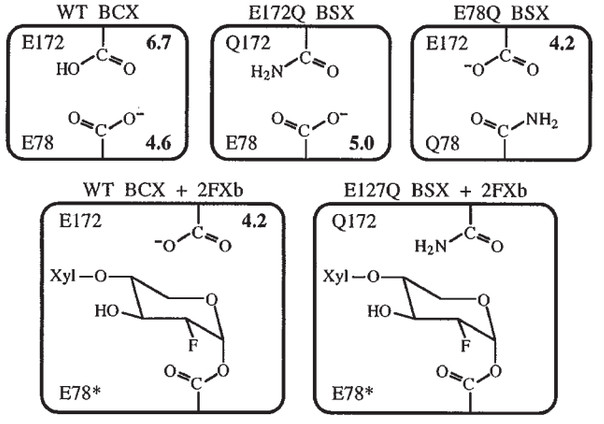

step, exactly as needed. It is of interest to consider the reasons for this abrupt change in pK_a. In the free enzyme the pK_a of Glu172 is raised above its normal value by the presence of the negative charge on Glu78, just as in any dicarboxylic acid. Good evidence for this is the fact that the pK_a of Glu172 in the Glu172Gln mutant, where the charge at that position has been removed, is 4.2 (Fig. 7). The shift in pK_a value upon formation of the intermediate therefore appears to be caused primarily by the removal of the charge on the catalytic nucleophile upon formation of the ester. In this way the enzyme automatically "cycles" the pK_a of the acid–base catalyst to suit its role at each step by an intrinsic mechanism involving the charge on the other key active-site residue. It is likely that this mechanism is quite general for retaining glycosidases, and possibly for other enzyme classes in which charge is masked in a covalent intermediate.

Glycosynthases: mutant glycosidases for oligosaccharide synthesis

The knowledge of the mechanism and the tools developed in the process were then put to use in the generation of a new class of mutant enzyme for the synthesis of oligosaccharides. There is a rapidly increasing interest in the use of oligosaccharides as possible therapeutics (32–34). However, the difficulties attendant in the large-scale synthesis of such molecules are slowing progress in this field. While classical organic synthetic approaches are able to yield almost any oligosaccharide needed, the quantities of compound available through such routes are typically very limited. Enzymatic synthesis provides an alternative approach, and indeed glycosyl transferases, Nature's own biosynthetic catalysts, are finding increasing application as they become available in greater numbers (35–38). However, the cost of the nucleotide diphosphosugars is still prohibitive. Glycosidases run "in reverse" are another alternative, indeed, one that has been pursued for over 85 years (38–40). There are two basic approaches that can be followed, one being an equilibrium approach in which very high concentrations of the sugars of interest are mixed and reaction allowed to approach equilibrium. This typically nets very low yields and complex product mixtures. The other is the kinetic approach in which the glycosyl–enzyme intermediate is formed using a reactive glycosyl donor and then intercepted with a second sugar acceptor molecule rather than water. This is the more useful approach as it can give very specific products. However, again yields are typically rather low unless some device is used to limit product hydrolysis. *Based on our observations*,

© 1999 NRC Canada

Fig. 8. Mechanism of glycoside synthesis with a glycosynthase. Taken from ref. 41.

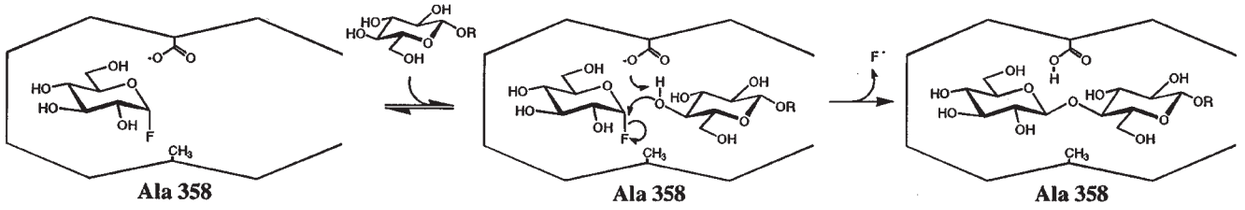

Table 1. Glycosynthase-catalyzed transglycosylations using α-galactosyl fluoride as donor. Taken from ref. 41.

No.	Acceptor	Products (% yield) β-1,4 linked (unless otherwise stated)
		Disaccharide
1	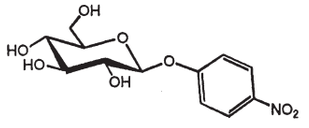	**84%**
2	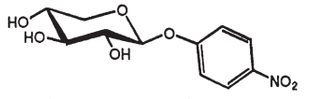	**81%** (β-1,3 linked)
3	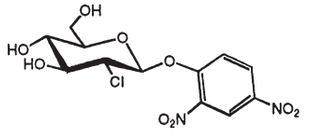	**64%**
4	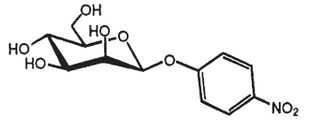	**66%**
		Trisaccharide
5	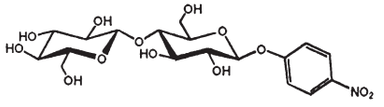	**92%**
6	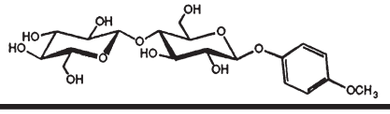	**88%**

we sought a mutant that would catalyse the formation of oligosaccharides while minimizing product hydrolysis.

The best method for completely eliminating activity in a retaining glycosidase through a single mutation, while keeping the structure intact, is to mutate the catalytic nucleophile to a non-nucleophilic residue such as alanine. If this mutation and purification are carried out with considerable care to minimize the amount of translational misincorporation and of contamination from wild-type enzyme or other active mutants during purification, then such Ala mutants of retaining glycosidases are essentially devoid of activity, having maximal rates at least 10^5 times lower than the wild-type enzyme (5). The protein active site so generated might therefore provide a useful environment in which to carry out the synthetic reaction, the mutant being folded correctly, as evidenced by CD measurements, and even X-ray crystallographic analyses in several cases (G. Brayer, D. Rose, and S.G. Withers. Unpublished results). Such a protein has an active site, capable of binding both the glycone and aglycone moieties, that is optimized for stabilization of the oxocarbenium ion-like transition state (although lacking the negative charge from the carboxylate). It also contains an acid–base residue that, due to the absence of a charged nucleophile, is likely in the deprotonated form, therefore is optimally set up as a base catalyst. In full, therefore, the enzyme is set up to carry out the transglycosylation step, but cannot do so because it has not formed a reactive α-glycosyl–enzyme intermediate. The answer to the problem was to provide the mutant with a glycosyl donor that was a chemical mimic of this reactive α-glycosyl–enzyme intermediate, incorporating a leaving group that is sufficiently small to fit into the space in the active site generated by removal of the catalytic nucleophile. The reagent of choice was an α-glycosyl fluoride since such compounds are reactive

© 1999 NRC Canada

Table 2. Glycosynthase-catalyzed transglycosylations using α-glucosyl fluoride as donor. Taken from ref. 41.[a]

		Products (% yield) β-1,4 linked			
No.	**Acceptor**	Disaccharide	Trisaccharide	Tetrasaccharide	Total yield
7	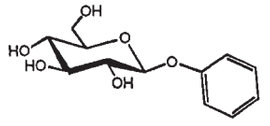	48%	34%	—	**82%**
8	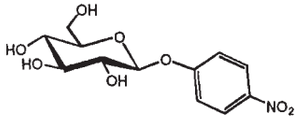	38%	24%	10%	**72%**
9	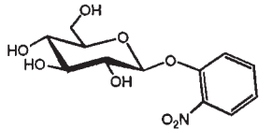	41%	29%	6%	**76%**
10	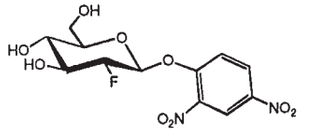	38%	42%	4%	**84%**
11 a b	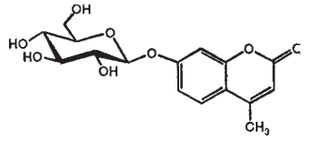	—	75% * 23% *	8%* 54%*	**83%*** **77%***
12 a b	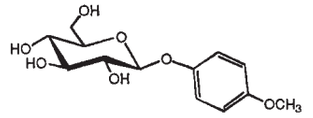	44% 12%*	29% 66%*	— 8%*	**73%** **86%***
13	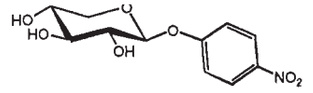	12%	51%	3%	**66%** β-1,3 linked
14	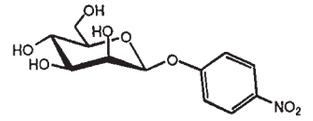	31%	42%	6%	**79%**
15 a b	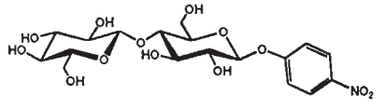		79% 8%*	13% 64%*	**92%** **72%***
16	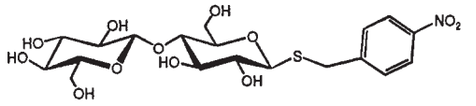		64%	21%	**85%**
17	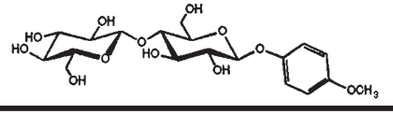		59%	12%	**71%**

[a]Reactions were performed with 1–1.4 equiv. of glycosyl donor, except for those marked with an asterisk, which were carried out with 2.2–3.0 equiv. of glycosyl donor.

glycosyl donors with a very small substituent/leaving group, fluoride, and are very readily synthesized. Incubation of the mutant with this donor in the presence of a suitable glycosyl acceptor should lead to product formation as shown in Fig. 8.

© 1999 NRC Canada

This approach was first established (41) with the β-glucosidase from *Agrobacterium sp.* (Abg), a Family 1 β-glycosidase with broad specificity that has been studied extensively in our group (11, 14, 42–45). The buffer chosen was either 150 mM sodium phosphate, or 150 mM ammonium bicarbonate, the latter being preferred due to its volatility. High buffer concentrations are required in order to neutralize the HF released stoicheometrically. As an illustration of this approach on the 2 mL scale, the Glu358Ala mutant of Abg was incubated with α-galactosyl fluoride (40 mM) as donor and *p*-nitrophenyl β-cellobioside (30 mM) as acceptor in the presence of AbgGlu358Ala (0.01 mg) in 150 mM ammonium bicarbonate buffer. After 8 h, TLC analysis indicated that reaction was complete and the reaction was worked up by ultrafiltration to remove the enzyme (which can be reused). Lyophilization, then HPLC purification, yielded 34 mg (92% isolated yield) of Gal-β-1,4-Glu-β-1,4-Glu-β-*p*-nitrophenyl.

The enzyme was shown to be capable of transferring galactose residues to a range of different acceptors, as shown in Table 1. The products formed were poor acceptors for the enzyme (as also is galactose), thus reaction terminated after a single transfer. α-Glucosyl fluoride also acts as an excellent donor. However, in this case the products, being glucosides, are also excellent acceptors, resulting in longer oligomers. The size of the oligosaccharide product can be controlled to a reasonable extent through the number of equivalents of donor employed, though such control is not perfect. Examples are shown in Table 2. A final interesting example, which illustrates the power of this approach, is that of the synthesis of some 2-fluorocello-oligosaccharide based cellulase inactivators. Incubation of AbgGlu358Ala with 2,4-dinitrophenyl 2-deoxy-2-fluoro β-glucoside plus 1.5 equiv. of α-glucosyl fluoride yielded an intentional mixture of 2,4-dinitrophenyl 2-deoxy-2-fluoro β-cellobioside and trioside (84% total yield) that was readily separated by HPLC. It is interesting to note that this reaction could not be carried out by standard glycosidase transglycosylation since the 2-fluorosugar would have inactivated the enzyme, a process that is not possible with the mutant.

As is clear from the above data, this approach provides very good yields of product in a very simple reaction starting with easily accessible reagents. It therefore has good potential as a method for synthesis of oligosaccharides, particularly on the large scale. The approach has therefore been patented (U. S. Patent no. 5,716,812 (1998)) and work is currently ongoing to extend this approach to the synthesis of a range of different oligosaccharides.

Acknowledgments

This work was carried out in collaboration with a number of colleagues who have been named in the article. I owe my thanks to them and to all our graduate students, postdoctoral fellows, and technicians. Their names are apparent in the references quoted, or the references therein. The work was supported by research funds from the Natural Sciences and Engineering Research Council of Canada and the British Columbia Science Council. It was also supported by the Government of Canada's Network of Centres of Excellence programme supported by the Medical Research Council and the Natural Sciences and Engineering Research Council of Canada through PENCE Inc. (the Protein Engineering Network of Centres of Excellence of Canada).

References

1. B. Henrissat and A. Bairoch. Biochem. J. Lett. **316**, 695 (1996).
2. G. Davies and B. Henrissat. Structure, **3**, 853 (1995).
3. B. Henrissat, I. Callebaut, S. Fabrega, P. Lehn, J.P. Mornon, and G. Davies. Proc. Natl. Acad. Sci. U.S.A. **92**, 7090 (1995).
4. D.E. Koshland. Biol. Rev. **28**, 416 (1953).
5. Q. Wang, R.W. Graham, D. Trimbur, R.A.J. Warren, and S.G. Withers J. Am. Chem. Soc. **116**, 11594 (1994).
6. A. White, S.G. Withers, N.R. Gilkes, and D.R. Rose. Biochemistry, **33**, 12546 (1994).
7. J. McCarter and S.G. Withers. Curr. Opin. Struct. Biol. **4**, 885 (1994).
8. G.J. Davies, M.L. Sinnott, and S.G. Withers. *In* Comprehensive biological catalysis. Vol. 1. *Edited by* M.L. Sinnott. Academic Press, London. Chap. 3, pp. 119–208.
9. G. Legler. Adv. Carbohydr. Chem. Biochem. **48**, 319 (1990).
10. R. Wolfenden and W.M. Kati. Acc. Chem. Res. **24**, 209 (1991).
11. M.N. Namchuk and S.G. Withers. Biochemistry, **34**, 16194 (1995).
12. J. McCarter, M. Adam, and S.G. Withers. Biochem. J. **286**, 721 (1992).
13. S.G. Withers and R. Aebersold. Protein Sci. **4**, 361 (1995).
14. I.P. Street, J.B. Kempton, and S.G. Withers. Biochemistry, **31**, 9970 (1992).
15. L.F. Mackenzie, G.S. Brooke, J.F. Cutfield, P.A. Sullivan, and S.G. Withers. J. Biol. Chem. **272**, 3161 (1997).
16. L.F. Mackenzie, G.J. Davies, M. Schulein, and S.G. Withers. Biochemistry, **36**, 5893 (1997).
17. J.D. McCarter, D.L. Burgoyne, S.C. Miao, S.Q. Zhang, J.W. Callahan, and S.G. Withers. J. Biol. Chem. **272**, 396 (1997).
18. C. Braun, G. Brayer, and S.G. Withers. J. Biol. Chem. **270**, 26778 (1995).
19. J.D. McCarter and S.G. Withers. J. Am. Chem. Soc. **118**, 241 (1996).
20. J.D. McCarter and S.G. Withers. J. Biol. Chem. **271**, 6889 (1996).
21. D. Tull, S. Miao, S.G. Withers, and R. Aebersold. Anal. Biochem. **224**, 509 (1994).
22. A. White, D. Tull, K. Johns, N.R. Gilkes, S.G. Withers, and D.R. Rose. Nat. Struct. Biol. **3**, 149 (1996).
23. V. Notenboom, C. Birsan, R.A.J. Warren, S.G. Withers, and D.R. Rose. Biochemistry, **37**, 4751 (1998).
24. A.M. Macleod, D. Tull, K. Rupitz, R.A.J. Warren, and S.G. Withers. Biochemistry, **35**, 13165 (1996).
25. V. Notenboom, C. Birsan, M. Nitz, D.R. Rose, R.A.J. Warren, and S.G. Withers. Nat. Struct. Biol. **5**, 812 (1998).
26. J.P. Guthrie. Chem. Biol. **3**, 163 (1996).
27. J.A. Gerlt, M.M. Kreevoy, W. Cleland, and P.A. Frey. Chem. Biol. **4**, 259 (1997).
28. G.J. Davies, L.F. Mackenzie, A. Varrot, M. Dauter, A.M. Brzozowski, M. Schulein, and S.G. Withers. Biochemistry, **37**, 11707 (1998).
29. L.P. McIntosh, G. Hand, P.E. Johnson, M. Joshi, M. Korner, L.A. Plesniak, L. Ziser, W.W. Wakarchuk, and S.G. Withers. Biochemistry, **35**, 9958 (1996).
30. W.W. Wakarchuk, R.L. Campbell, W.L. Sung, J. Davoodi, and M. Yaguchi. Protein Sci. **3**, 467 (1994).
31. L.A. Plesniak, W.W. Wakarchuk, and L.P. Mcintosh. Protein Sci. **5**, 1118 (1996).
32. P.M. Simon. Drug Discovery Today, **1**, 522 (1996).

© 1999 NRC Canada

33. P. Sears and C.H. Wong. Proc. Natl. Acad. Sci. U.S.A. **93**, 12086 (1996).
34. D. Zopf and S. Roth. Lancet, **347**, 1017 (1996).
35. Y. Ichikawa, G.C. Look, and C.H. Wong. Anal. Biochem. **202**, 215 (1992).
36. Y. Ichikawa, Y.C. Lin, D.P. Dumas, G.J. Shen, E. Garcia-Junceda, M.A. Williams, R. Bayer, C. Ketcham, L.E. Walker, J.C. Paulson, and C.H. Wong. J. Am. Chem. Soc. **114**, 9283 (1992).
37. C.H. Wong, R.L. Halcomb, Y. Ichikawa, and T. Kajimoto. Angew. Chem. Int. Ed. Engl. **34**, 521 (1995).
38. J. Thiem. FEMS Microbiol. Rev. **16**, 193 (1995).
39. E. Bourquelot and M.J. Bridel. J. Pharm. Chim. (Paris), **7**, 569 (1912).
40. K.G.I. Nilsson. Trends Biotechnol. **6**, 256 (1988).
41. L.F. Mackenzie, Q. Wang, R.A.J. Warren, and S.G. Withers. J. Am. Chem. Soc. **120**, 5583 (1998).
42. S.G. Withers, K. Rupitz, D. Trimbur, and R.A.J. Warren. Biochemistry, **31**, 9979 (1992).
43. Q. Wang and S.G. Withers. J. Am. Chem. Soc. **117**, 10137 (1995).
44. Q. Wang, D. Trimbur, R.A.J. Warren, and S.G. Withers. Biochemistry, **34**, 14554 (1995).
45. J.B. Kempton and S.G. Withers. Biochemistry, **31**, 9961 (1992).

© 1999 NRC Canada

Ryanoids and related compounds. Isolation and characterization of four minor ryanoids from the plant *Ryania speciosa* Vahl: 8,9-didehydroryanodine, 10-*O*-acetylryanodol, 3-*O*-benzoylryanodol, and a first natural 4-deoxyryanoid: 4-deoxy-8_{ax}-hydroxy-10-*O*-methyl-10-epiryanodine (4-deoxyester A)[1]

Luc Ruest, Carl Berthelette, Marco Dodier, Laurence Dubé, and David St-Martin

Abstract: In a search for minor ryanoids from the plant *Ryania Speciosa* Vahl, we characterized four new members of that family of natural compounds: 8,9-didehydroryanodine (**5**), 10-*O*-acetylryanodol (**6**), 3-*O*-benzoylryanodol (**9**), and the first member of the natural 4-deoxyryanoid series: 4-deoxy-8_{ax}-hydroxy-10-*O*-methyl-10-epiryanodine (**10**) (4-deoxyester A).

Key words: natural ryanoids, ryanodine, deoxyryanoids, ryanodol derivatives.

Résumé : En cherchant à identifier les ryanoïdes mineurs de la plante *Ryania Speciosa* Vahl, nous avons caractérisé quatre nouveaux membres de cette famille de produits naturels : la 8,9-didéhydroryanodine (**5**), le 10-*O*-acétylryanodol (**6**), le 3-*O*-benzoylryanodol (**9**) et un tout premier membre de la série 4-déoxyryanoïde : la 4-déoxy-8_{ax}-hydroxy-10-*O*-méthyl-10-épiryanodine (**10**) (4-déoxyester A).

Mots clés : ryanoïdes naturels, ryanodine, déoxyryanoïdes, dérivés du ryanodol.

Introduction

Ryanodine (**1**) (Fig. 1) is known to be a potent modulator of the sarcoplasmic reticulum calcium release channel (1). After ryanodine structure elucidation by Wiesner (2), a few groups (3–12) reported that this complex polycyclic, polyhydroxylic compound was not the sole insecticidal principle in the plant *Ryania speciosa* Vahl. In a recent review on the pharmacology of ryanodine and related compounds (1), 18 structurally related compounds, the ryanoids, were reported. These structures have been elucidated by extensive NMR analysis and also by X-ray diffraction (12, 13). These natural compounds represent very interesting molecules in which the ryanodine molecule is slightly modified by different orientations of the functional groups and the nature of the functional groups (e.g., **1–4**, **7**, **8**). Most of the natural ryanoids would be very difficult to obtain by multistep transformations of ryanodine (**1**) or of 9,21-didehydroryanodine (**2**), the two most abundant ryanoids in that plant. The total syntheses of ryanodol (**3**) (14) and 3-epiryanodine (not shown)(15) from ryanodol (**3**) have been reported.

The biological activities of these metabolites and of several of their derivatives have been studied (ref. 1, and references therein). A number of hypotheses have been formulated regarding the effects of specific structural moieties on the binding affinity of these compounds at the ryanodine binding site (1, 15–27).

In a search for other members of this family, we have very recently identified new ryanoids **5**, **6**, **9**, and **10** (Fig. 1) in the extracts of the plant. Compound **10** represents the first known member of a novel series: the 4-deoxyryanoids. These four metabolites are very minor components, each one representing ~1–5 ppm quantities (w/w) of the dried powdered wood, compared to approximately 500–800 ppm for **1** and **2**.

Results and discussion

The observation of the presence of the new ryanoids came after usual separation of the known major ones. In the mother liquors of crystallization of 9,21-didehydroryanodine (**2**), the already known natural 9α,21-epoxyryanodine (**4**, ref. 12) and the new 8,9-didehydroryanodine (**5**) were observed.

Received July 6, 1998.

L. Ruest,[2] C. Berthelette,[3] M. Dodier, L. Dubé,[3] and D. St- Martin.[3] Département de chimie, Université de Sherbrooke, Sherbrooke, QC J1K 2R1, Canada.

[1]Taken in part from M. Dodier, M.Sc. Thesis, 1996.

[2]Author to whom correspondence may be addressed. Telephone: (819) 821-7922. Fax: (819) 821-8017. e-mail: Luc.Ruest@courrier.usherb.ca
[3]B.Sc. student.

© 1999 NRC Canada

Fig. 1. Structures of the new metabolites **5**, **6**, **9**, and **10**, together with some relevant known structures.

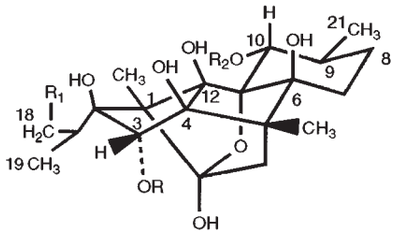

1: $R_1 = R_2 = H$; R = Pyr: Ryanodine
3: $R_1 = R_2 = R = H$: Ryanodol
6: $R = R_1 = H$; $R_2 = -CO-CH_3$
7: $R_1 = OH$; $R_2 = H$; R = Bz
9: $R_1 = R_2 = H$; R = Bz

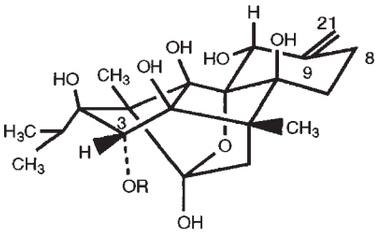

2: R = Pyr: 9,21-Didehydroryanodine

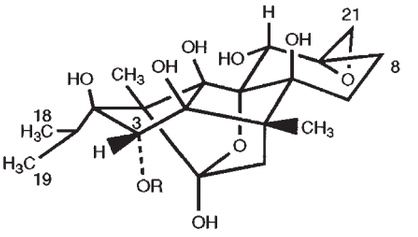

4: R = Pyr: 9α,21-Epoxyryanodine

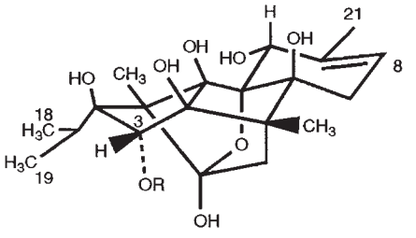

5: R = Pyr: 8,9-Didehydroryanodine

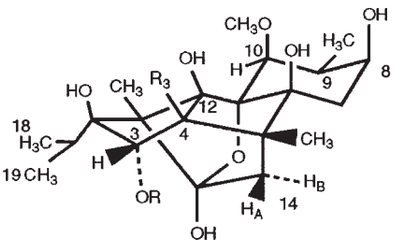

8: R = Pyr; R_3 = OH: Ester A
10: R = Pyr; R_3 = H: 4-Deoxy-Ester A

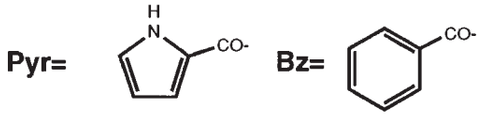

This latter compound had been obtained previously by palladium-catalyzed isomerization of the 9,21 double bond of compound **2**. (4, 25). Its identification was thus highly facilitated.

The new 10-*O*-acetylryanodol (**6**) was first detected by NMR and TLC analysis of the mother liquors of crystallization of ryanodine, together with the previously described 18-hydroxy-3-*O*-benzoylryanodol (**7**, ref. 12). It is very slightly less polar than ryanodine and undetectable by usual UV light detection. Combining HPLC and multiple preparative TLC, we finally obtained this new natural compound in a pure form. Compound **6** and ryanodol (**3**) show very similar NMR spectra, the sole major differences being the position of the HC10 doublet (at δ 5.23 for **6**) and the presence of a new singlet (3H) of an acetyl group at δ 2.04. The structure of compound **6** was confirmed by chemical correlation with ryanodol (**3**) from which 10-*O*-acetyl-4-*O*,15-*O*-dibenzylryanodol (**11**) was obtained following a reported method (14*b*) (Scheme 1). Derivative **11** gave compound **6** under hydrogenolysis of the benzyl ether moieties. It had been shown previously that direct acetylation of ryanodol leads to a complex mixture of di-, tri-, and tetraacetate derivatives (14*b*). The present strategy makes it possible to obtain a good yield of single specific derivatives of ryanodol at position 10.

During the purification of 8_{ax}-hydroxy-10-*O*-methyl-10-epiryanodine (**8**), the so-called ester A (4, 10), by HPLC techniques combined with plate chromatography, we observed the presence of two new ryanoids: 3-*O*-benzoylryanodol (**9**), a compound slightly more polar than ester A, and 4-deoxyester A (**10**), slightly less polar than ester A. Compound **9** and ryanodine show very similar NMR spectra, differing mainly in the typical aromatic hydrogens of a benzoic ester moiety and in the downfield chemical shift of HC3 (δ 5.76 compared to δ 5.62 for ryanodine). Compound **10** shows an NMR spectrum very close to that of ester A (**8**), but an unusual doublet at δ 5.68 (8.4 Hz) for HC3 revealed the presence of a vicinal hydrogen atom (at C2 or C4) appearing as a doublet of doublets at δ 3.24 (8.4 and 1.6 Hz). By means of COSY experiments, it was shown that the small coupling constant is due to a long-range interaction (W-coupling) with one of the protons at position 14 (H_BC14).

The biological activities and affinities to ryanodine binding sites of the new ryanoids **5**, **6**, **9,** and **10** are currently under analysis in the laboratories of Professor William Welch, Department of Biochemistry, University of Nevada, Reno, Nevada.

Experimental section

Melting points were recorded on a Reichert hot-stage apparatus and are uncorrected. Mass spectra (MS) and peak matching (HRMS) data were determined at 70 eV on a VG Micromass ZAB-1F spectrometer. The ^1H (300 MHz) NMR

© 1999 NRC Canada

Scheme 1. Synthesis of the new ryanoid **6** from ryanodol (**3**).

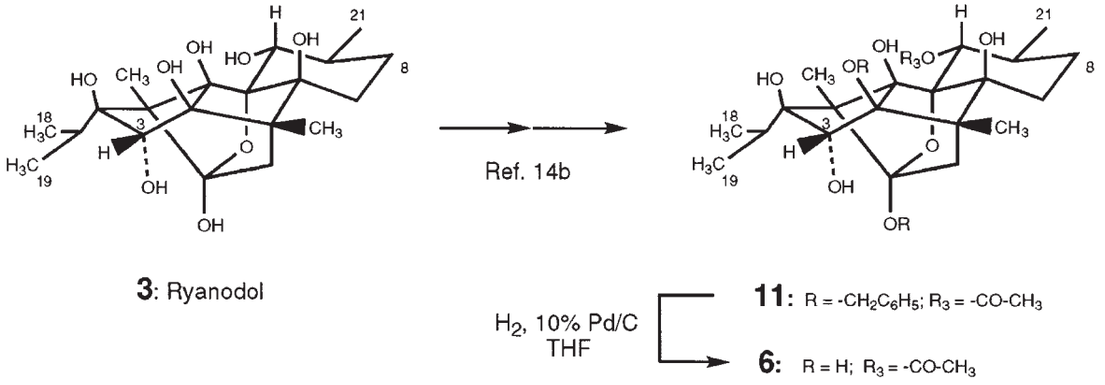

spectra were recorded on a Bruker AC-300 instrument (with CHD_2OD as internal standard centered at δ 3.30). The usual standard abbreviations have been used to indicate the multiplicity of the proton signals. Analytical and preparative thin-layer chromatography were done on 0.25 or 0.5 mm glass plates precoated with silica gel 60F-250 (Merck). A typical solvent was a mixture of 5–15% of methanol in chloroform to which may be added 0.5–2.0% of commercial 40% aqueous methylamine. Column chromatography (flash) was performed with Merck silica gel (200–400 mesh). High-performance liquid chromatography (HPLC) utilized a Waters model 510 instrument equipped with a Vydac C18 reverse-phase preparative column (15 μm, 2.5 × 25 cm) and a Waters 484 tunable UV detector set at 254 nm. A typical solvent for HPLC preparative separation was a mixture of 40% methanol in water. All reactions were performed under argon atmosphere and in solvents purified by standard methods. Reaction mixtures were extracted with at least five portions of distilled ethyl acetate. Solutions in organic solvents were washed with brine, dried over anhydrous magnesium sulfate or anhydrous sodium sulfate, filtered, and then stripped of solvents with a rotatory evaporator connected to a water aspirator.

Isolation of the new ryanoids

Extraction of powdered Ryania wood was carried out as previously described in ref. 11. The isolation of each of the new ryanoids was done as described above.

*8,9-Didehydroryanodine (**5**)*

By TLC analysis, compound **5** is very slightly more polar than 9,21-didehydroryanodine (**2**). The spectroscopic and physical properties of synthetic **5** have been reported previously (4).

*10-*O*-Acetylryanodol (**6**)*

This compound was obtained from the extracts by HPLC techniques combined with careful multi-elution preparative thin-layer chromatography using a mixture of chloroform–methanol (9:1) as a solvent: mp 220–224°C (MeOH); ^{1}H NMR (CD_3OD, δ ppm): 5.23 (d, 11.6 Hz, 1H, HC10), 4.06 (s, 1H, HC3), 2.52 (d, 13.4 Hz, 1H, H_AC14), 2.13 (m, 1H, HC13), 2.13–1.95 (m, 2H, $H_{ax}C7$, HC9), 2.04 (s, 3H, -CO-CH_3), 1.74 (d, 13.4 Hz, 1H, H_BC14), 1.55 (m, 2H, $H_{eq}C7$, $H_{ax}C8$), 1.33 (s, 3H, CH_3C1), 1.29 (m, 1H, $H_{eq}C8$), 1.11 (s, 3H, CH_3C5), 1.07 (d, 6.8 Hz, 3H, CH_3C9), 0.98 (d, 6.5 Hz, 3H, CH_3C13), 0.83 (d, 6.6 Hz, 3H, CH_3C13); MS *m/e*: 406 ($M^+ - 2H_2O$); HRMS calcd. for $C_{22}H_{30}O_7$ ($M^+ - 2H_2O$): 406.1991; found: 406.1994.

Synthesis of **6** from compound **11**, obtained from ryanodol as described in ref. 14*b*, was as follows:

At ambient temperature, a solution of ryanodol derivative **11** (20 mg, 0.032 mmol) in tetrahydrofuran (THF) was transferred (canula) to a stirred suspension of prehydrogenated (15 min) catalyst (10% Pd/C, 20 mg) in THF (5 mL). The mixture was stirred under hydrogen atmosphere for 24 h, then filtered, and the solvent was evaporated. The crude product was purified by preparative thin-layer chromatography (10% methanol in chloroform, two elutions) to give compound **6** (13.5 mg, 95%).

*3-*O*-Benzoylryanodol (**9**)*

Amorphous solid; ^{1}H NMR (CD_3OD, δ ppm): 8.05 (app d, 7.3 Hz, 2H, *o*-ArH), 7.65 (app t, 7.4 Hz, 1H, *p*-ArH), 7.53 (app t, 7.8 Hz, 2H, *m*-ArH), 5.76 (s, 1H, HC3), 3.79 (d, 10.2 Hz, 1H, HC10), 2.56 (d, 14.0 Hz, 1H, H_AC14), 2.29 (m, 1H, HC13), 2.09 (m, 1H, $H_{ax}C7$), 1.94 (d, 14.0 Hz, 1H, H_BC14), 1.84 (m, 1H, HC9), 1.6–1.4 (m, 2H, $H_{eq}C7$, $H_{ax}C8$), 1.40 (s, 3H, CH_3C1), 1.35–1.20 (m, 1H, $H_{eq}C8$), 1.13 (d, 6.7 Hz, 3H, H_3C18), 1.00 (d, 6.5 Hz, 3H, CH_3C9), 0.81 (s, 3H, CH_3C5), 0.72 (d, 6.4 Hz, 3H, H_3C19); MS *m/e*: 504 (M^+); HRMS calcd. for $C_{27}H_{36}O_9$: 504.2359; found: 504.2345.

*4-Deoxy-8$_{ax}$-hydroxy-10-*O*-methyl-10-epiryanodine (4-deoxyester A) (**10**)*

Amorphous solid; ^{1}H NMR (CD_3OD, δ ppm): 7.00, 6.84, and 6.22 (3 dd for pyrrole ring hydrogens), 5.68 (d, 8.4 Hz, 1H, HC3), 3.89 (m, 1H, HC8), 3.49 (s, 3H, CH_3-O-C10), 3.42 (d, 3.2 Hz, 1H, HC10), 3.24 (dd, 8.4 and 1.6 Hz, 1H, HC4), 2.36 (m, 1H, HC13), 2.34 (d, 13.7 Hz, 1H, H_AC14), 2.20 (dd, 13.7 and 3.7 Hz, 1H, $H_{ax}C7$), 2.12 (m, 1H, HC9), 1.68 (br d, 13.7 Hz, 2H, H_BC14 and $H_{ax}C7$), 1.34 (s, 3H, CH_3C1), 1.19 (d, 7.3 Hz, 3H, H_3CC9), 1.13 (d, 6.7 Hz, 3H, H_3C18), 0.83 (d, 6.4 Hz, 3H, H_3C19), 0.79 (s, 3H, CH_3C5); MS *m/e*: 507 (M^+); HRMS calcd. for $C_{26}H_{37}O_9N$: 507.2468; found: 507.2471.

© 1999 NRC Canada

Acknowledgments

We wish to thank Mr. N. Pothier and Mr. G. Boulé, Département de chimie, Université de Sherbrooke, for their technical assistance (NMR spectroscopy and mass spectrometry). We are grateful to Professor W. Welch, Department of Biochemistry, Unversity of Nevada, Reno, who made this work possible by funding us with research subcontracts from the National Science Foundation (NSF) and the American Heart Association (AHA). We also thank the Université de Sherbrooke for financial support from the Fonds de Recherche à Allocation Interne (FRAI).

References

1. J.L. Sutko, J.L. Airey, W. Welch, and L. Ruest. Pharmacol. Rev. **49**, 53 (1997).
2. K. Wiesner. Adv. Org. Chem. **8**, 295 (1972).
3. A.L. Waterhouse, I. Holden, and J.E. Casida. J. Chem. Soc. Chem. Commun. 1265 (1984).
4. L. Ruest, D.R. Taylor, and P. Deslongchamps. Can. J. Chem. **63**, 2840 (1985).
5. A.L. Waterhouse, I. Holden, and J.E. Casida. J. Chem. Soc. Perkin Trans. 2, 1011 (1985).
6. A.L. Waterhouse, I.N. Pessah, A.O. Francini, and J.E. Casida. J. Med. Chem. **30**, 710 (1987).
7. R.A. Humerickhouse, J. Paschal, T. Elvey, D. Berry, and H.R. Besch, Jr. Pharmacologist, **31,** 185, 1989 (Program and Abstracts ASPET, Abstracts 363).
8. P.R. Jefferies, R.F. Toia, and J.E. Casida. J. Nat. Prod. **54**, 1147 (1991).
9. P.R. Jefferies, R.F. Toia, B. Brannigan, I.N. Pessah, and J.E. Casida. J. Agric. Food Chem. **40**, 142 (1992).
10. P.R. Jefferies, W.-W. Lam, R.F. Toia, and J.E. Casida. J. Agric. Food Chem. **40**, 509 (1992).
11. R.A. Humerickhouse, H.R. Besch, Jr., K. Gerzon, L. Ruest, J.L. Sutko, and J.T. Emmick. Mol. Pharmacol. **44**, 412 (1993).
12. L. Ruest and M. Dodier. Can. J. Chem. **74**, 2424 (1996).
13. M. Drouin, M. Dodier, and L. Ruest. Acta Crystallogr. Sect. C: Cryst. Struct. Commun. **C54**, 687 (1998).
14. (*a*) A. Bélanger, D.J.F. Berney, H.J. Borschberg, R. Brousseau, A. Doutheau, R. Durand, H. Katayama, R. Lapalme, D.M. Leturc, C.C. Liao, F.N. MacLachlan, J.P. Maffrand, F. Marazza, R. Martino, C. Moreau, L. St-Laurent, R. Saintonge, P. Soucy, L. Ruest, and P. Deslongchamps. Can.J. Chem. **57**, 3348 (1979); (*b*) P. Deslongchamps, A. Bélanger, D.J.F. Berney, H.J. Borschberg, R. Brousseau, A. Doutheau, R. Durand, H. Katayama, R. Lapalme, D.M. Leturc, C.C. Liao, F.N. MacLachlan, J.P. Maffrand, F. Marazza, R. Martino, C. Moreau, L. Ruest, L. St-Laurent, R. Saintonge, and P. Soucy. Can. J. Chem. **68**, 115 (1990) (a series of four papers).
15. L. Ruest and P. Deslongchamps. Can. J. Chem. **71**, 634 (1993).
16. D.E. Mais, N. Bowling, and A.M. Watanabe. Biochem. Biophys. Res. Commun. **183**, 462 (1992).
17. P.R. Jefferies, E. Lermberg, W.-W. Lam, and J.E. Casida. J. Med. Chem. **36**, 1128 (1993).
18. R.A. Humerickhouse, K.R. Bidasee, K. Gerzon, J.T. Emmick, S. Kwon, J.L. Sutko, L. Ruest, and H.R. Besch, Jr. J. Biol. Chem. **269**, 30242 (1994).
19. W. Welch, S. Ahmad, J.A. Airey, K. Gerzon, R.A. Humerickhouse, H.R. Besch, Jr., L. Ruest, P. Deslongchamps, and J.L. Sutko. Biochemistry, **33**, 6074 (1994).
20. D.R. Witcher, P.S. McPherson, S.D. Kahl, T. Lewis, P. Bentley, M.J. Mullinnix, J.D. Windass, and K.P. Campbell. J. Biol. Chem. **269**, 13076 (1994).
21. S.D. Kahl, P.S. McPherson, T. Lewis, P. Bentley, M.J. Mullinnix, J.D. Windass, and K.P. Campbell. Anal. Biochem. **218**, 55 (1994).
22. K.R. Bidasee, H.R. Besch, Jr., K. Gerzon, and R.A. Humerickhouse. Mol. Cell. Biochem. **149/150**, 145 (1995).
23. W. Welch, J.L. Sutko, K.E. Mitchell, J. Airey, and L. Ruest. Biochemistry, **35**, 7165 (1996).
24. S. Tinker, J.L. Sutko, L. Ruest, P. Deslongchamps, W. Welch, J.A. Airey, K. Gerzon, K.R. Bidasee, H.R. Besch, Jr., and A.J. Williams. Biophys. J. **70**, 2110 (1996).
25. W. Welch, A.J. Williams, A. Tinker, K.E. Mitchell, P. Deslongchamps, J. Lamothe, K. Gerzon, K.R. Bidasee, H.R. Besch, Jr., J.A. Airey, J.L. Sutko, and L. Ruest. Biochemistry, **36**, 2939 (1997).
26. P.R. Jefferies, P. Yu, and J.E. Casida. Pestic. Sci. **51**, 33 (1997).
27. B. Tanna, W. Welch, L. Ruest, J.L. Sutko, and A.J. Williams. J. Gen. Physiol. **112**, 55 (1998).

© 1999 NRC Canada

Distortions in square-planar palladium(II) halides: a nonempirical molecular orbital model study

Pierre D. Harvey and Christian Reber

Abstract: Density functional theory is used to characterize the lowest energy excited spin triplet orbital configurations of square-planar halide complexes of palladium(II). Calculations for the $e_g \rightarrow b_{1g}$ orbital excitation (D_{4h} labels) predict a non-totally symmetric distortion along the b_{1g} normal coordinate, leading to unequal bond lengths for perpendicular metal–ligand bonds (D_{2h} symmetry). Calculated bond length changes are 0.15 Å (0.11 Å) and 0.05 Å (0.00 Å) for $PdCl_4^{2-}$ ($PdBr_4^{2-}$). These values compare favorably to the emitting-state distortions of 0.12 Å and 0.09 Å for K_2PdCl_4 (0.12 Å, and 0.07 Å for K_2PdBr_4) determined from resolved single-crystal luminescence spectra. The calculations indicate that the non-totally symmetric distortion is an intrinsic molecular property of these complexes.

Key words: palladium(II) complexes, excited state distortions, density functional theory.

Résumé : La théorie de fonctionnelle de la densité est appliquée à la caractérisation des premières configurations triplet excitées de deux complexes plan-carrés du palladium(II). Les calculs pour l'excitation $e_g \rightarrow b_{1g}$ (groupe ponctuel D_{4h}) prédisent une distorsion le long de la coordonnée normale b_{1g}. Cette distorsion mène à des longueurs de liaison inégales pour liaisons métal–ligand perpendiculaires (groupe ponctuel D_{2h}). Les changements calculés sont de 0,15 Å (0,11 Å) et 0,05 Å (0,00 Å) pour $PdCl_4^{2-}$ ($PdBr_4^{2-}$). Ces valeurs sont proches aux distorsions de l'état émissif de 0,12 Å et 0,09 Å pour K_2PdCl_4 (0,12 Å et 0,07 Å pour K_2PdBr_4), déterminées à partir des spectres de luminescence de monocristaux. Les calculs indiquent que la distorsion de symétrie non-totale est une propriété intrinsèque de ces complexes.

Mots clés : complexes du palladium(II), distorsions des états excités, théorie de fonctionnelle de la densité.

Introduction

Modern theoretical methods such as density functional theory have become powerful tools to characterize challenging molecules, including transition metal complexes and organometallic compounds (1). Their large number of electrons and energetically close excited states have until recently limited theoretical studies to semiempirical methods such as the Extended Hückel approach, which can not be used to reliably calculate structures of the ground and excited electronic states (2). Over the past few years, density functional theory has provided reliable excited-state structures for a number of octahedral and tetrahedral coordination compounds (3–6), for organometallic molecules such as ruthenocene (7, 8), and for polynuclear palladium complexes with metal–metal bonds (9).

Square-planar palladium(II) and platinum(II) complexes with four identical monodentate ligands are attractive molecules for a density functional study of the ground and excited orbital configurations. Resolved absorption and luminescence spectra of crystalline solids at low temperature are reported for a series of complexes, leading to quantitative excited-state energies and distortions, an important prerequisite for a detailed comparison of calculated and experimental quantities (10–21). In several square-planar complexes, most notably K_2PtCl_4, K_2PdCl_4, and K_2PdBr_4, unusual non-totally symmetric distortions along the b_{1g} mode were analyzed in the resolved luminescence spectra (18, 20, 21). In addition, a distortion along the totally symmetric a_{1g} normal coordinate is expected if antibonding orbitals such as the b_{1g} ($d_{x^2-y^2}$) LUMO orbital of the title compounds are occupied.

In this study, we use a simplified approach to the calculation of structural changes as a consequence of electronic excitations in $PdBr_4^{2-}$ and $PdCl_4^{2-}$, isolated square-planar complexes with the [Kr]4d^8 electron configuration. In D_{4h} symmetry, the d orbitals split into the occupied a_{1g} (d_{z^2}), b_{2g} (d_{xy}), and e_g (d_{xz},d_{yz}) orbitals at lower energy than the empty b_{1g} ($d_{x^2-y^2}$) orbital. This splitting pattern has been discussed extensively in the literature and orbital energies have been calculated with a variety of computational methods, as sum-

Received June 8, 1998.

This paper is dedicated to Professor Dennis R. Salahub on the occasion of his nomination to the Royal Society of Canada.

P.D. Harvey.[1] Département de chimie, Université de Sherbrooke, Sherbrooke, QC J1K 2R1, Canada.
C. Reber.[2] Département de chimie, Université de Montréal, Montréal, QC H3C 3J7, Canada.

[1]Telephone: (819) 821-7092. Fax: (819) 821-8017. e-mail: pharvey@courrier.usherb.ca
[2]Telephone: (514) 343-7332. Fax: (514) 343-7586. e-mail: reber@chimie.umontreal.ca

 © 1999 NRC Canada

Fig. 1. One-dimensional potential energy surfaces for $PdCl_4^{2-}$ (*a*), (*c*) and $PdBr_4^{2-}$ (*b*), (*d*). The dots indicate calculated energies for the $a_{1g}{}^2b_{2g}{}^2e_g{}^3b_{1g}{}^1$ triplet excited configuration along the totally symmetric $Q_{a_{1g}}$ (*a*), (*b*) and the non-totally symmetric $Q_{b_{1g}}$ (*c*), (*d*) normal coordinates, which are given in dimensionless units. The ground state molecular structure defines the origin of the abscissa in panels (*a*)–(*d*). The totally symmetric a_{1g} and non-totally symmetric b_{1g} vibrational modes are illustrated schematically in panels (*a*) and (*c*), respectively. Panel (*d*) shows the molecular structures corresponding to the two potential minima and the structure at the crossing point of the potential energy curves.

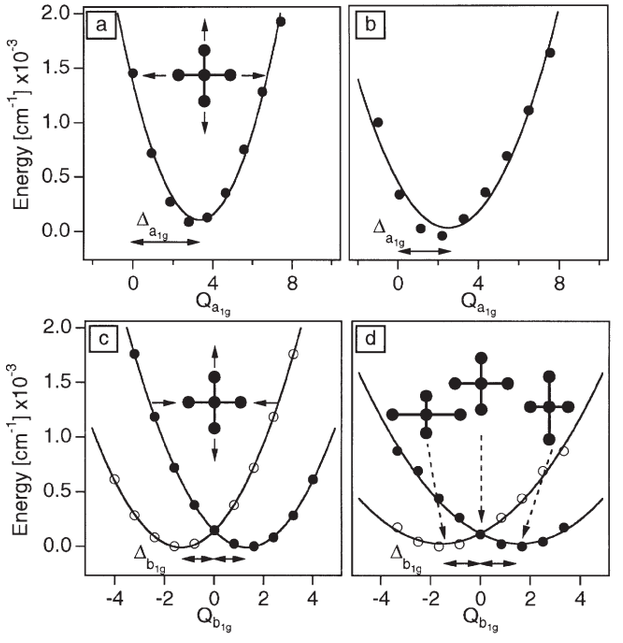

marized in ref. 22. Three one-electron excitations are possible within these orbital energy levels. We limit our study to these changes in the orbital populations and focus on the energetically most favorable structure of the spin triplet configuration arising from the $e_g \rightarrow b_{1g}$ excitation, leading to the lowest energy ^3E_g excited state. This is the only configuration in which non-totally symmetric distortions can occur. The limitation to orbital configurations is a dramatic simplification of the physical situation and prevents us from calculating accurate energies of electronic transitions, but it has an intuitive appeal with respect to the characterization of metal–ligand bonds. It is particularly appropriate for the title compounds with only one set of doubly degenerate orbitals, in contrast to octahedral and tetrahedral complexes where both HOMO and LUMO orbitals are degenerate. Models based on empirical *orbital* parameters such as 10*Dq* have been successfully used to rationalize overall bond length changes in excited states of these high-symmetry molecules, further supporting the approach chosen for this study (23).

Computational methodology

All molecular orbital calculations were carried out using the HFS-LCAO program system A-MOL (Amsterdam density functional: ADF program), developed by Baerends et al. (24, 25) and vectorized by Ravenek (26). The numerical integration procedure applied for the calculations was developed by te Velde and co-workers (27). The electronic configurations of the molecular systems were described by an uncontracted double-ζ STO basis set (28, 29) for 4*s*, 4*p*, 5*s*, and triple-ζ for 5*d*. The double-ζ STO basis sets (30–32) for chloride (3*s*, 3*p*) and bromide (4*s*, 4*p*) were augmented with single 4*d* and 5*d* polarization functions for Cl and Br, respectively. No polarization function was used for palladium. The $1s^22s^22p^63s^23d^{10}$ configuration of the palladium center, the $1s^22s^2$ configuration of chloride, and the $1s^22s^22p^63s^2$ configuration of bromide were treated by the frozen-core approximation. A set of auxiliary (33) s, *p*, *d*, *f*, and *g* STO functions, centered on all nuclei, was used to fit the molecular density and represent Coulomb and exchange potentials accurately in each self-consistent field (SCF) cycle. Energy differences were calculated by including the local exchange-correlation potential by Vosko et al. (34) with Becke's (35) nonlocal exchange corrections and Perdew's (36) nonlocal correlation correction. The three lowest energy spin triplet configurations used for our calculations are of different symmetries and can therefore easily be obtained from DFT calculations.

The potential energy surfaces for the $a_{1g}{}^2b_{2g}{}^2e_g{}^3b_{1g}{}^1$ spin triplet excited configuration for both PdX_4^{2-} complexes (X = Cl, Br) have been calculated using the complex total energies as a function of the Pd—X distances ranging from 2.30 to 2.66 Å for $PdCl_4^{2-}$ and from 2.42 to 2.72 Å for $PdBr_4^{2-}$. Bond length increments of 0.03 Å were used for both compounds. The results are reported as one-dimensional potential energy curves in Fig. 1 and as contour maps of the full grid of molecular geometries using 200 cm^{-1} energy intervals between contour lines in Fig. 2. The origin of the coordinate system in Fig. 2 indicates the calculated ground state minimum energy position. The molecular structures of $PdCl_4^{2-}$ and $PdBr_4^{2-}$ at the calculated potential energy minima are summarized in Fig. 3, with a definition of the molecular axes used in the following.

The most important simplification made for this study is the limitation to one-electron excitations. To justify this approach, we present full crystal field calculations using the angular overlap formalism (37). We reproduce the energies given for selected states of square-planar palladium(II) and platinum(II) complexes in the literature (16) to within 10 cm^{-1}. In the following, we use the parameters derived from our low-temperature absorption and luminescence spectra (21). The Racah parameters *B* and *C* are identical to those determined earlier from absorption spectra (16). Our e_σ and e_π angular overlap parameters vary by less than 5% from those in ref. 16. These small variations were made to better account for the weak low-energy absorption bands and for the lower limit to excited state energies imposed by the luminescence spectra. The complete results of these calculations are presented in Tables 1 and 2 and are intended to link this work to the extensive literature on crystal field states of square-planar complexes with the d^8 electron configuration. Only partial listings of the energies of crystal field states have been published before, often omitting the orbital parentage of the calculated excited states.

© 1999 NRC Canada

Fig. 2. Two-dimensional potential energy surfaces for the component of the $a_{1g}{}^2b_{2g}{}^2e_g{}^3b_{1g}{}^1$ triplet excited configuration given by black dots in Fig. 1. Surfaces are given for both $PdCl_4{}^{2-}$ (*a*) and $PdBr_4{}^{2-}$ (*b*). The position of the ground-state potential energy minima is at the origin of the Δr_i coordinate system. The minimum of the potential surfaces in the figure is set to an energy of 0 cm^{-1} and contours are shown at an interval of 200 cm^{-1}. Calculations were made in steps of 0.03 Å along the horizontal and vertical axes, as indicated by the tick marks. The directions of the normal coordinates $Q_{a_{1g}}$ and $Q_{b_{1g}}$ in Fig. 1 are indicated for comparison.

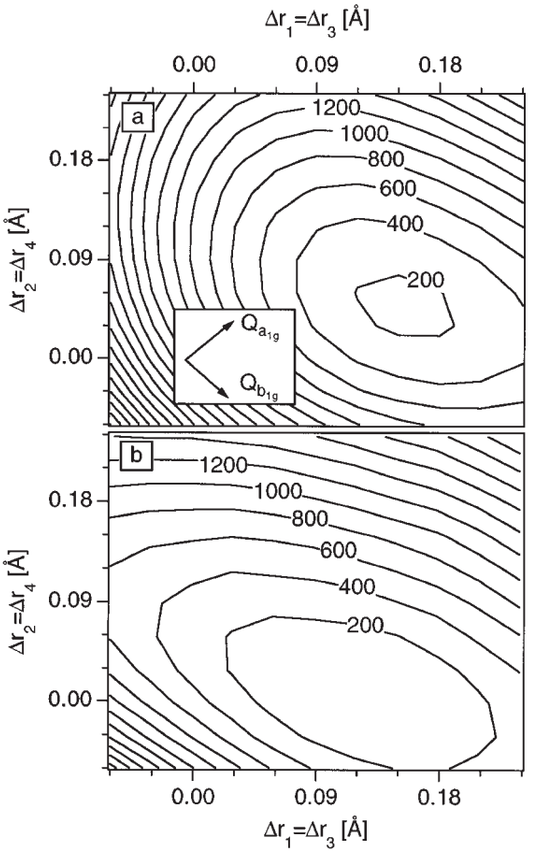

Fig. 3. Calculated molecular distortions for the excited $a_{1g}{}^2b_{2g}{}^2e_g{}^3b_{1g}{}^1$ orbital configuration of $PdCl_4{}^{2-}$ and $PdBr_4{}^{2-}$. The coordinate system schematically defines the axes used in Fig. 2.

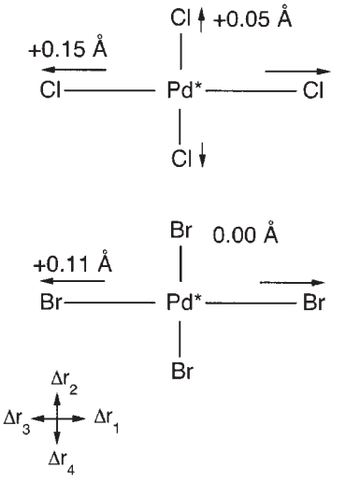

Results and discussion

(a) Crystal field calculations and orbital excitations

Square-planar complexes such as the title compounds present a very particular energy order of their excited states. Tables 1 and 2 summarize all crystal field excited states with their strong field electron configurations. An inspection of the states calculated without spin-orbit coupling shows that all three low-energy spin triplet excited states correspond to almost pure one-electron excitations. They are separated by more than 20 000 cm^{-1} from higher energy triplet states of the same symmetry, formally arising from two-electron excitations. This large energy difference justifies the limitation to orbital excitations, which can be expected to reveal the most important structural characteristics of the low-energy spin triplet excited states.

Of particular interest to us is the structure of the lowest energy ^3E_g excited state arising from the $a_{1g}{}^2b_{2g}{}^2e_g{}^3b_{1g}{}^1$ configuration, because this state is susceptible to a Jahn–Teller effect that can involve both the b_{1g} and b_{2g} modes in addition to the elongation of all palladium–halide bonds along the a_{1g} normal coordinate. The Jahn–Teller effect lifts the degeneracy of the e_g orbitals, leading to a net stabilization because of the asymmetric occupation of these orbitals. Orbitally nondegenerate electronic states can only undergo distortions along the totally symmetric a_{1g} normal coordinate. The distortions of the $a_{1g}{}^2b_{2g}{}^2e_g{}^3b_{1g}{}^1$ configuration along the different normal coordinates are therefore intrinsic and not resulting from interactions with other states of the same symmetry. We have recently shown for a series of octahedral nickel(II) complexes with the same d^8 electron configuration as the title compounds that distortions can be induced by spin-orbit coupling between excited states of the same symmetry separated by less than 2000 cm^{-1} (38). The vibronic progression observed in an electronic spectrum for the state with only a small or no distortion is determined by another state of identical symmetry with a large offset along one or more normal coordinates. This situation does not apply here because the nearest ^3E_g state arises from a double excitation, corresponding to the $a_{1g}{}^2b_{2g}{}^1e_g{}^3b_{1g}{}^2$ electron configuration, and it is calculated at energies higher by 22 783 cm^{-1} and 22 159 cm^{-1} than the first ^3E_g state for $PdCl_4{}^{2-}$ and $PdBr_4{}^{2-}$, respectively. The energy difference between the two ^3E_g states is larger by more than an order of magnitude than for states where the distortions are significantly influenced by spin-orbit coupling, leading to weak or negligible effects. Every triplet state has a corresponding singlet excited state approximately 5000 to 7000 cm^{-1} higher in energy. A comparison of the electron configurations of these states in Tables 1 and 2 shows that their configurations are almost identical to those of the corresponding triplet states. Singlet and triplet states have therefore very similar potential energy surfaces and their interactions do not significantly influence

© 1999 NRC Canada

Table 1. Calculated crystal field states with electron configurations for K_2PdCl_4 (D_{4h} point group symmetry) with the parameters e_σ(Cl) = 10 340 cm^{-1}, e_π(Cl) = 1980 cm^{-1}, $\sigma_{sd} = e_\sigma$(Cl), B = 540 cm^{-1}, C = 2400 cm^{-1}.

State	Electron configuration				Calcd. energy	State	Calcd. energy
(ζ = 0)	a_{1g} (d_{z^2})	b_{2g}(d_{xy})	e_g ($d_{xz,yz}$)	b_{1g}($d_{x^2-y^2}$)	(cm^{-1})	(ζ = 900 cm^{-1})	(cm^{-1})
$^1A_{1g}$	1.992	1.998	3.984	0.026	0	A_{1g}	0
^3E_g	1.994	1.996	3.000	1.009	15 566	A_{1g}	14 839
						A_{2g}	15 042
						E_g	15 247
						B_{2g}	15 699
						B_{1g}	16 105
$^3A_{2g}$	2.000	1.015	3.970	1.015	16 382	E_g	16 647
						A_{1g}	16 823
$^3B_{1g}$	1.000	2.000	4.000	1.000	18 218	E_g	18 417
						B_{2g}	18 820
$^1A_{2g}$	2.000	1.000	4.000	1.000	21 577	A_{2g}	21 765
^1E_g	1.999	1.995	3.000	1.006	23 774	E_g	24 001
$^1B_{1g}$	1.006	2.000	3.988	1.006	27 191	B_{1g}	27 348
^3E_g	1.942	1.059	3.000	1.998	38 349	A_{1g}	37 961
						A_{2g}	38 207
						E_g	38 237
						B_{1g}	38 303
						B_{2g}	38 756
$^3B_{2g}$	1.000	1.000	4.000	2.000	41 318	E_g	41 570
						B_{1g}	41 975
$^3A_{2g}$	2.000	1.985	2.030	1.985	43 333	E_g	43 383
						A_{1g}	43 449
$^1A_{1g}$	1.950	0.250	3.800	2.000	44 372	A_{1g}	44 653
^1E_g	1.991	1.015	3.000	1.995	47 047	E_g	47 431
$^1B_{2g}$	1.429	1.429	3.142	2.000	48 818	B_{2g}	48 238
^3E_g	1.064	1.944	3.000	1.992	51 078	B_{1g}	50 141
						E_g	51 257
						A_{1g}	51 543
						B_{2g}	51 558
						A_{2g}	51 644
$^1B_{1g}$	1.994	2.000	2.012	1.994	51 125	B_{1g}	52 010
$^1B_{2g}$	1.571	1.571	2.858	2.000	52 598	B_{2g}	52 812
^1E_g	1.010	1.990	3.000	1.999	56 132	E_g	56 348
$^1A_{1g}$	1.175	1.957	2.870	1.998	56 799	A_{1g}	56 996
$^1A_{1g}$	0.883	1.795	3.346	1.976	68 719	A_{1g}	69 092

the positions of the potential minima along the normal coordinates.

Spin-orbit coupling has an important influence on the energetic order of the states arising from the low-energy spin triplet configurations. It is important to realize that a distortion of the ^3E_g state (other than a bond elongation along the totally symmetric normal coordinate) can not be induced by spin-orbit coupling with a nearby orbitally nondegenerate state. The crystal field calculations show that the orbital occupations of the antibonding b_{1g} orbital for the low-energy

© 1999 NRC Canada

Table 2. Calculated crystal field states with electron configurations for K_2PdBr_4 (D_{4h} point group symmetry) with the parameters e_σ(Br) = 9900 cm^{-1}, e_π(Br) = 1800 cm^{-1}, $\sigma_{sd} = e_\sigma$(Br), B = 530 cm^{-1}, C = 2200 cm^{-1}.

State	Electron configuration				Calcd. energy	State	Calcd. energy
$\zeta = 0$)	(a_{1g} (d_{z^2})	b_{2g}(d_{xy})	e_g ($d_{xz,yz}$)	b_{1g}($d_{x^2-y^2}$)	(cm^{-1})	(ζ = 500 cm^{-1})	(cm^{-1})
$^1A_{1g}$	1.992	1.998	3.986	0.025	0	A_{1g}	0
^3E_g	1.994	1.996	3.000	1.010	15 232	A_{1g}	14 864
						A_{2g}	14 934
						E_g	15 118
						B_{2g}	15 380
						B_{1g}	15 533
$^3A_{2g}$	2.000	1.016	3.968	1.016	16 313	E_g	16 398
						A_{1g}	16 458
$^3B_{1g}$	1.000	2.000	4.000	1.000	17 552	E_g	17 627
						B_{2g}	17 768
$^1A_{2g}$	2.000	1.000	4.000	1.000	21 112	A_{2g}	21 172
^1E_g	1.999	1.995	3.000	1.006	22 979	E_g	23 052
$^1B_{1g}$	1.006	2.000	3.988	1.006	26 047	B_{1g}	26 098
^3E_g	1.937	1.065	3.000	1.998	37 391	A_{1g}	37 187
						A_{2g}	37 269
						E_g	37 344
						B_{1g}	37 430
						B_{2g}	37 597
$^3B_{2g}$	1.000	1.000	4.000	2.000	40 052	E_g	40 145
						B_{1g}	40 285
$^3A_{2g}$	2.000	1.984	2.032	1.984	42 042	E_g	42 058
						A_{1g}	42 082
$^1A_{1g}$	1.947	0.256	3.796	2.000	43 210	A_{1g}	43 297
^1E_g	1.990	1.016	3.000	1.994	45 647	E_g	45 767
$^1B_{2g}$	1.429	1.429	3.142	2.000	47 102	B_{2g}	46 898
$^1B_{1g}$	1.994	2.000	2.012	1.994	49 368	B_{1g}	48 806
^3E_g	1.069	1.939	3.000	1.992	49 384	E_g	49 441
						B_{2g}	49 457
						A_{1g}	49 633
						A_{2g}	49 665
						B_{1g}	49 829
$^1B_{2g}$	1.571	1.571	2.858	2.000	50 812	B_{2g}	50 880
^1E_g	1.011	1.989	3.000	1.999	54 001	E_g	54 071
$^1A_{1g}$	1.155	1.960	2.886	1.998	54 656	A_{1g}	54 719
$^1A_{1g}$	0.906	1.786	3.332	1.997	65 774	A_{1g}	65 895

triplet states change by less than 0.007 as a consequence of spin-orbit coupling, indicating that all these excited states involve almost exclusively one-electron excitations. We describe here one of very few situations where it is possible to gain insight on excited state distortions from a study limited to orbital excitations. We note that crystal field calculations involving only the electron configurations corresponding to one-electron excitations (21, 39) lead to energies of the first excited states that are higher by approximately 500 cm^{-1} than those of the full calculations in Tables 1 and 2. This is

© 1999 NRC Canada

the likely origin of a recent controversy over crystal field calculations on square-planar complexes (40–42). The small differences of less than 3% of the excited state energies calculated from different crystal field models are further evidence confirming that the following analysis of orbital configurations is physically reasonable for the title compounds.

(b) Density functional calculations of excited spin triplet configurations

In a first series of molecular orbital calculations, we use the density functional approach to calculate palladium–halide distances for the electronic ground state of the two target molecules. We obtain values of 2.360 and 2.482 Å for $PdCl_4^{2-}$ and $PdBr_4^{2-}$, respectively. These values compare favorably with the crystallographic bond lengths of 2.313 and 2.444 Å for K_2PdCl_4 and K_2PdBr_4 (43, 44). The small differences of approximately 0.05 Å qualitatively indicate that the molecular and overall electronic structures for the complexes in condensed phases and for the isolated molecules used for our model systems are comparable, an important foundation for the following analysis. This similarity is experimentally confirmed by the resemblance of absorption spectra measured in solution and in the solid state (11–14). A sophisticated density functional study (5) of octahedral complexes of chromium(III), including the electrostatic effects of the crystal lattice, has led to differences between calculated and crystallographic bond lengths of less than 0.01 Å, again underlining the approximate nature of our model study.

The calculated energy differences between the occupied e_g orbital and the lowest unoccupied b_{1g} orbital are 15 240 and 14 430 cm^{-1} for $PdCl_4^{2-}$ and $PdBr_4^{2-}$, respectively. Without taking into account the singlet–triplet state interactions and the total energies of the complexes in their ground and excited electronic configurations, these values compare favorably to the energy range of the first absorption bands (21). Detailed discussions of calculated orbital energies for the title compounds are given in the literature (11, 22) but the comparison between the energies of experimental transition energies and the calculated differences between occupied and empty orbitals is not the focus of the present work. The density functional calculations predict an energy difference between the e_g and b_{1g} orbitals that is higher by 810 cm^{-1} for $PdCl_4^{2-}$ than for $PdBr_4^{2-}$. In the angular overlap approach, this difference is equal to $3e_\sigma - 2e_\pi$ (16). The energy difference from density functional calculations compares favorably with the difference of 960 cm^{-1} calculated from the crystal field parameters in Table 1 and is also in good agreement with the value of 1133 cm^{-1} determined from an alternative angular-overlap analysis (22) of the absorption spectra. It is within an order of magnitude of the difference of 210 cm^{-1} between the electronic origins of the luminescence spectra of K_2PdCl_4 and K_2PdBr_4 (21). The electronic origins are experimentally well defined and are therefore much better suited to a semiquantitative comparison with calculated energies than the maxima of broad bands, which are notoriously hard to determine accurately. Preliminary calculations for the platinum(II) analogs of the title compounds have led to energy differences higher by approximately 2500 cm^{-1} than for the palladium halides, again comparable to the experimental emission energies that are higher by 1500 cm^{-1} for the platinum(II) complexes (15, 18). These trends confirm that density functional theory and our orbital model provide a good representation of the low-energy electronic excitations.

(c) Potential energy surfaces from density functional calculations

We have made density functional calculations for a series of geometries and for all three low-energy spin triplet configurations of $PdCl_4^{2-}$ and $PdBr_4^{2-}$ in D_{4h} symmetry. Average bond length increases of 0.12 and 0.10 Å are calculated for the chloride and bromide complexes, respectively, with variations of less than 0.01 Å between the different orbital configurations. Three low-energy absorption bands to the first three triplet excited states are resolved in the low-temperature spectrum of K_2PdBr_4 (21). Their widths and vibronic patterns are similar, a qualitative experimental confirmation of the very small variation of calculated bond length changes for the three spin triplet configurations. The calculated values are within the range determined from broad *d–d* bands in a variety of transition metal complexes, further underlining that our simplified model produces physically reasonable structural characterizations of the excited complexes. Identical changes of all four palladium–halide bonds are the only structural variations possible for the $a_{1g} \rightarrow b_{1g}$ and $b_{2g} \rightarrow b_{1g}$ orbital excitations, leading to the parent configurations of nondegenerate electronic states.

The most interesting orbital excitation is $e_g \rightarrow b_{1g}$, because the resulting $a_{1g}^2 b_{2g}^2 e_g^3 b_{1g}^1$ configuration gives rise to orbitally degenerate excited states. We first examine its energy in wavenumber units as a function of the dimensionless normal coordinates Q_i (i: a_{1g} or b_{1g}) in Fig. 1. This choice of units allows for easy comparisons to similar diagrams derived from electronic spectra in the literature (18, 20, 21) and to the energies summarized in Tables 1 and 2. The potential minima Δ_i and vibrational frequencies $\hbar\omega_i$ associated with the potentials in Fig. 1 are obtained from the equation:

$$[1] \qquad E_i = 0.5\ \hbar\omega_i\ (Q_i - \Delta_i)^2$$

where E_i is the energy calculated along Q_i with the adjustable parameters Δ_i and $\hbar\omega_i$. All calculated energies shown as solid dots in Fig. 1 were used for the least-squares refinement of the parameters and the resulting harmonic potentials reproduce the calculated energies well.

The curves in Fig. 1 can be regarded as cross sections through the full configurational space defined by the plane of the complexes and shown in detail in Fig. 2. Figure 1 shows the schematic definition of both relevant normal coordinates and the calculated energies as the title complexes are deformed along both coordinates. The fits using eq. [1] lead to vibrational frequencies of 227 and 133 cm^{-1} for $PdCl_4^{2-}$ and $PdBr_4^{2-}$, respectively. These values are lower by approximately 30% than the experimental Raman frequencies of 303.6 and 187.4 cm^{-1} (45) or 307 and 190 cm^{-1} (46). Lower vibrational frequencies are expected for the title compounds because of the increased population of the antibonding b_{1g} orbital. The calculations probably overestimate the decrease: a density functional study on octahedral complexes of chro-

© 1999 NRC Canada

mium(III) reports ground state vibrational frequencies that are lower by 20% than the experimental values (6). The ratio of the Raman frequencies of the a_{1g} modes of $PdCl_4^{2-}$ and $PdBr_4^{2-}$ is 0.62, very similar to the ratio of 0.59 obtained for the calculated frequencies. The minima $\Delta_{a_{1g}}$ of the potentials along $Q_{a_{1g}}$ are at 3.33 and 2.50 for $PdCl_4^{2-}$ and $PdBr_4^{2-}$, respectively, again in reasonable agreement with the spectroscopic values of 3.68 and 3.90, especially in view of the limitation to orbital configurations. The two potentials along the b_{1g} coordinate represent a simple Jahn–Teller situation. The molecule has D_{4h} symmetry at the crossing point and distorts to D_{2h} symmetry at the two potential minima, as indicated in Fig. 1*d*. The two minima are offset by the same amount from the crossing point, denoted by the horizontal arrows. Minima along the $Q_{b_{1g}}$ coordinate are calculated at ±1.35 and ±1.61 for $PdCl_4^{2-}$ and $PdBr_4^{2-}$. Both the magnitude of $\Delta_{b_{1g}}$ for each complex and the trend between the two title compounds are in good agreement with the spectroscopic values of ±1.18 and ±1.73 for $\Delta_{b_{1g}}$ in $PdCl_4^{2-}$ and $PdBr_4^{2-}$, respectively (21). Figure 1 illustrates that the calculated vibrational frequency of the b_{1g} mode is lower than that of the totally symmetric a_{1g} mode. Calculated vibrational frequencies for the b_{1g} mode are 170 and 133 cm^{-1} for $PdCl_4^{2-}$ and $PdBr_4^{2-}$, respectively. Raman spectroscopy gives frequencies of 269.9 cm^{-1} (45) or 274 cm^{-1} (46) for $PdCl_4^{2-}$ and 166.6 cm^{-1} (45) or 171 cm^{-1} (46) for $PdBr_4^{2-}$. The calculated potential curves in Fig. 1 are in qualitative agreement with the spectroscopic results obtained for a series of square-planar halide complexes and confirm the observation of distortions along both the a_{1g} and b_{1g} coordinates (18, 20, 21).

The main results of our study are represented as a full two-dimensional potential energy surface in Fig. 2, showing the energy of this configuration for both target complexes as a function of the length change of all four palladium–halide bonds. Only one of the two surfaces illustrated by the one-dimensional cross sections in Figs. 1*c* and 1*d* is included in Fig. 2. It is obvious from the symmetry of the surfaces in Figs. 1*c* and 1*d* that this is sufficient to determine structural distortions of this excited configuration. The origin of the coordinate system is at the calculated bond lengths for the ground state orbital configuration and calculations were made every 0.03 Å. The energy minima correspond to rhombus structures with pairs of opposite palladium–halide bonds of equal length (18). This structure involves distortions of similar magnitude along both the totally symmetric $Q_{a_{1g}}$ and the non-totally symmetric $Q_{b_{1g}}$ normal coordinates. The directions of both normal coordinates are given in Fig. 2. Bond length changes Δr_i and changes along normal coordinates ΔQ_i of the excited orbital configuration are related by:

$$[2] \qquad \Delta Q_{a_{1g}} = 1/2(\Delta r_1 + \Delta r_2 + \Delta r_3 + \Delta r_4)$$

$$[3] \qquad \Delta Q_{b_{1g}} = 1/2(\Delta r_1 - \Delta r_2 + \Delta r_3 - \Delta r_4)$$

$\Delta Q_{a_{1g}}$ is determined by moving across the potential energy surfaces in Fig. 2 along the $Q_{a_{1g}}$ axis from the origin to the energy minimum. The values for Δr_i can then be read directly from the horizontal and vertical axes. Moving along the $Q_{b_{1g}}$ direction from the minimum along $Q_{a_{1g}}$ leads to the global minimum of the potential energy surface, and the corresponding values of Δr_i can again be directly determined from the figure. The structures corresponding to the energy minimum for this excited orbital configuration are summarized in Fig. 3. The calculated bond length changes of 0.15 and 0.05 Å for perpendicular bonds in $PdCl_4^{2-}$ are remarkably close to the experimental emitting state distortions of 0.12 and 0.09 Å in K_2PdCl_4 (21). The calculated bond length changes for $PdBr_4^{2-}$ are 0.11 and 0.00 Å, in fair agreement with the emitting state bond length changes of 0.12 and 0.07 Å in K_2PdBr_4 (21). We note that the potential energy minimum for $PdBr_4^{2-}$ in Fig. 2*b* is shallow because of the lower vibrational frequencies of this complex, a situation that could lead to larger uncertainties in the Δr_i values than for $PdCl_4^{2-}$.

The "valley" in Fig. 2 is oriented along the b_{1g} coordinate, and its minimum corresponds to the total excited state distortions, as described before. The b_{1g} mode is therefore in fact the most important non-totally symmetric distortion, in agreement with the spectroscopic results (21). The density functional approach consistently determines the dominant Jahn–Teller active mode as the in-plane b_{1g} stretching vibration and not the b_{2g} bending mode. A significant distortion along this additional normal coordinate would lead to an orientation of the "valley" that deviates from $Q_{b_{1g}}$. A small distortion along $Q_{b_{2g}}$ cannot be excluded from the calculations; especially in $PdBr_4^{2-}$ the orientation of the calculated "valley" appears to deviate somewhat from the $Q_{b_{1g}}$ direction. Indirect spectroscopic evidence for a small distortion involving the b_{2g} mode is discussed in ref. 21. Our simplified model cannot be used to prove the presence of such a minor distortion, especially in view of a recent detailed density functional study on ruthenocene illustrating that non-totally symmetric excited state distortions can be induced by the environment of the molecule in a crystal, an effect neglected here for the title compounds (8).

Potential energy barriers along $Q_{b_{1g}}$ can be estimated as the difference between the global energy minimum and the energy minimum along the $Q_{a_{1g}}$ axis on the surfaces in Fig. 2, leading to values of 150 and 110 cm^{-1} for $PdCl_4^{2-}$ and $PdBr_4^{2-}$, respectively. These values compare very favorably to the crossing point of the diabatic surfaces of the emitting states of K_2PdCl_4 and K_2PdBr_4 (21), determined from the spectra as 190 and 280 cm^{-1}. Preliminary calculations for $PtCl_4^{2-}$ have led to a barrier of approximately 140 cm^{-1}, lower by an order of magnitude than the experimentally determined barrier of 2600 cm^{-1} (20). This discrepancy could be due to the lack of precise relativistic corrections for the 5*d* metal center, but it is important to note that the non-totally symmetric distortion is again predicted from the calculations to occur along $Q_{b_{1g}}$ in the platinum(II) complex, in agreement with the distortions derived from spectroscopic data (18).

Density functional calculations on the title compounds show that the non-totally symmetric distortion along the $Q_{b_{1g}}$ normal coordinate is a direct consequence of the molecular electronic structure. This dominant Jahn–Teller active mode is determined from the potential energy surfaces, illustrating that density functional calculations correctly predict Jahn–Teller distortions for square-planar compounds with D_{4h} point group symmetry, in agreement with density functional

© 1999 NRC Canada

studies on Jahn–Teller distortions in octahedral and tetrahedral transition metal complexes (4–6).

Acknowledgment

This work was made possible by research grants from the Natural Sciences and Engineering Research Council of Canada.

References

1. C. Daul. Int. J. Quantum Chem. **52**, 867 (1994).
2. J. Simons. J. Phys. Chem. **95**, 1017 (1991).
3. A.C. Stückl, C.A. Daul, and H.-U. Güdel. Int. J. Quantum Chem. **61**, 579 (1997).
4. R. Bruyndonckx, C. Daul, and P.T. Manoharan. Inorg. Chem. **36**, 4251 (1997).
5. F. Gilardoni, J. Weber, K. Bellafrouh, C. Daul, and H.-U. Güdel. J. Chem. Phys. **104**, 7624 (1996).
6. K. Bellafrouh, C. Daul, H.-U. Güdel, F. Gilardoni, and J. Weber. Theor. Chim. Acta, **91**, 215 (1995).
7. C. Daul, H.-U. Güdel, and J. Weber. J. Chem. Phys. **98**, 4023 (1993).
8. F. Gilardoni, J. Weber, A. Hauser, and C. Daul. J. Chem. Phys. **109**, 1425 (1998).
9. R. Provencher and P.D. Harvey. Inorg. Chem. **35**, 2113 (1996).
10. E. Francke and C. Moncuit. C. R. Acad. Sci. Paris Sér. B: **271**, 741 (1970).
11. D.S. Martin. Inorg. Chim. Acta Rev. **5**, 107 (1971).
12. H.H. Patterson, J.J. Godfrey, and S.M. Kahn. Inorg. Chem. **11**, 2872 (1972).
13. R.M. Rush, D.S. Martin, and R.G. LeGrand. Inorg. Chem. **14**, 2543 (1975).
14. W. Tuszynski and G. Gliemann. Z. Naturforsch.A: Phys. Phys. Chem. Kosmophys. **34A**, 211 (1979).
15. H. Yersin, H. Otto, J.I. Zink, and G. Gliemann. J. Am. Chem. Soc. **102**, 951 (1980).
16. L.G. Vanquickenborne and A. Ceulemans. Inorg. Chem. **20**, 796 (1981).
17. G. Gliemann and H. Yersin. Struct. Bonding (Berlin), **62**, 87 (1985).
18. D.M. Preston, W. Güntner, A. Lechner, G. Gliemann, and J.I. Zink. J. Am. Chem. Soc. **110**, 5628 (1988).
19. W. Güntner, G. Gliemann, H. Kunkely, C. Reber, and J.I. Zink. Inorg. Chem. **29**, 5238 (1990).
20. C. Reber and J.I. Zink. J. Phys. Chem. **95**, 9151 (1991).
21. Y. Pelletier and C. Reber. Inorg. Chem. **36**, 721 (1997).
22. A.J. Bridgeman and M. Gerloch. Mol. Phys. **79**, 1195 (1993).
23. M.A. Hitchman. Inorg. Chem. **21**, 821 (1981).
24. E.J. Baerends, D.E. Ellis, and P. Ros. Chem. Phys. **2**, 41 (1973).
25. E. J. Baerends. Thesis, Vrije Universiteit Amsterdam, 1975.
26. W. Ravenek. Algorithms and applications on vector and parallel computers. Elsevier, Amsterdam. 1987.
27. P.M. Boerrigter, G. te Velde, and E.J. Baerends. Int. J. Quantum Chem. **33**, 87 (1988).
28. G.J. Snijders, E.J. Baerends, and P. Vernooijs. At. Nucl. Data Tables, **26**, 483 (1982).
29. P. Vernooijs, G.J. Snijders, and E.J. Baerends. Internal Report, Vrije Universiteit Amsterdam. 1981.
30. L. Noodleman and J.G. Norman. J. Chem. Phys. **70**, 4903 (1979).
31. L. Noodleman. J. Chem. Phys. **74**, 5737 (1981).
32. L. Noodleman and E.J. Baerends. J. Am. Chem. Soc. **106**, 2316 (1984).
33. J. Krijn and E.J. Baerends. Internal Report, Vrije Universiteit Amsterdam. 1984.
34. S.H. Vosko, L. Wilk, and M. Nusair. Can. J. Phys. **58**, 1200 (1980).
35. A.D. Becke. Phys. Rev. A: Gen. Phys. **38**, 3098 (1988).
36. J.P. Perdew. Phys. Rev. B: Condens. Matter, **33**, 8822 (1986).
37. H. Adamsky. AOMX, version 20/1/96. The program package is documented at http://www.theochem.uni-duesseldorf.de/Computing/Progs/aomx/Welcome.html.
38. G. Bussière and C. Reber. J. Am. Chem. Soc. **120**, 6306 (1998).
39. E. Francke and C. Moncuit. Theor. Chim. Acta, **29**, 319 (1973).
40. A.J. Bridgeman and M. Gerloch. J. Chem. Soc. Dalton Trans. 197 (1995).
41. J.I. Zink. J. Chem. Soc. Dalton Trans. 4027(1996).
42. A.J. Bridgeman and M. Gerloch. J. Chem. Soc. Dalton Trans. 4027 (1996).
43. R.H. Mais, P.G. Owston, and A.M. Wood. Acta Crystallogr. Sect. B: Struct. Crystallogr. Cryst. Chem. **B28**, 393 (1972).
44. D.S. Martin, J.L. Bonte, R.M. Rush, and R.A. Jacobson. Acta Crystallogr. Sect. B: Struct. Crystallogr. Cryst. Chem. **B31**, 2538 (1975).
45. Y. Bosworth and R.J.H. Clark. Inorg. Chem. **14**, 170 (1975).
46. Y. Chen, D.H. Christensen, O.F. Nielsen, J. Hyldtoft, and C.J.H. Jacobsen. Spectrochim. Acta, Part A: **51A**, 595 (1995).

© 1999 NRC Canada

Accurate density-functional calculation of core-electron binding energies with a scaled polarized triple-zeta basis set. VI: Extension to boron-containing molecules

Germán Cavigliasso and Delano P. Chong

Abstract: Our procedure for calculating core-electron binding energies (CEBEs), based on the unrestricted generalized transition state model using B88/P86 functional, was extended to boron-containing molecules. Both unscaled (cc-pVTZ, cc-pVQZ, cc-pV5Z) and scaled (scaled-pVTZ and scaled-pVQZ) basis sets were used. The average absolute deviation from experiment for boron CEBEs with the scaled-pVTZ basis set was found to be 0.24 eV, compared to 0.23 eV for the much larger cc-pV5Z basis set.

Key words: DFT, boron, core-electron binding energies.

Résumé : Notre méthode de calcul des énergies de liaison des électrons de coeur (ELEC), basée sur le modèle de l'état de transition généralisé sans restriction en utilisant une fonctionnelle B88/P86, a été étendue aux molécules contenant du bore. On a utilisé aussi bien des ensembles de base non gradués (cc-pVTZ, cc-pVQZ, cc-pV5Z) et gradués (p-VTZ et p-VQZ gradués). La déviation absolue moyenne par rapport aux expériences pour les ELEC avec l'ensemble de base p-VTZ gradué est de 0,24 eV; elle se compare avantageusement à la valeur de 0,23 eV obtenue avec l'ensemble de base cc-pV5Z beaucoup plus gros.

Mots clés : théorie de la densité fonctionnelle (TDF); énergies de liaison des électrons de coeur.

[Traduit par la rédaction]

1. Introduction

Accurate calculations of core-electron binding energies (CEBEs) have been recently shown to be a valuable tool for analytical purposes. Investigations of the CEBEs of isomers of C_2H_4O, C_3H_3NO, C_3H_6O, and C_6H_6 (1, 2) have provided results that support the possible use of electron spectroscopy for chemical analysis (ESCA). Surface science is also an important area for ESCA applications. Studies by Bureau and coworkers (3, 4) have shown that the use of CEBEs determined by an accurate computational approach for the interpretation of XPS spectra on a molecular scale provides a useful method for tracing the interactions of molecules with a surface. Also, this approach has been shown to assist the interpretation of XPS spectra of compounds for which there is no gas-phase reference spectrum (4).

The present work is an extension of the recent studies by Chong et al. (1, 2, 5–11) on the use of density functional theory (DFT) and the unrestricted generalized transition state (uGTS) (12) model for the accurate calculation of core-electron binding energies. Our experiences have shown that the best procedure for calculating CEBEs involves the uGTS model combined with Becke's 1988 exchange functional and Perdew's 1986 correlation functional. Calculations were initially performed for C, N, O, and F employing large basis sets and the average absolute deviation (AAD) from experiment for over 50 computed CEBEs was found to be 0.2 eV (6). More recently, a more efficient basis set was proposed and tested. It consists of Dunning's correlation-consistent polarized valence triple-zeta (cc-pVTZ) basis for the neutral parent molecule and the same basis scaled for the atom with the partial core-hole according to the screening constants derived by Clementi and Raimondi (13). Our initial investigation (1, 9) of over 60 cases showed that the AAD from experiment remains at 0.2 eV for CEBEs calculated with this scaled basis set.

The purpose of this work is to extend our uGTS-based density functional method of calculating core-electron binding energies to boron-containing molecules.

2. Computational approach

In the unrestricted generalized transition-state model, Williams et al. (12) extended Slater's transition-state method to approximate the endothermiticity of vertical ionization by

$$[1] \qquad E_{\lambda=1} - E_{\lambda=0} = \frac{1}{4}\left(\frac{\partial E}{\partial \lambda}\right)_{\lambda=0} + \frac{3}{4}\left(\frac{\partial E}{\partial \lambda}\right)_{\lambda=2/3}$$

where λ is assumed to be a continuous variable, with $E_{\lambda=0}$ and $E_{\lambda=1}$ denoting the total energies of the neutral molecule

Received October 28, 1998.

G. Cavigliasso and D.P. Chong.[1] Department of Chemistry, University of British Columbia, 2036 Main Mall, Vancouver, BC V6T 1Z1, Canada.

[1] Corresponding author: **Telephone:** (604) 822-5754 **FAX:** (604) 822-2847 **e-mail:** chong@chem.ubc.ca

© 1999 NRC Canada

Table 1. Basis set convergence in the calculation of B 1*s* energies (in eV) with unscaled basis sets.

Molecule	cc-pVTZ	cc-pVQZ	cc-pV5Z	Experiment [a]
B F_3	202.42	202.19	202.15	202.78
B Cl_3	199.81	199.48	199.43	199.68
B Br_3	199.17	198.82	198.78	198.98
B I_3	198.23	197.84	197.78	197.78
$\mathbf{B}_2H_6$	196.82	196.57	196.54	196.48
B H_3CO	195.57	195.32	195.29	195.13
B H_3NH_3	194.44	194.15	194.12	193.71
B H_3CNCH_3	194.05	193.80	193.76	193.58
B H_3PF_3	195.14	194.82	194.77	194.67
B F_3PH_3	199.52	199.29	199.26	

[a] Relativistic effects removed (see text).

and cation, respectively. For the ionization of an electron from the *k*th molecular orbital (MO) ψ_k, λ represents the fraction of electron removed from this MO. $\partial E/\partial\lambda$ is the negative of the orbital energy $\epsilon_k(\lambda)$ according to Janak's theorem (14).

The uGTS approach involves a partial core-ionized cation. We used scaled basis functions to account for the different screening that electrons experience in these cations. For Gaussian-type orbital (GTO) basis functions, the scaling factor for the exponent is the square of the ratio of the effective nuclear charge

$$[2] \qquad scaling = \left(\frac{Z-\sigma'}{Z-\sigma}\right)^2$$

where Z is the nuclear charge of the atom considered, σ and σ' are the screening constants of the neutral molecule and the partial core-ionized cation, respectively. The screening constants for the partial core-ionized atoms were determined using the formulas provided by Clementi and Raimondi (13) with a reduced screening by the 1*s* electron (1).

3. Calculations

In the present study, experimental geometries (15) of the neutral parent molecules were used in the calculations. The deMon density functional program (16) was used, with extrafine nonrandom grid and the auxiliary fitting functions denoted by (3,1;3,1) for H, (4,4;4,4) for B, C, N, O, and F, (5,4;5,4) for P and Cl, and (5,5;5,5) for Br and I. The basis sets used were the *s*, *p*, *d* parts of the correlation-consistent (cc) polarized valence (pV) basis set given by Dunning and co-workers (17–19). The *d*-type basis funtions consisted of six Cartesian components. Calculations were carried out for cc-pVTZ, cc-pVQZ, and cc-pV5Z, and for scaled pVTZ and scaled pVQZ basis sets. For Br and I, the polarized valence double-zeta basis sets in the deMon program were used. All calculations were performed with the DFT functional labeled as B88/P86, which consists of Becke's 1988 exchange functional (20) and Perdew's 1986 correlation functional (21).

Table 2. Calculations of B core-electron binding energies (in eV) with scaled basis sets.

Molecule	Scaled-pVTZ	Scaled-pVQZ	Experiment [a]
B F_3	202.21	202.17	202.78
B Cl_3	199.52	199.48	199.68
B Br_3	198.84	198.81	198.98
B I_3	197.87	197.82	197.78
$\mathbf{B}_2H_6$	196.61	196.56	196.48
$\mathbf{B}_5H_9$ − *apex*	194.24		194.18
$\mathbf{B}_5H_9$ − *base*	196.25		196.08
B H_3CO	195.35	195.31	195.13
B H_3NH_3	194.18	194.14	193.71
B H_3CNCH_3	193.83	193.79	193.58
B H_3PF_3	194.88	194.81	194.67
B $H_3N(CH_3)_3$	193.55		193.35
B $H_3P(CH_3)_3$	192.98		192.91
$1,5-\mathbf{B}_3C_2H_5$	196.26		195.98
$1,6-\mathbf{B}_4C_2H_6$	195.65		195.38
B $(CH_3)_3$	195.89		196.38
B $(OCH_3)_3$	197.50		197.78
B F_3PH_3	199.28	199.26	
$\mathbf{B}_3N_3H_6$	196.06		

[a] Relativistic effects removed (see text).

For the calculation of partial core-hole states, difficulties for converging the density functional SCF procedure were sometimes encountered in molecules with two or more identical atoms, both in cases where these atoms were chemically equivalent and distinct. Our general solution to this problem was to restart the computation with the density of a partial core-hole state artificially created with fictitious nuclear charge. To obtain this density we replaced the atom with its isoelectronic cationic or anionic counterpart (e.g., N^+ or B^- for C) and computed the starting uGTS density with two-thirds of an electron removed from the corresponding fictitious core orbital.

4. Results and discussion

The results of CEBEs of boron are summarized in Tables 1 and 2. The range of experimental CEBEs is almost 10 eV, from 192.9 eV for $BH_3P(CH_3)_3$ to 202.8 eV for BF_3. The CEBEs of C, N, O, and F were also calculated and are shown

©1999 NRC Canada

Table 3. Basis set convergence in the calculation of C, N, O, and F 1*s* energies (in eV) with unscaled basis sets.

Molecule	cc-pVTZ	cc-pVQZ	cc-pV5Z	Experiment [a]
BH_3 **C** O	295.98	295.69	295.65	296.13
BH_3 **C** NCH_3	293.31	293.07	293.02	293.38
BH_3CN **C** H_3	294.16	293.86	293.82	294.01
BH_3 **N** H_3	408.53	408.14	408.09	408.30
BH_3C **N** CH_3	407.32	406.97	406.92	407.02
BH_3C **O**	542.09	541.67	541.60	541.85
B **F** $_3$	694.90	694.38	694.31	694.46
BH_3P **F** $_3$	695.07	694.55	694.48	693.96
B **F** $_3PH_3$	692.24	691.76	691.69	

[a] Relativistic effects removed (see text).

Table 4. Calculations of C, N, O, and F core-electron binding energies (in eV) with scaled basis sets.

Molecule	Scaled-pVTZ	Scaled-pVQZ	Experiment [a]
BH_3 **C** O	295.69	295.67	296.13
BH_3 **C** NCH_3	293.07	293.05	293.38
BH_3CN **C** H_3	293.88	293.85	294.01
$BH_3N($ **C** $H_3)_3$	292.22		291.92
$BH_3P($ **C** $H_3)_3$	291.23		290.91
$1,5-B_3$ **C** $_2H_5$	290.47		290.15
$1,6-B_4$ **C** $_2H_6$	291.54		291.25
$B(O$ **C** $H_3)_3$	292.31		292.15
BH_3 **N** H_3	408.17	408.12	408.30
BH_3C **N** CH_3	406.97	406.94	407.02
BH_3 **N** $(CH_3)_3$	407.12		406.57
BH_3C **O**	541.66	541.63	541.85
$B($ **O** $CH_3)_3$	538.29		538.10
B **F** $_3$	694.37	694.35	694.46
BH_3P **F** $_3$	694.54	694.51	693.96
B **F** $_3PH_3$	691.69	691.72	
B_3 **N** $_3H_6$	404.90		

[a] Relativistic effects removed (see text).

in Tables 3 and 4. The experimental CEBEs were taken from the compilation by Jolly et al. (22) and from the article by Beach and Jolly on borane adducts (23).

The results of our calculations are compared with experimental CEBEs modified by the exclusion of approximate relativistic corrections. These corrections are based on the studies by Pekeris (24) for two-electron ions and were estimated with the following empirically derived equation (6)

$$[3] \quad C_{\text{rel}} = K\, I_{\text{nrel}}^{N}$$

where C_{rel} is the relativistic correction, I_{nrel} is the nonrelativistic CEBE in eV, $K = 2.198 \times 10^{-7}$, and $N = 2.178$. K and N are two fitting parameters of the relation between the relativistic correction and the nonrelativistic CEBEs for Pekeris' two-electron ions. The "experimental" CEBEs listed in Tables 1–4 were obtained by subtracting the relativistic corrections from the original data.

For the phosphine–trifluoroborane adduct and for borazine, experimental CEBEs have not been reported. Therefore, these results represent our predictions for the CEBEs of boron-containing molecules.

Average absolute deviations (AAD) and maximum deviations (MD) of the calculated CEBEs from the experimental values and from the estimated complete basis set (CBS) limits are given in Table 5. The estimated CBS limits for 19 of the test cases were determined from the results of the corresponding cc-pVTZ, cc-pVQZ, and cc-pV5Z calculations, according to the empirically derived equation (25)

$$[4] \quad A(x) = A(\infty) + B\, \mathrm{e}^{-Cx}$$

where x is the cardinal number of the basis set (3, 4, 5 for TZ, QZ, 5Z, respectively) and $A(\infty)$ is the estimated CBS limit for the property.

For the 9 cases studied with the cc-pVQZ and cc-pV5Z basis sets and the 17 cases investigated with the cc-pVTZ basis set, the AAD from experiment for the boron CEBEs is smallest for cc-pV5Z, and the cc-pVQZ performance is almost as good as that of cc-pV5Z. It is also observed that with exponent scaling the results from the triple-zeta basis set (scaled-pVTZ) significantly improve upon those from the corresponding unscaled basis set (cc-pVTZ), and they are very close to the results obtained from cc-pV5Z calculations. Exponent scaling does not have an appreciable effect on the performance of the pVQZ basis set as far as agreement with experimental results is concerned. However, comparisons with the estimated CBS limits are more meaningful if the aim is to design an efficient basis set applicable to large molecules. Also, experimental observations are affected by experimental error whereas the CBS limit gives a fixed value. The cc-pV5Z basis set approximates the CBS limit very well and the scaled-pVTZ basis set also performs well. The scaled-pVQZ results do show some improvement upon those from cc-pVQZ calculations when compared with the CBS limit.

The effect of relativistic corrections is either very small or negligible for boron CEBEs. This was expected from the fact that the relativistic correction calculated via eq. [3] was found to be only 0.02 eV for the boron 1s energies.

©1999 NRC Canada

Table 5. Average absolute deviation (in eV) and maximum deviation (in eV) of calculated core-electron binding energies from experiment and from CBS.

Basis set	Deviations from experiment		Deviations from CBS	
	AAD	MD	AAD	MD
Boron test cases [a]				
cc-pVTZ	0.36 (17)	+ 0.73	0.34 (10)	0.46
cc-pVQZ	0.24 (9)	− 0.59	0.05 (10)	0.07
cc-pV5Z	0.23 (9)	− 0.63	0.01 (10)	0.01
Scaled-pVTZ	0.24 (17)	− 0.57	0.07 (10)	0.10
Scaled-pVQZ	0.24 (9)	− 0.64	0.03 (10)	0.06
CBS	0.23 (9)	− 0.64		
All test cases [a]				
cc-pVTZ	0.41 (32)	+ 1.11	0.38 (19)	0.60
cc-pVQZ	0.25 (17)	± 0.59	0.06 (19)	0.08
cc-pV5Z	0.26 (17)	− 0.63	0.01 (19)	0.01
Scaled-pVTZ	0.26 (32)	+ 0.58	0.07 (19)	0.10
Scaled-pVQZ	0.24 (17)	− 0.61	0.04 (19)	0.06
CBS	0.26 (17)	− 0.64		

[a] Number of cases given in parentheses.

The results for the CEBEs of all five second-period elements investigated — 32 cases with pVTZ and 17 cases with pVQZ and pV5Z — gave an AAD from experiment of 0.26 eV for both the cc-pV5Z and scaled-pVTZ basis sets. This compares very well with our previous study (9) of 66 CEBEs of small closed-shell molecules, in which the AAD was found to be 0.22 eV.

5. Conclusions

The results presented here confirm that the excellent approach of density functional theory combined with the unrestricted generalized transition-state model can be extended to the calculation of the CEBEs of boron-containing molecules.

The scaled-pVTZ calculations for boron 1*s* energies gave an average absolute deviation of 0.07 eV from the estimated complete basis set limit, confirming that this is a highly accurate procedure for describing the core-hole state. Very good agreement with experiment — comparable to that obtained for cc-pV5Z calculations — is also observed for the scaled basis sets.

Acknowledgements

The authors thank Dr. D.R. Salahub for an early version of the deMon DFT program. Financial support from the Natural Sciences and Engineering Research Council (NSERC) of Canada is acknowledged.

References

1. D.P. Chong, C-H. Hu, and P. Duffy. Chem. Phys. Lett. **249**, 491 (1996), part I of this series.
2. D.P. Chong and C-H. Hu. J. Chem. Phys. **108**, 8950 (1998), part IV of this series.
3. C. Bureau and D.P. Chong. Chem. Phys. Lett. **264**, 186 (1997).
4. S. Kranias, C. Bureau, D. P. Chong, V. Brenner, I. George, P .Viel, and G. Lecayon. J. Phys. Chem. B, **101**, 10254 (1997).
5. D.P. Chong. Chem. Phys. Lett. **232**, 486 (1995).
6. D.P. Chong. J. Chem. Phys. **103**, 1842 (1995).
7. D.P. Chong. Can. J. Chem. **74**, 1005 (1996).
8. C-H. Hu and D.P. Chong. Chem. Phys. Lett. **262**, 733 (1996).
9. M. Pulfer, C-H. Hu, and D.P. Chong. Chem. Phys. **216**, 91 (1997), part II of this series.
10. C-H. Hu and D.P. Chong. Chem. Phys. **216**, 99 (1997), part III of this series.
11. C. Bureau, D.P. Chong, G. Lecayon, and J. Delhalle. J. Electron Spectrosc. Rel. Phenom. **83**, 227 (1997), part V of this series.
12. A.R. Williams, R.A. deGroot, and C.B. Sommers. J. Chem. Phys. **63**, 628 (1975).
13. E. Clementi and D.L. Raimondi. J. Chem. Phys. **38**, 2686 (1963).
14. J.F. Janak. Phys. Rev. B: Condens. Matter, **18**, 7165 (1978).
15. O. Madelung (*Editor*). Landolt–Börnstein numerical data and functional relationship in science and technology. New series, Group II. Vol. 21. Springer, Berlin. 1992.
16. A. St-Amant and D.R. Salahub. Chem. Phys. Lett. **169**, 387 (1990).
17. T.H. Dunning, Jr. J. Chem. Phys. **90**, 1007 (1989).
18. R.A. Kendall, T.H. Dunning, Jr., and R.J. Harrison. J. Chem. Phys. **96**, 6796 (1992).
19. D.E. Woon and T.H. Dunning, Jr. J. Chem. Phys. **98**, 1358 (1993).
20. A.D. Becke. Phys. Rev. A: Gen. Phys. **38**, 3098 (1988).
21. J.P. Perdew. Phys. Rev. B: Solid State, **33**, 8822 (1986).
22. W.L. Jolly, K.D. Bomben, and C.J. Eyermann. At. Data Nucl. Data Tables, **31**, 433 (1984).
23. D.B. Beach and W.L. Jolly. Inorg. Chem. **24**, 567 (1985).
24. C.L. Pekeris. Phys. Rev. **112**, 1649 (1958).
25. K.A. Peterson, and T.H. Dunning, Jr. J. Phys. Chem. **99**, 3898 (1995).

©1999 NRC Canada

Quantum molecular similarity. Part 2: The relation between properties in BCP space and bond length

Sean E. O'Brien and Paul L.A. Popelier

Abstract: In previous work we introduced an abstract space of bond critical point properties, called BCP space, to measure the similarity between molecules. In this contribution we critically examine the dependence of properties in BCP space on equilibrium bond length, a topic which has been extensively investigated in the literature. For that purpose we have designed a data set of 57 molecules yielding 731 bond critical points. We confirm the existence of *local* linear relationships provided the bonds vary little in their chemical surroundings. Such relationships break down completely for larger subsets of bond critical points encompassing a wider variety of bonds. The patterns observed in the global picture show so little correlation that one may safely conclude that BCP properties cannot be trivially recovered or even predicted by knowledge of bond length alone.

Key words: atoms in molecules, molecular similarity, bond critical points.

Résumé : Dans un travail antérieur, on a introduit un espace abstrait des propriétés de points critiques des liaisons dans le but de mesurer la similarité entre les molécules; on l'a appelé espace « BCP ». Dans ce travail, on examine d'une façon critique la dépendance des propriétés dans l'espace BCP sur la longueur de la liaison à l'équilibre, un sujet qui a été examiné d'une façon extensive dans la littérature. À cette fin, on a mis au point un ensemble de données relatives à 57 molécules qui nous ont permis d'extraire 731 points critiques de liaison. Nous pouvons confirmer l'existence de relations linéaires *locales*, à la condition que l'environnement chimique des liaisons varie peu. Ce type de relation n'existe plus avec des sous ensembles plus larges de points critiques de liaison comprenant une variété plus grande de liaisons. Les patrons observés pour l'ensemble montre qu'il y a peu de corrélation et on peut conclure qu'il n'est pas possible de récupérer facilement les propriétés BCP ou même de les prédire par la connaissance uniquement de la longueur de liaison.

Mots clés : atomes dans les molécules, similarité moléculaire, points critiques de liaison.

[Traduit par la Rédaction]

1. Introduction

This contribution is the second in a series of papers proposing a useful and feasible method to measure molecular similarity employing ab initio calculations. In the previous paper (P.L.A. Popelier. J. Phys. Chem. In press.) we explained the main idea behind our approach and systematically delineated some practical questions that will arise during the full implementation of the intended program. This paper addresses a technical, but fundamental, issue arising within the context of the method that we are currently developing. In essence we employ the theory of "Atoms in Molecules" (AIM) (1) to represent the electronic structure of molecules in a reliable and compact way. We then define a molecular similarity measure that operates directly on this AIM representation.

Received July 30, 1998.

S.E. O'Brien and P.L.A. Popelier.[1] Department of Chemistry, University of Manchester Institute of Science and Technology, 88 Sackville Street, Manchester M60 1QD, U.K.

[1]Author to whom correspondence may be addressed. Telephone: 0044 161 2004511. e-mail: pla@umist.ac.uk

On several occasions it has been suggested in the literature that many simple (e.g., linear) relationships exist between the magnitudes constituting the AIM representation and the equilibrium bond length. Although we confirm the existence of these relationships, we have proven that they occur only *locally*, in other words within a restricted subset of bonds sharing roughly the same chemical environment. When a much wider class of bonds is included a different *global* picture emerges. Much more complex relationships — if any — are seen between the AIM-based values and the bond length. Consequently we invalidate the possible objection that our AIM representation can be trivially recovered from known (linear) relationships acting on tabulated bond lengths. All this will become much clearer below where we briefly review our approach and expound the broader picture into which the present contribution fits.

Bioisosterism (2) is the concept that similar molecules can exhibit comparable biological activities. This traditional idea has often been used in pharmaceutical, agrochemical, and other industries to improve drug design. A description of relative activity, or a similarity index, can be attained by examining several different and varied physical and chemical properties. It is in the search for a fundamental, underlying quantity to describe molecules that Carbó et al. (3) examined the electron density and proposed a similarity index between

© 1999 NRC Canada

Table 1. Basis sets selected for testing.

Label	Basis set	
A	B3LYP/6–311++G(3df,3pd)	//B3LYP/6–311++G(3df,3pd)
B	B3LYP/6–311++G(3df,3pd)	//B3LYP/6–31G(d)
C	B3LYP/6–311+G(2d,p)	//B3LYP/6–311+G(2d,p)
D	B3LYP/6–311+G(2d,p)	//HF/6–31G(d)
E	B3LYP/6–311+G(d,p)	//HF/3–21G(d)
Z	HF/6–31G(d,p)	//HF/6–31G

Note: Basis sets **A–E** were selected after consulting ref. 13. **Z** was used by Bader in studies on substituted benzenes (16).

Fig. 1. Data set generation. The amino acid aspartate is cleaved in positions **1**–**4** and the resulting fragments capped with a hydrogen atom to produce the following molecules: **1**, ethanoic acid; **2**, methanoic acid; **3**, water; **4**, hydrogen.

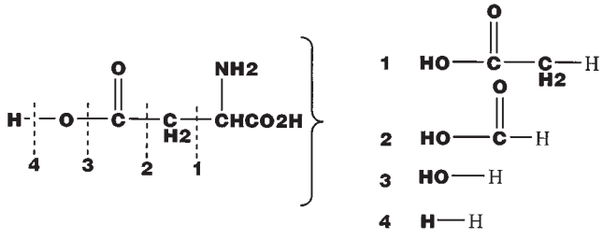

two molecules in terms of electron density overlap integrals. Although the main idea behind this similarity measure has shown its merit (4), the method has proved to be time consuming and suffers from certain technical difficulties.

Major problems arise from the superimposition of two electron densities that are overlaid so as to maximize the similarity index. This procedure is extremely expensive and can also produce multiple (undesirable) maxima. In addition, it is unclear whether the comparisons should be limited to small regions or performed over the whole molecule. Finally, the measure is severely biased by core densities (near nuclei). Although several methods (5–9) have sought to solve these problems, difficulties still remain. Therefore we propose to utilize the tools provided by the theory of Atoms in Molecules (AIM)(1) to extract information about similarities concealed within the electron density.

One of the innovations of AIM is the rigorous division of a molecule into its constituent atomic fragments. These atomic basins are linked by a number of bond paths from which one can construct a molecular graph. This describes the network of bonds that link the atoms in a molecule at its equilibrium geometry and recovers our experimentally obtained view of atoms linked by chemical bonds. Each bond path contains a point of special interest — a bond critical point (BCP) — at which the bond can be characterized. These BCPs occur at the point of minimal electron density, along the bond path, but at a point of maximal density perpendicular to the bond path.

It is possible to evaluate certain properties at these BCPs such as ρ, the electron density; $\nabla^2\rho$, the Laplacian of ρ; ε, the ellipticity (10) of the bond; and K and G, the kinetic energy densities. These local properties constitute an accurate and unique quantum chemical fingerprint of any particular BCP and hence any bond can be represented in terms of the properties at its BCP. Some of these properties were reported to depend linearly on the bond length but, as mentioned above,

Fig. 2. Molecules used for basis set testing.

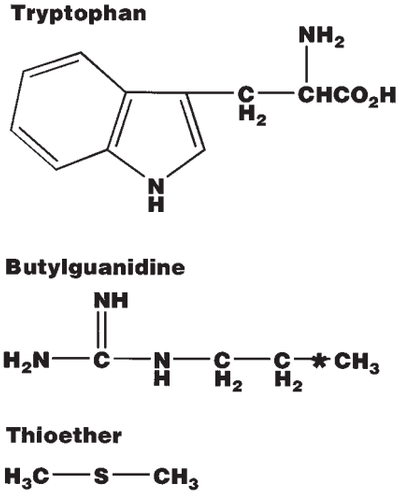

we will demonstrate in this paper that this no longer holds provided we look at a large set of bonds in very different chemical surroundings. The properties at bond critical points span a hyperspace in which any molecule or molecular fragment can be represented discretely. It is by representing molecules as they appear in "BCP space" that we aim to develop a similarity index.

First we introduce the collection of molecules from which a vast set of BCPs was drawn, followed by an investigation justifying the level of calculation to be used throughout our BCP-space research program. We refer to this collection of molecules as the *data set* in this and future work. Subsequently each of the five properties listed above is systematically investigated for all C—C and C=O bonds in turn. By focusing on certain subsets of the data set, we reveal typical, local relationships occurring between these BCP properties and equilibrium bond length.

2. Data set

To properly explore BCP space a large, consistent group of molecules that gradually varied was required. To this end a set of molecules was generated from the 20 natural amino acids. How this is done becomes clear with Fig. 1. The bond between the C_α and the side chain of each amino acid was cleaved (bond **1**) and the chain fragment was capped with a hydrogen atom. Cutting and capping was continued in this manner, along the side chain, away from the C_α (following the sequence of bonds **2, 3,** and **4** on Fig. 1), until the small-

© 1999 NRC Canada

Fig. 3. The quantities ρ, Laplacian, and ellipticity are shown for nitrobenzene, relative to the values calculated for benzene in the appropriate basis set **C**, **D**, and **Z**. Each BCP number is marked on the molecule shown in the figure above. The trends in BCP properties are shown as they vary around the ring structure. It is clear that qualitatively each basis set reveals the same picture. In fact, sets **C** and **D** often produce indistinguishable points.

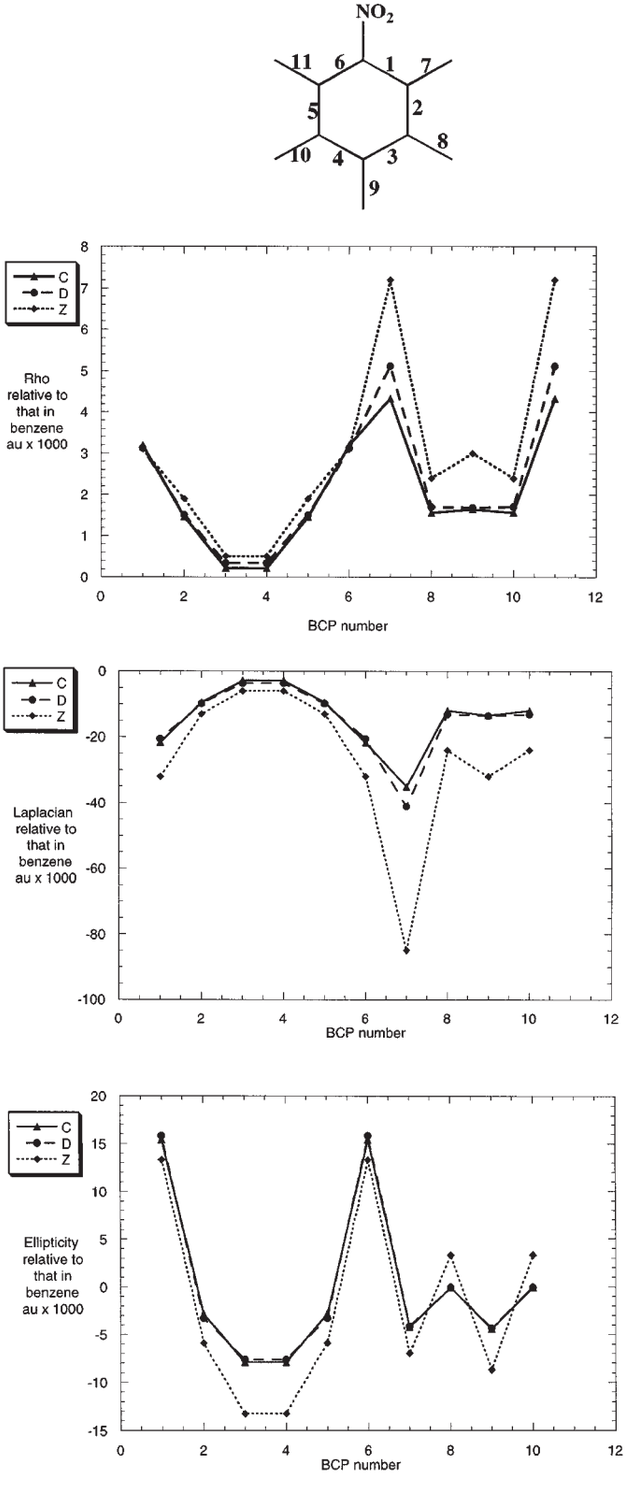

est possible molecule was produced. During this process only single bonds were sliced, i.e., all double bonds and ring structures were left intact, and any molecule duplicated was included only once. Together with the 20 original amino acids, this process left us with a data set of 57 unique molecules. Once evaluated, this set contained 731 BCPs.

3. Level of calculation

To include the effects of electron correlation it was decided to use Density Functional Theory (DFT). It is computationally less demanding than MP2 and QCISD, especially for large systems, and has been found to yield comparable results for BCP properties (11, 12). Of the available functionals, B3LYP has been found to have the best overall coherence with MP2 for properties at the BCPs (12),and a better overall performance than other functionals in general (13). All wave functions were generated via the program GAUSSIAN94 (14) and the BCPs were obtained using MORPHY98 (15).

Employing the above level of theory, the wave functions, and then the properties at the BCPs, of three molecules were calculated at five different basis set levels. This was to discover if (and, if so, how) altering the basis set changed the values of the said properties. The molecules tested were representative of the data set (Fig. 2). They included all types of atoms present, both rings and chains, and were of varying sizes. The basis set levels (Table 1) were selected after consulting ref. 13. Basis set **A** was the largest available and was used as a benchmark from which to calculate the deviations of the other basis sets. The selections decrease steadily in size from **B** to **E,** varying both the level of optimization and the level of single point calculation.

From running the above calculations it can be observed that the properties at the BCPs vary significantly from basis set to basis set. Table 2 shows the values obtained at the five levels **A–E** for a C—C bond (marked with * in Fig. 2) of butylguanidine. This is an example of a common bond showing typical basis set error. The bond is not particularly exotic and yet produces some strikingly large deviations between the basis sets. Taking into account all the bonds studied, there is no regular shift from the benchmark value within a particular set, i.e., **C** does not always calculate ρ_b to deviate from **A** by 2.2%. Several conclusions can be drawn from these results. The first is that the absolute values of BCP properties are highly basis set dependent. It must, however, be stated that the "Pople" basis sets used in this study, and frequently elsewhere, are not large enough to achieve the HF limit. If basis sets of sufficiently large size are employed, BCP properties will eventually converge to physically limiting values. This fact does not negate the above conclusion, as the values of most BCP properties calculated today will be largely affected by choice of basis set. Secondly, the relative stabilities of these properties to the choice of basis set are also revealed; $\rho_b > G_b$, $\nabla^2\rho_b$, $K_b > \varepsilon_b$, with ρ_b being the most steady. The ellipticity is seen to be most unstable although the extent of this instability can be misleading if only the percentage deviation is studied. Small and physically insignificant ellipticities, i.e., ~ <0.1 au, tend to show much larger percentage deviations. Finally, in general, the larger the basis set, the smaller the difference from **A**.

© 1999 NRC Canada

Table 2. Basis set and BCP properties of a C—C bond (marked with an asterisk in Fig. 2).

Basis set	ρ_b	$\nabla^2\rho_b$	ε_b	K_b	G_b
A	0.244 43	0.567 01	0.006 75	0.200 37	0.058 61
B	0.246 13	0.575 85	0.006 72	0.203 33	0.059 35
B – A	0.001 7	0.008 84	–0.000 03	0.002 96	0.000 74
%	**0.7**	**1.56**	**–0.44**	**1.48**	**1.26**
C	0.249 86	0.627 52	0.008 12	0.220 04	0.063 23
C – A	0.005 43	0.060 51	0.001 37	0.019 67	0.004 62
%	**2.22**	**10.67**	**20.30**	**9.82**	**7.88**
D	0.249 65	0.626 15	0.008 25	0.219 61	0.06306
D – A	0.005 22	0.059 14	0.001 5	0.019 24	0.004 45
%	**2.14**	**10.43**	**22.22**	**9.60**	**7.59**
E	0.255 33	0.656 14	0.009 22	0.228 84	0.064 79
E – A	0.010 9	0.089 13	0.002 47	0.028 47	0.006 18
%	**4.46**	**15.72**	**36.59**	**14.21**	**10.54**

Note: This demonstrates the effect of changing basis set on the values of BCP properties. For each basis set the calculated value is subtracted from that found using set **A**. The percentage differences are marked in bold. These particular figures come from looking at the C—C bond in butylguanidine marked by an asterisk in Fig. 2. All values are in au.

Fig. 4. *para* C—H bond ellipticities for Ph-X substituted benzenes calculated at basis sets **C**, **D**, and **Z** are plotted versus the Taft resonance parameter σ_R^0. The trends shown by all three basis sets are the same. Note that sets **C** and **D** hardly deviate from each other The values for **D** correlate fairly well with σ_R^0 (r = 0.972).

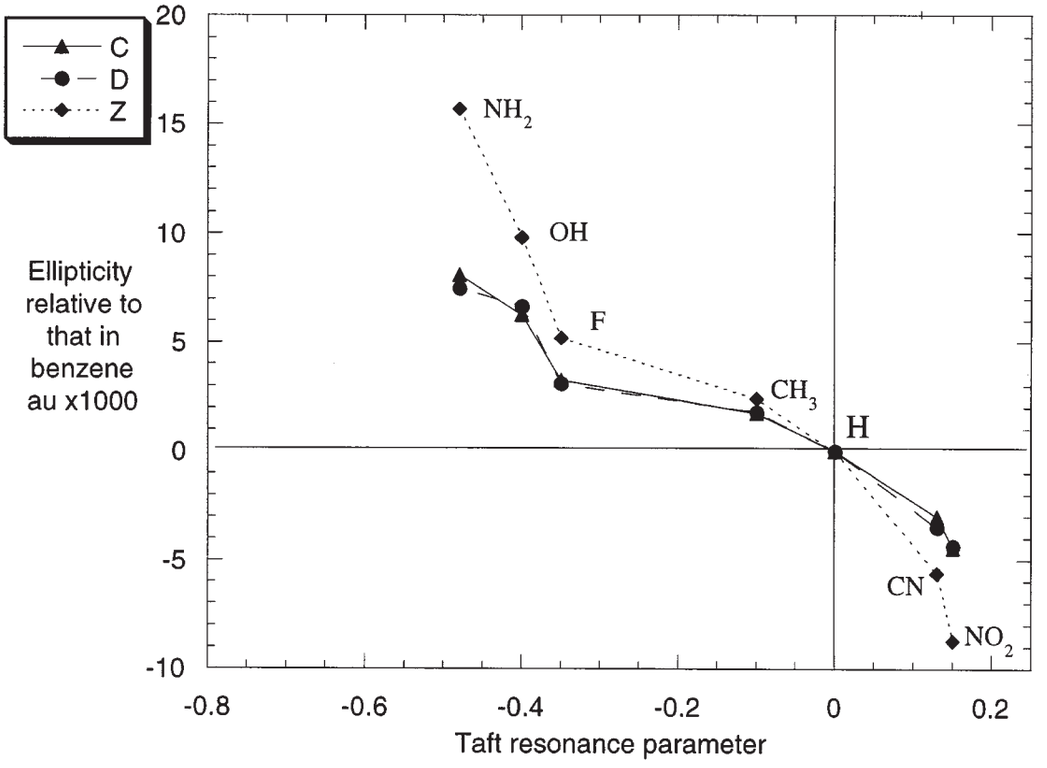

One feature of B3LYP that became apparent (and has been noted before for more general molecular properties (13)) is its relative insensitivity to the level of optimization, i.e., for a more accurate result it is more important to increase the level of the single point calculation than that of the optimization. As a consequence, sets **D** and **E** show fairly similar results. However, the maximum error for **E** is larger (cf. ref. 13). Due to the unfeasibility of **A** owing to its large size, SCF convergence problems when using **B** and **C,** and the larger maximum error found when using **E,** it was decided to use level **D** — B3LYP/6-311+G(2d,p)//HF/6-31G(d) for the data set calculations.

Although this study provided a probable choice of basis set, it also revealed the need for further investigation. If the choice of basis set could alter the values of BCP properties, sometimes drastically, could observations made while using one basis set still be valid when using another? In comparing BCP properties between benzene and substituted

© 1999 NRC Canada

Fig. 5. Plots of BCP properties against equilibrium bond length. Amongst this set of 160 C—C bonds strong correlation can be seen between ρ_b, $\nabla^2\rho_b$, ε_b, K_b, and G_b and *R*e. Although some graphs (especially 5*e*) might appear to obey a power law relationship better than a linear one, this does not prove to be the case with this data set. A gradual change in the magnitude of each property can be seen as the longer single-bond lengths shorten to become aromatic.

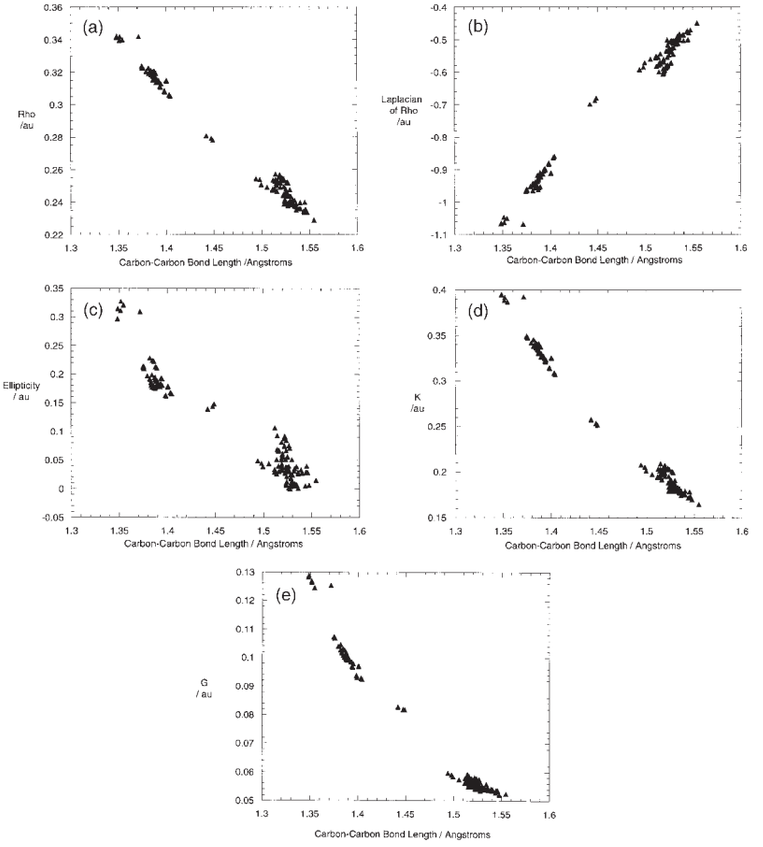

benzenes (16), Bader found that ρ_b and $\nabla^2\rho_b$ paralleled small changes in bond length and that C—H bond ellipticities recovered the relative directing abilities of the ipso substituents. Could Bader's following of substituent effects by analysis of the properties at BCPs be reproduced using other basis sets? To answer this question a set of substituted benzenes Ph-X (where X = NH_2, OH, F, CH_3, H, CN, and NO_2) were examined. Bader and Chang used the following level of theory, HF/6-31G(d,p)//HF/6-31G, which we denote by **Z.** Their results were compared to those obtained using sets **C** and **D**. As before, the absolute values of the relevant properties tended to differ. However, when plotted against each other (Fig. 3), it is clear that the way in which ρ_b, $\nabla^2\rho_b$, and ε_b vary around the benzene ring is similar in all three basis sets. The trends shown are the same. The basis set HF/6-31G(d,p)//HF/6-31G, which is the smallest, has a tendency to exaggerate the peaks and troughs when compared to the set of points produced by **C** and **D.** Although the graph appears slightly stretched for the latter levels, the patterns seen are the same. In spite of Edgecombe's demonstration of the need for "large basis sets to avoid significant basis set errors"(17) it is worth knowing that Stutchbury and Cooper (18) noted how even a set as small as 4-31(G) is sufficient to preserve trends seen in electron density properties. Hence we can conclude that observations made about relative BCP properties are consistently reproduced whichever basis set is being used.

Table 3. Pearson correlation coefficients for BCP properties vs. bond length along the C—C, C—O, C—OH bond paths and for all the bonds in the data set.

Bond	ρ_b	$\nabla^2\rho_b$	ε_b	K_b	G_b
C—C	–0.994	0.993	–0.958	–0.994	–0.989
C—O	–1.000	–0.983	–0.990	–1.000	–0.999
C—OH	–0.984	–0.188	–0.140	–0.980	–0.950
All	–0.647	0.687	0.505	–0.463	0.050

As noted by Bader and Chang (16), the C—H bond path acts as a "probe of the interatomic surface" of the attached carbon atom. The ellipticity at the C—H BCP distinguishes between the directing abilities of the π-donating (OH, CH_3, F, NH_2) and π-abstracting (CN, NO_2) substituents. In fact, they mirror the experimentally obtained Taft resonance parameter (σ_R^0) (19).This is a measure of the F NMR shift in *meta*- and *para*-substituted fluorobenzenes. As this is zero for X = H, all values are relative to nonsubstituted benzene. As σ_R^0 parallels the directing abilities of the various substituents, so does the C—H bond ellipticity for the *para* carbon (this BCP is in the same position as the one numbered 9

© 1999 NRC Canada

Fig. 6. Plots of BCP properties versus equilibrium bond lengths for 51 C—O bonds. It is clear that there are two groups of bonds present. Obvious linear relationships appear in 6*a*, 6*d*, and 6*e*. The patterns (if any) present in 6*b* and 6*c* are not so apparent.

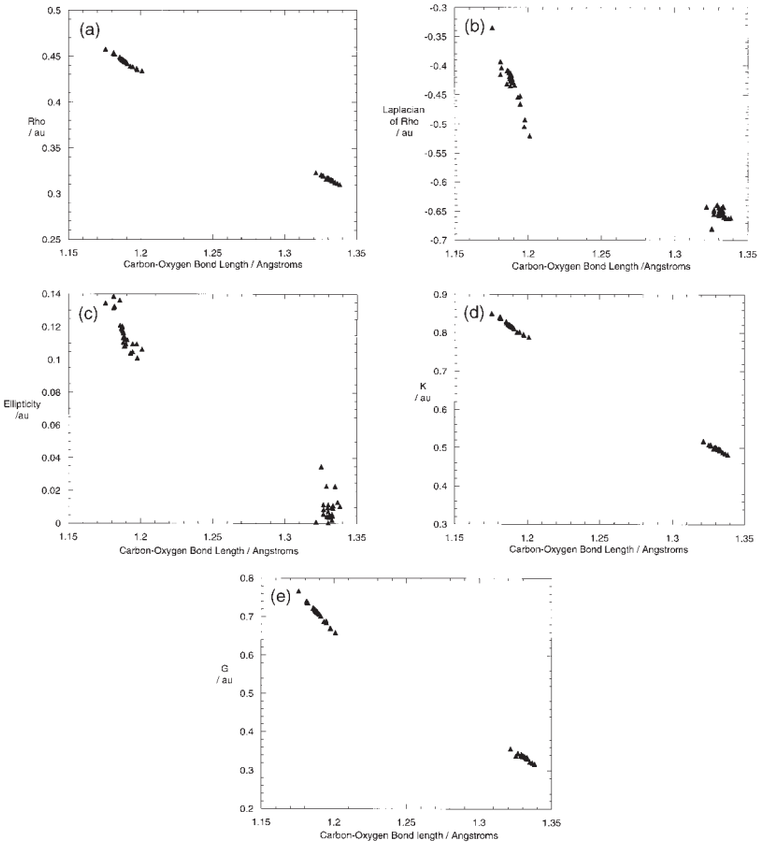

in Fig. 3). Figure 4 shows how these values compare at all three basis sets used (**C, D, Z**). Rather than producing perfectly linear relationships, this graph clearly shows the trends in site activation of the ipso substituents. As seen in Figs. 3 and 4, the patterns produced by each basis set are similar. However, these trends appear more pronounced when calculated using **Z**. Basis sets **C** and **D** regularly produce overlapping points and hence virtually identical patterns. Although equivalent pictures are given by all basis sets, the comparatively large fluctuations produced by smaller sets probably serve to exaggerate and distort these trends. Set **C**, as well as being unfeasible due to SCF convergence problems, gives no clearer picture than **D**. There is no discernible advantage to be gained in using the larger basis set. Hence in all further data set calculations B3LYP/6-311+G(2d,p)//HF/6-31G(d) was used.

4. BCP space

To fully understand BCP space it is necessary to explore its dimensions. We need to see how each property relates to each of the others and how they might be related to any external observables. If any of these are correlated in a simple manner it will affect the final dimensionality of BCP space. It is unnecessary and in fact can be highly misleading to have linked parameters. Examining how variables are interrelated enables us to construct a multidimensional property space that has orthogonal axes and contains no redundant information. Simultaneously it would be pointless calculating the values of a BCP property if these could easily be obtained from an already known quantity. It was for these reasons that the relationships between BCP properties and equilibrium bond length (R_e) were examined.

Bader et al. (20) first mention a highly linear correlation between R_e and ρ_b for C—C bonds in ethane, benzene, and ethylene. As conjectured, ρ_b increases as the bond length decreases — the electron density between the nuclei balances the forces of repulsion, which augment as the atoms move closer. It is important to note that when strained hydrocarbons such as cyclopropane are fitted into this scheme the relationship no longer holds. However, when geometrical bond length is replaced with bond path length (R_b) a linear relationship is once more observed (10). In the majority of cases $R_e = R_b$ and this problem does not arise. Knop and Boyd (21) suggest a power law relationship of the form $\rho_b = AR_e^{-B}$. This was originally observed as being a better fit than a linear one for several S—S bond lengths. They propose that this "relationship may hold for any class of (binary) bond." This phenomenon has now been recorded for several different classes of bonds and has been observed with both experimental (22, 23) and calculated (24–28) densities. In his examination of condensed aromatic systems (28) Wiberg

© 1999 NRC Canada

Fig. 7. The graphs are shown for the reduced C—O group. This now contains only C—OH bonds. In focusing on this subset, no apparent relationship can be seen between $\nabla^2\rho_b$ or ε_b and R_e. This demonstrates that any line fits (linear or power law) are only valid within the appropriate data set. Any resizing of the group, or altering of its boundaries, can lead to considerable changes in observed relationships. Compare 7*a* and 7*b* to 6*b* and 6*c*.

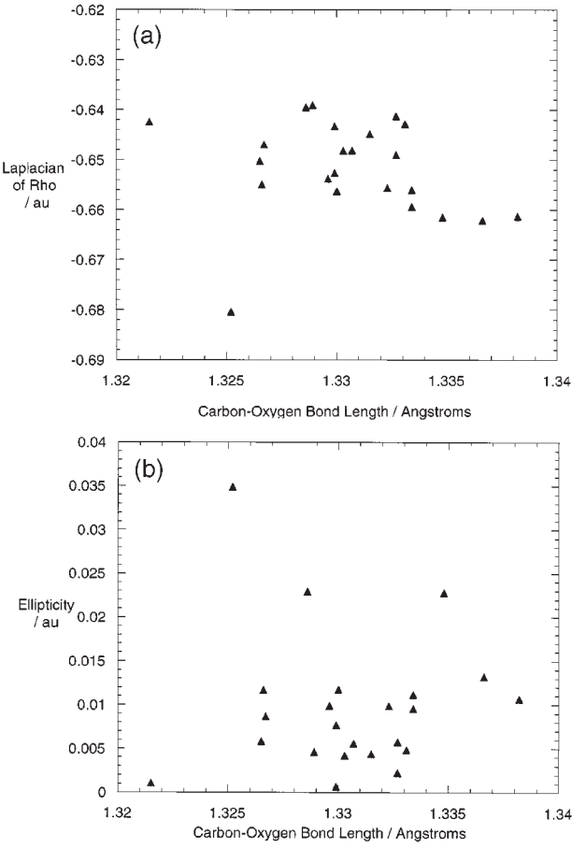

shows a linear graph of ρ_b vs. R_e and also includes a plot of ellipticity vs. bond length that shows a clear relationship between the two quantities. Howard's study of benzenoid hydrocarbons (26) also produces excellent linear correlations between the bond length, ρ_b (r = –0.998), ε_b (r = –0.978), and even $\nabla^2\rho_b$ (r = 0.997).

Within our amino acid based data set we also recover such relationships. However, these are found not only for the properties mentioned immediately above but also for K_b and G_b. This is demonstrated graphically for carbon–carbon bonds in Fig. 5 and also for carbon–oxygen bonds in Fig. 6. The linear relationships can immediately be seen from these plots and from the table of correlation coefficients (Table 3). The C—C set consists of 160 C—C bond critical points that encompass "pure" single bonds (longer bond length, lower ρ_b) through to aromatic BCPs (shorter bond length, higher ρ_b). In a similar fashion the C—O set comprises 51 BCPs. This includes C=O bonds present as aldehydes, ketones, and carboxylic acids (shorter bond length, higher ρ_b) and C—OH bonds both in amino acids and alcohols (longer bond length, lower ρ_b).

In general, the correlations between the BCP properties and R_e indicate excellent linear relationships. These can be verified by comparison with Figs. 5 and 6. If there always were a good correlation between a particular BCP property and bond length then one would expect the coefficients for the C—C set to be very similar to those in the C—O set. For the most part this is the case. The one striking exception is found to be $\nabla^2\rho_b$. The correlation completely switches sign when calculated for the two classes of bonds. Although $\nabla^2\rho_b$ and R_e still show a relatively linear relationship for C—O bonds it is now *opposite* to that observed for the C—C bonds. It is known that $\nabla^2\rho_b$ indicates the degree of covalency of a bond (1).The lower, or more negative, the value of $\nabla^2\rho_b$, the more covalent the bond. For C—C bonds, the shorter the bond, the higher the degree of covalency and thus the positive correlation seen. However, for C—O bonds, the shorter bond is C=O. This is known to exhibit some degree of ionic character (hence its frequent representation as $C^{\delta+}=O^{\delta-}$), and therefore has a higher, or less negative, value of $\nabla^2\rho_b$ than the C—OH bond.

Upon inspection of Figs. 5*c*, 6*b*, and 6*c* the validity of the correlation coefficients can be called into question. It is well known (29) that this regression statistic can be misleading and the use of graphical methods for reviewing data is recommended. When used with caution, however, the statistic can equally be very revealing. It is the ellipticities for both bonds and the previously mentioned values of $\nabla^2\rho$ at the C—O BCPs that need more examination. For these bonds, shorter bond lengths are characterized by increased π-character. The subsequent shift of the bond shape (perpendicular to the bond path) from circular to ovoid is reflected in higher values of ε_b. This is true for both sets of bonds. A lower correlation between ε_b and R_e than between ρ_b and R_e or $\nabla^2\rho_b$ and R_e is seen here and was also observed by Howard (26) for a set of C—C bonds. The linear relationships appearing in both sets of data are very similar, Howard's values showing slightly higher correlation than ours. This may be due to the more varied nature of the bonds featured in our set.

To obtain a clearer picture of the anomalies revealed in the C—O set the C=O bonds were removed. If the 27 C—OH are examined separately, a completely different picture emerges for $\nabla^2\rho_b$ and ε_b. Figure 7 shows how there is a complete lack of structure in the set of values now present. This is reflected in the C—OH correlation coefficients (Table 3). Note especially the values for $\nabla^2\rho_b$ and ε_b, which are completely different from before and are now negligible. Those for the other quantities, while still indicating strong correlation, have also changed. These last results indicate that one must be very careful in assigning any significance to such relationships. What may appear a strong correlation when observed from one perspective can in fact be much altered when viewed from another. Similarly, what is a perfectly valid conclusion at a small scale can appear hopelessly inadequate in the larger picture.

When all 731 BCPs are included, the bigger picture becomes apparent (Fig. 8). There is quite obviously no simple relationship (linear, power law, or otherwise) between BCP properties and bond length. Table 3 confirms this impression, showing no correlations of any significance. If any small cluster visible on these graphs were examined more

© 1999 NRC Canada

Fig. 8. The graphs shown are for the complete data set of amino acid derived molecules. Each BCP property is plotted versus equilibrium bond length. They each contain data from 731 BCPs. None suggest any simple relationships between the plotted quantities. The bond lengths around 2–2.5 Å belong to hydrogen bonds that appear in the calculated amino acid structures. They show low values of all quantities except ε_b in 8*c*. Higher values of ellipticity have been associated with relative instability (1).

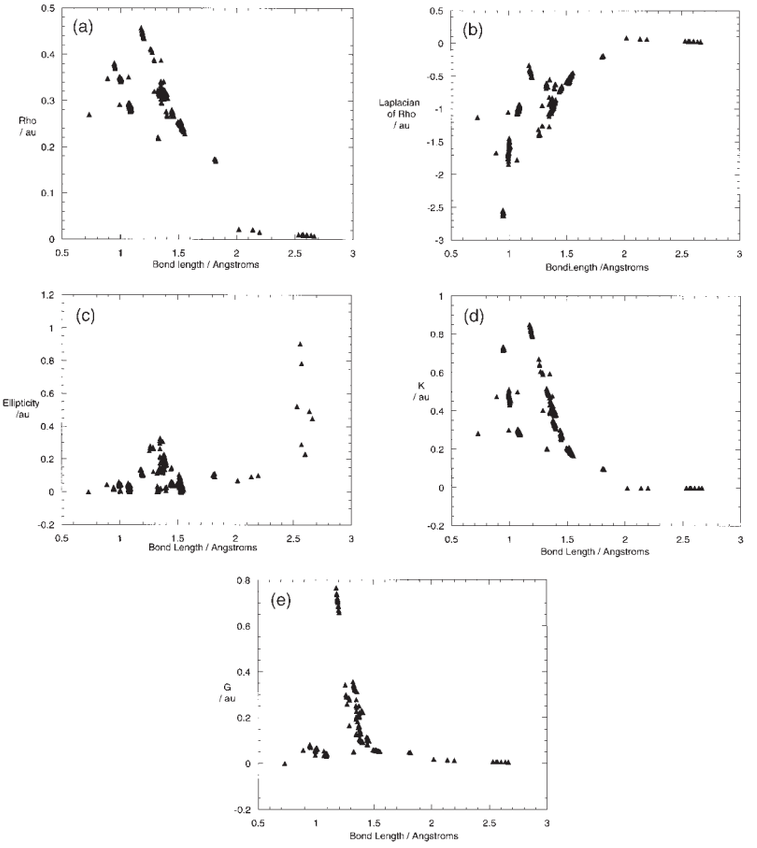

closely one might find some form of relationship between a BCP property and bond length. However, when viewed outside the boundaries of the chosen cluster, do the observations still hold?

It seems likely that ρ_b is always related to R_e for any "class of (binary) bond." Whether this can be expressed as a power law or in a linear way may be dependent on the range of bond lengths covered in the data set. Once this particular relationship is known for any class of bond, then bond lengths may indeed be "estimated from a single parameter"(ρ_b)(21) — though it seems more likely one would wish to use the relationship to discover ρ_b rather than R_e. On the other hand, $\nabla^2\rho_b$ has been shown to be unpredictable even within the confines of a particular class of bond. The ellipticity correlations appear to deviate wildly when altering the boundaries of a (small) group. It seems improbable that a reliable $\nabla^2\rho_b$ vs. R_e or ε_b vs. R_e relationship can be established. At first glance it might seem likely that the kinetic energy density K_b is related to R_e in the same way as ρ_b. Both have graphs that are remarkably similar in form for all sets shown. For the C—C and C—O sets, they correlate identically with R_e (Table 3) and on such a basis it would not be unreasonable to assume that they were closely linked. However, their correlation values with R_e are not the same when viewed in the context of the whole data set (Table 3). Thus they cannot be linked as closely as one might have previously thought. Similarly R_e and G_b show very strong correlation within given boundaries but exhibit absolutely none in the larger picture.

5. Conclusion

As part of our molecular similarity program we attempt to understand BCP space better. One particular question that arises is how properties in BCP space are correlated with bond length. Based on a set of bonds larger than any previously published we are able to say that one cannot predict any BCP property on the basis of bond length alone. A set of bonds has to be defined and coefficients fitted (linear, power law, or other) before this is feasible. The definition of any set has also to include the basis set, as we have seen that choice of basis set can greatly distort BCP properties. The relationships between ρ_b and bond length for given systems seem to be pretty robust, as they have often been quoted in the literature although they only hold within a given basis set. It has been shown that, even within a given subset of bonds, $\nabla^2\rho_b$ and ε_b cannot be reliably linked to bond length. Within the limits provided by the C—O and C—C data sets the kinetic energy densities K_b and G_b do appear to obey highly linear relationships with R_e.

© 1999 NRC Canada

Acknowledgement

Ms F.M. Aicken is thanked for help in generating the wave functions of the data set. Gratitude is expressed to the Engineering and Physical Sciences Research Council for a studentship (GR/L65895).

References

1. R.F. W. Bader. Atoms in molecules: a quantum theory. Clarendon Press, Oxford. 1990.
2. H.L. Friedman. N.A.S. – N.R.S. Publ. **206**, 295 (1951).
3. R. Carbo, L. Leyda, and M. Arnau. Int. J. Quantum Chem. **17**, 1185 (1980).
4. M. Sola, J. Mestres, R. Carbo, and M. Duran. J. Am. Chem. Soc. **116**, 5909 (1994).
5. E.E. Hodgkin and W.G. Richards. J. Chem. Soc. Chem. Commun. 1342 (1986).
6. E.E. Hodgkin and W.G. Richards. Int. J. Quantum Chem. **31**, 105 (1987).
7. C. Lee and S. Smithline. J. Phys. Chem. **98**, 1135 (1994).
8. A.M. Richard and J.R. Rabinowitz. Int. J. Quantum Chem. **31**, 309 (1987).
9. P.E. Bowen-Jenkins and W.G. Richards. J. Chem. Soc. Chem. Commun. 133 (1986).
10. R.F.W. Bader, T.S. Slee, D. Cremer, and E. Kraka. J.Am. Chem. Soc. **105**, 5061 (1983).
11. T. Ziegler. Chem. Rev. **91**, 651 (1991).
12. X. Lopez, J.M. Ugalde, C. Sarasola, and F.P. Cossio. Can. J. Chem. **74**, 1032 (1996).
13. J.B. Foresman and A. Frisch. Exploring chemistry with electronic structure methods. 2nd ed. Gaussian Inc., Pittsburgh, Pa. 1996.
14. M.J. Frisch, G.W. Trucks, H.B. Schlegel, P.M.W. Gill, B.G. Johnson, M.A. Robb, J.R. Cheeseman, T. Keith, G.A. Petersson, J.A. Montgomery, K. Raghavachari, M.A. Al-Laham, V.G. Zakrzewski, J.V. Ortiz, J.B. Foresman, J.Cioslowski, B.B. Stefanov, A. Nanayakkara, M. Challacombe, C.Y. Peng, P.Y. Ayala, W. Chen, M.W. Wong, J.L. Andres, E.S. Replogle, R. Gomperts, R.L. Martin, D.J. Fox, J.S. Binkley, D.J. Defrees, J. Baker, J.P. Stewart, M. Head-Gordon, C. Gonzalez, and J.A. Pople. Gaussian94. Gaussian, Inc., Pittsburgh Pa. 1995.
15. P.L.A. Popelier. MORPHY98 — a program written by P.L.A. Popelier with a contribution from R.G.A. Bone. UMIST, Manchester, England.
16. R.F.W. Bader and C. Chang. J. Phys. Chem. **93**, 2946 (1989).
17. K.E. Edgecombe and R.J. Boyd. Int. J. Quantum Chem**. 1986**, **29**, 959 (1986).
18. N.C.J. Stutchbury and D.L. Cooper. J. Chem. Phys. **79**, 4967 (1983).
19. R.W. Taft, E. Price, I.R. Fox, I.C. Lewis, K.K. Andersen, and G.T. Davis. J. Am. Chem. Soc. **85**, 3146 (1963).
20. R.F. Bader, T.H. Tang, Y. Tal, and F.W. Biegler König. J. Am. Chem. Soc. **104**, 946 (1982).
21. O. Knop, R.J. Boyd, and S.C. Choi. J. Am. Chem. Soc. **110**, 7299 (1988).
22. R. Destro and F. Merati. Acta Crystallogr. Sect. B: Struct. Sci. **B51**, 559 (1995).
23. P. Roversi, M. Barzaghi, F. Merati, and R. Destro. Can. J. Chem. **74**, 1145 (1996).
24. R.J. Boyd and S.C. Choi. Chem. Phys. Lett. **120**, 80 (1985).
25. R.J. Boyd and K.E. Edgecombe. J. Comput. Chem. **8**, 489 (1987).
26. S.T. Howard and T.M. Krygowski. Can. J. Chem. **75**, 1174 (1997).
27. O. Knop, T.S. Cameron, P.K. Bakshi, W. Kwiatkowski, S.C. Choi, and D. Adhikesavalu. Can. J. Chem. **71**, 1495 (1993).
28. K.B. Wiberg. J. Org. Chem. **62**, 5720 (1997).
29. D. Livingstone. Data analysis for chemists. 1st ed. Oxford University Press, Oxford. 1995.

© 1999 NRC Canada

Synthesis, structure, and reactivity of macrocyclic heterobimetallic complexes of (Co, Cu), (Co, Ni), (Co, Zn), (Zn, Cu), (Zn, Ni) combinations

H. Golchoubian, W.L. Waltz, and J.W. Quail

Abstract: A series of macrocyclic heterobimetallic complexes of type $[M_c(tntnam)M_o](PF_6)_n$ and $[M_c'(tntnim)Ni](PF_6)_n$ where M_c = Co(III) and Zn(II), M_c' = Co(II), Co(III), and Zn(II), and M_o = Ni(II), Cu(II), and Zn(II) have been synthesized and characterized. The macrocyclic ligands tntnim **2** and tntnam **3** contain two geometrically distinct compartments, 6-coordinate (closed site) and 4-coordinate (open site), which are bridged by phenolic oxygens. The heterobimetallic complexes with Zn(II) or Ni(II) in the open site are primarily formed as 5-coordinate with a chloride ion as a fifth ligand; the latter can be removed by Ag^+ ion. The crystal structures of $[Zn(tntnim)NiCl]PF_6\cdot C_2H_5OH$, **5**, $[Zn(tntnam)Ni](PF_6)_2$, **11**, $[Zn(tntnam)Cu](PF_6)_2$, **12**, and $[Co(tntnam)Ni(H_2O)](PF_6)_3\cdot 4H_2O$, **14** were determined. Crystal data for **5**: monoclinic, T = 123 K, a = 15.822(2), b = 15.6230(10), c = 16.432(2) Å, β = 104.570(10)°, Z = 4, space group Pc, R = 0.0371 ($wR2$ = 0.0843) for 5826 reflections with $I \geq 2\sigma(I)$. Crystal data for **11**: tetragonal, T = 123 K, $a = b$ = 24.122(2), c = 14.397(7) Å, Z = 8, space group $P4_12_12$, R = 0.0625 ($wR2$ = 0.1549) for 3250 reflections with $I \geq 2\sigma(I)$. Crystal data for **12**: tetragonal, T = 123 K, $a = b$ = 24.180(2), c = 14.281(4) Å, Z = 8, space group $P4_12_12$, R = 0.0588 ($wR2$ = 0.1219) for 3452 reflections with $I \geq 2\sigma(I)$. Crystal data for **14**: triclinic, T = 287 K, a = 12.664(2), b = 12.983(2), c = 16.216(3) Å, α = 80.317(14)°, β = 69.585(12)°, γ = 74.791(12)°, Z = 2, space group $P\bar{1}$, R = 0.0573 ($wR2$ = 0.1332) for 3443 reflections with $I \geq 2\sigma(I)$. The structures were solved by direct methods and refined by full-matrix least-squares procedures. The crystal structures demonstrate that the expected *trans* pyridine structures are formed. The magnetic moments, electrospray mass spectra, electronic absorption and emission spectra, and redox couples are reported.

Key words: cobalt, copper, nickel, zinc, heterobimetallic, macrocycle.

Résumé : On a synthétisé et caractérisé une série de complexes macrocycliques hétérobimétalliques du type $[M_c(tntnam)M_o](PF_6)_n$ et $[M_c'(tntnim)Ni](PF_6)_n$ dans lesquels M_c = Co(III) et Zn(II), M_c' = Co(II), Co(III) et Zn(II) et M_o = Ni(II), Cu(II) et Zn(II). Les ligands macrocycliques tntnim, **2**, et tntnam, **3**, contiennent deux compartiments géométriquement distincts à coordination de 6 (site fermé) et à coordination de 4 (site ouvert) qui sont reliés par les oxygènes phénoliques. Les complexes hétérobimétalliques avec le Zn(II) ou le Ni(II) dans le site ouvert existent principalement sous une forme pentacoordinée dans laquelle l'ion chlorure agit comme cinquième ligand; on peut récupérer ce dernier à l'aide de l'ion Ag^+. On a déterminé les structures cristallines des complexes $[Zn(tntnim)NiCl]PF_6\cdot C_2H_5OH$, **5**, $[Zn(tntnam)Ni](PF_6)_2$, **11**, $[Zn(tntnam)Cu](PF_6)_2$, **12**, et $[Co(tntnam)Ni(H_2O)](PF_6)_3\cdot 4H_2O$, **14**. Les données cristallographiques pour **5** : monoclinique, T = 123 K, a = 15,822(2), b = 15,6230(10) et c = 16,432(2) Å, β = 104,570(10)°, Z = 4, groupe d'espace Pc, R = 0,0371 ($wR2$ = 0,0843) pour 5826 réflexions avec $I \geq 2\sigma(I)$. Les données cristallographiques pour **11** : tétraédrique; T = 123 K, $a = b$ = 24,122(2) et c = 14,397(7) Å, Z = 4, groupe d'espace $P4_12_12$, R = 0,0625 ($wR2$ = 0,1549) pour 3250 réflexions avec $I \geq 2\sigma(I)$. Les données cristallographiques pour **12** : tétraédrique; T = 123 K, $a = b$ = 24,180(2) et c = 14,281(4) Å, Z = 8, groupe d'espace $P4_12_12$, R = 0,0588 ($wR2$ = 0,1219) pour 3452 réflexions avec $I \geq 2\sigma(I)$. Les données cristallographiques pour **14** : triclinique, T = 287 K, a = 12,664(2), b = 12,983(2) et c = 16,216(3) Å, α = 80,317(14)°, β = 69,585(12)° et γ = 74,791(12)°, Z = 2, groupe d'espace $P\bar{1}$, R = 0,0573 ($wR2$ = 0,1332) pour 3443 réflexions avec $I \geq 2\sigma(I)$. On a résolu les structures par des méthodes directes et on les a affinées par les méthodes des moindres carrés (matrice complète). Les structures cristallines démontrent qu'il y a formation des structures attendues à pyridine *trans*. On a aussi déterminé les moments magnétiques, les spectres de masse, les spectres d'absorption électronique et les spectres d'émission ainsi que les couples redox.

Mots clés : cobalt, cuivre, nickel, zinc, hétérobimétallique, macrocycle.

[Traduit par la Rédaction]

Received July 22, 1998.

H. Golchoubian, W.L. Waltz,[1] and J.W. Quail. Department of Chemistry, University of Saskatchewan, 110 Science Place, Saskatoon, SK S7N 5C9, Canada.

[1]Author to whom correspondence may be addressed. Telephone: (306) 966-4708. Fax: (306) 966-4730. e-mail: waltz@sask.usask.ca

 © 1999 NRC Canada

Scheme 1.

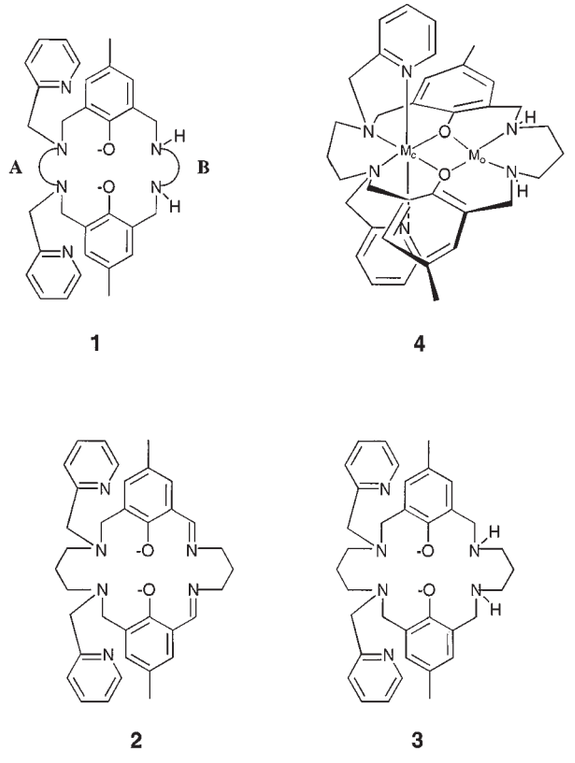

Introduction

Heterobimetallic complexes are of interest because of the unique physicochemical properties that arise from metal–metal interaction (1–6) and their potential as sources for multielectron transfers (7–9). In particular, the recent recognition of heterobimetallic cores at the active sites of purple acid phosphatase (FeZn) (10), human calcineurin (FeZn) (11), and human protein phosphatase 1 (MnFe) (12) has stimulated study in the functions of heterobimetallic core complexes. Macrocycles with dissimilar coordination sites are a great advantage for the studies of heterobimetallic complexes because such macrocyclic complexes are thermodynamically stabilized and kinetically retarded toward metal dissociation or substitution relative to complexes of the corresponding noncyclic ligands (macrocyclic effects) (13). Phenol-base bimetallic macrocycles have often been used for the study of bimetallic complexes (14–33). Macrocycles of the type **1** (Scheme 1), whose two metal-binding sites are dissimilar with respect to their coordination environments around each metal, have been studied by Bosnich and co-workers (34, 35) and Busch and co-workers (14). This macrocyclic ligand contains two compartments, a sexadentate closed site and a contiguous quadridentate open site. The nomenclature introduced by McCollum et al. (36) to describe the heterobimetallic complexes is designed, first, to designate the closed-site metal, M_c, followed by the closed-site link, A, the open-site link, B, and then followed by im or am to designate the diimine or diamine, the open-site metal, M_o, and followed by ligand L (where it exists), i.e., [M_c(closed-site link) (open-site link) (im or am) M_oL].

One of the objectives of this work has been to synthesize heterobimetallic complexes of the Bosnich's ligands tntnim[2] **2** and tntnam[3] **3**. These ligands, both having trimethylenediamine (tn) links, have been found in other systems to provide one topological isomer among three possible isomers with *trans*-disposed pyridine and *cis*-phenolate groups as shown in **4** (36). For purposes of characterization and comparison, investigations both of liquid solutions and of the solid state have been made. The relatively close juxtaposition of the two metal centers is favorable towards the coordination of small molecules, and we have investigated this facet in regard to the photoactivation of dioxygen.

Experimental

Apparatus and procedures

Conductance measurements were made at 25°C with a Wayne Kerr 6425 conductance meter on 1.00×10^{-3} M samples in CH_3CN. Infrared spectra were recorded in KBr mixtures by the diffuse reflectance technique on a single-beam Bio-Rad FTS-40 FTIR. The UV–VIS–NIR solution spectra were obtained on a Varian (Cary) 2315 spectrophotometer using spectral grade CH_3CN. Electrospray mass spectral studies were conducted on a VG Quattro II (Fision) triple–quadruple electrospray mass spectrometer with 100% methanol as the mobile phase. The compounds were dissolved in a mixture of acetonitrile and methanol (1:1) and in some cases acetonitrile:methanol:formic acid (1:1:1). The dissolved compounds were injected directly into the spectrometer via a Rheodyne injector using a Fision LC syringe pump to deliver the solution at a flow rate of 20 μL s^{-1}. Nitrogen was used for nebulization and as a drying gas with flow rates of approximately 20 and 250 L h^{-1}, respectively. Elemental analyses were performed on a Perkin–Elmer 2400 CHN elemental analyzer. ^{1}H NMR and ^{13}C NMR spectra were recorded on a Bruker 300 Fourier transform spectrometer. All samples were dried to constant weight under vacuum prior to analysis. Magnetic susceptibilities of the samples in solution were measured by the modified Evans method (37) using the above-mentioned constant field, 300 Fourier transform instrument. Coaxial NMR tubes were used with tetramethylsilane (TMS) as an internal reference. The inner tube contained acetone-d_6 (CD_3COCD_3) and TMS (1% v/v) while the outer tube contained the same matrix plus sample. Magnetic susceptibilities of powder samples were measured at 20°C using a Johnson Matthey magnetic susceptibility balance.[4] Diamagnetic corrections were made using Pascal's constant (38). All electrochemical experiments were done using a setup consisting of a PC 486, 66 MHz, microcomputer equipped with a data acquisition board (POL-818PG,

[2] μ-[11,23-Dimethyl-15,19-bis(2-pyridinylmethyl)-3,7,15,19-tetraazatricyclo[19.3.1.^{9,13}]hexacosa-1(25),2,7,9,11,13(26),21,23-octaene-25,26-diolato(2–)-N^3,N^7,O^{25},O^{26}:N^{15},$N^{15'}$,N^{19},$N^{19'}$,O^{25},O^{26} or tntnim.

[3] μ-[11,23-Dimethyl-15,19-bis(2-pyridinylmethyl)-3,7,15,19-tetraazatricyclo[19.3.1.^{9,13}]hexacosa-1(25),9,11,13(26),21,23-hexaene-25,26-diolato(2–)-N^3,N^7,O^{25},O^{26}:N^{15},$N^{15'}$,N^{19},$N^{19'}$,O^{25},O^{26} or tntnam.

[4] Department of Chemistry, University of British Columbia, Vancouver.

© 1999 NRC Canada

PC-Labcard Co.) and a custom-made potentiostat (39). The data acquisition and data processing program used in the electrochemical measurements was developed by A. Baranski.[5] Cyclic voltammograms that were 0.1 M in *n*-Bu_4NPF_6 supporting electrolyte and 1×10^{-3} M in sample were recorded in the range of +2 to –2 V in deaerated CH_3CN solution. Redox potentials were measured using a Pt disk electrode (0.25 mm in diameter), a tungsten wire as a pseudo-reference electrode, and another tungsten wire as an auxiliary electrode. They were standardized with a ferrocene internal and in some cases external standard (40). Acetonitrile used in the electrochemistry experiments was distilled twice over CaH_2.

Emission spectra were obtained on a Spex Flurolog Fl 221 with a cooled photomultiplier R928 using software DM 3000, version 3.3, SPEX Inc. Time-resolved experiments were carried out using a DL2160B Phase-R coaxial flash-lamp dye laser. The absorbances of the irradiated solutions were set at $A = 0.4$ for a wavelength of 490 nm (the wavelength of the irradiation laser light). After oxygenation for 1 h, the solution was irradiated by laser pulses (2.3 J $pulse^{-1}$). The same experiments were performed on deaerated solutions. In the deaeration process, a stream of argon presaturated with acetonitrile was passed through the solution during the course of the experiment. A C30642 planar PIN InGaAs photodiode detector, which was constructed by Dr. E. Janata,[6] was used to monitor the phosphorescence of singlet molecular oxygen, O_2 ($^1\Delta_g$), at a wavelength of 1270 nm. The electronic spectra of the solutions were studied, by UV–VIS spectrophotometry, before and after the laser pulses.

In the steady-state photolysis experiments, a 10 cm Pyrex-jacketed cell was filled with the solution. The concentration of the solution was adjusted so that the absorbance of the solution was 2.0 at 25°C. A 1000 W Hg–Xe lamp (Oriel 6293) was used for quantum yield measurements. To filter out infrared and UV light, a water cell and another cell containing an aqueous solution of 0.1 M $CuSO_4$ were placed in front of the beam. Subsequently an interference filter (Edmund Scientific Co., CWL 415, λ_{max} = 415 nm, fwhm 12 nm) was placed immediately prior to the photocell. Oxygenation was achieved by passing a stream of O_2 presaturated with water through the solution during the course of the experiment. A sample of solution was maintained in the dark at the same temperature in order to provide a control for any thermal component of the reaction and to serve as a reference for the spectrophotometric measurement. During the photolysis, the solution was stirred with a small magnetic bar. After a suitable irradiation period, the irradiated solution was analyzed for the concentration of peroxide species as follows: to the irradiated and control solutions were added solutions of KI (5.00 mL, 0.200 mol L^{-1}) and acetic acid (1.0 mL, 1.00 mol L^{-1}). The solutions were allowed to stand for 30 min for the colour development of I_3^- (41). The resulting solutions were extracted with CCl_4 (4 × 5 mL) and the combined organic fractions were made up to 25 mL. The absorbance of the organic solutions was measured at a wavelength of 517 nm against the control sample. This method provides a limit of detection of 5×10^{-6} mol L^{-1} for the peroxide. Quantum yields of reaction ($\Phi_{peroxide}$) were determined using ferrioxalate actinometry (42).

Materials

All solvents used in reactivity studies were distilled twice. Ethanol used in this work refers to absolute ethanol. Acetone was dried over 4 Å molecular sieves. Other solvents were of BDH (Omnisolv) grade. Water purified by a Millipore Super-Q system was used to prepare the aqueous solutions. All preparations of Co(II) complexes were conducted under argon using deaerated solvents and standard Schlenk techniques (43). Yields of compounds were calculated after purification. The physical data (elemental analyses, molar conductance, and ^1H NMR data) are detailed below for each complex. The identity of each compound was confirmed by electrospray mass spectrometry, and these data are given in the results and discussion section. The compounds $[Co(tntnim)(H^+)_2](PF_6)_2$ (36), $[Co(tntnam)(H^+)_2](PF_6)_3$ (35), $[Zn(tntnim)(H^+)_2](PF_6)_2$ (36), and $[Zn(tntnam)(H^+)_2](PF_6)_2$ (35) were prepared by standard methods found in the literature.

Preparation of imine complexes, $[M_c(diimine)M_o]^{q+}$ complexes

The complexes are air stable as solids. Unless indicated otherwise, each of the heterobimetallic complexes was purified by recrystallization from CH_3CN–ethanol using one of two general procedures.

Method 1: The crude salt was dissolved in a minimal volume of CH_3CN (ca. 2 mL for each 0.15 g of complex) at room temperature and the solution was filtered. To the CH_3CN solution was added absolute ethanol (ca. 5 mL). A steady stream of argon was passed over the solution in order to reduce the CH_3CN content, and additional aliquots of ethanol (3 × 3 mL) were added over time. The solution was typically allowed to stand overnight. The crystalline complex was then collected and washed with ethanol (3 × 3 mL), ether (2 × 3 mL), and pentane (2 × 3 mL) and was dried under vacuum for 5–6 h.

Method 2: The crude compound was dissolved in CH_3CN (ca. 2 mL for each 0.200 g of complex) at room temperature and the solution was filtered. To the CH_3CN solution was added absolute ethanol (ca. 4 mL) and the resulting solution was placed in a small flask, which was then put in a jar containing ethanol (ca. 25 mL). This jar was capped to allow for slow diffusion of ethanol into the solution. After several days, the crystalline complex was collected and washed with ethanol (3 × 3 mL), Et_2O (2 × 3 mL), and pentane (2 × 3 mL) and dried under vacuum for 5–6 h.

$[Zn(tntnim)NiCl]PF_6 \cdot C_2H_5OH$, ***5***

To a solution of the $[Zn(tntnim)(H^+)_2](PF_6)_2$ (189 mg, 0.20 mmol) in CH_3CN (5 mL) was added a solution of $NiCl_2 \cdot 6H_2O$ (52.3 mg, 0.22 mmol) in ethanol (10 mL) and Et_3N (55.7 mL, 0.40 mmol). The yellow-green mixture was stirred for 12 h. During the course of the reaction, small

[5] Department of Chemistry, University of Saskatchewan, Saskatoon.
[6] Hahn–Meitner-Institut Berlin, Postfach 39 28 01, 14109 Berlin, Germany.

© 1999 NRC Canada

amounts of a gelatinous green compound precipitated that was discarded after filtration. NH_4PF_6 (140 mg, 0.86 mmol) in ethanol (5 mL) was added to the resultant solution. The solution was partially concentrated at room temperature to reduce the CH_3CN content; ethanol was then added in portions (2 × 10 mL), and the solution allowed to stand overnight. The solid was collected and washed with water (2 × 5 mL), ethanol (2 × 10 mL), ether (2 × 10 mL), and pentane (2 × 10 mL). The crude compound was recrystallized by method 1 to give green polyhedra (76%). Crystals suitable for X-ray crystal structure determination were grown by vapour diffusion of ethanol into a CH_3CN:ethanol solution of the complex. Λ_m = 170 Ω^{-1} mol^{-1} cm^2. Anal. calcd. for $C_{36}H_{40}N_6O_2PF_6ClZnNi\cdot C_2H_5OH$: C 48.59, H 4.94, N 8.95; found: C 48.59, H 4.78, N 8.99.

[Zn(tntnim)Ni](PF$_6$)$_2$, ***6***

The [Zn(tntnim)NiCl]PF_6 (90 mg, 0.10 mmol) was dissolved in acetone (5 mL) and an acetonitrile solution of $AgPF_6$ (25 mg, 0.10 mmol) was added to precipitate chloride ion. The resultant cloudy brown solution was stirred for 30 min, then filtered through Celite, and concentrated by passing a stream of argon over the surface of the solution at room temperature. The green residue was dissolved in acetone (ca. 2 mL) and filtered through Celite again, and was then reconcentrated. The green residue was recrystallized by method 2, which yielded [Zn(tntnim)Ni]$(PF_6)_2$ as brown needles (77%). Λ_m = 272 Ω^{-1} mol^{-1} cm^2. Anal. calcd. for $C_{36}H_{40}N_6O_2P_2F_{12}ZnNi$: C 43.12, H 4.02, N 8.38; found: C 43.23, H 4.10, N 8.34.

[Co(tntnim)NiCl]PF$_6$, ***7***

[Co(tntnim)NiCl]PF_6 was prepared by the general procedure described for **5** except that the reaction mixture was stirred for 30 min. The crude compound was purified by method 2 and yielded an orange solid (70%). Λ_m = 163 Ω^{-1} mol^{-1} cm^2. Anal. calcd. for $C_{36}H_{40}N_6O_2PF_6CoClNi$: C 48.76, H 4.55, N 9.48; found: C 48.68, H 4.55, N 9.43.

[Co(tntnim)Ni](PF$_6$)$_2$, ***8***

The [Co(tntnim)NiCl]PF_6 was dechlorinated by the procedure described for **6** to yield [Co(tntnim)Ni]$(PF_6)_2$, **8**, as a dark-red solid (51%). This cobalt(II) compound is sensitive to air in the solid state and in solution and turns to a black compound over a period of time. Anal. calcd. for $C_{36}H_{40}N_6O_2P_2F_{12}CoNi$: C 43.40, H 4.05, N 8.44; found: C 42.74, H 3.80, N 8.31.

[Co(tntnim)Ni](PF$_6$)$_3$, ***9***

To an acetone solution (5 mL) of **8** (199 mg, 0.20 mmol) under argon was added ferrocenium hexafluorophosphate, $[Cp_2Fe]PF_6$ (66.4 mg, 0.20 mmol), in deaerated acetonitrile (ca. 2 mL). The dark-green solution was stirred under argon for 15 min, then opened to air, and concentrated in vacuo. The black residue was triturated with ether until washes were colourless. The crude compound was recrystallized by method 2. [Co(tntnim)Ni]$(PF_6)_3$, **9**, was obtained as a black needle-like solid (96%). Λ_m = 372 Ω^{-1} mol^{-1} cm^2. Anal. calcd. for $C_{36}H_{40}N_6O_2P_3F_{18}CoNi$: C 37.89, H 3.53, N 7.36; found: C 38.03, H 3.80, N 7.50.

Preparation of amine complexes, [M$_c$(diamine)M$_o$]$^{q+}$

All of the diamine complexes showed a characteristic intense absorption band in the electronic spectrum at λ_{max} 293–307 nm (ε ca. 6 × 10 ^{3} L mol^{-1} cm^{-1}) in CH_3CN solution, whereas for diimine the most intense bands and those assigned to the azomethine $\pi \rightarrow \pi^*$ transition (44) occur at longer wavelengths in the range 330–352 nm (ε ca. 1 × 10^4 L mol^{-1} cm^{-1}).

The crude materials were purified by one of two procedures.

Method 1: The crude compound was dissolved in CH_3CN (ca. 2 mL for ca. 0.200 g of complex) at room temperature and the solution was filtered. To the CH_3CN solution was added absolute ethanol–Et_2O (50:50) (ca. 4 mL), and the resulting solution was placed in a small flask, which was then put in a jar containing ethanol–Et_2O (50:50), (ca. 25 mL). After several days the crystalline complex was collected and washed with ethanol–Et_2O (50:50) (3 × 3 mL), Et_2O (2 × 3 mL), and pentane (2 × 3 mL) and dried under vacuum for 5–6 h.

Method 2: The crude compound was dissolved in acetone (ca. 5 mL for each 0.100 g of complex) at room temperature and the solution was filtered. To the acetone solution was added about 5 mL of absolute ethanol. This solution was placed in a small flask, inside a jar containing diethyl ether (ca. 25 mL). After 3 days the crystalline material was collected and washed with ethanol (3 × 3 mL), Et_2O (2 × 3 mL), and pentane (2 × 3 mL) and dried under vacuum for 5–6 h.

The [M(tntnam)MCl]$^{q+}$ complexes were generally prepared by the procedure described below for [Zn(tntnam)NiCl]PF_6, **10,** with minor variations being noted for some complexes. Dechlorination of [M(tntnam)MCl]$^{q+}$ complexes followed the procedure described above for the imine complex [Zn(tntnim)Ni]$(PF_6)_2$, **8**.

[Zn(tntnam)NiCl]PF$_6$, ***10***

[Zn(tntnam)$(H^+)_2$]$(PF_6)_2$ (100 mg, 0.10 mmol) was dissolved in CH_3CN (5 mL), followed by addition of $NiCl_2\cdot 6H_2O$ (24.3 mg, 0.10 mmol) in methanol (5 mL). To the stirred reaction mixture was added $LiOH\cdot H_2O$ (8.6 mg, 0.20 mmol) in methanol (1.5 mL), dropwise over 5 min. The resulting yellow-green solution was stirred for 30 min and then NH_4PF_6 (81.5 mg, 0.50 mmol) in methanol (2 mL) was added. After 10 min, the green solution was taken to dryness in vacuum. The resultant pale green residue was washed with EtOH (2 × 2 mL), Et_2O (2 × 2 mL), and pentane (2 × 2 mL) and dried under vacuum. The compound was recrystallized by method 2. [Zn(tntnam)NiCl]PF_6, **10**, was obtained as pale pink solid (55%). Λ_m = 157 Ω^{-1} mol^{-1} cm^2. Anal. calcd. for $C_{36}H_{44}N_6O_2PF_6NiZnCl$: C 48.19, H 4.94, N 9.37; found: C 47.94, H 4.95, N 9.26.

[Zn(tntnam)Ni](PF$_6$)$_2$, ***11***

[Zn(tntnam)Ni]$(PF_6)_2$, **11** (44%), was obtained as dark pink polyhedral crystals from dechlorination of compound **10** followed by recrystallization using method 2. This compound is very sensitive to solvent: it is purple in CH_3CN, pink-violet in acetone, and yellow in ethanol. Crystals suitable for X-ray structure determination were obtained upon a

© 1999 NRC Canada

second recrystallization. Λ_m = 276 Ω^{-1} mol^{-1} cm^2. Anal. calcd. for $C_{36}H_{44}N_6O_2P_2F_{12}NiZn$: C 42.95, H 4.41, N 8.35; found: C 42.71, H 4.27, N 8.15.

*[Zn(tntnam)Cu](PF$_6$)$_2$, **12***

$Cu(OAc)_2 \cdot H_2O$ was used instead of $CuCl_2$ as starting material because of the greater solubility of the former compound. The [Zn(tntnam)Cu](PF$_6$)$_2$, **12** (71%), was obtained, after recrystallization by method 1, as a gray-red crystalline solid that was suitable for X-ray structure determination. Λ_m = 248 Ω^{-1} mol^{-1} cm^2. Anal. calcd. for $C_{36}H_{44}N_6O_2P_2F_{12}CuZn$: C 42.76, H 4.38, N 8.31; found: C 42.74, H 4.32, N 8.28.

*[Co(tntnam)NiCl](PF$_6$)$_2$·H$_2$O, **13***

[Co(tntnam)NiCl](PF$_6$)$_2$·H$_2$O**, 13** (55%), was obtained as a dark-green solid after recrystallization. For recrystallization, method 2 was used and recrystallization typically took several days. Λ_m = 281 Ω^{-1} mol^{-1} cm^2. Anal. calcd. for $C_{36}H_{46}N_6O_3ClP_2F_{12}CoNi$: C 41.03, H 4.40, N 7.97, Co 5.59, Ni 5.57; found: C 41.08, H 3.82, N 7.59, Co 5.52, Ni 5.26.

*[Co(tntnam)Ni(H$_2$O)](PF$_6$)$_3$·4H$_2$O, **14***

[Co(tntnam)Ni(H$_2$O)](PF$_6$)$_3$·2H$_2$O (30%) was obtained as a green powder after recrystallization by method 2. Elemental analyses indicated that there are two molecules of water along with the complex. Green polyhedron crystals with four water molecules suitable for X-ray structure determination were obtained by recrystallization of the product three more times. Λ_m = 387 Ω^{-1} mol^{-1} cm^2. Anal. calcd. for $C_{36}H_{50}N_6O_5P_3F_{18}CoNi$: C 36.05, H 4.20, N 7.01, Co 4.91, Ni 4.86; found: C 36.17, H 4.15, N 7.02, Co 4.96, Ni 4.91.

*[Co(tntnam)Cu](PF$_6$)$_3$, **15***

[Co(tntnam)Cu](PF$_6$)$_3$, **15** (17%), was obtained as a dark-green solid after recrystallization twice by method 1. Λ_m = 378 Ω^{-1} mol^{-1} cm^2. Anal. calcd. for $C_{36}H_{44}N_6O_2P_3F_{18}CoCu$: C 37.59, H 3.86, N 7.31; found: C 37.80, H 4.08, N 7.09.

*[Co(tntnam)ZnCl](PF$_6$)$_2$, **16***

The diamagnetic [Co(tntnam)ZnCl](PF$_6$)$_2$, **16** (52%), was obtained as dark-green needles after recrystallization by method 1. Λ_m = 281 Ω^{-1} mol^{-1} cm^2. ^{1}H NMR (300 MHz, CD_3COCD_3), δ 1.87 (m, H), 1.98 (m, H), 2.08 (s, 3H), 2.28 (s, 3H), 2.44 (m, 4H), 2.59 (m, H), 2.75 (d, *J* = 13.4 Hz, H), 2.85 (m, 2H), 3.44 (m, 5H), 3.78 (t, d, *J* = 12.1, 1.7 Hz, H), 4.19 (m, 6 H), 4.43 (t, d, *J* = 12.1, 1.7 Hz, H), 4.71 (t, *J* = 11.9 Hz, H), 4.92 (d, *J* = 17.7 Hz, H), 5.32 (d, *J* = 18.9 Hz, H), 6.74 (s, H), 6.91 (s, H), 6.99 (s, H), 7.12 (s, H), 7.28 (d, *J* = 7.9 Hz, H), 7.42(t, *J* = 6.4 Hz, H), 7.82 (d, *J* = 7.4 Hz, 2H), 7.91 (t, *J* = 7.6 Hz, H), 8.31 (t, *J* = 7.6, H), 8.44 (d, *J* = 5.8, H), 9.42 (d, *J* = 5.2 Hz, H). Anal. calcd. for $C_{36}H_{44}N_6O_2ClP_2F_{12}CoZn$: C 41.48, H 4.25, N 8.06; found: C 41.38, H 4.15, N 7.91.

*[Co(tntnam)Zn](PF$_6$)$_3$·CH$_3$CN, **17***

The diamagnetic cobalt(III) complex [Co(tntnam)Zn](PF$_6$)$_3$·CH$_3$CN, **17** (67%), was obtained as a black needle-like solid after recrystallization by method 1. Λ_m = 368 Ω^{-1} mol^{-1} cm^2. ^{1}H NMR (300 MHz, CD_3CN), δ 1.19 (m, 2H), 2.16 (s, 6H), 2.24 (m, 2H), 2.62 (m, 4H), 2.94 (m, 2H), 3.23 (d, *J* = 15.0 Hz, 4H), 3.41 (d, *J* = 13.1 Hz, 2H), 3.87 (m, 2H), 3.94 (d, *J* = 4.2 Hz, 2H), 3.98 (s, 2H), 4.31, 4.48 (syst AB, J_{AB} = 18.3 Hz, 4H), 6.84 (s, 2H), 6.94 (s, 2H), 7.41 (d, *J* = 7.8 Hz, 2H), 7.62 (t, *J* = 6.3 Hz, 2H), 8.03 (t, *J* = 7.8 Hz, 2H), 8.53 (d, *J* = 5.6 Hz, 2H). Anal. calcd. for $C_{36}H_{44}N_6O_2P_3F_{18}CoZn \cdot CH_3CN$: C 38.26, H 3.97, N 8.22; found: C 38.21, H 3.74, N 8.22.

Crystallography

The single-crystal X-ray diffraction structures of complexes **5**, **11,** and **12** were determined at 123(2) K and corrected for absorption using the ψ-scan method (45). Data for complex **14** was collected at 287(2) K and no absorption correction applied because the crystal was lost before a ψ-scan could be collected. The crystallographic data are summarized in Table 1. For compound **14**, most reflections beyond θ = 23.8° were insufficiently intense to give meaningful observations.

Data were collected on an Enraf–Nonius CAD-4 diffractometer, using the CAD-4 Express operating system (46). Three standard reflections were checked every 200 reflections. Data were processed using XTAL3.5 (47) and the structure solved using NRCVAX (48). The structures were refined by full-matrix least squares on F^2 using SHELXL-97 (49). The methyl H atoms were positioned geometrically in a staggered conformation using a riding model and all other H atoms were placed in calculated positions using a riding model with U(H) = 1.2 U_{eq}(attached atom). The bond lengths assumed were sp^3(methyl), C—H = 0.98 Å at 123 K and 0.96 Å at 287 K; sp^3(methylene), C—H = 0.99 Å at 123 K and 0.97 Å at 287 K; sp^2, C—H = 0.95 Å at 123 K and 0.93 Å at 287 K; sp^3, N—H = 0.93 Å at 123 K and 0.91 Å at 287 K;

Three of the compounds ([Zn(tntnam)Cu](PF$_6$)$_2$, [Zn(tntnam)Ni](PF$_6$)$_2$, and [Zn(tntnim)NiCl](PF$_6$)·C$_2$H$_5$OH) crystallize in acentric space groups ($P4_12_12$, $P4_12_12$, and *Pc*, respectively), even though the compounds are prepared as racemic mixtures. These acentric structures were refined for racemic twinning. The PF_6^- units were all disordered to various extents. For example, in [Zn(tntnam)Cu](PF$_6$)$_2$ and [Zn(tntnam)Ni](PF$_6$)$_2$ (isomorphous and almost isostructural), the P of one PF_6^- ion (P(2)) is very close to a special position (~0.25 Å from $\bar{x}$+1/2, *x*+1/2, 1/4), resulting in an occupancy of 0.5 and disorder. Another PF_6^- in this structure (P3) is lying on a special position (*x*+1/2, $\bar{x}$+1/2, 3/4) with large resultant disorder. Many attempts were made to model the disorder of the PF_6^- units with partially occupied isotropic atom sites, but none of these models improved the agreement factors without introducing many more variables into the refinement. It was concluded that the anisotropic temperature factors for the fluorine atoms best described the PF_6^- units with the fewest variable parameters. Some of the fluorine thermal ellipsoids are very large and elongated (e.g., F(31) and F(34) of **11**), but it was believed that this refinement allowed the best determination of the structure of the bimetallic cation. In addition, in [Zn(tntnim)NiCl](PF$_6$)·C$_2$H$_5$OH, half of the ethanol solvate molecules were disordered and in [Co(tntnam)Ni](PF$_6$)$_3$·4 H$_2$O the water solvate molecules were disordered. The bimetallic complex ions are generally well behaved and there is only one example of refineable disorder (C(26) in [Zn(tntnam)Cu](PF$_6$)$_2$ has two positions of nearly equal occupancy). Many alternative models of the

© 1999 NRC Canada

Table 1. Crystallographic data.

Compound	[Zn(tntnim)NiCl](PF$_6$)·C$_2$H$_5$OH, **5**	Zn(tntnam)Ni](PF$_6$)$_2$, **11**	Zn(tntnam)Cu](PF$_6$)$_2$, **12**	Co(tntnam)Ni(H$_2$O)](PF$_6$)$_3$·4H$_2$O, **14**
Formula	$C_{38}H_{46}N_6O_3ZnNiClPF_6$	$C_{36}H_{44}N_6O_2ZnNiP_2F_{12}$	$C_{36}H_{44}N_6O_2ZnCuP_2F_{12}$	$C_{36}H_{54}N_6O_7CoNiP_3F_{18}$
fw	939.327	1006.801	1011.637	1235.394
Temperature (K)	123(2)	123(2)	123(2)	287(2)
Crystal system	Monoclinic	Tetragonal	Tetragonal	Triclinic
Space group	*Pc*	$P4_12_12$	$P4_12_12$	$P\bar{1}$
a, Å	15.822(2)	24.122(6)	24.180(6)	12.664(2)
b, Å	15.6230(10)	24.122(6)	24.180(6)	12.983(2)
c, Å	16.432(2)	14.397(7)	14.281(4)	16.216(3)
α,°	90	90	90	80.317(14)
β,°	104.570(10)	90	90	69.585(12)
γ,°	90	90	90	74.791(12)
V, Å^3	3931.2(0.7)	8377(5)	8350(4)	2402.4(0.7)
Cell parameters from	25 reflections, 10.31° < Θ < 18.00°	15 reflections, 8.82° < Θ < 10.81°	15 reflections, 11.85° < Θ < 12.47°	25 reflections, 9.98° < Θ < 17.94°
Z	4	8	8	2
D_x, g cm^{-3}	1.587	1.597	1.609	1.708
D_m, g cm^{-3}	Not measured	Not measured	Not measured	Not measured
μ, cm^{-1}	1.273	1.193	1.255	0.960
F(000)	1936	4112	4120	1260
Crystal size, mm	0.45 × 0.35 × 0.25	0.40 × 0.25 × 0.20	0.40 × 0.35 × 0.25	0.45 × 0.35 × 0.30
Crystal color and shape	Green polyhedron	Dark-pink polyhedron	Smokey grey, slightly pink polyhedron	Green polyhedron
Θ_{max}, deg	26.2	25.98	28.42	23.8
Data collected	±*h*, +*k*, +*l*	+*h*, +*k*, +*l*	+*h*, +*k*, +*l*	+*h*, ±*k*, ±*l*
Reflections collected	7179	9752	11314	7406
Unique reflections	6453	4612	4871	7114
R_{merge}	0.031	0.0328	0.0486	0.042
No. with $I \geq 2\sigma(I)$	5826	3250	3452	3443
Completeness to Θ_{max}	81.3%	99.7%	83.1%	95.8%
Abs corr. method	ψ-scan	ψ-scan	ψ-scan	No abs. corr.
Transmission factors	1.0000–0.9334	1.0000–0.9460	1.0000–0.9393	No abs. corr.
Crystal decay, %	Negligible	Negligible	Negligible	13
Data /restraints /parameters	6453 / 2 / 1025	4612 / 0 / 535	4871 / 0 / 542	7114 / 0 / 643
Weighting function, *w* = where $P = (F_o^2 + 2F_c^2)/3$	$1/[\sigma^2(F_o^2)+(0.0491\ P)^2 +1.7271\ P]$	$1/[\sigma^2(F_o^2)+(0.0939\ P)^2 +18.8793\ P]$	$1/[\sigma^2(F_o^2)+(0.0575\ P)^2 +12.7120\ P]$	$1/[\sigma^2(F_o^2)+(0.0671\ P)^2]$
R on F^2 ($I \geq 2\sigma(I)$)	*R* = 0.0371, *wR*2 = 0.0843	*R* = 0.0625, *wR*2 = 0.1549	*R* = 0.0588, *wR*2 = 0.1219	*R* = 0.0573, *wR*2 = 0.1332
R on F^2 (all data)	*R* = 0.0452, *wR*2 = 0.0881	*R* = 0.1034, *wR*2 = 0.1768	*R* = 0.0965, *wR*2 = 0.1366	*R* = 0.1933, *wR*2 = 0.1715
gof on F^2 (all data)	1.064	1.030	1.016	0.941
Max Δ/σ (final cycle)	0.003	0.020	0.000	0.001
Racemic twin components	0.53, 0.47(3)	0.56, 0.44(4)	0.51, 0.49(3)	Centrosymmetric
Abs. struct. parameter	0.0(2)	0.0(3)	0.0(10)	No twinning
Residual den., e/Å^3	0.38, –0.60	1.22, –1.14	0.91, –0.68	0.68, –0.52

Enraf–Nonius CAD-4 diffractometer, Mo K_α radiation (λ = 0.71069 Å), graphite monochromator, ω-scans, $R = \sum ||F_o| - |F_c|| / \sum |F_o|$, $wR2 = \{\sum [w(F_o^2 - F_c^2)^2] / \sum [w(F_o^2)^2]\}^{1/2}$, gof = $\{\sum [w (F_o^2 - F_c^2)^2] / (n - p)\}^{1/2}$, where *n* is the number of reflections and *p* is the total number of parameters refined.

© 1999 NRC Canada

disorders were tried. The models reported in this paper gave the most reasonable results with the simplest models.[7]

Results and discussion

An extensive study on the effect of the closed-site link on the topology of mono- and bimetallic complexes by McCollum et al. has shown that the presence of a 6-membered ring such as trimethylenediamine, tn, at the closed-site link results in mono- and bimetallic complexes that adapt a C_2 symmetrical structure with *trans*-disposed pyridine groups (35, 36) as shown in **4** (Scheme 1). This topological isomer results regardless of the nature of the metal used at the closed site. It has been shown that no scrambling occurs in the preparation of heterobimetallic complexes bearing labile metals (50). Our solid- and liquid-phase results support the absence of scrambling. The diimine groups located at the open site were reduced to amine groups to provide the flexibility required for the bond-length contraction associated with change in oxidation state of metals at the closed and open sites.

Synthesis

Diimine heterobimetallic complexes were prepared by a general method as exemplified in eq. [1]

$$[1] \quad [\text{M(diimine ligand)}(H^+)_2]^{2+} + NiCl_2 \rightleftharpoons [\text{M(diimine ligand)NiCl}]^+ + HCl$$

where M is Co(II) or Zn(II). To drive the reaction to completion, two equivalents of trimethylamine were added. The heterobimetallic complexes prepared in this way contain chloride ion that is bound to the open-site metal at a fifth coordination position. In acetonitrile, all of the chloro complexes were found to be 1:1 electrolytes, indicating that the chloride ligand is bound to the metal in this solvent. The chloride ligand was removed by Ag^+ as a white precipitate in the acetonitrile–acetone solution and gave heterobimetallic complexes of the type $[M^{II}(\text{diimine})Ni]^{2+}$ with molar conductances expected of 2:1 electrolytes in acetonitrile solution (51). The cobalt(II)–nickel(II) complex **7** appears to be reasonably air-stable both in the solid state and in acetonitrile and acetone solutions; however, upon removal of coordinated Cl^- ligand from this complex using Ag^+ salt and exposure to air, a darkening of the solution occurs, suggesting oxidation of the closed-site Co(II). Consistent with this is that compound **8** can be oxidized to the Co(III) complex by ferrocinium ion.

The general method for preparation of diamine heterobimetallic complexes is analogous to the method used for diimine heterobimetallic complexes except that a stronger base, such as LiOH, is required to drive the reaction to completion. Generally the diamine heterobimetallic complexes proved to be more soluble but also more difficult to crystallize than their diimine analogues. All Co(III) heterobimetallic complexes are slightly soluble in water. Aqueous solutions of **13** and **16** undergo loss of chloride ligand over a period of the time as evidenced by increases in molar conductance of the solution and by comparing the UV–VIS spectra of the products with those of **14** and **17**, respectively.

Crystal structures

The fractional atomic coordinates of complexes **5**, **11**, **12,** and **14** are given in Table 2. A number of features of the crystal structures bear noting. First, the structures consist of two metal centres bridged by two phenoxide oxygen atoms. Secondly, the two pyridine groups are bound to the closed-site metals in a *trans* fashion, but there is considerable deviation from ideal octahedral geometry as shown by comparison of the apical angles. Thirdly, the 1,3-diaminopropane in the closed-site link has a skew conformation rather than chair as required for *trans* disposition of the pyridine groups. The bond lengths for M—N, M—O, and M—Cl are generally in the range expected.

*Structure of [Co(tntnam)Ni(H_2O)](PF_6)$_3$·4H_2O, **14***

Two views of the cation of **14** along with the numbering scheme are given in Fig. 1 and selected bond lengths and bond angles are listed in Table 3. The results demonstrate that a molecule of water is bound to the Ni(II) atom at the open site and it is H-bonded to other molecules of water in the lattice. The least-squares plane determined by N(2), N(3), Co, and Ni has all atoms within 0.112(8) Å of the plane. Relative to this plane the distances to O(1), O(2), O(3), N(5) and N(6) are –0.160(6), –0.073(6), 1.502(8), –1.462(8), and 0.248(10) Å, respectively. As a result the Ni(II) at the open site is a five-coordinate ion with a distorted trigonal bipyramidal environment. The Co(III) ion is located in the plane defined by O(1), O(2), N(2), N(3), and the Ni(II) ion is 0.252(6) Å above this plane. The two metal centres are separated by 3.0904(15) Å with Co-O-Ni bridge angles of 102.4 (2)° and 105.1 (2)°. The O(1)-Ni-O(2) angle is compressed to 73.77(18)° whereas the N(5)-Ni-N(6) angle is broadened to 96.7 (3)°. The amine groups at the closed site and open site are in *S*,*S* and *R*,*S* configurations, respectively, for the isomer whose topological chirality about the Co(III) ion is Λ, and vice versa for the Δ isomer.

*Structure of [Zn(tntnim)NiCl]PF_6·C_2H_5OH, **5***

Two views of the cation of **5** along with the numbering scheme are given in Fig. 2. Selected bond lengths and bond angles are listed in Tables 4 and 5. There are two crystallographically different cations in the asymmetric unit (molecule A and molecule B) whose geometric parameters are slightly different (see Tables 4 and 5). In the isomer in which the Zn(II) ion has a Δ configuration, the configuration about the nitrogen atoms of the amine group in the closed-site link are *S*,*S*, and vice versa for the Λ isomer. In mole-

[7] Supplementary material available: tables of anisotropic displacement parameters, hydrogen coordinates and isotropic displacement parameters, torsion angles and planes involving metal atoms for compounds **5**, **11**, **12**, and **14** have been deposited, and may be purchased from: The Depository of Unpublished Data, Document Delivery, CISTI, National Research Council Canada, Ottawa, Canada K1A 0S2. The tables of crystal data and refinement, atomic coordinates, bond lengths and angles, and hydrogen atom coordinates have also been deposited with the Cambridge Crystallographic Data Centre, and can be obtained on request from The Director, Cambridge Crystallographic Data Centre, University Chemical Laboratory, 12 Union Road, Cambridge, CB2 1EZ, U.K.

© 1999 NRC Canada

Table 2. Atomic coordinates ($\times 10^4$) and equivalent isotropic displacement parameters ($Å^2 \times 10^3$). *U*(eq) is defined as one third of the trace of the orthogonalized U_{ij} tensor.

	x	*y*	*z*	*U*(eq)
[Zn(tntnim)NiCl](PF$_6$)·C$_2$H$_5$OH, 5				
ZnA	6323(1)	6212(1)	6912(1)	16(1)
NiA	8044(1)	5074(1)	7393(1)	19(1)
ClA	8629(1)	5054(1)	6253(1)	31(1)
O(1A)	6686(3)	4939(3)	7138(3)	21(1)
O(2A)	7653(3)	6332(3)	7322(3)	17(1)
N(1A)	6277(4)	6358(3)	8213(3)	20(1)
N(2A)	6052(3)	7576(3)	6968(4)	20(1)
N(3A)	4980(3)	5896(3)	6369(3)	19(1)
N(4A)	6297(4)	6246(3)	5585(3)	20(1)
N(5A)	9068(4)	5350(4)	8377(3)	24(1)
N(6A)	8101(4)	3784(4)	7589(4)	24(1)
C(1A)	6590(4)	5764(5)	8809(4)	27(2)
C(2A)	6850(5)	5957(6)	9652(5)	36(2)
C(3A)	6778(5)	6810(5)	9894(5)	32(2)
C(4A)	6472(5)	7409(5)	9297(5)	32(2)
C(5A)	6208(4)	7175(4)	8455(4)	21(2)
C(6A)	5853(4)	7810(4)	7765(4)	25(2)
C(7A)	5366(4)	7875(5)	6232(4)	24(2)
C(8A)	4469(4)	7452(5)	6123(5)	29(2)
C(9A)	4406(4)	6597(5)	6530(4)	27(2)
C(10A)	6938(4)	6552(4)	5254(4)	24(2)
C(11A)	6771(5)	6777(5)	4422(5)	32(2)
C(12A)	5946(5)	6696(5)	3899(4)	32(2)
C(13A)	5298(4)	6377(5)	4237(4)	26(2)
C(14A)	5497(4)	6144(4)	5078(4)	22(2)
C(15A)	4835(5)	5711(5)	5460(4)	26(2)
C(16A)	6890(4)	7995(4)	6909(4)	22(2)
C(17A)	8021(4)	6988(4)	7795(4)	15(1)
C(18A)	8781(4)	6892(4)	8464(4)	17(1)
C(19A)	9162(4)	7610(4)	8920(4)	21(1)
C(20A)	8818(4)	8425(4)	8761(4)	23(2)
C(21A)	8058(4)	8508(4)	8137(4)	21(1)
C(22A)	7661(4)	7821(4)	7637(4)	16(1)
C(23A)	9222(5)	9192(5)	9272(5)	33(2)
C(24A)	9236(4)	6088(4)	8707(4)	20(1)
C(25A)	9741(5)	4695(5)	8725(5)	35(2)
C(26A)	9367(5)	3802(5)	8788(5)	37(2)
C(27A)	8960(5)	3400(5)	7954(5)	30(2)
C(28A)	7469(5)	3247(4)	7318(4)	25(2)
C(29A)	6557(5)	3424(5)	6957(4)	25(2)
C(30A)	6021(5)	2708(4)	6695(4)	26(2)
C(31A)	5141(5)	2771(5)	6429(4)	30(2)
C(32A)	4752(5)	3585(5)	6465(5)	28(2)
C(33A)	5266(4)	4305(4)	6719(4)	22(2)
C(34A)	6183(5)	4255(4)	6940(4)	19(1)
C(35A)	4571(6)	1995(5)	6119(5)	45(2)
C(36A)	4791(4)	5117(5)	6831(4)	25(2)
ZnB	1134(1)	1349(1)	1917(1)	16(1)
NiB	2687(1)	25(1)	2337(1)	20(1)
ClB	3442(2)	–12(1)	1335(2)	52(1)
O(1B)	1355(3)	54(3)	2226(3)	23(1)
O(2B)	2450(3)	1318(3)	2225(3)	21(1)
N(1B)	1200(3)	1683(3)	3237(3)	19(1)
N(2B)	1071(4)	2753(3)	1875(4)	18(1)
N(3B)	–243(4)	1173(3)	1460(3)	18(1)
N(4B)	1015(4)	1208(4)	576(3)	22(1)
N(5B)	3522(4)	191(4)	3449(4)	31(1)
N(6B)	2603(4)	–1283(4)	2498(4)	31(2)
C(1B)	1470(4)	1117(5)	3870(4)	27(2)
C(2B)	1821(5)	1376(5)	4687(5)	35(2)
C(3B)	1917(5)	2234(5)	4862(5)	37(2)
C(4B)	1646(4)	2831(5)	4221(4)	28(2)
C(5B)	1284(4)	2518(4)	3413(4)	25(2)
C(6B)	959(4)	3118(4)	2681(4)	22(2)
C(7B)	377(4)	3046(4)	1147(4)	21(2)
C(8B)	–554(4)	2759(4)	1165(4)	22(2)
C(9B)	–692(4)	1968(4)	1626(4)	23(2)
C(10B)	1660(5)	1359(4)	195(4)	26(2)
C(11B)	1493(5)	1531(5)	–654(5)	31(2)
C(12B)	635(5)	1557(5)	–1124(4)	29(2)
C(13B)	–20(5)	1389(4)	–751(4)	25(2)
C(14B)	186(4)	1210(4)	110(4)	18(1)
C(15B)	–506(4)	962(4)	548(4)	21(1)
C(16B)	1939(4)	3023(4)	1748(4)	20(1)
C(17B)	2912(4)	1933(4)	2694(4)	20(1)
C(18B)	3605(4)	1769(4)	3400(4)	22(2)
C(19B)	4074(4)	2454(5)	3856(4)	26(2)
C(20B)	3862(4)	3292(4)	3649(4)	24(2)
C(21B)	3161(4)	3453(4)	2966(4)	23(2)
C(22B)	2686(4)	2804(4)	2477(4)	19(1)
C(23B)	4358(5)	4023(5)	4167(5)	33(2)
C(24B)	3854(5)	914(5)	3741(4)	29(2)
C(25B)	3883(6)	–575(5)	3932(6)	51(2)
C(26B)	4135(5)	–1236(5)	3368(6)	46(2)
C(27B)	3401(5)	–1791(5)	2891(6)	49(2)
C(28B)	1915(5)	–1729(5)	2181(5)	31(2)
C(29B)	1040(5)	–1414(4)	1854(5)	26(2)
C(30B)	403(5)	–2037(4)	1534(4)	27(2)
C(31B)	–477(5)	–1865(5)	1333(5)	29(2)
C(32B)	–722(5)	–1040(4)	1497(4)	25(2)
C(33B)	–127(4)	–405(4)	1802(4)	21(1)
C(34B)	774(5)	–570(4)	1959(4)	23(2)
C(35B)	–1176(5)	–2517(5)	938(5)	36(2)
C(36B)	–462(4)	467(4)	1985(4)	20(1)
P(1)	2279(1)	4031(1)	9125(2)	37(1)
P(2)	6650(1)	9855(1)	348(1)	33(1)
F(11)	2792(3)	4655(3)	9863(3)	52(1)
F(12)	3035(3)	4155(3)	8642(3)	56(1)
F(13)	1769(3)	3405(3)	8395(3)	56(1)
F(14)	1534(3)	3901(3)	9608(3)	51(1)
F(15)	2803(3)	3231(3)	9620(3)	56(1)
F(16)	1766(3)	4829(3)	8633(3)	52(1)
F(21)	5941(4)	10003(4)	866(4)	76(2)
F(22)	6875(4)	8938(3)	753(3)	56(1)
F(23)	5923(4)	9457(3)	–414(3)	61(2)
F(24)	6413(4)	10778(3)	–58(4)	65(2)
F(25)	7373(4)	10264(4)	1096(4)	86(2)
F(26)	7343(4)	9717(4)	–182(4)	70(2)
O(40)	324(5)	5671(5)	784(4)	72(2)
C(40)	982(6)	5548(5)	1546(5)	50(2)
C(41)	1868(6)	5721(7)	1365(7)	62(3)

© 1999 NRC Canada

Table 2 (*continued*).

	x	*y*	*z*	*U*(eq)
O(50A)	7717(9)	8526(9)	3580(9)	69(4)
C(50A)	7096(14)	9082(14)	3073(14)	57(6)
C(51A)	6333(15)	9408(15)	2979(15)	47(7)
O(50B)	7784(15)	8813(15)	3181(14)	91(6)
C(50B)	7152(14)	8896(14)	3354(14)	32(5)
C(51B)	6269(19)	9504(19)	2778(19)	40(8)
[Zn(tntnam)Ni](PF$_6$)$_2$, 11				
Zn	7706(1)	4412(1)	1025(1)	22(1)
Ni	8160(1)	3319(1)	238(1)	30(1)
P(1)	1403(1)	6524(1)	1937(2)	34(1)
P(2)	5079(3)	5074(3)	2670(6)	62(2)
P(3)	1997(2)	8003(2)	7500	54(1)
F(11)	1328(3)	6273(3)	2962(4)	50(2)
F(12)	1002(3)	7016(3)	2186(5)	61(2)
F(13)	1801(3)	6012(4)	1705(5)	67(2)
F(14)	894(3)	6164(3)	1585(5)	42(2)
F(15)	1492(3)	6764(3)	905(4)	56(2)
F(16)	1919(3)	6875(4)	2299(5)	72(3)
F(21)	5400(5)	5387(5)	1887(11)	169(7)
F(22)	4858(5)	5505(5)	3127(11)	167(7)
F(23)	5524(7)	4849(7)	3137(10)	228(12)
F(31)	2356(7)	7644(7)	7500	610(60)
F(32)	1606(5)	7584(4)	6995(6)	90(3)
F(33)	1766(12)	7862(14)	8258(7)	490(30)
F(34)	1631(4)	8369(4)	7500	480(50)
O(1)	8391(3)	4061(3)	412(4)	23(2)
O(2)	7490(3)	3589(3)	781(5)	27(2)
N(1)	7326(3)	4607(3)	–324(5)	28(2)
N(2)	6896(3)	4670(3)	1439(6)	28(2)
N(3)	8113(3)	5170(3)	1343(5)	23(2)
N(4)	8017(3)	4233(3)	2401(5)	22(2)
N(5)	7777(4)	2655(4)	–67(7)	44(2)
N(6)	8885(4)	3118(3)	–218(6)	30(2)
C(1)	7533(4)	4427(4)	–1135(7)	30(2)
C(2)	7202(5)	4405(5)	–1926(8)	43(3)
C(3)	6660(5)	4540(6)	–1861(8)	51(3)
C(4)	6438(5)	4720(5)	–1019(8)	40(3)
C(5)	6788(4)	4730(4)	–273(7)	31(2)
C(6)	6581(4)	4929(5)	679(7)	32(2)
C(7)	6933(4)	5046(4)	2249(7)	32(2)
C(8)	7243(5)	5594(4)	2066(8)	38(3)
C(9)	7680(4)	5609(4)	1301(7)	32(2)
C(10)	7918(4)	3771(4)	2895(7)	30(2)
C(11)	8059(4)	3717(4)	3815(7)	31(2)
C(12)	8293(5)	4166(5)	4264(8)	38(3)
C(13)	8391(4)	4641(4)	3769(6)	28(2)
C(14)	8260(4)	4660(4)	2821(6)	25(2)
C(15)	8406(4)	5162(4)	2245(6)	27(2)
C(16)	6618(4)	4142(4)	1733(7)	28(2)
C(17)	6969(4)	3474(4)	523(7)	28(2)
C(18)	6861(4)	3099(4)	–208(7)	27(2)
C(19)	6315(5)	2992(5)	–464(8)	38(3)
C(20)	5872(4)	3245(5)	–37(8)	34(2)
C(21)	5989(4)	3619(5)	678(7)	36(3)
C(22)	6520(4)	3738(4)	954(7)	29(2)
C(23)	5280(5)	3117(6)	–329(9)	52(3)
C(24)	7333(4)	2823(4)	–711(7)	34(2)

Table 2 (*continued*).

	x	*y*	*z*	*U*(eq)
C(25)	8058(5)	2166(5)	–394(10)	53(3)
C(26)	8528(7)	2250(5)	–980(10)	62(4)
C(27)	9028(5)	2537(5)	–515(10)	47(3)
C(28)	9300(5)	3309(4)	450(8)	39(3)
C(29)	9370(4)	3926(4)	503(6)	23(2)
C(30)	9904(4)	4169(4)	545(7)	31(2)
C(31)	9980(4)	4734(4)	595(7)	26(2)
C(32)	9522(4)	5053(4)	601(6)	21(2)
C(33)	8975(4)	4857(4)	545(7)	23(2)
C(34)	8900(4)	4276(4)	478(6)	20(2)
C(35)	10558(5)	4975(4)	611(7)	33(2)
C(36)	8502(4)	5245(4)	540(6)	23(2)
[Zn(tntnam)Cu](PF$_6$)$_2$, 12				
Zn	7698(1)	4422(1)	1018(1)	20(1)
Cu	8157(1)	3325(1)	211(1)	23(1)
P(1)	1398(1)	6551(1)	1991(2)	35(1)
P(2)	5082(2)	5074(2)	2664(4)	41(1)
P(3)	2068(1)	7932(1)	7500	34(1)
F(11)	1326(3)	6303(3)	3025(4)	61(2)
F(12)	976(3)	7024(3)	2225(5)	69(2)
F(13)	1806(3)	6054(4)	1759(5)	82(3)
F(14)	903(2)	6166(2)	1629(5)	53(2)
F(15)	1471(3)	6773(3)	943(4)	59(2)
F(16)	1896(3)	6923(4)	2320(4)	98(3)
F(21)	5388(3)	5371(4)	1867(8)	146(5)
F(22)	4863(4)	5504(4)	3137(8)	127(4)
F(23)	5535(5)	4858(5)	3144(7)	163(6)
F(31)	2534(3)	7466(3)	7500	152(8)
F(32)	1666(3)	7507(3)	6983(4)	56(2)
F(33)	1641(3)	8359(3)	7500	197(11)
F(34)	1902(5)	7666(5)	8423(5)	144(5)
O(1)	8397(2)	4079(2)	400(4)	22(1)
O(2)	7479(2)	3603(2)	765(4)	22(1)
N(1)	7320(3)	4612(3)	–353(4)	19(2)
N(2)	6891(3)	4686(3)	1413(5)	24(2)
N(3)	8104(3)	5181(3)	1337(5)	23(2)
N(4)	8008(3)	4242(3)	2415(5)	23(2)
N(5)	7763(3)	2647(3)	–163(7)	44(2)
N(6)	8912(3)	3096(3)	–116(7)	46(2)
C(1)	7527(3)	4427(3)	–1170(5)	22(2)
C(2)	7195(3)	4387(4)	–1956(6)	30(2)
C(3)	6644(4)	4524(4)	–1899(7)	40(2)
C(4)	6428(4)	4698(4)	–1063(7)	33(2)
C(5)	6782(4)	4736(4)	–307(6)	28(2)
C(6)	6567(4)	4943(4)	641(6)	28(2)
C(7)	6928(4)	5064(4)	2227(6)	30(2)
C(8)	7224(4)	5622(4)	2027(7)	38(2)
C(9)	7676(4)	5625(3)	1284(6)	32(2)
C(10)	7914(4)	3771(3)	2888(6)	27(2)
C(11)	8064(3)	3720(4)	3820(6)	28(2)
C(12)	8310(4)	4168(4)	4261(6)	34(2)
C(13)	8393(4)	4646(4)	3776(6)	30(2)
C(14)	8253(3)	4671(3)	2835(6)	22(2)
C(15)	8379(4)	5178(3)	2261(6)	27(2)
C(16)	6607(4)	4167(4)	1720(6)	28(2)
C(17)	6952(3)	3480(4)	511(6)	27(2)
C(18)	6842(3)	3105(3)	–202(6)	26(2)

© 1999 NRC Canada

Table 2 (*continued*).

	x	*y*	*z*	*U*(eq)
C(19)	6298(4)	2988(4)	–447(7)	35(2)
C(20)	5857(4)	3248(4)	–9(6)	28(2)
C(21)	5973(4)	3627(4)	679(6)	31(2)
C(22)	6509(3)	3750(3)	958(6)	25(2)
C(23)	5267(4)	3122(5)	–292(7)	45(3)
C(24)	7305(4)	2828(4)	–726(7)	38(2)
C(25)	8071(4)	2168(4)	–565(9)	54(3)
C(26A)	8649(8)	2110(9)	–180(16)	37(5) occ. = 0.47
C(26B)	8569(9)	2252(8)	–937(15)	45(5) occ. = 0.53
C(27)	9033(5)	2510(4)	–387(9)	54(3)
C(28)	9289(4)	3314(4)	549(8)	47(3)
C(29)	9375(4)	3937(3)	540(6)	26(2)
C(30)	9904(4)	4158(4)	598(6)	29(2)
C(31)	9987(4)	4733(3)	653(5)	21(2)
C(32)	9522(4)	5066(3)	644(6)	23(2)
C(33)	8986(3)	4859(3)	579(5)	18(2)
C(34)	8907(3)	4285(3)	505(5)	18(2)
C(35)	10564(4)	4982(4)	673(7)	35(2)
C(36)	8503(4)	5253(3)	560(6)	23(2)
[Co(tntnam)Ni(H_2O)][(PF_6)$_3$·4H_2O, 14				
P(1)	1988(2)	9731(2)	6257(2)	54(1)
P(2)	9049(2)	6907(2)	7641(2)	64(1)
P(3)	3904(3)	7720(2)	9253(2)	64(1)
F(11)	2470(6)	8656(5)	5818(6)	128(3)
F(12)	3260(5)	9939(5)	5855(4)	93(2)
F(13)	1748(5)	10257(7	5364(4)	125(3)
F(14)	724(5)	9550(5)	6631(5)	104(2)
F(15)	1560(6)	10836(6	6628(6)	150(4)
F(16)	2237(6)	9207(8)	7113(5)	150(3)
F(21)	10362(4)	6928(4)	7328(4)	84(2)
F(22)	9328(5)	6110(5)	6901(5)	101(2)
F(23)	8840(5)	7882(4)	6960(4)	96(2)
F(24)	7736(5)	6889(6)	7976(6)	134(3)
F(25)	9299(7)	5898(6)	8282(5)	139(3)
F(26)	8797(7)	7710(7)	8332(5)	146(3)
F(31)	3820(6)	8439(5)	8384(4)	100(2)
F(32)	2656(6)	8291(7)	9741(5)	137(3)
F(33)	4008(7)	7000(6)	10122(4)	120(3)
F(34)	3457(9)	6863(5)	8980(5)	145(3)
F(35)	4403(10)	8545(7)	9495(6)	169(4)
F(36)	5138(7)	7132(8)	8733(6)	173(4)
Ni	4885(1)	4233(1)	7689(1)	40(1)
Co	5669(1)	1884(1)	7214(1)	28(1)
O(1)	4638(4)	3202(4)	6989(3)	32(1)
O(2)	6042(4)	2880(4)	7752(3)	32(1)
O(3)	4499(6)	4427(5)	9007(4)	69(2)
O(4)	2299(11)	4948(11)	12(9)	212(6)
O(5)	940(2)	128(2)	1087(17)	412(15)
O(6)	629(5)	528(5)	928(4)	750(40)
O(7)	87(2)	643(2)	939(2)	237(10) occ. = 0.64
O(8)	151(4)	718(4)	860(3)	243(18) occ. = 0.36
N(1)	6952(5)	2148(5)	6187(4)	32(2)
N(2)	6841(5)	642(4)	7519(4)	30(2)
N(3)	5053(5)	1034(4)	6651(4)	29(2)
N(4)	4418(5)	1626(4)	8271(4)	31(2)
N(5)	6008(6)	5215(5)	7282(4)	45(2)
N(6)	3499(6)	5344(5)	7567(5)	51(2)

Table 2 (*concluded*).

	x	*y*	*z*	*U*(eq)
C(1)	6919(7)	3006(6)	5598(5)	39(2)
C(2)	7904(8)	3237(7)	4968(6)	47(2)
C(3)	8962(8)	2568(8)	4937(6)	54(2)
C(4)	8987(7)	1687(7)	5532(6)	47(2)
C(5)	7970(6)	1493(6)	6148(5)	30(2)
C(6)	7940(6)	513(6)	6769(5)	40(2)
C(7)	6419(7)	–369(6)	7765(5)	41(2)
C(8)	6232(7)	–780(6)	7018(6)	52(2)
C(9)	5895(7)	32(6)	6319(6)	42(2)
C(10)	4192(7)	1984(6)	9057(5)	41(2)
C(11)	3260(7)	1831(8)	9754(6)	55(2)
C(12)	2495(8)	1320(8)	9644(6)	63(3)
C(13)	2716(7)	940(7)	8845(6)	51(2)
C(14)	3680(6)	1119(6)	8166(5)	32(2)
C(15)	3952(6)	766(6)	7269(5)	38(2)
C(16)	7086(7)	884(6)	8313(5)	38(2)
C(17)	7091(6)	2804(6)	7821(5)	33(2)
C(18)	7620(6)	3684(6)	7594(6)	41(2)
C(19)	8640(7)	3566(8)	7768(6)	53(2)
C(20)	9182(7)	2612(8)	8109(6)	54(2)
C(21)	8676(7)	1742(7)	8277(6)	48(2)
C(22)	7651(6)	1824(6)	8128(5)	35(2)
C(23)	10293(8)	2509(9)	8306(8)	84(4)
C(24)	7239(7)	4668(7)	7034(6)	53(2)
C(25)	5831(9)	6055(7)	6573(7)	68(3)
C(26)	4607(9)	6710(8)	6725(7)	71(3)
C(27)	3726(9)	6099(7)	6781(7)	63(3)
C(28)	2557(7)	4823(7)	7659(6)	54(3)
C(29)	2774(6)	4151(6)	6915(5)	39(2)
C(30)	1928(7)	4286(7)	6512(6)	47(2)
C(31)	1999(7)	3635(7)	5918(6)	50(2)
C(32)	2952(7)	2802(6)	5696(5)	42(2)
C(33)	3847(6)	2643(6)	6048(5)	35(2)
C(34)	3758(6)	3328(6)	6650(5)	32(2)
C(35)	1042(8)	3769(9)	5509(8)	85(4)
C(36)	4816(6)	1686(6)	5843(5)	36(2)

cule A, the least-squares plane determined by N(2), N(3), Zn, and Ni has all atoms within 0.003(6) Å of the plane. Relative to this plane, the distances to O(1), O(2), N(5), N(6), and Cl are +0.433(6), –0.116(6), +0.954(8), +0.564(8), and –2.165(2) Å, respectively. In molecule B, the least-squares plane determined by N(2), N(3), Zn, and Ni has all atoms within 0.060(8) Å of the plane. Relative to this plane, the distances to O(1), O(2), N(5), N(6), and Cl are +0.434(6), –0.095(6), +1.440(7), +0.367(9), and –1.990(3) Å, respectively. As a result, the open-site metal has a distorted trigonal bipyramidal environment. The imine bond lengths, C(28A)—N(6A), C(24A)—N(5A), C(28B)—N(6B), and C(24B)—N(5B) are 1.294(9), 1.274(9), 1.287(10), and 1.287(9) Å, respectively, and are shorter with respect to the amine bond lengths C(36A)—N(3A), C(16A)—N(2A), C(36B)—N(3B), and C(16B)—N(2B) with 1.503(9), 1.504(8), 1.493(8), 1.501(8) Å, respectively. The intermetallic separations between Zn(II) and Ni(II) ions in molecules A and B are 3.1811(11) and 3.1526(11) Å, respectively.

© 1999 NRC Canada

Fig. 1. Two views of the molecular structure of the bimetallic cation of $[Co(tntnam)Ni(H_2O)](PF_6)_3 \cdot 4H_2O$, **14**, drawn with 30% probability ellipsoids. The hydrogen atoms have been deleted for clarity.

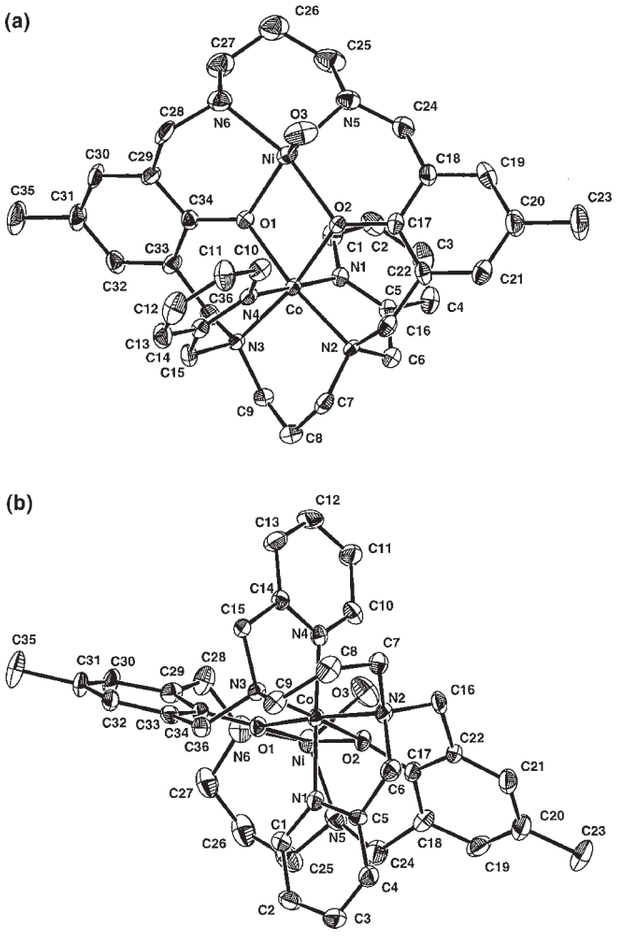

Fig. 2. Two views of the molecular structure of the bimetallic cation of $[Zn(tntnim)NiCl](PF_6) \cdot C_2H_5OH$, **5,** drawn with 50% probability ellipsoids. The hydrogen atoms have been deleted for clarity.

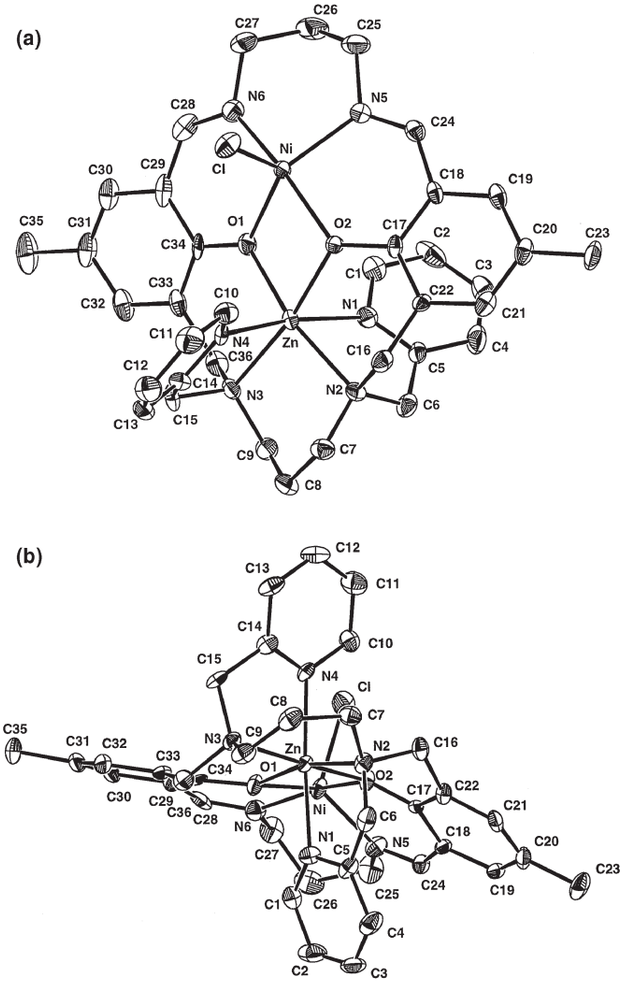

*Structure of [Zn(tntnam)Ni]$(PF_6)_2$, **11***

Two views of the cation of **11** along with the numbering scheme are given in Fig. 3 and selected bond lengths and bond angles are listed in Table 6. The isomer whose topological chirality about the Zn(II) ion is Λ has the *R,R* configuration for both nitrogen atoms of the amine groups at the closed site and the open site, and vice versa for the Δ isomer. The Zn(II) and Ni(II) ions are in the macrocyclic plane defined by N(2), N(3), O(1), O(2), N(5), and N(6) atoms. The O(2)-Ni-N(6) and O(1)-Ni-N(5) bond angles are 172.6 (3)° and 166.3 (4)°, respectively. The two metal centres are separated by 3.0711(18) Å with Zn-O-Ni bridge angles of 102.1 (3)° and 100.5 (3)°. The O(1)-Ni-O(2) angle is compressed to 82.6(3)° whereas the N(5)-Ni-N(6) angle is broadened to 98.6(4)°.

*Structure of [Zn(tntnam)Cu]$(PF_6)_2$, **12***

Two views of the cation of **12** along with the numbering scheme are given in Fig. 4. Selected bond lengths and bond angles are listed in Table 7. The isomer whose topological chirality about the Zn(II) ion is Λ has the *R,R* configuration for both nitrogen atoms of the amine groups at the closed site and the open site, and vice versa for the Δ isomer. Both Zn(II) and Cu(II) ions are in the same plane defined by N(2), N(3), O(1), O(2), N(5), and N(6) atoms. The O(2)-Cu-N(6) bond angle is 168.5 (3)° and the opposing angle O(1)-Cu-N(5) is 165.5 (3)°. The Cu atom and four of the atoms of the open-site link (N(5), N(6) C(25), and C(27)) are located in the same plane, but the disordered atom C(26) is out of the plane. The crystal structure data indicate that there are two different conformers of the open-site link. The only difference between these two conformers is the position of the C(26) atom. With respect to the plane defined by the open-site link, C(26) is above the plane in one conformer but below in the other. The intermetallic distance between the two metal centres is close to that found in compound **11** at 3.0983(15) Å.

IR spectra

The infrared spectra of imine and amine bimetallic complexes are generally similar but at the same time compli-

© 1999 NRC Canada

Table 3. Selected bond distances and angles for $[Co(tntnam)Ni(H_2O)](PF_6)_3 \cdot 5H_2O$, **14**[a]

Bond distances (Å)			
Co—Ni	3.0904(15)	Ni—O(1)	2.039(5)
Co—O(1)	1.927(5)	Ni—O(2)	1.984(4)
Co—O(2)	1.909(5)	Ni—O(3)	2.063(6)
Co—N(1)	1.935(6)	Ni—N(5)	2.025(6)
Co—N(2)	2.009(5)	Ni—N(6)	2.005(7)
Co—N(3)	1.987(6)	O(1)—C(34)	1.369(8)
Co—N(4)	1.936(6)	O(2)—C(17)	1.349(8)
Bond angles (deg)			
O(1)-Co-O(2)	78.03(19)	Ni-O(1)-Co	102.4(2)
O(1)-Co-N(3)	92.8(2)	Ni-O(2)-Co	105.1(2)
O(1)-Co-N(4)	86.8(2)	O(1)-Ni-N(6)	92.4(2)
O(1)-Co-N(1)	94.1(2)	O(1)-Ni-O(3)	136.0(2)
O(1)-Co-N(2)	171.6(2)	O(1)-Ni-N(5)	128.9(2)
O(2)-Co-N(2)	93.6(2)	O(2)-Ni-O(3)	92.4(2)
O(2)-Co-N(3)	170.6(2)	O(2)-Ni-N(5)	96.5(2)
O(2)-Co-N(4)	92.2(2)	O(2)-Ni-N(6)	165.1(2)
O(2)-Co-N(1)	85.9(2)	O(3)-Ni-N(5)	93.5(3)
N(1)-Co-N(2)	84.4(2)	O(3)-Ni-N(6)	93.7(3)
N(1)-Co-N(3)	97.1(2)	N(5)-Ni-N(6)	96.7(3)
N(1)-Co-N(4)	177.7(3)	Ni-O(2)-C(17)	125.5(4)
N(2)-Co-N(3)	95.5(2)	Ni-O(1)-C(34)	128.2(4)
N(2)-Co-N(4)	94.5(2)	Co-O(2)-C(17)	124.8(4)
N(3)-Co-N(4)	85.0(2)	Co-O(1)-C(34)	127.4(4)
O(1)-Ni-O(2)	73.77(18)		

[a]Estimated standard deviations are given in parentheses.

Table 4. Selected bond distances and angles for $[Zn(tntnim)NiCl]PF_6 \cdot C_2H_5OH$, **5**, molecule A.[a]

Bond distances (Å)			
Zn(A)—Ni(A)	3.1811(11)	Ni(A)—Cl(A)	2.288(2)
Zn(A)—O(1A)	2.078(4)	Ni(A)—N(5A)	2.026(6)
Zn(A)—O(2A)	2.050(5)	Ni(A)—N(6A)	2.040(6)
Zn(A)—N(1A)	2.170(6)	O(1A)—C(34A)	1.322(7)
Zn(A)—N(2A)	2.180(5)	O(2A)—C(17A)	1.328(7)
Zn(A)—N(3A)	2.146(5)	N(2A)—C(16A)	1.504(8)
Zn(A)—N(4A)	2.171(6)	N(3A)—C(36A)	1.502(9)
Ni(A)—O(1A)	2.095(5)	N(5A)—C(24A)	1.274(9)
Ni(A)—O(2A)	2.055(4)	N(6A)—C(28A)	1.294(9)
Bond angles (deg)			
O(1A)-Zn(A)-O(2A)	79.31(16)	Ni(A)-O(1A)-Zn(A)	99.34(18)
O(1A)-Zn(A)-N(3A)	93.07(19)	Ni(A)-O(2A)-Zn(A)	101.60(18)
O(1A)-Zn(A)-N(4A)	97.91(91)	O(1A)-Ni(A)-N(6A)	86.2(2)
O(1A)-Zn(A)-N(1A)	90.0(2)	O(1A)-Ni(A)-N(5A)	139.0(2)
O(1A)-Zn(A)-N(2A)	167. (2)	O(2A)-Ni(A)-N(5A)	90.6(2)
O(2A)-Zn(A)-N(2A)	95.38(18)	O(2A)-Ni(A)-N(6A)	162.6(2)
O(2A)-Zn(A)-N(3A)	170.1(2)	O(1A)-Ni(A)-Cl(A)	116.18(14)
O(2A)-Zn(A)-N(4A)	95.0(2)	O(2A)-Ni(A)-Cl(A)	98.36(15)
O(2A)-Zn(A)-N(1A)	87.3(2)	N(5A)-Ni(A)-Cl(A)	104.45(17)
N(1A)-Zn(A)-N(2A)	78.4(2)	N(6A)-Ni(A)-Cl(A)	96.07(17)
N(1A)-Zn(A)-N(3A)	99.1(2)	N(5A)-Ni(A)-N(6A)	95.1(2)
N(1A)-Zn(A)-N(4A)	172.02(19)	Ni(A)-O(2A)-C(17A)	128.5(4)
N(2A)-Zn(A)-N(3A)	93.3(2)	Ni(A)-O(1A)-C(34A)	130.8(4)
N(2A)-Zn(A)-N(4A)	93.7(2)	Zn(A)-O(2A)-C(17A)	121.7(4)
N(3A)-Zn(A)-N(4A)	79.7(2)	Zn(A)-O(1A)-C(34A)	127.4(4)
O(1A)-Ni(A)-O(2A)	78.78(17)		

[a]Estimated standard deviations are given in parentheses.

© 1999 NRC Canada

Table 5. Selected bond distances and angles for [Zn(tntnim)NiCl]$PF_6 \cdot C_2H_5OH$, **5**, molecule B.[a]

Bond distances (Å)			
Zn(B)—Ni(B)	3.1526(11)	Ni(B)—Cl(B)	2.265(2)
Zn(B)—O(1B)	2.093(4)	Ni(B)—N(5B)	1.984(6)
Zn(B)—O(2B)	2.015(5)	Ni(B)—N(6B)	2.069(6)
Zn(B)—N(1B)	2.207(5)	O(1B)—C(34B)	1.336(8)
Zn(B)—N(2B)	2.197(5)	O(2B)—C(17B)	1.331(8)
Zn(B)—N(3B)	2.135(6)	N(2B)—C(16B)	1.501(8)
Zn(B)—N(4B)	2.175(6)	N(3B)—C(36B)	1.493(8)
Ni(B)—O(1B)	2.070(5)	N(5B)—C(24B)	1.287(9)
Ni(B)—O(2B)	2.055(4)	N(6B)—C(28B)	1.287(10)
Bond angles (deg)			
O(1B)-Zn(B)-O(2B)	79.47(18)	Ni(B)-O(1B)-Zn(B)	98.45(19)
O(1B)-Zn(B)-N(3B)	93.14(19)	Ni(B)-O(2B)-Zn(B)	101.5(2)
O(1B)-Zn(B)-N(4B)	96.6(2)	O(1B)-Ni(B)-N(6B)	86.3(2)
O(1B)-Zn(B)-N(1B)	91.50(19)	O(1B)-Ni(B)-N(5B)	120.3(2)
O(1B)-Zn(B)-N(2B)	167.5(2)	O(2B)-Ni(B)-N(5B)	91.1(2)
O(2B)-Zn(B)-N(2B)	93.84(19)	O(2B)-Ni(B)-N(6B)	165.1(2)
O(2B)-Zn(B)-N(3B)	169.41(19)	O(1B)-Ni(B)-Cl(B)	130.39(16)
O(2B)-Zn(B)-N(4B)	94.2(2)	O(2B)-Ni(B)-Cl(B)	94.48(15)
O(2B)-Zn(B)-N(1B)	88.2(2)	N(5B)-Ni(B)-Cl(B)	108.8(2)
N(1B)-Zn(B)-N(2B)	77.6(2)	N(6B)-Ni(B)-Cl(B)	86.3(2)
N(1B)-Zn(B)-N(3B)	99.7(2)	N(5B)-Ni(B)-N(6B)	93.5(3)
N(1B)-Zn(B)-N(4B)	171.8(2)	Ni(B)-O(2B)-C(17B)	126.6(4)
N(2B)-Zn(B)-N(3B)	94.78(19)	Ni(B)-O(1B)-C(34B)	127.9(4)
N(2B)-Zn(B)-N(4B)	94.4(2)	Zn(B)-O(2B)-C(17B)	120.8(4)
N(3B)-Zn(B)-N(4B)	79.0(2)	Zn(B)-O(1B)-C(34B)	124.5(4)
O(1B)-Ni(B)-O(2B)	79.12(18)		

[a]Estimated standard deviations are given in parentheses.

cated. Significant differences between the imines and amines in the spectra are the emergence of a sharp, but weak, band at 3268 cm^{-1}, which is attributed to the N–H stretch of the quaternized amine, and the disappearance of the strong band at 1643 cm^{-1}, corresponding to the C=N stretch of the imine groups (52). Appearance of a band near 1550 cm^{-1} for all of the complexes is assigned to the skeletal vibration of the aromatic rings (53). A broad signal centred at around 3500 cm^{-1} for **14** is likely the stretching modes for the mixed form of coordinated and uncoordinated water. The presence of a sharp band at 2316 cm^{-1} for **17** is due to the presence of lattice CH_3CN.

Electrospray mass spectra

Electrospray mass spectrometry is proving to be a very powerful analytical tool for characterization of macrocyclic complexes in the liquid phase because it allows for transfer of preexisting ions from solution to the gas phase with minimal fragmentation. All major signals for the complexes, including the assignments, are listed in Table 8. Particularly noteworthy is that the presence of a given metal centre is accompanied by a set of signals for each *m*/*z* due to relative isotope abundance. The number and relative intensities of these peaks are unique for each bimetallic complex and thus indicative of the formation of the expected heterobimetallic complexes. Multiply charged ions are usually harder to observe and they give signals of low intensities in ESMS because of the formation of ion-pair adducts with counterions in the solution (54). Proton loss, as observed here in some cases, is also a common mechanism in the ESMS as it reduces the charge on the multicharged compounds (55).

Magnetic moments

The magnetic susceptibilities of all of the paramagnetic complexes were determined in acetone solution at 25°C by the Evans ^1H NMR method (56). These are tabulated in Table 9, together with the magnetic susceptibilities of selected complexes in the solid state and the calculated spin-only values for these complexes. All of the Co(III) complexes are found to be spin paired. For the bimetallic complexes containing Co(III) or Zn(II) at the closed site, the calculated magnetic moments fall within the ranges expected for magnetically dilute complexes containing a single paramagnetic ion (38). A magnetic moment of 1.6 BM for **12** and **15** indicates the presence of one unpaired electron per molecule. The solution magnetic moments of heterobimetallic complexes with Ni(II) at the open site are normal for two unpaired electrons per molecule. However, **6** exhibits a diamagnetic property in the solid state. The different magnetic behaviour of **6** in the solid state and in solution may be due to a change in coordination geometry of the Ni(II) ion in solution as a result of coordination of solvent molecule(s). The cobalt(II)–nickel(II) complex **7**, which contains two paramagnetic ions, exhibits a magnetic moment of 5.3 BM, which is slightly less than the spin-only value. This suggests that a weak antiferromagnetic exchange coupling exists between neighbouring paramagnetic ions, presumably through the phenoxide bridging ligands (57–60).

© 1999 NRC Canada

Fig. 3. Two views of the molecular structure of the bimetallic cation of $[Zn(tntnam)Ni](PF_6)_2$, **11**, drawn with 50% probability ellipsoids. The hydrogen atoms have been deleted for clarity.

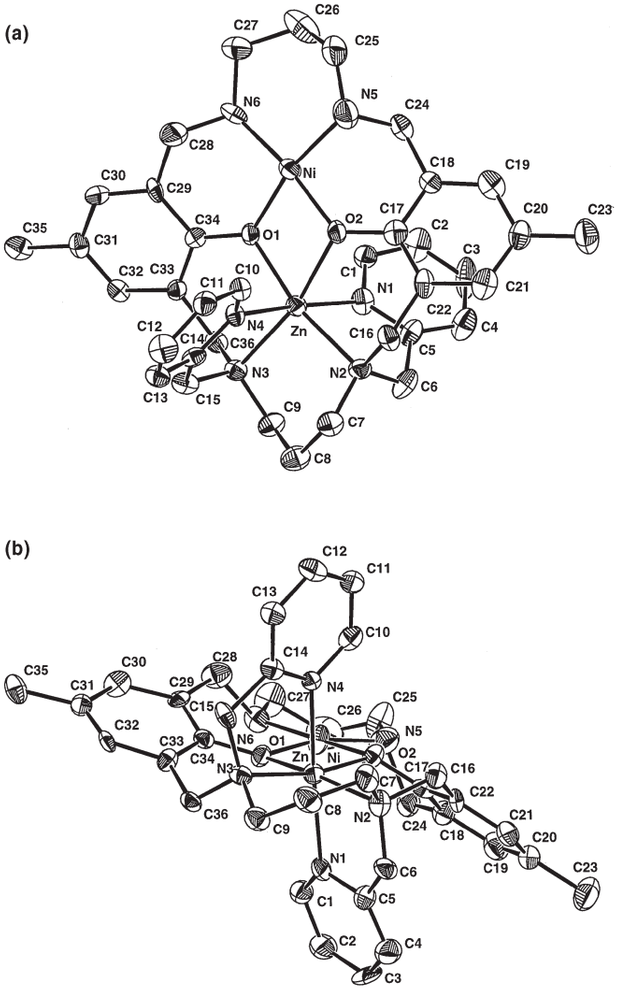

Table 6. Selected bond distances and angles for $[Zn(tntnam)Ni](PF_6)_2$, **11**.[a]

Bond distances (Å)			
Zn—Ni	3.0711(18)	Ni—O(1)	1.892(6)
Zn—O(1)	2.056(6)	Ni—O(2)	1.910(7)
Zn—O(2)	2.081(7)	Ni—N(5)	1.901(10)
Zn—N(1)	2.198(8)	Ni—N(6)	1.930(9)
Zn—N(2)	2.135(8)	O(1)—C(34)	1.337(11)
Zn—N(3)	2.126(8)	O(2)—C(17)	1.340(12)
Zn—N(4)	2.161(8)		
Bond angles (deg)			
O(1)-Zn-O(2)	74.7(2)	N(3)-Zn-N(4)	79.2(3)
O(1)-Zn-N(3)	94.3(3)	O(1)-Ni-O(2)	82.6(3)
O(1)-Zn-N(4)	91.9(3)	Ni-O(1)-Zn	102.1(3)
O(1)-Zn-N(1)	92.5(3)	Ni-O(2)-Zn	100.5(3)
O(1)-Zn-N(2)	167.2(3)	O(1)-Ni-N(6)	90.9(3)
O(2)-Zn-N(2)	95.5(3)	O(1)-Ni-N(5)	166.3(4)
O(2)-Zn-N(3)	166.5(3)	O(2)-Ni-N(5)	88.3(4)
O(2)-Zn-N(4)	93.0(3)	O(2)-Ni-N(6)	172.6(3)
O(2)-Zn-N(1)	87.2(3)	N(5)-Ni-N(6)	98.6(4)
N(1)-Zn-N(2)	78.6(3)	Ni-O(2)-C(17)	127.5(6)
N(1)-Zn-N(3)	101.4(3)	Ni-O(1)-C(34)	130.3(6)
N(1)-Zn-N(4)	175.5(3)	Zn-O(2)-C(17)	118.7(6)
N(2)-Zn-N(3)	96.4(3)	Zn-O(1)-C(34)	123.3(5)
N(2)-Zn-N(4)	96.9(3)		

[a]Estimated standard deviations are given in parentheses.

NMR spectra

The bimetallic complexes of macrocyclic amine ligands are potentially more complicated than their imine analogues. This complexity arises from the chirality of the nitrogen atoms of the amine groups at the open site coupled with the topology of the closed site. McCollum et al. (35) have shown that with a single chiral isomer for the closed-site bimetallic complexes type **18**, the open-site nitrogen groups can be (*S*,*S*), (*R*,*R*), or (*R*,*S*). The first two are C_2 symmetric and the third is C_1. The aforementioned isomers can be identified by the chemical shifts of the α-pyridyl and *p*-tolylmethyl proton signals. The ^{1}H NMR and ^{13}C NMR spectra of the diamagnetic **16**, obtained in acetone-d_6 solution at 25°C, indicate a structure of C_1 symmetry, but upon addition of 1 equiv. of $AgPF_6$ to remove the coordinated chloride, the ^{1}H NMR and ^{13}C NMR spectra become consistent with a C_2 symmetric complex. Also, equilibrium among isomers has been reported for di-zinc complexes (35). However, the presence of other isomers was not detected in **16** and **17**. Since ^{1}H NMR spectroscopy does not distinguish between the (*S*,*S*) and (*R*,*R*) diastereomers, the assignment of the isomer remains open, but these results do indicate that the structures of cobalt(III)–zinc(II) complexes in solution contain *trans*-disposed pyridine ligands above and below the mean macrocyclic plane as in **4**, Scheme 1.

Electronic absorption spectroscopy

The purpose of this study was to correlate the *d*–*d* transi-

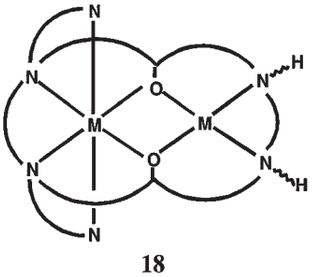

18

tions with the geometries of the metal ions and to determine whether any intravalence transitions occurred in the bimetallic complexes (61). However, the latter do not appear to be present. The electronic absorption spectra of **5–17** were recorded in room-temperature acetonitrile solution over the range 300–2000 nm. These regions encompass the *d*–*d* transitions at the lower energies and some of the metal–ligand charge-transfer bands and the $\pi \rightarrow \pi^*$ azomethine transitions at higher energies (62). Table 10 lists the positions and intensities of azomethine, phenolate charge-transfer, and the *d*–*d* bands observed in the spectra of bimetallic complexes. The azomethine chromophores in all of the diimine com-

© 1999 NRC Canada

Fig. 4. Two views of the molecular structure of the bimetallic cation of $[Zn(tntnam)Cu](PF_6)_2$, **12**, drawn with 50% probability ellipsoids. The hydrogen atoms have been deleted for clarity.

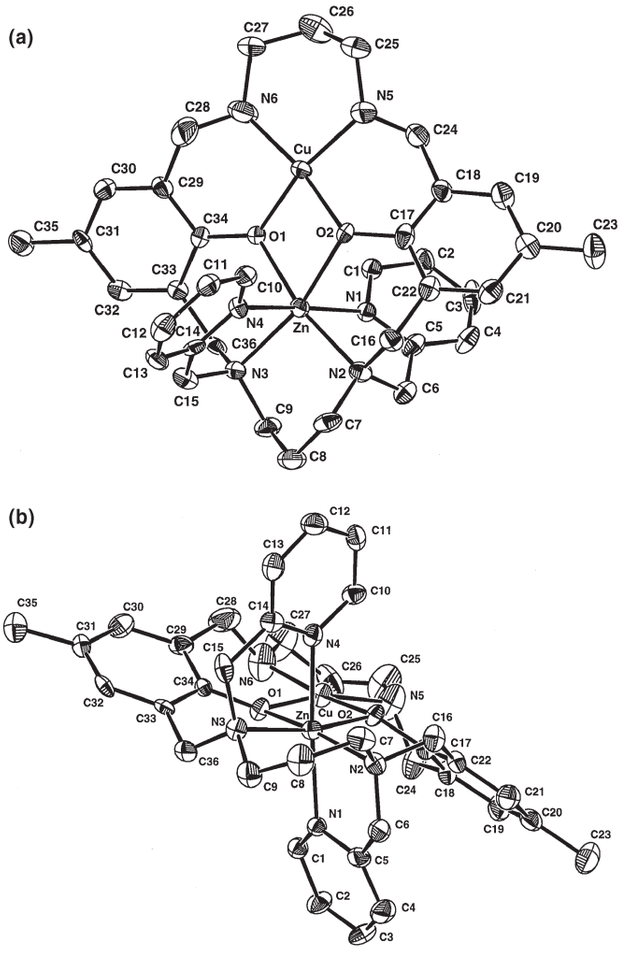

plexes appear as intense bands in the 330–355 nm region as the dominating UV feature for all spectra of the complexes. All mono- and bimetallic complexes with Co(III) at the closed site have similar visible spectra. Their characteristic features consist of intense absorption bands at 420–435 nm (ε ca. 2000–4000 M^{-1} cm^{-1}) due to phenolate–cobalt(III) charge transfer and another band at 565–600 nm (ε ca. 800–1800 M^{-1} cm^{-1}) attributed to the *d–d* transition of Co(III) (35). The high molar absorptivity of this latter band might be due to structural deviation as shown in Table 3. All heterobimetallic complexes of Zn(II)–Ni(II) display bands that are characteristic of a 5-coordinated spin-free Ni(II) structure in the acetonitrile solvent although it is difficult to distinguish clearly between trigonal bipyramidal and square pyramidal structures for Ni(II) (63, 64). In the near-infrared region, the heterobimetallic complexes of Co(III)–Ni(II) have similar band positions and shapes as those for the analogous Zn(II)–Ni(II) complexes, but the higher energy bands of Ni(II) at the open site are obscured by the intense bands of Co(III) at the closed site. The cobalt(II)–nickel(II) compound **7** displays five bands in the absorption spectrum. A

Table 7. Selected bond distances and angles for $[Zn(tntnam)Cu](PF_6)_3$, **12**.[a]

Bond distances (Å)			
Zn—Cu	3.0983(15)	Cu—O(1)	1.932(5)
Zn—O(1)	2.078(6)	Cu—O(2)	1.941(5)
Zn—O(2)	2.081(6)	Cu—N(5)	1.970(8)
Zn—N(1)	2.210(7)	Cu—N(6)	1.962(8)
Zn—N(2)	2.130(7)	O(1)—C(34)	1.340(9)
Zn—N(3)	2.130(7)	O(2)—C(17)	1.358(9)
Zn—N(4)	2.175(7)		
Bond angles (deg)			
O(1)-Zn-O(2)	75.7(2)	N(3)-Zn-N(4)	79.5(3)
O(1)-Zn-N(3)	93.4(2)	O(1)-Cu-O(2)	82.5(2)
O(1)-Zn-N(4)	91.7(2)	Zn-O(1)-Cu	101.1(2)
O(1)-Zn-N(1)	92.5(2)	Zn-O(2)-Cu	100.7(2)
O(1)-Zn-N(2)	167.6(2)	O(1)-Cu-N(6)	91.2(3)
O(2)-Zn-N(2)	95.6(2)	O(1)-Cu-N(5)	165.5(3)
O(2)-Zn-N(3)	166.9(2)	O(2)-Cu-N(5)	89.4(3)
O(2)-Zn-N(4)	93.3(2)	O(2)-Cu-N(6)	168.5(3)
O(2)-Zn-N(1)	86.5(2)	N(5)-Cu-N(6)	98.8(3)
N(1)-Zn-N(2)	78.0(3)	Cu-O(2)-C(17)	127.5(6)
N(1)-Zn-N(3)	101.5(2)	Cu-O(1)-C(34)	130.0(5)
N(1)-Zn-N(4)	175.6(3)	Zn-O(2)-C(17)	119.5(5)
N(2)-Zn-N(3)	96.2(3)	Zn-O(1)-C(34)	123.6(5)
N(2)-Zn-N(4)	97.6(3)		

[a]Estimated standard deviations are given in parentheses.

characteristic transition for cobalt(II) at the closed site is a band in the 960–1000 nm region (35); however, because open-site Ni(II) has an absorption band in the same region, the assignment of the near IR is problematical. Upon removal of chloride ion and oxidation of the cobalt(II) centre with ferrocinium ion, the absorption in the visible region changes to that characteristic of Co(III) at the closed site.

The zinc–copper complex **12** displays three bands at 350, 410, and 614 nm. The weak band at 614 nm occurs in the expected *d–d* transition region and is assigned accordingly (65, 66). The two other bands are assigned as metal to phenolate charge transfer (67–70). Both of these charge-transfer bands are relatively weak, which is not unusual for these types of ligands because the major source of intensity of these transitions is the promotion of an electron from d_{xz}, d_{yz} orbitals of the copper ion (68, 71). The position of the *d–d* band suggests that the Cu(II) ions may have a square-planar environment at the open site (65, 66). Three bands are resolved for **15** at 357, 414, and 576 nm. The moderately strong band at 414 nm is probably associated with phenolate–cobalt(III) charge transfer and the broad band at 576 nm is attributed to the *d–d* transition of Co(III), which tails into the near-IR region and tends to obscure the weaker *d–d* transition of Cu(II). The band at higher energy seems to be due to Cu(II) because neither compound **17** nor $[Co^{III}(tntnam)(H^+)_2]^{3+}$ shows such a band in this region, and it is probably associated with metal to phenolate charge transfer.

Redox properties

One of our objectives has been to develop a heterobimetallic system in which both metals contribute to the oxidative addition of reactants such as dioxygen. For such a process to occur, both of the metals at their respective open

© 1999 NRC Canada

Table 8. Electrospray mass spectral data for bimetallic complexes of ligands tntnam and tntnim.

Compound	Ions (ESMS) (m/z) [a]
$[Co(tntnam)Ni(H_2O)](PF6)_3$, **14**	$\{[Co(tntnam)Ni] - 2H^+\}^+$ (707.2)
	$\{[Co(tntnam)Ni] - H^+\}^{2+}$ (354.2)
$[Co(tntnam)NiCl](PF_6)_2$, **13** [b]	$\{[Co(tntnam)Ni] - 2H^+\}^+$ (707.2)
	$\{[Co(tntnam)Ni] - H^+\}^{2+}$ (354.2)
$[Zn(tntnim)Ni](PF_6)_2$, **6**	$\{[Zn(tntnim)Ni] - H^+\}^+$ (713.1)
	$[Zn(tntnim)Ni]^{2+}$ (356.2)
$[Zn(tntnim)NiCl]PF_6$, **5**	$[Zn(tntnim)NiCl]^+$ (747.1)
	$\{[Zn(tntnim)Ni] - H^+\}^+$ (713.1)
$[Zn(tntnam)Ni](PF_6)_2$, **11**	$\{[Zn(tntnam)Ni] - H^+\}^+$ (715.2)
	$[Zn(tntnam)Ni]^{2+}$ (357.1)
$[Zn(tntnam)NiCl]PF_6$, **10** [b]	$\{[Zn(tntnam)Ni] - H^+\}^+$ (715.2)
	$[Zn(tntnam)Ni]^{2+}$ (357.1)
$[Co(tntnim)Ni](PF_6)_3$, **9**	$\{[Co(tntnim)Ni]–2H^+\}^+$ (703.2)
	$\{[Co(tntnim)Ni] - H^+\}^{2+}$ (352.7)
$[Co(tntnim)NiCl]PF_6$, **7**	$[Co(tntnim)NiCl]^+$ (740.2)
$[Co(tntnam)Cu](PF_6)_3$, **15**	$\{[Co(tntnam)Cu](PF_6)_2\}^+$ (1003.9)
	$\{[Co(tntnam)Cu] - 2H^+\}^+$ (713.0)
	$\{[Co(tntnam)Cu] - H^+\}^{2+}$ (357.2)
$[Zn(tntnam)Cu](PF_6)_2$, **12**	$\{[Zn(tntnam)Cu]PF_6\}^+$ (866.1)
	$\{[Zn(tntnam)Cu] - H^+\}^+$ (720.2)
$[Co(tntnam)ZnCl](PF_6)_2$, **16**	$[Co(tntnam)ZnCl]^{2+}$ (375.1)
	$\{[Co(tntnam)ZnCl]PF_6\}^+$ (897.35)
$[Co(tntnam)Zn](PF_6)_3$, **17**	$\{[Co(tntnam)Zn] - H^+\}^{2+}$ (356.9)

[a]Most intense peak of isotopic mass distribution.

[b]The chloride ion fragments were not observed due to use of formic acid as mobile phase, which more than likely resulted in removal of the bound chloride; however, the presence of chloride ions was confirmed by precipitation of AgCl from bimetallic complexes as a result of treatment with $AgPF_6$.

Table 9. Magnetic moments for bimetallic complexes.

Complex	μ_{eff} [a] (BM) Solution [b]	Solid [c]	$\mu_{s.o.}$ [d] (BM)	n [e]
$[Co^{III}(tntnam)\ Ni(H_2O)](PF_6)_3$, **14**	2.7		2.83	2
$[Co^{III}(tntnam)NiCl](PF_6)_2$, **13**	2.9	3.0	2.83	2
$[Co^{III}(tntnam)Cu](PF_6)_3$, **15**	1.6		1.73	1
$[Co^{III}(tntnim)Ni](PF_6)_3$, **9**	3.0	3.1	2.83	2
$[Co^{II}(tntnim)NiCl]PF_6$, **7**	5.3		5.92	5
$[Zn(tntnim)NiCl]PF_6$, **5**	2.3		2.83	2
$[Zn(tntnam)Cu](PF_6)_2$, **12**	1.6		1.73	1
$[Zn(tntnam)NiCl]PF_6$, **10**	2.3		2.83	2
$[Zn(tntnam)Ni](PF_6)_2$, **11**	2.3	2.8	2.83	2
$[Zn(tntnim)Ni](PF_6)_2$, **6**	2.3	— [f]	2.83	2

[a]Approximate error = ±0.1 BM.

[b]Magnetic susceptibilities were determined at 25°C by the Evans ^1H NMR method on samples dissolved in CD_3COCD_3.

[c]Magnetic susceptibilities were determined at 20°C by Evans balance method.

[d]Spin-only values are determined for the bimetallic ensemble, where $\mu_{s.o} = (n(n+2)+2))^{1/2}$ and n = total number of unpaired spins (e.g., for Co(II)–Ni(II) complex, $n = 5$).

[e]Total number of unpaired spins.

[f]No paramagnetism.

and closed coordination sites must be capable of transferring electrons to the dioxygen molecule. To investigate cooperative interaction of metals for the electron transfer process, we studied the change in redox properties of an invariant metal by variations of the neighbouring metal in bimetallic complexes. Cyclic voltammetry was used to measure the formal potentials, E_f, of the metal ions. The open-site Ni(II)/Ni(I) and Cu(II)/Cu(I) couples were monitored for three series, $[M(ligand)Ni]^{q+}$, $[M(ligand)NiCl]^{q+}$, and $[M(ligand)Cu]^{q+}$, where M = Co(III) and Zn(II) and ligand = tntnim or tntnam. The cyclic voltammograms were measured at 25°C in acetonitrile solution containing 0.1 M n-Bu_4NPF_6 as the supporting electrolyte. Cyclic voltammograms were recorded using a tungsten reference electrode. All potentials E_f reported or discussed are adjusted relative to the ferrocenium/ferrocene (Fc^+/Fc) couple that was used as an

© 1999 NRC Canada

Table 10. Electronic absorption maxima and intensities of the charge-transfer and *d–d* transitions for bimetallic complexes.[a]

Complex	λ_{max}, (ε, L mol^{-1} cm^{-1})				
[Co^{III}(tntnam)Ni(H$_2$O)](PF$_6$)$_3$, **14**	422 (3330)	596 (sh, 1240)			1025 (35)
[Co^{III}(tntnim)Ni](PF$_6$)$_3$, **9**	332 (8650)	424 (3020)	590 (sh, 800)	825 (11)	982 (23)
[Co^{III}(tntnam)(H$^+$)$_2$](PF$_6$)$_3$ [b]	438 (3930)	565 (1750)	628 (1550)		
[Co^{III}(tntnam)Zn](PF$_6$)$_3$, **17**	432 (1960)	582 (782)			
[Co^{III}(tntnam)ZnCl](PF$_6$)$_2$, **16**	432 (2150)	583 (824)			
[Co^{III}(tntnam)NiCl](PF$_6$)$_2$, **13**	434 (3560)	600 (1570)			1070 (22)
[Co^{III}(tntnam)Cu](PF$_6$)$_3$, **15**	357 (4250)	414 (sh, 2980)	576 (804)[c]		
[Co^{II}(tntnim)NiCl]PF$_6$, **7**	355 (8570)	400 (sh, 1070)	570 (sh, 48)	828 (7)	998 (12)
[Zn(tntnam)Cu](PF$_6$)$_2$, **12**	350 (1340)	410 (sh, 285)	614(80)		
[Zn(tntnam)NiCl]PF$_6$, **10**	396 (500)	572 (12)	670 (sh, 8)	830 (9)	1030 (17)
[Zn(tntnim)NiCl]PF$_6$, **5**	350 (7790)	608 (17)	745 (sh, ~8)	829 (4)	1010 (7)
[Zn(tntnam)Ni](PF$_6$)$_2$, **11**	391 (570)	607 (19)	767 (sh, 9)	830 (9)	970 (9)
[Zn(tntnim)Ni](PF$_6$)$_2$, **6**	352 (3500)	400 (sh, 500)	607 (21)	829 (5)	985 (8)

[a]Spectra were run in CH_3CN.

[b]See ref. 35.

[c]Tail into NIR region.

Table 11. Redox potentials and peak separations for mono- and bimetallic complexes of tntnam and tntnim.[a]

	E_f,[b] V ($E_{pa} - E_{pc}$, V)	
	Closed-site	Open-site
Complex	Co(III/II) couple	M(II/I) couple
[Co^{III}(tntnam)Ni(H$_2$O)](PF$_6$)$_3$, **14**	–0.24 (0.139)	–1.72 (0.090)
[Zn(tntnam)Ni](PF$_6$)$_2$, **11**	—	–1.65 (0.220)
[Co^{III}(tntnam)NiCl](PF$_6$)$_2$, **13**	–0.24 (0.122)	–1.74 (0.133)
[Zn(tntnam)NiCl]PF$_6$, **10**	—	–1.65 (0.213)
[Co^{III}(tntnam)Zn](PF$_6$)$_3$, **17**	–0.11 (0.280)	—
[Co^{III}(tntnam)Cu](PF$_6$)$_3$, **15**	–0.20 (0.238)	–1.23 (0.182)
[Zn(tntnam)Cu](PF$_6$)$_2$, **12**	—	–1.04 (0.188)
[Co^{III}(tntnam)ZnCl](PF$_6$)$_2$, **16**	–0.31 (0.216)	—
[Co^{III}(tntnam)(H$^+$)$_2$](PF$_6$)$_3$	–0.41 (0.497)	—
[Co^{III}(tntnim)Ni](PF$_6$)$_3$, **9**	–0.18 (0.148)	–1.45 (0.114)
[Zn(tntnim)Ni](PF$_6$)$_2$, **8**	—	–1.26 (0.116)
[Zn(tntnim)NiCl]PF$_6$, **5**	—	–1.14 (0.092)
[Co^{II}(tntnim)NiCl]PF$_6$, **7**	0.09 (0.227)	–1.18 (0.121)
[Co^{II}(tntnim)(H$^+$)$_2$](PF$_6$)$_2$	0.03 (0.240) [c]	—

[a]1.0 mM sample, 0.1 M *n*-Bu_4NPF_6 in CH_3CN. Scan rate: 100 mV/s. Solutions were deaerated with Ar for 10 min prior to each run.

[b]Reduction potentials are reported relative to the ferrocenium/ferrocene (Fc^+/Fc) couple, assigned a value of 0.00 V.

[c]Scan rate: 200 mV/s.

internal reference (40) except for those of the macrocyclic Co(II) complexes. In the case of Co(II) complexes, the redox waves corresponding to the ferrocene internal reference coincide with Co(III)/Co(II) waves for the complexes, and thus here the Fc^+/Fc couple was used as an external reference (40). Table 11 lists the redox couples E_f found in acetonitrile solutions. Most of the compounds gave quasi-reversible waves, with clear anodic and cathodic peak separations, $E_{pa} - E_{pc}$. The Co(III)/Co(II) couple of $[Co(tntnam)(H^+)_2]^{3+}$ appears as a broad quasi-reversible wave. The waves at –0.65 to –0.15 V are ascribed to the Co(III)/Co(II) couples (35). It appears that the Co(III) ions in the bimetallic complexes are more difficult to reduce than that in the monometallic Co(III) complex. This may be due to more flexibility in the monometallic complex. Bimetallic complexes are constrained by the presence of a second metal ion at the open site. The cyclic voltammograms of selected Cu(II) complexes are shown in Fig. 5. The complex **15** shows two redox couples. We ascribe the quasi-reversible wave at –0.20 V to the Co(III)/Co(II) couple and that at –1.23 V to the Cu(II)/Cu(I)couple. The voltammogram of **12** also contains a quasi-reversible wave at –1.04 V and is assigned to the copper ion at the open site. There are no significant differences in Co(III)/Co(II) and Cu(II)/Cu(I) couples for **15** compared to **12** (Zn–Cu) and **17** (Co–Zn). These results point to a lack of substantial cooperative interaction between the two metal centres.

Complexes of **10**, **11**, **13**, **14**, **16,** and **17** were prepared in order to assess the Co(III)–Ni(II) interaction with reference to redox properties in amine complexes. The crystal structures of the **5**, **11**, and **14** complexes show *trans*-disposed pyridines and it is likely that other complexes have a *trans* configuration. This was also observed in other bimetallic complexes with trimethylenediamine at the open- and closed-

© 1999 NRC Canada

Fig. 5. The cyclic voltammograms of selected Co(III)– and Cu(II)–tntnam complexes in acetonitrile solutions referenced to Fc^+/Fc.

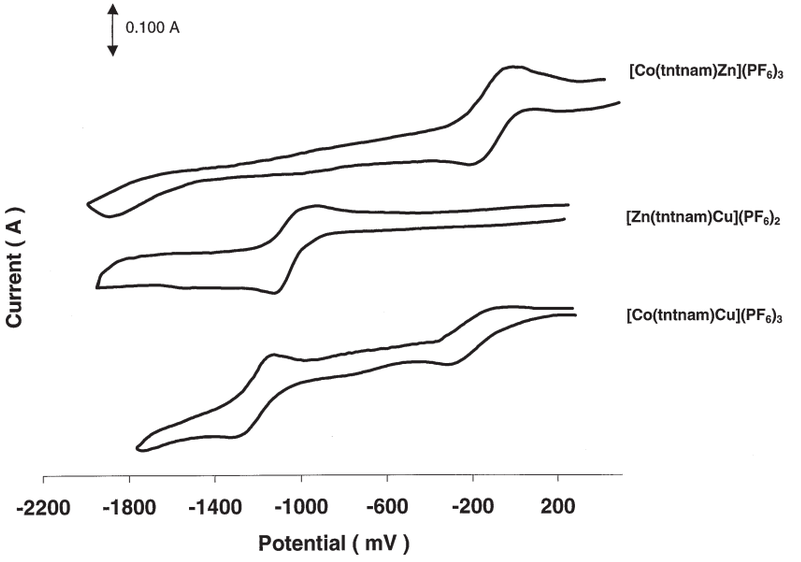

Fig. 6. The cyclic voltammograms of selected Co(III)– and Ni(II)–tntnam complexes in acetonitrile solutions referenced to Fc^+/Fc.

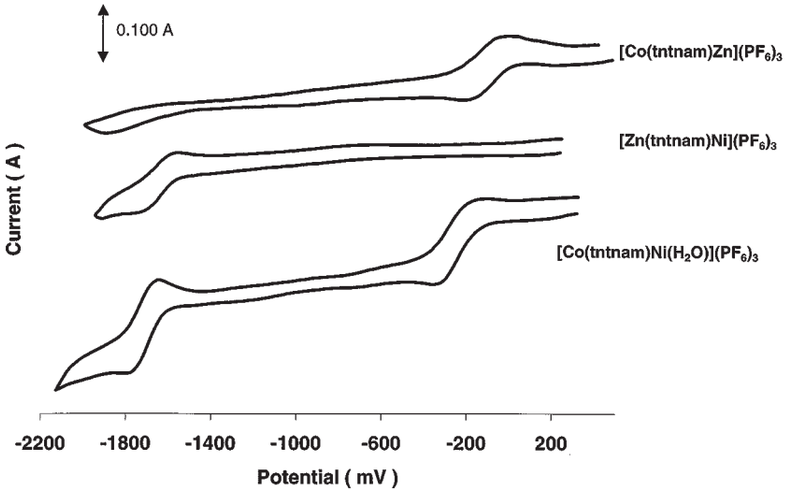

site links (36). As a result, there may be some slight structural differences in the closed-site Co(III) ion as the open-site metal is varied. Representative collections of cyclic voltammograms are given in Fig. 6. In addition to the waves ascribed to the Co(III)/Co(II) couple at –0.24 V, redox couples were also observed at –1.72 and –1.74 V arising from the open-site Ni(II) complexes in **13** and **14,** respectively. Redox couples were observed at similar potentials for analogous closed-site Zn(II) complexes **10** and **11**.

The analogous amine complexes of Ni(II) show more negative potentials than their imine counterparts. Presumably the more negative Ni(II)/Ni(I) potentials observed for amine complexes are related, at least in part, to the increased flexibility provided in the open-site link for diamine as compared to diimine. As a result, the diamine linkage at the open site is expected to be better able to adjust to the bond length changes accompanying the Ni(II) $\rightarrow$ Ni(I) transformation. Another observation that is apparent from the data in Table 11 is the variation of the closed-site Co(III)/Co(II) potential between diamine and diimine complexes of $[Co(ligand)NiCl]^{q+}$. Compound **13** has a redox couple that is significantly more negative than the ferrocenium/ferrocene couple and is consistent with ready oxidation of the Co(II) analogue with the ferrocenium ion. In the diimine analogue **7**, however, the Co(III)/Co(II) couple occurs at a much more positive potential, 0.09 V. It is not surprising, therefore, that we were unable to oxidize **7** with the ferrocenium ion. Upon removal of the coordinated Cl^- ligand, the resulting **8** is very sensitive to air and is readily oxidized to **9** by ferrocenium ion as evidenced by the redox potential of **9** in Table 11. Complex **9** shows two waves in the voltammogram, including one at –1.45 V attributable to the Ni(II)/Ni(I) couple of the open site, and the second one at –0.18 V that is ascribed to the closed-site Co(III)/Co(II) couple. The waves corre-

© 1999 NRC Canada

sponding to Ni(III)/Ni(II) and Cu(III)/Cu(II) in heterobimetallic complexes containing Ni(II) and Cu(II) were not observed in the potential range studied. It appears that oxidation of a metal at the given site deactivates the oxidation of metal at the other site (35).

Although the Co(II) oxidation state is expected to be more stereochemically labile than that of Co(III), it seems unlikely that the ligand coordination rearranges from the original C_2-symmetric structure of $[Co^{III}(ligand)M^{II}]^{3+}$ and $[Co^{III}(ligand)M^{II}Cl]^{2+}$ to the unsymmetrical structure, with *cis*-disposed pyridyl ligands, on the time scale of the electrochemical experiment (38, 56). Such extensive rearrangement, were it to occur, would likely give almost irreversible waves, which were not observed.

Reactivities towards molecular oxygen

The emission spectra of room temperature aerated and deaerated solutions of heterobimetallic complexes **9**, **11**, **13**, **14**, and **15** and free ligand tntnamH_2 were recorded in aqueous and acetonitrile solutions. An emission band occurred in all of the bimetallic complexes and for the free ligand at 416–526 nm upon excitation of the charge transfer bands of the compounds. The emission intensities significantly depend on molecular oxygen and decrease when the solutions are saturated with oxygen. No emission was observed from excitation of the *d–d* bands of the metal complexes. The origin of the emission band seems to be the intraligand charge transfer of the ligand system.

Time-resolved studies were carried out on the heterobimetallic complexes in oxygenated acetonitrile solutions to investigate the possible formation of singlet molecular oxygen, O_2 ($^1\Delta_g$), as a result of oxygen quenching. However, we were unable to detect the presence of singlet molecular oxygen.

To investigate the possibility of the formation of peroxide species as a result of oxidative quenching of the emission of the heterobimetallic complex in the aerated media, aqueous solutions of complexes **9**, **13**, and **14** were irradiated by visible light (415 nm) and the formation of the peroxide species was monitored by a standard method (41). The results show that the quantum yields for the production of hydrogen peroxide are less than 10^{-5}. This is in keeping with the absence of oxidation waves for Ni(II)/Ni(III) couples in the cyclic voltammetry experiments. The general observation that the absorption spectra remain unchanged upon extensive irradiation also shows the robust character of these complexes.

Acknowledgement

We express appreciation to the Natural Sciences and Engineering Research Council of Canada and the Ministry of Culture and Higher Education of the Islamic Republic of Iran for financial support. We also thank Professor A.S. Baranski for useful suggestions and discussions in the electrochemistry work. The authors gratefully acknowledge the assistance of Dr. Peter Wassell in measuring the magnetic susceptibility of the powdered samples. We wish also to thank Professor G. McKay and Dr. K. Lee for performing the electrospray mass analysis of the samples.

References

1. O. Kahn. Struct. Bonding (Berlin), **68**, 89 (1987).
2. E. Sinn and C.M. Harris. Coord. Chem. Rev. **4**, 391 (1969).
3. U. Casellato, P.A. Vigato, and M. Vidali. Coord. Chem. Rev. **23**, 31 (1977).
4. P. Zanello, S. Tamburini, P.A. Vigato, and G.A. Mazzocchin. Coord. Chem. Rev. **77**, 165 (1987).
5. F. Arena, C. Floriani, A. Chiese-Villa, and C. Guastini. Inorg. Chem. **25**, 4586 (1986).
6. Y. Aratake, H. Okawa, E. Asato, M. Sakiyama, M. Kodera, S. Kida, and M. Sakamoto. J. Chem. Soc. Dalton Trans. 2941 (1990).
7. N. Kitajima and Y. Moro-oka. Chem. Rev. **94**, 737 (1994).
8. B. Jung, K.D. Karlin, and A.D. Zuberbühler. J. Am. Chem. Soc. **118**, 3763 (1996).
9. S. Fox, A. Nanthakumar, M. Wilkistörn, K.D. Karlin, and A.J. Blackburn. J. Am. Chem. Soc. **118**, 24 (1996).
10. N. Stater, T. Klabunde, P. Tucker, H. Witzel, and B. Krebs. Science, **268**, 1489 (1995).
11. C.R. Kissinger, H.E. Parge, D.R. Knighton, C.T. Lewis, L.A. Pelletier, A. Tempczyk, V.J. Kalish, K.D. Tucker, R.E. Showalter, E.W. Moomaw, L.N. Gastinel, N. Habuka, X. Chen, F. Maldonado, J.E. Barker, R. Bacquet, and L.E. Villafranca. Nature (London), **378**, 41 (1995).
12. M.P. Egloff, P.T.W. Cohen, P. Reinemer, and D. Barford. J. Mol. Biol. **254**, 942 (1995).
13. J.D. Lamb, R.M. Izatt, J.J. Christensen, and D. J. Eatough. *In* Coordination chemistry of macrocyclic compounds. *Edited by* G.A. Melson. Plenum Press, New York. 1979. p. 145.
14. E.V. Rybak-Akimova, N.W. Alcock, and D.H. Busch. Inorg. Chem. **37**, 1563 (1998).
15. S. Ohtsuka, M. Kodera, K. Motoda, M. Ohba, and H. Okawa. J. Chem. Soc. Dalton Trans. 1599 (1995).
16. A. Aono, H. Wada, Y. Aratake, N. Matsumoto, H. Okawa, and M. Matsuda. J. Chem. Soc. Dalton Trans. 25 (1996).
17. H. Okawa, J. Nishio, M. Ohba, M. Tadokoro, N. Matsumoto, M. Koikawa, S. Kida, and D.E. Fenton. Inorg. Chem. **32**, 2949 (1993).
18. K.K. Nanda, S. Mohanta, S. Ghosh, M. Mukherjee, M. Helliwell, and K. Nag. Inorg. Chem. **34**, 2861 (1995).
19. J. Nishio, H. Okawa, S. Ohtsuka, and M. Tomono. Inorg. Chim. Acta, **218**, 27 (1994).
20. K.K. Nanda, A.W. Addison, N. Paterson, E. Sinn, L.K. Thompson, and U. Sakaguchi. Inorg. Chem. **37**, 1028 (1998).
21. K.K. Nanda, R. Das, K. Venkatsubramanian, and K. Nag. Proc. Indian Acad. Sci. Chem. Sci. **106**, 673 (1994).
22. A.J. Atkins, D. Black, A.J. Blake, A. Martin-Becerra, S. Parsons, L. Ramirez, and M. Schroeder. Chem. Commun. 457 (1996).
23. K. Nag. Proc. Indian Acad. Sci. Chem. Sci. **102**, 269 (1990).
24. P.A. Vigato, S. Tamburini, and D.E. Fenton. Coord. Chem. Rev. **106**, 25 (1990).
25. U. Casellato, P.A. Vigato, D.E. Fenton, and M. Vidali. Chem. Soc. Rev. **8**, 199 (1978).
26. S.E. Groh. Isr. J. Chem. **15**, 277 (1976/77).
27. M. Bell, A.J. Adwards, B. Hoskins, E.H. Kachab, and R. Robson. J. Am. Chem. Soc. **111**, 3603 (1989).
28. S.S. Tandon, L.K. Thompson, and N.J. Bridson. J. Chem. Soc. Chem. Commun. 911 (1992).
29. H. Sakayama, K. Matoda, H. Okawa, and S. Kida. Chem. Lett. 1133 (1991).
30. S.S. Tandon and V. McKee. J. Chem. Soc. Chem. Commun. 385 (1988).
31. R. Das, K.K. Nanda, I. Paul, S. Bitalik, and S. Nag. Polyhedron, **13**, 2639 (1994).

© 1999 NRC Canada

32. S.K. Dutta, J. Ensling, R. Werner, U. Floerke, W. Haase, P. Gutlich, and K. Nag. Angew. Chem. Int. Ed. Engl. **36**, 152 (1997).
33. S.K. Dutta, R. Werner, U. Floerke, S. Mohanta, K.K. Nanda, W. Haase, and K. Nag. Inorg. Chem. **35**, 2292 (1996).
34. C. Fraser, L. Johnston, A.L. Rheingold, B.S. Hagerty, G. K. Williams, L. Whelan, and B. Bosnich. Inorg. Chem. **31**, 1835 (1992).
35. D.G. McCollum, G.P.A. Yap, A.L. Rheingold, and B. Bosnich. J. Am. Chem. Soc. **118**, 1365 (1996).
36. D.G. McCollum, L. Hall, C. White, R. Ostrander, A.L. Rheingold, J. Whelan, and B. Bosnich. Inorg. Chem. **33**, 924 (1994).
37. K.S. Sandip. J. Magn. Reson. **82**, 169 (1997).
38. A. Earnshaw. Introduction to magnetic chemistry. Academic Press, New York. 1968. p 115.
39. A.S. Baranski and A. Szulborska. J. Electroanal. Chem. **373**, 157 (1994).
40. R.R.Grane, C.A. Koval, and G.C. Lisensky. Inorg. Chem. **19**, 2854 (1980).
41. H. Jeffery, J. Bassett, J. Mendham, and R.C. Denney. Vogel's textbook of quantitative chemical analysis. John Wiley & Sons Inc., New York. 1989. pp. 372–394.
42. C.G. Hatchard and C.A. Parker. Proc. R. Soc. London, Ser. A: **235**, 518 (1959).
43. D.F. Shriver. The manipulation of air-sensitive compounds. McGraw–Hill, Inc., New York. 1969.
44. B. Bosnich. J. Am. Chem. Soc. **90**, 627 (1968).
45. A.C.T. North, D.C. Phillips, and F.S. Mathews. Acta. Crystallogr. **24**, 351 (1968).
46. Enraf–Nonius (1992). CAD-4 EXPRESS. Version 1.1. Enraf–Nonius, Delft, The Netherlands.
47. S.R. Hall, G.S.D. King, and J.M. Stewart. The XTAL system, University of Western Australia, Australia. 1997.
48. E.J. Gabe, Y. LePage, J.P. Charland, F.L. Lee and S.P. White. J. Appl. Crystallogr. **22**, 384 (1989).
49. G.M. Sheldrick. SHELXL-97. Program for the refinement of crystal structures. University of Göttingen, Germany. 1997.
50. C. Fraser and B. Bosnich. Inorg. Chem. **33**, 338 (1994).
51. R.A.Q. Walton. Rev. Chem. Soc. **19**, 126 (1965).
52. A.J. Gordon and R.A. Ford. The chemist's companion. John Wiley & Sons, New York. 1972.
53. H. Okawo and S. Kida. Bull. Chem. Soc. Jpn. **45**, 1759 (1972).
54. R. Colton, A. Dagostino, and J.C. Traeger. Mass Spectrom. Rev. **14**, 79 (1995).
55. I.I. Stewart and G. Horlick. Trends Anal. Chem. **15**, 80 (1996).
56. E.A. Boudreaux and L.N. Mulary. Theory and applications of molecular paramagnetism. John Wiley & Sons, Inc., New York. 1976.
57. B.J. Hathaway. *In* Comprehensive coordination chemistry. Vol. 5. *Edited by* G. Wilkinson. Pergamon Press, New York. 1987. pp. 533-774.
58. D.H. Live and S.I. Chan. Anal. Chem. **42**, 791 (1970).
59. L. Banci, A. Bencini, C. Benelli, D. Gatteschi, and C. Zanchine. Struct. Bonding (Berlin), **52**, 37 (1982).
60. L. Sacconi, F. Mani, and A. Bencini. *In* Comprehensive coordination chemistry. Vol. 5. *Edited by* G. Wilkinson. Pergamon Press, New York. 1987. p. 533.
61. M.B. Robin and P. Day. Adv. Inorg. Chem. Radiochem. **10**, 247 (1967).
62. D. Heinert and A.E. Martell. J. Am. Chem. Soc. **84**, 3257 (1962).
63. A.B.P. Lever. Inorganic electronic spectroscopy. Elsevier, Amsterdam. 1984. p. 521.
64. L. Sacconi, F. Mani, and A. Bencini. *In* Comprehensive coordination chemistry. Vol. 5. *Edited by* G. Wilkinson. Pergamon Press, New York. 1987. p. 60.
65. M. Yonemura, Y. Matsumura, M. Ohba, H. Okawa, and D. Fenton. Chem. Lett. 601 (1996).
66. M. Yonemura, Y. Matsumura, M. Ohba, H. Okawa, and D. Fenton. Inorg. Chem. **36**, 2711 (1997).
67. B. Adhikary, S.K. Mondal, and K. Nag. J. Chem. Soc. Dalton Trans. 935 (1998).
68. A.R. Amundsen, J. Whelan, and B. Bosnich. J. Am. Chem. Soc. **99**, 6730 (1977).
69. E.W. Ainscough, A.G. Bingham, A.M. Brodie, J.M. Husbands, and J.E. Plowman. J. Chem. Soc. Dalton. Trans. 1701 (1981).
70. E.I. Solomon, K.W. Penfield, and D.E. Wilcox. Struct. Bonding (Berlin), **53**, 1 (1983).
71. A.B.P. Lever. Inorganic electronic spectroscopy. Elsevier, Amsterdam. 1984. p. 314.

© 1999 NRC Canada

Kinetics and mechanism of the reduction of Cr^{VI} to Cr^{III} by D-ribose and 2-deoxy-D-ribose

Verónica Daier, Sandra Signorella, Marcela Rizzotto, María Inés Frascaroli, Claudia Palopoli, Carlos Brondino, Juan Manuel Salas-Peregrin, and Luis F. Sala

Abstract: The oxidation of D-ribose and 2-deoxy-D-ribose by Cr^{VI} yields the aldonic acid and Cr^{3+} as final products when an excess of sugar over Cr^{VI} is used. The redox reaction occurs through $Cr^{VI}\rightarrow Cr^{III}$ and $Cr^{VI}\rightarrow Cr^{V}\rightarrow Cr^{III}$ paths. The complete rate laws for the Cr^{VI} oxidation reactions are expressed by $-d[Cr^{VI}]/dt = k_H[H^+]^2$ [ribose][Cr^{VI}], where $k_H = (5.9 \pm 0.1) \times 10^{-2}$ mol^{-3} dm^9 s^{-1}, and $-d[Cr^{VI}]/dt = (k_0 + k_H'[H^+]^2)$ [2-deoxyribose][Cr^{VI}], where $k_0 = (1.3 \pm 0.5) \times 10^{-3}$ mol^{-1} dm^3 s^{-1} and $k_H' = (4.2 \pm 0.1) \times 10^{-2}$ mol^{-3} dm^9 s^{-1}, at 33°C. An intermediate sugar alkoxide radical could be trapped with DMPO and observed by EPR as a multiline signal at $g = 2.003$. Cr^V is formed in a rapid step by reaction of the sugar radical with Cr^{VI}. Cr^V reacts with the substrate faster than Cr^{VI} does. The EPR spectra show that five- and six-coordinate oxochromate(V) intermediates are formed, and the distribution of these Cr^V species in the reaction mixture essentially depends on the solution acidity.

Key words: ribose, 2-deoxyribose, chromium, redox, mechanism, kinetics.

Résumé : L'oxydation du D-ribose et du 2-désoxy-D-ribose par le Cr^{VI} conduit aux acides aldoniques et au Cr^{3+} lorsque le sucre est en excès par rapport au Cr^{VI}. La réaction redox se produit par les voies $Cr^{VI}\rightarrow Cr^{III}$ et $Cr^{VI}\rightarrow Cr^{V}\rightarrow Cr^{III}$. Les lois de vitesse complètes pour les réactions d'oxydation par le Cr^{VI} s'expriment par les équations $-d[Cr^{VI}]/dt = k_H[H^+]^2$[ribose][$Cr^{VI}$] dans laquelle $k_H = (5{,}9 \pm 0{,}1) \times 10^{-2}$ mol^{-3} dm^9 s^{-1} et $-d[Cr^{VI}]/dt = (k_0 + k_H'[H^+]^2)$ [2-désoxyribose][Cr^{VI}] dans laquelle $k_0 = (1{,}3 \pm 0{,}5) \times 10^{-3}$ mol^{-1} dm^2 s^{-1} et $k_H' = (4{,}2 \pm 0{,}1) \times 10^{-2}$ mol^{-3} dm^9 s^{-1}, à 33°C. Faisant appel au DMPO, il est possible de piéger un radical alcoolate intermédiaire du sucre et de l'observer par RPE sous la forme d'un signal multiligne à $g = 2{,}003$. Le Cr^V se forme dans une étape rapide par réaction du radical avec du Cr^{VI}. La vitesse de réaction du Cr^V réagit avec le substrat est plus grande que celle du Cr^{VI}. Le spectre RPE montre qu'il y a formation d'intermédiaires oxochromates(V) penta- et hexacoordinés et que la distribution de ces espèces Cr^V dans le milieu réactionnel dépend essentiellement de l'acidité de la solution.

Mots clés : ribose, 2-désoxyribose, chrome, redox, mécanisme, cinétiques.

[Traduit par la Rédaction]

Introduction

Hexavalent chromium, in many different compounds, is a well-established carcinogen and mutagen (1–5). The observation of Cr^V and Cr^{IV} intermediates in the selective oxidation of organic substrates by Cr^{VI} and their implication in the mechanism of Cr-induced cancers (6–8) has generated a considerable amount of interest in their chemistry and biochemistry (9–12).

Received July 7, 1998.

V. Daier, S. Signorella, M. Rizzotto, M.I. Frascaroli, C. Palopoli, and L.F. Sala.[1] Departamento de Química, Facultad de Ciencias Bioquímicas y Farmacéuticas, UNR, Suipacha 531, 2000 Rosario, Argentina.
C. Brondino. Instituto de Desarrollo Tecnológico para la Industria Química, Güemes 3450, 3000 Santa Fe, Argentina.
J.M. Salas-Peregrin. Departamento de Química Inorgánica, Facultad de Ciencias, Universidad de Granada, Fuentenueva s/n, 18071 Granada, Spain.

[1]Author to whom correspondence may be addressed.
Telephone and fax: 54-341-4350214.
e-mail: inquibir@satlink.com

The biological reduction of Cr^{VI} to lower states has been observed with a wide variety of naturally occurring cellular reductants (13–15). Ligands that possess two oxygen atoms able to form five-membered rings about the metal ion, such as 1,2-diols and α-hydroxyacids, are effective as nonenzymatic reductants and complexation agents towards hypervalent chromium and can stabilize the labile oxidation states of chromium (12, 16–19). For this reason sugars, or their derivatives, may play an important role in the chemistry of Cr^{VI}.

We are studying the possible fate of Cr^{VI} and Cr^V in biological systems by examining reactions of Cr^{VI} with low-molecular-weight biological and model reductants, as a means of more fully understanding the processes involved in the genotoxicity of chromium. In previous work we have found that the stereochemistry of the sugars or their derivatives affects the Cr^{VI} reduction rate (20–27). In any case, the first reaction step involves the formation of a Cr^{VI} ester, which is followed by the slow redox steps. For aldohexoses, this precursor is formed in rapid pre-equilibrium, and C(1)O, C(2)O, and in a little extent, C(6)O have been found to be the preferred coordination sites either in the Cr^{VI} or Cr^V electron-transfer precursors (20, 24). On the other hand, 2-deoxyaldohexoses form with Cr^{VI} a precursor ester, which

 © 1999 NRC Canada

behaves as a steady state, and they yield several Cr^{V} intermediate complexes which are in rapid pre-equilibria before the slow redox steps take place, with C(1)O and C(6)O being the preferred coordination sites (21, 22). In this paper, we compare the Cr^{VI} reduction by D-ribose and 2-deoxy-D-ribose, and provide with new information on the influence of the furanose hydroxyl groups on the reaction kinetics and mechanism as well as on the nature and reactivity of the intermediate Cr^{V} species.

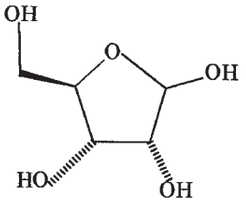

D-Ribose

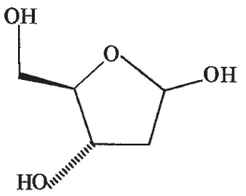

2-deoxy-D-Ribose

Experimental

Materials

D-Ribose (Rib) (Sigma grade), 2-deoxy-D-Ribose (2dRib) (Sigma grade), potassium dichromate (BDH), sodium perchlorate (Fluka grade), acrylonitrile (Aldrich grade), and perchloric acid (P.A. Merck) were used without further purification.

For experiments performed in the 2–7 pH range, the pH of the solutions was adjusted by addition of 0.5 mol dm^{-3} NaOH and 0.5 mol dm^{-3} $HClO_4$.

The spin trap 5,5-dimethyl-1-pyrroline *N*-oxide (DMPO) (Aldrich grade) was purified by charcoal decolorization. The method consists of successively treating the DMPO with activated charcoal until all free-radical impurities disappeared by EPR spectroscopy (28).

Warning: chromic acids and acrylonitrile are toxic and carcinogens.

Spectrophotometric measurements

Kinetics measurements were made at 350 nm, by monitoring the absorbance changes on a Guilford Response II spectrophotometer with fully thermostated cell compartments. The reactions were followed under pseudo-first-order conditions, using at least a 25-fold excess of sugar over Cr^{VI}. Mixtures of sodium perchlorate and perchloric acid were used to maintain a constant ionic strength (*I*) of 1.0 mol dm^{-3}. Reactant solutions were previously thermostated and transferred into a cell of 1 cm path length immediately after mixing. Experiments were performed at 33°C unless otherwise mentioned.

Disappearance of Cr^{VI} was followed at 350 nm until at least 80% conversion. In most experiments the concentration of Cr^{VI} was kept constant at 8×10^{-4} mol dm^{-3} while the sugar concentration was varied from 0.02 to 0.16 mol dm^{-3}. The observed pseudo-first-order rate constants (k_{obs}), determined from the linear part of plots of ln (A_{350}) vs. time, were deduced from multiple determinations and were within ±5% of each other. The first-order dependence of the rate upon $[Cr^{VI}]$ was verified. The k_{obs} were calculated at various $[Cr^{VI}]_0$, but at constant temperature, $[sugar]_0$, $[H^+]$, and *I*. As expected on the basis of a $-d(\ln [Cr^{VI}])/dt = k_{obs}$ rate law, where $k_{obs} = f([sugar][H^+])$, k_{obs} was found to be essentially constant with increasing $[Cr^{VI}]_0$. The formation of Cr^{III} was monitored at 570 nm. At the end of the reaction the two d–d bands ascribed to Cr^{III} were observed at λ_{max} = 410 nm (ε = 18 dm^3 mol^{-1} cm^{-1}) and 576 nm (ε = 15.5 dm^3 mol^{-1} cm^{-1}) ($[HClO_4]$ = 0.5 mol dm^{-3}). Both, visible and UV spectral maxima and intensities, are in close agreement (vide infra) with those observed for the $[Cr(H_2O)_6]^{3+}$ ion. The assignment was verified by comparing the spectral features with those of the acid solutions of independently synthesized $[Cr(RibaH_{-3})(H_2O)_2]$ (λ_{max} = 421 nm (ε = 27.4 dm^3 mol^{-1} cm^{-1}) and 573 nm (ε = 25.8 dm^3 mol^{-1} cm^{-1})), $K[Cr_2(OH)(Riba)_2(Rib)_2]$ (λ_{max} = 408 nm (ε = 452 dm^3 mol^{-1} cm^{-1}) and 571 nm (ε = 146 dm^3 mol^{-1} cm^{-1})) (29), and $Na_3[Cr(RibH_{-2})_2(OH)_2]$ (λ_{max} = 298 nm (ε = 137 dm^3 mol^{-1} cm^{-1}) and 576 nm (ε = 15.5 dm^3 mol^{-1} cm^{-1})) complexes.

Products analysis

Under the conditions used in the kinetic measurements (ratios of Rib (2dRib) to Cr^{VI} from 25:1 to 200:1), qualitative identification of D-ribonic acid (Riba) (or 2-deoxy-D-ribonic acid (2dRiba)) as the reaction product was carried out by paper chromatography. Riba (2dRiba) was identified against an authentic sample using *n*-butanol/acetic acid/water (4:1:5) as eluent. Paper chromatograms were visualized by two kinds of development reagents: a three-stage dip of silver nitrate, sodium hydroxide, and sodium thiosulphate and *p*-anisidine reagent (30, 31). Riba (2dRiba) identification as the only reaction product was also made by ^{13}C NMR. A mixture of Rib (2dRib) (13.2×10^{-3} mol) and potassium dichromate (6.6×10^{-3} mol) in 1 mol dm^{-3} $HClO_4$ (10 cm^3) was allowed to react at 33°C. After the reaction had proceeded to completion the mixture was stirred with a Dowex 50W-X8 cation exchange resin until all the Cr^{III} was removed from the solution and a concentrated sample was analysed by ^{13}C NMR. Riba (2dRiba) and unreacted Rib (2dRib) were identified by comparing against authentic samples.

The presence of free radicals was tested for in the reaction of Rib (2dRib) with Cr^{VI}. To a solution of potassium dichromate (0.005 mmol) and Rib (2dRib) (0.1 mmol) in 4 cm^3 of 0.25 mol dm^{-3} $HClO_4$ was added acrylonitrile (0.5 cm^3) at 33°C. After a few minutes a white precipitate appeared. Control experiments (without potassium dichromate or reductant present) did not show the formation of a precipitate.

EPR spectroscopy

The EPR spectra were obtained on a Bruker ESP 300 E spectrometer. The microwave frequency was generated with a Bruker 04 ER (9–10 GHz) and measured with a Racal–Dana frequency meter. The magnetic field was measured with a Bruker NMR-probe Gauss meter. All of the EPR experiments were carried out at room temperature.

Results and discussion

Cr^{VI} reduction by Rib and 2dRib

Over the whole range of $HClO_4$ concentrations used in the kinetic measurements, spectrophotometric studies showed

© 1999 NRC Canada

Table 1. Observed pseudo-first-order rate constants (k_{obs}) for different concentrations of $HClO_4$ and organic substrate. T = 33°C; $[Cr^{VI}]_0 = 3.6 \times 10^{-4}$ mol dm^{-3}; I = 1.00 mol dm^{-3}.

	$10^4\ k_{obs}{}^a$ (s^{-1}) for $[HClO_4]$/ mol dm^{-3} of						
[Rib]/mol dm^{-3}	0.10	0.25	0.50	0.60	0.75	0.90	1.00
0.02	—	1.35	3.89	5.33	7.80	10.1	14.1
0.04	—	2.31	7.49	10.6	13.5	19.2	24.2
0.08	1.02	4.12	13.7	20.2	28.2	39.9	47.3
0.12	1.42	5.61	20.0	25.1	40.6	52.6	72.1
0.14	1.55	6.35	23.7	31.7	49.1	68.6	85.3
0.16	1.75	6.63	26.4	36.2	52.6	69.8	92.2
	$10^4\ k_{obs}'$ (s^{-1}) for $[HClO_4]$/ mol dm^{-3} of						
[2dRib]/mol dm^{-3}	0.10	0.15	0.25	0.50	0.75	1.00	
0.02	—	—	0.97	2.87	5.70	9.68	
0.04	—	0.74	1.73	5.35	10.1	16.7	
0.08	0.78	1.51	3.48	10.5	20.5	33.7	
0.12	1.05	2.05	4.84	14.3	30.5	50.3	
0.16	1.32	2.65	6.79	21.4	40.7	69.3	

[a]Rate constants obtained from multiple determinations.

Fig. 1. Time evolution of the UV-vis spectrum of a mixture of Rib (0.2 mol dm^{-3}) and Cr^{VI} (8×10^{-3} mol dm^{-3}). $[HClO_4]$ = 0.25 mol dm^{-3}; T = 25°C, over a period of ca. 113 min, showing the Cr^{III} growth and Cr^{VI} decay with one isosbestic point.

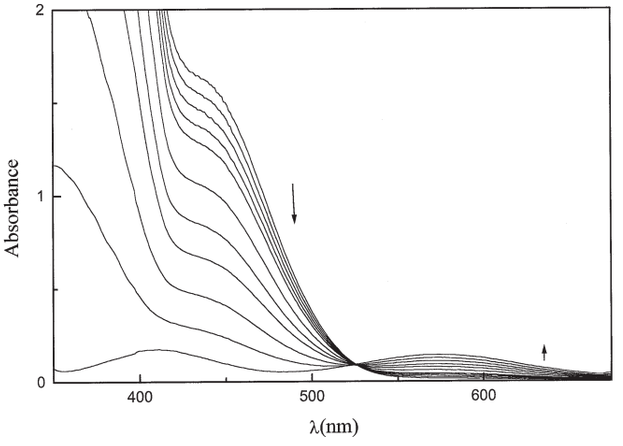

Fig. 2. Effect of [Rib] on k_{obs} at 33°C, I = 1.00 mol dm^{-3}, and $[H^+]$ (mol dm^{-3}): (*a*) 0.10; (*b*) 0.25; (*c*) 0.50; (*d*) 0.60; (*e*) 0.75; (*f*) 0.90; (*g*) 1.00.

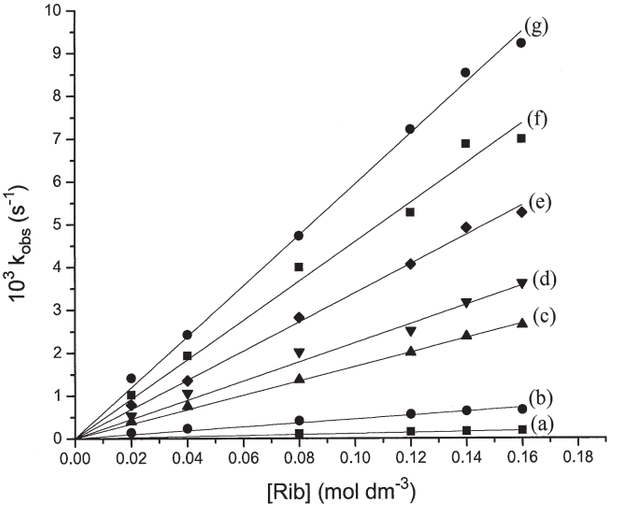

that the reaction of the sugar and Cr^{VI} resulted in an absorbance band at 350 nm and a shoulder at 420–500 nm. The absorbance vs. time curves at 350 nm exhibit a monotonic decrease. At this wavelength, kinetic traces show an initial deviation from first-order decay over short time periods. It is known that Cr^V species absorb strongly at 350 nm and may superimpose Cr^{VI} absorbance yielding the wrong interpretation of spectrophotometric absorbance decay values (32). However, if Cr^V reacts faster than Cr^{VI} and exists in solution in a sufficiently small concentration, changes in absorbance at 350 nm essentially reflect changes in Cr^{VI} concentration. We calculated pseudo-first-order rate constants from the slope of the linear part of the ln (Abs) vs. time curves; a good criterion only if Cr^V decays faster than Cr^{VI}. The relative values of the Cr^{VI} vs. Cr^V reduction rate constants obtained from the Cr^V EPR signal intensity variation during the reaction course (discussed below) demonstrate this is the case for the present reaction. Besides, we have followed the formation of Cr^{III} at 570 nm, and we have found that the rate of Cr^{III} formation equals the rate of Cr^{VI} decay. This is consistent with the observation of an isosbestic point at 525 nm (Fig. 1) and implies a low $[Cr^V]$ throughout the reaction in the $[H^+]$ range used in the kinetic measurements.

Table 1 summarizes values of k_{obs} for various concentrations of Rib at fixed concentrations of $HClO_4$. Plots of k_{obs} vs. [Rib] (Fig. 2) gave good straight lines from which values of k were determined (Table 2). Figure 3 shows the dependence of k with $[HClO_4]$, which may be expressed as in eq. [1].

$$[1] \qquad k = k_H[H^+]^2$$

where $k_H = (5.9 \pm 0.1) \times 10^{-2}$ mol^{-3} dm^9 s^{-1}.

The complete rate law is then given by

© 1999 NRC Canada

Table 2. Values of k and k' for different $[HClO_4]$. T = 33°C; $[Cr^{VI}]_0 = 3.6 \times 10^{-4}$ mol dm^{-3}; I = 1.00 mol dm^{-3}.

$[HClO_4]$/ mol dm^{-3}	0.10	0.15	0.25	0.50	0.60	0.75	0.90	1.00
10^3 k/mol^{-1} dm^3 s^{-1}	1.13(3)	—	4.5(2)	16.8(2)	22.3(5)	34.0(5)	45.9(1)	59.4(6)
10^3 k'/mol^{-1} dm^3 s^{-1}	0.86(4)	1.66(4)	4.20(6)	12.9(3)	—	25.5(1)	—	42.7(4)

Fig. 3. Effect of acidity on k (■) and k' (●).

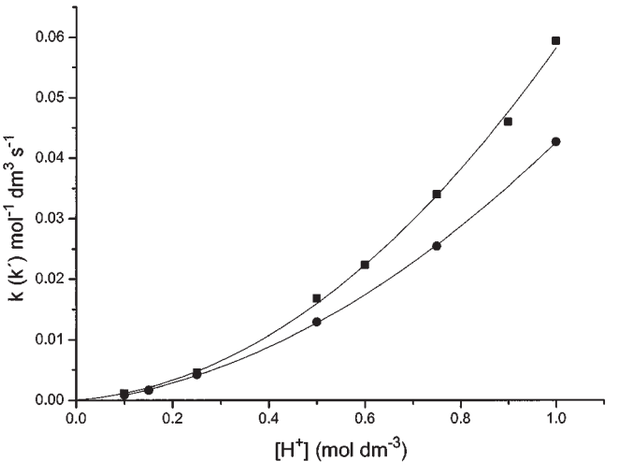

[2] $$-d[Cr^{VI}]/dt = k_{obs}[Cr^{VI}]_T = k_H[H^+]^2[Rib][Cr^{VI}]_T$$

where $[Cr^{VI}]_T$ represents the total Cr^{VI} concentration.

For the oxidation of 2dRib, plots of k_{obs}' (Table 1) vs. [2dRib] (Fig. 4) gave straight lines with zero intercept from which values of k' were determined (Table 2). A plot of k' vs. $[H^+]^2$ gave a straight line with a positive intercept, showing that the second-order rate constant may be expressed as consisting of an acidity independent and an acidity dependent term:

[3] $$k' = k_0 + k_H'[H^+]^2$$

where $k_0 = (1.3 \pm 0.5) \times 10^{-3}$ mol^{-1} dm^3 s^{-1} and $k_H' = (4.2 \pm 0.1) \times 10^{-2}$ mol^{-3} dm^9 s^{-1}.

The complete rate law is then given by

[4] $$-d[Cr^{VI}]/dt = k_{obs}'[Cr^{VI}]_T = (k_0 + k_H'[H^+]^2)[2dRib][Cr^{VI}]_T$$

The rate laws for the oxidation of Rib and 2dRib by Cr^{VI} differ in that, for the second, a term independent of $[H^+]$ is observed. These two terms in the rate law (eq. [4]) for 2dRib result from the fact that there are at least two transition states, differing in composition but similar in energy, through which the reduction of Cr^{VI} can proceed. Thus, the oxidation of 2dRib by Cr^{VI} should occur through two parallel slow steps leading to the redox products. In the case of Rib, the redox reaction proceeds through one path of consecutive reactions leading to the products only after protonation of the 1:1 Rib–Cr^{VI} intermediate species. This fact explains why at high pH the oxidation of 2dRib occurs faster than that of Rib. For both sugars, in the range of substrate concentrations employed, only substrate first-order dependence was observed and Riba (or 2dRiba) was the only detected reaction product. A mechanism taking account of these facts is proposed for Rib and 2dRib in Scheme 1.

Fig. 4. Effect of [2dRib] on k_{obs}' at 33°C, I = 1.00 mol dm^{-3}, and $[H^+]$ (mol dm^{-3}): (*a*) 0.10; (*b*) 0.15; (*c*) 0.25; (*d*) 0.50; (*e*) 0.75; (*f*) 1.00.

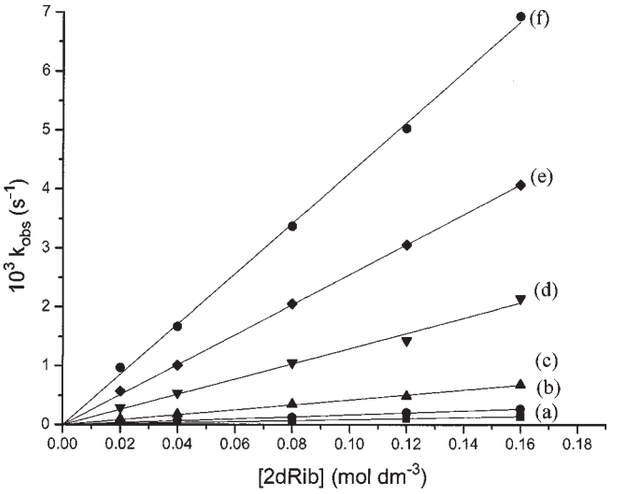

In the $[H^+]$ range studied, Cr^{VI} exists mainly as $HCrO_4^-$ (33). Thus, the first step of the mechanism proposed in Scheme 1(*a*) may be interpreted as the formation of a monochelate with Rib acting as a bidentate ligand bound to Cr^{VI} at C1-O and C2-O to yield the anionic species A^-. Even when several linkage isomers might be formed by coordination of the sugar with Cr^{VI} via any properly disposed hydroxyl groups, we think that the complex with the anomeric hydroxyl group bound to Cr^{VI} should be the precursor of the slow redox steps. Then, the monoprotonated form of this intermediate (AH) yields the redox product through an acid catalyzed step.

The rate law corresponding to this mechanism may be expressed as in eq. [5]:

[5] $$-d[Cr^{VI}]/dt = k_2K_1K_2[H^+]^2[Rib][Cr^{VI}]$$

where $k_2K_1K_2 = k_H$ of the experimental rate law.

An alternative mechanism might involve the formation of an intermediate bis-chelate Cr^{VI}-Rib_2, where only one of the two Rib molecules involved in the Cr^{VI} complex formation is oxidized to Riba through the two-electron intramolecular redox path.

The first step of the mechanism proposed for the oxidation of 2dRib in Scheme 1(*b*) corresponds to the formation of a 1:1 2dRib–Cr^{VI} binary complex, with 2dRib acting as a monodentate ligand bound to Cr^{VI} at the anomeric hydroxyl group to yield the anionic species B^-. This intermediate may decompose directly to the products or give BH. This monoprotonated intermediate yields the redox products

© 1999 NRC Canada

Scheme 1. $A^- = [(RibH_{-2})CrO_2(H_2O)OH]^-$, $B^- = [(2dRibH_{-1})\ CrO_2(H_2O)(OH)_2]^-$.

(a) $Rib + Cr^{VI} \overset{K_1}{\rightleftharpoons} A^- \overset{K_2, H^+}{\rightleftharpoons} AH \overset{k_2, H^+}{\longrightarrow} Cr^{IV} + Riba$

(b)
$$2dRib + Cr^{VI} \overset{K_a}{\rightleftharpoons} B^- \overset{k_a}{\longrightarrow} Cr^{IV} + 2dRiba$$
$$K_b \Big\downarrow H^+$$
$$BH \overset{k_b, H^+}{\longrightarrow} Cr^{IV} + 2dRiba$$

through an acid-catalyzed step. The rate law corresponding to this mechanism may be expressed as in eq. [6]:

[6] $$-d[Cr^{VI}]/dt = (k_aK_a + k_bK_aK_b[H^+]^2)[2dRib][Cr^{VI}]$$

where $k_aK_a = k_0$ and $k_bK_aK_b = k_H'$ of the experimental rate law.

For either Rib or 2dRib, after the slow steps, reactions [7]–[9] may take place.

[7] $$Sugar + Cr^{IV} \rightarrow sugar^{\cdot} + Cr^{III}$$

[8] $$Sugar^{\cdot} + Cr^{VI} \rightarrow sugar\ acid + Cr^{V}$$

[9] $$Sugar + Cr^{V} \rightarrow sugar\ acid + Cr^{III}$$

Cr^{IV} formed in the slow steps yields the final Cr^{III} and the $sugar^{\cdot}$ radical in a subsequent fast step. The formation of these sugar radicals is supported by the observed polymerization after addition of acrylonitrile. Besides, DMPO was used to detect any sugar radical intermediate formed during the reduction of Cr^{VI} by Rib. The addition of DMPO to the reaction mixture resulted in the appearance of a spin adduct signal at $g = 2.003$ (Fig. 5) with splitting constants of $a_N = 7.48 \times 10^{-4}$ cm^{-1}, $a_H = 3.65 \times 10^{-4}$ cm^{-1} (× 2). This is the first time that a signal corresponding to a DMPO/sugar radical adduct is reported, and confirms our proposal. Cr^V formed by rapid reaction of the radical and Cr^{VI} can further oxidize the sugar to yield the final redox products.

Unlike Rib, aldohexoses kinetic profiles yield saturation curves (20, 24). This means that aldohexoses form more "stable" intermediate Cr^{VI} complexes (with higher K). But, also, under the same reaction conditions, the kinetic parameter (kK) for the $[H^+]^2$ dependent term is, at least, six times lower for aldohexoses than for Rib. Thus, the $k_{ox}/K_{complexation}$ ratio is higher for the Rib/Cr^{VI} system, meaning that intramolecular electron transfer paths are faster within the less stable Cr^{VI} intermediate complexes. The same difference was observed when 2-deoxy-glucose/Cr^{VI} and glucose/Cr^{VI} systems were compared (21, 22). The more stable the intermediate Cr^{VI} complex, precursor of the redox steps, the higher the energy barrier to overcome in the slow electron transfer steps. Comparing the kinetic parameters of the acidity dependent term for Rib and 2dRib it can be observed that they are of the same order of magnitude, meaning that, in this case, k and K compensate each other, yielding a similar value for the kK product.

Fig. 5. EPR spectrum recorded from a 0.1 mol dm^{-3} $HClO_4$ solution containing 25 mmol dm^{-3} Cr^{VI}, 250 mmol dm^{-3} Rib, and 73 mmol dm^{-3} DMPO. The spectrum was recorded 3 min after mixing. Modulation amplitude: 0.514 G, centre field: 3450 G, frequency = 9.66 GHz.

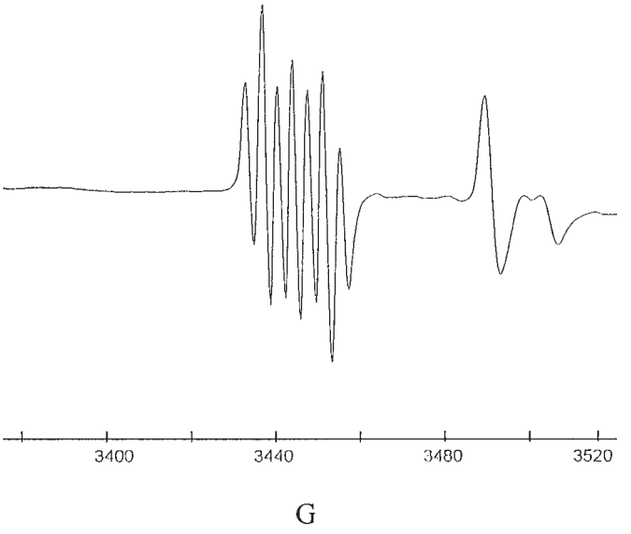

It must be noted that the slow redox steps, involving either A^- or B^- (BH) intermediate complexes, are two electron steps, and the final chromium species, Cr^{III}, is formed through either a $Cr^{VI} \rightarrow Cr^{IV} \rightarrow Cr^{III}$ or a $Cr^{VI} \rightarrow Cr^{V} \rightarrow Cr^{III}$ path.

Intermediacy of Cr^V

The reaction of Cr^{VI} with an excess of 5–100 times of Rib, in the 4–7 pH range, at 25°C, generates an EPR spectrum dominated by a single detectable signal at $g_{iso} = 1.9787$ (Fig. 6) with the four weak ^{53}Cr (9.55% abundance, $I = 3/2$) hyperfine peaks at 15.7×10^{-4} cm^{-1} spacing, typical of five-coordinate oxochromate(V) complexes (34–36). In this pH range, Cr^V remains in solution several days. We found that varying the modulation amplitude, the superhyperfine (shf) pattern partially resolved, and the Cr^V EPR spectrum

© 1999 NRC Canada

Fig. 6. X-band EPR signal of a mixture of Rib (3.75×10^{-1} mol dm^{-3}) and Cr^{VI} (3.75×10^{-2} mol dm^{-3}) at different [H^+]. T = 25°C, modulation amplitude = 4 G, centre field = 3550 G; frequency = 9.85 GHz.

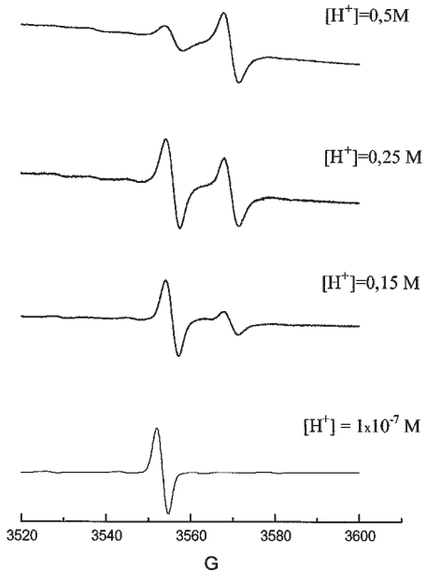

Fig. 7. X-band EPR signal of a mixture of 2dRib (3.75×10^{-1} mol dm^{-3}) and Cr^{VI} (3.75×10^{-2} mol dm^{-3}) at different pH. T = 25°C, modulation amplitude = 8 G, centre field = 3550 G; frequency = 9.84 GHz.

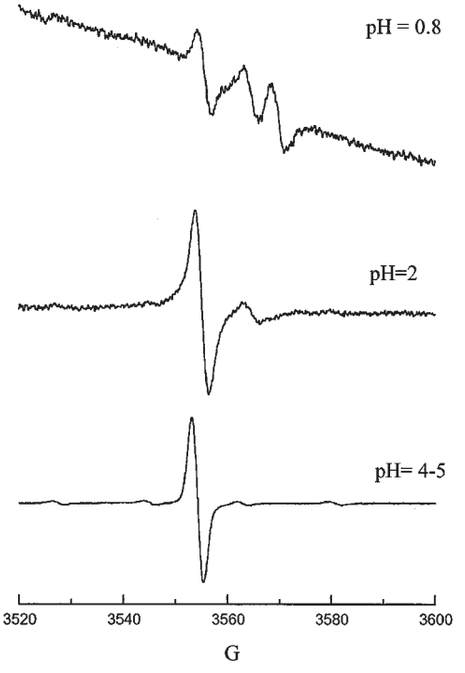

resulted to be a composite of several Cr^V species. Even when the complex chemistry of the Cr^V-Rib species present in solution makes accurate determinations of g_{iso} values difficult, specially due to the overlap of the shf coupling, the g_{iso} values for all of these signals are in the range of those expected for five-coordinate oxochromate(V) complexes (34).

At [$HClO_4$] ≥ 0.1 M, the reaction of Cr^{VI} with excess Rib resulted in the formation of two types of relatively long-lived Cr^V species. The relative intensity of the two Cr^V EPR signals, at g_1 = 1.9787 and g_2 = 1.9711, depends on the [H^+] (Fig. 6), but is independent of the rib:Cr^{VI} ratio employed (from 5:1 to 100:1). The g_2 value is significantly lower than the values observed for the five-coordinate oxochromate(V) complexes, and since the g values of the Cr^V species are very sensitive to coordination (37), it may be assigned to a six-coordinate oxochromate(V) complex (35). However, the lack of a resolved shf pattern from the protons prevented a more detailed analysis of this signal. For [H^+] = 0.1–0.15 M, the five-coordinate species (g_1) is the major one; it forms rapidly (the maximum concentration is reached at t < 3 min) and decays slowly. Under these conditions, the minor species always decays with time. At [H^+] = 0.25 M, the total amount of Cr^V reached a maximum concentration at t < 1 min, and both signals always decay with time. In the [H^+] range 0.25–1.0 M the six-coordinate species (g_2) is the major one, i.e., at [H^+] = 1 M, after 6 min of reaction, the g_1/g_2 signal ratio was 0.07. Thus, the five-coordinate oxochromate(V) complexes are formed at any [H^+], whereas the formation of the six-coordinate species requires acid conditions. At each pH, the two Cr^V signals decay at different rates, and these rates increase with decreasing pH, indicating that proton catalysis is present in the oxidation of the sugar by Cr^V. The observed behavior seems to indicate that both types of complexes, five- and six-coordinate, are formed independently and they yield the final Cr^{III} by two parallel paths.

In the 4–7 pH range, the sugar should essentially form binary Rib:di-oxochromate(V) complexes, with the sugar binding Cr^V as a bidentate ligand at a 1,2-diolate moiety, or bound to Cr^V at a 1,2,3-triolate moiety (34). The appearance of the six-coordinate Cr^V species at high [H^+] might be interpreted as the consequence of the protonation of the anionic dioxochromate(V) species, yielding the monooxochromate(V) complexes with the sixth coordination position occupied by an additional solvent molecule.

The reaction of Cr^{VI} with an excess of 2dRib, in the 4–7 pH range, at 25°C, results in only one Cr^V intermediate species, with g_{iso} = 1.9791 and A_{iso} = 16.6×10^{-4} cm^{-1} (Fig. 7), typical of a five-coordinate oxochromate(V) complex (34). In this case, the signal did not split when the modulation amplitude was lowered. So, probably, only one species is responsible for this EPR signal. At pH = 2, a minor signal at g_2 = 1.9735 appears, and when the [H^+] > 0.1 M a third signal at g_3 = 1.9707 is observed. The g_{iso} values of the two signals at higher field may be assigned to six-coordinate oxochromate(V) complexes (34). The relative proportions of the three species depend essentially on the acidity. The time course of the peak-to-peak height of the first derivative of the signals as a function of time for an initial ratio 2dRib:Cr^{VI} = 10:1, at different pH, revealed that the two (or three) signals decay at comparable rates; therefore, these Cr^V intermediates are in rapid equilibrium compared to the time scale of their subsequent reduction to Cr^{III}. Again, these rates increased with decreasing pH, indicating that proton catalysis is also present in this case. A similar behavior had

© 1999 NRC Canada

Fig. 8. Peak-to-peak heights of Cr^{V} EPR signals vs. time. [Rib] = 3.75×10^{-1} mol dm^{-3}; [Cr^{VI}] = 3.75×10^{-2} mol dm^{-3}; [H^{+}] = 0.15 mol dm^{-3}; I = 1 mol dm^{-3}; T = 25°C. T_{max} = 4.4 min.

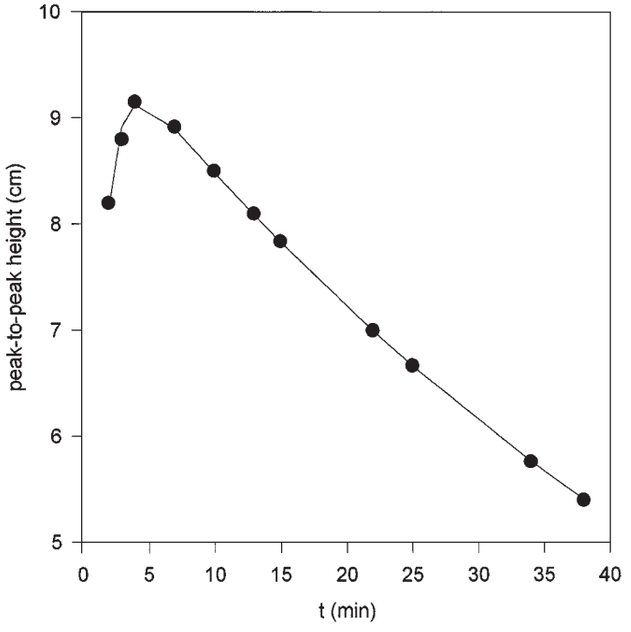

been previously observed for the reaction of 2dGlc and Cr^{VI} (21).

For the reduction of Cr^{VI} by either Rib or 2dRib, the time of maximum Cr^{V} concentration is very short compared to the time required for the reaction completion. At [H^{+}] = 0.15 mol dm^{-3}, [Rib] = 0.375 mol dm^{-3} and $[Cr^{VI}]_0$ = 0.0375 mol dm^{-3}, at room temperature, Cr^{VI} requires 12 h to be completely reduced to Cr^{III}. Figure 8 shows a curve for peak-to-peak height of Cr^{V} EPR signal vs. time obtained on a reacting solution. Values of the rate constant for the disappearance of Cr^{VI} (k_6) and Cr^{V} (k_5), respectively, may be calculated by eq. [10] (26, 38), which fits well the experimentally observed Cr^{V} intermediate growth and decay curve in Fig. 8.

$$[10] \quad h = Ak_6(\exp(-k_5t) - \exp(-2k_6t))/(2k_6 - k_5)$$

In eq. [10], h is the peak-to-peak height, and A depends on the spectrometer settings and is adjusted by the fitting program.

For conditions stated in the figure, $k_6 = 1.35 \times 10^{-4}$ s^{-1} and $k_5 = 1.57 \times 10^{-2}$ s^{-1}, and the time of maximum Cr^{V} concentration, T_{max}, is 14.4 min. To verify if this assignment of the rate constant values — and not the reverse one — was correct, we have evaluated k_{obs} ($2k_6$) spectrophotometrically at 25°C under conditions used in the EPR experiments, and we have reproduced the k_{obs} ($2k_6$) value. Thus, the fact that k_5 is 116 times higher than k_6 justifies our initial assumption that changes in absorbance at 350 nm essentially reflect changes in Cr^{VI} concentration.

The ultimate fate of the chromium in these reactions is a Cr^{III} species and a typical broad Cr^{III} EPR signal centered at g ~1.98 is always observed at later time points.

Conclusions

These results show that Cr^{V}, generated by reaction of the sugar radical with Cr^{VI}, oxidizes Rib (or 2dRib) to the sugar acid faster than Cr^{VI} does. The reduction of both Cr^{VI} and Cr^{V} by the furanose is acid catalysed and yields the same oxidized product. Comparing the Cr^{VI} redox rates with those of allose (Allo) — the aldohexose with the same configuration of C2 and C3 — the second-order rate constant (k, M^{-1} s^{-1}) is six-fold higher for Rib than for Allo, a fate probably resulting from the furanose vs. pyranose forms of these two sugars. That the furanose ring favors oxidation vs. complexation processes might be interpreted as the consequence of the influence of the strain-induced instability of the chromate ester on the redox rate. This effect is enhanced in the Cr^{V}–furanose species, as evidenced when k_5 and k_6 for pyranose vs. furanose forms are compared. In the chromic oxidation of aldohexoses (pyranose form), k_5 values are no more than 10 times higher than k_6; whereas in the present case, $k_5 > 100k_6$.

Acknowledgements

We thank the National Research Council of Argentina (CONICET), the Third World Academy of Sciences (TWAS), the National University of Rosario, Antorchas Foundation, and the International Foundation for Sciences (IFS) for financial support. V. Daier thanks CONICET and FOMEC for a fellowship.

References

1. M. Costa. Crit. Rev. Toxicol. **27**, 431 (1997).
2. S.J. Stohs and D. Bagchi. Free Radicals Biol. Med. **18**, 321 (1995).
3. R. Von Burg and D. Liu. J. Appl. Toxicol. **13**, 225 (1993).
4. S. Langard. Am. J. Ind. Med. **17**, 189 (1990).
5. S. De Flora, M. Bagnasco, D. Serra, and P. Zanacchi. Mutat. Res. **238**, 99 (1990).
6. K.D. Sugden and K.E. Wetterhahn. Chem. Res. Toxicol. **10**, 1397 (1997).
7. S. Moghaddas, E. Gelerinter, and R.N. Bose. J. Inorg. Biochem. **57**, 135 (1995).
8. S.L. Scott, A. Bakac, and J.H. Espenson. J. Am. Chem. Soc. **114**, 4205 (1992).
9. M. Ciéslak-Golonka. Polyhedron, **15**, 3667 (1996).
10. R.N. Bose, B. Fonkeng, G. Barr-David, R.P. Farrell, R.J. Judd, P.A. Lay, and D.F. Sangster. J. Am. Chem. Soc. **118**, 7139 (1996).
11. E.S. Gould. Coord. Chem. Rev. **135**/**136**, 651 (1994).
12. L. Zhang and P.A. Lay. J. Am. Chem. Soc. **118**, 12 624 (1996).
13. D.H. Stearns and K.E. Wetterhahn. Chem. Res. Toxicol. **7**, 219 (1994).
14. K.E. Wetterhahn Jannette. J. Am. Chem. Soc. **104**, 874 (1982).
15. P. O'Brien, J. Barrett, and F. Swanson. Inorg. Chim. Acta, **108**, L19 (1985).
16. M. Krumpolc, B.G. de Boer, and J. Rocek. J. Am. Chem. Soc. **100**, 145 (1978).
17. S.L. Brauer and K.E. Wetterhahn. J. Am. Chem. Soc. **113**, 3001 (1991).
18. D.M.L. Goodgame, P.B. Hayman, and D.E. Hathaway. Polyhedron, **1**, 497 (1982).
19. D.M.L. Goodgame and A.M. Joy. J. Inorg. Biochem. **26**, 219 (1986).

© 1999 NRC Canada

20. L.F. Sala, S.R. Signorella, M. Rizzotto, M.I. Frascaroli, and F. Gandolfo. Can. J. Chem. **70**, 2046 (1992).
21. S. Signorella, M. Rizzotto, V. Daier, M.I. Frascaroli, C. Palopoli, D. Martino, A. Bousseksou, and L.F. Sala. J. Chem. Soc. Dalton Trans. 1607 (1996).
22. M. Rizzotto, S. Signorella, M.I. Frascaroli, V. Daier, and L.F. Sala. J. Carbohydr. Chem. **14**, 45 (1995).
23. L.F. Sala, C. Palopoli, and S. Signorella. Polyhedron, **14**, 1725 (1995).
24. M. Rizzotto, M.I. Frascaroli, S. Signorella, and L.F. Sala. Polyhedron, **15**, 1517 (1996).
25. S. Signorella, S. García, and L.F. Sala. Polyhedron, **16**, 701 (1997).
26. S.R. Signorella, M.I. Santoro, M.N. Mulero, and L.F. Sala. Can. J. Chem. **72**, 398 (1994).
27. S. Signorella, M. Santoro, C. Palopoli, C. Brondino, J.M. Salas-Peregrin, M. Quirós and L.F. Sala. Polyhedron, **17**, 2739 (1998).
28. G.R. Buettner and L.W. Oberley. Biochem. Biophys. Res. Commun. **83**, 69 (1978).
29. S.P. Kaiwar, M.S.S. Raghavan, and C.P. Rao. J. Chem. Soc. Dalton Trans. 1569 (1995).
30. M.E. Trevelyan, D.P. Procter, and J.S. Harrison. Nature (London), **166**, 444 (1950).
31. L. Haugh, J.K.N. Jones, and W.H. Wadman. J. Chem. Soc. 1702 (1950).
32. G.P. Haight, G.M. Jursich, M.T. Kelso, and P.J. Merrill. Inorg. Chem. **24**, 2740 (1985).
33. N.E. Brasch, D.A. Buckingham, A.B. Evans, and C.R. Clark. J. Am. Chem. Soc. **118**, 7969 (1996).
34. G. Barr-David, M. Charara, R. Codd, R.P. Farrell, J.A. Irwin, P.A. Lay, R. Bramley, S. Brumby, J.Y. Ji, and G.R. Hanson. J. Chem. Soc. Faraday Trans. **91**, 1207 (1995).
35. R.P. Farrell, R.J. Judd, P.A. Lay, R. Bramley, and J.Y. Ji. Inorg. Chem. **28**, 3401 (1989).
36. M. Branca, A. Dessí, H. Kozlowski, G. Micera, and J. Swiatek. J. Inorg. Biochem. **39**, 217 (1990).
37. R. Bramley, J.Y. Ji, R.J. Judd, and P.A. Lay. Inorg. Chem. **29**, 3089 (1990).
38. S. Signorella, S. García, and L.F. Sala. Polyhedron, **11**, 1391 (1992).

© 1999 NRC Canada

The energy barrier for CO migration in $Mn_2(CO)_6(H_2PCH_2PH_2)_2$: a PM3(tm) study

Stephen A. Decker and Mariusz Klobukowski

Abstract: Carbonyl fluxionality in $Mn_2(CO)_6(dhpm)_2$ (dhpm = bis(dihydrophosphino)-methane), serving as a model of $Mn_2(CO)_6(dppm)_2$ (dppm = bis(diphenylphosphino)-methane), was studied using both the PM3(tm) semiempirical method and the DFT//PM3(tm) approach. When the PM3(tm) method is used for both geometry optimization and energy determination, the most stable conformer of $Mn_2(CO)_6(dppm)_2$ is predicted to possess six planar carbonyls, two of which are symmetrically bridging the Mn atoms, in contrast to the usually assumed planar all-terminal structure of $Mn_2(CO)_6(dppm)_2$. Carbonyl scrambling via the pairwise exchange mechanism in $Mn_2(CO)_6(dppm)_2$ is predicted to occur as follows at the PM3(tm)//PM3(tm) level: lowest energy, planar symmetrically di-bridged conformer → planar, all-terminal conformer → lowest energy, planar symmetrically di-bridged conformer. The corresponding barrier to the exchange process is 32 kcal/mol, much higher than the experimental value of 10 kcal/mol in the related $Mn_2(CO)_6(dppm)_2$ complex. Calculation of the total energies using density functional theory at the PM3-optimized geometries improves results in two ways. Firstly, the energy barrier to scrambling is reduced to only 15–19 kcal/mol depending on the functional employed. Secondly, the energy ordering of the conformers is reversed, with the planar, all-terminal structure of $Mn_2(CO)_6(dppm)_2$ being more stable than the bridging structure. The resulting mechanism is identical to that found in our earlier work on $Mn_2(CO)_{10}$. When DFT is used to optimize the conformer geometries, the energy barrier is further reduced to 13 kcal/mol.

Key words: PM3(tm) semiempirical method, density functional theory, carbonyl scrambling.

Résumé : Faisant appel à la méthode semiempirique PM3(tm) et à l'approche DFT//PM3(tm), on a étudié la fluxionalité du carbonyl dans le $Mn_2(CO)_6(dhpm)_2$ (dhpm = bis(dihydrophosphino)-méthane) qui sert de modèle pour le $Mn_2(CO)_6(dppm)_2$ (dppm = bis(diphénylphosphino)-méthane). Quand on utilise la méthode PM3(tm) tant pour l'optimisation de la géométrie que pour la détermination de l'énergie, on prévoit que le conformère le plus stable du $Mn_2(CO)_6(dhpm)_2$ comportera six carbonyls planaires, deux formant un pont symétrique entre les atomes de Mn; ceci est en opposition avec l'hypothèse habituelle selon laquelle le $Mn_2(CO)_6(dppm)_2$ assumerait une structure planaire dans laquelle tous les substituants seraient terminaux. Les calculs au niveau PM3(tm)//PM3(tm) permettent de prédique que, dans le $Mn_2(CO)_6(dhpm)_2$, un mécanisme d'échange par paire conduira à un mélange des groupes carbonyls : conformère biponté planaire et symétrique de plus faible énergie → conformère planaire avec tous les substituants terminaux → conformère biponté planaire et symétrique de plus basse énergie. La barrière correspondant au processus d'échange est de 32 kcal/mol, beaucoup plus élevée que la valeur expérimentale de 10 kcal/mol observée dans le complexe apparenté $Mn_2(CO)_6(dppm)_2$. Le calcul des énergies globales en utilisant la théorie de la densité fonctionnelle avec des géométries optimisées au niveau PM3 permet d'améliorer les calculs de deux façons : premièrement, la barrière d'énergie du brouillage est réduite à 15 à 19 kcal/mol suivant la fonctionnelle utilisée; deuxièmement, l'énergie de mise en ordre des conformères est renversée alors que la structure planaire avec tous les groupements en positions terminales du $Mn_2(CO)_6(dhpm)_2$ est plus stable que la structure pontée. Le mécanisme qui en résulte est identique à celui trouvé dans nos travaux antérieurs sur le $Mn_2(CO)_{10}$. Lorsqu'on utilise l'approche DFT pour optimiser les géométries des conformères, la barrière d'énergie est encore réduite à 13 kcal/mol.

Mots clés : méthode semiempirique PM3(tm), théorie de la densité fonctionnelle, brouillage des carbonyls.

[Traduit par la Rédaction]

1. Introduction

The last decade has seen a dramatic increase in the application of computational chemistry to the study of the properties and reactions of transition metal complexes (see, for instance, the review by Veillard (1)). This may be attributed to advances in theory, in particular density functional theory (DFT) methodologies (illustrated in the review of Ziegler (2)) and pseudopotential techniques (see the recent reviews by Frenking et al. (3) and Cundari et al. (4)), coupled with

Received May 7, 1998.

S.A. Decker[1] and M. Klobukowski.[2] Department of Chemistry, University of Alberta, Edmonton, AB T6G 2G2, Canada.

[1]Harry Emmett Gunning Graduate Fellow 1994–1996.
[2]Author to whom correspondence may be addressed. Telephone: (403) 492-2568. Fax: (403) 492-8231.
e-mail: Mariusz.Klobukowski@UAlberta.CA

© 1999 NRC Canada

technological advances in computer hardware and computational chemistry software. Currently nonlocal, gradient-corrected DFT is the method of choice for studies on transition metal compounds. However, using the workstation hardware typically available in research groups, the computational cost of DFT often makes it prohibitively expensive for modelling the large systems encountered in transition metal chemistry. The need for more cost-efficient techniques for studies of transition metal complexes has prompted the development of semiempirical methods, of which the PM3(tm) method available in the Spartan program[3] is frequently used. The semiempirical PM3(tm) method requires much less computing time; however, its reliability in applications to molecules containing transition metals has not yet been fully evaluated. A search of the literature shows only two papers that probe the utility of the PM3(tm) method in calculations involving transition metal complexes. Adam et al. (5) studied the ability of PM3(tm) to predict molecular structures of high- and low-spin nickel(II) teraaza macrocycle complexes. Looking only at geometry structures, they found PM3(tm) to be inferior to an extended MM2 molecular mechanics force field, derived for macrocycles of low-spin nickel(II). Børve et al. (6) performed a comparative study of PM3(tm) vs. DFT in calculations of Ti, Cr, and Zr complexes. They found the PM3(tm) method to be quite successful in predicting geometries of stable, closed-shell complexes, in close agreement with both experiment and DFT calculations. However, they also found that PM3(tm) gave poor relative energies and activation barriers for ethylene insertion reactions. Single-point energy calculations, using nonlocal density functional theory at the PM3(tm) optimized geometries, yielded more reliable and accurate activation barriers, reasonably close to those obtained if the DFT method were used throughout. Their approach may be denoted as the DFT//PM3(tm) method. In the current paper we use the DFT//PM3(tm) method in modelling carbonyl scrambling in transition metal dimer complexes.

Carbonyl scrambling has been found in all types of transition metal complexes of varying nuclearity, from simple mononuclear complexes to clusters containing many metal atoms (7, 8). There are two accepted mechanistic schemes for carbonyl scrambling: pairwise exchange and one-for-one exchange. In the pairwise exchange mechanism, proposed by Adams and Cotton (9) in the early 1970s, two of the migrating ligands are mutually exchanged between the two metal atoms. Symmetrical ligand bridges are opened and closed pairwise in a *trans*, coplanar, concerted fashion. This is the most common mechanism proposed for carbonyl migration, and may proceed from either an all-terminal or symmetrically bridging conformation. In the one-for-one mechanism, first proposed by Evans et al. (10) for carbonyl exchange in *trans*-$(\eta^5\text{-}C_5H_5)_2Rh_2(CO)_3$ and $(\eta^5\text{-}C_5H_5)_2Rh_2\text{-}(CO)_2P(OC_6H_5)_3$, the migrating ligands are not coplanar and are exchanged unsymmetrically in a stepwise fashion. The conventional experimental means of studying the dynamic fluxionality of ligands is NMR spectroscopy. To be detected by NMR, the exchange process must have a rate in the range 10^{-1}–10^6 s^{-1} (7). Furthermore, the solvents employed in NMR restrict the range of temperatures at which the process can be followed, thereby imposing limitations on the activation energy. The activation energy ($\Delta G^{\ddagger}$) for these fluxional processes must fall within the range 3–25 kcal/mol in order for the process to be studied by NMR (7).

The two Mn complexes, $Mn_2(CO)_{10}$ and $Mn_2(CO)_6(dppm)_2$, where dppm denotes bis(diphenylphosphino)-methane, show very different fluxional behaviour in solution. The carbonyl ligands in $Mn_2(CO)_{10}$ remain fixed up to a temperature of 130°C, as shown by ^{13}C and ^{17}O NMR studies (11). However, when four of the carbonyl ligands are replaced with two bidentate dppm ligands, then carbonyl fluxionality is observed, both by ^{13}C and ^{31}P NMR, down to a temperature as low as –75°C (12). Marsella and Caulton(12) proposed that carbonyl scrambling in $Mn_2(CO)_6(dppm)_2$ proceeds via the pairwise exchange (merry-go-round) mechanism from the most stable all-terminal conformer through a symmetrically di-bridged transition state or intermediate with an energy barrier of 10.2 kcal/mol. Conformational differences between $Mn_2(CO)_6(dppm)_2$ and the parent species $Mn_2(CO)_{10}$ were thought to be the driving force behind the observed difference in fluxional behaviour. In the lowest-energy conformer of $Mn_2(CO)_{10}$ the equatorial carbonyls are staggered and must undergo an initial rotation about the Mn—Mn bond to give the eclipsed conformation required for the merry-go-round scrambling of the carbonyls; this rotation would then contribute to the overall activation energy for the exchange process. On the other hand, in $Mn_2(CO)_6(dppm)_2$ the six carbonyls are believed to be already coplanar in the most stable conformer, and may proceed directly to scrambling without any prerequisite rotation about the Mn—Mn bond.

Our previous calculations (13), employing nonlocal density functionals for both geometry optimization and total energy evaluation, predicted that carbonyl migration in $Mn_2(CO)_{10}$ proceeds from the most stable staggered (D_{4d}) conformation, Fig. 1(*a*), to the eclipsed (D_{4h}) conformation, Fig. 1(*b*), via rotation about the Mn—Mn bond, with a barrier of only 5–6 kcal/mol, and then on to the planar, di-bridged (D_{2h}) conformer, Fig. 1(*c*), with an additional barrier of 14–15 kcal/mol. The overall activation barrier for carbonyl scrambling in $Mn_2(CO)_{10}$ via the pairwise exchange mechanism was therefore calculated from the total energies to be about 19–21 kcal/mol, close to the upper limit of 25 kcal/mol (7) for the process to be detected experimentally by NMR. The PM3(tm) method gave structural parameters that were close to both experimental data and the results from the DFT calculations; however, the PM3(tm) energy barrier for the rotation about Mn—Mn bond (converting the staggered and eclipsed conformers) was found to be 11 kcal/mol, about twice the DFT values. Using the DFT//PM3(tm) approach, we obtained an energy barrier of 3.8 kcal/mol, much closer to the value computed using the DFT//DFT approach.

In the present paper we use the PM3(tm)//PM3(tm), DFT//PM3(tm), and DFT//DFT energies to compute the energy barrier to CO migration in the $Mn_2(CO)_6(dppm)_2$ model system, in order to gauge the predictability of each method. The paper is divided into two sections, the first dealing with

[3] Spartan 4.0.3. Wavefunction, Inc., Irvine, CA 92715, U.S.A. 1995.

© 1999 NRC Canada

Fig. 1. The conformers of $Mn_2(CO)_{10}$ involved in CO migration: (*a*) staggered (D_{4d}), (*b*) eclipsed (D_{4h}), and (*c*) symmetrically bridged (D_{2h}).

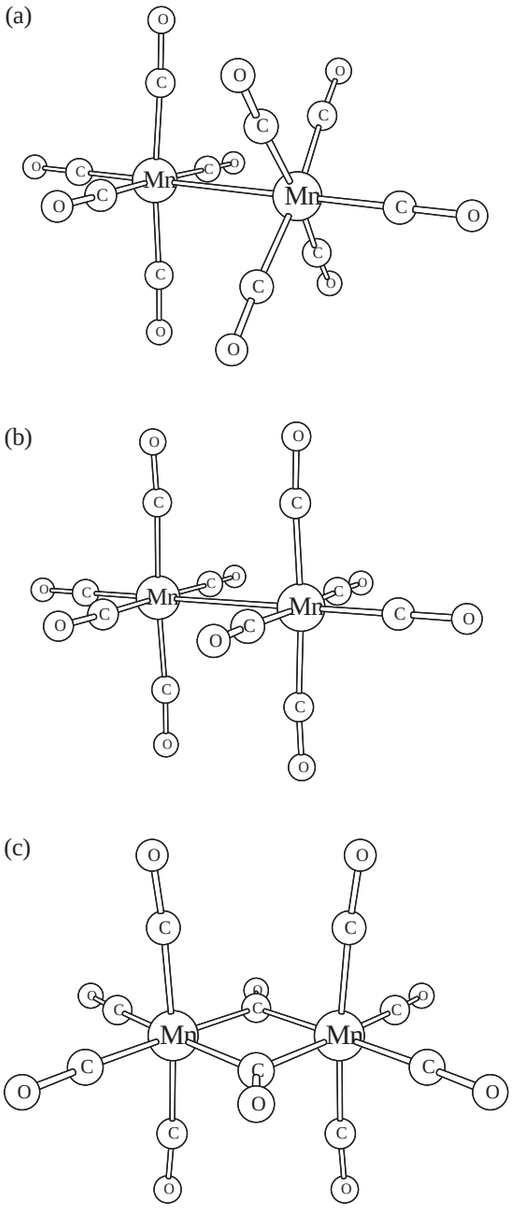

geometric structures and the second discussing the relative energies of the conformers involved in the scrambling process and the resulting activation barrier for the process.

2. Computational methods

To simplify the problem and reduce the computational cost, the phenyl rings of the bidentate dppm ligand were replaced with hydrogen atoms, giving the bis(dihydrophosphino)-methane (dhpm) ligand. Assuming that carbonyl scrambling in both the experimental $Mn_2(CO)_6(dppm)_2$ and model $Mn_2(CO)_6(dppm)_2$ systems proceeds via the pairwise exchange (merry-go-round) mechanism, the PM3(tm) semiempirical method was employed to optimize the geometries and determine the energies of the conformers that play an integral role in the scheme. In addition, structural parameters were optimized for $Mn_2(CO)_5(dhpm)_2$ and the parent $Mn_2(CO)_6(dppm)_2$ system. All geometries, with the exception of one of the $Mn_2(CO)_6(dppm)_2$ conformers with constrained angles (see below), were fully optimized using analytical gradient techniques, and the nature of the resulting stationary point was characterized by harmonic vibrational analysis at the PM3(tm) level. The Hessian was not obtained for the $Mn_2(CO)_6(dppm)_2$ conformers due to their significant size and the computational cost involved, even at the semiempirical level of theory. The choice of semiempirical method was based solely on the availability of parameters for Mn, and the unpublished PM3(tm) parameters in the Spartan program[3] were used.

To obtain a more reliable estimate of the activation barrier, the total energies of the $Mn_2(CO)_6(dppm)_2$ conformers involved in the carbonyl migration were computed via single-point energy calculations at their respective PM3-optimized geometries using density functional theory. Several density functionals were employed: BLYP (Becke's nonlocal exchange functional (14) in conjunction with the nonlocal correlation functional of Lee, Yang, and Parr (15)), BP86 (Becke's nonlocal exchange functional (14) coupled with Perdew's nonlocal correlation functional (16)), B3LYP (comprised of Becke's three-parameter hybrid gradient-corrected exchange functional (17) coupled with the gradient-corrected correlation functional of Lee, Yang, and Parr (15)), and B3PW91 (Becke's three-parameter hybrid gradient-corrected exchange functional (17) in conjunction with the gradient-corrected correlation functional of Perdew and Wang (18)). The effective core potentials (ECPs) of Stevens et al. (19) were used for all heavy atoms. In DFT calculations, ECPs have been shown to yield results close to experiment and of equivalent accuracy to that of all-electron calculations for a variety of transition metal complexes at a much reduced computational cost (3, 4). The valence space contractions used were as follows: P, C, and O (31/31/1*) and Mn (4211/4211/3111). The *d* polarization functions for the main-group elements were taken from the compilation of Huzinaga (20). The 3-21G basis set was used for the H atoms (21). The same basis set was used in DFT calculations with the BLYP functional to optimize the geometries of the conformers involved in the scrambling process, yielding a DFT//DFT value for the energy barrier. All of the DFT calculations were carried out using the Gaussian94 program (22).

3. Results of calculations and discussion

A. PM3(tm) Predicted structures

1. $Mn_2(CO)_6(dppm)_2$

The geometrical parameters of five different conformers of $Mn_2(CO)_6(dppm)_2$ and the lowest energy conformer of $Mn_2(CO)_5(dhpm)_2$, as calculated with the PM3(tm) method, are listed in Table 1 along with the experimental crystal structure values from the related complex $Mn_2(CO)_5(dppm)_2$ (23). Conformers A and B (Figs. 2(*a*) and 2(*b*)), differing only in the orientation of the methylene unit, have a planar

© 1999 NRC Canada

Table 1. Structural parameters of the $Mn_2(CO)_n(dhpm)_2$ conformers (n = 6, 5).[a]

	$n = 6$[b]							$n = 5$[c]	
	A		B	C	D	E		F	
Parameter	PM3	DFT	PM3	PM3	PM3	PM3	DFT	PM3	Expt.[d]
Mn—Mn	2.988	2.878	2.986	3.101	3.101	3.077	3.288	3.328	2.934
$Mn—C_{ax}$				1.722	1.722	1.731	1.802	1.729	1.73
$Mn—C_{eq/term}$	1.743	1.825	1.742	1.818	1.817	1.821	1.852	1.728	1.67
$Mn—C_{br}$	2.112	2.096	2.112					2.042	1.93
Mn—P	2.245	2.322	2.245	2.221	2.221	2.219	2.298	2.212	2.272
$C_{ax}—O_{ax}$				1.194	1.193	1.192	1.191	1.194	1.20
$C_{eq/term}—O_{eq/term}$	1.189	1.188	1.187	1.179	1.802	1.178	1.189	1.192	1.18
$C_{br}—O_{br}$	1.198	1.211	1.195					1.232	1.10
P—H	1.274	1.447	1.273	1.277	1.278	1.280	1.446	1.274	
$P—CH_2$	1.860	1.898	1.859	1.866	1.866	1.855	1.899	1.867	1.83
$Mn\text{-}Mn\text{-}C_{eq/term}$	133.5	132.4	133.4	86.4	86.4	90.0[e]	85.8	96.4	94
$O_{eq/term}\text{-}C_{eq/term}\text{-}Mn$	178.1	179.3	178.1	175.8	175.8	174.8	174.4	170.9	176
$O_{ax}\text{-}C_{ax}\text{-}Mn$				180.0	180.0	179.7	179.9	168.9	173
$O_{br}\text{-}C_{br}\text{-}Mn$	135.0	136.6	135.0					125.5	173
$P\text{-}Mn\text{-}C_{eq/term}$	89.0	89.4	88.9	90.0	90.0	90.0[e]	89.8	95.2	
$P\text{-}Mn\text{-}C_{ax}$				90.4	90.4	90.0[e]	92.6	91.3	
$P\text{-}CH_2\text{-}P$	113.4	106.3	113.5	115.5	115.5	112.4	108.1	117.9	113.2
H-P-H	97.9	96.9	97.9	97.8	97.8	97.6	96.7	98.2	
$H\text{-}CH_2\text{-}H$	106.0	110.0	106.0	106.0	106.0	106.2	109.5	106.1	
Mn-P-P-Mn	0.1	0.1	0	18.9	18.4	0.0[e]	0.1	0.1	
$C_{eq/term}\text{-}Mn\text{-}Mn\text{-}C_{eq/term}$	0.1	0.1	0	19.6	19.2	0.0[e]	0.2	0.1	

[a]Bond lengths in Å, bond angles in deg.

[b]The $Mn_2(CO)_6(dppm)_2$ conformers are: (A) *cis*-$Mn_2(CO)_4(\mu_2\text{-}CO)_2(dhpm)_2$ (planar, bridging), Fig. 2(*a*). (B) *trans*-$Mn_2(CO)_4(\mu_2\text{-}CO)_2(dhpm)_2$ (planar, bridging), Fig. 2(*b*). (C) *cis*-$Mn_2(CO)_6(dppm)_2$ (nonplanar, nonbridging), Fig. 2(*c*). (D) *trans*-$Mn_2(CO)_6(dppm)_2$ (nonplanar, nonbridging), Fig. 2(*d*). (E) *cis*-$Mn_2(CO)_6(dppm)_2$ (planar, nonbridging), Fig. 2(*e*).

[c]The lowest energy conformer of $Mn_2(CO)_5(dhpm)_2$ (conformer F), Fig. 3.

[d]Values taken from the experimental crystal structure of the related complex $Mn_2(CO)_5(dppm)_2$ (23).

[e]Parameter fixed during optimization.

arrangement of the CO ligands with two of them symmetrically bridging the Mn atoms. In conformers C and D (Figs. 2(*c*) and 2(*d*)), all of the CO ligands are in the terminal positions but they adopt a pseudo-staggered arrangement, similar to the staggered conformer of $Mn_2(CO)_{10}$ in Fig. 1(*a*). In conformer E (Fig. 2(*e*)), all of the CO ligands occupy terminal positions in a planar arrangement. The following naming convention for the carbonyl ligands is used: In the all-terminal conformers (C and D, Figs. 2(*c*), 2(*d*); E, Fig. 2(*e*)) the *axial* carbonyls are defined to be colinear to the Mn—Mn bond, while the remaining carbonyls are labelled as *equatorial*. In the planar, di-bridged conformers (A and B, Figs. 2(*a*), 2(*b*)) *bridged* is used to label the two μ_2-carbonyls, while *terminal* labels the remaining four carbonyls. For the $Mn_2(CO)_5(dhpm)_2$ complex (conformer F, Fig. 3) *bridged* labels the lone μ_2-CO, *axial* labels the two CO ligands colinear to the Mn—Mn bond, while the two remaining carbonyls are labelled *equatorial*.

Interestingly, whenever the geometry optimization was commenced from a structure in which the six carbonyls were coplanar, the carbonyls in the final optimized structure remained coplanar and two of them became symmetrically bridged (conformers A and B, Figs. 2(*a*), 2(*b*)). This planarity was maintained even though no symmetry constraints were placed on the system (i.e., C_1 point group was used). When the optimization was initiated from a structure with the six carbonyls in a pseudo-staggered arrangement, then the final optimized structure was also pseudo-staggered with all carbonyls in the terminal positions (conformers C and D, Figs. 2(*c*), 2(*d*)). The coplanar, all-terminal species (conformer E, Fig. 2(*e*)) could only be obtained by constraining certain angles. Such behaviour could indicate that the molecule has a very complicated potential energy hypersurface with a large number of local minima.

As illustrated in Table 1, the PM3(tm) method predicts structural parameters that agree reasonably well with the corresponding parameters of $Mn_2(CO)_5(dppm)_2$ (23) given the steric differences between the two phosphine ligands and the presence of a semibridging CO ligand in the experimental complex. This semibridging carbonyl would make the experimental structure resemble a conformation intermediate between the computed symmetrically di-bridging (A, B) and planar, all-terminal (E) conformers. PM3(tm) overestimates the experimental Mn—Mn bond distance by 0.14 Å in the planar, all-terminal conformer (E), not surprisingly, as the semibridging CO ligand should act to bring the Mn atoms closer. The deviation between the experimental Mn—Mn distance and that predicted by PM3(tm) is smaller for the symmetrically di-bridged conformers, around 0.05 Å. The difference could be ascribed to either the shortcomings of PM3(tm), or to crystal packing effects, or both. There also appears to be a significant difference between the computed and experimental Mn—C distance for the equatorial or terminal CO ligands. The experimental distance is much

© 1999 NRC Canada

Fig. 2. The conformers of $Mn_2(CO)_6(dppm)_2$: (*a*) *cis*-$Mn_2(CO)_4(\mu_2\text{-}CO)_2(dhpm)_2$ (Conformer A), (*b*) *trans*-$Mn_2(CO)_4(\mu_2\text{-}CO)_2(dhpm)_2$ (Conformer B),(*c*) *cis*-$Mn_2(CO)_6(dhpm)_2$ (Conformer C), (*d*) *trans*-$Mn_2(CO)_6(dhpm)_2$ (Conformer D), (*e*) planar, all-terminal $Mn_2(CO)_6(dppm)_2$ (Conformer E).

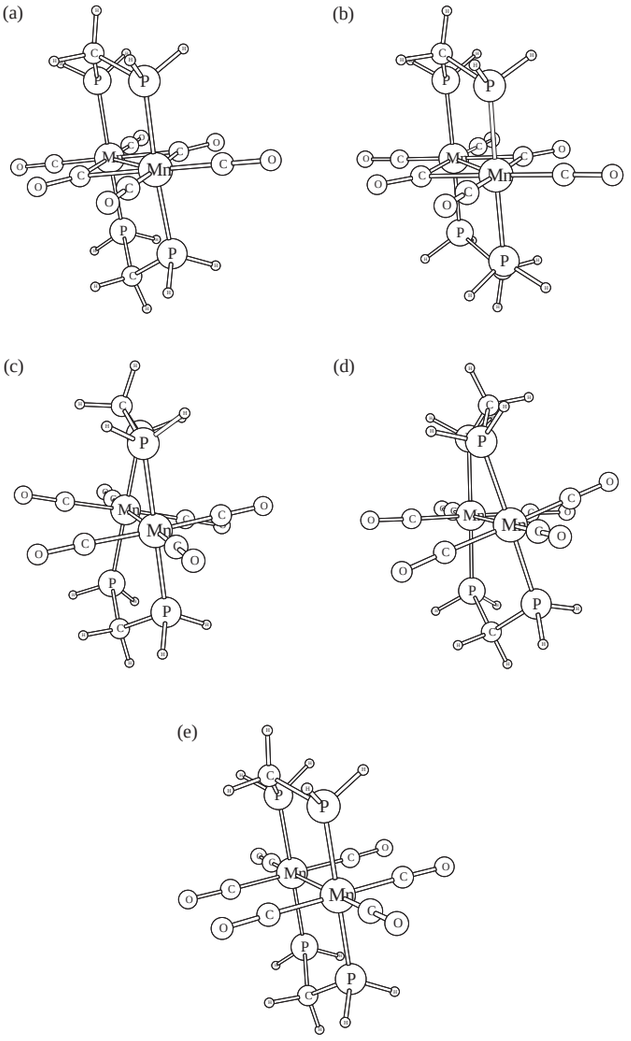

shorter (0.07–0.15 Å) than the computed values, and may be due to the different coordination at the Mn atoms in the experimental structure. The Mn atoms have different coordination numbers in the experimental $Mn_2(CO)_5(dppm)_2$ structure and the computed $Mn_2(CO)_6(dppm)_2$ structure. The loss of an equatorial CO ligand in the experimental species should make the Mn atoms more electron rich and thus more capable of back-donation to the remaining equatorial carbonyls, resulting in a shorter Mn—C_{eq} distance. However, as with the Mn—Mn distance, both crystal packing effects and PM3(tm) deficiencies could be contributing to this disagreement. There is good agreement between the PM3(tm)-computed values and experimental values for those parameters least sensitive to the semibridging CO ligand and the differing steric demands of the phosphines, e.g., the Mn—C_{ax}, Mn—P, P—CH_2, and C—O distances.

Fig. 3. The lowest energy conformer of $Mn_2(CO)_5(dhpm)_2$ (Conformer F).

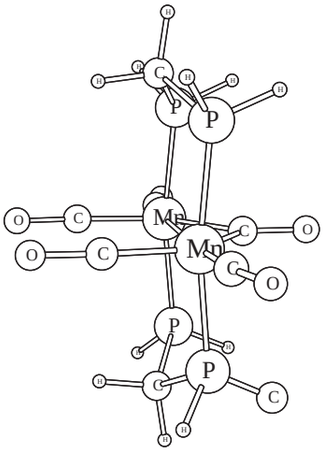

As a further test of the ability of the PM3(tm) method to predict geometric structures of transition metal complexes, we removed one of the bridging CO ligands from conformer A and optimized the resultant $Mn_2(CO)_5(dhpm)_2$ complex (shown in Fig. 3 and labeled as conformer F in Table 1) for comparison with the respective experimental crystal structure. As seen in Fig. 3, the bridging CO ligand is oriented symmetrically between the two Mn atoms, normal to the Mn—Mn bond. As discussed above, the experimental structure, on the other hand, shows the semibridging nature of the CO ligand (being bound to one of the Mn atoms through the C atom and to the other through the C—O triple bond). Apart from the Mn—Mn and Mn—C_{br} distances, predicted to be too long by 0.39 Å and 0.11 Å, respectively, there is quite good agreement between the computed and experimental values for the remaining geometric parameters, with deviations of 0.06 Å or less. Of course the deviation between the computed and experimental Mn-C_{br}-O_{br} bond angle is largest, 125° vs. 173°, reflecting the different bonding nature of the bridging carbonyl ligands. There is reasonable aggreement between computation and experiment for the remaining bond angles, typically less than 5°.

It must be added that conformer F is a minimum on the potential energy surface, reached from several different initial geometries with no symmetry constraints imposed on the system (i.e., C_1 symmetry), as indicated by the results of the harmonic vibrational analysis. One of the lowest frequency modes (42 cm^{-1}) corresponds to the Mn–Mn stretch. This indicates that the potential energy hypersurface is very flat and that the molecule may be easily compressed by the crystal-

© 1999 NRC Canada

Fig. 4. The two conformers of $Mn_2(CO)_6(dppm)_2$.

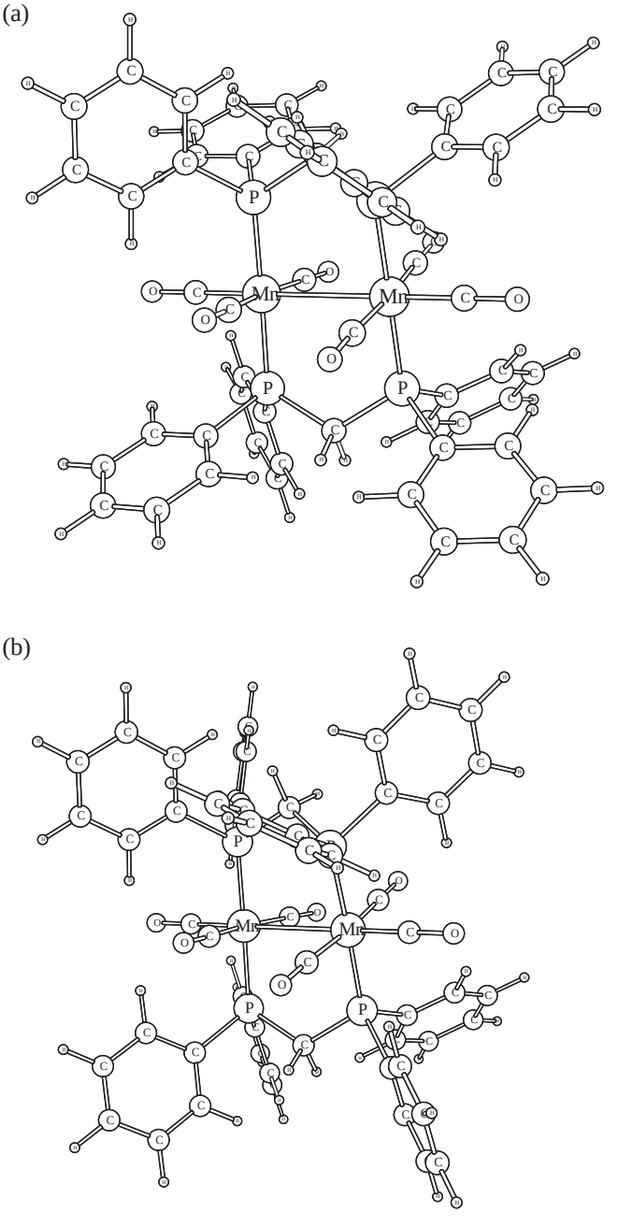

line environment, perhaps explaining why in the gas phase our PM3(tm) calculations exaggerate the Mn—Mn distance. As seen in Table 1, this compression may be simulated in the gas phase by the addition of a second bridging carbonyl. Furthermore, several other higher energy conformers, differing in the orientation of the lone bridging CO ligand with respect to the CH_2 groups of the dhpm ligands, were also located.

A comparison of the Mn—Mn distance in the bridged (A and B) and nonbridged, all-terminal (C, D, and E) conformers shows that the formation of the μ_2-carbonyls results in a shortening of the Mn—Mn distance by over 0.1 Å. Contrary to what one would expect from steric and electrostatic considerations, the conversion from a staggered conformation (C and D) to an eclipsed conformation (E) shortens the

Table 2. Structural parameters of two different conformers of $Mn_2(CO)_6(dppm)_2$.[a]

	Conformer[b]		
Parameter	A	B	Expt.[c]
Mn—Mn	3.166	3.187	2.934
Mn—C_{ax}	1.733	1.732	1.73
Mn—C_{eq}	1.836	1.843	1.67
Mn—P	2.215	2.217	2.272
C_{ax}—O_{ax}	1.191	1.191	1.20
C_{eq}—O_{eq}	1.172	1.171	1.18
P—CH_2	1.865	1.866	1.83
P—CPh	1.873	1.855	1.82
CPh—HPh	1.095	1.098	
(C—H)CH_2	1.106	1.182	
Mn-Mn-C_{eq}	86.9	84.6	
O_{eq}-C_{eq}-Mn	176.5	176.9	176
O_{ax}-C_{ax}-Mn	180.0	179.7	173
C_{ax}-Mn-C_{eq}	93.1	93.7	
P-Mn-C_{eq}	92.8	92.0	
P-Mn-C_{ax}	90.29	90.93	
P-CH_2-P	118.7	119.3	113
CPh-P-CPh	99.4	97.5	103
Mn-P-P-Mn	11.0	13.3	
C_{eq}-Mn-Mn-C_{eq}	13.8	17.0	

[a]Bond lengths in Å, bond angles in deg.

[b]The two conformers are shown in Fig. 4.

[c]Values taken from the crystal structure of the related complex $Mn_2(CO)_5(dppm)_2$ (23).

Mn—Mn bond by 0.02 Å. From the calculated Mn—C distances one can conclude that the terminal carbonyls in the di-bridged conformers (A and B) are bound more strongly to Mn than the equatorial carbonyls, but more weakly than the axial carbonyls of the pseudo-staggered conformers (C and D). In accord with experimental data for symmetrically bridged species (24), the PM3(tm) calculations predict the bridging carbonyls to have the longest Mn—C and C—O distances.

Interestingly, the arrangement of the phosphine moiety is slightly different in the five conformers: the Mn—P distance is shorter, by over 0.02 Å, in the pseudo-staggered conformers (Fig. 3) than in the planar, dibridged species (Fig. 2). Furthermore, the P-CH_2-P angle appears to be more affected by the planarity of the six carbonyls (conformers A, B, and E versus C and D), than the *cis* or *trans* arrangement of the methylene unit in the bidentate phosphine ligand (conformers A, C, and E versus B and D).

At the PM3(tm) level the stationary points corresponding to the optimized geometries of conformers A, B, C, and D were all found by harmonic vibrational analysis to be local minima. The planar all-terminal conformer E was found to be a second-order saddle point (with very small imaginary frequencies of 25*i* and 13*i* cm^{-1}). The vibrational mode for the frequency of 25*i* corresponds to the scrambling motion of the carbonyls towards the planar, di-bridged conformer A, while the other one corresponds to rotation about the Mn—Mn bond to form the pseudo-staggered conformer C. Furthermore, in each conformer about one third of the computed vibrational frequencies are smaller than 500 cm^{-1}, in-

© 1999 NRC Canada

Table 3. Relative energies of the $Mn_2(CO)_6(dhpm)_2$ conformers.

Conformer	Relative energy[a]				
	PM3(tm)[b]	BLYP[c]	BP86[c]	B3LYP[c]	B3PW91[c]
B. *trans*-$Mn_2(CO)_4(\mu_2\text{-}CO)_2(dhpm)_2$ (planar, bridging)	0.1				
C. *cis*-$Mn_2(CO)_6(dhpm)_2$ (nonplanar, nonbridging)	29.3	–16.9	–14.2	–18.3	–16.2
D. *trans*-$Mn_2(CO)_6(dhpm)_2$ (nonplanar, nonbridging)	29.3				
E. *cis*-$Mn_2(CO)_6(dppm)_2$ (planar, nonbridging)	32.2	–17.4 (–13.1)[d]	–14.9	–18.6	–16.8

[a]In kcal/mol, calculated with respect to conformer A (Fig. 2(*a*)), *cis*-$Mn_2(CO)_4(\mu_2\text{-}CO)_2(dhpm)_2$ (planar, di-bridged conformation).
[b]Values computed from PM3(tm) energies at the PM3(tm)-optimized geometries. The PM3(tm) reference energy is $\Delta H° = -555.3$ kcal/mol.
[c]Values computed from the DFT total energies at their respective PM3(tm)-optimized geometries. The reference energies are: E(BLYP) = –381.538 66 E_h; E(BP86) = –382.696 65 E_h; E(B3LYP) = –382.038 84 E_h; E(B3PW91) = –382.398 17 E_h.
[d] Computed from BLYP energies at their respective BLYP-optimized geometries. The BLYP//BLYP reference energy is E(BLYP) = –381.693 54 E_h.

dicating a very flat potential energy hypersurface near the local minima.

The DFT-optimized Mn—Mn bond length in conformer A was shorter than the value obtained using the PM3(tm) method, while in conformer E DFT predicts a longer Mn—Mn bond than PM3(tm). As discussed above for the $Mn_2(CO)_5(dhpm)_2$ system (conformer F), the absence of bridging carbonyls in conformer E brings about a longer Mn—Mn bond. Compared with PM3(tm), DFT also predicts longer Mn—C distances for the axial and equatorial/terminal carbonyls for both conformers, and a shorter Mn—C_{br} distance in conformer A. Interestingly, in both conformers the geometry of the dhpm ligand computed at the DFT level is different from its PM3(tm) geometry, as indicated by the significant changes in the Mn—P and P—CH_2 distances and the P-CH_2-P angle. As illustrated in Table 1, all of the remaining DFT-optimized bond lengths and angles agree reasonably well with their PM3(tm) counterparts.

2. $Mn_2(CO)_6(dppm)_2$

Geometry optimizations at the PM3 level of theory were performed for the two different conformers of $Mn_2(CO)_6(dppm)_2$ shown in Fig. 4, differing only in the tilt angle of the plane of the phenyl rings. For both conformers, the PM3 calculations (Table 2) predict a pseudo-staggered arrangement of carbonyls, similar to that observed in the $Mn_2(CO)_6(dppm)_2$ system (Figs. 2(*c*) and 2(*d*)), with dihedral angles deviating from planarity by 14°–17°. (The pseudo-staggered conformation was obtained even when the optimization was initiated from a structure with a coplanar arrangement of carbonyls.) The differences in bond lengths between the axial and equatorial carbonyls and the Mn atom suggest stronger binding of the axial carbonyls to the metal atom, as observed in the dhpm conformers. As stated before, there is no experimental structure known for $Mn_2(CO)_6(dppm)_2$, and although the X-ray crystal structure is known for $Mn_2(CO)_5(dppm)_2$ (23), the presence of the semibridging CO ligand is expected to induce a number of structural changes, as discussed above for the dhpm complex. As seen in comparison with the computed dhpm structures, the experimental Mn—Mn distance is shorter than that predicted by the PM3(tm) calculations. Again, the agreement is quite satisfactory for those parameters least likely to be affected by the semibridging carbonyl (M—C_{ax}, P—C, and C—O distances). The agreement becomes worst for the M—P distance and M—CO_{eq} distance, perhaps reflecting the sensitivity of these parameters to the presence of the semibridging CO ligand, the tilt of the phenyl rings of the dppm ligands, and, possibly, crystal packing effects or shortcomings of the PM3(tm) methodology.

The differences in the geometric structures of the two conformers are negligible, with conformer A more stable by 5 kcal/mol. It is interesting to note that a slight change in the tilt of the phenyl rings was a sufficient structural perturbation to locate a completely different stationary point on the potential energy hypersurface. This, along with the fact that we failed to locate a structure with a planar conformation of CO ligands, again suggests a very complicated potential energy hypersurface with a large number of shallow local minima, leading to significantly different structures with similar total energies. The size of these systems prevented the characterization of the stationary points corresponding to the optimized geometries by harmonic vibrational analysis, even at the PM3(tm) level.

B. Relative energies and the barrier to CO migration

The relative energies of the different conformers of $Mn_2(CO)_6(dhpm)_2$ are shown in Table 3. The PM3(tm)//PM3(tm) calculations predict conformers A and B with a coplanar arrangement of CO ligands, two of which are symmetrically bridging the two Mn atoms, to be the lowest in energy. The total energy of the planar, all-terminal conformer E is 32 kcal/mol above the energy of conformer A. The pseudo-staggered conformers C and D have energies about 29 kcal/mol higher than that of A. The PM3(tm)//PM3(tm) approach finds a slight preference for a *cis* arrangement of the methylene units in the two bidentate dhpm ligands, in agreement with the arrangement found in the crystal structure of $Mn_2(CO)_5(dppm)_2$.

The results obtained at the PM3(tm)//PM3(tm) level imply that carbonyl scrambling in the model $Mn_2(CO)_6(dppm)_2$ system proceeds from the coplanar, symmetrically bridged conformation (A and B) to the coplanar, all-terminal conformer E, and then back to A/B, with an activation barrier of about 32 kcal/mol. This energy barrier is higher than the upper limit for an NMR-detectable process (ca. 25 kcal/mol (7)) and much higher than the barrier of 10 kcal/mol reported by Marsella and Caulton (12). This finding is consistent with the overestimated PM3(tm)//PM3(tm) energy barrier for rotation about the Mn—Mn bond in $Mn_2(CO)_{10}$ (13).

We employed the DFT//PM3(tm) scheme, with several density functionals, to calculate the total energies and the energy barrier to carbonyl scrambling in the model

© 1999 NRC Canada

$Mn_2(CO)_6(dppm)_2$ system. The results, collected in Table 3, show that all of the density functionals predict a stability trend opposite to that found at the PM3(tm)//PM3(tm) level. The planar, all-terminal conformer E is found to have the lowest energy, smaller by 15–19 kcal/mol than the energy of the planar, symmetrically bridged conformer A. The DFT//PM3(tm) calculations predict the pseudo-staggered conformer C to lie 0.3–0.7 kcal/mol above the lowest-energy conformer E. Hence, based solely on the computed energy differences, the DFT//PM3(tm) approach models the carbonyl scrambling in $Mn_2(CO)_6(dppm)_2$ as proceeding from the planar, all-terminal conformer E to the planar, di-bridged conformer A, and back to conformer E. This mechanism is similar to that predicted for carbonyl scrambling in $Mn_2(CO)_{10}$ in our previous DFT//DFT study (13). Depending on the functional used, the DFT//PM3(tm) approach yields an energy barrier of 15–19 kcal/mol for carbonyl migration in the $Mn_2(CO)_6(dppm)_2$ system, nearly halved with respect to the PM3(tm)//PM3(tm) barrier. These values are smaller than the upper limit for NMR detectable processes (25 kcal/mol (7)) and closer to the value of 10 kcal/mol estimated from NMR experiments by Marsella and Caulton (12). Using the total energies of conformers A and E at their respective DFT-optimized geometries (DFT//DFT), the energy barrier for scrambling is reduced to only 13 kcal/mol. We expected a further lowering of the DFT//PM3(tm) energy barrier upon reoptimization of the geometries using the DFT approach since the PM3(tm) parameters were not trained on any bridging systems similar to the one studied here.[4]

4. Conclusions

The PM3(tm) semiempirical method successfully locates the local minima involved in CO migration, and gives an indication of the flatness of the surface, as illustrated by the large number of low vibrational frequencies. Although the experimental structure data were obtained from a crystal structure of $Mn_2(CO)_5(dppm)_2$ (23) in which one of the carbonyls was semibridging in nature, the agreement between the experimental and the PM3(tm)-optimized $Mn_2(CO)_6(dppm)_2$ and $Mn_2(CO)_5(dhpm)_2$ geometries was very good for those structural parameters least likely to be affected by the presence of the semibridging carbonyl and the different steric demands of the dppm ligand. The deviations are largest for the Mn—Mn, Mn—CO_{br}, and Mn—CO_{eq} distances, and may be attributed to the chemical differences between the experimental and calculated complexes, and to shortcomings of the PM3(tm) method. In addition, crystal packing effects may be quite large for the flat $Mn_2(CO)_n(dhpm)_2$ potential energy hypersurfaces.

The PM3(tm)//PM3(tm) energy barrier of 32 kcal/mol for CO scrambling in $Mn_2(CO)_6(dppm)_2$ is vastly overestimated compared to the experimental value of 10 kcal/mol. The barrier was reduced by a factor of two using energies from DFT calculations at the PM3(tm)-optimized geometries. In addition, the relative energy ordering of conformers was changed. Using the DFT//PM3(tm) scheme, carbonyl scrambling was found to proceed in a manner similar to that predicted for $Mn_2(CO)_{10}$ using the DFT//DFT approach: from the planar, all-terminal conformation to a planar, di-bridged conformation and then back to the original conformation with an energy barrier of 15–19 kcal/mol, depending on the functional employed. The DFT//PM3(tm) method successfully improves the energy barrier obtained when the PM3(tm) is used throughout; however, the barrier is still overestimated by 5–10 kcal/mol. This value was reduced even further to 13 kcal/mol upon optimization of the structures using DFT, overestimating experiment by only 3 kcal/mol. This improvement was expected, since the training set used to develop the PM3(tm) parameters contained more complexes with terminal carbonyls than bridging carbonyls; as a result the lowest energy all-terminal conformer E should be better represented at the PM3(tm) level than the symmetrically bridged conformer A.

Since semiempirical methods rely on experimental data for the training of parameters, the results of these semiempirical calculations will be close to experiment as long as the calculated molecules resemble those in the training set. It has been established that the modern DFT approach brings about results close to experiment for a variety of transition metal complexes (2). Given the sparsity of reliable structural data, especially for molecules containing transition metal atoms, an alternative approach to the parametrization of semiempirical methods could utilize these reliable DFT results. In this approach, the semiempirical parameters would be derived not from experimental data, but rather from quantities calculated using accurate DFT methods in conjunction with very large extended basis sets, leading to a *semitheoretical method*.

Acknowledgments

This study was inspired by a lecture given by Professor J. Takats at the University of Alberta. Subsequent discussions with Professor Takats are gratefully acknowledged. M.K. is grateful to Professor W.A.G. Graham for enlightening comments on the nature of bridging carbonyls. The calculations were done on the IBM RS/6000 workstations and on the IBM SP2 installation at the University of Alberta. This work was financed partly by a research grant from the Natural Sciences and Engineering Research Council of Canada (NSERC), and partly by the University of Alberta. S.A.D. would also like to thank the Faculty of Graduate Studies at the University of Alberta for a scholarship and the Department of Chemistry for the Harry Emmett Gunning Graduate Fellowship.

References

1. A. Veillard. Chem. Rev. **91**, 743 (1991).
2. T. Ziegler. Chem. Rev. **91**, 651 (1991).
3. G. Frenking, I. Antes, M. Böhme, S. Dapprich, A.W. Ehlers, V. Jonas, A. Neuhaus, M. Otto, R. Stegmann, A. Veldkamp, and S.F. Vyboishchikov. *In* Reviews in computational chemis-

[4] J. Yu, Wavefunction, Inc. Personal communication: The only bridged Mn dimers included in the PM3(tm) parameterization were $Mn_2(CO)_8(\mu_2\text{-}Br)_2$ and $Mn_2(\mu_2\text{-}C\text{-}CH_2)$. However, there were a number of terminal carbonyl complexes included in the training set: $Mn_2(CO)_{10}$, $(CO)_4MnCl[P(Ph)_3]$, $(CO)_2(PMe_3)_2MnOOCMe$, and $(CO)_4(Br)Mn[CCP(Ph)_3]$.

© 1999 NRC Canada

try. Vol. 8. *Edited by* K.B. Lipkowitz and D.B. Boyd. VCH Publishers, Inc., New York. 1996. p. 63.
4. T.R. Cundari, M.T. Benson, M.L. Lutz, and S.O. Sommerer. *In* Reviews in computational chemistry. Vol. 8. *Edited by* K.B. Lipkowitz and D.B. Boyd. VCH Publishers, Inc., New York. 1996. p. 145.
5. K.R. Adam, I.M. Atkinson, and L.F. Lindoy. J. Mol. Struct. **384**, 183 (1996).
6. K.J. Børve, V.R. Jensen, T. Karlsen, J.A. Støvneng, and O. Swang. J. Mol. Model. **3**, 193 (1997).
7. E. Band and E.L. Muetterties. Chem. Rev. **78**, 639 (1978).
8. P. de Mayo (*Editor*). Rearrangements in ground and excited states. Academic, New York. 1980.
9. R.D. Adams and F.A. Cotton. J. Am. Chem. Soc. **95**, 6589 (1973).
10. (*a*) J. Evans, B.F.G. Johnson, J. Lewis, and J.R. Norton. Chem. Commun. **73**, 79 (1973); (*b*) J. Evans, B.F.G. Johnson, J. Lewis, and T.W. Matheson. Chem. Commun. **75**, 576 (1975).
11. (^{13}C) L.J. Todd and J.R. Wilkinson J. Organomet. Chem. **77**, 1 (1974); (^{17}O) S. Aime, L. Milone, D. Osella, G.E. Hawkes, and E.W. Randall. J. Organomet. Chem. **178**, 171 (1979).
12. J.A. Marsella and K.G. Caulton. Organometallics, **1**, 274 (1982).
13. S.A. Decker, O. Donini, and M. Klobukowski. J. Phys. Chem. A **101**, 8734 (1997).
14. A.D. Becke. Phys. Rev. A: Gen. Phys. **38**, 3098 (1988).
15. C. Lee, W. Yang, and R.G. Parr. Phys. Rev. B: Condens. Matter, **37**, 785 (1988).
16. J.P. Perdew. Phys. Rev. B: Condens. Matter, **33**, 8822 (1986).
17. A.D. Becke. J. Chem. Phys. **98**, 5648 (1993).
18. J.P. Perdew and Y. Wang. Phys. Rev. B: Condens. Matter, **45**, 13244 (1992).
19. (*a*) W.J. Stevens, H. Basch, and M. Krauss. J. Chem. Phys. **81**, 6026 (1984); (*b*) W.J. Stevens, H. Basch, M. Krauss, and P. Jasien. Can. J. Chem. **70**, 612 (1992); (*c*) T.R. Cundari and W.J. Stevens. J. Chem. Phys. **98**, 5555 (1993).
20. S. Huzinaga (*Editor*). Gaussian basis sets for molecular calculations. Elsevier, Amsterdam. 1984.
21. (*a*) J.S. Binkley, J.A. Pople, and W.J. Hehre. J. Am. Chem. Soc. **102**, 939 (1980); (*b*) M.S. Gordon, J.S. Binkley, J.A. Pople, W.J. Pietro, and W.J. Hehre. J. Am. Chem. Soc. **104**, 2797 (1982); (*c*) W.J. Pietro, M.M. Francl, W.J. Hehre, D.J. Defrees, J.A. Pople, and J.S. Binkley. J. Am. Chem. Soc. **104**, 5039 (1982).
22. M.J. Frisch, G.W. Trucks, H.B. Schlegel, P.M.W. Gill, B.G. Johnson, M.A. Robb, J.R. Cheeseman, T. Keith, G.A. Petersson, J.A. Montgomery, K. Raghavachari, M.A. Al-Laham, V.G. Zakrzewski, J.V. Ortiz, J.B. Foresman, J. Cioslowski, B.B. Stefanov, A. Nanayakkara, M. Challacombe, C.Y. Peng, P.Y. Ayala, W. Chen, M.W. Wong, J.L. Andres, E.S. Replogle, R. Gomperts, R.L. Martin, D.J. Fox, J.S. Binkley, D.J. Defrees, J. Baker, J.P. Stewart, M. Head-Gordon, C. Gonzalez, and J.A. Pople. GAUSSIAN 94, Revision D.3. Gaussian, Inc., Pittsburgh, Pa. 1995.
23. C.J. Commons and C.F. Hoskins. Aust. J. Chem. **28**, 1663 (1975).
24. J.P. Collman, L.S. Hegedus, J.R. Norton, and R.G. Finke. Principles and applications of organotransition metal chemistry. University Science Books, Mill Valley, Calif. 1987.

© 1999 NRC Canada

Dioxirane oxidation of nitrosoamines. An ab initio study

Gennady V. Shustov and Arvi Rauk

Abstract: Pathways for oxidation of the parent nitrosoamine **2**, nitrosodimethylamine **3**, and *anti*-nitrosoethylmethylamine **4** by the parent dioxirane **1** have been explored computationally using the B3LYP hybrid density functional theoretical method in conjunction with the 6-31G* and 6-311+G** basis sets. Oxygen transfer from **1** to the nitrogen of the NO group (NO oxidation), yielding nitroamines **5**, **7**, and **10**, has the lowest activation barrier (15, 12.8, and 12 kcal mol^{-1} for **2**, **3**, and *anti*-**4**, respectively). Oxidation of the amine nitrogen (N oxidation) in **2**, **3** leads to nitric oxide and nitroxyl radicals **6**, **8** and is characterized by the highest activation energy: 28.5 kcal mol^{-1} for **2**, 22.3 kcal mol^{-1} for **3**. The potential barrier to hydroxylation of the methyl groups in **3** (CH oxidation) is intermediate — ca. 19 kcal mol^{-1}. Introduction of a methyl group to the carbon reaction centre decreases the activation barrier of the *anti*-CH oxidation by 2–3 kcal mol^{-1}. In **3**, a gas-phase small preference for *anti*-CH oxidation over *syn*-CH oxidation, 0.1 kcal mol^{-1}, is predicted to increase dramatically to 4.7 kcal mol^{-1} when the reaction is carried out in a dielectric medium (acetone, IPCM model). In general, polar solvents (CH_2Cl_2, acetone) lower the activation barriers for the NO, N, and CH oxidations, more so for the species of higher polarity than those of lower polarity (reactive complexes (**1+3**), (**1**+*anti*-**4**), transition state *anti*,*syn*-$\mathbf{TS_{CH}}$ **(1+4)**]. However, the chemoselectivity ($E_a^{NO} < E_a^{anti\text{-}CH} < E_a^{syn\text{-}CH} < E_a^{N}$) in the polar solvents is predicted to be the same as in the gas phase.

Key words: dioxirane, nitrosoamines, oxidation, ab initio, computation.

Résumé : En se basant sur des calculs faisant appel à la méthode théorique de la densité fonctionnelle hybride B3LYP en conjonction avec des ensembles de base 6-31G* et 6-311+G**, on a examiné les diverses voies réactionnelles pour l'oxydation de la nitrosamine (**2**), de la nitrosodiméthylamine (**3**) et de l'*anti*-nitrosoéthylméthylamine (**4**) par le dioxirane (**1**). Le transfert d'oxygène de **1** vers l'azote du groupe NO (oxydation de NO), conduisant aux nitramines **5**, **7** et **10** donne lieu à la barrière d'oxydation la plus faible (respectivement 15, 12,8 et 12 kcal mol^{-1} pour **2**, **3** et *anti*-**4** respectivement). L'oxydation de l'azote de l'amine (oxydation de l'azote) des composés **2** et **3** conduit à l'oxyde nitrique et aux radicaux nitroxyles **6** et **8** et elle est caractérisée par une énergie d'activation plus élevée 28,5 kcal mol^{-1} pour **2** et 22,3 kcal mol^{-1} pour **3**. La barrière de potentiel pour l'hydroxylation des groupes méthyles de **3** (oxydation d'un CH) est intermédiaire, soit environ 19 kcal mol^{-1}. L'introduction d'un groupe méthyle au centre réactionnel carboné diminue la barrière d'activation de l'oxydation du *anti*-CH par 2 à 3 kcal mol^{-1}. Lors de l'oxydation du composé **3** en phase gazeuse, on prévoit une légère préférence (0,1 kcal mol^{-1}) pour l'oxydation du CH *anti* par rapport au CH *syn*; cette différence croît d'une façon dramatique (à 4,7 kcal mol^{-1}) lorsque la réaction serait effectuée dans un milieu diélectrique (acétone, modèle IPCM). En général, les solvants polaires (CH_2Cl_2, acétone) conduisent à des barrières d'activation plus faibles pour les oxydations de NO, de N ou de CH; ceci est plus vrai pour les espèces de polarité élevée que pour celles de faible polarité (complexes réactifs (**1+3**), (**1**+*anti*-**4**) état de transition *anti*,*syn*-$\mathbf{ET_{CH}}$ **(1+4)**). Toutefois, on prévoit que la chimiosélectivité sera la même dans des solvants polaires qu'en phase gazeuse ($E_a^{NO} < E_a^{anti\text{-}CH} < E_a^{syn\text{-}CH} < E_a^{N}$).

Mots clés : dioxirane, nitrosamines, oxydation, ab initio, calcul théorique.

[Traduit par la Rédaction]

Introduction

Oxidation of nitrosodialkylamines continues to be a matter of intense, current interest, mainly because it is the main path of metabolism and metabolic activation (1–5). In addition, oxidation is offered (6–8) as one of the most effective methods for removing these highly carcinogenic, mutagenic, and toxic substances from wastewater of rocket fuel, metallurgical and food industries. Finally, oxidation of nitrosodialkylamines can be used for the preparation of *N*-nitroamines — highly energetic materials (9–12).

In general, two kinds of oxidative processes have been studied. The first one is the reactions of nitrosodialkylamines with various oxidants (O_2, H_2O_2, PhIO, hydroperoxides, peracids) in the presence of catalysts — salts (13, 14) and complexes of metals (Fe, Mn) (15). In the catalytic processes, oxidation of an alkyl group of a nitrosodialkylamine occurs usually at the α-carbon atom, forming α-hydroxy-*N*-nitro-

Received July 29, 1998.

V. Shustov and A. Rauk.[1] Department of Chemistry, University of Calgary, Calgary, AB T2N 1N4, Canada.

[1]Author to whom correspondence may be addressed. Telephone: (403) 220-6247. Fax: (403) 289-9488. e-mail: rauk@chem.ucalgary.ca

© 1999 NRC Canada

Scheme 1.

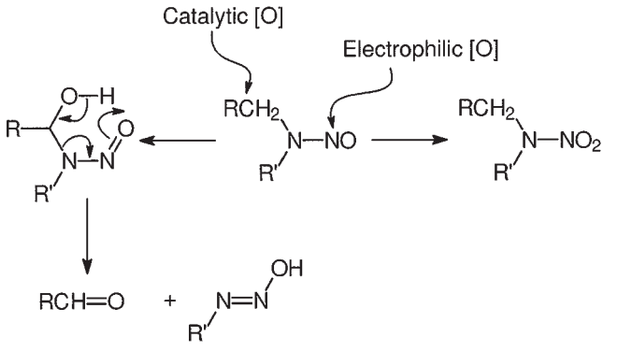

soamines which undergo further fragmentation (Scheme 1) (16–18). This kind of oxidation includes also metabolic degradation mediated by cytochromes P-450 (1–5).

The second kind is electrophilic oxidation by peracids (9–11) or concentrated HNO_3 in the presence of trifluoroacetic anhydride (12). The electrophilic oxidants attack the nitrogen of the nitroso group, yielding the corresponding *N*-nitroamines (Scheme 1).

Dioxiranes, which have proved to be powerful and selective oxidants (18–23), nevertheless, have not yet been employed for oxidation of nitrosodialkylamines. It was reported that the efficacy of the dioxirane oxidation of aliphatic CH bonds in organic substrates approaches the efficacy of enzyme oxidation (18–25). The presence of an electron-donating group in the α-position to the CH bond accelerates the dioxirane oxidation (24). At the same time, in reactions with alkylamines, dioxiranes behave as electrophilic oxidants and attack the nitrogen atom of the amino group (26–28). Electrophilicity of dioxiranes reveals itself also in reactions with sulfides and sulfoxides (29, 30). Hence, in nitrosodialkylamines, the probable points for the dioxirane attack can be both nitrogen atoms as well as an α-CH bond. It is not obvious which of these sites is the most vulnerable because, unlike the nitrogen in alkylamines, the nitrogens in nitrosodialkylamines are substantially less nucleophilic. In addition, the reactivity of the CH bonds in *syn*- and *anti*-alkyl groups should be different. Therefore, it is of interest to study, firstly, the mechanism of the dioxirane oxidation of nitrosoamines and, secondly, the chemo- and regioselectivity of this oxidation. Knowledge of the selectivity is important for the practical use of dioxiranes for oxidation of nitrosodialkylamines.

Here we describe a theoretical study of the dioxirane oxidation of nitrosoamines. Reactions of the parent dioxirane **1** with the parent nitrosoamine **2**, nitrosodimethylamine **3**, and *anti*-nitrosoethylmethylamine **4** were chosen as theoretical models.

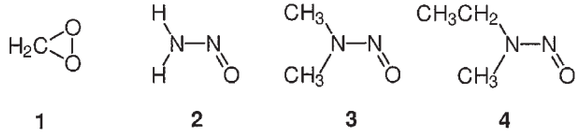

1 **2** **3** **4**

Scheme 2.

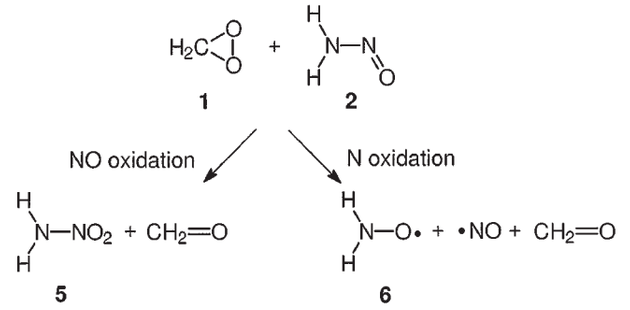

5 **6**

Earlier, theoretical studies of the dioxirane oxidations of heteroatoms in organic substrates were performed using the B3LYP hybrid density functional theory (28) and MP2 methods (28, 30). Recently, we showed (24) that the MP2 method is not appropriate for the description of the dioxirane oxidation of aliphatic CH bonds, whereas the B3LYP method gives results agreeing with experiment. Therefore, the latter method was employed in the present work.

Computational methods

All calculations presented here were performed with the Gaussian 94 system of programs (31). The geometry optimizations and frequency calculations were carried out at the B3LYP hybrid density functional theory level with the internal 6-31G* and 6-311+G** basis sets using procedures implemented in the Gaussian molecular orbital package. Harmonic frequency analysis verified the nature of the stationary points as minima (all real frequencies) or as transition structures (one imaginary frequency) and was used to provide an estimate of the zero-point vibrational energies (ZPVE). Zero-point corrections (ΔZPVE) were scaled by a 0.98 factor. Total energies and ZPVEs of all species are given in Tables S-1, S-2, and S-3, which are included as supplementary material.[2]

The intrinsic reaction coordinate (IRC) (32, 33) path was traced in order to check the B3LYP/6-31G* energy profiles for the reactions of the parent dioxirane **1** with nitrosoamine **2**.

The effects of dielectric medium were simulated at the B3LYP/6-311+G** level by single-point SCRF calculations with the IPCM model (34) as implemented in Gaussian 94.

Results and discussion

Parent nitrosoamine – parent dioxirane

For the parent system, dioxirane **1** – nitrosoamine **2**, the possibility of the dioxirane attack on the two sites of nitrosoamine **2** — on the nitrogen of the nitroso group (NO oxidation) and on the amine nitrogen (N oxidation) — has been explored (Scheme 2).

NO oxidation

Dioxirane **1** attacks the nitrogen of the nitroso group along the axis of the nitrogen lone pair, revealing itself as an electrophilic oxidant. A substantial elongation of the O—O

[2] Supplementary material may be purchased from: The Depository of Unpublished Data, Document Delivery, CISTI, National Research Council Canada, Ottawa, Canada, K1A 0S2.

© 1999 NRC Canada

Fig. 1. B3LYP structures of the reactive complex ((*a*) IRC structure, (*b*) fully optimized structure) and concerted transition states for the NO and N oxidations of the parent nitrosoamine **2** with the parent dioxirane **1** calculated with the 6-31G* and 6-311+G** (in parentheses) basis sets. Bond lengths are given in angstroms and angles in degrees.

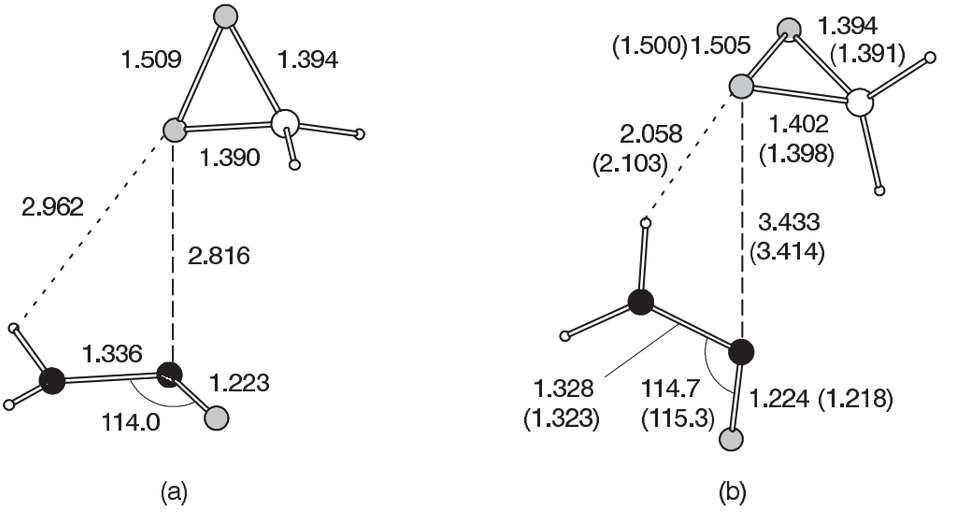

reactive complex (1+2)

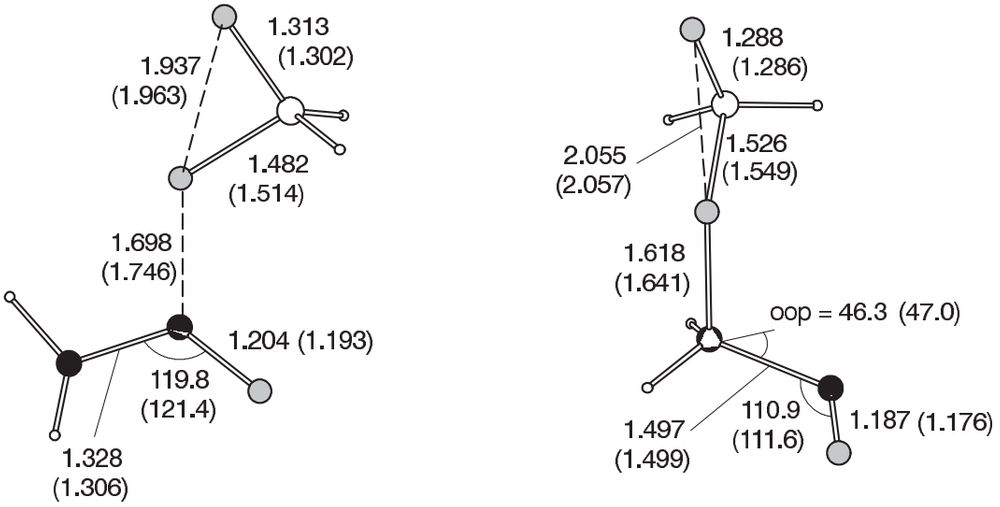

TS_{NO}(1+2) **TS_{N}(1+2)**

bond in the transition state of the NO oxidation, **TS_{NO}(1+2)** (Fig. 1), indicates a dominant role of the antibonding σ^*_{OO} orbital, which determines the electrophilic properties of the dioxirane. The dioxirane ring takes up a position in the average plane of the nitrosoamine group.

The path of the reaction of dioxirane **1** with nitrosoamine **2** to nitroamine **4** via transition state **TS_{NO}(1+2)** was confirmed by the IRC-B3LYP/6-31G* calculation. It was found that the reactants form a reactive complex **(1+2)** (Fig. 1*a*), which lies somewhat lower in energy (–2.9 kcal mol^{-1}) than its predecessors. It is interesting that in this complex, the dioxirane ring settles in a plane, which is almost perpendicular to the average plane of the nitrosoamine. Full geometry optimization of complex **(1+2)** led to formation of the hydrogen bond between an oxygen of the dioxirane ring and the *anti*-hydrogen of the nitrosoamine (Fig. 1*b*). The relative energy of the complex was decreased to –5.5 kcal mol^{-1}, apparently owing to this hydrogen bond.

In **TS_{NO}(1+2)**, the σ^*_{OO} orbital of dioxirane **1** interacts with the nonbonding orbital of the nitrogen of the nitroso

© 1999 NRC Canada

Chart 1.

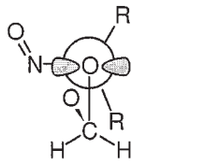

R = H, **TS_N(1+2)**

R = CH_3, **TS_N(1+3)**

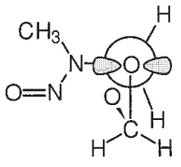

anti-**TS_{CH}(1+3)**

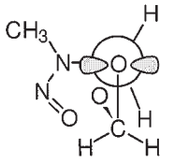

syn-**TS_{CH}(1+3)**

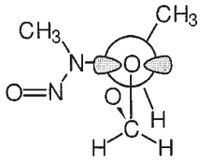

anti,anti-**TS_{CH}(1+4)**

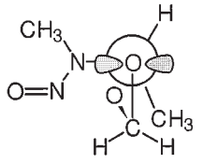

anti,syn-**TS_{CH}(1+4)**

group, which is a principal component of the HOMO of nitrosoamine **2**. Hence, the NO oxidation is characterized by a rather low potential barrier (15.0 kcal mol^{-1}). This barrier is close to the barrier (12.2 kcal mol^{-1}) of the N oxidation of methylamine with dimethyldioxirane, calculated at the same theoretical level (28). However, the reaction with nitrosoamine is substantially more exothermic (–48.5 kcal mol^{-1}) than the reaction with methylamine (–18.9 kcal mol^{-1}) (28).

N oxidation

Upon formation of the transition state for the oxidation of the amino N (N oxidation), **TS_N(1+2)**, dioxirane **1** approaches also along the axis of the nitrogen lone pair (Fig. 1). The *gauche*-orientation of the dioxirane ring with respect to the N—N bond is apparently caused by a secondary interaction of the nonbonded orbital (*n*) of the dioxirane oxygen atom with the antibonding σ* orbital of this bond (Chart 1).

Investigation of the reaction path of the N oxidation by means of an IRC-B3LYP/6-31G* calculation revealed that the products of the reaction, besides formaldehyde, are nitroxyl **5** and nitric oxide (Fig. 2). This implies that the expected nitrosoamine N-oxide is not a minimum on the $CH_2N_2O_3$ potential-energy surface.

The nonbonding orbital of the amine nitrogen of nitrosoamine **2** is in conjugation with the π^*_{NO} orbital making this nitrogen a poor electron donor. As a result, the activation barrier for the N oxidation is almost twice as high as the barrier for the NO oxidation (Table 1). As in the case of methylamine oxidation, the exothermicity of the reaction is lower than the exothermicity of the NO oxidation.

Table 1. Relative energies[a] (kcal mol^{-1}) of the reactants, products, and transition states for the parent nitrosoamine **2** – dioxirane **1** system.

Species	B3LYP/6-31G*	B3LYP/6-311+G**
1 + **2**	0.0	0.0
Reactive complex **(1+2)**	–5.5	–4.0
TS_{NO}(1+2)	17.7	15.0
TS_N(1+2)	30.1	28.5
5 + CH_2O	–44.9	–48.5
6 + NO + CH_2O	–12.1	–19.6

[a]Including 0.98 × ΔZPVE.

Table 2. Relative energies[a] (kcal mol^{-1}) of the reactants, products, and transition states for the nitrosodimethylamine **3** – parent dioxirane **1** system.

Species	B3LYP/6-31G*	B3LYP/6-311+G**
1 + **3**	0.0	0.0
Reactive complex **(1+3)**	–3.4	–2.8
TS_{NO}(1+3)	15.5	12.8
TS_N(1+3)	24.9	22.3
anti-**TS_{CH}(1+3)**	25.5	18.6
syn-**TS_{CH}(1+3)**	25.5	18.7
7 + CH_2O	–42.8	–46.1
8 + NO + CH_2O	–15.7	–22.8
anti-**9** + CH_2O	–61.2	–69.8
syn-**9** + CH_2O	–60.7	–68.8

[a]Including 0.98 × ΔZPVE.

Nitrosodimethylamine 3 – parent dioxirane

Besides the NO and N oxidations, the CH oxidation of the *syn*- and *anti*-methyl groups has been studied in nitrosodimethylamine **3** (Scheme 3).

NO and N oxidations

Introduction of the methyl groups to the amine nitrogen leads to a decrease of the potential barriers of the NO and N oxidations by ca. 2 and 5.5 kcal mol^{-1}, respectively. Naturally, the barrier of the amino N oxidation is more sensitive because the introduction is carried out directly at the reaction centre. In spite of this, the energy of activation for the NO oxidation remains substantially lower than the energy of activation for the N oxidation (Table 2).

Qualitatively the geometries of transition states **TS_{NO}(1+3)** and **TS_N(1+3)** (Fig. 3) are similar to those for the parent system, whereas the geometry of the reactive complex of the NO oxidation is quite different. For the dimethyl system, this complex has a "proper" geometry, i.e., the dioxirane ring settles in the average plane of the nitrosoamino group as it does in **TS_{NO}(1+3)**. Complex **(1+3)** is relatively less stable with respect to its precursors (Table 2) than complex **(1+2)** because of the lack of the hydrogen bond, which stabilizes the latter.

CH oxidation

It was recently shown (24, 25) that the transition state of the dioxirane oxidation of aliphatic CH bonds corresponds

© 1999 NRC Canada

Fig. 2. Schematic representation of the N oxidation pathway for the parent system nitrosoamine-dioxirane derived with the IRC-B3LYP/6-31G* calculation. Bond lengths are given in angstroms.

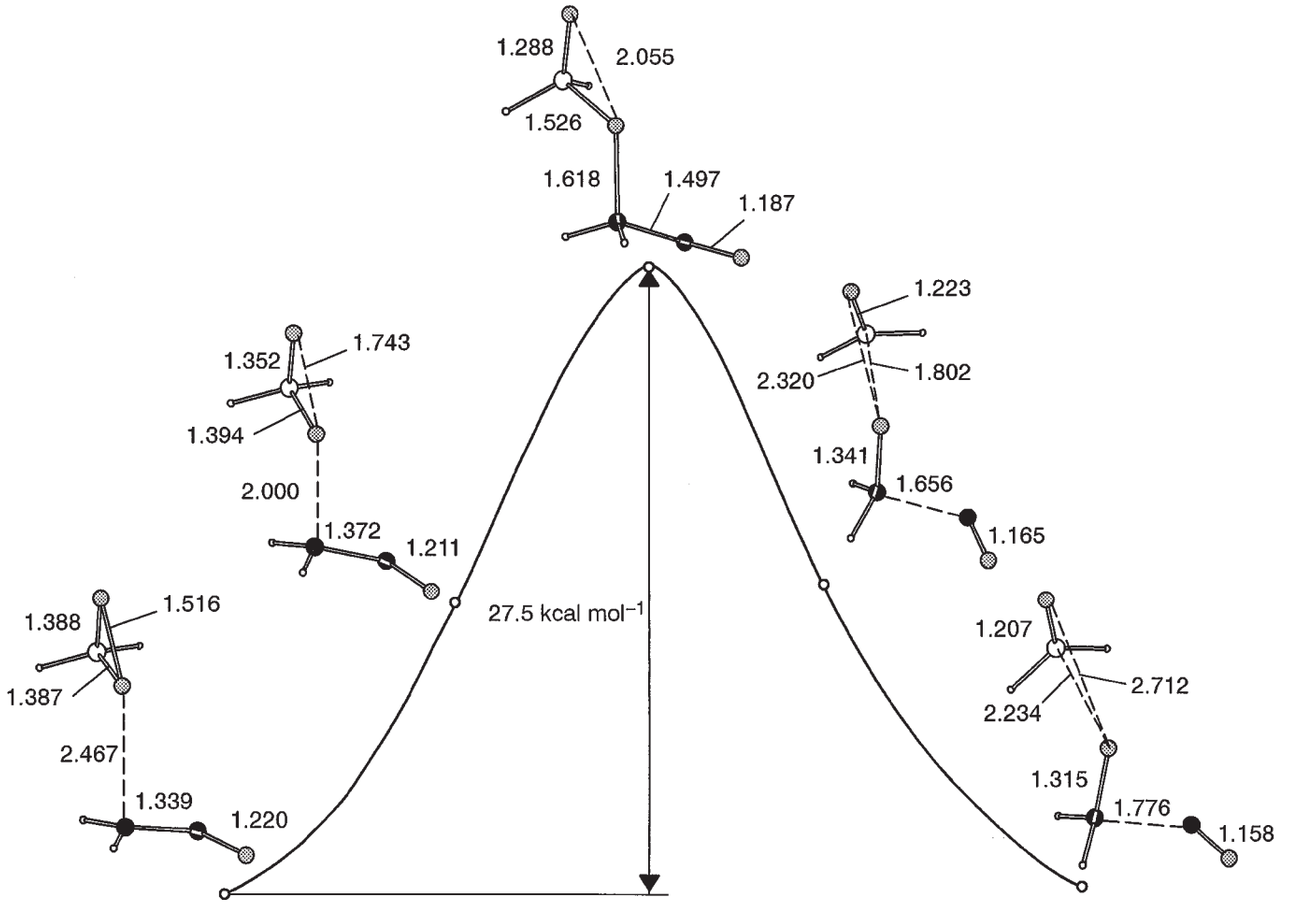

Scheme 3.

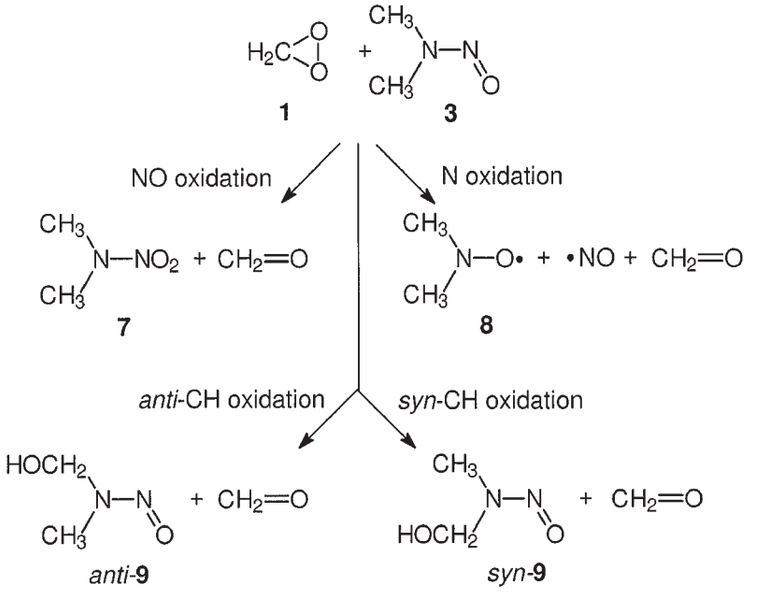

© 1999 NRC Canada

Fig. 3. B3LYP structures of the reactive complex and concerted transition state for the NO and N oxidations of nitrosodimethylamine **3** with the parent dioxirane **1** calculated with the 6-31G* and 6-311+G** (in parentheses) basis sets. Bond lengths are given in angstroms and angles in degrees.

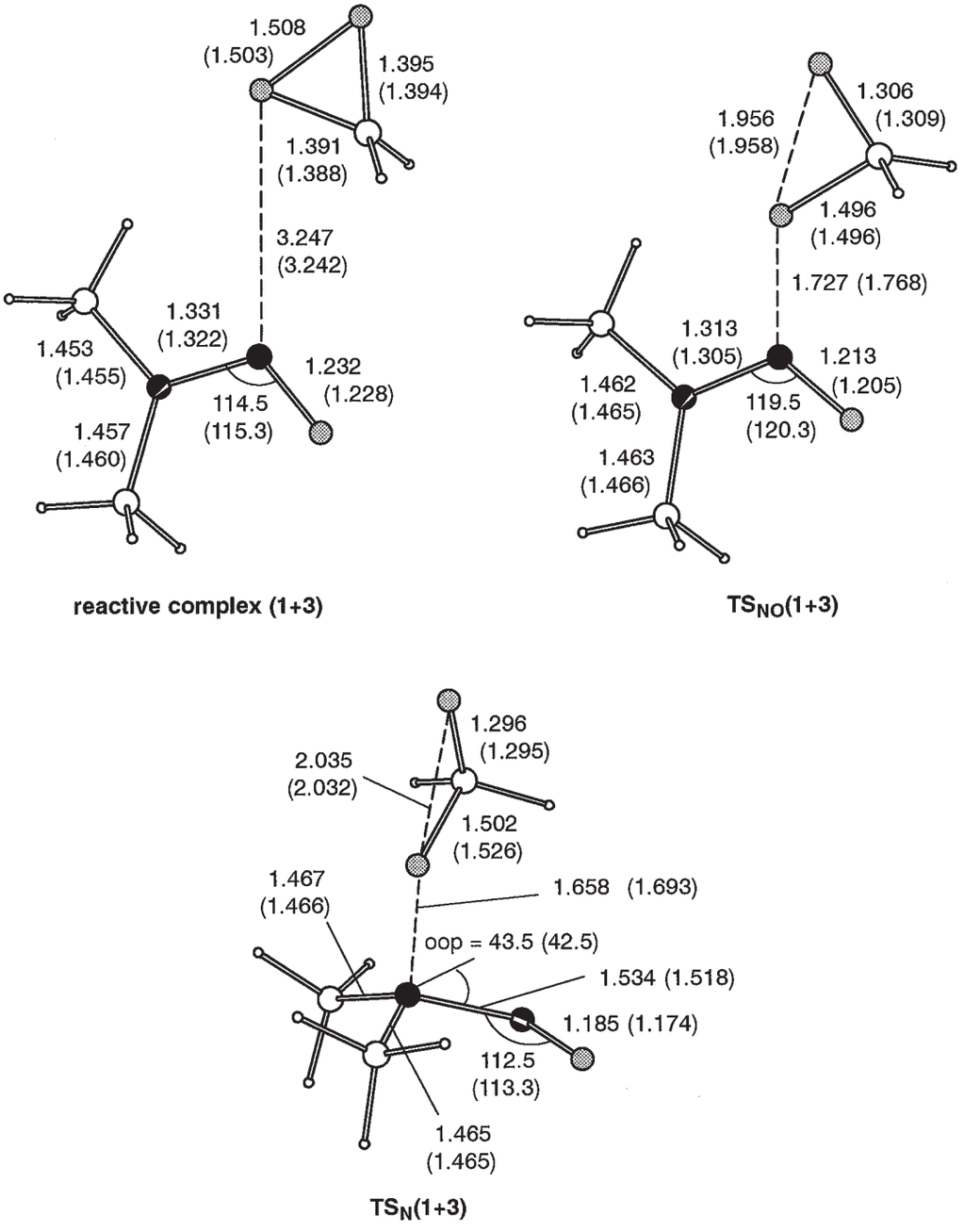

to electrophilic oxygen insertion with a pronounced hydride transfer character and some diradical character. Electron-donating substituents at the reaction carbon atom of the substrate decrease the activation barrier for this reaction.

A similar nature is apparently inherent in the transition state of the oxidation of the CH bonds in nitrosoamine **3**. In both isomers, *syn*- and *anti*-$\mathbf{TS_{CH}(1+3)}$, the breaking CH bond settles almost perpendicularly to the average plane of the nitrosoamine group (Fig. 4). In such geometry, the orbital interactions between the reaction centre and the amine nitrogen is maximum, although the *n* orbital of this nitrogen is involved in the competitive conjugation with π^* orbital of the N=O bond. As a result of this conjugation, the ability of the amine nitrogen to stabilize the hydride transfer is weakened. In fact, the activation barrier for the dioxirane oxidation of the CH bonds in nitrosodimethylamine **3** (ca. 19 kcal mol^{-1})

© 1999 NRC Canada

Fig. 4. B3LYP structures of the concerted transition state for the CH oxidations of nitrosodimethylamine **3** and nitrosoethylmethylamine **4** with the parent dioxirane **1** calculated with the 6-31G* and 6-311+G** (in parentheses) basis sets. Bond lengths are given in angstroms and angles in degrees.

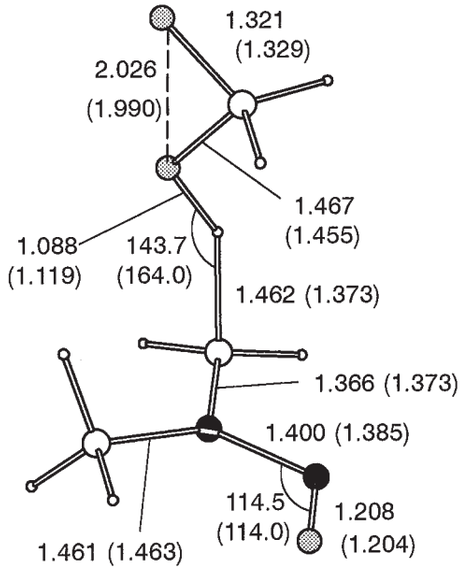

anti–TS_{CH}**(1+3)**

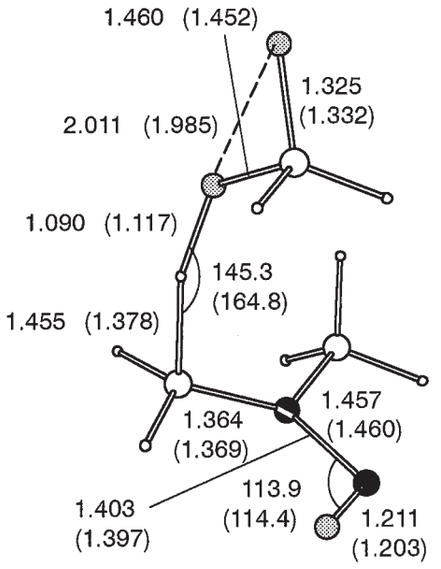

syn–TS_{CH}**(1+3)**

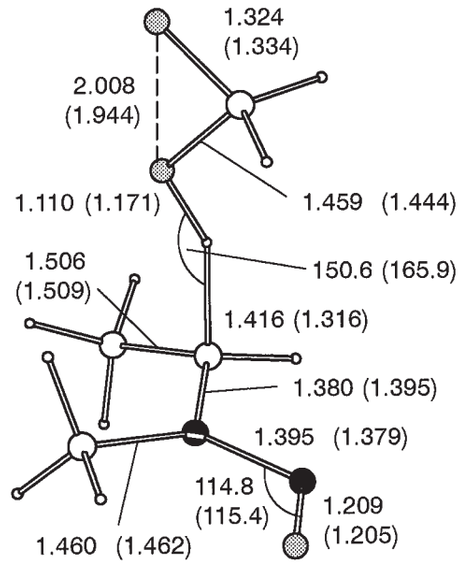

anti,anti–TS_{CH}**(1+4)**

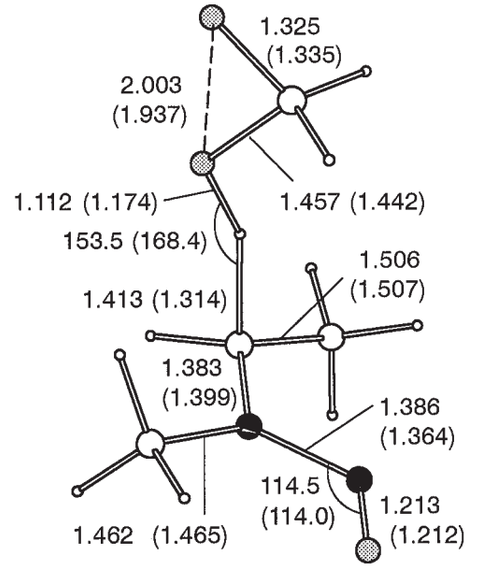

anti,syn–TS_{CH}**(1+4)**

is closer to the barrier for methanol (19.9 kcal mol^{-1}) than for methylamine (10.4 kcal mol^{-1}), calculated at the same theoretical level (24).

The *gauche* orientation of the dioxirane ring with respect to the C—N bond in *syn*- and *anti*- TS_{CH}**(1+3)** (Chart 1, Fig. 4) is determined by the secondary n-σ^* orbital interaction, as in the case of the CH oxidation of methanol (24).

The mechanism of the dioxirane oxidation of the aliphatic CH bonds and, correspondingly, the intrinsic nature of its transition state continues to be a matter of lively discussion (24, 25, 35). Experimental data may be interpreted (19–23, 35) so as to support both electrophilic oxygen insertion and a free-radical mechanism via a molecule-induced homolysis of the O—O bond of the dioxirane (35). The discovery (24)

© 1999 NRC Canada

Scheme 4.

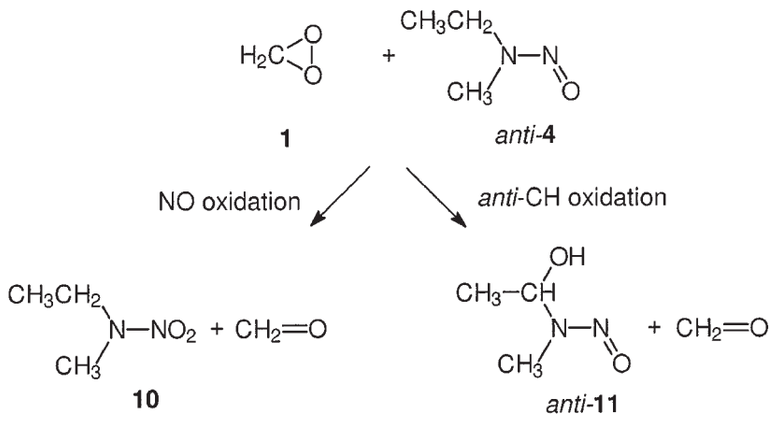

Chart 2.

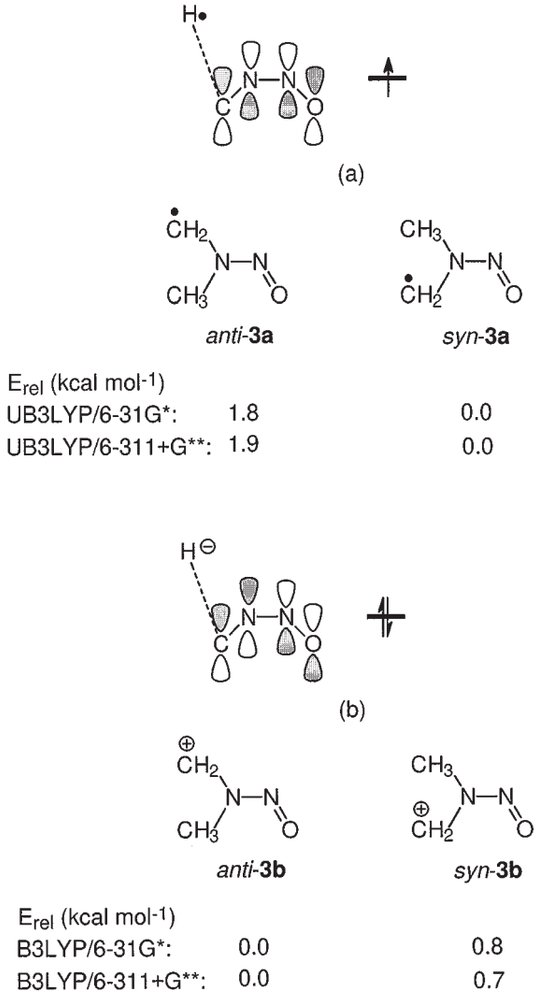

of a bifurcation in the reaction path subsequent to the transition state for CH oxidation of methane suggests a mechanistic compromise. At the bifurcation point, the system can convert into a radical pair or relax straightforwardly into the products of electrophilic oxygen insertion, i.e., the corresponding alcohol and carbonyl compound. Obviously, a greater diradical character of the transition state increases the probability of the conversion into the radical pair at the bifurcation point and vice versa.

The dominant character of the transition state for the CH oxidation of nitrosoamine **3** can be revealed from the *syn*- versus *anti*-regioselectivity of the reaction. Let us examine nodal characteristics of the highest occupied π-like orbitals of the nitrosoamine fragment of $\mathbf{TS_{CH}(1+3)}$. These will be different depending on whether the transition state involves primarily hydrogen atom transfer (i.e., has free-radical character) (Chart 2*a*) or hydride transfer (i.e., has electrophilic character) (Chart 2*b*). In the first case, the singly occupied fragment orbital is in phase at the two ends, and one can expect an extra stabilization of the *syn*-transition state.[3] In the second case, the frontier orbital is doubly occupied, out of phase at the two ends, and the *syn*-transition state would be destabilized by the out-of-phase interaction of the terminal p AOs. This qualitative picture is confirmed by calculations of the relative stability of the *syn*,*anti*-isomers of model compounds — C-radical **3a** and C-cation **3b**. It was found that the *syn*-isomer is more stable for C-radical **3a**, whereas C-cation **3b** prefers the *anti*-configuration (Chart 2). Thus, dominant radical character in $\mathbf{TS_{CH}(1+3)}$ should lead to *syn*-regioselectivity and dominant hydride transfer character to the *anti*-regioselectivity.

The calculations at the B3LYP/6-311+G** level give a small preference (0.1 kcal mol^{-1}) to *anti*-$\mathbf{TS_{CH}(1+3)}$ over its *syn*-isomer in the gas phase. However, as it will be shown below, the *anti*-regioselectivity becomes considerable when the influence of a dielectric medium is taken into account. All these data confirm the supposition that the transition state of the dioxirane oxidation of the aliphatic CH bonds has mainly the hydride transfer character.

anti-Nitrosoethylmethylamine – parent dioxirane

As it follows from above, the oxidations of the nitroso group and the C—H bond of the *anti*-methyl group are the

[3] Such stabilization was considered earlier for *syn*-α-C anions of nitrosodialkylamines (36).

© 1999 NRC Canada

Fig. 5. B3LYP structures of the reactive complex and concerted transition state for the NO oxidation of nitrosoethylmethylamine **4** with the parent dioxirane **1** calculated with the 6-31G* and 6-311+G** (in parentheses) basis sets. Bond lengths are given in angstroms and angles in degrees.

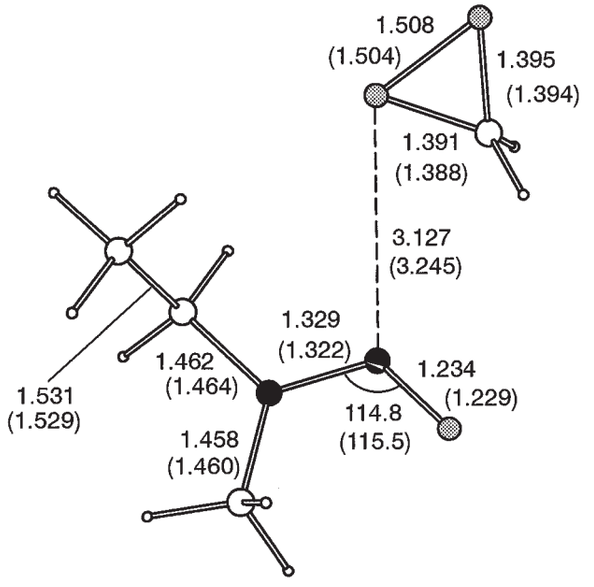

reactive complex (1+*anti*–4)

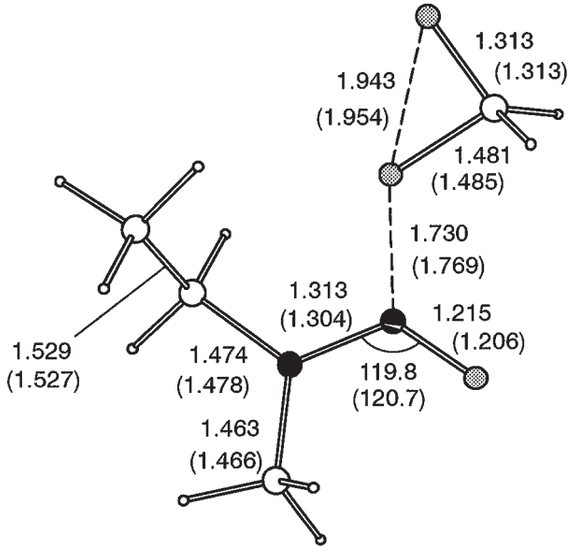

***anti*–TS$_{NO}$(1+4)**

main competing processes in the interaction of dioxirane **1** with nitrosodimethylamine **3**. A difference in activation energies of these processes is 5.8 kcal mol^{-1} in favor of the NO oxidation. It was earlier (24) found for the CH oxidations of methanol and ethanol by dioxirane **1** that the introduction of the methyl group to the reaction centre of the substrate decreases the potential barrier for the reaction by 5.5 kcal mol^{-1} (B3LYP/6-311+G**, gas phase) owing to the electron donor ability of the methyl group. Hence, one can suppose equalization of the rates of the NO and *anti*-C oxidations or inversion of their ratio in higher nitrosodialkylamines. To check this supposition, we have studied the NO and *anti*-C oxidations in *anti*-nitrosoethylmethylamine **4** (Scheme 4).

© 1999 NRC Canada

Table 3. Relative energies[a] (kcal mol^{-1}) of the reactants, products, and transition states for the *anti*-nitrosoethylmethylamine **4** – parent dioxirane **1** system.

Species	B3LYP/6-31G*	B3LYP/6-311+G**
1 + *anti*-**4**	0.0	0.0
Reactive complex **(1**+*anti*-**4)**	–3.6	–2.9
anti-$\mathbf{TS_{NO}(1+4)}$	14.3	12.0
anti,anti-$\mathbf{TS_{CH}(1+4)}$	21.8	16.0
anti,syn-$\mathbf{TS_{CH}(1+4)}$	22.5	16.8
10 + CH_2O	–42.9	–46.1
anti-**11** + CH_2O	–63.8	–72.2

[a]Including 0.98 × ΔZPVE.

Table 4. Energies[a] (kcal mol^{-1}) and dipole moments (debye) of the transition states and reactive complexes for oxidation of nitrosodimethylamine (**3**) and *anti*-nitrosoethylmethylamine (**4**) by the parent dioxirane (**1**) derived with the IPCM model of dielectric medium at the B3LYP/6-311+G** level.

	Gas phase		CH_2Cl_2 (ε = 9.08)		Acetone (ε = 20.7)	
Species	E_{rel}	μ	E_{rel}	μ	E_{rel}	μ
Reactive complex **(1+3)**	–2.8	4.17	–0.9	5.18	–0.8	5.32
$\mathbf{TS_{NO}(1+3)}$	12.8	8.64	6.8	11.68	6.0	12.05
$\mathbf{TS_{N}(1+3)}$	22.3	7.83	15.9	11.34	15.2	11.75
anti-$\mathbf{TS_{CH}(1+3)}$	18.6	5.98	10.4	11.04	9.3	11.74
syn-$\mathbf{TS_{CH}(1+3)}$	18.7	6.14	15.9	9.73	14.0	10.24
Reactive complex **(1**+*anti*-**4)**	–2.9	4.23	–0.6	4.87	–0.4	4.92
anti-$\mathbf{TS_{NO}(1+4)}$	12.0	8.29	7.2	11.85	6.5	12.31
anti,anti-$\mathbf{TS_{CH}(1+4)}$	16.0	5.56	12.5	9.48	11.9	10.02
anti,syn-$\mathbf{TS_{CH}(1+4)}$	16.8	5.28	17.3	6.80	17.3	7.00

[a]Relative to the reactants, including 0.98 × ΔZPVE.

NO oxidation

The optimized geometries of reactive complex **(1**+*anti*-**4)** and transition state *anti*-$\mathbf{TS_{NO}(1+4)}$ (Fig. 5) are practically the same as in the case of nitrosodimethylamine **3** (Fig. 3). The C-methyl group takes a position almost perpendicularly to the average plane of the nitrosoamine group and does not impede the dioxirane attack on the nitroso group that proceeds in this plane. As a result, the relative energies of complex **(1**+*anti*-**4)** and *anti*-$\mathbf{TS_{NO}(1+4)}$ are very close to the relative energies of the corresponding species for nitrosoamine **3** (Tables 2, 3).

CH oxidation

For the CH oxidation of the methylene group in *anti*-**4**, two transition states, *anti,anti*-$\mathbf{TS_{CH}(1+4)}$ and *anti,syn*-$\mathbf{TS_{CH}(1+4)}$ (Fig. 4), were found. These differ by the mutual orientation of the C-methyl and nitroso groups, *anti* in the first and *syn* in the second. In both transition states, the dioxirane ring is in the *gauche*-position with respect to the C—N bond due to the *n*-σ* orbital interaction (Chart 1).

Selectivity for CH oxidation in nitrosoamines **3**, **4** is not as great as was observed in alcohols. The greatest difference (2.6 kcal mol^{-1}) in energies of the transition states (of the *anti*-CH oxidations) of nitrosodimethylamine **3** and nitrosoethylmethylamine **4**, is notably smaller than the difference (5.5 kcal mol^{-1}) for the CH oxidation of methanol versus ethanol (24). We assume that in the case of nitrosoamines **3**, **4**, the electronic stabilizing effect from the introduction of the methyl group is compensated to a substantial extent by steric repulsion with the N substituents. Indeed, flattening of the carbon reaction centre upon formation of the transition state of the *anti*-CH oxidation of nitrosoamine **4** must lead to an increase of the steric interactions of the C-methyl group with the N-methyl group in *anti,anti*-$\mathbf{TS_{CH}(1+4)}$ and with the nitroso group in *anti,syn*-$\mathbf{TS_{CH}(1+4)}$. Such steric strains cannot arise in the transition state of the CH oxidation of ethanol, which has only the hydrogen of the OH group instead of the bulky N-methyl and nitroso groups in **4**. To judge from the relative energies of *anti,anti*- and *anti,syn*-$\mathbf{TS_{CH}(1+4)}$, the MeC---NO steric repulsion is rather greater than the MeC---MeN one.

Chemo- and regioselectivity of the oxidation of 3 and *anti*-4 in a dipolar medium

Solvent polarity has been shown experimentally (19–23, 37, 38) and theoretically (24, 28, 30) to have a substantial influence on the rate and selectivity of dioxirane oxidations. In all these works, a decrease of the activation barrier for the reaction in polar solvents has been noted, presumably due to a higher polarity of the transition state.

The transition states of the NO, N, and CH oxidations of nitrosoamine **3** are also characterized by a high polarity, and the SCRF calculations, using the IPCM model of a dielectric medium, predict a considerable decrease of the potential barriers for these reactions upon transition from the gas phase into such solvents as methylene chloride and acetone (Table 3). The greatest decrease of the barrier is observed for *anti*-CH oxidation of nitrosoamine **3** — by 9.3 kcal mol^{-1} (gas phase → acetone). By contrast, the barrier for the *syn*-CH oxidation of **3** is decreased to the least extent — by

© 1999 NRC Canada

4.7 kcal mol^{-1}. Thus, the *anti*-regioselectivity of the CH oxidation is predicted to increase dramatically in polar solvents. Equally affected by solvent polarity are the activation energies for the NO and N oxidations of nitrosoamine **3**, which are each decreased by ca. 6–7 kcal mol^{-1}, i.e., to a more moderate extent than the activation energy for the *anti*-CH oxidation in the polar solvents. However, in spite of the differential solvation effects, the chemoselectivity order remains the same as in the gas phase, i.e., the nitrogen of the nitroso group should be oxidized most readily, followed by the CH bond of the *anti*-methyl group.

The introduction of the methyl group to the *anti*-(to NO)-carbon atom decreases the polarity of the transition states of both NO and CH oxidations. As a result, a relatively smaller influence of the polar solvents on the potential barriers of the oxidations of nitrosoethylmethylamine **4** is observed (Table 4). For the least polar transition state *anti*,*syn*-$\mathbf{TS_{CH}(1+4)}$, as well as for the relatively low polar reactive complexes **(1+3)** and **(1+*anti*-4)**, the SCRF calculations even predict an increase of the relative energies in the polar solvents.

Conclusions

According to the present B3LYP study, in the reactions with nitrosodialkylamines, dioxiranes behave as electrophilic oxidants. The nitrogen of the nitroso group is the most readily attacked. The α-CH bond of the *anti*-alkyl group is the second probable site for the oxidation, and the amine nitrogen is the least reactive. In accord with the electrophilic character of the dioxirane, the transition state of the CH oxidation of nitrosodialkylamines **3**, **4** has mainly hydride transfer character with a concomitant electron deficiency on the reaction carbon atom of the substrate. The introduction of an additional methyl group to the *anti*-α-carbon atom leads to a narrowing of the difference between the potential barriers of the NO and *anti*-C oxidations but not a reversal. The electronic stabilizing effect of the methyl group is compensated to a substantial extent by steric repulsions.

The decrease of the difference in the activation barriers for the NO and *anti*-CH oxidations of nitrosodimethylamine **3** from 5.8 kcal mol^{-1} in the gas phase to 3.3 kcal mol^{-1} in acetone (IPCM model) presupposes the possibility of actually reversing the chemoselectivity in experimental conditions, depending on the solvent. However, on the basis of our results on the ethylmethyl system, **4**, this seems improbable for higher nitrosodialkylamines, which form less polar transition states of the dioxirane CH oxidations. For example, the difference in the barriers for the NO and *anti*-CH oxidations is predicted to increase when the reaction is transferred from the gas phase (4.0 kcal mol^{-1}) into CH_2Cl_2 (5.3 kcal mol^{-1}) or acetone (5.4 kcal mol^{-1}).

On the basis of the calculated activation energies for the NO oxidation in solution (6–7 kcal mol^{-1}), one can predict that dialkyldioxiranes would be effective reagents for the conversion of nitrosodialkylamines into nitrodialkylamines. This reaction can be used also for removing highly hazardous nitrosodialkylamines from wastewater taking into account the possibility of the generation of dialkyldioxiranes in situ in aqueous solutions, and a low commercial cost of the reagents (22).

Acknowledgment

The financial support of the Natural Sciences and Engineering Research Council of Canada is gratefully acknowledged.

References

1. Y. Tan, S.P. White, S.R. Paranawithana, and C.S. Yang. Xenobiotica, **27**, 287 (1997).
2. V.M. Lee, L.K. Keefer, and M.C. Archer. Chem. Res. Toxicol. **9**, 1319 (1996).
3. L.K. Keefer, M.B. Kroeger-Koepke, H. Ishizaki, C.J. Michejda, J.E. Saavedra, J.A. Hrabie, C.S. Yang, and P.P. Roller. Chem. Res. Toxicol. **3**, 540, (1990).
4. P. Fournier. J. Toxicol. Clin. Exp. **10**, 283, (1990).
5. B.C. Challis and J.A. Challis. *In* The chemistry of amino, nitroso and nitro compounds and their derivatives. Suppl. F. *Edited by* S. Patai. John Wiley, New York. 1982. pp 1151–1223.
6. E.S. Fleming, J.C. Pennington, R.A. Howe, M.R. Colsman, K.E. Garrett, and B.G. Wachob. Hazard. Ind. Wastes, **26**, 285 (1994).
7. W. Mcphee, L. Wagg, and P. Martin. Chem. Oxid. **3**, 249 (1993); Chem. Abstr. **121**, 41 926s (1994).
8. B.J. Jody, R.J. Dihu, H. Judeikis, and H. Takimoto. Proc. Int. Pyrotech. Semin. **18**, 483 (1992); Chem. Abstr. **118**, 197 329y (1993).
9. W.D. Emmons. J. Am. Chem. Soc. **76**, 3468 (1954).
10. K. Yoshida, T. Nabeshima, and Y. Yano. J. Chem. Res. Synop. 192 (1991).
11. G.V. Shustov and A. Rauk. J. Org. Chem. **60**, 5891 (1995).
12. A.P. Marchand, D. Rajagopal, S.G. Bott, and T.G. Archibald. J. Org. Chem. **59**, 1608 (1994); **59**, 5499 (1994).
13. S.-T. Hsieh, P.L. Kraft, M.C. Archer, and S.R. Tannenbaum. Mutat. Res. **35**, 23 (1976).
14. D.A. Wink, R.W. Nims, J.E. Saavedra, W.E. Utermahlen, Jr., and P.C. Ford. Proc. Natl. Acad. Sci. U.S.A. **91**, 6604 (1994).
15. J.R. L. Smith, M.W. Nee, J.B. Noar, and T.C. Bruice. J. Chem. Soc. Perkin Trans. 2, 255 (1984).
16. P.P. Roller, D.R. Shimp, and L.K. Keefer. Tetrahedron Lett. **16**, 2065 (1975).
17. M. Mochizuki, T. Anjo, and M. Okada. Tetrahedron Lett. **21**, 3693 (1980).
18. M. Poulson, D. Spangler, and G. Loew. Mol. Toxicol. **1**, 35 (1987).
19. R.W. Murray. Chem. Rev. **89**, 1187 (1989).
20. R. Curci. *In* Advances in oxygenated processes. Vol. 2. *Edited by* A.L. Baumstark. JAI Press Ltd., Greenwich, Conn. 1990. Chap. 1.
21. W. Adam, L.P. Hadjiarapoglou, R. Curci, and R. Mello. *In* Organic peroxides. *Edited by* W. Ando. John Wiley, New York. 1992. pp. 195–219.
22. W. Adam and L. Hadjiarapoglu. Top. Curr. Chem. **164**, 45 (1993).
23. R. Curci, A. Dinoi, and M.F. Rubino. Pure Appl. Chem. **67**, 811 (1995).
24. G.V. Shustov and A. Rauk. J. Org. Chem. **63**, 5413 (1998).
25. X. Du and K.N. Houk. J. Org. Chem. **63**, 6480 (1998).

© 1999 NRC Canada

26. R.W. Murray, S.N. Rajadhyaksha, and L. Mohan. J. Org. Chem. **54**, 5783 (1989).
27. R.W. Murray and M. Singh. Tetrahedron Lett. **29**, 4677 (1988).
28. K. Miaskiewicz, N.A. Teich, and D.A. Smith. J. Org. Chem. **62**, 6493 (1997).
29. R.W. Murray, R. Jeyaraman, and M.K. Pillay. J. Org. Chem. **52**, 746 (1987).
30. J.J.W. McDouall. J. Org. Chem. **57**, 2861 (1992).
31. M.J. Frisch, G.W. Trucks, H.B. Schlegel, P.M.W. Gill, B.G. Johnson, M.A. Robb, J.R. Cheeseman, T. Keith, G.A. Petersson, J.A. Montgomery, K. Raghavachari, M.A. Al-Laham, V.G. Zakrzewski, J.V. Ortiz, J.B. Foresman, J. Cioslowski, B.B. Stefanov, A. Nanayakkara, M. Challacombe, C.Y. Peng, P.Y. Ayala, W Chen, M.W. Wong, J.L. Andres, E.S. Replogle, R. Gomperts, R.L. Martin, D.J. Fox, J.S. Binkley, D.J. Defrees, J. Baker, J.P. Stewart, M. Head-Gordon, C. Gonzalez, and J.A. Pople. Gaussian 94 (Revision E.2). Gaussian, Inc., Pittsburgh, Pa. 1995.
32. C. Gonzalez and H.B. Schlegel. J. Phys. Chem. **94**, 5523 (1990).
33. C. Gonzalez and H.B. Schlegel. J. Phys. Chem. **95**, 5853 (1990).
34. J.B. Foresman, T.A. Keith, K.B. Wiberg, J. Snoonian, and M.J. Frisch. J. Phys. Chem. **100**, 16 098 (1996).
35. A. Bravo, F. Fontana, G. Fronza, F. Minisci, and L. Zhao. J. Org. Chem. **63**, 254 (1998), and refs. cited therein.
36. R.R. Fraser and L.K. Ng. J. Am. Chem. Soc. **98**, 5895 (1976).
37. R.W. Murray and D. Gu. J. Chem. Soc. Perkin Trans. 2, 2203 (1993).
38. W. Adam and A.K. Smerz. J. Org. Chem. **61**, 3506 (1996).

© 1999 NRC Canada

Can there be more than a single definition of an atom in a molecule?

R.F.W. Bader

Abstract: Arguments are presented that the theoretical definition of an atom in a molecule or of a functional grouping of atoms that derive from experimental chemistry must be unique. Definitions based on the orbital model or, as recently proposed, in terms of domains defined by isovalued density envelopes fail for a number of reasons, among them being their failure to enable a quantum mechanical description of the atomic or group properties. Chemistry is concerned with the observation and measurement of properties. Definitions that do not predict the measurable, additive properties found for atoms in molecules fail to recover the essence of the atomic concept and can play no operational or predictive role in chemistry. Atoms exist in real space and their form determines their properties. There is but a single definition for an atom, free or bound, that meets this essential requirement.

Key words: atoms in molecules, proper open systems.

Résumé : On présente des arguments pour que la définition théorique d'un atome dans une molécule ou dans un groupe fonctionnel d'atomes qui dérive de la chimie expérimentale soit unique. Les définitions basées sur le modèle des orbitales ou, comme il l'a été récemment proposé, en fonctions de domaines définis par des enveloppes de densité de valeurs égales ne sont pas appropriées pour un certain nombre de raisons; une d'elles est leur inhabilité à fournir une description de mécanique quantique des propriétés atomiques ou du groupe. La chimie s'intéresse à l'observation et à la mesure de propriétés. Les définitions qui ne permettent pas de prédire des propriétés additives, mesurables observées pour des atomes dans des molécules faillissent à la tâche de récupérer l'essence du concept atomique et elles ne peuvent jouer aucun rôle prédictif ou opérationnel en chimie. Les atomes existent dans des espaces réels et leurs formes déterminent leurs propriétés. Il n'y a qu'une seule définition pour un atome, libre ou non libre, qui rencontre cette exigence essentielle.

Mots clés : atomes dans les molécules, systèmes ouverts appropriés.

[Traduit par la Rédaction]

The definition of a functional group

The concept of a functional group — that an atom or linked grouping of atoms can exhibit a set of characteristic properties — is central to our understanding and prediction of chemical behaviour. Since this behaviour is observed experimentally, it must be definable in terms of quantum mechanics. Indeed, the definition of a functional group must meet well-defined theoretical as well as experimental constraints if it is to recover the chemical characteristics associated with such groups and, in particular, recover their measured values in systems where additivity of properties is experimentally observed (1, 2). If theory is to apply, then the definition of a functional group must be such that the expectation values and the associated equations of motion be uniquely defined for all observables. Experiment requires: (*a*) that the properties so defined be characteristic and additive, the group properties summing to yield the corresponding value for the total system, (*b*) that the group properties be as transferable from one system to another as is the form of the group in real space, that is, as is the group's charge distribution in real space, and (*c*) that its definition maximize its extent of transferability from one system to another. Thus the definition of a functional group is not arbitrary, at least not if one wishes to recover the functional groups of chemistry.

It has been shown that groups composed of atoms defined as proper open systems meet the above constraints (1–3). A proper open system (4) is a region of real space Ω bounded by a surface $S(\Omega,\boldsymbol{r})$ exhibiting a local zero flux in the gradient vector field of the electron density, as stated in eq. [1]:

$$[1] \qquad \nabla\rho(\boldsymbol{r})\cdot\boldsymbol{n}(\boldsymbol{r}) = 0 \;\forall\; \boldsymbol{r} \quad S(\Omega,\boldsymbol{r})$$

Equation [1] is a statement of the boundary condition for obtaining Schwinger's principle of stationary action for an open system from the quantum action principle (5). While no one has disputed the finding that proper open systems faithfully recover the characteristics of the functional groups of chemistry, other definitions have been put forth. Indeed, Liu and Parr (6) overlook the derivation of a proper open system obtained from the action principle, in expressing the opinion "The atom (or functional group) in a molecule is not easily defined. There are always subjective factors for any definition, or strict partition of the molecule. What model one chooses is subject to one's particular needs." This state-

Received July 21, 1998.

R.F.W. Bader.[1] Department of Chemistry, McMaster University, Hamilton, ON L8S 4M1, Canada.

[1]Telephone: (905) 525-9140, ext. 23499. Fax: (905) 522-2509.

© 1999 NRC Canada

ment is scientifically acceptable only to the extent that "one's needs" are satisfied by a definition of a functional group that recovers its chemical characteristics and by the requirement that the group and its properties be defined by quantum mechanics. Schwinger's principle of stationary action (5), along with Feynman's equivalent path integral approach (7), are considered by some (8) to provide the true foundation of quantum mechanics. The use of Schwinger's principle to define both the atom and its properties through its identification with a proper open system removes any and all "subjectivity" in the definition of an atom in a molecule (3, 4).

The definition of a functional group obtained from the quantum action principle is the only physically acceptable one. The description of a system provided by physics is unique. When alternative formulations are provided, such as the Heisenberg and Schrödinger representations of quantum mechanics or Schwinger's and Feynman's reformulation of quantum mechanics using the action principle, they are found to be equivalent. Thus there are no other definitions of a group that will yield its energy, magnetic susceptibility, polarizability, and all other properties as they are defined by quantum mechanics for a proper open system. It is the values of the properties defined in this manner that are found to be in agreement with the experimentally measured group properties, measurements that are possible in those cases where the properties of a group are found to be transferable, as well as additive (1, 3). The definition of a functional group as a quantum mechanical proper open system is thus unique and no other definition can recover its properties. To demonstrate this uniqueness we show the inadequacy of alternative definitions and provide a further example of how the properties of a proper open system are determined by its form, a consequence of the truism that two identical pieces of matter exhibit identical properties.

Orbital and overlapping models of atoms in a molecule

The quotation by Liu and Parr is from a paper in which they report calculations of atomic and orbital electronegativities and hardnesses for an atom in a molecule (6). Ideally, they wish to consider the ground state of an atom with N electrons (not necessarily integer) in an external potential that in principle is chosen to be "appropriate for the molecular environment." The authors do not explicitly take account of the potential exerted by the environment. Instead, their model of an atom in a molecule consists of an isolated atom with continuously variable orbital occupation numbers. It is their contention that the effect of the environment is reflected in the variation of the orbital occupation numbers. While the population of an open system is variable, it changes only in response to changes in its surroundings. Their model, however, takes no account of the contribution to the potential of the open system from its environment, the single most important feature of an open, as opposed to an isolated, system. Indeed, it is a property of a quantum open system that it changes only in response to changes in the forces exerted on its surface by its surroundings, a property of an open system in classical mechanics, as well (3). The transferable behaviour exhibited by atoms is a consequence of the energy and form of the atoms responding only to the change in the net virial of the forces exerted by its surroundings, the external virial, but not to the individual contributions to that change (3, 4). The atom of Liu and Parr (6) is in reality not an open system, but simply an isolated atom with a population that is arbitrarily varied at will.

Parr et al. (9, 10) equate the electronegativity to the negative of the Lagrange multiplier μ introduced into density functional theory as a constraint that the density integrate to N, the total number of electrons in a system. They argue that μ is the derivative $\partial E/\partial N$, where E is the total energy, and should be identified with the chemical potential. In thermodynamics, the chemical potential is defined as the rate of change of the total energy with respect to a change in the average number of particles of a particular component of the total system or of a bounded open system contained within the total system, the other thermodynamic variables being fixed in value. In the model of the atom used by Liu and Parr (6), the orbital electronegativity is equated to the negative of the corresponding chemical potential in a process that involves taking the derivative of the energy of the atom with respect to the orbital occupation number with the orbitals held fixed, an expression due to Janak (11). Thus the thermodynamic analogy in this case would lead one to identify the atom with the total system and the orbitals with the open components, since it is the energy of the atom that is differentiated with respect to the orbital occupation numbers.

The interpretation given to μ by Parr and co-workers has been questioned for two reasons (12). (*a*) The identification assumes that N in a closed quantum mechanical system is a continuously variable property. (*b*) It was shown that the value of μ is, at the point of variation, independent of the value of the normalization constraint placed on the density, that is, independent of N, the number of electrons in the system. In fact, the normalization constraint may be assigned any arbitrary value λ without affecting the value of μ, as λ is a purely mathematical parameter without physical significance. The same paper shows how the theory of atoms in molecules enables one, in principle, to determine the necessary derivative of a molecule's total energy with respect to the average population of any of its constituent atoms, each of which is a bounded proper open system. This would yield a quantity in formal accord with the thermodynamic definition of the chemical potential, although whether it would satisfy the property of equalization of atomic chemical potentials as suggested by Parr et al. (9, 10) remains to be determined.

Parr et al. (9, 10) previously considered the problem of defining an atom in a molecule as an open system, based on the premise that "at equilibrium" one will have an equality in the chemical potentials of all the atoms in the molecule corresponding to the equalization of their electronegativities. Their model requires an undefined partitioning of the total density into a sum of atomic contributions that are not assumed to be disjoint, and perhaps involving some "bond charge" as well. They conclude (10) that "partitionings with overlapping atoms also have advantages," as opposed to the disjoint partitioning of space achieved through eq. [1].

Both of the models by Parr et al. are readily demonstrated to be incompatible with the physics of an open system, one because of its orbital basis, the other because of the related

© 1999 NRC Canada

problem of overlapping atomic domains. Starting with Schrödinger's equation one derives, in a few steps, the result that a quantum mechanical expectation value and its time rate of change are determined only for open systems that are bounded in real space. In addition to excluding the models proposed by Parr et al. (6, 9, 10), the result has broader implications, namely, that one must forego all definitions of an atom in a molecule based on the orbital model or on partitionings of the basis sets used in their expansion, as these definitions assume the atom to be without boundaries and to extend over all space.

Schrödinger's equation yields the result given in eq. [2] that describes the time rate of change of the value of some property G in an infinitesimal volume element, $d\tau$ (3):

$$[2] \qquad d\rho_G(\boldsymbol{r})/dt = (1/2)\{(i/\hbar)N\int d\tau' \Psi^* [\hat{H}, \hat{G}(\boldsymbol{r})]\Psi - \nabla \cdot \boldsymbol{j}_G(\boldsymbol{r}) + cc\}$$

In this equation $\rho_G(\boldsymbol{r})$ is the density of property G represented by the quantum observable $\hat{G}(\boldsymbol{r})$ and $\boldsymbol{j}_G(\boldsymbol{r})$ is the current density of G, where the densities are defined in eqs. [3] and [4]:

$$[3] \qquad \rho_G(\boldsymbol{r}) = (N/2)\int d\tau' \{\Psi^* \hat{G}(\boldsymbol{r})\Psi + (\hat{G}(\boldsymbol{r})\Psi)^* \Psi\}$$

$$[4] \qquad \boldsymbol{j}_G(\boldsymbol{r}) = (\hbar/2mi)N\int d\tau' \{\Psi^* \nabla(\hat{G}(\boldsymbol{r})\Psi) - (\nabla\Psi^*)\hat{G}(\boldsymbol{r})\Psi\}$$

The mode of integration denoted by $N\int d\tau'$ implies a summation over all spins and an integration over all coordinates save those denoted by the vector $\boldsymbol{r}$ (the coordinate of the electron whose ultimate integration is restricted to the open system) followed by multiplication by N, the number of electrons. This mode of integration is not arbitrary but follows directly from the field theoretic derivation of the principle of stationary action wherein every operator $\hat{G}(\boldsymbol{r})$ is identified with a generator that acts on a single field point (4). It is this feature of the theory that yields a spatial density $\rho_G(\boldsymbol{r})$ and a current $\boldsymbol{j}_G(\boldsymbol{r})$ describing its flow for every property G (2). Equation [2] equates the local change in the density of property G to a contribution arising from within the volume element $d\tau$, as determined by the commutator, and to a contribution from the net flux in the current of G through the surface bounding $d\tau$, as determined by the divergence of the current density. If $\hat{H}$ and $\hat{G}(\boldsymbol{r})$ commute, then eq. [2] reduces to the corresponding equation of continuity for property G, relating its time rate of change to the divergence of its current. For example, if $\hat{G}(\boldsymbol{r})$ equals the unit operator then $\rho_G(\boldsymbol{r})$ and $\boldsymbol{j}_G(\boldsymbol{r})$ reduce to the electron density and its current to yield the equation of continuity for $\rho(\boldsymbol{r})$.

Integration of the densities in eq. [2] over a region Ω yields eq. [5], the Heisenberg equation of motion for $\hat{G}(\boldsymbol{r})$ for an open system. The equation is expressed in the Schrödinger representation in terms of average values.

$$[5] \qquad \int_\Omega d\boldsymbol{r}\partial\rho_G(\boldsymbol{r})/\partial t = (1/2)\{(i/\hbar)\langle\Psi, [\hat{H}, \hat{G}(\boldsymbol{r})]\Psi\rangle_\Omega - \oint dS(\Omega, \boldsymbol{r})\, \boldsymbol{j}_G \cdot \boldsymbol{n}(\boldsymbol{r}) + cc\}$$

The derivation of eq. [5] from Schwinger's principle of stationary action (5) is, however, restricted to a proper open system, one bounded by a zero-flux surface, as stated in eq. [1] (2–4). The surface bounding the total system at infinity also satisfies eq. [1] and thus a single principle determines the properties of the total system and its constituent proper open systems. The surface term vanishes for the total system and eq. [5] then corresponds to the usual statement of the Heisenberg equation of motion for an observable.

The terms in eq. [5] have the same meaning as in eq. [2], with Gauss' theorem being used to replace the volume integral of the divergence of the current with a corresponding surface term relating the change in G to the flux in its current density through the surface of the open system. Equations [2] and [5] demonstrate that, in addition to the total system that is bounded at infinity, the quantum mechanical description of a property and its time rate of change are determined only for bounded regions of real space, be they of infinitesimal or finite extent, and that an essential part of this description is provided by the flux in the associated current density through the surface of an open system. Thus if one's ultimate goal is to use quantum mechanics to define the properties of an atom in a molecule, then one must forego the use of orbitals or of the basis functions used in their expansion in the definition, as these functions extend over all space. A partitioning based on overlapping atomic domains is similarly excluded.

Prefacing their modelling of an atom as an open system, Parr and Yang (10) pose the question "…what is an atom in a molecule? How can one find it in the Schrödinger equation? The problem is a profound one." However, this problem has already been solved by the definition of a proper open system using Schwinger's principle of stationary action. This was first demonstrated for a system in a stationary state (13) in which case the derivation of Schwinger's principle in fact reduces to a corresponding generalization of Schrödinger's derivation of his "wave equation." This work is described in ref. 3 and was recently reviewed in ref. 2. In 1926 Schrödinger showed that making an energy functional, which he termed the Hamilton integral, stationary with respect to first-order variations in the wave function and subject to the constraint that ψ remain normalized, yielded $\hat{H}\psi = E\psi$ as the Euler equation. Repeating Schrödinger's variation of the same functional used in this original paper, but expressed for an open system satisfying the zero-flux boundary condition, eq. [1], yields not only Schrödinger's equation but, in addition, the stationary state expression of Schwinger's principle (2, 3, 13). This principle may be stated as in eq. [6], the stationary state form of eq. [5],

$$[6] \qquad (1/2)\{(i/\hbar)\langle\Psi, [\hat{H}, \hat{G}(\boldsymbol{r})]\Psi\rangle_\Omega + cc\} = (1/2)\{\oint dS(\Omega, \boldsymbol{r})\, \boldsymbol{j}_G \cdot \boldsymbol{n}(\boldsymbol{r}) + cc\}$$

Equation [6], together with the wave equation, completely determines the physics of a proper open system in a stationary state, that is, the physics of an atom in a molecule. When Ω refers to all space the surface integral in eq. [6] vanishes and one recognizes the hypervirial theorem for the observable $\hat{G}(\boldsymbol{r})$. Thus the principle of stationary action generalizes the variation of the energy functional for a stationary state or

© 1999 NRC Canada

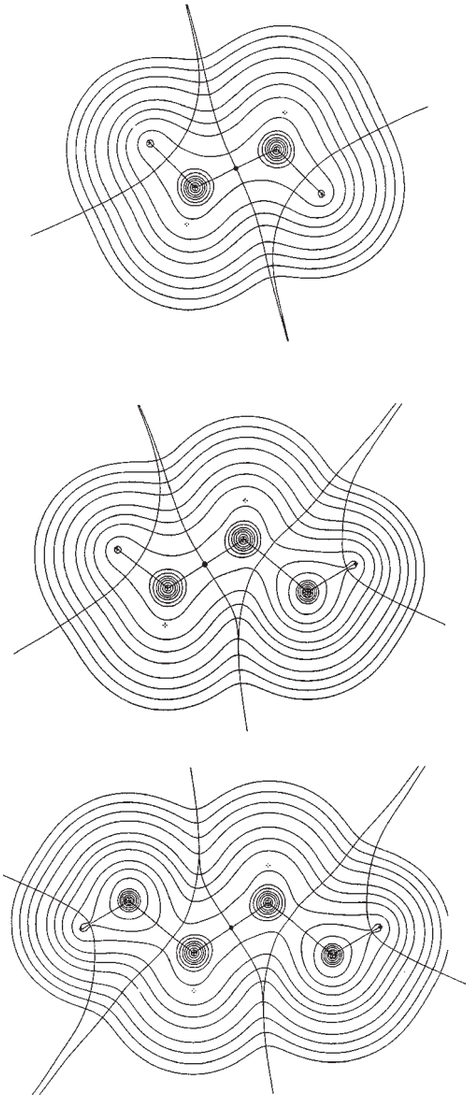

Fig. 1. Contour maps of the electron density for ethane in the H-C-C-H plane, ethanol in the H-C-C-O-H plane, and ethylene glycol in the H-O-C-C-O-H plane, showing the bond paths and the intersections of the interatomic surfaces with the plane of the diagram. The bcp of each C|C surface is denoted by a dot. The density contours of the methyl and the methylenehydroxy groups up to the C|C interatomic surface in the hybrid molecule ethanol are close to being superimposable on the corresponding contours of the related group in ethane and ethylene glycol, significant differences being found only in a small region of the C|C surface beginning with the 0.02 au contour outwards to lower values in the lower portion of the ethanol diagram. The C|H, C|O, and O|H surfaces in the hybrid molecule are separately superimposable with those in the parent molecules. Geometry changes in forming the hybrid, while present, are so small as to be nearly undetectable in these diagrams. The reader may check the transferability of the density distributions by making a copy of the diagram and superimposing it on the original. The final contour to encompass the H-C-C-O-H nuclei in the diagram for ethanol has the value 0.200 au. All the density beyond this contour and some of the density lying within it, up to that at the C—O bcp, would be excluded from the CH_3CH_2 and OH groups defined as density domains using a value for the density somewhat greater than that for the C—O bcp.

of the action integral for a time-dependent system, so that one obtains the equation of motion not only for the state function, but also for each of the observables, eqs. [5] and [6]. This result is obtained only for a proper open system. Thus the principle of stationary action defines both the atom and its properties and this is how one finds an atom in a molecule "in the Schrödinger equation" — by retracing Schrödinger's path. Indeed, it is the extension of Schrödinger's variation to an open system that leads one to Schwinger's principle (13). The extension to an open system necessarily includes a variation of its surface and retention of the variation of the state function on this surface, followed by the identification of these surface variations with the action of infinitesimal generators, the very steps that Schwinger purposefully takes in his generalization of the action principle. One may use the stationary state form of Schwinger's variational principle to obtain Schrödinger's equation together with all properties for the total system by restricting the variations to the basin of a proper open system interior to the total system.

Definition of a functional group as a density domain

We consider next a definition of a functional group proposed by Mezey (14). While he defines a group to be a bounded region of real space, the definition is arbitrary and consequently the groups so defined do not recover nor reflect the observed chemistry. His definition equates a functional group to a "density domain," a region of space enveloped by a closed isovalued surface of the electron density. As one progressively decreases the value of the density $\rho(\boldsymbol{r})$ that is used to define the surfaces within a molecule, starting from a value that typically yields surfaces that separately envelope the individual nuclei, the enveloped regions expand. When $\rho(\boldsymbol{r})$ attains its minimum value along a line of maximum density linking two nuclei, that is, when it attains the value of the density at a bond critical point (bcp) (3) denoted by ρ_b, the envelope will expand to encompass both nuclei or however many equivalent pairs of nuclei as are linked by the same value of the density at their bcps. Thus pairs of nuclei are linked in order of the decreasing value of the density at the associated bcp to yield linked groupings of nuclei of increasing size, a process that terminates when a single envelope encompasses all of the nuclei in the molecule. Reference to the electron density of ethane in Fig. 1, for example, shows that in this case the first polynuclear groups defined in this manner would be two groups of CH_3 nuclei; all C—H bond paths have the same ρ_b value, one that is greater than that for the C—C interaction, Table 1. The program EXTREME (15) of the theory of atoms in molecules locates and characterizes all cps in a density distribution, enabling one to determine all bcps and arrange them in order of decreasing value, and thereby determining the order of the creation and merging of density domains. While

© 1999 NRC Canada

Table 1. Values of electron density at bond critical points in atomic units.[a]

	CH_3CH_2OH	CH_3CH_2OH	CH_3CH_3	$HOCH_2CH_2OH$
Link[b]	Basis a	Basis b	Basis b	Basis b
C—H	0.2785	0.2898	0.2913	
C—H	0.2806	0.2920	0.2913	
C—H	0.2876	0.2993		0.3008
C—C	0.2669	0.2692	0.2569	0.2775
C—O	0.2608	0.2650		0.2662
O—H	0.3780	0.4046		0.4036

[a]Basis set a is 6-31G*; basis set b is 6-311++G(3df,2p).

[b]The first two C—H values are for CH_3: in ethanol, the first is *trans* to the O—H, the second is for the two equivalent C—H bond paths. The third C—H listing is for the CH_2OH group.

Mezey does not associate the merging of domains with the density attaining the value at a bcp, it is the analytical way of determining this information.

Mezey applies his criterion for a group to the electron density in the ethanol molecule and comes to the somewhat surprising conclusion (14) that "the methyl group does not appear as a formal functional group of separate entity within the ethanol molecule." This statement is followed by "This result is in good agreement with chemical practice: few organic chemists would attempt to use ethanol as a methylating agent for incorporation of methyl group into another molecule." This latter statement confuses the concept of a functional group — a linked set of atoms exhibiting a characteristic set of properties in different molecules — with the use of a group in a form that enables one to transfer it in a particular chemical reaction. The methyl and methylene groups in saturated hydrocarbons, while generally unreactive, provided the first quantitative experimental examples of the transferability and additivity of group properties and played an essential role in the development of the concept of a functional group. The presence of a carbonyl group, an example of a chemically more reactive group, is readily recognized by its characteristic infrared and NMR spectroscopic properties and by its chemical susceptibility to protonation at oxygen and nucleophilic attack at carbon, regardless of whether or not the group is chemically transferable in a particular chemical reaction.

In actual fact the methyl group in ethanol, when defined as a proper open system, exhibits characteristic properties as anticipated for a functional group. This has been exemplified by showing that not only is the methyl group defined in the series of molecules CH_3CH_2X where X = H, CH_3, NH_2, OH, and F, but that it contributes nearly identical amounts to their heats of formation, magnetic susceptibilities, and volumes, as well as exhibiting characteristic external contributions to the ^{13}C chemical shift, in spite of the very different nature of X (16, 17).

Mezey's analysis of the density domains in the ethanol molecule (14) is discussed using the electron density for this molecule displayed in Fig. 1. In ethanol, the first binuclear density domain obtained links O to H, as this bond path has the greatest ρ_b value (Table 1). This is followed by the progressive separate linking of each C to its neighbouring protons to yield the nuclear sets CH_3, CH_2, and OH at an intermediate stage, followed next by the linking of the two carbons and finally of C to O, the order determined by the decrease in the ρ_b values, Table 1. Unfortunately, Mezey apparently did not consider the equilibrium geometry or made an error in interpreting his visual displays of the envelopes, as he links the carbons before linking the carbon of methyl to its unique H. This is an incorrect result and, as pointed out above, one that is easily avoided through the use of the program EXTREME. The ρ_b values for C—H bonds in saturated hydrocarbons exceed those for C—C single bonds for equilibrium geometries at any basis set and this result remains true for ethanol. The ρ_b values for ethanol using the 6-31G* set employed by Mezey are also listed in Table 1. The values for the C—H bond paths range from 0.279 to 0.281 au, compared to 0.267 au for C—C. Thus the finding by Mezey that the methyl group is not defined by a density domain in ethanol is incorrect. Ignoring the error in Mezey's conclusion resulting from the incorrect assignment of the value of ρ_b for the C—C link, there are a number of general criticisms that can be made of his procedure, in addition to the obvious one that it misses the known chemistry of the methyl group as determined by its characteristic properties, properties that are necessarily recovered in the transferable forms exhibited by these groups when defined as proper open systems.

(*a*) One cannot assign meaningful values to the properties of groups defined as density domains, however the properties themselves are defined, since the group properties can never sum to yield the corresponding values for the total system. This is a result of electron density being excluded from groups that are separately defined by any isodensity envelope with a value greater than zero. Only the envelope at infinity or, operationally, one that encompasses all of the nuclei, can effectively contain all of the density in the entire system. In the case of ethanol, for example, the OH and CH_3CH_2 groupings of nuclei are separately defined by the surface with a density value lying between 0.269 and 0.265 au, the values of the density at the C—C and C—O bcps, respectively. Thus all density with a value less than ~0.267 au is necessarily excluded if the two groupings of nuclei are to be separately defined, a sizeable fraction of the valence density as is obvious by reference to the contour map in Fig. 1.

(*b*) There is no physical basis for separating groups of atoms on the basis of ρ_b, the value of the density at the bcp. The value of ρ_b provides a qualitative relative measure of bond strength (3, 18) and the use of an isovalued density surface for the definition of a group would forbid the existence of any group that contained, interior to it, a bond with a ρ_b value less than (that is, a bond weaker than) those linking it to the rest of the molecule. The value of ρ_b for the C—C link in ethanol exceeds that for the C—O link by only 0.004 au using the larger basis set, a difference that hardly seems to justify, on any physical grounds, denying the existence of the latter link in preference to the former.

(*c*) The dependence of ρ_b on internuclear separation represents another shortcoming of the use of isodensity envelopes to define a group, in that existing groups would disappear and new groups would appear as the molecule underwent vibrational motions, the resulting changes in molecular geometry changing the order of the *relative* values of ρ_b. The definition of a group and the associated definition of molecular structure provided by the theory of atoms in molecules,

© 1999 NRC Canada

on the other hand, frees these concepts from the classical notion of a molecular geometry by associating a group and a molecular structure with an open region of nuclear configuration space, removing thereby even the need of invoking the Born–Oppenheimer approximation (3). Molecular and group structure is generic and persists over nuclear vibrations, until progress along a given reaction coordinate leads to a catastrophic change in the topology of the system's electron density distribution that leads to the creation of a new structure (3).

Utilizing the transferability of the methyl group in a theoretical synthesis

A simple theoretical synthesis is used to illustrate that the methyl group is not only definable in ethanol but that it emulates the essential feature required of a functional group by chemistry, namely, that its properties mirror its form in real space. Figure 1 shows the electron density distributions for ethane ($CH_3|CH_3$) and ethylene glycol ($HOCH_2|CH_2OH$), considered as parent molecules, together with the density for the hybrid molecule, ethanol ($CH_3|CH_2OH$). The vertical bar in each formula denotes the C|C zero-flux interatomic surface. It is clear from the three diagrams that the density distributions of the $HOCH_2|$ and $|CH_3$ groups are little changed upon transfer from their defining molecules to the hybrid. Consequently one could imagine performing a theoretical synthesis of ethanol by combining the methyl and the methylene hydroxyl groups defined as proper open systems by the C|C interatomic surface in each of the two original molecules. For this to be a useful procedure would require the properties of ethanol to be the arithmetic mean of the properties of the two parent molecules, a situation that is very closely obeyed (16). Thus one finds the error incurred in the estimate of the energy of ethanol by this procedure is –0.33 kcal/mol, compared to –0.32 kcal/mol obtained using experimental values of heats of formation (19). The error incurred in the magnetic susceptibility is 0.1 u out of a total value of 37.8 u (u = -1×10^{-6} emu) and the error in the van der Waals volume is 0.36 au out of a value of 81.69 au. The calculations use a 6-311++G(3df,2p) basis and incorporate self-consistent virial scaling to ensure satisfaction of the virial theorem.[2]

This synthesis provides an example of compensatory transferability wherein each group changes in response to its new neighbor in such a way as to minimize the overall change, the more prevalent response of a group to a change in environment (16). The electron population is necessarily conserved in forming the heteromolecule, with –0.047 e being transferred from $CH_3|$ to $HOCH_2|$, but what is perhaps surprising is the extent to which other properties are nearly similarly conserved. The apparent additivity of their properties is a result of the small changes in the properties of one group being nearly nullified by compensatory changes in its new neighbor. Thus the energies of $CH_3|$ and $|CH_2OH$ change by –2.6 and +1.9 kcal/mol, their magnetic susceptibilities by +0.28 and –0.18 u, and the van der Waals volumes by –3.14 and +3.50 au, respectively. (The difference in the sum of the changes in the group energies, obtained by numerical integration over the separate atomic basins, differs from that calculated by subtracting the total energies by 0.4 kcal/mol, a measure of the accuracy of the atomic integrations.)

While a simple empirical averaging of the properties of the two parent molecules would yield the results described above, such a procedure would have no physical basis. The procedure would correspond to the use of fragments obtained by a partitioning in the plane perpendicular to the bond midpoint in each of the parent molecules, as opposed to use of the interatomic surfaces that reflect the alternating symmetry axes present in the parent molecules. As a result, the density contours would not match across the interfragment surface in the hybrid and the partitioning would result in a portion of the oxygen basin becoming part of the "methyl" fragment and a portion of the carbon basin becoming part of the "methylene hydroxyl" fragment. In addition, of course, the properties of such improper fragments are not defined by theory. Thus the properties assigned to the fragments in this empirical procedure would not reflect their charge distributions, and form would not determine property as found in nature.

The second-order properties induced by an applied magnetic field are determined by the induced magnetization density $\boldsymbol{r} \times \boldsymbol{j}^{[1]}(\boldsymbol{r})$, where $\boldsymbol{j}^{[1]}(\boldsymbol{r})$ is the first-order induced current (17). The magnetic shielding σ_A of nucleus A is determined by the integration of the shielding density $\boldsymbol{r}_A \times \boldsymbol{j}^{[1]}(\boldsymbol{r})/r^3_A$, with origin at nucleus A, over the basin of each atom, enabling one to determine the atomic contributions to σ_A (20). A carbon nucleus in ethane, with a shielding constant σ_C = 181 ppm, is more shielded than the methyl carbon in ethanol by 12 ppm (20). It is a property of a given nucleus in a functional group that all of the shift in its shielding occurs as a consequence of small perturbations to the shielding density within the atomic basin containing the nucleus in question, the contributions from the remaining atoms in the system, regardless of their number and kind, contributing a nearly constant amount to the shielding and exhibiting variations of less than 1 ppm (20). Thus the external contribution to the shielding of a carbon nucleus of a terminal methyl group in saturated hydrocarbons or their corresponding normal alcohols varies from 17.0 to 17.8 ppm, equaling 17.4 in ethane and 17.0 in ethanol, with the three methyl hydrogens contributing 4.2 ppm in both cases. The internal contributions to σ_C predict C in ethanol to be less shielded than C in ethane, by 8 ppm compared to the experimental 12 ppm (20).

The transferable nature of the groups illustrated here and elsewhere is a consequence of their being bounded by a zero-flux surface. Any other choice of surface would result in a loss of transferability, as would any attempt to define the atoms as unbounded overlapping systems using, for example, a Mulliken partitioning of a set of basis functions into gross atomic sets by the equal division of the overlap terms between two participating nuclear centres. This latter approach is still frequently employed and is the method used by Walker and Mezey in their MEDLA approach to obtaining molecular density fragments for use in the construction

[2] T.A. Keith. Private communication.

© 1999 NRC Canada

of large molecules (21). Such a partitioning eschews the very property of the density that forms the core of the concept of an atom in a molecule — namely, that it can exhibit characteristic properties in spite of changes in its neighbouring atoms. To take a simple example, one that contributed to the observational basis underlying the theory (22), consider the Li atom in LiH and LiF. The distribution of the electron density over the basin of the Li atom up to its interatomic surface is so similar in the two molecules, when the Li atom is defined as a proper open system, that it must be considered truly remarkable, considering the very different natures of its bonded neighbours (2, 3, 22). Contrawise, the density distributions in the basins of the neighbouring hydrogen and fluorine atoms are completely different. However, since properties follow form in real space, the expectation values of all observables are very similar for the Li atom in the two molecules, in spite of the very different distributions of density in the neighbouring atomic basins (22). Thus the integration of the density over the Li basin in LiF yields 2.06 electronic charges and a net charge on Li of +0.94e, compared to a net charge of +0.91e in LiH. The electronic kinetic energies of the Li atoms differ by 9 kcal/mol, a value that, by the atomic virial theorem, equals the magnitude of the difference in their total energies (3).

If, however, the atomic density distributions are defined in terms of nuclear centred basis functions, then the physical similarity observed in real space is lost: in one case the Li density includes contributions from the density in the hydrogen basin while in the other it includes density lying within the basin of the F atom. The distribution of the density in the H basin is very different from that in the F basin and hence the density ascribed to the Li atom by this procedure is different for the two molecules. In addition, of course, differing amounts of density within the Li basin are assigned to the H and F atoms, with the net result that the densities assigned to the Li atoms do not appear similar. In fact, the net charges for Li determined by the Mulliken partitioning are +0.59e in LiF and +0.37 in LiH, compared to charges that differ by only 0.03e when the Li atom is defined as a proper open system. In addition to judging the atom to be different in the two molecules, neither charge gives any indication of the close approach of the density of the Li atom to that of the core density associated with a Li^+ ion that is evident in the contour maps for the two molecules (2, 3, 22).

The one-electron density matrix, whose diagonal elements determine the electron density, determines the quantum stress tensor. The stress tensor, through the local expressions of the equations of motion for the force and virial operators, determines the kinetic and potential energy densities and thus the mechanics of a molecule. It has been demonstrated that the one-electron density matrix is short-sighted (23) and thus the transferable nature of an atom or a functional group is a consequence of the parallel short-range behaviour of the density and its local energy contributions that is observed for proper open systems (2, 4, 23, 24). The effective potential field experienced by a single electron in a many-electron system is determined by the virial field. The virial field is a dressed real-space density (2, 3) that determines all of the complex interactions between the electrons and nuclei that are determined by the many-electron wave function. It provides the most short-range description possible of the interactions experienced by an element of the density, because it integrates to the total potential energy, including the nuclear repulsion energy. Not only does the virial field, like the kinetic energy density, mimic the transferable nature of the electron density, the negative of the virial field has been shown to be structurally homeomorphic with $\rho(\boldsymbol{r})$ (24). Thus a density that has the appearance of a scaled version of $\rho(\boldsymbol{r})$ has the property of integrating to twice the total energy of the molecule.

Conclusions

The philosophy of Parr and others such as March (25), concerning the definition of an atom in a molecule, is summarized (26) in the statement "what an atom in a molecule is must be defined and there is no unique definition." The argument presented here is that if one wishes to define the atoms of chemistry, those that meet the necessary experimental and theoretical constraints outlined in the introduction, then one has no freedom of choice. Instead, like all true physical concepts, that is, those determined by observation, the choice is dictated by physics and the definition of an atom in a molecule is unique. Specifically, it has been shown that Parr's proposal (6, 10, 26) that a molecular density be partitioned into overlapping atoms, however this might be done, precludes the use of quantum mechanics in the definition of the contributions the atoms make to the measurable properties of a system. Parr has used the model of overlapping atoms to define the energy required to promote an atom in a molecule into a non-quantum mechanical "valence state" (26, 27), and the same model, supplemented with an intervening bond density, has been employed in a discussion of force constants (28). One should not attempt to justify one's desire to formulate a subjective model of an atom for use in a particular problem by the premise that a unique definition of the atoms of experimental chemistry is impossible.

Conceptually, models that partition a molecular density into distinct contributions from overlapping atoms and from bonds derive from the orbital model of electronic structure. The atoms and the bonds correspond to the atomic and overlap contributions to the density that are obtained from the expansion of the orbitals using atomic centred basis functions. Historically, the notion of a "bond" as being separate from the atoms it links traces back to the ball and stick model of molecular structure. The adoption of the theory of atoms in molecules requires the replacement of any model of structure that imparts an existence to a *bond* as being separate from the atoms it links with the concept of *bonding*; two atoms are bonded if they share an interatomic surface and hence are linked by a bond path, as illustrated in Fig. 1. The presence of a bond path — a line of maximum density linking neighbouring nuclei in an equilibrium geometry — provides a universal indicator of bonding between atoms (29), but does not itself represent a bond or any finite amount of electronic charge. The interatomic surfaces separating neighbouring basins appear to some to cut the bond paths, causing Parr and Yang (10), in a critique of the theory of atoms in molecules, to state "···and the chemical bond itself seems to

© 1999 NRC Canada

have disappeared into thin air." This is a valid comment but they fail to add that the resulting theory of molecular structure and structural stability obtained by replacing the notion of "a bond" with that of "bonding" yields the first and so far the only theory of structure and structural stability that recovers and quantifies all of the structural concepts of chemistry, one that defines all possible structures and all possible mechanisms of structural change (3, 30) for a given system.

While Mezey defines an atom or a functional group to be a bounded region of space, the resulting density domains do not recover the properties associated with the functional groups of chemistry, one reason being that they exhaust neither the total system nor its properties. Also, according to Mezey's stated findings (14), the methyl group is not definable as a density domain in ethanol. Yet physically, the space occupied by the electron density of the atoms associated with the CH_3 grouping exhibits nearly identical properties in ethanol as in ethane, where the group is represented by a density domain. In fact, when defined as a proper open system the methyl group of ethanol is found to exhibit properties characteristic of the methyl group in hydrocarbons and substituted hydrocarbons. Density domains may be of use in the topological characterization of molecular shape and similarity (14), but the concept cannot be used to define a functional group of chemistry. Thus Mezey's concluding remark "by this criterion, the electron density distribution does not justify regarding the terminal CH_3 moiety as a formal functional group" is at variance with the demonstration that it is possible to define a methyl group in ethanol whose form and properties are characteristic of those exhibited by the methyl group in other molecules, that is, it behaves as a functional group of chemistry.

Mezey's statements (14) that the electron density is "fuzzy" and that the Heisenberg uncertainty principle somehow limits one's ability to employ the density to obtain physical definitions that are not in conflict with quantum mechanics are misleading. The electron density is the measurable expectation value of the density operator (31), an operator that is both linear and Hermitian, the requirements placed by Dirac on the definition of an observable (32). Our ability to measure or calculate this expectation value is not limited by any inherent quantum uncertainty but rather, as for other properties, only by our experimental abilities (33). Even the position of a single electron can be measured (a process that has nothing to do with the measurement of the many-electron density). What one cannot do is simultaneously measure its momentum with unlimited accuracy. The overuse of the "fuzzy" aspect of quantum mechanics is discussed by Feshbach and Weisskopf (34) in an article entitled "Ask a foolish question." In particular, the representation of a molecular structure in terms of an equivalence class of molecular graphs defined by the topology of the density (3, 30) is in complete accord with quantum mechanics, even though an individual molecular graph, as defined by the network of bond paths, is a portrayal of the "skeletal" image of structure that Mezey (14) claims to be incompatible with physics and an impediment to our thinking.

Acknowledgements

The author wishes to thank Maggie Austen for her careful reading of the manuscript and for her many useful comments and Dr. G.L. Heard for help with the diagrams.

References

1. R.F.W. Bader, P.A.L. Popelier, and T.A. Keith. Angew. Chem. Int. Ed. Engl. **33**, 620 (1994).
2. R.F.W. Bader. Can. J. Chem. **76**, 973 1998.
3. R.F.W. Bader. Atoms in molecules — a quantum theory. Oxford University Press, Oxford. 1990.
4. R.F.W. Bader. Phys. Rev. B: Condens. Matter, **49**, 13348 (1994).
5. J. Schwinger. Phys. Rev. **82**, 914 (1951).
6. G.H. Liu and R.G. Parr. J. Am. Chem. Soc. **117**, 3179 (1994).
7. R.P. Feynman. Rev. Mod. Phys. **20**, 367 (1948).
8. M. Gell-Mann. Phys. Today, **42**, 50 (1989).
9. R.G. Parr, R.A. Donnelly, M. Levy, and W.E. Palke. J. Chem. Phys. **68**, 3801 (1978).
10. R.G. Parr and W. Yang. Density functional theory in atoms and molecules. Oxford University Press, Oxford. 1989.
11. J.F. Janak. Phys. Rev. B: Condens. Matter, **18**, 7165 (1978).
12. T.T. Nguyen-Dang, R.F.W. Bader, and H. Essen. Int. J. Quantum Chem. **22**, 1049 (1982).
13. S. Srebrenik and R.F.W. Bader. J. Chem. Phys. **63**, 3945 (1975).
14. P.G. Mezey. Can. J. Chem. **72**, 938 (1994).
15. F.W. Biegler-König, R.F.W. Bader, and T.-T. Tang. J. Comput. Chem. **3**, 317 (1982).
16. R.F.W. Bader and F.J. Martín. Can. J. Chem. **76**, 284 (1998).
17. T.A. Keith and R.F.W. Bader. J. Chem. Phys. **99**, 3669 (1993).
18. R.J. Boyd, O. Knop, and S.C. Choi. J. Am. Chem. Soc. **110**, 7299 (1988).
19. S.W. Benson, F.R. Cruichshank, D.M. Golden, G.R. Haugen, H.E. O'Neal, A.S. Rodgers, R. Shaw, and R. Walsh. J. Chem. Rev. **69**, 279 (1969).
20. T.A. Keith and R.F.W. Bader. Can. J. Chem. **74**, 185 (1996).
21. P.D. Walker and P.G. Mezey. J. Am. Chem. Soc. **116**, 12022 (1994).
22. R.F.W. Bader and P.M. Beddall. J. Chem. Phys. **56**, 3320 (1972).
23. R.F.W. Bader. Int. J. Quantum Chem. **56**, 409 (1995).
24. T.A. Keith, R.F.W. Bader, and Y. Aray. Int. J. Quantum Chem. **57**, 183 (1996).
25. N.H. March. Electron density of atoms and molecules. Academic Press, London. 1992. pp. 80–81.
26. J. Rychlewski and R.G. Parr. J. Chem. Phys. **84**, 1696 (1986).
27. L. Li and R.G. Parr. J. Chem. Phys. **84**, 1704 (1986).
28. R.F. Borkman and R.G. Parr. J. Chem. Phys. **48**, 1116(1968); R.F. Borkman, G. Simons, and R.G. Parr. J. Chem. Phys. **50**, 58 (1969).
29. R.F.W. Bader. J. Phys. Chem. A, **102**, 7314 (1998).
30. R.F.W. Bader, T.T. Nguyen-Dang, and Y. Tal. Rep. Prog. Phys. **44**, 893 (1981).
31. R.F.W. Bader and P.F. Zou. Chem. Phys. Lett. **191**, 54 (1992).
32. P.A.M. Dirac. The principles of quantum mechanics. Oxford University Press, Oxford. 1958.
33. P. Coppens. X-ray charge densities and chemical bonding. Oxford Science Publications, Oxford University Press, Oxford. 1997.
34. H. Feshbach and V.F. Weissfopf. Phys. Today, **41**, 9 (1988).

© 1999 NRC Canada

Preparation of *N*-aryl-4-oxo-4*H*-1-benzothiopyran-2-acetamides from trilithiated acetoacetanilides and lithiated methyl thiosalicylate

April J. Angel, Anne E. Finefrock, Kristen L. French, Douglas R. Hurst, Angela R. Williams, Mary E. Rampey, Shannon L. Studer-Martinez, and Charles F. Beam

Abstract: Acetoacetanilide and substituted acetoacetanilides were trilithiated in excess lithium diisopropylamide, and the polylithiated intermediates were regioselectively condensed with lithiated methyl thiosalicylate, followed by acid cyclization to afford substituted *N*-aryl-4-oxo-4*H*-1-benzothiopyran-2-acetamides (thiochromone-2-acetamides).

Key words: thiochromones, strong-base multiple anion synthesis, Claisen-type condensation.

Résumé : On a effectué une trilithiation de l'acétoacétanilide et d'acétoacétanilides substitués en procédant dans un excès de diisopropylamidure de lithium, et les intermédiaires polylithiés ont subi une condensation régiosélective par réaction avec du thiosalicylate de méthyle lithié, suivie d'une cyclisation acide conduisant à des *N*-aryl-4-oxo-4*H*-1-benzothiopyran-2-acétamides (thiochromon-2-acétamides).

Mots clés : thiochromones; synthèse, base forte anion multiple; condensation du type de Claisen.

[Traduit par la Rédaction]

Introduction

Chromones (4*H*-1-benzopyran-4-ones) have been extensively investigated regarding their synthesis, their isolation as secondary metabolites, and their potential for broad spectrum biological activity (1, 2). In comparison, thiochromones (4*H*-1-benzothiopyran-4-ones) have received considerably less investigative attention (3, 4). These compounds have been prepared and studied for their biological potential, especially as bacteriocides and anticancer agents (5–8). Very few thiochromone-2-acetic acid derivatives (e.g., thiochromone-2-acetic acid, ethyl ester and related esters) have been reported (9–11). These compounds have been prepared by the condensation–cyclization of phenyl mercaptan with β-oxocarboxylic acid esters (9). Also, 3-carboethoxy- (10) or 3-carbomethoxy- (11) thiochrome-2-acetic acid, ethyl or methyl esters, have been prepared by the condensation–cyclization of methyl thiosalicylate with either 1,3-dicarbethoxyallene or 1,3-dicarbmethoxyallene, respectively.

Thiochromone-2-acetic acid has not been reported, but related thiochromone acetic acids or their derivatives have been made for which the acetic acid or acetamido moiety was in the 3-, 5-, 6-, or 8-position (12–15). These materials were also studied for their antitumor, schistosomicidic, or hypolipemic activity. Generally, biological and other studies involving thiochromones have lagged behind chromones, due in part to the lack of synthetic routes or the availability of starting materials to these compounds (3).

In our initial study (16), we trilithiated acetoacetanilide and treated this intermediate with select electrophilic reagents in order to prepare new products such as chromone-2-acetamides (*N*-aryl-4-oxo-4*H*-1-benzopyran-2-acetamides). A part of the initial study dealt with the condensation–cyclization of trilithiated acetoacetanilide with lithiated salicylate esters.

These electrophilic reagents presented a challenge because of the potential for diminished electrophilicity and reactivity of the carboxyl carbon, which is in a resonance position relative to the phenoxide ion portion of the electrophilic substrate (17–19). The condensation–cyclization of these trianion-type intermediates with lithiated methyl thiosalicylate (20) was not attempted at that time, and such an investigation offered the potential for the preparation of thiochromone-2-acetamides (*N*-aryl-4-oxo-4*H*-1-benzothiopyran-2-acetamides) that may be difficult to prepare by traditional procedures.

Results and discussion

During the current investigation, 11 acetoacetanilides were trilithiated with excess LDA and condensed with lithiated methyl thiosalicylate (Fig. 1). This was followed by neutral-

Received August 19, 1998.

A.J. Angel, A.E. Finefrock, K.L. French, D.R. Hurst, A.R. Williams, M.E. Rampey, S.L. Studer-Martinez,[1] and C.F. Beam.[1] Department of Chemistry and Biochemistry, College of Charleston, Charleston, SC 29424, U.S.A.

[1]Authors to whom correspondence may be addressed. Fax: (843) 953-1404.

© 1999 NRC Canada

Fig. 1. Synthesis of *N*-aryl-4-oxo-4*H*-1-benzothiopyran-2-acetamides **1**–**11**.

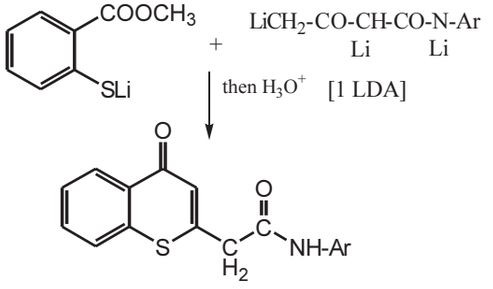

1-11, Ar listed below

1. C_6H_5 **2.** 2-$CH_3C_6H_4$
3. 4-ClC_6H_4 **4.** 4-$CH_3C_6H_4$
5. 4-$CH_3OC_6H_4$ **6.** 2,5-$(CH_3O)_2C_6H_3$
7. 2,5-$(CH_3O)_2C_6H_3$ **8.** 2,5-$(CH_3)_2C_6H_3$
9. 4-BrC_6H_4 **10.** 2-Cl-C_6H_4
11. 4-$CH_3C_6H_4$

ization of *C*-acylated intermediates and cyclization with aqueous hydrochloric acid to afford products **1**–**11**.

All of the thiochromone-2-acetamides **1**–**11** prepared by this strong-base procedure are new, and they were characterized by absorption spectra with support from combustion analyses for C, H, and N. The infrared spectra displayed a number of absorptions between 1600 and 1700 cm^{-1} that were attributed to the thiopyranone carbonyl, the amide carbonyl group, or aromatic absorptions. Proton magnetic resonance absorptions displayed sharp singlets for the methylene hydrogens (CH_2CO) ranging from δ 3.81 to δ 4.01 ppm, and the thiopyranone ring C_3-H singlets, δ 7.01–7.05 ppm, were usually upfield and distinguishable from aromatic absorptions. Pendant group hydrogen absorptions were noted as singlets for $ArCH_3$ and $ArOCH_3$ ranging from δ 2.17 to 2.24 and δ 3.67 to 3.86 ppm, respectively. In each instance the NH was displayed as a sharp singlet distinctly downfield from aromatic absorptions ranging from δ 9.53 to 10.73 ppm. Representative ^{13}C NMR absorptions were noted for methylene carbons ranging from δ 40.4 to 44.5 ppm, ring carbonyl carbons from δ 165.1 to 166.2 ppm, and amide carbonyl carbon primarily at δ 179.0 ppm.

Conclusions

The yields of thiochromone-2-acetamides **1**–**11** ranged from 38 to 92%, which indicates that the general experimental procedure is satisfactory for the expedient preparation of gram quantities of the desired products. This is especially attractive for characterization, biological testing, and other uses; however, it may not necessarily represent the optimum conditions for the preparation of each individual compound. Most reagents used in the preparation are commercially available, and the substituted acetoacetanilides for **9** and **11** were prepared by one-step documented procedures (21–23). The strong-base procedure is general enough so that it is readily reproducible by someone not necessarily familiar with these techniques, and it does not require an elaborate experimental setup.

Experimental

Melting points were obtained with a Mel-Temp II melting point apparatus in open capillary tubes and are uncorrected. Fourier Transform infrared spectra were obtained on a Nicolet Impact 410 FT-IR spectrometer (paraffin oil mull for each compound). Proton and ^{13}C nuclear magnetic resonance spectra were obtained with a Varian Associates Mercury Oxford 300 MHz nuclear magnetic resonance spectrometer, and chemical shifts are recorded in δ ppm downfield from an internal tetramethylsilane (TMS) standard (dimethyl sulfoxide-d_6, solvent for each compound).

Combustion analyses were performed by Quantitative Technologies, Inc., P.O. Box 470, Salem Industrial Park, Bldg. 5, Whitehouse, NJ 08888, U. S. A. The tetrahydrofuran (THF) was distilled from sodium (benzophenone ketyl) prior to use, and chemicals were obtained from Aldrich Chemical Co. and Pfaltz and Bauer, Inc. The acetoacetanilides, *N*-(4-bromophenyl)-3-oxo-butanamide and *N*-(4-methylphenyl)-3-oxo-butanamide, for the preparation of thiochromone-2-acetamides **9** and **11**, were made by the condensation of *p*-bromoaniline or *p*-toluidine with ethyl acetoacetate (21–23).

General experimental procedure for preparing *N*-aryl-4-oxo-4*H*-1-benzothiopyran-2-acetamides 1–11

In a typical experiment, the acetoacetanilide was added to excess lithium diisopropylamide (LDA), followed by the thiosalicylate ester (entry compound:LDA:ester, 1:5:1), and then acid-cyclized to the product. The LDA was prepared by adding 5.37 g (0.0525 mol) of diisopropylamine, dissolved in 45–55 mL of dry THF, to 33 mL (0.0525 mol) of *n*-butyllithium (1.6 M, N_2, 0°C). After 20 min, 0.0100 mol of the acetoacetanilide, dissolved in 35–45 mL of THF, was added at a fast dropwise rate (5 min). After stirring at 0° C for 3 h, 1.82 g (0.0105 mol) of methyl thiosalicylate, dissolved in 25–35 mL of THF, was added at a fast dropwise rate (5 min), and the resulting mixture was stirred at 0°C for an additional 2 h. The mixture was quenched by addition of 100 mL of 3 N hydrochloric acid, and the resulting two-phase mixture was stirred and heated under reflux for 1 h. The mixture was then poured into a large flask containing ice (ca. 100 g) and, after adding solvent-grade ether (ca. 100 mL), it was neutralized with solid sodium bicarbonate. The layers were separated, the aqueous layer was extracted with ether (2 × 75 mL), and the ether extracts were combined and evaporated. The resulting solid or oil was crystallized from routine solvents.

*Preparation of 4-oxo-*N*-phenyl-4*H*-1-benzothiopyran-2-acetamide (1)*

Compound **1** was prepared by the general procedure from the condensation–cyclization of 0.0100 mol of trilithiated acetoacetanilide (3-oxo-*N*-phenyl-butanamide) and 0.0105 mol of lithiated methyl thiosalicylate. Yield: 2.21 g (75%); mp 214–216°C (95% ethanol). IR (cm^{-1}): 3311, 1691, 1606, and 1585; ^1H NMR δ (ppm): 3.90 (s, 2H, CH_2), 7.03 (s, 1H, C_3-H), 7.07–7.90, 8.34-8.37 (m, 9H, ArH), and 10.41 (s, 1H, NH); ^{13}C NMR δ (ppm): 44.5, 119.1, 123.6, 125.7, 126.8, 127.5, 127.9, 129.9, 131.9, 137.0, 138.6, 149.4, 165.6, and 179.0. Anal. calcd. for $C_{17}H_{13}NO_2S$: C 69.13, H 4.44, N 4.74; found: C 69.03, H 4.34, N 4.69.

© 1999 NRC Canada

Preparation of
N-*(2-methoxyphenyl)-4-oxo-4*H-*1-benzothiopyran-2-acetamide (**2**)*

Compound **2** was prepared by the general procedure from the condensation–cyclization of 0.0100 mol of trilithiated *o*-acetoacetanisidide (*N*-(2-methoxyphenyl)-3-oxo-butanamide) and 0.0105 mol of lithiated methyl thiosalicylate. Yield: 2.99 g (92%); mp 205–207°C (95% ethanol). IR (cm^{-1}): 3265, 1651, 1626, and 1593; ^{1}H NMR δ (ppm): 3.86 (s, 3H, OCH_3), 3.99 (s, 2H, CH_2), 7.02 (s, 1H, C_3-H), 6.88–6.94, 7.05–7.14, 7.59–7.94, and 8.32–8.35 (m, 8H, ArH), and 9.66 (s, 1H, NH); ^{13}C NMR δ (ppm): 44.0, 55.7, 111.1, 120.1, 122.0, 124.8, 125.5, 126.6, 126.8, 127.4, 127.8, 129.9, 131.9, 137.1, 149.6, 149.8, 165.9, and 179.0. Anal. calcd. for $C_{18}H_{15}NO_3S$: C 66.44, H 4.65, N 4.30; found: C 66.27, H 4.65, N 4.21.

Preparation of
N-*(4-chlorophenyl)-4-oxo-4*H-*1-benzothiopyran-2-acetamide (**3**)*

Compound **3** was prepared by the general procedure from the condensation–cyclization of 0.0100 mol of trilithiated acetoacet-*p*-chloroanilide (*N*-(4-chlorophenyl)-3-oxo-butanamide) and 0.0105 mol of lithiated methyl thiosalicylate. Yield: 2.17 g (66%); mp 217–219°C (95% ethanol). IR (cm^{-1}): 3304, 1694, 1611, and 1591; ^{1}H NMR δ (ppm): 3.91 (s, 2H, CH_2), 7.02 (s, 1H, C_3-H), 7.23–7.90, 8.32–8.34 (m, 8H, ArH), and 10.73 (s, 1H, NH); ^{13}C NMR δ (ppm): 44.4, 120.7, 125.8, 126.8, 127.1, 127.5, 127.9, 128.6, 129.9, 131.9, 137.0, 137.5, 149.1, 165.8, and 179.0. Anal. calcd. for $C_{17}H_{12}ClNO_2S$: C 61.91, H 3.67, N 4.25; found: C 61.78, H 3.72, N 4.11.

Preparation of
N-*(2-methylphenyl)-4-oxo-4*H-*1-benzothiopyran-2-acetamide (**4**)*

Compound **4** was prepared by the general procedure from the condensation–cyclization of 0.0100 mol of trilithiated *o*-acetoacetotoluidide (*N*-(2-methylphenyl)-3-oxo-butanamide) and 0.0105 mol of lithiated methyl thiosalicylate. Yield: 2.60 g (84%); mp 197–199°C (95% ethanol). IR (cm^{-1}): 3265, 1651, 1621, and 1591; ^{1}H NMR δ (ppm): 2.22 (s, 3H, CH_3), 3.90 (s, 2H, CH_2), 7.03 (s, 1H, C_3-H), 7.09–7.92, 8.32–8.34 (m, 8H, ArH), and 9.75 (s, 1H, NH); ^{13}C NMR δ (ppm): 39.0, 44.2, 125.3, 125.8, 125.9, 126.2, 127.1, 127.8, 128.2, 130.2, 130.6, 132.1, 132.2, 135.9, 137.4, 150.0, 166.1, and 179.3. Anal. calcd. for $C_{18}H_{15}NO_2S$: C 69.88, H 4.89, N 4.53; found: C 69.66, H 4.74, N 4.40.

Preparation of
N-*(4-methoxyphenyl)-4-oxo-4*H-*1-benzothiopyran-2-acetamide (**5**)*

Compound **5** was prepared by the general procedure from the condensation–cyclization of 0.0100 mol of trilithiated *p*-acetoacetanisidide (*N*-(4-methyoxyphenyl)-3-oxo-butanamide) and 0.0105 mol of lithiated methyl thiosalicylate. Yield: 2.28 g (70%); mp 179–182°C (95% ethanol). IR (cm^{-1}): 3312, 1680, 1611, and 1591; ^{1}H NMR δ (ppm): 3.72 (s, 3H, CH_3O), 3.81 (s, 2H, CH_2), 6.89–6.99, 7.49–7.90, 8.32–8.35 (m, 9H, C_3-H and ArH), and 10.23 (s, 1H, NH); ^{13}C NMR δ (ppm): 44.4, 55.2, 113.8, 120.7, 125.6, 126.8, 127.5, 127.9, 129.9, 131.7, 131.9, 137.1, 149.6, 155.3, 165.1, and 179.0. Anal. calcd. for $C_{18}H_{15}NO_3S$: C 66.44, H 4.65, N 4.30; found: C 66.26, H 4.43, N 4.07.

Preparation of
N-*(2,5-dimethoxyphenyl)-4-oxo-4*H-*1-benzothiopyran-2-acetamide (**6**)*

Compound **6** was prepared by the general procedure from the condensation–cyclization of 0.0100 mol of trilithiated acetoacet-2,4-dimethoxyanilide (*N*-(2,4-dimethoxyphenyl)-3-oxo-butanamide) and 0.0105 mol of lithiated methyl thiosalicylate. Yield: 2.70 g (76%); mp 134–136°C (95% ethanol). IR (cm^{-1}): 3270, 1694 shoulder, 1684, 1660, 1625, and 1598; ^{1}H NMR δ (ppm): 3.67 (s, 3H, CH_3O), 3.81 (s, 3H, CH_3O), 4.01 (s, 2H, CH_2), 6.64–6.68 (m, vinyl), 6.97–7.01, 7.60–7.90, 8.32–8.35 (m, 8H, C_3-H and ArH), and 9.94 (s, 1H, NH); ^{13}C NMR δ (ppm): 44.1, 55.3, 56.2, 108.5, 111.8, 125.6, 126.8, 127.4, 127.5, 127.8, 129.9, 131.9, 137.1, 143.4, 149.7, 152.7, 166.1, and 179.0. Anal. calcd. for $C_{19}H_{17}NO_4S$: C 64.21, H 4.82, N 3.94; found: C 63.84, H 4.92, N 3.67.

Preparation of
N-*(2,4-dimethoxyphenyl)-4-oxo-4*H-*1-benzothiopyran-2-acetamide (**7**)*

Compound **7** was prepared by the general procedure from the condensation–cyclization of 0.0100 mol of trilithiated acetoacet-2,4-dimethoxyanilide (*N*-(2,4-dimethoxyphenyl)-3-oxo-butanamide) and 0.0105 mol of lithiated methyl thiosalicylate. Yield: 2.95 g (83%); mp 188–190°C (95% ethanol – benzene). IR (cm^{-1}): 3276, 1651, 1629, and 1614; ^{1}H NMR δ (ppm): 3.75 (s, 3H, CH_3O), 3.84 (s, 3H, CH_3O), 3.92 (s,CH_2), 6.47–6.50 (m, vinyl), 7.01 (s, 1H, C_3-H), 7.59–7.91, 8.32–8.35 (m, 7H, ArH), and 9.53 (s, 1H, NH); ^{13}C NMR δ (ppm): 40.1, 40.4, 55.3, 55.7, 119.7, 123.7, 126.8, 127.5, 127.9, 129.9, 131.9, 137.1, 150.0, 151.4, 156.9, 165.6, and 179.0. Anal. calcd. for $C_{19}H_{17}NO_4S$: C 64.21, H 4.82, N 3.94; found: C 64.19, H 4.63, N 3.76.

Preparation of
N-*(2,5-dimethylphenyl)-4-oxo-4*H-*1-benzothiopyran-2-acetamide (**8**)*

Compound **8** was prepared by the general procedure from the condensation–cyclization of 0.0100 mol of trilithiated acetoacet-*p*-xylidide (*N*-(2,4-dimethylphenyl)-3-oxo-butanamide) and 0.0105 mol of lithiated methyl thiosalicylate. Yield: 1.29 g (40%); mp 212°C (95% ethanol). IR (cm^{-1}): 3271, 1653, 1624, and 1593; ^{1}H NMR δ (ppm): 2.17 (s, 3H, CH_3), 2.24 (s, 3H, CH_3), 3.87 (s, 2H, CH_2), 6.96–7.03, 7.22–7.22, 7.60–7.91, 8.32–8.35 (m, 8H, C_3-H and ArH), and 9.68 (s, 1H, NH); ^{13}C NMR δ (ppm): 17.8, 20.6, 43.9, 125.0, 125.6, 126.4, 126.8, 127.5, 127.9, 129.9, 130.8, 131.8, 131.9, 133.0, 134.6, 137.1, 149.8, 165.7, and 179.0. Anal. calcd. for $C_{19}H_{17}NO_2S$: C 69.83, H 5.24, N 4.39; found: C 70.09, H 4.93, N 4.16.

Preparation of
N-*(4-bromophenyl)-4-oxo-4*H-*1-benzothiopyran-2-acetamide (**9**)*

Compound **9** was prepared by the general procedure from the condensation–cyclization of 0.0100 mol of trilithiated

© 1999 NRC Canada

acetoacet-*p*-bromoanilide *(N*-(4-bromophenyl)-3-oxo-butanamide) and 0.0105 mol of lithiated methyl thiosalicylate. Yield: 2.43 g (65%); mp 234–235°C (95% ethanol). IR (cm^{-1}): 3332, 1682, 1622, and 1591; ^{1}H NMR δ (ppm): 3.90 (s, 2H, CH_2), 7.02 (s, 1H, C_3-H), 7.51–7.90, 8.33–8.36 (m, 8H, ArH), and 10.55 (s, 1H, NH); ^{13}C NMR δ (ppm): 44.4, 115.2, 121.1, 125.8, 126.8, 127.5, 127.9, 129.9, 131.5, 131.9, 137.0, 137.9, 149.1, 165.8, and 179.0. Anal. calcd. for $C_{17}H_{12}BrNO_2S$: C 54.56, H 3.23, N 3.74; found: C 54.94, H 3.20, N 3.51.

Preparation of
N-*(2-chlorophenyl)-4-oxo-4*H-*1-benzothiopyran-2-acetamide (**10**)*

Compound **10** was prepared by the general procedure from the condensation–cyclization of 0.0100 mol of trilithiated acetoacet-*o*-chloroanilide (*N*-(2-chlorophenyl)-3-oxo-butanamide) and 0.0105 mol of lithiated methyl thiosalicylate. Yield: 1.71 g (52%); mp 188–190°C (methanol–toluene). IR (cm^{-1}): 3272, 1653, 1614, and 1591; ^{1}H NMR δ (ppm): 3.98 (s, 2H, CH_2), 7.05 (s, 1H, C_3-H), 7.20–7.91, 8.33–8.36 (m, 8H, ArH), and 10.02 (s, 1H, NH); ^{13}C NMR δ (ppm): 43.7, 125.7, 126.3, 126.7, 126.8, 127.5, 127.9, 129.5, 129.9, 131.9, 134.3, 137.1, 149.3, 166.2, and 179.0. Anal. calcd. for $C_{17}H_{12}ClNO_2S$: C 61.91, H 3.67, N 4.25; found: C 62.07, H 3.71, N 4.22.

Preparation of
N-*(4-methylphenyl)-4-oxo-4*H-*1-benzothiopyran-2-acetamid e (**11**)*

Compound **11** was prepared by the general procedure from the condensation–cyclization of 0.0100 mol of trilithiated *p*-acetoacetotoluidide (*N*-(4-methylphenyl)-3-oxo-butanamide) and 0.0105 mol of lithiated methyl thiosalicylate. Yield: 1.17 g (38%); mp 203–204°C (95% ethanol). IR (cm^{-1}): 3307, 1689, 1603, and 1593; ^{1}H NMR δ (ppm): 2.26 (s, 3H, CH_3), 3.86 (s, 2H, CH_2), 7.01 (s, 1H, C_3-H),7.12–7.90, 8.32–8.36 (m, 8H, ArH), and 10.30 (s, 1H, NH); ^{13}C NMR δ (ppm): 20.5, 44.4, 119.2, 125.6, 126.8, 127.5, 127.8, 129.1, 129.9, 131.9, 132.5, 136.0, 137.1, 149.5, 165.3, and 179.0. Anal. calcd. for $C_{18}H_{15}NO_2S$: C 69.88, H 4.89, N 4.53; found: C 69.78, H 4.85, N 4.28.

Acknowledgements

This work was supported by grants from the Donors of the Petroleum Research Fund, Administered by the American Chemical Society, NSF-RUI grant, CHE-9708014, and the American Heart Association – South Carolina Affiliate. The acquisition of the recently installed 300 MHz NMR spectrometer was made possible through National Science Foundation's Division of Undergraduate Education through grant DUE no. 9750721.

References

1. G.P. Ellis. *In* Comprehensive heterocyclic chemistry. Vol. 3. Part 2B. *Edited by* A.R. Katritzky and C.W. Rees. Pergamon Press, New York. 1984. pp. 695–718.
2. J.P. Hepworth. *In* Comprehensive heterocyclic chemistry. Vol. 3. Part 2B. *Edited by* A.R. Katritzky and C.W. Rees. Pergamon Press, New York. 1984. pp. 816–830 and 874–883.
3. J.P. Hepworth, *In* Comprehensive heterocyclic chemistry. Vol. 3. Part 2B. *Edited by* A.R. Katritzky and C.W. Rees. Pergamon Press, New York. 1984. pp. 918–919.
4. A.H. Ingall. *In* Comprehensive heterocyclic chemistry. Vol. 3. Part 2B. *Edited by* A.R. Katritzky and C.W. Rees. Pergamon Press, New York. 1984. pp. 941–942.
5. H. Nakazumi, T. Ueyama, and T. Kitao. J. Heterocycl. Chem. **21**, 193 (1984).
6. H. Nakazumi, T. Ueyama, and T. Kitao. J. Heterocycl. Chem. **22**, 1593 (1985).
7. H.-K. Wang, K.F. Bastow, K.F. Cosentino, and K.H. Lee. J. Med. Chem. **39**, 1975 (1996).
8. L.J. Loeffler and I.H. Hall. J. Med. Chem. **24**, 853 (1981).
9. F. Bossert. Ann. Chem. **680**, 40 (1964).
10. Y. Tamura, T. Tsugoshi, S. Morhi, and Y. Kita. J. Org. Chem. **50**, 1542 (1985).
11. G.J.S. Doad, D.I. Okar, F. Scheinmann, P.A. Bates, and M.B. Hursthouse. J. Chem. Soc. Perkin Trans. 1, 2993 (1988).
12. F. Bossert and R. Goennert. Med. Chem. Abhandl. Med.-Chem. Forschungsstaetten Farbwerke Hoechst AG, **7**, 367 (1963); Chem. Abstr. **60**, 9238d (1964).
13. T. Nambra, Y. Takemori, and S. Okamoto. Yakugaku Zasshi, **81**, 1 (1961); Chem. Abstr. **55**, 12397g (1961).
14. G.J. Atwell, G.W. Rewcastle, B.C. Baguley, and A. Denny. Anti-Cancer Drug Des. **4**, 161 (1989).
15. K. Tomizawa, K. Kammeo, H. Saito, and K. Hatayama. Jpn Kokai Tokkyo Koho JP 02, 255, 676 (1990); Chem. Abstr. **114**, P228737d (1991).
16. C.F. Beam, M.A. Hines, C.L. Mazat, D.C. Duncan, D. Beckman, R.J. Lachicotte, R.C. Tummons, and N.D. Heindel. Chem. Ind. (London), 727 (1989).
17. M.J. Livingston, M.F. Chick, E.O. Shealy, D.J. Park, T.D. Fulmer, and C.F. Beam. J. Heterocycl. Chem. **19**, 215 (1982).
18. A.M. Huff and C.F. Beam. J. Heterocycl. Chem. **23**, 1343 (1986).
19. C.L. Mazat, C.F. Beam, and M.A. Hines. Synth. Commun. **20**, 253. (1990).
20. K.L. French, A.J. Angel, A.R. Williams, D.R. Hurst, and C.F. Beam. J. Heterocycl. Chem. **35**, 45 (1998).
21. C.R. Hauser and G.A. Reynolds. J. Am. Chem. Soc. **70**, 2402 (1948).
22. M.L. Gnanadoss and M. Radha. J. Org. Chem. **48**, 570 (1983).
23. M. Zanger, W.V. Simons, and A.R. Gennaro. J. Org. Chem. **33**, 3673 (1968).

© 1999 NRC Canada

Réactions d'addition conjuguée d'organolithiens aux acides carboxyliques α, β-insaturés

Jacques Mortier, Michel Vaultier, Barbara Plunian et Sourisak Sinbandhit

Résumé : Les organolithiens et les acides carboxyliques α,β-insaturés non protégés donnent des réactions d'addition conjuguée dans le tétrahydrofurane à –78°C. Les réactions des acides 1- et 2-naphtoïques avec divers organolithiens et réactifs électrophiles sont présentées. Deux études de diffraction des rayons X montrent que la réaction s'effectue avec une excellente diastéréosélectivité : l'énolate de dilithium intermédiairement formé additionne exclusivement le réactif électrophile par la face opposée à celle d'entrée de l'organolithien. L'étude des spectres de résonance magnétique nucléaire du proton des produits obtenus permet de mettre en évidence l'existence d'une conformation privilégiée de ces composés en solution. La protonolyse de l'énolate intermédiaire par l'acide trifluoroacétique en mode inverse donne accès à des dihydronaphtalènes disubstitués en 1 et 2. Avec les acides carboxyliques α,β-insaturés acycliques, la réaction présente une diastéréosélectivité faible. Avec le butyllithium secondaire, la protonolyse des énolates intermédiaires donne les produits d'addition 1,4 avec une diastéréosélectivité moyenne. La réaction de l'acide phénylpropiolique avec le butyllithium conduit à la formation d'un produit résultant de la *trans* addition de l'organolithien à la triple liaison, l'organolithien additionnant en α de la fonction acide carboxylique.

Mots clés: réactions d'addition 1,4; acides carboxyliques; organolithiens.

Abstract: In THF at –78°C, organolithium derivatives and unprotected α,β-unsaturated carboxylic acids give a conjugated addition reaction. Reactions of 1- and 2-naphthoic acids with various organolithium derivatives and electrophiles are reported. Two X-ray studies show that the reaction occurs with a good diastereoselectivity: the dilithiated enolate formed as an intermediate adds the electrophile exclusively via the face opposite to that of the organolithium. A study of the ^{1}H NMR spectra of the products obtained shows that these compounds adopt a preferred conformation in solution. The protonolysis of the intermediate enolate by trifluoroacetic acid in an inverted mode gives rise to the formation of 1,2-disubstituted dihydronaphthalenes. With acyclic α,β-unsaturated carboxylic acids, the diastereoselectivity of the reaction is marginal. With secondary butyllithium, the protonolysis of the intermediate enolates gives a 1,4-addition and an average diastereoselectivity. Reaction of phenylpropiolic acid with butyllithium gives rise to the formation of a product resulting from a *trans* addition to the triple bond; the organolithium derivative adds in α to the carboxylic group.

Key words: 1,4-addition reactions, carboxylic acids, organolithium derivatives.

[Journal translation]

1. Introduction

La réaction d'addition de Michael constitue une méthode chimique générale de formation de la liaison carbone–carbone (1). Les réactifs organométalliques les plus couramment mis à contribution dans ce type de transformation sont ceux contenant du lithium, du magnésium et du cuivre. En regard de la terminologie HSAB de Pearson (2), la molesse des composés organométalliques croît dans l'ordre lithium → magnésium → cuivre (3). Il en résulte que les réactivités chimiques de ces réactifs sont différentes et donc souvent complémentaires les unes des autres. Les dérivés carbonylés α,β-insaturés constituent probablement la classe d'accepteurs de Michael la mieux étudiée. Avec ces composés, les réactifs organométalliques moux donnent d'une manière générale des réactions d'addition 1,4 alors que les dérivés organométalliques durs produisent préférentiellement les composés résultant d'une addition 1,2 (revues concernant les réactions d'addition conjuguée des organolithiens : voir réf. 4).

Ainsi, la réaction des organocuprates de lithium avec les esters éthyléniques chiraux et achiraux conduit aux produits d'addition 1,4 avec une stéréosélectivité généralement excellente (réf. 1, chap. 4, pp. 218–225). Les énolates lithiés de cétones stabilisés par conjugaison π réagissent préférentiellement en 1,4 avec les esters éthyliques et méthyliques (5, 6), les nitriles (réf. 6, p. 687, et réf. 7) et les amides tertiaires (8) α,β-insaturés. Le crotonamide de diméthyle conduit ainsi à des adduits *syn* avec de bons rendements après réaction avec les électrophiles (8). Les énolates lithiés d'esters et d'amides tertiaires réagissent de façon similaire avec les es-

Reçu le 15 avril 1998.

J. Mortier,[1] M. Vaultier et B. Plunian. Université Rennes-1, Synthèse et électrosynthèse organiques, Unité mixte de recherche associée au Centre national de la recherche scientifique, campus de Beaulieu, 35042 Rennes Cedex, France.
S. Sinbandhit. Université Rennes-1, Centre régional de mesures physiques de l'Ouest, campus de Beaulieu, 35042 Rennes Cedex, France.

[1]Auteur à qui adresser toute correspondance.
Tél : +33 2 99 28 62 76. Téléc : +33 2 99 28 69 55.

© 1999 CNRC Canada

Schéma 1.

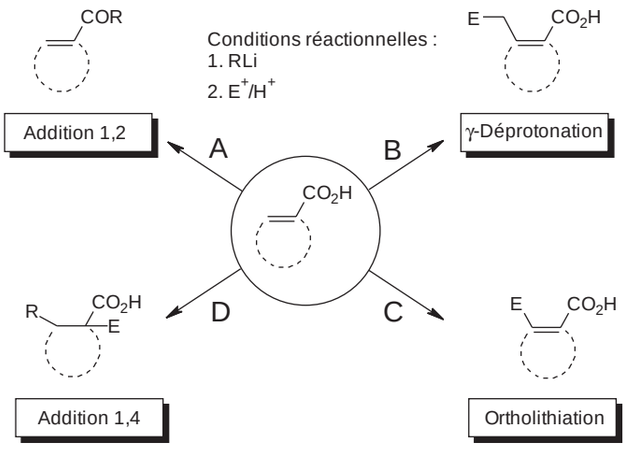

ters α,β-insaturés (9). Les carbanions lithiés d'α-cyanoamines réagissent également en 1,4 avec les esters éthyliques α,β-insaturés donnant accès à des γ-oxoalcénoates après hydrolyse acide (10). Les nitroalcanes présentent une réactivité analogue avec les esters α,β-insaturés en présence d'une quantité catalytique de bases telles que HCO_2Na (11), TBAB (12), TBAF (13), NEt_3 (14) et AcOK (15). De même, les carbanions α-thiosulfonylés stabilisés par conjugaison π additionnent les esters α,β-insaturés (16). Corey et Hegedus ont montré que les anions acyles masqués par un atome de nickel ($RCO\text{-}Ni(CO)_3$) additionnent en β le crotonate de méthyle (17). Enfin, les allylsilanes donnent des réactions d'addition 1,4 avec les dérivés d'acrylate et d'acrylonitrile en présence d'une quantité catalytique d'ion fluorure (18). D'excellentes revues concernant l'addition conjuguée stéréosélective des énolates et des organocuprates achiraux aux esters éthyléniques chiraux ou de carbanions chiraux à des esters α,β-insaturés achiraux sont parues (1).

Les composés organométalliques durs donnent préférentiellement des réactions d'addition 1,2 avec les composés α,β-insaturés du type C=C-COR, C=C-CHO et $C{=}C\text{-}CO_2Et$. Un groupement protecteur encombrant permet de diminuer la nucléophilie de la fonction CO facilitant l'addition du réactif organométallique en β (4). Les amides et les thioamides secondaires et tertiaires α,β-insaturés constituent de bons accepteurs de Michael avec les nucléophiles durs tels que les alkylithiens non stabilisés (4, 19). La formation de produits d'addition conjuguée peut également être favorisée en utilisant des groupements protecteurs de carbonyle du type $C{=}C\text{-}COCPh_3$ (20) et $C{=}C\text{-}CO_2Ar$ (Ar = 2,6-di-*tertio*-butyl-4-méthoxyphényle) (21). Les (*E*)-alcényloxazolines chirales et les organolithiens non stabilisés donnent des réactions d'addition 1,4 avec de très bonnes stéréosélectivités (22, 23).

Les acides carboxyliques α,β-insaturés *non protégés* ($C{=}C\text{-}CO_2H$) réagissent avec les organolithiens selon quatre grandes voies (schéma 1). À une température comprise entre –40 et 0°C dans l'éther ou le THF, l'addition 1,2 de l'organolithien est essentiellement observée et la méthode donne accès à des cétones α,β-insaturées (voie A) (24, 25). À température plus élevée (i.e., T = +20°C) dans le THF, le butyllithium additionne de façon compétitive la fonction acide carboxylique *préalablement* à l'étape de déprotonation, conduisant à l'espèce PhC(OLi)(OH)Bu (26). Les acides carboxyliques comportant un hydrogène acide en position γ sont déprotonés par le LDA dans le THF à –78°C (voie B) (mise au point : réf. 27). L'énolate formé réagit avec les composés carbonylés par le carbone α ou par le carbone γ en fonction des conditions réactionnelles utilisées (28). Nous avons montré récemment que les acides benzoïques *ortho*-fonctionnalisés peuvent être obtenus par lithiation d'acides benzoïques non protégés, via un intermédiaire dianionique *ortho*-lithio benzoate de lithium, sans protection préalable de la fonction acide carboxylique (voie C) (29, 30). Le traitement à –90°C d'un acide benzoïque par 2,2 équivalents du complexe 1 : 1 butyllithium secondaire (*s*-BuLi)/TMEDA dans le THF conduit, après réaction avec des électrophiles variés à –78°C, à des acides benzoïques *ortho*-substitués (applications à la synthèse de pesticides : réf. 31).

Quelques rares exemples de la littérature montrent que les composés organiques possédant une fonction acide carboxylique α,β-insaturée sont susceptibles de donner des réactions d'addition conjuguée avec les composés organométalliques *sans protection préalable de la fonction acide*. Les chlorures de phényle et de *tertio*-butyle magnésium donnent des produits d'addition 1,4 avec des rendements faibles par réaction avec les acides carboxyliques α,β-insaturés (32). Des réactions d'addition conjuguée ont également été observées entre les acides carboxyliques α,β-insaturés et $RCu{\cdot}BF_3$ (33). La réaction de MeCu avec l'acide phénylpropiolique conduit à un énolate de configuration stable à température ambiante (32*c*). Cet énolate donne l'acide *Z*-β-méthylcinnamique après hydrolyse.

L'addition conjuguée des organolithiens aux acides carboxyliques α,β-insaturés a été décrite dans quelques rares cas (voie D). Snieckus et Majewski ont montré que le traitement de l'acide (*E*)-3-méthylbut-2-énoïque avec le 2-lithiodithiane dans le THF à 0°C conduit au produit d'addition 1,4 avec un rendement de 65 % (34). La réaction de l'acide (*E*)-3-triméthylsilylpropénoïque avec le butyllithium dans le THF–hexane à –70°C donne un mélange en produits d'addition 1,2 (55 %) et 1,4 (45 %) (35). L'addition 1,4 des organolithiens aux acides carboxyliques α,β-insaturés α-silyciés s'effectue avec des rendements médiocres. Dans ce cas, l'addition 1,2 est rendue plus difficile par la présence de l'atome de silicium qui augmente la densité de charge en α de la fonction carbonyle (36).

Dans cet article, nos travaux concernant l'étude de la réactivité des acides 1- et 2-naphtoïques et des acides carboxyliques α,β-insaturés acycliques avec divers organolithiens et réactifs électrophiles dans le THF à basse température (–78°C) sont présentés. La stéréosélectivité de la réaction est excellente avec les acides 1- et 2-naphtoïques.

2. Synthèse d'acides dihydronaphtoïques 1,1,2- et 1,2,2-trisubstitués

L'addition nucléophile de complexes organométalliques au système π de naphtalènes permet l'introduction régio et stéréosélective de substituants alicycliques dans le squelette naphtalène (schéma 2). Les études effectuées dans ce domaine concernent en particulier l'addition d'alkyllithiens au naphtalène non substitué (37), l'addition de réactifs de Gri-

© 1999 CNRC Canada

Schéma 2.

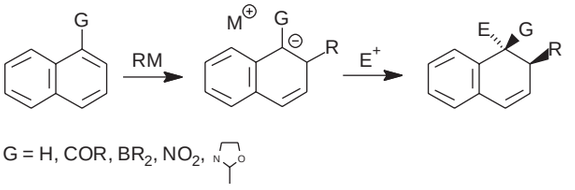

Schéma 3.

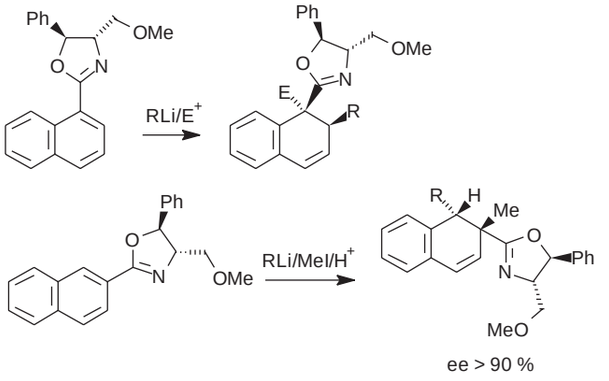

Schéma 4.

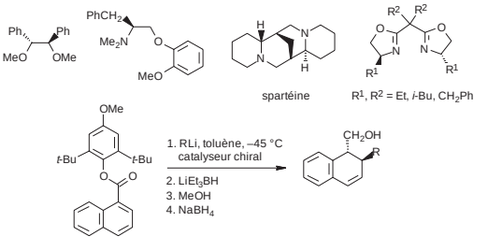

Fig. 1. ORTEP de **4a**.

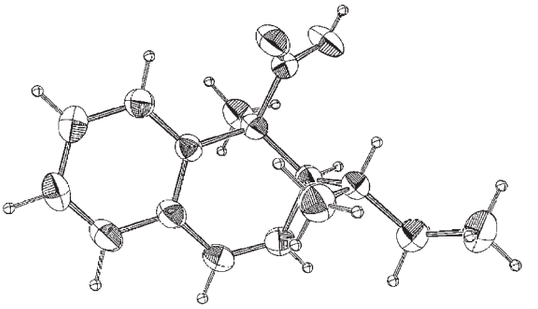

gnard aux acylnaphtalènes (38), aux nitronaphtalènes (39) et aux 1(2)-naphtyloxazolidines (40), et les réactions de complexes « ate » de boranes avec le fluorosulfonate de méthyle (41).

Kündig a montré que les organolithiens donnent des réactions d'addition conjuguées avec les complexes benzène–$Cr(CO)_3$ et naphtalène–$Cr(CO)_3$ (42). Alors que les phényloxazolines peuvent être *ortho*-métallées puis alkylées par les réactifs électrophiles (43), les 1-naphtyloxazolines présentent une réactivité différente : les organolithiens additionnent stéréosélectivement ces composés et conduisent à des 1,2-dihydronaphtalènes trisubstitués après piégeage de l'intermédiaire azaénolate par un réactif électrophile (44). Lorsque l'oxazoline est chirale, la méthode permet de préparer des composés optiquement actifs avec d'excellents excès énantiomériques (schéma 3) (44). Dans ces réactions, le réactif électrophile réagit avec l'énolate en *anti* par rapport à l'organolithien. Les organolithiens et les 2-naphtyloxazolines possèdent une réactivité similaire (45). Meyers a utilisé cette réaction comme étape clé dans la synthèse totale de composés d'intérêt biologique accessibles à partir de précurseurs possédant le squelette 1,2-dihydronaphtalène (44).

Les benzamides tertiaires peuvent être facilement *ortho*-métallés (46). Les 1-naphtylamides tertiaires présentent une réactivité analogue (47). Des travaux de Tomioka et coll. (48) et de Denmark et al. (49) montrent qu'en présence d'une quantité stœchiométrique ou catalytique de ligands chiraux tels que ceux représentés au schéma 4, les organolithiens réagissent avec l'ester 2,6-di-*tertio*-butyl-4-méthoxyphénylnaphtalène pour donner les adduits correspondants avec des excès énantiomériques compris entre 60 et 95 %.

Nous montrons dans ce travail que l'addition des organolithiens aux acides 1- et 2-naphtoïques (**1** et **2**, schéma 5) et le piégeage des énolates de dilithium **3** et **5** (communication préliminaire : réf. 50) par un réactif électrophile conduisent à des dihydronaphtalènes trisubstitués (**4** et **6**). Dans la littérature, ce type d'énolates est également obtenu par déprotonation d'acides alcanoïques par le LDA (51).

Avec le butyllithium secondaire à –78°C dans le THF, l'acide 1-naphtoïque **1** conduit à la formation d'un couple de diastéréoisomères **4a** et **4a′** dans le rapport 9 : 1 via l'énolate **7** (schéma 6 et entrée 1 du tableau 1).[2] La stéréochimie de l'isomère majoritaire **4a** isolé pur par recristallisation fractionnée a été déterminée par analyse cristallographique aux rayons X dont l'ORTEP est représenté à la fig. 1. Cette analyse montre que les groupes butyle secondaire en C2 et méthyle en C1 ont une géométrie *trans*. Cette étude permet également de préciser la configuration relative du carbone C2′. La stéréochimie au niveau des carbones C1 et C2 est confirmée par RMN ^{1}H (effet Overhauser entre l'hydrogène en C2 et le groupe méthyle en C1 de 13 %). Dans les mêmes conditions réactionnelles, le butyllithium conduit à un isomère unique **4e** (entrée 5). Comme l'étude RMN ^{1}H montre que dans ce cas également l'hydrogène en C2 et le groupe méthyle en C1 ont une géométrie *cis* (éclipsée) (effet Overhauser de 10 %), l'isomère minoritaire **4a′** obtenu avec le butyllithium secondaire diffère vraisemblablement de l'isomère majoritaire **4a** par la configuration relative du carbone latéral C2′. Avec l'iodoéthane et le disulfure de diméthyle (entrées 2 et 3), l'introduction du carbone latéral dissymétrique de l'organolithien s'effectue avec une moins bonne stéréosélectivité (75 : 25 et 65 : 35, respectivement). Compte tenu des résultats obtenus avec l'iodométhane, il est raisonnable de proposer une géométrie *cis* aux groupes butyle se-

[2] De façon standard, l'acide naphtoïque en solution dans le THF est ajoute au goutte-a-goutte à une solution de l'organolithien dans le THF prealablement refroidie à –78°C (voir partie experimentale). Le réactif électrophile est ajouté à la solution résultante à la même température. Un changement de température lors de la derrière addition affecte peu le rendement de la transformation et pratiquement pas la diastéréosélectivité. L'addition de HMPT ou de TMEDA est également sans effet sur le cours de la réaction.

© 1999 CNRC Canada

Schéma 5.

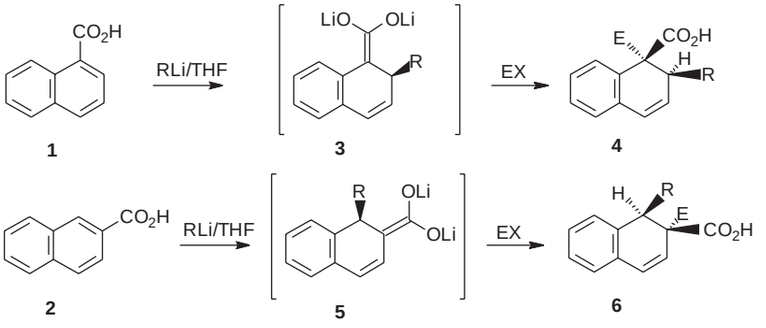

Schéma 6.

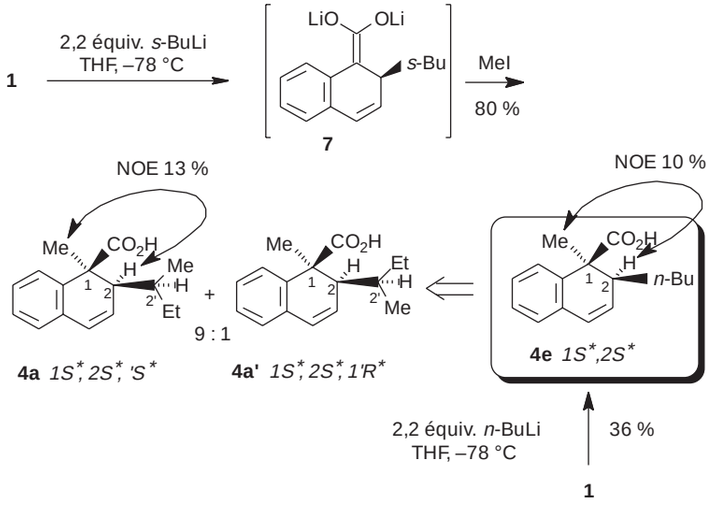

Tableau 1. Réactions d'addition d'organolithiens aux acides 1- et 2-naphtoïques. Piégeage du dianion intermédiaire par les réactifs électrophiles.

Entrée	RLi[a]	Substrat	EX/E	Produit	Rdt (%)[b]	Rapport diast.[c]
1	*s*-BuLi	**1**	MeI/Me	**4a,a′**	80	90 : 10
2	*s*-BuLi	**1**	EtI/Et	**4b,b′**	44	75 : 25
3	*s*-BuLi	**1**	Me_2S_2/MeS	**4c,c′**	82	65 : 35
4	*s*-BuLi	**1**	C_2Cl_6/Cl	**9**	70[d]	—
5	BuLi	**1**	MeI/Me	**4e**	36	—
6	*s*-BuLi	**2**	MeI/Me	**6a,a′**	90	70 : 30
7	*s*-BuLi	**2**	C_2Cl_6/Cl	**10**	78[d]	—
8	BuLi	**2**	MeI/Me	**6c**	38	—

[a]BuLi dans l'hexane; *s*-BuLi dans un mélange cyclohexane–hexane; 2,2 équiv. de RLi sont utilisés.
[b]Rendements en produits purifiés.
[c]Les rapports diastéréoisomériques sont déterminés par RMN ^{1}H du mélange réactionnel brut.
[d]Les produits d'addition 1,**4 4d,d′** et **6b,b′**n'ont pas été isolés mais sont détectables par analyse RMN ^{1}H du mélange brut réactionnel.

condaire en C2 et CO_2H en C1. La réaction du dianion dérivé de l'acide 1-naphtoïque avec l'hexachloroéthane ne conduit pas aux produits d'addition 1,4 attendus **4d,d′** mais à l'acide 2-(2-méthylpropyl)naphtoïque **9** (schéma 7 et entrée 4, tableau 1). Ce dernier composé résulte vraisemblablement de la déshydrohalogénation de **4d,d′** dans les conditions réactionnelles basiques.

Avec l'acide 2-naphtoïque **2**, des résultats analogues sont observés. L'énolate **8** résultant de l'addition du butyllithium secondaire conduit, après piégeage par l'iodométhane, aux diastéréoisomères **6a** et **6a′** dans le rapport 7 : 3 (schéma 8). L'analyse cristallographique aux rayons X de l'isomère majoritaire **6a** isolé pur par recristallisation fractionnée permet de montrer que dans ce cas également les groupements butyle secondaire en C1 et méthyle en C2 ont une géométrie *trans* (fig. 2). L'électrophile réagit par la face opposée à la face d'entrée de l'organolithien. Comme le composé **6c** est uniquement obtenu lorsque le butyllithium est utilisé comme nucléophile, l'isomère minoritaire **6a′** formé avec le butyllithium secondaire diffère vraisemblablement de l'isomère

© 1999 CNRC Canada

Schéma 7.

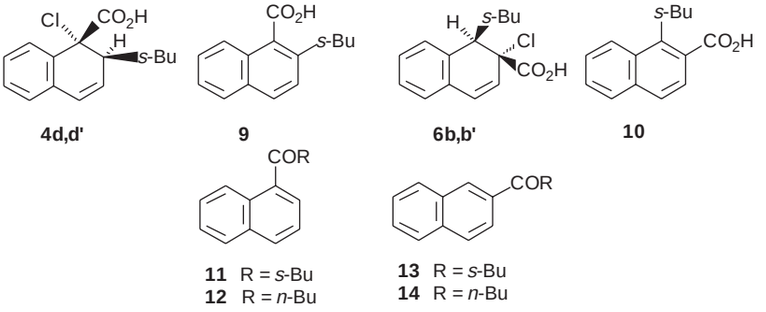

Schéma 8.

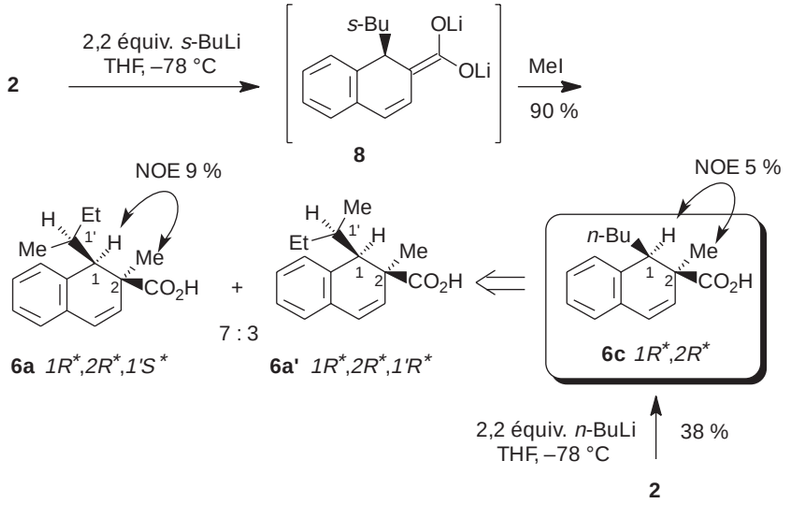

majoritaire **6a** par sa configuration au niveau du carbone latéral C1′. L'hexachloroéthane conduit au produit d'aromatisation **10** dans les conditions réactionnelles basiques (schéma 7 et entrée 7, tableau 1). Dans chacun des exemples étudiés, les produits d'addition 1,**2 11**–**14** sont obtenus avec des rendements inférieurs à 10 %.

3. Synthèse d'acides dihydronaphtoïques 1,2-disubstitués

La protonolyse des énolates résultant de l'addition du butyllithium secondaire à l'acide 1-naphtoïque **1** à –78°C dans le THF conduit à un mélange de dihydronaphtalènes 1,2-disubstitués diastéréoisomères **15a,a′,b,b′** (78 %) dans les proportions 56 : 14 : 24 : 16 (schéma 9). Comme ces produits sont susceptibles d'épimérisation ou (et) d'aromatisation dans les conditions réactionnelles basiques ou au cours de la protonolyse, l'acide trifluoroacétique dont la base conjuguée est faible a été utilisé. Lorsque l'acide trifluoroacétique en solution dans le THF est ajouté au goutte-à-goutte à l'énolate, le dihydronaphtalène formé peut être épimérisé également par l'énolate présent en excès dans le milieu. Cette éventualité n'est pas envisagée par Meyers et al. dans leurs travaux concernant la préparation de naphtyloxazolines 1,2-disubstituées chirales (44*a*).

Fig. 2. ORTEP de **6a**.

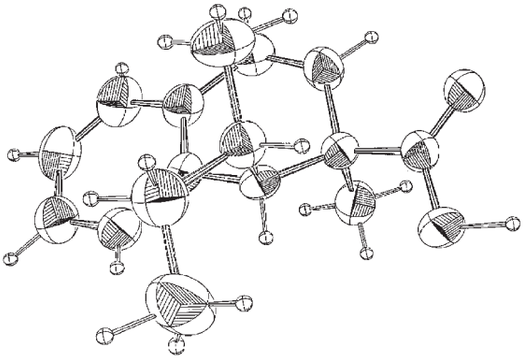

L'énolate de dilithium est préparé en additionnant le butyllithium secondaire à une solution préalablement refroidie à –78°C d'acide 1-naphtoïque dans le THF (mode inverse).[3] Cette solution est ultérieurement ajoutée au goutte-à-goutte à une solution d'acide trifluoroacétique (4 équivalents molaires) en solution dans le THF préalablement refroidi à –78°C.

[3] L'appareillage utilisé permet le transfert aisé en mode inverse de substances peu ou pas solubles et (ou) thermiquement instables. Voir la réf. 52.

© 1999 CNRC Canada

Schéma 9.

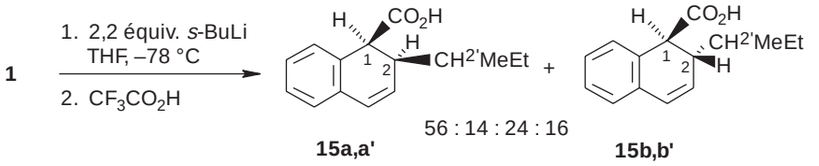

Schéma 10.

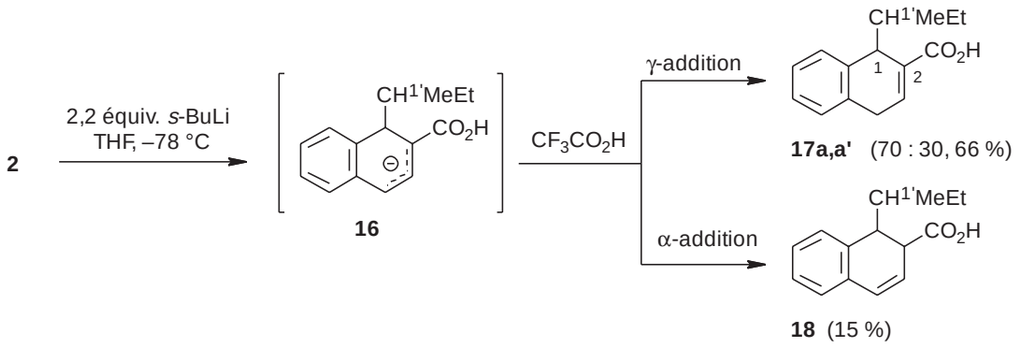

Tableau 2. δ (ppm/TMS) et *J* (Hz).

Produit	H1 (d)	H2 (ddt)	H3 (dd)	H4 (dd)	H2'	*J*
cis-maj **15a**	3,86	2,59	5,96	6,48	1,83	*J*(1,2) 6,5; *J*(2,3) 3,0; J(2,4) 2,8; *J*(2,2') 9,0; *J*(3,4) 9,8
cis-min **15a′**	3,79	2,51	5,98	6,48	1,83	*J*(1,2) 6,2; *J*(2,3) 2,6; J(2,4) 3,0; *J*(2,2') 10,3; *J*(3,4) 9,7
trans-maj **15b**	3,76	2,86	5,90	6,48	1,44	*J*(1,2) 4,1; *J*(2,3) 5,1; *J*(2,4) 1,2; *J*(2,2') 5,4; J(3,4) 9,8
trans-min **15b′**	3,77	2,79	5,94	6,46	1,44	*J*(1,2) 2,6; *J*(2,3) 5,5; J(2,4) 0,8; *J*(2,2') 5,5; *J*(3,4) 9,7

Une chromatographie sur colonne de silice du mélange brut réactionnel permet d'isoler chacun des deux couples qui diffèrent par leurs configurations au niveau des carbones C1 et C2. Leurs configurations respectives ont été établies à partir des spectres RMN ^{1}H et ^{13}C (vide infra). Nous avons pu vérifier que les isomères **15a,a′,b,b′** sont obtenus dans les mêmes proportions mais avec un rendement moins bon (59 %) lorsque l'acide trifluoroacétique en solution dans le THF est ajouté à l'énolate à –78°C (mode d'addition normal). Aucune équilibration n'est observée lorsque chaque couple de diastéréoisomères est placé dans les conditions réactionnelles basiques.

La réaction de l'acide 2-naphtoïque avec le butyllithium secondaire conduit, en mode d'addition inverse, à un couple de diastéréoisomères **17a,a′** qui diffèrent par leurs configurations au niveau des carbones C1 et C1′ (66 %, 70 : 30) (schéma 10). Ces deux composés résultent de la protonation en position γ de l'anion allylique **16**. Une réactivité analogue a été observée par Meyers et al. avec les 2-naphtyloxazolines (53). La présence de deux doublets dédoublés à 6,47 (*J* = 9,4 et *J* = 3,1 Hz) et 6,23 ppm (*J* = 9,4 et *J* = 1,8 Hz) dans le spectre de RMN ^{1}H du mélange brut réactionnel montre que le produit d'addition conjugué **18** résultant de la protonation en position α de l'anion allylique **16** a également été formé (15 %). La stéréochimie de ce composé (mélange de diastéréoisomères) n'a pas été déterminée.

4. Analyse conformationnelle des composés 15a,a′,b,b′ et 4a,a′ dans le chloroforme deutérié par la spectroscopie RMN ^{1}H et ^{13}C

4-1. Étude des composés 15a,a′ et 15b,b′

L'analyse des constantes de couplage des spectres RMN ^{1}H effectués dans le chloroforme deutérié permet d'obtenir des informations intéressantes concernant la stéréochimie des composés synthétisés. Dans certains cas, il est même possible de mettre en évidence l'existence de conformations privilégiées.

© 1999 CNRC Canada

Fig. 3.

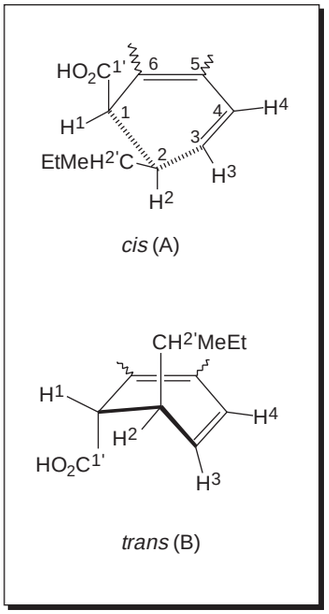

Les déplacements chimiques et les constantes de couplage des composés **15a,a′** et **15b,b′** sont indiqués dans le tableau 2. Pour **15a**, l'irradiation du multiplet à 2,59 ppm correspondant au proton H2 entraîne un effet Overhauser de 9 % au niveau du doublet de H1 à 3,86 ppm. Ce composé possède donc les deux protons H1 et H2 en *cis* et peut présenter deux conformations privilégiées A ou B éventuellement en équilibre (fig. 3). Pour chacune des deux conformations, les carbones C1 et C3–C6 sont quasi coplanaires, le carbone C2 étant situé au dessous (conformère A) ou au dessus du plan (conformère B). Dans le cas du conformère A, la valeur de l'angle dièdre formé par les plans H1-C1-C2 et C1-C2-H2 de 47° déterminée à partir du modèle moléculaire (Dreiding) et la valeur de la constante de couplage mesurée $J(1,2)$ = 6,5 Hz, sont en accord avec la relation de Karplus (54) adaptée empiriquement par Bothner-By (54*b*). La constante de couplage entre les protons H2 et H3, $J(2,3)$ = 3 Hz, est également compatible avec un angle dièdre formé par les plans H3–C3–C2 et C3–C2-H2 mesuré de 110° (55). En RMN ^{13}C, la constante de couplage entre le carbone du carbonyle C1′ et le proton H2, J(C1′,H2) = 11 Hz, est en accord avec l'angle déterminé à l'aide du modèle moléculaire (environ 180°). Par contre, cette constante de couplage de 11 Hz est incompatible avec l'angle mesuré pour une conformation B de la molécule (C1′ équatorial-H2 équatorial). De plus, dans l'hypothèse d'une conformation B, l'angle dièdre formé par les plans H3-C3-C2 et C3-C2-H2 mesuré de 25° n'est pas non plus compatible avec la valeur de la constante de couplage $J(2,3)$ de 3 Hz. En conséquence, le diastéréoisomère majoritaire **15a** possède en solution dans le chloroforme une géométrie *cis* au niveau des carbones C1 et C2 pour une conformation bloquée A.

Dans le cas de l'isomère minoritaire **15a′**, l'irradiation du signal à 2,51 ppm attribuable au proton H2 entraîne une augmentation de 10 % de l'intensité du signal de H1 à 3,79 ppm

Fig. 4.

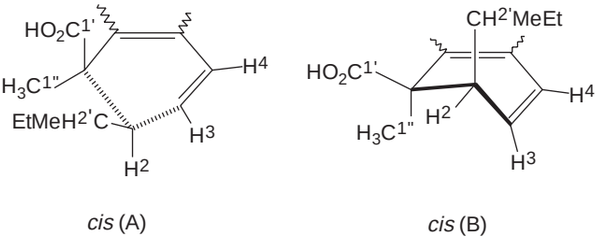

par effet Overhauser. Les constantes de couplage $J(1,2)$ = 6,2 Hz et $J(2,3)$ = 2,6 Hz sont compatibles avec la conformation A. Ce diastéréoisomère possède donc la même géométrie *cis* au niveau des carbones C1 et C2 et se présente sous une conformation privilégiée identique à celle de l'isomère majoritaire **15a**. Les deux diastéréoisomères **15a** et **15a′** ne diffèrent que par la configuration du carbone C2′.

Le couple d'isomères **15b,b′** correspond alors, soit à une structure de géométrie *cis* (au niveau des carbones C1 et C2) de conformation B (fig. 3), soit à une structure de géométrie *trans* de conformation A ou B. Un effet Overhauser de 5 % est observé entre les protons H1 (3,76 ppm) et H2′ (1,44 ppm) de l'isomère majoritaire **15b**. Les protons H1 et H2′ doivent être proches dans l'espace, ce qui implique une géométrie *trans* au niveau des carbones C1 et C2. Le composé **15b** possède l'une des deux conformations privilégiées A ou B. La valeur de la constante de couplage $J(1,2)$ de 4,1 Hz n'est pas compatible avec une géométrie axiale–axiale des protons H1 et H2 (conformation A). L'angle dièdre mesuré entre les plans H1-C1-C2 et C1-C2-H2 de 60° (H1 et H2 en positions équatoriales) dans le cas de la conformation B est par contre cohérent avec cette valeur. De plus, la valeur de la constante de couplage $J(2,3)$ de 5,1 Hz est en accord avec l'angle dièdre formé par les plans H3-C3-C2 et C3-C2-H2 (25°). La proximité de H2 et H3 est confirmée par un effet NOE de 5 % entre ces deux protons. En RMN ^{13}C, le couplage J(C1′,H2) égal à 5 Hz est également compatible avec les positions C1′ axiale et H2 équatoriale. La même étude effectuée avec l'isomère minoritaire **15b′** conduit à des résultats similaires. Le couple de composés **15b,b′** possède une géométrie *trans* au niveau des carbones C1 et C2 et la conformation privilégiée des deux diastéréoisomères est B.

4-2. Étude des composés 4a,a′

Dans le cas de l'isomère majoritaire **4a** résultant de la réaction de l'énolate **7** avec l'iodométhane, les conformères *cis* (A) et *cis* (B) sont compatibles avec un effet Overhauser de 13 % observé au niveau du proton H2 lorsque le groupe méthyle en C1 à 1,57 ppm est irradié (fig. 4). En RMN ^{13}C, dans le cas du conformère A, la constante de couplage entre le carbone du carbonyle C1′ et le proton H2, J(C1′,H2) de 1 Hz ne correspond pas à l'angle déterminé à l'aide du modèle moléculaire (environ 180°). La constante de couplage entre les protons H2 et H3, $J(2,3)$ = 5,7 Hz, n'est pas non plus en accord, d'après la relation de Karplus adaptée empiriquement par Garbisch, avec l'angle dièdre formé par les plans H2-C2-C3 et C2-C3-H3 (110°). Pour la conformation B, le même angle qui a pour valeur 30° est compatible avec la constante de couplage $J(2,3)$ = 5,7 Hz. Par contre, l'angle

© 1999 CNRC Canada

Schéma 11.

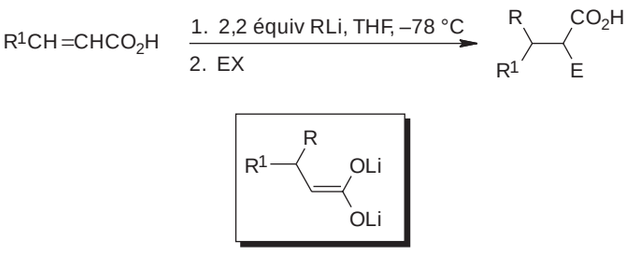

R = *n*-Bu, *s*-Bu, Ph
R^1 = H, Me, Ph

Schéma 12.

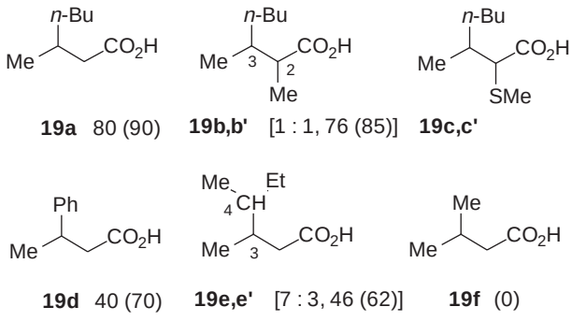

[ratio, rendement purifié (rendement brut[a]) %]
[a] déterminé par RMN-^{1}H

dièdre formé par les plans C1′′-C1-C2 et C1-C2-H2 de 62° n'est pas cohérent avec le fort effet Overhauser observé (13 %). Le cyclohexadiène est vraisemblablement légèrement déformé par des effets stériques tendant à diminuer l'angle entre les plans C1′′-C1-C2 et C1-C2-H2. Ce résultat est confirmé par les valeurs mesurées par analyse cristallographique aux rayons X : les angles 41,9° pour les plans C1′′-C1-C2 et C1-C2-H2, 75,1° pour les plans C1′-C1-C2 et C1-C2-H2 et 35,3° pour les plans H2-C2-C3 et C2-C3-H3 sont compatibles avec les constantes de couplage observées J(2,3) = 5,7 Hz, J(C1′,H2) = 1 Hz et avec l'effet Overhauser de 13 %. Le composé **4a** possède vraisemblablement la conformation privilégiée B.

5. Addition stéréosélective d'organolithiens aux acides carboxyliques α,β-insaturés acycliques

Les acides carboxyliques α,β-insaturés acycliques et les organolithiens donnent préférentiellement des réactions d'addition conjuguée dans le THF à –78°C (56) (schéma 11). Avec l'acide crotonique, le butyllithium, le phenyllithium et le butyllithium secondaire, les produits **19a,d,e,e′** sont obtenus avec de bons rendements, après piégeage de l'énolate de dilithium intermédiaire par l'acide trifluoroacétique (schéma 12). Le méthyllithium ne réagit pas dans les mêmes conditions et conduit au produit d'addition sur la fonction carbonyle par réaction à température plus élevée (24). L'énolate de dilithium formé intermédiairement peut être protoné par l'acide trifluoroacétique, méthylé par l'iodométhane ou méthylsulfénylé par le disulfure de diméthyle. La réaction du butyllithium et de l'iodométhane conduit avec un bon rendement purifié (76 %) à un mélange de composés diastéréoisomères **19b** et **19b′** dans le rapport 1 : 1 qui diffèrent au niveau de leurs carbones C2 et C3. Le disulfure de diméthyle conduit dans les mêmes conditions aux deux diastéréoisomères **19c** et **19c′** avec un rendement brut moyen 3 : 2 (50 %). La réaction du butyllithium secondaire suivie d'une protonolyse conduit aux diastéréoisomères **19e** et **19e′** qui diffèrent au niveau de leurs carbones C3 et C4 (7 : 3, 46 %).

Schéma 13.

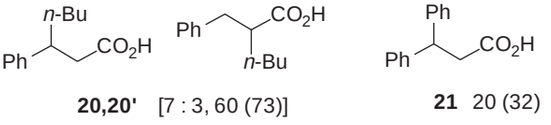

[ratio, rendement purifié (rendement brut[a]) %]
[a] déterminé par RMN-^{1}H

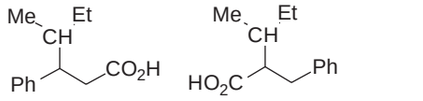

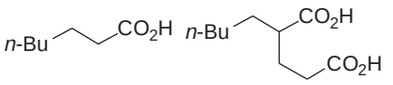

La réaction du butyllithium et du butyllithium secondaire avec l'acide (*E*)-3-phénylpropénoïque conduit dans chaque cas à la formation de deux isomères de position, l'addition en β de la fonction acide carboxylique étant majoritaire (schéma 13). Quelques rares exemples de la littérature décrivent l'addition conjuguée d'organolithiens en position β d'un groupe phényle (35, 57). Les structures **20** et **20'** peuvent être facilement différenciées en RMN ^{13}C par la multiplicité et par le déplacement chimique du signal du carbone de la fonction acide carboxylique. L'acide acrylique réagit avec le butyllithium dans le THF à –78°C et les acides **24** et **25** sont obtenus avec des rendements de 50 % et 30 % respectivement. Le composé **25** résulte de la double addition de l'énolate intermédiaire à l'acrylate de lithium (autres méthodes de préparation du composé **25** : réf. 58).

La réaction de l'acide phénylpropiolique **26** avec le butyllithium dans le THF à –78°C et la protonolyse par l'acide trifluoroacétique à la même température conduisent à la formation exclusive du composé **27** facilement purifiable par recristallisation (heptane – acétate d'éthyle) (70 %, schéma 14).[4,5] Le dianion **28** résultant de la *trans* addition du butyllithium au phénylpropiolate de lithium est formé préférentiellement. Il est intéressant de noter l'analogie structurale existant entre **28** et le dianion *ortho*-lithio benzoate de lithium **29** obtenu par traitement de l'acide benzoïque avec le complexe 1 : 1 *s*-BuLi/TMEDA (29, 30). L'interaction forte — responsable

© 1999 CNRC Canada

Schéma 14.

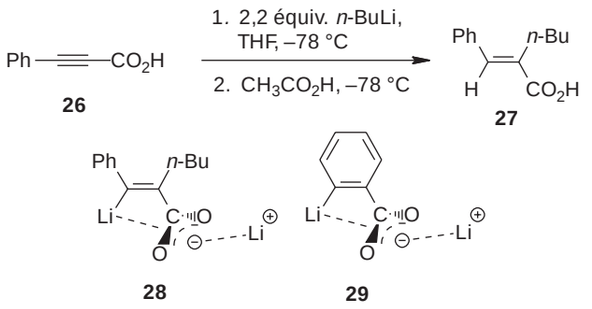

de l'effet CIPE observé (60) — existant à –78°C entre le carboxylate et le cation lithium contribue probablement à augmenter la stabilité des dianions **28** et **29**.

6. Partie expérimentale

Le butyllithium secondaire (1,3 M en solution dans un mélange cyclohexane–hexanes), le butyllithium (1,6 M en solution dans l'hexane) et le méthyllithium (1 M en solution dans l'éther) commercialisés par Acros Chemicals et Aldrich Chemical Company, sont titrés périodiquement par l'alcool 2,5-diméthoxybenzylique. Le THF est distillé sur sodium–benzophénone. Les spectres de RMN ont été enregistrés sur un spectromètre Bruker ARX 200 ou Bruker AM 300 opérant à 200 et 300 MHz pour le proton et à 50,3 et 75,5 MHz pour le carbone-13. Les déplacements chimiques δ sont exprimés en ppm par rapport au tétraméthylsilane (TMS) utilisé comme référence interne lorsque $CDCl_3$ est le solvant. Les constantes de couplage sont exprimés en Hz. Les abréviations suivantes sont utilisées : s (singulet), sl (singulet large), d (doublet), dl (doublet large), dd (doublet dédoublé), t (triplet), q (quadruplet), m (multiplet). Les spectres SM-EI ont été réalisés sur un spectromètre Varian MAT 311.

Les (flash) chromatographies sur colonne ont été effectuées sur gel de silice 60 Merck (70–230 mesh et 230–400 mesh). Les plaques Merck en aluminium recouvertes de gel de silice 60 F 254 (0,2 torr (1 torr = 133,3 Pa)) sont utilisées pour les chromatographies analytiques sur couche mince. Les éluants et solvants de recristallisation (éther, heptane, acétate d'éthyle) sont utilisés sans purification préalable. Les points de fusion ont été déterminés à l'aide d'un appareil Büchi 510. Les distillations sont effectuées au four tubulaire Büchi GRK 50. Les points d'ébullition sont déterminés à ±10 degrés. Les analyses centésimales ont été réalisées par le Service central d'analyse du CNRS de Gif-sur-Yvette.

Synthèse d'acides dihydronaphtoïques — Mode opératoire général

Dans un ballon de 250 mL à tubulure latérale muni d'une ampoule à addition isobare sous argon, sont introduits successivement le THF et l'organolithien à –30 à 40°C. Le mélange est refroidi à –78°C et l'acide 1- ou 2-naphtoïque en solution dans le THF (20 mL) est ajouté au goutte-à-goutte. Le mélange est agité pendant une heure à –78°C puis le réactif électrophile en solution dans le THF (20 mL) est additionné lentement. Le milieu réactionnel est amené à température ambiante sous agitation puis traité par de l'eau (30 mL). La phase aqueuse est lavée deux fois avec de l'éther (40 mL). Le séchage et l'évaporation du solvant permettent d'isoler le produit d'addition 1,2 avec un rendement généralement compris entre 3 et 10 % après chromatographie sur colonne de silice (heptane – acétate d'éthyle). La phase aqueuse est acidifiée par HCl 2 M (40 mL) puis additionnée d'éther (40 mL). La phase organique est séparée, lavée par une solution saturée de bicarbonate de sodium (40 mL) et par de l'eau (40 mL) puis séchée sur $MgSO_4$. La filtration du sel et l'évaporation du solvant conduisent à un mélange brut constitué des adduits 1,4 qui peuvent être isolés et purifiés par recristallisation ou chromatographie.

trans-*1-Carboxy-1-méthyl-2-(2-méthylpropyl)-1,2-dihydronaphtalènes (**4a,a′**)*

Selon le mode opératoire général, la réaction de l'acide 1-naphtoïque (2,58 g, 15 mmol) et du butyllithium secondaire (25,4 mL d'une solution 1,3 M dans un mélange cyclohexane–hexanes, 33 mmol) dans le THF (60 mL) et le traitement de l'énolate résultant par l'iodométhane (8,52 g, 60 mmol) dans le THF (20 mL) conduisent au composé **4a** obtenu pur (2,64 g, 72 %) après recristallisation fractionnée (heptane – acétate d'éthyle) (**4a**,**4a′** 9 : 1). Les caractéristiques spectroscopiques de l'isomère minoritaire **4a′** (8 %) sont obtenues par différence à partir des spectres du mélange.

4a : Solide blanc. *F* = 175–176°C. RMN ^{1}H (300 MHz) δ ppm : 11,61 (sl, 1H), 7,43 (m, 1H), 7,22–7,13 (m, 2H), 7,04 (m, 1H), 6,56 (dl, 1H, *J* = 9,9 Hz), 5,79 (dd, 1H, *J* = 9,9 et 5,7 Hz), 2,65 (ddd, 1H, *J* = 5,5, 3,2 et 0,9 Hz), 1,59 (m, 1H), 1,57 (s, 3H), 1,35 (m, 1H), 1,25 (m, 1H), 0,91 (t, 3H, *J* = 7,4 Hz), 0,61 (d, 3H, *J* = 6,6 Hz). RMN ^{13}C (75,5 MHz) δ ppm : 181,1 (*J* = 1 Hz); 137,0; 132,5; 128,4; 127,7; 127,1; 126,8; 124,7; 124,7; 50,5; 48,1; 38,6; 28,4; 28,1; 13,8; 12,3. SM-HR calc. pour $C_{16}H_{20}O_2$: 244,1463; tr. : 244,1456. Anal. calc. pour $C_{16}H_{20}O_2$: C 78,65; H 8,25; tr. : C 78,64; H 8,11.

4a′ : Solide blanc. RMN ^{1}H (300 MHz) δ ppm : 11,61 (sl, 1H), 7,43 (m, 1H), 7,22–7,13 (m, 2H), 7,04 (m, 1H), 6,51 (d, 1H, *J* = 9,9 Hz), 5,89 (dd, 1H, *J* = 9,9 et 5,6 Hz), 2,54 (ddd, 1H, *J* = 5,5, 3,2 et 1 Hz), 1,59 (m, 1H), 1,56 (s, 3H), 1,32 (m, 1H), 1,25 (m, 1H), 0,98 (d, 3H, *J* = 6,9 Hz), 0,65 (t, 3H, *J* = 7,3 Hz). RMN ^{13}C (75,5 MHz) δ ppm : 181,5; 137,9; 132,4; 125,2; 51,1; 50,7; 39,0; 28,4; 28,4; 17,8; 12,3.

*2-Méthyl-1-naphtalèn-1-yl-butan-1-one (**11**)*

Chromatographie sur colonne de silice (95 : 5 heptane – acétate d'éthyle), 0,25 g (8 %). Huile incolore. RMN ^{1}H (200 MHz) δ ppm : 8,32 (m, 1H), 7,98–7,74 (m, 3H), 7,58–7,46 (m, 3H), 3,37 (m, 1H), 1,88 (m, 1H), 1,53 (m, 1H), 1,24 (d, 3H, *J* = 7 Hz), 0,96 (t, 3H, *J* = 7,5 Hz).

trans-*1-Carboxy-1-éthyl-2-(2-méthylpropyl)-1,2-dihydronaphtalènes (**4b,b′**)*

Selon le mode opératoire général, la réaction de l'acide 1-naphtoïque (2,58 g, 15 mmol) et du butyllithium secondaire (25,4 mL d'une solution 1,3 M dans un mélange cyclohexane–hexanes, 33 mmol) dans le THF (60 mL) et le traitement de l'énolate résultant par l'iodoéthane (9,36 g, 60 mmol) dans le THF (20 mL) conduisent au composé **4b**

© 1999 CNRC Canada

obtenu pur (1,7 g, 44 %) après recristallisation fractionnée (heptane – acétate d'éthyle) de (**4b,b′** 75 : 25). Les caractéristiques spectroscopiques de l'isomère minoritaire **4b′** sont obtenues par différence à partir des spectres du mélange.

4b : Solide blanc. *F* = 125–127°C. RMN ^{1}H (200 MHz) δ ppm : 10,47 (sl, 1H), 7,53 (m, 1H), 7,25–7,01 (m, 3H), 6,55 (d, 1H, *J* = 10 Hz), 5,78 (dd, 1H, *J* = 10 et 6 Hz), 2,69 (dd, 1H, *J* = 6 et 3,5 Hz), 2,00 (m, 2H), 1,53 (m, 1H), 1,33 (m, 1H), 1,22 (m, 1H), 0,89 (t, 3H, *J* = 7 Hz), 0,73 (t, 3H, *J* = 7 Hz), 0,54 (d, 3H, *J* = 6,5 Hz). RMN ^{13}C (50,3 MHz) δ ppm : 180,9; 134,7; 132,8; 129,3; 128,5; 126,9; 126,6; 126,4; 125,1; 55,5; 48,6; 39,3; 32,4; 28,1; 13,91; 12,3; 9,8. SM-HR calc. pour $C_{17}H_{22}O_2$: 258,1620; tr. : 258,1616. Anal. calc. pour $C_{17}H_{22}O_2$: C 79,09; H 8,58; tr. : C 79,16; H 8,44.

4b′ : Solide blanc. RMN ^{1}H (200 MHz) δ ppm : 10,47 (sl, 1H), 7,25–7,01 (m, 3H), 7,53 (m, 1H), 6,48 (d, 1H, *J* = 10 Hz), 5,99 (m, 1H), 2,60 (m, 1H), 1,90 (m, 2H), 1,53 (m, 1H), 1,33 (m, 1H), 1,22 (m, 1H), 0,89 (t, 3H, *J* = 7 Hz), 0,73 (t, 3H, *J* = 7 Hz), 0,54 (d, 3H, *J* = 6,5 Hz).

trans-*1-Carboxy-1-méthylthio-2-(2-méthylpropyl)-1,2-dihydronaphtalènes (**4c,c′**)*

Selon le mode opératoire général, la réaction de l'acide 1-naphtoïque (1,72 g, 10 mmol) et du butyllithium secondaire (117 mL d'une solution 1,3 M dans un mélange cyclohexane–hexanes, 22 mmol) dans le THF (20 mL) et le traitement de l'énolate résultant par le disulfure de diméthyle (3,76 g, 40 mmol) dans le THF (20 mL) conduisent au mélange des deux composés **4c,c′** (2,36 g, 65 : 35, 82 %) après recristallisation (heptane – acétate d'éthyle). Les caractéristiques RMN ^{1}H et ^{13}C de chacun des deux isomères sont facilement obtenus par analyse des mélanges.

4c : Solide blanc. RMN ^{1}H (300 MHz) δ ppm : 10,55 (sl, 1H), 7,68 (m, 1H), 7,24–7,21 (2H), 7,11 (m, 1H), 6,66 (d, 1H, *J* = 10 Hz), 5,90 (dd, 1H, *J* = 10, 6 Hz), 2,96 (dd, 1H, *J* = 6 et 3,5 Hz), 1,94 (s, 3H), 1,69 (m, 1H), 1,38 (m, 1H), 1,23 (m, 1H), 0,91 (t, 3H, *J* = 7,5 Hz), 0,53 (d, 3H, *J* = 6,5 Hz). RMN ^{13}C (75,5 MHz) δ ppm : 176,3; 132,7; 131,9; 128,9; 127,9; 127,7; 127,6; 126,8; 124,6; 59,9; 46,1; 39,2; 28,2; 14,6; 13,9; 12,3. SM-HR calc. pour $C_{16}H_{20}O_2S$: 276,1183; tr.: 276,1172. Anal. calc. pour $C_{16}H_{20}O_2S$: C 69,53; H 7,29; tr. : C 69,79; H, 7,32.

4c′ : Solide blanc. RMN ^{1}H (300 MHz) δ ppm : 10,55 (sl, 1H), 7,68 (m, 1H), 7,24–7,21 (2H), 7,11 (m, 1H), 6,63 (d, 1H, *J* = 10 Hz,), 6,00 (dd, 1H, *J* = 10 et 6 Hz), 2,86 (dd, 1H, *J* = 5,5 et 4 Hz), 1,94 (s, 3H), 1,69 (m, 1H), 1,4 (m, 1H), 1,23 (m, 1H), 0,91 (t, 3H, *J* = 4,5 Hz), 0,53 (d, 3H, *J* = 6,5 Hz). RMN ^{13}C (75,5 MHz) δ ppm : 176,2; 132,7; 131,9; 128,9; 127,9; 127,7; 127,6; 126,8; 125,2; 59,9; 49,4; 39,6; 20,9; 17,5; 13,9; 12,1.

trans-*1-Carboxy-1-méthyl-2-butyl-1,2-dihydronaphtalène (**4e**)*

Selon le mode opératoire général, la réaction de l'acide 1-naphtoïque (1,72 g, 10 mmol) et du butyllithium (13,7 mL d'une solution 1,6 M dans l'hexane, 22 mmol) dans le THF (60 mL) et le traitement de l'énolate résultant par l'iodométhane (5,68 g, 40 mmol) dans le THF (20 mL) conduisent au composé **4e** obtenu pur (0,87 g, 36 %) après chromatographie (heptane – acétate d'éthyle). Huile incolore. RMN ^{1}H (300 MHz) δ ppm : 9,36 (sl, 1H), 7,03 (m, 1H), 7,19–7,16 (m, 2H), 7,43 (m, 1H), 6,41 (dd, 1H, *J* = 10 et 2 Hz), 5,94 (dd, 1H, *J* = 10 et 4 Hz), 2,41 (m, 1H), 1,60 (s, 3H), 1,48-1,32 (m, 2H), 1,30–1,10 (m, 4H), 0,79 (t, 3H, *J* = 7 Hz). RMN ^{13}C (75,5 MHz) δ ppm : 181,0; 136,9; 133,0; 130,2; 127,5; 127,3; 127,0; 126,9; 126,5; 49,8; 43,7; 30,8; 29,8; 24,6; 22,8; 14,1. SM-HR calc. pour $C_{16}H_{20}O_2$: 244,1463; tr. : 244,1459. Anal. calc. pour $C_{16}H_{20}O_2$: C 78,65; H 8,25; tr. : C 78,34; H 8,30.

*1-Naphtalèn-1-yl-pentan-1-one (**12**)*

Chromatographie sur colonne de silice (95 : 5 heptane – acétate d'éthyle), 0,25 g (8 %). Huile incolore (Autres méthodes de préparation : réf. 61). RMN ^{1}H (200 MHz) δ ppm : 8,53 (m, 1H), 7,90–7,81 (m, 3H), 7,62–7,44 (m, 3H), 3,05 (t, 2H, *J* = 7,5 Hz), 1,78 (m, 2H), 1,43 (m, 2H), 0,95 (t, 3H, *J* = 7,5 Hz).

trans-*2-Carboxy-2-méthyl-1-(2-méthylpropyl)-1,2-dihydronaphtalènes (**6a,a′**)*

Selon le mode opératoire général, la réaction de l'acide 2-naphtoïque (2,58 g, 15 mmol) et du butyllithium secondaire (25,4 mL d'une solution 1,3 M dans un mélange cyclohexane–hexanes, 33 mmol) dans le THF (60 mL) et le traitement de l'énolate résultant par l'iodométhane (8,52 g, 60 mmol) dans le THF (20 mL) conduisent au composé **6a** obtenu pur (2,31 g, 70 : 30, 63 %) après recristallisation fractionnée (heptane – acétate d'éthyle). Les caractéristiques spectroscopiques de l'isomère minoritaire **6a′** (27 %) sont obtenues par différence à partir des spectres du mélange.

6a : Solide blanc. *F* = 113–115°C. RMN ^{1}H (300 MHz) δ ppm : 12,42 (sl, 1H), 7,03–7,21 (m, 4H), 6,4 (d, 1H, *J* = 10 Hz), 6,35 (dd, 1H, *J* = 1 et 10 Hz), 3,02 (dd, 1H, *J* = 1 et 2,5 Hz), 1,66 (m, 1H, *J* = 2,5 Hz), 1,43 (m, 1H), 1,34 (s, 3H), 1,08 (m, 1H), 0,92 (t, 3H, *J* = 7 Hz), 0,65 (d, 3H, *J* = 7 Hz). RMN ^{13}C (75,5 MHz) δ ppm : 183,3; 133,5; 132,4; 131,4; 130,3; 126,9; 126,8; 126,7; 126,0; 50,2; 48,4; 38,8; 29,1; 25,5; 15,2; 12,2. SM-HR calc. pour $C_{16}H_{20}O_2$: 244,1463; tr. : 244,1456. Anal. calc. pour $C_{16}H_{20}O_2$: C 78,65; H 8,25; tr. : C 78,26; H 7,94.

6a′ : Solide blanc. RMN ^{1}H (300 MHz) δ ppm : 12,42 (sl, 1H), 7,03–7,21 (m, 4H), 6,40 (d, 1H, *J* = 10 Hz), 6,35 (dd, 1H, *J* = 1 et 10 Hz), 2,91 (dd, 1H,, 3 Hz), 1,66 (m, 1H, *J* = 2,5 Hz), 1,43 (m, 1H), 1,23 (s, 3H), 1,08 (m, 1H), 0,94 (t, 3H, *J* = 7 Hz), 0,65 (d, 3H, *J* = 7 Hz). RMN ^{13}C (75,5 MHz) δ ppm : 183,3; 133,1; 132,4; 131,4; 130,5; 126,9; 126,8; 126,7; 126,0; 52,8; 48,4; 39,1; 25,6; 24,2; 18,6; 15,3.

*2-Méthyl-1-naphtalèn-2-yl-butan-1-one (**13**)*

Chromatographie sur colonne de silice (95 : 5 heptane – acétate d'éthyle), 0,22 g (7 %). Huile incolore. RMN ^{1}H (200 MHz) δ ppm : 8,45 (s, 1H), 8,00–7,80 (m, 4H), 7,54–7,50 (m, 2H), 3,54 (m, 1H), 1,89 (m, 1H), 1,52 (m, 1H), 1,24 (d, 3H, *J* = 7 Hz), 0,93 (t, 3H, *J* = 7,5 Hz). RMN ^{13}C (50,3 MHz) δ ppm : 204,4; 135,5; 134,1; 132,6; 129,6; 129,5; 128,4; 128,3; 127,7; 126,6; 124,2; 42,1; 26,8; 16,9; 11,7.

© 1999 CNRC Canada

trans-*2-Carboxy-2-méthyl-1-butyl-1,2-dihydronaphtalène (**6c**)*

Selon le mode opératoire général, la réaction de l'acide 2-naphtoïque (1,72 g, 10 mmol) et du butyllithium (13,7 mL d'une solution 1,6 M dans l'hexane, 22 mmol) dans le THF (60 mL) et le traitement de l'énolate résultant par l'iodométhane (5,68 g, 40 mmol) dans le THF (20 mL) conduisent au composé **6c** obtenu pur (0,92 g, 38 %) après chromatographie sur colonne de silice (heptane – acétate d'éthyle). Huile incolore. RMN ^{1}H (300 MHz) δ ppm : 10,36 (sl, 1H), 7,20–7,05 (m, 4H), 6,44 (d, 1H, *J* = 10 Hz), 6,3 (dd, 1H, *J* = 10 et 1 Hz), 2,84 (dd, 1H, *J* = 2,5 et 8 Hz), 1,44 (m, 2H), 1,29 (s, 3H), 1,20 (m, 4H), 0,79 (t, 3H, *J* = 7 Hz). RMN ^{13}C (50,3 MHz) δ ppm : 181,9; 135,3; 130,4; 129,5; 128,6; 125,9; 125,5; 125,2; 124,9; 47,8; 46,2; 29,9; 28,7; 22,8; 21,6; 12,9. SM-HR calc. pour $C_{16}H_{20}O_2$: 244,1463; tr. : 244,1471. Anal. calc. pour $C_{16}H_{20}O_2$: C 78,65; H 8,25; tr. : C 78,34; H 8,26.

*2-Naphtalèn-2-yl-pentan-1-one (**14**)*

Chromatographie sur colonne de silice (95 : 5 heptane – acétate d'éthyle), 0,11 g (5 %). Huile incolore (61*b*). RMN ^{1}H (200 MHz) δ ppm : 8,44 (s, 1H), 8,03–7,82 (m, 4H), 7,58–7,48 (m, 2H), 3,06 (t, 2H, *J* = 7,5 Hz), 1,77 (m, 2H), 1,43 (m, 2H), 0,97 (t, 3H, *J* = 7,5 Hz). RMN ^{13}C (75,5 MHz) δ ppm : 200,5; 135,5; 133,4; 132,5; 129,6; 129,5; 128,4; 128,3; 127,8; 126,7; 124,0; 38,4; 26,7; 22,6; 14,1.

*Acide 2-(2-méthylpropyl)-1-naphtoïque (**9**)*

Selon le mode opératoire général, la réaction de l'acide 1-naphtoïque (1,72 g, 10 mmol) et du butyllithium secondaire (17 mL d'une solution 1,3 M dans un mélange cyclohexane–hexanes, 22 mmol) dans le THF (60 mL) et le traitement de l'énolate résultant par l'hexachloroéthane (9,46 g, 40 mmol) dans le THF (20 mL) conduisent au composé **9** obtenu pur (2,39 g, 70 %) après recristallisation (heptane – acétate d'éthyle). Solide blanc. *F* = 166–168°C. RMN ^{1}H (300 MHz) δ ppm : 11,10 (sl, 1H), 8,01 (d, 1H), 7,90 (d, 1H), 7,83 (d, 1H), 7,59–7,43 (m, 3H), 3,11 (m, 1H), 1,81–1,67 (m, 2H), 1,36 (d, 3H, *J* = 7 Hz), 0,87 (t, 3H, *J* = 7 Hz). RMN ^{13}C (75,5 MHz) δ ppm : 176,2; 142,5; 131,8; 130,5; 129,6; 129,2; 128,1; 127,2; 125,8; 124,8; 123,6; 39,2; 30,8; 22,2; 12,4. SM-HR calc. pour $C_{15}H_{16}O_2$: 228,1150; tr. : 228,1159. Anal. calc. pour $C_{15}H_{16}O_2$: C 78,92; H 7,01; tr. : C 79,15; H 6,95.

*Acide 1-(2-méthylpropyl)-2-naphtoïque (**10**)*

Selon le mode opératoire général, la réaction de l'acide 2-naphtoïque (1,72 g, 10 mmol) et du butyllithium secondaire (17 mL d'une solution 1,3 M dans un mélange cyclohexane–hexanes, 22 mmol) dans le THF (60 mL) et le traitement de l'énolate résultant par l'hexachloroéthane (9,46 g, 40 mmol) dans le THF (20 mL) conduisent au composé **10** obtenu pur (1,78 g, 78 %) après recristallisation (heptane – acétate d'éthyle). Solide blanc. *F* = 117–118°C. RMN ^{1}H (200 MHz) δ ppm : 10,70 (sl, 1H), 8,4 (m, 1H), 7,87 (m, 1H), 7,78–7,69 (m, 2H), 7,58–7,49 (m, 2H), 3,89 (m, 1H), 2,09 (m, 2H), 1,65 (d, 3H, *J* = 7 Hz), 0,90 (t, 3H, *J* = 7 Hz). RMN ^{13}C (50,3 MHz) δ ppm : 176,1; 144,4; 135,6; 131,7; 129,2; 129,1; 126,9; 125,8; 125,3; 38,4; 29,7; 20,5; 13,3. SM-HR calc. pour $C_{15}H_{16}O_2$: 228,1150; tr. : 228,1161. Anal. calc. pour $C_{15}H_{16}O_2$: C 78,92; H 7,01; tr. : C 78,85; H 6,93.

1-Carboxy-2-(2-méthylpropyl)-1,2-dihydronaphtalènes (15a,a′ et 15b,b′) — addition de l'énolate au réactif électrophile en mode inverse

L'appareillage pour addition inverse utilisé est décrit à la réf. 52. Dans un ballon B de 250 mL à trois tubulures muni d'une ampoule à addition isobare sous argon, sont introduits successivement le THF (60 mL) et le butyllithium secondaire (22,7 mL d'une solution 1,4 M dans un mélange cyclohexane–hexanes, 33 mmol) à –30 à 40°C. Le mélange est refroidi à –78°C et l'acide 1-naphtoïque (2,58 g, 15 mmol) en solution dans le THF (20 mL) est ajouté au goutte-à-goutte. Le milieu réactionnel est agité pendant 1 h à –78°C. Dans un ballon A de 250 mL à deux tubulures et purgé sous argon est placé l'acide trifluoroacétique (4,6 mL, 60 mmol) en solution dans le THF (20 mL). La solution résultante est refroidie à –78°C. À cette solution est ajoutée au goutte-à-goutte l'énolate précédemment préparé. Le milieu réactionnel est amené lentement à température ambiante puis traité par une solution de HCl 2 M (40 mL). La phase aqueuse est lavée avec de l'éther (40 mL). Les phases organiques sont rassemblées et lavées par une solution saturée de bicarbonate de sodium (20 mL) et par de l'eau (40 mL) puis séchée sur $MgSO_4$. La filtration du sel et l'évaporation du solvant conduisent à un mélange brut constitué des adduits **15a,a′** et **15b,b′** (78 %, 56 : 14 : 24 : 16) purifiés par chromatographie sur colonne de silice (gradient d'élution 9 : 1 → 7 : 3, heptane – acétate d'éthyle). Les couples de diastéréoisomères **15a,a′** et **15b,b′** sont isolés avec des rendements respectifs de 30 et 16 %. Huiles rouge-ocre.

15a : RMN ^{1}H (300 MHz) δ ppm : 8,80 (sl, 1H), 7,26–7,04 (m, 4H), 6,48 (dd, 1H, *J*(2,4) = 2,8 et *J*(3,4) = 9,8 Hz), 5,96 (ddl, 1H, *J*(2,3) = 3,0 Hz et *J*(3,4) = 9,8 Hz), 3,86 (d, 1H, *J*(1,2) = 6,5 Hz), 2,59 (dddd, 1H, *J*(2,4) = 2,8; *J*(2,3) = 3,0; *J*(1,2) = 6,5 et *J*(2,2′) = 9,0 Hz), 1,83 (m, 1H), 1,64 (m, 1H), 1,26 (m, 1H), 0,95 (d, 3H, *J* = 6,6 Hz), 0,89 (t, 3H, *J* = 7,3 Hz). RMN ^{13}C (75,5 MHz) δ ppm : 178,3 (*J* = 11 Hz); 134,1; 132,5; 129,8; 128,3; 128,0; 127,4; 127,2; 126,3; 46,6; 41,7; 34,6; 26,8; 16,4; 10,6. SM-HR calc. pour $C_{15}H_{18}O_2$: 230,1306; tr. : 230,1318.

15a′ : RMN ^{1}H (300 MHz) δ ppm : 8,80 (sl, 1H), 7,26–7,04 (m, 4H), 6,46 (dd, 1H, *J*(2,4) = 3,0 et *J*(3,4) = 9,7 Hz), 5,98 (ddl, 1H, *J*(2,3) = 2,6 et *J*(3,4) = 9,7 Hz), 3,79 (d, 1H, *J*(1,2) = 6,2 Hz), 2,51 (dddd, 1H, *J*(2,3) = 2,6; *J*(2,4) = 3,0; *J*(1,2) = 6,2 et *J*(2,2′) = 10,3 Hz), 1,83 (m,1H), 1,64 (m, 1H), 1,26 (m, 1H), 1,03 (d, 3H, *J* = 6,6 Hz), 0,89 (t, 3H, *J* = 7,5 Hz). RMN ^{13}C (75,5 MHz) δ ppm : 178,3; 134,2; 132,7; 130,4; 128,6; 128,1; 127,5; 127,1; 126,3; 46,5; 41,9; 34,6; 26,6; 17,0; 10,7.

15b : RMN ^{1}H (300 MHz) δ ppm : 9,05 (sl, 1H), 7,26–7,02 (m, 4H), 6,48 (dd, 1H, *J*(2,4) = 1,2 et *J*(3,4) = 9,8 Hz), 5,90 (dd, 1H, *J*(2,3) = 5,1 et *J*(3,4) = 9,8 Hz), 3,76 (d, 1H, *J*(1,2) = 4,1 Hz), 2,86 (dddd, 1H, *J*(2,4) = 1,2; *J*(1,2) = 4,1; *J*(2,3)

© 1999 CNRC Canada

= 5,1 et $J(2,2')$ = 5,4 Hz), 1,48–1,39 (m, 2H), 1,29 (m, 1H), 0,86 (t, 3H, J = 7,3 Hz), 0,82 (d, 3H, J = 6,7 Hz). RMN ^{13}C (75,5 MHz) δ ppm : 180,6 (J = 5 Hz); 133,4; 131,0; 128,8; 128,8; 127,9; 127,5; 127,5; 126,3; 47,5; 40,8; 38,5; 26,7; 15,8; 11,5.

15b′ : RMN ^1H (300 MHz) δ ppm : 9,05 (sl, 1H), 7,26–7,02 (m,4H), 6,46 (dd, 1H, $J(2,4)$ = 0,8 et $J(3,4)$ = 9,7 Hz), 5,94 (dd, 1H, $J(2,3)$ = 5,5 et $J(3,4)$ = 9,7 Hz), 3,77 (d, 1H, $J(1,2)$ = 2,6 Hz), 2,79 (dddd, 1H, $J(2,4)$ = 0,8; $J(1,2)$ = 2,6; $J(2,2')$ = 5,5 et $J(2,3)$ = 5,5 Hz), 1,48-1,39 (m, 2H), 1,19 (m, 1H), 0,86 (t, 3H, J = 7,3 Hz), 0,80 (d, 3H, J = 6,6 Hz).

*2-Carboxy-1-(2-méthylpropyl)-1,4-dihydronaphtalènes (**17a,a′**)*

Selon le mode opératoire précédent (addition inverse de l'énolate), la réaction de l'acide 2-naphtoïque (1,72 g, 10 mmol) et du butyllithium secondaire (17 mL d'une solution 1,3 M dans un mélange cyclohexane–hexanes, 22 mmol) dans le THF (60 mL) et le traitement de l'énolate résultant par l'acide trifluoroacétique (1,58 mL, 40 mmol) dans le THF (20 mL) conduisent au mélange non séparables des composés **17a** et **17a′** (**17a,a′** 70 : 30) purifiés par recristallisation (heptane – acétate d'éthyle) (66 %). Solide blanc.

17a : RMN ^1H (300 MHz) δ ppm : 11,50 (sl, 1H), 7,48 (dd, 1H, J = 5,9 et J = 2,5 Hz), 7,21–7,16 (m, 4H), 3,98 (m, 1H, J = 3 et J = 1,5 Hz,), 3,61 (dd, 1H, J = 22,5; J = 2,5 et J = 3 Hz), 3,49 (dd, 1H, J = 22,5; J = 5,9 et J = 1,5 Hz), 1,79 (m, 1H), 1,55 (m, 1H), 1,22 (m, 1H), 0,97 (t, 3H, J = 7,3 Hz), 0,57 (d, 3H, J = 7 Hz). RMN ^{13}C (75,5 MHz) δ ppm : 172,6; 141,2; 136,2; 134,4; 133,4; 129,4; 127,7; 126,2; 125,9; 43,7; 42,2; 32,4; 27,8; 14,4; 12,3. SM-HR calc. pour $C_{15}H_{18}O_2$: 230,1306; tr. : 230,1307.

17a′ : RMN ^1H (300 MHz) δ ppm : 11,50 (sl, 1H), 7,48 (dd, 1H, J = 5,9 et 2,5 Hz), 7,21–7,16 (m, 4H), 3,93 (m, 1H), 3,61 (dd, 1H, J = 22,5; J = 2,5 et J = 3 Hz), 3,49 (dd, 1H, J = 22,5; J = 5,9 et J = 1,5 Hz), 1,79 (m, 1H), 1,49 (m, 1H), 0,90 (d, 3H, J = 7 Hz), 0,81 (t, 3H, J = 7 Hz), 0,73 (m, 1H). RMN ^{13}C (75,5 MHz) δ ppm : 172,9; 141,4; 137,6; 134,0; 132,9; 129,2; 127,6; 126,1; 125,9; 45,0; 42,9; 32,3; 25,2; 16,6; 12,1.

Synthèse d'acides alkanoïques acycliques — mode opératoire général

Dans un ballon de 250 mL à tubulure latérale muni d'une ampoule à addition isobare sous argon, sont introduits successivement le THF (50 mL) puis l'organolithien à –30 à 40°C. Le milieu réactionnel est refroidi à –78°C et l'acide carboxylique α,β-insaturé en solution dans le THF (20 mL) est ajouté au goutte-à-goutte. Le mélange est agité pendant 1 h à –78°C puis le réactif électrophile en solution dans le THF (20 mL) est additionné lentement. Le milieu réactionnel est amené à température ambiante sous agitation puis traité par une solution de HCl 2 M (40 mL). La phase aqueuse est lavée avec de l'éther (40 mL). Les phases organiques sont rassemblées, lavées trois fois par une solution saturée de bicarbonate de sodium (20 mL). La phase aqueuse est séparée, acidifiée par une solution de HCl 2 M (60 mL) puis additionnée d'éther (60 mL). La phase organique est séparée puis séchée sur $MgSO_4$. La filtration du sel et l'évaporation du solvant permettent de récupérer après recristallisation ou distillation les produits de réaction purs.

*Acide 3-méthylheptanoïque (**19a**)*

Selon le mode opératoire général, la réaction de l'acide crotonique (1,29 g, 15 mmol) et du butyllithium (20 mL d'une solution 1,6 M dans l'hexane, 33 mmol) dans le THF (60 mL) et le traitement de l'énolate résultant par l'acide trifluoroacétique (2,31 mL, 33 mmol) dans le THF (20 mL) conduisent au composé **19a** obtenu pur (1,72 g, 80 %) après distillation (Eb = 75–80°C/1 torr). Huile incolore. RMN ^1H (200 MHz) δ ppm : 11,80 (sl, 1H), 2,36 (dd, 1H, J = 6 et 15 Hz), 2,14 (dd, 1H, J = 8 et 15 Hz), 1,96 (m, 1H), 1,36–1,21 (m, 6H), 0,96 (d, 3H, J = 6,5 Hz), 0,89 (t, 3H, J = 6 Hz). RMN ^{13}C (50,3 MHz) δ ppm : 180,3; 41,7; 36,4; 30,2; 29,1; 22,8; 19,7; 14,1. SM-HR calc. pour $C_4H_7O_2$ [M – $C_4H_9]^+$: 87,0446; tr. : 87,0445.

*Acides 2,3-diméthylheptanoïques (**19b,b′**)*

Selon le mode opératoire général, la réaction de l'acide crotonique (1,29 g, 15 mmol) et du butyllithium (16,5 mL d'une solution 2 M dans l'hexane, 33 mmol) dans le THF (60 mL) et le traitement de l'énolate résultant par l'iodométhane (3,73 mL, 60 mmol) dans le THF (20 mL) conduisent au mélange des diastéréoisomères **19b** et **19b′** purifiés par distillation (1,28 g, 54 %) (Eb = 70°C/0,01 torr). Huile incolore. RMN ^1H (200 MHz, mélange) δ ppm : 11,36 (br, 2H), 2,40 (m, 2H), 2,00–1,67 (m, 2H), 1,46-1,17 (m, 12H), 1,13 (d, 3H, J = 7 Hz), 1,08 (d, 3H, J = 7 Hz), 0,98–0,86 (m, 12H). RMN ^{13}C (50,3 MHz, mélange) δ ppm : 183,5; 183,2; 44,7; 44,0; 35,8; 35,1; 34,5; 32,9; 29,5; 29,2; 22,9; 22,8; 17,2; 15,6; 14,1; 13,6; 11,7. SM-HR calc. pour $C_5H_9O_2$ [M – $C_4H_9]^+$: 101,0602; tr. : 101,0592.

*Acide 2-méthylthio-3-méthylheptanoïque (**19c,c′**)*

Selon le mode opératoire général, la réaction de l'acide crotonique (1,29 g, 15 mmol) et du butyllithium (17,8 mL d'une solution 1,85 M dans l'hexane, 33 mmol) dans le THF (60 mL) et le traitement de l'énolate résultant par le disulfure de diméthyle (5,32 mL, 60 mmol) dans le THF (20 mL) conduisent au mélange des composés **19c,c′** (1,42 g, 40 : 60 (rapport diastéréoisomérique déterminé sur le mélange distillé), 50 %) purifiés par distillation (Eb = 55–65°C/0,1 torr). Huile jaune. RMN ^1H (200 MHz, mélange) δ ppm : 11,00 (sl, 1H), 3,00 (d, 1H, J = 8,3 Hz), 2,16 (s, 3H), 1,43–0,89 (m, 13H). RMN ^{13}C (50,3 MHz) δ ppm : 178,8; 178,6; 54,5; 54,2. SM-HR calc. pour $C_9H_{18}O_2S$: 190,1027; tr : 190,1030.

*Acide 3-phénylbutyrique (**19d**)*

Selon le mode opératoire général, la réaction de l'acide crotonique (1,29 g, 15 mmol) et du phényllithium (33 mL d'une solution 1 M dans l'éther, 33 mmol) dans le THF (60 mL) et le traitement de l'énolate résultant par l'acide trifluoroacétique (4,62 mL, 60 mmol) dans le THF (20 mL) conduisent au composé **19d** obtenu pur (0,95 g, 40 %) après distillation (Eb = 90°C/0,1 torr). Huile incolore. RMN ^1H (200 MHz) δ ppm : 10,00 (sl, 1H), 7,35–7,16 (m, 5H), 3,26 (m, 1H), 2,68 (dd, 1H, J = 15,7 et 7 Hz), 2,56 (dd, 1H, J = 15,7 et 8,5 Hz), 1,31 (d, 3H, J = 7 Hz). RMN ^{13}C (50,3 MHz) δ ppm : 178,7; 145,4; 128,6; 126,7; 126,5; 42,6;

© 1999 CNRC Canada

36,1; 21,8. SM-HR calc. pour $C_{10}H_{12}O_2$: 164,0837; tr : 164,0843. Anal. calc. pour $C_{10}H_{12}O_2$: C 73,15; H 7,37; O 19,49; tr. : C 72,91; H 7,19; O 19,23.

*Acides 2,3-diméthylhexanoïques (**19e,e′**)*

Selon le mode opératoire général, la réaction de l'acide crotonique (1,29 g, 15 mmol) et du butyllithium secondaire (25,4 mL d'une solution 1,3 M dans un mélange cyclohexane–hexanes, 33 mmol) dans le THF (60 mL) et le traitement de l'énolate résultant par l'acide trifluoroacétique (2,31 mL, 33 mmol) dans le THF (20 mL) conduisent à un mélange des composés **19e** et **19e′** purifiés par distillation (1,00 g, 46 %, Eb = 65–70°C/0,01 torr). Huile incolore. RMN ^{1}H (200 MHz, mélange) δ ppm : 11,67 (sl, 1H), 0,96–0,79 (m, 9H), 1,47-1,04 (m, 3H), 2,41–1,94 (m, 3H). SM-HR calc. pour $C_6H_{11}O_2$ $[M - C_2H_5]^+$: 115,0759; tr : 115,0760.

19e : RMN ^{13}C (50,3 MHz) δ ppm : 180,6; 39,9; 38,7; 33,7; 27,2; 14,6; 14,2; 12,0.

19e′ : RMN ^{13}C (50,3 MHz) δ ppm : 180,9; 39,3; 38,0; 34,4; 26,0; 17,0; 15,6; 12,0.

*Acides 3-phényl-heptanoïque (**20**) et 2-benzyl-hexanoïque (**20′**)*

Selon le mode opératoire général, la réaction de l'acide (*E*)-3-phénylpropénoïque (2,22 g, 15 mmol) et du butyllithium (20 mL d'une solution 1,6 M dans l'hexane, 33 mmol) dans le THF (60 mL) et le traitement de l'énolate résultant par l'acide trifluoroacétique (4,62 mL, 60 mmol) dans le THF (20 mL) conduisent au mélange d'isomères **20** et **20′**. Le composé **20** peut être obtenu pur après distillation : Eb = 90°C/0,1 torr (litt. (62) Eb = 118°C/0,3 torr) et chromatographie sur colonne de silice (95 : 5 heptane – acétate d'éthyle) (1,64 g, 48 %). Huile incolore. RMN ^{1}H (300 MHz) δ ppm : 9,90 (sl, 1H), 7,28–7,15 (m, 5H), 3,10–3,01 (m, 1H, *J* = 7 et 8 Hz), 2,66 (dd, 1H, *J* = 7 et 15,5 Hz), 2,59 (dd, 1H, *J* = 8 et 15,5 Hz), 1,73-1,52 (m, 2H), 1,35–1,04 (m, 4H), 0,82 (t, 3H, *J* = 7 Hz). RMN ^{13}C (75,5 MHz) δ ppm : 178,4; 143,9; 128,5; 127,4; 126,5; 41,8; 41,5; 35,9; 29,5; 22,5; 13,9. SM-HR calc. pour $C_{13}H_{18}O_2$: 226,1307; tr. : 226,1313.

20′ : RMN ^{1}H (200 MHz) δ ppm : 11,60 (sl, 1H), 7,83–7,14 (m, 5H), 2,94 (m, 1H), 2,77–2,62 (m, 2H), 1,69–1,58 (m, 2H), 1,31–1,08 (m, 4H), 0,86 (t, 3H, *J* = 6,5 Hz). RMN ^{13}C (50,3 MHz) δ ppm : 182,4; 139,1; 128,9; 128,4; 126,4; 47,4; 38,1; 31,4; 29,3; 22,5; 13,8. SM-HR calc. pour $C_{13}H_{18}O_2$: 226,1307; tr. : 226,1313.

*Acide 3,3-diphényl-propionique (**21**)*

Selon le mode opératoire général, la réaction de l'acide (*E*)-3-phénylpropénoïque (2,22 g, 15 mmol) et du phényllithium (33 mL d'une solution 1 M dans l'éther, 33 mmol) dans le THF (40 mL) et le traitement de l'énolate résultant par l'acide trifluoroacétique (4,62 mL, 60 mmol) dans le THF (20 mL) conduisent au composé **21** obtenu pur (0,68 g, 20 %) après recristallisation dans un mélange toluène–hexane. Poudre blanche. *F* = 154–156°C (litt. (63) *F* = 155°C). RMN ^{1}H (200 MHz) δ ppm : 10,90 (br, 1H), 7,32–7,14 (m, 10 H), 4,52 (t, 1H, *J* = 8 Hz), 3,08 (d, 2H, *J* = 8 Hz). RMN ^{13}C (50,3 MHz) δ ppm : 177,0; 143,2; 128,6; 127,6; 126,6; 46,6; 40,3.

*Acides 3-phényl-4-méthylhexanoïques (**22′,22″,23′,23″**)*

Selon le mode opératoire général, la réaction de l'acide (*E*)-3-phénylpropénoïque (2,22 g, 15 mmol) et du butyllithium secondaire (25,4 mL d'une solution 1,3 M dans un mélange cyclohexane–hexanes, 33 mmol) dans le THF (60 mL) et le traitement de l'énolate résultant par l'acide trifluoroacétique (4,62 mL, 60 mmol) dans le THF (20 mL) conduisent au mélange des diastéréosomères **22′,22″,23′,23″** (42 : 22 : 23 : 13, détermination RMN ^{13}C) purifiés par distillation (2,37 g, 70 %, Eb = 110°C/0,3 torr). Huile incolore. SM-HR calc. pour $C_{13}H_{18}O_2$: 226,1307; tr. : 226,1310.

*Acides hexanoïque (**24**) et 2-pentyl-glutarique (**25**)*

Selon le mode opératoire général, la réaction de l'acide acrylique (1,03 mL, 15 mmol) et du butyllithium (16,5 mL d'une solution 2 M dans l'hexane, 33 mmol) dans le THF (40 mL) et le traitement de l'énolate résultant par l'acide trifluoroacétique (4,62 mL, 60 mmol) dans le THF (20 mL) conduisent à un mélange des composés **24** et **25** (5 : 3, proportions déterminées par RMN ^{1}H) non séparable par distillation (Eb = 90–92°C/0,1 torr) (80 %) (58). Huile jaune.

24 : RMN ^{1}H (300 MHz) δ ppm : 10,54 (sl, 1H), 2,35 (t, 2H, *J* = 7,6 Hz), 1,63 (q, 2H), 1,38–1,25 (m, 6H), 0,85 (t, 3H, *J* = 6,8 Hz).

25 : RMN ^{1}H (300 MHz) δ ppm : 10,54 (sl, 2H), 2,44 (t, 2H, *J* = 7,3 Hz), 2,42 (m, 1H), 2,02–1,81 (m, 2H), 1,68 (m, 1H), 1,48 (m, 1H), 1,25–1,38 (m, 6H), 0,88 (t, 3H, *J* = 6,8 Hz).

24, ***25*** : RMN ^{13}C (50,3 MHz) δ ppm : 182,3; 180,6; 179,6; 44,7 (**25**); 34,1 (**24**); 32,0; 31,9 (**25**); 31,7; 31,4; 28,7; 26,8; 26,6 (**25**); 22,5 (**24**); 14,0 (**24**, **25**).

SM-HR calc. pour $C_{10}H_{17}O_3$ $[M - OH]^+$: 185,1178; tr : 185,1194.

*Acide 2-butyl-3(*E*)-phényl-but-3-en-2-one (**27**)*

Selon le mode opératoire général, la réaction de l'acide phénylpropiolique (2,19 g, 15 mmol) et du butyllithium (20,6 mL d'une solution 1,6 M dans l'hexane, 33 mmol) dans le THF (60 mL) et le traitement de l'énolate résultant par l'acide trifluoroacétique (2,31 mL, 30 mmol) dans le THF (20 mL) conduisent au composé **27** purifié par recristallisation (heptane – acétate d'éthyle) (1,6 g, 52 %). *F* = 82–84°C (litt. (64) *F* = 83–84°C). Solide blanc. RMN ^{1}H (300 MHz) δ ppm : 11,3 (sl, 1H), 7,81 (s, 1H), 7,41–7,30 (m, 5 H), 2,57–2,52 (m, 2H), 1,64–1,53 (m, 2H), 1,46–1,34 (m, 2H), 0,93 (t, 3H, *J* = 7 Hz). RMN ^{13}C (50,3 MHz) δ ppm : 174,3; 140,9; 135,6; 132,9; 129,4; 128,7; 128,5; 31,3; 27,0; 22,9; 13,8. SM-HR calc. pour $C_{13}H_{16}O_2$: 204,1150; tr. : 204,1139.

Bibliographie

1. P. Perlmutter. *Dans* Conjugate addition reactions in organic synthesis. Tetrahedron Organic Chemistry Series. Vol. 9. *Éditeurs :* J.E. Baldwin et P.D. Magnus. Pergamon Press, Oxford. 1992.
2. R.G. Pearson. J. Am. Chem. Soc. **85**, 3533 (1963).

© 1999 CNRC Canada

3. T.-L. Ho. Tetrahedron, **85**, 3533 (1963).
4. (*a*) D.A. Hunt. Org. Prep. Proced. Int. **21**, 705 (1989); (*b*) J.V.N. Vara Prasad et C.N. Pillai. J. Organomet. Chem. **259,** 1 (1983).
5. (*a*) S. Kim et P.H. Lee. Tetrahedron Lett. **29**, 5413 (1988); (*b*) C. Najera et M. Yus. Tetrahedron Lett. **30**, 173 (1989).
6. B.S. Furniss, A.J. Hannaford, P.W.G. Smith et A.R. Tatchell. *Dans* Vogel's Textbook of Pratical Organic Chemistry. Longman, Burnt Mill. 1989. p. 718.
7. D.A. Dickman et C.H. Heathcock. J. Am. Chem. Soc. **111**, 1528 (1989).
8. G.B. Mpango, K.K. Mahalanabis, Z. Mahdavi-Damghani et V. Snieckus. Tetrahedron Lett. **21**, 4823 (1980).
9. M. Yamaguchi, M. Tsukamoto et I. Hirao. Chem. Lett. 375 (1984).
10. H. Ahlbrecht et H.-M. Kompter. Synthesis, 645 (1983).
11. J. Nogami, T. Sonoda et S. Wakabayashi. Synthesis, 763 (1983).
12. W.T. Monte, M.M. Baizer et R.D. Little. J. Org. Chem. **48**, 803 (1983).
13. K. Matsumoto. Angew.Chem. Int. Ed. Engl. **20**, 770 (1981).
14. J.L. Zeistra et J.B.F.N. Egberts. J. Org. Chem. **39**, 3215 (1974).
15. M. Mikolajczyk et P. Balczewski. Synthesis, 691 (1984).
16. J.E. Richman, J.L. Herrmann et R.H. Schlessinger. Tetrahedron Lett. **14**, 3271 (1973).
17. E.J. Corey et L.S. Hegedus. J. Am. Chem. Soc. **91**, 4926 (1969).
18. G. Majetich, A.M. Casares, D. Chapman et M. Behnke. Tetrahedron Lett. **24**, 1909 (1983).
19. (*a*) J.E. Baldwin et W.A. Dupont. Tetrahedron Lett. **21**, 1881 (1980); (*b*) Y. Tamaru, T. Harada, H. Iwamoto et Z.-i. Yoshida. J. Am. Chem. Soc. **100**, 5221 (1978); (*c*) G.B. Mpango et V. Snieckus. Tetrahedron Lett. **21**, 4827 (1980).
20. D. Seebach, M. Ertas, R. Locher et W.J. Schweitzer. Helv. Chim. Acta, **68**, 264 (1985).
21. P. Manning et M.P. Cooke, Jr. J. Org. Chem. **51**, 1637 (1986).
22. K.A. Lutomski et A.I. Meyers. *Dans* Asymmetric synthesis. Vol. 3, partie B. *Éditeur :* J.D. Morrison. Academic Press, New York. 1984. Chap. 3, pp. 259–274.
23. (*a*) A.I. Meyers, G. Knaus, K. Kamata et M.E. Ford. J. Am. Chem. Soc. **98**, 567 (1976); (*b*) A.I. Meyers, R.K. Smith et C.E. Witten. J. Org. Chem. **44**, 2250 (1979).
24. M.J. Jorgenson. Org. React. **18**, 1 (1970).
25. T. Ahn et T. Cohen. Tetrahedron Lett. **35**, 203 (1994) et références citées.
26. C. Einhorn, J. Einhorn et J.-L. Luche. Tetrahedron Lett. **32**, 2771 (1991).
27. N. Petragnani et M. Yonashiro. Synthesis, 521 (1982).
28. J.A. Katzenellenbogen et A.L. Crumrine. J. Am. Chem. Soc. **98**, 4925 (1976).
29. J. Mortier, J. Moyroud, B. Bennetau et P.A. Cain. J. Org. Chem. **59**, 4042 (1994).
30. (*a*) J. Moyroud, J.-L.Guesnet, B. Bennetau et J. Mortier. Tetrahedron Lett. **36**, 881 (1995); (*b*) B. Bennetau, J. Mortier, J. Moyroud et J.-L. Guesnet. J. Chem. Soc. Perkin Trans. 1, 1265 (1995); (*c*) J. Moyroud, J.-L. Guesnet, B. Bennetau et J. Mortier. J. Bull. Soc. Chim. Fr. **133**, 133 (1996); (*d*) G. Ameline, M. Vaultier et J. Mortier. Tetrahedron Lett. **37**, 8175 (1996).
31. (*a*) R. Cantegril, D. Croisat, P. Desbordes, F. Guigues, J. Mortier, R. Peignier et J.-P. Vors. Brevet mondial W0932287 (1993); (*b*) R. Cantegril, J. Mortier, D. Croisat et R. Peignier. Brevet mondial WO9602138 (1996); (*c*) J. Moyroud, A. Chene, J.-L. Guesnet et J. Mortier. Heterocycles, **43**, 221 (1996).
32. (*a*) J.H. Wotiz, J.S. Matthews et H. Greenfield. J. Am. Chem. Soc. **75**, 6342 (1953); (*b*) J. Klein. Tetrahedron, **20**, 465 (1964); (*c*) J. Klein et R.M. Turkel. J. Am. Chem. Soc. **91**, 6186 (1969); (*d*) J. Klein et N. Aminadav. J. Chem. Soc. 1380 (1970); (*e*) J. Klein et S. Zitrin. J. Org. Chem. **35**, 666 (1970).
33. (*a*) Y. Yamamoto et K. Maruyama. J. Am. Chem. Soc. **100**, 3240 (1978); (*b*) Y. Yamamoto, S. Yamamoto, H. Yatagai, Y. Ishihara et K. Maruyama. J.Org.Chem. **47**, 119(1982).
34. M. Majewski et V. Snieckus. J. Org. Chem. **49**, 2682 (1984).
35. K. Kruithof, A. Mateboer, M. Schakel et G. Klumpp. Recl. Trav. Chim. Pays-Bas, **105**, 62 (1986).
36. M.P. Cooke, Jr. J. Org. Chem. **52**, 5729 (1987).
37. R.L. Eppley et J.A. Dixon. J. Am. Chem. Soc. **90**, 1606 (1968).
38. R.C. Fuson, B.C. McKusick et F.W. Spangler. J. Am. Chem. Soc. **67**, 597 (1945).
39. G. Bartoli, M. Bosco et G. Baccolini. J. Org. Chem. **45**, 2649 (1980).
40. L.D. Pridgen, M.K. Mokhallalati et M.-J. Wu. J. Org. Chem. **57**, 1237 (1992).
41. E.-i. Negishi et R.E. Merrill. J. Chem. Soc. Chem. Commun. 860 (1974).
42. (*a*) E.P. Kündig, A. Ripa, R. Liu et G. Bernardinelli. J. Org. Chem. **59**, 4773 (1994) et références citées; (*b*) D. Amurrio, K. Khan et E.P. Kündig, J. Org. Chem. **61**, 2258 (1996).
43. (*a*) G.W. Gschwend et Hamden, J. Org. Chem. **40**, 2008 (1975); (*b*) A.I. Meyers et E.D. Mihelich. J. Org. Chem. **40**, 3158 (1975).
44. (*a*) A.I. Meyers, G.P. Roth, D. Hoyer, B.A. Barner et D. Laucher. J. Am. Chem. Soc. **110**, 4611 (1988); (*b*) A.I. Meyers, W. Schmidt et M.J. McKennon. Synthesis, 250 (1993); (*c*) A.N. Hulme, S.S. Henry et A.I. Meyers. J. Org. Chem. **60**, 1265 (1995) et références citées.
45. A.I. Meyers et D. Hoyer. Tetrahedron Lett. **25**, 3667 (1984).
46. P. Beak et R.A. Brown. J. Org. Chem. **42**, 1823 (1977).
47. M. Watanabe et V. Snieckus. J. Am. Chem. Soc. **102**, 1457 (1980).
48. I. Inoue, M. Shindo, K. Koga et K. Tomioka. Tetrahedron, **50**, 4429 (1994) et références citées.
49. S.E. Denmark, N. Nakajima et O.J.-C. Nicaise. J. Am. Chem. Soc. **116**, 8797 (1994).
50. B. Plunian, J. Mortier, M. Vaultier et L. Toupet. J. Org. Chem. **61**, 5206 (1996).
51. (*a*) P.L. Creger. J. Am. Chem. Soc. **89**, 2500 (1967); (*b*) P.E. Pfeffer et L.S. Silbert. J. Org. Chem. **35**, 262 (1970).
52. J. Mortier, M. Vaultier, R. Cantegril et P. Dellis. Aldrichimica Acta, **30**, 34 (1997).
53. (*a*) A.I. Meyers, K.A. Lutomski et D. Laucher. Tetrahedron, **44**, 3107 (1988); (*b*) A.I. Meyers. J. Org. Chem. **56**, 7098 (1991).
54. (*a*) M. Karplus. J. Chem. Phys. **30**, 11 (1959); (*b*) A.A. Bothner-By. Adv. Magn. Reson. **1**, 195 (1965); (*c*) M. Karplus. J. Am. Chem. Soc. **85**, 2870 (1963).
55. E.W. Garbish, Jr. J. Am. Chem. Soc. **86**, 5561 (1964).
56. B. Plunian, M. Vaultier et J. Mortier. J. Chem. Soc. Chem. Commun. 81 (1998).
57. (*a*) J.A. Landgrebe et J.D. Shoemaker. J. Am. Chem. Soc. **89**, 4465 (1967); (*b*) H. Okamoto, M. Kato et H. Yuki. Bull. Chem. Soc. Jpn. **42**, 760 (1969).
58. (*a*) S. Roberts. J. Chem. Soc. 2842 (1950); (*b*) P. R. Stapp. J. Org. Chem. **34**, 479 (1969).
59.(*a*) E.J. Corey et J.A. Katzenellenbogen. J. Am. Chem. Soc. **91**, 1851 (1969). (*b*) B.M. Trost, C.D. Shuey et F. DiNinno, Jr. J. Am. Chem. Soc. **101**, 1284 (1979).
60. P. Beak et A.I. Meyers. Acc. Chem. Res. **19**, 356 (1986).
61. (*a*) H. Nunn. J. Org. Chem. **12**, 540 (1947); (*b*) G.B. Arrowsmith. J. Chem. Soc. 2072 (1965).

© 1999 CNRC Canada

62. S.R. Jensen. Acta Chem. Scand. **24**, 2641 (1970).
63. (*a*) E. Ulman, E. Babad et M. Sung. J. Am. Chem. Soc. **91**, 5792 (1969); (*b*) A. Patra et S. Misra. Magn. Reson. Chem. **9**, 749 (1981).
64. M.-P. Teulade, P. Savignac, E. About-Jaudet et N. Collignon. Synth. Commun. **19**, 71 (1989).

© 1999 CNRC Canada

A versatile synthetic route to 1,5-dithiocins from *o*-mercapto aromatic aldehydes[1]

Ian W.J. Still, Rosanne Natividad-Preyra, and F. Dean Toste

Abstract: An earlier procedure for the facile preparation of benzo-fused 1,5-dithiocins **2a–2c** from *o*-mercapto-benzaldehydes has been improved and shown to be capable of extension to the preparation of several naphthalene-derived analogues. The general method also afforded several N-alkylated 1,5-dithiocins **4, 5** by replacing NH_3 with the appropriate primary amine. It was found that N-acylation of the 1,5-dithiocins was successful only with methyl chloroformate. Attempted N-phenylation met with limited success but was shown to be unnecessary since even the less reactive aniline readily undergoes the general reaction of primary amines. When simple α-amino acids, or their methyl esters, were employed as the primary amine in the reaction with *o*-mercaptobenzaldehyde, the formation of the N-alkylated 1,5-dithiocins **4a**, **17a**, **17b** with accompanying loss of -COOH or -COOMe was observed, in preparatively useful yields. A mechanism is proposed for this interesting transformation.

Key words: 1,5-dithiocins, α-amino acids, N-acylation, decarboxylation.

Résumé : On a amélioré une méthode proposée antérieurement pour préparer facilement des benzo-1,5-dithiocines, **2a–2c**, à partir des *o*-mercaptobenzaldéhydes et on a démontré qu'on peut l'étendre à la préparation de plusieurs dérivés du naphtalène. La méthode générale permet aussi d'obtenir plusieurs 1,5-dithiocines *N*-alkylées (**4, 5**) en remplaçant le NH_3 par l'amine primaire appropriée. On a observé que la *N*-acylation des 1,5-dithiocines ne se fait correctement qu'avec du chloroformiate de méthyle. Des essais en vue d'effectuer une *N*-phénylation ont conduit à des résultats mitigés; toutefois, cette limitation ne présente pas de problèmes puisque l'on peut obtenir le même produit en procédant à la réaction générale en présence d'aniline, même si celle-ci est moins réactive. Lorsqu'on utilise des acides α-aminés simples ou leurs esters méthyliques comme amine primaire dans la réaction avec l'*o*-mercaptobenzaldéhyde, on observe la formation des 1,5-dithiocines *N*-alkylées, **4a, 17a**, **17b**, avec des rendements préparativement utiles. On propose un mécanisme pour cette transformation intéressante.

Mots clés : 1,5-dithiocines, acides α-aminés, *N*-acylation, décarboxylation.

[Traduit par la Rédaction]

Introduction

Molecules possessing a structurally well-defined, V-shaped molecular cleft have recently attracted considerable attention due to their application toward problems in the areas of molecular recognition, self-assembly, and supramolecular chemistry (1, 2). Molecules possessing molecular chirality in addition are of interest as potential chiral ligands and solvating agents. Chiral molecules that lock two aromatic rings in almost perpendicular planes, such as Tröger's base **1** (3) are of special interest as DNA probes owing to their different possible modes of interaction with DNA and to their chiral properties (4, 5). We felt that it would be advantageous to prepare this type of compound containing a readily functionalized group (such as a secondary amine) for which a variety of derivatives could easily be produced. The preparation of the racemic 6,12-imino-6*H*,12*H*-dibenzo[*b*,*f*]-1,5-dithiocins **2a–2c**, representing easily obtained examples of such compounds, was reported earlier by us (6).

The preparation of the imino-bridged, 1,5-dithiocin ring system was reported as early as 1958 (7) and that of the dibenzo[*b*,*f*] analog **2b** by Gol'dfarb et al. (8) in 1966. These synthetic procedures, and the later serendipitous preparations of dibenzo[*b*,*f*]-1,5-dithiocins by Corrigan and West (9) and, more recently, Brieaddy and Donaldson (10), were of limited utility. Moreover, structural proof, notably the absence of NMR spectra in the earlier papers cited, was inadequate. Our previous work (6) was therefore important not only in establishing the structure of **2b** and its analogues by X-ray analysis but also in making available a general synthetic approach to such molecules.

We describe herein an improved experimental procedure for the preparation of **2a–2c** that also allows the facile preparation of N-alkyl and N-aryl analogues of these molecules. We also describe our attempts to prepare N-acyl analogues and the ready extension of our methodology to several

Received August 4, 1998.

I.W.J. Still,[2] R. Natividad-Preyra, and F.D. Toste. Department of Chemistry, University of Toronto at Mississauga, 3359 Mississauga Road, Mississauga, ON L5L 1C6, Canada.

[1]Taken in part from the M.Sc. thesis of R. Natividad, University of Toronto, l997.

[2]Author to whom correspondence may be addressed. Telephone: (905) 828-5354. Fax: (905) 828-5425. e-mail: istill@credit.erin.utoronto.ca

© 1999 NRC Canada

naphtho-fused analogues of **2a**. Finally, the results of our attempts to prepare chiral N-alkylated analogues of **2a** *directly* by utilizing natural α-amino acids or their methyl esters in our general approach will be discussed.

Results and discussion

The benzo-fused 1,5-dithiocins **2a–2c** were prepared, as reported previously (6), starting from the appropriate thiol and carrying out a selective *ortho* formylation via a doubly lithiated (S,C-) intermediate. We have found that yields in the formylation could be almost doubled (to 63–81%) if *N*-formylpiperidine was used as the formylating agent, in place of DMF. We have also discovered that the subsequent cyclization step converting **3a–3c** into **2a–2c** is more conveniently achieved with NH_4OAc in refluxing ethanol rather than in nitromethane, presumably by the mechanism we had previously outlined (6). The reaction was also attempted using other amonium salts (e.g., NH_4Cl, NH_4SCN) but, with the exception of NH_4HCO_3, only the acetate seems to offer the right balance between acid and base catalysis, which seems to be crucial.

By modifying the reaction of **3a** or **3b** and replacing the ammonium acetate with a mixture of primary amine and acetic acid (1:4) we have been able to prepare the N-alkyl analogues **4a–4c** and **5a**, **5b** in excellent yields (83–91%). Interestingly, **4a** could also be obtained in the absence of acetic acid but in a very much lower yield (27%).

It was felt that the creation of the naphtho-fused analogues of these 1,5-dithiocins would provide molecules with more pronounced clefts and potentially more interesting solvating effects. We accordingly undertook the synthesis of the three isomeric *ortho*-mercaptonaphthaldehydes **6–8**. Compound **6** was readily obtained from 1-naphthalenethiol,[3] by our general procedure using *N*-formylpiperidine, in 43% yield. It was found in the naphthalene series that a slightly higher molar ratio of both the *n*-butyllithium and the TMEDA complexing agent gave the best results (2.5 equiv. of each, vs. 2.2 equiv. for the benzene analogues).

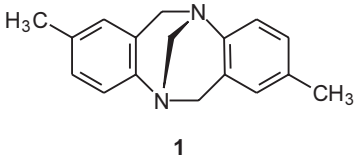

1

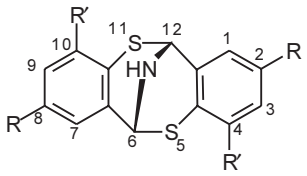

2a R= R′= H
b R= CH_3, R′= H
c R= CH_3, R′= S^{t}Bu

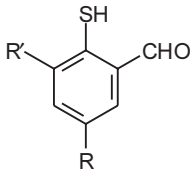

3a R= R′= H
b R= CH_3, R′ = H
c R = CH_3, R′= S^{t}Bu

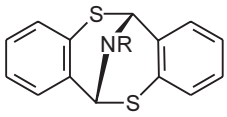

4a R= $CH_2CH_2C_6H_5$
b R= $CH_2CH(CH_3)_2$
c R= $C(CH_3)_3$
d R= C_6H_5

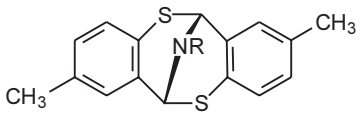

5a R= $CH_2CH_2C_6H_5$
b R= $CH_2CH(CH_3)_2$

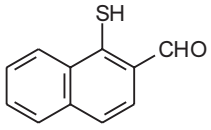

6

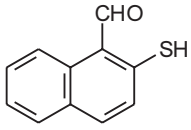

7

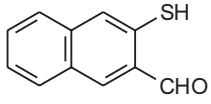

8

[3] 1-Naphthalenethiol is a relatively expensive reagent, which may be conveniently prepared, in 89% yield, by reduction of 1-naphthalenesulfonyl chloride with tin and concentrated HCl (see experimental section).

© 1999 NRC Canada

Scheme 1.

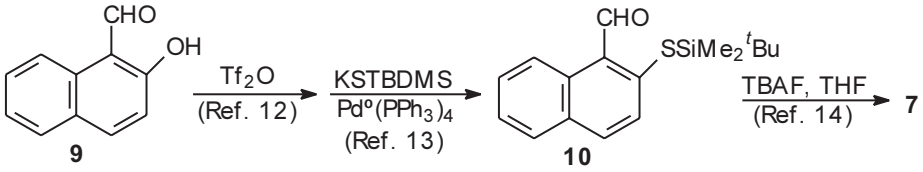

Application of our general formylation procedure to the isomeric 2-naphthalenethiol afforded the two isomeric aldehydes **7** and **8**, in isolated yields of 45% and 30%, respectively. That the major isomer was the (expected) result of 1-formylation of the naphthalene nucleus was confirmed by an unambiguous synthesis of **7** from 2-hydroxy-1-naphthaldehyde **9** in 42% overall yield, by the three-step sequence shown in Scheme 1 (11), slightly modified in Step 2 (see Experimental).

With the necessary three naphthaldehydes in hand, we were able to complete our synthesis of the three isomeric naphtho-fused 1,5-dithiocins **11**–**13**, from **6**, **7**, and **8**, respectively. The same experimental procedure was used as for the benzo-fused analogues **2a**–**2c** and excellent yields (>90%) of these crystalline solids were obtained for all three cases. Recently, Biehl et al. (15) reported the synthesis of the 1,5-dioxocin **14a** (analogous to **12**) by the reaction of **9** with ammonium acetate, accompanied by a small amount of the O-bridged derivative **14b**. The mechanism proposed by these authors for the formation of **14a** is essentially identical to that which we had earlier proposed (6), differing only in the order of the steps involved.

Attempts have been made to introduce an N-acyl group into these imino-bridge molecules. Using **4b** as a representative example, we sought to introduce N-benzoyl and N-propanoyl groups by reaction of **4b** with benzoyl chloride and propanoic acid–DCC, respectively, but failed to obtain the amides in preparatively useful yields. When methyl chloroformate was used, however, in refluxing acetone with K_2CO_3 (or, better still, Cs_2CO_3 (16)) as the base, we ob-

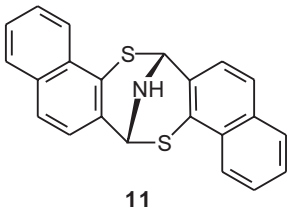

11

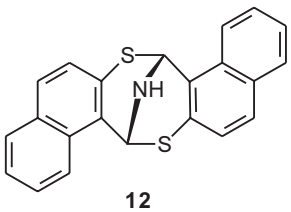

12

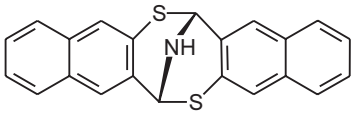

13

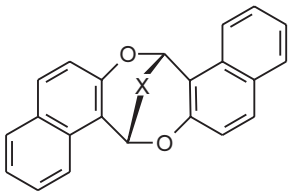

14a X = NH
b X = O

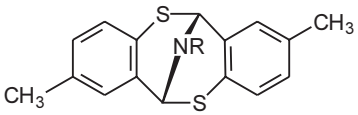

15
R = CO_2Me

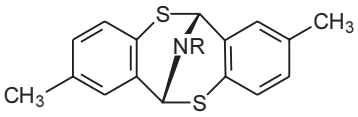

16 R = $CH(CH_3)C_6H_5$

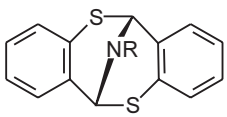

17a R = $CH_2CH_2CH(CH_3)_2$
b R = CH_2CH_2OH
c R = $CHCH_2CH(CH_3)_2$
$CO_2{}^tBu$

© 1999 NRC Canada

Scheme 2.

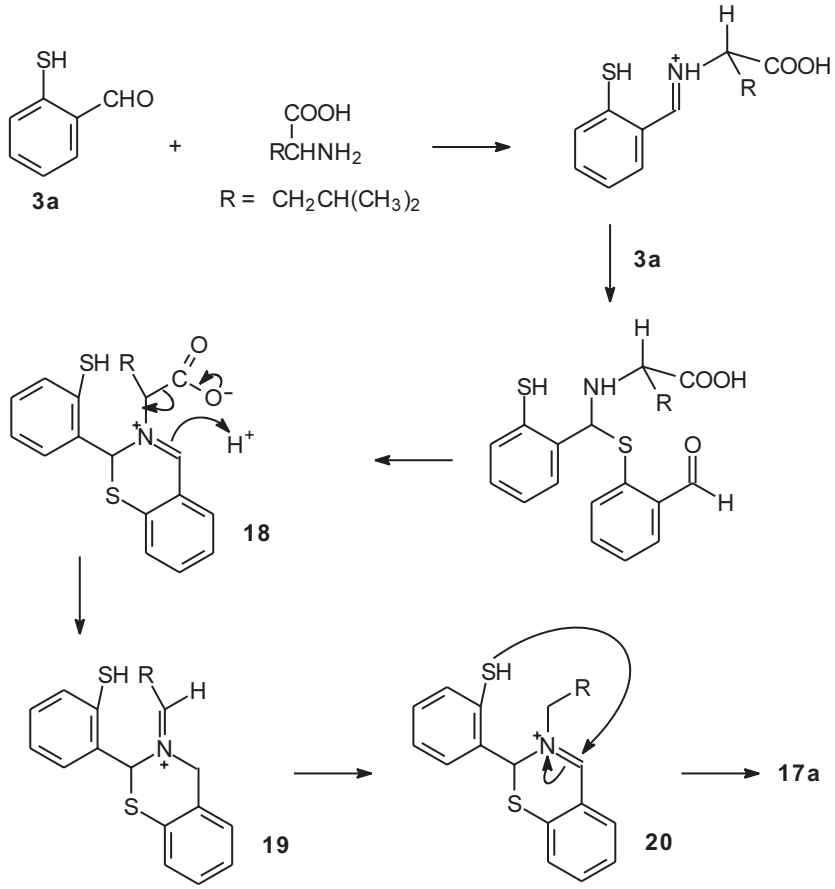

tained the expected carbamate **15** in over 60% yield. Unlike the starting imino analogue and its congeners, **15** shows the two methine protons, in addition to the expected downfield shift, as nonequivalent (δ_H = 6.74, 6.57), presumably due to restricted bond rotation in the N—CO_2Me bond.

We have also attempted to introduce an N-phenyl substituent in the 1,5-dithiocins. Using a procedure described by Barton et al. (17) we first attempted this with **2a**, using Ph_3Bi as phenylating agent, with $Cu(OAc)_2$ as the catalyst. The reaction mixtures obtained in various trials were complex and in no case was more than 25% of the desired **4d** present. Accordingly, we reverted to our standard methodology, using **3a**, aniline, and a somewhat longer reflux period, and were rewarded by obtaining the crystalline **4d** in 75% yield.

One potential application of our 1,5-dithiocins was in the area of asymmetric base-catalyzed reactions. The early work of Noyori and coworkers (18) established (–)-sparteine, a readily available alkaloid, as a potential agent for enantioinduction at carbanion centres and several recent reports have made good use of this type of methodology (refs. 19 (for recent reviews) and 20). For our compounds to be useful in this type of application, it will be necessary to prepare enantiomerically pure 1,5-dithiocins. As one approach to this problem we decided to investigate the use of enantiomerically pure amines in our general method since, in principle, the diastereomeric dithiocins so obtained should be readily separable.

Our first attempt along these lines employed *R*-1-phenylethylamine as the derivatizing amine, in a reaction with **3b**. Disappointingly, however, we were unable to achieve a complete separation of the diastereomeric pair of dithiocins **16** so formed, under a variety of conditions. We next decided to use one of the readily available, inexpensive, α-amino acids to achieve our purpose. Reaction of **3a** with L-leucine under the usual conditions led, much to our surprise, to a benzo-fused dithiocin which showed no evidence for -COOH either in the IR or the proton NMR. The structure of the product has been established as **17a**, the *N*-(3′-methylbutyl) analogue of the N-alkylated series, formed here in 68% yield. When the reaction was repeated using L-leucine methyl ester the same product was obtained. Thus, formation of the N-alkylated 1,5-dithiocins in these reactions from α-amino acids *or* their methyl esters is accompanied by loss of the carboxylate moiety.

Confirmation that the structural assignment to the products of this new reaction was correct came from the reaction of **3a** with L-phenylalanine methyl ester. The product, obtained in 63% yield, was identical in all respects with **4a**, obtained independently as described above. A further example of this interesting reaction was shown by the formation of the 2′-hydroxyethyl analogue **17b** in 75% yield when **3a** was allowed to react with L-serine methyl ester under the usual conditions.

We propose that this novel reaction may proceed by a mechanism akin to the known enzymatic decarboxylation of

© 1999 NRC Canada

Table 1. Physical data and ^{1}H NMR chemical shifts for 1,5-dithiocins **2**, **4**, **5**, **11–13**, **15**.

			δ		
Compound	Yield (%)	Melting point (°C)	$=NCH_2$ or =NH	Aromatic	=CH—S
2a	89	131–133	2.88	7.28(2H), 7.04(6H)	5.73
2b	91	205–206	2.83	7.08(2H), 6.91(4H)	5.67
2c	90	45–47	4.33	7.15(4H)	5.66
4a	84	147–150	3.01	7.24(2H), 7.05(6H)	5.45
4b	83	129–131	2.87, 2.48	7.25(2H), 7.00(6H)	5.38
4c	87	136–138	—	7.28(2H), 6.69(6H)	5.87
4d	75	70–72	—	7.32(4H), 7.13(4H)	6.15
5a	83	132–134	2.94	7.04(2H), 6.88(4H)	4.92
5b	86	Oil	2.83, 2.46	7.05(2H), 6.89(4H)	5.31
11	92	168–170	Not observed	7.95(4H), 7.78(2H) 7.75(2H), 7.53(2H), 7.44(2H)	6.05
12	94	160–163	Not observed	7.83(4H), 7.62(4H) 7.48(2H), 7.02(2H)	6.45
13	96	170–172	Not observed	7.76(4H), 7.62(4H) 7.38(4H)	6.03
15	67	143–146	—	7.18(2H), 6.93(4H)	6.74, 6.57

α-amino acids, catalyzed by pyridoxal phosphatase (21). The key intermediate in our proposed mechanism for the reaction with L-leucine (Scheme 2) is the initial iminium ion **18**, which, under the approximately neutral pH conditions employed, leads to decarboxylation and a second iminium species **19**, which undergoes a protropic rearrangement to the more stable iminium ion **20** and is trapped by thiol (thiolate), leading to the 1,5-dithiocin in the usual way. Since thiolate ions are known to be excellent nucleophiles it is quite conceivable that intramolecular demethylation could first occur in the analogous reaction with the methyl ester, leading to the same carboxylate species **18**. Indirect support for this hypothesis came from a preliminary reaction using L-leucine *tert*-butyl ester, which should be stable to thiolate ion attack. Gratifyingly, the N-alkylated dithiocin **17c**, obtained in 71% yield, showed no loss of the -COO^{t}Bu group. As expected, signals for the diastereomeric methine protons in **17c** were observable (δ_H = 5.78, 5.70) in the ^{1}H NMR spectrum, indicating a 70:30 ratio of the diastereomers. Further work is under way to optimize this finding using the *tert*-butyl esters of other natural amino acids. Effective separation of the presumably scalemic diastereomers is also a prerequisite for the successful application of this approach.

Work is continuing in our attempts to prepare enantiomerically pure examples of the 1,5-dithiocins from readily accessible starting materials. We also plan to investigate the solvating and metal-complexing properties of these interesting molecules.

Experimental

General information

For all anhydrous reactions, glassware was dried in the oven overnight at 120°C prior to its use. All anhydrous reactions were run under an argon atmosphere. DMF and nitromethane were distilled from P_2O_5 and stored over 3Å sieves. Methanol was distilled from magnesium turnings and stored over activated 3Å sieves. Hexanes, THF, toluene, and diethyl ether were distilled from sodium – benzophenone ketyl. Triethylamine and TMEDA were distilled from calcium hydride prior to use. Alkyllithium solutions were obtained from Fluka and were titrated regularly (22). Work-up procedures involving the drying of organic extracts utilized Na_2SO_4. Purification was initially carried out by (flash) column chromatography, using Merck 40–60 μm silica gel or aluminum oxide and the appropriate solvent system (q.v.)

IR spectra were obtained as neat films or as KBr pellets, as indicated, and data were recorded in cm^{-1}. ^{1}H NMR spectra were recorded at 200 MHz in $CDCl_3$, unless otherwise stated. ^{13}C NMR and DEPT spectra were run at 100.6 MHz. High- and low-resolution mass spectra were obtained at 70 eV. Elemental analyses were performed by the Guelph Chemical Laboratories Ltd., Guelph, Ontario. Compounds for which high-resolution mass measurements are given were homogeneous by TLC analysis and gave satisfactory ^{1}H and (or) ^{13}C NMR spectra indicative of their purity. ^{1}H NMR data for compounds **2a–2c**, **4a–4d**, **5a**, **5b**, **11**, **12**, **13**, and **15** have been collected in Table 1.

2-Mercaptobenzaldehyde 3a

To a solution of thiophenol (2.00 mL, 19.47 mmol) in 45 mL of dry hexanes under argon, TMEDA (6.43 mL, 42.83 mmol) was added via addition funnel. The clear solution was stirred for 5 min and cooled to 0°C. The 2.2 M *n*-BuLi (19.47 mL, 42.83 mmol) was added with a syringe over a period of 20 min, giving the solution a yellow colour. The mixture was stirred for an additional 0.5 h at 0°C, warmed to room temperature, and stirred for 17 h. The resulting solution turned white and became very thick in appearance. On cooling to 0°C, *N*-formylpiperidine (4.34 mL, 38.94 mmol) was slowly added, forming a red solution and an orange pastelike precipitate. The reaction mixture was stirred at 25°C for 18 h, then acidified with 1 M HCL (2 × 25 mL), extracted with CH_2Cl_2 (4 × 25 mL), and washed with saturated NaCl (25 mL). The solution was dried and concentrated to afford a dark orange-brown oil (2.77 g,

© 1999 NRC Canada

93%). Flash chromatography, eluting with CH_2Cl_2 (R_f = 0.35) afforded an oil (2.42 g, 81%). IR (film), ν: 3085, 2839, 2750, 1680, 1590, 1560, 850, 750; ^{1}H NMR, δ: 10.25 (s, 1H), 7.89 (dd, 1H, *J* = 7.5, 1.6 Hz), 7.80 (dd, 1H, *J* = 7.8, 1.6 Hz), 7.50 (td, 1H, *J* = 7.8, 1.6 Hz), 7.39 (td, 1H, *J* = 7.5, 1.6 Hz), 5.49 (s, 1H).

2-Mercapto-5-methylbenzaldehyde 3b

This aldehyde was prepared according to the same procedure. A crude orange-brown oil (1.19 g, 88%) was obtained from the solution. Flash chromatography, eluting with CH_2Cl_2 (R_f = 0.39), afforded a yellow oil (1.01 g, 75%). IR (film), ν: 3018, 2925, 2875, 2545, 1665, 815, 780; ^{1}H NMR, δ: 9.99 (s, 1H), 7.52 (d, 1H, *J* = 2.6 Hz), 7.19 (m, 2H), 5.31 (s, 1H), 2.37 (s, 3H).

3-(*tert*-Butylthio)-2-mercapto-5-methylbenzaldehyde 3c

To a solution of *p*-thiocresol (0.30 g, 2.40 mmol) in 30 mL of dry hexanes under argon, TMEDA (0.80 mL, 5.32 mmol) was added via addition funnel. The clear solution was stirred for 5 min and was cooled to 0°C. The 1.6 M *n*-BuLi (3.32 mL, 5.32 mmol) was added with a syringe, over a period of 20 min, giving the solution a yellow colour. The mixture was stirred for an additional 0.5 h at 0°C, warmed to room temperature, and stirred for 17 h. The resulting solution turned white and, was cooled to –10°C. Slow addition of freshly distilled *tert*-butyl disulfide (0.74 mL, 3.84 mmol) turned the mixture red in colour and stirring was continued for 16 h. The solution was washed with 1 M HCl (2 × 20 mL), saturated NaCl (20 mL), dried, and evaporated to afford a brown oil (0.38 g, 81%). Kugelrohr distillation afforded 2-(*tert*-butylthio)-4-methylbenzenethiol (0.33 g, 70%), bp 130–134°C/7 Torr (1 Torr = 133.3 Pa). IR (film), ν: 2961, 2934, 2518, 818; ^{1}H NMR, δ: 7.41 (d, 1H, *J* = 1.5 Hz), 7.29 (d, 1H, *J* = 7.8 Hz), 7.04 (dd, 1H, *J* = 7.8, 1.5 Hz), 4.77 (s, 1H), 2.33 (s, 3H), 1.39 (s, 9H).

The thiol so obtained (0.20 g, 0.94 mmol) was lithiated in dry hexanes (20 mL) and TMEDA (0.33 mL, 2.17 mmol), using 2.2 M *n*-BuLi (0.98 mL, 2.17 mmol) as in the general procedure. The resulting orange mixture was treated with *N*-formylpiperidine (0.21 mL, 1.88 mmol) at 25°C. The mixture turned yellow and was stirred for 18 h. The solution was washed with 1 M HCl (2 × 15 mL), saturated NaCl (15 mL), dried, and concentrated to afford a brown oil (0.16 g, 74%). Flash chromatography, eluting with CH_2Cl_2 (R_f = 0.45), yielded a yellow oil (0.13 g, 63%). IR (film), ν: 2960, 2925, 2893, 2480, 1684, 1672, 769; ^{1}H NMR, δ: 10.05 (s, 1H), 7.63 (d, 1H, *J* = 1.6 Hz), 7.56 (d, 1H, *J* = 1.6 Hz), 6.98 (s, 1H), 2.15 (s, 3H), 1.33 (s, 9H).

6,12-Imino-6*H*,12*H*-dibenzo[*b*,*f*]-1,5-dithiocin 2a

The thiosalicylaldehyde **3a** (0.90 g, 6.52 mmol) dissolved in absolute ethanol (30 mL) was treated with ammonium acetate (0.55 g, 7.17 mmol), the solution turning a yellow colour. The solution was refluxed for 3.5 h and cooled to room temperature, resulting in the formation of a white precipitate. Filtration and drying afforded a yield of (0.75 g, 89%), mp 131–133°C (lit. (6) mp 130–132°C). IR (KBr), ν: 3334, 3115, 3005, 1595, 1499, 763.

2,8-Dimethyl-6,12-imino-6*H*,12*H*-dibenzo[*b*,*f*]-1,5-dithiocin 2b

The same procedure as that used for the preparation of **2a** was employed. A white solid was obtained directly from the reaction mixture (0.85 g, 91%), mp 205–206°C (lit. (6) mp 206–206.5°C). IR (KBr), ν: 3358, 3056, 2965, 1482, 796.

4,10-Bis(*tert*-butylthio)-2,8-dimethyl-6,12-imino-6*H*,12*H*-dibenzo[*b*,*f*]-1,5-dithiocin 2c

The same procedure as that used for the preparation of **2a** was employed. A yellow solid was obtained from the reaction mixture (0.05 g, 90%), mp 45–47°C (lit. (6) mp 44–46°C). IR (KBr), ν: 3054, 2920, 2874, 1493, 804, 737.

***N*-(2′-Phenylethyl)-6,12-imino-6*H*,12*H*-dibenzo[*b*,*f*]-1,5-dithiocin 4a**

Method A

To a solution of thiosalicylaldehyde **3a** (0.04 g, 0.28 mmol) in absolute ethanol (10 mL), 0.5 mL of HOAc was added. Addition of the phenethylamine (0.02 mL, 0.15 mmol) to the above reaction vessel immediately turned the yellow solution orange in colour. The mixture was refluxed for 3.5 h, quenched with H_2O (5 mL), and extracted with CH_2Cl_2 (2 × 10 mL). The organic layer was dried and concentrated to afford a brown oil. Flash chromatography, eluting with CH_2Cl_2–hexanes (4:1) (R_f = 0.52), yielded a light yellow solid, (0.04 g, 84%), mp 147–150°C. IR (KBr), ν: 3116, 3032, 2996, 1625, 1487, 815. Exact Mass calcd. for $C_{22}H_{19}NS_2$: 361.0959; found: 361.0954. Anal. calcd. for $C_{22}H_{19}NS_2$: S 17.74; found: S 18.14.

Method B

A mixture of **3a** (0.14 g, 1.03 mmol), L-phenylalanine methyl ester hydrochloride (0.09 g, 0.57 mmol), and absolute ethanol (15 mL) was refluxed for 2.5 h. The clear yellow solution was cooled to room temperature and the solvent was evaporated to yield a yellow-brown oil. The oil was dissolved in CH_2Cl_2 (15 mL) and the organic layer washed with saturated $NaHCO_3$ (15 mL). Drying and concentration afforded a white powdery solid (0.12 g, 63%). Flash chromatography, eluting with CH_2Cl_2–hexanes (85:15) (R_f = 0.57) gave white crystals (0.10 g, 51%), mp 149–151°C, identical in all respects with **4a** prepared above.

***N*-(Isobutyl)-6,12-imino-6*H*,12*H*-dibenzo[*b*,*f*]-1,5-dithiocin 4b**

To a solution of **3a** (0.05 g, 0.35 mmol) in absolute ethanol (8 mL), 0.5 mL of HOAc was added. Addition of isobutylamine (0.02 mL, 0.19 mmol) to the above reaction vessel immediately turned the yellow solution orange in colour. Reaction was carried out as in Method A above and, after flash chromatography, eluting with CH_2Cl_2–hexanes (4:1) (R_f = 0.52), gave **4b** as a yellow solid (0.04 g, 83%), mp 129–131°C. IR (film), ν: 3053, 2456, 1515, 1489, 792, 743. Exact Mass calcd. for $C_{18}H_{19}NS_2$: 313.0958; found: 313.0956.

***N*-(*tert*-Butyl)-6,12-imino-6*H*,12*H*-dibenzo[*b*,*f*]-1,5-dithiocin 4c**

To a solution of **3a** (0.06 g, 0.40 mmol) in absolute ethanol (10 mL), 0.5 mL of HOAc and *tert*-butylamine

© 1999 NRC Canada

(0.02 mL, 0.22 mmol) were added. Reaction and work-up procedure identical with those for **4a**, **4b** afforded, on flash chromatography, eluting with CH_2Cl_2–hexanes (4:1) (R_f = 0.56), **4c** as a yellow solid (0.04 g, 87%), mp 136–138°C. IR (film), ν: 3322, 3057, 2970, 2924, 1695, 1589, 1463, 819. Exact Mass calcd. for $C_{18}H_{19}NS_2$: 313.0958; found: 313.0968.

N-Phenyl-6,12-imino-6*H*,12*H*-dibenzo[*b*,*f*]-1,5-dithiocin 4d

A mixture of **3a** (0.23 g, 1.64 mmol), aniline (0.08 g, 0.90 mmol), acetic acid (0.5 mL), and absolute ethanol (15 mL) was refluxed for 6.5 h. The clear yellow solution was cooled to room temperature and the solvent was evaporated to yield a brown oil (0.24 g, 87%). Flash chromatography, eluting with CH_2Cl_2–hexanes (4:1) (R_f = 0.58), resulted in a white solid (0.20 g, 75%), mp 70–72°C. IR (KBr), ν: 3075, 2961, 835; ^{13}C NMR, δ: 147.1s, 133.3s, 130.3s, 129.5d, 128.6d, 128.0d, 127.9d, 125.0d, 123.0d, 119.5d, 61.1d. Exact Mass calcd. for $C_{20}H_{15}NS_2$: 333.0645; found: 333.0651. Anal. calcd. for $C_{20}H_{15}NS_2$: C 72.12, H 4.54, N 4.20, S 19.25; found: C 71.63, H 4.51, N 3.93, S 19.78.

N-(2′-Phenylethyl)-2,8-dimethyl-6,12-imino-6*H*,12*H*-dibe nzo[*b*,*f*]-1,5-dithiocin 5a

The same procedure was used as in the formation of **4a**. A crude yellow oil was obtained (0.06 g, 96%). Flash chromatography, eluting with CH_2Cl_2–hexanes (4:1) (R_f = 0.58), yielded a beige solid (0.05 g, 83%), mp 132–134°C. Exact Mass calcd. for $C_{24}H_{23}NS_2$: 389.1272; found: 389.1263.

N-Isobutyl-2,8-dimethyl-6,12-imino-6*H*,12*H*-dibenzo[*b*,*f*]-1,5-dithiocin 5b

The same procedure as for the formation of **4b** was used. Flash chromatography of the crude product, eluting with CH_2Cl_2–hexanes (4:1) (R_f = 0.60), yielded a yellow oil (0.06 g, 86%) bp 150–153°C/5 Torr. Exact Mass calcd. for $C_{20}H_{23}NS_2$: 341.1272; found: 341.1270.

1-Naphthalenethiol

Concentrated hydrochloric acid (11.40 mL) was added to crushed ice (30 g) in a round-bottom flask, with stirring. 1-Naphthalenesulfonyl chloride (1.00 g, 4.41 mmol) was added portionwise via spatula, making sure that the solution was kept below 0°C. Tin (6.30 g, 53.04 mmol) was added to the vessel, turning the solution yellow. The mixture was refluxed for 6 h and the solution became clear. The solution was then extracted with CH_2Cl_2 (2 × 20 mL), washed with saturated NaCl solution, dried, and concentrated to yield a yellow oil (0.63 g, 89%), bp 138–140°C/7 Torr (lit. (23) bp 138–140°C/2 Torr).

1-Mercapto-2-naphthaldehyde 6

1-Naphthalenethiol (0.94 g, 5.87 mmol) was dissolved in dry hexanes (50 mL) under argon, and TMEDA (2.20 mL, 14.67 mmol) was added to the mixture. The reaction was cooled to 0°C and 1.6 M *n*-BuLi (9.17 mL, 14.67 mmol) was added dropwise. The solution initially turned cloudy white and eventually became yellow and clear. The mixture was then stirred for 0.5 h at 0°C, then warmed to room temperature before stirring for an additional 16 h. *N*-Formylpiperidine (1.11 mL, 9.98 mmol) was added via syringe and a dark red paste resulted. Vigorous stirring for 10 h formed a yellow mixture, which was then washed with 1 M HCl (2 × 25 mL) and extracted with CH_2Cl_2 (4 × 25 mL). Additional washing with saturated NaCl (25 mL), drying, and concentration yielded a brown oil (0.62 g, 56%). Chromatography on aluminum oxide, eluting with CH_2Cl_2–MeOH (95:5) (R_f = 0.45), gave a yellow oil (0.47 g, 43%), bp 139–142°C/7 Torr. IR (film), ν: 3050, 2924, 2864, 1682, 1495, 825, 753; ^{1}H NMR, δ: 9.82 (s, 1H), 8.33 (m, 2H), 7.95 (m, 2H), 7.66 (m, 1H), 7.31 (m, 1H), 5.31 (s, 1H). Exact Mass calcd. for $C_{11}H_8OS$: 188.0288; found: 188.0283.

2-Mercapto-1-naphthaldehyde 7 and 3-mercapto-2-naphthaldehyde 8

2-Naphthalenethiol (2.00 g, 12.48 mmol) was ground and dissolved in dry hexanes (80 mL), under argon, and TMEDA (4.69 mL, 31.20 mmol) was added to the mixture. The mixture was cooled to 0°C and 1.6 M *n*-BuLi (19.50 mL, 31.20 mmol) was added dropwise. The solution initially turned a cloudy white colour and eventully became yellow and clear. The mixture was then stirred for 0.5 h at 0°C and warmed to room temperature before stirring for an additional 16 h. *N*-Formylpiperidine (2.78 mL, 24.96 mmol) was added via syringe and a dark red paste resulted. Vigorous stirring for 10 h formed a yellow mixture, which was washed with 1 M HCl (2 × 30 mL) and extracted with CH_2Cl_2 (4 × 30 mL). Washing with saturated NaCl (30 mL), drying, and concentration afforded a brown oil (1.76 g, 75%). Chromatography on aluminum oxide, eluting with CH_2Cl_2–MeOH (95:5) (R_f = 0.64), resulted in compound **7** (0.70 g, 45%), mp 122–124°C. IR (film), ν: 2957, 2924, 2851, 2725, 2555, 1722,774; ^{1}H NMR, δ: 11.03 (s, 1H), 8.66 (d, 1H, *J* = 7.5 Hz), 7.84 (d, 1H, *J* = 7.6 Hz), 7.63 (m, 1H), 7.48 (m, 1H), 7.34 (d, 1H, *J* = 7.5 Hz), 7.31 (d, 1H, *J* = 7.7 Hz), 4.85 (s, 1H). Exact Mass calcd. for $C_{11}H_8OS$: 188.0288; found: 188.0285.

An earlier fraction obtained on eluting with CH_2Cl_2 –MeOH (95:5) (R_f = 0.33) resulted in **8** (0.47 g, 30%), mp 134–136°C. IR (film), ν: 2970, 2930, 2850, 2578, 1708, 1525, 734; ^{1}H NMR, δ: 10.15 (s, 1H), 8.26 (s, 1H), 7.89 (d, 1H, *J* = 3.9 Hz), 7.73 (m, 1H), 7.68 (m, 1H), 7.52 (d, 1H, *J* = 7.6 Hz), 7.45 (dd, 1H, *J* = 7.6, 3.8 Hz), 5.48 (s, 1H). Exact Mass calcd. for $C_{11}H_8OS$: 188.0288; found: 188.0281.

Synthesis of 7 by an alternative route, from 2-hydroxy-1-naphthaldehyde 9

*A. 2-(*tert*-Butyldimethylsilylthio)-1-naphthaldehyde **10***

To a solution of 2-hydroxy-1-naphthaldehyde (1.00 g, 5.81 mmol), in 16 mL of pyridine at 0°C, triflic anhydride (1.09 mL, 6.45 mmol) was slowly added. Evolution of a white gas occurred and the resulting mixture was stirred at 0°C for an additional 5 min. The mixture was then warmed to room temperature and stirred for 24 h. Water (15 mL) was added to the solution, which was extracted with diethyl ether (2 × 15 mL), washed with H_2O (15 mL), 10% aqueous HCl, and then with saturated NaCl (15 mL). The organic layer was dried and concentrated to obtain a brown, foamy solid (1.32 g, 75%). Recrystallization from CH_2Cl_2–hexanes af-

© 1999 NRC Canada

forded a beige solid (1.15 g, 65%). IR (KBr), ν: 3160, 2834, 2755, 1702, 1587, 856, 784; ^{1}H NMR, δ: 10.81 (s, 1H), 8.45 (d, 1H, *J* = 6.3 Hz), 8.25–7.17 (m, 5H).

Dry THF (25 mL) was saturated with H_2S gas, and the reaction vessel was then cooled to –78°C. The 1.6 M *n*-BuLi (8.00 mL, 13.00 mmol) was added dropwise to the above solution, which was allowed to warm to 0°C, with stirring for 0.5 h. The mixture was then recooled to –78°C and TBDMS-Cl (1.68 g, 11.11 mmol) was added portionwise with a spatula. The yellow mixture was warmed to room temperature and was partitioned between pentane (50 mL) and H_2O (25 mL). The organic layer was extracted and washed with H_2O (20 mL), dried, and concentrated to afford TBDMS-SH as a clear oil (83%). IR (film), ν: 2737, 2560; ^{1}H NMR, δ: 0.97 (s, 9H),0.29 (s, 6H), 0.11 (s, 1H).

Potassium hydride (0.31 g, 7.69 mmol), was initially washed with dry pentane (3 × 20 mL) and was placed in a flask with 10 mL of pentane. The silanethiol above (1.13 g, 7.63 mmol) was added slowly to the reaction mixture at 0°C and stirring was continued for 2 h. Solvent was removed and a white solid was obtained (0.98 g, 69%). The salt was recrystallized from toluene to yield white crystals of TBDMS-SK (0.87 g, 61%).

A solution of this salt (0.12 g, 0.66 mmol) in dry THF (15 mL) was added to tetrakis(triphenylphosphine)palladium (0) (0.06 g, 0.05 mmol) and the triflate obtained above (0.20 g, 0.66 mmol) in toluene (20 mL). The brown solution was refluxed for 5 h, after which it was partitioned between H_2O (25 mL) and ethyl acetate (25 mL). The organic layer was washed with H_2O (2 × 15 mL), dried, and concentrated to afford a brown oil (0.14 g, 73%). Flash chromatography, eluting with CH_2Cl_2 (R_f = 0.44), afforded **10** as a yellow oil (0.10 g, 52%). IR (film), ν: 2990, 2946, 2856, 2725, 1722, 1597, 1517; ^{1}H NMR, δ: 10.85 (s, 1H), 8.35 (d, 1H, *J* = 8.2 Hz), 7.98 (d, 1H, *J* = 7.1 Hz), 7.78 (dd, 1H, *J* = 8.1, 4.0 Hz), 7.60 (m, 1H), 7.41 (m, 1H), 7.17 (dd, 1H, *J* = 7.0, 3.9 Hz), 1.05 (s, 9H), 0.48 (s, 6H).

*B. Deprotection of **10** to give **7***

To a solution of the protected thiol **10** (0.53 g, 0.18 mmol) in THF (10 mL) at 0°C, tetrabutylammonium fluoride (0.20 mL, 0.19 mmol) was added dropwise. The mixture was stirred for 3 h, eventually turning a deep yellow colour. The reaction mixture was washed with saturated NH_4Cl (10 mL) and extracted with CH_2Cl_2 (3 × 10 mL), dried, and concentrated to afford a brown oil (0.30 g, 90%). Flash chromatography, eluting with CH_2Cl_2 (R_f = 0.48), resulted in a yellow solid (76% yield), mp 124–126°C. This product was identical (mixture mp, IR, ^{1}H NMR) with the *2-mercapto-1-naphthaldehyde* **7** prepared as described above.

8,16-Imino-8*H*,16*H*-dinaphtho [2,1-*b*,*f*]-1,5-dithiocin 12

A mixture of the naphthaldehyde **7** (0.04 g, 0.20 mmol) and ammonium acetate (0.02 g, 0.20 mmol) in absolute ethanol (15 mL) was refluxed for 3.5 h. The solution was cooled and the ethanol was removed. The yellow solid was recrystallized from methanol to give **12** (0.03 g, 94%), mp 160–163°C. IR (KBr), ν: 3356, 2952, 1583, 835, 806. Exact Mass calcd. for $C_{22}H_{15}NS_2$: 357.0646; found: 357.0647.

8,16-Imino-8*H*,16*H*-dinaphtho [1,2-*b*,*f*]-1,5-dithiocin 11

The same procedure outlined for compound **12** was used for the formation of **11**. Yellow crystals were obtained (0.03 g, 92%) mp 168–170°C. IR (KBr), ν: 3033, 2953, 2846, 1529, 818. Exact Mass calcd. for $C_{22}H_{15}NS_2$: 357.0646; found 357.0643.

8,16-Imino-8*H*,16*H*-dinaphtho [2,3-*b*,*f*]-1,5-dithiocin 13

The same procedure was used for the formation of **13**. Yellow crystals were obtained, recrystallized from methanol (0.04 g, 96%), mp 170–172°C. IR (KBr), ν: 3197, 2953, 1590, 1495, 1492, 805. Exact Mass calcd. for $C_{22}H_{15}NS_2$: 357.0646; found: 357.0640.

8,16-Imino-8*H*,16*H*-dinaphtho[2,1-*b*,*f*]-1,5-dioxocin 14a

A mixture of 2-hydroxy-1-naphthaldehyde (1.72 g, 10.00 mmol) and ammonium acetate in 15 mL of ethanol was refluxed for 4.5 h, then cooled to room temperature. The ethanol was partially evaporated and the yellow solid was recrystallized to yield **14a** (1.55 g, 95%), mp 241–243°C (lit. (15) mp 240–242°C). IR (KBr), ν: 3332, 1616, 955; ^{1}H NMR, δ: 8.18 (d, 2H, *J* = 6.0 Hz), 7.72 (t, 4H, *J* = 5.8 Hz), 7.59 (d, 2H, *J* = 6.0 Hz), 7.36 (d, 2H, *J* = 5.8 Hz), 7.05 (d, 2H, *J* = 5.8 Hz), 6.63 (d, 2H, *J* = 2.5 Hz), 3.00 (br s, 1H); ^{13}C NMR, δ: 150.3s, 131.5s, 131.0d, 128.9s, 128.4d, 127.2d, 123.7d, 121.9d, 118.3d, 112.4s, 75.6d. Exact Mass calcd. for $C_{22}H_{15}NO_2$: 325.1101; found: 325.1093.

***N*-(Methoxycarbonyl)-2,8-dimethyl-6,12-imino-6*H*,12*H*-dibenzo[*b*,*f*]-1,5-dithiocin 15**

The amine **2b** (0.20 g, 0.70 mmol) was dissolved in acetone (15 mL), then cesium carbonate (1.37 g, 4.20 mmol) was added to the solution, which was stirred for 5 min. Slow addition of methyl chloroformate (0.22 mL, 2.80 mmol) with a syringe resulted in a red-coloured solution. The mixture was refluxed for 16 h under argon. Removal of the Cs_2CO_3 by gravity filtration and evaporation of the acetone solution yielded an orange oil. A solution of 4% NaOMe in methanol was added to the oil and stirring was continued for 2 h. A white precipitate was obtained (0.16 g, 67%), which was filtered off and recrystallized from CH_2Cl_2–hexanes, mp 143–146°C. IR (KBr), ν: 3347, 2975, 2846, 1698, 1503, 731. Exact Mass calcd. for $C_{18}H_{17}NO_2S_2$: 343.0700; found: 343.0702.

***N*-(1′-Phenylethyl)-2,8-dimethyl-6,12-imino-6*H*,12*H*-dibenzo[*b*,*f*]-1,5-dithiocin 16**

To thiosalicylaldehyde **3b** (0.11 g, 0.69 mmol) dissolved in 20 mL of absolute ethanol and 1 mL of acetic acid, the *R*-(+)-1-phenylethylamine (0.05 mL, 0.38 mmol) was added dropwise. The solution turned an orange colour and was then refluxed for 4.5 h. The mixture was washed with H_2O (10 mL), extracted with CH_2Cl_2 (3 × 15 mL), dried, and concentrated to yield a brown oil (0.12 g, 86%). Flash chromatography, eluting with ethyl acetate – hexanes (1:1) (R_f = 0.57), gave a foamy beige solid (0.10 g, 77%), mp 81–83°C. IR (KBr), ν: 3367, 2949, 1485; ^{1}H NMR, δ: 7.39 (m, 4H), 6.92 (m, 7H), 5.53, 5.48 (2s, 2H), 4.17, 3.90 (2q, 1H, *J* = 7.8 Hz), 2.25 (s, 6H), 1.61, 1.55 (2d, 3H, *J* = 7.8 Hz); ^{13}C NMR, δ: 143.2s, 134.3s, 133.1s, 129.8d, 129.2d, 127.6d, 127.5d, 127.4s, 127.2d, 126.5d, 60.0d, 59.3d, 22.5q, 20.9q.

© 1999 NRC Canada

Exact Mass calcd. for $C_{24}H_{23}NS_2$: 389.1272; found: 389.1264.

_N_-(3′-Methylbutyl)-6,12-imino-6_H_,12_H_-dibenzo[_b_,_f_]-1,5-dithiocin 17a

A mixture of thiosalicylaldehyde **3a** (0.12 g, 0.85 mmol), L-leucine (0.06 g, 0.47 mmol), and absolute ethanol (30 mL) was refluxed for 4.5 h. The clear yellow solution was cooled to room temperature and the solvent was evaporated to yield a yellow oil (0.09 g, 68%). Flash chromatography, eluting with CH_2Cl_2 – hexanes (85:15) (R_f = 0.52), gave a yellow oil (0.08 g, 60%). IR (film), ν: 3057, 2945, 2853, 830, 742; ^{1}H NMR, δ: 7.28 (m, 2H), 7.0 (m, 6H), 5.41 (s, 2H), 2.98 (m, 1H), 1.62 (m, 4H), 0.91 (d, 6H, J = 7.5 Hz). Exact Mass calcd. for $C_{19}H_{21}NS_2$: 327.1115; found: 327.1112.

_N_-(2′-Hydroxyethyl)-6,12-imino-6_H_,12_H_-dibenzo[_b_,_f_]-1,5-dithiocin 17b

A mixture of **3a** (0.14 g, 1.03 mmol), L-serine methyl ester hydrochloride (0.09 g, 0.57 mmol), and absolute ethanol (15 mL) was refluxed for 4.5 h. The clear yellow solution was cooled to room temperature and the solvent was evaporated to yield a yellow-brown oil. This was dissolved in CH_2Cl_2 (15 mL) and the organic layer was washed with saturated $NaHCO_3$ (15 mL), dried, and concentrated to afford a yellow oil (0.14 g, 88%). Flash chromatography, eluting with CH_2Cl_2–hexanes (85:15) (R_f = 0.57), gave white needle crystals (0.11 g, 75%), mp 165–167°C. IR (film), ν: 3395, 2993, 1626, 1505, 806; ^{1}H NMR, δ: 7.82 (dd, 4H, J = 7.8, 7.6 Hz), 7.32 (dt, 4H, J = 7.8, 7.7 Hz), 6.21 (s, 2H), 4.35 (m, 2H), 3.50 (m, 3H).

_N_-(1′-_tert_-Butyloxycarbonyl-3′-methylbutyl)-6,12-imino-6_H_,12_H_-dibenzo[_b_,_f_]-1,5-dithiocin 17c

A mixture of **3a** (0.22 g, 1.60 mmol), L-leucine *tert*-butyl ester (0.19 g, 0.88 mmol), and absolute ethanol (15 mL) was refluxed for 4.5 h. Work-up as for **17b**, followed by flash chromatography, eluting with CH_2Cl_2–hexanes (85:15) (R_f = 0.67), gave a yellow solid (0.24 g, 71%), mp 154–156°C. ^{1}H NMR, δ: 7.33 (m, 4H), 7.01 (m, 4H), 5.78, 5.70 (2s, 2H), 3.65 (t, 1H, J = 9.1 Hz), 1.82 (m, 1H), 1.64 (m, 2H), 1.20 (s, 9H), 0.90 (d, 6H, J = 9.4 Hz). Exact Mass calcd. for $C_{24}H_{29}NO_2S_2$: 427.1639; found: 427.1644.

Acknowledgements

Support of this work by a Natural Sciences and Engineering Research Council of Canada research grant is gratefully acknowledged. One of us (F.D.T.) acknowledges the award of an Ontario Graduate Scholarship.

References

1. (*a*) M. Harmata, C.L. Barnes, S.R. Karra, and S. Elahmad. J. Am. Chem. Soc. **116**, 8392 (1994); (*b*) S. Paliwal, S. Geib, and C.S. Wilcox. J. Am. Chem. Soc. **116**, 4497 (1994); (*c*) D. St. C. Black, D.C. Craig, N. Kumar, and D.B. McConnell. Tetrahedron Lett. **37**, 241 (1996); (*d*) K. Mitra and K.S. Gates. Tetrahedron Lett. **36**, 1391 (1995); (*e*) B.G. Bag and U. Maitra. Synth. Commun. **25**, 1849 (1995).
2. J. Rebek, Jr. Acc. Chem. Res. **23**, 399 (1990).
3. (*a*) J. Tröger. J. Prakt. Chem. **36**, 225 (1887); (*b*) M.A. Spielman. J. Am. Chem. Soc. **57**, 583 (1935); (*c*) V. Prelog and P. Wieland. Helv. Chim. Acta, **27**, 1127 (1944).
4. H. Salez, A. Wardani, M. Demeunynck, A. Tatibouet, and J. Lhomme. Tetrahedron Lett. **36**, 1271 (1995).
5. S.H. Wilen, J.Z. Qi, and P.G. Williard. J. Org. Chem. **56**, 485 (1991).
6. F.D. Toste, A.J. Lough, and I.W.J. Still. Tetrahedron Lett. **36**, 6619 (1995).
7. (*a*) F. Asinger and M. Theil. Angew. Chem. **70**, 667 (1958); (*b*) M. Theil, F. Asinger, and G. Trümpler. Liebigs Ann. Chem. **619**, 137 (1958).
8. Y.L. Gol'dfarb, A.E. Skorova, and M.K. Kirmalova. Izv. Akad. Nauk SSSR, Ser. Khim. 1421 (1966); 1426 (1966).
9. M.F. Corrigan and B.O. West. Aust. J. Chem. **29**, 1413 (1976).
10. L.E. Brieaddy and K.H. Donaldson. J. Heterocycl. Chem. **32**, 1683 (1995).
11. J.C. Arnould, M. Didelot, C. Cadilhac, and M.J. Pasquet. Tetrahedron Lett. **37**, 4523 (1996).
12. P.J. Stang, M. Hanack, and L.R. Subramanian. Synthesis, 85 (1982).
13. (*a*) E.I. Miranda, M.J. Diaz, I. Rosado, and J.A. Soderquist. Tetrahedron Lett. **35**, 3221 (1994); (*b*) A.M. Rane, E.I. Miranda, and J.A. Soderquist. Tetrahedron Lett. **35**, 3225 (1994).
14. T.D. Nelson and R.D. Crouch. Synthesis, 1031 (1996).
15. E.R. Biehl, H.M. Refat, A.A. Fadda, and Y. Lu. Heterocycles, **43**, 977 (1996).
16. (*a*) E.J. Corey, M.G. Bock, A.P. Kozikowski, A.V. Rao, D. Floyd, and B. Lipshutz. Tetrahedron Lett. 1051 (1978); (*b*) K.J. Butcher. Synlett, 825 (1994).
17. (*a*) D.H.R. Barton, J.-P. Finet, and J. Khamsi. Tetrahedron Lett. **28**, 887 (1987); (*b*) D.H.R. Barton, N. Ozbalik, and M. Ramesh. Tetrahedron Lett. **29**, 857 (1988).
18. H. Nozaki, T. Aratani, T. Toraya, and R. Noyori. Tetrahedron, **27**, 905 (1971).
19. (*a*) P. Beak, A. Basu, D.J. Gallagher, Y.S. Park, and S. Thayumanaran. Acc. Chem. Res. **29**, 552 (1996); (*b*) D. Hoppe. Angew. Chem. Int. Ed. Engl. **36**, 2282 (1997).
20. (*a*) M. Oestreich, R. Fröhlich, and D. Hoppe. Tetrahedron Lett. **39**, 1745 (1998); (*b*) K.M.B. Gross, Y.M. Jun, and P. Beak. J. Org. Chem. **62**, 7679 (1997); (*c*) S. Norsikian, I. Marek, and J.-F. Normant. Tetrahedron Lett. **38**, 7523 (1997); (*d*) K. Nishimura, M. Ono, Y. Nagaoka, and K. Tomioka. J. Am. Chem. Soc. **119**, 12974 (1997); (*e*) N. Voyer, J. Roby, S. Chénard, and C. Barberis. Tetrahedron Lett. **38**, 6505 (1997); (*f*) D.E. Ward and W.-L. Lu. J. Am. Chem. Soc. **120**, 1098 (1998).
21. E.E. Snell and S.J. di Mari. Enzymes, **2**, 335 (1976).
22. M. Casey, J. Leonard, and B. Lygo. Advanced practical organic chemistry. Chapman and Hall, New York. 1990. p. 230.
23. The Merck Index. 12th ed. Whitehouse, N.J. 1996. p. 1095.

List of abbreviations

TMEDA: *N*,*N*,*N*′,*N*′-tetramethylethylenediamine
TBAF: tetra-*n*-butylammonium fluoride
TBDMS: *tert*-butyldimethylsilyl
Tf: trifluoromethanesulfonyl
Triflate: trifluoromethanesulfonate
DCC: dicyclohexylcarbodiimide

© 1999 NRC Canada

The molecular complexes of deoxycholic acid and cholesterol with CH_3COOD studied by infrared spectroscopy

Alpha O. Diallo, Claude Meyer, and Nguyen Van-Thanh

Abstract: The frequencies of the O-D stretching vibrations of CH_3COOD have been measured in the liquid and vapour phases and in the form of molecular associations with deoxycholic acid and cholesterol. The spectra confirm that the vapour phase is a mixture of monomeric and dimeric forms at room temperature. The vibrational assignment made for the gaseous phase is used in conjunction with prior data available on the monomeric O-D stretching frequencies in solutions to explain the spectroscopic behaviour of the molecular complexes. The pattern of frequency shifts suggests that deuterium bonding links the cholesterol and CH_3COOD in the hydrophilic regions and that the self association of the heavy acid is limited to the dimeric species in the complex with deoxycholic acid. Extra absorption bands observed in the spectral region characteristic of the deuterium bond vibrations are tentatively considered to arise from O-D groups in different local environments with different vibrational energies compared with the D-bonded species. Further evidence for steroid–CH_3COOD interactions is obtained from a study of the O-H and C=O stretching vibrations of the compounds.

Key words: acetic acid-*d*, complexation with deoxycholic acid and cholesterol, infrared spectroscopy.

Résumé : Les fréquences des vibrations d'élongation O-D de CH_3COOD ont été étudiées dans les états gazeux et liquide et sous la forme de complexes avec l'acide deoxycholique et le cholestérol. Les spectres confirment que la phase gazeuse est un mélange de formes monomères et dimères à la température ambiante. L'interprétation des vibrations O-D à l'état gazeux est utilisée de concert avec les fréquences des monomères étudiées antérieurement en solutions pour expliquer les propriétés spectroscopiques des composés moléculaires. Les modèles des déplacement des fréquences suggèrent que le cholestérol et CH_3COOD sont associés par liaison deutérium dans les régions hydrophiles et que l'autoassociation de l'acide lourd est limitée à la dimérisation dans le complexe formé avec l'acide deoxycholique. Des bandes d'absorption en surnombre observées dans le domaine spectral caractéristique des vibrations de la liaison deutérium sont considées comme provenant des groupements O-D dans des environnements différents avec des énergies vibrationnelles différentes comparées avec les espèces associées. En outre, l'étude des vibrations de valence des liaisons O-H et C=O des composés a permis de mettre en évidence quelques interactions entre CH_3COOD et les stéroides dans les complexes.

Mots clés : acide-*d* acétique, complexation avec l'acide déoxycholique et le cholestérol, spectroscopie infrarouge.

1. Introduction

The vibrational spectra of aliphatic carboxylic acids, RCOOH, have been extensively studied with special emphasis on the location of the monomeric O-H and O-D stretching bands and the frequency shifts of these bands by change of the external conditions (1–4). It is well known that the molecules in the solid and liquid states are different from the molecules in the gas phase due to their association through hydrogen bonding. These differences are reflected in the relatively different vibrational spectra. For both the O-H and O-D groups, the vibrational frequencies referred to above, are lowered with increasing strength of the O-H(D)···O bonding on going from the gaseous to the condensed phase spectra. For the O-H group, the most thoroughly investigated, the condensed phase spectra generally appear as broad absorptions consisting in some cases of many sub-bands. The interpretation of these complex spectra has been attempted but cannot be said to have been satisfactorily resolved (3, 4).

We have measured the infrared spectra of acetic acid-*d*, CH_3COOD, in the liquid and vapour phases and in the form

Received July 28, 1998.

A.O. Diallo[1] and N. Van-Thanh. Laboratoire de Photophysique Moléculaire, UPR 3661 du C.N.R.S., Université de Paris-Sud, Centre d'Orsay, Bât. 350, 91405 Orsay Cedex, France.
C. Meyer. Laboratoire de Chimie Bio-organique et Bio-inorganique, Université de Paris-Sud, Centre d'Orsay, Bât. 420, 91405 Orsay Cedex, France.

[1]Author to whom correspondence may be addressed. Telephone: 0169157526. Fax: 0169157530.
e-mail: annette.mont-reynaud@lppm.u-psud.fr

 © 1999 NRC Canada

Table 1. Stretching frequencies ν_{OD} (cm^{-1}) of CH_3COOD in various conditions.

	Solvent[b]			Complexed[a] with	
Vapour[a]	*o*-$C_6H_4(COOCH_3)_2$	CH_3CN	$(CH_3)_2CO$	Cholesterol	DCA[c]
2641					
	2472				2490
		2437		2432	
			2370		2397
2306					
2274					2271
				2222	

[a]Present work.
[b]Reference 13.
[c]Deoxycholic acid.

of complexes with deoxycholic acid, DCA, and cholesterol, to obtain additional information on the spectroscopic behaviour of deuterium bond forming molecules. The results of the investigation are presented below.

2. Experimental

All the reagents were Aldrich commercial compounds. The molecular complexes were obtained from recrystallization of the steroids in the acid (5, 6). All the manipulations necessary in the preparation of the solutions were carried out in a dry nitrogen atmosphere using glove boxes. The steroids are not very soluble in the medium. The powdered solid (~0.5–1.0 g) was suspended in 5–10 mL of the acid, and the flasks were stopped in the glove boxes. The suspensions were warmed on a steam bath (~50°C) until complete dissolution. The resulting clear solutions were allowed to cool to room temperature, protected against light and set aside for crystallization. The solid crystals were collected by suction filtration, dried under a well ventilated hood, and stored in a closed container. These crystals can be handled at room temperature, but they decompose on heating. Since the composition may vary in a way mentioned later, it is difficult to determine the true dissociation temperature accurately. The addition compound from cholesterol and CH_3COOD separates into the component molecules by the action of high vacuum and by strongly pressing the crystals. That formed from deoxycholic acid and CH_3COOD is quite stable under the same conditions. The spectra of the complexes were obtained as solids ground in nujol and in KBr pressed disks. The liquid and vapour phases were examined in conventional cells.

The set IR measurements at ambient temperature has been carried out on a Bruker IFS66V Fourier transform spectrometer. It was equipped with a vacuum bench which was pumped to better than 1 Torr. The standard mid-IR source was a current stabilized water-cooled SiC glowbar. For the 1500–4000 cm^{-1} spectral range, the detector was a room-temperature DTGS equipped with a KBr window. The beamsplitter material was KBr. All the spectra measured in the present work were apodized and obtained at a resolution (full width at half maximum) of 0.5 cm^{-1} in the considered spectral window. Thirty-two scans were superimposed to yield each interferogram, and a four-point apodization function was used. The ratio of the spectral slit width to the band system width is less than 1×10^{-2}. This is sufficiently small to avoid line-shape corrections due to the finite slit width. The absolute calibration of the wave numbers was accomplished using the well-known positions of lines to the 1←0 band of $^{12}C^{16}O$.

The absorption coefficient $k(\nu)$ at the frequency $\nu(cm^{-1})$ was obtained from the measurement of incident and transmitted, I_0 and I_t, respectively, corresponding to:

$$k(\nu)(cm^{-1}) = l^{-1} \ln (I_0/I_t)$$

where l is the optical path length.

Each absorption spectrum $I_t(\nu)$ of the gas, liquid, or solid sample was digitally divided by a background $I_o(\nu)$ of the same sample cell that was emptied. This resulted in a transmittance:

$$T(\nu) = I_t(\nu)/I_o(\nu)$$

The experimental results are given in Table 1 and illustrated in Figs. 1–5 which include the O-D, O-H, and C=O absorption bands.

3. Discussion

a. General considerations

The behaviour of CH_3COOH (guest) with regard to the formation of addition compounds with deoxycholic acid and cholesterol (hosts) have been previously described (5, 6). The complex of deoxycholic acid and CH_3COOH appears to be of an inclusion type, according to X-ray crystallographic study (7). The CH_3COOH molecules linked together into long chains by hydrogen bonding, as in the crystal structure of the acid itself, are held in channels between stacked sheets of the deoxycholic acid bound head-to-tail by hydrogen bonds. Likewise, by means of thermal gravimetric analysis of the adduct of cholesterol and CH_3COOH, the host–guest stoichiometry of the complex was established as 2:1 (6). The crystal structure is not known but it is probable that hydrogen bonds link the constituent species in the hydrophilic regions, perhaps with alternating arrangements of the molecules (6).

From the above information it is a great tentation to assume that similar structures are also obtained for the D-analogue. However, it is not clear how far the analogy can be taken with safety, as the arrangement of the molecules is not determined by van der Waals forces between them, but by hydrogen bondings between electronegative groups. For example, microwave studies of hydrogen-bonded simple car-

© 1999 NRC Canada

Fig. 1. IR absorption bands in the expected positions of the (O-D) stretching frequencies of CH_3COOD: (*a*) gas; (*b*) liquid; (*c*) complexed with deoxycholic acid.

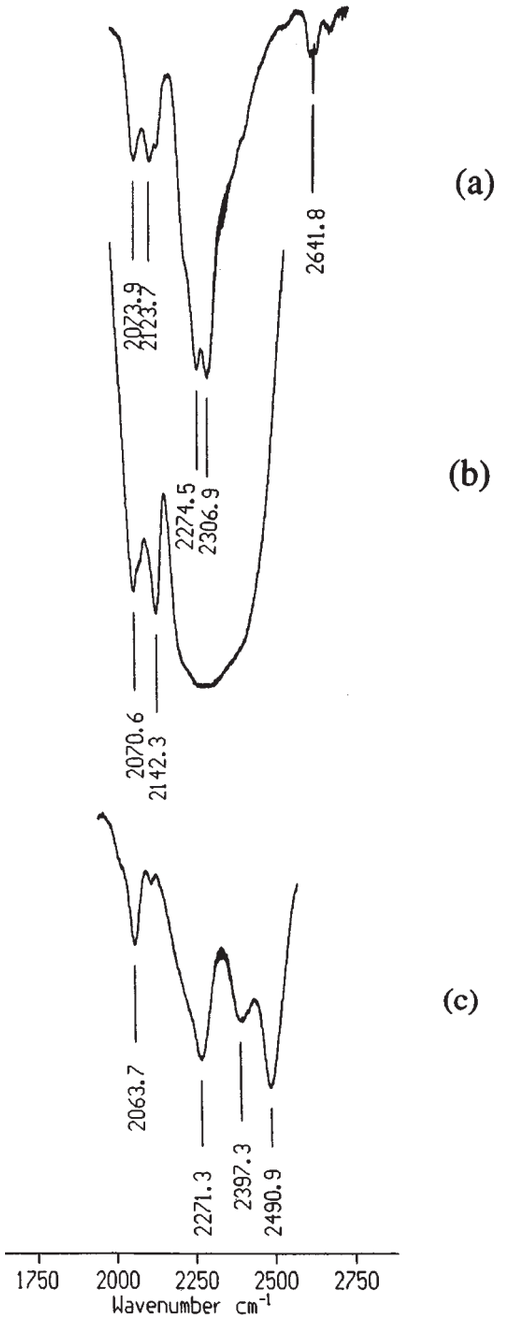

Fig. 2. IR absorption bands in the expected positions of the (O-D) stretching frequencies of CH_3COOD: (*a*) gas; (*b*) liquid; (*c*) complexed with cholesterol.

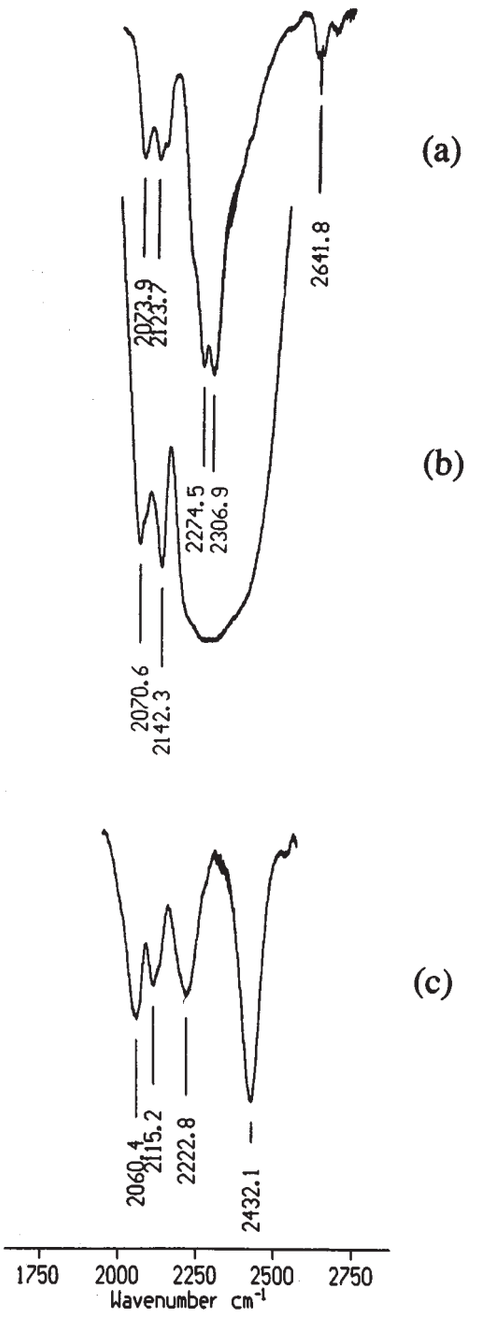

boxylic acids have shown that the O-H(D)···O distances are longer for D-bonding than for H-bonding (8).

Therefore it is impossible to be sure whether the D-bonds might be strong enough to maintain long and flexible chain molecules in their ordered crystalline-like state, as in the case of CH_3COOH referred to above. On the other hand, the possibility of isotopic exchange reaction such as

$$\text{-COOD} + \text{HO-host} \rightarrow \text{-COOH} + \text{DO-host}$$

between the carboxyl deuterium of the guest and the hydroxyl group of the host cannot be surely excluded. Such isotopic exchange, if it occurs, is likely to affect in an impredictable fashion the intermolecular host–guest organization. As will be shown later, it is hazardous to predict the way in which the molecules are arranged in the complexes under investigation. Because of this, an empirical approach to an understanding of the observed spectra seems more profitable at present. Of particular interest in our IR spectra

© 1999 NRC Canada

Fig. 3. IR absorption bands in the expected positions of the (O-D) stretching frequencies of CH_3COOD: (*a*) complexed with deoxycholic acid; (*b*) complexed with cholesterol.

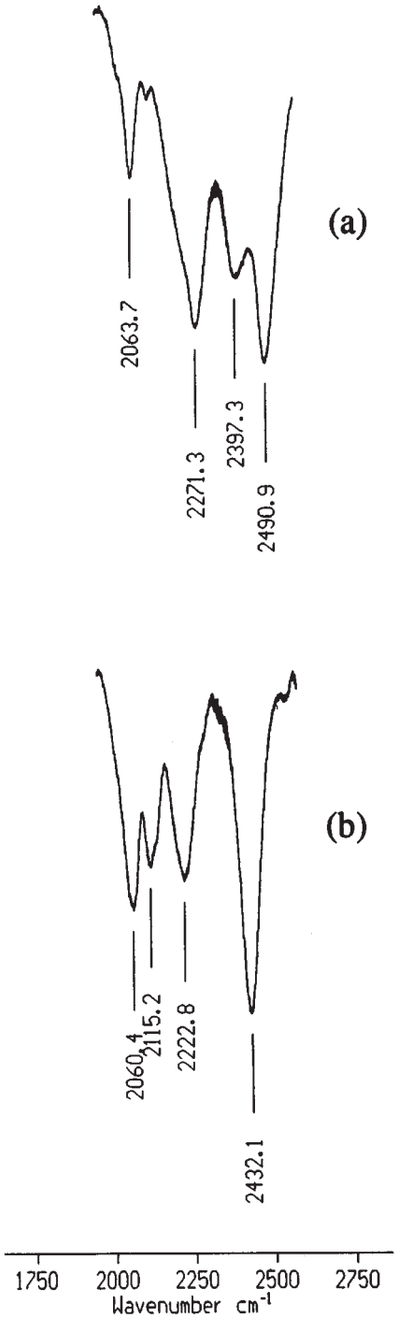

Fig. 4. IR absorption bands in the expected positions of the (O-H) stretching frequencies of deoxycholic acid: (*a*) uncomplexed species; (*b*) complexed with CH_3COOD.

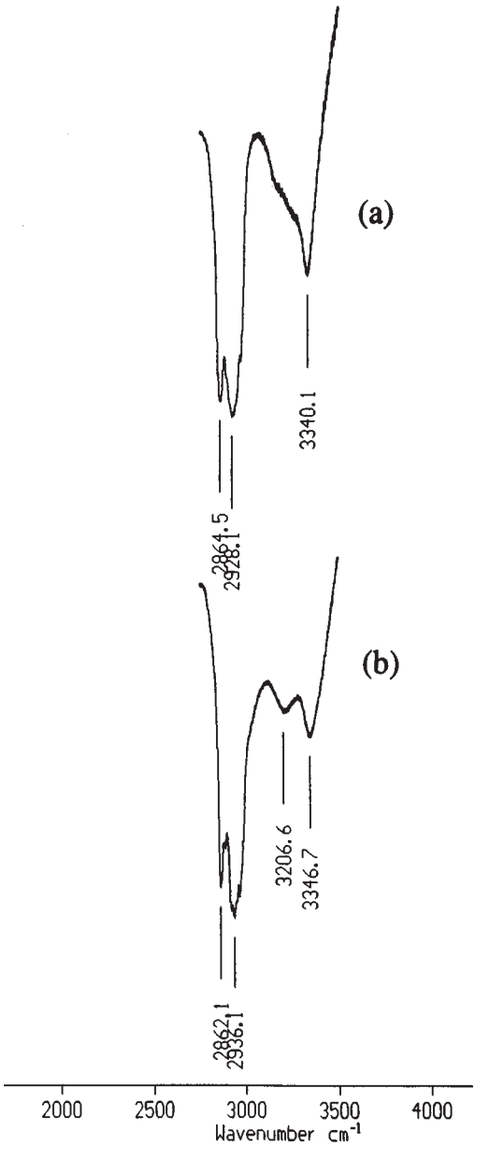

are the frequencies of the O-D, O-H, and C=O stretching vibrations usually considered as characteristic frequencies.

b. Interpretation of the spectroscopic results

Region associated with the O-D stretching vibrations

The monomeric O-D stretching frequencies of aliphatic carboxylic acids are most easily identified in the gaseous phase at high temperature. Experiments of this type have been made in earlier IR studies of the CH_3COOD molecules. The O-D fundamental vibration was assigned to a band observed at ≈2642 cm^{-1} (9, 10). In the present investigation of the vapour-phase spectrum of the molecules at ambient temperature, a weak absorption is clearly observable at the expected position (see Figs. 1*a* and 2*a*). The band appears to have a PQR contour, with the Q-branch located at 2641 cm^{-1}. We therefore accept this band as due to the monomeric stretching vibration.

The effect of D-bond formation on the position of the O-D absorption is to shift this band to lower frequencies (see Introduction). For example, the dimeric CH_3COOD and the polymeric HCOOD have been reported to show the

© 1999 NRC Canada

Fig. 5. IR absorption bands in the expected positions of the (O-H) stretching frequencies of cholesterol: (*a*) uncomplexed species; (*b*) complexed with CH_3COOD.

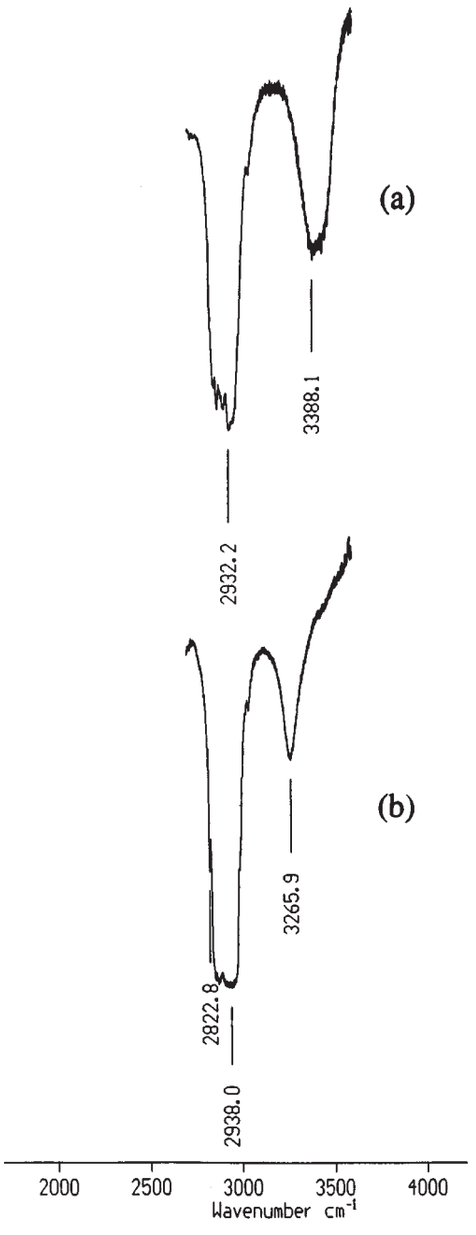

bonded O-D absorptions at 2268 and 2160 cm^{-1}, respectively (10, 11).

Actually, as can be seen in Figs. 1–3, there is a series of bands extending from 2060 to 2490 cm^{-1} in our spectra. The bands on the low-frequency side (viz. 2063–2142 cm^{-1}) are observed in all the curves with variable distribution of intensity from one spectrum to another. The intensity changes shift the relative position of the ν_{max} within the band system. However, the effects are small and the absorptions can be considered together. The intensities seem somewhat low for fundamental vibrations. We tentatively consider this group of bands as due to summation and (or) overtones of fundamentals, although the combinations responsible for them are difficult to ascertain.

In contrast to the above, on the high-frequency side from 2500 to 2200 cm^{-1} the spectra are extremely sensitive to the experimental conditions (compare Figs. 1–3).These observations agree qualitatively with the expected spectral behaviour of the O-D stretching modes of D-bonded species (see Introduction). Thus, these bands may be considered as the shifted O-D fundamentals involved in some type of intermolecular interactions, the nature of which remains to be determined.

In a number of previous works (3, 4), the band-width phenomena of the liquid phase and the multiplicity of peaks which occur in the vibrational studies of hydrogen-bonded systems, as observed here, have been interpreted in terms of anharmonic coupling between the O-H fundamentals and low-frequency motions of the molecules together with Fermi resonance involving levels of the same species.

Unfortunately, the pattern of frequency shifts of the O-D stretching modes presented in Fig. 3 is not easily accounted for in terms of such processes. Consequently, a different interpretation of the spectroscopic effects reported here, susceptible of experimental examination, is proposed below.

We deal with the vapour- and liquid-phase frequencies of CH_3COOD first. In the spectral region under consideration, the vapour-phase spectrum shows an incompletely resolved doublet with the two peaks located at 2306 and 2274 cm^{-1} (see Figs. 1*a* and 2*a*). As mentioned earlier, the lower of these frequencies falls close to the frequency assigned by previous authors (10) to the O-D stretching vibration of the dimeric species at 2268 cm^{-1}. The occurrence of a pair of bands, only 30 cm^{-1} apart, could indicate that more than one structure is represented. We therefore believe that a mixture of two kinds of dimers — for example, a cyclic and an open structure — is most likely, since higher polymers can be expected to have stronger D-bonds and hence to absorb at lower frequencies (12). Similarly the O-D bandwidth in liquid CH_3COOD (see Figs. 1*b* and 2*b*) may be explained by supposing, as above, that the acids are associated through deuterium bonds to a different extent into various polymeric species distributed at random. On this assumption the broad region of absorption represents the envelope of many unresolved sub-bands. The same type of explanation has been used before by Bellamy (3) to account for the broad character of the ν_{OH} bands in the spectra of aliphatic alcohols in the liquid state.

The spectra of the complexes are more difficult to explain because of the relatively wide separation of the bands and the multiplicity of peaks (see Fig. 3). Factor group splitting of the O-D stretching vibrations seems improbable, since similar frequencies are seen in the vapour and dilute solution spectra (see below). The only source of information available that might be used as guide in interpreting the observations are the vapour-phase spectrum referred to above and a study of solvent effects on the spectra of CH_3COOD reported by Bellamy et al.(13). These authors have carried out measurements of the O-D sretching frequencies attributable to the monomeric structure in solvents with different polar

© 1999 NRC Canada

properties. Some of their results are reproduced in Table 1 for comparison.

Comparison of the spectra of the gas and the complexes

Once more, reference to the frequencies assigned to the O-D stretching vibrations of the dimeric CH_3COOD shows that the band at 2274 cm^{-1} has a close counterpart at 2271 cm^{-1} in the spectrum of the molecular association with deoxycholic acid (compare Figs. 1*a* and *c*), but it is absent from the spectrum of the addition product with cholesterol. Instead a new band is observed at 2222 cm^{-1} (Fig. 2*c*). The fact that the band positions are relatively independent of whether the acid is in the vapour or the complexes would seem to imply that they have similar origin. Thus the presence of the dimeric CH_3COOD in the inclusion complex with deoxycholic acid is suggested by the experimental results. With regard to the combination with cholesterol, the postulation of intermolecular deuterium bonding between the carboxyl deuterium of CH_3COOD and the hydroxyl oxygen atom in the 3-position of the steroid would account for the observed frequency.

The remaining IR absorption bands of the complexed CH_3COOD molecules appear at higher frequencies than those of the vapour phase and cannot be ascribed to dimerization (see Figs. 1, 2 and Table 1). Of course, the frequency shifts of the dimer would be expected to differ from those of higher polymers presumed to have linear D-bonds. However, as already noted above, the O-D stretching absorptions should occur at lower frequencies as the extent of polymerization increases (12).

The frequency rise, as compared with the dimeric CH_3COOD, is probably a result of an increase of the force constant for the vibration and hence a weakening of the intermolecular D-bonding. In this respect, CH_3COOD differs strikingly from CH_3COOH. The light acetic acid molecules hydrogen bond with each other to form polymeric chains held in tunnels between hydrogen-bonded sheets of deoxycholic acid (7).

Comparison of the spectra of the complexes and the solutions

The possibility that the frequencies higher than those of the dimeric CH_3COOD are influenced by some new factors is strongly suggested by the data available on the monomeric stretching frequencies measured in a range of solvents already referred to in the foregoing. An examination of Table 1 reveals, indeed, that some of the solution frequencies are of the same order of magnitude as those found here. Thus, the comparison shows that the O-D stretching frequency at 2437 cm^{-1} in CH_3CN is nearly the same as the frequency at 2432 cm^{-1} in the spectrum of the addition compound with cholesterol. Similarly the monomeric stretching frequencies at 2472 and 2370 cm^{-1} in *o*-$C_6H_4(COOCH_3)_2$ and $(CH_3)_2CO$, respectively, have parallels at 2490 and 2397 cm^{-1} in the spectrum of the complex formed between CH_3COOD and deoxycholic acid.

The above qualitative similarities between low solute concentration spectra and those of the complexed species are consistent with the view that D-bonding intermolecular interactions between adjacent CH_3COOD molecules do not play a significant part in determining the band positions under discussion. Of course, the two effects may be caused by different mechanisms. The solvent effects observed have been ascribed to local interactions with the solutes (13). In the case of the complexed CH_3COOD, it is also quite possible that the regions of the hosts surrounding the O-D groups play some role in the spectra. Accordingly, the spectroscopic results can be understood by assuming that the variations in frequencies reflect the extent to which the local environment of the individual O-D groups affects the vibrations independently of D-bonding. Such specific effects, if any, would then result in a loss of the ability of the acids to associate further and a corresponding increase of the O-D stretching frequencies over those of the dimeric CH_3COOD.

Unfortunately, the intermolecular effects in inclusion complexes have not been made the subject of a systematic study (14). For this reason the specific intermolecular forces between structural units, considered above, cannot be discussed usefully at present. Further experimental work is necessary before the factors responsible for the observed frequency shifts can be correlated with the structure around the O-D groupings.

However, in order to see whether the IR absorption characteristics of the steroids are also affected by the effects of complexation, we have examined other regions of the spectra from which additional informations may be obtained.

Regions asociated with the O-H stretching vibrations of the steroids

The O-H bands of deoxycholic acid: According to X-ray diffraction study of several deoxycholic acid complexes, previously reported (7, 14), the steroid molecules hydrogen bond only with each other. The O-H···O bonding structure includes the -COOH group of the side chain and the hydroxyl -OH groups in the 3- and 12-positions of the A and C rings, respectively. Such information is of particular interest in the present case, since the above-mentioned individual OH groups may be expected to have different vibrational frequencies in the 3 μm region (3).

Actually, in the spectrum of deoxycholic acid a strong and unsymmetrical band with a broad shoulder on the low-frequency side occurs at 3340 cm^{-1} (Fig. 4*a*). Considering this unresolved band as being due to the overlapping of at least two components, the observed frequencies are consistent with the expectation for hydrogen-bonded O-H vibrations of the steroid molecules (3).

In the spectrum of its molecular association with CH_3COOD, the absorptions appear as a doublet with the maxima at 3346 and 3206 cm^{-1} (Fig. 4*b*). It seems likely that these bands arise from two kinds of O-H···O bonds different in strength. Since the OH vibration frequencies are not appreciably altered on going from one spectrum to the other, we must assume that the hydrogen-bonding arrangement of the deoxycholic acid molecules persists after complexation. As will be seen from Figs. 4*a* and *b* the essential difference between the spectra of the complexed and uncomplexed species lies in the fact that the former shows much better defined vibrational bands than the latter. This change in the band contours suggests that the molecular association is accompanied by the formation of a more organized crystal structure of these compounds.

© 1999 NRC Canada

Fig. 6. IR absorption bands in the expected positions of the (C=O) stretching frequencies of deoxycholic acid and CH_3COOD: (*a*) CH_3COOD gas; (*b*) uncomplexed deoxycholic acid; (*c*) complexed species.

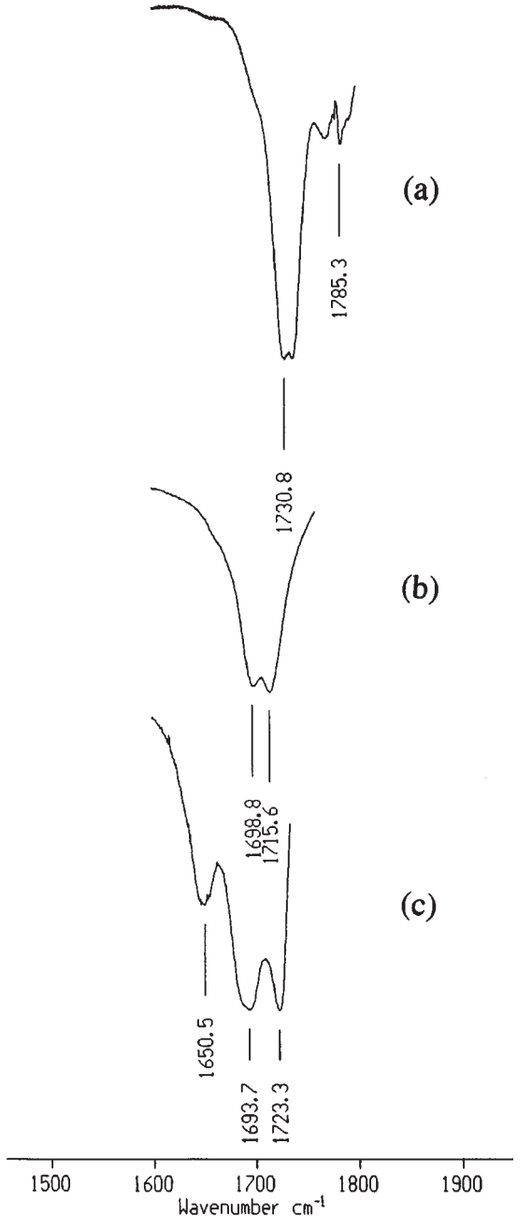

The OH bands of cholesterol: The crystal structure of anhydrous cholesterol has been determined by X-ray diffraction analysis (15). Hydrogen bondings of the same kind and strength link the molecules into separate chains forming a bilayer arrangement. In accord with this only a single absorption band attributable to the O-H···O stretching vibrations occurs at 3388 cm^{-1} in the IR spectrum of the steroid (Fig. 5*a*). In the complexed state the band is found to be shifted at 3265 cm^{-1} (Fig. 5*b*). This displacement of the OH absorption band is presumably due to the formation of an additional D bonding to the same hydroxyl oxygen atom already mentioned in the comparison of the spectra of the gas and the complexes (16).

Region associated with the C=O stretching vibrations: The IR absorption bands observed in the region of the C=O stretching frequencies are shown in Fig. 6. Acetic acid-*d*, as a gas, absorbs at 1785 cm^{-1} (Q-branch) and at 1730 cm^{-1} (doublet contour Fig. 6*a*). The former frequency can be assigned to the vibration of the free carbonyl of the monomeric species. The latter frequency could be caused by the similar vibration of the dimeric forms shifted by D bonding effect.

In the spectrum of deoxycholic acid there are two strong bands at 1715 and 1698 cm^{-1} (Fig. 6*b*).When the steroid forms complex with CH_3COOD it absorbs strongly at 1723 and 1693 cm^{-1} (Fig. 6*c*). A weaker additional band, separated enough from those mentioned above to make it distinguishable, appears at 1650 cm^{-1}. This latter band is believed to arise from the carboxyl carbonyl vibration of the CH_3COOD molecules. It is not known whether the large displacement of the frequency from its positions in the gaseous phase (Fig. 6*a*) is an indication of intermolecular interactions or whether it reflects the influence of structural change around the carboxyl group on the carbonyl frequency. The comparison of the spectra of the steroid and its complex shows some resemblance though there is a significant difference. The C=O stretching frequencies of the two main bands are not appreciably altered on going from one spectrum to another (compare Figs. 6*b* and *c*). However, their relative intensities are markedly different. The most remarkable difference is an increase of the bandwidth of the lower frequency absorption at 1693 cm^{-1} (Fig. 6*c*).

From these last results it may be concluded once again that the assumption of some type of steroid–CH_3COOD interactions accounts for the apparent spectroscopic behaviour of these molecular compounds. Since the nature of the intermolecular forces involved cannot be determined from vibrational spectroscopy alone, it is highly desirable that the crystal structures should be investigated.

Acknowledgments

The sample of cholesterol used in the present work was kindly supplied to us by Professor Lutton, Laboratoire de Physiologie de la Nutrition, Campus d'Orsay, Bât. 447, 91405 Orsay.

References

1. G.C. Pimentel and A.L. McClellan. The hydrogen bond. W.H. Freeman Co., San Francisco. 1959.
2. L. Pauling. The nature of the chemical bond. Cornell University Press, New York. 1960.
3. L.J. Bellamy. Infrared spectra of complex molecules. Methuen & Co. Ltd., London. 1959.
4. N. Sheppard. *In* Symp. hydrogen bonding. *Edited by* D. Hadzi. Pergamon Press, New York. 1959. p. 85.
5. W.C. Herndon. J. Chem. Educ. **44**, 724 (1967).
6. F. Toda, K. Tanaka, H. Krupitsky, and I. Goldberg. Bull. Chem. Soc. Jpn. **66**, 320 (1993).
7. B.M. Craven and G.T. De Titra. J. Chem. Soc. Chem. Commun. 530 (1972).

© 1999 NRC Canada

8. J.C. Costain and G.P. Srivastava. J. Chem. Phys. **35**, 1903 (1961).
9. H.M. Randall, N. Fuson, R.G. Fowler, and J.R. Dangl. Infrared determination of organic structures. D. Van Nostrand Co., Inc. New York. 1949.
10. M. Haurie and A. Novak. J. Chim. Phys. **62**, 137 (1965).
11. Y. Mikawa, J.W. Brasch, and R.J. Jakobsen. J. Mol. Spectrosc. **24**, 314 (1967).
12. N.V. Thiel, E.D. Beker, and G.C. Pimentel. J. Chem. Phys. **27**, 95 (1957).
13. L.J. Bellamy, A.R. Osborn, and R.J. Pace. J. Chem. Soc. 3749 (1963).
14. R. Popowitz-Biro, C.P. Tang, H.C. Chang, M. Lahav, and L. Leiserowitz. J. Am. Chem. Soc. **107**, 4043 (1985).
15. H.S. Shieh, L.G. Hoard, and C.E. Norman. Acta Crystallogr. Sect. B: Struct. Crystallogr. Cryst. Chem. **B37**, 1538 (1981).
16. L.P. Hammet. Physical organic chemistry. McGraw–Hill Book Co., New York. 1970. p. 227.

© 1999 NRC Canada

^{13}C NMR and crystallographic evidence of push–pull effects in furoindolic β-enamino esters

Martha S. Morales-Ríos, Oscar R. Suárez-Castillo, Celina Alvarez-Cisneros, and Pedro Joseph-Nathan

Abstract: A series of cyclic enamine derivatives, stabilized through conjugation with an electron-attracting CO_2Me group at the β-carbon of the enamine system, has been prepared. The influence of substituents at the vinylogous donor NH_2 group on ^{13}C chemical shifts has been investigated, and the results analyzed on the basis of resonance and steric effects on the dipolar charge distribution in the molecule. Intramolecular H-bonding was established for the *N*-methylated enamines **4a** and **4b** based on the high-frequency shift of the NH proton and its solvent immutability. Several deuterium-induced isotope effects on ^{13}C chemical shift [$^n\Delta$C(ND)] due to deuteration at the enamine nitrogen have been measured. The crystal structures of the enamine **1b** and the *N*,*N*-diacetylated enamine **3a**, determined by X-ray analyses, show that these compounds, in the solid state, adopt an *s-trans* disposition around the C—C=O bond, with the carbonyl ester group and the C=C double bond in an almost coplanar conformation. Comparison of bond lengths of **1b** and **3a** in the crystalline state provides information on changes in the extent of *n*–π delocalization arising from the nature of the *N*-substituent.

Key words: β-enamino esters, furo[2,3-*b*]indoles, push–pull effects, ^{13}C NMR, X-ray.

Résumé : On a préparé une série d'énamines cycliques, stabilisées par conjugaison avec un groupe CO_2Me, attracteur d'électron, situé en position β du système énamine. On a étudié l'influence des substituants attachés au groupe NH_2 vinylogue donneur sur les déplacements chimiques en RMN du ^{13}C et on a analysé les résultats en fonction de la résonance et des effets stériques sur la distribution de la charge dipolaire dans la molécule. En se basant sur le déplacement du proton NH vers une haute fréquence et sur son immutabilité dans les solvants, on a pu mettre en évidence la présence d'une liaison hydrogène intramoléculaire dans les énamines *N*-méthylées **4a** et **4b**. Lors de la deutération de l'azote de l'énamine, on a pu mesurer plusieurs effets isotopiques induits par le deutérium sur le déplacement chimique du ^{13}C [$^n\Delta$C(ND)]. Faisant appel à la diffraction des rayons X, on a déterminé les structures cristallines de l'énamine **1b** et de l'énamine *N*,*N*-diacétylée, **3a**; elles montrent que, à l'état solide, ces composés adoptent une disposition *s-trans* autour de la liaison C—C=O alors que le groupe carbonyle de l'ester et la double liaison C=C se trouvent pratiquement dans une conformation coplanaire. Une comparaison des longueurs des liaisons dans les composés **1b** et **3a** à l'état solide fournit de l'information sur les changements dans l'amplitude de la délocalisation *n*–π découlant de la nature du substituant fixé sur l'azote.

Mots clés : β-énaminoesters, furo[2,3-*b*]indoles, effet «push–pull», RMN du ^{13}C, rayons X.

[Traduit par la Rédaction]

Introduction

The structures of β-enamino esters (see reviews, ref. 1) have been extensively studied, considering a variety of factors such as hydrogen-bond pattern (2), tautomerism involving the imine–enamine forms (3), *cis*/*trans* isomerism about the olefinic C=C double bond (4), and barriers to rotation around the N—C(sp^2) and C(sp^2)—CO_2R single bonds (5) in combination with the electron distribution inside these mesomeric systems. As in similar push–pull olefins, NMR spectroscopy combined with X-ray studies can provide information on these matters. In continuation of our studies on furoindolic β-enamino esters (6), we present herein detailed assignment of the ^{13}C NMR spectra of dihydro-2-amino-3-carbomethoxyfuro[2,3-*b*]indoles **1a**–**1d**. We also discuss the ^{13}C chemical shift variations in the so-called push–pull system caused by changing one or both protons attached to the vinylogous donor NH_2 group for electron-releasing and electron-withdrawing substituents in the series **1a**–**1d** (Scheme 1). The corresponding mono and doubly acetylated β-enamino esters were prepared by treatment with acetic anhydride (7). In this work, we emphasize the importance of bond lengths, obtained by X-ray analyses, in revealing the extent of *n*–π delocalization of the enaminocarbonyl framework (N—C=C—C=O). Thus, an increase in *n*–π overlap is expected to be accompanied by a shortening of the N—C and C—C single bond distances, and by a lengthening of the C=C double bond distance (8).

Received June 18, 1998.

M.S. Morales-Ríos, O.R. Suárez-Castillo, C. Alvarez-Cisneros, and P. Joseph-Nathan.[1] Departamento de Química del Centro de Investigación y de Estudios Avanzados, Instituto Politécnico Nacional, Apartado 14-740, México, D.F., 07000 México.

[1]Author to whom correspondence may be addressed. Telephone: (52) 5747-7112. Fax: (52) 5747-7113. e-mail: pjoseph@nathan.chem.cinvestav.mx

© 1999 NRC Canada

Scheme 1. Reagents and conditions: *i*, AcONa, Ac_2O, 90°C, 4 h; *ii*, pyridine, Ac_2O, 110°C, 1 h; *iii*, K_2CO_3, Me_2SO_4, acetone, 50°C, 8 days.

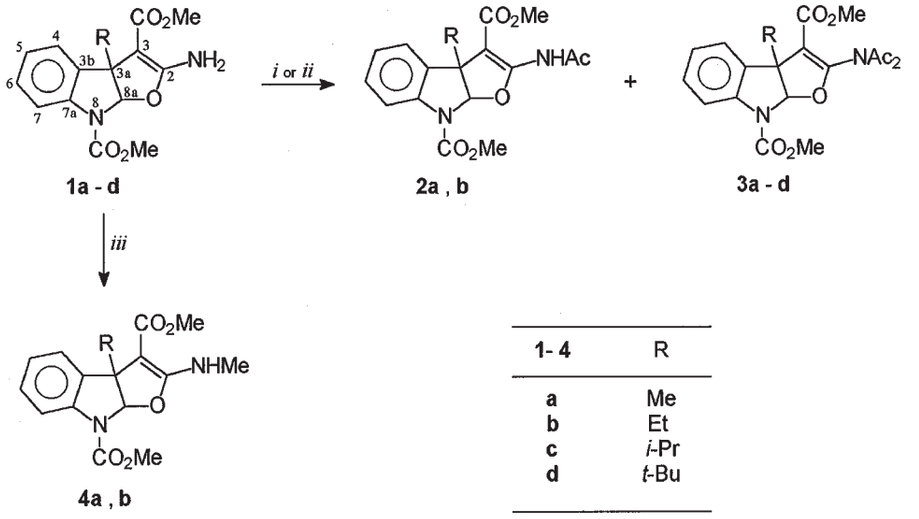

1- 4	R
a	Me
b	Et
c	*i*-Pr
d	*t*-Bu

The intramolecular H-bonding in aminocarbonyl systems has been recently approached by the study of secondary deuterium isotope effects on the ^{13}C, ^{15}N, and ^{17}O nuclear shielding [$^n\Delta X(ND)$] (9, 10). In the case of the ^{13}C nuclear shielding, it has been shown that the deuteration of the amino nitrogen, involved in an intramolecular H-bond, produces a relatively large low-frequency shift on the resonance of the nitrogen-bearing carbon atom, the magnitude of which correlates with the H-bond energy (11). To evaluate the substituent effects on H-bonding, the ^{13}C NMR spectra of the β-enamino esters **1b**, **2b**, and **4b**, partially deuterated at the enamine nitrogen, have been investigated.

Results and discussion

Preparation of *N*-substituted enamines 2–4

Furoindolic β-enamino esters **1a**–**1d** (R = Me, Et, i-Pr, *t*-Bu) were synthesized by rearrangement of the corresponding α-cyano-γ-butyrolactones (6). Critical reaction conditions were required for the preparation of *N*-acetyl and *N*,*N*-diacetyl substituted enamines **2** and **3.** The significant stability of the amino group and, therefore, the rather weak nucleophilicity of the nitrogen atom arise from an expected extended conjugation of the enamine moiety with the carbonyl ester group, which increases the *n*–π overlap in the system. Treatment of β-enamino esters **1a**,**1b** (R = Me, Et) with acetic anhydride and sodium acetate afforded a mixture of monoacetylated compounds **2a**,**2b** and the corresponding diacetylated compounds **3a**,**3b** in an overall yield of ca. 80%, and in a nearly 1:1 ratio, as determined by ^1H NMR analysis of the crude reaction outcome. These reactions were conducted in the presence of 0.1 equiv. of NaOAc at 90°C and were completed within 1 h, as revealed by TLC. The reactions can easily be monitored by TLC, since enamines are more polar than their corresponding diacetylated derivatives, but less polar than the monoacetylated compounds. An increase either in the reaction time, sodium acetate amount, or in the reaction temperature results in significant decomposition. The conversion of enamines **1a–1d** to the corresponding diacetyl derivatives **3a**–**3d** was improved using pyridine instead of sodium acetate. In this way yields increased from 40% to 75–85% at the expense of the monoacetyl derivatives **2**, which were formed in yields ranging from 2 to 11%. It should be noted that the pyridine-catalyzed reaction occurs at 110°C. Pure samples of each of these compounds were obtained after chromatographic separation.

N-Alkylation of enamines with a tetrasubstituted double bond, **1a**,**1b,** was carried out by treatment with excess dimethyl sulfate, at reflux in dry acetone for 8 days. In this way, only the corresponding monosubstituted compounds **4a**,**4b** were obtained in a nearly quantitative yield.

^{13}C NMR and push–pull effect

The pertinent ^{13}C chemical shifts for compounds in series **1–4** are summarized in Table 1. Straightforward evidence for the assignment of the ^{13}C resonances was obtained from selective double resonance ^1H,^{13}C experiments, C–H coupling constants, deuterium isotope effects, and the usual expectation of self-consistent substituent chemical shift effects. From the ^1H and ^{13}C NMR spectra it follows that the *Z*-fixed cyclic β-enamino esters **1–4** appear to exist in $(CD_3)_2SO$ solution exclusively as the enamino tautomer, and rotamers around the C2—N and C3—CO_2Me bonds were not found. The protonated carbons were assigned from HETCOR experiments and the unprotonated carbons were assigned with the aid of multiple-bond ^1H,^{13}C FLOCK correlation experiments. These experiments, for **1a–4a**, showed relevant cross peaks corresponding to $^3J_{CH}$ couplings between the protons of the methyl group attached to C3a and the carbons C3 and C3b. Informative cross peaks, which allow differentiation between C3b and C7a, were also visible between H5/C3b and H5/C7. The signal due to the carbonyl ester group, which appears to be very close or coincident with that owing to C2 in compounds **1a**–**1d** and **4a**, was identified by its long-range coupling $^3J_{CH}$ to the CO_2Me protons. In addition, H8a showed a cross peak to the C2 and C3 carbons in compound **3a**. The ^{13}C NMR spectra display the carbamate carbonyl signal in the expected chemical shift region

© 1999 NRC Canada

Table 1. ^{13}C NMR chemical shifts (ppm) of β-enamino esters **2–4** and chemical shift difference $\Delta\delta = \delta_{C2} - \delta_{C3}$.

Compound	C2	C3	C3a	C3b	C4	C5	C6	C7	C7a	C8a	Δδ
1a	166.2	79.5	53.0	138.0	124.1	123.8	127.8	114.2	139.2	99.7	86.7
1b	165.8	76.9	57.4	136.9	123.9	123.5	127.5	113.9	139.5	96.9	88.9
1c	165.7	77.4	61.4	136.7	123.6	123.5	127.6	113.8	139.5	93.8	88.3
1d	166.1	77.2	63.9	133.6	126.9	122.6	127.4	113.8	140.2	96.1	88.9
2a	158.0	92.0	52.9	136.0	124.1	123.8	128.1	114.3	139.5	100.4	66.0
2b	158.2	90.1	57.6	135.0	124.1	123.7	128.1	114.2	139.9	97.9	68.1
3a	156.4	108.2	54.5	133.9	124.3	123.7	128.5	114.1	139.9	99.5	48.2
3b	156.9	106.6	59.5	133.2	124.4	123.8	128.6	114.2	140.2	97.1	50.3
3c	156.5	107.1	63.4	132.7	124.0	123.9	128.6	114.0	140.2	94.0	49.4
3d	157.0	107.2	66.2	130.1	127.5	123.0	128.5	114.0	140.7	96.2	49.8
4a	165.9	78.4	52.7	138.0	123.7	123.6	127.4	114.1	138.9	99.9	87.5
4b	166.1	76.2	57.4	137.2	123.9	123.7	127.5	114.1	139.4	97.4	89.9

Note: **1a**: CO 166.2, NCO 152.9, 2 OMe (carbamate, ester) 53.3, 49.9, Me 24.2. **1b**: CO 166.5, NCO 152.5, 2 OMe 53.0, 49.5, *C*H_2CH$_3$ 27.8, CH$_2$*C*H$_3$ 8.8. **1c**: CO 166.2, NCO 152.4, 2 OMe 53.1, 49.6, CH 30.1, 2 Me 17.5, 16.4. **1d**: CO 167.4, NCO 152.4, 2 OMe 53.2, 49.4, *C*Me$_3$ 36.8, C*Me*$_3$ 26.4. **2a**: *C*OMe 167.5, CO 165.2, NCO 152.6, 2 OMe 53.3, 50.1, CO*Me* 24.1, Me 23.6. **2b**: COMe 167.4, CO 165.1, NCO 152.5, 2 OMe 53.2, 50.8, *C*H_2CH$_3$ 27.6, CO*Me* 24.0, CH$_2$CH$_3$ 8.6. **3a**: 2 *C*OMe 169.9, CO 162.3, NCO 152.5, 2 OMe 53.2, 51.5, 2 CO*Me* 24.7, Me 23.0. **3b**: 2 *C*OMe 170.0, CO 162.4, NCO 152.5, 2 OMe 53.3, 51.7, *C*H$_2$CH$_3$ 27.9, 2 CO*Me* 24.8, CH$_2$*C*H$_3$ 8.9. **3c**: 2 *C*OMe 169.9, CO 162.3, NCO 152.2, 2 OMe 53.4, 51.7, CH 30.9, 2 CO*Me* 24.8, 2 Me 17.7, 15.8. **3d**: 2 *C*OMe 170.0, CO 163.2, NCO 152.1, 2 OMe 53.4, 51.7, *C*Me$_3$ 37.0, C*Me*$_3$ 26.0, 2 CO*Me* 24.8. **4a**: CO 165.9, NCO 152.6, 2 OMe 53.1, 49.4, NMe 28.0, Me 24.0. **4b**: CO 166.1, NCO 152.6, 2 OMe 53.2, 49.5, NMe 28.0, *C*H_2CH$_3$ 27.9, CH$_2$*C*H$_3$ 8.8.

Table 2. Mulliken atomic charges of enamines **1a–4a**.

	C2	C3		C2	C3
1a	0.125	–0.362	**3a**	0.190	–0.266
2a	0.158	–0.372	**4a**	0.148	–0.373

of δ 153–155 ppm (12). Assignment of the two coincident acetyl carbonyl peaks in **3a–3d** was assisted by considering their relative intensities and the two-bond coupling constants. The values of these coupling constants further allowed assignment of the acetyl carbonyl in **2a**,**2b**. The olefinic carbons in compounds **1b**, **2b**, and **4b** were further evidenced, in some cases, by the resolved deuterium isotope shift effects, which caused additional splitting of both C2 and C3 resonances.

Comparison of the data in Table 1 reveals the β- and γ-effects exerted by the alkyl group on the chemical shifts in series **1a**–**1d** and **3a**–**3d**. These effects are the result of adding methyl groups on going through the series Me, Et, i-Pr, *t*-Bu. Thus, C3a moves to lower frequency as the alkyl group increases, while for C3 and C3b the reverse situation is true. Although the chemical shift variations of C8a are less systematic than those observed for C3 and C3b, the tendency to higher frequency is also seen. The chemical shifts for the remaining carbons are almost unchanged.

Series **1–4** provide a useful set for investigating the push–pull effect. It is apparent from analysis of the ^{13}C chemical shifts for the donor- and acceptor-substituted carbons C2 and C3 that the C2 signal (165.9 ± 0.2 ppm) in **1a–1d** is significantly less shielded than the corresponding C2 signal in dihydrofuran (145.6 ppm). At the same time, the signal due to the acceptor-substituted carbon C3 (78.2 ± 1.3 ppm) for the same compounds is significantly more shielded than the corresponding C3 signal in dihydrofuran (98.4 ppm) (13). These differences demonstrate, as in other push–pull olefins (14), a strong *n*–π delocalization with appreciable charge polarization of the enaminocarbonyl framework. The electron delocalization in these compounds is reflected in a large chemical shift difference (Δδ) (15) of ca. 88 ppm between the olefinic C2 and C3 carbons ($\Delta\delta = \delta_{C2} - \delta_{C3}$). This Δδ is in the range of other push–pull alkenes in which the acceptor ester group at C3 promotes more extensive charge delocalization (14*a*). These findings are, further, in accord with the observed reactivity described above for the β-enamino esters **1a–1d**.

Inspection of Table 1 shows that for R = Me in **1–3**, the *N*-acetyl substitution causes a dramatic effect on the C3 chemical shifts. The C3 carbon signal moves gradually to a higher frequency in the order NH_2 < NHAc < NAc_2, whereas that of the C2 carbon is shifted to a lower frequency. This difference is attributed to the electron-withdrawing and steric effects of the *N*-acetyl group that reduce or prevent the conjugation of the nitrogen electron lone pair with the enamine double bond, thus resulting in a large redistribution of π-electron charge density within this residue. The pronounced twisting of the NAc_2 group out of the plane of the C=C-CO_2Me system in **3a**, with the consequent nil *n*–π overlap, was confirmed by X-ray analysis and geometry optimization using MO calculation, vide infra. The ^{13}C chemical shift difference Δδ in compounds **1a–3a** varies from 86 to 48 ppm. This variation is associated with the decreasing polarization of the enamine double bond in the order NH_2 > NHAc > NAc_2. Similar results were observed for R = Et in **1–3**. Methyl substitution at the vinylogous donor NH_2 group has only a small effect on the chemical shifts. When comparing **4a**, **4b** with **1a**, **1b** in Table 1, we note a very small lower frequency shift of C3, leading to an increase in Δδ of about 1 ppm.

The results (Table 2) of PM3 semiempirical calculation of the atomic charges in compounds **1a–4a** are in line with the expected electronic behavior of the β-enamino esters studied, where C2 is positive while C3 is negative. The largest positive charge at C2 (0.190) as well as the smallest negative charge at C3 (0.266) were obtained for the diacetylated enamine **3a**. The Mulliken atomic charge difference between C2 and C3 decreases in the order **1a** > **4a** > **2a** > **3a**, in ac-

© 1999 NRC Canada

Table 3. Deuterium-induced isotope effects on ^{13}C chemical shifts ($^{n}\Delta$, in ppb) and N*H* chemical shifts (δ, in ppm) of enamines **1b**, **2b,** and **4b.**

	$^{2}\Delta$			$^{3}\Delta$		δ N*H*	
	C2	C=O	Me	C3	Me	In $CDCl_3$	In DMSO-d_6
1b[a]	–75	—	—	–11	—	5.80 very br	7.19br
2b[b]	–135	–64	—	[c]	–45	9.94br	9.95br
4b[a]	[d]	[d]	–66	–29	—	7.15br	7.20

[a] $^{n}\Delta$ in DMSO-d_6, where n = number of intervening bonds.

[b] $^{n}\Delta$ in $CDCl_3$.

[c] Not resolved.

[d] Overlapped.

cord with the decreasing polarization of the enamine double bond.

Isotope effects and hydrogen bonding

A summary of deuterium isotope effects on ^{13}C chemical shifts due to partial deuteration at the enamine nitrogen atom [$^{n}\Delta$C(ND)] for compounds **1b**, **2b**, and **4b**, measured in either DMSO-d_6 or $CDCl_3$, as well as the corresponding NH proton chemical shifts, measured in both DMSO-d_6 and $CDCl_3$, is given in Table 3. Only low-frequency deuterium-induced chemical shifts were observed (negative sign). For **1b**, both amino protons may be partially deuterium exchanged, and therefore the signals due to C2 and C3 in the ^{1}H decoupled ^{13}C NMR spectra show three resonances per nucleus, owing to the isotopomeric ternary mixture constituted by the NH_2, NHD, and ND_2 species. In these multiplets the signal at lower frequency arises from the ND_2 species. The two-bond isotope effect on C2 ($^{2}\Delta$C2 = –75 ppb) was small, as judged from the effects normally found for hydrogen-bonded enamino esters (–156 to –214 ppb) (9*a*, 9*c*, 16). The small isotope effect at C2, as well as the observed low-frequency shift of the NH_2 protons in $CDCl_3$ (δ = 5.80 ppm) must be average values resulting from an exchange between the free hydrogen and its hydrogen-bonded partner. A small three-bond isotope effect on C3 ($^{3}\Delta$C3 = –11 ppb) was also observed.

Measurement of the ^{13}C NMR spectrum of partially deuterated **2b** in DMSO-d_6 shows the ^{13}C lines substantially broadened, and therefore the $^{n}\Delta$C(ND) values were determined in $CDCl_3$. The relatively large $^{2}\Delta$C2 effect caused by deuterium substitution of the amide NH proton can be associated with the corresponding high-frequency shift of this NH proton (δ = 9.94 ppm in $CDCl_3$). We have already demonstrated that $^{2}\Delta$C(ND) are valuable in describing cross-conjugated systems of the type C(sp^2)-NH(D)-C(sp^2), such as indoles, acetanilides, and benzanilides (17*a*–*d*). In this work, we further described the application of $^{2}\Delta$ isotope effects to account for the competitive interplay of electronic delocalization. Thus, an interesting feature is that the $^{2}\Delta$ isotope effect at C2 in **2b** (–135 ppb) is significantly larger than that observed at the amide carbonyl carbon ($^{2}\Delta$C=O = –64 ppb), the origin of this large difference (71 ppb) can be attributed to a strong conjugative interaction between the nitrogen lone pair and the C2=C3-CO_2Me fragment (17*b*, *c*), and consequently an increase in the N—C2 bond order. The three-bond isotope effect $^{3}\Delta$C3 was not resolved in **2b**.

Compounds **4a** and **4b** exist in the *Z-s-cis* conformation as a result of stabilization through the intramolecular H-bond between the C=O oxygen and the NH hydrogen. The H-bond formation in the *N*-methylated enamines **4a** and **4b** has been established, based on the observed high-frequency shift of the N-H proton chemical shift (δ = 7.15 ppm in $CDCl_3$) when compared with those of related compounds (18). The same conclusion is reached from the observed immutability of the corresponding ^{1}H NMR spectra (in $CDCl_3$) upon dilution. The H-bonding formation in compounds **4a**, **4b** is further related to the donor nature and steric requirements of the methyl group, which contribute to the approach of the groups involved in the H-bonding. It is worth noting that the corresponding $^{2}\Delta$ isotope effects in **4a** and **4b** cannot be seen as the N*H* resonance is somewhat broad and the signals owing to the olefinic C2 carbon and the carbonyl ester group overlapped. Isotope effects at the olefinic C3 carbon and at the *N*-Me group were measured in compound **4b** ($^{3}\Delta$ = –29 and $^{2}\Delta$ = –66 ppb, respectively).

X-ray structure determination

The higher degree of n–π overlap of enamines **1** as compared to the corresponding mono- or diacetylated enamines **2** or **3**, initially inferred from ^{13}C NMR evidence, was fully corroborated by single-crystal X-ray analysis of **1b** and **3a**. The molecular structures are shown in Figs. 1 and 2, respectively. Details of the structure determination are found in Table 4.[2] Selected bond lengths and angles are compared in Table 5. The molecular structures exhibit a *syn*-periplanar orientation of the C13 carbon atom of the alkyl group and the H8a proton along the C3a—C8a bond (dihedral angle C13-C3a-C8a-H8a of 9.9° for **1b** and of 3.2° for **3a**). The two virtually planar pyrrole and furane rings are *cis* ring-fused. The overall shape of the molecules is therefore bent. The carbonate N8 atom has, in both cases, a trigonal planar geometry, with an average of bond angles around N8 close to 120°. The short N8—C11 bond lengths (1.362(6), 1.361(6) Å), as compared with a carbon–nitrogen single bond (1.477–1.467 Å) (19), are indicative of the participation of the nitrogen lone pair in the respective N8—C11

[2] Tables of atomic coordinates, complete bond lengths and angles, and other refinement data may be purchased from: The Depository of Unpublished Data, Document Delivery, CISTI, National Research Council Canada, Ottawa, Canada K1A 0S2. This supplementary material has also been deposited with the Cambridge Crystallographic Data Center, and can be obtained on request from The Director, Cambridge Crystallographic Data Center, University Chemical Laboratory, 12 Union Road, Cambridge, CB2 1EZ, U. K.

© 1999 NRC Canada

Fig. 1. Perspective view of **1b**.

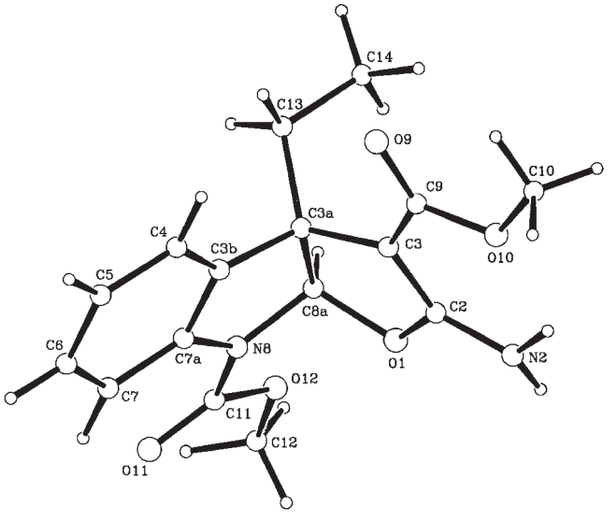

Fig. 2. Perspective view of **3a**.

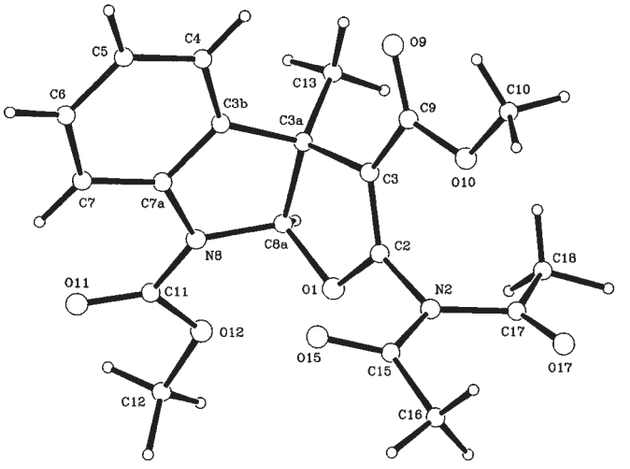

bonds. The carbonyl carbamate group is in an *E* configuration with C8a along the N8—C11 bond (dihedral angle, O11-C11-N8-C8a of –179.3° for **1b** and of –176.2° for **3a**).

A feature that is apparent from Fig. 1 is that one of the N—H bonds in **1b** almost eclipses the C2=C3 bond (dihedral angle C3-C2-N2-H2a is –13.8°), whereas molecule **3a** (Fig. 2) adopts a conformation in which the double bond C2=C3 bisects the C15-N2-C17 angle (dihedral angles C3-C2-N2-C15 and C3-C2-N2-C17 of 96.7° and –75.5°, respectively) in order to minimize the steric strain introduced by the relatively bulky acetyl groups at N2 (20). These results are in agreement with the PM3 geometry optimization (dihedral angles C3-C2-N2-C15 and C3-C2-N2-C17 of 97.2° and –75.2°, respectively). It is also clear from the molecular diagram of **3a** (Fig. 2) that the O15 atom of an acetyl group is oriented to the concave side of the molecule, and exhibits a *syn*-periplanar conformation with the C2—N2 bond (dihedral angle C2-N2-C15-O15 of –0.7°), whereas in the other acetyl group the O17 atom is oriented away from the C2—N2 bond (dihedral angle C2-N2-C17-O17 of 163.2°). A comparison of the bond lengths in **1b** and **3a** provides information on changes in the extent of n–π overlap in these enamine systems (8, 21). An increase in n–π overlap in **1b** with respect to **3a** is accompanied by a shortening of both the N(2)—C(2) and C(3)—C(9) distances by 0.08 and 0.04 Å, respectively, while the C(2)—C(3) bond is lengthened by about 0.03 Å. The geometry around the enamine N2 atom in **3a** is similar to N8, trigonal planar (sum of the angles 359.3°). As far as the carbonyl ester group is concerned, in both compounds **1b** and **3a**, it is found in an almost *anti*-periplanar conformation with the C=C double bond (dihedral angle C2-C3-C9-O9 of 176.3 for **1b** and of –175.5° for **3a**).

Experimental

Analytical TLC was carried out on precoated plates (Aldrich silica gel 60 F 254) and the products were visualized with UV light (254 nm). Silica gel used for column chromatography was Merck 60. Melting points were measured on a microscopic Fisher–Johns apparatus and are uncorrected. IR spectra were obtained using a Perkin Elmer 727B spectrophotometer; only diagnostic peaks are reported. ^{1}H and ^{13}C NMR spectra were recorded on a Varian XL300GS spectrometer working at 300 and 75.4 MHz, respectively, in DMSO-d_6 solutions with $SiMe_4$ as internal standard. Multiplicities are indicated by one or more of the following: s (singlet), d (doublet), t (triplet), h (heptet), m (multiplet), br (broad); the list of coupling constants (J in Hz) corresponds to the order of the multiplicity assignment. Elemental analysis was performed by the MHW Laboratories, Phoenix, Ariz., U.S.A. Electron impact mass spectra (EIMS) were recorded on a Hewlett Packard 5989A spectrometer. High-resolution mass spectra (HRMS) were measured on a Jeol JMS-SX 102A spectrometer. Semiempirical MO calculations were performed by using the PM3 program (22). The dihydro-2-amino-3-carbomethoxyfuro[2,3-*b*]indoles **1a–1d** were prepared as previously described (6).

General procedure for the acetylation of *cis*-(±)-dimethyl 3a,8a-dihydro-3a-alkyl-2-amino-8*H*-furo[2,3-*b*]indole-3,8-dicarboxylates 1a–1d

Method A

The appropriate furoindolic β-enamino ester (**1a** or **1b**) (0.30 mmol) was stirred with sodium acetate (0.1 equiv.) in acetic anhydride (5 mL) at 90°C for 4 h until TLC analysis indicated complete loss of starting material. The solvent was evaporated under reduced pressure and the residue was dissolved in ethyl acetate, washed with saturated NH_4Cl solution (2 × 10 mL), dried (Na_2SO_4), and evaporated. The oily residue was chromatographed on silica gel eluting with hexane – diethyl ether (2:3) to afford successively the corresponding diacetylated (**3a** or **3b**) and monoacetylated (**2a** or **2b**) compounds in a ratio of ca. 1:1.

Method B

The appropriate furoindolic β-enamino ester (**1a–1d**) (0.30 mmol) was dissolved in a mixture of acetic anhydride (5 mL) and pyridine (1 mL). The solution was stirred at

© 1999 NRC Canada

Table 4. Crystallographic data.

Compound	**1b**	**3a**
A. Crystal parameters		
Formula	$C_{16}H_{18}N_2O_5$	$C_{19}H_{20}N_2O_7$
fw	318. 33	388.38
Crystal system	Monoclinic	Monoclinic
Space group	$P2_1/a$	$P2_1/c$
Crystal size, mm	0.04 × 0.20 × 0.40	0.12 × 0.06 × 0.28
a, Å	13.232(4)	7.795(5)
b, Å	7.080(2)	19.89(1)
c, Å	18.090(6)	12.276(7)
β, deg	116.40(2)	95.45(3)
V, Å^3	1518(1)	1894(3)
ρ_{calc}, g cm^{-3}	1. 393	1.361
Z	4	4
F(000)	672	816
B. Data collection parameters		
μ, cm^{-1}	8.31	8.43
Temperature, K	298	298
2θ range, deg	3–110	3–110
Scan speed, deg min^{-1}	3.0 (in 2θ)	3.0 (in 2θ)
Absorption correction	Empirical	Empirical
Exposure time, h	39.5	48.5
Reflections collected	2212	2683
Unique reflections	1910	2378
Data with $I \geq 3\sigma(I)$	1445	1733
C. Structure refinement		
Reflections for final refinement	1182	1416
Solution method	Direct methods	Direct methods
Parameters refined	208	253
R (*F*)[a], %	5.3	5.3
R (*W*)[b], %	6.1	6.3
Goodness of fit for the last cycle	1.716	1.844
Residual electron density, e Å^{-3}	0.61	0.36

[a]$R\ (F) = \Sigma\ ||F_o| - |F_c|| / \Sigma|F_o|$.

[b]$R\ (W) = (\Sigma w\ (|F_o| - |F_c|)^2 / \Sigma w|F_o|^2)^{1/2}$.

Table 5. Selected bond distances (Å) and angles (°).

Bond(s)	**1b**	**3a**	Bond(s)	**3a**
C(2)—C(3)	1.367(6)	1.340(5)	N(2)—C(15)	1.409(6)
N(2)—C(2)	1.320(6)	1.402(6)	N(2)—C(17)	1.413(6)
C(3)—C(9)	1.413(6)	1.455(6)	C(15)—O(15)	1.218(6)
C(9)—O(9)	1.219(5)	1.218(5)	C(17)—O(17)	1.196(6)
N(8)—C(11)	1.362(6)	1.361(6)		
C(11)—O(11)	1.197(6)	1.196(6)		
C(7a)-N(8)-C(8a)	110.4(4)	110.2(3)	C(2)-N(2)-C(15)	114.3(4)
C(7a)-N(8)-C(11)	125.4(4)	125.1(4)	C(2)-N(2)-C(17)	120.2(4)
C(8a)-N(8)-C(11)	124.1(4)	124.0(4)	C(15)-N(2)-C(17)	125.0(4)

110°C for 1 h until TLC analysis indicated complete loss of starting material. After work-up as in method A, the oily residue was chromatographed on silica gel eluting with hexane – diethyl ether (2:3) to afford the corresponding compounds **3a–3d** along with small amounts of **2a**–**2d**.

***cis*-(±)-Dimethyl 3a,8a-dihydro-2-acetylamino-3a-methyl-8*H*-furo[2,3-*b*]indole-3,8-dicarboxylate (2a)**

The title compound was prepared by methods A and B in 37 and 11% yield, respectively. The product was obtained as

© 1999 NRC Canada

a colourless oil. IR ν_{max} /cm^{-1}: 1729, 1665, 1624; ^{1}H NMR δ: 9.88 (1 H, s, NHAc), 7.67 (1 H, br s, H7), 7.52 (1 H, dd, *J* 7.6, 1.2, H4), 7.24 (1 H, td, *J* 7.6, 1.2, H6), 7.04 (1 H, td, *J* 7.6, 1.0, H5), 6.44 (1 H, s, H8a), 3.83 (3 H, s, OMe carbamate), 3.71 (3 H, s, OMe ester), 2.06 (3 H, s, COMe), 1.64 (3 H, s, Me); MS *m*/*z*: 346.3 (M$^+$, 28%) and 255.3 (100); HRMS calcd. for $C_{17}H_{18}O_6N_2$, *M*: 346.1165; found: 346.1170.

***cis*-(±)-Dimethyl 3a,8a-dihydro-2-acetylamino-3a-ethyl-8*H*-furo[2,3-*b*]indole-3,8-dicarboxylate (2b)**

The title compound was prepared by methods A and B in 38 and 5% yield, respectively. The product was crystallized from diethyl ether – hexane as colourless crystals, mp 135–137°C; IR ν_{max} /cm^{-1}: 1728, 1670, 1624; ^{1}H NMR δ: 9.95 (1 H, s, NHAc), 7.71 (1 H, br s, H7), 7.51 (1 H, dd, *J* 7.6, 1.0, H4), 7.26 (1 H, td, *J* 7.8, 1.3, H6), 7.06 (1 H, td, *J* 7.5, 1.0, H5), 6.51 (1 H, s, H8a), 3.86 (3 H, s, OMe carbamate), 3.72 (3 H, s, OMe ester), 2.23 and 1.92 (2 H, 2 m, *C*H$_2$CH$_3$), 2.09 (3 H, s, COMe), 0.78 (3 H, t, CH$_2$*C*H$_3$); MS *m*/*z*: 360.3 (M$^+$, 24%) and 269.3 (100); HRMS calcd. for $C_{18}H_{20}O_6N_2$, *M*: 360.1321; found: 360.1321.

***cis*-(±)-Dimethyl 3a,8a-dihydro-2-diacetylamino-3a-methyl-8*H*-furo[2,3-*b*]indole-3,8-dicarboxylate (3)**

The title compound was prepared by methods A and B in 40 and 82% yield, respectively, and crystallized from diethyl ether – hexane as colourless crystals, mp 152–155°C; IR ν_{max}/cm^{-1}: 1728, 1656; ^{1}H NMR δ: 7.73 (1 H, br d, *J* 6.0, H7), 7.54 (1 H, dd, *J* 7.5, 1.2, H4), 7.28 (1 H, td, *J* 7.5, 1.2, H6), 7.07 (1 H, td, *J* 7.5, 1.1, H5), 6.57 (1 H, s, H8a), 3.82 (3 H, s, OMe carbamate), 3.69 (3 H, s, OMe ester), 2.20 (6 H, br s, 2 COMe), 1.72 (3 H, s, Me); MS *m*/*z*: 388 (M$^+$, 4%), 287 (100), and 255 (93); HRMS calcd. for $C_{19}H_{20}O_7N_2$, *M*: 388.1271; found: 388.1268. Anal. calcd. for $C_{19}H_{20}O_7N_2$: C 58.76, H 5.19, N 7.21; found: C 58.80, H 5.30, N 7.21.

***cis*-(±)-Dimethyl 3a,8a-dihydro-2-diacetylamino-3a-ethyl-8*H*-furo[2,3-*b*]indole-3,8-dicarboxylate (3b)**

The title compound was prepared by methods A and B in 41 and 75% yield, respectively, and crystallized from diethyl ether – hexane as colourless crystals, mp 118–120°C; IR ν_{max} /cm^{-1}: 1728, 1654; ^{1}H NMR δ: 7.73 (1 H, br d, *J* 6.8, H7), 7.50 (1 H, dd, *J* 7.2, 1.0, H4), 7.28 (1 H, td, *J* 7.5, 1.3, H6), 7.06 (1 H, td, *J* 7.5, 1.0, H5), 6.62 (1 H, s, H8a), 3.82 (3 H, s, OMe carbamate), 3.68 (3 H, s, OMe ester), 2.34 and 1.92 (2 H, 2 m, *C*H$_2$CH$_3$), 2.19 (6 H, br s, 2 COMe), 0.86 (3 H, t, CH$_2$*C*H$_3$); MS *m*/*z*: 402.3 (M$^+$, 35%) and 269.3 (100); HRMS calcd. for $C_{20}H_{22}O_7N_2$, *M*: 402.1427; found: 402.1415.

***cis*-(±)-Dimethyl 3a,8a-dihydro-2-diacetylamino-3a-isopropyl-8*H*-furo[2,3-*b*]indole-3,8-dicarboxylate (3c)**

The title compound was prepared by method B in 75% yield as an oil; IR ν_{max}/cm^{-1}: 1728, 1656; ^{1}H NMR δ: 7.79 (1 H, br d, *J* 8.0, H7), 7.56 (1 H, d, *J* 8.0, H4), 7.34 (1 H, td, *J* 8.0, 1.3, H6), 7.14 (1 H, td, *J* 8.0, 1.0, H5), 6.65 (1 H, s, H8a), 3.86 (3 H, s, OMe carbamate), 3.70 (3 H, s, OMe ester), 2.93 (1 H, h, CH), 2.19 (6 H, br s, 2 COMe), 1.05 and 0.57 (6 H, 2 d, *J* 7.0, 2 Me); MS *m*/*z*: 416.3 (M$^+$, 9.5%) and 283.3(100); HRMS calcd. for $C_{21}H_{24}O_7N_2$, *M*: 416.1584; found: 416.1587.

***cis*-(±)-Dimethyl 3a,8a-dihydro-2-diacetylamino-3a-*tert*-butyl-8*H*-furo[2,3-*b*]indole-3,8-dicarboxylate (3d)**

The title compound was prepared by method B in 85% yield and crystallized from diethyl ether – hexane as colourless crystals, mp 104–106°C; IR ν_{max}/cm^{-1}: 1728, 1642; ^{1}H NMR δ: 7.85 (1 H, d, *J* 8.0, H4), 7.77 (1 H, br d, *J* 8.0, H7), 7.31 (1 H, td, *J* 8.0, 1.3, H6), 7.09 (1 H, td, *J* 8.0, 1.1, H5), 6.62 (1 H, s, H8a), 3.86 (3 H, s, OMe carbamate), 3.65 (3 H, s, OMe ester), 2.20 (6 H, br s, 2 COMe), 1.02 (9 H, s, CMe$_3$); MS *m*/*z*: 430.3 (M$^+$, 6.3%) and 273.3 (100); HRMS calcd. for $C_{22}H_{26}O_7N_2$, *M*: 430.1740; found: 430.1746.

***cis*-(±)-Dimethyl 3a,8a-dihydro-2-methylamino-3a-methyl-8*H*-furo[2,3-*b*]indole-3,8-dicarboxylate (4a)**

A solution of **1a** (90 mg, 0.3 mmol) in 40 mL of acetone was treated with K_2CO_3 (165 mg, 1.2 mmol) and dimethyl sulfate (0.1 mL, 1.1 mmol). The mixture was stirred at reflux and the reaction followed by TLC. After the starting material disappeared (8 days), the solvent was evaporated under reduced pressure and the residue was dissolved in ethyl acetate (60 mL), washed twice with brine (15 mL), dried (Na_2SO_4), and concentrated. The residue was crystallized in diethyl ether – hexane to give **4a** as colourless crystals. Yield 98%; mp 175–177°C; IR ν_{max} /cm^{-1}: 3682, 3336, 1722, 1674, 1632; ^{1}H NMR δ: 7.64 (1 H, br s, H7), 7.54 (1 H, br d, *J* 7.3, H4), 7.21 (1 H, td, *J* 8.0, 1.4, H6), 7.20 (1 H, br s, N*H*Me),7.02 (1 H, td, *J* 8.0, 1.0, H5), 6.29 (1 H, s, H8a), 3.85 (3 H, s, OMe carbamate), 3.63 (3 H, s, OMe ester), 2.77 (3 H, d, J 5.0, NH*Me*), 1.61 (3 H, s, Me); MS *m*/*z*: 318.3 (M$^+$, 28.5%) and 255.3 (100); HRMS calcd. for $C_{16}H_{18}O_5N_2$, *M*: 318.1216; found: 318.1219.

***cis*-(±)-Dimethyl 3a,8a-dihydro-3a-ethyl-2-methylamino-8*H*-furo[2,3-*b*]indole-3,8-dicarboxylate (4b)**

The title compound was prepared following the above procedure starting from **1b**. After work-up, the oily residue was chromatographed on silica gel eluting with hexane – diethyl ether (2:3) to afford **4b** as a colourless oil, in 92% yield; IR ν_{max} /cm^{-1}: 3480, 3336, 1720, 1667; ^{1}H NMR δ: 7.66 (1 H, br s, H7), 7.52 (1 H, br d, *J* 7.1, H4), 7.21 (1 H, td, *J* 7.8, 1.3, H6), 7.21 (1 H, br s, N*H*Me),7.03 (1 H, td, *J* 7.5, 1.0, H5), 6.34 (1 H, s, H8a), 3.87 (3 H, s, OMe carbamate), 3.64 (3 H, s, OMe ester), 2.79 (3 H, d, J 5.1, NH*Me*), 2.16 and 1.90 (2 H, 2 m, *C*H$_2$CH$_3$), 0.73 (3 H, t, CH$_2$*C*H$_3$); MS *m*/*z*: 332.3 (M$^+$, 100%), 301.3 (27), and 269.3 (62).

X-ray crystallographic analyses

Crystallographic data appear in Table 3. The X-ray structures were determined using a Nicolet R3m diffractometer with the θ–2θ scan technique, Cu-Kα radiation (λ = 1.54178 Å), graphite monochromator. The final unit-cell parameters

© 1999 NRC Canada

were obtained by least squares on the setting angles for 9 reflections for **1b** and for 16 reflections for **3a**. The intensities of two standard reflections, measured every 98 reflections throughout the data collections, showed no significant variation. The data were corrected for Lorentz and polarization effects and for absorption (based on azimuthal scans).

The structures were solved by direct methods using SHELX86. The hydrogen atoms were refined isotropically. The hydrogen atoms for the NH_2 group in **1b** and one hydrogen atom for all the methyl groups in **1b** and **3a** were located on a difference map, and all remaining hydrogen atoms of both compounds were fixed in calculated positions with C—H = 1.00 Å. Non-hydrogen atoms were refined anisotropically. Values given for $R(F)$, $R(W)$, and goodness of fit are based on those reflections with $I \geq 3\sigma(I)$. After removal of the redundant reflections, a few additional reflections were also removed by hand to improve the final fit.

Acknowledgments

This work was supported in part by CONACYT México. We thank I.Q. Luis Velasco Ibarra (Instituto de Química, UNAM) for recording the HRMS.

References

1. (*a*) J.L. Chiara and A. Gómez-Sánchez. *In* The chemistry of enamines. *Edited by* Z. Rappoport. Wiley, Chichester, U.K. 1994. Chap. 5, pp. 353–360; (*b*) H. Wamhoff. Adv. Heterocycl. Chem. **38**, 300 (1985).
2. (*a*) G.O. Dudek. J. Org. Chem. **30**, 548 (1965); (*b*) G.O. Dudek and G.P. Volpp. J. Am. Chem. Soc. **85**, 2697 (1963); (*c*) A. Gómez Sánchez and A. M. Valle. J. Chem. Soc. Perkin Trans. 2, 15 (1973).
3. F. Korte and K. Trautner. Chem. Ber. **95**, 281 (1962); **95**, 295 (1962).
4. (*a*) A. Gómez Sánchez, A.M. Valle, and J. Bellanato. J. Chem. Soc. (B), 2330 (1971); (*b*) A. Gómez Sánchez, M. Tena Aldave, and U. Scheidegger. J. Chem. Soc. (C), 2570 (1968).
5. (*a*) G. Bartoli, C. Cimarelli, R. Dalpozzo, and G. Palmieri. Tetrahedron, **51**, 8613 (1995); (*b*) L. Kozerski, K. Kamienska-Trela, L. Kania, and W. von Philipsborn. Helv. Chim. Acta, **66**, 2113 (1983).
6. O.R. Suárez-Castillo, M. García-Velgara, M.S. Morales-Ríos, and P. Joseph-Nathan. Can. J. Chem. **75**, 959 (1997).
7. F. Korte and H. Wamhoff. Chem. Ber. **97**, 1970 (1964).
8. K.L. Brown, L. Damm, J.D. Dunitz, A. Eschenmoser, R. Hobi, and C. Kratky. Helv. Chim. Acta, **61**, 3108 (1978).
9. (*a*) P.E. Hansen, R. Kawecki, A. Krowczynski, and L. Kozerski. Acta Chem. Scand. **44**, 826 (1990); (*b*) P.E. Hansen, A. Kolonicny, and A. Lycka. Magn. Reson. Chem. **30**, 786 (1992); (*c*) P.E. Hansen, S. Bolvig, F. Duus, M.V. Petrova, R. Kawecki, R. Krajewski, and L. Kozerski. Magn. Reson. Chem. **33**, 621 (1995).
10. (*a*) L. Koserski and W. von Philipsborn. Org. Magn. Reson. **17**, 306 (1981); (*b*) Helv. Chim. Acta, **65**, 2077 (1982); (*c*) J.-C. Zhuo. Magn. Reson. Chem. **35**, 21 (1997).
11. J. Reuben. J. Am. Chem. Soc. **109**, 316 (1987).
12. E. Pretsch, J. Seibl, W. Simon, and T. Clerc. *In* Spectral data for structure determination of organic compounds. Springer-Verlag, Berlin. 1983. p. C185.
13. F.T. Oakes and J.F. Sebastian. J. Org. Chem. **45**, 4959 (1980).
14. (*a*) J.L. Mueller, M.S. Gibson, and J.S. Hartman. Can. J. Chem. **74**, 1329 (1996); (*b*) P. Marchand, M.-C. Frageau-Bellassoued, C. Bellec, and G. Lhommet. Synthesis, 1118 (1994).
15. (*a*) G. Fischer, W.-D. Rudorf, and E. Kleinpeter. Magn. Reson. Chem. **29**, 212 (1991); (*b*) E. Kleinpeter, S. Thomas, G. Uhlig, and W.-D. Rudorf. Magn. Reson. Chem. **31**, 714 (1993).
16. J.L. Chiara, A. Gómez-Sánchez, F.-J. Hidalgo, and J. Bellanato. J. Chem. Soc. Perkin Trans. 2, 1691 (1988).
17. (*a*) M.S. Morales-Ríos, R.E. del Rio, and P. Joseph-Nathan. Magn. Reson. Chem. **27**, 1039 (1989); (*b*) M.S. Morales-Ríos and P. Joseph-Nathan. Magn. Reson. Chem. **29**, 49 (1991); (*c*) M.S. Morales-Ríos, P. Joseph-Nathan, B. Wrackmeyer, and E. Kupce. Magn. Reson. Chem. **31**, 238 (1993); (*d*) M.S. Morales-Ríos, V. Pérez-Alvarez, P. Joseph-Nathan, and L. Zepeda. Magn. Reson. Chem. **32**, 228 (1994).
18. H. Wamhoff, H.W. Dürbeck, and P. Sohár. Tetrahedron, **27**, 5873 (1971).
19. International tables for X-ray crystallography. Vol. 3. D. Reidel Publishing Company, Dordrecht. 1985. p. 276.
20. J.E. Anderson, D. Casarini, and L. Lunazzi. Tetrahedron Lett. **29**, 3141 (1988).
21. K. Müller and L.D. Brown. Helv. Chim. Acta, **61**,1407 (1978).
22. J.J.P. Stewart. J. Comput.-Aided Mol. Des. **4**, 1 (1990).

© 1999 NRC Canada

Heterocyclic aromatic amide protecting groups for aryl and phthalocyaninesulfonic acids

Zhaopeng Li, Johan van Lier, and Clifford C. Leznoff

Abstract: Pyrroles, indole, imidazole, and a pyrazole were treated with 3,4-dibromobenzenesulfonyl chloride to form 3,4-dibromobenzenesulfonamides. The 1-(3,4-dibromophenylsulfonyl)pyrrole and 1-(3,4-dibromophenylsulfonyl)indole were stable to CuCN in DMF to produce 1-(3,4-dicyanophenylsulfonyl)pyrrole and 1-(3,4-dicyanophenylsulfonyl)indole, which upon treatment with ammonia in 2-*N*,*N*-dimethylaminoethanol gave the protected phthalocyanine-2,9,16,23-tetrasulfonamides. Base cleavage of these sulfonamides yielded the free acids. A mixed condensation of 4,5-diheptylphthalonitrile and 1-(3,4-dicyanophenylsulfonyl)pyrrole gave 9,10,16,17,23,24-hexakis(1-heptyl)-2-(1-pyrrolylsulfonyl)phthalocyanine. Cleavage of the latter yielded the lithium salt of the monosulfonic acid.

Key words: sulfonic acid blocking groups, phthalocyanine sulfonic acids, 1-(3,4-dicyanophenylsulfonyl)pyrrole, 1-(3,4-dicyanophenylsulfonyl)indole.

Résumé : La réaction du chlorure de 3,4-dibromobenzènesulfonyle avec des pyrroles, l'indole, l'imidazole et un pyrazole conduit à la formation de 3,4-dibromobenzènesulfonamides. Le 1-(3,4-dibromophénylsulfonyl)pyrrole et du 1-(3,4-dibromophénylsulfonyl)indole ont été soumis à l'action du CuCN dans le DMF pour produire du 1-(3,4-dicyanophénylsulfonyl)pyrrole et du 1-(3,4-dicyanophénylsulfonyl)indole qui, par traitement avec de l'ammoniac dans le 2-*N*,*N*-diméthylaminoéthanol conduit aux phtalocyanine-2,9,16,23-tétrasulfonamides protégés. Le clivage basique de ces sulfonamides conduit aux acides libres. Une condensation mixte du 4,5-diheptylphtalonitrile et du 1-(3,4-dicyanophénylsulfonyl)pyrrole conduit à la 9,10,16,17,23,24-hexakis(1-heptyl)-2-(1-pyrrolylsulfonyl)phtalocyanine. Le clivage de cette dernière fournit le sel de lithium de l'acide monosulfonique.

Mots clés : acide sulfonique comme agents bloqueurs, acides phtalocyanine sulfoniques, 1-(3,4-dicyanophénylsulfonyl)pyrrole, 1-(3,4-dicyanophénylsulfonyl)indole.

[Traduit par la Rédaction]

Introduction

Phthalocyanine (Pc) sulfonic acids have potential as photodynamic therapy (PDT) agents of cancer tumours (1, 2). Although phthalocyanine -2,9,16,23-tetrasulfonic acid is commercially available as a mixture of isomers, it has been shown that phthalocyanine-2-sulfonic acid and phthalocyanine-2,9-disulfonic acid are more effective for direct cell kill (3–9). Unfortunately, only small samples obtained by high-performance liquid chromatography (HPLC) of these unsymmetrical phthalocyanine sulfonic acids (6–8) were available for PDT studies (9, 10). Some recent attempts at preparing mono sulfonated Pcs by the oxidation of sulfides (11) or trisulfonated Pcs (12, 13) via subphthalocyanines (14, 15) gave Pcs in low yield.

One roadblock in the development of a rich variety of readily available sulfonated Pcs is the paucity of suitable blocking groups or precursors of sulfonic acids. Sulfonamides are common compounds made from sulfonyl chlorides and amines, and sulfonamides are widely used as blocking groups of amines. Cleavage (16) of sulfonamides to recover the free amines is not a trivial operation, but a large number of sophisticated procedures (17) have been used to accomplish this task, often requiring harsh conditions such as the use of concentrated acid and high temperatures (18), or reducing agents (19). In most of these procedures little attention is paid to the sulfonic acid residue remaining after the cleavage, and indeed, the sulfonic acid group is often transformed in the process (17–19). The recent description of a neopentyl ester group as a blocking group (20) of sulfonic acid seemed interesting to us but early experiments indicated it to be unsuitable for phthalocyanine synthesis.

Aryl sulfonyl chlorides have been used as blocking groups of five-membered ring aromatic amines such as imidazole, (21, 22), pyrrole (23), and indole (24), and these were cleaved under a variety of conditions, liberating both the amine and recovered sulfonic acids, and hence we directed our attention to the use of these five-membered heterocyclic amines as blocking groups of aryl sulfonic acids. It proved to be essential to develop an aryl sulfonic acid blocking group that was stable to both phthalonitrile and phthalo-

Received July 15, 1998.

Z. Li and C.C. Leznoff.[1] Department of Chemistry, York University, Toronto, ON M3J 1P3 Canada.
J. van Lier. MRC Group in the Radiation Sciences, Faculty of Medicine, Université de Sherbrooke, PQ J1N 5N4, Canada.

[1]Author to whom correspondence may be addressed. Telephone: (416) 736-2100, ext. 33838. Fax: (416) 736-5936.
e-mail: leznoff@yorku.ca

© 1999 NRC Canada

cyanine formation and yet could be cleaved under conditions in which the sulfonic acid groups remained intact.

Results and discussion

Chlorosulfonation of 1,2-dibromobenzene (**1**) readily gave 3,4-dibromobenzenesulfonyl chloride (**2**) (25). Solov'eva et al. (25) described the synthesis of a wide variety of *N*,*N*-dialkyl-3,4-dibromobenzenesulfonamides for use in phthalonitrile and phthalocyanine synthesis, but these sulfonamides are *not* readily cleaved to the free acids. We first decided to try to see if aryl groups such as diphenylamine (**3**) used in making *N*,*N*-diphenylbenzenesulfonamide would be useful in phthalocyanine synthesis and at the same time compare that analog with a series of heteroarylbenzenesulfonamides derived from pyrrole (**4**), 2-ethylpyrrole (**5**), 3,5-dimethylpyrazole (**6**), imidazole (**7**), and indole (**8**).

Treatment of sulfonyl chloride **2** with **3** in refluxing $CHCl_3$ and pyridine (py) afforded 3,4-dibromo-*N*,*N*-diphenylbenzenesulfonamide (**9**) in high yield. On the other hand, pyrroles **4** and **5** were first treated with NaH in tetrahydrofuran (THF) to form the sodium derivatives, which then reacted with **2** at room temperature to give 1-(3,4-dibromophenylsulfonyl)pyrrole (**10**), 1-(3,4-dibromophenylsulfonyl)-2-ethylpyrrole (**11**), and 1-(3,4-dibromophenylsulphonyl)-3,5-dimethylpyrazole (**12**) in 50, 3, and 84% yields, respectively. The reaction of imidazole (**7**) and indole (**8**) with base in $CHCl_3$ likewise gave 1-(3,4-dibromophenylsulfonyl)imidazole (**13**) and 1-(3,4- dibromophenylsulfonyl)indole (**14**) in 34 and 50% yields, respectively (Scheme 1). The low yield of **11** precluded further work on this compound, although we had envisioned that the ethyl group of **5** would afford enhanced solubility to the subsequent phthalonitrile and phthalocyanine.

At this point it was important to test the stability of sulfonamides **9**, **10,** and **12**–**14** to the conditions of (*i*) the Rosenmund – von Braun reaction (CuCN, 200°C, DMF) (26), (*ii*) phthalocyanine formation (MOR or NH_3), and (*iii*) sulfonamide cleavage. Sulfonamides **9**, **10**, **13**, and **14** were stable to the Rosemund – von Braun reaction, but **12** was not and was abandoned for further consideration. Sulfonamides **9**, **10,** and **14** were stable to $NaOCH_3$ at room temperature and NH_3 in 2-*N*,*N*-dimethylaminoethanol (DMAE), possible methods for use in phthalocyanine formation but **13** did not survive these conditions (Table 1) and was dropped as a potential candidate for Pc formation. Sulfonamides **10** and **14** were solvolyzed by $NaOCH_3$ in refluxing methanol to give 3,4-dibromophenylsulfonic acid (**15**) (27), but again **12** and **13** gave **15** simply upon stirring at room temperature as above (Table 1). All sulfonamides were stable to concentrated HCl at room temperature. Thus, only sulfonamides **9**, **10**, and **14** were suitable substrates for development for phthalocyanine synthesis.

The dibromosulfonamides **9**, **10**, and **14** were readily converted via CuCN in DMF to 3,4-dicyano-*N*,*N*-diphenylbenzenesulfonamide (**16**), 1-(3,4-dicyanophenylsulfonyl)pyrrole (**17**), and 1-(3,4-dicyanophenylsulfonyl)indole (**18**) in 29, 43, and 45% yields, respectively (Scheme 2). The *N*,*N*-diphenylsulfonamide **16** readily formed *N*,*N*,*N*′,*N*′,*N*″,*N*″,*N*‴,*N*‴-octaphenylphthalocyanine-2,9,16,23-tetrasulfonamide (**19**) in 50% yield when treated with lithium in DMAE at 70°C (28).

Scheme 1.

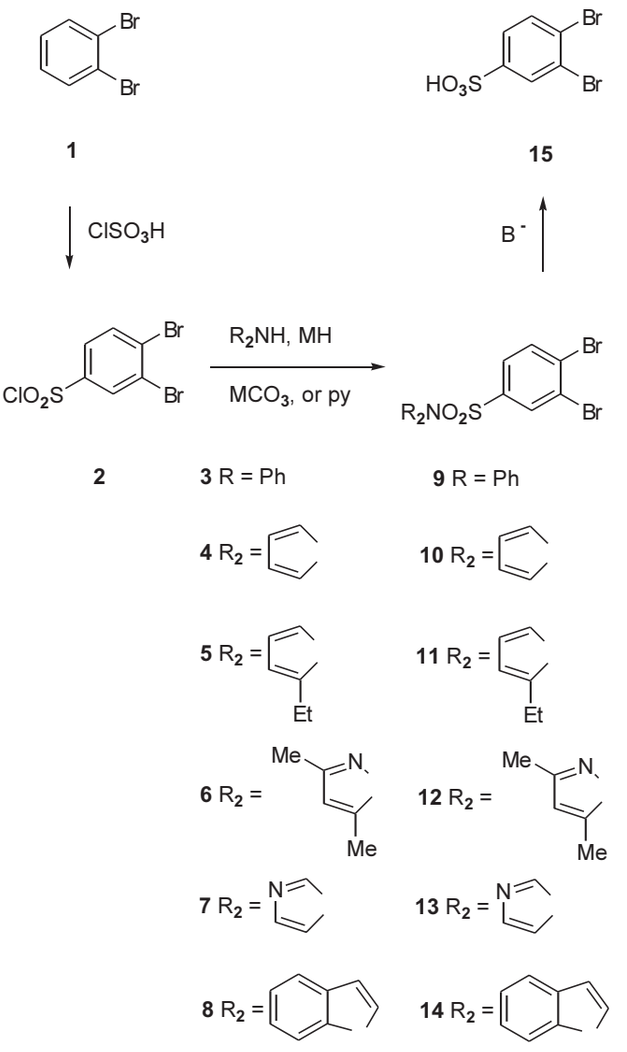

Since we had already shown that **10** and **14** are cleaved by metal alkoxides at refluxing methanol conditions, we treated **17** and **18** with NH_3 in DMAE to form *N*,*N*′,*N*″,*N*‴-tetrakis-(1-pyrrolyl)phthalocyanine-2,9,16,23-tetrasulfonamide (**20**) and *N*,*N*′,*N*″,*N*‴-tetrakis-(1-indolyl) phthalocyanine-2,9, 16,23-tetrasulfonamide (**21**) in 33 and 42% yields, respectively. Under similar conditions to the formation of **21** and **22**, but with the addition of $Zn(OAc)_2$, **17** and **18** were converted directly to *N*,*N*′,*N*″,*N*‴-tetrakis- (1-pyrrolyl)phthalocyanine-2,9,16, 23-tetrasulfonamide zinc(II) (**22**) and *N*,*N*′,*N*″,*N*‴-tetrakis-(1-indolyl)phthalocyanine-2, 9,16, 23-tetrasulfonamide zinc(II) (**23**) in 32 and 68% yields, respectively (Scheme 2).

As expected Pc **19** proved to be resistant to solvolysis, but Pc sulfonamides **20** and **21** were readily converted to phthalocyanine-2,9,16,23-tetrasulfonic acid (**24**) by treatment with lithium 2-*N*,*N*-dimethylaminoethoxide in DMAE (for **20**) or lithium methoxide in THF–MeOH for **21** (Scheme 2).

Early experiments towards the synthesis of a phthalocyanine monosulfonic acid via a mixed condensation of **17** and phthalonitrile gave insoluble residues difficult to separate by chromatography. To increase the solubility of the

© 1999 NRC Canada

Table 1. Synthesis of 3,4-dibromosulfonamides and their stability to bases and the Rosenmund – von Braun reaction.

Compound	Method (base/solvent)	Yield (%)	Stability at 20°C		
			NaOMe	NH_3	CuCN–DMF[a]
9	py/$CHCl_3$	65	Stable	Stable	Stable
10	NaH/THF	50	Stable[b]	Stable	Stable
12	NaH/THF	84	Unstable	Stable	—
13	Na_2CO_3/$CHCl_3$[c]	34	Unstable	Unstable	—
14	NaOH/CH_2Cl_2[d]	57	Stable[b]	Stable	Stable

[a]Refluxed.
[b]Unstable in refluxing MeOH.
[c]With MeOH.
[d]Bu_4NHSO_4 phase transfer reagent.

phthalocyanine product, **17** was condensed with 4,5-diheptylphthalonitrile (**25**) (29), as for the formation of **22**, to give 9,10,16,17,23,24-hexakis(1-heptyl)phthalocyanine-2-(*N*-pyrrolyl)sulfonamide (**26**) in 14.7% yield. Treatment of **26** with $Zn(OAc)_2$ in DMF readily afforded 9,10,16,17, 23, 24-hexakis(1-heptyl)phthalocyanine-2-(*N*-pyrrolyl)sulfonamide zinc(II) (**27**) in 86% yield. Hydrolysis of **27** with lithium methoxide in methanol afforded lithium 9,10,16,17,23,24-hexakis(1-heptyl)phthalocyanine-2-sulfonate zinc(II) (**28**) in 85% yield (Scheme 3).

Spectral data of all new compounds were consistent with their structures (see Experimental). Pcs **19**–**23** exhibited multiplets in their NMR spectra, consistent with the fact that they exist as mixtures of isomers. Mass spectra of all sulfonamides exhibited ions showing loss of SO_2 and peaks representing both fragments (30).

We have demonstrated that indole and pyrrole moieties can be successfully used to form sulfonamides as blocking groups in the synthesis of phthalocyanine sulfonic acids.

Experimental

All organic solvents were dried by appropriate methods and distilled before use. All reagents were freshly distilled, or were recrystallized and then dried under reduced pressure, before use. Unless otherwise noted, magnetic stirring methods under an inert atmosphere (Matheson High Purity argon) were utilized during distillation or reaction processes, and round-bottom glass vessels chosen such that the quantity of reagents and solvent did not exceed half of the available volume. Water-cooled condensers were used if reaction processes were held near, or at, reflux conditions. Melting points were determined using a Kofler hot-stage melting point apparatus and are reported uncorrected. Infrared spectroscopy was performed on either a Pye Unicam SP3-2000 or a Perkin Elmer 1310 infrared spectrophotometer and FTIR spectroscopy was performed on a Unicam Matheson 3000 FTIR spectrometer, using samples prepared as KBr discs unless otherwise noted. Mass spectral analyses were performed by Dr. B. Khouw (York University, Toronto, Ontario), Dr. R. Smith (McMaster University, Hamilton, Ontario), and Dr. R.N. Cerny (Midwest Center for Mass Spectrometry, University of Nebraska–Lincoln, Lincoln, Nebraska). HRMS were preformed by Dr. R. Smith (McMaster University, Hamilton, Ontario). Nuclear magnetic resonance (NMR) spectroscopy was performed at 295–300 K unless otherwise noted, using a Bruker ARX 400 high-field Fourier transform instrument. Chemical shifts are reported in parts per million relative to a tetramethylsilane (TMS) internal standard.

3,4-Dibromobenzenesulfonyl chloride (2)

To a flask containing 1,2-dibromobenzene **(1)** (20 g, 88.47 mmol) and dry $CHCl_3$ (120 mL), which was cooled to ca. –10°C by an ice–NaCl bath, was added chlorosulfonic acid (30 g) over 20 min. The light brown solution was stirred at room temperature for 20 h. The reaction mixture turned red during this period. The solution was refluxed for 1 h. After cooling to room temperature, the vigorously stirred reaction mixture was poured onto crushed ice (200 g). The aqueous and organic layers were separated. The former was washed with CH_2Cl_2 (100 × 2 mL). The combined organic layer was washed with aqueous $NaHCO_3$ (10%, 150 mL) followed by water until pH neutral. After drying over $MgSO_4$, and evaporating the solvent, vacuum distillation afforded a colourless solid product (120–125°C/5 mmHg (1 mmHg = 133.3 Pa), 22.7 g, 85%), mp 31–33°C (lit. (27) mp 34°C); ^{1}H NMR ($CDCl_3$) δ 8.28 (d, J = 1.8, 1H, H_4), 7.91 (d, J = 8.4, 1H, H_6), 7.85 (dd, J_1 = 1.8, J_2 = 8.4, 1H, H_5).

3,4-Dibromo-*N*,*N*-diphenylbenzenesulfonamide (9)

To a solution of 3,4-dibromobenzenesulfonyl chloride (**2**) (1.0 g, 3.2 mmol) in dry $CHCl_3$ (10 mL) were added diphenylamine (**3**) (0.7 g, 3.0 mmol) and pyridine (0.5 mL). The solution was refluxed for 14 h, and cooled at room temperature, washed with aqueous HCl (5%, 10 mL) and water until neutral. After drying over $MgSO_4$ and evaporating the solvent, the crude product was recrystallized from ethanol to give colourless crystalline needles (0.9 g, 65%), mp 160–161°C; IR (KBr cm^{-1}): 1957, 1886, 1589, 1449, 1446, 1351; ^{1}H NMR ($CDCl_3$) δ 7.93 (d, J = 2.0, 1H), 7.74 (d, J = 8.0, 1H), 7.45 (dd, J_1 = 8.0, J_2 = 2.0, 1H), 7.31 (m, 10H); MS (*m*/*z*, relative intensity): 469 (M^+, 15), 467 (M^+, 30), 465 (M^+, 14), 167 (100). Anal. calcd. for $C_{18}H_{13}NBr_2NO_2S$: C 46.25, H 2.78, N 3.00; found: C 46.41, H 2.66, N 2.96.

1-(3,4-Dibromophenylsulfonyl)pyrrole) (10)

To freshly distilled pyrrole (**4**) (220 mg, 30 mmol) in dry THF (5 mL), cooled to 0°C, was added NaH (300 mg, 60%

© 1999 NRC Canada

Scheme 2.

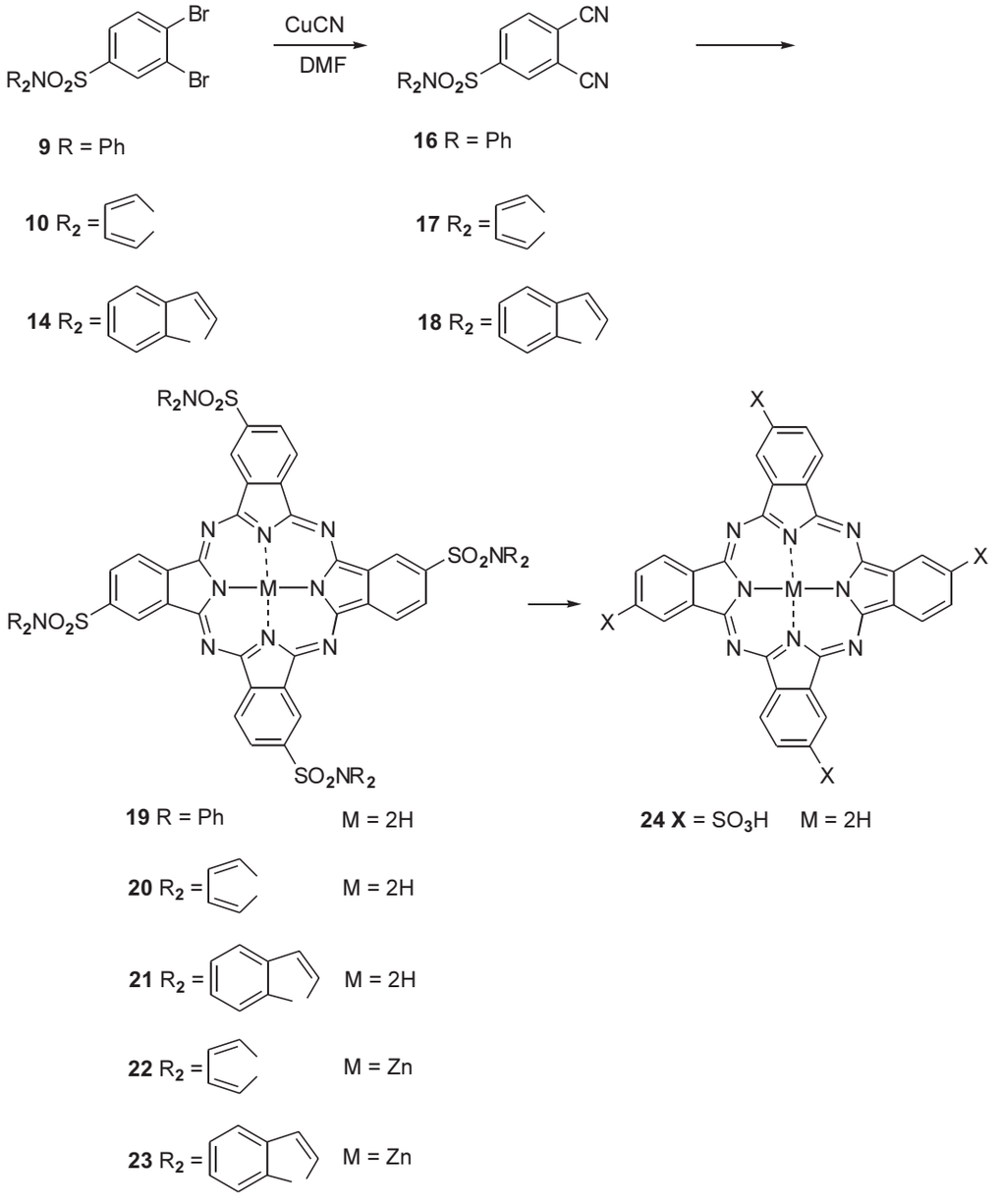

oil dispersion). 3,4-Dibromobenzenesulfonyl chloride (**2**) (1.0 g, 3.2 mmol) was added over 30 min. under Ar. After stirring at room temperature for 6 h, the brown reaction mixture was carefully poured into a saturated NH_4Cl solution (30 mL) placed in an ice bath. Ether (30 mL) was added and the aqueous layer was washed with ether (20 mL). The combined organic layer was washed with saturated NH_4Cl until neutral. After drying over $MgSO_4$ and evaporating the solvent, the crude product was recrystallized from ethanol to give colourless crystalline needles (545 mg, 50%), mp 141–142°C; IR (KBr cm^{-1}): 3075 (s, ArH), 1375 (s, SO_2N), 1186 (s, SO_2N); ^1H NMR ($CDCl_3$) δ 8.10 (d, J = 2.0, 1H), 7.77 (d, J = 8.4, 1H), 7.63 (dd, J_1 = 8.4, J_2 = 2.0, 1H), 7.16 (m, 2H), 6.36 (m, 2H); MS (*m*/*z*, relative intensity): 367 (M^+, 50), 365 (M^+, 95), 363 (M^+, 50), 299 (90), 235 (100). Anal. calcd. for $C_{10}H_7NBr_2$: C 32.88, H 1.92, N 3.84; found: C 33.72, H 1.87, N 3.91.

1-(3,4-Dibromophenylsulphonyl)-2-ethylpyrrole (11)

The crude product, obtained as described for **10** but using 2-ethylpyrrole (**5**), recrystallized from ethanol to give in 3% yield fine colourless crystals 78–79°C; IR (KBr cm^{-1}): 3074 (s, ArH), 1372 (s, SO_2N), 1180 (s, SO_2N); ^1H NMR ($CDCl_3$) δ 8.14 (d, J = 1.6, 1H), 8.03 (d, J = 7.8, 1H), 7.73 (dd, J_1 = 1.6, J_2 = 7.8, 1H), 7.41 (d, 1.7, 1H), 6.31 (t, 1H) (6.12 bs, 1H); 2.71 (q, J = 7.3, 2H), 1.24 (t, J = 7.3, 3H); MS (*m*/*z*,

© 1999 NRC Canada

Scheme 3.

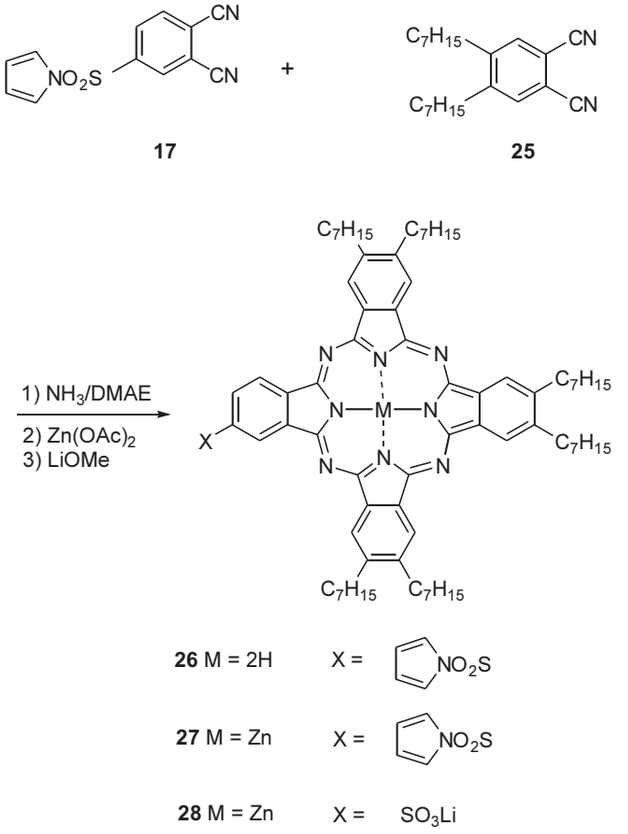

relative intensity): 393 (M^+, 75), 379 (70), 315 (67), 299 (70), 80 (100). Anal. calcd. for $C_{12}H_{11}Br_2NO_2S$: C 36.64, H 2.80, N 3.56; found: C 37.27, H 2.74, N 3.52.

1-(3,4-Dibromophenylsulphonyl)-3,5-dimethylpyrazole (12)

The crude product, obtained as described for **10** but using 3,5-dimethylpyrazole (**6**), was recrystallized from ethanol twice to give 0.98 g of **12** in 84% yield, mp 145–147°C; IR (KBr cm^{-1}): 3082 (s, ArH), 1374 (s, SO_2N), 1188 (s, SO_2N); ^1H NMR ($CDCl_3$) δ 8.19 (d, J = 1.5, 1H), 7.75 (m, 2H), 5.94 (s, ^1H), 2.51 (s, 3H), 2.22 (s, 31H); MS (*m*/*z*, relative intensity): 394 (M^+, 10), 328 (100), 299 (30), 250 (40), 236 (50). Anal. calcd. for $C_{11}H_{10}Br_2N_2O_2S$: C 33.50, H 2.54, N 7.11; found: C 33.72, H 2.30, N 7.14.

1-(3,4-Dibromophenylsulfonyl)imidazole (13)

To a solution of (**3**) (1.0 g, 3.2 mmol) in a mixture of chloroform (5 mL) and methanol (1 mL) was added imidazole (**7**) in chloroform (2 mL) and Na_2CO_3 (1.0 g). The mixture was stirred at room temperature for 22 h, filtered, and the filtrate was washed with HCl (10%, 20 mL) and water until neutral. After drying over $MgSO_4$ and evaporating the solvent, the crude product was chromatographed with 40% ethyl acetate – hexane to give pure **13** as fine, colourless crystals (320 mg, 34%), mp 119–120°C; IR (KBr cm^{-1}): 1938 (m), 1768 (m), 1564 (s), 1464 (s), 1381 (s, SO_2N); ^1H NMR ($CDCl_3$) δ 8.19 (d, J = 2.0, 1H), 8.04 (s, 1H), 7.85 (d, J = 8.0, 1H), 7.73 (dd, J_1 = 8.0, J_2 = 2.0, 1H), 7.32 (brs, 1H); 7.16 (brs, 1H); MS (*m*/*z*, relative intensity): 366 (M^+, 95) 299 (100), 235 (100). Anal. calcd. for $C_9H_6Br_2N_2O_2S$: C 29.51, H 1.64, N 7.65; found: C 29.61, H 1.46, N 7.61.

1-(3,4-Dibromophenylsulfonyl)indole (14)

Ground NaOH (2.0 g) was mixed with tetrabutylammonium hydrogen sulfate (140 mg) in CH_2Cl_2 (30 mL). The reaction flask was cooled by a salt–ice bath to 0–4°C after which indole (**8**) (1.85 g, 15.8 mmol) was added. Sulfonyl chloride (**7**) (5.0 g, 15.0 mmol) was added over 30 min. and stirred for an additional 30 min. in the ice bath. The solution was stirred at room temperature for 20 h, washed with HCl (10%, 20 mL) and with water until neutral. After drying over $MgSO_4$ and evaporating the solvent, the crude product was chromographed with 20% ethyl acetate – hexane to give **14** as a fine, colourless crystals (3.1 g, 50% mp) 125–126°C; IR (KBr cm^{-1}): 3140, 3081 (s, ArH), 1376 (s, SO_2N); ^1H NMR ($CDCl_3$) δ 8.13 (d, J = 2.0, 1H), 7.99 (d, J = 8.0, 1H), 7.66 (m, 2H), 7.56 (m, 2H), 7.37 (m, 1H); 7.29 (m, 1H), 6.74 (d, J = 4.0, 1H); MS (*m*/*z*, relative intensity): 417 (M^+, 45), 415 (M^+, 88) 413 (M^+, 43) 116 (100). Anal. calcd. for $C_{14}H_9Br_2NO_2S$: C 40.68, H 2.18, N 3.39; found: C 40.79, H 1.95, N 3.37.

3,4-Dibromobenzenesulfonic acid (15)

Compound **13** (50 mg, 0.14 mmol) was dissolved in methanol (5 mL) and NaOMe (40 mg, 0.74 mmol) was added.

© 1999 NRC Canada

The reaction solution was stirred at room temperature for 20 h. The solvent was evaporated. The residue was dissolved in water (50 mL) and washed with ether (10 mL) followed by neutralization with aqueous HCl (36%). The solvent was evaporated, the residue recrystallized from water, and the product was further purified by ion-exchange resin (Dowex 50X8-400). Recrystallization from EtOH (80%) afforded pale, yellow needles of **15** (26 mg, 60%), mp 64–66°C (lit. (27) mp 66.5–67.5°C); ^{1}H NMR (D_2O) δ 7.99 (s, 1H), 7.74 (d, 1H), 7.52 (dd, 1H). In a similar manner **12** gave **15** in 69% yield, while **10** and **14** were cleaved in methanol at reflux to give **15** in 72 and 57% yield, respectively.

3,4-Dicyano-*N*,*N*-diphenylbenzenesulfonamide (16)

To a solution of **9** (1.80 g, 3.87 mmol) in dry DMF (20 mL) was added CuCN (1.80 g, 20 mmol). The reaction solution was gently refluxed for 6 h, cooled to room temperature, and CH_2Cl_2 (200 mL) was added. A fine insoluble powder precipitated overnight. The crude product was purified by chromatography with 30% ethyl acetate – hexane as eluent to give colourless, scaly crystals (395 mg, 29%), mp 185–187°C; IR (KBr cm^{-1}): 3091 (s, ArH), 2235, (s, CN), 1360 (s, SO_2N), 1186 (s, SO_2N); ^{1}H NMR ($CDCl_3$) δ 7.90 (s, 1H), 7.82 (d, J = 8.0, 1H), 7.76 (d, J = 8.0), 7.19 (m, 5H), 7.07 (m, 5H); MS (*m*/*z*, relative intensity): 359 (M^+, 60), 168 (100). Anal. calcd. for $C_{20}H_{13}N_3O_2S$: C 66.85, H 3.62, N 11.70; found: C 66.36 H 3.33, N 11.56.

1-(3,4-Dicyanophenylsulfonyl)pyrrole (17)

In a manner identical to that of **16**, **10** gave a crude product **17**, which on flash chromatography with 30% ethyl acetate – hexanes as eluents yielded fine, colourless crystals (43%), mp 155–157°C; IR (KBr cm^{-1}): 2235 (s, CN), 1388, 1287 (s, SO_2N); ^{1}H NMR ($CDCl_3$) δ 8.22 (d, J = 1.2, 1H), 8.17 (dd, J_1 = 1.2, J_2 = 8.2, 1H), 7.97 (d, J = 8.2, 1H), 7.16 (d, J = 1.8, 2H), 6.41 (d, J = 1.8, 2H); MS (*m*/*z*, relative intensity): 257 (M^+, 100), 193 (70). Anal. calcd. for $C_{12}H_7N_3O_2S$: C 56.03, H 2.72, N 16.34; found: C 56.17 H 2.62, N 16.34.

1-(3,4-Dicyanophenylsulfonyl)indole (18)

As for **16** above, **14** gave a crude product, which on purification by flash chromatography with 30% ethyl acetate – hexane as eluents, yielded pale yellow, fine crystals (45%), mp 171–173°C; IR (KBr cm^{-1}): 3110 (s, ArH), 2242 (s, CN), 1391 (s, SO_2N); ^{1}H NMR ($CDCl_3$) δ 8.25 (s, 1H, H_1), 8.17 (dd, J_1 = 1.6, J_2 = 8.5, 1H, H_3), 7.96 (d, J = 8.5, 1H, H_2), 7.88 (d, J = 8.0, 1H, H_4), 7.58 (d, J = 7.7, 1H, H_7), 7.51 (d, J = 3.5, 1H, H_9), 7.40 (t, J_1 = 8.0, J_2 = 7.3, 1H, H_5), 7.32 (t, J_1 = 7.3, J_2 = 8.0, 1H, H_6), 6.79 (d, J = 3.5, 1H, H_8); MS (*m*/*z*, relative intensity): 3.07 (M^+, 53), 116 (52), 105 (100). Anal. calcd. for $C_{16}H_9N_3O_2S$: C 62.54, H 2.93, N 1368; found: C 62.95, H 2.81, N 13.62.

***N*,*N*,*N*′,*N*′,*N*″,*N*″,*N*‴,*N*‴-Octaphenylphthalocyanine-2,9,16,23-tetrasulfonamide (19)**

Small pieces of metal lithium (30 mg, 4.3 mmol) were dissolved in DMAE (2 mL) to which **16** (100 mg, 0.28 mmol) was added. The reaction solution was stirred at 60–70°C (oil bath) for 20 h, cooled to room temperature, and the sticky blue solution was poured into a mixture of ice (5 g) and aqueous HCl (10 mL, 4 M). The precipitate was collected by filtration, and the crude product was purified using flash chromatography with 5% THF–CH_2Cl_2 as eluent to give a dark blue, fine powder of **19** (11 mg, 11%), mp >310°C. IR (KBr cm^{-1}): 1394, 1164 (s, SO_2N); UV-vis (THF) (λ_{max}): 698, 664, 636, 604, 344, 238; ^{1}H NMR (pyridine-d_5): 8.91 (s) 8.46 (s), 7.85 (m), 7.37 (m), 6.96 (s); MS (FAB$^+$, *m*/*z* relative intensity): 1438 (M^+). Anal. calcd. for $C_{80}H_{54}N_{12}O_8S_4$: C 66.76, H 3.75, N 11.68; found: C 66.95, H 3.66, N 10.82.

2,9,16,23-Tetrakis(1-pyrrolysulfonyl)phthalocyanine (20)

Compound **17** (200 mg, 0.78 mmol) was dissolved in *N*,*N*-dimethylaminoethanol (DMAE) (2 mL). As ammonia gas was bubbled through, the reaction mixture was heated to 100–110°C (sand bath) for 1 h and then refluxed for 4 h. The reaction mixture was cooled to room temperature, the solvent evaporated, and water (10 mL) was added to the resulting sticky solution. The blue precipitate was collected by filtration or centrifugation and purified by flash chromatography using 5% THF–CH_2Cl_2 as eluent to give in the first fraction phthalocyanine **20** as dark blue crystals (66 mg, 33%), mp >310°C; IR (KBr cm^{-1}): 3141 (m, ArH), 1374 (s, SO_2N), 1191 (s, SO_2N); UV-vis (THF), (λ_{max}): 696, 662, 634, 608, 394, 348; ^{1}H NMR (THF-d_8) δ 9.40, 9.38, 8.45 (m, 4H, H_3), 7.79 (m, 4H, H_4), 6.95, 5.87 (m, 8H, H_1), 6.93 (m, 8H, H_2), 664 (m, 4H, H_5); MS (FAB$^+$, *m*/*z*, relative intensity): 1030 (M^+). Anal. calcd. for $C_{48}H_{130}N_{12}O_8S_4$: C 55.92, H 2.91, N 16.31; found: C 55.80, H 2.90, N 15.78.

2,9,16,23-Tetrakis(1-indolylsulfonyl)phthalocyanine (21)

As for **20**, but from **18**, phthalocyanine **21** was obtained as dark, blue crystals in 42% yield, mp >310°C; IR (KBr cm^{-1}): 1387 (s, SO_2N) 1173 (s, SO_2N); UV-vis (THF) (λ_{max}): 698, 666, 634, 612, 346, 248; ^{1}H NMR ($CDCl_3$) δ: 9.56 (m, br), 8.88 (m, br), 8.70 (m, br), 8.54 (m), 8.14 (m), 8.03 (m), 7.67(m), 7.55 (m), 7.01 (m), 6.92 (m); MS (FAB$^+$, *m*/*z*, relative intensity): 1230 (M^+, 40), 671 (70), 539 (100). Anal. calcd. for $C_{64}H_{38}N_{12}O_8S_4$: C 62.44, H, 3.09, N 13.66; found: C 62.85, H 3.32, N 13.27.

2,9,16,23-Tetrakis(1-pyrrolylsulfonyl)phthalocyanine zinc(II) (22)

Compound **17** (200 mg, 0.78 mmol) was dissolved in 2-*N*,*N*-dimethylaminoethanol (DMAE) (2 mL) containing anhydrous $Zn(OAc)_2$ (200 mg). The reaction mixture was heated to 100–110°C (sand bath) and kept at that temperature for 1 h while ammonia gas was bubbled through it. The solution was refluxed for 4 h and cooled to room temperature. The solvent was evaporated and water (10 mL) was added to the resulting sticky solution. The blue precipitate was collected by filtration or centrifugation and purified by flash column chromatography using 50% THF–CH_2Cl_2 as eluent to give in the first fraction **22** as dark crystals (68 mg, 32%), mp >310°C; IR (KBr cm^{-1}): 1371 (m, SO_2N) 1167 (s, SO_2N); UV-vis (THF) (λ_{max}): 672, 610, 350, 242; ^{1}H NMR (THF-d_8) δ 9.73 (br), 7.36–8.66 (m, br), 6.59–6.90 (m, br). MS (FAB$^+$, *m*/*z*, relative intensity): 1093 (M^+ + 1250), 964 (20), 625 (52) 558 (100). Anal. calcd. for $C_{48}H_{128}N_{12}O_8S_4Zn$: C 52.70, H 2.56, N 15.37; found: C 52.29, H 2.80, N 14.46.

© 1999 NRC Canada

2,9,16,23-Tetrakis(1-indolylsulfonyl)phthalocyanine zinc(II) (23)

As for **22**, **18** yielded a crude product which was purified by flash chromatography by using 40% THF–benzene as eluent to give **23** as dark blue crystals (68%), mp >310°C; IR (KBr cm^{-1}): 1376 (m, SO_2N), 1173 (s, SO_2N); UV-vis (THF) (λ_{max}): 676, 610, 360, 244; ^1H NMR ($CDCl_3$) δ 9.79 (m), 9.12 (m), 8.68 (m), 8.31 (m), 8.04 (m), 7.60 (m), 7.17 (m), 6.86 (m), 6.62 (m); MS (FAB+, *m*/*z*, relative intensity): 1293 (M^+, 60), 1113 (50), 919 (100). Anal. calcd. for $C_{64}H_{36}N_{12}O_8S_4Zn$: C 59.40, H 2.78, N 12.99; found: C 59.19; H 3.09, N 12.65.

Phthalocyanine-2,9,16,23-tetrasulfonic acid (24)

Method A

Small pieces of metal lithium (400 mg, 58 mmol) were dissolved in DMAE (20 mL) and **20** (100 mg, 0.097 mmol) was added. The solution was stirred at 60–70°C for 30 h. An aliquot was taken and added to a mixture of water and CH_2Cl_2. The organic solution appeared colourless. The reaction mixture was cooled to room temperature, water was added, and the solvent was reduced to half volume under vacuum. After acetone (15 mL) was added, the precipitates were separated by centrifugation and washed with aqueous HCl (36%, 5 × 3 mL). Drying under high vacuum gave a dark blue powder of **24** (25, 31) (70 mg, 86%), mp >310°C; IR (KBr cm^{-1}): 3400 (s, SO_3H), 1472 (s, SO_3H); UV-vis (MeOH) (λ_{max}): 692, 656; ^1H NMR (DMSO-d_6) δ 10.19 (br, 4H), 9.71 (br, 4H), 9.53 (m, 4H), 8.60 (m, 4H); MS (electrospray, *m*/*z*): 834.13 $(M + 1 - H)^-$, 753.50 $(M + 1 - H\text{-}SO_3H)^-$, 416.11 $(M - 2H)^{2-}$, 277.07 $(M - 3H)^{3-}$, 250.19 $(M + 1 - SO_3H\text{-}3H)^{3-}$, 207.49 $(M - 4H)^{4-}$.

Method B

Small pieces of metal lithium (40 mg, 5.8 mmol) were dissolved in a mixture of methanol (2 mL) and THF (2 mL) to which **21** (20 mg) was added. The solution was refluxed for 20 h. TLC with 5% THF–CH_2Cl_2 as eluent showed that the starting material had disappeared. The solvent was evaporated and the residue was washed with aqueous HCl (36%, 5 × 3 mL) to give a product identical with that from method A (23 mg, 84%).

9,10,16,17,23,24-Hexakis-(1-heptyl)-2-(1-pyrrolylsulfonyl)phthalocyanine (26)

Excess 4,5-diheptylphthalonitrile (**25**) (29), prepared by our previously described method (32), (200 mg, 0.69 mmol) and **17** (20 mg, 0.078 mmol) were dissolved in DMAE (3 mL). As ammonia gas was bubbled through, the reaction mixture was heated to 100–110°C (sand bath). After 1 h, the solution was raised to reflux temperatures and refluxed for 20 h. The reaction mixture was cooled to room temperature, ice (5 g) was added to the resulting sticky solution, and the precipitates were separated by centrifugation followed by sequential washing with water (10 × 2 mL) and methanol (10 × 2 mL). The blue precipitate was collected by filtration or centrifugation and purified by flash column chromatography using CH_2Cl_2 as eluent. After evaporation of the solvent, the residue was rechromatographed with 10% EtOAc–hexanes and then 5% THF–CH_2Cl_2 as eluents. The first fraction contained two spots, which was rechromatrographed later. The second fraction was a mixture of multisulfonate Pcs (8.7 mg). The first fraction was separated by column chromatography using 50% CH_2Cl_2–hexanes to give **26** (4.5 mg, 4.7%), mp >310°C; IR (KBr cm^{-1}): 1337 (m, SO_2N), 1167 (s, SO_2N); UV-vis (THF) (λ_{max}): 714, 692, 686, 656; ^1H NMR ($CDCl_3$) δ 9.54 (s, 1H), 9.03 (s, 1H), 8.71 (m 3H), 8.50 (m, 2H), 8.25 (d, *J* = 7.6, 1H), 7.69 (s, 1H), 7.57 (s, Py-H, 2H), 6.42 (s, Py-H, 2H), 3.15 (m, 12H), 1.49 (m, 78H); MS (FAB+ *m*/*z*): 1232 ($M^+ + 1$). Anal. calcd. for $C_{78}H_{105}N_9O_2S$: C 76.04, H 8.53, N 10.24; found: C 76.62, H 8.85, N 9.52.

9,10,16,17,23,24-Hexakis-(1-heptyl)-2-(1-pyrrolylsulfonyl)-phthalocyanine zinc(II) (27)

Metal-free Pc **26** (10 mg, 0.008 mmol) was dissolved in a mixture of toluene (3 mL) and DMF (3 mL) to which anhydrous $Zn(OAc)_2$ was added. The reaction solution was refluxed for 24 h, the solvent evaporated, and the residue washed with water (10 mL × 2) and methanol (10 mL × 2). After drying under vacuum, the crude product was purified by column chromatography using 5% THF–CH_2Cl_2 as eluent to give **27** as a dark blue powder (9 mg, 86%), mp >310°C; IR (KBr cm^{-1}): 1339, 1166 (s, SO_2N); UV-vis (THF) (λ_{max}): 692, 666, 634, 604, 354; ^1H NMR (C_6D_6) δ 9.96 (br, 1H), 9.10–8.12 (m, 8H), 7.45 (py-H, 2H), 6.13 (py-H, 2H), 3.15 (m, 12H), 1.70 (m, 60H), 1.01(m, 18H); MS (FAB+, *m*/*z*, relative intensity): 1295 ($M^+ + 1$, 100), 736 (60). Anal. calcd. for $C_{78}H_{103}N_9O_2SZn$: C 72.33, H 7.96, N 9.74; found: C 72.12, H 8.21, N 9.14.

Lithium 9,10,16,17,23,24-hexakis-(1-heptyl)phthalocyanine-2-sulfonate zinc(II) (28)

To a solution of lithium (40 mg) in MeOH (2 mL) was added **27** (17 mg). The solution was refluxed for 24 h, the solvent evaporated, and the crude product purified by column chromatography (Si-gel, 70–230 mesh) using 40% EtOAc–hexanes and methanol as eluents to give **28** as a dark blue fine powder (14 mg, 85%), mp >310°C; IR (KBr cm^{-1}): 1110 (s, SO_3Li). UV-vis (THF) (λ_{max}): 676, 616, 346, 240 (0.47); ^1H NMR (DMSO-d_6) δ 9.60 (br, 1H), 9.31 (d, *J* = 8.0, 1H), 9.15 (m, 6H), 8.42 (d, *J* = 8.0, 1H), 1.94 (m, 6H), 1.38 (m, 60H), 0.92 (m, br, 18H); MS (FAB+, *m*/*z*, relative intensity): 1251 (M^+, 100).

Acknowledgement

We are grateful to the Natural Sciences and Engineering Research Council of Canada for financial support of this research.

References

1. R.W. Boyle and D. Dolphin. Photochem. Photobiol. **64**, 469 (1996); T.J. Dougherty. Photochem. Photobiol. **58**, 895 (1993).
2. A.M. Fisher, A.L. Murphree, and C.J. Gamer. Lasers Surg. Med. **17**, 2 (1995).
3. C.J. Byrne, L.V. Marshallsay, S.Y. Sek, and A.P. Ward. *In* Photodynamic therapy of neoplastic disease. *Edited by* D. Kessel. CRC press, Boca Raton. 1990. pp. 133–144.
4. (*a*) J.D. Spikes. Photochem Photobiol. **43**, 691 (1986); (*b*) J.E. van Lier. *In* Photodynamic therapy of neoplastic disease.

© 1999 NRC Canada

Edited by D. Kessel. CRC Press, Boca Raton. 1990. pp. 279–290.
5. W.S. Chan, J.F. Marshall, R. Svensen, J. Bedwell, and I.R. Hart. Cancer Res. **50**, 4533 (1990).
6. N. Brasseur, H. Ali, R. Langlois, and J.E. van Lier. Photochem. Photobiol. **46**, 739 (1987).
7. B. Paquette, H. Ali, R. Langlois, and J.E. van Lier. Photochem. Photobiol. **47**, 215 (1988).
8. H. Ali, R. Langlois, J.R. Wagner, N. Brasseur, B. Paquette, and J.E. van Lier. Photochem. Photobiol. **47**, 713 (1988).
9. P. Margaron, P. Madarnas, R. Ouellet, and J.E. van Lier. Anticancer Res. **16**, 613 (1996).
10. W.-S. Chan, N. Brasseur, C. La Madeleine, and J.E. van Lier. Anticancer Res. **16**, 1998 (1996).
11. S.V. Kudrevich, H. Ali, and J.E. van Lier. J. Chem. Soc. Perkin Trans. 1, 2767 (1994).
12. S.V. Kudrevich, S. Gilbert, and J.E. van Lier. J. Med. Chem. **40**, 3897 (1997).
13. S.V. Kudrevich, N. Brasseur, C. La Madeleine, S. Gilbert, and J.E. van Lier. J. Med. Chem. **40**, 3897 (1997).
14. N. Kobayashi, R. Kondo, S. Nakajima, and T. Osa. J. Am. Chem. Soc. **112**, 9640 (1990).
15. A. Weitemeyer, H. Kliesch, and D. Wöhrle. J. Org. Chem. **60**, 4900 (1995); J. Rauschnabel and M. Hanack. Tetrahedron Lett. **36**, 1629 (1995).
16. S. Searles and S. Nukina. Chem. Rev. **59**, 1077 (1959).
17. E. Vedejs and S. Lin. J. Org. Chem. **59**, 1602 (1994); C. Goulaouic-Dubois, A. Guggisberg, and M. Hesse. J. Org. Chem. **60**, 5969 (1995).
18. J.E. Richmond and T.J. Atkins. J. Am. Chem. Soc. **96**, 2268 (1974); R.C. Roemmele and H. Rapoport. J. Org. Chem. **53**, 2367 (1988).
19. S. Ji, L.B. Gorther, A. Waring, A. Battisti, S. Bank, W.D. Closson, and P. Wriede. J. Am. Chem. Soc. **89**, 5311 (1967); B. Nyasse, L. Grehn, and U. Ragnarsson. J. Chem. Soc. Chem. Commun. **1017** (1997).
20. J.C. Roberts, H. Gao, A. Gopalsamy, A. Kongsjahju, and R.J. Patch. Tetrahedron Lett. 38, 355 (1997).
21. J.J. Plattner, P.A. Marcotte, H.D. Kleinert, H.H. Stein, J. Greer, G. Bolis, A.K.L. Fung, B.A. Bopp, J.R. Luly, H.L. Sham. D.J. Kempf, S.H. Rosenberg, J.F. Dullaria, B. De, I. Merits, and T.J. Perun. J. Med. Chem. **31**, 2277 (1988).
22. R.J. Sundberg. J. Heterocyclic Chem. **14**, 517 (1977).
23. (*a*) E.P. Papadopoulos and N.F. Haidar. Tetrahedron Lett. 1721 (1968); (*b*) M. Kakushima, P. Hamel, R. Frenette, and J. Rokach. J. Org. Chem. **48**, 3214 (1983); (*c*) H.J. Gogan, R. McDonald, and L.G. Edwards. Can. J. Chem. **63**, 896 (1985).
24. (*a*) V.D. Illi. Synthesis, **136** (1979); (*b*) D.M. Ketcha and G.W. Gribble. J. Org. Chem. **50**, 5451 (1985); J.-Y Mérour, B. Malapel, and E. Desarbe. Synth. Commun. **26**, 3267 (1996).
25. L.I. Solov'eva, S.A. Mikhalenko, E.V. Chernykh, and E.A. Luk'yanets. Zh. Obshch. Khim. **52**, 90 (1982).
26. (*a*) Ellis and Romney-Alexander. Chem. Rev. **87**, 779 (1987); (*b*) M. Hu, N. Brasseur, S.Z. Yildiz, J.E. van Lier, and C.C. Leznoff. J. Med. Chem. **41**, 1789 (1998).
27. (*a*) C. Goslich. Ann. **186**, 148 (1877); (*b*) L. Spiegelberg. Ann. **197**, 257 (1879).
28. C.C. Leznoff, M. Hu, and K.J.M. Nolan. J. Chem. Soc. Chem. Commun. 1245 (1996).
29. H. Mishi, N. Azuma, and K. Kitahara. J. Heterocycl. Chem. **29**, 475 (1992).
30. V.M. Negrimousky, V.M. Derkacheva, E.A. Luk'yanets, A. Weitemeyer, D. Wöhrle, and G. Schneider. Phosphorus Sulfur Silicon Relat. Elem. **104**, 161 (1995).
31. R.P. Linstead and F.T. Weiss. J. Chem. Soc. 2975 (1950).
32. D.S. Terekhov, K.J.M. Nolan, C.R. McArthur, and C.C. Leznoff. J. Org. Chem. **61**, 3034 (1996).

© 1999 NRC Canada

The total synthesis of a technetium chelate – tamoxifen complex

Russell A. Bell, Kieran C. Dickson, and John F. Valliant

Abstract: A potential agent for imaging breast cancer has been synthesized by derivatization of the anti-estrogen tamoxifen. A multistep synthesis was required to conjugate a technetium chelate to tamoxifen in such a fashion that the biodistribution of the complex should mimic that of the parent compound.

Key words: tamoxifen, radioimaging, technetium, synthesis.

Résumé : En procédant à la préparation d'un dérivé du tamoxifène, un anti-estrogène, on a synthétisé un agent pouvant éventuellement être utilisé dans l'imagerie du cancer du sein. Il a fallu recourir à une synthèse en plusieurs étapes pour conjuguer un chélate du technétium au tamoxifène d'une façon telle que la biodistribution du complexe puisse ressembler à celle du composé parent.

Mots clés : tamoxifène, radioimagerie, technétium, synthèse.

[Traduit par la Rédaction]

Introduction

One method of developing a site-specific radioimaging agent is to derivatize a drug or bioactive molecule with a chelate – radio nuclide complex (1). To maintain receptor selectivity the chelate must be attached to the biomolecule at a point distant from the part of the molecule which binds to the receptor. One bioactive compound of particular interest is tamoxifen (Fig. 1), a drug used for the treatment of hormone dependent breast cancer (2). An imaging agent based on tamoxifen could potentially detect tumours in their infancy, which is crucial if chemotherapy is to be effective (3).

Tamoxifen, (*Z*-1(*p*-(2-dimethylaminoethoxy)phenyl)-1,2-diphenylbut-1-ene) exerts its biological effect by binding to estrogen receptors which, for certain types of cancers, are more numerous in cancer cells than normal cells (4). ^{131}I derivatives of *E* and *Z* tamoxifen were used successfully to image tumours in mice (5); however, there was insufficient uptake in human cancer patients to develop a commercial imaging agent. The location of the iodine label and the loss of iodine due to the relatively weak carbon–iodine bond could explain the insufficient tumour uptake in human breast cancer tumours. One method of overcoming these problems is to covalently attach a chelate, the technetium complex of which is known to be stable in vivo, to a site in which substituents do not tend to affect the biodistribution of the parent molecule.

Substitution on ring B of tamoxifen is not feasible because data from binding assays of tamoxifen derivatives suggests that ring B derivatives alter the pharmacological activity of tamoxifen (6). From the aforementioned binding studies of tamoxifen derivatives, ring A appears to be a more attractive location for conjugation to a chelate. *E*-2-methyl-tamoxifen, where the methyl substituent was in the *ortho* position of ring A, had an estrogen receptor binding affinity identical to that of tamoxifen (7). From this, we concluded that the *ortho* position of ring A would be a logical site, through a spacer chain, to attach a chelate.

Received June 18, 1998.

R.A. Bell, K.C. Dickson, and J.F. Valliant.[1] Department of Chemistry, McMaster University, 1280 Main St. West, Hamilton, ON L8S 4M1, Canada.

[1]Author to whom correspondence may be addressed. Telephone: (905) 525-9140, ext. 23303. Fax: (905) 522-2509. e-mail: valliant@chemistry.mcmaster.ca

Results and discussion

The diamido dithiol (DADT) chelate (**4**, Scheme 1) (8), which is known to bind ^{99m}Tc ($t_{1/2}$ = 6.0, γ = 140 KeV), the most commonly used radionuclide in diagnostic imaging, was synthesized by modifying the approach used by Bell et al. (9). 2,3-Diaminopropionic acid (**1**) was converted to the methyl ester **2** via a Fisher esterification with *p*-toluenesulfonic acid prior to reaction with the *N*-hydroxysuccinimido ester of *S*-triphenylmethylmercaptoacetic acid (1). In preparation for conjugation to the tamoxifen derivative (vide infra) the methyl ester **3** was hydrolysed by reaction with aqueous sodium hydroxide in THF to produce the desired chelate **4**.

Two approaches to the synthesis of DADT-tamoxifen conjugate were used; approach A involved the total synthesis of the tamoxifen derivative before coupling to the chelate, while strategy B entailed coupling of a chloro-tamoxifen species to the chelate prior to the addition of the dimethylamine moiety.

The synthesis, based on the approach of McCague and co-worker (10) (Scheme 2) began by following the literature procedure for the mono substitution of 1,2-dichloroethane by phenolate under phase transfer conditions (11). The chloroether was subsequently subjected to Friedel–Crafts acylation (12) by use of either (±)-2-phenylbutyric acid and trifluoroacetic anhydride (TFAA) or the acid chloride of

 © 1999 NRC Canada

Scheme 1. Synthesis of DADT (**4**).

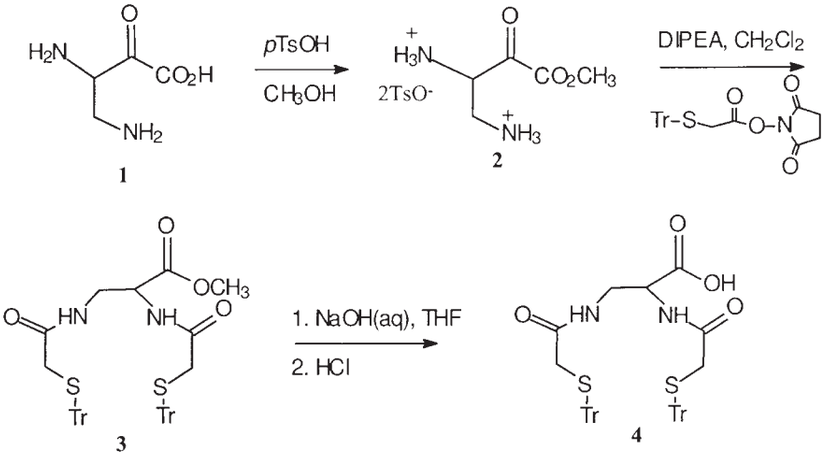

Fig. 1. Tamoxifen.

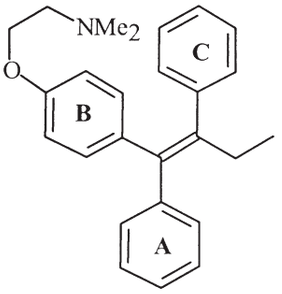

(±)-2-phenylbutyric acid and aluminum trichloride in carbon disulfide (12) to give **6** in 79 and 57% yields, respectively. Evidence from ^{1}H and ^{13}C NMR confirmed that the acylation product was entirely *para* substituted. The linker arm for the chelate was now added in the form of the *tert*-butyldimethylsilyl ether of 2-bromophenethyl alcohol (13), the nucleophile being generated by metal halogen exchange. The anion reacted with the ketone **6** to generate two diasteriomeric alcohols **9**, which were not normally isolated but converted directly to the alkenes **10** by reaction with thionyl chloride and pyridine at –10°C. These milder elimination conditions were used because the literature procedure employing concentrated HCl in ethanol caused the loss of the silyl protecting group and subsequent elimination of the resultant alcohol. The silyl group of **10** was removed in good yield (96%) by the use of tetrabutylammonium fluoride in THF (13).

The chemical shift of the proton and carbon atoms of each diasteriomer of **10**, at 200 MHz and 50 MHz, respectively, were significantly different and each isomer could be distinguished readily. To assign the signals of each isomer required the use of a two-dimensional nuclear Overhauser effect (2-D NOE) experiment (NOESY). From the ^{1}H spectrum the pair of doublets at 6.812 and 6.50 ppm were assigned to the AB spin system of ring B. The doublet at 6.812 ppm exhibited a NOE correlation to signals in the aromatic region but showed no correlation to the methylene of the ethyl group of tamoxifen; this confirmed that these signals belonged to the *E*-isomer. The COSY spectrum was then used to assign the remaining signals belonging to that isomer, and it was concluded that the major isomer, as Cram's rules (14) predicted, was the *E*-isomer in a ratio of approximately 5:1.

Fatty acid derivatives were selected as the spacer chain because the length of the spacer can be altered easily as there are numerous fatty acid derivatives which are commercially available. Once the general synthetic route was developed, varying lengths of spacers can be tested until the optimum length associated with high binding efficiency is found. In the present synthesis (Scheme 3), bromododecanoic acid was converted to the azide prior to reaction with thionyl chloride. The acid chloride was then converted to an ester by reaction with alcohol **11**. An unexpected advantage of using the long-chain fatty acid was that small quantities of each isomer of **12** could be separated by radial chromatography. During the development of the synthetic methodology towards **15**, a relatively large quantity of **12** was required, and for practical purposes, the nonenriched 5:1 *E*:*Z* ratio, material was used. Should the results of the biodistribution studies show promise, the isomers of **12** can be separated and pure *E*-**15** and *Z*-**15** synthesized. Because of the ratio of 5:1 for *E*:*Z* isomers, it was possible to assign many of the NMR signals for each isomer in mixtures of compounds **13**–**17**.

In approach A, the azido-chloride species **12** was converted to the dimethylamino species **13** by reaction with dimethylamine in ethanol at an elevated temperature. If extensive reaction times were used (greater than 4 days) a minor byproduct occurred as a result of cleavage of the ester bond by either a dimethylamine or ethoxide nucleophile with the resulting species being the phenethyl alcohol **11**. The azide **13** was reduced by the use of triphenylphosphine (15) because other methods (lithium aluminum hydride and catalytic hydrogenation) would cause reduction of the alkene and (or) ester groups. Reduction appeared to occur quantitatively as indicated by TLC, however, isolation of the resulting amine was difficult, and only a low yield of product was isolated (25%). The amine **14** was immediately coupled to the chelate (**4**) by the use of EDC (16) in good yield, as judged by thin-layer chromatography. Again, however, puri-

© 1999 NRC Canada

Scheme 2. Synthesis of **11**.

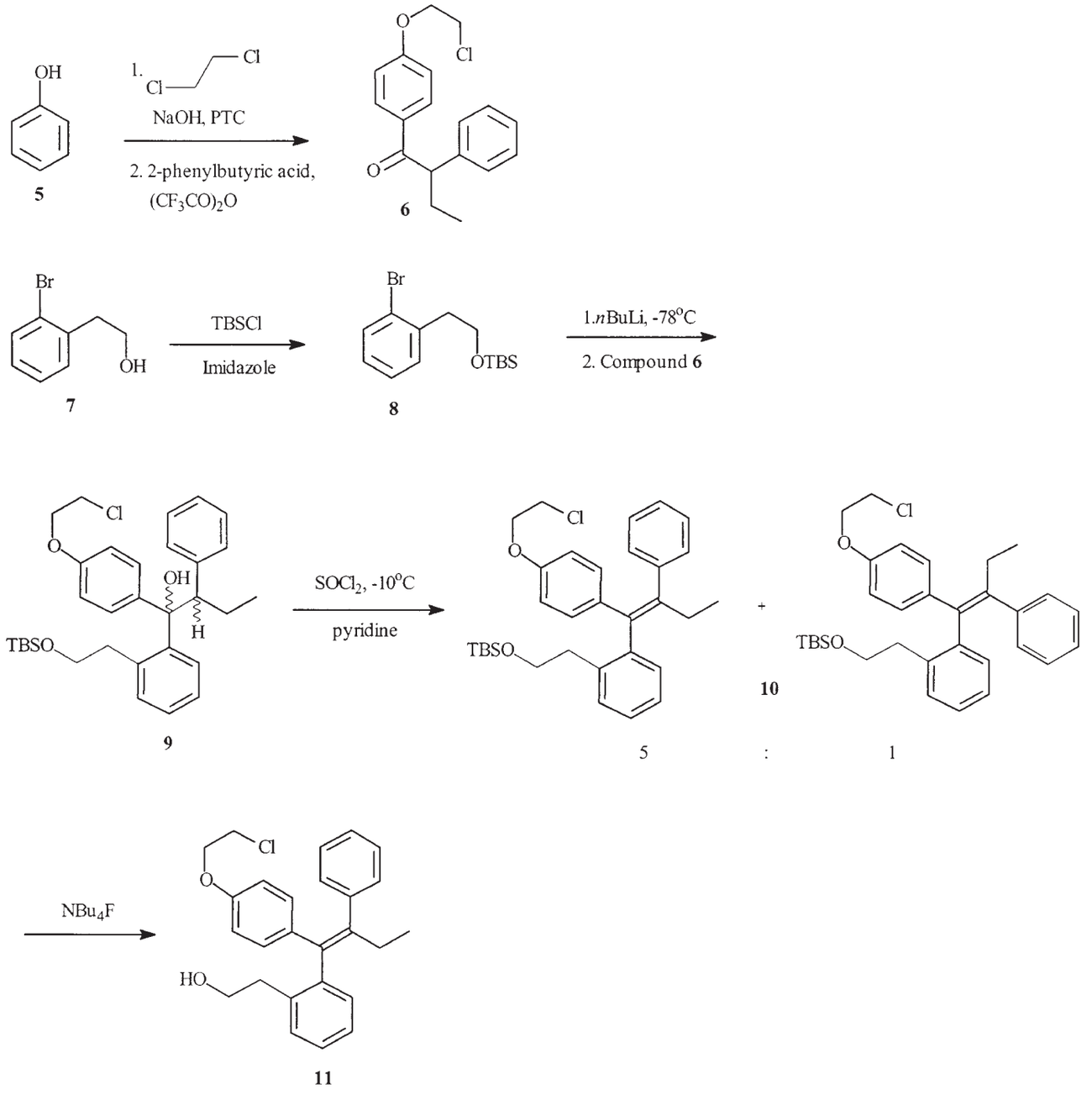

fication of the product proved difficult and resulted in a low yield of the desired product (26%).

In an attempt to improve the yields of synthesis A, strategy B was developed. The azide **12** was reduced by the use of the aforementioned triphenylphosphine approach (Scheme 4). Formation of the phosphonium salt from the alkyl chloride fragment was not a concern because the reduction was carried out at room temperature. The resulting amine **16** was coupled to the chelate in good yield (76%), and replacement of the chloro substituent with dimethylamine also occurred in good yield (60%). There was no evidence for decomposition of the ester or amide bonds so long as the reaction time was kept to a reasonable length (20–24 h).

The addition of dimethylamine to **17** could be observed in the ^{1}H NMR as the two singlets at 2.325 and 2.267 ppm, corresponding to the two isomers, were assigned to the *N*-methyl protons. There was also a significant shift of the methylene protons adjacent to the dimethylamine moiety, upon substitution, the protons shifted upfield by approximately 1 ppm. The ^{13}C NMR contained no ambiguities, the resonances associated with the *N*-methyl protons were ob-

© 1999 NRC Canada

Scheme 3. Synthesis of **15**, approach A.

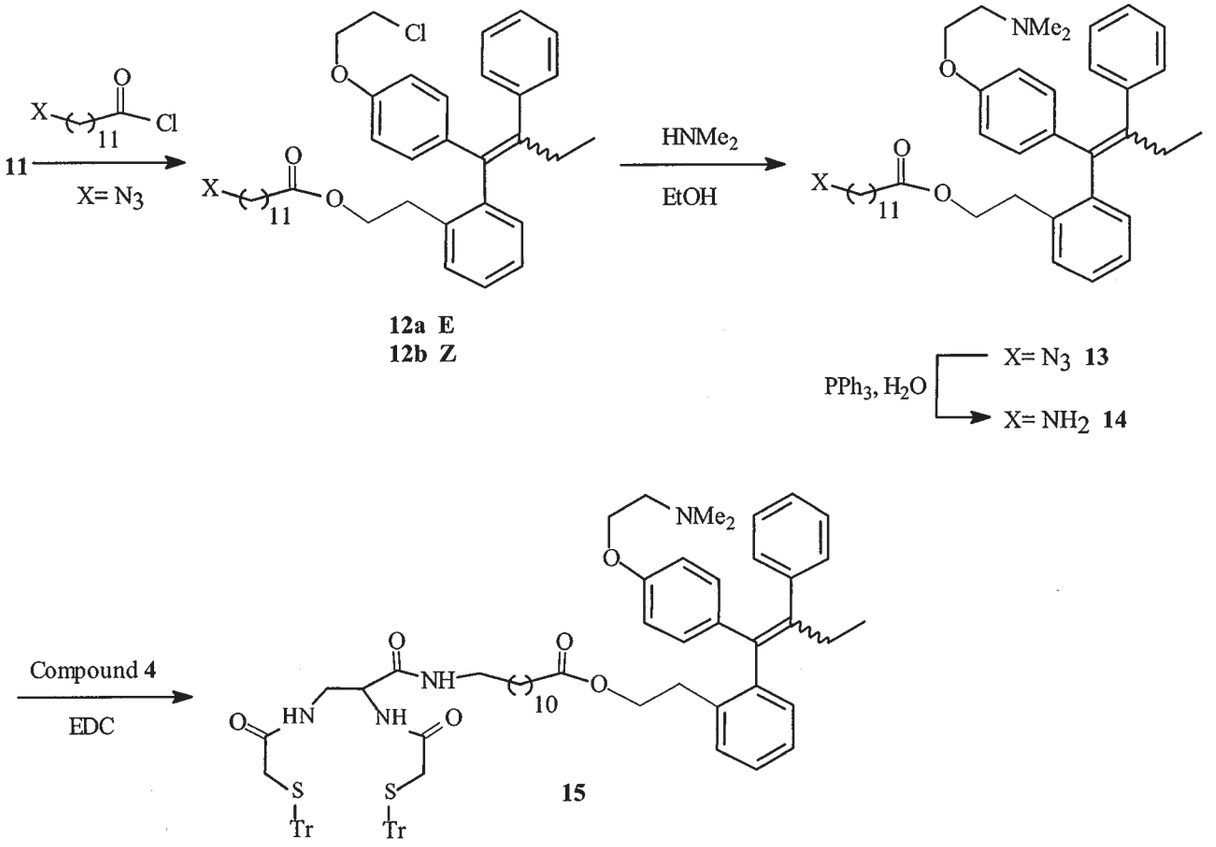

served at 45.80 ppm. The methylene protons adjacent to the *N*-methyl moiety shifted downfield upon substitution of the chloro group from 41.99 ppm to 58.18 ppm.

Experimental section

Analytical TLC was performed on silica gel 60-F_{254} (Merck) with detection by long wavelength ultraviolet light. Chromatography was performed with a chromatotron (Harrison Research Model 7924T) that used a 4 mm plate (EM Science silica gel 60 PF_{254} that contained gypsum). All commercial reagents were used as supplied. Solvents were distilled, under nitrogen, from calcium hydride. Nitrogen was dried by passing it through calcium sulphate. All reactions were protected from light and carried out under a slow flow of nitrogen. Solvents were evaporated with a rotary evaporator (20 mmHg (1 mmHg = 133.3 Pa)) at moderate temperatures (30–50°C).

Selected NMR spectra were recorded on a Bruker Avance DRX-500 spectrometer. Proton spectra were acquired at 500.130 MHz with a 5 mm broadband inverse probe with triple-axis gradient capability. Spectra were obtained in 8 scans in 32K data points over a 4.006 kHz spectral width (4.096 s acquisition time). The compounds used in this study were dissolved in $CDCl_3$ (Isotec, Inc.) to a concentration of approximately 15.0 mg mL^{-1}. Chemical shifts are reported in ppm relative to TMS. The residual solvent signals at 7.24 and 77.0 ppm were used as internal references for the ^1H and ^{13}C spectra, respectively. Coupling constants are given in Hertz (Hz). All other NMR spectra were recorded on a Bruker AC-200 spectrometer. Proton spectra were acquired at 200.133 MHz with a 5 mm dual frequency probe. Spectra were obtained in 8 scans in 16K data points over a 2.403 KHz spectral width (3.408 s acquisition time). Spectra were acquired at ambient probe temperature. The free induction decay (FID) was processed with exponential multiplication (line broadening: 0.1 Hz) and was zero-filled to 32K before Fourier transformation. Carbon-13 NMR spectra were recorded at 50.323 MHz with the 5 mm QNP probe. The spectra were acquired over a 12.195 kHz spectral width in 16K data points (0.672 s acquisition time).

Synthetic procedures

Methyl 2,3-diaminopropanoate p-*toluenesulfonate salt (**2**)*

To 2.0 g (14.28 mmol) of (±) 2,3-diaminopropionic acid monhydrochloride suspended in methanol (60 mL), *p*-toluenesulfonic acid was added (10.82 g, 56.9 mmol). After the solution was heated at reflux for 24 h it was evaporated to dryness at reduced pressure, and the remaining solid was washed with diethyl ether (200 mL), rendering the methyl ester as colourless crystals. Yield: 6.5 g, 99%; mp 200°C (decomp.); ^1H NMR (CD_3OD) (200 MHz) δ 7.719 (d, J = 8.3, 2H, H-*ortho*), 7.251 (d, 2H, H-*meta*), 5.003 (brd, NH), 4.494 (m, 1H, C*H*), 3.853 (s, 3H, OCH_3), 3.529 (m, 2H, CH_2), 2.354 (s, 3H, PhCH_3); ^{13}C NMR (CD_3OD)

© 1999 NRC Canada

Scheme 4. Synthesis of **15**, approach B.

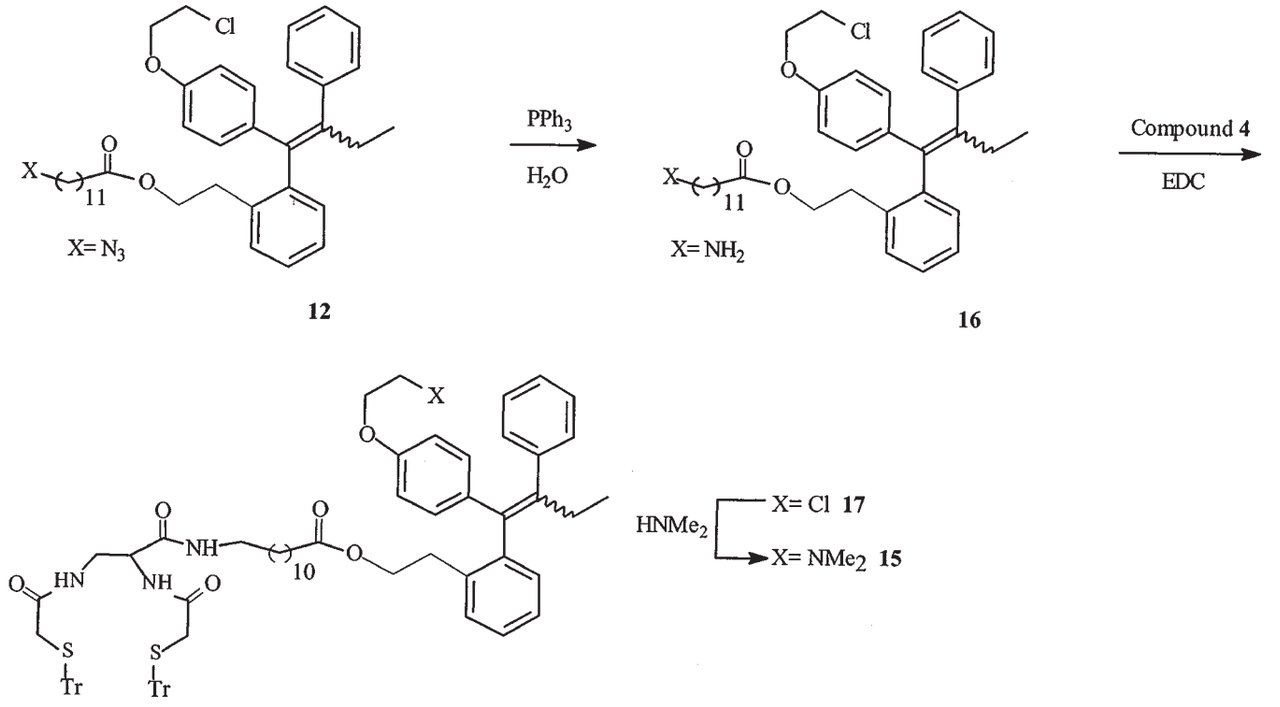

(50 MHz) δ: 167.99 (*C*OOMe), 143.00 (C-*para*), 141.99 (C-*ipso*), 129.91 (C-*meta*), 126.90 (C-*ortho*), 54.55 (*C*H), 51.14 (O*C*H$_3$), 39.51 (*C*H$_2$), 21.32 (Ph-*C*H$_3$).

Methyl 2,3-bis(triphenylmethylthioacetylamino)propanoate (3)

To 3.62 g (8.40 mmol) of 2-(triphenylmethylthio)ethanoic acid-*N*-hydroxysuccinimido ester (1) dissolved in dichloromethane (50 mL), 1.92 g (4.16 mmol) of **2** was added. To the rapidly stirred mixture, diisopropylethylamine (DIPEA) (1.34 mL, 7.69 mmol) was added and the solution heated to reflux for 8 h. The solution was cooled and extracted with 1 M HCl (2 × 10 mL), 1 M NaHCO$_3$ (2 × 10 mL), and distilled water (distilled water) (3 × 15 mL). The solution was evaporated to dryness at reduced pressure, and the solid was washed with distilled water (200 mL), methanol (5 mL), and ether (5 mL). The colourless solid was recrystallized from acetone and subsequently dried in vacuo to give 2.2 g (78%) of **3**. The compound showed mp 68–70°C; TLC: R_f = 0.44 (2% CH$_3$OH–CH$_2$Cl$_2$); ^{1}H NMR (CDCl$_3$) (200 MHz) δ: 7.324–7.075 (m, 17H, H-*aryl*), 6.708 (d, *J* = 6.7, 1H, CHN*H*), 6.094 (m, 1H, CH$_2$N*H*), 4.064 (m, 1H, C*H*), 3.087 (m, 2H, CHC*H*$_2$), 2.934 (s, 2H, C*H*$_2$); ^{13}C NMR (CDCl$_3$) (50 Mhz) δ: 170.06 (*C*OOMe), 168.55, 168.89 (*C*(O)NH), 143.87 (C-*ipso*), 129.50 (C-*ortho*), 128.09 (C-*meta*), 126.98 (C-*para*), 67.71 (Ph$_3$*C*), 52.72 (*C*H and O*C*H$_3$), 41.24 (CH*C*H$_2$), 35.93 (*C*H$_2$), 35.72 (S*C*H$_2$).

2,3-Bis(triphenylmethylthioacetylamino)propanoic acid (4)

To 1.0 g (1.33 mmol) of **3** in a 1:1 mixture of THF and water (80 mL), 100 mg (2.5 mmol) of NaOH was added. After the mixture was heated to reflux for 3 h under an atmosphere of nitrogen, the solution was cooled, acidified to pH 3.9 using 6 M HCl, and concentrated to 30 mL under reduced pressure. The precipitate that formed was collected by filtration, and the colourless solid washed with distilled water (100 mL) and sparingly with ether (5 mL). The filtrate was concentrated and diluted with methanol (15 mL) and refrigerated overnight. The resulting solid was collected by filtration and washed again with distilled water and ether as above, yielding an additional crop of the title compound. Yield 900 mg, (97%); mp 214–215°C; TLC: R_f = 0.22 (10% CH$_3$OH–CH$_2$Cl$_2$); ^{1}H NMR (CD$_3$OD) (200 MHz) δ 7.643 (m, 15H, H-*aryl*), 4.590 (m, 1H, C*H*), 4.063 (m, 2H, C*H*$_2$CH), 3.269 (m, 2H, TrSC*H*$_2$); ^{13}C NMR (CD$_3$OD) (50 MHz) δ 171.21 (C-*C*OOH), 168.90, 168.55 (*C*(O)NH), 143.87 (C-*ipso*), 129.50 (C-*ortho*), 128.09 (C-*meta*), 126.98 (C-*para*), 65.88 (Ph$_3$*C*), 52.05 (*C*H), 43.96 (*C*H$_2$CH), 35.85, 32.33 (TrS*C*H$_2$).

(2-Chloroethoxy)benzene

The procedure described by McCague (10) was used. Phenol (28.2 g, 300 mmol), dimethyldioctadecylammonium bromide (1.8 g, 3.0 mmol), sodium hydroxide (24.0 g, 600 mmol) in distilled water (225 mL), and 1,2-dichloroethane (225 mL) were heated to reflux for 48 h. The organic phase was separated, dried with magnesium sulfate, and concentrated under reduced pressure to produce a translucent yellow oil. This crude product was subsequently purified by vacuum distillation to give the title compound as a colourless oil (35.6 g, 76%). The compound showed bp 100–102°C @ 12 mmHg; ^{1}H NMR (CDCl$_3$) (200 MHz) δ: 7.30 (m, 5H, H-*aryl*), 4.23 (t, 2H, OC*H*$_2$), 3.81 (t, 2H, *J* = 5.9, C*H*$_2$Cl); ^{13}C NMR (CDCl$_3$) (50 MHz) δ 159.8 (C- *ipso*), 131.0 (C-*meta*), 122.5 (C-*para*), 118.3 (C-*ortho*), 67.86 (O*C*H$_2$), 41.86 (*C*H$_2$Cl).

© 1999 NRC Canada

*1-[4-(2-Chloroethoxy)phenyl]-2-phenyl-1-butanone (**6**)*

The procedure developed by McCague was used (10). 1-Chloro-2-phenoxyethane (21.8 g, 140 mmol), (±)-2-phenylbutyric acid (20.2 g, 120 mmol), and trifluoroacetic anhydride (27.3 g, 130 mmol) were mixed and stirred magnetically at 20°C for 70 h. The reaction mixture was then poured slowly into distilled water (150 mL) to give a pink solid which was collected and recrystallized from ethanol to give colourless crystals (28.8 g, 79%). The compound showed mp 65–70°C; TLC: R_f = 0.79 (100% CH_2Cl_2); ^{1}H NMR ($CDCl_3$) (200 MHz) δ: 7.98–6.85 (m, 9H, H-*aryl*), 4.39 (t, 1H, *J* = 7.3, PhC*H*), 4.24 (t, 2H, OCH_2), 3.80 (t, 2H, *J* = 5.8, CH_2Cl), 2.02 (m, 2H, CH_2CH$_3$), 0.89 (t, 3H, *J* = 7.4, CH_3); ^{13}C NMR ($CDCl_3$) (50 MHz) δ: 198.07 (*C*(O)), 162.11–107.38 (*C*-aryl), 67.53 (*C*HPhCH$_2$CH$_3$), 55.17 (OCH_2), 41.39 (*C*H$_2$Cl), 26.48 (*C*H$_2$), 12.15 (*C*H$_3$).

*2-(2-Bromophenyl)-*O*-(*tert*-butyldimethylsilyl)ethan-2-ol (**8**)*

The procedure developed by Corey and Venkateswarlu (13) was used. 2-Bromophenethyl alcohol (2.0 g, 9.95 mmol) and imidazole (1.02 g, 14.9 mmol) were dissolved in dichloromethane (30 mL) under nitrogen and cooled over ice before *tert*-butyldimethylsilyl chloride (2.25 g, 14.9 mmol) was added. After 8 h the reaction mixture was filtered and the residue washed with dichloromethane (25 mL). The filtrate was extracted with distilled water (3 × 30 mL), concentrated to 1 mL, and passed down a silica column (petroleum ether – dichloromethane). The first band to elute from the column was collected, evaporated to dryness, and dried under high vacuum until the odour of the silicon starting material could no longer be detected (2–3 h). The product, a colourless oil (2.6 g, 83%), showed TLC: R_f = 0.66 (50:50 v/v CH_2Cl_2/hexanes); ^{1}H NMR ($CDCl_3$) (200 MHz) δ: 7.58–6.99 (m, 4H, H-*aryl*), 3.85 (t, 2H, *J* = 8.8, CH_2O), 2.99 (t, 2H, PhCH_2), 0.90 (s, 9H, SiC(CH_3)$_3$), 0.03 (s, 6H, Si(CH_3)$_2$); ^{13}C NMR ($CDCl_3$) (50 MHz) δ 138.29 (C-2), 131.7, 132.6 (C-3, C-6), 127.8, 127.1, (C-4, C-5), 124.56 (C-*ipso* i.e., C-1), 62.40 (*C*H$_2$O), 53.27 (Si*C*(CH$_3$)$_3$), 39.59 (PhCH$_2$), 25.89 (SiC(*C*H$_3$)$_3$), 18.22 (Si(*C*H$_3$)$_2$); MS (NH$_3$ DCI) *m*/*z* (RI%): 334 (100) (M + 2H$^+$ + NH$_3$), 332 (89) (M + NH$_3$), 331 (20) (M + NH$_3$ – H$^+$), 317 (100) (M + 2H$^+$), 315 (90) (M).

*1-[4-(2-Chloroethoxy)phenyl]-1-[2-(*O*-(*tert*-butyldimethylsilyl)ethyl)phenyl]-2-phenyl butan-1-ol (**9**)*

Compound **8** (2.02 g, 6.41 mmol) was dissolved in 5 mL of dry THF in a flame-dried flask under an argon atmosphere and cooled to –78°C. When *n*-butyllithium (4.0 mL, 1.6 M solution in hexanes) was added via syringe the solution became heterogeneous; it was left to stir for an additional 20 min. After the addition of compound **6** (1.09 g, 3.6 mmol in 5 mL dry THF) the solution cleared. The solution was allowed to gradually warm to room temperature and after 12 h the reaction was complete. Distilled water (50 mL) was added slowly and the solution extracted with ether (3 × 50 mL). The organic layers were combined, dried over sodium sulfate, filtered, and evaporated to dryness. The resulting oil was used without further purification or characterization.

*1-[4-(2-Chloroethoxy)phenyl]-1-[2-(*O*-(*tert*-butyldimethylsilyl)ethyl)phenyl]-2-phenyl but-1-ene (**10**)*

Compound **9** was dissolved in freshly distilled pyridine (10 mL) and cooled to –10°C; thionyl chloride (788 µL, 10.8 mmol) was added and the mixture stirred under argon for 3 h. The yellow–orange coloured solution was diluted cautiously with distilled water (20 mL) and extracted with diethyl ether (4 × 40 mL). The organic layers were combined and evaporated to dryness. The product was isolated by radial chromatography (10:1 low boiling petroleum ether/ether). The compound, a yellow oil (1.18 g, 64%), showed TLC: R_f = 0.72 (10:90 v/v ether/petroleum ether); ^{1}H NMR ($CDCl_3$) (200 MHz) δ:7.102 (m, H-aryl), 6.500 (d, 2H, H-*ortho* ring B), 4.189 (t, *J* = 3.9, 2H, *Z*-isomer OCH_2CH$_2$Cl), 4.042 (t, *J* = 3.8, 2H, *E*-isomer OCH_2CH$_2$Cl), 3.910 (m, 1H, SiOCH_2), 3.769 (t, *J* = 3.9, 2H, *Z*-isomer CH_2Cl), 3.672 (t, *J* = 4.0, 2H, *E*-isomer CH_2Cl), 3.449 (m, TBSOCH_2), 2.867 (t, *J* = 3.6, 2H, *E*-isomer CH_2Ph), 2.787 (m, 1H, *E*-isomer CH_2CH$_3$), 2.686 (t, *J* = 4.9, 2H, *E*-isomer CH_2Ph), 2.560 (m, 1H, *Z*-isomer CH_2CH$_3$), 2.276 (m, 2H, *Z*-isomer CH_2CH$_3$), 1.007 (t, *J* = 4.9, CH_3), 0.814 (m, SiC(CH_3)$_3$), 0.02 (s, Si-CH_3); ^{13}C NMR ($CDCl_3$) (50 MHz) δ 156.77, 156.06, 142.77, 142.53, 142.16, 141.89, 141.74, 137.55, 136.95, 135.97, 134.77, 131.71, 131.55, 130.65, 130.42, 130.01, 129.73, 129.46, 128.96, 128.26, 127.97, 127.47, 126.95, 126.20, 126.0, 125.36, 120.05, 117.0, 114.18, 113.505 (C-*aryl*), 67.93 (*Z*-isomer OCH$_2$CH$_2$Cl), 67.70 (*E*-isomer OCH$_2$CH$_2$Cl), 63.43 (*E*-isomer SiOCH$_2$), 63.20 (*Z*-isomer SiOCH$_2$), 41.76 (*C*H$_2$Cl), 36.72 (*E*-isomer *C*H$_2$Ph), 36.43 (*Z*-isomer *C*H$_2$Ph), 29.51 (*C*H$_2$CH$_3$), 25.93 (SiC(*C*H$_3$)$_3$), 18.31 (Si*C*H$_3$), 13.80 (*Z*-isomer CH$_2$*C*H$_3$), 12.93 (*E*-isomer CH$_2$*C*H$_3$); MS (NH$_3$ DCI) *m*/*z* (RI%): 538 (100) (M + NH$_3$), 520 (80) (M), 406 (85) (M – TBS + H).

*1-[4-(2-Chloroethoxy)phenyl]-1-[2-(hydroxyethyl)phenyl]-2-phenyl but-1-ene (**11**)*

The procedure developed by Corey and Venkateswarlu (13) was used. To compound **10** (800 mg, 1.54 mmol) in 10 mL of THF, tetrabutylammonium fluoride (5.07 mL, 1.0 M solution in THF) was added. The reaction was allowed to stir for 24 h before dilution with distilled water (20 mL) and extraction with diethyl ether (4 × 25 mL). The organic layer was concentrated to a volume of 2 mL and the product isolated by radial chromatography (hexanes–dichloromethane). The title compound (600 mg, 96%), an oil, showed TLC: R_f = 0.15 (100% CH_2Cl_2); ^{1}H NMR ($CDCl_3$) (200 MHz) δ: 7.20 (m, H-*aryl*), 6.520 (d, 2H, H-*ortho* ring B), 4.143 (t, *J* = 5.9, *Z*-isomer, OCH_2CH$_2$Cl), 3.996 (t, *J* = 5.9, 2H, *E*-isomer OCH_2CH$_2$Cl), 3.725 (t, *J* = 5.8, 2H, *Z*-isomer CH_2Cl), 3.629 (t, *J* = 5.9, 2H, *E*-isomer CH_2Cl), 3.425 (m, *E*/*Z*, CH_2OH), 2.711, 2.200 (m, overlap, CH_2Ph, CH_2CH$_3$), 0.954 (t, *J* = 7.5, 3H, *Z*-isomer CH_3), 0.769 (t, *J* = 7.4, 3H, *E*-isomer CH_3); ^{13}C NMR ($CDCl_3$) (50 MHz) δ: 156.10, 156.06, 142.98, 142.69, 142.05, 141.70, 136.65, 136.37, 136.15, 135.86, 134.60, 132.01, 131.50, 130.35, 130.24, 129.65, 128.87, 127.98, 127.52, 127.22, 126.50, 126.26, 126.06, 125.64, 114.24, 113.52 (C-*aryl*), 67.93 (*Z*-isomer OCH_2CH$_2$Cl), 67.67 (*E*-isomer OCH_2CH$_2$Cl), 62.63 (*E*-isomer *C*H$_2$OH), 62.41 (*Z*-isomer *C*H$_2$OH), 41.79 (*C*H$_2$Cl), 36.47 (*E*-isomer PhCH$_2$), 36.14 (*Z*-isomer PhCH$_2$),

© 1999 NRC Canada

29.49 (*E*-isomer CH_2CH_3), 28.04 (*Z*-isomer CH_2CH_3), 13.77 (*Z*-isomer CH_3), 12.92 (*E*-isomer CH_3).

12-Azido-dodecanoic acid

Sodium azide (4.7 g, 72.3 mmol) was added to a solution of 12-bromododecanoic acid (2.0 g, 7.16 mmol) in DMF (45 mL). After heating at 80°C for 12 h, the reaction mixture was cooled to room temperature and poured into distilled water (100 mL). The solution was extracted with ether (2 × 70 mL) and the organic fractions pooled and evaporated in vacuo. The resulting yellow oil was diluted with a 3:1 mixture of water/brine (10 mL) and refrigerated overnight. The resulting colourless precipitate was collected by filtration, washed with cold water (30 mL), and dried in air. The compound (1.56 g, 90%) showed ^{1}H NMR ($CDCl_3$) (200 MHz) δ: 3.320 (t, *J* = 6.8, 2H, CH_2-N_3), 2.313 (t, *J* = 7.4, 2H, CH_2COOH), 1.570 (m, 4H, CH_2), 1.257 (m, 18H, CH_2); ^{13}C NMR ($CDCl_3$) (50 MHz) δ: 180.04 (*C*OOH), 51.45 (CH_2-N_3), 34.15 (CH_2COOH), 29.40, 29.18, 29.09, 29.02, 28.8, 26.67, 24.68 (CH_2); MS(ES) *m*/*z* (RI%): 241.4 (18) (M), 240.4 (100) (M – H).

*1-[4-(2-Chloroethoxy)phenyl]-1-[2-[(12-azidododecanoyl)oxyethyl)phenyl]-2-phenyl but-1-ene (**12**)*

12-Azido-dodecanoic acid (500 mg, 2.07 mmol) was dissolved in thionyl chloride (8 mL) and heated to reflux under nitrogen for 1 h. Residual thionyl chloride was evaporated in vacuo and the residue dissolved in dry dichloromethane (25 mL), which was subsequently evaporated. The oily residue was redissolved in dry dichloromethane (20 mL) and compound **11** (766 mg, 1.89 mmol) in dry dichloromethane (5 mL) was added. The solution was heated to reflux for 12 h before the slow addition of 10% Na_2CO_3 (20 mL). The solution was extracted with chloroform (2 × 50 mL), and the organic layers were pooled, concentrated to 2 mL, and the product, a yellow oil (766 mg, 64%), isolated by radial chromatography (petroleum ether – ether). Samples of pure *E*-12 and pure *Z*-12 can be isolated by using a new chromatatron plate (activated with petroleum ether), a very gradual gradient of 100% petroleum ether up to 10% ether and collecting small aliquots as the major product band elutes from the chromatatron. The compound showed MS (HRDEI): obs: 629.33695, calcd.: 629.3384. *E*-Isomer: ^{1}H NMR ($CDCl_3$) (500 MHz) δ: 7.280 (m, H-*aryl*), 6.764 (d, *J* = 9.3, 2H, H-*meta*- ring B), 6.512 (d, 2H, H-*ortho*- ring B), 4.117 (m, 1H, OCH_2CH_2Ph), 4.063 (m, 2H, OCH_2CH_2Cl), 3.914 (m, 1H, OCH_2CH_2Ph), 3.694 (t, 2H, *J* = 6.0, CH_2Cl), 3.233 (t, 2H, CH_2N_3), 2.734 (m, 2H, OCH_2CH_2Ph), 2.325 (m, 1H, CH_2CH_3), 2.224 (t, *J* = 6.2, 2H, $CH_2C(O)$), 2.211 (m, 1H, CH_2CH_3), 1.564, 1.344, 1.245 (m, CH_2), 0.810 (t, *J* = 7.4, 3H, CH_3); ^{13}C NMR ($CDCl_3$) (125 MHz) δ 173.61 (*C*OOR), 156.13, 142.68, 142.28, 141.76, 136.50, 135.82, 134.48, 131.53, 130.28, 130.20, 129.70, 128.00, 127.20, 126.44, 126.28, 113.60 (C-*aryl*), 67.78 (OCH_2CH_2Cl), 63.71 (OCH_2CH_2Ph), 51.48 (CH_2N_3), 41.78 (CH_2Cl), 34.32 ($CH_2OC(O)$), 32.48 OCH_2CH_2Ph), 29.42, 29.38, 29.23, 29.10 (CH_2), 28.82 (CH_2CH_3), 26.69, 24.94 (CH_2), 12.90 (CH_3). *Z*-Isomer: ^{1}H NMR ($CDCl_3$) (500 MHz) δ: 7.00 (m, H-*aryl*), 4.166 (t, *J* = 6.0, 2H, OCH_2CH_2Cl), 3.816 (m, OCH_2CH_2Ph), 3.746 (t, *J* = 6.0, 2H, OCH_2CH_2Cl), 3.652 (m, OCH_2CH_2Ph), 3.191 (t, *J* = 7.0, 2H, CH_2N_3), 2.801, 2.620, 2.553 (m, overlap, OCH_2CH_2Ph and CH_2CH_3), 2.192 (t, *J* = 7.6, 2H, $CH_2C(O)$), 1.511, 1.288 (m, CH_2), 0.960 (t, *J* = 7.4, 3H, CH_3); ^{13}C NMR ($CDCl_3$) (125 MHz) δ: 173.60 (*C*OOR), 142.92, 142.01, 137.18, 135.65, 131.95, 130.39, 129.71, 128.95, 127.54, 126.52, 126.12, 125.80, 114.35 (C-*aryl*), 68.05 (OCH_2CH_2Cl), 63.72 (OCH_2CH_2Ph), 51.48 (CH_2N_3), 41.83 (CH_2Cl), 34.33 ($CH_2OC(O)$), 32.05 (OCH_2CH_2Ph), 29.45, 29.25, 29.13, 28.82 (CH_2), 26.70 (CH_2CH_3), 24.95 (CH_2), 13.79 (CH_3).

*1-[4-(2-Dimethylaminoethoxy)phenyl]-1-{2-[(12-azidododecanoyl)oxyethyl]phenyl}-2-phenyl but-1-ene (**13**)*

The procedure developed by McCague (10) was used. In a round-bottom flask fitted with a dry ice condenser, compound **12** (150 mg, 0.235 mmol) was dissolved in dimethylamine (20 mL, 5.6 M solution in ethanol) and the mixture was heated to reflux for 2 days. The solution was evaporated to dryness, the residue dissolved in DCM (2 mL), and the title compound isolated by centrifugal chromatography ($CHCl_3$–MeOH). The title compound, a yellow oil (76 mg, 50%), showed ^{1}H NMR ($CDCl_3$) (500 MHz) δ: 7.298 (m, H-*aryl*), 6.934 (d, *J* = 8.9, 2H, *H-meta* ring A), 6.512 (d, 2H, H-*ortho*, ring A), 4.110 (m, OCH_2CH_2Ph), 3.916 (overlap, t, *J* = 6.0, $OCH_2CH_2NMe_2$, and m, OCH_2CH_2Ph), 3.242 (t, *J* = 6.8, 2H, CH_2N_3), 2.713 (m, OCH_2CH_2Ph), 2.644 (t, *J* = 5.7, 2H, CH_2NMe_2), 2.210 (m, overlap, CH_2CH_3, CH_2COOR, NCH_3), 1.331 (m, $(CH_2)_n$), 0.813 (t, *J* = 7.2, 3H, CH_2CH_3); ^{13}C NMR ($CDCl_3$) (125 MHz) δ: 173.59 (*C*OOR), 156.69, 142.72, 141.88, 141.74, 136.57, 135.76, 133.68, 131.33, 130.21, 130.11, 129.65, 128.89, 127.90, 127.46, 127.07, 126.34, 126.14, 114.05 (C-*aryl*), 65.52 ($OCH_2CH_2NMe_2$), 63.67 (OCH_2CH_2Ph), 58.13 (CH_2N), 51.38 (CH_2N_3), 45.73 (NCH_3), 34.25 (CH_2COOR), 32.42 (OCH_2CH_2Ph), 29.37, 29.18, 29.05 ($(CH_2)_n$), 28.75 (CH_2CH_3), 26.63, 24.88 ($(CH_2)_n$), 12.90 (CH_2CH_3); MS (HRDEI): obs: 638.4190, calcd.: 638.4196.

*1-[4-(2-Dimethylaminoethoxy)phenyl]-1-{2-[(12-aminododecanoyl)oxyethyl]phenyl]-2-phenyl but-1-ene (**14**)*

To compound **13** (69 mg, 0.108 mmol) in THF (1 mL), triphenylphosphine (29 mg, 0.110 mmol) followed by distilled water (3.0 μL) were added. The reaction was allowed to stir for 24 h whereupon an additional aliquot of triphenylphosphine (29 mg, 0.110 mmol) and water (3.0 μL) were added. After an additional 24 h the solution was evaporated to dryness, diluted with chloroform (1 mL), and the title compound isolated by centrifugal chromatography (16 mg, 25%). The compound showed ^{1}H NMR ($CDCl_3$) (500 MHz) δ 7.230 (m, H-*aryl*), 6.691 (d, *J* = 8.8, 2H, *H-meta* ring A), 6.488 (d, 2H, H-*ortho*, ring A), 4.036 (m, OCH_2CH_2Ph), 3.832 (overlap, t, *J* = 5.8, $OCH_2CH_2NMe_2$, and m, OCH_2CH_2Ph), 2.637 (m, overlap, CH_2NH_2, OCH_2CH_2Ph, CH_2NMe_2), 2.197 (m, CH_2CH_3, CH_2COOR, NCH_3), 1.492, 1.353, 1.182 (m, $(CH_2)_n$), 0.743 (t, *J* = 7.2, 3H, CH_2CH_3); ^{13}C NMR ($CDCl_3$) (125 MHz) δ: 173.64 (*C*OOR), 156.73, 142.72, 141.87, 141.76, 136.58 135.77, 133.66, 131.33, 130.22, 130.22, 130.11, 129.66, 128.25, 127.91, 127.07, 126.34, 126.14, 113.34 (C-*aryl*), 65.60 ($OCH_2CH_2NMe_2$), 63.68 (OCH_2CH_2Ph), 58.18 (CH_2N), 45.78 (NCH_3), 42.08 (H_2NCH_2), 34.27 (CH_2COOR), 33.69 ($(CH_2)_n$), 32.42

© 1999 NRC Canada

(OCH_2CH_2Ph) 29.44, 29.21(($CH_2)_n$), 29.06 (CH_2CH_3), 26.82, 24.89 (($CH_2)_n$), 12.91 (CH_2CH_3); MS (NH_3 DCI) *m*/*z* (RI%): 613 (100) (M + 1), 541 (14) (M – $CH_2CH_2NMe_2$).

*1-[4-(2-Dimethylaminoethoxy)phenyl]-1-{2-[(12-((2,3-bistriphenylmethylthioacetylamino)propanamido)dodecanoyloxy)ethyl]phenyl}-2-phenyl but-1-ene (**15**)*

Compound **14** (16 mg, 0.026 mmol) was dissolved in DCM (10 mL) and triethylamine was added (1 mL), followed by compound **4** (20 mg, 0.027 mmol). To this well stirred solution, EDC (19 mg, 0.099 mmol) was added slowly. The reaction mixture was stirred for 48 h before dilution with DCM (10 mL) and extraction with brine (3 × 10 mL). The organic phase was concentrated to 1 mL and an impure fraction of the title compound isolated by radial chromatography ($CHCl_3$–MeOH). This fraction was concentrated to 0.5 mL, and a pure sample of the title compound isolated by preparative TLC (silica). The title compound was a yellow oil (9 mg, 26%).

*1-[4-(2-Chloroethoxy)phenyl]-1-{2-[(12-aminododecanoyl)oxyethyl]phenyl}-2-phenyl but-1-ene (**16**)*

Triphenylphosphine (326 mg, 1.24 mmol) was added to a solution of compound **12** (710 mg, 1.13 mmol) in THF (2 mL) and water (50 μL). The solution was stirred (protected from light) for 12 h before concentration of the solvent under reduced pressure. The oily residue was dissolved in chloroform (2 mL), and the product, a yellowish oil (450 mg, 66%), was isolated by radial chromatography ($CHCl_3$–MeOH) and used immediately after isolation.

*1-[4-(2-Chloroethoxy)phenyl]-1-[2-((12-((2,3-bistriphenylmethylthioacetylamino)propanamide)dodecanoyl)oxyethyl)phenyl]-2-phenyl but-1-ene (**17**)*

To a dichloromethane solution (10 mL) of compound **16** (180 mg, 0.298 mmol) and compound **4** (264 mg, 0.36 mmol), EDC (70 mg, 0.36 mmol) and triethylamine (1 mL) were added. The mixture was allowed to stir for 48 h whereupon the solvent was evaporated at reduced pressure, the oily residue dissolved in chloroform (2 mL), and the product isolated by radial chromatography (hexanes–chloroform). The compound, a yellow oil (300 mg, 76%), showed ^{1}H NMR ($CDCl_3$) (500 MHz) δ: 7.250 (m, H-*aryl*), 6.755 (d, *J* = 8.9, 2H, H-*meta* ring A), 6.491 (d, 2H, H-*ortho*, ring A), 4.150 (t, *J* = 5.8, 2H, *Z*- OCH_2CH_2Cl), 4.118 (m, overlap, OCH_2CH_2Ph), 4.028 (t, *J* = 3.9, 2H, *E*-OCH_2CH_2Cl), 3.771 (m, overlap, $CHCH_2$ and OCH_2CH_2Ph), 3.761 (t, *J* = 4.2, *Z*-OCH_2CH_2Cl), 3.665 (t, *J* = 5.8, 2H, *E*- OCH_2CH_2Cl), 3.181 (m, 2H, $CHCH_2$), 2.971 (s, 4H, CH_2S), 2.718 (m, overlap, *E*/*Z* OCH_2CH_2Ph), 2.246 (m, overlap, *E*/*Z* CH_2CH_3), 2.179 (t, *J* = 5.6, 2H, CH_2COOR), 1.534, 1.385, 1.200 (m, $(CH_2)_n$), 0.988 (t, *J* = 7.5, 3H, *Z*-CH_2CH_3), 0.793 (t, *J* = 7.3, 3H, CH_2CH_3); ^{13}C NMR ($CDCl_3$) (125 MHz) δ 173.54 (ester *C*(O)), 169.71, 169.08, 168.88 (amide C(O)), 156.00, 143.81, 142.78, 142.56, 142.15, 141.63, 136.39, 135.69, 134.32, 131.43, 130.21, 130.08, 129.60, 129.42, 129.35, 128.85, 128.02, 127.45, 127.12, 126.90, 126.36, 126.19, 125.71, 114.22, 113.46 (C-*aryl*), 83.14 (CPh_3), 67.65 (*Z*-OCH_2CH_2Cl), 67.62 (*E*-OCH_2CH_2Cl), 63.61 (OCH_2CH_2Ph), 51.11 ($CHCH_2$), 41.99 (*Z*-CH_2Cl), 41.76 (*E*-CH_2Cl), 39.55 ($CHCH_2$), 36.04, 35.74 (SCH_2), 34.22 (CH_2COOR), 32.38 (OCH_2CH_2Ph), 30.81, 29.42, 29.18, 26.79 (($CH_2)_n$), 29.03 (CH_2CH_3), 26.79, 24.86 (($CH_2)_n$), 13.05 (*Z*-CH_2CH_3); 12.85 (*E*-CH_2CH_3).

*1-[4-(2-Dimethylaminoethoxy)phenyl]-1-{2-[(12-((2,3-bistriphenylmethylthioacetylamino)propanamide)dodecanoyl)oxyethyl]phenyl}-2-phenyl but-1-ene (**15**)*

A sample of 300 mg (0.227 mmol) of **17** was dissolved in a 5.6 M solution of dimethylamine in ethanol (5 mL) in a round-bottom flask that was fitted with a dry-ice condenser. The solution was heated to reflux for 24 h when, after cooling, the solvent was evaporated in vacuo. The product, a dark oily semi-solid (181 mg, 60%), was isolated by radial chromatography (chloroform–methanol). The compound showed TLC: R_f = 0.36 (10% CH_3OH–CH_2Cl_2); ^{1}H NMR ($CDCl_3$) (500 MHz) δ: 7.250 (m, H-*aryl*), 6.735 (d, *J* = 8.9, H, *H-meta* ring A), 6.505 (d, 2H, H-*ortho*, ring A), 4.122 (m, overlap, OCH_2CH_2Ph,$CHCH_2$), 4.055 (m, *Z*-OCH_2CH_2N), 3.926 (m, overlap, OCH_2CH_2Ph), 3.896 (t, *J* = 5.9, *E*-OCH_2CH_2N), 3.194 (m, $CHCH_2$), 2.985 (s, 4H, CH_2S), 2.718 (m, overlap, *Z*-OCH_2CH_2N and OCH_2CH_2Ph), 2.625 (t, *J* = 5.8, 2H, *E*-OCH_2CH_2N), 2.325 (s, *Z*-NCH_3), 2.267 (*E*-NCH_3), 2.211 (m, overlap, *E*/*Z* CH_2CH_3, CH_2COOR), 1.540, 1.407, 1.213 (m, $(CH_2)_n$), 0.994 (t, *J* = 7.4, 3H, *Z* = CH_2CH_3), 0.797 (t, *J* = 7.5, 3H, CH_2CH_3); ^{13}C NMR ($CDCl_3$) (125 MHz) δ 173.63 (ester *C*(O)), 169.86, 169.21, 168.96 (amide *C*(O)), 156.73, 143.87, 142.75, 141.92, 136.60, 135.82, 133.72, 131.37, 130.26, 129.69, 129.50, 129.42, 128.94, 128.11, 126.98, 126.38, 126.19, 114.10, 113.39, (C-*aryl*), 67.73 (CPh_3), 65.57 (OCH_2CH_2N), 63.70 (OCH_2CH_2Ph), 58.18 (CH_2N), 54.55 ($NHCH_2$), 45.80 (NCH_3), 42.07 ($CHCH_2$), 39.64 ($CHCH_2$), 36.10, 35.79 (SCH_2), 34.31 (CH_2COOR), 32.45 (OCH_2CH_2Ph), 29.48, 29.26 (($CH_2)_n$), 29.03 (CH_2CH_3), 26.86, 24.94 (($CH_2)_n$), 13.05 (*Z*-CH_2CH_3); 12.95 (*E*-CH_2CH_3). C, H analysis: calcd. for $C_{85}H_{94}N_4S_2O_6 \cdot 2.5H_2O$: C 74.06, H 7.42%; obs.: C 74.18, H 7.20%.

Conclusions

Using approach B, a 5:1 *E*:*Z* sample of compound 15 was synthesized in 18 steps in reasonable yield. It is was also discovered that the *E* and *Z* isomers of compound 12 could be separated by radial chromatography. This work is an example of a total synthesis of a biomolecule–chelate complex for the purpose of developing a site-specific radioimaging agent. Testing of compound 15 in tumour models remains work in progress.

Acknowledgements

We acknowledge, with thanks, financial support of this work by the Natural Sciences and Engineering Research Council of Canada and the grant of an NSERC postgraduate fellowship to J.F.V.

References

1. R.K. Hom and J.A. Katzenellenbogen. Nucl. Med. Biol. **24**, 485 (1997); W.A. Volkert and S. Jurisson. Top. Curr. Chem. **176**, 124 (1996); R.A. Bell, D.W. Hughes, C.J.L. Lock, and J.F. Valliant. Can J. Chem. **74**, 1503 (1996).

© 1999 NRC Canada

2. B.J.A. Furr and V.C. Jordan. Pharmacol. Ther. **25**, 127 (1984).
3. C.L. Carter, G.Allen, and D.E. Henderson. Cancer, **63**,181 (1989).
4. P. Feherty, G. Farrer-Brown, and A.E. Kellie. Br. J. Cancer, **25**, 697 (1971).
5. L.A. Strickland, Y.Z. Ponce, D.H. Hunter, P.L. Zabel, G.M. Powe, A.A. Driedger, and M.J. Chamberlain. Drug Des. Delivery, **6**, 195 (1990).
6. V.C. Jordan. Pharm. Rev. **36**(4) (1984).
7. R. McCague, M. Jarman, On-Tai Leung, A.B. Foster, G. Leclercq, and S. Stoessel. J. Steroid Biochem. **31**, 4B (1988); **31**, 545 (1988).
8. A. Davison, A.G. Jones, C. Orvig, and M. Sohn. Inorg. Chem. **20**, 1629 (1981).
9. R.A. Bell, A. Capretta, and R.B. Maharajh. Carbohydr. Res. **267**, 49 (1995).
10. G.A. Potter and R. McCague. J. Org. Chem. **55**, 6184 (1990); R. McCague. J. Chem. Res. Synop. **58**, 771 (1986); J. Chem. Soc. Perkin Trans 1, 1011 (1987)
11. R. McCague. J. Chem. Res. 771 (1980).
12. F.R. Jensen and G. Goldman. Friedel-Crafts and related reactions. Vol. 2. *Edited by* G. Olah. Wiley Interscience, New York. 1964. Chap. 36.
13. E.J. Corey and A. Venkateswarlu. J. Am. Chem. Soc. **94**, 6190 (1972).
14. D.J. Cram and F.A. Abd Elhafez. J. Am. Chem. Soc. **74**, 5828 (1952).
15. H. Staudinger and J. Meyer. Helv. Chim. Acta, **2**, 635 (1919); M. Vaultier, N. Knouzi, and R. Carrie. Tetrahedron Lett. **24**, 763 (1983).
16. J.C. Sheehan and S.L. Ledis. J. Am. Chem. Soc. **95**, 875 (1973).

© 1999 NRC Canada

COMMUNICATION

Self-assembly of one-dimensional polymers by coordination and hydrogen bonding in palladium(II) complexes

Zengquan Qin, Hilary A. Jenkins, Simon J. Coles, Kenneth W. Muir, and Richard J. Puddephatt

Abstract: The ligands L = pyridine- or quinoline-carboxylic acid easily give complexes *trans*-[$PdCl_2L_2$], which self-assemble through hydrogen bonding between carboxylic acid groups to give one-dimensional polymers, as proved by structure determinations when L = NC_5H_4COOH-4, NC_5H_4COOH-3, and 2-Ph-NC_9H_5COOH-4.

Key words: polymer, hydrogen-bonding, palladium, coordination.

Résumé : Les ligands L = acide pyridine-3-carboxylique, acide pyridine-4-carboxylique ou acide quinoléine-4-carboxylique donnent facilement des complexes *trans*-[$PdCl_2L_2$], qui s'auto-assemblent, au moyen de liaisons hydrogènes entre les groupes carboxyliques, pour donner des polymères unidimensionnels comme le démontrent les déterminations de structure lorsque L = NC_5H_4-4-COOH, NC_5H_4-3-COOH et 2-Ph-NC_9H_5-4-COOH.

Mots clés : polymère, liaison hydrogène, palladium, coordination.

[Traduit par la Rédaction]

The design of supramolecular architectures that self-assemble in a predictable way presents a challenge in modern chemistry (1). Hydrogen bonding is known to control organic structures in both natural (2) and synthetic (3) systems, resulting in the formation of one-, two-, and three-dimensional architectures of many kinds. The use of coordination chemistry in self-assembly is also developing rapidly (4), based on the easy templating effect of the metal centres, the opportunity that metal centers in neighbouring molecules can be linked through interactions that have strengths similar to those of hydrogen bonds, and the potential importance of new metal-containing materials in electronic, optical, or sensing devices. The combination of both coordination chemistry and hydrogen-bonding approaches is particularly powerful (5, 6) but relatively little work has yet been reported on the use of hydrogen bonding between simple carboxylic acid groups as substituents in coordination compounds to give supramolecular arrays (6). This communication reports the synthesis and characterization of one-dimensional polymers based on *trans*-[$PdCl_2L_2$] complexes, where L is a ligand containing both a pyridine donor and a free carboxylic acid group.

Several new *trans*-[$PdCl_2L_2$] complexes, including **1**, L = NC_5H_4COOH-4; **2**, L = NC_5H_4COOH-3, and **3**, L = 2-Ph-NC_9H_5COOH-4, were prepared by displacement of the weakly bound benzonitrile ligands in *trans*-[$PdCl_2(NCPh)_2$] by the corresponding ligand L. All the new complexes are yellow, air-stable solids. These complexes are expected to self-assemble in the solid state but it proved difficult to grow crystals suitable for structure determination since the complexes were essentially insoluble in most organic solvents. They do dissolve in dimethyl sulfoxide (DMSO) or *N*,*N*-dimethylformamide (DMF), but these solvents may displace the pyridine ligands and certainly break up the presumed polymeric structures by acting as hydrogen-bond acceptors. Thus, crystals of **2**·2DMSO and **3**·4DMF were

Received December 8, 1998.

Z. Qin, H.A. Jenkins, and R.J. Puddephatt.[1] Department of Chemistry, University of Western Ontario, London, ON N6A 5B7, Canada.
K.W. Muir.[1] Department of Chemistry, University of Glasgow, Glasgow G12 8QQ, U.K.
S.J. Coles. CLRC Daresbury Laboratory, Warrington WA4 4AD, U.K.

[1]Authors to whom correspondence may be addressed: R.J.P.: Telephone: (519) 679-2111, ext. 6336. Fax: (519) 661-3022. e-mail: pudd@uwo.ca. K.W.M.: Telephone: 0141-330-5345. Fax: 0141-330-4888. e-mail: ken@chem.gla.ac.uk

© 1999 NRC Canada

Chart 1. Structures showing H bonding in the DMSO and DMF solvates.

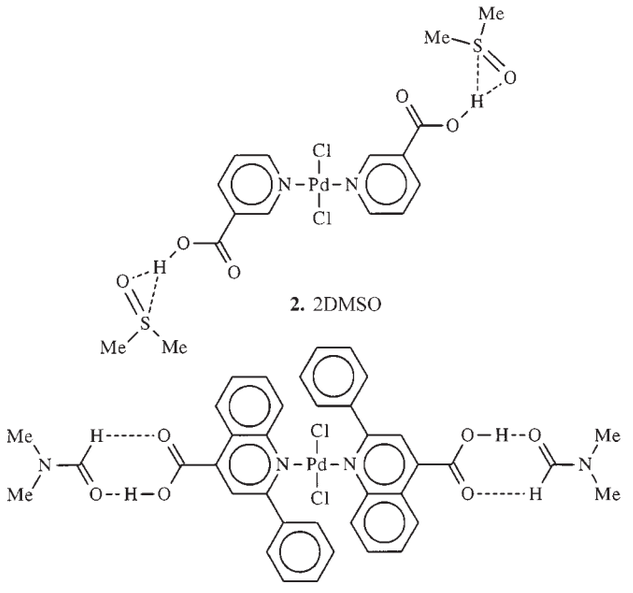

shown to contain molecular units only, as depicted in Chart 1;[2] the ligand displacement was also a significant problem with DMSO solvent but it was possible to characterize the complexes in DMF-d_7 solution by ^{1}H NMR.[3]

Finally, a method for obtaining single crystals of complexes **1**, **2**, and **3** was discovered, in which separate solutions of *trans*-[$PdCl_2(NCPh)_2$] in acetone and the ligand L in water were allowed to diffuse together slowly in a narrow-bore glass tube; crystals formed over a period of several weeks close to the interface where the ligand substitution occurred, and proved suitable for structure determinations.[2] All three complexes self-assemble into infinite one dimensional polymeric arrays through intermolecular hydrogen-bonding as shown in Fig. 1. In each case, the palladium atom lies on a cystallographic inversion centre so the angles N-Pd-N and Cl-Pd-Cl are 180°. Crystals of **1** contain strictly

Fig. 1. Views of the 1-D chain structures of the H-bonded polymers showing 30% probability ellipsoids for all non-H atoms. Selected bond distances (Å) and angles (°):
(*a*) *trans*-[$PdCl_2(NC_5H_4COOH\text{-}4)_2$], **1**: Pd—N = 2.021(2) Å, Pd—Cl = 2.3051(7) Å, N-Pd-Cl = 90.5(1)°.
(*b*) *trans*-[$PdCl_2(NC_5H_4COOH\text{-}3)_2$], **2**: Pd—N = 2.022(2) Å, Pd—Cl = 2.305(1) Å, N-Pd-Cl = 90.1(1)°.
(*c*) *trans*-[$PdCl_2$(2-Ph-$NC_9H_5COOH\text{-}4)_2$], **3**: Pd—N = 2.035(2) Å, Pd—Cl = 2.308(1) Å, N-Pd-Cl = 91.8(1)°

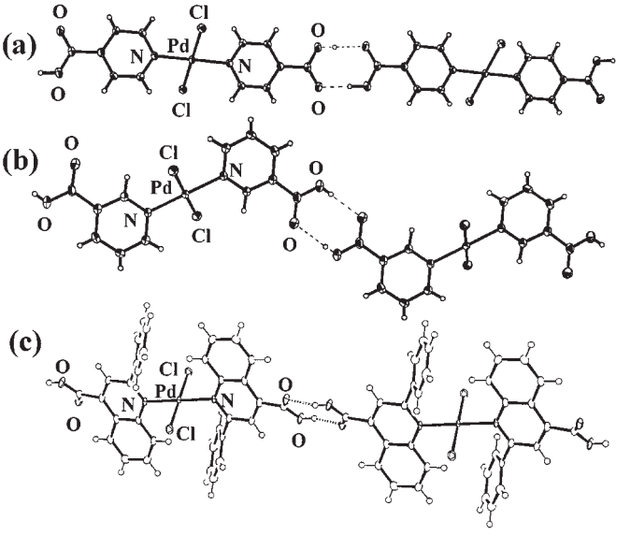

linear chains of molecules (Fig. 1*a*) and the O···O distances in hydrogen-bonded OH···O groups are 2.637(4) Å, typical of such distances in carboxylic acids (1–3). Complex **2**, with L = $NC_5H_4CO_2H$-3, naturally gives zigzag chains; the hydrogen bonding is similar to that in **1**, with intermolecular distances O···O = 2.634(3) Å (Fig. 1*b*). Complex **3**, with L = 2-Ph-NC_9H_5COOH-4, again gives a structure that is remarkably similar to that of **1**, with strictly linear chains assembled through hydrogen bonding and with O···O distances of 2.655(3) Å (Fig. 1*c*). In the solid state structures of both **1** and **2**, there are other short non-bonded contacts involving C-H groups and Pd-Cl groups of neighbouring chains and

[2] Crystal data: **1**, $C_{12}H_{10}Cl_2N_2O_4Pd$, M = 423.52, triclinic, space group P-1, a = 3.9554(2), b = 7.4830(4), c = 12.5456(7) Å, α = 75.625(3)°, β = 88.898(3)°, γ = 80.313(3)°, V = 354.47(3) Å^3, Z = 1, D_c = 1.984 Mg/m^3, μ = 1.701 mm^{-1}, T = 295(2) K, $R1$ = 0.0238 for 1250 data with $I > 2\sigma(I)$; **2**, $C_{12}H_{10}Cl_2N_2O_4Pd$, M = 423.52, monoclinic, space group $P2_1/c$, a = 3.9234(1), b = 13.5352(6), c = 13.4180(6) Å, β = 96.052(1)°, V = 708.58(5) Å^3, Z = 2, D_c = 1.985 Mg/m^3, μ = 1.702 mm^{-1}, T = 295(2) K, $R1$ = 0.0275 for 1610 data with $I > 2\sigma(I)$; **2**·2DMSO: $C_{16}H_{22}Cl_2N_2O_6PdS_2$, M = 579.78, triclinic, space group P-1, a = 4.772(1), b = 10.139(2), c = 12.788(3) Å, α = 107.35(1)°, β = 90.55(1), γ = 96.331(1)°, V = 586.4(2) Å^3, Z = 1, D_c = 1.642 Mg/m^3, μ = 1.23 mm^{-1}, T = 294(2) K, $R1$ = 0.0278 for 1933 data with $I > 2\sigma(I)$; in this structure O-H···O H-bonding appears stronger than O-H···S with O···O = 2.55, O···S = 3.464 Å, O-H···O = 170.5°, O-H···S = 158.1° (Chart 1). **3**, $C_{32}H_{22}Cl_2N_2O_4Pd$, M = 675.82, triclinic, space group P-1, a = 8.145(2), b = 9.422(2), c = 10.092(2) Å, α = 65.601(2)°, β = 75.142(2)°, γ = 78.015(3)°, V = 677.2(3) Å^3, Z = 1, D_c = 1.657 Mg/m^3, μ = 0.925 mm^{-1}, T = 150(2) K, $R1$ = 0.0364 for all 2752 unique data. **3**·4DMF: $C_{44}H_{50}Cl_2N_6O_8Pd$, M = 968.2, triclinic, space group $P1$, a = 7.9009(2), b = 9.3964(2), c = 15.9253(2) Å, α = 77.992(1)°, β = 77.342(1)°, γ = 82.234(1)°, V = 1123.34(3) Å^3, Z = 1, D_c = 1.431 Mg/m^3, μ = 0.590 mm^{-1}, T = 294(2) K, $R1$ = 0.0304 for 7077 data with $I > 2\sigma(I)$. Note that in this structure **2** DMF are H-bonded and **2** are not (Chart 1). Complete X-ray data are available as supplementary material, which may be purchased from: The Depository of Unpublished Data, Document Delivery, CISTI, National Research Council Canada, Ottawa, Canada K1A 0S2. These data have also been deposited with the Cambridge Crystallographic Data Centre, and can be obtained on request from: The Director, Cambridge Crystallographic Data Centre, University Chemical Laboratory, 12 Union Road, Cambridge, CB2 1EZ, U.K.

[3] Selected ^{1}H NMR data in DMF-d_7: **1**, δ(^{1}H): 9.10 (d, ^3J(HH) = 7 Hz, 4H, H^{2,6}), 8.07 (d, ^3J(HH) = 7 Hz, 4H, H^{3,5}); **2**, δ(^{1}H): 9.41 (d, ^4J(HH) = 2 Hz, 2H, H^2), 9.13 (dd, ^3J(HH) = 6 Hz, ^4J(HH) = 1 Hz, 2H, H^6), 8.58 (ddd, ^3J(HH) = 8 Hz, ^4J(HH) = 2 Hz, ^4J(HH) = 1 Hz, 2H, H^4), 7.83 (dd, ^3J(HH) = 8 Hz, ^3J(HH) = 6 Hz, 2H, H^5); **3**, δ(^{1}H): 9.11 (d, ^3J(HH) = 8 Hz, 2H, H^8), 8.71 (dd, ^3J(HH) = 8 Hz, ^4J(HH) = 1 Hz, 2H, H^5), 8.21–8.30 (br, m, 4H, H^{6,7}), 7.78–8.14 (br, m, 12H, H^3 and C_6H_5). Satisfactory C, H, and N analyses were obtained for all new complexes.

© 1999 NRC Canada

these, though clearly weak, may be attractive, thereby contributing to the insolubility of the complexes. Hence the complex **3** was prepared in the hope that the bulky substituents might prevent these secondary intermolecular interactions and so lead to enhanced solubility. It is clear from Fig. 1*c* that the bulky substituents do indeed protect the palladium centres and so prevent intermolecular association through these atoms, but the complex is still insoluble in organic solvents that are not capable of breaking down the intermolecular hydrogen bonding. We conclude therefore that the polymerization through hydrogen bonding alone is sufficient to lead to the observed insolubility of these and similar complexes.

In conclusion, this work shows that both linear and zigzag one-dimensional hydrogen-bonded polymers can be prepared by self-assembly from very simple ligands by using palladium(II) centres as templates. The hydrogen bonding in these polymers is strong and leads to insolubility of the complexes. The inability to recrystallize these compounds presented a problem in the development of this chemistry, but it is now shown that single crystals can be grown in situ by slow diffusion of the reagents together. Clearly, the method can be extended to create many more complex supramolecular arrays by using different metal centres as templates.

Acknowledgements

R.J.P. thanks the Natural Sciences and Engineering Research Council of Canada and K.W.M. thanks Engineering and Physical Sciences Research Council (U.K.) for financial support.

References

1. (*a*) J.-M. Lehn. Angew. Chem. Int. Ed. Engl. **29**, 1304(1990); (*b*) M.M. Conn and J. Rebek, Jr. Chem. Rev. **97**, 1647(1997); (*c*) G.R. Desiraju. Angew. Chem. Int. Ed. Engl. **34**, 2311(1995); (*d*) D. Philp and J.F. Stoddart. Angew. Chem. Int. Ed. Engl. **35**, 1154(1996); (*e*) D.S. Lawrence, T. Jiang, and M. Levett. Chem. Rev. **95**, 2229(1995).
2. G.A. Jeffery. An introduction to hydrogen bonding. Oxford University Press, Oxford. 1997.
3. (*a*) R. Alcala and S. Martines-Carrera. Acta Crystallogr. Sect. B: Struct. Crystallogr. Cryst. Chem. **B28**, 1671(1972); (*b*) D.J. Duchamp and R.E. Marsh. Acta Crystallogr. Sect. B: Struct. Crystallogr. Cryst. Chem. **B25**, 5(1969); (*c*) J. Yang, J.-L. Marendaz, S.J. Geib, and A.D. Hamilton. Tetrahedron Lett. **35**, 3665(1994); (*d*) A. Zafar, J. Yang, S.J. Geib, and A.D. Hamilton. Tetrahedron Lett. **37**, 2327(1996); (*e*) S.V. Kolotuchin, E.E. Fenlon, S.R. Wilson, C.J. Loweth and S.C. Zimmerman. Angew. Chem. Int. Ed. Engl. **34**, 2654(1995); (*f*) P.R. Ashton, A.N. Collins, M.C.T. Fyfe, S. Menzer, J.F. Stoddart, and D.J. Williams. Angew. Chem. Int. Ed. Engl. **36**, 735(1997); (*g*) S.C. Zimmerman, F. Zeng, D.E.. Reichert, and S.V. Kolotuchin. Science, **271**, 1095(1996); (*h*) M. Simard, D. Su, and J.D. Wuest. J. Am. Chem. Soc. **113**, 4696(1991).
4. (*a*) J.-M. Lehn. Supramolecular chemistry — concepts and perspectives. VCH Publishers, New York. 1995; (*b*) R. J. Puddephatt. Chem. Commun. 1055(1998); (*c*) J.E. Kickham and S.J. Loeb. Inorg. Chem. **34**, 5656 (1995).
5. (*a*) D. Braga, F. Grepioni, and G.R. Desiraju. Chem. Rev. **98**, 1375(1998); (*b*) A.D. Burrows, C.W. Chan, M.M. Chowdhry, J.E. McGrady, and D.M.P. Mingos. Chem. Soc. Rev. 329(1995); (*c*) C.B. Aakeroy and A.M. Beatty. Chem. Commun. 1067(1998); (*d*) M.M. Chowdhry, D.M.P. Mingos, A.J.P. White, and D.J. Williams. Chem. Commun. 899(1996); (*e*) W.T.S. Huck, R. Hulst, P. Timmerman, F.C.J.M. van Veggel, and D.N. Reinhoudt. Angew. Chem. Int. Ed. Engl. **36**, 1006(1997); (*f*) M. Munakata, L.-P. Wu, M. Yamamoto, T. Kuroda-Sowa, and M. Maekawa. J. Am. Chem. Soc. **118**, 3117(1996); (*g*) R.K. Kumar, S. Balasubramanian, and I. Goldberg. Inorg. Chem. **37**, 541(1998); (*h*) K. Biradha and M.J. Zaworotko. Cryst. Eng. **1**, 67(1998).
6. (*a*) D. Braga, L. Maini, and F. Grepioni. Angew. Chem. Int. Ed. Engl. **37**, 2240(1998); (*b*) P. Stepnicka, J. Podlaha, R. Gyepes, and M. Polasek. J. Organomet. Chem. **552**, 293(1998); (*c*) P. Bishop, P. Marsh, A.K. Brisdon, B.J. Brisdon, and M.F. Mahon. J. Chem. Soc. Dalton Trans. 675(1998); (*d*) P.G. Desmartin, A.F. Williams, and G. Bernardinelli. New J. Chem. **19**, 1109(1995).

© 1999 NRC Canada

1998 Alfred Bader Award Lecture
Tangents and targets: The synthetic highway from natural products to medicine[1]

Alex G. Fallis

Abstract: Synthetic studies directed toward various classes of compounds including taxoids and enediyne systems are described. These investigations include tether-controlled imtramolecular Diels–Alder reactions, carbometallation routes to dienes and furans, the use of carbohydrate building blocks, pentadienyl indium reagents for tandem cycloadditions to steroid and triterpenoid skeletons, and the synthesis of taxamycins and revolveneynes and related cyclophanes.

Key words: cycloaddition, taxoids, enediyne, cyclophanes, carbometallation.

Résumé : On décrit des études orientées vers la synthèse de diverses classes de composés, y compris des systèmes taxoïdes et ènediynes. Ces recherches comprennent des réactions de Diels–Alder intramoléculaires sous contrôle d'attaches, des voies de carbométallation conduisant à des dienes et à des furanes, l'utilisation de synthons dérivés des sucres, de réactifs pentadiényl-indium pour les cycloadditions en tandem conduisant aux squelettes des stéroïdes et aux triterpénoïdes ainsi que la synthèse de taxamycines, de révolvèneynes et de cyclophanes apparentés.

Mots clés : cycloaddition, taxoïdes, ènediyne, cyclophanes, carbométallation.

[Traduit par la Rédaction]

Introduction

Synthetic organic chemistry occupies a significant position in many diverse scientific disciplines and related areas of modern society in addition to its importance in its own right. This central role involves key interactions and overlap with pharmaceutical discovery and development, medical research, molecular biology, and material science. Nature has often provided the impetus for synthesis due to the complex, biologically active molecules that are produced and the significant preparative challenge these structures present.

A frequent advantage of synthetic investigations is the unexpected discoveries and developments that result from adversity. Woodward pointed out that "*the specific objective which the synthetic chemist uses as the excuse for his (her) activity is often not of special importance in the general sense; rather the important things are those that he finds out in the course of attempting to reach his (her) objective*." In this respect targets become vehicles for discovery and the tangents and cul de sacs encountered stimulate new chemistry. In addition, "systematic serendipity" provides new insights and opportunities for further investigation. In this regard, our studies directed toward the total synthesis of taxoids have been particularly rewarding.

In the course of these investigations, the following topics have been developed: (*a*) studies of cyclic α-diazoketones and reactions with enol ethers to afford unstable donor–acceptor cyclopropanes as precursors to dihydrofurans; (*b*) oxetane synthesis by epoxide rearrangement; (*c*) diene preparation by palladium coupling; (*d*) routes to taxane Ring A building blocks; (*e*) carbometallation of alkynes with organomagnesium reagents for the synthesis of dienes, enediynes, and furans; (*f*) development of tether-control groups for a variety of stereocontrolled cycloadditions; (*g*) indium-mediated additions to aldehydes for dienes and trienes; (*h*) increased knowledge of Diels–Alder reactions in diverse ring systems; (*i*) development of tandem cycloadditions for steroid and triterpenoid skeletons; (*j*) synthesis of novel enediyne systems such as taxamycins and revolveneynes.

The yew tree has played an important role in human history and since antiquity has been honoured for its longevity (Druids) and practical applications due to the density of its wood (1). The European yew (*Taxus baccata*) has been detected in Triassic fossils from 200 million years ago and, in an early example of superior armaments, the English employed long bows from yew trees to defeate the French at the battle of Crécy in 1346. In Britain, ancient yew trees predate the birth of Julius Caesar. An aqueous extract from the needles of *Taxus canadensis* was used by Canadian Indians for the treatment of rheumatism and as a tea after childbirth. Taxol® (paclitaxel) was first detected in the Pacific yew (*Taxus brevifolia*) in 1964, its structure published in 1971 (2), its novel mode of action determined in 1979 (3), and its approval as a drug attained in 1993. Initially public controversy surrounded the interactions between competing groups, including loggers, environmentalists (the yew forest

Received September 15, 1998.

A.G. Fallis.[2] Ottawa–Carleton Chemistry Institute, Department of Chemistry, University of Ottawa, 10 Marie Curie, Ottawa, ON K1N 6N5, Canada.

[1]This paper is based on the Alfred Bader Award Lecture presented June 1, 1998, by Professor Fallis at the 81st Annual Conference of the Canadian Society for Chemistry, Whistler, British Columbia.

[2]Telephone: (613) 562-5732. Fax: (613) 562-5170. e-mail: afallis@science.uottawa.ca

© 1999 NRC Canada

Fig. 1. Tubulin active cytotoxic agents.

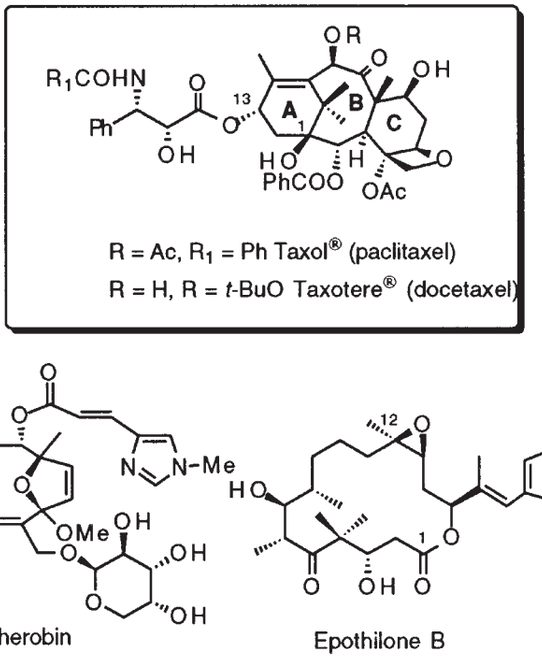

Scheme 1. Various cycloadditions for tricyclo[9.3.1.0^{3,8}]pentadecenes.

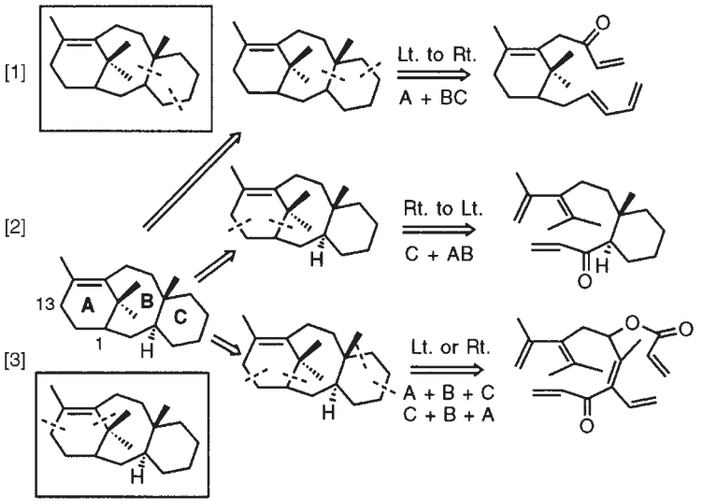

is home of the endangered spotted owl), and drug firms. This was a consequence of the large numbers of yew trees that had to be sacrificed to obtain material for the initial clinical trials (4).

The development of screening methods for taxoid activity have revealed new structures such as the epothilones (5), discodermolide (6), and eleutherobin (7) with similar biological profiles (Fig. 1).

Taxoid synthesis

We, in common with several other research groups, have been interested in the synthetic challenge presented by the taxoids. The proven clinical utility of the potent anti-tumor agents paclitaxel (Taxol®) and docetaxel (Taxotere®) for the treatment of ovarian and breast cancer has established these compounds as an important new class of chemotherapeutic agents. These antimitotic drugs alter the equilibrium between soluble tubulin dimers and polymerized microtubule structures. The microtubules are stabilized, depolymerization suppressed, and cell division inhibited (3, 8). This novel mode of action, plus the significant synthetic challenge presented by the sterically congested multicyclic structure, has stimulated worldwide interest in these molecules (9). Our initial approach to the tricyclo[9.3.1.0^{3,8}]pentadecene nucleus was based on a left-to-right sequence (ring A to BC) intramolecular Diels–Alder strategy in which ring A cyclohexene building blocks were selected as anchors to facilitate the construction of the B and C rings simultaneously (Scheme 1, eq. [1]) (10). A very large number of [4 + 2]

© 1999 NRC Canada

Scheme 2. Taxoid model cycloadddition.

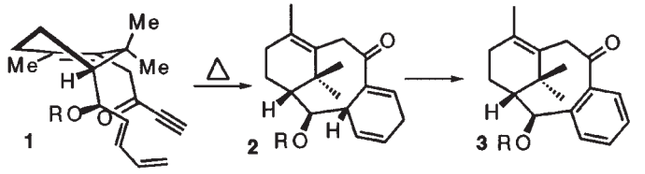

Scheme 3. Convergent A to BC intramolecular Diels–Alder approach.

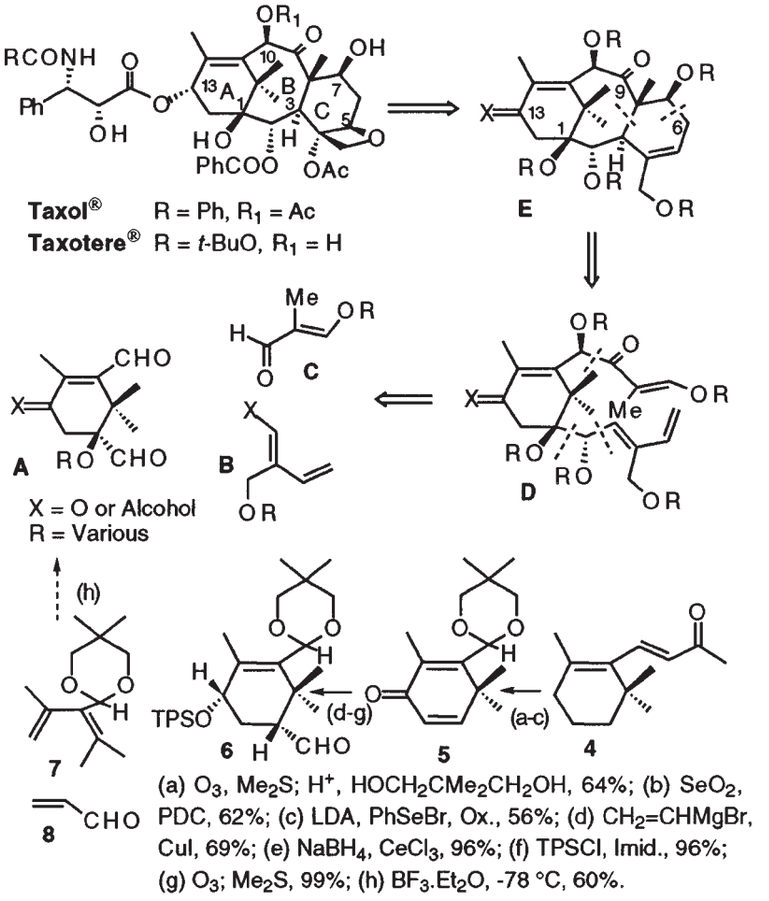

combinations may be envisioned for the tricyclic skeleton. Our investigations have evolved to encompass aspects of several diverse cycloaddition strategies (eqs. [1]–[3]), but many other variations, such as those in the boxes, have not been examined.

In previous studies, the C ring has been constructed using a bicyclo[2.2.2]octene precursor as an scaffold (11). It was assumed that the rigid geometry imparted by this bicyclic framework was required to hold the diene in an axial orientation. This maintains the close proximity of the reactive components in order to achieve the proper alignment for the cyclization transition state and overcome the entropic difficulties that were believed to be associated with a conformationally mobile ring system such as a cyclohexene. Conformational analysis of substituted cyclohexenes suggested that additional ring constructions should not be required to access the transition state geometry for ring C directly, when the diene and dienophile are attached to a cyclohexene. To further encourage the cycloaddition, the rotational parameters normally encountered with olefinic partners were minimized by selecting an acetylenic dienophile. Model studies using this convergent approach led to the successful preparation of the functionalized tricyclo-[9.3.1.$0^{3,8}$]pentadecatriene adduct **2** from **1,** and the structure was confirmed by conversion to the aromatic system **3** (Scheme 2) (10). The C_2 stereocentre controls the adduct stereochemistry from an *endo* transition state in accord with other studies concerning the π-facial selectivity of related cycloadditions (12).

A more detailed retrosynthetic analysis requires replacement of the ester side chain by a carbonyl or alcohol and removal of the ring D oxetane to afford the tricyclic skeleton **E** (Scheme 3). Subsequent double disconnection between C_6–C_7 and C_3–C_8 in ring C (retro-Diels–Alder) in this

© 1999 NRC Canada

Table 1. Representative condensations.

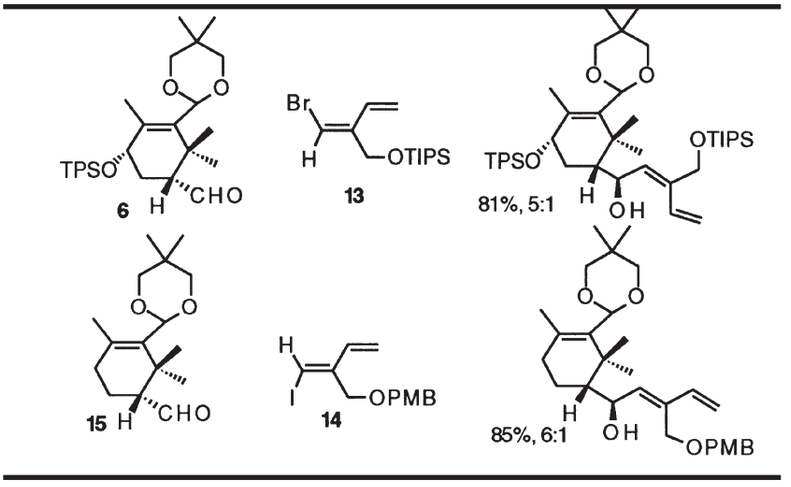

Scheme 4. Halodiene syntheses.

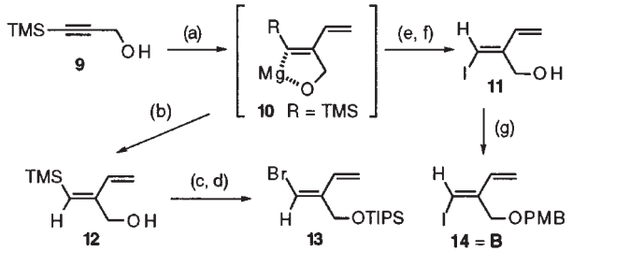

(a) CH_2=CHMgCl, THF, 0-67 °C, 16 h; (b) Aq. NH_4Cl, 0 °C, 2 min., 75%; (c) TIPSCl, imidazole, CH_2Cl_2, 0 °C, 2.3 h, 88%; (d) NBS, DMF, 21 °C, 1 h, 87%; (e) I_2, THF, -78 °C, 1.5 h, 53-60%; (f) MeOH, NaOMe, 65 °C, 45 min., 87%; (g) NaH, THF, 0 °C, DMF, 4-MeOBnCl, Bu_4NI, 21 °C, 18 h, 97%.

intermediate suggests a precursor related to the tetraene **D** (Scheme 3). In principle this intermediate could contain the majority of the paclitaxel (Taxol®) oxygen substituents, although in practice the use of less substituted systems appeared more prudent. Construction of **D** may be envisaged in a direct manner from further disconnections between C_1–C_2 or C_2–C_3 and C_9–C_{10}. In total, this leads to a highly convergent approach to the taxane nucleus from a suitably functionalized ring A building block in the form of a masked dialdehyde synthon related to **A** followed by attachment of the lower diene and upper dienophile units **B** and **C**, respectively.

The extension of this chemistry required the introduction of more oxygen functionality and a hydroxymethyl diene substituent (such as **B**) for the eventual introduction of the oxetane. As our research has progressed, the field has advanced rapidly and a better understanding of the factors that must be considered in any synthetic approach to the taxoids has emerged. In particular, it has proven difficult to manipulate many of the required oxygen-containing centres in the intact nucleus. Consequently, it appeared preferable to carry several of these functional groups from an early stage.

The required ring A building blocks were constructed using β-ionone (**4**) to give **6**, or, more directly, by the Diels–Alder reaction between an appropriate trimethyl-substituted diene-acetal **7** and acrolein (**8**) under Lewis acid catalyzed conditions (Scheme 3) (13).

Scheme 5. Representative attempted cycloadditions.

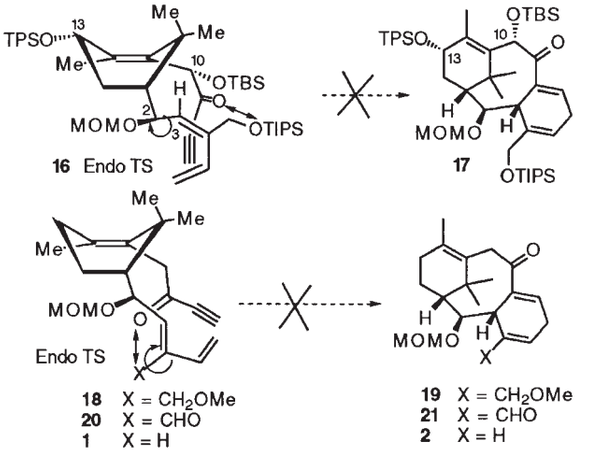

The required dienes **B** were initially synthesized by palladium-mediated addition and coupling of the appropriate alkene unit followed by halodesilylation (14). However, a more versatile route employed the addition of vinylmagnesium chloride to trimethylsilylpropargyl alcohol (**9**) via the putative magnesium chelate **10** to afford the (*E*) and (*Z*) dienes **13** or **14** as required (Scheme 4) (15). Condensation of the derived vinyl anion with the appropriate ring A aldehyde proceeded in yields of 80–95% with a diastereoselectivity of ~5:1 (Table 1), and attachment of the upper acetylenic dienophile afforded the cycloaddition precursors in Scheme 5 (16).

It was anticipated that cyclization of these compounds would provide the desired tricyclic nucleus. Molecular models and computer modeling suggested the cycloaddition transition states illustrated (Scheme 5) should be preferred. These reactions failed. Initially it appeared the potential 1,3 interaction between the C_{13} ether and the axial bond connecting the diene side chain was the culprit. However, this is not the case, since after completion of these investigations, Winkler et al. (17) reported the successful cyclization of a closely related example **22** to **23** (Scheme 6) with an *endo* C_{13} ether substituent. Danishefsky and co-workers (18) dis-

© 1999 NRC Canada

covered that an epimeric ether (compared to Taxol®) at C_{10} (as contained in **16**) inhibited the Diels–Alder cyclization of ring A in a steroid-based model. This was not the problem in this case, as compound **18** differs from the successful model system **1** only by the inclusion of the methoxymethyl ether diene substituent in place of hydrogen (X = CH_2OMe vs. X = H). The preferred transition state in which the cyclohexene is distorted into a boatlike conformation allows reasonable alignment between the acetylenic ketone and the diene unit. However, the substituent (X = CH_2OMe), due to its rapid free rotation, inhibits the close approach of the dienophile. Even the sterically less demanding aldehyde **20** (X = CHO) did not cyclize to **21**, in spite of the fact that carbonyl groups in the 2-position of dienes usually render them particularly reactive (19). The Winkler results (17) confirm that the diene substituent is the problem, as the diene in **22** (Scheme 6) is both more reactive and lacks this substituent. A revision of our approach to the challenging tricyclo-[9.3.1.$0^{3,8}$]pentadecene nucleus was required.

Tether control groups

In related research we are developing various "tether-control groups" (Table 2) for intramolecular reactions (pericyclic, free radical, dipolar, enolate, metal mediated, etc.) (20). These constructs are useful, as intramolecularity by itself is often insufficient to ensure the best levels of stereoselectivity in complex reactions. Functional groups that limit the flexibility of the side chain and impose a restricted geometry on the reactive components will facilitate the achievement of the requisite transition state and lower the activation barrier. When a chiral group is employed it will induce the desired enantioselectivity to afford chiral nonracemic products. In addition, the group should be selected so the product will contain useful functionality for subsequent synthetic manipulation.

The effect on intramolecular [4 + 2] cycloadditions will be significant, provided the group selected promotes the achievement of a dominant transition state. For example, Diels–Alder cycloaddition of simple trienes to generate decalins often requires long reaction times, high temperatures, and the selectivity is often disappointing (21). However, limiting the flexibility in the side chain, through the incorporation of a planar moiety (such as an olefin or aromatic or heterocyclic ring), should enhance the transition state interaction between the reactive components (A, B) and facilitate a variety of intramolecular reactions. Various examples of this beneficial template effect have appeared in the literature, but a systematic study does not appear to have been reported. Representative reactions include intramolecular alkylations for 10-membered rings (22), radical cyclizations (23), olefin metathesis (24), and cycloadditions of metal carbenes (25). Chiral, nonracemic tartrate- and carbohydrate-derived isopropylidene acetals also fulfill the criteria above and can be synthesized easily. In addition, they are usually available in both optical series and these groups supply useful functionality.

Previous strategies to increase the level of regio- and stereochemical control in intramolecular cycloadditions have included the use of cleavable control groups such as silyl acetal tethers (26) that may contain stereocenters (27*a*), conformationally restricted diester spacers (27*b*), as well as chiral Lewis acids (28), chiral auxiliaries (29), magnesium chelation (30), and chiral copper complexes (31). The ring cleavage products, from removal of the control group of appropriate adducts, constitute an intermolecular cyclohexene synthesis, while the bicyclo[4.4.0] nucleus can be used independently or expanded.

Scheme 6. Diels–Alder cycloaddition (17).

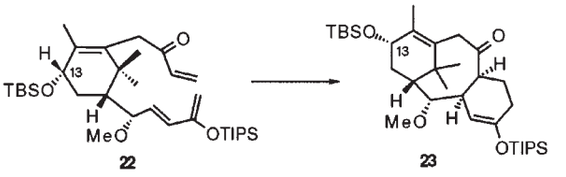

The following examples illustrate the utility of planar control groups. Thus with a benzene group in the tether the cycloaddition illustrated (**24** to **26**, Scheme 7) occurred readily during oxidation with Dess–Martin periodinane (2 h, 48°C, 95% yield) to give a single diastereomer (X-ray) (20). This result illustrated the dramatic improvement that arose from the restricted rotational freedom in the side chain due to the presence of the aromatic ring. Thus, the required diene–dienophile interaction was readily achieved. This adduct arose from preferential addition *anti* to the methoxymethyl ether substituent via an *endo* transition state as illustrated. This orientation places the OR_1 group in an axial position. Thus the 1,3-allylic interaction with the bulky group on the diene (arrow) that occurs in the *endo* approach from the opposite face (hydrogen and ether are interchanged) is avoided. Varying the ether substituents (PMB, Bn, Bz) in **24** did not alter the π-facial selectivity observed, but the yields were reduced (52–83%). This stereochemical preference is consistent with related diene – allylic ether cycloadditions (12).

A *cis*-olefin produced a similar beneficial effect in refluxing dichloromethane and provided the adduct **27** in 73% yield but with lower selectivity (2:1). Cyclopentadiene reacted readily with the enone **27** at 0°C in the presence of diethylaluminum chloride to generate the expected tetracyclic ketone in 87% yield (*syn/anti*, 9:1) as a consequence of *endo* addition of the cyclopentadiene *syn* to the methoxymethyl ether substituent.

New taxoid approach

Encouraged by these results, a new convergent, double, intramolecular Diels–Alder strategy for taxoids has been devised that proceeds in a right-to-left (C to BA) direction (Scheme 1, eq. [2]) (32). A key feature of this route is the use of a chiral isopropylidene acetal tether control group in **30** (Scheme 8) to impart asymmetry, facilitate the attainment of the requisite transition state for the intramolecular cycloaddition to form the C ring, and introduce latent functionality for subsequent ring cleavage to a substituted cyclohexene. Thus functional group modification of **31** leads to a second Diels–Alder precursor **29**. An ester group was selected as a surrogate for the C_{19} methyl group in order to facilitate the chelated transition state illustrated in Scheme 9 (**32**). Lewis acid coordination should occur between this ester and the dienophilic carbonyl to give the desired adduct

© 1999 NRC Canada

Table 2. Tether-control groups.

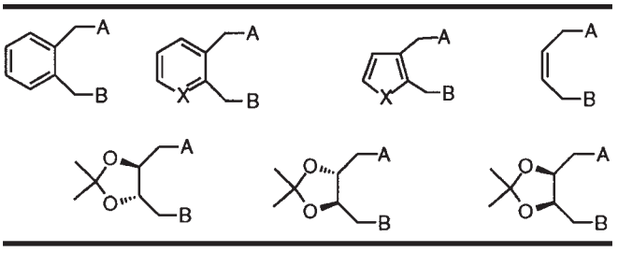

Scheme 7. Aromatic and alkene tether-controlled cycloadditions.

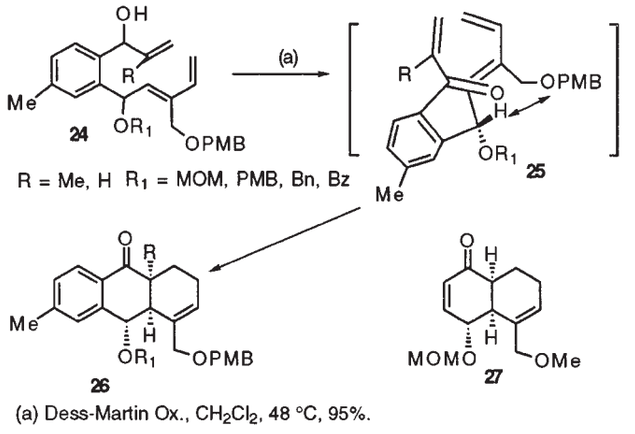

Scheme 8. Tether-controlled acetal Diels–Alder approach.

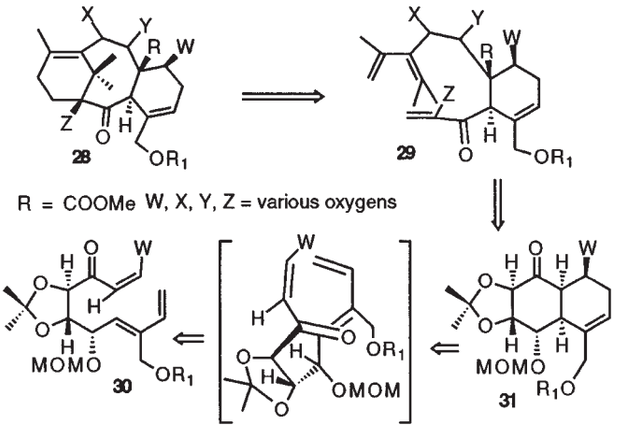

33. However, careful choice of the reactive components is required, as certain substitution patterns have been found to afford the unnatural (C-1 epimeric) stereochemistry from an *exo–anti* cyclization (Scheme 10) (33*a*).

Isopropylidene acetals hold promise for the control of many intramolecular reactions although only a few cases of this beneficial effect have appeared in the literature and a systematic study does not appear to have been reported. Representative examples include radical cyclizations (34) and 2-azaallyl cycloadditions (35). In addition, the behavior of 1,7,9-decatriene-3-ones bearing isopropylidene acetals adjacent to the diene have been examined by Roush and coworkers (36) in their synthesis of nargenicin A_1. However, as discussed below, placement of the acetonide β to both the diene and dienophile improved the stereoselectivity for the synthesis of substituted decalins.

The required trienol precursors related to **30** were prepared from the known *tert*-butyldimethylsilyl ether-aldehyde **36** (Scheme 11) (37). Condensation of this aldehyde with the organolithium reagent derived from the halogen–metal exchange with butadiene **14** (15) afforded the secondary alcohol as a 2:1 epimeric mixture. The major diastereomer was separated and protected as its methoxymethyl ether to give **37**. Desilylation was effected with *n*-tetrabutylammonium fluoride to give **38** (94%). Subsequent Swern oxidation and vinyl magnesium bromide addition yielded the trienol **39** (38). To ascertain the potential influence of the methoxymethyl ether substituent upon the stereoselectivity of the cycloaddition in this *trans* series, the trienol **43** was synthesized from (L)-ascorbic acid via the epoxide intermediate **40** (39), followed by epoxide ring opening by butadienyllithium addition (40) to give **41**. Subsequent isomerization afforded **42**, while oxidation to the aldehyde and condensation with vinyl magnesium chloride gave **43**.

Swern oxidation of **39** afforded ketone **44**, which cyclized readily to afford **45** (X-ray) as a single enantiomer (Scheme 12). Acid hydrolysis of the acetal and lead tetraacetate cleavage of the resulting diol in methanol gave the ester-aldehyde **46.** Wittig condensation with **46** afforded the alkene **47**. Unfortunately, base-catalyzed methods to introduce the diene side chain were unsatisfactory and it was necessary to add this component as a vinyl anion. The methyl-substituted diene-vinyl iodide appendage **52** required for the taxane nucleus was synthesized by a copper-mediated addition followed by coupling of **50** and **51** as illustrated (Scheme 13) and demonstrates the power of modern organometallic chemistry for the facile preparation of these triene systems. Thus the parallel sequence to Scheme 12 provided the pentadiene ketone **55**. The results from several *trans* isopropylidene acetal mediated cycloadditions are listed in Table 3 (38). In favourable cases the intermediate ketones were not isolated, but were cyclized directly to avoid a mixture of adduct and enone. The efficient cyclization of **55** to the adduct **56** (97%) under mild conditions and without recourse to Lewis acid was particularly gratifying. Thus the stage appeared to be set for conversion of this material to the taxane nucleus.

These decalin adducts **45**, **54**, and **56** arose from preferential addition via an *endo* transition state in which the side chain adopted a chairlike conformation, as illustrated in **59**. The number of possible transition states was reduced due to the presence of the *trans* isopropylidene unit in which the

© 1999 NRC Canada

Scheme 9. Proposed ring A cycloaddition.

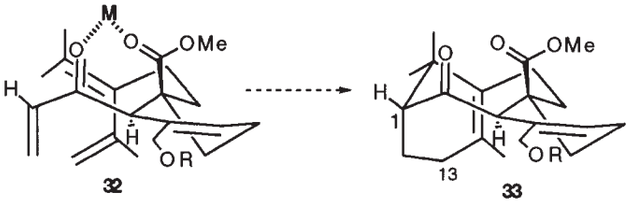

Scheme 10. *exo* Ring A cycloaddition.

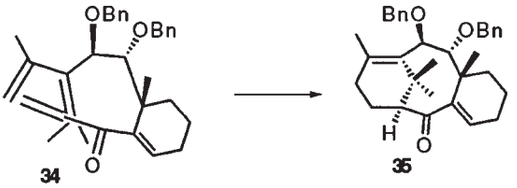

oxygen substituents were constrained to a diequatorial orientation. The altertative *endo* transition state **60** prefers a boatlike conformation with a 1,3-allylic interaction between the ether substituents. In the case of **57**, which lacks both the secondary ether and the vinyl substituent, the stereoselectivity of the cycloaddition might be expected to be reduced. However, the interactions between these groups were less important due to the overriding influence of the cyclic acetal, which afforded the same predominant stereochemistry in the adduct **58**.

Treatment of **56** (Scheme 14) with aqueous acid generated the diol **61**. Unfortunately, in contrast to the model studies with **45**, the oxidative cleavage of this diol with lead tetraacetate was very troublesome and did not afford the desired ester-aldehyde **62**, but instead gave only a low yield (~20%) of the acetal-lactone **63** from capture of the methoxyhemiacetal by the carboxylic acid. The diol was inert to treatment with sodium metaperiodate and related reagents even at elevated temperatures. This lack of reactivity is a consequence of the preferred conformation of **61** in which the methoxymethyl ether and the diene substituent adopt equatorial positions to minimize their steric interactions. This places the adjacent hydroxyl functions in a diaxial orientation. Thus reagents that require a cyclic intermediate prior to bond cleavage will not be effective. Oxidation of **61** to the triketone was not a clean reaction, and reduction with sodium borohydride to the triol followed by cleavage experiments was also unsatisfactory. Consequently, the best alternative, to capitalize on the chemistry we have developed, is the use of a "*cis*-tartrate" precursor for the cycloaddition.

The required *cis* substrates for the model studies were synthesized as summarized in Scheme 15 following a sequence that was developed from (L)-arabinose (41), or alternatively from (L)-gulonolactone via the bis acetal **69** (42), followed by reduction and protection to give **70** and selective periodic acid oxidation to generate the aldehyde **71**. Unfortunately the Horner–Emmons reaction with **64** could not be scaled up efficiently nor was it possible to selectively protect the primary alcohol due to the preference of **64** to exist in the closed hemiacetal form. In addition, our desire to have a hydroxymethyl substituent was thwarted by the instability of the required reagents. Thus a novel pentadienyl indium synthon has been developed to introduce the triene unit via the intermediacy of the homo-allylic alcohol **66**, followed by elimination of water to afford **67** (Y = $CH{=}CH_2$). These versatile building blocks hold promise for diverse transformations, particularly tandem cycloadditions of the triene unit. In contrast to pentadienyllithium reagents, these indium species add selectively at the γ position (43). To complete the synthesis of these tetraenols, the upper dienophyllic units were added as described above.

As listed in Table 4, the *cis* isopropylidene acetal systems cyclized readily at mild temperatures to afford the single adducts **73**, **75**, **78**, and **79** in good yield. The cycloadditions of **76** and **77** were particularly expedient and the enone was not detected. Thus epimerization of an acetal centre improved the efficiency of the reaction and led to the same stereochemical result as above from the preferred transition state **80**, via a boatlike conformer that placed the diene and dienophile in close proximity for facile cyclization. Other transition states such as **81** are disfavoured due to the significant nonbonded interactions illustrated. Scheme 16 outlines the anticipated route for the preparation of the desired taxoid skeleton **84**.

The versatility of **68** derived from the pentadienyl indium reagent is illustrated (Scheme 17) by the rapid assembly of highly oxygenated, nor-methyltriterpenoid and steroid type skeletons from a double cycloaddition sequence. Thus the synthesis of **85** and **86** from **68** arises directly from a tandem cycloaddition to afford tetracyclic systems enantioselectively. The fourth ring added from the most accessible convex face of **78** in an *endo* fashion. In addition, the diketone ring in **85** may be viewed as either the A or the D ring component depending upon the synthetic objective. Furthermore, the ring fusion may be adjusted due to the presence of the adjacent ketone functionality. Less complex triene units allow the rapid construction of multicyclic skeletons by tandem cycloadditions with the same dienophile.

Enediynes

The enediyne family of anticancer antibiotics continues to be a topic of considerable current interest. This is a consequence of their novel mechanism of DNA cleavage involving cycloaromatization to benzyne diradicals and the synthetic challenge presented by the natural products themselves. This has also stimulated the design and synthesis of simpler less toxic analogs (44). Esperamicin (45) and calicheamicin (46) in particular have received widespread attention. In addition, preliminary studies on a number of hybrid structures that mimic established biologically active agents have been reported. These include incorporation of part of

© 1999 NRC Canada

Scheme 11. Synthesis of *trans* acetal trienols.

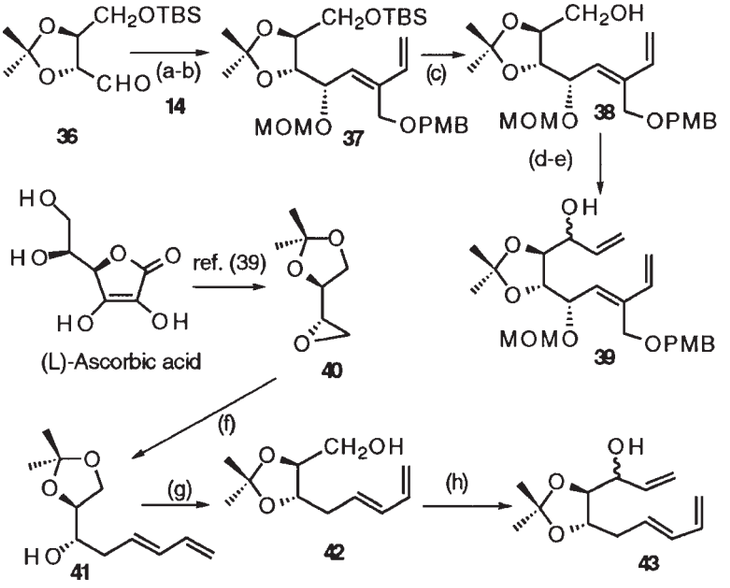

(a) *s*-*B*uLi, **14**, THF, -78 °C, ~2:1, 93%; (b) MOMCl, *i*-Pr_2EtN, CH_2Cl_2,77%; (c) *n*-Bu_4NF, THF, 94%; (d) $(COCl)_2$, DMSO, CH_2Cl_2, -78 °C, 40 min; Et_3N, 93%; (e) CH_2=CHMgBr,THF, -78 °C, 97%; (f) *n*-BuLi, THF, Bu_3SnCH=CH-CH=CH_2, 2-thienylCu(CN)Li, $BF_3.Et_2O$, 66%; (g) *p*-TsOH, MeCOMe, 70%; (h) 2 eq. $(COCl)_2$, CH_2Cl_2, 3 eq. DMSO, -78 °C; 4 eq. Et_3N, 21 °C; 4 eq. $BrMgCH=CH_2$, 0 °C, 82%.

Scheme 12. Initial cycloaddition and cleavage studies.

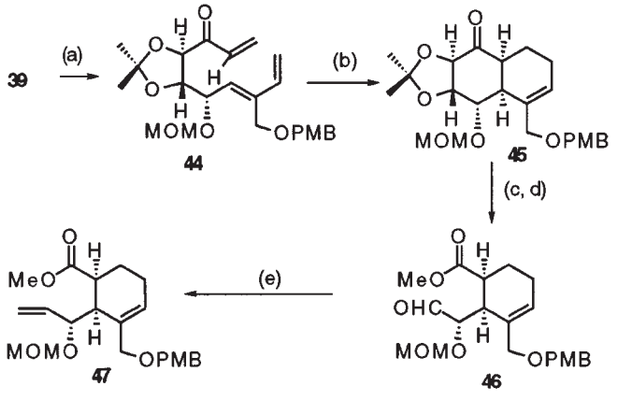

(a) Swern Ox, 63%; (b) C_6H_6, 80°C, 20 h, 75%; (c) Aq HCl, THF, 91%; (d) $Pb(OAc)_4$, MeOH, C_6H_6, 84%; (e) $Ph_3PCH_3^+I^-$, $KN(TMS)_2$, C_6H_6, 68%.

the steroid nucleus (estramycins) (47), β-lactams (lactendiynes) (48), and enediynes linked to diethylstilbestrol (49).

We have designed a new family of potential anti-tumor agents (taxamycins (**88**), Scheme 18) (50) that combine aspects of the important pharmacophores in both the taxoid and enediyne families in which suitable functionality should facilitate tubulin binding and cycloaromatization would induce cell damage. In addition, it was hoped that the 12-membered ring system might suffice for the synthesis of aromatic taxanes (Scheme 18).

To investigate this potential, the 12-, 11-, and 10-membered ring species have been prepared. Condensation of our triisopropylsilyl-enediyne building block **87** with suitable ring A precursors allowed conversion to suitable iodoacetylene aldehydes. The best cyclization conditions involved the use of the $[CrCl_2(THF)_2]$ complex to afford the bridged bicyclic systems (Scheme 19) (51). Thermolysis of **93** gave only small amounts (5%) of aromatic material. As Table 5 indicates, the c–d separation exceeds the 3.1 Å distance required for spontaneous cyclization, and thus removal of the bridgehead double bond will be required for facile cycloaromatization.

It was anticipated, by analogy with taxoid systems, that allylic oxidation of **96** and **101** would introduce the desired oxygen at C_{13} (taxane numbering) for attachment of the appropriate side chain. However, oxidation by reagents such as CrO_3 or PCC resulted only in recovery of starting material. Treatment of the acetate **96** with selenium dioxide in dioxane at 60–70°C afforded exclusively the C_2 ketone **97** in 89% yield. The strain and lack of orbital overlap in this ring system is reflected in the carbonyl IR band at 1740 cm^{-1}. Initially it appeared that the acidity of the reaction medium had resulted in hydrolysis of the MOM ether followed by oxidation of the resulting alcohol. However, this was not the case, as a parallel oxidation of the methyl ether **101** with excess SeO_2, in dioxane at reflux for 2 h, also gave the corresponding ketone **102** in a yield of 77% (Scheme 20). Consistent with the accepted mechanism of selenium dioxide oxidations (52) these reactions likely proceeded via an ene reaction to form the allene intermediate **99**, followed by

© 1999 NRC Canada

Scheme 13. Synthesis of vinyl iodide **52**.

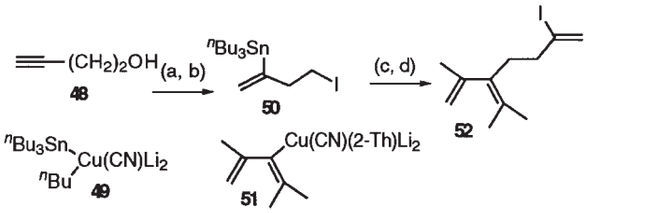

(a) **49**, THF, -78 °C, 1 h, 49%; (b) $Ph_3.I_2$, Et_3N, CH_2Cl_2, 21 °C, 5 h, 96%; (c) **51**, THF, -78 °C,15 min, 21 °C, 65 h, 86%; (d) I_2 (1 eq), CH_2Cl_2, 21 °C, 10 min, 99%

Table 3. Tether-controlled *trans* acetal cycloadditions.

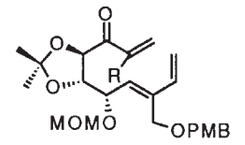 **44** R = H **53** R = CH_2CH_2OTPS **55** R = CH_2CH_2C-$(CMe{=}CH_2){=}CMe_2$	48 °C, 4 h 110 °C, 18.5 h 110 °C, 17 h	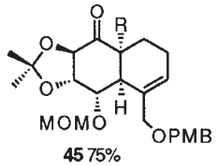 **45** 75% **54** 82% **56** 97%
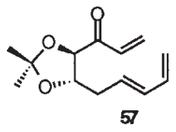 **57**	48 °C, 21 h	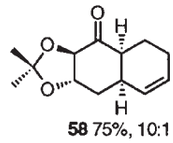 **58** 75%, 10:1
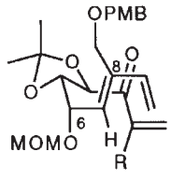 **59**		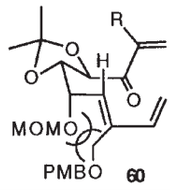 **60**

Scheme 14. Modification of adduct **56**.

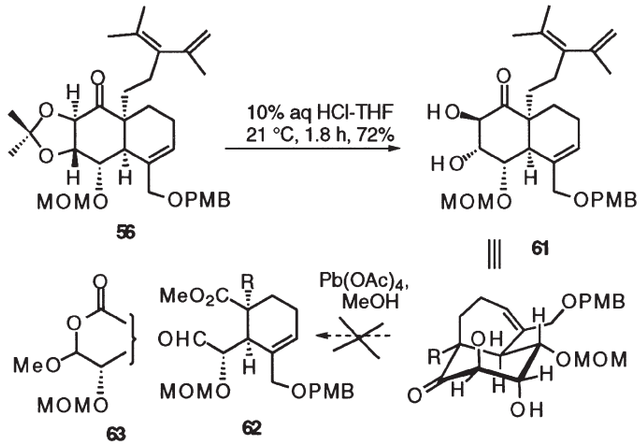

© 1999 NRC Canada

Scheme 15. Synthesis of *cis* acetal trienols.

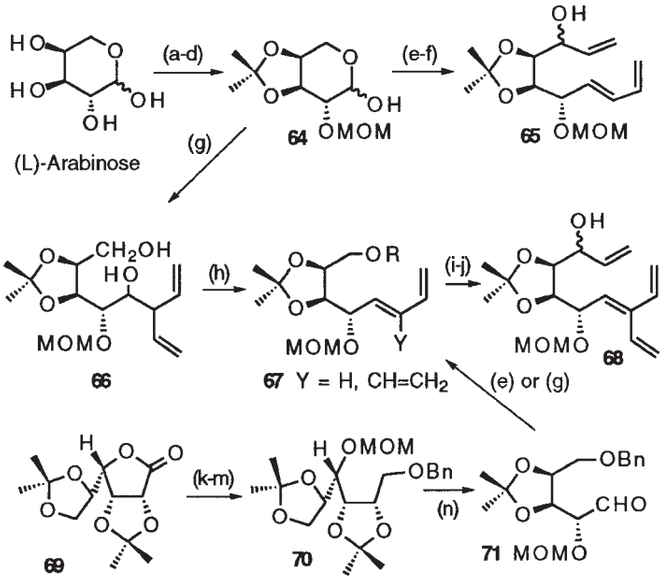

(a) BnOH, HCl, 21 °C, 16 h, 88%; (b) Me_2CO, $CuSO_4$, H_2SO_4, 21 °C, 20 h, 75%; (c) MOMCl, *i*-Pr_2EtN, CH_2Cl_2, 96%; (d) Na/NH_3, Et_2O, 97%; (e) 3 eq. CH_2=CH-$CH_2P(O)(OEt)_2$, 3 eq. *n*-BuLi, THF, -78-21 °C, 77%; (f) 1.5 eq. $(COCl)_2$, CH_2Cl_2, 3 eq. DMSO, -78 °C; 7 eq. Et_3N, 21 °C; 4 eq. $BrMgCH=CH_2$, 0 °C,72%; (g) $In_{(s)}$, $BrCH_2CH=CHCH=CH_2$, DMF, 21 °C, 96%; (h) Et_3N, DMAP, TBSCl; Ph_3P, DEAD, C_6H_6, 80 °C, 96%; (i) Bu_4NF, THF 0 °C, 99%; (j) 1.5 eq. $(COCl)_2$, CH_2Cl_2, 3 eq. DMSO, -78 °C; 7 eq. Et_3N, 21 °C; 4 eq. $BrMgCH=CH_2$, 0 °C, 93%; (k) $LiAlH_4$, THF, 95%; (l) Et_3N, DMAP, TBSCl or BnBr, NaH; (m) MOMCl, NaH, THF, 82%; (n) 3 eq. H_5IO_6, Et_2O, 49%.

Table 4. Tether-controlled *cis* acetal cycloadditions.

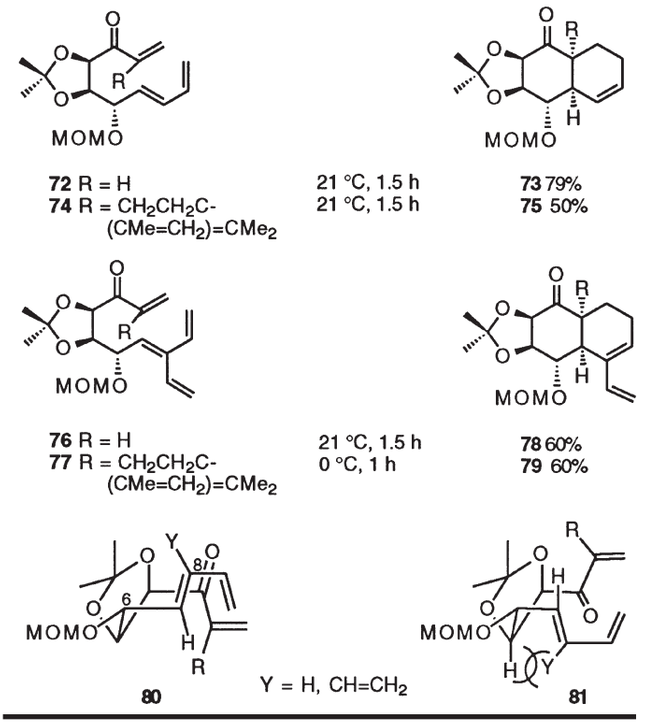

© 1999 NRC Canada

Scheme 16. Proposed ring cleavage and ring A cycloaddition.

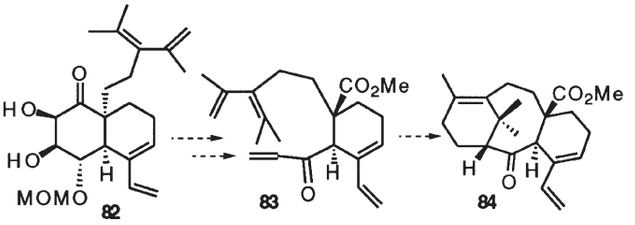

rearrangement to the acetal species **100** and hydrolysis to the ketones upon aqueous work-up. The double bond in the A ring is hindered by both the enediyne bridge on one face and by the sterically demanding *gem* dimethyl group on the other. These features apparently inhibit the approach of the SeO_2 and thus the rearrangement pathway is observed. In principle, the generation of the allene should facilitate the cycloaromatization (Myers cyclization), but this was not observed due to the presence of the bridgehead olefin. However, this oxidation sequence may have potential as a trigger mechanism in other cases.

For proper evaluation, the synthesis of these taxoid mimics (taxamycins) requires the incorporation of a paclitaxel or docetaxel side chain at C_{13} of the bicyclic enediyne framework. In view of the failure to introduce oxygen as described above, the bis-nor methyl system **104** was synthesized (53). The intramolecular coupling of the iodoacetylene **103** proceeded readily, based on our previous research (50, 51) with freshly prepared $[CrCl_2(THF)_2]$ complex (51) in THF to afford the bicyclic system **104** as a single diastereomer in 76% yield. Reasonable yields (60–70%) were also obtained with commercial anhydrous (toluene azeotrope) $CrCl_2$. In contrast to the more sterically demanding cyclizations examined earlier (51), catalytic $NiCl_2$ was not required in these decaenediyne systems. This is consistent with related 10-membered ring enediyne cyclizations (54), although the mechanistic role of Ni(II) in these reactions remains obscure, as many cases require a catalytic amount of $NiCl_2$ (55). A 60% yield of **104** was also achieved from treatment of the aldehyde **103** (R = H) with KHMDS at –78°C, although the anhydrous fluoride-mediated cyclization procedure on the corresponding silylacetylene-aldehyde failed.

Conversion of **104** to its acetate **105** set the stage for oxygen introduction. Oxidation with SeO_2 provided the allylic alcohol **106** (Scheme 21) as a single diastereomer in a yield of 66%. Consistent with a related example (56), this oxidation occurred from the top face as a consequence of the steric hindrance of the enediyne bridge. The diastereomeric alcohol **108** was prepared by oxidation of **106** with Dess–Martin periodinane to afford the crystalline cyclohexenone **107**. X-ray analysis of **107** confirmed the structures in this series. Reduction of the ketone **107** with sodium borohydride in the presence of $CeCl_3$ resulted in the preferential formation of alcohol **108** accompanied by its diastereoisomer (60:40 ratio).

Independently, the two alcohols **106** and **108** were coupled with the oxazolidine **109** (57) (a protected form of the Taxotere® side chain) to provide two separate diastereomeric mixtures (1:1) in quantitative yield represented by the hetero-

Scheme 17. Tandem cycloadditions to nor-triterpenoids and steroids.

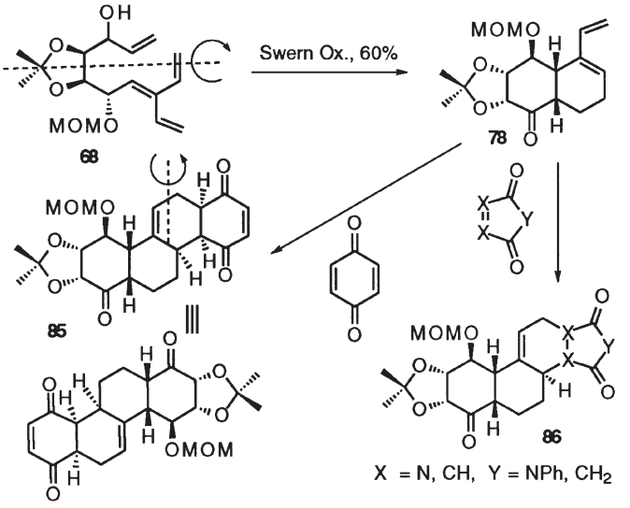

cyclic ester **110.** Acid-catalyzed ring opening afforded the four distinct esters that were resolved by chromatography (SiO_2). The individual silyl ether isomers were converted to their C_1 alcohols upon exposure to *n*-tetrabutylammonium fluoride in THF. For clarity, only the taxamycin-10 **111**, possessing the Taxotere® side chain, is illustrated. The stereochemical and electronic features of this compound most closely mimic those of the natural products.

Compared to Taxol®, compound **111** displayed negligible effects on tubulin polymerization and in protecting against Ca^{2+} induced depolymerization. This established that even a functionalized A ring (side chain, double bond, C_1-OH, C_{10}-OAc) is insufficient for tubulin binding. This information will help delineate the structural and functional features required for future investigation. Cytotoxic activity with the HT-29 human cancer cell line was too weak to be useful. This cytotoxic activity should increase in the presence of a cycloaromatization initiator that removes the bridgehead double bond. This double bond was inert to hydrogenation, a feature consistent with hyperstable alkenes (58), and activation by oxidation of the vinyl methyl group failed (SeO_2, CrO_3, PCC).

It was anticipated that formation of a five-membered ring, such as **112**, by conjugate addition, would induce cyclization due to the induced proximity of the terminal acetylenes (Scheme 22). However, generation of the anionic intermediate from the alcohol derived by hydrolysis of acetate **107** after treatment with carbon disulfide resulted in cyclization onto the acetylenic bond to generate **113** instead. Additional efforts to induce cycloaromatization included both intramolecular [4 + 2] and [2 + 2] cycloadditions as well as radical cyclizations. These were not successful and nature, as usual, knows best, since the sulfur anion in the natural products is oriented so that it approaches the double bond in a perfectly perpendicular direction as required for reaction.

Our next goal is to synthesize and examine compounds that possess both antiestrogenic and cytotoxic activity as illustrated in the general concept outlined in Scheme 23. Thus a simpler enediyne **117** has been synthesized as outlined. It

© 1999 NRC Canada

Scheme 18. Taxamycins (taxoid–enediyne hybrids).

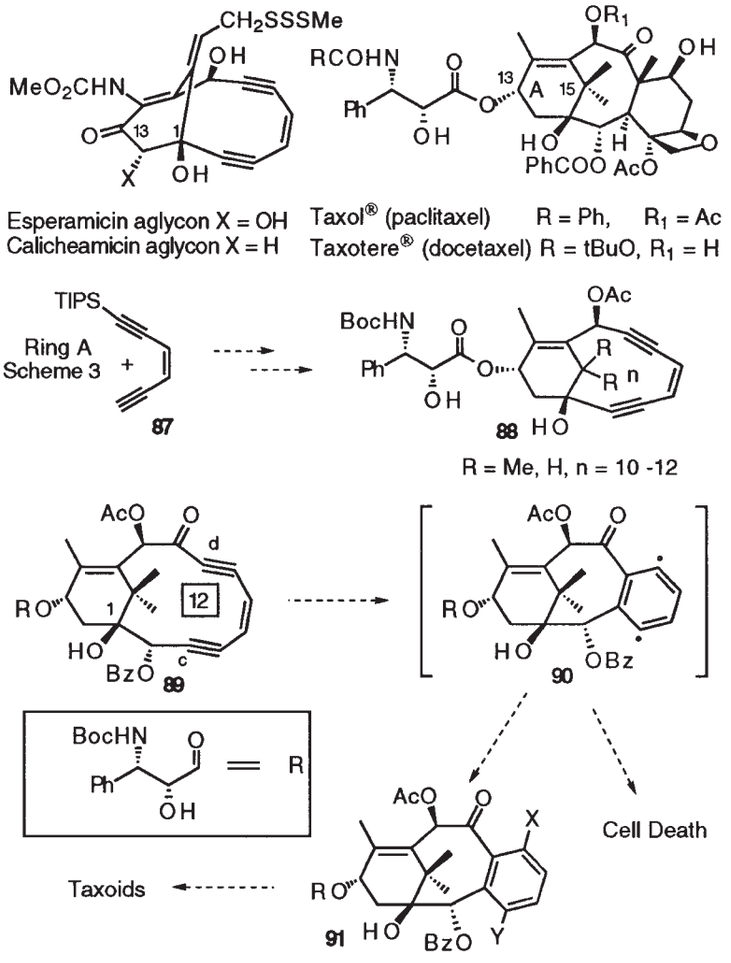

Scheme 19. Synthesis of taxamycin-12 and -11 ring cores.

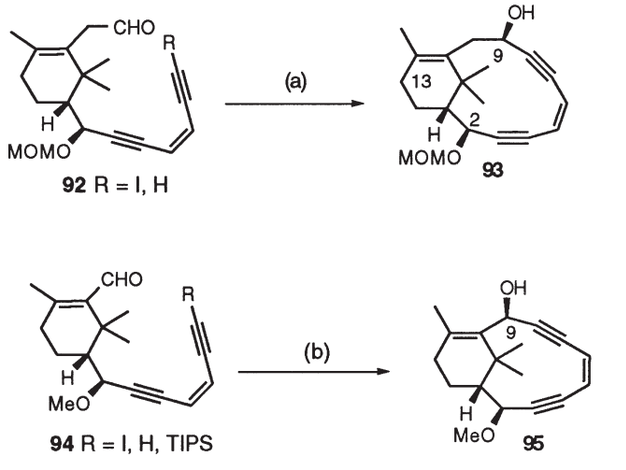

should undergo cycloaromatization below 50°C. The acetal in **115** acted as both a chiral auxiliary and a control group to facilitate the cyclization. In addition, the strain inherent in the *trans* isopropylidene moiety should inhibit Bergman cyclization initially but allow the close acetylene contact required upon hydrolysis. The enediyne will be linked to a steroidal mimic such as Toremifene®, which is known to interact with the breast cancer receptor. A more interesting and potent combination is to combine a modified form of the new Canadian drug **EM-652** with **117** to generate a viable mimic with therapeutic potential for the treatment of breast cancer.

Enediyne cyclophanes

Diverse families of cyclophanes and assorted cage compounds with novel structures and properties continue to be topics of widespread current interest. (59). We have synthesized the first members of a novel class of enediyne cyclophanes (60) by sequential palladium- or copper-mediated coupling. In contrast to normal [*n.m*]paracyclophanes, the rotation of the ring is not restricted by the bridge. In these compounds the benzene rings rotate freely, and as a consequence of this "skipping rope" property (61), in which the bridging units and one ring may swing around the other, we call these structures revolveneynes. These compounds are

© 1999 NRC Canada

Table 5. Summary of calculated c–d separations.

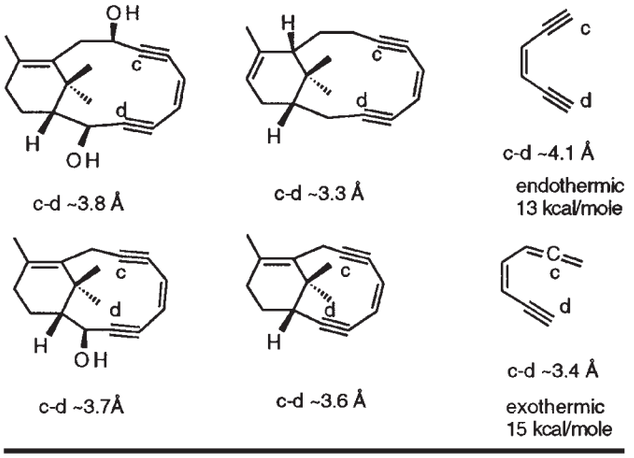

Scheme 20. Selenium dioxide oxidations.

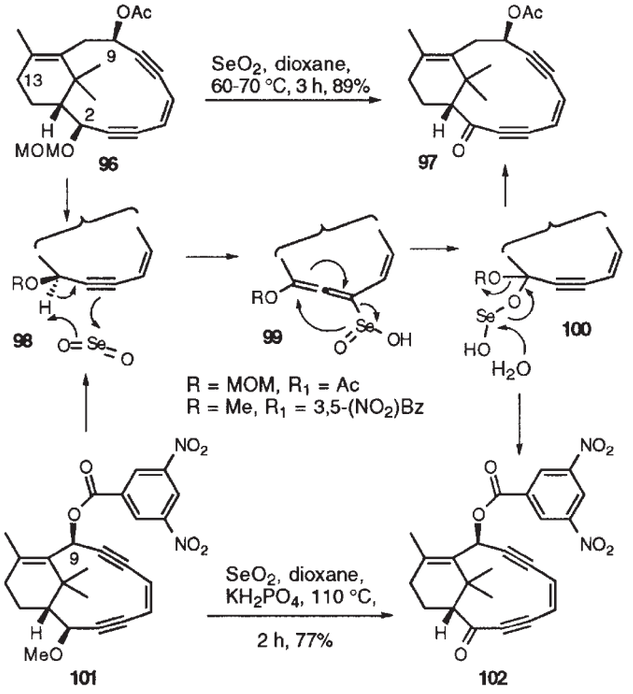

helical and thus chiral. These arrays have considerable potential as liquid crystals, as hosts when heteroatoms are present, possibly as chiral sources of Rh and Pd for catalytic transformations, and for carbon networks including fullerenes.

A double Wittig reaction on 1,4-benzenedicarboxaldehyde afforded the *Z*-dibromodiene **118** in 42% isolated yield. Palladium(0)-based coupling of **118** with trimethylsilylacetylene generated the TMS-protected diacetylene **119,** and the silyl groups were removed with K_2CO_3 in methanol at 21°C to give **119** (R = H) (Scheme 24). The synthesis of **120** was effected by palladium-mediated coupling of the dibromide **118** and the diacetylene in 9% yield. The dimer **121** was synthesized directly (50%) by oxidative coupling. A parallel sequence commencing with 1,2-dibromocyclopentene pro-

Scheme 21. Synthesis of taxamycin-10.

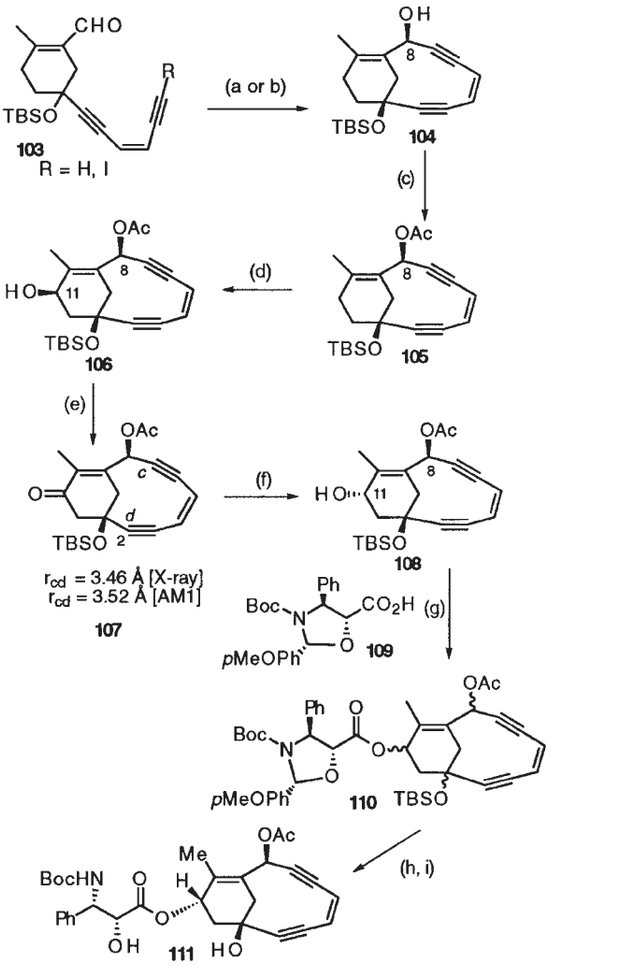

(a) $[CrCl_2(THF)_2]$ (8 equiv.), THF, 30 min, 76%; (b) KHMDS, THF, -78 °C, 60%; (c) Ac_2O, DMAP (cat.), Py, 21 °C, 15 h, 99%; (d) SeO_2, dioxane, 70 °C, 30 min, 66%; (e) Dess-Martin periodinane, CH_2Cl_2, 21 °C, 45 min., 99%; (f) $NABH_4$, MeOH, $CeCl_3$, 0 °C, 41%; (g) DCC, **109**, DMAP (cat.), toluene, 21 °C, 30 min, 99%,(1:1); (h) PTSA, MeOH, 21°C, 1.5 h, 94%; (i) TBAF, THF, 21 °C, 30 min, 75%.

Scheme 22. Attempted cycloaromatization.

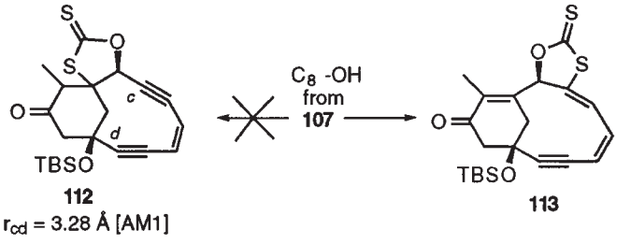

vided the diene-tetrayne system **124** (12%) accompanied by the dimer **121** (15%).

Rigid "Dreiding type" molecular models revealed that the unsaturated linkage imparted a helical twist to these structures similar to related D_2 symmetric olefinic paracyclophanes (62). Thus, the strain is relieved by rotation of one benzene ring with respect to the other about an axis that

© 1999 NRC Canada

Scheme 23. Antiestrogen–enediyne hybrids.

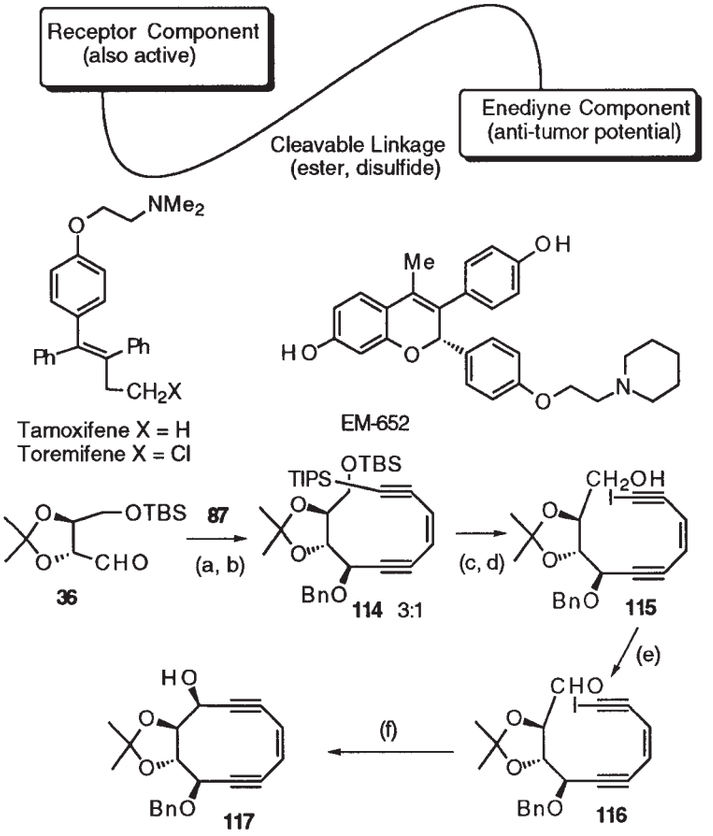

(a) *n*-BuLi, **87**, THF, -78 °C, 80%; (b) NaH, BnBr, THF, 0-21 °C,16 h, 88%; (c) TBAF, THF, -78 - 0 °C, 0.5 h, 98%; (d)LDA, I_2, morpholine C_6H_6, -78 -21 °C, 2.5 h, 93%; (e) Dess-Martin periodinane CH_2Cl_2, $NaHCO_3$, 45 min, 81%; (f) $NiCl_2$ (0.3 equiv.), $CrCl_2$, (9 equiv.) THF, 21 °C, 1.5h, 71%.

passes through the centre of both rings. This gyrochiral property implies that at suitable temperatures the enantiomers with substituents or additional bridges may also be resolvable (**122**). As illustrated, the two rings are offset slightly with respect to one another. These structures possess accordionlike flexibility and yet the rigid nature of the bridge presents a large cavity for complexation (inclusion) (63). For example, structures derived from the bipyridine **123** would possess different reactive sites for subsequent functionalization.

In an extension of these studies the diacetylene **127** was prepared and the oxidative coupling examined with the expectation that the dimer **128** would be produced (Scheme 25). Instead, the strained monomer **129** was formed in 91% yield when the reaction was conducted at 80°C. Using similar chemistry, the trienetriyne compound **132** was synthesized from the appropriate Wittig combination (Scheme 26). The reactions in the boxes lacked stereocontrol. Under carefully controlled conditions **132** gave rise to the triply bridged dimer **133.** The hexasubstituted systems have the potential for more complex structures. Thus, by modification of literature protocol (64), the building block **137** was constructed from simpler units (Scheme 27) in the hope that under appropriate conditions it could be trimerized to a hexasubstituted benzene ring. Unfortunately, it was unstable above 40°C and despite a huge effort and a wide range of catalysts (Co, Pd, Pt, Ni, Ti, Ag) the silyl-protected version of **139** was not detected. The synthesis of **139** is being purused by other routes since, as illustrated in Scheme 28, oxidative dimerization of **139** should give **140** by analogy with our previous studies. Bromination–dehydrobromination of the styrenyl bonds should introduce the triple bonds to give the C_{60} allotrope **141** (30 acetylenic bonds, strain energy ~500 kcal/mol greater than C_{60}, (Buckminsterfullerene)) (65). C_{60} sits in a potential well, and by analogy with earlier studies with adamantane (66), thermal rearrangement of **141** should give the spherical C_{60} system. This route has a high probability of providing interesting inclusion compounds (endohedral fullerenes) if complexation precedes rearrangement, as well as more complex fullerenes of higher molecular weight.

Carbometallation studies

We continue to search for short direct routes to the taxane nucleus that may be adapted to prepare analogs, as well as improved methods to prepare Diels–Alder components. In this context, we have further expanded our study of the magnesium chelates used earlier for the synthesis of our dienes

© 1999 NRC Canada

Scheme 24. Synthesis of revolvenynes (eneynecyclophanes).

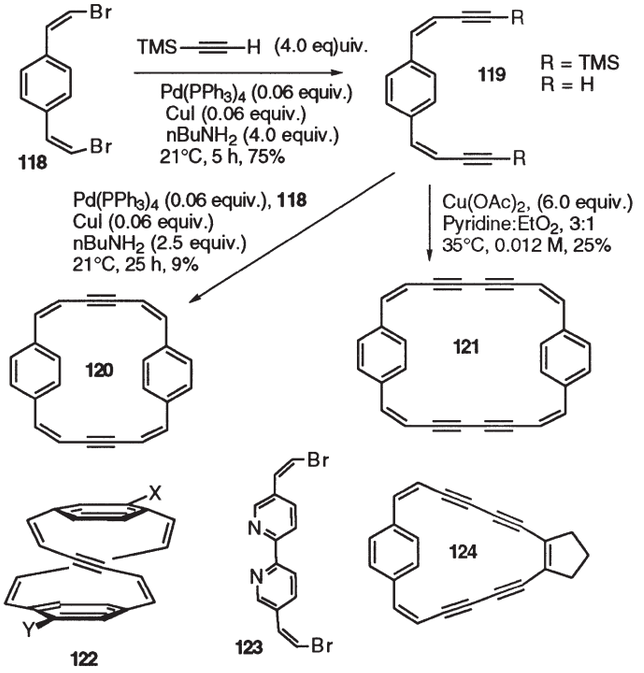

Scheme 25. Synthesis of novel cyclophanes.

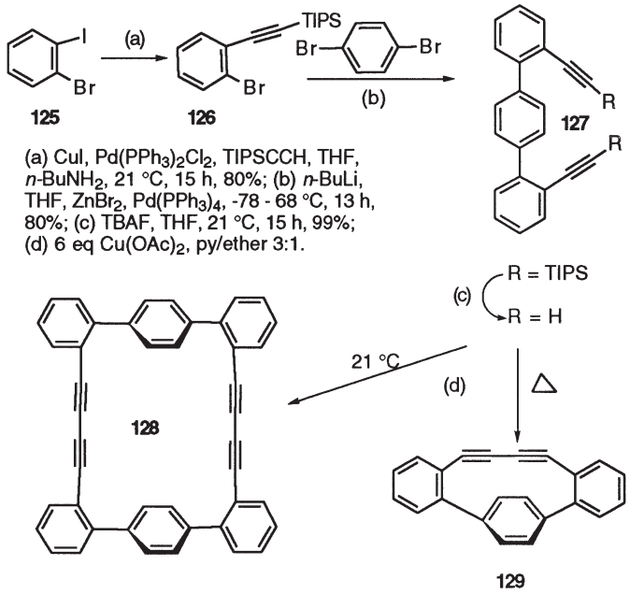

(Scheme 4, **10**). Procedures have been developed for the direct condensation of this putative intermediate with aldehydes by conducting the reaction in cyclohexane. Thus direct condensation of **10** (Scheme 29) with the hemiacetal **143** afforded a 40% yield (3:1) of the diene triol **146**. If **10** is reacted directly with DMF, the resultant hemiacetal **142** is converted to the furan **144** (90%) upon acidic work-up. Alternatively, condensation with a nitrile leads to substituted furans of type **145**. These furans may serve as precursors for double cycloaddition reactions (vinyl group, then furan, after isomerization of the exocyclic double bond) and (or) natural products by modification of the substitution pattern. It should be possible to modify these methods for the synthesis of thiophenes and pyrroles.

A further refinement is to generate the key intermediate **10** (Scheme 30) in a different manner by commencing with a lithium acetylide **147**. Condensation with the aldehyde **148** afforded the lithium alkoxide **149**. Subsequent addition of vinylmagnesium chloride and condensation of **10** with nitriles has allowed the synthesis of tetra-substituted furans (**145**) in one reaction pot, a significant improvement over current routes to furans. If **150** is added to trimethylsilylpenta-2,4-diynyl alcohol (**151**), the interesting enediyne alcohol **152** (66) can be prepared in a single step. This type of synthon has many potential applications.

Finally, a potentially short, versatile, strategy for synthesis of taxane systems is being developed based on the following combination. Sequential reaction of the components in Box A (Scheme 31) afforded the diol-pentaene **153** in which R is phenyl. With a methyl group, the corresponding compound **154** (R = Me) has been prepared in a stepwise fashion. After conversion to **154** it is anticipated that the planar tether will facilitate the cycloaddition to **155,** and a final ring C cyclization in either an inter- or, preferably, intramolecular manner may provide **156**. Alternatively, these cyclization steps could be reversed; however, this remains to be tested experimentally.

Concluding comment

In summary, modern life has been greatly enriched by the achievements and discoveries derived from synthetic organic chemistry. It is an important area of investigation in its own right and occupies a key role in a myriad of other disciplines that range from medicine to molecular biology to materials

© 1999 NRC Canada

Scheme 26. Synthesis of a triple-bridged hexaeneyne cyclophane.

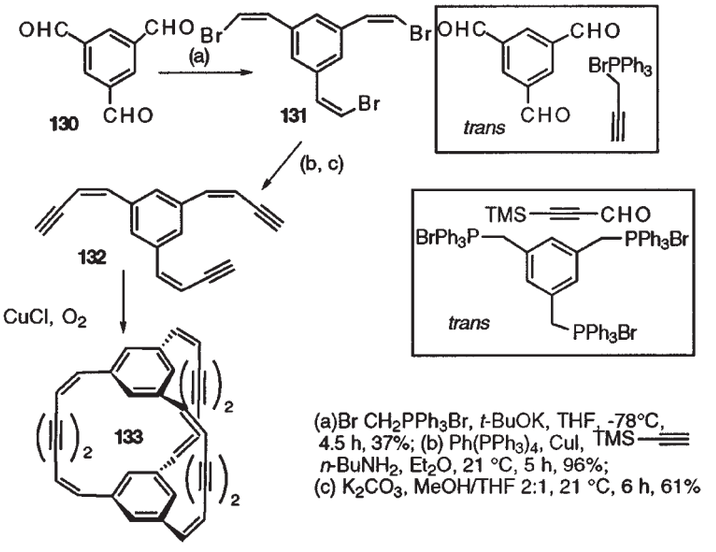

Scheme 27. Preparation of dienetriyne synthon.

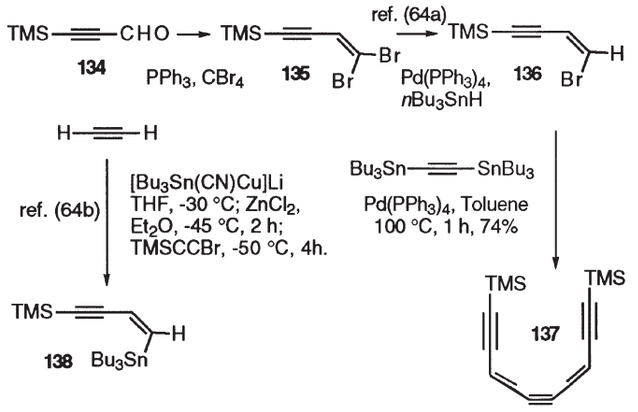

Scheme 28. Potential route to C_{60} (Buckminsterfullerene).

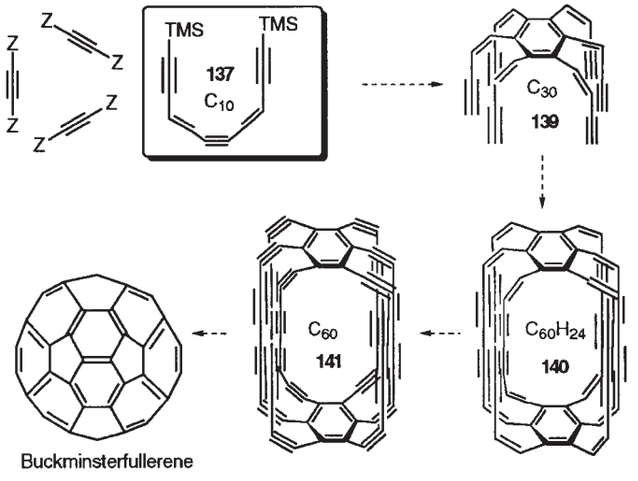

Scheme 29. Carbometallation routes to diols and furans.

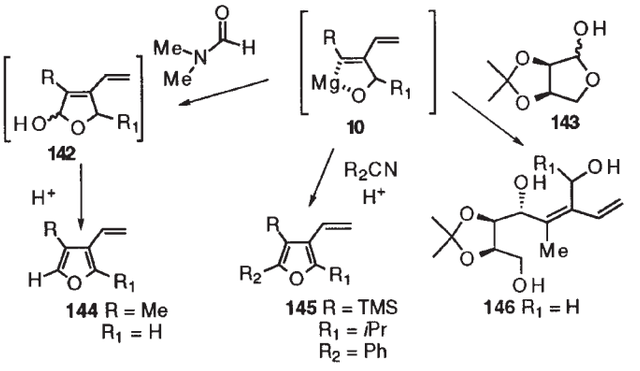

Scheme 30. Further carbometallation routes.

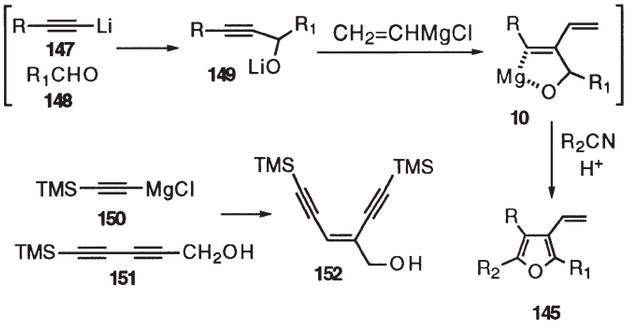

© 1999 NRC Canada

Scheme 31. Potential carbometallation route to taxoids.

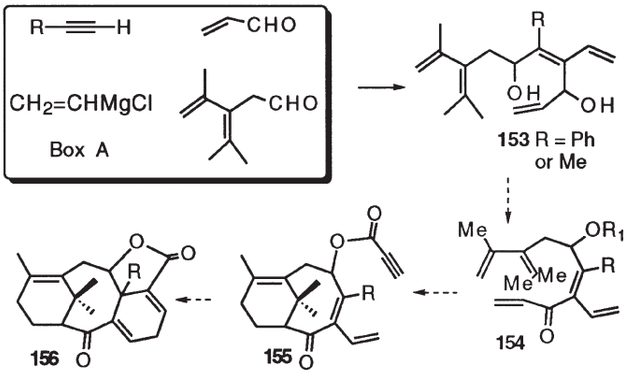

science. The strategies and synthetic methods discussed above should prove of general utility for a variety of synthetic objectives. These investigations contribute to our understanding of organic chemistry and provide an excellent vehicle for the education of students.

Acknowledgments

I wish to thank a very dedicated group of collaborators whose names are listed in our publications (or will be in the future!) for their intellectual and experimental contributions to our research program. We are grateful to the Natural Sciences and Engineering Research Council of Canada, Rhône-Poulenc Rorer, Torcan Chemical, the Canadian Breast Cancer Research Initiative (NCI, Canada), and the Saunders–Matthey Foundation for Breast Cancer Research for financial support of this research.

References

1. H. Hartzell. The yew tree, a thousand whispers. Hulogosi, Eugene, Oregon. 1991.
2. M.C. Wani, H.L. Taylor, M.E. Wall, P. Coggan, and A.T. McPhail. J. Am. Chem. Soc. **93**, 2325 (1971).
3. (*a*) P.B. Schiff, J. Fant, and S.B. Horwitz. Nature, **277**, 665 (1979); (*b*) G.I. Georg, T.T. Chen, I. Ojima, and D.M. Vyas (*Editors*). Taxane anticancer agents: basic science and current status. ACS Symp. Ser. **583**. American Chemical Society, Washington. 1994; (*c*) M.L. Rothenberg. Curr. Opin. Invest. Drugs **2,** 1269 (1993); (*d*) J.J. Manfredi and S.B. Horwitz. Pharmacol. Ther. **25**, 83 (1984).
4. E.K. Rowinsky, L.A. Cazenave, and R.C. Donehower. J. Natl. Cancer Inst. **82**, 1247 (1990).
5. G. Hofle, N. Bedorf, H. Steinmetz, D. Schomburg, K. Gerth, and H. Reichenbach. Angew. Chem. Int. Ed. Engl. **35**, 1567 (1996).
6. E. ter Haar, R.J. Kowalski, E. Hamel, C.M. Lin, R.E. Longley, S.P. Gunasekera, H.S. Rosenkranz, and B.W. Day. Biochemistry, **35**, 243 (1996).
7. T. Lindel, P.R. Jensen, W. Fenical, B.H. Long, A.M. Casazzza, J. Carboni, and C.R. Fairchild. J. Am. Chem. Soc. **119**, 8744 (1997).
8. F. Lavelle, F. Guéritte-Voegelin, and D. Guénard. Bull. Cancer, **80**, 326 (1993).
9. (*a*) A.N. Boa, P.R. Jenkins, and N.J. Lawerence. Contemp. Org. Synth. **1**, 47 (1994); (*b*) K.C. Nicolaou, W.-M. Dai, and R.K. Guy. Angew. Chem. Int. Ed. Engl. **33**, 15 (1994); for total syntheses see (*c*) R.A. Holton, C. Somoza, H.B. Kim, F. Liang, R.J. Biediger, P.D. Boatman et al. J. Am. Chem. Soc. **116**, 1597 (1994); (*d*) R.A. Holton, H.B. Kim, C. Somoza, F. Liang, R.J. Biediger, P.D. Boatman et al. J. Am. Chem. Soc. **116**, 1599 (1994); (*e*) K.C. Nicolaou, Z. Yang, J.J. Liu, H. Ueno, P.G. Nantermet, R.K. Guy et al. Nature, **367**, 630 (1994); (*f*) K.C. Nicolaou, P.G. Nantermet, H. Ueno, R.K. Guy, and E.A. Sorensen. J. Am. Chem. Soc. **117**, 624 (1995); (*g*) K.C. Nicolaou, J.J. Liu, Z. Yang, H. Ueno, E.J. Sorensen, C.F. Claiborne et al. J. Am. Chem. Soc. **117**, 634 (1995); (*h*) K.C. Nicolaou, Z. Yang, J.J. Liu, P.G. Nantermet, C.F. Claiborne, J. Renaud, R.K. Guy, and K. Shibayama. J. Am. Chem. Soc. **117**, 645 (1995); (*i*) K.C. Nicolaou, H. Ueno, J.J. Liu, P.G. Nantermet, Z. Yang, J. Renaud, K. Paulvannan, and R. Chadha.. J. Am. Chem. Soc. **117**, 653 (1995); (*j*) J.J. Masters, J.T. Link, L.B. Snyder, W.B. Young, and S.J. Danishefsky. Angew. Chem. Int. Ed. Engl. **34**, 1723 (1995); (*k*) S.J. Danishefsky, J.J. Masters, W.B. Young, J.T. Link, L.B. Snyder, T.V. Magee et al. J. Am. Chem. Soc. **118**, 2843 (1996); (*l*) P.A. Wender, N.F. Badham, S.P. Conway, P.E. Floreancig, T.E. Glass, C. Gränicher et al. J. Am. Chem. Soc. **119**, 2755 (1997); (*m*) P.A. Wender, N.F. Badham, S.P. Conway, P.E. Floreancig, T.E. Glass, J.B. Houze et al. J. Am. Chem. Soc. **119**, 2757 (1997); (*n*) T. Mukaiyama, I. Shiyama, H. Iwadare, H. Sakoh, Y. Tan, M. Hasegawa, and K. Saitoh. Proc. Jpn. Acad. Ser. B. **73**, 95 (1997); (*o*) T. Mukaiyama, I. Shiina, H. Iwadare, M. Saitoh, T. Nishimura, N. Ohkawa et al. Chem. Eur. J. **5**, 121 (1999); (*p*) K. Morihira, R. Hara, S. Kawahara, T. Nishimori, N. Nakamura, H. Kusama, and I. Kuwajima. J. Am. Chem. Soc. **120**, 12890 (1998).
10. (*a*) Y.-F. Lu and A.G. Fallis. Tetrahedron Lett. **34**, 3367 (1993); (*b*) Can. J. Chem. **73**, 2239 (1995).
11. (*a*) K. Sakan and B.M. Craven. J. Am. Chem. Soc. **105**, 3732 (1983); (*b*) K. Sakan, D.A. Smith, S.A. Babirad, F.R. Fronczek, and K.N. Houk. J. Org. Chem. **56**, 2311 (1991).
12. A.G. Fallis and Y.-F. Lu. *In* Advances in cycloadditions. Vol. 3. *Edited by* D.P. Curran. JAI Press, Greenwich, Conn. 1993. pp. 1–66.
13. (*a*) M.W. Tjepkema, P.D. Wilson, T. Wong, M.A. Romero, H. Audrain, and A.G. Fallis. Tetrahedron Lett. **36**, 6039 (1995); (*b*) M.W. Tjepkema, P.D. Wilson, T. Wong, H. Audrain, and A.G. Fallis. Can. J. Chem. **75**, 1215 (1997).
14. T. Wong, M.A. Romero, and A.G. Fallis. J. Org. Chem. **59**, 5527 (1994).
15. T. Wong, M.W. Tjepkema, H. Audrain, P.D. Wilson, and A.G. Fallis. Tetrahedron Lett. **37**, 755 (1996).
16. M.W. Tjepkema, T. Wong, P.D. Wilson, and A.G. Fallis. Can. J. Chem. **38**, 1542 (1997).
17. J.D. Winkler, S.K. Bhattacharya, and R.A. Batey. Tetrahedron Lett. **37**, 8069 (1996).
18. I.J. Kim, T.K. Park, and S.J. Danishefsky. Tetrahedron Lett. **36**, 1015 (1995).
19. (*a*) C. Spino and J. Crawford. Can. J. Chem. **71**, 1094 (1993); (*b*) C. Spino, J. Crawford, and J. Bishop. J. Org. Chem. **60**, 844 (1995).
20. S. Millan, T. Pham, J. Lavers, and A.G. Fallis. Tetrahedron Lett. **38**, 795 (1997).
21. (*a*) A.G. Fallis. Can. J. Chem. **62**, 183 (1984); (*b*) E. Ciganek. Org. React. **32**, 1 (1984); (*c*) D. Craig. Chem. Soc. Rev. **16**, 187 (1987); (*d*) M. Hirama and M. Uei. J. Am. Chem. Soc. **104**, 4251 (1982).
22. P. Deslongchamps, S. Lamothe, and H.-S. Lin. Can. J. Chem. **65**, 1298 (1987).

© 1999 NRC Canada

23. D.L. Boger and R.J. Mathvink. J. Org. Chem. **53**, 3377 (1988).
24. (*a*) S.J. Miller, S.-H. Kim, Z.-R. Chen, and R.H. Grubbs. J. Am. Chem. Soc. **117**, 2108 (1995); (*b*) D.J. O'Leary, S.J. Miller, and R.H. Grubbs. Tetrahedron Lett. **39**, 1689 (1998).
25. M.P. Doyle, M.N. Protopopova, C.S. Peterson, J.P. Vitale, M.A. McKervey, and C.F. Garcia. J. Am. Chem. Soc. **118**, 7865 (1996).
26. (*a*) K. Tamao, K. Kobayashi, and Y. Ito. J. Am. Chem. Soc. **111**, 6478 (1989); (*b*) K.J. Shea, K.S. Zandi, A.J. Staab, and R. Carr. Tetrahedron Lett. **31**, 5885 (1990); (*c*) D. Craig and J.C. Reader. Tetrahedron Lett. **31**, 6586 (1990); (*d*) J.W. Gillard, R. Fortin, E.L. Grimm, M. Maillard, M. Tjepkema, M.A. Bernstein, and R. Glaser. Tetrahedron Lett. **32**, 1145 (1991); (*e*) G. Stork, T.Y. Chan, and G. Breault. J. Am. Chem. Soc. **114**, 7578 (1992).
27. (*a*) D. Craig and J.C. Reader. Tetrahedron Lett. **33**, 6165 (1992); (*b*) D. Craig, M.J. Ford, and J.A. Stones. Tetrahedron Lett. **37**, 535 (1996).
28. (*a*) H.B. Kagan and O. Riant. Chem. Rev. **92**, 1007 (1992); (*b*) M. Sawamura and Y. Ito. Chem. Rev. **92**, 857 (1992); (*c*) U. Pinder, G. Lutz, and C. Otto. Chem. Rev. **93**, 741 (1993); (*d*) E.J. Corey, A. Guzman-Perez, and T.-P. Loh. J. Am. Chem. Soc. **116**, 3611 (1994); (*e*) D. Seebach, R. Dahinder, R.E. Marti, A.K. Beck, D.A. Plattner, and F.N.M. Kühnk. J. Org. Chem. **60**, 1788 (1995); (*f*) D.A. Evans, J.A. Murry, P. von Matt, R.D. Norcross, and S.J. Miller. Angew. Chem. Int. Ed. Engl. **34**, 398 (1995).
29. (*a*) D.A. Evans, K.T. Chapman, and J. Bisaha. Tetrahedron Lett. **25**, 4071 (1984); (*b*) D.A. Evans, K.T. Chapman, and J. Bisaha. J. Am. Chem. Soc. **106**, 4261 (1984); (*c*) I. Alsono, J.C. Carretero, and J.L. Garcia Ruano. J. Org. Chem. **59**, 1499 (1994); (*d*) W. Oppolzer, B.M. Seletsky, and G. Bernardinelli. Tetrahedron Lett. **35**, 3509 (1994).
30. G. Stork and T.Y. Chan. J. Am. Chem. Soc. **117**, 6595 (1995).
31. D.A. Evans and J.S. Johnson. J. Org. Chem. **62**, 786 (1997).
32. A.G. Fallis. Pure Appl. Chem. **69**, 495 (1997).
33. (*a*) R.W. Jackson and K.J. Shea. Tetrahedron Lett. **35**, 1317 (1994); for previous, representative Ring A cycloadditions see (*b*) K.J. Shea and P.D. Davis. Angew. Chem. Int. Ed. Engl. **22**, 419 (1983); (*c*) K.J. Shea and J.W. Gilman. Tetrahedron Lett. **25**, 2451 (1984); (*d*) K.J. Shea, J.W. Gilman, C.D. Haffner, and T.K. Dougherty. J. Am. Chem. Soc. **108**, 4953 (1986); (*e*) R.V. Bonnert and P.R. Jenkins. J. Chem. Soc. Chem. Commun. 1540 (1987); (*f*) R.V. Bonnert and P.R. Jenkins. J. Chem. Soc. Perkin Trans. 1, 413 (1989); (*g*) R.W. Jackson, R.G. Higby, J.W. Gilman, and K.J. Shea. Tetrahedron, **48**, 7013 (1992); (*h*) C.A. Alaimo, C.A. Coburn, and S.J. Danishefsky. Tetrahedron Lett. **35**, 6603 (1994); (*i*) S.M. Rubenstein and R.M. Williams. J. Org. Chem. **60**, 7215 (1995).
34. J. Marco-Contelles, C. Destabel, P. Callego, J.L. Chiara, and M.J. Bernabé. J. Org. Chem. **61**, 1354 (1996).
35. W.H. Pearson and F.E. Lovering. J. Am. Chem. Soc. **117**, 12336 (1995).
36. (*a*) W.R. Roush, M. Kageyama, R. Riva, B.B. Brown, J.S. Warmus, and K.J. Moriarty. J. Org. Chem. **56**, 1192 (1991); (*b*) W.R. Roush, K. Koyama, M.L. Curtin, and K.J. Moriarty. J. Am. Chem. Soc. **118**, 7502 (1996); (*c*) J.W. Coe and W.R. Roush. J. Org. Chem. **54**, 915 (1989).
37. (*a*) J.A. Musich and H. Rapoport. J. Am. Chem. Soc. **100**, 4865 (1976); (*b*) H. Iida, N. Yamazaki, and C. Kibayashi. J. Org. Chem. **52**, 3337 (1987).
38. T. Wong, P.D. Wilson, S. Woo, and A.G. Fallis. Tetrahedron Lett. **38**, 7045 (1997).
39. E. Abushanab, P. Vemishetti, R.W. Leiby, H.K. Singh, A.B. Mikkileni, D.C.-J. Wu, R. Saibaba, and R.P. Panzica. J. Org. Chem. **53**, 2598 (1998).
40. P.A. Wender, S.M. Sieburth, J.J. Petraitis, and S.K. Singh. Tetrahedron, **37**, 3967 (1987).
41. C.E. Ballou. J. Am. Chem. Soc. **79**, 165 (1957).
42. G.W.J. Fleet, N.G. Ramsden, and D.R. Witty. Tetrahedron, **45**, 319 (1989).
43. For leading references to allylindium additions see (*a*) C.J. Li and T.-H. Chan. Tetrahedron Lett. **32**, 7017 (1991); (*b*) T.-H. Chan, C.J. Li, M.C. Lee, and Z.Y. Wei. Can. J. Chem. **72**, 1181 (1994); (*c*) L.A. Paquette and T.M. Mitzel. Tetrahedron Lett. **36**, 6863 (1995); (*d*) X.-R. Li and T.P. Loh. Tetrahedron Asymmetry, **7**, 1535 (1996).
44. (*a*) D.B. Borders and T.W. Doyle (*Editors*). Enediyne antibiotics as antitumor agents. Marcel Dekker Inc., New York. 1995; (*b*) K.C. Nicolaou and A.L. Smith. *In* Modern acetylene chemistry. *Edited by* P.J. Stang and F. Diederich. VCH, Weinheim. 1995. pp. 203–279; (*c*) H. Lhermitte and D.S. Grierson. Contemp. Org. Synth. **3**, 41 (1996); (*d*) Contemp. Org. Synth. **3**, 43 (1997); (*e*) S.J. Danishefsky and M.D. Shair. J. Org. Chem. **61**, 16 (1996).
45. (*a*) J. Golik, J. Clardy, G. Dubay, G. Groenewold, H. Kawaguchi, M. Konishi, B. Krishnan, H. Ohkuma, K.I. Saitoh, and T.W. Doyle. J. Am. Chem. Soc. **109**, 3461 (1987); (*b*) J. Golik, G. Dubay, G. Groenewold, H. Kawaguchi, M. Konishi, B. Krishnan, H. Ohkuma, K.I. Saitoh, and T.W. Doyle. J. Am. Chem. Soc. **109**, 3462 (1987).
46. (*a*) M.D. Lee, T.S. Dunne, M.M. Siegel, C.C. Chang, G.O. Morton, and D.B. Borders. J. Am. Chem. Soc. **109**, 3464 (1987); (*b*) M.D. Lee, T.S. Dunne, C.C. Chang, G.A. Ellestad, M.M. Siegel, G.O. Morton, W.J. McGahren, and D.B. Borders. J. Am. Chem. Soc. **109**, 3466 (1987).
47. (*a*) J. Wang and P.J. De Clercq. Angew. Chem. Int. Ed. Engl. **34**, 1749 (1995); (*b*) Tetrahedron Lett. **37**, 3395 (1995).
48. L. Banfi and G. Guanti. Angew. Chem. Int. Ed. Engl. **34**, 2393 (1995).
49. G.B. Jones, R.S. Huber, J.E. Mathews, and A. Li. Tetrahedron Lett. **37**, 3643 (1996).
50. (*a*) Y.-F. Lu, C.W. Harwig, and A.G. Fallis. J. Org. Chem. **58**, 4202 (1993); (*b*) Can. J. Chem. **73**, 2253 (1995).
51. C.W. Harwig, S. Py, and A.G. Fallis. J. Org. Chem. **62**, 7902 (1997).
52. (*a*) K.B. Sharpless and R.F. Lauer. J. Am. Chem. Soc. **94**, 7154 (1972); (*b*) D. Arigoni, A. Vasella, K.B. Sharpless, and H.P. Jensen. J. Am. Chem. Soc. **95**, 7917 (1973).
53. S. Py, C.W. Harwig, and A.G. Fallis. Tetrahedron Lett. **39**, 6139 (1998).
54. T. Nishikawa, S. Shibuya, S. Hosokawa, and M. Isobe. Synlett, 485 (1984).
55. (*a*) Y. Okude, S. Hirano, T. Hiyama, and H. Nozaki. J. Am. Chem. Soc. **99**, 3179 (1977); (*b*) T. Hiyama, K. Kimura, and H. Nozaki. Tetrahedron Lett. **22**, 1037 (1981); (*c*) K. Takai, K. Kimura, T. Kuroda, T. Hiyama, and H. Nozaki. Tetrahedron Lett. **24**, 5281 (1983). (*d*) K. Takai, T. Kuroda, S. Nakatsukasa, K. Oshima, and H. Nozaki. Tetrahedron Lett. **26**, 5585 (1985); (*e*) H. Jin, J. Uenishi, W.J. Christ, and Y. Kishi. J. Am. Chem. Soc. **108**, 5644 (1986); (*f*) K. Takai, M. Yagashira, T. Kuroda, K. Oshima, K. Uchimoto, and H. Nozaki. J. Am. Chem. Soc. **108**, 6048 (1986); (*g*) P. Cintas. Synthesis, 248 (1992); (*h*) D.M. Hodgson. J. Organomet. Chem. **476**, 1 (1994); (*i*) C. Crevisy and J.-M. Beau. Tetrahedron Lett. **32**, 3171 (1991); (*j*) K.C. Nicolaou, A. Liu, Z. Zeng, and S.J.

© 1999 NRC Canada

McComb. J. Am. Chem. Soc. **114**, 9279 (1992); (*k*) M.E. Maier and T. Brandstetter. Tetrahedron Lett. **33**, 7511 (1992); (*l*) A.G. Meyers and N.S. Finney. J. Am. Chem. Soc. **114**, 10986 (1992); (*m*) M. Eckhardt, R. Brückner, and J. Suffert. Tetrahedron Lett. **36**, 5167 (1995).

56. J.F. Kadow, D.J. Cook, T.W. Doyle, D.R. Langley, K.M. Pham, D.M. Vyas, and M.D. Wittman. Tetrahedron, **30**, 3499 (1989).
57. E. Didier, E. Fouque, I. Taillepied, and A. Commerçon. Tetrahedron Lett. **35**, 2349 (1994).
58. W.F. Maier and P.v.R. Schleyer. J. Am. Chem. Soc. **103**, 1891 (1981).
59. (*a*) F. Vögtle. Top. Curr. Chem. **113**, 72 (1983); (*b*) P.M. Keehn and S.M. Rosenfeld (*Editors*). Cyclophanes. Academic Press, New York. 1983; (*c*) F. Diederich. Cyclophanes. Royal Society of Chemistry, Cambridge. U.K. 1991; (*d*) C. Seel and F. Vögtle. Angew. Chem. Int. Ed. Engl. **31**, 528 (1992); (*e*) H.J. Sneider and H. Dürr (*Editors*). Frontiers in supramolecular organic chemistry and photochemistry. VCH, Weinheim. 1991; (*f*) J.M. Coterón, C. Vicent, C. Bosso, and S. Penadés. J. Am. Chem. Soc. **115**, 10066 (1993); (*g*) P.J. Stang and F. Diederich (*Editors*). Modern acetylene chemistry. VCH, Weinheim. 1995.
60. M.A. Romero and A.G. Fallis. Tetrahedron Lett. **35**, 4711 (1994).
61. (*a*) A. Nikon and E.F. Silversmith. Organic chemistry: the name game. Pergamon Press, Oxford. 1987. pp. 22–23; (*b*) H.S. Brown, C.P. Muenchavsen, and L.R. Sousa. J. Org. Chem. **45**, 1682 (1980).
62. (*a*) D.J. Cram and C.K. Dewhirst. J. Am. Chem. Soc. **81**, 5963 (1959); (*b*) J. Abell and D.J. Cram. J. Am. Chem. Soc. **76**, 4406 (1954).
63. K. Odashima, A. Itai, Y. Iitaka, and K. Koga. J. Am. Chem. Soc. **102**, 2504 (1980).
64. (*a*) J. Uenishi, R. Kawahama, and O. Yonemitsu. J. Org. Chem. **61**, 5716 (1996); (*b*) P.A. Magriotis, M.E. Scott, and K.D. Kim. Tetrahedron Lett. **32**, 6085 (1991).
65. For related ideas see (*a*) Y. Rubin, T.C. Parker, S.I. Khan, C.L. Holliman, and S.W. McElvany. J. Am. Chem. Soc. **118**, 5308 (1996); (*b*) Y. Rubin. Chem. Eur. J. **3**, 1009 (1997); (*c*) R. Boese, A.J. Matzger, and K.P.C. Vollhard. J. Am. Chem. Soc. **119**, 2052 (1997); (*d*) Y. Rubin, T.C. Parker, S.J. Pastor, S. Jalisatgi, C. Boulle, and C.L. Wilkins. Angew. Chem. Int. Ed. Engl. **37**, 1226 (1998); (*e*) Y. Tobe, N. Nakagawa, K. Naemura, T. Wakabayashi, T. Shida, and Y. Achiba. J. Am. Chem. Soc. **120**, 4544 (1998).
66. (*a*) P.v.R. Schleyer. J. Am. Chem. Soc. **79**, 3292 (1957); (*b*) M.A. McKervey. Chem. Soc. Rev. **3**, 479 (1974).
67. A.G. Meyers, P.M. Harrington, and E.Y. Kuo. J. Am. Chem. Soc. **113**, 694 (1991).

© 1999 NRC Canada

C(2)-H isotopic exchange in coordinated imidazoles revisited. The case of the $[Co(NH_3)_5ImH]^{3+}$ ion

Charles R. Clark, Allan G. Blackman, M. Ross Grimmett, and Akbar Mobinikhaledi

Abstract: The temperature dependence of the acid ionization constants of $[Co(NH_3)_5ImH]^{3+}$ in H_2O (I = 1.0 M ($NaClO_4$)): pK_a (°C) = 10.10 ± 0.04 (25.0), 9.92 ± 0.03 (30.0), 9.82 ± 0.02 (35.0), 9.62 ± 0.03 (40.0), and $[Co(ND_3)_5ImD]^{3+}$ in D_2O (I = 0.35 M ($NaClO_4$)): pK_a (°C) = 10.58 ± 0.06 (25.0), 9.46 ± 0.08 (60.0) is reported. Observed first-order rate constants for H/D exchange at C-2 in $[Co(ND_3)_5ImD]^{3+}$ over the pD range 8.08–11.20 (60.0°C, I = 0.35 M ($NaClO_4$)) follow an equation of the form: $k_{obs} = k_{OD}K_w/(a_{D+} + K_a)\gamma_{\pm}$, with k_{OD} (0.27 ± 0.06 M^{-1} s^{-1}) corresponding to the rate constant for OD^--catalyzed abstraction of H-2 in $[Co(ND_3)_5ImD]^{3+}$, and K_a ((2.8 ± 0.7) × 10^{-10} M, pK_a = 9.55 ± 0.13) to the acid ionization constant of this species. No evidence was found for a pathway to H/D exchange in the imidazolate moiety of $[Co(ND_3)_5Im]^{2+}$.

Key words: kinetics, H/D-exchange, imidazole, metal complex.

Résumé : On a la relation entre la température et les constantes d'ionisation acide du $[Co(NH_3)_5ImH]^{3+}$ dans l'eau (I = 1,0 M ($NaClO_4$)): pK_a (°C) = 10,10 ± 0,04 (25,0), 9,92 ± 0,03 (30,0), 9,82 ± 0,02 (35,0), 9,62 ± 0,03 (40,0) et du $[Co(ND_3)_5ImD]^{3+}$ dans le D_2O (I = 0,35 M ($NaClO_4$)): pK_a (°C) = 10,58 ± 0,06 (25,0), 9,46 ± 0,08 (60,0). Les constantes de vitesses du premier ordre observées pour l'échange H/D en C-2 du $[Co(ND_3)_5ImD]^{3+}$, à des pD allant de 8,08 à 11,20 (60,0°C, I = 0,35 M ($NaClO_4$)), obéissent à une équation de la forme: $k_{obs} = k_{OD}K_w/(a_{D+} + K_a)\gamma_{\pm}$ dans laquelle k_{OD} (0,27 ± 0,06 M^{-1} s^{-1}) correspond à la constante de vitesse de la réaction d'ablation du H-2 du $[Co(ND_3)_5ImD]^{3+}$ par OH^- et K_a ((2,8 ± 0,7) × 10^{-10} M, pK_a = 9,55 ± 0,13) à la constante d'ionisation acide de cette espèce. On n'a observé aucune voie permettant l'échange H/D de la portion imidazolate du $[Co(ND_3)_5ImD]^{3+}$.

Mots clés : cinétiques, échange H/D, imidazole, complexe métallique.

[Traduit par la Rédaction]

Introduction

There have been a number of studies focusing on isotopic hydrogen exchange in coordinated imidazoles (1–7). Such exchange is base-catalyzed, is favored for C-2 rather than C-4, C-5 (5), and appears to involve rate-determining formation of ylide intermediates (5–7). One such investigation, which has laid the foundation for knowledge in this area, is that by Buncel et al. (7), who described the pathways leading to detritiation of the substitution inert complex $[Co(NH_3)_5[2\text{-}^3H]ImH]^{3+}$ (cf. Fig. 1). Two routes to exchange were reported to be involved: for weakly alkaline solutions reactivity was said to be dominated by an OH^--catalyzed reaction on the $[Co(NH_3)_5[2\text{-}^3H]ImH]^{3+}$ ion, whereas for pH > 10 it was stated that a similar process on the conjugate base, $[Co(NH_3)_5[2\text{-}^3H]Im]^{2+}$, became increasingly important. The latter result was most surprising since OH^--catalyzed H-atom abstraction from the anionic imidazolate center would be expected to be very unfavorable from the energetic point of view. We have had occasion to re-examine C(2)-H exchange in $[Co(NH_3)_5ImH]^{3+}$, and our findings are at odds with those originally reported. Our results derive from a kinetic study of H/D exchange in $[Co(NH_3)_5ImH]^{3+}$ and are given below.

Received September 14, 1998.

C.R. Clark,[1] A.G. Blackman,[1] M.R. Grimmett, and A. Mobinikhaledi. The Department of Chemistry, University of Otago, P.O. Box 56, Dunedin, New Zealand.

[1]Authors to whom correspondence may be addressed. Telephone: 64-3-479-7930. Fax: 64-3-479-7906. e-mail: charles.clark@stonebow.otago.ac.nz

Experimental

Caution: Although no problems were encountered in the synthesis and handling of the materials described below, those containing perchlorate are potentially explosive and should be handled with great care.

$[Co(NH_3)_5ImH](ClO_4)_3$ (8) and $[Co(NH_3)_5ImCo(NH_3)_5](ClO_4)_5$ (9) were prepared using standard procedures. Both were purified by recrystallization from water. D_2O (99.9 atom% D) and NaOD solution (30 wt.%, 99+ atom% D) were obtained from Aldrich. ^1H NMR spectra were recorded using a Varian VXR 300 spectrometer.

Rates of H/D exchange at C-2 for $[Co(NH_3)_5ImH]^{3+}$ in D_2O were obtained by following the decay of the H-2 signal by ^1H NMR spectroscopy. For kinetic runs at pD < 9.3 solutions of the complex (0.05 M, 350 μL) and $NaClO_4$ (0.40 M, 350 μL) in D_2O were mixed, and the pD adjusted to the required value with NaOD (1.0 M). The resultant solution

© 1999 NRC Canada

Fig. 1. Atom numbering scheme for imidazole coordinated to the $Co(NH_3)_5$ center.

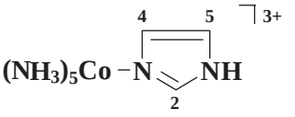

was placed in a sealed NMR tube and maintained at 60.0 ± 0.1°C (water bath). At known time intervals the room temperature ^{1}H NMR spectrum of the sample was recorded. For reactions carried out at pD > 9.3 direct integration failed to give reliable peak areas, owing to increasing broadness of the signals. In these cases a quench method was employed. A reaction mixture consisting of 3.0 mL of complex (0.05 M), and 3.0 mL of $NaClO_4$ (0.40 M) in D_2O was maintained at 60.0 ± 0.1°C. At various times aliquots (700 μL) were placed in an NMR tube, and DCl (30–40 μL, 0.9 M) was added. The ^{1}H NMR spectrum of the acidic solution was then recorded and peak areas obtained by integration as before. H-2 signal areas were measured relative to nonexchanging H-4 and H-5. Plots of ln (normalized peak area) versus time were linear over $3t_{1/2}$, and rate constants were obtained from their slopes.

pD measurements were made using a Radiometer PHM 82 pH meter fitted with G2040B glass and K4040 calomel electrodes. Measurements were carried out using a salt bridge (NH_4NO_3 = 1.6 M, $NaNO_3$ = 0.2 M) to separate the test solution from the calomel electrode. The system was standardized using 0.025 M Na_2HPO_4 – 0.025 M KH_2PO_4 (pH 6.865 (25°C), 6.836 (60°C)) and 0.0100 M Borax buffers (pH 9.185 (25°C), 8.962 (60°C)). pD was obtained using the empirical relationship $pD = pH_{meter\ reading} + 0.40$ (10). Rate constants were calculated using $pK_w(D_2O) = 13.918$ at 60.0 °C (11) and a value for $\gamma_\pm$ of 0.67 at I = 0.35 M $NaClO_4$ (interpolated from data given by ref. 12).

pK_a values are given as mixed constants, i.e., $K_a(D_2O) = a_{D+}[A^-]/[DA]$, $K_a(H_2O) = a_{H+}[A^-]/[HA]$. For $[Co(NH_3)_5\ ImH](ClO_4)_3$ in D_2O the pK_a was determined at 25.0 and 60.0°C (I = 0.35 M, $NaClO_4$) by potentiometric titration of 0.0183 M solutions (10 mL) with standardized NaOD (0.283 M). Data were treated by the method of Albert and Serjeant (13). The pK_a of $[Co(NH_3)_5ImH](ClO_4)_3$ in H_2O was similarly determined at 25.0 (10.10 ± 0.04), 30.0 (9.92 ± 0.03), 35.0 (9.82 ± 0.02), and 40.0°C (9.62 ± 0.03) for I = 1.0 M ($NaClO_4$).

Results and discussion

In neutral to alkaline D_2O solution all ammine–amine hydrogens in $[Co(NH_3)_5ImH]^{3+}$ exchange rapidly with solvent. Thus, for this condition the species finally present is the $[Co(ND_3)_5ImD]^{3+}$ ion.[2] Potentiometric titration of ca. 0.02 M solutions of the complex in D_2O (I = 0.35 M ($NaClO_4$)) established pK_a = 10.58 ± 0.06 at 25.0°C and pK_a = 9.46 ± 0.08 at 60.0°C, cf. eq. [1]. These data indicate a temperature dependence for the pK_a of –0.032 units/°C, which compares

Table 1. Observed and calculated rate constants for H/D exchange at C-2 in $[Co(ND_3)_5ImD]^{3+}$ at 60.0°C, D_2O solution, I = 0.35 M ($NaClO_4$).

pD[a]	$10^9 a_{D^+}$/M	$10^6 k_{obs}/s^{-1}$	$10^6 k_{calc}/s^{-1}$[b]
8.08	8.32	1.25	0.986
8.32	4.79	2.36	1.67
8.64	2.29	2.78	3.29
8.79	1.62	4.17	4.45
8.98	1.05	6.22	6.36
9.19	0.646	8.94	9.11
9.54	0.288	15.0	14.8
9.78	0.166	17.5	18.8
9.90	0.126	21.4	20.6
10.09	0.0813	26.9	23.1
10.57	0.0269	27.8	27.2
10.99	0.0102	27.5	28.7
11.20	0.00631	27.8	29.1

[a]Obtained from pD measurements at 25.0°C using a correction factor for the $[Co(ND_3)_5ImD]^{3+}$–$[Co(ND_3)_5Im]^{2+}$ buffer system of –0.032 pD units/°C.

[b]Calculated using eq. [2] and the values of the constants given in the text.

$$[1] \quad [Co(ND_3)_5Imd]^{3+} + D_2O \overset{K_a}{\rightleftharpoons} [Co(ND_3)_5Im]^{2+} + D_3O^+$$

with –0.032 units/°C for ionization of $[Co(NH_3)_5ImH]^{3+}$ in H_2O, see above. Thus, the deutero substrate in D_2O (pK_a = 10.58, 25.0°C) is a somewhat weaker acid than its protio counterpart in H_2O (pK_a = 10.10, 25.0°C, I = 1.0 M $NaClO_4$), as is usually observed (14). Also, the acidity difference ($\Delta pK_a \approx 0.5$) is of the expected magnitude; e.g., $[Co(ND_3)_5OD_2]^{3+}$ in D_2O, pK_a = 6.70; $[Co(NH_3)_5OH_2]^{3+}$ in H_2O, pK_a = 6.22 (25.0°C, I = 0.30 M $NaClO_4$) (15).

Rate data for H/D exchange at C-2 were obtained using ^{1}H NMR spectroscopy over the pD range 8.08–11.20 at 60.0°C for self-buffered solutions of $[Co(ND_3)_5ImD]^{3+}$–$[Co(ND_3)_5Im]^{2+}$. Under these conditions H-4 and H-5 do not exchange to any measurable extent. For pD > 9.3 the ^{1}H NMR signals of the heterocyclic ligand were increasingly broadened, presumably from quadrupolar coupling by imidazolate nitrogen; however, acid quenching of the kinetic solutions resulted in sharpened signals with a concomitant improvement in integration quality. No evidence was found for complex decomposition at high alkalinity, as has been reported for the protic system (7). Observed first-order rate constants, Table 1, vary according to eq. [2] and are plotted as log k_{obs} versus pD in Fig. 2. Least-squares fitting of the data to eq. [2] using the known

$$[2] \quad k_{obs} = \frac{k_{OD}K_w}{(a_{D^+} + K_a)\gamma_\pm}$$

value for $K_w(D_2O)$ of 2.08×10^{-14} M^2 (i.e., pK_w = 13.918, 60°C, (11)) gave k_{OD} = 0.27 ± 0.06 M^{-1} s^{-1} and K_a = (2.8 ± 0.7) × 10^{-10} M (i.e., pK_a = 9.55 ± 0.13). We interpret these results in terms of the mechanism given in Scheme 1, with exchange at C-2 occurring exclusively via an OD^--catalyzed

[2] Such exchange necessarily results in isotopic dilution of solvent D_2O. For the 0.02–0.05 M $[Co]_T$ solutions used in the present study deuteration at the ammine–amine centers introduces 0.29–0.72 atom% H into the solvent.

© 1999 NRC Canada

Fig. 2. Plot of log k_{obs} versus pD for exchange of H-2 in $[Co(ND_3)_5ImD]^{3+}$ (D_2O, 60.0°, I = 0.35 M ($NaClO_4$)). The points are experimental, and the curve is drawn using eq. [2] and the values of the constants given in the text.

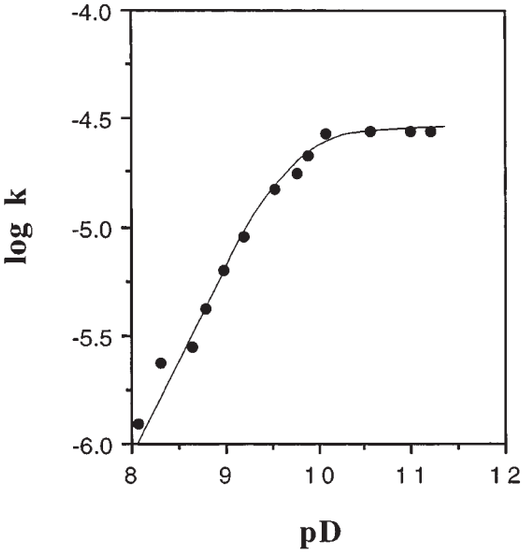

reaction (k_{OD}) on $[Co(ND_3)_5ImD]^{3+}$. The value of the kinetically defined acidity constant is in excellent agreement with that obtained by independent potentiometric measurements for the same conditions (i.e., pK_a = 9.46, 60.0°C, I = 0.35 M). Also, and most importantly, the data appear to exclude a pathway involving OD^--catalyzed exchange in the $[Co(ND_3)_5Im]^{2+}$ ion.

In the earlier study (7) it was claimed that observed rate constants for detritiation of $[Co(NH_3)_5[2\text{-}^3H]ImH]^{3+}$ in H_2O at 60.0°C followed the rate law given by eq. [3], with k_{OH} (= 1.24 M^{-1} s^{-1}) and

$$[3] \qquad k_{obs} = \frac{k_{OH}K_w + k'_{OH}K_a[OH^-]}{[H^+] + K_a}$$

k'_{OH} (= 1.21 × 10^{-3} M^{-1} s^{-1}), respectively, representing the rate constants for OH^--catalyzed detritiation of $[Co(NH_3)_5[2\text{-}^3H]ImH]^{3+}$ and its conjugate base, $[Co(NH_3)_5[2\text{-}^3H]Im]^{2+}$. However, for this interpretation to be valid the pH-rate profile is required to be sigmoidal (cf. eq. [3]), and the certain reactivity of the $[Co(NH_3)_5[2\text{-}^3H]Im]^{2+}$ ion is demonstrated only if a first-order in $[OH^-]$ dependence is observed at high pH. The *experimental data* of the earlier study did not support the proposal, since k_{obs} tended toward a limiting value at pH ≈ 9.5 but never exhibited the necessary first order in $[OH^-]$ behavior at higher pH.[3] This, taken with the present results, argues against an exchange pathway involving Co(III)-coordinated imidazolate. On the assumption that reaction by this route could make a 5% contribution to the observed rate at pD 11.2 and remain undetected we calculate a maximum value for k'_{OD} (cf. k'_{OH} of eq. [3] but for H/D exchange) of ≤5 × 10^{-4} M^{-1} s^{-1}. This finding is in agreement with expectations for this system.

Scheme 1.

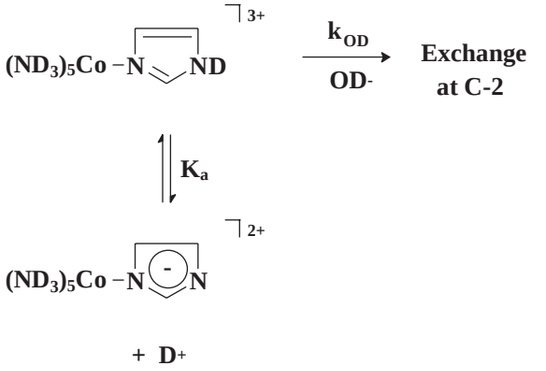

H/D exchange rates in imidazoles are reasonably well correlated with ^1H NMR signal positions.[4] The latter provide a measure of electron density at C-2, with any increase in electron withdrawal from the heterocyclic ring manifesting itself in a down-field shift in H-2 and favoring OD^- attack. This is readily seen when data for the dimethylimidazolium and methylimidazolium ions (k_{OD} = 10^3–10^4 M^{-1} s^{-1}, 60°C; H-2, δ (D_2O) = 8.65–8.68 ppm), for various substitution-inert Pt(II)- and Co(III)-imidazole and -*N*-methylimidazole complexes (k_{OD} = 1–10^{-2} M^{-1} s^{-1}, 60°C; H-2, δ (D_2O) = 8.06–7.73 ppm), and for *N*-methylimidazole (k_{OD} = 5 × 10^{-5} M^{-1} s^{-1}, 60°C; H-2, δ (D_2O) = 7.59 ppm) are compared (these data are given in ref. 5, but see also ref. 16). The absence of a detectable pathway for H/D exchange in the $[Co(ND_3)_5Im]^{2+}$ ion (H-2, δ (D_2O) = 7.44 ppm, (2)) is not unexpected when the above trends are considered. Finally, it is of interest to note that we were unable to find evidence for H-2 exchange (<10%) in $[Co(ND_3)_5ImCo(ND_3)_5]^{5+}$ (H-2, δ (D_2O) = 7.77 ppm) after 170 h in 0.10 M NaOD solution at 60°C. This result implies that k_{OD} must take a value of less than 2 × 10^{-5} M^{-1} s^{-1}, and indicates that the total charge carried by a metal–imidazole complex is not a factor in determining exchange rate, nor H-2 signal position an unequivocal guide. Indeed, for $[Co(ND_3)_5ImCo(ND_3)_5]^{5+}$, hydrogen bonding of the incoming base to amine centres of the flanking $Co(ND_3)_5$ substituents might well provide an effective barrier to H-atom abstraction. Work in this area is continuing.

References

1. D.H. Buisson, J.R. Jones, and S.E. Taylor. J. Chem. Soc. Chem. Commun. 856 (1975).

[3] A limiting rate is certainly indicated when errors in the observed rate constants given in ref. 7 are taken into account. The reported reactivity of $[Co(NH_3)_5[2\text{-}^3H]Im]^{2+}$ derives solely from a possible superiority in the least-squares fit of the data (six points) to eq. [3] compared to an equation of the form given by eq. [2]. It is also noted that in this case the kinetically determined pK_a (8.0, 60°C) appears to be too low when compared with that calculated (9.0 ± 0.1) from the temperature dependence of $[Co(NH_3)_5ImH]^{3+}$ acidity, see above.

[4] Available data do not always allow quantitative comparisons. Reported k_{OD} values (= $k_{obs}/[OD^-]$) for H/D exchange at elevated temperatures often appear to have been erroneously calculated by using solution OD^- concentrations applicable to the 25°C situation. The use of such uncorrected data can lead to order of magnitude errors in k_{OD}.

© 1999 NRC Canada

2. N.S. Rowan, C.B. Storm, and R. Rowan. J. Inorg. Biol. Chem. **14**, 59 (1981).
3. N.R. Brodsky, N.M. Nguyen, C.B. Storm, and E. Sinn. Inorg. Chem. **23**, 891 (1986).
4. E. Buncel, H.A. Joly, and D.C. Yee. Can. J. Chem. **67**, 1426 (1989).
5. O. Clement, A.W. Roszak, and E. Buncel. J. Am. Chem. Soc. **118**, 612 (1996).
6. E. Buncel, O. Clement, and I. Onyido. J. Am. Chem. Soc. **114**, 2679 (1994).
7. E. Buncel, F. Yang, R.Y. Moir, and I. Onyido. Can. J. Chem. **73**, 781 (1995).
8. J.M. Harrowfield, V. Norris, and A.M. Sargeson. J. Am. Chem. Soc. **98**, 7282 (1976).
9. A.G. Blackman, D.A. Buckingham, C.R. Clark, and J. Simpson. J. Chem. Soc. Dalton Trans. 3031 (1991).
10. P.K. Glascoe and F.A. Long. J. Chem. Phys. **64**, 188 (1960).
11. R.E. Mesmer and D.L. Herting. J. Solution Chem. **7**, 901 (1978)
12. N. Linnet. *In* pH measurements in theory and practice. Radiometer, Copenhagen. 1970. p. 173.
13. A. Albert and E.P. Serjeant. Ionization constants of acids and bases. Methuen, London. 1962.
14. K.B. Wiberg. Chem. Rev. **55**, 713 (1955).
15. R.C. Splinter, S.J. Harris, and R.S. Tobias. Inorg. Chem. **7**, 897 (1968).
16. J.L. Wong and J.H. Keck, Jr. J. Org. Chem. **39**, 2398 (1974).

© 1999 NRC Canada

Porphyrins incorporating heterocyclic *N*-oxides: (oxidopyridyl)porphyrins, porphyrin-*N*-oxides, and a tirapazamine–porphyrin conjugate

Jeffrey J. Posakony, Russell C. Pratt, Steven J. Rettig, Brian R. James, and Kirsten A. Skov

Abstract: Porphyrins containing one to four 4-pyridyl groups as *meso*-substituents were synthesized via a mixed aldehyde condensation, and then "*N*-oxidized" with *m*-chloroperbenzoic acid to produce five novel (oxidopyridyl) porphyrins and seven porphyrin-*N*-oxides, which were characterized by analysis and spectroscopic methods, especially NMR; an X-ray crystal structure of 5-(1-oxido-4-pyridyl)-10,15,20-triphenylporphyrin was also obtained. Crystals of (oxidopyridyl)triphenylporphyrin are tetragonal, $a = b = 15.174(1)$, $c = 13.709(1)$ Å, $Z = 4$, space group *I*2*d*. The structure was solved by direct methods and refined by full-matrix least-squares procedures to $R = 0.031$ ($R_w = 0.026$) for 685 reflections with $I \geq 3\sigma(I)$. Sulfonation of two of the (oxidopyridyl)porphyrins was achieved readily with no loss of oxygen from the oxidopyridyl groups. Tirapazamine (3-amino-1,2,4-benzotriazine-1,4-di-*N*-oxide) was treated with triphosgene to yield the previously reported 2*H*-[1,2,4]oxadiazolo[3,2-*c*][1,2,4]benzotriazin-2-one-5-oxide (**1**); this reacts like an isocyanate and with 5-(4-aminophenyl)-10,15,20-triphenylporphyrin yields a tirapazamine-porphyrin conjugate (**2**).

Key words: porphyrin-*N*-oxides, (oxidopyridyl)porphyrins, tirapazamine.

Résumé : Faisant appel à une condensation mixte d'aldéhyde, on a synthétisé des porphyrines contenant d'un à quatre groupes 4-pyridyles comme substituants *méso* et on les a ensuite oxydées à l'aide d'acide *m*-chloroperbenzoïque pour produire cinq nouvelles (oxydopyridyl)porphyrines et sept *N*-oxydes de porphyrine que l'on a caractérisés par analyse et par spectroscopie, principalement la RMN; on a aussi déterminé la structure cristalline de la 5-(1-oxydo-4-pyridyl)-10,15,20-triphénylporphyrine par diffraction des rayons X. Les cristaux de la (oxydopyridyl)triphénylporphyrine sont tétragonaux, groupe d'espace *I*2*d*, avec $a = b = 15{,}174(1)$ et $c = 13{,}709(1)$ Å et $Z = 4$. On a résolu la structure par des méthodes directes et on l'a affinée par la méthode des moindres carrés (matrice entière) jusqu'à des valeurs de $R = 0{,}031$ et $R_w = 0{,}026$ pour 685 réflexions avec $I \geq 3\sigma(I)$. On a effectué la sulfonation de deux des oxydopyridylporphyrines facilement, sans perte d'oxygène à partir des groupes oxydopyridyles. On a traité la tirapazamine (le 1,4-dioxyde de la 3-amino-1,2,4-benzotriazine) avec du triphosgène pour obtenir la 5-oxyde de la 2*H*-[1,2,4]oxadiazolo[3,2-*c*][1,2,4]benzotriazine-2-one (**1**) rapportée antérieurement; celle-ci réagit comme un isocyanate et, avec la 5-(4-aminophényl)-10,15,20-triphénylporphyrine, elle fournit une tirapazamine–porphyrine conjuguée.

Mots clés : *N*-oxyde de porphyrine, (oxydopyridyl)porphyrine, tirapazamine.

[Traduit par la Rédaction]

Introduction

One advantage of porphyrin-based, cancer therapies is that neoplastic tissue has been reported to accumulate many porphyrins to a greater degree than many normal tissues; this phenomenon also occurs with other aromatic macrocycles (e.g., naphthalocyanines, phthalocyanines, and chlorins) (1, 2). The mechanisms of tumor localization of such aromatic macrocycles have been discussed and are complex (2–5).

Received July 20, 1998.

J.J. Posakony, R.C. Pratt, S.J. Rettig, and B.R. James.[1] Department of Chemistry, University of British Columbia, Vancouver, BC V6T 1Z1, Canada.
K.A. Skov. B.C. Cancer Research Centre, Vancouver, BC V5Z 1L3, Canada.

[1]Author to whom correspondence may be addressed. Telephone: (604) 822-6645. Fax: (604) 822-2847. e-mail: brj@chem.ubc.ca

Heterocyclic *N*-oxides, most notably aromatic tirapazamine (6) and RB90740 (6, 7) have been investigated as radiosensitizers and hypoxia-selective agents. Thus, because of our ongoing interest in the development of porphyrin-based anticancer agents (8–10), we have pursued porphyrins incorporating heterocyclic *N*-oxides, as this might improve the delivery of heterocyclic *N*-oxides to neoplastic tissue. Herein, we describe the *N*-oxidation of several *meso*-pyridyl porphyrins to yield their corresponding (oxidopyridyl)porphyrins and their corresponding porphyrin-*N*-oxides, and the conjugation of tirapazamine to a porphyrin.

Experimental

All solvents were reagent grade or better. Unless otherwise indicated, all commercial chemicals were used as purchased from Aldrich Chemical Co., Strem, or Sigma Chemical Co. Pyrrole was dried over and distilled from CaH_2 or vacuum-transferred before use. Benzaldehyde, 4-pyridine-

 © 1999 NRC Canada

Table 1. Abbreviations used for the *meso*-pyridyl porphyrins, and corresponding (oxidopyridyl)porphyrins and porphyrin-*N*-oxides.

Porphryin precursor	Abbrev.	Oxidopyridyl abbrev.	Corresponding porphyrin-*N*-oxide abbrev.
5,10,15-Triphenyl-20-(4-pyridyl)porphyrin	TrPhPyP	OPyTrPhP	OPyTrPhP-21O, OPyTrPhP-23O
5,15-Diphenyl-10,20-bis(4-pyridyl)porphyrin	*t*-DPhBPyP[a]	*t*-BOPyDPhP	Not isolated
5,10-Diphenyl-15,20-bis(4-pyridyl)porphyrin	*c*-DPhBPyP	*c*-BOPyDPhP	*c*-BOPyDPhP-21O, *c*-BOPyDPhP-22O, *c*-BOPyDPhP-24O
5-Phenyl-10,15,20-tris(4-pyridyl)porphyrin	PhTrPyP	TrOPyPhP	TrOPyPhP-21O, TrOPyPhP-23O
5,10,15,20-Tetrakis(4-pyridyl)porphyrin	TPyP	TOPyP	Not isolated

[a]Present in small amounts as an impurity in TrPhPyP.

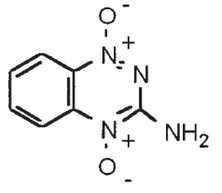

Tirapazamine

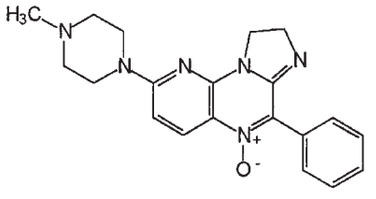

RB90740

carboxaldehyde, and trifluoroacetic acid (TFA) were freshly distilled before use. Tirapazamine (3-amino-1,2,4-benzotriazine-1,4,-di-*N*-oxide) was a gift from Dr. M. Tracy (SRI International, Menlo Park, Calif.). Reaction products were dried in vacuo at 78°C overnight, unless otherwise noted.

The alumina used for chromatography was Fisher, activity I, and was deactivated by adding water to give a standard range of activities (11). Unless otherwise noted, the silica gel used in the chromatographies was Merck Silica Gel 60, 230–400 mesh, whilst R_f values were measured on Merck silica TLC Al sheets (silica gel 60 F_{254}). Preparative TLCs of porphyrin free bases were performed with Merck silica gel 60, 0.5 mm plates (without indicator, to avoid metallation of the products). In general, the visualization of non-porphyrinic compounds was achieved with the aid of a UV lamp. Dialysis tubing (SpectraPor) used in the purification of the sulfonated porphyrins had a molecular weight cutoff of 1000.

^{1}H and ^{13}C NMR spectra were recorded on a BRUKER AC-200, a Varian XL-300, or a BRUKER WH-400 instrument, and UV-vis spectra on an HP8452A photo-diode array spectrophotometer (± 2 nm) with molar absorptivity (ϵ) values recorded for analytically pure porphyrins. IR spectra were recorded as KBr pellets or as a thin film on a KBr disk (from slow evaporation of a solution of the compound on the surface of a KBr disk) on an AIT Mattson Genesis Series FTIR instrument. Elemental analyses were performed by Mr. P. Borda of the Department of Chemistry (UBC). High- (HR-MS) and low-resolution (LR-MS) mass spectra were obtained on a KRATOS MS50 (EI), a KRATOS MS80 (CI), a KRATOS Concept IIHQ (LSIMS), or a BRUKER Biflex MALDI-TOF mass spectrometer. When analyzed with EI techniques, the mass spectra of free-base porphyrins often showed a peak at 61 *m*/*z* higher ($M^+ - 2H + Cu$) than the parent mass due to a gas phase metallation reaction with Cu from the ionization source.

Porphyrin precursors

The *meso*-pyridyl porphyrins were synthesized according to literature methods (8, 12); the abbreviations used for these porphyrins and the corresponding (oxidopyridyl)porphyrin and porphyrin-*N*-oxide derivatives are given in Table 1.

***N*-Oxidations**

Based on published procedures for the preparation of pyridine-*N*-oxide (13), excess *meta*-chloroperoxybenzoic acid (*m*-CPBA, 60–85%, the rest being benzoic acid and H_2O) was added to a stirred solution of the starting porphyrin in CH_2Cl_2 or CH_2Cl_2–MeOH at room temperature (r.t.). Addition of 1–2 equiv. aliquots of *m*-CPBA gave the (oxidopyridyl)porphyrins, while a single addition of several equivalents gave the corresponding porphyrin-*N*-oxides in low and variable yield. The reactions were monitored by TLC on silica (CH_2Cl_2:MeOH 100:1 to 10:1); Et_3N was added to the final reaction mixture, and the product was purified by chromatography after preadsorbing the product mixture on silica. With very polar eluent mixtures, metallation (with Zn from the fluorescent indicator in the silica) occurred on the TLC plate. In such cases, analytical TLC plates without indicator were used. Tables 2–6 summarize, respectively, ^{1}H NMR data for the (1-oxido-4-pyridyl)porphyrins, ^{1}H NMR data for some porphyrin-*N*-oxides, UV-vis data, elemental analyses, and mass spectrometry data; the ^{1}H NMR assignments are considered in Results and Discussion. IR data for the (oxidopyridyl)porphyrins and the two sulfonated derivatives (Table S1) and the porphyrin-*N*-oxides (Table S2) are available as supplementary material.[2]

If the porphyrin-*N*-oxides were not produced or their isolation was not pursued, the product was purified by first removing the solvent under reduced pressure, and the residue

[2]Copies of material on deposit may be purchased from: The Depository of Unpublished Data, Document Delivery, CISTI, National Research Council Canada, Ottawa, Canada, K1A 0S2. Tables of hydrogen atom coordinates have also also been deposited with the Cambridge Crystallographic Data Centre and can be obtained on request from: The Director, Cambridge Crystallographic Data Centre, University Chemical Laboratory, 12 Union Road, Cambridge, CB2 1EZ, U.K.

© 1999 NRC Canada

Table 2. ^{1}H NMR data for the (1-oxido-4-pyridyl)porphyrins.[a]

Porphyrin (MHz, solvent)	β-Pyrrole[b]	2,6-OPy 3,5-OPy[c]	2,6-Ph (or 2,6-SPh) 3,4,5-Ph (or 3,5-SPh)[d]	Pyrrole N-H
OPyTrPhP (200, $CDCl_3$)	8.92 d (2), 8.84 s (4), 8.82 d (2)	8.64 dd (2) 8.11 dd (2)	8.18 d (6) 7.76 m (9)	–2.82 s (~1.5)
t-BOPyDPhP (200, $CDCl_3$)	8.94 d (4), 8.83 d (4)	8.62 dd (4) 8.10 dd (4)	8.18 d (4) 7.80 m (6)	–2.87 s (~1.5)
c-BOPyDPhP (300, $CDCl_3$)	8.94 d (2), 8.93 s (2), 8.86 s (2), 8.83 d (2)	8.63 dd (4) 8.10 dd (4)	8.18 d (4) 7.78 m (6)	–2.85 s (~1.5)
TrOPyPhP (400, $CDCl_3$)	8.95 d (2), 8.94 s (4), 8.83 d (2)	8.63 dd (6) 8.10 dd (6)	8.18 d (2) 7.8 m (3)	–2.88 s (~1.5)
TOPyP (400, $CDCl_3$–CD_3OD)	8.95 s br (8)	8.67 dd (8) 8.19 dd (8)		None observed in $CDCl_3$–CD_3OD
OPyTrSPhP (200, DMSO-d_6)	9.05 d (2), 8.88 d (2), 8.85 s (4)	8.63 d (2) 8.17 d (2)	8.17 d (6) 8.05 d (6)	–2.96 s br (1.7)
c-BOPyBSPhP (200, DMSO-d_6)[e]	9.10 s (2), 9.05 d (2), 8.87 m (4)	8.64 d (4) 8.25 d (4)	8.18 d (4) 8.05 d (4)	–2.95 s br (1.6)

[a]Measured at r.t.; δ in ppm, signal pattern (number of protons). An H_2O signal was generally observed in the spectra.
[b]*J* values typically ~5 Hz (*meso*-phenyl derivatives) or ~6 Hz (*meso*-(4-sulfonatophenyl) derivatives).
[c]Typically, J_1 = 7 Hz, J_2 = 1 Hz.
[d]*J* values typically ~8 Hz.
[e]Impurity peaks appeared near δ ~7.8 and 8.4 (<0.5 H each by integration).

Table 3. ^{1}H NMR data for the porphyrin-*N*-oxides.[a]

Porphyrin	β-Pyrrole[b]	2,6-OPy 3,5-OPy[c]	2,6-Ph 3,4,5-Ph	β-Pyrrole-NO[d]	Pyrrole N-H
OPyTrPhP-23O	9.07 d (1), 9.00 d (1), 8.8 overlapping doublets (2), 8.75 d (1), 8.66 d (1)	8.63 d (2) 8.10 d (2)	8.5 m (6) 7.9 m (9)	7.5 s (2)	1.6 s br (>2)[e]
OPyTrPhP-21O	8.97 overlapping doublets (2), 8.91 d (1), 8.83 d (1), 8.65 m (2)	Under β-pyrrole signal at 8.65 Under 2,6-Ph signal at 8.17	8.23 d (2), 8.17 d (4) 7.8 m (9)	7.56 d (1), 7.50 d (1)	~1.7 s br (>2)[e]
TrOPyPhP-21O	9.06 overlapping doublets (2), 8.92 d (1), 8.85 d (1), 8.73 m (2)	8.64 m (6) 8.14 d (2), 8.07 d (4)	8.22 d (2) 7.83 m (3)	7.60 d (1), 7.54 d (1)	N-H peak not assigned because of large H_2O peak
TrOPyPhP-22O[f]	9.07 d, 9.00 d, 8.94 d, 8.92 d, 8.74 d, 8.63 d	8.6 m 8.14 m, 8.05 d	Under 8.14 m 7.8 m	7.61 s	N-H peak not assigned because of large H_2O peak

[a]Measured at r.t. in $CDCl_3$ (400 MHz); δ in ppm, signal pattern (number of protons). An H_2O signal was observed in all spectra.
[b]*J* values typically ~5 Hz.
[c]*J* values typically ~7 Hz.
[d]*J* values typically ~6 Hz; addition of D_2O changed these signals to broad multiplets.
[e]Integration includes H_2O peak; the peak disappeared when D_2O was added.
[f]Integrations did not match.

then being washed with acetone. The resulting solid contained mostly the (oxidopyridyl)porphyrin, while the filtrate contained the corresponding porphyrin-*N*-oxides and other reaction byproducts (e.g., large amounts of *m*-chlorobenzoic acid (*m*-CBA)). Excess *m*-CBA complicated the chromatography, and also could be removed by washing the reaction mixture with dilute aq. NaOH. In some cases, mixtures of porphyrins (e.g., *c*-DPhBPyP and PhTrPyP) were treated with *m*-CPBA to give mixtures of (oxidopyridyl)porphyrins and the corresponding porphyrin-*N*-oxides. The mixtures were separated by chromatography, but no yield was determined for the minor components, as the molar ratio of the compounds was not determined prior to the reaction.

Because of the polar solvent mixtures used in chromatography, the porphyrin samples were often contaminated with silica. To obtain analytically pure material, the porphyrin was allowed to crystallize slowly (days to weeks) from a CH_2Cl_2:MeOH (~10:1) solution in a vial placed in a chamber containing EtOH.

The (oxidopyridyl)porphyrins were deoxygenated under the conditions of EI or LSIMS mass spectrometry and had to be analyzed by MALDI-TOF mass spectrometry. The corresponding porphyrin-*N*-oxides were deoxygenated to a lesser degree, and in some cases the parent peaks were intense enough to be analyzed by HR-MS (EI).

5-(1-Oxido-4-pyridyl)-10,15,20-triphenylporphyrin (OPyTrPhP)

TrPhPyP (0.223 g, 0.36 mmol) was dissolved in CH_2Cl_2 (150 mL), and treated with excess *m*-CPBA (3 × 0.1 g aliquots)

© 1999 NRC Canada

Table 4. UV-vis data for the (1-oxido-4-pyridyl)porphyrins and porphyrin-*N*-oxides.

Porphyrin (solvent)	*N*-Oxide region (log ϵ)	Soret (log ϵ)	Q bands (log ϵ)
OPyTrPhP[a] (CH_2Cl_2:MeOH 20:1)	274 (4.32)	420 (5.60)	516 (4.35), 552 (3.95), 590 (3.80), 646 (3.67)
t-BOPyDPhP[b] (CH_2Cl_2:MeOH 10:1)	274, 310 (weak)	426	516, 556, 602, 648
c-BOPyDPhP[a] (CH_2Cl_2:MeOH 10:1)	272 (4.49)	422 (5.57)	518(4.30), 556 (4.00), 592 (3.85), 650 (3.59)
TrOPyPhP[a] (CH_2Cl_2:MeOH 10:1)	274 (4.61)	424 (5.65)	518 (4.33), 554 (4.07), 594 (3.87), 650 (3.65)
TOPyP[a] (CH_2Cl_2:MeOH 10:1)	274 (4.66)	424 (5.63)	518 (4.3), 554 (4.03), 594 (3.85), 650 (3.56)
OPyTrPhP-23O[c] (CH_2Cl_2)	282 (4.30)	420 (5.14)	518 (3.77), 544 (3.76), 594 (3.85), 684 (3.41)
OPyTrPhP-21O (CH_2Cl_2)	280	420	516, 548, 596, 684
OPyTrPhPZn-23O[d,e] (CH_2Cl_2:MeOH 5:1)	272 (4.35), 322 (4.26)	436 (5.27)	574 (3.89), 622 (3.91)
OPyTrPhPZn-21O (CH_2Cl_2:MeOH 5:1)	276, 330	438	574, 622
c-BOPyDPhP-O mixture (CH_2Cl_2)	280, 342 (weak)	422	514, 550, 594, 688
TrOPyPhP-21O (CH_2Cl_2)	283, 334 (weak)	424	518, 548, 600, 685
TrOPyPhP-22O (CH_2Cl_2)	280, 348 (weak)	424	518, 552, 598, 685
OPyTrSPhP[f] (H_2O)	258 (4.32), 306 (4.27)	414 (5.59)	516 (4.14), 554 (3.84), 580 (3.81), 636 (3.57)
c-BOPyBSPhP (H_2O)	258, 306	418	520, 560, 586, 646

[a]Soret ϵ determined at 2×10^{-6} M; ϵ of other bands determined at 2×10^{-5} M.
[b]The C, H, and N elemental analyses were ~0.5% too low (see Table 5); ϵ values were not determined.
[c]The C and N elemental analyses were ~0.5 and 1.26% too low, respectively (see Table 5).
[d]Soret ϵ determined at 5×10^{-6} M; ϵ of other bands determined at 5×10^{-5} M.
[e]Prepared from a known concentration of OPyTrPhP-23O and excess $Zn(OAc)_2$.
[f]ϵ determined at 1.0×10^{-6} M.

Table 5. Elemental analyses for the (1-oxido-4-pyridyl)porphyrins and porphyrin-*N*-oxides.[a]

Porphyrin (formula)	C (%)	H (%)	N (%)
OpyTrPhP ($C_{43}H_{29}N_5O$)	81.53 (81.75)	4.63 (4.88)	11.09 (11.10)
OpyTrPhP-23O ($C_{43}H_{29}N_5O_2 \cdot 1H_2O$)	77.58 (77.12)	4.69 (4.65)	10.52 (9.26)
t-BOPyDPhP ($C_{42}H_{28}N_6O_2 \cdot 2H_2O$)	73.67 (73.12)	4.71 (4.24)	12.27 (11.86)
c-BOPyDPhP ($C_{42}H_{28}N_6O_2 \cdot H_2O$)	75.66 (75.83)	4.54 (4.41)	12.60 (12.73)
c-BOPyDPhP-O mixture ($C_{42}H_{28}N_6O_3 \cdot 1.5H_2O$)	72.93 (72.71)	4.52 (4.46)	12.60 (12.73)
TrOPyPhP ($C_{41}H_{27}N_7O_3 \cdot 1.5H_2O$)	71.09 (71.04)	4.37 (4.31)	14.15 (13.93)
TOPyP ($C_{40}H_{26}N_8O_4 \cdot 2H_2O$)	68.56 (68.55)	4.03 (3.98)	15.99 (15.75)
OpyTrSPhP ($C_{43}H_{26}N_5Na_3O_{10}S_3 \cdot 11H_2O$)	45.46 (45.72)	4.26 (4.11)	6.16 (6.12)
c-BOPyBSPhP ($C_{42}H_{26}N_6Na_2O_8S_2 \cdot 4.5H_2O$)	54.02 (54.28)	3.78 (3.66)	9.00 (8.80)

[a]Calculated (found); not obtained for OPyTrPhP-23O, TrOPyPhP-21O, and TrOPyPhP-22O.

over 1–2 h while the solution was stirred. Et_3N (20 mL) was then added, and the product was preadsorbed on silica and chromatographed on silica ($CHCl_3$: pyridine 10:1). The solvent was removed from the main product band to yield 0.128 g (56% yield) of OPyTrPhP. The reaction was scaled up to ~0.5 g of TrPhPyP with similar results. Slow solvent evaporation from a CH_2Cl_2–MeOH solution of the porphyrin yielded analytically pure crystals which were studied by X-ray crystallography.

5-(1-Oxido-4-pyridyl)-10,15,20-triphenylporphyrin-21-oxide (OPyTrPhP-21O), and -23-oxide (OPyTrPhP-23O)

From reactions in which several equivalents of *m*-CPBA were added all at once to a solution of TrPhPyP in CH_2Cl_2:MeOH, two additional products were isolated (~5% yield each) after OPyTrPhP was first isolated chromatographically. The two bands following that of OPyTrPhP were collected; the solvent was removed, and a second chromatography column silica (CH_2Cl_2:THF:MeOH 100:5:2.5) was used to separate two isomers. The less polar band was OPyTrPhP-23O, and the more polar band was OPyTrPhP-21O.

The porphyrin-*N*-oxides metallated rapidly when mixed with $Zn(OAc)_2$ in CH_2Cl_2–MeOH to give OPyTrPhPZn-21O and OPyTrPhPZn-23O (see Table 4 for UV-vis data). Attempts to grow crystals of the free-base porphyrin-*N*-oxides or Zn-porphyrin-*N*-oxides were unsuccessful.

5,15-Bis(1-oxido-4-pyridyl)-10,20-diphenylporphyrin (*t*-BOPyDPhP)

t-BOPyDPhP was prepared in the same manner as OPyTrPhP. The *m*-CPBA was added in 1–2 equiv. aliquots to a solution of an impure sample of TrPhPyP containing a small amount of *t*-DPhBPyP. The products were purified by column chromatography on silica; OPyTrPhP was eluted from the column with $CHCl_3$:pyridine (10:1), and *t*-BOPyDPhP was eluted with $CHCl_3$:pyridine (10:3). The yield was not determined. Because only small amounts of *t*-DPhBPyP were obtained from the mixed-aldehyde synthesis (8, 12), the synthesis of the corresponding porphyrin-*N*-oxide was not pursued.

5,10-Bis(1-oxido-4-pyridyl)-15,20-diphenylporphyrin (*c*-BOPyDPhP)

c-BOPyDPhP was synthesized in the same manner as OPyTrPhP. To a solution of *c*-DPhBPyP (0.5 g, 0.8 mmol,

© 1999 NRC Canada

Table 6. Mass spectrometry data for (1-oxido-4-pyridyl)porphyrins and porphyrin-*N*-oxides.

Porphyrin	LR-MS, m/z[a] (intensity %, assignment)	Formula HR-MS, calcd. (found)
OPyTrPhP[b]	632 (88, M^{+1}), 616 (36, $M^{+1} - O$)	Not obtained
OPyTrPhP-21O[c]	692 (2, $M^+ - O - 2H + Cu$), 676 (5, $M^+ - 2O - 2H + Cu$), 647 (4, M^+), 631 (10, $M^+ - O$), 615 (100, $M^+ - 2O$)	$C_{43}H_{29}N_5O_2$ 647.232 12 (647.232 07)
OPyTrPhP-23O[c]	692 (1, $M^+ - O - 2H + Cu$), 677 (2, $M^+ -2O - 2H + Cu$), 647 (1, M^+), 631 (20, $M^+ - O$), 615 (100, $M^+ - 2O$)	$C_{43}H_{29}N_5O_2$ 647.232 12 (647.229 65) $C_{43}H_{29}N_5O$ 631.237 18 (631.237 01)
t-BOPyDPhP[b,d]	650 (100, M^{+1}), 634 (62, $M^{+1} - O$), 614 (19, $M^{+1} - 2O$)	Not obtained
c-BOPyDPhP[b,d]	649 (100, M^{+1}), 633 (86, $M^{+1} - O$), 617 (27, $M^{+1} - 2O$)	Not obtained
c-BOPyDPhP-NO mixture[c]	677 (5, $M^+ - 2O - 2H + Cu$), 693 (2, $M^+ - O -2H + Cu$), 664 (1, M^+), 648 (5, $M^+ - O$), 632 (29, $M^+ - 2O$), 616 (100, $M^+ - 3O$)	$C_{42}H_{28}O_3N_6$ 664.222 29 (664.219 42) $C_{42}H_{28}O_2N_6$ 648.227 36 (648.225 16)
TrOPyPhP[b,d]	666 (87, M^{+1}), 650 (100, $M^{+1} - O$), 634 (66, $M^{+1} - 2O$), 618 (33, $M^{+1} - 3O$)	Not obtained
TrOPyPhP-21O[c]	710 (1, $M^+ - 2O - 2H + Cu$), 694 (7, $M^+ - 3O - 2H + Cu$), 678 (8, $M^+ - 4O - 2H + Cu$), 665 (1, $M^+ - O$), 649 (11, $M^+ - 2O$), 633 (80, $M^+ - 3O$), 617 (100, $M^+ - 4O$)	$C_{41}H_{27}O_3N_7$ 665.217 53 (665.217 19) $C_{41}H_{27}O_3N_7$ 649.222 60 (649.222 10)
TrOPyPhP-22-NO[c]	678 (20, $M^+ - 4O -2H + Cu$), 665 (2, $M^+ - O$), 649 (9, $M^+ - 2O$), 633 (10, $M^+ - 3O$), 617 (100, $M^+ - 4O$)	$C_{41}H_{27}O_3N_7$ 665.217 53 (665.215 11) $C_{41}H_{27}O_3N_7$ 649.222 60 (649.221 75)
TOPyP[b]	683 (51, M^{+1}), 666 (84, $M^{+1} - O$), 650 (99, $M^{+1} - 2O$), 635 (100, $M^{+1} - 3O$), 619 (79, $M^{+1} - 4O$)	Not obtained
c-BOPyBSPhP[f]	875 (0.1, $M^{+1} + Na$), 859 (0.1, $M^{+1} + Na - O$), 853 (0.1, M^{+1}), 837 (0.1, $M^{+1} - O$)	Not obtained

[a] M^{+1} implies $(M + H)^+$.
[b] MALDI-TOF mass spectroscopy.
[c] EI mass spectroscopy.
[d] Dimer peaks (5–10% intensity, due to combinations of the species listed in the LR-MS column) are observed.
[e] (+)CI mass spectroscopy.
[f] (+)LSIMS mass spectroscopy.

but containing a small percentage of PhTrPyP) in CH_2Cl_2:MeOH (125:25 mL) was added excess *m*-CPBA (4 × ~1.25 g aliquots), and the reaction monitored by TLC. Et_3N (~10 mL) was added; the product was preadsorbed on silica and intially chromatographed on silica (CH_2Cl_2:pyridine:MeOH 20:1:2 to 20:1:3). The product bands were poorly resolved, possibly because of large amounts of residual *m*-CPBA and *m*-CBA; the porphyrin-containing fractions were washed with dilute aq. NaOH. The product mixture was rechromatographed on silica (CH_2Cl_2:pyridine:MeOH 10:1:2.5); *c*-BOPyDPhP eluted first (~0.27 g, ~50% yield), followed by a mixture of porphyrin-*N*-oxides, and then a small amount (~20 mg) of TrOPyPhP. A *c*-BOPyDPhP sample of analytical purity was obtained by slow crystallization from a solution of the compound in CH_2Cl_2:MeOH.

5,10-Bis(1-oxido-4-pyridyl)-15,20-diphenylporphyrin-21-oxide (*c*-BOPyDPhP-21O), -22-oxide (*c*-BOPyDPhP-22O), and -24-oxide (*c*-BOPyDPhP-24O)

A mixture of porphyrin-*N*-oxides was isolated (~30 mg, ~5%) from the reaction of *c*-DPhBPyP with a large excess of *m*-CPBA (see above). Attempts to separate the mixture on

© 1999 NRC Canada

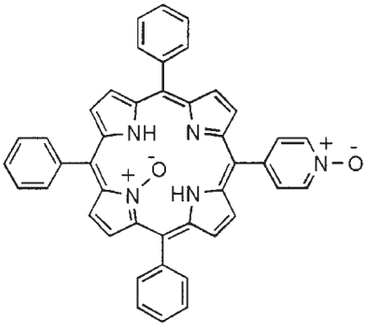

OPyTrPhP-23O

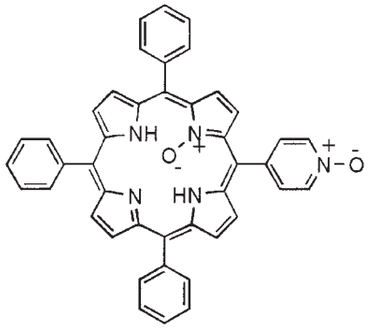

OPyTrPhP-21O

silica (CH_2Cl_2:pyridine:MeOH 20:1:2.5) were unsuccessful. There are three possible porphyrin-*N*-oxides isomers: *c*-BOPyDPhP-21O, *c*-BOPyDPhP-22O, and *c*-BOPyDPhP-24O.

The ^{1}H NMR data given below support the presence of at least two of these. The two doublets for the β-pyrrole-NO protons (δ 7.57 and 7.51) indicate the presence of *c*-BOPyDPhP-21O, while the corresponding singlet at δ 7.60 indicates the presence of either *c*-BOPyDPhP-22O or *c*-BOPyDPhP-24O, or both. ^{1}H NMR (400 MHz, $CDCl_3$) δ 9.05 (d, J = 5 Hz), 8.99 (overlapping ds, J = 5 Hz), 8.93 (d, J = 5 Hz), 8.91 (d, J = 5 Hz), 8.85 (d, J = 5 Hz), 8.74 (d, J = 5 Hz), 8.65 (m), 8.22 (dd, J_1 = 6 Hz, J_2 = 1.5 Hz), 8.15 (m), 8.08 (d), 7.8 (m), 7.60 (s), 7.57 (d, J = 6 Hz), 7.51 (d, J = 6 Hz). Because the ratio of products is unknown, the ^{1}H NMR signals are not assigned; general δ_H values for the (oxidopyridyl)porphyrins and porphyrin-*N*-oxides can be found in Tables 2 and 3.

5,10,15-Tris(1-oxido-4-pyridyl)-20-phenylporphyrin (TrOPyPhP)

TrOPyPhP was produced in the same manner as OPyTrPhP. PhTrPyP was present in small amounts in the sample of *c*-DPhBPyP used above, and TrOPyPhP was isolated from the reaction mixture. The yield was not determined. A sample of analytical purity was obtained by slow crystallization from CH_2Cl_2–MeOH.

5,10,15-Tris(1-oxido-4-pyridyl)-20-phenylporphyrin-21-oxide (TrOPyPhP-21O), and -22-oxide (TrOPyPhP-22O)

TrOPyPhP-21O and TrOPyPhP-22O were prepared in the same manner as the porphyrin-*N*-oxides of OPyTrPhP. The product was purified by preparative TLC on silica (CH_2Cl_2:MeOH 10:1 to 5:1). Only ~1 mg of each porphyrin-*N*-oxide was obtained (<5% yield).

5,10,15,20-Tetrakis(1-oxido-4-pyridyl)porphyrin (TOPyP)

Oxidation of TPyP

TOPyP was prepared in the same manner as OPyTrPhP. TPyP (0.35 g, 0.57 mmol) was dissolved in CH_2Cl_2:MeOH (150:25 mL) and excess *m*-CPBA (6 × 0.5 g) was added in aliquots over 3 h to the stirred mixture. TLC showed at least four intermediates as the reaction progressed. Et_3N (~20 mL) was added to the reaction mixture and the solvent was removed. The residual solid was rinsed with MeOH, acetone, and H_2O, and air-dried. Further purification was achieved by dissolving the product in H_2O:TFA (20:1), neutralizing the solution (NaOH), and subsequently filtering off the crude TOPyP precipitate; total yield 0.275 g (0.40 mmol, ~70%). Analytically pure TOPyP was obtained by slow crystallization from CH_2Cl_2:MeOH. Alternatively, small amounts of the product could be chromatographed on Al_2O_3(III) (CH_2Cl_2:MeOH 20:1). TOPyP was insoluble in $CDCl_3$, and thus its ^{1}H NMR spectrum was measured in $CDCl_3$–CD_3OD.

*Acid-catalyzed condensation of pyrrole and 4-pyridinecarboxaldehyde-*N*-oxide*

Attempts were also made to prepare TOPyP via acid-catalyzed condensation of pyrrole and 4-pyridinecarboxaldehyde-*N*-oxide. Pyrrole (0.3 mL, 0.4 mmol) and 4-pyridinecarboxal-

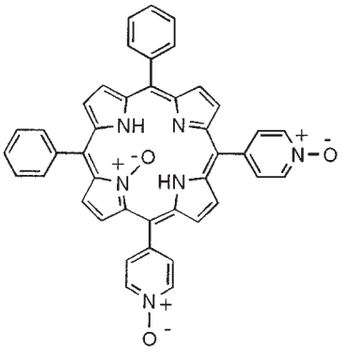

c-BOPyDPhP-21O

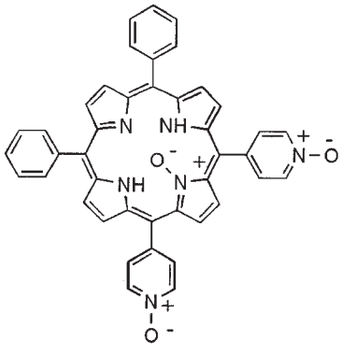

c-BOPyDPhP-22O

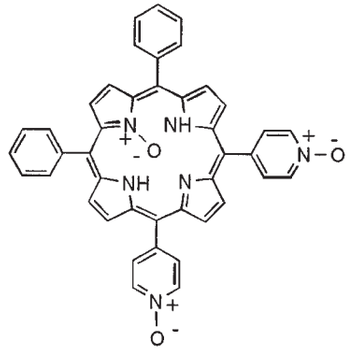

c-BOPyDPhP-24O

© 1999 NRC Canada

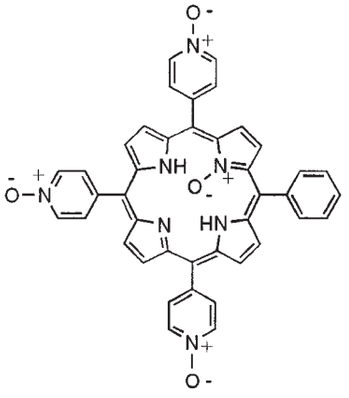

TrOPyPhP-21O

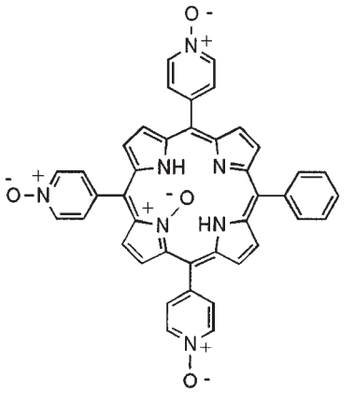

TrOPyPhP-22O

dehyde-*N*-oxide (0.05 g, 0.4 mmol) were dissolved in propionic acid (2 mL), and the solution was refluxed for ~50 min. UV-vis spectroscopy indicated that a porphyrin had formed (Soret 418 nm), but TLC analysis of the mixture on silica (CH_2Cl_2–MeOH) indicated numerous side products and so further isolation was not attempted. Attempts to synthesize TOPyP with Lindsey-type conditions in CH_2Cl_2 with pyrrole and 4-pyridinecarboxaldehyde (4 or 8 mM), using TFA or BF_3·MeOH and subsequent oxidation with 2,3,5,6-tetrachloro-1,4-benzoquinone (TCQ), yielded only traces of porphyrin by UV-vis spectroscopy.

TPyP synthesis via Lindsey conditions

When Lindsey conditions (14) were applied to the synthesis of TPyP using trichloroacetic acid, TFA, or BF_3·MeOH catalysis, TPyP was produced when aliquots of the reaction mixture were treated with TCQ, which showed that the precursor porphyrinogen was forming. However, the porphyrinogen was eventually consumed by a side reaction that gave a very polar, unidentified, blue compound. The rate of the side reaction increased with increasing acid strength and concentration.

Sulfonations

Sodium 5-(1-oxido-4-pyridyl)-10,15,20-tris(4-sulfonatophenyl)porphyrin (OPyTrSPhP)

Based on the literature procedure for the sulfonation of 5,10,15,20-tetraphenylporphyrin (TPhP) (8), OPyTrPhP (0.535 g, 0.85 mmol) was dissolved in conc. H_2SO_4 (10 mL), and the solution was heated at 110°C for 4 h. The reaction was monitored by first neutralizing an aliquot of the mixture (using aq. Na_2CO_3), then analyzing by TLC on silica (CH_2Cl_2:MeOH 100:1 to 5:1). The reaction mixture was cooled with an ice-bath, and cold, distilled H_2O (50 mL) was added, with the pH of the solution being adjusted to 7–8 with aq. NaOH and aq. Na_2CO_3. The solvent was removed and the porphyrin washed from the residue with MeOH. Then the MeOH was removed and the porphyrin subsequently dialyzed in dialysis tubing in a beaker of distilled H_2O to yield 0.51 g (~53% yield) of OPyTrSPhP·$11H_2O$. The ^{1}H NMR signals were assigned with the help of a ^{1}H-2D-COSY spectrum.

*Sodium 5,10-bis(1-oxido-4-pyridyl)-15,20-bis(4-sulfonatophenyl)porphyrin (*c*-BOPyBSPhP)*

c-BOPyDPhP (0.10 g, 0.15 mmol) was sulfonated in the same manner used for OPyTrSPhP. The reaction was monitored by TLC; an intermediate band appeared between that of the starting material and the baseline, and heating was continued ~0.5 h after the intermediate had disappeared (6 h total). After dialysis of the worked up product, its ^{1}H NMR spectrum revealed the presence of an impurity. Redissolving the product in conc. H_2SO_4 and heating at 100°C for another 2 h with the same work-up procedure did not remove the impurity (i.e., it is not a monosulfonatophenyl product). Attempts to purify by chromatography on silica MeOH or by recrystallization from MeOH–acetone were unsuccessful. The results of the elemental analysis (Table 5) suggest that the composition of the impurity does not differ significantly from that of *c*-BOPyBSPhP. Careful TLC analysis of the sample of *c*-BOPyDPhP used here showed the presence of another compound with an R_f nearly identical to that of *c*-BOPyDPhP; the presence of the impurity was not evident in the ^{1}H NMR spectrum ($CDCl_3$).

2*H*-[1,2,4]Oxadiazolo[3,2-*c*][1,2,4]benzotriazin-2-one-5-oxide (1)

Based on a literature reaction between phosgene and tirapazamine (15), a suspension of tirapazamine (0.3 g, 1.7 mmol) in dry toluene (5 mL) was heated to 90°C, and triphosgene (0.173 g, 0.58 mmol) was added. Within 5 min, the suspension turned from orange to yellow and TLC indicated near quantitative conversion to **1** (R_f = 0.75 silica (CH_2Cl_2:MeOH ~50:1)). (When the solution was heated for ~2 h, TLC indicated that some **1** had been reconverted to tirapazamine (R_f = 0.18).) The reaction mixture was cooled, and the precipitate was filtered off and washed with hexanes to yield 0.324 g (1.59 mmol, 94% yield) of **1** as a yellow–brown solid, which contained a small amount of tirapazamine (by TLC). The product was used without further purification in subsequent reactions. Compound **1** was reconverted to tirapazamine when exposed to H_2O vapor or when co-spotted with H_2O on a TLC plate, and tirapazamine was isolated in variable amounts from subsequent reactions involving **1**. IR (KBr pellet): 3460 w br, 3170 w, 3067 w, 1814 vs, 1598 s, 1541 vs, 1437 vw, 1386 s,1344 s, 1226 m,

© 1999 NRC Canada

Table 7. ^{1}H NMR data for the benzotriazine-dioxide compounds.[a]

Compound (solvent)	-CON*H*	Benzotriazine ring *H*[b]	Other substituent
Tirapazamine (acetone-d_6)[c]		8.28 t of d (2), 7.98 t of d (2), 7.64 t of d (2)	7.38 s br (2, -NH_2)
1 (acetone-d_6)		8.47 d (1), 8.27 t of d (1), 7.97 d of d (1), 7.80 t of d (1)	
2 ($CDCl_3$)	9.71 s (1), 8.81 s (1)	7.27 t(1), 7.04 m (2), 6.63 t (1)	8.91 s br (4), 8.84 s (4), β-pyrrole *H*; 8.35 d (2, *J* 8, 2,6-RNHPh-*H*); 8.25 m (6, 2,6-Ph-*H*); 8.00 d (2, *J* 8, 3,5-RNHPh-*H*); 7.78 m (9, 3,4,5-Ph-*H*); –3.19 s br (2, pyrrole N-*H*)

[a]Measured at r.t. at 400 MHz; δ in ppm, signal pattern (number of protons).
[b]Typical *J* values for doublets or triplets 8–9 Hz; for a doublet or triplet of doublets $J_1 \sim 9$, $J_2 \sim 1$ Hz.
[c]The ^{1}H NMR data are similar to those reported in the literature (recorded in TFA), ref. 15*b*.

1196 m, 1149 m, 1110 m, 772 m, 734 m; IR of tirapazamine (thin film on a KBr disk): 3411 w, 3274 w br, 3098 w, 1594 vs, 1408 vs, 1362 vs, 1105 vs, 1025 w, 828 w, 723 w. For **1**, LR-MS (+CI): 205 (30, M^{+1}), 163 (100, M^{+1} – NCO), 147 (75, M^{+1} – NCO – O). HR-MS (+CI) calcd. for $C_8H_5N_4O_3$: 205.03616; found 205.03622. The ^{1}H NMR data for **1** (not reported previously) and for tirapazamine appear in Table 7.

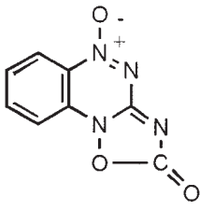

1

5-(4-*N*-(*N*′-(1,4-dioxido-1,2,4-benzotriazin-3-yl)aminocarbonyl)aminophenyl)-10,15,20-triphenylporphyrin (2)

To a solution of 5-(4-aminophenyl)-10,15,20-triphenylporphyrin (APhTrPhP) (8) (31 mg, 0.05 mmol) in dry DMF (3 mL) was added **1** (11 mg, 0.055 mmol), and the mixture was stirred at r.t. in the dark for 26 h. TLC (silica (CH_2Cl_2:MeOH 100:2–3)) showed a new product (R_f = 0.4), some APhTrPhP (R_f = 0.65), but little **1**; so another 1.0 equiv. of **1** was added, and the mixture was stirred another 24 h. The solvent was removed, and the desired product was isolated from several minor products by preparative TLC on silica (CH_2Cl_2:MeOH 100:2–3). The isolated product was washed with hexanes, dissolved in CH_2Cl_2:MeOH (20:1), and the solution was washed with H_2O. The solvent was removed to yield 20 mg of a purple powder (~50%). IR (KBr pellet, cm^{-1}): 3312 w, 1709 m, 1597 m, 1526 vs, 1405 m, 1332 m, 1311 m, 1225 m, 1181 w, 964 m, 799 m, 727 m, 701 m; UV-vis (2.4×10^{-6} M, CH_2Cl_2:MeOH (100:1)) corresponding to the tirapazamine moiety: 280 (log ε: 4.65), 478 (4.26) nm, corresponding to the porphyrin core: 418 (5.81), 514 (4.54), 550 (4.28), 586 (4.16), 646 (4.03). LR-MS (+LSIMS): 834 (0.25, M^{+1}), 818 (1, M^{+1} – O), 802 (0.25 M^{+1} – 2O), 656 (12, M^{+1} – tirapazamine). HR-MS (+LSIMS) calcd. for $C_{52}H_{36}N_9O_3$: 834.29411, found: 834.29456; calcd. for $C_{52}H_{36}N_9O_2$: 818.29919, found 818.29953. Anal. calcd. for $C_{52}H_{35}N_9O_3 \cdot 0.5H_2O$: C 74.10, H 4.30, N 14.96; found: C 73.96, H 4.18, N 14.41%. The ^{1}H NMR data for **2** appear in Table 7.

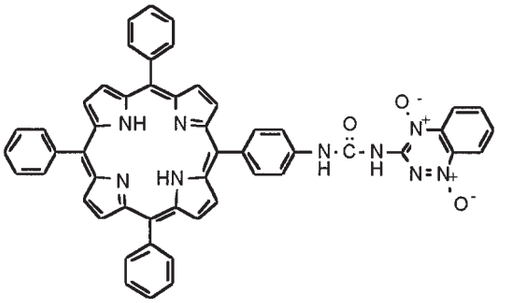

2

X-ray crystallographic analysis of OPyTrPhP

Crystallographic data appear in Table 8. The final unit-cell parameters were obtained by least squares on the setting angles for 25 reflections with $2\theta = 45.4 – 80.4°$. The intensities of three standard reflections, measured every 200 reflections throughout the data collection, showed only small random fluctuations. The data were processed[3] corrected for Lorentz and polarization effects and absorption (based on azimuthal scans).

The space group ambiguity (space groups $I4_1md$ and $I2d$ are possible) was resolved by trial and error. The structure was solved by direct methods, the coordinates of the non-hydrogen atoms being determined from *E*-maps or from subsequent difference Fourier syntheses. The molecule is centred at a point of crystallographic S_4 symmetry, thus the pyridine-*N*-oxide ligand and the N-H protons are statistically disordered. Position C(9)/N(2) was refined as 0.75C and 0.25N; the N and C atoms are too close to resolve. The oxygen position is 1/4 occupied and the N-H proton position is half occupied. All non-hydrogen atoms were refined with anisotropic thermal parameters. The full-occupancy hydrogen atoms were refined isotropically and the N-H and C(9)-H hydrogen atoms were fixed in calculated positions with C—H = 0.98 Å, N—H = 0.91 Å and $B_H = 1.2B_{\text{bonded atom}}$. A correction for secondary extinction was applied (Zachariasen type, isotropic, Gaussian), the final value of the extinction

[3]*teXsan*: Crystal structure analysis package. Unix version 1.7. Molecular Corporation. The Woodlands, Tex., U.S.A. 1995.

© 1999 NRC Canada

Table 8. Crystallographic data for OpyTrPhP.[a]

Compound	OPyTrPhP
Formula	$C_{43}H_{29}N_5O$
fw	631.73
Crystal system	Tetragonal
Space group	*I*2*d* (no. 122)
a, Å	15.174(1)
c, Å	13.709(3)
V, Å^3	3156.3(9)
Z	4
ρ_{calc}, g/cm^3	1.329
F(000)	1320
μ(Cu K_α), cm^{-1}	6.41
Crystal size, mm	0.20 × 0.35 × 0.45
Transmission factors	0.87–1.00
Scan type	ω-2θ
Scan range, deg in ω	1.00 + 0.20 tan θ
Scan speed, deg/min	32 (up to 9 scans)
Data collected	
$2\theta_{max}$, deg	155
Crystal decay, %	Negligible
Total reflections	998
Total unique reflections	998
Reflections with $I \geq 3\sigma(I)$	685
No. of variables	143
R	0.031
R_w	0.026
gof	2.2
Max Δ/σ (final cycle)	0.0008
Residual density, e/Å^3	–0.07 to 0.09

[a]Temperature 294 K, Rigaku AFC6S diffractometer, Cu K_α radiation (λ = 1.54178 Å), graphite monochromator, takeoff angle 6.0°, aperture 6.0 × 6.0 mm at a distance of 285 mm from the crystal, stationary background counts at each end of the scan (scan/background time ratio 2:1), $\sigma^2(F^2) = [S^2(C + 4B)]/Lp^2$ (S = scan rate, C = scan count, B = normalized background count), function minimized $\Sigma w(|F_o| - |F_c|)^2$ where $w = 4F_o^2/\sigma^2(F_o^2)$, $R = \Sigma||F_o| - |F_c||/\Sigma|F_o|$, $R_w = (\Sigma w(|F_o| - |F_c|)^2/\Sigma w|F_o|^2)^{1/2}$, and gof = $[\Sigma w(|F_o| - |F_c|)^2/(m - n)]^{1/2}$. Values given for R, R_w, and gof are based on those reflections with $I \geq 3\sigma(I)$.

coefficient being 1.54(5) × 10^{-6}. A parallel refinement of the mirror image gave marginally larger residuals (by a factor of 1.001). Neutral atom scattering factors for all atoms and anomalous dispersion corrections for the non-hydrogen atoms were taken from ref. 16. Final atomic coordinates and equivalent isotropic thermal parameters, bond lengths and bond angles appear in Tables 9–11, respectively. Infrared spectroscopy data, hydrogen atom parameters, anisotropic thermal parameters, torsion angles, intermolecular contacts, and least squares planes are included as supplementary material.[2]

Results and discussion

Porphyrin-*N*-oxides and (1-oxido-4-pyridyl)porphyrins

Porphyrin-*N*-oxides have been reported in the literature. Octaethylporphyrin-*N*-oxide (OEP-O) was first prepared by Bonnet et al. (17, 18) by treating OEP with hypofluorous acid (in 64% yield) or a peroxyacid (26% using *m*-CPBA, to 68% using permaleic acid). In studies relating to the active site of cytochrome P-450 enzymes, metal complexes of OEP-O (Ni, Mn, Co, Cu) (19–22), an Fe tetramesitylporphyrin-*N*-oxide complex Fe(TMP-O) (23–26), and a Ti tetraphenylporphyrin-*N*-oxide complex Ti(TPhP-O) (27) have been reported. With OEP-O, the metal was introduced after *N*-oxidation, while Fe(TMP-O) was produced by treating Fe(TMP) with *m*-CPBA, and Ti(TPhP-O) was prepared by photolysis of Ti(TPhP)(O_2). TMP-O was produced by oxidation of TMP, or demetallation of Fe(TMP-O) with HCl–HOAc (23), and Ti(TPhP-O) spontaneously demetallated in ethanol (27). In the metal complexes, the oxygen remains on one face of the porphyrin but, in the free-base porphyrin-*N*-oxides, the oxygen rapidly moves through the center of the porphyrin in a fluxional inversion process (19).

In contrast, (oxidopyridyl)porphyrins have not been reported, although a related compound (**3**) was obtained by Milgrom et al. (28) from the aerial oxidation of a (1-benzyl-4-pyridyl)porphyrin, this procedure leading also to further benzylation of the macrocyclic nitrogens.

Tetraarylporphyrin syntheses

The precursor *meso*-phenyl/pyridyl porphyrins and (aminophenyl)triphenylporphyrin were synthesized according to published procedures (8). The synthesis of (oxidopyridyl)porphyrins via acid-catalyzed condensation of pyrrole, benzaldehyde and 4-pyridinecarboxaldehyde-*N*-oxide was also attempted, but a significant percentage of the oxidopyridyl groups was deoxygenated in refluxing propionic acid. However, acid-catalyzed condensation of pyrrole and 4-pyridinecarboxaldehyde-*N*-oxide did produce at least one porphyrin, probably TOPyP, but this compound was much more conveniently prepared by *N*-oxidation of TPyP.

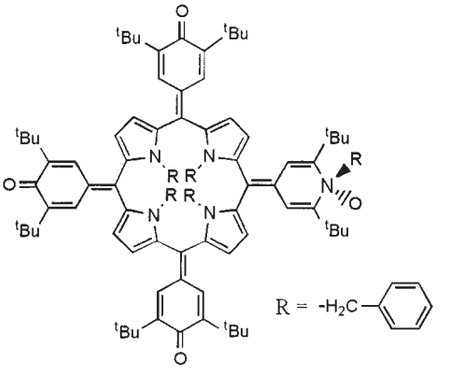

3

The synthesis of TPyP, via Lindsey conditions was hampered by a side reaction that produced an unidentified, blue compound. It has been noted that under Lindsey conditions, numerous heterocyclic aldehydes fail to give porphyrins but no explanation was suggested (14). *N*-Substitution on the pyridine nitrogen (as in *N*-oxides, and alkyl or acyl pyridinium salts) greatly activates the pyridine ring to nucleophilic addition at the α and γ positions (29). Thus, in situ formation of a pyridinium salt via protonation of (or BF_3 coordination to) the pyridine lone pair under high [H^+] and subsequent reaction (at the pyridine ring and aldehyde substituent) with pyrrole could explain the results obtained here. The side re-

© 1999 NRC Canada

Table 9. Final atomic coordinates (fractional) and B_{eq} (10^3 Å^2).[a]

Atom	*x*	*y*	*z*	B_{eq}	Occupancy
O(1)	0.5590(4)	0.3378(6)	0.1417(9)	8.0(3)	1/4
N(1)	0.0680(1)	0.3847(1)	0.2468(2)	4.68(5)	
N(2)	0.4789	0.3672	0.1491	6.61	1/4
C(1)	0.0344(2)	0.3027(2)	0.2670(2)	4.78(6)	
C(2)	0.1059(2)	0.2406(2)	0.2692(2)	5.60(8)	
C(3)	0.1804(2)	0.2851(2)	0.2478(3)	5.65(7)	
C(4)	0.1574(2)	0.3759(2)	0.2349(2)	4.71(7)	
C(5)	0.2170(2)	0.4450(2)	0.2217(2)	4.74(7)	
C(6)	0.3096(2)	0.4202(2)	0.1961(2)	4.95(7)	
C(7)	0.3305(2)	0.3948(2)	0.1022(3)	6.10(9)	
C(8)	0.4147(2)	0.3695(3)	0.0789(3)	7.4(1)	
C(9)	0.4789(2)	0.3672(2)	0.1491(3)	6.61(9)	3/4
C(10)	0.4600(2)	0.3928(3)	0.2407(3)	7.2(1)	
C(11)	0.3762(2)	0.4195(3)	0.2645(3)	6.90(9)	

[a] $B_{eq} = (8/3)\pi^2\Sigma\Sigma(U_{ij}a_ia_j(\mathbf{a}_i\mathbf{a}_j))$.

Table 10. Bond lengths (Å) with estimated standard deviations in parentheses.[a]

Bond	Length	Bond	Length
O(1)—N(2)	1.299(7)	N(1)—C(1)	1.372(3)
N(1)—C(4)	1.374(3)	N(2)—C(8)	1.369(4)
N(2)—C(10)	1.346(4)	C(1)—C(2)	1.438(4)
C(1)—C(5)′	1.398(4)	C(2)—C(3)	1.349(4)
C(3)—C(4)	1.433(4)	C(4)—C(5)	1.396(3)
C(5)—C(6)	1.496(4)	C(6)—C(7)	1.381(4)
C(6)—C(11)	1.378(4)	C(7)—C(8)	1.372(4)
C(9)—C(10)	1.346(5)	C(10)—C(11)	1.375(4)

[a] Symmetry operation: (′) $-1/2 + y$, $1/2 - x$, $1/2 - z$.

action did not occur using weaker acids (e.g., dichloroacetic acid), but these were not able to catalyze the formation of a porphyrinogen, and thus no TPyP was observed when TCQ was added.

N-Oxidations

N-Oxidation of the pyridyl substitutents was accomplished using *m*-CPBA; the oxidations were sluggish at 0°C, but proceeded readily at r.t. When the peroxyacid was added in small aliquots, only the (oxidopyridyl)porphyrins were obtained, while the single addition of *m*-CPBA generated the corresponding porphyrin-*N*-oxides in low but variable yield, as pyrrole nitrogens were also oxidized. Use of the same conditions with TPhP gave no significant amount of TPhP-oxide, and continued addition of *m*-CPBA only led to the degradation of the porphyrin. As an oxidopyridyl group is more electron-withdrawing than a phenyl group, the (oxidopyridyl)porphyrins are more resistant to oxidative degradation, and thus the (oxidopyridyl)porphyrin-*N*-oxides could be isolated.

Thermal deoxygenation is commonly observed with heterocyclic *N*-oxides (13), but no deoxygenation was observed (by ^{1}H NMR studies) when a solid sample of OPyTrPhP was heated at 100°C overnight in vacuo. Porphyrin-*N*-oxides deoxygenate at milder conditions (18), and were thus kept below 30°C. Deoxygenation was observed in the mass spectra of the (oxidopyridyl)porphyrins and their *N*-oxides. The elemental analyses of these compounds, and the presence of H_2O peaks in their ^{1}H NMR spectra were consistent with water being present; of note, pyridine-*N*-oxide itself is hygroscopic and freely soluble in water (13).

The porphyrin-*N*-oxides are much more soluble in weakly polar solvents (CH_2Cl_2, $CHCl_3$) than their parent oxidopyridyl compounds, and are soluble in MeOH. OPyTrPhP has good solubility in CH_2Cl_2 or $CHCl_3$, but with increasing numbers of oxidopyridyl groups, increasing amounts of MeOH are required as a cosolvent to ensure dissolution. For

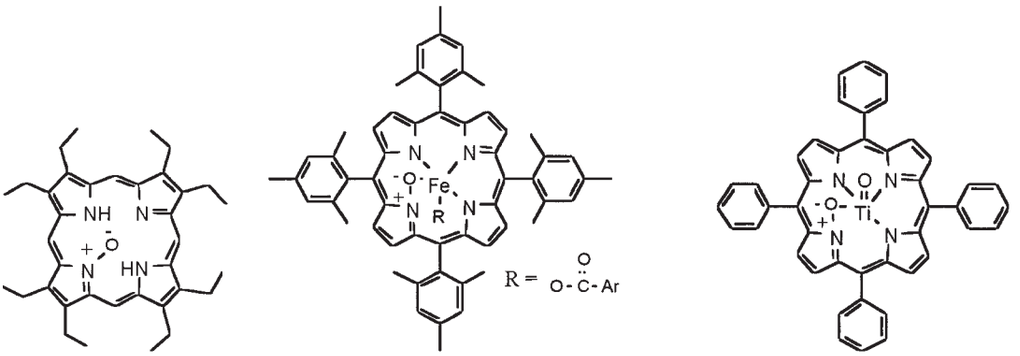

OEP-O Fe(TMP-O) Ti(TPhP-O)

© 1999 NRC Canada

Fig. 1. ORTEP view of OPyTrPhP; 33% probability thermal ellipsoids are shown for the non-hydrogen atoms. The disorder is not shown for the sake of clarity.

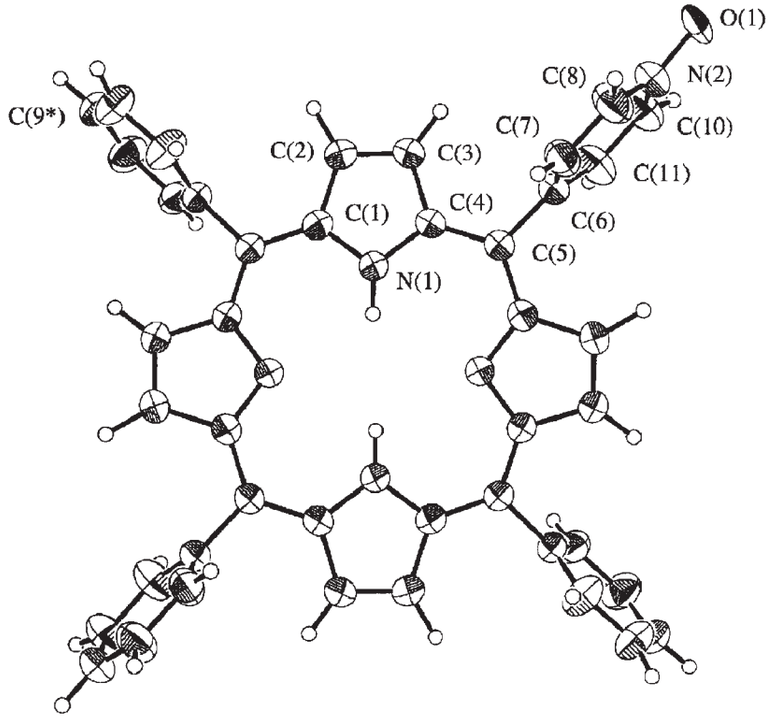

Table 11. Bond angles (deg) with estimated standard deviations in parentheses.[a]

Bonds	Angle	Bonds	Angle
C(1)-N(1)-C(4)	107.7(2)	O(1)-N(2)-C(8)	128.3(6)
O(1)-N(2)-C(10)	111.8(5)	C(8)-N(2)-C(10)	119.8(2)
N(1)-C(1)-C(2)	108.6(2)	N(1)-C(1)-C(5)′	125.2(2)
C(2)-C(1)-C(5)′	126.1(2)	C(1)-C(2)-C(3)	107.4(3)
C(2)-C(3)-C(4)	107.7(2)	N(1)-C(4)-C(3)	108.6(2)
N(1)-C(4)-C(5)	125.7(2)	C(3)-C(4)-C(5)	125.5(2)
C(1)″-C(5)-C(4)	125.1(2)	C(1)″-C(5)-C(6)	118.1(2)
C(4)-C(5)-C(6)	116.8(2)	C(5)-C(6)-C(7)	120.3(3)
C(5)-C(6)-C(11)	122.1(3)	C(7)-C(6)-C(11)	117.7(3)
C(6)-C(7)-C(8)	120.6(3)	C(9)-C(8)-C(7)	120.4(3)
C(8)-C(9)-C(10)	119.8(3)	C(9)-C(10)-C(11)	120.2(3)
C(6)-C(11)-C(10)	121.3(4)		

[a]Symmetry operations: (′) –1/2 + *y*, 1/2 – *x*, 1/2 – *z*; (″) 1/2 – *y*, 1/2 + *x*, 1/2 – *z*.

example, TOPyP is insoluble in $CDCl_3$ but dissolution (required for ^{1}H NMR measurement) occurs readily on addition of a few drops of CD_3OD. The difference in solubility may be related to less aggregation in the porphyrin-*N*-oxides because of steric effects of the macrocyclic oxygens; also, these oxygens may well be involved in hydrogen-bonding.

X-ray crystallography

The X-ray structure of OPyTrPhP is shown in Fig. 1. The morphology of the porphyrin core and the orientation of the aryl groups do not differ significantly from those of TPhP (30). The porphyrin ring is nearly planar, and the dihedral angle of the oxidopyridyl group and the porphyrin plane is 78°. The N(2)—O(1) bond length (1.299(7) Å) is significantly shorter than that in pyridine-*N*-oxide (1.34 Å), but lies within the range of N—O distances in a variety of substituted pyridine-*N*-oxides (13, 19).

^{1}H NMR spectra

^{1}H NMR spectroscopy (Tables 2, 3) was very useful for characterization of the (oxidopyridyl)porphyrins and enabled the porphyrin-*N*-oxide isomers to be identified.

Oxidopyridyl groups

Compared to the δ_H values for the unoxidized pyridyl group, the 2-*H* and 6-*H* protons of the oxidopyridyl groups were shifted upfield by ~0.4 ppm, while the 3-*H*- and 5-*H*-oxidopyridyl protons were shifted <0.1 ppm (see Fig. 2). Similar shift changes, observed for pyridine-*N*-oxide versus pyridine (13), were rationalized in terms of additional electron density at the 2, 4, and 6 positions resulting from mesomeric structures (Fig. 3). The splitting patterns and δ values for the phenyl and sulfonatophenyl signals of the (oxidopyridyl)porphyrins correspond well to those of the phenyl-(pyridyl)- and (pyridyl)(sulfonatophenyl)porphyrins, respectively (8).

Pyrrole-*N*-oxides

The β-pyrrole protons of the pyrrole-*N*-oxide of the porphyrin-*N*-oxides are shifted upfield to δ ~7.5 compared to those of the nonoxidized pyrroles (Fig. 4, Δ ~ 1.4 ppm). Similar δ values were noted for the β-pyrrole-oxide positions in TMP-O (δ 7.49) (23) and Ti(TPhP-O) (δ 7.26) (27). Based

© 1999 NRC Canada

Fig. 2. The aromatic region of the ^{1}H NMR spectrum TrPhPyP and OPyTrPhP in $CDCl_3$.

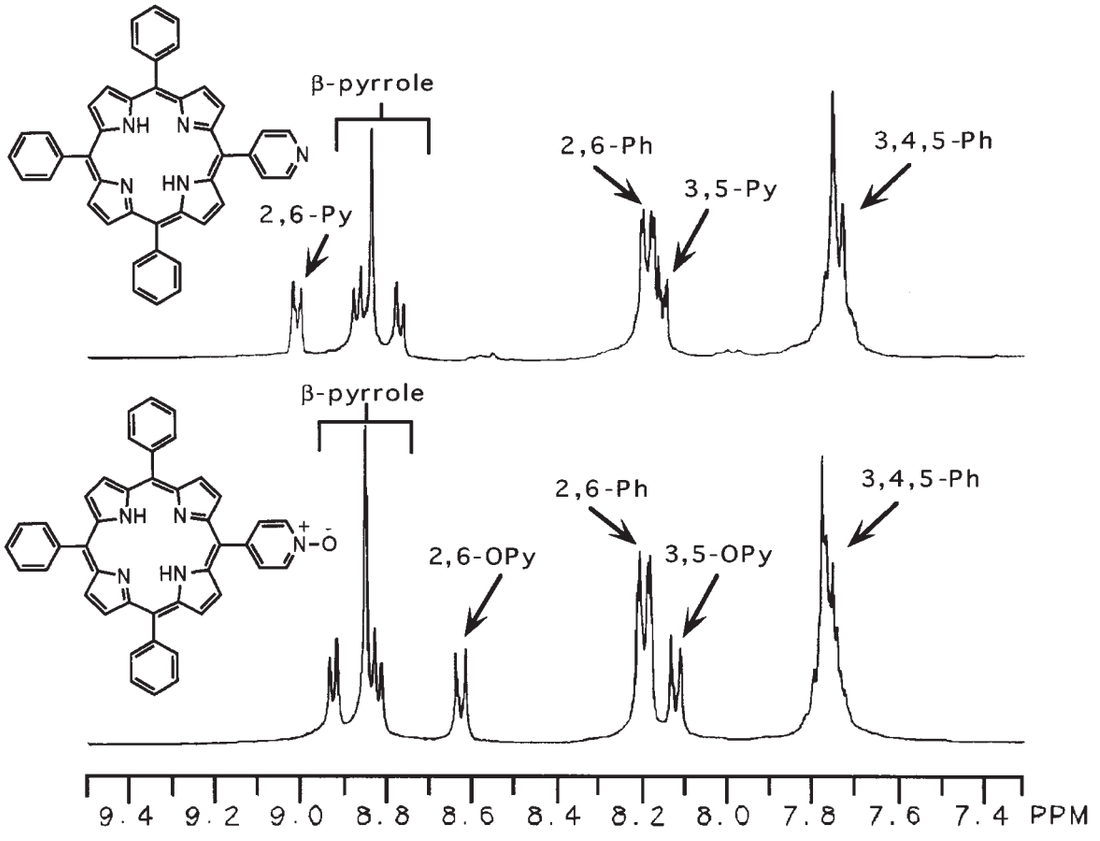

Fig. 3. Mesomeric forms of pyridine-*N*-oxide.

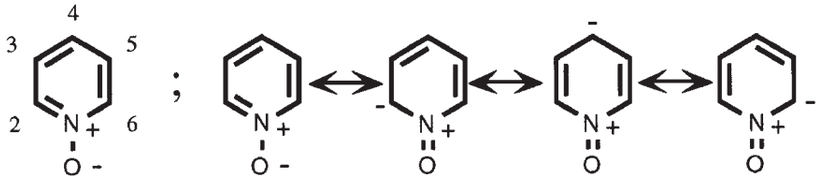

solely on inductive effects, such shifts are opposite to those expected by incorporation of an O-atom, and are unlikely due to partial negative charges for mesomeric forms (cf. Fig. 3), as these would tend to be delocalized over the whole macrocycle. An out-of-plane tilt of the pyrrole-*N*-oxide could explain the upfield shift, as the β-pyrrole protons would then experience less deshielding from the induced ring current. However, in the solid state, the pyrrole-*N*-oxide ring in OEP-O is tipped out of the porphyrin plane only 6.1° (20), which is similar to that of 6.6° found in two of the pyrrole rings of TPhP (30), and such a small tilt in solution is unlikely to explain the large $\Delta\delta$. In the dynamic porphyrin inversion process, in which the oxygen atom moves through the center of the porphyrin (19), the pyrrole groups may be tilted far enough for such a loss of deshielding, and in support of this a similar loss of deshielding is noted for the methylene groups in the Ni(II) complex of OEP-O, where a large pyrrole-*N*-oxide tilt (38.3°) is observed and inversion does not occur (19, 20). A large tilt of the pyrrole-*N*-oxide unit is also expected in Ti(TPhP-O) where a $\Delta\delta$ of ~2 is observed (27).

As in the corresponding pyridyl(phenyl)- and (oxidopyridyl)(phenyl)porphyrin series, the β-pyrrole protons show a singlet when situated between two idendical *meso*-substituents, and an AB spectrum when between two different *meso*-subsituents (8). The rest of the β-pyrrole region is complex because of the inequivalence introduced by the proximity of the oxidopyrrole group and different *meso*-subsitutents.

The inner N-H protons of the porphyrin-*N*-oxides appear as broad singlets at δ ~1.6, which disappear in the presence of D_2O. Compared to the (oxidopyridyl)porphyrins (where δ_{NH} is ~–2.85), the induced ring current is presumably slightly disrupted because of the out-of-plane pyrrole-*N*-oxide ring. The inner N-H signals of OEP-O and TMP-O appear at δ 0.8 (19) and δ 1.75 (23), respectively.

In the ^{1}H NMR spectrum of TOPyP in $CDCl_3$–CD_3OD, the β-pyrrole protons appear as a broad singlet and no N-H

© 1999 NRC Canada

Fig. 4. The aromatic region of the ^{1}H NMR spectrum of OPyTrPhP-23O and -21O.

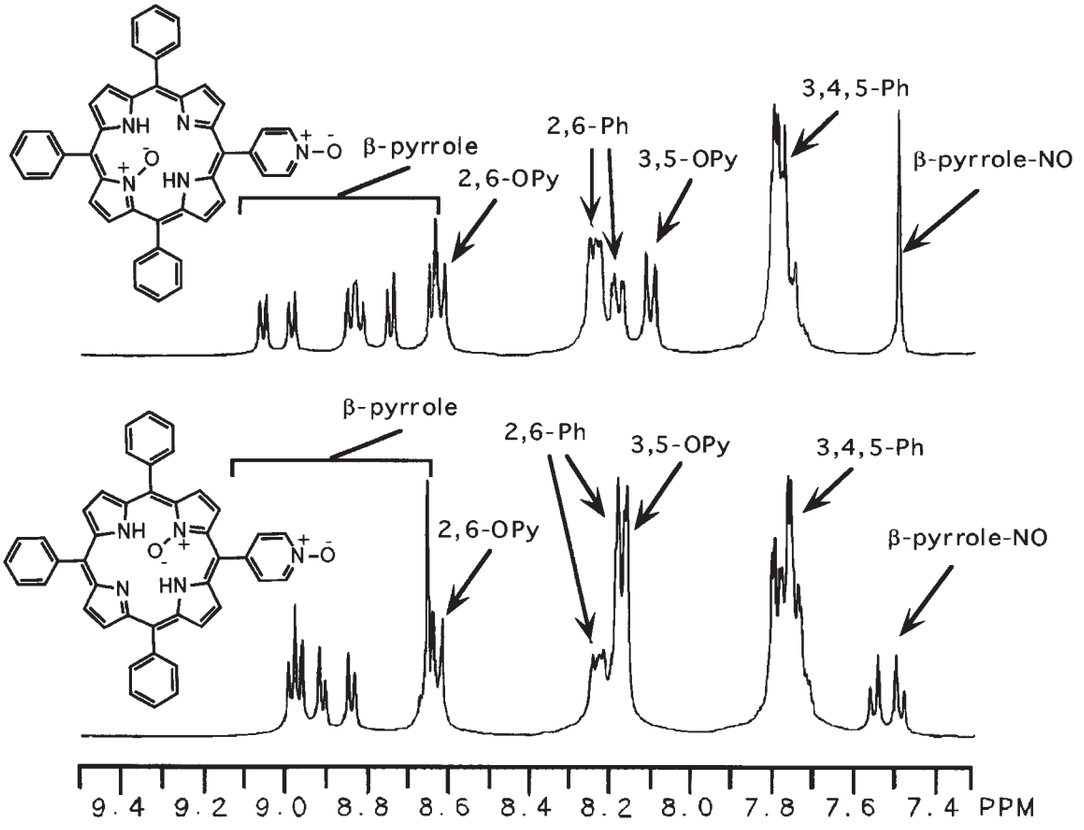

Fig. 5. UV-vis spectrum of TPhPyP (2.3×10^{-6} M) in CH_2Cl_2.

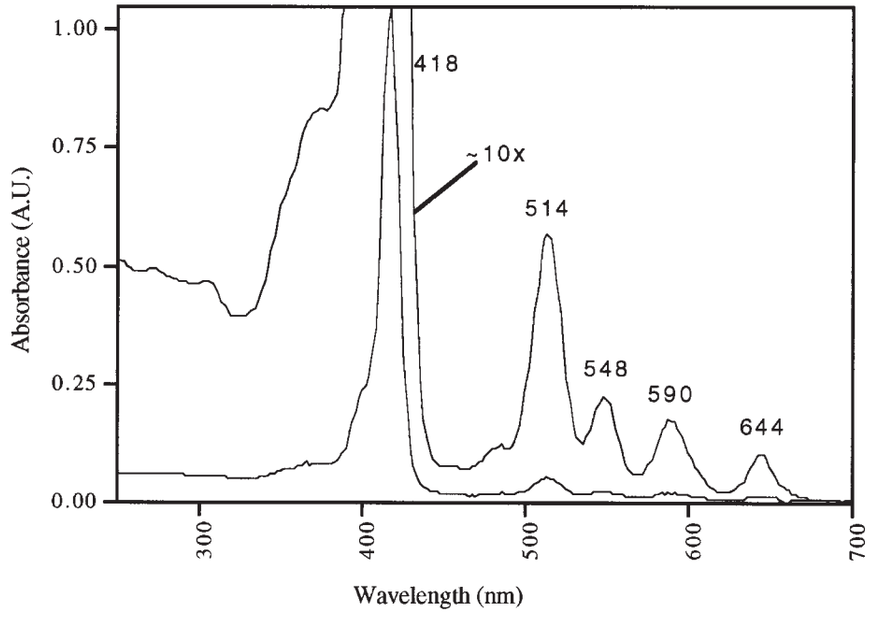

signals are seen. Similar data were obtained when D_2O or CD_3OD was added to the $CDCl_3$ solutions of TrPhPyP, OPyTrPhP, *t*-DPBPyP, *t*-BOPyDPhP, *c*-DPhBPyP, or *c*-BOPyDPhP, and reflect H/D exchange with the N-H protons. The β-pyrrole protons are weakly coupled to the N-H protons but rapid tautomerism prevents any observable

© 1999 NRC Canada

Fig. 6. UV-vis spectrum of OPyTrPhP (2.6×10^{-6} M) in CH_2Cl_2.

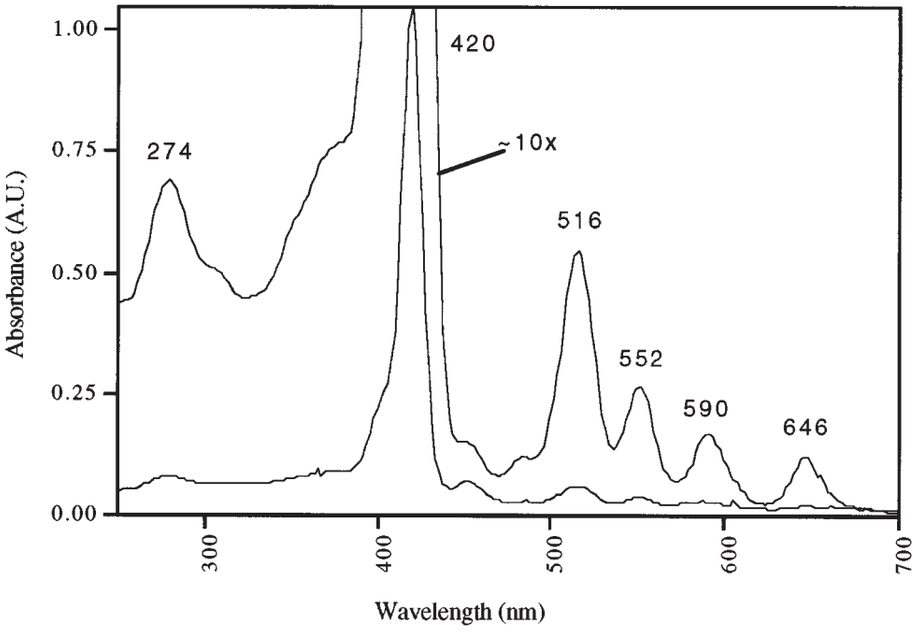

Fig. 7. UV-vis spectrum of OPyTrPhP-23O (~7.6×10^{-6} M) in CH_2Cl_2. (At ~2.8×10^{-5} M, an additional, small peak is observed at 518 nm.)

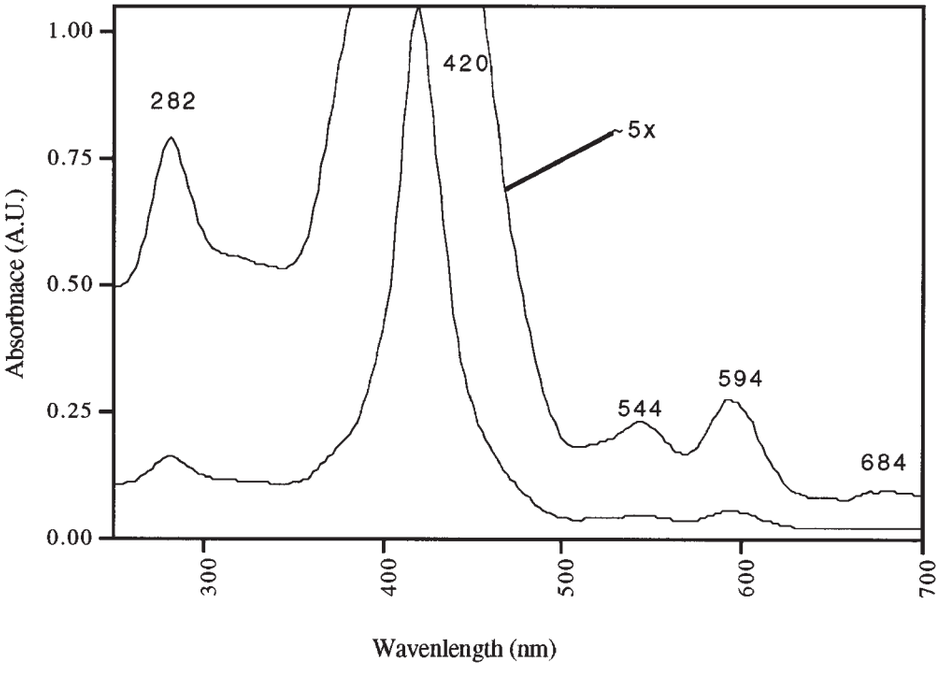

splitting at room temperature; with N-D, the tautomerism is slower (k_H/k_D ~ 12.1 at 35°C) (31), and coupling to the D-atoms broadens the β-pyrrole signals.

UV-vis spectroscopy

Pyridine-*N*-oxide displays an absorbance maximum (log ϵ > 4) in the 255–285 nm region and a weaker (log ϵ ~ 2) absorbance maximum near 350 nm; in polar solvents, the longer wavelength band is blue-shifted and can be hidden by the shorter wavelength absorption maximum (13). The shorter wavelength maximum appears at ~275 nm for the (oxidopyridyl)porphyrins and the corresponding porphyrin-*N*-oxides (see Table 4); and the corresponding longer wavelength band is sometimes observed in the ~310–350 nm

© 1999 NRC Canada

Fig. 8. UV-vis spectrum of OPyTrPhPZn-23O (~1.0×10^{-5} M) in CH_2Cl_2.

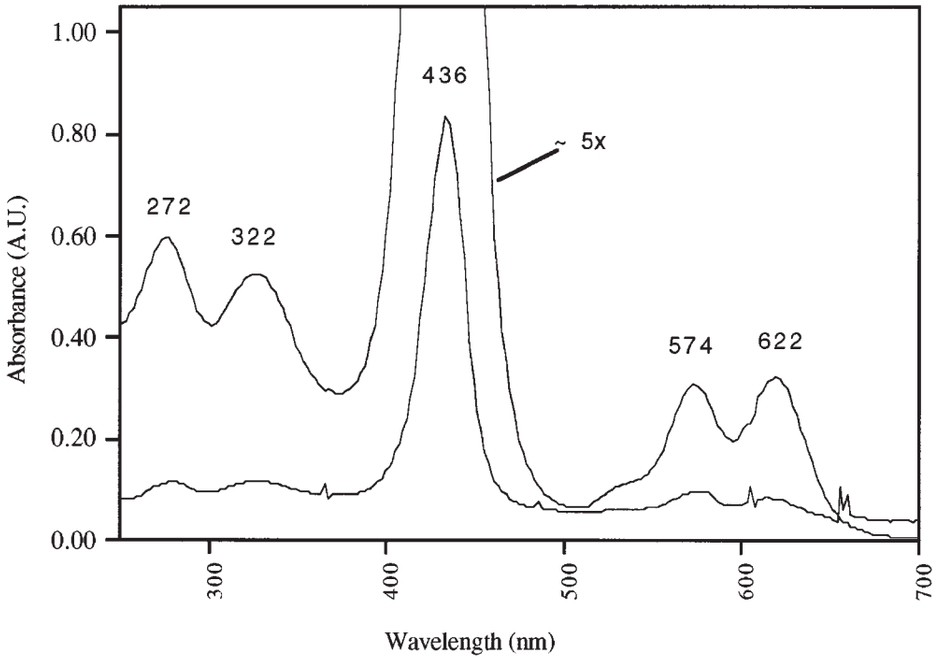

region, although this is usually masked by the "background" absorbance from the porphyrin moiety (see Figs. 5 and 6). With the exception of the UV region, the spectra of the (oxidopyridyl)porphyrins are similar to those of free-base tetraarylporphyrins.

The presence of the Soret bands for the porphyrin-*N*-oxides suggests that the conjugation of the macrocycle is uninterrupted (18); however, the Soret bands are broadened, and the Q bands are not as intense as those in the parent (oxidopyridyl)porphyrins (Fig. 7). The Soret and Q-bands in the spectra of OPyTrPhPZn-21O and -23O are similarly broad and diminished in intensity, but the peaks at 320–330 nm are more prominent (see Fig. 8). There is no evidence for a band assignable to any electronic transition of the pyrrole-*N*-oxide group.

Infrared spectroscopy

The *N*-oxide moiety exhibits an intense, characteristic band in the 1200–1350 cm^{-1} region attributed to ν(N-O) (13), and the IR spectra of the (oxidopyridyl)porphyrins show an intense band in the 1221–1261 cm^{-1} region due to the pyridyl-*N*-oxide stretch; for the sulfonated derivatives, the values are about 20 cm^{-1} lower than for the corresponding nonsulfonated porphyrins (see Table S1)[2]. Porphyrin- *N*-oxide stretches for OEP-O (18) and TMP-O (23) appear at 1265 and 1273 cm^{-1}, respectively. Intense bands for the porphyrin-*N*-oxides synthesized here are in the range 1238–1261 cm^{-1}, and these likely result from overlap of the porphyrin- and pyridine-*N*-oxide stretches. The other spectral bands common to the porphyrin ring structure can be assigned according to the literature (32).

Mass spectrometry

The oxidopyridyl groups were deoxygenated using EI and LSIMS techniques and no moleular ion peak was seen, but this could be observed using MALDI-TOF mass spectrometry (using a dihydroxybenzoic acid matrix) (Table 6). Some of the parent peaks for the porphyrin-*N*-oxides were observed under EI ionization conditions (see Fig. 9), and HR-MS analyses were obtained for these species (Table 6).

Sulfonation reactions

Sulfonation of the phenyl groups of OPyTrPhP and *c*-BOPyDPhP was achieved readily in hot, conc. H_2SO_4. Like the pyridyl subsituent, the oxidopyridyl group was not sulfonated under these conditions, and the *N*-oxide was retained. The pyridine nitrogen (or oxygen in the oxidopyridyl group) is certain to be protonated under the sulfonation conditions, thus making the pyridyl group unreactive towards electrophilic addition.

The sulfonated porphyrins, when isolated by solvent removal from an aqueous solution, retained several mole equivalents of water as judged by elemental analysis. This behavior for sulfonated porphyrins has been noted previously by our group (9).

Tirapazamine chemistry

Patents and publications on the biological activity of tirapazamine have appeared (33–35), and the desire to incorporate tirapazamine into a porphyrin was noted in the introduction. The use of triphosgene, a crystalline compound (36), in place of the highly toxic, gaseous phosgene, for reaction with tirapazamine, provided an effective, rapid route to **1**, although the product contained a small amount of tirapazamine. Compound **1** had previously been made in a 4 h reaction using phosgene, and its structure proposed (15) on IR data: ν(C=O) 1814 cm^{-1}, ν(C=N) 1541 cm^{-1}, and the absence of ν(NCO) bands at 2273–2000 cm^{-1} (37). Reaction of an amine with phosgene typically generates an isocyanate, and despite its cyclic structure, **1** does react like an

© 1999 NRC Canada

Fig. 9. Low-resolution mass spectrum (EI) of OpyTrPhP-21O.

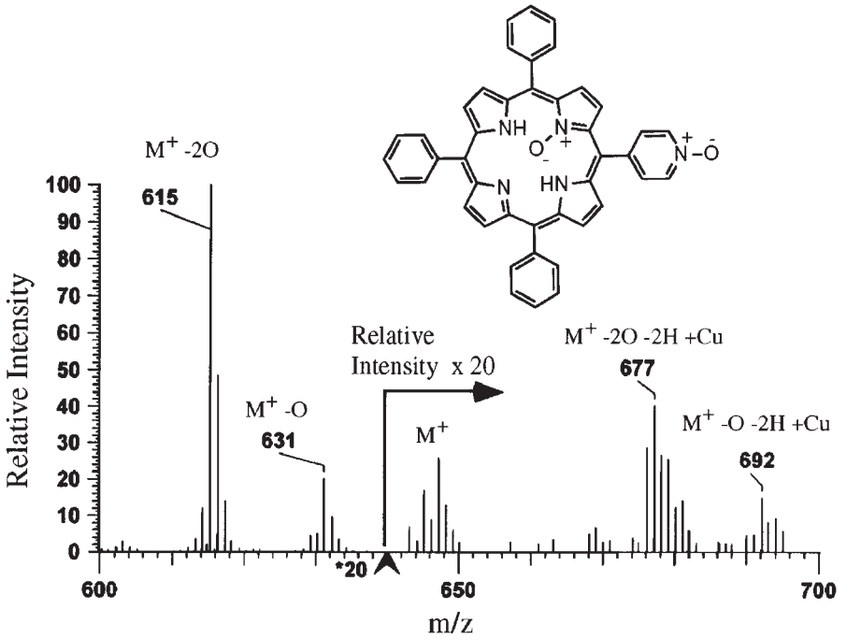

isocyanate and produce ureas and carbamates when mixed with amines and alcohols, respectively, undergoing a ring-opening process (15, 33). Also typical of an isocyanate, **1** reacts with water (even on a TLC plate) to regenerate the amine tirapazamine.

The porphyrin bearing an amino group, APhTrPhP, was mixed with **1** to yield **2** in ~50% isolated yield. An IR peak seen at 1225 cm^{-1} due to ν(NO) was not observed in the aminophenyl porphyrin (38). Peaks attributed to tirapazamine appeared in the UV-vis spectrum, but these were in a region of relatively high background absorbance from the porphyrin core.

Conclusions

Porphyrins containing one to four pyridyl groups were synthesized and *N*-oxidized with *m*-CPBA to produce five novel (oxidopyridyl)porphyrins and seven porphyrin-*N*-oxides (including three from a *c*-BOPyBPhP-O mixture). Only three free-base porphyrin-*N*-oxides have been reported previously (OEP-O, TMP-O, and TPhP-O). The (oxidopyridyl)porphyrins and porphyrin-*N*-oxides were well characterized and an X-ray crystal structure of OPyTrPhP was obtained. Sulfonation of OPyTrPhP and *c*-BOPyDPhP was achieved readily under standard conditions with no loss of oxygen from the oxidopyridyl groups.

The product **1** from tirapazamine and triphosgene reacts like an isocyanate, reacting with porphyrins bearing amines and alcohols; the best results were obtained using APhTrPhP to produce the novel porphyrin conjugate **2**. The electrochemical and in vitro evaluation of these porphyrins incorporating *N*-oxide functionalities (39) will be published elsewhere.

Acknowledgments

We thank the Natural Sciences and Engineering Research Council and Medical Research Council of Canada for financial support, and Dr. M. Tracy for the sample of tirapazamine.

References

1. R. Boyle and D. Dolphin. Photochem. Photobiol. **64**, 469 (1996).
2. J. Moan and K. Berg. Photochem. Photobiol. **55**, 931 (1992).
3. M.R. Hamblin and E.L. Newman. J. Photochem. Photobiol. B, **23**, 3 (1994).
4. H. Pass. J. Nat. Cancer Inst. **85**, 443 (1993).
5. M. Ochsner. J. Photochem. Photobiol. B, **39**, 1 (1997).
6. P. Wardman, K.I. Priyadarsini, M.F. Dennis, S.A. Everett, M.A. Naylor, K.B. Patel, I.J. Stratford, M.R.L. Stratford, and M. Tracy. Br. J. Cancer, **74**, S70 (1996).
7. W.A. Denny, W.R. Wilson, and M.P. Hay. Br. J. Cancer, **74**, S32 (1996).
8. G.G. Meng, B.R. James, and K.A. Skov. Can. J. Chem. **72**, 1894 (1994).
9. G.G. Meng, B.R. James, K.A. Skov, and M. Korbelik. Can. J. Chem. **72**, 2447 (1994).
10. B.R. James, G.G. Meng, J.J. Posakony, J.A. Ravensbergen, C.J. Ware, and K.A. Skov. Met.-Based Drugs, **3**, 85 (1996).
11. D.C. Harris. Quantitative chemical analysis. W.H. Freeman, New York. 1987. p. 644.
12. R.G. Little, J.A. Anton, P.A. Loach, and J.A. Ibers. J. Heterocycl. Chem. **12**, 343 (1975).
13. A. Albini and S. Pietra. Heterocyclic *N*-oxides. CRC Press, Boca Raton. 1991. pp. 7–31.
14. J.S. Lindsey. *In* Metalloporphyrins catalyzed oxidations. *Edited by* F. Montanari and L. Casella. Kluwer Academic Publishers, Dortdrecht. 1994. p. 49.

© 1999 NRC Canada

15. (*a*) F. Seng and K. Ley. Angew. Chem. Int. Ed. Eng. **11**, 1009 (1972); (*b*) J.C. Mason and G. Tennant. J. Chem. Soc. B, 911 (1970).
16. (*a*) International tables for X-ray crystallography. Vol. 4. Kynoch Press, Birmingham, U.K. (present distributor Kluwer Academic Publishers, Boston, Mass., U.S.A.). 1974. pp. 99–102; (*b*) International tables for crystallography. Vol. C. Kluwer Academic Publishers, Boston, Mass., U.S.A. 1992. pp. 200–206.
17. R. Bonnet and R. Ridge. J. Chem. Soc. Chem. Commun. 310 (1978).
18. L.E. Andrews, R. Bonnet, R. Ridge, and E.H. Appelman. J. Chem. Soc. Perkin Trans. 1, **1983**, 103 (1983), and refs. therein.
19. A.L. Balch, C.Y.-W., M. Olmstead, and M.W. Renner. J. Am. Chem. Soc. **107**, 2393 (1985).
20. A.L. Balch, Y.-W. Chan, and M.M. Olmstead. J. Am. Chem. Soc. **107**, 6510 (1985).
21. A.L. Balch and Y.W. Chan. Inorg. Chim. Acta, **115**, L45 (1986).
22. R.D. Arasasingham, A.L. Balch, M.M. Olmstead, and M.W. Renner. Inorg. Chem. **26**, 3562 (1987).
23. J.T. Groves and Y. Watanabe. J. Am. Chem. Soc. **108**, 7836 (1986).
24. J.T. Groves and Y. Watanabe. J. Am. Chem. Soc. **110**, 8443 (1988).
25. Y. Mizutani, Y. Watanabe, and T. Kitagawa. J. Am. Chem. Soc. **116**, 3439 (1994), and refs. therein.
26. K. Rachlewicz and L. Latos-Grazynski. Inorg. Chem. **35**, 1136 (1996).
27. M. Hoshino, K. Yamamoto, J.P. Lillis, T. Chijimatsu, and J. Uzawa. Inorg. Chem. **32**, 5002 (1993).
28. L.R. Milgrom, J.P. Hill, and P.J.F. Dempsey. Tetrahedron, **47**, 13 477 (1994).
29. J.A. Joule, K. Mills, and G.F. Smith. Heterocyclic chemistry. Chapman and Hall, London. 1995. p. 95.
30. S.J. Silvers and A. Tulinsky. J. Am. Chem. Soc. **89**, 3331 (1967).
31. H. Scheer and H. Katz. *In* Porphyrins and metalloporphyrins. *Edited by* K.M. Smith. Elsevier, Amsterdam. 1975. p. 399.
32. J.O. Alben. *In* The porphyrins. *Edited by* D. Dolphin. Academic Press, New York. 1978. Vol. 3. p. 323.
33. (*a*) F. Seng, K. Ley, and K.G. Metzger. U.S. Patent 3,957,779 (1976) and 4,027,022 (1977); (*b*) F. Seng, K. Ley, B. Hamburger, and B. Franz. U.S. Patent 3,991,189 (1976).
34. E.M. Zeman, M.A. Baker, M.J. Lemmon, C.I. Pearson, J.A. Adams, J.M. Brown, W.W. Lee, and M. Tracy. Int. J. Radiat. Oncol. Biol. Phys. **16**, 977 (1989).
35. A.I. Minchinton, M.J. Lemmon, M. Tracy, D.J. Pollart, A.P. Martinez, L.M. Tosto, and M.J. Brown. Int. J. Radiat. Oncol. Biol. Phys. **22**, 701 (1992).
36. H. Eckert and B. Foster. Angew. Chem. Int. Ed. Engl. **26**, 894 (1987).
37. R.M. Silverstein, G.C. Bassler, and T.C. Morrill. Spectrometric identification of organic compounds. John Wiley and Sons, New York. 1991. p. 419.
38. G.G. Meng. Ph.D. thesis, University of British Columbia. 1993.
39. J.J. Posakony. Ph.D. thesis, University of British Columbia. 1998.

© 1999 NRC Canada

Reactions of $(\eta^5\text{-}C_9H_7)Rh(\eta^2\text{-}C_2H_4)_2$ with quinones: molecular structure of $[(\eta^5\text{-}C_9H_7)Rh(2,3,5,6\text{-}C_6O_2(CH_3)_4)]$

Stephen A. Westcott, Nicholas J. Taylor, and Todd B. Marder

Abstract: Reactions of $(\eta^5\text{-}C_9H_7)Rh(\eta^2\text{-}C_2H_4)_2$ (**1**) with quinones were investigated. Substitution of the labile ethylene ligands was observed upon addition of either duroquinone (2,3,5,6-tetramethyl-1,4-benzoquinone) or 1,4-benzoquinone to complex **1**. The molecular structure of neutral $(\eta^5\text{-}C_9H_7)Rh(2,3,5,6\text{-}C_6O_2(CH_3)_4)$ (**3**), determined by X-ray diffraction, shows that the duroquinone ligand lies in a plane nearly parallel to the indenyl group. The carbonyl moieties of duroquinone lie in a plane incorporating Rh, C2, and the midpoint between C3a and C7a of the indenyl ring. The slip parameter (Δ = *d*(average Rh-C3a,7a) – *d*(average Rh-C1,3)) was calculated to be 0.112(2) Å; whereas a value of ca. 0.05 Å had been obtained previously from film data. Values for the hinge angle (HA = angle between normals to the least-squares planes defined by C1, C2, C3 and C1, C7a, C3a, C3) and fold angle (FA = angle between normals to the least-squares planes defined by C1, C2, C3 and C3a, C4, C5, C7, C7a) are 7.2° and 4.0°, respectively.

Key words: indenyl, rhodium, quinones, ring-slippage, ground-state distortion.

Résumé : On a étudié les réactions du composé $(\eta^5\text{-}C_9H_7)Rh(\eta^2\text{-}C_2H_4)_2$ (**1**) avec les quinones. On a observé la substitution des ligands éthylène labiles lors de l'addition de l'éther duroquinone (2,3,5,6-tétraméthyl-1,4-benzoquinone) ou de la 1,4-benzoquinone sur le complexe **1**. La structure moléculaire du composé neutre $(\eta^5\text{-}C_9H_7)Rh(2,3,5,6\text{-}C_6O_2(CH_3)_4)$ déterminée par diffraction de rayons X, révèle que le ligand duroquinone est lié dans un plan quasi parallèle au groupe indényle. Les unités carbonyle de la duroquinone sont liées dans un plan incorporant Rh, C2 et le point milieu entre C3a et C7a du cycle indényle. On a trouvé un paramètre de glissement (Δ = (moyenne Rh-C3a, 7a) – (moyenne Rh-C1,3)) de 0,112 (2) Å; alors qu'on a obtenu antérieurement une valeur d'environ 0,05 Å à partir des données de film. Les valeurs de l'angle d'articulation (AA = angle entre le plan normal et celui des moindres carrés défini par C1, C2, C3 et C1, C7a, C3a) et l'angle de pliement (AP = angle entre le plan normal et celui des moindres carrés défini par (C1, C2, C3 et C3a C4, C5, C7, C7a) sont respectivement de 7,2° et de 4,0°.

Mots clés : indényle, rhodium, quinones, glissement de cycle, distorsion de l'état fondamental.

[Traduit par la Rédaction]

Introduction

Indenylcobalt and rhodium complexes are known to display enhanced catalytic activities compared to their cyclopentadienyl analogues for a number of important organic reactions (1). This rate enhancement, or indenyl effect, (2) occurs in both associative (S_N2) and dissociative (S_N1) reaction pathways and, for the associative process, has been attributed to a low-energy barrier associated with an $\eta^5 \rightarrow \eta^3$ indenyl ring slippage, where the metal centre avoids an unfavourable 20-electron transition state. The relative stability of the η^3-intermediate arises from resonance stabilization of the benzene ring in the indenyl ligand (Fig. 1). Indeed, the molecular structures of several η^3-indenyl metal complexes have been reported (2*c*, 3).

Interestingly, η^5-indenyl d^8-ML_2 complexes all display a certain degree of ground-state distortion towards this allylic bonding mode within the five-membered ring of the indenyl ligand (4, 5). We have been examining the degree of this distortion as a function of the electronic nature of the ancillary ligands (4). While a significant amount of distortion was found for $(\eta^5\text{-}C_9H_7)Rh(CO)_2$ (4*d*), an early report using film data suggested that the slip-fold distortion in $(\eta^5\text{-}C_9H_7)Rh(2,3,5,6\text{-}C_6O_2(CH_3)_4)$ was unusually small (6), making this compound the least distorted of all d^8-ML_2-indenyl complexes. As the range of values was important to us, this "limiting" value represented a critical number, and it was thus decided to re-examine the structure of this compound. In this article, however, we report that the degree of distortion in this latter quinone compound is con-

Received September 15, 1998.

S.A. Westcott,[1,3] N.J. Taylor, and T.B. Marder.[2,3] Department of Chemistry, University of Waterloo, ON N2L 3G1, Canada.

[1]Current address: Department of Chemistry, Mount Allison University, Sackville, NB E4L 1G8, Canada.
[2]Current address: Department of Chemistry, University of Durham, South Road, Durham DH1 3LE, England.
[3]Authors to whom correspondence may be addressed. SAW: Telephone (506) 364–2372. Fax: (506) 364–2313. e-mail: swestcott@mta.ca; TBM: Telephone (44) 191–374–3137. Fax: (44) 191–386–1127. e-mail: todd.marder@durham.ac.uk

 © 1999 NRC Canada

Fig. 1. Two of the possible bonding modes in $(\eta^5\text{-}C_9H_7)ML_2$ complexes.

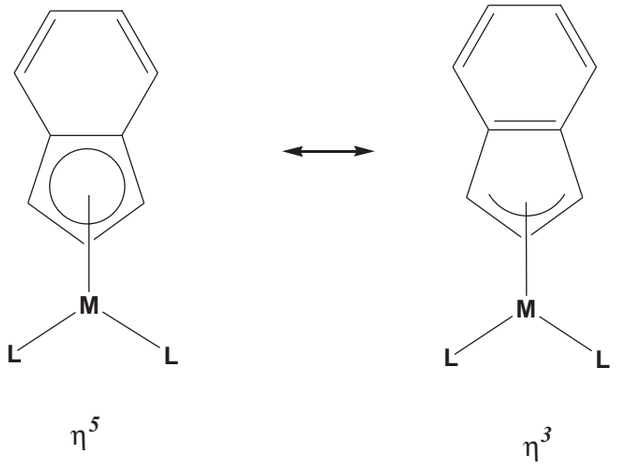

siderably more pronounced than initially reported, thus reducing the range of values known to date.

Experimental

General procedures

NMR spectra were recorded on Bruker WM250 (^{1}H at 250 MHz, $^{13}C\{^1H\}$ at 63 MHz, $^{31}P\{^1H\}$ at 101 MHz), and Nicolet NMC-300 (^{1}H at 250 MHz, $^{13}C\{^1H\}$ at 75.4 MHz, $^{31}P\{^1H\}$ at 121 MHz) spectrometers. ^{1}H NMR chemical shifts are reported in ppm relative to external TMS and were referenced to residual protons in the solvent; coupling constants are in Hz. Multiplicities are reported as (s) singlet, (d) doublet, (t) triplet, (q) quartet, (m) multiplet, (br) broad, and (ov) overlapping. THF and hexane were freshly distilled from sodium benzophenone ketyl. Benzoquinone, duroquinone, and TCNQ (Aldrich Chemical Co.) were used as received. $(C_9H_7)Rh(\eta^2\text{-}C_2H_4)_2$ (**1**) was prepared by established methods (7).

*Preparation of $(\eta^5\text{-}C_9H_7)Rh(C_6O_2H_4)$ (**2**)*

$(\eta^5\text{-}C_9H_7)Rh(C_6O_2H_4)$ was prepared by allowing 1,4-benzoquinone ($C_6O_2H_4$) (119 mg, 1.1 mmol) to react with $(\eta^5\text{-}C_9H_7)Rh(C_2H_4)_2$ (274 mg, 1 mmol) in THF at room temperature. After stirring for 12 h, the solvent was removed in vacuo. The residue was washed with cold hexane (2 × 5 mL) and dissolved in THF/hexane (5/1). An orange–yellow product (271 mg, 83% yield) was obtained after cooling to –10°C. Selected spectroscopic data: IR (CH_2Cl_2, cm^{-1}): 1631 (s sh), 1614 (s), 1578 (m); ^{1}H NMR (CD_2Cl_2) δ: 7.36–7.30 (m), 7.29–7.24 (m), 6.06 (d, J = 3 Hz), 5.74 (q, $J_{H-Rh=H-H}$ = 3 Hz), 5.00 (s); $^{13}C\{^1H\}$ NMR (CD_2Cl_2): 160.6 (C=O), 128.9, 121.3, 107.5 (d, J_{C-Rh} = 5 Hz), 90.8 (d, J_{C-Rh} = 7 Hz), 82.1 (d, J_{C-Rh} = 8 Hz), 78.6 (d, J_{C-Rh} = 7 Hz) ppm.

*Preparation of $(\eta^5\text{-}C_9H_7)Rh(2,3,5,6\text{-}C_6O_2(CH_3)_4)$ (**3**)*

$(\eta^5\text{-}C_9H_7)Rh(2,3,5,6\text{-}C_6O_2(CH_3)_4)$ was prepared by allowing duroquinone ($2,3,5,6\text{-}C_6O_2(CH_3)_4$) (180 mg, 1.1 mmol) to react with $(\eta^5\text{-}C_9H_7)Rh(C_2H_4)_2$ (274 mg, 1 mmol) in THF at room temperature. After stirring for 12 h, the solvent was removed in vacuo. The residue was washed with cold hexane (2 × 5mL) and dissolved in THF/hexane (10/1). Orange–yellow crystals of the product (138 mg, 36% yield) were obtained after cooling to –10°C. Selected spectroscopic data: IR (CH_2Cl_2, cm^{-1}): 1587 (s), 1426 (m), 1369 (m); ^{1}H NMR (CD_2Cl_2) δ: 7.63–7.59 (m), 7.39–7.35 (m), 5.91 (q, $J_{H-Rh=H-H}$ = 3 Hz), 5.68 (d, J = 3 Hz), 2.07 (s) ppm; $^{13}C\{^1H\}$ NMR (CD_2Cl_2): 140.5 (C=O), 123.7, 119.5, 112.3, 91.9 (d, J_{C-Rh} = 5 Hz), 78.8 (d, J_{C-Rh} = 4 Hz), 43.8 (d, J_{C-Rh} = 12 Hz), 12.3 ppm.

Table 1. Crystallographic data collection parameters for $(\eta^5\text{-}C_9H_7)Rh(2,3,5,6\text{-}C_6O_2(CH_3)_4)$ (**3**).

Formula	$C_{19}H_{19}O_2Rh$
fw	382.3
Crystal system	Monoclinic
Space group	$P2_1/c$
a, Å	7.932(2)
b, Å	17.879(5)
c, Å	11.074(3)
β, deg	96.88(2)
V, Å^3	1559.1(8)
Z	4
ρ_{calcd}, g cm^{-3}	1.628
Crystal size, mm	0.34 × 0.39 × 0.30
Temperature, K	295
Radiation	MoKα (λ = 0.710 73)
μ, cm^{-1}	10.81
Max 2θ, deg	60.0
Data collection method	ω
Scan speed, deg/min	2.93–29.30
Scan width, deg	1.20
Total unique reflections measured	4545
Total observed reflections[a]	3651
Max./min. transmission factor[b]	0.550, 0.586
No. of variables	276
Final max. Δ/σ	0.023
Max. res. density/hole, e Å^{-3}	0.41, –0.28
R[c]	0.0224
R_w	0.0231
GoF[d]	1.55

[a] $F_o > 6\sigma(F_o)$.
[b] Absorption correction by ψ-scan semi-empirical method.
[c] $R = \Sigma||F_o| - |F_c||/\Sigma|F_o|$; $Rw = [\Sigma(w(|F_o| - |F_c|)^2/\Sigma(w|F_o|)^2]^{1/2}$.
[d] $[\Sigma(w(|F_o| - |F_c|)^2/(NO - NV)]^{1/2}$.

Molecular structure determination

Crystals of **3** suitable for X-ray diffraction studies were obtained by crystallization from a THF–hexane solution at –10°C. A summary of the crystal data and parameters for data collection is given in Table 1. Data were collected at room temperature on a Nicolet R3m/V diffractometer using graphite-filtered MoKα radiation (λ = 0.710 73 Å) and the ω scan method. The data and refinement were performed on a VAX 3100 computer using Siemens SHELXTL (VAX) software.[4] The structure was solved using Patterson and

[4] G.M. Sheldrick. SHELXTL-Plus. Version 4.21/v. Siemens Analytical X-Ray Instruments, Inc. Madison, Wisconsin, U.S.A. 1990.

© 1999 NRC Canada

Table 2. Bond distances (Å) and selected bond angles (deg) for (η^5-C_9H_7)Rh(2,3,5,6-$C_6O_2(CH_3)_4$) (**3**).

Rh(1)—C(1)	2.164(4)	C(4)—C(5)	1.329(7)
Rh(1)—C(2)	2.207(4)	C(5)—C(6)	1.408(7)
Rh(1)—C(3)	2.191(4)	C(6)—C(7)	1.347(8)
Rh(1)—C(3A)	2.297(3)	C(7)—C(7A)	1.422(5)
Rh(1)—C(7A)	2.281(3)	C(8)—C(9)	1.474(4)
Rh(1)—C(8)	2.447(3)	C(8)—C(13)	1.468(4)
Rh(1)—C(9)	2.198(3)	C(8)—O(14)	1.237(4)
Rh(1)—C(10)	2.181(3)	C(9)—C(10)	1.422(4)
Rh(1)—C(11)	2.490(3)	C(9)—C(15)	1.494(5)
Rh(1)—C(12)	2.195(3)	C(10)—C(11)	1.469(4)
Rh(1)—C(13)	2.197(3)	C(10)—C(16)	1.505(5)
C(1)—C(2)	1.399(7)	C(11)—C(12)	1.480(4)
C(1)—C(7A)	1.443(5)	C(11)—O(17)	1.230(4)
C(2)—C(3)	1.420(5)	C(12)—C(13)	1.412(4)
C(3)—C(3A)	1.435(5)	C(12)—C(18)	1.507(4)
C(3A)—C(4)	1.412(5)	C(13)—C(19)	1.501(4)
C(3A)—C(7A)	1.432(4)		
C(1)-Rh(1)-C(2)	37.3(2)	C(1)-Rh(1)-C(11)	126.8(1)
C(1)-Rh(1)-C(3)	63.2(1)	C(2)-Rh(1)-C(11)	113.7(1)
C(2)-Rh(1)-C(3)	37.7(1)	C(3)-Rh(1)-C(11)	127.3(1)
C(1)-Rh(1)-C(3A)	62.5(1)	C(3A)-Rh(1)-C(11)	160.8(1)
C(2)-Rh(1)-C(3A)	61.9(1)	C(7A)-Rh(1)-C(11)	160.9(1)
C(3)-Rh(1)-C(3A)	37.2(1)	C(8)-Rh(1)-C(11)	72.0(1)
C(1)-Rh(1)-C(7A)	37.8(1)	C(9)-Rh(1)-C(11)	64.3(1)
C(2)-Rh(1)-C(7A)	61.9(1)	C(10)-Rh(1)-C(11)	35.9(1)
C(3)-Rh(1)-C(7A)	62.0(1)	C(1)-Rh(1)-C(12)	154.8(1)
C(3A)-Rh(1)-C(7A)	36.4(1)	C(2)-Rh(1)-C(12)	121.9(1)
C(1)-Rh(1)-C(8)	136.2(1)	C(3)-Rh(1)-C(12)	109.7(1)
C(2)-Rh(1)-C(8)	173.1(1)	C(3A)-Rh(1)-C(12)	127.9(1)
C(3)-Rh(1)-C(8)	142.4(1)	C(7A)-Rh(1)-C(12)	162.9(1)
C(3A)-Rh(1)-C(8)	114.2(1)	C(8)-Rh(1)-C(12)	65.0(1)
C(7A)-Rh(1)-C(8)	111.5(1)	C(9)-Rh(1)-C(12)	80.7(1)
C(1)-Rh(1)-C(9)	109.7(1)	C(10)-Rh(1)-C(12)	68.1(1)
C(2)-Rh(1)-C(9)	141.1(1)	C(11)-Rh(1)-C(12)	36.1(1)
C(3)-Rh(1)-C(9)	168.3(1)	C(1)-Rh(1)-C(13)	167.6(1)
C(3A)-Rh(1)-C(9)	131.9(1)	C(2)-Rh(1)-C(13)	149.0(1)
C(7A)-Rh(1)-C(9)	106.5(1)	C(3)-Rh(1)-C(13)	116.4(1)
C(8)-Rh(1)-C(9)	36.5(1)	C(3A)-Rh(1)-C(13)	109.1(1)
C(1)-Rh(1)-C(10)	105.5(1)	C(7A)-Rh(1)-C(13)	130.1(1)
C(2)-Rh(1)-C(10)	116.6(1)	C(8)-Rh(1)-C(13)	36.4(1)
C(3)-Rh(1)-C(10)	150.4(1)	C(9)-Rh(1)-C(13)	68.3(1)
C(3A)-Rh(1)-C(10)	163.2(1)	C(10)-Rh(1)-C(13)	80.6(1)
C(7A)-Rh(1)-C(10)	126.9(1)	C(11)-Rh(1)-C(13)	64.2(1)
C(8)-Rh(1)-C(10)	65.3(1)	C(12)-Rh(1)-C(13)	37.5(1)
C(9)-Rh(1)-C(10)	37.9(1)		

Fourier techniques, and refinement was performed using full-matrix least squares on *F*, with anisotropic thermal parameters for all non-hydrogen atoms. The hydrogen atoms were located on the Fourier difference electron-density maps and included in the structure model. The maximum residue and hole are proximate to the rhodium atom. Selected bond distances and angles are given in Table 2, and final atomic coordinates are given in Table 3. Complete tables of bond distances and angles, anisotropic thermal parameters for the non-hydrogen atoms, hydrogen atom positions, atomic coordinates, isotropic thermal parameters, crystal data, refinement parameters, and alternative views of **3** have been deposited.[5]

[5] A complete set of data may be purchased from: The Depository of Unpublished Data, Document Delivery, CISTI, National Research Council Canada, Ottawa, Canada, K1A 0S2. With the exception of thermal parameters, these have also been deposited with the Cambridge Crystallographic Data Centre, and can be obtained on request from: The Director, Cambridge Crystallographic Data Centre, University Chemical Laboratory, 12 Union Road, Cambridge, CB2 1EZ, U.K.

© 1999 NRC Canada

Table 3. Atomic coordinates (× 10^4) and equivalent isotropic displacement coefficients for (η^5-C_9H_7)Rh(2,3,5,6-$C_6O_2(CH_3)_4$) (**3**).

	x	*y*	*z*	*U* (eq)
Rh(1)	7280.9(2)	998.2(1)	2207.6(2)	24.42(8)
C(1)	8307(5)	1491(3)	667(3)	46(1)
C(2)	8758(5)	734(3)	695(3)	50(1)
C(3)	9766(4)	592(2)	1820(4)	42(1)
C(3A)	10122(4)	1290(2)	2436(3)	33.2(8)
C(4)	11055(5)	1496(3)	3553(3)	48(1)
C(5)	11076(7)	2202(3)	3927(4)	66(2)
C(6)	10184(7)	2763(3)	3223(6)	71(2)
C(7)	9275(6)	2605(2)	2148(6)	59(1)
C(7A)	9212(4)	1856(2)	1712(3)	36.4(9)
C(8)	5754(4)	1447(2)	3860(3)	32.2(8)
C(9)	5037(4)	1632(2)	2605(3)	31.2(8)
C(10)	4529(4)	1049(2)	1766(3)	31.4(8)
C(11)	4605(4)	265(2)	2164(3)	32.6(8)
C(12)	5998(3)	126(2)	3152(3)	29.7(7)
C(13)	6521(4)	700(2)	3990(3)	29.0(7)
O(14)	5977(4)	1924(1)	4673(2)	51.6(8)
C(15)	4724(6)	2439(2)	2312(4)	46(1)
C(16)	3644(5)	1203(3)	511(3)	46(1)
O(17)	3790(4)	–243(2)	1618(3)	53.4(9)
C(18)	6578(6)	–674(2)	3321(4)	47(1)
C(19)	7725(5)	568(2)	5122(3)	45(1)

Results and discussion

The addition of 1,4-benzoquinone ($C_6O_2H_4$) and duroquinone (2,3,5,6-tetramethyl-1,4-benzoquinone, $C_6O_2(CH_3)_4$) to (η^5-C_9H_7)Rh(C_2H_4)$_2$ (**1**) gave the corresponding metal complexes (η^5-C_9H_7)Rh($C_6O_2H_4$) (**2**) and (η^5-C_9H_7)Rh(2,3,5,6-$C_6O_2(CH_3)_4$) (**3**) (Scheme 1), respectively, where the quinone acts as a four-electron diene ligand.

An early report (6) described only a minimum amount of distortion within the indenyl ring in complex **3**, which is not consistent with data obtained with other (η^5-C_9H_7)RhL_2 complexes where significant slip-fold distortions are observed (1–5). These distortions arise as the ML_2 fragment slips from a pure η^5-bonding mode towards the allylic η^3-mode, whereby the indenyl ring loses planarity, and as result, the six-membered ring folds away slightly from the bulky metal fragment. One spectroscopic tool that has proven useful in determining the degree of slip-fold distortion in solution is $^{13}C\{^1H\}$ NMR spectroscopy (4*f*, 5*b*, 8). The slip distortion has been correlated with the $^{13}C\{^1H\}$ chemical shifts of the ring-junction carbons C3a,7a where larger distortions result in significant downfield shifts. Interestingly, the chemical shifts for the quaternary carbons in benzoquinone complex **2** at δ 107.5 ppm are significantly upfield from starting complex **1** at δ 112.2 ppm (7). This result is significant in that it suggests that the amount of distortion in this quinone complex is much less than that observed in the bis(ethylene) complex (η^5-C_9H_7)Rh(C_2H_4)$_2$.

$^{13}C\{^1H\}$ NMR data have also been used to describe the amount of distortion observed in quinones when these ligands coordinate to metal centres (9). Upon complexation, a marked deviation in the quinone from the D_{2h} symmetry of the free ligand is observed as the carbonyl moieties bend away from the metal. This distortion has been attributed to a repulsive interaction of the metal *d* orbitals with the filled $2b_{1u}$ and empty $2b_{2g}$ orbitals of the quinone (10). As a result of this distortion, the $^{13}C\{^1H\}$ NMR chemical shifts for this carbonyl fragments shift significantly upfield. For instance, the carbonyl groups in (η^5-C_5H_5)Rh($C_6O_2H_4$) are observed at δ 161.6 ppm, compared to free 1,4-benzoquinone at δ 187.0 ppm. A chemical shift at δ 160.6 ppm for **2** suggests that, like (η^5-C_5H_5)Rh($C_6O_2H_4$), only a minor distortion from planarity exists within the quinone ligand for this complex (9).

Although a minimal amount of distortion was reported earlier for (η^5-C_9H_7)Rh(2,3,5,6-$C_6O_2(CH_3)_4$) (**3**) (6), the $^{13}C\{^1H\}$ NMR data for both the indenyl ring and the quinone ligand in this complex suggest otherwise. Indeed, chemical shifts for the indenyl ring-junction carbons at δ 112.3 ppm implies that the degree of slip-fold distortion in **3,** at least in solution, is comparable to complex **1**. Likewise, the carbonyl groups of the quinone ligand have shifted by 36.8 ppm in complex **3** (δ 140.5 ppm) compared to free duroquinone (δ 187.3 ppm). To understand the nature of this discrepancy, we decided to reinvestigate the solid-state structure of **3**.

Figure 2 presents a view of the molecular structure with the atomic numbering scheme. Compound **3** consists of a (η^5-C_9H_7)Rh(2,3,5,6-$C_6O_2(CH_3)_4$) unit with the duroquinone ligand lying in a plane nearly parallel to the indenyl group. The carbonyl moieties of duroquinone lie on a plane incorporating Rh, C2, and the midpoint of the C3a–C7a vector of the indenyl ring. Duroquinone behaves as a 1,4-diolefin where the rhodium–carbon bond distances to the olefinic carbons C9, C10, C12, C13 of 2.194(2), 2.100(2), 2.201(2), and 2.195(2) Å (Rh—C_{ave} = 2.193(2) Å) are typical for those found in other d^8-π-quinone complexes (11). As expected from $^{13}C\{^1H\}$ NMR data, a significant distortion of the quinone ligand away from the plane is observed with the carbonyl groups bending away from the indenylrhodium fragment. The distances Rh—C8 of 2.448 (2) Å and Rh—C11 of 2.450(2) Å are approximately 0.276 Å longer than those to the olefinic carbons. In addition to this distortion from planarity, the unsaturated C=C bond distances within the duroquinone ligand (mean value 1.417 Å) are also elongated considerably compared to free quinone (1.341 Å) (12).

In contrast to previous work, we find that a modest amount of distortion in the indenyl ring is present in the ground-state structure of (η^5-C_9H_7)Rh(2,3,5,6-$C_6O_2(CH_3)_4$), which contains three "short" and two "long" rhodium–carbon distances. The value of the slip-distortion is Δ = 0.112(3) Å, where Δ = *d*(average Rh—C3a,7a) – *d*(average Rh—C1,3). While a hinge angle of 7.2° (HA = angle between planes defined by C1, C2, C3 and C1, C7a, C3a, C3) and a fold angle of FA = 4.0° (FA = angle between planes defined by C1, C2, C3 and C3a, C4, C5, C6, C7, C7a) also suggest a slight distortion towards an allylic bonding mode, there is clearly bonding between the metal atom and ring junction carbons C3a and C7a, as required to attain an 18-electron configuration at the metal. This level of distortion still makes the title compound the least distorted d^8-RhL_2 indenyl complex to have been structurally characterized to date.

© 1999 NRC Canada

Scheme 1.

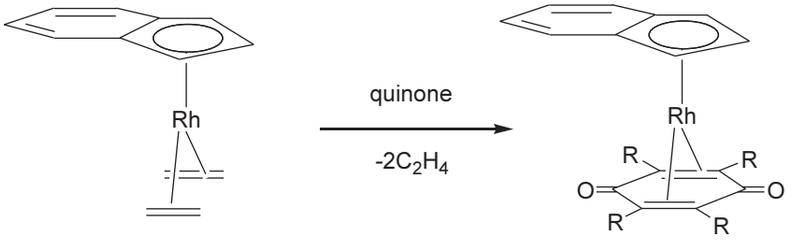

1 **2**, R = H; **3**, R = CH_3

Fig. 2. Molecular structure of (η^5-C_9H_7)Rh(2,3,5,6-$C_6O_2(CH_3)_4$) (**3**).

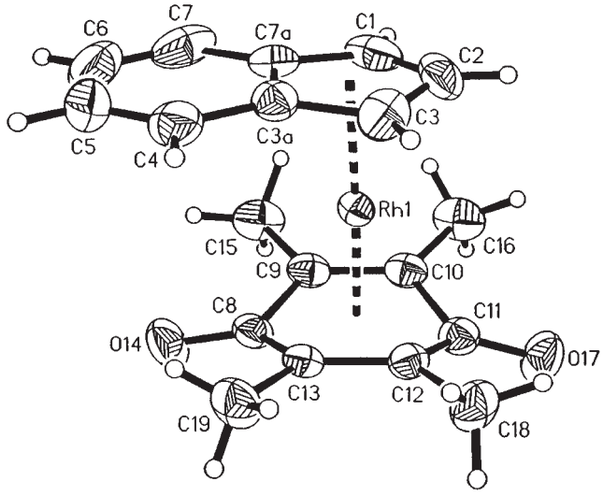

It is interesting to note that the degree of ground-state distortion in **3** does not correlate well with solution data and is still somewhat less pronounced than in the bis(ethylene) complex **1** (Δ = 0.161 Å, HA = 8.08°, FA = 7.40°) (4*b*, 13). It is plausible that this anomaly arises from the π-accepting ability of the quinone ligand, whereby π-backbonding removes electron density from the Rh(I) centre (towards a formal Rh(III) configuration) and thus strengthening the metal–ligand interactions and affecting the shift correlation. This type of interaction would also result in an increase in contribution from an "aromatic" resonance structure of the quinone ligand, as shown by the pronounced lengthening of the C=C bonds in **3**. Reactions with related 7,7′,8,8′-tetracyanoquinodimethane (TCNQ) gave highly coloured insoluble powders, where the quinone is now so strongly oxidizing that it appears to gives products arising from just charge-transfer chemistry (14[6]). Unfortunately, attempts to grow single crystals of less sterically hindered **2** suitable for X-ray diffraction studies, in order to compare solution and solid-state distortions, proved unsuccessful. In conclusion, the results described herein narrow significantly the range of these distortions, making correlations between ligand electronic and steric parameters and the degree of ground state distortion in d^8-ML_2 indenyl complexes much more difficult to assess.

Acknowledgements

T.B.M. acknowledges support from the Petroleum Research Fund, administered by the American Chemical Society. T.B.M. and S.A.W. also thank the Natural Sciences and Engineering Research Council of Canada and Johnson Matthey Ltd. for a loan of $RhCl_3 \cdot 3H_2O$. We thank the referees for helpful suggestions and Jacquelyn Burke for assistance with the literature search.

References

1. (*a*) P. Caddy, M. Green, L.E. Smart, and N. White. J. Chem. Soc. Chem. Commun. 839 (1978); (*b*) A. Borrini, P. Diversi, G. Ingrosso, A. Lucherini, and G. Serra. J. Mol. Catal. **30**, 181 (1985); (*c*) H. Bönneman. Angew. Chem. Int. Ed. Engl. **24**, 248 (1985); (*d*) T.B. Marder, D.C. Roe, and D. Milstein. Organometallics, **7**, 1451 (1988); (*e*) T. Foo and R.G. Bergman. Organometallics, **11**, 1811 (1992); (*f*) G.H. Llinas, R.O. Day, M.D. Rausch, and J.C.W. Chien. Organometallics, **12**, 1283 (1993); (*g*) B.Y. Lee, Y.K. Chung, N. Jeong, Y. Lee, and S.H. Hwang. J. Am. Chem. Soc. **116**, 8793 (1994); (*h*) M.A. Schmid, H.G. Alt, and W. Milius. J. Organomet. Chem. **514**, 45 (1996); (*i*) C.E. Garrett and G.C. Fu. J. Org. Chem. **63**, 1370 (1998).
2. (*a*) M.E. Rerek and F. Basolo. Organometallics, **3**, 740 (1984); (*b*) J. Am. Chem. Soc. **106**, 5908 (1984); (*c*) J.M. O'Connor and C.P. Casey. Chem Rev. **87**, 307 (1987), and refs. therein.
3. (*a*) J.S. Merola, R.T. Kacmarcik, and D. Van Engen. J. Am. Chem. Soc. **108**, 329 (1986); (*b*) R.M. Kowalewski, A.L. Rheingold, W.C. Trogler, and F. Basolo. J. Am. Chem. Soc. **108**, 2460 (1986); (*c*) T.C. Forschner, A.R. Cutler, and R.K. Kullnig. Organometallics, **6**, 889 (1987); (*d*) R. Poli, S.P. Mattamana, and L.R. Falvello. Gazz. Chim. Ital. **112**, 315 (1992); (*e*) T. Le Husebo and C.M. Jensen. Organometallics, **14**, 1087 (1995); (*f*) M.J. Calhorda, C.A. Gamelas, I.S. Gonçalves, E. Herdtweck, C.C. Romão, and L.F. Veiros. Organometallics, **17**, 2597 (1998), and refs. therein.
4. (*a*) R.D. Barr, M. Green, T.B. Marder, and F.G.A. Stone. J. Chem. Soc. Dalton Trans. 1261 (1984); (*b*) T.B. Marder, J.C. Calabrese, D.C. Roe, and T.H. Tulip. Organometallics, **6**, 2012 (1987); (*c*) A.K. Kakkar, N.J. Taylor, and T.B. Marder. Organometallics, **8**, 1765 (1989); (*d*) A.K. Kakkar, N.J. Taylor,

[6] S.A. Westcott and T.B. Marder. Unpublished results. For leading references on the radical anion chemistry of TCNQ, see ref. 14.

© 1999 NRC Canada

J.C. Calabrese, W.A. Nugent, D.C. Roe, E.A. Connaway, and T.B. Marder. J. Chem. Soc. Chem. Commun. 990 (1989); (*e*) A.K. Kakkar, S.F. Jones, N.J. Taylor, S. Collins, and T.B. Marder. J. Chem. Soc. Chem. Commun. 1454 (1989); (*f*) S.A. Westcott, A.K. Kakkar, G. Stringer, N.J. Taylor, and T.B. Marder. J. Organomet. Chem. **394**, 777 (1990), and refs. therein; (*g*) A.K. Kakkar, N.J. Taylor, T.B. Marder, J.K. Shen, N. Hallinan, and F. Basolo. Inorg. Chim. Acta, **198**–**200**, 219 (1992); (*h*) D. O'Hare, J.C. Green, T.B. Marder, S. Collins, G. Stringer, A.K. Kakkar, N. Kaltsoyannis, A. Kuhn, R. Lewis, C. Mehnert, P. Scott, and S. Pugh. Organometallics, **11**, 48 (1992); (*i*) T.M. Frankcom, J.C. Green, A. Nagy, A.K. Kakkar, and T.B. Marder. Organometallics, **12**, 3688 (1993); (*j*) S.A. Westcott, G. Stringer, S. Anderson, N.J. Taylor, and T.B. Marder. Inorg. Chem. **33**, 4589 (1994); (*k*) A.K. Kakkar, G. Stringer, N.J. Taylor, and T.B. Marder. Can. J. Chem. **73**, 981 (1995).

5. (*a*) R. Cramer, J.B. Kline, and J.D. Roberts. J. Am. Chem. Soc. **91**, 2519 (1969); (*b*) R.T. Baker and T.H. Tulip. Organometallics, **5**, 839 (1986); (*c*) A. Habib, R.S. Tanke, E.M. Holtz, and R.H. Crabtree. Organometallics, **8**, 1225 (1989); (*d*) F. Morandini, G. Pilloni, G. Consiglio, A. Sironi, and M. Moret. Organometallics, **12**, 3495 (1993); (*e*) D. Rau and U. Behrens. J. Organomet. Chem. **454**, 151 (1993); (*f*) Z. Zhou, C. Jablonski, and J. Bridson. J. Organomet. Chem. **461**, 215 (1993); (*g*) M. Bassetti, P. Casellato, M.P. Gamasa, J. Gimeno, C. González-Bernardo, and B. Martín-Vaca. Organometallics, **16**, 5470 (1997); (*h*) M. Stradiotto, D.W. Hughes, A.D. Bain, M.A. Brook, and M.J. McGlinchey. Organometallics, **16**, 5563 (1997); (*i*) M.C. Comstock and J. R. Shapley. Organometallics, **16**, 4816 (1997), and refs. therein; (*j*) T.A. Huber, M. Bayrakdarian, S. Dion, I. Dubuc, F. Bélanger-Gariépy, and D. Zargarian. Organometallics, **16**, 5811 (1997); (*k*) P. Cecchetto, A. Ceccon, A. Gambaro, S. Santi, P. Ganis, R. Gobetto, G. Valle, and A. Venzo. Organometallics, **17**, 752 (1998), and refs. therein.
6. G.G. Aleksandrov, Y.T. Struchkov, V.S. Khandkarova, and S.P. Gubin. J. Organomet. Chem. **25**, 243 (1970).
7. (*a*) H. Eshtiagh-Hosseini and J.F. Nixon. J. Less Common Met. **61**, 107 (1978); (*b*) P. Caddy, M. Green, E. O'Brien, L. E. Smart, and P. Woodward. Angew. Chem. Int. Ed. Engl. **16**, 648 (1977); J. Chem. Soc. Dalton Trans. 962 (1980).
8. F.H. Köhler. Chem. Ber. **107**, 570 (1974).
9. G.M. Bodner and T.R. Englemann. J. Organomet. Chem. **88**, 391 (1975).
10. G.N. Schrauzer and K.C. Dewhirst. J. Am. Chem. Soc. **86**, 3265 (1964).
11. (*a*) V.A. Uchtman and L.F. Dahl. J. Organomet. Chem. **40**, 403 (1972); (*b*) M.J. Chetcuti, J.A. Howard, M. Pfeffer, J.L. Spencer, and F.G.A. Stone. J. Chem. Soc. Dalton Trans. 276 (1981); (*c*) M. Cocivera, G. Ferguson, B. Kaitner, F.J. Lalor, D.J. O'Sullivan, M. Parvez, and B. Ruhl. Organometallics, **1**, 1132 (1982); (*d*) M. Valderrama, M. Scotti, R. Ganz, L.A. Oro, F.J. LaHoz, C. Foces-Foces, and F.H. Cano. J. Organomet. Chem. **288**, 97 (1985).
12. D. Rabinovich, G.M.J. Schmidt. and E. Ubell. J. Chem. Soc. B, 131 (1967).
13. M. Mlekuz, P. Bougeard, B.G. Sayer, M.J. McGlinchey, C.A. Rodger, M.R. Churchill, J.W. Ziller, S-K. Kang, and T.A. Albright. Organometallics, **5**, 1656 (1986).
14. (*a*) H. Zhao, R. A. Heintz, K. R. Dunbar, and R.D. Rogers. J. Am. Chem. Soc. **118**, 12844 (1996); (*b*) P.J. Kunkeler, P.J. van Koningsbruggen, J.P. Cornelissen, A.N. van der Horst, A.M. van der Kraan, A.L. Spek, J.G. Haasnoot, and J. Reedijk. J. Am. Chem. Soc. **118**, 2190 (1996).

© 1999 NRC Canada

Synthesis, structure, and solution dynamics of indenyl rhodium complexes containing bulky phosphine ligands: molecular structures of $(\eta^5\text{-}1\text{-}CH_3\text{-}C_9H_6)Rh(\eta^2\text{-}C_2H_4)(PCy_3)$ (Cy = cyclohexyl) and $(\eta^5\text{-}1\text{-}CH_3\text{-}C_9H_6)Rh(dcpe)$ (dcpe = $Cy_2PCH_2CH_2PCy_2$)

Stephen A. Westcott, Ashok K. Kakkar, Nicholas J. Taylor, D. Christopher Roe, and Todd B. Marder

Abstract: Reactions of $(\eta^5\text{-}1\text{-}CH_3\text{-}C_9H_6)Rh(\eta^2\text{-}C_2H_4)_2$ with PCy_3 (Cy = cyclohexyl) and 1,2-bis(dicyclohexylphosphino)ethane (dcpe = $Cy_2PCH_2CH_2PCy_2$) gave complexes $(\eta^5\text{-}1\text{-}CH_3\text{-}C_9H_6)Rh(\eta^2\text{-}C_2H_4)(PCy_3)$ (**1**) and $(\eta^5\text{-}1\text{-}CH_3\text{-}C_9H_6)Rh(dcpe)$ (**2**), respectively, in high yields. Complexes **1** and **2** were characterized by x-ray diffraction studies and by multinuclear NMR spectroscopy. Variable temperature $^{31}P\{^1H\}$ NMR spectra allowed for evaluation of energy barriers associated with indenyl ring rotation. While **1** and **2** displayed similar degrees of slip-fold distortion with respect to bonding of the indenyl ligand to the RhL_2 fragment, a lower energy barrier to ring rotation was calculated for the mixed ethylene-phosphine complex **1**. Yellow crystals of **1** are orthorhombic, *Pbca* with 16 molecules per unit cell of dimensions a = 11.341(3), b = 32.915(10), and c = 29.413(9) Å. Yellow crystals of **2** are triclinic, $P\bar{1}$ with two molecules per unit cell dimensions a = 9.327(3), b = 10.117(3), c = 18.934(6) Å, α = 104.28(2)°, β = 101.34(2)°, and γ = 92.99(2)°.

Key words: indenyl, rhodium, phosphines, ring-slippage.

Résumé : Les réactions du $(\eta^5\text{-}1\text{-}CH_3\text{-}C_9H_6)Rh(\eta^2\text{-}C_2H_4)_2$ avec le PCy_3 et le 1,2-bis(dicyclohexylphosphino)éthane (dope = $Cy_2PCH_2CH_2PCy_2$) fournissent les complexes $(\eta^5\text{-}1\text{-}CH_3\text{-}C_9H_6)Rh(\eta^2\text{-}C_2H_4)(PCy_3)$ (**1**) et $(\eta^5\text{-}1\text{-}CH_3\text{-}C_9H_6)Rh(dope)$ (**2**) respectivement, avec des rendements élevés. On a caractérisé les complexes **1** et **2** par des études de diffraction des rayons X et par spectroscopie RMN multinucléaire. Les spectres RMN $^{31}P\{^1H\}$ à température variable ont permis d'évaluer les barrières d'énergie associées à la rotation du noyau indényle. Même si les complexes **1** et **2** présentent des degrés semblables de distorsion par glissement/plissement par rapport à la liaison du ligand indényle sur le fragment RhL_2, on a calculé que l'énergie de la barrière à la rotation du cycle est plus faible pour le complexe de l'éthylène phosphine mixte (**1**). Les cristaux du composé **1** sont de couleur jaune, orthorhombiques, de groupe d'espace *Pbca* avec 16 molécules par maille de dimensions a = 11,341(3), b = 32,915(10) et c = 29,413(9) Å. Les cristaux de couleur jaune du complexe **2** sont tricliniques, groupe d'espace $P\bar{1}$ avec deux molécules par maille de dimensions a = 9,327(3), b = 10,117(3) et c = 18,934(6) Å, α = 104,28(2), β = 101,34(2) et γ = 92,99(2)°.

Mots clés : indényle, rhodium, phosphines, glissement de cycle.

[Traduit par la Rédaction]

Received September 15, 1998.

S.A. Westcott,[1,2] A.K. Kakkar,[3] N.J. Taylor, and T.B. Marder.[1,4] Department of Chemistry, University of Waterloo, Waterloo, ON N2L 3G1, Canada.
D.C. Roe. Central Research and Development, Corporate Catalysis Center, Dupont Science and Engineering Laboratories, Experimental Station, Wilmington, DE 19880–0328, U.S.A.

[1]Authors to whom correspondence may be addressed. SAW: Telephone: (506) 364-2372. Fax: (506) 364-2313. e-mail: swestcott@mta.ca; TBM: Telephone: (44) 191-374-3137. Fax: (44) 191-386-1127. e-mail: todd.marder@durham.ac.uk
[2]Current address: Department of Chemistry, Mount Allison University, Sackville, NB E4L 1G8, Canada.
[3]Current address: Department of Chemistry, McGill University, Montreal, PQ H3A 2K6, Canada.
[4]Current address: Department of Chemistry, University of Durham, South Road, Durham DH1 3LE, England.

© 1999 NRC Canada

Introduction

The enhanced reactivity of η^5-indenyl transition metal complexes compared with their more common η^5-C_5R_5 (R = H, Me) analogues is well documented (1–5) and has been attributed to the facile ring slippage from $\eta^5 \rightarrow \eta^3$ in an associative transition state (2, 5*c*). As part of our ongoing investigation into transition metal indenyl chemistry we have prepared and examined a number of (η^5-indenyl)RhL_2 complexes and examined the factors effecting ground-state distortion and related ligand dynamics (5). While much effort has focused on measuring the energy barriers associated with olefin rotation in indenyl complexes (see ref. 6*c* for leading refs.), relatively few reports describe the barrier to rotation about the metal-ring axis. (4*a*, *b*, *d*, 6) This latter process has a lower activation energy for bis(ethylene) complex (η^5-C_9H_7)Rh(η^2-C_2H_4)$_2$ ($\Delta G_{190}^{\ddagger}$ = 8.5 ± 0.4 kcal mol^{-1}) compared to $\Delta G_{240}^{\ddagger}$ = 10.4 ± 0.4 kcal mol^{-1} observed for olefin rotation (6*c*) (Fig. 1).

Molecular orbital arguments (5*e*, 6*e*, 7) suggest a preferred ground-state conformation where the d^8-ML_2 unit lies parallel to a plane through the C3a-C7a ring-junction carbons of the indenyl ring straddling the C_s mirror plane of the molecule. This orientation best stabilizes the indenyl HOMO while minimizing a four-electron destabilizing π-interaction between the indenyl second HOMO and metal d_{xz}. Rotation of the ML_2 fragment by 90° therefore results in a net destabilization of the molecule. We have prepared a monophosphine complex (η^5-1-CH_3-C_9H_6)Rh(η-C_2H_4)(PCy_3) (Cy = cyclohexyl) (**1**) and a diphosphine analogue, (η^5-1-CH_3-C_9H_6)Rh(dcpe) (dcpe = $Cy_2PCH_2CH_2PCy_2$) (**2**), where incorporation of the methyl substituent at C1 of the indenyl ligand breaks the ground-state C_s symmetry of both molecules. Variable temperature $^{31}P\{^1H\}$ NMR studies have been conducted, allowing us to assess the energy barriers associated with indenyl ring rotation, the results of which, along with the molecular structures of complexes **1** and **2**, are presented herein.

Experimental section

General procedures

NMR spectra were recorded on Bruker WM250 (^{1}H at 250 MHz, $^{13}C\{^1H\}$ at 63 MHz, $^{31}P\{^1H\}$ at 101 MHz), and Nicolet NMC-300 (^{1}H at 250 MHz, $^{13}C\{^1H\}$ at 75.4 MHz, $^{31}P\{^1H\}$ at 121 MHz) spectrometers. ^{1}H NMR chemical shifts are reported in ppm relative to external TMS and were referenced to residual protons in the solvent; coupling constants are in hertz. Multiplicities are reported as (s) singlet, (d) doublet, (t) triplet, (q) quartet, (m) multiplet, (br) broad, and (ov) overlapping. $^{31}P\{^1H\}$ chemical shifts are reported in ppm relative to the external standard 85% H_3PO_4. THF was freshly distilled from sodium benzophenone ketyl. PCy_3 and dcpe (Strem Chemical Co.) were used as received. (η^5-1-Me-C_9H_6)Rh(η^2-C_2H_4)$_2$ was prepared by established methods (6*c*).

Preparation of (η^5-1-CH_3-C_9H_6)Rh(η-C_2H_4)(PCy_3) (1)

A solution of PCy_3 (140 mg, 0.5 mmol) in 10 mL of THF was added dropwise to a solution of (η^5-1-CH_3-C_9H_6)Rh(η^2-C_2H_4)$_2$ (144 mg, 0.5 mmol) in 10 mL of THF at ambient temperature. After stirring for 12 h, the solution was concentrated in vacuo to 5 mL, hexane (20 mL) was added, and the solution cooled to –30°C for 48 h. The resulting orange–red crystals were collected by filtration, washed with hexane (2 × 10 mL), and dried in vacuo to yield 238 mg (88%) of **1**. Selected NMR spectroscopic data: $^{31}P\{H\}$ (THF-d_8, 298 K) δ: 53.9 (d, J_{P-Rh} = 209 Hz); ^{1}H (C_6D_6, 298 K) δ: 0.83–1.19 (br ov m), 1.34 (d, *J* = 5 Hz), 1.40 (br), 1.65 (m), 2.03 (m), 5.47 (d, *J* = 3 Hz, H2, 1H), 5.73 (dd, *J* = 3,1 Hz, H3, 1H), 6.73 (ov m, H4–6, 3H), 7.07 (m, H7, 1H); $^{13}C\{^1H\}$ (THF-d_8, 298 K) δ: 9.6 (d, *J* = 2.3 Hz), 14.3 (s), 23.1 (s), 26.0 (s), 27.2 (s), 28.3 (dd, *J* = 10, 4 Hz), 30.5 (d, *J* = 26 Hz), 32.0 (s), 36.1 (d, *J* = 18 Hz), 38.2 (s), 72.9 (d, *J* = 5 Hz), 83.1 (dd, *J* = 15, 4 Hz), 95.3 (d, *J* = 6 Hz), 114.4 (s), 114.5 (s), 118.3 (s), 119.7 (s), 120.0 (s), 122.5 (s).

Fig 1. ML_2 rotation with respect to the indenyl ligand.

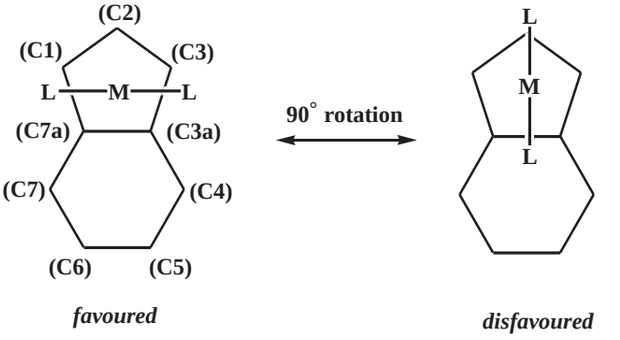

Preparation of (η^5-1-CH_3-C_9H_6)Rh(dcpe) (2)

A solution of dcpe (211 mg, 0.5 mmol) in 10 mL of THF was added dropwise to a solution of (η^5-1-CH_3-C_9H_6)Rh(η^2-C_2H_4)$_2$ (144 mg, 0.5 mmol) in 10 mL of THF at ambient temperature. After stirring for 12 h, the solution was concentrated in vacuo to 5 mL, hexane (20 mL) was added, and the solution was cooled to –30°C for 48 h. The resulting red crystals were collected by filtration, washed with hexane (2 × 10 mL), and dried in vacuo to yield 258 mg (79%) of **2**. Selected NMR spectroscopic data: $^{31}P\{^1H\}$ (THF-d_8, 298 K) δ: 93.7 (d, J_{P-Rh} = 217 Hz); ^{1}H (THF-d_8, 298 K) δ: 0.86–1.34 (br ov m), 1.55–1.88 (br ov m), 2.30 (br s), 5.27 (s, 1H), 5.74 (s, 1H), 6.62 (app q, *J* = 7 Hz, 1H), 6.66 (app q, *J* = 7 Hz, 1H), 6.95 (d, *J* = 8 Hz, 1H), 7.06 (d, *J* = 8 Hz, 1H). $^{13}C\{^1H\}$ (THF-d_8, 298 K) δ: 1.41 (s, CH_3), 23.5 (d t, J_{C-P} = 19 Hz, J_{C-Rh} = 4 Hz), 25.2 (t, *J* = 20 Hz), 27.4 (d, J_{C-P} = 26 Hz), 27.8 (t, *J* = 11 Hz), 29.7 (q, *J* = 14 Hz), 38.5 (app q), 65.2 (d, J_{C-Rh} = 4 Hz), 84.4 (s), 96.2 (d, J_{C-Rh} = 5 Hz), 115.4 (s), 117.0 (s), 117.2 (s), 118.8 (s), 118.9 (s), 119.0 (s).

Molecular structure determination

Crystals of **1** and **2** suitable for X-ray diffraction studies were obtained by recrystallization from THF–hexane solution at –30°C. A summary of the crystal data and parameters for data collection is given in Table 1. Data were collected at room temperature on a Nicolet R3m/V diffractometer using graphite-filtered MoKα radiation (λ = 0.710 73 Å) and the ω scan method. The data and refinement of **1** and **2** were performed on an VAX 3100 computer using Siemens SHELXTL (VAX) software as described elsewhere (5, 8).

© 1999 NRC Canada

Table 1. Crystallographic data collection parameters for (η^5-1-CH_3-C_9H_6)Rh(η^2-C_2H_4)(PCy_3) (**1**) and (η^5-1-CH_3-C_9H_6)Rh(dcpe) (**2**).

Complex	**1**	**2**
Formula	$C_{30}H_{46}PRh$	$C_{36}H_{57}P_2Rh$
fw	540.5	654.7
Crystal system	Orthorhombic	Triclinic
Space group	*Pbca*	$P\bar{1}$
a, Å	11.341(3)	9.327(3)
b, Å	32.915(10)	10.117(3)
c, Å	29.413(9)	18.934(6)
α, deg		104.28(2)
β, deg		101.34(2)
γ, deg		92.99(2)
V, Å^3	10 980(6)	1688.0(9)
Z	16	2
ρ_{calcd}, g cm^{-3}	1.308	1.288
Crystal size, mm	0.29 × 0.31 × 0.40	0.40 × 0.45 × 0.47
Temperature, K	295	295
Radiation	MoKα (λ = 0.710 73)	MoKα (λ = 0.710 73)
μ, cm^{-1}	6.96	6.12
Max 2θ, deg	50.0	60.0
Data collection method	ω	ω
Scan speed, deg/min	2.93–29.30	2.93–29.30
Scan width, deg	1.20	1.20
Total unique reflections measured	9672	9843
Total observed reflections[a]	4903	8047
Max./min. transmission factor[b]	0.721, 0.671	0.795, 0.645
No. of variables	669	410
Final max. Δ/σ	0.011	0.002
Max. res. density/hole, e Å^{-3}	0.57, –0.36	0.39, –0.38
R[c]	0.0398	0.0279
R_w	0.0327	0.0291
GoF[d]	1.46	1.85

[a] $F_o > 6\sigma(F_o)$.

[b] ψ-Scan semi-empirical method.

[c] $R = \Sigma||F_o| - |F_c||/\Sigma|F_o|$; $Rw = [\Sigma(w(|F_o| - |F_c|)^2/\Sigma(w|F_o|)^2]^{1/2}$.

[d] $[\Sigma(w(|F_o| - F_c|)^2/(NO - NV)]^{½}$.

The structure was solved using Patterson and Fourier techniques, and refinement was performed using full-matrix least squares on *F*, with anisotropic thermal parameters for all non-hydrogen atoms and isotropic thermal parameters for the hydrogen atoms (riding model). The function minimized was $\Sigma w(F_o - F_c)^2$ with the weights, $w^{-1} = \sigma^2(F)$ for both **1** and **2**. Selected bond distances and angles are given in Table 2, and final atomic coordinates are given in Tables 3 and 4. Crystal data, complete tables of bond distances and angles, atomic coordinates, anisotropic thermal parameters for the non-hydrogen atoms, and hydrogen atom positions, isotropic thermal parameters, and NMR data have been deposited.[5]

Results and discussion

Synthesis of rhodium(I) indenyl complexes

Complexes **1** and **2** were prepared directly by addition of 1 equiv. of the corresponding phosphines to (η^5-1-CH_3-C_9H_6)Rh(η-C_2H_4)$_2$ (**3**) (9). Attempts to prepare the sterically encumbered (η^5-1-CH_3-C_9H_6)Rh(PCy_3)$_2$ by addition of excess PCy_3 to **3** at ambient or elevated temperatures, however, proved unsuccessful, generating only the mixed ethylene–phosphine complex **1** (Fig. 2).

Molecular structures

The crystal structure of **1** contains two independent molecules in the asymmetric unit, which differ in respect to the stereochemistry of the phosphine ligands. Selected bond distances and angles are given in Table 2, and a view of the two molecules is provided in Fig. 3. The two molecules are chemically equivalent with the ethylene and phosphine ligands straddling a plane incorporating Rh and C2 of the indenyl ligand and bisecting the C3a-C7a vector. The ethylene ligands lie directly below the methyl substituent of the indenyl group having an average carbon–carbon bond length of 1.390(11) Å. These bonds are significantly longer than

[5] A complete set of data may be purchased from: The Depository of Unpublished Data, Document Delivery, CISTI, National Research Council Canada, Ottawa, Canada, K1A 0S2. With the exception of anisotropic and isotropic thermal parameters and NMR data, these have also been deposited with the Cambridge Crystallographic Data Centre and can be obtained on request from: The Director, Cambridge Crystallographic Data Centre, University Chemical Laboratory, 12 Union Road, Cambridge, CB2 1EZ, U.K.

© 1999 NRC Canada

Table 2. Bond distances (Å) and angles (deg) for (η^5-1-CH_3-C_9H_6)Rh(η^2-C_2H_4)(PCy_3) (**1**) and (η^5-1-CH_3-C_9H_6)Rh(dcpe) (**2**).

(η^5-1-CH_3-C_9H_6)Rh(η^2-C_2H_4)(PCy_3) (**1**)			
Molecule 1		Molecule 2	
Rh(1)—P(1)	2.271(2)	Rh(1)B—P(1)B	2.260(2)
Rh(1)—C(1)	2.206(7)	Rh(1)B—C(1)B	2.275(7)
Rh(1)—C(2)	2.220(7)	Rh(1)B—C(2)B	2.230(7)
Rh(1)—C(3)	2.272(7)	Rh(1)B—C(3)B	2.207(7)
Rh(1)—C(3a)	2.463(7)	Rh(1)B—C(3a)B	2.411(7)
Rh(1)—C(7a)	2.410(7)	Rh(1)B—C(7a)B	2.423(7)
Rh(1)—C(9)	2.098(7)	Rh(1)B—C(9)B	2.126(7)
Rh(1)—C(10)	2.107(7)	Rh(1)B—C(10)B	2.113(7)
P(1)—C(11)	1.864(6)	P(1)B—C(11)B	1.876(6)
P(1)—C(17)	1.852(6)	P(1)B—C(17)B	1.870(5)
P(1)—C(23)	1.869(6)	P(1)B—C(23)B	1.849(6)
C(1)—C(2)	1.407(11)	C(1)B—C(2)B	1.423(11)
C(1)—C(7a)	1.444(10)	C(1)B—C(7a)B	1.446(11)
C(1)—C(8)	1.487(12)	C(1)B—C(8)B	1.494(11)
C(2)—C(3)	1.409(11)	C(2)B—C(3)B	1.412(12)
C(3)—C(3a)	1.460(10)	C(3)B—C(3a)B	1.443(11)
C(3a)—C(4)	1.409(11)	C(3a)B—C(4)B	1.409(12)
C(3a)—C(7a)	1.395(10)	C(3a)B—C(7a)B	1.419(12)
C(4)—C(5)	1.362(13)	C(4)B—C(5)B	1.368(13)
C(5)—C(6)	1.388(15)	C(5)B—C(6)B	1.393(16)
C(6)—C(7)	1.364(12)	C(6)B—C(7)B	1.366(13)
C(7)—C(7a)	1.412(11)	C(7)B—C(7a)B	1.413(11)
C(9)—C(10)	1.385(11)	C(9)B—C(10)B	1.395(11)
C(11)—C(12)	1.520(9)	C(11)B—C(12)B	1.530(9)
C(11)—C(16)	1.522(8)	C(11)B—C(16)B	1.537(9)
C(12)—C(13)	1.535(9)	C(12)B—C(13)B	1.510(10)
C(13)—C(14)	1.507(10)	C(13)B—C(14)B	1.517(12)
C(14)—C(15)	1.516(11)	C(14)B—C(15)B	1.542(10)
C(15)—C(16)	1.534(10)	C(15)B—C(16)B	1.520(9)
C(17)—C(18)	1.535(8)	C(17)B—C(18)B	1.534(9)
C(17)—C(22)	1.539(8)	C(17)B—C(22)B	1.527(9)
C(18)—C(19)	1.529(9)	C(18)B—C(19)B	1.535(9)
C(19)—C(20)	1.514(10)	C(19)B—C(20)B	1.506(10)
C(20)—C(21)	1.517(9)	C(20)B—C(21)B	1.497(12)
C(21)—C(22)	1.532(9)	C(21)B—C(22)B	1.532(9)
C(23)—C(24)	1.530(8)	C(23)B—C(24)B	1.500(10)
C(23)—C(28)	1.524(9)	C(23)B—C(28)B	1.534(9)
C(24)—C(25)	1.527(10)	C(24)B—C(25)B	1.536(11)
C(25)—C(26)	1.497(12)	C(25)B—C(26)B	1.523(11)
C(26)—C(27)	1.506(10)	C(26)B—C(27)B	1.489(12)
C(27)—C(28)	1.523(10)	C(27)B—C(28)B	1.555(11)
Molecule 1		Molecule 2	
P(1)-Rh(1)-C(1)	167.8(2)	P(1)B-Rh(1)B-C(1)B	158.3(2)
P(1)-Rh(1)-C(2)	132.6(2)	P(1)B-Rh(1)B-C(2)B	121.5(2)
C(1)-Rh(1)-C(2)	37.1(3)	C(1)B-Rh(1)B-C(2)B	36.8(3)
P(1)-Rh(1)-C(3)	106.1(2)	P(1)B-Rh(1)B-C(3)B	100.6(2)
C(1)-Rh(1)-C(3)	61.7(3)	C(1)B-Rh(1)B-C(3)B	62.1(3)
C(2)-Rh(1)-C(3)	36.5(3)	C(2)B-Rh(1)B-C(3)B	37.1(3)
P(1)-Rh(1)-C(3a)	111.7(2)	P(1)B-Rh(1)B-C(3a)B	115.3(2)
C(1)-Rh(1)-C(3a)	58.9(3)	C(1)B-Rh(1)B-C(3a)B	59.1(3)
C(2)-Rh(1)-C(3a)	58.6(2)	C(2)B-Rh(1)B-C(3a)B	59.2(3)
C(3)-Rh(1)-C(3a)	35.6(2)	C(3)B-Rh(1)B-C(3a)B	36.1(3)
P(1)-Rh(1)-C(7a)	139.4(2)	P(1)B-Rh(1)B-C(7a)B	148.1(2)
C(1)-Rh(1)-C(7a)	36.1(3)	C(1)B-Rh(1)B-C(7a)B	35.7(3)
C(2)-Rh(1)-C(7a)	59.1(3)	C(2)B-Rh(1)B-C(7a)B	59.2(3)
C(3)-Rh(1)-C(7a)	58.8(3)	C(3)B-Rh(1)B-C(7a)B	59.8(3)

© 1999 NRC Canada

Table 2 (*continued*).

(η^5-1-CH_3-C_9H_6)Rh(η^2-C_2H_4)(PCy_3) (**1**)			
Molecule 1		Molecule 2	
C(3a)-Rh(1)-C(7a)	33.2(2)	C(3a)B-Rh(1)B-C(7a)B	34.1(3)
P(1)-Rh(1)-C(9)	97.2(2)	P(1)B-Rh(1)B-C(9)B	98.4(2)
C(1)-Rh(1)-C(9)	93.3(3)	C(1)B-Rh(1)B-C(9)B	101.4(3)
C(2)-Rh(1)-C(9)	106.6(3)	C(2)B-Rh(1)B-C(9)B	134.8(3)
C(3)-Rh(1)-C(9)	142.2(3)	C(3)B-Rh(1)B-C(9)B	158.1(3)
C(3a)-Rh(1)-C(9)	150.3(3)	C(3a)B-Rh(1)B-C(9)B	124.2(3)
C(7a)-Rh(1)-C(9)	117.5(3)	C(7a)B-Rh(1)B-C(9)B	98.3(3)
P(1)-Rh(1)-C(10)	94.6(2)	P(1)B-Rh(1)B-C(10)B	95.4(2)
C(1)-Rh(1)-C(10)	97.5(3)	C(1)B-Rh(1)B-C(10)B	94.8(3)
C(2)-Rh(1)-C(10)	129.1(3)	C(2)B-Rh(1)B-C(10)B	111.4(3)
C(3)-Rh(1)-C(10)	157.7(3)	C(3)B-Rh(1)B-C(10)B	148.2(3)
C(3a)-Rh(1)-C(10)	128.0(3)	C(3a)B-Rh(1)B-C(10)B	148.6(3)
C(7a)-Rh(1)-C(10)	99.8(3)	C(7a)B-Rh(1)B-C(10)B	114.4(3)
C(9)-Rh(1)-C(10)	38.5(3)	C(9)B-Rh(1)B-C(10)B	38.2(3)
(η^5-1-CH_3-C_9H_6)Rh(dcpe) (**2**)			
Rh(1)—P(1)	2.216(1)	C(11)—C(12)	1.529(3)
Rh(1)—P(2)	2.210(1)	C(11)—C(16)	1.530(3)
Rh(1)—C(1)	2.274(2)	C(12)—C(13)	1.525(3)
Rh(1)—C(2)	2.246(2)	C(13)—C(14)	1.514(4)
Rh(1)—C(3)	2.227(2)	C(14)—C(15)	1.513(4)
Rh(1)—C(3A)	2.424(2)	C(15)—C(16)	1.524(3)
Rh(1)—C(7A)	2.432(2)	C(17)—C(18)	1.513(4)
P(1)—C(9)	1.851(2)	C(17)—C(22)	1.503(3)
P(1)—C(11)	1.856(2)	C(18)—C(19)	1.534(5)
P(1)—C(17)	1.861(2)	C(19)—C(20)	1.507(4)
P(2)—C(10)	1.853(2)	C(20)—C(21)	1.499(5)
P(2)—C(23)	1.859(2)	C(21)—C(22)	1.542(5)
P(2)—C(29)	1.865(2)	C(23)—C(24)	1.532(3)
C(1)—C(2)	1.400(4)	C(23)—C(28)	1.531(3)
C(1)—C(7A)	1.452(3)	C(24)—C(25)	1.518(3)
C(1)—C(8)	1.500(4)	C(25)—C(26)	1.521(3)
C(2)—C(3)	1.398(4)	C(26)—C(27)	1.519(4)
C(3)—C(3A)	1.436(4)	C(27)—C(28)	1.528(3)
C(3A)—C(4)	1.396(4)	C(29)—C(30)	1.530(3)
C(3A)—C(7A)	1.427(4)	C(29)—C(34)	1.530(2)
C(4)—C(5)	1.353(6)	C(30)—C(31)	1.525(3)
C(5)—C(6)	1.383(8)	C(31)—C(32)	1.510(3)
C(6)—C(7)	1.380(5)	C(32)—C(33)	1.513(4)
C(7)—C(7A)	1.396(4)	C(33)—C(34)	1.530(3)
C(9)—C(10)	1.523(3)		
P(1)-Rh(1)-P(2)	85.9(1)	P(2)-Rh(1)-C(3A)	143.8(1)
P(1)-Rh(1)-C(1)	164.2(1)	C(1)-Rh(1)-C(3A)	59.1(1)
P(2)-Rh(1)-C(1)	107.6(1)	C(2)-Rh(1)-C(3A)	58.8(1)
P(1)-Rh(1)-C(2)	128.3(1)	C(3)-Rh(1)-C(3A)	35.6(1)
P(2)-Rh(1)-C(2)	132.0(1)	P(1)-Rh(1)-C(7A)	145.1(1)
C(1)-Rh(1)-C(2)	36.1(1)	P(2)-Rh(1)-C(7A)	114.6(1)
P(1)-Rh(1)-C(3)	104.9(1)	C(1)-Rh(1)-C(7A)	35.8(1)
P(2)-Rh(1)-C(3)	168.0(1)	C(2)-Rh(1)-C(7A)	58.6(1)
C(1)-Rh(1)-C(3)	60.9(1)	C(3)-Rh(1)-C(7A)	59.0(1)
C(2)-Rh(1)-C(3)	36.4(1)	C(3A)-Rh(1)-C(7A)	34.2(1)
P(1)-Rh(1)-C(3A)	114.3(1)		

those observed for typical uncoordinated C=C distances (cf. 1.335 Å) (6*c*). The geometries about the ethylene ligands are typical for $d\pi$–π^* metal–alkene back-donation interactions (10).

© 1999 NRC Canada

Table 3. Atomic coordinates ($\times 10^4$) and equivalent isotropic displacement coefficients for (η^5-1-CH_3-C_9H_6)Rh(η^2-C_2H_4)(PCy_3) (**1**).

	x	*y*	*z*	*U* (eq)
Molecule 1				
Rh(1)	6686.8(5)	1255.5(1)	1227.0(2)	34.4(2)
P(1)	5164(2)	1465.7(5)	1669.9(5)	30.8(5)
C(1)	7866(6)	995(2)	707(2)	48(3)
C(2)	6837(7)	1131(2)	487(2)	54(3)
C(3)	5865(7)	903(2)	643(2)	51(3)
C(3a)	6340(6)	571(2)	916(2)	49(3)
C(4)	5807(9)	224(2)	1108(3)	66(4)
C(5)	6494(9)	–38(3)	1350(3)	81(4)
C(6)	7690(9)	37(3)	1406(3)	73(4)
C(7)	8244(9)	364(2)	1218(3)	63(3)
C(7a)	7553(7)	633(2)	955(2)	47(3)
C(8)	9110(8)	1121(4)	630(4)	93(5)
C(9)	7828(6)	1741(2)	1367(3)	54(3)
C(10)	8001(6)	1440(2)	1689(3)	52(3)
C(11)	4781(5)	1104(2)	2135(2)	34(2)
C(12)	5877(6)	989(2)	2403(2)	45(3)
C(13)	5621(7)	682(2)	2783(2)	55(3)
C(14)	5075(7)	302(2)	2588(3)	59(3)
C(15)	3949(7)	411(2)	2338(3)	59(3)
C(16)	4171(6)	723(2)	1961(2)	46(3)
C(17)	3747(5)	1517(2)	1363(2)	32(2)
C(18)	3821(6)	1759(2)	917(2)	42(3)
C(19)	2680(6)	1712(2)	645(2)	47(3)
C(20)	1609(7)	1834(2)	921(2)	55(3)
C(21)	1537(6)	1606(2)	1368(2)	50(3)
C(22)	2675(5)	1655(2)	1644(2)	41(3)
C(23)	5438(6)	1950(2)	1985(2)	37(2)
C(24)	5322(6)	2327(2)	1684(2)	45(3)
C(25)	5831(9)	2702(2)	1919(3)	76(4)
C(26)	5224(9)	2771(2)	2364(3)	81(4)
C(27)	5269(8)	2401(2)	2666(2)	70(4)
C(28)	4787(8)	2024(2)	2430(2)	53(3)
Molecule 2				
Rh(1)B	1698.1(5)	3554.3(1)	993.3(2)	33.6(2)
P(1)B	3103(2)	4020.8(5)	1150.4(5)	32.7(6)
C(1)B	616(7)	2976(2)	1067(3)	49(3)
C(2)B	1528(7)	2985(2)	1399(3)	54(3)
C(3)B	2633(7)	2990(2)	1178(3)	45(3)
C(3a)B	2416(7)	2916(2)	701(3)	46(3)
C(4)B	3167(9)	2835(2)	331(3)	66(4)
C(5)B	2684(10)	2768(2)	–89(3)	77(4)
C(6)B	1472(10)	2783(2)	–163(3)	77(4)
C(7)B	719(9)	2859(2)	189(3)	61(4)
C(7a)B	1178(7)	2918(2)	631(3)	44(3)
C(8)B	–674(7)	2948(3)	1165(4)	78(4)
C(9)B	497(6)	3938(2)	642(3)	53(3)
C(10)B	259(6)	3949(2)	1107(3)	52(3)
C(11)B	2847(6)	4546(2)	923(2)	37(2)
C(12)B	3037(7)	4576(2)	409(2)	54(3)
C(13)B	2545(10)	4969(2)	226(3)	76(4)
C(14)B	3150(11)	5330(2)	444(3)	85(5)
C(15)B	3041(8)	5308(2)	966(2)	62(3)
C(16)B	3485(7)	4905(2)	1151(2)	52(3)
C(17)B	3277(6)	4107(2)	1775(2)	36(2)
C(18)B	2118(6)	4253(2)	1989(2)	45(3)
C(19)B	2272(7)	4338(2)	2498(2)	57(3)

© 1999 NRC Canada

Table 3 (*continued*).

	x	*y*	*z*	*U* (eq)
Molecule 1				
C(20)B	2739(8)	3973(2)	2749(2)	66(3)
C(21)B	3862(8)	3820(3)	2543(2)	65(3)
C(22)B	3731(7)	3736(2)	2033(2)	53(3)
C(23)B	4603(5)	3860(2)	983(2)	42(2)
C(24)B	4716(6)	3728(3)	497(2)	61(3)
C(25)B	5872(6)	3495(3)	417(3)	66(3)
C(26)B	6926(6)	3759(3)	545(3)	74(4)
C(27)B	6848(7)	3898(3)	1026(3)	69(3)
C(28)B	5665(5)	4123(2)	1116(2)	50(3)

Table 4. Atomic coordinates (× 10^4) and equivalent isotropic displacement coefficients for (η^5-1-CH_3-C_9H_6)Rh(dcpe) (**2**).

	x	*y*	*z*	*U* (eq)
Rh(1)	941.0(2)	768.7(2)	2478.9(1)	29.67(5)
P(1)	2848.5(5)	566.7(5)	1937.2(3)	30.7(2)
P(2)	2463.8(5)	483.5(5)	3470.2(3)	28.5(1)
C(1)	–1192(2)	1353(2)	2822(1)	46.4(8)
C(2)	–851(2)	2149(3)	2357(2)	53.9(9)
C(3)	–844(2)	1291(3)	1655(1)	57(1)
C(3A)	–1416(2)	–70(3)	1630(1)	50.4(8)
C(4)	–1767(3)	–1291(4)	1064(2)	81(1)
C(5)	–2291(4)	–2432(4)	1222(3)	111(2)
C(6)	–2483(3)	–2428(3)	1928(3)	101(2)
C(7)	–2153(2)	–1244(3)	2504(2)	70(1)
C(7A)	–1617(2)	–42(2)	2361(1)	43.1(8)
C(8)	–1441(3)	1883(4)	3597(2)	77(1)
C(9)	4423(2)	25(2)	2522(1)	37.3(7)
C(10)	4385(2)	527(2)	3345(1)	36.3(7)
C(11)	2629(2)	–706(2)	1020(1)	36.0(7)
C(12)	4032(3)	–925(2)	722(1)	50.2(9)
C(13)	3721(3)	–1905(3)	–57(1)	58(1)
C(14)	2912(3)	–3261(3)	–88(2)	68(1)
C(15)	1547(3)	–3064(3)	230(1)	62(1)
C(16)	1880(3)	–2093(2)	1011(1)	45.8(8)
C(17)	3656(2)	2118(2)	1735(1)	36.5(7)
C(18)	2500(3)	2758(3)	1285(2)	66(1)
C(19)	3162(3)	3977(3)	1065(2)	73(1)
C(20)	4033(4)	5031(3)	1743(2)	75(1)
C(21)	5183(4)	4393(3)	2182(2)	88(1)
C(22)	4496(4)	3187(3)	2411(2)	77(1)
C(23)	2602(2)	1797(2)	4368(1)	32.2(6)
C(24)	2777(2)	3253(2)	4274(1)	41.9(7)
C(25)	2698(3)	4314(2)	4985(1)	52.5(9)
C(26)	3816(3)	4160(2)	5654(1)	62(1)
C(27)	3689(3)	2712(2)	5746(1)	50.4(8)
C(28)	3772(2)	1652(2)	5028(1)	42.5(7)
C(29)	2210(2)	–1148(2)	3744(1)	32.2(6)
C(30)	964(2)	–1173(2)	4161(1)	40.3(7)
C(31)	747(3)	–2540(2)	4351(1)	49.7(9)
C(32)	450(3)	–3732(2)	3661(1)	56(1)
C(33)	1679(3)	–3740(2)	3245(1)	56(1)
C(34)	1934(3)	–2374(2)	3056(1)	44.8(8)

Although the substituted indenyl ligand is bound to the rhodium centre in an η^5-fashion, there is a certain amount of distortion towards an η^3-bonding mode. Both rhodium atoms have three short Rh—C distances (average = 2.235(7) Å)

© 1999 NRC Canada

Fig 2. Complexes (η^5-1-CH_3-C_9H_6)Rh(η^2-C_2H_4)(PCy_3) (**1**) and (η^5-1-CH_3-C_9H_6)Rh(dcpe) (**2**).

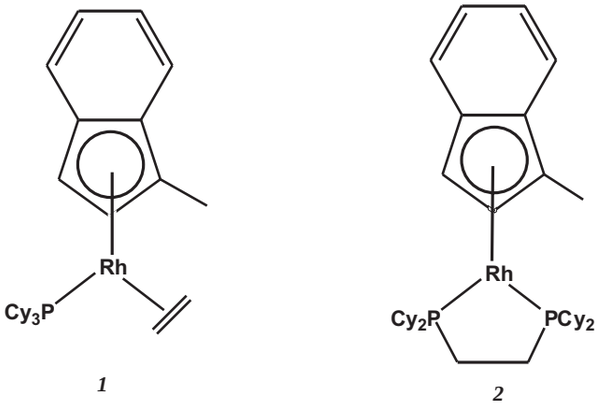

1 *2*

and two longer Rh—C distances (average = 2.427(7) Å); the latter bonds involving the bridge head atoms C3a, C7a. The slip parameter (Δ = *d*(average Rh—C3a,7a) – *d*(average Rh—C1,3)) was calculated to be 0.198(7) Å for molecule A and 0.176(7) Å for molecule B, giving an average value of 0.187(7) Å. Average values for the hinge angle (HA = angle between normals to the least-squares planes defined by C1, C2, C3 and C1, C7a, C3a, C3) and fold angle (FA = angle between normals to the least-squares planes defined by C1, C2, C3 and C3a, C4, C5, C7, C7a) are 8.9 and 10.5°, respectively. Such distortions towards η^3-allyl systems are well-established for d^8-ML_2 compounds (1–6). The degree of distortion in the solid state has been correlated with the electronic nature of the ML_2 fragment where, in general, the greater the electron-donating ability of the fragment, the higher the degree of slip-fold distortion (6*d*).

A fourth type of distortion is also present in **1** as the RhL_2 fragment is skewed slightly towards one side of the five-membered ring of the indenyl ligand. This skew-distortion has been reported recently for analogous nickel indenyl (6*h*) and cyclopentadienyl systems (11). This distortion in **1** appears to be a function of the disposition of the bulky cyclohexyl groups of the phosphine ligand. In molecule A one cyclohexyl ring lies roughly parallel with the Rh—C2 bond under the cyclopentadienyl fragment of the indenyl ring, while in molecule B this ring is rotated approximately 180° and lies under the six-membered ring of the indenyl group. As a result, the Rh—C1 bond (2.206(7) Å) in molecule A is slightly shorter than the corresponding Rh—C3 bond (2.272(7) Å), whereas in molecule B the Rh—C1(b) bond (2.275(7) Å) is somewhat longer than the Rh—C3(b) bond (2.207(7) Å).

Slip-fold distortions are also present in bis(phosphine) complex **2**. Selected bond distances and angles are given in Table 2, and a view of **2** is provided in Fig. 4. The bonding of the RhP_2 fragment is again unsymmetric with respect to the indenyl ligand, containing three short Rh—C distances (average = 2.249(2) Å) and two long Rh—C distances (average = 2.428(2) Å). The slip parameter was calculated to be 0.179(2) Å whereas values for the hinge angle and fold angle are 9.2° and 9.5°, respectively. Interestingly, the degree of slip-fold distortion in **2** is approximately equal to that observed in **1**, where the effect of replacing the second ethylene ligand with a more basic phosphine moiety appears to be minimal at least in the solid state. A pronounced skew-distortion in **2** attests to the influence the unsymmetrical indenyl ligand has on the rhodium–carbon bond distances.

Fig 3. Molecular structure of the two molecules of **1** with the hydrogen atoms omitted for clarity.

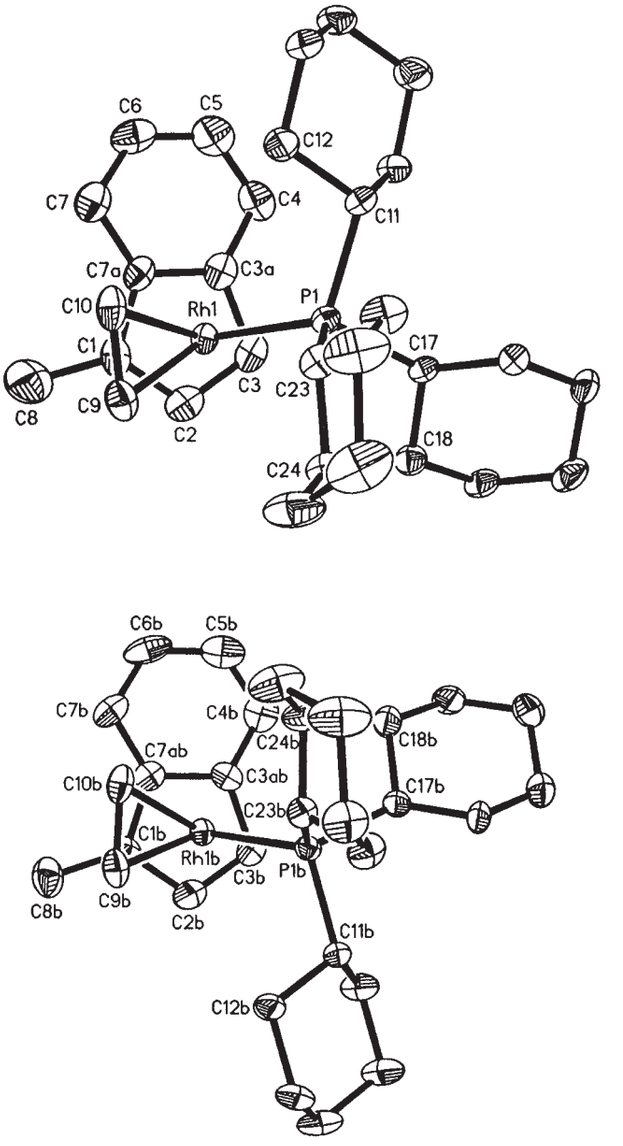

NMR spectroscopic studies

It has been reported that two separate resonances are observed in the ^{1}H NMR spectra of d^8-indenyl metal ethylene complexes for the inner and outer protons of the ethylene moiety (6*c*, *e*). The inner ethylene protons are shielded due to their proximity to the overlying indenyl group and are reported at approximately 0.5–2.0 ppm. Conversely, the outer protons are deshielded and resonate at approximately 2.5–3.0 ppm. Unfortunately, unequivocal assignment of the

© 1999 NRC Canada

Table 5. $^{13}C\{^1H\}$ NMR data for the indenyl ring in complexes **1–3**[a].

Complex	C_1	C_2	C_3	C_{3a}, C_{7a}	C_4, C_7	C_5, C_6
1	83.1	95.3	72.9	114.4, 118.3	114.4, 119.7	120.0, 122.5
2	84.4	96.2	65.2	117.2, 118.8	115.4, 117.0	118.9, 119.0
3[b]	88.8	93.3	76.7	112.1, 112.9	117.9, 119.9	123.6, 127.7

[a]Spectra were recorded at 63 and 75 MHz, and chemical shifts are referenced to residual protiated solvents.
[b]Reference 6*b*.

Fig 4. Molecular structure of **2** with hydrogen atoms omitted for clarity.

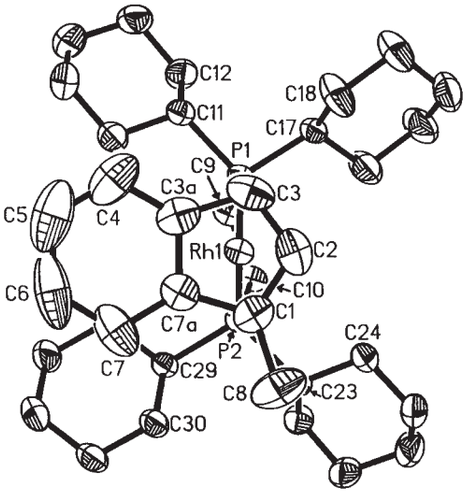

inner protons is complicated by nearby resonances due to the cyclohexyl groups of the phosphine ligand. For this reason, energy barriers associated with ethylene rotation could not be obtained.

While slippage of the indenyl ring from planar η^5 towards allylic η^3-bonding is observed in the solid state, this distortion is also thought to persist to some extent in solution (1–6, 12). Indeed, $^{13}C\{^1H\}$ NMR spectroscopy can be used as a diagnostic tool to measure the degree of hapticity of the indenyl ligand in solution (4, 6*b*). The chemical shifts of the indenyl ring junction carbons are compared to those for sodium indenide, a standard for planar η^5 bonding (6*b*, 12). The quaternary carbon (C3a, C7a) chemical shifts for **1** are observed at δ 114.5 and 118.3 ppm and are consistent with a slight distortion towards the η^3 form in solution. Likewise, chemical shifts observed for the analogous ring-junction carbons in **2** at δ 117.2 and 118.8 ppm also suggest a certain degree of distortion. For comparison, in the complex $(\eta^3\text{-}C_9H_7)Ir(PMe_2Ph)_3$, which contains a true η^3-indenyl ligand, these carbon resonances are observed at δ 156.7 ppm (13). $^{13}C\{^1H\}$ NMR data pertaining to the indenyl ring for complexes **1** and **2** are provided in Table 5, and are compared to values for the bis(ethylene) complex $(\eta^5\text{-}1\text{-}CH_3C_9H_6)Rh(\eta^2\text{-}C_2H_4)_2$ (**3**). It is interesting to note that addition of a second phosphine moiety has little effect on the carbon chemical shifts as evidenced by similar resonances observed for both the mixed phosphine–ethylene complex **1** and the bis(phosphine) complex **2**. As expected, however, a significant change in chemical shift is observed on going from the strong π-accepting bis(ethylene) complex to the σ-donating phosphine-containing products. The chemical shift difference between indenyl C2 and C3 nuclei is yet another parameter that has been used to measure the degree of distortion within metal–indenyl complexes (4, 6*f*).

Energy barriers to indenyl ring rotation

The 121 MHz $^{31}P\{^1H\}$ spectrum of **1** at room temperature exhibits a doublet (J_{P-Rh} = 209 Hz) at 53.9 ppm split by ^{103}Rh (I = 1/2, 100% abundant). Variable temperature $^{31}P\{^1H\}$ NMR measurements have allowed an evaluation of the barrier to RhL_2 rotation about the indenyl–rhodium axis, where incorporation of the methyl substituent at Cl of the indenyl ligand breaks the ground-state *Cs* symmetry of the molecule. The low temperature limiting spectrum obtained at –100°C displays a pair of doublets with an intensity ratio of approximately 1:2 (δ 54.9 and 53.0 ppm with J_{P-Rh} = 209 Hz). Only minor changes in rotamer populations were observed over the temperature range examined (i.e., 40:60 at –125°C and 44:56 at –75°C). Taking this into account, along with a slight temperature dependence of chemical shifts, a $\Delta G^{\ddagger}_{193}$ value of 8.6 ± 0.05 kcal mol^{-1} has been calculated for indenyl ring rotation. An Eyring plot for the kinetic data for **1** and a linear least-squares analysis of these data gives values of $\Delta H^{\ddagger}$ = 10.5 ± 0.8 kcal mol^{-1} and $\Delta S^{\ddagger}$ = 9.7 ± 4.4 cal mol^{-1} K^{-1}.

It seemed possible that the dynamic process could have involved a hindered rotation about the Rh—P bond, resulting in an exchange of the two distinct species observed in the solid state. Likewise, a dynamic process involving dissociation and flipping the indenyl ring by 180° would also account for the formation of two rotamers. However, the data are completely consistent with the more reasonable explanation of hindered indenyl rotation as observed in all other d^8-ML_2 complexes of 1-Me-indene. Indeed, in a similar study, a barrier of $\Delta G^{\ddagger}_{190}$ = 9.7 ± 0.4 kcal mol^{-1} was measured for rotation about the metal-ring axis in $(\eta^5\text{-}C_9H_7)Rh(\eta\text{-}C_2H_4)_2$ (6*c*). It is interesting to note that a higher energy process ($\Delta G^{\ddagger}_{240}$ = 10.4 ± 0.5 kcal mol^{-1}) was observed in this complex and attributed to an olefin rotation process. As mentioned previously, obstruction of the ethylene resonances in the ^1H NMR by overlapping cyclohexyl resonances from the phosphine ligand precluded similar measurements for complex **1**.

The room temperature $^{31}P\{^1H\}$ spectrum of **2** consists of a doublet at 93.7 ppm (J_{P-Rh} = 217 Hz). The corresponding low-temperature spectrum exhibits two doublet of doublets at δ 98.0 and 89.3 ppm with J_{P-Rh} = 217 Hz arising from the ABX spin systems. While replacement of one of the ethylene moieties with a basic phosphine ligand seems to have little effect on the barrier to indenyl ring rotation, higher energy barriers are observed for bis(phosphine) complexes. Thus, the free energy of activation for ring rotation in **2** was

© 1999 NRC Canada

calculated to be $\Delta G^{\ddagger}_{253} = 10.8 \pm 0.2$ kcal mol^{-1}. This value is comparable to energies observed for the analogous bis(phosphine) complex (η^5-1-CH_3-C_9H_6)Rh(PMe_3)$_2$ ($\Delta G^{\ddagger}_{253} = 11.2 \pm 0.03$ kcal mol^{-1}) (6*d*) and bis(carbonyl) complex (η^5-1-CH_3-C_9H_6)Rh(CO)$_2$ ($\Delta G^{\ddagger}_{213} = 11.27 \pm 0.09$ kcal mol^{-1}) (6*e*). Barriers of approximately 11 kcal mol^{-1} have also been observed in bimetallic Rh–Cr complexes (6*a*, *f*). Although it is difficult to assess the factors governing these energy barriers, it is of interest to note that much lower barriers are obtained for complexes containing ancillary ethylene ligands. Further work is therefore required to gain a better understanding of the factors effecting the barrier to indenyl ring rotation in these systems.

Conclusions

We have prepared the mixed phosphine–ethylene complex (η^5-1-CH_3-C_9H_6)Rh(η-C_2H_4)(PCy_3) (**1**) and bis(phosphine) complex (η^5-1-CH_3-C_9H_6)Rh(dcpe) (**2**) in high yields. Single crystal X-ray diffraction and $^{13}C\{^1H\}$ NMR spectroscopic studies have been used to demonstrate that complexes **1** and **2** show a similar degree of slip-fold distortion in both the solid and solution states, towards an η^3-allylic bonding mode with respect to the indenyl ligand. Variable temperature $^{31}P\{^1H\}$ NMR studies were conducted on both complexes as well. From this data, energy barriers associated with rotation about the indenyl ring – rhodium axis were calculated to be approximately 8.5 and 10.8 kcal mol^{-1} for complexes **1** and **2**, respectively. While $\Delta G^{\ddagger}$ does not appear to be correlated with the degree of slip-fold distortion, lower energies are observed for indenyl rhodium complexes containing ethylene ligands.

Acknowledgements

T.B.M. acknowledges support from the Petroleum Research Fund, administered by the American Chemical Society. T.B.M. and S.A.W. also thank the Natural Sciences and Engineering Research Council of Canada and Johnson Matthey Ltd. for a loan of $RhCl_3 \cdot 3H_2O$. We thank Jan Venne (U. of W.) and Christopher M. Vogels (MtA) for technical assistance and Dr. R. Tom Baker (Los Alamos National Laboratories) for helpful discussions.

References

1. (*a*) R. Cramer, J.B. Kline, and J.D. Roberts. J. Am. Chem. Soc. **91**, 2519 (1969); (*b*) H. Eshtiagh-Hosseini and J.F. Nixon. J. Less Common Met. **61**, 107 (1978); (*c*) A. Borrini, P. Diversi, G. Ingrosso, A. Lucherini, and G. Serra. J. Mol. Catal. **30**, 181 (1985); (*d*) J.M. O'Connor and C.P. Casey. Chem Rev. **87**, 307 (1987), and refs. therein for early metal indenyl chemistry.
2. (*a*) M.E. Rerek and F. Basolo. Organometallics, **3**, 740 (1984); (*b*) J. Am. Chem. Soc. **106**, 5908 (1984).
3. (*a*) A. Habib, R.S. Tanke, E.M. Holtz, and R.H. Crabtree. Organometallics, **8**, 1225 (1989); (*b*) J.S. Merola and R.T. Kacmarcik. Organometallics, **8**, 778 (1989); (*c*) L.P. Szajek, R.J. Lawson, and J.R. Shapley. Organometallics, **10**, 357 (1991); (*d*) T. Foo and R.G. Bergman. Organometallics, **11**, 1811 (1992); (*e*) F. Morandini, G. Pilloni, G. Consiglio, A. Sironi, and M. Moret. Organometallics, **12**, 3495 (1993); (*f*) D. Rau and U. Behrens. J. Organomet. Chem. **454**, 151 (1993); (*g*) Z. Zhou, C. Jablonski, and J. Bridson. J. Organomet. Chem. **461**, 215 (1993); (*h*) M. Bassetti, L. Mannina, and D. Monti. Organometallics, **13**, 3293 (1994); (*i*) E. Hauptman, S. Sabo-Etienne, P.S. White, M. Brookhart, J.M. Garner, P.J. Fagan, and J.C. Calabrese. J. Am. Chem. Soc. **116**, 8038 (1994); (*j*) T. Le Husebo and C. M. Jensen. Organometallics, **14**, 1087 (1995); (*k*) M. Bassetti, P. Casellato, M.P. Gamasa, J. Gimeno, C. González-Bernardo, and B. Martín-Vaca. Organometallics, **16**, 5470 (1997); (*l*) M. Stradiotto, D.W. Hughes, A.D. Bain, M.A. Brook, and M.J. McGlinchey. Organometallics, **16**, 5563 (1997); (*m*) M.C. Comstock and J. R. Shapley. Organometallics, **16**, 4816 (1997); (*n*) R. Vollmerhaus, F. Bélanger-Gariépy, and D. Zargarian. Organometallics, **16**, 4762 (1997); (*o*) S-M. Yang, M.C-W. Chan, S-M. Peng, and C-M. Che. Organometallics, **17**, 151 (1998); (*p*) C.E. Garrett and G.C. Fu. J. Org. Chem. **63**, 1370 (1998); (*q*) M.J. Calhorda, C.A. Gamelas, I.S. Conçalves, E. Herdtweck, C.C. Romão, and L.F. Veiros. Organometallics, **17**, 2597 (1998).
4. (*a*) A. Ceccon, A. Gambaro, S. Santi, G. Valle, and A. Venzo. J. Chem. Soc. Chem. Commun. 51 (1989); (*b*) A. Ceccon, C.J. Elsevier, J.M. Ernsting, A. Gambaro, S. Santi, and A. Venzo. Inorg. Chim. Acta, **204**, 15 (1993); (*c*) C. Bonifaci, A. Ceccon, A. Gambaro, P. Ganis, L. Mantovani, and S. Santi. J. Organomet. Chem. **475**, 267 (1994); (*d*) C. Bonifaci, A. Ceccon, A. Gambaro, P. Ganis, S. Santi, G. Valle, and A. Venzo. J. Organomet. Chem. **492**, 35 (1995); (*e*) C. Bonifaci, A. Ceccon, A. Gambaro, P. Ganis, S. Santi, and A. Venzo. Organometallics, **14**, 2430 (1995); (*f*) C. Bonifaci, G. Carta, A. Ceccon, A. Gambaro, S. Santi, P. Ganis, and A. Venzo. Organometallics, **15**, 1630 (1996); (*g*) L. Mantovani, A. Ceccon, A. Gambaro, S. Santi, P. Ganis, and A. Venzo. Organometallics, **16**, 2682 (1997); (*h*) C. Amatore, A. Ceccon, S. Santi, and J.-N. Verpeaux. Chem. Eur. J. **3**, 279 (1997); (*i*) P. Cecchetto, A. Ceccon, A. Gambaro, S. Santi, P. Ganis, R. Gobetto, G. Valle, and A. Venzo. Organometallics, **17**, 752 (1998).
5. (*a*) A.K. Kakkar, N.J. Taylor, and T.B. Marder. Organometallics, **8**, 1765 (1989); (*b*) S.A. Westcott, A.K. Kakkar, G. Stringer, N.J. Taylor, and T.B. Marder. J. Organomet. Chem. **394**, 777 (1990), and refs. therein; (*c*) A.K. Kakkar, N.J. Taylor, T.B. Marder, J.K. Shen, N. Hallinan, and F. Basolo. Inorg. Chim. Acta, **198**–**200**, 219 (1992); (*d*) D. O'Hare, J.C. Green, T.B. Marder, S. Collins, G. Stringer, A.K. Kakkar, N. Kaltsoyannis, A. Kuhn, R. Lewis, C. Mehnert, P. Scott, and S. Pugh. Organometallics, **11**, 48 (1992); (*e*) T.M. Frankcom, J.C. Green, A. Nagy, A.K. Kakkar, and T.B. Marder. Organometallics, **12**, 3688 (1993); (*f*) S.A. Westcott, G. Stringer, S. Anderson, N.J. Taylor, and T.B. Marder. Inorg. Chem. **33**, 4589 (1994); (*g*) A.K. Kakkar, G. Stringer, N.J. Taylor, and T.B. Marder. Can. J. Chem. **73**, 981 (1995).
6. (*a*) R.D. Barr, M. Green, T.B. Marder, and F.G.A. Stone. J. Chem. Soc. Dalton Trans. 1261 (1984); (*b*) R.T. Baker and T.H. Tulip. Organometallics, **5**, 839 (1986); (*c*) M. Mlekuz, P. Bougeard, B.G. Sayer, M.J. McGlinchey, C.A. Rodger, M.R. Churchill, J.W. Ziller, S-K. Kang, and T.A. Albright. Organometallics, **5**, 1656 (1986); (*d*) T.B. Marder, J.C. Calabrese, D.C. Roe, and T.H. Tulip. Organometallics, **6**, 2012 (1987); (*e*) A.K. Kakkar, N.J. Taylor, J.C. Calabrese, W.A. Nugent, D.C. Roe, E.A. Connaway, and T.B. Marder. J. Chem. Soc. Chem. Commun. 990 (1989); (*f*) A. Ceccon, A. Gambaro, S. Santi, A. Venzo. J. Mol. Catal. **69**, L1 (1991); (*g*) L.P. Szajek, and J.R. Shapley. Organometallics, **13**, 1395 (1994); (*h*) T.A. Huber, M. Bayrakdarian, S. Dion, I. Dubuc, F.

© 1999 NRC Canada

Bélanger-Gariépy, and D. Zargarian. Organometallics, **16**, 5811 (1997).
7. (*a*) T.A. Albright and R. Hoffmann. Chem. Ber. **111**, 1578 (1978); (*b*) D.M.P. Mingos, M.I. Forsyth, and A.J. Welch. J. Chem. Soc. Dalton Trans. 1363 (1978).
8. D.T. Cromer and J.T. Waber. International Tables for X-ray Crystallography. Vol. 4. Kynoch Press, Birmingham. 1974. Table 2.2B.
9. P. Caddy, M. Green, L.E. Smart, and N. White. J. Chem. Soc. Chem. Commun. 839 (1978).
10. J. Chatt and L.A. Duncanson. J. Chem. Soc. 2939 (1953).
11. P.L. Holland, M.E. Smith, R.A. Anderson, and R.G. Bergman. J. Am. Chem. Soc. **119**, 12 815 (1997).
12. F.H. Köhler. Chem. Ber. **107**, 570 (1974).
13. J.S. Merola, R.T. Kacmarcik, and D. Van Engen. J. Am. Chem. Soc. **108**, 329 (1986).

© 1999 NRC Canada

Synthesis of 5-phenyl-10-methyl-7*H*-pyrimido[4,5-*f*][1,2,4]triazolo[4,3-*a*][1,4]diazepine and its evaluation as an anticonvulsant agent

Oludotun A. Phillips, K.S. Keshava Murthy, Charles Y. Fiakpui, and Edward E. Knaus

Abstract: The homolytic benzoylation (benzoyl radical) of 5-*tert*-butylcarbonylaminopyrimidine (**6**, 1 equiv.) in the presence of benzaldehyde (3 equiv.), water, sulfuric acid, and acetic acid, upon treatment with $FeSO_4 \cdot 7H_2O$ (3 equiv.) and 70% *t*-BuOOH (3 equiv.) at 5–10°C for 10 min afforded a mixture of 4-benzoyl-5-*tert*-butylcarbonylaminopyrimidine (**7**, 23%), 4,6-dibenzoyl-5-*tert*-butylcarbonylaminopyrimidine (**8**, 44%), and 4-benzoyl-5-*tert*-butylcarbonylamino-6-methylpyrimidine (**9**, 10%). When a similar reaction was performed using 1 equiv. each of PhCHO, $FeSO_4 \cdot 7H_2O$, and *t*-BuOOH, to prevent formation of the 4,6-dibenzoyl product **8**, the monobenzoyl (**7**, 38%) and 4-benzoyl-6-methyl (**9**, 6%) products were obtained. A similar homolytic benzoylation of 5-bromopyrimidine (**10**) using 1.5 equiv. of reagents to generate the benzoyl radical afforded 4-benzoyl-5-bromopyrimidine (**11**, 61%) as the predominant product. Elaboration of **11** via a six-step reaction sequence afforded 2-hydrazino-5-phenyl-3*H*-pyrimido[5,4-*e*][1,4]diazepine (**17**) in 5.2% overall yield. The acid-catalyzed reaction of **17** with triethyl orthoacetate gave the title compound 5-phenyl-10-methyl-7*H*-pyrimido[4,5-*f*][1,2,4]triazolo[4,3-*a*][1,4]diazepine (**18**, 62%). The triazolo compound **18** was more potent than valproic acid (Depakene®) in both the subcutaneous metrazol (scMet) and maximal electroshock (MES) anticonvulsant screens, and more potent than clonazepam in the MES anticonvulsant screen but less potent than clonazepam in the scMet anticonvulsant screen.

Key words: homolytic benzoylation, pyrimidines, pyrimidodiazepines, anticonvulsants.

Résumé : La benzoylation homolytique (radical benzoyle) de la 5-*tert*-butylcarbonylaminopyrimidine (**6**, 1 équiv.), en présence de benzaldéhyde (3 équiv.), d'eau, d'acide sulfurique et d'acide acétique, par réaction avec du $FeSO_4 \cdot 7H_2O$ (3 équiv.) et du *t*-BuOOH à 70% (3 équiv.) à 5–10°C pendant 10 min conduit à un mélange de 4-benzoyl-5-*tert*-butylaminopyrimidine (**7**, 23%), de 4,6-dibenzoyl-5-*tert*-butylaminopyrimidine (**8**, 44%) et de 4-benzoyl-5-*tert*-butylamino-6-méthylpyrimidine (**9**, 10%). Quand on effectue la même réaction en utilisant un équivalent chacun de PhCHO, $FeSO_4 \cdot 7H_2O$ et *t*-BuOOH pour empêcher la formation du produit 4,6-dibenzoylé **8**, on obtient les produits monobenzoyle (**7**, 38%) et 4-benzoyl-6-méthyle (**9**, 6%). Une benzoylation homolytique semblable de la 5-bromopyrimidine (**10**) en utilisant 1,5 équiv. des réactifs pour générer le radical benzoyle conduit à la formation de la 4-benzoyl-5-bromopyrimidine (**11**, 61%) comme produit principal. Une séquence de synthèse en six étapes à partir du produit **11** permet d'obtenir la 2-hydrazino-5-phényl-3*H*-pyrimido[5,4-*e*][1,4]diazépine (**17**) avec un rendement global de 5,2%. La réaction acidocatalysée de **17** avec l'orthoacétate de triéthyle fournit le composé mentionné dans le titre, la 5-phényl-10-méthyl-7*H*-pyrimido[4,5-*f*][1,2,4]triazolo[4,3-*a*][1,4]diazépine (**18**, 62%). Le composé triazolo **18** est plus actif que l'acide valproïque (Depakenc®) dans les épreuves sous-cutanées métrazel (« scMet ») que dans celles anticonvulsantes avec électrochocs maximaux (« MES »); comparé au clonazépame, il est plus actif dans les épreuves anticonvulsantes MES, mais moins actif dans l'épreuve anticonvulsante scMet.

Mots clés : benzoylation homolytique, pyrimidines, pyrimidodiazépines, anticonvulsants.

[Traduit par la Rédaction]

Introduction

Structure–activity studies for the benzo[1,4]diazepin-2-one class of compounds (**1**) indicated that an electronegative X-substituent at C-7 is an essential requirement for anticonvulsant, sedative, hypnotic, and muscle relaxant activities (1–3). In earlier studies, we showed that the 1,3-dihydro-5-phenyl-2*H*-pyrido[3,4-*e*][1,4]diazepin-2-one (**2**)

Received July 20, 1998.

O.A. Phillips and C.Y. Fiakpui. SynPhar Laboratories Inc., 4290–92A Street, Edmonton, AB T6E 5V2, Canada.
K.S.K. Murthy. Brantford Chemicals Inc., 34 Spalding Drive, Brantford, ON N3T 6B8, Canada.
E.E. Knaus.[1] Faculty of Pharmacy and Pharmaceutical Sciences, University of Alberta, Edmonton, AB T6G 2N8, Canada.

[1]Author to whom correspondence may be addressed. Telephone: (780) 492–5993. Fax: (780) 492–1217.
e-mail: eknaus@pharmacy.ualberta.ca

© 1999 NRC Canada

Fig. 1. A comparison of the inductive and resonance effects exhibited by the chlorophenyl substituent in chlorobenzene (**1**) and the ring nitrogens in pyrimidine (**15**).

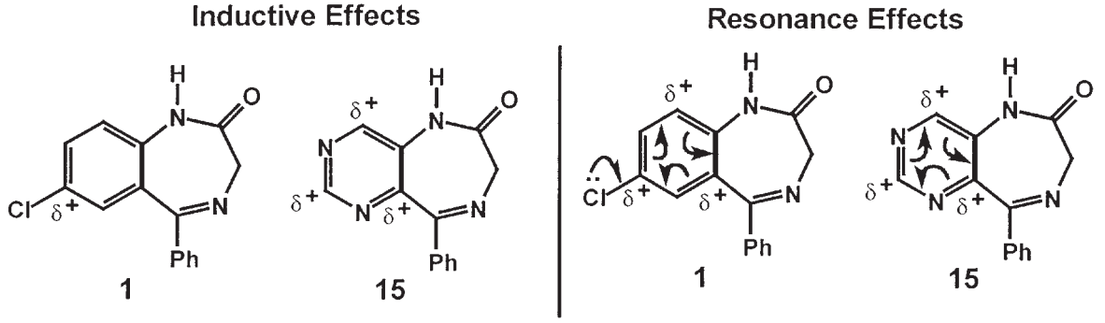

and 1,3-dihydro-5-phenyl-2*H*-pyrido[3,2-*e*][1,4]diazepin-2-one (**3**) classes of compounds, which are electronically analogous to 7-chloro(nitro)-benzo[1,4]diazepin-2-one (**1**), exhibited anticonvulsant activity (4, 5). It was therefore of interest to extend these structure–activity relationships to include the 1,3-dihydro-5-phenyl-2*H*-pyrimido[5,4-*e*][1,4]diazepin-2-one (**15**) class of compounds, which also are electronically analogous to the chlorophenyl analog (**1**, X = Cl), since they possess similar electron-density profiles at equivalent positions. When the inductive and resonance effects of a chloro substituent (**1**, X = Cl) and the pyrimido ring nitrogen atoms of the pyrimido compound (**15**) are compared, the resulting electron densities are qualitatively similar for the chlorophenyl and pyrimido ring systems at equivalent positions as illustrated in Fig. 1. This study was therefore initiated to determine whether the chlorophenyl and pyrimido ring systems are bioisosteric with respect to anticonvulsant activities, since these ring systems are similar in size and shape (phenyl and pyrimido), and they possess similar electron-density profiles at equivalent positions. Furthermore, the pyrimido nitrogen atom free-electron pairs have the potential to act as H-bond acceptors, which may provide a receptor binding interaction that is not possible with a chlorophenyl ring. Accordingly, it is plausible that the chlorophenyl (**1**) and pyrimido (**15**) classes of compounds could interact with the same receptor site(s) to elicit anticonvulsant activities.

Chemistry

In earlier studies, we developed synthetic methodologies, involving *ortho*-directed lithiation of 3-*tert*-butylcarbonylaminopyridine, that were applicable to the preparation of 3-*tert*-butylcarbonylamino-4-benzoylpyridines (6, 7). In contrast, all attempts to prepare 4-benzoyl-5-*tert*-butylcarbonylaminopyrimidine (**7**) using a similar *ortho*-directed lithiation of 5-*tert*-butylcarbonylaminopyrimidine (**6**), prepared by the Pd/C catalyzed dechlorination of 5-amino-4,6-dichloropyrimidine (**4**), which was elaborated to 5-*tert*-butylcarbonylaminopyrimidine (**6**) upon reaction with trimethylacetyl chloride and Et_3N, were unsuccessful. Although *ortho*-lithiation occurs at the C-4 position of **6**, this lithio, or radical anion, species attacks either the highly electron-deficient C-4, or C-2, position of **6** to exclusively afford bis(5-*tert*-butylcarbonylaminopyrimidine) products prior to addition of an electrophilic reagent such as benzaldehyde. Similar self-condensation coupling reactions of pyrimidine and pyridine derivatives in the presence of lithium diisopropylamide have been reported (8–10).

To overcome the formation of bis(5-*tert*-butylcarbonylaminopyrimidine) self-condensation products during the *ortho*-directed lithiation of 5-*tert*-butylcarbonylaminopyrimidine (**6**), the nucleophilic character of an acyl radical generated in a one-step reaction (11) from an aldehyde in water containing sulfuric acid, *tert*-butylhydroperoxide, ferrous sulfate, and acetic acid reported for the acylation of quinoline (11, 12), 4-cyanopyridine (13), 2-substituted-pyrazines (14, 15), and quinoxaline (16) was investigated. Accordingly, this selective homolytic acylation of protonated heteraromatic bases was used for the benzoylation of 5-*tert*-butylcarbonylaminopyrimidine (**6**). Thus, the homolytic benzoylation of **6** (1 equiv.) in the presence of benzaldehyde (3 equiv.), water, sulfuric acid, and acetic acid, upon treatment with $FeSO_4 \cdot 7H_2O$ (3 equiv.) and 70% *t*-BuOOH (3 equiv.) at 5–10°C for 10 min afforded a mixture of 4-benzoyl-5-*tert*-butylcarbonylaminopyrimidine (**7**, 23%), 4,6-dibenzoyl-5-*tert*-butylcarbonylaminopyrimidine (**8**, 44%), and 4-benzoyl-5-*tert*-butylcarbonylamino-6-methylpyrimidine (**9**, 10%) (see Scheme 1). Introduction of the 6-methyl substituent into **9** likely arises from decomposition of *t*-BuOOH to acetone and a methyl radical which adds to the C-6 position of 4-benzoyl-5-*tert*-butylcarbonylaminopyrimidine (**7**). When the reaction was performed using 1 equiv. each of PhCHO, $FeSO_4 \cdot 7H_20$ and *t*-BuOOH, to prevent the formation of the 4,6-dibenzoyl product **8**, the monobenzoyl prod-

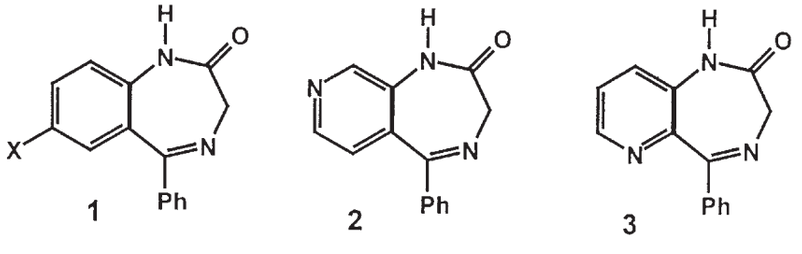

© 1999 NRC Canada

Scheme 1. Reagents: i, 10% Pd/C, 20% w/v aqueous NaOH, H_2 gas at 30 psi, Et_2O, 25°C; ii, Me_3COCl, Et_3N, CH_2Cl_2, 0°C for 30 min and then 25°C for 3 h; iii, H_2O, concentrated H_2SO_4, PhCHO (3 equiv.), HOAc, 0°C and then $FeSO_4 \cdot 7H_2O$ (3 equiv.), 70% w/v *t*-BuOOH (3 equiv.), 5–10°C, 10 min.

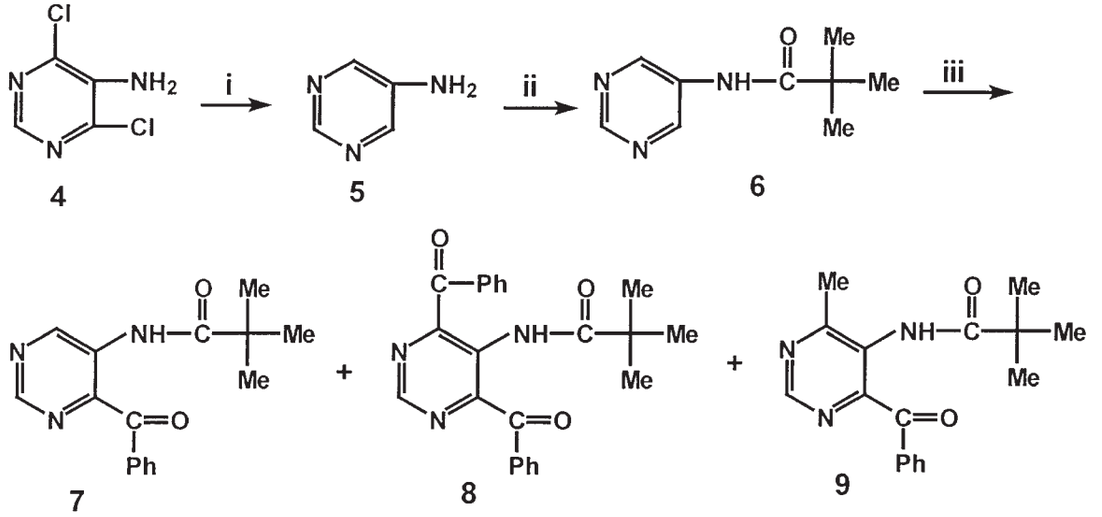

uct **7**, the 4-benzoyl-6-methyl product **9**, and unreacted **6** were obtained in 38, 6, and 23% (recovery) chemical yields, respectively. It has been reported that the yield of monoacylation product can be increased by replacement of HOAc with CH_2Cl_2 in homolytic acylation reactions (15). When HOAc is used, the reaction mixture is homogenous. Alternatively, in the absence of HOAc a heterogeneous medium is obtained, which has be proposed to result in the monoacylation product being extracted into the organic layer (CH_2Cl_2) where it is more soluble thereby protecting the monoacylation product from further acylation. However, in this study, replacement of HOAc by CH_2Cl_2 was not successful, since no reaction occurred and the starting material **6** was recovered.

A similar homolytic benzoylation (benzoyl radical) of 5-bromopyrimidine (**10**) was investigated with the objective of increasing the yield of the monoacylation product and preventing the formation of the dibenzoylation (**8**) and methyl radical (**9**) products previously observed upon reaction with 5-*tert*-butylcarbonylaminopyrimidine (**6**). This rationale is based on the premise that (*i*) a bromo substituent should direct predominately *ortho*-substitution and (*ii*) the bromo substituent can be displaced by a nitrogen nucleophile (14). Accordingly, homolytic benzoylation of 5-bromopyrimidine (**10**) with a benzoyl radical, as described previously (see Scheme 1) afforded 4-benzoyl-5-bromopyrimidine (**11**) as the predominant, or exclusive, product which was readily purified by silica-gel column chromatography (61% yield) (see Scheme 2). Amination of **11** using aqueous NH_4OH in the presence of $CuSO_4 \cdot 5H_2O$ yielded 5-amino-4-benzoylpyrimidine (**12**, 22%). The subsequent reduction of **12** with $NaBH_4$ in MeOH gave 5-amino-4-(α-hydroxybenzyl)pyrimidine (**13**, 75%), which was converted to 4-benzoyl-5-benzyloxycarbonylaminomethylcarbonylaminopyrimidine (**14**, 84%) by coupling to the carboxyl group of $PhCH_2OCONHCH_2CO_2H$ in the presence of dicyclohexylcarbodiimide (DCC) and then oxidation of the alcohol using MnO_2. Cyclization of **14** with 33% w/v HBr in HOAc afforded 1,3-dihydro-5-phenyl-2*H*-pyrimido[5,4-*e*][1,4]diazepin-2-one (**15**, 67%), which was elaborated to the corresponding 2-thione derivative (**16**, 70%). Reaction of **16** with $H_2NNH_2 \cdot H_2O$ in MeOH gave the 2-hydrazino-5-phenyl-3*H*-pyrimido[5,4-*e*][1,4]diazepine (**17**, 80%), which was immediately converted to 5-phenyl-10-methyl-7*H*-pyrimido[4,5-*f*][1,2,4]triazolo[4,3-*a*][1,4]diazepine (**18**, 62%) upon reaction with triethyl orthoacetate in the presence of concentrated H_2SO_4.

Biological evaluation of 5-phenyl-10-methyl-7*H*-pyrimido[4,5-*f*][1,2,4]triazolo[4,3-*a*][1,4]diazepine (18) as an anticonvulsant agent

The anticonvulsant activities of 5-phenyl-10-methyl-7*H*-pyrimido[4,5-*f*][1,2,4]triazolo[4,3-*a*][1,4]diazepine (**18**) were determined by the Antiepileptic Drug Development (ADD) Program that is administered by the Section on Epilepsy, United States National Institutes of Health, Bethesda, Md. Anticonvulsant activities against subcutaneous metrazol (scMet) and maximal electroshock (MES) induced seizures, which are models for absence (petit mal) and generalized tonic clonic (grand mal) seizures, respectively, were measured in mice and (or) rats at various time intervals after intraparietoneal (ip), or oral (po), administration of the test compound **18** using procedures previously reported (7). In the Phase II quantitative screen in mice, **18** was moderately active (ED_{50} = 79.5 mg/kg ip at 1 h post drug administration) against MES-induced seizures, very active (ED_{50} = 6.2 mg/kg ip at 15 min post drug administration) against scMet-induced seizures, and it was nontoxic (TD_{50} > 150 mg/kg ip at 15 min post drug administration in mice). The ED_{50} values for the standard reference drugs in these anticonvulsant screens were clonazepam (scMet, ED_{50} = 0.02 mg/kg; MES, ED_{50} = 86.6 mg/kg) and valproic acid (scMet, ED_{50} = 148.6 mg/kg; MES, ED_{50} = 271.7 mg/kg). In

© 1999 NRC Canada

Scheme 2. Reagents: i, PhCHO (1.5 equiv.), HOAc, 4N H_2SO_4 and then $FeSO_4 \cdot 7H_2O$ (1.5 equiv.), H_2O, 70% *t*-BuOOH (1.5 equiv.), 0–5°C for 0.5 h and then 25°C for 2 h; ii, 37% w/v aqueous NH_4OH, $CuSO_4.5H_2O$, 0.5 h at 25°C and then 90°C for 20 h; iii, $NaBH_4$, MeOH, 0–5°C and then 25° for 1.5 h; iv, dicyclohexylcarbodiimide, THF–CH_2Cl_2 (1:1, v/v), $PhCH_2OCONHCH_2CO_2H$, 20 min at 25°C and then 2.5 h at reflux; MnO_2, $CHCl_3$, 25°C, 20 h; v, 33% w/v HBr in HOAc, 25°C, 2.5 h and then Et_2O, 10% w/v aqueous MeOH, NH_4OH, 25°C, 6 h; vi, Lawesson's reagent (2,4-bis(4-methoxyphenyl)-1,3-dithia-2,4-diphosphetane-2,4-disulfide), benzene, reflux under argon, 1 h; vii, $H_2NNH_2 \cdot H_2O$, MeOH, 25°C, 2h; viii, triethyl orthoacetate, EtOH, concentrated H_2SO_4, 0°C → 25°C, 4 h.

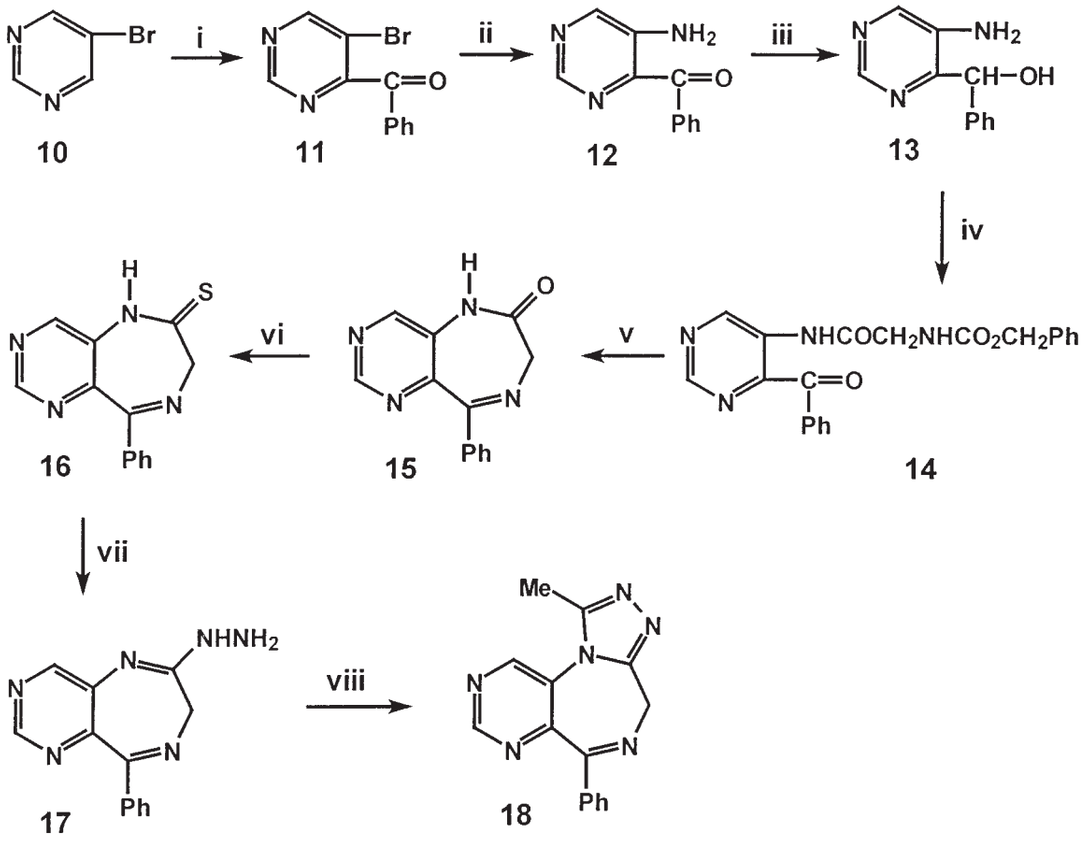

addition, **18** also exhibited good anticonvulsant activity in the Phase VIa rat oral screen where a 50 mg/kg oral dose protected 2/4, 2/4, and 1/4 rats against seizures at 15 min, 1 h, and 4 h post drug administration, respectively, in the MES screen, and 4/4, 4/4, and 2/4 rats were protected at 15 min, 1 h and 4 h post drug administration, respectively, in the scMet screen.

The ability of **18** to prevent convulsions induced by other convulsion-inducing agents was also investigated in mice at 15 min following an ip dose of **18** (sc bicuculline test: ED_{50} > 10 mg/kg; sc picrotoxin test: ED_{50} = 7.72 mg/kg; and sc strychnine test: ED_{50} > 10 mg/kg). Bicuculline blocks γ-aminobutyric acid (GABA) receptors and this interferes with GABA inhibitory function thereby inducing both clonic and tonic extensor convulsions. Picrotoxin interferes with chloride channels that are regulated by GABA receptors thereby inducing minimal threshold seizures.

The ability of **18** to displace 50% of 10 nM [^{3}H]flunitrazepam from mouse whole brain P_2 pellets (IC_{50} = 72 μM) indicates it has a weaker affinity for the benzodiazepine receptor site(s) as compared to the reference drug clonazepam (5-(2-chlorophenyl)-7-nitrobenzo[1,4]diazepin-2-one, IC_{50} = 0.003 μM).

The results of this study indicate **18** is more potent than valproic acid (Depakene®) in both the scMet and MES screens, more potent than clonazepam in the MES screen, but less potent than clonazepam in the scMet screen.

Experimental

Melting points were determined using a Buchi capilliary apparatus and are uncorrected. Nuclear magnetic resonance spectra (^{1}H NMR, ^{13}C NMR) were determined on a Bruker AM-300 spectrometer. The assignment of exchangeable protons (O*H*, N*H*) was confirmed by the addition of D_2O. ^{13}C NMR spectra were acquired using the *J* modulated spin-echo technique where methyl and methine carbon resonances appear as positive peaks, and methylene and quaternary carbon resonances appear as negative peaks. Infrared (IR) spectra were acquired using a Nicolet 550 Series II Magna FT-IR spectrometer. Silica-gel column chromatography was carried out using Merck 7734 silica gel (60–200 mesh). Preparative

© 1999 NRC Canada

thin-layer chromatography (TLC) was performed using Keiselgel silica-gel (Camag) plates, 1.0 mm in thickness. All reagents were purchased from the Aldrich Chemical Co.

5-Aminopyrimidine (5)

A solution of 5-amino-4,6-dichloropyrimidine (2.0 g, 12.2 mmol) in ether (240 mL) and then 10% palladium-on-charcoal (160 mg) was added to a solution of 20% w/v NaOH (8 g) in water (32 mL) in a low-pressure hydrogenation bottle, and the mixture was agitated at 25°C under hydrogen gas at 30 psi (1 psi = 6.895 kPa) until the uptake of hydrogen gas had ceased. The reaction mixture was filtered through a celite pad which was then washed with warm water (2 × 16 mL). The pH of the combined filtrates was made strongly alkaline by addition of NaOH at less than 5°C. Ether (20 mL) was added, the mixture was extracted by stirring overnight at 25°C, the ether layer was separated, and the aqueous fraction was further extracted with ether (3 × 80 mL). The combined ether extracts were dried ($MgSO_4$), and the solvent was removed in vacuo to give **5** as colorless crystals after recrystallization from benzene containing a few drops of methanol (1.1 g, 95%); mp 170–171°C (lit. mp 171–172°C (17)); ^{1}H NMR ($CDCl_3$) δ: 3.80 (br s, 2H, N*H*$_2$), 8.25 (s, 2H, H-4, H-6), 8.70 (s, 1H, H-2).

5-*tert*-Butylcarbonylaminopyrimidine (6)

A solution of trimethylacetyl chloride (1.67 g, 13.9 mmol) in dry CH_2Cl_2 (1.5 mL) was added dropwise to an ice-cooled solution of **5** (1.2 g, 12.6 mmol) and Et_3N (1.6 g, 15.8 mmol) in dry CH_2Cl_2 (25 mL) at 0°C with stirring during 30 min. The reaction was allowed to proceed with stirring at 25°C for 3 h, and the reaction mixture was poured onto water (40 mL). Extraction with CH_2Cl_2 (2 × 100 mL), washing the combined CH_2Cl_2 extracts with 10% w/v $NaHCO_3$, and then brine (25 mL), drying the CH_2Cl_2 fraction (Na_2SO_4) and removal of the solvent in vacuo gave a yellow–brown viscous oil that was purified by preparative TLC using MeOH–EtOAc (1:20, v/v) as development solvent. Extraction of the band (R_f = 0.56) gave a yellow oil which was recrystallized from EtOAc–hexane (1:3, v/v) to afford **6** as needle-like crystals (1.14 g, 50%); mp 120–121°C; IR ($CHCl_3$): 3442 (NH), 1693 (C=O) cm^{-1}; ^{1}H NMR ($CDCl_3$) δ: 1.36 (s, 9H, C*Me*$_3$), 7.40 (br s, 1H, N*H*), 8.98 (s, 1H, H-2), 9.00 (s, 2H, H-4, H-6). Anal. calcd. for $C_9H_{13}N_3O$: C 60.31, H 7.31, N 23.45; found: C 60.46, H 7.39, N, 23.24.

4-Benzoyl-5-*tert*-butylcarbonylaminopyrimidine (7), 5-*tert*-butylcarbonylamino-4,6-dibenzoylpyrimidine (8) and 4-benzoyl-5-*tert*-butylcarbonylamino-6-methylpyrimidine (9)

A saturated solution of $FeSO_4 \cdot 7H_2O$ (0.93 g, 3.26 mmol) in water (12 mL) and 70% w/v *t*-BuOOH (303 mg, 3.36 mmol) were added simultaneously to a mixture containing **6** (0.20 g, 1.12 mmol), water (2 mL), concentrated H_2SO_4 (80 μL), benzaldehyde (357 mg, 3.36 mmol), and HOAc (3 mL) at 5–10°C with stirring. The reaction was allowed to proceed at 5–10°C for 10 min with stirring prior to neutralization with saturated aqueous $NaHCO_3$ at 0°C. Extraction with EtOAc (3 × 100 mL), drying the EtOAc extract (Na_2SO_4), and removal of the solvent in vacuo yielded an oil which was separated by preparative TLC using benzene–EtOAc (1:1, v/v) as development solvent. Extraction of the band having R_f 0.69 yielded **7** (73 mg, 23%); mp 84–85°C (EtOAc–hexane); IR (CCl_4): 3320 (NH), 2967 (CH), 1742 (C=O), 1703 (CONH) cm^{-1}; ^{1}H NMR ($CDCl_3$) δ: 7.54 (t, *J* = 9.0 Hz, 2H, phenyl H-3, H-5), 7.64–7.68 (m, 1H, phenyl H-4), 8.04 (dd, *J* = 2.0, 9.0 Hz, 2H, phenyl H-2, H-6), 9.06 (s, 1H, H-2), 10.24 (s, 1H, H-6), 10.85 (br s, 1H, N*H*). Anal. calcd. for $C_{16}H_{17}N_3O_2$: C 67.82, H 6.05, N 14.83; found: C 68.10, H 6.07, N 14.80. Extraction of the band having R_f 0.86 afforded **8** (190 mg, 44%); mp 166–167°C (EtOAc–hexane); IR (CCl_4): 3361 (NH), 2969 (CH), 1691 (br, C=O and CONH) cm^{-1}; ^{1}H NMR ($CDCl_3$) δ: 1.24 (s, 9H, C*Me*$_3$), 7.55 (t, *J* = 8.7 Hz, 4H, phenyl H-3, H-5), 7.68 (t, *J* = 8.7 Hz, 2H, phenyl H-4), 8.08 (d, *J* = 8.7 Hz, 4H, phenyl H-2, H-6), 9.18 (s, 1H, H-2), 10.30 (br s, 1H, N*H*). Anal. calcd. for $C_{23}H_{21}N_3O_3$: C 71.30, H 5.46, N 10.85; found: C 70.93, H 5.34, N 10.67. Extraction of the band having R_f 0.38 yielded **9** (33 mg, 10%); mp 144–145°C (hexane–EtOAc); IR (CCl_4): 3407 (NH), 2968 (CH), 1742 (C=O), 1699 (CONH) cm^{-1}; ^{1}H NMR ($CDCl_3$) δ: 1.28 (s, 9H, C*Me*$_3$), 2.56 (s, 3H, C-6 Me), 7.52 (t, *J* = 7.0 Hz, 2H, H-3, H-5), 7.66 (t, *J* = 7.0 Hz, 1H, phenyl H-4), 8.01 (d, *J* = 7.0 Hz, 2H, phenyl H-2, H-6), 8.70 (br s, 1H, N*H*), 9.06 (s, 1H, H-2). Anal. calcd. for $C_{17}H_{19}N_3O_2$: C 68.67, H 6.44, N 14.13; found: C 68.62, H 6.38, N 13.95.

4-Benzoyl-5-bromopyrimidine (11)

Solutions of $FeSO_4 \cdot 7H_2O$ (110 g, 396 mmol) in water (280 mL) and *t*-BuOOH (54 mL of 70% w/v, 394 mmol) were added simultaneously to an ice-cooled solution of **10** (42 g, 264 mmol) and benzaldehyde (40 mL, 394 mmol) in HOAc (280 mL) and sulfuric acid (182 mL of 4.5 N) with stirring during 20 min. After 30 min, the cooling bath was removed, and the reaction was allowed to proceed for 2 h at 25°C. Extraction with EtOAc (4 × 200 mL), and removal of the solvents including acetic acid in vacuo at 40°C gave a residue which was neutralized by treatment with saturated aqueous $NaHCO_3$ solution prior to extraction with EtOAc (4 × 100 mL). The combined EtOAc extracts were washed with water (100 mL), brine (60 mL), and the EtOAc fraction was dried (Na_2SO_4). Removal of the solvent in vacuo gave a residue which was purified by silica-gel column chromatography (4 × 30 cm column) using EtOAc–hexane (1:9, v/v) as eluant to yield **11** (42.2 g, 61%) as an apparently homogeneous oil (silica-gel TLC, EtOAc–hexane (4:1, v/v) as development solvent, R_f = 0.38). This oil, upon standing in hexane at 25°C crystallized as colorless crystals after several hours; mp 41–42°C; IR (KBr): 1680 (C=O) cm^{-1}; ^{1}H NMR ($CDCl_3$) δ: 7.42–7.60 (m, 2H, phenyl H-3, H-5), 7.65 (dt, *J* = 7.5, 1.5 Hz, 1H, phenyl H-4), 7.78–7.80 (m, 2H, phenyl H-2, H-6), 9.00 (s, 1H, H-6), 9.21 (s, 1H, H-2); ^{13}C NMR ($CDCl_3$) δ: 117.02, 128.82 (2C), 130.11 (2C), 133.64, 134.63, 156.26, 159.97, 162.54, 190.73 (*C*=O). Anal. calcd. for $C_{11}H_7BrN_2O$: C 50.22, H 2.68, N 10.65; found: C 49.94, H 2.61, N 10.62.

5-Amino-4-benzoylpyrimidine (12)

A mixture of **11** (12.0 g, 46 mmol), aqueous NH_4OH (100 mL of a 37% w/v solution), and $CuSO_4 \cdot 5H_2O$ (1.1 g, 44 mmol) were placed in a glass pressure flask, and the

© 1999 NRC Canada

reaction was allowed to proceed with stirring at 25°C for 30 min, and then at 90°C for 20 h. After cooling to 10°C, the reaction mixture was transferred to a separatory funnel, the pressure flask was rinsed with chloroform (2 × 40 mL), and the chloroform solution was transferred to the separatory funnel. The organic fraction was separated, and the aqueous fraction was extracted with chloroform (4 × 50 mL). The combined organic extracts were dried (Na_2SO_4), and the solvent was removed in vacuo to give a gummy yellow solid which was purified by silica-gel column chromatography (4.5 × 30 cm column) using EtOAc–hexane (3:2, v/v) as eluant to afford **12** (2.0 g, 22%) as bright yellow needles; mp 109–110°C (ether–hexane); R_f = 0.56 (EtOAc–hexane, 4:1, v/v as development solvent); IR (KBr): 3451, 3328 (NH_2), 1630 (C=O) cm^{-1}; ^1H NMR ($CDCl_3$) δ: 6.03 (br s, 2H, N*H*$_2$), 7.40–7.60 (m, 3H, phenyl H-3, H-4, H-5), 8.00–8.10 (m, 2H, phenyl H-2, H-6), 8.44 (s, 1H, H-6), 8.64 (s, 1H, H-2); ^{13}C NMR ($CDCl_3$) δ: 127.95 (2C), 130.69 (2C), 132.53, 137.21, 137.26, 142.63, 146.28, 148.92, 196.21 (C=O). Anal. calcd. for $C_{11}H_9N_3O$: C 66.32, H 4.55, N 21.09; found: C 66.12, H 4.60, N 21.07.

5-Amino-4-(α-hydroxybenzyl)pyrimidine (13)

Sodium borohydride (1.5 g, 40 mmol) was added to an ice-cooled solution of **12** (3.0 g, 15 mmol) in methanol (80 mL), and the reaction was allowed to proceed for 1.5 h with stirring. Saturated aqueous NH_4Cl (30 mL) was added, the mixture was stirred for 3 h at 25°C, most of the MeOH was removed in vacuo, and the aqueous residue was extracted with chloroform (6 × 50 mL). The combined chloroform extracts were washed with water (50 mL), brine (50 mL), and the chloroform fraction was dried (Na_2SO_4). Removal of the solvent in vacuo gave a residue which was purified by either recrystallization from chloroform–hexane, or by silica-gel column chromatography using EtOAc as eluant, to afford **13** as a colorless crystalline solid (2.27 g, 75%); mp 148–149°C; IR (KBr): 3425, 3312, 3181, 2853, 1630, 1573 cm^{-1}; ^1H NMR (DMSO-d_6) δ: 5.46 (br s, 2H, N*H*$_2$), 5.79 (d, *J* = 5.0 Hz, 1H, C*H*-OH), 6.37 (d, *J* = 5.0 Hz, 1H, CH-O*H*), 7.15–7.37 (m, 3H, phenyl H-3, H-4, H-5), 7.37–7.50 (m, 2H, phenyl H-2, H-6), 8.10 (s, 1H, H-6), 8.36 (s, 1H, H-2); ^{13}C NMR (DMSO-d_6) δ: 74.40, 126.06 (2C), 127.03, 127.90 (2C), 139.78, 141.72, 143.34, 146.16, 152.64. Anal. calcd. for $C_{11}H_{11}N_3O$: C 65.66, H 5.51, N 20.88; found: C 65.29, H 5.51, N 20.93.

4-Benzoyl-5-benzyloxycarbonyl-aminomethylcarbonylaminopyrimidine (14)

N-Benzyloxycarbonylglycine (10.5 g, 50 mmol) was added in small aliquots to a solution of dicyclohexylcarbodiimide (10.3 g, 50 mmol) in dry THF–CH_2Cl_2 (1:1, v/v, 200 mL) at which time a white solid separated in a few minutes after mixing the two reagents. The resulting suspension was stirred for 20 min at 25°C, **13** (7.0 g, 34.8 mmol) was added as a single aliquot, and the reaction mixture was heated at reflux for 2.5 h. The reaction mixture was cooled to 25°C, the solid was removed by filtration, and the solvent was removed in vacuo to give an oily residue that was purified by silica-gel column chromatography (4.5 × 30 cm column). Elution with EtOAc–hexane (1:1, v/v) eluted impurities which were discarded. Further elution with EtOAc–hexane (9:1, v/v) afforded the hydroxy intermediate as an oil which was dissolved in chloroform (250 mL). Activated MnO_2 (16.0 g, 200 mmol) was added, and the oxidation reaction was allowed to proceed at 25°C for 20 h with stirring. The reaction mixture was filtered through a small celite pad, the celite pad was washed with chloroform (2 × 20 mL), and the chloroform filtrate was filtered. Removal of the solvent in vacuo gave an oily residue which was purified by silica-gel column chromatography (4.5 × 26 cm column) using EtOAc–hexane (7:3, v/v) as eluant to afford **14** (11.5 g, 84%); mp 86–87°C; IR (KBr): 3312, 3058, 1712, 1655, 1565 cm^{-1}; ^1H NMR ($CDCl_3$) δ: 4.05 (d, *J* = 6.0 Hz, 2H, C*H*$_2$NH), 5.14 (s, 2H, OC*H*$_2$), 5.73 (t, *J* = 6.0 Hz, 1H, CH$_2$N*H*), 7.10–7.42 (m, 5H, CH$_2$*Ph*), 7.47 (t, *J* = 7.5 Hz, 2H, benzoyl H-3, H-5), 7.62 (t, *J* = 7.5 Hz, 1H, benzoyl H-4), 7.95 (d, *J* = 8.0 Hz, 2H, benzoyl H-2, H-6), 8.05 (s, 1H, H-6), 9.09 (s, 1H, H-2), 10.86 (br s, 1H, N*H*COCH$_2$); ^{13}C NMR ($CDCl_3$) δ: 45.51, 67.56, 128.21 (2C), 129.48, 131.22 (2C), 133.73, 133.85, 135.68, 135.91, 143.77, 151.95, 152.07, 156.60, 168.72, 195.74. Anal. calcd. for $C_{21}H_{18}N_4O_4$: C 64.61, H 4.65, N 14.35; found: C 64.58, H 4.74, N 14.66.

1,3-Dihydro-5-phenyl-2*H*-pyrimido[5,4-*e*][1,4]diazepin-2-one (15)

A solution of 32% w/v HBr in HOAc (120 mL) was added to **14** (10.0 g, 25.6 mmol), and the reaction was allowed to proceed at 25°C for 2.5 h with stirring. Ether (100 mL) and 10% aqueous NaOH (200 mL) were added, and the mixture was cooled in an ice-bath prior to neutralization with aqueous NH_4OH. The resulting mixture was allowed to stand for 6 h at 25°C, extracted with chloroform (6 × 60 mL), the combined chloroform extracts were dried (Na_2SO_4), and the solvent was removed in vacuo to afford a viscous oil. Purification by silica-gel column chromatography (4.5 × 30 cm column) using EtOAc as eluant gave **15** (4.5 g, 67%); mp 184–185°C (CH_2Cl_2–hexane); IR (KBr): 3156, 1696, 1622 cm^{-1}; ^1H NMR ($CDCl_3$) δ: 4.42 (s, 2H, C*H*$_2$), 7.30–7.50 (m, 3H, phenyl H-3, H-4, H-5), 7.50–7.60 (m, 2H, phenyl H-2, H-6), 8.75 (s, 1H, H-9), 9.08 (s, 1H, H-7), 10.21 (br s, 1H, N*H*); ^{13}C NMR ($CDCl_3$) δ: 56.51, 128.22 (2C), 129.43 (2C), 130.92, 133.50, 136.70, 149.58, 150.94, 153.23, 169.10, 171.71. Anal. calcd. for $C_{13}H_{10}N_4O$: C 65.54, H 4.23, N 23.52; found: C 65.29, H 4.00, N 23.44.

1,3-Dihydro-5-phenyl-2*H*-pyrimido[5,4-*e*][1,4]diazepin-2-thione (16)

A mixture of **15** (5.65 g, 23.7 mmol) and Lawesson's reagent (2,4-bis(4-methoxyphenyl)-1,3-dithia-2,4-diphosphetane-2,4-disulfide) (5.0 g, 12.3 mmol) in benzene (150 mL) was refluxed for 1 h under argon, the resulting dark-colored solution was cooled to 25°C, and EtOAc (150 mL) was added. This mixture was washed with 10% w/v aqueous NaOH (150 mL), water (50 mL), and the aqueous fractions were combined. The combined aqueous fractions were neutralized with 1N HCl, and this mixture was extracted with EtOAc (3 × 50 mL). The combined EtOAc extracts were washed with brine (50 mL) and the EtOAc extract was dried (Na_2SO_4). Removal of the solvent in vacuo at 25°C gave a semi-solid residue which was purified by silica-gel column chromatography (4.5 × 30 cm column) using EtOAc–hexane

© 1999 NRC Canada

(2:3, v/v) as eluant to yield **16** (4.2 g, 70%) as a yellow solid; mp 198–205°C (dec.) (MeOH–hexane); ^{1}H NMR (MeCOMe-d_6) δ: 4.86 (s, 2H, CH_2), 7.32–7.50 (m, 3H, phenyl H-3, H-4, H-5), 7.60–7.70 (s, 2H, phenyl H-2, H-6), 8.97 (s, 1H, H-9), 9.04 (s, 1H, H-7), 11.50 (br s, 1H, N*H*); ^{13}C NMR (MeCOMe-d_6) δ: 64.75, 128.74 (2C), 128.40, 130.38 (2C), 131.25, 135.00, 138.19, 151.59, 151.88, 152.80, 169.14. Product **16** was used immediately in the subsequent reaction for the preparation of **17**.

2-Hydrazino-5-phenyl-3*H*-pyrimido[5,4-*e*][1,4]diazepine (17)

Hydrazine monohydrate (7.4 mL, 151 mmol) was added dropwise using a syringe to a solution of **16** (4.0 g, 15.7 mmol) in MeOH (100 mL) at 25°C with stirring, and the reaction was allowed to proceed at 25°C with stirring for 2 h prior to pouring onto ice-water (100 mL). Methanol was removed from the mixture in vacuo at 25°C, and the aqueous residue was extracted with chloroform (4 × 60 mL). The combined chloroform extracts were washed with water (40 mL), brine (40 mL), and the chloroform fraction was dried (Na_2SO_4). Removal of the solvent in vacuo yielded **17** (3.17 g, 80%) as a yellow solid; ^{1}H NMR ($CDCl_3$) δ: 3.60–4.70 (br m, 5H, N*H*NH_2, H-3), 7.26–7.70 (m, 5H, phenyl hydrogens), 8.74 (s, 1H, H-9), 8.90 (s, 1H, H-7). Since **17** was quite pure (^{1}H NMR) and since it decomposes slowly on standing in air, or in chloroform solution at 25°C, it was used immediately in the subsequent reaction for the preparation of **18**.

5-Phenyl-10-methyl-7*H*-pyrimido[4,5-*f*][1,2,4]triazolo[4,3-*a*][1,4]diazepine (18)

Concentrated H_2SO_4 (1.2 mL) was added dropwise with stirring to an ice-bath cooled solution of **17** (3.0 g, 11.9 mmol) and triethyl orthoacetate (11.0 mL, 60 mmol) in 98% EtOH (120 mL), and the reaction was allowed to proceed at 25°C for 4 h. The reaction mixture was neutralized with a saturated solution of aqueous $NaHCO_3$ and the mixture was concentrated in vacuo at 25°C. The residue was extracted with chloroform (3 × 50 mL), the combined chloroform extracts were washed with water (50 mL), brine (50 mL), and the chloroform fraction was dried (Na_2SO_4). Removal of the solvent in vacuo, and purification of the product by silica-gel column chromatography using EtOAc–methanol (4:1, v/v) as eluant afforded **18** (2.0 g, 62%); mp 223–224°C (CH_2Cl_2–hexane); ^{1}H NMR ($CDCl_3$) δ: 2.68 (s, 3H, CH_3), 4.19 (d, *Jgem* = 12 Hz, 1H, H-7′), 5.59 (d, *Jgem* = 12 Hz, 1H, H-7″), 7.30–7.50 (m, 3H, phenyl H-3, H-4, H-5), 7.55–7.62 (m, 2H, phenyl H-2, H-6), 9.02 (s, 1H, H-1), 9.35 (s, 1H, H-3); ^{13}C NMR ($CDCl_3$) δ: 12.09, 46.08, 128.25 (2C), 129.17 (2C), 129.39, 131.10, 136.74, 149.94, 151.94, 152.63, 155.02, 156.76, 166.89. Anal. calcd. for $C_{15}H_{12}N_6$: C 65.21, H 4.38, N 30.42; found: C 64.83, H 4.26, N 30.46.

Acknowledgments

We are grateful to the Medical Research Council of Canada (grant no. MT-4888) for financial support of this research, to the Alberta Heritage Foundation for Medical Research for a Fellowship to one of us (C.Y.F.), and to the Anticonvulsant Drug Development Program, Epilepsy Branch, NINCDS, Bethesda, for anticonvulsant testing.

References

1. L.O. Randall, W. Schallek, L.H. Sternbach, and R.Y. Ning. *In* Psychopharmacological agents. *Edited by* M. Gordon. Academic Press. New York. 1974. pp. 175–281.
2. L.H. Sternbach. J. Med. Chem. **22**, 1 (1979).
3. M. Williams. J. Med. Chem. **26**, 619 (1983), and refs. cited therein.
4. C.Y. Fiakpui, O.A. Phillips, K.S.K. Murthy, and E.E. Knaus. Drug Des. Discovery, **10**, 45 (1993).
5. C.Y. Fiakpui and E.E. Knaus. Drug Des. Discovery, **10**, 173 (1993).
6. C.Y. Fiakpui and E.E. Knaus. Can. J. Chem. **65**, 1158 (1987).
7. C.Y. Fiakpui, M.N. Namchuk, and E.E. Knaus. Drug Des. Delivery, **6**, 111 (1990).
8. T.J. Kress. J. Org. Chem. **44**, 2081 (1979).
9. G.R. Newkome and D.C. Hager. J. Org. Chem. **47**, 599 (1982).
10. T. Kauffmann, B. Greving, J. Konig, A. Mitschker, and A. Woltermann. Angew. Chem. Intl. Ed. Engl. **14**, 713 (1973).
11. T. Caronna, G.P. Gardini, and F. Minisci. Chem. Commun. 201 (1969).
12. T. Caronna, G. Fronza, F. Minisci, and O. Porta. J. Chem. Soc. Perkin Trans. 2, 1477 (1972).
13. G. Heinisch and G. Lotsch. Angew. Chem. Intl. Ed. Engl. **24**, 692 (1985).
14. Y. Houminer, E.W. Southwick, and D.L. Williams. J. Org. Chem. **54**, 640 (1989).
15. Y. Houminer, E.W. Southwick, and D.L. Williams. J. Heterocyl. Chem. **23**, 497 (1986).
16. G.P. Gardini and F. Minisci. J. Chem. Soc. C, 929 (1970).
17. N. Whittaker. J. Chem. Soc. 1565 (1951).

© 1999 NRC Canada

Chemoenzymatic enantioselective synthesis of (–)-enterolactone

Robert Chênevert, Ghodsi Mohammadi-Ziarani, Dave Caron, and Mohammed Dasser

Abstract: Enterolactone, a lignan isolated from biological fluids of animals and humans, was synthesized via enzymatic desymmetrization of 2-(3-methoxybenzyl)-1,3-propanediol.

Key words: enterolactone, synthesis, lipase, desymmetrization, lignan.

Résumé : L'entérolactone, une lignane isolée des fluides biologiques des animaux et des humains, a été préparée via une désymétrisation enzymatique du 2-(3-méthoxybenzyl)-1,3-propanediol.

Mots clés : entérolactone, synthèse, lipase, désymétrisation, lignane.

Introduction

Lignans, naturally occurring secondary plant metabolites consisting of two phenylpropanoid units, are widely distributed in the plant kingdom (1). Enterolactone and enterodiol were the first lignans to be found in humans and animals (2, 3). Enterolactone, like other lignans, exhibits a wide range of biological activity (inhibition of cardiac Na^+, K^+-ATPase, antiestrogenic properties, platelet activating factor antagonist, inhibitor of human estrogen aromatase) and has attracted great interest on account of its cancer-protective properties (4). Epidemiological studies reveal a lowered risk of hormone-dependent cancers (breast, prostate) among vegetarians consuming large amount of lignans. Enterolactone and enterodiol are formed in the intestinal tract by the action of bacteria on precursors present in the diet (5).

Many syntheses of racemic enterolactone have been reported (6) but only a few enantioselective syntheses have been achieved (7). We report here a chemoenzymatic enantioselective synthesis of enterolactone via enzymatic desymmetrization of 2-(3-methoxybenzyl)-1,3-propanediol.

Results and discussion

The known diester **1** (8) was reduced to the diol **2** by lithium aluminum hydride in ether (Scheme 1). Diol **2** was subjected to enzyme-catalyzed esterification (for related desymmetrization of propane-1,3-diol derivatives, see ref. 9) by treatment with *Pseudomonas cepacia* lipase using vinyl acetate as acyl donor and solvent to give the optically active monoester (*R*)-(+)-**3** in quantitative yield. The enantiomeric composition of **3** was measured by ^{19}F NMR (282 MHz, in benzene-d_6) analysis of the corresponding (+)-α-methoxy-α-trifluoromethyl-α-phenyl acetate (MTPA, Mosher's ester). The enantiomeric excess was determined to be 94% (10). (The accuracy of this method is ±3%.) The absolute configuration of monoester **3** (*R*; $[\alpha]_D^{25}$ +26.8 (*c* 2.26, $CHCl_3$)) was determined by correlation with enterolactone **8** of known absolute configuration (the absolute configuration of enterolactone was established by X-ray crystal diffraction (11)). The use of *Pseudomonas fluorescens* lipase gave similar results (quantitative yield, ee = 92%, reaction time = 6.5 h).

Monoester (*R*)-(+)-**3** was treated with mesyl chloride in the presence of triethylamine to give mesylate (*S*)-(+)-**4** (Scheme 2). Displacement of the mesylate with cyanide in DMSO afforded nitrile (*R*)-(–)-**5**. Hydrolysis of the nitrile and the acetate groups in acidic medium was followed by ring closure in a one-pot procedure to give lactone (*R*)-(+)-**6**, $[\alpha]_D^{25}$ +6.15 (*c* 1.86, $CHCl_3$) (lit. (7*e*) $[\alpha]_D^{24}$ 6.06 (*c* 7.92, $CHCl_3$).

The anion of lactone **6** was generated by treatment with lithium diisopropylamide and stereoselectively alkylated with *m*-methoxybenzyl bromide (7*c*) to give lactone (*R*,*R*)-(–)-**7**, $[\alpha]_D^{25}$ –39.0 (*c* 2.5, $CHCl_3$) (lit. (7*a*) $[\alpha]_D^{23}$ –39.2 (*c* 0.78, $CHCl_3$)). Demethylation of lactone **7** with boron tribromide provided enterolactone (*R*,*R*)-(–)-**8**. Comparison of the optical rotation values ($[\alpha]_D^{25}$ –38.4 (*c* 0.37, $CHCl_3$)) for the sample obtained with those reported in the literature (7*a*) ($[\alpha]_D^{23}$ –38.4 (*c* 0.25, $CHCl_3$)) confirmed the absolute configuration of (–)-**8** to be (*R*,*R*), which requires that the enzymatic desymmetrization of **2** leads to diol (+)-**3** with *R* configuration at the newly created stereogenic center.

In conclusion, we have completed the enantioselective synthesis (ee = 94%) of (*R*,*R*)-(–)-enterolactone in seven steps and 35% yield from diester **1**. The key step is the enzymatic desymmetrization of diester **2**.

Experimental section

Melting points were recorded on a Thomas–Hoover apparatus, and are uncorrected. Infrared spectra were recorded

Received August 4, 1998.

R. Chênevert,[1] G. Mohammadi-Ziarani, D. Caron, and M. Dasser. Département de chimie, Faculté des sciences et de génie, Université Laval, Québec, QC G1K 7P4, Canada.

[1]Author to whom correspondence may be addressed. Telephone: (418) 656-3283. Fax: (418) 656-7916. e-mail: robert.chenevert@chm.ulaval.ca

© 1999 NRC Canada

Scheme 1.

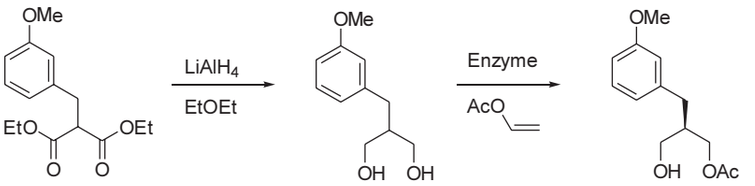

Scheme 2.

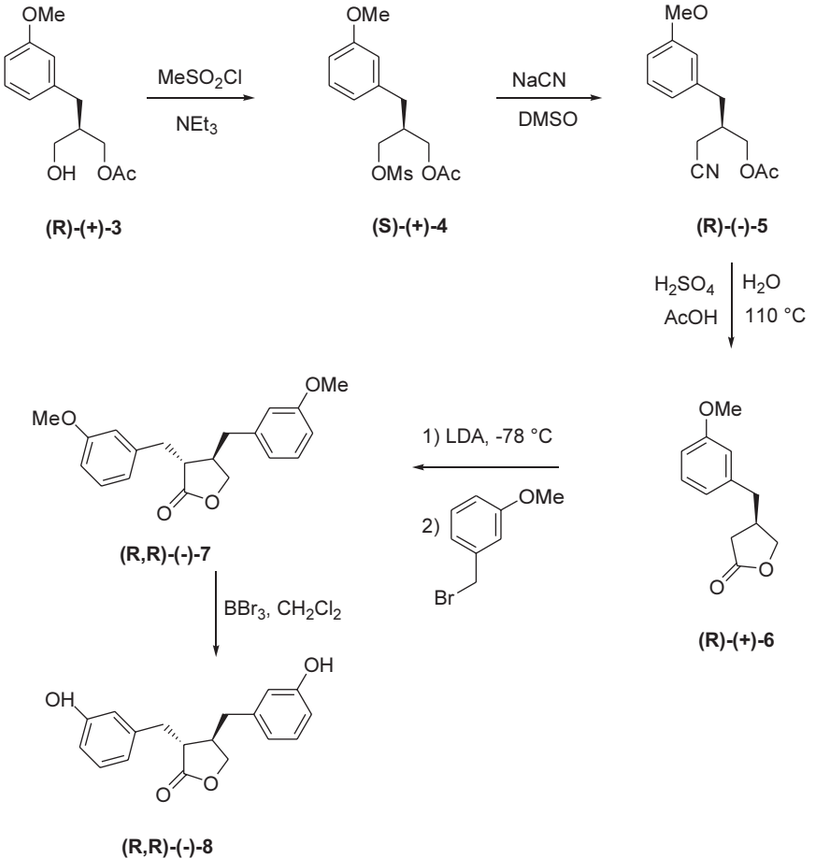

using a Perkin Elmer 781 spectrometer. NMR spectra were recorded in $CDCl_3$ solutions at 300 MHz (^1H), 282 MHz (^{19}F), 75 MHz (^{13}C) on a Bruker AC-300 instrument. Optical rotation values were obtained from a JASCO DIP-300 polarimeter. Column purifications were conducted by flash chromatography on silica gel 60 (230–400 mesh). *Pseudomonas cepacia* lipase and *Pseudomonas fluorescens* lipase were purchased from Amano and Aldrich, respectively.

2-(3-Methoxybenzyl)-propane-1,3-diol (2)

Lithium aluminum hydride (1.825 g, 48.0 mmol) was suspended in anhydrous ether (100 mL) at 0°C under a dry N_2 atmosphere. Diester **1** (3.37 g, 12.0 mmol) was added dropwise and the reaction mixture was stirred at 25°C for 4 h. The mixture was cooled and acidified with 3 N HCl (65 mL), filtered through a bed of Celite, and then extracted with ethyl acetate (2 × 100 mL). The combined extracts were washed with saturated aqueous $NaHCO_3$ (2 × 50 mL) and brine (2 × 50 mL), dried ($MgSO_4$), and evaporated. The crude product was purified by flash chromatography (ethyl acetate:hexane 2:3, to pure ethyl acetate) to yield diol **2** as a white solid (1.76 g, 75%); mp 82°C (recrystallized from ether) (lit. (6*l*) mp 81–82°C). IR (KBr): 3350, 3020–2800, 1605, 1588, 1491, 1264, 1036, 873, 778, 695 cm^{-1}; ^1H NMR (MeOD): 1.90 (1H, m), 2.61 (2H, d, J = 7.0 Hz), 3.54 (4H, d, J = 5.6 Hz), 3.74 (3H, s), 6.76 (3H, m), 7.15 (1H, m); ^{13}C NMR ($CDCl_3$): 34.17, 43.75, 55.03, 64.49, 111.17, 114.77, 121.55, 129.28, 141.49, 159.49.

Lipase-catalyzed acylation of diol 2. 3-Hydroxy-2-(3-methoxybenzyl)propyl acetate ((*R*)-3)

To a solution of diol **2** (40 mg, 0.167 mmol) in vinyl acetate (3 mL) was added *Pseudomonas cepacia* lipase (35 mg), and the mixture was stirred at room temperature. The prog-

© 1999 NRC Canada

ress of the reaction was monitored by TLC and the reaction was stopped after disappearance of the starting material (26 min). The enzyme was filtered and washed with diethyl ether. The solvent was evaporated and the crude product was purified by flash chromatography (ethyl acetate:hexane, 10:90 to 50:50) to give monoester (*R*)-(+)-**3** as a colorless oil in quantitative yield (ee = 94%). The use of *Pseudomonas fluorescens* lipase gave similar results (quantitative yield, ee = 92%, reaction time 6.5 h). $[\alpha]_D^{25}$ +26.8 (*c* 2.26, $CHCl_3$); IR (neat): 3425, 1738, 1605, 1588, 1491, 1043 cm^{-1}; ^1H NMR ($CDCl_3$): 2.07 (3H, s), 2.10 (2H, m), 2.62 (2H, m), 3.50 (1H, dd, *J* = 11.2 Hz, *J* = 6.2 Hz), 3.60 (1H, dd, *J* = 11.2 Hz, *J* = 4.5 Hz), 3.79 (3H, s), 4.07 (1H, dd, *J* = 11.1 Hz, *J* = 6.5 Hz), 4.18 (1H, dd, *J* = 11.1 Hz, *J* = 4.6 Hz), 6.76 (3H, m), 7.21 (1H, t, *J* = 7.5 Hz); ^{13}C NMR ($CDCl_3$): 20.71, 34.25, 42.22, 55.01, 61.95, 63.92, 111.39, 114.76, 121.31, 129.32, 140.86, 159.63, 171.45; HRMS (EI) calcd. for $C_{13}H_{18}O_4$ (M^+): 238.1205; found: 238.1199.

1-Acetoxy-2-(3-methoxybenzyl)-3-(mesyloxy)propane ((*S*)-4)

A solution of **3** (296.4 mg, 1.244 mmol) in anhydrous THF (10 mL) was prepared under nitrogen. The solution was cooled to 0°C and triethylamine (0.184 mL, 1.32 mmol) was added first, and then methanesulfonyl chloride (0.152 mL, 1.96 mmol) was added dropwise. The solution was stirred for 2 h while the temperature was increased to 25°C. The solvent was evaporated and the residue was taken up in ether. The organic phase was washed with a 1 N HCl solution, with a saturated $NaHCO_3$ solution (three times), dried, and concentrated. The crude product was purified by flash chromatography (silica gel, elution with hexanes:ethyl acetate, 3:1) to yield (*S*)-(+)-**4** (380 mg, 97%) as a colorless oil. $[\alpha]_D^{25}$ 5.40 (*c* 2.34, $CHCl_3$); IR (neat): 3100–3000, 3000–2800, 1738, 1602, 1587, 1490, 1350, 1155 cm^{-1}; ^1H NMR ($CDCl_3$): 1.99 (3H, s), 2.32 (1H, m), 2.63 (2H, d, *J* = 7.4 Hz), 2.91 (3H, s), 3.71 (3H, s), 3.93–4.16 (4H, m), 6.69 (3H, m), 7.14 (1H, t, *J* = 7.8 Hz); ^{13}C NMR ($CDCl_3$): 20.58, 33.78, 36.85, 39.32, 54.96, 62.78, 68.57, 111.83, 114.63, 121.16, 129.52, 139.47, 159.68, 170.54; HRMS (EI) calcd. for $C_{14}H_{20}O_6$ S (M^+): 316.0980; found: 316.0990.

4-Acetoxy-3-(3-methoxybenzyl)butyronitrile ((*R*)-(–)-5)

To a solution of mesylate **4** (152.8 mg, 0.483 mmol) in anhydrous DMSO (5 mL) was added finely pulverized sodium cyanide (31.9 mg, 0.651 mmol). The solution was stirred at 45°C for 12 h. Ethyl acetate (200 mL) was added and the organic layer was washed with water (8 × 50 mL) dried ($MgSO_4$), and evaporated. The crude product was purified by flash chromatography (silica gel, hexane:ethyl acetate, 3:1) to give nitrile (*R*)-(–)-**5** (118.4 mg, 99%) as a colorless oil. $[\alpha]_D^{25}$–10.77 (*c* 1.96, $CHCl_3$); IR (neat): 3100–3000, 3000–2800, 2250, 1742, 1604, 1589, 1493, 1250–1040 cm^{-1}; ^1H NMR ($CDCl_3$): 2.07 (3H, s), 2.13–2.42 (2H, m), 2.38 (1H, m), 2.66 (1H, dd, *J* = 13.7 Hz, *J* = 7.4 Hz), 2.76 (1H, dd, *J* = 13.7 Hz, *J* = 6.3 Hz), 3.77 (3H, s), 3.98 (1H, dd, *J* = 11.5 Hz, *J* = 6.7 Hz), 4.17 (1H, dd, *J* = 11.5 Hz, *J* = 4.4 Hz), 6.72 (3H, m), 7.22 (1H, m); ^{13}C NMR ($CDCl_3$): 18.94, 20.62, 36.44, 36.61, 55.05, 64.99, 112.06, 114.62, 117.73, 121.13, 129.71, 138.94, 159.80, 170.51; HRMS (EI) calcd. for $C_{14}H_{17}O_3N$ (M^+): 247.1208; found: 247.1200.

4-[(3-Methoxyphenyl)methyl]dihydro-2(3*H*)-furanone ((*R*)-(+)-6)

Nitrile **5** (114 mg, 0.461 mmol) was dissolved in water (5 mL), acetic acid (10 mL), and concentrated sulfuric acid (1 mL). The solution was stirred at 110°C for 2 h. Ethyl acetate (300 mL) and 2 M NaOH (60 mL) were added to the solution and the layers were decanted. The organic layer was washed with water (3 × 50 mL), dried ($MgSO_4$), and evaporated. The crude product was purified by flash chromatography (silica gel, ethyl acetate:hexane, 1:4) to afford lactone (*R*)-(+)-**6** (89.4 mg, 94%) as a colorless oil. $[\alpha]_D^{25}$ +6.15 (*c* 1.86, $CHCl_3$) (lit. (7*e*) $[\alpha]_D^{24}$ 6.06 (*c* 7.92, $CHCl_3$) (lit. (7*d*) $[\alpha]_D^{20}$ +6.41 (*c* 2.08, $CHCl_3$)). IR (film): 3100–3000, 3000–2800, 1775, 1601, 1584, 1492, 1300–1000 cm^{-1}; ^1H NMR ($CDCl_3$): 2.24 (1H, dd, *J* = 17.5 Hz, *J* = 7.2 Hz), 2.57 (1H, dd, *J* = 17.2 Hz, *J* = 7.6 Hz), 2.71 (2H, dd, *J* = 9.3 Hz, *J* = 3.2 Hz), 2.81 (1H, m), 3.76 (3H, s), 4.00 (1H, dd, *J* = 9.1 Hz, *J* = 6.3 Hz), 4.31 (1H, d, *J* = 8.7 Hz, *J* = 6.9 Hz), 6.74 (3H, m), 7.22 (1H, m); ^{13}C NMR ($CDCl_3$): 34.10, 36.92, 38.78, 55.06, 72.53, 111.73, 114.47, 120.85, 129.68, 139.76, 159.75, 176.77.

3,4-Bis[(3-methoxyphenyl)methyl]-dihydro-2(3*H*)-furanone (3*R*,4*R*)-(–)-7

To lactone **6** (40.2 mg, 0.195 mmol) in anhydrous THF (1.5 mL) at –78°C was added LDA (2 M solution in CH_2Cl_2, 0.176 mL, 0.351 mmol) and HMPA (0.105 mL, 0.585 mmol). The solution was stirred for 0.5 h at –78°C and 3-methoxybenzyl bromide (70.6 mg, 0.351 mmol) in anhydrous THF (0.5 mL) was added in one portion. The mixture was stirred overnight (15 h) at –78°C and then warmed slowly to 0°C. The excess of base was neutralized at 0°C with a saturated aqueous NH_4Cl solution (3 mL) and the mixture was extracted with ether (5 mL) and ethyl acetate (2 × 10 mL). The combined organic layer was washed with water (3 × 20 mL) and brine (10 mL), dried ($MgSO_4$), and evaporated under reduced pressure. The crude product was purified by flash chromatography (pure hexane, to ether:hexane, 15:85) to give lactone **7** (38 mg, 60%) as a colorless oil. $[\alpha]_D^{25}$ –39.0 (*c* 2.5, $CHCl_3$) (lit.(7*a*) $[\alpha]_D^{23}$ –39.2 (*c* 0.78, $CHCl_3$)). IR(neat): 3100–3000, 3000–2800, 1770, 1600, 1585, 1490, 1300–1100, 870, 782, 696 cm^{-1}; ^1H NMR ($CDCl_3$): 2.43–2.64 (4H, m), 2.91 (1H, dd, *J* = 13.9 Hz, *J* = 7.0 Hz), 3.06 (1H, dd, *J* = 13.9 Hz, *J* = 5.0 Hz), 3.76 (3H, s), 3.78 (3H, s), 3.78 (1H, dd, *J* = 15.0 Hz, *J* = 6.2 Hz), 4.10 (1H, dd. *J* = 9.0 Hz, *J* = 6.8 Hz), 6.76 (4H, m), 6.56 (2H, m), 7.20 (2H, m). ^{13}C NMR ($CDCl_3$): 35.01, 38.43, 41.14, 46.22, 55.00, 55.03, 71.05, 111.74, 112.24, 114.39, 114.72, 120.77, 121.47, 129.53, 129.59, 139.42, 139.17, 159.70, 178.32.

3,4-Bis[(3-hydroxyphenyl)methyl]dihydro-2(3*H*)-furanone (enterolactone, 8)

A solution of BBr_3 in CH_2Cl_2 (1 M, 0.421 mL, 0.421 mmol) was added dropwise to a solution of lactone **7** (34.3 mg, 0.105 mmol) in anhydrous CH_2Cl_2 at 0°C. The solution was stirred at 0°C for 1 h and then at –18°C for 12 h. Water (1 mL) was added to the solution and the aqueous

© 1999 NRC Canada

layer was extracted with CH_2Cl_2 (3 × 5 mL). The combined organic layers were washed with brine, dried ($MgSO_4$), and evaporated. The crude product was purified by flash chromatography (ethyl acetate:hexane, 3:7) to yield enterolactone **8** (26.9 mg, 86%) as a white solid; mp 140–142°C (lit. (6*l*) mp 141–143°C). $[\alpha]_D^{25}$ –38.4 (*c* 0.37, $CHCl_3$) (lit. (7*a*) $[\alpha]_D^{23}$ –38.4 (*c* 0.25, $CHCl_3$)). IR (KBr): 3350, 3100–3000, 3000–2800, 1760, 1595, 1485, 1460, 1350, 1230, 875, 785, 698 cm^{-1}; ^1H NMR (acetone-d_6): 2.46–3.01 (6H, m), 3.85–4.08 (2H, m), 6.5–7.2 (8H, m), 8.34 (2H, s); ^{13}C NMR (acetone-d_6): 35.20, 38.57, 42.04, 46.69, 71.38, 114.15, 114.36, 116.34, 117.01, 120.51, 121.36, 130.19, 130.28, 140.72, 141.21, 158.32, 178.65.

Acknowledgments

We acknowledge the financial support of this work by the Natural Sciences and Engineering Research Council of Canada. G.M.Z. is grateful to the Ministry of Culture and Higher Education of Iran and Al-Zahra University for a fellowship.

References

1. R.S. Ward. Nat. Prod. Rep. **14**, 43 (1997).
2. S.R. Stitch, J.K. Toumba, M.B. Groen, C.W. Funke, J. Leemhuis, J. Vink, and G.F. Woods. Nature, **287**, 738 (1980).
3. K.D.R. Setchell, A.M. Lawson, F.L. Mitchell, H. Adlercreutz, D.N. Kirk, and M. Axelson. Nature, **287**, 740 (1980).
4. S.E. Rickard and L.V. Thompson. *In* Antinutrients and phytochemicals in food. *Edited by* F. Shahidi. ACS Symp. Ser. 662 (1997).
5. J.T. Kumpulainen and J.T. Salonen. Natural antioxidants and food quality in atherosclerosis and cancer prevention. The Royal Society of Chemistry, Cambridge. 1996.
6. (*a*) A. Srikrishna, S. Venkateswarlu, S. Danieldoss, and J.A. Sattigeri. Indian J. Chem. **34B**, 679 (1995); (*b*) J.P. Robin and Y. Landais. Tetrahedron, **48**, 819 (1992); (*c*) M. Bambagiotti-Alberti, S.A. Coran, F.F. Vincieri, N. Mulinacci, and G.M.L. Pieraccini. Heterocycles, **27**, 2185 (1988); (*d*) M. Bambagiotti-Alberti, S.A. Coran, F.F. Vincieri, and P. Lo Nostro. Heterocyles, **26**, 1735 (1987); (*e*) J.L. Belletire and S.L. Fremont. Tetrahedron Lett. **27**, 127 (1986); (*f*) D.N. Kirk, L.M. McLaughlin, A.M. Lawson, K.D.R. Setchell, and S.K. Patel. J. Chem. Soc. Perkin Trans. 1, 35 (1985); (*g*) A. Pelter, R.S. Ward, P. Satyanarayana, and P. Collins. J. Chem. Soc. Perkin Trans. 1, 643 (1983); (*h*) K.K. Mahalanabis, M. Muntaz, and V. Snieckus. Tetrahedron Lett. **23**, 3975 (1982); (*i*) P.A. Ganeshpure and R. Stevenson. Chem. Ind. (London), 778 (1981); (*j*)A. Pelter, P. Satyanarayana, and R.S. Ward. Tetrahedron Lett. **22**, 1549 (1981); (*k*) G. Colley, R.D. Farrant, D.N. Kirk, and S. Wynn. Tetrahedron Lett. **22**, 349 (1981); (*l*) M.B. Groen and J. Leemhuis. Tetrahedron Lett. **21**, 5043 (1980).
7. (*a*) J.W. Bode, M.P. Doyle, M.N. Protopopova, and Q.L. Zhou. J. Org. Chem. **61**, 9146 (1996); (*b*) M.P. Doyle, M.N. Protopopova, Q.L. Zhou, J.W. Bode, S.H. Simonsen, and V. Lynch. J. Org. Chem. **60**, 6654 (1995); (*c*) A. van Oeveren, J.F.G.A. Jansen and B.L. Feringa. J. Org. Chem. **59**, 5999 (1994); (*d*) H. Yada, H. Kitayama, T. Katagiri and K. Takabe. Tetrahedron, **48**, 3313 (1992); (*e*) M. Asaoka, N. Fujii, K. Shima and H. Takei. Chem. Lett. 805 (1988).
8. J.M. Bruce, D. Creek, and K. Dawes. J. Chem. Soc. C, 3749 (1971).
9. (*a*) E. Schoffers, A. Golebiowski, and C.R. Johnson. Tetrahedron, **52**, 3769 (1996); (*b*) T. Itoh, J. Chika, Y. Takagi, and S. Nishiyama. J. Org. Chem. **58**, 5717 (1993); (*c*) S. Shiotani, H. Okada, T. Yamamoto, K. Nakamata, J. Adachi, and H. Nakamoto. Heterocycles, **43**, 113 (1996).
10. S. Yamaguchi. *In* Asymmetric synthesis. Vol. 1. *Edited by* J.D. Morrison. Academic Press, New York. 1983. Chap. 7, pp. 125–152.
11. G. Cooley, R.D. Farrant, D.N. Kirk, S. Patel, S. Wynn, M.J. Buckingham, G.E. Hawkes, M.B. Hursthouse, A.M.R. Galas, A.M. Lawson, and K.D.R. Setchell. J. Chem. Soc. Perkin Trans. 2, 489 (1984).

© 1999 NRC Canada

A capillary electrophoretic determination of the kinetics of tetradecanedisulfate hydrolysis

Richard A. Walker, D. Gerrard Marangoni, and Truis Smith-Palmer

Abstract: Capillary electrophoresis was used to follow the decrease in concentration of tetradecanedisulfate as a function of time during its hydrolysis in 0.5 M sulfuric acid solution at 60, 75, and 90°C. The hydrolyses were mostly carried out at premicellar concentrations of surfactant, from 1 to 7.5 mM. Large increases of rate occurred at higher concentrations (at least 15 mM). The reaction was found to be first order in tetradecanedisulfate. The activation energy and entropy of activation were calculated to be 97 kJ mol^{-1} and –55 J K^{-1} mol^{-1}, respectively.

Key words: capillary electrophoresis, surfactant, acid hydrolysis, tetradecanedisulfate, activation energy, entropy of activation.

Résumé : On a utilisé l'électrophorèse capillaire pour suivre la diminution de concentration du tétradécanedisulfate en fonction du temps lors de son hydrolyse dans de l'acide sulfurique à 0,5 M, à 60, 75 et 90°C. Les hydrolyses ont été réalisées principalement à des concentrations prémicellaires d'agent de surface, soit de 1 à 7,5 mM. On observe d'importantes augmentations de vitesse aux concentrations les plus élevées (au moins 15 mM). On a trouvé que la réaction est du premier ordre en tétradécanedisulfate. On a calculé que l'énergie et l'entropie d'activation sont respectivement égales à 97 kJ mol^{-1} et –55 J K^{-1} mol^{-1}.

Mots clés : électrophorèse capillaire, agent de surface, hydrolyse acide; tétradécanedisulfate, énergie d'activation, entropie d'activation.

[Traduit par la Rédaction]

Introduction

Despite the tremendous utility of single-headed surfactants in consumer and industrial applications, very little research dealing with the synthesis and properties of surfactants containing two typical anionic head groups such as sulfate, sulfonate, carboxylate, or phosphate has been reported in the literature. Comeau et al. (1) and Boucher et al. (2) have examined the micellar properties of a series of two-headed surfactants: the disodium alkanedisulfates (critical micelle concentration (cmc) values and degrees of counterion binding) and the disodium 3-sulfanato-4-alkylsuccinates (cmc's, aggregation numbers, and degrees of counterion binding). These authors concluded that the addition of the second polar head group made micelle formation thermodynamically less favoured (i.e., the cmc values were higher when compared to their single-headed counterparts). They also concluded that the surface charge densities were higher, while the aggregation numbers were smaller, than those of the single-headed counterparts of comparable chain length. Hence, it appears likely that the structure of the micelles formed by two-headed surfactants is not significantly different from that of the single-headed surfactants, i.e., two-headed surfactants will form small, spherical micelles where the head groups are heavily hydrated.

Sodium alkanedisulfates have been synthesized by El Sawy et al. (3) and in the labs of Marangoni (1) and Smith-Palmer (4) in our department. Two-headed sulfate surfactants offer greater water solubility than their single-headed counterparts, and are more resistant to precipitation in the presence of calcium ions (3, 5). These are properties that could make their use desirable in certain industrial or analytical processes. However, there is some question as to the stability of these species to hydrolysis. One drawback to using SDS, one of the best-known single-headed surfactants, is its propensity to hydrolyze slowly when left to sit in water, and at a considerably faster rate when placed in acid (6–11). Although El Sawy reported that the alkanedisulfates "were completely stable to hydrolysis," the indications in the accompanying data table were that they underwent significant hydrolysis in 40 min in 0.5 M sulfuric acid (3). It was thus of interest to study the stability of these surfactants in various aqueous solutions.

In a previous study, we demonstrated that we were able to separate hydroxy- alkanesulfate and alkanedisulfate using capillary electrophoresis (CE). We were then able to show that the alkanedisulfates were stable in base (but not in acid), and that the constitutional isomers 1-hydroxy-2-alkanesulfate and 2-hydroxy-1-alkanesulfate were able to be hydrolyzed in both acid and base (4).

In this study we determined the rates of acid hydrolysis of tetradecanedisulfate (TDDS) at three temperatures by means of capillary electrophoresis. The results are compared to those reported by El Sawy et al. (3), and to literature rates

Received June 26, 1998.

R.A.Walker, D.G. Marangoni, and T. Smith-Palmer.[1]
Chemistry Department, St Francis Xavier University, Box 5000, Antigonish, NS B2G 2W5, Canada.

[1]Author to whom correspondence may be addressed.
Telephone: (902) 867-2270. Fax: (902) 867-2414.
e-mail: tsmithpa@stfx.ca

© 1999 NRC Canada

for the hydrolysis of various alkanesulfates (6–10). Although CE has already been used to study reaction kinetics (12–15), its utility in this regard is yet to be fully exploited, and the demonstration that we could use CE for this purpose was an important facet of our work. Thermodynamic calculations were also done.

Experimental

Reagents

Chlorosulfonic acid and diethylbarbituric acid were from BDH, Mississauga, Ont.; 1,2-tetradecanediol, anhydrous diethyl ether, and *n*-butanol were from Aldrich, Mississauga, Ont., and sodium hydroxide was from J.T. Baker Chemical Co., Phillisburg, N.J. Ethanol was obtained from Commercial Alcohols, Boucherville, Que., and concentrated sulfuric acid and pure cellulose Soxhlet extraction thimbles were from Fisher Scientific, Nepean, Ont. Sodium chromate tetrahydrate was from Anachemia, Mississauga, Ont. CIA-Pak™ OFM Anion-BT solution was obtained from Waters (Millipore), Milford, Mass.The reverse-phase columns were 15g Supelclean Envi-Carb solid phase extraction columns from Supelco, Bellefonte, Pa.

All water used was 10 MΩ cm resistivity (Millipore 4000S purification system).

Preparation of TDDS: 1,2-Tetradecanediol (2.3 g, 10 mmol) was dissolved in 50 mL ether cooled in an ice bath, and chlorosulfonic acid (1.5 mL, 22 mmol) was added dropwise. The reaction mixture was stirred for 10 min and then neutralised with 8 M sodium hydroxide. The white precipitated surfactant was collected and vacuum dried. A portion (0.083g) was diluted to 25 mL and checked for purity by CE.

Purification by reverse phase extraction columns: The crude product was dissolved in 100 mL water and loaded onto the column, which was then washed with water in 10 50-mL aliquots.

Purification by Soxhlet extraction: Crude product was placed in a thimble and extracted with *n*-butanol. The product remaining in the thimble was then extracted with ethanol.

Instrumentation

Capillary zone electrophoresis (CZE) was carried out on a Waters Quanta 4000 capillary electrophoresis system using a 75 μm fused silica capillary (Polymicro Technologies Inc., Phoenix, Ariz.), hydrostatic injection mode for 30 s, and indirect photometric detection at 254 nm. The data were collected using LabCalc software (Galactic, Salem, N.H.) with 1 V equal to 1 au.

For anion analysis (to check salt content of surfactant preparations), the applied voltage was –20 kV, and the buffer was a chromate solution containing CIA-Pak™ OFM-BT solution, prepared as described by Waters (16). The capillary was 58 cm to the detector.

For surfactant analysis, the applied voltage was +25 kV, and the buffer was a diethylbarbiturate solution prepared by dissolving 0.0554 g diethylbarbituric acid in 30 mL water, adjusting the pH to 8.6, then making the volume up to 50 mL. The pH was readjusted to 8.6 (17), and the buffer was filtered through a 45 μL syringe filter and sonicated for 3 min prior to use. Prior to each run the capillary (52 cm to detector) was rinsed for 2 min with each of 0.1 M sodium hydroxide, water, and buffer.

The water bath was a HAAKE G water circulator employing a digital HAAKE D8 thermostat and containing a 1:1 solution of ethylene glycol and water. A Digi-Sense digital pH/mV/ORP meter was used to record and adjust all pH's.

Hydrolyses

A sulfuric acid solution was prepared from concentrated sulfuric acid and standardized to be 1.002 M using 8.2168 M sodium hydroxide in a Hach model 16900–01 digital titrator (Loveland, Colo.). A 10 mL aliquot was pipetted into a large test tube sealed with a rubber stopper. A balloon on a syringe needle was inserted to allow for expansion and the tube was equilibrated for 10 min at the desired temperature (60, 75, or 90°C). Surfactant solutions of concentrations between 2 and 35 mM were also equilibrated at the chosen temperature for 10 min before a 10 mL aliquot was added to the acid and the time and initial pH recorded. Approximately 2 mL aliquots were taken via syringe from the reaction mix at recorded time intervals. Each aliquot was placed in a 15 mL beaker. From this, 1 mL was pipetted into 30 mL water, the time was noted and the pH was recorded. The 30 mL solutions were neutralized using 1 M and 0.1 M sodium hydroxide and diluted to 50 mL. Samples were analyzed by taking 100 μL of the above solution and running it in the CE as described above. The peak areas and migration times were recorded and the concentration was determined by reference to a standard curve of peak area/migration time versus concentration. This standard curve was prepared by diluting surfactant with sulfuric acid at room temperature and immediately neutralizing and diluting samples as done in the actual hydrolyses experiments.

Results and discussion

Reaction rates of substances are greatly changed when the substances in question are incorporated into micelles. These substances may enter the micelle and thus be held in a more hydrophobic environment where the reagent is more or less soluble, or, as in the case of TDDS, the substance of interest may be the surfactant actually forming the micelles. The charge on the surface of a micelle will strongly attract or repel charged reagents. In the case of acid hydrolysis we would expect the protons to be attracted to the negatively charged surface of the micelle, thus producing rate enhancement at surfactant concentrations above the cmc. Such a phenomenon has been well documented in the case of alkanesulfate hydrolysis (8, 9, 11). Some investigators of alkanesulfate hydrolysis have only used concentrations above the cmc (7) while others have conducted studies at lower concentrations (9–11). It was our intention to carry out our study in a concentration region considerably lower than the cmc in order to avoid micellar rate enhancement. We chose our experimental setup to mimic conditions used by El Sawy et al. (3), so that comparisons would be valid. To this end, we chose TDDS as the substrate because it was the shortest-chain disulfate reported in their paper. Because of having the shortest chain, it was found to have the lowest surface tension and be the best emulsifying agent of the

© 1999 NRC Canada

Fig. 1. Plots of reaction rate versus concentration for TDDS in 0.5 M sulfuric acid at 60°C (●), 75°C (△), and 90°C (■).

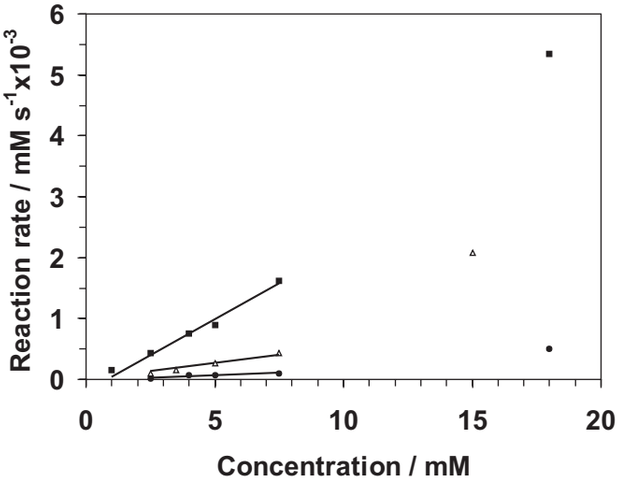

alkanedisulfates that they prepared. Although we have prepared even shorter-chain analogues, it is more difficult to purify them and so the choice of TDDS as substrate was convenient from all standpoints.

Our method of synthesizing alkanedisulfates involves the reaction of chlorosulfonic acid with the appropriate diol. The end product can contain unreacted diol, singly sulfated product, and chloride and sulfate (4). A variety of ways to purify these surfactants were investigated. The use of C18 reverse-phase columns gave some pure product, but at high cost on a scale sufficient for our kinetic experiments. We believe that the main problem in the purification process is the high solubility conferred by the presence of the second sulfate. The sodium TDDS is extremely soluble in water, and only slightly soluble in ethanol. Sodium chloride is similarly soluble, while sodium sulfate, also very soluble in water, is less soluble in ethanol. As the length of the hydrocarbon tail is decreased, this problem is exacerbated. Soxhlet extractions were found to be the most useful method of purification. The impurity in product tended to vary, but a typical crude product might contain TDDS, hydroxytetradecanesulfate, chloride, and sulfate in a mole ratio of 2.2:1:2:2.4 as determined using CE (using a run in BARB buffer and a run in chromate buffer). As the diol is neutral, it is not separated from the water peak in our buffers. However, the presence of diol is shown by the cloudiness of an aqueous solution of the product. Soxhlet extraction with butanol removed hydroxytetradecanesulfate isomers and unreacted diol into the butanol. The TDDS was separated from inorganic impurities in a subsequent Soxhlet extraction with ethanol. Although longer refluxing times yield more product, the cleanest TDDS (96%) was obtained using a 1 h refluxing time. It was not possible to remove all the chloride.

The final concentration of acid used in the kinetic runs was set at 0.5 M sulfuric, as used by El Sawy et al.(3). This concentration was high enough above the concentrations of surfactant used in the main experiments (1 mM – 7.5 mM) to give us pseudo-first-order conditions.

The reaction was followed by monitoring the disappearance of TDDS as determined by CE using a BARB buffer. Quantitation was by peak area divided by migration time, and an internal standard was not found to be necessary. The reproducibility of runs was generally a few per cent. We assumed that the high concentration of acid being used would override ionic strength effects from using different concentrations of surfactant. Indeed, we checked this assumption by carrying out a run using 10 mL of 10 mM TDDS with an added 0.01 g L^{-1} Na_2SO_4. No significant difference in rate was found.

The presence of the high concentration of sulfuric acid in the reaction mixture necessitated neutralization and dilution of samples before analysis, and limited the concentration of acid that we could use. Hydrolyses of submicellar concentrations of alkanesulfates of interest to us, such as tetradecanesulfate, were not able to be followed by CE using our particular instrument because the sample concentrations were lower than the limit of detection after the necessary neutralisation and dilution of the sulfuric acid reaction matrix. The CMC for tetradecanesulfate in water is 2.2 mM while that for tetradecanedisulfate in water is 11.6 mM (1).

The temperatures were chosen to be well above room temperature so that the reactions went rapidly enough to be followed in reasonable time periods. Preliminary experiments at 40°C, the temperature used by El Sawy et al., gave inconveniently slow reaction rates. They reported the time for cloudiness to appear in a reaction flask containing 5 mM TDDS in 0.5 M sulfuric acid to be 41 min (3). We were not able to duplicate this result. No cloudiness was detected even after 6 days under the prescribed conditions. In their discussion, they stated that the TDDS was stable to hydrolysis, but this is also not completely true, as cloudiness is seen in less than 2 h if the hydrolysis is carried out at 90°C.

The initial rate curves for various concentrations of TDDS at the chosen temperatures of 60, 75, and 90°C were measured, plotted, and the slopes obtained by linear fitting of the points. The fit was very good, with R for the lines ranging from 0.987 to 1.000.

The observed pseudo-first-order rate constant for hydrolysis can be written (18) as

$$k_{obs} = k_0 + k_{H^+}[H^+] + k_{OH^-}[OH^-]$$

We previously reported that we were unable to detect basic hydrolysis of TDDS, and here we are working in acid conditions where $[OH^-]$ will be very low. This is in agreement with the zero values Kurz (7) assigned to the k_{OH}'s for alkanesulfates with carbon chains of 10 and longer. The values of k_0, the first-order rate constant for uncatalyzed hydrolysis, decrease with increasing hydrocarbon chain length for the alkanesulfates and do not seem to be dependent on micellization. The value of k_0 given for SDS at 90°C is 0.27×10^{-7} (7), and thus the value for tetradecanesulfate would be expected to be smaller and even less significant in comparison to k_{H^+}. We will make the assumption that k_0 is also much smaller than k_{H^+} $[H^+]$ for TDDS. Thus we can say

$$k_{obs} = k_{H^+}[H^+]$$

In Fig. 1, the rates obtained from the initial rate curves are plotted as a function of concentration for the three different reaction temperatures. We see a linear dependence on concentration until a concentration of 7.5 mM is reached. We

© 1999 NRC Canada

Fig. 2. Plots of log reaction rate versus log concentration for TDDS in 0.5 M sulfuric acid at 60°C (●), 75°C (△), and 90°C (■).

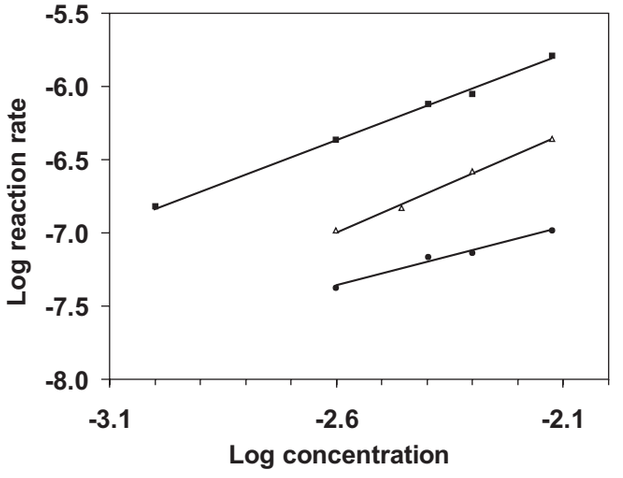

Fig. 3. Plot of ln rate constant versus reciprocal temperature (K^{-1}) for TDDS in 0.5 M sulfuric acid.

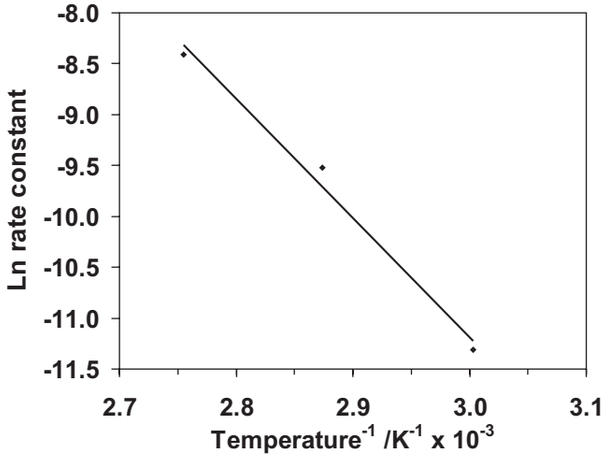

expect that the rate would increase once micelle formation starts to occur because the surface of the micelle would have many negative charges and thus strongly attract the hydrogen ions. Although Marangoni's group reported the cmc to be 11.6 mM for TDDS in aqueous solution (1), the cmc in the 0.5 M sulfuric acid used for the hydrolysis experiment will be quite different. We would expect that the sulfuric acid would act to lower the cmc, as cmc's are known to decrease in the presence of salts. Increasing the temperature generally has the opposite effect (19). To be sure that we were working in the premicellar region under our conditions, one higher concentration was used at each temperature. The increase in rate over that expected shows that micellization was occurring at the higher concentration, and thus we feel confident that our results for 1–7.5 mM are those for premicellar conditions. The sudden jump in rate that is characteristic of micellization occurred between the last two points on each plot shown in Fig. 1. We have not drawn a line between these points, because all we can really say from our results is that there is a change in the rate constant at some point between them.

The premicellar reaction rates at 60, 75, and 90°C were 1.2×10^{-5}, 6.8×10^{-5}, and 2.2×10^{-4} M s^{-1}, respectively. As our concentration of acid ($[H^+]$) is 1 M, these translate to specific acid rate constants of the same numerical value. These k_{H^+}'s are about 10 times larger than corresponding values that have been reported for SDS (9). A better comparison would be with rates for the hydrolysis of tetradecanesulfate, but little information is available. Kurz made some comparisons of hydrolysis rates between SDS and tetradecanesulfate, but the extra carbon never made more than a 50% difference to the rate (7). We can thus assume that the increase in hydrolysis rate as compared to SDS is much more because of the extra sulfate than the extra CH_2. The extra sulfate will increase the electrostatic attraction of the proton to the surfactant. This is the same phenomenon that is responsible for the increase in hydrolysis rate upon micellization, but on a much smaller scale. In addition, the presence of two sulfate groups gives two places for hydrolysis to occur, in a sense doubling the chance of reaction. Once one of the sulfate groups is hydrolyzed, the resulting hydroxytetradecanesulfate hydrolyzes very rapidly, as was previously reported for hydroxydecanesulfate (4).

Plots of log rate versus log concentration for the sets of reactions at 60, 75, and 90°C are shown in Fig. 2. Assuming that the mechanism is the same at all three temperatures, the slopes of 0.86, 1.34, and 1.16, respectively, were averaged to give a value of 1.12. This indicates that the hydrolysis reaction is first order with respect to TDDS. Motsavage and Kostenbauder found that premicellar acid hydrolysis of SDS was first order with respect to SDS at 50 and 70°C (9). Muramatsu and Inoue (10) reported that SDS hydrolysis was second order in surfactant, with the difference being that their results were obtained at 40°C. In addition, they followed the reaction using a radiotracer method after precipitation of sulfate with barium chloride. It seems unlikely that the reaction mechanism changes at this point, and the difference is much more likely to be due to the different methods of obtaining the kinetic data. In addition, the hydrolysis of *s*-butyl hydrogen sulfate is also first order in substrate.

The Arrhenius equation tells us (20) that

$$\ln k = \ln A - E_a/RT$$

where A is the pre-exponential factor and E_a is the activation energy. By plotting $\ln k_{H^+}$ versus the reciprocal of the temperature (Fig. 3) we obtained a value of 96 J mol^{-1} for the activation energy of the hydrolysis reaction. In comparison, an E_a of 120 kJ mol^{-1} was reported for the slower hydrolysis of SDS (9).

The enthalpy of activation in liquid systems can be calculated from the activation energy as follows (21):

$$\Delta H^{o\ddagger} = E_a - RT$$

where R is the gas constant and T is the temperature in degrees Kelvin.

For the acid hydrolysis of TDDS, our calculated values were 94.7, 94.5, and 94.4 kJ mol^{-1} at 60, 75, and 90°C, respectively. Kurz reported an enthalpy of activation of 112

© 1999 NRC Canada

kJ mol^{-1} for SDS at 90°C (7), slightly larger than the value obtained by us for TDDS under the same conditions.

The entropy of activation can be calculated using the following equation:

$$k_{H^+} = kT/\hbar\, e^{-\Delta H_a/RT} e^{-\Delta S_a/R}$$

where k is the Boltzmann constant (21).

The entropy of activation for the hydrolysis of TDDS was thus found to be –55 J K^{-1} mol^{-1}. Such a decrease in entropy on formation of the activated complex is common. A decrease in entropy corresponds to formation of a more ordered configuration in the transition state. A large negative energy may signify an association reaction, where the preliminary binding of the two reagents in a transition state considerably reduces their freedom. A large negative activation entropy may also occur when the activated complex can be more solvated than are the reagents. This electrostriction of water is usually attributed to the distribution of charges in the activated state, suggestive of a bimolecular transition state (22).The more tightly bound the complex, the lower will be its entropy (21). In contrast to our results, Motsavage and Kostenbauder reported a positive entropy of activation of 13 J K^{-1} for hydrolysis of premicellar SDS, with an even more positive value for SDS concentrations above the cmc (9). Positive activation entropies have also been reported for the hydrolysis of steroidal hydrogen sulfate, although solvents other than pure water were used (23). The second charged sulfate group presumably makes a big difference to the electrostriction of water, to the binding of the initial H^+, and to the charge separation in the actual transition state.

Conclusions

CE was used to follow the decrease in concentration of TDDS as a function of time and thus obtain kinetic data for the hydrolysis of TDDS. The hydrolyses were considerably slower than those measured by El Sawy et al. (3) at lower temperature (40°C) but otherwise similar conditions. The majority of the rate measurements were carried out using premicellar concentrations of TDDS. Under these conditions, the rate was found to be first order in TDDS. Hydroxytetradecanesulfate hydrolyzes much more quickly than TDDS, so the hydrolysis of the first sulfate is presumed to be the rate-determining step. Comparison to data in the literature shows that TDDS hydrolyzed more quickly than SDS (and, by inference, more quickly than tetradecanesulfate) under the same conditions. This was attributed to the presence of the second sulfate increasing the overall negative charge (and thus attraction of protons) and providing twice the number of sites for the initiation of hydrolysis. Further rate enhancement is seen at high TDDS concentrations, where we assume micellization has occurred, further increasing the overall negative charge density and the attraction of protons.

The activation energy for the reaction was determined to be 97 kJ mol^{-1}, while the entropy of activation was –55 J K^{-1} mol^{-1}. The high activation energy is in accord with the reaction being very slow, while the entropy change suggests a complex transition state involving restricted motion of the various species involved.

Acknowledgements

The authors thank the Natural Sciences and Engineering Research Council of Canada and the St Francis Xavier University Council for Research for funding.

References

1. E.K. Comeau, E.J. Beck, J.F. Caplan, C.V. Howley, and D.G. Marangoni. Can. J. Chem. **73**, 1741 (1995).
2. G.D. Boucher, A.C. MacDonald, B. Hawrylak, and D.G. Marangoni. Can. J. Chem. **76**, 1266 (1998).
3. A.A. El-Sawy, S.A. Essaway. M.M. El-Sukkary, and A.M.F. Eissa. Hung. J. Ind. Chem. **20**, 25 (1992).
4. R.A. Walker, A.C. MacDonald, T. MacGillivray, D.G. Marangoni, and T. Smith-Palmer. Can. J. Chem. **76**, 292 (1998).
5. P.A. Kooreman and J.B.F.N. Engberts. Recl. Trav. Chim. Pays-Bas, **113**,163 (1994).
6. R.R. Read and W.G. Fredell. Toilet Goods Assoc. **30**, 11 (1958).
7. J.L. Kurz. J. Phys. Chem. **66**, 2239 (1962).
8. H. Nogami, S. Awazu, and Y. Kanakubo. Chem. Pharm. Bull. **11**, 13 (1963).
9. V.S. Motsavage and H.B. Kostenbauder. J. Colloid Sci. **18**, 603 (1963).
10. M. Muramatsu and M. Inoue. J. Colloid Interface Sci. **55**, 80 (1976).
11. M. Nakagaki and S. Yokoyama. J. Pharm. Sci. **74**, 1047 (1985).
12. A. Hilmi, J.H.T. Long, and A. Nguyen. Chemosphere, **36**, 3137 (1998).
13. G. Dinelli, A. Vicari, A. Bonetti, and P. Catizone. J. Agric. Food Chem. **45**, 1940 (1997).
14. P. Seng and R.A. Hartwick. J. Chromatogr. A, **695**, 279 (1995).
15. W.T. Lowther and B.M. Dunn. Lett. Pept. Sci. **1**, 89 (1994)).
16. Method no. N–601. *In* Waters innovative methods for ion analysis. Waters, Milford, Mass. 1989.
17. M.W.F. Nielen. J. Chromatogr. **588**, 321 (1991).
18. K.J. Laidler. Reaction kinetics. Vol. II. Reactions in solution. Pergamon Press, New York. 1963. p. 54.
19. D.J. Shaw. Introduction to colloid and surface chemistry. 4th ed. Butterworth-Heinemann, Oxford, U.K. 1992. p. 86.
20. W.J. Moore. Physical chemistry. 4th ed. Longman Group, London. 1963. p. 273.
21. W.J. Moore. Physical Chemistry. 4th ed. Longman Group, London. 1963. pp. 297–299.
22. K.J. Laidler. Reaction kinetics. Vol. II. Reactions in solution. Pergamon Press, New York. 1963. pp. 13–15.
23. S. Burstein and S. Lieberman. J. Am. Chem. Soc. **80**, 5235 (1958).

© 1999 NRC Canada

Thermodynamics of the interaction of HCl with D-xylose in water at 278.15–318.15 K

Jianji Wang, Kelei Zhuo, Qiufen Zhang, and Jinsuo Lu

Abstract: The thermodynamic parameters of interaction of HCl with D-xylose in water were determined from electromotive force measurements from 278.15 to 318.15 K. The correlation between the pair interaction Gibbs free energy parameters for HCl–sugar (g_{HCl-S}) and the mean number (n(*e*-OH)) of equatorial hydroxy groups in sugar molecules was found to be g_{HCl-S}/J kg mol^{-2} = (41.2 ± 2.1) + (16.88 ± 0.52)n(*e*-OH). Refractive indices of aqueous D-xylose solutions were measured and used to evaluate the polarizability of D-xylose molecule in water. Several theoretical models were used to calculate the salting constant of D-xylose. The results show that the calculated values are reasonably in agreement with the experimental ones.

Key words: thermodynamics, HCl, D-xylose, interaction parameter, salting constant.

Résumé : Utilisant des mesures de force électromotrice faites entre 278,15 et 318,15 K, on a déterminé les paramètres thermodynamiques de l'interaction HCl avec le D-xylose. On a trouvé que la corrélation entre les paramètres d'énergie libre de Gibbs pour l'interaction de la paire HCl–sucre (g_{HCl-S}) et le nombre moyen de groupes hydroxyles équatoriaux [n(*e*-OH)] dans les molécules de sucre est donnée par l'équation suivante: g_{HCl-S}/J kg mol^{-2} = (41,2 ± 2,1) + (16,88 ± 0,52)n(*e*-OH). On a mesuré les indices de réfraction de solutions aqueuses de D-xylose et on les a utilisées pour évaluer la polarisabilité de la molécule de D-xylose dans l'eau. On a utilisé plusieurs modèles théoriques pour calculer la constante de salaison du D-xylose. Les résultats montrent que les valeurs calculées sont en bon accord avec les données expérimentales.

Mots clés : thermodynamique, HCl, D-xylose, paramètre d'interaction, constante de salaison.

[Traduit par la Rédaction]

Introduction

The hydration of sugars (S) depends on their stereochemistry (1, 2). Several attempts have been made to rationalize the hydration characteristics of sugars (2–4). Franks et al. (5) and Suggett (6) introduced the important distinction between equatorial (*e*-OH) and axial hydroxy (*a*-OH) groups. Uedaira and Uedaira (7*a*) predicted that any properties that depend on the sugar hydration will correlate well with the number n(*e*-OH) of *e*-OH groups in sugar molecules. Examples have been given for diffusion coefficients (7*a*) and partial molar heat capacities (7*b*) of some mono-, di-, and trisaccharides in water.

In an earlier paper (8), we found a linear relation between the pair interaction Gibbs free energy parameters for electrolyte (E) – D-glucose (G) and those for E–sucrose (E = HCl, NaCl, KCl, $MgCl_2$, and $CaCl_2$) at 298.15 K. The slope of this linear equation was calculated to be the mean *e*-OH group number ratio of sucrose to glucose. In our recent papers (9), the thermodynamic parameters of interaction were reported between HCl and some sugars. In this work, we report the interaction parameters for the HCl – D-xylose (X) pair in water from 278.15 to 318.15 K. This not only would provide additional information on the interaction between HCl and D-xylose in water, but also enable us to examine the possible relationship between g_{HCl-S} and n(*e*-OH).

Electromotive forces (emf) measurements of the cells A and B without liquid junction

$$\text{A: Pt, } H_2(g, p^\circ)|\text{HCl}(m_{HCl})|\text{AgCl–Ag}$$

$$\text{B: Pt, } H_2(g, p^\circ)|\text{HCl}(m_{HCl}), \text{X}(m_X)|\text{AgCl–Ag}$$

at m_{HCl}(A) = m_{HCl}(B) were carried out at 10 K intervals from 278.15 to 318.15 K, where p° = 101.325 kPa, m_{HCl} and m_X are the molalities of HCl and D-xylose, respectively, with respect to a kilogram of pure water, m_{HCl} = 0.005–0.1 mol kg^{-1}, m_X = 0.2–0.8 mol kg^{-1}.

Experimental section

D-Xylose (Biochemical reagent, Quzhou Chemical Co.) was purified by recrystallization from aqueous solution of ethanol (80%) at low temperature. Then it was dried under vacuum at 343 K to constant weight and stored over P_2O_5 in a desiccator. The data of elemental analysis (C = 39.927%, H = 6.743%, O = 53.33%) are in good agreement with the theoretical values of xylose (C = 40.002%, H = 6.714%, O = 53.284%). This shows that thus-obtained xylose is anhydrous. Water with specific conductivity of (1.0–1.2) × 10^{-4} Ω^{-1} m^{-1} at room temperature was used in this work. Purification and standardization of hydrochloric acid have been described elsewhere (9).

Received June 10, 1998.

J. Wang,[1] K. Zhuo, Q. Zhang, and J. Lu. Department of Chemistry, Henan Normal University, Xinxiang, Henan 453002, P.R. China.

[1]Author to whom correspondence may be addressed. Telephone (86) 373-3383000-5779. Fax: (86) 373-3383145.

© 1999 NRC Canada

Table 1. The emf (in mV) values of the cells A and B for the HCl–D-xylose–water system from 278.15 to 318.15 K.

		T (K)				
m_{HCl} (mol kg^{-1})	m_X (mol kg^{-1})	278.15	288.15	298.15	308.15	318.15
0.005 000	0.0000	0.491 79	0.495 40	0.498 54	0.501 04	0.502 91
	0.2016	0.490 99	0.494 61	0.497 73	0.500 08	0.501 61
	0.3954	0.490 04	0.493 65	0.496 74	0.499 26	0.500 87
	0.5923	0.489 32	0.492 89	0.496 02	0.498 16	0.499 86
	0.7932	0.488 48	0.491 83	0.495 00	0.497 47	0.499 02
0.010 000	0.0000	0.459 62	0.462 23	0.464 17	0.465 62	0.466 50
	0.1801	0.458 78	0.461 46	0.463 31	0.464 86	0.465 29
	0.3944	0.458 04	0.460 50	0.462 34	0.463 61	0.464 14
	0.598	0.456 89	0.459 58	0.461 38	0.462 62	0.463 23
	0.7942	0.456 15	0.458 75	0.460 61	0.461 88	0.462 41
0.030 000	0.0000	0.409 66	0.410 52	0.410 73	0.410 26	0.409 32
	0.19	0.408 93	0.409 75	0.409 80	0.409 33	0.408 10
	0.3939	0.407 98	0.408 77	0.409 02	0.408 39	0.407 28
	0.6176	0.406 83	0.407 61	0.407 92	0.407 26	0.405 92
	0.7861	0.405 91	0.406 76	0.407 09	0.406 39	0.405 31
0.05 000	0.0000	0.386 30	0.386 53	0.385 82	0.384 66	0.382 87
	0.1985	0.385 37	0.385 56	0.384 83	0.383 59	0.381 73
	0.3966	0.384 44	0.384 65	0.383 96	0.382 55	0.380 63
	0.6138	0.383 22	0.383 52	0.382 80	0.381 49	0.379 60
	0.7996	0.382 54	0.382 74	0.382 02	0.380 66	0.378 70
0.10 000	0.0000	0.355 00	0.354 02	0.352 43	0.350 23	0.347 56
	0.2004	0.353 84	0.352 95	0.351 37	0.349 14	0.346 35
	0.3858	0.353 01	0.352 11	0.350 52	0.348 34	0.345 61
	0.6068	0.351 97	0.351 03	0.349 44	0.347 27	0.344 53
	0.7849	0.351 08	0.350 08	0.348 42	0.346 21	0.343 56

The AgCl–Ag electrodes were of the thermal electrolytic type (10). They were aged in 0.1 mol kg^{-1} HCl(aq), which was deoxygenated by bubbling hydrogen. Three days after preparation, the finished electrodes were intercompared and the bias potentials were usually less than 0.05 mV. Only those AgCl–Ag electrodes whose bias potentials were less than 0.02 mV were used. Standard potentials of these electrodes in water were determined by the method of Bates and Robinson (11). They are in excellent agreement with the literature values (12) within experimental error. The hydrogen electrodes were lightly coated with platinum black in terms of the Hills and Ives method (13). High-purity hydrogen served as the source of hydrogen. The cells were of all-glass construction with four isothermal presaturators containing the test solution, as described by Yang et al. (14). These cells were thermostated at each temperature with an accuracy of ±0.02 K. The test solutions were freshly prepared. All measures were made using two Ag–AgCl electrodes and two hydrogen electrodes. Equilibrium was reached in about 4–5 h after the initiation of hydrogen bubbling. This allows for the anomeric equilibrium to be reached. The other experimental apparatus and experimental procedures were the same as previously described (9). The observed emf values were corrected to the values at 101.325 kPa of hydrogen. These corrected emf values are listed in Table 1.

Refractive indices of aqueous solutions of D-xylose were measured by a 2WA-J-type refractometer (Shanghai) at 298.15 K from 2 to 24 wt.%.

Results

The transfer Gibbs free energies of electrolyte from water (W) to aqueous nonelectrolyte solutions (W + N) may be expressed as (9)

$$[1]\qquad \Delta_t G_E(W \rightarrow W + N) = -nF\Delta E = 2\nu g_{EN} m_N + 6\nu^2 g_{EEN} m_E m_N + 3\nu g_{ENN} m_N^2$$

where n and F have their usual meaning, ΔE is the difference of the emf values. In the present case, $\Delta E = E_B - E_A$ at $m_E(A) = m_E(B)$; ν is the number of ions into which the electrolyte dissociates; g_{EN}, g_{EEN}, and g_{ENN} are pair and triple interaction Gibbs free energy parameters that take into account for all new sources of nonideality in the ternary system. The higher terms have been neglected in eq. [1]. The Gibbs free energy parameters for the HCl–D-xylose–water system were obtained by least squares and given in Table 2. In this work, we are yet interested in the pair parameters which are most important in dilute solutions.

The relationship between g_{EN} and thermodynamic temperature T can be well represented by the empirical equation (9)

$$[2]\qquad g_{EN} = a + bT + cT^2$$

The coefficients a = 3876.8 J kg mol^{-2}, b = –26.279 J kg mol^{-2} K^{-1}, c = 0.045 714 J kg mol^{-2} K^{-2} were obtained by least squares for the HCl–D-xylose pair, with a standard deviation of the fit of 2.0 J kg mol^{-2}.

© 1999 NRC Canada

Table 2. Interaction free energy parameters for the HCl–D-xylose–water system from 278.15 to 318.15 K.

T (K)	g_{EN} (J kg mol^{-2})	g_{EEN} (J kg^2 mol^{-3})	g_{ENN} (J kg^2 mol^{-3})	δ^a (mV)	R^b
278.15	103±4	37.7±4.7	–0.03±3.96	0.10	0.996
288.15	102±3	27.3±3.4	0.12±2.91	0.07	0.998
298.15	105±3	24.5±3.9	2.23±3.27	0.08	0.998
308.15	118±5	14.7±5.1	–3.55±4.32	0.11	0.996
318.15	144±5	–4.19±5.97	–17.43±5.05	0.12	0.994

[a] δ is the standard deviation of the fit.
[b] R is the correlation coefficient.

Table 3. Pair interaction parameters for HCl–D-xylose from 278.15 to 318.15 K.

T (K)	Ts_{EN} (J kg mol^{-2})	h_{EN} (J kg mol^{-2})	$c_{p,EN}$ (J kg mol^{-2} K^{-1})	k_S (kg mol^{-1})
278.15	236	340	–25.4	0.178
288.15	–19	81	–26.3	0.170
298.15	–292	–187	–27.3	0.169
308.15	–584	–464	–28.2	0.184
318.15	–894	–750	–29.1	0.218

Substituting these coefficients to the following equations (9)

$$[3] \quad s_{EN} = -(b + 2cT)$$

$$[4] \quad h_{EN} = a - cT^2$$

$$[5] \quad c_{p,EN} = -2cT$$

Values of s_{EN}, h_{EN}, and $c_{p,EN}$, which are, respectively, pair interaction entropic, enthalpic, and isobaric capacity parameters for the HCl–D-xylose pair, were calculated and given in Table 3.

The salting constant, k_S, defined by Friedman (15) can be obtained from

$$[6] \quad RTk_S = 2\nu g_{EN}$$

at low values of both m_N and m_E (16, 17). The k_S values for the HCl–D-xylose–water system were obtained and also given in Table 3.

Discussion

Data in Table 2 show that $g_{HCl-X} > 0$ at the temperatures concerned. This means that D-xylose is being salted out by HCl in water (thermodynamic repulsion). Similar phenomena have been found for the HCl–alcohol (17), NaCl–alcohol (18), and HCl–sugar (D-glucose (9*a*), D-fructose (F) (9*b*)) pairs in water. However, the temperature dependence of g_{HCl-X} is different from g_{HCl-G} (see Fig. 1). Similar to g_{HCl-F}, g_{HCl-X} increases with increasing temperature (although it varies slightly from 278.15 to 298.15 K), whereas g_{HCl-G} decreases with increasing temperature. Data in Table 3 show that h_{HCl-X} and Ts_{HCl-X} decrease rapidly with increasing temperature (from positive to negative). Similar tendency exists also for the HCl–alcohol and HCl–sugar pairs in water.

In our previous papers, the structure interaction and electrostatic models were used to interpret the signs and temperature dependence of the interaction parameters for the HCl–alcohol (17) and HCl–D-glucose (9*a*) pairs. Therein, the interactions between HCl and hydroxy compounds were divided into four types: H^+–R (alkyl group); Cl^-–R; H^+–O (O stands for OH, C=O, and -O- groups); and Cl^-–O interactions. It seems that the interaction parameters for the HCl–X pair are mainly determined at low temperature (278.15 K) by the Cl^-–S (Cl^-–R, Cl^-–O) interactions which contribute a positive value to h_{HCl-X} and Ts_{HCl-X}. On the contrary, they are mainly determined at high temperatures (298.15, 308.15, and 318.15 K) by the H^+-O interaction which contributes a negative value to h_{HCl-X} and Ts_{HCl-X}. Meanwhile, the free energy is controlled by enthalpy at lower temperatures (278.15, 298.15 K) and by entropy at higher temperatures (298.15, 308.15, and 318.15 K). On these ideas, the experimental results obtained for the HCl–xylose–water system can be easily understood. In addition, the negative $c_{p,HCl-X}$ values mean that the HCl–X interaction results in a reduction in structure of the solution.

It is also noted that values of g_{HCl-X} are larger than those of g_{HCl-F} over the investigated temperatures, although D-xylose is a pentose, a molecule of which contains a CHOH group less than D-fructose (hexose). This is due to the difference in their stereochemistry as discussed below.

Correlation between pair interaction parameters and the mean number of *e*-OH groups

Hydration of sugars depends on stereochemistry of sugar molecules, especially on the compatibility of their conformation with water structure (1, 5, 6, 19). Therefore, the ratio of *e*-OH and *a*-OH groups seems to be an important factor which determines sugar hydration (7). To calculate the mean number of *e*-OH groups in sugar molecules, we recall the simplified assumption by Lemieux (20; see also ref. 7*a*) that the number of quasi-equatorial hydroxy groups in a molecule for both α- and β-furanose are regarded to be 1.25. On

© 1999 NRC Canada

Fig. 1. Temperature dependence of g_{HCl-S}: ◆, HCl–D-glucose (9*a*); ■, HCl–D-fructose (9*b*); ▲, HCl–D-xylose.

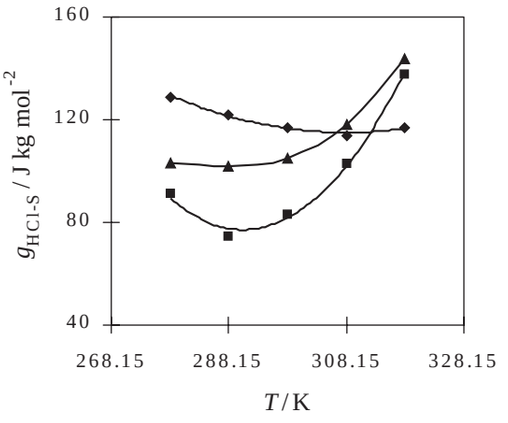

Fig. 2. Correlation between g_{HCl-S} and the mean number n(*e*-OH) of equaterial hydroxy groups in sugar molecules. 1, D-arabinose (unpublished datum from the laboratory of the authors); 2, D-fructose (9*b*); 3, D-xylose; 4, D-glucose (9*a*); 5, sucrose (22).

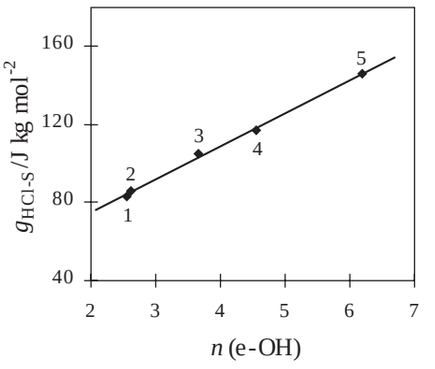

the basis of this assumption and the percentage ratio of anomers in aqueous solutions (1), the values of n(*e*-OH) were calculated as follows: 4.56 for D-glucose, 2.56 for D-fructose, 3.67 for D-xylose, 2.61 for D-arabinose, and 6.2 for sucrose (7*b*, 21).

The g_{HCl-S} values are plotted against n(*e*-OH) in Fig. 2. Evidently, a good linear correlation between g_{HCl-S} and n(*e*-OH) can be observed. By fitting these data to a linear equation, we get

$$[7] \quad g_{HCl-S}/\text{J kg mol}^{-2} = (41.2 \pm 2.1) + (16.88 \pm 0.52)n(e\text{-OH})$$

with a correlation coefficient of 0.999 and a standard deviation of fit of 1.6 J kg mol^{-2}. The equation shows that (*i*) the g_{HCl-S} values are strongly affected by n(*e*-OH); (*ii*) the increase in g_{HCl-S} for each *e*-OH group is about 17 J kg mol^{-2}. This also confirms the suggestion that the hydration characteristics of sugars can be rationalized by the ratio of *e*- to *a*-OH groups (5–7). Furthermore, we can conclude that the dehydration of sugar molecules arising from the interaction between HCl and hydrated sugar molecules should give a significant contribution to g_{HCl-S}. It should be mentioned that such a good correlation is possibly because few data points were used in the fit. More measurements are to be made in the laboratory of the authors.

In previous papers (9), a so-called "H^+-induced structure changes" model was proposed to interpret the interaction of HCl with sugars. In fact, the structure change of sugar molecules will dispel the compatibility between the OH groups on ring sugar molecules and the three-dimensional hydrogen-bonded structure of water, and result in some changes of hydration shell of sugar molecules. This is equivalent to the decrease in the mean number of *e*-OH groups. Accordingly, the g_{HCl-S} values will decrease.

Now return our attention to the difference between HCl–D-xylose and HCl–D-fructose interactions. It can be seen from eq. [7] that the larger value of g_{HCl-X} is due to the larger n(*e*-OH) values of D-xylose compared with D-fructose, although a D-xylose molecule contains one CHOH group less than D-fructose. In other words, because D-xylose is more compatible with water structure, the changes in its hydration shell should contribute a larger value to g_{HCl-X} than would D-fructose.

Theoretical calculation of salting constants

In the preceding paper (22), we calculated the salting constants of three sugars (D-glucose, D-fructose, sucrose) by HCl in water from the Debye–MacAulay theory (DMT) (23), Conway–Desnoyers–Smith theory (CDST) (24), the internal pressure theory (IPT) (25), and the scaled particle theory (SPT) (26). The results showed that the calculated values are reasonably in agreement with the experimental ones.

It has been noted that selecting the required molecular parameters is very important in the calculation. Especially, the parameters of oxonium ion (H_3O^+), such as radius, seriously affect the calculated results. The methods described in the preceding paper (22) for obtaining these molecular parameters have also been used in this work.

The polarizability of D-xylose molecule was obtained by the following processes: first, using the measured refractive indices of pure water (1.3336), the polarizability of water molecule was calculated from the Lorenz–Lorentz equation (27); then, the polarizability of water and the refractive indices of aqueous D-xylose solutions were used to evaluate polarizabilities of D-xylose molecule at various concentrations; finally, the polarizability at infinite dilution for D-xylose was obtained by fitting these data and extrapolating it to zero concentration. The molecular parameters used in the calculation are presented in Table 4.

Using these parameters, the salting constants at 298.15 K calculated from the theoretical models mentioned above are 0.244 (CDST), 0.203 (IPT1),[2] 0.097 (IPT2),[2] and 0.127

[2] IPT1 refers to the equation (25): $[V_n^\circ(V_s - V_s^\circ)]/(RT\beta^\circ)$, where V_n° and V_s° are the standard molal volume (= limiting apparent molal volume V_Φ^∞) of nonelectrolyte and electrolyte, respectively. V_s is the molal volume of the electrolyte as in the molten state and β° the compressibility of pure water. V_{HCl} and V_{HCl}° were, respectively, taken as 20.5 and 18.1 cm^3 mol^{-1} (25*a*). IPT2 refers to the equation (25): $\{[V_n^\circ(V_s - V_s^\circ)]/(RT\beta^\circ)\}[a/(a + b)]$, where a is the average radius of the cation and anion, and b is the radius of the nonelectrolyte (sugar). In the present paper, they were taken as the hydrated radius.

© 1999 NRC Canada

Table 4. Molecular parameters used in the theoretical calculation of salting constants at 298.15 K.

	σ^a (10^{-8} cm)	α^b (10^{-24} cm^{-3})	ϵ/k^c (K)	$r_p{}^d$ (10^{-8} cm)	$r_h{}^e$ (10^{-8} cm)	$V_m{}^{\circ f}$ (cm^3 mol^{-1})
H_3O^{+g}	2.43	1.30	519.1	1.22	2.82[j]	12.5
Cl^-	3.62[h]	3.02[h]	226	1.81[h]	3.32[j]	23.7
H_2O	2.75[h]	0.21[h]	85.3[h]			18.1
D-Xylose	6.56[k]	10.7	519		3.28[k]	95.5[i]

[a]σ is the diameter used in the SPT.

[b]α is the polarizability used in the CDST and SPT.

[c]ϵ/k is the energy parameter which were calculated from the Mavroyannis–Stephen formula (28) except for water.

[d]Pauling radius.

[e]r_h is the hydrated radius.

[f]V_m° is the standard partial molal volume in water (22).

[g]The method for obtaining the parameters was presented in ref. 22.

[h]From ref. 26.

[i]From ref. 32.

[j]From ref. 29.

[k]Hydrodynamic radius or diameter was evaluated from the Stokes–Einstein equation (30) using the diffusion coefficients (31).

(SPT), respectively. Clearly, the theoretical values of k_S are reasonably in agreement with the experimental (0.169). This shows that these salt effect theories are suitable not only for hexoses but also for pentose, D-xylose. In the following work, the interaction of HCl with other pentoses will be investigated.

Acknowledgments

Financial support from the National Natural Science Foundation of China (grant no. 29573102) and the Science Foundation of the National Education Commission of China is gratefully acknowledged.

References

1. (*a*) G. Barone. Thermochim. Acta, **162**, 17 (1990); (*b*) F. Franks. Pure Appl. Chem. **59**, 1189 (1987).
2. (*a*) S.A. Galema, M.J. Blandamer, and J.B.F.N. Engberts. J. Am. Chem. Soc. **112**, 9665 (1990); (*b*) J. Org. Chem. **57**, 1995 (1992); (*c*) S.A. Galema, H. Høiland. J. Phys. Chem. **95**, 5321 (1991).
3. F. Franks. *In* Polysaccharides in food. *Edited by* J.M.V. Blanshard and L.R. Mitchel. Butterworths Publication Ltd., London and Boston. 1979. p. 33.
4. M.D. Walkinsaw. J. Chem. Soc. Perkin Trans. **2**, 1903 (1987).
5. (*a*) F. Franks, J.R. Ravenhill, and D.S. Reid. J. Solution Chem. **1**, 3 (1972); (*b*) M.J. Tait, A. Suggett, F. Franks, S. Ablett, and P.A. Quickenden. J. Solution Chem. **1**, 131 (1972).
6. (*a*) A. Suggett and A.U. Clark. J. Solution Chem. **5**, 1 (1976); (*b*) A. Suggett. J. Solution Chem. **5**, 33 (1976).
7. (*a*) H. Uedaira and H. Uedaira. J. Solution Chem. **14**, 27 (1985); (*b*) J. Chem. Thermodyn. **17**, 901 (1985).
8. J. Wang, L. Zeng, W. Liu, and J. Lu. Thermochim. Acta, **224**, 261 (1993).
9. (*a*) K. Zhuo, J. Wang, J. Zhou, and J. Lu. J. Phys. Chem. B, **101**, 3447 (1997); (*b*) K. Zhuo, J. Wang, Y. Cao, and J. Lu. J. Phys. Chem. B, **102**, 3574 (1998).
10. R.G. Bates. *In* Determination of pH. John Wiley and Sons Inc., New York. 1964. p. 281.
11. R.G. Bates and R.A. Robinson. J. Solution Chem. **9**, 455 (1980).
12. D.R. While, R.G. Bates, and R.A. Robinson. J. Solution Chem. **9**, 457 (1980).
13. G.J. Hills and D.J.G. Ives. *In* Reference electrodes. *Edited by* D.J.G. Ives and G.J. Janz. Academic Press, New York. 1960. p. 107.
14. J. Yang, D. Men, C. Liang, L. Zhang, L. He, and A. Sun. J. Phys. Chem. **93,** 7248 (1989).
15. (*a*) H.L. Friedman. J. Solution Chem. **1**, 387 (1972); (*b*) *In* The physics and chemistry of aqueous ionic solutions. *Edited by* M.C. Bellissent-Funel and G.W. Noilsons. D. Reidel Publishing Co., Dordrecht, The Netherlands. 1987. p. 61.
16. (*a*) G. Perron, D. Joly, J.E. Desnoyers, L. Avedikian, and J.P. Morel. Can. J. Chem. **56**, 552 (1978); (*b*) J.P. Morel, C. Lhermet, and N. Morel-Desrosiers. J. Chem. Soc. Faraday Trans. 1, **84**, 2567 (1988).
17. (*a*) K. Zhuo, J. Wang, and J. Lu. J. Chem. Soc. Faraday Trans. **92**, 41 (1996); (*b*) J. Chem. Soc. Faraday Trans. **92**, 3363 (1996).
18. H. Piekarski. Can. J. Chem. **64,** 2127 (1986).
19. G. Barone, G. Castronuovo, D. Doucas, V. Elia, and C.A. Mattia. J. Phys. Chem. **87**, 1931 (1983).
20. R.U. Lemieux. *In* Molecular rearrangements. *Edited by* P. de Mayo. Wiley Interscience, New York. 1963. p. 713.
21. D. Lu, S. Ni, Z. Li, and R. Liu. Chem. J. Chin. Univ. **10**, 845 (1989).
22. J. Wang, K. Zhuo, Q. Zhang, Z. Yan, and H. Wang. J. Chem. Soc. Faraday Trans. **94**, 3359 (1998).
23. P. Debye and J. MacAulay. Phys. Z. **26**, 22 (1925).
24. B.E. Conway, J.E. Desnoyers, and A.C. Smith. Philos. R. Soc. London, **256**, 389 (1964).
25. (*a*) W.F. McDevit and F.A. Long. J. Am. Chem. Soc. **74**, 1773 (1952). (*b*) W. Xie, J. Su, and X. Xie. Thermochim. Acta, **169**, 271 (1990).
26. W.L. Masterton and T.P. Lee. J. Phys. Chem. **74**, 1776 (1970).
27. C.J.F. Böttcher. *In* Theory of dielectric polarization. 4th ed. Elservier Science Publishing Co., New York. 1973. p. 190.
28. C. Mavroyannis and M. Stephen. J. Mol. Phys. **5**, 629 (1962).
29. E.R. Nightingale. J. Phys. Chem. **63**, 1381 (1959).
30. R.A. Robinson and R.H. Stokes. *In* Electrolyte solutions. Butterworths Publication Ltd., London. 1955, p. 43.
31. H. Uedaira and H. Uedaira. J Phys Chem. **74**, 2211 (1970).
32. R.N. Goldberg. J. Phys. Chem. Ref. Data, **18**, 809 (1989).

© 1999 NRC Canada

Photochemical reaction of β-ionone derivatives in the presence of oxygen. A convenient synthesis of substituted 1,2,4-trioxanes

Mirta P. Mischne, Silvia N. Huber, and Juan Zinczuk

Abstract: This paper describes a simple and convenient method for the preparation of substituted 1,2,4-trioxanes. The scope of the one-pot photooxidation of β-ionones has been extended to include derivatives bearing additional functionalities in the β-ionone ring. The relative stereochemistry of the products has been established by analysis of ^{1}H and ^{13}C NMR spectra.

Key words: 1,2,4-trioxanes, photooxidation, cyclic peroxides, tetrahydrobenzopyranes, antimalarials.

Résumé : Dans ce travail, on décrit une méthode simple et convenable de préparer des 1,2,4-trioxanes substitués. On a élargi la domaine d'application de la réaction d'oxydation photochimique de façon à inclure des dérivés de la β-ionone qui possèdent des fonctionalités additionnelles sur le cycle. La stéréochimie relative des produits a été déterminée par analyse des résultats obtenus par RMN du ^{1}H et du ^{13}C.

Mots clés : 1,2,4-trioxanes, photooxydation, peroxydes cycliques, tétrahydrobenzopyranes, antipaludéens.

During the last two decades, the recognition of the importance of peroxide-containing natural products possessing biological activities has brought a resurgence in the chemistry of cyclic peroxides and related compounds (1). The discovery that the natural product artemisinin (**1**) is a potent antimalarial drug and that the presence of the 1,2,4-trioxane moiety is responsible for the pharmacological activity (2) has led to new syntheses of compounds containing this oxygenated system.

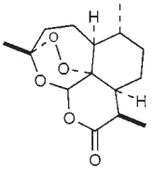

1

Examples of reported methods for preparing 1,2,4-trioxanes include the trapping of Paterno–Büchi 1,4 diradicals by molecular oxygen (3), autoxidation of imines in the presence of aldehydes (4), cyclization of vicinal hydroxyhydroperoxides with ketones (5), cyclization of hydroperoxyacetals with olefins (6) or epoxides (7), trapping of β-peroxy carbocations or equivalents with aldehydes and ketones (8), cationic ring expansion of ozonides (9), and singlet oxygen addition to pyranes (10). However, in spite of these efforts, there still remains a need to develop more efficient and operationally simple procedures for the preparation of this kind of peroxides.

We have recently reported a simple diastereoselective preparation of the 1,2,4-trioxanes **2a** and **2b** by irradiation of β-ionone type compounds **3a** and **3b** in the presence of oxygen (11).

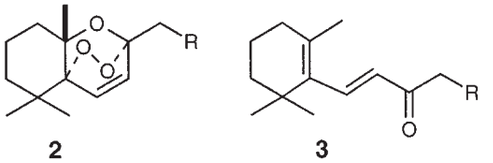

2 **3**

a R=H
b R=CO_2Me

These compounds were previously prepared by singlet oxygenation of the corresponding tetrahydrobenzopyranes and the stereochemistry of the singlet oxygen addition was assigned by comparing the ^{1}H NMR spectra of the olefinic compounds **2a** and **2b** with their corresponding saturated analogues (10*b*).

Because of the continuous interest on the chemistry and biological activity of cyclic peroxides and in line with our preliminary report, we decided to extend the scope of our methodology to prepare 1,2,4-trioxanes that contain additional functionality. Starting with the readily available ionone

Received July 14, 1998.

M.P. Mischne, S.N. Huber,[1] and J. Zinczuk.[2] Instituto de Química Orgánica de Síntesis (CONICET-UNR) Facultad de Ciencias Bioquímicas y Farmacéuticas, Casilla de Correo 991, 2000 Rosario, Argentina.

[1]This paper includes part of the results of the Doctoral Thesis of S.N.H. (Universidad Nacional de Rosario).

[2]Author to whom correspondence may be addressed. Telephone: 54-41-804600. Fax: 54-41-370477. e-mail: jzinczuk@fbioyf.unr.edu.ar

© 1999 NRC Canada

Fig. 1. Relative stereochemistry of compound **2b** and proton–proton through-space connectivities, obtained by NOE difference experiments.

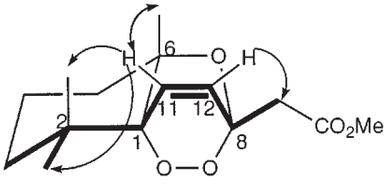

derivatives **4**, a series of 1,2,4-trioxanes **5** was obtained. The stereochemical outcome of the reaction was determined by a careful ^{1}H and ^{13}C NMR analysis of the products, which gives further support to the proposed mechanism for the formation of the trioxane compounds.

Results and discussion

β-Ionone derivatives **4a–4e** were prepared according to literature methods (12*a*–12*d*). Irradiation at λ 350 nm of a 0.01 M toluene solution of **4a–4e** for 6 h, while bubbling oxygen, gave, after purification by column chromatography, compounds **5a–5e** in 35–86% yield. The structures of the products were established based on analytical and spectral data.

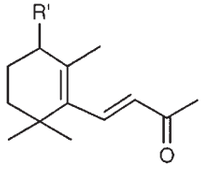

E-**4**

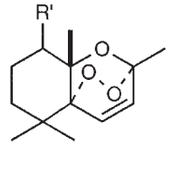

5

a R' = OH
b R' = OMe
c R' = OAllyl
d R' = OAc
e R' = O

a$_a$ R' = ax-OH
a$_e$ R' = eq-OH
b$_a$ R' = ax-OMe
b$_e$ R' = eq-OMe
c$_a$ R' = ax-OAllyl

c$_e$ R' = eq-OAllyl
d$_a$ R' = ax-OAc
d$_e$ R' = eq-OAc
e R' = O

The spectral analysis, necessary for the unambiguous determination of the relative stereochemistry of compounds **5a–5e**, was initiated with the previously described ester **2b**. The ^{1}H and ^{13}C NMR signals of compound **2b** were assigned on the basis of chemical shift considerations, and by HETCOSY, ^{1}H–^{13}C COLOQ, and a series of nuclear Overhauser enhancement (NOE) experiments, which further confirm the relative stereochemistry at C-1, C-6, and C-8 of this compound. Irradiation of the singlet at δ 1.11, attributed to the methyl of C-6, showed NOE with the H-11 signal, while irradiation at δ 6.54 (H-11) enhanced the signals of the C-2α, C-2β, and C-6 methyl protons. In addition, when the signal at δ 6.77 corresponding to H-12 was irradiated, the signal at δ 2.78 attributed to the methylene group of the ester moiety was enhanced (Fig. 1).

These results, which establish the *anti* relationship between the angular methyl group and the peroxide bridge, are in agreement with the conclusion reported previously by using an indirect method (10*b*).

In addition, NOE experiments were performed on compounds **5b**, **5d**$_a$, **5d**$_e$, and **5e**. In particular, strong reciprocal NOE were observed between the signals due to 11-H (δ 6.50) and the methyl groups bonded to C-2 and C-6 (δ 1.00–1.17). No enhancement of these signals was expected in the alternative position of the peroxide bridge. The results support the proposed relative configuration of 1,2,4-trioxanes **5**.

Further evidence for the diastereoselective outcome of the reaction was obtained by analyzing the products of the irradiation of the hydroxy-β-ionone **4a**. In this case, only two of the four possible isomers of 1,2,4-trioxanes were obtained. The resulting trioxanes **5a**$_a$ and **5a**$_e$ were analyzed by ^{1}H and ^{13}C NMR.[3] Thus, alcohol **5a**$_a$ was confirmed as being axial based on its ^{1}H NMR spectral data. While the signal at δ 3.80 is a broad singlet with $W_{1/2}$ = 6.8 Hz, clearly indicating an equatorial methine proton, in compound **5a**$_e$ the corresponding signal appears as a doublet of doublets centered at δ 4.34 (J = 4 and 12 Hz) with characteristic couplings of an axial proton (14). The observed downfield shift of the methine signal could be explained by the deshielding effect of the axial peroxide bridge. Moreover, the distinghishing feature in the ^{1}H NMR spectrum of **5a**$_a$ is a sharp doublet centered at δ 3.56 (J = 6 Hz). This signal, attributed to the hydroxyl proton resonance, is characteristic of an intramolecular hydrogen bond, coupled with the C-5 methine proton and bonded to one oxygen atom of the peroxide bridge. As expected, the signal disappeared upon treatment with deuterium oxide. On the other hand, the corresponding signal of **5a**$_e$ appears as a broad singlet centered at δ 2.45. The presence of an intramolecular hydrogen bond in alcohol **5a**$_a$ is also supported by comparing its IR spectrum with that of **5a**$_e$. The hydroxyl stretching band of **5a**$_a$ at 3575 cm^{-1} agrees with the expected value for an intramolecular hydrogen bond peak. On the other hand, the absorption band for **5a**$_e$ at 3610 cm^{-1} is characteristic of a free hydroxyl group (15). Therefore we must conclude that, in compound **5a**$_a$, the peroxide bridge must be on the same side as the hydroxyl group and, because of the geometrical constraint of the tricyclic system, the angular methyl group must occupy the axial position, which is *anti* to both the hydroxyl group and the peroxide bridge. The conformation of **5a**$_a$, suggested on the basis of the spectral analysis discussed above, is in agreement with conformational calculations performed by the MMX molecular mechanics program (16). The minimum-energy conformation calculated for the alcohol **5a**$_a$ is shown in Fig. 2.

The photooxidation of alkoxy-β-ionones **4b–4c** afforded the corresponding alkoxy-trioxanes **5b–5c** in low yield. The presence of a donor group in the ring makes the substrates more sensible to overoxidation by molecular oxygen and, consequently, to the formation of unidentified products. The formation of the equatorial isomers is preferred with the increasing steric demand of the alkoxy group and the lack of stabilization that is present in the axial isomer **5a**$_a$ because of the intramolecular hydrogen bond. Accordingly, **5b**$_e$ and traces of axial isomer **5b**$_a$ were formed from **4b** (R = OMe),

[3] The spectral data obtained are coincident with those reported by Jeger and co-workers (13) for the same compounds, although no stereochemical assignment was proposed by these authors. In addition, the ^{13}C NMR data of **5a**$_e$ were erroneously assigned to **5a**$_a$.

© 1999 NRC Canada

Scheme 1.

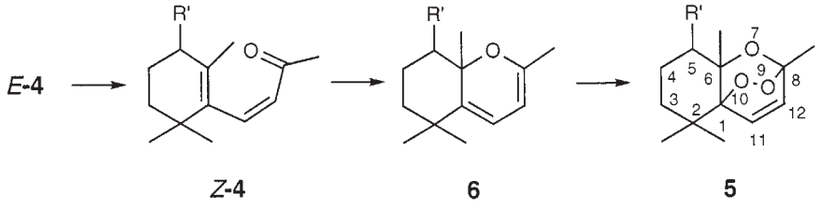

Fig. 2. Projection of the lowest-energy conformation of $\mathbf{5a}_a$ predicted on the basis of molecular mechanics calculations.

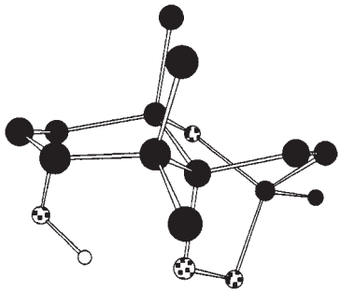

and for **4c** (R = allyloxy) only the equatorial isomer $\mathbf{5c}_e$ was obtained.

Significantly higher yields of 1,2,4-trioxanes were obtained by introducing deactivating groups into the β-ionone moiety. Thus, photooxidation of acetoxy-β-ionone **4d** afforded the corresponding acetoxytrioxanes in 74% yield as a 1:2 mixture of diastereoisomers $\mathbf{5d}_a$ and $\mathbf{5d}_e$. Moreover, the ketotrioxane **5e** was obtained from **4e** with excellent yield (86%).

On the basis of the results described above, the mechanism of formation of 1,2,4-trioxanes **5** could be explained by a rapid *E* to *Z* exocyclic double bond isomerization (*E*-**4** to *Z*-**4**), followed by a tandem process, involving an electrocyclic reaction to give the pyrane intermediates **6** and a Diels–Alder type singlet oxygen reaction addition (Scheme 1).

Although no extra sensitizer was used in the reaction, we conclude that is likely that the substrates may act as sensitizers and generate singlet oxygen.[4] The quantitative formation of **2a** from β-ionone **3a**, bearing an *anti* relationship between the angular methyl group and the peroxide bridge, allowed us to postulate that the oxygen molecule approaches the pyrane **6** (R′ = H) exclusively from the less hindered side. The angular methyl group blocks the attack from one face of the diene system. All the trioxanes obtained, **5a–5e**, show the same relative configuration as **2a** and further support the diastereoselectivity for the oxygen attack. We rationalized the intermediacy of the pyrane based on the reported formation of 1,2,4-trioxanes by sensitized oxygenation of such compounds. In this way, Jeger and co-workers (13) irradiated the epoxy-ionone **7**, to obtain a mixture of hydroxypyranes, **6a** (R′ = OH), which, after purification, were photooxygenated in the presence of a sensitizer to give the trioxanes **5a** in moderate yield.

In our case, when **7** was submitted to reaction with oxygen, the trioxanes **5a** were isolated in very low yield. Instead, the major components of the reaction mixture were the peroxyketal **8** and the hydroperoxide **9** (55% and 10% yield, respectively).

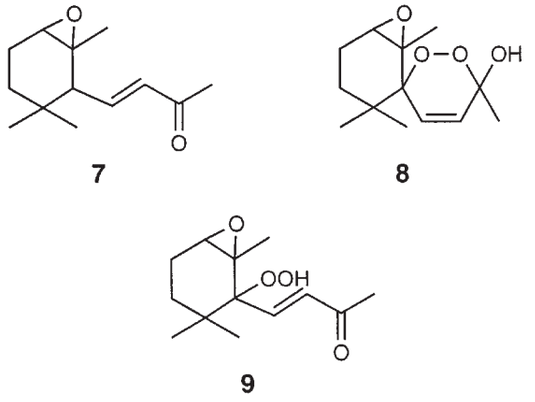

The formation of the spiro-peroxyketal **8** is probably due to the reaction of oxygen with the diradical **10**, formed from *Z*-**7**. The reaction of **10** with oxygen would give the intermediate hydroperoxide **9** that, subsequently, undergoes cyclization to **8**. This pathway is clearly favored over the formation of the hydroxytrioxanes **5a**, which would require the rupture of the C—O bond of the oxirane diradical **10**, necessary to afford the *Z*-hydroxy-β-ionone *Z*-**4a** that would yield the trioxanes **5a** through the intermediacy of the hydroxypyranes **6a** (Scheme 2).

Experimental section

Melting points were determined on an Electrothermal 9100 apparatus and are uncorrected. IR spectra were recorded on a Beckman Acculab 8 spectrometer. The ^{1}H and ^{13}C NMR spectra were measured at 200.1 and 50.3 MHz on a Bruker AC 200-E NMR spectrometer in $CDCl_3$ solutions, with TMS as internal standard. For the COSY, COLOQ, and NOE experiments Bruker standard software was employed. Assignments marked with *, **, or *** may be, correspondingly, interchanged. Column chromatography was performed on silica gel 60H, slurry packed, run under low pressure of nitrogen and employing increasing amounts of EtOAc in hexane as solvent. Analytical TLC was carried out using Kielselgel Merck GF_{254} of thickness 0.20 mm. EI-MS were measured on a ZAB-SEQ4F instrument (LANAIS,

[4] Jeger and co-workers (17) reported the formation of small amounts of the corresponding trioxane, when they photolyzed 7-Me-β-ionone without excluding oxygen from the reaction mixture.

© 1999 NRC Canada

Scheme 2.

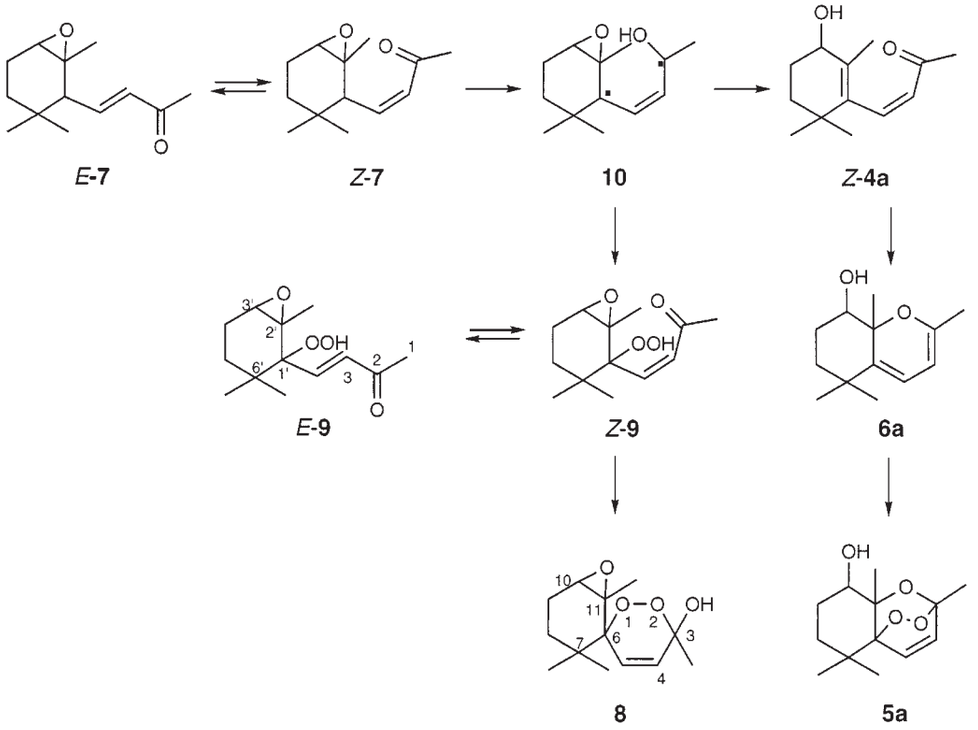

Universidad de Buenos Aires). Elemental analysis were performed by Atlantic Microlab, Inc., Norcross, U.S.A.

General procedure for the photooxidation of 5a–e

The irradiations were performed at λ 350 nm, in a Rayonet RPR 100 photochemical reactor, in which a transparent Pyrex vessel containing a 0.01 M solution of ketone **4** in toluene was placed. A stream of oxygen was bubbled through the solution at room temperature. After 6 h the solvent was evaporated under reduced pressure, and the photoproducts were isolated by column chromatography. The crude products were purified by crystallization to constant mp (solid) or by column chromatography (oily samples).

The following compounds were prepared from this general method.

8-Methoxycarbonylmethyl-2,2,6-trimethyl-7,9,10-trioxatricyclo[6.2.2.0^{1,6}]dodec-11-ene, ***2b****:* ^{1}H nmr δ: 1.00 (3H, s, 2-αMe), 1.10 (3H, s, 6-Me), 1.14 (3H, s, 2-βMe), 1.20 (1H, dt, *J* = 12.3, 3.8 Hz, 5-βH),1.48 (1H, dt, *J* = 10, 3.3 Hz, 3-βH), 1.50 (1H, m, 5-αH), 1.63 (1H, m, 3-αH), 1.79 (1H, dt, *J* = 12.4, 4.1 Hz, 4-βH), 2.14 (1H, dt, *J* = 12.4, 4.1 Hz, 4-αH), 2.78 (2H, s, 8-CH_2), 3.70 (3H, s, OMe), 6.54 (1H, d, *J* = 8.5 Hz, 11-H), 6.77 (1H, d, *J* = 8.5 Hz, 12-H). ^{13}C nmr δ: 82.57 (C-1), 35.58 (C-2), 25.18 (2-αMe), 26.45 (2-βMe), 19.08 (C-3), 34.45 (C-4), 34.38 (C-5), 76.40 (C-6), 24.32 (6-Me), 94.34 (C-8), 39.19 (8-CH_2), 128.02 (C-11), 131.98 (C-12), 51.88 (OMe), 168.09 (CO).

syn-*5-Hydroxy-2,2,6,8-tetramethyl-7,9,10-trioxatricyclo-[6.2.2.0^{1,6}]dodec-11-ene,* ***5a****$_a$:* Yield 18%, conversion 85%. IR ($CHCl_3$): 3575, 2940, 1160, 1070 cm^{-1}.^{1}H nmr δ: 1.02 (3H, s, Me), 1.12 (3H, s, Me), 1.12 (3H, s, Me), 1.59 (3H, s, Me), 1.50–2.10 (4H, m, 2 × CH_2), 3.56 (1H, d, *J* = 6 Hz, OH), 3.80 (1H, br s, $W_{1/2}$ = 6.8 Hz, 5-H), 6.53 (AB, *J* = 8 Hz, δ_A = 6.48, δ_B = 6.59, 11-H, 12-H). ^{13}C nmr δ: 82.94 (C-1), 35.29 (C-2), 24.30* (2-Me), 26.18* (2-Me), 25.71** (C-3), 28.98** (C-4), 71.33 (C-5), 78.61 (C-6), 20.62* (6-Me), 95.02 (C-8), 26.24* (8-Me), 129.13*** (C-11), 133.40*** (C-12).

anti-*5-Hydroxy-2,2,6,8-tetramethyl-7,9,10-trioxatricyclo-[6.2.2.0^{1,6}]dodec-11-ene,* ***5a****$_e$:* Yield 19%. IR ($CHCl_3$): 3610, 2950, 1115, 1040 cm^{-1}. ^{1}H nmr δ: 1.00 (3H, s, Me), 1.07 (3H, s, Me), 1.12 (3H, s, Me), 1.51 (3H, s, Me), 1.20–2.10 (4H, m, 2 × CH_2), 2.45 (1H, br s, OH), 4.34 (1H, dd, *J* = 12, 4 Hz, 5-H), 6.48 (AB, *J* = 8 Hz, δ_A = 6.43, δ_B = 6.53, 11-H, 12-H). ^{13}C nmr δ: 83.10 (C-1), 35.48 (C-2), 20.71* (2-Me), 24.46*(2-Me), 33.58**(C-3), 26.71** (C-4), 73.64 (C-5), 80.79 (C-6), 19.42* (6-Me), 94.91 (C-8), 26.00* (8-Me), 128.56*** (C-11), 133.24*** (C-12).

5-Methoxy-2,2,6,8-tetramethyl-7,9,10-trioxatricyclo-[6.2.2.0^{1,6}]dodec-11-ene, ***5b****:* Yield 36%, conversion 90%. Colorless solid, mp 75–76°C (from diisopropyl ether). IR (KBr): 2950, 1390, 1080 cm^{-1}. ^{1}H nmr δ: 1.00 (3H, s, Me), 1.07 (3H, s, Me), 1.11 (3H, s, Me), 1.52 (3H, s, Me), 1.25–2.00 (4H, m, 2 × CH_2), 3.52 (3H, s, OMe), 3.86 (1H, dd, *J* = 12, 4 Hz, 5-H), 6.47 (AB, *J* = 8 Hz, δ_A = 6.44, δ_B = 6.50, 11-H, 12-H). ^{13}C nmr δ: 83.28 (C-1), 35.32 (C-2), 20.74* (2-Me), 24.28* (2-Me), 24.83** (C-3), 33.45** (C-4), 82.73 (C-5), 81.02 (C-6), 19.84* (6-Me), 94.58 (C-8), 25.97* (8-Me), 128.20*** (C-11), 133.36*** (C-12), 58.38 (OMe). Anal. calcd. for $C_{14}H_{22}O_4$: C 66.12, H 8.72; found: C 66.09, H 8.67.

© 1999 NRC Canada

5-Allyloxy-2,2,6,8-tetramethyl-7,9,10-trioxatricyclo-[6.2.2.0^{1,6}]dodec-11-ene, ***5c****:* Yield 41%, conversion 70%. Colorless oil. IR (film): 2950, 1460, 1395 cm^{-1}. ^{1}H nmr δ: 1.00 (3H, s, Me), 1.09 (3H, s, Me), 1.11 (3H, s, Me), 1.51 (3H, s, Me), 1.25–2.00 (4H, m, 2 × CH_2), 4.03 (1H, dd, *J* = 12, 6 Hz, 5-H), 4.10–4.37 (2H, m, OCH_2), 5.12–5.36 (2H, m, CH=CH_2), 5.87–6.04 (1H, m, C*H*=CH_2). 6.47 (AB, *J* = 8 Hz, δ_A = 6.44, δ_B = 6.51, 11-H, 12-H). ^{13}C nmr δ: 83.34 (C-1), 35.23 (C-2), 20.74* (2-Me), 23.90*(2-Me), 25.90** (C-3), 33.52** (C-4), 80.53 (C-5), 81.22 (C-6), 20.04* (6-Me), 94.57 (C-8), 25.97* (8-Me), 128.22*** (C-11), 134.36*** (C-12), 71.80 (OCH_2), 116.05 (*C*H_2 = CH), 135.61 (CH_2 = *C*H). EI-HRMS calcd. for $C_{16}H_{24}O_4$ (M^+): 280.167460; found: 280.167455.

syn-*5-Acetoxy-2,2,6,8-tetramethyl-7,9,10-trioxatricyclo-[6.2.2.0^{1,6}]dodec-11-ene,* ***5d****$_a$:* Yield 24%, conversion 95%. Colorless solid, mp 90–90.5°C. IR (film): 2970, 1750, 1730, 1390 cm^{-1}. ^{1}H nmr δ: 1.04 (3H, s, Me), 1.14 (3H, s, Me), 1.17 (3H, s, Me), 1.45 (3H, s, Me), 1.50–2.10 (4H, m, 2 × CH_2), 2.18 (3H, s, MeCO), 5.12 (1H, t, 5-H), 6.48 (AB, *J* = 8 Hz, δ_A = 6.41, δ_B = 6.51, 11-H, 12-H). ^{13}C nmr δ 80.99 (C-1), 35.02 (C-2), 21.41* (2-Me), 24.11* (2-Me), 29.74** (C-3), 23.64** (C-4), 70.77 (C-5), 65.68 (C-6), 20.43* (6-Me), 94.32 (C-8), 26.24* (8-Me), 128.88*** (C-11), 133.40*** (C-12), 26.24* (MeCO), 171.19 (CO). Anal. calcd. for $C_{15}H_{22}O_5$: C 63.81, H 7.85; found: C 63.97, H 8.04.

anti-*5-Acetoxy-2,2,6,8-tetramethyl-7,9,10-trioxatricyclo-[6.2.2.0^{1,6}]dodec-11-ene,* ***5d****$_e$:* Yield 50%. Colorless solid, mp 104.3–104.9°C (from diisopropyl ether). IR (KBr): 2960, 1750, 1390 cm^{-1}. ^{1}H nmr δ: 1.01 (3H, s, Me), 1.13 (3H, s, Me), 1.13 (3H, s, Me), 1.47 (3H, s, Me), 1.60–2.10 (4H, m, 2 × CH_2), 2.08 (3H, s, MeCO), 5.49 (1H, dd, *J* = 12, 4 Hz, 5-H), 6.47 (AB, *J* = 8 Hz, δ_A = 6.44, δ_B = 6.50, 11-H, 12-H). ^{13}C nmr δ: 83.02 (C-1), 35.35 (C-2), 20.56* (2-Me), 21.26* (2-Me), 24.91** (C-3), 33.23** (C-4), 76.93 (C-5), 77.56 (C-6), 20.44* (6-Me), 94.70 (C-8), 24.32* (8-Me), 128.01*** (C-11), 133.84*** (C-12), 25.98* (MeCO), 170. 20 (CO). Anal. calcd. for $C_{15}H_{22}O_5$: C 63.81, H 7.85; found: C 63.95, H 7.85.

5-Keto-2,2,6,8-tetramethyl-7,9,10-trioxatricyclo-[6.2.2.0^{1,6}]dodec-11-ene, ***5e****:* Yield 86%, conversion 88%. Colorless solid, mp 131.7–132.7°C (from ethanol). IR (KBr): 2940, 1730, 1110 cm^{-1}. ^{1}H nmr δ 1.09 (3H, s, Me), 1.25 (3H, s, Me), 1.35 (3H, s, Me), 1.58 (3H, s, Me), 2.10–2.80 (4H, m, 2 × CH_2), 6.50 (2H, s, 11-H, 12-H). ^{13}C nmr δ: 85.10 (C-1), 35.48 (C-2), 24.35* (2-Me), 24.35* (2-Me), 34.46** (C-3), 34.70** (C-4), 207.37 (C-5), 82.85 (C-6), 20.35* (6-Me), 95.14 (C-8), 25.50* (8-Me), 126.06*** (C-11), 134.73*** (C-12). Anal. calcd. for $C_{13}H_{18}O_4$: C 65.53, H 7.61; found: C 65.63, H 7.61.

3,7,7,11-Tetramethyl-10,11-epoxy-1,2-dioxaspiro[5.5]undec-4-en-3-ol, ***8****:* Yield 55%. Colorless solid, mp 117–119°C (from ethanol). IR (KBr): 3360, 2980, 1250 cm^{-1}. ^{1}H nmr δ: 0.98 (3H, s, Me), 1.04 (3H, s, Me), 1.24 (3H, s, Me), 1.43 (3H, s, Me), 1.90–1.95 (2H, m, CH_2), 3.03 (1H, s, OH), 3.08 (1H, m, 10-H), 6.10 (AB, *J* = 10 Hz, δ_A = 6.06, δ_B = 6.14, 11-H, 12-H). ^{13}C nmr δ 95.03 (C-3), 19.31* (3-Me), 127.90** (C-4), 128.97** (C-5), 81.77 (C-6), 35.75 (C-7), 22.54* (7-Me), 22.28* (7-Me), 21.00*** (C-8), 30.51*** (C-9), 60.87 (C-10), 60.41 (C-11), 27.27* (11-Me). Anal. calcd. for $C_{13}H_{20}O_4$: C 64.98, H 8.39; found: C 65.08, H 8.33.

E-*4-(2′,3′-Epoxy-1′-hydroperoxy-2′,6′,6′-trimethylcyclohexyl)-3-buten-2-one,* ***9****:* Yield 10%. IR (film): 3450, 2980, 1670 cm^{-1}. ^{1}H nmr δ: 1.01 (3H, s, Me), 1.04 (3H, s, Me), 1.34 (3H, s, Me), 1.40–2.10 (4H, m, 2 × CH_2), 2.33 (3H, s, COMe), 3.13 (1H, t, *J* = 2 Hz, 3′-H), 6.42 (1H, d, *J* = 16 Hz, 3-H), 6.84 (1H, d, *J* = 16 Hz, 4-H). ^{13}C nmr δ: 19.82* (C-1), 199.09 (C-2), 130.97 (C-3), 145.02 (C-4), 85.77 (C-1′), 61.02 (C-2′), 60.51 (C-3′), 27.74* (2′-Me) 20.82** (C-4′), 32.08** (C-5′), 37.21 (C-6′), 23.87* (6′-Me), 26.64* (6′-Me).

Conclusions

We report here a convenient and simple route to 1,2,4-trioxanes from substituted β-ionones. The products, which belong to a class of compounds with interesting pharmacological properties, were formed in a one-pot reaction by irradiation in the presence of molecular oxygen. The new compounds were fully characterized by spectroscopic methods. Though we postulated the presence of singlet oxygen in the addition reaction to the pyrane intermediates, no external sensitizer was needed to afford the trioxanes. The diastereoselectivity of the reaction is controlled by the angular methyl group of the in situ generated pyrane intermediate, which directs the approach of the oxygen molecule from the opposite side, giving exclusively the *anti* isomer. High yields of trioxanes were obtained from β-ionones bearing an electron-withdrawing group, which reduces the electron density and prevents the oxidative degradation of the substrate.

The proposed methodology avoids the preparation of the pyranes as starting materials and the use of sensitizers. It also opens up the way for possibile synthesis of properly substituted 1,2,4-trioxanes with potential use as model compounds for biological evaluation.

Acknowledgements

We thank CONICET (Consejo Nacional de Investigaciones Científicas y Técnicas) and UNR (Universidad Nacional de Rosario) for financial support and fellowship (S.N.H.). Comments and suggestions from Professor W. Adam were most appreciated. We also thank Professor M. González Sierra for the measurement and interpretation of the NMR experiments.

References

1. (*a*) K.J. McCullough. Contemp. Org. Synth. **2**, 225 (1995); (*b*) H. Ziffer, R.J. Highet, and D.L. Kulgman. Prog. Chem. Org. Nat. Prod. **72**, 123 (1997); (*c*) J.N. Cumming, P. Ploypradith, and G.H. Posner. Adv. Pharmacol. **37**, 253 (1997); (*d*) G.H. Posner, H. O'Dowd, P. Ploypradith, J.N. Cumming, S. Xie, and T.A. Shapiro. J. Med. Chem. **41**, 2164(1998); (*e*) M.D. Bachi, E.E. Korshin, P. Ploypradith, J.N. Cumming, S. Xie, T.A. Shapiro, and G.H. Posner. Bioorg. Med. Chem. Lett. **8**, 903 (1998).
2. D.L. Klayman. Science, **228**, 1049 (1985).
3. W. Adam, U. Kliem, T. Mosandl, E-M. Peters, K. Peters, and H.G. von Schnering. J. Org. Chem. **53**, 4986 (1988).

© 1999 NRC Canada

4. H. Yamamoto, M. Akutagawa, H. Aoyama, and Y. Omote. J. Chem. Soc. Perkin Trans. 1, 2300 (1980).
5. (*a*) C. Singh, D. Misra, G. Saxena, and S. Chanda. Bioorg. Med.Chem. Lett. **2**, 497 (1992); (*b*) Bioorg. Med. Chem. Lett. **5**, 1913 (1995).
6. (*a*) A.J. Bloodworth, T. Hagen, K.A. Johnson, I. LeNoir, and C. Moussy. Tetrahedron Lett. **38**, 635 (1997), and references therein; (*b*) P.H. Dussault and D.R. Davies. Tetrahedron Lett. **37**, 463 (1996).
7. M. Miura, M. Nojima, and S. Kusabayashi. J. Chem. Soc. Chem. Commun. 581 (1981).
8. (*a*) C.W. Jefford, S.-J. Jin, and G. Bernardinelli. Tetrahedron Lett. **32**, 7243 (1991); (*b*) G.H. Posner, C.H. Oh, L. Gerena, and W.K. Milhous. J. Med. Chem. **35**, 2459 (1992).
9. W.H. Bunnelle, T.A. Isbell, C.L. Barnes, and S. Qualls. J. Am. Chem. Soc. **113**, 8168 (1991).
10. (*a*) H. Etoh, K. Ina, and M. Iguchi. Agric. Biol. Chem. **37**, 2241 (1973); (*b*) J.A. Kepler, A. Philip, Y.W. Lee, M.C. Morey, and F.I. Carrol. J. Med. Chem. **31**, 713 (1988).
11. S.N. Huber and M.P. Mischne. Nat. Prod. Lett. **7**, 43 (1995).
12. (*a*) A. Haag, W. Eschenmoser, and C.H. Eugster. Helv. Chim. Acta, **63**, 10 (1980); (*b*) A. Merz. Angew. Chem. Int. Ed. Engl. **12**, 846 (1973); (*c*) D.A. Hartman and D.W. Curley, Jr. Tetrahedron Lett. **30**, 645 (1989); (*d*) H. Henbest. J. Chem. Soc. 1074 (1951).
13. P. Mathies, B. Frei, and O. Jeger. Helv. Chim. Acta, **68**, 192 (1985).
14. N.S. Bhacca and D.H. Williams. Applications of NMR spectroscopy in organic chemistry. Holden-Day, San Francisco. 1964.
15. K. Nakanishi. Infrared absorption spectroscopy. Holden-Day, San Francisco. 1966.
16. N.L. Allinger and J.T. Spragne. J. Am. Chem. Soc. **95**, 3893 (1973).
17. P. Mathies, T. Nishio, B. Frei, and O. Jeger. Helv. Chim. Acta, **72**, 933 (1989).

© 1999 NRC Canada

Préparation du chlorure mercureux et mesure de sa pression de vapeur

Komla Oscar Awitor, Laurent Bernard, Olivier Bonnin, Bernard Coupat, Jean Paul Fournier et Philippe Verdier

Résumé : Le chlorure mercureux (Hg_2Cl_2), ou calomel, a été préparé par synthèse directe à partir de mercure et de chlorure mercurique commerciaux. La fraction massique en chlorure mercurique du produit synthétisé est particulièrement faible. La pression de vapeur du chlorure mercureux a été mesurée entre 353 et 453 K par la méthode d'effusion de Knudsen. Pour exploiter nos mesures, nous avons tenu compte de sa dissociation en phase vapeur, en mercure et chlorure mercurique. Nos résultats sont comparés à ceux existant dans la littérature.

Mots clés : chlorure mercureux, calomel, pression de vapeur, spectrométrie de masse, cellule de Knudsen.

Abstract: Mercurous chloride (Hg_2Cl_2), or calomel, was prepared by direct synthesis from commercial mercury and mercuric chloride. The mercuric chloride mass fraction in the synthesized material is particularly small. The mercurous chloride vapor pressure was measured between 353 and 453 K by the Knudsen cell method. In order to obtain the mercurous chloride vapor pressure, we took into account the dissociation in the vapor phase into mercury and mercuric chloride. Our results are compared with those in the literature.

Key words: mercurous chloride, calomel, vapor pressure, mass spectrometry, Knudsen cell.

1. Introduction

Le chlorure mercureux ou calomel, Hg_2Cl_2, est un matériau aux propriétés physiques remarquables (1). L'utilisation des monocristaux de Hg_2Cl_2 connaît un essor dans le domaine de la polarisation optique et acousto-optique (2), les applications étant limitées par la difficulté d'obtenir un matériau suffisamment pur. Le chlorure mercureux disponible dans le commerce est au mieux pur à 99,5 %, ce qui est insuffisant pour la cristallogénèse. L'objectif de ce travail est d'obtenir un matériau de grande pureté et de stœchiométrie parfaitement maîtrisée pour l'obtention de monocristaux de bonne qualité par croissance à partir de la phase vapeur. Après avoir caractérisé qualitativement la phase gazeuse nous exposons notre méthode de préparation du calomel, basée sur la synthèse directe à partir de mercure et de chlorure mercurique. La pression de vapeur du calomel obtenu a été mesurée entre 353 et 453 K par la méthode d'effusion de Knudsen.

2. Composition de la vapeur du chlorure mercureux

Il n'existe pas d'études expérimentales récentes sur la composition de la vapeur du chlorure mercureux, cependant il est sûr que la vapeur n'est pas formée de molécules HgCl qui, contenant un nombre impair d'électrons, seraient paramagnétiques (3). Des études anciennes ont montré que des traces d'humidité influencent fortement la vaporisation (4, 5).

Plus récemment, pour l'étude de la cristallogénèse du calomel à partir de sa phase vapeur, N.B. Singh et al. (6–11) supposent que la sublimation est congruente. Cette supposition, qui est à la base de tous leurs modèles de transport de matière en phase gazeuse, n'a pas été vérifiée.

Opperman et al. (12) ont montré, en comparant leurs mesures de pression de vapeur du calomel avec les données thermodynamiques, que la vapeur était complètement dissociée en mercure et chlorure mercurique pour des températures supérieures à 200°C.

Nous avons réalisé des analyses qualitatives par spectrométrie de masse à partir du produit commercial (Aldrich Chemical Company, Inc. 99,5+ %) longuement desséché sur anhydride phosphorique. Nous avons utilisé la méthode d'ionisation par impact électronique. Les mesures sont réalisées en augmentant la température de 30 à 500°C à raison de 1°C/s, une acquisition étant effectuée toutes les 5 s. L'énergie d'ionisation de 70 eV, couramment utilisée en spectrométrie de masse pouvant fragmenter d'éventuelles molécules Hg_2Cl_2, nous avons également travaillé à 50 et 12 eV.

Les spectres de masse correspondant à une température de 140°C sont présentés sur la figure 1, chaque massif étant repéré par son identité. Les abondances isotopiques relatives

Reçu le 24 juin 1998.

K.O. Awitor,[1] L. Bernard, O. Bonnin, B. Coupat, J.P. Fournier et P. Verdier. Laboratoire des sciences et matériaux pour l'électronique et d'automatique (LASMEA), UMR 6602 du Centre national de la recherche scientifique, Complexe Scientifique des Cézeaux, 63177 Aubière Cedex, France.

1.Auteur auquel la correspondance doit être adressée. Tél. : 33 04 73 40 71 18. Téléc. : 33 04 73 40 73 40. Mél. : awitor@lasmea.univ-bpclermont.fr

© 1999 CNRC Canada

Fig. 1. Spectres de masse du calomel pour différentes énergies d'ionisation.

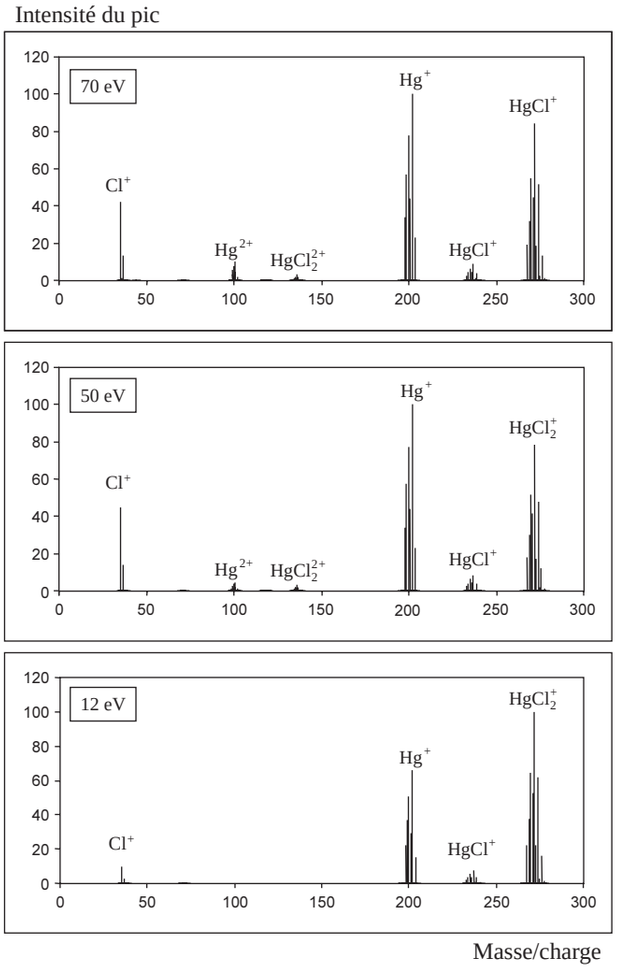

au mercure et au chlore, utiles pour interpréter les spectres de masse, sont données dans le tableau 1. Nous remarquons que le nombre de massifs diminue en même temps que l'énergie d'ionisation. Pour une énergie électronique de 12 eV, on ne détecte aucune masse supérieure à 300, ce qui élimine la présence de Hg_2Cl_2. Le massif aux environs de 237 correspond à l'ion $HgCl^+$ et non pas à l'ion doublement chargé $Hg_2Cl_2{}^{2+}$, car dans ce cas on devrait observer des rapports masse/charge demi-entiers et une répartition isotopique différente. Ces ions $HgCl^+$ ainsi que les ions Cl^+ proviennent de la fragmentation de molécules $HgCl_2$ par le faisceau d'électrons. De cette étude, il ressort que dans le domaine de température 30–500°C, le calomel est totalement dissocié en phase vapeur, la vapeur étant composée d'un mélange de mercure et de chlorure mercurique.

[1] $Hg_2Cl_{2\ solide} \leftrightarrow Hg_{gaz} + HgCl_{2\ gaz}$

3. Préparation du chlorure mercureux

Singh et al. (6) opèrent à partir de chlorure mercureux commercial et effectuent une purification par sublimations successives en tube scellé. Lors de nos tentatives à partir de

Tableau 1. Abondances isotopiques pour le mercure et le chlore.

Elément	Masse atomique	Abondance (%)
Hg	195,9658	0,15
	197,9667	9,97
	198,9683	16,87
	199,9683	23,10
	200,9703	13,18
	201,9706	29,86
	203,9735	6,87
Cl	34,9689	75,77
	36,9659	24,23

calomel commercial Aldrich Chemical Company Inc. à 99,5+ %, nous avons observé la formation de gouttelettes de mercure, ce qui laisse penser que le produit final n'est pas stœchiométrique. Ce problème nous a conduit à entreprendre la synthèse directe du calomel à partir des produits commerciaux Aldrich Chemical Company Inc. Le chlorure mercurique a une pureté de 99,999 %, celle du mercure étant de 99,9995 %, ce qui est bien supérieur à celle du calomel commercial.

Le protocole de la synthèse et de la purification est schématiquement représenté sur la figure 2. On commence par charger le compartiment de queue d'un tube Pyrex® à deux compartiments de façon équimolaire en mercure et chlorure mercurique (soit 6,5 g de mercure pour 8,8 g de chlorure mercurique). Après dégazage, les produits sont transportés vers le compartiment suivant par chauffage à 110°C sous vide secondaire dynamique. Le produit condensé est un mélange de calomel, de mercure et de chlorure mercurique. Les impuretés les plus volatiles sont évacuées vers le système de pompage et les moins volatiles isolées par scellage du compartiment de queue. L'ampoule est à nouveau dégazée durant 24 h et scellée sous vide secondaire.

On récupère dans le compartiment de chargement des impuretés de couleur noire provenant certainement en majeure partie de l'affinité du chlorure mercurique pour l'eau. Ces dépôts étant très peu abondants, il est difficile de les analyser et de les quantifier. Par ailleurs, une certaine quantité de mercure et de chlorure mercurique part vers le système de pompage durant les différentes phases de dégazage et de transport. Ces pertes vers le système de pompage sont certainement plus importantes en mercure qu'en chlorure mercurique et sont très difficiles à évaluer.

L'ampoule est ensuite insérée au 9/10^e dans un four maintenu à 200°C, l'extrémité étant laissée à l'air libre. Les produits sont transportés de la zone chaude vers la zone froide et se combinent lors de leur condensation. Lorsque le transport est terminé, l'ampoule est retournée pour un nouveau transport. Chaque étape de sublimation–condensation nécessite 24–72 h, la durée de l'opération augmentant en fonction de la proportion de calomel synthétisé. Après trois opérations, n'observant plus de traces de mercure, nous considérons que quatre transports suffisent.

Les premières analyses thermiques différentielles effectuées sur les produits de synthèse ont révélé que le produit final était un mélange de calomel et de chlorure mercurique. Pour éliminer l'excès de chlorure mercurique, nous effec-

© 1999 CNRC Canada

Fig. 2. Préparation du chlorure mercureux.

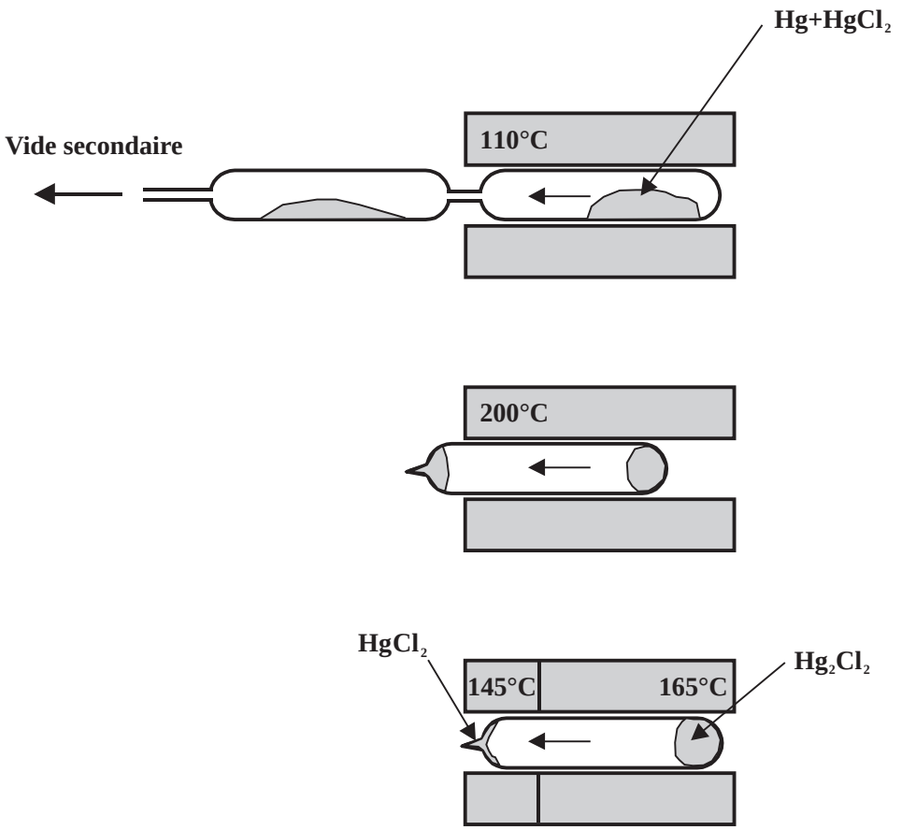

Fig. 3. Analyse thermique différentielle du matériau condensé dans la zone froide.

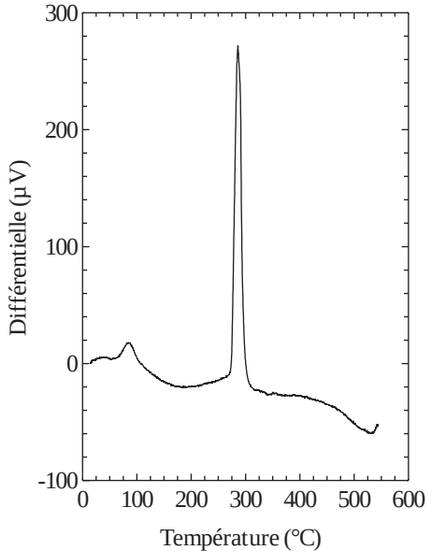

Fig. 4. Analyse thermique différentielle du calomel synthétisé.

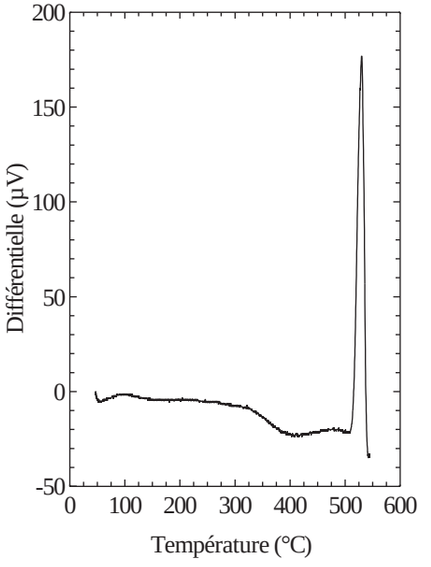

tuons un dernier transport pendant 24 h dans un four à deux zones isothermes maintenues respectivement à 165 et 145°C. Compte tenu des différences très importantes entre les pressions de vapeur du chlorure mercureux et du chlorure mercurique, ce dernier se condense majoritairement dans la zone froide de l'ampoule avec une faible partie du produit synthétisé. L'analyse thermique différentielle effectuée sur le matériau condensé dans la zone froide (fig. 3) montre qu'il s'agit bien de chlorure mercurique, le seul pic qui apparaît correspondant à la fusion de $HgCl_2$ aux environs de

© 1999 CNRC Canada

285°C. L'analyse du produit synthétisé (fig. 4) montre par ailleurs qu'il y a peu de chlorure mercurique, le pic près de 530°C correspondant à la transformation de Hg_2Cl_2 en deux phases liquides (13).

Nous avons déterminé précisément la fraction massique en chlorure mercurique des produits préparés (14). L'excès de chlorure mercurique est extrait par solubilisation dans l'éther et la quantité extraite est mesurée, après fixation des ions mercuriques sur un papier échangeur de cations, par spectrométrie d'émission de rayons X sur la raie $L\alpha_1$ du mercure. La fraction massique du chlorure mercureux synthétisé est de l'ordre de (3–4) × 10^{-5}.

4. Mesure de la pression de vapeur

4.1 Étude de la méthode

La méthode d'effusion, développée par Knudsen (15), repose sur la mesure de la perte de masse de la substance à travers un orifice vers une enceinte à basse pression. L'interprétation du phénomène met en jeu l'effusion moléculaire associée à un flux hydrodynamique, l'importance relative des deux termes dépendant de la pression mesurée et de la géométrie de l'orifice. Dans le cas du calomel, les pressions attendues sont très faibles, et compte tenu des caractéristiques de nos cellules de mesure, le terme hydrodynamique est négligeable.

Dans cette hypothèse, le flux d'effusion des molécules qui s'échappent d'une enceinte par un orifice de longueur L et de rayon r, exprimé en mol m^{-2} s^{-1} a pour expression (15, 16) :

$$[2] \qquad J = \frac{pW}{\sqrt{2\pi MRT}}$$

avec

p : pression de vapeur à l'intérieur de la cellule en pascal
M : masse molaire de la substance étudiée en kg mol^{-1}
R : constante molaire des gaz (8,314 J mol^{-1} K^{-1})
T : température en kelvin
W : facteur de Clausing dépendant de L et r (17)

Dans le cas du calomel, la formule [2] montre que le flux d'effusion du mercure est supérieur à celui du chlorure mercurique si leurs pressions partielles sont égales. Si par ailleurs la sublimation du matériau est stœchiométrique, l'apport à la phase gazeuse est équimolaire. Le régime d'effusion sera permanent si les flux d'effusion sont égaux au flux de sublimation du matériau et dans ce cas, les pressions partielles des deux espèces dans la cellule doivent, quant à elles, être différentes.

Si p désigne maintenant la pression de vapeur du calomel :

$$[3] \qquad p_{Hg} \cdot p_{HgCl_2} = \frac{p^2}{4}$$

et compte tenu de la relation [2] qui donne

$$[4] \qquad \frac{p_{Hg}}{\sqrt{M_{Hg}}} = \frac{p_{HgCl_2}}{\sqrt{M_{HgCl_2}}}$$

les pressions d'équilibre à l'intérieur de l'enceinte sont donc

$$[5] \qquad p_{Hg} = \frac{p}{2}\left(\frac{M_{Hg}}{M_{HgCl_2}}\right)^{1/4} \quad \text{et} \quad p_{HgCl_2} = \frac{p}{2}\left(\frac{M_{HgCl_2}}{M_{Hg}}\right)^{1/4}$$

Si n_c moles de calomel sont vaporisées par seconde, la variation du nombre de moles de l'espèce i (Hg ou $HgCl_2$) à l'intérieur de la cellule s'exprime :

$$[6] \qquad dn_i = n_c\, dt - J_i S\, dt$$

où S est l'aire de l'orifice.
Si V représente le volume de la cellule :

$$[7] \qquad J_i = \frac{Wn_i}{V}\sqrt{\frac{RT}{2\pi M_i}}$$

et ainsi

$$[8] \qquad dn_i = (n_c - \alpha_i n_i)\, dt \text{ avec } \alpha_i = \frac{WS}{V}\sqrt{\frac{RT}{2\pi M_i}}$$

À l'intérieur de la cellule :

$$n_{Hg} n_{HgCl_2} = \frac{p^2}{4}\left(\frac{V}{RT}\right)^2 = \beta \quad \text{donc}$$

$$[9] \qquad n_{Hg}\, dn_{HgCl_2} + n_{HgCl_2}\, dn_{Hg} = 0$$

En utilisant [8] on obtient :

$$[10] \qquad n_c = \frac{(\alpha_{Hg} + \alpha_{HgCl_2}) n_{Hg} n_{HgCl_2}}{n_{Hg} + n_{HgCl_2}}$$

Et en reportant cette valeur dans l'expression [8] on obtient l'équation différentielle :

$$[11] \qquad dn_{Hg} = \left(\frac{n_{Hg} n_{HgCl_2} \alpha_{HgCl_2} - n_{Hg}^2 \alpha_{Hg}}{n_{Hg} + n_{HgCl_2}}\right) dt$$

En intégrant cette expression on obtient l'équation :

$$[12] \qquad t + \frac{1}{2\alpha_{Hg}} \ln(n_{Hg}^2 \alpha_{Hg} - \beta\alpha_{HgCl_2}) + \frac{1}{2\alpha_{HgCl_2}} \ln\left(\frac{n_{Hg}^2 \alpha_{Hg} - \beta\alpha_{HgCl_2}}{n_{Hg}^2}\right) + C = 0$$

où la constante C peut être déterminée par la condition limite à $t = 0$.

Nous présentons sur la figure 5, pour une pression de vapeur du calomel égale à 0,53 Pa, l'évolution des pressions partielles du mercure et du chlorure mercurique dans une cellule de 3 cm^3 de volume et dont l'orifice mesure 0,085 mm de diamètre et 1 mm de longueur. Le temps d'établissement du régime permanent, de l'ordre de 100 s, est tout à fait négligeable par rapport aux temps de mesure de plusieurs heures que nous avons utilisés.

Dans ces conditions, la pression de vapeur du calomel s'exprime, en fonction de la masse effusée m et du temps de mesure t :

$$[13] \qquad p = \frac{\sqrt{8\pi RT}}{W}\frac{m}{tS}\frac{(M_{Hg} M_{HgCl_2})^{1/4}}{M_{Hg_2Cl_2}}$$

© 1999 CNRC Canada

Fig. 5. Évolution des pressions partielles de mercure et de chlorure mercurique dans la cellule de mesure.

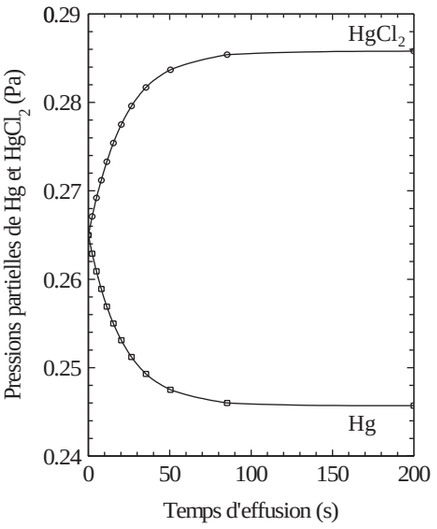

Tableau 2. Dimensions des cellules de Knudsen.

Cellules	C15	C25	M15
Longueur *L* (mm)	1,01	1,14	2,50
Rayon *r* (mm)	0,085	0,120	0,214

Tableau 3. Pertes de masse expérimentales et pressions de vapeur du chlorure mercureux.

Cellules	*T* (K)	*m* / *t* (mg/h)	*p* (Pa)
C15	423,8	0,6684	14,9±0,45
	433,4	1,1766	26,5±0,80
	443,6	2,0611	47,0±1,46
	453,5	3,5455	81,8±2,53
C25	373,4	0,0587	0,52±0,01
	383,5	0,1315	1,18±0,03
	393,5	0,2390	2,17±0,05
	403,4	0,4609	4,24±0,11
	413,4	0,8871	8,27±0,20
	423,5	1,6924	16,0±0,40
	433,3	2,9216	27,9±0,67
M15	353,2	0,0321	0,10±0,003
	363,2	0,0762	0,25±0,007
	373,2	0,1588	0,52±0,01
	383,2	0,3242	1,08±0,03
	393,2	0,6960	2,34±0,05
	403,2	1,2917	4,40±0,11

4.2 Résultats

Le dispositif expérimental et l'étalonnage des cellules de Knudsen ont fait l'objet d'une publication (18). Nous rappelons les dimensions des cellules utilisées (tableau 2).

Les pressions de vapeur du chlorure mercureux obtenues avec les trois cellules sont reportées dans le tableau 3 et représentées sur la figure 6. Le lissage du logarithme népérien en fonction de l'inverse de la température en kelvin conduit à

Fig. 6. Pression de vapeur du calomel.

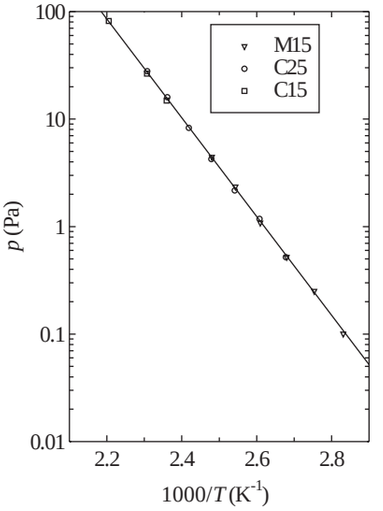

Fig. 7. Comparaison des données de la littérature avec nos valeurs expérimentales.

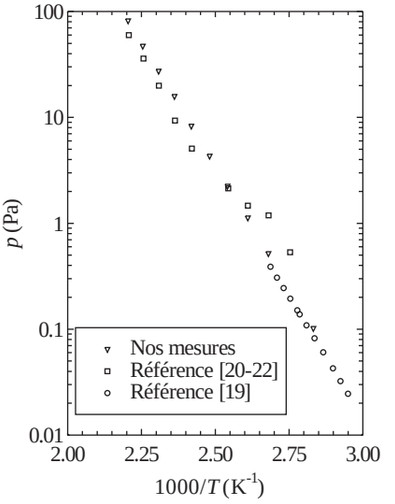

$$[14] \quad \ln p(\text{Pa}) = 27{,}7 - \frac{10571}{T(K)}$$

ce qui correspond à une enthalpie de sublimation égale à 87,9 kJ mol^{-1}.

Sur la figure 7, nous comparons nos résultats avec les pressions de vapeur mesurées par Neumann (19), Niederschulte (20), Niederschulte et Matthies (21) et Wiedemann et al. (22). Nous constatons un écart de 18 % à 363 K entre nos mesures et celles de la référence 19, l'écart avec celles des références 20–22 étant de 55 % à la même température.

Les pressions de vapeur mesurées par Oppermann et al. (12), pour les températures supérieures à 473 K, conduisent à

$$[15] \quad \ln p(\text{Pa}) = 27{,}8 - \frac{10546}{T(K)}$$

ce qui est très proche de nos résultats pour le domaine 353–453 K.

© 1999 CNRC Canada

5. Conclusion

La méthode de préparation du calomel que nous avons mise au point par synthèse directe à partir de mercure et du chlorure mercurique conduit à du calomel dont la fraction massique en chlorure mercurique est particulièrement faible. Nous avons confirmé la dissociation du calomel en phase vapeur, en mercure et chlorure mercurique, et mesuré sa pression de vapeur de 353 à 453 K. Ces résultats nous permettront de mieux maîtriser le transport et la croissance en phase vapeur pour l'obtention de monocristaux dont les études seront publiées prochainement.

Bibliographie

1. G.J. Rosasco, H.S. Parker, R.S. Roth, R.A. Forman et W.S. Brower. J. Phys. C : Solid State Phys. **11**, 35 (1978).
2. C. Barta et C. Barta, Jr. Mater. Sci. Forum, **61**, 93 (1990).
3. D'après P. Pascal : P.W. Selwood et R. Preckel. J. Am. Chem. Soc. **62**, 3055 (1940).
4. D'après P. Pascal : A. Smith et A.W.C. Menzies. Z. Phys. Chem. **76**, 713 (1911).
5. D'après P. Pascal : F.T. Gucker et R.H. Munch. J. Am. Chem. Soc. **59**, 1275 (1937).
6. N.B. Singh, R.H. Hoppkins, R. Mazelsky et M.E. Glicksman. Mater. Res. Soc. Symp. Proc. **87**, 71 (1987).
7. N.B. Singh. Mater. Sci. Forum, **50**, 29 (1989).
8. N.B. Singh, R. Mazelsky et M. E. Glicksman. PhysicoChem. Hydrodyn. **11**, 41 (1989).
9. N. B. Singh. Am. Inst. Aeronaut. Astronaut. Pap. (AIAA Pap.) 175 (1990).
10. N.B. Singh, M. Gottlieb, R.H. Hoppkins, R. Mazelsky, W.M.B. Duval et M.E. Glicksman. Prog. Cryst. Growth Charact. **27**, 201 (1993).
11. G.T. Kim, W.M.B. Duval, M.E. Glicksman et N.B. Singh. Modell. Simul. Mater. Sci. Eng. **3**, 331 (1995).
12. H. Oppermann, C. Barta et J. Trnka. Z. Anorg. Allg. Chem. **568**, 187 (1989).
13. C. Guminski. J. Phase Equilib. **15**, 101 (1994)
14. O. Bonnin, K.O. Awitor, J.P. Badaud, L. Bernard, B. Coupat, J. P. Fournier et P. Verdier. J. Chem. Phys. **94**, 181 (1997).
15. M. Knudsen. Ann. Phys. **28**, 909 (1909).
16. S. Dushman. Scientific foundations of vacuum technique. J. Wiley, New York. 1958.
17. P. Clausing. J. Vac. Sci. Technol. **8**, 636 (1971).
18. O. Bonnin, K.O. Awitor, J.P. Badaud, L. Bernard, B. Coupat, J.P. Fournier et P. Verdier. J. Phys. III, **7**, 311 (1997).
19. D'après P. Pascal : K. Neumann. Z. Phys. Chem. Abt. A: **191**, 284 (1942).
20. D'après P. Pascal : G. Niederschulte. Dissertation Erlangen, 1903.
21. D'après P. Pascal : G. Niederschulte et W. Matthies. Verh. Phys. Ges. **7**, 189 (1905).
22. D'après P. Pascal : E. Wiedemann, K. Stelzner et G. Niederschulte. Ber. **7**, 159 (1905).

© 1999 CNRC Canada

Energétique des liaisons inter- et intramoléculaires dans les trois acides carboxypyridiniques (acides picolinique, nicotinique et isonicotinique)

Raphaël Sabbah et Safi Ider

Résumé : Le présent travail porte sur l'étude thermodynamique des trois acides carboxypyridiniques de formule générale : $C_6H_5NO_2$. Il a été réalisé en utilisant quatre techniques : la calorimétrie de combustion de faibles quantités de substance (quelques milligrammes par essai), la calorimétrie de sublimation, la mesure de capacités calorifiques par la méthode de chute et l'analyse thermique différentielle. Cette étude nous a permis : de déterminer les enthalpies de combustion, de sublimation, de formation et de fusion de ces composés ainsi que la température de leur point triple; de préciser la stabilité relative des trois isomères et de les comparer à celle d'autres dérivés de la pyridine; de déterminer les énergies de conjugaison et de les comparer à celles d'autres dérivés de la pyridine; de déterminer les enthalpies d'atomisation des trois composés et la valeur enthalpique des liaisons du groupe (C-N=C); de déterminer qualitativement et quantitativement les interactions intermoléculaires.

Mots clés : thermodynamique, calorimétrie, analyse thermique différentielle, acides carboxypyridiniques, acide picolinique, acide nicotinique, acide isonicotinique, enthalpie de combustion, de sublimation, de fusion, de formation, des liaisons inter- et intramoléculaires, énergie de conjugaison, température du point triple, substance d'intercomparaison.

Abstract: The present work is concerned with a thermodynamic study of the three carboxypyridinic acids (general formula: $C_6H_5NO_2$). It was achieved using four techniques: combustion calorimetry of small amounts of substance (a few milligrams), sublimation calorimetry, heat capacity measurements by the drop method, and differential thermal analysis. From this study, it was possible to determine the enthalpies of combustion, sublimation, formation, and fusion of these compounds and their triple point temperatures; to discuss the relative stability of the three molecules and to compare it to those of other pyridine derivatives; to determine the resonance energy and to compare it to those of other pyridine derivatives; to determine the atomization enthalpies of our compounds and an enthalpy value for the bonds of the group (C-N=C); to determine the nature and the enthalpy of the intermolecular bonds.

Key words: thermodynamics, calorimetry, differential thermal analysis, carboxypyridinic acids, picolinic acid, nicotinic acid, isonicotinic acid, enthalpy of combustion, of sublimation, of fusion, of formation, of inter- and intramolecular bonds, resonance energy, triple point temperature, reference material.

1. Introduction

Dans le cadre de nos études sur l'énergétique des liaisons inter- et intramoléculaires dans les substances organiques visant la mise en évidence du lien existant entre grandeurs énergétiques et structure, nous avons souhaité nous intéresser à l'étude des trois acides picolinique, nicotinique et isonicotinique. Cette étude fait suite à celle que nous avons entreprise sur les trois isomères de l'aminopyridine (1).

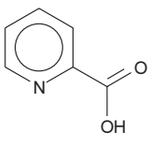

Acide picolinique
(isomère *ortho*)

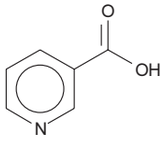

Acide nicotinique
(isomère *méta*)

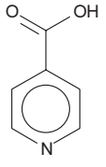

Acide isonicotinique
(isomère *para*)

Reçu le 23 juin 1998.

R. Sabbah[1] et S. Ider. Centre de thermodynamique et de microcalorimétrie du Centre national de la recherche scientifique, 26, rue du 141ème RIA, 13331 - Marseille, Cedex 03, France.

1.Auteur à qui adresser toute correspondance. Tél. : 33 4 91 28 20 62. Téléc. : 33 4 91 50 38 29.
Mél. : raphael·sabbah@ctm·cnrs-mrs·fr

© 1999 CNRC Canada

Sur le plan pratique l'acide nicotinique et ses dérivés, la nicotinamide par exemple, font partie du groupe de la vitamine B. Ils sont principalement utilisés en pharmacie et comme additifs dans l'alimentation humaine et animale. On évalue les besoins mondiaux en acide nicotinique et ses dérivés à environ 100 000 t/an (2). Entrant dans la constitution de certains coenzymes (NADH, NADP), une carence alimentaire en acide nicotinique induit une pathologie : la pellagre associant aux lésions dermatologiques et digestives d'importants troubles mentaux (3). Signalons, au passage, que l'acide nicotinique a été étudié, au cours de ces dernières années, par calorimétrie de combustion dans le but de le proposer comme substance d'intercomparaison dans ce domaine calorimétrique pour les substances azotées (4).

Cette étude a été réalisée par calorimétrie de combustion de faibles quantités de substance, de sublimation et par analyse thermique différentielle : mesure du degré de pureté de l'échantillon soumis à l'étude, de son enthalpie de fusion ainsi que de la température de son point triple. Elle nous a permis, dans un premier temps, de déterminer certaines grandeurs énergétiques liées à la structure des molécules étudiées : énergie de conjugaison, enthalpie d'atomisation. À partir de cette dernière grandeur, il nous a été possible de déterminer l'enthalpie des liaisons du groupement (C-N=C). Une étude sur la stabilité relative des acides carboxypyridiniques et d'autres dérivés de la pyridine a aussi été réalisée. Elle a permis de mettre en évidence l'effet du substituant.

Enfin, à partir de l'enthalpie de sublimation, nous avons pu tirer des conclusions quantitatives relatives aux liaisons hydrogène inter- et intramoléculaires présentes dans les cristaux des trois acides.

Les données dans la littérature concernant les grandeurs thermodynamiques des substances étudiées sont inexistantes à l'exception de l'acide nicotinique pour lequel l'enthalpie de combustion et de formation à l'état condensé sont connues (5, 6). Par ailleurs, quelques résultats concernant la structure cristalline sont consignés dans les références 7 à 13.

2. Partie expérimentale

2.1. Produits

L'acide picolinique est un produit Aldrich. L'analyse thermique différentielle de l'échantillon de cet acide ayant donné un degré de pureté égal à 99,65 mol %, nous avons été amenés à repurifier le produit en le recristallisant trois fois dans l'éthanol absolu puis séché en l'abandonnant 8 h environ dans un dessiccateur à potasse maintenu sous pression réduite. Nous avons trouvé pour le produit ainsi purifié un degré de pureté de (99,92 ± 0,01) mol %.

L'acide nicotinique est un produit Fluka. Son analyse thermique différentielle ayant fourni un résultat satisfaisant pour son degré de pureté : (99,98 ± 0,01) mol %, nous l'avons utilisé tel que.

L'acide isonicotinique est un produit Fluka dont le degré de pureté, signalé sur le flacon, est ≥99 %. Compte tenu de son point de fusion élevé (592 K (14)) et de sa décomposition à la fusion, il ne nous a pas été possible de réaliser son analyse thermique différentielle. Selon la référence 13, l'acide isonicotinique pur est incolore. Comme notre produit avait une légère couleur brunâtre, nous l'avons repurifié à partir de quatre recristallisations dans l'eau distillée et déminéralisée suivies d'un séchage identique à celui qui a été pratiqué dans le cas de l'acide picolinique.

2.2. Appareillages, techniques et modes opératoires

2.2.1. Analyse thermique différentielle

Nous avons utilisé la version moyenne température de l'analyseur thermique différentiel et les cellules expérimentales en verre décrites dans la référence 15.

Dans toutes nos expériences : (*i*) la vitesse de montée en température du four a été de 0,2 K min^{-1}; (*ii*) la masse de substance utilisée a été d'environ 100 mg, déterminée par double pesée à l'aide d'une balance « Mettler», type M5, sensible au μg et dont l'exactitude des pesées est de ±2 μg; (*iii*) la préparation des échantillons et leur mise en container ont été conduites de la façon décrite dans la référence 15.

La mesure des températures a été faite à l'aide de deux thermocouples (thermocoax, type 2ABI 15), l'un est solidaire de l'échantillon, l'autre de la référence (alumine-α). La différence entre les f.é.m. délivrées par ces deux thermocouples est amplifiée par un microvoltmètre AOIP, type EVA, sensibilité 100 μV pleine échelle. Le signal ainsi amplifié est envoyé simultanément à un enregistreur Sefram, type Gépérac, pour le visualiser, et à un multimètre Keithley, modèle 175, pour le digitaliser. Un autre multimètre Keithley, modèle 196, sensibilité 300 mV (résolution 100 nV) est utilisé pour mesurer la f.é.m correspondant à la température de l'échantillon. Les données issues de ces deux multimètres sont envoyées vers un ordinateur en vue de leur traitement à l'aide d'un programme écrit et mis au point au laboratoire. En appliquant l'équation de Clausius–Clapeyron et la loi de Raoult, ce programme permet de déterminer la pureté de l'échantillon, son enthalpie de fusion ainsi que la température de son point triple.

Comme indiqué dans la référence 15, l'étalonnage (*i*) en température, de notre analyseur thermique a été réalisé à partir d'échantillons rigoureusement purs de naphtalène, de fluorène, d'acides benzoïque, diphénylacétique et anisique, de carbazole et d'anthraquinone, dont la température de leur point triple est bien connue dans la littérature; (*ii*) en énergie, a été réalisé à partir d'échantillons rigoureusement purs de naphtalène, de fluorène, d'acides benzoïque et diphénylacétique, dont l'enthalpie de fusion est bien connue dans la littérature.

2.2.2. Calorimétrie de combustion

Les enthalpies de combustion de nos composés ont été déterminées en utilisant un calorimètre isotherme, à flux thermique, monopile, basculant, CRMT (sensibilité : 0,0623 V W^{-1}) équipé d'une microbombe en acier inoxydable (Superimphy 625) de volume interne égal à 42,9 cm^3 à la température ambiante.

Le signal issu du calorimètre est amplifié par un microvoltmètre électronique AOIP, modèle EVA, sensibilité 30 mV pleine échelle, avant son envoi simultané sur un intégrateur électronique, conçu, réalisé et mis au point au laboratoire, qui détermine l'aire des thermogrammes $dQ/dt = f(t)$, et sur un enregistreur potentiométrique Sefram, modèle Servotrace, qui le visualise.

© 1999 CNRC Canada

La rotation du calorimètre suivant plusieurs plans permet à toutes les génératrices de la bombe d'être lavées par l'eau déminéralisée placée en son fond (1 cm^3).

Comme indiqué dans la référence 16, les substances à étudier sont mises sous forme de pastilles. À cet effet, nous avons utilisé un ensemble piston-moule façonné dans un acier trempé, ce qui a pour effet d'éviter l'entraînement dans les pastilles de traces de métal et d'augmenter ainsi la qualité des résultats.

Les pesées ont été effectuées sur une microbalance « Mettler», modèle UM3, équipée d'un jeu de poids étalonnés par le N.I.S.T. Sa portée est de 3 g et sa sensibilité de 0,1 µg. L'erreur commise avec cette balance sur une pesée de quelques milligrammes est de l'ordre de ±0,2 µg. Dans toutes nos pesées, nous avons tenu compte des corrections de poussée de l'air pour calculer les masses réelles.

Une fois garnie, la bombe est remplie d'oxygène sous une pression de 3,04 MPa. L'oxygène N45, utilisé à cet effet, provient de l'Air Liquide et son degré de pureté est supérieur à 99,995 % (fraction molaire d'azote $<10^{-5}$). La durée d'une expérience a toujours été de 90 min à partir du moment de la mise de feu.

Après chaque expérience, nous avons déterminé, dans la phase aqueuse, la concentration d'acide nitrique par titrage acido-basique en présence de phénolphtaléine avec une solution de soude préalablement titrée à l'aide de solutions d'acide oxalique de concentrations connues et avons vérifié, à l'aide des tubes de Dräger, l'absence d'oxyde de carbone et d'oxydes d'azote (NO, NO_2) dans la phase gazeuse (sensibilité des tubes <1 ppm pour CO et <0,1 ppm pour NO et NO_2).

2.2.3. Calorimétrie de sublimation

Nous avons utilisé un calorimètre Tian–Calvet (sensibilité 0,0188 V W^{-1} à 328,75 K et 0,0160 V W^{-1} à 362,15 K) associé à un montage différentiel doté de cellules d'effusion de Knudsen pour déterminer les enthalpies de sublimation de nos composés. L'étalonnage de notre système calorimétrique a été réalisé par effet Joule avant et après chaque série d'expériences. Le mode opératoire a été décrit dans la référence 17. Précisons que :

(*i*) le signal issu du calorimètre est amplifié par un nanovoltmètre Keithley modèle 147, sensibilité 30 µV pleine échelle, puis digitalisé par un multimètre numérique Keithley modèle 175 et enregistré sur un enregistreur potentiométrique Sefram, modèle Servotrace;

(*ii*) compte tenu de la faible pression de vapeur saturante de nos composés, l'isomère *ortho* a été étudié à 328,75 K et les deux autres isomères à 362,15 K. De plus, nous avons admis l'identité $\Delta_{sub}H_m(T) \equiv \Delta_{sub}H°_m(T)$;

(*iii*) le diamètre des trous d'effusion, pratiqués dans des joints en téflon de 0,3 mm d'épaisseur, sont respectivement de 0,5, 1 et 2,5 mm dans le cas des isomères *ortho*, *méta* et *para*.

(*iv*) l'ouverture et la fermeture de l'orifice d'effusion des cellules sont pilotées par l'ordinateur;

(*v*) toutes les pesées ont été effectuées à l'aide d'une balance « Mettler », type UM3.

L'acquisition et le traitement des données sont réalisés à l'aide de l'ordinateur et d'un programme conçu et mis au point au laboratoire. Il permet, entre autres, de déterminer la pression de vapeur saturante, l'aire des thermogrammes et, à partir du coefficient d'étalonnage, l'enthalpie de sublimation de nos composés à la température de l'expérience $\Delta_{sub}H°_m(T)$.

2.2.4. Mesure des capacités calorifiques

Pour calculer $\Delta_{sub}H°_m$ (298,15 K) à partir de $\Delta_{sub}H°_m(T)$, il est nécessaire de connaître : (*i*) le comportement thermique de nos substances entre 298,15 K et *T*. Nous nous sommes donc assurés que nos substances ne présentaient aucun changement de phase dans cet intervalle; (*ii*) la capacité calorifique à pression constante des phases condensée et gazeuse des substances étudiées à 298,15 K et *T* de façon à pouvoir appliquer la relation suivante :

$$\Delta_{sub}H°_m(298{,}15\ \mathrm{K}) = \Delta_{sub}H°_m(T) + \int_T^{298{,}15K} [C°_{p,m}(g) - C°_{p,m}(cr)]dT$$

La différence enthalpique $H°_m(T) - H°_m(298{,}15\ K)$ à l'état solide a été calculée par la méthode de chute à l'aide d'un calorimètre Tian–Calvet et d'un four maintenus respectivement à 298,15 K et *T*. Le calorimètre a été préalablement étalonné en utilisant des échantillons d'alumine-α.

Quant aux valeurs des capacités calorifiques à l'état gazeux $C°_{p,m}(g)$ et aux températures 298,15 K et *T*, elles ont été déterminées à partir d'une méthode incrémentale en utilisant, à chacune de ces deux températures, les capacités calorifiques à l'état gazeux des molécules de benzène et de l'acide benzoïque (18). Ceci nous a permis, dans un premier temps et à chacune de ces deux températures, de déterminer la part du chaînon COOH, puis de calculer une valeur moyenne de $C°_{p,m}$ pour les trois acides en ajoutant cette quantité au $C°_{p,m}$ de la pyridine.

Les différents calorimètres et analyseur thermique, leurs périphériques ainsi que les balances sont placés dans des salles thermorégulées à (19,0 ± 0,2)°C.

3. Résultats

Les constantes physiques des trois acides ayant fait l'objet de ce mémoire sont rassemblées dans le tableau 1.

3.1. Analyse thermique différentielle

Les résultats obtenus sont consignés dans le tableau 2. Les trois isomères se décomposent à la fusion en prenant une coloration brune. L'acide isonicotinique n'a pas pu être étudié car sa décomposition entraînait une explosion de l'ampoule.

Le manque de données de la littérature relatives à l'enthalpie de fusion de ces acides ne nous a pas permis d'en faire une comparaison avec nos valeurs expérimentales.

Quant aux températures de leur point triple, la référence 14 indique les valeurs suivantes : acide picolinique : 409–410 K, acide nicotinique : 509–510 K et acide isonicotinique : 592 K. Comme nous pouvons le constater, nos résultats expérimentaux sont tout à fait compatibles avec ces données.

3.2. Calorimétrie de combustion

L'équivalent énergétique du système calorimétrique (U_{calor}) a été déterminé à partir de sept combustions d'acide benzoïque échantillon 39 i du N.I.S.T. pour lequel $\Delta_c u°$(cr, 298,15 K) = (–26 414 ± 3) J g^{-1} (21). Dans chaque expérience, nous avons utilisé environ 5 mg d'acide et 0,2 mg de

© 1999 CNRC Canada

Tableau 1. Grandeurs physiques des substances utilisées à 298,15 K.

Substance	Formule	M [a] / g mol^{-1}	ρ / g cm^{-3}	$-(\partial U/\partial P)_T$ / J g^{-1} MPa^{-1}
Acide benzoïque	$C_7H_6O_2$	122,1234	1,32(19)	0,12(19)
Coton	$CH_{1.791}O_{0.850}$	27,4157	1,50(19)	0,29(19)
Acide picolinique	$C_6H_5NO_2$	123,1112	1,571 [b]	0,13 [c]
Acide nicotinique	$C_6H_5NO_2$	123,1112	1,333 [b]	0,13 [c]
Acide isonicotinique	$C_6H_5NO_2$	123,1112	1,488(13)	0,13 [c]

[a]Calculée à partir du tableau des masses atomiques de 1993 (20).
[b]Valeurs déterminées par nos soins.
[c]Valeurs estimées.

coton (dont l'énergie de combustion, préalablement déterminée au laboratoire, a pour valeur $\Delta_c u°$(cd, 298,15 K) = (–16 399 ± 23) J g^{-1} (22). Nous avons trouvé U_{calor} = (16,028 ± 0,004) J V^{-1} s^{-1}.

Les enthalpies standard de combustion de nos composés concernent la réaction suivante :

$$C_6H_5NO_2(cr) + 25/4\ O_2\ (g) \rightarrow 6\ CO_2\ (g) + 5/2\ H_2O\ (l) + 1/2\ N_2\ (g)$$

et sont calculées, à l'aide de l'ordinateur et d'un programme écrit et mis au point au laboratoire, à partir de nos valeurs expérimentales en tenant compte des corrections dites de Washburn.

La combustion des trois isomères s'est révélée complète, aucune trace de cendre ne subsistant dans le corps de la bombe et dans le creuset, une fois l'expérience terminée et les dosages par tubes colorimétriques de Dräger n'ayant révélé aucune présence de CO et d'oxydes d'azote dans la phase gazeuse.

Les résultats relatifs à ces manipulations sont rassemblés dans les tableaux 3–5.

L'enthalpie de formation à l'état condensé de nos trois acides a été calculée à partir de leur enthalpie de combustion et des valeurs de l'enthalpie de formation de l'eau : $\Delta_f H°_m$(l, 298,15 K) = (–285,830 ± 0,042) kJ mol^{-1} et du dioxyde de carbone : $\Delta_f H°_m$(g, 298,15 K) = (–393,51 ± 0,13) kJ mol^{-1} (23).

Nous avons remarqué qu'environ 12 % de l'azote contenu dans nos composés se trouvaient, à l'issue de la combustion, sous forme d'acide nitrique. L'expérience a montré que la quantité d'acide nitreux formé est excessivement faible et peut être négligée.

Comme nous l'avons précisé dans l'introduction, seul l'acide nicotinique a fait l'objet de deux études réalisées par calorimétrie de combustion en bombe statique en vue de sa proposition comme substance d'intercomparaison dans ce domaine calorimétrique pour les substances azotées. C'est ainsi que Johnson propose en 1975 (5) la valeur $\Delta_f H°_m$(cr, 298,15 K) = (–2730,67 ± 0,57) kJ mol^{-1} et Sato-Toshima et al. proposent en 1983 (6) la valeur $\Delta_f H°_m$(cr, 298,15 K) = (–2730,83 ± 0,48) kJ mol^{-1}. Comme nous pouvons le constater ces deux valeurs sont tout à fait compatibles à la nôtre $\Delta_f H°_m$(cr, 298,15 K) = (–2731,19 ± 0,79) kJ mol^{-1}.

Tableau 2. Analyse thermique différentielle des acides étudiés.

Substance	Pureté / mol %	T_{pt} [a] / K	$\Delta_{fus}H_m$ / kJ mol^{-1}
Acide picolinique	99,92±0,02	410,23±0,04	14,47±0,11
Acide nicotinique	99,98±0,01	509,16±0,01	13,01±0,32

[a] Températures du point triple définies par rapport à l'EIT-90.

3.3. Calorimétrie de sublimation.

L'ensemble des résultats est consigné dans le tableau 6. Malheureusement le manque de données dans la littérature relatives à l'enthalpie de sublimation et à la pression de vapeur saturante des trois acides carboxypyridiniques ne nous a pas permis d'en faire une comparaison avec nos valeurs expérimentales. À partir de nos essais, il nous a été possible d'évaluer la pression de vapeur saturante de nos trois acides en utilisant la relation :

$$P(T) \approx \Delta P = \mathrm{d}m/\mathrm{d}t\ (2\pi RT / M)^{1/2} 1/aF$$

dans laquelle ΔP est la pression de part et d'autre du trou d'effusion; $P(T)$, la pression mesurée par effusion à la température T; $\mathrm{d}m/\mathrm{d}t$, la masse effusée par unité de temps; R, la constante des gaz parfaits; M, la masse molaire de la substance; a, l'aire de l'orifice d'effusion; F, le facteur de Clausing.

3.4. Enthalpie de formation à l'état gazeux

En utilisant les résultats expérimentaux obtenus par calorimétrie de combustion et de sublimation, nous avons calculé l'enthalpie molaire standard de formation à l'état gazeux de chacun des trois isomères. Celle-ci est égale à (–245,0 ± 0,9) kJ mol^{-1}, (–239,3 ± 1,0) kJ mol^{-1} et (–240,3 ± 1,0) kJ mol^{-1} respectivement pour les isomères *ortho*, *méta* et *para*.

3.5. Enthalpie d'atomisation

À une température donnée, la réaction d'atomisation des acides étudiés dans ce mémoire s'écrit :

$$C_6H_5NO_2(g) \rightarrow 6\ C(g) + 5\ H(g) + N(g) + 2\ O(g)$$

En conséquence, à 298,15 K, l'enthalpie liée à cette réaction est égale à :

$$\Delta_a H°_m(g) = 6\Delta_f H°_m C(g) + 5\Delta_f H°_m H(g) + \Delta_f H°_m N(g) + 2\Delta_f H°_m O(g) - \Delta_f H°_m C_6H_5O_2N(g)$$

© 1999 CNRC Canada

Tableau 3. Combustion de l'acide picolinique (isomère *ortho*) à 298,15 K.

m_{subst}	m_{coton}	n (HNO_3)	A	$-\Delta U$	$-W_1$	W_2	$-\Delta_c U°_m$
mg	mg	10^{-6} mol	V s	J	J	J	kJ mol^{-1}
7,0192	0,1352	7,45	9,907245	158,790	2,217	0,634	2735,03
5,9476	0,1335	6,88	8,431185	135,132	2,190	0,570	2740,01
7,4184	0,1456	7,64	10,493439	168,185	2,388	0,657	2740,57
6,1673	0,1293	6,88	8,728518	139,898	2,121	0,576	2738,79
5,8866	0,0937	6,30	8,287905	132,836	1,537	0,534	2734,79
6,2468	0,1671	6,88	8,878794	142,306	2,741	0,580	2739,12
5,6952	0,1037	5,35	8,049306	129,012	1,701	0,473	2741,81
5,2016	0,1406	5,73	7,388838	118,426	2,309	0,482	2736,83
5,0680	0,0903	5,16	7,153461	114,653	1,481	0,444	2738,38
7,5250	0,1482	7,64	10,641621	170,560	2,431	0,660	2739,85

$-\Delta_c U$(cr,298,15 K)/kJ mol^{-1} = 2738,52 ± 0,73
$-\Delta_c H$(cr,298,15 K)/kJ mol^{-1} = 2737,96 ± 0,73
$-\Delta_f H$(cr,298,15 K)/kJ mol^{-1} = 337,73 ± 0,73
A = aire des thermogrammes, ΔU = variation de l'énergie interne de la bombe et de son contenu, W_1 = énergie de combustion du coton, W_2 = corrections pour passer à l'état de référence.

Tableau 4. Combustion de l'acide nicotinique (isomère *méta*) à 298,15 K.

m_{subst}	m_{coton}	n (HNO_3)	A	$-\Delta U$	$-W_1$	W_2	$-\Delta_c U°_m$
mg	mg	10^{-6} mol	V s	J	J	J	kJ mol^{-1}
6,1029	0,0976	6,11	8,572344	137,395	1,601	0,529	2728,64
6,4085	0,1558	6,88	9,067806	145,336	2,555	0,584	2731,68
7,0258	0,1525	6,69	9,917505	158,954	2,501	0,590	2731,15
6,0255	0,1158	6,69	8,490999	136,091	1,899	0,561	2730,30
5,4839	0,1264	5,16	7,749681	124,209	2,073	0,456	2731,66
5,1415	0,1354	6,69	7,297641	116,964	2,221	0,536	2734,65
5,5873	0,1457	5,73	7,922163	126,974	2,390	0,493	2734,24

$-\Delta_c U$(cr,298,15 K)/kJ mol^{-1} = 2731,76 ± 0,79
$-\Delta_c H$(cr,298,15 K)/kJ mol^{-1} = 2731,19 ± 0,79
$-\Delta_f H$(cr,298,15 K)/kJ mol^{-1} = 344,48 ± 0,79
A = aire des thermogrammes, ΔU = variation de l'énergie interne de la bombe et de son contenu, W_1 = énergie de combustion du coton, W_2 = corrections pour passer à l'état de référence.

Tableau 5. Combustion de l'acide isonicotinique (isomère *para*) à 298,15 K.

m_{subst}	m_{coton}	n (HNO_3)	A	$-\Delta U$	$-W_1$	W_2	$-\Delta_c U°_m$
mg	mg	10^{-6} mol	V s	J	J	J	kJ mol^{-1}
6,6658	0,1226	6,30	9,378564	150,316	2,011	0,557	2728,79
5,8860	0,1778	5,73	8,340882	133,685	2,916	0,502	2724,64
5,4115	0,1343	4,39	7,635474	122,379	2,203	0,409	2724,68
5,8374	0,1439	6,49	8,239944	132,067	2,360	0,545	2724,04
6,2735	0,1382	5.92	8,844485	141,756	2,267	0,523	2727,07
6,6323	0,1109	6,49	9,304860	149,135	1,819	0,566	2724,02
6,4366	0,1199	6,30	9,041061	144,907	1,967	0,550	2723,47
8,4330	0,1509	9,55	11,849523	189,920	2,475	0,797	2724,82
6,5235	0,1486	6,30	9,182025	147,166	2,437	0,553	2720,88

$-\Delta_c U$(cr,298,15 K)/kJ mol^{-1} = 2724,71 ± 0,74
$-\Delta_c H$(cr,298,15 K)/kJ mol^{-1} = 2724,09 ± 0,74
$-\Delta_f H$(cr,298,15 K)/kJ mol^{-1} = 351,54 ± 0,74
A = aire des thermogrammes, ΔU = variation de l'énergie interne de la bombe et de son contenu, W_1= énergie de combustion du coton, W_2 = corrections pour passer à l'état de référence.

Les valeurs de $\Delta_a H°_m$(298,15 K) sont respectivement égales à (6606,0 ± 1,6) kJ mol^{-1}, (6600,3 ± 1,7) kJ mol^{-1} et (6601,3 ± 1,7) kJ mol^{-1} pour les acides picolinique, nicotinique et isonicotinique. Elles ont été calculées en utilisant les valeurs de $\Delta_f H°_m$(g,298,15K) de C, H, N et O consignées dans la référence 23 et qui valent respectivement (716,67 ± 0,44), (217,997 ± 0,006), (472,68 ± 0,40) et (249,17 ± 0,10) kJ mol^{-1}.

© 1999 CNRC Canada

Tableau 6. Sublimation des acides picolinique, nicotinique et isonicotinique.

Isomère	T	m	$\Delta_{sub}H_m(T)$	$\Delta_{sub}\overline{H}_m(T)$	$\int_{298,15K}^{T} C^\circ_{p,m}(g)dT$	$\int_{298,15K}^{T} C^\circ_{p,m}(cr)dT$	$\Delta_{sub}H^\circ_m(298,15\ K)$	$P_s(T)$
	K	mg	kJ mol^{-1}	kJ mol^{-1}	kJ mol^{-1}	kJ mol^{-1}	kJ mol^{-1}	Pa
ortho	328,75	20,9578	92,60					
		20,3792	91,22					
		20,8570	89,13					
		20,8562	90,39	91,00±0,50	3,14±0,15	4,86±0,02	92,72±0,52	1,9
		21,0406	92,71					
		21,1240	91,08					
		22,6783	89,90					
méta	362,15	9,4256	100,98					
		10,2895	99,93					
		9,7803	99,97	101,12±0,61	7,05±0,15	11,10±0,06	105,17±0,63	0,31
		10,6050	103,11					
		10,1439	100,13					
		11,6030	103,74					
		11,8446	99,97					
para	362,15	4,1015	107,87					
		3,5774	106,76					
		3,7896	106,11					
		5,0566	109,43					
		5,1588	105,93					
		3,7730	106,39	107,74± 0,68	7,05± 0,15	10,59± 0,03	111,28± 0,70	0,015
		5,5268	106,33					
		5,0398	110,60					
		4,3480	106,71					
		3,3775	104,30					
		3,1835	110,04					
		4,0754	112,40					

Tableau 7. Enthalpies de formation à l'état gazeux et à 298,15 K des trois isomères de différents dérivés de la pyridine.

Dérivé	$\Delta_fH^\circ_m$(g, 298,15 K) kJ mol^{-1}			Référence
	ortho	*méta*	*para*	
Méthylpyridines	99,2	106,4	104,1	24
Aminopyridines	107,5	141,4	125,9	1
Hydroxypyridines			–30,3	25
Carboxypyridines	–245,0	–239,3	–240,3	Ce travail

Dans le présent travail, l'incertitude qui accompagne les résultats expérimentaux représente l'écart moyen, $\sigma_m = \pm\{\Sigma(x - x_0)^2 / n(n-1)\}^{1/2}$, x étant chacune des n valeurs entrant dans le calcul de la moyenne x_0. Lorsque la valeur expérimentale est fonction de plusieurs variables, l'incertitude calculée tient compte de l'erreur sur chacune de ces variables.

4. Discussion

4.1. Enthalpie de formation à l'état gazeux

Nous avons voulu comparer entre elles les valeurs de l'enthalpie de formation à l'état gazeux et à 298,15 K des trois isomères de différents dérivés de la pyridine se différenciant par la nature du substituant. Ces différentes valeurs sont rassemblées dans le tableau 7. Cette comparaison nous permet de faire les constatations suivantes :

1. Les substances étudiées dans le présent travail sont les plus stables. Les valeurs de leur $\Delta_fH^\circ_m$(g, 298,15 K) sont négatives et élevées (en valeur absolue). La stabilité semble décroître dans l'ordre suivant : carboxypyridines, hydroxypyridines, méthylpyridines et aminopyridines.

2. Quelle que soit la famille considérée, l'isomère *ortho* paraît être le plus stable. Comme il en sera question plus loin dans le texte, ceci peut être dû à la présence d'une liaison hydrogène intramoléculaire entre l'atome d'hydrogène de la fonction acide et l'atome d'azote de l'hétérocycle créant ainsi un second cycle et renforçant, de ce fait, la conjugaison. Par ailleurs, cette stabilité décroît dans le sens *ortho*, *para*, *méta*.

4.2. Liaisons intramoléculaires dans les acides carboxypyridiniques

Par définition, l'enthalpie d'atomisation d'une molécule est égale à la somme des liaisons intramoléculaires compte tenu des facteurs de stabilisation et de déstabilisation.

À partir de cette grandeur thermodynamique et compte tenu du principe de transférabilité, nous avons pu déterminer la valeur enthalpique de l'ensemble des liaisons comprises

© 1999 CNRC Canada

Tableau 8. Energie de conjugaison des trois isomères de différents dérivés de la pyridine.

Dérivé	E_{conj} kJ mol^{-1}		
	ortho	*méta*	para
Méthylpyridines	169,9	153,6	160,5
Aminopyridines	182,6	168,2	182,9
Hydroxypyridines			161,9
Carboxypyridines	252,9	240,1	241,1

dans le groupement (C-N=C) dans chacun des trois acides. Pour ce faire, nous avons défalqué de $\Delta_a H°_m$(298,15 K) la valeur des différentes autres liaisons intramoléculaires précédemment déterminées au laboratoire (26) : H(C_b—C_b) = 504,97 kJ mol^{-1}, H(C_b—H) = 415,88 kJ mol^{-1}, H(C_b—C) = 351,56 kJ mol^{-1}, H(COOH) = 1657,35 kJ mol^{-1}. Nous trouvons pour H(C-N=C) la valeur moyenne 910,22 kJ mol^{-1} qui est en très bon accord avec les valeurs trouvées précédemment au laboratoire pour ce même ensemble (902,18 kJ mol^{-1} (26), 924,2 kJ mol^{-1} (27)) ou consignées dans la littérature (valeur moyenne 903 kJ mol^{-1} (28)).

4.3. Energie de conjugaison

L'énergie de conjugaison est la différence entre l'énergie réelle de la molécule et l'énergie qu'elle aurait si les divers systèmes insaturés qu'elle comporte étaient indépendants. Pratiquement, pour la déterminer, il suffit d'utiliser les enthalpies standard de combustion à l'état gazeux de la molécule réelle et de la molécule fictive non conjuguée. La première de ces grandeurs s'obtient expérimentalement et la seconde nécessite le recours aux systématiques. En ce qui nous concerne, nous avons utilisé celle de Klages qui est consignée dans la référence 29 compte tenu des modifications relatives aux liaisons C—N et C=N indiquées dans la référence 30.

Les valeurs de l'énergie de conjugaison des trois acides étudiés dans ce mémoire sont consignées dans le tableau 8 avec celles de différents dérivés de la pyridine. Ce tableau nous permet de faire les constatations suivantes :

1. Les carboxypyridines sont les dérivés les plus conjugués. Ceci est vraisemblablement dû au fait que le groupement (COOH), donneur d'électrons, consolide la conjugaison du cycle.

2. Quelle que soit la famille considérée, l'isomère *ortho* est plus le conjugué.

3. L'énergie de conjugaison des aminopyridines est plus élevée que celles des hydroxypyridines (à noter que la littérature ne propose de valeur sûre que pour l'isomère *para*). Ceci peut s'expliquer si l'on considère l'électronégativité des atomes d'azote de la fonction amine (NH_2) et d'oxygène de la fonction hydroxyle (OH). En effet, le doublet électronique porté par chacun de ces deux atomes est plus délocalisé dans le cas de NH_2 que dans celui de OH.

4. Le groupement CH_3 ne participant éventuellement à la conjugaison que par l'effet d'hyperconjugaison fait que les méthylpyridines apparaissent comme les dérivés les moins conjugués.

4.4. Liaisons intermoléculaires dans les acides carboxypyridiniques

4.4.1. Liaisons hydrogène intermoléculaires

L'enthalpie de sublimation d'une substance organique est liée aux interactions intermoléculaires comprenant la part énergétique due aux forces de van der Waals (de dispersion et dipolaires) et, le cas échéant, celle qui est relative aux liaisons hydrogène.

Un procédé de calcul, plusieurs fois utilisé avec succès au laboratoire (1, 31–38), nous a permis de déterminer la part énergétique due aux liaisons hydrogène intermoléculaires. Il consiste, dans notre cas, à comparer l'enthalpie de sublimation de nos molécules à celle d'une molécule isoélectronique (ici la molécule de nitrobenzène) possédant les mêmes forces de dispersion et d'interactions dipolaires. Ce composé étant liquide à 298,15 K, nous avons déterminé son enthalpie de sublimation à partir de son enthalpie de vaporisation à 298,15 K et de son enthalpie de fusion à T_{fus} = 278,85 K en utilisant, en première approximation, la relation suivante :

$$\Delta_{sub}H°_m(298{,}15\ \text{K}) = \Delta_{vap}H°_m(298{,}15\ \text{K}) + \Delta_{fus}H_m(298{,}15\ \text{K})$$

avec $\Delta_{vap}H°_m$(298,15 K) = 55,0 kJ mol^{-1} (24) et $\Delta_{fus}H_m$(278,85 K) = 11,59 kJ mol^{-1} (39). Cette dernière valeur a été ramenée à 298,15 K en appliquant la relation de Sidgwick (40) :

$$\Delta_{fus}H_m(298{,}15\ \text{K}) = \Delta_{fus}H_m(278{,}85\ \text{K}) - 0{,}055\ (278{,}85 - 298{,}15)$$

Nous obtenons $\Delta_{fus}H_m$(298,15 K) = 12,65 kJ mol^{-1} et $\Delta_{sub}H°_{m.}$(298,15 K) = 67,65 kJ mol^{-1}. Cette dernière valeur correspond, en première approximation, à la part des forces de dispersion et dipolaires dans le cristal des trois acides carboxypyridiniques. Malheureusement, il ne nous a pas été possible de départager ces deux types d'interactions. En effet, la littérature ne propose aucune valeur de l'enthalpie de vaporisation et de fusion du 2-phénylpropène qui nous auraient permis de déterminer son enthalpie de sublimation à 298,15 K. Cette grandeur est, rappelons-le, en première approximation égale à la part énergétique due aux forces de dispersion dans les cristaux des acides carboxypyridiniques. Il s'en suit que la part énergétique due aux liaisons hydrogène intermoléculaires dans les isomères *ortho*, *méta* et *para* est respectivement égale à 25,07 kJ mol^{-1}, 37,52 kJ mol^{-1} et 43,63 kJ mol^{-1}.

Si l'on considère la molécule d'isomère *para* dans laquelle il ne peut y avoir que des liaisons hydrogène intermoléculaires, la part énergétique due à ces liaisons est relativement élevée par rapport à celles qui ont été trouvées jusqu'ici au laboratoire (41) ou consignées dans la littérature (42). On pourrait expliquer cette anomalie si l'on considère les rares résultats de la littérature à propos de la structure cristalline des trois acides carboxypyridiniques (10, 11, 13). En effet, ces résultats font tous état de liaisons hydrogène intermoléculaires entre l'atome d'azote d'une molécule et l'atome d'oxygène de la fonction OH d'une molécule voi-

© 1999 CNRC Canada

sine. D'après Takusagawa et Shimada (13), à ces liaisons viennent s'ajouter, dans le cas de l'acide isonicotinique (isomère *para*), deux autres faibles liaisons hydrogène entre chacun des atomes de carbone du cycle, situés de part et d'autre de l'atome d'azote, et l'atome d'oxygène de la fonction carbonyle de molécules voisines. En estimant que la liaison N···H—O, ayant une longueur N···H de 1,51 Å (13), possèderait une enthalpie de 29 kJ mol^{-1} (42), à chacune des deux liaisons C—H···O, ayant une longueur O···H de 2,46 Å (13), serait associée une enthalpie d'environ 7,5 kJ mol^{-1}.

4.4.2. Liaisons hydrogène intramoléculaire dans l'isomère ortho

À la suite de leur travail sur la structure de l'acide picolinique, Pâris et al. (7) concluent que cet acide présente une chélation à l'état solide par formation d'une liaison hydrogène intramoléculaire entre l'atome d'azote de l'hétérocycle et l'atome d'hydrogène de la fonction carboxylique.

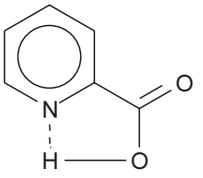

Un moyen simple de pouvoir quantifier cette chélation consiste à comparer entre elles les valeurs de l'enthalpie de sublimation des isomères *ortho* et *para*. La différence observée, dans le cas présent, est de 18,56 kJ mol^{-1} et doit être attribuée, compte tenu de la chélation, au fait que la molécule d'acide picolinique possède moins de liaisons hydrogène intermoléculaires que les deux autres isomères. La valeur trouvée est tout à fait compatible avec celles qui ont été précédemment déterminées au laboratoire dans le cas des acides hydroxybenzoïques (17,8 kJ mol^{-1} (43)), des acides aminobenzoïques (11,2 kJ mol^{-1} (44)) et des nitrophénols (20,1 kJ mol^{-1} (33)).

D'autres observations faites sur les propriétés physicochimiques de l'acide picolinique tendent à prouver l'existence de cette liaison intramoléculaire.

1. À partir de nos expériences de sublimation, il s'avère que la pression de vapeur saturante de l'isomère *ortho*, est, quelle que soit la température, toujours supérieure à celle des deux autres isomères.

2. La température du point triple et l'enthalpie de fusion sont plus faibles dans le cas de l'isomère *ortho* qu'elles ne le sont dans celui des deux autres isomères (cf. tableau 2).

3. La valeur du pK_a de l'acide picolinique (5, 32) est supérieure à celle des deux autres acides (nicotinique : 4,81, isonicotinique : 4,86) (45).

4. Au cours de nos expériences, nous avons constaté que la solubilité de l'acide picolinique dans un solvant apolaire comme le benzène est plus forte que celle de l'isomère *para* dans le même solvant.

4.5. Peut-on ériger l'acide nicotinique au rang de substance d'intercomparaison en calorimétrie de combustion des substances azotées ?

À la suite de leurs travaux, plusieurs chercheurs (5, 6, 46, 47) ont en fait la proposition.

L'étude des trois acides carboxypyridiniques nous a montré qu'ils sont stables à température ambiante, non hygroscopiques et ont une faible pression de vapeur saturante. Par contre, les expériences réalisées avec ces substances par calorimétrie de combustion nous ont permis de constater que :

1. les pastilles d'acide isonicotinique ont tendance à s'effriter;
2. des combustions incomplètes ont quelquefois été observées avec l'acide picolinique.

Enfin, on trouve dans le commerce des échantillons d'acide nicotinique très purs, ce qui permet de les utiliser sans purification.

Compte tenu de ce qui précède, nous pensons aussi que l'acide nicotinique peut être retenu comme substance d'intercomparaison en calorimétrie de combustion des substances azotées dont le rapport N/C est faible.

Bibliographie

1. R. Sabbah et M.E.S. Eusébio. Can. J. Chem. **76**, 18 (1998).
2. K. Weissermel et H.J. Arpe. Chimie organique industrielle. Principaux produits de base et intermédiaires. Masson, Paris. 1981.
3. P. Magnin. Les vitamines. Collection Que sais-je ? P.U.F., Paris. 1992.
4. ICTAC working group « thermochemistry». Reference materials for calorimetry and differential thermal analysis. Thermochim. Acta. Numéro spécial, sous presse.
5. W.H. Johnson. J. Res. Natl. Bur. Stand. **79A**, 425 (1975).
6. T. Sato-Toshima, A. Kamaguchi, K. Nishiyama, M. Sakiyama et S. Seki. Bull. Chem. Soc. Jpn. **56**, 51 (1983).
7. M. Pâris, G. Thomas et J.C. Merlin. Bull.Soc. Chim. Fr. 707 (1961).
8. F. Takusagawa et A Shimada. Chem. Lett. 1089 (1973).
9. W.B. Wright et G.S.D. King. Acta Crystallogr. **3**, 31 (1950).
10. W.B. Wright et G.S.D. King. Acta Crystallogr. **6**, 305 (1953).
11. M.P. Gupta et P. Kumar. Cryst. Struct. Commun. **4**, 365 (1975).
12. A. Kutoglu et C. Scheringer. Acta Crystallogr. Sect. C : Cryst. Struct. Commun.**C39**, 232 (1983).
13. F. Takusagawa et A. Shimada. Acta Crystallogr. Sect. B : Struct. Crystallogr. Cryst. Chem. **B32**, 1925 (1976).
14. D.L. Lide. Handbook of chemistry and physics. 71^{e} éd. CRC, Boca Raton, Fla. 1990–1991.
15. (*a*) R. Sabbah et L. El Watik. J. Therm. Anal. **36**, 2291 (1990); (*b*) R. Sabbah et I. Antipine. J. Therm. Anal. **32**, 1929 (1987).
16. R. Sabbah et I. Antipine. Bull. Soc. Chim. Fr. **3**, 392 (1987).
17. R. Sabbah, I. Antipine, M. Coten et L. Davy. Thermochim. Acta, **115**, 153 (1987).
18. D.R. Stull, E.F. Westrum, Jr. et G.C. Sinke. The chemical thermodynamics of organic compounds. Wiley, New York. 1969.
19. W.D. Good et N.K. Smith. J. Chem. Eng. Data, **14**, 102 (1969).
20. Atomic weights of the elements. Pure Appl. Chem. **66**, 2423 (1994).
21. J.D. Cox et G. Pilcher. Themochemistry of organic and orgametallic compounds. Academic Press, London. 1970.
22. R. Sabbah et M. Coten. Thermochim. Acta, **49**, 307 (1981).
23. Report of the codata task group on key values of thermodynamics 1977. J. Chem. Thermodyn. **10**, 903 (1978).
24. J.B. Pedley, R.D. Naylor et S.P. Kirby. Thermochemical data of organic compounds. 2^{e} éd. Chapman et Hall, New-York. 1986.
25. M.A.V. Ribeiro da Silva, M. Agostinha, R. Matos, Yang Meng-Yan et G. Pilcher. J. Chem. Thermodyn. **24**, 107 (1992).
26. R. Sabbah et M. Laffitte. Thermochim. Acta, **25**, 376 (1978).
27. R. Sabbah et L. El Watik. Thermochim. Acta, **176**, 163 (1991).

© 1999 CNRC Canada

28. D.M. McEachern, O. Sandoval et J.C. Iniguez. J. Chem. Thermodyn. **7**, 299 (1975).
29. G.W. Wheland. Resonance in organic chemistry. Wiley, New York. 1955. Chap. 3.
30. M. Nabavian, R. Sabbah, R. Chastel et M. Laffitte. J. Chim. Phys. **74**, 115 (1977).
31. R. Sabbah et L. Perez. Can. J. Chem. **75**, 357 (1997).
32. R. Sabbah et M. Gouali. Can. J. Chem. **74**. 500 (1996).
33. R. Sabbah et M. Gouali. Aust. J. Chem. **47**, 1651 (1994).
34. R. Sabbah et O. Pemenzi. C.R. Acad. Sci. Sér. II : Méc. Phys. Chim. Sci. Terre Univers, **317**, 575 (1993).
35. R. Sabbah et E.N.L.E. Buluku. Can. J. Chem. **69**, 481 (1991).
36. P. Knauth et R. Sabbah. Can. J. Chem. **68**, 731 (1990).
37. P. Knauth et R. Sabbah. Bull Soc. Chim. Fr. **5**, 834 (1988).
38. S. Skoulika et R. Sabbah. Thermochim. Acta, **61**, 203 (1983).
39. W.E. Acree, Jr. Thermochim. Acta, **18**9 37 (1991).
40. T.L. Cottrell. The strengths of chemical bonds. 2^{e} éd. Butterworths, London. 1958.
41. R. Sabbah et M. Gouali. Thermochim. Acta, **30**3 107 (1997).
42. A. Julg. Chimie théorique. Dunod, Paris. 1964.
43. R. Sabbah et T.H.D. Le. Can. J. Chem. **71**, 1378 (1993).
44. R. Sabbah, R. Chastel et M. Laffitte. Can. J. Chem. **52**, 2201 (1974).
45. J.J. Christensen, R.M. Izatt, D.P. Wrathall et L.D. Hansen. J. Chem. Soc. A, 1212 (1969).
46. G.T. Armstrong et W.H. Johnson. Proc. Int. Conf. Chem. Thermodyn. 3^{e}, Baden. 1973. **8**, 55 (1973).
47. J.D. Cox. Experimental thermodynamics. Vol. I : Combustion calorimetry. *Édité par* S. Sunner et M. Månsson. Pergamon, Oxford. 1979.

© 1999 CNRC Canada

Ether synthesis using trifluoromethanesulfonic anhydride or triflates under mild reaction conditions

Tomihiro Nishiyama, Hideaki Kameyama, Hideki Maekawa, and Kouhei Watanuki

Abstract: Reactions of magnesium alkoxides with trifluoromethanesulfonic anhydride or triflates gave corresponding symmetrical or unsymmetrical ethers in moderate to good yields under mild reaction conditions. The scope and limitations of the reaction are discussed.

Key words: ethers, trifluoromethanesulfonic anhydride, triflates, magnesium alkoxides.

Résumé : Les réactions des alcoolates de magnésium avec l'anhydride trifluorométhanesulfonique ou avec les triflates dans des conditions douces conduit aux éthers symétriques ou non symétriques avec des rendements qui vont de modérés à bons. On discute de la portée et des limitations de la réaction.

Mots clés : éthers, anhydride trifluorométhanesulfonique, triflates, alcoolates de magnésium.

[Traduit par la Rédaction]

Introduction

Conversion of an alcohol to the corresponding ether is a widely used functional transformation in organic synthesis, and several methods are available to accomplish an *O*-alkylation reaction under a variety of conditions. For example, the Williamson ether synthesis, with its modifications (1, 2), is one of the most useful synthetic methods for the formation of a carbon–oxygen bond. The attack of alkoxides on alkyl halides, however, is synthetically useful only when the alkyl halide is primary (3). Moreover, the standard Williamson ether synthesis requires rigorous reaction conditions. The condensation of alcohols and their salts with aldehydes (4), olefins (5), *p*-toluene sulfonic acid (6), nitro compounds (7), and dialkyl phosphates (8) are also reported to be useful methods for the *O*-alkylation reaction.

Other approaches have been demonstrated by either the trimethylsilyl triflate- or trimethylsilyl iodide-catalyzed reductive coupling of carbonyl compounds with trialkylsilanes (9). Noyori and co-workers (10) have shown that acetals can be conveniently reduced to ether with trimethylsilane catalyzed by trimethylsilyl trifluoromethanesulfonate. This method is extremely mild and provides nearly equal quantitative yields of symmetrical and unsymmetrical ethers from the corresponding acetals.

Received June 18, 1998.

T. Nishiyama.[1] High Technology Research Center, Kansai University, Suita, Osaka 564-0073, Japan.
H. Kameyama, H. Maekawa, and K. Watanuki. Department of Applied Chemistry, Faculty of Engineering, Kansai University, Suita, Osaka 564-0073, Japan.

[1]Author to whom correspondence may be addressed. Telephone:(06) 6368–0901. Fax: (06)6339-4026. e-mail: organic@ipcku.kansai-u.ac.jp

In this paper, we report a simple procedure for the preparation of symmetrical and unsymmetrical ethers by the reaction of magnesium alkoxides with trifluoromethanesulfonic anhydride (Tf_2O) or triflates (Scheme 1). The scope and limitations of this procedure are also discussed.

Results and discussion

Table 1 summarizes the products and yields obtained from the reaction of magnesium alkoxides with Tf_2O, and scope of the present method. The reaction of Tf_2O in dry ether with in situ generated magnesium di(benzyl alcoholate) proceeded smoothly to yield dibenzyl ether **2a**. The reaction was completed in 30 min at 5°C, and an 80% isolated yield of dibenzyl ether could be obtained. In this reaction, a stoichiometric amount of Tf_2O was necessary for the reaction. After treatment of magnesium di(benzyl alcoholate) with 0.5 equiv. of Tf_2O, the isolated yield of symmetrical ether decreased to 35% (entry 2). The trifluoromethanesulfonic acid (TfOH) and toluene-4-sulfonic anhydride (TS_2O) were less effective (entries 3 and 4), and the reaction required longer reaction times and a higher temperature to attain a comparable yield (entry 4). With other magnesium alkoxides such as 2-phenylethanol **1b** and hexanol **1c**, the corresponding symmetrical ethers, diphenethyl ether **2b** and dihexyl ether **2c**, were obtained in high yields. The reactions of magnesium alkoxides with Tf_2O were usually carried out at 5°C for 30 min, although in one case, a higher temperature provided better yields. When a mixture of magnesium di(hexanolate) and Tf_2O was stirred at 40°C for 1h, **2c** was obtained in 90% yield. Similarly, a branched primary magnesium alkoxide gave the symmetrical ether **2d** as a mixture of diastereomers (ratio 1:1) in 60% yield (entry 7). In contrast to results obtained with primary magnesium alkoxides, the reactions with secondary magnesium alkoxides such as 2-hexanol **1e** and

© 1999 NRC Canada

Table 1. Synthesis of symmerical ethers.[a]

Entry	Alcohol	Additive	Product	Yield (%)[b]
1	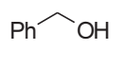 **(1a)**	Tf_2O	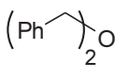 **(2a)**	85 (80)
2		Tf_2O		39 (35)[c]
3		TfOH		23 (19)
4		TS_2O		86 (80)[d]
5	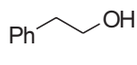 **(1b)**	Tf_2O	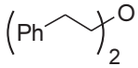 **(2b)**	86 (72)
6	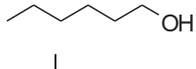 **(1c)**	Tf_2O	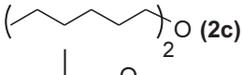 **(2c)**	98 (90)[e]
7	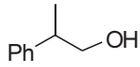 **(1d)**	Tf_2O	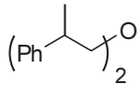 **(2d)**	71 (60)[f]
8	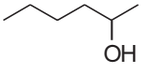 **(1e)**	Tf_2O	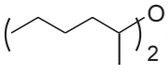 **(2e)**	30 (25)[f]
9	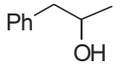 **(1f)**	Tf_2O	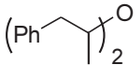 **(2f)**	45 (37)[f]

[a]Unless otherwise indicated, all reactions were carried out at 5°C for 30 min.
[b]GLC yield based on Tf_2O. Value in parentheses indicates yield after purification.
[c]The amount of Tf_2O was 0.5 equiv. Yield based on Mg.
[d]The reaction was carried out at 40°C for 15 h.
[e]The reaction was carried out at 40°C for 1 h.
[f]1:1 diastereomeric ratio. The ratios of two diastereomers were estimated by GLC.

Scheme 1.

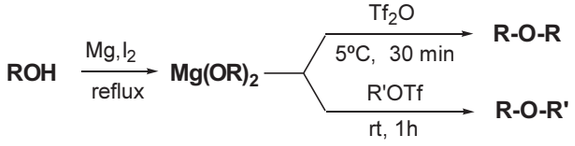

3-phenyl-2-propanol **1f** gave bis(2-hexyl) ether **2e** and bis(3-phenyl-2-propyl) ether **2f** as a mixture of diastereomers (ratio 1:1) in low yields. However, tertiary alcohol and phenol failed to give the corresponding ethers. No product was obtained upon heating magnesium di(1,1-dimethyl-2-phenylethanolate) and Tf_2O, even after several hours.

We next turned our attention to the synthesis of unsymmetrical ethers. An unsymmetrical ether can be obtained in moderate yields when an alkyl triflate is used in place of Tf_2O in the reaction. These results are summarized in Table 2. The addition of 1 equiv. of pentyl triflate in dry ether to magnesium di(benzyl alcoholate) in benzyl alcohol **1a** solution at room temperature for 1 h gave benzyl pentyl ether **3a** in 87% yield. The reaction is much less successful with mesylate or tosylate than with triflate. In the case of pentyl mesylate, the reaction required longer reaction times and a higher temperature to obtain an unsymmetrical ether (entry 2). Pentyl tosylate did not give an unsymmetrical ether even at 60°C for 17 h (entry 3). The treatment of 2 equiv. of magnesium di(2-phenylethanolate) with ditriflate at room temperature for 6 h gave symmetrical bis(phenethoxy)butane **3c** in 60% yield. When branched magnesium di(2-phenyl-1-propanolate) was used, the corresponding pentyl 2-phenyl-1-propyl ether **3d** was obtained in 88% yield. For the reactions of secondary magnesium alkoxides with triflate, the corresponding ethers **3e** and **3f** were isolated in 85 and 76% yields, respectively (entries 7 and 8). With tertiary magnesium alkoxide such as 1,1-dimethyl-2-phenylethanol **1h**, the yield was not satisfactory (entry 9). The results in Table 2 indicate that this reaction sequence is applicable to primary and secondary magnesium alkoxides in moderate yields.

In conclusion, we report a simple procedure for the preparation of symmetrical and unsymmetrical ethers by the reaction of magnesium alkoxides with Tf_2O or triflates. This method has the advantage that the reaction rapidly and cleanly takes place under mild reaction conditions.

Experimental

General methods

NMR spectra were recorded in $CDCl_3$ on a JEOL GSX-400 spectrometer operating at 400 and 100 MHz for ^1H and ^{13}C, respectively. Chemical shifts for NMR spectra were referenced to internal $(CH_3)_4Si$. Mass spectra were measured

© 1999 NRC Canada

Table 2. Synthesis of unsymmetrical ethers.[a]

Entry	Alcohol	Triflate	Product	Yield (%)[b]
1	**1a**	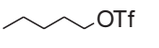	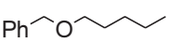 **(3a)**	98 (87)
2		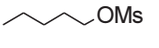		52 (42) [c]
3		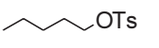		N.R [c]
4	**1b**	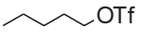	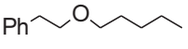 **(3b)**	99 (94)
5		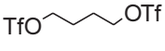	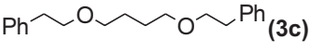 **(3c)**	66 (60) [d]
6	**1d**	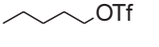	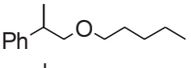 **(3d)**	92 (88)
7	**1g** [e]		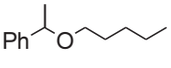 **(3e)**	96 (85)
8	**1f**		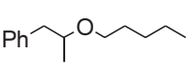 **(3f)**	86 (76)
9	**1h** [f]		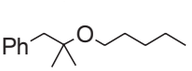 **(3g)**	52 (40)

[a]Unless otherwise indicated, all reactions were carried out at room temperature for 1 h.
[b]GLC yield based on triflate. Value in parentheses indicates yield after purification.
[c]The reaction was carried out at 60°C for 17 h.
[d]The reaction was carried out at room temperature for 6 h.
[e]1-Phenylethanol.
[f]1,1-Dimethyl-2-phenylethanol.

with a Perkin–Elmer model 910 spectrometer operating in the electron impact mode (70 eV). IR spectra were recorded on a Perkin–Elmer model 1600 spectrophotometer. Gas chromatography was carried out on a 20 m × 0.22 mm capillary column packed with methyl silicone.

Materials

Triflates, mesylates, and tosylates were prepared in the same manner as described in the literature (11, 12). All reagents were reagent grade materials purchases obtained from Tokyo Kasei Kogyo Co. Ltd. (Tokyo) and used without further purification.

General procedure for the synthesis of symmetrical ethers

The following experimental procedure is representative. The precursor, the magnesium alkoxides, were prepared by using a slight modification of the procedure described in the literature (13). A mixture of benzyl alcohol **1a** (2.16 g, 0.02 mol), magnesium (0.24 g, 0.01 mol), and iodine (50 mg, 0.2 mmol) was stirred at 60°C for 1 h. To this solution were added **1a** (2.16 g, 0.02 mol), and the reaction mixture was refluxed until the magnesium was digested. After the reaction mixture cooled to ice-water temperature, a solution of Tf_2O (2.8 g, 0.01 mol) in dry ether (10 mL) was added, and the mixture was then stirred continuously for 30 min at 5°C. The reaction was quenched by the addition of water and extracted with ether. The extract was washed with water, and concentrated in vacuo. The residue was chromatographed on silica gel using hexane/ethyl acetate (80/20) to give dibenzyl ether **2a** in 80% yield as a colorless oil.

Dibenzyl ether (2a) (14)

^{1}H NMR δ: 4.54 (s, 4H), 7.24–7.37 (m, 10H); ^{13}C NMR δ: 72.1,127.6, 127.8, 128.4, 138.3; MS *m*/*z* (rel. intensity): 107(19), 92(100), 91(98), 79(29), 77(28), 65(31), 51(12).

Diphenethyl ether (2b) (15)

^{1}H NMR δ: 2.87 (t, *J* = 7.3 Hz, 4H), 3.64 (t, *J* = 7.3 Hz, 4H), 7.18–7.28 (m, 10H); ^{13}C NMR δ: 36.4, 71.9, 126.2, 128.3, 128.9, 139.1; MS *m*/*z* (rel. intensity): 226 (M^+, 1), 135(11), 134(11), 106(10), 105(100), 104(12), 103(13), 91(25), 77(19).

Dihexyl ether (2c) (14, 15)

^{1}H NMR δ: 0.89 (t, *J* = 7.0 Hz, 6H), 1.28–1.36 (m, 12H), 3.39 (t, *J* = 7.0 Hz, 4H); ^{13}C NMR δ: 14.1, 22.7, 25.9, 29.8, 31.8, 71.0; MS *m*/*z* (rel. intensity): 85(84), 84(21), 83(22), 69(15), 59(21), 56(43), 55(23), 43(100).

Bis(2-phenyl-1-propyl) ether (2d) (16*a*)

^{1}H NMR δ: 1.09 (d, *J* = 6.6 Hz, 3H), 1.23 (d, *J* = 6.6 Hz, 3H), 2.58 (dd, *J* = 6.6, 13.5 Hz, 1H), 2.62 (dd, *J* = 6.6, 13.5 Hz, 1H), 2.83 (dd, *J* = 6.6 Hz, 1H), 2.86 (dd, *J* = 6.6, 13.5 Hz, 1H), 3.53–3.63 (m, 2H), 7.09–7.29 (m, 10H); ^{13}C NMR δ: 18.3, 18.3, 19.4, 19.5, 40.3, 40.4, 43.1, 43.2, 74.7, 74.8, 76.9, 77.1, 125.9, 126.0, 126.2, 127.3, 127.4, 128.1,

© 1999 NRC Canada

128.2, 128.3, 129.4, 129.5, 139.1, 144.6, 144.7; MS *m/z* (rel. intensity): 163(12), 119(42), 105(13), 91(100), 77(10).

Bis(2-hexyl) ether (2e) (16*b*)
^{1}H NMR δ: 0.89 (t, *J* = 7.0 Hz, 3H), 1.10 (t, *J* = 6.2 Hz, 3H), 1.09 (d, *J* = 5.9 Hz, 3H), 1.11 (d, *J* = 6.2 Hz, 3H), 1.21–1.38 (m, 10H), 1.45–1.49 (m, 2H), 3.39–3.42 (m, 2H); ^{13}C NMR δ: 14.1, 20.5, 21.1, 22.8, 22.9, 27.9, 28.1, 36.9, 37.3, 72.9, 73.4; MS *m/z* (rel. intensity): 152(10), 137(20), 129(17), 85(100), 69(11), 57(17).

Bis(3-phenyl-2-propyl) ether (2f)
IR (neat, cm^{-1}): 2960, 2920, 1599, 1495, 1450, 1370, 1122, 749, 709; ^{1}H NMR δ: 0.98 (d, *J* = 5.9 Hz, 3H), 1.10 (d, *J* = 5.9 Hz, 3H), 2.50 (dd, *J* = 6.6, 13.2 Hz, 1H), 2.60 (dd, *J* = 6.6, 13.2 Hz, 1H), 2.74 (dd, *J* = 6.2, 13.2 Hz, 1H), 2.84 (dd, *J* = 6.2, 13.2 Hz, 1H), 3.54–3.62 (m, 2H), 7.08–7.27 (m, 10H); ^{13}C NMR δ: 20.2, 20.7, 43.8, 43.9, 74.9, 75.4, 126.0, 128.1, 128.2, 129.5, 129.6, 139.3; MS *m/z* (rel. intensity): 163(24), 119(51), 92(9), 91(100), 65(9). Anal. calcd. for $C_{18}H_{22}O$: C 84.99, H 8.72; found: C 84.87, H 8.97.

General procedure for the synthesis of unsymmetrical ethers

Unsymmetrical ethers were prepared using triflates in place of Tf_2O. To a solution of magnesium di(benzyl alcoholate), generated in situ from **1a** (2.16 g, 0.02 mol), magnesium (0.24 g, 0.01 mol), and iodine (50 mg, 0.2 mmol) in benzyl alcohol (2.16 g, 0.02 mol) was added dropwise a solution of pentyl triflate (2.2 g, 0.01 mol) in 5 mL of dry ether. The mixture was stirred at room temperature for 1 h, the reaction was quenched by the addition of water. After the usual work-up, chromatography of the residue with hexane/ethyl acetate (80/20) afforded benzyl pentyl ether **3a** (1.55 g, 87%).

Benzyl pentyl ether (3a) (17)
^{1}H NMR δ: 0.89 (t, *J* = 7.0 Hz, 3H), 1.29–1.35 (m, 4H), 1.57–1.64 (m, 2H), 3.46 (t, *J* = 6.6 Hz, 2H), 4.50 (s, 2H), 7.25–7.34 (m, 5H); ^{13}C NMR δ: 14.1, 22.5, 28.4, 29.5, 36.4, 71.1, 71.8, 126.1, 128.3, 128.9, 139.1; MS *m/z* (rel. intensity): 92(61), 91(100), 77(9), 65(15).

Pentyl phenetyl ether (3b)
IR (neat, cm^{-1}): 2910, 2840, 1598, 1492, 1449, 1360, 1110, 743, 695; ^{1}H NMR δ: 0.89 (t, *J* = 7.3 Hz, 3H), 1.28–1.32 (m, 4H), 1.55–1.59 (m, 2H), 2.87 (t, *J* = 6.9 Hz, 2H), 3.42 (t, *J* = 6.9 Hz, 2H), 3.63 (t, *J* = 6.9 Hz, 2H), 7.17–7.29 (m, 5H); ^{13}C NMR δ 14.1, 22.5, 28.4, 29.5, 36.4, 71.1, 71.9, 126.1, 128.3, 128.9, 139.1; MS *m/z* (rel. intensity): 192 (M$^+$, 19), 174(8), 106(38), 105(44), 104(17), 103(18), 101(11), 92(24), 91(54), 79(21), 78(16), 77(28), 71(100), 69(18), 65(17), 55(9), 51(9), 43(63). Anal. calcd for $C_{13}H_{20}O$: C 81.19, H 10.48; found: C 81.01, H 10. 35.

Bis(phenethoxy) butane (3c)
IR (neat, cm^{-1}): 2920, 2845, 1732, 1598, 1595, 1450, 1364, 1109, 749, 699; ^{1}H NMR δ 1.60–1.62 (m, 4H), 2.87 (t, *J* = 7.0 Hz, 4H), 3.46 (t, *J* = 7.0 Hz, 4H), 3.61 (t, *J* = 7.0 Hz, 4H); ^{13}C NMR δ: 26.5, 36.4, 70.7, 71.8, 126.1, 128.3, 128.9, 139.1; MS *m/z* (rel. intensity): 207(8), 107(25), 92(12), 91(100), 73(17), 65(17). Anal. calcd. for $C_{20}H_{26}0_2$: C 85.06, H 9.28; found; C 85.11, H 9.19.

Pentyl 2-phenyl-1-propyl ether (3d)
IR (neat, cm^{-1}): 2945, 2850, 1721, 1595, 1491, 1445, 1388, 1105, 755, 696; ^{1}H NMR δ: 0.88 (t, *J* = 7.3 Hz, 3H), 1.29 (d, *J* = 6.9 Hz, 3H), 1.25–1.30 (m, 4H), 1.53–1.55 (m, 2H), 2.98–3.02 (m, 1H), 3.38–3.45 (m, 3H), 3.53 (dd, *J* = 9.3, 6.1Hz, 1H), 7.18–7.31 (m, 5H); ^{13}C NMR δ 14.1, 18.4, 22.5, 28.4, 29.4, 71.2, 126.3, 127.4, 128.3, 144.7; MS *m/z* (rel. intensity): 206 (M$^+$, 8), 120(17), 106(12), 105(100), 104(36), 91(50), 79(16), 78(12), 77(23), 71(80), 69(13), 43(32). Anal. calcd. for $C_{14}H_{22}O$: C 81.49, H 10.75; found: C 81.20, H 10.45.

Pentyl 1-phenylethyl ether (3e)
IR (neat, cm^{-1}): 2910, 2850, 1600, 1492, 1451, 1370, 1105, 760, 703; ^{1}H NMR δ: 0.88 (t, *J* = 7.3 Hz, 3H), 1.28–1.34 (m, 4H), 1.42 (d, *J* = 6.6 Hz, 3H), 1.55–1.56 (m, 2H), 4.37 (q, *J* = 6.6 Hz, 1H), 3.28 (t, *J* = 6.6 Hz, 2H), 7.23–7.35 (m, 5H); ^{13}C NMR δ: 14.0, 22.6, 24.3, 28.4, 29.5, 29.7, 68.8, 126.1, 127.3; MS *m/z* (rel. intensity): 121(13), 104(24), 105(100), 91(10), 79(18), 77(34). Anal. calcd. for $C_{13}H_{20}O$: C 81.19, H 10.48; found: C 81.13, H 10.26.

1-(3-Phenyl-2-propoxy) pentane (3f)
IR (neat, cm^{-1}): 2920, 2810, 1719, 1590, 1485, 1442, 1365, 1101, 735, 693; ^{1}H NMR δ: 0.88 (t, *J* = 7.3 Hz, 3H), 1.27–1.31 (m, 7H), 1.53–1.55 (m, 2H), 2.98–3.01 (m, 1H), 3.38–3.44 (m, 3H), 3.52–3.55 (m, 1H), 7.18–7.31 (m, 5H); ^{13}C NMR δ: 14.1, 19.6, 22.5, 28.4, 29.8, 43.2, 68.8, 76.7, 126.0, 128.2, 129.5, 139.3; MS *m/z* (rel. intensity): 206 (M$^+$, 4), 115(95), 97(14), 92(28), 91(100), 77(10), 72(18), 71(98), 65(21), 55(16), 45(93), 43(99). Anal. calcd. for $C_{14}H_{22}O$: C 81.49, H 10.75; found: C 81.12, H 11.01.

1-(2-Methyl-3-phenyl-2-propoxy) pentane (3g)
IR (neat, cm^{-1}): 2906, 2850, 1595, 1490, 1448, 1375, 1359, 1222, 1145, 1122, 1080, 725, 698; ^{1}H NMR δ: 0.91 (t, *J* = 6.9 Hz, 3H), 1.12 (s, 6H), 1.32–1.35 (m, 6H), 2.77 (s, 2H), 3.39 (t, *J* = 6.6 Hz, 2H), 7.19–7.25 (m, 5H); ^{13}C NMR δ: 14.1, 25.2, 28.6, 30.3, 47.1, 61.4, 71.0, 74.9, 125.9, 127.8, 130.6, 138.7; MS *m/z* (rel. intensity): 135(7), 130(8), 129(82), 117(8), 92(11), 91(53), 71(14), 65(10), 60(10), 59(100), 55(10), 43(34). Anal. calcd. for $C_{15}H_{24}O$: C 81.76, H 10.98; found: C 82.02, H 11.01.

References

1. H.H. Freedman and R.A. Dubois. Tetrahedron Lett. **38**, 3251 (1975).
2. M. Yamashita and Y. Takegami. Synthesis, 803 (1977).
3. J. March. *In* Advanced organic chemistry, reactions, mechanisms, and structure. 2nd ed. McGraw–Hill Book Company, New York. 1978. pp. 357–358.
4. S. Torii, S. Takagishi, T. Inokuchi, and H. Okumoto. Bull. Chem. Soc. Jpn. **60**, 775 (1987).
5. F.M. Callahan, G.W. Anderson, R. Paul, and J.E. Zimmerman. J. Am. Chem. Soc. **85**, 201 (1963).
6. F. Toda, H. Takumi, and M. Akehi. J. Chem. Soc. Chem. Commun. 1270 (1990).

© 1999 NRC Canada

7. P.G. Sammers, D. Thetford, and M. Voyle. J. Chem. Soc. Chem. Commun. 1373 (1987).
8. Y. Kashman. J. Org. Chem. **37**, 912 (1972).
9. M.B. Sassaman, K.D. Kotian, G.K.S. Prakash, and G.A. Olar. J. Org. Chem. **52**, 4314 (1987).
10. T. Tsunoda, M. Suzuki, and R. Noyori. Tetrahedron Lett. 4679 (1979).
11. K. Ritter. Synthesis, 735 (1993), and refs. therein.
12. P.J. Stang, M. Hanack, and L.R. Subramanian. Synthesis, 85 (1982), and refs. therein.
13. Japan Patent P58-41832, Idemitsu Kosan Co Ltd., 1983; Chem. Abstr. **99**, 104 778 (1983).
14. C.J. Pouchert. The Aldrich library ^{13}C and ^{1}H FT NMR. Aldrich Chemical Company Inc., Milwaukee. 1993.
15. D.R. Lide. Handbook of data on common organic compounds. Vol. 1. CRC Press, Boca Raton, Fla. 1995.
16. (*a*) F. Richter. Beilsteins Handbuch der Organischen Chemie. Verlag von Julius Springer, Berlin. **6**(I), 250 (1952); (*b*) Beilsteins Handbuch der Organischen Chemie. Verlag von Julius Springer, Berlin. **1**(II), 438 (1952).
17. J.I. Cadogan. Dictionary of organic compounds. 6th ed. Chapman and Hall, London. 1996.

© 1999 NRC Canada

α-Halogenohydrazides: useful starting material for the synthesis of hydrazinoazapeptides and azauracils

Catherine Barré, Sophie Carret, Michel Guerro, Philippe Le Grel, and Michèle Baudy-Floc'h

Abstract: An efficient method for the synthesis of pseudodipeptides, which combines an aza glycine residue with various hydrazinoacid moieties by simple substitution of the halogen of α-halohydrazides, is described. Some of these hydrazinoazapeptides lead to hydrazones by oxidation or to azaaminouracils by cyclization.

Key words: hydrazinohydrazides, hydrazones, hydrazinoazapeptides, azaaminouracils, pseudopeptides.

Résumé : Une méthode de synthèse efficace de pseudopeptides, combinant une unité azaglycine avec divers hydrazinoacides, est décrite. Celle-ci consiste en une simple réaction de substitution de l'halogène de divers α-halohydrazides. Nous montrons également que certains de ces hydrazinoazapeptides peuvent conduire à des hydrazones par oxydation et par cyclisation intramoléculaire à des hétérocyles très peu représentés, les azaaminouracils.

Mots clés : hydrazinohydrazides, hydrazones, hydrazinoazapeptides, azaaminouracils, pseudopeptides.

Introduction

Following our studies on the high lability of the chloro or bromo atom of α-halogenohydrazides **1** (1, 2), which occurs under basic conditions with rapid substitution of the halogen by nucleophiles, we focussed our attention on the reaction of various substituted hydrazines. Here is a full report of the reaction of hydrazines, hydrazides, or carbazates **2** with α-halogenohydrazides **1**, which affords hydrazinoazapeptides **3**, **4**, or azauracils **9**. Such pseudopeptides are interesting since hydrazinopeptides (3), as well as azapeptides (4), are analogues of peptides in which the modification of the amide bond decreases the enzymatic biodegradability (5). Moreover, though azauracils are well known compounds (6), only a few of them are *N*-amino substituted and they have been shown to act as herbicidal agents (7).

Results

α-Hydrazinohydrazides **3** or **4** are readily obtained via a simple procedure that involves stirring the starting α-halogenohydrazides **1** with an excess of nucleophiles **2** (typically 3- to 6-fold excess) at room temperature. The basicity of most of the hydrazine derivatives **2** means that only in the case of the lowest basic hydrazides or carbazates must some additional base (NEt_3) be added to promote the reaction.

Most of the cases we have examined give moderate to good yields (Tables 1 and 2). It is interesting to note that monoalkylated hydrazines **2** react either exclusively (R^3 = Me, CH_2Ph; R^4 = H; only one isomer **4** is observed by ^1H NMR spectra of the crude reaction mixture) or predominantly ($R^3 = CH_2CF_3$; R^4 = H) through the substituted nitrogen, the most nucleophilic one being due to the electron donor substituent (Table 2). In the former case, both isomers **3** and **4**, which can be separated by column chromatography, are formed in the proportion 3:7. The structure **4** was proved by NMR spectroscopy as well as by condensation with an aldehyde or a ketone to give **5** (Scheme 1).

Some exceptions to the general reaction must be noted. (*i*) The use of *N*-aminotriazole **6** affords the triazolium salt **7** instead of the expected α-hydrazino compound (Scheme 2). This structure was confirmed by ^1H NMR spectroscopy; in particular, the CH at 6.75 ppm is in accord with a proton in the α position of a pyridinium salt (8). (*ii*) The reaction with phenylhydrazine **2** (R^3 = Ph, R^4 = H) leads to the corresponding hydrazone **8** (*syn* and *anti*) probably via the oxidation of an α-hydrazino intermediate **3** (Scheme 3). (*iii*) In some cases (Table 3), if the reaction is run in refluxing toluene, the formation of *N*-aminoazauracil **9** was observed even under a nitrogen or argon atmosphere. This reaction probably takes place through the oxidation of the primary α-hydrazinohydrazide **3**. It was possible to isolate **3** at room temperature and to show that the α-hydrazinohydrazide can be oxidized by DDQ to yield the hydrazone **8**, which affords *N*-aminoazauracil **9** by cyclization in the presence of NEt_3 (Scheme 4).

Regarding the peptidomimic properties of the resulting compounds **3** and **4**, it appears that a lot of them are interesting pseudopeptidic building blocks that combine an

Received October 6, 1998.

C. Barré, S. Carret, M. Guerro, P. Le Grel, and M. Baudy-Floc'h.[1] Groupe de synthèse et électrosynthèse organique, UMR 6510 au Centre national de la recherche scientifique, Université de Rennes I, Campus de Beaulieu, F-35042 Rennes Cédex, France.

[1]Author to whom correspondence may be addressed.
Fax: +(33)0299286738.
e-mail: Michele.Baudy-Floch@univ-rennes1.fr

© 1999 NRC Canada

Table 1. Yields for compounds **3a–3q.**

Compound	R^1	R^2	R^3	R^4	Yield, %
3a	$pClC_6H_4$	Ph	CO_2Me	H	70
3b	$pMeC_6H_4$	Ph	CO_2Me	H	72
3c	$pMeC_6H_4$	OMe	CO_2Me	H	55
3d	$pMeC_6H_4$	OtBu	CO_2Me	H	60
3e	$pClC_6H_4$	OtBu	CO_2Me	H	82
3f	$pClC_6H_4$	Ph	COPh	H	65
3g	$pMeC_6H_4$	OMe	COPh	H	70
3h	$pClC_6H_4$	OMe	COPh	H	78
3i	$pClC_6H_4$	Ph	CO_2Et	H	69
3j	$pMeC_6H_4$	Ph	CO_2Et	H	71
3k	$pMeC_6H_4$	OMe	CO_2tBu	H	60
3l	$pClC_6H_4$	OMe	CO_2tBu	H	88
3m	$pMeC_6H_4$	OMe	Me	Me	48
3n	$pClC_6H_4$	OMe	Me	Me	44
3o	2,4-$Cl_2C_6H_3$	OMe	$(CH_2)_2O(CH_2)_2$		40
3p	$pMeC_6H_4$	Ph	$(CH_2)_5$		74
3q	$pMeC_6H_4$	OMe	CF_3CH_2	H	27

Table 2. Yields for compounds **4a–4n**.

Compound	R^1	R^2	R^3	Yield
4a	$pClC_6H_4$	OMe	Me	73
4b	$pMeC_6H_4$	OMe	Me	70
4c	$pClC_6H_4$	Ph	Me	68
4d	Et	Ph	Me	68
4e	$pClC_6H_4$	Me	Me	47
4f	$pClC_6H_4$	O*t*Bu	Me	93
4g	$pMeC_6H_4$	O*t*Bu	Me	70
4h	Et	O*t*Bu	Me	70
4i	H	O*t*Bu	Me	76
4j	$pClC_6H_4$	OCH_2Ph	Me	78
4k	$pMeC_6H_4$	OCH_2Ph	Me	60
4l	$pClC_6H_4$	OMe	$PhCH_2$	55
4m	$pMeC_6H_4$	OMe	$PhCH_2$	41
4n	$pMeC_6H_4$	OMe	CF_3CH_2	63

azaglycine residue (ester form) with various hydrazinoarylglycine moieties in racemic form (Scheme 5). Such association of aza aminoacids and hydrazino acids has not been previously reported; moreover, substituted phenylglycine derivatives have been described as potent agonists or antagonists of the glutamate receptors of the central nervous system (9).

It is important to note that although the presence of an additional nitrogen makes their incorporation into peptidic backbones (10) difficult, such pseudodipeptides **(3** and **4)** could be linked to aminoacids (3*b*). For example the *N* extremity could be coupled with the free carboxylic acid function of protected aminoacids or peptides. Alternatively, the Boc-hydrazino (11) or Bz-hydrazino (12) moiety could be deprotected, leading to an hydrazido extremity that could react with isocyano aminoester (13). Of course these two aspects could be combined to integrate the pseudodipeptides into elaborated peptidic analogues. This last promising aspect is under investigation in our laboratory.

Experimental section

General procedures

^1H NMR spectra were recorded at 80 MHz on a Bruker WP 80 or at 300 MHz on a Bruker AM 300 spectrometer and ^{13}C NMR spectra at 75 MHz on a Bruker AM 300 spectrometer with tetramethylsilane as internal reference. Mass spectra were determined with a Varian Mat 311 spectrometer from the Centre Régional de Mesures Physiques de l'Ouest. IR spectra were determined with a Perkin–Elmer 225 or 1420 spectrometer. Elemental analyses were performed by the analytical laboratory, CNRS (Lyon). Melting points were taken with a Kofler hot stage apparatus. α-Halohydrazides **1** (X = Cl or Br) were prepared as previously described (14).

Preparation of hydrazinoazapeptides 3a–3e

A mixture of α-halohydrazide **1** (8 mmol), methylhydrazinocarboxylate **2** ($R^3 = CO_2Me$, $R^4 = H$) (32 mmol), and NEt_3 (32 mmol) was stirred for 16 h in CH_3CN (50 mL). After removal of the solvent under reduced pressure, the residue was diluted in CH_2Cl_2 (100 mL), and the organic layer was washed with an aqueous solution of HCl (100 mL) and water (100 mL) and then dried (Na_2SO_4). Evaporation afforded the α-hydrazinohydrazide **3**.

3a *(R^1 = pClC_6H_4, $R^2 = Ph$, $R^3 = CO_2Me$, $R^4 = H$)*: Yield 70%, mp 144°C ($CHCl_3$–Et_2O). IR (Nujol), ν: 3270, 3200, 3100, 1695, 1655 cm^{-1}. ^1H NMR (80 MHz, DMSO-d_6), δ: 3.57 (s, 3 H), 4.72 (s, 1 H), 5.27 (br, 1 H), 7.45–7.95 (m, 9 H), 8.45 (br, 1 H), 10.12 (s, 1 H), 10.40 (s, 1 H). Anal. calcd. for $C_{17}H_{17}N_4O_4Cl$: C 54.18, H 4.52, N 14.87, Cl 9.43%; found: C 54.41, H 4.82, N 15.08, Cl 9.36%.

3b *(R^1 = pMeC_6H_4, $R^2 = Ph$, $R^3 = CO_2Me$, $R^4 = H$)*: Yield 72%, mp 105°C ($CHCl_3$–Et_2O). IR (Nujol), ν: 3220, 1720, 1685, 1645 cm^{-1}. ^1H NMR (80 MHz, DMSO-d_6), δ: 2.30 (s, 3 H), 3.57 (s, 3 H), 4.65 (s, 1 H), 5.12 (br, 1 H), 7.10–7.92 (m, 9 H), 8.42 (br, 1 H), 10.02 (br, 1 H), 10.40 (br, 1 H). Anal. calcd for $C_{18}H_{20}N_4O_4$: C 60.66, H 5.65, N 15.72%; found: C 60.31, H 5.73, N 15.14%.

© 1999 NRC Canada

Scheme 1.

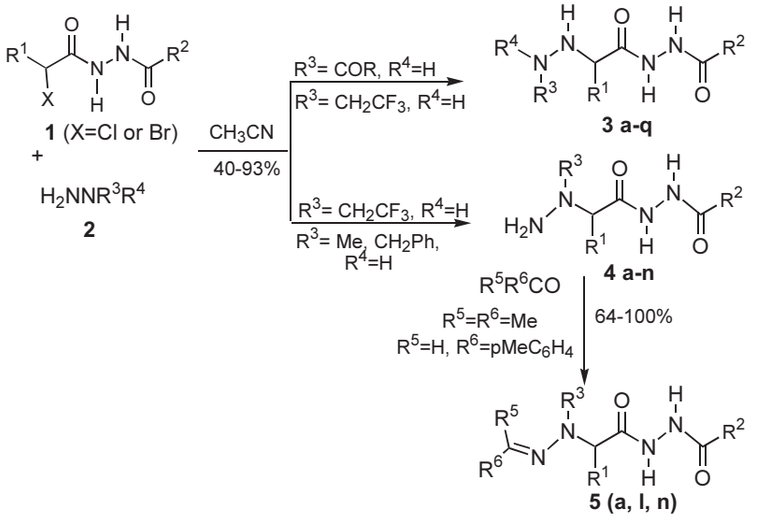

Scheme 2.

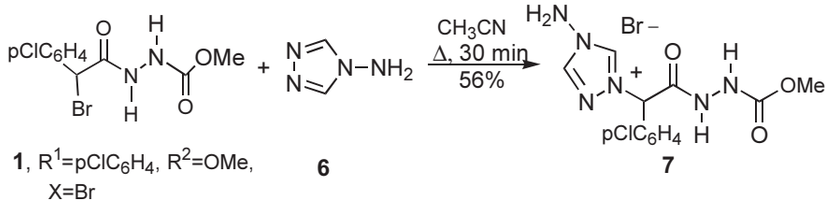

Scheme 3.

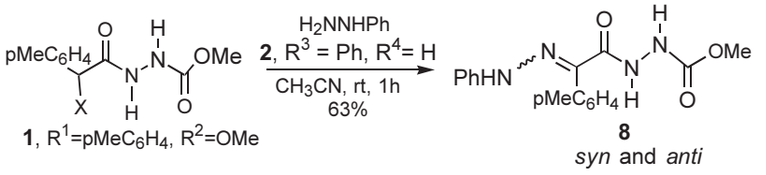

Table 3. Yields for compounds **9a–9d**.

Compound	R^1	R^2	R^3	Yield, %
9a	pClC$_6$H$_4$	Ph	OMe	61
9b	pMeC$_6$H$_4$	Ph	OMe	40
9c	mClC$_6$H$_4$	Me	OMe	42
9d	pClC$_6$H$_4$	Me	OMe	40

3c *(R^1 = pMeC_6H_4, R^2 = OMe, R^3 = CO_2Me, R^4 = H)*: Yield 55%, mp 99°C ($CHCl_3$–Et_2O). IR (Nujol), ν: 3340, 3305, 3270, 1760, 1740, 1710, 1650 cm^{-1}. ^{1}H NMR (80 MHz, $CDCl_3$ + CF_3CO_2H), δ: 2.37 (s, 3 H), 3.80 (s, 6 H), 5.30 (s, 1 H), 7.30 (s, 4 H). Anal. calcd. for $C_{13}H_{18}N_4O_5$: C 49.36, H 5.70, N 17.72%; found: C 50.35, H 5.63, N 18.24%.

3d *(R^1 = pMeC_6H_4, R^2 = $OtBu$, R^3 = CO_2Me, R^4 = H)*: Yield 60%, mp 100°C ($CHCl_3$–Et_2O). IR (CCl_4), ν: 3405, 3310, 1720, 1700 cm^{-1}. ^{1}H NMR (80 MHz, $CDCl_3$), δ: 1.45 (s, 9 H), 2.32 (s, 3 H), 3.67 (s, 3 H), 4.67 (s, 1 H), 6.80 (br, 1 H), 7.07–7.40 (m, 6 H), 8.30 (br, 1 H). Anal. calcd. for $C_{16}H_{24}N_4O_5$: C 54.56, H 6.82, N 15.91%; found: C 54.86, H 6.83, N 16.12%.

3e *(R^1 = pClC_6H_4, R^2 = $OtBu$, R^3 = $CO2Me$, R^4 = H)*: Yield 82%, mp 113°C ($CHCl_3$–Et_2O). IR (CCl_4), ν: 3410, 3280, 1735, 1715 cm^{-1}. ^{1}H NMR (80 MHz, $CDCl_3$), δ: 1.40 (s, 9 H), 3.65 (s, 3 H), 4.67 (s, 1 H), 6.85 (br, 1 H), 7.15–7.47 (m, 6 H), 8.95 (br, 1 H). Anal. calcd. for $C_{15}H_{21}N_4O_5Cl$: C 48.32, H 5.64, N 15.03, Cl 9.53%; found: C 48.42, H 5.83, N 15.12, Cl 9.64%.

Preparation of hydrazinoazapeptides 3f–3h

The α-halohydrazide **1** (6 mmol) was added to a solution of benzoylhydrazine **2** (R^3 = COPh, R^4 = H) (18 mmol) and NEt_3 (18 mmol) in toluene (30 mL). The mixture was then heated for 24 h. Cooling afforded a precipitate of α-hydrazinohydrazide **3**, which was filtered and dried.

© 1999 NRC Canada

Scheme 4.

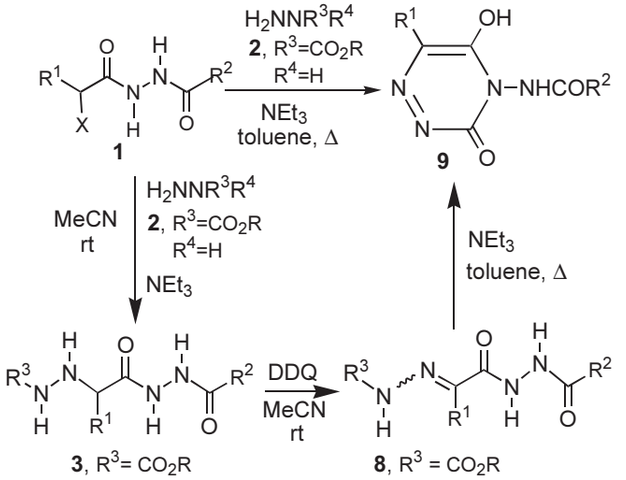

3f *(R^1 = pClC_6H_4, R^2 = Ph, R^3 = COPh, R^4 = H)*: Yield 65%, mp 247°C. IR (CCl_4), ν: 3280, 3262, 3240, 1678, 1630, 1605 cm^{-1}. ^1H NMR (80 MHz, DMSO-d_6), δ: 4.85 (s, 1 H), 5.25–4.62 (br, 1 H), 7.25–8.00 (m, 14 H), 10.00 (s, 1 H), 10.25 (s, 1 H), 10.40 (s, 1 H). Anal. calcd. for $C_{23}H_{22}N_4O_3$: C 62.48, H 4.50, N 13.25, Cl 8.40%; found: C 62.52, H 4.33, N 13.43, Cl 8.54%.

3g *(R^1 = pMeC_6H_4, R^2 = OMe, R^3 = COPh, R^4 = H)*: Yield 70%, mp 154°C. IR (Nujol), ν: 3310, 3260, 3190, 1678, 1630, 1605 cm^{-1}. ^1H NMR (80 MHz, DMSO-d_6), δ: 2.30 (s, 3 H), 3.55 (s, 3 H), 4.70 (s, 1 H),5.60 (br, 1 H), 7.07–7.85 (m, 9 H), 9.02 (s, 1 H), 9.95 (s, 2 H). ^{13}C NMR (75 MHz, DMSO-d_6), δ: 170 (d, ^2J = 9 Hz), 165, 156, 137 (q, ^2J = 6 Hz), 134, 133 (t, ^2J = 8 Hz), 131 (dt, ^1J = 205 Hz, ^2J = 8 Hz), 128 (dd, ^1J = 161 Hz, ^2J = 7 Hz), 65 (d, ^1J = 142 Hz), 52 (q, ^1J = 157 Hz), 20 (q, ^1J = 117 Hz). HRMS, $M^{+\bullet}$ calcd. for $C_{18}H_{20}N_4O_4$: 356.1484; found: 356.1489. Anal. calcd.: C 60.67, H 5.62, N 15.73%; found: C 60.29, H 5.62, N 14.95%.

3h *(R^1 = pClC_6H_4, R^2 = OMe, R^3 = COPh, R^4 = H)*: Yield 78%, mp 199°C. IR (Nujol), ν: 3310, 3240, 3180, 1725, 1680, 1645 cm^{-1}. ^1H NMR (80 MHz, DMSO-d_6), δ: 3.55 (s, 3 H), 4.75 (d, 1 H, ^3J = 6 Hz), 5.72 (t, 1 H, ^3J = 6 Hz,), 7.32–7.85 (m, 9 H), 9.05 (br s, 1 H), 10.02 (br s, 2 H). Anal. calcd. for $C_{17}H_{17}N_4O_4Cl$: C 54.18, H 4.51, N 14.87, Cl 9.43%; found: C 54.25, H 4.62, N 15.11, Cl 9.60%.

Preparation of hydrazinoazapeptides 3i–3j

To a mixture of ethylhydrazinocarboxylate **2** (R^3 = CO_2Et, R^4 = H) (30 mmol) and NEt_3 (30 mmol) in CH_3CN (30 mL) was added the α-halohydrazide **1** (10 mmol). After 24 h stirring at room temperature the solvent was removed under reduced pressure. The residue was diluted in CH_2Cl_2 (50 mL). The organic layer was washed with an aqueous solution of HCl (50 mL) and with water (50 mL) and then dried (Na_2SO_4). Evaporation of the solvent afforded the α-hydrazinohydrazide **3.**

Scheme 5.

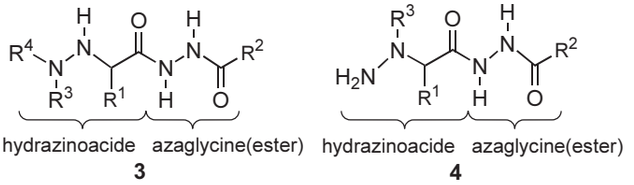

3i *(R^1 = pClC_6H_4, R^2 = Ph, R^3 = CO_2Et, R^4 = H)*: Yield 69%, mp 152°C (EtOH). IR (Nujol), ν: 3280, 3240, 3210, 1700, 1675, 1655 cm^{-1}. ^1H NMR (80 MHz, DMSO-d_6), ν: 1.22 (t, 3 H, ^3J = 8 Hz), 4.07 (q, 2 H, ^3J = 8 Hz), 4.72 (s, 1 H), 5.12 (br s, 1 H), 7.30–7.97 (m, 9 H), 8.35 (br s, 1 H), 10.10 (br s, 1 H), 10.40 (br s, 1 H). Anal. calcd. for $C_{18}H_{19}N_4O_4Cl$: C 55.31, H 4.86, N 14.34, Cl 9.10%; found: C 55.00, H 4.97, N 14.01, Cl 8.99%.

3j *(R^1 = pMeC_6H_4, R^2 = Ph, R^3 = CO_2Et, R^4 = H)*: Yield 71%, mp 136°C (CH_2Cl_2). IR (Nujol), ν: 3310, 3280, 3210, 1660, 1655 cm^{-1}. ^1H NMR (80 MHz, DMSO-d_6), δ: 1.20 (t, 3 H, ^3J = 8 Hz), 2.30 (s, 3 H), 4.05 (q, 2 H, ^3J = 8 Hz), 4.65 (s, 1 H), 5.10 (br s, 1 H), 7.07–7.95 (m, 9 H), 8.37 (br s, 1 H), 10.00 (br s, 1 H), 10.35 (br s, 1 H). Anal. calcd. for $C_{19}H_{22}N_4O_4$: C 61.62, H 5.95, N 15.14%; found: C 61.50, H 5.89, N 15.25%.

Preparation of hydrazinoazapeptides 3k–3l

To a mixture of tertiobutylhydrazino carboxylate **2** (R^3 = CO_2tBu, R^4 = H) (30 mmol) and NEt_3 (30 mmol) in CH_3CN (10 mL) was added the α-halohydrazide **1** (10 mmol). After 24 h stirring at room temperature the solvent was removed under reduced pressure, and the residue was diluted in CH_2Cl_2 (50 mL). The organic layer was washed with an aqueous solution of HCl (50 mL) and with water (50 mL) and finally dried (Na_2SO_4). Evaporation afforded the α-hydrazinohydrazide **3**, pure enough for analysis.

3k *(R^1 = pMeC_6H_4, R^2 = OMe, R^3 = CO_2tBu, R^4 = H)*: Yield 60%, mp 112°C. IR (CCl_4), ν: 3410, 3300, 1745, 1720 cm^{-1}. ^1H NMR (80 MHz, $CDCl_3$), δ: 1.42 (s, 9 H), 2.27 (s, 3 H), 3.40 (br s, 1 H), 3.67 (s, 3 H), 4.62 (s, 1 H), 6.82 (s, 1 H), 7.00–7.45 (m, 5 H), 9.07 (br s, 1 H). Anal. calcd. for $C_{16}H_{24}N_4O_5$: C 54.54, H 6.82, N 15.91%; found: C 54.35, H 6.79, N 15.97%.

3l *(R^1 = pClC_6H_4, R^2 = CO_2Me, R^3 = CO_2tBu, R^4 = H)*: Yield 88%, mp 128°C. IR (CCl_4), ν: 3410, 3300, 1750, 1715 cm^{-1}. ^1H NMR (80 MHz, $CDCl_3$), δ: 1.42 (s, 9 H), 3.60 (s, 3 H), 4.60 (s, 1 H), 4.90 (br s, 1 H), 7.40 (m, 4 H), 7.97 (br s, 1 H), 8.97 (br s, 2 H), 9.82 (br s, 1 H). Anal. calcd. for $C_{15}H_{21}N_4O_5Cl$: C 48.32, H 5.64, N 15.03, Cl 9.53%; found: C 48.35, H 5.78, N 15.12, Cl 9.78%.

Preparation of hydrazinoazapeptides 3m and 3n

To a solution of *N*,*N*-dimethylhydrazine **2** (R^3 = R^4 = Me) (30 mmol) in CH_3CN (10 mL) was added the α-halohydrazide **1** (5 mmol). The α-hydrazinohydrazide **3** precipitated after 16 h (R^1 = *p*ClC_6H_4) or 60 h (R^1 = *p*MeC_6H_4) of stirring at room temperature and was then filtered and dried (pure enough for analysis).

© 1999 NRC Canada

3m *(R^1 = pMeC_6H_4, R^2 = OMe, R^3 = R^4 = Me)*: Yield 48%, mp 171°C. IR (Nujol), ν: 3260, 3180, 1740, 1696 cm^{-1}. ^1H NMR (80 MHz, $CDCl_3$ + CF_3CO_2H), δ: 2.40 (s, 3 H), 3.27 (s, 3 H), 3.47 (s, 3 H), 3.72 (s, 3 H), 5.62 (s, 1 H), 7.40–7.60 (m, 4 H). Anal. calcd. for $C_{13}H_{20}N_4O_3$: C 55.71, H 7.14, N 17.14%; found: C 55.72, H 7.32, N 17.29%.

3n *(R^1 = pClC_6H_4, R^2 = OMe):* Yield 44%, mp 180°C. IR (Nujol), ν: 3280, 3240, 3180, 3140, 1700 cm^{-1}. ^1H NMR ($CDCl_3$ + DMSO-d_6), δ: 2.97 (s, 3 H), 3.37 (s, 3 H), 3.52 (s, 3 H), 4.98 (s, 1 H), 6.61 (br s, 2 H), 7.61 (A_2B_2, 4 H, ^3J = 4 Hz), 8.45 (br s, 1 H). Anal. calcd. for $C_{12}H_{17}N_4O_3Cl$: C 47.92, H 5.69, N 18.63, Cl 11.78%; found: C 47.72, H 5.70, N 18.46, Cl 11.87%.

Preparation of α-hydrazinohydrazide 3o

To a solution of *N*-aminomorpholine **2** (R^3, R^4 = -$(CH_2)_2O(CH_2)_2$-) (25 mmol) in CH_3CN (10 mL) was added the α-halohydrazide **1** (5 mmol). After 16 h stirring at room temperature the solvent was removed under reduced pressure, the residue was partially dissolved in CH_2Cl_2 (10 mL), the halohydrate of *N*-aminomorpholine was filtered, and the filtrate saturated by addition of petroleum ether. Cooling afforded a precipitate of α-hydrazinohydrazide **3o.**

3o *(R^1 = 2,4-$Cl_2C_6H_3$, R^2 = OMe, R^3, R^4 = -$(CH_2)_2O(CH_2)_2$-)*: Yield 40%, mp 149°C (CH_2Cl_2 – petroleum ether). IR (Nujol), ν: 3362, 3270, 3227, 1728, 1700 cm^{-1}. ^1H NMR (80 MHz, $CDCl_3$ + CF_3CO_2H), δ: 2.72 (m, 4 H), 3.57 (m, 4 H), 3.60 (s, 3 H), 4.87 (s, 1 H), 7.28–7.77 (m, 3 H), 9.00 (br s, 1 H), 9.85 (br s, 1 H). HRMS, $M^{+\bullet}$ calcd for $C_{14}H_{18}N_4O_4Cl_2$: 376.0705; found: 376.0721. Anal. calcd.: C 44.57, H 4.80, N 14.85, Cl 18.80%; found: C 44.32, H 4.84, N 14.62, Cl 19.26%.

Preparation of α-hydrazinohydrazide 3p

To a solution of *N*-aminopiperidine **2** (R^3, R^4 = -$(CH_2)_5$) (25 mmol) in CH_3CN (10 mL) was added the α-halohydrazide **1** (5 mmol). After 16 h stirring at room temperature a first precipitate of α-hydrazinohydrazide **3p** was filtered, the solvent was then evaporated, the residue dissolved in CH_2Cl_2 (50 mL) and thenwashed by water (50 mL). The organic layer was dried (Na_2SO_4) and concentrated by evaporation of the solvent. Addition of acetone and cooling afforded a new fraction of **3p**.

3p *(R^1 = pMeC_6H_4, R^2 = Ph, R^3, R^4 = -$(CH_2)_5$)*: Yield 74%, mp 201°C (acetone). IR (Nujol), ν: 3321, 3255, 3200, 3155, 1695, 1670 cm^{-1}. ^1H NMR (80 MHz, $CDCl_3$ + CF_3CO_2H), δ: 2.00 (m, 6H), 2.42 (s, 3H), 3.47–4.00 (m, 4H), 5.96 (s, 1H), 7.27–7.90 (m, 9H). HRMS, $M^{+\bullet}$ calcd. for $C_{21}H_{26}N_4O_2$: 366.2055; found: 366.2065. Anal. calcd. for $C_{21}H_{26}N_4O_2 \cdot HBr$: C 56.37, H 6.08, N 12.52, Br 17.86%; found: C 56.09, H 6.06, N 12.59, Br 17.41%.

Preparation of hydrazinoazapeptides 4a–4k

To a solution of methylhydrazine **2** (R^3 = Me, R^4 = H) (30 mmol) in CH_3CN (10 mL) was added the α-halohydrazide **1** (5 mmol). When R^2 = OMe, Me, Ph, or CH_2Ph, after 2 h stirring at room temperature, the α-hydrazinohydrazide **4** precipitated and was filtered. When R^2 = O*t*Bu or R^1 = H the solution was evaporated and the residue was dissolved in CH_2Cl_2 (50 mL) and washed with water (50 mL). The organic layer was dried (Na_2SO_4) and concentrated by evaporation of the solvent. Addition of ether afforded **4**.

4a *(R^1 = pClC_6H_4, R^2 = OMe, R^3 = Me)*: Yield 73%, mp 178°C (EtOH). IR (Nujol), ν: 3310, 3250, 3150, 1730, 1670 cm^{-1}. ^1H NMR (80 MHz, $CDCl_3$ + DMSO-d_6), δ: 2.31 (s, 3 H), 3.25 (br, 1 H),3.60 (s, 3 H), 3.96 (s, 1 H), 4.15–5.47 (br, 1 H), 8.50–9.50 (br, 1 H), 7.41 (m, 4 H). ^{13}C NMR (75 MHz, DMSO-d_6–D_2O), δ: 45 (q, ^1J = 135 Hz), 52 (q, ^1J = 148 Hz), 75 (d, ^1J = 136 Hz), 128 (d, ^1J = 168 Hz), 130 (d, ^1J = 138 Hz), 133, 134, 157, 171. HRMS, $M^{+\bullet}$ calcd. for $C_{11}H_{15}N_4O_3Cl$: 286.0832; found: 286.0823. Anal. calcd.: C 46.07, H 5.24, N 19.55, Cl 12.39%; found: C 46.16, H 5.30, N 19.44, Cl 12.56%.

4b *(R^1 = pMeC_6H_4, R^2 = OMe)*: Yield 70%, mp 158°C (EtOH). IR (Nujol), ν: 3318, 3180, 3150, 1732, 1670 cm^{-1}. ^1H NMR (80 MHz, $CDCl_3$ + DMSO-d_6), δ: 2.30 (s, 3 H), 2.32 (s, 3 H), 3.57 (s, 3 H), 3.95 (s, 1 H), 4.25–5.25 (br, 1 H), 9.00 (br, 1 H), 7.25 (A_2B_2, 4 H, ^3J = 8 Hz). Anal. calcd. for $C_{12}H_{18}N_4O_3$: C 54.13, H 6.76, N 21.05%; found: C 53.73, H 6.55, N 20.81%.

4c *(R^1 = pClC_6H_6, R^2 = Ph)*: Yield 68%, mp 132°C (EtOH). IR (Nujol), ν: 3275, 3210, 1695, 1645 cm^{-1}. ^1H NMR (80 MHz, $CDCl_3$ + DMSO-d_6), δ: 2.32 (s, 3H), 3.30 (br, 2H), 4.07 (s, 1H), 7.32–8.10 (m, 9H), 10.50 (br, 1H). Anal. calcd. for $C_{16}H_{17}N_4O_2Cl + H_2O$: C 54.77, H 5.46, N 15.97, Cl 10.10%; found: C 54.68, H 5.36, N 15.99, Cl 10.09%.

4d *(R^1 = Et, R^2 = Ph)*: Yield 68%, mp 132°C (EtOH). IR (Nujol), ν: 3290, 3160, 1685, 1645 cm^{-1}. ^1H NMR (80 MHz, $CDCl_3$ + DMSO-d_6), δ: 0.92 (t, 3 H, ^3J = 6 Hz), 1.65 (m, 2 H), 2.50 (s, 3 H), 3.00 (t, 1 H, ^3J = 7 Hz), 5.55–7.05 (br, 3 H), 7.70 (m, 5 H). Anal. calcd. for $C_{12}H_{18}N_4O_2$: C 57.60, H 7.20, N 22.40%; found: C 57.34, H 7.46, N 22.32%.

4e *(R^1 = pClC_6H_4, R^2 = Me)*: Yield 47%, mp 188°C (EtOH). IR (Nujol): ν: 3280, 3210, 3180, 1690, 1650 cm^{-1}. ^1H NMR (80 MHz, $CDCl_3$ + CF_3CO_2H), δ: 2.17 (s, 3 H), 2.87 (s, 3 H), 5.00 (s, 1 H), 7.45 (m, 4 H). Anal. calcd. for $C_{11}H_{15}N_4O_2Cl$: C 48.80, H 5.54, N 20.70, Cl 13.12%; found: C 48.70, H 5.83, N 20.54, Cl 13.41%.

4f *(R^1 = pClC_6H_4, R^2 = O*t*Bu)*: Yield 93%, mp 166°C (toluene). IR (Nujol), ν: 3300, 3170, 1720, 1675 cm^{-1}. ^1H NMR (80 MHz, $CDCl_3$ + CD_3COCD_3), δ: 1.42(s, 9 H), 2.22 (s, 3 H), 4.05 (s, 1 H), 7.35 (m, 4 H), 7.67 (s, 1 H). ^{13}C NMR (75 MHz, CD_3COCD_3), δ: 28 (q, ^1J = 125 Hz), 44(q, ^1J = 140 Hz), 75 (d, ^1J = 130 Hz), 80 (q, ^3J = 4 Hz), 129 (d, ^1J = 159 Hz), 129.5 (d, ^1J = 166 Hz), 132, 134, 156, 167. HRMS, $M^{+\bullet}$ calcd. for $C_{14}H_{21}N_4O_3Cl$: 328.1302; found: 328.1301. Anal. calcd.: C 51.14, H 6.44, N 17.04, Cl 10.78%; found: C 51.24, H 6.52, N 16.70, Cl 10.97%.

4g *(R^1 = pMeC_6H_4, R^2 = O*t*Bu)*: Yield 70%, mp 135°C (toluene). IR (Nujol), ν: 3370, 3300, 1720, 1705, 1685 cm^{-1}. ^1H NMR (80 MHz, $CDCl_3$), δ: 1.40 (s, 9 H), 2.29 (s, 3 H), 2.35 (s, 3 H), 3.76 (s, 1 H), 7.17 (m, 4 H). ^{13}C NMR (75 MHz, $CDCl_3$), δ: 21 (q, 1*J* = 126 Hz), 28 (q, ^1J = 127 Hz), 46 (q, ^1J = 136 Hz), 76 (d, ^1J = 136 Hz), 81 (q, ^3J = 4 Hz), 128 (d, ^1J = 156 Hz), 129 (d, ^1J = 153 Hz), 131,

© 1999 NRC Canada

138 (q, ^3J = 7 Hz), 155, 171. HRMS, $M^{+\bullet}$ calcd. for $C_{15}H_{24}N_4O_3$: 308.1848; found: 308.1835. Anal. calcd.: C 58.42, H 7.84, N 18.17%; found: C 58.54, H 7.88, N 18.02%.

4h *(R^1 = Et, R^2 = OtBu)*: Yield 70%, mp 121°C (toluene). IR (Nujol), ν: 3310, 3160, 1720, 1715, 1680 cm^{-1}. ^{1}H NMR (80 MHz, $CDCl_3$), δ: 1.00 (t, 3 H, ^3J = 3 Hz),1.51 (s, 9 H), 2.65 (s, 3 H), 2.78 (m, 2 H), 3.00 (t, 1 H, ^3J = 7 Hz), 6.9 (s, 1 H). ^{13}C NMR (75 MHz, $CDCl_3$), δ: 10 (q, ^1J = 126 Hz), 22 (t, ^1J = 128 Hz), 28 (q, ^1J = 125 Hz), 45 (q, ^1J = 135 Hz), 72 (d, ^1J = 137 Hz), 81, 155, 172. Anal. calcd. for $C_{10}H_{22}N_4O_3$: C 48.78, H 8.94, N 22.76%; found: C 48.29, H 9.00, N 22.65%.

4i *(R^1 = H, R^2 = OtBu)*: Yield 76%, mp 103°C (toluene). IR (Nujol), ν: 3340, 3310, 1730, 1705, 1680, 1650 cm^{-1}. ^{1}H NMR (80 MHz, $CDCl_3$), δ: 1.45 (s, 9 H), 2.57 (s, 3 H), 3.25 (s, 2 H). ^{13}C NMR (75 MHz, $CDCl_3$), δ: 10 (q, ^1J = 126 Hz), 22 (t, ^1J = 128 Hz), 28 (q, ^1J = 125 Hz), 45 (q, ^1J = 135 Hz), 72 (d, ^1J = 137 Hz), 81, 155, 172. Anal. calcd. for $C_8H_{18}N_4O_3$: C 44.03, H 8.26, N 25.69%; found: C 43.92, H 8.03, N 25.53%.

4j *(R^1 = pClC_6H_4, R^2 = OCH_2Ph)*: Yield 78%, mp 169°C (EtOH). IR (Nujol), ν: 3295, 3115, 1715, 1660 cm^{-1}. ^{1}H NMR (80 MHz, $CDCl_3$ + CF_3CO_2H), δ: 2.66 (s, 3 H), 4.98 (s, 1 H), 5.03 (s, 2 H) 7.29 (m, 9 H). ^{13}C NMR (75 MHz, $CDCl_3$ + CF_3CO_2H), δ: 42 (q, ^1J = 138 Hz), 68 (t, ^1J = 151 Hz), 70 (d, ^1J = 139 Hz), 127 (d, ^1J = 164 Hz), 128 (d, ^1J = 165 Hz), 129.2 (d, ^1J = 160 Hz), 129.6 (d, ^1J = 159 Hz), 130 (d, ^1J = 160 Hz), 134.2, 134.8, 136, 156, 169. Anal. calcd. for $C_{17}H_{19}N_4O_3Cl$: C 56.27, H 5.28, N 15.44, Cl 9.77%; found: C 56.05, H 5.07, N 15.45, Cl 9.72%.

4k *(R^1 = pMeC_6H_4, R^2 = OCH_2Ph)*: Yield 60%, mp 148°C (EtOH). IR (Nujol), ν: 3290, 3140, 1725, 1660, 1685 cm^{-1}. ^{1}H NMR (80 MHz, $CDCl_3$ + CF_3CO_2H), δ: 2.36 (s, 3 H), 2.81 (s, 3 H), 5.04 (s, 1 H), 5.14 (s, 2 H), 7.26 (m, 9 H). Anal. calcd. for $C_{18}H_{22}N_4O3$: C 58.42, H 7.84, N 18.17%; found: C 58.54, H 7.88, N 18.02%.

Preparation of hydrazinoazapeptides 4l–4m

To a suspension of benzylhydrazine dihydrochloride **2**·2HCl (R^3 = $PhCH_2$, R^4 = H) (9 mmol) in CH_3CN (15 mL) was added NEt_3 (27 mmol) and water (1 mL) to afford a homogeneous solution, after which the α-halohydrazide **1** (3 mmol) was added in small portions. After 6 h stirring at room temperature the solution was evaporated and the residue dissolved in CH_2Cl_2 (30 mL) and then washed with water (2 × 30 mL). The organic layer was dried (Na_2SO_4) and concentrated by evaporation of the solvent. Addition of ether afforded **4**.

4l *(R^1 = pClC_6H_4, R^2 = OMe)*: Yield 55%, mp 179°C (EtOH). IR (Nujol), ν: 3335, 3310, 3280, 3200, 1735, 1705, 1665 cm^{-1}. ^{1}H NMR (80 MHz, $CDCl_3$ + CF_3CO_2H), δ: 3.69 (s, 3 H), 4.03 (br, 2 H), 5.00 (s, 1 H), 7.29–7.42 (m, 9 H). HRMS, $M^{+\bullet}$ calcd. for $C_{17}H_{19}N_4O_3Cl$: 362.1145; found: 362.1135. Anal. calcd.: C 56.27, H 5.24, N 15.48, Cl 9.80%; found: C 56.29, H 5.17, N 15.42, Cl 9.51%.

4m *(R^1 = pMeC_6H_4, R^2 = OMe)*: Yield 41%, mp 158°C (EtOH). IR (Nujol), ν: 3340, 3300, 3200, 1730, 1700, 1665 cm^{-1}. ^{1}H NMR (80 MHz, $CDCl_3$ + CF_3CO_2H), δ: 2.37 (s, 3H), 3.80 (s, 3H), 4.15 (s, 2H), 7.05–7.47 (m, 9H). Anal. calcd. for $C_{18}H_{22}N_4O_3$: C 63.14, H 6.47, N 16.36%; found: C 62.89, H 6.42, N 16.18%.

Preparation of hydrazinoazapeptides 3q and 4n

To a solution of **2** (R^3 = CF_3CH_2, R^4 = H) (36 mmol, in solution in water 60%) in CH_3CN (10 mL) was added the α-halohydrazide **1** (6 mmol). After 12 h stirring at room temperature the solvent was evaporated and the residue dissolved in CH_2Cl_2 (100 mL) and washed with water (2 × 50 mL). The organic layer was dried (Na_2SO_4) and then concentrated by evaporation of the solvent. The oil was separated by silica gel chromatography, and eluted by 80:20 Et_2O:petroleum ether to afford **4n** (R_f 0.18) and **3q** (R_f 0.12).

4n *(R^1 = pMeC_6H_4, R^2 = OMe)*: Yield 63%, mp 122°C. IR (Nujol), ν: 3410, 3330, 3250, 1745, 1697 cm^{-1}. ^{1}H NMR (80 MHz, $CDCl_3$), δ: 2.33 (s, 3 H), 3.21 (q, 2 H, $^3J_{HF}$ = 18), 3.70 (br, 2 H), 3.71 (s, 3 H), 4.50 (s, 1 H), 7.15–7.29 (m, 5 H), 8.60 (br, 1 H). ^{13}C NMR (75 MHz, $CDCl_3$): δ: 21 (q, ^1J = 128 Hz), 53.1 (q, ^1J = 148 Hz), 57 (tq, ^1J = 138 Hz, $^2J_{CF}$ = 30 Hz), 74 (d, ^1J = 139 Hz), 125 (q, $^1J_{CF}$ = 279 Hz), 129 (d), 129.6 (d), 130, 138.9, 157.1, 171. HRMS $M^{+\bullet}$ calcd. for $C_{13}H_{17}N_4O_3F_3$: 334.1252; found: 334.1249. Anal. calcd.: C 46.70, H 5.13, N 16.76, F 17.05%; found: C 46.78, H 5.04, N 16.70, F 16.99%.

3q *(R^1 = pMeC_6H_4, R^2 = OMe)*: Yield 27%, oil. IR (Nujol), ν: 3410, 3220, 1745, 1697 cm^{-1}. ^{1}H NMR (80 MHz, $CDCl_3$), δ: 2.30 (s, 3 H), 3.30 (q, 2 H, $^3J_{HF}$ = 18 Hz), 3.69 (s, 3 H), 4.47 (s, 1 H), 7.10–7.47 (m, 7 H), 8.75 (br, 1 H). ^{13}C NMR (75 MHz, $CDCl_3$), δ: 21 (q, ^1J = 126 Hz), 53 (q, ^1J = 147 Hz), 52 (tq, ^1J = 122 Hz, $^2J_{CF}$ = 26 Hz), 67 (d, ^1J = 141 Hz), 125.2 (q, $^1J_{CF}$ = 278 Hz), 129 (d), 129.6 (d), 132, 138.6, 157, 172. HRMS, $M^{+\bullet}$ calcd. for $C_{13}H_{17}N_4O_3F_3$: 334.1252; found: 334.1249. Anal. calcd.: C 46.70, H 5.13, N 16.76; F 17.05%; found: C 46.27, H 5.45, N 16.32, F 16.44%.

Preparation of hydrazone 5a

A mixture of α-hydrazinohydrazide **4a** (2 mmol) and *p*-tolualdehyde (2.5 mmol) in MeCN was stirred for 15 h at room temperature. After evaporation of the solvent, the crude product afforded the hydrazone **5a**, by trituration with ether.

5a *(R^1 = pClC_6H_4, R^2 = OMe, R^3 = Me, R^5 = pMeC_6H_4, R^6 = H)*: Yield 64%, mp 100°C (CH_2Cl_2). IR (Nujol), ν: 3400, 3260, 1750, 1670 cm^{-1}. ^{1}H NMR (80 MHz, DMSO-d_6 – $CDCl_3$), δ: 2.25 (s, 3 H), 2.75 (s, 3 H), 3.62 (s, 3 H), 5.22 (s, 1 H), 7.02–7.47 (m, 9 H), 8.84 (br, 1 H), 9.65 (s, 1 H). ^{13}C NMR (75 MHz, $CDCl_3$), δ: 21 (q, ^1J = 126 Hz), 36 (q, ^1J = 136 Hz), 73 (d, ^1J = 136 Hz), 126 (d), 128 (d), 129 (d), 130, 132 (d), 133, 134, 137 (d, ^1J = 160 Hz), 138, 156, 170. HRMS, $M^{+\bullet}$ calcd. for $C_{19}H_{21}N_4O_3Cl$: 388.1302; found: 388.1283.

Preparation of hydrazones 5l, 5n

α-Hydrazinohydrazide **4** (2 mmol) was refluxed in acetone (25 mL) for 30 min. After evaporation of the solvent the crude product, by trituration with ether, afforded the hydrazone **5** (R^5 = R^6 = Me).

© 1999 NRC Canada

5l *(R^1 = pClC_6H_4, R^2 = OMe, R^3 = $PhCH_2$, R^5 = Me, R^6 = Me)*: Yield 100%, mp 108°C. IR (Nujol), ν: 3410, 3360, 3230, 1770, 1670 cm^{-1}. ^1H NMR ($CDCl_3$), δ: 1.35 (s, 3 H), 1.52 (s, 3 H), 3.27–3.77 (m, 2 H), 3.67 (s, 3 H), 4.22 (s, 1 H), 6.97–7.40 (m, 11 H). ^{13}C NMR ($CDCl_3$), δ: 24 (q, ^1J = 125 Hz), 53 (q, ^1J = 147 Hz), 58 (t, ^1J = 135 Hz), 77 (d, ^1J = 136 Hz), 127, 128.2, 128.6, 128.9, 129, 129.2, 130, 134, 136, 157, 168. HRMS, $M^{+\bullet}$ calcd. for $C_{20}H_{23}N_4O_3Cl$: 402.1458; found: 402.1442.

5n *(R^1 = pMeC_6H_4, R^2 = OMe, R^3 = CF_3CH_2, R^4 = H, R^5 = Me, R^6 = Me)*: Yield 100%, mp 195°C. IR (Nujol), ν: 3480, 3220, 3170, 1715, 1650 cm^{-1}. ^1H NMR (80 MHz, $CDCl_3$), δ: 1.42 (s, 3 H), 1.57 (s, 3 H), 2.32 (s, 3 H), 3.02 (q, 2 H, ^3J = 10 Hz), 3.72 (s, 3 H), 4.45 (s, 1 H), 6.77 (s, 1 H), 7.25 (m, 5 H). ^{13}C NMR (75 MHz, $CDCl_3$), δ: 20 (q, ^1J = 126 Hz), 24.1 (q, ^1J = 129 Hz), 24.3 (q, ^1J = 129 Hz), 53 (q, ^1J = 147 Hz), 58 (t, ^1J = 132 Hz), 71 (d, ^1J = 135 Hz), 124 (q, $^1J_{CF}$ = 281 Hz), 128.2 (d, ^1J = 157 Hz), 128.7 (d, ^1J = 158 Hz), 137, 138, 156, 167. HRMS, calcd. for $C_{13}H_{16}N_2F_3$: 257.1265; found, M^+ – $CONHNHCO_2Me$: 257.1263.

Preparation of triazolium salt 7

To a solution of 4-amino-4*H*-1,2,4-triazole **6** (28 mmol) in CH_3CN (20 mL) was added α-halohydrazide **1** (9 mmol) under stirring, and the solution was then heated (water bath) for 30 min. After 16 h stirring at room temperature the precipitate of salt **7** was filtered, and washed with hot CH_3CN.

7 *(R^1 = pClC_6H_4, R^2 = OMe)*: Yield 56%, mp 234°C (EtOH). IR (Nujol), ν: 3260, 3110, 3020, 1690, 1612 cm^{-1}. ^1H NMR (DMSO–$CDCl_3$), δ: 3.57 (s, 3 H), 6.75 (s, 1 H), 7.10 (br, 2 H), 7.57 (A_2B_2, 4 H, ^3J = 8 Hz), 9.20 (br, 2 H), 10.25 (s, 1 H), 10.52 (s, 1 H). ^{13}C NMR (DMSO-d_6), δ: 52 (q, ^1J = 147 Hz), 65 (d, ^1J = 146 Hz), 129 (d, ^1J = 169 Hz), 131 (d, ^1J = 160 Hz), 130, 134, 143 (d, ^1J = 229 Hz), 145 (d, ^1J = 228 Hz), 156, 164. Anal. calcd. for $C_{12}H_{14}N_6O_3BrCl$: C 35.5, H 3.45, N 20.70, Cl 18.75, Br 19.73%; found: C 35.68, H 3.59, N 20.38, Cl 8.81, Br 19.25%.

Preparation of hydrazone 8

NEt_3 (20 mmol) was added to a solution of α-halohydrazide **1** (7 mmol) and phenylhydrazine **2** (R^3 = Ph, R^4 = H) (20 mmol) in toluene (20 mL) and refluxed for 65 h. The solvent was then removed and the residue was dissolved in Et_2O (60 mL) and washed with water (2 × 50 mL). The organic layer was dried (Na_2SO_4), and concentrated by evaporation of the solvent. The oil was resolved by silica gel chromatography, eluted by 50:50 Et_2O:petroleum ether to afford *syn* and *anti* **8**. It was not possible to determine which was the *syn* or the *anti* isomer.

8 *(R^1 = pMeC_6H_4, R^2 = OMe, R^3 = Ph)*: R_f 0.38, yield 38%. IR (Nujol), ν: 3420, 3270, 1740, 1710, 1640 cm^{-1}. ^1H NMR (80 MHz, $CDCl_3$), δ: 2.37 (s, 3 H), 3.77 (s, 3 H), 6.80–7.62 (m, 11 H), 12.30 (s, 1 H). ^{13}C NMR (75 MHz, DMSO), δ: 20 (q, ^1J = 126 Hz), 51 (q, ^1J = 146 Hz), 112 (d, ^1J = 161 Hz), 120 (d, ^1J = 159 Hz), 125 (d, ^1J = 159 Hz), 129(d), 131, 137, 138, 144, 156, 164. HRMS, $M^{+\bullet}$ calcd. for $C_{17}H_{18}N_4O_3$: 326.1378; found: 326.1375.

8 *(R^1 = pMeC_6H_4, R^2 = OMe, R^3 = Ph)*: R_f 0.10, yield 25%. IR (Nujol), ν: 3420, 3260, 1735, 1665, 1610 cm^{-1}. ^1H NMR (80 MHz, $CDCl_3$), δ: 2.37 (s, 3 H), 3.72 (s, 3 H), 6.87–7.35 (m, 10 H), 8.15 (s, 1 H), 8.62 (s, 1 H). ^{13}C NMR (75 MHz, DMSO), δ: 20 (q, ^1J = 126 Hz), 51 (q, ^1J = 146 Hz), 114 (d, ^1J = 162 Hz), 120 (d, ^1J = 161 Hz), 127 (d, ^1J = 156 Hz), 127, 129(d), 135, 138, 144, 157, 164. HRMS,$M^{+\bullet}$ calcd. for $C_{17}H_{18}N_4O_3$: 326.1378; found: 326.1375.

Preparation of hydrazones 8 by oxydation of 3

To a solution of DDQ (dichloro-2,3-dicyano-5,6-parabenzoquinone) (12 mmol) in CH_3CN (150 mL) was added the α-halohydrazide **1** (12 mmol). After 1 h stirring the solvent was removed under reduced pressure and the residue dissolved in CH_2Cl_2 (60 mL), and washed by $NaHCO_3$ (2 × 50 mL). The organic layer was dried (Na_2SO_4), and concentrated by evaporation of the solvent to afford **8** as a mixture of two isomers, *syn* and *anti*, in the ratio 6:4. NMR data of only the major isomer are reported.

8a *(R^1 = pMeC_6H_4, R^2 = Ph, R^3 = OMe)*: Yield 60%, mp 130°C. IR (Nujol), ν: 3420, 3260, 1735, 1665, 1610 cm^{-1}. ^1H NMR (80 MHz, DMSO-d_6), δ: 2.37 (s, 3 H), 3.72 (s, 3 H), 7.32–7.47 (m, 9 H), 10.22 (s, 1 H), 10.54 (s, 1 H) ; 10.75 (s, 1 H). ^{13}C NMR (75 MHz, DMSO-d_6), δ: 21 (q, ^1J = 129 Hz), 52 (q, ^1J = 146 Hz), 127.5, 127.6, 128.7, 131, 131.5, 132.5, 135, 143, 154, 163, 167, 169. Anal. calcd. for $C_{18}H_{18}N_4O_4$: C 61.02, H 5.08, N 15.82%; found: C 60.86, H 4.95, N 15.96%.

8b *(R^1 = pClC_6H_4, R^2 = Ph, R^3 = OMe)*: Yield 60%, mp 100°C. IR (Nujol), ν: 3420, 3260, 1735, 1665, 1610 cm^{-1}. ^1H NMR (80 MHz, DMSO-d_6), δ: 3.80 (s, 3 H), 7.18–7.79 (m, 9 H), 8.31 (s, 1 H), 9.09 (s, 1 H), 9.85 (s, 1 H). ^{13}C NMR (75 MHz, DMSO), δ: 54 (q, ^1J = 146 Hz), 125.5, 127.5, 128.7, 129.8, 130, 131.5, 132.5, 137, 141.7, 153, 161, 166. Anal. calcd. for $C_{17}H_{15}N_4O_4Cl$: C 54.47, H 4.01, N 14.95, Cl 9.48%; found: C 54.68, H 3.94, N 15.03, Cl 9.03%.

Preparation of azaaminouracils 9

General procedure

NEt_3 (12 mmol) was added to a mixture of α-halohydrazide **1** (4 mmol) and hydrazine **2** (R^3 = OMe, R^4 = H) (12 mmol) in toluene (25 mL) and refluxed for 20 h. After cooling, the solvent was removed and the residue dissolved in CH_2Cl_2 (60 mL). Addition of acidified water (4 N HCl) afforded a precipitate of **9**.

Via the hydrazone 8

NEt_3 (14 mmol) was added to hydrazone **8** (7 mmol) in toluene (80 mL) and refluxed for 24 h. After cooling, the azaaminouracil **9** was filtered.

9a *(R^1 = pClC_6H_4, R^2 = Ph)*: Yield 61%, mp > 260°C (ethyl acetate). IR (Nujol) ν: 3378, 3300, 3120, 1752, 1730, 1675 cm^{-1}. ^1H NMR (80 MHz, DMSO–$CDCl_3$), δ: 7.40–8.00 (m, 9 H), 11.28 (s, 1 H), 13.06 (s, 1 H). ^{13}C NMR (75 MHz, DMSO-d_6), δ: 127.8, 128.3, 128.6, 129, 130.8 (t, J = 7 Hz), 131 (t, J = 8 Hz), 132, 134 (t, J = 11 Hz), 140 (d, J = 7 Hz), 148 (d, J = 7 Hz), 154.2, 165 (d, J = 7 Hz), 156, 164.

© 1999 NRC Canada

HRMS, $M^{+\bullet}$ calcd. for $C_{16}H_{11}N_4O_3Cl$: 342.0519; found: 342.0509. Anal. calcd.: C 56.06, H 3.23, N 16.35, Cl 10.34%; found: C 56.11, H 3.22, N 16.47, Cl 10.23%.

9b *(R^1 = pMeC_6H_4, R^2 = Ph)*: Yield 40%, mp 240°C (ethyl acetate). IR (Nujol), ν: 3185, 3120, 1720, 1670, 1650 cm^{-1}. ^1H NMR (80 MHz, DMSO-d_6 – $CDCl_3$), δ: 2.35 (s, 3 H), 7.28–7.58 (m, 4 H), 7.81–8.02 (m, 4 H), 11.47 (s, 1 H), 13.13 (s, 1 H). ^{13}C NMR (75 MHz, DMSO), δ: 20.8 (q, ^1J = 127 Hz), 127.7 (d, ^1J = 161 Hz), 127.8 (d, ^1J = 162 Hz), 128.6 (d, ^1J = 162 Hz), 128.8 (d, ^1J = 160 Hz), 129.2, 131, 132.6 (d, ^1J = 162 Hz), 139.6, 141, 148.2, 154.3, 164.9. HRMS, $M^{+\bullet}$ calcd. for $C_{17}H_{14}N_4O_3$: 322.1066; found: 322.1052. Anal. calcd.: C 63.35, H 4.35, N 17.39%; found: C 63.52, H 4.36, N 17.28%.

9c *(R^1 = mClC_6H_4, R^2 = Me)*: Yield 42%, mp 209°C (ethyl acetate). IR (Nujol): ν = 3290, 3200, 3110, 1732, 1660, 1675 cm^{-1}. ^1H NMR (80 MHz, DMSO – $CDCl_3$), δ: 2.05 (s, 3 H), 7.30–7.97 (m, 4 H), 12.77 (s, 1 H), 13.05 (br,1 H). HRMS, $M^{+\bullet}$ calcd. for $C_{11}H_9N_4O_3Cl$: 280.0363; found: 280.0411. Anal. calcd.: C 47.14, H 3.21, N 20.00, Cl 12.70%; found: 280.0411. C 47.23, H 3.43, N 19.58, Cl 12.68%.

9d *(R^1 = pClC_6H_4, R^2 = Me)*: Yield 40%, mp > 209°C (ethyl acetate). IR (Nujol), ν: 3230, 3130, 1730, 1680 cm^{-1}. ^1H NMR (80 MHz, DMSO-d_6 – $CDCl_3$), δ: 2.02 (s, 3 H), 7.67 (m, 4 H), 10.67 (s, 1 H), 12.97 (s, 1 H). HRMS, $M^{+\bullet}$ calcd. for $C_{11}H_9N_4O_3Cl$: 280.0363; found: 280.0379. Anal. calcd.: C 47.14, H 3.21, N 20.00, Cl 12.70%; found: C 47.07, H 3.23, N 19.96, Cl 12.63%.

References

1. P. Le Grel, M. Baudy-Floc'h, and A. Robert. Tetrahedron, **15**, 4805 (1988).
2. C. Barré, P. Le Grel, A. Robert, and M. Baudy-Floc'h. J. Chem. Soc. Chem. Commun. 607 (1994).
3. (*a*) M. Sletzinger, R.A. Firestone, D.F. Reinhold, and C.S. Rooney. J. Med. Chem. **11**, 261 (1968); (*b*) A. Amour, A. Collet, C. Dubar, and M. Reboud-Ravaux. Int. J. Pept. Protein Res. **43**, 297 (1994); L. Guy, J. Vidal, A. Collet, A. Amour, and M. Reboud-Ravaux. J. Med. Chem. **41**, 4833 (1998).
4. (*a*) J. Gante, M. Krug, G. Lauterbach, and R. Weitzel. Liebigs Ann. Chem. 1231 (1994); (*b*) M. Quibell, W.G. Turnell, and T. Johnson. J. Chem. Soc. Perkin Trans. 1, 2843 (1993).
5. M. Marraud, V. Dupont, V. Grand, S. Zerkout, A. Lecoq, G. Boussard, J. Vidal, A. Collet, and A. Aubry. Biopolymers, **33**, 1135 (1993).
6. (*a*) A.K. Mansour, M.M. Eid, R.A. Hassan, A. Haemers, S.R. Pattyn, D.A. Vanden Berghe, and L. Van Hoff. J. Heterocycl. Chem. **25**, 279 (1988); (*b*) Y.A. Ibrahim, M.M. Eid, M.A. Badawi, and S.A.L. Abdel-Hady. J. Heterocycl. Chem. **18**, 953 (1981).
7. (*a*) Bayer. US Patent 3 966 715 (1976); (*b*) Y. Nakayama, Y. Sanemitsu, H. Yoshioka, and A. Nishinaga. Tetrahedron Lett. **23**, 2499 (1982).
8. C. Florac, P. Le Grel, M. Baudy-Floc'h, and A. Robert. J. Chem. Soc. Perkin Trans. 1, 1143 (1991).
9. M.J. Garcia and R. Azerad. Tetrahedron Asymmetry, **8**, 85 (1997).
10. (*a*) H. Niedrich. Chem. Ber. **100**, 3273 (1967); (*b*) H. Niedrich and G. Koller. J. Prakt. Chem. **316**, 729 (1974).
11. (*a*) K.D. Kopple, T.J. Scamper, and A. Go. J. Am. Chem. Soc. **96**, 2597 (1974); (*b*) S.F. Brady, S.L. Varga, R.M. Friedinger, D.A. Schwenk, M. Mendlowski, F.W. Holly, and D.F. Veber. J. Org. Chem. **44**, 3101 (1979).
12. B. El Amin, G.M. Anatharamaiah, G.P. Royer, and G.E. Means. J. Org. Chem. **44**, 3442 (1979).
13. J. Gante. Synthesis, 405 (1989)
14. P. Le Grel, M. Baudy-Floc'h, and A. Robert. Synthesis, 306 (1987).

© 1999 NRC Canada

An ether-linked tetrafunctional acylating reagent and its cross-linking reactions with hemoglobin

Ronald Kluger, Krisztina Paal, and J. Gordon Adamson

Abstract: A new type of tetrafunctional reagent for cross-linking proteins has been prepared and used to modify human hemoglobin A. DPEE (1,2-bis{2-[3,5-bis(3,5-dibromosalicyloxycarbonyl) phenoxy]ethoxy}ethane)) has two separate pairs of reacting sites connected by a flexible tetraether chain. DPEE is capable of connecting a cross-link within a protein to another cross-link, either within the same protein molecule or between molecules. DPEE was readily prepared by esterification of a tetraether-linked bisphthalate (prepared by coupling of 1,2-bis(2-iodoethoxy)ethane and 5-hydroxyisophthalic acid). DPEE reacts with deoxy hemoglobin to produce a mixture of modified proteins. Ion-exchange HPLC was used to separate the modified proteins in the mixture. The most abundant products were selected for structural analysis, which used data from reverse-phase chromatography and tryptic peptide mapping. To prevent dissociation of the modified proteins during analysis, the products were further reacted with the bifunctional reagent, bis(3,5-dibromosalicyl) fumarate, which produces fumaryl cross-links between α-subunits. From peptide analysis of the separated products, the major modified protein from DPEE was identified as a novel species with four links within the same $\alpha_2\beta_2$ tetramer. In addition, a minor product that involves cross-links in two different proteins was observed. These results imply that the reagent reacts primarily in a folded state within the protein.

Key words: acylation: cross-linking, multifunctional, hemoglobin, reaction pattern.

Résumé : On a préparé un nouveau type de réactif tétrafonctionnel pour effectuer la réticulation des protéines et on l'a utilisé pour modifier de l'hémoglobine humaine A. Le DPEE (1,2-bis{2-[3,5-bis(3,5-dibromosalicyloxycarbonyl) phénoxy]éthoxy}éthane) possède deux paires séparées de sites réactionnels liés par une chaîne tétraéther flexible. Le DPEE peut relier une réticulation à l'intérieur d'une protéine avec une autre réticulation de la même molécule de protéine ou entre des molécules. On peut facilement préparer le DPEE par estérification d'un bisphtalate relié à un tétraéther (préparé par couplage du 1,2-bis(2-iodoéthoxy)éthane et de l'acide 5-hydroxy-isophtalique). Le DPEE réagit avec la désoxyhémoglobine pour produire un mélange de protéines modifiées. On a fait appel à la CLHP par échange d'ions pour séparer les protéines modifiées présentes dans le mélange. On a choisi les produits les plus abondants pour réaliser une analyse structurale en utilisant des données obtenues par chromatographie en phase inversée et par cartographie d'un peptide tryptique. Dans le but d'empêcher la dissociation des protéines modifiées au cours de l'analyse, on a fait réagir les produits avec le réactif bifonctionnel, fumarate de bis(3,5-dibromosalicyle) qui produit des réticulations fumaryles entre les sous-unités α. Sur la base de l'analyse peptidique des produits séparés, on a déterminé que la protéine principale découlant de la modification par le DPEE est une nouvelle espèce comportant quatre liaisons à l'intérieur du même tétramère $\alpha_2\beta_2$. On a aussi observé la présence d'un produit mineur qui comporte des réticulations dans deux protéines différentes. Ces résultats impliquent que le réactif agit principalement dans un état replié de la protéine.

Mots clés : acylation : réticulation, multifonctionnel, hémoglobine, patron de réaction.

[Traduit par la Rédaction]

Introduction

Human hemoglobin A is an $\alpha_2\beta_2$ tetramer that reversibly dissociates into αβ dimers (1, 2). Cross-linking prevents dissociation into dimers while providing the possibility for systematic alteration of the protein's properties (3-8). Cross-linked hemoglobins are of special interest since they may have clinical significance as red cell substitutes in transfusion medicine (9–11). A minimal reagent that prevents hemoglobin from dissociating into dimers contains two reactive functional groups that create a cross-link (12–14). The properties of the resulting altered protein depend on the sites that are connected and the structure of the link (7, 14–18). Reagents with three reactive functional groups can produce a cross-link between two sites within a protein, leaving a functional group available for bioconjugation (19). Alternatively, all three groups can react within the protein, creating a novel cross-linked structure (7, 20, 21).

Received October 13, 1998.

K. Paal and R. Kluger.[1] Lash Miller Laboratoires, Department of Chemistry, University of Toronto, Toronto, ON M5S 3H6, Canada.
J.G. Adamson. Hemosol, Inc., 115 Skyway Avenue, Toronto, ON M9W 4Z4, Canada.

[1]Author to whom correspondence may be addressed. Telephone: (416) 978-3582. e-mail: rkluger@chem.utoronto.ca

 © 1999 NRC Canada

Reagents with four reactive centers present additional possibilities for creating novel modified proteins (22, 23). A reagent that has two pairs of connected reactive sites can produce two cross-links that are connected by the core of the reagent. Depending on the geometry of the core, the two cross-links can form within one protein molecule or in two separate molecules, resulting in modified-connected proteins. If one or two functional groups of the reagent remain intact in the reaction with the protein these sites can be utilized for further conjungation reactions.

We have reported that a relatively small reagent with four reactive groups, BTDS (3,5,3′,5′-biphenyltetracarbonyl tetrakis(3,5-dibromosalicylate)), reacts with deoxy hemoglobin to give principally a product that has a stable cross-link between the β-subunits. The two additional reactive groups of the reagent do not combine with the protein (22). It is likely that once reaction has occurred at two of the groups, the geometric relationship of the remaining groups prevents them from being in proximity to nucleophiles in the same protein or in a second protein.

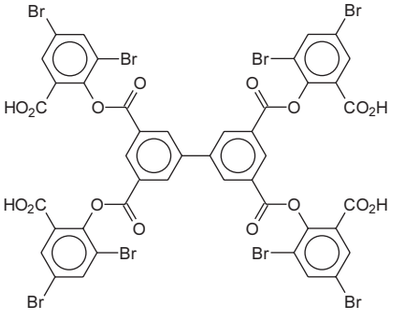

BTDS

To arrive at new types of altered proteins from a reagent with four reactive groups, we therefore assumed that a greater separation of the groups is necessary. In this paper we report the synthesis of DPEE (1,2-bis{2-[3,5-bis(3,5-dibromosalicyloxycarbonyl) phenoxy]ethoxy}ethane). DPEE contains isophthalyl dibromosalicylate reaction sites, as in BTDS, but they are connected in a longer, more flexible, and more hydrophilic array.

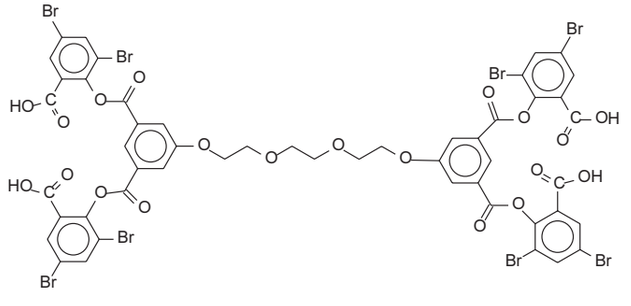

DPEE

Chemically modified hemoglobins are readily amenable to ion spray mass spectral analysis (21, 24, 25). Combining the results of such an analysis for separated materials with results from size-exclusion chromatography and tryptic peptide mapping (26) enables us to propose structures for the major modified proteins that result from reaction of DPEE and hemoglobin.

Experimental

Commercial reagents and chemicals were used without further purification. Solvents were dried prior to use. Reagents for preparation of buffers were analytical grade or better. Purified human hemoglobin A was from Hemosol, Inc. Proton NMR spectra were obtained at 400 MHz or 200 MHz and ^{13}C NMR spectra at 100 MHz.

The structures of the materials associated with the synthesis of the DPEE are shown in Schemes 1 and 2 in the Results section. The synthesis of the linked esters follows the general procedure of Collman et al. (4).

Synthesis of 1,2-bis{2-[3,5-bis(ethoxycarbonyl) phenoxy]-ethoxy}ethane (2)

Diethyl 5-hydroxyisophthalate (0.95 g, 0.0040 mol) and potassium *tert*-butoxide (0.47 g, 0.0042 mol) were stirred in 20 mL anhydrous tetrahydrofuran at room temperature for 30 min. A solution of 0.74 g (0.0020 mol) of 1,2-bis(2-iodoethoxy)ethane (**1**) in 20 mL anhydrous tetrahydrofuran was added and the reaction mixture was refluxed for 48 h under nitrogen. Water was added and the product was extracted with ether. The solution was dried over magnesium sulfate, filtered, and the solvent removed. Separation on a silica column (3 cm × 30 cm, hexanes – ethyl acetate 1:1) produced a white powder (0.60 g, 51%). ^1H NMR ($CDCl_3$) δ: 8.25 (2 H, t, J = 1.2 Hz, ArH), 7.74 (4 H, d, J = 1.2 Hz, ArH), 4.36 (8 H, q, J = 6.9 Hz, CH_2), 4.20 (4 H, t, J = 5.6 Hz, CH_2), 3.87 (4 H, t, J = 5.6 Hz, CH_2), 3.75 (4 H, s, CH_2), 1.36 (12 H, t, J = 6.9 Hz, CH_3).

1,2-Bis[2-(3,5-dicarboxyphenoxy) ethoxy]ethane (3)

The tetraethyl ester (0.60 g, 0.0010 mol, **2**) was dissolved in 30 mL ethanol. The solution was heated to 65°C. Then 0.25 g (0.0060 mol) sodium hydroxide dissolved in 1 mL water was added and the reaction mixture kept at 65°C for 22 h. The resulting white precipitate was filtered and dissolved in 10 mL of water. The tetraacid (**3**) was precipitated by addition of concentrated hydrochloric acid and filtered. The product was dried under vacuum (0.46 g, 95%). ^1H NMR (DMSO-d_6) δ: 8.05 (2 H, s, ArH), 7.62 (4 H, s, ArH), 4.19 (4 H, s, CH_2), 3.75 (4 H, s, CH_2), 3.60 (4 H, s, CH_2); a broad band is also present under the three high-field signals.

1,2-Bis{2-[3,5-bis(chlorocarbonyl) phenoxy]ethoxy}-ethane (4)

The tetraacid (0.23 g, 0.0047 mol, **3**) was dissolved in 15 mL thionyl chloride containing three drops of dimethylformamide. The solution was refluxed under nitrogen for 5 h and then the solvent was evaporated. The product (yellow oil) was dried under vacuum and solidified overnight (0.26 g, 100%). ^1H NMR ($CDCl_3$) δ: 8.43 (2 H, t, J = 1.6 Hz, ArH), 7.90 (4 H, d, J = 1.6 Hz, ArH), 4.24 (4 H, t, J = 5 Hz, CH_2), 3.89 (4 H, t, J = 5 Hz, CH_2), 3.74 (4 H, s, CH_2). This tetraacid tetrachloride was used without further purification.

© 1999 NRC Canada

1,2-Bis{2-[3,5-bis(3,5-dibromosalicyloxycarbonyl) phenoxy]ethoxy}ethane (DPEE, 6)

tert-Butyl 3,5-dibromosalicylate (0.66 g, 0.0019 mol) (27, 28) and potassium *tert*-butoxide (0.21 g, 0.0019 mol) were stirred in 15 mL anhydrous tetrahydrofuran at room temperature for 30 min. Then a solution of 0.26 g (0.00047 mol) of **4** in 15 mL anhydrous tetrahydrofuran was added and the reaction mixture was stirred at room temperature overnight. Water was added and the product was extracted with ether. The extract was dried over magnesium sulfate, filtered, and the solvent removed, leaving the tetra *tert*-butyl ester (**5**). The white solid was dissolved in 15 mL anhydrous trifluoroacetic acid (to convert the *tert*-butyl ester to the free acid) and left at room temperature for 2.5 h. Dry ether was added (15 mL) and a white precipitate formed. The product (**6)**, DPEE, was filtered and dried in vacuum (white powder, 0.55 g, 74%). IR (KBr): 3177 (br s, ν_{OH}), 1736 (s, $\nu_{C=O}$), 1195 (s, $\nu_{C—O}$) cm^{-1}; ^1H NMR (DMSO-d_6) δ: 8.36 (2 H, t, J = 1.4 Hz, ArH), 8.33 (4 H, d, J = 2.5 Hz, ArH), 8.09 (4 H, d, J = 2.5 Hz, ArH), 7.98 (4 H, d, J = 1.4 Hz, ArH), 4.31 (4 H, br s, CH_2), 3.79 (4 H, br s, CH_2), 3.63 (4 H, s, CH_2); a broad band is also present under the three high-field signals; ^{13}C NMR (acetone-d_6) δ: 163.57, 163.25, 160.59, 148.36, 140.13, 134.68, 131.79, 128.06, 124.54, 122.12, 120.29, 120.06, 71.50, 70.29, 69.47; MS (negative FAB), M – 1 calcd. for $C_{50}H_{30}Br_8O_{20}$: 1589; found: 1589.

Reactions of human hemoglobin A with DPEE were carried out as described previously (22). A typical example is described here. A solution of carbonmonoxy hemoglobin (2.0 mL, 1.25 mM, 0.000025 M) in 50 mM Bis-Tris buffer (pH 6.5) was passed through a Sephadex G-25 column (2.5 × 15 cm) equilibrated with 50 mM sodium borate buffer (pH 8.0). The carbonmonoxy hemoglobin was converted to oxy hemoglobin by irradiation under flowing oxygen at 0°C for 2 h. The solution was then kept under flowing nitrogen at 37°C for 2 h to convert the hemoglobin to the deoxy form. DPEE (0.0080 g, 5.0×10^{-6} mol) was dissolved in 1.0 mL of dioxane, and 3.0 mL of 50 mM sodium borate buffer (pH 8.0) was added. Oxygen was removed from the solution by evacuation followed by addition of nitrogen. This was repeated three times. The material was then added under nitrogen to the deoxy hemoglobin solution. The reaction mixture was kept at 37°C for 20 h with humidified nitrogen flowing through the rotating flask. The flask was then flushed with carbon monoxide. The solution of modified carbonmonoxy hemoglobin was passed through a Sephadex G-25 column (2.5 × 15 cm) equilibrated with 50 mM sodium phosphate buffer (pH 7.5) to remove residual reagent. (The resulting material is referred to as DPEE-Hb.) C-4 reverse-phase HPLC columns were used to separate heme and the various modified and native globin chains under denaturing conditions. Hemoglobins of different molecular weights were resolved using gel filtration chromatography, both with high concentrations of magnesium salt that lead to dissociation into $\alpha\beta$ dimers (29) as well as under nondissociating conditions where the tetramers remain intact.

Analysis of modified hemoglobin

General procedures for structural analysis were as previously reported (22). The product mixture was separated on a C-4 reverse-phase HPLC column. In addition to known peaks corresponding to heme and native globin chains, new peaks appeared that correspond to cross-linked globin chains. The molecular weights of these materials were determined by ion spray mass spectrometry (30, 31). The sites of modification were deduced by comparison of peptide patterns (reverse-phase HPLC) from digestion of native and modified chains with trypsin and endoproteinase Glu-C (14, 22, 32–34) along with ion spray mass spectral results as has been described in detail for other cross-linked hemoglobins (24, 27). Reference data for weights and mass spectra of native globin chains are conveniently summarized in the work of Adamczyk and Gebler (25). Size exclusion chromatography was used to distinguish materials by their approximate molecular weights (35). Columns were calibrated with cross-linked and oligomerized hemoglobin.

The formation of a cross-link between α-subunits of DPEE-Hb with fumaryl bis(3,5-dibromosalicylate) was accomplished by the procedure described for production of doubly cross-linked hemoglobin (14). After the 20 h incubation period of deoxy hemoglobin with DPEE (described above), a deoxygenated solution of fumaryl bis(3,5-dibromosalicylate) (0.0035 g, 5.0×10^{-6} mol) in 4.0 mL 50 mM sodium borate buffer (pH 8.0) was added to the hemoglobin reaction solution under nitrogen. (This reagent should introduce a cross-link between the ε-amino groups of the α-99 lysyl residues of hemoglobin (14, 16). It is effective if the sites in the β-subunits that make up the DPG-binding site (3, 36) are blocked.) The mixture was kept at 37°C for 2 h and then the flask was flushed with carbon monoxide. The solution of twice-modified carbonmonoxy hemoglobin was passed through a Sephadex G-25 column (2.5 × 15 cm) equilibrated with 50 mM sodium phosphate buffer (pH 7.5) in order to remove residual reagent. (The resulting material is referred to as XL2-Hb.) C-4 reverse-phase HPLC columns were used to separate the hemes and the globin chains. In another set of analyses of XL2-Hb, gel filtration chromatography was used to separate modified hemoglobins by their gross molecular weight (size). We used size-exclusion columns under conditions that dissociate the $\alpha\beta$ dimers from hemoglobin that is not cross-linked between these dimers, and also used conditions under which hemoglobin remains tetrameric ("nondissociating conditions"). Elution was under isocratic conditions. The nondissociating eluent was 0.050 M pH 7.0 sodium phosphate with 0.15 M sodium chloride flowing through a PSEC-12 column at 0.5 mL min^{-1}. The dissociating eluent was 0.025 M pH 7.2 Tris with 0.5 M magnesium chloride flowing through a TSK G2000 swxl column at 0.2 mL min^{-1}.

Results

The synthesis of DPEE efficiently introduces the necessary paired reactive functional groups for cross-linking onto a flexible linking chain. The route could be extended to produce a reagent library by varying the length of the polyether linker. The synthesis of the ether is based on Collman's method for producing a tetraether-linked tetraester (4). The reactive groups are conveniently introduced by Klotz's procedure for forming dibromosalicylates (28) (Schemes 1 and 2).

© 1999 NRC Canada

Scheme 1.

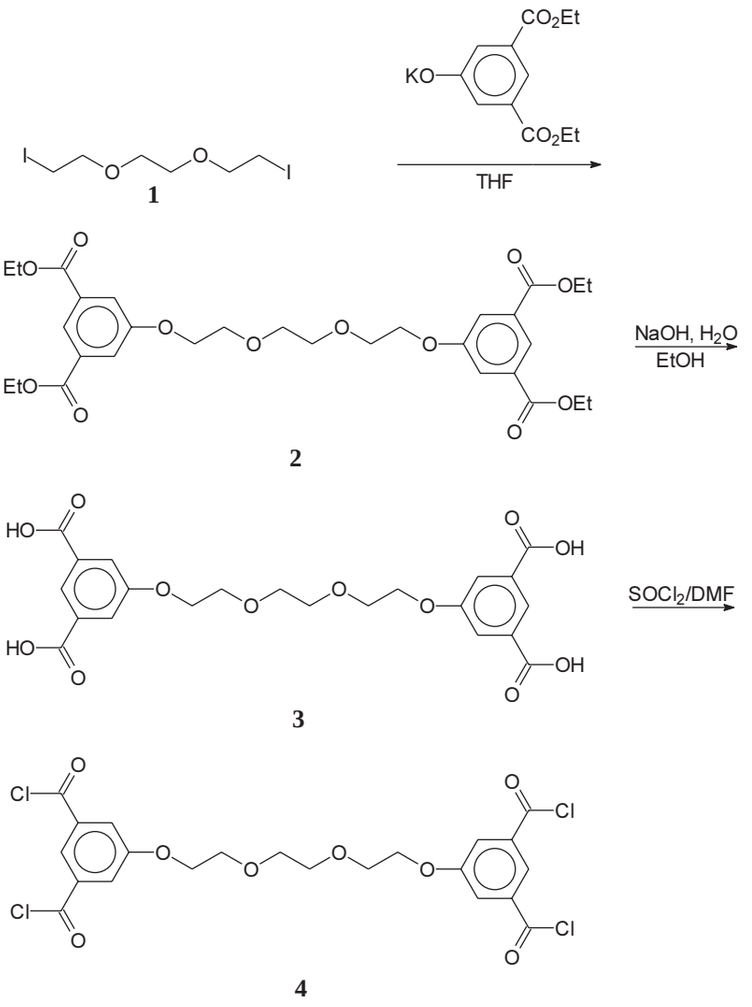

DPEE reacts with deoxy hemoglobin but not with carbonmonoxy hemoglobin, based on analysis of the resulting globin chains by C-4 reverse-phase HPLC. This is consistent with reaction occurring at the binding site for DPG in hemoglobin, which is more accessible in the deoxy form (37). The observed product pattern of the reaction remained constant as the ratio of the reagent to hemoglobin was varied from 1:2 to 2:1 and temperature was changed from 37 to 50°C. The reaction mixture appears to contain a considerable variety of altered protein products. The relative amounts were estimated based on peak areas in the chromatograms. We chose the materials in the largest peaks for structural analysis.

The heme and globin chains were separated on a C-4 reverse-phase HPLC column (see Fig. 1). The products in the largest peaks were detected and their molecular weights were determined from the parent peaks of ion spray mass spectra. Table 1 summarizes the ion spray mass spectral assignments associated with major peaks that were observed on reverse-phase HPLC analysis. The product from the largest chromatographic peak (**7**) is a tetraamide formed by acylation at four amino groups of two β-subunits. Products from other peaks retain one or more 3,5-dibromosalicyl (DBS) esters from DPEE or are partially hydrolyzed. Structures consistent with the observed masses are indicated as substituted derivatives of the core structure below:

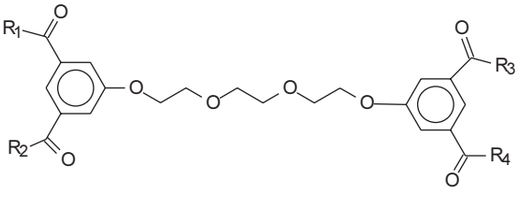

7–13

The mass of the linked globin chain that is proposed as the structure of the major product (**7**) is consistent with the electrospray mass spectral peak. This is a dimer of two β-subunits linked by four amide connections derived from the core of DPEE (**14**), which has a molecular mass of 410. The molecular mass of a β-subunit is 15 868 and that of the α-subunit is 15 126. Combining the masses of two β-subunits and **14**, less the mass of hydrogens that are dissociated from

© 1999 NRC Canada

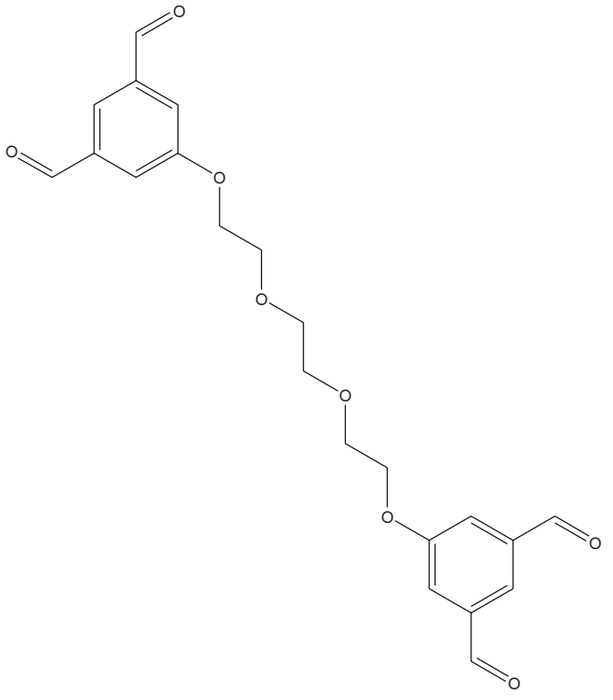

14

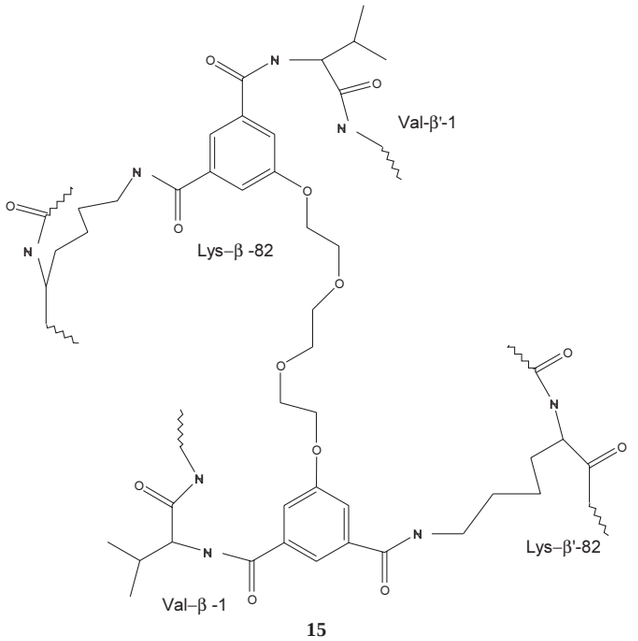

15

each resulting amide, gives a predicted mass of 32 142 for **7**. This is consistent with what is observed.

Scheme 2.

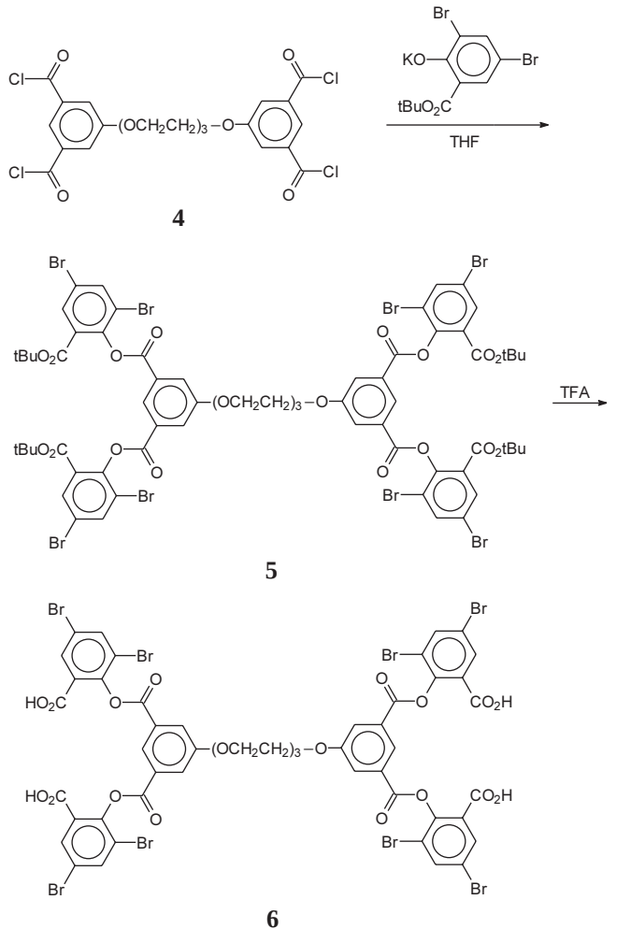

4

5

6

To determine the residues within hemoglobin that are modified by DPEE in **7**, the material from the peak corresponding to the cross-linked β-subunits was subject to tryptic digestion and peptide mapping. The products of digestion were separated by C-18 reverse-phase HPLC and the peptides were compared to those from digestion of the unmodified β chain (26). Three fragments of the native β digest were absent from that of the modified β-subunits: β-T1, β-T9, and β-T10a′. β-T1 is the amino terminus (Val-β-1) and β-T9 is connected to β-T10a′ through the β-Lys-82 residue, indicating that the amino termini of both β-subunits as well as the ε-amino groups of both β-Lys-82 residues are acylated by DPEE (Fig. 2). (The other peaks listed in Table 1 represent smaller quantities and the structural assignments are based on masses, with attachment sites based on the consistent patterns of modification seen with other reagents with similar functionality. Digests were not performed for these.) The results for **7** indicate that there are two sets of cross-links connecting positions 1 and 82 of β-subunits introduced by a single tetrafunctional reagent (**15**).

Formation of bis tetramers

The four functional groups of DPEE are arranged so that it is possible for them to produce a connection between tetramers. If we assume that reaction occurs at positions 1 or

© 1999 NRC Canada

Table 1. Ion spray mass spectral assignments for altered globin chains derived from the reaction of DPEE with hemoglobin. The structures are indicated based on the core structure above connected to hemoglobin β-subunits at the indicated amino group. A hydrolyzed site is indicated as "OH" and an intact ester as "DBS". Mass assignments for the native peaks are based on literature summations (25). The structure **12** is listed as two possibilities where either ester group from DPEE has undergone hydrolysis.

Mass (found)	Mass (calcd.)	Label	R_1	R_2	R_3	R_4
32 140	32 142	**7**	NH(ε)-β-Lys-82	NH(α)-β′-Val-1	NH(ε)-β′-Lys-82	NH(α)-β-Val-1
32 163	32 160	**8**	NH(ε)-β-Lys-82	NH(α)-β′-Val-1	NH(ε)-β′-Lys-82	OH
16 421	16 420	**9**	NH(ε)-α-Lys-99	DBS	DBS	DBS
30 971	30 972	**10**	NH(ε)-α-Lys-99	NH(ε)-α′-Lys-99	DBS	OH
31 250	31 250	**11**	NH(ε)-α-Lys-99	NH(ε)-α′-Lys-99	DBS	DBS
31 713	31 714	**12a**	NH(ε)-β-Lys-82	DBS	NH(ε)-α′-Lys-99	OH
31 713	31 714	**12b**	NH(ε)-β-Lys-82	OH	NH(ε)-α′-Lys-99	DBS
31 444	31 436	**13**	NH(ε)-β-Lys-82	OH	NH(ε)-α′-Lys-99	OH

Fig. 1. Globin chain separation after reaction of deoxy hemoglobin with DPEE: 20 h at pH 8.0 and 37°C

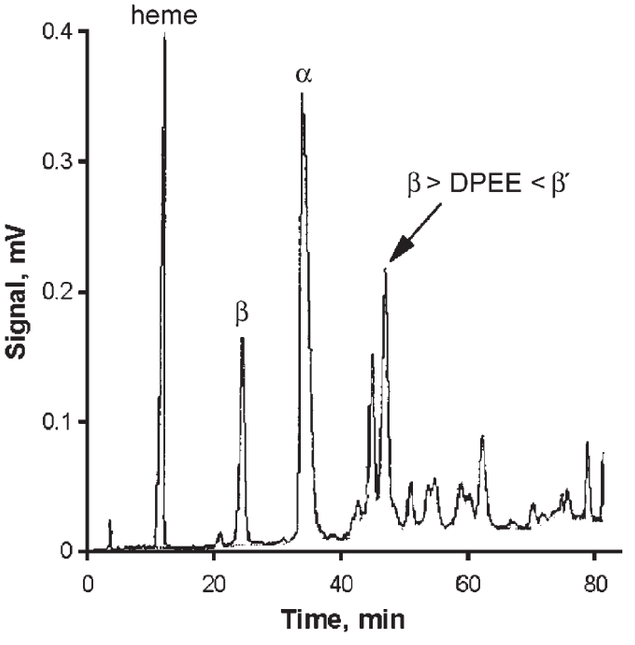

82 of β-subunits, and the product is symmetrical, schematic structures **16** or **17** are possible. To determine whether any bis tetramer formed, we analyzed the reaction solutions on size exclusion columns that give an indication of mass based on calibrated globular size. Since hemoglobin tetramers (64 000 Da) are in equilibrium with αβ dimers (32 000 Da) (38), cross-linking between two β-subunits or between two α-subunits prevents dissociation while a link within a subunit does not. Addition of magnesium chloride to the solution influences the equilibrium toward dissociation into dimers (29). Thus, **16** will dissociate into dimers while **17** will not.

Hemoglobins that are doubly cross-linked, with a link in between α- as well as β-subunits, can be prepared by addition of the reagent bis(3,5-dibromosalicyl)fumarate (DBBF), to a ββ-cross-linked hemoglobin (14). Thus when the α-subunits of **16** are subsequently cross-linked by reaction with DBBF, the tetrameric protein will no longer dissociate into dimers. In the possible cross-linked tetrameric structures, shown as **18** and **19,** reaction with all four sites of DPEE

Table 2. Expected masses (kDa) of peaks of modified hemoglobins. Addition of 0.5 M magnesium chloride causes dimers that are not cross-linked to separate from tetramer. See text for details (indicated as "dissociating").

Structure	Mass	Mass (dissociating)	Mass (dissociating) after formation of α–α cross-link
16	128	64, 32	128
17	128	128	128
18	64	64	64
19	64	64	64

will give material that does not dissociate into dimers. Therefore, introducing the α–α cross-link should not change the effect of adding magnesium chloride. These possibilities are summarized in Table 2.

We note that α–α cross-linking permits separations that

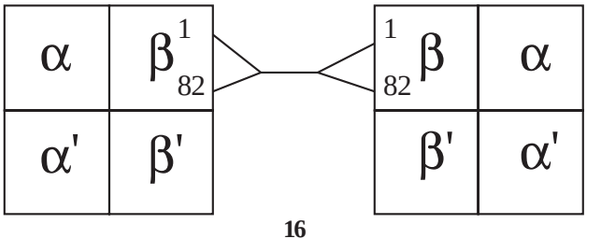

16

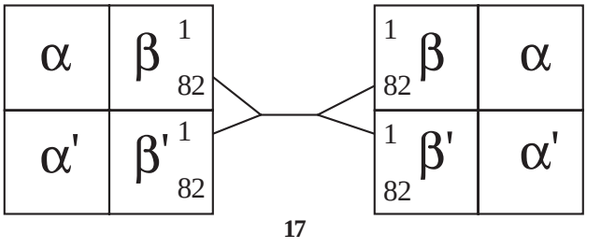

17

distinguish **16** from **17**. Structure **17** has cross-links between β-subunits, preventing dissociation into dimers. Cross-linking between the α-subunits does not change the results for dissociation. Therefore, formation of **17** should not change the apparent product–mass distribution. However, two of the four αβ dimers of **16** can dissociate. If an α–α cross-link is

© 1999 NRC Canada

Fig. 2. Tryptic-Glu-C peptides of the β-subunits linked at four sites by DPEE. Comparison is noted against native protein digest.

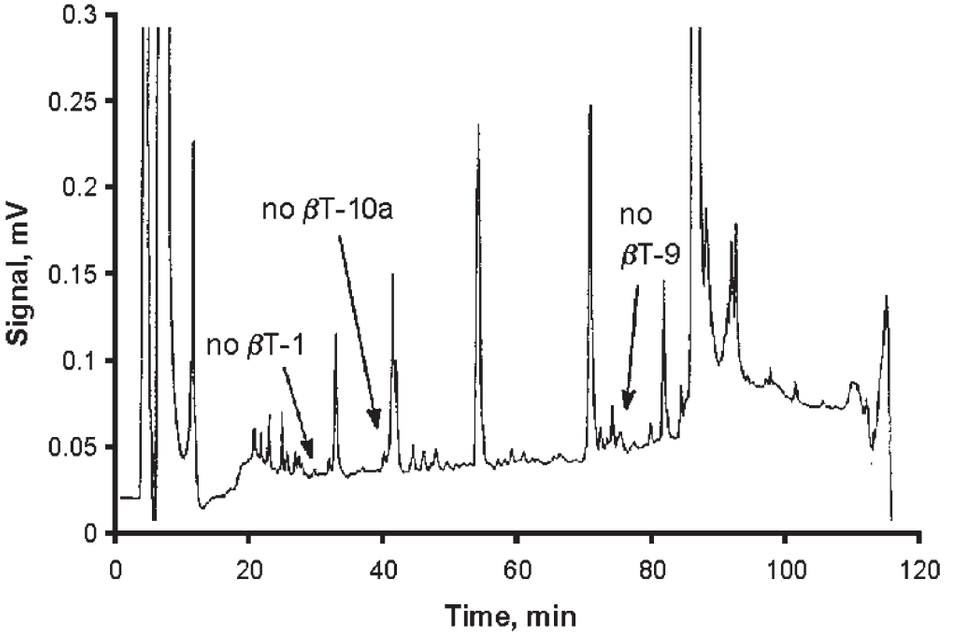

introduced, there will be a decrease in the amount of 32K material present.

Structures **18** and **19** are both capable of generating the major product. Both are fully cross-linked and will not dissociate into dimers. Both have a molecular mass of 64K. Both have all the β-1 and β-82 amino groups converted to amides.

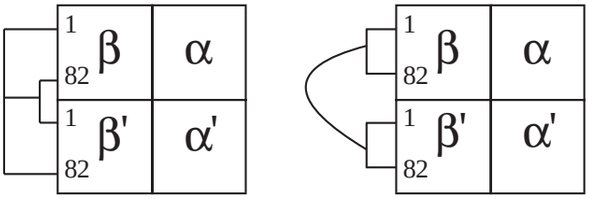

18

19

Separation of the globin chains by C-4 reverse-phase HPLC, before and after treatment of the reaction product with DBBF, shows that the reagent completely converts all native α-subunits in the product solution. The results of analysis by size exclusion chromatography are given in Table 3.

Discussion

DPEE appears to react with amino groups in the β-subunits of deoxyhemoglobin within its DPG-binding site as do other 3,5-dibromosalicylate esters. However, unlike BTDS, which reacts at only two of its four ester sites, major products include species in which all four esters are converted to amide derivatives of hemoglobin. The reaction of DPEE with deoxy hemoglobin gives one major product (>50%) and several minor products, including β–β, α–β, and α–α cross-linked products. Even after a long reaction period, considerable amounts of native protein subunits are found on reverse-phase HPLC analysis. The rates of the reactions between hemoglobin and DPEE are considerably slower than with other reagents that have the same dibromosalicyl leaving groups on aromatic hydrocarbon cores (trimesyl and biphenyl) (22, 27). These cross-linkers readily react with hemoglobin and reactions go to completion within a few hours. It is very likely that the slow reaction of DPEE would be the result of the hydrophobic end groups of DPEE stacking on one another, blocking its accessibility, and controlling its reaction patterns.

Our data show that the major product is a β–β′ cross-linked tetraamide containing one tetraacyl unit derived from DPEE. Several different modified hemoglobins could give data consistent with our results. From the mass and tryptic digestion analyses we know that cross-links are only between β-subunits, and all four amino groups from β-Val-1 (N-terminal α-amino group) and β-Lys-82 (ε-amino group) of both chains must be acylated. From the reaction patterns of other reagents, we know that the acyl groups on *meta* positions of a substituted benzene can connect ε-amino groups of the lysyl residues at position 82 of each β-subunit. They also can connect the α-amino group of the N-terminal valine of one β-subunit and the ε-amino group of Lys-82 of the other β-subunit. The same amino groups can also be connected within the same subunit. The β-Val-1 amino groups are too far apart to be connected by the *meta*-substituent groups.

If one end of DPEE has reacted between amino groups of Val-1 and Lys-82 on different β-subunits, then the other end must react with the alternative Val-1 and Lys-82 amino groups (**18**). The schematic diagrams for **20** and **21** (for **18** and **19**) are shown in terms of functional groups (following page).

The alternative products (**19** and **21**)) have the *meta*-substituted dicarbonyls from one end of DPEE connected as amides on the same β-subunit to Val-1 and Lys-82. The other end of DPEE is then connected to the other β-subunit in the

© 1999 NRC Canada

Table 3. Size exclusion chromatography analysis of relative amounts of various modified hemoglobins (DPEE-Hb) and those that have been reacted further to cross-link their α-subunits (HBXL2). Results are for distribution of relative amounts, according to their mass. Dissociating conditions refer to the presence of 0.5 M magnesium chloride.

Hemoglobin	Conditions	% ≥128 kDa	% 64 kDa	% 32 kDa
Native (human)	Dissociating	0.7	15.3	82.0
DPEE-Hb	Dissociating	2.5	89.3	8.2
DPEE-Hb	Nondissociating	5.7	87.7	6.6
HBXL2	Dissociating	5.2	82.4	12.4
HBXL2	Nondissociating	6.1	86.3	7.6

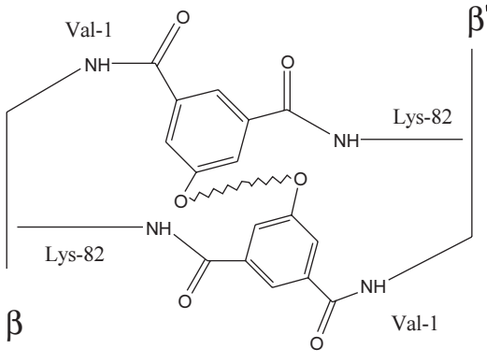

20

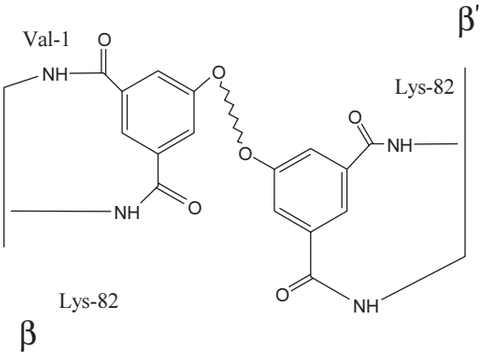

21

same manner. Based on the reaction patterns of other isophthalyl-DBS esters, we know that the ε-amino group of a β-Lys-82 is most likely to be converted to an amide. Since the α-amino groups of each N-terminal β-Val-1 are also modified in the product, and the *meta*-substituted reagent cannot span the distance between the two N-termini, these must react more quickly than does the other β-Lys-82 ε-amino group with the same end of DPEE. The reagent must arrange itself within the DPG binding site in order to achieve this selectivity, perhaps directed by hydrogen-bonding interactions.

The data in Table 3 show that a portion of the reaction products consists of two connected β-subunits, derived from different tetramers, producing a bis tetramer (mass: 128 kDa). Such a species of connected tetramers should be of interest for studies of cooperativity (1) as well as for analysis of physiological effects. Approximately half of the 128 kDa material found in DPEE-Hb under nondissociating conditions is converted to 64 and 32 kDa species under dissociating conditions (Table 3). This scenario is consistent with structure **16** (Table 2). The portion of 128 kDa species that is present under dissociating conditions could be explained by structure **17**, which should be stable under such conditions.

The introduction of cross-links between α-subunits holds the tetrameric structure together regardless of whether cross-linking has occurred between the β-subunits (14, 18). Stabilization of DPEE-Hb by α–α cross-linking, giving HBXL2, makes the 128 kDa species stable under dissociating conditions. These findings are also consistent with structure **16**. In such a case, the reagent would have had to join Val-1 and Lys-82 on the same subunit within each tetramer. Structure **17** remains intact under dissociating conditions, requiring that the cross-linking of each tetramer be between different β-subunits. The results from size exclusion chromatography confirm that at least one of the minor but significant products is a bis tetramer.

While these assignments are self-consistent, we know that other difunctional *meta*-substituted DBS reagents react between the ε-amino groups of each of the β-Lys-82 residues only (14, 22, 27, 33). The formation of such a product within one tetramer would require that the two β-Val-1 amino groups be connected at *meta* substituents. This is most unlikely since the distance between the amino termini of the two β chains of hemoglobin is too great (18.4 Å in the deoxy and 19.9 Å in the oxy conformation) (37) to be spanned by the isophthalyl group. No reagent that we have examined, even with a larger span (32), connects the N-termini of two β-subunits.

The slow rate of the reaction of DPEE with deoxyhemoglobin is consistent with either of the four-way cross-linked tetramers (**18** and **19**) being the product. Since movement of the bulky reagent inside the DPG binding site is likely to be restricted, it should be in a folded conformation as it enters the cavity. In addition, there is probably a limited orientation by which DPEE can get into the DPG site, once it is in an appropriate overall conformation.

Conclusion

The reaction of DPEE with deoxy hemoglobin is slower than that of smaller reagents, suggesting that the reagent is less accessible to the protein, presumably because it exists in a folded state. This has consequences in the reaction pattern as well. The major product from the reaction of DPEE with hemoglobin has four amino groups of the $\alpha_2\beta_2$ tetramer, two from each β-subunit, modified and cross-linked by a single molecule of reagent. In contrast, the rigid reagent derived from a symmetrical biphenyl tetracarboxylate (BTDS), which is unable to fold onto itself, reacts with hemoglobin primarily at only two sites in any modification process. The "knotted" species from the DPEE reaction may present an

© 1999 NRC Canada

interesting basis for studies of the protein's structural dynamics. Our results show that DPEE is sufficiently long to produce bis tetramers but the product is not present to a large extent, consistent with a predominant folded state of the reagent. A long but rigid reagent will give such products in greater proportion.

Acknowledgements

This work was supported by the Natural Sciences and Engineering Research Council of Canada (Strategic Project).

References

1. M. Perutz. Nature (London), **228**, 1 (1970).
2. R.E. Dickerson and I. Geis. Hemoglobin: structure, function, evolution, and pathology. The Benjamin/Cummings Publishing Co., Menlo Park, Calif. 1983. p. 1.
3. A. Arnone, R.E. Benesch, and R. Benesch. J. Mol. Biol. **115**, 627 (1977).
4. J.P. Collman, J.I. Brauman, J.P. Fitzgerald, P.D. Hampton, Y. Naruta, J.W. Sparapany, and J.A. Ibers. J. Am. Chem. Soc. **110**, 3477 (1988).
5. S. Miura and C. Ho. Biochemistry, **23**, 2492 (1984).
6. R. Kluger, R.T. Jones, and D.T. Shih. Artif. Cells Blood Substitutes Immobilization Biotechnol. **22**, 415 (1994).
7. M.A. Schumacher, M.M. Dixon, R. Kluger, R.T. Jones, and R.G. Brennan. Nature (London), **375**, 84 (1995).
8. M.A. Schumacher, E.E. Zheleznova, K.S. Poundstone, R. Kluger, R.T. Jones, and R.G. Brennan. Proc. Natl. Acad. Sci. U.S.A. **94**, 7841 (1997).
9. R.M. Winslow. Hemoglobin-based red cell substitutes. Johns Hopkins University Press, Baltimore, Md. 1995.
10. M. Jing, F.G. Panico, J.L. Panico, M.A. Ledvina, S. Bina, and S.M. Muldoon. Artif. Cells Blood Substitutes Immobilization Biotechnol. **24**, 621 (1996).
11. S.M. Cohn and T.J. Farrell. J. Trauma, **39**, 210 (1995).
12. K. Kikugawa, K. Adachi, H. Kosugi, and T. Asakura. Hemoglobin, **7**, 533 (1983).
13. I.M. Klotz, D.N. Haney, and L.E. Wood. J. Biol. Chem. **260**, 16215 (1985).
14. R.T. Jones, D.T. Shih, T.S. Fujita, Y. Song, H. Xiao, C. Head, and R. Kluger. J. Biol. Chem. **271**, 675 (1996).
15. E. Bucci, A. Razynska, H. Kwansa, B. Matheson-Urbaitis, M. O'Hearne, J.A. Ulatowski, and R.C. Koehler. J. Lab. Clin. Med. **128**, 146 (1996).
16. J.A. Walder, R.H. Zaugg, R.Y. Walder, J.M. Steele, and I.M. Klotz. Biochemistry, **18**, 4265 (1979).
17. Y. Zheng and K.W. Olsen. Artif. Cells Blood Substitutes Immobilization Biotechnol. **24**, 587 (1996).
18. S.R. Snyder, E.V. Welty, R.Y. Walder, L.A. Williams, and J.A. Walder. Proc. Natl. Acad. Sci. U.S.A. **84**, 7280 (1987).
19. R. Kluger and Y. Song. J. Org. Chem. **59**, 733 (1994).
20. K.W. Olsen, Q.Y. Zhang, H. Huang, G.K. Sabaliauskas, and T. Yang. Biomater. Artif. Cells Immobilization Biotechnol. **20**, 283 (1992).
21. R. Kluger, J. Wodzinska, R.T. Jones, C. Head, T.S. Fujita, and D.T. Shih. Biochemistry, **31**, 7551 (1992).
22. K. Paal, R.T. Jones, and R. Kluger, J. Am. Chem. Soc. **118**, 10380 (1996).
23. P.A. Pavlik, M.K. Boyd, and K.W. Olsen. Biopolymers, **39**, 615 (1996).
24. Z. Yu, G. Friso, J.J. Miranda, M.J. Patel, T. Lo-Tseng, E.G. Moore, and A.L. Burlingame. Protein Sci. **6**, 2568 (1997).
25. M. Adamczyk and J.C. Gebler. Bioconjugate Chem. **8**, 400 (1997).
26. R.T. Jones. Methods Enzymol. **231**, 322 (1994).
27. R. Kluger, Y. Song, J. Wodzinska, C. Head, T.S. Fujita, and R.T. Jones. J. Am. Chem. Soc. **114**, 9275 (1992).
28. E.J. Delaney, S.E. Massil, G.Y. Shi, and I.M. Klotz. Arch. Biochem. Biophys. **228**, 627 (1984).
29. G. Guidotti. J. Biol. Chem. **242**, 3685 (1967).
30. J.B. Fenn, M. Mann, C.K. Meng, and S.F. Wong. Mass Spectrom. Rev. **9**, 37 (1990).
31. J.B. Fenn, M. Mann, C.K. Meng, S.F. Wong, and C.M. Whitehouse. Science (Washington, D.C.), **246**, 64 (1989).
32. R.T. Jones, C.G. Head, T.S. Fujita, D.T. Shih, J. Wodzinska, and R. Kluger. Biochemistry, **32**, 215 (1993).
33. R. Kluger, L. Shen, H. Xiao, and R.T. Jones. J. Am. Chem. Soc. **118**, 8782 (1996).
34. M.P. Kavanaugh, D.T. Shih, and R.T. Jones. Biochemistry, **27**, 1804 (1988).
35. H. Pötzschke, W.K.R. Barnikol, R.G. Kirste, and M. Rosenbaum. Macromol. Chem. Phys. **197**, 1419 (1996).
36. R. Benesch and R.E. Benesch. Biochem. Biophys. Res. Commun. **26**, 162 (1967).
37. G. Fermi and M.F. Perutz. J. Mol. Biol. **175**, 159 (1984).
38. J.M. Manning, L.R. Manning, S. Morgan, R.C. Beavis, and B. Chait. Proc. Natl. Acad. Sci. U.S.A. **88**, 3329 (1991).

© 1999 NRC Canada

1998 W.A.E. McBryde Medal Lecture Searching for the Holy Grail in analytical separations[1]

Charles A. Lucy, Ken K.-C. Yeung, Shilin Fu, Dongmei Li, Tracey L. Henselwood, and Royale S. Underhill

Abstract: This paper describes the chemistry presented during the W.A.E. McBryde Medal address given at the 81st Chemistry in Canada Conference held in Whistler. The narrative chronicles our Quest to perform isotopic separations in the solution phase using as our Excalibur, capillary zone electrophoresis. The narrative takes you through the highs of our early success in separating $^{35}Cl^-$ and $^{37}Cl^-$. This separation was achieved by adjusting the electroosmotic flow to be equal in magnitude but opposite in direction to the chloride mobility. The narrative then takes you through the dark days, when we could not extend the isotopic separations to cationic species or even explain why there was an isotopic effect on mobility. Since those dark days, we have made numerous discoveries that have aided our Quest. Firstly, the development of mixed surfactant wall coating procedures yielded control of the reversed electroosmotic flow. This control enabled us to perform isotopic separations of systems such as ^{15}N-/^{14}N-aniline and $^{15}NH_4^+/^{14}NH_4^+$. In terms of understanding electrophoretic mobility, we demonstrate the importance of dielectric friction to mobility. Further, the effect of ionic strength in capillary zone electrophoresis is explained using the Pitts treatment, which is analogous to the extended Debye–Hückel equation for ionic activity. So, have we completed our Quest? Read on.

Key words: capillary zone electrophoresis, isotopic, electroosmotic flow, mobility modeling, ionic strength.

Résumé : Ce travail décrit la chimie décrite au cours de la conférence W.A.E. McBryde présentée lors de la 81ème Conférence de chimie au Canada qui s'est tenue à Whistler. La narration fait la chronique des événements qui ont accompagné notre quête en vue de réaliser des séparations isotopiques en solution en utilisant comme Excalibur l'électrophorèse en zone capillaire. Cette narration vous guide vers les sommets de nos succès préliminaires dans la séparation du $^{35}Cl^-$ et du $^{37}Cl^-$. Cette séparation a été effectuée en ajustant l'écoulement électroosmotique de façon à rendre son amplitude égale, mais direction opposée, à la mobilité des ions chlorures. Cette narration vous entraîne ensuite vers les jours sombres vécus lorsque nous avons été dans l'impossibilité d'étendre la portée des séparations isotopiques à des espèces cationiques ou même d'expliquer pourquoi il n'y avait pas d'effet isotopique sur la mobilité. Depuis ces jours sombres, nous avons fait de nombreuses découvertes qui nous ont aidés dans notre quête. Premièrement, le développement des méthodes impliquant le recouvrement des surfaces avec des agents de surface mixtes a permis de contrôler l'écoulement électroosmotique inversé. Ce contrôle nous a permis d'effectuer des séparations isotopiques de systèmes telles que les ^{15}N-/^{14}N-anilines et $^{15}NH_4^+/^{14}NH_4^+$. En termes de compréhension de la mobilité électrophorétique, on a démontré l'importance de la friction diélectrique pour la mobilité. De plus, on a expliqué l'effet de la force ionique dans l'électrophorèse en zone capillaire en faisant appel au traitement de Pitts qui est analogue à l'équation étendue de Debye–Hückel pour l'activité ionique. Nous avons donc complété notre quête. Lisez.

Mots clés : électrophorèse en zone capillaire, isotopique, écoulement électroosmotique, modélisation de la mobilité, force ionique.

[Traduit par la Rédaction]

Introduction

The nature of research, like that of quests, depends heavily upon the character and the background of the protagonist. This particular quest had its beginnings during Dr. Lucy's time with Atomic Energy of Canada Ltd. (AECL Research) in Chalk River, Ont. AECL Research produces a wide array of radioisotopes for medicinal and other peaceful applica-

Received October 21, 1998.

C.A. Lucy,[2] K.K.-C. Yeung, S. Fu, D. Li, T.L. Henselwood, and R.S. Underhill. Department of Chemistry, University of Calgary, Calgary, AB T2N 1N4, Canada.

[1]This paper is an invited review article based on the W.A.E. McBryde Medal Lecture presented by Professor Lucy at the 81st Annual Conference of the Canadian Society for Chemistry, Whistler, British Columbia, June 1998.

[2]Author to whom correspondence may be addressed. Telephone (403) 220-7795. Fax: (403) 289-9488. e-mail: lucy@ucalgary.ca

© 1999 NRC Canada

Fig. 1. Schematic diagram of a capillary electrophoresis instrument. Inset is an expanded view of a section of the capillary.

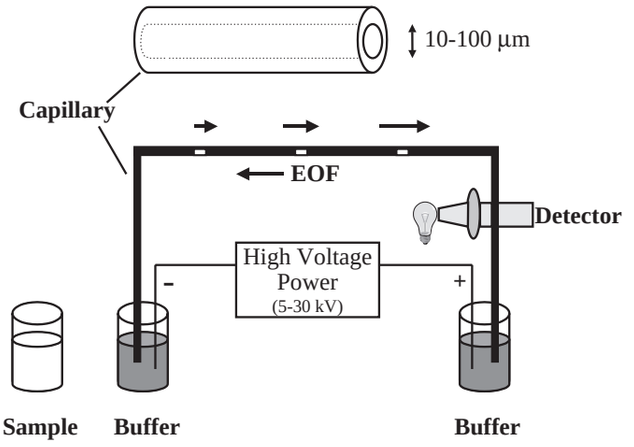

tions. For instance, AECL produces most of the world's molybdenum-99 which is used to generate technicium-99m for radiodiagnostic scans of the brain, bones, heart, lungs, gall bladder, and virtually every other organ of the body.

At AECL Dr. Lucy developed production methods for new radioisotope products. During this time Dr. Lucy became intrigued by the work of Tanaka et al. (1) and by technique of capillary electrophoresis. Tanaka et al. (1) demonstrated that isotopic induced differences in acid dissociation constants for species such as aniline and benzoic acid could be used to separate the isotopic species using high-performance liquid chromatography, albeit the separations took hours. At the same time, the scientific literature was rife with papers on capillary zone electrophoresis (CZE). CZE offers 10–100 times the separation power of high-performance liquid chromatography.

Thus, when Dr. Lucy joined the faculty at The University of Calgary in 1992, his "Holy Grail" was to separate isotopic species using as our "Excalibur" capillary zone electrophoresis. This paper details our efforts towards that goal, and some of the integral tangents that arose from this work. Indeed the work has taken many tangents, which through the skills, perseverance, and ingenuity of the "knights and squires" in our laboratory, have lead to many fascinating and unexpected results.[3]

Introduction to capillary zone electrophoresis

Electrophoresis is simply defined as the migration of ions in an applied electric field. Anions will migrate towards the anode (positive electrode), and cations toward the cathode (negative electrode). The rate of migration will be a function of the size of the ions, and the net charge on the ion. This is illustrated by the Hückel equation

$$[1] \qquad \mu_e = \frac{q}{6\pi\eta r_s}$$

where μ_e is the electrophoretic mobility of an ion, q is the charge on the molecule, η is the solvent viscosity, and r_S is the Stokes or hydrated radius of the ion. The time necessary to perform a separation is related to the velocity with which the ions move. This ion velocity (ν) is a simple function of the ionic mobility (μ) and the applied voltage V

$$[2] \qquad \nu = \frac{\mu V}{L_t}$$

where L_t is the total length of solution over which the voltage is applied. In classical electrophoresis, such as used for DNA fingerprinting, about 300 V is applied and yields separations in hours to days.

In *capillary zone electrophoresis* (CZE) the goal is to perform separations in minutes. Thus, as shown in Fig. 1, 5 000–30 000 V are applied across the capillary, causing the ions to migrate rapidly. Unfortunately, such high voltages generate significant Joule heating, such that the solution will heat or even boil. The use of narrow (10–100 μm) capillaries effectively dissipates that heat, making possible the use of high voltages.

A typical CZE experiment starts with the voltage off. The left-hand buffer vial is replaced with a sample vial, and a pressure (0.5 psi) is applied for a few seconds to hydrodynamically push a few nanoliters of sample onto the capillary. The sample vial is then replaced with the buffer vial, and the voltage (5–30 kV) is applied. Ions are then separated based on differences in their electrophoretic mobilities, i.e., effectively their *charge-to-mass* ratios, as depicted by the vectors in Fig. 1. Near the right-hand end of the capillary, a detector monitors the absorbance of the ion bands.

The resultant signals are known as *electropherograms*. Electropherograms, such as those presented in Fig. 2, appear very much like traditional *chromatograms*. The features that distinguish electropherograms from chromatograms are the rapid separation times (Fig. 2*A*) and the extremely high separation efficiencies (Fig. 2*B*). In Fig. 2, the solutes range from inorganic anions to macromolecules. Furthermore, these separations are complete in minutes and display efficiencies as high as 300 000 plates. The performance in Fig. 2 is by no means unusual. CZE separations have been performed in as little as a millisecond (2) and can achieve efficiencies over 1 000 000 theoretical plates (3).

So, this is the Excalibur with which we were going to take up the quest for the Holy Grail in analytical separations, the separation of isotopic species. However, as with any weapon as powerful as Excalibur, it is essential to understand its subtleties to fully exploit its power. The most important subtlety in CZE is that a flow is generated within the capillary when a voltage is applied. This *electroosmotic flow* (EOF) is caused by the intrinsic negative charge on the capillary walls. This negative charge arises from the weakly acidic silanol (-SiOH) groups on the surface of the fused silica. An excess of cationic charge will build up in the solution near

[3] We were not able to include the wonderful work done by the following members of our group: Dr. Liwen Ye, Wayne E. Rae, Dr. Susan Varkey, Huyen Dinh, Brian P. Hausermann, Roger Brown, Jennifer E. Wong, Angela N. Ko, Anne Co, Dr. Quanji Wu, Julie Hickey, Monica Fernandez, Yusuf Muombwa, and Jinglan Yan.

© 1999 NRC Canada

Fig. 2. Examples of capillary electrophoretic separations. (*A*) Separation of inorganic anions. Experimental conditions: applied voltage, –20 kV; capillary, 57 cm of 75 μm i.d. (50 cm to detector); temperature, 25°C; detection, indirect at 254 nm; buffer, 5.0 mM potassium chromate and 0.5 mM CAS U with pH adjusted to 8.0 using phosphoric acid; sample, 5 ppm mixed anion solution. Reprinted from ref. 16. Copyright 1998, with permission from Elsevier Science. *(B)* Separation of cationic proteins. Experimental conditions: applied voltage, –15 kV; capillary, 47 cm of 75 μm i.d. (40 cm to detector); temperature, 25°C; detection, 214 nm; buffer, 10 mM sodium phosphate with pH adjusted to 7.2 using sodium hydroxide and ionic strength adjusted to 50 mM with NaCl; sample, 0.1 mg/mL of lysozyme and α-chymotrypsinogen A. Reprinted with permission from ref. 18. Copyright 1997 American Chemical Society.

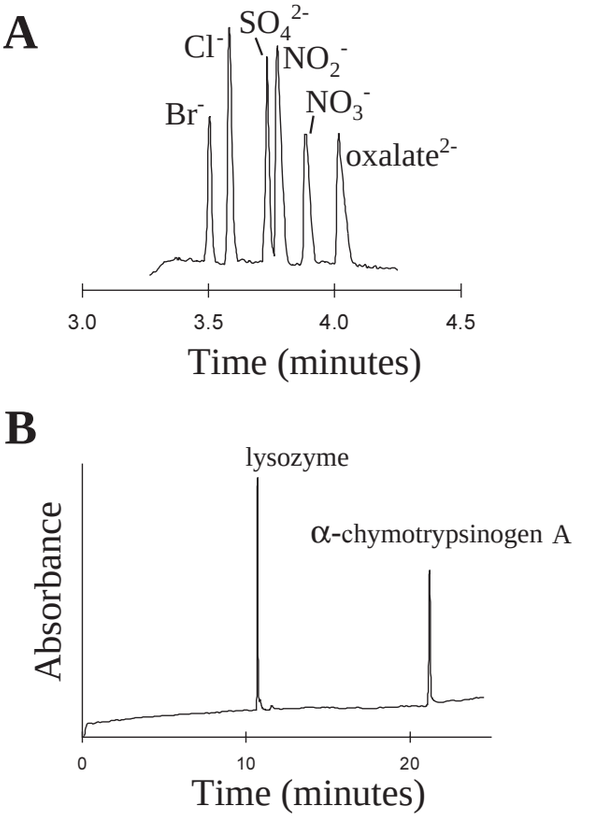

the capillary wall. When a voltage is applied, these excess cations within the diffuse layer of the solution migrate towards the cathode (to the left in Fig. 1). As the cations in the diffuse layer move toward the cathode, they drag with them their hydration spheres. These hydration spheres in turn generate a viscous drag on the bulk solution within the capillary. The net effect is a plug flow of buffer towards the cathode that is larger in magnitude that the mobility of most anions. The velocity of this flow can be described in terms of an electroosmotic mobility (μ_{eof}).

The electrophoretic mobilities and the electroosmotic flow mobility are vectoral functions. The net or apparent mobility ($\mu_{apparent}$) is the sum of the two mobilities:

$$[3] \quad \mu_{apparent} = \mu_e + \mu_{eof}$$

where μ_e is the electrophoretic mobility of the ion (eq. [1]), and μ_{eof} is the electroosmotic flow mobility.

With a bare fused silica capillary, the electroosmotic flow mobility is large and towards the cathode. The electroosmotic flow is so large that almost all ions are swept towards the cathode. Thus, if an injection is made at the anode and the detector is positioned at the cathode (opposite configuration to that shown in Fig. 1), cations, neutral molecules, and slow anions can all be detected in the same electropherogram. Only small inorganic anions such as chloride and sulfate have an electrophoretic mobility greater than the electroosmotic flow. Thus only these anions migrate towards the anode. As such, fast anions such as chloride and sulfate are injected at the cathode and migrate to the detector positioned at the anode to generate the electropherogram in Fig. 2*A*. This is the instrument configuration used for most of the work discussed herein.

Seeking the Holy Grail

In capillary electrophoresis, the resolution between two peaks is expressed as (4)

$$[4] \quad R_S = \frac{\sqrt{N}}{4}\frac{\Delta\nu}{\bar{\nu}}$$

where N is the average number of theoretical plates as defined in chromatography, $\Delta\nu$ is the difference in the peak velocities, and $\bar{\nu}$ is the average peak velocity. Recalling that the electromigration is accompanied by electroosmotic flow, the zone velocity is given by (3)

$$[5] \quad \nu = (\mu_e + \mu_{eof})\frac{V}{L_t}$$

where V is the applied voltage and L_t is the total length of the capillary.

Typical efficiencies in capillary electrophoresis are on the order of 100 000–1 000 000 theoretical plates. However, even such high efficiencies by themselves are not sufficient to separate isotopic species. With isotopic separations, the difference in the electrophoretic mobilities will be very small. For instance, there is only a 0.12–0.26% difference in the zone velocity ($\Delta\nu$) between $^{35}Cl^-$ and $^{37}Cl^-$ (5). Nonetheless, Avdalovic et al. (6) had observed a partial separation of $^{35}Cl^-$ and $^{37}Cl^-$ using capillary electrophoresis with suppressed conductivity detection. The key to performing ultrahigh resolution capillary electrophoretic separations is to adjust the average zone velocity ($\bar{\nu}$) in eq. [4] to near zero (7). As indicated by eq. [5], a near zero zone velocity can be achieved by adjusting the electroosmotic flow to be equal in magnitude but opposite in direction to the ionic migration of the sample.

In an untreated capillary, the electroosmotic flow coefficient is given by (8)

$$[6] \quad \mu_{eof} = \frac{\sigma_{SiO^-}\kappa^{-1}}{\eta}$$

where σ_{SiO^-} is the surface charge density which is related to the degree of ionization of the silanol groups on the capillary wall, η is the viscosity, and κ^{-1} is the double layer thick-

© 1999 NRC Canada

Fig. 3. Separation of the isotopes of chloride using capillary zone electrophoresis. Experimental conditions: applied voltage, –20 kV; capillary, 47 cm of 75 μm i.d. (40 cm to detector); temperature, 25°C; detection, indirect at 254 nm; buffer, 5.0 mM potassium chromate and 3.0 mM borate at pH 9.2; sample, 20 ppm of natural abundance chloride. Reprinted with permission from ref. 9. Copyright 1995 American Chemical Society.

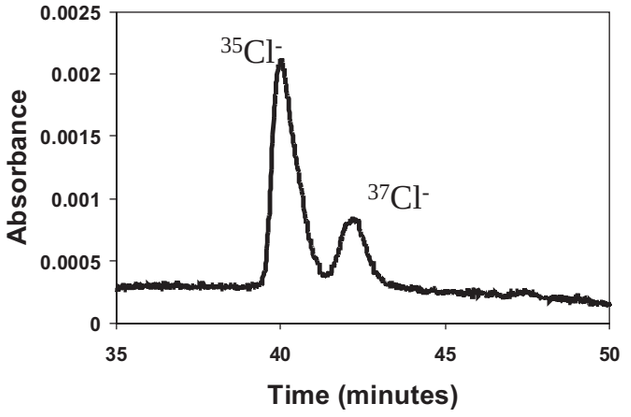

ness which is inversely related to the square root of the buffer ionic strength. Based on eq. [6], Tracey Henselwood (née McDonald) adjusted the ionic strength (altering κ^{-1} in eq. [6]) and pH (altering σ_{SiO^-}) of a chromate buffer to match the electroosmotic flow to the mobility of chloride ions. The resultant separation is shown in Fig. 3.

We achieved baseline separation of the isotopes of chloride based solely on the intrinsic mobility differences of the isotopes (9)! The response to this result was overwhelming. The work was highlighted in Chemical and Engineering News (10), and a copy of Fig. 3 was incorporated into popular undergraduate texts in analytical chemistry with the caption *This impressive separation was done by an undergraduate student at the University of Calgary* (see Fig. 18–14 in ref. 11).

We had achieved our Holy Grail of isotopic separations in the solution phase…

The dark days

…but just as quickly doubts started to descend upon the lab. You see, it should have been possible to extend ultra-high resolution capillary electrophoresis to cations. Indeed, the isotopic difference in mobility between $^{39}K^+$ and $^{41}K^+$ is almost twice that of chloride (5). But we could not do it. One of the primary reasons that we could not perform cation isotopic separations is that we could not control the electroosmotic flow in the opposite direction.

To make matters worse, we really could not explain why the separation of the chloride isotopes was even possible! Why did one isotope migrate faster than another did? One could simply say "charge-to-mass," but mass does not appear in the expressions for electrophoretic mobility (e.g., Hückel equation, eq. [1]). To account for isotopic fractionation in geological groundwaters, geologists had invoked the concept of ion filtration (12) and even Graham's law (5, 13). While these arguments successfully predicted that the lighter isotope migrates faster, they were ineffective at given a clear understanding of the factors that control mobility.

Fig. 4. Models for reversal of electroosmotic flow by cationic surfactants. *(A)* Bilayer model and *(B)* hemi-micelle model. See text for details.

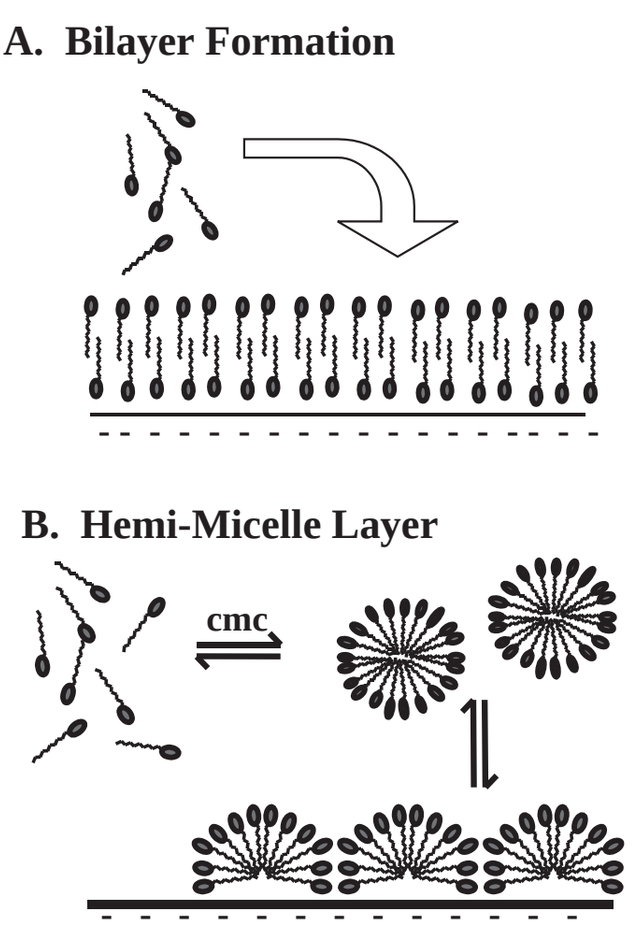

So, at this point we had to retrench. We set out three goals. Firstly, to gain control of reversed electroosmotic flow. Secondly, to achieve isotopic separations of cationic species. Finally, to gain an understanding of the factors affecting electrophoretic mobility.

Seeking control of reversed electroosmotic flow

Figure 1 depicts the migration of anions in an untreated capillary. With cationic separations, the migration of the ions will be reversed. Therefore, similarly it is necessary to reverse the electroosmotic flow. It had been reported that addition of cationic surfactants such as cetyltrimethylammonium bromide (CTAB) and tetradecyltrimethylammonium bromide (TTAB) to the electrophoretic buffer reverses the electroosmotic flow (14). The conventional explanation for this electroosmotic flow reversal was as depicted in Fig. 4*A*. The cationic surfactants adsorb onto the anionic capillary wall to form a *bilayer.* That is, there is a first monolayer of surfactant in which each cationic head group is associated with

© 1999 NRC Canada

a silanol on the wall. The hydrophobic tail of the surfactant is left extending out into solution. A second monolayer of surfactants associates their tails with those of the first monolayer, leaving their cationic head groups extending out into the solution. The net result of such bilayer formation is that each anionic site on the wall is replaced with a positive charge.

So, the bilayer model was our initial model for the reversal of electroosmotic flow. We reasoned that, given this model, it should be possible to alter the magnitude of the reversed flow simply by varying the pH of the buffer. Alteration of the pH would change the anionic charge on the capillary wall. This in turn would alter the population of cationic surfactant in the bilayer. Thus, simply varying the pH of CTAB containing buffers should adjust the magnitude of the reversed electroosmotic flow. It did not work! Varying the buffer pH had almost no effect on the magnitude of the reversed electroosmotic flow (15).

Thus, a new model of the cationic surfactant induced electroosmotic flow reversal was needed. Extensive review of the colloid and interface literature indicated that a "hemi-micelle model" should be a better descriptor of this behavior. In the hemi-micelle model, no reversal of the electroosmotic flow is expected below the critical micelle concentration of the surfactant. Indeed, little alteration of the flow was observed below the critical micelle concentration (15). However, once the critical micelle concentration was exceeded, micelles form in the buffer solution (Fig. 4*B*). These polycationic micelles are attracted to the negative capillary wall, and condense onto the wall to form a "hemi-micelle" layer (Fig. 4*B*). The properties of this hemi-micelle layer are then governed by the properties of the micelle and surfactant, and not affected by the underlying anionic charge (so long as there is sufficient anionic wall charge to anchor the micelles to the wall).

Thus, the hemi-micelle model explained why the surfactant-induced electroosmotic flow reversal was pH independent. Further it was found that variation of other conditions such as the buffer anion and the surfactant length had little effect on the magnitude of the reversed electroosmotic flow (15).

Still questing for control of reversed electroosmotic flow

Thus, while we now understood the mechanism for flow reversal using cationic surfactants, we still required a means to easily alter the magnitude of the reversed electroosmotic flow. Fortunately, we realized that the electroosmotic flow resulting from the hemi-micelle layer was a function of the electrostatic properties of the layer. The electrostatic properties of the hemi-micelle layer could be altered by adding another surfactant bearing a different charge, i.e., create a mixed surfactant system. The zwitterionic surfactant coco amidopropylhydroxyldimethyl sulfobetaine (CAS U, Witco) was successfully incorporated into the cationic hemi-micelle to alter the effective wall charge. Variation of the CAS U to cationic surfactant ratio (at concentrations above the critical micelle concentrations of the surfactants) allowed monotonic variation in the electroosmotic flow from near zero to full reversed (16). Thus, we had achieved the first of the three challenges that we foresaw — control of reversed electroosmotic flow. We have successfully applied this reversed electroosmotic flow to the optimization of separations of inorganic anions (16) and cationic proteins (17).

Meandering along the path to the Holy Grail

One surprising aside from this work was the observation that CAS U itself adsorbed onto the capillary walls to form a hemi-micelle. This hemi-micelle formation reduced the electroosmotic flow to ~10% of its normal (i.e., untreated capillary) value (18). We believe the hemi-micelle formation increased the ionic strength in the vicinity of the capillary wall, as depicted in Fig. 4*B*. The hemi-micelle formation lowers the double layer thickness (κ^{-1}), and thus the electroosmotic flow (eq. [6]). The hypothesis of a localized high ionic strength was very important.

Cationic proteins are very difficult to separate by capillary electrophoresis. The strong electrostatic attraction between these proteins and the anionic capillary wall results in severe peak distortion and even irreversible loss of the protein. One solution to this problem was to use extremely high ionic strength buffers (>2 M) (19). Despite the *Herculean* nature of this approach, it has been commercialized by Waters as Z1 Methyl Additive, and is widely used. We argued that if our zwitterionic surfactant hemi-micelle layer increases the localized ionic strength at the capillary walls, might it not also prevent adsorption of cationic proteins. Indeed addition of 0.002 M CAS U to our buffers yielded over 750 000 plates per meter for lysozyme and α-chymotrypsinogen A, as evident in Fig. 2*B* (18). This was the highest efficiency ever reported for separation of these proteins. Further, recoveries of protein from the capillary were quantitative (18).

Retrieving the Holy Grail

To perform isotopic separations of cationic species we needed an electroosmotic flow that was equal in magnitude, but opposite in direction to the migration of the cations. The zwitterionic–cationic surfactant systems described above gave us the electroosmotic flow control needed for this application.

But what cationic isotopic separation should we apply this technique to? The advent of Inductively Coupled Plasma – Mass Spectroscopy (ICP–MS) has rekindled the use of tracers, albeit stable isotopes, by once again demonstrating their great value in practical applications such as environmental studies (20). However, ICP–MS and other mass spectroscopic techniques are expensive, and so are all too often unavailable to experimentalists, thus limiting the use of stable-isotope labeling. Also, with isotope species like $^{15}NH_4^+/^{14}NH_4^+$ sample handling can be complex (21). Thus it would be extremely useful if capillary electrophoresis could be used to separate isotopically labeled ammonium. Further, the work of Tanaka et al. (1) has demonstrated that there is an isotope-induced shift in the pK_a of amines that can be exploited for such separations.

Figure 5 shows a preliminary separation of $^{15}NH_4^+$ and $^{14}NH_4^+$ achieved by Ken Yeung using mixed surfactant hemi-micelle wall coatings to control the reversed electroosmotic

© 1999 NRC Canada

Fig. 5. Separation of isotopically labeled ammonium ($^{15}NH_4^+$) from natural ammonium ($^{15}NH_4^+$). Experimental conditions: applied voltage, –15 kV; capillary, 47 cm of 50 μm i.d. (40 cm to detector); temperature, 25°C; detection, indirect at 214 nm; buffer, 10 mM borate with 0.5 mM CAS U with pH adjusted to 9.55 using benzyltributyl ammonium hydroxide; sample, 0.1 mM $^{15}NH_4^+$ and 0.2 mM $^{14}NH_4^+$.

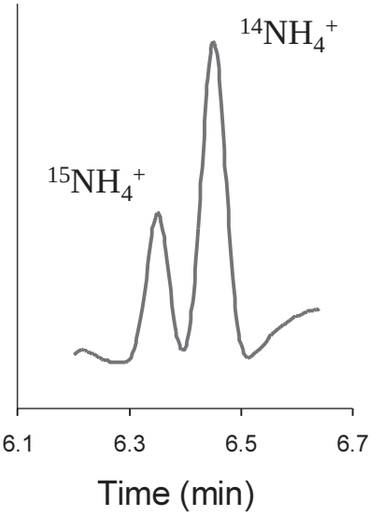

flow. As predicted (1), the ^{15}N retains its hydrogen more strongly, and so has a slightly higher effective charge than $^{14}NH_4^+$, and thus migrates more quickly. Further work is being done to fully characterize this analysis (22). The same approach has been applied to other ^{15}N-labeled compounds such as aniline (23).

Thus, we now have overcome two of the hurdles that we foresaw. Firstly, we have gained control over the magnitude of the reversed electroosmotic flow. Secondly, we have used that flow control to separate cationic isotopic species. The only quest that yet remains is an understanding of what actually controls electrophoretic mobility.

Questing for an understanding of electrophoretic mobility

The mobility of an ion is a function of its charge (z) and a frictional drag (f):

$$[7] \qquad \mu \alpha \frac{z}{f}$$

The most common hydrodynamic model for mobility is related to the Stokes–Einstein diffusion model, and is known as the Hückel equation:

$$[8] \qquad \mu_0 = \frac{ze}{6\pi\eta r_s}$$

where z is the valence number of the molecule, e is the charge of an electron, η is the viscosity of the solution, and r_S is the Stokes radius. The denominator is the frictional coefficient (f) as predicted by Stokes law for moving a hypothetical spherical molecule of radius r_s at a uniform velocity through a continuum of viscosity η.

Fig. 6. Correlation of the mobilities predicted using the Hückel equation (eq. [8]) with the infinite dilution mobilities for 34 aliphatic monoamines. The line is the expected behaviour for perfect correlation between the literature and predicted values. Reprinted with permission from ref. 24. Copyright 1998 American Chemical Society.

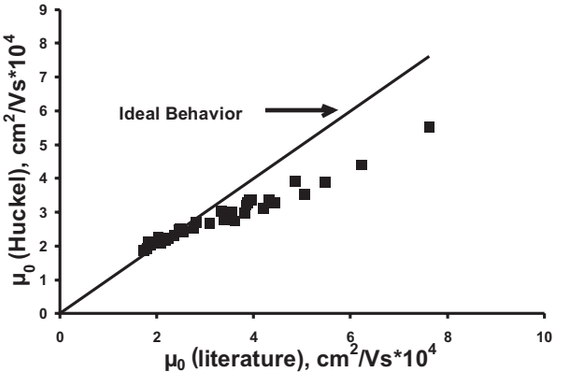

While the Hückel equation is widely quoted, it is not highly effective even for simple organic ions, as is shown in Fig. 6. Figure 6 shows the infinite dilution mobilities calculated using the Hückel equation (eq. [8]) plotted versus the literature mobilities for 34 aliphatic monoamines (24). The Stokes radii were derived from the van der Waals volume of the molecule calculated using the Bondi increments. The line in Fig. 6 indicates the ideal correlation (i.e., if the calculated mobilities precisely matched the literature mobilities). Clearly, the mobilities determined using the Hückel equation (eq. [8]) deviate significantly from the literature values. The average relative error in mobility prediction using the Hückel equation (eq. [8]) is 13.9% (24).

In retrospect, it seemed obvious why the Hückel equation failed. Molecules are not spherical! Thus, our second attempt at modeling the mobility of these simple aliphatic monoamines was to use the Perrin model (25). In the Perrin model, the shape of the molecule is approximated as an ellipsoid. Generally the frictional resistance of the ellipsoid is expressed relative to the resistance of moving a sphere of the same volume (i.e., f/f_0 where f is the frictional coefficient of the ellipsoid, and f_0 is the frictional coefficient for a sphere of the same volume). Thus Perrin's equation has the form:

$$[9] \qquad \mu = \frac{ze}{6\pi\eta r_s(f/f_0)}$$

The frictional ratio factor (f/f_0) is related to the dimensions of the ellipsoid (length, width, and depth) through elliptical functions of the first kind. So, molecular modeling was used to determine the dimensions of the molecule, and then nontrivial mathematics were used to convert these dimensions into a frictional factor.

After all this effort, the Perrin ellipsoidal model provided little improvement over the Hückel model (24). The average relative error of mobilities predicted for the aliphatic monoamines by the Perrin model was 10.0% (24). Furthermore, use of the Perrin model induced greater deviation in

© 1999 NRC Canada

the prediction of the mobility of large monoamines, where shape was expected to be most important!

At times like these one forsakes the wisdom of Merlin, and relies on the brawn of Lancelot. Numerous empirical expressions have been developed for predicting electrophoretic mobility (26). A common feature of these is that the mobility is found to depend upon the molecular volume to a power greater than the minus one third suggested by the Hückel equation (eq. [8]). Similarly, empirical expressions for diffusion, which is related to electrophoretic mobility through the Einstein relation, have consistently yielded surprisingly high power dependencies on the radius and (or) volume (27). Therefore, it was decided to try to fit the literature mobilities for the aliphatic monoamines to an expression in which the dependence on volume was allowed to vary. The resultant expression for monoamines (z = +1) was (24)

$$[10] \quad \mu_0 = \frac{3.66 \pm 0.27 \times 10^{-3}}{V^{0.481 \pm 0.016}} \quad (\mathrm{cm^2\ V^{-1}\ s^{-1}})$$

where V is the van der Waals volume of the molecule calculated using the Bondi increments. The average error for infinite dilution mobilities predicted using eq. [10] was 6.6%. This error was much reduced from that of the Hückel (eq. [8]) (13.9%) or Perrin (eq. [9]) (10.0%) equations.

However, there were still significant problems with our mobility predictions. Firstly, eq. [10] was purely empirical. In all likelihood the power dependence on volume was biased by other factors affecting mobility. Secondly, there are significant errors in the mobilities predicted by eq. [10]. Surprisingly, these errors did not seem to relate to shape. What else could influence mobility? Well, obviously hydration! An ion in solution will cause water molecules to reorient in response to the ion charge. Generally, we refer to the first shell of such solvation as the "*primary hydration sphere*." But how do you calculate the primary hydration sphere for an organic molecule? Fortunately, our molecular modeling program (Molecular Modeling Pro™, Version 1.44, WindowChem Software, Fairfield, Calif.) provided the McGowan waters of hydration. In this procedure, each functionality within a molecule is associated with a certain number of waters of hydration. For instance, CH_n has 0 waters, ROH has 1, NH_4^+ has 12, R-NH_3^+ has 9, $R_2NH_2^+$ has 6, R_3NH^+ has 3, and R_4N^+ has 3. The summation of such increments over the functional groups of a molecule gives the total waters of hydration for that molecule.

Allowing for the influence of hydration on mobilities of ions, the general expression for mobility (eq. [7]) becomes

$$[11] \quad \mu \propto \frac{z}{f_{\mathrm{hydrodynamic}} + f_{\mathrm{hydration}}}$$

where $f_{\mathrm{hydrodynamic}}$ is the frictional drag due to the volume of the ion, and $f_{\mathrm{hydration}}$ is the frictional drag caused by the waters of hydration. Incorporating the McGowan waters of hydration (H) into our empirical expression for the mobility of aliphatic monoamines (z = +1) yielded

$$[12] \quad \mu_0 = \frac{(7.8 \pm 1.2) \times 10^{-3}}{V^{(0.619 \pm 0.028)} + (0.286 + 0.087)H} \quad (\mathrm{cm^2\ V^{-1}\ s^{-1}})$$

This expression significantly lowered the error in our predicted mobilities, to about 5% (24). Further, this expression was the most effective predictor for mobilities of a test set of other aliphatic monoamines (5.2%) (24).

So, we seem to have identified the primary factors governing mobility — the volume-related hydrodynamic friction and the hydration friction. We decided to test this model on another class of ions, aliphatic carboxylates. It is obvious that more than just hydrodynamic friction governs the mobility of carboxylates. For instance, CCl_3COO^- and n-$C_4H_9COO^-$ have about the same molecular volume (104.3 and 105.3 Å^3, respectively). However, the infinite dilution mobility of CCl_3COO^- (3.62×10^{-4} cm^2 V^{-1} s^{-1}) is much higher than that of n-$C_4H_9COO^-$ (2.98×10^{-4} cm^2 V^{-1} s^{-1})). Thus, it would appear that a hydration friction is operative with carboxylates, as well as with the amines discussed above. However, the McGowan waters of hydration list carboxylates as 5 waters of hydration. There is no variation. It is then not possible to explain the mobility differences between CCl_3COO^- and n-$C_4H_9COO^-$.

At about this same time we started to become aware of the "semi-empirical" nature of the McGowan waters of hydration. This is not surprising since even with simple ions such as K^+ and F^- there is tremendous variation in the quoted hydration numbers (see Table 15 in ref. 28). Thus, while the McGowan waters of hydration worked very effectively for the aliphatic monoamines (24), it was evident that we needed to find a more sophisticated or appropriate manner to describe the charge induced friction of an ion.

And as is often the case with such incantations, we found the answer in old lost scrolls. In 1920 Max Born proposed a model to explain the mobilities of the alkali metal ions ($K^+ > Na^+ > Li^+$). He postulated that an additional *dielectric* friction is caused by the orientation of the solvent dipoles in response to the ionic charge. After the ion passes, energy is dissipated during the relaxation of the solvent to its equilibrium polarization. This additional energy dissipation enhances the overall friction experienced by the ion. That is, the mobility of an ion is governed by both a hydrodynamic ($f_{\mathrm{hydrodynamic}}$) and a dielectric friction ($f_{\mathrm{dielectric}}$):

$$[13] \quad \mu_0 \propto \frac{z}{f_{\mathrm{hydrodynamic}} + f_{\mathrm{dielectric}}}$$

The hydrodynamic friction is related to the molecular volume, while the dielectric friction is related to the ion charge.

Born's idea has been further developed by numerous workers using the assumption of point charges within a continuum medium (29). The most advanced formulations of this approach are the Zwanzig and Hubbard–Onsager expressions, which have the general form:

$$[14] \quad \mu_0 = \frac{ze}{6\pi\eta r_i + \left(\frac{B'\eta}{r_i^3}\right)}$$

where z is the valence number of the ion charge, e is the charge on the electron, η is the solvent viscosity and r_i is the crystallographic radius. The constant B' is

© 1999 NRC Canada

Fig. 7. Correlation of the mobilities predicted using eq. [16] with the infinite dilution mobilities for 15 aliphatic carboxylates. The symbol ◆ indicates nonhalogenated aliphatic carboxylates, and other symbols indicate halogenated aliphatic carboxylates. The line is the linear regression between the predicted and literature mobilities. Reprinted with permission from ref. 31. Copyright 1998 Royal Society of Chemistry.

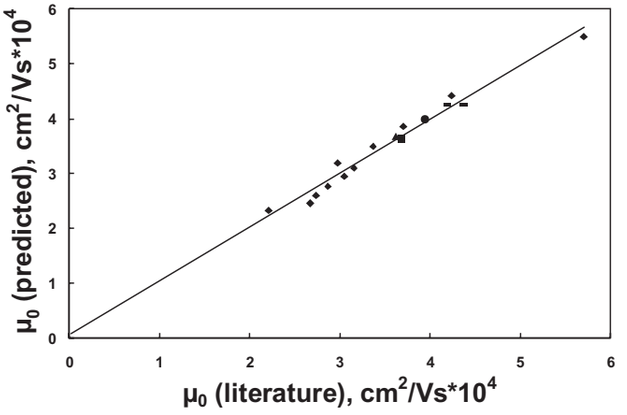

$$[15] \quad B' = H(ze)^2 \frac{\tau}{\eta} \frac{\varepsilon_0 - \varepsilon_\infty}{\varepsilon_0^2}$$

where τ is the solvent dielectric relaxation time, and ε_0 and ε_∞ are the low- and high-frequency dielectric constants, respectively. The constant H is 3/8 for the Zwanzig model and 1/16.5 for the Hubbard–Onsager model (29).

One of the most striking features of eqs. [14] and [15] is that the dielectric friction is related to z^2/r^3. This is, in effect, a charge density. So, if we can calculate the charge density of an amine or a carboxylate functionality, we should be able to predict the mobility of the molecule. However, such calculations would be long and tedious. It would be much more straightforward and simple to use nature's explicit statement of the charge density in a functional group — the acid dissociation constant (30). For instance, for acetic acid the charge can only be distributed within the carboxylate. As a result, the pK_a is quite high, 4.72. With chloroacetic acid, the chloro group helps disperse the carboxylate charge. This stabilizes the conjugate base form of the molecule, and lowers the pK_a to 2.87.

Based on the above rationale, we developed expressions for mobility incorporating the volume to reflect the hydrodynamic friction and the pK_a to reflect the charge density that governs the dielectric friction. The resultant expression for carboxylates was (31)

$$[16] \quad \mu_0 = \frac{(6.8 \pm 1.2) \times 10^{-3}}{V^{(0.62 \pm 0.04)} + (0.66 \pm 0.24) \mathrm{p}K_a} \quad (\mathrm{cm}^2\ \mathrm{V}^{-1}\ \mathrm{s}^{-1})$$

Volumes were calculated using the Bondi increments, and pK_a values were taken from the literature. This expression successfully described the infinite dilution mobilities of aliphatic carboxylates, as can be seen in Fig. 7. The average relative error between the predicted and literature absolute mobilities is only 3.7%. This is approximately the error associated with the literature absolute mobilities.

However, what was more exciting than the accuracy of the predictions given by eq. [16] was the commonalities between this expression for aliphatic carboxylates, and that determined for aliphatic monoamines (31):

$$[17] \quad \mu_0 = \frac{(7.8 \pm 1.3) \times 10^{-3}}{V^{(0.62 \pm 0.03)} + (0.66 \pm 0.23) \times \mathrm{p}K_b} \quad (\mathrm{cm}^2\ \mathrm{V}^{-1}\ \mathrm{s}^{-1})$$

and that for sulfonates (32):

$$[18] \quad \mu_0 = \frac{(5.5 \pm 0.6) \times 10^{-3}}{V^{(0.57 \pm 0.02)} + 0} \quad (\mathrm{cm}^2\ \mathrm{V}^{-1}\ \mathrm{s}^{-1})$$

In eq. [17], the pK_b is used as the measure of the charge density on the amine.

There are numerous points of commonality within eqs. [16]–[18]. Firstly, the numerators are similar. Secondly, the power dependence on volume is statistically equivalent in the three cases. The only differences in the equation lies in their dielectric friction terms. The use of pK_a and pK_b as measures of the charge density on ionized carboxylates and amines make chemical sense (31). The lack of a dielectric friction term for the sulfonates requires a bit more reflection. Sulfonates are fully dissociated in aqueous solution. Thus, their pK_a will be very low (≈0). Thus, in analogy to eq. [16], such a low pK_a would make the dielectric effect negligible.

The strong commonalities between eqs. [16]–[18] suggest that we have reduced the mobility behaviour down to its fundamental form. But, as has been discussed previously, it is the physical significance of the parameters and not the quality of fit that is the true test of a model (33). So what is the significance of the parameters in eqs. [16]–[18]? Well, the power dependence on volume is probably the most interesting. In eqs. [16]–[18], the mobility of aliphatic carboxylates, amines, and sulfonates depends on $\sim V^{-0.6}$. This is very close to the $V^{-0.66}$ that is theoretically predicted if the mobility of these ions were governed by the radius of gyration of the flexible tail of these aliphatic molecules (31). But what then of aromatic molecules. Their structure is much more rigid, and so will not be free to gyrate. Preliminary results with aromatics indicate that their mobility is well modeled by the Perrin equation (eq. [9]) modified to include the effect of dielectric friction (34).

Thus, we now have a better understanding of the form of the hydrodynamic friction for organic molecules and an appreciation for the importance of dielectric friction. We are now in a position to estimate the mobility of organic ions at infinite dilution.

Is the knowledge of Merlin useful to Lancelot?

The work described in the last section all focused on predicting mobilities at infinite dilution. However interesting and worthwhile this might be, practical analysts must work in more concentrated buffers — generally 5–100 mM in concentration. At such concentrations ionic strength and ion association will alter the observed mobilities from that observed at infinite dilution. As can be seen in Fig. 8*A*, the

© 1999 NRC Canada

Fig. 8. Dependence of the mobility of multivalent carboxylate on: *(A)* the buffer concentration; *(B)* the square root of ionic strength ($\sqrt{I}$); and *(C)* $\sqrt{I}/(1 + 2.4\sqrt{I})$. Solutes: ●, 1,2,4,5-benzenetetracarboxylate; ▲, 1,2,4-benzenetricarboxylate; ■, phthalate; ◆, benzoate. Curves are second-order polynomial fits in plots *A* and *B* and linear regression in plot *C*. Experimental conditions: detection, direct UV at 214 nm; applied voltage, +5 kV; capillary, 37 cm (30 cm to detector); buffer, sodium borate (pH = 10); temperature, 25°C; sample concentration, 0.0001 M. Reprinted with permission from ref. 36. Copyright 1999 American Chemical Society.

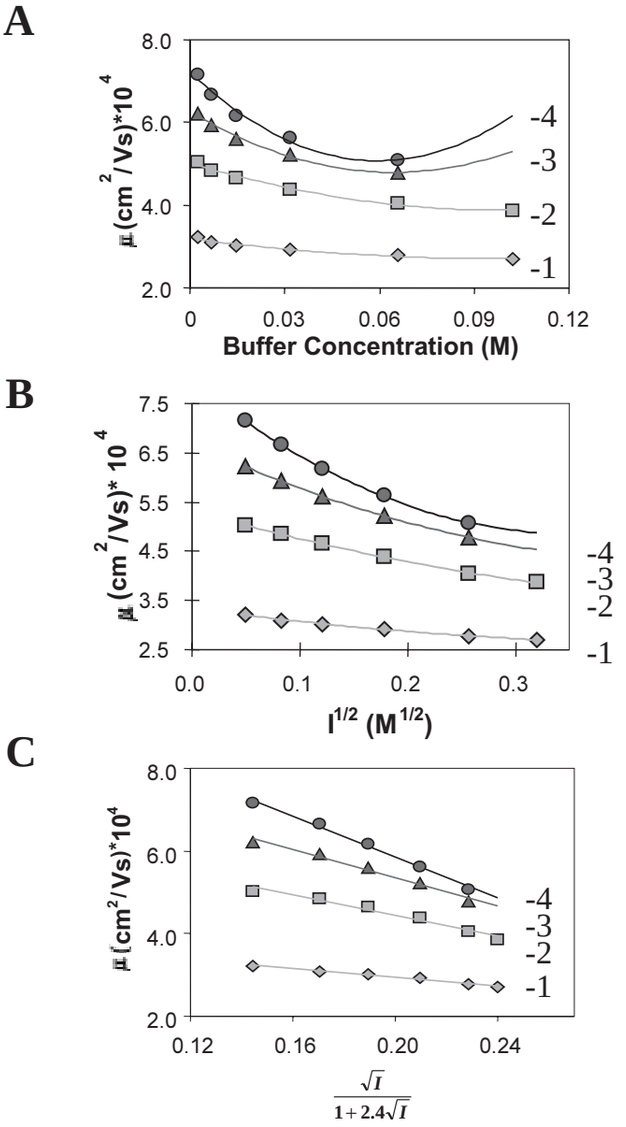

mobility of ions, and particularly highly charged ions, decrease rapidly as the buffer concentration is increased.

Traditionally in capillary electrophoresis, the effect of ionic strength has been described using the Onsager law. This model is analogous to the Debye–Hückel limiting law for ionic activity. It is postulated that the ion is a point charge surrounded by an ionic atmosphere of opposite charge. Based on these assumptions, the apparent mobility ($\mu_{apparent}$) is related to the square root of the buffer ionic strength ($\sqrt{I}$). Figure 8*B* replots the mobility observed in Fig. 8*A* in this fashion (36). Nonlinearity is still apparent in Fig. 8*B*. Thus, the Onsager equation was only partially successful in correcting for the effect of ionic strength.

What is needed to fully correct for the effect of ionic strength on mobility is an allowance for the size of the central ion. In discussions of ionic activity, such allowances are made in the Debye–Hückel extended law. In this model, the central ion is considered to have a finite radius and is then surrounded by an ionic atmosphere. The mobility model that is equivalent to the Debye–Hückel extended law once again comes from the ancient scrolls (1950s) and is known as the Pitts equation (35). The predicted ionic strength dependence is then

$$[19] \quad \mu \propto \frac{\sqrt{I}}{1 + Ba\sqrt{I}}$$

where I is the ionic strength, B is a constant for a given solvent related to the dielectric constant, temperature and viscosity, and a is an ionic size parameter related to the hydrated radius of the ion. While eq. [19] is simple, I do not want to trivialize this expression. Generation of this expression from Pitts' work required 2 months of effort using Mathematica.

For aromatic carboxylates, the constant Ba was found to have an empirical value of 2.4 (36). Figure 8*C* shows the mobility data from Fig. 8*A* replotted using the Pitts equation (eq. [19]). This expression successfully linearized the ionic strength behaviour. Furthermore, the slope of the ionic strength dependence in Fig. 8*C* was within 20% of that predicted by the Pitts equation (36). This is remarkable when one considers that the Pitts equation was actually derived to describe equivalent conductivity. That is, it was derived to describe the mobility of the *buffer*, not the mobilities of *analytes* within a buffer.

While the success of the Pitts equation is remarkable, the uncertainty in the predicted behaviour is still sufficient to allow the relative mobilities of similar ions to reverse. There remain numerous factors which can alter selectivity including ion association and other secondary equilibrium effects. Thus, we are not yet at the stage where we can predict the absolute migration order of ions within a buffer. Nonetheless, our work acts as a guide to help analytical chemists understand some of the key factors affecting electrophoretic mobility.

Conclusions

So concludes our narrative for today. Were we successful in our quest? Well, we have achieved control of the reversed electroosmotic flow, and we have demonstrated separations of isotopic species ranging from chloride to ammonium. We have even made progress in understanding the factors affecting the mobility of ions, albeit we still cannot explain the isotopic effect on mobility.

But then none of this was really what the quest was all about. In reality, the quest for the Holy Grail has always symbolized the quest for knowledge. For it is only with knowledge and understanding that one can wield the full

© 1999 NRC Canada

power of an Excalibur such as capillary electrophoresis. In that quest we have had some success, as is being recognized by the W.A.E. McBryde Medal. However, it is not a quest that we have completed, nor ever hope to complete.

Finally, given the theme of this presentation, I suspect a number of you now know what my middle initial stands for.

Acknowledgments

The foundations for this work were laid during my squireship under the tutelage of Prof. Fred Cantwell at the University of Alberta and Prof. Pete Carr at the University of Minnesota (Minneapolis). However, many other individuals including Janis Gulens, Howard Yeager, and Penny Codding greatly aided me with their sage advise and wisdom.

The work described herein has had many patrons. These include the Natural Sciences and Engineering Research Council of Canada (NSERC), The University of Calgary, the Province of Alberta, the Government of Canada, and Syncrude Research. This support is gratefully acknowledged. K.K.-C.Y. also thanks NSERC, the Killam Foundation, and Glaxo Wellcome for their support. Finally, I would like to thank Hewlett–Packard for sponsoring the W.A.E. McBryde Medal, and for their support of the Canadian Analytical Chemistry Community in general.

References

1. (*a*) N. Tanaka, K. Hosoya, K. Nomura, T. Yoshimura, T. Ohki, R. Yamaoka, K. Kimata, and M. Araki. Nature (London), **341**, 727 (1989); (*b*) N. Tanaka and M. Araki. J. Am. Chem. Soc. **107**, 7780 (1985); (*c*) N. Tanaka, A. Yamaguchi, and M. Araki. J. Am. Chem. Soc. **107**, 7781 (1985); (*d*) N. Tanaka, A. Yamaguchi, K. Hashizume, M. Araki, A. Wada, and K. Kimata. J. High Resolut. Chromatogr. Chromatogr. Commun. **9**, 683 (1986).
2. S.C. Jacobson, C.T. Culbertson, J.E. Daler, and J.M. Ramsey. Anal. Chem. **70**, 3476 (1998).
3. J.W. Jorgenson and K.D. Lukacs. Science (Washington, D.C.) **222**, 266 (1983).
4. (*a*) J.C. Giddings. Sep. Sci. **4**, 181 (1969); (*b*) A.G. Ewing, R.A. Wallingford, and T.M. Olefirowicz. Anal. Chem. **61**, 292A (1989).
5. (*a*) S.L. Madorsky and S. Straus. J. Res. Natl. Bur. Stand. **38**, 185 (1947); (*b*) B.P. Konstantinov and E.A. Bakulin. Russ. J. Phys. Chem. **39**, 315 (1965); (*c*) D.E. Desaulniers, R.S. Kaufmann, J.A. Cherry, and H.W. Bentley. Geochim. Cosmochim. Acta, **50**, 1757 (1986).
6. N. Avdalovic, C.A. Pohl, R.D. Rocklin, and J.R. Stillian. Anal. Chem. **65**, 1470 (1993).
7. S. Terabe, T. Yashima, N. Tanaka, and M. Araki. Anal. Chem. **60**, 1673 (1988).
8. P.D. Grossman. *In* Capillary electrophoresis: theory and practice. *Edited by* P.D. Grossman and J.C. Colburn. Academic Press, San Diego. 1992. Chap. 1.
9. C.A. Lucy and T.L. McDonald. Anal. Chem. **67**, 1074 (1995).
10. Chem. Eng. News, **73** (13), 20 (1995).
11. D.C. Harris. Exploring chemical analysis. Freeman, New York. 1997.
12. F.M. Phillips and H.W. Bentley. Geochim. Cosmochim. Acta, **51**, 683 (1987).
13. F.E. Senftle and J.T. Bracken. Geochim. Cosmochim. Acta, **7**, 61 (1955).
14. (*a*) T. Tsuda. J. High Resolut. Chromatogr. Chromatogr. Commun. **10**, 622 (1987); (*b*) K.D. Altria and C.F. Simpson. Chromatographia, **24**, 527 (1987); (*c*) X. Huang, J.A. Luckey, M.J. Gordon, and R.N. Zare. Anal. Chem. **61**, 766 (1989).
15. C.A. Lucy and R.S. Underhill. Anal. Chem. **68**, 300 (1996).
16. K. K.-C. Yeung and C.A. Lucy. J. Chromatogr. A, **804**, 319 (1998).
17. C.A. Lucy and K.K.-C. Yeung. Proc. Third Int. Symp. Miniatured Anal. Syst. Banff, Alta., Oct. 1998.
18. K.K.-C. Yeung and C.A. Lucy. Anal. Chem. **69**, 3435 (1997).
19. (*a*) J.S. Green and J.W. Jorgenson. J. Chromatogr. **478**, 63 (1989); (*b*) M.M. Bushey and J.W. Jorgenson. J. Chromatogr. **480**, 301 (1989).
20. A. Date and A.L. Gray. Applications of inductively coupled plasma mass spectroscopy. Blackie, Glasgow. 1988.
21. W.S. Gardner, L.R. Herche, P.A. St. John, and S.P. Seitzinger. Anal. Chem. **63**, 1838 (1991).
22. K.K.-C. Yeung and C.A. Lucy. Electrophoresis. In press.
23. K.K.-C. Yeung and C.A. Lucy. Anal. Chem. **70**, 3286 (1998).
24. S. Fu and C.A. Lucy. Anal. Chem. **70**, 173 (1998).
25. (*a*) F. Perrin. J. Phys. Radium, **5**, 497 (1934); (*b*) J. Phys. Radium, **7**, 1 (1936).
26. (*a*) R.E. Offord. Nature (London), **211**, 591 (1966); (*b*) N. Adamson, P.F. Riley, and E.C. Reynolds. J. Chromatogr. A, **646**, 391 (1993); (*c*) H.G. Lee and D.M. Desiderio. J. Chromatogr. A, **666**, 271 (1994); (*d*) V. Kašicka, Z. Prusík, P. Mudra, and J. Štepánek. J. Chromatogr. A, **709**, 31 (1995); (*e*) R.C. Rowe, S.A.C. Wren, and A.G. McKillop. Electrophoresis, **15**, 635 (1994); (*f*) V. Jokl. J. Chromatogr. **13**, 451 (1964); (*g*) P.D. Grossman, J.C. Colburn, and H.H. Lauer. Anal. Biochem. **179**, 28 (1989).
27. (*a*) C.R. Wilke and P. Chang. AIChE J. **1**, 264 (1955); (*b*) W. Hayduk and H. Laudie. AIChE J. **20**, 611 (1974).
28. Y. Marcus. Ion properties. Marcel Dekker, New York. 1997.
29. R.L. Kay. Pure Appl. Chem. **63**, 1393 (1991).
30. D.D. Perrin, B. Dempsey, and E.P. Serjeant. pK_a prediction for organic acids and bases. Chapman and Hall, New York. 1981.
31. S.Fu, D. Li, and C.A. Lucy. Analyst, **123**, 1487 (1998).
32. S. Fu. M.Sc. thesis, The University of Calgary, 1998.
33. C.A. Lucy, J.L. Wade, and P.W. Carr. J. Chromatogr. **484**, 61 (1989).
34. D. Li and C.A. Lucy. 81st Can. Soc. Chem. Conf. Exhibition. Poster 386. Whistler, B.C., June 1998.
35. (*a*) E. Pitts. Proc. Roy. Soc. **A217**, 43 (1953); (*b*) E. Pitts; B.E. Tabor, and J. Daly. Trans. Faraday Soc. **66**, 693 (1970).
36. D. Li, S.Fu, and C.A. Lucy. Anal. Chem. **71**, 687 (1999).

© 1999 NRC Canada

Theoretical studies of heterofullerenes $C_{68}X_2$ (X = N, B)

Zhongfang Chen, Keqin Ma, Yinming Pan, Xuezhuang Zhao, and Auchin Tang

Abstract: A systematic investigation on the molecular structures of the possible energetically favored isomers of $C_{68}X_2$ (X = N, B) have been performed using the semiempirical MNDO, AM1, and PM3 methods. The most stable isomer of $C_{68}X_2$ was computed, and the static properties such as heats of atomization, ionization potentials, electron affinities, absolute electronegativities, and global hardness have been predicted theoretically. The proposition that the changes of hybridization from sp^2 to sp^3 are the predominant factors of the regiochemistry for both $C_{60}X_2$ and $C_{58}X_2$ are supported by the calculations, and the regioselectivity of the doped fullerenes may be deduced in light of the knowledge of the fullerene adducts based on this proposition.

Key words: $C_{68}N_2$, $C_{68}B_2$, MNDO, AM1, PM3.

Résumé : Utilisant des méthodes de calculs semi-empiriques, comme MNDO, AM1 et PM3, on a effectué une étude systématique des structures moléculaires des isomères énergétiquement favorisés possibles pour le $C_{68}X_2$ (X = N, B). On a déterminé par calcul la nature de l'isomère le plus stable du $C_{68}X_2$ et l'on a prédit d'une façon théorique ses propriétés statiques, telle que chaleur d'atomisation, potentiel d'ionisation, affinité électroniques, électronégativité absolue et dureté globale. L'hypothèse selon laquelle les changements d'hybridation de sp^2 à sp^3 sont les facteurs prédominants dans la région chimie tant du $C_{60}X_2$ que du $C_{58}X_2$ est supportée par les calculs et, en utilisant cette hypothèse, on peut déduire la régiosélectivité de fullerènes dopés à la lumière d'une connaissance des adduits du fullerène.

Mots clés : $C_{68}N_2$, $C_{68}B_2$, MNDO, AM1, PM3.

[Traduit par la Rédaction]

1. Introduction

The synthesis and characterization of the so-called heterohedral fullerenes, which have one or more of the carbon atoms substituted by other elements such as boron and nitrogen, have become the new hot topic soon after the discovery of C_{60} (1–13), since the incorporation of heteroatoms into the fullerene skeleton is expected to modify its structural and electronic properties. The first substituted fullerenes $C_{60-x}B_x$ (x = 1–6) were produced by Smalley and co-workers (1) in 1991. Later in the same year Rao and co-workers (2) reported the preparation of a number of C_nN_m fullerenes. The production of the first substituted fullerenes in 1991 opened up new avenues in materials science and organic chemistry, raised new fundamental questions about their ability, morphology, electronic behavior, and the basic features of the chemical bonding. All of these revealed another inspiring world for scientists to explore. Since then much experimental and theoretical work has been done in this new field. The verification of $C_{59}N$ was reported by Mattay and co-workers (3) in 1995, and the fullerenes substituted with one nitrogen atom $C_{59}N$ were synthesized and characterized by Yu et al. (4) at about the same time. Also in this year, the synthesis of $C_{59}N$ in the dimer form $(C_{59}N)_2$ was achieved by Hummelen et al. (5). Later the synthesis and isolation of heterofullerenes $(C_{59}N)_2$ and $(C_{69}N)_2$ and their adducts $RC_{59}N$ and $RC_{69}N$ were achieved by Nuber and Hirsh (6) in 1996. The potassium-intercalated $K_6C_{59}N$ solid was prepared and structurally characterized by Prassides et al. (7) with $(C_{59}N)_2$ as precursor. The hydrogenated azafullerene $C_{59}NH$, which can be a suitable source of $C_{59}N$ radical when it is deprotonated, was isolated and fully characterized by Wudl and co-workers (8) in 1997. The derivatization of $C_{59}N$ has been achieved from $(C_{59}N)_2$ and $C_{59}NH$ also by Wudl and his group (9) in 1997. More recently Nuber and Hirsch (10) reported the successful synthesis of arylated heterofullerenes $ArC_{59}N$ with $(C_{59}N)_2$ as precursor. The experimental work about boron-substituted fullerenes will also make great progress with the macroquantivity synthesis of $C_{60-n}B_n$ and $C_{70-n}B_n$ (11).

On the theoretical side, the stabilities, electronic properties, band structures, and the third-order polarizability of the heterohedral fullerenes have been studied, and some intriguing properties different from the all carbon fullerenes are predicted (14–32). However, theoretical studies on the molecular properties, including all the static properties and most kinetic properties, largely depend on the accuracy and reliability of the equilibrium geometries, the properties of

Received September 8, 1998.

Z. Chen, K. Ma, Y. Pan, and X. Zhao.[1] Dept. of Chemistry, Nankai University, Tianjin 300071, P.R. China.
A. Tang. Theoretical Institute of Chemistry, Jilin University, Changchun 110023, P.R. China.

[1]Author to whom correspondence may be addressed. Telephone: 0086-022-23501771. Fax: 0086-022-23504853. e-mail: zhaoxuezhuang@263.net

© 1999 NRC Canada

Fig. 1. The planar nets of C_{70}. (The numbers of the circles are used to characterize the 70 carbon atoms of C_{70}. C_I, C_{II}, C_{III}, C_{IV}, and C_V are defined as the five unique carbon atoms in C_{70}.)

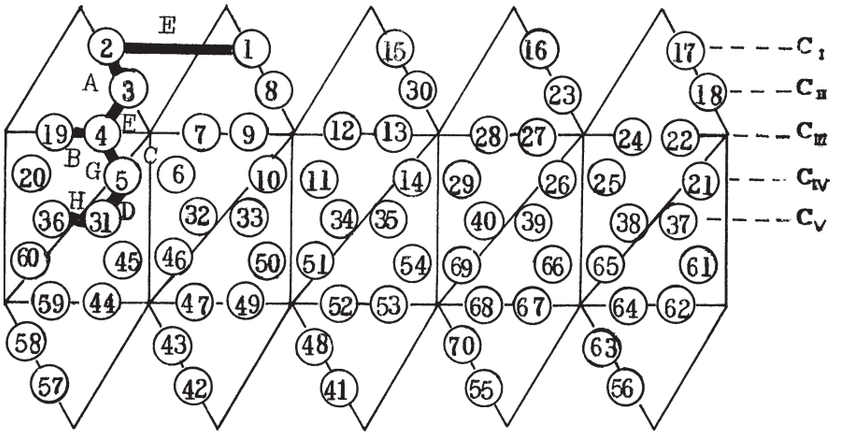

the heterofullerenes predicted so far are all based on the arbitrarily assigned geometries, which often give ambiguous and contradictory results. Hence, it is an urgent task for us to determine the stable species of the doped fullerenes.

In our previous work (32), heterofullerenes $C_{58}X_2$ (X = N, B) have been investigated systematically. The aim of the present theoretical work is to extend our investigations on heterofullerenes to the studies of $C_{68}X_2$ (X = N, B) to find the most stable isomers and predict their electronic properties. The semiempirical MNDO, AM1, and PM3 methods were used to perform a systematic investigation on the molecular structures of the possible energetically favored isomers of $C_{68}X_2$ (X = N, B). The equilibrium geometrical structures, heats of formation, HOMO–LUMO gap energies, heats of atomization, ionization potentials, electron affinities, absolute electronegativities, and global hardness will be predicted theoretically.

2. Computational details

Closed-shell SCF calculations were performed with the standard MNDO, AM1, and PM3 parameters as implemented in the MOPAC 6.0 program,[2] using the PRECISE option in order to decrease the gradient norm. The full optimizations were carried out without any symmetry constraints in Cartesian coordinates, and initial input geometries were based on the optimized C_{70} with specific carbon atoms displaced by B and N. The ab initio 3-21G computations on the two lowest energy isomers of $C_{68}X_2$ were performed with the G94 program package (33) in the optimized MNDO geometries as single-point calculations only.

3. Results and discussion

There are 143 structurally distinct isomers for $C_{68}X_2$. Time required for the computation makes it impossible to calculate all the isomers of the systems studies in this paper. Nevertheless, in our previous studies (32) we have found that the isomer corresponding to 1,4-substitution to the cyclohexatriene unit is the most stable isomer among 23 possible isomers of $C_{58}X_2$ (X = N, B), and the stabilities decrease with the increasing of the distance between the heteroatoms. These results permit a reliable search of the ground state of $C_{68}X_2$ with little effort. All the isomers resulting from 1,2-substitution across the 6,6-fusion and from the 1,4-substitution across 6-rings will be calculated; the other isomers, except 1,2- and 1,4-substitution to the cyclohexatriene units, will also be considered in this paper. These isomers are listed in Table 1 and designed as follows. First, the carbon atoms are numbered as indicated in the planar net of C_{70}. An isomer of $C_{68}X_2$ is characterized by the position of the substitution, and a comma is used for 1,2-isomers, a slash (/) is used for 1,4-isomers, a semicolon (;) is used for other isomers except 1,2- and 1,4-substitution to the cyclohexatriene units. For example, $C_{68}X_2(2,3)$ means that the carbon atoms numbered 2 and 3 in C_{70} are substituted by X atoms, and this isomer is 1,2-substitution. $C_{68}X_2(2/19)$ means that the carbon atoms numbered 2 and 19 in C_{70} are substituted by X atoms, and this isomer is 1,4-substitution (see Fig. 1).

3.1. Heats of formations and HOMO–LUMO energy gaps

The heats of formation and HOMO–LUMO gap energies of $C_{68}X_2$ are listed in Table 1. All the calculations indicate that $C_{68}X_2(6/45)$ and (2/19), which correspond to 1,4-substitution to the cyclohexatriene unit, have the lowest heats of formation among all the isomers that resulted from substitution to the cyclohexatriene units, thus the most stable isomers. The isomer 6/45 is favored by several kcal/mol over 2/19 according to both semiempirical and ab initio calculations, and is predicted to be the ground state.

In our previous paper (32) we have proposed that the changes of hybridization from sp^2 to sp^3 may be the underlying reason why 1,4-substitution is favored in $C_{58}N_2$ and $C_{58}B_2$. Our recent calculations of $C_{58}P_2$ also confirmed this proposition. Therefore, the most stable isomers may be found out in the light of the regioselectivity of $C_{60}X_2$, since the same hybridization changes occur at the carbon atoms where the addends are added in $C_{60}X_2$. Now let us try finding the most stable isomers of $C_{68}X_2$ in light of the regioselectivity of $C_{70}X_2$. Up to now, many theoretical stud-

[2] J.J.P. Stewart. MOPAC version 6.0 QCPE455 (1990).

© 1999 NRC Canada

Table 1. Heats of formation, energies, and related static properties for $C_{68}X_2$ (X = N, B) (units, kcal/mol for HF, RHF, H_{at}, and RE; eV for gap, IP, AE, η, and χ).

	MNDO										
Species	HF	RHF	Gap	IP	AE	η	χ	H_{at}	AM1 RHF	PM3 RHF	HF/3-21G RE
C_{70}	939.44		5.82	8.67	2.85	2.91	5.76	–14 025.16			
$C_{68}N_2$(2,3)	957.86	16.40	5.47	8.47	3.00	2.74	5.74		18.90	22.43	
$C_{68}N_2$(4,19)	952.87	11.41	5.72	8.65	2.93	2.86	5.79		14.01	17.25	
$C_{68}N_2$(5,31)	976.82	35.36	5.48	8.42	2.94	2.74	5.68		33.93	37.49	
$C_{68}N_2$(31,36)[a]	954.59	13.13	5.86	8.75	2.89	2.93	5.82		3.89	31.14	
$C_{68}N_2$(2/19)[a]	944.94	3.48	5.31	8.29	2.98	2.66	5.64	–13 946.32	5.49	5.48	8.97
$C_{68}N_2$(6/45)	941.46	0.00	5.32	8.26	2.94	2.66	5.60	–13 949.80	0.00	0.00	0.00
$C_{68}N_2$(4/36)	959.25	17.79	5.19	8.11	2.92	2.60	5.52		11.66	16.93	
$C_{68}N_2$(3/18)	949.62	8.16	5.04	8.09	3.05	2.52	5.57		9.18	9.89	
$C_{68}N_2$(5/20)	962.08	20.62	4.81	7.86	3.05	2.41	5.46		23.86	26.65	
$C_{68}N_2$(31/32)	973.07	31.61	5.28	8.20	2.92	2.64	5.56		23.20	27.69	
$C_{68}N_2$(1;2)	971.43	29.97	5.44	8.48	3.04	2.72	5.76		32.38	35.03	
$C_{68}N_2$(2;4)	966.84	25.38	4.41	7.69	3.28	2.21	5.49		27.12	23.49	
$C_{68}N_2$(2;18)	964.44	22.98	4.77	7.86	3.09	2.39	5.48		27.87	25.16	
$C_{68}N_2$(4;20)	954.25	12.79	4.86	7.87	3.01	2.43	5.44		15.58	11.65	
$C_{68}N_2$(4;31)	977.93	36.47	4.31	7.46	3.15	2.16	5.31		31.35	31.79	
$C_{68}N_2$(4;5)	983.81	42.35	4.65	7.91	3.26	2.33	5.59		35.14	45.09	
$C_{68}N_2$(5;6)	962.16	20.70	5.51	8.46	2.95	2.76	5.71		23.11	22.86	
$C_{68}N_2$(5;32)	973.21	31.75	4.67	7.61	2.94	2.34	5.28		25.93	22.41	
$C_{68}N_2$(5;45)	963.12	21.66	4.48	7.51	3.03	2.24	5.27		24.14	20.63	
$C_{68}B_2$(2,3)	936.45	24.53	5.61	8.54	2.93	2.81	5.74		11.34		
$C_{68}B_2$(4,19)	937.84	25.92	5.70	8.67	2.97	2.85	5.82		13.49		
$C_{68}B_2$(5,31)	940.59	28.67	5.47	8.69	3.22	2.74	5.96		19.11		
$C_{68}B_2$(31,36)	960.34	48.42	5.16	8.72	3.56	2.58	6.14		49.28		
$C_{68}B_2$(2/19)	919.61	7.69	5.50	8.67	3.17	2.75	5.92	–13 888.83	10.49		13.75
$C_{68}B_2$(6/45)	911.92	0.00	5.60	8.73	3.13	2.80	5.93	–13 896.52	0.00		0.00
$C_{68}B_2$(4/36)	925.69	13.77	5.37	8.68	3.31	2.69	6.00		20.68		
$C_{68}B_2$(3/18)	922.84	10.92	5.45	8.52	3.07	2.73	5.80		13.12		
$C_{68}B_2$(5/20)	930.96	19.04	5.03	8.53	3.50	2.52	6.02		22.13		
$C_{68}B_2$(31/32)	921.20	9.28	5.43	8.69	3.26	2.72	5.98		16.51		
$C_{68}B_2$(1;2)	946.50	34.58	5.30	8.67	3.37	2.65	6.02		28.20		
$C_{68}B_2$(2;4)	942.53	30.61	4.73	8.56	3.83	2.37	6.20		45.54		
$C_{68}B_2$(2;18)	941.91	29.99	4.83	8.57	3.74	2.42	6.16		43.63		
$C_{68}B_2$(4;20)	938.44	26.52	4.82	8.60	3.78	2.41	6.19		41.55		
$C_{68}B_2$(4;31)	945.66	33.74	4.88	8.70	3.82	2.44	6.32		53.04		
$C_{68}B_2$(4;5)	964.04	52.12	4.08	8.12	4.04	2.04	6.08		44.61		
$C_{68}B_2$(5;6)	934.70	22.78	5.53	8.73	3.20	2.77	5.97		12.93		
$C_{68}B_2$(5;32)	934.26	22.34	4.97	8.64	3.67	2.49	6.04		39.83		
$C_{68}B_2$(5;45)	933.58	21.66	4.68	8.48	3.80	2.34	6.14		32.72		

[a]Note that the heats of formation of $C_{68}N_2$(31,36) and (2/19) obtained by AM1 are almost the same, the single point energies (3-21G) based on the optimized geometries of $C_{68}N_2$(31,36) and (2/19) are –2668.5070 and –2668.5438 au, respectively. The energy order is not consistent with AM1 results but agrees with the MNDO and PM3 results.

ies on $C_{70}X_2$ have been performed. For example, Henderson et al. (34) have found that 4 of 143 $C_{70}H_2$ isomers have particularly low heats of formation based on the PM3 results, and these isomers represent either 1,2-addition across 6:6 ring fusion or 1,4-addition across a six-membered ring. It is feasible to find the most stable isomer of $C_{68}X_2$ from the four isomers in which the heteroatoms substitute the carbon atoms where the H atoms are added in the four most stable isomers of $C_{70}H_2$. Considering that the N—N and B—B bonds will tend to destabilize the structures and should be avoided, we can draw the conclusion that the two isomers of 1,4-substitution across a six-membered ring, i.e., $C_{68}X_2$(2/19), $C_{68}X_2$(6/45), are the most energetically favored. Hence, the knowledge of the regioselectivity of fullerenes can be useful to find the stable isomers of the doped fullerenes.

If the carbon C2 in C_{70} was substituted by heteroatom X, and the substitution positions of the second heteroatom fall approximately on the circumference connecting C2 and C42, the distance between the heteroatoms can be approximately represented by the number of C—C bonds between the two heteroatoms. The dependence of H_f and *E*(HOMO)/*E*(LUMO) obtained by MNDO method on the number of

© 1999 NRC Canada

Fig. 2. Dependence of H_f on the number of C—C bond separating the heteroatoms in $C_{68}N_2$ (top) and $C_{68}B_2$ (bottom).

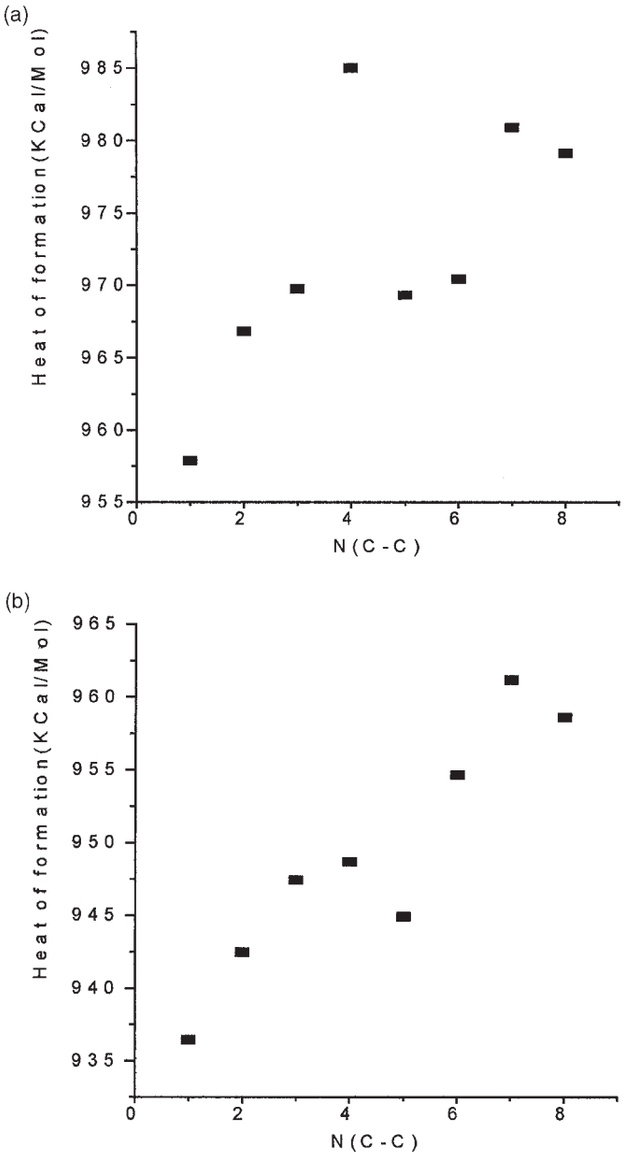

Fig. 3. Dependence of E(HOMO)/E(LUMO) on the number of C—C bonds separating the heteroatoms in $C_{68}N_2$ (top) and $C_{68}B_2$ (bottom).

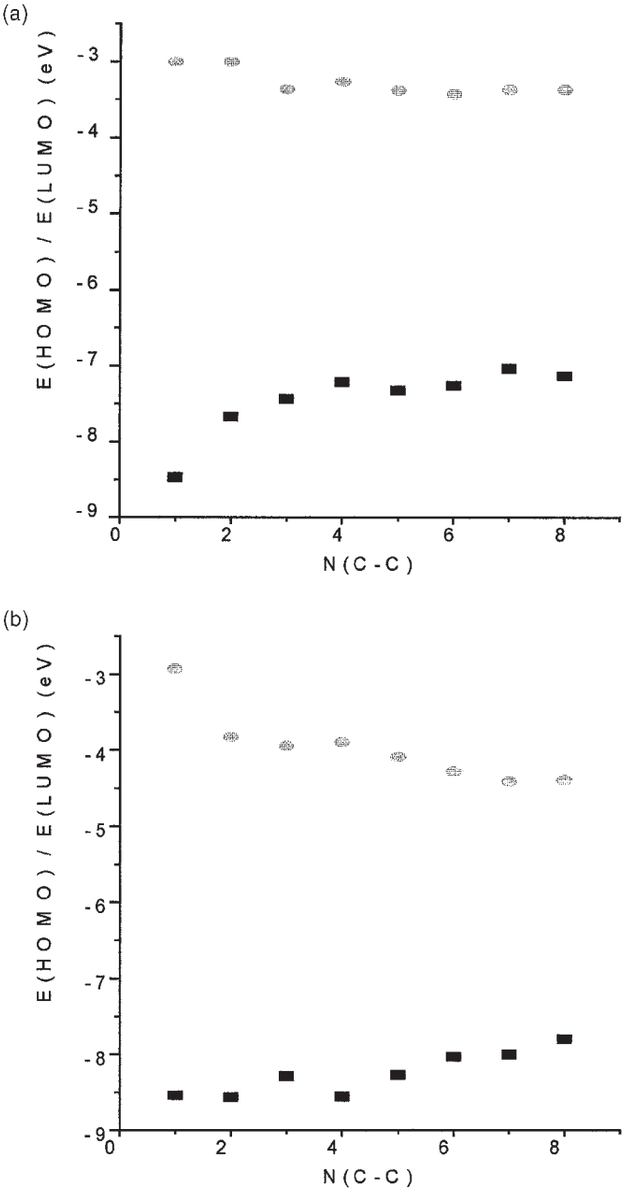

C—C bond separating the heteroatoms in $C_{68}X_2$ were shown in Figs. 2 and 3, respectively. Although there are some oscillations, the general trend is that the heats of formation increase (or stabilities decrease), and the HOMO–LUMO gap energies decrease with increasing number of intervening bonds. This indicates that the stabilities of $C_{68}X_2$ (X = N, B) decrease with increasing the distance between the heteroatoms, which is similar to the findings for the analogous $C_{58}X_2$ (X = N, B) systems (32). These results can also be seen as further confirmation of the stability order.

The HOMO–LUMO energy gapes are associated with chemical stabilities against electronic excitation. Generally speaking, the larger the gap, the more chemically stable the compound is. The HOMO–LUMO energy gaps of the most stable species of $C_{68}X_2$ are all smaller than that of C_{70}. This means that it is easier to excite the electrons in $C_{68}X_2$ from the HOMO to the LUMO than in C_{70}; in other words, the electrons in the HOMO of $C_{68}X_2$ are easier to remove from its molecular potential surfaces than C_{70} by some distance.

3.2. Heats of atomization of $C_{68}X_2$ and C_{70}

For hetero-clusters, the stability should be indicated by a greater negative value of the heat of atomization H_{at}. The heat of formation H_{at} can be calculated according to the gas-phase reaction: nC + mX = C_nX_m; this means that $H_{at}(C_nX_m) = H_f(C_nX_m) - nH_f(C) - mH_f(X)$. The heats of atomization of

© 1999 NRC Canada

the most stable isomers of $C_{68}X_2$ (X = B, N) and C_{70} are summarized in Table 1. Similar to C_{60} and its substituted fullerenes, C_{70} also can not be stabilized by doping nitrogen or boron atoms, and the nitrogen-doped species are more stable than their boron-doped analogues. Considering the successful synthesis of $C_{68}B_2$ (11), it is reasonable to expect that $C_{68}N_2$ would be synthesized and detected experimentally if appropriate synthetic protocols can be achieved. The preparation of heteroatom-doped fullerenes has been one of the challenges in the fullerene field. Up to now there are several experimental methods to prepare heterofullerenes. One convenient way is the contact-arc vaporization method. For instance, the nitrogen-doped fullerenes have been synthesized by arcing a graphite rod in a pure nitrogen atmosphere (4). Some macroscopic amounts of boron-doped fullerenes such as $C_{60-n}B_n$ and $C_{70-n}B_n$ (n = 1, 2, 3) have been synthesized by the DC arc-burning method using highly pure graphite rod and B_4C/graphite composite rod as electrodes (11). The alternative method may be the derivativation of some suitable precursors for the doped fullerenes. A good example for this procedure is the ongoing investigation on the uses of the pyrrole-embedded [60]fullerenes as potential precursors for $C_{58}N_2$ derivatives formed by an azide addition–dechlorination sequence (35).

3.3. Frontier orbital energies, ionization potentials, electron affinities, global hardness, and absolute electronegativities

The substitutional perturbation affects both HOMO and LUMO orbitals of $C_{68}X_2$. In general, the HOMO become less bound while the LUMO become more bound with increasing H_f (i.e., decrease in stabilities).

Now we discuss the reactivities of $C_{68}X_2$ based on the Frontier Orbital (FO) theory of Fukui (36). This theory considers the distribution of the HOMO density as being most important for electrophile attack, and the LUMO density for neucleophile attack. For the most stable species of $C_{68}X_2$ and C_{70}, the energy sequence of HOMO is $C_{68}N_2$ (–8.26 eV) > C_{70} (–8.67 eV) > $C_{68}B_2$ (–8.73 eV), while the energy sequence of LUMO is $C_{68}B_2$ (–3.13 eV) < $C_{68}N_2$ (–2.94 eV) < C_{70} (–2.85 eV). Thus towards an electrophile, $C_{68}N_2$ is the more reactive than C_{70}, and C_{70} is more reactive than $C_{68}B_2$; towards a nucleophile, both $C_{68}B_2$ and $C_{68}N_2$ are more reactive than all-carbon fullerene C_{70}, and $C_{68}B_2$ is the most reactive.

IP and EA are two well-known quantities and are of considerable interest from a theoretical viewpoint. The ionization potentials and electron affinities from Koopmans theorem for $C_{68}X_2$ (X = N, B) are summarized in Table 1. It can be seen that for the most stable species both $C_{68}N_2$ and $C_{68}B_2$ have bigger affinity energies than C_{70}, which suggests that $C_{68}X_2$ can obtain electrons easier to form anions, i.e., it is more easier to reduce $C_{68}X_2$ relative to C_{70}. While the sequence of ionization potentials is $C_{68}N_2$ < C_{70} < $C_{68}B_2$, which suggests that $C_{68}N_2$ loses electrons more readily to form positive ions than C_{70}, i.e., it is more easier to oxide $C_{68}N_2$, while $C_{68}B_2$ loses electrons difficultly to some extent. In our previous work we have found that $C_{58}X_2$ (X = N, B) have somewhat smaller ionization potentials and bigger electron affinities compared with C_{60} (32), which indicates that it is more easy to oxidize and reduce $C_{58}X_2$ relative to C_{60}. Thus we can draw the conclusion that doping may have different effects in substituted C_{60} systems and substituted C_{70} systems.

Fig. 4. The absolute electronegativities of the doped fullerenes. (The arrows show the electron transfer directions when the dimers are formed.)

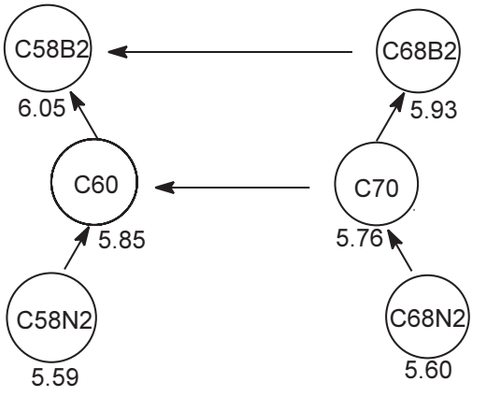

Recently the concept of chemical hardness has been of great interests (37). The quantities of the global hardness (η) and absolute electronegativity (χ) have been defined as $\eta = (1/2)(\partial^2 E/\partial N^2)$ and $\chi = (\partial E/\partial N)$ where E being the energy and N being the number of electrons in the system considered. In a finite difference approximation using integer values for N, the expressions can be rewritten as η = (IP – EA)/2 and χ = (IP + EA)/2. The hardness is the resistance of the chemical potential to change in the number of electrons, the absolute electronegativity is a good measure of the ability of the molecule to attract electrons to itself. Table 1 summarizes the calculated global hardness and absolute electronegativity of the heterofullerenes $C_{68}X_2$ (X = N, B). It can be found that the most stable isomer has the biggest global hardness among all the 1,4-isomers. This is consistent with the principle of maximum hardness (PMH) (37). Since Choho et al. (38) have found that the reactivity of the larger fullerenes can still be governed by the hard–hard interactions as described in the HSAB principle (39), i.e., hard acids prefer to coordinate to hard bases and soft acids to soft bases, the global hardness is also considered here to study the reactivities of the heterofullerenes. The sequence of the most stable species of the doped fullerenes under investigation according to the global hardness can be found in Table 1. For both $C_{68}N_2$ and $C_{68}B_2$, the most stable isomer has smaller hardness as compared to C_{70}, and the sequence of hardness is C_{70} > $C_{68}B_2$ > $C_{68}N_2$. If we take the global hardness as the measure for the reactivity, $C_{68}X_2$ (X = N, B) should have smaller reactivity towards a nucleophile relative to C_{70}; this is contrary to the reactivity order based on the Frontier Orbital theory. The local hardness may be better descriptor of the reactivity of $C_{68}X_2$, and the reactivity sequence similar to that of FO theory is expected, based on the local hardness because the reactions occur only at specific positions.

From Table 1 we can find that there are remarkable differences between the absolute electronegativities of the doped fullerenes. Since the absolute electronegativity is a good measure of the ability of the molecule to attract electrons to

© 1999 NRC Canada

Fig. 5. Calculated bond lengths (Å) and atomic charges of $C_{68}X_2$.

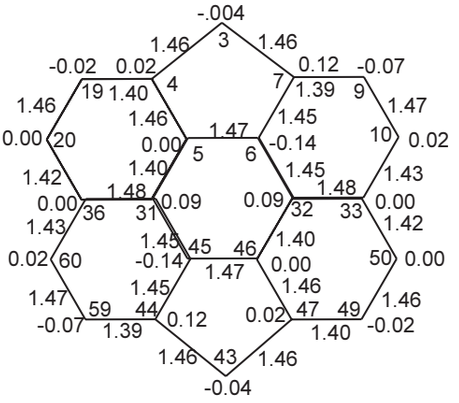

$C_{68}N_2(6/45)$

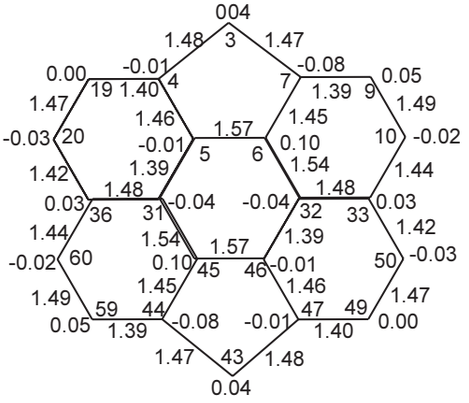

$C_{68}B_2(6/45)$

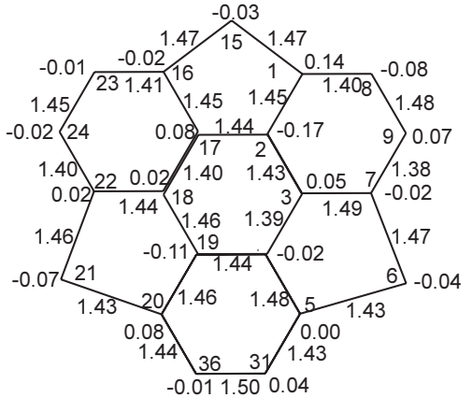

$C_{68}N_2(2/19)$

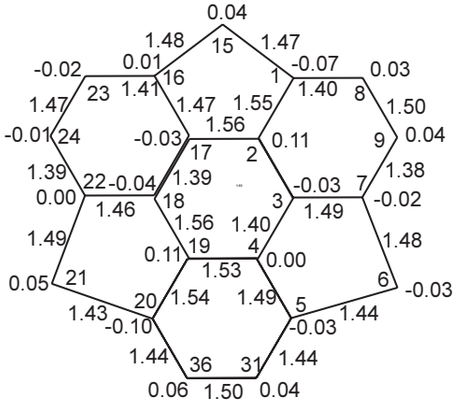

$C_{68}B_2(2/19)$

itself, the existence of these differences suggests that there should be electron transfer when the dimers such as $C_{68}N_2$–$C_{68}B_2$, $C_{68}N_2$–C_{70} are formed. These dimers formed should be donor–acceptor salts. The absolute electronegativities of the most stable doped fullerenes under investigation were summarized in Fig. 4 from which we can see the electron transfer directions. There should be significant electron transfer in the complexes between the all carbon fullerenes and B- or N-doped fullerenes or between the boron-doped fullerenes and their nitrogen analogues. Moreover we can find that the electrons will flow from C_{70} and its B-doped fullerene to C_{60} and its B-doped fullerene when the dimers between them are formed.

3.4. Geometric structures of $C_{68}X_2$ (X = N, B)

The cluster geometry is seriously affected by the substitution. The significant distortion occurs at the heteroatom site for all the isomers of the doped fullerenes. We mainly discuss the structures of two lowest energy isomers of $C_{68}X_2$ (isomer 6/45 and 2/19) obtained by MNDO method.

The calculated bond lengths and atomic charges of $C_{68}N_2$ and $C_{68}B_2$ are shown in Fig. 5 for the region where the heteroatoms substitute the carbon atoms. In $C_{68}N_2$ (6/45), the calculated angle sums for N6 and N45 are 332.2° and 332.3°, respectively. In $C_{68}B_2$(6/45), the calculated angle sums for B6 and B45 are 346.7° and 346.8°, respectively, whereas the corresponding values in C_{70} are 348.3° and 353.0°. Significant deviations from the values for C_{70} indicates that the heteroatoms lie well outside the mean surface of the fullerene skeleton. Hence, some angle strain in C_{70} is relieved upon the substitution, similar to the addition of a double bond of C_{70}. In both cases, heteroatom substitution or addition, the hybridization states change from sp^2 to sp^3. As expected, the comparison of charge density distributions in C_{70} and $C_{68}X_2$ clearly demonstrates the larger amount of charges around the N and B nuclei, since there are differences between the electronegativities of boron, nitrogen, and that of carbon element. The calculated atomic charges of –0.14*e* for each nitrogen atom in $C_{68}N_2$ and +0.10*e* for each boron atom in $C_{68}B_2$ can be found.

The geometries of $C_{68}X_2$(2/19) show the same deformation as shown in $C_{68}X_2$(6/45), with the angle sums of the heteroatoms smaller than those of the corresponding carbons in C_{70}. For $C_{68}N_2$, the calculated angle sums for N2 and N19 are 339.2° and 327.2°, respectively. For $C_{68}B_2$, the calculated angle sums for B2 and B19 are 346.0° and 343.6°,

© 1999 NRC Canada

respectively, whereas the corresponding values in C_{70} are 347.2 and 348.3. For $C_{68}N_2$, the atomic charges at N2 and N19 are –0.17*e* and –0.11*e*, respectively, and the carbon atoms connecting the nitrogen atoms show positive charges. For $C_{68}B_2$, the atomic charges at boron atoms are +0.11*e* on each, and the neighboring atoms show negative charges. The charge distribution in $C_{68}X_2$(2/19) can also be explained by the differences between the electronegativities of the heteroatoms and those of the carbon atoms.

Symmetry lowering with respect to C_{70} is also responsible for the existence of permanent dipole moments in heterofullerenes. The calculated values (MNDO) are 1.132 D for $C_{68}N_2$(6/45), 1.303 D for $C_{68}N_2$(2/19). The dipole moments for $C_{68}B_2$ are relatively smaller, 0.417 and 0.340 D for isomers 6/45 and 2/19, respectively.

4. Conclusions

The equilibrium geometrical structures of $C_{68}X_2$ (X = N, B) were fully optimized at MNDO, AM1, and PM3 level. The heats of formation, HOMO–LUMO gap energies, heats of atomization, ionization potentials, electron affinities, absolute electronegativities, and global hardness for doped fullerenes $C_{68}X_2$ (X = N, B) have been predicted theoretically. The calculation results show that the heterofullerenes $C_{68}X_2$ are less stable than their all carbon analogue C_{70}, and the nitrogen-doped fullerenes $C_{68}N_2$ should be of greater thermodynamic stabilities than their boron analogues $C_{68}B_2$. The isomers 6/45 and 2/19, which correspond to 1,4- substitution to the cyclohexatriene unit, are the most stable isomers for both $C_{68}N_2$ and $C_{68}B_2$, and the isomer 6/45 is the ground state. Although there are some oscillations, the stabilities decrease with the increasing of the distance between the heteroatoms. The redox characteristics of fullerenes can be enhanced by doping. The reactivities towards a nucleophile or electrophile attack are considered according to the frontier molecular orbital (FMO) theory and the HSAB principle. Based on the absolute electronegativities the electron transfer directions in dimer fullerenes are predicted. Our previous proposition that the changes of hybridization from sp^2 to sp^3 are the predominant factors of the regiochemistry for both $C_{60}X_2$ and $C_{58}X_2$ are supported by the calculation results presented in this paper. The regioselectivity of the doped fullerenes may be deduced in light of the knowledge of the fullerene adducts based on this proposition.

Acknowledgments

This work was supported by the National Nature Science Foundation of China.

References

1. T. Guo, C. Jin, and R.E. Smally. J. Chem. Phys. **95**, 4948 (1991).
2. T. Pradeep, V. Vijayakrishnan, A.K. Santra, and C.N.R. Rao. J. Phys. Chem. **95**, 10 564 (1991).
3. J. Averdung, H. Luftmann, I. Schachter, and J. Mattay. Tetrahedron, **51**, 6977 (1995).
4. R. Yu, M. Zhan, D. Cheng, S. Yang, Z. Liu, and L. Zheng. J. Phys. Chem. **99**, 1818 (1995).
5. J.C. Hummelen, B. Knight, J. Pavlovich, R. Gonzalez, and F. Wudl. Science (Washington, D.C.) **269**, 1554 (1995).
6. B. Nuber and A. Hirsh. Chem. Commun. 1421 (1996).
7. K. Prassides, M. Keshavarz-K, J.C. Hummelen, W. Andreoni, P. Giannozzi, E. Beer, C. Bellavia, L. Cristofolini, R. Gonzalez, A. Lappas, Y. Murata, M. Malecki, V. Srdanov, and F. Wudl. Science (Washington, D.C.) **271**,1833 (1996).
8. C. Bellavia-Lund, M. Keshavarz-K, T. Collins, and F. Wudl. J. Am. Chem. Soc. **119**, 8101 (1997).
9. C. Bellavia-Lund, R. Gonzalez, J.C. Hummelen, R.G. Hicks, A. Sastre, and F. Wudl. J. Am. Chem. Soc. **119**, 2946 (1997).
10. B. Nuber and A. Hirsch. Chem. Comm. 405 (1998).
11. B. Cao, X. Zhou, Z. Shi, Z. Jin, Z. Gu, H. Xiao, and J. Wang. Acta Phys.-Chim. Sin. **13**, 204 (1997).
12. M. Keshavarz-K, M. Gonzalez, R.G. Hicks, G. Srdanov, V.I. Srdanov, T.A. Collins, J.C. Hummelen, C. Bellavia-Lund, J. Pavlovich, and F. Wudl. Nature (London), **383**, 147 (1996).
13. A. Gruss, K.-P. Dinse, A. Hirsch, B. Nuber, and U. Reuther. J. Am. Chem. Soc. **119**, 8728 (1997).
14. J.R. Bowser, D.A. Jeleski, and T.F. George. Inorg. Chem. **31**, 154 (1992).
15. Y. Miyamoto, N. Hamada, A. Oshiyama, and S. Saito. Phys. Rev. B: Condens. Matter, **46**, 1749 (1992).
16. N. Kurita, K. Koboyyashi, H. Kumabora, K.Tago, and K.Ozawa. Chem. Phys. Lett. **198**, 95 (1992).
17. J. Lin, B. Gu, and R. Han. Solid State Commun. **84**(8), 807 (1992).
18. X. Xia, D.A. Jelski, J.R. Bowser, and T.F. George. J. Am. Chem. Soc. **114**, 6493 (1992).
19. W. Andreoni, F. Gygi, and M. Parrinello. Chem. Phys. Lett. **190**, 159 (1992).
20. N. Kurita, K. Kobayashi, H. Kumabora, and K. Tago. Phys. Rev. B: Condens. Matter, **48**, 4850 (1993).
21. F. Chen, D. Singh, and S. Jansen. J. Phys. Chem. **97**, 10 958 (1993).
22. K. Esfarjani, K. Ohmo, and Y. Kawazoe. Phys. Rev. B: Condens. Matter, **50**, 17 830 (1994).
23. S.H. Wang, F. Chen,Y.-C. Fann, M. Kashani, M. Malaty, and S.A. Jansen. J. Phys. Chem. **99**, 6801 (1995).
24. J. Dong, J. Jiang, Z.D. Wang, and D.Y. Xing. Phys. Rev. B: Condens. Matter, **51**, 1977 (1995).
25. W. Andreoni, A. Curioni, K. Holczer, K. Prassides, M. Keshavarz-K, J.C. Hummelen, and F. Wudl. J. Am. Chem. Soc. **118**, 11 335 (1996).
26. Q. Xu, J. Dong, J. Jiang, and D.Y. Xing. J. Phys. B: At. Mol. Opt. Phys. **29**, 1563 (1996).
27. J. Piechota, P. Byszewski, R. Jablonski, and K. Antonova. Fullerene Sci. Technol. **4**(3), 491 (1996).
28. B.C. Wang, L.J. Yu, and W.J. Wang. Int. J. Quantum Chem. **57**, 465 (1996).
29. S.J. Zhong and C.W. Liu. J. Mol. Struct. (Theochem), **392**, 125 (1997).
30. Z. Chen, K. Ma, L. Chen, H. Zhao, Y. Pan, X. Zhao, A. Tang, and J. Feng. J. Mol. Struct. (Theochem), **452**, 219 (1998).
31. Z. Chen, K. Ma, H. Zhao, Y. Pan, X. Zhao, A. Tang, and J. Feng. J. Mol. Struct. (Theochem). In press.
32. Z. Chen, K. Ma, Y. Pan, X. Zhao, A. Tang, and J. Feng. J. Chem. Soc. Faraday Trans. **94**, 2269 (1998).
33. M.J. Frisch, G.W. Trucks, H.B. Schlegel, P.M.W. Gill, B.G. Johnson, M.A. Robb, J.R. Cheeseman, T. Keith, G.A. Petersson, J.A. Montgomery, K. Raghavachari, M.A. Al-Laham, V.G. Zakrzewski, J.V. Ortiz, J.B. Foresman, C.Y. Peng, P.Y. Ayala, W. Chen, M.W. Wong, J.L. Andres, E.S. Replogle, R. Gomperts, R.L. Martin, D.J. Fox, J.S. Binkley,

© 1999 NRC Canada

D.J. Defrees, J. Baker, J.P. Stewart, M. Head-Gordon, C. Gonzalez, and J.A. Pople. Gaussian 94. Gaussian, Inc., Pittsburgh, Pa. 1995.
34. C.C. Henderson, C.M. Rohlfing, and P.A. Cahill. Chem. Phys. Lett. **213**, 383 (1993).
35. U. Reuther and A. Hirsch. Chem. Commun. 1401 (1998).
36. K. Fukui. Science (Washington, D.C.) **217**, 747 (1982).
37. R.G. Pearson. J. Chem. Educ. **64**, 561 (1987).
38. K. Choho, W. Langenaeker, G.V.D. Woude, and P. Geerling. J. Mol. Struct. (Theochem), **338**, 293 (1995).
39. R.G. Pearson. J. Am. Chem. Soc. **85**, 3533 (1963).

© 1999 NRC Canada

Excess molar volumes of liquid 1-bromoalkane + alkane mixtures. Nitta–Chao characterization of the bromine–bromine and bromine–methylene interactions in binary 1-bromoalkane + alkane mixtures

J. García, M.J. Comuñas, L. Lugo, E.R. López, and J. Fernández

Abstract: Excess molar volumes at 298.15 K for the binary mixtures of a 1-bromoalkane with a *n*-alkane are reported. The V^E values were obtained from measurements of the density with an Anton Paar densimeter. Literature data of excess Gibbs energies, excess enthalpies, excess volumes, and activity coefficients at infinite dilution for this kind of mixtures together with molar volumes and vaporization enthalpies of pure bromoalkanes were used to calculate the characteristic parameters of the Nitta–Chao group contribution model. With the obtained parameters, this model consistently describes the experimental data of the 1-bromoalkane + *n*-alkane mixtures. Furthermore, we have determined the energetic parameters for the Larsen version of the UNIFAC model.

Key words: liquids, mixtures, thermodynamics, group contributions.

Résumé : On presente les volumes molaires d'excès, V^E, à 298.15 K des mélanges binaires de 1-bromoalcane avec un *n*-alcane. Les valeurs de V^E ont éte obtenues a partir des mesures de densité faites avec un densimètre Anton–Paar. Les données disponibles dans la littérature relatives aux énergies de Gibbs en excès, aux enthalpies en excès, aux volumes en excès et aux coefficients d'activité à dilution infini pour cette type de melanges aussi bien que les volumes molaires et les enthalpies de vaporisation ont été uti1lisees pour determiner les paramètres characteristiques du modèle de contribution de groupe de Nitta–Chao. Ce modèle décrit d'une façon consistante les données expérimentales des mélanges 1-bromoalcane + *n*-alcane. Nous avons determiné aussi les paramètres energetiques pour la version de Larsen du modèle de UNIFAC.

Mots clés : liquides, mélanges, thermodynamique, contributions de groupes.

1. Introduction

In previous papers (1, 2), thermodynamic properties of mixtures involving a 1-chloroalkane or a α,ω-dichloroalkane with a *n*-alkane were used to determine the characteristic parameters of the chlorine group and of its interaction with the methyl and methylene groups for the Nitta–Chao (3) model. To continue with the study of mixtures containing other halogenoalkanes, we have determined in this paper, for the first time, the characteristic parameters of the bromine group and of its interaction with the methyl and methylene groups, using the Nitta–Chao model and the Larsen et al. (4) version of UNIFAC. Moreover, in the present work we have measured the excess volumes at 298.15 K and atmospheric pressure of 1-bromoheptane + hexane, heptane, and dodecane and of 1-bromooctane + hexane, octane, and dodecane, since we have not found excess molar volumes in the literature for 1-bromoalkane + alkane systems. The obtained experimental values are compared with those predicted by the Nitta–Chao model.

Kehiaian and Velasco (5) have presented a literature survey until 1987 of the VLE, excess enthalpy, and activity coefficients at infinite dilution. These authors have also determined the dispersive and quasichemical parameters for bromine–bromine and bromine–methylene interactions using the DISQUAC model (6). After 1987, we have only found in the literature VLE data of 1-bromobutane + (hexane, heptane) measured by Rambabu et al. (7) and of 1-bromopropane + heptane obtained by Wisniak et al. (8).

Concerning the UNIFAC model, there are parameters available of bromine–methylene interactions for the original (9), Dang and Tassios (10), and Gmehling et al. (11) versions, whereas there are not published parameters for the Larsen et al. (4, 12) version. In this paper we compare the

Received September 4, 1998

J. García,[1] M.J. Comuñas, L. Lugo, E.R. López, J. Fernández.[2] Laboratorio de Propiedades Termofísicas, Departamento de Física Aplicada, Facultad de Física, Universidad de Santiago, E-15706 Santiago de Compostela, Spain.

[1]Current address: Departamento de Física Aplicada, Facultad de Ciencias, Universidad de Vigo, E-36280 Vigo, Spain.
[2]Author to whom correspondence may be addressed. Telephone number: 34-981-563100, ext. 14046.
Fax: +34-981-520676. e-mail: fajferna@usc.es

© 1999 NRC Canada

Fig. 1. Experimental excess molar volumes, V^E, at 298.15 K and Nitta–Chao predictions of x 1-bromoalkane + $(1 - x)$ alkane against x, the mole fraction of the 1-bromoalkane: (*a*) 1-bromoheptane + hexane (●), heptane (■), dodecane (▲); (*b*) 1-bromooctane + hexane (●), octane (◆), dodecane(▲). ---, Nitta–Chao model; —, Redlich–Kister fits.

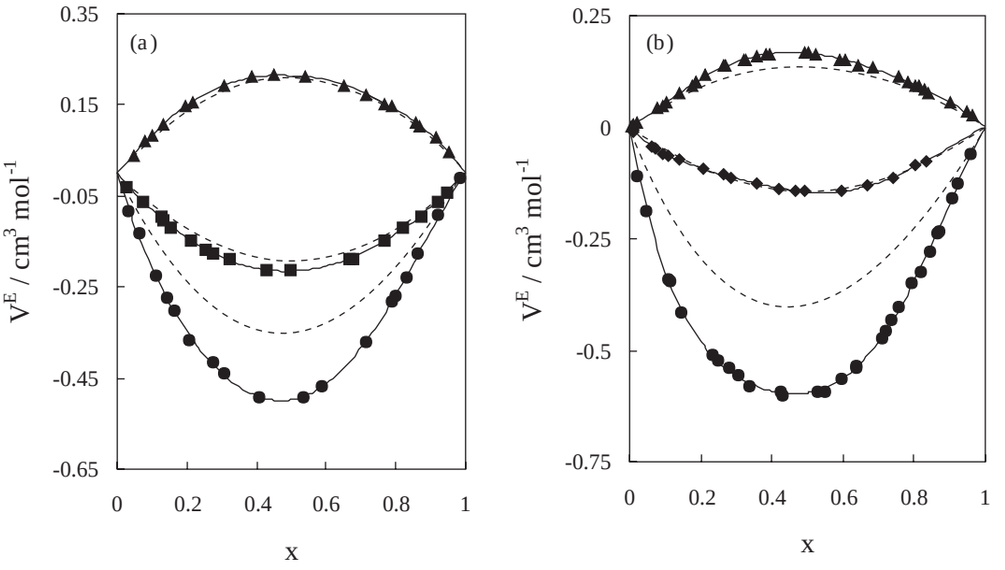

predictions of the UNIFAC versions (Tassios, Gmehling, and Larsen) and the DISQUAC and Nitta–Chao models.

2. Experimental

The sources and the purities of the chemicals were *n*-hexane, *n*-heptane, *n*-octane (Fluka, puriss 99.5%), *n*-dodecane, 1-bromooctane (Aldrich, puriss 99%), and 1-bromoheptane (Fluka, puriss >98%). All liquids were used without purification, but prior to the measurements they were kept over Union Carbide 0.4 nm molecular sieves (Fluka) and degassed. The purities of the chemical products were verified by measurement of the densities at 298.15K, which were in agreement with literature values (13–16).

Excess molar volumes were calculated from density measurements made using an Anton–Paar DMA 60/602HP densimeter at 298.15 K. The temperature inside the vibrating tube was measured with an Anton Paar CKT 100 thermometer and was regulated to better than ±0.01 K using a Polyscience PS 9110 thermostat.

Before each series of measurements the instrument was calibrated at atmospheric pressure with air, heptane, and water, which was purified using a Milli-Q Plus System. Liquid mixtures were prepared by weight using a precision digital Sartorius 210-P balance with an accuracy of $\pm 10^{-5}$ g. The possible error in the mole fractions is estimated to be less than 10^{-5}, and the precision of V^E was estimated better than ±0.002 cm^3 mol^{-1}. All molar quantities are based on the IUPAC relative atomic mass table.

3. Experimental results and discussion

The experimental results for the excess molar volumes at 298.15 K are listed in Table 1. A Redlich–Kister equation was fitted to the excess volume values for the binary systems:

$$[1] \qquad V^E/(\text{cm}^3\ \text{mol}^{-1}) = x(1 - x)\ \Sigma A_i(2x - 1)^i$$

where x is the mole fraction of the 1-bromoalkane. The coefficients A_i and the standard deviations given in Table 2 were calculated by the unweighted least-squares method, the degree of the polynomial having been optimized by applying the *F*-test. A graphical representation of the experimental values together with the fitted curves is shown in Fig. 1. We have not found in the literature V^E data for any 1-bromoalkane + alkane mixture.

The excess molar volumes of 1-bromoheptane and 1-bromooctane + alkane present a similar behaviour. The $V^E(x)$ curves are quite symmetrical about $x = 0.5$. Furthermore, the V^E data increase when the size of the alkane grows, being negative for the shorter alkanes and positive for the dodecane. The trend of the excess molar volumes with the bromoalkane length is opposite to the trend with the alkane size, and thus, the V^E values increase when the alkane length increases and the bromoalkane size decreases.

In the literature (4, 17, 18), contrary to the excess volumes, the excess enthalpies for all the mixtures of this type are positive over the whole range of composition. The positive values of the excess enthalpies indicate that the breaking of the pure bromoalkanes and the dispersive interactions of the pure alkanes are more important than the negative contributions due to the formation of dipole–dipole interactions in the bromoalkanes. Besides, the excess enthalpies for the 1-bromoalkane + alkane systems decrease when the length of the 1-bromoalkane chain decreases and the alkane chain increases.

4. The Nitta–Chao model

4.1. Theory

It is a remarkable characteristic of the Nitta–Chao model (3) that the same set of interaction parameters can be used to represent rather accurately the thermodynamic properties of

© 1999 NRC Canada

Table 1. Experimental excess molar volumes, V^E, of 1-bromoalkane + alkane at 298.15 K and atmospheric pressure.

x	V^E/cm^3 mol^{-1}	x	V^E/cm^3 mol^{-1}	x	V^E/cm^3 mol^{-1}	x	V^E/cm^3 mol^{-1}
			x 1-Bromoheptane + (1– x) hexane				
0.031 04	–0.084	0.207 40	–0.368	0.584 80	–0.466	0.861 54	–0.178
0.064 02	–0.131	0.272 60	–0.416	0.713 53	–0.371	0.922 91	–0.090
0.112 52	–0.226	0.304 48	–0.441	0.788 79	–0.280	0.985 32	–0.012
0.141 99	–0.273	0.405 87	–0.492	0.799 72	–0.271		
0.164 20	–0.300	0.532 47	–0.491	0.833 15	–0.229		
			x 1-Bromoheptane + (1– x) heptane				
0.027 81	–0.029	0.211 01	–0.148	0.495 01	–0.214	0.870 90	–0.095
0.075 50	–0.063	0.255 20	–0.170	0.665 05	–0.188	0.918 20	–0.061
0.129 20	–0.097	0.276 80	–0.178	0.677 72	–0.187	0.945 80	–0.042
0.134 37	–0.103	0.323 50	–0.189	0.768 62	–0.147		
0.151 92	–0.118	0.426 20	–0.211	0.820 10	–0.127		
			x 1-Bromoheptane + (1– x) dodecane				
0.046 52	0.039	0.214 40	0.154	0.650 88	0.192	0.869 83	0.103
0.078 30	0.070	0.305 05	0.193	0.714 36	0.173	0.914 32	0.080
0.097 99	0.083	0.385 40	0.210	0.769 69	0.151	0.952 41	0.047
0.131 63	0.107	0.451 24	0.215	0.786 61	0.146		
0.194 23	0.148	0.538 25	0.210	0.855 57	0.111		
			x 1-Bromooctane + (1– x) hexane				
0.023 11	–0.111	0.305 04	–0.557	0.637 36	–0.541	0.865 63	–0.237
0.048 81	–0.189	0.334 79	–0.579	0.708 73	–0.472	0.870 51	–0.232
0.110 20	–0.341	0.427 39	–0.591	0.718 70	–0.456	0.905 30	–0.159
0.112 89	–0.347	0.430 18	–0.599	0.737 29	–0.431	0.924 46	–0.125
0.147 00	–0.416	0.528 17	–0.594	0.758 97	–0.405	0.960 15	–0.058
0.231 26	–0.512	0.551 18	–0.592	0.793 23	–0.351		
0.248 06	–0.521	0.595 74	–0.566	0.816 43	–0.323		
0.279 15	–0.541	0.635 61	–0.537	0.843 20	–0.278		
			x 1-Bromooctane + (1– x) octane				
0.012 50	–0.010	0.205 20	–0.092	0.492 45	–0.143	0.868 80	–0.058
0.063 70	–0.043	0.262 80	–0.106	0.597 50	–0.144	0.902 60	–0.046
0.073 60	–0.048	0.285 80	–0.115	0.668 80	–0.132	0.921 30	–0.034
0.091 70	–0.058	0.359 30	–0.126	0.740 70	–0.114	0.931 40	–0.029
0.110 60	–0.065	0.419 60	–0.138	0.804 80	–0.086	0.972 90	–0.011
0.140 20	–0.072	0.466 20	–0.141	0.836 50	–0.075		
			x 1-Bromooctane + (1– x) dodecane				
0.005 79	0.003	0.188 20	0.101	0.494 82	0.167	0.803 00	0.093
0.009 62	0.005	0.212 49	0.116	0.504 16	0.166	0.811 00	0.093
0.020 35	0.009	0.263 10	0.137	0.522 15	0.165	0.830 10	0.083
0.075 40	0.042	0.270 40	0.138	0.588 32	0.152	0.841 90	0.079
0.091 43	0.049	0.321 66	0.151	0.605 70	0.152	0.902 40	0.055
0.101 18	0.054	0.328 06	0.151	0.643 27	0.140	0.961 30	0.025
0.137 42	0.078	0.355 88	0.159	0.681 60	0.135		
0.176 05	0.094	0.385 66	0.164	0.755 00	0.114		
0.186 17	0.100	0.396 02	0.163	0.784 73	0.100		

the mixtures: excess Gibbs energies, G^E, excess enthalpies, H^E, excess volumes, V^E, heat capacities, $C_p{}^E$, and activity coefficients at infinite dilution, γ^∞; as well as thermodynamic properties of the pure liquids such as molar volumes and vaporization enthalpies.

In the Nitta–Chao model (3) the hard-core volume V_i^* has a temperature dependence given by the empirical expression:

$$[2] \qquad V_i^* = V_{i0}^* \exp\left[a_i\left(\frac{1}{T} - \frac{1}{T_0}\right)\right]$$

where V_{i0}^* is the hardcore volume at temperature T_0 (normally 298.15 K), and a_i gives the dependence of V_i^* with the temperature. Both parameters (V_{i0}^*, a_i) and the number of ex-

© 1999 NRC Canada

Table 2. Coefficients A_i for the Redlich–Kister equation and standard deviation, s, for x 1-bromoalkane + $(1 - x)$ alkane.

System	A_1	A_2	A_3	A_4	A_5	s
1-Bromoheptane + hexane	–1.9909	0.2581	0.2007	0.4589		0.006
1-Bromoheptane + heptane	–0.8599	0.0467				0.002
1-Bromoheptane + dodecane	0.8551	–0.1204	0.1381	0.2060		0.002
1-Bromooctane + hexane	–2.3837	0.2471	–0.5605	1.2719		0.005
1-Bromooctane + octane	–0.5800	–0.1147	0.0741	0.3433	–0.1127	0.001
1-Bromooctane + dodecane	0.6633	–0.1450	–0.0657	–0.2294	–0.0291	0.002

Table 3. Characteristic parameters of the Nitta–Chao model for 1-bromoalkane + alkane mixtures.

Group	$V^*_{i,0}$/cm^3 mol^{-1}	a_i /K	c_i	q_i
-CH_3	13.460 (3)	23.700(3)	0.338 (3)	6.71
-CH_2	10.250 (3)	23.700(3)	0.093 (3)	4.27
-Br	15.493[a]	81.774[a]	0.376 (3)	6.58
	ε_{BrBr}/J mol^{-1}	ε_{CH2Br}/J mol^{-1}	σ_{BrBr}/J mol^{-1}	σ'_{BrBr}/J mol^{-1}
	5756[a]	3598[a]	250[a]	801[a]

[a]This work.

Table 4. Geometrical parameters ($(z/2)q_i$, r_i) and interaction parameters ($a_{mn,i}$) for 1-bromoalkane + alkane for the Larsen model.

$(z/2)q_i$	r_i	Subgroup	Main group	CH_2	$BrCH_2$
0.848	0.9011	CH_3		0	260.8456
			CH_2	0	–0.4319
0.540	0.6744	CH_2		0	6.6523
1.372	1.6236	$BrCH_2$	$BrCH_2$	–79.8505	0
				–0.1417	0
				–11.9832	0

ternal degrees of freedom of the group (c_i) are determined by fitting the theoretical equations to the experimental data.

The energy of pairwise interaction between groups (Φ_{ij}) is the sum of two contributions:

$$[3] \qquad \Phi_{ij} = -\frac{\varepsilon_{ij}}{\tilde{\nu}} \exp\left(\frac{\kappa}{\tilde{\nu}}\right) - \sigma_{ij}$$

with ε_{ij} being the dispersive interaction energy parameter, κ a constant whose value is 0.7, and σ_{ij} being the nondispersive energy which is temperature dependent and given by

$$[4] \qquad \frac{\sigma_{ij}}{T} = \frac{\sigma^0_{ij}}{T_0} + \sigma'_{ij}\left(\frac{1}{T} - \frac{1}{T_0}\right)$$

where σ^0_{ij} and σ'_{ij} are characteristic parameters of this model. For nonassociating pairs $\sigma_{ij} = 0$, and all the energy is dispersive. However, for associating pairs or polar–polar interactions $\varepsilon_{ij} \neq 0$, and the dispersive energy still gives a contribution.

4.2. Estimation of the characteristic parameters of the Nitta–Chao model and Larsen version of UNIFAC

As for the DISQUAC (6) model and the Tassios and Gmehling versions of UNIFAC (9–11) model, the bromoalkanes were considered, in the Nitta–Chao model, as being formed by a bromine group (Br) and methyl (CH_3) and methylene (CH_2) groups. The number of the contacts of the groups, q_i, is determined by means of the Bondi (19) method. The hardcore volumes, the number of external degrees of freedom of these groups, and the energetic parameter, ε_{CH2CH2}, were taken from Nitta et al. (3). For this reason, only the V^*_{Br}, a_{Br}, c_{Br}, ε_{BrBr}, ε_{BrCH2}, σ^0_{BrBr}, σ'_{BrBr}, parameters need to be fitted to the thermodynamic properties of pure bromoalkanes and of bromoalkanes + alkanes mixtures.

Similarly to what is done in the Larsen version for the chlorine group ($ClCH_2$) we have considered the bromine group as $BrCH_2$.

Furthermore, as in other group contribution models, the energetic parameters involving the groups CH_2 and CH_3 have the same values. In order to keep a low number of characteristic parameters we have made all them independent of the length of the 1-bromoalkanes.

In both models the parameters (Tables 3, 4) were fitted using a database containing the thermodynamical properties of the 1-bromoalkane + alkane systems and a Marquardt (20) optimization algorithm. For the Nitta–Chao model, the constraints imposed by the physical significance of the parameters (1), have also been considered.

The database contains excess Gibbs energies (5, 7, 8), excess enthalpies (5), and activity coefficients at infinite dilution (5) of 1-bromoalkane + alkane mixtures for the two models. Furthermore, for the Nitta–Chao model, vaporization enthalpies (21), excess molar volumes (this work), and molar volumes (15) of pure 1-bromoalkanes have been introduced in the database.

We have not included thermodynamical properties of 1-bromoalkane + cycloalkane systems for the determination of the group parameters, because the methylene group of a cycloalkane is different from the methylene group of a normal alkane in both models.

To analyze the significance of the parameters obtained in the case of the Nitta–Chao model, we have compared the energetic parameters of the chlorine and bromine groups. It is important to point out that the dispersive interaction energies increase in the order Cl < Br, and the nondispersive interaction energies decrease in the order Cl > Br, for 1-halogenoalkanes + alkanes mixtures. These sequences are the

© 1999 NRC Canada

Fig. 2. Experimental and theoretical molar volumes, V_m, of 1-bromoalkane against n, the number of carbons of the 1-bromoalkane. (*a*) T = 293.15 K: ◇, ref. 15; T = 323.15 K: ○, ref. 14. (*b*) T = 298.15 K: ◇, ref. 15; △, ref. 14; ○, ref. 13; +, this work. —, Nitta–Chao model.

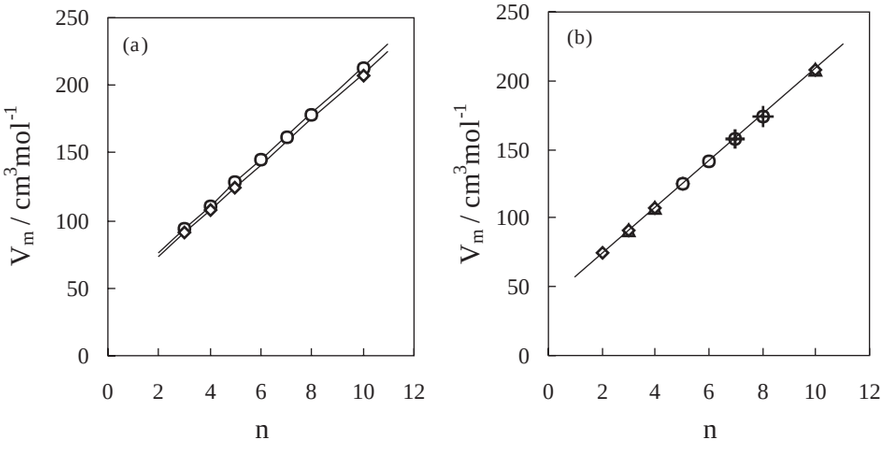

Fig. 3. Experimental and theoretical vaporization enthalpies, H_v, of 1-bromoalkane against the temperature. Bromoethane: ●, ref. 21; ○, ref. 15. 1-Bromopropane: ■, ref. 21; □, ref. 15. 1-Bromobutane: ◆, ref. 21; ◇, ref. 15. —, Nitta–Chao model.

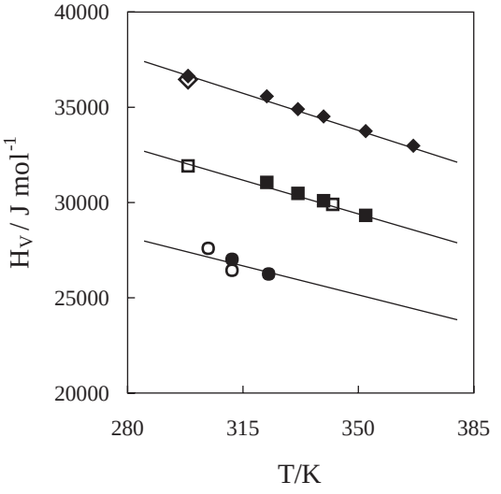

same as those previously obtained by Kehiaian and Velasco (5) for the dispersive and quasichemical interchange energies of the DISQUAC model. These authors explained these trends by taking into account the dipole moments of the molecules and the cohesive energy density of the pure liquids.

5. Theoretical results and discussion

To compare the predictions of all the thermodynamic properties with the Nitta–Chao model with the Larsen version, and with other group contribution models, we have used the percentage mean deviation, PMD defined by

$$[5] \qquad \mathrm{PDM} = \frac{100}{N_Y} \sum \frac{\left| Y_{\mathrm{exp}} - Y_{\mathrm{theo}} \right|}{\left| Y_{\mathrm{exp}} \right|}$$

where Y_{exp} and Y_{theo} are, respectively, the experimental and predicted values for the thermodynamic property Y and N_Y is the number of experimental values for this property.

Pure liquids

The percentage mean deviations between experimental (15, 21) and predicted values for the molar volumes, V_m, and the vaporization enthalpies, H_v, are about 0.9 and 1.2%, respectively. It can be seen in Figs. 2 and 3 that the Nitta–Chao model with the parameters calculated in this work gives a very good representation of the variation of these properties with the length of the 1-bromoalkane chain and with the temperature.

Mixtures

In Tables 5–7 the theoretical predictions obtained in this work for equimolar composition of the mixing properties of the 1-bromoalkane + alkane systems, using the parameters calculated by us, are presented. For comparison we have also listed the theoretical predictions using DISQUAC and the Tassios and Gmehling versions of the UNIFAC model.

The overall percentage mean deviations obtained for the excess Gibbs energies, G^E, are 13, 21, 21, and 26% for the Nitta–Chao model and the Larsen version with our parameters, the DISQUAC model, and the Gmehling version, respectively. In Table 5 we can see that all models reproduce the temperature dependence of the excess Gibbs energy for 1-bromopentane + pentane; this property decreases when the temperature increases. In Fig. 4 we show that the Nitta–Chao and DISQUAC models reproduce remarkably well the magnitude and the symmetry of the $G^E(x)$ curves.

For the excess enthalpies, H^E, the percentage mean deviations are 8% for the Nitta–Chao model with our parameters, DISQUAC model, and Tassios version, 9% for the Larsen version with our parameters, and 19% for the Gmehling version. In Table 6 it is possible to observe that the Nitta–Chao model and the Larsen version correctly predict the sequences with the length of the 1-bromoalkane and alkane chains. The other models reproduce also the above mentioned sequences. Figure 5 shows the predictions obtained

© 1999 NRC Canada

Table 5. Excess Gibbs energies, G^E, of 1-bromoalkane + alkane mixtures at various temperatures and equimolar composition. Comparison between the experimental and the calculated values using the Gmehling and Larsen versions of UNIFAC model and DISQUAC and Nitta–Chao models; *n* is the number of carbon atoms of the alkane.

		G^E/J mol^{-1}				
			Calc.			
System	*T*/K	Expt.	Gmehling	DISQUAC	Nitta	Larsen
Bromoethane						
n = 7	303.15	262 (22)	232	358	304	331
1-Bromopropane						
n = 7	352.22	266 (8)	149	273	213	289
1-Bromobutane						
n = 6	298.15	296 (7)	230	298	294	249
n = 7	298.15	229 (7)	226	300	274	259
	323.15	277 (22)	196	279	247	280
1-Bromopentane						
n = 5	223.15	394 (23)	274	269	340	289
	273.15	338 (23)	237	237	305	217
	293.15	329 (23)	220	225	293	193

Table 6. Excess enthalpies, H^E, of 1-bromoalkane + alkane mixtures 298.15 K and equimolar composition. Comparison between the experimental and the calculated values using the Gmehling, Tassios, and Larsen versions of UNIFAC model and DISQUAC and Nitta–Chao models; *n* is the number of carbon atoms of the alkane.

		H^E/J mol^{-1}					
			Calc.				
System	*T*/K	Expt.	Gmehling	Tassios	DISQUAC	Nitta	Larsen
Bromoethane							
n = 6	298.15	767 (17)	757	788	792	900	739
n = 12	298.15	960 (17)	1051	1015	1015	1132	977
n = 16	298.15	1134 (17)	1175	1103	1104	1238	1073
1-Bromobutane							
n = 6	298.15	522 (17)	576	534	522	573	527
n = 12	298.15	704 (17)	819	714	701	731	719
n = 16	298.15	867 (17) 810 (5)	925	788	776	814	800
1-Bromohexane							
n = 6	303.15	401 (18)	450	374	376	421	356
1-Bromododecane							
n = 6	298.15	242 (17)	249	187	186	272	200
n = 12	298.15	267 (17)	379	275	277	274	298
n = 16	298.15	338 (17)	443	317	320	299	344
1-Bromohexadecane							
n = 6	298.15	232 (17)	181	129	131	252	141
n = 12	298.15	199 (17)	283	196	200	215	216
n = 16	298.15	215 (17)	334	229	235	224	253

for two examples. The symmetry of the curves is reproduced quite well by the Nitta–Chao model.

In the case of the logarithm of the activity coefficients at infinite dilution, the percentage mean deviations are 19, 37, 79, and 21% for the Nitta–Chao model and Larsen version with our parameters, DISQUAC model, and Gmehling version, respectively.

The excess molar volumes (Table 8) measured in this work present a percentage mean deviation of about 14% with the Nitta–Chao model and the parameters calculated by us. The poorer results are obtained in systems containing hexane, as can be seen in Figs. 1 and 6. The mean deviation is reduced until 5% if the mixtures containing *n*-hexane are excluded. We think that the Nitta–Chao model can not reproduce well the excess volumes for the systems that present a great packing effect, such as the systems composed by a large 1-halogenoalkane and a short alkane. In fact, for 1-chloroalkane + alkane mixtures (1), the overall mean deviations for V^E were 21%, but for the case with the bigger packing effect for which there are available V^E data (1-chlorohexane + hexane), the deviation increases until 100%.

Finally, we can see that the Nitta–Chao model, for all properties, gives the best description and that only this model is able to predict excess molar volumes. Although the

© 1999 NRC Canada

Table 7. Activity coefficients at infinite dilution, ln γ^{∞}, of 1-bromoalkane + alkane mixtures at various temperatures. Comparison between the experimental and the calculated values using the Gmehling and Larsen versions of UNIFAC model and DISQUAC and Nitta–Chao models; *n* is the number of carbon atoms of the alkane.

			Calc.			
System	*T*/K	Expt.	Gmehling	DISQUAC	Nitta	Larsen
			ln γ_1^{∞}			
Bromoethane						
n = 6	301.00	0.482 (24)	0.438	0.554	0.438	0.503
	314.30	0.432 (24)	0.375	0.501	0.385	0.460
	332.00	0.315 (24)	0.301	0.439	0.321	0.425
	340.30	0.231 (24)	0.269	0.412	0.294	0.414
n = 7	293.15	0.482 (25)	0.439	0.521	0.417	0.505
n = 8	293.15	0.482 (25)	0.403	0.455	0.369	0.472
1-Bromopropane						
n = 24	353.15	–0.194 (26)	–0.213	–0.415	–0.301	–0.041
n = 28	353.35	–0.305 (27)	–0.289	–0.539	–0.393	–0.110
n = 30	353.15	–0.357 (26)	–0.323	–0.595	–0.436	–0.141
n = 36	353.15	–0.504 (26)	–0.419	–0.749	–0.555	–0.228
			ln γ_2^{∞}			
1-Bromononane						
n = 5	303.65	0.212 (28)	0.133	–0.024	0.244	0.122
n = 6	303.65	0.211 (28)	0.157	0.069	0.256	0.142
1-Bromohexadecane						
n = 7	318.15	0.072 (29)	–0.003	–0.199	0.065	0.062

Fig. 4. Experimental and theoretical excess Gibbs energies, G^E, of *x* 1-bromobutane + (1 – *x*) hexane at 298.15 K: ●, experimental points (ref. 7). —, Nitta–Chao; – – –, DISQUAC; ---, Gmehling predictions.

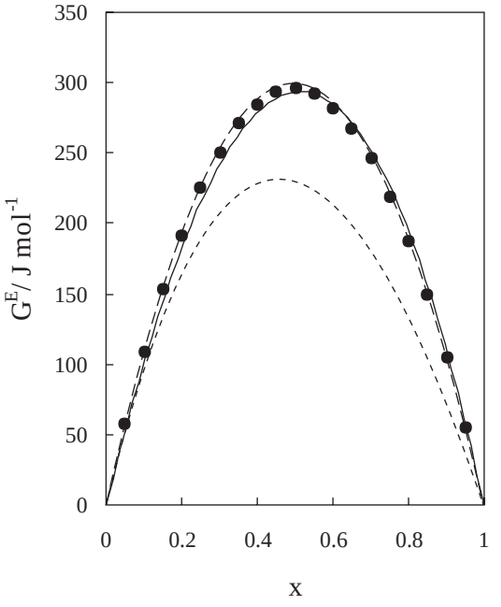

DISQUAC model predicts excess Gibbs energies and excess enthalpies with a precision better than the Larsen and Gmehling versions, for the activity coefficients at infinite dilution the best results are obtained with this last version. These results confirm that the Nitta–Chao and DISQUAC models are more appropriate for mixtures containing a polar molecule, bromoalkanes in this case, due to the inclusion in the expression for the interaction energies of a nondispersive term (σ^0_{BrBr} and σ'_{BrBr} for the Nitta–Chao model and C^{quac} for the DISQUAC model).

6. Conclusions

We have determined, for the Nitta–Chao model, the structural parameters for the bromine group and its interaction with the methyl or methylene groups for 1-bromoalkane + alkane binary systems by using an updated database of excess enthalpies, excess Gibbs energies, and excess volumes for the mixtures, together with vaporization enthalpies and molar volumes of the pure 1-bromoalkanes. Moreover we have calculated, for the first time in the literature, the energetic parameters between the bromine and methyl or methylene groups of the Larsen version of UNIFAC.

Compared with other group contribution models such as DISQUAC and UNIFAC (in Tassios, Larsen, and Gmehling versions), the Nitta–Chao model with our parameters is distinguished, since this model gives the best results and the other models cannot predict the excess volumes, vaporization enthalpies, and molar volumes.

In the future, we will try to extend the parameter matrix for the Nitta–Chao model, by determining the structure-dependent interaction parameters for the α,ω-dibromoalkane + alkane mixtures in order to improve the predictions for this kind of mixtures, as was done for α,ω-dichloroalkane + alkane systems (2). In addition, we will extend this study to mixtures containing other halogenoalkanes (iodoalkanes and fluoroalkanes).

© 1999 NRC Canada

Fig. 5. Experimental excess molar enthalpies, H^E, of (*a*) *x* 1-bromoalkane + (1 – *x*) hexane and (*b*) 1-bromoalkane + dodecane at 298.15 K. ●, 1-bromobutane; ◆, 1-bromododecane (ref. 17). —, Nitta–Chao predictions.

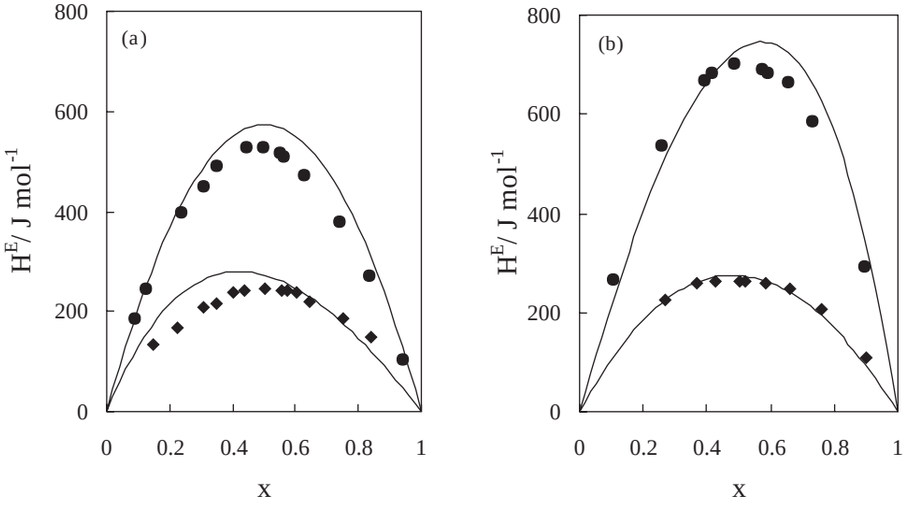

Table 8. Excess volumes, V^E (x = 0.5) of 1-bromoalkane + alkane mixtures at 298.15 K. Comparison between the experimental and the Nitta–Chao (calc.) values; *n* is the number of carbon atoms of the alkane.

	V^E/cm^3 mol^{-1}	
System	Expt.	Calc.
1-Bromoheptane		
n = 6	–0.498	–0.343
n = 7	–0.215	–0.193
n = 12	0.214	0.213
1-Bromooctane		
n = 6	–0.596	–0.397
n = 8	–0.145	–0.142
n = 12	0.167	0.135

Fig. 6. Experimental and Nitta–Chao (—) predicted values of V^E (x = 0.5) at 298.15 K against *n*, the number of carbon atoms of the alkane. ●, 1-bromoheptane + alkane; ◆, 1-bromooctane + alkane.

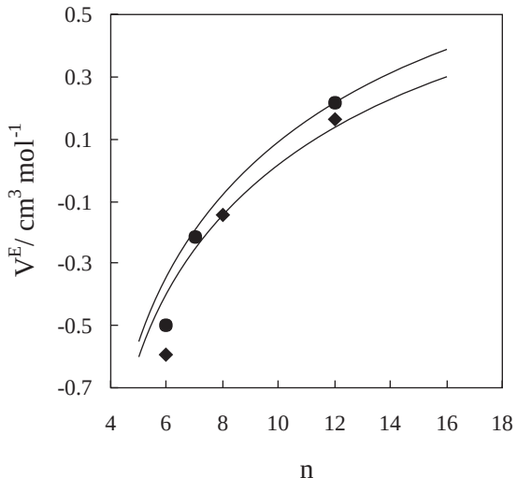

Acknowledgements

This work was carried out under the research project PB94-1083-C03-C02-DGICYT-Spain. The authors wish to express their gratitude to Miss Silvia Miramontes for her experimental assistance.

References

1. J. Fernandez, L. Pias, M.I. Paz Andrade, J.L. Legido, T. Lorenzana, and J. Diez. Ber. Bunsenges Phys. Chem. **97**, 106 (1993).
2. J. Garcia, E.R. Lopez, J.L. Legido, and J. Fernandez. Fluid Phase Equilib. **110**, 31 (1995).
3. T. Nitta, E.A. Turek, R.A. Greenkorn, and K.C. Chao. AIChE. J. **23**, 144 (1977).
4. B.L. Larsen, P. Rasmussen, and A. Fredenslund. Ind. Eng. Chem. Res. **26**, 2274 (1987).
5. H.V. Kehiaian and I. Velasco. Fluid Phase Equilib. **38**, 227, (1987).
6. H.V. Kehiaian, J.P.-E. Grolier, and G.C. Benson. J. Chem. Phys. **75**, 1031 (1978).
7. K. Rambabu, G.K. Raman, and Y.V.L. Ravikumar. Phys. Chem. Liq. **26**, 39 (1993).
8. J. Wisniak, A. Apelblat, J. Zabicky, and I. Feingold. J. Chem. Eng Data, **40**, 120 (1995).
9. A. Fredenslund, J. Gmehling, and P. Rasmusen. Vapour-liquid equilibria using UNIFAC. Elsevier, Amsterdam. 1977.
10. D. Dang and P. Tassios. Ind. Eng. Chem. Process. Des. Dev. **25**, 22 (1986).
11. J. Gmehling, J. Li, and M. Schiller. Ind. Eng. Chem. Res. **32**, 178 (1993).
12. B.L. Larsen. Ph.D. thesis. Predictions of phase equilibria and heat effects of mixing with a modified UNIFAC model. Technical University of Denmark, Lyndby. 1986.
13. L.M. Ellis and E.E. Reid. J. Am. Chem. Soc. **54**, 1674 (1932).
14. S.K. Begum, S. Akhtar, M. Habibullah, and M.A. Saleh. Phys. Chem. Liq. **30**, 177 (1995).
15. J.A. Riddick, W.B. Bunger, and T.K. Sakano. Org. Solvents, **2** (1986).
16. TRC. Selected values of properties of chemical compounds. Manufacturing chemists association research project. Thermo-

© 1999 NRC Canada

dynamics Research Center, Texas A and M University, College Station. 1958.
17. J. Valero, M. Gracia, and C. Gutiérrez-Losa. J. Chem. Thermodyn. **12**, 627 (1980).
18. A. De Torre, I. Velasco, S. Otín, and G. Gutiérrez Losa. J. Chem. Thermodyn. **12**, 87 (1980).
19. A. Bondi. J. Phys. Chem. **68**, 441 (1964).
20. D.W. Marquardt. J. Soc. Indust. Appl. Math. **11**, 431 (1963).
21. V. Majer and V. Svobdoda. Enthalpies of vaporization of organic compounds. Blackwell Scientific, Oxford. 1985.
22. C.P. Smyth and E.W. Engel. J. Am. Chem. Soc. **51**, 2646 (1929).
23. U.T. Kreibich, K. Schäfer, and A. Höpfner. Ber. Bunsenges. Phys. Chem. **74**, 1020 (1970).
24. E.R. Thomas, B.A. Newman, G.L. Nicolaides, and C.A. Eckert. J. Chem. Eng. Data, **27**, 233 (1982).
25. E.R. Thomas, B.A. Newman, T.C. Long, D.A. Wood, and C.A. Eckert. J. Chem. Eng. Data, **27**, 399 (1982).
26. Y.B. Tewari, J.P. Sheridan, and D.E. Martire. J. Phys. Chem. **74**, 3263 (1970).
27. U. Weidlich. Ph.D. thesis. Experimentelle und Theoretische untersuchungen zur erweiterung der gruppenbeitragsmethode UNIFAC. University of Dortmund, Germany. 1985.
28. A.N. Korol. Neftekhimiya, **3**, 635 (1963).
29. G.M. Janini and D.E. Martire. J. Phys. Chem. **78**, 1644 (1974).

Appendix: symbols

A_i Parameters of the eq. [1]
a_i Coefficient to express change of hardcore volume with changing temperature
c_i External degrees of freedom of i
G^E Excess molar Gibbs energy
H^E Excess molar enthalpy
N Number of molecules
N_A Avogadro constant
k_B Boltzmann constant
q_i Number of contacts of group i
r_i Volume parameter of group i
T Absolute temperature
T_0 Reference temperature (298.15 K)
V_i^* Hardcore volume of group i
V_{i0}^* Hardcore volume at reference temperature T_0
V_m Molar volume
$\tilde{v}$ Reduced volume
V^E Excess molar volume
x Mole fraction
z Lattice coordination number

Greek letters
ε_0 Permittivity of vacuum
γ^∞ Activity coefficient at infinite dilution
ε_{ij} Dispersive interaction energy parameter of groups i and j
κ Constant equal to 0.7
σ_{ij} Nondispersive energy of groups i and j
σ_{ij}^0 Nondispersive energy at T_0
σ'_{ij} Coefficient to express change of σ with T
Φ_{ij} Energy of ij pairwise interaction

© 1999 NRC Canada

Oxidation of secondary alcohols and ethers by dimethyldioxirane

Alfons L. Baumstark, Franci Kovac, and Pedro C. Vasquez

Abstract: The oxidation of several series of secondary alcohols **2**–**9**, ethers **10**–**17**, and related derivatives **18** and **19**, by dimethyldioxirane, **1**, in acetone at 25°C produced the corresponding ketones in good to excellent yields for all but two cases. (The exceptions: oxidation of 1-methoxy-2-methyl-1-phenylpropane (48%) and 1-methoxy-2,2-dimethyl-1-phenylpropane (24%).) The oxidation of the secondary alcohols was found to yield k_2 values that were roughly 10-fold greater than those of the corresponding methyl ethers. The rate constant for oxidation of a silyl ether was slightly lower than that for the corresponding methyl ether while that for the ester derivative was roughly half the value. For oxidation of alcohols and methyl ethers, the k_2 values became smaller as the R″ series (Me, Et, *n*Pr, iPr, and *t*Bu) increased in steric bulk ($\rho^* = 1.7$; $r = 0.998$ and $\rho^* = 3.2$; $r = 0.95$, respectively). The Hammett study for the oxidation of the methyl ethers of α-methyl-*p*-benzyl alcohols (**10**, **20**–**25**) yielded a ρ value of –0.74. The activation parameters for oxidation of the parent compound of the ether series (1-methoxy-1-phenylethane) were $\Delta H^{\ddagger} = 14.8 \pm 0.5$ kcal/mol, $\Delta S^{\ddagger} = -21.9$ eu, $\Delta G^{\ddagger} = 21.3$ kcal/mol, k_2 (25°C) = 1.6×10^{-3} M^{-1} s^{-1}. The mechanistic aspects of the oxidation are discussed in relation to two mechanistic extremes: (*a*) direct insertion of the oxygen atom into the C—H bond and (*b*) direct abstraction of the H by dimethyldioxirane to yield a caged-radical pair, with subsequent coupling to hemi-ketal intermediates that fragment to yield acetone, alcohol or water, and ketone as the final products.

Key words: dimethyldioxirane, oxidation.

Résumé : L'oxydation de plusieurs séries d'alcools secondaires (**2**–**9**), d'éthers (**10**–**17**) et de dérivés apparentés (**18** et **19**), par le diméthyldioxirane (**1**) dans l'acétone, à 25°C, conduit aux cétones correspondantes avec des rendements allant de bons à excellents (à l'exception des deux cas suivants : 1-méthoxy-2-méthyl-1-phénylpropane (48%) et 1-méthoxy-1-phénylpropane (24%)). On a observé que les valeurs de k_2 des alcools secondaires sont environ 10 fois plus élevées que celles des éthers méthyliques correspondants. La constante de vitesse d'oxydation d'un éther silylé est légèrement inférieure à celle de l'éther méthylique correspondant alors que celle du dérivé ester est approximativement égale à la moitié de la valeur. Pour l'oxydation des alcools et des éthers méthyliques, les valeurs de k_2 deviennent de plus en plus faibles avec une augmentation de l'empêchement stérique (Me, Et, *n*Pr, iPr, *t*-Bu) de la série R″ ($\rho^* = 1{,}7$; $r = 0{,}998$ et $\rho^* = 3{,}2$; $r = 0{,}95$ respectivement). Une étude de Hammett pour l'oxydation des éthers méthyliques des alcools benzyliques **10** et **20–25** conduit à une valeur de ρ de –0,74. Les paramètres d'activation pour l'oxydation du produit parent de la série des éthers (1-méthoxy-1-phényléthane) sont: $\Delta H = 14{,}8 \pm 0{,}5$ kcal/mol, $\Delta S = 21{,}9$ ue; $\Delta G = 21{,}3$ kcal/mol et k_2 (25°C) = $1{,}6 \times 10^{-3}$ M^{-1} s^{-1}. On discute des aspects mécanistiques de l'oxydation en relation avec deux mécanismes extrêmes : (*a*) insertion directe de l'atome d'oxygène dans la liaison C—H et (*b*) enlèvement direct de l'hydrogène par le diméthyldioxirane, conduisant à une paire de radicaux en cage, suivie d'un couplage subséquent formant des intermédiaires hémicétals qui se fragmentent ensuite pour donner de l'acétone, de l'alcool ou de l'eau et la cétone comme produits finals.

Mots clés : diméthyldioxirane, oxydation.

[Traduit par la Rédaction]

Introduction

Dimethyldioxirane, **1**, has become an extremely versatile reagent for the fast, mild oxidation of a great variety of organic substrates (for reviews, see ref. 1) since the initial report of its isolation and characterization (2, 3). Although considerably less reactive than methyl(trifluoromethyl)dioxirane (4), dimethyldioxirane is often the reagent of choice because of its facile, inexpensive preparation. For example, dimethyldioxirane has been shown to be useful (1) for olefin epoxidation, heteroatom oxidation, and oxidation of C—H bonds of saturated hydrocarbons, phenyl-substituted hydro-

Received September 2, 1998.

A memorial to Professor P.D. Bartlett. Your teaching continues to inspire!

A.L. Baumstark,[1] F. Kovac, and P.C. Vasquez. Department of Chemistry, Laboratory for BCS (Biological and Chemical Sciences), Georgia State University, Atlanta, GA 30303, U.S.A.

[1]Author to whom correspondence may be addressed. Telephone: (404) 651-1716. Fax: (404) 651-1416. e-mail: chealb@panther.gsu.edu

 © 1999 NRC Canada

Table 1. Second-order rate constants and product (ketone) yields for the oxidation of secondary alcohols, ethers, and related compounds by dimethyldioxirane in acetone at 25°C.

	R′	R″	Z	k_2 (M^{-1} s^{-1}) [a]	% Yield [b]	Relative reactivity
Alcohol						
2 [c]	Ph	Me	H	$(2.24\pm0.06) \times 10^{-2}$	98	≅1.00
3	Ph	Et	H	$(1.48\pm0.03) \times 10^{-2}$	92	0.66
4	Ph	*n*Pr	H	$(1.45\pm0.03) \times 10^{-2}$	92	0.65
5	Ph	iPr	H	$(1.02\pm0.02) \times 10^{-2}$	90	0.46
6	Ph	*t*Bu	H	$(6.9\pm0.1) \times 10^{-3}$	90	0.31
7	Ph	Ph	H	$(8.9\pm0.1) \times 10^{-3}$	96	0.40
8	Ph	Cyclopropyl	H	$(1.97\pm0.03) \times 10^{-2}$	92	0.88
9	Bz	Me	H	$(7.1\pm0.1) \times 10^{-3}$	85	0.32
Ethers						
10	Ph	Me	Me	$(1.63\pm0.03) \times 10^{-3}$	90	0.073
11	Ph	Et	Me	$1.03\pm0.02 \times 10^{-3}$	81	0.046
12	Ph	*n*Pr	Me	$(7.6\pm0.1) \times 10^{-4}$	86	0.034
13	Ph	iPr	Me	$(2.76\pm0.03) \times 10^{-4}$	48	0.012
14	Ph	*t*Bu	Me	$(2.23\pm0.03) \times 10^{-4}$	24	0.010
15	Ph	Ph	Me	$(1.79\pm0.04) \times 10^{-3}$	84	0.080
16	Ph	Cyclopropyl	Me	$(1.52\pm0.03) \times 10^{-3}$	88	0.068
17	Bz	Me	Me	$(8.4\pm0.1) \times 10^{-4}$	80	0.038
Miscellaneous						
18	Ph	Me	$SiMe_3$	$(1.48\pm0.03) \times 10^{-3}$	95	0.066
19	Ph	Me	Ac	$(9.2\pm0.1) \times 10^{-4}$	96	0.041

[a]Obtained under pseudo-first-order conditions; errors are the standard deviations between duplicate experiments.

[b]NMR yield (±4%) from reactions with at least a 3 to 1 ratio of dioxirane to substrate.

[c]Reference 5*f*.

carbons, aldehydes, and alcohols (5). In addition, there have been several reports on the use of **1** for the removal of benzyl protecting groups of alcohols (6) as well as the oxidation of other ethers, acetals, and orthoesters (7). Similar conversions have been carried out with methyl(trifluoromethyl)dioxirane (8). An earlier study (5*e*) of the reaction of **1** with benzaldehydes to produce benzoic acids indicated that the formal CH insertion process involved radical intermediates. Recently, a mechanistic study (5*f*) on the reaction of substituted α-methylbenzyl alcohols with dimethyldioxirane yielded results that could be interpreted as consistent with a direct reaction to yield caged-radical pairs. CH insertion studies on more difficult-to-oxidize positions by dioxiranes have been interpreted (8) to be consistent with a concerted insertion process. We report here a study of the oxidation of a series of secondary alcohols, the corresponding ethers, and related compounds by dimethyldioxirane in acetone.

Results

The reaction of excess dimethyldioxirane, **1**, with secondary alcohols (1-phenylethan-1-ol, **2**; 1-phenylpropan-1-ol, **3**; 1-phenylbutan-1-ol, **4**; 1-phenyl-2-methylpropan-1-ol, **5**; 1-phenyl-2,2-dimethylpropan-1-ol, **6**; benzhydrol, **7**; α-cyclopropylbenzyl alcohol, **8**; 1-phenyl-2-propanol, **9**), corresponding methyl ethers, **10**–**17**, and related compounds (1-trimethylsilyloxy-1-phenylethane, **18**; 1-acetoxy-1-phenylethane, **19**; 1-(*p*-anisyl)-1-methoxyethane, **20**; 1-(*p*-tolyl)-1-methoxyethane, **21**; 1(*p*-fluorophenyl)-1-methoxyethane, **22**; 1-(*p*-chlorophenyl)-1-methoxyethane, **23**; 1-(*p*-bromophenyl)-1-methoxyethane, **24**; 1-(*p*-trifluoromethylphenyl)-1-methoxyethane, **25**) produced the corresponding ketones in good to excellent yields in most cases (reaction [1]). Generally, under similar conditions the yields of ketones were higher from the oxidation of alcohols **2**–**9** than from that of the methyl ethers **10**–**17**.

In most cases, at least a threefold excess of **1** was necessary to achieve efficient conversion. For all but the slowest oxidation reactions, use of an inert (N_2) atmosphere resulted in product yields within experimental error of those obtained when open to the atmosphere. Low yields of ketones were obtained in two cases, the dimethyldioxirane oxidation of 1-methoxy-2-methyl-1-phenylpropane, **13**, and 1-methoxy-2,2-dimethyl-1-phenylpropane, **14** (48% and 24%, respectively). The products (ketones) were isolated and identified by comparison of NMR and GC–MS data with those of authentic samples. The product yields are listed in Table 1.

Kinetic studies of the oxidation of **2**–**19** were carried out in acetone at 25°C by UV techniques. Excellent linear correlations were obtained under pseudo-first-order conditions with either the dioxirane or the substrate in at least a 10-fold

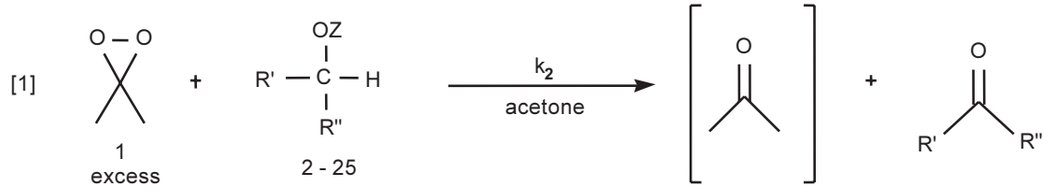

© 1999 NRC Canada

Table 2. Effect of temperature and added solvents on the second-order rate constants for oxidation of 1-methoxy-1-phenylethane (**10**) by dimethyldioxirane.

k_2 (M^{-1} s^{-1})	Temperature ±0.3°C	Solvent
(1.37±0.03) × 10^{-3}	20.0°C	Acetone
(1.63±0.03) × 10^{-3}	25.0°C	Acetone
(2.59±0.03) × 10^{-3}	30.0°C	Acetone
(4.65±0.05) × 10^{-3}	35.0°C	Acetone
(5.74±0.06) × 10^{-3}	40.0°C	Acetone
(1.05±0.01) × 10^{-2}	45.0°C	Acetone
(2.44±0.03) × 10^{-3}	25.0°C	H_2O–acetone (1.0:5.5 by vol)
(1.73±0.03) × 10^{-3}	25.0°C	CH_2Cl_2–acetone (1.0:1.0 by vol)
(1.82±0.02) × 10^{-3}	25.0°C	$CHCl_3$–acetone (1.0:1.0 by vol)

Table 3. Product yields (ketone) and second-order rate constants for the oxidation of 1-methoxy-1-arylethanes (secondary *p*-substituted benzyl methyl ethers) by dimethyldioxirane in acetone at 25°C.

Compound	*p*-X	% Yield [a]	k_2 (M^{-1} s^{-1}) [b]
20	MeO	98 (98)	(3.10±0.05) × 10^{-3}
21	Me	84 (94)	(2.22±0.05) × 10^{-3}
10	H	83 (90)	(1.63± 0.03) × 10^{-3}
22	F	76 (89)	(1.31±0.03) × 10^{-3}
23	Cl	78 (82)	(1.21±0.03) × 10^{-3}
24	Br	74 (80)	(1.11±0.03) × 10^{-3}
25	CF_3	61 (62)	(7.2±0.1) × 10^{-4}

[a] ±4% under N_2 (O_2); 3 to 1 ratio of dioxirane to substrate.

[b] Pseudo-first-order conditions with 10-fold excess of dioxirane.

excess. Either approach yielded k_2 values within experimental error (±5%) as expected for this second-order reaction. For convenience, most experiments were carried out with a 10-fold excess of dioxirane. Reproducibility between duplicate runs was excellent (generally 1–2%). In general, the k_2 values for oxidation of the alcohol series were at least 10-fold greater than those for the corresponding methyl ether series. The k_2 values for **13** and **14**, the only compounds for which the product yields were poor, were the lowest in the entire set of data. Formal replacement of the methyl ether in **10** by either the trimethylsilyl ether (**18**) or the acetate (**19**) yielded k_2 values that were slightly lower with excellent product yields. Formal replacement of the phenyl group in compounds **2** and **10** by a benzyl group (**9** and **17**) produced k_2 values that were three- and twofold slower, respectively. Oxidation of both the alcohol and methyl ether series showed the same general trend: as the alkyl group in the α-position (R″, Table 1) becomes bulkier, the k_2 value becomes smaller (Me > Et > *n*Pr > iPr > *t*Bu). An excellent correlation (r = 0.998) was obtained for a plot of log k_2 vs. σ* with a Taft ρ* value of 1.7 for compounds **2**–**6**. The corresponding methyl ether series, **10**–**14**, showed a marginal correlation (r = 0.95) with a ρ* of 3.2. The k_2 value for R″= cyclopropyl in both series is only slightly lower than for R = methyl, and higher than for R″ = ethyl. A minor discrepancy between the two series is for R″ = phenyl: k_2 for **7** falls between **5** (R″ = iPr) and **6** (R″ = *t*Bu); and k_2 for **15** is slightly faster than that for **10** (R″ = Me). The kinetic data (second-order rate constants k_2) are summarized in Table 1.

The oxidation reaction of 1-methoxy-1-phenylethane (**10**) and *p*-substituted analogs **20**–**25** by dimethyldioxirane was chosen for futher characterization. Unlike epoxidation reactions (5*e)* with **1**, the ether oxidations did not show large changes in rate upon addition of water to the solvent. This result is similar to that found (5*f*) for the dimethyldioxirane oxidation of α-methylbenzyl alcohols. Rate accelerations that correlated with the hydrogen bond donor capacity of the medium have been noted (5*c*) for the reaction of **1** with *cis*-1,2-dimethylcyclohexane. Additional solvent effect studies including some intramolecular hydrogen-bonding effects have been described (*5g*). The rate constants for the oxidation of **10** were determined at 5° intervals from 20° to 45°C (see Table 2). The activation parameters determined by the Arrhenius method were found to be $\Delta H^{\ddagger}$ = 14.8 ± 0.5 kcal/mol; $\Delta S^{\ddagger}$ = –21.9 e.u.; $\Delta G^{\ddagger}$ = 21.3 kcal/mol; k_2 (25°C) = 1.63 × 10^{-3} M^{-1} s^{-1}. In addition, the oxidation of *p*-substituted analogs of **10** showed that electron-donating groups increased the rate of oxidation while electron-withdrawing groups decreased it. A Hammett plot of the second-order rate constants at 25°C for oxidation of **10** and **20**–**25** by **1** showed an excellent LFER against σ_p constants with a ρ value of –0.74 ± 0.03. These data are shown in Table 3.

Discussion

The oxidations of secondary alcohols and hydrocarbons by **1** and methyl(trifluoro-methyl)dioxirane have been interpreted (1, 5*a*–*d*, 8) in terms of direct reaction without involvement of a chain process. Recently, Ingold and coworkers (9) have shown, based on radical rearrangement arguments, that the oxidation of 2-cyclopropylpropane by **1** is not a free-radical chain process. Historically, the AIBN catalyzed O_2 oxidation of benzyl methyl ether was found (10*a*) to be faster than that of benzyl alcohol. The direct reaction of **1** with secondary methyl ethers also shows different characteristics from those of free-radical chain processes. The results clearly show that the oxidation of secondary alcohols by **1** is at least 10-fold faster than that of the corresponding methyl ethers and related derivatives. The Hammett ρ value of –0.74 for oxidation of methyl ethers **10** and **20**–**25** by **1** is essentially equivalent to that of –0.7, as was obtained (5*f* : note, the ρ value reported was off by 2.303; correct value is –0.7) for the oxidation of alcohol **2** derivatives. Free-radical reactions on benzyl ethers, hydrogen atom abstraction by alkyl peroxy radicals on benzyl phenyl ether (5, 9*a*), or by benzoyloxy radicals on dibenzyl ether (5, 10*b*), were found to show ρ values of –0 and –0.65, respectively. The direct reaction of *p*-nitroperbenzoic acid with substituted benzyl

© 1999 NRC Canada

Scheme 1.

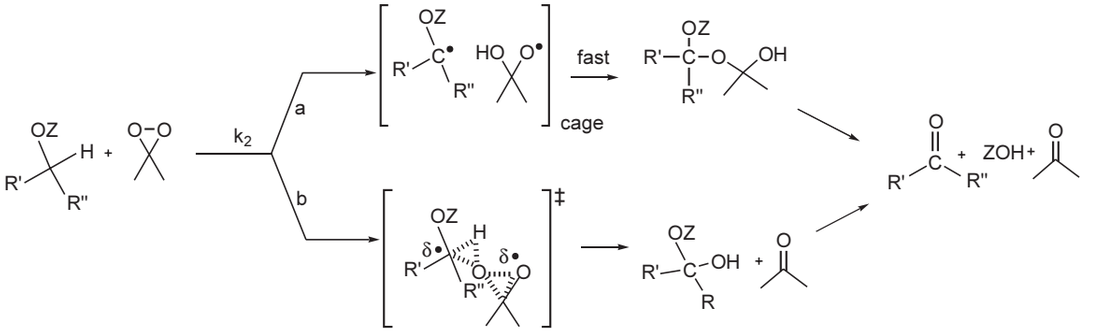

methyl ethers was found (11*a*) to show a ρ^+ value of –0.9. The differences in activation parameters for oxidation of the secondary methyl ethers by **1** vs. those of the secondary alcohols (5*f*) are roughly an increase of 3 kcal/mol in $\Delta H^{\ddagger}$ and a decrease in $\Delta S^{\ddagger}$ (less negative). A $\Delta S^{\ddagger}$ of approximately –15 eu has been estimated (8) for the oxidation of cyclohexanol by methyl(trifluoromethyl)dioxirane. The relative reactivity as a function of R″ within the alcohol and methyl ether series shows similar trends. Plots of log k_2 vs. σ^* constants give reasonable correlations with the greater sensitivity found in the ether series. The sign of the ρ^* is opposite that of the Hammett ρ value and opposite that found (11*b)* for ρ^* for the reaction of *p*-nitroperbenzoic acid with substituted alkenes. The ρ^* of reaction [1] presumably is strongly influenced by steric effects. The data showed a poor correlation with the Taft steric parameter (E_S). The lower reactivity of methyl ether series coupled with the larger range of relative reactivity could be viewed as a steric effect. Alternatively, it could be argued that the alcohols undergo faster oxidation by **1** due to hydrogen bonding with **1** and (or) the solvent. Our deuterium isotope effect study (5*f*) for the oxidation of **2** with dimethyldioxirane has shown a k_{OH}/k_{OD} value of 1.09. This value could represent a large secondary effect or perhaps an extremely small primary effect, indicative of a hydrogen bond between the alcohol OH and the dioxirane in the transition state.

The reaction of dimethyldioxirane with secondary alcohols, ethers, and related derivatives can be viewed in terms of two mechanistic extremes: (*a*) a direct insertion process and (*b*) a caged-radical process (Scheme 1). The direct insertion process has been postulated (1, 8) to involve an "oxenoid" atom insertion into the side of the C—H bond via a multicentered transition state. Our previous study (5*f*) of the oxidation of α-methylbenzyl alcohols by **1** was interpreted in terms of a caged-radical process in which direct reaction of **1** and the substrate yields a singlet pair of radicals that are not solvent separated. For the caged-radical process to be valid, combination of the radicals must be faster than both rearrangement of the carbon-based radical and escape from the cage. In addition, for the oxidation of methyl ethers (Z = Me), the caged-radical process must yield a hemiketal, which would be expected to rapidly fragment to the final products. The concerted process has been favored (8) as the simplest explanation due, in part, to the lack of detection of (hemiketal) intermediates for secondary alcohol and hydrocarbon oxidation. At present, the data do not clearly distinguish between these two possibilities. Note that for secondary ether oxidation, hemiketal intermediates must be formed regardless of pathway. The two mechanisms are not necessarily mutually exclusive. The trajectory of approach of the dioxirane to the C—H bond remains to be elucidated.

In conclusion, the oxidation of secondary alcohols, methyl ethers, and related derivatives with excess dimethyldioxirane generally produces high yields of ketones. Reaction times are convenient if a 10-fold excess of dioxirane is employed. The differences in reactivity with each series and between different series of compounds show the method to be of synthetic utility.

Experimental

A. General

Infrared spectra were recorded on a Perkin–Elmer system 2000 FT-IR spectrophotometer. All ^{1}H NMR and ^{13}C NMR spectra were obtained in chloroform-d_1 at 30°C on a Varian 300 MHz spectrometer. The GS–MS data were obtained on a Shimadzu GC-17A gas chromatograph coupled to a Shimadzu QP-5000 mass spectrometer.

All solvents were either spectral or HPLC grade (Aldrich). Dimethyldioxirane (**1**) was prepared and isolated by a modified version (12) of the general method developed by Murray and Teyaraman (3*a*). The redistilled acetone solution (≤0.1 M) of **1** was stored at –20°C with little or no decomposition after several weeks (over $MgSO_4$). Initial dioxirane concentration was determined by NMR techniques (integration of thioanisole and oxidation product signals) for reaction of the stock solution with a known quantity of thioanisole. The value was within experimental error (±5%) of that determined by monitoring the change in absorbance at 330 nm before and after reaction with excess 2,3-dimethyl-2-butene (added neat via syringe) and dividing by the ε value of 12.9. All the final products (ketones) and alcohols **2**, **3**, **6**, **7**, and **9** were commercially available (Aldrich) and were used without further purification. Alcohols **4**, **5**, and **8** were prepared from the corresponding ketones (Aldrich) by conventional $NaBH_4$ reduction and were purified by vacuum distillation. Methyl ethers **10**–**17** and **20**–**25** were prepared in ~65% yields by a two-step procedure: first, the parent ketones of alcohols **2–9** were converted to their corresponding dimethyl ketals (13) by treatment with methyl orthoformate in methanol (HCl catalyst); after purification by vacuum distillation the dimethyl ketals were converted to the corresponding methyl ethers (14*a*) by treatment with $AlCl_3$ in ethyl ether, followed by $LiAlH_4$; the methyl ethers were purified by vacuum distillation. The boiling points of the methyl ethers were in good agreement with literature values (14). Silyl

© 1999 NRC Canada

ether **18** and acetate **19** were prepared from alcohol **2** by standard silylation (Me_3SiCl–Et_3N) and acylation (Ac_2O) procedures, and were purified by vacuum distillation. All compounds were characterized by physical and spectral (^1H NMR, IR, and GC–MS) data.

B. Kinetic studies

Kinetic experiments were performed using a Shimadzu UV-3101PC UV-VIS-NIR scanning spectrometer. The cell temperature (25°C unless specified) was maintained via a constant temperature circulating bath (± 0.3°C) and was checked before and after each kinetics run using a YSI model 425C telethermometer with a number 423 probe. The following is a general, representative procedure for the kinetics studies: dimethyldioxirane solutions (1.000 mL, 10 equiv.) of known concentration (≤0.100 M) in dried acetone were placed in a 1 cm UV cell at the desired temperature. After temperature equilibration, 1.0 equiv. of the substrate in 0.100 mL acetone was added via syringe and the solution was rapidly mixed by bubbling air via disposable pipet. The reaction was monitored by measuring the change in absorbance at 380 nm vs. time (pseudo-first-order conditions). The ε value at 380 nm for **1** is 4.51 ± 0.03. The value of the relative absorbance was determined by subtraction of the final value from the instantaneous value as a function of time. The pseudo-first-order rate constants (k_{obs}) were calculated by plotting the ln (relative absorbance) versus time and were linear for at least two half-lives. The second-order rate constants (k_2) were calculated by dividing the pseudo-first-order rate constant (k_{obs}) by the initial concentration of dimethyldioxirane. Reproducibility between runs was generally better than 5% of the k_2 value. Correlation coefficients were excellent for all experiments. Several experiments were repeated under pseudo-first-order conditions with the substrate in 10-fold excess. The rate constants were found to be essentially identical (within experimental error) to those determined with **1** in excess, confirming the validity of the approach.

C. Product studies

The products from the reaction of compounds **2**–**25** with 3 equiv. of isolated dimethyl-dioxirane at room temperature (~1.5 mmol of substrate) were analyzed after 6–24 h by GC–MS. The GC–MS data showed the ketones to be formed in high yield in all cases except for oxidation of **13** and **14**. The GC–MS data were in excellent agreement with those of authentic ketone samples. After removal of the solvent (acetone), the residue was taken up in $CDCl_3$ and then was analyzed by ^1H NMR spectroscopy. The ^1H NMR data were in agreement with those of authentic (commercial) ketone samples. For most cases (within experimental error), little or no reduction in final ketone yields was observed for reactions carried out under inert (N_2) atmosphere. The percentage yields (±4%) were determined (with anisole as added internal standard) from the ^1H NMR spectral data.

Acknowledgments

Acknowledgment is made to the National Science Foundation (CHE-9017230), to the U.S. Army ERDEC SEAS subcontract via Clark Atlanta University (DAAA 15–94-K–0004), and to the Georgia State University Research Fund for financial support of this work.

References

1. (*a*) R. Curci. *In* Advances in oxygenated processes. Vol. 2. *Edited by* A.L. Baumstark. JAI Press, Greenwich, Conn. 1990; (*b*) R.W. Murray. Chem. Rev. **89**, 1187 (1989); (*c*) W. Adam, L.P. Hadjiarapoglou, R. Curci, and R. Mello. *In* Organic peroxides. *Edited by* W. Ando. Wiley and Sons, Chichester, England. 1992. Chap. 4.
2. (*a*) J.O. Edwards, R.H. Pater, R. Curci, and F.D. Fusca. Photochem. Photobiol. **30**, 63 (1979); (*b*) R. Curci, M. Fiorentino, L. Froisi, J.O. Edwards, and R.H. Pater. J. Org. Chem. **45**, 4758 (1980).
3. (*a*) R.W. Murray and R. Teyaraman. J. Org. Chem. **50**, 2847 (1985); (*b*) R.W. Murray, R. Jeyaraman, and L. Mohan. Tetrahedron Lett. **27**, 2335 (1986).
4. R. Mello, M. Fiorentino, O. Sciacovelli, and R. Curci. J. Org. Chem. **53**, 3890 (1988).
5. (*a*) R.W. Murray, R. Jeyaraman, and R. Mohan. J. Am. Chem. Soc. **108**, 2470 (1986); (*b*) R. Mello, M. Fiorentino, C. Fusco, and R. Curci. J. Am. Chem. Soc. **111**, 6749 (1989); (*c*) R.W. Murray and Gu. Daquan. J. Chem. Soc. Perkin Trans. 2, 451 (1994); (*d*) D. Kuck, A. Schuster, C. Fusco, M. Fiorentino, and R. Curci. J. Am. Chem. Soc. **116**, 2375 (1994); (*e*) A.L. Baumstark, M. Beeson, and P.C. Vasquez. Tetrahedron Lett. **30**, 5567 (1989); (*f*) A.L. Baumstark and F. Kovac. Tetrahedron Lett. **35**, 8751 (1994); (*g*) R.W. Murray and H. Gu. J. Phys. Org. Chem. **2**, 751 (1996).
6. (*a*) R. Csuk and P. Dörr. Tetrahedron, **50**, 9983 (1994); (*b*) B.A. Marples, J.P. Muxworthy, and K.H. Baggaley. Synlett, 646 (1992).
7. (*a*) R. Curci, L. D'Accolti, M. Fiorentino, C. Fusco, W. Adam, M.E. Gonzalez-Nunez, and R. Mello. Tetrahedron Lett. **33**, 4225 (1992); (*b*) A. Messegues, M. Fener, F. Sanchez-Baeza, and J. Casas. Tetrahedron Lett. **35**, 2981 (1994).
8. (*a*) R. Curci, M. Fiorentino, C. Fuseo, and R. Mello. *In* Dioxygen activation and homogenous catalytic oxidation. *Edited by* L.I. Simándi. Elsevier Science Publishers B.V., Amsterdam. 1991. pg. 147; (*b*) W. Adam and L.P. Hadjiarapoglou. Top. Curr. Chem. **164**, 45 (1993); (*c*) R. Curci, A. Dinoi, and M.F. Rubino. Pure Appl. Chem. **67**, 811 (1995).
9. R. Vanni, S.J. Garden, J.T. Banks, and K.U. Ingold. Tetrahedron Lett. 7999 (1995).
10. (*a*) G.A. Russell and R.C. Williamson, Jr. J. Org. Chem. **12**, 2357 (1964); (*b*) R.L. Huang, H.H. Lee, and S.H. Ong. J. Chem. Soc. 3336 (1962).
11. (*a*) H.J. Schneider, A. Ahlhelm, and W. Mueller. Chem. Ber. 3297 (1984); (*b*) H.J. Schneider and W. Mueller. J. Org. Chem. **50**, 4609 (1985).
12. (*a*) A.L. Baumstark and C.J. McCloskey. Tetrahedron Lett. 3311 (1987); (*b*) W. Adam, L. Hadjiarapoglou, and J. Bialas. Chem. Ber. **124**, 2377 (1991).
13. C.E. Kaslow and W.R. Lawton. J. Am. Chem. Soc. **72**, 1723 (1950).
14. (*a*) E.L. Eliel, V.G. Badding, and M.N. Rerick. J. Am. Chem. Soc. **84**, 2371 (1962); (*b*) M. Shi, Y. Okamoto, and S. Takamuku. J. Org. Chem. **55**, 3821 (1990); (*c*) J.P. McCormick and D.L. Barton. J. Org. Chem. **45**, 2566 (1980).

© 1999 NRC Canada

One-dimensional ribbons of solvated Ag sulfonates

George K.H. Shimizu, Gary D. Enright, Gabriela S. Rego, and John A. Ripmeester

Abstract: Single crystal X-ray structure determinations of two solvated silver sulfonates have been obtained and these compounds have been shown to adopt infinite one-dimensional motifs. $\{AgOTs(MeCN)\}_\infty$ (OTs = *p*-toluenesulfonate) crystallizes in the monoclinic space group, $P2_1$, a = 8.4278(5) Å, b = 5.7413(3) Å, c = 12.1057(7) Å, β = 109.24(1)°. $\{Ag(NDSA)(MeCN)_2(H_3O)(H_2O)_2\}_\infty$ (NDSA = 1,5-naphthalenedisulfonate) crystallizes in the triclinic space group, $P\bar{1}$, a = 8.3407(4) Å, b = 10.4374(5) Å, c = 12.3399(6) Å, α = 101.941(8)°, β = 109.24(1)°, γ = 102.190(8)°. Despite one compound containing a monosulfonate and the other a disulfonate, both complexes form infinite one-dimensional arrays.

Key words: silver, sulfonates, coordination polymer.

Résumé : Une détermination de structure de deux sulfonates d'argent solvatés par rayons X sur un cristal unique montre que ces composés adoptent un motif infini unidimensionnel. Le composé $\{AgOTs(MeCN)\}_\infty$ (OTs = *p*-toluènesulfonate) cristallise dans le groupe d'espace monoclinique $P2_1$, avec a = 8,4278(5) Å, b = 5,7413(3) Å, c = 12,1057(7) Å, β = 109,24(1)°. Le composé $\{Ag(NDSA)(MeCN)_2(H_2O)_2\}_\infty$ (NDSA = 1,5-naphtalènedisulfonate) cristallise dans le groupe d'espace triclinique $P\bar{1}$, avec a = 8,3407(4) Å, b = 10,4374(5) Å, c = 12,3399(6) Å, α = 101,941(8)°, β = 109,24(1)°, γ = 102,190(8)°. En dépit du fait qu'un composé soit un monosulfonate et l'autre un disulfonate, les deux complexes forment une chaîne infinie à une dimension.

Mots clés : argent, sulfonates, polymère de coordination.

[Traduit par la Rédaction]

Introduction

The coordinate covalent bond is increasingly being recognized as a powerful tool in the generation of ordered solid state arrays (1). We are in the process of probing the chemistry of silver(I) with sulfonate anions (2). These compounds form a layered network bearing a strong structural analogy to the much studied Zr phosphonates (3). A characteristic of silver(I) is its rather pliant coordination sphere. Coordination numbers ranging from two to four are common and even five- and six-coordinate complexes have been observed (4). In a positive light, this imparts an element of versatility to the frameworks. However, this flexibility comes at the cost of predictability of the overall structure, a crucial factor for crystal engineering (5). Elucidation of the fundamental bonding interactions, which exist in solution prior to crystallization, is critical if a true element of structural control is to be achieved.

Received August 20, 1998.

G.K.H. Shimizu,[1] G.D. Enright, G.S. Rego, and J.A. Ripmeester. Steacie Institute for Molecular Sciences, National Research Council of Canada, Ottawa, ON K1A 0R6, Canada.

[1]Author to whom correspondence may be addressed. Current address: Department of Chemistry, University of Calgary, 2500 University Drive N.W., Calgary, AB T2N 1N4, Canada. Telephone: (403) 220-5347. Fax: (403) 289-9488. e-mail: gshimizu@ucalgary.ca

Silver *p*-toluenesulfonate, AgOTs, forms an infinite lamellar structure containing 7-coordinate silver(I) and a fivefold bridging sulfonate group (2). This crystal structure was obtained from relatively non-coordinating solvents (MeOH, ether). As part of our ongoing examination of solvent effects on the structures of silver sulfonates, we present the coordination polymer structures of two silver sulfonates, $\{AgOTs(MeCN)\}_\infty$, **1**, and $\{Ag(NDSA)(MeCN)_2(H_3O)(H_2O)_2\}_\infty$ (NDSA = 1,5-naphthalenedisulfonate), **2**, grown from solutions of a coordinating nitrile solvent. Despite one compound containing a monosulfonate and the other a disulfonate, both complexes form infinite one-dimensional arrays.

Results and discussion

Crystallographic data for **1** and **2** are presented in Tables 1–5.

Structure of $\{AgOTs(MeCN)\}_\infty$, 1

Commercially available AgOTs was dissolved in MeCN and single crystals were grown by the slow diffusion of isopropyl ether into this solution. Figure 1 shows the structure of the resulting one-dimensional array. Each Ag(I) ion adopts a distorted tetrahedral geometry comprising three sulfonate oxygen atoms (Ag—O distances are 2.308(2), 2.364(3), and 2.438(3) Å), each from a different OTs group, and a nitrogen donor from a coordinated MeCN molecule (2.187(2) Å). Bond angles around Ag range from 94.94(9)°

© 1999 NRC Canada

Table 1. Crystallographic data for **1** and **2**.

Formula	$C_9H_{10}NSO_3Ag$ **1**	$C_{14}H_{19}N_2S_2O_9Ag$ **2**
fw	320.11	531.29
Crystal system	Monoclinic	Triclinic
Space group	$P2_1$	$P\bar{1}$
a (Å)	8.4278(5)	8.3407(4)
b (Å)	5.7413(3)	10.4374(5)
c (Å)	12.1057(7)	12.3399(6)
α(degrees)		101.94(1)
β (degrees)	109.24(1)	96.835(8)
γ(degrees)		102.19(1)
V (Å^3)	553.05(5)	1012.33(8)
Z (molecules/unit cell)	2	2
D_{calc} (g/cm^3)	1.922	1.743
μ (mm^{-1})	1.99	1.25
Crystal dimensions (mm^3)	0.10 × 0.16 × 0.25	0.07 × 0.20 × 0.30
Radiation, λ (Å)	0.7093	0.7093
2θ (max)	57.7	57.3
Reflections with $I > 2.5\sigma I$	2712	4445
Total unique reflections	2827	5180
Total measured reflections	6372	11908
R_f (sig. reflections)	0.02	0.035
R_w (sig. reflections)	0.022	0.04
Maximum shift / σ ratio	0.003	0.036
Goodness of fit	1.77	2.35
Last *D*-map (e/Å^3)		
Deepest hole	–0.490	–0.570
Highest peak	0.520	0.740

$R_f = (\sum (F_o - F_c) / \sum (F_o)$; $R_w = (\sum w (F_o - F_c)^2 / \sum w(F_o)^2)^{0.5}$

Table 2. Atomic bond distances for **1**.

Bond	Length (Å)
Ag—N	2.186(2)
Ag—O1	2.364(3)
Ag—O2	2.308(2)
Ag—O2a	2.483(3)
S—O1	1.452(3)
S—O2	1.495(2)
S—O3	1.444(3)
O1—Aga	2.364(3)
O2—Agb	2.438(3)
N—C8	1.136(4)
C8—C9	1.470(4)
C1—C2	1.388(5)
C1—C6	1.382(5)
C2—C3	1.388(5)
C3—C4	1.389(5)
C4—C5	1.386(6)
C4—C7	1.515(5)
C5—C6	1.384(5)

Table 3. Atomic bond angles for **1**.

Bonds	Angle (deg)	Bonds	Angle (deg)
N-Ag-O2	131.9(1)	Ag-O2-Agb	112.3(1)
N-Ag-O2a	108.9(2)	Ag-O2-S	119.6(1)
N-Ag-O1b	112.3(1)	Agb-O2-S	120.0(2)
O2-Ag-O2a	96.02(9)	Aga-O1-S	130.5(2)
O2-Ag-O1b	94.94(9)	C1-C6-C5	119.8(5)
O2a-Ag-O1b	110.89(9)	S-C1-C6	119.8(3)
O2-S-O1	110.7(2)	S-C1-C2	119.8(2)
O2-S-O3	112.0(2)	C6-C1-C2	120.3(3)
O2-S-C1	103.7(1)	C2-C3-C4	120.9(3)
O1-S-O3	114.0(2)	C1-C2-C3	119.3(3)
O1-S-C1	107.5(2)	C3-C4-C5	118.9(3)
O3-S-C1	108.3(2)	C4-C5-C6	120.7(4)
Ag-N-C8	166.6(2)	C3-C4-C7	120.7(4)
N-C8-C9	176.5(8)	C5-C4-C7	120.4(4)

to 131.9(1)°. Each toluenesulfonate ion is coordinated, via two of the oxygen atoms, to two different silver(I) centers. Figure 2 shows the packing, along the *b* axis, of the one-dimensional arrays. There are no interactions, save for van der Waals' contacts, between adjacent 1-D polymers. It should be noted that the MeCN in this structure is lost quite readily to afford a white solid. This desolvated product has been determined, by powder X-ray diffraction, to have the same layered structure as single crystals grown from a methanolic solution.

Structure of $\{Ag(NDSA)(MeCN)_2(H_7O_3^+)\}_\infty$, 2

Large block-like crystals of $\{Ag(NDSA)(MeCN)_2(H_7O_3^+)\}_\infty$, **2**, were grown by diffusion of diethyl ether into a MeCN solution consisting of 2 equiv. of $AgBF_4$ and 1 equiv. of the

© 1999 NRC Canada

Table 4. Atomic bond distances for **2**.

Bond	Length (Å)	Bond	Length (Å)
Ag—O1	2.439(2)	C1—C5	1.371(3)
Ag—O6a	2.380(2)	C4b—C5	1.397(40
Ag—N1	2.204(3)	C6—C7	1.440(3)
Ag—N2	2.220(2)	C6—C10	1.367(4)
S1—C1	1.775(2)	C7—C8	1.423(3)
S1—O1	1.461(2)	C8—C9	1.363(4)
S1—O2	1.448(2)	C2—C2b	1.416(5)
S1—O3	1.453(2)	C7—C7c	1.421(5)
S2—O4	1.455(2)	C9—C10c	1.410(4)
S2—O5	1.459(2)	C9c—C10	1.410(4)
S2—O6	1.450(2)	C11—C12	1.458(4)
S2—C6	1.778(3)	C11—N1	1.126(4)
C1—C2	1.435(3)	C13—C14	1.450(4)
C2—C3	1.427(3)	C13—N2	1.133(4)
C3—C4	1.378(3)	Agd—O6	2.380(2)
C4—C5b	1.397(4)		

Table 5. Atomic bond angles for **2**.

Bonds	Angle (deg)	Bonds	Angle (deg)
O1-Ag-O6a	84.98(6)	C7-C8-C9	120.7(2)
O1-Ag-N1	122.05(8)	C3-C4-C5b	120.7(2)
O1-Ag-N2	92.79(8)	S1-C1-C2	121.6(2)
O6a-Ag-N1	106.02(8)	S1-C1-C5	117.4(2)
O6a-Ag-N2	116.02(9)	C2-C1-C5	121.0(2)
N1-Ag-N2	127.34(9)	C4-C3-C2	120.2(2)
C1-S1-O1	106.7(1)	C1-C2-C3	122.3(2)
C1-S1-O2	105.8(1)	C1-C2-C2b	118.1(2)
C1-S1-O3	106.2(1)	C3-C2-C2b	119.6(2)
O1-S1-O2	111.8(1)	C6-C7-C8	122.6(2)
O1-S1-O3	112.8(1)	C6-C7-C7c	117.9(2)
O2-S1-O3	112.8(1)	C8-C7-C7c	119.6(2)
C6-S2-O4	106.2(1)	C4b-C5-C1	120.5(2)
C6-S2-O5	106.3(1)	C8-C9-C10c	120.5(2)
C6-S2-O6	106.5(1)	N2-C13-C14	179.6(3)
O4-S2-O5	112.6(1)	C6-C10-C9c	120.5(2)
O4-S2-O6	113.1(1)	Ag-O1-S1	126.0(1)
O5-S2-O6	111.5(1)	Agd-O6-S2	132.4(1)
S2-C6-C7	120.8(2)	Ag-N1-C11	177.35(2)
S2-C6-C10	118.4(2)	Ag-N2-C13	176.4(3)
C7-C6-C10	120.8(2)	N1-C11-C12	179.4(3)

sodium salt of 1,5-naphthalenedisulfonic acid tetrahydrate. Interestingly, the formulation of the crystals contains only a 1:1 ratio of metal to disulfonate. To achieve charge balance, a single hydronium ion, originating from the hydrate molecules of the starting sulfonate salt, is present in the unit cell.

The structure of **2** reveals another one-dimensional polymeric structure. The nature of the extended system is fundamentally different than that in **1** as, in this case, there are two different sulfonate groups on each ligand. Figure 3 shows that each sulfonate group functions in a monodentate manner coordinating to a single silver(I) center (Ag—O = 2.380(2) and 2.439(2)Å). In **1**, the multidentate coordination mode of the SO_3 groups is the basis of the polymeric architecture. The coordination environment around silver is a tetrahedron comprised of two sulfonate oxygen atoms, from different disulfonate molecules, and two MeCN molecules (Ag—N = 2.204(3) and 2.220(2)Å). As the sulfonate ligand is dianionic and only a single silver(I) ion is present for each of these molecules, a hydronium ion (H_3O^+) is also present. The hydronium ion, along with two water molecules, forms part of a hydrogen-bonded $H_7O_3^+$ bridge between sulfonyl oxygen atoms of adjacent $Ag(NDSA)^-$ ribbons, as shown in Fig. 4. O—O distances in the H-bonded array range from 2.459(2) to 2.703(2) Å. Figure 5 shows the overall packing motif of **2**, where $(Ag\text{-}NDSA)^-$ layers alternate with layers of $H_7O_3^+$ units.

Fig. 1. Single crystal X-ray structure of **1**, showing the infinite one-dimensional array and coordination of MeCN at silver(I). Hydrogen atoms omitted for clarity.

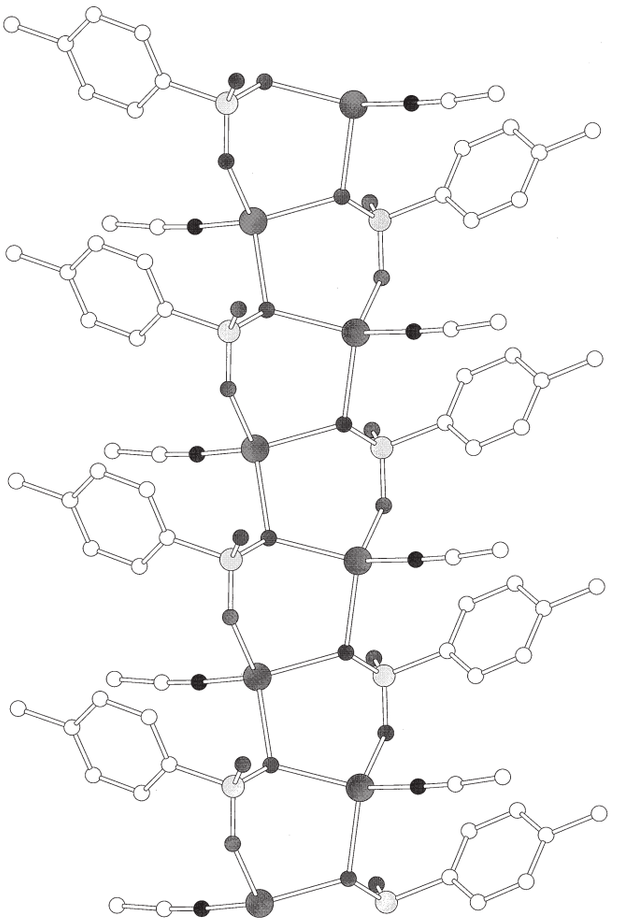

Crystals of **2** lose solvent readily, as did the crystals of **1**, to afford a white powder. Our attempts to index the powder X-ray diffraction pattern of this compound have not been successful, possibly indicating the presence of lower symmetry. However, the present results lend encouragement towards the prospect of forming infinite lamellar networks with the disulfonate ligands, where the disulfonate moieties would act to "pillar" the interlayer region (6). Further studies on the effects of different solvents and anhydrous conditions are in progress.

© 1999 NRC Canada

Fig. 2. View down the *b* axis, showing the packing of **1** in three dimensions. Hydrogen atoms omitted for clarity.

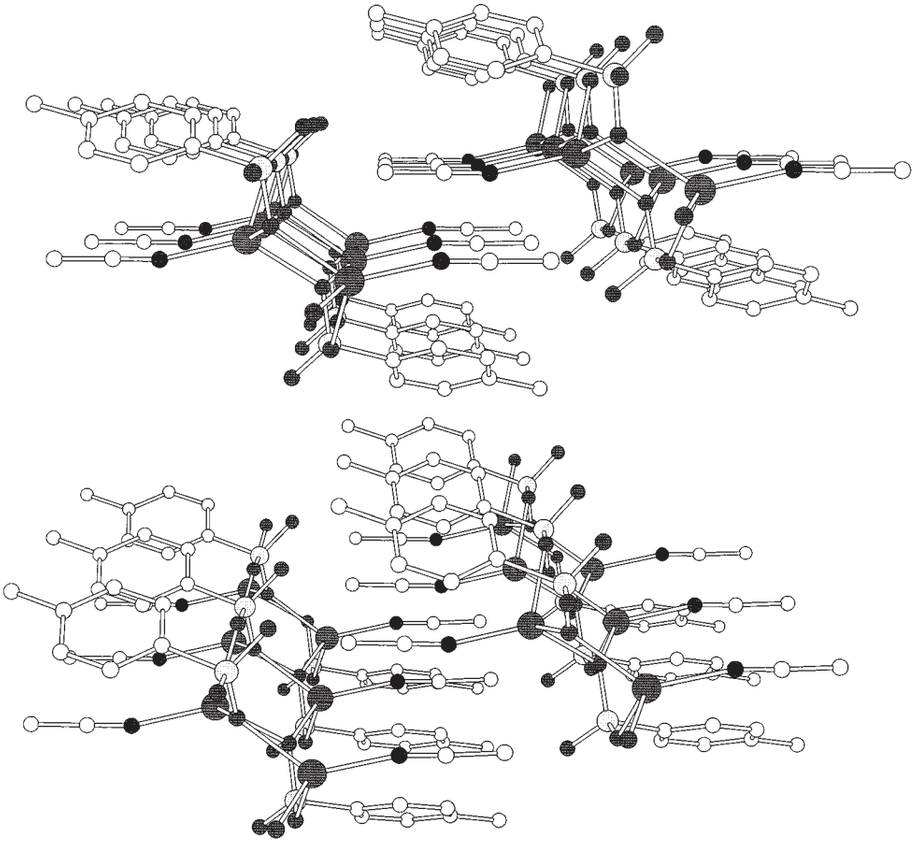

Fig. 3. ORTEP plot of the unique unit of **1**, showing the atom numbering scheme. Ellipsoids of 30% probability are shown. H atoms omitted for clarity.

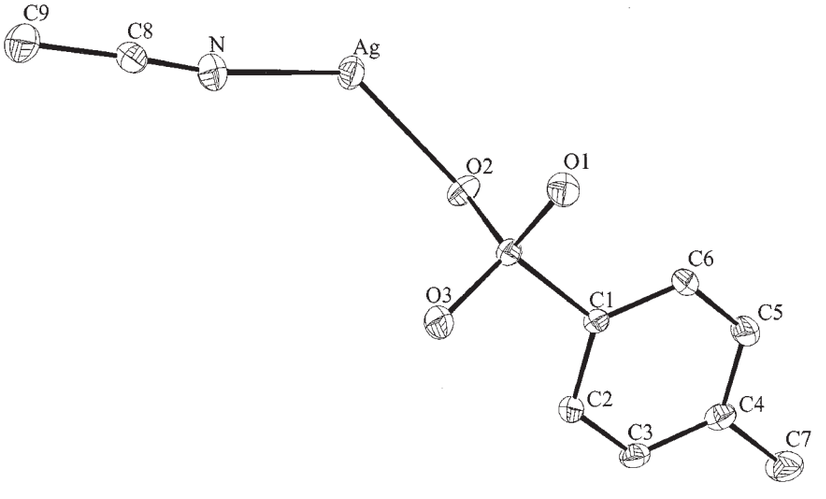

Experimental

Silver tetrafluoroborate, silver *p*-toluenesulfonate, and sodium 1,5-naphthalenedisulfonic acid tetrahydrate were obtained from Aldrich Chemical Company and used as received.

1: Large block crystals of $\{AgOTs(MeCN)\}_\infty$ were grown by slow diffusion of isopropyl ether into a MeCN solution of AgOTs.

2: A 2:1 molar ratio of $AgBF_4$ and sodium 1,5-disulfonate tetrahydrate was stirred in MeCN until a homogeneous solu-

© 1999 NRC Canada

Fig. 4. Single crystal X-ray structure of **2**, showing the coordination of the NDSA units and two molecules of MeCN to Ag(I), resulting in a one-dimensional array. Hydrogen atoms omitted for clarity.

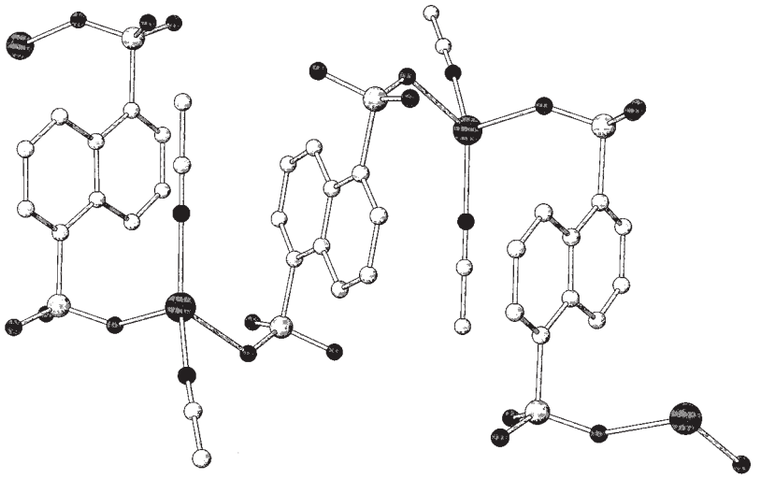

Fig. 5. View of **2**, down the *a* axis, showing the alternating layer structure of $(Ag\text{-}NDSA)^-$ and $H_7O_3^+$ units. MeCN molecules omitted for clarity.

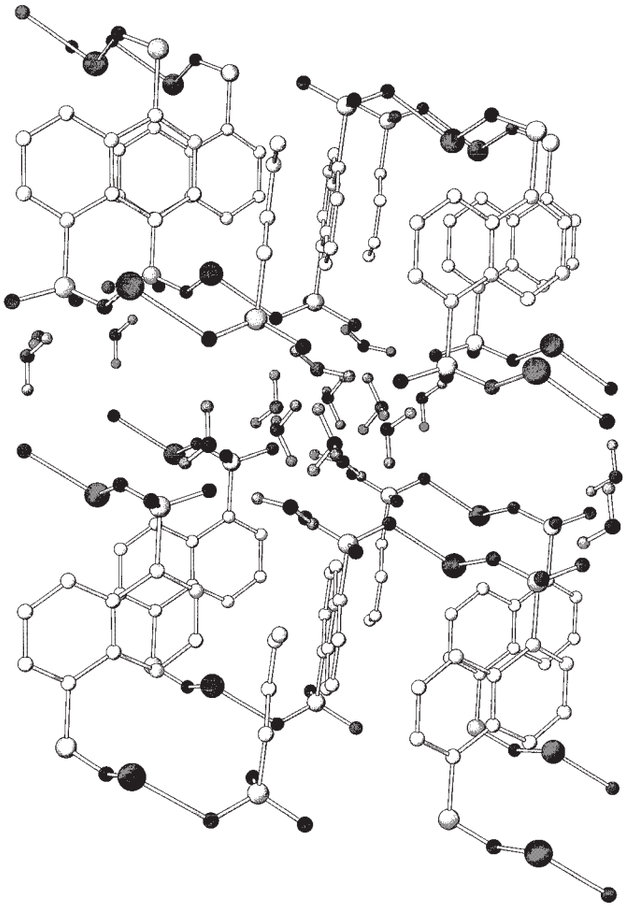

Fig. 6. View of the $H_7O_3^+$ unit of **2**, showing the H-bonded array linking the SO_3^- groups of two different NDSA ligands.

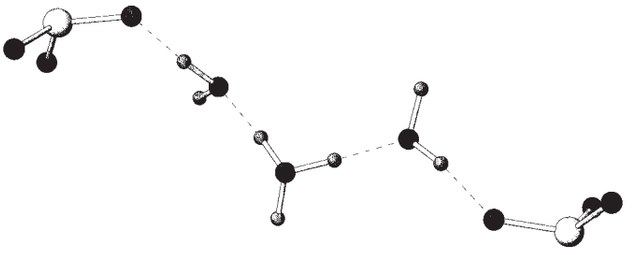

Fig. 7. ORTEP plot of the unique unit of **2**, showing the atom numbering scheme. Ellipsoids of 30% probability are shown. H atoms omitted for clarity.

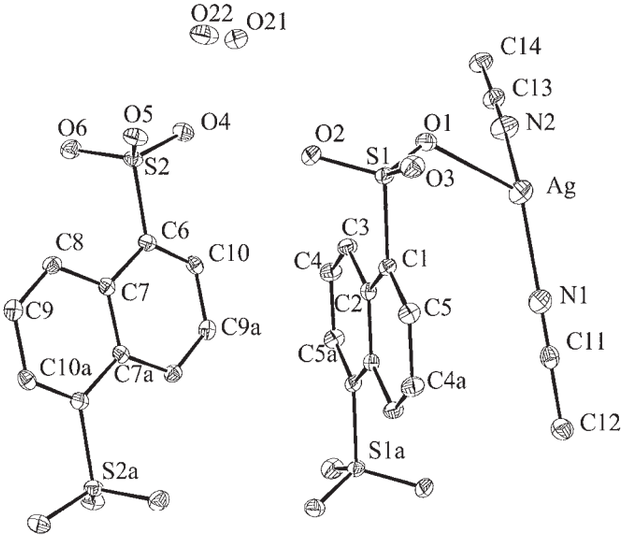

© 1999 NRC Canada

tion was obtained. Diffusion of diethyl ether into this solution resulted in the growth of colourless block crystals of $\{Ag(NDSA)(MeCN)_2(H_7O_3^+)\}_\infty$.

X-ray data collection and structure determination

A summary of the crystallographic data is given in Table 1. The data were collected on a Siemens SMART CCD diffractometer using the ω scan mode ($3° < 2\theta < 57.3°$) and solved using the NRCVAX suite of programs. The hydrogen atoms of **2** were located on a density map and moved to calculated positions. For the NRCVAX system, see ref. 7.

References

1. C.L. Bowes and G.A. Ozin. Adv. Mater. **8**, 13 (1996); G.K.H. Shimizu, G.D. Enright, C.I. Ratcliffe, J.A. Ripmeester, and D.D.M. Wayner. Angew. Chem. Int. Ed. Engl. **37**, 1407 (1998); M. Munakata, L.P. Wu, T. Kuroda-Sowa, M. Maekawa, K. Moriwaki, and S. Kitagawa. Inorg. Chem. **36**, 5416 (1997); B.F. Abrahams, S.J. Egan, B.F. Hoskins, and R. Robson. Chem. Commun. 1099 (1996); D.M. Young, U. Geiser, A.J. Schultz, and H.H. Wang. J. Am. Chem. Soc. **120**, 1331 (1998); H. Li, C.E. Davis, T.L. Groy, D.G. Kelley, and O.M. Yaghi. J. Am. Chem. Soc. **120**, 2186 (1998); K.N. Power, T.L. Hennigar, and M.J. Zaworotko. Chem. Commun. 595 (1998); R.K. Kumar, S. Balasubramanian, and I. Goldberg. Inorg. Chem. **37**, 541 (1998); K.A. Hirsch, S.R. Wilson, and J.S. Moore. Chem. Eur. J. **3**, 765 (1997); M. Kondo, T. Yoshitomi, K. Seki, H. Matsuzaka, and S. Kitagawa. Angew. Chem. Int. Ed. Engl. **36**, 1725 (1997); D.M L. Goodgame, S. Menzer, A M. Smith, and D.J. Williams. J. Chem. Soc. Dalton Trans. 3213 (1997).
2. G.K.H. Shimizu, G.D. Enright, C.I. Ratcliffe, G.S. Rego, J.L. Reid, and J.A. Ripmeester. Chem. Mater. In press.
3. G. Alberti. *In* Comprehensive supramolecular chemistry. Vol. 7. *Edited by* J.L. Atwood, J.E.D. Davies, D.D. MacNicol, and F. Vögtle. Elsevier Science, New York. 1996. Chap. 5, pp. 151–189, and refs. therein.
4. L. Carlucci, G. Ciani, D.M. Proserpio, and A. Sironi. Angew. Chem. Int. Ed. Engl. **34**, 1895 (1995); K.A. Hirsch, S.R. Wilson, and J.S. Moore. Inorg. Chem. **36**, 2960 (1997).
5. V.A. Russell, M.C. Etter, and M.D. Ward. J. Am. Chem. Soc. **116**, 1941 (1994); M. Munakata, L.P. Wu, and T. Kuroda-Sowa. Bull. Chem. Soc. Jpn. **70**, 1727 (1997).
6. I.V. Mitchell. Pillared layered structures. Elsevier Appl. Science, New York. 1990.
7. E.J. Gabe, Y. LePage, J.-P. Charland, F.L. Lee, and P.S. White. J. Appl. Crystallogr. **32**, 384 (1989).

© 1999 NRC Canada

Preparation, isolation, and characterization of permethylated galactosides and fucosides

Daniel D. Asres and Hélène Perreault

Abstract: Sugar analysis involving permethylation followed by methanolysis can lead to significant results, given that permethylated monosaccharide standards are available for comparison of spectral and chromatographic data. Such standards are not readily commercially available, especially the furanoside forms. This note describes the isolation and characterization of permethylated pyranoside and furanoside species of D(+)-galactose and L(–)-fucose. Separation of the isomers was optimized using a combination of column chromatography and continuous elution thin-layer chromatography (TLC). TLC, gas chromatography – mass spectrometry, and ^{1}H nuclear magnetic resonance (NMR) spectroscopy were used as the characterization methods. The isolation of furanosides is emphasized, since no specific NMR data have been reported on those to date, while several reports have already discussed the structural aspects of pyranosides.

Key words: permethylation, monosaccharide, GC–MS, TLC, NMR.

Résumé : Une analyse des sucres faisant intervenir une perméthylation suivie d'une méthanolyse peut donner des résultats significatifs en autant que des standards de monosaccharides perméthylés soient disponibles pour comparer les données spectrales et chromatographiques. De tels standards ne sont pas facilement accessibles commercialement surtout en ce qui a trait aux formes furannosides. Ce travail décrit l'isolement et la caractérisation de furannosides et de pyrannosides perméthylés du D(+)-galactose et du L(–)-fructose. On a optimisé la séparation des isomères en utilisant une combinaison de chromatographie sur colonne et de chromatographie en couche mince avec élution continue (TLC). On a utilisé comme méthodes d'analyse : la TLC, la chromatographie en phase gazeuse couplée avec la spectrométrie de masse et la RMN du ^{1}H. On a mis l'accent sur l'isolement des furannosides pour lesquels aucune donnée spécifique de RMN n'existe jusqu'à ce jour dans la littérature, alors que l'on dispose de plusieurs données relatives aux aspects structuraux des pyrannosides.

Mots clés : perméthylation, monosaccharide, GC–MS, TLC, RMN.

[Traduit par la Rédaction]

Introduction

Methylation analysis has, for more than 40 years, played an important role in the characterization of carbohydrates. Methylated sugar derivatives are in general less polar and more volatile than their unmodified analogs, which makes their characterization more feasible by a variety of methods. Gas chromatography – mass spectrometry (GC–MS) is one of the most popular techniques used to identify and quantify methylated sugars. Several methylation procedures have been established, some yielding partially methylated products (1–3) and others producing permethylation (4–8). Several articles (e.g., refs. 9–12) reported that permethylation of a monosaccharide produces at least two, and up to four isomers, which are five- and six-membered ring compounds. The formation of seven-membered ring permethylated sugars has also been discussed (13).

In our hands, using the Ciucanu and Kerek permethylation method (7), mainly furanosides and pyranosides are obtained (12). We recently reported on the influence of permethylation reaction conditions upon the isomeric ratios obtained for two monosaccharides, D(+)-galactose and L(–)-fucose (12). We can take advantage of these experimental conditions and apply them to permethylation toward preparation of pure, single galactosides and fucosides. In this paper, we report on inexpensive methods of preparing pure permethylated hexosides of D(+)-galactose and L(–)-fucose. These methods include (*i*) permethylation of commercially available methyl pyranosides, and (*ii*) permethylation of hexoses followed by separation of isomers by column chromatography or continuous elution thin-layer chromatography (TLC). Such separations of permethylation products of monosaccharides have already been reported (14–18), although the emphasis was on recovery of permethylated pyranoside isomers and no

Received July 13, 1998.[1]

D.D. Asres and H. Perreault.[2] Department of Chemistry, University of Manitoba, 144 Dysart Road, Winnipeg, MB R3T 2N2, Canada.

[1]Revision received January 18, 1999.

[2]Author to whom correspondence may be addressed. Telephone: (204) 474-7418. Fax: (204) 474-7608. e-mail: perreau@cc.umanitoba.ca

© 1999 NRC Canada

Fig. 1. Thin-layer chromatographic patterns for the elution of (*a*) a mixture of permethylated galactoside isomers (12 consecutive elutions) and (*b*) a mixture of permethylated fucoside isomers (8 consecutive elutions). Eluent: 1:9:4 isopropanol – ethyl acetate – hexanes. **1**: β-Galactofuranoside; **2**: β-galactopyranoside; **3**: α-galactopyranoside; **4**: α-galactofuranoside; **5**: β-fucofuranoside; **6**: β-fucopyranoside; **7**: α-fucopyranoside; **8**: α-fucofuranoside.

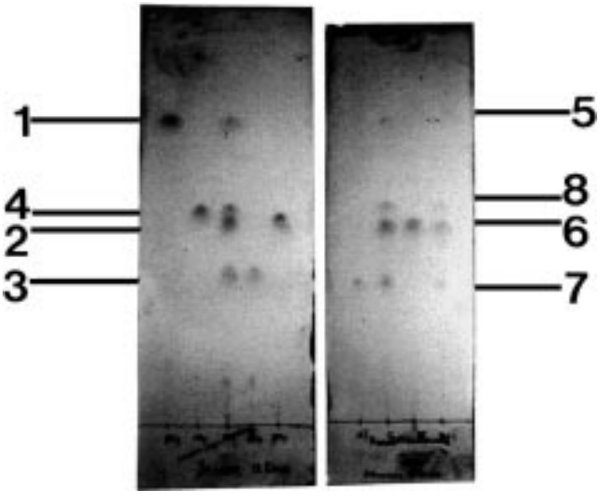

mention was made about isolation of the furanosides (15–18). The initiative for achieving this work thus came from the great difficulty in locating reference ^{1}H nuclear magnetic resonance (NMR) and mass spectral data for the furanoside isomers produced by permethylation of galactose and fucose. Extensive ^{1}H and ^{13}C NMR studies on permethylated pyranosides have been reported (15–18), and their electron impact mass spectra are available from a library (19).

Experimental

Materials

D(+)-Galactose and L(–)-fucose were purchased from Sigma (St. Louis, Mo.). Methyl iodide (CH_3I) was obtained from Aldrich Chemicals (St. Louis, Mo.). The α and β forms of methyl galacto- and fucopyranoside were from Sigma. The α and β forms of methyl galactofuranoside and methyl-β-fucofuranoside were purchased from Color Your Enzyme (Kingston, Ont.). Dimethyl sulfoxide (DMSO) was obtained from Pierce Chemicals (Rockport, Ill.). The other solvents were glass-distilled or HPLC grade and obtained from Mallinckrodt (Paris, Ky.). Water was obtained from a Barnstead Nanopure II^{TM} purification system fed with water purified by reverse osmosis. Small TLC plates were cut from aluminium sheets coated with silica gel 60 F_{254} (E. Merck, Darmstadt, Germany). Silica gel 60, 230–400 mesh, 40–63 μm, used for column chromatography was obtained from Mallinckrodt. The large TLC plates (20 cm × 20 cm, glass coated with a 1 mm thick layer of silica gel 60) were obtained from E. Merck.

Permethylation of the hexoses and preparation of reference standards

D(+) Galactose and L(–) fucose were permethylated based on the method developed by Ciucanu and Kerek (7), and specific sets of experimental conditions as reported by us previously (12) were used. Permethylation of methyl glycoside standards of known anomericity was also effected using conditions based on the method developed by Ciucanu and Kerek (7). Essentially no epimerization or degradation was observed.

GC–MS

The apparatus used consisted of a Varian 3400 chromatograph and Finnigan Mat Ion Trap Detector 800. A 30 m long DB-5 column (95% methyl-, 5% phenyl-silicon, J&W Scientific) with 250 mm i.d. and 0.25 μm film thickness was used. The oven temperature programming was as follows: initial temperature of 80°C kept constant for 10 min, followed by linear ramp to 270°C at the rate of 7°C/min, and final temperature of 270°C maintained constant for 10 min. The data system used was a Finnigan Mat ITDS, version 4.10.

TLC

Characterization experiments were carried out with silica-coated aluminum plates with 8 to 12 successive elutions. The solvent system was 1:9:40 isopropanol – ethyl acetate – hexanes.

Column chromatography

A 0.7 × 20 cm glass column packed with 10 g of silica was used. The solvent was 3:1 cyclohexane – ethyl acetate. The amount of sample applied to the column for one separation was of the order of 5–7 mg.

Continuous elution TLC

The solvent was 1:9:40 isopropanol – ethyl acetate – heptane. The galactose isomers required 12–15 h of continuous development, whereas in the case of fucose only 7–9 h were necessary.

^{1}H NMR

The instrument used was a Bruker AM 300 FT spectrometer (Bruker Inc., Billerica, Mass.). Samples were in concentrations of 1 mg/mL or less. The solvent used was deuterated chloroform, $CDCl_3$.

Results and discussion

Although a number of reports mention the use of TLC and silica column chromatography for the separation of monosaccharide permethylation mixtures (15–18), no details are given about elution order, chromatographic behavior, or resolution. We wish to provide more details on these procedures, which constitute an important step in the preparation of permethylated monosaccharides.

In a previous report (12), we discussed the relative abundances of permethylated galactoside and fucoside isomers formed with different sets of reaction conditions. The permethylated galactoside isomers observed by GC–MS were, in increasing order of retention time: β-galactofuranoside

© 1999 NRC Canada

Fig. 2. GC–MS total ion chromatograms of permethylated galactoside standards. (*a*) Mixture of the four standards named: (*b*) β-galactofuranoside (β-GF) isolated from mixture, (*c*) β-galactopyranoside (β-GP) isolated from mixture, (*d*) α-galactopyranoside (α-GP) isolated from mixture, and (*e*) α-galactofuranoside (α-GF) isolated from mixture.

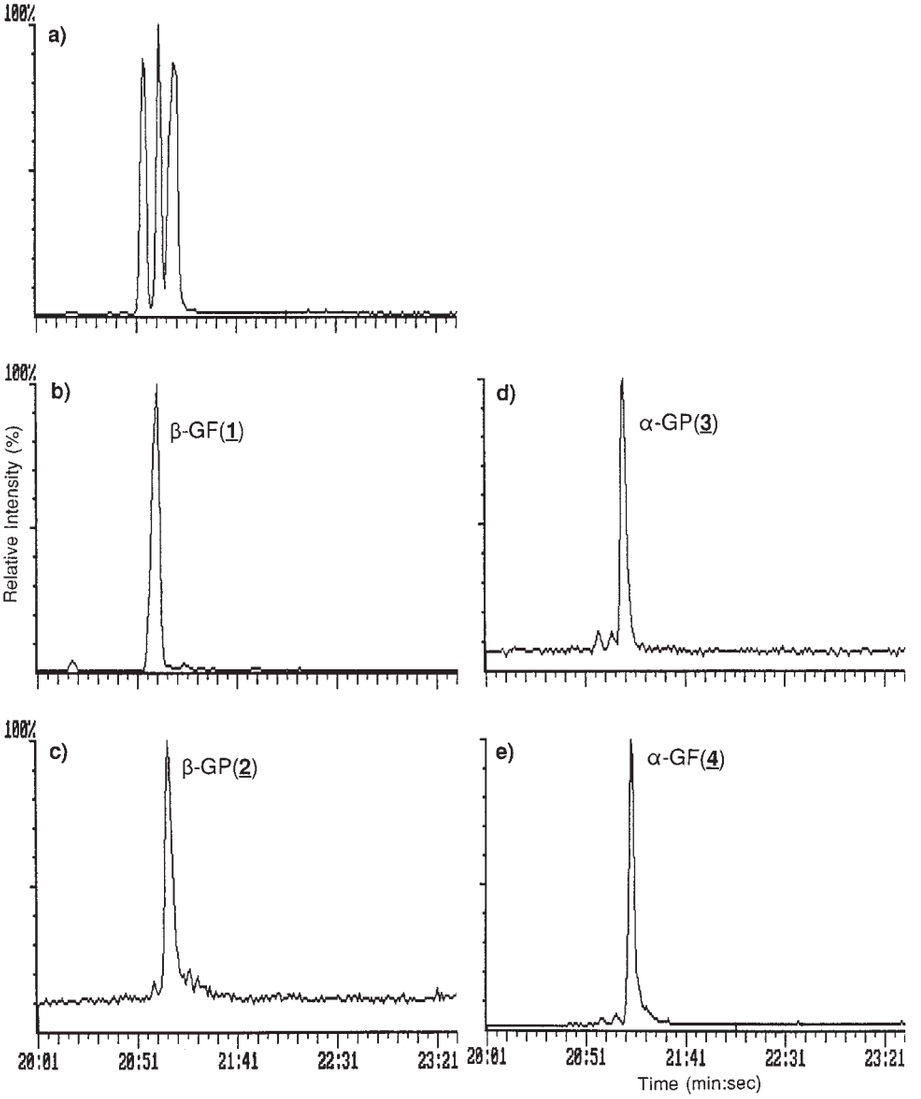

Table 1. Best isolation method found for individual permethylated galactosides and fucosides.

Compound No.	Name of compound (Permethylated)	Compound better isolated by
1	β-Galactofuranoside	Column chromatography
2	β-Galactopyranoside	Continuous elution TLC
3	α-Galactopyranoside	Either of the above
4	α-Galactofuranoside	Continuous elution TLC
5	β-Fucofuranoside	Column chromatography
6	β-Fucopyranoside	Continuous elution TLC
7	α-Fucopyranoside	Either of the above
8	α-Fucofuranoside	Continuous elution TLC

(**1**), β-galactopyranoside (**2**), α-galactopyranoside (**3**), and α-galactofuranoside (**4**). In the case of the fucosides, the GC retention order was similar, i.e.: β-fucofuranoside (**5**), β-fucopyranoside (**6**), α-fucopyranoside (**7**), and α-fucofuranoside (**8**).

For the work discussed here, permethylation reaction conditions were chosen to favor production of (*a*) selective isomer(s), as described previously (12). However, a variation of the conditions did not have a significant influence on the amounts of **1**, **3**, and **5** obtained. The three latter were produced in very low amounts (≤4% of the products) and thus were difficult to isolate as pure substances at the low-milligram level.

Gee (14) observed that the TLC separation of products **1–4** on silica was restricted by the tendency of **2** and **4** to coelute. In our hands, the compounds were eluted as follows: **1**, R_f = 0.280; **4**, R_f = 0.195; **2**, R_f = 0.190; **3**, R_f =

© 1999 NRC Canada

Fig. 3. GC–MS total ion chromatograms of the permethylation products of D(+)-galactose. (*a*) Product mixture, (*b*) β-galactofuranoside (β-GF) isolated from mixture, (*c*) β-galactopyranoside (β-GP) isolated from mixture, (*d*) α-galactopyranoside (α-GP) isolated from mixture, and (*e*) α-galactofuranoside (α-GF) isolated from mixture.

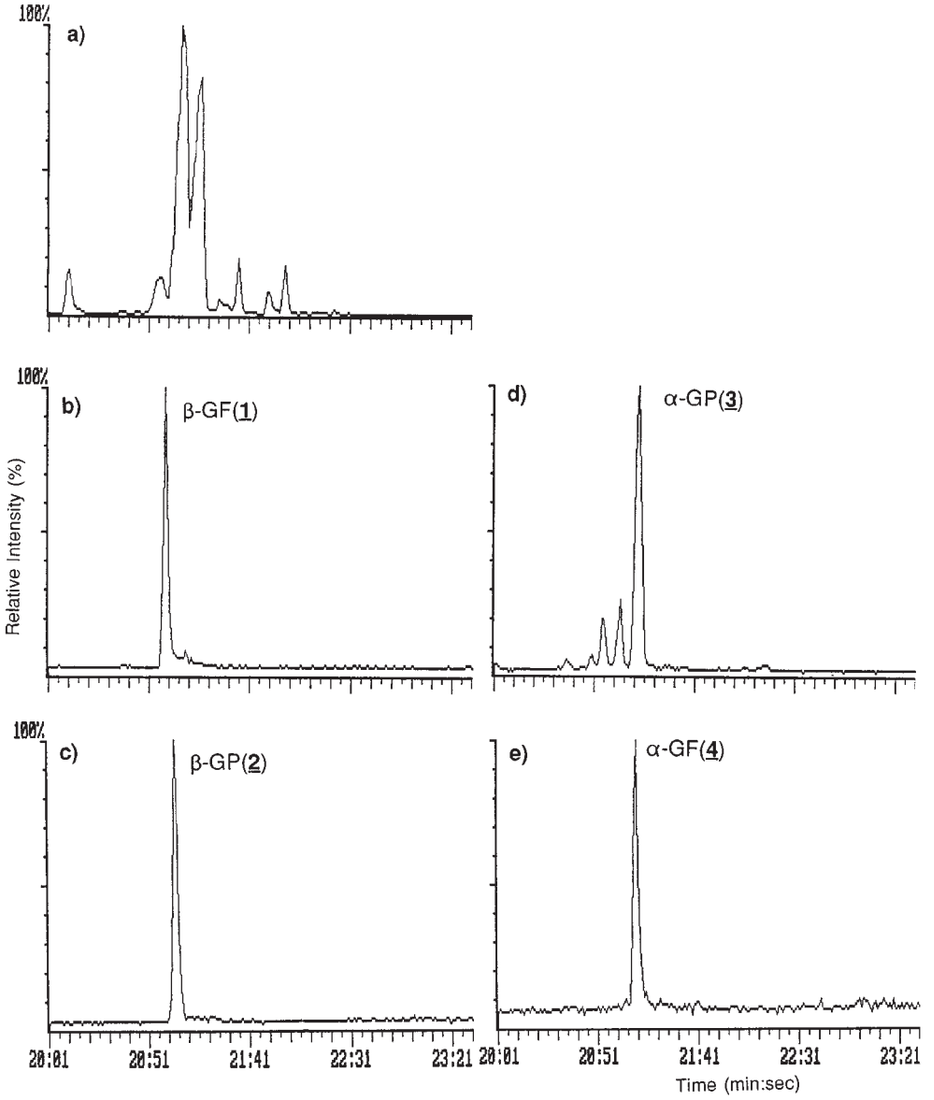

0.145, for the galactosides, and **5**, R_f = 0.565; **8**, R_f = 0.310; **6**, R_f = 0.245; **7**, R_f = 0.150, for the fucosides. Figure 1*a* shows the TLC elution pattern obtained for the permethylated galactoside isomers and emphasizes the difficulty of separating **2** and **4**. This separation is, however, better than reported by Gee (14). Figure 1*b* shows the elution pattern of the permethylated fucoside isomers, whose separation was easier to achieve.

Column chromatography of the mixture of permethylated galactosides allowed isolation of pure **1** and **3**; however, **2** and **4** could not be separated when 5–7 mg of products were applied to the column. The fucoside isomers could be separated more easily under the same conditions.

In our hands, continuous elution TLC was the most efficient method of separating the isomers. This technique yielded reasonably good separation of **2** and **4**, with quantities of material ranging from 5 to 30 mg. The fucoside isomers were separated using the same method. For either galactosides or fucosides, the fastest moving isomer had to be discarded, due to its migration to the top of the plate along with the impurities. Table 1 lists each of the eight compounds discussed in this study, along with the method that we considered the most efficient for its isolation.

The use of reversed phase high-performance liquid chromatography (HPLC) as a preparative method for the separation of the isomers was also investigated. Detection based on ultraviolet absorption was made difficult by the absence of suitable chromophores on the galactosides, and refractive index detection became possible only when milligram quantities of sample were loaded onto the column, at which point no separation was obtained. The only way to detect a good separation of the four isomers was by on-line HPLC – electrospray mass spectrometry, and injections of less than 1 picomol of each component were necessary to baseline-

© 1999 NRC Canada

Fig. 4. GC–MS total ion chromatograms of the permethylation products of L(–)-fucose and of the permethylated fucoside standards. (*a*) Mixture of the four standards named as those isolated: (*b*) β-fucofuranoside (β-FF) isolated from permethylation mixture, (*c*) β-fucopyranoside (β-FP) isolated from permethylation mixture, (*d*) permethylation products of L(–)-fucose, (*e*) α-fucopyranoside (α-FP) isolated from permethylation mixture, and (*f*) α-fucofuranoside (α-FF) isolated from the permethylation mixture.

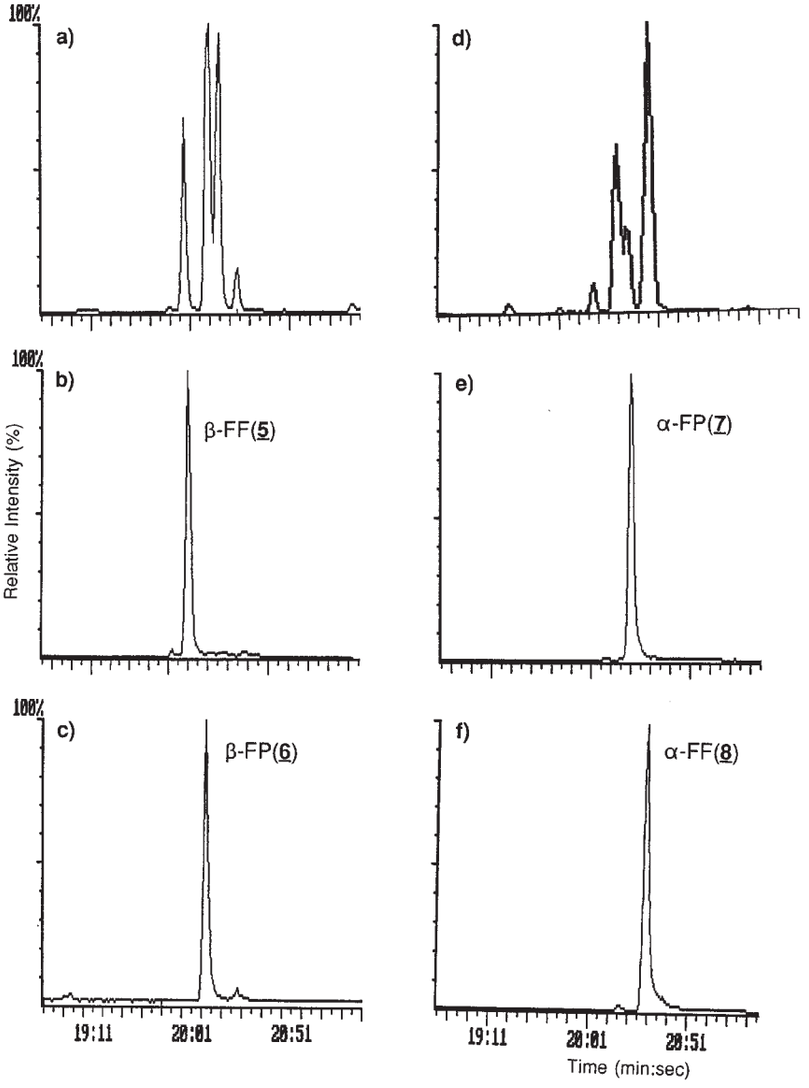

resolve the isomers. The practicability of this approach was questioned, and finally we decided not to use this method for the purposes of the present report.

Figure 2*a* shows the GC–MS total ion current (TIC) traces obtained for a mixture of the four permethylated galactoside standards.Traces (*b*)–(*e*) show the elution of each standard, once isolated, according to the methods listed in Table 1. Compound **1** was isolated with the highest purity level, while compounds **2**, **3**, and **4** contained very low levels of the other components due to band broadening on column or TLC.

Figure 3*a* shows the GC–MS TIC trace obtained for the permethylation products of D-(+)-galactose, and traces (*b*)–(*e*) correspond to the products isolated using the same methods as the standards. Compound **3** was the least abundant with each permethylation condition set used (12), and thus it was impossible to perfectly isolate this product from the rest of the permethylated mixture.

Figure 4*a* shows the elution (GC–MS) of the four permethylated fucoside standards. The first one, **5**, contained a high proportion of **8** from an impurity of methyl α-fucofuranoside in the starting material. Figure 4*d* shows the GC–MS trace obtained for the permethylation products of fucose, in one specific set of permethylation conditions (12). The isolation of the four main components from this product mixture resulted in the chromatograms presented in Fig. 4, (*b*), (*c*), (*e*), and (*f*). We successfully isolated milligram quantities of **7**, which we could not readily obtain from a commercial source. The production of compound **5** by permethylation of fucose was very difficult to enhance and

© 1999 NRC Canada

Table 2. ^{1}H NMR data (chemical shifts in ppm and coupling constants in Hz) obtained for permethylated D(+)-galacto- and L(–)-fucopyranosides.

Per-*O*-methyl derivative of	Compound no.	MeO1[a]	MeO2[a]	MeO3[a]	MeO4[a]	MeO6[a]	Me5[a]	H1	J_{12}[b]	H2	J_{23}[b]	H3	J_{34}[b]	H4	J_{45}[b]	H5	$J_{56,6'}$[b]	H6,6'
α-D(+)GP	**3**	3,42	3,515	3,515	3,57	3,41		4.87d	3	3.64dd	10	3.55dd	3	3.685dd	1	3.86td	6,2	3.46–3.60
β-D(+)GP	**2**	3,51	3,59	3,52	3,56	3,4		4.15d	7	3.315dd	9,2	3.145dd	3	3.655dd	0,8	3.485td	6,2	3.50–3.63
α-L(–)FP	**7**	3,4	3.505[c]	3.51[c]	3,6		1.26d	4.84d	4	3.62dd	10	3.54dd	2,9	3.425dd	1,1	3.85qd	6,5	
β-L(–)FP	**6**	3,51	3,595	3,525	3,585		1.32d	4.19d	7	3.30dd	9,2	3.15dd	3	3.365dd	1,2	3.47qd	6,5	

[a]Assigned with the help of ref. 15.

[b]Assigned with the help of ref. 17.

[c]Uncertainty in the peak assignments (may be reversed).

GP = galactopyranoside, FP = fucopyranoside.

d = doublet, dd = double doublet, td = triple doublet, qd = quadruple doublet.

Table 3. ^{1}H NMR data (chemical shifts in ppm and coupling constants in Hz) obtained for permethylated D(+)-galacto- and L(–)-fucofuranosides.

Per-*O*-methyl derivative of	Compound no.	MeO	Me5 (H6)	H1	J_{12}	H2	J_{23}	H3	J_{34}	H4	J_{45}	H5	J_{56}, $J_{56'}$	H6,6'
α-D(+)GF	**4**	3.38, 3.455, 3.465, 3.48, 3.54		4.90d	4.25	3.50dd	10	3.41dd	2.0	3.55dd	0.9		3.78–3.97 ppm	
β-D(+)GF	**1**	3.375, 3.38, 3.41, 3.43, 3.54		4.87d	<1.0			3.42–3.56 ppm			0.9	4.00td	4.3,6.3	3.67–3.72
α-L(–)FF	**8**	3.40, 3.505, 3.51, 3.60	1.26d	4.835d	3.1	3.635dd	9.5	3.54dd	2.9	3.43dd	0.9	3.85qd	7.0	

GF = galactofuranoside, FF = fucofuranoside.

d = doublet, dd = double doublet, td = triple doublet, qd = quadruple doublet.

© 1999 NRC Canada

was maximized as shown in Fig. 4*d*. Therefore, we collected enough of this compound for a GC–MS analysis (Fig. 4*b*), but insufficient for NMR characterization.

Each of the separated isomers of permethylated D(+)-galactose and L(–)-fucose were subjected to ^{1}H NMR analysis. The results obtained for the pyranoside isomers are presented in Table 2. The values related to the methoxy groups closely matched those already reported by Streefkerk and Stephen (15) with $CDCl_3$ as the solvent. For other non-methoxy protons, values were available from the literature but only with acetonitrile-d_3 or benzene-d_6 as the solvent (16, 17), while we used $CDCl_3$. The values presented in Table 3, to our knowledge, are the first NMR data to have been reported on permethylated galacto- and fucofuranosides. Our assignments of the ring proton peaks (H2, H3, and H4) were made based on their respective coupling constants. In the case of compound **1**, the assignment of the peaks due to these protons was only possible within a range, since the peaks of interest were burried under the methoxy proton peaks. In general, the chemical shift of the H1 signal and its associated coupling constants were sufficient to identify the hexoside under investigation.

Conclusions

We have described an inexpensive method for the preparation of single isomers of permethylated D(+)-galactosides and L(–)-fucosides, to be used as standards in GC experiments as part of methylation analysis. Starting from D(+)-galactose and L(–)-fucose, we can control to some extent the proportions of the four isomers obtained in each case, by varying parameters in the permethylation reaction. Most products can then be separated in milligram quantities by silica column chromatography or continuous elution TLC. Two of the galactosides, β-galactopyranoside and α-galactofuranoside, were difficult to separate and were not recoverable as pure species on a column. They were isolated as almost pure compounds, however, using continuous elution TLC. The fucoside isomers lent themselves better to separation, although there was still a slight overlap between β-fucopyranoside and α-fucofuranoside; however, this was much less than for the galactoside isomers. We are in the process of using this method for preparing single permethylated hexoside isomers for glucose, *N*-acetylgalactosamine, *N*-acetylglucosamine, sialic acid, and mannose.

Acknowledgments

The authors wish to thank W. Buchannon of the Chemistry Department, University of Manitoba, for technical assistance during the GC–MS experiments. We acknowledge the help of D. Kunec in preparing some of the permethylated compounds of interest to this study. Thanks are also addressed to P. Hultin for advice regarding chromatographic methods using silica, and to R. Wallace for kindly scanning and editing pictures for Fig. 1. Finally, the authors wish to thank the Natural Sciences and Engineering Research Council of Canada and the University of Manitoba for their financial support.

References

1. W.N. Haworth. J. Chem. Soc. **107**, 8 (1915).
2. R. Kuhn, H. Trischmann, and I. Löw. Angew. Chem. **67**, 32 (1955).
3. Y.S. Ovodov and A.F. Pavelenko. J. Chromatogr. **36**, 531 (1968).
4. H.G. Walker, M. Gee, and R.M. McCready. J. Org. Chem. **27**, 2100 (1962).
5. S. Hakomori. J. Biochem. **55**, 205 (1964).
6. J. Finne, T. Krusius, and H. Rauvala. Carbohydr. Res. **80**, 336 (1980).
7. I. Ciucanu and F. Kerek. Carbohydr. Res. **131**, 209 (1984).
8. G. Larsson, H. Karlsson, G. Hansson, and W. Pimlott. Carbohydr. Res. **161**, 281 (1987).
9. M. Gee and H.G. Wlaker, Jr. Anal. Chem. **34**, 650 (1962).
10. H.W. Kircher. Anal.Chem. **32**, 1103 (1960).
11. D.D. Asres and H. Perreault. Can. J. Chem. **74**, 1512 (1996).
12. D.D. Asres and H. Perreault. Can. J. Chem. **75**, 1385 (1997).
13. K. Heyns, D. Müller, R. Stute, and H. Paulsen. Chem. Ber. **100**, 2664 (1967).
14. M. Gee. Anal. Chem. **35**, 350 (1963).
15. D.G. Streefkerk and A.M. Stephen. Carbohydr. Res. **49**, 13 (1976).
16. J. Haverkamp, J.P.C.M. van Dongen, and J.F.G. Vliegenthart. Carbohydr. Res. **33**, 319 (1974).
17. J. Haverkamp, M.J.A. de Bie, and J.F.G. Vliegenthart. Carbohydr. Res. **39**, 201 (1975).
18. E.B. Rathbone and A.M. Stephen. Tetrahedron Lett. **16**, 1339 (1970).
19. NIST Standard Reference Data Base, MS Search Library Version 1.6, 1997.

© 1999 NRC Canada

Free radicals formed by H(Mu) addition to pyrene

Paul W. Percival, Brenda Addison-Jones, Jean-Claude Brodovitch, Khashayar Ghandi, and Joachim Schüth

Abstract: Muonium addition to pyrene has been investigated by means of transverse field muon spin rotation and muon level-crossing spectroscopy. Two hydropyrenyl radicals are produced and easily detected while a third is formed in low abundance. Muon and proton hyperfine constants were experimentally determined and compared with semiempirical and ab initio calculations. It is concluded that the radicals are of cyclohexadienyl type, i.e., the Mu adds only to carbon atoms that can assume a tetrahedral -CHMu- configuration without distorting the planar carbon skeleton of pyrene.

Key words: muonium, pyrene, radical, hyperfine.

Résumé : L'addition du muonium au pyrène a été étudiée à la fois par la spectroscopie de rotation du spin du muon en champ transverse et par celle de résonance de croisement de niveaux en champ longitudinal. Parmi les radicaux hydropyrényles qui sont produits, deux sont facilement détectés alors qu'un troisième n'est formé qu'en très faible quantité. Les valeurs des constantes hyperfines du muon et du proton obtenues expérimentalement ont été comparées à celles fournies par des calculs semi-empiricaux et ab initio. On en déduit que les espèces observées sont des radicaux cyclohexadiényles, ou encore, que Mu ne s'additionne qu'aux atomes de carbone dont la position permet au groupe -CHMu- de prendre un configuration tétrahédrale sans déformation du plan défini par les atomes de carbone du pyrène.

Mots clés : muonium, pyrène, radical, hyperfine.

Introduction

It has been well established that fullerene, C_{70}, has five chemically distinct carbon atoms. Hence, up to five isomeric radicals could be formed by addition of a single hydrogen atom or other free radical. Four of the H adducts have been detected by electron spin resonance (ESR) (1) and four (2) or five (3) of the muonium adducts have been detected by muon spin rotation (μSR). Assignment of the structures is not at all straightforward, and there is disagreement (1, 4, 5) on whether addition occurs at the "equatorial" carbon (labelled E in Fig. 1(*a*)). This carbon differs from the others (A–D) in being at the intersection of three six-membered rings. As such, it is similar to the central carbons, 15 and 16, of pyrene (see Fig. 1(*b*)). The A–D fullerene sites each involve two six- and one five-membered ring. It is the latter that provide curvature to the fullerene skeleton, and not surprisingly the curvature in C_{70} is least at E. The question of how curvature of the carbon skeleton influences reactivity has prompted us to extend our μSR studies of fullerene radicals (2, 6, 7) to planar and curved polyaromatics, selected to represent sub-units of the C_{70} molecule. In this context, the pyrene molecule may be considered a fragment of C_{70} (as emphasized in Fig. 1), and its reactivity may guide us in understanding the behaviour of the fullerene.

Pyrene is a planar polycyclic aromatic hydrocarbon with five chemically distinct carbons. In an ESR study of γ-irradiated pyrene single crystals Kawakubo (8) concluded that two H-adduct radicals are formed (1-hydro- and 4-hydropyrenyl). In contrast, a more recent pulse radiolysis study of pyrene in liquid methanol was interpreted (9) in terms of a single radical product, 1-hydropyrenyl. By drawing analogies with the benzene H adduct, cyclohexadienyl (10), and the two radicals formed from naphthalene (11), we might expect three radicals from pyrene, corresponding to addition at sites 1, 2, and 4, where the resulting radicals can have a tetrahedral C-CH_2-C configuration without disturbing the planarity of the carbon skeleton. The remaining two sites (11 and 15) are considered less likely because of the rigidity of the planar carbon skeleton at the points of ring fusion. On the other hand, in the case of fullerenes, whose framework is an assembly of curved unsaturated carbon rings, it is precisely these trigonal carbon sites that are attacked.

In our investigation, pyrenyl radicals were generated from the parent pyrene molecule by addition of muonium (Mu) instead of the H atom. Muonium is the single-electron atom with a positive muon as nucleus and can be considered a light isotope of hydrogen. The short lifetime of the muon (2.2 μs) and the availability of spin-polarized beams (the muon has spin 1/2) makes it particularly suited as a probe of transient radicals (12). Although the experimental probe (the muon) and the data acquisition techniques have their roots in particle physics, the principles of μSR are the same as magnetic resonance (12, 13). In particular, the hyperfine interac-

Received October 13, 1998.

P.W. Percival,[1] B. Addison-Jones, J.-C. Brodovitch, K. Ghandi, and J. Schüth.[2] Department of Chemistry and TRIUMF, Simon Fraser University, 8888 University Drive, Burnaby, BC V5A 1S6, Canada.

[1]Author to whom correspondence may be addressed. Telephone: (604) 291-4477. Fax: (604) 291-3765. e-mail: percival@sfu.ca

© 1999 NRC Canada

Fig. 1. (*a*) Classification of C_{70} carbon atoms. (*b*) The pyrene numbering system used in this paper.[3]

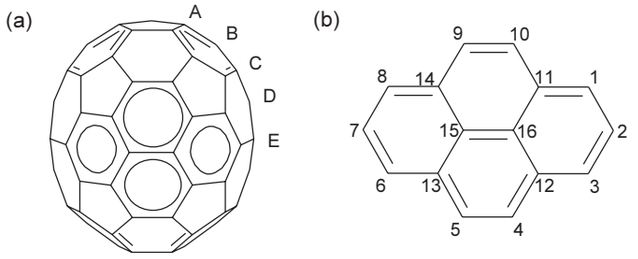

tion between a muon and the unpaired electron of a free radical can be deduced from the frequencies of muons precessing in a magnetic field transverse to their spin polarization (transverse-field muon spin rotation, TF-μSR). A related technique, muon level-crossing resonance (μLCR) can be used to determine the hyperfine constants (hfcs) for other magnetic nuclei in the muonium-labelled molecule, here, specifically, the protons of a pyrenyl radical. Thus, these two μSR techniques complement each other to provide information similar to ESR. An advantage of μLCR over conventional ESR is the ready determination of the sign of the hfc.

Muon spin rotation and muon level-crossing resonance experiments

Experiments were performed at one of the muon beam lines of the TRIUMF cyclotron in Vancouver. TF-μSR and μLCR measurements were made with the same sample, a degassed 1.04 M solution of pyrene in tetrahydrofuran (THF), sealed in a stainless steel vessel fitted with a thin foil window (14). Both types of measurements were made in the same spectrometer, HELIOS, based on a superconducting solenoid magnet arranged such that the muon beam travels along its axis and stops in the sample placed at its centre. A plastic scintillator detector in front of the sample signals muons incident on the sample, while other scintillators are used to detect the muon decay positrons. For TF-μSR the spin polarization of the muon beam was rotated roughly 90° from its momentum, and four positron detectors were arranged around the sample in a circular array perpendicular to the beam. For μLCR measurements, the spin polarization was kept parallel to the beam momentum; the positron detectors were moved in a downstream direction and used with an upstream set to provide a forward–backward counter geometry (13, 14).

In TF-μSR the elapsed time between the stop of each muon and the detection of its decay positron is measured, and the data are collected as a histogram of frequency of occurrence (counts) against time. The probability of detecting the decay positron in a given direction varies with time due to the radioactive decay of the muon and, more interestingly, to the muon spin precession in the magnetic field. Thus the μSR histogram obtained from each positron detector contains oscillations in the muon lifetime spectrum, and these oscillations correspond to the time dependence of the muon spin polarization. The general form of the histogram is

$$[1] \qquad N(t) = B_g + N_0 e^{-t/\tau_\mu}[1 + A(t)]$$

where B_g represents a small constant background count, N_0 is a normalization factor, τ_μ is the muon lifetime, and $A(t)$ is a sum of decaying oscillations — the precession signals. $A(t)$ may be Fourier transformed to provide a frequency spectrum similar to NMR and ESR spectra.

For typical organic solvents, such as the THF used in this work, roughly two thirds of the incoming muons become incorporated in diamagnetic molecules (15). The resulting diamagnetic signal precesses at the muon Larmor frequency, $\nu_\mu = \gamma_\mu H$ ($\gamma_\mu = 0.01355$ MHz G^{-1}). The remaining muons form muonium, which rapidly reacts with unsaturated molecules such as pyrene. Muons in free radicals are subject to a hyperfine interaction with the unpaired electron in addition to the Larmor interaction with the external magnetic field. At high magnetic fields two precession frequencies ensue:

$$[2] \qquad \nu_{R1} = \nu_{mid} - \tfrac{1}{2}A_\mu \text{ and } \nu_{R2} = \nu_{mid} + \tfrac{1}{2}A_\mu$$

where

$$[3] \qquad \nu_{mid} = \tfrac{1}{2}\{[A_\mu^2 + (\nu_e + \nu_\mu)^2]^{1/2} - \nu_e + \nu_\mu\}$$

is close to the muon Larmor frequency. A_μ is the isotropic muon hyperfine constant; ν_e and ν_μ are the electron and muon Larmor frequencies. The experimentally measurable quantities are ν_μ, ν_{R1}, and ν_{R2}. Equations [2] and [3] show that A_μ can be determined from the difference of ν_{R1} and ν_{R2} or from a combination of one of these and the diamagnetic frequency.

If A_μ is larger than $2\nu_{mid}$, then ν_{R1} is negative, i.e., precession occurs in the opposite sense to the diamagnetic muon signal. Whether this can be detected in practice depends on the experimental setup. In our experiments data from four positron detectors were combined to produce time signals in quadrature, thus permitting use of complex Fourier transformation and providing the ability to distinguish negative frequencies.

The symmetrical placement of radical frequencies around the diamagnetic peak is evident in the Fourier transform TF-μSR spectrum shown in Fig. 2. The presence of two pairs of peaks clearly signals the existence of two radicals (**I** and **II**) with different hyperfine constants. The low intensity of the high-frequency peaks is due to limited time resolution of the apparatus. Careful inspection of a series of spectra revealed consistent weak signals that we interpret as a third radical (**III**). One of the peaks due to **III** can be seen in the expanded portion of the figure; the corresponding peak on the high-frequency side of the diamagnetic signal is too weak to detect.

Quantitative data evaluation was done by fitting histograms in the time domain, using initial parameters derived from the Fourier transform. Comparison of the statistically independent results from the four detectors provided a consistency check that further confirmed the third radical signal. The hyperfine frequencies (A_μ) determined at 20° C are **I**: 263.44 ± 0.01 MHz; **II**: 347.06 ± 0.01 MHz; **III**: 530.52 ±

[3] The carbons labeled 11–16 here correspond to 10a, 3a, 5a, 10c, and 10b, respectively, according to standard rules for numbering fused rings.

© 1999 NRC Canada

Fig. 2. Fourier power TF-μSR spectrum from 1 M pyrene in tetrahydrofuran at 20°C in an applied magnetic field of 15.4 kG. The peaks labelled **I**, **II**, and **III** are due to free radicals.

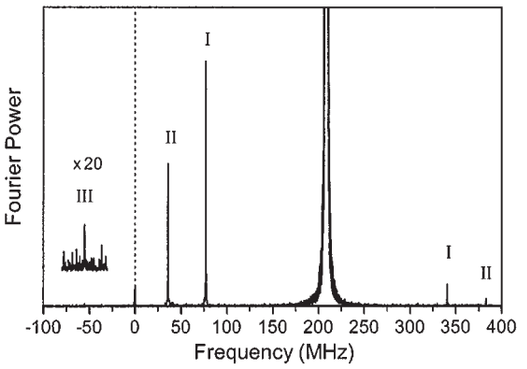

Table 1. Assignment of muon level-crossing resonance fields (B_{LCR}) to the two principal pyrenyl radicals, and the corresponding proton hyperfine constants (A_ρ) calculated from eq. [4].

Radical **I**		Radical **II**	
A_μ = 263.44 ± 0.01 MHz		A_μ = 347.06 ± 0.01 MHz	
B_{LCR} / kG [a]	A_ρ / MHz [b]	B_{LCR} / kG [a]	A_ρ / MHz [b]
10.492	67.27	13.982	85.66
14.725	–11.18	19.530	–17.15
14.837	–13.25	19.627	–18.95
14.903 [c]	–14.47 [c]	20.696	–38.76
15.073	–17.62		

[a] Uncertainty ≤3 G.
[b] Uncertainty ≤0.06 MHz.
[c] Doubly degenerate.

0.07 MHz. The relative radical abundances derived from the fitted signal amplitudes are **I** : **II** : **III** = 1.00 ± 0.02 : 0.71 ± 0.02 : 0.08 ± 0.03.

In contrast to TF-μSR, which involves spin precession in a fixed magnetic field, in μLCR the longitudinal muon spin polarization is monitored as the magnetic field is swept. The polarization is determined from the difference in decay positrons detected in the forward and reverse directions with respect to the applied field. Resonances occur at values of the magnetic field where a muon transition frequency is matched to that of some other nucleus in the coupled spin system of a radical. The mixing of a pair of otherwise degenerate levels results in an avoided crossing. This mixing couples the muon and nuclear spin functions, with the net result that there is an effective loss of muon spin polarization integrated over the muon lifetime. The field at resonance is primarily determined by the difference between the hyperfine constants of the muon and that (A_n) of the nucleus (or magnetically equivalent nuclei) involved in the resonance:

$$[4] \qquad B_{LCR} = \frac{1}{2}\left[\frac{A_\mu - A_n}{\gamma_\mu - \gamma_n} - \frac{A_\mu^2 - 2MA_n^2}{\gamma_e(A_\mu - A_n)}\right]$$

where M is the z-component of the total spin, γ_e, γ_μ, and γ_n refer to the magnetogyric ratios of the electron, muon, and other nucleus, respectively, and $\gamma_e \gg \gamma_\mu, \gamma_n$. It is possible to use μLCR to determine ^{13}C hyperfine constants (7, 16) if ^{13}C-enriched samples are available, but in this study of pyrene radicals only proton hfcs were determined.

Fig. 3. Part of the μLCR spectrum obtained from 1 M pyrene in tetrahydrofuran. The resonance labelled **II** is assigned to the -CHMu- group of radical **II**, while the set of four resonances marked **I** are due to different -CH- sites in radical **I**.

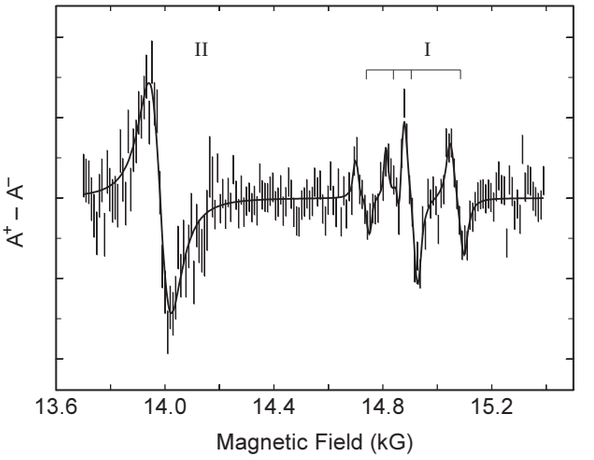

μLCR investigation of the sample of pyrene in tetrahydrofuran revealed at least nine resonances in a range of fields from 8 to 22 kG (see Table 1). Part of the spectrum is shown in Fig. 3. (The differential lineshape of the resonances is a consequence of the field modulation used to suppress baseline fluctuations.) On the basis of the TF-μSR results it is assumed that only radicals **I** and **II** give rise to the μLCR signals. Nevertheless, there is inherent ambiguity in using eq. [4] to deduce the proton hyperfine constants, since it is not known a priori to which radical (therefore which value of A_μ) a given resonance belongs.

Part of the problem is resolved by predicting the proton hfcs of the methylene (-CHMu-) groups on the basis of results for cyclohexadienyl (12, 17). After accounting for the "trivial" isotope effect caused by the ratio of magnetic moments of the muon and the proton (3.183) the "reduced" muon hyperfine constant, $A_\mu' = A_\mu / 3.183$, in cyclohexadienyl is 28% larger than the proton hfc. By assigning the 14 kG pyrenyl resonance (see Fig. 3) to radical **II** we deduce an isotope effect of 27%. Similarly, assignment of a resonance detected at 10.5 kG to radical **I** results in an isotope effect of 23%. No other assignment gives acceptable values.

The remaining resonances must all be due to α protons (protons attached to a carbon carrying significant unpaired spin density) whose hfcs are typically negative (17, 18). By rejecting atypical alternatives we assigned the resonances to radicals **I** and **II** as shown in Table 1. In one case, the resonance at 14.9 kG, the signal intensity did not match prediction until two protons were assumed (details of the method are given in ref. 19).

The uncertainties of the calculated proton hfcs are dominated by the calibration and reproducibility of the magnetic field, estimated to be about 3 G, which corresponds to 0.06 MHz in hfc.

© 1999 NRC Canada

Table 2. Heats of formation and RHF unpaired spin distribution (in percent). [a]

	1-Hydropyrenyl	4-Hydropyrenyl	2-Hydropyrenyl pyrenyl	11-Hydropyrenyl	15-Hydropyrenyl
ΔH_f / kJ mol^{-1}	317.94	319.26	357.89	388.1	407.26
Carbon					
1	—	—	22.9	25.0	—
2	7.3	—	—	—	—
3	—	—	22.9	36.7	—
4	—	—	2.3	3.1	8.3
5	14.7	41.4	—	—	—
6	12.2	19.0	—	—	—
7	—	—	5.0	3.1	26.3
8	11.5	17.9	—	—	—
9	13.5	—	—	—	—
10	—	—	2.2	—	8.3
11	17.3	2.5	—	—	—
12	19.6	—	—	—	—
13	—	—	5.6	5.1	22.0
14	—	—	5.6	2.4	22.0
15	—	9.6	—	—	—
16	—	—	25.1	17.0	5.7

[a]Spin densities less than 2% omitted.

Table 3. Muon hyperfine constants (in MHz) of isomeric pyrenyl radicals: predictions and proposed assignment of experimental values

	1-Mu-pyrenyl	4-Mu-pyrenyl	2-Mu-pyrenyl	11-Mu-pyrenyl	15-Mu-pyrenyl
Spin factor [a]	0.47	0.57	0.92	1.10	1.39
Predicted hfc [b]	275	336	536	642	812
Calcd. hfc [c]	263	337	513	664	802
Expt.	263	347	531	—	—

[a]Based on RHF unpaired spin densities from Table 2. See text.

[b]Scaled to equate the 1-Mu-pyrenyl hfc to that of the most abundant MuC_{70} radical.

[c]Single-point UB3LYP/6-31G** on UB3LYP/STO-3G optimized geometry; includes a factor of 1.20 to account for the isotope effect.

Computation and discussion

The foregoing analysis of experimental results clearly shows that two of the five possible Mu adducts of pyrene are readily formed, and a third isomer is formed in low abundance. To assign individual structures it is necessary to turn to model calculations. We employed both semiempirical RHF-PM3 (20) and ab initio density functional (DFT) methods (21). Relevant results are summarized in Tables 2–4, and compared with the experimentally determined hyperfine constants to justify our assignments.

Consideration of the relative heats of formation of the isomeric radicals immediately suggests that the two abundant radicals, **I** and **II**, correspond to 1-Mu- and 4-Mu-pyrenyl, and that **III** could be 2-Mu-pyrenyl. Further support and, in particular, evidence to distinguish between the 1-Mu and 4-Mu isomers comes from the predictions of unpaired electron spin distribution (Table 2). It is well established that α-proton hyperfine constants in π-radical systems are proportional to the unpaired spin density on the carbons to which they are bound (18):

$$[5] \qquad A_H = Q_\alpha \rho_\alpha, \quad Q_\alpha \approx -75 \text{ MHz}$$

Given that only carbons 1–10 have attached protons, the expected pattern of negative hyperfine constants is four medium and one small for 1-Mu-pyrenyl; one very large and two medium for 4-Mu-pyrenyl; two degenerate values for 2-Mu-pyrenyl; two large for 11-Mu-pyrenyl; and a single large value for 15-Mu-pyrenyl. The first two patterns match the experimental results for radicals **I** and **II** (Table 1), respectively.

The unpaired electron spin estimates can also be used to predict the methylene (-CHMu-) hfcs in the β position, although the relationship is more complicated. Whiffen showed (22) that the CH_2 proton hfcs in cyclohexadienyl depend on the π-orbital coefficients of the two neighbouring carbons; we extended his argument to predict how the proton hfc in $C_{60}H$ depends on the unpaired spin densities of the three carbons adjacent to the CH site (6):

$$[6] \qquad A_\beta \propto \left(\rho_{\alpha 1}^{1/2} + \rho_{\alpha 2}^{1/2} + \rho_{\alpha 3}^{1/2}\right)^2$$

A difficulty in applying eq. [6] to the hydropyrenyls is that the proportionality constant is expected to vary with the local molecular geometry, because the hfc depends on the degree of orbital overlap between the C—H bond and the π orbital containing the unpaired electron. (This is also affected by the curvature of the carbon skeleton, as noted by Borghi et al. (5)). However, with these considerations in mind it is still instructive to predict the trend in hfcs. The

© 1999 NRC Canada

Table 4. Calculated muon and proton hyperfine constants (in MHz) of the assigned pyrenyl radicals compared with experimental values.

1-Mu-pyrenyl				4-Mu-pyrenyl			
Nucleus	Site	hfc[a]	Expt.	Nucleus	Site	hfc[a]	Expt.
Mu	C1	263.0[b]	263.4	Mu	C4	336.8[b]	347.1
H	C1	64.7[c]	67.3	H	C4	82.9[c]	85.7
H	C4	9.0	—[d]	H	C7	8.9	—[d]
H	C10	7.7	—[d]	H	C10	5.0	—[d]
H	C7	7.7	—[d]	H	C1	3.1	—[d]
H	C3	6.6	—[d]	H	C3	3.0	—[d]
H	C2	–15.2	–11.2	H	C2	–3.7	—[d]
H	C9	–17.0	–13.3	H	C9	–4.6	—[d]
H	C8	–18.1	–14.5	H	C6	–21.2	–17.2[e]
H	C6	–18.2	–14.5	H	C8	–21.8	–19.0[e]
H	C5	–20.6	–17.6	H	C5	–45.7	–38.8

[a]Single-point UB3LYP/6-31G** on UB3LYP/STO-3G optimized geometry.

[b]Includes factor of 1.20 to account for primary isotope effect.

[c]Includes factor of 0.94 to account for secondary isotope effect.

[d]Corresponding resonance not detected.

[e]Calculated values too close for unambiguous assignments.

Fig. 4. Principal sites of unpaired π-spin density in radicals **I** and **II.** The shaded areas are proportional to the spin densities determined from the hyperfine constants through eq. [5]. The sites were determined from the results of RHF calculations.

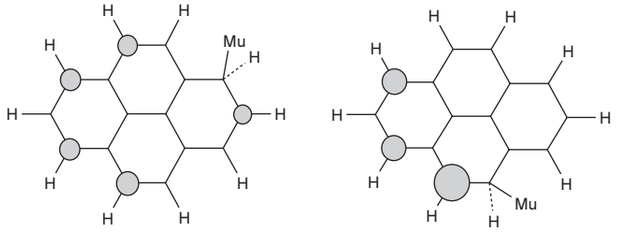

I II

spin factors listed in Table 3 correspond to the right-hand side of eq. [6]. In the next line of the table the spin factors have been converted to hfc predictions with a proportionality factor chosen so that the muon hfc in 1-Mu-pyrenyl is 275 MHz, the value for the most abundant C_{70}Mu radical (2, 23). Once again, the conclusion is that radicals **I**, **II**, and **III** should be assigned as 1-Mu-, 4-Mu-, and 2-Mu-pyrenyl, respectively.

An alternative to the above semiempirical calculations of spin density is direct calculation of hyperfine constants ab initio. We performed unrestricted open-shell calculations using the UB3LYP density functional provided with the Gaussian 94W package (21). The geometry of each hydropyrenyl isomer was first optimized using the STO-3G basis set, and then the hyperfine constants were computed in a single-point Fermi contact analysis using the 6-31G** basis. The program outputs values of spin density at each nucleus. These were converted from atomic units to hyperfine constants with the conversion factors 14229.0 MHz for Mu and 4469.9 MHz for H (24). Muon hfcs were then adjusted by a factor of 1.20 to account for the isotope effect. Similarly, a correction factor of 0.94 was applied to the proton hfc of the -CHMu- group to mimic the isotope effect found for the muonium-substituted cyclohexadienyl (12, 16).

Considering the different methods employed, there is remarkable accord (see Table 3) between the density functional calculations of muon hfcs and the semiempirical estimates. The DFT results for all the hfcs of 1-Mu- and 4-Mu-pyrenyl are listed in Table 4. The α-H values do not match the experimental results quite as well as the β-H and muon values, but the correspondence still provides convincing evidence for the assignment of these two isomers.

Conclusions

Addition of muonium to pyrene results in 1-Mu-pyrenyl and 4-Mu-pyrenyl in large abundance and a small amount of 2-Mu-pyrenyl. Taking into account degeneracies (there are twice as many sites equivalent to carbons 1 and 4 as for carbon 2), the relative reactivities of carbons 1, 4, and 2 are 1.00 ± 0.02 : 0.71 ± 0.02 : 0.16 ± 0.06.

Having assigned the spectra, it is possible to deduce the distribution of unpaired π-spin density in the radicals from the experimentally determined hyperfine constants. Figure 4 shows the results for the two principal pyrenyls.

There is no evidence for addition at one of the trigonal carbon sites (15 and 16 in Fig.1(*b*)). This supports the conclusion that the HC_{70} isomer not detected by ESR (1) corresponds to addition at the E carbon (Fig.1(*a*)).

Acknowledgements

We thank Syd Kreitzman and the staff of the TRIUMF μSR Facility for technical support. This research was financially supported by the Natural Sciences and Engineering Research Council of Canada and, through TRIUMF, by the National Research Council of Canada. J. Schüth was the recipient of a NATO postdoctoral fellowship administered by DAAD (Deutscher Akademischer Austauschdienst).

© 1999 NRC Canada

References

1. J.R. Morton, F. Negri, and K.F. Preston. Chem. Phys. Lett. **218**, 467 (1994).
2. B. Addison-Jones, P.W. Percival, J.-C. Brodovitch, F. Ji, S. Wlodek, J.P. Selegue, M.S. Meier, and J.B. Wakefield. Hyperfine Interact. **86**, 817 (1994).
3. A. Lappas, K. Vavekis, and K. Prassides. J. Chem. Soc. Chem. Commun. 2743 (1994).
4. R. Borghi, L. Lunazzi, G. Placucci, P.J. Krusic, D.A. Dixon, and L.B. Knight, Jr. J. Phys. Chem. **98**, 5395 (1994).
5. R. Borghi, L. Lunazzi, G. Placucci, P.J. Krusic, D.A. Dixon, N. Matsuzawa, and M. Ata. J. Am. Chem. Soc. **118**, 7608 (1996).
6. P.W. Percival and S. Wlodek. Chem. Phys. Lett. **196**, 317 (1992).
7. P.W. Percival, B. Addison-Jones, J.-C. Brodovitch, F. Ji, P.J. Horoyski, M.L.W. Thewalt, and T.R. Anthony. Chem. Phys. Lett. **245**, 90 (1995).
8. T. Kawakubo. Annu. Rep. Res. Reactor Inst. Kyoto Univ. **10**, 84 (1977).
9. G. Zhang and J.K. Thomas. J. Phys. Chem. **98**, 11714 (1994).
10. M.B. Yim and D.E. Wood. J. Am. Chem. Soc. **97**, 1004 (1975).
11. I.D. Reid and E. Roduner. Struct. Chem. **2**, 419 (1991).
12. E. Roduner. The positive muon as a probe in free radical chemistry. Lect. Notes Chem. **49**, 1988.
13. E. Roduner. Appl. Magn. Reson. **13**, 1 (1997).
14. P.W. Percival, J.-C. Brodovitch, S.K. Leung, D. Yu, R.F. Kiefl, G.M. Luke, K. Venkateswaran, and S.F.J. Cox. Chem. Phys. **127**, 137 (1988).
15. D.C. Walker, J. Phys. Chem. **85**, 3960 (1981).
16. R.F. Kiefl, P.W. Percival, J.-C. Brodovitch, S.K. Leung, K. Yu, K. Venkateswaran, and S.F.J. Cox. Chem. Phys. Lett. **143**, 613 (1988).
17. P.W. Percival, R.F. Kiefl, S.R. Kreitzman, D.M. Garner, S.F. Cox, G.M. Luke, J.H. Brewer, K. Nishiyama, and K. Venkateswaran. Chem. Phys. Lett. **133**, 465 (1987).
18. J.E. Wertz and J.R. Bolton. Electron spin resonance. Elementary theory and practical applications. McGraw–Hill, New York. 1972. Chap. 6.
19. P.W. Percival, B. Addison-Jones, J.-C. Brodovitch, F. Ji, P.J. Horoyski, M.L.W. Thewalt, and T.R. Anthony. *In* Fullerenes: recent advances in the chemistry and physics of fullerenes. *Edited by* R.S. Ruoff and K.M. Kadish. Proc. Electrochem. Soc. **95-10,** 343 (1995).
20. J.J.P. Stewart. MOPAC 93. Fujitsu Limited, Tokyo, Japan. 1993.
21. M.J. Frisch, G.W. Trucks, H.B. Schlegel, P.M.W. Gill, B.G. Johnson, M.A. Robb, J.R. Cheeseman, T.A. Keith, G.A. Petersson, J.A. Montgomery, K. Raghavachari, M.A. Al-Laham, V.G. Zakrzewski, J.V. Ortiz, J.B. Foresman, C.Y. Peng, P.Y. Ayala, M.W. Wong, J.L. Andres, E.S. Replogle, R. Gomperts, R.L. Martin, D.J. Fox, J.S. Binkley, D.J. Defrees, J. Baker, J.P. Stewart, M. Head-Gordon, C. Gonzalez, and J.A. Pople. Gaussian 94 (Revision D.1). Gaussian, Inc., Pittsburgh, Pa. 1995.
22. D. Whiffen. Mol. Phys. **6**, 223 (1963).
23. Ch. Niedermayer, I.D. Reid, E. Roduner, E.J. Ansaldo, C. Bernhard, U. Binninger, H. Glückler, E. Recknagel, J.I. Budnick, and A. Weidinger. Phys. Rev. B: Condens. Matter, **47**, 10923 (1993).
24. D. Buttar and B.C. Webster. J. Chem. Soc. Faraday Trans. **87**, 2901 (1991).

© 1999 NRC Canada

Complete determination of the solid (RI)–liquid equilibria of four consecutive *n*-alkane ternary systems in the range $C_{14}H_{30}$–$C_{21}H_{44}$ using only binary data

Valérie Metivaud, Fazil Rajabalee, Harry A.J. Oonk, Denise Mondieig, and Yvette Haget

Abstract: The liquidus surfaces and thermal windows of four ternary systems implying consecutive *n*-alkanes (for *n* between 14 and 21 carbon atoms) have been studied combining Differential Scanning Calorimetry (DSC), X-ray experiments, and calculation using the program Txy-CALC. From the DSC measurements, the transition temperatures as well as the melting enthalpies have been determined. X-ray experiments performed at temperatures just below melting have shown that there is almost complete syncrystallization in the rotator form RI. The calculation of the RI → L liquidus surfaces has been made with temperature-independent as well as temperature-dependent excess Gibbs energies. In both cases, the agreement between experimental and calculated data is very good, the average temperature difference being within the uncertainty of the former.

Key words: *n*-alkanes, ternary mixtures, liquidus and solidus surfaces, rotator phase, thermodynamic analysis.

Résumé : Les surfaces de liquidus et les fenêtres thermiques de quatre systèmes ternaires impliquant des alcanes normaux consécutifs (de 14 à 21 atomes de carbone) ont été étudiées en combinant l'analyse enthalpique différentielle (AED), les mesures aux rayons X et le calcul thermodynamique. Les températures et les enthalpies de fusion ont été déduites des mesures AED. Les expériences aux rayons X, réalisées à des températures proches de la fusion, ont montré qu'il y a syncristallisation quasi-totale sous forme rotatoire RI. Les surfaces de liquidus RI → L ont été calculées en utilisant les énergies de Gibbs d'excès aussi bien indépendantes que dépendantes de la température. Dans les deux cas l'accord calcul–expérience est excellent, l'écart moyen entre les températures restant dans la limite des erreurs expérimentales.

Mots clés : *n*-alcanes, alliages ternaires, surfaces de liquidus et de solidus, phase rotatoire, analyse thermodynamique.

Introduction

The study of *n*-alkanes and their mixtures, which is one of the main research topics in our group, is of great interest both from a fundamental and a practical point of view. Fundamental because knowledge of the behaviour of *n*-alkanes and their systems can serve as a basis for understanding the behaviour of systems composed of more complex molecules, such as alkanes with one or more characteristic groups. Practical because the systems of *n*-alkanes lead to MAPCM (Molecular Alloy Phase Change Materials), which are suitable for the storage of energy and for thermal protection (1–4). One of the main characteristics of MAPCM is that they are thermo-adjustable by means of their composition. High-performance MAPCM that can be used for the applications mentioned must meet two important criteria, which are (*i*) a transition with an important latent heat, in combination with (*ii*) a narrow thermal window (temperature difference between solidus and liquidus at a certain composition). Research is necessary to investigate which compositions of what system of *n*-alkanes have these characteristics. Because many combinations of *n*-alkanes are possible, it would be useful to have a thermodynamic model to make reliable predictions of the desired characteristics. With such a model,

Received August 2, 1998.

V. Metivaud, F. Rajabalee, D. Mondieig,[1] and Y. Haget. Centre de Physique Moléculaire Optique et Hertzienne, UMR 5798 au Centre National de la Recherche Scientifique, Université Bordeaux I, 351 cours de la libération, 33405 Talence Cedex, France.
H.A.J. Oonk. Department of Interfaces and Thermodynamics, Faculty of Chemistry and Petrology Group, Faculty of Earth Sciences, Utrecht University, Budapestlaan 4, 3584 CD Utrecht, The Netherlands.

[1]Author to whom correspondence may be addressed. Telephone: (33) 556-846-988. e-mail: dmondiei@frbdx11.cribx1.u-bordeaux.fr
[2]Experimental data are from ref. 5.

 © 1999 NRC Canada

suitable systems could be selected without the need of testing all systems in detail experimentally.

The present work concerns the experimental determination and thermodynamic calculation of four ternary systems of consecutive *n*-alkanes from $C_{14}H_{30}$ to $C_{21}H_{44}$ (hereafter denoted by C14 to C21): the systems C14-C15-C16,[2] C16-C17-C18, C18-C19-C20, and C19-C20-C21. This paper focuses on solid–liquid equilibria. From the application point of view, these systems cover a large temperature range, roughly from 0 to 50 degrees Celsius.

Experimental

The compounds were purchased from Aldrich (C14, C16, C17, and C20) and from Fluka (C15, C18, C19, and C21), with purity grades >99% as certified by gas chromatography and mass spectrometry.

For the systems implying at least one solid component at room temperature, mixtures were prepared according to the melting–quenching method: the components are weighed in the desired proportion, melted, mixed to get an entirely homogeneous sample, and then quenched into liquid nitrogen (in the case of the system C14-C15-C16, the components are already liquid at room temperature).

Calorimetric measurements were carried out using a Perkin–Elmer DSC7 differential scanning calorimeter, operating in the subambient mode. The instrument was calibrated with substances of known transition temperatures and enthalpies (indium, naphthalene, and water). Samples were introduced at room temperature in aluminium pans, which were subsequently hermetically closed. The following conditions were adopted: sample weight ≈4.0 mg, each time, precision ±0.1 mg; heating rate, 2 K/min; at least four independent measurements for each composition.

Liquidus temperatures were determined from the DSC curves using the shape-factor method (6, 7). The random part of the uncertainties was estimated using Student's method with 95% threshold of reliability.

X-ray experiments were performed at specified constant temperatures using a Siemens D500 vertical powder diffractometer, which operates in the reflection mode with CuK α radiation (λ = 1.5406 Å). The temperature was controlled with a low-temperature Anton Paar KG device. The data were collected with 0.04° 2θ–step and 3 s interval time.

Pure component properties

The structural and thermodynamic properties of the *n*-alkanes considered in this work have been described previously in detail (8–10). In the range $n \leq 21$, *n*-alkanes can be divided into two groups according to the parity of the number of carbon atoms.

Odd-numbered alkanes have an orthorhombic crystal structure Oi at low temperature (space group *Pcam*, $Z = 4$). With increasing temperature, the structure becomes face-centred orthorhombic (*Fmmm*, $Z = 4$). This form, which is called rotator I (RI), presents orientational disorder (11, 12). Even-numbered alkanes have a triclinic structure Tp ($P\bar{1}$, $Z = 1$), the RI form being metastable.

Stable and metastable (RIm → L) melting points ($T_{melting}$) and enthalpies of melting ($\Delta H_{melting}$) of the pure components are reported in Table 1, together with the entropies of melting ($\Delta S_{melting} = \Delta H_{melting}/T_{melting}$). Thermophysical characteristics relative to the Oi → RI transition are given elsewhere (8).

Table 1. Thermophysical characteristics of the pure components ($T_{melting}$ are in K, $\Delta H_{melting}$ in kJ mol^{-1}, and $\Delta S_{melting}$ in J mol^{-1} K^{-1}).

C*n*	$T_{melting}$	$\Delta H_{melting}$	$\Delta S_{melting}$	Transition
C14	278.3±0.4	42.8±0.3	154±2	Tp → L
	276.0±0.6	31.7±1.5	115±6	RI* → L
C15	282.7±0.4	34.2±0.8	121±3	RI → L
C16	290.7±0.4	53.0±0.5	182±2	Tp → L
	289.2±0.6	36.9±1.5	128±8	RI* → L
C17	294.8±0.3	39.4±0.9	134±3	RI → L
C18	301.1±0.2	59.8±1.4	199±5	Tp → L
	299.5±0.6	41.3±1.5	138±5	RI* → L
C19	304.4±0.3	42.7±1.0	140±3	RI → L
C20	309.7±0.2	68.1±1.6	220±5	Tp → L
	308.7±0.5	44.9±1.0	145±3	RI* → L
C21	313.0±0.3	46.6±1.1	149±4	RI → L

* is related to the metastable form RI.

The constituent binary systems

Experimental data

The solid–liquid phase diagrams of the 11 binary subsystems are represented in Fig. 1. The diagrams C14-C15, C15-C16, C14-C16, C18-C19, and C18-C20 are taken from refs. 5, 9, and 13).

In all cases, the mixed crystalline state in the rotator I form is stable over a large part of the composition range, even when both components do not show that stable phase (C14-C16 and C18-C20). When the two components present the RI phase, the miscibility is total (C19-C21). One could say that compositional disorder tends to stabilize forms with orientational disorder.

Calculation

The equilibria between solid (RI) and liquid were analysed using the program LIQFIT (which stands for LIQuidus FITting) (14): an iterative method of thermodynamic phase diagram analysis, with intermediate phase diagram calculation, in which the calculated liquidus curve is made to pass through the experimental liquidus points. It provides a thermodynamically sound solidus together with the difference in excess Gibbs energy between the liquid and the solid state for the mean temperature of the solid–liquid two-phase region (eq. [1]).

$$[1] \qquad \Delta^{liq}_{sol} G^E(T,x) = G^{E,liq}(T,x) - G^{E,sol}(T,x)$$

If the excess Gibbs energy of one of the states is known, then the excess Gibbs energy difference function provides the excess Gibbs energy of the other state. In the case of *n*-alkane systems, the thermodynamic excess functions of liquid mixtures are so small that these mixtures can safely be taken as ideal, i.e., $G^{E,liq=0}$. Then, as expressed in eq. [2]:

$$[2] \qquad \Delta^{liq}_{sol} G^E(T,x) = -G^{E,sol}(T,x)$$

© 1999 NRC Canada

Fig. 1. Experimental solid–liquid phase diagrams of the binary systems involved in the four ternary systems.

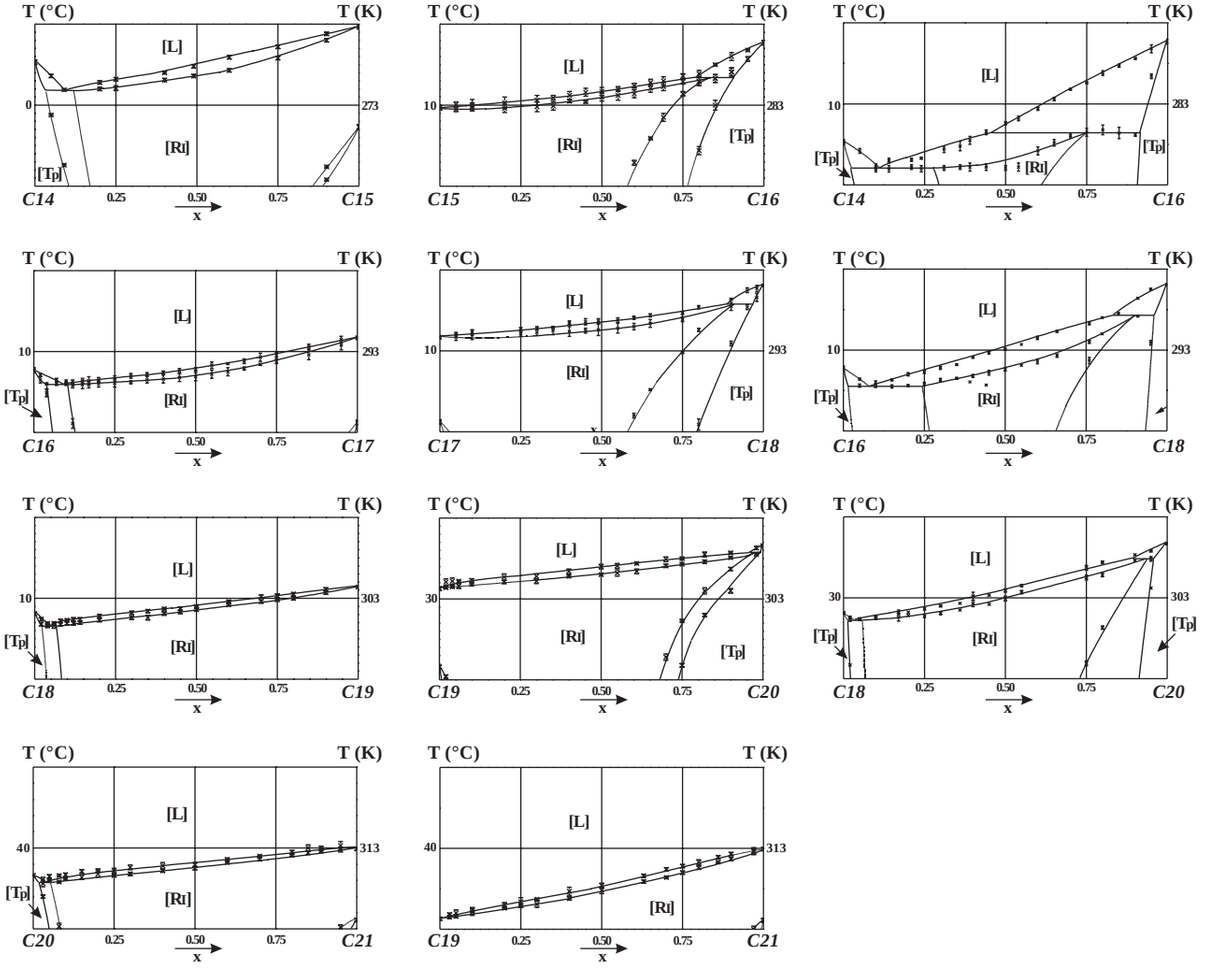

The calculation of the solid state excess Gibbs energy by means of LIQFIT was made in two different ways, hereafter denoted by case 1 and case 2.

In case 1 (eq. [3]), the excess Gibbs energy is taken to be independent of temperature.

$$[3] \qquad G^{E,sol}(T,x) = G^{E,sol}(x)$$

And it means that the outcome of the computation corresponds to an excess Gibbs energy function that is representative of the mean temperature of the input data.

In case 2 (eq. [4]), the excess Gibbs energy is taken to be linearly dependent upon temperature.

$$[4] \qquad G^{E,sol}(T,x) = H^{E,sol}(x) - TS^{E,sol}(x)$$

In this case, the experimental $H^{E,sol}$ (excess enthalpy depending on heat of mixing) is part of the input for LIQFIT and the program is used to calculate the excess entropy ($S^{E,sol}$).

The thermodynamic excess functions were expressed as a second-order Redlich–Kister polynomial (eq. [5], (15)).

$$[5] \qquad Z^E = x(1 - x)[Z1 + Z2(1 - 2x)]$$

In eq. [5], Z^E stands for any thermodynamic excess function such as G^E, H^E, or S^E, x is the mole fraction of the component with the greatest number of carbon atoms, and $Z1$ and $Z2$ the so-called Redlich–Kister coefficients of the excess property.

Solid (RI) excess coefficients of most of the binary systems involved in this work have already been determined previously within our research group and published by Mondieig et al. (16) and Oonk et al. (17). However, recent complementary studies performed on pure *n*-alkanes have allowed a refinement of the even alkane metastable (RI $\rightarrow$ L) transition temperatures. These metastable values have been used as input for new LIQFIT computations in order to refine excess coefficients. The results of the computations for case 1 (eq. [3]) are given in Table 2. Uncertainties relative to these excess parameters are about 20 J mol^{-1} for $G1$ and 40 J mol^{-1} for $G2$. For case 2 (eq. [4]), the computed entropy coefficients are given in Table 3 along with the input enthalpy coefficients. Uncertainties relative to the $H1$ and $H2$ experimental excess values and to the $S1$ and $S2$ computed values are about 0.5 kJ mol^{-1}, 0.8 kJ mol^{-1}, 10 J mol^{-1} K^{-1}, and 20 J mol^{-1} K^{-1}, respectively.

© 1999 NRC Canada

Table 2. Computed Redlich–Kister coefficients of excess Gibbs energy valid for the mean temperatures of the individual systems ($G1$ and $G2$ are in J mol^{-1}).

Binary systems	$G1$	$G2$
C14-C15	930	150
C15-C16	760	–360
C14-C16	2070	100
C16-C17	680	–90
C17-C18	310	–170
C16-C18	1370	300
C18-C19	200	0
C19-C20	–160	150
C18-C20	500	0
C20-C21	–290	–160
C19-C21	360	–90

Table 3. Computed Redlich–Kister coefficients of excess entropy along with the experimental coefficients of the excess enthalpy used as input for the computations ($H1$ and $H2$ are in kJ mol^{-1}, $S1$ and $S2$ in J mol^{-1} K^{-1}).

Binary systems	$H1$	$H2$	$S1$	$S2$
C14-C15	6.5	0.2	20	1
C15-C16	5.0	2.8	15	11
C14-C16	13.4	–18.3	41	–66
C16-C17	4.7	1.8	14	7
C17-C18	5.2	1.2	17	5
C16-C18	12.2	0.3	37	1
C18-C19	3.6	0.0	11	0
C19-C20	4.7	3.7	16	12
C18-C20	11.2	8.3	35	28
C20-C21	4.8	1.6	16	6
C19-C21	10.3	7.0	32	23

Although these new values are slightly different from those published in refs 16 and 17, the conclusions given in these two papers remain totally the same.

The ternary solid–liquid equilibria

Experimental

For each ternary system, experiments were carried out for at least 11 ternary compositions. Liquidus temperatures and thermal windows were determined from the DSC curves. The expected existence of large ternary stability regions of the rotator I mixed crystalline state was confirmed by X-ray diffraction. As an example, in Fig. 2, X-ray patterns corresponding to a central composition are given for the four systems.

Calculation

Calculations of the RI $\rightarrow$ L equilibria of the different ternary systems were performed using the program Txy-CALC (18, 19). In common practice, the ternary excess Gibbs energy needed for the calculations is composed of the binary functions and eventually extended with ternary interaction functions. The latter, as a rule, are added if the ensemble of binary functions fails to yield a correct description of the equilibria for compositions inside the ternary triangle. Out of the various methods of adding binary excess functions (20), we opted for the method proposed by Kohler (21).

As was done for the binary systems, two different approaches were considered. In the first case, the excess Gibbs energy was taken as temperature independent and in the second case as temperature dependent. Two main parameters were calculated: the liquidus surfaces and the thermal windows. The comparison between experimental and calculated temperatures is given in Tables 4–7 for the systems C14-C15-C16, C16-C17-C18, C18-C19-C20, and C19-C20-C21, respectively. Isotherm liquidus lines calculated in case 1 are represented in Figs. 3*a*–6*a* for the systems C14-C15-C16, C16-C17-C18, C18-C19-C20, and C19-C20-C21, respectively, together with the analysed compositions. Lines of thermal windows of equal width calculated in case 1 are represented in Figs. 3*b*–6*b*.

Fig. 2. X-ray diffraction patterns performed at temperatures just below the melting (RI form, space group *Fmmm*, $Z = 4$).
(*a*) C14(0.32)C15(0.24)C16(0.44), T = 274 K;
(*b*) C16(0.33)C17(0.33)C18(0.34), T = 285 K;
(*c*) C18(0.33)C19(0.33)C20(0.34), T = 301 K;
(*d*) C19(0.29)C20(0.28)C21(0.43), T = 306 K.

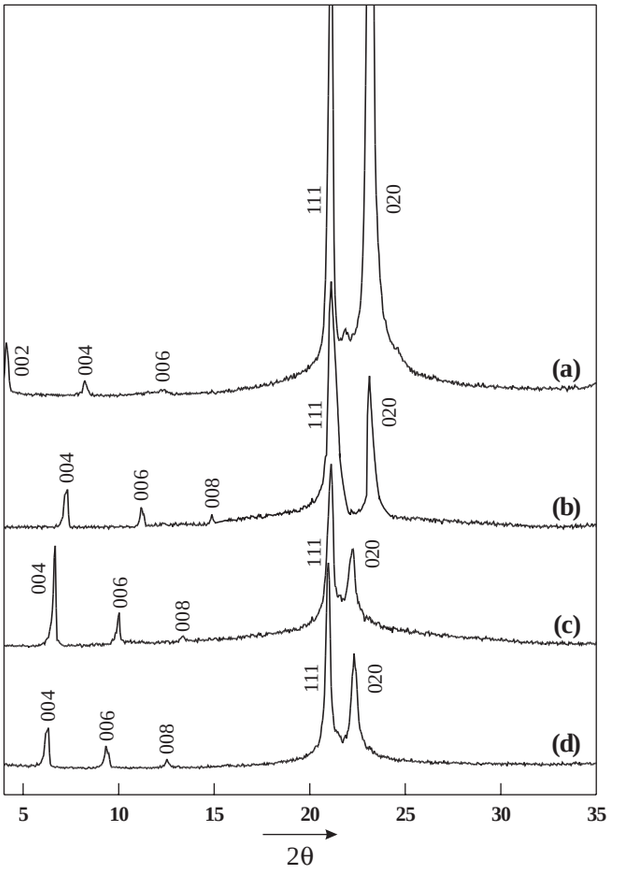

© 1999 NRC Canada

Table 4. Experimental and calculated temperatures (in K) of the system C14-C15-C16.

					Case 1		Case 2	
	C14	C15	C16	*T*exp	*T*calc	*T*exp — *T*calc	*T*calc	*T*exp – *T*calc
1	0.06	0.57	0.37	283.4±0.2	283.4	0.0	283.4	0.0
2	0.14	0.23	0.63	284.6±0.4	284.5	0.1	284.7	–0.1
3	0.17	0.06	0.77	285.5±0.3	285.8	–0.3	285.8	–0.3
4	0.24	0.33	0.43	282.2±0.2	282.0	0.2	282.1	0.1
5	0.21	0.56	0.23	281.2±0.2	281.3	–0.1	281.3	–0.1
6	0.27	0.66	0.07	280.4±0.3	280.2	0.2	280.2	0.2
7	0.37	0.05	0.58	282.6±0.2	282.4	0.2	282.7	–0.1
8	0.32	0.24	0.44	281.5±0.3	281.3	0.2	281.4	0.1
9	0.43	0.33	0.24	279.2±0.2	279.0	0.2	279.0	0.2
10	0.57	0.17	0.26	278.0±0.4	277.7	0.3	277.7	0.3
11	0.73	0.14	0.13	276.3±0.2	276.1	0.2	276.2	0.1

Table 5. Experimental and calculated temperatures (in K) of the system C16-C17-C18.

					Case 1		Case 2	
	C16	C17	C18	*T*exp	*T*calc	*T*exp – *T*calc	*T*calc	*T*exp – *T*calc
1	0.10	0.10	0.80	297.8±0.6	297.6	0.2	297.6	0.2
2	0.10	0.75	0.15	294.3±0.6	294.5	–0.2	294.5	–0.2
3	0.10	0.80	0.10	294.6±0.7	294.3	0.3	294.3	0.3
4	0.11	0.39	0.50	295.8±0.7	295.8	0.0	295.8	0.0
5	0.20	0.20	0.60	295.8±0.9	295.8	0.0	295.7	0.1
6	0.20	0.60	0.20	293.7±0.7	293.8	–0.1	293.8	–0.1
7	0.33	0.33	0.34	293.3±0.8	293.4	–0.1	293.2	0.1
8	0.40	0.10	0.50	293.6±0.6	293.8	–0.2	293.7	–0.1
9	0.40	0.40	0.20	291.9±0.5	292.2	–0.3	292.2	–0.3
10	0.60	0.20	0.20	290.8±0.7	290.8	0.0	290.9	–0.1
11	0.80	0.10	0.10	289.5±0.8	289.5	0.0	289.6	–0.1

Table 6. Experimental and calculated temperatures (in K) of the system C18-C19-C20.

					Case 1		Case 2	
	C18	C19	C20	*T*exp	*T*calc	*T*exp – *T*calc	*T*calc	*T*exp – *T*calc
1	0.02	0.02	0.96	309.0±0.5	308.5	0.5	308.5	0.5
2	0.05	0.05	0.90	308.5±0.4	308.1	0.4	308.2	0.3
3	0.05	0.90	0.05	304.7±0.4	304.5	0.2	304.4	0.3
4	0.10	0.10	0.80	307.5±0.3	307.6	–0.1	307.6	–0.1
5	0.10	0.40	0.50	306.3±0.2	306.6	–0.3	306.5	–0.2
6	0.10	0.55	0.35	305.9±0.3	305.7	0.2	305.6	0.3
7	0.14	0.73	0.13	304.4±0.3	304.4	0.0	304.4	0.0
8	0.15	0.15	0.70	307.3±0.3	307.0	0.3	307.0	0.3
9	0.20	0.20	0.60	306.3±0.2	306.4	–0.1	306.4	–0.1
10	0.20	0.60	0.20	304.9±0.3	304.5	0.4	304.5	0.4
11	0.26	0.26	0.48	305.5±0.2	305.6	–0.1	305.6	–0.1
12	0.33	0.33	0.34	304.3±0.4	304.6	–0.3	304.5	–0.2
13	0.40	0.10	0.50	304.6±0.2	304.9	–0.3	304.8	–0.2
14	0.43	0.43	0.14	302.8±0.2	303.0	–0.2	303.0	–0.2
15	0.48	0.15	0.37	303.8±0.4	303.4	0.4	303.5	0.3
16	0.60	0.20	0.20	302.3±0.2	302.5	–0.2	302.5	–0.2
17	0.79	0.11	0.10	301.4±0.5	301.5	–0.1	301.5	–0.1
18	0.90	0.05	0.05	300.6±0.4	300.2	0.4	300.2	0.4

© 1999 NRC Canada

Table 7. Experimental and calculated temperatures (in K) of the system C19-C20-C21.

					Case 1		Case 2	
	C19	C20	C21	*T*exp	*T*calc	*T*exp – *T*calc	*T*calc	*T*exp – *T*calc
1	0.05	0.05	0.90	312.9±0.3	312.5	0.4	312.5	0.4
2	0.05	0.89	0.06	309.4±0.3	309.1	0.3	309.1	0.3
3	0.10	0.40	0.50	310.9±0.3	311.0	–0.1	311.0	–0.1
4	0.10	0.80	0.10	309.5±0.3	309.2	0.3	309.2	0.3
5	0.12	0.10	0.78	312.1±0.3	311.7	0.4	311.8	0.3
6	0.19	0.50	0.31	309.9±0.2	309.9	0.0	309.9	0.0
7	0.20	0.21	0.59	310.9±0.2	310.8	0.1	310.7	0.2
8	0.20	0.60	0.20	309.3±0.2	309.3	0.0	309.3	0.0
9	0.29	0.28	0.43	309.7±0.3	309.8	–0.1	309.8	–0.1
10	0.39	0.10	0.51	309.5±0.1	309.6	–0.1	309.5	0.0
11	0.39	0.50	0.11	307.8±0.3	308.1	–0.3	308.1	–0.3
12	0.49	0.20	0.31	308.1±0.2	308.3	–0.2	308.2	–0.1
13	0.50	0.40	0.10	307.4±0.4	307.5	–0.1	307.5	–0.1
14	0.60	0.20	0.20	307.3±0.4	307.3	0.0	307.3	0.0
15	0.80	0.10	0.10	306.0±0.3	305.9	0.1	305.9	0.1
16	0.90	0.05	0.05	305.5±0.4	305.2	0.3	305.2	0.3

Fig. 3. (*a*) Analysed points (numbers correspond to compositions given in Table 4) and liquidus surfaces of the ternary system C14-C15-C16 calculated in case 1. The lines are isotherms. (*b*) Thermal windows of the ternary system C14-C15-C16 calculated in case 1. The lines connect points with thermal windows of equal width.

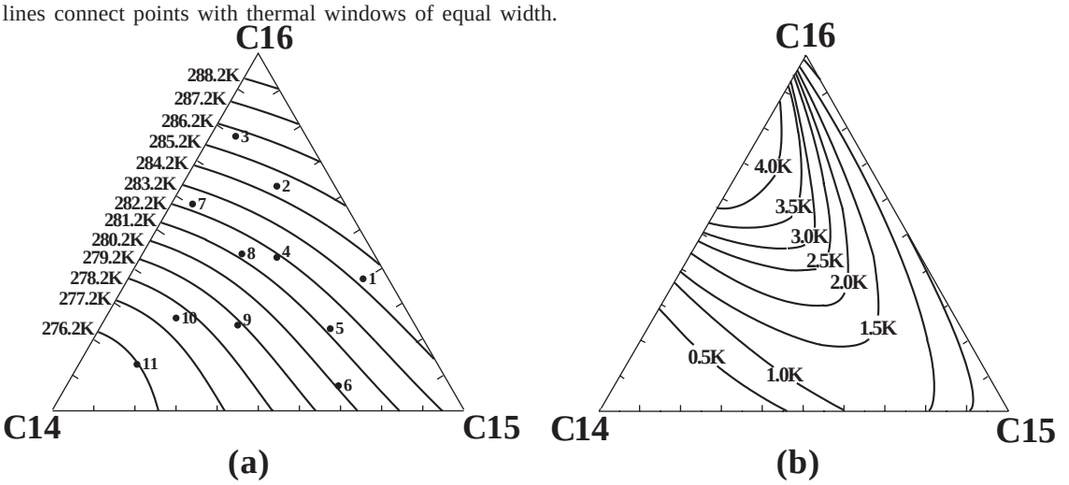

Fig. 4. (*a*) Analysed points (numbers correspond to compositions given in Table 5) and liquidus surfaces of the ternary system C16-C17-C18 calculated in case 1. The lines are isotherms. (*b*) Thermal windows of the ternary system C16-C17-C18 calculated in case 1. The lines connect points with thermal windows of equal width.

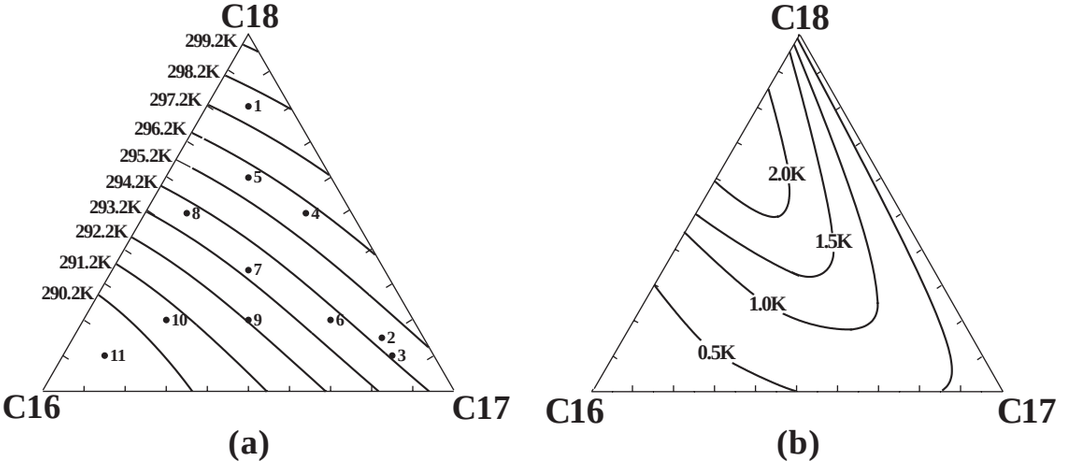

© 1999 NRC Canada

Fig. 5. (*a*) Analysed points (numbers correspond to compositions given in Table 6) and liquidus surfaces of the ternary system C18-C19-C20 calculated in case 1. The lines are isotherms. (*b*) Thermal windows of the ternary system C18-C19-C20 calculated in case 1. The lines connect points with thermal windows of equal width.

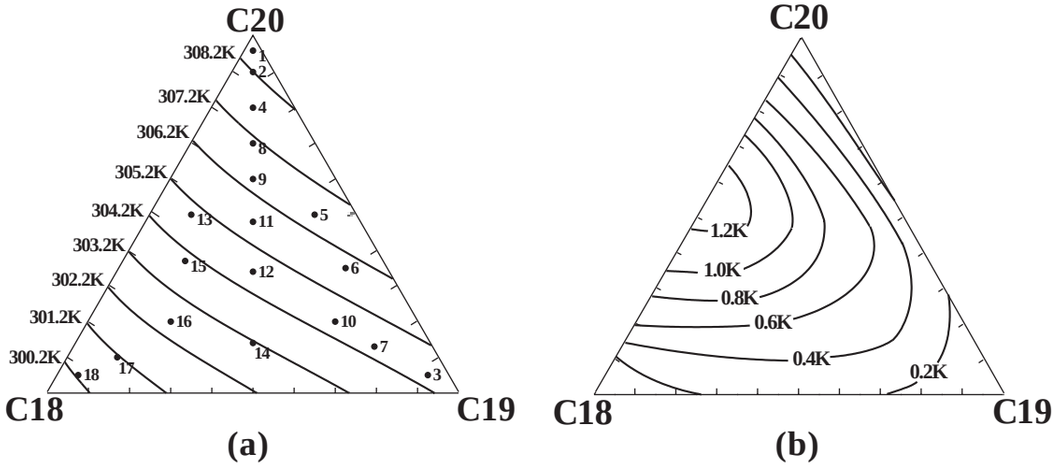

Fig. 6. (*a*) Analysed points (numbers correspond to compositions given in Table 7) and liquidus surfaces of the ternary system C19-C20-C21 calculated in case 1. The lines are isotherms. (*b*) Thermal windows of the ternary system C19-C20-C21 calculated in case 1. The lines connect points with thermal windows of equal width.

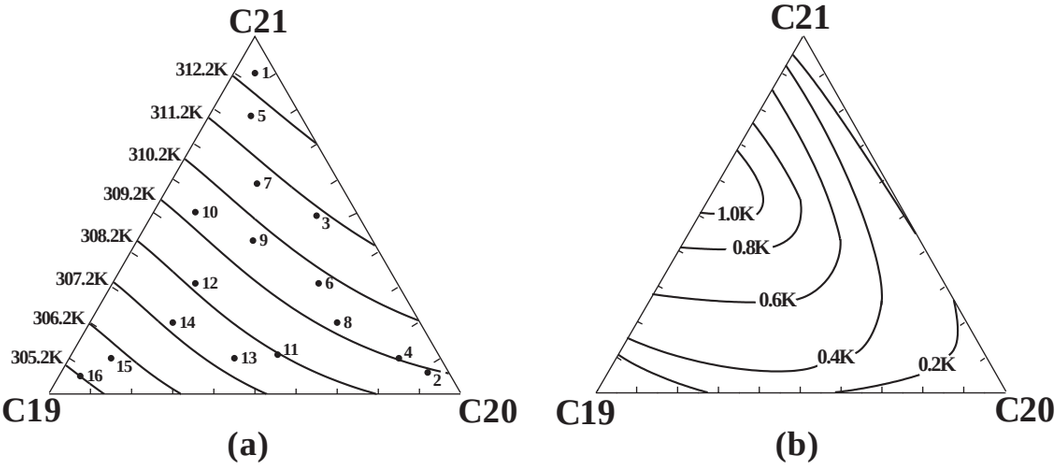

Discussion

The average differences between experimental and calculated liquidus temperatures are reported for each system in Table 8.

The agreement between experimental and calculated data is very good in all cases, the maximum average difference being 0.3 K. All these differences are within the experimental uncertainties of the liquidus temperatures. Moreover, no systematic shift is observed; in other words, it was not necessary to introduce a ternary interaction parameter. From Fig. 7, in which the experimental thermal windows are plotted against the calculated ones, it can be concluded that the agreement between the two is quite satisfactory. It means, among other things, that the experimental procedures for the melting process in the alkane systems, in combination with the shape-factor method, are capable of giving consistent solidus and liquidus temperatures.

Table 8. Average differences between experimental and calculated liquidus temperatures.

	Liquidus temperatures	
Ternary systems	Case 1	Case 2
C14-C15-C16	0.2	0.2
C16-C17-C18	0.1	0.1
C18-C19-C20	0.3	0.2
C19-C20-C21	0.2	0.2

Another observation that can be made, in the case of the melting in alkane systems, is that, for predictive computations from binary data, it is not necessary to take into account the temperature dependence of the excess Gibbs energies. This follows from the fact that the case 2 calculations did not produce better results than the case 1 calculations. In addition, computations made earlier on the system C15-C16-C17 gave rise to the same conclusions (22).

© 1999 NRC Canada

Fig. 7. Experimental thermal windows (l_{exp}) against the calculated ones (l_{calc}).

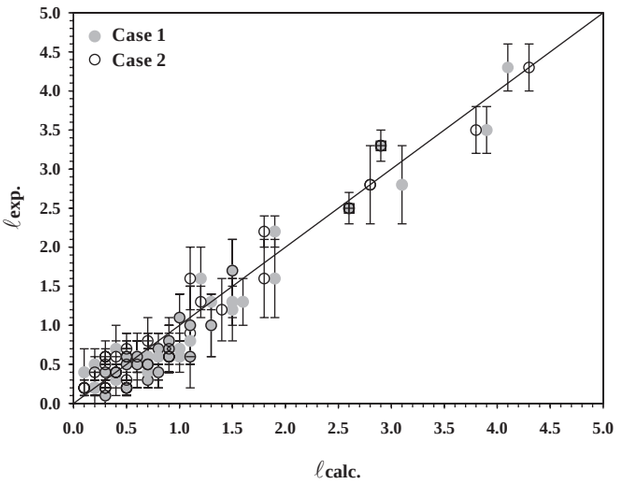

The general conclusion of the underlying research could be that the equilibria between solid and liquid in ternary systems of consecutive *n*-alkanes can be reliably predicted from the binary data, i.e., without the need of experimentally verifying the computational results.

References

1. Y. Haget, D. Mondieig, and M.A. Cuevas-Diarte. CNRS Patent FR91/08695 and foreign co-pending patent applications.
2. D. Mondieig, Y. Haget, M. Labrador, M.A. Cuevas-Diarte, P.R.Van der Linde, and H.A.J. Oonk. Mater. Res. Bull. **26**, 1091 (1991).
3. P. Espeau, D. Mondieig, Y. Haget, and M.A. Cuevas-Diarte. Packag. Technol. Sci. **10**, 253 (1997).
4. D. Mondieig, A. Marbeuf, L. Robles, P. Espeau, B. Poirier, Y. Haget, T. Calvet-Pallas, and M.A. Cuevas-Diarte. High Temp. – High Pressures, **29**, 385 (1997).
5. P. Espeau. European Thesis of the University Bordeaux I, France. 1995. pp. 194–197.
6. R. Courchinoux, N.B. Chanh, Y. Haget, E. Tauler, and M.A. Cuevas-Diarte. Thermochim. Acta, **128**, 45 (1988).
7. R. Courchinoux, N.B. Chanh, Y. Haget, T. Calvet, E. Estop, and M.A. Cuevas-Diarte. J. Chim. Phys. **86**, 561 (1989).
8. P. Espeau, L. Robles, D. Mondieig, Y. Haget, M.A. Cuevas-Diarte, and H.A.J. Oonk. J. Chim. Phys. **93**, 1217 (1996).
9. L. Robles-Beneyt. European Thesis of the University Bordeaux I, France. 1995. pp. 71–100.
10. F. Rajabalee. European Thesis of the University Bordeaux I, France. 1998. pp. 25–55.
11. E.B. Sirota, H.E. King, Jr., D.M. Singer, and H.H. Shao. J. Chem. Phys. **98**, 5809 (1993).
12. E.B. Sirota, H.E. King, Jr., H.H. Shao, and D.M. Singer. J. Phys. Chem. **99**, 798 (1995).
13. L. Robles, D. Mondieig, Y. Haget, M.A. Cuevas-Diarte, and X. Alcobe. Mol. Cryst. Liq. Cryst. **281**, 279 (1996).
14. M.H.G. Jacobs and H.A.J. Oonk. LIQFIT, a computer program for the thermodynamic assessment of T-X liquidus or solidus data. Utrecht University. 1990.
15. O. Redlich and A.T. Kister. Ind. Eng. Chem. **40**, 345 (1948).
16. D. Mondieig, P. Espeau, L. Robles, Y. Haget, H.A.J. Oonk, and M.A. Cuevas-Diarte. J. Chem. Soc. Faraday Trans. **93**, 3343 (1997).
17. H.A.J Oonk, D. Mondieig, Y. Haget, and M.A. Cuevas-Diarte. J. Chem. Phys. **108**, 715 (1998).
18. M.H.G. Jacobs and H.A.J. Oonk. Txy-CALC, a computer program for the calculation of thermodynamic function and phase equilibria in binary and ternary systems. Utrecht University. 1995.
19. M.H.G. Jacobs, R. Jelleria, and H.A.J. Oonk. CALPHAD: Comput. Coupling Phase Diagrams Thermochem. **20**, 79 (1996).
20. M.H.G. Jacobs. Thesis of Utrecht University, The Netherlands. 1190. pp. 19–24.
21. F. Kohler. Monatsh. Chem. **91**, 738 (1960).
22. R. Stolk, F. Rajabalee, M.H.G. Jacobs, P. Espeau, D. Mondieig, H.A.J. Oonk, and Y. Haget. CALPHAD: Comput. Coupling Phase Diagrams Thermochem. **21**, 401 (1997).

© 1999 NRC Canada

The properties of a family of two-headed surfactant systems: the 4-alkyl-3-sulfosuccinates 2. Surface properties of alkyl sulfosuccinate micelles

Judith A. MacInnis, Greg D. Boucher, R. Palepu, and D. Gerrard Marangoni

Abstract: The micellar properties of a family of two-headed surfactants, the alkyl sulfosuccinates, were investigated employing fluorescence, ultra-violet spectroscopy, and acid–base titrations, as a function of the chain length of the surfactant. Polarity of the micellar interior was investigated using pyrene and the ionic probe 8-anilino-1-naphthalensulfonic acid ammonium salt (ANS). Pyrene I_1/I_3 ratios were used to probe the microenvironment of the probe in the palisade layer of the micelle. The pK_a values of both of the anionic head groups were determined using acid–base titrations. Surface potential measurements were obtained from the measurement of the pK_a of the hydrophobic indicator, 7-hydroxycoumarin, at the sulfosuccinate micellar interface. All of these results were used to examine the surface properties of the alkyl sulfosuccinate micelles and the polarity of the micellar interior.

Key words: micellization, pK_a, surface potential, surface charge density, 7-hydroxycoumarin, pyrene.

Résumé : Faisant appel à la fluorescence, à la spectroscopie ultraviolette et à des titrages acide/base, on a étudié les propriétés micellaires d'une famille d'agents de surface à deux têtes, les sulfosuccinates d'alkyle, en fonction de la longueur de la chaîne de l'agent de surface. On a étudié la polarité de l'intérieur de la micelle en utilisant le pyrène et une sonde ionique, le sel d'ammonium de l'acide 8-anilinonaphtalène-1-sulfonique (ANS). On a utilisé les rapports I_1/I_3 du pyrène pour évaluer le microenvironnement de la sonde dans la couche palissade de la micelle. On a déterminé les valeurs des pK_a des deux têtes ioniques à partir de mesures de pK_a de la 7-hydroxycoumarine, un indicateur hydrophobe, à l'interface micellaire du sulfosuccinate. On a utilisé l'ensemble de ces résultats pour étudier les propriétés superficielles des micelles de sulfosuccinate d'alkyle et la polarité de l'intérieur de la micelle.

Mots clés : micellisation, pK_a, potentiel de surface, densité de charge de surface, 7-hydroxycoumarine, pyrène.

[Traduit par la Rédaction]

1. Introduction

Micelles in ionic detergent solutions are generally considered to be excellent models for the study of colloidal and detergent properties due to the ease of creating stable colloidal aggregates with definite surface properties. There have been a number of papers in the literature describing the synthesis and micellar and solution properties of novel two-headed surfactant systems (1–4). However, much of this work has focused on the synthesis, critical micelle concentration values (cmc), and the degrees of counter ion binding (β values) of two-headed surfactants. Although the β values provide some information on the surface charge densities of the micelles, direct measurements of the surface properties of the two-headed surfactants are essential to evaluate the unique structure of the interface between water and the micelles of these two-headed surfactants (5–17). Surface potential measurements using solubilized pH indicators have often been used to examine the properties of micelles and model lipid membranes. The micelle–water interface possesses properties that are distinctly different from those of the bulk solution and the micellar interior. Understanding the surface properties of micelles may play an important role in applications such as micellar catalysis, transport phenomena, anesthetic properties, and colloid stability in mixed electrolyte solutions, where surface micellar effects have been recognized as being important. Surface potential measurements may also shed some light on the hard-water tolerance of two-headed surfactants (3). The present paper involves the examination of a family of two-headed surfactants, the disodium 4-alkyl 3-sulfosuccinate surfactants (Fig. 1). These two-headed surfactants are of interest because the addition of a second negatively charged head group adjacent to an existing anionic surfactant increases the cmc and lowers the Kraft point of the two-headed surfactants (1–4). The alkyl sulfosuccinate surfactants have negatively charged sulfonate and carboxylate groups separated by two carbon atoms on the alkyl chain (4), and hence may also have interesting micellar properties as a function of the pH.

In this paper, the micellar surface properties and the micropolarity of a family of two-headed surfactants, the alkyl sulfosuccinates, were investigated using fluorescence

Received September 15, 1997.

J.A. MacInnis, G.D. Boucher, R. Palepu, and D.G. Marangoni.[1] Chemistry Department, St. Francis Xavier University, Antigonish, NS B2G 2W5, Canada.

[1]Author to whom correspondence may be addressed. Telehone: (902) 867-2324. Fax: (902) 867-2414. e-mail: gmarango@stfx.ca

© 1999 NRC Canada

Fig. 1. Structural formula of alkyl sulfosuccinate surfactants (R = alkyl group).

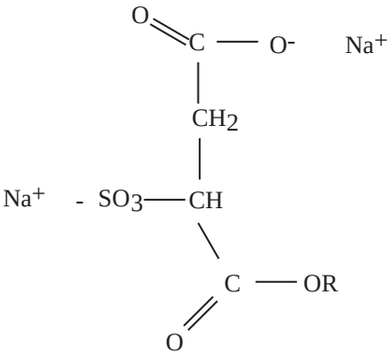

spectroscopy, ultra-violet spectroscopy, and acid–base titrations of surface solubilized indicator 7-hydroxycoumarin. As a first step in determining the micellar properties of the sulfosuccinate surfactants, as a function of pH, we have also determined the pK_a values of both of the anionic head groups of the alkyl sulfosuccinates, employing acid–base titrations. Pyrene I_1/I_3 ratios and the luminescent intensities of ANS were used to determine the polarity of the microenvironment of the micelle. The measurement of the pK_a of hydrophobic indicator, 7-hydroxycoumarin, at the sulfosuccinate micellar surface, was used to determine the micellar surface potentials. All of these properties are discussed in terms of the influence of having two negatively charged head groups on the surfactant chain. Nuclear magnetic resonance spectroscopy was also used to investigate the location of a typical aromatic probe (benzene) in the surfactant micelles.

2. Experimental

The alkyl sulfosuccinates were synthesized using the following general procedure. Equimolar amounts of maleic anhydride and an alcohol were heated for 20 min, with constant stirring, in a 500 mL round bottom flask. An equimolar amount of an aqueous sodium metabisulfite solution was added, and the mixture was neutralized to pH ≅ 7–9. The mixture was then allowed to reflux for 20–24 h. The progress of the reaction was monitored by running a UV spectrum on the reaction mixture to confirm the absence of the maleic anhydride double bond. The resulting surfactants were purified through Soxhlet extraction with diethyl ether for at least 72 h. The structures of these surfactants were confirmed by nuclear magnetic resonance and FT-IR spectroscopy.

The pK_a values of the respective anionic head groups were determined as follows. Aqueous surfactant solutions, with concentrations twice the critical micelle concentration, were titrated with standardized sodium hydroxide (0.10 M, Fisher Scientific A.C.S.) and were used to obtain the titration curve data. The pH of the solution was measured using a glass electrode and a Cole–Palmer Digi-Sens pH/mv meter. The electrode was calibrated using pH 4 and 10 buffer solutions (Fisher Scientific). The pH values were reproducible to ±0.15 pH units.

The luminescence probing experiments to obtain the pyrene I_1/I_3 ratios in the sulfosuccinate micellar interior were carried out as follows. Pyrene (Aldrich, 99%) was purified through sublimation and recrystallization (twice) with ethanol. The pyrene probe was held at a constant concentration of 2×10^{-5} M. A small amount of a pyrene–ethanol solution was placed in a small flask, and the solvent was allowed to evaporate, depositing the pyrene as a monolayer at the bottom of the flask.

The stock aqueous solution of the surfactant was added to the flask containing the pyrene; this solution was stirred overnight to ensure complete dissolution of the pyrene in the surfactant solution. Steady-state pyrene emission spectra were recorded on a Perkin–Elmer MPF-66 spectrophotometer, using an excitation wavelength of 338 nm and scanning the emission spectra from 350 to 500 nm. The intensities of the first and third peaks of the emission spectra were recorded and used to determine the I_1/I_3 ratio and hence, an estimate of the micropolarity of the micellar interior.

The ANS polarity studies were carried out as follows: 8-anilino-1-naphthalenesulfonic acid ammonium salt was purchased from Aldrich and was used as received. A stock solution of the probe (10^{-5} M) was prepared in absolute ethanol. Micellar solutions of ANS were prepared by taking an aliquot of the stock solution and adding the surfactant solution. The resulting solutions were sonicated for 5 min. Fluorescence measurements were made using an excitation wavelength of 389 nm and the emission spectra was obtained from 400 to 525 nm.

The nmr spectra (^{1}H and proton decoupled ^{13}C) were obtained on a Bruker AC-200. D_2O was used as a solvent for all of the sulfosuccinate experiments. The ^{1}H spectra were referenced to the HOD peak (δ = 4.81 ppm), while the ^{13}C chemical shift signals were referenced to the deuterium lock signal. Two sets of nmr experiments were carried out to determine the location of a typical aromatic probe (benzene) in the surfactant micellar interior.

(*a*) Benzene solubilization studies: The alkyl sulfosuccinate solutions were prepared, at a concentration of twice the critical micelle concentration. To 1 mL of each of these solutions was added 10 or 20 μL of benzene (Aldrich), and the mixture was stirred for 30 min.

(*b*) Surfactant Studies: At least five solutions, up to twice the critical micelle concentration were prepared in D_2O. To 1 mL of each of these solutions was added 10 mL of benzene.

Surface potential measurements were carried out as follows. Sodium dodecyl sulfate (Aldrich, 99%) was recrystallized twice from absolute ethanol. The nonionic surfactant octaethylene glycol decyl ether ($C_{10}E_8$) was supplied by Fluka and was used without further purification. The acid–base indicator 7-hydroxycoumarin was obtained from Aldrich Chemical Co. and was used without further purification. The pH was adjusted by NaOH (A.C.S. Reagent Fisher Scientific) or HCl (A.C.S. Reagent Fisher Scientific). NaCl (A.C.S. Fisher Scientific) was used to adjust the ionic strength of the surfactant solutions. Solutions were titrated from high pH to low pH by the addition of small amounts of NaOH or HCl solutions (0.10 M). After the addition of either NaOH or HCl the pH of the solution was recorded, and the degree of ionization of the indicator was

© 1999 NRC Canada

Fig. 2. Sodium hydroxide titration curves of the alkyl sulfosuccinate surfactants.

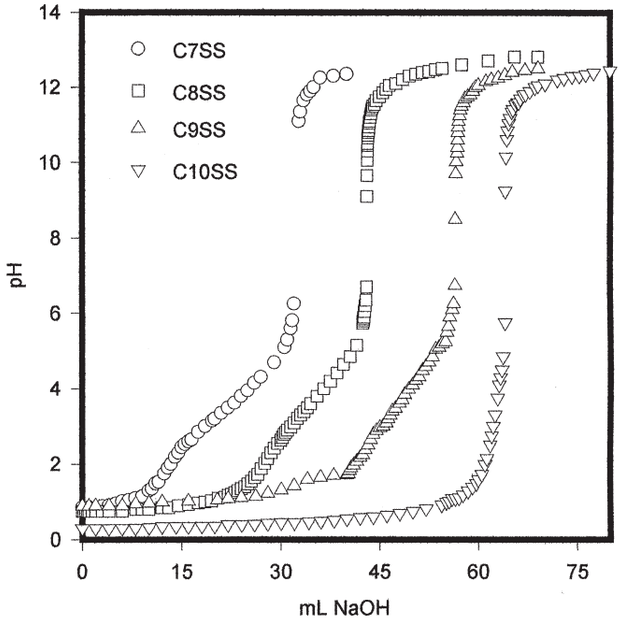

Table 1. pK_a values of alkyl sulfosuccinates.

No. of carbons	Sulfonate group	Carboxylate group
7	1.51	4.86
8	1.66	5.15
9	1.74	5.21
10	1.85	5.39

obtained by measuring the intensities of the peak at 373 nm as a function of pH using the HP 8450A diode array spectrophotometer.

3. Results

3.1. pK_a determination

Aqueous solutions of the alkyl sulfosuccinates were prepared at twice the critical micelle concentration, and the resulting solutions were titrated using 0.1 M NaOH. The pK_a values for the carboxylate and the sulfonate anionic head groups were determined from the apparent breaks that occur in the titration curves (Fig. 2), and these values are given in Table 1.

The pK_a values (Fig. 3) increase with increasing carbon number for both the carboxylate and sulfonate head groups. There is an observed dependence on increasing chain length for the pK_a values, and these values are in agreement with the literature values. These pK_a values depend slightly on the alkyl chain length (18). Hence, we can clearly see from Fig. 1 that when the pH is high (>9.6), the sulfosuccinates are in the form of two-headed anionic surfactants. Varying the pH of the solution should change the properties of the sulfosuccinate micelles as the degree of ionization of the ionizable carboxylate head group is changed; this is currently under investigation.

Fig. 3. pK_a values of the alkyl sulfosuccinate surfactants, as a function of carbon number.

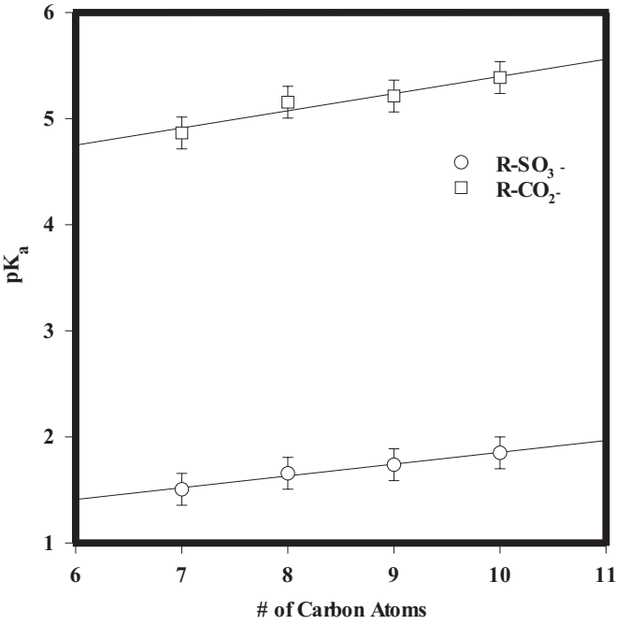

Fig. 4. Pyrene I_1/I_3 ratios of alkyl sulfosuccinates.

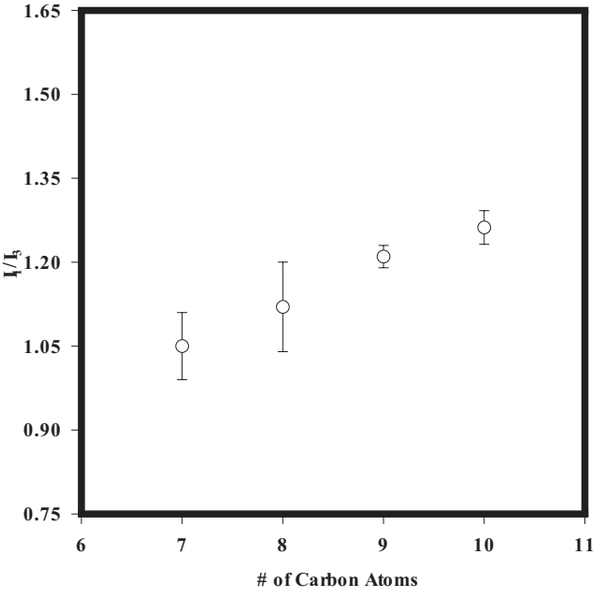

3.2. Fluorescence studies

3.2.1. Pyrene

The pyrene I_1/I_3 ratios were determined for the alkyl sulfosuccinates (Fig. 4) and are given in Table 2.

3.2.2. 8-Anilino-1-naphthalenesulfonic acid ammonium salt

To verify the polarity of the microenvironment, the photophysical behavior of an ionic probe, ANS, was investigated with the two-headed surfactants under study. The relative intensity of the probe in the presence of the alkyl

© 1999 NRC Canada

Table 2. Aggregation numbers (N_s), size of sulfosuccinate micelles, and I_1/I_3 pyrene ratios.

No. of carbons	N_s[a]	R (Å)	a_0 (Å^2)	v/a_0l_c	I_1/I_3
7	12±3	8.52	76.01	0.16	1.05 ± 0.06
8	20±5	10.50	69.27	0.19	1.12 ± 0.09
9	29±4	12.32	65.76	0.21	1.21 ± 0.02
10	42±5	14.38	61.87	0.23	1.26 ± 0.03
Water	—	—	—	—	1.81 ± 0.04

[a]Reference 1.

Fig. 5. Relative intensity ANS + alkyl sulfosuccinate surfactants and ANS + alkyl sulphate surfactants.

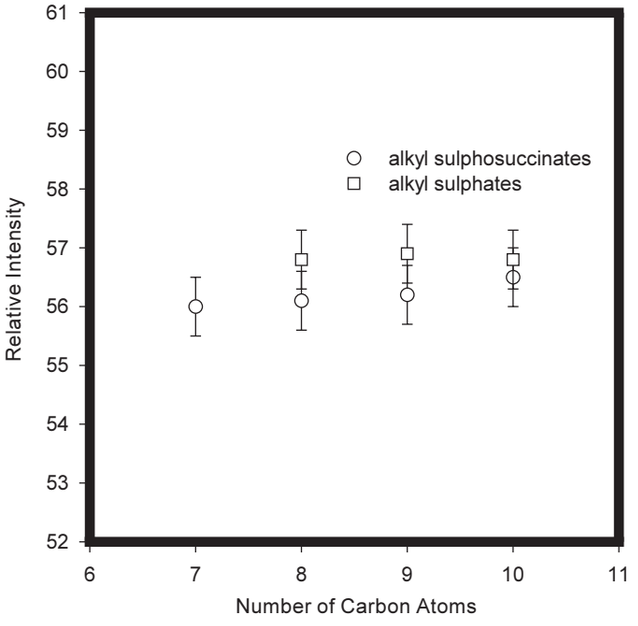

sulfosuccinates and the alkyl sulphate surfactants is shown in Fig. 5.

3.3. Surface potential measurements

The measurement of the surface potential of a micellar system will provide information on the surface charge density – surface potential relationships for these novel two-headed surfactants. 7-Hydroxycoumarin and its derivatives have been used, in the literature, to investigate the interfacial microenvironment of a large number of monolayers (8–12). The electrostatic surface potential of a charged interface can be calculated using the following expression:

$$[1] \qquad \Psi_0 = \frac{2.303RT}{F}(pK_a^i - pK_a^{obs})$$

where ψ_0 is the surface potential, pK_a^{obs} is the apparent pK_a value of the 7-hydroxycoumarin at the charged surface, pK_a^i is the apparent pK_a of the 7-hydroxycoumarin at the surface when $\psi_0 = 0$ and F, R, and T are the Faraday constant, the universal gas constant, and the absolute temperature, respectively. The pK_a values of 7-hydroxycoumarin are a function of the dielectric constant of the medium. The pK_a^i of the indicator is determined from the pK_a^{obs} in the presence of a nonionic surfactant. The nonionic surfactant micelle acts as a zero potential reference state for determining the pK_a^i values of 7-hydroxycoumarin in anionic micelles. The absorption spectrum of 7-hydroxycoumarin was obtained as a function of pH; the UV spectrum shows two characteristic peaks that are pH dependent (Fig. 6).

Fig. 6. UV/vis adsorption spectrum for 7-hydroxycoumarin in aqueous solution at a pH of 2.0 (λ_{max} = 320 nm) and a pH of 10.0 (λ_{max} = 370 nm).

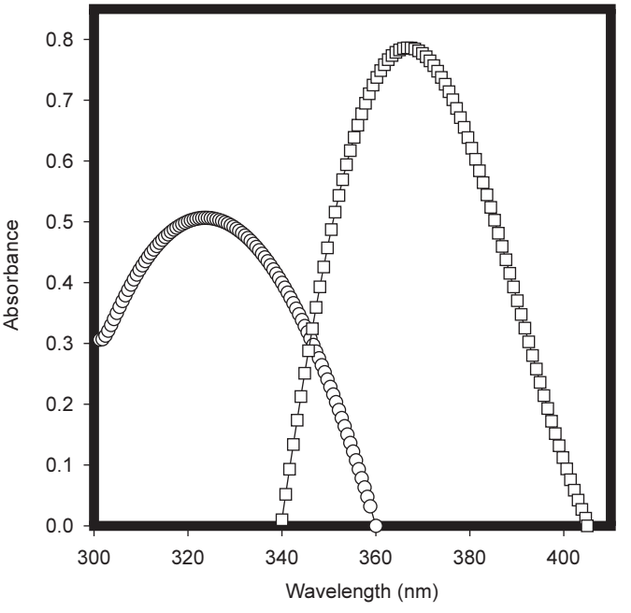

The protonated 7-hydroxycoumarin (pH < 6) exhibits an intense absorption band with λ_{max} at 324–330 nm, with a log $\varepsilon \sim 4.1$. In basic solution (pH > 8) the absorption band that appears at λ_{max} 365–370 nm, with log $\varepsilon \sim 4.2$, is assigned to the anionic form of the indicator that is formed from the dissociation of the acidic phenolic proton at position seven (19).

The results for the λ_{max} of the acid form and the λ_{max} of the anionic form of the indicator are in excellent agreement with the literature. The absorbance spectrum (1.0 cm cells) of a 6.0×10^{-5} M solution as a function of pH at 370 and 320 nm is given in Fig. 7.

The observed pK_a for 7-hydroxycoumarin was determined from the absorption spectra using the following equation:

$$[2] \qquad pK_a = pH - \log\left(\frac{\alpha}{100 - \alpha}\right)$$

where α is the percentage of 7-hydroxycoumarin that has been ionized. The maximum absorbance of the 7-hydroxycoumarin at the λ_{max} of the probe, as a function of the solution pH, was taken as the 100% ionization value and the minimum absorbance as the 0% ionization value. At least six different a values between 0 and 100 were examined for each solution.

For the alkyl sulfosuccinate surfactants the ionic strength, I, of the bulk solution is given by

$$[3] \qquad I = 10^{(pH_i - 14)} + [NaCl] + cmc + 1/2(\Sigma Z^2\ cmc)$$

© 1999 NRC Canada

Fig. 7. Absorbance of 7-hydroxycoumarin as a function of pH at 320 and 370 nm.

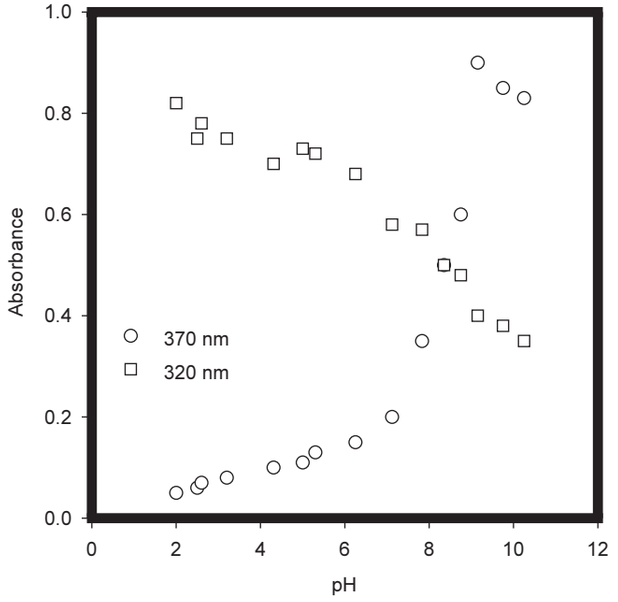

Fig. 8. Surface potentials of sodium dodecyl sulphate at various ionic strengths.

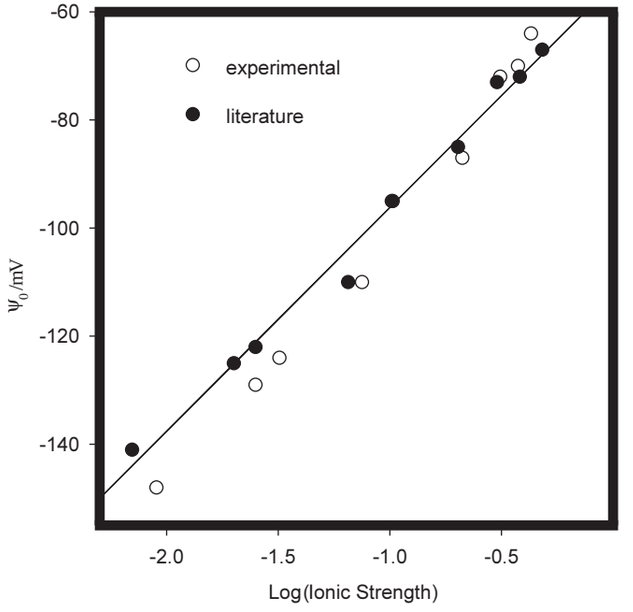

where pH_i is the initial pH, [NaCl] is the concentration of added NaCl, and the last term is due to the contributions of the negatively charged head groups ($Z = -2$). This equation neglects the contribution to the ionic strength from the micelles and the dissociated counter ions (6).

The experimental surface potentials of 0.02 M SDS solutions, of varying ionic strength, were determined using the above method. The measured values for SDS are in excellent agreement with those reported in the literature. These are shown in Fig. 8. The potentials were calculated using

Fig. 9. Surface potentials of the alkyl sulfosuccinates at varying ionic strength.

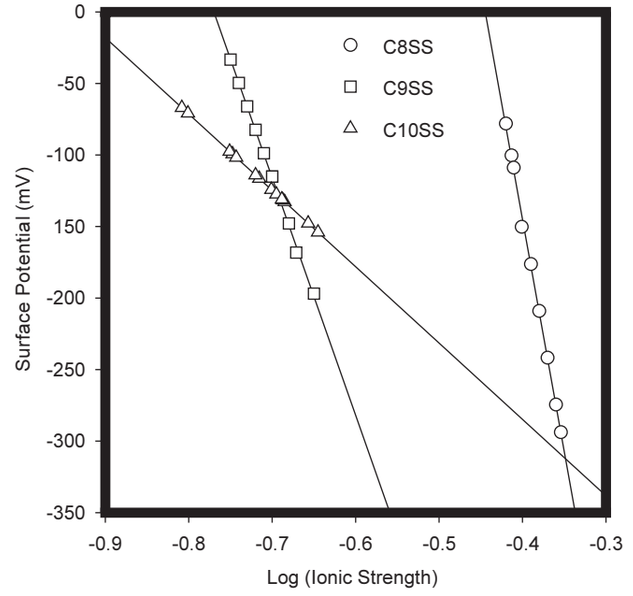

Table 3. Surface charge densities of the alkyl sulfosuccinates.

No. of carbons	N_s[a]	R (Å)	β[a]	σ_o (C/m^2)
7	12	8.52	0.60	–0.061 ± 0.005
8	20	10.50	0.66	–0.058 ± 0.005
9	29	12.32	0.70	–0.053 ± 0.005
10	42	14.38	0.87	–0.025 ± 0.005

[a]Reference 1.

eq. [1] based on the pK_a of 7-hydroxycoumarin, in 5×10^{-3} mol/L $C_{10}E_8$, of 9.12 ± 0.15 (pK_a^0). This value was found to be constant by up to an ionic strength of 4 M NaCl. The experimental surface potentials for the alkyl sulfosuccinates are shown in Fig. 9, and as both the un-ionized and ionized forms of the indicator partition into the micellar phase and reside within the interfacial region of the anionic micelles (8, 9, 11, 12), the differences between pK_a^i and pK_a^0 should reflect the difference in the surface potential of the two-headed surfactants vs. the nonionic reference micelle. The above expression assumes that the dielectric constant of the medium directly surrounding the probe is relatively the same in both micellar systems. This has been verified for SDS and DTAB micelles (8, 12, 14) and should be a reasonable assumption for the sulfosuccinate micelles.

The surface charge density was calculated using the following equation:

$$[4] \qquad \sigma_0 = \frac{-eN_s(1-\beta)}{4\pi a^2}$$

where N_s is the aggregation number, and β is the fraction of surfactant ions in the micelle that are electrically neutralized by the specific binding of a counter ion. These values are given in Table 3 (Fig. 10).

© 1999 NRC Canada

Fig. 10. Surface charge density of the alkyl sulfosuccinates.

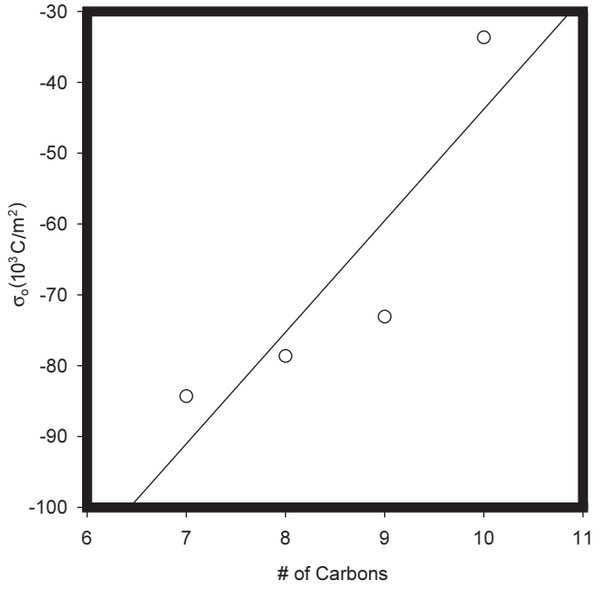

Fig. 11. Surface area per head group alkyl sulfosuccinates.

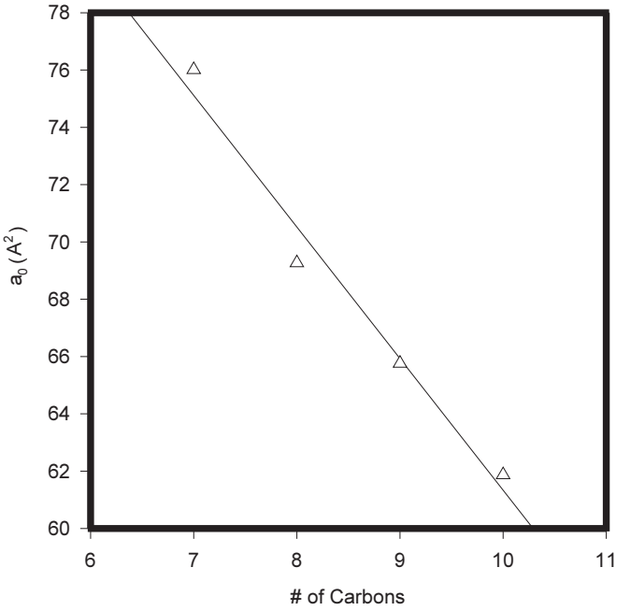

4. Discussion of results

The pK_a values of the sulfonate and carboxylate head groups of the alkyl sulfosuccinates increase as the number of carbons is increased on the hydrocarbon chain (Table 2, Fig. 3). The titration of the alkyl sulfosuccinates produces a curve that is similar to that of a weak acid titrated with a strong base. The break points that occur in the curve are due to the neutralization of the carboxylate and sulfonate head groups. The pK_a values are in good agreement with those for the aliphatic carboxylic acids (18). The pK_a values for the sulfonic acid group is slightly higher than the pK_a values for benzenesulfonic and toluenesulfonic acids (18). There is also an observed dependence on increasing chain length for the pK_a values, which is in reasonable agreement with the literature.

The use of luminescence probing experiments to determine a number of important properties of surfactant micelles is well established (19–29). The ability of pyrene to sense the polarity of its microenvironment is also well established (22–29). Since the pyrene I_1/I_3 ratios reflect the polarity of the microenvironment around the probe, it can, therefore, detect changes in polarity in micelles. Analysis of the pyrene I_1/I_3 ratios (Table 2, Fig. 4) gives information about the polarity of the microenvironment surrounding the solubilized probe in the micelle. It is known that pyrene is solubilized in the palisade layer of micelles, near the polar head groups, where it senses a relatively high polar environment (30). In the present study, it is evident that the pyrene senses a very similar degree of polarity in the microenvironment surrounding the probe in all of the sulfosuccinate micelles. This may be attributed to the inability of the pyrene to penetrate deeply into the micelle, and hence the pyrene senses the same degree of polarity due to the location of the pyrene near the micelle–water interface.

The surface area per head group for the sulfosuccinate micelles has been estimated as follows. The hydrophobic chain volume of the micelle (v) and the critical chain lengths (l_c) were obtained using Tanford equations (30):

[5] $v = 27.4 + 26.9n$ (Å^3)

[6] $l_c = 1.5 + 1.265n$ (Å)

where n is the number of carbon atoms of the chain. The micellar radius, r, and the surface area per head group (a_0) were obtained assuming spherical shape. The aggregation numbers were determined by fitting the C-13 measurements to the mass action model (1). The values of r and a_0 ($(4\pi r^2)/N_{agg}$) along with the critical packing parameter ($v/(a_0 l_c)$), which is a parameter-controlling micelle shape, are presented in Table 3 (30). The increase in the critical packing parameter indicates the formation of larger spherical micelles; however, we estimate that the surface area per head group decreases linearly with an increase in carbon number. This is shown in Fig. 11.

The ionic probe, ANS, has been known to interact with anionic micelles such as sodium dodecyl sulphate (31). The spectral behavior of ANS is interesting because the emission properties are sensitive not only to the polarity of the microenvironment but to the microviscosity of the environment of the probe. ANS is almost nonfluorescent in aqueous solutions, but it exhibits a fluorescence enhancement upon binding to the micellar surface. This fluorescence enhancement is due to the polarity-dependent twisted intramolecular charge transfer (TICT) (32). When the ANS molecules are transferred from the highly polar aqueous media to the relatively nonpolar micellar surface, the reduction in polarity and the increase in microviscosity leads to a decrease in the rate of the TICT process. Inhibition of nonradiative TICT pathways results in an increase of the emission quantum yield lifetime.

In examining Fig. 5 it can be seen that the members of the alkyl sulfosuccinate family experience the same polarity in the microenvironment surrounding the ANS probe. The same

© 1999 NRC Canada

Fig. 12. (*a*) Changes in proton chemical shifts upon addition of benzene (C8SS). (*b*) Changes in proton chemical shifts upon increasing surfactant (C8SS) concentration (benzene concentration = 10 μL/mL).

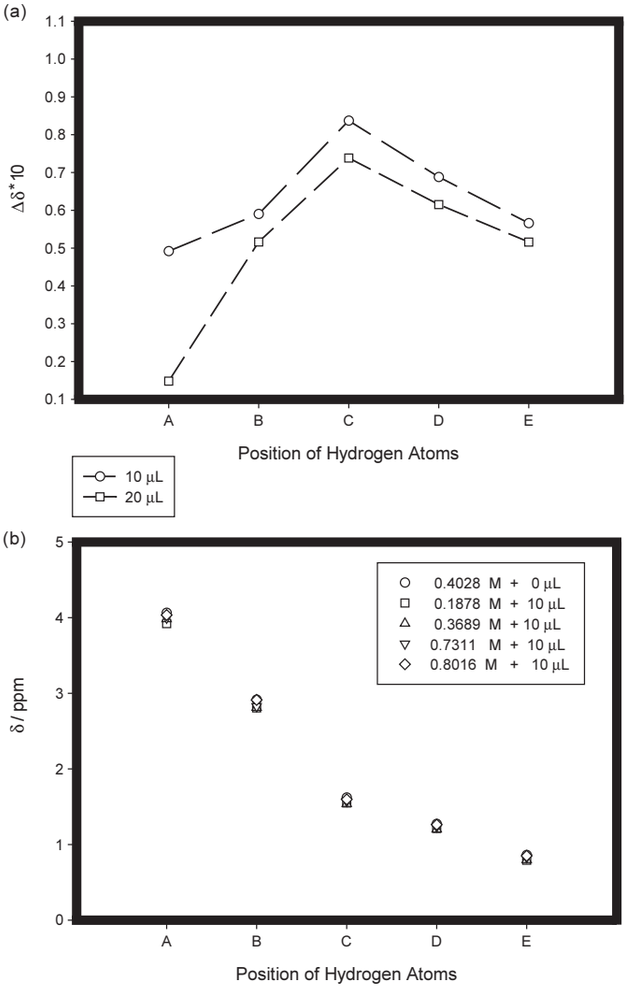

is also true for the alkyl sulfate surfactants. These results agree with those obtained from the pyrene polarity study.

Before we discuss the surface potentials of the sulfosuccinate surfactants, certain facts must be considered when examining the use of a probe for surface potential measurements. To calculate the surface charge density the radius of the micelle hydrophobic core is needed. Because of changes at the micelle surface, its shape is not known exactly (22, 23); also the exact position of the 7-hydroxycoumarin at the micelle surface is also not known. If the indicator resides outside the micelle surface it will sense a surface potential lower than the true value (1). There have been extensive nmr studies carried out with aromatic molecules solubilized in SDS micelles (33) in the literature. These studies have indicated that the aromatic molecules with ionizable hydroxy groups sit in the plane of the sulphate head groups in the SDS micelle. Therefore, it is reasonable to assume in our present investigation that the 7-hydroxycoumarin indicator will also sit in this plane and hence, respond to the true surface potential.

Table 4. Changes in proton chemical shift (ppm) due to added benzene (μL, in parentheses).

Hydrogen position	δ (0)	Δδ ×10 (+10)	Δδ ×10 (20)
(*a*) C7SS			
Alpha	4.0187	0.4920	0.1480
Beta	2.9144	0.5900	0.5160
C	1.6208	0.8370	0.7380
D	1.2715	0.6880	0.6150
CH_3	0.8042	0.8092	0.5160
(*b*) C8SS			
Alpha	4.0876	0.4180	0.7140
Beta	2.8923	–0.3690	–0.3200
C	1.6355	0.7870	0.8110
D	1.3010	0.8110	0.8110
E CH_3	0.8706	0.5650	0.5900
(*c*) C10SS			
Alpha	3.9769	–0.2460	–0.3470
Beta	2.8923	–0.7380	–0.3440
C	1.5013	–0.6045	–0.1625
D	1.2543	0.2700	0.6390
E CH_3	0.8436	0.3200	0.6150

Although the locus of solubilization may not be the same for benzene and other aromatic molecules (pyrene or 7-hydroxycoumarin), one should be able to obtain a fairly reasonable qualitative estimate of the location of aromatic molecules in the sulfosuccinate surfactant micelle interior from the nmr studies of benzene solubilized in the alkyl sulfosuccinate micelles. It can be seen from Fig. 12(*a*) that the magnitude of the alpha proton chemical shift (i.e., head group region) are greater than those of the other proton shifts, that occur due to added benzene (Table 4), suggesting that the benzene is residing in the head group region of the micelle. The second area of the nmr study involved keeping the benzene concentration constant and increasing the surfactant concentration. From this study it was concluded that the proton chemical shifts are not influenced by the increasing surfactant concentration (Fig. 12(*b*)). These studies indicate, in the range of ion concentrations studied, that the benzene is located within the head group region of the surfactant micelle. From this we can conclude that the acid–base indicator 7-hydroxycoumarin should also be located in the same region of the micelle.

It is clear from the surface potential values, in the anionic sulfosuccinate micelles, that these surfactants must have relatively low degrees of counter ion binding, as the surface potential values are two to three times larger than those of sodium dodecyl sulphate at comparable ionic strengths. In addition, the dependence of the surface potential on ionic strength is significantly different for these two-headed surfactants vs. the single-headed surfactants. In the case of the two-headed surfactants, the ψ_0 values decrease with an increase in ionic strength, whereas for the single-headed surfactants, the ψ_0 values increase with increasing ionic strength. This may indicate a significant difference in the properties of two-headed surfactant micelles, as a function

© 1999 NRC Canada

of increasing salt concentration, vs. single-headed surfactant micelles like sodium dodecyl sulphate.

It is also important to note that the differences in the surface potential values between the members of the alkyl sulfosuccinate family are due to several important factors:

1. The various micellar solutions have different ionic strengths due to the fact that the members of the sulfosuccinate family have different cmc values.

2. The degree of counter ion binding is different for each member of the sulfosuccinate family.

3. The sulfosuccinate micelles may have slightly different sizes and shapes.

5. Conclusions

It has therefore been shown that the alkyl sulfosuccinate surfactants exhibit characteristics that are distinctive of a family of surfactants that contain two negatively charged head groups.

The micellar properties of these two-headed anionic surfactants have therefore been shown to be influenced by the pH of the solution. Also the presence of this second negatively charged head group affects not only the polarity of the microenvironment of the micelle, but it also increases the surface potential of the head-group region.

Acknowledgments

The financial support of the Natural Science and Engineering Research Council of Canada (NSERC) and St. F.X. University in the grant of a James Chair Research Fellowship to R.P. are greatly appreciated. The authors would also like to thank Andrew P. Rodenhiser of Dalhousie University for supplying the sample of the nonionic surfactant octaethylene glycol decyl ether ($C_{10}E_8$) used in this study.

References

1. G. Boucher, B. Hawrylak, A. MacDonald, and D.G. Marangoni. Can. J. Chem. **76**, 1266 (1998).
2. E.K. Comeau, E.J. Beck, J.F. Caplan, C.V. Howley, and D.G. Marangoni. Can. J. Chem. **73**, 1741 (1995).
3. P.A. Kooreman and J.F.B.N. Engberts. Recl. Trav. Chim. Pays-Bas, **113**, 163 (1994).
4. D.J. Jobe and V.C. Reinsburough. Aust. J. Chem. **37**, 303 (1984).
5. G.V. Hartland, F. Grieser, and L.R. White. J. Chem. Soc. Faraday Trans. **83,** 591 (1987).
6. P. Mukerjee and K. Banerjee. J. Phys. Chem. **68**, 3567 (1964).
7. D. Stinter and K.J. Mysels. J. Colloid Interface Sci. **59**, 45 (1955).
8. C.J. Drummond, F. Grieser, and T.H. Healy. Faraday Discuss. Chem. Soc. **81**, 95 (1986).
9. C.J. Drummond and F. Grieser. J. Phys. Chem. **92**, 5589 (1988).
10. E.F. Williams, N.T. Woodberry, and J.K. Dixon. J. Colloid Sci. **12**, 452 (1957).
11. C.J. Drummond and F. Grieser. Photochem. Photobiol. **45**, 19 (1987).
12. C.J. Drummond, F. Grieser, and T.H. Healy. Chem. Phys. Lett. **140**, 493 (1987).
13. D. Stigter. J. Phys. Chem. **68**, 3606 (1964).
14. F. Grieser and C.J. Drummond J. Phys. Chem. **92**, 5580 (1988).
15. D.J. Shaw. Introduction to colloid and surface chemistry. Butterworths, London. 1966. pp. 148–182.
16. D.S. Karpovich and G.J. Blanchard. J. Phys. Chem. **99**, 3951 (1995).
17. D.C. Dong and M.A. Winnik. Can. J. Chem. **62**, 2560 (1984).
18. R.C. West (*Editor*). CRC handbook of chemistry and physics. 70th ed. CRC Press, Boca Raton, Fla. 1990.
19. D.W. Fink and W.R. Koehler. Anal. Chem. **42**, 990 (1970).
20. Z. Zicmanis, T. Hamaide, C. Graillat, C. Monnet, S. Abele, and A. Guyot. Colloid Polym. Sci. **275**, 1 (1997).
21. M. Almgren and S. Shanti. J. Colloid Interface Sci. **91**, 256 (1983).
22. F. Grieser, C.J. Drummond, G.G. Warr, B.W. Ninham, and D. Evans. J. Phys. Chem. **89**, 2103 (1985).
23. J. Kibblewhite, C.J. Drummond, F. Grieser, and T.H. Healy. J. Phys. Chem. **91**, 4658 (1987).
24. C.J. Drummond and F. Grieser. Langmuir, **3**, 855 (1987).
25. C.J. Drummond, F. Grieser, and T.H. Healy. J. Phys. Chem. **92**, 2604 (1988).
26. G.E.A. Aniansson. J. Phys. Chem. **82**, 2805 (1978).
27. S. Ljungren, and J.C. Eriksson J. Chem. Soc. Faraday Trans., **2**, 498 (1984).
28. B. Lovelock, F. Grieser, and T.W. Healy. J. Phys. Chem. **89**, 501 (1985).
29. M. Almgren, F. Grieser, and J.K. Thomas. J. Am. Chem. Soc. **101**, 279 (1979).
30. C. Tanford. The hydrophobic effect. Wiley, New York. 1980. pp. 42–59.
31. R.C. Carnero. Colloid Polym. Sci. **273**, 1033 (1995).
32. K. Bhattacharyya and M. Chowdhury. Chem. Rev. **93**, 507, (1993).
33. K.N. Ganesh, P. Mitra, and D. Balasubramanian. J. Phys. Chem. **86**, 279 (1982).

© 1999 NRC Canada

Energetics of the encapsulation of *o*-, *m*-, and *p*-hydroxybenzoic acids by β-cyclodextrin and its methylated and hydroxypropylated derivatives in aqueous solution

Elena Junquera, Valentin G. Baonza, and Emilio Aicart

Abstract: A fully computerized potentiometric technique has been used to analyze the energetics of the encapsulation of *o*-, *m*-, and *p*-hydroxybenzoic acids by β-cyclodextrin (β-CD) and (or) two of its most used derivatives: 2,6-di-*O*-methyl-β-cyclodextrin (DIMEB) and hydroxypropyl-β-cyclodextrin (HPBCD). The study has been carried out by measuring the pH of aqueous solutions of the three hydroxyacids in the absence of cyclodextrin at 25°C, and in the presence of cyclodextrin at several temperatures ranging from 15 to 40°C, keeping constant the concentration of the guest. The dissociation constant of the acids and the binding constants of the inclusion complexes formed have been simultaneously determined at all the temperatures by using a model previously derived by us. The carboxylic forms have been found to bind the CD with higher affinities than the carboxylate partners do, irrespective of the temperature, the cyclodextrin used, and the position of the substituents on the guest molecules. The formation of the inclusion complexes studied in this work has been found to be enthalpy driven, with a favorable enthalpic term dominant over an unfavorable entropic one. The effect of the substituents of both guest and host molecules on the thermodynamics of the inclusion processes has been analyzed.

Key words: binding constant, β-cyclodextrin, hydroxybenzoic acid, inclusion complex, substituent effect.

Résumé : On a utilisé une technique potentiométrique entièrement automatisée pour analyser le bilan énergétique de l'inclusion des acides *o*-, *m*- et *p*-hydroxybenzoïques dans la β-cyclodextrine (β-CD) et (ou) dans deux de ses dérivés les plus utilisés : la 2,6-di-*O*-méthyl-β-cyclodextrine (DIMEB) et la hydroxypropyl-β-cyclodextrine (HPBCD). On a réalisé l'étude en mesurant le pH des solutions aqueuses de trois hydroxyacides en l'absence de la cyclodextrine à 25°C, et en présence de la cyclodextrine à différentes températures allant de 15 à 40°C, tout en maintenant constante la concentration de l'entité moléculaire invitée. On a déterminé simultanément, à toutes les températures, la constante de dissociation des acides et la constante de liaison des complexes d'inclusion formés, en utilisant un modèle mis au point antérieurement dans ce laboratoire. On a trouvé que les formes carboxyliques sont liées dans la CD avec des affinités plus grandes que les formes carboxylates quelles que soient la température, la cyclodextrine utilisée et la position des substituants sur la molécule-hôte. On a trouvé que la formation des complexes d'inclusion étudiés dans ce travail dépend de l'enthalpie avec un terme enthalpique favorable qui a préséance sur un terme entropique défavorable. On a étudié l'effet des substituants, aussi bien sur la molécule hôte que sur la molécule invitée, sur le bilan thermodynamique du processus d'inclusion.

Mots clés : constante de liaison, β-cyclodextrine, acide hydroxybenzoïque, complexe d'inclusion, effet de substituant.

[Traduit par la Rédaction]

Introduction

Non-covalent interactions, with water solvent playing an important and decisive role, are known to be the main driving forces in most recognition processes at the biological level (1, 2). Highly specific biological processes make extensive use of molecular complexation. It is thus necessary to have as much information as possible regarding the contribution of, for example, of van der Waals contacts, hydrophobic and solvent effects, electrostatic interactions, etc., in the energetics of these processes (3). However, this is not a simple task, and very often scientists turn to designing sim-

Received July 13, 1998.

E. Junquera, V.G. Baonza, and E. Aicart.[1] Departamento de Química Fisica I, Facultad de Ciencias Químicas, Universidad Complutense de Madrid, 28040-Madrid, Spain.

[1]Author to whom correspondence may be addressed. Telephone: 34-91-3944208. Fax: 34-91-3944135. e-mail: aicart@eucmax.sim.ucm.es

 © 1999 NRC Canada

Scheme 1.

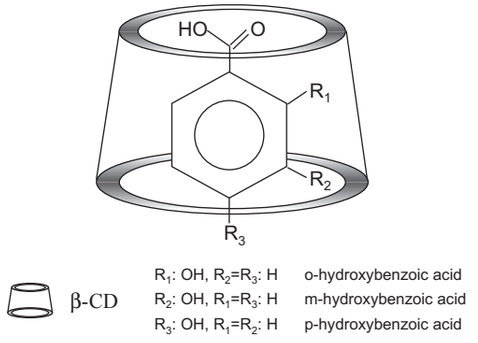

ple synthetic model systems that somehow mimic the biological interaction (4, 5). In this context, cyclodextrins (CDs) have been widely used as simple model receptors to study the nature of the binding process of apolar organic molecules in aqueous solutions (6). These cyclic oligosaccharides are well known for including a wide variety of guest molecules in their toroidal cavity with only the concurrence of non-covalent intermolecular forces, and with clearly changing effects on the physicochemical properties of the guest. This feature has been profitably used by the cosmetic, agro-alimentary, and pharmaceutical industries (6–8) to improve the bioavailability of their products.

A number of structural and thermodynamic studies have been carried out in the last decade with different experimental techniques to elucidate the rules that govern the association process in these model systems (9–14). Parameters such as stoichiometry of the complex (*A*), binding constant ($K_{CD:Substrate}$), and enthalpy ($\Delta H°$), entropy ($\Delta S°$), and heat capacity (ΔC_p^o) changes upon binding are of crucial importance to understand how the different intermolecular forces contribute to the overall free energy of complexation ($\Delta G° = -RT \ln K_{CD:Substrate}$). Several methods and mathematical models for determining association constants can be found in the literature (6, 15), while the thermodynamic magnitudes ΔH^o and ΔS^o can be obtained either directly from calorimetric experiments, or indirectly from van't Hoff plots, which give $-\Delta H^o$ as the slope and $\Delta S°$ as the intercept of a plot of $R \ln K$ vs. $1/T$. Some authors use the comparison of ΔH^o obtained from both calorimetric and van't Hoff methods to extract information about the possible contribution of concomitant processes to the associations studied (10*c*, 16–21).

We recently (13) derived a model to obtain simultaneously the binding constants for the inclusion of the non-ionized and ionized forms of the guest into the CD cavity from pH potentiometric data when the guest is an acid–base conjugated system. In the present work, this model has been applied to study the encapsulation of three derivatives of benzoic acid, the *o*-, *m*-, and *p*-hydroxybenzoic acids, by the β-CD and two derivatives, DIMEB and HPBCD (see Scheme 1, as an example). Previous studies (11, 22–34) on the complexation of benzoic acid and phenol derivatives by CDs revealed that the thermodynamic parameters of the association process are quite sensitive to the type, position, and orientation of the substituents introduced in both host and guest molecules. However, systematic studies have not been done with the hydroxy derivatives of benzoic acid. We expect that the determination of the association constants of the inclusion complexes studied in this work as a function of temperature will improve our understanding of the effect of substitution and position of substituents on the energetics of the CD:hydroxybenzoic acid interaction.

Experimental

Materials

The *o*-, *m*-, and *p*-hydroxybenzoic acids, with purities greater than 99%, were purchased from Sigma. β-CD was from Aldrich; HPBCD, containing an average of 0.4 hydroxypropyl groups per glucopyranose unit, was from Janssen Biotech, and DIMEB was from Cyclolab. β-CD, HPBCD, and DIMEB have been found (through a thermogravimetric (TG) analysis) to consist of 13.6%, 3.4%, and 1.7% mass of water content, respectively, which was used to calculate solute concentrations. Distilled water was further treated with a Super Q Millipore ion exchange purification system. To assure the homogeneity of the initial solutions, they were sonicated during 1 h in an ultrasonic bath.

Potentiometric measurements

Potentiometric data were collected with a Metrohm 713 ion meter, using a combined glass electrode filled with 3 M KCl solution. Calibration of both the asymmetry potential and the Nernst slope of the electrode was made daily using three Metrohm buffer solutions at pH = 1, 4, and 7. The equipment and the experimental procedure have been described in detail elsewhere (13). Mixtures were prepared with a Metrohm digital burette, whose cylinder was kept at the same constant temperature as that of the measuring cell. The pH ion meter and the burette were operated via RS-232C interfaces. The whole measuring process is controlled through a computer program developed by us. The accuracy on the molarity of the solutions is better than 1×10^{-5} M, in both the cell and the burette. The thermostatic system holds the temperature constant within ±1 mK. The pH data, obtained as an average of 250 measurements for each concentration, are reproducible within 0.0003 units. pH measurements were made as a function of cyclodextrin concentration, keeping constant the guest concentration around 4 mM. Cyclodextrin concentrations were chosen to cover at least 80% of the saturation curve to guarantee a proper determination of binding constants (35).

Determination of the association constants from potentiometric data

Several models have been developed in the literature to determine the binding constants of host–guest systems from pH potentiometric measurements (13, 22, 36, 37). Particularly when the guest is an acid–base conjugated system, both acid (HA) and base (A^-) species are present in the aqueous solution and can be included by the cyclodextrin. Several equilibria are then involved in the encapsulation process: (*a*) those for the association of both acid and base species of the guest with the cyclodextrin, and (*b*) those for the dissociation of the acid species in both their free and complexed forms, as indicated in the following scheme:

© 1999 NRC Canada

Scheme 2.

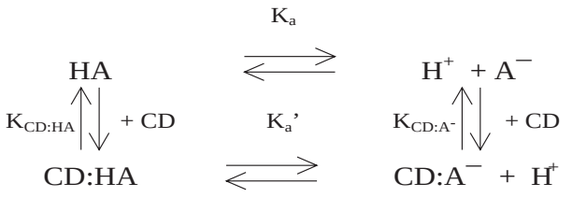

Fig. 1. Plot of pH vs. the concentration of *o*-, *m*-, and *p*-hydroxybenzoic acid, in aqueous solution at 25°C.

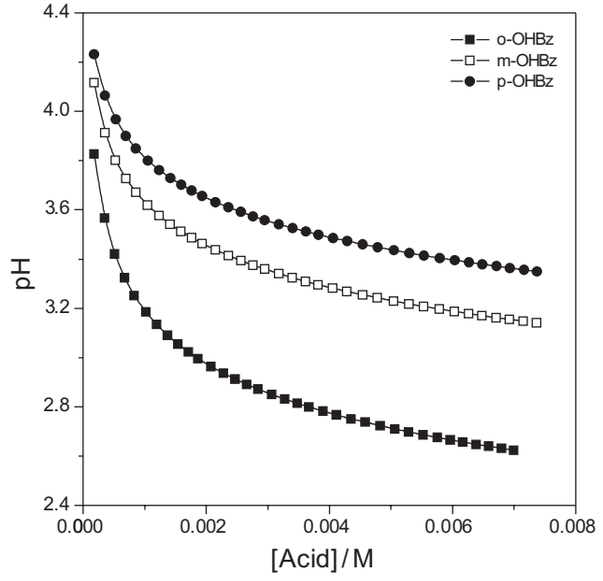

The equilibrium constants that govern these equilibria can be expressed as a function of the activity of the species as follows,

[1] $K_a = (a_{H+}a_{A}\text{-})/a_{HA}$

[2] $K_{CD:HA} = a_{CD:HA} / (a_{CD}\, a_{HA})$

[3] $K_{CD:A}\text{-} = a_{CD:A}\text{-} / (a_{CD}\, a_{A}\text{-})$

The dissociation constant for the complexed acid species (K_a') is related to the previous equilibrium constants by a simple expression. Any valuable model must check the formation of complexes with stoichiometries different than those shown in the previous scheme. In our model, eqs. [1]–[3], those for the activity coefficients (using the Debye–Hückel theory), and the corresponding mass and charge balances, allow for simultaneous determination of these binding constants and the dissociation constant of the uncomplexed hydroxyacid by fitting the experimental pH data with a nonlinear regression method (NLR), based on a Marquardt algorithm. The numerical procedure includes the determination of uncertainties due to pH measurements and statistical errors inherent in the NLR method. These uncertainties are 5% in the dissociation constants for the pure acids and 10–25% in the constants for the ternary systems. This model (13) was derived on the basis of that of Gelb et al. (22), although improvements were successfully included, the most relevant being: (*i*) the numerical procedure assigns negligible values to those binding constants of association processes (1:1, 1:2, 2:1, etc.) that either do not take place or occur with negligible affinities; and (*ii*) the simultaneous determination of the dissociation constant of the guest (K_a) constitutes a control for the suitability of the method, since these values can be compared either with literature values or with those obtained for the pure acids in the absence of cyclodextrin.

Fig. 2. Plot of pH vs. [DIMEB] for aqueous solutions of *p*-hydroxybenzoic acid where [*p*-OHBz] is kept constant at ~4 × 10^{-3} M, at different temperatures ranging from 15 to 40°C.

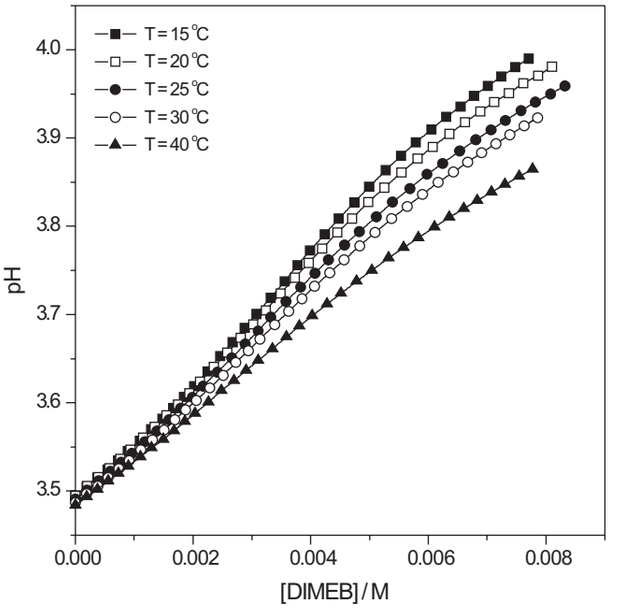

Results and discussion

The pH of the aqueous solutions of *o*-, *m*-, and *p*-hydroxybenzoic acids has been measured in the absence of cyclodextrin at 25°C, and in the presence of β-CD, DIMEB, or HPBCD at 15, 20, 25, 30, and 40°C, at constant hydroxyacid concentration.

Figure 1 shows the data for pH as a function of *o*-, *m*-, and *p*-hydroxybenzoic acid concentration at 25°C. From the experimental pH data, the dissociation constants of the three hydroxyacids have been determined for our model in its simplest version. There is only one fitting parameter, K_a, provided that only one equilibrium must be considered in the absence of cyclodextrin. Values of 2.9, 4.1, and 4.6 have been obtained, at 25°C, for the pK_a of *o*-, *m*-, and *p*-hydroxybenzoic acids, respectively. The acid character increases with the proximity of the -OH and -COOH groups in the aromatic ring, since the formation of a hydrogen bond between the hydroxyl and carboxylic groups stabilizes the ionized species.

Figure 2 shows, as an example, the pH curves of an aqueous solution of *p*-hydroxybenzoic acid, at a constant concentration of ~4 mM, as a function of DIMEB concentration, the temperature ranging from 15 to 40°C. In contrast with Fig. 1, when the DIMEB is added several equilibria are

© 1999 NRC Canada

Table 1. Values of the dissociation constant (K_a) of *o*-, *m*-, and *p*-hydroxybenzoic acids, and the association constants of the 1:1 inclusion complexes formed by β-cyclodextrin and the acidic and basic forms of *o*-, *m*-, and *p*-hydroxybenzoic acids, as a function of temperature.

[Guest] / mM	T / °C	10^5 K_a	$K_{CD:OHBz}$ / M^{-1}	$K_{CD:OHBz^-}$ / M^{-1}
		β-CD + *o*-hydroxybenzoic		
4.05	15	120 ± 10	1160 ± 120	120 ± 20
4.00	20	115 ± 10	940 ± 90	110 ± 20
4.04	25	125 ± 10	780 ± 80	90 ± 20
3.96	30	120 ± 10	630 ± 60	70 ± 15
3.92	40	140 ± 10	450 ± 40	45 ± 10
		β-CD + *m*-hydroxybenzoic		
3.99	15	7.8 ± 0.1	840 ± 80	55 ± 12
3.97	20	7.8 ± 0.1	640 ± 60	30 ± 6
4.03	25	7.9 ± 0.1	530 ± 50	29 ± 6
4.03	30	8.1 ± 0.1	450 ± 40	12 ± 4
4.03	40	8.1 ± 0.1	290 ± 30	<5
		β-CD + *p*-hydroxybenzoic		
4.05	15	2.9 ± 0.1	1330 ± 130	100 ± 20
4.05	20	2.8 ± 0.1	1110 ± 110	85 ± 20
4.02	25	2.8 ± 0.1	910 ± 90	75 ± 15
4.00	30	2.9 ± 0.1	790 ± 80	50 ± 10
3.98	40	2.9 ± 0.1	500 ± 50	48 ± 10

Table 2. Values of the dissociation constant (K_a) of *o*-, *m*-, and *p*-hydroxybenzoic acids, and the association constants of the 1:1 inclusion complexes formed by 2,6-di-*O*-methyl-β-cyclodextrin (DIMEB) and the acidic and basic forms of *o*-, *m*-, and *p*-hydroxybenzoic acids, as a function of temperature.

[Guest] / mM	T / °C	10^5 K_a	$K_{CD:OHBz}$ / M^{-1}	$K_{CD:OHBz^-}$ / M^{-1}
		DIMEB + *o*-hydroxybenzoic		
3.93	15	120 ± 10	2140 ± 210	170 ± 30
3.62	20	120 ± 10	1840 ± 200	130 ± 20
4.14	25	125 ± 10	1570 ± 150	105 ± 20
4.16	30	130 ± 10	1380 ± 140	95 ± 20
4.03	40	125 ± 10	1060 ± 100	70 ± 15
		DIMEB + *m*-hydroxybenzoic		
4.02	15	7.9 ± 0.1	1800 ± 180	27 ± 6
4.01	20	7.7 ± 0.1	1400 ± 140	9 ±3
3.94	25	7.9 ± 0.1	1190 ± 120	8 ±3
3.98	30	8.0 ± 0.1	1000 ± 100	5 ±3
3.95	40	8.0 ± 0.1	690 ± 70	<5
		DIMEB + *p*-hydroxybenzoic		
3.99	15	2.8 ± 0.1	2530 ± 250	42 ± 8
3.96	20	2.8 ± 0.1	2120 ± 210	29 ± 6
4.01	25	2.8 ± 0.1	1830 ± 180	24 ± 6
4.00	30	2.9 ± 0.1	1610 ± 160	18 ± 4
4.04	40	2.9 ± 0.1	1150 ± 120	9 ± 3

involved, since both non-ionized (*p*-OHBz) and ionized (*p*-$OHBz^-$) forms of the guest can be encapsulated by DIMEB, the pH data in Fig. 2 being the result of shifting of the equilibria with the addition of cyclodextrin. The binding constants, $K_{CD:OHBz}$ and $K_{CD:OHBz^-}$, as well as K_a of the guests, were determined by fitting the pH data as a function of cyclodextrin concentration using our model (13). The results obtained are shown in Tables 1–3, and can be summarized as follows: (*i*) stoichiometries higher than 1:1 have not been found in any of the complexes, confirming the validity of Scheme 1; (*ii*) values of $K_{CD:guest}$ smaller than 5 are not considered representative, since they are within the uncertainty of the fit; (*iii*) the dissociation constants of *o*-, *m*-, and *p*-hydroxybenzoic acid (K_a) are in excellent agreement with those found in the study made in the absence of cyclodextrin, confirming the suitability of the method; and (*iv*) the carboxylic species are encapsulated by either β-CD or its derivatives with a higher stability than their ionized counterparts in all the systems studied.

The behavior described above has been previously observed (22, 31, 38, 39) for other carboxylic derivatives, and is explained in terms of the way these guest molecules penetrate the cyclodextrin cavity. It is believed that carboxylic species are encapsulated with the carboxylic group end first,

© 1999 NRC Canada

Table 3. Values of the dissociation constant (K_a) of *o*-, *m*-, and *p*-hydroxybenzoic acids, and the association constants of the 1:1 inclusion complexes formed by hydroxypropyl-β-cyclodextrin (HPBCD) and the acidic and basic forms of *o*-, *m*-, and *p*-hydroxybenzoic acids, as a function of temperature.

[Guest] / mM	T / °C	10^5 K_a	$K_{CD:OHBz}$ / M^{-1}	$K_{CD:OHBz^-}$ / M^{-1}
		HPBCD + *o*-hydroxybenzoic		
3.99	15	115 ± 10	980 ± 100	140 ± 30
3.96	20	110 ± 10	890 ± 90	110 ± 20
4.09	25	125 ± 10	740 ± 70	90 ± 20
3.98	30	125 ± 10	720 ± 70	70 ± 15
4.15	40	135 ± 10	440 ± 50	37 ± 8
		HPBCD + *m*-hydroxybenzoic		
4.01	15	8.0 ± 0.1	720 ± 70	<5
3.99	20	7.8 ± 0.1	620 ± 60	<5
4.01	25	8.0 ± 0.1	530 ± 50	<5
4.04	30	8.0 ± 0.1	450 ± 40	<5
4.04	40	7.8 ± 0.1	300 ± 30	<5
		HPBCD + *p*-hydroxybenzoic		
4.01	15	2.8 ± 0.1	1100 ± 110	<5
3.97	20	2.8 ± 0.1	940 ± 90	<5
4.02	25	2.8 ± 0.1	880 ± 90	<5
4.03	30	2.9 ± 0.1	730 ± 70	<5
4.02	40	2.9 ± 0.1	520 ± 50	<5

Table 4. Comparison of the binding constants obtained in this work with available literature values at 25°C.

CD	Guest	$K_{CD:Guest}$ / M^{-1}	
		This work	Literature
β-CD	*o*-OHBz	780 ± 80	700 (27)
	o-$OHBz^-$	90 ± 20	51 (32), 105(33)
	o-OHBz / *o*-$OHBz^-$		426 (23), 378 (32), 130 (41)
	m-OHBz	530 ± 50	
	m-$OHBz^-$	29 ± 6	
	m-OHBz / *m*-$OHBz^-$		288 (24)
	p-OHBz	910 ± 90	
	p-$OHBz^-$	75 ± 15	
	p-OHBz / *p*-$OHBz^-$		252 (41), 247 (29), 531 (24)
DIMEB	*o*-OHBz	1570 ± 150	
	o-$OHBz^-$	105 ± 20	140 (33)
HPBCD	*o*-OHBz	740 ± 70	1200 (34)
	o-$OHBz^-$	90 ± 20	220 (34)

which means that the ionizable group is inside the cavity. Some authors (38) attribute the lower stability of the CD:carboxylate complexes to the random character of the inclusion and (or) to the energy balance of transferring species from the bulk to the CD cavity, and others (31) to the repulsive interaction between the negative charge on the anionic species and the negatively charged end of the CD dipole, which is located at the wider end of the cavity. In a previous article (13), we pointed out slight differences in the entropic balance upon binding, related to the water structure-breaking character of carboxylate anions, as an additional factor for such a pattern.

Table 4 compares the values of the association constants found in the literature for some of the systems studied in this work with the values obtained here. It must be emphasized that whenever the binding constants obtained with different experimental techniques are to be compared, the same interval of the degree of saturation must be covered, preferably within the optimum range (20–80%) (35), and in experimental conditions that are as similar as possible (40). Keeping this in mind, the values in Table 4 call for some comment. First of all, it can be observed that those *K* values obtained from experiments where the solution is unbuffered (Lach and Cohen (23), Harata (24), and Kajtar et al. (41)) are always intermediate between the binding constants for the inclusions of the acid and basic forms. Actually, those values correspond to apparent constants that average both inclusion processes. The values obtained by Sideris et al. (32) for the β-CD:*o*-OHBz complex determined at pH = 1.5, and by Kamiya et al. (29) for the β-CD:*p*-$OHBz^-$ complex determined at pH = 6.2, are affected by a certain contribution of both the base and acid forms, since the fixed pH is not different enough (34) from the pK_a of the guest. On the other hand, those association constants obtained under such condi-

© 1999 NRC Canada

Table 5. Values of the enthalpy ($\Delta H°$) and entropy ($\Delta S°$) changes upon binding, obtained from the slope and the intercept of the corresponding van't Hoff plots, respectively. Uncertainties have been estimated with 95% confidence.

CD	Guest	$\Delta H°$ / kJ mol^{-1}	$\Delta S°$ / J mol^{-1} K^{-1}
β-CD	*o*-OHBz	–29 ± 1	–42 ± 4
	o-OHBz$^-$	–29 ± 8	–63 ± 20
	m-OHBz	–29 ± 4	–50 ± 8
	m-OHBz$^-$	–67 ± 40	–200 ± 160
	p-OHBz	–29 ± 4	–42 ± 17
	p-OHBz$^-$	–25 ± 12	–46 ± 42
DIMEB	*o*-OHBz	–21 ± 1	–8 ± 4
	o-OHBz$^-$	–25 ± 4	–50 ± 12
	m-OHBz	–28 ± 2	–37 ± 8
	m-OHBz$^-$	–75 ± 50	–240 ± 160
	p-OHBz	–23 ± 2	–17 ± 4
	p-OHBz$^-$	–46 ± 8	–130 ± 20
HPBCD	*o*-OHBz	–25 ± 4	–29 ± 12
	o-OHBz$^-$	–38 ± 8	–96 ± 25
	m-OHBz	–25 ± 4	–33 ± 12
	p-OHBz	–21 ± 4	–17 ± 16

tions that only the acid (or the base) form of the guest is present are in better agreement with the values reported herein, the level of agreement depending mainly on the degree of saturation covered in each experiment.

Van't Hoff analysis

As shown in Tables 1–3, the dissociation constants of the three monohydroxybenzoic acids are temperature independent within the uncertainty of the K_a values, while $K_{CD:OHBz}$ and $K_{CD:OHBz}$- decrease with temperature independently of the position of the substituents on the guest or the cyclodextrin. In all cases, valuable thermodynamic information can be extracted through the corresponding van't Hoff plots ($R \ln K$ vs. $1/T$). Figure 3 shows, for example, this plot for the system formed by DIMEB with *o*-, *m*-, and *p*-hydroxybenzoic acids in both the non-ionized and ionized forms. It is well known (16) that this procedure assumes that both $\Delta H°$ and $\Delta S°$ are independent of temperature, which means that the association process runs with no change in the molar heat capacity $\Delta C_p^o (\sim 0)$, an assumption that is not always correct (10, 14, 17, 42). In any case, if a reasonable linearity is observed for the plot over a given range of temperatures, it can be assumed that both $\Delta H°$ and $\Delta S°$ are essentially constant in the temperature range of the experiments.

Table 5 reports the $\Delta H°$ and $\Delta S°$ values determined for all the complexes studied in this work. These data reveal that both non-ionized and ionized species, irrespective of the *ortho*, *meta*, and *para* position of the substituents in the aromatic ring, bind to β-CD or DIMEB with a favorable enthalpic term ($\Delta H° < 0$) and an unfavorable entropic term ($\Delta S° < 0$). In the case of HPBCD, the non-ionized and ionized forms of the *ortho* isomer, and only the non-ionized forms of the *meta* and *para* isomers bind and have similar characteristics. Thus, the encapsulation processes are exothermic and enthalpy driven ($|\Delta H°| > T|\Delta S°|$), following the behavior found for associations of small guest molecules and cyclodextrins in aqueous solution (9–14). This thermodynamic pattern, which contrasts with a typical hydrophobically driven process (43), has been attributed (9–14) to the contribution of different driving forces to the overall free energy of binding: the hydrophobic effect, van der Waals contacts between the host and the guest, and the solvent reorganization. A clear trend for $\Delta H°$ of the non-ionized complexes with respect to the ionized ones is not found in Table 5. However, negative values are always obtained for $\Delta S°$, being more negative for the complexed anions. This energy balance translates into a decrease of the overall stability of the ionized complexes with respect to the non-ionized ones. This picture indicates that the difference found between the entropic terms could be responsible for such a pattern, as previously reported for other CD:carboxylate systems (13). This behavior has been attributed to the water structure-breaking character of carboxylate anions, which tend to orient water molecules radially with respect to their electrostatic field (44).

Fig. 3. van't Hoff plots for the associations of DIMEB with the nonionized and the ionized forms of *o*-, *m*-, and *p*-hydroxybenzoic acids.

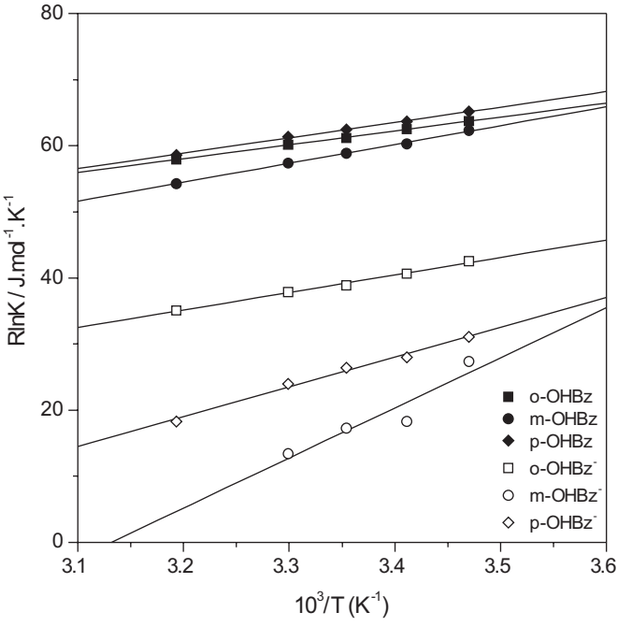

Effect of the position of the substituents of the guest molecule

The data in Tables 1–3 show that the stability of the inclusion complexes CD:OHBz and CD:OHBz$^-$ (CD is β-CD or HPBCD or DIMEB) decreases in the order *p*-OHBz > *o*-OHBz > *m*-OHBz, and *o*-OHBz$^-$ > *p*-OHBz$^-$ > *m*-OHBz$^-$, irrespective of the temperature and the cyclodextrin. Some different and probably opposite contributions may be responsible for such a pattern for the stability of the complexes, depending on the positions of the substituents on the guest molecule. It seems clear that the *m*-hydroxybenzoic, in both the ionized and non-ionized forms, is the guest that binds a cyclodextrin with less affinity, pointing to the important role of a steric factor in the interactions of CD:hydroxybenzoic derivatives. In addition, the slightly higher

© 1999 NRC Canada

stability of the inclusion complexes formed with the *p*-hydroxybenzoic with respect to the *o*-hydroxybenzoic in the acid forms (inverted in the case of the anionic forms) could be related to the presence or absence of the hydrogen bond between the -OH and -COOH groups of these molecules.

Effect of the substituents of the β-CD molecule

The binding constants reported in Tables 1–3 reveal that, independently of the temperature and of the position of the substituents on the guest molecule, the trend observed for the acid species is $K_{\text{DIMEB:OHBz}} > K_{\beta\text{-CD:OHBz}} \approx K_{\text{HPBCD:OHBz}}$. The higher affinity found for the DIMEB:OHBz inclusion complexes may be reasonably explained in terms of the substitution of 14 H per β-CD molecule by 14 CH_3 groups. The methyl groups increase the hydrophobicity of the CD cavity by providing an extension of the cavity when introducing nonpolar methyl groups at the 2 and 6 positions of the glucopyranose units. This cavity lengthening may promote van der Waals contacts between the host and the guest. However, it seems that the substitution of 3 H per β-CD molecule by 3 hydroxypropyl groups (β-CD → HPBCD) does not affect the interaction with the guest very much. In contrast, for a given cyclodextrin, clear stabilizing effects have been reported (40) when the guests are elongated rather than globular molecules, as in the case of surfactant molecules. This feature indicates that 3 hydroxypropyl "tails" on the CD cavity entrance clearly favor van der Waals contacts with the guest when it is long enough, but in the case of globular molecules the steric hindrance of the hydroxypropyl groups and the rigidity of the macrocycle (45) could be competing with its ability to extend the hydrophobic cavity. On the other hand, a clear trend cannot be found for the *K* values of the ionized species, revealing the differences in the molecular mechanism that governs the inclusion process with respect to their non-ionized counterparts, although some structural information would be clarifying.

Conclusions

The results reported can be summarized as follows: (*i*) the three monohydroxybenzoic acids are encapsulated by β-CD, DIMEB, and HPBCD with 1:1 stoichiometries. Higher stoichiometries have not been found; (*ii*) in all cases, the carboxylic forms of the guests bind a cyclodextrin with higher affinities than do the carboxylate partners, independently of the temperatures and of the substituents of both host and guest molecules; (*iii*) all the association processes have been found to be exothermic and enthalpy driven, with favorable enthalpic terms dominant over unfavorable entropic terms. The affinities of binding decrease with increasing temperature, indicating the contribution of van der Waals contacts, hydrophobic effect, and solvent reorganization as the main driving forces governing the interactions; (*iv*) the higher affinity shown by the acid forms on binding the DIMEB, relative to β-CD and HPBCD, has been attributed to the lengthening of the apolar CD cavity by the substitution of 14 H atoms by 14 methyl groups. On the other hand, the anionic forms present a more random behavior, with the particularity shown by HPBCD, which does not encapsulate the *m*-$OHBz^-$ and *p*-$OHBz^-$; (*v*) the effect of a steric factor, and possibly the presence of hydrogen bonding between the -OH and -COOH groups of the guest molecules, depending on their position, could be beyond the trends found for the CD:OHBz or CD:$OHBz^-$ affinities; and (*vi*) it is worth noting the importance of analyzing the encapsulation processes of non-ionized and ionized forms of the guest, when they occur, if clear and reasonable conclusions are required.

Acknowledgment

The authors acknowledge the financial support of the Ministerio de Educación y Cultura of Spain through DGES Project No. PB95-0356.

References

1. R.U. Lemieux, L.T.J. Delbarre, H. Beierbeck, and U. Spohr. *In* Host–guest molecular interactions: from chemistry to biology. *Edited by* D. Chadwick and K. Widdows. Ciba Found. Symp. **158**, 231 1991.
2. H. Dugas. Bioorganic chemistry: a chemical approach to enzyme action. Springer-Verlag, New York. 1989.
3. H.J. Schneider. Angew. Chem. Int. Ed. Engl. **30**, 1417 (1991).
4. (*a*) J.M. Lehn. Angew. Chem. Int. Ed. Engl. **27**, 89 (1988); (*b*) Angew. Chem. Int. Ed. Engl. **29**, 1304 (1990).
5. D.J. Cram. Angew. Chem. Int. Ed. Engl. **27**, 1009 (1988).
6. J. Szejtli and T. Osa. Comprehensive supramolecular chemistry. Vol. 3. Cyclodextrins. Elsevier Science Ltd., Oxford. 1996.
7. D.O. Thompson. CRC Crit. Rev. Ther. Drug Carrier Syst. **14**, 1 (1997).
8. L. Luzzi and A. Palmieri. Biomedical applications of microencapsulation.CRC Press, Boca Ratón, Fla. 1984.
9. (*a*) Y. Inoue, T. Hakushi, Y. Liu, L.-H. Tong, B.-J. Shen, and D.-S. Jin. J. Am. Chem. Soc. **115**, 475 (1993); (*b*) Y. Inoue, Y. Liu, L.-H. Tong, B.-J. Shen, and D.-S. Jin. J. Am. Chem. Soc. **115**, 10637 (1993).
10. (*a*) M.V. Rekharsky, F.P. Schwarz, Y.B. Tewari, R.N. Goldberg, M. Tanaka, and Y. Yamashoji. J. Phys. Chem. **98**, 4098 (1994); (*b*) M.V. Rekharsky, F.P. Schwarz, Y.B. Tewari, and R.N. Goldberg. J. Phys. Chem. **98**, 10282 (1994); (*c*) P.D. Ross and M.V. Rekharsky. Biophys. J. **71**, 2144 (1996); (*d*) M.V. Rekharsky, R.N. Goldberg, F.P. Schwarz, Y.B. Tewari, P.D. Ross, Y. Yamashoji, and Y. Inoue. J. Am. Chem. Soc. **117**, 8830 (1995).
11. G.L. Bertrand, J.R. Faulkner, S.M. Han, and D.W. Armstrong. J. Phys. Chem. **93**, 6863 (1989).
12. (*a*) D. Salvatierra, C. Jaime, A. Virgile, and D. Sánchez-Ferrando. J. Org. Chem. **61**, 9578 (1996); (*b*) G. Castronuovo, V. Elia, D. Fessas, A. Giordano, and F. Velleca. Carbohydr. Res. **272**, 31 (1995); (*c*) A. Szafranek and J. Szafranek. J. Inclusion Phenom. **15**, 351 (1993); (*d*) A.F.D. De Namor, R. Traboulssi, and D.F.V. Lewis. J. Am. Chem. Soc. **112**, 8442 (1990).
13. E. Junquera and E. Aicart. J. Phys. Chem. **101**, 7163 (1997).
14. (*a*) E. Junquera, J. Laynez, M. Menéndez, S. Sharma, and S. Penadés. J. Org. Chem. **61**, 6790 (1996); (*b*) J. Jiménez-Barbero, E. Junquera, M. Martín-Pastor, S. Sharma, C. Vicent, and C. Penadés. J. Am. Chem. Soc. **117**, 11198 (1995).
15. (*a*) K.A. Connors. Binding constants: the measurement of molecular complex stability. Wiley, New York. 1987; (*b*) K.A. Connors. Chem. Rev. **97**, 1325 (1997).
16. R.E. Stauffer, R.E. Barrans, and D.A. Dougherty. J. Org. Chem. **55**, 2762 (1990).
17. B.W. Sigurskjold and D.R. Bundle. J. Biol. Chem. **267**, 8371 (1992).

© 1999 NRC Canada

18. D.B. Smithrud, T.B. Wyman, and F.J. Diederich. J. Am. Chem. Soc. **113**, 5420 (1991).
19. H. Naghiti, A. Tamura, and J.M. Sturtevant. Proc. Natl. Acad. Sci. U.S.A. **92**, 5597 (1995).
20. B.W. Sirgurskjold, C.R. Berland, and B. Svensson. Biochemistry, **33**, 10191 (1994).
21. Y. Lin and J.M. Sturtevant. Protein Sci. **4**, 2559 (1995).
22. (*a*) R.A. Gelb, L.M. Scwartz, B. Cardelino, H.S. Fuhrman, R.F. Johnson, and D.A. Laufer. J. Am. Chem. Soc. **103**, 1750 (1981); (*b*) R.A. Gelb, L.M. Schwartz, R.F. Johnson, and D.A. Laufer. J. Am. Chem. Soc. **101**, 1869 (1979).
23. J.L. Lach and J. Cohen. J. Pharm. Sci. **52**, 137 (1963).
24. K. Harata. Bioorg. Chem. **10**, 255 (1981).
25. A. Buvari and L. Barcza. J. Chem. Soc. Perkin Trans. 2, 543 (1988).
26. R.J. Clarke, J.H. Coates, and S.F. Lincoln. Adv. Carbohydr. Chem. Biochem. **46**, 205 (1988).
27. H. Vromans, A.C. Eissens, and C.F. Lerk. Acta Pharm. Technol. **35**, 250 (1989).
28. Y. Cai, S.U. Gaffney, T.-H. Lilley, D. Magnolato, R. Martin, C.M. Spencer, and E. Haslam. J. Chem. Soc. Perkin Trans. 2, 2197 (1990).
29. M. Kamiya, S. Mitsuhashi, M. Makino, and H. Yoshioka. J. Phys. Chem. **96**, 95 (1992).
30. S.E. Brown, J.H. Coates, P.A. Duckworth, S.F. Lincoln, C.J. Easton, and B.L. May. J. Chem. Soc. Faraday Trans. **89**, 1035 (1993).
31. D. Martin-Davies and J.R. Savage. J. Chem. Soc. Perkin Trans. 2, 1525 (1994).
32. E.E. Sideris, C.A. Georgiou, M.A. Koupparis, and P.E. Macheras. Anal. Chim. Acta, **289**, 87 (1994).
33. (*a*) E. Junquera, L. Peña, and E. Aicart. J. Pharm. Sci. **87**, 86 (1998); (*b*) E. Junquera and E. Aicart. J. Inclusion Phenom. **29**, 119 (1997).
34. K.A. Connors. J. Pharm. Sci. **84**, 843 (1995).
35. D.A. Deranleau. J. Am. Chem. Soc. **91**, 4044 (1969).
36. K.A. Connors, S.F. Lin, and A.B. Wong. J. Pharm. Sci. **71**, 217 (1982).
37. P. Boudeville and J.L. Burgot. J. Pharm. Sci. **84**, 1083 (1995).
38. R.J. Bergeron, M.A. Channing, and K.A. McGovern. J. Am. Chem. Soc. **100**, 2878 (1978).
39. W.C. Cromwell, K. Byström, and M.R. Eftink. J. Phys. Chem. **89**, 326 (1985).
40. E. Junquera, L. Peña, and E. Aicart. Langmuir, **11**, 4685 (1995).
41. M. Kajtar, C. Horvath-Toro, E. Kuthi, and J. Szjetli. Acta Sci. Hung. **110**, 327 (1982).
42. J.C. Harrison and M.R. Eftink. Biopolymers, **21**, 1153 (1982).
43. C. Tanford. The hydrophobic effect: formation of micelles and biological membranes. Wiley, New York. 1980.
44. J.E. Desnoyers, M. Arel, G. Perron, and C. Jolicoeur. J. Phys. Chem. **73**, 3346 (1969).
45. G. Wenz. Angew. Chem. Int. Ed. Engl. **33**, 803 (1994)

© 1999 NRC Canada

Tetraorganodichalcogenoimidodiphosphinato derivatives of dimethyltellurium(IV) compounds. Crystal structures of $Me_2Te[(SPPh_2)_2N]_2$, $Me_2TeCl[(SPPh_2)_2N]$, $Me_2TeI[(SPPh_2)_2N]$, and $Me_2TeCl[(OPPh_2)(SPPh_2)N]$

John E. Drake, Robert J. Drake, Anca Silvestru, and Jincai Yang

Abstract: Isolation of $Me_2Te[(SPPh_2)_2N]_2$, $Me_2Te[(OPPh_2)(SPPh_2)N]_2$, and the halo derivatives $Me_2TeX[(SPPh_2)_2N]$ and $Me_2TeX[(OPPh_2)(SPPh_2)N]$, where X = Cl, Br, I, was attempted. Four of these were characterized by single crystal X-ray diffraction, while the formation of the others was confirmed by multinuclear NMR spectroscopy. $Me_2Te[(SPPh_2)_2N]_2$, **1**; $P2_1/n$ (No. 14) with cell parameters a = 14.908(3) Å, b = 11.122(5) Å, c = 30.384(6) Å, β = 92.67(2)°, V = 5032(2) Å^3, Z = 4, R = 0.0661, R_w = 0.0696. $Me_2TeCl[(SPPh_2)_2N]$, **2**; $P\bar{1}$ (No. 2) with cell parameters a = 10.553(2) Å, b = 15.512(2) Å, c = 8.769(3) Å, α = 103.19(2)°, β = 94.27(2)°, γ = 85.76(2)°, V = 1391.3(7) Å^3, Z = 2, R = 0.0377, R_w = 0.0328. $Me_2TeI[(SPPh_2)_2N]$, **4**; $P\bar{1}$ (No. 2) with cell parameters a = 10.954(3) Å, b = 15.580(3) Å, c = 8.751(3) Å, α = 103.49(2)°, β = 93.11(3)°, γ = 87.33(2)°, V = 1449.3(7) Å^3, Z = 2, R = 0.0586, R_w = 0.0613. $Me_2TeCl[(OPPh_2)(SPPh_2)N]$, **6**; $P2_1/c$ (No. 14) with cell parameters a = 10.441(9) Å, b = 13.672(10) Å, c = 19.521(9) Å, β = 97.16(6)°, V = 2764(3) Å^3, Z = 4, R = 0.0546, R_w = 0.0572. The immediate environment about Te is that of a sawhorse structure in which the lone pair is apparently stereochemically active and occupying an equatorial position in a distorted trigonal bipyramid. In **1**, **2**, and **4**, one sulfur atom of $(SPPh_2)_2N$ occupies an axial position. If the second sulfur atom is included in the coordination sphere, then the environment about Te becomes distorted octahedral, for **1**, and square pyramidal, for **2** and **4**. By contrast, in $Me_2TeCl[(OPPh_2)(SPPh_2)N]$, **6**, the oxygen atom, rather than sulfur, is bound to tellurium in the axial position, with the S atom, at best, having a very weak interaction with Te.

Key words: structure, tellurium, methyl, tetraphenyldichalogenoimidodiphosphinates.

Résumé : On a tenté d'isoler le $Me_2Te[(SPPh_2)_2N]_2$, le $Me_2Te[(OPPh_2)_2(SPPh_2)N]_2$ et les dérivés halogénés $Me_2TeX[(SPPh_2)_2N]$ et $Me_2TeX[(OPPh_2)(SPPh_2)_2N]$ dans lesquels X = Cl, Br, I. On a caractérisé quatre de ces complexes par diffraction des rayons X de monocristaux alors que la formation des autres a été confirmée par spectroscopie RMN multinucléaire. $Me_2Te[(SPPh_2)_2N]_2$ (**1**), $P2_1/n$ (No. 14), avec a = 14,908(3), b = 11,122(5) et c = 30,384(6) Å, β = 92,67(2)°, V = 5032(2) Å^3, Z = 4, R = 0,0661 et R_w = 0,0696. $Me_2TeCl(SPPh_2)_2N]$ (**2**), $P\bar{1}$ (No. 2), avec a = 10,553(2), b = 15,512(2) et c = 8,769(3) Å, α = 103,19(2)°, β = 94,27(2)° et γ = 85,76(2)°, V = 1391,3(7) Å^3, Z = 2, R = 0,0377, R_w = 0,0328. $Me_2TeI(SPPh_2)_2N]$ (**4**), $P\bar{1}$ (No. 2), avec a = 10,954(3), b = 15,580(3) et c = 8,751(3) Å, α = 103,49(2)°, β = 93,11(3)° et γ = 87,33(2)°, V = 1449,3(7) Å^3, Z = 2, R = 0,0586, R_w = 0,0613. $Me_2TeCl(OPPh_2)_2(SPPh_2)_2N$ (**6**), $P2_1/n$ (No. 14), avec a = 10,441(9), b = 13,672(10) et c = 19,521(9) Å, β = 97,16(6)°, V = 2764(3) Å^3, Z = 4, R = 0,0546 et R_w = 0,0572. L'environnement immédiat autour du Te correspond à une structure en chevalet dans laquelle la paire d'électron non pairée est apparemment stéréochimiquement active alors qu'elle occupe une position équatoriale dans une bipyramide trigonale déformée. Dans les composés **1**, **2** et **4**, un atome de soufre du groupe $(SPPh_2)_2N$ occupe une position axiale. Si le deuxième atome de soufre est inclus dans la sphère de coordination, l'environnement autour du Te devient alors un octaèdre déformé (composé **1**) et une pyramide carrée (composés **2** et **4**). Par opposition, dans le composé $Me_2TeCl(OPPh_2)_2(SPPh_2)_2N$ (**6**), c'est l'atome d'oxygène plutôt que l'atome de soufre qui est lié en position axiale du tellure; dans les meilleures conditions, l'atome de S n'offre qu'une faible interaction avec le Te.

Mots clés : structure, tellure, tétraphényldichalcogénoimidodiphophinates.

[Traduit par la Rédaction]

Received October 26, 1998.

J.E. Drake,[1] R.J. Drake, and J. Yang. Department of Chemistry and Biochemistry, University of Windsor, Windsor, ON N9B 3P4, Canada.
A. Silvestru. Department of Chemistry, Babes-Bolyai University, RO-3400, Cluj-Napoca, Romania.

[1]Author to whom correspondence may be addressed. Telephone: (519) 253-4232, ext. 3551. Fax: (519) 973-7098. e-mail: ak4@uwindsor.ca

 © 1999 NRC Canada

Introduction

The importance of supramolecular associations in molecular compounds of tellurium complexes with sulfur ligands has been recently reviewed (1). Several reports have appeared on organotellurium(IV) derivatives with 1,1-dithio ligands including *O*-alkyl dithiocarbonates (2–7), *N*,*N*-dialkyl dithiocarbamates (5–16), pyrrolidyl and piperidyl dithioformates (17), and dithiophosphates (18). Many of these sulfur-bonding derivatives of diorganotellurium(IV) display varying tendencies to undergo reductive elimination. The bonding can usually be described as anisobidentate (one strong and one weaker interaction with tellurium) and the ligands have similarly restricted bite lengths. We were therefore interested to see whether such features would be maintained using tetraphenylmono- and -di-thioimidodiphosphinates, which have relatively unrestricted bite lengths. We have reported on the molecular structures of triphenyltellurium derivatives $Ph_3Te[(SPPh_2)_2N]$, $Ph_3Te[(OPPh)_2(SPPh_2)N]$ and $Ph_3Te[(OPPh_2)_2N]$ (19, 20), and we now describe attempts to synthesize and spectroscopically characterize the dimethylbis(tetraorganodichalogenoimidodiphosphinato)tellurium(IV) compounds, $Me_2Te[(SPPh_2)_2N]_2$ and $Me_2Te[(OPPh_2)(SPPh_2)N]_2$, as well as the corresponding halodimethyl compounds, $Me_2TeX[(SPPh_2)_2N]$ and $Me_2TeX[(OPPh_2)(SPPh_2)N]$, where X = Cl, Br, I. X-ray crystal structures are included for $Me_2Te[(SPPh_2)_2N]]_2$, **1**, $Me_2TeCl[(SPPh_2)_2N]$, **2**, $Me_2TeI[(SPPh_2)_2N]$, **4**, and $Me_2TeCl[(OPPh_2)(SPPh_2)N]$, **6**.

Experimental

Materials

$TeCl_4$, and Me_4Sn were obtained from Aldrich, and $TeBr_4$ and Me_2TeI_2 from Alfa and Organometallics, Inc., respectively, all starting materials being used as supplied. Me_2TeCl_2 and Me_2TeBr_2 were prepared by adaptation of the method described in the literature for the preparation of Ph_2TeCl_2 (21) involving the reaction of $TeCl_4$ or $TeBr_4$ with Me_4Sn in toluene at 60°C under reflux for 4 h. The salts $K[(SPPh_2)_2N]$ and $Na[(OPPh_2)(SPPh_2)N]$ were prepared as described previously (22, 23). All solvents were dried and distilled prior to use and all reactions were carried out under anhydrous conditions. Elemental analyses were performed at Guelph Chemical Laboratories, Guelph, Ontario.

Preparation of $Me_2Te[(SPPh_2)_2N]_2$, 1, and $Me_2Te[(OPPh_2)(SPPh_2)N]_2$, 5

Typically, Me_2TeCl_2 (0.048 g, 0.167 mmol) and $K[(SPPh_2)_2N]$ (0.170 g, 0.350 mmol) were placed in a flask followed by the addition of toluene (15 mL). The mixture was stirred at room temperature for 1 h before being filtered to remove KCl and unreacted materials. The filtrate was concentrated by pumping off the solvent, followed by the addition of *n*-hexane (5 mL), and then left in the refrigerator at 5°C to allow the formation of $Me_2Te[(SPPh_2)_2N]_2$, **1**; yellow crystals; mp (dec.) 152°C, 0.153 g, 0.140 mmol, yield 84%. ^{1}H NMR ($CDCl_3$) δ: 2.42 (6H, Te-CH_3), 7.29 (24H, P(S)-C_6H_5, *m* + *p*), 7.85 (16H, P(S)-C_6H_5, *o*). ^{13}C NMR ($CDCl_3$) δ: 22.03 (Te-CH_3), 128.14 (C_m, P(S)-C_6H_5), 130.64 (C_p, P(S)-C_6H_5), 131.18 (C_o, P(S)-C_6H_5). ^{31}P NMR ($CDCl_3$) δ: 35.8 (*P*(S)-C_6H_5). ^{125}Te NMR ($CDCl_3$) δ: 566. Anal. calcd. for $C_{50}H_{46}N_2P_4S_4Te$: C 56.94, H 4.40, N 2.66; found: C 57.15, H 4.48, N 2.65. Similarly, starting with Me_2TeCl_2 and a twofold excess of $Na[(OPPh_2)(SPPh_2)N]$, was formed $Me_2Te[(OPPh_2)(SPPh_2)N]_2$, **5**; yellow viscous material. ^{1}H NMR ($CDCl_3$) δ: 2.69 (6H, Te-CH_3), 7.28 (P(O)-C_6H_5, *m* + *p*, and P(S)-C_6H_5, *m* + *p*), 7.68 (8H, P(O)-C_6H_5, *o*), 7.94 (8H, P(S)-C_6H_5, *o*), along with peaks attributable to toluene. ^{13}C NMR ($CDCl_3$) δ: 25.80 (Te-CH_3), 127.94 (C_m, P(O)-C_6H_5), 128.20 (C_m, P(S)-C_6H_5), 130.82, 130.95 (C_p, P(O)-C_6H_5 and P(S)-C_6H_5), 131.29, 131.42 (C_o, P(O)-C_6H_5 and P(S)-C_6H_5), along with peaks attributable to toluene. ^{31}P NMR ($CDCl_3$) δ: 21.3 (*P*(O)-C_6H_5), 39.7 (*P*(S)-C_6H_5). ^{125}Te NMR ($CDCl_3$) δ: 571. Attempts to recrystallize as described above did not yield X-ray quality crystals, but resulted in decomposition.

Preparation of $Me_2TeCl[(SPPh_2)_2N]$, 2, and $Me_2TeCl[(OPPh_2)(SPPh_2)N]$, 6

Typically, Me_2TeCl_2 (0.039 g, 0.135 mmol) and $K[(SPPh_2)_2N]$ (0.066 g, 0.135 mmol) were placed in a flask followed by the addition of toluene (15 mL). The mixture was stirred at room temperature for 2 h before being filtered to remove KCl and unreacted materials. The filtrate was concentrated by pumping off solvent, followed by the addition of *n*-hexane (5 mL) and then left in the refrigerator at 5°C to allow the formation of $Me_2TeCl[(SPPh_2)_2N]$, **2**; colorless crystals; mp (dec.) 106°C, 0.075 g, 0.117 mmol, yield 87%. ^{1}H NMR ($CDCl_3$) δ: 2.72 (6H, Te-CH_3), 7.31 (12H, P(S)-C_6H_5, *m* + *p*), 7.86 (8H, P(S)-C_6H_5, *o*). ^{13}C NMR ($CDCl_3$) δ: 23.39 (Te-CH_3), 128.16 (C_m, P(S)-C_6H_5), 130.10 (C_p, P(S)-C_6H_5), 131.20 (C_o, P(S)-C_6H_5). ^{31}P NMR ($CDCl_3$) δ: 43.2 (*P*(S)-C_6H_5). ^{125}Te NMR ($CDCl_3$) δ: 618. Anal. calcd. for $C_{26}H_{26}NP_2S_2ClTe$: C 48.67, H 4.08, N 2.18; found: C 48.88, H 4.01, N 2.01. Similarly, starting with Me_2TeCl_2 (0.101 g, 0.350 mmol) and $Na[(OPPh_2)(SPPh_2)N]$ (0.159 g, 0.350 mmol), was formed $Me_2TeCl[(OPPh_2)(SPPh_2)N]$, **6**; colorless crystals; mp (dec.) 130°C, 0.189 g, 0.302 mmol, yield 86%. ^{1}H NMR ($CDCl_3$) δ: 2.80 (6H, Te-CH_3), 7.30 (12H, P(O)-C_6H_5, *m* + *p*, and P(S)-C_6H_5, *m* + *p*), 7.70 (4H, P(O)-C_6H_5, *o*), 7.90 (4H, P(S)-C_6H_5, *o*). ^{13}C NMR ($CDCl_3$) δ: 26.00 (Te-CH_3), 128.10 (C_m, P(O)-C_6H_5), 128.34 (C_m, P(S)-C_6H_5), 129.13, 129.75 (C_p, P(O)-C_6H_5 and P(S)-C_6H_5), 131.23, 131.94 (C_o, P(O)-C_6H_5 and P(S)-C_6H_5). ^{31}P NMR ($CDCl_3$) δ: 21.8 (*P*(O)-C_6H_5), 39.8 (*P*(S)-C_6H_5). ^{125}Te NMR ($CDCl_3$) δ: 580. Anal. calcd. for $C_{26}H_{26}NOP_2SClTe$: C 49.92, H 4.19, N 2.24; found: C 49.68, H 4.12, N 2.18.

Formation of $Me_2TeBr[(SPPh_2)_2N]$, 3 and $Me_2TeBr[(OPPh_2)(SPPh_2)N]$, 7

Typically, Me_2TeBr_2 (0.062 g, 0.195 mmol) and $K[(SPPh_2)_2N]$ (0.095 g, 0.195 mmol) were placed in a flask followed by the addition of toluene (15 mL). The mixture was stirred at room temperature for 2 h before being filtered to remove KBr and unreacted materials. The solvent was pumped off to give $Me_2TeBr[(SPPh_2)_2N]$, **3**, a yellow viscous material that darkened with time. ^{1}H NMR ($CDCl_3$) δ: 2.77 (6H, Te-CH_3), 7.37 (12H, P(S)-C_6H_5, *m* + *p*), 7.89 (8H, P(S)-C_6H_5, *o*), along with peaks attributable to toluene. ^{13}C NMR ($CDCl_3$) δ: 22.64 (Te-CH_3), 128.55 (C_m, P(S)-C_6H_5), 130.68 (C_p, P(S)-C_6H_5), 131.12 (C_o, P(S)-C_6H_5), along with peaks attributable to toluene. ^{31}P NMR ($CDCl_3$) δ: 43.3

© 1999 NRC Canada

(P(S)-C_6H_5). ^{125}Te NMR ($CDCl_3$) δ: 590. Similarly, starting with Me_2TeBr_2 and an equimolar amount of Na[($OPPh_2$)($SPPh_2$)N], was formed Me_2TeBr[($OPPh_2$)($SPPh_2$)N], **7**, a pale yellow viscous material that darkened with time. ^{1}H NMR ($CDCl_3$) δ: 2.87 (6H, Te-CH_3), 7.33 (12H, P(O)-C_6H_5, m + p, and P(S)-C_6H_5, m + p), 7.79 (4H, P(O)-C_6H_5, o), 7.864 (4H, P(S)-C_6H_5, o), along with peaks attributable to toluene. ^{13}C NMR ($CDCl_3$) δ: 25.29 (Te-CH_3), 128.36 (C_m, P(O)-C_6H_5 and C_m, P(S)-C_6H_5), 130.80, 130.99 (C_p, P(O)-C_6H_5 and P(S)-C_6H_5), 131.15, 131.24 (C_o, P(O)-C_6H_5 and P(S)-C_6H_5), along with peaks attributable to toluene. ^{31}P NMR ($CDCl_3$) δ: 20.3 (P(O)-C_6H_5), 39.7 (P(S)-C_6H_5). ^{125}Te NMR ($CDCl_3$) δ: 578. Attempts to recrystallize **3** and **7** as described above for **2** and **6** resulted in decomposition.

Preparation of $Me_2TeI[(SPPh_2)_2N]$, 4, and $Me_2TeI[(OPPh_2)(SPPh_2)N]$, 8

Typically, Me_2TeI_2 (0.125 g, 0.304 mmol) and K[$(SPPh_2)_2$N] (0.148 g, 0.304 mmol) were placed in a flask followed by the addition of toluene (15 mL). The mixture was stirred at room temperature for 1 h before being filtered to remove KI and unreacted materials. The filtrate was concentrated by pumping off solvent, followed by the addition of *n*-hexane (5 mL), and was then left in the refrigerator at 5°C to allow the formation of $Me_2TeI[(SPPh_2)_2N]$, **4**, yellow crystals, mp (dec.) 105°C, to form a brown solid that darkened considerably at 230°C, 0.190 g, 0.259 mmol, yield 86%. ^{1}H NMR ($CDCl_3$) δ: 2.76 (6H, Te-CH_3), 7.35 (12H, P(S)-C_6H_5, m + p), 7.88 (8H, P(S)-C_6H_5, o). ^{13}C NMR ($CDCl_3$) δ: 20.74 (Te-CH_3), 128.44 (C_m, P(S)-C_6H_5), 131.04 (C_p, P(S)-C_6H_5), 131.18 (C_o, P(S)-C_6H_5). ^{31}P NMR ($CDCl_3$) δ: 33.6 (P(S)-C_6H_5). ^{125}Te NMR ($CDCl_3$) δ: 557. Anal. calcd. for $C_{26}H_{26}NP_2S_2ITe$: C 42.60, H 3.58, N 1.91; found: C 42.76, H 3.62, N 1.83. Similarly, starting with Me_2TeI_2 and an equimolar amount of Na[($OPPh_2$)($SPPh_2$)N] was formed, Me_2TeI[($OPPh_2$)($SPPh_2$)N], **8**; brown viscous material. ^{1}H NMR ($CDCl_3$) δ: 2.84 (6H, Te-CH_3), ca. 7.20 (P(O)-C_6H_5, o), 7.40 (4H, P(S)-C_6H_5, o), 7.60 (8H, P(O)-C_6H_5, o and P(S)-C_6H_5, o). ^{13}C NMR ($CDCl_3$) δ: 23.39 (Te-CH_3), 127.68 (C_m, P(O)-C_6H_5), 127.88 (C_m, P(S)-C_6H_5), 128.60 (C_p, P(O)-C_6H_5), 130.62 (C_p, P(S)-C_6H_5), 131.42, 131.90 (C_o, P(O)-C_6H_5 and P(S)-C_6H_5)]. ^{125}Te NMR ($CDCl_3$) δ: 525. Attempts to recrystallize as described above resulted in decomposition.

Physical measurements

^{1}H and ^{13}C {H} NMR spectra were recorded on a Bruker 300 FT/NMR spectrometer at 300.133 and 75.471 MHz, respectively, in $CDCl_3$ using Me_4Si as internal standard. The ^{31}P and ^{125}Te NMR spectra were recorded on a Bruker 200 FT/NMR spectrometer in $CDCl_3$ using 85% H_3PO_4 and Me_2Te, respectively, as external standard. All NMR spectra were run at ambient temperature under standard operating conditions. The melting points were determined on a Fisher–Johns apparatus.

X-ray crystallographic analysis

Yellow block crystals of $Me_2Te[(SPPh_2)_2N]_2$, **1**, and $Me_2TeI[(SPPh_2)_2N]$, **4**, and colorless block crystals of $Me_2TeCl[(SPPh_2)_2N]$, **2**, and $Me_2TeCl[(OPPh_2)(SPPh_2)N]$, **6**, were mounted on glass fibres and sealed with epoxy glue. Data were collected on a Rigaku AFC6S diffractometer, with graphite-monochromated Mo Kα radiation operating at 50 kV and 35 mA. Cell constants corresponded to monoclinic (for **1** and **6**), and triclinic (for **2** and **4**) cells whose dimensions are given in Table 1, along with other experimental parameters. Based on the appropriate systematic absences for **1** and **6**, statistical analyses of intensity distributions, and the successful solution and refinement of the structures, the space groups were determined to be $P2_1/n$ and $P2_1/c$ (No. 14) for **1** and **6**, respectively, and $P\bar{1}$ (No. 2) for **2** and **4**. The data were corrected for Lorentz and polarization effects and an empirical absorption correction was applied. The structures were solved by direct methods (24) and all calculations were performed using the TEXSAN (25) crystallographic software package of the Molecular Structure Corp.[2] For **1**, the phenyl groups were treated as fixed rings with the C—C distances set at 1.40 Å. Hydrogen atoms attached to carbon were included in their idealized positions with C—H set at 0.95 Å and with isotropic thermal parameters set at 1.2 times that of the carbon atom to which they were attached. All non-hydrogen atoms were refined anisotropically for **2** and **6**, all non-hydrogen atoms except carbon for **1**, and only the tellurium and iodide atoms for **4**.

The unweighted and weighted agreement factors and standard deviations of an observation of unit weight[3] are given in Table 1. Plots of $\Sigma w(|F_o| - |F_c|)^2$ versus $|F_o|$, reflection order in data collection, sin θ/λ, and various classes of indices showed no unusual trends. Selected distances and bond angles are given in Tables 2–4 and ORTEP diagrams in Figs. 1 and 2. Additional crystallographic data are available as supporting information. Tables of final atomic coordinates and equivalent isotropic thermal parameters for the non-hydrogen atoms, final anisotropic thermal parameters of non-hydrogen atoms, final fractional coordinates and thermal parameters of hydrogen atoms, and all bond distances and angles have been deposited.[4]

Calculation of Pauling partial bond orders

We have introduced an adjustment to Pauling's calculation of partial bond orders (26), which was essentially based on the C—C single bond, to readily obtain estimates of the partial bond orders within these tellurium complexes (2). Thus,

[2] Least squares: function minimized: $\Sigma w(|F_o| - |F_c|)^2$, where $w = 4F_o^2(F_o^2)$, $\sigma^2(F_o^2) = [S^2(C + R^2B) + (pF_o^2)^2]/(Lp)^2$, S = scan rate, C = total integrated peak count, R = ratio of scan time to background counting time, Lp = Lorentz-polarization factor, and p = p factor.

[3] Standard deviation of an observation of unit weight: $\Sigma w(|F_o| - |F_c|)^2/N_o - N_v)^{1/2}$, where N_o = number of observations and N_v = number of variables.

[4] Copies of material deposited (tables of fractional atomic coordinates, isothermal parameters and anisotropic thermal parameters, interatomic bond distances and angles) may be purchased from: The Depository of Unpublished Data, Document Delivery, CISTI, National Research Council of Canada, Ottawa, ON K1A 0S2, Canada. Tables of atomic coordinates and of bond distances and angles have also been deposited with the Cambridge Crystallographic Centre, and can be obtained on request from The Director, Cambridge Crystallographic Centre, University Chemical Laboratory, 12 Union Road, Cambridge, CB2 1EZ, UK. Structure factor amplitudes are no longer being deposited and may be obtained directly from the author.

© 1999 NRC Canada

Table 1. Summary of crystal data, intensity collection, and structural refinement for $Me_2Te[(SPPh_2)_2N]_2$, **1**, $Me_2TeCl[(SPPh_2)_2N]$, **2**, $Me_2TeI[(SPPh_2)_2N]$, **4**, and $Me_2TeCl[(OPPh_2)(SPPh_2)N]$, **6**.

	1	**2**	**4**	**6**
Cell constants				
a (Å)	14.908(3)	10.553(2)	10.954(3)	10.441(9)
b (Å)	11.122(5)	15.512(4)	15.580(3)	13.672(10)
c (Å)	30.384(6)	8.769(3)	8.751(3)	19.521(9)
α (deg)	90.00	103.19(2)	103.49(2)	90.00
β (deg)	92.67(2)	94.27(2)	93.11(3)	97.16(6)
γ (deg)	90.00	85.76(2)	87.33(2)	90.00
Cell volume (Å^3)	5032(2)	1391.3(7)	1449.3(7)	2764(3)
Space group	$P2_1/n$	$P\bar{1}$	$P\bar{1}$	$P2_1/c$
Z	4	2	2	4
Mol. wt (g mol^{-1})	1054.66	641.62	733.07	625.56
ρ_{calcd} (g cm^{-3})	1.39	1.53	1.68	1.50
T,°C	23	23	23	23
Radiation	MoKα 0.71609 Å			
Monochromator	Highly oriented graphite			
Scan method	ω-2θ			
Max 2θ angle	50	50	50	50
Absorption coefficient μ (cm^{-1})	9.10	14.46	23.61	13.83
Transmission factors	0.59–1.00	0.83–1.00	0.73–1.00	0.61–1.00
Total reflections measured	8034	5204	4317	5097
Unique data used ($I > 3\sigma$)	1970	3407	1199	1154
No. of parameters refined	204	298	143	143
$R = \Sigma \|\|F_o\| - \|F_c\|\| / \|F_o\|$	0.0661	0.0377	0.0586	0.0546
$R_w = [(\Sigma\, w(\|F_o\| - F_c\|)^2 / \Sigma\, wF_o^2)]^{1/2}$	0.0696	0.0328	0.0615	0.0572
Goodness of fit	2.05	1.72	1.60	1.63
Largest shift / e.s.d in final cycle	0.001	0.001	0.001	0.001
Largest residual electron density	0.59	0.93	0.74	0.49

Pauling's relationship is modified so that for $n = 10^X$, $X = [1.54(d - d_n)/d]/0.6$ or $X = 2.57(d - d_n)/d$, where d_n is the bond length for bond number *n*, and *d* is the length of the single bond of the same type. Based on the assumption that in these compounds the appropriate Te—S single bond length has an average value of 2.62 Å in **1**, **2**, and **3**, typical calculated values of the lengths of Te—S partial bonds for various values of *n* are as follows: 2.62 Å (*n* = 1.0), 2.75 (0.75), 2.93 (0.50), 3.24 (0.25), and 3.64 Å (*n* = 0.10). Similarly, based on the assumption that the appropriate Te—Cl, Te—Br, and Te—I single bond lengths are those found in the corresponding Me_2TeX_2 compounds of 2.51, 2.68, and 2.92 Å, respectively, for X = Cl, Br, and I, typical calculated values of the lengths of Te—X partial bonds for various values of *n* are as follows: for Te—Cl, 2.51 Å (*n* = 1.0), 2.63 (0.75), 2.80 (0.50), 3.10 (0.25), and 3.49 Å (*n* = 0.10); for Te—Br, 2.68 Å (*n* = 1.0), 2.81 (0.75), 2.99 (0.50), 3.31 (0.25), and 3.71 Å (*n* = 0.10); and for Te—I, 2.92 Å (*n* = 1.0), 3.06 (0.75), 3.26 (0.50), 3.60 (0.25), and 4.06 Å (*n* = 0.10). The corresponding "valences" for partial bonds, which were calculated for the Te—I bonds in TeI_4, gave 3.16 (0.40) and 3.50 Å (0.20) (27).

Results and discussion

Preparation of the tetraphenyldi- and -mono-thioimidodiphosphinate bis derivatives of dimethyltellurium(IV), $Me_2Te[(SPPh_2)_2N]_2$, **1**, and $Me_2Te[(OPPh_2)(SPPh_2)N]_2$, **5**, is achieved by the reaction of an excess of the potassium or sodium salt of the appropriate imidodiphosphinate with dimethyltellurium dichloride in toluene in accord with eq. [1]:

[1] $$Me_2TeCl_2 + 2M[(EPPh_2)(SPPh_2)N] = Me_2Te[(EPPh_2)(SPPh_2)N]_2 + 2MCl$$

(M = Na or K; E = S or O)

Halodimethyl(tetraphenyldi- and -mono-thioimidodiphosphinato)tellurium(IV) compounds, $Me_2TeCl[(SPPh_2)_2N]$, **2**, $Me_2TeBr[(SPPh_2)_2N]$, **3**, $Me_2TeI[(SPPh_2)_2N]$, **4**, $Me_2TeCl[(OPPh_2)(SPPh_2)N]$, **6**, $Me_2TeBr[(OPPh_2)(SPPh_2)N]$, **7**, and $Me_2TeI[(OPPh_2)(SPPh_2)N]$, **8**, can be similarly prepared by the reaction of equimolar amounts of the appropriate salt with dimethyltellurium dihalide in accord with eq. [2]:

[2] $$Me_2TeX_2 + M[(EPPh_2)(SPPh_2)N] = Me_2TeX[(EPPh_2)(SPPh_2)N] + MX$$

(X = Cl, Br, or I; M = Na or K; E = S or O)

However, four of these products, notably **3**, **5**, **7** and **8**, were not isolated in a pure state totally free of solvent because of a tendency to decompose when attempts were made to recrystallize or remove the last traces of solvent. By contrast, **1**, **2**, **4**, and **6** were isolated in good yields (ca. 85%) and were obtained as X-ray quality crystals on recrystallization from mixed toluene–*n*-hexane solvents. None showed signs of decomposition during X-ray data collection, which was carried out at room temperature.

© 1999 NRC Canada

Table 2. Selected interatomic distances (Å) and bond angles (°) in $Me_2Te[(SPPh_2)_2N]_2$, **1**, with standard deviations in parentheses.[a]

Atoms	Distance	Atoms	Distance
Te(1)—S(1)	2.655(6)	Te(1)—S(3)	2.631(7)
Te(1)—C(1)	2.13(3)	Te(1)—C(2)	2.13(3)
S(1)—P(1)	2.039(9)	S(3)—P(3)	2.05(1)
S(2)—P(2)	1.96(1)	S(4)—P(4)	1.964(8)
N(1)—P(1)	1.58(2)	N(2)—P(3)	1.54(2)
N(1)—P(2)	1.61(2)	N(2)—P(4)	1.63(2)
Te(1)—S(2)	3.345(8)	Te(1)—S(4)	3.527(6)
Te(1)—S(3)′	5.100(7)		
Bonds	**Angle**	**Bonds**	**Angle**
S(1)-Te(1)-S(3)	169.6(2)	C(1)-Te(1)-C(2)	90(1)
S(1)-Te(1)-C(1)	83.3(6)	S(3)-Te(1)-C(2)	82.9(7)
S(3)-Te(1)-C(1)	90.5(6)	S(1)-Te(1)-C(2)	88.7(7)
P(1)-N(1)-P(2)	129(1)	P(3)-N(2)-P(4)	133(1)
S(1)-Te(1)—S(2)	90.1(2)	S(3)-Te(1)—S(4)	88.4(2)
S(1)-Te(1)—S(4)	98.3(2)	S(3)-Te(1)—S(2)	94.3(2)
C(1)-Te(1)—S(2)	166.7(7)	C(2)-Te(1)—S(4)	164.9(7)
C(1)-Te(1)—S(4)	77.4(6)	C(2)-Te(1)—S(2)	78.0(8)
S(2)—Te(1)—S(4)	115.1(2)		

[a]Symmetry equivalent position (–*x*, 1 – *y*, –*z*) is denoted by a prime.

Table 3. Selected interatomic distances (Å) and bond angles (°) for compounds **2** and **4**, with standard deviations in parentheses.[a]

$Me_2TeCl[(SPPh_2)_2N]$, **2**		$Me_2TeI[(SPPh_2)_2N]$, **4**	
Atoms	**Distance**	**Atoms**	**Distance**
Te(1)—Cl(1)	2.526(2)	Te(1)—I(1)	2.900(3)
Te(1)—S(1)	2.607(2)	Te(1)—S(1)	2.633(8)
Te(1)—C(1)	2.105(6)	Te(1)—C(1)	2.15(3)
Te(1)—C(2)	2.110(6)	Te(1)—C(2)	2.11(3)
S(1)—P(1)	2.047(2)	S(1)—P(1)	2.05(1)
S(2)—P(2)	1.964(2)	S(2)—P(2)	1.97(1)
N(1)—P(1)	1.571(4)	N(1)—P(1)	1.56(2)
N(1)—P(2)	1.599(4)	N(1)—P(2)	1.62(2)
Te(1)—S(2)	3.367(2)	Te(1)—S(2)	3.361(8)
Te(1)—S(1)′	4.620(2)	Te(1)—S(1)‴	4.607(8)
Te(1)—Cl(1)″	5.442(2)	Te(1)—I(1)′‴′	5.679(3)
Bonds	**Angle**	**Bonds**	**Angle**
Cl(1)-Te(1)-S(1)	172.18(6)	I(1)-Te(1)-S(1)	172.7(2)
Cl(1)-Te(1)-C(1)	89.9(2)	I(1)-Te(1)-C(1)	90.0(8)
Cl(1)-Te(1)-C(2)	86.1(2)	I(1)-Te(1)-C(2)	88.6(8)
S(1)-Te(1)-C(1)	86.7(2)	S(1)-Te(1)-C(1)	87.0(8)
S(1)-Te(1)-C(2)	87.2(2)	S(1)-Te(1)-C(2)	85.1(8)
C(1)-Te(1)-C(2)	95.3(3)	C(1)-Te(1)-C(2)	95(1)
P(1)-N(1)-P(2)	139.1(3)	P(1)-N(1)-P(2)	138(1)
Cl(1)-Te(1)—S(2)	102.60(6)	I(1)-Te(1)—S(2)	101.4(2)
S(1)-Te(1)—S(2)	79.43(5)	S(1)-Te(1)—S(2)	80.4(2)
C(1)-Te(1)—S(2)	162.9(2)	C(1)-Te(1)—S(2)	164.2(8)
C(2)-Te(1)—S(2)	74.3(2)	C(2)-Te(1)—S(2)	74.8(7)

[a]Symmetry equivalent position (–*x*, 1 – *y*, –*z*) is denoted by a prime, (1 – *x*, 1 – *y*, –*z*) by a double prime, (–*x*, –*y*, –*z*) by a triple prime, and (1 – *x*, –*y*, –*z*) by a quadruple prime.

Table 4. Selected interatomic distances (Å) and bond angles (°) for $Me_2TeCl[(OPPh_2)(SPPh_2)N]$, **6**, with standard deviations in parentheses.[a]

Atoms	Distance	Atoms	Distance
Te(1)—Cl(1)	2.464(8)	Te(1)—O(1)	2.14(2)
Te(1)—C(1)	2.10(2)	Te(1)—C(2)	2.11(2)
O(1)—P(1)	1.56(1)	S(1)—P(2)	1.973(8)
N(1)—P(1)	1.56(2)	N(1)—P(2)	1.64(2)
Te(1)—S(1)	3.413(7)	Te(1)—Cl(1)″	7.577(8)
Te(1)—S(1)′	6.261(6)		
Bonds	**Angle**	**Bonds**	**Angle**
Cl(1)-Te(1)-O(1)	168.9(4)	C(1)-Te(1)-C(2)	98.8(9)
Cl(1)-Te(1)-C(1)	89.1(7)	Cl(1)-Te(1)-C(2)	87.8(8)
O(1)-Te(1)-C(1)	82.9(8)	O(1)-Te(1)-C(2)	85.9(8)
Te(1)-O(1)-P(1)	127.1(8)	S(1)-P(2)-N(1)	116.8(7)
O(1)-P(1)-N(1)	119(1)	P(1)-N(1)-P(2)	129(1)
Cl(1)-Te(1)—S(1)	108.2(2)	O(1)-Te(1)—S(1)	78.9(4)
C(1)-Te(1)—S(1)	161.1(6)	C(2)-Te(1)—S(1)	75.0(7)

[a]Symmetry equivalent position (2 – *x*, –*y*, –*z*) denoted by a prime and (2 – *x*, *y* – 1/2, ½ – *z*) denoted by a double prime.

Crystal structures of $Me_2Te[(SPPh_2)_2N]_2$, 1, $Me_2TeCl[(SPPh_2)_2N]$, 2, $Me_2TeI[(SPPh_2)_2N]$, 4, and $Me_2TeCl[(OPPh_2)(SPPh_2)N]$, 6

$Me_2Te[(SPPh_2)_2N]_2$, **1**, crystallizes in the space group $P2_1/n$. The ORTEP diagram in Fig. 1*a* illustrates that the immediate environment about tellurium is the sawhorse structure typical of tellurium(IV) compounds, at least in the gas phase, in which the lone pair is assumed to be active stereochemically and occupying an equatorial position in a distorted trigonal bipyramid approximately at the location of the Te(1) label. The two methyl groups occupy the other two equatorial positions with the Te—C bond length of 2.13(3) Å essentially the same as those in related dithio derivatives. The C(1)-Te(1)-C(2) bond angle of 90(1)° is much closer to 90° than is normally found, as exemplified by angles of 96.2(2)°, 97.1(1)°, and 96.6(3)°, respectively, for $Me_2Te[S_2COEt]_2$ (2), $Me_2Te[S_2CN(CH_2)_3CH_2]_2$ (17), and $Me_2Te[S_2POCH_2CEt_2CH_2O]_2$ (18). The axial positions are occupied by one sulfur atom from each of the $(SPPh_2)_2N$ groups. The S(1)-Te(1)-S(3) bond angle of 169.6(2)° is the same as in $Me_2Te[S_2POCH_2CEt_2CH_2O]_2$, close to those in $Me_2Te[S_2CN(CH_2)_4CH_2]_2$ (17) and $Me_2Te[S_2POCMe_2CMe_2O]_2$ (18), (173.1(1) and 173.26(7)°, respectively) and larger than in $Me_2Te[S_2CN(CH_2)_3CH_2]_2$, 162.2(3)°. The average length of these axial Te—S bonds, 2.64(1) Å, is longer than has generally been reported for related dithio derivatives and one of these bonds is clearly longer than the other. When the two Te—S bond lengths differ, the sulfur atom of the longer bond has frequently been associated with the tellurium atom of an adjacent molecule at contact distances less than the sum of the van der Waals radii of 3.86 Å. However, this is not the case in **1**, as has also been found for other derivatives with bulky ligands such as $Me_2Te[S_2CN(CH_2)_4CH_2]_2$, $Me_2Te[S_2CN(CH_2)_3CH_2]_2$, $Me_2Te[S_2POCMe_2CMe_2O]_2$, and $Me_2Te[S_2POCH_2CEt_2CH_2O]_2$ (17, 18).

The apparently nonbonded S(2) and S(4) atoms are both oriented toward the tellurium center at Te—S distances of 3.345(8) and 3.572(6) Å, which are at the high end of the

© 1999 NRC Canada

Fig. 1. ORTEP plots of the molecules (*a*) $Me_2Te[(SPPh_2)_2N]_2$, **1**; (*b*) $Me_2TeCl[(SPPh_2)_2N]$, **2**; and (*c*) $Me_2TeCl[(OPPh_2)(SPPh_2)N]$, **6**, showing the immediate environment about tellurium. Atoms are drawn with 30% probability ellipsoids and spheres with hydrogen atoms omitted for clarity.

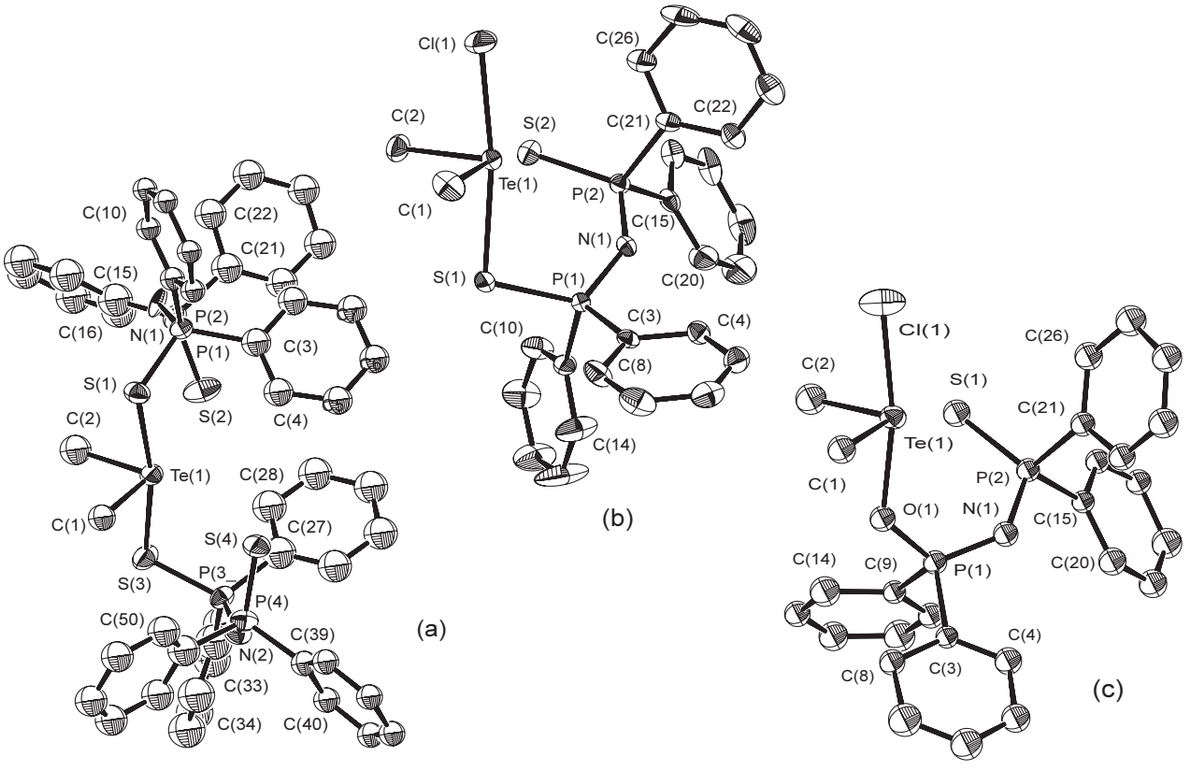

range of those found in related dithio derivatives, 3.162(4)–3.33(1) Å. These distances correspond to normalized Pauling partial bond orders of less than 0.25, but are still compatible with their being part of the coordination sphere as demonstrated in Fig. 2*a*. The orientation of the two unsymmetrical bidentate or anisobidentate $(SPPh_2)_2N$ groups results in a distorted octahedral environment about Te(1), the distortion being much less than has been previously found in, for example, $Me_2Te[S_2CN(CH_2)_4CH_2]_2$ (17), suggesting an essentially inactive lone pair, or one with a high percentage of *s*-character. The Te-S-P angles of the two ligands are 107.7(3)° and 108.2(3)°, leading to S-Te—S bite angles of 90.1(2)° and 88.4(2)° and S—S bite lengths of 4.27(1) and 4.343(9) Å. This is in contrast to typical bite angles and lengths of ca. 60° and ca. 2.99 Å, respectively, found with the more restricted S_2COR and S_2CNR_2 ligands (2, 8, 15, 17). The more flexible $(SPPh_2)_2N$ fragments should be capable of forming bidentate ligands but instead appear to establish similar anisobidentate distances with the Te—S anisobond essentially *trans* to a methyl group and *cis* to the "fully bonded" sulfur atom of the adjacent ligand with S(2)—Te(1)-S(3) and S(4)—Te(1)-S(1) being 94.3° and 98.3(2)°, respectively. In $Me_2Te[S_2CN(CH_2)_4CH_2]_2$, the corresponding angles are more distorted from 90°, with values of 123.1(1)° and 121.6(1)° (17).

$Me_2TeCl[(SPPh_2)_2N]$, **2**, and $Me_2TeI[(SPPh_2)_2N]$, **4**, both crystallize in the space group $P\bar{1}$. The ORTEP diagram of **2** in Fig. 1*b* illustrates that, as for **1**, the immediate environment about tellurium for **2** and **4** is again the sawhorse structure but with the halogen atoms now occupying one of the axial positions to give X(1)-Te(1)-S(1) angles of 172.18(6)° and 172.7(2)°, respectively, for **2** and **4**. The average Te—C bond length of 2.12(1) Å is essentially the same as in **1**, but the C(1)-Te(1)-C(2) angles, with an average of 95.2(2)°, are no longer as close to 90° as they were in the bis compound. The average Te(1)—S(1) distance of 2.62(2) Å in **2** and **4** is similar to those in **1**, whereas in the corresponding $Me_2TeX[S_2COEt]$ and $Me_2TeX[S_2CN(CH_2)_nCH_2]$ species there was considerable shortening of the Te—S bond, with distances of ca. 2.51 Å indicating much stronger bonds in these halo derivatives with estimated bond orders of up to 1.30 (17, 28). In $Me_2TeX[S_2COEt]$ and $Me_2TeX[S_2CN(CH_2)_nCH_2]$ derivatives, the Te—X bonds were found to be distinctly longer than in related R_2TeX_2 species, an average of 2.670(7) Å for Te—Cl bonds compared to 2.51(4) Å for Me_2TeCl_2 (29), and an average of 3.05(3) Å for Te—I bonds compared to a range of 2.885(3) to 2.994(3) Å in Me_2TeI_2 (30). This shortening of the Te—S bond and lengthening of the Te—X bonds appeared to be a general example of the *trans* influence operating on a main group metal for such derivatives of tellurium. Therefore, by contrast and, surprisingly, in $Me_2TeX[(SPPh_2)_2N]$, the Te(1)—Cl(1) bond in **2** is, within experimental error, the same length as in Me_2TeCl_2, and the Te(1)—I(1) bond in **4** at 2.900(3) Å is within the range of the bond lengths in Me_2TeI_2. This suggests that the sulfur atoms in $(SPPh_2)_2N$ have far less *trans*

© 1999 NRC Canada

Fig. 2. ORTEP plots of the molecules (*a*) $Me_2Te[(SPPh_2)_2N]_2$, **1**; (*b*) $Me_2TeI[(SPPh_2)_2N]$, **4**; and (*c*) $Me_2TeCl[(OPPh_2)(SPPh_2)N]$, **6**, showing the stereochemistry about tellurium when the intramolecular interactions leading to unsymmetrical bidentate ligands are included. The atoms are drawn with 30% probability ellipsoids and spheres. Hydrogen atoms and the carbon atoms of the phenyl rings other than those attached to phosphorus are omitted for clarity.

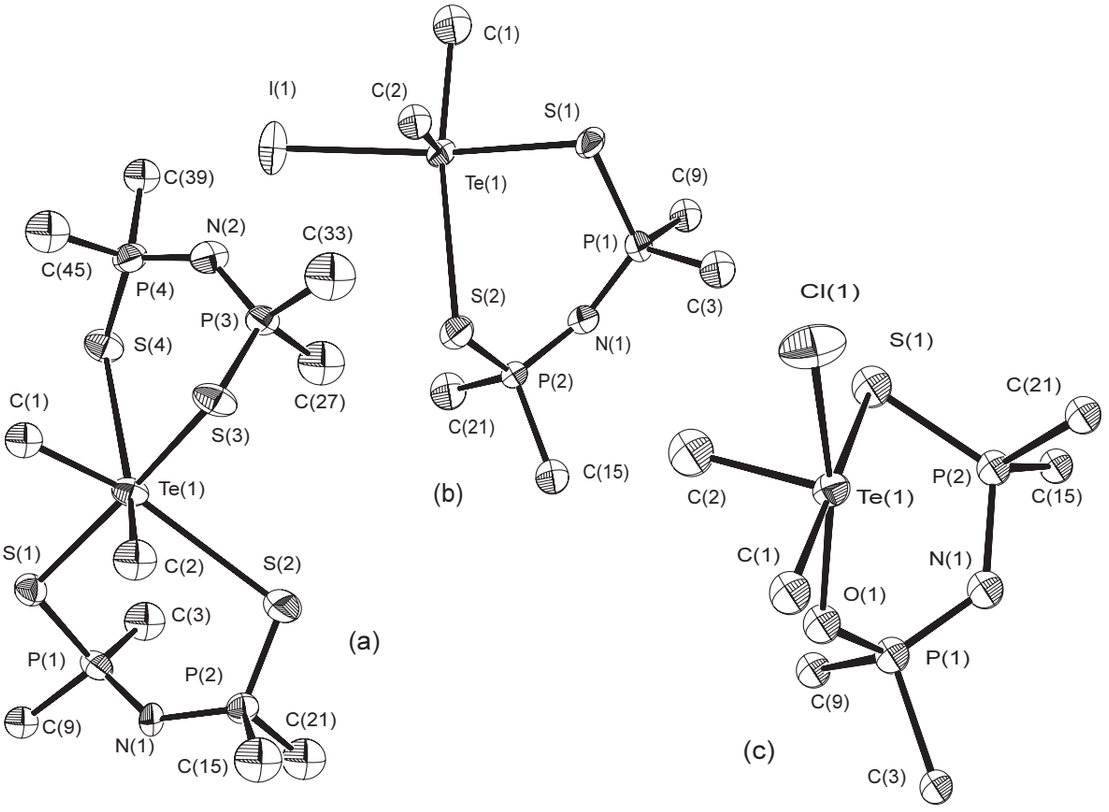

influence than in halo-dithiocarbonates and -dithiocarbamates and the Te—S bonds are generally weaker in these dithioimido compounds.

As with **1**, the $(SPPh_2)_2N$ group in **2** and **4** can be treated as an unsymmetrical bidentate ligand with the pendant S atom as part of the coordinating sphere to give Te—S anisobonds of similar length, Te(1)—S(2) 3.367(2) Å in **2** and 3.361(8) Å in **4**, respectively. The orientation of the phosphorus ligand is identical in **2** and **4**, giving rise to a distorted square pyramidal arrangement about tellurium in both cases or a distorted pseudo-octahedral arrangement if the lone pair is now assumed to be occupying the position *trans* to C(2), as is illustrated for **4** in Fig. 2*b*. The Te-S-P angles in **2** and **4** of 103.49(7)° and 102.7(4)°, respectively, are slightly smaller than in **1**, resulting in smaller S(1)-Te(1)—S(2) bite angles of 79.43(5)° and 80.4(2)°, respectively, and S(1)—S(2) bite lengths of 3.862(2) and 3.91(1) Å, respectively. As with **1**, the P—S(Te) bonds are longer, 2.045(7) Å for **1**, 2.047(2) Å for **2**, and 2.05(1) Å for **4**, than those of the aniso *P*=S—(Te) bonds, 1.962(3) for **1**, 1.964(2) Å for **2**, and 1.97(1) Å for **4**.

The weak intramolecular Te—S interactions, which range from 3.345(8) to 3.527(6) Å in **1**, **2**, and **4**, are of the same magnitude as in $Ph_3Te[(SPPh_2)_2N]$, 3.331–3.655 Å (19). The short and long tellurium–sulfur distances correspond with long and short phosphorus–sulfur bonds, which are typical for P—S single and P=S double bonds (P—S (avg.) 2.047(5) Å, P=S (avg.) 1.965(4) Å); cf. $MeS\text{-}PPh_2\text{=}N\text{-}Ph_2P\text{=}S$:[5] P—S 2.069(3) Å, P=S 1.9563(3) Å). Consequently, the phosphorus–nitrogen bond lengths are also different, corresponding to P=N double and P—N single bonds (P=N (avg.) 1.563(17) Å, P—N (avg.) 1.615(13) Å); cf. $MeS\text{-}PPh_2\text{=}N\text{-}Ph_2P\text{=}S$:[5] P=N 1.568(4) Å, P—N 1.610(4) Å). As expected, the PNP unit in the dithioimidodiphosphinato ligands is angular and the magnitude of the P-N-P angle, which ranges from 129(1)° in **1**, to 139.1(3)° in **2**, is consistent with the high flexibility of the SPNPS fragment. The resulting TeS_2P_2N rings display different conformations (Table 5). Thus in **1**, both six-membered rings may be discussed in terms of a boat with a variable degree of distortion (Fig. 3*a*, *b*), while in both halo derivatives the TeS_2P_2N rings are folded along the S(1)—-S(2) axis (Fig. 3*c*, *d*) as was found in the $Ph_3Te[(SPPh_2)_2N]$ derivative (Fig. 3*e*) (19). The TeS_2/S_2P_2N dihedral angle is 104.9° in **2**, 104.4° in **4**, and 114.4° in $Ph_3Te[(SPPh_2)_2N]$.

$Me_2TeCl[(OPPh_2)(SPPh_2)N]$, **6**, crystallizes in the space group $P2_1/c$ and the ORTEP diagram, Fig. 1*c*, illustrates that, as with **2** and **4**, the immediate environment about tellurium is the sawhorse structure with the chlorine atom now occupying one of the axial positions. However, in contrast to

[5] R. Rosler, C. Silvestru, and G. Espinosa-Oerez. Unpublished results.

© 1999 NRC Canada

Table 5. Torsion angles (°) for compounds **1**, **2**, **4**, and **6**, for comparison with those of Ph_3TeL and Ph_3TeL' where L = $[(SPPh_2)_2N]$ and L′ = $[(OPPh_2)(SPPh_2)N]$. [a–e]

	1 [a]	**2** [c]	**4** [c]	Ph_3TeL [c]		**6** [d]	Ph_3TeL' [e]
S(2)Te(1)S(1)P(1)	–14.0	61.1	59.5	37.7	S(1)Te(1)O(1)P(1)	44.5	6.8
Te(1)S(1)P(1)N(1)	67.7	–24.2	–21.9	13.1	Te(1)O(1)P(1)N(1)	5.9	0.1
Te(1)S(2)P(2)N(1)	24.9	50.6	47.6	71.2	Te(1)S(1)P(2)N(1)	47.9	65.1
S(1)P(1)N(1)P(2)	–90.7	–41.8	–49.8	–63.4	O(1)P(1)N(1)P(2)	–62.2	34.7
S(2)P(2)N(1)P(1)	26.4	12	18.9	3.4	S(1)P(2)N(1)P(1)	7.8	–88.3
S(1)Te(1)S(2)P(2)	–22.4	–77.1	–78.0	68.3	O(1)Te(1)S(2)P(2)	–65.8	–29.5
	1 [b]						
S(4)Te(1)S(3)P(3)	–25.7						
Te(1)S(3)P(3)N(2)	74.5						
Te(1)S(4)P(4)N(2)	47.2						
S(3)P(3)N(2)P(4)	–58.0						
S(4)P(4)N(2)P(3)	–20.8						
S(3)Te(1)S(4)P(4)	–18.3						

[a]In **1**, one ring is a boat with S(2) and P(1) on vertices.

[b]In **1**, the second ring is a twisted boat with S(4) and P(3) on vertices.

[c]In **2**, **4**, and $Ph_3Te[(SPPh_2)_2N]$ the ring is folded about the S(1)—-S(2) axis.

[d]In **6** the ring is folded about the O(1)—-S(1) axis.

[e]In $Ph_3Te[(OPPh_2)(SPPh_2)N]$ the ring is folded about the N(1)—-S(1) axis.

the halo-dithioimidodiphosphinato derivatives and any other related monothio derivatives such as the $Me_2TeX[SCONEt_2]$ (31) and $Me_2TeX[SCO_2R]$ series (32), the oxygen atom in **6** forms the primary bond in the axial position to give a Cl(1)-Te(1)-O(1) angle of 168.9(4)° with the sulfur atom forming a Te—S aniso-bond. This is also contrary to what was observed in $Ph_3Te[(OPPh_2)(SPPh_2)N]$ where neither chalcogen forms a short bond. However, it is consistent with the generally weaker Te—S bonds in the $Me_2TeX[(SPPh_2)_2N]$ species and the lack of a *trans* influence. The Te—O distance of 2.14(2) Å is similar to the lengths of the primary Te—O bonds in $Ph_2Te(O_2CCH_3)_2$ (2.160 Å) (33) and $Ph_2Te(O_2CCCl_3)_2$ (2.156 Å) (34). The Te—Cl bond (2.464(8) Å) is clearly not longer than in Me_2TeCl_2 (2.51(4) Å), confirming that the imidodiphosphinato ligands are demonstrating different behavior from other monothio derivatives because the Te—Cl bonds in $Me_2TeCl[SCONEt_2]$ and $Me_2TeCl[SCO_2Me]$ are considerably longer at 2.792(2) and 2.703(3) Å, respectively.

When the relatively long Te(1)—S(1) aniso-bond (3.413(7) Å) is included in the coordination sphere it gives rise to the same distorted square pyramidal arrangement about tellurium as was found with **2** and **4** (see Fig. 2*c*). The primary coordination of $(OPPh_2)(SPPh_2)N$ through oxygen is consistent with the length of the P(1)—O(1) bond (1.56(1) Å), which is typical for a single P—O bond, whereas the P(2)—S(1) bond length (1.973(8) Å) is similar to that of the aniso-bonded sulfur atom in **1**, **2**, and **4**, and is typical for a P=S bond (cf. $PPh_2(=S)OMe$ (35): P—O 1.60(2) Å; $(OPPh_2)(SPPh_2)NH$ (23): P=O (avg.) 1.503(16), P=S (avg.) 1.925(14) Å; $Na(OPPh_2)(SPPh_2)N$ (36): P=O 1.494(7), P=S 1.979(4) Å). Again, the different phosphorus–nitrogen bond lengths are consistent with P=N double and P—N single bonds (P(1)=N(1) 1.56(2) Å, P(2)—N(1) 1.64(2) Å); cf. $MeS\text{-}PPh_2{=}N\text{-}Ph_2P{=}S$:[5] P=N 1.568(4), P—N 1.610(4) Å). The conformation of the $TeOSP_2N$ ring is similar to those displayed by the $Me_2TeX[(SPPh_2)_2N]$ derivatives (Table 5) being folded along the O(1)—-S(1) axis (Fig. 3*f*), but quite different from that observed for $Ph_3Te[(OPPh_2)(SPPh_2)N]$ where the ring is folded about the N(1)—-S(1) axis (Fig. 3*g*). This behavior again confirms the high flexibility of the XPNPY fragment in this class of ligands.

Nuclear magnetic resonance spectra

The ^1H, ^{13}C, ^{31}P, and ^{125}Te NMR spectra presented in the experimental section are assigned based on the spectra taken as quickly as possible immediately after dissolving the compounds in $CDCl_3$. For **1**, **2**, **4**, and **6** the integration of the peaks in the ^1H NMR spectra confirms the presence of the assigned compound in solution and the absence of other peaks indicates greater than 99% purity relative to other H-containing species. The integration also confirms the presence of **3**, **5**, **7**, and **8**, the overlap with the toluene peaks being somewhat limited. In general, the quality of the ^{31}P and ^{125}Te NMR spectra was much poorer for **3**, **5**, **7**, and **8**. In the ^1H NMR spectra, all of the derivatives show a sharp peak attributable to the methyl group attached to tellurium, and the C*H*$_3$-Te chemical shift of 2.42 ppm in $Me_2Te[(SPPh_2)_2N]_2$, **1**, is close to the values observed for Me_2TeL_2 species, where L = $S_2P(OPh)_2$ (18) (2.40 ppm), S_2CNR_2 (15, 17) (2.46–2.49 ppm), and S_2COR (2) (2.52–2.55 ppm), but somewhat lower than for S_2POGO (18) (2.68–2.69 ppm for G = CMe_2CMe_2, CHMeCHMe, $CH_2CMe_2CH_2$, and $CH_2CEt_2CH_2$) all of which have anisobidentate ligands, with short and long Te—S distances similar to those in **1**. The chemical shifts of the $Me_2TeX[(SPPh_2)_2N]$ species **2**–**4** range from 2.72 to 2.77 ppm, which is a similar range to those observed for the Me_2TeXL species, where L = S_2CNR_2 (15, 17) (2.75–2.81 ppm) and S_2COR (28) (2.79–2.87 ppm). By contrast with the chemical shift of **1**, that of $Me_2Te[(OPPh_2)(SPPh_2)N]_2$, **5**, is 2.69 ppm, putting it near the range of many partially halogenated species. But for the exception of the $Me_2Te[S_2POGO]_2$ species, it would be reasonable to suggest that this reflects the fact that, in contrast to **1** and the

© 1999 NRC Canada

Fig. 3. The conformations of the TeS_2P_2N and $TeOSP_2N$ rings in (*a*) and (*b*) $Me_2Te[(SPPh_2)_2N]_2$, **1**, (*c*) $Me_2TeCl[(SPPh_2)_2N]$, **2**, (*d*) $Me_2TeI[(SPPh_2)_2N]$, **4**, and (*f*) $Me_2TeCl[(OPPh_2)(SPPh_2)N]$, **6**, with those of (*e*) $Ph_3Te[(SPPh_2)_2N]$ and (*g*) $Ph_3Te[(OPPh_2)(SPPh_2)N]$ for comparison.

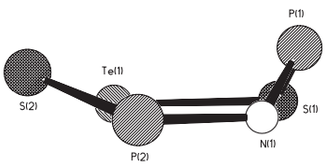

(a)

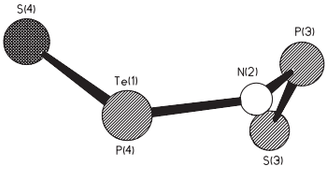

(b)

$Me_2Te[(SPPh_2)_2N]_2$ (1)

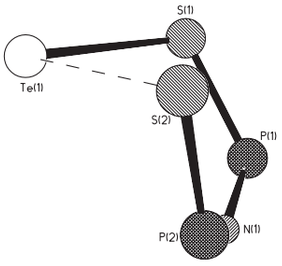

(c)

$Me_2TeCl[(SPPh_2)_2N]$ (2)

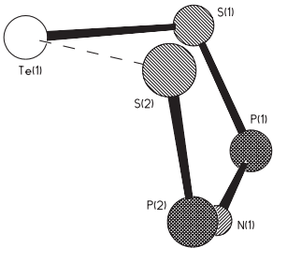

(d)

$Me_2TeI[(SPPh_2)_2N]$ (4)

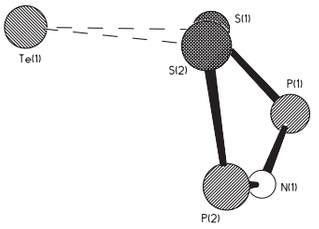

(e)

$Ph_3Te[(SPPh_2)_2N]$

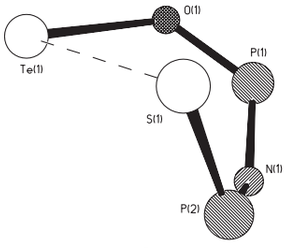

(f)

$Me_2TeCl[(OPPh_2)(SPPh_2)N]$ (6)

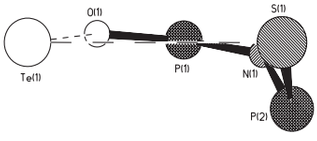

(g)

$Ph_3Te[(OPPh_2)(SPPh_2)N]$

other Me_2TeL_2 species, the primary bond may well be with the more electronegative oxygen atom, as it is in the solid state structure of **6**. In other related monothio derivatives such as $Me_2Te[SCONR_2]_2$ (31) and $Me_2Te[SCO_2R]_2$ (32),

© 1999 NRC Canada

where the primary bond is Te—S, the chemical shifts are again closer to 2.42, at ca. 2.45 and 2.57 ppm, respectively. The ^{125}Te–^{1}H coupling, with *J*(TeH) ca. 26-29 Hz, is observed in the spectra of the $(SPPh_2)_2N$ derivatives but not in those of $(OPPh_2)(SPPh_2)N$. The peaks in the phenyl region of the spectra are similar to those found for other tetraphenyldichalcogenoimidodiphospinato derivatives, but are more poorly resolved.

In the ^{13}C NMR spectra of the Me_2TeL_2 species, the *C*H_3-Te chemical shifts are ca. 14.8, 15.1, 15.5, 17.0, and 19.2 ppm, respectively, for L = $SCONR_2$, SCO_2R, S_2COR, S_2CNR_2, and S_2POGO, respectively. The values of 22.03 and 25.80 ppm for **1** and **5** appear to be an extension to the series. The corresponding Me_2TeXL series range from ca. 18.9 to 16.9, 20.0 to 17.3, 21.4 to 18.0, and 20.7 to 18.2 for L = $SCONR_2$, SCO_2R, S_2COR, and S_2CNR_2, respectively, as X goes from Cl to I, so, relatively, the range of shifts in **2–4** and **6–8** of 26.00 for **6** to 20.74 for **4** is as might be expected. The peaks in the phenyl region of the spectrum are similar to those found for other tetraphenyldichalcogenoimidodiphospinato derivatives (19, 20, 23, 36) but are again more poorly resolved so that the phosphorus–carbon coupling was ill defined and the *ipso* carbon signals were not observed. The chemical shifts for C_m, C_p, and C_o are similar in $Me_2Te[(OPPh_2)(SPPh_2)N]_2$ and the $Me_2TeX[(OPPh_2)(SPPh_2)N]$ series to those reported for $Me_2Sn[(OPPh_2)(SPPh_2)N]_2$ (36) in which the imidodiphosphinate groups are clearly bidentate, but are much broader than in the tin analogue. The chemical shifts differ from those in $Ph_3Te[(OPPh_2)(SPPh_2)N]$ (20) in which there are no short Te—S or Te—O bonds. The ^{31}P NMR signals were not always of good quality, presumably at least in part because of decomposition. The chemical shift for Ph_2PO is quite close to that of $Me_2Sn[(OPPh_2)(SPPh_2)N]_2$ (δ_P 20.0) but the shift for Ph_2PS is in general closer to that of $Me_3Sn[(OPPh_2)(SPPh_2)N]$ (δ_P 39.7) (36). The values of the ^{125}Te NMR chemical shifts cover similar ranges to those of the previously studied Me_2TeL_2 and Me_2TeXL species, as exemplified by the $Me_2TeX[S_2CO(i\text{-}Pr)]$ series where δ_{Te} ranges from 577 to 525 for X = Cl and I, respectively, compared to 580 for **6** to 525 for **8**. The resonance for **6** is shielded by 38 ppm relative to that for **2**. In contrast, the resonance for **5** is slightly deshielded relative to that for **1**, suggesting that in **5** the diphosphinates might be S-bonded rather than O-bonded.

Concluding comments

This study was initiated to examine the differences that might result from the use of more flexible ligands with the potential for a wide range of bite lengths and angles in the formation of Me_2TeL_2 and Me_2TeXL species as compared to the many dithio and monothio ligands that we had studied previously. Despite the flexibility for both L = $(SPPh_2)_2N$ and $(OPPh_2)(SPPh_2)N$, the ligands are still anisobidentate. However, the bite angles and lengths are larger so that, although the Te—S aniso bonds are still long (avg. 3.40(7) Å), the angles about Te are less distorted. In previous studies with Me_2TeXL dithio derivatives, there was a marked "*trans* influence" in the shortening of the Te—X bond and lengthening of the Te—S bond but no such effect was observed in this study. With $Me_2TeCl[(OPPh_2)(SPPh_2)N]$, the primary bond is Te—O rather than Te—S, which is contrary to what has been observed in related monothio derivatives such as $Me_2TeX[SCONEt_2]$ (31) and $Me_2TeX[SCO_2R]$ (32), where Te—S is the primary bond.

Acknowledgements

We wish to thank the Natural Sciences and Engineering Research Council of Canada for financial support (J.E.D, R.J.D, J.Y.); the financial support offered by the Romanian Academy and the Romanian National Council for University Scientific Research (CNCSU) is also warmly acknowledged by A.S.

References

1. I. Haiduc, R.B. King, and M.G. Newton. Chem. Rev. **94**, 301 (1994).
2. J.H.E. Bailey, J.E. Drake, L.N. Khasrou, and J. Yang. Inorg. Chem. **34**, 124 (1995).
3. M. Wieber, E. Schmidt, and C. Burschka. Z. Anorg. Allg. Chem. **525**, 127 (1985).
4. A.K. Singh, J.K. Basumatary, T.P. Singh, and B. Padmanabhan. J. Organomet. Chem. **424**, 33 (1993).
5. S. Husebye, K. Maartmann-Moe, and O. Mikalsen. Acta Chem. Scand. **44**, 464 (1990).
6. D. Dakternieks, R. Di Giacomo, R.W. Gable, and B.F. Hoskins. J. Am. Chem. Soc. **110**, 6753 (1988).
7. A.K. Singh and J.K. Basumatary. J. Organomet. Chem. **364**, 73 (1989).
8. D. Dakternieks, R. Di Giacomo, R.W. Gable, and B.F. Hoskins. J. Am. Chem. Soc. **110**, 6762 (1988).
9. D. Dakternieks, R. Di Giacomo, R.W. Gable, and B.F. Hoskins. J. Organomet. Chem. **349**, 305 (1988).
10. J.H.E. Bailey, J.E. Drake, A.B. Sarkar, and M.L.Y. Wong. Can. J. Chem. **67**, 1735 (1989).
11. J.H.E. Bailey, J.E. Drake, and M.L.Y. Wong. Can. J. Chem. **69**, 1948 (1991).
12. J.E. Drake and M.L.Y. Wong. J. Organomet. Chem. **377**, 43 (1989).
13. S. Husebye, K. Maartmann-Moe, and W. Steffenson. Acta Chem. Scand. **44**, 139 (1990).
14. S. Husebye, K. Maartmann-Moe, and W. Steffenson. Acta Chem. Scand. **44**, 579 (1990).
15. J.H.E. Bailey and J.E. Drake. Can. J. Chem. **71**, 42 (1993).
16. T.N. Srivastava, R.C. Srivastava, and A. Bhargava. Indian J. Chem. Sect. A: Inorg. Phys. Theor. Anal. **18A**, 236 (1979).
17. J.E. Drake and J. Yang. Inorg. Chem. **36**, 1890 (1997).
18. J.E. Drake, L.N. Khasrou, A.G. Mislankar, and R. Ratnani. Can. J. Chem. **72**, 1328 (1994).
19. A. Silvestru, I. Haiduc, R.A. Toscano, and H.J. Breunig. Polyhedron, **14**, 2047 (1995).
20. J.E. Drake, A. Silvestru, J.Yang, and I. Haiduc. Inorg. Chim. Acta, **271**, 75 (1998).
21. R.C. Paul, K.K. Bhasin, and R.K. Chadha. J. Inorg. Nucl. Chem. **37**, 2337 (1975).
22. R. Rosler, C. Silvestru, I. Haiduc, M. Gielen, F. Kayser, and B. Mahieu. Main Group Metal Chem. **16**, 435 (1993).
23. J. Yang, J.E. Drake, S. Hernandez-Ortega, R. Rosler, and C. Silvestru. Polyhedron, **16**,4061 (1997).
24. G.M. Sheldrick. Acta Crystallogr. Sect. A: Found. Crystallogr. **A46**, 467 (1990).

© 1999 NRC Canada

25. TEXSAN-TEXRAY structure analysis package; Molecular Structure Corp., The Woodlands, Tex. 1985.
26. L. Pauling. J. Am. Chem. Soc. **69**, 542 (1947); *In* The nature of the chemical bond. 3rd ed. Cornell University Press, Ithaca, N.Y. 1960. p. 255.
27. I.D. Brown. Acta Crystallogr. Sect. B: Struct. Crystallogr. Cryst. Chem. **B33**, 1305 (1977).
28. J.E. Drake, R.J. Drake, L.N. Khasrou, and R. Ratnani. Inorg. Chem. **35**, 2831 (1996).
29. G.D. Christofferson, R.A. Sparks, and J.D. McCullough. Acta Crystallogr. **11**, 782 (1958).
30. G.D. Christofferson and J.D. McCullough. Acta Crystallogr. **11**, 249 (1958).
31. J.E. Drake, L.N. Khasrou, A.G. Mislankar, and R. Ratnani. Inorg. Chem. **33**, 6154 (1994).
32. J.E. Drake, R.J. Drake, L.N. Khasrou, A.G. Mislankar, R. Ratnani, and J. Yang. Can. J. Chem. **74**, 1968 (1996).
33. N.W. Alcock, W.D. Harrison, and C. Howes J. Chem. Soc. Dalton Trans. 1709 (1984).
34. N.W. Alcock, J. Culver, and S.M. Ross. J. Chem. Soc. Dalton Trans. 1477 (1992).
35. G. Lepicard, D. de Saint-Ginez-Liebig, A. Laurent, and C. Rerat. Acta Crystallogr. Sect. B: Struct. Crystallogr. Cryst. Chem. **B25**, 617 (1969).
36. R. Rosler, J.E. Drake, C. Silvestru, J. Yang, and I. Haiduc. J. Chem. Soc. Dalton Trans. 391 (1996).

© 1999 NRC Canada

Computational study on small water clusters using a semiempirical valence bond approach

Youliang Wang and John R. Gunn

Abstract: Small clusters of water $(H_2O)_n$, $n = 3$–8, are studied using a semiempirical valence bond approach to investigate the bonding energy contribution and hydrogen-bonding structure in the most stable conformation. The energy contribution was decomposed into electron pair–pair interactions and valence-bond energy for each water monomer. Our study shows that there is significant bonding difference between small clusters ($n \leq 5$) of water and larger clusters ($n > 5$). In the larger clusters, there are structures containing tetravalent oxygen centers, which is impossible in the small clusters. The contribution to the binding energy from each H-bond varies from −4.7 kcal/mol to −7.3 kcal/mol in the water clusters considered here. The contribution of −5.9 kcal/mol per H-bond in the cubic octamer is comparable to the experimental value (−6.7 kcal/mol) of the binding energy in ice.

Key words: semi-empirical, valence bond, hydrogen bonding, water clusters.

Résumé: On a étudié des petits agrégats d'eau $(H_2O)_n$, $n = 3$–8, en utilisant une méthode semi-empirique de liaison de valence afin d'évaluer les contributions à l'énergie des liaisons et de la disposition des ponts hydrogène dans les structures les plus stables. L'énergie a été décortiquée en énergie de liaison des doublets et interaction entre doublets pour chaque monomère. Notre étude démontre qu'il y a une différence significative entre les plus petits ($n \leq 5$) et les plus grands ($n > 5$) agrégats d'eau. Dans ce dernier cas, il existe des atomes d'oxygène liés à quatre hydrogènes, ce qui est impossible dans les petits agrégats. La contribution à l'énergie due à chaque pont hydrogène varie de −4,7 kcal/mol jusqu'à −7,3 kcal/mol dans les agrégats considérés ici. La contribution de −5,9 kcal/mol par pont hydrogène dans l'octamère cubique se compare avec la valeur expérimentale de −6,7 kcal/mol pour l'énergie de liaison dans la glace.

Mots clés: semi-empirique, liaison de valence, pont hydrogène, agrégats d'eau.

1. Introduction

Small clusters of water molecules are of great interest due to the importance of water as a universal solvent. An understanding of the water–water interactions is fundamental to the problems of solvation and hydration in chemistry, ice structures in physics, and enzymatic mechanisms and protein and RNA folding in biology. The structural properties and cooperative effects of intermolecular interactions have also been studied in the case of small neutral water clusters $(H_2O)_n$ ($n = 2$–6) (1–4), where the magnitudes of the two- through six-body energy terms and their contribution to the interaction energy have been calculated at various levels of theory. Hydrogen-bonded water complexes $H^+(H_2O)_n$ ($n = 2$–6) have been used as models to study the mechanism of proton transport through biological membranes (5–9). It is known that the potential energy surface (PES) is extremely flat and anharmonic along the motion of the proton in both the dimer and trimer, which may be adequately described with the treatment of electron correlation at the second-order Møller–Plesset perturbation (MP2) level (10,11). However, it is unrealistic to carry out a dynamics calculation at that level due to the computational expense.

Water–water effective pair potentials have been widely used for liquid water simulations. In the model "Transferable Intermolecular Potential" functions (TIPS2, TIP3P, TIP4P) by Jorgensen et al. (12), the water–water interaction energy is calculated from the electrostatic energy between the point charges on the atoms and a Lennard–Jones (LJ) interaction between oxygen atoms, based on the experimental H_2O geometry. In the model of "Empirical Potential using Electrons and Nuclei" (EPEN) by Scheraga and co-workers (13), the empirical potential was developed by the charge distribution of their pair potentials, which involves the nuclei of oxygen and hydrogen, the binding electron pairs and the lone pairs. A number of researchers have derived potential schemes based on ab initio calculations, such as the MCY potentials (14), and ASP (for anisotropic potential) (15).

Most of those potentials are based directly on simple physical models rather than on principles of chemical bonding. High-level ab initio calculations (MP2 and density functional (DFT) with large basis sets including basis-set superposition error (BSSE) correction) are also making it more and more difficult to relate energies to qualitative ideas about chemical bonding. It is necessary to explore the conceptual interpretations that allow for the development of a corresponding chemical intuition. It was Pauling (16) who first gave a proper description of the structures of water and water clusters based on valence bond (VB) theory, introducing the hybridization and hydrogen bond concepts. Classical valence bond theory

Received June 22, 1998.

Y. Wang and J.R. Gunn.[1] Département de Chimie, Université de Montréal, C.P. 6128, Succursale Centre-Ville, Montréal, QC H3C 3J7, Canada and Centre de Recherche en Calcul Appliqué, 5160 Boulevard Décarie, Bureau 400, Montréal, QC H3X 2H9, Canada.

[1] Corresponding author: **Telephone:** (514) 343-7636; **FAX:** (514) 343-7586; **e-mail:** gunnj@cerca.umontreal.ca

© 1999 NRC Canada

is very successful in providing a qualitative explanation for many aspects. Chemists are familiar with the localized molecular orbitals and the classical VB resonance concepts. When modern accurate wave functions are represented in terms of such well-known concepts, chemical intuition and experience can be given a firm theoretical basis.

Most theoretical structural studies have been based on ab initio calculations but these have been limited, especially for large clusters where such calculations are very demanding. Both empirical potential and ab initio calculations (1–4, 17–25), as well as far-infrared spectroscopic results (26–28) have indicated that the trimer, tetramer, and pentamer have the cyclic structure as the most stable structure. However, the water hexamer is much harder to characterize since a large number of nearly isoenergetic minima are too close for the most stable structure to be definitely determined theoretically. A recent combined experimental and theoretical study (far-infrared and diffusion Monte Carlo, respectively) has identified a "cage" structure. Based on the ASP potential, a diffusion quantum Monte Carlo calculation by Gregory and Clary (29) has confirmed that a noncyclic cagelike structure is the most stable for the hexamer due to a relatively low zero-point energy (ZPE). Their calculation gave similar results for the 3D prismatic structure, which is also found to be the absolute minimum in the extended MP2 analysis on the water hexamer of Tsai and Jordan (30). The cagelike structure is consistent with the far-infrared spectrum, which shows a prolate symmetric top and has been used (31) to extract geometrical parameters for the structure of Gregory and Clary. However, a recent DFT calculation by Estrin et al. (32) reported that the optimized 3D prismlike structure is lower by 1.4 kcal/mol than the energy of the cyclic structure when no corrections are applied. The zero-point energy correction is larger than the value for the cyclic structure, and by including the BSSE correction, the energy is -38.0 kcal/mol (D_0) compared to -39.8 kcal/mol (D_0) for the chairlike geometry, in contradiction to the results of other theoretical methods. Although the ZPE correction is clearly important in resolving the exact energy differences among these structures, it has not been calculated in the present work. The contribution of the ZPE to the cluster binding energies is largely due to the intermolecular (H-bond) modes, which are notoriously flat and anharmonic. For this reason, an estimate using harmonic normal modes would not be appropriate and a thorough sampling of the energy surface is required. This is beyond the scope of the present work, and the results presented here will therefore be compared with classical potential minima whenever possible.

It has been observed that the O—O distances decrease as the number of water molecules increases in the cyclic structures, in agreement with experiment, giving values of 2.84, 2.80, and 2.76 Å for the trimer, tetramer, and pentamer, respectively (31). As expected, different binding energies result from different methods for the clusters ($n = 2$–8). For instance, for the water cyclic hexamer, the plane-wave-DFT simulation yields $D_0 = -45.5$ kcal/mol and the Hartree–Fock (HF) $D_0 = -20.6$ kcal/mol, to be compared with $D_0 = -39.9$ kcal/mol from DFT–PP (Perdew–Perdew gradient-corrected exchange-correlation functional) (32).

Due to the inconsistent results for the binding energy and stable structures of the larger water clusters, it is of interest to investigate the structural characteristics from the viewpoint of the chemical bonds. To study the characteristic features in the different conformations, we derive a semiempirical valence bond method for water clusters based on LMP2/6-31G** (localized MP2 with the 6-31G** Gaussian basis set) calculations and investigate the individual contributions from each electron pair, especially from the H-bonds, contributed from each water monomer. This will also be useful in establishing the principles that underly the formation of different types of structures, thereby determining guidelines for predicting the likely minima for larger clusters. This would also greatly simplify the search for the global minimum by reducing the number of possibilities that need to be considered.

Section 2 briefly outlines the computational method. The benchmark calculation results and discussion of the water trimer are given in Sect. 3. Section 4 presents the results and discussion for the water tetramer, pentamer, hexamer, and octamer. The conclusions are given in Sect. 5.

2. Computational method

A semiempirical scheme for generalized valence bond (GVB) calculations of large systems has been proposed, based on a GVB wave function and fitted to high-level ab initio potential energy surfaces. Although the details of this methodology have been given previously (33), it is useful to give a brief description of the basic features of the VB wave function, energy decomposition, and semiempirical evaluation formula.

2.1. Valence bond wave function

With the assumption that each atom has only *s* and *p* atomic orbitals in its valence shell, a set of four hybrid atomic orbitals is generated based on the local geometry. The assigned hybrid orbitals are oriented along the internuclear vectors, forming σ bonds, and the hybrid orbitals on each atom are related to one another by orthonormality.

The GVB wave function for an A–B bond is thus constructed directly from two atomic hybrid orbitals ϕ_A and ϕ_B,

$$[1] \quad \psi_{AB} = [\sigma_1(\phi_A\phi_B + \phi_B\phi_A) + \sigma_2\phi_A\phi_A + \sigma_3\phi_B\phi_B](\alpha\beta - \beta\alpha)$$

where each term corresponds to the electronic structures A–B, $A^- B^+$, and $A^+ B^-$, respectively, with the coefficients (σ_i, $i = 1, 3$) being determined variationally by solving a 3×3 secular matrix equation.

In general, this VB wave function for a three-body fragment A–X–B is

$$[2] \quad \psi_{A-X-B} = \mathcal{A}[\psi_{A-X}\psi_{B-X}]$$

©1999 NRC Canada

which is a multiconfiguration form. Typically for a three-center four-electron hydrogen bond system, for instance, $[F–H–F]^-$, our VB wave function has a total of 6 degrees of freedom with 9 configurations, as compared to 2 degrees of freedom with 3 configurations in the extended valence bond (EVB) model (34,35). In addition, our VB wave function has a strong orthogonality restriction imposed as in the GVB–PP (perfect pairing) wave function (36). However, with more degrees of freedom in determining configurations in our procedure, only the configuration coefficients are variationally determined, as opposed to optimizing both the starting orbitals and configuration coefficients, resulting in a substantial cut in the computing time.

2.2. Energy components

For a closed-shell system, the seGVB total energy is calculated by summing the valence-bond energies over all pairs of electrons and the interactions between the different pairs of electrons. The general expression for the seGVB total energy is therefore

$$[3] \qquad E = E_{\mathrm{nr}} + \sum_{\mu} E_{\mu} + \sum_{\mu<\nu} E_{\mu\nu}$$

where E_μ is the GVB pair energy for each electron pair (bonding or lone pair), $E_{\mu\nu}$ the interaction between the different pairs of electrons, and E_{nr} the internuclear repulsion. The energy contributed by a specific electron pair μ can be calculated by the sum of its GVB pair energy E_μ and its interactions with all other pairs of electrons,

$$[4] \qquad E'_{\mu} = E_{\mu} + \sum_{\nu} E_{\mu\nu}$$

where E'_μ is the quantity that is variationally minimized.

The advantages of this energy expression are (i) the transferability of a valence bond can be used to compute the energy for large systems; (ii) a distance cutoff can be employed in evaluating the pair–pair interactions to substantially decrease the computing time; and (iii) the characteristic change in the potential energy surface in conformational changes and reactions can be easily analyzed. The first two advantages have been used in other VB or similar methods (35, 37). For the third, many energy decomposition schemes (38) have been applied to hydrogen-bonded systems. Virtually all decompose the total energy into components such as Coulomb interaction, polarization, exchange repulsion, charge transfer, and electron density deformation. The method of localized charge distributions has been used to analyze the localized MP2 pair energies for the hydrogen bond in the water dimer (39). The energy form used in our scheme is rather different in that it highlights the characteristic contribution from each pair of electrons.

In this study of water clusters, the following energy terms have been defined. The total bonding energy of each water monomer (e.g., monomer 1) in clusters was calculated as $\sum_{\mu\in \mathrm{O1}} E_\mu$, which is the bonding energy of the four pairs of electrons of each oxygen in the water cluster. The total pair–pair interaction energy between water monomers in a cluster was calculated as $\sum_{\mu\in \mathrm{O1},\nu\in \mathrm{O2}} E_{\mu\nu}$. The total binding energy is defined as $\Delta E = E[(H_2O)_n] - nE[H_2O]$.

2.3. Semiempirical evaluation and parameterization

The calculation of the Hamiltonian in the secular equation is based on the evaluation of the one-center and two-center energy integrals. The one-center energy integrals (h_{AA}, J_{AA}) are calculated using similar formulae to those in AM1 (40,41) and PM3 (42). The functional forms for evaluating two-center energy integrals and overlap integrals used in our previous work (33) have been modified for a better description of the angular dependence. Defining $\boldsymbol{\mu}_\mathrm{A}$ and $\boldsymbol{\mu}_\mathrm{B}$ as unit vectors in the direction of the major lobes of each hybrid orbital in an A–B bond and $\boldsymbol{R}_{\mathrm{AB}}$ as the separation vector between centers A and B, the two-center energy integrals can be generally expressed as

$$[5] \qquad T_{\mathrm{AB}} = F(n_\mathrm{A}, n_\mathrm{B}, \boldsymbol{\mu}_\mathrm{A}, \boldsymbol{\mu}_\mathrm{B}, \boldsymbol{R}_{\mathrm{AB}})$$

where n_A and n_B are used to quantify the hybridization of sp^n-type orbitals. This function can be simplified by using the angles θ_A, θ_B, and θ_{AB} with the definition that $\cos\theta_\mathrm{A} = \cos\theta_\mathrm{B} = \cos\theta_{\mathrm{AB}} = 1$ for "head-to-head" σ bonding, such that

$$[6] \qquad T_{\mathrm{AB}} = F_1(n_\mathrm{A}, n_\mathrm{B}, \cos\theta_\mathrm{A}, \cos\theta_\mathrm{B}, \cos\theta_{\mathrm{AB}}) F_2(R_{\mathrm{AB}})$$

Therefore, the approximation formulae for two-center energy integrals and overlap integrals are

$$[7] \qquad h_{\mathrm{AB}} = \frac{\alpha^{ss}_{\mathrm{AB}} + \sqrt{n_\mathrm{A}}\cos\theta_\mathrm{A}\alpha^{ps}_{\mathrm{AB}} + \sqrt{n_\mathrm{B}}\cos\theta_B\alpha^{sp}_{\mathrm{AB}} + \sqrt{n_\mathrm{A}n_\mathrm{B}}\cos\theta_{\mathrm{AB}}\alpha^{pp}_{\mathrm{AB}}}{1 + \sqrt{n_\mathrm{A}} + \sqrt{n_\mathrm{B}} + \sqrt{n_\mathrm{A}n_\mathrm{B}}} f_1(R_{\mathrm{AB}})$$

$$[8] \qquad J_{\mathrm{AB}} = \frac{\beta^{ss}_{\mathrm{AB}} + n_\mathrm{A}\cos^2\theta_\mathrm{A}\beta^{ps}_{\mathrm{AB}} + n_\mathrm{B}\cos^2\theta_\mathrm{B}\beta^{sp}_{\mathrm{AB}} + n_\mathrm{A}n_\mathrm{B}\cos^2\theta_{\mathrm{AB}}\beta^{pp}_{\mathrm{AB}}}{1 + n_\mathrm{A} + n_\mathrm{B} + n_\mathrm{A}n_\mathrm{B}} \left(f_2(R_{\mathrm{AB}}) + C_{-1}\frac{1}{R_{\mathrm{AB}}} \right)$$

©1999 NRC Canada

$$[9] \quad K_{AB} = \frac{\gamma_{AB}^{ss} + n_A \cos^2\theta_B \gamma_{AB}^{ps} + n_B \cos^2\theta_B \gamma_{AB}^{sp} + n_A n_B \cos^2\theta_{AB} \gamma_{AB}^{pp}}{1 + n_A + n_B + n_A n_B} f_3(R_{AB})$$

$$[10] \quad S_{AB} = \frac{S_{AB}^{ss} + \sqrt{n_A}\cos\theta_A S_{AB}^{ps} + \sqrt{n_B}\cos\theta_B S_{AB}^{sp} + \sqrt{n_A n_B}\cos\theta_{AB} S_{AB}^{pp}}{1 + \sqrt{n_A} + \sqrt{n_B} + \sqrt{n_A n_B}} f_4(R_{AB})$$

The function $f(R_{AB})$ is

$$f(R_{AB}) = e^{-\zeta_{AB} R_{AB}} (c_0 + c_1 R_{AB} + c_2 R_{AB}^2 + \cdots + c_5 R_{AB}^5)$$

The bonding orbital exponent ζ_{AB} in the expression for $f(R_{AB})$ is defined as

$$[11] \quad \zeta_{A-B} = \frac{\zeta_{AB}^{ss} + \sqrt{n_A}\cos\theta_B \zeta_{AB}^{ps} + \sqrt{n_B}\cos\theta_B \zeta_{AB}^{sp} + \sqrt{n_A n_B}\cos\theta_{AB} \zeta_{AB}^{pp}}{1 + \sqrt{n_A} + \sqrt{n_B} + \sqrt{n_A n_B}}$$

The parameters α_{AB}, β_{AB}, γ_{AB}, S_{AB}, and ζ_{AB} are obtained by fitting to model ab initio calculations, for instance, LMP2/6-31G** calculations in most cases due to the vast amount of available data and their reliability.

In our work, the model ab initio calculations at the LMP2/6-31G** level were carried out using the PSGVB (43) programs. Due to the BSSE in ab initio calculations of the total energy for complexes, the interaction energy with counterpoise corrections is the target to be fit by our seGVB parameterization.

3. Benchmark calculations of water trimer

The seGVB potential energy functions are evaluated based on their ability to reproduce the LMP2/6-31G** geometries and energies for the water monomer and dimer. The parameters that have been given in an earlier paper (33) are used here for calculating the water clusters. In this section, the results and discussion of the benchmark calculations of the water trimer are given.

There have been a number of previous ab initio theoretical studies on the water trimer. Notably, the early studies by Clementi and co-workers (44) had already established a cyclic structure as the global minimum; in the minimum energy structure one O—H bond from each monomer contributes to a hydrogen bond to form a nearly equilateral triangle, with the other O—H bond remaining free. Two of the free O—H bonds are above the O–O–O plane, the third below, i.e., (uud). Mó et al. (18) recently investigated the PES over a wide range of configurations at the MP4 level. In addition to the cyclic minimum, the linear water chain can be considered as a model for the study of proton transfer along a proton wire and in the study of the binding energy for water clusters (33).

As a benchmark calculation, we analyzed the energy contributions in seGVB calculations for four different typical structures of water trimer, which are labeled as linear I, linear II, cyclic I, and cyclic II as shown in Fig. 1. H_2O has the experimental geometry, and each H-bond distance is 1.95 Å.

To simplify the analysis, each of the valence bond electron pairs can be described as one of four types: free O—H bonds (OH); free lone pairs (LP); and hydrogen bonds, which consist of an O—H donor (OH-D) and a lone pair acceptor (LP-A). Each water monomer thus comprises two pairs of type OH or OH-D and two pairs of type LP or LP-A, giving a total of nine distinct molecule types. These can be labeled as hydrogen-bond donors (D) and acceptors (A), as well as the combinations AA, DA, DD, DAA, and DDA. The remaining two possibilities correspond to free and bulk configurations.

Fig. 1. The equilibrium structures of water trimers. (*a*) Linear I; (*b*) linear II; (*c*) cyclic I; (*d*) cyclic II.

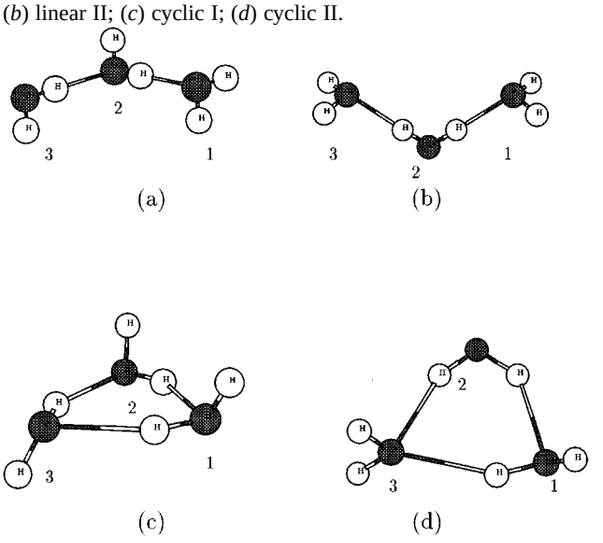

The electron-pair binding energies are shown in Table 1 for each of the trimers, listed according to pair type. These terms represent the two-electron VB energy levels. The total binding energies for each monomer are given in Table 2, along with the intra- and inter-molecular pair–pair repulsion energies. These are the sums of the two-pair terms, $\sum_{\mu,\nu} E_{\mu\nu}$, for all μ and ν on the same center in the case of intramolecular repulsions,

©1999 NRC Canada

and for all μ on one center and all ν on a second center, as described in Sect. 2.2, in the case of intermolecular repulsions.

The results clearly show the direct effects of the formation of a hydrogen bond. The energies of the interacting pairs, OH-D and LP-A, are lower than the corresponding OH and LP energies. In addition, the intramolecular pair repulsion energies are lower in both the donor and acceptor due to the delocalization of electron density into the bonding region. This effect is greater for the acceptor because the lone pairs represent the dominant contribution to the repulsions. For an isolated water molecule, this term is 5.44 a.u., which indicates that the effects of the hydrogen bond are very nearly additive, roughly 0.35 and 0.95 a.u. for the donor and acceptor, respectively. Larger clusters also give values for the DDA and DAA monomers that follow the same trend.

There is a significant difference, however, between the total binding energies of the donor and acceptor molecules. For the donor, the difference with respect to an isolated water molecule, which has a binding energy of −30.711 161 a.u., is 0.317 529 a.u., which is entirely due to the difference between the OH and OH-D pairs. For the acceptor, on the other hand, the energies of all VB pairs are lowered with respect to an isolated molecule. In fact, the energy of an OH pair in an H-bond acceptor is actually lower than that of an OH-D. This suggests that the effect of the polarization of the acceptor by the shared hydrogen is more important than the contribution of the bonds that are directly involved. The linear I trimer was constructed with monomers of types A, DA, and D forming two hydrogen bonds that are held to be perfectly linear with an O—O distance of 2.907 Å. Although this structure collapses readily to the cyclic structure described below, it is an important benchmark for describing cumulative hydrogen bonds. The binding energy for this trimer structure is −12.2 kcal/mol, or −6.1 kcal/mol per H-bond. At the same geometry, the sum of the binding energies for two isolated H-bonded dimers is −8.8 kcal/mol, showing that the nonadditive energy contribution due to the cooperative effect is −3.4 kcal/mol in the trimer. Again, this is due to the increased polarization of the central molecule.

The linear II structure with three monomers of types A, DD, and A forming two hydrogen bonds, as shown in Fig. 1 (*b*), is different from the linear I structure in that monomer 2 of type DD maintains two O—H bonds and two lone pairs as in H_2O, while it is connected to monomer 1 of type A and monomer 3 of type A through H-bonds. Despite the difference in connectivity, the individual VB pairs are virtually the same as in the linear I structure, with the only difference being between the terminal and central LP-A pairs, the latter being absent in the linear II case. The binding energy is virtually the same, −12.0 kcal/mol, or −6.0 kcal/mol per H-bond, giving a nonadditive contribution of −3.2 kcal/mol. The dominant feature of both linear structures is the presence of two different acceptor molecules.

The other possible linear structure, with a D, AA, D connectivity, would be expected to be much higher in energy because even though there are the same number of H-bonds, there is only one (double) acceptor molecule and, therefore, fewer pairs next to the LP-A pairs, which are themselves neighbors. In fact, this structure is not even a local minimum with respect to the cyclic II structure, which is itself higher in energy than the other linear structures despite the presence of a third H-bond. The preference for accepting rather than donating hydrogen bonds can be understood in terms of the nucleophilicity of water, which is known to be greater than its electrophilicity (18). The fact that structures with multiple acceptors are less stable than those with multiple donors does not contradict this principle — monomers which are multiple acceptors are indeed lower in energy. However, the underlying driving force is to maximize the total number of acceptor *molecules* and, since the total number of acceptor and donor *sites* are necessarily equal, this leads to a preference for single acceptors and multiple donors rather than the inverse.

The most stable structure for water trimer is the cyclic I structure with three monomers of type DA forming three hydrogen bonds. In this structure, each water monomer of type DA is connected to the two others, acting as both an H-bond donor and acceptor. With one more H-bond formed in the cyclic structure, the binding energy becomes −15.0 kcal/mol, or −5.0 kcal/mol per H-bond. As compared to the linear structures, the stability of each H-bond is actually decreased due to the increase in the pair–pair interaction as the calculated results of VB energy decomposition indicated; however, this cost is offset by the addition of the third hydrogen bond. The pair–pair repulsion in this case is simply a reflection of the nonlinearity of the H-bonds; while the OH–D and LP–A distances remain the same, the two oxygen centers are closer together along with all other electron pairs that do not participate in the H-bond. The advantage of having a third acceptor molecule is partially offset by the increased intermolecular repulsions due to the confined geometry. The linear is therefore not the stable equilibrium structure, and will go instead to the cyclic structure through a transition state as calculated by Mó et al. (18) on the full potential energy surface.

In the cyclic II structure with three monomers of types DA, DD, and AA forming three hydrogen bonds, monomer 2 of type DD maintains two O—H bonds and two lone pairs as in H_2O. This structure is energetically not as stable as the cyclic I, even though they both have three H-bonds. Our results give a binding energy of −11.9 kcal/mol, or −4.0 kcal/mol per H-bond. In comparing the two cyclic structures, the large difference is clearly seen to be due to the presence of only two acceptor molecules instead of three. Although the LP-A energies are lower in the AA molecule, giving it the lowest binding energy (−34.413 207), this can only partially compensate for the higher pair energies in the DD molecule that lose the secondary stabilization.

No experimental indications of the trimer binding energy have been reported so far although the cyclic structure has been confirmed experimentally (26). For the stable cyclic structure, the most recent high-level ab initio calculations give a binding energy of −12.71 kcal/mol (DFT with ZPE and BSSE correction) (44), −16.6 kcal/mol (MP2), −11.2 kcal/mol(MP2 with

©1999 NRC Canada

Table 1. The decomposition of monomer valance bond energies in the water trimer. Pair types are shown with the monomer number in parentheses, and the energies are shown with the molecule types in parentheses. The monomers are labeled as shown in Fig. 1. See the text for an explanation of the symbols. All values are in atomic units.

Electron pair type	Linear I		Linear II		Cyclic I		Cyclic II	
OH (1)	−8.498960	(A)	−8.508532	(A)	−8.504674	(DA)	−8.505480	(DA)
OH (1)	−8.515868	(A)	−8.508523	(A)				
OH (2)	−8.515868	(DA)			−8.504674	(DA)		
OH (3)	−8.041411	(D)	−8.508532	(A)	−8.504674	(DA)	−8.969018	(AA)
OH (3)			−8.508523	(A)			−8.969018	(AA)
OH-D (1)					−8.905106	(DA)	−9.071871	(DA)
OH-D (2)	−8.806915	(DA)	−8.358430	(DD)	−8.905106	(DA)	−8.448058	(DD, to 1)
OH-D (2)			−8.358430	(DD)			−8.620816	(DD, to 3)
OH-D (3)	−8.358940	(D)			−8.905106	(DA)		
LP (1)	−7.819290	(A)	−7.819290	(A)	−7.819290	(DA)	−7.819290	(DA)
LP (2)	−7.819290	(DA)	−7.314170	(DD)	−7.819290	(DA)	−7.314170	(DD)
LP (2)			−7.314170	(DD)			−7.314170	(DD)
LP (3)	−7.314170	(D)	−7.819290	(A)	−7.819290	(DA)		
LP (3)	−7.314170	(D)						
LP-A (1)	−8.129834	(A)	−7.939164	(A)	−8.226248	(DA)	−8.016565	(DA)
LP-A (2)	−7.936819	(DA)			−8.226248	(DA)		
LP-A (3)			−7.939164	(A)	−8.226248	(DA)	−8.545622	(AA, to 1)
LP-A (3)							−8.344555	(AA, to 2)

ZPE and BSSE correction) (22), and −10.8 kcal/mol (MP4 with ZPE and BSSE correction) (18).

4. Results and discussion

Our benchmark calculations of the water trimer are not only in good agreement with the previous high-level calculations, but also allow the electronic structure to be interpreted in terms of the stability and interactions of individual chemical bonds. Based on these results, this investigation can now be extended to larger water clusters. In this study, some typical structures of water tetramer, pentamer, hexamer, and octamer have been considered, with the goal of studying the relationship between bonding structure and energy. H_2O has the experimental geometry, and each H-bond distance is 1.95 Å.

4.1. Water tetramer

It is known that the cyclic water tetramer is the most stable structure, with shorter H-bonds than in the trimer (27). Four water tetramer structures were calculated in this work: the linear and three different cyclic structures as studied earlier by Clementi et al. (1). These structures are illustrated in Fig. 2.

The energy decomposition (Table 3) shows that the same valence-bond energies observed for the trimer are generally transferable to the tetramer. The linear structure contains four monomers of types A, DA, DA, and D forming three hydrogen bonds, analogous to the trimer. The total bonding energies for monomers 1, 3, and 4 are virtually the same as those of monomers 1, 2, and 3 in the trimer, respectively. The difference arises for monomer 2 in the tetramer, which, although still of type DA, has another DA as a donor rather than a D as is the

Fig. 2. The equilibrium structures of water tetramers. (*a*) Linear; (*b*) cyclic I; (*c*) cyclic II; (*d*) cyclic III.

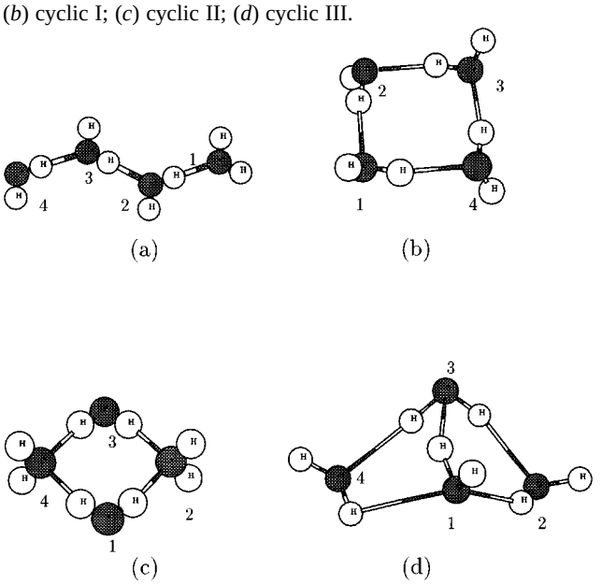

case for monomer 3. The calculated binding energy for the linear tetramer is −20.4 kcal/mol, or −6.8 kcal/mol per H-bond, with a cooperative effect of −8.2 kcal/mol. Compared to the linear I trimer, the fourth water monomer stabilizes the cluster by 0.7 kcal/mol per H-bond. The average H-bond strength has been increased in going to the linear tetramer from the linear trimer, due to the cumulation of the H-bonds.

The most stable structure is the cyclic I structure with four

©1999 NRC Canada

Table 2. The energy contribution in atomic units from the VB calculation of the water trimer. The monomers are labeled as shown in Fig. 1, with the molecule types given in parentheses. See the text for the definitions of each term. Values are in atomic units unless specified otherwise.

	Linear I	Linear II	Cyclic I	Cyclic II
Monomer binding energy				
1	−32.963952 (A)	−32.775518 (A)	−33.455118 (DA)	−33.413207 (DA)
2	−33.078892 (DA)	−31.345199 (DD)	−33.455118 (DA)	−31.697213 (DD)
3	−31.028690 (D)	−32.775518 (A)	−33.455118 (DA)	−34.413207 (AA)
Monomer pair repulsion				
1	4.443088 (A)	4.442156 (A)	4.152690 (DA)	4.148141 (DA)
2	4.128324 (DA)	4.748604 (DD)	4.152690 (DA)	4.745021 (DD)
3	5.095836 (D)	4.442156 (A)	4.152690 (DA)	3.496646 (AA)
Intermolecular pair repulsion				
1–2	1.723773	1.639209	1.810095	1.721415
1–3	0.187832	0.233908	1.807606	1.929947
2–3	1.636343	1.639209	1.807634	1.725326
Binding energy				
ΔE (kcal/mol)	−12.2	−12.0	−15.0	−11.9

Table 3. The energy contribution in atomic units from the VB calculation of the water tetramer. The monomers are labeled as shown in Fig. 2, with the molecule types given in parentheses. See the text for the definitions of each term. Values are in atomic units unless specified otherwise.

	Linear	Cyclic I	Cyclic II	Cyclic III
Monomer binding energy				
1	−32.963868 (A)	−33.347651 (DA)	−31.713705 (DD)	−35.057571 (DAA)
2	−33.271733 (DA)	−33.347651 (DA)	−34.679140 (AA)	−33.600405 (DA)
3	−33.078720 (DA)	−33.347651 (DA)	−31.713705 (DD)	−33.962712 (DDA)
4	−31.028604 (D)	−33.347651 (DA)	−34.679140 (AA)	−33.540809 (DA)
Total pair repulsion				
	23.257391	24.402744	23.965614	25.007106
Binding energy				
ΔE (kcal/mol)	−20.4	−23.9	−20.6	−21.2

monomers of type DA forming four hydrogen bonds, as shown in Fig. 2(*b*). In this form, each water monomer is connected to two others through H-bonds as in the cyclic I trimer, acting as both an H-bond donor and acceptor. As in the trimer, the individual H-bonds are weaker than in the linear structures, but there is an overall stabilization due to the additional H-bond. The calculated binding energy is −23.9 kcal/mol, or −6.0 kcal/mol per H-bond. Compared to the cyclic I trimer, the fourth water monomer stabilizes the cluster by 1.0 kcal/mol per H-bond. The cyclic structure also benefits from reduced repulsion in a more relaxed geometry.

The cyclic II structure, as shown in Fig. 2 (*c*), has two monomers of type AA and two of type DD. As is the case in the trimer, the energy of the LP pairs of the donors is higher, and is not completely compensated by the adjacent LP-A pairs of the acceptors. Although the total number of H-bonds is the same as in cyclic I, the total bonding energy is smaller. The calculated binding energy is −20.6 kcal/mol, or −5.2 kcal/mol per H-bond.

The cyclic III structure with four monomers of types DAA, DA, DDA, and DA forms five hydrogen bonds, as shown in Fig. 2 (*d*). The formation of an additional H-bond lowers the monomer energies relative to the cyclic I structure, since each monomer is still at least a single acceptor, and the DAA monomer 1 has the lowest monomer energy of any structure. However, the pair repulsion is also increased, and in particular the nuclear repulsion is higher due to the central hydrogen. The resulting binding energy is −21.2 kcal/mol, or −4.2 kcal/mol per H-bond. The higher coordination of the DAA and DDA monomers in this case leads to a strained geometry; however, as is the case with the cyclic structures, this would be expected to be more favorable in a larger cluster.

HF, MP2, and DFT calculations all give similar cyclic structures as the equilibrium conformation. The binding energy varies from −24.6 to −29.1 kcal/mol (44). With BSSE and ZPE correction, MP2 gives a binding energy of −16.1 kcal/mol. There is no experimental binding energy value to compare with. The energy spread reported in the literature for the tetramer shows that the binding energy is very sensitive to the level of theory.

4.2. Water pentamer

The most stable pentamer is cyclic (28). The results for the cyclic and linear (Fig. 3) pentamers are listed in Table 4. For the linear structure as shown in Fig. 3 (*a*), the binding energy is −27.2 kcal/mol, or −6.8 kcal/mol per H-bond, which is similar

©1999 NRC Canada

Table 4. The energy contribution in atomic units from the VB calculation of the water pentamer. The monomers are labeled as shown in Fig. 3, with the molecule types given in parentheses. See the text for the definitions of each term. Values are in atomic units unless specified otherwise.

	Linear	Cyclic
Monomer binding energy		
1	−32.963868 (A)	−33.304688 (DA)
2	−33.271733 (DA)	−33.304688 (DA)
3	−33.271733 (DA)	−33.304688 (DA)
4	−33.078720 (DA)	−33.304688 (DA)
5	−31.028604 (D)	−33.304688 (DA)
Total pair repulsion		
	29.251156	30.630271
Binding energy		
ΔE (kcal/mol)	−27.2	−33.7

Fig. 3. The equilibrium structures of water pentamers. (*a*) Linear; (*b*) cyclic.

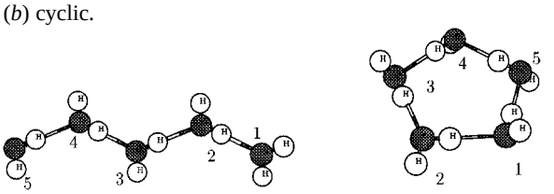

(a) (b)

Fig. 4. The equilibrium structures of water hexamers. (*a*) Linear; (*b*) cyclic; (*c*) prism; (*d*) book.

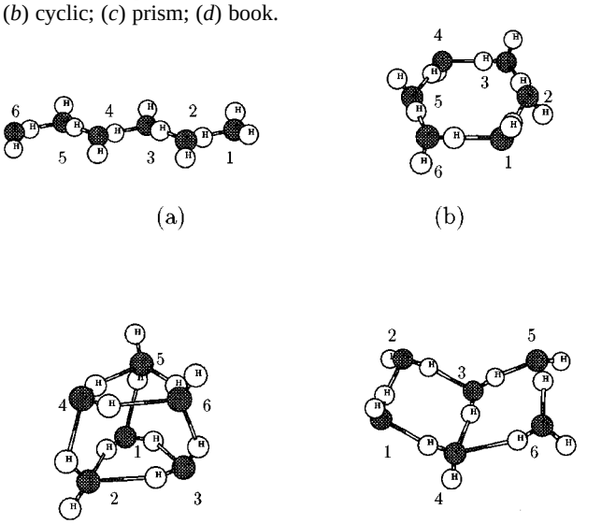

(a) (b) (c) (d)

to that in the linear tetramer. For the cyclic structure with five monomers of type DA forming five hydrogen bonds, as shown in Fig. 3 (*b*), the calculated binding energy is −33.7 kcal/mol or −6.7 kcal/mol per H-bond. Compared with the cyclic tetramer, the fifth water stabilizes the cluster by 0.7 kcal/mol per H-bond. The H-bond strength has been substantially increased in the five-water cyclic structure from the four-water cyclic structure. The nearly identical values for the H-bond energies in the linear and cyclic structures indicates that the ring strain is minimal in this case and that the H-bond geometries are nearly optimal.

Although many other types of structures have been calculated, none has been found so far to have a lower energy than the cyclic structure. This includes structures having a triply H-bonded monomer, consistent with our above observation that this type of bonding will lead to a twisted structure that will only be stable in a larger, more relaxed system.

4.3. Water hexamer

The water hexamer has served as a prototype for analyzing the bonding in ice. It is well known that there exist a number of distinct and almost isoenergetic structures for the hexamer based on a number of theoretical studies. This cluster is particularly interesting because it represents the transition between two- and three-dimensional H-bonding networks with a near trade-off between the additional energy of new H-bonds and the repulsion associated with the geometrical strain and nonlinearity. Four different characteristic structures are investigated in this work: the linear, cyclic, prism, and book structures as shown in Fig. 4. The analysis of VB energy decomposition are listed in Table 5.

For the linear structure in Fig. 4 (*a*), the binding energy is −35.2 kcal/mol, or −7.0 kcal/mol per H-bond. Compared with the linear pentamer, the sixth water stabilizes the cluster by 0.2 kcal/mol H-bond. The binding energy is −41.0 kcal/mol for the cyclic structure as shown in Fig. 4 (*b*), or −6.8 kcal/mol per H-bond. Compared with the cyclic pentamer, the sixth water stabilizes the cluster by 0.1 kcal/mol per H-bond. This structure consists of six nearly equivalent DA monomers, with H-bond energies approaching those of the linear chain, indicating minimal strain as in the case of the pentamer.

©1999 NRC Canada

Table 5. The energy contribution in atomic units from the VB calculation of the water hexamer. The monomers are labeled as shown in Fig. 4, with the molecule types given in parentheses. See the text for the definitions of each term. Values are in atomic units unless specified otherwise.

	Linear	Cyclic	Prism	Book
Monomer binding energy				
1	−32.963868 (A)	−33.714636 (DA)	−34.020033 (DDA)	−33.961987 (DA)
2	−33.271733 (DA)	−33.770287 (DA)	−35.440289 (DAA)	−33.786636 (DA)
3	−33.271733 (DA)	−33.733174 (DA)	−34.140269 (DDA)	−34.404830 (DDA)
4	−33.271733 (DA)	−33.733589 (DA)	−34.421124 (DDA)	−35.605611 (DAA)
5	−33.078720 (DA)	−33.854997 (DA)	−35.605136 (DAA)	−33.775722 (DA)
6	−31.028604 (D)	−33.736858 (DA)	−35.200174 (DAA)	−33.813066 (DA)
Total pair repulsion				
	35.244965	37.747424	41.105215	39.400281
Binding energy				
ΔE (kcal/mol)	−35.2	−41.0	−42.6	−39.3

The book structure shown in Fig. 4 (*d*) adds one additional H-bond with the creation of a bridgehead pair of DDA and DAA monomers. As expected, these monomers have a greater bonding energy (the double acceptor in particular); however, this is offset by the additional repulsion caused by a more compact geometry. The binding energy is −39.3 kcal/mol, or −5.6 kcal/mol per H-bond.

The prism structure shown in Fig. 4 (*c*) consists of all DDA and DAA monomers, with a total of nine H-bonds. The repulsion is again increased, but in this case the marginal cost is less than the benefit of the added H-bonds. The value of the binding energy drops to −4.7 kcal/mol; however, the total of −42.6 kcal/mol surpasses that of the cyclic structure. The intermediate case, with two DA, two DAA, two DDA monomers, and a total of eight H-bonds, corresponds to the cage structure proposed by Gregory and Clary (29), which they found to be intermediate in energy between the book and prism forms. Their conclusion that the cage structure would be the ground state was based on a detailed calculation of the zero-point energy using diffusion Monte Carlo (DMC) with an empirical potential surface. Such effects are clearly important when the differences in energy minima are so small; however, this calculation was not carried out in the present work in which the goal is to reproduce the underlying potential energy surface with the seGVB calculation.

There is a large spread in the binding energies for the hexamer as reported in the literature. MP2 calculations for the cyclic and prism structures, respectively, give $D_e = -47.4$ and −46.1 kcal/mol (29) and $D_e = -39.8$ and −40.2 kcal/mol (30). The corresponding DFT-PP values are $D_e = -52.0$ and −52.4 kcal/mol (32), and the ASP results are $D_e = -45.8$ and −50.2 kcal/mol (29). Our results are in relatively good agreement with the MP2 calculations, as would be expected since MP2 results for the dimer were used in the parameterization. Estimates of the ZPE correction, for the cyclic and prism structures, respectively, range from 17.6 and 17.0 kcal/mol from the DMC simulations to 14.4 and 12.1 kcal/mol from harmonic analysis of the DFT-PP frequencies.

Fig. 5. The equilibrium structures of water octamers. (*a*) Linear; (*b*) cubic D_2d; (*c*) cubic S_4.

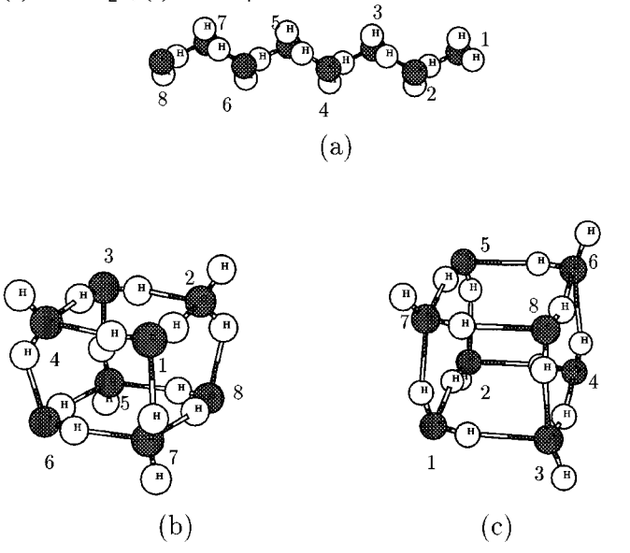

4.4. Water octamer

We have investigated three structures of the water octamer: one linear and two cubic structures, of D_{2d} and S_4 symmetry, as shown in Fig. 5 and listed in Table 6. The binding energy for the linear octamer is −51.0 kcal/mol, or −7.3 kcal/mol per H-bond.

For the D_{2d} and S_4 structures, four monomers are of type DDA and four others of type DAA. The sum of the binding energies for monomers of type DDA (−34.350 144 a.u. for D_{2d} and −34.345 135 a.u. for S_4) is smaller than that for monomers of type DAA (−35.560615 a.u. for D_{2d} and −35.477 311 a.u. for S_4), respectively, as would be expected. Both cubic structures have 12 hydrogen bonds, with very similar binding energies of −70.4 and −71.1 kcal/mol, respectively, or −5.9 kcal/mol per H-bond. Since the valence bond structure is the same in both cases, the small difference is likely due to struc-

©1999 NRC Canada

Table 6. The energy contribution in atomic units from the VB calculation of the water octamer. The monomers are labeled as shown in Fig. 5, with the molecule types given in parentheses. See the text for the definitions of each term. Values are in atomic units unless specified otherwise.

	Linear	Cubic S_4	Cubic D_{2d}
Monomer binding energy			
1	−32.963868 (A)	−34.350144 (DDA)	−34.345135 (DDA)
2	−33.271733 (DA)	−35.560615 (DAA)	−35.477311 (DAA)
3	−33.271733 (DA)	−35.574924 (DAA)	−34.366937 (DDA)
4	−33.271733 (DA)	−34.340470 (DDA)	−35.446727 (DAA)
5	−33.271733 (DA)	−34.304567 (DDA)	−35.489770 (DAA)
6	−33.271733 (DA)	−35.579963 (DAA)	−34.379159 (DDA)
7	−33.078720 (DA)	−35.557189 (DAA)	−35.500625 (DAA)
8	−31.028604 (D)	−34.385913 (DDA)	−34.336845 (DDA)
Total pair repulsion			
	47.232582	57.304378	57.464885
Binding energy			
ΔE (kcal/mol)	−51.0	−71.1	−70.4

tural relaxation and reduced repulsion in the lower symmetry structure.

The binding energy varies from −59 to −70 kcal/mol in ab initio HF, MP2, and DFT calculations. The energy contribution of −5.9 kcal/mol from each H-bond in the cubic octamer is of the order of the experimental value (−6.7 kcal/mol) of the binding energy in ice (45).

5. Conclusions

Based on the valence bond calculations, several basic principles emerge that determine the structures and relative energies of small water clusters. The energy of a hydrogen bond is largely determined by the polarization of the acceptor by the donor. For this reason small clusters form cyclic structures in which the hydrogen bonds are aligned with each molecule acting as both donor and acceptor, and structures with multiple donors and acceptors are less favorable. There is also a nonadditive energy due to the fact that the charge transfer that occurs in hydrogen bonding is stabilized by the presence of other molecules. This has the effect of increasing the effective acidity or basicity of molecules that are already hydrogen bonded, as observed by Mó et al. (18). There is also a secondary next-nearest-neighbour effect, which favours "head-to-tail" H-bonding patterns.

In larger clusters, more hydrogen bonds can be formed by creating polycyclic structures; however, the individual bonds are weaker. Again, structures with each molecule acting as both donor and acceptor are favored in order to maximize the nonadditive energy. Because the polycyclic structures have a higher electronic and nuclear repulsion, only structures with a high connectivity (prism, cube) will be lower in energy than the cyclic structures, although the energy differences are often quite small.

Although water clusters generally maximize the number of hydrogen bonds, because of the polarization effects the energy of each bond depends strongly on the geometry and pattern of connectivity. In the systems studied here, the contribution to the binding energy from each H-bond varies from −4.7 to −7.3 kcal/mol. The contribution of −5.9 kcal/mol per H-bond in the cubic octamer can be compared to the experimental value (−6.7 kcal/mol) of the binding energy in ice.

Acknowledgements

This work was funded by grants from the Natural Sciences and Engineering Research Council of Canada (NSERC) and the Fonds pour la formation de chercheurs et l'aide à la recherche (Québec).

References

1. K.S. Kim, M. Dupuis, C.C. Lie, and E. Clementi. Chem. Phys. Lett. **131**, 451 (1986).
2. J.G.C.M. van Duijneveldt-van de Rijdt and F.B. van Duijneveldt. Chem. Phys. **175**, 271 (1993).
3. S.S. Xantheas. J. Chem. Phys. **100**, 7523 (1994).
4. J.H. Jensen and M.S. Gordon. J. Phys. Chem. **99**, 8091 (1995).
5. K. Luth and S. Scheiner. J. Chem. Phys. **97**, 7507 (1992).
6. D. Wei and D.R. Salahub. J. Chem. Phys. **101**, 7633 (1994).
7. G. Corongiu, R. Kelterbaum, and E. Kochanski. J. Phys. Chem. **99**, 8038 (1995).
8. H.-P. Cheng, R.N. Barnett, and U. Landman. Chem. Phys. Lett. **180**, 161 (1995).
9. R. Pomes and B. Roux. J. Chem. Phys. **100**, 2519 (1996).
10. S.S. Xantheas and T.H. Dunning, Jr. J. Chem. Phys. **99**, 8774 (1993).
11. T. Komatsuzaki and I. Ohmine. Chem. Phys. **180**, 239 (1994).
12. W.L. Jorgensen. J. Am. Chem. Soc. **103**, 335 (1981); J. Chem. Phys. **77**, 4156 (1982); W.L. Jorgensen, J. Chandrasekhar, J.W. Madura, R.W. Impey, and M.L. Klein. J. Chem. Phys. **79**, 926 (1983).
13. J.C. Owicki, L.L. Shipman, and H.A. Scheraga. J. Phys. Chem. **79**, 1794 (1975); J. Snir, R.A. Nemenoff, and H.A. Scheraga. J. Phys. Chem. **82**, 2497 (1978).
14. O. Matsuoka, E. Clementi, and M. Yoshimine. J. Chem. Phys. **64**, 1351 (1976).

©1999 NRC Canada

15. C. Millot and A.J. Stone. Mol. Phys. **77**, 439 (1992).
16. L. Pauling. Nature of the chemical bond. 3rd ed. Cornell University Press, Ithaca, N.Y. 1960.
17. R.O. Watts. Chem. Phys. **26**, 367 (1977).
18. O. Mó, M. Yáñez, and J. Elguero. J. Chem. Phys. **97**, 6628 (1992).
19. D.J. Wales and I. Ohmine. J. Chem. Phys. **98**, 7245 (1993).
20. S. Scheiner. Annu. Rev. Phys. Chem. **45**, 23 (1994) and references therein.
21. J.K. Gregory and D.C. Clary. J. Chem. Phys. **103**, 8924 (1995).
22. S.S. Xantheas. J. Chem. Phys. **102**, 4505 (1995).
23. K.A. Franken, M. Jalaie, and C.E. Dykstra. Chem. Phys. Lett. **198**, 59 (1992).
24. C.J. Tsai and K.D. Jordan. J. Chem. Phys. **95**, 3850 (1991).
25. C.J. Tsai and K.D. Jordan. J. Phys. Chem. **97**, 5208 (1993).
26. M.R. Viant, J.D. Cruzan, D.D. Lucas, M.G. Brown, K. Liu, and R.J. Saykally. J. Phys. Chem. **101**, 9032 (1997).
27. J.D. Cruzan, M. R. Viant, M. G. Brown, and R. J. Saykally. J. Phys. Chem. **101**, 9022 (1997).
28. K. Liu, M.G. Brown, J.D. Cruzan, and R.J. Saykally. J. Phys. Chem. **101**, 9011 (1997).
29. J.K. Gregory and D.C. Clary. J. Phys. Chem. **100**, 18014 (1996).
30. C.J. Tsai and K.D. Jordan. Chem. Phys. Lett. **213**, 181 (1993).
31. K. Liu, M.G. Brown, and R.J. Saykally. J. Phys. Chem. **101**, 8995 (1997).
32. D.A. Estrin, L. Paglieri, G. Corongiu, and E. Clementi. J. Phys. Chem. **100**, 8701 (1996).
33. Y. Wang and J.R. Gunn. J. Chem. Phys. **106**, 3248 (1997).
34. T. Wesolowski, R.P. Muller, and A. Warshel. J. Phys. Chem. **100**, 15444 (1996).
35. A. Warshel. Computer modeling of chemical reactions in enzymes and solutions. John Wiley, New York. 1991.
36. F.W. Bobrowicz and W.A. Goddard III. *In* Methods of electronic structure theory. *Edited by* H.F. Schaefer III. Plenum, New York. 1977. p. 79.
37. J.J.P. Stewart. Int. J. Quantum Chem. **58**, 133 (1996).
38. K. Morokuma. J. Chem. Phys. **55**, 1236 (1971).
39. J.H. Jensen and M.S. Gordon. J. Phys. Chem. **99**, 8091 (1995).
40. M.J.S. Dewar and N.L. Hojvat. J. Chem. Phys. **34**, 1232 (1961).
41. R.C. Bingham, M.J.S. Dewar, and D.H. Lo. J. Am. Chem. Soc. **97**, 1285 (1975).
42. J.J.P. Stewart. J. Comput. Chem. **10**, 209 (1989).
43. M.N. Ringnalda, J.-M. Langlois, B.H. Greeley, R.B. Murphy, T.V. Russo, C. Cortis, R.P. Muller, B. Marten, R.E. Donnelly, Jr., D.T. Mainz, J.R. Wright, W.T. Pollard, Y. Cao, Y. Won, G.H. Miller, W.A. Goddard III, and R.A. Friesner. PS-GVB v2.1, Schrodinger, Inc., Pasadena, Calif. 1995.
44. H. Kistenmacher, G.C. Lie, H. Popkie, and E. Clementi. J. Chem. Phys. **61**, 546 (1974).
45. D. Eisenbag and W. Kanzmann. The structure and properties of water. Clarendon, Oxford. 1969.

©1999 NRC Canada

Cyclic voltammetry of ferrocene-containing β-diketones as a tool to obtain group electronegativities. The structure of 3-ferrocenoyl-1,1,1-trifluoro-2-hydroxyprop-2-ene

W.C. (Ina) du Plessis, Johannes J.C. Erasmus, Gert J. Lamprecht, Jeanet Conradie, T. Stanley Cameron, Manuel A.S. Aquino, and Jannie C. Swarts

Abstract: Formal reduction potentials ($E^{\circ\prime}$ values vs. Ag/Ag^+ given in parentheses) in acetonitrile of 1-ferrocenyl-4,4,4-trifluorobutane-1,3-dione (ferrocenoyltrifluoroacetone, Hfctfa, 0.394 V), 1-ferrocenyl-4,4,4-trichlorobutane-1,3-dione (ferrocenoyltrichloroacetone, Hfctca, 0.370 V), 1-ferrocenylbutane-1,3-dione (ferrocenoylacetone, Hfca, 0.313 V), 1-ferrocenyl-3-phenylpropane-1,3-dione (benzoylferrocenoylmethane, Hbfcm, 0.306 V), and 1,3-diferrocenylpropane-1,3-dione (diferrocenoylmethane, Hdfcm, 0.265 and 0.374 V for the two electrochemically nonequivalent ferrocenyl groups) were determined. A linear relationship between observed group electronegativity, χ, and $E^{\circ\prime}$ as well as observed infrared carbonyl stretching frequencies of methyl esters of the type RCOOMe resulted in average χ-values, on the Gordy scale, of 1.87 for the ferrocenyl group and 2.82 for the ferrocenium group. A single crystal X-ray structure determination of Hfctfa (monoclinic, $P2_1/n$, $Z = 4$, $R = 0.029$) showed that this β-diketone crystallizes in the enol form. Asymmetric enolization in a direction furthest from the aromatic ferrocenyl group was observed.

Key words: ferrocene, β-diketone, group electronegativity, cyclic voltammetry.

Résumé : On a déterminé les potentiels de réduction formelle (valeurs de $E^{\circ\prime}$ en fonction de Ag/Ag^+ données entre parenthèses), dans l'acétonitrile, des 1-ferrocényl-4,4,4-trifluorobutane-1,3-dione (ferrocényltrifluoroacétone, Hfctfa, 0,394 V), 1-ferrocényl-4,4,4-trichlorobutane-1,3-dione (ferrocényltrichloroacétone, Hfctca, 0,370 V), 1-ferrocénylbutane-1,3-dione (ferrocénylacétone, Hfca, 0,313 V), 1-ferrocényl-3-phéhylpropane-1,3-dione (benzoylferrocénylméthane, Hbfcm, 0,306 V) et 1,3-diferrocénylpropane-1,3-dione (diferrocénylméthane, Hdfcm, 0,265 et 0,374 V respectivement pour les deux groupes ferrocényles électrochimiquement non équivalents). On a observé une relation linéaire entre l'électronégativité des groupes, χ, et $E^{\circ\prime}$ ainsi qu'avec les fréquences d'élongation du carbonyle observées dans l'infrarouge pour les esters méthyliques du type RCOOMe; sur l'échelle de Gordy, les valeurs moyennes de χ seraient respectivement 1,82 pour le groupe ferrocényle et 2,82 pour le groupe ferrocénium. On a déterminé la structure cristalline du Hfcta par diffraction des rayons X (monoclinique $P2_1/n$, $Z = 4$, $R = 0,029$); elle montre que cette β-dicétone cristallise sous la forme énolique. On observe une énolisation asymétrique dans la direction opposée au groupe ferrocényle aromatique.

Mots clés : ferrocène, β-dicétone, électronégativité d'un groupe, volvampérométrie cyclique.

[Traduit par la Rédaction]

Introduction

β-Diketones may exist in equilibrium with two possible enol isomers according to eq. [1].

[1] $$R'C(OH)=CHCOR \rightleftharpoons R'COCH_2COR \rightleftharpoons R'COCH=C(OH)R$$

Two driving forces that will determine the preferred enol isomer were recently (1) defined. The first is labelled an electronic driving force in which the formation of the preferred enol isomer is controlled by the group electronegativity of the substituents R and R′ on the β-diketone $R'COCH_2COR$. Regarding the keto isomer (eq. [1]), when the group electronegativity of R′ is less than that of R, the

Received October 14, 1998.

W.C. (Ina) du Plessis, J.J.C. Erasmus, G.J. Lamprecht, J. Conradie, and J.C. Swarts.[1] Department of Chemistry, University of the Orange Free State, Bloemfontein, 9300, Republic of South Africa.
T.S. Cameron. Department of Chemistry, Dalhousie University, Halifax, NS B3H 4J3, Canada.
M.A.S. Aquino. Department of Chemistry, St. Francis Xavier University, P.O. Box 5000, Antigonish, NS B2G 2W5, Canada.

[1]Author to whom correspondence may be addressed. Telephone: ++27-51-4012781. Fax: ++27-51-4307805.
e-mail: swartsjc@cem.nw.uovs.ac.za

© 1999 NRC Canada

Scheme 1. Claisen condensation of acetylferrocene (**1**) with appropriate esters to give β-diketones Hfctfa (**2**, R = CF_3), Hfctca (**3**, R = CCl_3), Hfca (**4**, R = CH_3), Hbfcm (**5**, R = phenyl), and Hdfcm (**6**, R = ferrocenyl). ^{1}H NMR studies indicated that asymmetric enolization as shown dominates. Aldol self-condensation of **1** leads to the side product **7**. The base used was either sodium ethoxide or lithium diisopropylamide. Abbreviations are defined in the abstract.

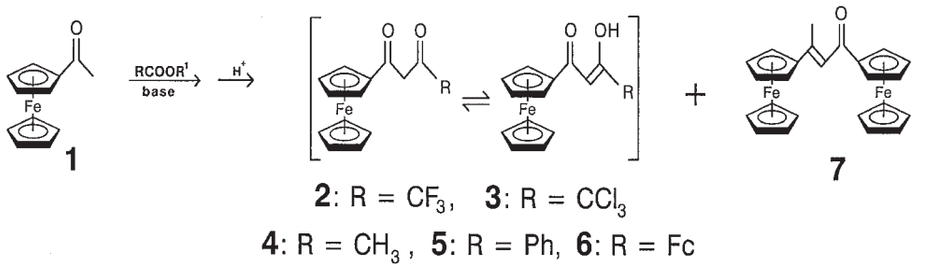

carbon atom of the carbonyl group adjacent to R′ will be less positive in character than the carbon atom of the other carbonyl group. Consequently, from an electronic point of view, the dominant enol isomer should be R′C(OH)=CHCOR. However, this driving force was not found to apply to β-diketones with R′ = ferrocenyl or phenyl. In a recent paper (1) we have shown that, in chloroform solutions, the only observable enol isomer of β-diketones of the type $FcCOCH_2COR$ (Fc = ferrocenyl, R = CF_3, CCl_3, CH_3 (Me), phenyl (Ph), and Fc) is FcCOCH=C(OH)R. In the same paper, apparent group electronegativities, χ, measured on the Gordy scale, for all R groups were obtained from a linear relationship between χ and apparent pK_a' determinations of the β-diketones and also from a linear relationship between χ and carbonyl IR stretching frequencies of esters of the type RCOOMe. The term "apparent pK_a'" is used because no distinction is made between the pK_a of enol and keto isomers. Rather, pK_a' refers to the acidic behaviour of the conjugated keto–enol system. The apparent group electronegativity, χ, of the ferrocenyl group was found to be lower than χ for all the indicated R substituents of $FcCOCH_2COR$. Hence, if the electronic driving force was dominant in this system, the expected enol isomer should be FcC(OH)=CHCOR and not the one found. Consequently, the existence of a second driving force, the resonance driving force, was defined. The resonance driving force implies that the formation of different canonical forms of a specific enol isomer will lower the energy of this specific isomer enough to allow it to dominate over the existence of other isomers. Indirect evidence for the canonical forms was from the crystal structure determination (2) of the enol form of Hfca, FcCOCH=C(OH)Me. However, the apparent Gordy group electronegativities of the ferrocenyl and methyl groups of Hfca are not that different (χ_{Fc} = 1.87 and χ_{Me} = 2.34). There is a need to demonstrate that the resonance driving force arguments put forward by us (1) are also valid for ferrocene-containing β-diketones in which the other β-diketone substituent, R, has a marked larger group electronegativity than that of the ferrocenyl group. Hfctfa, with R = CF_3, would be particularly suitable for this purpose because the CF_3 group has one of the largest group electronegativities known. However, there exists an uncertainty in the group electronegativity of the CF_3 group (estimated values vary between 3.01 (1) and 3.35 (3)) primarily because of the method of group electronegativity determination. With respect to ref. 1, this uncertainty is due to the uncertainty of the structure of CF_3-containing β-diketones (1) in basic aqueous solutions, which resulted in an unreliable apparent pK_a' for $FcCOCH_2COCF_3$. The CF_3 group electronegativity obtained from IR carbonyl measurements was more satisfactory, but still open to criticism since CF_3COOMe is too volatile for convenient experiments. Instead, the ethyl ester was used. This makes direct comparisons with the other methyl esters unsatisfactory. We now demonstrate that cyclic voltammetry can be used to determine accurate apparent group electronegativities, including that of the CF_3 group. From the crystal structure determination of $FcCOCH=C(OH)CF_3$ we conclude that the resonance driving force overrules the electronic driving force in determining the preferred enol isomer of β-diketones where different canonical forms lower the energy of a specific enol isomer even if group electronegativities are markedly in favour of the electronic driving force.

Results and discussion

Claisen condensation of acetylferrocene, **1**, with an appropriate ester according to the general procedure outlined in Scheme 1, gave the β-diketones Hfctfa, **2**, Hfctca, **3**, Hfca, **4**, Hbfcm, **5,** and Hdfcm, **6**. β-Diketones **2–6** exist in solution (1) predominantly as one enol tautomer. The aldol condensation product, **7**, was invariably isolated when lithium diisopropylamide was the base used to initiate Claisen condensation.

Cyclic voltammetry results are summarized in Table 1. The difference in peak anodic, E_{pa}, and peak cathodic, E_{pc}, potentials, ΔE_p, for all β-diketones indicates reasonable electrochemical reversibility: Electrochemical reversibility (4) of a one-electron process at 25°C is characterized by ΔE_p = 59 mV and is independent of scan speed. The biggest E_{pa} drift detected was 6 mV for E_{pa} of Hfctca when the scan rate was increased from 50 to 200 mV s^{-1}, but this did not influence $E^{o'}$. All $E^{o'}$ values remained constant between scan rates of 50 and 200 mV s^{-1} and indicate that the group electronegativities obtained from formal reduction potentials are independent of scan rates within the indicated range. The ratio i_{pc} / i_{pa} (i_{pc} and i_{pa} are the peak cathodic and anodic currents) was in all cases close to unity, implying that the electrochemical oxidation of the iron(II) nucleus of the ferrocenyl groups is not followed by a chemically induced reduction (5) of the Fe(III) nucleus of the ferrocenium group by the hydroxyl group of the enol form of the β-diketone, a reaction that has been observed in other ferrocenyl / hydroxyl

© 1999 NRC Canada

Table 1. Peak anodic potentials, E_{pa} (versus the ferrocene/ferrocenium couple); difference in peak anodic and peak cathodic potentials, ΔE_p; formal reduction potentials, $E^{\circ\prime}$; peak anodic currents, i_{pa}; and peak anodic/peak cathodic current ratios, i_{pa} / i_{pc}, for the indicated compounds (concentrations 2.0 mmol dm^{-3} unless otherwise indicated) in acetonitrile with 0.1 mol dm^{-3} tetrabutylammonium hexafluorophosphate as supporting electrolyte at 25°C. Ferrocene itself, under identical conditions, showed reversible electrochemical behaviour (ΔE_p, = 73–76 mV, i_{pa} / i_{pc}, 0.97–1.00 at scan speeds v = 50, 100, 150, and 200 mV s^{-1}, $E^{\circ\prime}$ = 0.077 V versus a Ag/Ag$^+$ reference electrode).

v/mV s^{-1}	E_{pa}/V	ΔE_p/mV	$E^{\circ\prime}$/V	i_{pa}/μA	i_{pa}/i_{pc}	E_{pa}/V	ΔE_p/mV	$E^{\circ\prime}$/V	i_{pa}/μA	i_{pa}/i_{pc}
Ferrocenoyltrifluoroacetone						Ferrocenoyltrichloroacetone				
50	0.354	74	0.317	10.53	0.96	0.332	78	0.293	12.08	0.98
100	0.352	74	0.317	14.46	0.97	0.334	83	0.293	17.03	0.97
150	0.356	77	0.317	17.56	0.98	0.336	87	0.293	20.59	0.98
200	0.357	80	0.317	20.24	0.98	0.338	91	0.293	23.76	0.95
Ferrocenoylacetone						Benzoylferrocenoylmethane				
50	0.279	86	0.236	12.46	0.99	0.267	73	0.230	11.58	0.97
100	0.282	92	0.236	16.86	0.99	0.271	81	0.231	16.40	1.01
150	0.286	98	0.237	20.52	1.02	0.271	82	0.231	20.37	1.01
200	0.283	102	0.237	23.60	1.03	0.273	86	0.231	23.53	1.02
Diferrocenoylmethane[a]										
50	0.220	66	0.187	10.00	1.00	0.333	72	0.297	12.14	1.02
100	0.221	67	0.188	14.28	1.03	0.333	73	0.297	16.67	1.04
150	0.221	67	0.188	17.38	1.04	0.334	76	0.296	17.38	1.04
200	0.222	68	0.188	19.52	1.00	0.337	79	0.298	23.33	1.04
1-Ferrocenoyl-2-ferrocenylprop-2-ene,[a] 1.3mmol dm^{-3}										
50	0.142	73	0.106	7.40	0.91	0.306	70	0.271	7.66	1.07
100	0.143	74	0.106	10.30	0.88	0.307	71	0.271	10.59	1.09
150	0.143	74	0.106	12.63	0.89	0.307	72	0.271	13.30	1.09
200	0.143	72	0.107	14.41	0.88	0.307	72	0.271	14.74	1.08

[a] The first set of electrochemical data refers to the electrochemical process taking place when the first ferrocenyl group is oxidized, while the second set of data refers to the oxidation of the second ferrocenyl group.

systems (6). Since i_{pc} could not always be measured with accuracy, the i_{pc} / i_{pa} ratio was estimated using eq. [2] with $i_{pc,0}$, the peak cathodic current, measured from the base line (i.e., where zero current flows) and $i_{pa,0}$, the current flowing at the potential where the sweep is reversed, also measured from the baseline (7).

$$[2] \qquad \frac{i_{pa}}{i_{pc}} = \frac{i_{pc,0}}{i_{pa}} + \frac{0.485 i_{pa,0}}{i_{pa}} + 0.086$$

That Hdfcm shows two formal reduction potentials ($E^{\circ\prime}$ = ½(E_{pc} + E_{pa})), one at 0.266 and one at 0.375 V versus Ag/Ag$^+$ (Fig. 1, Table 1), is in contrast to ^{1}H NMR measurements (1) that could not differentiate between the two ferrocenyl groups. The observed inequality is most likely due to the improbability of both ferrocenyl groups of the same molecule, Hdfcm, coming simultaneously in reaction contact with the electrode to invoke two simultaneous one-electron transfer processes. Therefore, when only one of the ferrocenyl groups is oxidized, the newly formed intermediate is the mixed valent β-diketone $FcCOCH_2COFc^+$. Good communication between Fc and Fc^+ for this intermediate leads to oxidation of the second ferrocenyl group at a different potential than was observed for the first ferrocenyl oxidation in Hdfcm. Electrochemical inequality of the ferrocenyl groups was also observed for **7** (Fig. 2, $E^{\circ\prime}$ = 0.183 and 0.348 V vs. Ag/Ag$^+$, respectively) and various other diferrocenyl-containing compounds (8). The spread of formal reduction potentials of the ferrocenyl group of β-diketones **2–6** is large. The least positive formal reduction potential is 0.266 V for Hdfcm whereas the most positive is 0.395 V for Hfctfa. This large spread in $E^{\circ\prime}$ is the result of good communication between the ferrocenyl group and the R substituent on β-diketones **2–6** via the backbone of the pseudo-aromatic β-diketone core. The ferrocenyl group on **2–6** becomes increasingly difficult to oxidize the more electron density is withdrawn from it by the substituent, R. This observation implies that communication between the ferrocenyl group and the other β-diketone substituent R is sufficient to allow determination of group electronegativities of the R groups by measuring formal reduction potentials, $E^{\circ\prime}$, of the ferrocenyl group on these β-diketones by means of cyclic voltammetry. Of great interest is the large positive potential required to oxidize the second ferrocenyl group on Hdfcm (and **7**) compared to the oxidation of the first. The formal reduction potential of the more difficultly oxidized ferrocenyl group of Hdfcm is only 20 mV less positive than that of the ferrocenyl group of Hfctfa. This indicates that the electron-withdrawing properties of the positively charged ferrocenium radical-cation, formed during the easy oxidation of the first ferrocenyl group of Hdfcm, is almost as powerful as that of the trifluoromethyl group. The relative ease of oxidation of the first ferrocenyl group of Hdfcm as compared to that of all the other β-diketones investigated here further indicates that the electron-donating properties of the ferrocenyl group substantially overshadow those of the other β-diketone side groups, R, used in this study.

The formal reduction potentials obtained for the ferrocenyl and ferrocenium groups of **2–6** were used to determine group electronegativities, χ_R, on the Gordy scale for

© 1999 NRC Canada

Fig. 1. Cyclic voltammograms of 2 mmol dm^{-3} solutions of ferrocene, Fc, and β-diketones in acetonitrile containing 0.100 mol dm^{-3} tetrabutylammonium hexafluorophosphate at 25°C at a scan rate of 50 mV s^{-1}on a Pt working electrode.

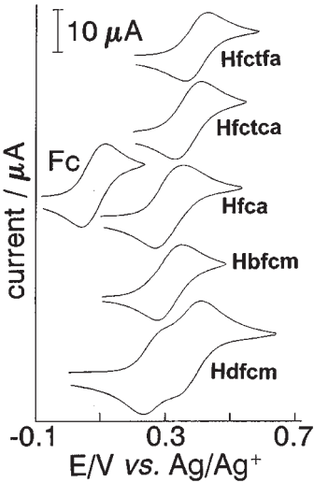

Fig. 2. Cyclic voltammograms of 1-ferrocenoyl-2-ferrocenylprop-2-ene, **7**, in CH_3CN (1.3 mmol dm^{-3}) containing 0.100 mol dm^{-3} tetrabutylammonium hexafluorophosphate at scan rates of 50 (smallest i_p values), 100, 150, 200, 250, 300, and 350 mV s^{-1} on a Pt working electrode at 25°C.

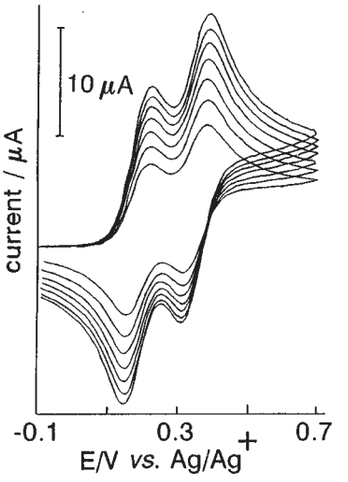

the substituents R on the β-diketone as well as the ferrocenium radical-cation. (3) Utilizing literature values (1, 3) for apparent group electronegativities, a straight line was generated by the linear fit of $E^{\circ\prime}$ (vs. Ag/Ag^+) and χ_R (R = Ph, CH_3 and CCl_3). It should be noted that χ_{Ph} was the observed value (1), χ_{Ph} = 2.21, and not the original value obtained from the IR spectra of $O{=}PPh_3$ or Ph-H (3*a*, *c*, *d*). The linear relationship obtained, $E^{\circ\prime}$ = 115.5χ_R + 47.9 mV, allowed the determination of the apparent group electronegativities of the ferrocenyl, ferrocenium radical-cation and the CF_3 group as $\chi_{ferrocenyl}$ = 1.87, $\chi_{ferrocenium}$ = 2.82, and $\chi_{trifluoromethyl}$ = 3.01, respectively. The results obtained for the ferrocenyl and CF_3 groups are mutually consistent with values obtained by utilizing the linear relationship, $\nu(C{=}O)_R$ = 74.5χ_R + 1560.7 cm^{-1}, between the carbonyl stretching frequency, $\nu(C{=}O)_R$, of methyl esters of the indicated R groups (Fig. 3) and apparent group electronegativities, χ_R. A polarographically determined group electronegativity for the ferrocenyl group was reported (9) to be 2.08. Since $E°$ and pK_a are thermodynamic quantities linked by the equation (10) $E° = (RT/nF)\ln(K_a)$ or, rearranged, $pK_a = -(nF/2.303RT)E°$, a graph of $E^{\circ\prime}$ versus pK_a' should be linear (by using $E^{\circ\prime}$ rather than $E°$ and also pK_a' rather than pK_a, the slope of the graph would be affected but not its linearity). The validity of the pK_a' values determined (1) is demonstrated by the linear relationship obtained (Fig. 4). In particular, it appears as if a pK_a' value of 5.65 for Hfctfa would be more appropriate than the observed (1) value of 6.53. The reason for the scattering of pK_a' values of CF_3-containing β-diketones is probably centred on the reversible formation of new CF_3 complexes when the β-diketone interacts with the base used to titrate it, as described elsewhere (1, 11). The pK_a' value of the mixed valent β-diketone $FcCOCH_2COFc^+$ ($Hdfcm^+$) is estimated as 6.80. Spectroscopic, pK_a', and group electronegativity results are summarized in Table 2.

The X-ray crystal structure of [Rh(fca)(cod)] has been reported (12*a*). Two molecules *within the same* unit cell were observed, one of which (molecule A) approached very closely the extreme case of asymmetric coordination with rhodium. As a result, for molecule A, the geometry of the coordinated fca ligand is very similar to that found for the asymmetrically enolized free (uncoordinated) ligand (2), Hfca. The geometry of the fctfa ligand coordinated to the Rh(I) centre is also known (12*b*). It was established spectroscopically (1) that uncoordinated Hfctfa enolizes in a direction away from the ferrocenyl group. Here we confirm this spectroscopic result by reporting the structure of Hfctfa (**6**, R = CF_3). Crystal data are summarized in Table 3, selected bond lengths and angles can be found in Table 4, and a perspective view of Hfctfa showing atom labelling is presented in Fig. 5. Unlike what was found (12*b*) in [Rh(fctfa) $(CO)(PPh_3)$], the trifluoromethyl group in free Hfctfa is disordered. The bond length C12—C13 (1.345(6) Å) is notably shorter than C11—C12 (1.432(6) Å), indicating that Hfctfa, like Hfca (2), is enolized asymmetrically in a direction away from the ferrocenyl group. Angle C11-C12-C13 (120.0(4)°) is, within experimental error, the theoretical value (120°) expected for sp^2 hybridization. The O1—O2 distance of 2.549(6) Å provides further support for the enolic structure of Hfctfa. β-Diketones in the keto form have O—O distances (12*c*) of ca. 3.05 Å. From the difference map, H11 is shown to be approximately 0.33 Å further away from O1 than from O2 with H11—O2 ca. 1.15 Å. The cyclopentadienyl rings of the ferrocenyl group deviated only 2.17(1)° (Fig. 5) from an eclipsed conformation although the energy barrier to cyclopentadienyl rotation (12*d*) in ferrocene (which includes conversion from the eclipsed to the staggered conformation) is very small (4 ± 1 kJ mol^{-1}). The structural details that may be used to explain the spectroscopically observed (1) direction of asymmetrical enolization are, however, centred on the longer bond length C13—C14 (1.515(7) Å) as compared to C11—C1 (1.448(6) Å) and the dihedral angle of 7.84° between the pseudo-aromatic system forming plane 1 defined by atoms O1-C11-C12-C13-O2 (Fig. 5) and the planar cyclopentadienyl ring of the aromatic ferrocenyl moiety bound to it. These two structural details emphasize the effective

© 1999 NRC Canada

Fig. 3. Apparent group electronegativities, χ_R, obtained by spectroscopic techniques, viz., the stretching frequency of the carbonyl group in methyl esters of the type $RCOOCH_3$ (right axis, lower graph), or electrochemical techniques, viz., cyclic voltammetry to obtain formal reduction potentials, $E^{o\prime}$ (left axis, upper graph), of β-diketones of the type $FcCOCH_2COR$ are mutually consistent. R = ferrocenyl (Fc), phenyl (Ph), H, CH_3, $CHCl_2$, CCl_3, Cl, ferrocenium (Fc^+), and CF_3 as indicated.

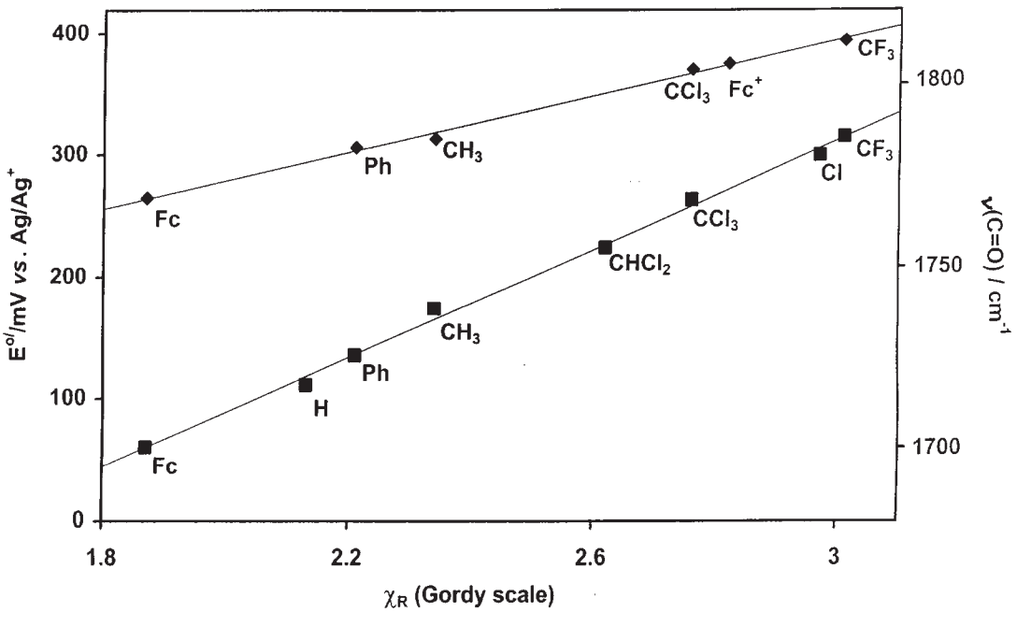

Fig. 4. The linear dependence of pK_a' of β-diketones with respect to formal reduction potential, $E^{o\prime}$ (points indicated as ■), predicts an apparent pK_a' of 5.65 for Hfctfa ($FcCOCH_2COCF_3$) and 6.80 for $FcCOCH_2COFc^+$ (points indicated as ●). The point indicated as ▲ is the measured pK_a' of Hfctfa (6.53).

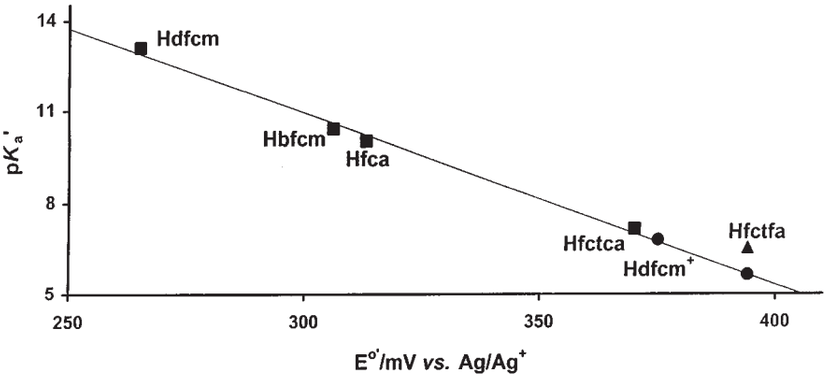

conjugation by the ferrocenyl group into the pseudo-aromatic system of plane 1. This conjugation can take place in at least two ways, as demonstrated with the formation of canonical forms **III** and **IV** of the two theoretically possible enol forms **I** and **II** of Hfctfa (Scheme 2). Either the enol isomer **I** can convert to one of its canonical forms, **III**, or isomer **II** will convert to canonical form **IV**. Both these conversions will lower the energy of the system. To decide which of these energy-lowering processes is favoured, the bond lengths O1—C11 (1.277(5) Å) and O2—C13 (1.297(5) Å) play a pivotal role. Typical β-diketone C=O bond lengths are 1.206 Å (see, for example, ref. 12*c*), whereas C—O (enol) bond lengths are in the region of 1.300 Å. For Hfctfa, C13—O2 (1.297(5) Å) is perfectly normal, but C11—O1 (1.277(5) Å) does not remotely resemble typical β-diketone C=O bond lengths. In fact, this bond is so long that it approaches typical single, enol, C—O, bond lengths, a situation that can only arise if canonical form **IV** makes a large contribution to the overall structure of Hfctfa. We therefore conclude as before (1) that, despite the large difference in group electronegativities of the ferrocenyl and trifluoromethyl groups, resonance driving forces always will carry priority over electronic driving forces to determine which enol form of a β-diketone possessing aromatic side groups is favoured. Zwitterionic canonical structures resembling **IV** are key intermediates in the enolization process of ferrocenyl- and phenyl-containing β-diketones. It should be noted that, although the canonical forms indicated in Scheme 2 explain the ^1H NMR and crystallographically observed dominance of isomer **II** over **I**, they by no means

© 1999 NRC Canada

Table 2. Group electronegativities, χ_R, for the indicated R groups; pK_a' values; IR carbonyl stretching frequencies, $\nu(C{=}O)_R$, of esters of the type $RCOOCH_3$; and formal reduction potentials, $E^{o\prime}$ vs. Ag/Ag^+, of β-diketones of the type $FcCOCH_2COR$. Fc = ferrocenyl, Fc^+ = ferrocenium, Ph = phenyl.

R	χ_R	pK_a'	$\nu(C{=}O)_R/cm^{-1}$	$E^{o\prime}/V$
CF_3	3.01[b]	6.53±0.03[a] or 5.65[c]	1785[a]	0.394[b]
Cl	2.97[a]	—	1780[a]	—
Fc^+	2.82[b]	6.80[c]	—	—
CCl_3	2.76[b]	7.15±0.02[a]	1768[a]	0.370[b]
$CHCl_2$	2.62[a]	—	1755[a]	—
CH_3	2.34[b]	10.01±0.02[a]	1738[a]	0.313[b]
Ph	2.21[b]	10.41±0.02[a]	1725[a]	0.306[b]
H	2.13[a]	—	1717[a]	—
Fc	1.87[b]	13.1±0.1[a]	1700[a]	0.265[b]; 0.374[b]

[a] Reference 1.
[b] Results from this study.
[c] An estimated value from cyclic voltammetry data, this study.

Table 3. Crystal data and structure refinement for Hfctfa.

Empirical formula	$C_{14}\ H_{11}F_3Fe\ O_2$	Cu K_α wavelength; μ	1.54178 Å; 97.12 cm^{-1}
Formula weight	324.08	$F(000)$	656
Temperature	296(1) K	Scan type; $2\theta_{max}$	ω–2θ; 130°
Crystal size, mm^3	0.40 × 0.14 × 0.10	Scan width	(1.37 + 0.35 tan θ)°
Crystal system	Monoclinic	Scan rate (in ω)	16.0°/min (up to 6 scans)
Space group	$P2_1/n$(No. 14)	Take-off angle	6°
Unit cell dimensions	a = 5.991(1) Å	Refl. Collected	2275
	b = 10.235(2) Å	Unique refl.	2056 (R(int) = 0.044)
	c = 21.076(1) Å	Refinement method	Full-matrix least squares on F
	β = 90.84(1)°	Data ($I > 3\sigma(I)$); parameters	949; 208
Volume	1292.3(3) $Å^3$	Goodness-of-fit on F	1.36
Density (calculated)	1.666 g/cm^3	Final R indices ($I > 3\sigma(I)$)[a]	R = 0.029,
Z	4		R_w = 0.030
		Largest diff. peak / hole	0.20/–0.19 e $Å^{-3}$

[a] $R = \Sigma\ ||F_o| - |F_c|| / \Sigma|F_o| = 0.029$ and $R_w = [\Sigma w(|F_o| - |F_c|)^2 / \Sigma wF_o^2]^{0.5} = 0.030$.

imply that other canonical forms and relationships do not also exist.

The geometry of Hfctfa as a free ligand and coordinated to the Rh(I) nucleus in [Rh(fctfa)(CO)(PPh_3)] follows the same general trends, especially the carbon–carbon bond lengths. In the complex, the CF_3 group is also further from the pseudo-aromatic β-diketone core than the ferrocenyl group. Like C12—C13, the corresponding bond length in the complex is also shorter than the other C—C bond of the β-diketone skeleton. The only obvious difference lies in the C—O bond lengths. In the complex, these bond lengths are equal (1.266(5) and 1.264(5) Å, respectively). This is expected and normal (12*e*) for β-diktone complexes of rhodium(I). It appears that, even in complexed form, canonical structures resembling **IV** (Scheme 2) play an important role. The structure of **7**, Scheme 1, is discussed elsewhere (12*f*).

Experimental

Materials

Solid reagents (Merck, Strem, or Aldrich) were used without further purification. Liquid reactants and solvents were distilled prior to use; water was double distilled. Dry, air-free acetonitrile was obtained by refluxing under nitrogen over calcium hydride, distilled onto alumina for storage, and redistilled just prior to use.

Spectroscopy

Proton NMR spectra at 298 K were recorded either on a Bruker AM-300 or a WP-80 instrument while chemical shifts are presented as δ values referenced to $SiMe_4$ at 0.00 ppm. IR spectra (KBr pellets or chloroform solutions) were recorded on a Hitachi model 270–50 spectrometer with data processor.

Cyclic voltammetry

Measurements on ca. 2 mmol dm^{-3} β-diketone solutions in acetonitrile with 0.100 mol dm^{-3} tetra-*n*-butylammonium hexafluorophosphate (Fluka, electrochemical grade) as supporting electrolyte were conducted under a blanket of purified argon at 25.0°C utilizing a BAS model CV-27 voltammograph interfaced with a personal computer. A three-electrode cell, which utilized a Pt auxiliary electrode, a Pt working electrode with surface area 0.0707 cm^2, and a Ag/Ag^+ (0.0100 mol dm^{-3}, $AgNO_3$) reference electrode (13) mounted on a Luggin capillary (4, 5), was employed. Data,

© 1999 NRC Canada

uncorrected for junction potentials, were collected with an Adalab-PC™ and Adapt™ data acquisition kit (Interactive Microwave, Inc.) with locally developed software, and analysed with Hyperplot (JHM International, Inc.). All temperatures were kept constant to within 0.5°C.

Structure determination

Crystals of Hfctfa were obtained by recrystallizing from acetone–hexane (1:5 by volume). A dark red crystal was mounted on a glass fiber and intensity data were collected on a Rigaku AFC5R diffractometer using graphite monochromated Cu-K_α radiation and a rotating anode generator. Cell constants and an orientation matrix for data collection were obtained from a least-squares refinement using the setting angles of 25 carefully centered reflections in the range $62.88° < 2\theta < 74.41°$. Data were corrected for Lorentz and polarization effects. A correction for secondary extinction was applied. The structure was solved by direct methods (14) and expanded using Fourier techniques (15). The non-hydrogen atoms were refined anisotropically. Hydrogen atoms were included but not refined. The locations of H10 and H11 (Fig. 5) were estimated from a difference Fourier synthesis (see supplementary material).[2] Neutral atom scattering factors were taken from Cromer and Waber (16). Anomalous dispersion effects were included in F_{calc} (17); the values for $\Delta f'$ and $\Delta f''$ were those of Creagh and McAuley (18). The values for the mass attenuation coefficients are those of Creagh and Hubell (19). All calculations were performed using the teXsan (20) crystallographic software package of the Molecular Structure Corporation. Crystallographic detail and refinement parameters are reported in Table 3.

Table 4. Bond lengths (Å) and angles (deg) for Hfctfa. The standard deviation of the last decimal is given in parentheses.

Atoms	Bond	Atoms	Bond
Fe—C(1)	2.020(4)	Fe—C(6)	2.041(5)
Fe—C(2)	2.019(4)	Fe—C(7)	2.033(5)
Fe—C(3)	2.048(5)	Fe—C(8)	2.037(4)
Fe—C(4)	2.049(5)	Fe—C(9)	2.032(5)
Fe—C(5)	2.048(5)	Fe—C(10)	2.028(5)
C(1)—C(2)	1.420(6)	C(6)—C(7)	1.395(7)
C(2)—C(3)	1.410(7)	C(7)—C(8)	1.395(7)
C(3)—C(4)	1.398(7)	C(8)—C(9)	1.399(7)
C(4)—C(5)	1.405(7)	C(9)—C(10)	1.395(7)
C(5)—C(1)	1.436(6)	C(10)—C(6)	1.418(7)
O(1)—C(11)	1.277(5)	O(2)—C(13)	1.297(5)
C(11)—C(12)	1.432(6)	C(1)—C(11)	1.448(6)
C(12)—C(13)	1.345(6)	C(13)—C(14)	1.515(7)
C(14)—F(1)	1.306(7)	C(14)—F(4)	1.27(1)
C(14)—F(2)	1.336(8)	C(14)—F(5)	1.35(1)
C(14)—F(3)	1.267(7)	C(14)—F(6)	1.177(8)
O(1)—O(2)	2.549(6)		
Atoms	**Angle**	**Atoms**	**Angle**
O(1)-C(11)-C(12)	120.0(4)	O(2)-C(13)-C(12)	126.3(4)
O(1)-C(11)-C(1)	119.0(4)	O(2)-C(13)-C(14)	112.3(4)
C(1)-C(11)-C(12)	121.0(4)	C(12)-C(13)-C(14)	121.4(4)
C(11)-C(12)-C(13)	120.0(4)	C(6)-C(7)-C(8)	108.1(4)
C(2)-C(1)-C(5)	107.3(4)	C(7)-C(6)-C(10)	107.5(4)
C(3)-C(4)-C(5)	108.6(5)	F(2)-C(14)-C(13)	112.4(5)
C(5)-C(1)-C(11)	125.3(4)	F(3)-C(14)-C(13)	114.8(5)
F(1)-C(14)-C(13)	110.6(5)	F(5)-C(14)-C(13)	108.0(6)
F(4)-C(14)-C(13)	112.4(6)	F(6)-C(14)-C(13)	115.5(6)

Synthesis

Hfctfa (**2**), Hfca (**4**), Hbfcm (**5**), and Hdfcm (**6**) were synthesized according to published (1) procedures. The procedure for Hfctca is as follows: A light yellow solution of $LiNPr^i_2$ was prepared under nitrogen by adding *n*-butyllithium (20 cm^3 of a 1.6 mol dm^{-3} solution in hexane) to an ice-cooled solution of freshly distilled diisopropylamine (3.41 g, 33.6 mmol) in dry THF (60 cm^3). The $LiNPr^i_2$ solution was added at 0°C to a solution of acetylferrocene (6.81 g, 29.87 mmol) in THF (50 cm^3) and stirred at room temperature for 20 min before methyl trichloroacetate (5.00 g, 3.36 cm^3, 28 mmol) dissolved in 40 cm^3 THF was added. Stirring of the resulting reaction mixture continued for 4 h before it was shaken with 250 cm^3 of 1 mol dm^{-3} HCl and immediately extracted with ether (5×200 cm^3). The combined ether extracts were thoroughly washed with water and dried ($MgSO_4$), and the solvent was removed under reduced pressure. Chromatography of the residue (R_f = 0.58) on Sephadex with eluant ethanol:hexane (1:6 by volume) afforded spectroscopically pure Hfctca (1.78 g, 16%) as a dark purple liquid that crystallized over 3 weeks at 4°C, mp 52°C. ν_{max}(KBr)/cm^{-1}: 1620 (C=O); δ_H (300 MHz, $CDCl_3$): 4.14 (0.1 H, s, keto-CH_2), 4.22 (5 H, s, C_5H_5), 4.62 (2 H, t, C_5H_4), 4.86 (2 H, t, C_5H_4), and 6.35 (0.95 H, s, enol CH). Anal. calcd. for $C_{14}H_{11}FeCl_3O_2$: Fe 14.95; found: Fe 14.8%. Compound **7** was isolated from the reaction mixture in yields up to 10%, mp116°C. ν_{max}(KBr)/cm^{-1}: 1630 (C=O); δ_H (300 MHz, $(CD_3)_2CO$): 2.55 (3 H, d, CH_3), 4.19 (5 H, s, C_5H_5 on the alkenyl side), 4.22 (5 H, s, C_5H_5 of ferrocenoyl), 4.46 (2 H, t, C_5H_4 on the alkenyl side), 4.57 (2 H, t, C_5H_4 of ferrocenoyl), 4.79 (2 H, t, C_5H_4 on the alkenyl side), 4.88 (2 H, t, C_5H_4 of ferrocenoyl) and 6.89 (1 H, q, CH). Anal. calcd. for $C_{24}H_{22}Fe_2O$: Fe 26.21; found: 26.1 %.

Summary

The formal reduction potentials, $E^{\circ\prime}$, of five different synthesized ferrocene-containing β-diketones and the carbonyl IR stretching frequencies of eight different methyl esters independently extrapolate to mutually consistent group electronegativities whereas the single crystal structure deter-

[2] Supplementary material (a complete X-ray structure report for $C_{14}H_{11}O_2FeF_3$ including experimental details, tables of atomic coordinates, bond lengths and angles, anisotropic displacement parameters, torsion angles, and least-squares planes) may be purchased from: The Depository of Unpublished Data, Document Delivery, CISTI, National Research Council Canada, Ottawa, Canada K1A 0S2. With the exception of the tables of anisotropic displacement parameters, torsion angles, and least-squares planes, this material has also been deposited with the Cambridge Crystallographic Data Centre, and can be obtained on request from: The Director, Cambridge Crystallographic Data Centre, University Chemical Laboratory, 12 Union Road, Cambridge, CB2 1EZ, U.K.

© 1999 NRC Canada

Fig. 5. A perspective view of Hfctfa showing atom labelling. The view from above down the C_5 ferrocenyl axis (top right) highlights the eclipsed conformation of the ferrocenyl group and the asymmetric enolization of the molecule.

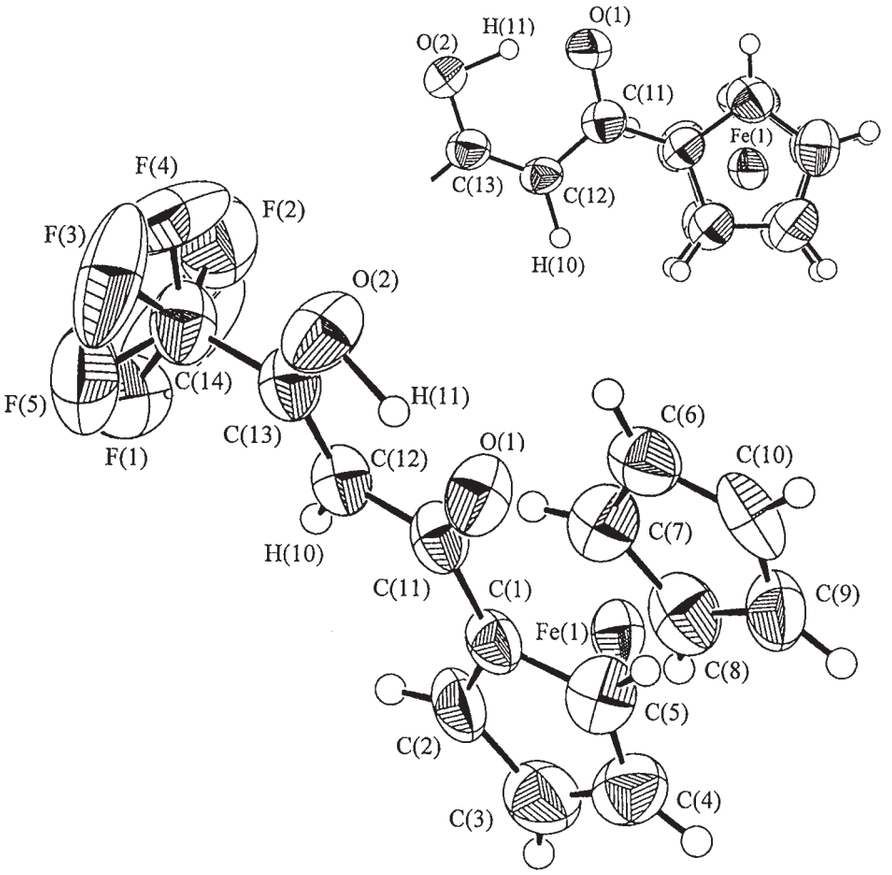

Scheme 2. Electronic considerations in terms of electronegativity, χ, favour **I** as the enol form of Hfctfa. However, structure **II** was shown by crystallography and NMR to be dominant, implying that the equilibrium between **I** and **II** lies far to the right. A dihedral angle of 7.84° between the aromatic ferrocenyl group and the pseudo-aromatic β-diketone core imply that energy-lowering canonical forms such as **IV** make a noticeable contribution to the overall existence of Hfctfa. For clarity, the ferrocenyl group in **II** and **IV** is shown in just one canonical form but in both cases the iron atom can be bound to any of the five cyclopentadienyl carbon atoms as indicated in **I.** Likewise, the positive charge of **IV** is also not confined to the single position shown but rather oscillates between C(2) and C(5) (it cannot be on C(1), atom numbers are indicated next to individual atoms) to give rise to four different canonical forms as indicated in **III**. $\chi_{trifluoromethyl} = 3.01$, $\chi_{ferrocenyl} = 1.87$.

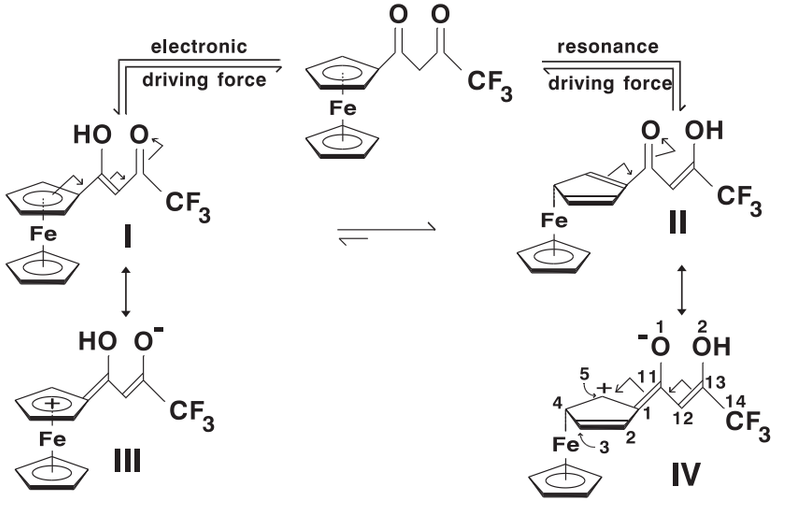

© 1999 NRC Canada

mination of the CF_3 derivative confirms that asymmetric enolization takes place in a direction away from the ferrocenyl group.

Acknowledgements

The authors gratefully acknowledge financial support from the Foundation for Research and Development and the Central Research Fund of the University of the Orange Free State. Generous financial support over a four year period by Henkel South Africa is also greatly appreciated. T.S.C. and M.A.S.A. thank the Natural Sciences and Engineering Research Council of Canada for financial support.

References

1. W.C. Du Plessis, T.G. Vosloo, and J.C. Swarts. J. Chem. Soc. Dalton Trans. 2507 (1998).
2. W. Bell, J.A. Crayston, C. Glidewell, M.A. Mazid, and M.B. Hursthouse. J. Organomet. Chem. **434**, 115 (1992).
3. (*a*) P.R. Wells. Prog. Phys. Org. Chem. **6**, 111 (1968); (*b*) R.E. Kagarise. J. Am. Chem. Soc. **77**, 1377 (1955); (*c*) J.K. Wilmshurst. J. Chem. Phys. **28**, 733 (1957); (*d*) J.V. Bell, J. Heisler, H. Tannenbaum, and J. Goldenson. J. Am. Chem. Soc. **76**, 5185 (1954); (*e*) W. Gordy. Phys. Rev. **69**, 604 (1946).
4. D.H. Evans, K.M. O'Connell, R.A. Peterson, and M.J. Kelly. J. Chem. Educ. **60**, 291 (1983); P.T. Kissinger and W.R. Heineman. J. Chem. Educ. **60**, 702 (1983); J.J. van Benschoten, J.Y. Lewis, and W.R. Heineman. J. Chem. Educ. **60**, 772 (1983); D.T. Sawyer and J.L. Roberts, Jr. Experimental electrochemistry for chemists. Wiley, New York. 1974. p. 118.
5. G.A. Mabbott. J. Chem. Educ. **60**, 697 (1983).
6. J.C. Swarts, E.W. Neuse, and G.J. Lamprecht. J. Inorg. Organomet. Polym. **4**, 143 (1994).
7. R.S. Nicholson. Anal. Chem. **37**, 1351 (1965).
8. G.M. Brown, T.J. Meyer, D.O. Cowan, C. Le Vanda, F. Kaufman, P.V. Roling, and M.D. Rausch. Inorg. Chem. **14**, 506 (1975); W.H. Morrison, Jr., S. Krogsrud, and D.N. Hendrickson. Inorg. Chem. **12**, 1998 (1973).
9. M.A. Bannett, M.I. Bruce, and T.W. Matheson. *In* Comprehensive organometallic chemistry. Vol. 4. *Edited by* G. Wilkinson. Pergamon Press, Oxford. 1982. Chap. 32, p. 765.
10. P.W. Atkins. Physical chemistry. Oxford University Press, Oxford. 1994. p. 345; D.J. Shaw and H.E. Avery. Physical chemistry. Macmillan, New York. 1991. p. 193.
11. M. Ellinger, H. Duschner, and K. Starke. J. Inorg. Nucl. Chem. **40**, 1063 (1978); H. Duschner and K. Starke. J. Inorg. Nucl. Chem. **40**, 1387 (1978); S. Aygen, E.F. Paulus, Y. Kitamura, and R. van Eldik. Inorg. Chem. **26**, 769 (1987); W. Purcell, J.G. Leipoldt, and Y. Kitamura. Inorg. Chim. Acta, **177**, 151 (1990).
12. (*a*) J.C. Swarts, T.G. Vosloo, J.G. Leipoldt, and G.J. Lamprecht. Acta Crystallogr. Sect. C: Cryst. Struct. Commun. **49**, 760 (1993); (*b*) G.J. Lamprecht, J.C. Swarts, J. Conradie, and J.G. Leipoldt. Acta Crystallogr. Sect. C: Cryst. Struct. Commun. **49,** 82 (1993); (*c*) C. Glidewell and C.M. Zakaria. Acta Crystallogr. Sect. C: Cryst. Struct. Commun. **50**, 1673 (1994); (*d*) A. Haaland and J. Nilsson. J. Chem. Soc. Chem. Commun. 88 (1968); (*e*) J.G. Leipoldt, S.S. Basson, and J.T. Nel. Inorg. Chim. Acta, **74**, 85 (1983); J.G. Leipoldt, S.S. Basson, and J.H. Potgieter. Inorg. Chim. Acta, **117**, L3 (1986); J.G. Leipoldt, S.S. Basson, L.D.C. Bok, and T.I.A. Gerber. Inorg. Chim. Acta, **26**, L35 (1978); (*f*) J.J.C. Erasmus, J.C. Swarts, A. Roodt, A. Oskarsson, and G.J. Lamprecht. Acta Crystallogr. Sect. C: Cryst. Struct. Commun. **C52**, 3000 (1996).
13. D.T. Sawyer and J.L. Roberts, Jr. Experimental electrochemistry for chemists. Wiley, New York. 1974. p. 54.
14. A. Altomare, M. Cascarano, C. Giacovazzo, and A. Guagliardi. J. Appl. Crystallogr. **26**, 343 (1993).
15. P.T. Beurskens, G. Admiraal, G. Beurskens, W.P. Bosman, R. de Gelder, I. Israel, and J.M.M. Smits. The DIRDIF-94 program system. Technical Report of the Crystallography Laboratory, University of Nijmegen, The Netherlands. 1994.
16. D.T. Cromer and J.T. Waber. International tables for X-ray crystallography. Vol. IV. The Kynoch Press, Birmingham. 1974. Table 2.2 A.
17. J.A. Ibers and W.C. Hamilton. Acta Crystallogr. **17**, 781 (1964).
18. D.C. Creagh and W.J. McAuley. International tables for crystallography. Vol. C. *Edited by* A.J.C. Wilson. Kluwer Academic Publishers, Boston. 1992. Table 4.2.6.8, pp. 219–222.
19. D.C. Creagh and J.H. Hubbell. International tables for crystallography. Vol. C. *Edited by* A.J.C. Wilson. Kluwer Academic Publishers, Boston. 1992. Table 4.2.4.3, pp. 200–206.
20. TeXan for windows: crystal structure analysis package. Molecular Structure Corporation, The Woodlands, Tex. 1997.

© 1999 NRC Canada

Apparent molar volumes of glycine, L-alanine, and L-serine in water + ethanol mixtures at 298.15 K

Xiaoling Ren, Ruisen Lin, Yaming Ni, and Hanxing Zong

Abstract: Densities of glycine, L-alanine, and L-serine have been measured with an oscillating-tube densimeter at 298.15 K in water + ethanol (EtOH) mixtures ranging from pure water to 45% ethanol by mass. From these densities, apparent molar volumes and limiting apparent molar volumes of the three amino acids in the mixtures have been calculated. Transfer volumes are interpreted in terms of the structure-making or structure-breaking effects of water on addition of these amino acids in the mixtures. The relative contributions of hydrophilic and hydrophobic interactions in these solutions have been inferred.

Key words: glycine, L-alanine, L-serine, water + ethanol mixtures, densities.

Résumé : Opérant à 298,15 K et faisant appel à un densimètre à tube oscillant, on a mesuré les densités de solutions de glycine, de L-alanine et de L-sérine dans des mélanges d'eau + éthanol (EtOH) contenant de 0 à 45% (en poids) d'éthanol. Utilisant ces densités, on a calculé les volumes molaires apparents et les volumes molaires apparents limites de ces trois acides aminés dans les mélanges. On interprète les volumes de transfert en fonction des effets de formation ou de bris de structures provoqués par l'eau lors de l'addition de ces acides aminés dans les mélanges. On a déduit les contributions relatives des interactions hydrophiles et hydrophobes dans ces solutions.

Mots clés : glycine, L-alanine, L-sérine, mélanges eau + éthanol, densités.

[Traduit par la Rédaction]

Introduction

Amino acids are the monomers that constitute proteins and are considered to be model compounds for proteins. There are extensive volumetric property studies of aqueous amino acid systems, but few of amino acids in mixed aqueous solvents (1–4). Water + alcohol mixtures have proved to be the most interesting due to the unique structural relationship of alcohols with pure water. The present work reports the apparent molar volumes of some amino acids in H_2O + ethanol (EtOH) mixtures.

Experimental

Analytical reagent grade glycine, L-alanine, and L-serine were recrystallized twice from ethanol + water mixtures. The materials were used after drying at 100°C for 6 h and then in vacuo over silica gel at room temperature for a minimum of 24 h. Ethanol (purity > 99.9 mass percent) was controlled by GLC. Freshly prepared twice-distilled water was used in all experiments. H_2O + EtOH mixtures were prepared by mass. The mass percentage of ethanol in these mixtures ranged in 10% increments from 5% to 45%. Solutions of amino acids were made by mass on the molality concentration scale. They were stored in sealable vials prior to use. Uncertainties in solution concentrations were estimated at ±0.000 02 mol kg^{-1} in calculations.

The sample densities were measured with an Anton Paar DMA 55 densimeter thermostatted to better than ±0.01°C. The temperature inside the densimeter cell was monitored with an Anton Paar DT 100-20 digital thermometer. The densimeter was calibrated with twice-distilled water and dry air. The accuracy of density values was $\pm 10^{-5}$ g cm^{-3}. The density of pure water at 298.15 K was taken as 0.99705 g cm^{-3} (5).

Results and discussion

Densities for solutions of glycine, L-alanine, and L-serine in H_2O + EtOH mixtures are shown in Tables 1–3. For the variation of densities of H_2O + EtOH mixtures with ethanol content, the results obtained in this work are in good agreement with those of Naize et al. (6), Sandhu et al. (7) and Bateman (8) (see Fig. 1). Our measured density of pure ethanol is 0.785 12, the value found by Treszczanowicz et al. (9) is 0.785 12, and that of Marsh et al. (10) is 0.785 08. Apparent molar volumes V_ϕ are calculated from these data (11) using the equation:

$$[1] \qquad V_\phi = \frac{1}{m}\left[\frac{1000 + mM}{d} - \frac{1000}{d_0}\right]$$

Received January 25, 1998.[1]

X.L. Ren[2] and Y.M. Ni. Department of Chemistry, Tongji University, 200092, Shanghai, China.
R.S. Lin and H.X. Zong. Department of Chemistry, Zhejiang University, 310027, Hangzhou, China.

[1]Revision received January 13, 1999.
[2]Author to whom correspondence may be addressed. Fax: +86 021 65028965.

© 1999 NRC Canada

Table 1. Densities and apparent molar volumes of glycine in H_2O + EtOH mixtures at 298.15 K.

m (mol kg^{-1})	d (g cm^{-3})	V_ϕ (cm^3 mol^{-1})	m (mol kg^{-1})	d (g cm^{-3})	V_ϕ (cm^3 mol^{-1})	m (mol kg^{-1})	d (g cm^{-3})	V_ϕ (cm^3 mol^{-1})
Gly + H_2O			**Gly + 5% EtOH**			**Gly + 15% EtOH**		
0	0.997 05		0	0.988 23		0	0.973 52	
0.024 94	0.997 86	42.59	0.025 05	0.989 04	42.82	0.024 97	0.974 26	45.81
0.051 32	0.998 71	42.68	0.050 07	0.989 84	42.97	0.050 22	0.975 01	45.74
0.075 14	0.999 47	42.79	0.075 31	0.990 64	43.09	0.075 45	0.975 77	45.54
0.101 21	1.000 29	42.95	0.100 78	0.991 44	43.21	0.100 74	0.976 53	45.44
0.124 58	1.001 03	42.98	0.126 38	0.992 22	43.46	0.126 01	0.977 30	45.28
0.150 38	1.001 83	43.11	0.151 36	0.993 00	43.48	0.151 50	0.978 08	45.14
0.203 62	1.003 46	43.35	0.177 25	0.993 78	43.66	0.177 29	0.978 88	44.96
Gly + 25%EtOH			**Gly + 35%EtOH**			**Gly + 45%EtOH**		
0	0.959 20		0	0.942 22		0	0.921 93	
0.049 91	0.960 53	49.23	0.045 00	0.943 06	58.60	0.049 71	0.922 40	70.27
0.075 28	0.961 22	49.00	0.075 31	0.943 78	56.25	0.074 71	0.922 95	65.29
0.100 40	0.961 91	48.79	0.100 61	0.944 36	55.59	0.099 17	0.923 47	63.05
0.125 75	0.962 62	48.53	0.125 31	0.945 03	54.25	0.125 09	0.924 07	61.16
0.151 25	0.963 33	48.38	0.151 59	0.945 73	53.40	0.150 37	0.924 62	60.20
0.176 77	0.964 06	48.14	0.177 38	0.946 55	51.94			

Table 2. Densities and apparent molar volumes of L-alanine in H_2O + EtOH mixtures at 298.15 K.

m (mol kg^{-1})	d (g cm^{-3})	V_ϕ (cm^3 mol^{-1})	m (mol kg^{-1})	d (g cm^{-3})	V_ϕ (cm^3 mol^{-1})	m (mol kg^{-1})	d (g cm^{-3})	V_ϕ (cm^3 mol^{-1})
Ala + H_2O			**Ala + 5%EtOH**			**Ala + 15%EtOH**		
0	0.997 05		0	0.988 23		0	0.973 58	
0.007 41	0.997 26	60.84	0.079 90	0.990 55	60.29	0.099 89	0.976 47	60.81
0.009 90	0.997 33	60.90	0.100 02	0.991 14	60.19	0.120 26	0.977 06	60.77
0.025 16	0.997 77	60.53	0.119 81	0.991 73	60.04	0.140 21	0.977 65	60.64
0.050 21	0.998 49	60.43	0.140 21	0.992 33	59.97	0.159 92	0.978 22	60.62
0.074 95	0.999 22	60.11	0.158 87	0.992 89	59.84	0.180 38	0.978 82	60.54
0.101 51	1.000 01	59.85				0.200 57	0.979 41	60.49
0.123 27	1.000 67	59.61						
Ala + 25%EtOH			**Ala + 35%EtOH**			**Ala + 45%EtOH**		
0	0.959 18		0	0.942 16		0	0.921 81	
0.080 27	0.961 53	60.92	0.080 55	0.944 19	66.04	0.040 01	0.922 44	78.07
0.107 63	0.962 34	60.78	0.100 41	0.944 69	66.01	0.060 05	0.922 94	74.42
0.120 71	0.962 76	60.43	0.120 40	0.945 27	65.26	0.079 75	0.923 53	71.14
0.139 98	0.963 35	60.25	0.139 80	0.945 82	64.82	0.099 95	0.924 12	69.29
0.161 14	0.964 01	60.01	0.159 61	0.946 45	64.00	0.119 69	0.924 65	68.52
			0.179 71	0.947 05	63.59	0.139 82	0.925 23	67.62

Fig. 1. Densities of H_2O + EtOH mixtures at 298.15 K: (○) this work, (×) ref. 6, (+) ref.(7), (△) ref. 8.

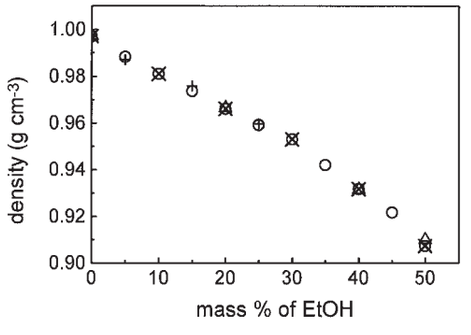

where m is the molality, M is the molecular weight of solute, and d_0 and d are the densities of solvent and solution, respectively. Calculated apparent molar volumes for amino acids are also listed in Tables 1–3. The results can be fitted by the equation

$$[2] \qquad V_\phi = V_\phi^0 + b_v m$$

where V_ϕ^0 is the apparent molar volume at infinite dilution and b_v is an experimentally determined parameter.

V_ϕ^0 and b_v values of eq. [2] have been evaluated by least squares and are listed in Table 4. Literature values for V_ϕ^0 and b_v of the three amino acids in water are also given in Table 4. The agreement between V_ϕ^0 values in water obtained in this work and those reported in the literature is good.

© 1999 NRC Canada

Table 3. Densities and apparent molar volumes of L-serine in H_2O + EtOH mixtures at 298.15 K.

m (mol kg^{-1})	d (g cm^{-3})	V_ϕ (cm^3 mol^{-1})	m (mol kg^{-1})	d (g cm^{-3})	V_ϕ (cm^3 mol^{-1})	m (mol kg^{-1})	d (g cm^{-3})	V_ϕ (cm^3 mol^{-1})
Ser + H_2O			**Ser + 5%EtOH**			**Ser + 15%EtOH**		
0	0.997 05		0	0.988 23		0	0.974 00	
0.010 09	0.997 50	60.51	0.099 93	0.992 60	61.29	0.100 18	0.977 91	66.49
0.025 08	0.998 17	60.41	0.119 83	0.993 48	61.15	0.120 15	0.978 75	65.90
0.050 23	0.999 29	60.41	0.139 98	0.994 40	60.83	0.140 28	0.979 61	65.36
0.075 25	1.000 41	60.28	0.160 28	0.995 30	60.74	0.160 14	0.980 51	64.61
0.100 99	1.001 56	60.21	0.180 10	0.996 17	60.71	0.180 25	0.981 37	64.31
0.126 53	1.002 70	60.14	0.199 91	0.997 04	60.67	0.199 95	0.982 22	64.02
Ser + 25%EtOH			**Ser + 35%EtOH**			**Ser + 45%EtOH**		
0	0.959 35		0	0.941 86		0	0.921 55	
0.099 69	0.963 41	65.02	0.100 18	0.946 06	64.03	0.079 72	0.924 65	68.02
0.120 21	0.964 31	64.38	0.120 47	0.946 90	64.07	0.099 77	0.925 44	67.84
0.140 36	0.965 17	64.10	0.140 09	0.947 71	64.11	0.119 91	0.926 24	67.64
0.160 01	0.966 00	63.94	0.160 59	0.948 55	64.16	0.139 85	0.927 03	67.49
0.180 04	0.966 84	63.84	0.180 01	0.949 35	64.16	0.159 82	0.927 84	67.23
0.200 57	0.967 72	63.65	0.199 62	0.950 15	64.20	0.179 96	0.928 66	67.00

Table 4. V_ϕ^0 and b_v values for amino acids in H_2O + EtOH mixtures at 298.15 K.

Mass% EtOH	V_ϕ^0 (cm^3 mol^{-1})	b_v (cm^3 mol^{-2} kg)	V_ϕ^0 (cm^3 mol^{-1})	b_v (cm^3 mol^{-2} kg)	V_ϕ^0 (cm^3 mol^{-1})	b_v (cm^3 mol^{-2} kg)
	Gly		**L-Ala**		**L-Ser**	
0	42.48(0.02) [a]	4.26(0.16)	60.92(0.04)	–10.64(0.63)	60.53(0.02)	–3.07(0.29)
	43.09 [b]	0.59	60.62(0.05) [d]	0.79	60.52 [c]	–3.52
	43.16 [c]	4.34	60.53 [e]		60.62(0.01) [f]	1.27(0.02)
5	42.69(0.04)	5.51(0.31)	60.74(0.04)	–5.65(0.32)	61.86(0.19)	–6.44(1.24)
15	45.99(0.02)	–5.65(0.22)	61.14(0.04)	–3.28(0.29)	68.95(0.30)	–25.57(1.94)
25	49.64(0.03)	–8.53(0.24)	61.92(0.18)	–11.86(1.46)	66.00(0.34)	–12.28(2.19)
35	60.33(0.39)	–47.34(3.26)	68.47(0.34)	–27.02(2.50)	63.87(0.02)	1.68(0.16)
45	73.60(1.83)	–96.25(17.30)	80.75(1.53)	–102.82(15.88)	68.85(0.05)	–10.10(0.40)

[a]Entries in parentheses are the standard errors on each coefficient.
[b]Reference 2.
[c]Reference 13.
[d]Reference 14.
[e]Reference 3.
[f]Reference 12.

Fig. 2. Transfer volumes ΔV_ϕ^0 of amino acids versus mass% of EtOH at 298.15 K: (■) L-Gly, (▲) L-Ala, (●) L-Ser.

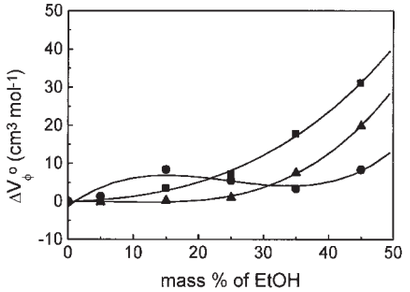

Transfer volumes of amino acids, ΔV_ϕ^0, from H_2O to H_2O + EtOH mixtures are calculated from

[3] $$\Delta V_\phi^0(H_2O \rightarrow H_2O + EtOH) = V_\phi^0(\text{in } H_2O + EtOH) - V_\phi^0(\text{in } H_2O)$$

The results are illustrated in Fig. 2.

It is well known that at infinite dilution solute–solute interactions are absent and, therefore, the observed transfer volumes are due to the solute–cosolvent–solvent interactions. As can be seen in Fig. 2, transfer volumes of the three amino acids are positive except one for L-alanine at 5 mass% of ethanol. Addition of a small amount of ethanol in water enhances the structure of water, resulting in a more structured solvent (15). When ethanol molecules interact with the charged centers of amino acids, some of the previously electrostricted water molecules around these centers return to their normal structure due to the hydration cosphere overlap effect. This decrease in electrostriction gives rise to an increase in volume, and demonstrates that the three amino acids are "structure makers" for the water in H_2O + EtOH mixtures.

Transfer volumes of glycine and L-alanine increase monotonically with increasing ethanol content in mixed solvents (Fig. 2). This suggests that the decrease in electrostriction

© 1999 NRC Canada

Fig. 3. Contribution of R groups to transfer volumes ΔV_ϕ^0(R) versus mass% of EtOH at 298.15 K: (▲) L-Ala, (●) L-Ser.

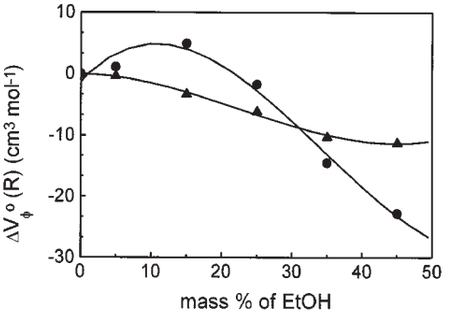

increases rapidly and the structure-making effects of water on addition of glycine and L-alanine increase rapidly with increasing ethanol content in mixed solvents.

Besides the electrostricted water around the charged zwitterionic centers, there exists a hydrophobic hydration cosphere for the -CH_3 side chain of L-alanine. In the case of overlap of the ethanol cosphere with that of L-alanine, some water molecules are also released from the cosphere of the side chains, making a negative contribution to ΔV_ϕ^0. This gives rise to a decrease in the ΔV_ϕ^0 of L-alanine against glycine. The structure-making effect of water on addition of L-alanine is weaker than that on addition of glycine. At 5 mass% of ethanol, the negative contribution is bigger than the positive contribution to ΔV_ϕ^0 of L-alanine in mixed solvents. This results in a small decrease in volume and L-alanine has a small effect on the structure breaking of water.

It can be seen that the variation of ΔV_ϕ^0 of L-serine with ethanol content is complex. The values first increase to a maximum at 15 mass% of ethanol, and then decrease to a minimum at 35 mass% of ethanol (Fig. 2). Besides the electrostricted water around the charged zwitterionic centers, there exists a hydrophilic hydration cosphere for the -CH_2OH sidechain of L-serine. In the case of overlap of ethanol cospheres with that of L-serine, some water molecules are also released from the cosphere of the side chains, making a positive contribution to ΔV_ϕ^0. This positive contribution is dominant in the "rich" water region and reaches a maximum at 15 mass% of ethanol. L-Serine has the strongest effect on making water structure at 15 mass% of ethanol. The collapse of the hydrophobic hydration co-sphere of ethanol due to charged portions of L-serine gives rise to a decrease in volume in the region of rich ethanol. At 35 mass% of ethanol, this negative contribution to ΔV_ϕ^0 is maximum and L-serine has the weakest effect on "making" water structure. As compared with glycine and L-alanine, L-serine contributes more effectively to enhancing water structure in the region of rich water (L-serine > glycine > L-alanine), but is less effective in the region rich in ethanol (glycine > L-alanine > L-serine) (Fig. 2).

It is of interest to examine the contribution to transfer volumes of R groups on the α-carbon of amino acids. For this purpose, the V_ϕ^0 of glycine is subtracted from that of the other two amino acids

$$[4] \qquad V_\phi^0(\mathrm{R}) = V_\phi^0(\text{amino acids}) - V_\phi^0(\text{glycine})$$

where V_ϕ^0(R) is the R group contribution to V_ϕ^0. In this calculation, it is being assumed that the volume contribution of the -H in glycine can be neglected. The results are shown in Fig. 3.

Contributions of the -CH_3 of L-alanine to transfer volumes are significant and negative. With increasing ethanol content in mixed solvents, the values of ΔV_ϕ^0(-CH_3) decrease rapidly, and the structure-making effect of water on addition of L-alanine increases rapidly.

The contributions of the -CH_2OH of L-serine to transfer volumes are significant and positive up to 22.5 mass% of ethanol. At 15 mass% of ethanol, the ΔV_ϕ^0(-CH_2OH) value is maximum, and the structure-making of water on addition of L-serine is also maximum. The positive ΔV_ϕ^0(-CH_2OH) values indicate that L-serine is a more effective water structure maker than glycine in the region of rich water. After 22.5 mass% of ethanol, the values of ΔV_ϕ^0(-CH_2OH) decrease rapidly.

Acknowledgment

This work was supported by the National Natural Science Foundation of China, grant No. 29773041.

References

1. C. Jolicoeur, B. Riedl, D. Desrochers, L. L. Lemelin, R. Zamojska, and O. Enea. J. Solution Chem. **15**, 109 (1986).
2. K.B. Belibagli and E. Ayranci. J. Solution Chem. **19**, 867 (1990).
3. R.K. Wadi and R.K. Goyal. J. Solution Chem. **21**, 163 (1992).
4. R. Bhat, N. Kishore, and J.C. Ahluwalia. J. Chem. Soc. Faraday Trans. 1, **84**, 2651 (1988).
5. G.S. Kell. J. Chem. Eng. Data, **20**, 97 (1975).
6. M.S.K. Naize, S.S. Shah, J. Ali, and M.Z.. Khan. J. Solution Chem. **19**, 623 (1990).
7. J.S. Sandhu, U. Kashyap, and R.K. Wadi. J. Indian Chem. Soc. **60**, 192 (1983).
8. R.L. Bateman. J. Am. Chem. Soc. **74**, 5516 (1952).
9. A.J. Treszczanowicz and G.C. Benson. J. Chem. Thermodyn. **9**, 1189 (1977).
10. K.N. Marsh and A.E. Richards. Aust. J. Chem. **33**, 2121 (1980).
11. F.J. Millero. *In* Structure and transport process in water and aqueous solutions. *Edited by* R.A. Horne. Wiley Press, New York. 1972. Chap. 12.
12. C. Jolicoeur and J. Boileau. Can. J. Chem. **56**, 2707 (1978).
13. H.Y. Yang, J.P. Zhao, and M. Dai. Huaxue Xuebao, **51**, 112 (1993).
14. A.W. Hakin, M.M. Duke, S.A. Klassen, R.M. McKay, and K.E. Preuss. Can. J. Chem. **72**, 362 (1994).
15. T.T. Herskovit and T.M. Kelly. J. Phys. Chem. **77**, 381 (1973).

© 1999 NRC Canada

Estimation of hydrocarbon types in light gas oils and diesel fuels by ultraviolet absorption spectroscopy and multivariate calibration

Peter D. Wentzell, Darren T. Andrews, Jennifer M. Walsh, Jean M. Cooley, and Paige Spencer

Abstract: Ultraviolet absorption spectra are used in conjunction with multivariate calibration methods to predict the percent content of saturates (61–99%), monoaromatics (1–34%), diaromatics (0–5%), and polyaromatics (0–1%) in light gas oil and diesel fuel samples. A total of 114 samples taken from three pilot plant studies between 1992 and 1994 were used to develop the calibration models. Supercritical fluid chromatography with flame ionization detection was employed as the reference method for quantifying hydrocarbon types. Several multivariate calibration methods (classical least squares, multiple linear regression, principal components regression (PCR), and partial least squares (PLS)) were examined. PCR and PLS gave the best overall performance, with root-mean-squared errors of prediction (absolute) of 0.9% (saturates), 0.8% (monoaromatics), 0.2% (diaromatics), and 0.05% (polyaromatics) based on 44 prediction samples. Relative errors (absolute × 100/range) for these same species were 2.4%, 2.4%, 3.2%, and 5.3%.

Key words: light gas oil, diesel, hydrocarbon content, UV spectroscopy, multivariate calibration, aromatics, petroleum.

Résumé : On a utilisé conjointement les spectres d'absorption ultraviolets et des méthodes de calibration à multivariables pour prédire le pourcentage de produits saturés (61–99%), monoaromatiques (1–34%), diaromatiques (0–5%) et polyaromatiques (0–1%) contenus dans des échantillons de diesel et de gazole léger. Pour développer les méthodes de calibration, on a utilisé cent quatorze (114) échantillons recueillis à partir de trois usines pilotes entre 1992 et 1994. On a fait appel à la chromatographie fluide supercritique avec détection à ionisation de flamme comme méthode de référence pour la quantification des divers types d'hydrocarbures. On a étudié plusieurs méthodes de calibration à multivariables (moindres carrés classiques, régression linéaire multiple, régression des principaux composants (RPC) et moindres carrés partiels (MCP). Les méthodes RCP et PLS donnent les meilleures performances globales avec des erreurs quadratiques moyennes de prédiction (absolues) de 0,9% (saturés), 0,8% (monoaromatiques), 0,2% (diaromatiques) et 0,05% (polyaromatiques) sur la base de quarante-quatre (44) échantillons de prédiction. Pour les mêmes espèces, les erreurs relatives (absolues × 100/écart) sont respectivement 2,4%, 2,4%, 3,2% et 5,3%.

Mots clés : gazole léger, contenu en hydrocarbures, spectroscopie UV, calibration à multivariables, aromatiques, pétrole.

[Traduit par la Rédaction]

1. Introduction

Transportation fuels such as gasoline, diesel, and jet fuels must meet detailed specifications for their quality. Such specifications ensure, for example, that the fuel will be suitable for the engine for which it is intended, will be stable over a reasonable time frame, and will meet certain environmental standards. Some of the analytical tests developed to monitor adherence to these specifications are rapid, simple, and require very little sample, while other assays require a more significant amount of fuel and specialized test equipment. Obviously, it is desirable to replace the latter test with the former wherever possible, not only to reduce costs and delays in analysis, but also to facilitate more efficient quality control at the processing stage.

One specification for transportation fuels that is becoming more important is the quantity of aromatic compounds present. This is often measured by fluorescent indicator analysis (FIA) (ASTM D1319 or UOP 501), a classical technique that is time consuming and, for the higher boiling samples (e.g., diesel), is difficult to perform reliably. A more recently developed method to measure aromatic content is based on analysis by supercritical fluid chromatography (SFC) (1, 2). In addition to being more rapid and reliable, this technique has the advantage of being able to speciate aromatics into mono-, di- and polyaromatics. However, it requires more

Received July 7, 1998.

P.D. Wentzell,[1] D.T. Andrews, and J.M. Walsh. Trace Analysis Research Centre, Department of Chemistry, Dalhousie University, Halifax, NS B3H 4J3, Canada.
J.M. Cooley and P. Spencer. Syncrude Canada Ltd., Edmonton Research Center, 9421 – 17 Avenue, Edmonton, AB T6N 1H4, Canada.

[1]Author to whom correspondence may be addressed. Telephone: (902) 494-3708. Fax: (902) 494-1310.
e-mail: peter.wentzell@dal.ca

© 1999 NRC Canada

complex instrumentation than techniques like FIA and is not available in many labs. Other techniques, such as high-performance liquid chromatography, mass spectrometry, and nuclear magnetic resonance spectroscopy, have also been used to determine aromatic content, but these methods face similar drawbacks.

An alternative approach to predict the aromatic content, as well as other properties of refinery products, is the use of spectroscopic techniques, and such methods have been widely reported in the literature. Near-infrared, Fourier transform infrared (FTIR), and Raman spectroscopy have been used most extensively for this purpose, especially with gasoline, aviation fuel, and other light products (3–10). Typically, these spectroscopic methods are used in conjunction with a variety of multivariate calibration techniques that can extract the desired information from the mixtures. The general consensus of these studies is that spectroscopy can be used as a rapid and simple means to predict certain properties of hydrocarbon mixtures provided that a training set of samples that is representative of future samples is available.

Fewer studies on the spectroscopic prediction of properties from heavier refinery products such as diesels have been carried out (11, 12). Quantitation of the hydrocarbon types in diesel fuels is becoming more important since future regulations on diesel properties may make it necessary to reduce the aromatic content in order to meet fuel specifications. A few studies have examined the application of ultraviolet absorption spectroscopy to the prediction of diesel and gas oil properties (13–15). These studies have been limited in scope and often restricted to a few wavelengths, without taking full advantage of multivariate calibration methods.

In this paper, a method for the spectroscopic determination of hydrocarbon types in light gas oils and diesel fuels is evaluated. The present study can be distinguished from many of the earlier works in three ways: (*i*) it utilizes ultraviolet (UV) absorption measurements as opposed to the more commonly employed IR or NIR measurements, (*ii*) it is applied to middle distillates as opposed to gasoline, (*iii*) aromatic content is subdivided into mono-, di-, and polyaromatics (saturated hydrocarbon content is also determined), and (*iv*) a large number of chemically diverse samples with a wide range of aromatic content were available for calibration. Five methods of multivariate calibration are applied to the spectroscopic data and compared for their ability to predict the four properties of interest.

2. Multivariate calibration techniques

Multivariate calibration techniques are now widely used in many practical applications, not the least of which is the petroleum industry. Whereas traditional univariate calibration relies on a single scalar measurement for each sample, multivariate calibration methods utilize a vector (or matrix) of data for each sample, such as a spectrum, which permits analysis in the presence of multiple interferences. In general, the object is to obtain an $n\times1$ vector of regression coefficients, **b**, such that

$$[1] \qquad \hat{y}_{unk} = \mathbf{x}^{T}\mathbf{b}$$

where $\hat{y}_{unk}$ is the estimated value of the property of interest (e.g., % monoaromatics) for an unknown sample and **x** is an $n\times1$ vector of responses for the sample measured at n channels (e.g., the spectrum measured at n wavelength channels). (In this paper, scalars will be indicated by lower case italic symbols, vectors by boldface lower case symbols, and matrices with boldface upper case symbols. The superscript "T" will be used to indicate the transpose of a matrix or vector.) A wide range of calibration techniques are now available, with the main differences being the methods that they employ to determine the regression vector, **b**.

In most cases, the calibration procedure is as follows. First, a set of samples is obtained that is representative of the range of compositions that are likely to be encountered in practice. Spectra (or other vectorial measurements) are then recorded for each sample. The property of interest is also measured for each of these samples by an independent reference method (in this work, supercritical fluid chromatography). The samples are then divided into two groups, one that is used to build the calibration model (the training or calibration set) and another that is used to independently assess the performance of the model (the validation or prediction set).

This study focuses on the evaluation of a few key multivariate calibration methods for the problem of interest. These are: (*i*) classical least squares (CLS), (*ii*) forward selection multiple linear regression (FS-MLR), (*iii*) stepwise selection multiple linear regression (SS-MLR), (*iv*) principal components regression (PCR), and (*v*) partial least-squares regression (PLS). These techniques have been reviewed in the literature (16–21), but will be described briefly here in the context of the present study.

2.1. Classical least squares

Classical least squares (CLS), also known as the K-matrix method, assumes that the observed responses are linearly related to the component concentrations and that the concentrations of all components in the mixtures are known for the calibration set. The most common example of this is the multivariate form of Beer's Law, which relates a matrix of spectra, **X**, to a matrix of concentrations, **Y**, through:

$$[2] \qquad \mathbf{X} = \mathbf{YK}$$

Here, **X** is an $m\times n$ matrix of mixture spectra (m samples measured at n wavelength channels), **Y** is an $m\times p$ matrix of component concentrations (p components for each of m samples), and **K** is the $p\times n$ matrix of pure component spectra (molar absorptivities, assuming a unit path length). Unless pure component spectra are known, **K** is normally calculated from the calibration data by solving the system of linear equations. From there it is a straightforward procedure to obtain the regression vectors for each component.

CLS can be an effective method when all components in the mixture contributing to the spectra have been identified and can be quantitated, but it is less useful when these conditions are not met because the model is incomplete. Furthermore, the model really only applies when the property of interest (e.g., concentration) can be associated with a component with a clearly defined spectrum, and its utility for more general properties (e.g., cetane number) is questionable. In the present study, it might be argued that the properties measured (saturates and aromatics) approximate a

© 1999 NRC Canada

complete set of "components" for UV spectroscopy, so the potential of CLS was explored.

2.2. Multiple linear regression

Perhaps the most serious deficiency of CLS is that it requires a knowledge of all of the components in the mixture, while there may be only a few properties of interest. Multiple linear regression (MLR), sometimes called the P-matrix method, circumvents this problem by assuming a model of the form:

$$\mathbf{Y} = \mathbf{XP} \quad [3]$$

where **Y** is the $m \times p$ matrix of properties to be estimated (p properties for m samples), **X** is the $m \times n$ matrix of spectra, and **P** is the $n \times p$ matrix of regression coefficients. This is sometimes referred to as the "inverse model," since **X** and **Y** are reversed from the CLS model in eq. [2], and MLR is sometimes referred to as inverse least squares. A distinct advantage of MLR is that it permits the determination of the regression vector (**b** in eq. [1]) for a desired component or property without requiring a complete knowledge of all components. It is therefore possible to apply this equation using only reference values for the property of interest. Unfortunately, reliable estimation requires that m, the number of samples in the calibration set, is substantially greater than n, the number of wavelength channels. Since modern spectrometers can have hundreds to thousands of channels, this condition is seldom met and it is necessary to select a much smaller subset of the wavelength channels. The channel selection is key, and in this work two common methods of variable selection were used: forward selection (FS) and stepwise selection (SS).

Forward selection is a screening procedure that selects the best variables (wavelength channels in this case) and adds them to the regression model one at a time until no additional improvement in model performance is found (17). This point is often determined using a standard F-test, but with a large number of wavelength channels, this test breaks down due to the statistical problem of multiple testing (17, 22). In this work, the alternative approach of internal validation was used. In this procedure, the calibration set is further subdivided into two parts, one that is used to build the models (calibration subset) and the other that is used to determine when to stop adding variables (prediction subset). Note that the latter is not the same as the prediction set described earlier, since the calibration procedure must remain blind to the data set used for validation. Variables are added to the calibration model by FS using the calibration subset as described above. For each new set of variables, the regression vector is calculated and the prediction subset is used to calculate the root-mean-squared standard error of prediction (rmsep) from:

$$\text{rmsep} = \sqrt{\frac{\left(\mathbf{y}_{\text{pred}} - \mathbf{X}_{\text{pred}}\hat{\mathbf{b}}\right)^{\text{T}}\left(\mathbf{y}_{\text{pred}} - \mathbf{X}_{\text{pred}}\hat{\mathbf{b}}\right)}{n_{\text{pred}}}} \quad [4]$$

where n_{pred} is the number of samples in the prediction subset. Note that in this case, the rows of **X** do not contain the full spectra of the prediction samples, only those variables selected by the FS procedure. The rmsep is a measure of the predictive ability of the model and will generally pass through a minimum when plotted against the number of variables added to the model, indicating that additional variables are overfitting. The minimum is used to determine the optimum number of wavelength channels. The FS procedure is then repeated using the full calibration set and terminating at this number of variables.

The technique of stepwise selection is fundamentally the same as FS for the addition of variables, but it allows one to check the significance of previously added variables after a new one is added (17). As with FS-MLR, the internal validation procedure was used to select the optimum number of variables for SS-MLR.

2.3. Principal component regression

Principal component regression (PCR) has emerged as one of the tools of choice for the multivariate calibration problems in chemistry. In PCR, the overall dimensionality of the data is reduced to only a few variables, thereby addressing the rank deficiency problem inherent in MLR. Unlike the variable selection procedures used for MLR, variable reduction in PCR occurs by combining those variables that exhibit strong correlations into *latent variables*, so information is not lost through the elimination of wavelength channels. The first step in PCR is to decompose the $m \times n$ matrix of calibration responses, **X**, using principal component analysis (PCA) to give scores and loadings matrices:

$$\mathbf{X} = \mathbf{TL} \quad [5]$$

Assuming that $m < n$, PCA returns the scores matrix, **T** ($m \times m$), and the loadings matrix, **L** ($m \times n$). In order to retain p latent variables for the regression, these matrices are then truncated by removing the right-hand columns and bottom rows to give $\tilde{\mathbf{T}}$ ($m \times p$) and $\tilde{\mathbf{L}}$ ($p \times n$). The latent variables selected in this way form an orthogonal set and are the linear combinations of the original variables that account for the largest amount of variance in the data. Because of this, these variables are likely to be useful in developing a model. The matrix $\tilde{\mathbf{T}}$ is analogous to the matrix **X**, except that it has fewer columns, making it more readily employed in MLR. The corresponding regression model is:

$$\mathbf{y} = \tilde{\mathbf{T}}\mathbf{q} \quad [6]$$

where **q** is the $p \times 1$ vector of regression coefficients. Solution of eq. [6] for **q**, the regression vector for the scores, and its transformation to **b**, the regression vector in terms of the original variables, is straightforward.

An important consideration in PCR is the number of latent variables used in the regression. In this work, this parameter was determined by *leave-one-out cross-validation*. In this procedure, the calibration is carried out using all but one of the calibration samples. This sample is then predicted using the model determined and the difference between the predicted and reference values of y is determined. This process is repeated m times, each time leaving out a different calibration sample. All of the prediction errors are then combined to give the root-mean-squared error of cross-validation (rmsecv):

© 1999 NRC Canada

$$[7] \qquad \text{rmsecv} = \sqrt{\sum_{i=1}^{m} (y_i - \hat{y}_i)^2 / m}$$

Here y_i is the observed value of the property of interest for calibration sample i, $\hat{y}_i$ is the predicted value of the property, and m is the number of calibration samples. A plot of the rmsecv vs. the number of latent variables should pass through a minimum at the optimum number of latent variables. This approach is similar to the internal validation procedure used for variable selection in MLR, but is often considered more reliable because more samples are used to build the model. For MLR, cross-validation cannot generally be used for variable selection, since a new group of variables may be selected on each iteration of the process.

2.4. Partial least-squares regression

One weakness of PCR is that it extracts the latent variables, which are linear combinations of the original variables, on the basis of the amount of variance in **X** that they encompass. Therefore, wavelength channels with large variations in response over the calibration set tend to be weighted most heavily. However, these wavelengths are not necessarily the ones that are most useful in predicting the desired property. To mitigate this problem, the technique of partial least-squares regression (PLS) can be used (16). In recent years, PLS has become one of the most widely used regression techniques in chemistry. In many instances, PCR and PLS produce comparable results, but in certain cases PLS will exhibit superior performance and often can produce a model with fewer latent variables.

Regression with PLS is very similar to PCR, with latent variables being extracted from the calibration data and used in the regression model. However, while PCR extracts the latent variables to maximize the variance in **X**, PLS generates the latent variables by maximizing the covariance between **X** and **y**. In this way, variables that have good predictive abilities are given a greater weight. The latent variables, or scores, in PLS can be calculated by a variety of algorithms (16), the details of which will not be discussed here. As with PCR, it is necessary to determine the optimum number of latent variables by cross-validation.

3. Experimental

3.1. Data

There were a total of 115 samples from pilot plant studies available for study in this work. These consisted of two sets of light gas oil samples (boiling range 195–343°C) and one set of diesel samples (boiling range 177–343°C). Fifty-nine light gas oil samples were obtained from a pilot plant program conducted at Syncrude Canada Ltd. to evaluate three different catalysts. The project consisted of 20 mass balances and included temperatures ranging from 320 to 400°C, pressures ranging from 6.9 to 13.8 MPa, and liquid hourly space velocities ranging from 0.7 to 1.3 mL L^{-1} mL^{-1}. A further 26 samples were obtained from a subsequent program, which used a different feed as well as different catalysts. Finally, 30 diesel samples were obtained from a third pilot study that involved very severe treating of light gas oil samples with an aim of significantly reducing aromatic content. The use of three separate pilot plant studies ensured chemical diversity in the samples studied.

The reference values for percentages of saturates, monoaromatics, diaromatics, and polyaromatics were determined by supercritical fluid chromatography (1) using an HP model G1205A supercritical fluid chromatograph (Hewlett–Packard, Palo Alto, Calif.) equipped with an autosampler. The oils were separated neat on a 250 × 4.6 mm HP hydrocarbon group separation column using carbon dioxide as the carrier (2 mL min^{-1}). The oven temperature was 35°C and the outlet pressure was 150 bar. Quantitation was performed with a flame ionization detector (FID). To obtain the weight percentages of each of the four groups, the FID signal was integrated over ranges specified by the CGSB for each group. This area was then ratioed to the total area for the chromatogram. The ranges obtained for the samples were as follows: saturates, 60.6–99.0%; monoaromatics, 0.8–34.1%; diaromatics, 0–5.0%; polyaromatics, 0–0.9%. The wide range of concentrations is an asset in the construction of reliable models.

For the spectral analysis, approximately 0.12 g of each sample was accurately weighed into a 25 mL volumetric flask and diluted with HPLC grade cyclohexane. This solution was further diluted by a factor of 1/200 with cyclohexane before running the spectra. (In preliminary studies, higher concentrations had also been employed, but the lower concentrations were found to be more useful.) Spectra were obtained on a Cary 3 UV–visible spectrophotometer (Varian Instruments, San Fernando, Calif.) in a 1 cm flow-through cell. Scanning parameters were: spectral band width, 0.5 nm; signal averaging time, 0.1 s; data interval, 0.35 nm; scan rate, 21 nm min^{-1}; range, 200–400 nm. There were a total of 572 points acquired for each spectrum. Each spectrum was normalized to an initial concentration of 0.1 g/25 mL by multiplying the absorbance readings by 0.1/(sample mass).

3.2. Data pretreatment

The data for the original 115 samples were first analyzed to identify the presence of outliers using the procedure outlined by Martens and Næs (16). In this procedure, samples that are highly influential (high leverage) and have large studentized residuals are flagged as outliers. Only one sample was identified as an outlier and eliminated from subsequent analysis. This corresponded to a feed sample that was expected to have a considerably different composition from the other samples. The UV spectra for the remaining 114 samples used in this work are shown in Fig. 1.

Prior to regression analysis, the spectra were adjusted by subtracting the mean absorbance at each wavelength from all of the measurements at that wavelength. This preprocessing step, called column mean-centering, is commonly employed with spectroscopic data to eliminate intercept terms from the model. Likewise, each of the four groups of reference measurements was centered about its mean value. In the final prediction, a correction for the offset was made.

For the regression analysis, it was necessary to divide the full data set into a calibration set and a prediction set for purposes of validation. For this work, the sizes of the calibration and prediction sets were chosen to be 70 and 44 samples, respectively. To ensure that each set is representative of the other, the subset selection procedure of Kennard

© 1999 NRC Canada

Fig. 1. Spectra of 114 samples used in the study (outlier excluded). Spectra were normalized to a concentration of 0.02 g L^{-1}.

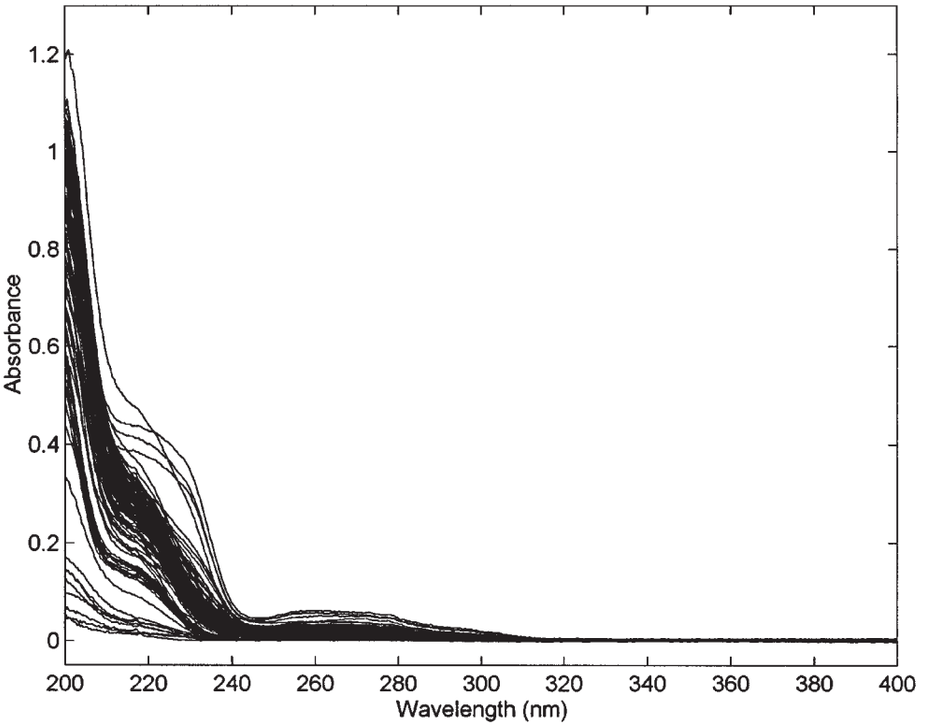

and Stone was used (23) to split the data. Visual verification of the representativity was also made by examining two-dimensional projections of the samples after PCA. For FS-MLR and SS-MLR, further splitting of the calibration set was necessary for internal validation, giving a calibration subset of 50 samples and a prediction subset of 20 samples. The same method was used for obtaining these subsets.

3.3. Computational aspects

All of the results presented here were obtained on a Pentium-based personal computer using programs written in Matlab v4.2x (The Math Works, Natick, Mass.). All programs were written by the authors, except for the PLS routines, which were taken from the PLS Toolbox for Matlab (Eigenvector Research Inc., Manson, Wash.). Computation times for building the models varied with the regression technique, but all were under an hour. Once the regression coefficients are computed, calcualtion of results for new samples is computationally trivial.

4. Results and discussion

Initially, the feasibility of using UV spectroscopic data to predict aromatic content was evaluated by calculating the correlation coefficient between the absorbance at each wavelength and the reference value for each of the four properties to be predicted. The data were mean-centered for these calculations. Figure 2 shows the correlation coefficient plotted as a function of wavelength for the four properties. Each of the properties exhibits regions where there is a high degree of positive or negative correlation, indicating that these data may be useful in the development of a regression model. For the three classes of aromatics, correlation is high at short wavelengths and the maximum shifts to longer wavelengths with increasing aromaticity. This is consistent with the observed transitions for aromatic compounds and the bathochromic shift that occurs with increasing conjugation. For saturates, there is a strong negative correlation in this region, since these compounds do not absorb in this part of the spectrum and the content is essentially correlated with the absence of aromatics. For all constituents, the degree of correlation falls off with increasing wavelength until it is effectively zero above 350 nm.

Despite the high degree of correlation found, attempts to use single wavelengths to model the properties of interest were unsuccessful, generally resulting in nonlinear plots. This led to the application of the multivariate methods described above.

Table 1 summarizes the results obtained by the various calibration methods. The table is divided by constituent and calibration method and gives the prediction errors in each case, along with other relevant parameters. The errors presented in the table are rmsep values obtained using the prediction set of 44 samples, which were completely excluded from the calibration process. Therefore, these values should be good estimates of the true predictive ability of each model in this sample domain. Both absolute errors (% content of constituent) and relative errors (% of range of predicted value) are shown. The relative error is often a better means of evaluating the predictive ability of the model since it takes into account the range of values to be predicted. Also given in the table are the number of wavelength channels selected, the corresponding wavelengths (MLR), and the number of latent variables used (PCR and PLS). The

© 1999 NRC Canada

Fig. 2. Correlation of properties to be estimated with absorbance at each wavelength: (*a*) % saturates, (*b*) % monoaromatics, (*c*) % diaromatics, (*d*) % polyaromatics. Data were column mean-centered prior to calculation.

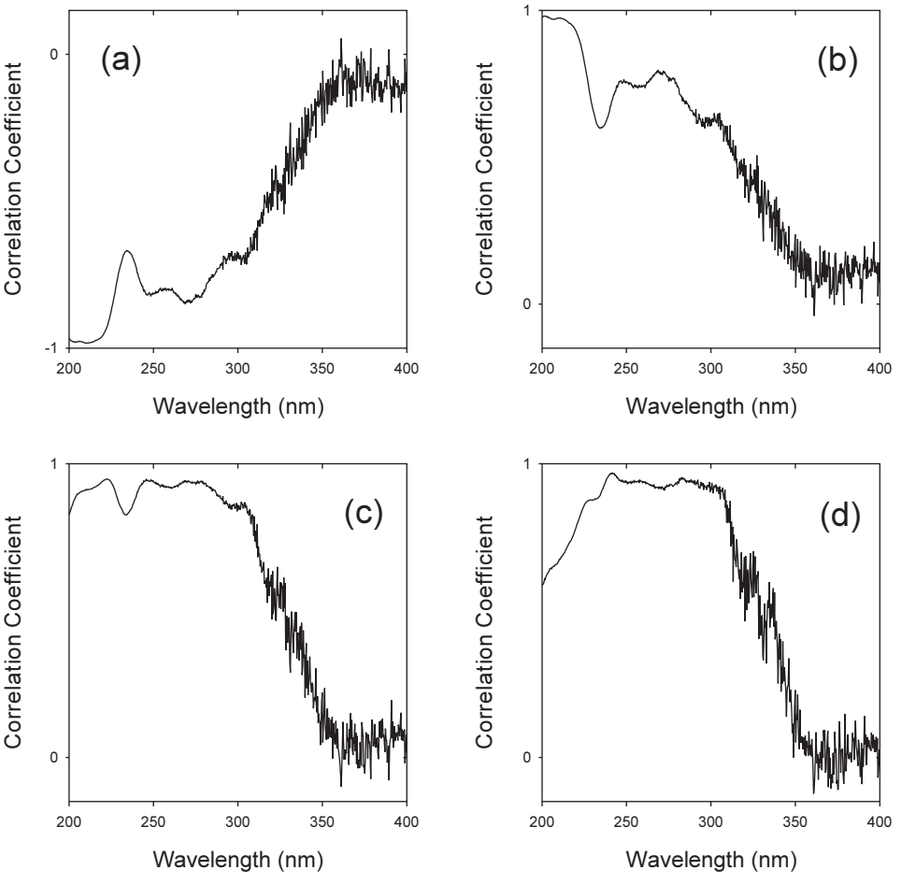

Table 1. Comparison of calibration methods for the prediction set (44 samples) for each of the compound classes.

Property	Method[a]	Absolute error[b]	% Relative error[c]	Wavelengths used
Saturates	CLS	1.24	3.24	
	FS-MLR (12)	1.27	3.32	204 211 327 346 360 371 373 380 381 385 394 398
	SS-MLR (12)	1.27	3.32	As for FS-MLR
	PCR (10)	0.94	2.45	
	PLS (6)	0.93	2.42	
Monoaromatics	CLS	1.35	4.06	
	FS-MLR (2)	0.78	2.33	201 319
	SS-MLR (2)	0.78	2.33	201 319
	PCR (10)	0.8	2.41	
	PLS (9)	0.81	2.44	
Diaromatics	CLS	0.226	4.51	
	FS-MLR (9)	0.184	3.67	200 204 208 223 246 261 270 283 308
	SS-MLR (4)	0.292	5.85	246 261 270 308
	PCR (6)	0.159	3.19	
	PLS (4)	0.16	3.21	
Polyaromatics	CLS	0.134	14.84	
	FS-MLR (1)	0.058	6.4	242
	SS-MLR (1)	0.058	6.4	242
	PCR (5)	0.051	5.66	
	PLS (5)	0.048	5.34	

[a]Numbers in parentheses indicate the number of wavelength channels selected (MLR) or the number of latent variables used (PCR and PLS).

[b]Values given are the root-mean-squared errors of prediction (rmsep) for % content.

[c]Calculated from (rmsep/range) × 100.

© 1999 NRC Canada

Fig. 3. Graphical comparison of relative prediction errors from multivariate calibration.

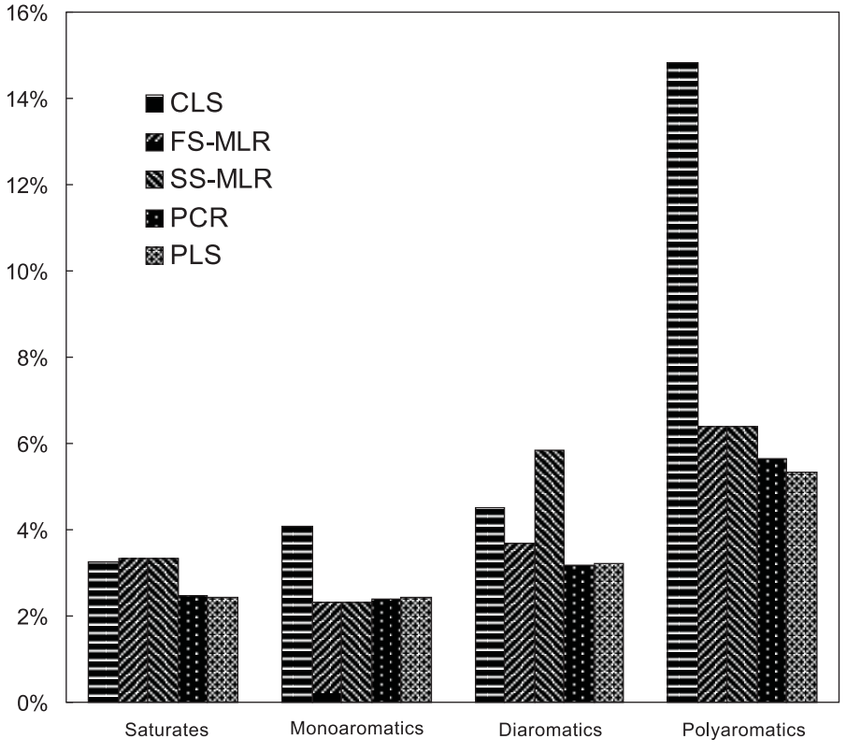

wavelengths have been rounded to the nearest nanometre to save space. The predictive abilities are also summarized in the bar chart in Fig. 3 for easy comparison.

All of the methods used were able to quantitate the four hydrocarbon types reasonably well, with the possible exception of the polyaromatic content, which was below 1% in all of the samples examined. For the other three groups of compounds, all of the relative prediction errors are below 6% and often below 4%. CLS performed better than expected, probably because the aromatic classes approximate a complete set of absorbers in the UV. FS-MLR and SS-MLR yielded the same wavelength subsets (and hence the same predictive abilities) in all cases except the diaromatics, with SS generating a subset of the FS case with poorer predictive ability. Only two wavelengths were selected for the monoaromatics and a single wavelength was found to be sufficient for the polyaromatics. While it is tempting to try to interpret the selected wavelengths from a chemical perspective, this is difficult to do because the wavelengths with the best predictive ability do not necessarily correspond to the peak maximum for a given class of compounds in a complex mixture.

In general, PCR and PLS performed the best of the five methods tested, but the improvement was only marginal. These two methods gave similar results but, as is common, PLS often required fewer latent variables. The regression vectors obtained by PCR and PLS can often yield information about important regions of the spectrum and suggest critical measurement regions for lower resolution instruments. These regression vectors are plotted for each of the hydrocarbon classes in Fig. 4. There appears to be good agreement in the general shape of the regression vectors (with the possible exception of the monoaromatics), which explains their similar performance. These plots suggest that shorter wavelengths are more important, as expected. Beyond this, it is difficult to say much about the shape of the curves, but it is likely that the oscillating structure of the regression coefficients is the result of regularly spaced bands for the aromatic species present. It is possible that restricting the wavelength range to shorter wavelengths prior to calibration may further improve the results, but this was not attempted in this work.

Finally, as a typical example, Fig. 5 shows results for predicted vs. measured properties for the PLS method. The plot distinguishes among calibration and prediction samples and the three different data subsets in order to convey information about the distribution of samples. Note that the correlation between measured and predicted values is very good for the first three constituents and there is no suggestion of bias. The agreement is not as good for the polyaromatics, but the figure makes it clear that one of the reasons for this is digitization error in the reference method arising from the low concentrations of these species within the samples, which is anticipated for light gas oils.

5. Conclusions

The results presented here demonstrate that UV spectroscopic measurements, in conjunction with multivariate calibration methods, can be used to predict the aromatic content of intermediate petroleum distillates with good reliability. The models were constructed and validated using two differ-

© 1999 NRC Canada

Fig. 4. PCR and PLS regression vectors: (*a*) and (*b*) % saturates, (*c*) and (*d*) % monoaromatics, (*e*) and (*f*) % diaromatics, (*g*) and (*h*) % polyaromatics.

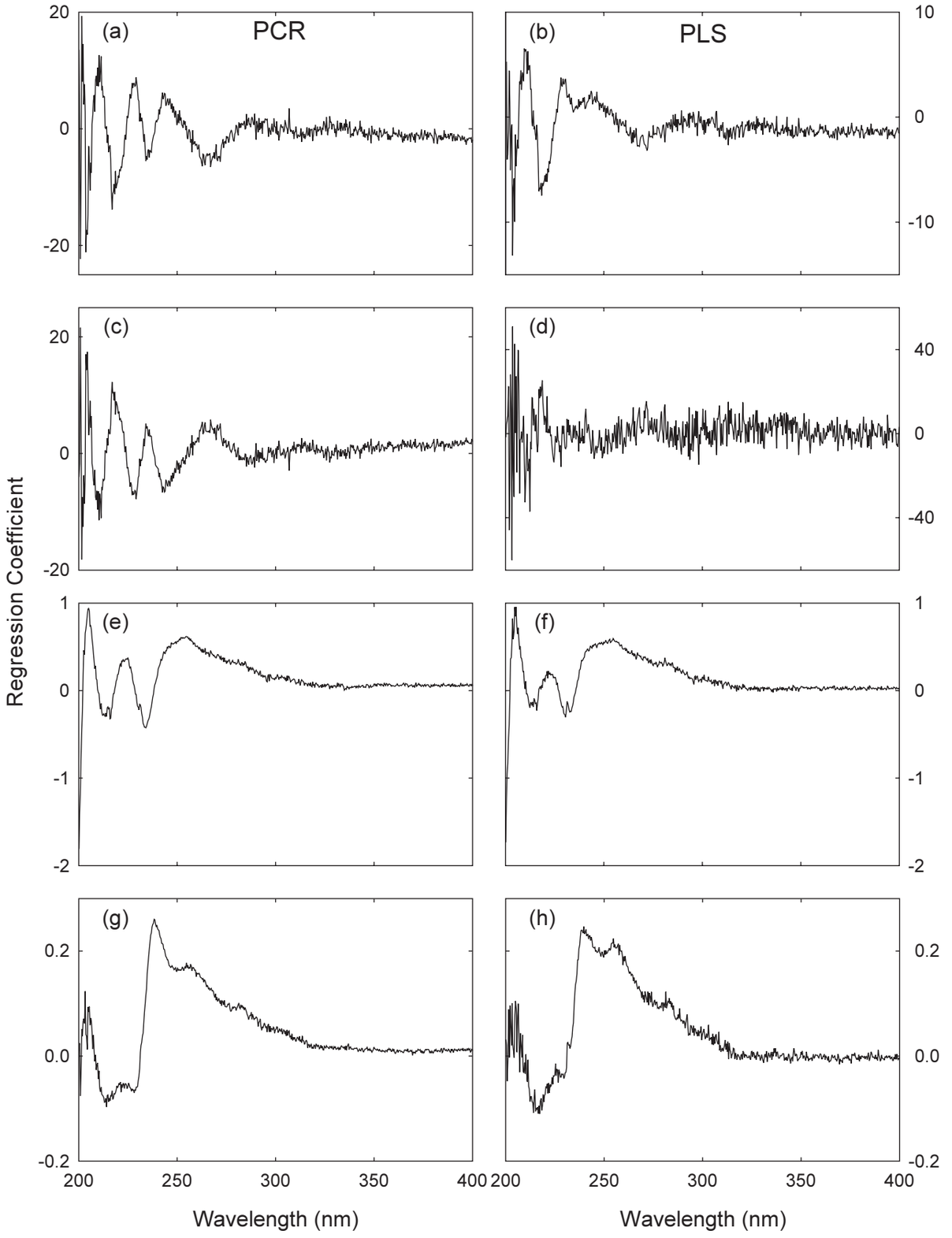

© 1999 NRC Canada

Fig. 5. Comparison of predicted vs. measured properties using the PLS regression model. △ 1992 pilot plant data, □ 1993 pilot plant data, ○ 1994 pilot plant data. Filled symbols indicate prediction samples, open symbols indicate calibration samples. Note that all of the observed measurements were rounded to the nearest 0.1%.

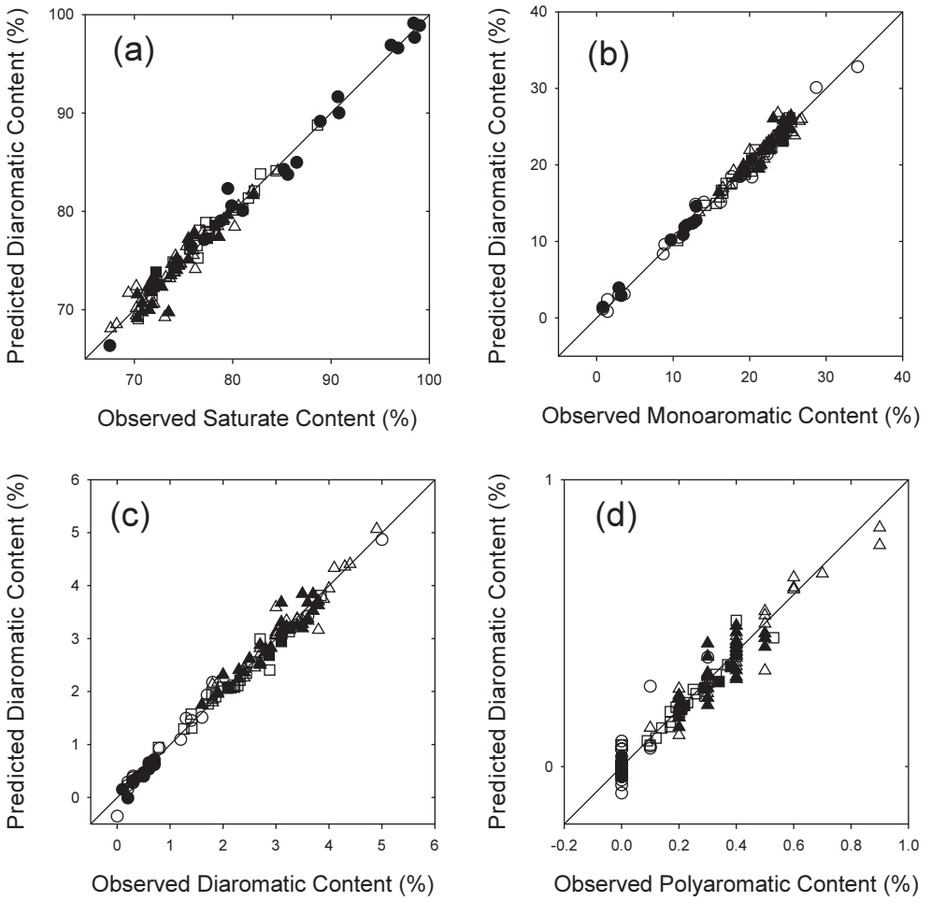

ent sets of light gas oil samples and one set of diesel samples. In addition to different boiling ranges, the samples are also chemically different due to severe hydrotreating/ hydrocracking of the diesel samples. Therefore, this data set should represent a fairly rigorous test of the multivariate modeling methods. Furthermore, unlike some earlier studies that only quantified total aromatics, this work was able to differentiate among three different classes of aromatic compounds. With the exception of polyaromatic content, which suffered from imprecision in the reference method, relative prediction errors for PCR and PLS were around 3%, which is quite good for this type of analysis and comparable to current methods for diesel aromatics. The absolute errors were similar to the repeatability specifications for the SFC method, suggesting that uncertainty in the reference method may be a significant contributor to the prediction error.

The use of an ultraviolet spectrometer to measure aromatic content has potential advantages over SFC and other techniques. UV spectrometers are relatively inexpensive, rugged, and simple to use, making them more suitable for on-site measurements. In this work, spectroscopic measurements were carefully made on a high-quality instrument to ensure reliable data. It is likely, however, that comparable results can be obtained with faster scans on lower resolution instruments. Of course, steps would need to be taken to ensure that the calibration models exhibit good long-term reliability with changes in plant operating conditions and feedstocks. Nevertheless, this study has shown the feasibility of estimating hydrocarbon content through UV spectroscopy.

Acknowledgments

The authors gratefully acknowledge the support of Natural Sciences and Engineering Research Council of Canada. D.T.A. was partially supported by a fellowship from the Sumner Foundation. P.S. was employed at Syncrude in conjunction with the Chemistry Industrial Internship Program at the University of Alberta. The authors thank Syncrude Canada Ltd. for permission to publish this work.

References

1. Methods of testing petroleum and associated products: standard test method for the determination of aromatic hydrocarbons by their ring number in petroleum middle distillates by supercritical fluid chromatography Canadian General Standards Board CAN/CGSB-3.0, No. 15.0–94 (1994).

© 1999 NRC Canada

2. Standard test method for determination of the aromatic content and polynuclear aromatic content of diesel fuels and aviation turbine fuels by supercritical fluid chromatography. ASTM D5186–96.
3. J.J. Kelly and J.B. Callis. Anal. Chem. **62**, 1444 (1990).
4. S.J. Swarin and C.A. Drumm. Spectroscopy, **7**, 42 (1992).
5. M.J. Lysaght, J.J. Kelly, and J.B. Callis. Fuel, **72**, 623 (1993).
6. S. Garrigues, J.M. Andrade, M. de la Guardia, and D. Prada. Anal. Chim. Acta, **317**, 95 (1995).
7. J.B. Cooper, K.L. Wise, J. Groves, and W.T. Welch. Anal. Chem. **67**, 4096 (1995).
8. G.E. Fodor, K.B. Kohl, and R.L. Mason. Anal. Chem. **68**, 23 (1996).
9. A. Iob, M.A. Ali, B.S. Tawabini, S. Bassam, and N.M. Abbas. Fuel, **75**, 1060 (1996).
10. P.E. Flecher, W.T. Welch, S. Albin, and J.B. Cooper. Spectrochim. Acta, Part A: **53A**, 199 (1997).
11. S.J. Foulk and B.E. DeSimas. Process Control Qual. **2**, 69 (1992).
12. G.E. Fodor and K.B. Kohl. Energy Fuels, **7**, 598 (1993).
13. B.K. Bailey and K.B. Kohl. Chemical analysis of aromatics in diesel fuels. Final report, contract no. A932–125, Southwest Research Institute, San Antonio, Tex. 1991.
14. T. Zerlia and G. Pinelli. Fuel, **72**, 505 (1993).
15. L. Dixit, R.B. Gupta, S. Ram, and P. Kumar. Fuel Sci. Technol. Int. **12**, 171 (1994).
16. H. Martens and T. Næs. *In* Multivariate calibration. Wiley, New York. 1989.
17. S. Weisberg. *In* Applied linear regression. 2nd ed. Wiley, New York. 1985.
18. E.V. Thomas. Anal. Chem. **66**, 795A (1994).
19. B.R. Kowalski and M.B. Seasholtz. J. Chemom. **5**, 129 (1991).
20. E.V. Thomas and D.M. Haaland. Anal. Chem. **62**, 1091 (1990).
21. K.R. Beebe and B.R. Kowalski. Anal. Chem. **59**, 1007A (1987).
22. R.W. Butler. J. Am. Stat. Assoc. **79**, 341 (1984).
23. R.W. Kennard and L.A. Stone. Technometrics. **11**, 137 (1969).

© 1999 NRC Canada

The adsorption of carbon dioxide by tertiary alkanolamines

M. Teresa S.R. Gomes, Cristina M.F. Barros, M. Graça O. Santana-Marques, and João A.B.P. Oliveira

Abstract: The quantification of gaseous carbon dioxide, CO_2, adsorbed by tertiary alkanolamines was performed using a quartz crystal microbalance. Carbon dioxide was injected over piezoelectric quartz crystals coated with different amounts of *N*,*N*,*N*′,*N*′-tetrakis(2-hydroxyethyl)ethylenediamine (THEED), *N*,*N*,*N*′,*N*′-tetrakis(2-hydroxypropyl)ethylenediamine (Quadrol), and triethanolamine (TEA), and the frequency decrease of the crystals was recorded. The nature of the interaction of the alkanolamines with CO_2 was investigated by nuclear magnetic resonance spectroscopy (NMR), Fourier transform infrared spectroscopy (FTIR), fast atom bombardment mass spectrometry (FABMS), and mass spectrometry/mass spectrometry (MS/MS).

Key words: alkanolamine, quartz crystal microbalance, piezoelectric quartz crystal.

Résumé : On a déterminé la quantité de dioxyde de carbone gazeux absorbé par les alcanolamines tertiaires à l'aide d'une microbalance à cristal de quartz. On a injecté le dioxyde de carbone sur un cristal de quartz piézoélectrique enrobé de différentes quantités de *N*,*N*,*N*′,*N*′-tétrakis(2-hydroxyéthyl)éthylènediamine (THEED), de *N*,*N*,*N*′,*N*′-tétrakis(2-hydroxypropyl)éthylènediamine (Quadrol) et de triéthanolamine (TEA), et on a enregistré la diminution de fréquence des cristaux. Pour déterminer la nature des interactions des alcanolamines avec le CO_2, on a utilisé la spectroscopie de résonnance magnétique nucléaire (RMN), la spectroscopie infrarouge avec transformation de Fourrier (IR FT), la spectrométrie de masse à bombardement par des atomes rapides (FABMS) et la combinaison spectrométrie de masse/spectrométrie de masse (MS/MS).

Mots clés : alcanolamine, microbalance à cristal de quartz, cristal de quartz piézoélectrique.

[Traduit par la Rédaction]

Introduction

N,*N*,*N*′,*N*′-Tetrakis(2-hydroxyethyl)ethylenediamine (THEED) interacts in a reversible way with carbon dioxide, and previous studies have shown that THEED is a suitable coating for piezoelectric quartz crystals used for carbon dioxide monitoring (1–3).

Although amines are widely used for CO_2 adsorption in a variety of industrial processes, there is a lack of information on the nature of the interaction of amines with CO_2, in the absence of water.

Tertiary amines do not react with carbon dioxide in the absence of water (4, 5), but tertiary alkanolamines can react with CO_2, due to the presence of the hydroxyl groups, and form alkyl carbonates, $R_2NROCOO^-$. However, these carbonates are not stable at pH values lower than 10 and, in an acidic, neutral, or slightly basic medium, the hydroxyl group can be regarded as inert (6–10). This is why, in aqueous solutions, triethanolamine (TEA), $(HOCH_2CH_2)_3N$, showed qualitatively the same behaviour as triethylamine, $(CH_3CH_2)_3N$, when reacting with CO_2 (8). In the absence of solvent either a small interaction between TEA and CO_2 (1) or no interaction at all (11, 12) has been reported.

In the absence of water a very small interaction between *N*,*N*,*N*′,*N*′-tetrakis(2-hydroxypropyl)ethylenediamine (Quadrol) and CO_2 has been reported in the literature (12, 13). The similarity of structures (Scheme 1) and of the chemical and physical properties of TEA, THEED, and Quadrol makes the study of their interactions with CO_2 particularly interesting.

The quartz crystal microbalance (QCM) is known for its remarkable sensitivity and was used to monitor the mass change of a crystal coated with known quantities of these alkanolamines in the presence of CO_2. The results obtained allowed the comparison of the three alkanolamines in terms of the extent of their interactions with CO_2. To obtain information about the nature of these interactions, in the absence of solvents, nuclear magnetic resonance spectroscopy (NMR), Fourier transform infrared spectroscopy (FTIR), fast atom bombardment mass spectrometry (FABMS), and mass spectrometry/mass spectrometry (MS/MS) were used.

Received July 29, 1998.

M.T.S.R. Gomes,[1] C.M.F. Barros, M.G.O. Santana-Marques, and J.A.B.P. Oliveira. Department of Chemistry, University of Aveiro, 3810-193 Aveiro, Portugal.

[1]Author to whom correspondence may be addressed. Telephone: +351 34 370722. Fax: +351 34 370084. e-mail: mtgomes@dq.ua.pt

Experimental

Reagents

N,*N*,*N*′,*N*′-Tetrakis(2-hydroxyethyl)ethylenediamine (THEED) and *N*,*N*,*N*′,*N*′-tetrakis(2-hydroxypropyl)ethylenediamine (Quadrol) were purchased from Fluka, and triethanolamine (TEA) from Merck. The three alkanolamines were used

© 1999 NRC Canada

Scheme 1.

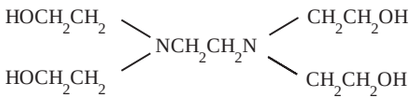

THEED

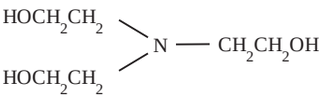

TEA

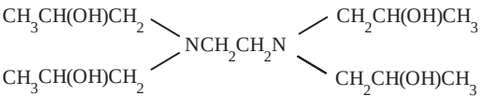

Quadrol

without further purification. In all experiments no solvent was added to the amines, except for spray coating, for which they were dissolved in absolute ethanol (purchased from Merck). Nitrogen was R grade, carbon dioxide was N45, and both were purchased from ArLíquido.

Apparatus

Each piezoelectric crystal was coated with a solution of the alkanolamine in absolute ethanol on one of its faces, using a commercial air brush and a rotating plate with orifices that held the crystal upright. After coating, the crystal was placed in a glass cell through which a constant nitrogen flow of 50 cm^3 min^{-1} was maintained. The flow rate was controlled with a variable area flow meter (Cole Parmer). Both the spraying device and the glass cell have been described elsewhere (14).

CO_2 was injected into the nitrogen flow, through an Omnifit septum injector fitted in front of the crystal cell. The syringes were SGE (Scientific Glass Engineering, Ltd), gas tight, with valve.

The piezoelectric crystals were 9 MHz (SIWARD) and the frequency was monitored with a frequency counter (Leader).

The infrared spectra were recorded on a Nicolet Magma 550 Fourier transform infrared spectrometer. The sample was introduced into a liquid cell (Spectra Tech) with CaF_2 windows.

The NMR spectra were obtained using a Bruker AMX 300 spectrometer tuned at 75 MHz to detect ^{13}C. The sample was placed in a 5 mm NMR tube with a coaxial tube for the external reference of $CDCl_3$.

FAB mass spectra and MS/MS spectra were acquired with a VG AutoSpecQ used as a EBE geometry instrument. It was equipped with a cesium ion gun, and the intensity of the Cs^+ beam was 3 μA at 15 kV. The applied accelerating voltage was 8 kV. The mass spectrometer was operated at a nominal mass resolution of 1000 (10% valley).

Samples were placed directly on the probe tip. MS/MS spectra were acquired with and without collision gas (Ar, 50% of signal attenuation). Precursor ion spectra were obtained by a linked scan of B^2/E.

Procedure

Quartz crystal microbalance measurements

The frequency of three new and similar crystals, which had been previously washed with absolute ethanol and dried, was measured under a nitrogen flow of 50 cm^3 min^{-1}.

One of the quartz crystals was sprayed on one of its faces with a 1% (w/v) solution of one of the alkanolamines in absolute ethanol. The coated crystal was again placed in the glass cell, through which the nitrogen flow was maintained. The frequency of the crystal was continuously monitored and a sudden rise in the frequency, corresponding to solvent evaporation, was observed. After frequency stabilization, corresponding to complete solvent evaporation, the frequency of the coated crystal was recorded. The frequency decreases due to coating were calculated by subtracting the recorded stabilized value from the initial frequency of the uncoated crystal.

After complete evaporation of the solvent, 5.0 cm^3 of CO_2 was injected into the nitrogen flow, and, as soon as it reached the crystal, a sudden decrease in the frequency was observed and recorded.

The crystal was washed and dried and its frequency monitored, to insure that the initial frequency of the uncoated crystal was reached. It was then coated with a different amount of the same amine, by varying the exposure of the crystal to the spray, and the experiment with CO_2 was repeated as before.

The overall procedure was repeated for the other two alkanokamines and, to prevent contamination, a new crystal was used for each amine.

NMR spectra

The NMR tube was filled with THEED, and nitrogen was bubbled in to displace atmospheric CO_2. An external reference of $CDCl_3$ was placed inside the coaxial tube, to prevent contact with the amine. The ^{13}C NMR spectrum of THEED was then recorded. The spectrum of THEED with CO_2 was recorded after bubbling CO_2 into the previous sample.

© 1999 NRC Canada

Fig. 1. Frequency of a crystal coated with THEED when 5.0 cm^3 of CO_2 are injected into the nitrogen flow.

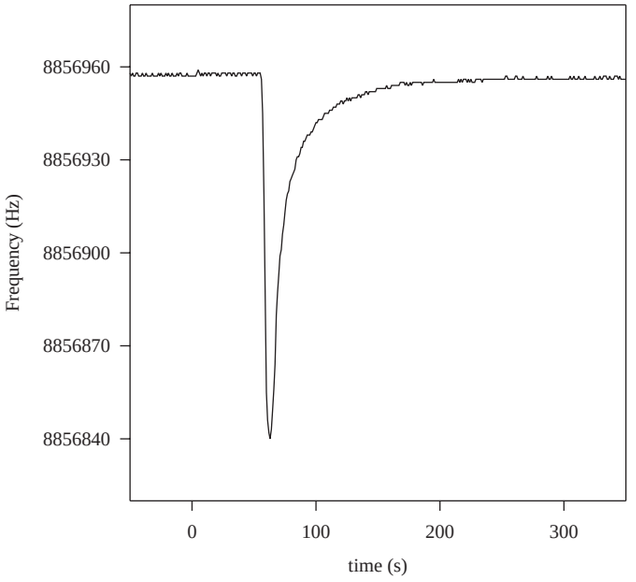

Fig. 2. Frequency decrease of a crystal coated with THEED with successive injections of different amounts of CO_2.

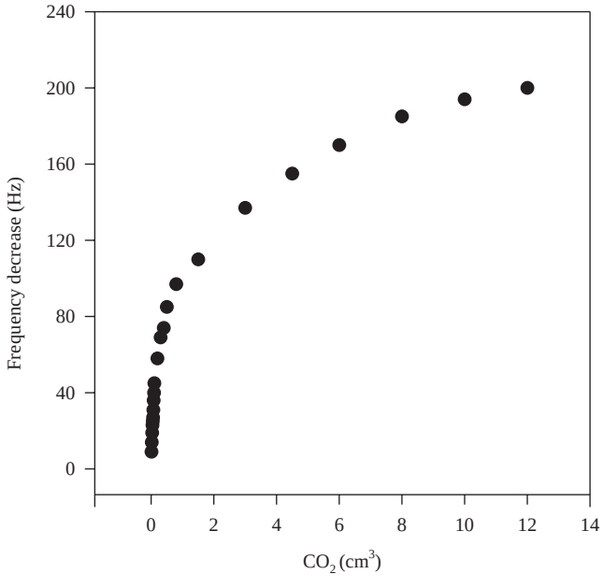

MS spectra

FAB mass spectra were recorded after bubbling N_2 and CO_2 into aliquots of the alkanolamine. The samples were applied directly to the tip of the FAB probe without adding matrix or cosolvent. Positive and negative ion spectra were recorded.

MS/MS experiments, both in the positive and in the negative mode, were performed, selecting the ions with the EB section of the mass spectrometer. Product ions of the metastable or collision-induced decompositions of the selected ions were obtained by a scan of the second electric sector.

Fig. 3. Frequency decrease observed when 5.0 cm^3 of CO_2 are injected over crystals coated with different amounts of THEED, TEA, and Quadrol.

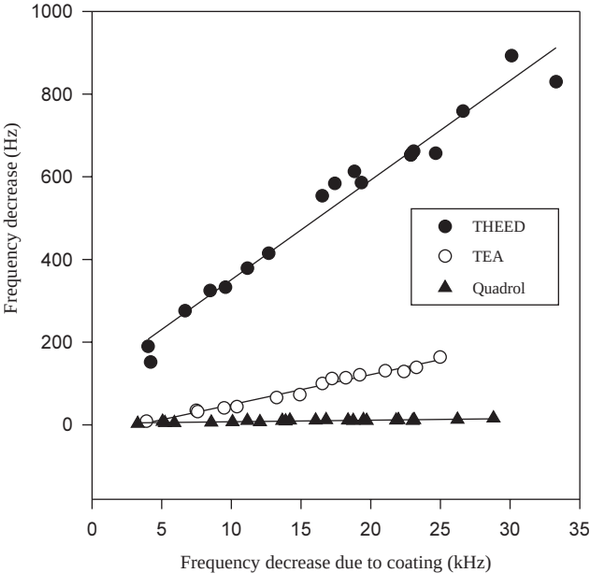

Precursor ion spectra were obtained by a linked scan of B^2/E.

FTIR spectra

THEED was introduced into the liquid cell and either N_2 was passed through the cell, or CO_2 was introduced through a Luer fitting.

The single beam IR spectra were saved after fixed time intervals. The resolution was 4 cm^{-1} and 100 interferograms were accumulated for each spectrum.

Results and discussion

Quartz crystal microbalance experiments

Figure 1 shows the frequency of a piezoelectric crystal coated with THEED, when 5.0 cm^3 of CO_2 was injected into the nitrogen carrier gas passing through the crystal cell, and impinging on both faces of the crystal. The frequency of the crystal decreases, after CO_2 injection, due to the increase of mass on the surface of the electrodes. As the nitrogen continues to flow through the crystal cell, CO_2 is slowly displaced from the coated crystal, and the frequency rises to the base-line value, which corresponds to the initial frequency of the crystal. The reversibility of the interaction of CO_2 with THEED, as long as coating stability is maintained, allows successive injections of different amounts of CO_2. As can be seen in Fig. 2, the observed frequency is proportional to the amount of injected CO_2, as long as saturation of the coating is prevented.

Figure 3 shows the response of crystals coated with different amounts of the three alkanolamines to 5.0 cm^3 CO_2 injections. For the same amount of injected CO_2, the frequency decrease is proportional to the coating amount. Although the precision of the data shown in Fig. 3 is not as good as that of Fig. 2, the coating procedure used is repro-

© 1999 NRC Canada

ducible enough, as far as concerns the coating distribution over the electrode area of the piezoelectric crystal, to allow us to compare the response of the three amines to CO_2 injection. If other widely known coating procedures, such as smearing, dipping, or syringe deposition, were used, no comparison would be possible. The plots in Fig. 3 show that THEED has the highest sensitivity to CO_2 and that the interaction with CO_2 of both TEA and Quadrol is very weak, especially in the case of Quadrol, which can be regarded as practically inert.

The higher sensitivity of THEED when compared with the other two alkanolamines is obviously related to its surface physicochemical properties. Parameters such as the diffusivity of the gas in the liquid film should be taken into account. The latter is inversely proportional to the viscosity of the liquid.

All experiments were carried out at room temperature, and the viscosities of the alkanolamines decrease in the following order: Quadrol > THEED > TEA, so the highest adsorption should be expected for TEA. This implies that other parameters must be taken into account.

Primary and secondary amines can react directly with CO_2 in the absence of water, forming carbamates ($RNHCOO^-$ or R_2NCOO^-) but, as mentioned before, tertiary amines do not react with CO_2 in the absence of water. If the observed interaction between THEED and CO_2 is chemical, either it occurs with HCO_3^- formation (eq. [1]) from absorbed water, because the alkanolamines are hygroscopic, or it involves the hydroxyl groups of the alkanolamines, probably leading to formation of an alkylcarbonic acid or alkyl carbonate (eq. [2]).

$$[1] \qquad CO_2 + H_2O \rightleftharpoons HCO_3^- + H^+$$

$$[2] \qquad R_2NROH + CO_2 \rightleftharpoons R_2NROCOOH$$

Although the amines were used without any previous purification or drying procedure, and contact with the atmosphere during spraying could not be avoided, it is not probable that the observed interaction is only, or even predominantly, due to the presence of absorbed water. Even when the quartz crystals coated with THEED were kept for several days at 44°C with a constant flow of N45 impinging on the coated face, the magnitude of the signals obtained after CO_2 injection showed only a slight decrease in comparison with those obtained at room temperature, already expected in exothermic processes governed by adsorption.

NMR and IR spectroscopy experiments

Figure 4 shows the NMR spectra of THEED after bubbling in N_2 (*a*), and CO_2 (*b*). The acquisition time for the spectrum in Fig. 4*b* was longer (1 night) than the acquisition time for the spectrum in Fig. 4*a* (2 h) due to a lower signal-to-noise ratio caused by the increased viscosity of the sample after CO_2 bubbling. In Fig. 4*b* we can observe a signal at 163.877 ppm that does not appear in Fig. 4*a*. This signal cannot be assigned to gaseous CO_2 (15, 16), but the possibility of the signal being due to HCO_3^- cannot be excluded (15, 16). On the other hand, the presence of H_2CO_3 is out of the question, as the signal of H_2CO_3 as reported in the literature would appear at 153 ppm (16). This signal can also be due to alkyl carbonate formation (17).

Figure 5 shows the infrared spectra of a THEED sample recorded in a sequence of different experiments, and Fig. 6 a detail of the same spectra in the range from 1000 to 1800 cm^{-1}. After the spectrum of the THEED sample in contact with the atmosphere was recorded, a flow of CO_2 through the cell was maintained for 5 min, after which a new spectrum was acquired. A third spectrum was acquired after 120 min of constant nitrogen flow through the infrared cell.

A few changes induced by CO_2 can be observed by comparing the spectra. The presence of gaseous CO_2 is easily recognised by the two signals at 2340 and 2362 cm^{-1}. A signal due to HCO_3^- would have appeared at 1360 ± 3 cm^{-1}; however, no significant change is observed in this region. This is evidence that formation of HCO_3^- from absorbed water does not occur to a significant extent.

The wide absorption band near 3300 cm^{-1}, from the OH stretching vibration, shows considerable broadening, downward frequency shift, and intensification with CO_2, which is characteristic of hydrogen bonding (18).

The two intense bands at 1069 and 1040 cm^{-1} can be attributed to C–N vibration (doublet for tertiary amines) (19), and the band at 1040 cm^{-1} to C–O stretching and O–H deformation, characteristic of primary alcohols (18). The decrease in the intensity of the band at 1040 cm^{-1} with CO_2 introduction can be interpreted as evidence of the involvement of the OH group in the interaction with CO_2.

Near 1300 cm^{-1} an absorption band that can be attributed to C–O stretching (20), and also to C–N vibration, increases with CO_2 introduction. This increase is consistent with alkyl carbonate formation.

Two bands at 1643 and 1574 cm^{-1}, which are almost nonexistent in the absence of CO_2, show a marked increase with its introduction. The band at 1643 cm^{-1} can be attributed to carbonyl group stretching, shifted to lower frequencies because of random formation of hydrogen bonds with the neighbouring molecules; if we assume that the compound also exists as the β-ammonium carboxylate zwitterion, the band at 1574 cm^{-1} can be assigned as the antisymmetrical stretching vibration.

The appearance of both the ionized and non-ionized carboxyl absorptions in the infrared spectra is not common, but has been reported before for noncrystalline aminoacids (18).

Zwitterionic forms also appear for EDTA (ethylenediaminetetraacetic acid) and related compounds in aqueous solution as their α-ammonium carboxylates, with carboxylate antisymmetrical stretching frequencies in the range 1630–1620 cm^{-1} (21). This shift is due to the inductive effect of the positive charge in the α quaternary nitrogen, and would not be expected to occur to the same extent for the β-ammonium carboxylates.

The data recorded in the literature for alkyl carbonates report carbonyl group absorptions from 1787 cm^{-1} up to 1819 cm^{-1}. Although these are not observed in our experiments, this does not exclude the formation of an alkyl carbonate type compound with the neutral carbonic acid in equilibrium with its zwitterion.

The spectrum obtained after the N_2 flow confirms the reversibility of the interaction between THEED and CO_2, already demonstrated by the quartz crystal microbalance experiments, although reversibility was not complete in 120 min.

© 1999 NRC Canada

Fig. 4. ^{13}C NMR spectra of THEED (*a*) after bubbling in N_2; (*b*) after bubbling in CO_2.

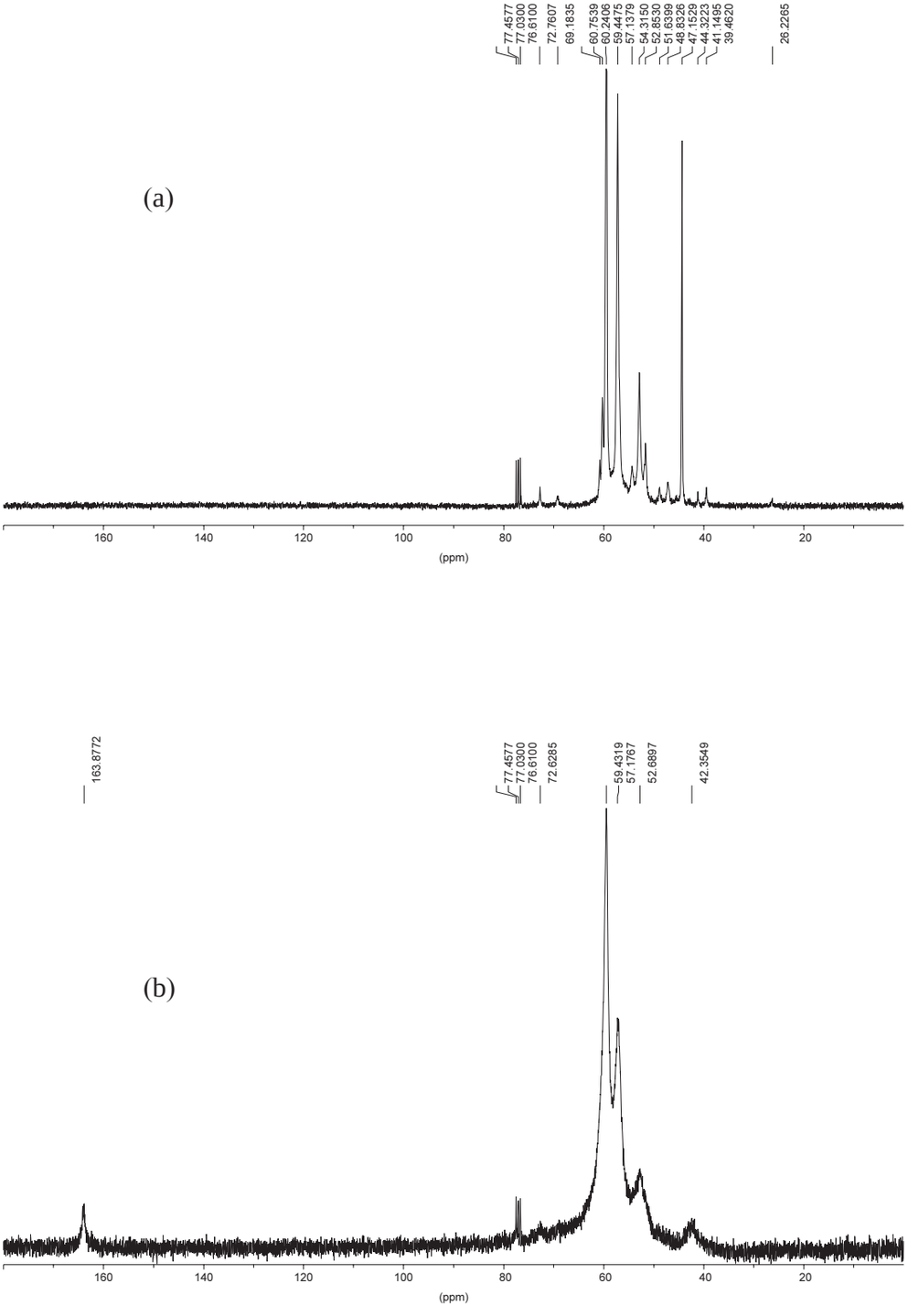

Mass spectrometry experiments

Figure 7 shows the positive ion FAB mass spectrum of THEED after CO_2 was bubbled in. The protonated THEED molecule, $[M + H]^+$, of *m/z* 237, is the third most abundant ion in the spectrum. The base peak is the ion of *m/z* 132 and the second most abundant ion is that of *m/z* 118. The spectrum also shows two ions of *m/z* 281 and of *m/z* 325, with masses, respectively, 44 and 88 Da higher than the mass of the protonated molecule of THEED, the last ion having a low relative abundance.

In the FAB mass spectrum of TEA, obtained after CO_2 was bubbled in, and using the same experimental conditions, no ions with masses 44 and 88 Da higher than the mass of the protonated molecule are observed. The positive ion mass

© 1999 NRC Canada

Fig. 5. Infrared spectra of THEED in different environments.

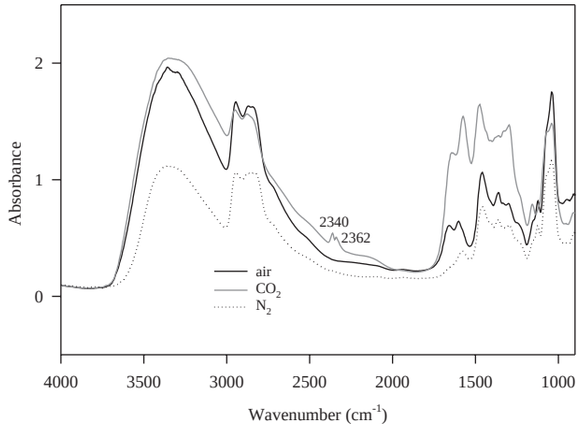

Fig. 6. Detail of the spectrum of Fig. 5 in the frequency range from 1000 to 1800 cm^{-1}.

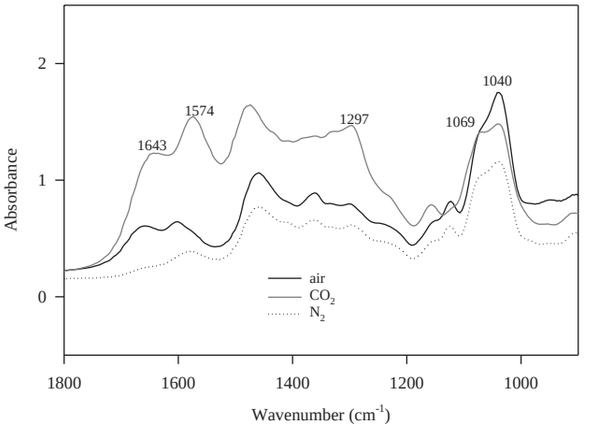

spectrum of TEA shows the protonated molecule $[M + H]^+$, of *m/z* 150, which is the base peak, and the other three most abundant ions are the $[M - H]^+$ ion, of *m/z* 148, and ions of *m/z* 132 and of *m/z* 118.

The collisionally activated MS/MS spectra of the ions of *m/z* 118 formed from both TEA and THEED are identical, and the same occurs for the collisionally activated MS/MS spectra of the ions of *m/z* 132. Based on these data we propose the following structures for these ions:

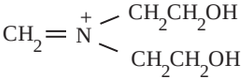

118

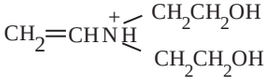

132

The collisionally activated MS/MS spectra of the ions of *m/z* 281, $[M + H + 44]^+$, and of *m/z* 325, $[M + H + 88]^+$, from THEED, both show abundant product ions of *m/z* 162 and of *m/z* 176. These data and the data from the collisionally activated MS/MS spectra of the ions of *m/z* 162 and of *m/z* 176, allow us to propose the following structures for the ions:

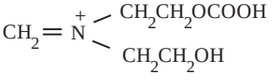

162

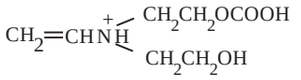

176

The proposed structures are consistent with the hypothesis of alkyl carbonate formation, and are the carbonated homologues of the structures proposed above for the ions of *m/z* 118 and of *m/z* 132.

The collisionally activated MS/MS spectrum of the ion of *m/z* 325 also shows other two product ions of *m/z* 206 and of *m/z* 220, with lower relative abundances, and with masses 44 Da higher than those of the ions of *m/z* 162 and of *m/z* 176, respectively. These other two product ions, of *m/z* 206 and of *m/z* 220, can be explained by the reaction of a second OH group with CO_2, with formation of a second alkyl carbonate group. If we compare the relative abundances of the ions of *m/z* 281 and of *m/z* 325 in Fig. 7, the second alkyl carbonate group is formed to a much smaller extent than the first alkyl carbonate group.

Figure 8 shows the spectra obtained by subtracting the negative ion FAB spectra of THEED, acquired without bubbling CO_2, from the spectra acquired after CO_2 was bubbled. The changes due to CO_2 are shown in this spectrum and the most important change is the formation of the ion of *m/z* 103, which was absent in the negative ion mass spectrum of THEED before CO_2 was bubbled in. The ion of *m/z* 339, also absent in the negative ion mass spectrum of THEED before CO_2 was introduced, can be observed, although with much lower relative abundance than the ion of *m/z* 103. An increase in the relative abundances of the ions of *m/z* 147 and *m/z* 191 is also observed.

The precursor ion spectrum of the ion of *m/z* 103 shows that this ion is formed by fragmentation of the ions of *m/z* 147 and of *m/z* 339. The ion of *m/z* 339 is probably the proton-bound dimer of the ions of *m/z* 103 and $[M - H]^-$ (of *m/z* 235). The precursor ion spectrum of the ion of *m/z* 147 shows that its main precursor ion is the ion of *m/z* 191.

The fragmentation of the $[M - H]^-$ ion of THEED, of *m/z* 235, can be rationalized by successive elimination of CH_2CH_2O, with hydrogen migration to the nitrogen atoms. On the basis of these data and the data obtained from the precursor ion spectra, we propose for the ions of *m/z* 191 and *m/z* 147 the following structures:

$H_2NCH_2CH_2N(CH_2CH_2OH)CH_2CH_2OCOO^-$

m/z 191

$H_2NCH_2CH_2NHCH_2CH_2OCOO^-$

m/z 147

The structure of the ion of *m/z* 103 is not obvious, although one possibility is the distonic ion $H_2NCH_2\dot{C}HOCOO^-$.

From analysis of the data from the negative ion spectra it is clear that a reaction between THEED and CO_2 occurs. The data are not inconsistent with alkyl carbonate formation, notwithstanding the fact that the ions, with masses 44 and 88 Da higher than the mass of the $[M - H]^-$ ion, are not observed in the negative ion spectra. The reason is perhaps a

© 1999 NRC Canada

Fig. 7. FAB positive ion mass spectrum of THEED after CO_2 interaction.

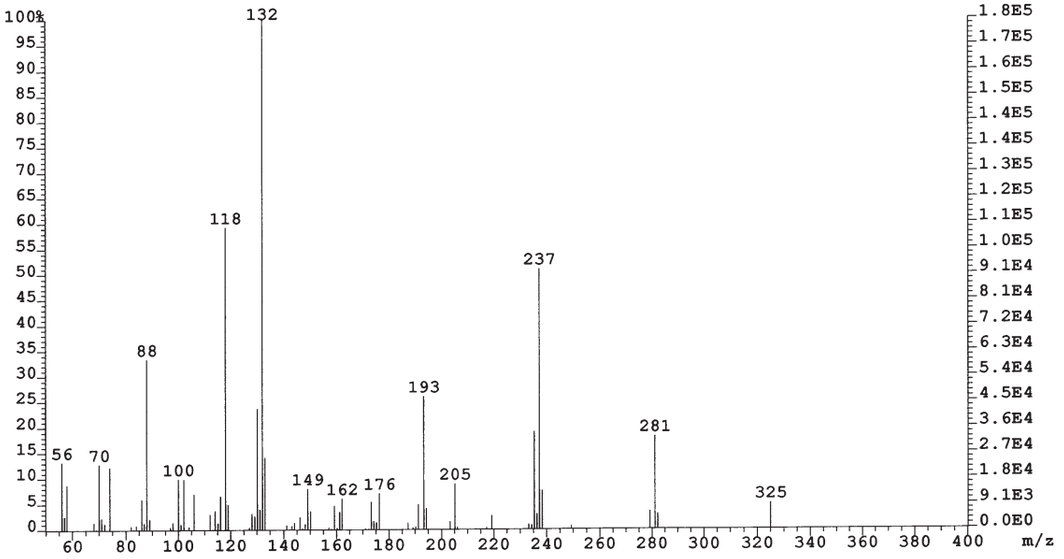

Fig. 8. Spectrum obtained by subtracting the FAB negative ion mass spectrum of THEED before CO_2 interaction from the FAB negative ion mass spectrum of THEED after CO_2 interaction.

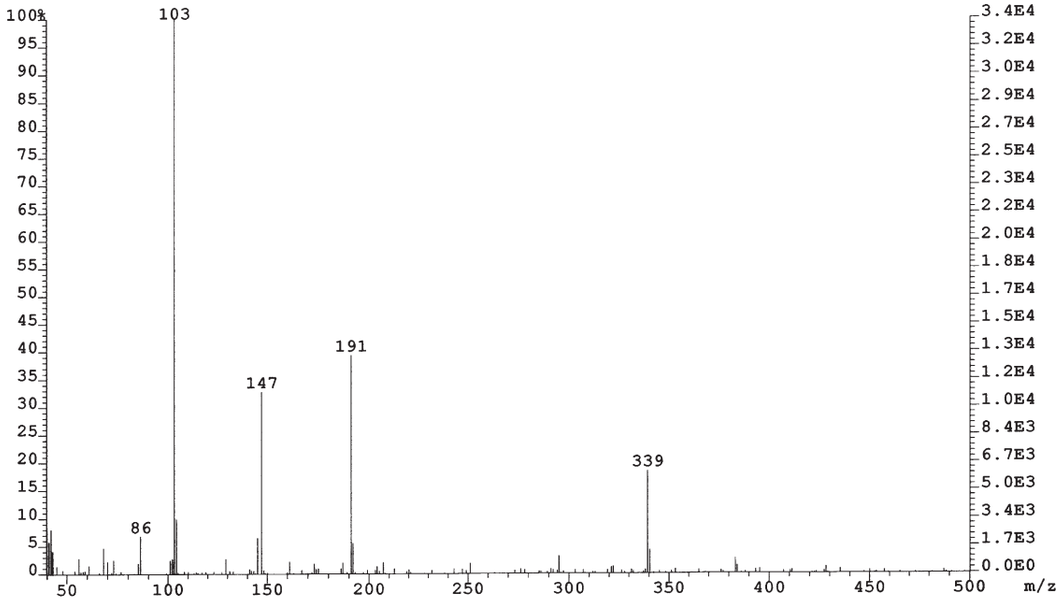

more extensive fragmentation in the negative mode, occurring mainly by successive elimination of CH_2CH_2O.

To test whether the ions observed were the result of FAB-induced "delayed chemistry" (22), we plotted the total ionic current and the currents of the ions of *m*/*z* 103 and *m*/*z* 339, formed after CO_2 absorption, vs. the elapsed time (Fig. 9). The ionic currents are approximately constant for the duration of the experiment (94 s), showing that the ions are not the result of a delayed chemistry process. They may exist as preformed ions in the condensed phase or they are formed in the selvedge in a "prompt chemistry process." Either way, they are much more closely related to their counterparts in the condensed phase than would be the case if they were the result of a FAB-induced delayed reaction.

The FAB mass spectrum of Quadrol, obtained without bubbling in of CO_2, has a very low signal-to-noise ratio, and no significant information could be retrieved from it. No spectrum could be obtained after introducing CO_2, because the signal-to-noise ratio is even lower.

Conclusions

THEED in the absence of water interacts reversibly, and to a great extent, with CO_2. Alkyl carbonate formation is a

© 1999 NRC Canada

Fig. 9. Ionic current: (*a*) total ion current; (*b*) current of the ion *m*/*z* 339; (*c*) current of the ion *m*/*z* 103.

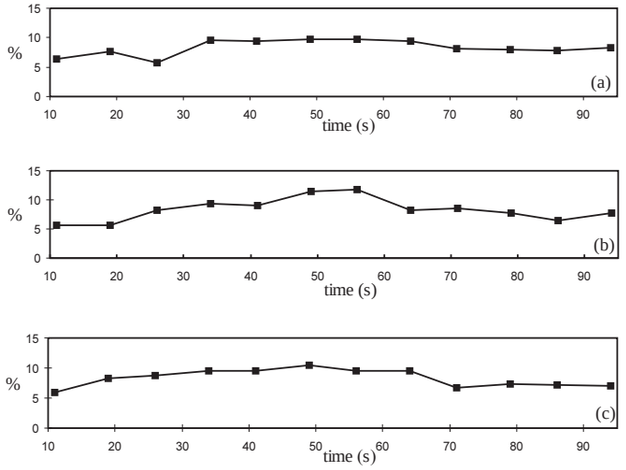

hypothesis that agrees with the results obtained. The other two tertiary alkanolamines TEA and Quadrol interact to such a small extent with CO_2 that for TEA no evidence of the interaction was found by using mass spectrometry, and for Quadrol practically no mass increase with CO_2 injections was detected. Quadrol has a high viscosity, which makes the bubbling of CO_2 difficult. Also the FAB mass spectrum of Quadrol has a very low signal-to-noise ratio, and no reliable information could be obtained from it.

An effective balance between physical and chemical parameters is perhaps the explanation for the highest sensitivity of THEED. Quadrol is the most viscous of the three alkanolamines, so the diffusivity of CO_2 is low. The highest diffusivity in TEA is probably overcome by the lesser availability of its OH groups, because TEA possess more intramolecular hydrogen bonding than THEED.

The ranking of the three alkanolamines in relation to the extent of their interaction with CO_2 was inferred from QCM experiments. However, we have to bear in mind that the QCM responds not only to mass change but also to changes in viscosity. This is not a problem when the interaction of CO_2 with a single alkanolamine is used, because it increases the sensitivity to the changes, but it can influence comparison of results obtained with different alkanolamines.

One should also note the differences in molecular organization depending upon whether the experiments were carried out with the QCM or with the spectrometers. In the first case the reaction took place at the surface, while in the second it occurred in the bulk of the alkanolamine.

Acknowledgements

The authors acknowledge the contributions of Dr. Artur Silva for collecting the NMR spectra, Emanuela Alexandra Santos for collecting some of the IR spectra, and Anabela Novo for assistance in sensor data collection.

References

1. O. Fatibello-Filho, J.F. Andrade, A.A. Suleiman, and G.G. Guilbault. Anal. Chem. **61**, 746 (1989).
2. M.T. Gomes, A.C. Duarte, and J.P. Oliveira. Sens. Actuators B: **B26**, 191 (1995).
3. M.T. Gomes, A.C. Duarte, and J.P. Oliveira. Anal. Chim. Acta, **327**, 95 (1996).
4. G.F. Versteeg and W.P.M. van Swaaij. Chem. Eng. Sci. **43**, 587 (1988).
5. H. Bosch, G.F. Versteeg, and W.P.M. van Swaaij. Chem. Eng. Sci. **44**, 2723 (1989).
6. R.N. Maddox, G.J. Mains, and A.R. Mahmud. Ind. Eng. Chem. Res. **26**, 27 (1987).
7. P.M.M. Blauwhoff, G.F. Versteeg, and W.P.M. van Swaaij. Chem. Eng. Sci. **39**, 207 (1984).
8. D. Barth, C. Tondre, G. Lappal, and J.-J. Delpuech. J. Phys. Chem. **85**, 3660 (1981).
9. T.L. Donaldson and Y.N. Nguyen. Ind. Eng. Chem. Fundam. **19**, 260 (1980).
10. J.L. Sotelo, F.J. Benitez, J. Beltran-Heredia, and C. Rodriguez. An. Quím. **87**, 212 (1991).
11. J.L. Cheney and J.B. Homolya. Anal. Lett. **8**, 175 (1875).
12. F. Benmakroha, T. Boudjerda, R. Boufenar, H. Allag, F. Djerboua, and J.J. MacCallum. Analyst, **118**, 401 (1993).
13. K.H. Karmarkar and G.G. Guilbault. Anal. Chim. Acta, **71**, 419 (1974).
14. M.T. Gomes, A.C. Duarte, and J.P. Oliveira. Anal. Chim. Acta, **300**, 329 (1995).
15. R. Quinn, J.B. Appleby, and G.P. Pez. J. Am. Chem. Soc. **117**, 329 (1995).
16. T.M. Abbott, G.W. Buchanan, P. Kruus, and K. Lee. Can. J. Chem. **60**, 1000 (1082).
17. H.-O. Kalinowski, S. Berger, and S. Braun. *In* Carbon-13 NMR spectroscopy. John Wiley & Sons, Great Britain. 1988.
18. L.J. Bellamy. *In* The infrared spectra of complex molecules. 3rd ed. Chapman and Hall, London. 1975.
19. W.J. Cridle and G.P. Ellis. *In* Spectral and chemical characterization of organic compounds. A laboratory handbook. John Wiley & Sons, London. 1976.
20. R.M. Silverstein, G.C. Bassler, and T. Morril. *In* Spectrometric identification of organic compounds. 5th ed. John Wiley & Sons, Inc., Singapore. 1991.
21. K. Nakamoto. *In* Infrared and Raman spectra of inorganic and coordination compounds. Part B: Applications in coordination, organometallic and bioinorganic chemistry. 5th ed. John Wiley & Sons, New York. 1997.
22. J. Sunner. Org. Mass Spectrom. **28**, 805 (1993).

© 1999 NRC Canada

Partial leaching as an aid to slurry nebulization for the analysis of soils by ICP-MS with flow injection and mixed-gas plasmas

Anthony Treveidi Persaud, Diane Beauchemin, Heather Edith Jamieson, and Robert J.C. McLean

Can. J. Chem. Downloaded from www.nrcresearchpress.com by University Town Library of Shenzhen on 09/05/12
For personal use only.

Abstract: Acid leaching (with 1 mol dm^{-3} HNO_3) was combined with slurry nebulization in inductively coupled plasma mass spectrometry, with mixed-gas plasmas and flow injection, in an attempt to facilitate the quantitative analysis of heterogeneous materials such as soils. Matrices analyzed ranged from marine sediment to metal-contaminated soil, and were chosen for their variety in elemental composition and matrix structure. Slurries were prepared by first grinding the material to less than 3 μm in high-purity water and then diluting to 0.1% (w/v) with 1 mol dm^{-3} HNO_3, which served as both a dispersing and a leaching agent. The resulting slurries were injected (0.25 cm^3) into a deionized distilled water carrier. Under these conditions, the sensitivity was about 85% of that achieved by continuous nebulization. Multivariate optimization of the nitrogen percentage, forward torch power, and aerosol carrier gas flow rate was conducted to find conditions maintaining sensitivity constant between different slurries. Since no set of conditions was optimal for all elements, a compromise set was selected, which resulted in accurate results for La and Pb in a series of reference materials, by calibrating with aqueous standards. On the other hand, the results for V and Cr were almost systematically low, indicating that the compromise plasma conditions did not allow complete atomization/ionization of these elements.

Key words: inductively coupled plasma mass spectrometry, slurry nebulization, flow injection, mixed-gas plasma.

Résumé : Un lessivage acide (par HNO_3 1 mol dm^{-3}) fut combiné à la nébulisation de suspension, les plasmas mixtes et la technique d'injection en flot continu dans le but de façiliter l'analyse quantitative de matériaux hétérogènes, tels que des sols, par la spectrométrie de masse à plasma couplé inductivement. Les matrices analysées vont des sédiments marins aux sols contaminés par des métaux; elles furent choisies pour leur variété en composition élémentaire et en structure. Des suspensions furent préparées en broyant d'abord chaque matériau jusqu'à moins de 3 μm dans de l'eau de haute pureté, et en diluant ensuite jusqu'à 0.1% (m/v) avec HNO_3 1 mol dm^{-3} qui servit d'agent de dispersion et de dissolution. Les suspensions résultantes furent injectées (0.25 cm^3) dans un flot d'eau distillée déionisée. Dans ces conditions, la sensibilité était environ 85% de celle obtenue par nébulisation continue. Une optimisation multifactorielle du pourcentage d'azote, de la puissance appliquée et du débit du gaz de nébulisation fut conduite afin de déterminer des conditions maintenant la sensibilité constante pour diverses suspensions. Comme aucun ensemble de conditions ne s'est révélé optimal pour tous les éléments, un ensemble compromis fut selectionné et donna des résultats exacts pour La et Pb dans une série de matériaux de référence, par étalonnage avec des solutions étalons. D'un autre côté, les résultats pour V et Cr furent presque systématiquement bas, ce qui indique que les conditions compromises du plasma n'ont pas permis une atomisation/ionisation complète de ces éléments.

Mots clés : spectrométrie de masse à plasma couplé inductivement, nébulisation de suspension, injection en flot continu, plasmas mixtes.

Introduction

Inductively coupled plasma mass spectrometry (ICP-MS) is a method with low detection limits, a wide linear dynamic range, and high sample throughput (1). However, the accuracy of results obtained using solutions of rocks or minerals depends on the dissolution method, which can cause loss of volatile analytes (2). Incomplete transfer of elements to solution is also possible for mineral phases that are highly resistant to acid attack, such as chromium or vanadium oxides (2).

Although ICP-MS was originally designed to analyze solutions, analysis of other matrices is possible, as long as the

Received July 31, 1998.

A.T. Persaud and D. Beauchemin.[1] Department of Chemistry, Queen's University, Kingston, ON K7L 3N6, Canada.
H.E. Jamieson. Department of Geological Sciences, Queen's University, Kingston, ON K7L 3N6, Canada.
R.J.C. McLean. Department of Biology, Southwest Texas State University, 601 University Drive, San Marcos, TX 78666-4615, U.S.A.

[1]Author to whom correspondence may be addressed. Telephone: (613) 545-2619. Fax: (613) 545-6669.
e-mail: beauchmn@chem.queensu.ca

 © 1999 NRC Canada

Can. J. Chem. Downloaded from www.nrcresearchpress.com by University Town Library of Shenzhen on 09/05/12
For personal use only.

Table 1. FI-ICP-MS operating conditions used throughout this work.

Rf forward power/kW	1.2,[a] 1.3, 1.4
Rf reflected power/W	<15
Outer gas flow rate/dm^3 min^{-1}	12 or 15[a]
% N_2 in Ar outer gas	0, 5, 10, 15[a]
Ar auxiliary gas flow rate/dm^3 min^{-1}	2[a]
Ar aerosol carrier flow rate/dm^3 min^{-1}	0.8[a]–1.1
DDW carrier flow rate/cm^3 min^{-1}	1, 2, 3[a]
Sample loop volume/μL	50, 100, 250, 500[a]
Bessel box barrel/V	1.72
Einzel lenses 1 and 3/V	–6.14
Bessel box end lenses/V	–20.1
Bessel box stop/V	–4.93
Ni sampler orifice diameter/mm	1.14
Ni skimmer orifice diameter/mm	0.89
Interface pressure/Torr	1
Mass spectrometer pressure/Torr	10^{-6}–10^{-5}
Resolution (at 10% peak height)	1.1

[a] Optimum conditions for the analysis of slurries.

sample can be introduced into the gas flow (3). In particular, slurry analysis is similar enough to solution analysis that conventional instruments can be used with little modification and calibration may be accomplished with aqueous standards (4). The approach was recently thoroughly reviewed by Ebdon et al. (4).

Slurry preparation, which can be as simple as the "bottle-and-bead" approach of Williams et al. (5), has the advantage of involving few chemicals. In comparison to total dissolution approaches, sample preparation is simplified, so slurry nebulization can be used to avoid analyte loss, contamination, incomplete dissolution, and the hazardous use of $HClO_4$ and (or) HF (6).

ICP-MS analysis of some slurry-nebulized reference soils was carried out previously using continuous nebulization (5) and flow injection (FI) (7). No sampler cone blockage occurred during the continuous nebulization of 0.05% w/v slurries of soil with particle sizes of <3 μm (5). Of the six trace elements determined using an external calibration with aqueous standards, the results for V, Cr, and Ni were in agreement with the certified values whereas those for Cu, Co, and Zn were higher than expected.

Flow injection (7) allowed the analysis of 1% w/v slurries, which would have resulted in blockage after about 30 min of continuous nebulization (5). Furthermore, under appropriate conditions, 0.5 cm^3 injections provided the same signal as for continuous nebulization of the same solutions, while reducing sample consumption and eliminating blockage problems (7). Under these conditions, accurate analysis of two reference soil slurries could be achieved, using a conventional calibration with standard solutions (7). However, only two trace elements, V and Cu, were determined.

For a calibration using standard solutions to be successful for the analysis of slurries, several parameters have to be considered (4). Amongst the most important are the particle size, the dispersion, i.e., colloidal stability of the slurry, and the ICP system (i.e., nebulizer, spray chamber, and torch injector), which determine the particle size that will ultimately reach the plasma (4). Ideally, to minimize transport interferences, a single particle should be present within each aerosol droplet, and the size of that particle should be such that the overall density of the droplet is not significantly different from that of a particle-free droplet (8). Under these conditions, the slurry aerosol would behave like a solution aerosol in the sample introduction system.

Because of the heterogeneous nature of soils and the varying density of the particles, segregation of different analyte-containing phases may occur during aerosol transport to the plasma. The smallest possible solid particle size is therefore recommended, to minimize variations in densities amongst the resulting aerosol droplets (8). One way to reduce particle size further from that achieved by grinding is to perform a leaching of the slurry with an acid. This approach was recently used for the quantitative determination of As in cigarette tobaccos by hydride generation atomic absorption spectrometry (9).

It is combined here to ICP-MS with FI for sample introduction of the slurries into a mixed-gas plasma. The latter has indeed been demonstrated to reduce atomization interferences during the ICP-AES (atomic emission spectroscopy) analysis of highly refractory firebrick particles (10). The intent of this paper is therefore to minimize transport effects by using FI of acid-leached slurries and to minimize atomization interferences with the mixed-gas plasma so as to provide a fast, reliable ICP-MS method for trace-element determination in soils by calibration using standard aqueous solutions.

Experimental

Reagents

Multielemental standard solutions were prepared by dilution of 1000 ± 5 mg dm^{-3} monoelemental stock solutions (Spex Industries, Edison, N.J.) with high-purity nitric acid (Seastar, Sidney, B.C.) and deionized distilled water (DDW) (Milli-Q+, Millipore, Mississauga, Ont.).

Standard reference materials (SRMs)

A variety of SRMs were used: soils GSS-1, -2, -4, and -7 from the Institute of Geophysical and Geochemical Prospection (IGGE), Ministry of Geology, and the Institute of Rock and Mineral Analysis (IRMA) in China; soils SRM-2710 and -2711 from the U.S. National Institute of Standards and Technology (NIST); marine sediment PACS-1 from the National Research Council of Canada (NRC). Two rock SRMs were also included in the study: basalt SRM-688 from NIST and syenite SY-2 from the Canadian Certified Reference Materials Project (CCRMP) of the Canada Centre for Mineral and Energy Technology (CANMET).

Slurry preparation

The bottle-and-bead method (5), with 30 cm^3 stoppered polypropylene bottles and 1.4–3.35 mm (in diameter) zirconia beads (Geneq Inc., Montréal, Que.), was used for slurry preparation. The bottles and zirconia beads were rinsed with 1 mol dm^{-3} HNO_3, before 0.25 g soil, 5 g zirconia beads, and 10 cm^3 DDW were placed in each bottle. Shaking was accomplished with a wrist action shaker for 24 h. The slurries were recovered into 250 cm^{-3} volumetric flasks that were filled to volume with 1 mol dm^{-3} HNO_3. The beads

© 1999 NRC Canada

Can. J. Chem. Downloaded from www.nrcresearchpress.com by University Town Library of Shenzhen on 09/05/12
For personal use only.

Fig. 1. Average count rate observed for 10 injections of a control (◆) and for 5 injections of a slurry of PACS-1 (▲) and of GSS-1 (×).

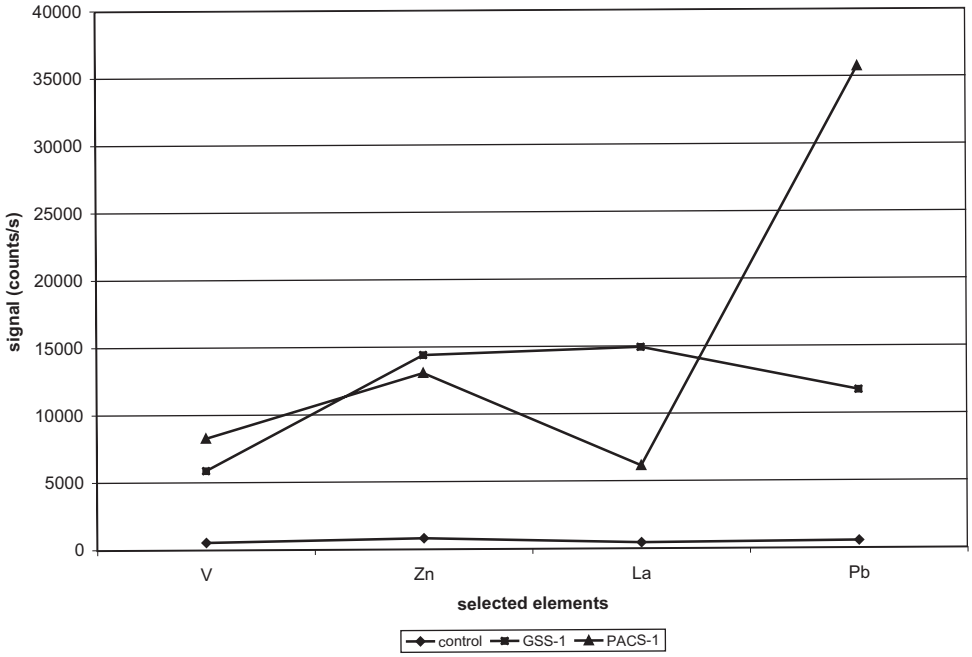

Table 2. Percentage of metal leached from 3 SRMs by dispersing agents.

	DDW			1 M HNO_3		
Element	PACS-1	NIST-2710	NIST-2711	PACS-1	NIST-2710	NIST-2711
V	4		1	33	19	11
Cr	2		0	45	57	19
Zn	13	6	11	>100	86	>100
Mo	30	6	46	77	96	21
La	NA[a]	0	2	NA	62	51
Pb	2	2	6	68	74	67

[a]No expected concentration was available.

were removed by decanting the slurry and rinsing the bottle at least 3 times, with each rinse also decanted into the volumetric flask. The slurries were then transferred to polypropylene bottles. An ultrasonic bath was employed to keep the slurries dispersed during ICP-MS analysis. Controls were prepared by following exactly the same procedure without soil.

Acids other than HNO_3 were not tried, since most would contribute additional peaks to the background spectrum and thereby result in spectroscopic interferences on many trace elements determined. More concentrated HNO_3 solutions than 2 mol dm^{-3} were also avoided since they would not only increase corrosion of the MS interface, but would also increase sample preparation cost.

Some slurries were centrifuged at 10 000 G (Beckman induction drive centrifuge, model J2–21M, used with Beckman Rotor JA-14, Spinco Division of Beckman Instruments Inc., Palo Alto, Calif.) for 1 h and decanted for supernatant analysis to determine the efficiency of the acid leaching.

Equipment

An ELAN 500 ICP-MS instrument (Perkin–Elmer SCIEX, Thornhill, Ont.) was used, with several modifications. A homemade x–y–z translation stage under the torch box allowed precise alignment of the plasma with respect to the interface. A low-flow PlasmaTherm (SCP Science, Montreal, Que.) torch was used instead of the standard ICP-MS one. The standard Meinhard C-3 concentric nebulizer (which is connected to a Scott double-pass spray chamber) was replaced by a Conespray nebulizer (Perkin–Elmer, Norwalk, Conn.). A mass flow controller (model 1259B, MKS Instruments, Andover, Mass.) regulated the aerosol carrier gas flow rate. A specified N_2 percentage was added to the outer plasma gas using a gas proportioner (model 7371, Matheson of Canada Ltd., Whitby, Ont.). A peristaltic pump (Minipuls 3, Gilson Medical Electronics Inc., Middleton, Wis.) kept the sample uptake or carrier flow rate constant at 3 cm^3 min^{-1}.

Flow injection setup

A single-line FI manifold was used, which consisted of a valve (model 5020, Rheodyne Inc., Cotati, Calif.) installed on an automatic switching module (Universal module, Anachem, Luton, U.K.) downstream of the peristaltic pump. The sample injection valve was connected to the nebulizer with 1 m of 0.8 mm i.d. Teflon tubing, similarly to the earlier FI study (7). The sample injection loop was filled by suction into a syringe directly from the sample bottle, to prevent contaminations incurred by syringe injection. The

© 1999 NRC Canada

input line to the FI loop was cleaned by flushing with 1 mol dm^{-3} HNO_3 between injections to minimize memory effects. All FI-ICP-MS operating conditions are summarized in Table 1.

Initial optimization

An Ar plasma was ignited at 1.2 kW with 9 dm^3 min^{-1} outer gas flow rate, which was then increased to either 12 dm^3 min^{-1} or 15 dm^3 min^{-1} upon ignition. The highest flow rate was used whenever power was increased and (or) a mixed-gas plasma was formed, to avoid torch melting. A 100 μg dm^{-3} standard solution of Li^+, Rh^+, and Pb^+ in 1% v/v HNO_3 was aspirated while manual triaxial plasma–MS interface alignment was conducted to optimize the Rh^+ signal. The voltages to the ion lenses were then adjusted, if needed, to equalize the Li^+ and Pb^+ signals. Then, the aerosol carrier gas flow rate was adjusted to maximize all three ion signals. This resulted in the best compromise conditions for multielemental analysis of supernatant solutions.

For the analysis of slurries, the optimization was performed similarly, except that the optimal aerosol carrier gas flow rate was determined by repeated injection of a slurry at various aerosol carrier gas flow rates. The flow rate giving maximum transient peak height for most analytes was selected.

Mixed-gas plasma formation

Nitrogen was slowly added to the outer gas stream of an already ignited Ar plasma, until the desired N_2 percentage was reached. Care was required to prevent plasma extinction as a result of the sudden plasma shrinkage that occurred when N_2 was initially added. Reflected power was kept lower than 15 W by manual fine tuning.

Experimental design

The percentage of N_2 in the outer plasma gas (5, 10, or 15%), forward power (1.2, 1.3, or 1.4 kW), and nebulizer gas flow rate (0.800, 0.900, or 1.00 dm^3 min^{-1}) were optimized together, because they were critically interdependent. Three values were considered sufficient to detail the effects of each parameter, with the addition of a 1.2 kW Ar-only plasma as a reference. To minimize instrumental drift, conditions were randomly selected from the 36 possible parameter combinations until all had been tested, while maintaining the optimum conditions previously determined for other experimental parameters (see Table 1). The study was carried out for each of three SRMs (GSS-7, PACS–1, and NIST-2710). For each set of conditions, the relative standard deviation (RSD) of the average sensitivity obtained for the three slurries was calculated for each element.

Data acquisition and processing

The "Graphics" program of the Elan 5000 multielement data acquisition software, Version 2, was used in the "Measurement" scanning mode, with 50 ms dwell time, 1 sweep per reading, and 1 measurement per peak (at the assumed peak centre).

In-house DOS GWBASIC programs were used to process the FI peaks. Polynomial smoothing was first performed with a seven-point moving window. Background-subtracted peak height was then determined (using the background on both sides of the peak to linearly interpolate that corresponding to the peak maximum).

The analysis of soil slurries was carried out by injecting a solution blank followed by the corresponding standard solution, a control, and then the slurries. Each blank or control count rate was then subtracted from the corresponding solution or slurry count rates.

Given the wide linear dynamic range of ICP-MS, sensitivity was determined for soil SRM slurries, using a one-point calibration. All sensitivity comparisons were carried out during the same day to minimize instrumental drift and changes in sensitivity associated with regular instrumental maintenance (i.e., change or cleaning of torch, sampler, skimmer, etc.). Detection limits (expressed with respect to the undiluted solid) were calculated as three standard deviations of the control count rate divided by the sensitivity.

Results and discussion

Slurry preparation

The grinding time was selected by examining backscattered electron images of ground samples and comparing them to that of a reference grid. Samples of sandy soil, but not of other soils, were ground down to 3 μm in 2 h. However, after 24 h of grinding, no samples (including peat- and clay-rich samples) had particles larger than 3 μm. Increasing the grinding time to 48 h had no significant effect on either the particle size or the signal obtained from the slurry. Thus, 24 h (overnight) was used for the remainder of the work.

Although the addition of acid to the dispersing agent during the grinding of geochemical materials has been reported to significantly improve analyte recoveries (11, 12) or reduce the size of some especially difficult mineral phases (13), this approach was not selected here. Only DDW was used during grinding, with acid added afterward, to minimize background metal levels originating from the grinding beads (13). The relatively low signal obtained for a control compared to an uncontaminated soil SRM (GSS-1) in Fig. 1 shows that this procedure was adequate.

Nitric acid was used to leach out metals and to, possibly, further reduce the particle size through partial dissolution (although the particle size after leaching was not actually measured in this study). Table 2 shows that 1 mol dm^{-3} HNO_3 leached metals out of soils and sediments. Since 2 mol dm^{-3} HNO_3 did so to a similar extent, all slurries were made up in 1 mol dm^{-3} HNO_3 thereafter. This medium also provided the best compromise in terms of precision (i.e., RSD of seven injections), detection limit, sensitivity, and sensitivity equality between different slurries. This is in agreement with the literature since, at the corresponding slurry pH of approximately 1.5, the zeta potential is expected to be far away from the isoelectric point (i.e., the stability of the suspension is ensured through an electrostatic stabilizing mechanism (14)). The best signal-to-noise ratio in ICP–AES and stability (i.e., no aggregation or flocculation) were similarly obtained for an alumina slurry by adjusting the pH away from the isoelectric point, without using any other dispersant (15).

The leaching efficiency was also checked as a function of time. However, supernatants of slurries that were allowed to settle for 2 months showed essentially the same concentra-

© 1999 NRC Canada

Can. J. Chem. Downloaded from www.nrcresearchpress.com by University Town Library of Shenzhen on 09/05/12
For personal use only.

Can. J. Chem. Downloaded from www.nrcresearchpress.com by University Town Library of Shenzhen on 09/05/12
For personal use only.

Fig. 2. Examples of typical flow injection peaks that were obtained with sample injection volumes of 0.1 (■), 0.25 (▲), and 0.5 (×) cm^3. Here Zn was monitored during injections of a slurry of NIST-2710.

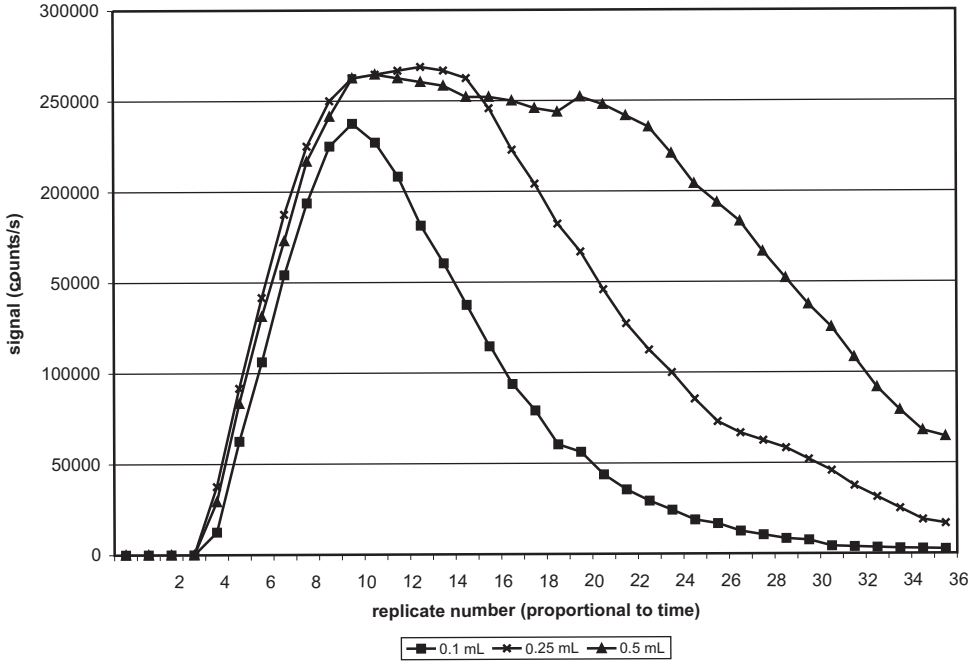

tion of metals as those of slurries that were immediately centrifuged. Very little signal was detectable in supernatant for some elements (e.g., V) due to the inability of these concentrations of HNO_3 to attack the silicates or relatively insoluble oxides in which they are found, while other elements are partially or fully leached. (The greater than 100% recoveries observed in some cases were the result of spectroscopic interferences, as discussed in greater detail below.)

Slurry flow injection

No blockage of either the sampler cone or the Conespray nebulizer was ever observed. However, despite the continuous rinsing by the DDW carrier, the first control injection immediately after a slurry sample injection was typically elevated in metal concentration, and was visually rejected in favour of an extra control injection.

Nonetheless, as shown in Fig. 2, a typical transient FI peak was observed upon injection of a 0.1 cm^3 (or 0.05 cm^3) aliquot of slurry. Larger volumes (0.25 and 0.5 cm^3) led to a wider transient signal, with a tendency to level into a plateau at its top. The plateau is particularly evident with 0.5 cm^3 injections, and was close to the signal that would be obtained if the slurry was continuously nebulized. Since, ideally, maximum sensitivity (i.e., that of continuous nebulization) is desired with the regular wash-out feature of flow injection, a 0.25 cm^3 loop was selected and used for the remainder of this work. It provided a dispersion coefficient (defined as the ratio of the steady-state signal from continuous nebulization over the height of the FI peak) of about 1.2 (as opposed to 1.7 for the 0.1 cm^3 loop), i.e., only a small sacrifice in sensitivity.

Wash-out time and peak reproducibility were the deciding factors when the DDW carrier flow rate was determined. Flow rates from 1 to 3 cm^3 min^{-1} resulted in similar signal intensity. (Even higher carrier flow rates were possible, but would have resulted in erratic nebulization since the nebulizer was designed to operate with 2–3 cm^3 min^{-1} sample uptake. Although a nebulizer can be starved, to an extent, by decreasing the sample uptake rate from its optimal value without a major sacrifice in sensitivity (16), it cannot be flooded.) However, 3 cm^3 min^{-1} gave more reproducible peaks than 2 cm^3 min^{-1}, and also provided faster wash-out times. It was therefore selected for the remainder of this study.

Table 3. Operating conditions resulting in the lowest relative standard deviation (RSD) in sensitivity between three slurries (or the next-to-lowest, in parentheses).

$\%N_2$	Rf power /kW	Aerosol carrier gas flow /cm^3 min^{-1}	Analytes
15	1.4	900	V, Cu, Zn, (Pb), (Mo)
0	1.2	800	Mo, Cr, Co
5	1.3	800	La, Co, (Ni)

Injection peak signals using 0.25 cm^3 sample loop volume, 3 cm^3 min^{-1} carrier flow rate, 900 cm^3 min^{-1} nebulizer gas flow rate, and an Ar-only plasma, showed that peak shape, width at half height, and the dispersion coefficient were very similar for solutions and soil slurries. This is in agreement with the dispersion behaviour reported for solid particles injected in a straight tube where, at a sufficiently high flow rate for the solid particle size, the soil slurry behaved like a solution (17). It further encouraged an attempt to calibrate soil slurries with aqueous solution standards.

Mixed-gas plasmas

Co-optimization of the percentage of N_2, the forward power, and the aerosol carrier gas flow rate, which was carried out

© 1999 NRC Canada

Can. J. Chem. Downloaded from www.nrcresearchpress.com by University Town Library of Shenzhen on 09/05/12
For personal use only.

Table 4. Comparison of the Pb and La concentrations found (± standard deviation, n = 5) and the certified (suggested) value (± confidence limits, 95% level[a]) in μg g^{-1} (in the solid).

SRM	Certified Pb	Pb found	Certified La	La found
NIST-2711	1162 ± 31	1263 ± 71	(40)	32 ± 2
NIST-2710	5532 ± 80	6750 ± 460	(34)	25 ± 2
GSS-1	98 ± 15	120 ± 9	34 ± 5	**30 ± 3**
GSS-2	20.2 ± 3.0	**20 ± 3**	164 ± 24	155 ± 10
GSS-4	58.5 ± 8.8	**67 ± 3**	53 ± 8	**52 ± 7**
GSS-7	13.6 ± 2.0	**15 ± 2**	45 ± 7	**50 ± 5**
PACS-1	404 ± 20	368 ± 8		
NIST-688	3.3 ± 0.2	4.0 ± 0.8		
SY-2	85 ± 8	66 ± 5	75 ± 9	**74 ± 2**

[a]The errors in the certified values for the GSS series are 15% relative uncertainties.

Table 5. Comparison of the Zn and Mo concentrations found[a] (n = 5) and the certified (suggested) value (± confidence limits, 95% level[b]) in μg g^{-1} (in the solid).

SRM	Certified Zn	Zn found	Certified Mo	Mo found
NIST-2711	350.4 ± 4.8	384	(1.6)	22
NIST-2710	6952 ± 91	9655	(19)	21
GSS-1	680 ± 100	854	1.4 ± 0.3	4
GSS-2	42 ± 6	**47**	1.0 ± 0.2	2
GSS-4	210 ± 32	312	2.6 ± 0.5	2
GSS-7	142 ± 21	249	2.9 ± 0.6	2
PACS-1	824 ± 22	773	12.3 ± 0.9	8
NIST-688	(58)	58		
SY-2	248 ± 15	231	1.8 ± 1.6	**2**

[a]The relative standard deviation was 2–10% for Zn and 10–20% for Mo.

[b]Errors on certified values for the GSS series are 15% relative uncertainties (20% for Mo).

to minimize the difference in sensitivities between 3 SRMs (PACS-1, GSS-7, and NIST-2710), did not result in a single set of optimal conditions for all the elements tested (V, Pb, Mo, La, Cr, Ni, Co, Cu, Zn). Factorial analysis was also unsuccessful (i.e., no suitable model could be found to fit the data). Table 3 shows three different sets of conditions that resulted in the least variation in sensitivity (or the next-to-least, in parentheses) for the various elements tested in the three slurries.

Analysis of SRMs

Compromise conditions were therefore required for multielemental analysis. The set of conditions providing the lowest average RSD for all the elements was selected: 15% N_2, 1.2 MW of torch power, with 800 cm^3 min^{-1} of aerosol carrier gas flow rate. Nine slurries were analyzed under these conditions, using an aqueous standard solution for external calibration. The results are summarized in Tables 4–6. In each case, averages that fall within the confidence limits of the corresponding certified value are highlighted in bold.

No accurate determination of Co, Ni, or Cu could be carried out using $^{59}Co^+$, $^{60}Ni^+$, and $^{63}Cu^+$ because of spectroscopic interferences from polyatomic species ($^{43}Ca^{16}O^+$ on $^{59}Co^+$, $^{44}Ca^{16}O^+$ on $^{60}Ni^+$, and $^{40}Ar^{23}Na^+$ on $^{63}Cu^+$) arising from the matrix. In fact, since Co is monoisotopic and all of the Ni isotopes are interfered with by CaO and (or) CaOH, the determination of these elements is precluded in Ca-containing matrices unless the Ca is removed. In the case of Cu, it may be possible to use $^{65}Cu^+$, with a concurrent sacrifice in sensitivity.

Table 4 shows that Pb and La may be accurately determined by this method. The results are particularly impressive for La where all the concentrations fall within the confidence interval of the certified values. Using five control replicates, detection limits in the solid of 7.1 μg g^{-1} for Pb and 2.7 μg g^{-1} for La were calculated. Calibration by a SRM (GSS-1) chosen for its uncontaminated, intermediate metal concentrations was also tried but was less accurate than calibration by aqueous standard for both Pb and La. This is not surprising since it is very likely that, for heterogeneous slurries, "elements will not be distributed uniformly and the particle size distributions and densities of elements within the sample may not be comparable to those for the slurry being analysed" (4).

In the case of Zn (Table 5), a positive bias was observed in most cases, as is also evident in the results obtained by continuous nebulization of soil slurries (5). This bias is very likely a result of spectroscopic interferences from the matrix. For instance, a $^{50}Ti^{16}O^+$ interference on $^{66}Zn^+$ led to 249 and 312 μg g^{-1} instead of 142 and 210 μg g^{-1} for GSS-7 and GSS-4, respectively, which are the two soils with the highest Ti content (2.01 and 1.08% w/w, respectively). Another positive bias may come from the interference of $^{40}Ar^{26}Mg^+$. Quantitative analysis (using $^{66}Zn^+$) is therefore possible only if the level of these sources of interferences is relatively low (as in GSS-2 and the two rock SRMs, NIST-688 and SY-2). An alternative would be to use $^{68}Zn^+$ for the determination, albeit with a sacrifice in sensitivity. Results in closer

© 1999 NRC Canada

Can. J. Chem. Downloaded from www.nrcresearchpress.com by University Town Library of Shenzhen on 09/05/12
For personal use only.

Table 6. Comparison of the V and Cr concentrations found[a] (n = 5) and the certified (suggested) value (± confidence limits, 95% level[b]) in μg g^{-1} (in the solid).

SRM	Certified V	V found	Certified Cr	Cr found
NIST-2711	81.6 ± 2.9	36	(47)	37
NIST-2710	76.6 ± 2.3	25	(39)	27
GSS-1	86 ± 13	49	62 ± 9	48
GSS-2	62 ± 9	35	47 ± 7	38
GSS-4	247 ± 37	381	370 ± 56	**366**
GSS-7	245 ± 37	438	410 ± 62	**364**
PACS-1	127 ± 5	66	113 ± 8	64
NIST-688	(250)	67	332 ± 9	93
SY-2	50 ± 8	3	9.5 ± 2.9	1

[a]The relative standard deviation was 2–10% for Cr and V.

[b]Errors on certified values for the GSS series are 15% relative uncertainties.

agreement with the certified values were obtained for Mo (Table 5). Although the Mo level was in general too low for accurate quantitative analysis, semi-quantitative analysis (i.e., within a factor of 2 of the expected concentration) was nonetheless possible.

In contrast, the V and Cr results were almost systematically low compared to the expected values (Table 6). The results for Cr were closer (or in agreement, for GSS-4 and GSS-7) than those for V, which is consistent with the higher percentage of Cr that was leached out (Table 2). A comparison of Table 6 with Table 2 also reveals that, at least for PACS-1, NIST-2710, and NIST-2711, the measured concentration corresponds to 12–33% more than the leachable concentration of these elements but the total is, in general, less than 100%. It suggests that the selected operating conditions did not allow complete atomization/ionization of the solid particles. However, quantitative analysis may still be possible if the optimal conditions found for these elements (see Table 3) were to be used instead of the compromise conditions. They indeed correspond to an increase in residence time in the plasma and should therefore reduce atomization interferences. A torch with a wider injector (than the 1 mm injector used in this work) could also be used to increase both the residence time in the plasma and the mean particle droplet size of the aerosol entering the plasma (4). Indeed, a 3 mm bore injector was previously used for the successful determination of V (5, 7) and Cr (5) in two SRM soils.

Conclusions

In comparison to earlier work on the analysis of soils by slurry nebulization ICP-MS (5, 7), the proposed approach allowed the quantitative determination of Pb and La, two elements that had not been previously looked at in this matrix. The determination of Zn and Mo should also be possible, based on the similar or better leaching efficiency observed for these elements in comparison to Pb and La (Table 2), provided that an interference-free isotope is used for the determination of Zn and the level of Mo can be detected (alternately, the concentration of the slurry could be increased to 1% w/v since the FI system can handle it).

On the other hand, the proposed approach degraded the determination of V and Cr, which had been successfully determined before. The most important difference between this work and previous studies is the smaller bore of the injector (1 mm vs. 3 mm), which restricted the mean particle droplet size reaching the plasma. Although acid-leaching the slurry was attempted to further reduce its particle size, and mixed-gas plasmas were used to minimize atomization differences between the various particles, the wider bore injector may be nonetheless required and will be the subject of a future study.

Acknowledgements

D.B. gratefully acknowledges funding from the Natural Sciences and Engineering Research Council of Canada (through Grant No. OGP0039487). The authors also sincerely thank Perkin–Elmer for the donation of ELAN 5000 software, and the National Research Council of Canada for the donation of PACS-1.

References

1. I. Jarvis and K.E. Jarvis. Chem. Geol. **95**, 1 (1992).
2. K.E. Jarvis and J.G. Williams. Chem. Geol. **77**, 53 (1989).
3. L. Ebdon, M.E. Foulkes, H.G.M. Parry, and C.T. Tye. J. Anal. At. Spectrom. **3**, 753 (1988).
4. L. Ebdon, M. Foulkes, and K. Sutton. J. Anal. At. Spectrom. **12**, 213 (1997).
5. J.G. Williams, A.L. Gray, P. Norman, and L. Ebdon. J. Anal. At. Spectrom. **2**, 469 (1987).
6. H.G.M. Parry and L. Ebdon. Anal. Proc. **25**, 69 (1988).
7. A.J. Ambrose, L. Ebdon, M.E. Foulkes, and P. Jones. J. Anal. At. Spectrom. **4**, 219 (1989).
8. P. Goodall, M.E. Foulkes, and L. Ebdon. Spectrochim. Acta, **48B**, 1563 (1993).
9. J. Mierzwa, S.B. Adeloju, and H.S. Dhindsa. Analyst, **122**, 539 (1997).
10. L. Ebdon and P. Goodall. J. Anal. At. Spectrom. **7**, 1111 (1992).
11. S.A. Darke, S.E. Long, C.J. Pickford, and J.F. Tyson. Fresenius' J. Anal. Chem. **337**, 284 (1990).
12. N.J. Miller-Ihli. J. Anal. At. Spectrom. **9**, 1129 (1994).
13. N.J. Miller-Ihli. Fresenius' J. Anal. Chem. **337**, 271 (1990).
14. J.C. Fariñas, R. Moreno, and J.-M. Mermet. J. Anal. At. Spectrom. **9**, 841 (1994).
15. J.H. Hyun, H.B. Lim, and C.H. Lim. Anal. Chim. Acta, **342**, 83 (1997).
16. M. Thompson and J.N. Walsh. Handbook of inductively coupled plasma spectrometry. 2nd ed. Blackie, Glasgow. 1989. pp. 68–71.
17. M. Hulsman, M. Bos, and W.E. van der Linden. Anal. Chim. Acta, **346**, 351 (1997).

© 1999 NRC Canada

Specific intramolecular interactions C—H···N in heteroaryl vinyl ethers and heteroaryl vinyl sulfides studied by ^{1}H, ^{13}C, and ^{15}N NMR spectroscopies and by ab initio calculations on molecular structures as well as on nuclear shieldings

Andrei V. Afonin, Alexander V. Vashchenko, Tatsuya Takagi, Atsuomi Kimura, and Hideaki Fujiwara

Can. J. Chem. Downloaded from www.nrcresearchpress.com by Peking University on 09/06/12
For personal use only.

Abstract: ^{1}H,^{13}C, and ^{15}N NMR spectra have been measured for a series of isostructural aryl (heteroaryl) vinyl sulfides and compared with analogues of vinyl ethers. It was found that "intramolecular interaction" of the α-hydrogen of the vinyl group with endocyclic nitrogen takes place in 2-vinylthiopyridines. This is in common with the findings for 2-vinyloxypyridine and the intramolecular interaction is shown to have a profile characteristic of hydrogen bonding. Also, the NMR spectral data show that this type of interaction is more intense (~1.5 times) in 2-vinyloxypyridine than in 2-vinylthiopyridine. This is probably due to the greater electronegative effect of oxygen compared to that of sulfur. To discuss these findings further in detail, ab initio calculations have been made, and the conformational energy map and the NMR chemical shifts have been discussed. The ab initio calculations, which were carried out on the D95++(d,p) basis set at the B3LYP level, confirm the planar structure of 2-vinyloxy- and 2-vinylthiopyridines, while other analogues of these ethers and sulfides were essentially nonplanar. Gauge-Independent Atomic Orbital (GIAO) calculations of the shielding constants, based on the same basis set, support the extraordinary low-field shift of the α-hydrogen in the vinyl group when it is situated close to endocyclic nitrogen. All these calculations support our proposal that the vinyl proton is involved in intramolecular hydrogen bonding in 2-vinyloxy- and 2-vinylthiopyridines.

Key words: NMR, intramolecular hydrogen bonding, ab initio calculation, GIAO.

Résumé : On a déterminé les spectres RMN du ^{1}H, du ^{13}C et du ^{15}N d'une série de sulfures d'aryle (hétéroaryle) et de vinyle et on les a comparés avec ceux de leurs analogues oxygénés. On a trouvé que, avec les 2-vinylthiopyridines, il se produit une « interaction intramoléculaire » de l'hydrogène-α du groupe vinyle avec l'azote endocyclique. Ceci se rapproche des observations faites avec la 2-vinyloxypyridine et l'interaction intramoléculaire est mise en évidence par un profil caractéristique de liaison hydrogène. Les données de spectroscopie RMN montrent aussi que ce type d'interaction est environ 1,5 fois plus intense dans la 2-vinyloxypyridine que dans la 2-vinylthiopyridine. Ce résultat est probablement dû à un effet électronégatif plus grand pour l'oxygène que pour le soufre. Dans le but d'analyser ces données plus en détail, on a effectué des calculs ab initio et on discute de la carte d'énergie conformationnelle et des déplacements chimiques en RMN. Les calculs ab initio, effectués au niveau B3LYP avec un ensemble de base D95++(d,p), confirment que les 2-vinyloxy- et 2-vinylthiopyridines existent dans une structure planaire alors que les autres analogues de ces éthers et de ces sulfures sont essentiellement non planaires. Les constantes d'écran calculées par la méthode « Gauge-Independent Atomic Orbital (GIAO) » en utilisant le même ensemble de bases sont en accord avec le fait que l'hydrogène α du groupe vinyle subit un déplacement extraordinaire vers les bas champs lorsqu'il est près de l'azote endocyclique. Tous les calculs théoriques sont en accord avec notre hypothèse selon laquelle le proton vinylique peut être impliqué dans une liaison hydrogène intramoléculaire dans la 2-vinyloxy- et la 2-vinylthio-pyridine.

Mots clés : RMN, liaison hydrogène intramoléculaire, calculs ab initio, « GIAO ».

[Traduit par la Rédaction]

Received September 9, 1998.

A.V. Afonin. Institute of Organic Chemistry, Favorsky St., 1, Irkutsk, 664033, Russia.
A.V. Vashchenko[1] and T. Takagi. Faculty of Pharmaceutical Sciences, Osaka University, 1–6 Yamada-Oka, Suita, Osaka, 565-0871 Japan.
A. Kimura and H. Fujiwara.[1] School of Allied Health Sciences, Faculty of Medicine, Osaka University, 1–7 Yamada-Oka, Suita, Osaka, 565-0871 Japan.

[1]Author to whom correspondence may be addressed. Telephone/Fax: (81) 06-6879-2577. e-mail: fujiwara@sahs.med.osaka-u.ac.jp

 © 1999 NRC Canada

Can. J. Chem. Downloaded from www.nrcresearchpress.com by Peking University on 09/06/12
For personal use only.

Introduction

Spectral (1) and crystallographic (2) data give evidence that polar C—H groups can form a weak hydrogen bond with heteroatom X (usually, X = N or O). For example, crystallographic data show that the H···X distance is significantly shorter than the sum of van der Waals radii in certain molecules, indicating the presence of inter- or intramolecular C—H···X hydrogen bonding (2). The clear nature of crystallographic data makes these investigations very attractive, but crystallographic data are not suited to detailed quantitative study and other spectroscopic studies necessary for discussion of all properties relevant to the C—H···X hydrogen bonding. It should also be stressed that the C—H···N interaction has not been investigated in detail although an overwhelming majority of studies have dealt with the C—H···O interaction (2). This paper is an attempt to compensate for this gap.

Hitherto, downfield shifts have been observed in the ^{1}H NMR signal (1*d*–1*h*) when hydrogen bonding of the type C—H···X (X = N or O) occurred. This trend is in common with the standard case of hydrogen bonding, O—H···X. Changes in the infrared frequencies have also been detected for the same case of hydrogen bonding C—H···X (1*a*–1*d*, 1*g*). However, such NMR and IR spectral effects are very small in the case of C—H···X compared to those observed in the standard case of O—H···X. This leads to ambiguity in an extended interpretation of the C—H···X hydrogen bonding. Probably, this C—H···X hydrogen bonding is weak and occupies a middle position on the energy scale between standard hydrogen bonding and nonspecific van der Waals interaction. Therefore it may be important to discuss such weak hydrogen bonding on the basis of advanced methods in molecular spectroscopy and molecular calculations.

Large numbers of aryl and heteroaryl vinyl ethers have recently been investigated by ^{1}H, ^{13}C, ^{15}N, and ^{17}O NMR spectroscopy and semiempirical quantum-chemical calculations (3). Statistical analysis of this quantity of structural data disclosed the presence of an anomaly in the NMR spectra. The anomaly, which appeared in the NMR parameters of the molecules under investigation, may be ascribed to the presence of weak intramolecular hydrogen bonding between the α-hydrogen of the vinyl group and the pyridine nitrogen atom (3).

Modern high-field NMR spectroscopy has proven to be an exceptionally powerful technique for detection of the weak interactions that occur between different molecules. Also, ab initio calculations in quantum chemistry are now becoming sufficiently accurate for the quantitative discussion of weak interactions in molecules (4, 5). Advances in these two different fields have promoted extensive studies on molecular properties and interactions in recent years. For example, the shielding tensor σ in nuclear magnetic resonance spectroscopy is one of the most important properties of a molecule, one that is closely related to the fine structure and chemical nature of the molecule, and hence has long been studied from the theoretical as well as the experimental point of view. As a consequence, a number of Hartree–Fock and post-Hartree–Fock calculations on the σ of different molecules have appeared in the literature. Among these, the GIAO method (6, 7) is very attractive to chemists since it is known to yield very accurate calculational results (8, 9). It was also shown (10) that density functional theory (DFT) tends to give more robust results than does the Hartree–Fock method: it provides calculations on geometrical structures, vibrational frequencies, and electronic structures that are reasonable compared with the results of experiment while the Hartree–Fock calculations fail to do so. Friedrich et al. (8) were the first to combine the GIAO method of Ditchfield (6) with DFT.

Scheme 1. Frameworks of the compounds used in the present study.

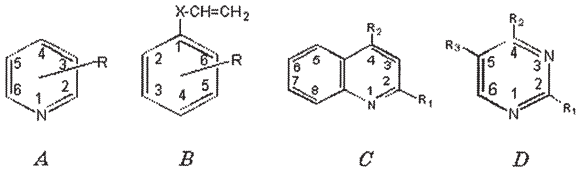

A *B* *C* *D*

Ethers (framework; substituent)	***Sulfides*** (framework; substituent)
1 (*A*; R: 2-O-CH=CH_2)	**16** (*A*; R: 2-S-CH=CH_2)
2 (*A*; R: 3-O-CH=CH_2)	**17** (*A*; R: 3-S-CH=CH_2)
3 (*A*; R: 4-O-CH=CH_2)	**18** (*A*; R: 4-S-CH=CH_2)
4 (*B*; R: 4-H, X=O)	**19** (*B*; R: 4-H, X=S)
5 (*B*; R: 4-Cl, X=O)	**20** (*B*; R: 4-Cl, X=S)
6 (*B*; R: 4-CH_3, X=O)	**21** (*B*; R: 4-H_2C-C$_6$H$_4$-S-CH=CH_2, X=S)
7 (*B*; R: 4-O-CH=CH_2, X=O)	**22** (*B*; R: 4-O-C$_6$H$_4$-S-CH=CH_2, X=S)
8 (*B*; R: 4-*Phthalamide*, X=O)	**23** (*B*; R: 4-C$_6$H$_4$-S-CH=CH_2, X=S)
9 (*B*; R: 4-Br, X=O)	**24** (*B*; R: 4-S-C$_6$H$_4$-S-CH=CH_2, X=S)
10 (*B*; R: 4-N=N-C$_6$H$_4$-N(CH_3)$_2$, X=O)	**25** (*B*; R: 4-N=N-C$_6$H$_4$-S-CH=CH_2, X=S)
11 (*B*; R: 5-$NHSO_2$-C$_6$H$_5$, X=O)	**26** (*B*; R: 5-NO_2, X=S)
12 (*B*; R: 4-NO_2, X=O)	**27** (*B*; R: 4-NO_2, X=S)
13 (*C*; R_1: O-CH=CH_2; R_2: H)	**28** (*C*; R_1: S-CH=CH_2; R_2: H)
14 (C, R_1: O-CH=CH_2, R_2: O-CH=CH_2)	
15 (*D*; R_1: O-CH=CH_2, R_2: O-CH=CH_2, R_3: CH_3)	

In the present study we investigated several isostructural molecules of 2-vinyloxypyridine and 2-vinylthiopyridine, 2-vinyloxyquinoline, and 2-vinylthioquinoline, together with other aromatic vinyl ethers and sulfides, and ab initio calculations were carried out to investigate how the intramolecular C—H···N interaction influences the molecular structure of 2-vinyloxy- and 2-vinylthiopyridines. Furthermore, the GIAO calculation of magnetic shielding tensors was applied on the basis of the ab initio wave functions, and the experimental data of ^{1}H, ^{13}C, ^{15}N, and ^{17}O NMR were discussed in relation to specific intramolecular hydrogen bonding.

Results and discussion

NMR data

The ^{1}H and ^{13}C NMR parameters of the vinyl group of ethers **1–15** and sulfides **16–28** (Scheme 1) are presented in Tables 1, 2, and 3.

The spectral anomalies in the ^1H_X, $^{13}C_\alpha$, and ^{15}N chemical shifts as well as the $^1J_{C_\alpha H_X}$ coupling constants were encountered in heteroaryl vinyl ethers **1** and **13–15**, which

© 1999 NRC Canada

Table 1. The ^1H and ^{13}C NMR parameters of vinyloxyl groups in ethers **1–15**.

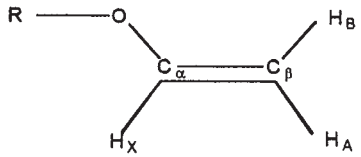

Compounds		δ / ppm							J / Hz		
		H_A	H_B	H_X	C_α	C_β	^{17}O	^{15}N	$^1JC_\beta H_A$	$^1JC_\beta H_B$	$^1JC_\alpha H_x$
1		4.49	4.87	7.55 <0.95>[a]	144.17	95.21	142	267.7 [–49.6][b]	162.1	157.9	188.3
2		4.51	4.81	6.62	147.48	96.72	112	320.0 [+2.7][b]	162.5	158.5	184.1
3		4.69	5.00	6.68	145.09	99.53	129	300.5 [–16.8][b]	162.5	158.9	186.0
4		4.35	4.69	6.57	148.37	95.07	125[c]	—	161.8	157.9	182.5
5		4.41	4.72	6.53	147.96	95.82	119[c]	—	162.1	158.3	183.3
6		4.33	4.67	6.57	148.79	94.27	118[c]	—	161.6	157.7	181.9
7		4.35	4.67	6.56	148.89	94.51	118[c]	—	161.7	157.8	182.5
8		4.49	4.83	6.66	147.84	96.27	—	—	161.9	158.0	183.7
9		4.44	4.75	6.55	147.77	95.93	—	—	162.1	158.3	183.3
10		4.49	4.82	6.69	147.46	96.64	—	—	161.7	158.0	183.9
11		4.45	4.75	6.49	147.40	96.64	—	—	161.9	158.2	183.8
12		4.68	4.97	6.68	146.13	99.11	139[c]	—	162.8	159.3	185.6
13		4.54	4.93	7.88	143.86	95.37	146	251.1 [–65.1]	162.1	157.9	189.2
14	**2**[d]	4.54	4.91	7.84	143.89	95.17	146	—	161.9	157.6	189.6
	4[d]	4.73	5.09	6.74	145.19	99.83	128	—	162.3	159.0	185.5
15	**2**[d]	4.55	4.94	7.63	144.23	96.12	—	—	162.2	158.5	190.4
	4[d]	4.67	5.01	7.50	142.96	97.46	—	—	162.6	158.7	192.1

[a]The deviation from average value is given in angle brackets.

[b]The increments of ^{15}N chemical shifts are presented in square brackets.

[c]These data are taken from ref. 23.

[d]**2** denotes the 2-vinyloxyl group and **4** denotes the 4-vinyloxyl group.

Scheme 2.

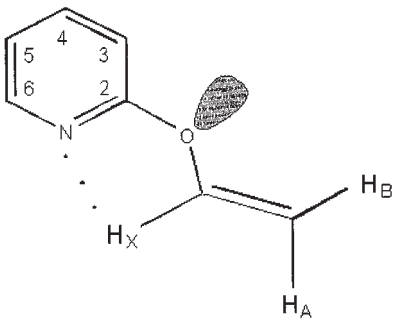

have a vinyloxyl group attached to the atom that is neighbour to the endocyclic nitrogen (Table 1). The spectral data listed suggest the presence of intramolecular hydrogen bonding between the pyridine nitrogen and the H_X proton in the s-*trans* conformation and a *syn* arrangement of nitrogen to the vinyl group as shown in Scheme 2. Various statistical treatments have been used to distinguish the effect of hydrogen bonding from the pure electronic effect of the aromatic system (3). The hydrogen bonding leads to a downfield shift of the α-proton signal by 1 ppm, and an upfield shift of the α-carbon and ^{15}N signals by 4–5 and 17–20 ppm, respectively. The increase in the $^1JC_\alpha H_X$ coupling constants amounts to 6-7 Hz.

The one-bond ^{13}C–^{13}C coupling constants in the aromatic ring of ethers **1–7**, **9**, and **12** are included in Table 2. The increment from the unsubstituted pyridine and benzene rings is also included in Table 2 (in parentheses). This increment is larger in all compounds listed in the Table 2 when the pertinent carbon is attached by such electronegative groups as vinyloxyl, halogen, and NO_2. This is due to the electronegative effect of the attached atoms (11, 13). This increment amounts to 11.6–13.0 Hz for compounds **2–7**, **9**, and **12**, but a much larger increment (18 Hz) is observed for compound **1**. It has been suggested (14) that the oxygen lone-pair electrons have introduced an additional positive contribution to the one-bond ^{13}C–^{13}C coupling constant when these lone-pair electrons are situated *cis* to this ^{13}C—^{13}C bond. The oxygen lone pair occupies just such a *cis* position relative to the C_2—C_3 bond in an s-*trans* conformation of a vinyloxyl group in the *syn* arrangement of the pyridine ring in 2-vinyloxypyridine (Scheme 2). It causes an additional positive contribution (5–6 Hz) to the $^1JC_2C_3$ coupling constant that results in an unusually large increment in this coupling. On the other hand, 3-vinyloxypyridine **2** should exist

Can. J. Chem. Downloaded from www.nrcresearchpress.com by Peking University on 09/06/12
For personal use only.

© 1999 NRC Canada

Can. J. Chem. Downloaded from www.nrcresearchpress.com by Peking University on 09/06/12
For personal use only.

Table 2. The one-bond ^{13}C–^{13}C coupling constants in ethers **1–7, 9,** and **12**.[a]

	J / Hz				
Compounds	$^1J_{C1C2}$	$^1JC_2C_3$	$^1JC_3C_4$	$^1JC_4C_5$	$^1JC_5C_6$
1	—	72.3	57.7	53.6	56.8
		(+18.0)	(+4.0)	(-0.1)	(+2.5)
2	—	67.2	65.7	55.2	54.8
		(+12.9)	(+12.0)	(+1.5)	(+0.5)
3	—	55.5	65.3	—	—
		(+1.2)	(+11.6)	—	—
4	67.8	57.0	56.1	—	—
	(+11.8)	(+1.0)	(+0.1)	—	—
5	68.8	57.8	66.4	—	—
	(+12.7)	(+1.5)	(+1.2)	—	—
6	68.3	58.0	57.6	—	—
	(+12.0)	(+1.5)	(-0.4)	—	—
7	69.1	—	—	—	—
	(+13.0)	—	—	—	—
9	68.8	57.1	64.7	—	—
	(+12.7)	(+1.7)	(+1.0)	—	—
12	68.1	57.1	68.9	—	—
	(+12.8)	(0.0)	(+1.5)	—	—

[a]Experimental values of one-bond ^{13}C–^{13}C coupling constants are taken from ref. 11 for **1** and **2**, and from ref. 13 for the other compounds. Increments for the vinyloxyl group are indicated in parentheses. The standard values of one-bond ^{13}C–^{13}C coupling constants are $^1JC_2C_3$ = 54.3 Hz and $^1JC_3C_4$ = 53.7 Hz (12), in the parent pyridine molecule and $^1J_{CC}$ = 56.0 Hz (24) in the parent benzene molecule.

Table 3. The ^1H and ^{13}C NMR parameters for vinylthio groups in sulfides **16–28**.

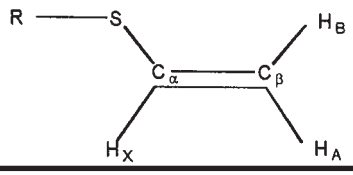

	δ / ppm[a]						*J* / Hz		
Compounds	H_A	H_B	H_X	C_α	$^C_\beta$	^{15}N	$^1JC_\beta H_A$	$^1JC_\beta H_B$	$^1JC\alpha H_X$
16	5.49	5.56	7.11 <0.58>[b]	128.17	116.33	302.5 [–14.8][b]	162.3	159.1	178.7
17	5.43	5.37	6.50	130.42	117.07	316.3 [–1.0]	162.2	159.6	174.9
18	5.64	5.68	6.57	126.98	121.93	309.7 [–7.6]	162.0	160.1	176.4
19	5.33	5.31	6.52	131.92	115.33	—	161.8	159.4	173.6
20	5.37	5.33	6.48	131.30	116.28	—	162.1	159.6	174.2
21	5.28	5.26	6.49	132.27	115.09	—	161.6	159.4	173.3
22	5.28	5.22	6.47	133.17	114.32	—	161.9	159.4	173.3
23	5.37	5.37	6.56	131.75	116.14	—	[c]	[c]	173.7
24	5.35	5.34	6.48	131.46	116.52	—	162.0	159.6	174.1
25	5.49	5.53	6.61	130.33	118.30	—	[c]	[c]	175.0
26	5.58	5.56	6.56	129.20	119.94	—	[c]	[c]	176.0
27	5.65	5.66	6.57	127.75	122.11	—	[c]	[c]	176.4
28	5.50	5.56	7.48 <0.95>[b]	127.84	115.98	290.6 [–25.6]	162.6	159.3	177.1

[a]Aromatic carbon chemical shifts are 157.39, 121.93, 136.36, 120.15, and 149.61 ppm for C_2, C_3, C_4, C_5 and C_6, respectively, in **16**; 150.83, 131.51, 137.84, 123.82, 148.02 ppm for C_2–C_6 in **17**; 149.53, 121.33, 147.25 ppm for C_2, C_3, and C_4, respectively, in **18**.

[b]See captions for Table 1.

[c]The analysis was complicated by peak overlapping.

as a rotamer mixture symbolized by the two ultimate conformers of the *syn* and *anti* forms (Scheme 3). These two forms are calculated to be in the global (*syn*) and the second (*anti*) minimum energies from the calculation of DFT/D95++. It should be taken into account that in these two ultimate conformers the structure is not planar and the

© 1999 NRC Canada

Scheme 3.

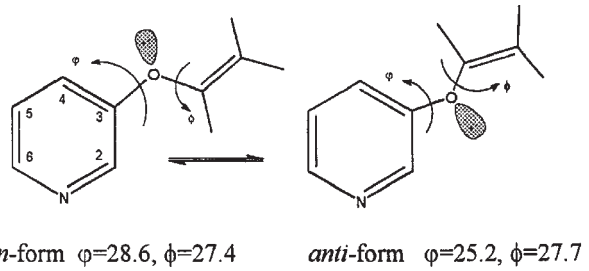

Scheme 4.

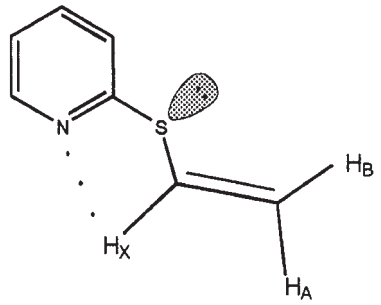

Scheme 5.

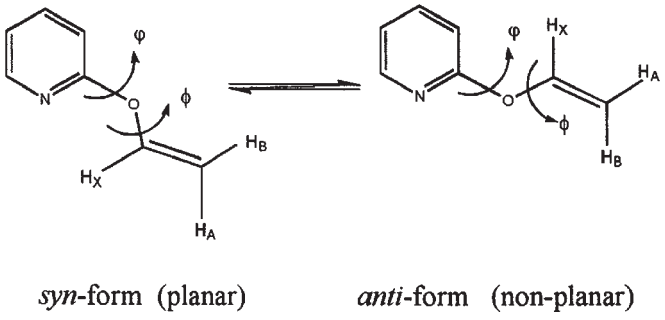

molecule is considered to have different local minima in the rotational equilibrium. Therefore, the extra contributions of the oxygen lone pair to the $^1JC_2C_3$ and $^1JC_3C_4$ coupling constants almost disappear. This situation is common to all the other compounds (**3**–**7**, **9**, and **12**).

The H_X signal in molecules **16** and **28**, in which the vinylthio group is attached to the *ortho* carbon of pyridine nitrogen, is found to be displaced by 0.6–1.0 ppm to the lower field with reference to other compounds **17–27** (Table 3). This characteristic result also supports the presence of intramolecular hydrogen bonding in this type of compound (Scheme 4).

It may be important to compare quantitatively the magnitude of the spectral anomalies observed in the intramolecularly hydrogen-bonded compounds of ethers **1** and **13** and sulfides **16** and **28**. The H_X signal is shifted to lower field by 0.95 and 1.28 ppm in ethers **1** and **13**, respectively, compared to other non-hydrogen-bonded compounds, since the average value of δH_X is 6.60 ppm for ethers **2**–**12** whereas in molecules **1** and **13** δH_X is equal to 7.55 and 7.88 ppm, respectively. This difference is reduced to 0.58 and 0.95 ppm for the sulfides when the data of **16** and **28** are compared with the averaged data (6.53 ppm) of **17–27**. Therefore the

Fig. 1. The function of potential energy of internal rotation in 2-vinyloxypyridine **1** and 2-vinyl-thiopyridine **16** around the C_2—O bond (D95 basis set).

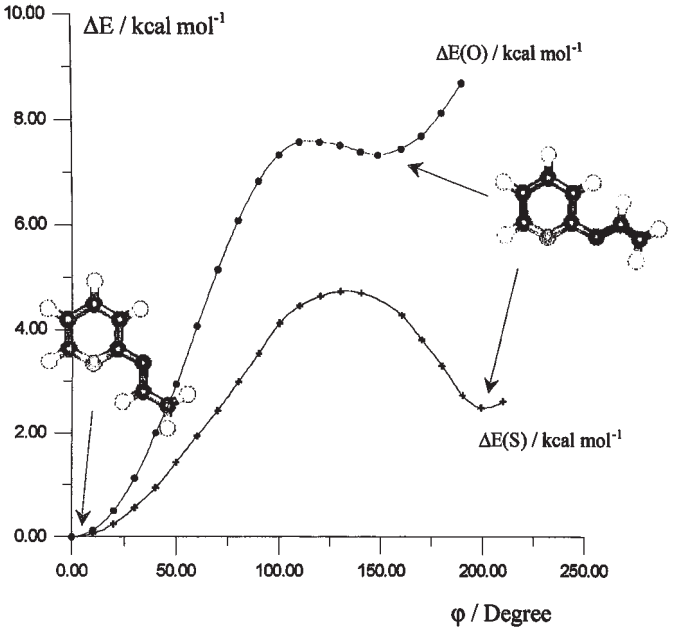

ratio of the downfield shift of δH_X is said to be larger by a factor of ca. 1.6 in ethers **1** compared to that in the sulfides. A similar ratio is observed for other spectral parameters: 1.4 times for the deviation in $\delta^{13}C_\alpha$ and 1.5 times for the deviation in the $^1JC_\alpha H_X$. Thus it is concluded that specific intramolecular hydrogen bonding will cause spectral changes in the ethers that is about 1.5 times stronger than that in the sulfides. A similar tendency may be expected in the difference of the interaction energy, which will be discussed below.

To estimate an additional contribution to the ^{15}N increment, the dependence of $\delta^{15}N$ increments for pyridine and quinolines ($\Delta\delta^{15}N$) versus ($\Delta\delta^{13}C$) for benzenes and naphthalenes upon the same substituents has been compared (3). Based on this dependence it is expected that the increment of the ^{15}N chemical shift for 2-vinylthiopyridine **16** would be 2.7 times larger in absolute magnitude than that for the C_3 carbon ($\delta^{13}C_3$, Table 3) (3). However, the observed value is 9 ppm less than this expectation (taking into consideration the sign of the increments). This suggests that the positive contribution to the ^{15}N shielding constant occurs because of the intramolecular C—H···N interaction. According to the theory of Li and Chesnut (15, 16) the shielding effect on the ^{15}N nucleus indicates the attractive nature of the interaction under discussion. The value of the positive contribution to the ^{15}N shielding constant is about 2 times smaller in 2-vinylthiopyridine **16** than that in 2-vinyloxy-pyridine **1**.

Ab initio calculations

To understand how the interaction under discussion influences the spatial structure of 2-vinyloxy- and 2-vinylthiopyridines ab initio calculations were carried out. The ab initio calculation is inevitable for the exact discussion of conformational energies as well as the NMR chemical shifts of sulfur compounds, especially when the sulfur is situated

Can. J. Chem. Downloaded from www.nrcresearchpress.com by Peking University on 09/06/12
For personal use only.

© 1999 NRC Canada

Table 4. The calculated torsion angles, energy difference, interatomic distances, and bond lengths in vinyl ethers and sulfides.

Compounds		Torsion angles, deg				Bond length, Å		
		φ	ϕ	Δ*E*, kcal/mol	Distance $H_X \cdots N$, Å	C_α—H_X	C_β—H_A	C_β—H_B
	syn	0[a]	0[a]	0[a]	2.39[a]	1.0687[a]	1.0716[a]	1.0722[a]
1		(0),[b] [0][b]	(0),[b] [0][b]	(0),[b] [0][b]	(2.32), [2.29]	(1.0738), [1.0847]	(1.0738), [1.0847]	(1.0755), [1.0868]
	anti	31.9	31.5	7.3	3.74	1.0742	1.0717	1.0719
		(33.6), [23.2]	(26.7), [25.8]	(4.7), [4.7]	(3.70), [3.76]	(1.0774), [1.0903]	(1.0742), [1.0850]	(1.0753), [1.0864]
	syn	27.1	33.6	0	4.57	1.0744	1.0716	1.0720
2		[28.6]	[23.8]	[0]	[4.76]	[1.0901]	[1.0848]	[1.0864]
	anti	27.3	36.3	0.26	4.77	1.0741	1.0716	1.0720
		[25.2]	[23.9]	[0.16]	[4.80]	[1.0903]	[1.0850]	[1.0864]
3		31.8	28.6		5.17	1.0742	1.0717	1.0721
4		26.1	34.5		—	1.0743	1.0717	1.0721
		(35.0)	(31.0)		—	(1.0776)	(1.0741)	(1.0754)
13 *syn*		(0.1)	(0)	—	(2.33)	(1.0711)	(1.0739)	(1.0755)
	syn	0	0	0	2.38	1.0693	1.0737	1.0741
16		(0), [0]	(0), [0]	(0), [0]	(2.37), [2.31]	(1.0727), [1.0869]	(1.0758), [1.0869]	(1.0771), [1.0881]
	anti	19.1	51.8	2.6	4.21	1.0731	1.0747	1.0734
		(16.5), [18.0]	(47.3), [36.1]	(1.3), [2.3]	(4.17), [4.12]	(1.0772), [1.0897]	(1.0769), [1.0877]	(1.0764), [1.0877]
17 *syn*		41.7	75.0		4.57	1.0723	1.0743	1.0736
18		46.8	37.0		5.17	1.0724	1.0744	1.0734
19		30.9	70.7		—	1.0725	1.0744	1.0737

[a] The HF/D95 basis set calculation.

[b]The values from the HF/D95++(d,p) basis set computation are indicated in parentheses and the values for the B3LYP/D95++(d,p) level are presented in square brackets.

Can. J. Chem. Downloaded from www.nrcresearchpress.com by Peking University on 09/06/12
For personal use only.

in a conjugated state with an aromatic ring, although for the discussion of the ether compounds in our previous study (3) a semiempirical AM1 calculation can offer a reasonable estimate of the conformational energy. The aryl and heteroaryl vinyl ethers have two degrees of freedom with regard to the flexible rotation angle. There is rotation around the O—C heteroaryl (aryl) bond and the O—C vinyl bond (the torsion angles φ and ϕ, respectively, Scheme 5). The search for the minimum in the potential energy hypersurface was carried out using the D95 basis set at full optimization of geometrical parameters. The global energy minimum in compounds **1, 13**, and **16** corresponds to a planar structure, i.e., both torsion angles φ and ϕ are equal to 0°. For comparison, the AM1 calculation of the global minimum gave φ and ϕ equal to 31° and 11°, respectively (3).

The segment of potential energy hypersurface was calculated in molecules **1** and **16** under varying torsion angles φ and full optimization of another geometry parameter. The results are shown in Fig. 1. The second energy minimum was found in the field of φ = 150°–160°. The local energy minimum is 7.3 kcal/mol higher in energy than the global one for 2-vinyloxypyridine **1**. The energy difference is reduced to 2.4 kcal/mol for 2-vinylthiopyridine **16**. The magnitudes of energy difference ensure that the population with the *anti* conformation is quite minor for both molecules (17), and compounds **1** and **16** are predominantly in the *syn* form.

The structure of the *anti* conformer differs considerably from that of the *syn* conformer in planarity, since the *anti* conformer is essentially nonplanar whereas the *syn* conformer is planar. The torsion angles φ and ϕ are equal to 30° and 31°, respectively, in the *anti* form of **1**. These angles are changed to φ = 20° and ϕ = 50° in compound **16**. To compare the structures of the other compounds under discussion, the equilibrium geometries were calculated for 3-, 4-vinyloxypyridines (**2** and **3),** phenyl vinyl ether **4**, 3-, 4-vinylthiopyridines (**17** and **18**), and phenyl vinyl sulfide **19**. The calculations are summarized in Table 4. The structures of these compounds are similar to those of the *anti* conformer of 2-vinyloxypyridine **1** and 2-vinylthiopyridine **16** but are strikingly different from those of the *syn* conformer.

The molecule of 3-vinyloxypyridine **2** should also have two distinguishable stereo orientations of the vinyloxyl group relative to the pyridine ring (Scheme 3). Indeed, the D95 calculation reveals two energy minima, which differ by only 0.26 kcal/mol, the *syn* conformer being lower in energy. Thus, the energy difference between *syn* and *anti* conformers is very small in 3-vinyloxypyridine **2** and the compound is considered to be present as a rotating mixture where rotation angles φ and ϕ are distributed over rather wide ranges.

To achieve a better description of the hydrogen-bonding interaction, diffuse functions were used (18) in the computation at the D95++(d,p) level. An appreciable reduction of the energy difference between the *syn* and *anti* conformers is observed in molecule **1** as well as molecule **16** in the extended basis set calculation: a reduction from 7.3 to 4.7 kcal/mol and from 2.6 to 1.3 kcal/mol is observed for **1** and **16**, respectively. To take into account an electron correlation effect, density functional theory was applied (19). No important change was observed in the equilibrium geometry of molecules **1** and **16** when calculations at the B3LYP/D95++(d,p) (19) as well as the HF/D95++(d,p) levels are compared with those at the HF/D95 basis set (Table 4).The computation for 3-vinyloxypyridine **2** at the B3LYP/D95++(d,p) level shows results similar to the computation at the D95

© 1999 NRC Canada

Table 5. The GIAO calculated values of the shielding constants (ppm).

	2-Vinyloxypyridine			3-Vinyloxypyridine		2-Vinylthiopyridine	
Atom	*syn*	30°[a]	*anti*	*syn*	*anti*	*syn*	*anti*
O	131.28	134.06	120.36	157.54	156.18	—	—
N	–25.95	–39.26	–50.56	–89.78	–90.70	–57.06	–73.54
C_α	42.17	38.95	39.30	38.55	38.95	52.00	50.24
C_β	94.36	91.62	90.77	91.45	91.00	79.42	68.81
H_A	27.05	26.93	26.90	26.90	26.87	26.09	25.89
H_B	26.53	26.38	26.26	26.32	26.26	26.01	25.57
H_X	22.70	24.43	24.76	24.66	24.77	23.10	24.67

[a]This corresponds to the *syn* conformer when both torsional angles are fixed at 30°.

Can. J. Chem. Downloaded from www.nrcresearchpress.com by Peking University on 09/06/12
For personal use only.

basis set: the torsional angles in both conformers differ only slightly and the energy difference amounts to only 0.16 kcal/mol (Table 4).

Another essential indication of the C—H···N interaction is the interatomic distance between H_X and nitrogen. The equilibrium distance H_X···N in 2-vinyloxypyridine **1** lies in the range 2.29–2.39 Å (depending on the basis set of the calculation) whereas the distance in 2-vinylthiopyridine **16** gives values between 2.31 and 2.38 Å (Table 4). The distance in 2-vinyloxyquinoline **13** is equal to 2.33 Å. The distance HX···N in all these molecules is much less than the sum of the van der Waals radii (2.75 Å) (2*a*). The short distance and planar structure of molecules **1**, **13**, and **16** completely support an attractive rather than a repulsive nature between C—H and N.

The NMR chemical shift can be discussed on the basis of ab initio theory in quantum chemistry through the use of an advanced version of nuclear shielding calculations. The calculations of shielding constants (SC) as a function of internal rotation for 2- and 3-vinyloxypyridines, **1** and **2**, and 2-vinylthiopyridine **16** by the GIAO method (9) are summarized in Table 5. The rotation of the vinyloxyl group seems not to affect the shielding constant in 3-vinyloxypyridine **2**: the changes in SC of H_A, H_B, and H_X are within 0.1 ppm. But closer examination of the calculated values discloses a few tendencies that are included in the calculation. The SC of $^{13}C_\beta$ is decreased by 0.40 ppm in the *anti* conformer compared to that in the *syn* conformer. This reflects an alteration in the *p*–π conjugation between the pyridine ring and the vinyloxyl group due to the change in spatial orientation. This decrease in the SC of $^{13}C_\beta$ is accompanied by an increase in the SC of $^{13}C_\alpha$, and it corresponds to the weakening of the *p*–π conjugation between the pyridine ring and the vinyl group. This tendency is in complete agreement with the observed experimental data (20). Very small changes in the SC of the *syn* and *anti* conformers of 3-vinyl-oxypyridine **2** indicate that these SC values can be treated as a suitable standard for the SC values, including no extra specific intramolecular interaction. When SC values calculated for 2-vinyloxypyridine **1** are compared on the basis of that standard, several characteristic profiles may be deduced. The H_X shielding constant is decreased by 2 ppm in the *syn* conformer of **1** while the H_A and H_B shielding constants remain almost unchanged. A decrease in the shielding constant means that the downfield chemical shift, and hence the experimentally observed downfield shift of the H_X proton (0.95 ppm), is supported by the theoretical calculations. It should also be noted that the H_X shielding constant in the *anti* conformer of 2-vinyloxypyridine **1** corresponds well with those calculated for the *syn* and *anti* conformers of 3-vinyloxypyridine **2** where a specific intramolecular interaction between the H_X proton and the nitrogen lone pair is impossible because of geometrical remoteness. The SC values of the C_α and C_β carbons in the *syn* conformer are increased relative to those in the *anti* conformer by 3.6 and 2.9 ppm, respectively. The increase in C_β shielding should be attributed to the intensification of the *p*–π conjugation with the vinyloxyl group in the planar *syn* conformation. However, the intensification of the *p*–π conjugation leads to the deshielding rather than the shielding of the C_α carbon (vide supra). The C_α atom shielding in the *syn* conformer comes from the intramolecular C—H···N interaction. The experimental shift of the C_α carbon and the change of shielding constants in the GIAO method are in an excellent agreement.

An important result is that the GIAO method predicts the increase of the ^{15}N SC by 24.6 ppm in going from the *anti* to the *syn* conformer of 2-vinyloxypyridine **1**. Therefore, the empirical estimate of the $\delta^{15}N$ upfield shift by 17–20 ppm is confirmed by the calculated data.

It is interesting to consider a hypothetical case in which the *syn*-conformer of 2-vinyloxypyridine **1** takes the "usual" structure, i.e., both torsional angles φ and ϕ are equal to 30°. The calculations for this hypothetical case are also given in Table 5. The increase in torsional angles results in an increase of intramolecular H_X···N distance (2.68 Å). Taking into account the angular factor (2*h*), this prevents hydrogen bond formation. In consequence, one can mark the sharp change of SC for atoms involved in the C—H···N interaction. The shielding constants of the H_X and C_α nuclei increase by 1.7 and 3.2 ppm, respectively, and have a value slightly different from that of the *anti* conformer. An increase in the torsional angles leads to the significant decrease of the ^{15}N shielding constant (13.3 ppm, see Table 5), indicating "release" from the attractive C—H···N interaction. The ^{17}O shielding in the hypothetical conformer is increased by 2.8 ppm, relative to that in the *syn* conformer. This supports the proper interpretation of the ^{17}O downfield shift in molecule **1** as a result of planar molecular structure (3). Similar regularities emerge from the comparison of calculated shielding constants in the *syn* and *anti* conformers of 2-vinylthiopyridine **16** (Table 5).

In Table 6 changes in the NMR parameters estimated for the hypothetical *syn* and *anti* conformers are compared with

© 1999 NRC Canada

Table 6. Comparison of the estimated changes in the NMR chemical shifts (ppm) between the *syn* and *anti* conformers.[a]

	$\delta H_X^{syn} - \delta H_X^{anti}$	$\delta C_\alpha^{syn} - \delta C_\alpha^{anti}$	$\delta N^{syn} - \delta N^{anti}$
Compound **1**	–2.06	2.87	24.61
Compound **16**	–1.57	1.76	16.48
Ratio	1.3	1.6	1.5

[a]An estimate is given only for those atoms that are common to the compounds and which can form an acyclic arrangement in the intramolecular hydrogen-bonded system:

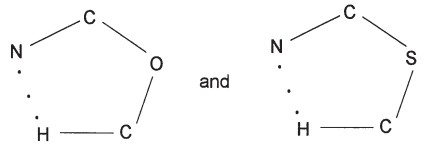

the nuclei that are directly engaged in intramolecular hydrogen bonding. The calculations are compared for compounds **1** and **16**. This *ratio* is based on the GIAO calculations and supposes that a change in the shielding constant of the *syn* conformer relative to that of the *anti* conformer of 2-vinyloxypyridine **1** is about 1.5 times larger than would be the case in 2-vinylthiopyridine **16**. This result corresponds well with the observed changes in the NMR parameters.

Experimental

Spectral measurements

The NMR spectra were recorded on a Bruker WP 200 SY spectrometer using ASPECT 2000 software system operating at 200 MHz for ^{1}H and 50.3 MHz for ^{13}C. All spectra were obtained under the same conditions. The solvent was $CDCl_3$ and the internal reference was given by HMDS. The concentration of solute molecules was 5% for the ^{1}H and 30% for the ^{13}C NMR experiments. The typical spectrometer conditions were as follows: ^{1}H NMR, spectral width 2500 Hz, pulse width 2 μs, flip angle 30°, number of scans 4, data points 32K; ^{13}C NMR, spectral width 10 000 Hz, pulse width 2.5 μs, flip angle 45°, relaxation delay 3 s, number of scans 100–400, data points 32K.

The proton-coupled spectra were obtained by gated decoupling techniques (21). The spectral width was contracted to 1000 Hz to reach the accuracy of ^{13}C–^{1}H coupling constant measurements, not less than ±0.1 Hz. The simulations of proton-coupled spectra were effected using Bruker's PANIC program. Some of the compounds were recorded on Tesla BS 567 A and Varian VXR 500 spectrometers (100 and 499.8 MHz for ^{1}H, 25.1 and 125.7 MHz for ^{13}C, respectively) under the same conditions as mentioned above. The conditions for ^{15}N and ^{17}O spectral measurements are given in ref. 3.

Computational details

All calculations were performed using Gaussian 94 (22) on a Silicon Graphics Indigo^2 computer at the Genome Information Research Center of Osaka University. The ab initio calculations were performed using D95 and D95++(d,p) basis sets at the Hartree–Fock level and at the B3LYP level of density functional theory (19). The geometries were fully optimized without any symmetry constraints. The shielding constants were calculated by the GIAO method (9) using the B3LYP/D95++(d,p) basis set.

References

1. (*a*) G.C. Pimentel and A.L. McClean. The hydrogen bond. W.H. Freeman, San Francisco. 1960; (*b*) R.D. Green. Hydrogen bonding by C—H groups. Macmillan, London. 1974; (*c*) S. Pinchas. J. Phys. Chem. **67**, 1862 (1963); (*d*) M.P. Sammes and R.L. Harlow, J. Chem. Soc. Perkin Trans. 2, 1130 (1976); (*e*) C. Li and M.P. Sammes. J. Chem. Soc. Perkin Trans. 1, 1303 (1983); (*f*) J. Chem. Soc. Perkin Trans. 1, 2193 (1983); (*g*) F.M. Slasinski, J.M. Tustin, F.J. Sweeney, A.M. Armstrong, Q.A. Ahmed, and J.P. Loran. J. Org. Chem. **41**, 2693 (1976); (*h*) R. Houssin and J.-P. Henichart. Org. Magn. Reson. **16**, 202 (1981); (*i*) H. Satonaka, K. Abe, and M. Hirota. Bull. Chem. Soc. Jpn. **61**, 2031 (1988).
2. (*a*) R. Taylor and O. Kennard. J. Am. Chem. Soc. **104**, 5063 (1982); (*b*) D.J. Sutor. J. Chem. Soc. 1105 (1963); (*c*) R.L. Harlow, S.H. Simonen, C.E. Pfluger, and M.P. Sammes. Acta Crystallogr. Sect. B: Struct. Crystallogr. Cryst. Chem. **B30**, 2264 (1974); (*d*) R.L. Harlow, S.H. Simonen, and M.P. Sammes. Acta Crystallogr. Sect. B: Struct. Crystallogr. Cryst. Chem. **B32**, 2690 (1974); (*e*) A.N. Chehlov, A. Ju. Aksinenko, A.N. Pushin, and V.B. Sokolov. Bull. Acad. Sci. USSR, Div. Chem. Sci. (Engl. Transl.) **44**, 1593 (1995); (*f*) T. Steiner. J. Chem. Soc. Perkin Trans. 2, **7**, 1315 (1995); (*g*) G.R. Desiraju. Acc. Chem. Res. **24**, 290 (1991); (*h*) Acc.Chem.Res. **29**, 441 (1996).
3. A.V. Afonin, A.V. Vashchenko, and H. Fujiwara. Bull. Chem. Soc. Jpn. **69**, 933 (1996).
4. F.P.S.C. Gil and J.J.C. Texeira-Dias. Theochem, **363**, 311 (1996).
5. R.V. Law and Y. Sasanuma. J. Chem. Soc. Faraday Trans. **92**, 4885 (1996).
6. R. Ditchfield. Mol. Phys. **27**, 789 (1974).
7. D.B. Chesnut and C.K. Foley. Chem. Phys. Lett. **118**, 316 (1985); D.B. Chesnut and K.D. Moore. J. Comput. Chem. **10**, 648 (1989).
8. K. Friedrich, G. Seifert, and G. Grossmann. Z. Phys. D: At. Mol. Clusters, **17**, 45 (1990).
9. K. Wolinski, J.F. Hinton, and P. Pulay. J. Am. Chem. Soc. **112**, 8251 (1990).
10. G. Schreckenbach and T. Ziegler. J. Chem. Phys. **99**, 606 (1995).
11. L.B. Krivdin and G.A. Kalabin. Zh. Org. Khim. **24**, 2268 (1988).
12. A. Yu. Denisov, V.J. Mamatyuk, and O.P. Shkurko. Khim. Geterocycl. Soed. 1383 (1985).
13. L.B. Krivdin, V.V. Scherbakov, I.A. Aliev, and G.A. Kalabin. Zh. Org. Khim. **23**, 569 (1987).
14. (*a*) G.A. Kalabin, L.B. Krivdin, V.V. Scherbakov, and B.A. Trofimov. J. Mol. Struct. **143**, 569 (1986); (*b*) L.B.Krivdin and G.A. Kalabin. Prog. Nucl. Magn. Reson. Spectrosc. **21**, 293 (1989).
15. S. Li and D.B. Chesnut. Magn. Reson. Chem. **23**, 625 (1985).
16. S. Li and D.B. Chesnut. Magn. Reson. Chem. **24**, 93 (1986).
17. W.J. Orville-Thomas. Internal rotation in molecules. John Wiley & Sons, London–New York–Sydney–Toronto. 1974.
18. (*a*) J.E. Del Bene, W.B. Person, and K. Szczepaniak. J. Phys. Chem. **99**, 10705 (1995); (*b*) S. Reiling, J. Brickman, M. Schlenkrich, and P.A. Bopp. J. Comput. Chem. **17**, 133 (1996); (*c*) A. Kovacs, J. Kolossvary, G.J. Csonka, and I. Hargittai. J. Comput. Chem. **17**, 1804 (1996).
19. C. Lee, W. Yang, and R.G. Parr. Phys. Rev. B: Condens. Matter, **37**, 785 (1988).

Can. J. Chem. Downloaded from www.nrcresearchpress.com by Peking University on 09/06/12
For personal use only.

© 1999 NRC Canada

20. O. Kajimoto, M. Kobayashi, and T. Fueno. Bull. Chem. Soc. Jpn. **46**, 1422 (1973).
21. P.E. Hansen. Prog. Nucl. Magn. Reson. Spectrosc. **14**, 1 (1981).
22. M.J. Frisch, G.W. Trucks, M. Head-Gordon, P.M.W. Gill, M.W. Wong, J.B. Foresman, B.G Johnson, H.B. Schlegel, M.A. Robb, E.S. Replogle, R. Gomperts, J.L. Andres, K. Raghavachari, J.S. Binkley, C. Gonzalez, R.L. Martin, D.J. Fox, D.J. Defrees, J. Baker, J.J.P. Stewart, and J.A. Pople. Gaussian 94, Revision B.3. Gaussian, Inc., Pittsburgh, Pa. 1995.
23. G.A. Kalabin, D.F. Kushnarev, R.B. Valeyev, B.A. Trofimov, and M.A. Fedotov. Org. Magn. Reson. **18**, 1 (1982).
24. V. Wray, L. Ernst, T. Lund, and H.J. Jakobsen. J. Magn. Reson. **40**, 55 (1980).

Can. J. Chem. Downloaded from www.nrcresearchpress.com by Peking University on 09/06/12
For personal use only.

© 1999 NRC Canada

Iron(II) 2-methylimidazolate and copper(II) 1,2,4-triazolate complexes: systems exhibiting long-range ferromagnetic ordering at low temperatures

Steven J. Rettig, Alan Storr, David A. Summers, Robert C. Thompson, and James Trotter

Can. J. Chem. Downloaded from www.nrcresearchpress.com by University Town Library of Shenzhen on 09/05/12
For personal use only.

Abstract: Crystals of [Fe(2-methylimidazolate)$_2$·0.13(FeCp$_2$)]$_x$, **1**, are orthorhombic, a = 8.0654(11), b = 15.3504(5), c = 19.3388(9) Å, Z = 8, space group *Pnnm*. The structure was solved by direct methods and refined by full-matrix least-squares procedures to R (F, $I \geq 3\sigma(I)$) = 0.057 (R_w (F^2, all data) = 0.142). The structure involves tetrahedral iron(II) centers linked in chains by single imidazolate ligand bridges. The chains are cross-linked by additional imidazolates to generate a complex 3-D network of linear channels in which ferrocene molecules are trapped. [Cu(1,2,4-triazolate)$_2$]$_x$, **2**, is shown by indirect evidence to have a polymeric structure in which copper(II) ions are bridged by triazolate ligands. Magnetic susceptibilities were measured on powdered samples over the temperature range 2–300 K at applied fields of 0–55 000 G. Both materials exhibit antiferromagnetic exchange at temperatures above a magnetic phase transition: 27 K for **1** and 35 K for **2**. At temperatures below these transitions the compounds exhibit weak ferromagnetism, likely resulting from canted spin structures. Cycling the applied magnetic field between +55 000 G and –55 000 G at 4.8 K generates hysteresis loops for both materials. Remnant magnetizations of 200 and 55 cm^3 G mol^{-1} and coercive fields of 5000 and 2500 G are obtained for **1** and **2**, respectively.

Key words: iron, 2-methylimidazolate, copper, 1,2,4-triazolate, canted spins, ferromagnets.

Résumé : Les cristaux du [Fe(2-méthylimidazolate)$_2$·0.13(FeCp$_2$)]$_x$, **1**, sont orthorhombiques, groupe d'espace *Pnnm*, avec a = 8,0654(11), b = 15,3504(5) et c = 19,3388(9) Å et Z = 8. On a résolu les structures par des méthodes directes et on les a affinées par la méthode des moindres carrés jusqu'à des valeurs de R (F, $I \geq 3\sigma(I)$) = 0,057 (R_w (F^2, toutes les données = 0,142). La structure implique des centres de fer(II) tétraédriques liés en chaînes par des ponts impliquant un seul ligand imidazolate. Les chaînes sont réticulées par des imidazolates additionnels qui génèrent un réseau tridimensionnel complexe de canaux linéaires dans lesquels les molécules de ferrocène sont enfermées. On a montré, grâce à des données indirectes, que le [Cu(1,2,4-triazolate)$_2$]$_x$, **2**, possède une structure polymérique dans laquelle les ions de cuivre(II) sont reliés par des ligands triazolates. On a mesuré les susceptibilités magnétiques d'échantillons en poudre à des températures allant de 2 à 300 K, à des champs appliqués allant de 0 à 55 000 G. Les deux matériaux donnent lieu à un échange antiferromagnétique aux températures supérieures à une transition de phase magnétique; 27 K pour le composé **1** et 35 K pour **2**. À des températures à ces transitions, ces composés présentent un faible ferromagnétisme qui résulte vraisemblablement de structures à spin oblique. En faisant faire un cycle au champ magnétique appliqué entre +55 000 G et –55 000 G, à 4,8 K, il y a génération d'un cycle d'hystérésis avec chacun des matériaux. On a observé des magnétisations résiduelles de 200 et 55 cm^3 G mol^{-1} et des champs coercifs de 5000 et 2500 G respectivement pour les composés **1** et **2**.

Mots clés : fer, 2-méthylimidazolate, cuivre, 1,2,4-triazolate, spins obliques, ferroaimants.

[Traduit par la Rédaction]

Introduction

The ability of diazolate ligands to bridge metal ions and to mediate magnetic interactions between paramagnetic centers is well documented (1–3). Studies on binary copper(II), cobalt(II), nickel(II), and manganese(II) pyrazolates show that the 1,2 positioning of the nitrogen atoms in the ligands leads to 1-D linear chain structures with double azolate bridges and antiferromagnetically coupled metal centers (4–9). In contrast, as has been recently discussed (10), the 1,3 positioning of the donor nitrogens in imidazolate ligands results in steric constraints that are likely to prevent the formation

Received January 14, 1999

S.J. Rettig, A. Storr,[1] D.A. Summers, R.C. Thompson,[1] and J. Trotter. Department of Chemistry, The University of British Columbia, Vancouver, BC V6T 1Z1, Canada.

[1]Authors to whom correspondence may be addressed. Telephone: R.C. Thompson: (604) 822-4979; A. Storr: (604) 822-3962. Fax: (604) 822-2847. e-mail: thompson@chem.ubc.ca and storr@chem.ubc.ca

 © 1999 NRC Canada

Can. J. Chem. Downloaded from www.nrcresearchpress.com by University Town Library of Shenzhen on 09/05/12
For personal use only.

Table 1. Crystallographic data.[a]

Compound	**1**
Formula	$C_{9.30}H_{11.30}Fe_{1.13}N_4$
fw	242.23
Crystal system	Orthorhombic
Space group	*Pnnm* (No. 58)
a, Å	8.0654(11)
b, Å	15.3504(5)
c, Å	19.3388(9)
V, Å^3	2394.3(3)
Z	8
ρ_{calc}, g cm^{-3}	1.344
F(000)	995.84
Radiation	Mo
μ, cm^{-1}	13.81
Crystal size, mm	0.15 × 0.15 × 0.25
Correction factors [b]	0.875–1.000
ϕ sweep range, deg (χ = –90°)	0–190
ω sweep range, deg (χ = –90°)	–22 – 18
Oscillation width, deg	0.5
Data images, exposure time	460, 100 s
$2\theta_{max}$, deg	63.8
Total reflections	25557
Unique reflections	3391 (to $2\theta_{max}$ = 60°)
R_{merge}	0.070
No. with $I \geq 3\sigma(I)$	1426
No. of variables	164
R (F) ($I \geq 3\sigma(I)$)	0.057
R_w (F^2) (all data)	0.142
gof	1.90
Max Δ/σ (final cycle)	0.07
Residual density e Å^{-3}	–1.70 to 2.96 (2.0 Å from Fe(2))

[a]Temperature 180 K, Rigaku/ADSC CCD diffractometer, Mo K_α (λ = 0.71069 Å), graphite monochromator, takeoff angle 6.0°, aperture 94.0 × 94.0 mm at a distance of 39.15(3) mm from the crystal, $\sigma^2(F^2) = (C + B)/Lp^2$ (C = scan count, B = background count), function minimized $\Sigma w(|F_o^2| - |F_c^2|)^2$ where $w = 1/\sigma^2(F_o^2)$, R (F) = $\Sigma||F_o| - |F_c||/\Sigma|F_o|$, R_w (F^2) = $(\Sigma w(|F_o^2| - |F_c^2|)^2/\Sigma w|F_o^2|^2)^{1/2}$, and gof = $[\Sigma w(|F_o^2| - |F_c^2|)^2/(m - n)]^{1/2}$.

[b]Includes crystal decay (if any), absorption, and scaling corrections performed in a single step.

of double azolate bridges. These ligands may then be expected to singly bridge metals with the potential of forming higher dimensional 2-D or 3-D structures and long-range magnetic interactions. As we reported previously, these structural and magnetic characteristics are exhibited by $[Fe_3(imid)_6(imidH)_2]_x$ (where imidH = imidazole), a compound in which iron(II) ions are singly bridged by imidazolate ligands in an extended 3-D lattice (10). Magnetic studies on this compound revealed antiferromagnetic coupling and a canted spin structure, leading to weak ferromagnetism and long-range magnetic ordering below a critical temperature of 17 K.

There is considerable interest in materials such as $[Fe_3(imid)_6(imidH)_2]_x$ (termed molecular magnets) from the joint perspectives of understanding factors that generate them and of their potential information storage applications (11). Hence we are expanding our studies on complexes of azolates, particularly those ligands in which the potentially bridging donor nitrogens are separated by one carbon in the heterocyclic ring. We report here the X-ray determined structure and magnetic characterization of an iron(II) complex of 2-methylimidazolate, $[Fe(2\text{-meimid})_2 \cdot 0.13Cp_2Fe]_x$ (2-meimid = 2-methylimidazolate and Cp = cyclopentadienyl), **1**. Stoichiometrically and structurally this compound is distinct from its imidazolate analogue, $[Fe_3(imid)_6(imidH)_2]_x$; nonetheless, it too is found to exhibit the properties characteristic of molecular magnets.

The 1,2,4 triazolate ligand (1,2,4-trz) is related to the imidazolates in that it too has two potentially bridging donor nitrogens separated by one carbon in the heterocyclic ring; it differs, of course, in that it has a third ring nitrogen. We are interested in studying complexes of this ligand and in making structural and magnetic comparisons with related imidazolate complexes. We chose to study first the known complex, Cu(1,2,4-trz)$_2$, **2**, since earlier magnetic characterization had involved only high-temperature measurements (12). In addition we hoped to determine its molecular structure. Unfortunately, in spite of repeated attempts involving a synthetic route that has been utilized very successfully to obtain single crystals of related copper(II) pyrazolate complexes (5*a*), we have been unable to obtain crystals of the compound suitable for single crystal X-ray studies. We have nonetheless completed extensive magnetic studies on this material. The magnetic properties parallel very closely those of **1**.

Experimental

Syntheses

Ferrocene (from Strem) and 2-methylimidazole (2-meimidH) and 1,2,4-triazole (1,2,4-trzH) (from Aldrich) were used as supplied. Copper metal beads were cleaned immediately prior to use by washing in 12 M HCl, followed by a thorough water wash and finally an acetone rinse. Solvents used were reagent grade and were dried and distilled under an atmosphere of dry dinitrogen before use.

$[Fe(2\text{-meimid})_2 \cdot 0.13Cp_2Fe]_x$, ***1***

Ferrocene (0.50 g, 2.6 mmol) and 2-methylimidazole (3.0 g, 37 mmol) were combined and sealed under vacuum in a Carius tube. The mixture was heated for 4 days at 160°C. Over this period the bright orange of the original solution of ferrocene in the molten 2-meimidH (mp 142°C) was discharged and pale yellow crystals were deposited from the solution. The product and excess 2-meimidH were allowed to cool to room temperature and the Carius tube was opened under a dinitrogen atmosphere. The excess 2-meimidH was extracted with dry and oxygen-free acetonitrile solvent and the remaining crystals were washed with benzene and hexanes. The product was isolated as pale yellow crystals. Anal. calcd. for $C_{9.3}H_{11.3}N_4Fe_{1.13}$: C 46.1, H 4.7, N 23.1; found: C 47.1, H 4.8, N 23.3.

$[Cu(1,2,4\text{-trz})_2]_x$, ***2***

Clean copper beads (ca. 1 g) were placed in a 20 mL round bottom flask. 1,2,4-Triazole (3 g, 0.15 mmol) was added to the flask, which was then fitted with a reflux condenser. The reaction mixture was heated under a dioxygen atmosphere to 140°C, causing the triazole to melt. The mixture was maintained at this elevated temperature, without stirring, for 5 days, during which time the copper beads became coated with a purple solid. The reaction mixture was

© 1999 NRC Canada

Can. J. Chem. Downloaded from www.nrcresearchpress.com by University Town Library of Shenzhen on 09/05/12
For personal use only.

Table 2. Final atomic coordinates (fractional) and B_{eq} (10^3 Å^2).[a]

Atom	*x*	*y*	*z*	B_{eq}	occ.
Fe(1)	0.20726(6)	0.16979(3)	0.34343(2)	1.925(9)	
Fe(2)	0.5000	0.5000	0.5000	5.03(8)	0.1298(10)
N(1)	0.3998(3)	0.1672(2)	0.27458(13)	2.27(6)	
N(2)	0.5662(3)	0.2333(2)	0.19818(15)	2.90(7)	
N(3)	0.2883(3)	0.1826(2)	0.44210(12)	2.27(6)	
N(4)	0.1285(7)	0.0435(3)	0.3439(3)	2.52(10)	1/2
N(5)	–0.0186(6)	–0.0832(3)	0.3411(3)	2.06(10)	1/2
C(1)	0.4911(4)	0.2381(2)	0.2609(2)	2.58(8)	
C(2)	0.5226(4)	0.1533(2)	0.1727(2)	2.57(8)	
C(3)	0.4203(4)	0.1127(2)	0.2185(2)	2.41(8)	
C(4)	0.5029(5)	0.3139(3)	0.3080(2)	4.03(10)	
C(5)	0.1982(6)	0.1916(3)	0.5000	1.89(9)	1/2
C(6)	0.4476(4)	0.1660(3)	0.4649(2)	3.78(9)	
C(7)	0.0165(6)	0.2072(4)	0.5000	3.35(12)	1/2
C(8)	–0.0250(7)	0.0062(4)	0.3454(3)	2.21(11)	1/2
C(9)	0.2344(10)	–0.0277(4)	0.3370(5)	2.7(2)	1/2
C(10)	0.1471(8)	–0.1051(4)	0.3393(5)	2.5(2)	1/2
C(11)	–0.1864(10)	0.0562(6)	0.3525(6)	3.1(3)	1/2
C(12)	0.6992(9)	0.4384(5)	0.4676(4)	3.9(2)	0.519
C(13)	0.6830(15)	0.5318(7)	0.4495(6)	8.4(3)	0.519
C(14)	0.6765(15)	0.5773(8)	0.5000	5.0(3)	0.260

[a] $B_{eq} = (8/3)\pi^2 \Sigma \Sigma (U_{ij} a_{i*} a_{j*} (\mathbf{a}_i . \mathbf{a}_j))$.

allowed to cool and solidify, and the unreacted triazole was removed by vacuum sublimation. The product was then physically separated from the copper beads as a purple powder. Anal. calcd. for $C_4H_4N_6Cu$: C 24.1, H 2.0, N 42.1; found: C 24.4, H 2.0, N 41.7.

Physical characterization

Differential scanning calorimetry (DSC; 35°C to 600°C) and thermal gravimetric analysis (TGA; 35°C to 800°C) measurements were made using a TA Instruments TGA 51 unit. Electronic spectra (200–3000 nm) were obtained at room temperature on Nujol mulls pressed between quartz plates using a Varian Cary 5 UV–Vis–NIR spectrophotometer. Infrared spectra (4000–400 cm^{-1}) were recorded at room temperature on a Bomen FTIR spectrophotometer using KBr disc samples.

Magnetic properties were examined using a Quantum Design (MPMS) SQUID magnetometer. Magnetic susceptibilities were measured at 500 and 10 000 G over the temperature range 2–300 K, magnetization studies as a function of field strength (0–55 000 G) were made at several temperatures, and hysteresis magnetization data were obtained by oscillating the applied magnetic field between +55 000 G and –55 000 G at 4.8 K. A specially designed sample holder, as described previously (5*d*), was used to minimize the background signal. Magnetic susceptibilities were corrected for background and for the diamagnetism of all atoms; corrections of 125×10^{-6} and 79.0×10^{-6} cm^3 mol^{-1} were employed for $[Fe(2\text{-meimid})_2 \cdot 0.13Cp_2Fe]_x$ and $[Cu(1,2,4\text{-trz})_2]_x$, respectively. Data reported here are on a per mole of monomer basis.

X-ray crystallographic analysis of $[Fe(2\text{-meimid})_2 \cdot 0.13Cp_2Fe]_x$, 1

Crystallographic data appear in Table 1. The final unit-cell parameters were obtained by least squares based on 16 071 reflections with $2\theta = 4.0$–63.8. The data were processed,[2] and corrected for Lorentz and polarization effects, and for absorption (semiempirical, multi-scan, based on analysis of symmetry-equivalent data).

The structure was solved by direct methods, the coordinates of the non-hydrogen atoms being determined from *E*-maps or from subsequent difference Fourier syntheses. A cavity in the structure is partially occupied by ferrocene. The site occupancy of the ferrocene iron atom (Fe(2), which lies at the intersection of two mirror planes) was refined and its final value of 0.130(1) corresponds to 52% of the maximum value of 0.25. One of the 2-methylimidazolate ligands (containing N(4)) was modeled as 1:1 twofold disordered with respect to rotation about a twofold axis. Bond length restraints (six in total) were imposed for the disordered 2-methylimidazolate moiety. The poorly resolved ferrocene carbon atoms were refined with isotropic thermal parameters while all remaining non-hydrogen atoms were refined with anisotropic thermal parameters. Hydrogen atoms were fixed in calculated positions with C—H = 0.98 Å and $B_H = 1.2B_{bonded\ atom}$. No corrections for secondary extinction were necessary. Neutral atom scattering factors for all atoms and anomalous dispersion corrections for the non-hydrogen atoms were taken from the *International tables for X-ray crystallography* (13). Final atomic coordinates and equivalent isotropic thermal parameters, bond lengths, and bond angles

[2] *teXsan: Crystal structure analysis package*. Molecular Structure Corporation, The Woodlands, Tex. 1985–1998, and *d*TREK: Area detector software*. Molecular Structure Corporation, The Woodlands, Tex. 1997.

© 1999 NRC Canada

Can. J. Chem. Downloaded from www.nrcresearchpress.com by University Town Library of Shenzhen on 09/05/12
For personal use only.

Table 3. Selected bond lengths (Å) with estimated standard deviations in parentheses.[a]

Bond	Length	Bond	Length
Fe(1)—N(1)	2.046(4)	Fe(1)—N(2)[b]	2.038(4)
Fe(1)—N(3)	2.027(3)	Fe(1)—N(4)	2.040(7)
Fe(1)—N(5)[c]	2.021(7)	Fe(2)—C(12)	1.967(10)
Fe(2)—C(13)	1.84(2)	Fe(2)—C(14)	1.85(2)
N(1)—C(1)	1.340(5)	N(1)—C(3)	1.380(5)
N(2)—C(1)	1.357(6)	N(2)—C(2)	1.369(5)
N(3)—C(5)	1.342(5)	N(3)—C(6)	1.382(5)
N(4)—C(8)	1.364(9)[e]	N(4)—C(9)	1.394(9)[e]
N(5)—C(8)	1.376(9)[e]	N(5)—C(10)	1.378(8)[e]
C(1)—C(4)	1.480(6)	C(2)—C(3)	1.362(6)
C(5)—C(7)	1.485(8)	C(6)—C(6)[d]	1.356(10)
C(8)—C(11)	1.518(9)[e]	C(9)—C(10)	1.382(9)[e]
C(12)—C(12)[d]	1.25(2)	C(12)—C(13)	1.48(2)
C(13)—C(14)	1.20(2)		

[a]Superscripts refer to symmetry operations.
[b]$-1/2 + x, 1/2 - y, 1/2 - z$.
[c]$-x, -y, z$.
[d]$x, y, 1 - z$.
[e]Restrained during refinement.

Table 4. Selected bond angles (deg) with estimated standard deviations in parentheses.[a]

Bonds	Angle (deg)	Bonds	Angle (deg)
N(1)-Fe(1)-N(2)[b]	100.4(2)	N(1)-Fe(1)-N(3)	111.69(14)
N(1)-Fe(1)-N(4)	102.8(2)	N(1)-Fe(1)-N(5)[c]	123.0(2)
N(2)[b]-Fe(1)-N(3)	118.75(15)	N(2)[b]-Fe(1)-N(4)	121.4(3)
N(2)[b]-Fe(1)-N(5)[c]	92.9(2)	N(3)-Fe(1)-N(4)	100.9(3)
N(3)-Fe(1)-N(5)[c]	109.1(2)	Fe(1)-N(1)-C(1)	122.0(3)
Fe(1)-N(1)-C(3)	127.9(3)	C(1)-N(1)-C(3)	105.7(4)
Fe(1)-N(2)-C(1)	124.2(3)	Fe(1)-N(2)-C(2)	131.0(3)
C(1)-N(2)-C(2)	104.8(4)	Fe(1)-N(3)-C(5)	128.4(3)
Fe(1)-N(3)-C(6)	125.7(3)	C(5)-N(3)-C(6)	104.8(4)
Fe(1)-N(4)-C(8)	133.0(7)	Fe(1)-N(4)-C(9)	123.6(6)
C(8)-N(4)-C(9)	103.3(7)	Fe(1)[c]-N(5)-C(8)	128.8(6)
Fe(1)[c]-N(5)-C(10)	124.8(6)	C(8)-N(5)-C(10)	106.3(7)
N(1)-C(1)-N(2)	112.2(4)	N(1)-C(1)-C(4)	123.4(4)
N(2)-C(1)-C(4)	124.3(4)	N(2)-C(2)-C(3)	109.4(4)
N(1)-C(3)-C(2)	107.8(4)	N(3)-C(5)-N(3)[d]	113.1(6)
N(3)-C(5)-C(7)	123.4(3)	N(3)-C(6)-C(6)[d]	108.6(2)
N(4)-C(8)-N(5)	112.5(7)	N(4)-C(8)-C(11)	124.6(9)
N(5)-C(8)-C(11)	122.9(8)	N(4)-C(9)-C(10)	111.0(10)
N(5)-C(10)-C(9)	106.6(9)	C(12)[d]-C(12)-C(13)	103.7(7)
C(12)-C(13)-C(14)	111.9(16)	C(13)-C(14)-C(13)[d]	108.8(22)

[a]Superscripts refer to symmetry operations.
[b]$-1/2 + x, 1/2 - y, 1/2 - z$.
[c]$-x, -y, z$.
[d]$x, y, 1 - z$ (due to disorder, Fe(1) atoms are bonded to either N(4) or N(5) but not to both).

appear in Tables 2–4, respectively. Complete tables of atomic coordinates, anisotropic thermal parameters, bond lengths and angles, torsion angles, intermolecular contacts, and least-squares planes are included as supplementary material.[3] Tables of structure factors may be obtained directly from the author.

Results and discussion

Syntheses and structures

The synthetic pathway in which metallocenes are reacted directly with molten azoles affords a clean and effective

[3]Copies of material on deposit may be purchased from: The Depository of Unpublished Data, Document Delivery, CISTI, National Research Council of Canada, Ottawa K1A 0S2, Canada. Tables of atomic coordinates and of bond lengths and angles have also been deposited with the Cambridge Crystallographic Centre, and can be obtained on request from: The Director, Cambridge Crystallographic Data Centre, University Chemical Laboratory, 12 Union Road, Cambridge, CB2 1EZ, U.K.

© 1999 NRC Canada

Can. J. Chem. Downloaded from www.nrcresearchpress.com by University Town Library of Shenzhen on 09/05/12
For personal use only.

Fig. 1. View of the repeat unit of **1** and atom numbering scheme (33% ellipsoids, 0.13 occupancy for ferrocene).

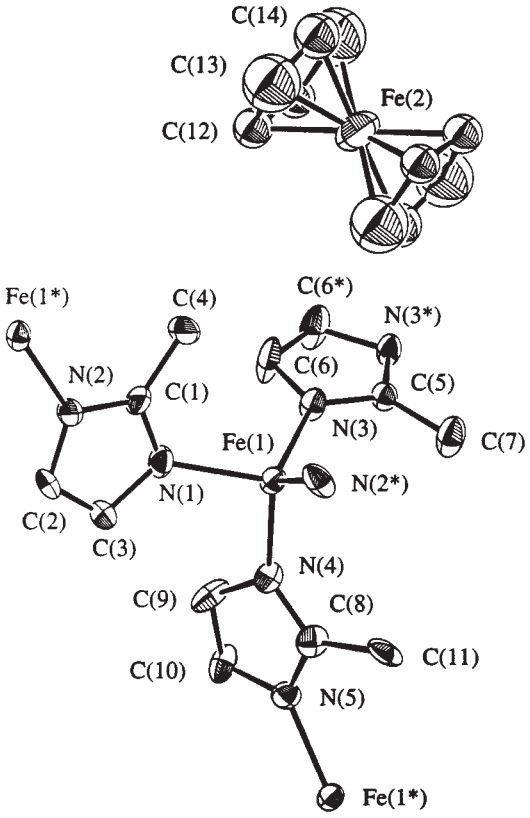

method for preparing divalent metal azolate polymers (9, 10). In the present work the reaction between ferrocene and excess molten 2-methylimidazole has afforded a crystalline polymeric Fe(II) material, $[Fe(2\text{-meimid})_2 \cdot 0.13Cp_2Fe]_x$, **1**, in which tetrahedral Fe(II) ions are linked via 2-methylimidazolate bridges. The electronic spectrum of **1** shows an absorption maximum at 1300 nm with a shoulder at about 1800 nm. This we assign to the $^5E \rightarrow {}^5T_2$ transition for (distorted) tetrahedral Fe(II) (14). The absence of a ν_{N-H} stretching vibration in both this spectrum and the infrared spectrum is indicative of the absence of neutral 2-methylimidazole in the product sample. Thermal gravimetric analysis (TGA) of the compound shows it to be thermally stable to 310°C. From 310 to 640°C the compound decomposes with a total weight loss over this range corresponding to 70% of the initial mass. This compares favorably with a 74% loss in mass that would occur if only iron metal remained after decomposition. Interestingly, the thermal analysis indicates that the ferrocene molecules trapped in the lattice (see below) are firmly held, at least up to 310°C. Loss of these, through sublimation for example, would be expected to result in a weight loss of 15% of the initial mass followed by decomposition of the covalent lattice material and further weight loss at higher temperatures. The carbon microanalysis was not in particularly good agreement with the value expected on the basis of the stoichiometry as determined by X-ray crystallography, suggesting the possibility that different crystals might have slightly different amounts of trapped ferrocene. However, both hydrogen and nitrogen analyses were in excellent agreement with the

Fig. 2. View of the crystal structure of **1** along the *a* axis. The stoichiometry is not shown as the ferrocene sites are only partially occupied, as described in the text.

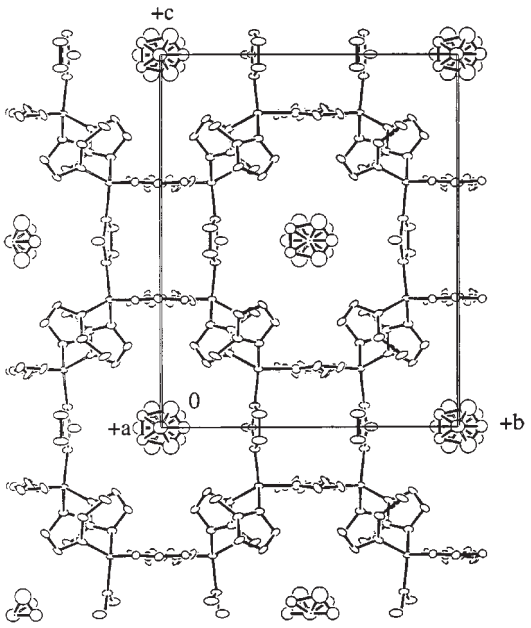

X-ray determined stoichiometry and hence this stoichiometry was used in the analysis of the magnetic data.

The structure of **1** was determined by single crystal X-ray diffraction and a section of it is shown with the atom numbering scheme in Fig. 1. Each of the tetrahedral Fe(II) ions is linked via single 2-meimid bridges to four other Fe(II) ions to form the 3-D polymer. A portion of the polymer structure is shown in Fig. 2. This structure again demonstrates how the 1,3 positioning of the nitrogens has prohibited the formation of a linear chain polymer with double azolate bridges between the M(II) ions as seen in previously described metal pyrazolate materials (4–9). Further insights into the nature of the 3-D lattice can be obtained from the iron atom connectivity diagram (Fig. 3). The structure involves the interconnection of 4-, 6- and 8-sided rings containing iron ions. A novel feature of this structure is the ferrocene molecules trapped in the lattice. These molecules may play a role in stabilizing the structure. Repeated preparations always generated the same material and, as described above, the ferrocenes cannot be removed by thermolysis without complete decomposition of the material.

$[Cu(1,2,4\text{-trz})_2]_x$, **2**, was prepared by the copper shot – molten azole method, which has been employed to obtain several copper(II) pyrazolate complexes, some in crystalline form suitable for X-ray structure determinations (5*a*, 5*d*). Unfortunately, all attempts to obtain the triazolate in a form suitable for definitive X-ray analysis were unsuccessful. These attempts generally involved modifications designed to reduce the rate of the reaction. This involved procedures such as lowering the temperature of the reaction (below that of the melting point of the azole) by adding small amounts of benzene or xylenes to the reaction mixture and reducing the concentration of dioxygen by employing atmospheric concentrations instead of a pure O_2 atmosphere. Although such attempts did produce the desired product, no macroscopic

© 1999 NRC Canada

Can. J. Chem. Downloaded from www.nrcresearchpress.com by University Town Library of Shenzhen on 09/05/12
For personal use only.

Fig. 3. Iron ion connectivity diagram for **1**.

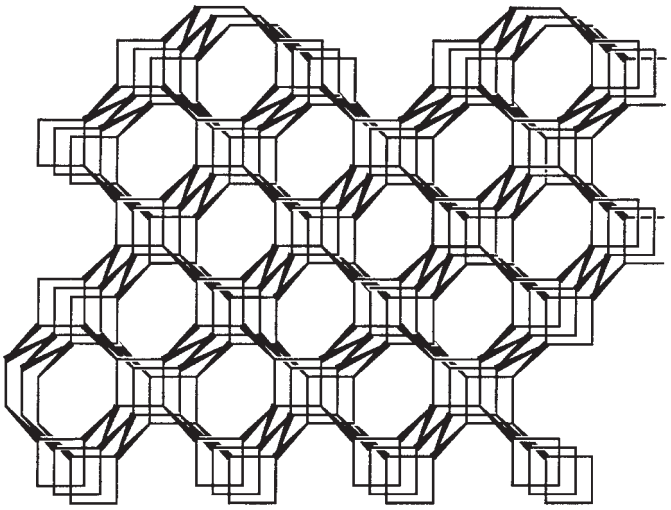

single crystals were obtained. The previously published route to this compound involving the reaction of an aqueous solution of the azole with an ammoniacal copper(II) sulfate solution (15) was also explored but yielded only microcrystalline powder.

Although the exact structure of **2** remains unknown, the polymeric nature of the material is indicated by its physical properties. The compound is stable both in air and in contact with moisture. It is insoluble in water and common organic solvents, involatile, and thermally robust. It dissolves with decomposition in concentrated mineral acids. Thermogravimetric analysis shows no mass loss due to thermal decomposition or sublimation below 320°C. Thermal decomposition appears to take place in two stages. There is a relatively rapid loss of about 40% of the initial mass between 320 and 380°C. The second stage is more gradual with about 30% of the initial mass being lost between 380 and 560°C. The 30% of the mass remaining corresponds closely to the 32% expected for a residue of copper metal.

The infrared spectrum of **2** does not contain the bands generated by ν_{N-H} stretching vibrations, thus indicating that all of the triazole is present in its deprotonated form. The electronic spectrum consists of an absorption at 35 700 cm^{-1} assigned to charge transfer and another at 17 400 cm^{-1} assigned to d→d transitions. Hathaway (16) published a correlation between band energies and stereochemistry for CuN_{4-6} chromophores. The value of 17 400 cm^{-1} obtained for the triazolate compound is consistent with six-coordination. This could be achieved if all three of the azolate nitrogen atoms are involved in binding to copper in a structure involving a 3-D covalent lattice. It should be noted, however, that two possible structures for this material were previously proposed based on evidence obtained from broad-line proton magnetic resonance spectroscopy (17). Both of these structures involved lower dimensional lattices and four coordinate copper ions.

Fig. 4. Magnetic susceptibility and χT versus temperature plots at 500 G for **1** (top) and **2** (bottom).

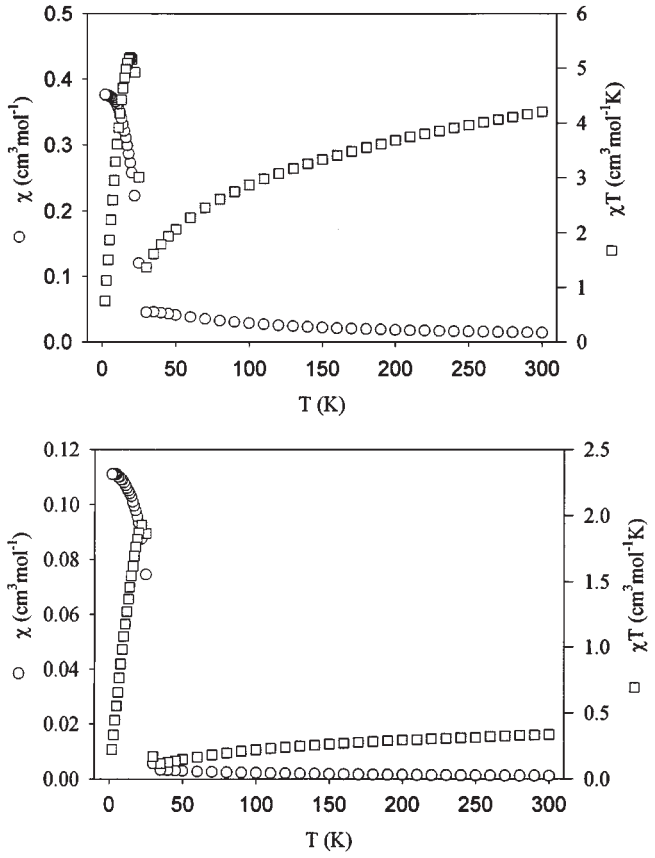

Magnetic properties

Magnetic susceptibility (χ) and χT versus T data on powdered samples of **1** and **2** in an applied field of 500 G are shown in Fig. 4. For both compounds χT decreases with decreasing temperature from 300 K to a critical temperature, T_c, (27 K and 35 K for **1** and **2**, respectively). Below T_c, χT increases abruptly to a maximum value (5.19 cm^3 mol^{-1} K at 19 K for **1** and 1.93 cm^3 mol^{-1} K at 22 K for **2**) before decreasing again as the temperature decreases to 2 K. The magnetic transition at T_c is also seen in the χ versus T plots (Fig. 4). The susceptibility, which increases with decreasing temperature below 300 K, shows an incipient maximum just above T_c for both compounds. Below T_c the susceptibility rises abruptly as the temperature decreases before levelling off and approaching a saturation value at the lowest temperatures studied. This magnetic behavior is very similar to that reported for $[Fe_3(imid)_6(imidH)_2]_x$ (10). It suggests a form of antiferromagnetic coupling in which perfect antiparallel alignment of spins on neighboring metal ions does not occur because of a canting of the spins. This leads to a residual spin on the metal centers and long-range ferromagnetic ordering of the spins generates weak ferromagnetism at low temperatures. Ferromagnetism is also evident in the magnetization versus field plots at several temperatures (Fig. 5). For both compounds these plots are linear above T_c and extrapolate to zero magnetization at zero applied field while below T_c they show extrapolated net magnetization at zero field. That these compounds are behaving as long-range or-

© 1999 NRC Canada

Can. J. Chem. Downloaded from www.nrcresearchpress.com by University Town Library of Shenzhen on 09/05/12
For personal use only.

Fig. 5. Magnetization versus applied field plots at different temperatures for **1** (top) and **2** (bottom).

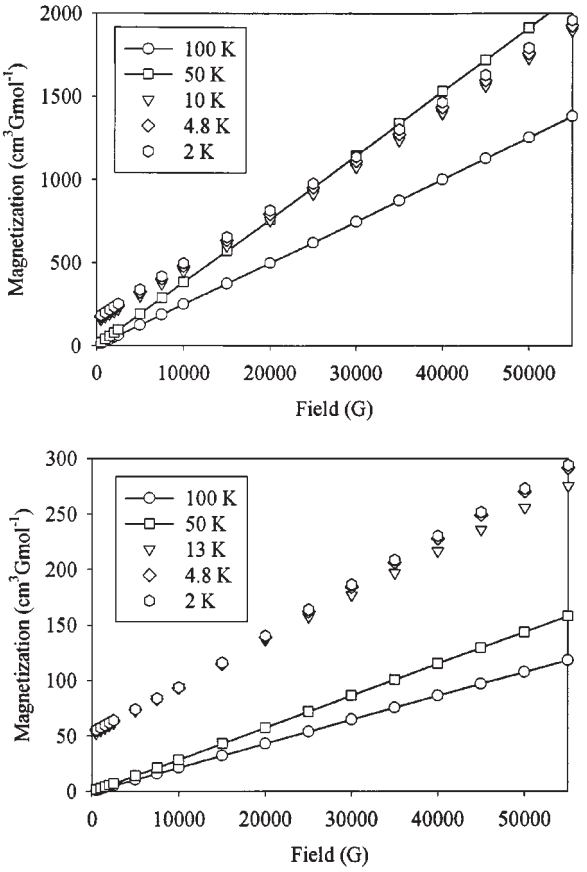

Fig. 6. Magnetic hysteresis plots at 4.8 K for **1** (top) and **2** (bottom).

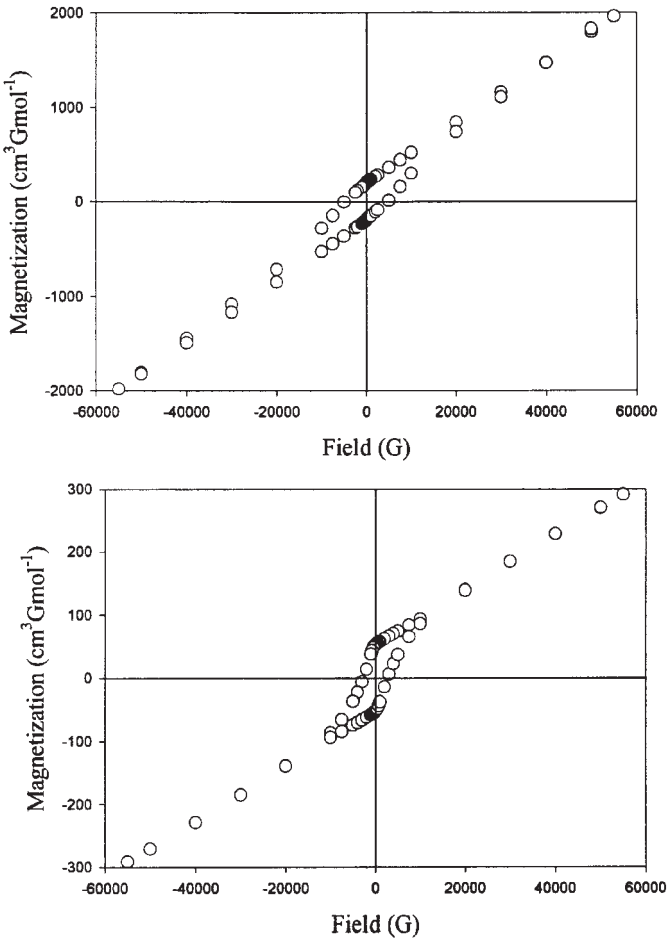

dered molecular magnets below T_c is further illustrated by hysteresis studies. In these studies, the magnetization was measured as the applied field was cycled between +50 000 G and –50 000 G at 4.8 K. The resulting hysteresis loops are shown in Fig. 6. These loops give remnant magnetizations of 200 and 55 cm^3 G mol^{-1} and coercive fields of 5000 and 2800 G for **1** and **2**, respectively.

Since the structure of **1** is known, the possibility exists of analyzing the antiferromagnetic exchange in the material by modeling the magnetic data at temperatures above T_c as was done earlier for $[Fe_3(imid)_6(imidH)_2]_x$ (10). Unfortunately, no theoretical expression is available for modeling the magnetism of a 3-D extended array of $S = 2$ ions. The structure itself revealed a feature that suggested the use of a simpler model. There are three different Fe–ligand–Fe distances in the compound: Fe···Fe = 5.95 Å (a chain along the *a* axis), and 6.06 and 6.19 Å (in the 4- and 8-membered rings). The structure is such that it can be considered as consisting of chains of ligand-bridged iron ions joined together by weaker Fe–ligand-bridged–Fe interactions. While exchange likely occurs via all three pathways, we considered the possibility that the shortest pathway dominates. Accordingly, we examined fits of the magnetic susceptibilities over the temperature range 30–300 K to the expression for a linear chain of antiferromagnetically coupled $S = 2$ centers (18). Employing an isotropic Hamiltonian of the form $H = -2\,J\,S_1S_2$ the equation for the magnetic susceptibility is

$$\chi = (Ng^2\beta^2/kT)\left[\frac{2 + 71.938x^2}{1 + 10.482x + 955.56x^3}\right]$$

where $x = |J|/kT$, J is the exchange coupling constant, g is the Landé factor, and the other symbols have their usual meaning.

To analyze the antiferromagnetic interactions in **1** using the above equation we employed susceptibility data obtained at 10 000 G. At this higher field the ferromagnetic ordering is repressed as evidenced by a less pronounced anomaly at 27 K in both the susceptibility and χT plots (Fig. 7). The best fit to these susceptibility data was obtained with $J = -2.75$ cm^{-1}, $g = 2.20$ (with $F = 0.010$), where F is the value of the function (given below) that was minimized in the fitting procedure. F also provides a measure of the goodness of fit.

$$F = \left[\frac{1}{n}\sum_{i=1}^{n}\left[\frac{\chi^i_{calc} - \chi^i_{obs}}{\chi^i_{obs}}\right]^2\right]^{1/2}$$

In the above expression n is the number of data points. The experimental and calculated susceptibility and χT data are compared in Fig. 7. In spite of the obvious limitations of

© 1999 NRC Canada

Table 5. Magnetic parameters for some azolate complexes showing low-temperature weak ferromagnetism.

Compound	Critical temperature (K)	Coercive field (G)	Remnant magnetization (cm^3 G mol^{-1})	Reference
$Fe(4\text{-imidac})_2 \cdot 2CH_3OH$	15	6200	1200	19
$Fe_3(imid)_6(imidH)_2$	17	200	2500	10
Fe(biimid)	25	2000	950	20
1	27	5000	200	This work
2	35	2800	55	This work

Abbreviations: 4-imidac = 4-imidazoleacetate, imid = imidazolate, biimid = biimidazolate.

Can. J. Chem. Downloaded from www.nrcresearchpress.com by University Town Library of Shenzhen on 09/05/12
For personal use only.

Fig. 7. Plots of magnetic susceptibility and χT versus temperature at 10 000 G for **1**. The solid lines are calculated from theory, for the temperature range 30–300 K, as described in the text.

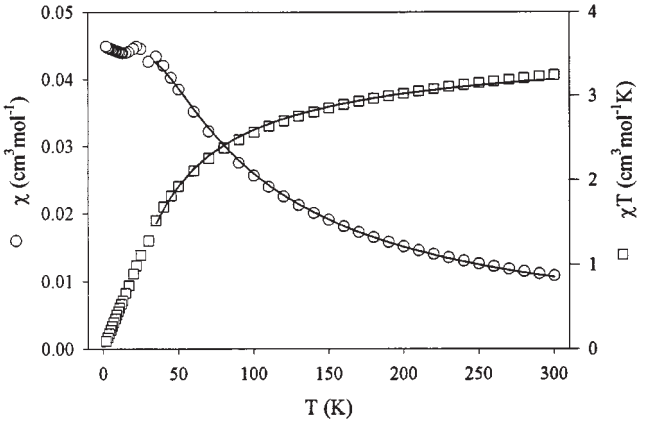

the model, which ignores interchain exchange, the agreement between experiment and theory is good. However, because of the limitations of the model not too much importance should be attached to the actual value of *J*. That *J* is, at least, a qualitative measure of the strength of the antiferromagnetic coupling, however, is indicated by the fact that it is of the same order of magnitude as that determined previously for $[Fe_3(imid)_6(imidH)_2]_x$ in which interacting Fe(II) centers are linked by single imidazolate bridges ($J = -2.3$ cm^{-1}) (10).

Magnetic parameters for five azolate compounds, including **1** and **2** and three other azolate compounds (10, 19, 20) that exhibit low-temperature ferromagnetic ordering and canted spin antiferromagnetism, are given in Table 5. The three compounds that have structures determined from X-ray studies illustrate the fact that the phenomenon is not restricted to covalent lattices of a particular dimensionality since the antiferromagnetic exchange processes in $[Fe_3(imid)_6(imidH)_2]_x$ (10), $[Fe(4\text{-imidazolacetate})_2]_x$ (19), and **1** are considered to involve 1-D, 2-D, and 3-D pathways, respectively. Unfortunately the number of compounds of this class with known structures is too small at this time to try to correlate magnetic parameters with detailed structural features.

In summary, the studies on **1** have supported the previously stated contention (10) that azolate ligands that bridge through nitrogen atoms separated by one carbon in the heterocyclic ring will generate structures with single azolate bridges and extended arrays. Moreover, it appears this bridge geometry can generate a systematic alternation in the relative orientation of neighboring metal chromophores. These characteristics facilitate a canting of spins and long-range magnetic ordering (10). The 1,2,4-triazolate ligand may have these desirable structural features also, although confirmation of this will require the X-ray structural determination of **2** or a related system.

Acknowledgements

Funding for the project was provided by the Natural Sciences and Engineering Research Council of Canada. P. Borda of this department is thanked for the C, H, N analyses.

References

1. S. Trofimenko. (*a*) Chem. Rev. **72**, 497 (1972); (*b*) Prog. Inorg. Chem. **34**, 115 (1986).
2. P.J. Steele. Coord. Chem. Rev. **106**, 227 (1990).
3. G. La-Monica and G.A. Ardizzoia. Prog. Inorg. Chem. **46**, 151 (1997).
4. M.K. Ehlert, A. Storr, D.A. Summers, and R.C. Thompson. Can. J. Chem. **75**, 491 (1997).
5. M.K. Ehlert, S.J. Rettig, A. Storr, R.C. Thompson, and J. Trotter. Can. J. Chem. (*a*) **67**, 1970 (1989); (*b*) **68**, 1444 (1990); (*c*) **68**, 1494 (1990); (*d*) **69**, 432 (1991); (*e*) **70**, 2161 (1992); (*f*) **71**, 1425 (1993).
6. M.K. Ehlert, A. Storr, and R.C. Thompson. Can. J. Chem. (*a*) **70**, 1121 (1992); (*b*) **71**, 1412 (1993).
7. M.K. Ehlert, S.J. Rettig, A. Storr, R.C. Thompson, F.W.B. Einstein, and R.J. Batchelor. Can. J. Chem. **71**, 331 (1993).
8. M.K. Ehlert, S.J. Rettig, A. Storr, R.C. Thompson, and J. Trotter. Acta. Crystallogr. Sect. C: Cryst. Struct. Commun. **C50**, 1023 (1994).
9. A. Storr, D.A. Summers, and R.C. Thompson. Can. J. Chem. **76**, 1130 (1998).
10. S.J. Rettig, A. Storr, D.A. Summers, R.C. Thompson, and J. Trotter. J. Am. Chem. Soc. **119**, 8675 (1997).
11. O. Kahn. Adv. Inorg. Chem. **9**, 11 (1995).
12. M. Inoue and M. Kubo. J. Coord. Chem. **6**, 157 (1977).
13. (*a*) International tables for X-ray crystallography. Vol. IV. Kynoch Press. Birmingham, U.K. (present distributor Kluwer Academic Publishers, Boston, Mass.). 1974. pp. 99–102; (*b*) International tables for crystallography. Vol. C. Kluwer Academic Publishers, Boston, Mass. 1992. ppp. 200–206.
14. A.P.B. Lever. Inorganic electronic spectroscopy. Elsevier, Amsterdam. 1984.
15. M. Inoue, M. Kashita, and M. Kubo. Inorg. Chem. **4**, 626 (1965).
16. B.J. Hathaway. J. Chem. Soc. Dalton Trans. 1196 (1972).
17. M. Inoue and M. Kubo. Inorg. Chem. **5**, 70 (1966).
18. W. Hiller, J. Strahle, A. Datz, M. Hanack, W.E. Hatfield, and P. Gutlich. J. Am. Chem. Soc. **106**, 329 (1984).

© 1999 NRC Canada

19. M.-A. Martinez-Lorente, V. Pétrouléas, J.-M. Savariault, R. Poinsot, and M. Drillon. Inorg. Chem. **30**, 3589 (1991).

20. M.-A. Martinez-Lorente, F. Dahan, Y. Sanakis, V. Pétrouléas, A. Bousseksou, and J.P. Tuchagues. Inorg. Chem. **34**, 5346 (1995).

Can. J. Chem. Downloaded from www.nrcresearchpress.com by University Town Library of Shenzhen on 09/05/12
For personal use only.

© 1999 NRC Canada

The methylgallium-2-carboxylatobenzimidazolato hexamer, $[MeGa{\cdot}C_8H_4N_2O_2]_6{\cdot}C_6H_6{\cdot}(Me_2C_6H_4)_2$; synthesis and X-ray crystal structure

Steven J. Rettig, Alan Storr, and James Trotter

Can. J. Chem. Downloaded from www.nrcresearchpress.com by Peking University on 09/06/12
For personal use only.

Abstract: The room-temperature reaction of Me_3Ga with benzimidazole 2-carboxylic acid in xylene solvent has yielded a novel crystalline hexameric gallium compound with "MeGa" moieties bridged by the doubly depronotated ligand precursor. Crystals of $[MeGa(4,5\text{-benzimidazolato-2-carboxylato})]_6{\cdot}(C_6H_6){\cdot}(m\text{-}Me_2C_6H_4)_2$ are monoclinic, a = 18.091(2), b = 17.094(2), c = 13.2215(5) Å, Z = 2, space group $C2/m$. The structure was solved by direct methods and refined by full-matrix least-squares procedures to R (F, $I \geq 3\sigma(I)$) = 0.064 (R_w (F^2, all data) = 0.134). The hexameric Ga complex contains a six-membered ring of Ga atoms, bridged by the benzimidazolate ligands with the benzo rings projecting alternately above and below the Ga plane, thus forming a ball-shaped molecule. The complex could have ideal D_{3d} symmetry, but it contains an encapsulated molecule of benzene, which distorts the regularity of the Ga_6 hexagon, and reduces the symmetry of the complex to the crystallographically observed C_{2h}. The coordination geometry at each of the two independent GaO_2N_2C centres approximates a trigonal bipyramid, with a N_2C trigonal plane, and the O atoms above and below; average dimensions are Ga—O = 2.176(2), Ga—N = 1.973(3), Ga—C = 1.927(5) Å, O-Ga-O = 165°. The unit cell also contains four *m*-xylene solvent molecules (outside the molecular cage).

Key words: gallium, crystal structure, benzene intercalate, benzimidazolecarboxylic acid.

Résumé : La réaction du Me_3Ga avec l'acide benzimidazole-2-carboxylique en solution dans le xylène, à la température ambiante, conduit à un nouveau composé hexamérique cristallin comportant des portions « MeGa » reliées par de ligand précurseur doublement déprotoné. Les cristaux du $[MeGa(4,5\text{-benzimidazolato-2-carboxylato})]_6{\cdot}(C_6H_6){\cdot}(m\text{-}Me_2C_6H_4)$ sont monocliniques, groupe d'espace $C2/m$, avec a = 18,091(2), b = 17,094(2) et c = 13,2215(5) Å et Z = 2. On a résolu les structures par des méthodes directes et on les a affinées par la méthode des moindres carrés jusqu'à des valeurs de R (F, $I \geq 3\sigma(I)$) = 0,064 (R_w (F^2, toutes les données = 0,134). Le complexe hexamère du Ga contient un cycle à six chaînons d'atomes de Ga reliés par ligands benzimidazolates dans lesquels les noyaux benzo sont projetés alternativement au-dessus et au-dessous du plan des Ga formant ainsi une molécule en forme de balle. Le complexe pourrait avoir une symétrie idéale D_{3d}; elle contient toutefois une molécule de benzène encapsulée qui déforme la régularité de l'hexagone Ga_6 et qui réduit ainsi la symétrie observée cristallographiquement du complexe à C_{2h}. La géométrie de coordination de chacun des deux centres GaO_2N_2C indépendantes correspond approximativement à une bipyramide trigonale avec un N_2C trigonal plan et les atomes d'O au-dessus et au-dessous; les dimensions moyennes sont : Ga—O = 2,176(2), Ga—N = 1,973(3), Ga—C = 1,927(5) Å et O-Ga-O = 165°. La maille élémentaire contient aussi quatre molécules du solvant (*m*-xylène) (en dehors de la cage moléculaire).

Mots clés : gallium, structure cristalline, benzène intercalé, acide benzimidazolecarboxylique.

[Traduit par la Rédaction]

Introduction

Our interest in ligands capable of giving polymeric transition metal complexes is well documented, particularly with pyrazolate and imidazolate bridging ligands (1–5). The present study was undertaken to explore the possibility of utilizing the 4,5-benzimidazole-2-carboxylic acid molecule as a ligand precursor. Reaction with 2 molar equivalents of Me_3Ga was anticipated to yield the bis-Me_2Ga complex, **A**, shown in eq. [1]:
since it is well documented that Me_3Ga readily loses one Me group in its reactions with active hydrogen species (6), whereas

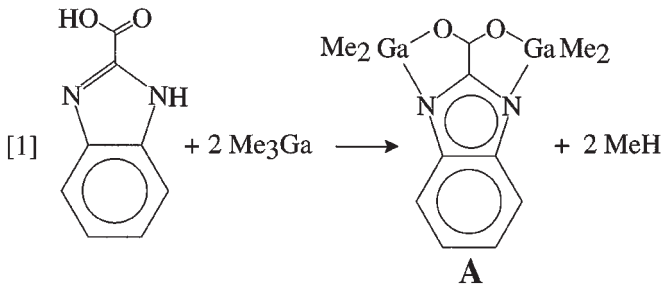

Received January 18, 1999.

S.J. Rettig, A. Storr,[1] and J. Trotter. Department of Chemistry, University of British Columbia, 2036 Main Mall, Vancouver, BC V6T 1Z1, Canada.

[1]Author to whom correspondence may be addressed. Telephone: (604) 822-3266. Fax: (604) 822-2847. e-mail: storr@chem.ubc.ca

© 1999 NRC Canada

Fig. 1. View of the hexameric Ga complex; (*a*) shows the crystallographic numbering scheme; (*b*) is a stereo view.

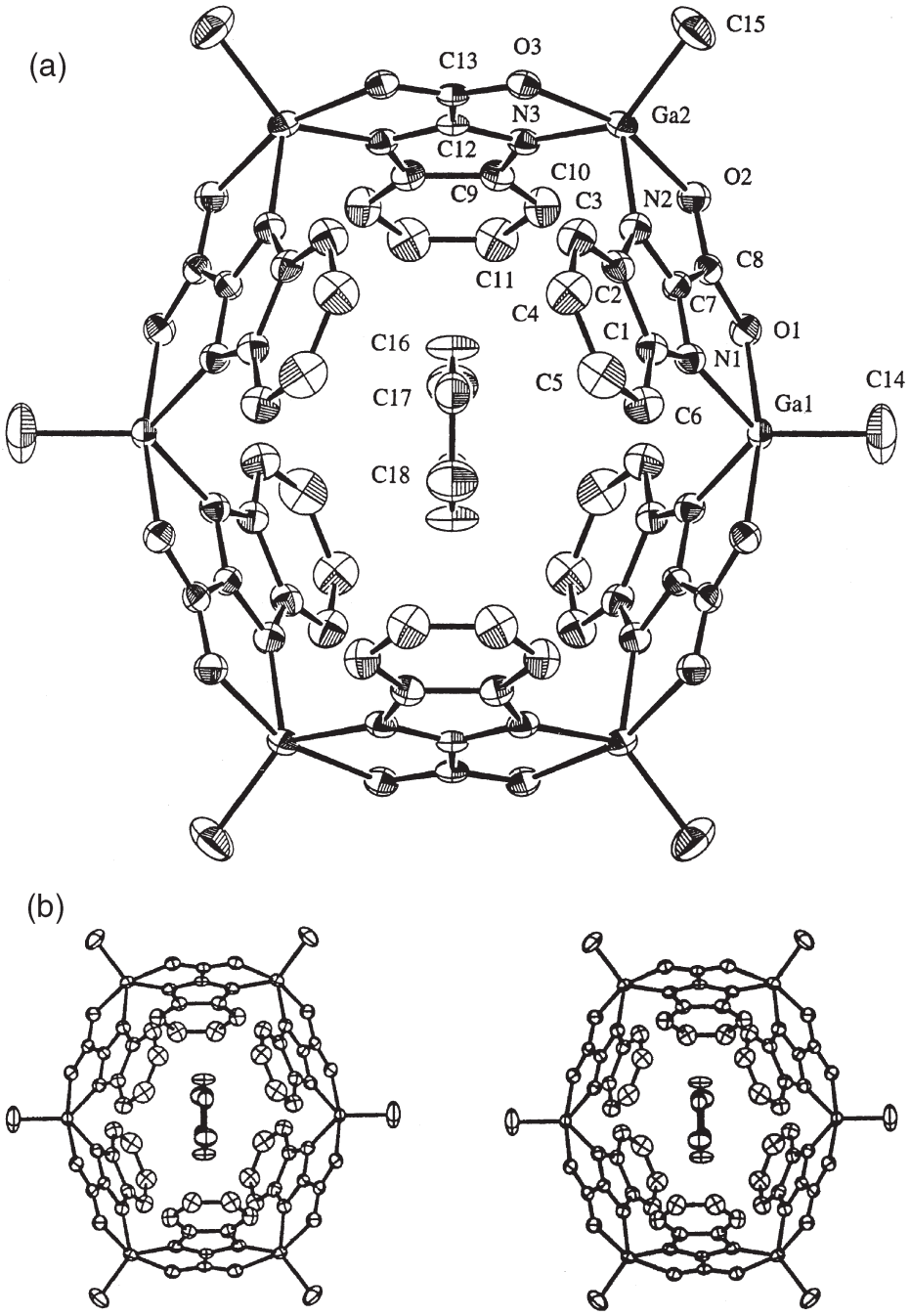

Can. J. Chem. Downloaded from www.nrcresearchpress.com by Peking University on 09/06/12
For personal use only.

the "Me_2Ga" moiety is quite robust and resists attack even by water (7). It was somewhat surprising, therefore, that the crystalline product isolated was a hexameric species containing only MeGa units bridged by doubly deprotonated ligand precursors (see Fig. 1). The entrapment of benzene molecules (from the xylene solvent) was also unexpected.

Experimental

Materials were handled in a conventional high-vacuum line or in a glove box under an atmosphere of oxygen-free dry dinitrogen. Solvents were dried and distilled before use. Gas volumes are at STP. Trimethylgallium was prepared as described previously, from gallium and dimethylmercury (8). The benzimidazole-2-carboxylic acid monohydrate (a gift from Dr. P.N. Preston of Heriot-Watt University, Edinburgh) was prepared by the method of Bistrzycki and Przeworski (9). The anhydrous compound was obtained by vacuum treatment of the hydrate at ~70ºC (N.B. Even at 100ºC the anhydrous material is prone to decarboxylation).

Preparation of $[MeGa{\cdot}C_8H_4N_2O_2]_6(C_6H_6)(m\text{-}Me_2C_6H_4)_2$

The anhydrous benzimidazole-2-carboxylic acid (0.162 g; 1.0 mmol) was transferred to a 250 mL round-bottomed flask fitted with break-seal side arm. Xylene solvent was added and the reaction flask was then cooled to –196ºC and

© 1999 NRC Canada

Can. J. Chem. Downloaded from www.nrcresearchpress.com by Peking University on 09/06/12
For personal use only.

Table 1. Crystallographic data.[a]

Formula	$C_{76}H_{68}Ga_6N_{12}O_{12}$
fw	1759.77
Crystal color, habit	Colorless, prism
Crystal dimensions (mm)	0.30 × 0.35 × 0.40
Crystal system	Monoclinic
Space group	*C2/m* (No. 12)
a, Å	18.091(2)
b, Å	17.094(2)
c, Å	13.2215(5)
β, deg	93.443(1)
V, Å^3	4081.2(5)
Z	2
ρ_{calc}, g/cm^3	1.432
F(000)	1780
Radiation	Mo
μ, cm^{-1}	20.16
Correction factors[b]	0.803–1.000
φ sweep range, deg (χ = –90°)	0–190
ω sweep range, deg (χ = –90°)	–23 – 18
Oscillation width, deg	0.5
Data images, exposure time	462, 90 s
$2\theta_{max}$, deg	60.2
Total reflections	18 744
Unique reflections	5480
R_{merge}	0.048
No. with $I \geq 3\sigma(I)$	4252
No. of variables	251
R (*F*) ($I \geq 3\sigma(I)$)	0.064
R_w (F^2) (all data)	0.134
gof	2.04
Max Δ/σ (final cycle)	0.02
Residual density e/Å^3	–0.98 to 1.29

[a]Temperature 180 K, Rigaku/ADSC CCD diffractometer, Mo K_α (λ = 0.7109 Å), graphite monochromator, takeoff angle 6.0°, aperture 94.0 × 94.0 mm at a distance of 39.15(3) mm from the crystal, $\sigma^2(F^2) = (C + B)/Lp2$ (C = scan count, B = background count), function minimized $\Sigma w(|F_o^2| - |F_c^2|)^2$ where $w = 1/\sigma^2(F_o^2)$, $R(F) = \Sigma||F_o| - |F_c||/\Sigma|F_o|$, $R_w(F^2) = (\Sigma w(|F_o^2| - |F_c^2|)^2/\Sigma w|F_o^2|^2)^{1/2}$, and gof = $[\Sigma w(|F_o^2| - |F_c^2|)^2/(m - n)]^{1/2}$.

[b]Includes crystal decay (if any), absorption, and scaling corrections performed in a single step.

evacuated. Me_3Ga (0.229 g; 2.0 mmol) was vacuum transferred into the reaction vessel, which was then flame-sealed. The contents of the flask were then warmed slowly to room temperature during which time gas evolution was observed. After remaining at room temperature overnight the product mixture was cooled to –196°C, the break-seal on the flask opened, and the volume of methane evolved in the reaction measured using a Toepler pump (found: 45.1 mL; calcd.: 44.8 mL (for 2 mmol)). The contents of the flask were then warmed to room temperature. The clear solution of the product was reduced in volume under vacuum and then placed in the glove box. Slow evaporation of further solvent led to the collection, in high yield, of colorless crystals of the solvated product $[MeGa{\cdot}C_8H_4N_2O_2]_6(C_6H_6)(m\text{-}Me_2C_6H_4)_2$. Anal. calcd.: C 51.9, H 3.9, N 9.6; found: C 52.3, H 4.2, N 9.7%. The air-stable colorless crystals were subjected to single crystal X-ray analysis (see below). The mass spectrum of the product did not show detectable signals due to the parent hexamer ion, but a weak group of signals around m/e 1228 corresponds to the $[MeGa.C_8H_4N_2O_2]_5^+$ cluster ion. A strong signal due to the monomeric species, $[MeGaC_8H_4N_2O_2]^+$ was also detected. The ^{1}H NMR spectrum of the complex in C_6D_6 solution showed one signal for the MeGa groups at δ 0.40, together with xylene Me signals at δ 2.20 and aromatic ring proton signals at δ ~7.0. The infrared spectrum (KBr disc) showed a characteristic Ga–C stretching vibration at 598 cm^{-1}. A thermal gravimetric analysis experiment revealed the compound to be thermally stable to 150°C. All solvated xylene and entrapped benzene were lost by ~230°C, and major cage breakdown was evident after ~320°C.

X-ray crystallographic analysis of $[MeGa(4,5\text{-benzimidazolato-2-carboxylato})]_6{\cdot}(C_6H_6){\cdot}(m\text{-}Me_2C_6H_4)_2$

Crystallographic data appear in Table 1. The final unit-cell parameters were obtained by least squares based on 18 744 reflections with 2θ = 4.0°–60.2°. The data were processed,[2] corrected for Lorentz and polarization effects, and for absorption (semiempirical, multi-scan, based on analysis of symmetry-equivalent data). Space group *C2/m* was deduced from the systematic absences, a statistical analysis of the intensity distribution, and successful solution and refinement of the structure.

The structure was solved by direct methods, the coordinates of the non-hydrogen atoms being determined from *E*-maps or from subsequent difference Fourier syntheses. Non-hydrogen atoms were refined with anisotropic thermal parameters. Hydrogen atoms were fixed in calculated positions with C—H = 0.98 Å and $B_H = 1.2\ B_{bonded\ atom}$. No corrections for secondary extinction were necessary. Neutral atom scattering factors for all atoms and anomalous dispersion corrections for the non-hydrogen atoms were taken from the *International tables for X-ray crystallography* (10). Final atomic coordinates and equivalent isotropic thermal parameters are in Table 2, and a summary of important bond lengths and angles in Table 3. Complete tables of atomic coordinates, anisotropic thermal parameters, bond lengths and angles, torsion angles, intermolecular contacts, and least-squares planes are included as supplementary material.[3]

Results and discussion

The reaction of Me_3Ga with ligands containing acidic hydrogen yields adducts that readily eliminate methane to produce cyclic products containing Me_2Ga moieties (6). The degree of association of the product materials is determined by a balance between steric effects, valency angle strain, and entropy factors (6, 11, 12). Thus, for example, the reaction

[2] *teXsan: Crystal structure analysis package*. Molecular Structure Corporation, The Woodlands, Tex. 1985–1998; and *d*TREK: Area detector software*. Molecular Structure Corporation, The Woodlands, Tex. 1997.

[3] Copies of material on deposit may be purchased from: The Depository of Unpublished Data, Document Delivery, CISTI, National Research Council of Canada, Ottawa, ON K1A 0S2, Canada. Tables of hydrogen atom coordinates and bond lengths and angles involving hydrogen atoms have also been deposited with the Cambridge Crystallographic Data Centre and can be obtained on request from The Director, Cambridge Crystallographic Data Centre, University Chemical Laboratory, 12 Union Road, Cambridge CB2 1EZ, U.K.

© 1999 NRC Canada

Can. J. Chem. Downloaded from www.nrcresearchpress.com by Peking University on 09/06/12
For personal use only.

Table 2. Final atomic coordinates (fractional) and B_{eq} (10^3 Å^2).[a]

Atom	*x*	*y*	*z*	B_{eq}
Ga(1)	0.5000	0.28693(3)	0.5000	1.969(11)
Ga(2)	0.64305(2)	0.15767(2)	0.19652(3)	2.126(9)
O(1)	0.61525(13)	0.27301(13)	0.4646(2)	2.21(5)
O(2)	0.67452(12)	0.22491(14)	0.3318(2)	2.29(5)
O(3)	0.59814(13)	0.06623(14)	0.0958(2)	2.29(5)
N(1)	0.48437(14)	0.2214(2)	0.3788(2)	1.96(6)
N(2)	0.54328(15)	0.1708(2)	0.2487(2)	2.03(6)
N(3)	0.68909(14)	0.0661(2)	0.2661(2)	1.85(5)
C(1)	0.4309(2)	0.1862(2)	0.3133(3)	2.05(7)
C(2)	0.4683(2)	0.1545(2)	0.2311(3)	2.15(7)
C(3)	0.4293(2)	0.1161(2)	0.1519(3)	2.86(8)
C(4)	0.3540(2)	0.1086(3)	0.1581(3)	3.37(9)
C(5)	0.3173(2)	0.1393(3)	0.2403(3)	3.66(9)
C(6)	0.3545(2)	0.1788(2)	0.3187(3)	2.77(8)
C(7)	0.5476(2)	0.2094(2)	0.3356(2)	1.85(6)
C(8)	0.6189(2)	0.2385(2)	0.3809(3)	1.93(6)
C(9)	0.7293(2)	0.0416(2)	0.3535(3)	2.07(6)
C(10)	0.7650(2)	0.0839(2)	0.4334(3)	2.71(8)
C(11)	0.7981(2)	0.0410(3)	0.5122(3)	3.23(8)
C(12)	0.6670(2)	0.0000	0.2200(3)	1.74(9)
C(13)	0.6173(2)	0.0000	0.1293(3)	1.89(9)
C(14)	0.5000	0.3996(4)	0.5000	5.2(2)
C(15)	0.6840(3)	0.2244(3)	0.0967(3)	4.12(10)
C(16)	0.5371(3)	0.0000	0.4147(5)	4.22(15)
C(17)	0.4615(3)	0.0000	0.4060(4)	3.38(12)
C(18)	0.4238(3)	0.0000	0.4939(6)	4.37(15)
C(19)	0.8714(8)	0.0000	0.1977(11)	9.6(4)
C(20)	0.8570(5)	0.0703(6)	0.1550(8)	9.8(3)
C(21)	0.8222(5)	0.0678(6)	0.0543(8)	9.7(3)
C(22)	0.8080(8)	0.0000	0.0053(13)	10.2(4)
C(23)	0.8786(7)	0.1356(7)	0.2051(11)	13.7(4)

[a] $B_{eq} = (8/3)\pi^2 \Sigma \Sigma(U_{ij} a_{i*} a_{j*} (\mathbf{a}_i \cdot \mathbf{a}_j))$.

Table 3. Selected bond lengths (Å) and angles (°), with estimated standard deviations in parentheses.

Lengths				
Ga—O	2.177(2)	2.172(2)	2.179(2)	mean 2.176(2)
Ga—N	1.962(3)	1.984(3)	1.973(3)	mean 1.973(3)
Ga—C	1.926(6)	1.927(4)		mean 1.927(5)
Angles				
O-Ga-O		167.5(1)	162.2(9)	mean 165
N-Ga-N		110.4(2)	107.2(1)	mean 109
N-Ga-C		124.8(1)	124.5(2)	128.3(2) mean 126

of pyrazoles with Me_3Ga yields, via methane elimination, dimeric products, $[Me_2Gapz]_2$, which contain six-membered Ga_2N_4 rings (13–15). On the other hand, the reaction of 2-methylimidazole or water with Me_3Ga results in the formation of the tetrameric products $[Me_2Ga{\cdot}Meimid]_4$ (16) and $[Me_2GaOH]_4$ (17), respectively.

The present study was designed to investigate the feasibility of using the doubly deprotonated benzimidazole-2-carboxylic acid dianion as a bridging ligand in the preparation of polymeric transition metal complexes. It was anticipated that in the 2:1 reaction (eq. [1]), each molecule of Me_3Ga would lose one Me group, resulting in the product **A**. It was somewhat surprising, therefore, when the isolated compound contained only MeGa moieties linked together by the deprotonated ligand precursor. (A 1:1 reaction also yielded the cyclic hexamer.) The observed cyclic hexamer (Fig. 1) was also unique in that within its central cavity was entrapped a benzene molecule. In addition, the isolated crystals contained two *m*-xylene molecules of crystallization per hexameric unit in the lattice; the encapsulated molecule is definitely benzene, with no electron-density peaks that could be interpreted as (ordered or disordered) xylenes.

Crystals of the product are built from hexameric molecules (Fig. 1) that contain a planar six-membered ring of Ga atoms, bridged by coordination with the N and O atoms of the benzimidazolate ligands. The benzo rings of the ligands project alternately above and below the Ga plane, thus forming a ball-shaped molecule, with the six Ga atoms around a central seam. The molecule could have ideal D_{3d} symmetry (Fig. 1 is a view along the possible C_3 axis), but it contains an encapsulated molecule of benzene, which distorts the regularity of the Ga_6 hexagon into an elliptical shape; the Ga···Ga distances remain all nearly equal at about 5.4 Å, but the Ga···Ga···Ga angles increase to 132° at the two Ga1 atoms, and decrease to 114° at the four Ga2 atoms. The symmetry of the complex is thus the crystallographically

© 1999 NRC Canada

Fig. 2. View of the unit cell of the hexameric Ga complex; the positive direction of the *c*-axis points away from the viewer.

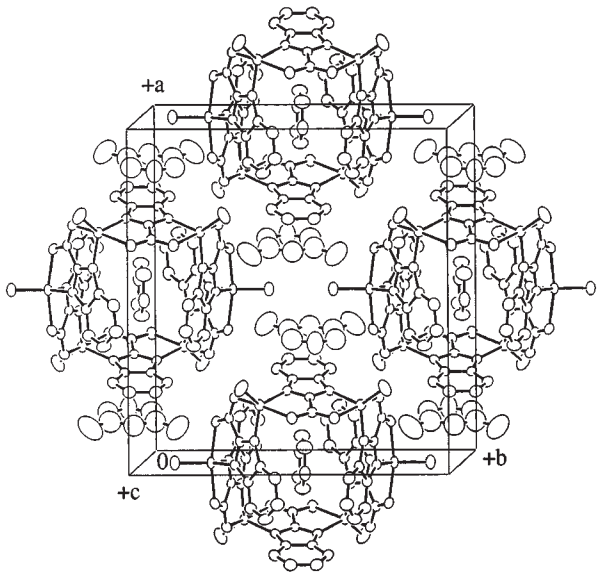

imposed C_{2h}, with the molecule and the encapsulated benzene situated on the 2/*m* site. The benzene is held in position only by van der Waals forces; the shortest C(benzene)···C(hexamer) distances are in the range 3.443–3.589(6) Å. Nevertheless the presence of benzene (or other possible intercalated molecule) may be crucial to formation of the hexamer.

The coordination geometry at each of the two independent GaO_2N_2C centres approximates a trigonal bipyramid, with a N_2C trigonal plane, and the O atoms above and below. Average dimensions are Ga—O = 2.176(2), Ga—N = 1.973(3), Ga—C = 1.927(5) Å, O-Ga-O = 165°; the O atoms are displaced away from the methyl C atoms. All the five- and six-membered rings in the molecule, including the chelate rings, are essentially planar (there are some minor foldings that are statistically significant, but not chemically important).

The crystal also contains *m*-xylene solvate molecules, which occupy positions across the mirror plane, but outside the Ga complex (Fig. 2). These solvate molecules exhibit rather high thermal parameters (Table 2), and their dimensions are less accurately determined.

These results are encouraging in that they demonstrate both the bridging capabilities and the flexibility of this novel ligand system. Currently work is in progress to incorporate magnetically interesting transition metal ions with this bridging anion in new polymeric materials.

Acknowledgements

Funding for the project was provided by the Natural Sciences and Engineering Research Council of Canada. P. Borda of this department is thanked for the C, H, N analyses.

References

1. S.J. Rettig, A. Storr, D.A. Summers, R.C. Thompson, and J. Trotter. Can. J. Chem. **75**, 949 (1997).
2. M.K. Ehlert, S.J. Rettig, A. Storr, R.C. Thompson, and J. Trotter. Can. J. Chem. (*a*) **67**, 1970 (1989); (*b*) **69**, 432 (1991); (*c*) **70**, 2161 (1992); (*d*) **71**, 1425 (1993).
3. M.K. Ehlert, A. Storr, and R.C. Thompson. Can. J. Chem. (*a*) **70**, 1121 (1992); (*b*) **71**, 1412 (1993).
4. M.K. Ehlert, A. Storr, D.A. Summers, and R.C. Thompson. Can. J. Chem. **75**, 491 (1997).
5. S.J. Rettig, A. Storr, D.A. Summers, R.C. Thompson, and J. Trotter. J. Am. Chem. Soc. **119**, 8675 (1997).
6. G.E. Coates and K. Wade. Organometallic compounds: Vol. 1. The main group elements. 3rd ed. Methuen, London. 1967. Chap. 3.
7. M.E. Kenny and A.W. Laubengayer. J. Am. Chem. Soc. **76**, 4839 (1954).
8. A. Storr and B.S. Thomas. Can. J. Chem. **48**, 3667 (1970).
9. A. Bistrzycki and G. Przeworski. Ber. Dtsch. Chem. Ges. **45**, 3483 (1912).
10. (*a*) International tables for X-ray crystallography. Vol. IV. Kynoch Press, Birmingham, U.K. (present distributor Kluwer Academic Publishers, Boston, Mass.). 1974. pp. 99–102; (*b*) International tables for crystallography. Vol. C. Kluwer Academic Publishers, Boston, Mass. 1992. pp. 200–206.
11. A. Storr and B.S. Thomas. J. Chem. Soc. (A), 3850 (1971).
12. M.F. Lappert, M.K. Majumdar, and B.P. Tilley. J. Chem. Soc. (A), 1590 (1966).
13. A. Arduini and A. Storr. J. Chem. Soc. Dalton Trans. 503 (1974).
14. D.F. Rendle, A. Storr, and J. Trotter. Can. J. Chem. (*a*) **53**, 2390 (1975); (*b*) **53**, 2944 (1975).
15. L.K. Peterson and K.I. The. Can. J. Chem. **57**, 2520 (1979).
16. K.R. Breakell, D.F. Rendle, A. Storr, and J. Trotter. J. Chem. Soc. Dalton Trans. 1584 (1975).
17. G.S. Smith and J.L Hoard. J. Am. Chem. Soc. **81**, 3907 (1959).

Can. J. Chem. Downloaded from www.nrcresearchpress.com by Peking University on 09/06/12
For personal use only.

© 1999 NRC Canada

Reaction of diphenylborinic acid with pyridinium and phosphonium bisacyl methylides. Crystal and molecular structures of resulting *B,N*- and *B,P*-betaines[1]

Johann Grünefeld, Wolfgang Kliegel, Steven J. Rettig, and James Trotter

Can. J. Chem. Downloaded from www.nrcresearchpress.com by Peking University on 09/06/12
For personal use only.

Abstract: Reaction of pyridinium and phosphonium 2-carboxy-1-formyl-2-oxoethylides with oxybis(diphenylborane) yields 5-(2-oxo-1-(pyridinio or phosphonio)ethylidene)-2,2-diphenyl-1,3-dioxa-2-borata-4-cyclopentanones, which represent novel types of boron nitrogen and boron phosphorus betaines, respectively. Crystals of 5-(2-oxo-1-pyridinioethylidene)-2,2-diphenyl-1,3-dioxa-2-borata-4-cyclopentanone, **1***a*, are monoclinic, a = 15.589(3), b = 12.366(2), c = 20.1869(11) Å, β = 111.227(2)°, Z = 8 (two independent molecules), space group $P2_1/a$; and those of 5-[2-oxo-1-(triphenylphosphonio)ethylidene]-2,2-diphenyl-1,3-dioxa-2-borata-4-cyclo-pentanone, **11**, are monoclinic, a = 9.6922(7), b = 25.027(2), c = 11.3041(4) Å, β = 92.1418(13)°, Z = 4 (two independent molecules), space group $P2_1$. The structures were solved by direct methods and refined by full-matrix least-squares procedures to R (F, $I \geq 3\sigma(I)$) = 0.047 and 0.042 (R_w (F^2, all data) = 0.096 and 0.088), respectively, for **1***a* and **11**.

Key words: pyridinium ylides, phosphonium ylides, bisacyl methylide diphenylboron chelates, boron nitrogen betaines, boron phosphorus betaines, organoboron compounds, crystal structures.

Résumé : Les réactions des 2-carboxy-1-formyl-2-oxoéthylures de pyridinium et de phosphonium avec l'oxybis(diphénylborane) conduisent aux 5-(2-oxo-1-pyridinio ou phosphonio)éthylidène)-2,2-diphényl-1,3-dioxa-2-borata-cyclopentan-4-ones respectivement qui correspondent à de nouveaux types de bétaïnes bore azote et bore phosphore. Les cristaux de la 5-(2-oxo-1-pyridinioéthylidène)-2,2-diphényl-1,3-dioxa-2-borata-cyclopentan-4-one, **1***a*, sont monocliniques, groupe d'espace $P2_1/a$, avec a = 15,589(3), b = 12,366(2) et c = 20,1869(11) Å, β = 111,227(2)° et Z = 8 (deux molécules indépendantes); celles de la 5-[2-oxo-1-(triphénylphosphonio)éthylidène]-2,2-diphényl-1,3-dioxa-2-borata-cyclopentan-4-one, **11**, sont monocliniques, groupe d'espace $P2_1$, avec a = 9,6922(7), b = 25,027(2) et c = 11,3041(4) Å, β = 92,1418(13)° et Z = 4 (deux molécules indépendantes). On a résolu les deux structures par des méthodes directes et on les a affinées par la méthode des moindres carrés jusqu'à des valeurs de R (F, $I \geq 3\sigma(I)$) = 0,047 et 0,042 (R_w (F^2, toutes les données = 0,096 et 0,088) respectivement pour **1a** et **11**.

Mots clés : ylures de pyridinium, ylures de phosphonium, chélates de biacylméthylure de diphénylbore, bétaïnes bore azote, bétaïnes bore phosphore, composés organiques du bore, structures cristallines.

[Traduit par la Rédaction]

Introduction

From a ring-opening reaction of pyridinium and phosphonium betaines of squaric acid the corresponding bisacyl methylides, **2** and **10**, were obtained (1). In these compounds both a formyl and an oxalyl group flank the ylidic carbon atom and contribute to the resonance stabilization. In the course of our investigations on stable boron nitrogen betaines (2), and also on the grounds of interest in zwitterionic boron phosphorus compounds (3), we employed these pyridinium and phosphonium ylides as bidentate ligands in reactions with diphenylborinic acid. Several modes of chelation are possible. The oxalyl moieties in **2** or **10** might lead to the formation of five-membered boron chelates[3] by replacement

Received February 16, 1999.

J. Grünefeld and W. Kliegel. Institut für Pharmazeutische Chemie der Technischen Universität Braunschweig, Beethovenstrasse 55, 38106 Braunschweig, Germany.
S. J. Rettig and J. Trotter.[2] Department of Chemistry, University of British Columbia, 2036 Main Mall, Vancouver, BC V6T 1Z1, Canada.

[1]Structural studies of organoboron compounds LXX. Previous paper in this series: ref. 17.
[2]Author to whom correspondence may be addressed. Telephone: (604) 822-4865. Fax: (604) 822-2847. e-mail: jtrt@xray4.chem.ubc.ca
[3]Here and elsewhere in this work the term "boron chelate" refers to a "chelate" of the Ph_2B^+ moiety. Considering the diphenylborenium moiety as a "pseudometal" explains much of the chemistry of these systems even though the bonding is (necessarily) quite different from that in metal complexes.

 © 1999 NRC Canada

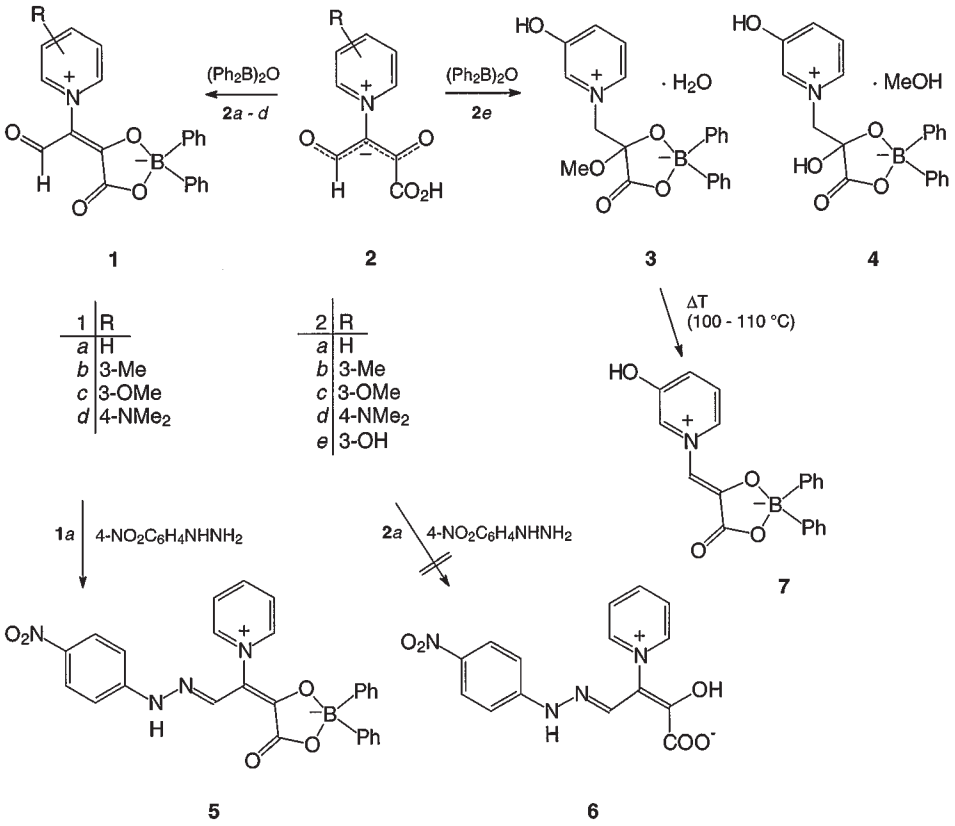

of the proton with a diphenylborenium (Ph_2B^+) ion, causing the migration of the (formal) negative charge from the mesomeric ylide system to the boron chelate ring and resulting in the hypothetical *B,N*- and *B,P*-betainic structures **1** and **11**, respectively. In addition to a five-membered chelate **1**, six- or seven-membered chelate rings as depicted in the pyridinium compounds **8** or **9**, and the analogous phosphonium derivatives, had to be taken into consideration. In the present study we describe the preparation of the desired diphenylboron chelates, some of their chemical and physical properties, and the unambiguous proof of two of the molecular structures by X-ray crystallographic analysis.

Experimental

General procedures

Compounds **2***a-e* and **10** were synthesized as described in the literature (1). Oxybis(diphenylborane) was prepared according to literature methods (4). All reactions were carried out under normal conditions, without protective gas atmosphere. Melting points (uncorrected): Linström apparatus. IR (KBr): Pye Unicam SP 3-100 and SP 3-200. ^{1}H and ^{13}C NMR: Bruker AM 400. ^{11}B and ^{31}P NMR: Bruker AC 200. MS: Finnigan MAT 8430. Elemental analyses: Carlo Erba CHNO elemental analyzer 1106-1 and 1106-2.

5-(2-Oxo-1-pyridinioethylidene)-2,2-diphenyl-1,3-dioxa-2-borata-4-cyclopentanone, 1*a*

Pyridinium (2-carboxy-1-formyl-2-oxoethylide) **2***a* (0.97 g, 5.0 mmol) is dissolved in 20 mL of methanol with heating and stirring. After addition of a solution of oxybis(diphenylborane) (0.87 g, 2.5 mmol) in 5 mL of methanol and refluxing with stirring for 15 min, the solvent is removed in vacuo to a residue of ca. 5 mL. The product crystallizes on cooling. Yield: 1.4 g (78%) of yellowish crystals; mp 215–217°C (dec.; from chloroform – diethyl ether). Infrared (KBr, cm^{-1}): 1735 (C=O), 1620 (C=C); ^{1}H NMR (400 MHz, DMSO-d_6–TMS), δ (ppm): 7.11–7.24 (m, 10 aromatic H), 8.30–8.34 (m, 2 aromatic H), 8.73–8.77 (m, 1 aromatic H), 8.99–9.01 (m, 2 aromatic H), 10.62 (s, CH=O). ^{13}C NMR (100 MHz, DMSO-d_6 –TMS), δ (ppm): 123.94 (s), 126.29 (d), 127.05 (d), 128.33 (d), 131.35 (d), 131.55 (s), 147.09 (d), 147.28 (d), 159.60 (s), 162.84 (s), 181.70 (d, CH=O). ^{11}B NMR (64.2 MHz, DMSO-d_6–Et_2OBF_3), δ (ppm): 9.9 ($W_{1/2}$ = 642 Hz). Mass spectrum (EI, 70 eV, 180°C), *m/z*: 357 (3%, M^+), 328 (3%, M^+ – CHO), 312 (7%, M^+ – CO_2H), 280 (100%, M^+ – Ph). Anal. calcd. for $C_{21}H_{16}BNO_4$: C 70.62, H 4.52, N 3.92; found: C 70.46, H 4.37, N 3.76.

The product gives a blue-colored solution upon the addition of diphenylcarbazone in ethanol, indicating the presence of the chelated diphenylborenium (Ph_2B^+) ion (5). Crystals suitable for X-ray analysis were obtained by slow crystallization from tetrahydrofuran – diethyl ether.

5-[2-Oxo-1-(3-methylpyridinio)ethylidene]-2,2-diphenyl-1,3-dioxa-2-borata-4-cyclopentanone, 1*b*

3-Methylpyridinium (2-carboxy-1-formyl-2-oxoethylide) **2***b* (1.0 g, 5.0 mmol) is reacted with oxybis(diphenylborane) (0.87 g, 2.5 mmol) as described above for **1***a*. Yield: 1.3 g (72%) of yellowish crystals; mp 186–187°C (dec.; from tetrahydrofuran – diethyl ether). Infrared (KBr, cm^{-1}): 1730 (C=O), 1615 (C=C); ^{1}H NMR (400 MHz, DMSO-d_6 –TMS), δ (ppm):

Can. J. Chem. Downloaded from www.nrcresearchpress.com by Peking University on 09/06/12
For personal use only.

© 1999 NRC Canada

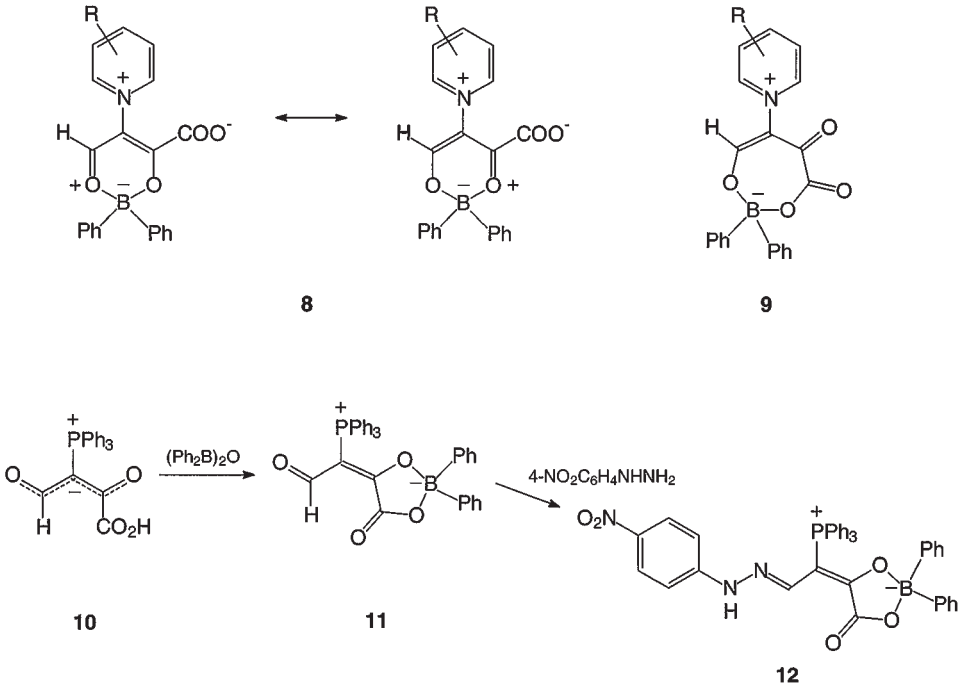

2.52 (s, CH_3), 7.12–7.24 (m, 10 aromatic H), 8.19–8.22 (m, 1 aromatic H), 8.58 (d, 1 aromatic H), 8.82 (d, 1 aromatic H), 8.90 (s, 1 aromatic H), 10.62 (s, CH=O). ^{13}C NMR (100 MHz, DMSO-d_6–TMS), δ (ppm): 17.81 (q, CH_3), 123.93 (s), 126.31 (d), 127.07 (d), 127.59 (d), 131.34 (d), 139.11 (s), 144.36 (d), 146.30 (d), 147.65 (d), 160.01 (s), 162.85 (s), 181.70 (d, CH=O). Mass spectrum (EI, 70 eV, 165°C), *m/z*: 371 (3%, M^+), 342 (2%, M^+ – CHO), 327 (1%, M^+ – CO_2), 312 (10%, 327 – CH_3), 294 (100%, M^+ – Ph). Anal. calcd. for $C_{22}H_{18}BNO_4$: C 71.19, H 4.89, N 3.77; found: C 70.93, H 4.66, N 3.72.

1*b* gives a blue-colored solution upon addition of diphenylcarbazone as described for **1***a*.

5-[2-Oxo-1-(3-methoxypyridinio)ethylidene]-2,2-diphenyl-1,3-dioxa-2-borata-4-cyclopentanone, 1*c*

3-Methoxypyridinium (2-carboxy-1-formyl-2-oxoethylide) **2***c* (1.1 g, 5.0 mmol) is reacted with oxybis(diphenylborane) (0.87 g, 2.5 mmol) as described above for **1***a*. Yield: 1.2 g (62%) of yellowish crystals; mp 190–191°C (dec.; from methanol – diethyl ether). Infrared (KBr, cm^{-1}): 1735 (C=O), 1615 (C=C). ^{1}H NMR (400 MHz, DMSO-d_6–TMS), δ (ppm): 3.99 (s, CH_3), 7.11–7.25 (m, 10 aromatic H), 8.22–8.25 (m, 1 aromatic H), 8.37–8.39 (m, 1 aromatic H), 8.62 (d, 1 aromatic H), 8.92 (d, 1 aromatic H), 10.60 (s, CH=O). ^{13}C NMR (100 MHz, DMSO-d_6–TMS), δ (ppm): 57.48 (q, CH_3), 124.18 (s), 126.27 (d), 127.02 (d), 128.57 (d), 131.38 (d), 132.01 (d), 134.83 (d), 139.60 (d), 158.27 (s), 159.92 (s), 162.87 (s), 181.50 (d, CH=O). Mass spectrum (EI, 70 eV, 170°C), *m/z*: 387 (3%, M^+), 358 (2%, M^+ – CHO), 310 (100%, M^+ – Ph). Anal. calcd. for $C_{22}H_{18}BNO_5$: C 68.24, H 4.69, N 3.62; found: C 67.74, H 4.70, N 3.49.

1*c* gives a blue-colored solution upon addition of diphenylcarbazone as described for **1***a*.

5-[2-Oxo-1-(4-dimethylaminopyridinio)ethylidene]-2,2-diphenyl-1,3-dioxa-2-borata-4-cyclopentanone, 1*d*

4-Dimethylaminopyridinium (2-carboxy-1-formyl-2-oxoethylide) **2***d* (1.2 g, 5.0 mmol) is reacted with oxybis(diphenylborane) (0.87 g, 2.5 mmol) as described above for **1***a*. Yield: 1.7 g (83%) of yellowish crystals; mp 258–260°C (dec.; from tetrahydrofuran – diethyl ether). Infrared (KBr, cm^{-1}): 1720 (C=O), 1640, 1610 (C=C). ^{1}H NMR (400 MHz, DMSO-d_6 –TMS), δ (ppm): 3.22 (s, CH_3), 7.08–7.26 (m, 12 aromatic H), 8.08 (d, 2 aromatic H), 10.60 (s, CH=O). ^{13}C NMR (100 MHz, DMSO-d_6–TMS), δ (ppm): 39.91 (q, CH_3), 107.42 (d), 122.59 (s), 126.15 (d), 126.99 (d), 131.37 (d), 143,66 (d), 156.01 (s), 160.10 (s), 163.46 (s), 183.20 (d, CH=O). Mass spectrum (EI, 70 eV, 230°C), *m/z*: 400 (2%, M^+), 371 (3%, M^+ – CHO), 323 (100%, M^+ – Ph). Anal. calcd. for $C_{23}H_{21}BN_2O_4$: C 69.02, H 5.29, N 7.00; found: C 68.92, H 5.43, N 6.81.

1*d* gives a blue-colored solution upon addition of diphenylcarbazone as described for **1***a*.

5-[2-(4-Nitrophenylhydrazono)-1-pyridinioethylidene]-2,2-diphenyl-1,3-dioxa-2-borata-4-cyclopentanone, 5

1*a* (0.36 g, 1.0 mmol) is dissolved in 20 mL of ethanol with heating and stirring. After addition of a hot solution of 4-nitrophenylhydrazine (0.15 g, 1 mmol) in 10 mL of ethanol and storage at room temperature for 7 days, the precipitated product is collected. Yield: 0.45 g (91%) of yellow crystals; mp 241–242°C (dec.; dimethylformamide–methanol). Infrared (KBr, cm^{-1}): 1690 (C=O), 1625 (C=C). ^{1}H NMR (400 MHz, DMSO-d_6–TMS), δ (ppm): 6.67 (d, 2 aromatic H), 7.07–7.22 (m, 8 aromatic H), 7.99 (d, 2 aromatic H), 8.36–8.39 (m, 2 aromatic H), 8.84 (t, 2 aromatic H + CH=N), 9.20 (d, 2 aromatic H), 11.51 (s, exchangeable, NH). ^{13}C NMR (100 MHz, DMSO-d_6–TMS), δ (ppm): 110.55 (d), 119.33 (s), 125.70 (d), 125.98 (d), 126.74 (d),

© 1999 NRC Canada

Can. J. Chem. Downloaded from www.nrcresearchpress.com by Peking University on 09/06/12
For personal use only.

Can. J. Chem. Downloaded from www.nrcresearchpress.com by Peking University on 09/06/12
For personal use only.

128.15 (d), 131,20 (d), 136.46 (d), 138.10 (s), 147.22 (d), 147.53 (d), 148.16 (s), 149.95 (s), 164.80 (s). Anal. calcd. for $C_{27}H_{21}BN_4O_5$: C 65.87, H 4.30, N 11.38; found: C 65.59, H 4.39, N 11.35.

5-Methoxy-5-(3-hydroxypyridiniomethyl)-2,2-diphenyl-1,3-dioxa-2-borata-4-cyclopentanone-hydrate, 3

3-Hydroxypyridinium (2-carboxy-1-formyl-2-oxoethylide) **2***e* (1.0 g, 5.0 mmol) is suspended in 20 mL of methanol with heating and stirring. After addition of a solution of oxybis(diphenylborane) (0.87 g, 2.5 mmol) in 5 mL of methanol and refluxing with stirring for 15 min, the solvent is removed in vacuo to a residue of ca. 5 mL. The product crystallizes on cooling. Yield: 1.3 g (66%) of colorless crystals; mp 90–100°C (from methanol). Infrared (KBr, cm^{-1}): 3400, 2750, 2640 (OH), 1695 (C=O). ^{1}H NMR (400 MHz, DMSO-d_6–TMS), δ (ppm): 2.89 (s, CH_3), 3.35 (s, broad, exchangeable, H_2O), 4.55–4.64 (q, CH_2), 6.89–7.08 (m, 8 aromatic H), 7.30–7.34 (m, 2 aromatic H), 7.45–7.49 (m, 1 aromatic H), 7.53–7.56 (m, 1 aromatic H), 8.10 (m, 2 aromatic H), 11.66 (s, broad, exchangeable, OH). ^{13}C NMR (100 MHz, DMSO-d_6–TMS), δ (ppm): 50.48 (q, CH_3), 63.92 (t, CH_2), 99.96 (s, *C*-OCH_3), 124.40 (d), 125.96 (s), 126.18 (d), 126.32 (d), 127.16 (d), 130.08 (d), 130.59 (d), 130.85 (d), 133.30 (d), 136.46 (d), 155.71 (s), 172.43 (s, C=O). Anal. calcd. for $C_{21}H_{22}BNO_6$: C 63.82, H 5.61, N 3.54; found: C 64.47, H 5.46, N 3.42.

5-(3-Hydroxypyridiniomethylene)-2,2-diphenyl-1,3-dioxa-2-borata-4-cyclopentanone, 7

3 (0.20 g, 5.0 mmol) is heated for 10 min, without solvent, to ca. 100–110°C. The residue is washed with hot methanol. Yield: 0.16 g (93%) of a pale yellow powder; mp 217–219°C (dec.; from tetrahydrofuran – diethyl ether). Infrared (KBr, cm^{-1}): 3420, 2840, 2720 (OH), 1680 (C=O), 1620 (C=C). ^{1}H NMR (400 MHz, DMSO-d_6–TMS), δ (ppm): 7.09–7.21 (m, 6 aromatic H), 7.28 (s, CH=), 7.36–7.38 (m, 4 aromatic H), 7.79–7.81 (q, 1 aromatic H), 7.93–7.97 (q, 1 aromatic H), 8.96 (d, 1 aromatic H), 9.22 (t, 1 aromatic H), 11.98 (s, broad, exchangeable, OH). ^{13}C NMR (100 MHz, DMSO-d_6–TMS), δ (ppm): 104.21 (d), 125.83 (d), 126.86 (d), 128.33 (d), 129.09 (d), 129.47 (d), 131.40 (d), 132.99 (d), 145.85 (s), 156.65 (s), 166.39 (s). Anal. calcd. for $C_{20}H_{16}BNO_4$: C 69.60, H 4.67, N 4.06; found: C 69.42, H 4.60, N 3.94.

5-[2-Oxo-1-(triphenylphosphonio)ethylidene]-2,2-diphenyl-1,3-dioxa-2-borata-4-cyclopentanone, 11

2,4-Dioxo-3-(triphenylphosphoranylidene)butanoic acid **10** (1) (0.38 g, 1.0 mmol) is dissolved in 20 mL of ethanol with heating and stirring. After addition of a solution of oxybis-(diphenylborane) (0.17 g, 0.5 mmol) in 5 mL of ethanol and refluxing with stirring for 15 min, the precipitated product is separated. Yield: 0.53 g (98%) of colorless crystals; mp 260–261°C (dec.; from 2-propanol – diethyl ether). Infrared (KBr, cm^{-1}): 1740 (C=O), 1650 (C=C). ^{1}H NMR (400 MHz, DMSO-d_6 –TMS), δ (ppm): 6.78–6.80 (m, 4 aromatic H), 7.02–7.06 (m, 6 aromatic H), 7.59–7.81 (m, 15 aromatic H), 10.96 (d, J = 22.1 Hz, CH=O). ^{13}C NMR (100 MHz, DMSO-d_6–TMS), δ (ppm): 119.92 (d, J = 91.1 Hz, =C-P), 125.90 (d), 126.63 (d), 129.46 (d), 129.59 (d), 130.70 (d), 133.55 (d), 133.65 (d), 133.74 (d), 133.77 (s), 188.57 (d, CH=O). ^{31}P NMR (81 MHz, DMSO-d_6–H_3PO_4), δ (ppm): 14.8. Mass spectrum (EI, 70 eV, 200°C), *m/z*: 540 (3%, M^+), 463 (100%, M^+ – Ph), 435 (12%, 463 – CO). Anal. calcd. for $C_{34}H_{26}BO_4P$: C 75.57, H 4.85; found: C 75.14, H 4.80.

Crystals suitable for X-ray analysis were obtained by slow crystallization from chloroform – diethyl ether.

5-[2-(4-Nitrophenylhydrazono)-1-(triphenylphosphonio)ethylidene]-2,2-diphenyl-1,3-dioxa-2-borata-4-cyclopentanone, 12

11 (0.54 g, 1.0 mmol) is dissolved in 20 mL of dichloromethane with heating and stirring. After addition of a hot solution of 4-nitrophenylhydrazine (0.15 g, 1.0 mmol) in 10 mL of ethanol and refluxing with stirring for 1 h, the solution is evaporated in vacuo to dryness. The solid residue is washed with methanol. Yield: 0.27 g (40%) of a yellow powder; mp 228–229°C (dec.; from dimethylformamide–methanol). Infrared (KBr, cm^{-1}): 1695 (C=O). ^{1}H NMR (400 MHz, DMSO-d_6–TMS), δ (ppm): 6.77–6.79 (m, 2 aromatic H), 6.97–7.02 (m, 4 aromatic H), 7.09–7.15 (m, 4 aromatic H), 7.39 (d, 2 aromatic H), 7.51–7.65 (m, 10 aromatic H), 7.74–7.86 (m, 8 aromatic H), 9.33 (d, CH=), 11.11 (s, broad, exchangeable, NH). Anal. calcd. for $C_{40}H_{31}BN_3O_5P$: C 71.12, H 4.63, N 6.22; found: C 70.57, H 4.49, N 6.19.

X-ray crystallographic analyses of 1*a* and 11

Crystallographic data appear in Table 1. The final unit-cell parameters were obtained by least squares based on 9640 reflections with 2θ = 4.0°–60.1° for **1***a* and 19 997 reflections with 2θ = 4.0°–60.2° for **11**. The data were processed,[4] corrected for Lorentz and polarization effects, and for absorption (based on analysis of symmetry-equivalent data).

The structures were solved by direct methods, the coordinates of the non-hydrogen atoms being determined from *E*-maps or from subsequent difference Fourier syntheses. There are two independent molecules in the asymmetric units of both **1***a* and **11**. For **11** the structure analysis was initiated in the noncentrosymmetric space group $P2_1$ on the basis of the *E*-statistics, this choice being validated by subsequent calculations. The two independent molecules in the asymmetric unit of **11** are mirror images of one another and are related by a non-crystallographic inversion centre. The non-hydrogen atoms were refined with anisotropic thermal parameters. Hydrogen atoms were fixed in calculated positions with C—H = 0.98 Å and B_H = 1.2 $B_{\text{bonded atom}}$. No corrections for secondary extinction were necessary. Neutral atom scattering factors for all atoms and anomalous dispersion corrections for the non-hydrogen atoms were taken from the *International tables for X-ray crystallography* (6). Parallel refinement of the mirror image of **11** resulted in marginally greater residuals (*R* and R_w ratios: both 1.001). This small difference is not unexpected in view of the pseudo-inversion centre and the small anomalous scattering effect. Final atomic coordinates and equivalent isotropic thermal parameters, selected bond lengths, selected bond angles, and intra-annular

[4] *teXsan: Crystal structure analysis package*. Unix version 1.7. Molecular Structure Corporation, The Woodlands, Tex. 1995; and *d*TREK: Area detector software*. Molecular Structure Corporation, The Woodlands, Tex. 1997.

© 1999 NRC Canada

Can. J. Chem. Downloaded from www.nrcresearchpress.com by Peking University on 09/06/12
For personal use only.

Table 1. Crystallographic data.[a]

Compound	**1***a*	**11**
Formula	$C_{21}H_{16}BNO_4$	$C_{34}H_{26}BO_4P$
fw	357.17	540.36
Crystal system	Monoclinic	Monoclinic
Space group	$P2_1/a$ (No. 14)	$P2_1$ (No. 4)
a, Å	15.589(3)	9.6922(7)
b, Å	12.366(2)	25.027(2)
c, Å	20.1869(11)	11.3041(11)
β, deg	111.227(2)	92.1418(13)
V, Å^3	3627.3(7)	2740.1(3)
Z	8[b]	4[b]
ρ_{calc}, g/cm^3	1.308	1.310
F(000)	1488	1128
Radiation	Mo	Mo
μ, cm^{-1}	0.90	1.39
Crystal size, mm	0.25 × 0.30 × 0.40	0.15 × 0.20 × 0.25
Correction factors[c]	0.83–1.00	0.80–1.00
φ sweep range, deg (χ = –90°)	0–190	0–190
ω sweep range, deg (χ = –90°)	–22 – 18	–22 – 18
Oscillation width, deg	0.5	0.5
Data images, exposure time	460, 80 s	460, 180 s
$2\theta_{max}$, deg	60.1	60.2
Total reflections	34142	25557
Unique reflections	9164	12473[d]
R_{merge}	0.058	0.052
No. with $I \geq 3\sigma(I)$	4283	7918[d]
No. of variables	487	720
R (F) ($I \geq 3\sigma(I)$)	0.047	0.042
R_w (F^2) (all data)	0.096	0.088
gof	1.80	1.48
Max Δ/σ (final cycle)	0.001	0.0007
Residual density e/Å^3	–0.47 to 0.50	–0.71 to 0.68

[a]Temperature 180 K, Rigaku/ADSC CCD diffractometer, Mo K_α (λ = 0.71069 Å), graphite monochromator, takeoff angle 6.0°, aperture 94.0 × 94.0 mm at a distance of 39.2 mm from the crystal, $\sigma^2(F^2) = (C + B)/Lp^2$ (C = scan count, B = background count), function minimized $\Sigma w(|F_o^2| - |F_c^2|)^2$ where $w = 1/\sigma^2(F_o^2)$, R (F) = $\Sigma||F_o| - |F_c||/\Sigma|F_o|$, R_w (F^2) = $(\Sigma w(|F_o^2| - |F_c^2|)^2/\Sigma w|F_o^2|^2)^{1/2}$, and gof = $[\Sigma w(|F_o^2| - |F_c^2|)^2/(m - n)]^{1/2}$.

[b]Two independent molecules.

[c]Includes crystal decay (if any), absorption, and scaling corrections performed in a single step.

[d]Includes Friedel pairs, 7586 are unique.

torsion angles appear in Tables 2–5, respectively. Complete tables of bond lengths and angles, hydrogen atom parameters, anisotropic thermal parameters, torsion angles, intermolecular contacts, and least-squares planes are available as supplementary material.[5]

Results and discussion

Reaction of the pyridinium ylides **2***a*–**2***d* with oxybis(diphenylborane) gives crystalline compounds having elemental analyses and ^{1}H NMR spectroscopic data consistent with the postulated diphenylboron chelate structure **1** as well as isomeric structures such as **8** and **9**. A chelate system with a tetracoordinated boron nucleus is also indicated by the ^{11}B NMR spectrum of **1***a*, displaying a typical ^{11}B NMR signal at $\delta(Et_2OBF_3)$ = 9.9 ppm. The intact diphenylboron moiety is confirmed by a color reaction with diphenylcarbazone, indicating the presence of the Ph_2B^+ ion via rechelatization (5). Strong absorption bands between 1720 and 1735 cm^{-1} in the infrared spectra indicate either free aldehyde groups as in **1**, and (or) boryloxyacyl moieties (B-O-C=O) as in **1** and **9**, respectively. Similar C=O stretching frequencies between 1700 and 1750 cm^{-1} have been noted for various diphenylboron chelates with one carboxylate ligand involved (7). Diphenylboron chelates of 1,3-dicarbonyl compounds, comparable to structure **8**, however, do not show any intense C=O absorptions at all in the range between 1600 and 2000 cm^{-1} (8). To provide a means of distinguishing be-

[5]Copies of material on deposit may be purchased from: The Depository of Unpublished Data, Document Delivery, CISTI, National Research Council of Canada, Ottawa, ON K1A 0S2, Canada. Tables of hydrogen atom coordinates and bond lengths and angles involving hydrogen atoms have also been deposited with the Cambridge Crystallographic Data Centre and can be obtained on request from The Director, Cambridge Crystallographic Data Centre, University Chemical Laboratory, 12 Union Road, Cambridge CB2 1EZ, U.K.

© 1999 NRC Canada

Table 2. Final atomic coordinates (fractional) and B_{eq} (10^3 Å^2).[a]

Atom	*x*	*y*	*z*	B_{eq}
		1*a*		
O(1)	0.35800(8)	0.31120(9)	0.51705(6)	2.68(3)
O(2)	0.32298(9)	0.28784(9)	0.39935(6)	3.28(3)
O(3)	0.22433(7)	0.40574(8)	0.51093(6)	2.27(3)
O(4)	0.05588(9)	0.38199(9)	0.26617(6)	3.37(3)
O(5)	0.34102(8)	0.20077(8)	0.99379(6)	2.67(3)
O(6)	0.41205(9)	0.23234(9)	1.11068(7)	3.35(3)
O(7)	0.21544(8)	0.10067(8)	1.00004(6)	2.36(3)
O(8)	0.29267(10)	0.09527(11)	1.24692(7)	5.03(4)
N(1)	0.06455(9)	0.44961(10)	0.39819(7)	1.96(3)
N(2)	0.16973(10)	0.04034(10)	1.11492(7)	2.26(3)
C(1)	0.30478(12)	0.31925(12)	0.44990(10)	2.42(4)
C(2)	0.21689(12)	0.37573(12)	0.44690(9)	2.09(4)
C(3)	0.14094(12)	0.39285(12)	0.38862(8)	2.12(4)
C(4)	0.12748(13)	0.36382(13)	0.31595(10)	2.83(5)
C(5)	–0.01326(12)	0.39579(12)	0.39161(9)	2.38(4)
C(6)	–0.08717(12)	0.45004(14)	0.39717(9)	2.66(4)
C(7)	–0.08039(12)	0.55989(13)	0.40975(9)	2.54(4)
C(8)	–0.00028(12)	0.61314(12)	0.41701(9)	2.58(4)
C(9)	0.07227(12)	0.55640(12)	0.41146(9)	2.38(4)
C(10)	0.37448(12)	0.45321(13)	0.61448(9)	2.48(4)
C(11)	0.45364(13)	0.49273(15)	0.60572(11)	3.77(5)
C(12)	0.50581(14)	0.5754(2)	0.64775(14)	4.88(6)
C(13)	0.47975(14)	0.62238(15)	0.69914(12)	4.42(6)
C(14)	0.40071(14)	0.58669(14)	0.70868(10)	3.69(5)
C(15)	0.34949(12)	0.50347(14)	0.66703(10)	2.96(4)
C(16)	0.28364(12)	0.26160(12)	0.60757(9)	2.34(4)
C(17)	0.21029(12)	0.19291(13)	0.57065(9)	2.94(4)
C(18)	0.18496(13)	0.10649(14)	0.60369(11)	3.69(5)
C(19)	0.2330(2)	0.08563(15)	0.67428(12)	4.08(6)
C(20)	0.3062(2)	0.1504(2)	0.71200(10)	4.02(5)
C(21)	0.33125(13)	0.23737(13)	0.67933(10)	3.11(5)
C(22)	0.35032(12)	0.19288(12)	1.06083(10)	2.47(4)
C(23)	0.26977(11)	0.12700(12)	1.06435(9)	2.10(4)
C(24)	0.25365(11)	0.10023(12)	1.12362(9)	2.23(4)
C(25)	0.31414(13)	0.12017(14)	1.19626(10)	3.30(5)
C(26)	0.08819(13)	0.09150(13)	1.09449(9)	2.80(4)
C(27)	0.00990(13)	0.03558(15)	1.08842(10)	3.47(5)
C(28)	0.01525(13)	–0.07324(15)	1.10326(10)	3.65(5)
C(29)	0.09905(15)	–0.12385(15)	1.12385(11)	4.04(5)
C(30)	0.17639(13)	–0.06567(14)	1.13014(11)	3.51(5)
C(31)	0.28152(12)	0.04301(13)	0.90608(9)	2.34(4)
C(32)	0.37254(13)	0.01399(14)	0.91808(10)	3.15(5)
C(33)	0.39447(13)	–0.07489(15)	0.88531(11)	3.63(5)
C(34)	0.32565(15)	–0.13727(14)	0.83934(10)	3.27(5)
C(35)	0.23494(14)	–0.11100(14)	0.82610(10)	3.43(5)
C(36)	0.21361(13)	–0.02251(13)	0.85932(10)	3.03(5)
C(37)	0.18391(12)	0.23108(13)	0.89620(9)	2.55(4)
C(38)	0.15184(13)	0.31408(14)	0.92860(10)	3.56(5)
C(39)	0.09110(15)	0.3916(2)	0.88994(15)	4.97(7)
C(40)	0.05931(15)	0.3897(2)	0.8173(2)	5.68(7)
C(41)	0.0898(2)	0.3103(2)	0.78295(12)	5.32(6)
C(42)	0.15178(14)	0.23132(14)	0.82243(10)	3.53(5)
B(1)	0.31357(13)	0.35858(15)	0.56701(10)	2.33(5)
B(2)	0.25531(14)	0.14379(15)	0.94445(10)	2.39(5)
		11		
P(1)	0.39237(7)	0.27860	0.07046(6)	1.453(14)

Can. J. Chem. Downloaded from www.nrcresearchpress.com by Peking University on 09/06/12
For personal use only.

© 1999 NRC Canada

Table 2 (*continued*).

Atom	*x*	*y*	*z*	B_{eq}
P(2)	0.18580(7)	0.52871(3)	0.34766(6)	1.497(14)
O(1)	0.4257(2)	0.31146(7)	0.50388(15)	1.69(4)
O(2)	0.6028(2)	0.35559(8)	0.4282(2)	2.48(5)
O(3)	0.3247(2)	0.27896(7)	0.32586(14)	1.47(4)
O(4)	0.6164(3)	0.36985(9)	0.0703(2)	4.75(7)
O(5)	0.1991(2)	0.49141(7)	0.7809(2)	1.82(4)
O(6)	0.3599(2)	0.43910(8)	0.7039(2)	2.46(5)
O(7)	0.1144(2)	0.53066(7)	0.60339(14)	1.50(4)
O(8)	0.3356(2)	0.41876(8)	0.3427(2)	3.70(6)
C(1)	0.4988(3)	0.32863(10)	0.4171(2)	1.55(6)
C(2)	0.4313(3)	0.30758(10)	0.3012(2)	1.35(5)
C(3)	0.4754(3)	0.31569(10)	0.1885(2)	1.40(6)
C(4)	0.5812(3)	0.35543(12)	0.1664(3)	2.49(7)
C(5)	0.2207(3)	0.30293(10)	0.0332(3)	1.85(6)
C(6)	0.1540(3)	0.28527(12)	–0.0717(3)	2.60(7)
C(7)	0.0197(3)	0.30145(13)	–0.0983(3)	2.99(8)
C(8)	–0.0471(3)	0.33457(13)	–0.0215(3)	3.28(8)
C(9)	0.0180(3)	0.35279(12)	0.0810(3)	3.11(8)
C(10)	0.1538(3)	0.33715(11)	0.1099(3)	2.33(7)
C(11)	0.4883(3)	0.28074(10)	–0.0621(2)	1.65(6)
C(12)	0.5831(3)	0.24012(11)	–0.0877(3)	2.03(6)
C(13)	0.6595(3)	0.24377(12)	–0.1874(3)	2.40(7)
C(14)	0.6437(3)	0.28727(11)	–0.2633(3)	2.30(7)
C(15)	0.5496(3)	0.32668(11)	–0.2399(3)	2.11(6)
C(16)	0.4717(3)	0.32402(10)	–0.1401(3)	1.82(6)
C(17)	0.3839(3)	0.20952(10)	0.1161(3)	1.64(6)
C(18)	0.4992(3)	0.18650(11)	0.1723(3)	2.11(7)
C(19)	0.4970(4)	0.13261(12)	0.2032(3)	3.01(8)
C(20)	0.3775(4)	0.10297(12)	0.1802(3)	3.33(9)
C(21)	0.2634(4)	0.12576(13)	0.1263(3)	3.26(8)
C(22)	0.2650(3)	0.17919(11)	0.0937(3)	2.35(7)
C(23)	0.1609(3)	0.31048(10)	0.4876(2)	1.52(6)
C(24)	0.0467(3)	0.30889(11)	0.4100(3)	1.82(6)
C(25)	–0.0777(3)	0.33290(11)	0.4375(3)	2.32(7)
C(26)	–0.0892(3)	0.35999(11)	0.5427(3)	2.44(7)
C(27)	0.0233(3)	0.36321(11)	0.6209(3)	2.45(7)
C(28)	0.1477(3)	0.33874(11)	0.5938(3)	2.07(6)
C(29)	0.3062(3)	0.21972(10)	0.5126(3)	1.65(6)
C(30)	0.2776(3)	0.17540(11)	0.4410(3)	2.36(7)
C(31)	0.2791(4)	0.12400(11)	0.4870(3)	3.36(8)
C(32)	0.3064(3)	0.11610(12)	0.6067(3)	3.23(8)
C(33)	0.3334(3)	0.15892(13)	0.6800(3)	3.14(8)
C(34)	0.3337(3)	0.21027(11)	0.6330(3)	2.37(7)
C(35)	0.2670(3)	0.47115(10)	0.6934(2)	1.71(6)
C(36)	0.2111(3)	0.49707(10)	0.5783(2)	1.40(6)
C(37)	0.2520(3)	0.48707(10)	0.4649(2)	1.55(6)
C(38)	0.3325(3)	0.43915(11)	0.4406(3)	2.44(7)
C(39)	0.0134(3)	0.51074(10)	0.3006(2)	1.61(6)
C(40)	–0.0466(3)	0.53426(11)	0.1982(2)	2.19(6)
C(41)	–0.1806(3)	0.52063(12)	0.1622(3)	2.41(7)
C(42)	–0.2540(3)	0.48419(11)	0.2268(3)	2.50(7)
C(43)	–0.1948(3)	0.46072(11)	0.3262(3)	2.38(7)
C(44)	–0.0609(3)	0.47379(10)	0.3645(2)	1.84(6)
C(45)	0.1921(3)	0.59680(10)	0.4002(2)	1.59(6)
C(46)	0.3138(3)	0.61530(10)	0.4563(3)	2.02(6)
C(47)	0.3225(3)	0.66825(12)	0.4946(3)	2.67(7)
C(48)	0.2113(4)	0.70182(11)	0.4774(3)	2.99(8)

Can. J. Chem. Downloaded from www.nrcresearchpress.com by Peking University on 09/06/12
For personal use only.

© 1999 NRC Canada

Table 2 (*concluded*).

Atom	*x*	*y*	*z*	B_{eq}
C(49)	0.0908(3)	0.68439(11)	0.4219(3)	2.86(8)
C(50)	0.0792(3)	0.63138(11)	0.3821(3)	2.15(6)
C(51)	0.2886(3)	0.52497(11)	0.2170(2)	1.66(6)
C(52)	0.3837(3)	0.56486(11)	0.1924(3)	2.05(6)
C(53)	0.4595(3)	0.56095(13)	0.0909(3)	2.64(7)
C(54)	0.4423(3)	0.51807(13)	0.0161(3)	2.81(7)
C(55)	0.3458(3)	0.47831(11)	0.0402(3)	2.58(7)
C(56)	0.2689(3)	0.48203(11)	0.1396(3)	2.12(7)
C(57)	0.1034(3)	0.58709(10)	0.7948(3)	1.60(6)
C(58)	0.0799(3)	0.63313(12)	0.7277(3)	2.38(7)
C(59)	0.0884(4)	0.68396(12)	0.7802(3)	3.19(8)
C(60)	0.1201(3)	0.68942(12)	0.8993(3)	3.01(8)
C(61)	0.1435(3)	0.64391(13)	0.9671(3)	2.81(8)
C(62)	0.1361(3)	0.59368(11)	0.9145(3)	2.16(7)
C(63)	–0.0626(3)	0.50168(10)	0.7556(3)	1.78(6)
C(64)	–0.1644(3)	0.49713(11)	0.6660(3)	2.30(7)
C(65)	–0.2917(3)	0.47303(12)	0.6866(3)	2.80(7)
C(66)	–0.3191(3)	0.45386(11)	0.7959(3)	2.82(8)
C(67)	–0.2203(4)	0.45735(12)	0.8860(3)	2.90(8)
C(68)	–0.0937(3)	0.48041(11)	0.8661(3)	2.32(7)
B(1)	0.3011(3)	0.27916(12)	0.4608(3)	1.41(6)
B(2)	0.0855(3)	0.52881(13)	0.7372(3)	1.72(6)

[a] $B_{eq} = (8/3)\pi^2 \Sigma \Sigma(U_{ij}a_{i*}a_{j*}(\mathbf{a}_i.\mathbf{a}_j))$.

Fig. 1. Stereoview of one of the two independent molecules of **1***a*; 50% probability thermal ellipsoids are shown for the non-hydrogen atoms.

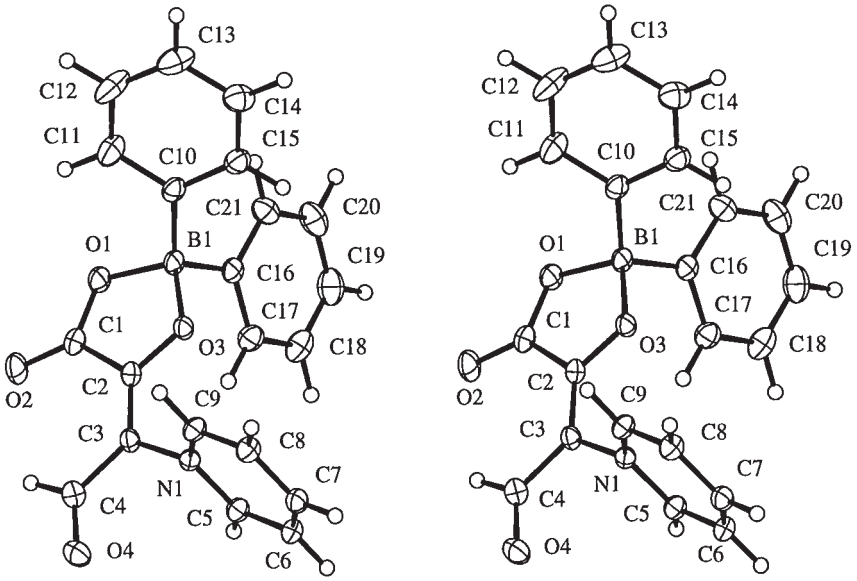

tween the possible isomers, an X-ray crystallographic analysis was performed on compound **1***a*, which gave suitable single crystals.

The X-ray analysis establishes the molecular structure **1***a* (Fig. 1), containing a five-membered boron chelate ring formed by the oxalyl residue of the ligand **2***a*.[6] The ylidic structure **2** has thus been transformed into the zwitterionic structure of **1**, a completely new type of boron nitrogen betaine (2*a*). Chelate structures analogous to **1***a* can also be ascribed with high probability to the substituted derivatives **1***b*–**1***d*.

The (*Z*)-configuration at the C(2)—C(3) double bond (C(23)—C(24) for the second independent molecule) allows an intramolecular C-H···O interaction between the formyl

[6] The chelating properties of the pyridinium ylides **2** might also be involved in the formation of a colored complex with $FeCl_3$ and the precipitation of reaction products with Cu(II), Ni(II), and Zn ions in aqueous solution (1).

© 1999 NRC Canada

Can. J. Chem. Downloaded from www.nrcresearchpress.com by Peking University on 09/06/12
For personal use only.

Table 3. Selected bond lengths (Å) with estimated standard deviations in parentheses.

Bond	Length	Bond	Length
	1*a*		
O(1)—C(1)	1.312(2)	O(5)—C(22)	1.311(2)
O(1)—B(1)	1.532(2)	O(5)—B(2)	1.520(2)
O(2)—C(1)	1.217(2)	O(6)—C(22)	1.215(2)
O(3)—C(2)	1.309(2)	O(7)—C(23)	1.309(2)
O(3)—B(1)	1.554(2)	O(7)—B(2)	1.560(2)
O(4)—C(4)	1.222(2)	O(8)—C(25)	1.225(2)
N(1)—C(3)	1.454(2)	N(2)—C(24)	1.458(2)
N(1)—C(5)	1.347(2)	N(2)—C(26)	1.344(2)
N(1)—C(9)	1.344(2)	N(2)—C(30)	1.342(2)
C(1)—C(2)	1.519(2)	C(22)—C(23)	1.520(2)
C(2)—C(3)	1.350(2)	C(23)—C(24)	1.350(2)
C(3)—C(4)	1.450(2)	C(24)—C(25)	1.449(2)
C(5)—C(6)	1.372(2)	C(26)—C(27)	1.369(2)
C(6)—C(7)	1.379(2)	C(27)—C(28)	1.375(2)
C(7)—C(8)	1.372(2)	C(28)—C(29)	1.370(3)
C(8)—C(9)	1.370(2)	C(29)—C(30)	1.370(3)
C(10)—B(1)	1.591(3)	C(31)—B(2)	1.597(3)
C(16)—B(1)	1.613(3)	C(37)—B(2)	1.602(3)
	11		
P(1)—C(3)	1.793(3)	P(2)—C(37)	1.786(3)
P(1)—C(5)	1.807(3)	P(2)—C(39)	1.792(3)
P(1)—C(11)	1.793(3)	P(2)—C(45)	1.805(3)
P(1)—C(17)	1.806(3)	P(2)—C(51)	1.815(3)
O(1)—C(1)	1.304(3)	O(5)—C(35)	1.310(3)
O(1)—B(1)	1.518(3)	O(5)—B(2)	1.514(4)
O(2)—C(1)	1.215(3)	O(6)—C(35)	1.209(3)
O(3)—C(2)	1.296(3)	O(7)—C(36)	1.298(3)
O(3)—B(1)	1.551(3)	O(7)—B(2)	1.550(3)
O(4)—C(4)	1.206(3)	O(8)—C(38)	1.219(3)
C(1)—C(2)	1.536(4)	C(35)—C(36)	1.535(4)
C(2)—C(3)	1.373(4)	C(36)—C(37)	1.378(4)
C(3)—C(4)	1.457(4)	C(37)—C(38)	1.462(3)
C(23)—B(1)	1.607(4)	C(57)—B(2)	1.604(4)
C(29)—B(1)	1.599(4)	C(63)—B(2)	1.608(4)

group involving C(4)—H(1) (C(25)—H(17)) and the carboxyl oxygen atom O(2) (O(6)). The geometry of this interaction is consistent with the presence of an intramolecular hydrogen bond with some contribution to the molecular arrangement (9) (C···O = 3.048(2) (3.025(2)) Å, H···O = 2.41 (2.39) Å, C-H···O = 122° (122°)).

The observed bond lengths are consistent with the distribution of double bonds depicted in formula **1**. Compared to the free ligand **2***a*, which displays nearly equal C—C bond lengths between the ylidic center carbon atom and both of the flanking carbonyl carbon atoms (average 1.405 Å) (1), the chelate **1***a* shows a short C—C bond with considerable double bond character between the (former) ylidic center carbon and the chelate ring carbon atom: C(3)—C(2) (C(24)—C(23)) = 1.350(2) Å (both), whereas the bond from the (former) ylidic center to the formyl group is lengthened: C(3)—C(4) (C(24)—C(25)) = 1.450(2) (1.449(2)) Å. The C=C bond length lies between the average C=C-OH (1.362 Å) and C=C-C=O (1.340 Å) bonds reported, and the C—C(formyl) single bond is similar to the average C—C distance for conjugated carbonyl compounds (1.464 Å) (10). Corresponding to the substantial double bond character of the C(3)—C(2) (C(24)—C(23)) bond, the C(2)—O(3) (C(23)—O(7)) bond shows a reduction of its carbonyl character with a bond distance of 1.309(2) Å (for both molecules), corresponding to a π-bond order of only 0.47, as estimated from a bond length vs. HMO–π-bond order plot (11) and calculated (12). This shift of electron density in the chelate **1**, relative to the ligand **2**, is coincident with the increase of the double bond character of the carbonyl C=O of the formyl group: C(4)—O(4) (C(25)—O(8)) = 1.222(2) (1.225(2)) Å, compared with 1.240 Å for the ligand **2***a* (1). The enhanced carbonyl activity of the formyl group in the chelate **1***a*, compared to the ligand **2***a*, is also confirmed by chemical means. The reaction of **2***a* with the carbonyl-detecting reagent 4-nitrophenylhydrazine did not lead to a corresponding hydrazone derivative **6** whereas **1***a* gave the hydrazone **5** under mild conditions. This indicates the enhanced reactivity of the aldehyde function, which interacts less with the adjacent (conjugated) groups in the chelate **1** than it does in the ylide **2**. An additional indication of the strengthened aldehyde function in **1** is given by the ^{1}H NMR

Can. J. Chem. Downloaded from www.nrcresearchpress.com by Peking University on 09/06/12
For personal use only.

© 1999 NRC Canada

Table 4. Selected bond angles (deg) with estimated standard deviations in parentheses.

Bonds	Angle (deg)	Bonds	Angle (deg)
	1*a*		
C(1)-O(1)-B(1)	112.57(13)	C(22)-O(5)-B(2)	112.60(13)
C(2)-O(3)-B(1)	110.41(12)	C(23)-O(7)-B(2)	110.20(13)
C(3)-N(1)-C(5)	119.98(13)	C(24)-N(2)-C(26)	120.38(13)
C(3)-N(1)-C(9)	118.83(13)	C(24)-N(2)-C(30)	118.50(14)
C(5)-N(1)-C(9)	121.16(14)	C(26)-N(2)-C(30)	121.09(15)
O(1)-C(1)-O(2)	126.1(2)	O(5)-C(22)-O(6)	125.7(2)
O(1)-C(1)-C(2)	107.45(14)	O(5)-C(22)-C(23)	107.67(15)
O(2)-C(1)-C(2)	126.4(2)	O(6)-C(22)-C(23)	126.6(2)
O(3)-C(2)-C(1)	109.56(14)	O(7)-C(23)-C(22)	109.62(14)
O(3)-C(2)-C(3)	123.54(15)	O(7)-C(23)-C(24)	123.85(15)
C(1)-C(2)-C(3)	126.90(15)	C(22)-C(23)-C(24)	126.5(2)
N(1)-C(3)-C(2)	117.50(14)	N(2)-C(24)-C(23)	117.71(15)
N(1)-C(3)-C(4)	115.38(14)	N(2)-C(24)-C(25)	115.80(14)
C(2)-C(3)-C(4)	127.1(2)	C(23)-C(24)-C(25)	126.4(2)
O(4)-C(4)-C(3)	122.7(2)	O(8)-C(25)-C(24)	121.9(2)
O(1)-B(1)-O(3)	99.37(12)	O(5)-B(2)-O(7)	99.88(13)
O(1)-B(1)-C(10)	111.38(14)	O(5)-B(2)-C(31)	111.17(14)
O(1)-B(1)-C(16)	109.43(13)	O(5)-B(2)-C(37)	109.78(13)
O(3)-B(1)-C(10)	110.14(13)	O(7)-B(2)-C(31)	108.71(13)
O(3)-B(1)-C(16)	107.54(14)	O(7)-B(2)-C(37)	107.30(14)
C(10)-B(1)-C(16)	117.41(15)	C(31)-B(2)-C(37)	118.32(15)
	11		
C(3)—P(1)—C(5)	112.50(12)	C(37)-P(2)-C(39)	112.28(12)
C(3)—P(1)—C(11)	111.96(12)	C(37)-P(2)-C(45)	107.45(12)
C(3)-P(1)-C(17)	107.88(12)	C(37)-P(2)-C(51)	112.41(12)
C(5)-P(1)-C(11)	107.24(13)	C(39)-P(2)-C(45)	110.76(12)
C(5)-P(1)-C(17)	109.78(12)	C(39)-P(2)-C(51)	106.22(12)
C(11)-P(1)-C(17)	107.36(12)	C(45)-P(2)-C(51)	107.68(12)
C(1)-O(1)-B(1)	112.5(2)	C(35)-O(5)-B(2)	111.9(2)
C(2)-O(3)-B(1)	111.0(2)	C(36)-O(7)-B(2)	110.6(2)
O(1)-C(1)-O(2)	125.2(3)	O(5)-C(35)-O(6)	125.2(3)
O(1)-C(1)-C(2)	107.6(2)	O(5)-C(35)-C(36)	107.7(2)
O(2)-C(1)-C(2)	127.2(3)	O(6)-C(35)-C(36)	127.0(3)
O(3)-C(2)-C(1)	108.9(2)	O(7)-C(36)-C(35)	108.9(2)
O(3)-C(2)-C(3)	124.1(2)	O(7)-C(36)-C(37)	123.8(2)
C(1)-C(2)-C(3)	127.0(2)	C(35)-C(36)-C(37)	127.4(2)
P(1)-C(3)-C(2)	117.8(2)	P(2)-C(37)-C(36)	118.4(2)
P(1)-C(3)-C(4)	121.7(2)	P(2)-C(37)-C(38)	121.2(2)
C(2)-C(3)-C(4)	120.4(2)	C(36)-C(37)-C(38)	119.9(2)
O(4)-C(4)-C(3)	125.7(3)	O(8)-C(38)-C(37)	123.1(3)
O(1)-B(1)-O(3)	99.9(2)	O(5)-B(2)-O(7)	100.4(2)
O(1)-B(1)-C(23)	110.4(2)	O(5)-B(2)-C(57)	111.3(2)
O(1)-B(1)-C(29)	111.4(2)	O(5)-B(2)-C(63)	109.8(2)
O(3)-B(1)-C(23)	110.1(2)	O(7)-B(2)-C(57)	110.4(2)
O(3)-B(1)-C(29)	110.7(2)	O(7)-B(2)-C(63)	109.5(2)
C(23)-B(1)-C(29)	113.6(2)	C(57)-B(2)-C(63)	114.6(2)

Can. J. Chem. Downloaded from www.nrcresearchpress.com by Peking University on 09/06/12
For personal use only.

spectra, which display the signal of the formyl proton at about 10.6 ppm, whereas the ligand **2** has the analogous signal in an upfield area around 9.2 ppm (1).

Unlike the formation of **1***a*–**1***d*, the reaction of the ylidic ligand **2***e* with diphenylborinic acid leads to the five-membered boron chelate **3**. This might originate from a solvolytic splitting off of the formyl group from **1** or **2** (presumbably as formic acid or methyl formate) with subsequent addition of the involved solvent methanol. Crystallizing with 1 mol of water, the compound **3** represents the diphenylboron chelate of a semi-acetal of an α-oxocarbonic acid derivative. The possible isomeric structure **4**, caused by the addition of water and crystallization with solvate methanol can be excluded by NMR spectroscopic observations. A distinct cross-correlation between the methoxy group and the acetalic carbonyl carbon atom can be seen in the C,H-COLOC spectrum. This proves the participation of methanol in the acetal group, and thus the structure **3**.

This deviating behavior in the reaction of **2***e* with oxybis(diphenylborane) might possibly be caused by the

© 1999 NRC Canada

Can. J. Chem. Downloaded from www.nrcresearchpress.com by Peking University on 09/06/12
For personal use only.

Table 5. Intra-annular torsion angles (deg) for **1***a* and **11** with standard deviations in parentheses.

Atoms	Value (deg)	Atoms	Value (deg)
	1*a*		
B(1)-O(1)-C(1)-C(2)	0.8(2)	B(2)-O(5)-C(22)-C(23)	0.4(2)
O(1)-C(1)-C(2)-O(3)	4.7(2)	O(5)-C(22)-C(23)-O(7)	–1.3(2)
C(1)-(2)-O(3)-B(1)	–8.0(2)	C(22)-C(23)-O(7)-B(2)	1.7(2)
C(2)-O(3)-B(1)-O(1)	7.9(2)	C(23)-O(7)-B(2)-O(5)	–1.37(15)
O(3)-B(1)-O(1)-C(1)	–4.9(2)	O(7)-B(2)-O(5)-C(22)	0.5(2)
	11		
B(1)-O(1)-C(1)-C(2)	–1.7(3)	B(2)-O(5)-C(35)-C(36)	4.3(3)
O(1)-C(1)-C(2)-O(3)	–0.9(3)	O(5)-C(35)-C(36)-O(7)	–0.1(3)
C(1)-C(2)-O(3)-B(1)	3.0(3)	C(35)-C(36)-O(7)-B(2)	–4.0(3)
C(2)-O(3)-B(1)-O(1)	–3.7(2)	C(36)-O(7)-B(2)-O(5)	6.1(3)
O(3)-B(1)-O(1)-C(1)	3.2(3)	O(7)-B(2)-O(5)-C(35)	–6.3(3)

Fig. 2. Stereoview of one of the two independent molecules of **11**; 50% probability thermal ellipsoids are shown for the non-hydrogen atoms.

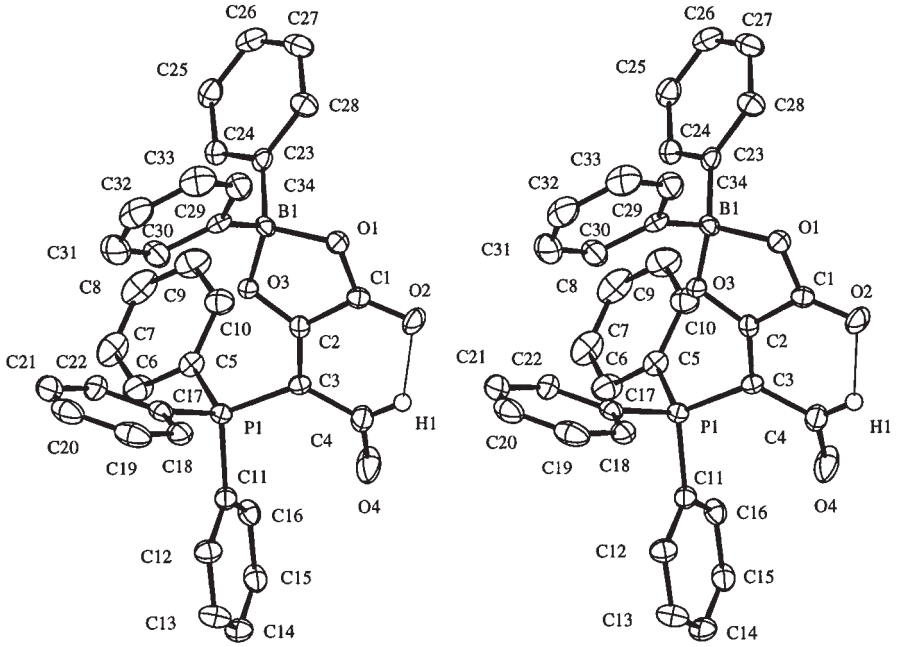

acidity of the free phenol group. All of the compounds of type **2** are hydrolyzed in acidic solution, giving formic acid and an α-oxocarbonic acid or its hydrate (1), a reaction that had already been observed by Kröhnke (13) with various bisacyl pyridinium ylides. Heating of **3** to ca. 110°C results in the elimination of methanol and the loss of solvate water, giving the very stable diphenylboron chelate **7**.[7]

The phosphonium ylide **10** reacts analogously to **2** with oxybis(diphenylborane) giving the *B,P*-betainic diphenylboron chelate **11** in high yield. In the ^{1}H NMR spectrum of **11** the signal of the formyl group proton appears at 10.96 ppm, distinctly downfield from the corresponding signal produced by the formyl proton of the uncomplexed ylide **10** at 8.72 ppm. This points to the enhanced aldehyde function of the formyl group, similar to that in the type **1** chelates, which is further supported by the formation of the 4-nitrophenylhydrazone **12**. The ^{31}P NMR spectrum of **11** shows only a minor change with respect to that of the ligand **10** (1), emphasizing the insignificant influence of the chelatization on the phosphonium moiety.

The X-ray analysis of **11** establishes the proposed molecular structure (Fig. 2), which is analogous to **1**. To the best of our knowledge, compound **11** represents a new type of boron chelate with a boron phosphorus betaine structure. As in **1***a*, an intramolecular C-H···O interaction is conspicuous. The C···O distances of 2.959(4) and 2.979(4) Å, respectively, for the two independent molecules, H···O distances of 2.24 and 2.30 Å, and the corresponding C-H···O angles of 129.6° and 125.6° might suggest somewhat stronger intramolecular hydrogen bonds between C(4) and O(2), and C(38) and O(6), than those existing in **1***a*.

In the triphenylphosphonium residue of **11** the P—C(phenyl) bond distances of about 1.800 Å (1.793(3)–1.815(3) Å) are of the same order as those observed in the

[7] A facile elimination of methanol and the formation of **7** can be observed even during storage at room temperature, monitored by infrared spectroscopy. A readdition of methanol is not achieved by the treatment of **7** with heated methanol.

© 1999 NRC Canada

triphenylphosphonium methylide adduct of boraadamantane (14). The P(1)—C(3) and P(2)—C(37) distances of 1.793(3) and 1.786(3) Å, respectively, are somewhat longer than the comparable P—C bond in the above-mentioned ylide adduct (14) (1.766 Å). Steric factors as well as loss of the ylide character might be responsible for the lengthening of this P—C bond in **11**. Free triphenylphosphonium methylide has a distinctly shorter comparable P—C bond of 1.661 Å (15), as does triphenylphosphonium dimethylallylide, P—C = 1.677 Å (16). The four substituents around the phosphorus atom are arranged in a nearly tetrahedral manner, the phenyl rings being oriented in a propeller arrangement.

The overall geometry of the boron chelate ring in **11** is similar to that observed for **1***a*. Obvious differences can be seen at the formyl group: C(4)—O(4) = 1.222(2) Å and C(25)—O(8) = 1.225(2) Å in **1***a*; C(4)—O(4) = 1.206(3) Å and C(38)—O(8) = 1.219(3) Å in **11.** The increased double bond character of the carbonyl C=O bond, having an estimated π-bond order of 0.85 (from a bond length vs. HMO–π-bond order plot (11)), points to the weaker influence of the phosphonium substituent in **11**, compared to the pyridinium substituent in **1***a*, upon the conjugated system that ends with the electron-withdrawing diphenylborinate moiety. The geometry around the boron nuclei in both compounds, **1***a* and **11,** is very similar, both displaying normal bond lengths and angles.

The structures of both **1***a* and **11** consist of discrete molecules, the most significant intermolecular interactions in the solid state corresponding to weak C-H···O interactions (C···O = 3.147(3)–3.441(2) Å, H···O = 2.44–2.53 ÅC–H···O = 125°–163°).

Acknowledgments

We thank the Natural Sciences and Engineering Research Council of Canada and the Fonds der Chemischen Industrie, Frankfurt am Main, for financial support. We are grateful to the Chemische Institute der Technischen Universität Braunschweig for ^{1}H, ^{11}B, ^{31}P, and ^{13}C NMR and mass spectra.

References

1. J. Grünefeld and P.G. Jones. J. Prakt. Chem. **338**, 718 (1996).
2. (*a*) W. Kliegel. Organomet. Chem. Rev. Sect. A: **8**, 153 (1972); (*b*) W. Kliegel, K. Drückler, S.J. Rettig, and J. Trotter. Can. J. Chem. **71**, 919 (1993), and references therein.
3. G.N. Nikonov and A.S. Balueva. Usp. Khim. **61**, 616 (1992); Russ. Chem. Rev. **61**, 335 (1992).
4. (*a*) R. Neu. Chem. Ber. **87**, 802 (1954); (*b*) G.N. Chremos, H. Weidmann, and H.K. Zimmerman. J. Org. Chem. **26**, 1683 (1961).
5. (*a*) R. Neu. Z. Anal. Chem. **176**, 334 (1960); (*b*) B. Friese and F. Umland. Anal. Chim. Acta, **96**, 303 (1978).
6. (*a*) International tables for X-ray crystallography. Vol. IV. Kynoch Press, Birmingham, U.K. (present distributor Kluwer Academic Publishers, Boston, Mass.). 1974. pp. 99–102; (*b*) International tables for crystallography. Vol. C. Kluwer Academic Publishers, Boston, Mass. 1992. pp. 200–206.
7. (*a*) E. Hohaus and F. Umland. Chem. Ber. **102**, 4025 (1969); (*b*) W. Kliegel and J. Graumann. Liebigs Ann. Chem. 950 (1983); (*c*) G.H.L. Nefkens and B. Zwanenburg. Tetrahedron, **39**, 2995 (1983).
8. (*a*) R. Köster and G.W. Rotermund. Liebigs Ann. Chem. **689**, 40 (1965); (*b*) I. Bally, A. Arsene, M. Bacescu-Roman, and A.T. Balaban. Tetrahedron Lett. 3929 (1965); (*c*) I. Bally, A. Arsene, M. Paraschiv, E. Romas, and A.T. Balaban. Rev. Roum. Chim. **11**, 1409 (1966); (*d*) I. Bally and A.T. Balaban. Rev. Roum. Chim. **16**, 739 (1971); (*e*) F. Umland, E. Hohaus, and K. Brodte. Chem. Ber. **106**, 2427 (1973); (*f*) T.S. Kopteva, V.G. Medvedeva, A.N. Radionov, N.I. Ruch'eva, A.P. Skoldinov, and D.N. Shigorin. J. Gen. Chem. USSR, **48**, 1453 (1978).
9. G.R. Desiraju. Acc. Chem. Res. **29**, 441 (1996).
10. F.H. Allen, O. Kennard, D.G. Watson, L. Brammer, A.G. Orpen, and R. Taylor. J. Chem. Soc. Perkin Trans. 2, S1 (1987).
11. G. Häfelinger. Chem. Ber. **103**, 2922 (1970).
12. J.P. Paolini. J. Comput. Chem. **11**, 1160 (1990).
13. (*a*) F. Kröhnke. Ber. Dtsch. Chem. Ges. **68**, 1177 (1935); (*b*) F. Kröhnke. Ber. Dtsch. Chem. Ges. **72**, 83 (1939).
14. M.V. Sergeeva, A.I. Yanovskii, Yu.T. Struchkov, B.M. Michailov, M.E. Gurskii, and D.G. Pershin. Bull. Acad. Sci. USSR, Div. Chem. Sci. **34**, 2296 (1985); Izv. Akad. Nauk SSSR, Ser. Khim. **34**, 2483 (1985).
15. J.C.J. Bart. J. Chem. Soc. B, 350 (1969).
16. B.L. Barnett and C. Krüger. Cryst. Struct. Commun. **3**, 427 (1973).
17. W. Kliegel, U. Riebe, S.J. Rettig and J. Trotter. Can. J. Chem. **76**, 1789 (1998).

Can. J. Chem. Downloaded from www.nrcresearchpress.com by Peking University on 09/06/12
For personal use only.

© 1999 NRC Canada

Kinetics of oxidation of hydrogen peroxide and ascorbic acid by a tribridged manganese(IV,IV) dimer in feebly acidic media

Anup Kumar Bhattacharya, Anath Bondhu Mondal, Anadi C. Dash, G.S. Brahma, and Rupendranath Banerjee

Can. J. Chem. Downloaded from www.nrcresearchpress.com by Peking University on 09/06/12
For personal use only.

Abstract: In weakly acidic, aqueous buffer ($MeCO_2^-$+ bipy), the complex ion $[Mn_2^{IV}(\mu\text{-}O)_2(\mu\text{-}MeCO_2)(bipy)_2(H_2O)_2]^{3+}$, **1** (bipy = 2,2′-bipyridine), coexists in rapid equilibrium with its hydrolytic derivatives, $[Mn_2^{IV}(\mu\text{-}O)_2(bipy)_2(H_2O)_4]^{4+}$, **2**, and $[Mn_2^{IV}(\mu\text{-}O)_2(\mu\text{-}MeCO_2)(bipy)(H_2O)_4]^{3+}$, **3**. The solution quantitatively oxidizes hydrogen peroxide to oxygen and ascorbic acid to dehydroascorbic acid, itself being reduced to Mn^{II}. In the presence of excess reductant, the reactions follow simple first-order kinetics with no evidence for the accumulation of a significant amount of any intermediate manganese complex. The ascorbate anion shows overwhelming kinetic dominance over ascorbic acid, but no evidence is available for deprotonation of hydrogen peroxide. The preferred intimate mechanism for hydrogen peroxide is inner sphere but that for ascorbic acid is uncertain. For both reductants, increased extent of aquation leads to increased kinetic activity in the order: **1** < **2** < **3**.

Key words: kinetics, manganese, ascorbic acid, hydrogen peroxide, 2,2′-bipyridine.

Résumé : En milieu faiblement acide, tampon aqueux (acétate + bipyridine), le complexe ionique $[Mn(IV)_2(\mu\text{-}O)(\mu\text{-}MeCO_2)(bipy)_2(H_2O)_2]^{3+}$ (**1** dans lequel bipy = 2,2'-bipyridine) coexiste en équilibre rapide avec ses dérivés d'hydrolyse, $[Mn(IV)_2(\mu\text{-}O)(bipy)_2(H_2O)_4]^{4+}$ (**2**) et $[Mn(IV)_2(\mu\text{-}O)_2(\mu\text{-}MeCO_2)(bipy)_2(H_2O)_4]^{3+}$ (**3**). La solution oxyde quantitativement le peroxyde d'hydrogène en oxygène et l'acide ascorbique en acide déhydroascorbique alors que le manganèse est réduit en Mn(II). En présence d'un excès de réducteur, les réactions suivent une cinétique du premier ordre simple, sans accumulation de quantités significatives de complexes de manganèse intermédiaires. L'anion ascorbate présente une dominance cinétique importante par rapport à l'acide ascorbique, mais on n'a pas pu mettre en évidence de déprotonation du peroxyde d'hydrogène. La sphère interne correspond au mécanisme intime préféré pour le peroxyde d'hydrogène; celui pour l'acide ascorbique est toutefois incertain. Pour les deux réducteurs, une augmentation de l'aquation conduit à une activité cinétique accrue dans l'ordre **1** < **2** < **3**.

Mots clés : manganèse, acide ascorbique, peroxyde d'hydrogène, 2,2′-bipyridine.

[Traduit par la Rédaction]

Introduction

The oxygen-evolving complex (OEC) in photosystem II (PS II) consists of a manganese cluster that binds substrate water molecules and accumulates oxidizing equivalents in a cyclic sequence of reactions known as the Kok or the S-state cycle (1). The OEC is made up of four manganese ions (2), held together by μ-oxo and carboxylate bridges, and a tetrameric structure was recently proposed on the basis of EXAFS and EPR data (3). ESSEM $^{14}N/^{15}N$ labelling studies (4) and ^{15}N ENDOR spectroscopy (5) have shown that nitrogen-containing ligands are bound to manganese in PS II. Oxo- and carboxylato-bridged manganese dimers (6) containing N-donor ligands are therefore considered as "molecular bricks" for the OEC. Investigation of the kinetics, equilibrium, and mechanism of the ligand substitution and redox reactions of such complexes is intrinsically interesting.

In addition to their significance in light-driven oxidation of water molecules to oxygen, these complexes are novel oxidants useful for the mechanistic studies of electron transfer reactions of higher-valent manganese in solution. We recently investigated the kinetics of reduction of two dioxo-bridged manganese(III,IV) dimers (7) and the tribridged $[Mn_2^{IV}(\mu\text{-}O)_2(\mu\text{-}MeCO_2)(bipy)_2(H_2O)_2]^{3+}$ ion (**1**; bipy = 2,2′-bipyridine; see Fig. 1) in aqueous media (8–10). We thus found that the Mn_2^{IV} species in excess bipy generate a $Mn^{III}Mn^{IV}$ dimer, $[(bipy)_2Mn^{IV}(\mu\text{-}O)_2Mn^{III}(bipy)_2]^{3+}$, as intermediate while reacting with thiosulfate and hydrazine but not with nitrite. From the observed proton dependence, the intimate mechanism for hydrazine appeared to be inner sphere. In this paper, we report the kinetics of reduction of **1** and its aqua derivatives by ascorbic acid (H_2A) and hydrogen peroxide in an attempt to further explore the reactivity pattern of higher-valent oxo-bridged manganese complexes.

Received July 6, 1998.

A.K. Bhattacharya, A.B. Mondal, and R. Banerjee.[1] Department of Chemistry, Jadavpur University, Calcutta-700032, India.
A.C. Dash[1] **and G.S. Brahma.** Department of Chemistry, Utkal University, Bhubaneswar-751004, India.

[1]Authors to whom correspondence may be addressed. e-mail (RB): rbju@yahoo.com; (ACD): dsthcr28@cal2.vsnl.net.in

 © 1999 NRC Canada

Fig. 1. Graphical structure for **1** drawn on the basis of its crystal structure.

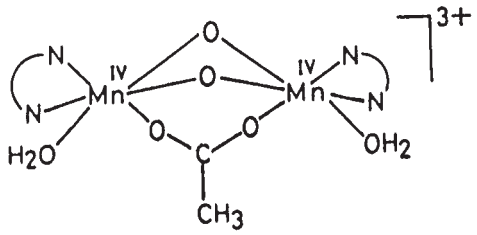

Experimental

Materials

The solutions of hydrogen peroxide were prepared by dilution of 30% (w/v) stabilizer-free hydrogen peroxide (G.R., E. Merck) and were standardized by iodometry using starch indicator (11). L-Ascorbic acid (A.R., S.R.L) was used without further purification. All other materials including the complex ion **1** have been described earlier (8). Solutions were prepared in doubly distilled water, generally just before use.

Physical measurements and kinetics

Kinetics were measured with a stopped-flow spectrophotometer (HITECH SF-51), interfaced with an Apple-II GS personal computer for data acquisition and analysis of absorbance–time data for the first-order rate constants. Five hundred and twelve data points were collected by the stopped-flow apparatus for each experiment. Excess reducing agent maintained pseudo-first-order conditions in a mixed ($MeCO_2H/MeCO_2^-$ + $Hbipy^+$/bipy) aqueous buffer medium in the pH range 4.2–5.5. Each reported first-order rate constant is the average of three to five replicate measurements for a given reaction mixture. We measured the solution pH with an Elico (L 1120) pH-meter (8, 12). The linearity of the electrode was established using pH 4, 7, and 9 buffers. The electrode was calibrated to read –log [H^+] directly using a series of acid solutions at the ionic strength used for kinetic measurements. Kinetics was measured at 25.0°C for hydrogen peroxide, but at 15.0°C for fast-reacting ascorbic acid.

Stoichiometries were determined under the kinetic conditions. An excess of a reducing agent, hydrogen peroxide or ascorbic acid, was added in a single portion to a solution of the Mn_2^{IV} complex **1**. The amount of hydrogen peroxide remaining after complete reaction was determined iodometrically(11). Ascorbate concentration in spent reaction mixtures was determined iodimetrically using starch indicator near the end point in a dilute sulphuric acid medium (13). Standard iodine solution rapidly and quantitatively oxidized ascorbic acid to dehydroascorbic acid (13, 14). Other materials present in the mixture did not interfere.

Results and discussion

Stoichiometry and reaction products

Each mole of the complex consumed two moles of H_2O_2 and thus suggests quantitative oxidation of H_2O_2 to O_2 (Table 1). The 1:2 stoichiometry was also observed for ascorbic acid (H_2A), indicating that dehydroascorbic acid (A), the most common oxidation product (14, 15) of H_2A, is produced in the present experiments.

Table 1. Stoichiometry of the reduction of Mn_2^{IV} complexes. [a]

$[Mn_2^{IV}]$	pH	[R]	$\Delta [Mn_2^{IV}]/\Delta[R]$
		R = H_2O_2	
0.2	4.53	0.8	0.48
0.6	4.79	1.4	0.52
0.8	4.85	1.8	0.49
1.0	4.96	2.4	0.47
1.2	5.12	2.8	0.51
			Avg. = 0.495 ± 0.02
		R = ascorbic acid	
0.2	4.48	0.7	0.49
0.4	4.52	1.2	0.47
0.9	4.87	2	0.52
1.2	5.05	2.8	0.48
1.6	5.23	3.8	0.51
			Avg. = 0.496 ± 0.02

[a] C_{bipy} = 35.0; all concentrations are in mmol dm^{-3} ; total volume, 100 mL.

Solution equilibria

The crystal structure of the complex salt $\mathbf{1}(ClO_4)_3 \cdot H_2O$ shows a bridging ethanoate ligand, a bis(μ-oxo) bridge, and two water molecules, each directly coordinated to one manganese(IV) ion (16). The ethanoate bridge and a bipy ligand are labile and dissociate in aqueous solution according to eqs. [1] and [2] (8).

[1] $$[Mn_2^{IV}(\mu-O)_2(\mu-MeCO_2)(bipy)_2(H_2O)_2]^{3+} + 2H_2O$$
$$\mathbf{1}$$
$$\overset{K_{12}}{\rightleftharpoons} [Mn_2^{IV}(\mu-O)_2(bipy)_2(H_2O)_4]^{4+} + MeCO_2^-$$
$$\mathbf{2}$$

[2] $$\mathbf{1} + 2\ H_2O \overset{K_{13}}{\rightleftharpoons} [Mn_2^{IV}(\mu-O)_2(\mu-MeCO_2)(bipy)(H_2O)_4]^{3+} + bipy$$
$$\mathbf{3}$$

[3] $$MeCO_2H \overset{K_{ea}}{\rightleftharpoons} MeCO_2^- + H^+$$

[4] $$Hbipy^+ \overset{K_{Hbipy}}{\rightleftharpoons} H^+ + bipy$$

The solution is otherwise stable under the present experimental conditions.

A labile ethanotate bridge is found also in the dinuclear Mn(III,IV) complex $[Mn_2(\mu\text{-}O)_2(\mu\text{-}MeCO_2)(\textit{fac}\text{-bpea})_2]^{2+}$ (bpea is *N*,*N*-bis(2-pyridylmethyl)ethylamine) and in its diferric analogue, $[Fe_2(\mu\text{-}O)(\mu\text{-}MeCO_2)_2(L)_2]^{2+}$ (L is substituted bpea) (17–19).

The chelating ligands in the complexes $[L'_2Mn^{III}(\mu\text{-}O)_2Mn^{IV}L'_2]^{3+}$ (L′ = 2,2′-bipyridine and 1,10-phenanthroline) are also labile (7, 20). The binding sites in the S_3-state (the S-state notation (1) identifies the number of oxidizing equivalents stored in the manganese cluster in the water oxidation

© 1999 NRC Canada

Can. J. Chem. Downloaded from www.nrcresearchpress.com by Peking University on 09/06/12
For personal use only.

Fig. 2. Variation of first-order rate constants for H_2O_2 with pH at a fixed C_{bipy}(0.035) and fixed C_{ea}(0.08) at 25.0°C (▽). Variation of first-order rate constants for ascorbic acid with pH at a fixed C_{bipy} (0.035) and C_{ea} (0.1) at 15.0°C (○).

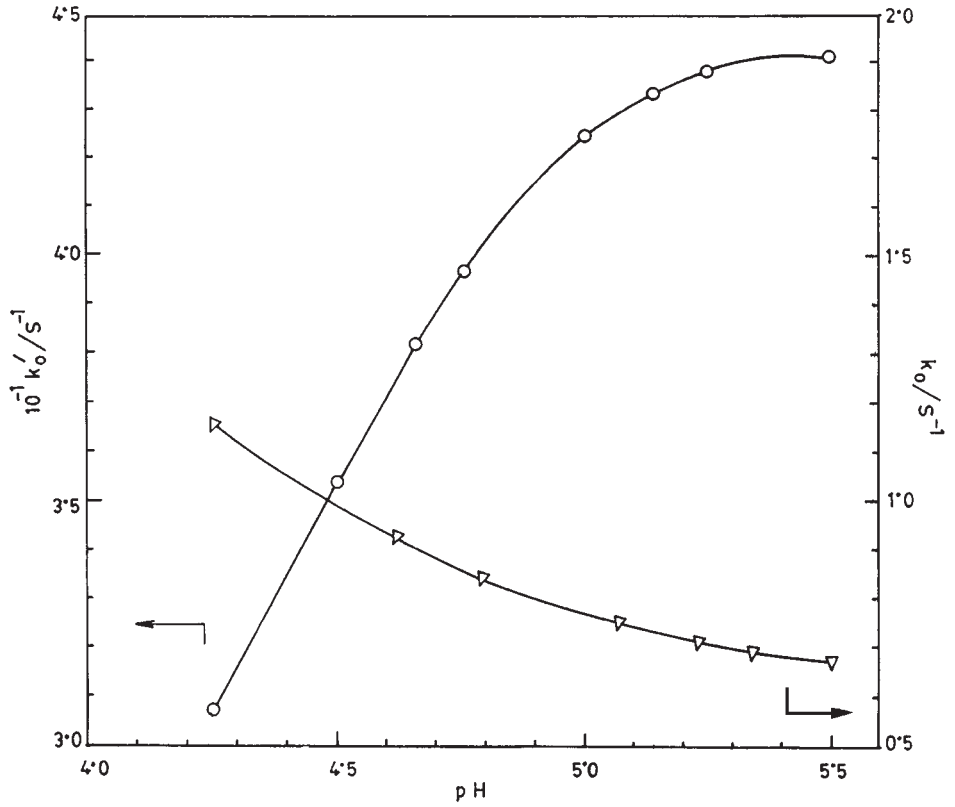

Can. J. Chem. Downloaded from www.nrcresearchpress.com by Peking University on 09/06/12
For personal use only.

complex of PS II) are labile and exchange ^{18}O-labeled water in less than 1 s (21). However, the bridging oxo-ligands are kinetically inert (22, 23). Interestingly, equilibrium as well as kinetic studies (8, 10) suggest that the coordinated water molecules in **1** and its aqua derivatives do not deprotonate, at least up to pH 5.5. Weak acidity of coordinated water is known also for $[Mn_3^{IV}(\mu\text{-}O)_4(bipy)_4(H_2O)_2]^{4+}$ (24) and $[Mn(pd)_2(H_2O)_2]^+$ (pd is pentane-2,4-dione). The latter complex has a pK_a value of 7.3 (25–27). The weak acidity observed is consistent with recent findings that the O—H bond strength in water coordinated to higher-valent manganese is comparable to the phenolic O—H bond strength in tyrosine (28, 29).

Kinetics and reaction schemes

All reactions in the presence of excess reducing agent obeyed first-order kinetics for at least 90% reaction. The first-order rate constants, k_0 for H_2O_2 and k_0' for ascorbic acid (see Table 2), increased with increasing concentration of the reducing agent but decreased with increasing [bipy] and [$MeCO_2^-$] at a fixed pH. However, pH change affects k_0 and k_0' differently. Increased pH decreases k_0 but increases k_0' (Fig. 2). The variations in k_0 can be explained on the basis of only equilibria [1]–[4], provided the hydrolytic derivatives **2** and **3** are kinetically more active than their parent, **1**. We therefore propose Scheme 1 as a simple model for the reaction of H_2O_2.

The pH dependence of the reactions of ascorbic acid can be reasonably explained if one assumes, along with equilibria [1]–[4], the deprotonation equilibrium of H_2A, eq. [8] (15), and an overwhelming kinetic dominance of the ascorbate ion, HA^-, over ascorbic acid, H_2A. (Scheme 2, eqs. [8]–[11]).

Scheme 1.

[5] **1** + H_2O_2 $\xrightarrow{k_A}$ Products (Mn^{II}, H^+, O_2)

[6] **2** + H_2O_2 $\xrightarrow{k_B}$ Products

[7] **3** + H_2O_2 $\xrightarrow{k_C}$ Products

Scheme 2.

[8] H_2A $\overset{K_a}{\rightleftharpoons}$ H^+ + HA^-

[9] **1** + HA^- $\xrightarrow{k_A'}$ Products (Mn^{II}, H^+, A)

[10] **2** + HA^- $\xrightarrow{k_B'}$ Products

[11] **3** + HA^- $\xrightarrow{k_C'}$ Products

© 1999 NRC Canada

Table 2. First-order rate constants for the reduction of Mn_2^{IV} complexes. [a]

pH	[bipy]	[$MeCO_2^-$]	[R]	k_0/s^{-1}
		Reducing agent (R), H_2O_2		
4.25	14.1	19.4	1.0	1.16 (1.13)
4.50	19.1	29.0	1.0	1.01 (0.99)
4.63	21.6	34.8	1.0	0.93 (0.91)
4.79	24.5	42.1	1.0	0.84 (0.82)
5.06	28.5	53.9	1.0	0.74 (0.73)
5.23	30.3	60.3	1.0	0.71 (0.69)
5.34	31.2	63.8	1.0	0.69 (0.68)
5.50	32.3	68.0	1.0	0.67 (0.66)
4.50	2.73	29.0	1.0	2.81 (2.68)
4.50	5.46	29.0	1.0	1.81 (1.78)
4.50	8.19	29.0	1.0	1.37 (1.43)
4.50	9.55	29.0	1.0	1.34 (1.32)
4.50	10.9	29.0	1.0	1.23 (1.24)
4.50	13.65	29.0	1.0	1.12 (1.26)
4.50	16.4	29.0	1.0	1.06 (1.09)
4.50	19.1	1.81	1.0	1.75 (1.76)
4.50	19.1	3.62	1.0	1.59 (1.61)
4.50	19.1	5.44	1.0	1.49 (1.50)
4.50	19.1	7.26	1.0	1.39 (1.41)
4.50	19.1	9.07	1.0	1.34 (1.33)
4.50	19.1	12.9	1.0	1.20 (1.22)
4.50	19.1	36.3	1.0	0.92 (0.94)
4.50	19.1	54.4	1.0	0.87 (0.86)
4.50	19.1	29.0	1.5	1.52 (1.48)
4.50	19.1	29.0	2.0	2.04 (1.98)
4.50	19.1	29.0	2.5	2.41 (2.47)
4.50	19.1	29.0	3.0	3.02 (2.97)
4.50	19.1	29.0	4.0	3.89 (3.96)
4.50	19.1	29.0	5.0	4.88 (4.95)
		Reducing agent, ascorbic acid		
pH	[bipy]	[$MeCO_2^-$]	[R]	$10^{-1}\ k_0'/s^{-1}$
4.25	14.1	24.2	1.0	3.07 (3.05)
4.50	19.1	36.3	1.0	3.54 (3.56)
4.67	22.4	45.8	1.0	3.81 (3.83)
4.75	23.8	50.3	1.0	3.99 (3.94)
5.00	27.7	64.3	1.0	4.25 (4.19)
5.13	29.3	70.8	1.0	4.35 (4.29)
5.25	30.5	76.2	1.0	4.39 (4.36)
5.50	32.3	85.1	1.0	4.41 (4.45)
4.50	2.73	36.3	1.0	5.18 (5.20)
4.50	5.46	36.3	1.0	4.40 (4.24)
4.50	8.19	36.3	1.0	3.99 (3.92)
4.50	9.55	36.3	1.0	3.84 (3.83)
4.50	13.65	36.3	1.0	3.65 (3.69)
4.50	17.2	36.3	1.0	3.62 (3.61)
4.50	19.1	1.81	1.0	3.99 (3.98)
4.50	19.1	3.63	1.0	3.91 (3.90)
4.50	19.1	5.44	1.0	3.87 (3.84)
4.50	19.1	13.8	1.0	3.68 (3.69)
4.50	19.1	23.6	1.0	3.57 (3.61)
4.50	19.1	54.4	1.0	3.43 (3.51)
4.50	19.1	36.3	1.5	5.21 (5.33)
4.50	19.1	36.3	2.0	7.21 (7.12)
4.50	19.1	36.3	2.5	8.96 (8.89)
4.50	19.1	36.3	3.0	10.5 (10.7)
4.50	19.1	36.3	4.0	14.3 (14.2)

Can. J. Chem. Downloaded from www.nrcresearchpress.com by Peking University on 09/06/12
For personal use only.

© 1999 NRC Canada

Table 2. (*concluded*).

pH	[bipy]	[$MeCO_2^-$]	[R]	k_0/s^{-1}
4.50	19.1	36.3	4.5	16.2 (16.0)
4.50	19.1	36.3	5.0	17.8 (17.8)

[a]Temperature, 25.0°C for H_2O_2; 15.0°C for ascorbic acid. [Mn_2^{IV}] = 0.10; all concentrations are in mmol dm^{-3} except I = 1.0 mol dm^{-3} ($NaNO_3$); λ, 420 nm for H_2O_2; 380 nm for ascorbic acid. Values in parentheses are calculated rate constants.

Schemes 1 and 2 lead to eqs. [12] and [13], respectively.

$$[12]\quad k_0 = \frac{\{k_A[MeCO_2^-][bipy] + k_BK_{12}[bipy] + k_CK_{13}[MeCO_2^-]\}[H_2O_2]}{[MeCO_2^-][bipy] + k_{12}[bipy] + k_{13}[MeCO_2^-]}$$

$$[13]\quad k_0' = \frac{\{K_ak_A'[MeCO_2^-][bipy] + K_ak_B'K_{12}[bipy] + K_aK_{13}k_C'[MeCO_2^-]\}C_a}{\{[H^+] + K_a\}\{[MeCO_2^-][bipy] + K_{12}[bipy] + K_{13}[MeCO_2^-]\}}$$

where C_a (= [H_2A] + [HA^-]) is the total analytical concentration for ascorbic acid. Equation [12] leads to eq. [14] and eq. [13] leads to eq. [15].

$$[14]\quad k_0([MeCO_2^-][bipy] + K_{12}[bipy] + K_{13}[MeCO_2^-])/[H_2O_2] = k_A[MeCO_2^-][bipy] + k_BK_{12}[bipy] + k_CK_{13}[MeCO_2^-]$$

$$[15]\quad k_0'([H^+] + K_a)([MeCO_2^-][bipy] + K_{12}[bipy] + K_{13}[MeCO_2^-])/C_aK_a = k_A'[MeCO_2^-][bipy] + k_B'K_{12}[bipy] + k_C'K_{13}[MeCO_2^-]$$

$[MeCO_2^-] = C_{ea}K_{ea}/([H^+] + K_{ea})$ and $[bipy] = C_{bipy}K_{Hbipy}/([H^+] + K_{Hbipy})$, where C_{ea} = ([$MeCO_2^-$] + [$MeCO_2^-$]) and C_{bipy} = ([$Hbipy^+$] + [bipy]) are the total analytical concentration of ethanoate and 2,2′-bipyridine, respectively. Values for the left-hand sides of eqs. [14] and [15] may be calculated using known rate constants (Table 2) and equilibrium constants (Table 3). The calculated left-hand sides of eqs. [14] and [15] each yielded excellent straight lines (Figs. 3 and 4) when plotted against [bipy] or [$MeCO_2^-$], thus justifying the proposed schemes. The slopes and intercepts of the straight lines yielded the specific rate constants k_A, k_B, k_C, k_A', k_B' and k_C' displayed in Table 4 along with known rate constants for comparable reactions. The rate law derived for an equivalent scheme admitting significant kinetic contribution from H_2A contains an additional term, first order in [H^+]. Such a rate law does not fit the experimental data.

The K_{12} and K_{13} values are available only at 25.0°C and were used in computing the k_n' values for ascorbic acid at 15.0°C. This difference in temperature is unlikely to introduce serious error. We verified that a simultaneous increase or decrease to the extent of 50% in K_{12} and K_{13} changes k_1' by only 12% even when k_2' and k_3' are kept fixed to see what happens if the whole thrust of the change in the two equilibrium constants are put on k_1' alone. Similar were the cases for k_2' and k_3'.

Intimate mechanism

Ascorbic acid can act both as an inner-sphere as well as an outer-sphere reducing agent (30). In the present study, labile coordination sites present in the metal complexes may induce an inner-sphere mechanism but it is not a trivial matter to pinpoint the mechanism. For example, Bansch et al. (31) have shown that oxidation of ascorbic acid by $[Fe(H_2O)_6]^{3+}$ ion follows an outer-sphere path, and oxidation by the $[Fe(H_2O)_5(OH)]^{2+}$ ion proceeds by an H-atom transfer from HA^- although both H_2A and HA^- are known (32) to be good ligands for Fe(III). Obviously, presence of a labile coordination site and the ability of the reductant to bind to a metal centre are insufficient information to decide in favour of one of the two intimate mechanisms — inner sphere or outer sphere. However, an H-atom transfer mechanism may be discarded since the Mn_2^{IV} complexes have no OH group.

The simple first-order kinetics observed by us, without any indication of rate saturation, only implies the validity of the inequality, $Q_x[HA^-] << 1$ for every individual value of Q_x, the formation quotient for adducts that may form between HA^- and the $Mn^{IV}{}_2$ complexes, **1**, **2**, **3**. In our experiments the maximum value for [HA^-] is 3.6×10^{-3} mol dm^{-3}. The inequality, therefore, imposes an upper limit on Q_x, 30 dm^3 mol^{-1}. The observed situation is similar to those for reduction of $[Mn_2^{III,IV}(\mu\text{-}O)_2(bipy)_4]^{3+}$, **4**, by hydroquinone and HSO_3^-. No rate saturation was observed in these two reactions, as was also the case in the reaction between HSO_3^- and **4**, and that between HA^- and the one-electron reduced $Mn^{III}{}_2$ form of **4** (33). However, the $(Mn^{III}{}_2)$–HSO_3^- adduct (Q = 450 dm^3 mol^{-1}), as well as that formed from **4** and ascorbic acid, is strong enough to permit their kinetic detection (33). Apparently, the Q values may be sufficiently different to evade rationalization even in closely related systems.

Oxidation of hydrogen peroxide is generally inner sphere (34) excepting when the oxidant is very powerful and coordinatively saturated, such as $[Ni^{III}(bipy)_3]$ (35). For example, the reactions of H_2O_2 with moderately oxidizing (36)

Can. J. Chem. Downloaded from www.nrcresearchpress.com by Peking University on 09/06/12
For personal use only.

© 1999 NRC Canada

Fig. 3. Variation of k_0 G / $[H_2O_2]$ with $[MeCO_2^-]$ at a fixed pH (4.50) and fixed C_{bipy} (0.035) (■). Variation of k_0 G / $[H_2O_2]$ with [bipy] at fixed pH (4.50) and fixed C_{ea} (0.08) (●). G = $[MeCO_2^-][bipy] + K_{12}[bipy] + K_{13}[MeCO_2^-]$. Other conditions: $[Mn_2^{IV}]$, 1.0×10^{-4}; *I*, 1.0; $[H_2O_2]$, 1.0×10^{-3}; temp., 25.0°C. All concentrations are in mol dm^{-3}.

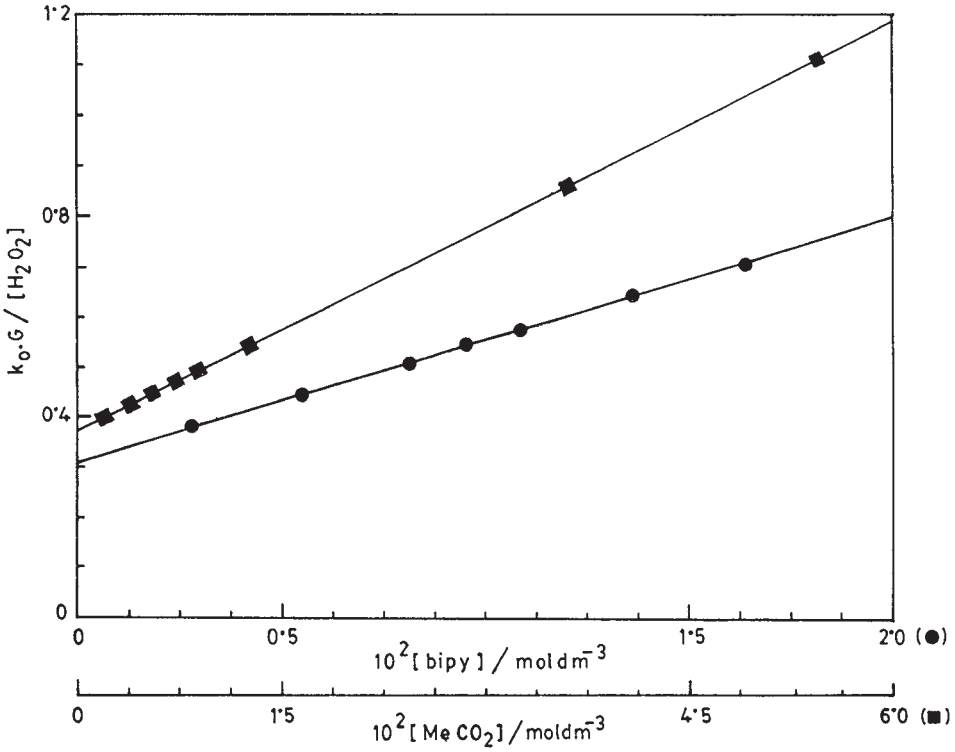

Table 3. Values of the equilibrium constants used.

Reaction	Temp./ °C	*I* / mol dm^{-3}	p*K*
Equation [1]	25	1.0	2.0[a]
Equation [2]	25	1.0	3.0[a]
Equation [3]	20	1.0	4.55[b]
Equation [4]	25	0.33	4.43[c]
	15	0.1	4.49[d]
Equation [8]	15	1.0	4.08[e]

[a]Reference 8 in the text.

[b]Reference 43. Change in temperature little affects the value; e.g, for $I \rightarrow 0$, the value over the temperature range 15–25°C is 4.756 ± 0.002 (44).

[c]Reference 45. Effect of *I* on p*K* is small; ±0.01 unit for a change in *I* from 0.33 to 0.1 mol dm^{-3}; cf. ref. 46.

[d]Reference 47. This value was used in calculations for ascorbic acid. Comparison with footnote *c* shows that the effect of temperature on p*K* is small.

[e]Reference 15 in the text.

complexes such as $[Mn(cydta)(H_2O)]^-$ (cydta is cyclohexyl ethylenediaminetetraacetate) (37) and solvolyzed **4** follow the inner-sphere path (7*d*, 36). Oxidation of potassium peroxymonosulfate to O_2 with solvolyzed **4** and its close analogues also follows the inner-sphere mechanism (38), and the same mechanism appears very likely for the reactions under the present investigation. Earlier examples of the inner-sphere mechanism for the Mn_2^{IV} complexes are their reactions with $N_2H_5^+$ (10).

In this study, no evidence is available for deprotonation of H_2O_2, though an inner-sphere mechanism implies a coordinated H_2O_2 and enhanced acidity. We recall that water molecules coordinated to Mn(IV) in **1** and its hydrolytic derivatives release no H^+ in the experimental range of pH. Similar behaviour is definitely expected for coordinated H_2O_2 and is not in contradiction with the proposed mechanism.

Table 4 shows that the kinetic activity of the Mn_2^{IV} complexes towards various reducing agents increases with increased extent of aquation in the order: **1** < **2** < **3**. Limburg et al. (38) as well as Banerjee and co-workers (7) noticed that, kinetically, **4** is a much inferior oxidant than its solvolyzed derivatives. Again, in a recent model for the mechanism of the OEC in PS II, it has been assumed that only the two terminal manganese atoms containing coordinated water in a ⊂-shaped tetranuclear cluster are redox active; the two central Mn^{4+} ions without coordinated water are inactive (23). A rationale for the greater kinetic activity of the aqua complexes was presented earlier (9).

Reduction of the Mn_2^{IV} complexes by $S_2O_3^{2-}$ and $N_2H_5^+$ produced the $Mn^{IV}Mn^{III}$ complex, **4**, as an intermediate, which subsequently oxidized additional molecules of reductant and thus decayed to Mn^{II}. No intermediate manganese complex could be detected in the present experiments. This, and the observed exponential profiles along with the absence of any absorbance drops immediately after mixing, suggests that generation of **4** and its subsequent reactions with ascorbic acid and hydrogen peroxide are kinetically insignificant in the present systems. It may be that the one-electron transfer products, the radicals $HO_2^\bullet$ and $A^{-\bullet}$ (generated in the rate-determining steps) rapidly react with the $Mn^{IV}Mn^{III}$ species. This is a strong possibility if the reactions are inner sphere, when rapid further reduction of the successor complex might

© 1999 NRC Canada

Can. J. Chem. Downloaded from www.nrcresearchpress.com by Peking University on 09/06/12
For personal use only.

Can. J. Chem. Downloaded from www.nrcresearchpress.com by Peking University on 09/06/12
For personal use only.

Fig. 4. Variation of k_0' D {[H^+] + K_a} / C_aK_a with [$MeCO_2^-$] at a fixed pH (4.50) and fixed C_{bipy} (0.035) (□). Variation of k_0' D {[H^+] + K_a} / C_aK_a [bipy] at a fixed pH (4.50) and fixed C_{ea} (0.1) (○). D = {[$MeCO_2^-$][bipy] + K_{12}[bipy] + K_{13}[$MeCO_2^-$]}. Other conditions: [Mn_2^{IV}], 1.0 × 10^{-4}; *I*, 1.0; C_{ea}, 1.0 × 10^{-3}; temp.,15.0°C. All concentrations are in mol dm^{-3}.

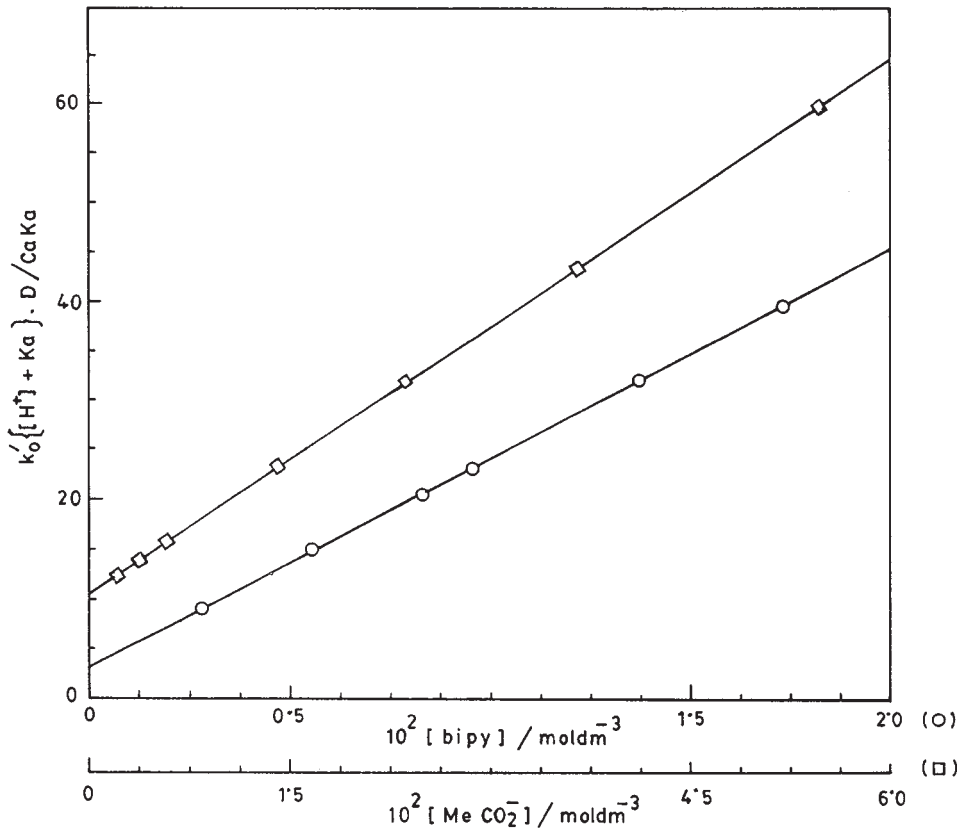

Table 4. Second-order rate constants (dm^3 mol^{-1} s^{-1}) for the reduction of different Mn_2^{IV} species by different reducing agents (R).

	Rate constant for			
R	**1**	**2**	**3**	Ref.
NO_2^-	(2.84 ± 0.13) × 10^{-3}	0.149 ± 0.007	2.07 ± 0.12	10
$N_2H_5^+$	—	(1.11 ± 0.08) × 10^{-3}	6.33 ± 0.2) × 10^{-3}	11
$S_2O_3^{2-}$	2.0 ± 0.02	40 ± 1	(1.45 ± 0.04) × 10^2	9
H_2O_2	(1.70 ± 0.08) × 10^2	(1.97 ±0.06) × 10^3	(1.02 ± 0.07) × 10^4	This work
HA^-	(4.22 ± 0.27) × 10^4	(5.62 ± 0.31) × 10^4	(9.20 ± 0.45) × 10^4	This work

occur before the radicals can escape into the bulk solvent (kind suggestion of a reviewer; see also ref. 39).

Such a mechanism, where the radicals are generated and consumed within the coordination sphere of the metal complex, is, however, closely analogous to and rarely distinguishable from a simultaneous two-electron transfer mechanism, proposed for different multinuclear manganese complexes. For example, Wieghardt et al. (40) isolated a peroxo-bridged complex, $[L_2'Mn_2^{IV}(\mu\text{-}O)_2(\mu\text{-}O_2)]^{2+}$ (L′ = trimethyl-1,4,7-triazacyclononane), which releases molecular oxygen rapidly in aqueous solution at 20°C by an intramolecular two-electron oxidation of coordinated O_2^{2-} with concomitant reduction of Mn_2^{IV} to a binuclear Mn_2^{III} complex. Peroxo-bridged Mn_4 clusters have recently been proposed to represent the S_4 state, in which intramolecular two-electron oxidation of the peroxo-bridge produces O_2 and the S_0 state is regenerated (23). The S_3 to S_4 transition may also be described as a probable two-electron oxidation of substrate ligands according to the Hoganson and Babcock model (23). It appears that a mechanism involving a pair of electron acceptors becomes necessary when the driving force for electron transfer from a multielectron donor becomes too small for free-radical production (41). In such situations, binuclear complexes may provide a low-energy pathway for two-electron transfer. Nevertheless, ascorbic acid rarely undergoes two-electron transfer (42). One suggested example involves a ferriporphyrin dimer(41).

Conclusions

Rapid reduction of the complex ion $[Mn_2^{IV}(\mu\text{-}O)_2(\mu\text{-}MeCO_2)(bipy)_2(H_2O)_2]^{3+}$ and its hydrolytic derivatives with hydrogen peroxide seems to be inner sphere, but the intimate mechanism for the reduction by ascorbic acid is uncertain. An increased number of coordinated water molecules in-

© 1999 NRC Canada

creases the kinetic activity of the host Mn(IV) site in these model complexes, as in the OEC.

Acknowledgment

R.B. is grateful to the Department of Science and Technology (New Delhi) for sponsoring the project under which the present work was done.

References

1. B. Kok, B. Forbush, and M. McGloin. Photochem. Photobiol. **11**, 457 (1970).
2. (*a*) M. Sivaraja and G.C. Dismukes. Biochemistry, **27**, 3467 (1988); (*b*) C.F. Yocum, C.T. Yerkes, R.E. Blankenship, R.R. Sharp, and G.T. Babcock. Proc. Natl. Acad. Sci. U.S.A. **78**, 7507 (1981); (*c*) G.M. Chenaic and I. Martin. Biochim. Biophys. Acta, **197**, 219 (1970); (*d*) N. Nurula, M. Miyo, T. Omata, H. Matsunami, and T. Kuwabara. Biochim. Biophys. Acta, **765**, 363 (1985).
3. (*a*) H. Dan, J.C. Andrews, T.A. Reolifs, M. Latimer, W. Liang, V.K. Yachandra, K. Sauer, and M.P. Klein. Biochemistry, **34**, 5274 (1995); (*b*) V.K. Yachandra, V.J. DeRose, M.J. Latimer, I. Mukherjee, K. Sauer, and M.P. Klein. Science, **260**, 675 (1993); (*c*) G.N. George, R.C. Prince, and S.P. Cramer. Science, **243**, 789 (1989).
4. (*a*) R.D. Britt, J.L. Zimmerman, K. Sauer, and M.P. Klein. J. Am. Chem. Soc. **111**, 3522 (1989); (*b*) V.J. DeRose, V.K. Yachandra, A.E. McDermott, R.D. Britt, K. Sauer, and M.P. Klein. Biochemistry, **30**, 1335 (1991).
5. X.S. Tang, M. Sivaraja, and G.C. Dismukes. J. Am. Chem. Soc. **115**, 2382 (1993).
6. (*a*) K. Weighardt. Angew. Chem. Int. Ed. Engl. **28**, 1153 (1988); (*b*) G. Christou. Acc. Chem. Res. **22**, 328 (1989); (*c*) G.C. Dismukes. Chem. Rev. **96**, 2909 (1996); (*d*) V.K. Yachandra, K. Sauer, and M.P. Klein. Chem. Rev. **96**, 2927 (1996); (*e*) W. Rittinger and GC. Dismukes. Chem. Rev. **97**, 1 (1997).
7. (*a*) S. Chaudhuri, S. Mukhopadhyay, and R. Banerjee. J. Chem. Soc. Dalton Trans. 621 (1995); (*b*) S. Kundu, A.K. Bhattacharya, and R. Banerjee. J. Chem. Soc. Dalton Trans. 3951 (1996); (*c*) B. Mondal, S. Kundu, and R. Banerjee. Polyhedron, **16**, 2199 (1997); (*d*) S. Kundu, B. Mondal, and R. Banerjee. J. Chem. Soc. Dalton Trans. 4341 (1997).
8. A.K. Bhattacharya, A.B. Mondal, and R. Banerjee. J. Chem. Soc. Dalton Trans. 2351 (1997).
9. S. Chaudhury, and R. Banerjee. Polyhedron, **16**, 3493 (1997).
10. A.B. Mondal, A.K.Bhattacharya, D. Maji, and R. Banerjee. Polyhedron, **17**, 1693 (1998).
11. A.I. Vogel. Quantitative inorganic analysis. 5th ed. English Language Book Society, London. 1989. p. 394.
12. S. Mukhopadhyay and R Banerjee. J. Chem. Soc. Dalton Trans. 1349 (1994).
13. The Indian pharmacopoeia. Vol. 1. 3rd ed. Government of India Publication, Publication and Information Directorate, New Delhi. 1985. p. 49.
14. I.L. Finar. Organic chemistry. Vol. 2. 4th ed. English Language Book Society, London. 1968. p. 268.
15. E. Pelizzetti, E. Mentasti, and P.R. West. Can. J. Chem. **17**, 1181 (1978).
16. K.R. Reddy, M.V. Rajasekharan, S. Padhye, F. Dahan, and J.P. Tuchagues. Inorg. Chem. **33**, 428 (1994).
17. S. Menge, J.M. Vincent, C. Lambeauz, G. Chottard, A. Grand, and M. Fontecave. Inorg. Chem. **32**, 4766 (1993).
18. S. Pal, M.M. Olmstead, and W.N. Armstrong. Inorg. Chem. **34**, 4708 (1995).
19. S. Ito, T. Okuno, H. Matsushima, T. Tokil, and Y. Nishida. J. Chem. Soc. Dalton Trans. 4037 (1996).
20. (*a*) R. Manchanda, G.W. Brudvig, and R.H. Crabtree. New J. Chem. **18**, 561 (1994); (*b*) S.R. Cooper and M. Calvin. J. Am. Chem. Soc. **99**, 6623 (1977).
21. (*a*) J. Messinger, M. Badger, and T. Wydrzynski. Proc. Natl. Acad. Sci. U.S.A. **92**, 3209 (1995); (*b*) J. Messinger, M. Hillier, M. Badger, and T. Wydrzynski. *In* Photosynthesis: from light to biosphere. Vol. 2. *Edited by* P. Mathis. Kluwer, Dordrecht, The Netherlands. 1995. pp. 283–286.
22. (*a*) G.S. Waldo, S. Yu, and J.E. Penner-Hahn. J. Am. Chem. Soc. **114**, 5869 (1992); (*b*) S. Khangulov, M. Sivraja, V.V. Barynin, and G.C. Dismukes. Biochemistry, **32**, 4912 (1993); (*c*) M. Shank, V. Barynin, and G.C. Dismukes. Biochemistry, **33**, 15433 (1994).
23. C.W. Hoganson and G.T. Babcock. Science, **227**, 1953 (1997).
24. J.E. Sarneski, H.H. Thorp,G.W. Brudvig, R.H. Crabtree, and G.K. Schulte. J. Am. Chem. Soc. **112**, 7255 (1990).
25. G.H. Cartledge. J. Am. Chem. Soc. **73**, 4416 (1951).
26. G.H. Cartledge. J. Am. Chem. Soc. **74**, 6015 (1952).
27. S. Mukhopadhyay and R. Banerjee. J. Chem. Soc. Dalton Trans. 933 (1993).
28. M.R.A. Blomberg, P.E.M. Siegbahn, S. Styring, G.T. Babcock, B. Akermark, and P. Korall. J. Am. Chem. Soc. **119**, 8285 (1997).
29. M.T. Caudle and V.L. Pecoraro. J. Am. Chem. Soc. **119**, 3415 (1997).
30. (*a*) S. Acharya, G. Neogi, and R.K. Panda. J. Chem. Soc. Dalton Trans., 1471 (1984); (*b*) M.J. Akhtar and A. Haim. Inorg. Chem. **27**, 1608 (1988); (*c*) E. Pelizzetti, E. Mentasti, and E. Pramauro. Inorg. Chem. **15**, 2898 (1976); (*d*) D.H. Macartney and N. Sutin. Inorg. Chim. Acta, **74**, 221 (1983).
31. B. Bsnsch, P. Martinez, D. Uribe, J. Zuluaga, and R. van Eldik. Inorg. Chem. **30**, 4555 (1991).
32. J. Xu and R.B. Jordan. Inorg. Chem. **29**, 4180 (1990).
33. M.C. Ghosh, J.W. Reed, R.N. Bose, and E.S. Gould. Inorg. Chem. **33**, 73 (1994).
34. D.G. Bray and R.C. Thompson. Inorg. Chem. **33**, 905 (1994).
35. A. McAuley, L. Spencer, and P.R. West. Can. J. Chem. **63**, 1198 (1985).
36. T.E. Jones, and R.E. Hamm. Inorg. Chem. **13**, 1940 (1974).
37. M.-N.C. Durrand Santhner, A. Deronzier, X. Pradon, S. Menge, and C. Philouze. J. Am. Chem. Soc. **119**, 3173 (1997).
38. J. Limberg, G.W. Brudvig, and R.H. Crabtree. J. Am. Chem. Soc. **119**, 2761 (1997).
39. R. Banerjee, A. Das, and A Dasgupta. J. Chem. Soc. Dalton Trans. 1645 (1989).
40. K. Wieghardt, U. Bassek, B. Nuber, J. Weiss, J. Bonvoisim, M. Corbella, S.E. Vitols, and J.J. Girerd. J. Am. Chem. Soc. **110**, 7398 (1988).
41. F.L. Haris and D.L. Toppen. Inorg. Chem. **17**, 74 (1978).
42. W. Weis. Ann. N.Y. Acad. Sci. **258,** 190 (1975).
43. D.D. Perrin, J. Phys. Chem. **62**, 767, (1958).
44. H.S. Harned and R.W. Ethlers. J. Am. Chem. Soc. **55**, 65 (1933)
45. P. Krumholz. Nature, **163**, 724 (1949); J. Am. Chem. Soc. **71**, 3654 (1949).
46. M. Yasuda, K. Sane and K. Yamaski, J. Phys. Chem., **60**, 1667 (1956).
47. G. Andergg. Helv. Chim. Acta, **46**, 2397 (1963).

Can. J. Chem. Downloaded from www.nrcresearchpress.com by Peking University on 09/06/12
For personal use only.

© 1999 NRC Canada

Solvent isotope effect on the hydroxide-ion-catalyzed hydration of ketenes in aqueous solution

J. Andraos, Y. Chiang, S.J. Eustace, A.J. Kresge, S.W. Paine, V.V. Popik, and K. Sung

Can. J. Chem. Downloaded from www.nrcresearchpress.com by Peking University on 09/06/12
For personal use only.

Abstract: Five ketenes, phenyl(ethyl)ketene, phenyl(methylthio)ketene, diphenylketene, pentafluorophenylketene, and 1-naphthylketene, were generated flash photolytically and solvent isotope effects (H_2O vs. D_2O) on their hydroxide-ion-catalyzed hydration in aqueous solution were determined. The values obtained are all weakly inverse and closely similar (k_{HO}/k_{DO} = 0.76–0.97), as expected for these fast, hydroxide-ion-consuming reactions, known to proceed by nucleophilic attack of hydroxide on the ketene carbonyl group. The characteristic magnitude of these isotope effects should prove useful in identifying new examples of this reaction.

Key words: ketenes, flash photolysis, photo-Wolff reaction, solvent isotope effects on hydroxide ion consumption.

Résumé : Faisant appel à la photolyse éclair, on a généré cinq cétènes (phényl(éthyl)cétène, phényl(méthylthio)cétène, diphénylcétène, pentafluorophénylcétène et 1-naphtylcétène) et on a déterminé les effets isotopiques de solvant (H_2O vs. D_2O) sur leur hydratation catalysée par l'ion hydroxyde, en solution aqueuse. Les valeurs obtenues sont toutes semblables, faibles et inverses (k_{HO}/k_{DO} = 0,76–0,97) comme on peut s'y attendre pour ces réactions rapides utilisant l'ion hydroxyde qui se produisent par une attaque nucléophile de l'hydroxyde sur le groupe carbonyle du cétène. L'amplitude caractéristique de ces effets isotopiques devrait s'avérer utile dans l'identification de nouveaux exemples de cette réaction.

Mots clés : cétènes, photolyse éclair, réaction de photo-Wolff, effets isotopique du solvant sur la consommation de l'ion hydroxyde.

[Traduit par la Rédaction]

Introduction

Solvent isotope effects on the hydration of ketenes to form carboxylic acids, eq. [1],

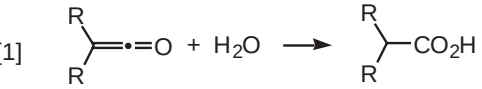

catalyzed by the hydronium ion, as well as on the uncatalyzed reaction, have proved to be useful in elucidating the mechanisms of these processes, and they have also served to help identify new examples (1). The same is not true of the hydroxide-ion-catalyzed reaction: we are aware of only one published determination of this isotope effect made prior to the present work, and that was done using a rather special substrate containing a second functional group that perturbed the isotope effect and gave it an atypical value (vide infra) (2).

Received December 10, 1998.

J. Andraos, Y. Chiang, S. J. Eustace, A. J. Kresge,[1] S. W. Paine, V. V. Popik, and K. Sung. Department of Chemistry, University of Toronto, Toronto, ON M5S 3H6, Canada.

[1]Author to whom correspondence may be addressed. Telephone: (416) 978-7259. Fax: (416) 978-7259. e-mail: akresge@chem.utoronto.ca

In the present paper we provide five unperturbed examples of this isotope effect, determined using the monofunctional ketene substrates phenyl(ethyl)ketene, **1**, phenyl(methylthio)-ketene, **2**, diphenylketene, **3**, pentafluorophenylketene, **4**, and 1-naphthylketene, **5**.

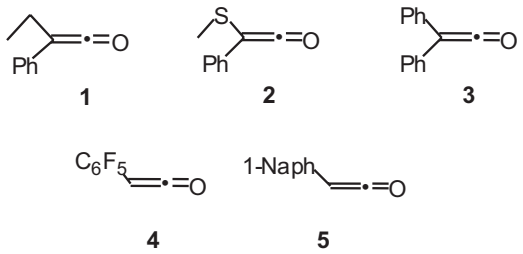

These ketenes were generated by photo-Wolff reactions, eq. [2],

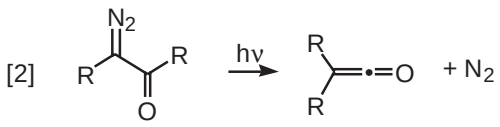

of the corresponding diazo compounds, α-diazobutyrophenone, **6**, *S*-methyl phenyldiazothioacetate, **7**, azibenzil, **8**, penta-

© 1999 NRC Canada

Can. J. Chem. Downloaded from www.nrcresearchpress.com by Peking University on 09/06/12
For personal use only.

Fig. 1. Relationship between sodium hydroxide concentration and observed first-order rate constants for the hydration of pentafluorophenylketene in aqueous solution at 25°C; O: H_2O, Δ: D_2O.

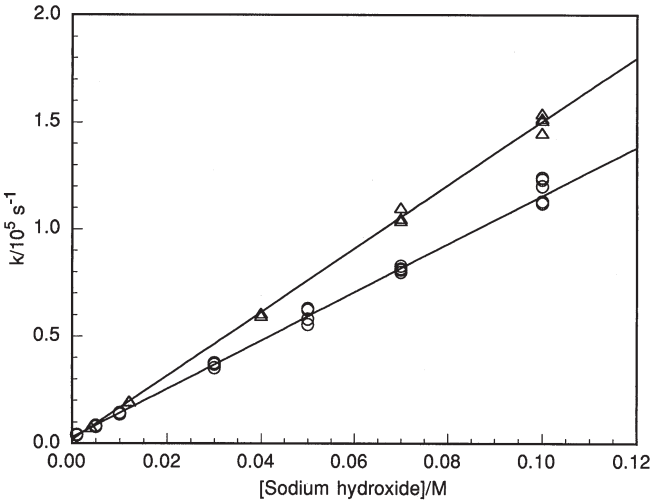

fluorobenzoyldiazomethane, **9**, and 1-naphthoyldiazomethane, **10**.

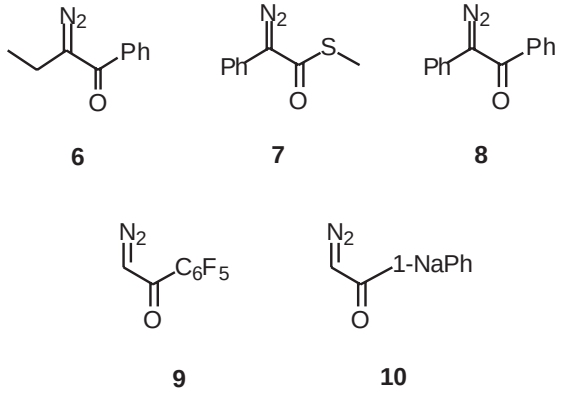

Because the reactions studied were fast, flash photolytic techniques were used to carry out rate measurements.

Experimental section

Materials

α*–Diazobutyrophenone*, **6**, was prepared by diazo group transfer from *p*-toluenesulfonyl azide to butyrophenone after the latter had been activated through introduction of an α-formyl group (3). Formylation was effected using ethyl formate as the formyl source and sodium hydride as the basic catalyst. The diazo compound, a yellow oil, was purified by column chromatography on silica gel using 80% chloroform – 20% hexane as the eluent. Its spectral properties are as follows: ^{1}H NMR (200 MHz, $CDCl_3$), δ/ppm: 7.50 (m, 5H, Ar), 2.57 (q, J = 7.4 Hz, 2H, CH_2), 1.20 (t, J = 7.4 Hz, 3H, CH_3); ^{13}C NMR (50 MHz, $CDCl_3$), δ/ppm: 189.4 (C=O), 137.8 (Ar), 131.2 (Ar), 128.4 (Ar), 127.0 (Ar), 68.3 (C=N_2), 17.0 (CH_2), 11.3 (CH_3); HRMS, M^+ for $C_{10}H_{10}N_2O$, *m/e*, calcd.: 174.0793; found: 174.0792.

Table 1. Sodium hydroxide catalytic coefficients and solvent isotope effects on ketene hydration in aqueous solution at 25°C.[a]

Substrate	k_{HO} / M^{-1} s^{-1}	k_{HO} / k_{DO}
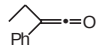	(6.05 ± 0.06) ×10^3	0.972 ± 0.012
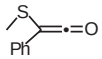	(1.89 ± 0.04) ×10^4	0.928 ± 0.026
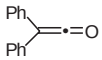	(4.64 ± 0.14) ×10^4	0.917 ± 0.051
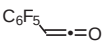	(1.13 ± 0.01) ×10^6	0.759 ± 0.009
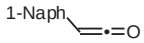	(1.18 ± 0.05) ×10^6	0.891 ± 0.063

[a]Ionic strength = 0.10 M.

Pentafluorobenzoyldiazomethane, **9**, has apparently been made before (4), but no details of its preparation nor of its spectral properties were given. It was synthesized here by treating pentafluorobenzoyl chloride with diazomethane. The product was a colorless crystalline solid, mp 45–46°C. Its spectral properties are as follows: IR (KBr), ν/cm^{-1} = 2123 (N≡N), 1650 (C=O); ^{1}H NMR (200 MHz, $CDCl_3$), δ/ppm: 5.71; ^{13}C NMR (50 MHz, $CDCl_3$), ^{19}F decoupled, ^{1}H not decoupled) δ/ppm: 176.8 (d, C=O), 144.3 (Ar), 142.7 (Ar), 137.6 (Ar), 113.3 (Ar), 60.1 (d, J = 204 Hz, C=N_2).

S-*Methyl phenyldiazothioacetate*, **7**, was made by diazo transfer from *p*-toluenesulfonyl azide to *S*-methyl phenylthioacetate in the presence of 1,8-diazobicyclo[5.4.0]undec-7-ene and 4-(*N,N*-dimethylamino)pyridine (5), and *azibenzil* was prepared by mercuric oxide oxidation of benzil monohydrazone (6*); 1-naphthoyldiazomethane* was a sample that had been prepared before (7). All other materials were best available commercial grades.

Kinetics

Flash photolytic generation of ketenes was performed using a conventional flash lamp system (8) and an excimer laser system (1*b*), operating at λ = 248 nm; these have already been described. With both systems, reaction mixtures were thermostatted at 25.0 ± 0.05°C. The ketene hydration reactions were followed by monitoring the decay of ketene absorbance at 250–270 nm for the phenyl-substituted substrates and at λ = 320–330 nm for the naphthyl derivative. All decays conformed well to the first-order rate law, and observed first-order rate constants were calculated by nonlinear least-squares fitting of exponential functions.

Results

Rates of hydration of the ketenes examined here were measured in dilute solutions of sodium hydroxide using H_2O and D_2O as the solvent. In all cases, a range of sodium hydroxide concentrations, usually spanning a variation of at least an order of magnitude, was employed. The ionic strength of these solutions was maintained at 0.10 M by adding sodium perchlorate as required. The data so obtained

© 1999 NRC Canada

Can. J. Chem. Downloaded from www.nrcresearchpress.com by Peking University on 09/06/12
For personal use only.

have been summarized, as supplementary material, in Table S1.[2]

As Fig. 1 illustrates, the observed first-order rate constants determined in this way are accurately proportional to sodium hydroxide concentration. Sodium hydroxide catalytic coefficients were therefore evaluated by linear least-squares analysis with proportional weighting, and solvent isotope effects were calculated as ratios of these catalytic coefficients. The results are listed in Table 1.

The sodium hydroxide catalytic coefficient for 1-naphthylketene in H_2O determined here, 1.18×10^6 M^{-1} s^{-1}, agrees well with that reported for this substrate before, 1.25×10^6 M^{-1} s^{-1} (7). The present values for diphenylketene, 4.64×10^4 M^{-1} s^{-1}, and phenyl(methylthio)ketene, 1.89×10^4 M^{-1} s^{-1}, are also consistent with previous determinations, 6.11×10^4 M^{-1} s^{-1} (9) and 3.09×10^4 M^{-1} s^{-1} (5), respectively.

Discussion

Each of the ketenes examined here reacts more rapidly in D_2O than in H_2O solutions of sodium hydroxide, and each consequently gives an inverse ($k_H/k_D < 1$) isotope effect. This is the expected direction for solvent isotope effects on hydroxide-ion-consuming reactions such as these. That follows from a model proposed by Gold and Grist (10), in which the hydroxide ion in aqueous solution is strongly solvated by three water molecules whose solvating O—H bonds are looser than the O—H bonds of bulk water. When such a hydroxide ion is consumed by reaction with a substrate, the solvating water molecules are transformed into bulk solvent, and they consequently move from a more loosely bound state to a more tightly bound state, thus producing an inverse isotope effect. This phenomenon has now been extensively documented (11).

The maximum magnitude of the solvent isotope effect on consumption of a hydroxide ion has been estimated as $k_{HO}/k_{DO} = 0.43$ (11*a*). The isotope effects observed here are much weaker than that, but they are on a rate process in whose transition state the hydroxide ion will be only partially consumed. The rates of the present reactions, moreover, are fast, and their transition states will consequently be especially reactant-like (12).

Another feature contributing to the weakness of the present isotope effects is the nucleophilic nature of the hydroxide ion plus ketene reaction (13): this generates negative charge on the ketene carbonyl oxygen atom, giving that atom alkoxide ion character, eq. [3]. Solvation of this charge, in much the same way as the hydroxide ion is solvated, then provides a normal component ($k_H/k_D > 1$) to the solvent isotope effect, which offsets the inverse factor given by hydroxide ion desolvation.

[3] 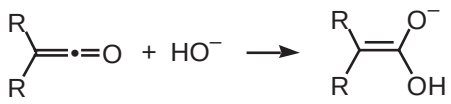

The present inverse isotope effects are quite different from the value, $k_{HO}/k_{DO} = 1.87$, reported for the only previous example of a solvent isotope effect on a ketene plus hydroxide ion reaction (2). The substrate in that case was acetylketene, **11**, and it was argued then that the acetyl group assisted hydroxide ion attack, as evidenced by its strong rate acceleration, by allowing strong hydrogen bond formation between the hydroxyl group and the acetyl oxygen atom in the transition state of this reaction, **12**, eq. [4]:

[4] 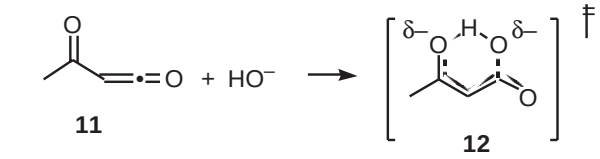

11 **12**

strong hydrogen bond formation is known to produce sizeable isotope effects in the normal direction (14). The inverse nature of the presently determined isotope effects reinforces this explanation.

It would seem fair to conclude, therefore, that solvent isotope effects on the reaction of hydroxide ion with simple, monofunctional, short-lived ketenes will be weakly inverse. This characteristic magnitude should be useful in identifying this reaction.

Acknowledgement

We are grateful to the Natural Sciences and Engineering Research Council of Canada for financial support of this research.

References

1. (*a*) S.H. Kabir, H.R. Seikaly, and T.T. Tidwell. J. Am. Chem. Soc. **101**, 1059 (1979); A.D. Allen and T.T. Tidwell. J. Am. Chem. Soc. **109**, 2774 (1987); A.D. Allen, A. Stevenson, and T.T. Tidwell. J. Org. Chem. **54**, 2843 (1989); J. Andraos and A.J. Kresge. J. Photochem. Photobiol. A: **57**, 165 (1991); (*b*) J. Andraos, Y. Chiang, C.-G. Huang, A.J. Kresge, and J.C. Scaiano. J. Am. Chem. Soc. **115**, 10605 (1993); (*c*) J. Andraos, A.J. Kresge, and N.P. Schepp. Can. J. Chem. **73**, 539 (1995); J. Andraos, Y. Chiang, A.J. Kresge, and V.V. Popik. J. Am. Chem. Soc. **119**, 8417 (1997); Y. Chiang, A.J. Kresge, V.V. Popik, and N.P. Schepp. J. Am. Chem. Soc. **119**, 10203 (1997).
2. Y. Chiang, H.-X. Guo, A.J. Kresge, and O.S. Tee. J. Am. Chem. Soc. **118**, 3386 (1996).
3. M. Regitz and G. Maas. Diazo compounds, properties and synthesis. Academic Press, New York, 1986, Chap. 13.
4. A.L. Fridman and N.A. Kolobov. Zh. Org. Khim. **12**, 228 (1976).
5. J. Jones, Jr. and A.J. Kresge. J. Org. Chem. **57**, 6467 (1992).

[2] Table S1 may be purchased from: The Depository of Unpublished Data, Document Delivery, CISTI, National Research Council of Canada, Ottawa, ON K1A OS2, Canada.

© 1999 NRC Canada

6. C.D. Nenitzescu and E. Solomonica. Organic synthesis. Collect. Vol. II. Wiley, New York. 1943. p. 496.
7. Y. Chiang, A.J. Kresge, and V.V. Popik. J. Am. Chem. Soc. **117**, 9165 (1995).
8. Y. Chiang, M. Hojatti, J.R. Keeffe, A.J. Kresge, N.P. Schepp, and J. Wirz. J. Am. Chem. Soc. **109**, 4000 (1987).
9. A.D. Allen, A.J. Kresge, N.P. Schepp, and T.T. Tidwell. Can. J. Chem. **65**, 1719 (1987).
10. V. Gold and S. Grist. J. Chem. Soc. Perkin Trans. 2, 89 (1972).
11. (*a*) A.J. Kresge, R.A. More O'Ferrall, and M.F. Powell. *In* Isotopes in organic chemistry. Vol. 7. *Edited by* E. Buncel and C.C. Lee. Elsevier, Amsterdam. 1987, pp. 177–273; (*b*) M.W. Washabaugh and W.P. Jencks. J. Am. Chem. Soc. **111**, 683 (1989).
12. G.S. Hammond. J. Am. Chem. Soc. **77**, 334 (1955).
13. T.T. Tidwell. Ketenes. Wiley–Interscience, New York. 1995. pp. 571–585.
14. M.M. Kreevoy and T.M. Liang. J. Am. Chem. Soc. **102**, 3315 (1980).

Can. J. Chem. Downloaded from www.nrcresearchpress.com by Peking University on 09/06/12
For personal use only.

© 1999 NRC Canada

Biotransformation of organic sulfides. Part 12. Conversion of heterocyclic sulfides to chiral sulfoxides by *Helminthosporium* sp. NRRL 4671 and *Mortierella isabellina* ATCC 42613

Herbert L. Holland, Carl D. Turner, Peter R. Andreana, and Doan Nguyen

Can. J. Chem. Downloaded from www.nrcresearchpress.com by University Town Library of Shenzhen on 09/05/12
For personal use only.

Abstract: The enantioselective oxidation of a series of heterocyclic prochiral sulfides to chiral sulfoxides has been examined using the fungal biocatalysts *Helminthosporium* species NRRL 4671 and *Mortierella isabellina* ATCC 42613. Methylthiofuranyl and -thiophenyl substrates gave (*S*)-configuration products in low to moderate enantiomeric purity on biotransformation with *H.* species, but pyridyl sulfides with the nitrogen atom located at an optimal distance of 8–10 Å from the sulfur centre gave (*S*) sulfoxides of high enantiomeric purity. The biotransformation of appropriately substituted benzothiane substrates by *M. isabellina* also gave products of high enantiomeric purity, but with (*R*) configuration at sulfur. The acceptability of the substrate and the configuration of sulfur oxidation by both *H.* species and *M. isabellina* for the range of substrates examined were found to be consistent with predictions based on cubic space models for these oxidations.

Key words: bioconversion, biotransformation, *Helminthosporium*, *Mortierella isabellina*, sulfide, sulfoxide.

Résumé : Utilisant les biocatalyseurs extraits des champignons *Helminthosporium* espèce NRRL 4671 et *Mortierella isabellina* ATCC 42613, on a étudié l'oxydation énantiosélective d'une série de sulfures hétérocycliques prochiraux en sulfoxydes chiraux. Lors des biotransformations à l'aide de l'espèce *H.* , les substrats méthylthiofuranyle et méthylthiophényle conduisent à des produits de configuration (*S*), avec des puretés énantiomériques qui vont de faibles à modérées; toutefois, les sulfures de pyridyle comportant un atome d'azote situé à une distance optimale de 8 à 10 Å du soufre conduisent à des sulfoxydes (*S*) de pureté énantiomérique élevée. La biotransformation de substrats benzothiane portant des substituants appropriés par *M. isabellina* fournit aussi des produits de pureté énantiomérique élevée; la configuration au niveau du soufre est toutefois (*R*). On a trouvé que, pour l'ensemble des produits étudiés, l'acceptabilité du substrat et la configuration du soufre oxydé par les espèces *H.* ainsi que par *M. isabellina* est en accord avec les prédictions faites sur la base de modèles spatiaux cubiques pour ces oxydations.

Mots clés : bioconversion, biotransformation, *Helminthosporium*, *Mortierella isabellina*, sulfure, sulfoxyde.

[Traduit par la Rédaction]

Introduction

Chiral sulfoxides have been used for many years as asymmetric starting materials for chemical synthesis (1–3). The enantioselective oxidation of prochiral sulfides by biocatalytic methods is one of the more versatile routes for the preparation of these chiral synthons (4, 5), and sulfoxides made in this way have been used in the preparation of (inter alia) chiral mevinic acid-type hypocholestemic agents (6, 7), cardiovascular agents related to the anti-anginal verapamil (8), and amino acid sulfoxides (9, 10).

Received January 6, 1999.

H.L. Holland,[1] C.D. Turner, P.R. Andreana, and D. Nguyen. Department of Chemistry, Brock University, St. Catharines, ON L2S 3A1, Canada.

[1]Author to whom correspondence may be addressed. Telephone: (905) 688-5550, ext. 3403. Fax: (905) 682-9020. e-mail: holland@chemiris.labs.brocku.ca

We have developed the use on a synthetic scale of the fungal biocatalysts *Helminthosporium* species NRRL 4671 for the preparation of phenyl alkyl and related sulfoxides of (*S*) configuration (5), and *Mortierella isabellina* ATCC 42613 for the oxidation of similar substrates to (*R*) sulfoxides (11, 12). These reactions, catalysed by oxygenase enzymes (13), are carried out using whole-cell methodology. This requirement is dictated by the intractable nature of the membrane-bound oxygenase enzymes, and by their (presumed) extensive cofactor requirements. A further consequence of this is the limitation of structural information for these enzymes, often resulting in difficulties in the prediction of suitable substrates and reaction products for biotransformations of this type: no data are available on the nature of the sulfoxidase enzymes from *Helminthosporium* or *M. isabellina*, and all attempts to date to isolate these enzymes have failed to produce viable catalysts. To address this problem we have developed predictive models based on cubic space descriptors for the sulfoxidation reactions carried out by both *Helminthosporium* species (5) and *Mortierella isabellina* (12), shown in Figs. 1 and 2, respectively. Such "active site" mod-

 © 1999 NRC Canada

Fig. 1. Model for sulfoxidation by *Helminthosporium* sp. and structurally comparable conformations of **16** and **17**.

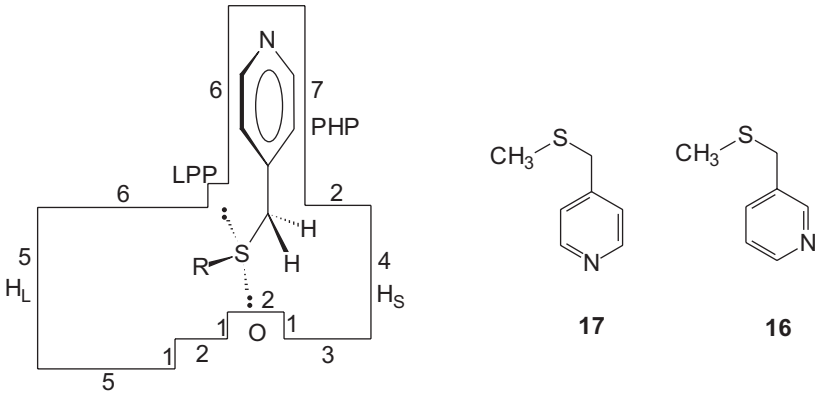

Model for oxidation by *Helminthosporium*
H_S: small hydrophobic pocket
H_L: large hydrophobic pocket
PHP: polar hydrophobic pocket
P: polar binding site
LPP: lone pair pocket
O: oxidation centre
dimensions in Angstrom

Fig. 2. Model for sulfoxidation by *Mortierella isabellina*.

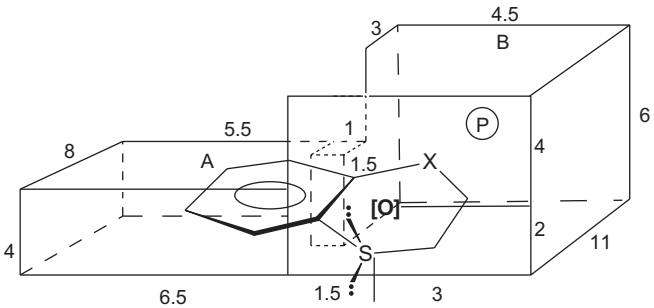

Model for oxidation by *M. isabellina*
A: aromatic binding pocket
B: aliphatic binding region
P: polar binding site
[O]: oxidising site
dimensions in Angstrom

els have been developed for a number of synthetically valuable enzymes, including horse liver alcohol dehydrogenase (14), lipase YS from *Pseudomonas fluorescens* (15), and *Candida rugosa* lipase (16), and have also been proposed for the analysis of whole-cell catalysed reactions for which no isolated enzymes are available, including steroid hydroxylations (17) and hydroxylations carried out by *Beauveria bassiana* (17). These models are widely used to predict and correlate substrate–product relationships for reactions catalysed by these enzymes and whole-cell biocatalysts. The model for *M. Isabellina* can also be applied to other reactions catalysed by the sulfoxidase enzyme, such as benzylic hydroxylation and epoxidation of suitable substrates (12), but the *Helminthosporium* system does not appear to possess substantial hydroxylase activity (18).

A feature of the models that we have proposed for sulfoxidations carried out by *H.* species and *M. isabellina* is the presence of a binding site for interaction with a polar site or group of the substrate. We have now specifically examined this feature of the models by the use of a range of sulfide substrates possessing heteroatom substituents at a defined distance from the site of oxidation, and present below results that confirm the location of such polar binding sites in the models for sulfoxidation by *H.* species and *M. isabellina*.

Results and discussion

The results of the biotransformations of substrates **1**–**26** are presented in Tables 1 and 2. In all cases, yields refer to isolated material and enantiomeric excesses are for homogenous product material prior to subsequent purification (e.g., crystallization) that might alter this value. The assignment of product structures relied heavily on NMR analysis, ^{1}H and ^{13}C spectral data being diagnostic of the oxidation state at sulfur. These data, together with supporting mass spectral data, are presented in the experimental section. The predominant configuration and enantiomeric excesses (e.e.) of the sulfoxide products were determined by analysis of their ^{1}H NMR spectra in the presence of the chiral shift reagents (*S*)-α-methoxyphenylacetic acid (MPAA) or (*R*)-*N*-(3,5-dinitrobenzoyl)-α-methylbenzylamine (DBMB), or by chiral stationary phase HPLC where appropriate. Use of the NMR shift reagents gave consistent, configurationally dependent shifts of signals for protons α to sulfur that have been correlated with data from sulfoxides of independently established configuration (19–21). Addition of MPAA, for example, causes the S-methyl signals of methyl sulfoxides to appear as two singlets with Δδ 0.02–0.03 ppm, cleanly resolved at 300 MHz: in over 50 such examples studied to date (5) the signal from the protons of the (*S*) enantiomer is at the higher field. The configurational assignments of Tables 1 and 2 are

© 1999 NRC Canada

Can. J. Chem. Downloaded from www.nrcresearchpress.com by University Town Library of Shenzhen on 09/05/12
For personal use only.

Can. J. Chem. Downloaded from www.nrcresearchpress.com by University Town Library of Shenzhen on 09/05/12
For personal use only.

Table 1. Biotransformations of sulfides **1**–**14** by *Helminthosporium*.

Substrate	Sulfoxide (% yield, configuration, e.e.)	Sulfone (%))
1	8, (*S*), 37	
2	78, (*S*), 16	
3	8, (*S*), 40	
4	45, (*S*), 68	
5	55, (*S*), 60	2
6	70, (*S*), 44	1
7	85, (*S*), 60	
8	99, (*S*), 22	0.4
9	30, (*S*), 40	
10	51, (*S*), 66	
11	31, (*S*), 75	1
12	22, (*S*), 6	
13	35, (*S*), 48	
14	37, (*S*), 34	

Table 2. Biotransformations of sulfides **15**–**27** by *Helminthosporium* and *M. isabellina*.

Substrate	Sulfoxide (% yield, configuration, e.e.)		Sulfone (%))
	Helminthosporium	*M. isabellina*	
15	56, (*S*), 73	53, (*R*), 42	
16	82, (*S*), >98	80, (*R*), 85	3 (*H.* sp.)
17	84, (*S*), 83	34, (*R*), 62	
18	31, (*S*), 43	<5	2 (*H.* sp.)
19	68, (*S*), 62 [a]	87, (*R*), 48 [a]	
20	42, (*S*), 5	34, (*R*), 47	
21	81	77	
22	92, (*S*), 11	72, (*R*), 40†	5 (*M.i.*)
23	6, (*S*), 25	45, (*R*), 88	
24	8, (*S*), 6	73, (*R*), 54	
25	4, (*R*), 2	52, (*R*), 81	
26	15, (*R*), 3	58, (*R*), 66	
27	34, (*S*), 7	89, (*R*), 60	

[a]Data from ref. 25.

in full agreement with the complexation model proposed for interaction of (*S*)-MPAA with sulfoxides (19).

Sulfone products were also obtained from a small number of substrates. In those cases, the enantiomeric purity of sulfoxide is unlikely to be substantially affected by the formation of sulfone as (*a*) the levels of sulfone were very low (≤5%), and (*b*) control experiments in which racemic sulfoxides were incubated with *Helminthosporium* have failed to detect enantiomeric enrichment of sulfoxide or the formation of substantial amounts of sulfone. This suggests that production of sulfone from sulfide occurs by a random, non-stereoselective reoxidation of the intermediate sulfoxide without the latter leaving the active site of the enzyme. Control experiments with autoclaved (deactivated) fungal biocatalyst indicate that conversion of sulfide to sulfoxide by autooxidation under the conditions of the biotransformation accounts for <2% of the sulfoxide product.

The models for oxidation of sulfides by *Helminthosporium* sp. and *M. isabellina* are presented in simplified versions in Figs. 1 and 2. The complete three-dimensional version of the model for *H.* sp. has been discussed in detail elsewhere (5); the top view of this model, presented in Fig. 1, is sufficiently detailed for the present analysis. A full analysis of the model for *M. isabellina*, shown in Fig. 2, has also been previously discussed (12). A feature of both these models is the presence of a site, P, specific for interaction with a polar group of the substrate. These sites are located in the polar hydrophobic pocket, PHP, of the *Helminthosporium* model at an optimal distance of 8–10 Å from the site of oxidation, and in the aliphatic binding region, B, of the model for *M. isabellina*.

The biotransformation of the heterocyclic methyl sulfides **1**–**14** (Table 1) and **15**–**17** (Table 2) by *Helminthosporium* was undertaken in order to investigate (*a*) the spatial relationship between a heteroatom of the substrate and the site of oxidation, and hence (*b*) the ability of a heteroatom to interact at site P of the model for oxidation by this biocatalyst. In all cases, sulfoxides of predominantly (*S*) configuration were obtained, and the results clearly demonstrate that good yields and the highest enantiomeric purities of product are obtained for those substrates (e.g., **16** and **17**, Table 2) in which the heteroatom is located at the optimal distance from the site of oxidation. Figure 1 shows the application of the sulfoxidation model to the biotransformation of 4-methylthiomethylpyridine (**17**) and illustrates the conformations of **16** and **17** that allow the optimal distance between the heteroatom and the site of oxidation to be attained.

The importance of the 8–10 Å separation between these two sites for efficient sulfoxidation by *Helminthosporium* is confirmed by analysis of the results of Table 2. The biotransformations of the five-membered heterocycles (**5**–**8** and **10**) and that of the carbocyclic substrate **11** illustrate that the presence of the heteroatom has little or no positive effect on the outcome of the biotransformation of the former group of substrates, whereas comparison of the results from the biotransformations of the thiomethylpyridines **15**–**17** with that of the corresponding carbocyclic sulfide **18** and benzyl methyl sulfide (**19**) (Table 2) confirms the spatial significance of the heteroatom: those substrates with the optimal spatial relationship of nitrogen to sulfur (**16** and **17**) are converted to sulfoxide in highest yield and e.e. A similar relationship exists in the case of *Helminthosporium*-catalysed oxidations of *ortho*, *meta*, and *para*-substituted benzyl methyl sulfides, where only the latter two substrate groups can be converted to sulfoxide in high e.e. (22). The influence of an electronic substituent effect on the outcome of sulfoxidation is possible for substrates **1**–**4**, **9**, **12**, and **13**, but no clear trends are apparent that would suggest such an effect, and in the absence of any information on the detailed mechanism of sulfoxidation the interpretation of any such effect would be difficult.

The pyridyl substrates **15**–**17** are converted to (*R*) sulfoxides by *M. isabellina* (Table 2), and the results generally confirm the earlier finding that a polar substituent on the aromatic ring does not have a profound effect on the outcome of this biotransformation (11, 12). The importance of the aromatic ring for effective biotransformation by *M. isabellina* is, however, emphasized by a comparison of the results from

© 1999 NRC Canada

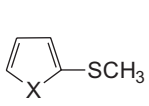

1, X = O
2, X = S

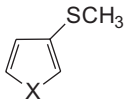

3, X = O
4, X = S

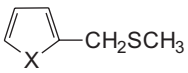

5, X = O
6, X = S

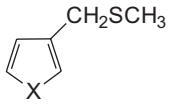

7, X = O
8, X = S

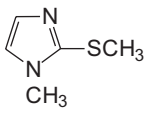

9

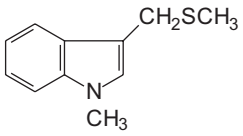

10

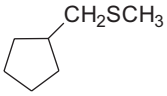

11

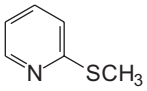

12

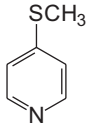

13

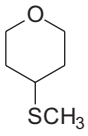

14

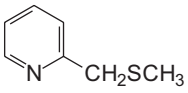

15

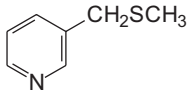

16

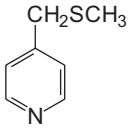

17

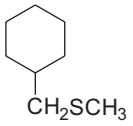

18

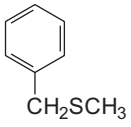

19

substrates **15**–**17** with that of the carbocycle **18**: the latter was converted to sulfoxide in only trace amount.

With the exception of the symmetrical sulfide **21**, the bicyclic substrates **20**–**27** were generally poor substrates for biotransformation by *Helminthosporium*, a result consistent with the model shown in Fig. 1 for oxidation by this biocatalyst: only **21** can be accommodated by the model with the aromatic ring in the PHP pocket and the sulfur atom close to the site of oxidation. Biotransformation of substrates **20**–**27** by *M. isabellina* was undertaken in order to investigate the spatial relationship between site P of the aliphatic binding region B (Fig. 2) and the site of oxidation by this biocatalyst. The positive effect of a heteroatom at position 4 of the heterocyclic ring on the stereoselectivity of sulfoxidation by *M. isabellina* is evident from a comparison of the outcome of the biotransformations of substrates **23**–**26** with those of substrates **20** and **27**. In all cases, (*R*)-configuration products of higher optical purity were obtained from the former group, and in two instances (sulfoxides from **23** and **25**) enantiopure materials could be obtained by a simple crystallization of the biotransformation products. In both **23** and **25**, the heteroatom substituent remote from sulfur is capable of acting as a hydrogen bond acceptor as shown in Fig. 2, and we postulate that this or a similar interaction with a suitable group in the enzyme's active site may be responsible for an enhancement of substrate binding, leading to an increase in the stereoselectivity of oxidation of these substrates.

Given careful choice of the nature and position of substitution present in the substrate, it is apparent that sulfoxides of high optical purity with (*R*) or (*S*) configuration may be obtained in good yield by biotransformations using *Mortierella isabellina* or *Helminthosporium* sp., respectively. This analysis facilitates the exploitation of these processes for the production of synthetically useful chiral sulfoxides.

© 1999 NRC Canada

Can. J. Chem. Downloaded from www.nrcresearchpress.com by University Town Library of Shenzhen on 09/05/12
For personal use only.

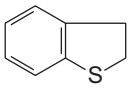

20

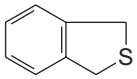

21

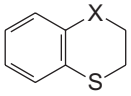

22, X = CH_2
23, X = O
24, X = S
25, X = NH
26, X = CH_3

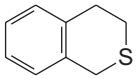

27

Experimental

Materials and methods

Melting points were determined on a Kofler hot stage and are uncorrected. The ^{1}H NMR spectra were recorded on a Bruker Avance series 300 spectrometer in $CDCl_3$ using residual $CHCl_3$ as the internal standard; chemical shifts are reported in parts per million (δ) and the signals are quoted as s (singlet), d (doublet), t (triplet), q (quartet), or m (multiplet). The ^{13}C NMR spectra were recorded at 75 MHz in $CDCl_3$ solution on the above spectrometer. Mass spectra were obtained in EI mode (unless otherwise stated) using a Kratos 1S spectrometer. IR spectra were obtained using a Mattson Research Series FTIR spectrometer. Optical rotations were recorded at ambient temperature in the stated solvent using a Rudolph Autopol 3 polarimeter. Enantiomeric excess (e.e.) was determined by ^{1}H NMR analysis in the presence of three equivalents of (*S*)-(+)-α-methoxyphenylacetic acid (MPAA) (19) or two equivalents of (*R*)-(–)-*N*-(3,5-dinitrobenzoyl)-α-methylbenzylamine (DBMB) (20), or by chiral stationary phase HPLC as described below. TLC was performed on Merck silica gel F_{254} plates, 0.2 mm, and column chromatography used Merck silica gel, 230–400 mesh. *Mortierella isabellina* ATCC 42613 and *Helminthosporium* species NRRL 4671 were maintained on malt agar slopes, grown at 27°C and stored at 4°C.

Preparation of substrates

Substrates **9**, **12**, and **13** were prepared by reaction of the appropriate thiol (1 equiv.), sodium ethoxide (1 equiv.), and iodomethane (1.5 equiv.) in the standard manner (23). Compounds **5**–**8**, **10**, **11**, and **14**–**18** were prepared starting from the appropriate alcohol or chloride using sodium thiomethylate, by the general procedure described below for **15**. The following were prepared by the published procedures: **20** (24), **21** (24), **22** (25), **23** (26), **24** (27), **25** (28), and **27** (29). All substrates gave spectral (IR, NMR, and MS) data consistent with their structures.

*2-Methylthiomethyl pyridine (**15**)*

A solution of 2-pyridyl carbinol (5.0 g, 45.8 mmol) in 75 mL dry THF under argon was treated with 1.1 equiv. of triethylamine (7.03 mL, 50.5 mmol) and the mixture was cooled to 0°C. Methanesulfonyl chloride (5.51 g, 48.1 mmol) was then added dropwise with stirring and the reaction mixture allowed to warm to room temperature. Stirring was continued for a further 1.5 h, and the solid was then removed by filtration. In a separate flask, sodium metal (1.16 g, 50.4 mmol) was dissolved in 100 mL absolute ethanol, and methanethiol (2.64 g, 55.0 mmol) was passed into the ethanolic solution. The THF solution of mesylate prepared earlier was then added directly to the preformed sodium methanethiolate solution via cannula, and the reaction mixture allowed to stir overnight. Distilled water (100 mL) was added and the mixture extracted with ethyl acetate (2 × 100mL). The combined organic layers were washed with saturated sodium bicarbonate solution (2 × 50 mL) and water, and then dried. The solvent was removed in vacuo, and the product purified on silica gel (EtOAc) to give 82% isolated yield of an oil; ^{1}H NMR δ: 2.06 (3H, s), 3.80 (2H, s), 7.16 (1H, ddd,), 7.36 (1H, d), 7.66 (1H, td), and 8.53 (1H, m) ppm; ^{13}C NMR δ: 15.5, 40.4, 122.3, 123.4, 137.1, 149.5, and 158.9 ppm; MS *m*/*z* (%): 139(4), 124(4), 93(100); HRMS, M^+ calcd. for C_7H_9NS: 139.04557; found: 139.04633.

*2-Methylthiofuran (**1**)*

Furan (2.38 g, 35.0 mmol) was dissolved in dry THF (75 mL) under an argon atmosphere and the solution was cooled to 0°C. A solution of *n*-butyllithium in hexane (35.0 mmol, 14.0 mL, 2.5 M) was added dropwise with stirring, followed by the addition of dimethyldisulfide (35.0 mmol, 3.15 mL), and the reaction mixture was then stirred for 2 h at 0°C. The mixture was allowed to warm to room temperature, an equal amount of distilled water was added, the layers separated, and the aqueous layer extracted with ether (2 × 50 mL). The combined organic layers were dried and the solvent was carefully removed in vacuo to give a volatile oil (2.51 g, 63%); ^{1}H NMR δ: 2.41 (3H, s), 6.38 (1H, m), 6.44 (1H, d), and 7.48 (1H, d) ppm; ^{13}C NMR δ: 19.2, 111.8, 114.7, 145.22, and 147.8 ppm; MS *m*/*z* (%): 114(100), 99(28), 83(23), 71(23); HRMS, M^+ calcd. for C_5H_6OS: 114.01394; found: 114.01402.

*2-Methylthiothiophene (**2**)*

Thiophene (4.2 g, 50.0 mmol) was dissolved in dry THF (50 mL) under an argon atmosphere and the solution was cooled to –10°C. A solution of *n*-butyllithium in hexane (1.6 M, 45.0 mmol, 28.1 mL) was added with stirring, and the reaction was kept between –5 and 0°C for 1.5 h and then cooled to –10°C. Dimethyldisulfide (4.1 mL, 45.0 mmol) was added slowly and the reaction stirred at –10°C for a further 1 h, whereupon water was added and the reaction mixture was allowed to warm to room temperature. The two layers were separated and the aqueous layer extracted with ether (75 mL). The combined organic layers were washed with saturated sodium bicarbonate (2 × 50 mL), brine (50 mL), dried, and the solvent was removed in vacuo to give a yellow oil (3.60 g, 67%); ^{1}H NMR δ: 2.48 (3H, s), 6.94 (1H, dd), 7.06 (1H, d), and 7.28 (1H, dd) ppm; ^{13}C NMR δ: 22.6, 127.8, 128.3, 131.4, and 137.6 ppm; MS *m*/*z* (%): 130(100), 115(61), 97(2), 71(11); HRMS, M^+ calcd. for $C_5H_6S_2$: 129.99109; found: 129.99178.

Can. J. Chem. Downloaded from www.nrcresearchpress.com by University Town Library of Shenzhen on 09/05/12
For personal use only.

© 1999 NRC Canada

Can. J. Chem. Downloaded from www.nrcresearchpress.com by University Town Library of Shenzhen on 09/05/12
For personal use only.

*3-Methylthiofuran (**3**)*

A solution of 3,4-dibromofuran (30) (5 g) in dry ether (50 mL) was cooled to –78°C, then treated with a solution of *tert*-butyllithium (13.0 mL, 1.7 M in pentane). The reaction mixture was stirred at –78°C for a further 30 min, then dimethyldisulfide (2.08 g) was added dropwise and the mixture was stirred for 1 h before warming to room temperature, where it was then stirred for a further 2 h. The reaction mixture was cooled to 0°C, quenched with saturated ammonium chloride solution, and then extracted with ether (2 × 40 mL). The combined organic extracts were dried and the solvent was removed in vacuo to give 3-bromo-4-methylthiofuran (70%), a solution of which (3 g) in dry ether (50 mL) was treated at –78°C with a solution of *tert*-butyllithium (10. 9 mL, 1.7 M in pentane). The reaction mixture was stirred for 1 h, allowed to reach 0°C, quenched with saturated ammonium chloride solution, and the product was then extracted into ether (2 × 40 mL). The combined organic extracts were dried and the solvent was removed in vacuo to give 1.4 g (73%) of an oil; ^{1}H NMR δ: 2.38 (3H, s), 6.44 (1H, br s), 7.37 (1H, br s), and 7.47 (1H, br s) ppm; ^{13}C NMR δ: 18.8, 112.8, 141.6, 141.9, and 143.93 ppm; MS *m*/*z* (%): 114(29), 99(100), 86(30), 71(25).

*3-Methylthiothiophene (**4**)*

3-Bromothiophene (1 g, 6.13 mmol) was dissolved in dry ether (30 mL) under an argon atmosphere, and the solution cooled to –78°C. A solution of *tert*-butyllithium in pentane (3.6 mL, 1.7 M, 6.13 mmol) was added dropwise with stirring and the reaction mixture was stirred at –78°C for a further 30 min. Dimethyldisulfide (0.57 g, 6.13 mmol) was then added dropwise and the reaction mixture stirred for 1 h before warming to room temperature, where it was stirred for a further 2 h. The mixture was then cooled to 0°C, quenched with saturated ammonium chloride solution, and extracted with ether (2 × 40 mL). The combined organic extracts were dried and the solvent was removed in vacuo to give an oil; ^{1}H NMR δ: 2.50 (3H, s), 7.0 (2H, br s), and 7.33 (1H, br s) ppm; ^{13}C NMR δ: 18.1, 119.7, 126.7, 128.4, and 134.6 ppm; MS *m*/*z* (%): 130(78), 115(100); HRMS, M^+ calcd. for $C_5H_6S_2$: 129.99109; found: 129.99149.

N-*Methyl-2,3-dihydrobenzo-1,4-thiazine (**26**)*

2,3-Dihydrobenzo-1,4-thiazine (**25**) (2.5 g, 16.6 mmol) was dissolved in dichloromethane (50 mL) and 1 M aqueous sodium hydroxide (6.64 g, 0.166 mol) was added with vigorous stirring. A catalytic amount of tetra *n*-butylammonium bromide was added, followed by iodomethane (23.6 g, 0.166 mol). The reaction mixture was stirred vigorously for a further 7 days and the organic layer separated. The aqueous layer was extracted with dichloromethane (1 × 50 mL), the combined organic layers were dried, and the solvent was removed in vacuo. The resulting brown oil was purified on silica gel (5% EtOAc – 95% hexane) to give 0.68 g of a yellow oil (25%); ^{1}H NMR δ: 2.87 (3H, s), 3.00 (2H, m), 3.46 (2H, m), 6.60 (2H, m), and 6.98 (2H, m) ppm; ^{13}C NMR δ: 26.9, 40.6, 52.1, 113.0, 119.1, 119.9, 126.4, 127.9, 129.9, and 145.3 ppm; MS *m*/*z* (%): 165(100), 150(62), 136(54), 91(31); HRMS, M^+ calcd. for $C_9H_{11}NS$: 165.06122; found: 165.06143.

Preparation of racemic sulfoxides from 1–27

Racemic sulfoxide standards were prepared from sulfides **1**–**27** by oxidation using sodium *meta*-periodate: to a stirred methanolic solution (5 mL) of sulfide (1.0 mmol) at 0°C was added dropwise an aqueous solution (5 mL) of sodium *m*-periodate (1.0 mmol). The reaction mixture was stirred at 0°C for 1 h and then allowed to warm to room temperature, whereupon it was extracted with dichloromethane (3 × 15 mL), the combined organic layers were dried, and the solvent was evaporated to leave the sulfoxide, which was sufficiently pure for use as a standard for chiral shift reagent ^{1}H NMR or chiral stationary phase HPLC analysis.

Biotransformations with *Helminthosporium* sp.

Two slopes of *Helminthosporium* sp. NRRL 4671 were used to inoculate 15 1-L Erlenmeyer flasks each containing 200 mL of an autoclaved medium composed of V-8 vegetable juice (200 mL) and calcium carbonate (3 g) per litre of distilled water, adjusted to pH 7.2 prior to sterilization by the addition of 1 M sodium hydroxide. The flasks were allowed to stand overnight at 27°C, were then placed on a rotary shaker at 180 rpm, and growth continued for a further 72 h at 27°C. The fungus was then harvested by filtration and resuspended in 15 1-L Erlenmeyer flasks each containing 200 mL of distilled water. Substrate (1 g in 30 mL of 95% ethanol) was then distributed among the flasks, which were replaced on the rotary shaker at 180 rpm, 27°C, for a further 48 h. The fungus and aqueous medium were then separated by filtration as before, the aqueous medium was extracted with dichloromethane (continuous extraction, 72 h), and the fungus discarded. Concentration of the medium extract gave the crude product, which was examined by TLC, using ether or 10% methanol – ether as solvent, and then submitted to flash chromatography using a hexane – ethyl acetate or benzene–ether 10% stepwise gradient, followed by an ethyl acetate – methanol or ether–methanol 5% stepwise gradient if necessary. The yields and e.e. values quoted in the tables refer to purified, homogeneous material and, unless otherwise stated, arise from the combination of (only) homogeneous column fractions without further purification (e.g., crystallization) that could lead to changes in stereochemical enrichment values (31). Spectral and optical rotation data for products are listed below.

Biotransformations with *Mortierella isabellina*

Two slopes of *M. isabellina* ATCC 42613 were used to inoculate 15 1-L Erlenmeyer flasks each containing 200 mL of an autoclaved medium composed of glucose (40 g), yeast extract (5 g), sodium chloride (5 g), dibasic potassium phosphate (5 g), and soya flour (5 g) per litre of distilled water. Subsequent manipulations were exactly as described in the preceding paragraph except that the fungal mycelia were harvested by centrifugation rather than filtration.

Characterization of products

Spectral data for the biotransformation products are listed under the appropriate substrate heading. All products gave satisfactory HRMS data for the establishment of elemental composition. Isolated yields are listed in Tables 1 and 2.

© 1999 NRC Canada

Can. J. Chem. Downloaded from www.nrcresearchpress.com by University Town Library of Shenzhen on 09/05/12
For personal use only.

2-Methylthiofuran (***1***): *2-methylsulfinylfuran*; oil, R_f 0.14 (Et_2O); ^{1}H NMR δ: 2.96 (3H, s), 6.53 (1H, dd), 6.94 (1H, d), and 7.66 (1H, s) ppm; ^{13}C NMR δ: 38.9, 111.8, 115.6, 147.1, and 153.0 ppm; MS *m*/*z* (%): 130(48), 115(78), 114(80), 99(28), 83(100). From *H*. sp., $[\alpha]_D$ –10.7 (*c* 1, EtOH), (*S*), e. e. 37% (DBMB, ^{1}H NMR SCH_3 δ 2.95 (major) and 2.97 (minor) ppm).

2-Methylthiothiophene (***2***): *2-methylsulfinylthiophene*; oil, R_f 0.14 (Et_2O); ^{1}H NMR δ: 2.93 (3H, s), 7.12 (1H, m), 7.48 (1H, dd), and 7.64 (1H, m) ppm; ^{13}C NMR δ: 44.8, 127.8, 129.7, 131.3, and 147.7 ppm; MS *m*/*z* (%): 146(35), 131(100), 115(13), 99(39). From *H*. sp. $[\alpha]_D$ –12.1 (*c* 1, EtOH), (*S*), e.e. 16% (MPAA ^{1}H NMR SCH_3 δ 2.915 (major) and 2.93 (minor) ppm).

3-Methylthiofuran (***3***): *3-methylsulfinylfuran*; oil, R_f 0.14 (Et_2O); ^{1}H NMR δ: 2.84 (3H, s), 6.74 (1H, br s), 7.57 (1H, t), and 7.81 (1H, br s) ppm; ^{13}C NMR δ: 42.2, 106.5, 143.2, 145.5, and 149.6 ppm; MS *m*/*z* (%): 130(100), 115(98). From *H*. sp., $[\alpha]_D$ –4.0 (*c* 1, $CHCl_3$), (*S*), e.e. 40% (DBMB, ^{1}H NMR SCH_3 δ: 2.83 (major) and 2.85 (minor) ppm).

3-Methylthiothiophene (***4***): *3-methylsulfinylthiophene*; oil, R_f 0.08 (EtOAc); ^{1}H NMR δ: 2.66 (3H, s), 7.27 (1H, d), 7.50 (1H, dd), and 7.75 (1H, d) ppm; ^{13}C NMR δ: 43.4, 123.5, 125.9, 129.0, and 145.3 ppm; MS (FAB) *m*/*z* (%): 147(M + H, 100); from *H*. sp. $[\alpha]_D$ –26.8 (*c* 1, EtOH), (*S*), e.e. 68% (DBMB, ^{1}H NMR SCH_3 δ: 2.81 (major) and 2.82 (minor) ppm).

2-Methylthiomethylfuran (***5***): *2-methylsulfinylmethylfuran*; oil; ^{1}H NMR δ: 2.35 (3H, s), 3.89 (2H, ABq), 6.22–6.25 (2H, m), and 7.27 (1H, s) ppm; ^{13}C NMR δ: 38.3, 52.8, 111.5, 111.6, 143.9, and 144.3 ppm; MS *m*/*z* (%): 144(2), 128(1), 81(100); from *H*. sp. $[\alpha]_D$ +14.3 (*c* 1.1, EtOH), –90.8 (*c* 1.52, $CHCl_3$), (*S*), e.e. 60% (MPAA, ^{1}H NMR SCH_3 δ: 2.57 (major) and 2.59 (minor) ppm). 2-Methylsulfonylmethylfuran; mp 49–51°C, ^{1}H NMR δ: 2.87 (3H, s), 4.35 (2H, s), 6.47, 6.55 (2H, m), and 7.49 (1H, s) ppm; ^{13}C NMR δ: 40.3, 54.8, 111.9, 112.7, 143.0, and 144.4 ppm; MS *m*/*z* (%): 160(5), 81(100).

2-Methylthiomethylthiophene (***6***): *2-methylsulfinylmethylthiophene*; mp 43–45°C, ^{1}H NMR δ: 2.50 (3H, s), 4.20 (2H, ABq), and 7.06–7.35 (3H, m) ppm; ^{13}C NMR δ: 37.7, 54.6, 127.2, 128.0, 129.2, and 130.5 ppm; MS *m*/*z* (%): 160(1), 144(1), 97(100); from *H*. sp. $[\alpha]_D$ +60.2 (*c* 1.1, EtOH), –55.3 (*c* 1.11, $CHCl_3$), (*S*), e.e. 44% (MPAA, ^{1}H NMR SCH_3 δ: 2.538 (major) and 2.553 (minor) ppm). *2-Methylsulfonylmethylthiophene*; mp 91–93°C, ^{1}H NMR δ: 2.83 (3H, s), 4.47 (2H, s), and 7.08–7.41 (3H, m) ppm; ^{13}C NMR δ: 39.1, 56.2, 128.1, 128.2, 129.1, and 130.5 ppm; MS *m*/*z* (%): 176(4), 97(100).

3-Methylthiomethylfuran (***7***): *3-methylsulfinylmethylfuran*; oil; ^{1}H NMR δ: 2.50 (3H, s), 3.85 (2H, ABq), 6.43 (1H, s), and 7.47–7.50 (2H, d) ppm; ^{13}C NMR δ: 37.7, 50.4, 111.8, 113.9, 142.3, and 144.2 ppm; MS *m*/*z* (%): 144(5), 81(100); from *H*. sp. $[\alpha]_D$ +47.7 (*c* 1, EtOH), –11.7 (*c* 1, $CHCl_3$), (*S*), e.e. 60% (MPAA, ^{1}H NMR SCH_3 δ: 2.538 (major) and 2.556 (minor) ppm).

3-Methylthiomethylthiophene (***8***): *3-methylsulfinylmethylthiophene*; oil; ^{1}H NMR δ: 2.46 (3H, s), 4.04 (2H, ABq), and 7.06–7.38 (3H, m) ppm; ^{13}C NMR δ: 37.7, 54.9, 125.6, 127.1, 128.9, and 129.9 ppm; MS *m*/*z* (%): 160(2), 144(1), 97(100); from *H*. sp. $[\alpha]_D$ +31.9 (*c* 1.3, EtOH), –36.1 (*c* 1.2, $CHCl_3$), (*S*), e.e. 22% (MPAA, ^{1}H NMR SCH_3 δ 2.512(major) and 2.533 (minor) ppm). *3-Methylsulfonylmethylthiophene*; mp 63–65°C; ^{1}H NMR δ: 2.78 (3H, s), 4.32 (2H, s), and 7.19–7.42 (3H, m) ppm; ^{13}C NMR δ: 39.4, 56.4, 126.9, 127.5, 128.5, and 129.0 ppm; MS *m*/*z* (%): 176(6), 97(100).

N-*Methyl-2-methylthioimidazole* (***9***): N-*methyl-2-methylsulfinylimidazole*; oil; ^{1}H NMR δ: 3.11 (3H, s), 3.96 (3H, s), and 7.0/7.14 (2H, ABq) ppm; MS *m*/*z* (%): 144(62), 129(99), 97(100); from *H*. sp. $[\alpha]_D$ –37.0 (*c* 0.6, EtOH), (*S*), e.e. 40% (DBMB, ^{1}H NMR SCH_3 δ: 3.069 (minor) and 3.082 (major) ppm).

N-*Methyl-3-methylthiomethylindole* (***10***): N-*methyl-3-methylsulfinylmethylindole*; oil; ^{1}H NMR δ: 2.44 (3H, s), 3.78 (3H, s), 4.12/4.26 (2H, ABq), 7.14 (1H, s), 7.18 (1H, m), 7.28 (1H, m), 7.35 (1H, d), and 7.58 (1H, d) ppm; ^{13}C NMR δ: 33.4, 37.8, 51.4, 102.5, 110.1, 119.0, 120.3, 122.6, 128.1, 129.8, and 137.4 ppm; MS *m*/*z* (%): 191(9), 173(6), 158(4), 144(100), 126(80); from *H*. sp. $[\alpha]_D$ –55.9 (*c* 3.6, $CHCl_3$), (*S*), e.e. 66% (MPAA, ^{1}H NMR SCH_3 δ: 2.50 (major) and 2.53 (minor) ppm).

Methylthiomethylcyclopentane (***11***): *methylsulfinylmethylcyclopentane*; oil; ^{1}H NMR δ: 1.15 (2H, m), 1.54 (4H, m), 1.80 (2H, m), 2.22 (1H, m), 2.48 (3H, s), 2.50 (2H, m), and 2.77 (1H) ppm; ^{13}C NMR δ: 25.2, 25.3, 32.6, 33.1, 35.1, 39.5, and 61.9 ppm; MS *m*/*z* (%): 146(8), 130(9), 83(58), 67(33), 55(100). From *H*. sp. $[\alpha]_D$ +76.2 (*c* 1, $CHCl_3$), + 103.3 (*c* 1.5, EtOH), (*S*), e.e. 75% (MPAA ^{1}H NMR SCH_3 δ: 2.497 (major) and 2.514 (minor) ppm). *1-Methylsulfonylmethylcyclopentane*; semisolid; ^{1}H NMR δ: 1.30 (2H, m), 1.60 (4H, m), 2.02 (2H, m), 2.43 (1H, m), 2.92 (3H, s), and 3.08 (2H) ppm; MS *m*/*z* (%): 162(12), 146(8), 83(100).

2-Methylthiopyridine (***12***): *2-methylsulfinylpyridine*; oil; ^{1}H NMR δ: 2.83 (3H, s), 7.32 (1H, m), 7.90 (1H, m), 8.02 (1H, d), and 8.59 (1H, d) ppm; MS *m*/*z* (%): 141(80), 126(35), 78(100). From *H*. sp. $[\alpha]_D$ –10.5 (*c* 0.53, EtOH), (*S*), e.e. 6% (DBMB, ^{1}H NMR SCH_3 δ: 2.795 (minor) and 2.811 (major) ppm).

4-Methylthiopyridine (***13***): *4-methylsulfinylpyridine*; oil; ^{1}H NMR δ: 2.76 (3H, s) and 7.52/8.78 (4H, ABq) ppm; MS *m*/*z* (%): 141(100), 126(28), 78(87). From *H*. sp. $[\alpha]_D$ –22.8 (*c* 0.3, EtOH), (*S*), e.e. 48% (DBMB, ^{1}H NMR SCH_3 δ: 2.740 (major) and 2.747 (minor) ppm).

4-Methylthiotetrahydropyran (***14***): *4-methylsulfinyltetrahydropyran*; oil; ^{1}H NMR δ: 1.65–1.82 (3H, m), 1.95–2.02 (1H, m), 2.51 (3H, s), 2.67–2.81 (1H, m), 3.37–3.48 (2H, m), and 4.01–4.12 (2H, m) ppm; ^{13}C NMR δ: 25.3, 26.2, 35.3, 58.2, 66.9, and 67.3 ppm; MS *m*/*z* (%): 148(3), 132(1), 85(37), 55(100). From *H*. sp. $[\alpha]_D$ +10.9 (*c* 0.94, $CHCl_3$), +19.4 (*c* 0.97, EtOH), (*S*), e.e. 34% (MPAA, ^{1}H NMR SCH_3 δ: 2.58 (major) and 2.61 (minor) ppm).

© 1999 NRC Canada

Can. J. Chem. Downloaded from www.nrcresearchpress.com by University Town Library of Shenzhen on 09/05/12
For personal use only.

2-Methylthiomethylpyridine (***15***): *2-methylsulfinylmethylpyridine*; oil; R_f 0.16 (EtOAc); ^{1}H NMR δ: 2.58 (3H, s), 4.18 (2H, dd), 7.28 (1H, dd), 7.38 (1H, d), 7.72 (1H, td), and 8.61 (1H, d) ppm; ^{13}C NMR δ: 38.1, 61.5, 123.4, 125.6, 136.8, 137.2, 150.1, and 150.9 ppm; MS *m*/*z* (%): 155(1), 139(1), 109(14), 92(100). From *H.* sp. $[\alpha]_D$ +105.5 (*c* 1, EtOH), (*S*), e.e. 73% (MPAA ^{1}H NMR SCH_3 δ: 2.48 (major) and 2.52 (minor) ppm); from *M. isabellina* $[\alpha]_D$ –66.6 (*c* 1, EtOH), (*R*), e.e. 42% (MPAA ^{1}H NMR SCH_3 δ: 2.48 (minor) and 2.52 (major) ppm).

3-Methylthiomethylpyridine (***16***): *3-methylsulfinylmethylpyridine*; oil; R_f 0.14 (20:80 MeOH:EtOAc); ^{1}H NMR δ: 2.47 (3H, s), 3.85 (1H, d), 3.98 (1H, d), 7.31 (1H, m), 7.67 (1H, m), 8.52 (1H, br s), and 8.59 (1H, dd) ppm; ^{13}C NMR δ: 37.8, 57.0, 124.0, 126.2, 138.1, 150.2, and 151.2 ppm; MS (FAB) *m*/*z* (%): 156(M + H,100), 140(9), 93(44); from *H.* sp. $[\alpha]_D$ +175.4 (*c* 1, EtOH), (*S*), e.e. >98% (MPAA, ^{1}H NMR SCH_3 δ: 2.47 ppm only); from *M. isabellina* $[\alpha]_D$ –146 (*c* 1.5, EtOH), (*R*), e.e. 85% (MPAA, ^{1}H NMR SCH_3 δ: 2.47 (minor) and 2.49 (major) ppm). *3-Methylsulfonylmethylpyridine*; mp 105–107°C; ^{1}H NMR δ: 2.80 (3H, s), 4.22 (2H, s), 7.4 (1H, m), 7.81 (1H, m), and 8.5–8.65 (2H, m) ppm; MS *m*/*z* (%): 171(6), 146(7), 131(12), 92(72) relative to 55(100).

4-Methylthiomethylpyridine (***17***): *4-methylsulfinylmethylpyridine*; oil; R_f 0.15 (10:80 MeOH:EtOAc) ^{1}H NMR δ: 2.51 (3H, s), 3.90 (1H, d), 3.99 (1H, d), 7.19 (2H, dd), and 8.61 (2H, dd) ppm; ^{13}C NMR δ: 38.1, 59.1, 125.3, 139.0, and 150.7 ppm; MS *m*/*z* (%): 155(37), 139(5), 124(2), 107(4), 92(100); from *H.* sp. $[\alpha]_D$ +133.8 (*c* 1, EtOH), (*S*), e.e. 83% (MPAA, ^{1}H NMR SCH_3 δ: 2.47 (major) and 2.56 (minor) ppm); from *M. isabellina* $[\alpha]_D$ –84.0 (*c* 1, EtOH), (*R*), e.e. 62% (MPAA, ^{1}H NMR SCH_3 δ 2.47 (minor) and 2.56 (major) ppm).

Methylthiomethylcyclohexane (***18***): *methylsulfinylmethylcyclohexane*; mp 41–43°C; ^{1}H NMR δ: 0.96–1.41 (5H, m), 1.65–2.05 (6H, m), 2.41–2.49 (1H, m), 2.59 (3H, s), and 2.72–2.78 (2H, m) ppm; ^{13}C NMR δ: 26.0, 26.3, 26.4, 32.8, 33.2, 33.8, 39.5, and 63.4 ppm; MS *m*/*z* (%): 160(8), 143(11), 97(69), 55(100); from *H.* sp. $[\alpha]_D$ +73.2 (*c* 1.2, EtOH), (*S*), e.e. 43% (MPAA, ^{1}H NMR SCH_3 δ 2.61 (major) and 2.635 (minor) ppm). *Methylsulfonylmethylcyclohexane*; semisolid; ^{1}H NMR δ: 0.90 (4H, m), 1.63–1.72 (4H, m), 2.02 (3H, m), 2.34–2.38 (2H, t), and 2.93 (3H, s) ppm; MS (FAB) *m*/*z* (%): 177(M+1, 100), 139(60), 97(48).

1-Thiaindan (***20***): *1-thiaindane* S-*oxide*; oil; ^{1}H NMR δ: 3.28 (3H, m), 3.82 (1H, m), 7.43 (3H, m), and 7.80 (1H, d) ppm; ^{13}C NMR δ: 31.8, 53.1, 126.5, 127.0, 128.6, 132.7, 143.65, and 145.0 ppm; MS (FAB) *m*/*z* (%): 153(M + H, 100), 136(14); from *H.* sp. $[\alpha]_D$ +11.3 (*c* 1, EtOH), (*S*), e.e. 5%; from *M. isabellina* $[\alpha]_D$ –135.0 (*c* 1, acetone), (*R*), e.e. 47% based on $[\alpha]_D$ –285 (acetone) for enantiopure (*R*) material (32).

2-Thiaindan (***21***): *2-thiaindane* S-*oxide*; mp 68–70°C (lit. (24) mp 90°C); ^{1}H NMR δ: 3.93 (2H, d), 4.03 (2H, d), and 7.21 (4H, m) ppm; ^{13}C NMR δ: 59.6, 126.9, 128.6, and 135.7 ppm; MS *m*/*z* (%): 152(55), 134(43), 104(100).

Thiochroman (***22***): *thiochroman* S-*oxide*; oil; ^{1}H NMR δ: 2.08 (2H, m), 2.55 (1H, m), 2.88 (1H, m), 3.01 (1H, m), 3.15 (1H, m), 7.23 (1H, d), 7.38 (2H, m), and 7.72 (1H, d) ppm; ^{13}C NMR δ: 14.4, 28.7, 46.6, 127.7, 130.7, 131.0, 131.9, 136.1, and 138.9 ppm; MS *m*/*z* (%): 166(34), 149(100), 137(30), 116(28); from *H.* sp. $[\alpha]_D$ +23.6 (*c* 1, acetone); (*S*), e.e. 11% based on $[\alpha]_D$ –202 (acetone) for enantiopure (*R*) material (32).

Benz-1,4-oxathiane (***23***): *benz-1,4-oxathian* S-*oxide*; mp 79°C, resolidifies and remelts at 105–110°C; ^{1}H NMR δ: 2.98 (1H, td), 3.12 (1H, m), 4.52 (1H, dt), 4.72 (1H, td), 6.98 (1H, d), 7.03 (1H, t), 7.41 (1H, td), and 7.57 (1H, dd) ppm; ^{13}C NMR: 44.0, 56.0, 119.5, 121.8, 123.6, 134.6, 133.1, and 153.0 ppm; MS *m*/*z* (%): 169(100), 152(12), 96(8); from *H.* sp. $[\alpha]_D$ +13.3 (*c* 1, EtOH) (*S*), e.e. 25% from HPLC, column Chirobiotic T™, solvent ACN:MeOH:TEA:AcOH (60:40:0.4:0.8), flow 0.5 mL/min, t_r 8.2 (major) and 9.6 (minor) min; from *M. isabellina* $[\alpha]_D$ –45.9 (*c* 1, EtOH), (*R*), e.e. 88% from HPLC as above, major enantiomer t_r 9.6 min. Crystallization from ethyl acetate – hexane gave enantiopure (*R*) material, $[\alpha]_D$ –52.2 (*c* 1, EtOH).

Benzo-1,4-dithiane (***24***): *benzo-1,4-dithiane*-S-*oxide*; oil; R_f 0.25 (EtOAc); ^{1}H NMR δ: 3.06 (2H, m), 3.38 (1H, m), 3.73 (1H, m), 7.26 (2H, m), 7.37 (1H, td), and 7.67 (1H, dd) ppm; ^{13}C NMR δ: 17.1, 45.0, 125.7, 129.0, 132.1, 132.3, 132.8, and 136.4 ppm; MS *m*/*z* (%): 184(21), 168(23), 153(24), 140(100); from *H.* sp. $[\alpha]_D$ –1.8 (*c* 1, EtOH), (*S*), e.e. 6% from HPLC, column Chirobiotic T™, solvent EtOH:hexane (20:80), flow 0.5 mL/min, t_r 23.2 (minor) and 26.2 (major) min; from *M. isabellina* $[\alpha]_D$ +16.1 (*c* 1, EtOH), (*R*), e.e. 54% from HPLC as above, major enantiomer t_r 23.2 min.

2,3-Dihydrobenzo-1,4-thiazine (***25***): *2,3-dihydrobenzo-1,4-thiazine*-S-*oxide*; mp 188–190°C; ^{1}H NMR δ: 2.61 (1H, td), 3.06 (1H, ddd), 3.46 (1H, dt), 3.88 (1H, dt), 6.57 (1H, d), 6.68 (1H, t), 7.19 (1H, td), and 7.47 (1H, dd) ppm; ^{13}C NMR δ: 30.8, 42.5, 116.9, 117.1, 120.2, 133.2, 133.9, and 143.4 ppm; ms *m*/*z* (%): 167(15), 151(100), 136(75); from *H.* sp. $[\alpha]_D$ +5.1 (*c* 3, EtOH), (*R*), e.e. 2% from HPLC, column Chirobiotic T™, solvent ACN:MeOH:TEA:AcOH (45:55:0.4:0.4), flow 0.5 mL/min, t_r 7.8 (major) and 9.2 (minor) min; from *M. isabellina* $[\alpha]_D$ +195.9 (*c* 1, EtOH), (*R*), e.e. 81% from HPLC as above, major enantiomer t_r 9.2 min. Crystallization from dichloromethane–hexane gave enantiopure (*R*) material, $[\alpha]_D$ +230.8 (*c* 1, EtOH).

N-*Methyl-2,3-dihydrobenzo-1,4-thiazine* (***26***): N-*methyl-2,3-dihydrobenzo-1,4-thiazine*-S-*oxide*; oil; R_f 0.22 (10:90 MeOH:EtOAc); ^{1}H NMR δ: 2.74 (1H, td), 3.07 (1H, m), 3.10 (3H, s), 3.44 (1H, dt), 4.10 (1H, td), 6.76 (2H, m), 7.38 (1H, m), and 7.54 (1H, dd) ppm; ^{13}C NMR δ: 40.1, 40.1, 42.5, 113.6, 116.6, 122.2, 133.6, 134.4; MS *m*/*z* (%): 181(20), 165(100), 164(92), 150(70), 131(50); from *H.* sp. $[\alpha]_D$ +2.2 (*c* 1, EtOH), e.e. 3% from HPLC, column Chirobiotic T™, solvent EtOH:hexane (20:80), flow 0.5 mL/min, t_r 53.8 (minor) and 66.5 (major) min; from *M. isabellina* $[\alpha]_D$ +116.8 (*c* 1, EtOH), e.e. 66% based on HPLC as above, major enantiomer t_r 53.8 min.

© 1999 NRC Canada

*Isothiochroman (**27**): isothiochroman* S-*oxide*; mp 73–75°C; ^{1}H NMR δ: 2.90 (3H, m), 3.27 (1H, m), 3.78 (1H, d), 4.02 (1H, d), and 7.14 (4H, m) ppm; ^{13}C NMR δ: 24.0, 47.4, 52. 5, 127.5, 127.6, 128.4, 129.0, 130.7, 135.5; MS *m*/*z* (%): 166(50), 149(13), 117(100), 104(42); from *H*. sp. $[\alpha]_D$ –4.0 (*c* 1, EtOH), (*S*), e.e. 7%, from HPLC, column Chiralcel OD™, solvent hexane:2-propanol (90:10), flow 1.0 mL/min, t_r 32.9 (major) and 34.5 (minor) min; from *M. isabellina* $[\alpha]_D$ +35.0 (*c* 1, EtOH), (*R*), e.e. 60% from HPLC as above, major enantiomer t_r 34.5 min.

Acknowledgments

This work was funded by the Natural Sciences and Engineering Research Council of Canada. We are grateful to Mr. T. Jones (Brock) for assistance with the acquisition of spectral data, and to Dr. P. Pasta (IBRM, CNR Milan) for determination of the e.e. of isothiochroman sulfoxide.

References

1. G. Solladié. Synthesis, 185 (1981).
2. Y. Arai. J. Synth. Org. Chem. Jpn. **56**, 798 (1998).
3. M.C. Carreno. Chem. Rev. **95**, 1717 (1995).
4. H.L. Holland. Chem. Rev. **88**, 473 (1988).
5. H.L. Holland, F.M. Brown, G. Lakshmaiah, B.G. Larsen, and M. Patel. Tetrahedron: Asymmetry, **8**, 683 (1997).
6. J. Beecher, I. Brackenridge, S.M. Roberts, J. Tang, and A.J. Willetts. J. Chem. Soc. Perkin Trans. 1, 1641 (1995).
7. J. Tang, I. Brackenridge, S.M. Roberts, J. Beecher, and A.J. Willetts. Tetrahedron, **51**, 13217 (1995).
8. H.L. Holland, J.-X. Gu, F. Orallo, M. Camiña, P. Fabeiro, and A. J. Willetts. Pharm. Res. **16**, 281 (1999).
9. H.L. Holland and F.M. Brown. Tetrahedron: Asymmetry, **9**, 535 (1998).
10. I. Koch and M. Keusgen. Pharmazie, **53**, 668 (1998).
11. H.L. Holland, H. Pöpperl, R.W. Ninniss, and P.C. Chenchaiah. Can. J. Chem. **63**, 1118 (1985).
12. H.L. Holland, L.J. Allen, M.J. Chernishenko, M. Diez, A. Kohl, J. Ozog, and J.-X. Gu. J. Mol. Cat. B: Enzym. **3**, 311 (1997).
13. H.L. Holland. Organic synthesis with oxidative enzymes. VCH, New York. 1992.
14. J.B. Jones and I.J. Jakovac. Can. J. Chem. **60**, 19 (1982).
15. K. Naemura, R. Fukuda, M. Konishi, K. Hirose, and T. Tobe. J. Chem. Soc. Perkin Trans. 1, 1253 (1994).
16. M. Cygler, P. Grochulski, R.J. Kazlauskas, J.D. Schrag, F. Bouthillier, B. Rubin, A.N. Serreqi, and A.K. Gupta. J. Am. Chem. Soc. **116**, 3180 (1994).
17. H.L. Holland. Adv. Appl. Microbiol. **44**, 125 (1997).
18. H.L. Holland, E.J. Bergen, P.C. Chenchaiah, S.H. Khan, B. Munoz, R.W. Ninniss, and D. Richards. Can. J. Chem. **65**, 502 (1987).
19. P.H. Buist, D. Marecak, H.L. Holland, and F.M. Brown. Tetrahedron: Asymmetry, **6**, 7 (1995).
20. M.N. Deshmukh, E. Dunach, S. Juge, and H.B. Kagan. Tetrahedron Lett. **25**, 3467 (1984).
21. H.L. Holland, F.M. Brown, B.G. Larsen, and M. Zabic. Tetrahedron: Asymmetry, **7**, 1569 (1995).
22. H.L. Holland, F. M. Brown, A. Kerridge and C. D. Turner. J. Mol. Cat. B: Enzym. In press (1999).
23. H.L. Holland and I.M. Carter. Can. J. Chem. **60**, 2420 (1982).
24. S.F. Birch, R.A. Dean, and E.V. Whitehead. J. Inst. Pet. **40**, 76 (1954).
25. H.L. Holland, C.G. Rand, P. Viski, and F.M. Brown. Can. J. Chem. **69**, 1989 (1991).
26. D. Greenwood and H.A. Stevenson. J. Chem. Soc. 1514 (1953).
27. W.E. Parham, T.M. Roder, and W.R. Hasek. J. Am. Chem. Soc. **75**, 1647 (1953).
28. J.F. Kerwin, J.E. McCarty, and C.A. Van der Werf. J. Org. Chem. **24**, 1719 (1959).
29. F.G. Holliman and F.G. Mann. J. Chem. Soc. 37 (1945).
30. M. Gorzynski and D. Rewicki. Liebigs Ann. Chem. 625 (1986).
31. P. Diter, S. Taudien, O. Samuel, and H.B. Kagan. J. Org. Chem. **59**, 370 (1994).
32. T. Takata, M. Yamazaki, K. Fujimori, Y.H. Kim, T. Iyangi, and S. Oae. Bull. Chem. Soc. Jpn. **56**, 2300 (1983).

Can. J. Chem. Downloaded from www.nrcresearchpress.com by University Town Library of Shenzhen on 09/05/12
For personal use only.

© 1999 NRC Canada

Studies of the photophysics and spectroscopy of alloxazine and related compounds in solution and in the solid state

M. Sikorski, E. Sikorska, F. Wilkinson, and R.P. Steer

Can. J. Chem. Downloaded from www.nrcresearchpress.com by University Town Library of Shenzhen on 09/05/12
For personal use only.

Abstract: The absorption and emission spectra and the fluorescence lifetimes and quantum yields of alloxazine and several of its N- and C- methyl-substituted derivatives, including two isoalloxazines, have been measured in a nonpolar solvent (1,2-dichloroethane), a polar aprotic solvent (acetonitrile), and a polar protic solvent (ethanol). The excited state decays are all single exponential, suggesting that only one emitting species is present in all cases. The spectroscopic data show that the emitting species is the π,π^* electronic excited state corresponding to the ground state of the absorbing molecule; there is no evidence of excited state proton transfer for any of these solutes in any of the three solvents. The longer lifetimes and larger fluorescence quantum yields of the isoalloxazines compared with the alloxazines can be attributed exclusively to significantly slower rates of radiationless relaxation in the excited isoalloxazines. The remission and emission spectra of these same compounds adsorbed on cellulose are similar to the corresponding absorption and emission spectra in homogeneous solution, suggesting that the emitting species are the same in the adsorbed state as they are in homogeneous solution. However, the adsorbed excited species exhibit non-exponential temporal decay, attributed to inhomogeneities in the binding of the chromophore to cellulose. The emission spectra of polycrystalline samples of alloxazine and lumichrome suggest the possible occurrence of double intermolecular excited state proton transfer, but this interpretation is not supported by the further photophysical data obtained here.

Key words: photophysics, spectroscopy, alloxazine, lumiflavin, cellulose.

Résumé : Opérant dans un solvant non polaire (1,2-dichloroéthane), dans un solvant polaire non protique (acétonitrile) et dans un solvant polaire protique (éthanol), on a mesuré les spectres d'absorption et d'émission, les temps de vie de fluorescence et les rendements quantiques de l'alloxazine et de plusieurs de ses dérivés portant des substituants N- et C-méthyles. Dans tous les cas, la décroissance de l'état excité est toujours à une seule exponentielle; ceci suggère que dans tous les cas, il n'y a qu'une seule espèce qui émet. Les donnes spectroscopiques montrent que l'espèce qui émet est l'état électronique excité π,π^* correspondant à l'état fondamental de la molécule qui absorbe; pour chacun de ces solutés dans les trois solvants, il n'y a aucune indication suggérant l'existence d'un transfert de proton dans l'état excité. Les temps de vie plus longs et les rendements quantiques de fluorescence plus élevés des isoalloxazines par comparaison avec les valeurs semblables des alloxazines peuvent être attribués entièrement aux vitesses plus lentes de la relaxation sans rayonnement dans les isoalloxazines excitées. Les spectres d'émission et de réémission des même composés adsorbés sur de la cellulose sont semblables aux spectres correspondants d'absorption et d'émission de solutions homogènes; ceci suggère que les espèces qui émettent sont les mêmes dans l'état adsorbé qu'en solution homogène. Toutefois, les espèces excitées adsorbées donnent lieu à une décroissance qui n'est pas exponentielle dans le temps et ce résultat est attribué à des inhomogénéités dans la fixation du chromophore sur la cellulose. Les spectres d'émission d'échantillons polycristallins d'alloxazine et de lumichrome suggèrent laissent croire qu'il existe peut-être un double transfert de proton intermoléculaire dans l'état excité; toutefois, cette interprétation n'est pas supportée par d'autres données photophysiques obtenues dans ce travail.

Mots clés : photophysique, spectroscopie, alloxazine, lumiflavine, cellulose.

[Traduit par la Rédaction]

Received November 16, 1998.

M. Sikorski.[1] Department of Chemistry, University of Saskatchewan, Saskatoon, S7N 5C9, Canada, and Faculty of Chemistry, A. Mickiewicz University, 60–780 Poznan, Poland.
E. Sikorska. Faculty of Commodity Science, Poznan University of Economics, 60-967 Poznan, Poland.
F. Wilkinson. Department of Chemistry, Loughborough University, Loughborough, Leicestershire, LE11 3TU, U.K.
R.P. Steer.[2] Department of Chemistry, University of Saskatchewan, Saskatoon, S7N 5C9, Canada.

[1]Present address: Department of Chemistry and Biochemistry, University of Notre Dame, Notre Dame, IN 46556, U.S.A.
[2]Author to whom correspondence may be addressed. Telephone: (306) 966-4667. Fax: (306) 966-4730. e-mail: steer@usask.ca

 © 1999 NRC Canada

Can. J. Chem. Downloaded from www.nrcresearchpress.com by University Town Library of Shenzhen on 09/05/12
For personal use only.

Fig. 1. Structures and abbreviations of the alloxazines and isoalloxazines employed in this study.

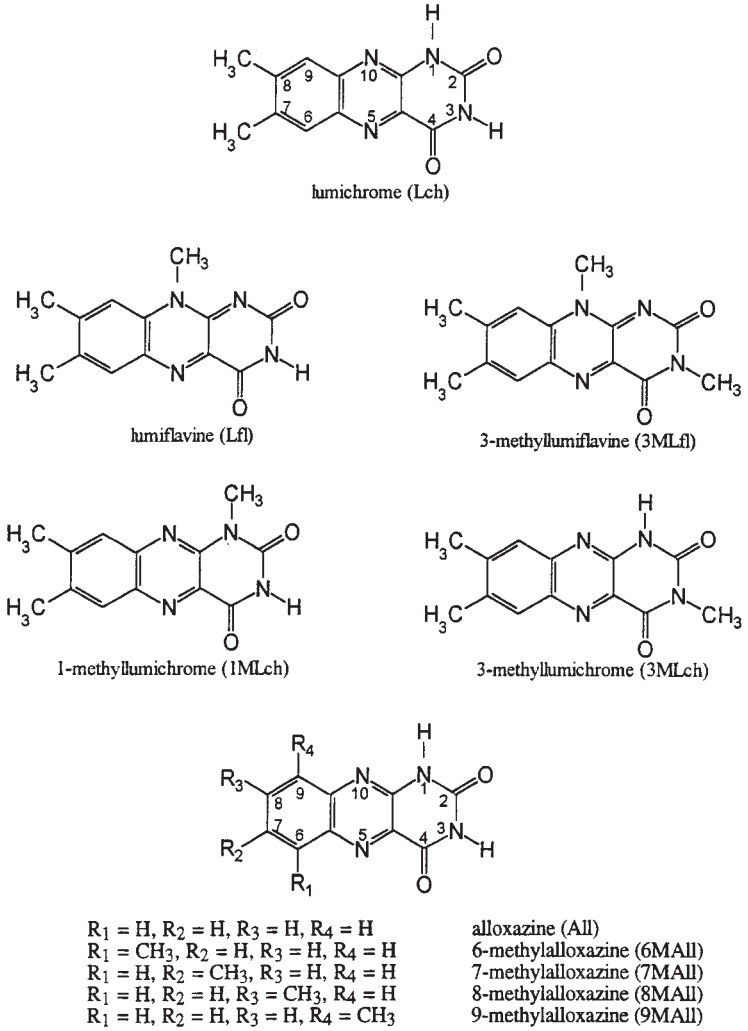

Introduction

Alloxazine and related compounds are numbered among an interesting group of species whose hydrogen-bonded complexes are capable of undergoing concerted intermolecular double proton transfer, and considerable work has been done to sort out the mechanism of photo-initiated double proton transfer in alloxazine – acetic acid and other complexes (1–8). The alloxazine system is a very useful one to model such processes because the isoalloxazine tautomer formed as a result of excited state proton transfer has a spectroscopically distinct emission spectrum (1, 6, 7). Recent work by one of us (1) has provided evidence that alloxazine – acetic acid complexes with appropriate structures for proton transfer can be formed in both the ground and excited states. The excited state reaction in solution is a two-step process involving, first, formation of a hydrogen-bonded structure that facilitates proton transfer, followed by proton transfer itself, with the former constituting the rate-determining step of the overall process.

The photophysics and photochemistry of alloxazine and its derivatives have been studied since 1966, when the proton transfer reactions in lumichrome and related compounds were first discovered (8). However, almost all of this previous work has been concerned with systems in homogeneous solution whereas current interests in the potential applications of photo-initiated processes are focussed largely on the solid state. Recently, Sarkar et al. (9) showed that lumichrome forms an inclusion complex with β-cyclodextrin (β-CD), and we studied the spectroscopic properties of this and several other complexes (lumichrome, Lch; 7-methylalloxazine, 7MAll; and 8-methylalloxazine, 8MAll — cf. Fig. 1) in both solution and the solid state (10). The formation of hydrogen bonds in the solid complexes was postulated to explain their ground-state absorption and steady-state fluorescence spectra, and spectroscopic evidence was found to support the existence of doubly hydrogen-bonded dimers of lumichrome capable of executing excited state double proton transfer in the solid state.

In this paper we present the results of a study of the photophysics of several alloxazines in both homogeneous solution and in the solid state, carried out with the objective of elucidating the structures and the dynamics of the excited species.

Experimental section

Materials

Alloxazine (Aldrich), lumichrome (Aldrich), and lumiflavine (Fluka) were purchased and used as received. The other

© 1999 NRC Canada

Fig. 2. The remission spectra of 1MLch on cellulose at a loading of 0.33 mg/g, 6MAll on cellulose at a loading of 1.0 mg/g, and 7MAll on cellulose at a loading of 0.8 mg/g. The corresponding spectra in acetonitrile are shown in the bottom panels.

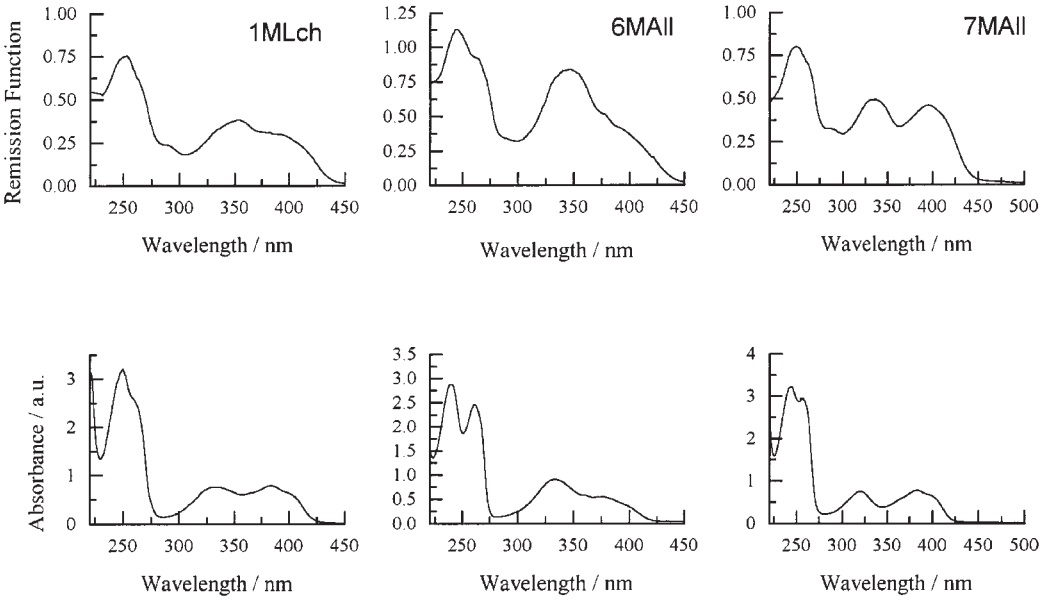

Can. J. Chem. Downloaded from www.nrcresearchpress.com by University Town Library of Shenzhen on 09/05/12
For personal use only.

alloxazines and 3-methyllumiflavine used in this study were available from previous work, and were synthesized and purified as described in ref. 6. Cellulose (20 μm powder, Aldrich), dry acetonitrile, 1,2-dichloroethane, and absolute ethanol were used as received.

Samples of microcrystalline cellulose were placed in a vacuum oven at 70°C for at least 24 h prior to use to remove adsorbed water. Samples of the alloxazines supported on cellulose were prepared by first dissolving a weighed amount of the adsorbate in a known volume of 3:1 acetonitrile:methanol solution, then adding an aliquot of this solution to a slurry consisting of a known weight of dried cellulose powder in a known volume of the same solvent. The resulting suspension was stirred periodically and allowed to evaporate slowly. After several hours the final traces of solvent were removed by placing the sample in a vacuum oven at 40°C for about 4 h. The loading of alloxazine on cellulose was between 0.3 and 1.0 mg/g, and typically 0.8 mg/g.

Equipment and methods

Ground state diffuse reflectance absorption (remission) spectra were recorded on either a PU 8800 UV–visible spectrophotometer equipped with an integrating sphere or on a Perkin Elmer LambdaBio 40 spectrophotometer equipped with a Labsphere reflectance attachment. The methods of obtaining corrected diffuse reflectance spectra have been described elsewhere (11, 12). Steady-state fluorescence spectra were obtained with a Spex Fluoromax spectrofluorometer. UV–visible absorption spectra were recorded on an HP 8453 diode array spectrophotometer.

The fluorescence decay curves of the alloxazines in acetonitrile (except for alloxazine itself) and in 1,2-dichloroethane were measured using an IBH model 5000U spectrometer, as previously described (1). Fluorescence decay curves of all other samples were measured by exciting at 340 nm using the frequency-doubled output of a mode-locked, synchronously pumped, cavity-dumped argon-ion/DCM dye laser system, and detecting emission with a Hamamatsu microchannel plate photomultiplier coupled to a time-correlated single-photon counting system. The pulse-shape mimic technique was used to obtain the instrument response function (13), and the fluorescence lifetimes were obtained by an iterative convolution method employing a least-squares fitting procedure. This measuring system has been described in detail in refs. 13 and 14.

Fluorescence quantum yields were obtained by the standard relative method using quinine sulfate in 1 N H_2SO_4 (ϕ_f = 0.546) as a reference (15).

All measurements were performed at room temperature with air-equilibrated samples.

Results and discussion

A total of 10 alloxazines and isoalloxazines (lumiflavines) were available for study. The diffuse reflectance spectra of three representative alloxazines, 1MLch, 6MAll, and 7MAll, on cellulose are shown in Fig. 2; the absorption spectra of the same compounds in acetonitrile are presented for comparison. The diffuse reflectance spectra are plotted in terms of the remission function, $F(R)$, as a function of wavelength. $F(R)$ is proportional to absorber concentration, and is defined in the Kubelka–Munk (11, 16) theory of the interaction of light with opaque materials as

$$[1] \qquad F(R) = (1 - R)^2/2R = K/S$$

where R is the observed diffuse reflectance from the surface of the sample, K is the absorption coefficient, and S is the scattering coefficient.

The normalized emission spectra of these same three compounds, excited at 355 nm on cellulose, are presented in Fig. 3, and the emission spectra of lumichrome and alloxazine on cellulose and in the polycrystalline solid state are shown in Fig. 4. The emission spectra of the isoalloxazines, lumiflavine and 3-methyllumiflavine, on cellulose are shown in Fig. 5. The spectroscopic data for all 10 compounds on cellulose and in ethanol are collected in Table 1.

© 1999 NRC Canada

Can. J. Chem. Downloaded from www.nrcresearchpress.com by University Town Library of Shenzhen on 09/05/12
For personal use only.

Fig. 3. Normalized fluorescence emission spectra of 1MLch, 6MAll, and 7MAll on cellulose. The loadings are the same as in Fig. 2.

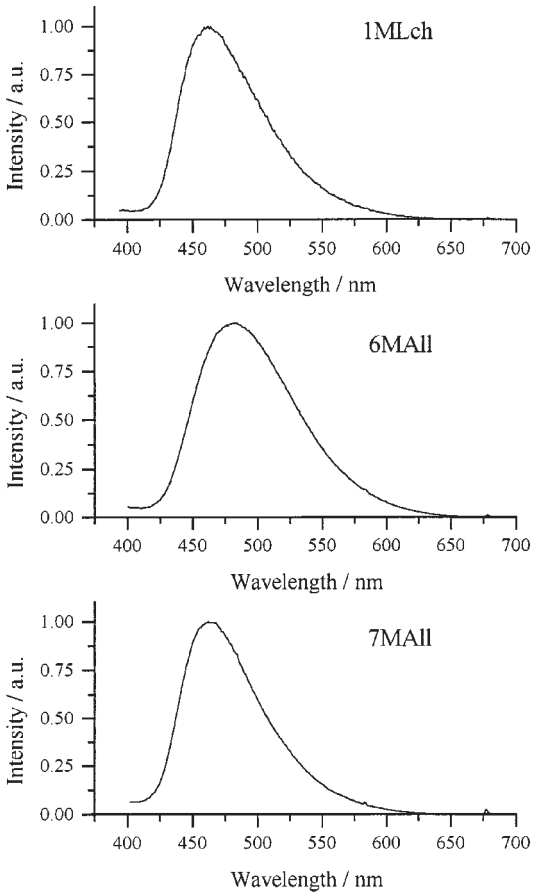

The strong UV–visible absorption and emission bands of these compounds are all assignable to electric dipole allowed $\pi \rightarrow \pi^*$ transitions (17, 18). Thus, in aprotic solvents the absorption bands will be expected to undergo small red shifts with increasing solvatochromism of the medium. If the medium can form hydrogen bonds with the alloxazine, the red shifts in the absorption spectra will be even greater and the emission spectra of the alloxazinic tautomer will exhibit increasing blue shifts in more strongly hydrogen-bonded media. Taken together, the previous spectroscopic data (1, 10) and the data in Table 1 are consistent with this straightforward interpretation. Allowing for small red shifts associated with methyl substitution, the absorption and emission spectra of the alloxazines are all similar to one another, but rather different from those of the isoalloxazines, which absorb and emit much further to the red (compare, for example, 1-methyllumichrome, an alloxazine, with its structural isomer lumiflavine, an isoalloxazine). Comparing these spectroscopic data with those obtained previously for the same compounds in β-CD inclusion complexes (10) and in 1,2-dichloroethane (1), one observes that 1,2-dichloroethane and acetonitrile give similar solvent shifts, but that *on average* the alloxazine is adsorbed in a more polar environment on cellulose than in either homogeneous acetonitrile solution or in β-CD inclusion complexes.

Note also that the emission spectra of the alloxazines on cellulose (Fig. 3) are typical of the emission spectra of the

Fig. 4. Normalized fluorescence emission spectra of Lch on cellulose and Lch crystals (top), and All on cellulose and All crystals (bottom).

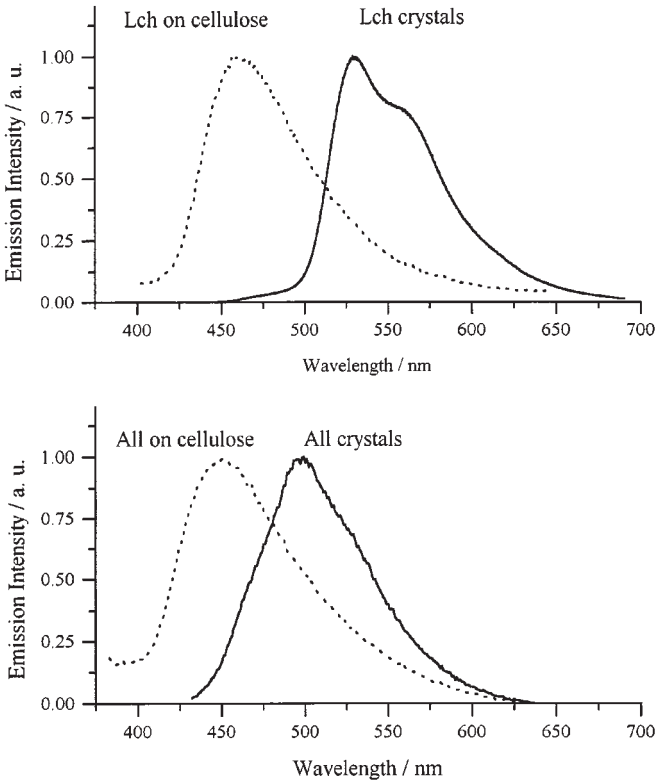

Fig. 5. Normalized fluorescence emission spectra of Lfl on cellulose (top), and 3MLfl on cellulose (bottom).

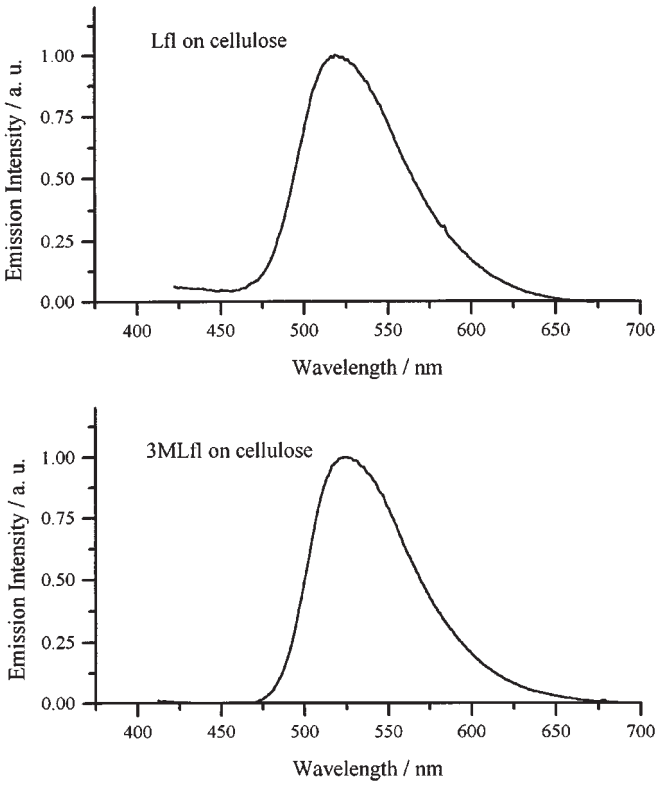

© 1999 NRC Canada

Can. J. Chem. Downloaded from www.nrcresearchpress.com by University Town Library of Shenzhen on 09/05/12
For personal use only.

Table 1. Spectral data for several alloxazines and isoalloxazines on cellulose and in ethanol. [a]

	Cellulose			Ethanol		
Compound	$\lambda_{max\ 2}$ (nm)	$\lambda_{max\ 1}$ (nm)	λ_F (nm)	$\lambda_{max\ 2}$ (nm)	$\lambda_{max\ 1}$ [b] (nm)	λ_F (nm)
Alloxazine	332	382	451	321	376 (6200)	445
6-Methylalloxazine	342	391(s) [c]	482	332	380	460
7-Methylalloxazine	335	395	463	321	386 (6100)	454
8-Methylalloxazine	358	389(s)	440	341	373 (8100)	436
9-Methylalloxazine	341	387	469	335	381 (4700)	465
Lumichrome	354	388	460	336	383 (8000)	453
1-Methyllumichrome	354	392	462	337	385 (7400)	459
3-Methyllumichrome	351	390	456	337	384 (8000)	453
Lumiflavine	—	447	520	346	444 (10 500)	515
3-Methyllumiflavine	—	451	523	349	446	515

[a]The maxima of the two strong long-wavelength bands in the absorption spectra are $\lambda_{max\ 1}$, $\lambda_{max\ 2}$; the fluorescence emission maximum is λ_F.

[b]Molar absorptivities (M^{-1} cm^{-1}) are given in parentheses.

[c](s) = shoulder.

excited alloxazine in a polar environment, whereas the emission spectra of the isoalloxazines (Fig. 5) are typical of the excited isoalloxazinic forms, i.e., lying much further to the red than those of their alloxazine tautomers. Thus the alloxazines adsorbed on cellulose do not produce significant emission from the isoalloxazinic tautomer following excitation. It is then tempting to suggest that no significant excited state intermolecular proton transfer occurs in the adsorbed molecules. However, one should be cautious in drawing such a conclusion on the basis of the spectra alone, because the quantum yields of emission from species produced on excitation of alloxazines adsorbed on cellulose have not been measured and may be quite different for the excited isoalloxazinic and alloxazinic forms (10).

The emission spectra of the polycrystalline samples of lumichrome and alloxazine are very different from the spectra obtained by exciting these same compounds on cellulose. In fact the emission spectra of these polycrystalline solids (Fig. 4) might suggest that the observed fluorescence should be assigned to the excited states of their isoalloxazinic tautomers (compare Figs. 3 and 5). Excited state intramolecular proton transfer cannot occur in these molecules. Therefore if the emission from the crystalline alloxazines were assignable to the excited isoalloxazinic forms, this would provide strong evidence for the existence of doubly hydrogen-bonded dimers in the crystalline solid that undergo intermolecular double proton transfer on excitation as previously suggested for lumichrome in various solid forms (10). Note, however, that the fluorescence decay data presented below do not sustain such a simple interpretation of the spectroscopic data.

The temporal profiles of the fluorescence of the alloxazines and lumiflavine were measured in acetonitrile, ethanol, and 1,2-dichloroethane solutions at room temperature using both conventional and ps laser-excited time-correlated single-photon counting methods. Logarithmic fluorescence decay plots are given in Fig. 6 for the representative alloxazines 6MAll and 9MAll and in Fig. 7 for the isoalloxazines Lfl and 3MLfl. In all cases the fluorescence decays are well modelled by single exponential functions, as shown by the usual statistical measures of "goodness-of-fit." The lifetime, τ_f, and corresponding fluorescence quantum yield, ϕ_f, data are collected in Table 2. Note that the excited alloxazines all exhibit considerably shorter decay times than the isoalloxazines, ranging from ca. 0.5 to 1 ns for the former, and from 6 to 7 ns for the latter. The existence of excellent single exponential fits of the decay data is good evidence for the presence of a single emitting species in each case.

Given the implied presence of only a single emitting species when each of the alloxazines and isoalloxazines is excited in homogeneous solution, the rate constants for their radiative and non-radiative relaxation processes may be calculated using the following well-known relationships:

$$[2] \qquad k_r = \phi_f/\tau_f \text{ and } \sum k_{nr} = (1 - \phi_f)/\tau_f$$

Here, k_r is the rate constant for radiative decay of the excited species and $\Sigma\, k_{nr}$ is the sum of all first-order and pseudo-first-order rate constants for its non-radiative decay. The values of k_r and $\Sigma\, k_{nr}$ are also tabulated in Table 2. The sum, $\Sigma\, k_{nr}$, could in principle contain contributions from pseudo-first-order concentration and oxygen quenching of the excited species. However, the concentrations of both the ground state chromophore ($<10^{-4}$ M) and oxygen ($<10^{-3}$ M) are too small to contribute significantly to the rates of decay of the excited molecules even if the quenching were diffusion limited. Thus the measured differences in $\Sigma\, k_{nr}$ can be attributed primarily to differences in the rates of intramolecular radiationless relaxation processes in the excited states of these compounds.

Note that, with the possible exception of alloxazine itself, the values of both k_r and $\Sigma\, k_{nr}$ differ by no more than a factor of about two in the three solvents employed, as expected of systems in which the excited state decay is dominated by intramolecular processes whose rates are only weakly varying functions of solvent–solute interaction energy (see, for example, ref. 19). Note in particular that the radiative rate constants of the excited states of the alloxazines are not significantly different from that of the isoalloxazine lumiflavine, consistent with the fact that both possess similar chromophores. The longer lifetimes of the excited isoalloxazines, Lfl and 3MLfl, compared with the excited alloxazines can therefore be ascribed exclusively to the slower rates of non-radiative decay of the former. In all of the alloxazinic com-

© 1999 NRC Canada

Can. J. Chem. Downloaded from www.nrcresearchpress.com by University Town Library of Shenzhen on 09/05/12
For personal use only.

Fig. 6. Normalized fluorescence emission decays of 6MAll in ethanol (left), and 9MAll in ethanol (right).

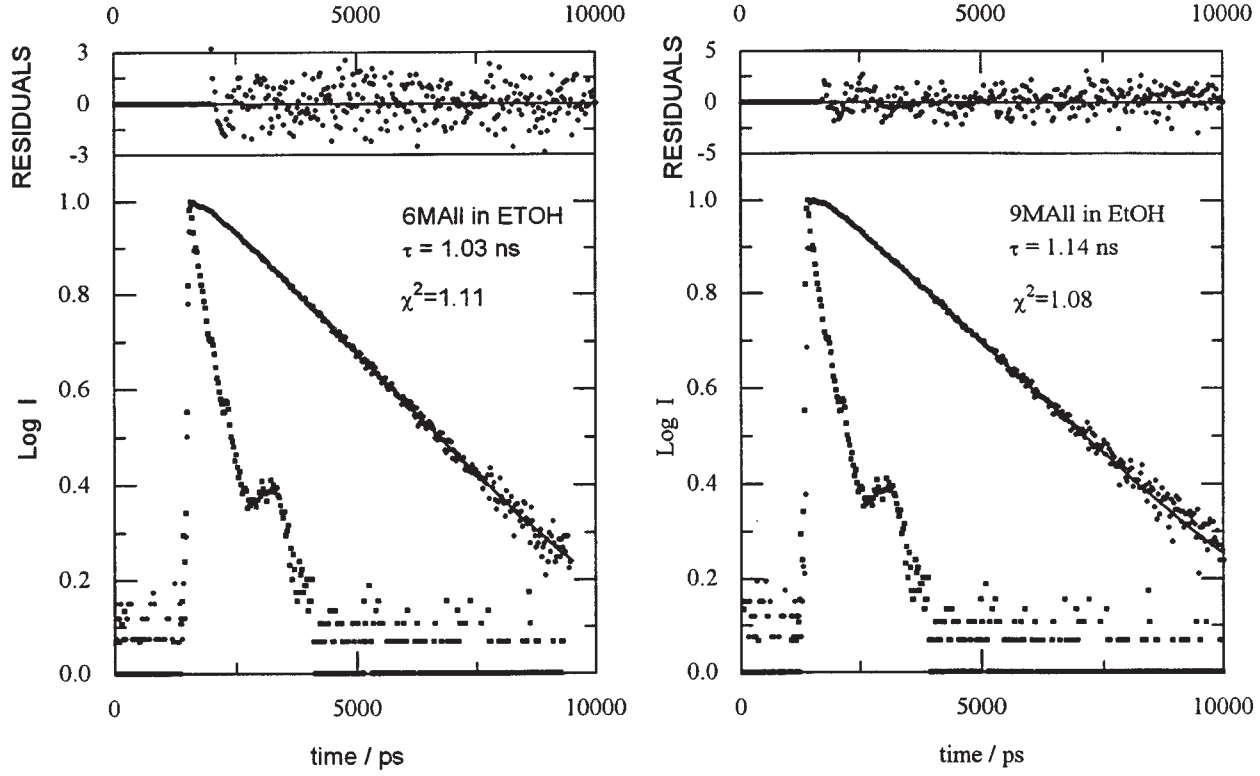

Fig. 7. Normalized fluorescence emission decays of Lfl in ethanol (left) and 3MLfl in ethanol (right).

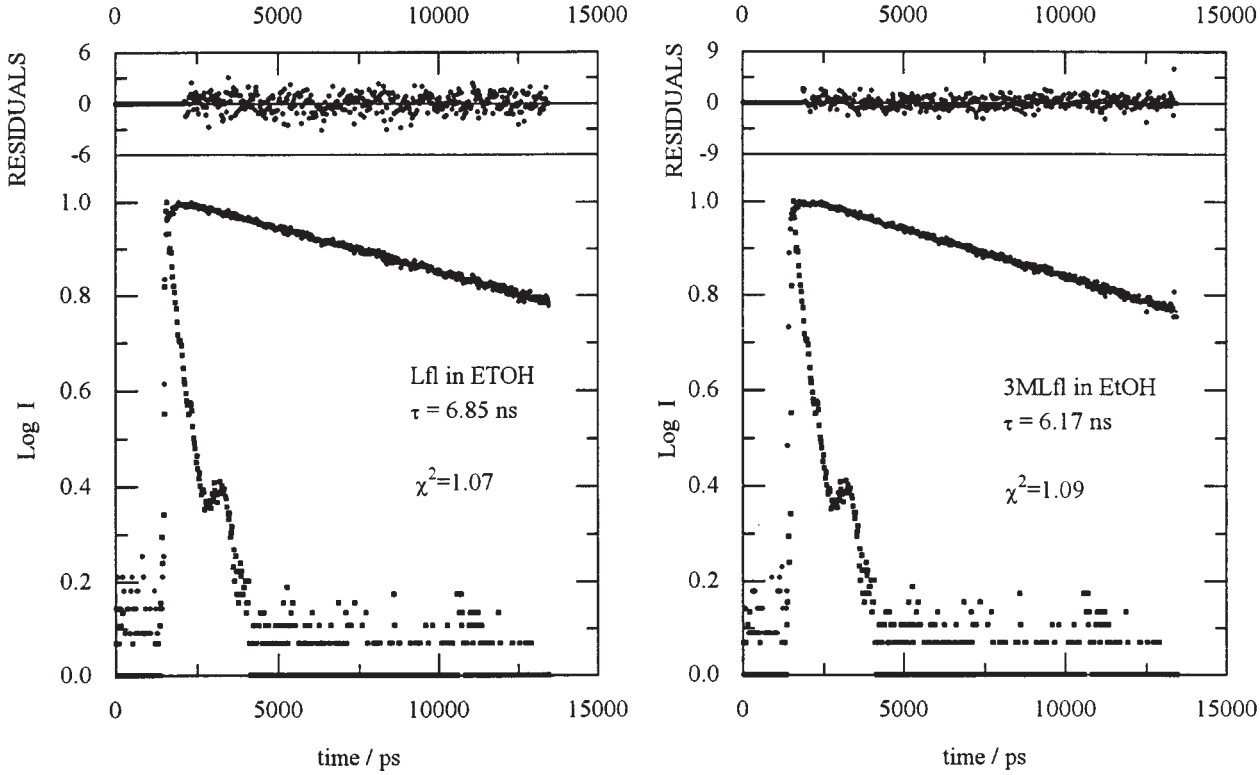

pounds examined here, non-radiative relaxation dominates the excited state decay.

Temporal fluorescence profiles were also measured for the alloxazines and isoalloxazines on cellulose, and for the polycrystalline samples of lumichrome and the parent compound itself, alloxazine. The fluorescence data, plotted in $\log_{10} I$ (relative intensity) vs. time form, are shown in Fig. 8 for 6MAll and 7MAll on cellulose and in Fig. 9 for Lch on

© 1999 NRC Canada

Table 2. Photophysical properties of several alloxazines and lumiflavine in homogeneous solution.

	1,2-Dichloroethane [a]				Acetonitrile				Ethanol			
Compound	τ (ns)	ϕ_F (10^{-2})	k_r (10^7 s^{-1})	Σk_{nr} (10^9 s^{-1})	τ (ns)	ϕ_F (10^{-2})	k_r (10^7 s^{-1})	Σk_{nr} (10^9 s^{-1})	τ (ns)	ϕ_F (10^{-2})	k_r (10^7 s^{-1})	Σk_{nr} (10^9 s^{-1})
All	0.19	2.3	12.0	5.1	0.35	0.9	2.6	2.8	—	—	—	—
6Mall	0.87	2.9	3.3	1.1	0.9	1.7	1.9	1.1	1.03	1.6	1.5	0.95
7Mall	0.49	3.4	6.9	2.0	0.6	2.5	4.2	1.6	0.85	4.6	5.4	1.12
8Mall	0.32	2.4	7.5	3.0	0.4	1.7	4.1	2.5	0.51	3.1	6.1	1.90
9Mall	0.74	2.8	3.8	1.3	0.6	1.8	2.9	1.6	1.35	3.0	2.2	0.72
Lc	0.61	2.6	4.3	1.6	0.7	2.8	4.2	1.4	0.88	5.8	6.6	1.07
1MLc	—	—	—	—	0.5	2.9	5.9	1.9	0.94	6.2	6.6	1.00
Lfl	6.71	—	—	—	7.64	20.9	3.8	0.09	6.85	4.2	6.1	0.08

[a] Except for Lfl, these data are from ref. 1.

Fig. 8. Normalized fluorescence emission decays of 6MAll on cellulose (left), and 7MAll on cellulose (right).

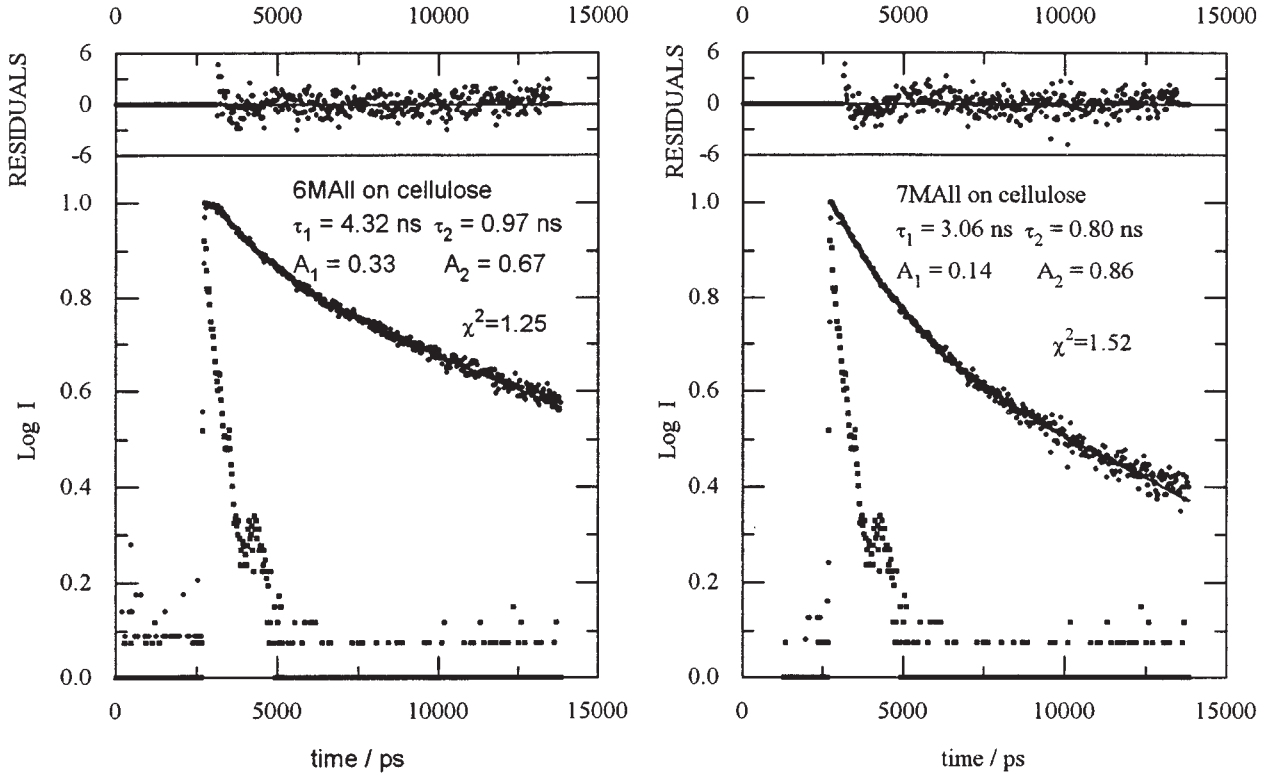

cellulose and Lch crystals. None of the data are well described by single exponential fluorescence decay functions, and fits to double exponential functions of the form

$$I(t) = a_1 \exp(-t/\tau_1) + a_2 \exp(-t/\tau_2)$$

were therefore attempted. The best numerical fits of the four constants in this equation to the experimental data are shown in the figures, together with the resulting distributions of weighted residuals. The values of the lifetimes, the reduced χ^2, and the fractions of the emission attributable to each emitter, $F_i = a_i\tau_i / \Sigma\, a_j\tau_j$, are given in Tables 3 and 4.

The fits are not perfect between these experimental data and those calculated for double-exponential decay functions. However, the existence of reasonable double-exponential fits provides a rationale for seeking a mechanism in which there are two distinct emitting species. Note that for the alloxazines on cellulose the shorter-lived component has a lifetime ranging from 0.67 to 0.93 ns whereas the longer-lived component has a lifetime of from 2.0 to 3.8 ns. Since these ranges of lifetimes are not too different from the ranges of lifetimes found when the alloxazines and isoalloxazines are separately excited in liquid solvents (cf. Table 2), it might be tempting to assign the shorter-lived component to the excited alloxazine and the longer-lived component to a separate excited species, perhaps formed as the result of intermolecular proton transfer between the alloxazine and the hydroxyl groups of cellulose. However, there are a number of reasons to believe this is not the correct interpretation of these data.

First, note that double-exponential decay is observed for 1MLch on cellulose, in which the substitution of a methyl group at N(1) prevents this compound from acting as a proton donor and acceptor. Thus the longer-lived component cannot be an excited isoalloxazine in this molecule, and a

© 1999 NRC Canada

Can. J. Chem. Downloaded from www.nrcresearchpress.com by University Town Library of Shenzhen on 09/05/12
For personal use only.

Can. J. Chem. Downloaded from www.nrcresearchpress.com by University Town Library of Shenzhen on 09/05/12
For personal use only.

Fig. 9. Normalized fluorescence emission decays of Lch on cellulose (left) and Lch crystals (right).

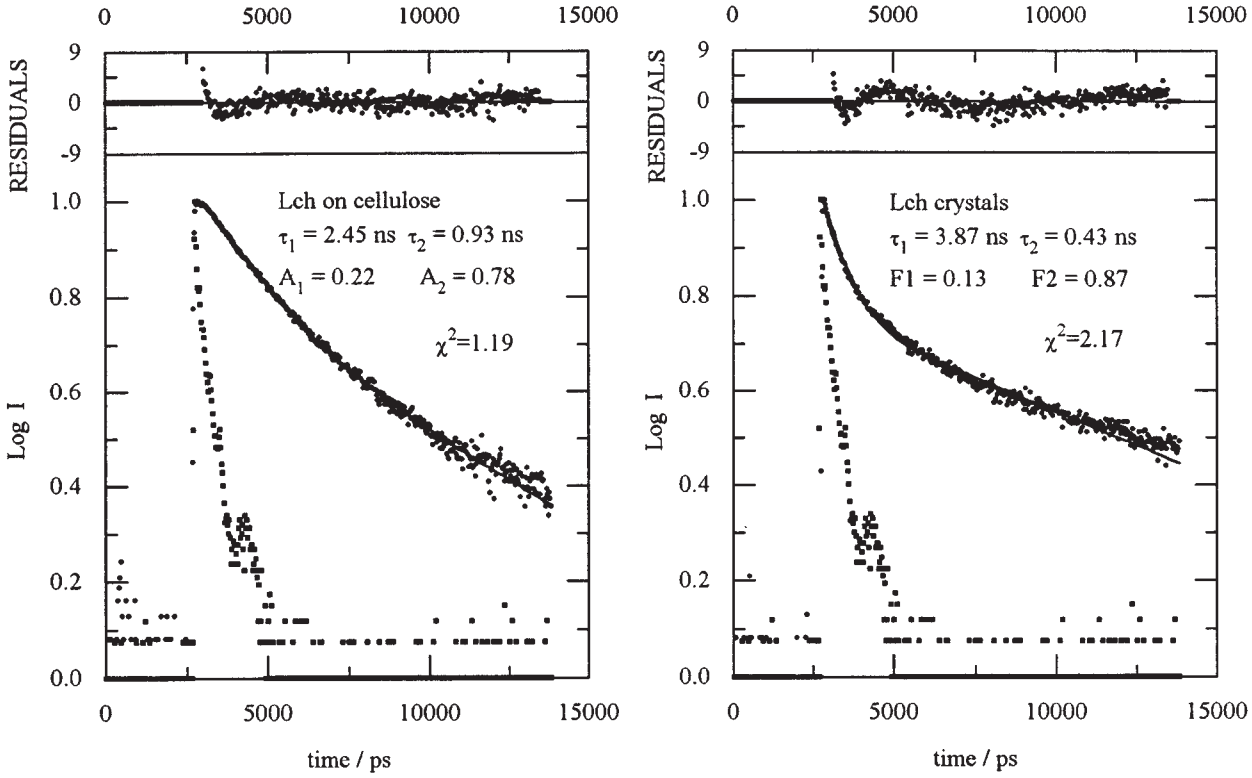

Table 3. Double-exponential decay analysis of the fluorescence of several alloxazines on cellulose at room temperature in air-equilibrated samples.

Compound	λ_F (nm)	τ_1 (F_1) (ns)	τ_2 (F_2) (ns)	χ^2
Alloxazine	451	3.77 (0.58)	0.67 (0.42)	1.46
6-Methylalloxazine	482	4.32 (0.69)	0.97 (0.31)	1.25
7-Methylalloxazine	463	2.46 (0.55)	0.91 (0.45)	1.19
8-Methylalloxazine	440	2.92 (0.34)	0.77 (0.66)	1.19
9-Methylalloxazine	469	3.76 (0.65)	0.97 (0.35)	1.19
Lumichrome	460	2.45 (0.43)	0.93 (0.57)	1.19
1-Methyllumichrome	462	1.97 (0.52)	0.67 (0.48)	2.24

Table 4. Double-exponential decay analysis of the fluorescence of crystalline alloxazine and lumichrome at room temperature in air-equilibrated samples.

Compound	λ_F (nm)	τ1 (*F*1) (ns)	τ2 (*F*2) (ns)	χ^2
Alloxazine	500	3.06 (0.51)	0.65 (0.49)	1.20
Lumichrome	525	3.87 (0.58)	0.43 (0.42)	1.24

different reason for at least its double-exponential fluorescence decay must be found. Second, for acetic acid – alloxazine complexes in which double excited state proton transfer does occur in solution, a rate of rise in the emission of the isoalloxazinic tautomer identical to the rate of decay of the excited alloxazinic form has been observed in some cases (1). No such precursor–product kinetic relationship is observed here, despite the fact that the emission was monitored at wavelengths that should have encompassed the emission of both excited tautomers, if present. Finally, the values of F_1 and F_2 (cf. Table 3) suggest that two species, if present, should contribute to the observed fluorescence with relative intensities in a range from about 2:1 to 1:2. Although the emission spectra of the alloxazines on cellulose are broad, there is no hint in these spectra that more than one species is present. If the longer-lived species are attributable to the excited isoalloxazinic tautomers, then, with up to two thirds of the total emission attributable to them, they should exhibit a second red-shifted band in the emission spectra. No such band is seen in the spectra of the alloxazines on cellulose.

We therefore seek an alternate explanation for the photophysical properties of these alloxazines and isoalloxazines adsorbed on cellulose. First, the moderately good fit of a double-exponential decay function to the decay data will not be interpreted in terms of two, and only two, emitting species. Rather, we assign the emission from the excited alloxazines on cellulose to species adsorbed in a range of environments. The values of $\Sigma\, k_{nr}$ of the methylalloxazines and Lc in ethanol are either the same or modestly smaller,

© 1999 NRC Canada

Can. J. Chem. Downloaded from www.nrcresearchpress.com by University Town Library of Shenzhen on 09/05/12
For personal use only.

compound for compound, compared with their values in 1,2-dichloroethane (cf. Table 2). We therefore tentatively conclude that polar protic environments have a stabilizing effect on the excited species. Because there is clear evidence that cellulose provides a stronger hydrogen-bonding environment than ethanol (see, for example, ref. 20), we thus assign the longer-lived species on cellulose to alloxazines, which are adsorbed at strongly hydrogen-bonding sites. The relative magnitudes of the values of F_1 and F_2 are then interpreted as indicating that cellulose provides relative numbers of highly polar and moderately polar binding sites for the alloxazines that are roughly in the ratio 1:1 to 1:2. The spectra of the ensemble of species will thus be expected to be broad, but species in different environments will have similar spectra, given that only solvatochromic shifts contribute to this breadth.

These results suggest that these heterogeneous systems would benefit from analysis using any of a number of methods for recovering underlying distributions of lifetimes from fluorescence decay data (21). To be of value, such analyses will require single-photon counting data acquired under conditions of better statistical reliability than presently available.

Finally, we note that the very different emission spectra of the polycrystalline samples of lumichrome and alloxazine, compared with their corresponding spectra in the adsorbed state (Fig. 4), might lead one to believe that these two compounds exhibit emission from their isoalloxazinic tautomers in the excited state of the crystals, or perhaps from stacked dimers. Note that their molecular structures admit the possibility of double excited state proton transfer, provided that a center of symmetry is found in the crystal structure at the geometric center of a planar arrangement of four nitrogen atoms (N(10), N(1), N′(10), N′(1)) from two adjacent molecules. However, a lack of clear confirmation from the lifetime data that the emission originates predominately from a single longer-lived species, which could be identified with the excited isoalloxazine, and our inability to date to obtain single crystals of these compounds for X-ray analysis makes such a simple interpretation problematic.

Conclusions

The absorption and emission spectra and the fluorescence lifetimes and quantum yields of alloxazine and several of its N- and C-methyl-substituted derivatives have been measured in a nonpolar solvent, a polar aprotic solvent, and a polar protic solvent. The photophysical data suggest that only one emitting species is present in all cases: the excited alloxazine when a ground state alloxazine is excited, and the excited isoalloxazine when a ground state lumiflavine is excited. There is no evidence of excited state proton transfer in any of these solutes in any of the three solvents. The longer lifetimes and larger fluorescence quantum yields of the isoalloxazines compared with the alloxazines can be attributed exclusively to significantly slower rates of radiationless relaxation in the excited isoalloxazines.

The remission and emission spectra of these same compounds adsorbed on cellulose are similar to the corresponding absorption and emission spectra in homogeneous solution, suggesting that the emitting species are the same in the adsorbed state as they are in solution. The adsorbed excited species exhibit non-exponential temporal decay. However, consistent with the spectra, this observation is attributed to inhomogeneities in the binding of the chromophore to the substrate, rather than to excited state intermolecular proton transfer.

The spectroscopic and photophysical data for polycrystalline samples of alloxazine and lumichrome do not admit a consistent interpretation of the excited state behaviour. The emission spectra suggest the possible occurrence of double intermolecular excited state proton transfer, but this interpretation is not clearly supported by the photophysical data. Further information, including crystal structures, will be necessary to advance this aspect of the work.

Acknowledgements

We thank Professors A. Koziolowa and J. Koziol for valuable discussions. Grants from the British Council and the Polish State Committee for Scientific Research to F.W. and M.S. are gratefully acknowledged. R.P.S. and M.S. thank the Natural Sciences and Engineering Research Council of Canada for continuing support.

References

1. E. Sikorska and A. Koziolowa. J. Photochem. Photobiol. A: Chem. **95**, 215 (1996).
2. M.M. Szafran, J. Koziol, and P. Heelis. Photochem. Photobiol. **52**, 353 (1990).
3. A. Koziolowa, A.J.W.G. Visser, and J. Koziol. Photochem. Photobiol. **48**, 7 (1988).
4. M. Kasha. J. Chem. Soc. Faraday Trans. 2, **82,** 2379 (1986).
5. J.D. Choi, R.D. Fugate, and P.S. Song. J. Am. Chem. Soc. **102**, 5293 (1980).
6. A. Koziolowa. Photochem. Photobiol. **29**, 459 (1979).
7. P.S. Song, M. Sun, A. Koziolowa, and J. Koziol. J. Am. Chem. Soc. **96**, 4119 (1974).
8. J. Koziol. Photochem. Photobiol. **5**, 41 (1966).
9. B. Sarkar, U. Das, S. Bhattacharyya, and S.K. Bose. Bull. Chem. Soc. Jpn. **68**, 1807 (1995).
10. M. Mir, E. Sikorska, M. Sikorski, and F. Wilkinson. J. Chem. Soc. Perkin Trans. 1095 (1997).
11. F. Wilkinson and G. Kelly. *In* Handbook of organic photochemistry. Vol. 1. *Edited by* J.C. Scaiano. CRC Press, Boca Raton, Fla. 1989. pp. 293–314.
12. F. Wilkinson. J. Chem. Soc. Faraday Trans. 2, **82**, 2073 (1986).
13. D.R. James, D.R.M. Demmer, R.E. Verrall, and R.P. Steer. Rev. Sci. Instrum. **54**, 1121 (1983).
14. W. Augustyniak, J. Koput, A. Maciejewski, M. Sikorski, R.P. Steer, and M. Szymanski. Pol. J. Chem. **67**, 1409 (1993).
15. S.R. Meech and D. Phillips. J. Photochem. **23**, 193 (1983).
16. P. Kubelka and F. Munk. Z. Tech. Phys. **12**, 593 (1931).
17. M. Sun, T.A. Moore, and P.S. Song. J. Am. Chem. Soc. **94**, 1730 (1972).
18. H. Szymusiak, J. Konarski, and J. Koziol. J. Chem. Soc. Perkin Trans. 2, 229 (1990).
19. B.D. Wagner, D. Tittelbach-Helmrich, and R.P. Steer. J. Phys. Chem. **96**, 7904 (1992).
20. M. Sikorski, F. Wilkinson, and R.P. Steer. J. Chem. Soc. Faraday Trans. **94**, 1855 (1998).
21. A. Siemiarczuk, B.D. Wagner, and W.R. Ware. J. Phys. Chem. **94**, 1661 (1990).

© 1999 NRC Canada

Determination of the configuration of ribitol in the C-polysaccharide of *Streptococcus pneumoniae* using a synthetic approach

Huiping Qin and T. Bruce Grindley

Can. J. Chem. Downloaded from www.nrcresearchpress.com by University Town Library of Shenzhen on 09/05/12
For personal use only.

Abstract: The C-polysaccharide is an antigen common to all known serotypes of *Streptococcus pneumoniae* bacteria and is a potential target for vaccine preparation. The final uncertainty in the structure of its repeating unit, a pentasaccharide phosphate containing two phosphorylcholine side chains, has been resolved by determining the configuration of ribitol. Assignment of configuration was performed by synthesis of the two trisaccharide phosphate fragments that have either D- or L-ribitol at their centers and comparison of their ^{1}H and ^{13}C NMR spectral data with that of the natural polysaccharide. The syntheses employed common synthons added in different orders to an asymmetrically substituted chiral ribitol derivative to obtain opposite chiralities in the ribitol segments. The data for the trisaccharide containing D-ribitol was almost identical to that of the natural material while that for the trisaccharide containing L-ribitol differed significantly. In particular, the chemical shift differences between the two protons of the primary carbons of ribitol units directly attached to the β-2-acetamido-2-deoxy-galactopyranosyl residue were 0.10, 0.12, and 0.33 ppm, in the natural polysaccharide, the D-ribitol-containing trisaccharide, and the L-ribitol-containing trisaccharide, respectively. The average difference between the ^{13}C NMR chemical shifts of corresponding ribitol carbons from the natural polysaccharide and the D-ribitol-containing trisaccharide phosphate was 0.034 ppm. This evidence indicates that ribitol in the C-polysaccharide has the D-configuration and that a very similar mixture of conformations in the ribitol portions is present for the natural polysaccharide and the D-ribitol-containing trisaccharide phosphate.

Key words: C-polysaccharide, *Streptococcus pneumoniae*, ribitol, dibutylstannylene acetal, determination of configuration.

Résumé : Le polysaccharide-C est un antigène commun à tous les sérotypes connus de la bactérie *Streptococcus pneumoniae* et est un objectif potentiel pour la préparation de vaccins. En déterminant la configuration du ribitol, on a levé la dernière incertitude dans la structure de son unité constitutive, un phosphate de polysaccharide contenant deux phosphorylcholine comme chaînes latérales. On a attribué la configuration en effectuant la synthèse des deux fragments de phosphate de trisaccharide comportant soit le D- soit le L-ribitol comme centres et en comparant les données de leurs spectres RMN du ^{1}H et du ^{13}C avec celles du polysaccharide naturel. On a réalisé la synthèse des trisaccharides en utilisant des synthons communs et un dérivé chiral du ribitol substitué d'une façon asymétrique qui ont été ajouté dans des ordres différents dans le but d'obtenir une chiralité différente dans ce segment. Les données obtenues avec le trisaccharide contenant du D-ribitol sont pratiquement identiques à celles du produit naturel alors que celles obtenues avec le trisaccharide contenant du L-ribitol présentent des différences significatives. En particulier, les différences de déplacements chimiques entre les deux protons des carbones primaires des unités ribitol attachées directement au résidu β-2-acétamido-2-désoxy-galactopyranosyle sont égales respectivement à 0,10, 0,12 et 0,33 ppm pour le polysaccharide naturel, le trisaccharide contenant le D-ribitol et le trisaccharide contenant le L-ribitol. La différence moyenne entre les déplacements chimiques en RMN du ^{13}C pour les carbones correspondants du ribitol du polysaccharide naturel et du trisaccharide contenant le D-ribitol sont de 0,034 ppm. Cette différence indique que le polysaccharide-C possède la configuration D et que le polysaccharide naturel et le phosphate du trisaccharide contenant le D-ribitol comportent des mélanges très semblables de conformations dans les portions du ribitol.

Mots clés : polysaccharide-C, *Streptococcus pneumoniae*, ribitol, acétal de dibutylstannylène, détermination de configuration.

[Traduit par la Rédaction]

Received October 16, 1998.

H. Qin and T.B. Grindley.[1] Department of Chemistry, Dalhousie University, Halifax, NS B3H 4J3, Canada.

[1]Author to whom correspondence may be addressed. Telephone: (902) 494-2041. Fax: (902) 494-1310.
e-mail: grindley@chem1.chem.dal.ca

 © 1999 NRC Canada

Scheme 1. The structure of the C-polysaccharide of *Streptococcus pneumoniae* with the configuration of ribitol shown as D.

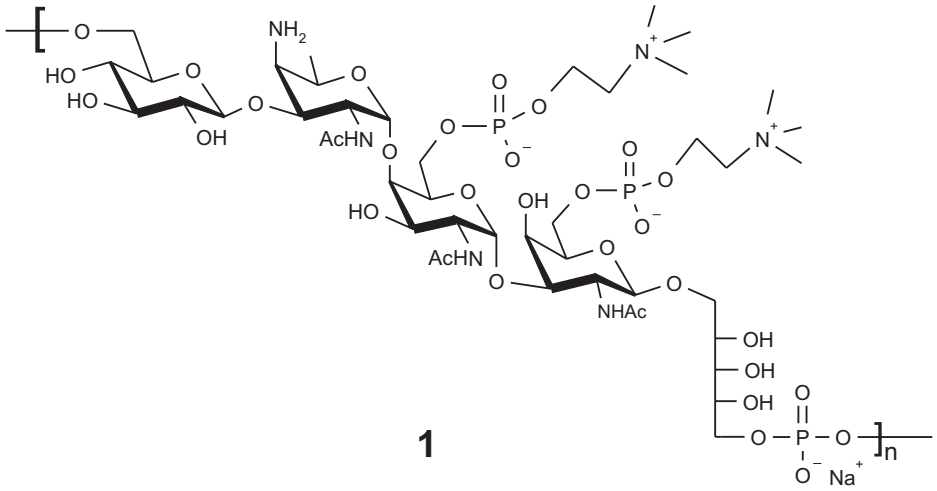

1

Introduction

The Gram-positive microorganism *Streptococcus pneumoniae* induces infections such as pneumonia, bacteremia, otitis media, and meningitis in human beings (1), and resistance to drug treatment is becoming an increasing problem. Ninety serologically defined types of these capsular bacteria have been described to date (2). The capsule of each serotype is a unique polysaccharide that extends outwards from the cell wall and current vaccines against this organism contain a mixture of 23 of the capsular polysaccharides of the most common serotypes. The C-polysaccharide, a common antigen of all the known serotypes of *Streptococcus Pneumoniae*, is distributed on both the inside and outside of the cell walls (3). A polysaccharide with the same repeating unit is covalently bonded to a lipid moiety in the plasmic membrane through a phosphodiester linkage (4), in which form it is called the F antigen. Its presence in all serotypes makes it an attractive target for vaccine preparation but attempts to date have not resulted in sufficient activity to yield commercial vaccines (1*c*, 5, 6). Structural studies (7–12) showed that the polysaccharide contained the pentasaccharide repeating unit shown in Scheme 1.

The configuration of ribitol in the structure was assumed to be D, based on schemes proposed for the biosynthesis of teichoic acids where the donors of glycerol and ribitol phosphate residues are CDP-glycerol and CDP-ribitol, respectively (8, 9, 13). Teichoic acids are major constituents of Gram-positive bacterial cell walls and consist of polymers of ribitol-5-phosphate or glycerol-3-phosphate with carbohydrates and alanine as substituents (13) and the C-polysaccharide was classified as a teichoic acid (8). The experimental evidence supporting this scheme is that CDP-ribitol is incorporated in polyribitol phosphate by cell-free enzymic preparations from various Gram-positive bacteria (14). It is not certain that this scheme would apply to the ribitol phosphate in the C-polysaccharide or other polymers where ribitol phosphate constitutes a small part of the polymer.

Although the absolute configuration of glycerol has been determined a number of times (15–22), the configuration of ribitol has never been determined for any compounds derived from Gram-positive bacteria. In fact, its configuration has only been determined three times; it was demonstrated to have the D-configuration in the capsular polysaccharide from type b *Haemophilus influenzae*, a Gram-negative organism (23), in a compound isolated from a lichen (24), and in CDP-ribitol (25). Glycerol-1-phosphate normally has the D-configuration (15, 17, 19–21) in agreement with the scheme proposed for its biosynthesis, but L-glycerol-1-phosphate is also known, in the membrane-bound teichoic acid from *Streptococcus lactis* (16) and in the cell wall of *Bacillus cereus* (22). It was discovered that the biosynthetic pathway leading to L-glycerol-1-phosphate was different from that proposed for its D-analogue (26) and the question naturally arises as to whether only one biosynthetic pathway leads to ribitol-5-phosphate.

Ribitol-5-phosphate is present in several of the capsular polysaccharides of *Streptococcus pneumoniae* as well as in the C-polysaccharide, and its configuration in these compounds has also been assumed to be D (27). In this publication, we outline the determination of the configuration of ribitol in the C-polysaccharide of *Streptococcus pneumoniae* through synthesis of the two trisaccharide portions of the natural C-polysaccharide that have D- and L-ribitol at the center. A tetrasaccharide portion of the repeating unit synthesized previously had D-ribitol at the nonreducing terminus, but no attempt was made to determine whether the configuration of ribitol matched that in the natural product (28).

Results and discussion

Synthetic strategy

To simulate the environment of the ribitol unit in the C-polysaccharide, two trisaccharide phosphate targets (**18** and **24**) were designed. In **18** and **24**, instead of linking to another 2-acetamido-2-deoxy-D-galactopyranose residue as in the C-polysaccharide, the 3″ position was substituted with a methyl group. A synthetic strategy to obtain **18** and **24** was developed that made the maximum use of synthons that were common to both trisaccharides and is shown in Scheme 2.

Synthesis of trisaccharide phosphates containing the D-ribitol unit (18)

Compound **12** was obtained from the known compound, *tert*-butyldimethylsilyl 2-azido-4,6-*O*-benzylidene-2-deoxy-β-D-galactopyranoside (29), as shown in Scheme 3. The anomeric

© 1999 NRC Canada

Can. J. Chem. Downloaded from www.nrcresearchpress.com by University Town Library of Shenzhen on 09/05/12
For personal use only.

Can. J. Chem. Downloaded from www.nrcresearchpress.com by University Town Library of Shenzhen on 09/05/12
For personal use only.

Scheme 2. Retrosynthetic analysis of synthesis of trisaccharide phosphates **18** and **24**.

© 1999 NRC Canada

Scheme 3. Synthesis of glycosyl donor **12**.

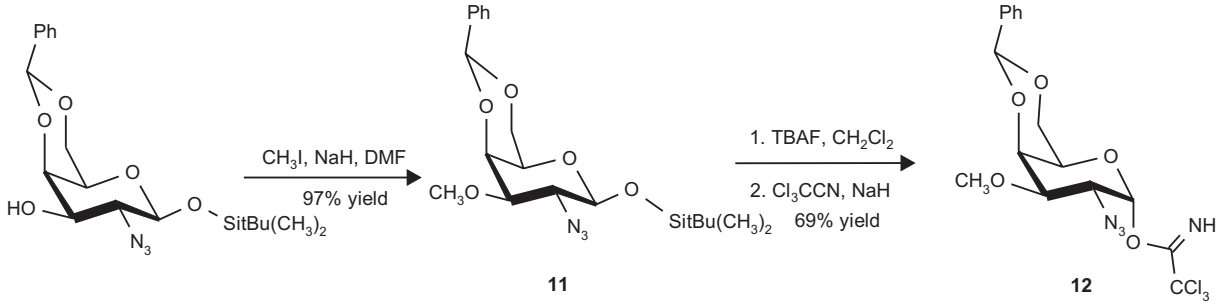

Scheme 4. Synthesis of key ribitol-containing intermediate **8**.

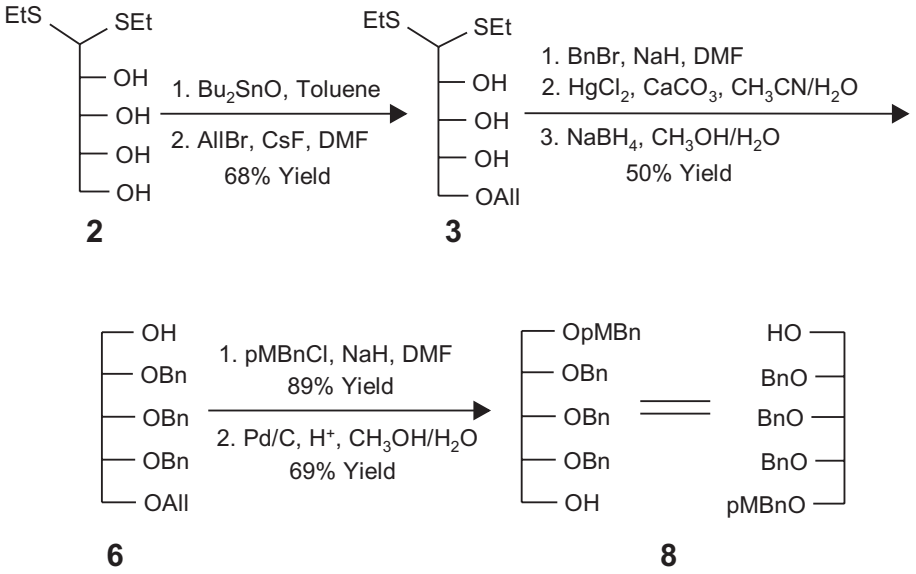

tert-butyldimethylsilyl group was stable in the presence of sodium hydride, allowing O-3 to be methylated in 97% yield with methyl iodide to provide **11**. Treatment of **11** with TBAF in dichloromethane successfully afforded the desired desilylated product. Subsequent reaction with trichloroacetonitrile in the presence of sodium hydride afforded the α-trichloroacetimidate **12** selectively in a 69% yield for the two steps.

Compound **8**, the key intermediate, could be converted into either D- or L-ribitol derivatives, depending on the order in which the differentially protected primary hydroxyl groups were functionalized. Its synthesis started with D-ribose diethyl dithioacetal (**2**), which was selectively allylated at the primary position via a stannylene acetal intermediate to give **3**. This is the first time that a dialkyldithioacetal derivative has been selectively protected at the primary position via a dibutylstannylene acetal intermediate (30) and this approach replaces a four-step preparation from D-ribose (31). As shown in Scheme 4, following benzylation of the selectively allylated **3**, the diethyl dithioacetal group was removed and reduction gave **6**. Compound **6** had previously been prepared in six steps from γ-ribonolactone, a relatively expensive starting material (32). Following *p*-methoxybenzylation of the free hydroxy group and deallylation, ribitol derivative **8** was obtained. Compound **8** is an L-derivative if the free hydroxyl group is at O-1 as numbered in Scheme 4 but a D-derivative if the *p*-methoxybenzyl group is at O-1 as numbered for **6**.

The D-ribitol-containing trisaccharide phosphate **18** was synthesized by glycosylation of a phosphorus-linked disaccharide **14** with trichloroacetimidate **12**. As shown in Scheme 5, the synthesis of the disaccharide glycosyl acceptor **14** was performed by phosphitylation of L-ribitol derivative **8** with **10**. Compound **10** was made from methyl 2,3,4-tri-*O*-benzyl-6-*O*-trityl-β-D-glucopyranoside (33) by a sequence that started with detritylation in 75% yield using 30% HBr in acetic acid, an improved method. The product, methyl 2,3,4-tri-*O*-benzyl-β-D-glucopyranoside (**9**), was reacted with chloro 2-cyanoethyl (*N*,*N*-diisopropyl)phosphoramidite (34) in the presence of diisopropylethylamine (DIPEA) to give **10** in an 83% yield. The reaction of **10** with **8** was followed by oxidation with *m*-chloroperbenzoic acid (MCPBA) in the same pot. The *p*-methoxybenzyl group survived the acidic conditions provided by both tetrazole and MCPBA, and was removed with 2,3-dichloro-4,5-dicyanoquinone (DDQ). These two steps afforded **14** in a 57% yield. The formation of the phosphorus linkage was clearly evident in the coupling of the phosphorus to the C-4 (doublet) and C-5 (doublet) of the ribitol unit and the disappearance of isopropyl group signals (δ 24, 43) in the ^{13}C NMR spectrum. Compound **14** was a mixture of epimers at phosphorus as indicated by the two signals (δ –0.72, –0.77) in the ^{31}P NMR spectrum.

Glycosylation of the disaccharide glycosyl acceptor **14** by **12** was successfully performed in an 82% yield. As antici-

© 1999 NRC Canada

Can. J. Chem. Downloaded from www.nrcresearchpress.com by University Town Library of Shenzhen on 09/05/12
For personal use only.

Can. J. Chem. Downloaded from www.nrcresearchpress.com by University Town Library of Shenzhen on 09/05/12
For personal use only.

Scheme 5. Synthesis of D-ribitol-containing trisaccharide phosphate **18**.

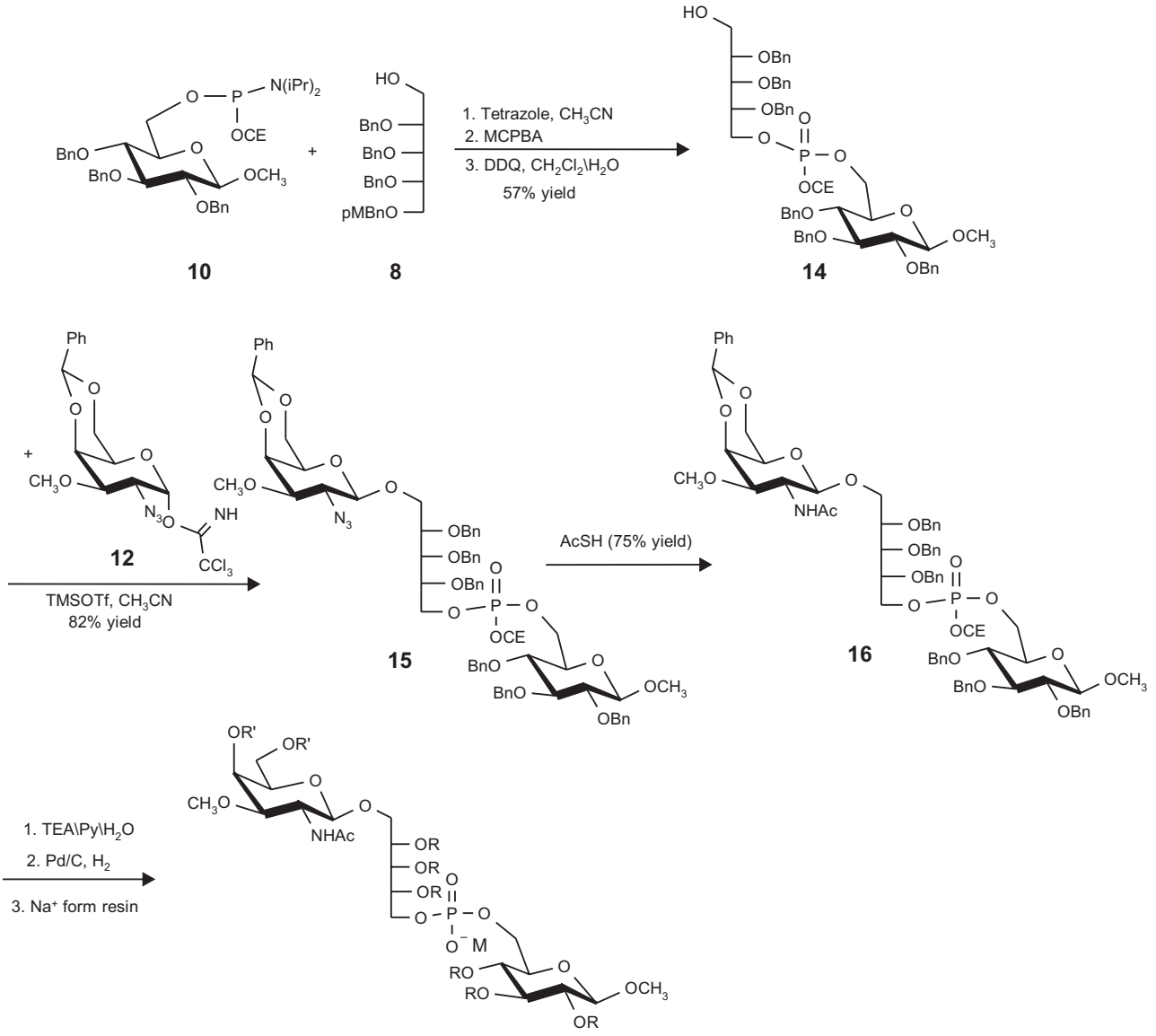

pated, solvent participation by acetonitrile (35) caused the β-linkage to be formed selectively, which was clearly shown by the observation of a large vicinal coupling constant of 7.8 Hz between H-1 and H-2. No products having an α-linkage were observed. In the transformation of the azido group to the acetamido group, the benzylidene ring surprisingly survived overnight treatment with thiolacetic acid at room temperature to give the reduction product in 75% yield.

Due to the stereogenic centre at phosphorus, **10**, **14**, and **15** are diastereomeric mixtures, as shown by their ^{31}P NMR spectra, each of which contained two peaks. This is also reflected in the appearance of two peaks in the ^{13}C NMR spectra for most of the carbons close to the phosphorus atoms. Surprisingly, on treatment of **15** with thiolacetic acid, another pair of peaks appeared. In the ^{31}P NMR spectrum of **16**, there are two large peaks (δ –0.68, –0.96) and two small peaks (δ 0.17, –0.73). A possible explanation is that both *E* and *Z* acetamido rotamers are being observed, perhaps due to hydrogen bond formation between the amide hydrogen and a phosphate oxygen in the normally less stable conformer.

The cyanoethyl (CE) group on phosphorus was removed by treatment with a triethylamine, pyridine, and water mixture for 2 h at room temperature and the product had only a single peak in its ^{31}P NMR spectrum (1.41 ppm), as expected for a product with no chirality at phosphorus. The disappearance of the CN (116 ppm) and two CH_2 (19 and 61 ppm) signals from the ^{13}C NMR spectrum confirmed the removal of this group. Hydrogenation removed the 4,6-*O*-benzylidene ring and all of the *O*-benzyl groups, as confirmed by disappearance of all of the signals assigned to aromatic proton and carbon signals in the ^{1}H and ^{13}C NMR

© 1999 NRC Canada

Scheme 6. Synthesis of the L-ribitol-containing trisaccharide phosphate **24**.

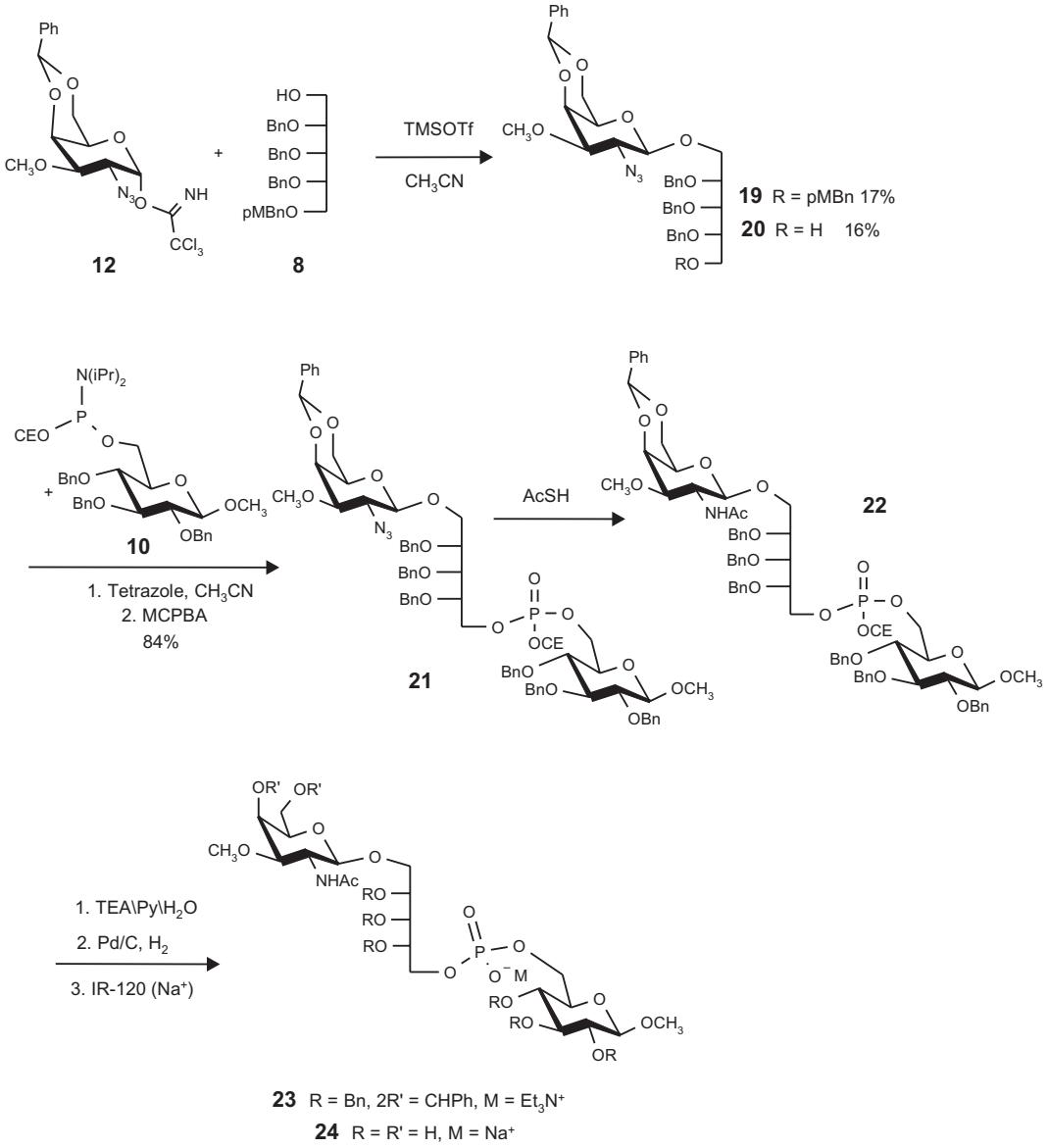

spectra, respectively. Treatment with Amberlite IR-120 (Na^+) resin afforded the target trisaccharide phosphate **18** in a quantitative yield. The disappearance of the signals for the ethyl group in the NMR spectra indicated the removal of the triethylammonium ion and the completion of the ion exchange reaction.

Synthesis of trisaccharide phosphate containing the L-ribitol unit (24)

The synthesis of the target trisaccharide phosphate **24** followed the reverse combination route outlined in Scheme 2. Though extra caution was exercised, coupling of **12** and **8** gave a low yield of a mixture of the expected product (**19**) and the product in which the *p*-methoxybenzyl group had been removed (**20**). Compound **19** was transformed into **20** by treatment with DDQ (63% yield) at room temperature. This observation confirms that compound **20** isolated from the coupling reaction was formed from **19** and, therefore, that formation of the glycosidic linkage was faster than the removal of the primary *p*-methoxybenzyl group under the coupling conditions. If the *p*-methoxybenzyl group had been cleaved at a rate comparable with or faster than glycoside formation, **20** and its diastereomer with the ribitol unit having the D-configuration would have been formed. The phosphotriester linkage between the disaccharide **20** and the phosphoramidite derivative **10** was formed as previously in an 84% yield. A diastereomeric mixture **21** having both configurations at phosphorus was obtained. The transformation of the azido group in **21** to an acetamido group and the subsequent transformation from **22** to **24**, as shown in Scheme 6, followed the same procedure as in Scheme 5.

Assignment of configuration

Complete assignments of all ^1H and ^{13}C NMR signals in the 500 and 125 MHz NMR spectra of the two trisaccharides **18** and **24** were made using a variety of 1D and 2D NMR

© 1999 NRC Canada

Can. J. Chem. Downloaded from www.nrcresearchpress.com by University Town Library of Shenzhen on 09/05/12
For personal use only.

Can. J. Chem. Downloaded from www.nrcresearchpress.com by University Town Library of Shenzhen on 09/05/12
For personal use only.

Table 1. ^{1}H NMR chemical shifts (ppm) for **PnC** (11), **18**, and **24**.

Comp.	Unit	H1a, H1b	H2	H3	H4	H5a, H5b	H6a, H6b
PnC	GalNAc	4.64	4.1	3.85	4.17	3.83	4.06, 4.06
	Rib	3.86, 3.96	3.99	3.76	3.88	3.98, 4.04	
	Glc	4.619	3.31	3.5	3.54	3.55	4.11, 4.11
18	GalNAc	4.49	3.93	3.44	4.22	3.66	3.77, 3.84
	Rib	3.83, 3.95	3.95	3.77	3.89	3.99, 4.06	
	Glc	4.39	3.28	3.5	3.5	3.58	4.07, 4.17
	ΔδRib[a]	–0.03, –0.01	0	+0.01	+0.01	+0.01, +0.02	
24	GalNAc	4.48	3.94	3.45	4.22	3.66	3.78, 3.83
	Rib	3.740, 4.07	3.95	3.744	3.93	3.98, 4.08	
	Glc	4.4	3.28	3.5	3.5	3.58	4.09, 4.18
	ΔδRib	–0.12, +0.11	0	0	+0.05	0.00, +0.04	

[a]ΔδRib refers to the chemical shift difference of the ribitol unit between **18**, **24**, and **PnC**. Digital resolution: 0.22 Hz/point for **18**, and 0.43 Hz/point for **24**.

Table 2. ^{13}C NMR chemical shifts (ppm) for **PnC** (11), **18**, and **24**.

Comp.	Unit	C1	C2	C3	C4	C5	C6
PnC	GalNAc	102.08	51.46	75.49	64.07	74.3	65.33
	Rib	71.46	71.35	72.23	71.46	67.46	
	Glc	104.81	73.79	76.37	69.68	75.22	64.92
18	GalNAc	102.67	51.99	80.7	64.35	75.78	61.88
	Rib	71.41	71.34	72.19	71.48	67.41	
	Glc	104.12	73.86	76.36	69.87	75.38	64.97
	ΔδRib[a]	–0.05	–0.01	0	+0.02	–0.1	
24	GalNAc	103.15	51.98	80.63	64.3	75.77	61.88
	Rib	71.7	71.34	72.41	71.67	67.36	
	Glc	104.15	73.89	76.39	69.87	75.38	64.96
	Δδ Rib	+0.24	–0.01	+0.18	+0.21	–0.1	

[a]Δ δRib refers to the chemical shift difference of the ribitol unit between **18**, **24**, and **PnC**. Digital resolution: 0.015 ppm/point for **18**, 0.0076 ppm/point for **24**.

techniques, including JMOD, COSY, TOCSY, HMBC, and HMQC experiments.[2] In accordance with the literature report detailing the spectral data for the C-polysaccharide (11), acetone was used as an internal reference, using chemical shifts of the methyl group at δ 2.225 and δ 31.07 in the ^{1}H and ^{13}C NMR spectra, respectively, as references and sample concentrations were also the same. A detailed outline of the procedures followed for signal assignment is provided in the supplementary material. Assignments are given for the ^{1}H and ^{13}C NMR spectra of **18**, **24**, and the corresponding segments of the natural polysaccharide (**PnC**) in Tables 1 and 2, respectively.

The ^{1}H NMR spectra of the final products **18** and **24** were similar, but there were small but significant differences in the section of the spectra where the ribitol signals appear. The chemical shifts for the galactosamine (GalNAc) and glucose (Glc) parts of **18** and **24** were the same within 0.02 ppm (see Table 1), which confirmed that the careful attention given to sample preparation, data point resolution, and referencing resulted in highly reproducible chemical shifts. The largest differences were observed for the signals of H-1a and H-1b of ribitol. Most chemical shifts were obtained from first-order analysis and from 2D experiments; those for the D-ribitol segment of the 500 MHz spectrum of **18** were obtained by simulation using the program LAME8 (36), because the chemical shifts of H-1b′ and H-2′ were virtually identical. The chemical shift differences (Δδ's) between the signals of the two H-1′s from the ribitol unit in the C-polysaccharide (**PnC**) and those from **18**, the D-ribitol derivative, were small, –0.03 ppm and –0.01 ppm; in contrast, the comparable differences between the data from **PnC** and that from **24**, the L-ribitol derivative, were much larger, –0.12 ppm and +0.11 ppm. Probably the most significant observations concern the chemical shift differences between the two H-1′ signals for each compound, being 0.10 ppm for **PnC**, 0.12 ppm for the D-ribitol derivative **18**, but much larger, 0.33 ppm, for the L-derivative **24**. The chemical shift differences were also somewhat larger for the signals of H-4′ and H-5b′ for **24** with respect to **PnC** than for **18**.

These observations clearly demonstrate that the data for the D-ribitol derivative **18** was very similar to that of **PnC**, whereas that of the L-ribitol derivative **24**, while still fairly similar to that of **PnC**, was less so. In fact, the chemical shift for every proton from the ribitol part of **18** is almost identical to that of the comparable proton in the natural polysaccharide; the largest Δδ was –0.04 ppm for H-2′.

As stated above, the most significant observation is that the chemical shift differences between the two C-1′ protons

[2] Discussion of spectral assignments of **18** and **24** with some of the supporting JMOD, TOCSY, and HMQC spectra (7 pages) is available as supplementary material and can be ordered from: The Depository of Unpublished Data, Document Delivery, CISTI, National Research Council of Canada, Ottawa, ON K1A 0S2, Canada.

© 1999 NRC Canada

Can. J. Chem. Downloaded from www.nrcresearchpress.com by University Town Library of Shenzhen on 09/05/12
For personal use only.

are virtually identical for **PnC** and the D-ribitol derivative **18**, being 0.10 and 0.12 ppm, respectively, whereas that for the L-ribitol derivative **24** is much larger, 0.33 ppm. This section of the spectrum of the natural polysaccharide might be different than that of the trisaccharide containing a ribitol segment of the same configuration if the size of the polysaccharide and the presence of other charged groups (phosphorylcholine groups) caused the composition of the conformational mixture for this region of the polysaccharide to be different than that present for the trisaccharide. The conformations and configuration of the ribitol segment and the conformation of the attached 2-acetamido-2-deoxy-β-D-galactopyranosyl unit will be most important in determining this chemical shift difference. The latter will be fixed in a $^4C_1$ conformation; the former, as an alditol with a β-1,3-O-O interaction in its Fischer projection, will be highly flexible (37). The ribitol segment should maintain this relative flexibility even if the remainder of the polysaccharide is less mobile. The near identity of the ^{1}H NMR chemical shifts of **PnC** and **18** supports the contention that the conformational mixtures present for both are almost identical, and the similar situation for ^{13}C chemical shifts, discussed in the following paragraph, provides further support. Therefore, the major factors influencing the H-1′ chemical shift differences will be the relative configurations at the anomeric centre of the 2-acetamido-2-deoxy-β-D-galactopyranosyl unit and those in ribitol, primarily at C-2′ but also at C-3′, and C-4′. These observations indicate that the configuration of ribitol in the natural material is D.

The ^{13}C NMR spectra of **18** and of **24** were also quite similar. The largest differences lie in the chemical shifts of C-1′ and C-4′ of the ribitol unit. The carbons of the glucopyranose units of **18** and **24** have almost the same chemical shifts, which indicates that there were no systematic shift differences between results from different samples (see Table 2). It was found that the chemical shifts of the carbons of ribitol in the synthetic D-trisaccharide phosphate **18** were almost identical to those from the corresponding part of the **PnC**; the average absolute deviation was 0.034 ppm. The chemical shifts for the same part of the L-trisaccharide phosphate **24** had an average absolute deviation of 0.15 ppm, with the largest differences at C-1 (+0.24 ppm), C-3 (+0.18 ppm), and C-4 (+0.21 ppm), respectively. All of these were less shielded than in the C-polysaccharide. ^{13}C NMR chemical shifts of carbons in acyclic systems are known (37*a*, 37*b*, 38) to be strongly dependent on the mixture of conformations present, particularly on the relative proportion of *gauche* and *anti* conformers. The close similarity of the chemical shifts of the corresponding carbons from the ribitol segments of **PnC**, **18**, and **24** to those from the first two, being identical within experimental error, strongly supports the contention that the conformational mixtures present for the ribitol segments of all three are identical. Therefore, this evidence supports the above conclusion that the ribitol unit in the C-polysaccharide of *Streptococcus pneumoniae* has the D-configuration.

Conclusions

From the differences in the NMR data of **18** and **24**, it was demonstrated that the configuration of the ribitol unit in these molecules had a significant influence on the chemical shifts of the corresponding ^{1}H and ^{13}C NMR signals. Of the two configurations, only one can be that present in the natural polysaccharide. The configuration for which the NMR data was in closer agreement to that of the corresponding part of the C-polysaccharide (**PnC**) should be the one present in the natural material as long as there is reasonable agreement. The ^{1}H and ^{13}C NMR chemical shift data for the D-ribitol derivative **18** showed remarkable agreement with that for **PnC**, with average chemical shift differences for the corresponding signals being 0.02 and 0.034 ppm, respectively; the agreement for the L-ribitol derivative **24** was significantly worse. Perhaps the most significant observation was that the chemical shift differences between the signals of the two primary hydrogens on the ribitol carbon closest to the anomeric center of the *N*-acetyl-β-D-galactopyranosyl unit were 0.10 ppm in the natural polysaccharide, 0.12 ppm in the D-ribitol derivative, but 0.33 ppm in the L-ribitol derivative. In view of the conformational flexibility of ribitol derivatives and the near identity of all ^{1}H and ^{13}C NMR chemical shifts in the D-ribitol derivative and the natural polysaccharide, it seems highly unlikely that there could be a conformational effect in the natural polysaccharide that could result in the two C-1 protons from the natural polysaccharide having a chemical shift difference markedly different than that of the trisaccharide containing ribitol with the same configuration. Thus, the ribitol unit in the C-polysaccharide of *Streptococcus pneumoniae* can now be reliably assigned the D-configuration.

Experimental section

General methods

Melting points were determined with a Fisher–Johns melting point apparatus and are uncorrected. Specific rotations were measured on Perkin–Elmer model 141 or 243 polarimeters. TLC was carried out on 0.20 mm thick Merck silica gel 60F-254 aluminum sheets cut to be approximately 7 cm long. Components were located by spraying with 2% ceric sulfate in 1 M sulfuric acid and heating on a hot plate until coloration occurred. Dry flash column chromatography was performed on silica gel 60 PF-254 for TLC. Low-pressure flash column chromatography was performed on silica gel Merck grade 9385, 230–400 mesh, 60 Å. The ^{1}H, ^{13}C, and ^{31}P NMR spectra were recorded on a Bruker AC-250 NMR spectrometer, unless otherwise noted. Some spectra were recorded on Bruker AMX-400 or AMX-500 NMR spectrometers. Solutions for NMR spectra were prepared in chloroform-*d* unless otherwise stated. Chemical shifts are reported in ppm downfield from internal TMS for ^{1}H and ^{13}C NMR spectra. The central peak for chloroform-*d*, at δ 77.0, was used as a secondary reference for ^{13}C NMR spectra. Phosphoric acid (25%) was used as an external chemical shift reference for ^{31}P NMR (δ 0.00). For **18** and **24**, acetone was used as an internal chemical shift reference for ^{1}H NMR (δ 2.225) and for ^{13}C NMR (δ 31.07). Exact masses for **3**, **5**, **6**, and **7** were measured on a JEOL AX505H mass spectrometer using fast atom bombardment (FAB) at the NRC in Ottawa. Exact masses for **10**, **11**, and **24** were measured on a Kratos IIH mass spectrometer using fast atom bombardment (FAB) at the University of Ottawa. The fast atom beam was provided by a cesium gun. Solvents for the matrix were

© 1999 NRC Canada

Can. J. Chem. Downloaded from www.nrcresearchpress.com by University Town Library of Shenzhen on 09/05/12
For personal use only.

glycerol and (or) 3-nitrobenzyl alcohol and combinations thereof. Exact masses for **15**, **16**, **17**, **18**, **21**, and **23** were measured on a Kratos MS50 mass spectrometer using electrospray ionization (ESI) at the University of Alberta. Electrospray ionization mass spectra for **8**, **14**, and **20** were run on a VG Micromass Quattro spectrometer in acetonitrile–water (1:1) using a loop injector. The solution concentration was approximately 5.21×10^{-4} M and injection was 10 μL. The sample capillary was at 3500 V, the sample cone was at 20 V, and the source temperature was at 100°C.

D-Ribose diethyl dithioacetal, 2

To a solution of D-ribose (30.0 g, 0.20 mol) and concentrated hydrochloric acid (36 mL) was added ethanethiol (36 mL) dropwise at 0°C over 15 min and the reaction mixture was stirred for another 30 min. Then a saturated sodium bicarbonate solution was added dropwise until the solution was neutral. The resulting solution was concentrated to a residue that was extracted with ethyl acetate. The insoluble inorganic salts were removed by filtration. The ethyl acetate filtrate was concentrated to solid **2**, and recrystallized from ethanol as needles (38.61 g, 75% yield): mp 82–83°C (lit. (39) mp 82–83°C).

5-*O*-Allyl D-ribose diethyl dithioacetal, 3

Dibutyltin oxide (0.248 g, 1.0 equiv.) and compound **2** (0.256 g, 1.0 mmol) were refluxed in toluene (20 mL) for 4 h in a Dean–Stark apparatus for the azeotropic removal of water. Then the solvent was evaporated and cesium fluoride (0.222 g, 1.45 equiv.) added. After the mixture had been kept under vacuum for 1 h, a solution of allyl bromide (0.12 mL, 1.3 equiv.) in DMF solution (6 mL) was added. The reaction mixture was stirred at room temperature for 1 h when TLC showed that all starting material had been consumed. The reaction solution was concentrated to a residue that was taken up in ethyl acetate (50 mL). The solution was dried (Na_2SO_4) and concentrated to a liquid residue that was purified by dry flash column chromatography to yield the title compound (**3**): yield 0.202 g (68%); $[\alpha]_D^{24}$ –17.4 (*c* 1.16, $CHCl_3$), ^{1}H NMR, same as ref. 31; ^{13}C NMR δ: 14.4, 14.5 (2 CH_3), 25.6 (2 CH_2S), 54.4 (C-1), 71.1 (C-4), 71.5 (C-5), 72.4 (**C**$\mathbf{H_2}$-All), 72.8 (C-3), 75.0 (C-2), 117.6 (CH_2=), 133.9 (-CH=). Exact Mass (FAB) calcd. for $C_{12}H_{24}O_4S_2Na$ $[M + Na]^+$: 319.1014; found: 319.1018.

5-*O*-Allyl-2,3,4-tri-*O*-benzyl-D-ribose diethyl dithioacetal, 4

A solution of compound **3** (0.425 g, 1.44 mmol) in DMF (5 mL) was treated with excess NaH (0.42 g, 60% suspension in mineral oil, washed with hexanes 3 times before use) at 0°C. The resulting mixture was stirred for 30 min. Then a solution of benzyl bromide (1.36 mL) in DMF (2 mL) was added dropwise. The reaction solution was stirred at 0°C for 3.5 h when TLC showed that all the starting material had been consumed. Cold water was added until the total volume was about 70 mL. The water layer was extracted with pentane (5 × 40 mL). The pentane solution was dried (Na_2SO_4) and concentrated to a liquid residue that was separated with dry flash column chromatography using a gradient elution from hexane to ethyl acetate. The title compound (**4**) was obtained as a syrup (0.514 g, 63% yield); $[\alpha]_D^{23}$ 24 (*c* 6.76, $CHCl_3$); ^{1}H NMR, same as ref. 31; ^{13}C NMR δ: 14.6 (2 CH_3 SEt), 24.8, 26.1 (2 **C**H_2 SEt), 53.8 (C-1), 69.3 (C-5), 72.0, 72.4, 73.4, 74.5 (3 **C**H_2Ph, 1 **C**H_2 All), 78.9, 79.8, 82.1 (C-2, C-3, C-4), 116.4 (**C**H_2=), 134.7 (-**C**H=), 127.2-128.7, 138.2, 138.3, 138.7 (C-Ph).

5-*O*-Allyl-2,3,4-tri-*O*-benzyl-D-ribose, 5

A solution of compound **4** (0.310 g, 0.55 mmol) in aqueous acetonitrile (7.25 mL CH_3CN + 0.72 mL H_2O) was treated with mercury(II) chloride (0.604 g, 2.21 mmol) and calcium carbonate (0.229 g, 2.29 mmol). The resulting mixture was stirred at room temperature for 1 h when TLC showed that all starting material had been consumed. The reaction mixture was filtered through Celite and the filtrate was concentrated to a residue that was taken up in dichloromethane (100 mL). The solution was subsequently washed with potassium iodide solution (1 M, 3 × 100 mL) and sodium thiosulfate solution (30%, 2 × 100 mL) and then dried (Na_2SO_4) and concentrated. The title compound (**5**) was obtained as a colourless liquid (0.216 g, 86% yield); $[\alpha]_D^{23}$ 20.5 (*c* 0.48, $CHCl_3$); ^{1}H NMR δ: 3.53 (dd, 1H, H-5_a, $J_{5a,5b}$ = –10.7 Hz, $J_{5a,4}$ = 4.6 Hz), 3.67 (dd, 1H, H-5_b, $J_{5b,4}$ = 2.1 Hz), 3.87–4.01 (m, 4H, H-3, H-4, C**H**$_2$ All), 4.09 (br d, 1H, H-2), 4.47–4.82 (m, 6H, 3 C**H**$_2$Ph), 5.11–5.26 (m, 2H, C**H**$_2$=), 5.78–5.93 (m, 1H, -C**H**=), 7.22–7.33 (m, 15H, H-Ph), 9.47 (br s, 1H, -C**H**=O); ^{13}C NMR δ: 69.0 (C-5), 72.1 (**C**H_2 All), 72.5, 72.7, 79.9 (3 **C**H_2Ph), 76.5, 80.3 (2C C-3, C-4), 82.2 (C-2), 116.8 (**C**H_2=), 134.6 (-**C**H=), 127.4–128.3, 137.3, 137.5, 137.9 (C-Ph), 200.9 (C-1, H**C**=O). Exact Mass (FAB) calcd. for $C_{29}H_{32}O_5Na$ $[M + Na]^+$: 483.2148; found: 483.2195.

5-*O*-Allyl-2,3,4-tri-*O*-benzyl-D-ribitol, 6

A solution of compound **5** (0.215 g, 0.47 mmol) in aqueous methanol (methanol:water 1:1, 3 mL) was stirred with sodium borohydride (0.032 g, 0.81 mmol) for 10 h. Then water (10 mL) was added and the resulting mixture was extracted with chloroform (3 × 10 mL). The combined extracts were dried (Na_2SO_4) and concentrated to a liquid residue that was purified with dry flash column chromatography to yield the title compound (**6**) (0.194 g, 90% yield); $[\alpha]_D^{23}$ –17 (*c* 2.52, $CHCl_3$) (lit. (31) $[\alpha]_D^{23}$ –23.2; lit. (32) $[\alpha]_D$ –15.0); ^{1}H (31, 32) and ^{13}C (32) NMR spectra same as literature values. Exact Mass (FAB) calcd. for $C_{34}H_{38}O_6Na$ $[M + Na]^+$:565.2566; found: 565.2544.

5-*O*-Allyl-2,3,4-tri-*O*-benzyl-1-*O*-*p*-methoxybenzyl-D-ribitol, 7

A solution of **6** (0.150 g, 0.325 mmol) in DMF (3 mL) was stirred with sodium hydride (0.06 g, 60% suspension in mineral oil, washed with hexanes before use) at 0°C for 20 min and a solution of *p*-methoxybenzyl chloride (300 μL, 2.21 mmol) in DMF (2 mL) was added dropwise in 6 min. The resulting mixture was stirred at room temperature for 4 h when TLC showed that all starting material had been consumed. Water (15 mL) was added and the resulting mixture was extracted with pentane (6 × 20 mL). The combined extracts were dried (Na_2SO_4) and concentrated to a liquid residue that was purified with dry flash column chromatography using a gradient elution from hexane to ethyl acetate to yield **7** (0.169 g, 89% yield); $[\alpha]_D^{24}$ –0.11 (*c* 2.48,

© 1999 NRC Canada

Can. J. Chem. Downloaded from www.nrcresearchpress.com by University Town Library of Shenzhen on 09/05/12
For personal use only.

$CHCl_3$); ^{1}H NMR δ: 3.63–3.70 (m, 4H, H-1, H-5), 3.75 (s, 3H, OC**H$_3$**), 3.85–3.95 (m, 5H, H-2, H-3, H-4, C**H$_2$** All), 4.42 (s, 2H, C**H$_2$**PhOCH$_3$-*p*), 4.57–4.72 (m, 6H, 3 **C**H$_A$H$_B$Ph, $J_{A,B}$ = –11.6 Hz, –11.9 Hz), 5.10–5.28 (m, 2H, **C**H$_2$=), 5.80–5.93 (m, 1H, -**C**H=), 6.82 (d, 2H, ½ AA′BB′ pattern, *p*MPh, *J* = 8.5 Hz), 7.18–7.25 (m, 17H, H-Ph); ^{13}C NMR δ: 55.1 (O**C**H$_3$), 69.6, 70.0 (C-1, C-5), 72.1, 72.2, 72.3, 73.7 (3 **C**H$_2$Ph, 1 **C**H$_2$ All), 72.8 (**C**H$_2$PhOCH$_3$-*p*), 78.4, 78.6 (C-2, C-3, C-4), 113.6 (2C *o*-**C**H *p*MBn), 116.6 (**C**H$_2$=), 134.8 (-**C**H=), 127.3–129.2, 130.4, 138.6, 159.0 (C-Ph). Exact Mass (FAB) calcd. for $C_{37}H_{42}O_6Na$ [M + Na]$^+$: 605.2879; found: 605.2936.

2,3,4-Tri-*O*-benzyl-5-*O*-*p*-methoxybenzyl-L-ribitol, 8

A solution of **7** (6.052 g, 10.4 mmol) in aqueous methanol (methanol:water 5:1, 55 mL) was stirred with Pd/C (10%, 0.60 g) at 60°C for 10 h. The reaction mixture was filtered through Celite and diluted with water (30 mL). The resulting mixture was extracted with dichloromethane (4 × 50 mL). The combined extracts were dried (Na_2SO_4), and concentrated to a liquid residue that was purified with dry flash column chromatography to yield **8** (3.88 g, 69% yield); $[\alpha]_D^{24}$ 11 (*c* 2.29, $CHCl_3$); ^{1}H NMR δ: 3.5–4.0 (m, 7H, H-1–H-5), 3.8 (s, 3H, OC**H$_3$**), 4.4 (s, 2H, C**H$_2$**PhOCH$_3$-*p*), 4.5–4.8 (m, 6H, 3 C**H$_2$**Ph), 6.82 (½ AA′BB′ pattern, 2H, *o*-C**H** *p*MBn, *J* = 8.5 Hz), 7.25 (m, 17H, H-Ph); ^{13}C NMR δ: 55.3 (O**C**H$_3$), 61.4 (C-1), 69.3 (C-5), 71.9, 72.4, 73.0, 74.0 (3 **C**H$_2$Ph, 1 **C**H$_2$PhOCH$_3$-*p*), 78.2, 78.9, 79.1 (3C, C-2, C-3, C-4), 113.8 (2C *o*-**C**H *p*MBn), 127.7–129.4, 130.3, 138.2, 138.3, 159.2 (C-Ph); ESI-MS (g/mol): 565 for $[C_{34}H_{38}O_6Na]^+$ [M + Na]$^+$ (100), isotopic peaks of [M + Na]$^+$: 566 (calcd. 38.6, measured 38.4), 567 (calcd. 8.5, measured 8.5), 568 (calcd. 1.3, measured 1.2); 581 for $[C_{34}H_{38}O_6K]^+$ [M + K]$^+$; calcd. mass 542.3 (M); ESI-MS (g/mol) (in the presence of trace amount of formic acid): 543 for $C_{34}H_{39}O_6$ [M + H]$^+$, 565 for $C_{34}H_{38}O_6Na$ [M + Na]$^+$, 581 for $C_{34}H_{38}O_6K$ [M + K]$^+$.

Methyl 2,3,4-tri-*O*-benzyl-β-D-glucopyranoside, 9

A solution of methyl 2,3,4-tri-*O*-benzyl-6-*O*-trityl-β-D-glucopyranoside (40) (19.52 g, 27.6 mmol) in glacial acetic acid (35 mL) was treated with a solution of HBr in acetic acid (30% w/v, 7.5 mL, 1.0 equiv.) at 0°C. The resulting precipitate was removed by filtration and washed with glacial acetic acid. The combined filtrate and washings were poured onto a mixture of ice and solid sodium carbonate and the resulting mixture was extracted with dichloromethane (3 × 100 mL). The combined extracts were washed with saturated sodium hydrogen carbonate solutions (2 × 100 mL), and water (3 × 100 mL), then dried (Na_2SO_4) and concentrated to a solid that was purified by flash chromatography using hexane and ethyl acetate (2:1) as eluent. The resulting solid (9.61 g, 75% yield) was recrystallized from ether and hexane to give fine needles of **9**: mp 90–91°C; $[\alpha]_D^{20}$ +8.8 (*c* 0.34, $CHCl_3$) (lit. (40) mp 91–92°C; $[\alpha]_D^{20}$ +9.9).

(Methyl 2,3,4-tri-*O*-benzyl-β-D-glucopyranosid-6-yl) 2-cyanoethyl (*N*,*N*-diisopropyl) phosphoramidite, 10

To a solution of **9** (3.25 g, 7.00 mmol) in dichloromethane (70 mL), stirred under argon at room temperature, were added diisopropylethylamine (DIPEA, 3.4 mL, 2.8 equiv.) and chloro 2-cyanoethyl (*N*,*N*-diisopropyl)phosphoramidite (34) (2.22 g, 1.3 equiv.). The reaction was complete in 30 min. The reaction solution was diluted with dichloromethane (30 mL), then washed with saturated sodium chloride containing 5% triethylamine (3 × 30 mL), and with tetraethylammonium bromide (TEAB, 2 M, 2 × 30 mL). The organic solution was dried ($MgSO_4$) and concentrated to a syrup that was purified with dry flash column chromatography using as eluant hexane:ethyl acetate 5:1 containing 4% triethylamine. Compound **10** was obtained as a colourless syrup (3.86 g, 83% yield); $[\alpha]_D^{20}$ 4.4 (*c* 3.03, $CHCl_3$); ^{1}H NMR δ: 1.14 (m, 12H, C**H$_3$** iPr), 2.48–2.60 (m, 2H, OCH$_2$C**H$_2$**CN), 3.36–4.05 (m, 13H, H-2–H-6, 2 C**H** iPr, OC**H$_2$**CH$_2$CN, OC**H$_3$**), 3.53 (s, OC**H$_3$**), 4.31 (d, 1H, H-1, $J_{1,2}$ = 7.6 Hz), 4.64–4.97 (m, 6H, 3 C**H$_2$**Ph), 7.15–7.37 (m, 15H, H-Ph); ^{13}C NMR δ: 19.9, 20.0 (OCH$_2$**C**H$_2$CN), 24.3, 24.4 (**C**H$_3$ *i*Pr), 42.7, 42.9, 43.1 (**C**H iPr), 56.5, 56.6 (O**C**H$_3$), 58.1, 58.4 (O**C**H$_2$CH$_2$CN), 62.2, 62.4, 62.7 (C-6), 74.3, 74.6, 75.3 (3 **C**H$_2$Ph, C-5), 77.5 (C-3), 82.1 (C-2), 84.26, 84.34 (C-4), 104.3 (C-1), 117.3, 117.5 (CN), 127.3–128.1, 137.9, 138.3 (C-Ph); ^{31}P NMR δ: 150.0, 149.4. Exact Mass (FAB) calcd. for $C_{37}H_{50}N_2O_7P$ [M + H]$^+$: 665.3356, $C_{37}H_{48}N_2O_7P$ [M – H]$^+$: 663.3199; found: 665.3323 [M + H]$^+$, 663.3210 [M – H]$^+$.

(*tert*-Butyldimethyl)silyl 2-azido-4,6-*O*-benzylidene-2-deoxy-3-*O*-methyl-β-D-galactopyranoside, 11

A solution of *tert*-butyldimethylsilyl 2-azido-4,6-*O*-benzylidene-2-deoxy-β-D-galactopyranoside (29) (3.14 g 7.71 mmol) in DMF (50 mL) was stirred with NaH (0.78 g, 60% suspension in mineral oil, washed with pentane 3 times before use) at 0°C for 0.5 h before methyl iodide (1.2 mL) was added. The reaction mixture was stirred at 0°C for 15 min, after which cold water (2 mL) was added. The resulting mixture was extracted with dichloromethane (3 × 30 mL). The combined extracts were dried (Na_2SO_4) and concentrated to a syrup that was purified by low-pressure flash column chromatography using as eluent hexane:ethyl acetate 4:1 to yield **11** as a syrup (3.14 g, 97% yield); $[\alpha]_D^{20}$ 8.5 (*c* 2.31, $CHCl_3$); ^{1}H NMR (400 MHz) δ: 0.10, 0.12 (2 s, 6H, C**H$_3$**Si), 0.88 (s, 9H, SiC(C**H$_3$**)$_3$), 3.03 (dd, 1H, H-3, $J_{2,3}$ = 10.5 Hz, $J_{3,4}$ = 3.7 Hz), 3.25 (br d, 1H, H-4,), 3.41 (s, 3H, O**C**H$_3$), 3.62 (dd, 1H, H-2, $J_{1,2}$ = 7.8 Hz), 3.97 (dd, 1H, H-6a, $J_{6a,6b}$ = 12.2 Hz, $J_{6a,5}$ = 2.0 Hz), 4.13–4.20 (m, 2H, H-5, H-6b), 4.47 (d, 1H, H-1), 5.50 (s, 1H, C**H**Ph), 7.25–7.45 (m, 5H, H-Ph); ^{13}C NMR δ: –4.87, –4.14 (2 **C**H$_3$Si), 18.0 (Si**C**(CH$_3$)$_3$), 25.6 (SiC(**C**H$_3$)$_3$), 57.2 (O**C**H$_3$), 64.3 (C-2), 66.5 (C-4), 69.3 (C-6), 71.7 (C-5), 79.6 (C-3), 97.3 (C-1), 101.2 (**C**HPh), 126.4, 128.7, 129.0, 137.7 (C-Ph). Exact Mass (FAB) calcd. for $C_{20}H_{30}N_3O_5Si$ [M – H]$^+$: 420.1955; found: 420.196.

2-Azido-4,6-*O*-benzylidene-2-deoxy-3-*O*-methyl-α-D-galactopyranosyl trichloroacetimidate, 12

A solution of **11** (1.53 g, 3.64 mmol) in dichloromethane (100 mL) was cooled to –25°C under argon and a solution of tetrabutylammonium fluoride (TBAF) in THF (1 M, 18.2 mL, 5 equiv.) was added dropwise. TLC analysis showed that all the starting material had been consumed in 10 min. The reaction mixture was poured into ice-water and the resulting mixture was extracted with dichloromethane (3 × 100 mL). The combined extracts were dried (Na_2SO_4) and concentrated to a residue, a mixture of anomers of 2-azido-

© 1999 NRC Canada

Can. J. Chem. Downloaded from www.nrcresearchpress.com by University Town Library of Shenzhen on 09/05/12
For personal use only.

4,6-*O*-benzylidene-2-deoxy-3-*O*-methyl-D-galactopyranose. To a solution of the anomeric mixture in dichloromethane (50 mL) was added trichloroacetonitrile (4.5 mL, 45 mmol). The solution was cooled to 0°C and sodium hydride (0.19 g, 60% suspension, washed with pentane three times before use) was added. After 1 h the reaction mixture was filtered through Celite and concentrated to a foam that was purified with low-pressure flash column chromatography, using hexane:ethyl acetate 5:1 as eluent, to yield **12** as a foam (1.14 g, 69% yield); $[\alpha]_D^{24}$ 128 (*c* 0.84, $CHCl_3$); ^{1}H NMR (400 MHz) δ: 3.56 (s, 3H, OC**H$_3$**), 3.87 (m, 2H, H-3, H-5), 4.08 (dd, 1H, H-6a, $J_{6a,6b}$ = -12.7 Hz, $J_{6a,5}$ = 1.5 Hz), 4.15 (dd, 1H, H-2, $J_{2,3}$ = 10.3 Hz), 4.32 (dd, 1H, H-6b, $J_{5,6b}$ = 1.5 Hz), 4.48 (br d, 1H, H-4, $J_{4,3}$ = 2.9 Hz), 5.59 (s, 1H, C**H**Ph), 6.51 (d, 1H, H-1, $J_{1,2}$ = 3.3 Hz), 7.34–7.53 (m, 5H, H-Ph), 8.52 (s, 1H, NH); ^{13}C NMR δ: 56.60 (O**C**H$_3$), 58.20 (C-2), 65.23(C-4), 69.04 (C-6), 71.78 (C-5), 76.26 (C-3), 95.64 (C-1), 101.1 (**C**HPh), 126.2, 128.2, 129.1, 137.4 (C-Ph), 160.59 (C=NH).

(Methyl 2,3,4-tri-*O*-benzyl-β-D-glucopyranosid-6-yl) 2-cyanoethyl 2,3,4-tri-*O*-benzyl-D-ribityl-5-phosphate, 14

To a stirred solution of **10** (0.412 g, 0.62 mmol) and **8** (0.343 g, 1.02 equiv.) in acetonitrile (10 mL) under argon was added tetrazole (77.5 mg, 1.8 equiv.). After 1 h, the reaction mixture was cooled to 0°C and a solution of *m*-chloroperbenzoic acid (MCPBA, 0.544 g, 2.6 equiv.) in dichloromethane was added dropwise. After 20 min, the reaction mixture was diluted with dichloromethane (20 mL) and the resulting solution was washed with TEAB (2 M, 1 × 20 mL) and water (1 × 30 mL). The dichloromethane solution was dried ($MgSO_4$) and concentrated to a residue that was purified by low-pressure flash column chromatography using hexane:ethyl acetate 1:1 as eluent. (Methyl 2,3,4-tri-*O*-benzyl-β-D-glucopyranosid-6-yl) 2-cyanoethyl 1-*p*-methoxybenzyl-2,3,4-tri-*O*-benzyl-D-ribityl-5-phosphate **(13)** was obtained as a colorless syrup (0.480 g, 69% yield); $[\alpha]_D^{20}$ 6.5 (*c* 3.72, $CHCl_3$); ^{1}H NMR (400 MHz) δ: 2.41 (m, 2H, OCH_2CH_2CN), 3.30–4.12 (m, H-1–H-5, H-1′–H-6′, O**CH$_2$**CH_2CN, OC**H$_3$**), 3.49, 3.51, 3.75 (3s, OC**H$_3$**), 4.39 (d, 1H, H-1, $J_{1,2}$ = 8.3 Hz), 4.15–4.95 (m, 14H, C**H$_2$**Ph), 6.79–6.84, 7.16–7.35 (m, 34H, H-Ph); ^{13}C NMR δ: 19.00 (OCH_2**C**H_2CN), 55.14, 57.03 (2 × O**C**H$_3$), 61.64 (O**C**H_2CH_2CN), 66.57, 67.45, 67.76 (C-5, C-6′), 69.20, 69.30 (C-1), 72.38, 72.89 (**C**H_2Ph), 73.35 (C-5′), 73.60, 73.69, 74.62, 74.90, 75.48 (**C**H_2Ph), 78.03 (C-2, C-3, C-4), 77.00, 82.11, 84.26, 84.33 (C-2′, C-3′, C-4′), 104.6 (C-1′), 116.3 (CN), 113.6, 127.6-129.2, 130.2, 137.8–138.4, 159.1 (C-Ph); ^{31}P NMR δ: –0.73, –0.81.

To a solution of **13** (0.330 g, 0.294 mmol) in dichloromethane (9 mL) was added water (0.5 mL) and 2,3-dichloro-5,6-dicyanoquinone (DDQ, 0.082 g, 1.2 equiv.) and the mixture was stirred vigorously for 4 h. The organic layer was extracted with saturated sodium hydrogen carbonate (3 × 50 mL), then dried (Na_2SO_4) and concentrated to a residue that was purified with low-pressure flash column chromatography to yield **14** as a colourless syrup (0.185 g, 63% yield); $[\alpha]_D^{20}$ 5.3 (*c* 1.36, $CHCl_3$); ^{1}H NMR (400 MHz) δ: 2.24, 2.29 (2 br t, 1H, 1-OH), 2.49 (m, 2H, OCH_2CH_2CN), 3.39 (m, 1H, H-2′), 3.45 (m, 1H, H-5′), 3.50, 3.52 (2s, 3H, OC**H$_3$**), 3.55 (br s, 1H, H-4′), 3.65 (m, 1H, H-3′), 3.86–3.95 (m, 1H, H-1), 3.99–4.05 (m, 2H, O**CH$_2$**CH_2CN), 4.18–4.50 (m, 3H, H-5, H-6′, H-1′, $J_{1',2'}$ = 7.9 Hz), 4.53–4.96 (m, 12H, C**H$_2$**Ph), 7.20–7.70 (m, 30H, H-Ph); ^{13}C NMR δ: 19.14 (OCH_2**C**H_2CN), 57.03 (O**C**H$_3$), 61.00, 61.05 (C-1), 61.62, 61.77 (O**C**H_2CH_2CN), 66.58, 67.23, 67.37 (C-5, C-6′), 72.00, 72.32, 72.43 (**C**H_2Ph), 73.30 (C-5′), 73.79, 73.90, 74.85, 74.91, 75.45 (**C**H_2Ph), 76.92 (C-4′), 77.73, 77.79, 78.03, 78.75, 78.85 (C-2, C-3, C-4), 82.06 (C-2′), 84.18, 84.25 (C-3′), 104.5 (C-1′), 116.3 (CN), 127.7–128.4, 137.6–138.3 (C-Ph); ^{31}P NMR δ: –0.72, –0.77; ESI-MS (g/mol) 1024 for $[C_{57}H_{64}O_{13}NPNa]^+$ $[M + Na]^+$ (100), isotopic peaks: 1025 (calcd. 65.2, measured 64.9), 1026 (calcd. 23.5, measured 23.5), 1027 (calcd. 5.7, measured 5.8); 1040 for $[C_{57}H_{64}O_{13}NPK]^+$ $[M + K]^+$; calcd. mass 1001.4 (M).

Following the same procedure, starting from **10** (1.389 g, 2.09 mmol) and **8** (1.133 g, 1.0 equiv.), **13** was obtained quantitatively and was treated with water and DDQ directly without further purification. Compound **14** was obtained in a 57% yield (1.190 g) based on **10**.

(Methyl 2,3,4-tri-*O*-benzyl-β-D-glucopyranosid-6-yl) 2-cyanoethyl 1-(2-azido-4,6-*O*-benzylidene-2-deoxy-3-*O*-methyl-β-D-galactopyranosyl) 2,3,4-tri-*O*-benzyl-D-ribityl-5-phosphate, 15

A solution of **14** (0.845 g, 0.844 mmol) and **12** (0.568 g, 1.2 equiv.) in acetonitrile (30 mL) was stirred with 4 Å molecular sieves for 2 h, then cooled to -40°C and treated with TMS triflate (120 μL, 0.74 equiv.). After 30 min, pyridine (1 mL) was added and the reaction mixture was filtered through Celite. The filtrate was washed with water (3 × 80 mL), dried (Na_2SO_4), and concentrated to a syrup. The product was purified with low-pressure flash column chromatography using hexane:ethyl acetate 1:1.3 as eluent. The title compound **15** was obtained as a colourless syrup (0.892 g, 82% yield); $[\alpha]_D^{20}$ 8.2 (*c* 3.40, $CHCl_3$); ^{1}H NMR δ: 2.39 (t, 2H, OCH_2CH_2CN, *J* = 6.4 Hz), 3.13 (dd, 1H, H-3″, $J_{2'',3''}$ = 10.27 Hz, $J_{3'',4''}$ = 3.4 Hz), 3.18 (br s, 1H, H-5″), 3.38 (t, 1H, H-2, $J_{1,2}$ = 8.3, $J_{2,3}$ = 8.8 Hz), 3.45 (m, 1H, H-5), 3.48, 3.50 (2 s, 6H, 2 OC**H$_3$**), 3.51 (m, 1H, H-4), 3.63 (t, 1H, H-3, $J_{3,4}$ = 8.8 Hz), 3.77 (dd, 1H, H-2″, $J_{1'',2''}$ = 7.8 Hz), 3.87 (dd, 1H, H-1′$_A$, $J_{1'A,1'B}$ = 10.8 Hz, $J_{1'A,2'}$ = 3.7 Hz), 3.98 (m, H-2, H-3, H-4, H-6′, O**CH$_2$**CH_2CN), 4.16 (dd, 1H, H-1′b, $J_{1'b,2'}$ = 3.7 Hz), 4.21 (m, H-5′a, H-4″), 4.26 (d, H-1″), 4.29 (d, H-1), 4.30 (m, H-6a), 4.37 (m, H-5′b), 4.48 (m, H-6b), 4.55–4.95 (m, 6 C**H$_2$**Ph), 5.53 (s, 1H, C**H**Ph), 7.2–7.6 (m, 35H, H-Ph); ^{13}C NMR δ: 19.0 (OCH_2**C**H_2CN), 57.1 (2 × O**C**H$_3$), 61.6 (O**C**H_2CH_2CN), 62.2 (C-2″), 66.4 (C-5″), 66.6 (C-5′), 67.4 (C-6), 68.3 (C-1′), 69.0 (C-6″), 71.5 (C-4″), 72.2 (2 **C**H_2Ph), 73.3 (C-5), 73.6, 74.6, 74.9, 75.4 (4 **C**H_2Ph), 77.0 (C-4), 77.8 (3C, C-2′, C-3′, C-4′), 79.9 (C-3″), 82.1 (C-2), 84.3 (C-3), 101.1 (**C**HPh), 101.9 (C-1″), 104.5 (C-1), 116.3 (CN), 126.3–128.9, 137.5–138.4 (C-Ph); ^{31}P NMR δ: –0.73, –0.83. Exact Mass (ESI) calcd. for $C_{71}H_{79}N_4O_{17}PNa$ $[M + Na]^+$: 1313.5076; found: 1313.5092.

(Methyl 2,3,4-tri-*O*-benzyl-β-D-glucopyranosid-6-yl) 2-cyanoethyl 1-*O*-(2-acetamido-4,6-*O*-ben-zylidene-2-deoxy-3-*O*-methyl-β-D-galactopyranosyl) 2,3,4-tri-*O*-benzyl-D-ribityl-5-phosphate, 16

A solution of **15** (0.651 g, 0.505 mmol) in thiolacetic acid (4 mL) was stirred under argon at room temperature for 17 h and then was concentrated to a liquid residue. Low-pressure

© 1999 NRC Canada

Can. J. Chem. Downloaded from www.nrcresearchpress.com by University Town Library of Shenzhen on 09/05/12
For personal use only.

flash column chromatography using ethyl acetate as eluent yielded **16** as a foam (0.493 g, 75% yield); $[\alpha]_D^{20}$ +22.3 (*c* 0.35, $CHCl_3$); ^{1}H NMR (400 MHz) δ: 1.80, 1.81 (2 s, 3H, C**H**$_3$CO), 2.32–2.36, 2.46-2.50 (m, 2H, $OCH_2C\mathbf{H}_2CN$), 3.41, 3.48, 3.51 (3 s, OC**H**$_3$), 5.527, 5.533, 5.539 (3s, C**H**Ph), 6.10, 6.38 (2 d, 1H, NH, $J_{NH,2''}$ = 6.8, 7.3 Hz), 7.20–7.48 (m, 35H, H-Ph); ^{13}C NMR δ: 18.99, 19.08, 19.15 ($OCH_2\mathbf{C}H_2CN$), 23.49 (**C**H_3CO), 54.31, 54.50, 54.62 (C-2″), 56.89, 57.06 (O**C**H_3), 61.78 (O**C**H_2CH_2CN), 66.39 (C-5″), 66.67 (C-5′), 67.60 (C-6), 68.41 (C-1′), 69.35 (C-6″), 71.89 (**C**H_2Ph), 72.36 (C-4″), 72.68 (**C**H_2Ph), 73.36 (C-5), 73.47, 74.93, 75.09, 75.49 (4 **C**H_2Ph), 77.0 (C-4), 77.61, 77.95, 78.20, 78.51, 78.66 (C-2′, C-3′, C-4′, C-3″), 82.13 (C-2), 84.27, 84.35 (C-3), 99.61, 99.89 (C-1″), 101.0 (**C**HPh), 104.6 (C-1), 116.5 (CN), 126.2–128.9, 137.8–138.4 (C-Ph), 170.9, 171.0 (CH_3**C**O); ^{31}P NMR δ: 0.17, –0.68, –0.73, –0.96. Exact Mass (ESI) calcd. for $C_{73}H_{83}N_2O_{18}PNa$ $[M + Na]^+$: 1329.5276; found: 1329.5275.

Triethylammonium (methyl 2,3,4-tri-*O*-benzyl-β-D-glucopyranosid-6-yl) 1-*O*-(2-acetamido-4,6-*O*-benzylidene-2-deoxy-3-*O*-methyl-β-D-galactopyranosyl) 2,3,4-tri-*O*-benzyl-D-ribityl-5-phosphate, 17

A solution of **16** (0.312 g, 0.239 mmol) in a mixture of triethylamine, pyridine, and water (3:1:1, 20 mL) was stirred at room temperature for 2 h. The reaction solution was concentrated to a foam of **17** (0.323 g, 99.6% yield); $[\alpha]_D^{25}$ –8.2 (*c* 0.48, CH_3OH); ^{1}H NMR (400 MHz, CD_3OD) δ: 1.22 (t, 3H, C**H**$_3CH_2$), 1.84 (s, 3H, C**H**$_3$CO), 2.95 (q, 2H, $CH_3C\mathbf{H}_2$), 3.15–3.55 (m, 12H, H-5″, H-2, H-3, H-3″, H-4, H-5, 2 OC**H**$_3$), 3.34, 3.38 (2 s, 2 × OC**H**$_3$), 3.88–4.36 (m, 14H, H-1′–H-5′, H-6″, H-6, H-2″, H-4″, H-1), 4.23 (d, H-1, $J_{1,2}$ = 7.3 Hz)), 4.05(br dd, H-2″, $J_{1'',2''}$ = 8.8 Hz, $J_{2'',3''}$ = 10.3 Hz), 4.53 (d, 1H, H-1″), 4.54–4.83 (m, 6 C**H**$_2$Ph), 5.54 (s, 1H, C**H**Ph), 7.10–7.48 (m, 35H, H-Ph); ^{13}C NMR (CD_3OD) δ: 9.31 (**C**H_3CH_2), 23.56 (**C**H_3CO), 47.72 ($CH_3\mathbf{C}H_2$), 52.77 (C-2″), 57.20, 57.52 (2 × O**C**H_3), 65.70, 66.32 (C-5′, C-6), 67.95 (C-5″), 69.81 (C-1′), 70.45 (C-6″), 72.91 (C-4″), 73.53, 74.86, 75.58 (4 **C**H_2Ph), 75.77 (C-5), 75.95, 76.48 (2 **C**H_2Ph), 79.22 (C-4), 80.10, 80.28, 80.60 (C-2′, C-3′, C-4′, C-3″), 83.47 (C-2), 85.73 (C-3), 102.2 (**C**HPh), 102.8 (C-1″), 105.9 (C-1), 127.2–129.9, 139.8–140.2 (C-Ph), 173.6 (**C** = O); ^{31}P NMR (CD_3OD) δ: 1.41. Exact Mass (ESI) calcd. for $C_{70}H_{79}NO_{18}PNa_2$ $[M - NHEt_3 + 2Na]^+$: 1298.4830; found: 1298.4814.

Sodium (methyl β-D-glucopyranosid-6-yl) 1-*O*-(2-acetamido-2-deoxy-3-*O*-methyl-β-D-galacto-pyranosyl)-D-ribityl-5-phosphate, 18

A solution of **17** (0.323 g, 0.238 mmol) in a mixture of ethyl acetate, methanol, and acetic acid (10:14.5:0.5, 25 mL) was stirred with Pd/C (10%, 0.38 g) under hydrogen (1 atm (= 101.3 kPa)) for 70 h. The reaction mixture was filtered through Celite and the filtrate was concentrated. A solution of the residue in water (3 mL) was stirred with Amberlite IR-120 (Na^+) resin overnight. The filtrate was concentrated to give **18** quantitatively; $[\alpha]_D^{20}$ –9.9 (*c* 0.68, H_2O); ^{1}H NMR (500 MHz, D_2O) δ: 2.04 (s, 3H, C**H**$_3$CO), 3.28 (m, 1H, H-2, $J_{2,3}$ = 9.4 Hz), 3.40 (s, 3H, 3″-O**C**H_3), 3.44 (dd, 1H, H-3″, $J_{2'',3''}$ = 10.9 Hz), 3.50 (m, 2H, H-3,4), 3.57 (s, 3H, 1-OC**H**$_3$), 3.58 (m, 1H, H-5), 3.66 (br dd, 1H, H-5″, $J_{5'',6a''}$ = 4.4 Hz, $J_{5'',6b''}$ = 8.1 Hz), 3.77 (dd, 1H, H-3′, $J_{2',3'}$ = 7.0 Hz, $J_{3',4'}$ = 4.8 Hz), 3.77 (dd, 1H, H-6″a, $J_{6a'',6b''}$ = 11.4 Hz), 3.83 (dd, 1H, H-2′, $J_{1',2'}$ = 6.4 Hz), 3.84 (dt, H-6″b), 3.89 (m, 1H, H-4′), 3.93 (dd, 1H, H-2″), 3.95 (d, 2H, H-1′), 3.99 (t, 1H, H-5′a, $J_{5'a,4'}$ = 6.1 Hz), 4.06 (m, 1H, H-5′b, $J_{5'b,5'a}$ = 10.4 Hz, $J_{5'b,4'}$ = 5.4 Hz), 4.07 (m, 1H, H-6a), 4.17 (dddd, 1H, H-6b, $J_{6b,6a}$ = 11.6 Hz, $J_{6b,5}$ = 5.2 Hz, $J_{6b,P}$ = 2.1 Hz), 4.22 (d, 1H, H-4″, $J_{4'',3''}$ = 3.3 Hz), 4.39 (d, 1H, H-1, $J_{1,2}$ = 8.0 Hz), 4.49 (d, 1H, H-1″, $J_{1'',2''}$ = 8.6 Hz); ^{13}C NMR (D_2O) δ: 23.94 (**C**H_3CO), 51.99 (C-2″), 57.18 (3″-O**C**H_3), 58.10 (1-O**C**H_3), 61.88 (C-6″), 64.35 (C-4″), 64.97 (d, C-6, $J_{6,P}$ = 4.8 Hz), 67.41 (d, C-5′, $J_{5',P}$ = 4.8 Hz), 69.87 (C-4), 71.34 (C-2′), 71.41 (C-1′), 71.48 (d, C-4′, $J_{4',P}$ = 7.6 Hz), 72.19, (C-3′), 73.86 (C-2), 75.38 (d, C-5, $J_{5,P}$ = 7.6 Hz), 75.78 (C-5″), 76.36 (C-3), 80.70 (C-3″), 102.67 (C-1″), 104.12 (C-1), 175.65 (**C** = O); ^{31}P NMR (D_2O) δ 1.73. Exact Mass (ESI) calcd. for $C_{21}H_{40}NO_{18}PNa$ $[M + H]^+$: 648.1881; found: 648.1900; calcd. for $C_{21}H_{39}NO_{18}PNa_2$ $[M + Na]^+$: 670.1700; found: 670.1697; calcd. for $C_{21}H_{38}NO_{18}PNa_3$ $[M - H + 2Na]^+$: 692.1519; found: 692.1536.

1-*O*-(2-Azido-4,6-*O*-benzylidene-2-deoxy-3-*O*-methyl-β-D-galactopyranosyl) 5-*O*-*p*-methoxybenzyl-2,3,4-tri-*O*-benzyl-L-ribitol, 19, and 1-*O*-(2-azido-4,6-*O*-benzylidene-2-deoxy-3-*O*-methyl-β-D-galactopyranosyl) 2,3,4-tri-*O*-benzyl-L-ribitol, 20

A solution of **12** (0.460 g, 1.02 mmol) and **8** (0.554 g, 1.02 mmol) in acetonitrile (20 mL) was stirred with 4 Å molecular sieves (1 g) for 1 h at room temperature. Then the solution was cooled to –50°C and trimethylsilyl trifluoromethanesulfonate (TMS triflate, 130 μL, 0.66 equiv.) was added. The reaction solution was stirred at –50°C for 40 min after which pyridine (1 mL) was added and the reaction mixture was filtered through Celite. The filtrate was washed with water (3 × 80 mL), dried (Na_2SO_4), and concentrated to a brownish syrup that was purified with low-pressure flash column chromatography using hexane:ethyl acetate 2:1 as eluent. Compound **19** was obtained as a syrup (0.145 g, 17% yield); $[\alpha]_D^{20}$ 2.2 (*c* 0.68, $CHCl_3$); ^{1}H NMR (400 MHz) δ: 3.11 (dd, 1H, H-3′, $J_{2',3'}$ = 10.3 Hz, $J_{3',4'}$ = 3.4 Hz), 3.20 (br s, 1H, H-5′), 3.49 (s, 3H, OC**H**$_3$), 3.61–4.06 (m, 11H, H-2, H-3, H-4, H-6′a, H-1a, H-5, H-2′, OC**H**$_3$), 3.75 (s, OC**H**$_3$), 4.18–4.34 (m, 4H, H-4′, H-6′b, H-1b, H-1′, $J_{1',2'}$ = 8.3 Hz), 4.42 (t, 2H, C**H**$_2$PhOMe-*p*), 4.55–4.84 (m, 6H, 3 C**H**$_2$Ph), 5.53 (s, 1H, C**H**Ph), 6.82 (d, 2H, AA′BB′ pattern, H*o*-*p*MPh, *J* = 8.8 Hz), 7.15–7.55 (m, 22H, H-Ph); ^{13}C NMR δ: 55.12, 57.14 (2 × O**C**H_3), 62.16 (C-2′), 66.34 (C-5′), 69.07, 69.44, 70.31 (C-1, C-6′, C-5), 71.63 (C-4′), 72.34, 72.56, 72.84, 73.53 (4 **C**H_2Ph), 78.22, 78.91, 79.03 (C-2, C-3, C-4), 80.07 (C-3′), 101.1 (**C**HPh), 102.3 (C-1′), 113.7, 127.2-129.7, 130.4, 137.6–138.7, 159.1 (C-Ph).

Another product (**20**) was obtained as a syrup (0.118 g, 16% yield); $[\alpha]_D^{24}$ –3.5 (*c* 0.31, $CHCl_3$); ^{1}H NMR (400 MHz) δ: 2.29 (br t, 5-OH), 3.14 (dd, 1H, H-3′, $J_{2',3'}$ = 10.3 Hz, $J_{3',4'}$ = 3.4 Hz), 3.26 (br s, 1H, H-5′), 3.50 (s, 3H, OC**H**$_3$), 3.65–4.07 (m, 8H, H-2, H-3, H-4, H-6′a, H-1a, H-5, H-2′), 4.18–4.34 (m, 4H, H-4′, H-6′b, H-1b, H-1′), 4.53–4.86 (m, 6H, 3 C**H**$_2$Ph), 5.58 (s, 1H, C**H**Ph), 7.15–7.55 (m, 20H, H-Ph); ^{13}C NMR δ: 57.19 (O**C**H_3), 61.25 (C-5), 62.16 (C-2′), 66.44 (C-5′), 69.45, 69.74 (C-1, C-6′), 71.63 (C-4′), 72.07, 72.70, 73.81 (3 **C**H_2Ph), 78.78, 79.09 (3C C-2, C-3,

© 1999 NRC Canada

Can. J. Chem. Downloaded from www.nrcresearchpress.com by University Town Library of Shenzhen on 09/05/12
For personal use only.

C-4), 80.07 (C-3′), 101.2 (**C**HPh), 102.2 (C-1′), 126.3–128.3, 137.6–138.4 (C-Ph); ESI-MS (g/mol): 706 for $[M + Na - N_2]^+$, 734 for $[M + Na]^+$, 750 for $[M + K]^+$; calculated mass: 711.3 (M).

A solution of **19** (0.107 g, 0.128 mmol) in dichloromethane (5 mL) was stirred with water (0.4 mL) and 2,3-dichloro-5,6-dicyano-quinone (DDQ, 0.0327 g, 1.1 equiv.) vigorously for 4 h. The reaction mixture was extracted with saturated sodium hydrogen carbonate (3 × 20 mL), then dried (Na_2SO_4) and concentrated to a syrup that was purified with low-pressure column chromatography using ethyl acetate and hexane (1:1.2) as eluent to yield **20** as a colourless syrup (0.059 g, 63% yield). The ^{1}H and ^{13}C NMR spectra of this product were identical in all respects to that of **20** above.

(Methyl 2,3,4-tri-*O*-benzyl-β-D-glucopyranosid-6-yl) 2-cyanoethyl 1-*O*-(2-azido-4,6-*O*-benzylidene-2-deoxy-3-*O*-methyl-β-D-galactopyranosyl) 2,3,4-tri-*O*-benzyl-L-ribityl-5-phosphate, 21

To a solution of **10** (0.105 g, 1.1 equiv.) and **20** (0.102 g, 0.144 mmol) in acetonitrile (20 mL) was added tetrazole (23.2 mg, 2.3 equiv.). The reaction solution was stirred under argon for 40 min. The reaction mixture was cooled to 0°C and a solution of *m*-chloroperbenzoic acid (MCPBA, 0.142 g, 2.6 equiv.) in dichloromethane (5 mL) was added dropwise. The reaction was complete in 20 min. The reaction mixture was diluted with dichloromethane (30 mL) and the organic layer was washed with TEAB (2 M, 1 × 30 mL) and water (1 × 30 mL), then dried ($MgSO_4$) and concentrated. The residue was purified with low-pressure flash column chromatography using hexane:ethyl acetate 1:2 as eluent. The title compound **21** was obtained as colourless foam (0.155 g, 84% yield); $[\alpha]_D^{25}$ 6.6 (*c* 0.33, $CHCl_3$); ^{1}H NMR (400 MHz) δ: 2.42–2.46 (m, 2H, $OCH_2C\mathbf{H_2}CN$), 3.14 (m, H-3″), 3.35 (br d, 1H, H-5″), 3.37 (m, 1H, H-2), 3.49 (m, 1H, H-4), 3.50 (s, $OC\mathbf{H_3}$), 3.63 (m, 1H, H-3), 3.75–3.86 (m, 2H, H-1′a, H-2″), 3.88–4.15 (m, H-2′, H-3′, H-4′, H-6″a, $OC\mathbf{H_2}CH_2CN$), 4.16–4.53 (m, H-1′b, H-6″b, H-5′, H-4″, H-1″, H-1, H-6), 4.54–4.96 (m, 6 $C\mathbf{H_2}$Ph), 5.54 (s, 1H, C**H**Ph), 7.2–7.6 (m, 35H, H-Ph); ^{13}C NMR δ: 19.24 ($OCH_2\mathbf{C}H_2CN$), 57.11, 57.24 (2 × $O\mathbf{C}H_3$), 61.96 ($O\mathbf{C}H_2CH_2CN$), 62.15 (C-2″), 66.45 (C-5″), 66.83 (C-5′), 67.39, 67.69 (C-6), 69.08 (C-6″), 69.59 (C-1′), 71.63 (C-4″), 72.46, 72.65 (2 $\mathbf{C}H_2$Ph), 73.30 (C-5), 73.56, 74.61, 74.94, 75.49 (4 $\mathbf{C}H_2$Ph), 77.0 (C-4), 77.62, 78.18, 78.45 (C-2′, C-3′, C-4′), 80.06 (C-3"), 82.06 (C-2), 84.26 (C-3), 101.1 (**C**HPh), 102.2 (C-1″), 104.5 (C-1), 116.2, 116.4 (CN), 126.2–134.4, 137.4–138.3 (C-Ph); ^{31}P NMR δ: –0.77, –1.28. Exact Mass (ESI) calcd. for $C_{71}H_{79}N_4O_{17}PNa$ $[M + Na]^+$: 1313.5076; found: 1313.5102.

Triethylammonium (methyl 2,3,4-tri-*O*-benzyl-β-D-glucopyranosid-6-yl) 1-*O*-(2-acetamido-4,6-*O*-benzylidene-2-deoxy-3-*O*-methyl-β-D-galactopyranosyl) 2,3,4-tri-*O*-benzyl-L-ribityl-5-phosphate, 23

A solution of **21** (0.139 g, 0.108 mmol) in thiolacetic acid (2 mL) was stirred under argon at room temperature for 17 h. Then the reaction mixture was concentrated and was purified by low-pressure flash column chromatography using ethyl acetate as eluent. (Methyl 2,3,4-tri-*O*-benzyl-β-D-glucopyranosid-6-yl) 2-cyanoethyl 1-*O*-(2-acetamido-4,6-*O*-benzylidene-2-deoxy-3-*O*-methyl-β-D-galactopyranosyl) 2,3,4-tri-*O*-benzyl-L-ribityl-5-phosphate (**22**) was obtained as a colourless foam (0.066 g, 47% yield); ^{1}H NMR (400 MHz) δ: 1.80, 1.84 (2 s, $C\mathbf{H_3}CO$), 2.34–2.46 (m, $OCH_2C\mathbf{H_2}CN$), 3.30–4.5 (m, H-1–H-6, H-1′–H-5′, H-1″–H-6″, $OC\mathbf{H_3}$, $OC\mathbf{H_2}CH_2CN$), 3.41 (s, $OC\mathbf{H_3}$), 4.52–4.96 (m, 6 $C\mathbf{H_2}$Ph), 5.54, 5.55 (2 s, C**H**Ph), 5.9, 6.2, 6.5 (2 br, NH), 7.2–7.6 (m, 35H, H-Ph); ^{13}C NMR δ: 19.13 ($OCH_2\mathbf{C}H_2CN$), 23.54 ($\mathbf{C}H_3CO$), 54.36 (C-2″), 56.88, 57.16 (2 × $O\mathbf{C}H_3$), 61.91 ($O\mathbf{C}H_2CH_2CN$), 66.46 (C-5″), 66.70, 67.30, 67.84 (C-5′, C-6), 68.63, 68.99, 69.40 (C-6″, C-1′), 72.23 (C-4″), 72.49 ($\mathbf{C}H_2$Ph), 73.32, 73.39 (C-5), 73.53, 74.59, 74.94, 75.50 (4 $\mathbf{C}H_2$Ph), 76.16, 77.00, 77.62, 78.15, 78.33, 78.49 (C-4, C-2′, C-3′, C-4′, C-3″), 82.10 (C-2), 84.28 (C-3), 99.52, 99.60 (C-1″), 100.9 (**C**HPh), 104.6 (C-1), 116.5 (CN), 126.2–128.8, 137.8–138.4 (C-Ph), 171.2 (**C**=O); ^{31}P NMR δ: –0.03, –0.58, –1.49, –1.50.

A solution of **22** (0.066 g, 0.051 mmol) in a mixture of triethylamine, pyridine, and water (3:1:1, 5 mL) was stirred at room temperature for 2 h. The solution was concentrated to a foam of **23** (0.068 g, 99.6% yield); $[\alpha]_D^{20}$ –7.9 (*c* 0.30, CH_3OH); ^{1}H NMR (400 MHz, CD_3OD) δ: 1.18 (t, 3H, $C\mathbf{H_3}CH_2$), 1.75 (s, 3H, $C\mathbf{H_3}CO$), 2.97 (q, 2H, $CH_3C\mathbf{H_2}$), 3.22 (dd, 1H, H-2, $J_{1,2}$ = 7.8 Hz, $J_{2,3}$ = 9.29 Hz), 3.35–3.45 (m, H-4,5,5″), 3.39, 3.43 (2 s, 2 × $OC\mathbf{H_3}$), 3.51 (m, H-3″,3), 3.75 (dd, 1H, H-1′, $J_{1'A,1'B}$ = –10.8 Hz, $J_{1'A,2'}$ = 6.4 Hz), 3.92 (m, H-3′,4′), 4.02 (m, H-2′,6), 4.25 (d, 1H, H-1), 4.40 (br d, 1H, H-4″, $J_{3'',4''}$ = 3.4 Hz), 4.52 (d, 1H, H-1″, $J_{1'',2''}$ = 8.8 Hz), 4.57–4.83 (m, 6 $C\mathbf{H_2}$Ph), 5.60 (s, 1H, C**H**Ph), 7.1–7.5 (m, 35H, H-Ph); ^{13}C NMR (CD_3OD) δ: 9.40 ($\mathbf{C}H_3CH_2$), 23.34 ($\mathbf{C}H_3CO$), 47.67 ($CH_3\mathbf{C}H_2$), 52.83(C-2″), 57.16, 57.57 (2 × $O\mathbf{C}H_3$), 65.85 (C-6), 66.39 (C-5′), 68.04 (C-5″), 70.54 (C-6″), 71.37 (C-1′), 72.93 (C-4″), 73.56, 73.77, 75.00, 75.50 (4 $\mathbf{C}H_2$Ph), 75.73 (C-5), 75.96, 76.41 (2 $\mathbf{C}H_2$Ph), 79.27 (C-4), 80.23 (3C C-3″, 2′, 3′, or 4′), 80.55 (C-3′ or 4′), 83.39 (C-2), 85.71 (C-3), 102.2 (**C**HPh), 103.1 (C-1″), 105.9 (C-1), 127.7–130.0, 138.5–140.5 (C-Ph), 173.5 (**C**=O); ^{31}P NMR (CD_3OD) δ: 1.22. Exact Mass (ESI) calcd. for $C_{70}H_{79}NO_{18}PNa_2$ $[M - NHEt_3 + 2Na]^+$: 1298.4830; found: 1298.4808.

Sodium (methyl β-D-glucopyranosid-6-yl) 1-*O*-(2-acetamido-2-deoxy-3-*O*-methyl-β-D-galactopyranosyl)-L-ribityl-5-phosphate, 24

A solution of **23** (0.323 g, 0.238 mmol) in a mixture of ethyl acetate, methanol, and acetic acid (10:14.5:0.5, 25 mL) was stirred with Pd/C (10%, 0.38 g) under hydrogen (1 atm) for 50 h. The reaction mixture was filtered through Celite and the filtrate was concentrated. A solution of the residue in water (3 mL) was stirred with Amberlite IR-120 (Na^+) resin overnight. The filtrate was concentrated to give **24** quantitatively; $[\alpha]_D^{20}$ –14.2 (*c* 0.12, H_2O); ^{1}H NMR (500 MHz) (D_2O) δ: 2.04 (s, 3H, $C\mathbf{H_3}CO$), 3.28 (m, 1H, H-2, $J_{2,3}$ = 9.4 Hz), 3.41 (s, 3H, 3"-$O\mathbf{C}H_3$), 3.45 (dd, 1H, H-3″, $J_{2'',3''}$ = 11.0 Hz), 3.50 (m, 2H, H-3,4), 3.57 (s, 3H, 1-$OC\mathbf{H_3}$), 3.58 (m, 1H, H-5), 3.66 (br dd, 1H, H-5″, $J_{5'',6a''}$ = 4.3 Hz, $J_{5'',6b''}$ = 6.9 Hz), 3.740 (dd, 1H, H-1′a, $J_{1'a,1'b}$ = 11.6 Hz, $J_{1'a,2'}$ = 6.3 Hz), 3.744 (t, 1H, H-3′, $J_{2',3'}$ = $J_{4',3'}$ = 6.4 Hz), 3.78 (dd, 1H, H-6″a, $J_{6a'',6b''}$ = 11.8 Hz, $J_{6''a,5''}$ = 4.3 Hz), 3.83 (dd, 1H, H-6″b, $J_{6''b,5''}$ = 7.9 Hz), 3.93 (m, 1H, H-4′), 3.94 (dd, H-2″, $J_{2'',3''}$ = 10.6 Hz), 3.95 (m, 1H, H-2′), 3.98 (m, 1H, H-5′a), 4.07 (dd, 1H, H-1′b, $J_{1'b,2'}$ = 5.2 Hz), 4.08 (m, H-5′b), 4.09

© 1999 NRC Canada

(dd, 1H, H-6a, $J_{6a,5}$ = 2.9 Hz), 4.18 (dddd, 1H, H-6b, $J_{6b,6a}$ = 11.6 Hz, $J_{6b,5}$ = 5.1 Hz, $J_{6b,P}$ = 2.1 Hz), 4.22 (d, 1H, H-4″, $J_{4'',3''}$ = 3.2 Hz), 4.40 (d, 1H, H-1, $J_{1,2}$ = 8.0 Hz), 4.48 (d, 1H, H-1″, $J_{1'',2''}$ = 8.5 Hz); ^{13}C NMR δ: 23.10 (**C**H_3CO), 51.98 (C-2″), 57.13 (3"-O**C**H_3), 58.14 (1-O**C**H_3), 61.88 (C-6″), 64.30 (C-4″), 64.96 (d, C-6, $J_{6,P}$ = 5.0 Hz), 67.36 (d, C-5′, $J_{5',P}$ = 6.3 Hz), 69.87 (C-4), 71.34 (C-2′), 71.67 (d, C-4′, $J_{4',P}$ = 7.7 Hz), 71.70 (C-1′), 72.41, (C-3′), 73.89 (C-2), 75.38 (d, C-5, $J_{5,P}$ = 7.8 Hz), 75.77 (C-5″), 76.39 (C-3), 80.63 (C-3″), 103.15 (C-1″), 104.15 (C-1), 175.72 (**C**=O); ^{31}P NMR (D_2O) δ: 1.71. Exact Mass (FAB) calcd. for $C_{21}H_{40}NO_{18}PNa$ [M + H]$^+$: 648.1881; found: 648.188.

Acknowledgments

We thank the Natural Sciences and Engineering Research Council of Canada (NSERC) for financial support, and Dr. M.D. Lumdson and Dr. I. Burton for recording some of the NMR spectra. We also thank the National Research Council in Ottawa, the University of Ottawa, and the University of Alberta for recording high-resolution MS spectra. Special thanks go to Dr. O. Hindsgaul for arranging for the MS to be run at the University of Alberta.

References

1. (*a*) J.B. Robbins, R. Austrian, C.-J. Lee, S.C. Rastogi, G. Schiffman, J. Henrichsen, P.H. Makela, C.V. Broome, R.R. Facklam, R.H. Tiesjema, and J.C. Parke, Jr. J. Infect. Dis. **148**, 1136 (1983); (*b*) E. Alonsodevelasco, A.F.M. Verheul, J. Verhoef, and H. Snippe. Microbiol. Rev. **59**, 591 (1995); (*c*) K.M. Zangwill, C.M. Vadheim, A.M. Vannier, L.S. Hemenway, D.P. Greenberg, and J.I. Ward. J. Infect. Dis. **174**, 752 (1996).
2. J. Henrichsen. J. Clin. Microbiol. 2759 (1995).
3. (*a*) U.B.S. Sorensen and J. Henrichsen. J. Clin. Microbiol. **25**, 1854 (1987); (*b*) U.B.S. Sorensen, J. Blom, A. Birch-Andersen, and J. Henrichsen. Infect. Immun. **56**, 1890 (1988).
4. (*a*) T. Behr, W. Fischer, J. Peter-Katalinic, and H. Egge. Eur. J. Biochem. **207**, 1063 (1992); (*b*) R.A. Klein, R. Hartmann, H. Egge, T. Behr, and W. Fischer. Carbohydr. Res. **256**, 189 (1994).
5. S.C. Szu, R. Schneerson, and J.B. Robbins. Infect. Immun. **54**, 448 (1986).
6. C.A. Laferriere, R.K. Sood, J.M. Demuys, F. Michon, and H.J. Jennings. Vaccine, **15**, 179 (1997).
7. (*a*) W.F. Goebel, T. Shedlovsky, G.I. Lavin, and M.H. Adams. J. Biol. Chem. **148**, 1 (1943); (*b*) E.C. Gotschlich and T.-Y. Liu. J. Biol. Chem. **242**, 463 (1967).
8. D.E. Brundish and J. Baddiley. Biochem. J. **110**, 573 (1968).
9. I.R. Poxton, E. Tarelli, and J. Baddiley. Biochem. J. **175**, 1033 (1978).
10. H.J. Jennings, C. Lugowski, and N.M. Young. Biochemistry, **19**, 4712 (1980).
11. M. Kulakowska, J.R. Brisson, D.W. Griffith, N.M. Young, and H.J. Jennings. Can. J. Chem. **71**, 644 (1993).
12. W. Fischer, T. Behr, R. Hartmann, J. Peter-Katalinic, and H. Egge. Eur. J. Biochem. **215**, 851 (1993).
13. (*a*) J. Baddiley. Acc. Chem. Res. **3**, 98 (1970); (*b*) H. Hussey and J. Baddiley. *In* The enzymes of biological membranes. Vol. 2. *Edited by* A. Martonosi. Plenum, New York. 1976. pp. 227–326.
14. (*a*) L. Glaser. J. Biol. Chem. **239**, 3178 (1964); (*b*) T. Chin, M.M. Burger, and L. Glaser. Arch. Biochem. Biophys. **116**, 358 (1966); (*c*) F. Fiedler and L. Glaser. J. Biol. Chem. **249**, 2684 (1974); (*d*) F. Fiedler and L. Glaser. J. Biol. Chem. **249**, 2690 (1974).
15. A.R. Archibald and H.E. Coapes. Biochem. J. **124**, 449 (1971).
16. H.U. Koch and W. Fischer. Biochemistry, **17**, 5275 (1978).
17. W. Fischer, M.A. Schmidt, B. Jann, and K. Jann. Biochemistry, **21**, 1279 (1982).
18. J.C. Richards and R.A. Leitch. Can. J. Chem. **68**, 1574 (1990).
19. (*a*) L.M. Beynon, J.C. Richards, and M.B. Perry. Eur. J. Biochem. **210**, 119 (1992); (*b*) L.M. Beynon, M.B. Perry, and J.C. Richards. Carbohydr. Res. **209**, 211 (1991).
20. L.M. Beynon and J.C. Richards. Carbohydr. Res. **252**, 263 (1994).
21. (*a*) T. Rundlöf and G. Widmalm. Anal. Biochem. **243**, 228 (1996); (*b*) T. Rundlof, A. Weintraub, and G. Widmalm. Carbohydr. Res. **291**, 127 (1996).
22. N. Kojima, Y. Araki, and E. Ito. Eur. J. Biochem. **148**, 479 (1985).
23. P. Branefors-Helander, C. Erbing, L. Kenne, and B. Lindberg. Carbohydr. Res. **56**, 117 (1977).
24. P.J. Garegg, B. Lindberg, K. Nilsson, and C.-G. Swahn. Acta Chem. Scand. **27**, 1595 (1973).
25. J. Baddiley, J.G. Buchanan, and B. Carss. J. Chem. Soc. 1869 (1957).
26. M.W. Ganfield and R.A. Pieringer. J. Biol. Chem. **255**, 5164 (1980).
27. (*a*) J.E.G. van Dam, J. Breg, R. Komen, J.P. Kamerling, and J.F.G. Vliegenthart. Carbohydr. Res. **187**, 267 (1989); (*b*) L. Kenne, B. Lindberg, and J.K. Madden. Carbohydr. Res. **73**, 175 (1979); (*c*) C. Jones. Carbohydr. Res. **269**, 175 (1995); (*d*) L. Kenne and B. Lindberg. Carbohydr. Res. **184**, 288 (1988); (*e*) L.M. Beynon, J.C. Richards, and M.B. Perry. Can. J. Chem. **73**, 41 (1995).
28. P. Smid, M. de Swart, W.P.A. Jörning, G.A. van der Marel, and J.H. van Boom. J. Carbohydr. Chem. **12**, 1073 (1993).
29. G. Grundler and R.R. Schmidt. Liebigs Ann. Chem. 1826 (1984).
30. (*a*) T.B. Grindley. Adv. Carbohydr. Chem. Biochem. **53**, 17 (1998); (*b*). *In* Synthetic oligosaccharides: indispensable probes for the life sciences. *Edited by* P. Kováč. ACS, Washington. 1994. pp. 51–76; (*c*) S. David and S. Hanessian. Tetrahedron, **41**, 643 (1985).
31. L. Chan and G. Just. Tetrahedron, **46**, 151 (1990).
32. J.P.G. Hermans, L. Poot, M. Kloosterman, G.A. van der Marel, C.A.A. van Boeckel, D. Evenberg, J.T. Poolman, P. Hoogerhout, and J.H. van Boom. Recl. Trav. Chim. Pays-Bas, **106**, 498 (1987).
33. B. Bernet and A. Vasella. Helv. Chim. Acta, **62**, 1990 (1979).
34. N.D. Sinha, J. Biernat, J. McManus, and H. Köster. Nucleic Acids Res. **12**, 4539 (1984).
35. R.R. Schmidt and W. Kinzy. Adv. Carbohydr. Chem. Biochem. **50**, 21 (1994).
36. C.W. Haigh. Annu. Rep. NMR Spectrosc. **4**, 311 (1971).
37. (*a*) S.J. Angyal, J.K. Saunders, C.T. Grainger, R. Le Fur, and P.G. Williams. Carbohydr. Res. **150**, 7 (1986); (*b*) S.J. Angyal and R. Le Fur. Carbohydr. Res. **84**, 201 (1980); (*c*) G.E. Hawkes and D. Lewis. J. Chem. Soc. Perkin Trans. 2, 2073 (1984); (*d*) G.A. Jeffrey and H.S. Kim. Carbohydr. Res. **14**, 207 (1970); (*e*) D. Lewis and S.J. Angyal. J. Chem. Soc. Perkin Trans. 2, 1763 (1989); (*f*) J.R. Synder. Carbohydr. Res. **198**, 1 (1990).
38. (*a*) G.W. Schnarr, D.M. Vyas, and W.A. Szarek. J. Chem. Soc. Perkin Trans. 1, 496 (1979); (*b*) J.K. Whitesell, T. LaCour, R.L. Lovell, J. Pojman, P. Ryan, and A. Yamada-Nosaka. J. Am. Chem. Soc. **110**, 991 (1988).
39. G.W. Kenner, H.J. Rodda, and A.R. Todd. J. Chem. Soc. 1613 (1949).
40. D. Keglević and D. Ljevakovic. Carbohydr. Res. **64**, 319 (1978).

© 1999 NRC Canada

Can. J. Chem. Downloaded from www.nrcresearchpress.com by University Town Library of Shenzhen on 09/05/12
For personal use only.

A structural investigation of the singly layered silicates, silinaite and makatite, by vibrational spectroscopy

Yining Huang, Zhimei Jiang, and Wilhelm Schwieger

Can. J. Chem. Downloaded from www.nrcresearchpress.com by Peking University on 09/06/12
For personal use only.

Abstract: The IR and Raman spectra of two singly layered silicates, silinaite and makatite, have been investigated. The vibrational spectra were assigned based on previous studies of various silicates. The correlation between vibrational modes and the structural properties of silicates under investigation has been made. The IR and Raman spectra of silinaite are in good agreement with the known structure. However, the observed vibrational data of makatite are not completely consistent with those predicted by a factor group analysis based on the published single-crystal data.

Key words: layered silicates, silinaite, makatite, vibrational spectroscopy.

Résumé : On a déterminé les spectres IR et Raman de deux silicates en monocouches, silinaite et makatite. Les spectres vibrationnels ont été attribués en se basant sur des études antérieures sur divers silicates. On a établi une corrélation entre les modes de vibration et les propriétés structurales des silicates. Les spectres IR et Raman de la silinaite sont en bon accord avec la structure connue. Toutefois, les données vibrationnelles observées avec la makatite ne sont pas en accord complet avec ceux prédits par une analyse de groupe factoriel basée sur les donnes relatives à un cristal unique.

Mots clés : silicates en couches, silinaite, makarite, spectroscopie vibrationnelle.

[Traduit par la Rédaction]

Introduction

Makatite, kanemite, magadiite, ilerite, and kenyaite are structurally related hydrous alkali silicates (1) and silinaite, a new addition to this family of layered materials, has recently been identified (2). With the exception of ilerite, all of the above-mentioned silicates are naturally occurring minerals, but they can be readily prepared in the laboratory by hydrothermal synthesis. These hydrated layered alkali metal silicates exhibit some interesting properties, such as interlamellar sorption of water and organic molecules and ion exchange of the surface cations. These properties suggest potential practical applications as ion exchangers, adsorbents, catalysts, and molecular sieves. Recently, these layered silicates have received much attention due to their ability to transform to layered silicic acids by proton exchange. Layered silicic acids are very useful hosts in the formation of pillared materials because of the presence of reactive silanol groups in their interlayer surfaces.

The structures of these silicates have been of continuous interest in past decades because the physical and chemical properties of these materials are largely structure dependent; however, single-crystal X-ray diffraction data are only available for makatite (3) and silinaite (4). The exact structures of magadiite, ilerite, kanemite, and kenyaite are unknown. Most of the structural information has been obtained by using techniques such as solid state NMR and powder X-ray diffraction. While the X-ray diffraction method detects long-range ordering and periodicity, vibrational spectroscopy, on the other hand, can provide complementary information on short-range ordering and local structures. As part of our ongoing project of investigating structure and bonding in the above-mentioned layered silicates, we have examined the vibrational spectra of silinaite and makatite with particular attention being paid to the correlation of the vibrational properties of these materials with their structural features. The IR spectra of silinaite and makatite have previously been reported (5), but no band frequencies or detailed assignments were given. To date, no Raman study has been performed on these silicates.

Experimental

Silinaite and makatite were synthesized according to refs. 5 and 6, respectively. The purity and crystallinity were

Received April 24, 1998.[1]

Y. Huang[2] and Z. Jiang.[3] Department of Chemistry, University of Western Ontario, London, ON N6A 5B7, Canada.
W. Schwieger. Martin-Luther-Universität Halle, Institut für Technische Chemie und Makromolekulare Chemie, Schlossberg 2, D-06108 Halle, Germany.

[1]Revision received February 9, 1999.
[2]Author to whom correspondence may be addressed. Telephone: (519) 679-2111, ext. 6384. Fax: (519) 661-3022.
e-mail: yhuang@julian.uwo.ca
[3]Present address: Department of Chemistry, University of Waterloo, Waterloo, ON N2L 3G1, Canada.

© 1999 NRC Canada

Fig. 1. IR (top) and Raman (bottom) spectra of silinaite.

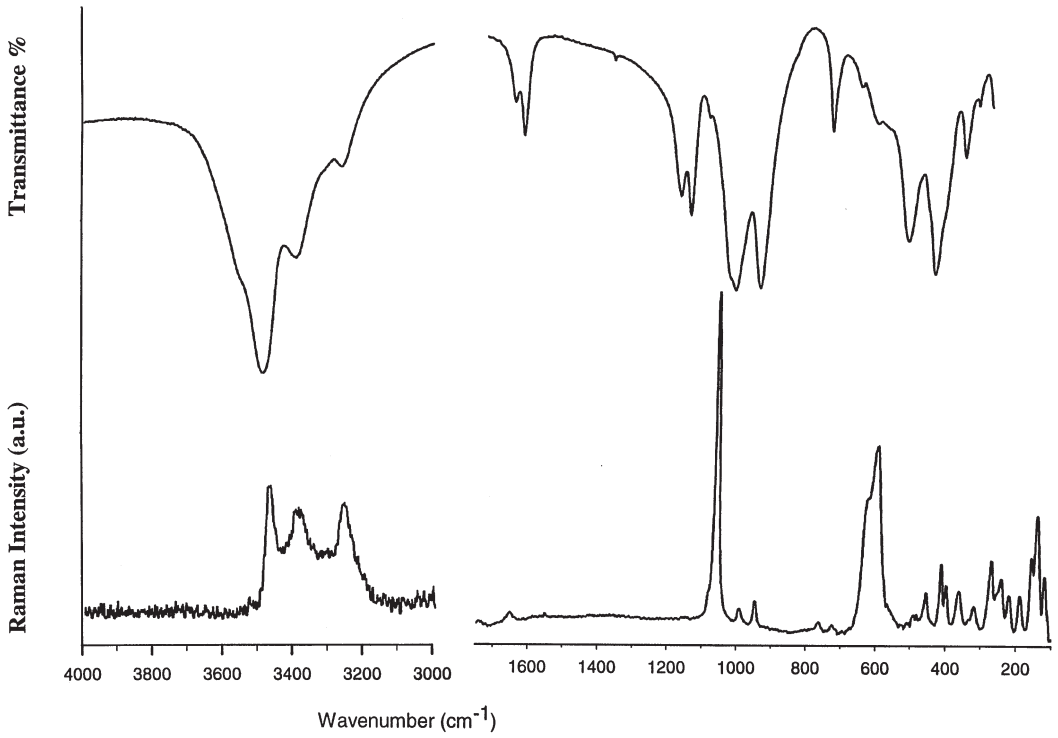

Can. J. Chem. Downloaded from www.nrcresearchpress.com by Peking University on 09/06/12
For personal use only.

checked by powder X-ray diffraction measurements (Philips PW 1830 powder diffractometer). The IR spectra (both 2 and 4 cm^{-1} resolution) were recorded on a Perkin–Elmer Paragon-1000 FT-IR spectrometer equipped with a DTGS detector. Samples were prepared using the standard KBr method. The Raman spectra were obtained on a Bruker RFS-100 FT-Raman spectrometer equipped with a Nd^{3+}:YAG laser (1064.1 nm) and a liquid nitrogen cooled Ge detector. The spectral resolution was 2 cm^{-1}, and 1000 scans were accumulated for the spectra. The precision for the band positions was ±1 cm^{-1}. All the measurements were performed at room temperature.

Results and discussion

1. Silinaite

The single-crystal X-ray study shows that silinaite is monoclinic with space group $A2/n$ (C_{2h}^6). There are four formula units ($NaLiSi_2O_5 \cdot 2H_2O$) per unit cell, $Z = 4$ (2, 4). The silicate consists of single layers of $[SiO_4]^{4-}$ tetrahedra. All Si sites are crystallographically equivalent and there are three different oxygen sites in the silicate layer. Each silicon atom forms three Si-O-Si bonds and only one $Si\text{-}O^{-}\text{-}M^{+}$ (M = Li or Na) bond, known as a Q^3 site. The silicate layers in silinaite are held together by $[LiO_4]$ tetrahedra in which the four terminal oxygen ions belong to four different $[SiO_4]^{4-}$ tetrahedra. The sodium ions between layers are octahedrally coordinated by interacting with four water molecules and two terminal oxygen ions that cross-link the $[LiO_4]$ tetrahedra. Each water molecule is also bonded to the silicate layer through hydrogen bonding (4).

The vibrational spectra of silinaite are shown in Fig. 1 and the corresponding IR and Raman frequencies are given in Table 1. The vibrational spectra can be divided into two regions. The first region covers the frequency range 4000–1600 cm^{-1} where stretching and bending vibrations of water molecules appear. The second region (below 1300 cm^{-1}) includes the vibrations due to the silicate layer and charge-balancing cations. Since the vibrations in these two regions are not normally coupled to one another, we shall discuss them separately.

Vibrations of silicate layer and associated cations

As mentioned earlier, the crystal structure of silinaite at ambient temperature is monoclinic with space group $A2/n$ (C_{2h}^6). One Bravais unit cell contains two formula units ($NaLiSi_2O_5 \cdot 2H_2O$). Within each Bravais unit cell, four Si atoms occupy the general positions. There are three types of crystallographically inequivalent oxygen atoms: O(1) and O(2) atoms are located at two different C_1 sites, while two O(3) atoms occupy C_i sites. Two Na and two Li ions lie on the positions with C_2 symmetry. Based on the above information, the vibrations due to the silicate layer and associated cations can be predicted by performing a factor group analysis.[4] Fifty-four vibrational bands due to the silicate layer and charge-balancing cations are expected in the IR and Raman spectra. Among them, 30 bands should be IR active while the Raman spectra should exhibit 24 bands:

$$\Gamma_{vib} = 11A_g(R) + 13B_g(R) + 14A_u(IR) + 16B_u(IR)$$

[4] Appendix 1 presents data for the factor group analysis of silinaite, while Appendix 2 gives the data for the factor group analysis of makatite. Appendices 1 and 2 are available as supplementary material and may be purchased from: The Depository of Unpublished Data, Document Delivery, CISTI, National Research Council Canada, Ottawa, Canada, K1A 0S2.

© 1999 NRC Canada

Table 1. Vibrational data (cm^{-1}) for silinaite and their assignments.[a]

IR	Raman	Assignment
3558 m (sh) 3490 s 3396 m 3265 m	3472 vw 3389 vw 3259 vw	νOH
1667 m 1639 m	1652vw	δHOH
1189 s 1159 s 1111 w 1042 vs (sh) 1026 vs 955 vs	1068 vs 1000 w 956 w	ν_{as} SiOSi and νSiO⁻
757 m 677 w 627 w	773 w 734 w 635 s (sh) 609 s	ν_s SiOSi
535 s 456 vs 375 m 339 w	501 vw 490 vw 466 m 423 m 408 m 371 m 342 vw 327 m 279 m 259 w (sh) 250 m 227 m 196 m 163 m 148 s 126 m 107 w	δSiO and νM-O

[a]Abbreviations: v, very strong; m, medium; w, weak; sh, shoulder; ν_{as} and ν_s, asymmetric and symmetric stretching; δ, bending mode.

where R and IR in parentheses denote Raman and IR activity, respectively. Experimentally, 13 IR bands were observed in the regions of 1300–300 cm^{-1} (Fig. 1 and Table 1). The number of observed bands is less than half of the number predicted by factor group analysis. This is due to several reasons: firstly, we were unable to obtain IR spectra below 300 cm^{-1}. In the far-IR range some silicon–oxygen bending and metal–oxygen stretching vibrations may occur (7). Secondly, accidental degeneracy and very weak intensities of certain modes may also be responsible for the observation of fewer bands. Furthermore, since IR bands are generally quite broad, it is likely that some bands are superimposed to give a broad spectral profile. The observed Raman spectrum contains 24 bands in the region of 1300–100 cm^{-1}. Some of these observed bands may be combinations or overtones.

According to the X-ray structure, the unit cell of silinaite is centrosymmetric. Therefore, the mutual exclusion rule should apply, i.e., no vibration can be active in both IR and Raman spectra. From Table 1, it is evident that all the observed IR bands indeed appear at different frequencies from those in the Raman spectrum. Therefore, the vibrational data are consistent with the X-ray result, and the unit cell of silinaite is indeed centrosymmetric.

The tentative assignments of vibrational bands in the spectra of silinaite are given in Table 1. According to previous studies (7), the various vibrations due to the silicate layer and associated cations follow the frequency order: ν_{as}SiOSi > νSiO⁻ > ν_sSiOSi > δSiO and νMO, where ν_{as}SiOSi and ν_sSiOSi refer to the asymmetric and symmetric stretching modes of Si-O-Si bridges; νSiO⁻ represents the stretch-

Can. J. Chem. Downloaded from www.nrcresearchpress.com by Peking University on 09/06/12
For personal use only.

© 1999 NRC Canada

Can. J. Chem. Downloaded from www.nrcresearchpress.com by Peking University on 09/06/12
For personal use only.

ing modes of terminal Si—O^- bonds; δSiO refers to the Si-O-Si and O-Si-O bending modes; and νMO represents the M–O stretching modes. There has been extensive discussion in the literature regarding the assignment of the bands of the IR and Raman spectra of various silicates (7–16). Silinaite bears some structural resemblance to sodium disilicate $Na_2Si_2O_5$ (4). Based on previous empirical assignments of the vibrational bands of α-$Na_2Si_2O_5$ and other silicates (7–16), the IR and Raman bands of silinaite can be tentatively assigned: the bands between 1300 and 950 cm^{-1} are due to the asymmetric stretching vibrations of Si-O-Si (ν_{as}SiOSi) and stretching vibrations of Si—O^- (νSiO); the bands between 780 and 600 cm^{-1} are associated with the symmetric stretching vibrations of Si-O-Si (ν_sSiOSi); the bands below 550 cm^{-1} are due to silicon–oxygen bending vibrations and the stretching vibrations arising from M—O bonds.

By studying the IR spectrum of pyrosilicates containing the Si_2O_7 group where ∠SiOSi = 180°, Lazarev has suggested that the appearance of IR bands in the frequency range between 1150 and 1200 cm^{-1} is associated with the existence of Si-O-Si bridges with an angle of 180° (or nearly so). This assumption has been extended to include other silicates with more complicated structures than pyrosilicates and has been confirmed by X-ray diffraction (7). Figure 1 shows that silinaite does exhibit two narrow intense IR bands centered at 1189 and 1159 cm^{-1}, respectively. The observation of these two bands is indicative of the existence of Si-O-Si bonds with an angle near 180°. This vibrational result is in good agreement with that obtained from the single-crystal X-ray study, which shows that the bond angle for the Si-O(3)-Si linkage is indeed 180°.

According to previous studies (7), the bands in the mid-frequency region may be assigned to the symmetric stretching vibrations, ν_sSiOSi. They are associated with the presence of bridging oxygens (Si-O-Si linkages) in the structure. For silinaite, we tentatively assign the bands between 780 and 600 cm^{-1} to ν_sSiOSi. A number of studies have shown that the band frequencies in this region are sensitive to the Si-O-Si bond angles (7, 12, 13). Lazarev (7) has pointed out that the ν_{as}SiOSi and ν_sSiOSi frequencies depend on the Si-O-Si bond angle and suggested an empirical relationship between the Si-O-Si angle and a quantity Δ, where $\Delta = (\nu_{as} - \nu_s)/(\nu_{as} + \nu_s)$. A large Si-O-Si angle corresponds to a large value of Δ. This means that an increase in the Si-O-Si angle will result in an increase in the ν_{as}SiOSi frequency and a decrease in the ν_sSiOSi frequency. It is reasonable to assume that for the linear Si-O-Si linkages the ν_sSiOSi should have a lower frequency than those of Si-O-Si units with angles less than 180°. Based upon this assumption, we assign the Raman band of silinaite at 609 cm^{-1}, which has the lowest frequency in the symmetric stretching region, to the ν_sSiOSi of linear Si-O-Si bonds.

Silinaite also contains two other inequivalent nonlinear Si-O-Si linkages. Their asymmetric vibrations (ν_{as}SiOSi) are assigned to the bands in the region 1100–950 cm^{-1}, where the Si–O^- stretching vibrations (νSiO^-) also appear. The IR spectrum of silinaite in the ν_sSiOSi frequency range has a strong band at 757 cm^{-1} and two weaker bands at lower frequency (676 and 630 cm^{-1}). They may be assigned to the symmetric stretching vibrations (ν_sSiOSi) arising from nonlinear Si-O-Si bridges.

In the Raman spectrum of silinaite, there is a very strong band located at 1068 cm^{-1}. We tentatively assign this band to the Si–O^- stretching vibration. This assignment is based on previous studies of crystalline silicates and silicate glasses containing $[SiO_4]^{4-}$ tetrahedra with one, two, three, and four nonbridging oxygens, respectively (9–13). These studies have shown that the dominant Raman bands at 1100–1050 cm^{-1}, 1000–950 cm^{-1}, near 900 cm^{-1}, and near 850 cm^{-1} are associated with the stretching vibrations (νSiO^-), due to Q^3, Q^2, Q^1 and Q^0 species, respectively. In the Raman spectrum of silinaite, only one strong band was observed at 1068 cm^{-1}, indicating that silinaite contains only Q^3 species, which is consistent with the result from single-crystal X-ray diffraction (4) and NMR studies (5) that silinaite has a single-layer structure.

Internal vibrations of water molecules

The internal vibrational modes of water molecules located between layers are worth mentioning. In addition to the molecular symmetry, the number of internal modes of water molecules in silinaite is also determined by the site (C_1) and unit cell (C_{2h}) symmetry. The scheme of correlation between the representations of the molecular, site, and factor group symmetries can be expressed as follows:

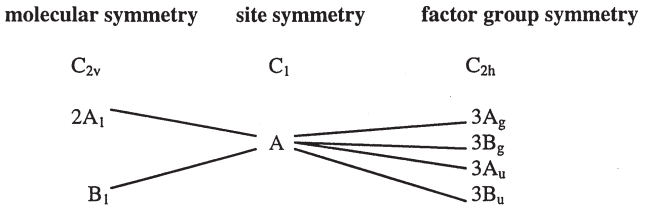

Since there are 4 water molecules per Bravais unit cell of silinaite (4), 12 crystal internal vibrations are expected:

$$\Gamma_{\text{Internal vib}} = 3A_g(R) + 3B_g(R) + 3A_u(IR) + 3B_u(IR)$$

The assignment of the fundamental vibrations of the free water molecule in the gas phase is well established. The band at 3651 cm^{-1} has been assigned to the symmetric stretching ν_1 (A_1), 1595 cm^{-1} to the bending ν_2 (A_1), and 3756 cm^{-1} to the asymmetric stretching ν_3 (B_1) (17). All three fundamentals are both Raman and IR active. From the above correlation diagram, we can see that each vibrational mode of free water molecule should split into four modes due to the correlation coupling. Among the four modes, two (A_g and B_g) are Raman active and the other two (A_u and B_u) are IR active. This factor group splitting can be clearly seen from the IR and Raman spectra of silinaite (Fig. 1). In the region of OH stretching vibrations (νOH), the IR spectrum shows four bands at 3558, 3490, 3396, and 3264 cm^{-1}, respectively. Because the frequencies of asymmetric stretching are normally higher than those of symmetric stretching, the above four bands may be assigned as follows: The bands at 3558 and 3490 cm^{-1} are due to the splitting of ν_3 (B_1 related species) and the bands at 3396 and 3265 cm^{-1} to the splitting of ν_1 (A_1 related species). In the Raman spectrum, three of the four predicted peaks were observed at 3472, 3389, and 3259 cm^{-1}. These peaks are also related to the ν_1 and ν_3 modes of free water molecules. The two bending bands, δHOH, in the IR spectrum at 1667 and 1639 cm^{-1} are corre-

© 1999 NRC Canada

Fig. 2. IR (top) and Raman (bottom) spectra of makatite.

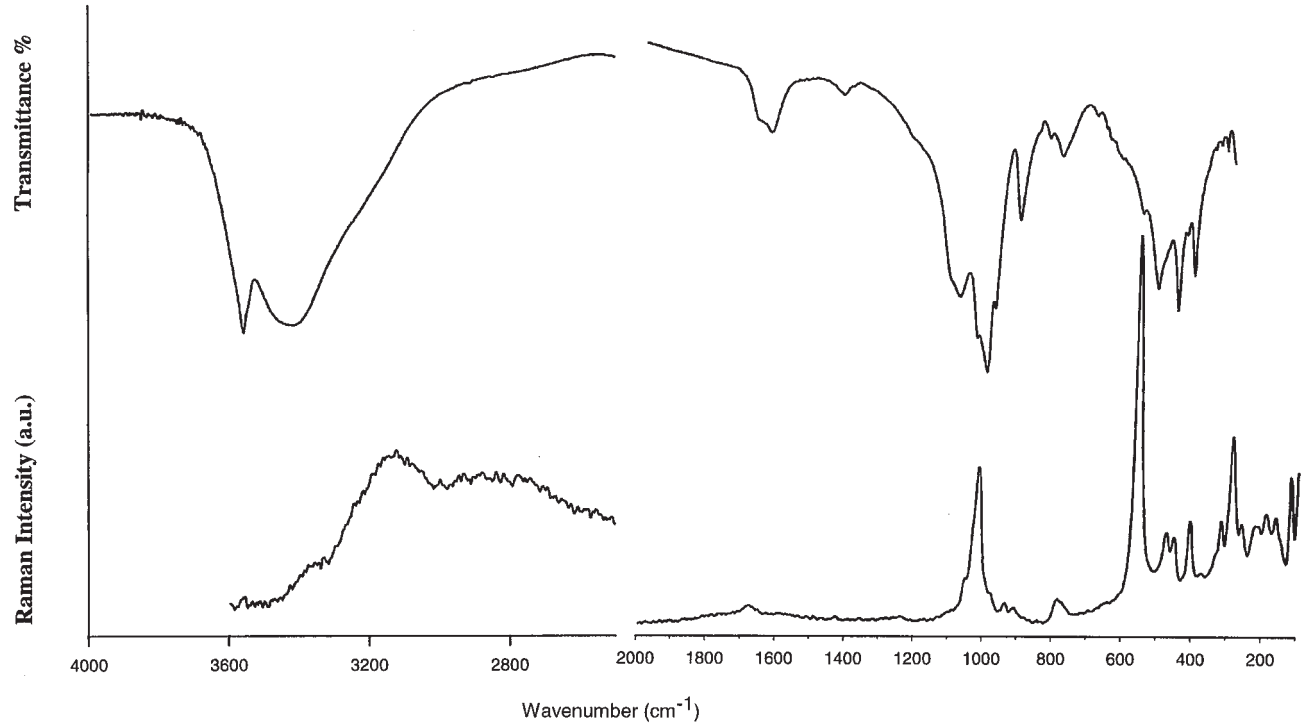

Can. J. Chem. Downloaded from www.nrcresearchpress.com by Peking University on 09/06/12
For personal use only.

lated with the splitting of the ν_2 fundamental mode for the free molecule. It is worth noting that the vibrational frequencies of IR and Raman bands of water molecules in silinaite are not coincident. This is again consistent with the fact that the unit cell of silinaite has a center of symmetry. The observed stretching frequencies in the IR and Raman spectra are lower than both ν_1 and ν_3 in free water molecules, due to the effect of hydrogen bonding between water and the silicate layer. These well-developed stretching and bending bands are sharp and intense, indicating that these vibrations are indeed due to the water molecules between layers that are part of the crystal.

In addition to the internal vibrations, factor group analysis predicts that water molecules in the crystal should also exhibit 24 external modes, including 12 rotational ($3A_g$(R) + $3B_g$(R) + $3A_u$(IR) + $3B_u$(IR)) and 12 translational ($3A_g$(R) + $3B_g$(R) + $3A_u$(IR) + $3B_u$(IR)) modes. However, we were unable to identify these lattice vibrations, since a majority of them would appear in the low-frequency region that is not accessible due to instrumental limitations.

In summary, the vibrational spectra of silinaite are consistent with the known structure obtained from the single-crystal X-ray study. IR and Raman frequencies of both the silicate layer and water molecules in silinaite are not coincident, suggesting that the unit cell is centrosymmetric. Observation of IR bands in the range 1150–1200 cm^{-1} indicates the existence of linear Si-O-Si linkages in silinaite. The strong band positioned at 1068 cm^{-1} in the Raman spectrum implies that silinaite contains Q^3 species.

Since all the above results are in good agreement with those obtained from single-crystal X-ray diffraction, we feel that the vibrational approach can now be used to probe those silicates with unknown or poorly defined structures.

2. Makatite

Makatite is also a single-layered silicate. Its composition is reported as $Na_2Si_4O_9 \cdot 5H_2O$ (18) and $Na_2Si_4O_8(OH)_2 \cdot 4H_2O$ (3). The early work by Sheppard et al. (18) suggested an orthorhombic symmetry for mineral makatite based on its powder X-ray diffraction data. A monoclinic structure with space group $P2_1/c$ (C_{2h}^5) was later proposed by Annehed et al. using the single-crystal X-ray diffraction technique (3). It seems that there is an ambiguity existing in the structure of makatite. Therefore, an IR and Raman spectroscopic study is particularly informative, since vibrational data may be used to verify the proposed structure.

According to the single-crystal data (3), makatite crystallizes in a space group of $P2_1/c$ with four units of $Na_2Si_4O_8(OH)_2 \cdot 4H_2O$ per primitive cell. Sixteen Si atoms occupy four crystallographically nonequivalent C_1 sites; Forty oxygen atoms are located at ten sets of different general positions. Four Na^+ ions lie on two different types of inversion centers and the remaining sodium ions are located in general positions. Eight hydrogen atoms in hydroxyl groups occupy C_1 sites. The contributing symmetry species of the silicon layer and charge-balancing cations at the center of the Brillouin zone are the following: $51A_g$(R) + $51B_g$(R) + $57A_u$(IR) + $57B_u$(IR). Sixteen water molecules located at eight nonequivalent C_1 sites can be treated separately. The irreducible representations including both internal and external modes are $36A_g$(R) + $36B_g$(R) + $36A_u$(IR) + $36B_u$(IR). The most important result of the factor group analysis is that the IR and Raman modes should not be coincident, since the proposed unit cell is centrosymmetric. The vibrational spectra of makatite are shown in Fig. 2 and the corresponding IR and Raman frequencies are given in Table 2. The experimentally observed frequency regions for IR and Raman spectra

© 1999 NRC Canada

Table 2. Vibrational data (cm^{-1}) for makatite and their assignments.

IR	Raman	Assignment
3563 vs 3424 vs, br[a]	3368 vw (sh), br 3122 w, br	νOH
1679 m (sh) 1639 m	1681 w	δHOH
1429 w 1115 sh 1089 s 1037 vs 1007 vs 987 s 918 s	1244 vw 1060 w 1025 s 986 w 945 w 919 w	ν_{as}SiOSi and νSiO$^-$
835 w 799 m 698 w 672 vw 661 vw 625 vw 564 w	793 w 567 vs	ν_sSiOSi
518 s 460 vs 436 vw 413 s 367 vw 355 vw 340 vw 323 w	482 m 460 m 414 m 381 w 339 vw 324 m 292 s 266 w 226 w 219 w 194 w 167 w 151 vw 122 m 100 m	δSiO and νMO

[a] br = broad.

are 4000–300 cm^{-1} and 3600–100 cm^{-1}, respectively. In their common region, 3600–300 cm^{-1}, 26 IR and 17 Raman bands were observed. Among them, 9 bands appear in both the IR and the Raman spectra. This means that about 35% of the IR and 54% of the Raman bands observed in the region 3600–300 cm^{-1} are coincident. The fact that many peaks have the same frequencies in both the IR and Raman spectra indicates that the unit cell of makatite may be noncentrosymmetric. If we consider the orthorhombic structure proposed by Sheppard et al. and assume the space group is noncentrosymmetric, the possible space groups may belong to *222* and *mm2* classes with factor group symmetries of D_2 and C_{2v}, respectively.

The tentative assignments for the spectra of makatite are given in Table 2. Similar to silinaite, the IR and Raman bands of makatite can be tentatively assigned as follows. The bands between 1300 and 900 cm^{-1} are assigned to the asymmetric stretching vibrations of Si-O-Si linkages and the stretching vibrations of the terminal Si—O^- bonds. The bands between 840 and 560 cm^{-1} are associated with the symmetric stretching vibrations of Si-O-Si bridges. The bands below 550 cm^{-1} are due to Si–O bending vibrations and the stretching vibrations arising from Na—O bonds.

Unlike silinaite, makatite does not have IR bands around 1150–1200 cm^{-1}. The absence of IR bands in this region suggests that makatite does not have Si-O-Si bonds with angles close to 180°.

In the Raman spectrum of makatite, two strong bands at 567 and 1025 cm^{-1} are worth mentioning. These bands can be assigned by comparison with some crystalline silicates and silicate glasses. The strongest band in the Raman spectrum is located at 567 cm^{-1}. Generally, it is believed that strong Raman bands in the 700–400 cm^{-1} region are associated with the presence of bridging oxygens in the structure

Can. J. Chem. Downloaded from www.nrcresearchpress.com by Peking University on 09/06/12
For personal use only.

© 1999 NRC Canada

(9). They are assigned to symmetric stretching vibrations of Si-O-Si linkages (ν_sSiOSi). McMillan (9, 11) has suggested that the bands in the range 520–600 cm^{-1} are related to ν_sSiOSi due to Q^3 species. Makatite exhibits one strong Raman band at 567 cm^{-1}, indicating that Q^3 species exist in the structure. Similar to the Raman band of silinaite at 1068 cm^{-1}, we can assign the strong Raman band at 1025 cm^{-1} as νSiO^- of Q^3 species, since makatite has a single-layer structure.

The bands below 550 cm^{-1} in the IR and Raman spectra of makatite are related to the bending vibrations of silicon–oxygen and stretching vibrations of sodium–oxygen. It is not easy to make a detailed assignment in this region, since those motions are likely mixed.

The bands in the 3700–3000 cm^{-1} region represent stretching vibrations of OH groups. The IR spectrum of makatite shows two OH stretching bands: a sharp band at higher frequency (3563 cm^{-1}) and a broad one centered at lower frequency (3424 cm^{-1}). The broad low-frequency band is related to the OH groups (both hydroxyl groups in Q^3 units and those in water) involved in interlayer hydrogen bonding. The narrow band at higher frequency can be assigned to the isolated surface OH groups, suggesting that not all the hydroxyl groups in Q^3 units are involved in hydrogen bonding.

In summary, unlike silinaite, the observed vibrational data of makatite are not consistent with those predicted by a factor group analysis based on the published single-crystal data. In particular, many peaks have the same frequencies in both the IR and Raman spectra, indicating that the unit cell of makatite may be noncentrosymmetric. Analysis of the vibrational data suggests that the possible space groups of makatite may be those of the *222* and *mm2* classes in the orthorhombic crystal system. Unlike silinaite, makatite does not have strong IR bands at very high frequency (around 1150–1200 cm^{-1}), indicating that there are no Si-O-Si bonds with angles near 180° existing in makatite. The strong bands positioned at 567 and 1025 cm^{-1} in the Raman spectrum imply that makatite contains Q^3 species.

Can. J. Chem. Downloaded from www.nrcresearchpress.com by Peking University on 09/06/12
For personal use only.

Acknowledgements

Y.H. acknowledges financial support from the Natural Sciences and Engineering Research Council of Canada. W.S. thanks the Alexander von Humboldt foundation for support. We also thank Dr. C.A. Fyfe for access to an FT-Raman spectrometer and Dr. N.T. Kawai (Bruker Optics) for obtaining the FT-Raman spectrum of makatite.

References

1. A. Brandt, W. Schwieger, and K.-H. Bergk. Rev. Chim. Miner. **5**, 564 (1987).
2. G.Y. Chao, J.D. Grice, and R.A. Gault. Can. Mineral. **29**, 359 (1991).
3. H. Annehed, L. Falth, and F.J. Lincoln. Z. Kristallogr. **159**, 203 (1982).
4. J.D. Grice. Can. Mineral. **29**, 363 (1991).
5. K. Beneke, P. Thiesen, and G. Lagaly. Inorg. Chem. **34**, 900 (1995).
6. W. Schwieger, D. Heidemann, and K.-H. Bergk. Rev. Chim. Miner. **22**, 639 (1985).
7. N. Lazarev. Vibrational spectra and structure of silicates. Consultants Bureau, New York. 1972.
8. P. Tarte, M.J. Pottier, and A.M. Proces. Spectrochim. Acta, **29A**, 1017 (1973).
9. P. McMillan. Am. Mineral. **69**, 622 (1984).
10. S.K. Sharma. Am. Mineral. **68**, 1113 (1983).
11. P.F. McMillan. Annu. Rev. Earth Planet. Sci. **17**, 255 (1989).
12. S.A. Brawer and W.B. White. J. Chem. Phys. **63**, 2421 (1975).
13. T. Furukawa, K.E. Fox, and W. B. White. J. Chem. Phys. **75**, 3226 (1981).
14. V.C. Farmer. The infrared spectra of minerals. Mineralogical Society, London. 1974.
15. R.K. Moore and W.B. White. Am. Mineral. **56**, 54 (1971).
16. W. Vedder. Am. Mineral. **49**, 736 (1964).
17. W.A. Senior and W.K. Thompson. Nature, **205**, 170 (1965).
18. R.A. Sheppard, A.J. Gude, and R.L. Hay. Am. Miner. **55**, 358 (1970).

© 1999 NRC Canada

A complex of gallium with a Schiff base – bis(orthoquinone) ligand

Martyn A Brown, Jesus A. Castro, Bruce R. McGarvey, and Dennis G. Tuck

Can. J. Chem. Downloaded from www.nrcresearchpress.com by University Town Library of Shenzhen on 09/05/12
For personal use only.

Abstract: The electrochemical oxidation of gallium in a cell containing a solution of 3,5-di-*tert*-butylcatechol (H_2dbc) in a mixture of liquid ammonia and diethyl ether gives rise to the complex Ga(dbqdi)$_2$, where dbqdi is a tridentate ligand formed by the condensation of two molecules of H_2dbc and ammonia. The same paramagnetic molecule can be prepared by treating $GaCl_3$ with H_2dbc in ethanol with concentrated aqueous ammonia, with subsequent aerial oxidation. The crystal parameters are triclinic, space group $P\bar{1}$, a = 11.6140(8), b = 12.3415(9), c = 20.765(1) Å, α = 89.491(1)°, β = 74.287(1)°, γ = 75.748(1)°, Z = 2, and R = 0.0542 for 7578 unique reflections. The structure, which is based on a GaO_4N_2 kernel, is discussed on the basis of crystallographic and ESR results.

Key words: gallium, electrochemical synthesis, electron spin resonance, X-ray crystallography.

Résumé : L'oxydation électrochimique du gallium dans une cellule contenant une solution de 3,5-di-*tert*-butylcatéchol (H_2dbc), dans un mélange d'ammoniac liquide et de méthoxyméthane, conduit à un complexe de Ga(dbqdi)$_2$ dans lequel dbqdi est un ligand tridentate formé par condensation de deux molécules de H_2dbc et d'ammoniac. On peut préparer la même molécule paramagnétique en traitant du $GaCl_3$ avec H_2dbc en solution dans l'éthanol avec de l'ammoniac concentré et en le soumettent ensuite à une oxydation par de l'air. Les cristaux sont tricliniques, groupe d'espace $P\bar{1}$, a = 11,6140(8) Å, b = 12,3415(9) Å et c = 20,765(1) Å, α = 89,49(1)°, β = 74,287(1)° et γ = 75,748(1)°, Z = 2 et R = 0,0542 pour 7578 réflexions uniques. Utilisant les données cristallographiques et les résultats de la RPE, on discute de la structure, qui est basée sur un noyau GaO_4N_2.

Mots clés : gallium, synthèse électrochimique, résonance paramagnétique électronique, diffraction des rayons X.

[Traduit par la Rédaction]

Introduction

As part of a continuing programme of work on electron transfer processes in compounds of Main Group elements, we recently prepared and characterized complexes of tin and lead with a tridentate ligand obtained by condensing two molecules of 3,5-di-*tert*-butylcatechol (dbc) with ammonia (1). This condensation product is formally the 3,5-di-*tert*-butyl-1,2-quinone-1-(2-hydroxy-3,5-di-*tert*-butylphenyl) imine anion, but in fact may exist in forms that vary in charge between +1 and –3, and that may have 0, 1,or 2 unpaired electrons.

We have labeled (Scheme 1) these dbqdi-I, -II, etc. in order to identify the possible complexes which may exist; certain of these isomers (e.g,. II, IV) can have other canonical forms resulting from rearrangement of the site of the unpaired electrons within the ring. The reaction of either $SnCl_2$ or PbF_2 with the appropriate H_2dbc–ammonia mixture gave structurally similar products with $M(O_2N)_2$ kernels, but the electron spin resonance (ESR) spectra showed the tin complex to be Sn^{IV} [dbqdi-V][dbqdi-VI], whereas lead yielded the diamagnetic Pb^{II} [dbqdi-III]$_2$. These results are in general agreement with those of earlier work with M^{2+} ions (see ref. 1).

We now report the preparation and characterization of an interesting complex of gallium with this ligand system. The compound can be obtained either by a simple chemical reaction, or by the method of direct electrochemical synthesis; this latter route is analogous to that used in the synthesis of indium(III) complexes by oxidizing the metal in liquid ammonia solutions of H_2dbc (2).

Experimental

Gallium metal (99.99% purity, Aldrich), and 3,5-di-*tert*-butylcatechol (99% purity, Aldrich) were used as supplied. Organic solvents were dried and distilled before use. For the electrochemical work, ammonia, supplied as the anhydrous gas, was condensed to the liquid in ca. 30 cm^3 quantities by passing it through a flask immersed in a solid CO_2–acetone bath.

Infrared spectroscopy involved the use of samples as KBr discs, with a Nicolet 5DX instrument. Electron spin resonance (ESR) spectra were run on a Bruker ESP-300 instru-

Received September 11, 1998.

M.A. Brown, J.A. Castro,[1] B.R. McGarvey, and D.G. Tuck.[2] Department of Chemistry and Biochemistry, University of Windsor, Windsor, ON N9B 3P4, Canada.

[1]Permanent address: Departamento de Quimica Inorganica, Universidade de Vigo, 36200 Vigo, Galicia, Spain.
[2]Author to whom correspondence may be addressed. Telephone: (519) 253-4232, ext. 3541. Fax: (519) 973-7098.
e-mail: dgtuck@uwindsor.ca

 © 1999 NRC Canada

Scheme 1.

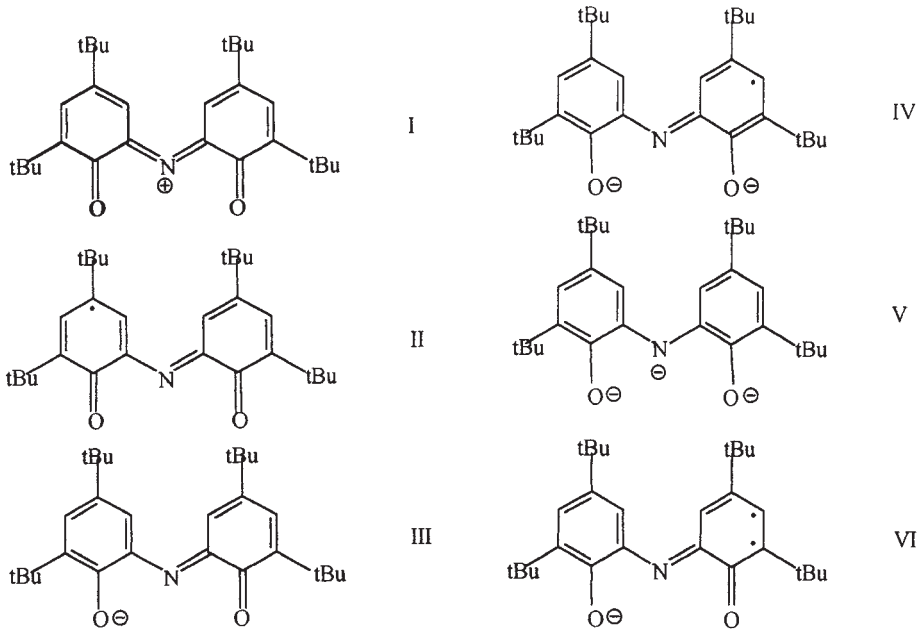

ment, using methods described previously (3). Microanalysis was performed by Canadian Microanalytical Services. Magnetic measurements were made on a VMS DMS 6000 instrument at the Universidade de Santiago de Compostela.

Electrochemical synthesis

The electrochemical cell was a round-bottomed flask (50 cm^3) with a Schlenk arm, and the anode was a gallium rod preformed onto a platinum wire, which passed through a rubber septum, while a second platinum wire formed the cathode. A solution of H_2dbc (0.5 g) in dry diethyl ether (30 cm^3) was placed in the flask, and ammonia condensed as described above. A Coutant LQ 50/50 power supply provided a current of 10–20 mA, which required an applied potential of 20–40 V. Typical current densities at the anode were in the order of 10 mA cm^{-2}. The total quantity of electricity passed through the cell during experiments, which lasted 2–4 h, was measured by means of a silver coulometer. The results of the measurement of electrochemical efficiency, derived from the measured weight loss at the anode, are discussed below. A stream of gas (dry nitrogen or air) was bubbled gently through the solution during the electrolysis.

As soon as current flowed through the cell, bubbles of gas were evolved at both anode and cathode. At the end of the experiment, the reaction mixture was evaporated to dryness, giving a mixture of crystals. Recrystallization from CH_2Cl_2 gave a dark green solid, identified as Ga(dbqdi)$_2$. (Anal. calcd. for $C_{56}H_{84}N_2O_4Ga$: C 73.2, H 9.20, N 3.05; found: C 72.2, H 9.10, N 3.23.) Yield 85%, based on quantity of gallium lost from the anode.

Chemical synthesis

Gallium metal (1.0 g, 14.3 mmol) was dissolved in 6 M aqueous hydrochloric acid (50 cm^3), and the resultant solution evaporated gently to dryness. The colourless product (hydrated $GaCl_3$) was suspended in 95% ethanol (50 cm^3), and H_2dbc (1.27 g, 5.72 mmol) in the same solvent was added, followed by concentrated aqueous ammonia (10 cm^3). A stream of air was bubbled through the stirred solution, which quickly became dark green; after 6 h, a dark green solid was collected by filtration, and further crystals were obtained by evaporating the filtrate. This product was identical to that from the electrochemical procedure (Anal. found: C 73.3, H 9.12, N 3.14). Yield 91%, based on the initial quantity of gallium.

Crystallographic analysis

Crystals of Ga(dbsqi)$_2$ prepared by the electrochemical route were recrystallized from dichloromethane. A single crystal, dimensions 0.30 × 0.30 × 0.20 mm, was attached to a quartz fiber and transferred to a Siemens SMART 3-circle diffractometer equipped with graphite monochromated Mo-Kα radiation and a CCD area detector and controlled by a Pentium-based PC running the SMART software package (4). Omega scans were used in such a way that an initial 180° scan range consisting of 0.3° intervals was followed by three further 120°, 180°, and 120° scans, with offsets of 88°, 180°, and 268°, respectively. This strategy samples the sphere of reciprocal space up to 2θ = 56.62°. Cell parameters were refined using the centroid values of 300 reflections with 2θ angles up to 56.62°. Raw frame data were integrated using the SAINT programme (5). The structure was solved by direct methods (6). An empirical absorption correction was applied to the data using the programme SADABS (7). The structure is disordered, but this was successfully modelled in terms of two equivalent *t*-C_4H_9 groups (C26–28 and C26″–28″) at C25.

Table 1 summarizes the crystal data and details of the structure refinement, Table 2 gives the atomic coordinates, and Table 3 reports the bond lengths and angles. Figure 1 shows the structure of the molecule. Tables of hydrogen atom coordinates and thermal parameters, thermal parameters

© 1999 NRC Canada

Can. J. Chem. Downloaded from www.nrcresearchpress.com by University Town Library of Shenzhen on 09/05/12
For personal use only.

Can. J. Chem. Downloaded from www.nrcresearchpress.com by University Town Library of Shenzhen on 09/05/12
For personal use only.

Table 1. Summary of crystal intensity data, collection and structural refinement for $Ga(dbqdi)_2$.

Chemical formula	$C_{56}H_{84}GaN_2O_4$
M	918.97
Temperature	298(2) K
Crystal system	Triclinic
Space group	$P\bar{1}$
Unit cell dimensions	*a* = 11.6140(8) Å
	b = 12.3415(9) Å
	c = 20.765(1) Å
	α = 89.491(1)°
	β = 74.287(1)°
	γ = 75.748(1)°
V (Å^3)	2771.6(3)
Z	2
D_c (g cm^{-3})	1.101
μ (mm^{-1})	0.539
F(000)	994
Crystal dimensions (mm)	0.30 × 0.30 × 0.20
θ range for data collection	1.71°–23.26°
Limiting indices	$-12 \le h \le 12$, $-8 \le k \le 13$, $-23 \le 1 \le 20$
Total reflections collected	10542
Independent reflections	7518
Data / restraints / parameters	7518 / 0 / 589
Final *R* indices ($I > 2\sigma(I)$)	*R*1 = 0.0542, *wR*2 = 0.1318
Largest diff. peak and hole	0.282 and –0.507 e Å^{-3}

Table 2. Final fractional coordinates (× 10^4) and thermal parameters (Å^2 × 10^3) for **1**.

	x	*y*	*z*	*U*(eq)
Ga	9872(1)	2668(1)	2506(1)	47(1)
O(1)	11278(1)	3289(1)	2107(1)	53(1)
O(2)	8412(1)	2088(2)	2616(1)	53(1)
O(3)	10934(2)	1148(1)	2476(1)	51(1)
O(4)	8844(2)	4181(1)	2836(1)	52(1)
N(1)	9839(3)	2612(2)	1534(1)	45(1)
N(2)	9931(3)	2626(2)	3470(1)	42(1)
C(1)	12420(4)	3933(3)	1114(2)	54(1)
C(2)	12602(4)	3979(4)	437(2)	63(1)
C(3)	11910(4)	3572(4)	74(2)	62(1)
C(4)	10996(4)	3108(4)	416(2)	60(1)
C(5)	10736(3)	3014(3)	1119(2)	49(1)
C(6)	11489(3)	3411(3)	1473(2)	47(1)
C(7)	13135(4)	4447(4)	1496(2)	73(1)
C(8)	13849(5)	3562(5)	1861(3)	97(2)
C(9)	12198(6)	5359(4)	2011(3)	98(2)
C(10)	14056(6)	5015(6)	1028(3)	113(2)
C(11)	12215(5)	3680(5)	–691(2)	84(2)
C(12)	13504(6)	2922(5)	–1010(3)	117(2)
C(13)	11273(7)	3365(8)	–975(3)	168(4)
C(14)	12224(6)	4902(5)	–847(3)	121(2)
C(15)	7200(4)	1379(3)	2054(2)	54(1)
C(16)	7034(4)	1188(4)	1434(2)	65(1)
C(17)	7768(4)	1442(3)	817(2)	62(1)
C(18)	8706(4)	1918(3)	828(2)	58(1)
C(19)	8953(4)	2152(3)	1439(2)	48(1)
C(20)	8181(3)	1876(3)	2066(2)	47(1)
C(21)	6403(5)	1075(4)	2713(2)	73(1)
C(22)	5406(6)	531(6)	2590(3)	121(2)
C(23)	7232(6)	204(5)	3036(3)	97(2)
C(24)	5757(5)	2108(5)	3186(3)	98(2)

© 1999 NRC Canada

Table 2 (*concluded*).

	x	*y*	*z*	*U*(eq)
C(25)	7504(5)	1169(5)	159(2)	79(1)
C(26)	8482(15)	1472(17)	–459(5)	99(4)
C(27)	7650(17)	–96(12)	104(7)	104(4)
C(28)	6252(14)	1807(15)	163(7)	94(4)
C(26″)	7143(30)	2220(14)	–160(10)	202(10)
C(27″)	8491(26)	355(28)	–267(13)	297(17)
C(28″)	6282(26)	785(33)	277(8)	262(15)
C(1′)	12037(3)	–157(3)	3081(2)	45(1)
C(2′)	12311(4)	–342(3)	3685(2)	51(1)
C(3′)	11841(3)	434(3)	4250(2)	47(1)
C(4′)	11057(3)	1427(3)	4193(2)	46(1)
C(5′)	10703(3)	1692(3)	3598(2)	42(1)
C(6′)	11232(3)	886(3)	3024(2)	42(1)
C(7′)	12529(4)	–1045(3)	2492(2)	56(1)
C(8′)	11428(5)	–1407(4)	2372(3)	79(1)
C(9′)	13217(4)	–578(4)	1856(2)	70(1)
C(10′)	13442(5)	–2083(4)	2643(2)	84(2)
C(11′)	12238(4)	153(3)	4891(2)	54(1)
C(12′)	13556(5)	245(5)	4769(3)	96(2)
C(13′)	11404(5)	954(5)	5489(2)	100(2)
C(14′)	12171(6)	–1029(5)	5074(3)	101(2)
C(15′)	7763(3)	5386(3)	3813(2)	51(1)
C(16′)	7544(4)	5490(3)	4500(2)	56(1)
C(17′)	8082(4)	4669(3)	4888(2)	52(1)
C(18′)	8863(4)	3706(3)	4565(2)	51(1)
C(19′)	9165(3)	3525(3)	3861(2)	43(1)
C(20′)	8588(3)	4373(3)	3476(2)	46(1)
C(21′)	7193(4)	6308(4)	3411(2)	66(1)
C(22′)	6252(5)	7296(4)	3869(3)	99(2)
C(23′)	6505(5)	5859(4)	2981(3)	88(2)
C(24′)	8231(5)	6762(4)	2958(2)	86(2)
C(25′)	7742(5)	4877(4)	5652(2)	68(1)
C(26′)	7820(6)	6034(4)	5838(2)	91(2)
C(27′)	8636(7)	4031(5)	5958(2)	123(3)
C(28′)	6443(6)	4761(6)	5950(3)	128(3)

for other atoms, and least-squares planes are available as supplementary data.[3]

Results and discussion

Preparative

The complex $Ga(dbqdi)_2$ can be prepared either by direct electrochemical synthesis starting from the metal, or by the reaction of gallium(III) with an aerated mixture of H_2dbc and ammonia in aqueous ethanol. Both procedures involve strongly basic media in which H_2dbc can be assumed to dissociate, or to react directly with gallium, or to condense with ammonia to give one or more of the polydentate ligands identified in Scheme 1.

The possible reactions which can occur in a solution containing H_2dbc and ammonia have been shown to include the formation of free radical intermediates, identified by ESR spectroscopy (1). In the case of lead(II), it was suggested that the final complexation step involves the ligand (dbqdi-III) in the reaction

[1] $Pb^{II} + 2(dbdqi\text{-}III] \rightarrow Pb(dbdqi\text{-}III)_2$

to give a diamagnetic lead(II) species. With the more strongly reducing tin(II), this is followed by intramolecular electron transfer reactions

[2] $Sn^{II}(dbqdi\text{-}III)_2 \rightarrow Sn^{IV}(dbqdi\text{-}IV)_2 \rightarrow Sn^{IV}(dbqdi\text{-}IV)(dbqdi\text{-}VI)$

to produce a diradical complex. Following these arguments, we suggest that the reaction of gallium(III) chloride under identical conditions follows a similar sequence.

[3] Tables of hydrogen atom coordinates and thermal parameters and of anisotropic displacement parameters are available as supplementary material, and may be purchased from: The Depository of Unpublished Data, Document Delivery, CISTI, National Research Council of Canada, Ottawa, ON K1A 0S2, Canada. The table of hydrogen atom coordinates has also been deposited with the Cambridge Crystallographic Data Centre and can be obtained on request from: The Director, Cambridge Crystallographic Data Centre, University Chemical Laboratory, 12 Union Road, Cambridge, CB2 1EZ, U.K.

Can. J. Chem. Downloaded from www.nrcresearchpress.com by University Town Library of Shenzhen on 09/05/12
For personal use only.

© 1999 NRC Canada

Table 3. Bond lengths (Å) and angles (°) for $Ga(dbqdi)_2$, with standard deviations in parentheses.

Ga—O(1)	1.9531(13)	Ga—O(2)	1.9547(13)
Ga—O(3)	1.9658(13)	Ga—O(4)	1.9661(13)
Ga—N(2)	2.023(3)	Ga—N(1)	2.030(3)
O(1)—C(6)	1.287(4)	O(2)—C(20)	1.287(4)
O(3)—C(6′)	1.294(4)	O(4)—C(20′)	1.292(4)
N(1)—C(19)	1.349(5)	N(1)—C(5)	1.354(5)
N(2)—C(19′)	1.349(4)	N(2)—C(5′)	1.349(4)
C(1)—C(2)	1.366(5)	C(1)—C(6)	1.427(5)
C(1)—C(7)	1.532(6)	C(2)—C(3)	1.415(6)
C(3)—C(4)	1.358(6)	C(3)—C(11)	1.543(6)
C(4)—C(5)	1.418(5)	C(5)—C(6)	1.454(5)
C(7)—C(8)	1.528(7)	C(7)—C(9)	1.544(7)
C(7)—C(10)	1.540(6)	C(11)—C(13)	1.505(8)
C(11)—C(12)	1.529(7)	C(11)—C(14)	1.542(8)
C(15)—C(16)	1.383(5)	C(15)—C(20)	1.426(5)
C(15)—C(21)	1.533(6)	C(16)—C(17)	1.414(6)
C(17)—C(18)	1.364(6)	C(17)—C(25)	1.537(6)
C(18)—C(19)	1.420(5)	C(19)—C(20)	1.458(5)
C(21)—C(24)	1.518(7)	C(21)—C(23)	1.535(7)
C(21)—C(22)	1.549(6)	C(25)—C(27″)	1.42(2)
C(25)—C(26")	1.47(2)	C(25)—C(28)	1.47(2)
C(25)—C(27)	1.53(2)	C(25)—C(28″)	1.56(2)
C(25)—C(26)	1.577(13)	C(1′)—C(2′)	1.378(5)
C(1′)—C(6′)	1.419(5)	C(1′)—C(7′)	1.536(5)
C(2′)—C(3′)	1.417(5)	C(3′)—C(4′)	1.360(5)
C(3′)—C(11′)	1.533(5)	C(4′)—C(5′)	1.415(5)
C(5′)—C(6′)	1.452(5)	C(7′)—C(8′)	1.533(6)
C(7′)—C(9′)	1.536(6)	C(7′)—C(10′)	1.539(6)
C(11′)—C(14′)	1.520(6)	C(11′)—C(12′)	1.514(6)
C(11′)—C(13′)	1.536(6)	C(15′)—C(16′)	1.381(5)
C(15′)—C(20′)	1.426(5)	C(15′)—C(21′)	1.529(6)
C(16′)—C(17′)	1.419(5)	C(17′)—C(18′)	1.356(5)
C(17′)—C(25′)	1.534(5)	C(18′)—C(19′)	1.413(5)
C(19′)—C(20′)	1.454(5)	C(21′)—C(24′)	1.536(6)
C(21′)—C(23′)	1.535(6)	C(21′)—C(22′)	1.545(6)
C(25′)—C(28′)	1.509(7)	C(25′)—C(26′)	1.514(6)
C(25′)—C(27′)	1.544(7)		
O(1)-Ga-O(2)	161.84(7)	O(1)-Ga-O(3)	92.75(5)
O(2)-Ga-O(3)	91.43(5)	O(1)-Ga-O(4)	89.95(5)
O(2)-Ga-O(4)	91.69(5)	O(3)-Ga-O(4)	161.41(7)
O(1)-Ga-N(2)	100.31(10)	O(2)-Ga-N(2)	97.80(10)
O(3)-Ga-N(2)	80.68(10)	O(4)-Ga-N(2)	80.74(10)
O(1)-Ga-N(1)	81.00(10)	O(2)-Ga-N(1)	80.98(10)
O(3)-Ga-N(1)	96.27(10)	O(4)-Ga-N(1)	102.31(10)
N(2)-Ga-N(1)	176.72(11)	C(6)-O(1)-Ga	115.0(2)
C(20)-O(2)-Ga	114.7(2)	C(6′)-O(3)-Ga	114.6(2)
C(20′)-O(4)-Ga	114.2(2)	C(19)-N(1)-C(5)	133.8(3)
C(19)-N(1)-Ga	113.1(2)	C(5)-N(1)-Ga	113.0(2)
C(19′)-N(2)-C(5′)	132.8(3)	C(19′)-N(2)-Ga	113.5(2)
C(5′)-N(2)-Ga	113.6(2)	C(2)-C(1)-C(6)	117.5(4)
C(2)-C(1)-C(7)	122.9(4)	C(6)-C(1)-C(7)	119.6(3)
C(1)-C(2)-C(3)	124.5(4)	C(4)-C(3)-C(2)	118.3(4)
C(4)-C(3)-C(11)	122.7(4)	C(2)-C(3)-C(11)	118.9(4)
C(3)-C(4)-C(5)	121.7(4)	N(1)-C(5)-C(4)	128.9(4)
N(1)-C(5)-C(6)	112.6(3)	C(4)-C(5)-C(6)	118.4(4)
O(1)-C(6)-C(1)	122.2(3)	O(1)-C(6)-C(5)	118.2(3)
C(1)-C(6)-C(5)	119.5(3)	C(1)-C(7)-C(8)	111.2(4)
C(1)-C(7)-C(9)	108.2(4)	C(8)-C(7)-C(9)	109.5(4)

Can. J. Chem. Downloaded from www.nrcresearchpress.com by University Town Library of Shenzhen on 09/05/12
For personal use only.

© 1999 NRC Canada

Can. J. Chem. Downloaded from www.nrcresearchpress.com by University Town Library of Shenzhen on 09/05/12
For personal use only.

Table 3. (*concluded*).

C(1)-C(7)-C(10)	112.0(4)	C(8)-C(7)-C(10)	108.4(4)
C(9)-C(7)-C(10)	107.4(4)	C(13)-C(11)-C(12)	110.6(6)
C(13)-C(11)-C(3)	111.4(4)	C(12)-C(11)-C(3)	108.1(4)
C(13)-C(11)-C(14)	108.2(6)	C(12)-C(11)-C(14)	109.0(5)
C(3)-C(11)-C(14)	109.6(4)	C(16)-C(15)-C(20)	117.0(4)
C(16)-C(15)-C(21)	123.5(4)	C(20)-C(15)-C(21)	119.5(3)
C(15)-C(16)-C(17)	124.7(4)	C(18)-C(17)-C(16)	118.2(4)
C(18)-C(17)-C(25)	122.0(4)	C(16)-C(17)-C(25)	119.8(4)
C(17)-C(18)-C(19)	121.5(4)	N(1)-C(19)-C(18)	128.7(4)
N(1)-C(19)-C(20)	112.4(3)	C(18)-C(19)-C(20)	118.8(4)
O(2)-C(20)-C(15)	121.9(3)	O(2)-C(20)-C(19)	118.5(3)
C(15)-C(20)-C(19)	119.7(3)	C(24)-C(21)-C(15)	110.8(4)
C(24)-C(21)-C(23)	110.5(4)	C(15)-C(21)-C(23)	108.8(4)
C(24)-C(21)-C(22)	108.4(5)	C(15)-C(21)-C(22)	111.3(4)
C(23)-C(21)-C(22)	107.0(4)	C(27″)-C(25)-C(26″)	114(2)
C(28)-C(25)-C(27)	112.0(9)	C(27″)-C(25″)-C(28″)	109(2)
C(26″)-C(25″)-C28″)	98.9(14)	C(27″)-C(25)-C(17)	112.7(8)
C(26″)-C(25)-C(17)	108.96	C(28)-C(25)-C(17)	109.6(6)
C(27)-C(25)-C(17)	107.3	C(28″)-C(25)-C(17)	112.6(7)
C(28)-C(25)-C(26)	109.7(9)	C(27)-C(25)-C(26)	107.9(9)
C(27″)-C(25)-C(28″)	109.3(16)	C(26″)-C(25)-C(28″)	98.9(14)
C(17)-C(25)-C(26)	110.4(5)	C(2′)-C(1′)-C(6′)	117.4(3)
C(2′)-C(1′)-C(7′)	122.7(3)	C(6′)-C(1′)-C(7′)	119.9(3)
C(1′)-C(2′)-C(3′)	124.6(3)	C(4′)-C(3′)-C(2′)	117.6(3)
C(4′)-C(3′)-C(11′)	122.3(3)	C(2′)-C(3′)-C(11″)	120.1(3)
C(3′)-C(4′)-C(5′)	122.2(3)	N(2)-C(5′)-C(4′)	128.9(3)
N(2)-C(5′)-C(6′)	112.6(3)	C(4′)-C(5′)-C(6′)	118.5(3)
O(3)-C(6′)-C(1′)	122.1(3)	O(3)-C(6′)-C(5′)	118.2(3)
C(1′)-C(6′)-C(5′)	119.7(3)	C(8′)-C(7′)-C(1′)	108.3(3)
C(8′)-C(7′)-C(9′)	110.2(4)	C(1′)-C(7′)-C(9′)	111.0(3)
C(8′)-C(7′)-C(10′)	108.6(4)	C(1′)-C(7′)-C(10′)	111.5(3)
C(9′)-C(7′)-C(10′)	107.3(4)	C(14′)-C(11′)-C(12′)	109.5(4)
C(14′)-C(11′)-C(3′)	110.5(3)	C(12′)-C(11′)-C(3′)	108.4(3)
C(14′)-C(11′)-C(13′)	107.6(4)	C(12′)-C(11′)-C(13′)	109.0(4)
C(3′)-C(11′)-C(13′)	111.7(3)	C(16′)-C(15′)-C(20′)	116.9(3)
C(16′)-C(15′)-C(21′)	123.0(3)	C(20′)-C(15′)-C(21′)	120.0(3)
C(15′)-C(16′)-C(17′)	124.8(3)	C(18′)-C(17′)-C(16′)	118.0(3)
C(18′)-C(17′)-C(25′)	122.3(4)	C(16′)-C(17′)-C(25′)	119.7(3)
C(17′)-C(18′)-C(19′)	121.7(3)	N(2)-C(19′)-C(18′)	128.5(3)
N(2)-C(19′)-C(20′)	112.2(3)	C(18′)-C(19′)-C(20′)	119.3(3)
O(4)-C(20′)-C(15′)	122.0(3)	O(4)-C(20′)-C(19′)	118.6(3)
C(15′)-C(20′)-C(19′)	119.4(3)	C(15′)-C(21′)-C(24′)	108.7(4)
C(15′)-C(21′)-C(23′)	111.1(4)	C(24′)-C(21′)-C(23′)	109.7(4)
C(15′)-C(21′)-C(22′)	112.1(4)	(24′)-C(21′)-C(22′)	108.0(4)
C(23′)-C(21′)-C(22′)	107.1(4)	C(28′)-C(25′)-C(26′)	109.8(4)
C(28′)-C(25′)-C(17′)	108.8(4)	C(26′)-C(25′)-C(17′)	111.0(4)
C(28′)-C(25′)-C(27′)	109.1(5)	C(26′)-C(25′)-C(27′)	106.9(5)
C(17′)-C(25′)-C(27′)	111.3(4)		

[3] $Ga^{3+} + Cl^- + 2(dbqdi\text{-}III)^- \rightarrow Ga(dbqdi\text{-}III)_2Cl$

[4] $Ga(dbqdi\text{-}III)_2Cl \rightarrow Ga(dbqdi\text{-}III)(dbqdi\text{-}IV) + Cl^-$

These processes lead to the formulation of the final product as a gallium(III) complex with one unpaired electron, in keeping with the structural and spectroscopic evidence discussed below.

The electrochemical procedures were similar to those described earlier (2), but with some significant detailed differences. An important parameter in such work is the electrochemical efficiency, E_F, defined as the quantity of metal dissolved from the anode per faraday of electricity flowing through the cell. When air or oxygen was bubbled through the solution phase during electrolysis, E_F was unusually low and variable from one experiment to another (~0.03–0.2 mol F^{-1}). For syntheses under nitrogen, the value of E_F was 0.31 ± 0.02 mol F^{-1}, although here again anomalous results (~0.05 mol F^{-1}) were recorded in a few experiments. In simpler solution systems, E_F can be interpreted in terms of the attack of a ligand L^{n-} on the sacrificial anode,

© 1999 NRC Canada

Can. J. Chem. Downloaded from www.nrcresearchpress.com by University Town Library of Shenzhen on 09/05/12
For personal use only.

Table 4. Possible ligand combinations for gallium(I), (II), and (III) in $Ga(dbqdi)_2$.

Oxidation state	L_2	Number of unpaired electrons	Average C—O bond order	Average C—N bond order
1	II +III	1	1.75	1.5
	II + VI	3	1.75	1.5
	I + IV	1	1.5	1.75
2	I + V	0	1.5	1.5
	II + IV	2	1.5	1.5
	III + III	0	1.5	1.5
	III + VI	2	1.5	1.5
	VI + VI	4	1.5	1.5
3	III + IV	1	1.25	1.5
	II + V	1	1.5	1.25
	IV + VI	3	1.25	1.5

Fig. 1. Structure of $Ga(dbqdi)_2$, with atoms shown as 30% probability ellipsoids. Hydrogen atoms have been omitted for clarity.

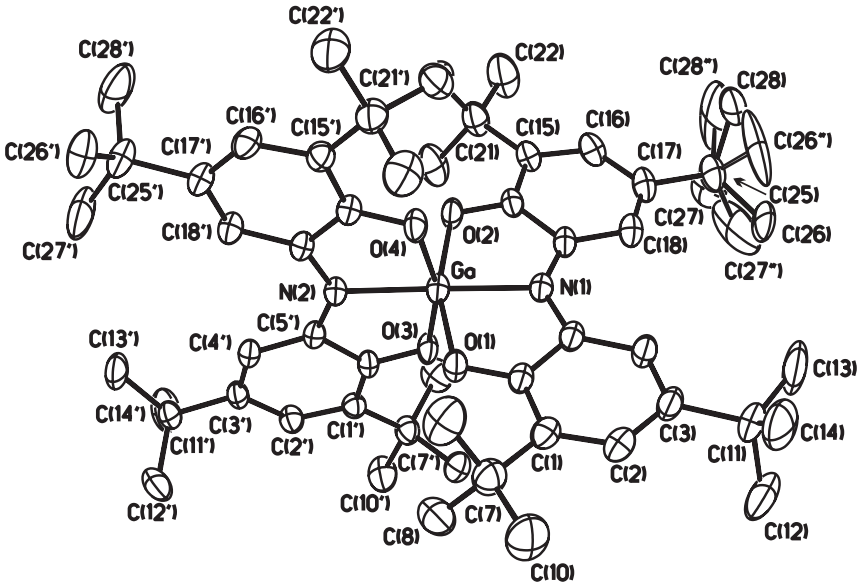

but this approach is not viable in the present case (cf. ref. 2), and the only reasonable conclusion is that the electrolysis gives rise to a gallium(III) species in the absence of oxygen.

In the earlier case of indium involving electrochemical oxidation in the presence of substituted catechols (H_2dbc; $X_4C_6(OH)_2$, X = Cl, Br), the products isolated from oxygen-free experiments were the ammonium salts of either $[In(O_2C_6X_4)_3]^{3-}$ or $[In_2(dbc)_4(NH_3)_2]^{2-}$ (2). These colourless diamagnetic complexes are air-sensitive, giving dark green paramagnetic products which were not identified, but which are presumably related to the gallium(III) complex isolated in the present work.

The structure of $Ga(dbqdi)_2$ in the solid state

To elucidate the structure of $Ga(dbqdi)_2$ in the solid state, it is necessary to consider crystallographic, magnetic, and spectroscopic results. The possible oxidation states of gallium are 1, 2, or 3, and Table 4 sets out the various combinations of dbqdi structures (Scheme 1) which can give rise to a neutral complex with each of these states. The experimental value of the magnetic moment of 1.70 B.M. establishes the presence of one unpaired electron in the molecule, and this eliminates structures based on gallium(II), and leaves two possibilities for both gallium(I) and (III).

The Ga—O bond distances to the two ligands are significantly different, with average values of 1.954(1) and 1.966(1) Å. The reason for these differences is not clear at this point, but the results are similar to those for the gallium(III) complexes $Ga(acac)_3$ (acac = 3,5-pentanedionate anion), for which *r*(Ga—O) = 1.952 Å(avg) (8), and $Ga(dbsq)_3$ (dbsq = 3,5-di-*tert*-butyl-1,2-semiquinonate) (9), where *r*(Ga—O) = 1.96(1) Å. We therefore identify **1** as a gallium(III) complex, which together with the magnetic moment implies that the ligand combinations can be either II + V or III + IV. In principle, it should be possible to distinguish between these on the basis of *r*(C—O) and *r*(C—N), and the distribution of *r*(C—C) values in the C_6 rings. The average C—O bond distance is 1.290(4) Å, with a narrow range 1.287(4)–1.294(4) Å, and this corresponds to the bond order of 1.5 found in *o*-semiquinonate complexes (10), and therefore favours the ligand combination II + V. The average *r*(C—N) is 1.350(5) Å, indicating a bond order close to that in nitrogen heterocycles, although similar distances are known (11) for

© 1999 NRC Canada

Can. J. Chem. Downloaded from www.nrcresearchpress.com by University Town Library of Shenzhen on 09/05/12
For personal use only.

Fig. 2. EPR spectrum of crystalline $Ga(dbqdi)_2$ at 303 K.

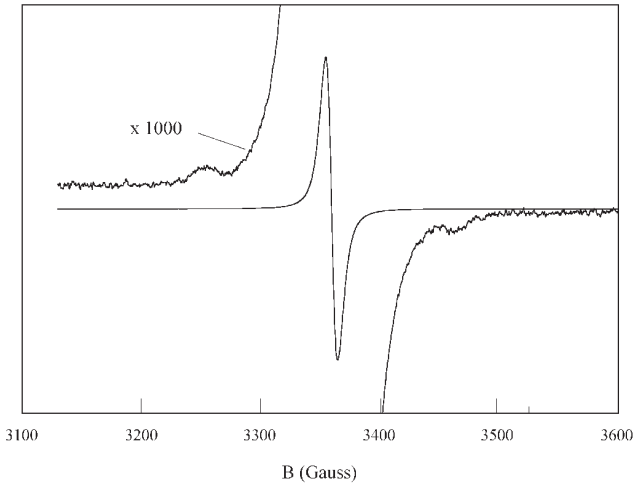

N—C=O in amides, and for H_2CN_2, so that this does not allow an unambiguous choice between the options, especially since the effects of Ga—N bonding, and of ring structure, are unknown. Equally, although a detailed analysis of the C—C bond distances predicted by III + IV or II + V reveals differences between the two, these are not sufficient to distinguish between the two possibilities. Given these uncertainties, we can only conclude that the overall evidence slightly favours the structure Ga^{III}[(dbqdi-III)(dbqdi-IV)] in the solid state, with one unpaired electron in the structure. As noted above, the preparative route in this and previous work is compatible with this formulation.

The ESR spectrum of crystalline $Ga(dbqdi)_2$ at 303 K, shown in Fig. 2, is apparently that of a monoradical species with a *g* value of 2.004 and a line width of 10 G. Figure 2 also suggests the presence of a biradical, $S = 1$, at sufficiently high gain, with two weak side resonances separated by 195 G. The presence of a biradical is confirmed by the observation of the forbidden half-field transition characteristic of $S = 1$ systems. Simulation of the spectrum in Fig. 2 indicates that the concentration of the $S = 1$ species is between 0.5% and 1% of that of the monoradical species. We have evaluated the *D* value in the spin Hamiltonian

$$[5] \qquad H = gS \cdot B + D\left[S_z^2 - \frac{1}{3}S(S+1)\right] + E[S_x^2 - S_y^2]$$

from both the splitting observed in Fig. 2, and from the displacement of the half-field transition from the true half field for temperatures from 103 to 363 K. The splitting in the main spectrum yields values of $D = 195 \pm 10$ G, while the half-field transition yields values of $(D^2 + 3E^2)^{1/2} = 180 \pm 20$ G. We have also measured the intensity of the half-field transition relative to the central transition over this same temperature range, and find that it remains constant, ruling out the possibility that the $S = 1$ species is a low-energy excited triplet state. It must therefore be due to an impurity. It cannot be a solid state phenomenon, because we were also able to detect a half-field transition in a concentrated frozen solution of $Ga(dbqdi)_2$ in toluene, and the intensity ratio to the central transition was the same as that observed in the spectrum of the crystalline material.

Fig. 3. EPR spectrum of a dilute solution of $Ga(dbqdi)_2$ in toluene. *A*, 103 K; *B*, 293 K.

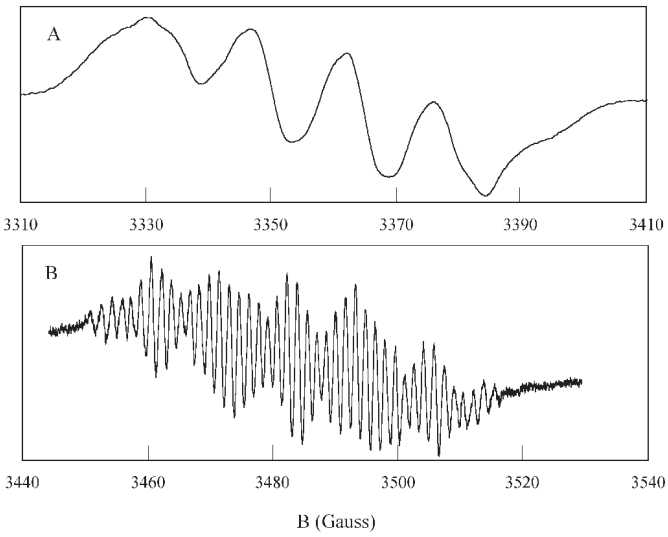

Scheme 2.

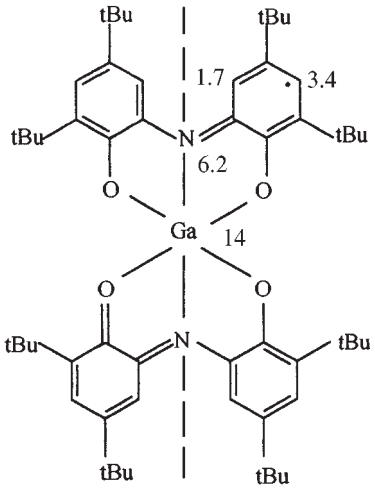

The monomer spectrum and the half-field spectrum in the solid state were quite narrow and showed no gallium hyperfine splitting. This has been shown to be due to exchange narrowing, because dilute and concentrated frozen solutions of $Ga(dbqdi)_2$ in toluene do show a hyperfine splitting for ^{69}Ga, ^{71}Ga of 14 G in the monomer spectrum (Fig. 3*A*). The half-field transition observed in concentrated solutions does not show a resolved hyperfine spectrum, but its increased line width, compared to the spectrum observed in the solid state, is best explained by an unresolved splitting of 14 G. The spectrum for a dilute toluene solution of $Ga(dbqdi)_2$ is given in Fig. 3*B*. Although it was not possible to get a perfect simulation, a reasonable fit was obtained with hyperfine constants for Ga splitting of 13.9 G, ^{14}N splitting of 6.2 G, and splittings of 3.4 G for two equivalent ^1H nuclei and of 1.7 G for a second pair of ^1H. This is compatible with the presence of the ligand in the form dbqdi-IV, a conclusion which agrees with the preparative and crystallographic results. The assignment of the hyperfine constants is shown in Scheme 2. The existence of pairs of H-atoms is

© 1999 NRC Canada

explicable in terms of a degeneracy equivalent to a twofold symmetry plane, indicated by the broken line.

Acknowledgements

This work was supported in part by Research Grants (to B.R.M. and D.G.T.) from the Natural Sciences and Engineering Research Council of Canada. One of us (J.A.C.) thanks Xunta de Galicia (Spain) for support. We thank Dr. Glenn Yap for assistance in the crystallographic analysis.

References

1. B.R. McGarvey, A. Ozarowski, Z. Tian, and D.G. Tuck. Can J. Chem. **75**, 1213 (1995).
2. T.A. Annan, J. Gu, Z. Tian, and D.G. Tuck. J. Chem. Soc. Dalton Trans. 306 (1992).
3. M.A. Brown, B.R. McGarvey, A. Ozarowski, and D.G. Tuck. J. Am. Chem. Soc. **118,** 9691 (1996).
4. Siemens SMART. Data collection software. Version 4.050. Siemens Analytical X-ray Instruments Inc., Madison, Wis., U.S.A. 1996.
5. Siemens SAINT. Data reduction software. Version 4.050. Siemens X-ray Instruments Inc., Madison Wis., U.S.A. 1996.
6. G.M. Sheldrick. SHELXTL 5.04/VMS. An integrated system for solving, refining and displaying crystal structures from diffraction data.. Siemens Analytical X-ray Instruments Inc., Madison, Wis., U.S.A. 1995.
7. G.M. Sheldrick. SADABS. Empirical absorption correction program. University of Gottingen, Germany. 1996.
8. K. Dymock and G.J. Palenik. Acta Crystallogr. Sect. B: Struct. Crystallogr. Cryst. Chem. **30**, 1364 (1974).
9. A. Ozarowski, B.R. McGarvey, A. El-Hadad, Z. Tian, D.G. Tuck, D.J. Krovich, and G.C. de Fotis. Inorg. Chem. **32**, 841 (1993).
10. (*a*) R.M. Buchanan and C.G. Pierpont. Coord. Chem. Rev. **38**, 401 (1981); (*b*) D.G. Tuck. Coord. Chem. Rev. **112**,, 215 (1992); (*c*) O. Carugo, C.B. Castellani, K. Djinovic, and M. Ruzzi. J. Chem. Soc. Dalton Trans. 837, (1992); (*d*) B.R. McGarvey, A. Ozarowski, and D.G. Tuck. Inorg. Chem. **32**, 4474 (1993).
11. Interatomic distances. Chemical Society Special Publication, London. 1965. p. 519.

Can. J. Chem. Downloaded from www.nrcresearchpress.com by University Town Library of Shenzhen on 09/05/12
For personal use only.

© 1999 NRC Canada

Electrochemistry of 1,2,5-thiadiazole 1,1-dioxide derivatives with 3,4 substituents presenting separated, connected, and fused π-systems

Esther Lea Svartman, José Alberto Caram, María Virginia Mirífico, and Enrique Julio Vasini

Can. J. Chem. Downloaded from www.nrcresearchpress.com by Peking University on 09/06/12
For personal use only.

Abstract: The voltammetric electroreduction properties of 1,2,5-thiadiazole 1,1-dioxide derivatives with different 3,4 substituents have been investigated in aprotic (mainly acetonitrile) solvent solution. The 3,4 substituents, selected according to the characteristics of their π-system, were phenanthro-9,10 (connected π-system) and acenaphtho-1,2 (fused π-system). New measurements are also presented for 3,4-diphenyl (separated π-systems). The basic properties of the substrates were investigated through voltammetry in acidic acetonitrile solutions. The substrates were more easily electroreduced (between –0.6 and –1.0 V vs. Ag/Ag^+, acetonitrile solvent) than the parent (non-1,1-dioxide) heterocycles (which are electroreduced at ca. –2.5 V). They were also more easily electroreduced (by ca. 0.4 V) than the corresponding diketones (benzil, 9,10-phenanthrenequinone, and acenaphthenequinone). The influence on voltammetric behavior of the electron-withdrawing properties of the 1,2,5-thiadiazole 1,1-dioxide ring and that of the structure of the molecules was analyzed in light of previous structural studies by X-ray crystallography and theoretical chemistry calculations. Bulk electrolysis experiments in acidic acetonitrile solutions of the phenanthro[9,10-*c*] derivative produced its previously unreported dihydrogenated derivative (thiadiazoline), which oxidizes easily. Infrared spectroscopy data suggested that the structure of this compound differs from that of 3,4-diphenyl-1,2,5-thiadiazoline 1,1-dioxide.

Key words: organic electrochemistry, 1,2,5- thiadiazoles, structure–reactivity relations.

Résumé : Opérant dans une solution dans un solvant aprotique (principalement l'acétonitrile), on a étudié les propriétés d'électroréduction voltampérométriques de dérivés du 1,1-dioxyde de 1,2,5-thiadiazole portant divers substituants dans les positions 3 et 4. Les substituants en 3,4, phénanthro-9,10 (lié à un système π) et acénaphto-1,2 (système π condensé) ont été choisis en fonction des caractéristiques de leur système π. On rapporte aussi les résultats de nouvelles mesures avec le 3,4-diphényle (systèmes π séparés). On a étudié les propriétés de base des substrats par le biais de la voltampérométrie de solutions acides dans l'acétonitrile. Les substrats sont électroréduits plus facilement (entre –0,6 et –1,0 V vs. Ag/Ag^+, acétonitrile comme solvant) que les hétérocycles parents (sans 1,1-dioxyde) qui sont électroréduits à environ –2,5 V. Ils sont aussi électroréduits plus facilement (par environ 0,4 V) que les dicétones correspondantes (benzil, 9,10-phénanthrènequinone et acénaphtènequinone). En se basant sur les résultats d'études cristallographiques et de calculs antérieurs, on a analysé l'influence des propriétés électroattractives du noyau 1,1-dioxyde de 1,2,5-thiadiazole et celle de la structure des molécules sur le comportement voltampérométrique. Des expériences d'électrolyse globale du dérivé phénanthro[9,10-*c*], en solutions acides dans l'acétonitrile, ont conduit à la formation du dérivé dihydrogéné (thiadiazoline) qui n'avait pas été rapporté antérieurement et qui s'oxyde facilement. Les données de spectroscopie infrarouge suggèrent que la structure de ce composé diffère de celle du 1,1-dioxyde de 3,4-diphényl-1,2,5-thiadiazoline.

Mots clés : électrochimie organique, 1,2,5-thiadiazoles, relations structure–réactivité.

[Traduit par la Rédaction]

Introduction

Thiadiazole derivatives have an actual or potential value as fine chemical intermediates and as molecules with pharmacological properties (1). Interest in these aspects, for the case of 1,1-dioxide derivatives, has been exemplified by recent publications on their use in β-lactams (2), in the synthesis of diaryl 1,2-diketones (3), or in their relation to potassium channel openers (4).

Our previous work (5, 6) on the electrochemical properties of 3,4-diphenyl-1,2,5- thiadiazole 1,1-dioxide (**1,** Scheme 1) in acetonitrile (ACN) solution, has shown that **1** is voltam-

Received August 16, 1998.

E.L. Svartman, J.A. Caram, M.V. Mirífico, and E.J. Vasini.[1] Instituto de Investigaciones Fisicoquímicas Teóricas y Aplicadas (INIFTA), Facultad de Ciencias Exactas, Departamento de Química, Universidad Nacional de La Plata, Casilla de Correo 16, Sucursal 4, (1900) La Plata, Argentina.

[1]Author to whom correspondence may be addressed. Telephone: 5.4-21-25-7430 / 7291. Fax: 54-21-25-4642. e-mail: vasini@isis.unlp.edu.ar

 © 1999 NRC Canada

Scheme 1.

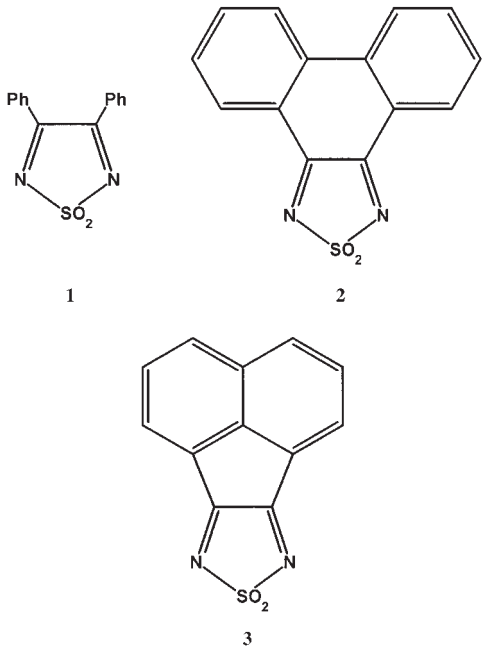

metrically reduced, in two reversible successive peaks, to the radical anion and to the dianion at ca. –0.8 and –1.6 V (vs. Ag/Ag^+, in ACN solvent, with $N(Et)_4ClO_4$ (TEAP) as supporting electrolyte). The peak potential of the second couple depends on the supporting electrolyte cation. It is shifted to higher potentials with the increasing Lewis acidity of the cation of the supporting electrolyte (6). This effect is due to stabilization of the basic dianion through complexation with the acid cations.

1 is a moderately strong base (pK_b [ACN] ≈ 12 (5)) and its electroreduction product in acidic ACN is the corresponding thiadiazoline $\mathbf{1}^{\bullet}H_2$.

The strong electron-withdrawing $>SO_2$ group of these substrates is an important factor in the voltammetric properties and the chemical reactivity for nucleophilic addition. The effect of the $>SO_2$ group can be modulated by electronic and steric effects of the substituents, such as the extent of their π-system, the degree of its conjugation with the C=N bonds of the heterocycle, and the feasibility of geometric changes upon reduction or nucleophilic addition.

To observe these effects, we studied the voltammetric electroreduction of phenanthro[9,10-*c*]-1,2,5-thiadiazole 1,1-dioxide (**2**, Scheme 1) and acenaphtho[1,2-*c*]-1,2,5-thiadiazole 1,1-dioxide (**3**, Scheme 1) in ACN solution. These systems were compared with the previously studied 3,4-diphenyl (**1**) (5, 6) derivative.

Experiments in which selected acids of varied strength were added to the ACN solution of the substrates were also performed to obtain information about their basic properties.

Experimental

Conventional cyclic voltammetry techniques were employed. A L.Y.P. M2 potentiostat, a three-module L.Y.P. sweep generator, and a Houston Omnigraphic 2000 pen recorder were used.

Fig. 1. Cyclic voltammograms (current function vs. potential) for the substrates in ACN solution. Working electrode: vitreous carbon disk; reference electrode: Ag^+ (0.1 M, ACN) / Ag; supporting electrolyte: 0.2 M TEAP; sweep rate: 0.2 V s^{-1}. 1c, 2c, 1a, 2a : first cathodic, second cathodic, first anodic, and second anodic peak potential regions. (—) **1**, 17 mM; (– – –) **2**, 1.6 mM; (- -·-) **3**, 2.1 mM.

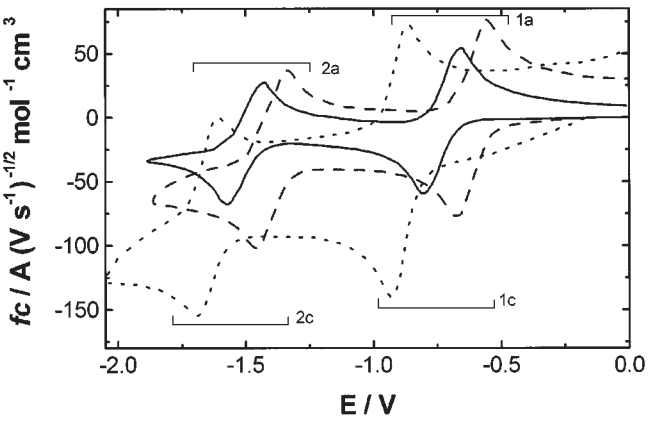

Experiments were performed in an undivided, gas-tight, glass cell swept by purified nitrogen and kept in a dry glove box, where all solution preparation and other experimental manipulations were made.

The reference electrode was Ag/ 0.1 M Ag^+ in ACN. It was separated from the cell solution by a porous-glass plug. A 2 cm Pt foil was the counter electrode and the working electrode was a Teflon encapsulated vitreous carbon disk of 0.074 cm^2 geometric area.

The substituted 1,1-dioxide thiadiazoles were synthesized and purified according to procedures reported by Wright (7) (**1** and **3**); and Vorreither and Ziegler (8) (**2**), respectively.

Results and discussion

General electrochemical and chemical properties

The aromatic character of the parent thiadiazole ring (9, 10), due to the contribution of one of the lone pairs of the sulfur atom to the π-system of the heterocycle, is lost in the 1,1-dioxide derivatives in which these lone pairs become bond pairs of the $>SO_2$ group. Thus, 1,1-dioxide thiadiazole derivatives have fewer delocalization possibilities than the parent ring for the extra charge of the radical anions formed by electroreduction.

However, the electroreduction of 1,2,5-thiadiazole derivatives was highly facilitated when the heterocyclic sulfur was replaced by the strongly electron-withdrawing (EWD) $>SO_2$ group, which was found to be the dominant factor determining the electroreduction potential. For example, the polarographic $E_{½}$ of the parent ring compound 1,2,5-thiadiazole is –2.52 V, and that of its 3,4-diphenyl derivative is –2.39 V (10), while the 1,1-dioxide heterocycles were typically electroreduced in the –0.6 to –1.0 V potential region (vs. 0.1 M Ag^+ (ACN)/ Ag), as shown in Fig. 1, where the cyclic voltammograms recorded in ACN solutions are presented. The voltammogram of **1** in ACN containing 0.2 M TBAP is also included for comparison (6).

The EWD character of the $>SO_2$ group causes the high electropositive character of the carbon atoms of the hetero-

© 1999 NRC Canada

Can. J. Chem. Downloaded from www.nrcresearchpress.com by Peking University on 09/06/12
For personal use only.

Can. J. Chem. Downloaded from www.nrcresearchpress.com by Peking University on 09/06/12
For personal use only.

Fig. 2. Influence of the solvent in the cyclic voltammogram of **3**, when $NaClO_4$ is used as supporting electrolyte. [$NaClO_4$] = 0.25 M; working electrode: vitreous carbon disk; reference electrode: Ag^+ (0.1 M, ACN) / Ag; sweep rate 0.010 V s^{-1}. (- - -) ACN solvent; (—) mixed solvent: ACN; 30 vol.% EtOH.

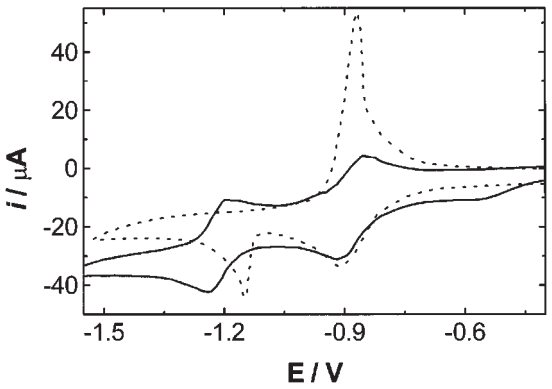

cycle and, of course, also affects the chemical behavior of 3,4-disubstituted 1,2,5-thiadiazole 1,1-dioxide derivatives. A study of structural effects on the nucleophilic addition to the heterocycle C=N double bond is under way in our laboratory. As a whole, the effect of the heterocycle on its 3,4 substituents has been compared to that of an acyl-like group (1, 11).

Voltammetric behavior of 2

2 was voltammetrically reduced to its radical anion and dianion at ca. –0.6 and –1.3 V, respectively (Fig. 1), in ACN solution with TEAP as supporting electrolyte. Both processes presented typical one-electron reversible behavior. A value of 2.0×10^{-5} cm^2 s^{-1} for the diffusion coefficient of **2** was calculated from its first cathodic peak (peak 1c**2**).

The peak potential of the second couple depended on the supporting electrolyte cation. It was shifted to ca. –0.9 V with $NaClO_4$ as supporting electrolyte. The effect is similar to that reported for 1 (**6**).

Voltammetric behavior of 3

The voltammetric response of **3** showed two diffusional couples at ca. –0.9 and –1.7 V vs. 0.1 M Ag^+ (ACN)/ Ag in TEAP as supporting electrolyte (Fig. 1). As for **1** and **2**, the second couple also shifted to higher potentials (ca. –1.2 V) when $NaClO_4$ was used as supporting electrolyte. In this case, the peaks of the second couple were sharp and symmetric and the anodic peak was shifted to higher potentials and overlapped with the anodic peak of the first couple. This was especially noticeable at low sweep rates (Fig. 2, broken line). The formation and adsorption of a complex or a salt of the dianion of the substrate with Na^+ might be responsible for the effect.

The addition of 30 wt.% of EtOH to the ACN solvent changed the voltammetric aspect of the second couple, which, in this solvent mixture, presented normal diffusional behavior and shifted to lower potential by ca. 0.1 V (Fig. 2, solid line). This change is probably caused by a decrease in the effective cation acidity through its interaction with ethanol.

From the *fc* of the first cathodic peak of **3**, a diffusion coefficient of 2.2×10^{-5} cm^2 s^{-1} in ACN was calculated for a one-electron reversible charge transfer.

Comparison of the voltammetric behavior of 2, 3, and 1

The E^o values for the first reduction peak of the compounds were, in decreasing potential order, **2** (–0.592 V), **1** (–0.822 V), and **3** (–0.892 V). The position of E^o**1** between E^o**2** and E^o**3** seemed to be in disagreement with the order expected when the delocalization possibilities of the charge added to the substrates to form the radical anion were considered.

As mentioned above, **1**, **2**, and **3** can be compared with strong electron-withdrawing substituted derivatives of their 3,4 substituents, such as the corresponding diketones. Thus, the potentials for the first cathodic voltammetric peak of these diketones were measured under the same experimental conditions at 0.2 V s^{-1}. The charge transfers were found to be reversible and the peak potentials followed the expected order: –1.06 V for 9,10-phenanthrenequinone; –1.27 V for acenaphthenequinone, and –1.54 V for benzil (**Bz**).

The diketones were found to be more difficult to electroreduce than the thiadiazoles. This was expected. The azomethine (>C=N-) group is generally more easily electroreduced than the carbonyl group from which it may be considered to derive (12), and the effect of the N-bonded, electron-withdrawing, $>SO_2$ group should also facilitate the electroreduction.

The differences in electroreduction potential (ΔE_R) between thiadiazoles and quinones were similar (ΔE_R [**2** – phenanthrenequinone] ≈ 0.47 V, ΔE_R [**3** – acenaphthenequinone] ≈ 0.38 V), but ΔE_R [**1** – Bz] (0.72 V) was significatively higher. Possible structural reasons for this difference are discussed below.

It is known (13) that the first step in quinone electroreduction in aprotic media is the formation of the semiquinone radical anion. Both **2** and **3**, which have been shown by X-ray crystallography to be planar (14), can produce upon one-electron transfer a "semiquinone-like" radical anion, as shown in Scheme 2. However, the comparison between the electroreduction of **Bz** and that of **1** can not be so direct.

The phenyl groups of **1** are restricted to a *cis* orientation with respect to the heterocyclic (C3—C4) carbon–carbon bond. They are also rotated out of the plane of the heterocycle by ca. 40°, as has been shown through X-ray difractommetry and molecular orbital calculations (14). Consequently, the resonance coupling between these phenyl groups and the C=N double bond is small. In contrast, benzil has a skew structure in which the strong conjugation of the carbonyl with phenyl apparently minimizes the conjugation of the two benzoyls with each other. The two benzoyl groups are twisted with respect to each other, perhaps by as much as 90° (15).

The radical anion of **Bz** ($\mathbf{Bz}^{\bullet-}$) presumably maintains the strong phenyl–carbonyl coupling and, although the radical anion is probably less twisted than **Bz** because of the advantage in further delocalizing the added charge, it will certainly not be planar. Thus, only one benzoyl π-system (or one plus a fraction) provides resonance stabilization for $\mathbf{Bz}^{\bullet-}$. **Bz** is therefore the most difficult to reduce.

Some of the classical Lewis structures that can be written for $\mathbf{1}^{\bullet-}$ are shown in Scheme 3.

It is clear from their symmetry that both phenyl groups and both nitrogen atoms participate equally in the can-

© 1999 NRC Canada

Scheme 2.

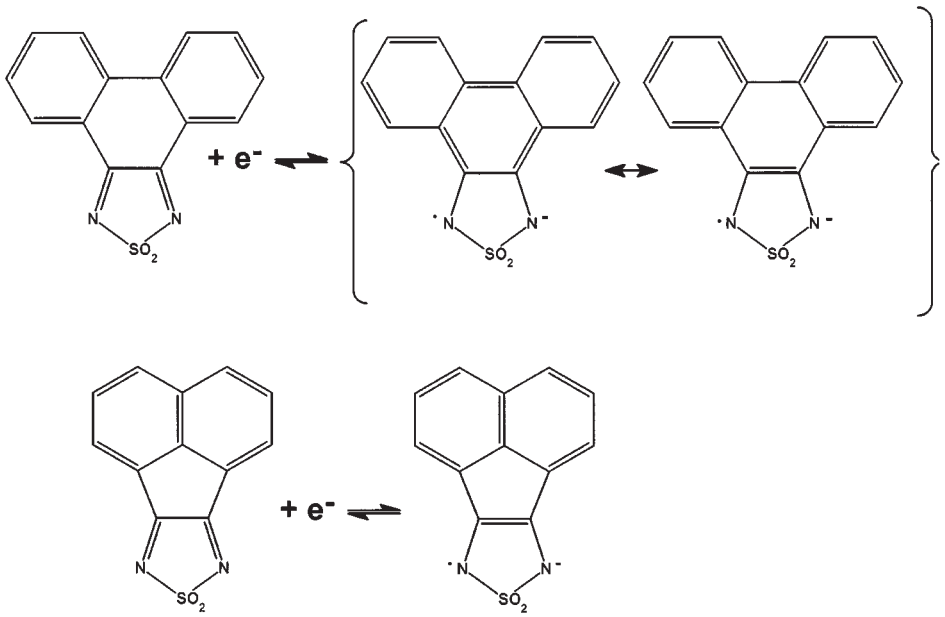

Scheme 3.

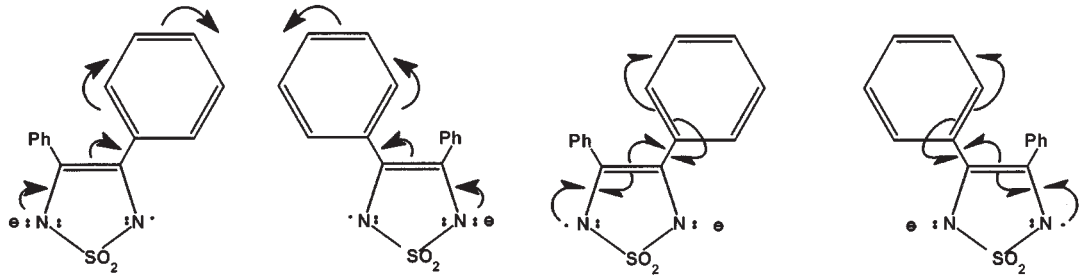

onical forms of these structures and cannot be distinguished from one another. The actual structure should contain a -NC(Ph)C(Ph)N- group sufficiently coupled (planar) to maximize the delocalization energy of the unpaired electron and sufficiently twisted to minimize repulsion, particularly between phenyl groups that are brought nearer together by the C3—C4 partial double bond character.

Thus, the free-energy difference between **1** and $\mathbf{1}^{\bullet-}$ should not be compared with that between **Bz** and $\mathbf{Bz}^{\bullet-}$, but with the free-energy difference between a hypothetical *cis*-benzil with a nearly zero carbonyl–carbonyl dihedral angle and its geometrically similar radical anion. The stabilization provided should correspond to somewhat less than two phenyl π-systems, but still more than an acenaphthene ring, thus making **1** more easily reducible than **3**.

Voltammetric results in ACN solutions with the addition of acids

The behavior of **2** and **3** in acidic ACN solution resembled that previously reported (5) for **1**. For small acid-to-substrate molar concentration ratios ([AH]/[**T**] ≤ 1, where **T** stands for any of the substrates), a prepeak at a higher potential with respect to E_p1c developed and the current intensity of peaks 1c and 2c decreased. The prepeak current intensity increased at the expense of the original substrate peaks and its peak potential shifted to higher potentials when the relative concentration of acid was increased. For molar concentration ratios of ca. 2, peaks 1c and 2c were barely detectable as shoulders of the prepeak at lower potential and the current intensity of the prepeak reached a higher limit of approximately twice that of the original peak 1c.

Voltammetric data corresponding to ca. 2×10^{-3} M ACN solutions of the substrates in the presence of several proton donors (AH) of varied strength, at a concentration ratio [AH]/[**T**] = 100 to ensure pseudo-first-order conditions, are presented in Fig. 3.

The proton donors used were phenol (PhOH, K_a (ACN) = 2.4×10^{-27}) (16), anhydrous benzoic acid (HBz, K_a (ACN) = 2×10^{-21}) (17), anhydrous trifluoracetic acid (TFA, K_a (ACN) = 4×10^{-8}) (18), and concentrated perchloric acid (K_a (ACN) = 1×10^{-2}) (16). The **1**–$HClO_4$ could not be studied because **1** reacted rapidly with the water contained in the concentrated perchloric acid added. In all cases, as expected, the cathodic peak potential increased with the strength of the added acid.

The shift to higher potentials, the doubled current intensity, and the demonstrated formation of $\mathbf{1}^{\bullet}H_2$ (5) and $\mathbf{2}^{\bullet}H_2$ (see below) indicate a 2 e, 2 H^+ process (Scheme 4), where the highly acid $\mathbf{T}H_2^{2+}$ and the highly basic $\mathbf{T}^{2-}$, which are improbable species under the conditions of these experiments, have been excluded.

The detailed analysis of Scheme 4 for each system is extremely complex. The voltammetric response depends on the equilibrium and kinetics of the charge transfers and chemical

© 1999 NRC Canada

Can. J. Chem. Downloaded from www.nrcresearchpress.com by Peking University on 09/06/12
For personal use only.

Fig. 3. Cyclic voltammograms of the substrates in ACN solution with different added acids in acid/substrate molar ratio = 100. Substrate concentration = 2 mM. Working electrode: vitreous carbon disk; reference electrode: Ag^+ (0.1 M, ACN) / Ag; supporting electrolyte: 0.2 M TEAP. Sweep rates: (—) : 0.2 V s^{-1}; (- - -): 0.02 V s^{-1}. Current values for the experiments at 0.02 V s^{-1} are multiplied by 3 to facilitate comparison. The added acid is indicated at the foot of each wave as follows: HBz: dry benzoic acid; TFA: dry trifluoracetic acid; $HClO_4$: concentrated perchloric acid. 3a: **2**; 3b: **3**; 3c: **1**.

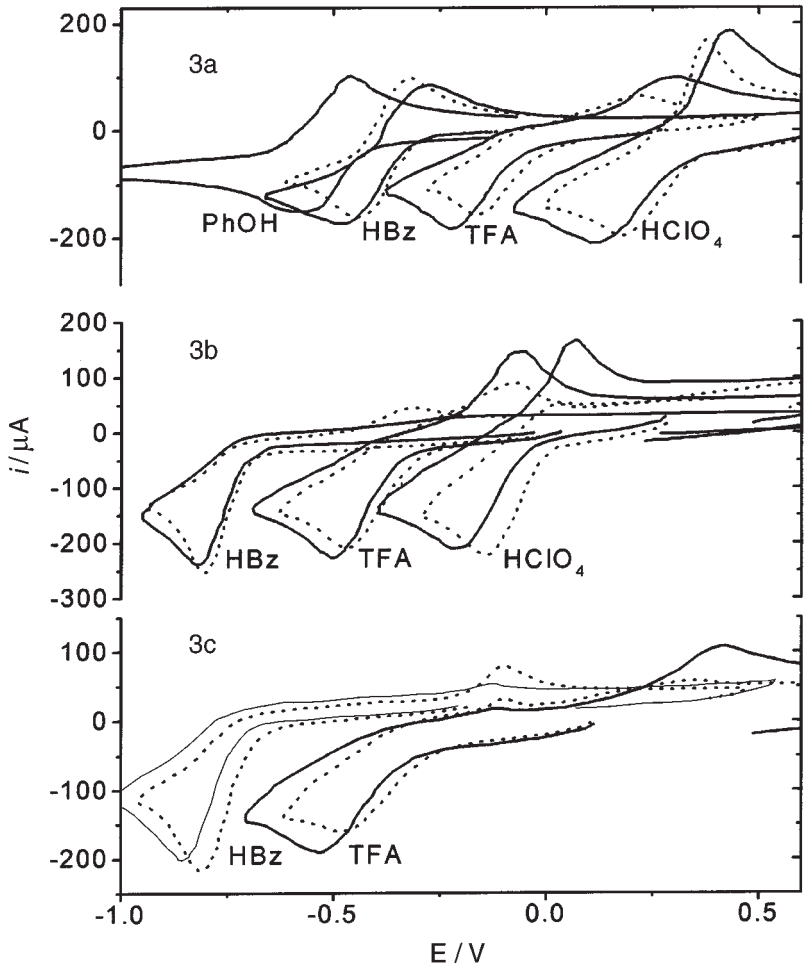

steps. It should also be noted that the deprotonation reactions indicated (with the possible exception of those in $HClO_4$ acid medium, since a high concentration of the ClO_4^- anion is provided by the supporting electrolyte) are of second kinetic order under our experimental conditions.

However, it seemed valuable to relate the observed voltammetric behavior of the **T**–HA systems to the relative acid–base properties of the species included in Scheme 4, as far as these properties can be rationalized according to the known structure of the thiadiazole substrates. Thus, **2** can efficiently stabilize the added charge in a **2**$^{\bullet}H^+$ cation through dispersal in its conjugated system. The π system available for the stabilization of a **3**$^{\bullet}H^+$ cation is less extended, while **1**$^{\bullet}H^+$ must be the strongest acid of the three since its charge can only be dispersed over one of the phenyl rings.

In the case of **1**, the minimum energy conformation postulated for its radical anion (Scheme 3), must change when **1**$^{\bullet}H^-$ is formed from it (reaction C_2**1** and charge transfer E_4**1**), since the delocalization of the added charge can only take place on one "side" of the molecule (Scheme 5). Of course, this does not apply to substrates **2** or **3**, since the structures of their monoprotonated anions can be easily de-

Scheme 4.

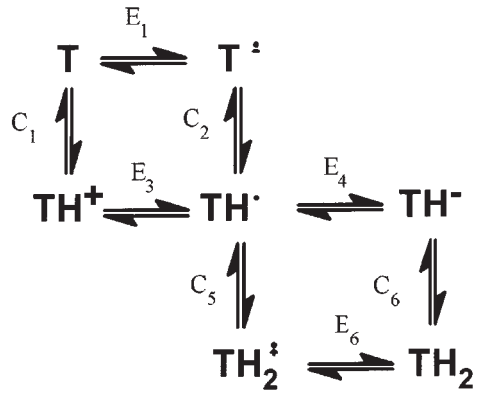

rived from those shown in Scheme 2 for the radical anions without structural changes.

Thus, in the **1**–HBz and the **1**–TFA systems, the reaction proceeds through a $E_1[C_2E_4]$ path to form **1**$^{\bullet}H^-$, which is further protonated to **1**$^{\bullet}H_2$.

© 1999 NRC Canada

Can. J. Chem. Downloaded from www.nrcresearchpress.com by Peking University on 09/06/12
For personal use only.

Scheme 5.

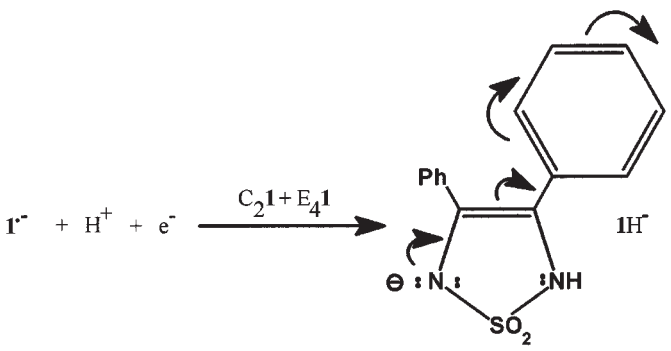

However, the anodic peak observed for the **1**–TFA system at ca. 0.4 V (Fig. 4, sweep rate: 0.2 V s^{-1}) cannot be assigned to the electrooxidation of **1**•H_2, since no anodic voltammetric signals were observed in ACN solutions of **1**•H_2 (5), with or without the addition of proton donors. Neither can this peak be caused by the electrooxidation of partially protonated species, such as **1**•H^-, which, if existent and electroxidable when TFA is added to an ACN solution of **1**, would also be present in the **1**–HBz system. It was also verified experimentally that the anodic peak did not correspond to benzil (a product of the eventual hydrolysis of **1** (19)) or its protonation products.

A controlled potential (at ca. –1.0 V) bulk electrolysis experiment of an ACN solution of **1**–TFA at a concentration ratio [TFA]/[**1**] = 50 was performed. Voltammograms scanned at selected time intervals during the electrolysis presented the same peaks shown in Fig. 3*c*. The cathodic peak continuously decreased during the electrolysis, while the anodic peak at ca. 0.4 V increased to about 60% of the initial value of the cathodic peak. Immediately after the end of the electrolysis, when the cathodic peak intensity was nearly zero, a voltammogram started in the anodic direction showed that scanning through the anodic peak caused the reappearance, in the subsequent cathodic scan, of the original cathodic peak at same potential, with about one half its initial (before electrolysis) current intensity. Neither peak could be observed in voltammograms run several hours after the electrolysis was finished. Although the electroreduction current of the acid interfered with the voltammetric observation of **1**•H_2 at ca. –1.7 V, a TLC run of the electrolyzed solution showed that **1**•H_2 was the only reaction product. The anodic peak at ca. 0.4 V must be assigned to a relatively stable intermediate in the formation of **1**•H_2 that is capable of being electrooxidized back to **1** at that potential. According to the structure assigned to **1**•H^-, the anion can be kinetically protonated in the nitrogen to give a tautomer of **1**•H_2 (**1**•H_2', Scheme 6), which would slowly transform into its stable structure[2] (**1**•H_2). The tautomer might be the species that is electrooxidable at 0.4 V.

The **2**–HA systems presented nearly reversible couples at low sweep rates in weak acids such as PhOH and HBz. A reversible $E_1\,C_2\,E_4$ might be the preferred reaction path but, in the case of the much stronger acids TFA and $HClO_4$, it is plausible that C_1**2** might precede the E_3**2** electroreduction, while the anodic process might start with the electrooxidation of **2**•H_2 (E_6**2**) at ca. 0.4 V. In the case of **3**–TFA and **3**–$HClO_4$ systems, the processes should be similar to those of **2** for the same acids. The reversibility should be decreased in the **3**–HBz system as compared with **2**–HBz, since C_2**3** should be more displaced towards the products than C_2**2** due to the higher basicity of **3**$^-$.

Fig. 4. Bulk electrolysis of the **2**–TFA system in ACN at –0.4 V. [**2**] = 2.16 mM; Electrolysis setup: divided cell; cathode: vitreous carbon rod; anode: Pt foil. Voltammetric setup (in the cathodic compartment of the electrolysis cell): working electrode: vitreous carbon disk; reference electrode: Ag^+ (0.1 M, ACN) / Ag; supporting electrolyte: 0.1 M TEAP; TFA acid = 0.1 M; sweep rate: 0.2 V s^{-1}. (*a*): Voltammogram before electrolysis; (*b*): voltammogram at the end of the electrolysis, started from the rest potential in the cathodic direction, (*c*): same in the anodic direction.

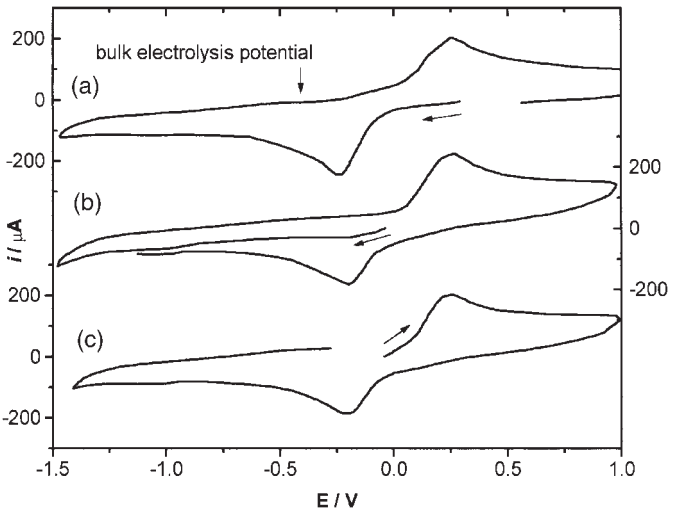

Bulk electrolysis and chemical reduction of 2: synthesis of 2•H_2

To the best of our knowledge, **2**•H_2 and **3**•H_2 have not been synthesized. The electrosynthesis of **2**•H_2 was attempted, by bulk electrolysis, on the **2**–TFA and the **2**–$HClO_4$ systems with similar results. The electrolysis was interrupted at selected time intervals to follow its course by cyclic voltammetry. The voltammograms showed that the cathodic peak current decreased, the anodic peak current increased correspondingly, and the characteristic bright red color of **2** faded as the electrolysis advanced. The initial and final voltammograms for the **2**–TFA system are shown in Fig. 4.

The electrolysis was concluded when the cathodic peak was almost undetectable in the first voltammetric sweep in the cathodic direction (Fig. 4*b*). At that time, the solution was colorless, the anodic peak had a current intensity similar to that of the original cathodic peak, and 2.05 F had been consumed per mole of **2** originally present. As shown in Fig. 4*c*, the results of a voltammetric cycle that started from the rest potential in an anodic direction indicated that the electrolysis product has been voltammetrically oxidized back to **2**.

However, only **2** and small amounts of an unidentified product could be recovered from the electrolyzed solution

[2] E.E. Castellano, O.E. Piro, J.A. Caram, M.V. Mirifico, S.L. Aimone, E.J. Vasini, and M.D. Glossman. Unpublished results.

© 1999 NRC Canada

Can. J. Chem. Downloaded from www.nrcresearchpress.com by Peking University on 09/06/12
For personal use only.

Scheme 6.

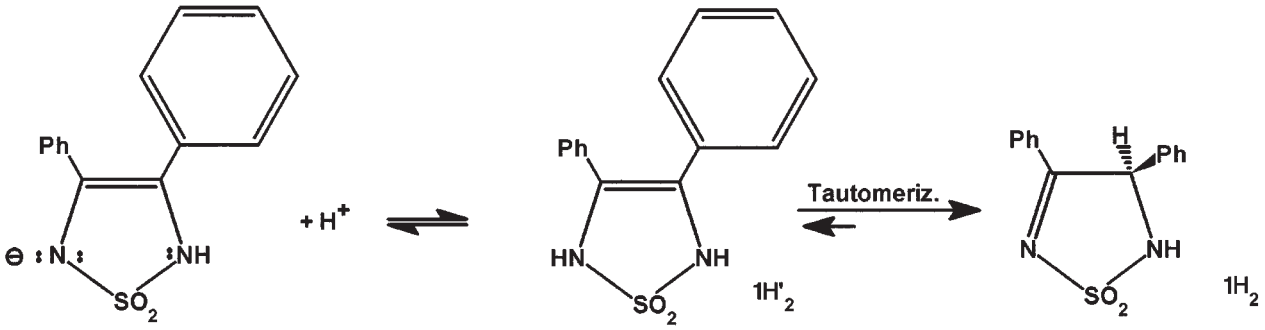

by normal work-up procedures (TLC analysis). It could be clearly observed that the chromatographic spot of the unidentified product changed from colorless to red on the layer. Bidimensional TLC analysis performed after this color change showed that the unidentified product had reverted to **2**.

It was found (TLC analysis) that **2** can be chemically reduced to the same product by metallic Zn in acidic ACN solution (obtained by the addition of dry TFA or by gaseous HCl bubbling). Vacuum evaporation of the resulting solution in the absence of air produced a white solid. An ACN solution of this white solid rapidly turned red in contact with air and, on vacuum evaporation, reverted to **2** (IR; TLC).

The IR spectrum (KBr pellet) of the white solid, which must be identified as **2**·H_2, presented an N–H IR band at 3150 cm^{-1}, along with characteristic $>SO_2$ bands at 1382 and 1172 cm^{-1}. No bands assignable to C=N (as those present at 1540 cm^{-1} in **2**, at 1560 cm^{-1} in **1**·H_2, or at 1610 and 1540 cm^{-1} in **1**) could be observed. No aliphatic C–H IR band was observed, in contrast with the IR spectrum of **1**·H_2.

The semiquinone-like structure schematized above for the radical anions $\mathbf{2}^-$ and $\mathbf{3}^-$ means that **2** and **3** can also form dianions, in which the added charges are placed on the heterocyclic nitrogen atoms, and dihydrogenated derivatives (thiadiazolines) with two N—H bonds, as suggested by the IR spectrum of **3**·H_2. In contrast, **1** is reduced to a thiadiazoline in which one of the -C=N- groups turns into a -CH-NH- group (5, 7). Thus **2**·H_2, and presumably **3**·H_2, should be considered as polycyclic derivatives of 2,1,3-benzothiadiazoline 2,2-dioxide (no C=N double bonds) while **1**·H_2 is a different thiadiazoline (one C=N double bond and one C—N single bond).

Acknowledgments

This work was financially supported by the Consejo Nacional de Investigaciones Científicas y Técnicas (CONICET), the Comisión de Investigaciones Científicas de la Provincia de Buenos Aires (CIC Pcia. Bs.As), and the University of La Plata (UNLP), Facultad de Ciencias Exactas, Departamento de Química. M.V.M and J.A.C. are researchers of CONICET and UNLP; E.L.S., S.L.A., and E.J.V. are researchers of CIC Pcia. Bs.As and UNLP.

References

1. V.J. Aran, P. Goya, and C. Ochoa. Adv. Heterocycl. Chem. **44**, 81 (1988).
2. Y.H. Lee, C.H. Lee, and W.S. Choi. Bull. Korean Chem. Soc. **17**, 290 (1996).
3. S.V. Pansare and M.G. Malusare. Synlett, 671 (1997).
4. L. Dupont, B. Pirotte, P. Detullio, and J. Delarge. Acta Crystallogr. Sect. C: Cryst. Struct. Commun. **52**, 1741 (1996).
5. M.V. Mirífico, J.A. Caram, and E.J. Vasini. Electrochim. Acta, **36**, 167 (1991).
6. J.A. Caram, M.V. Mirífico, and E.J. Vasini. Electrochim. Acta, **39**, 939 (1994).
7. J.B. Wright. J. Org. Chem. **29**, 1905 (1964).
8. H.K. Vorriether and E. Ziegler. Monatsh. Chem. **96**, 216 (1965).
9. I. Rozas. J. Phys. Org. Chem. **5**, 74 (1992).
10. H. Baumgartel and K. Retzlav. *In* Encyclopedia of the electrochemistry of the elements. Vol. 15. *Edited by* A.J. Bard and H. Lund. Marcel Dekker, New York. 1984. p. 168.
11. L.M. Weinstock and I. Shinkai. *In* Comprehensive heterocyclic chemistry. Vol. 6. *Edited by* K.T. Potts. Pergamon Press, Oxford. 1984. p. 514.
12. H. Lund. *In* Organic electrochemistry. 3rd ed. *Edited by* H. Lund and M. Baizer. M. Dekker Inc., New York. 1991. p. 465.
13. C.K. Mann and K.K. Barnes. Electrochemical reactions in non-aqueous systems. Dekker, New York. 1970. pp. 190–197.
14. E.E. Castellano, O.E. Piro, J.A. Caram, M.V. Mirifico, S.L. Aimone, E.J. Vasini, and M.D. Glossman. J. Phys. Org. Chem. **11**, 91 (1998).
15. H.H. Haffé and M. Orchin. Theory and applications of ultraviolet spectroscopy. J. Wiley & Sons, Inc., New York. 1965.
16. J.F. Coetzee. Prog. Phys. Org. Chem. **4**, 45 (1967).
17. I.M. Kolthoff and M.K. Chantooni, Jr. Anal. Chem. **39**, 1080 (1967).
18. G.A. Forcier and J.W. Olver. Electrochim. Acta, **15**, 1609 (1970).
19. M.V. Mirífico, E.J. Vasini, and J.E. Sicre. Int. J. Chem. Kinet. **23**, 197 (1991).

Can. J. Chem. Downloaded from www.nrcresearchpress.com by Peking University on 09/06/12
For personal use only.

© 1999 NRC Canada

Calculation of atomic recombination in a decaying high-temperature hydrogen gas column

Jörgen Stevefelt

Abstract: The temporal evolution of the concentration of atomic radicals [H] in a high-temperature hydrogen gas column has been evaluated, assuming an exponentially decaying temperature from 5000 K to 1000 K, and for constant pressures in the range from 0.125 to 2.0 bar (1 bar = 10^5 Pa). The initial concentration $[H]_{t=0}$, assumed to correspond to thermal equilibrium, would increase with pressure, but the termolecular recombination processes also become faster with increasing pressure. As a result, high concentration of atomic radicals rapidly becomes favoured by lower gas pressure after the temperature has decayed for a certain time. Also, operation at lower pressures would make the decay of [H] radicals less dependent upon the cooling rate of the gas.

Key words: high-temperature gas, atomic recombination, hydrogen radicals.

Résumé : L'évolution au cours du temps de la concentration des radicaux atomiques [H] dans une colonne de gaz d'hydrogène chaud a été évaluée en supposant une décroissance exponentielle de la température de 5000 K à 1000 K, et pour des pressions de gaz constantes, comprises entre 0,125 et 2.0 bar (1 bar = 10^5 Pa). La concentration initiale $[H]_{t=0}$, supposée correspondre à un équilibrium thermodynamique, augmente avec la pression, mais les processus termoléculaires de recombinaison deviennent également plus rapides. Il en résulte qu'une concentration élevée des radicaux atomiques est rapidement favorisée par des pressions plus basses à partir d'un certain temps pendant la décroissance de la température. L'utilisation des basses pressions permet également de rendre la décroissance de la concentration [H] moins dépendante de la vitesse de refroidissement du gaz.

Mots clés : gaz à haute température, recombinaison atomique, radicaux d'hydrogène.

Can. J. Chem. Downloaded from www.nrcresearchpress.com by Peking University on 09/06/12
For personal use only.

1. Introduction

Non-equilibrium gaseous media and plasmas, generally produced by various types of electrical discharges, are increasingly used as highly efficient sources of chemically active species. Of particular interest is the possibility of conducting selective chemical reactions at extremely high rates by a proper choice of experimental parameters such as pressure and temperature. The wide variety of potential applications has already stimulated much research, including experimental, theoretical, and modelling studies (1–5).

Highest energy efficiency is generally provided by pulsed discharge techniques, yielding conditions that may develop concentrations of active species which are far from thermodynamic equilibrium, at the same time as excessive gas heating is avoided. A very important property in bringing about the chemical reaction is then the lifetime of the desired active species against competing destruction processes. The rates of these processes are in general also dependent upon the average energy (the "temperature") of the active species, which decays after discharge cessation.

Received October 20, 1998.

J. Stevefelt.[1] Groupe de recherches sur l'énergétique des milieux ionisés, Université d'Orléans, 14 rue d'Issoudun, B.P. 6744, 45067 Orléans Cedex 2, France.

[1]Telephone: +33 (0) 238–49–46–15. Fax: +33 (0) 238–41–71–54. e-mail: jorgen.stevefelt@univ-orleans.fr

Reported here is a model calculation of the three-body recombination of atomic radicals in a typical environment of moderately high temperature, such as a column of hot gas at moderate pressures, created by the interruption of an electric arc discharge or by other means. Since the recombination reactions of hydrogen atoms,

[1] $$H + H + H \rightarrow H_2 + H$$

[2] $$H + H + H_2 \rightarrow H_2 + H_2$$

are well characterized in the literature, with equilibrium constants known from both spectroscopic (6) and thermochemical data (7), they were chosen for a first numerical application.

We shall first briefly discuss the values of these constants and the rate coefficients for reactions [1] and [2]. Then we shall proceed to a numerical simulation of the temporal evolution of the concentrations [H] and $[H_2]$ in a cooling gas, for several constant pressures and with gas temperature exponentially decaying from 5000 K to 1000 K in time intervals (up to a few milliseconds) that are typical in experimental situations. The concentrations will be assumed to initially correspond to themodynamic equilibrium, which may be reached by using a sufficiently long discharge pulse, with the purpose of studying how they will start deviating from equilibrium while the gas is cooling down. The results presented are of importance not only for describing hydrogen recombination, but for other gases as well. An example is fluorine atom recombination in plasma chemical cleaning

 © 1999 NRC Canada

Fig. 1. Concentrations of H and H_2 in thermal equilibrium as functions of the temperature, and for three different gas pressures: 2.0 bar, (___); 0.5 bar, (— —); 0.125 bar, (— - — -).

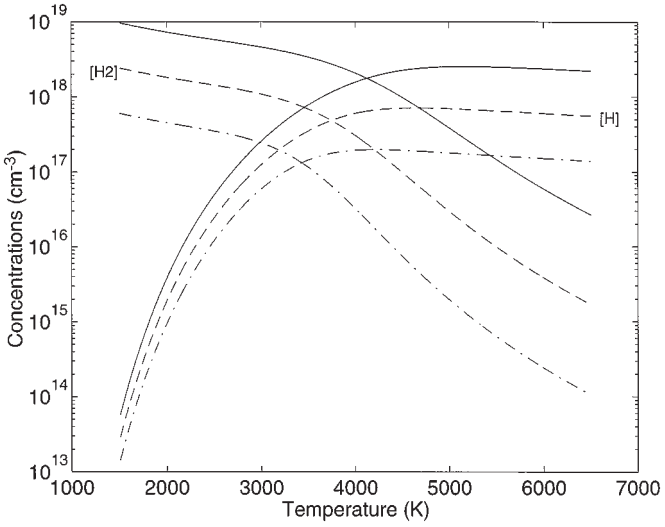

systems for applications in electronics, using remote plasma sources.

2. Rate coefficients for recombination and dissociation in hydrogen

Hydrogen atoms in a gaseous environment recombine to form diatomic molecules H_2 exclusively through the three-body processes [1] and [2], since removal of vibrational energy by radiation is impossible for a homonuclear molecule. It is conceivable that the rates of these processes are essentially determined by the efficient relaxation of the highest vibrational states of H_2 in collisions with the third body, for which the adiabaticity parameter is of order unity. This efficient VT energy transfer would yield a "vibrational temperature" for those states being close to the gas temperature. The same efficiency might be expected for electrons acting as third bodies, but these were neglected in the present work as being considered a minority species.

Several experimental determinations of the rate coefficients for processes [1] and [2] have been reported, sometimes with rather contradictory results. We have used the values recommended by Cohen and Westberg (7), based on an extensive literature review. For reaction [1]:

[3] $k_{r1} = 8.8 \times 10^{-33}$ cm^6 s^{-1}, 50 K < T < 5000 K

and for reaction [2]:

[4] $k_{r2} = 2.7 \times 10^{-31}\ T^{-0.6}$ cm^6 s^{-1}, 50 K < T < 5000 K

A more recent review paper by Baulch et al. (8) recommends the same expression for the rate coefficient of reaction [2].

For the inverse processes, i.e., the dissociation of hydrogen molecules H_2 in collisions with H and H_2, respectively, the rate coefficients can be obtained through the known equilibrium constant K for the processes, and by applying the principle of detailed balancing:

[5] $k_{d1} = k_{r1}/K$

[6] $k_{d2} = k_{r2}/K$

Cohen and Westberg (7) give an expression for the equilibrium constant K, based on thermo-chemical data:

[7] $K = 1.96 \times 10^{-25}\ T^{0.1} \exp(52530/T)$ cm^3

For the hydrogen molecule H_2, the spectroscopic constants $\omega_e = 4395.2$ cm^{-1} and $B_e = 60.809$ cm^{-1} related to vibration and rotation are well known (6), and from them the equilibrium constant can be accurately computed by means of the relation:

$$[8] \qquad K = \frac{Q_{H_2}}{(Q_H)^2} \exp(D_0/kT)$$

where the Q's indicate total partition functions and D_0 is the dissociation energy of H_2 in its ground vibrational state. For the atoms Q_H is just the translational partition function times the multiplicity 2 of the ground electronic state ^2S,

$$[9] \qquad Q_H = 2\left(\frac{2\pi m_H kT}{h^2}\right)^{3/2}$$

In the case of the H_2 ($^1\Sigma_g^+$) molecule the total partition function will be the multiplicity (= 1) times the product of the translational, vibrational, and rotational partition functions. The vibrational partition function is given by

$$[10] \qquad Q_V = 1/[1 - \exp(-hc\omega_e/kT)]$$

whereas the rotational partition function is obtained by the state sum

$$[11] \qquad Q_R = \sum_{J=0,1,\ldots} g_J \exp[-B_e J(J+1)hc/kT]$$

with $g_J = 2J + 1$ for the even and $g_J = 3(2J + 1)$ for the odd rotational levels J. The alternating statistical weights arise from the nuclear spin ½ of the proton H. For T > 1000 K, the sum in eq. [11] can be replaced by an integral, with an error <3%:

$$[12] \qquad Q_R = 2kT/hcB_e$$

so that we obtain

$$[13] \qquad K = \left(\frac{h^2}{\pi m_H kT}\right)^{3/2} \frac{kT}{2hcB_e} \frac{\exp(D_0/kT)}{1 - \exp(-hc\omega_e/kT)}$$

for the equilibrium constant.

With the known values for B_e, D_0, and ω_e, and with temperature in K, we find

$$[14] \qquad K = 8.50 \times 10^{-23}\ T^{-0.5}\ [1 - \exp(-6323.7/T)]^{-1} \times \exp(52530/T)\ \text{cm}^3$$

Obviously, eq. [7] is a rather poor approximation for the equilibrium constant, since in particular it has the wrong temperature dependence apart from the factor $\exp(D_0/kT)$. In the following we shall use the expression [14], derived from accurate spectroscopic data.

Can. J. Chem. Downloaded from www.nrcresearchpress.com by Peking University on 09/06/12
For personal use only.

© 1999 NRC Canada

Fig. 2. Calculated temporal evolutions of the atomic hydrogen concentration for the gas pressure 1.0 bar, and for different characteristic cooling times τ, defined by eq. [29]. T_0 = 5000 K, T_1 = 1000 K, and τ varies between 10 and 300 μs.

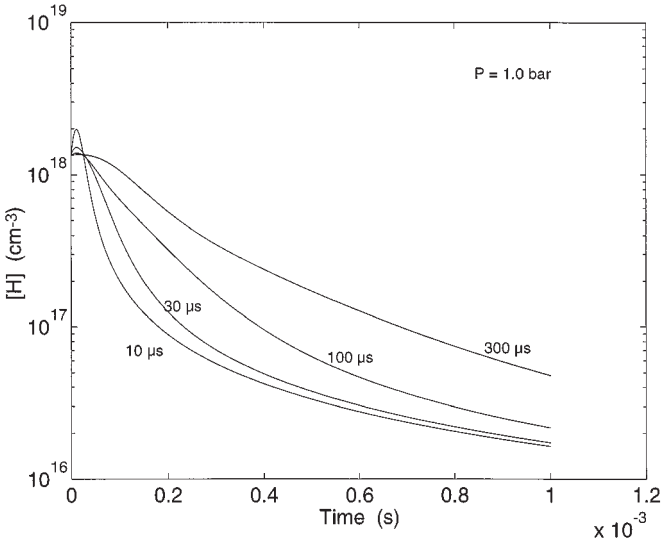

Fig. 3. Calculated temporal evolutions of the atomic hydrogen concentration for the gas pressure 0.25 bar, and for different characteristic cooling times τ, defined by eq. [29]. T_0 = 5000 K, T_1 = 1000 K, and τ varies between 10 and 300 μs.

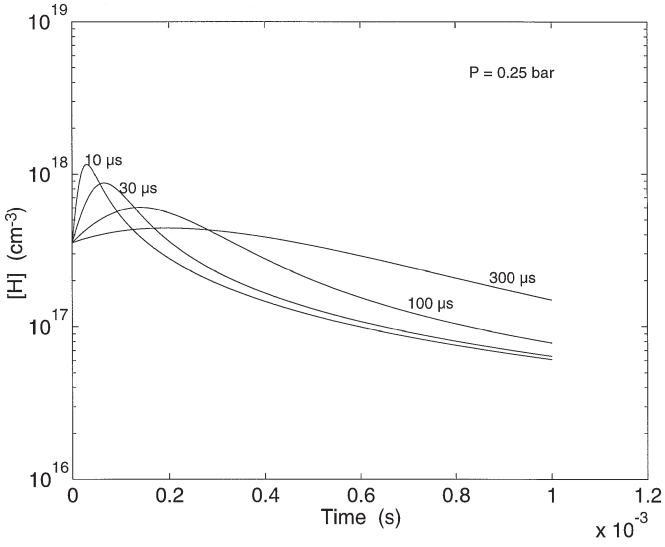

3. Temporal evolution of H and H_2 concentrations

3.1 Initial equilibrium concentrations

We have assumed that at the instant $t = 0$, the concentrations of atoms H and molecules H_2 will nearly be in thermodynamic equilibrium, such that

[15] $$[H_2]_0 / [H]_0^2 \approx K(T_0)$$

The gas pressure P at the temperature T is given by

[16] $$P = \{[H] + [H_2]\}\ kT$$

Combining eqs. [15] and [16] yields

[17] $$[H]_0 = \left\{\sqrt{1 + 4K(T_0)P/kT_0} - 1\right\}/2K(T_0)$$

[18] $$[H_2]_0 = P/kT_0 - [H]_0$$

These equilibrium concentrations are shown in Fig. 1 as functions of the temperature T_0 and for the three different gas pressures P = 0.125, 0.5, and 2.0 bar.

3.2 Theoretical formulation of the temporal evolution of atomic concentrations

For the numerical simulation of the temporal evolution of the concentrations [H] and [H_2], we considered a homogenous volume V of hydrogen gas, cooling down at constant pressure P. Then, since the total density of molecules ([H] + [H_2]) must increase with time, we had to include source terms due to the variation of the volume V in the kinetic equations for [H] and [H_2]:

[19]
$$\frac{d[H]}{dt} = -2k_{r1}[H]^3 - 2k_{r2}[H]^2[H_2] + 2k_{d1}[H][H_2] + 2k_{d2}[H_2]^2 + S_H$$
$$\frac{d[H_2]}{dt} = k_{r1}[H]^3 + k_{r2}[H]^2[H_2] - k_{d1}[H][H_2] - k_{d2}[H_2]^2 + S_{H_2}$$

If N_H and N_{H_2} are the total number of atoms and molecules in the volume V,

[20] $$[H] = N_H/V, \quad [H_2] = N_{H_2}/V$$

then

[21]
$$S_H = \frac{\partial[H]}{\partial V}\frac{dV}{dt} = -\frac{N_H}{V^2}\frac{dV}{dt} = -[H]\left(\frac{1}{V}\frac{dV}{dt}\right) \equiv s[H]$$
$$S_{H_2} = \frac{\partial[H_2]}{\partial V}\frac{dV}{dt} = -\frac{N_{H_2}}{V^2}\frac{dV}{dt} = -[H_2]\left(\frac{1}{V}\frac{dV}{dt}\right) \equiv s[H_2]$$

where

[22] $$s = -\left(\frac{1}{V}\frac{dV}{dt}\right)$$

If we further put

[23] $$C = k_{r1}[H]^3 + k_{r2}[H]^2[H_2] - k_{d1}[H][H_2] - k_{d2}[H_2]^2$$

then the eqs. [19] can be written

[24]
$$\frac{d[H]}{dt} = -2C + s[H]$$
$$\frac{d[H_2]}{dt} = C + s[H_2]$$

Adding together these two equations gives

© 1999 NRC Canada

Can. J. Chem. Downloaded from www.nrcresearchpress.com by Peking University on 09/06/12
For personal use only.

Table 1. Time elapsed in milliseconds, after which the atomic hydrogen concentration has decayed to 1/10 of its initial equilibrium value, for some gas pressures (P) and characteristic cooling times (τ).

	τ (μs)			
P (bar)	10	30	100	300
0.125	6.86	6.91	7.08	7.59
0.25	1.75	1.80	1.98	2.50
0.5	0.466	0.517	0.699	1.14
1.0	0.140	0.192	0.334	0.579
2.0	0.056	0.095	0.172	0.306

[25] $$\frac{dn}{dt} = -C + sn, \quad n = [H] + [H_2] = P/kT$$

Finally, by introducing

[26] $$[H] = xn$$
$$[H_2] = (1-x)\, n$$

we obtain the differential equation for the degree of dissociation x :

[27] $$\frac{dx}{dt} = \frac{1}{n}\frac{d[H]}{dt} - \frac{[H]}{n^2}\frac{dn}{dt} = \frac{C}{n}(x-2)$$

where the factor C can be expressed in terms of x :

[28] $$C = n^2[k_{r1}x + k_{r2}(1-x)]\left[nx^2 - \frac{1-x}{K}\right]$$

The gas density n, the reaction coefficient k_{r2}, and the equilibrium constant K are all functions of the temperature T, which in order to simulate the experimental situation of a gas column cooling by thermal conduction was modeled by the temporal evolution,

[29] $$T(t) = T_1 + (T_0 - T_1) \exp(-t/\tau)$$

where τ was varied between 10 and 300 μs. For a very rapid cooling, the product $v_{th}\tau$, where v_{th} is the thermal velocity of the molecules H_2 (= 5.6×10^5 cm s^{-1} at T = 3000 K), will be much smaller than the characteristic dimensions of the gas column, and the assumption of constant pressure is no longer justified.

The differential equation [27], with initial densities [H] and $[H_2]$ at time t = 0 given by the equilibrium relations [17] and [18] and temperature $T(t)$ modeled by eq. [29], allowed the numerical calculation of x, and then the temporal evolution of [H] and $[H_2]$ through the relations [26].

Results

The calculated temporal evolutions of the atomic hydrogen concentration [H] are shown in Figs. 2 and 3 for the two gas pressures 1.0 bar and 0.25 bar, respectively, and for different values of the characeristic cooling time τ. For each pressure, the initial [H] concentration is given by eq. [17], with the equilibrium constant $K(T)$ calculated by eq. [14] at an initial temperature T_0 = 5000 K. The gas temperature is then assumed to decay according to eq. [29] to a final temperature T_1 = 1000 K, while pressure remains constant.

Fig. 4. Calculated temporal evolutions of the atomic hydrogen concentration for a characteristic cooling time τ = 10 μs, and for different gas pressures.

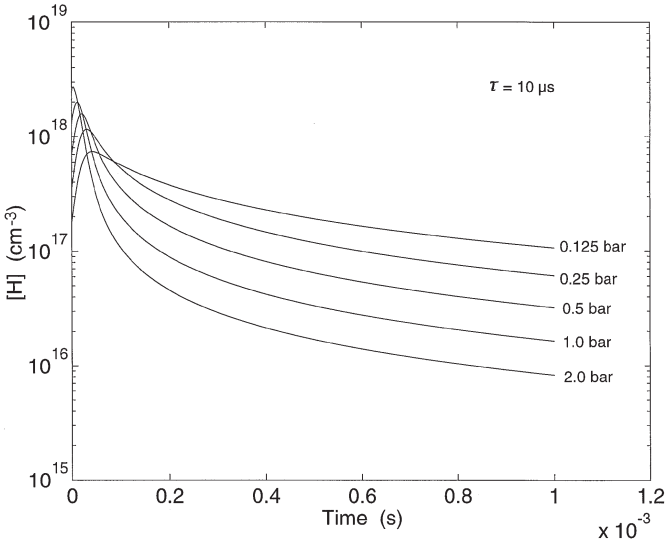

At very early times, the [H] concentration is first seen to increase. This effect is most pronounced for rapid gas cooling, and simply reflects the increasing total gas density. Rather soon, the equilibrium constant $K(T)$ increases rapidly and the recombination processes [1] and [2] will predominate over the inverse reactions. Because of their third-order character, they are most efficient at higher pressures, and at 1 bar (Fig. 2) the decay of radicals [H] depends strongly upon the cooling time τ. At first, hydrogen atoms will act as the main third body, and not until a large fraction (67–81%) of these have recombined will H_2 molecules take their place as predominant third bodies, the rate coefficient of process [2] being a factor of 4 slower than that of process [1] at $T \approx$ 3000 K. Fast atomic recombination will be accompanied by an important release of heat (4.53 eV = 7.25×10^{-19} J per recombination event) that would significantly slow down the gas cooling. However, the degree of dissociation will be far from equilibrium even at the slowest cooling time τ = 300 μs in Fig. 2: at the time t = 1 ms the gas temperature has decayed to T = 1143 K and the corresponding equilibrium concentration would be $[H]_{eq} = 1.65 \times 10^{11}$ cm^{-3}, compared to $[H] = 4.8 \times 10^{16}$ cm^{-3} obtained from the numerical calculation.

At the lower gas pressure of 0.25 bar (Fig. 3), the decay of [H] concentration is seen to be significantly slower, and to have a weaker dependence upon the cooling time τ. This can also be observed in Table 1, which shows the time θ required for the atomic hydrogen concentration to decay to 1/10 of its initial value at t = 0.

The influence of gas pressure on the decay of atomic hydrogen in the cooling gas column is further illustrated in Figs. 4 and 5 for two different characteristic times τ = 10 μs and τ = 300 μs, respectively.

Can. J. Chem. Downloaded from www.nrcresearchpress.com by Peking University on 09/06/12
For personal use only.

© 1999 NRC Canada

Fig. 5. Calculated temporal evolutions of the atomic hydrogen concentration for a characteristic cooling time τ = 300 μs, and for different gas pressures.

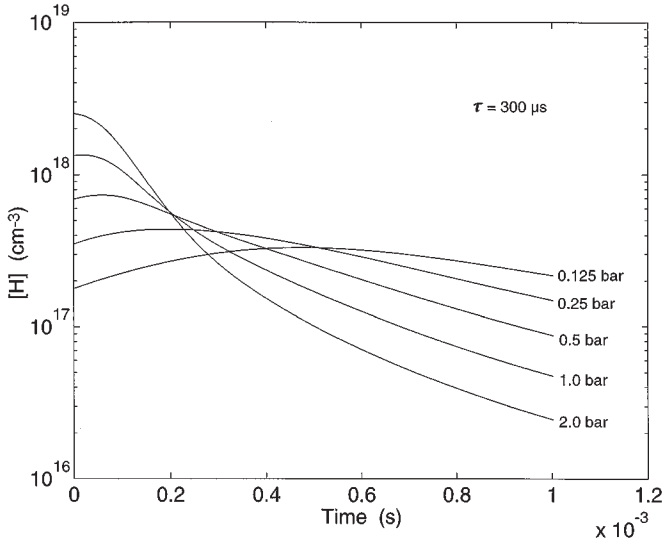

Conclusions

In summary, we have presented numerical solutions of a differential equation describing the temporal evolution of the concentration of atomic radicals [H] in a cooling hydrogen gas column. Even if the initial concentration, assumed to correspond to thermodynamic equilibrium at the temperature 5000 K, were to increase with gas pressure, this was found to be rapidly compensated by the increasing rate of three-body recombination. A further advantage of operating the chemical reactor at lower pressures was that this would make the decay of [H] radicals become less dependent upon the cooling rate of the gas.

While this study was made for a pure hydrogen gas where reaction rates for atomic recombination and molecular dissociation are well known, it is reasonable to assume that the general conclusions would also apply to other gases and gas mixtures. This would be of importance in many practical applications, where chemically active radicals are either injected into the reaction zone, or generated directly in this zone by an electrical discharge.

References

1. V.D. Rusanov, A.A. Fridman, and G.V. Sholin. Sov. Phys. Uspekhi, **24**, 447 (1981); A.A. Fridman and V.D. Rusanov. Pure Appl. Chem. **66,** 1267 (1994).
2. B. Eliasson, M. Hirth, and U. Kogelschatz. J. Phys. D: Appl. Phys. **20**, 1421 (1987); B. Eliasson and U. Kogelschatz. IEEE Trans. Plasma Sci. **19**, 309 (1991); L.M. Zhou, B. Xue, U. Kogelschatz, and B. Eliasson. Plasma Chem. Plasma Process. **18**, 375 (1998).
3. D. Evans, L.A. Rosocha, G.K. Anderson, J.J. Coogan, and M.J. Kushner. J. Appl. Phys. **74**, 5378 (1993).
4. A. Gicquel, K. Hassouni, S. Farhat, Y. Breton, C.D. Scott, M. Lefebvre, and M. Pealat. Diamond Relat. Mater. **3**, 581 (1994); K. Hassouni, O. Leroy, S. Farhat, and A. Gicquel. Plasma Chem. Plasma Process. **18**, 325 (1998).
5. B.M. Penetrante, M.C. Hsiao, J.N. Bardsley, B.T. Merritt, G.E. Vogtlin, A. Kuthi, C.P. Burkhart, and J.R. Bayless. Plasma Sources Sci. Technol. **6**, 251 (1997).
6. G. Herzberg. Molecular spectra and molecular structure: I. Spectra of diatomic molecules. Van Nostrand, New York. 1950.
7. N. Cohen and K.R. Westberg. J. Chem. Phys. Ref. Data, **12**, 531 (1983).
8. D.L. Baulch, C.J. Cobos, R.A. Cox, C. Esser, P. Frank, Th. Just, J.A. Kerr, M.J. Pilling, J. Troe, R.W. Walker, and J. Warnatz. J. Chem. Phys. Ref. Data, **21**, 411 (1992).

Can. J. Chem. Downloaded from www.nrcresearchpress.com by Peking University on 09/06/12
For personal use only.

© 1999 NRC Canada

ADDITIONS AND CORRECTIONS/AJOUTS ET CORRECTIONS

Additions and corrections: Estimation of hydrocarbon types in light gas oils and diesel fuels by ultraviolet absorption spectroscopy and multivariate calibration

Peter D. Wentzell, Darren T. Andrews, Jennifer M. Walsh, Jean M. Cooley, and Paige Spencer

Can. J. Chem. Downloaded from www.nrcresearchpress.com by Peking University on 09/06/12
For personal use only.

Ref.: Can. J. Chem. **77**, 391 (1999)

In Fig. 5, the vertical axes were incorrect and should read: (*a*) Predicted Saturate Content (%); (*b*) Predicted Monoaromatic Content (%); (*c*) Predicted Diaromatic Content (%); and (*d*) Predicted Polyaromatic Content (%). The correct figure appears as follows.

Fig. 5. Comparison of predicted vs. measured properties using the PLS regression model. ▵ 1992 pilot plant data, □ 1993 pilot plant data, ○ 1994 pilot plant data. Filled symbols indicate prediction samples, open symbols indicate calibration samples. Note that all of the observed measurements were rounded to the nearest 0.1%.

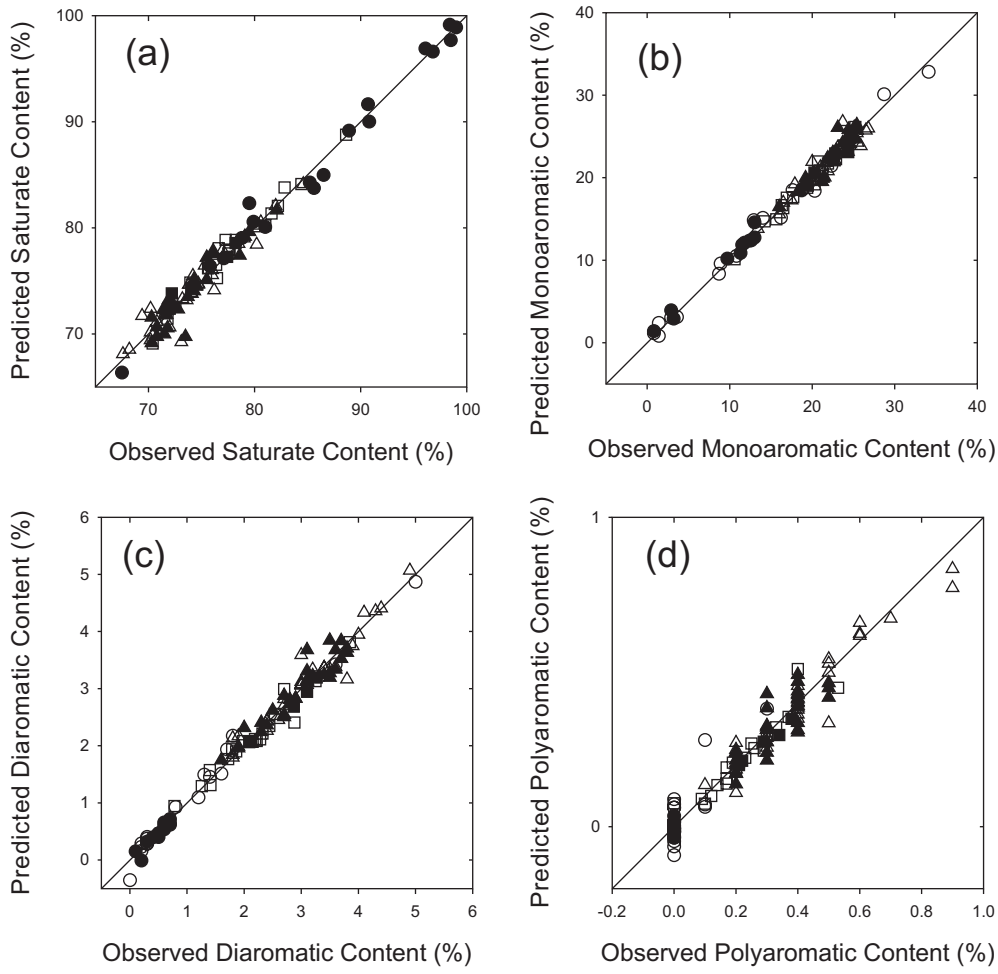

© 1999 NRC Canada

Preparation, ^{1}H and ^{13}C NMR, and ab initio/IGLO study of mono-*O*-protonated deltic acid and theoretical investigation of di-, tri-, and tetra-*O*-protonated deltic acids[1]

G.K. Surya Prakash, Golam Rasul, George A. Olah, Ronghua Liu, and Thomas T. Tidwell

Abstract: The hitherto elusive mono-*O*-protonated deltic acid $C_3O_3H_3^+$ was prepared by protolysis of di-*tert*-butoxy deltate in FSO_3H–SO_2ClF and in FSO_3H:SbF_5 (Magic Acid; 1:1 molar solution) in SO_2ClF as solvent at –78°C and was characterized by ^{1}H and ^{13}C NMR spectroscopy. The structure and NMR chemical shifts were also calculated by the ab initio/IGLO method. No NMR evidence was found for persistent di-*O*-protonated deltic acid under these conditions, although a limited equilibrium with the mono-*O*-protonated species can be involved. Di-, tri-, and tetra-*O*-protonated deltic acids were also studied by ab initio/IGLO method.

Key words: protonated deltic acid, aromaticity, superacids, NMR spectroscopy, ab initio and IGLO calculations.

Résumé : Procédant à –78°C, par protolyse du deltate de di-*tert*-butyle par du FSO_3H/SO_2ClF et dans FSO_3H/SbF_5 (Acide Magique; solution 1:1 molaire) dans du SO_2ClF comme solvant, on a préparé l'acide deltique mono-*O*-protoné (qui s'était avéré insaisissable jusqu'à maintenant) et on l'a caractérisé par spectroscopie RMN du ^{1}H et du ^{13}C. On a aussi calculé la structure et les déplacements chimiques en RMN à l'aide de la méthode ab initio/« IGLO ». La RMN n'a pas permis de déceler la présence soutenue d'acide deltique di-*O*-protoné même s'il est possible qu'un équilibre limité avec l'espèce mono-*O*-protonée soit possible. Faisant appel à la méthode ab initio/IGLO, on a aussi étudié les acides deltiques di-, tri- et tétra-*O*-protonés.

Mots clés : acide deltique protoné, aromaticité, superacides, spectroscopie RMN, calculs ab initio et IGLO.

[Traduit par la Rédaction]

Introduction

Although four-, five-, and six-membered cyclic protonated oxocarbons (2), di-*O*-protonated squaric acid (3,4-dihydroxy-3-cyclobutene-1,2-dione) **i**, tri-*O*-protonated croconic acid (4,5-dihydroxy-4-cyclopentene-1,2,3-trione) **ii**, and tetra-*O*-protonated rhodizonic acid (5,6-dihydroxy-5-cyclohexene-1,2,3,4-tetraone) **iii**, respectively, have been prepared and spectroscopically characterized (3) under long-lived ion conditions in solutions, the related three-membered cyclic mono-*O*-protonated deltic acid (2,3-dihydroxy-2-cyclopropenone) **iv** has never been observed. Ions **i**–**iv** are formally Hückeloid aromatic systems with significant delocalization of positive charges from the oxygen into the ring. Mono-*O*-protonated deltic **iv** acid is in fact a trihydroxy stabilized cyclopropenium ion, the smallest aromatic hydrocarbon.

Lien and Hopkinson (4) calculated the structures and energeties of mono-*O*-protonated deltic acid **iv** and its isomer trihydroxy propargyl cation **v** at the HF/6-31G*//HF/3-21G level. The OH substituents were found to be more stabilizing in the propargyl cation than in the cyclopropenium cation. This suggests that electron-donating OH substituents are relatively less effective at delocalization of the positive charge in the cyclopropenium ion (4).

We report now the preparation and ^{1}H and ^{13}C NMR spectroscopic characterization of mono-*O*-protonated deltic acid as a long-lived ion in superacid media and the study of its structure by theoretical methods.

Results and discussions

Protolytic ionization of di-*tert*-butoxy deltate (prepared as described (5)) in five-fold excess of FSO_3H:SbF_5 (magic acid; 1:1 molar solution) in SO_2ClF as solvent at –78°C resulted in the formation of mono-*O*-protonated deltic acid **1**. The 75 MHz ^{13}C NMR spectrum of the solution at –78°C

Received April 28, 1998.

This paper is dedicated to Jerry Kresge in recognition of his many fine contributions to physical organic chemistry.

G.K.S. Prakash, G. Rasul, and G.A. Olah.[2] Loker Hydrocarbon Research Institute and Department of Chemistry, University of Southern California, University Park, Los Angeles, CA 90089-1661, U.S.A.
R. Liu and T.T. Tidwell. Department of Chemistry, University of Toronto, 80 St. George St., Toronto, ON M5S 3H6, Canada.

[1]Considered as USC Stable Carbocations 306. Part 305 (see ref. 1).
[2]Author to whom correspondence may be addressed. Telephone: (213) 740-5976. Fax: (213) 740-6679.

 © 1999 NRC Canada

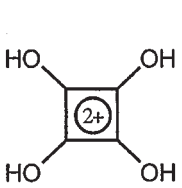

i

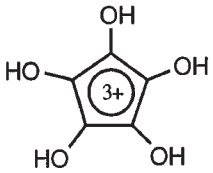

ii

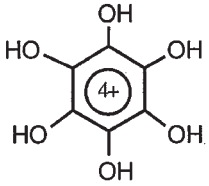

iii

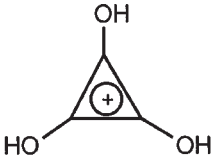

iv

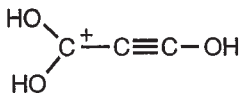

v

clearly showed the formation of *tert*-butyl cation $(CH_3)_3C^+$ at δ ^{13}C 334.6 (C^+, s) and 47.0 (CH_3, *q*), as well as a singlet at δ ^{13}C 128.7. We assign the peak at δ ^{13}C 128.7 to mono-*O*-protonated deltic acid. The 300 MHz ^{1}H NMR spectrum of the solution at –78°C exhibited a peak at δ ^{1}H 7.86 (*s*), besides the peaks resulting from the acid system (FSO_3H:SbF_5 (δ ^{1}H 12.91), H_3O^+ (δ ^{1}H 9.66)) and $(CH_3)_3C^+$ (δ ^{1}H 3.00). The magnetic equivalence of the three protons is in accordance with the C_{3h} symmetrical structure. When substantially less acidic FSO_3H (H_0 = –15) (6) was used in the place of Magic Acid (FSO_3H:SbF_5, H_0 = –22) (6) at –78°C with SO_2ClF as solvent, a slightly deshielded peak at δ ^{13}C 128.9 due to the mono-*O*-protonated deltic acid was observed.

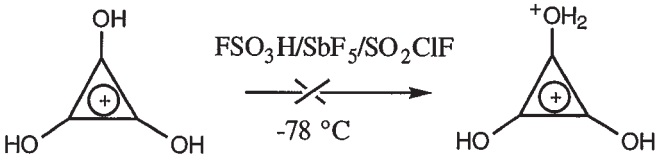

No persistent static di-*O*-protonated deltic acid, however, was observed even in stronger magic acid (compared to FSO_3H). The slightly shielded (by about 0.2 ppm) carbon peak in magic acid indicates either a proton exchange process occurring at the NMR time scale between the mono-*O*-protonated deltic acid and the acid or more probably an exchange involving a small equilibrium concentration of di-*O*-protonated deltic acid (or protosolvated dication) with the monocation.

The δ ^{13}C 128.7 of mono-*O*-protonated deltic acid is about 54.7, 45.7, and 35.7 ppm, respectively, shielded compared to that of di-*O*-protonated squaric acid **i**, tri-*O*-protonated croconic acid **ii,** and tetra-*O*-protonated rhodizonic acid **iii** (3).

To substantiate the observed experimental results, we have calculated the structures and ^{13}C NMR chemical shifts of mono-*O*-protonated deltic acid. The structures were fully optimized (Fig. 1) at the ab initio correlated MP2/6-31G* level. Consistent with the experimental results, the C_{3h} symmetry structure **1**, with C—C and C—O bond lengths of 1.389 and 1.301 Å, respectively, was found to be the global minimum for mono-*O*-protonated deltic acid. For comparison, the structures of deltic acid **2** and cyclopropenium ion **3** were also calculated. A calculated C_{2v} structure for **2** has also been reported (7), and resembles our C_s structure. The C—C bond distance of **1** (1.389 Å) is 0.031 Å shorter than the average of the three C—C bond distances of **2** (1.420 Å) and is 0.020 Å longer than that of cyclopropenium ion **3** (1.369 Å). The calculated bond distance of **1** and **2** (C_s) may be compared to those of **2** (C_{2v}) obtained by X-ray analysis (8). Interestingly the structure of crystalline **2**, which is strongly hydrogen bonded, is much closer to that of **1** than of **2** (in the idealized gas phase).

The ^{13}C NMR chemical shifts of **1**–**3** were calculated by the IGLO/II method (9) using the MP2/6-31G* optimized geometries (i.e., at the IGLO/II//MP2/6-31G* level) (Table 1). The IGLO calculated δ ^{13}C shift of **1** is 133.3, deviating by only 4.6 ppm from the experimentally observed value. We have now also calculated the ^{13}C NMR chemical shifts of **i**–**iii** at the same IGLO/II//MP2/6-31G* level and plotted in Fig. 2. The IGLO calculated chemical shifts of the protonated oxocarbons, even though they refer to the idealized gas phase, are in good agreement with the experimentally obtained values.

Diprotonated deltic acid **4** was calculated at the MP2/6-31G* level. The relatively long C1—O and C2—C3 bond lengths (1.420 and 1.451 Å) (Fig. 3) and short C2—O and C3—O bond lengths (1.266 and 1.267 Å) in ion **4** compared

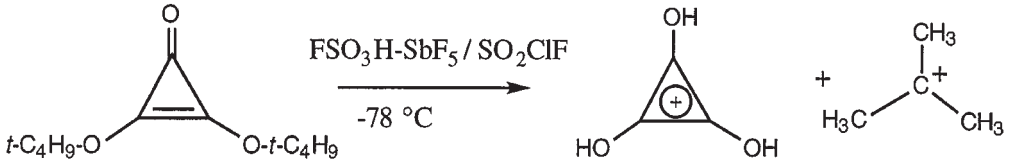

1

© 1999 NRC Canada

Fig. 1. MP2/6-31G* optimized structures of **1**–**3**.

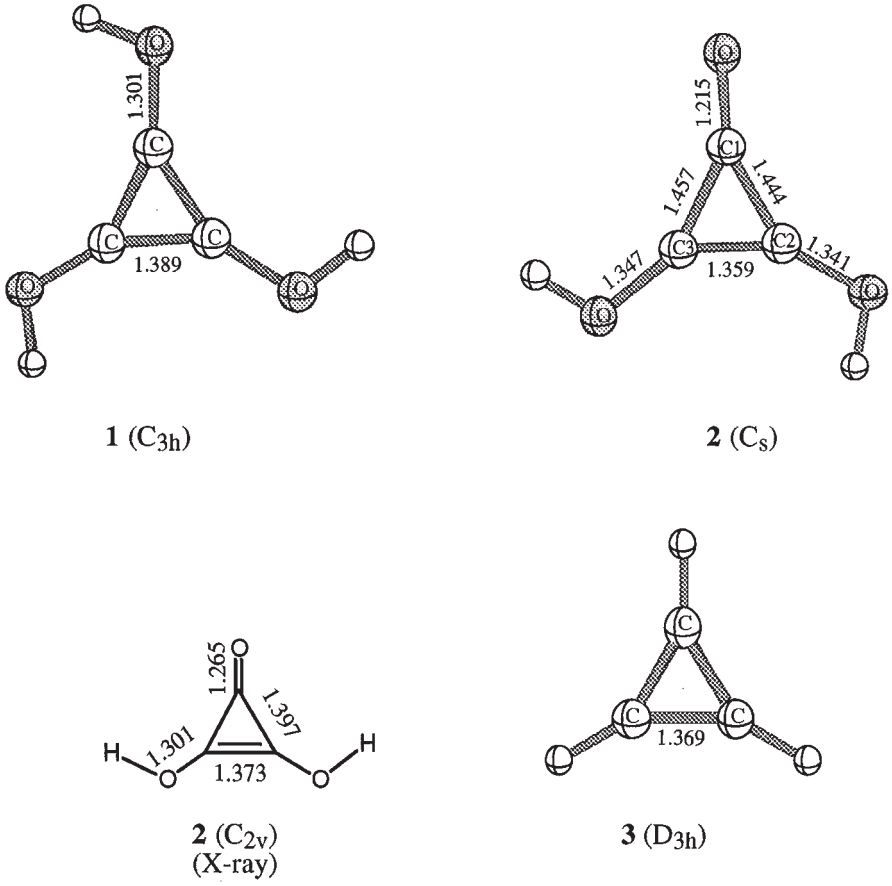

Table 1. Calculated and experimental ^{13}C NMR chemical shifts.[a]

Molecule	Atoms	Calc.	Expt.
1	C	133.3	128.7
2	C1	138.6	137.2[b]
	C2	131.6	127.2[b]
	C3	132.6	127.2[b]
3	C	171.8	
4	C1	104.7	
	C2	151.2	
	C3	152.1	
5	C1	120.2	
	C2	141.1	
	C3	147.7	
6	C	132.3	

[a]Chemical shifts were referenced to TMS, absolute shift IGLO II (i.e., σ(C) = 198.4). For numbering scheme see Figs. 1 and 3.

[b]Experimental data are for di-*tert*-butoxy deltate (ref. 5).

Fig. 2. Plot of experimental vs. IGLO calculated ^{13}C NMR chemical shifts of **1** and **i**–**iii**.

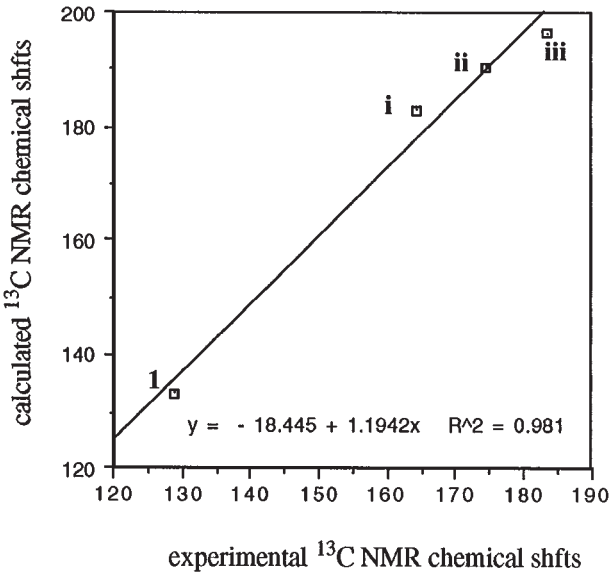

to those of monoprotonated deltic acid **1** indicates that one of its positive charges is localized on the -OH_2 group and the remaining one is delocalized over O-C_2-C_1-C_3-O atoms (i.e., dioxoallyl type resonance structure). Protonation of **1** to form **4** is calculated to be exothermic by 38.0 kcal/mol.

Calculated ^{13}C NMR chemical shifts of the C1, C2, and C3 carbons of diprotonated deltic acid **4** are 104.7, 151.2, and 152.1, respectively. The average δ ^{13}C of C1, C2, and C3 is 136.0, only 2.7 ppm deshielded compared to the protonated species **1** (δ ^{13}C 133.3).

We have also calculated the tri- and tetra-*O*-protonated deltic acids at the MP2/6-31G* level. The C_s symmetrical **5** and D_{3h} symmetrical **6** were found to be the energy minima

© 1999 NRC Canada

Fig. 3. MP2/6-31G* optimized structures of **4**–**6**.

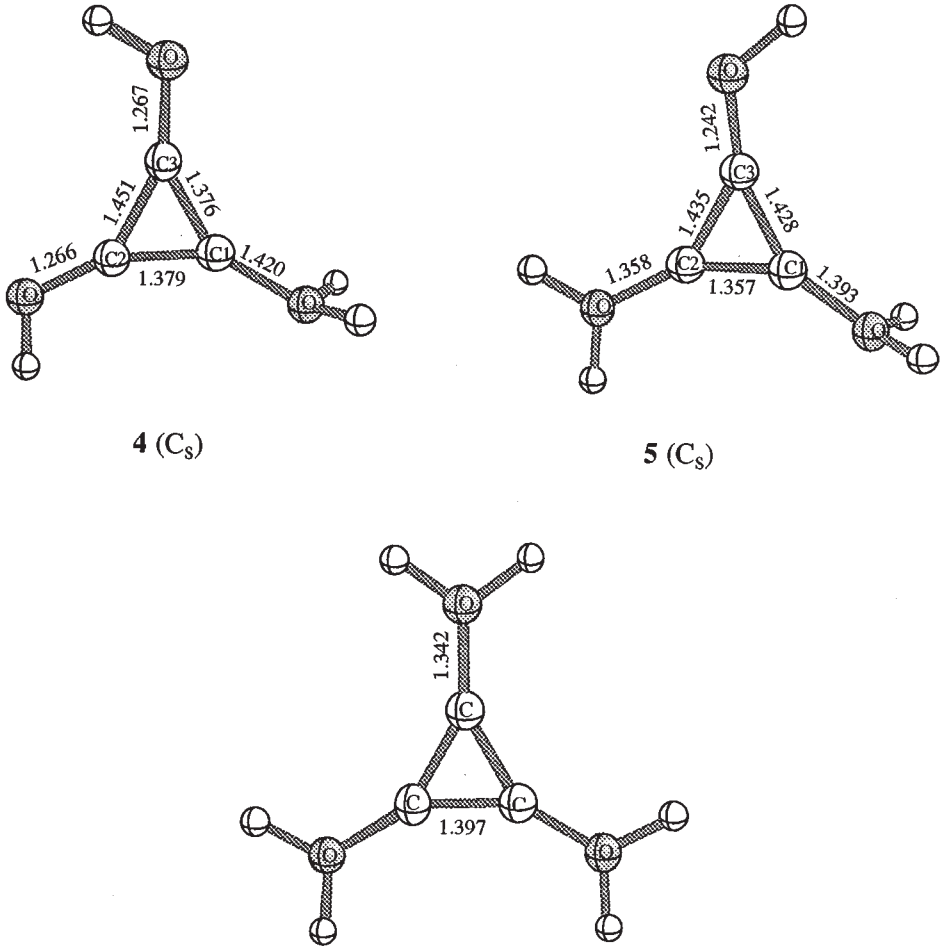

4 (C_s) **5** (C_s) **6** (D_{3h})

for tri- and tetra-*O*-protonated deltic acids, respectively. Protonation of **4** to form **5** and protonation of **5** to form **6** were calculated to be endothermic by 67.6 and 173.4 kcal/mol, respectively. Calculated structures of **5** and **6** are given in Fig. 1, and the calculated ^{13}C NMR chemical shift are listed in Table 1.

Experimental part

Preparation of di-*tert*-butoxy deltic acid

The di-*tert*-butoxy deltic acid was prepared according to the reported method (5).

Study of protonation of di-*tert*-butoxy deltic acid

Di-*tert*-butoxy deltate (~30 mg) was dissolved in approximately 0.5 mL of SO_2ClF in a 5 mm NMR tube and cooled to –78°C in a dry ice/acetone bath. Approximately 1.5 mL of 50% v/v solution of FSO_3H:SbF_5 (1:1 molar solution), FSO_3H in SO_2ClF, was added to the solution at –78°C. The ensuing mixture was vigorously stirred (Vortex stirrer) under periodic cooling prior to transfer to a precooled NMR probe.

^1H and ^{13}C NMR spectra were obtained on Varian Associates Model Unity 300 spectrometer equipped with a 5 mm variable temperature broadband probe at 300 and 75.4 MHz, respectively. ^1H and ^{13}C NMR spectra were obtained with respect to TMS by using an acetone-d_6 capillary as external standard.

Calculational methods, basis set, and geometry

Ab initio calculations were performed with the Gaussian 94 (10*a*) package of programs. Optimized geometries were obtained at the MP2/6-31G* level (11). Improved energies were obtained by single-point energy calculations at the MP4(SDTQ)/6-311G*//MP2/6-31G* level. Vibrational fre-

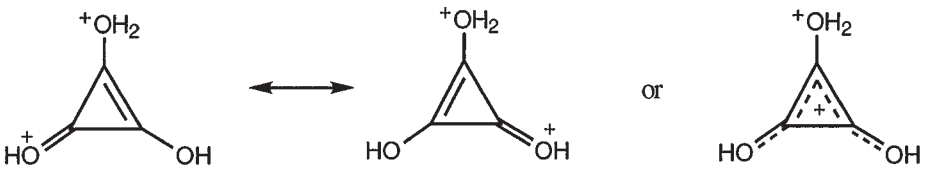

© 1999 NRC Canada

quencies at the MP2/6-31G*//MP2/6-31G* level were used to characterize stationary points as minima or transition state and to evaluate zero-point vibrational energies (ZPE) which were scaled by a factor of 0.93 (10*b*). Protonation energies were calculated at the MP4(SDTQ)/6-311G*//MP2/6-31G* + ZPE level. IGLO calculations were performed according to the reported method (9) at IGLO II levels using MP2/6-31G* geometries. Huzinaga (12) Gaussian lobes were used as follows. Basis II: C or O: 9s 5p 1d contracted to [51 111, 2111, 1]; d exponent: 1.0; H: 5s 1p contracted to [311, 1]; p exponent: 0.70. The calculated ^{13}C NMR chemical shifts (δ values) are referenced to TMS.

Conclusions

Mono-*O*-protonated deltic acid was prepared by protolysis of *di-tert*-butoxy deltate in FSO_3H/SO_2ClF and in $FSO_3H:SbF_5$ (magic acid; 1:1 molar solution) in SO_2ClF as solvent at –78°C and studied by ^1H and ^{13}C NMR spectroscopy and by ab initio calculations. No NMR evidence was found for the static diprotonated deltic acid under these conditions, although in highly acidic media the exchanging system may involve the dication in some limited equilibrium. The NMR chemical shifts were evaluated using the IGLO method and are compared to the experimental values. Structures and ^{13}C NMR chemical shifts of tri- and tetra-*O*-protonated deltic acids were also calculated.

Acknowledgment

Support of the work at the University of Southern California by the National Science Foundation and at the University of Toronto by the Natural Sciences and Engineering Research Council of Canada is gratefully acknowledged.

References

1. G.K.S. Prakash, G. Rasul, and G.A. Olah. J. Phys. Chem. A, **102**, 2579 (1998).
2. R. West and D.L. Powell. J. Am. Chem. Soc. **85**, 2577 (1963).
3. G.A. Olah, J. Bausch, G. Rasul, H. George, and G.K.S. Prakash. J. Am. Chem. Soc. **115**, 8060 (1993).
4. M.H. Lien and A.C. Hopkinson. J. Mol. Struct. (Theochem), **165**, 37 (1988).
5. A.D. Allen, J.D. Colomvakos, F. Diederich, I. Egle, X. Hao, R. Liu, J. Lusztyk, J. Ma, M.A. McAllister, Y. Rubin, K. Sung, T.T. Tidwell, and B.D. Wagner. J. Am. Chem. Soc. **119**, 12 125 (1997).
6. G.A. Olah, G.K.S. Prakash, and J. Sommer. Superacids. Wiley–Interscience, New York. 1985.
7. G. Maier and C. Rohr. Liebigs Ann. 307 (1996).
8. D. Semmingsen and P. Groth. J. Am. Chem. Soc. **109**, 7238 (1987).
9. W. Kutzelnigg. Isr. J. Chem. **19**, 193 (1980); W. Kutzelnigg, U. Fleischer, and M. Schindler. NMR: Basic Princ. Prog. **91**, 651 (1991); M. Schindler and W. Kutzelnigg. J. Chem. Phys. **76**, 1919 (1982).
10. (a) M.J. Frisch, G.W. Trucks, H.B. Schlegel, P.M.W. Gill, B.G. Johnson, M.A. Robb, J.R. Cheeseman, T.A. Keith, G.A. Peterson, J.A. Montgomery, K. Raghavachari, M.A. Al-Laham, V.G. Zakrzewski, J.V. Ortiz, J.B. Foresman, J. Cioslowski, B.B. Stefanov, A. Nanayakkara, M. Challacombe, C.Y. Peng, P.Y. Ayala, W. Chen, M.W. Wong, J.L. Andres, E.S. Replogle, R. Gomperts, R.L. Martin, D.J. Fox, J.S. Binkley, D.J. Defrees, J. Baker, J.J.P. Stewart, M. Head-Gordon, C. Gonzalez, and J.A. Pople. Gaussian 94 (Revision A.1) package of programs. Gaussian, Inc., Pittsburgh, Pa. 1995; (*b*) W.J. Hehre, L. Radom, P.v.R. Schleyer, and J.A. Pople. Ab initio molecular orbital theory. Wiley–Interscience, New York. 1986. p. 226.
11. S. Huzinaga. Approximate atomic wave function. University of Alberta, Edmonton. 1971.

© 1999 NRC Canada

The 4,4′-dimethoxytrityl carbenium ion by ionization of 4,4′-dimethoxytrityl alcohol in acetonitrile – aqueous perchloric and nitric acids containing electrolytes: kinetics, equilibria, and ion-pair formation

Juan Crugeiras and Howard Maskill

Abstract: We have studied the equilibration shown in eq. [3] of 4,4′-dimethoxytrityl alcohol in aqueous perchloric and nitric acids containing low proportions of acetonitrile using stopped-flow kinetics techniques. The rate constants for the overall progress to equilibrium, k_{obs}, have been resolved into forward and reverse components using the equilibrium UV absorbance and a value for the molar absorptivity of the 4,4′-dimethoxytrityl carbenium ion determined in concentrated aqueous perchloric acid. The forward reaction (rate constant k_f) is first order in both the alcohol and the acid concentrations; the reverse reaction (rate constant k_r) is pseudo first order with respect to the carbocation. At constant hydronium ion concentration, the forward rate constant increases linearly with the concentration of electrolyte, whereas the reverse rate constant decreases. These effects depend upon the nature of the anion, but not the cation, and are not ionic strength effects. At constant anion concentrations, k_f in both acids, and k_r in perchloric acid, are independent of hydronium ion concentration; however, k_r decreases with increasing hydronium ion concentration at constant nitrate concentration. At nonconstant ionic strength, changes in k_f and k_r observed in increasing concentrations of perchloric acid are attributable wholly to changes in perchlorate concentration. A mechanism is proposed which involves pre-equilibrium protonation of the alcohol, heterolysis of the protonated alcohol to give a 4,4′-dimethoxytrityl carbenium ion – water ion–molecule pair, then conversion of this into a dissociated carbenium ion in equilibrium with ion pairs. To account for the strong effects of perchlorate and nitrate upon the forward rate constants, it is proposed that these anions provide additional reaction channels from the ion–molecule pair. However, we find no evidence of acid catalysis in the reaction of the ion–molecule pair (in contrast to our finding for the reaction of the corresponding ion–molecule pair formed from dimethoxytritylamine in acidic media). Some of the elementary rate and equilibrium constants of the proposed mechanism have been evaluated.

Key words: trityl, carbenium ion, stopped-flow, ion pair, ion–molecule pair.

Résumé : Faisant appel à des techniques de cinétique à flux stoppé, on a étudié l'équilibre (représenté par l'équation 3) de l'alcool 4,4′-diméthoxytritylique dans les acides perchlorique et nitrique contenant de faibles quantités d'acétonitrile. Utilisant l'absorbance UV à l'équilibre et une valeur pour l'absorptivité molaire de l'ion 4,4′-diméthoxytritylcarbénium déterminé en solution aqueuse concentrée d'acide perchlorique, on a résolu les constantes de vitesse globales de réaction pour le déplacement vers l'équilibre, k_{obs}, en deux composantes, l'une pour réaction vers l'avant et l'autre pour l'inverse. La réaction vers l'avant (constante de vitesse k_a) est du premier ordre en concentrations tant d'alcool que d'acide; la réaction inverse (constante de vitesse k_i) est de pseudo premier ordre par rapport au carbocation. À concentration d'ion hydronium constante, la constante de vitesse vers l'avant augmente d'une façon linéaire avec la concentration de l'électrolyte alors que la constante de vitesse inverse diminue. Ces effets dépendent de la nature de l'anion, mais pas de celle du cation, et elles ne sont pas des effets de la force ionique. À des concentrations d'anion constantes, les valeurs de k_a dans les deux acides et les valeurs de k_i dans l'acide perchlorique sont indépendantes de la concentration en ion hydronium; toutefois, à concentration constante de nitrate, la valeur de k_i diminue avec une augmentation de la concentration en ion hydronium. À des forces ioniques qui ne sont pas constantes, on observe des changements dans les valeurs de k_a et de k_i lorsqu'on augmente la concentration de l'acide perchlorique; ces changements sont entièrement attribués à des changements dans la concentration du

Received September 24, 1998.

This paper is dedicated to Jerry Kresge in recognition of his many achievements in chemistry.

J. Crugeiras. Department of Physical Chemistry, University of Santiago de Compostela, 15706 Santiago de Compostela, Spain.
H. Maskill.[1] Chemistry Department, University of Newcastle upon Tyne, Newcastle upon Tyne NE1 7RU, U.K.

[1]Author to whom correspondence may be addressed. Telephone: 44-191-222-7088. Fax: 44-191-222-6929.
e-mail: h.maskill@ncl.ac.uk

 © 1999 NRC Canada

perchlorate. On propose un mécanisme qui implique un prééquilibre, protonation de l'alcool, une hétérolyse de l'alcool protoné pour donner une paire d'ion 4,4′-diméthytritycarbénium – molécule d'eau et finalement une transformation de celle-ci en un ion carbénium dissocié en équilibre avec des paires d'ions. Afin d'expliquer les effets importants des ions perchlorate et nitrate sur les constantes de vitesse vers l'avant, on suggère que ces anions fournissent des moyens additionnels de réaction pour la paire ion–molécule. Toutefois, on n'a pas mis en évidence de catalyse acide dans la réaction de la paire ion–molécule (en opposition avec les résultats que nous avons obtenus antérieurement pour la réaction de la paire ion-molécule correspondante formée à partir de la diméthoxytritylamine en milieu acide). On a évalué quelques-unes des constantes de vitesse élémentaire et d'équilibre du mécanisme proposé.

Mots clés : trityle, ion carbénium, flux stoppé, paire d'ion, paire ion–molécule.

[Traduit par la Rédaction]

Introduction

The kinetics and equilibria of ionization of substituted triphenylmethanols (substituted trityl alcohols) have been extensively studied, partly in connection with the development of the H_R acidity function (1, 2), and partly due to the importance of substituted trityl as a protecting group in organic synthesis (3). The H_R acidity function is based on the ionization equilibria of triarylmethanols, eq. [1], and equilibrium constants, K_{R^+}, for these reactions are given by eq. [2].

[1] $$Ar_3C^+ + H_2O \leftrightarrow Ar_3COH + H^+$$

[2] $$K_{R^+} = \frac{a_{Ar_3COH}\, a_{H^+}}{a_{Ar_3C^+}\, a_{H_2O}}$$

In a kinetic study of the ionization reaction of 4,4′,4′′-trimethoxytrityl alcohol (TMTOH) under acidic conditions, Postle and Wyatt (4) found that the addition of salts and nonelectrolytes has appreciable effects upon the forward and reverse rate constants of the reaction in eq. [1]. These effects were explained qualitatively in terms of the change in the activity of the water, changes in the activity coefficients of the different solutes involved in the equilibrium, and the formation of ion pairs. The effects are especially large in the case of perchlorate, an electrolyte regarded as inert in many contexts, but with an appreciable effect upon the ionization of neutral substrates where a delocalized positive charge is developed in a carbon residue in the transition state (5). Wyatt (6) proposed a value of 1.3 $dm^3\ mol^{-1}$ for the equilibrium constant for the formation of the ion pair $TMT^+ClO_4^-$ from dissociated ions in aqueous solution in order to bring the derived H_R values for aqueous perchloric acid onto the same water activity scale as that for aqueous sulfuric acid.

In other contexts, the formation of covalent organic perchlorates has been proposed in some reactions with carbocation intermediates (7). However, triarylmethyl perchlorates are fully ionic in the crystalline state and in solution in solvents of even low dielectric constant such as chloroform or dichloromethane (8).

In the investigation reported here, we have measured the overall rates of equilibration of 4,4′-dimethoxytrityl alcohol (DMTOH) in aqueous perchloric and aqueous nitric acid. From these rate constants and UV measurements at equilibrium, we have obtained experimental values for forward and reverse rate constants for the equilibrium reaction expressed as eq. [3].

[3] $$ROH + H_3O^+ \underset{k_r}{\overset{k_f}{\leftrightarrow}} R^+ + 2H_2O$$

Under the dilute acidic conditions of our investigations using the 4,4′-dimethoxytrityl system, activity coefficient effects are expected to be small and to cancel out. Consequently, thermodynamic equilibrium constants may be replaced by practical versions (9) in which activities of dilute solutes are replaced by molar concentrations, and water is referred to the mole fraction activity scale and given the value of unity.

This investigation is closely related to our prior study of the dimethoxytrityl carbenium ion generated by deamination of dimethoxytritylamine (10). In that study, we identified specific acid catalysis in the reaction of the substituted tritylammonium cation, and invoked the dimethoxytrityl carbenium ion – ammonia ion–molecule pair as a kinetically significant intermediate.

Experimental

Reagents

Aqueous solutions of nitric and perchloric acid were prepared from the commercial reagents (Merck 65 and 60%, respectively) and glass distilled water, and were titrated against solutions of sodium hydroxide previously standardized using standard solutions of potassium hydrogen phthalate. Electrolyte solutions were made from the commercial products of the highest purity available (Merck). 4,4′-Dimethoxytrityl alcohol was available from previous studies at Newcastle (10, 11).

Kinetics experiments

The rates of ionization of DMTOH were measured using an Applied Photophysics DX.17MV sequential stopped-flow spectrofluorimeter with an optical path length of 1 cm. One of the syringes of the stopped-flow device was filled with an aqueous solution of DMTOH (with 4% of CH_3CN to avoid solubility problems), and the aqueous acid ($HClO_4$ or HNO_3 with an appropriate concentration of $NaClO_4$, $Ba(ClO_4)_2$, or $NaNO_3$) was in the other syringe. The temperature of the solutions in the syringes and cell of the stopped-flow instrument was kept constant (25.0 ± 0.1°C) by circulating water from a thermostatted bath.

Spectra in Fig. 1 of the reaction mixture recorded at different times show the appearance of two absorption bands corresponding to the 4,4′-dimethoxytrityl carbocation. The reaction was studied by following the change with time in absorbance at the absorption maximum of the carbocation at 495 nm. The observed pseudo first-order rate constants (k_{obs}) were calculated by fitting the absorbance–time data to the integrated first-order rate law using a nonlinear regression

© 1999 NRC Canada

analysis program supplied by Applied Photophysics. The k_{obs} results are average values of 7–10 kinetic runs, and treatment of errors was by standard statistical procedures (12).

Results

Influence of electrolyte concentration

The influence of the electrolyte concentration upon the overall reaction rate constant (k_{obs}) was studied at 0.2 mol dm^{-3} perchloric acid by changing the concentration of sodium perchlorate, and at 0.2 mol dm^{-3} nitric acid by changing the concentration of sodium nitrate, but keeping the other reaction conditions constant in each series. We observe in Table 1 appreciable decreases in k_{obs} as the salt concentration increases for both acids. To study the effect of the charge on the cation of the electrolyte on the reaction rate, the influence of barium perchlorate concentration in perchloric acid was also investigated. These results are also included in Table 1 and show the same effect.

Influence of hydronium ion concentration

The effect of hydronium ion concentration upon the overall reaction rate constant (k_{obs}) was studied at a constant ionic strength of 1.0 mol dm^{-3} by changing the concentration of both perchloric acid (using sodium perchlorate to maintain constant ionic strength) and nitric acid (using sodium nitrate). The results obtained in these experiments are shown in Table 2. There is a distinct increase in k_{obs} with increasing perchloric acid concentration, but only a small increase for nitric acid. Analogous experiments were carried out using perchloric acid at nonconstant ionic strength; an appreciable decrease in k_{obs} with increasing acid concentration is now evident from the results in Table 3.

Kinetic analysis

The overall reaction may be described by the equilibrium in eq. [3] above where R stands for 4,4′-dimethoxytrityl, and R^+ does not imply any particular state of solvation or association. The rate equation for equilibration in terms of the changing concentration of carbenium ion is given in eq. [4].

$$[4] \qquad d[R^+]/dt = k_f[H_3O^+][ROH] - k_r[R^+]$$

Taking into account that

$$[ROH]_0 = [ROH] + [R^+]$$

where $[ROH]_0$ = the initial concentration of alcohol, and assuming that the only species absorbing at 495 nm is the carbocation ($A_{495} = [R^+]\varepsilon_{495}$ where A_{495} is the absorbance in the 1 cm cell and ε_{495} is the molar absorptivity (extinction coefficient) of the carbocation at 495 nm), then

$$dA_{495}/dt = \varepsilon_{495}d[R^+]/dt$$

hence,

$$[5] \qquad dA_{495}/dt = k_f[H_3O^+][ROH]_0\varepsilon_{495} - (k_f[H_3O^+] + k_r)A_{495}$$

Solution of this differential equation gives eq. [6]:

Fig. 1. Spectra of the reaction mixture at different times. $[DMTOH]_0 = 3.3 \times 10^{-5}$ mol dm^{-3}, $[HClO_4] = 0.5$ mol dm^{-3}, ionic strength = 1.0 mol dm^{-3} ($NaClO_4$), 25°C, time intervals = 0.01 s.

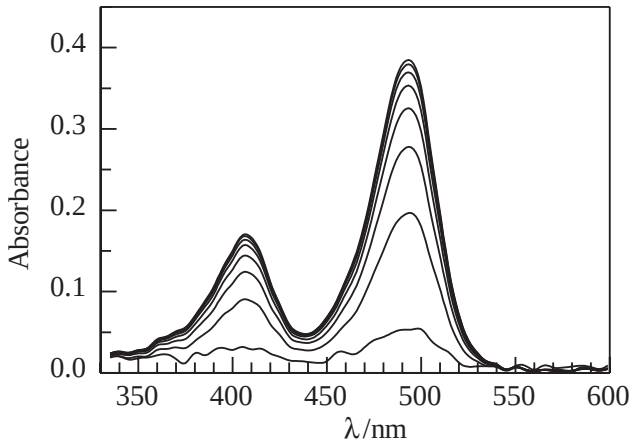

$$[6] \qquad A_{495} = \frac{k_f[H_3O^+][ROH]_0\varepsilon_{495}}{k_f[H_3O^+] + k_r}[1 - e^{-(k_f[H_3O^+]+k_r)t}]$$

Comparison of eq. [6] with eq. [7], the integrated first-order rate equation used to fit the experimental absorbance–time data,

$$[7] \qquad A_{495} = A_\infty - \Delta A e^{-k_{obs}t}$$

in which $\Delta A = A_\infty - A_0$, A_∞ is the absorbance at time = infinity, and A_0 (the absorbance at time = 0) is generally zero, leads to the relationships in eqs. [8] and [9] between the single experimental rate constant for equilibration, k_{obs}, the observed overall change in absorbance associated with the attainment of equilibrium, ΔA, and the attributed forward and reverse rate constants of eq. [3].

$$[8] \qquad k_f = \frac{\Delta A k_{obs}}{[H_3O^+][ROH]_0\varepsilon_{495nm}}$$

$$[9] \qquad k_r = k_{obs} - k_f[H_3O^+]$$

Taking the value for ε_{495} of DMT^+ in 70% perchloric acid obtained in this work (10) of 7×10^4 dm^3 mol^{-1} cm^{-1}, we obtain the results for k_f and k_r at different electrolyte concentrations summarized in Table 4. Clearly, the forward reaction rate constants, k_f, increase with the increasing electrolyte concentration, whilst the reverse reaction rate constants, k_r, decrease. However, the magnitudes of these effects depend upon the nature of the anion, whereas the identity of the cation in perchloric acid seems to be irrelevant.

The influence of perchloric and nitric acid concentrations on the forward and reverse rate constants k_f and k_r at constant ionic strength (1.0 mol dm^{-3}) were also investigated using eqs. [8] and [9], and results are shown in Table 5. We observe that, within experimental error, k_f remains constant with increasing concentrations of both acids, as does k_r for perchloric acid. In contrast, k_r decreases appreciably with increasing concentrations of nitric acid. Results for perchloric acid at nonconstant ionic strength are shown in Table 6, and we observe a modest increase in k_f and a pronounced decrease in k_r as the acid concentration increases.

© 1999 NRC Canada

Table 1. Influence of concentration of electrolytes NaX and BaX_2 on the observed reaction rate constant at $[H_3O^+]$ = 0.20 mol dm^{-3}, 2% CH_3CN, 25°C.[a]

Acid	Salt	$[X^-]_T$/M	μ[b]	ΔA	k_{obs}/s^{-1}
$HClO_4$	$NaClO_4$	0.20	0.20	0.051 ± 0.002	93 ± 1
		0.40	0.40	0.071 ± 0.005	76.5 ± 0.5
		0.70	0.70	0.107 ± 0.003	60.35 ± 0.05
		1.00	1.00	0.160 ± 0.010	49.9 ± 0.3
$HClO_4$	$Ba(ClO_4)_2$	0.20	0.20	0.051 ± 0.002	93 ± 1
		0.40	0.50	0.069 ± 0.001	77.9 ± 0.9
		0.70	0.95	0.103 ± 0.005	64 ± 1
		1.00	1.40	0.148 ± 0.006	53.3 ± 0.4
HNO_3	$NaNO_3$	0.20	0.20	0.040 ± 0.001	107 ± 3
		0.40	0.40	0.0496 ± 0.0001	93 ± 1
		0.70	0.70	0.0674 ± 0.0003	81 ± 1
		1.00	1.00	0.087 ± 0.002	73.4 ± 0.4

[a]$[DMTOH]_0 = 3.3 \times 10^{-5}$ mol dm^{-3}.
[b]Ionic strength (mol dm^{-3}).

Table 2. Influence of acid concentration upon the observed reaction rate constant; ionic strength = 1.0 mol dm^{-3} ($NaClO_4$ or $NaNO_3$), 2% CH_3CN, 25°C.[a]

Acid	Salt	$[H_3O^+]$/M	ΔA	k_{obs}/s^{-1}
$HClO_4$	$NaClO_4$	0.20	0.160 ± 0.010	49.9 ± 0.3
		0.40	0.318 ± 0.001	51.4 ± 0.4
		0.70	0.487 ± 0.001	55.2 ± 0.3
		1.00	0.633 ± 0.009	60.3 ± 0.2
HNO_3	$NaNO_3$	0.20	0.087 ± 0.002	73.4 ± 0.4
		0.40	0.1815 ± 0.0005	73.1 ± 0.3
		0.70	0.313 ± 0.001	74.4 ± 0.6
		1.00	0.417 ± 0.001	76.2 ± 0.2

[a]$[DMTOH]_0 = 3.3 \times 10^{-5}$ mol dm^{-3}.

Table 3. Influence of acid concentration upon the observed reaction rate constant; ionic strength not constant, 2% CH_3CN, 25°C.[a]

$[HClO_4]$/mol dm^{-3}	ΔA	k_{obs}/s^{-1}
0.20	0.051 ± 0.002	93 ± 1
0.40	0.139 ± 0.001	74.8 ± 0.3
0.70	0.351 ± 0.001	62.8 ± 0.3
1.00	0.633 ± 0.009	60.3 ± 0.2

[a]$[DMTOH]_0 = 3.3 \times 10^{-5}$ mol dm^{-3}.

Discussion

By analogy with the mechanism proposed for the deamination of 4,4′-dimethoxytritylammonium ions (10, 11), we propose the mechanism shown in Scheme 1 for the reaction of DMT alcohol.

In this mechanism, step (*i*) is the reversible protonation of the alcohol. The protonated alcohol then undergoes heterolysis in step (*ii*) to yield an ion–molecule pair, i.e., a discrete intermediate comprising a carbenium ion which has a special relationship with a single water molecule. Since the single water molecule of this ion–molecule pair is identical with the water molecules of the solvent (except regarding its unique relationship with the carbenium ion), this intermediate is intrinsically different from that implicated in the corresponding deamination reaction (10). In the latter, the molecule of the ion–molecule pair (NH_3) is different from the solvent molecules. Thus, the ion–molecule pair in deamination can undergo a diffusional separation, which is followed

Table 4. Influence of concentration of electrolytes NaX and BaX_2 on forward and reverse rate constants, k_f and k_r; $[H_3O^+]$ = 0.20 mol dm^{-3}, 2% CH_3CN, 25°C.[a]

Acid	Salt	$[X^-]_T$ /M	μ[b]	$k_f/M^{-1}s^{-1}$	k_r/s^{-1}
$HClO_4$	$NaClO_4$	0.20	0.20	10.2 ± 0.4	91 ± 1
		0.40	0.40	11.8 ± 0.8	74.1 ± 0.5
		0.70	0.70	14.0 ± 0.4	57.6 ± 0.1
		1.00	1.00	17 ± 1	46.4 ± 0.4
$HClO_4$	$Ba(ClO_4)_2$	0.20	0.20	10.2 ± 0.4	91 ± 1
		0.40	0.50	11.6 ± 0.2	75.6 ± 0.9
		0.70	0.95	14.3 ± 0.7	61 ± 1
		1.00	1.40	17.1 ± 0.7	49.8 ± 0.4
HNO_3	$NaNO_3$	0.20	0.20	9.3 ± 0.3	105 ± 3
		0.40	0.40	10.0 ± 0.1	91 ± 1
		0.70	0.70	11.8 ± 0.2	79 ± 1
		1.00	1.00	13.8 ± 0.3	70.6 ± 0.4

[a]$[DMTOH]_0 = 3.3 \times 10^{-5}$ mol dm^{-3}.
[b]Ionic strength (mol dm^{-3}).

Table 5. Influence of acid concentration upon forward and reverse rate constants, k_f and k_r; ionic strength = 1.0 mol dm^{-3} ($NaClO_4$ or $NaNO_3$), 2% CH_3CN, 25°C.[a]

Acid	Salt	$[H_3O^+]$/M	$k_f/M^{-1}s^{-1}$	k_r/s^{-1}
$HClO_4$	$NaClO_4$	0.20	17.5 ± 0.2	46.4 ± 0.4
		0.40	17.7 ± 0.1	44.3 ± 0.4
		0.70	16.6 ± 0.1	43.6 ± 0.3
		1.00	16.5 ± 0.2	43.8 ± 0.3
HNO_3	$NaNO_3$	0.20	13.8 ± 0.1	70.6 ± 0.4
		0.40	14.4 ± 0.1	67.4 ± 0.3
		0.70	14.4 ± 0.1	64.3 ± 0.6
		1.00	13.8 ± 0.1	62.4 ± 0.2

[a]$[DMTOH]_0 = 3.3 \times 10^{-5}$ mol dm^{-3}.

© 1999 NRC Canada

Table 6. Influence of perchloric acid concentration upon forward and reverse rate constants, k_f and k_r; 2% CH_3CN, 25°C (ionic strength not constant).[a]

$[HClO_4]$/mol dm^{-3}	k_f /M^{-1}s^{-1}	k_r /s^{-1}
0.20	10.2 ± 0.3	91 ± 1
0.40	11.3 ± 0.1	70.3 ± 0.3
0.70	13.6 ± 0.1	53.3 ± 0.3
1.00	16.5 ± 0.2	43.8 ± 0.3

[a] $[DMTOH]_0 = 3.3 \times 10^{-5}$ mol dm^{-3}.

by protonation of the ammonia under the acidic conditions, and full solvation of both cations by water molecules. In the corresponding reaction of the ion–molecule pair in Scheme 1, i.e., step (*iii*), the change is in the number of water molecules immediately around the carbenium ion and in the nature of the relationship of each of them with the carbenium ion. This step, therefore, rather than being a dissociation or diffusion apart, will involve the loosening of one water and the addition of further loosely held solvating water molecules around the cation. Two additional steps are included in Scheme 1 to accommodate the salt effects observed experimentally. Step (*iv*) is the formation of an ion pair from the protonated alcohol and the common anion of the acid and the salt present (we denote all types of ion pairs by $R^+||X^-$), and step (*v*) is the equilibrium formation of ion pairs from dissociated anion and carbenium ion regardless of their provenance. In principle, an additional step to include collapse of the ion pair to form a covalent compound, R-X, could be added to Scheme 1 (7). However, trityl perchlorate is fully ionic in the crystal state and in solvents of low dielectric constant such as chloroform or dichloromethane (8), and we found no spectroscopic evidence (^{13}C and ^{35}Cl NMR, IR, and UV-vis) for the existence of covalent compounds DMT-X when X = $OClO_3$ or Cl (using hydrochloric acid). Consequently, we omit this extra step.

Several approximations are now required in order to relate the experimental rate constants k_f and k_r to the elementary rate constants of the mechanism in Scheme 1. First, we assume that protonation of the alcohol is rapidly reversible, i.e., step (*i*) may be treated as a pre-equilibrium with equilibrium constant K_1 (equal to k_1/k_{-1}). Secondly, we assume that the steady-state approximation may be applied to the ion–molecule pair, $R^+\cdot OH_2$, in steps (*ii*) and (*iii*). Thirdly, we assume that the molar absorptivity of the ion R^+ is the same regardless of its solvolytic environment (13), i.e., ε_{495} for R^+ = ε_{495} for $R^+||X^-$, which we denote simply by ε_{495}, and hence $A_{495} = ([R^+] + [R^+||X^-])\varepsilon_{495}$. (Although in some cases there are appreciable changes in the spectra of carbocations on increasing the concentrations of added perchlorate (14), in our reactions the position of the main absorption maximum in spectra of solutions of the carbocation is essentially the same on changing the concentration of electrolyte from 0.5 to 3.5 mol dm^{-3}.) Finally, we assume that step (*v*) of Scheme 1 constitutes a postequilibrium with equilibrium constant K_5 (equal to k_5/k_{-5}), i.e., $[R^+||X^-] = K_5[R^+][X^-]$ and that maintenance of this equilibrium does not affect the overall rate of equilibration (13). With no further assumptions, these approximations allow derivation of the following equation:

Scheme 1.

$$\text{(i)}\quad H_3O^+ + ROH \underset{k_{-1}}{\overset{k_1}{\rightleftharpoons}} ROH_2^+ + H_2O$$

$$\text{(ii)}\quad ROH_2^+ \underset{k_{-2}}{\overset{k_2}{\rightleftharpoons}} R^+\cdot OH_2$$

$$\text{(iii)}\quad R^+\cdot OH_2 \underset{k_{-3}}{\overset{k_3}{\rightleftharpoons}} R^+ + H_2O$$

$$\text{(iv)}\quad ROH_2^+ + X^- \underset{k_{-4}}{\overset{k_4}{\rightleftharpoons}} R^+||X^- + H_2O$$

$$\text{(v)}\quad R^+ + X^- \underset{k_{-5}}{\overset{k_5}{\rightleftharpoons}} R^+||X^-$$

$$\frac{dA_{495}}{dt} = \frac{K_1(k_2k_3 + (k_{-2} + k_3)k_4[X^-])\varepsilon_{495}[ROH]_0[H_3O^+]}{(k_{-2} + k_3)(1 + K_1[H_3O^+])} - \left[\frac{K_1(k_2k_3 + (k_{-2} + k_3)k_4[X^-])[H_3O^+]}{(k_{-2} + k_3)(1 + K_1[H_3O^+])} + \frac{(k_{-2} + k_3)k_{-4}K_5[X^-] + k_{-2}k_{-3}}{(k_{-2} + k_3)(1 + K_5[X^-])}\right]A_{495}$$

Noting that K_1/dm^3 mol^{-1} will be less than 10^{-2} and possibly as low as 10^{-5} (15), $(1 + K_1[H_3O^+])$ will be approximately unity at the hydronium ion concentrations involved, so the above may be rewritten as eq. [10].

$$[10]\quad \frac{dA_{495}}{dt} = \frac{K_1(k_2k_3 + (k_{-2} + k_3)k_4[X^-])\varepsilon_{495}[ROH]_0[H_3O^+]}{(k_{-2} + k_3)} - \left[\frac{K_1(k_2k_3 + (k_{-2} + k_3)k_4[X^-])[H_3O^+]}{(k_{-2} + k_3)} + \frac{(k_{-2} + k_3)k_{-4}K_5[X^-] + k_{-2}k_{-3}}{(k_{-2} + k_3)(1 + K_5[X^-])}\right]A_{495}$$

Comparison of eq. [10] with eq. [5] now leads to eqs. [11] and [12] as the relationships for k_f and k_r in terms of the elementary rate constants in the mechanism of Scheme 1.

$$[11]\quad k_f = \frac{K_1k_2k_{-3}}{(k_{-2} + k_3)} + K_1k_4[X^-]$$

$$[12]\quad k_r = \frac{k_{-2}k_{-3}}{(k_{-2} + k_3)(1 + K_5[X^-])} + \frac{k_{-4}K_5[X^-]}{(1 + K_5[X^-])}$$

The linearity and finite intercept in the plot of k_f against $[X^-]$ shown in Fig. 2, using data from Table 4, provide experimental support for the validity of the mechanism in Scheme 1 and the derivations based upon it. Assuming that the collapse of the ion–molecule pair, $R^+\cdot OH_2$, back to the protonated alcohol is much faster than its further conversion to the solvated dissociated carbenium ion, i.e., $k_{-2} >> k_3$,

© 1999 NRC Canada

Fig. 2. Influence of anion concentration upon the forward reaction rate constant k_f at constant acid concentration (closed circles for perchlorate and closed squares for nitrate).

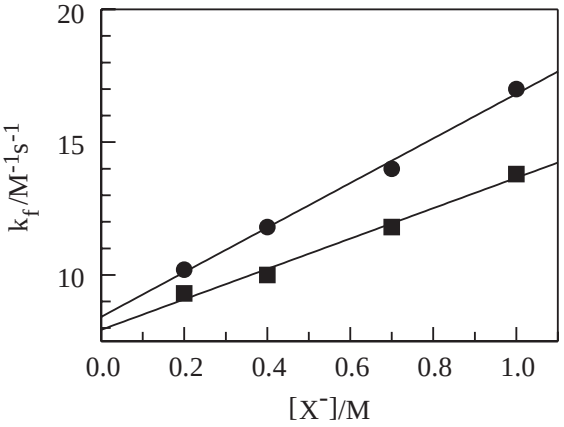

eq. [11] gives eq. [13] where $K_2 = k_2/k_{-2}$ and values for $K_1K_2k_3$ and K_1k_4 obtained by linear regression of k_f against

[13] $$k_f = K_1K_2k_3 + K_1k_4[X^-]$$

$[X^-]$ using the data of Table 4 are summarized in the columns 2 and 3 of Table 7. From column 2, we see that the product $K_1K_2k_3$ is, within experimental error, independent of the nature of the electrolyte as required by the mechanism. Furthermore, since virtually identical correlations are obtained for sodium and barium perchlorate, we conclude that k_f in these solutions is principally dependent upon concentration of perchlorate and not the ionic strength.

The same approximation ($k_{-2} >> k_3$,) applied to eq. [12] for the reverse rate constant, k_r, yields eq. [14].

[14] $$k_r = \frac{k_{-3} + k_{-4}K_5[X^-]}{(1 + K_5[X^-])}$$

Nonlinear regression analysis of k_r against $[X^-]$ using eq. [14] shows that $k_{-4}K_5$ is very much smaller than k_{-3}, so the second term of the numerator in eq. [14] may be neglected. By rearranging the simplified eq. [14], we obtain the linear relationship between $1/k_r$ and $[X^-]$ shown in eq. [15].

[15] $$\frac{1}{k_r} = \frac{1}{k_{-3}} + \frac{K_5}{k_{-3}}[X^-]$$

By plotting values of $1/k_r$ against the total concentration of the anion using data from Table 4, we get straight lines shown in Fig. 3 with a common intercept (same value of k_{-3}) but different gradients (different K_5 values according to the nature of X^-). These plots validate the approximations introduced and allow determination of k_{-3} and K_5, which are included in columns 4 and 5 of Table 7. The average value of $k_{-3} = 118\ s^{-1}$ compares with earlier results for the *overall reverse* rate constant k_r of eq. [3], i.e., the *overall forward* rate constant of eq. [1] when electrolyte effects are absent of 95 s^{-1} for reaction in water at 25°C (16), and 86 s^{-1} for reaction in 2:1 aqueous acetonitrile at 20°C (17). The average result of $K_5 = 1.45\ dm^3\ mol^{-1}$ for $X^- = ClO_4^-$ in aqueous solution compares very well with the value of 1.3 proposed by Wyatt (6) and the approximate result of 2.5 from our deamination studies (10). As expected, it is much smaller than the value of 795 $dm^3\ mol^{-1}$ reported for unsubstituted trityl perchlorate in the less polar 1,2-dichloroethane (8). The smaller value of $K_5 = 0.67\ dm^3\ mol^{-1}$ for $X^- = NO_3^-$ in water has not previously been measured as far as we are aware.

As we now have values for k_{-3} and $K_1K_2k_3$ (see Table 7), and noting that, according to the proposed mechanism of Scheme 1, $K_{R^+} = k_{-3}/K_1K_2k_3$, we can obtain practical values for the equilibrium constant K_{R^+}, which are shown in the penultimate column of Table 7. The average value of $K_{R^+} = 14.4 \pm 0.4$ ($pK_{R^+} = -1.16$) is in good agreement with literature results (1), which adds further support for the mechanism of Scheme 1 and the derivations arising from it.

Step (*iv*) of Scheme 1 could be considered either in terms of a nucleophilic attack by perchlorate anion on the protonated alcohol, water being the nucleofuge, or as a stabilization by the anion of the positive charge of the incipient carbocation in the heterolytic transition state. Sodium perchlorate is an electrolyte that has been used in kinetics and electrochemistry to control ionic strength. The term "inert electrolyte" has been used in many cases for this and other compounds used to keep ionic strength constant. But despite its low reactivity in general, there are isolated examples in the literature where perchlorate reacts with electrophiles faster than nucleophiles such as chloride (7). In such cases, and in our proposed mechanism, perchlorate acts by stabilizing the developing positive charge of nascent large nonpolarizing cations, especially those in which the positive charge is highly delocalized. From the results in column 3 of Table 7, and taking $K_1/dm^3\ mol^{-1} = 2.5 \times 10^{-3}$ (15), we calculate the values for k_4 shown in the final column of Table 7; perchlorate is more effective than nitrate. However, in spite of serious efforts, we found no spectroscopic evidence for the formation of fully covalent $DMTClO_4$ (see above).

Influence of hydronium ion concentration

As seen in Table 5, k_f is independent of the acid concentration as required by the mechanism in Scheme 1, which does not include a channel involving acid-catalyzed forward reaction of the ion–molecule pair. In this respect, therefore, the reaction of DMT alcohol is significantly different from the reaction of DMT amine (10); the latter includes a reaction channel involving acid-catalyzed separation of the cation–molecule pair. The average results obtained from Table 5 ($k_f = 17.1\ dm^3\ mol^{-1}\ s^{-1}$ for perchloric acid and 14.1 for nitric) at total electrolyte concentrations of 1 mol dm^{-3} are in excellent agreement with the ones obtained from the study of the influence of electrolyte concentration for total electrolyte concentration equal to 1.0 mol dm^{-3} and constant hydronium ion concentration (17.1 and 13.8 $dm^3\ mol^{-1}\ s^{-1}$, respectively) shown in Table 4.

The results of Table 5 also show that the concentration of perchloric acid has no effect upon k_r again as required by the mechanism. However, there is a noticeable decrease in k_r with increasing nitric acid concentration at constant total nitrate. We have no mechanistic explanation of this finding and assume, for the present, that under the particular experimental conditions of the reactions in nitric acid plus sodium nitrate, our total neglect of activity coefficient considerations is not justified.

© 1999 NRC Canada

Table 7. Derived rate and equilibrium parameters using data from Table 4 for the mechanism proposed in Scheme 1; 25°C.

Electrolyte	$K_1K_2k_3$/M^{-1} s^{-1}	K_1k_4/M^{-2} s^{-1}	k_{-3}/s^{-1}	K_5/M^{-1}	K_{R^+}/M[a]	k_4/M^{-1} s^{-1}[b]
$NaClO_4$	8.4 ± 0.3	8.4 ± 0.4	121 ± 2	1.60 ± 0.04	14.4 ± 0.6	3.4×10^3
$Ba(ClO_4)_2$	8.3 ± 0.2	8.7 ± 0.3	115 ± 2	1.30 ± 0.04	13.9 ± 0.4	3.5×10^3
$NaNO_3$	7.9 ± 0.3	5.7 ± 0.4	117 ± 3	0.67 ± 0.04	14.8 ± 0.6	2.3×10^3

[a]From the mechanism, $K_{R^+} = k_{-3}/K_1K_2k_3$.

[b]From results in column 3 using $K_1 = 2.5 \times 10^{-3}$ dm^3 mol^{-1} (see text).

Fig. 3. Plot of the inverse of k_r against the total anion concentration (closed squares for sodium perchlorate, triangles for barium perchlorate, and closed circles for sodium nitrate).

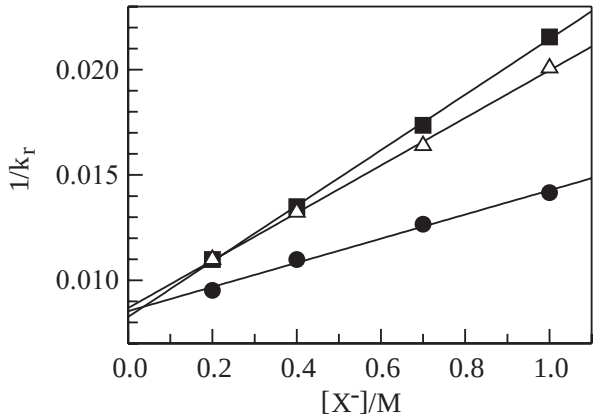

From the results for the influence of perchloric acid on the reaction parameters at nonconstant ionic strength (Table 6), we obtain the following using eq. [13] (linear regression of k_f against $[ClO_4^-]$) and eq. [15] (linear regression of $1/k_r$ against $[ClO_4^-]$): $K_1K_2k_3 = 8.3 \pm 0.4$ dm^3 mol^{-1} s^{-1}, $K_1k_4 = 7.9 \pm 0.6$ dm^6 mol^{-2} s^{-1}, $k_{-3} = 122 \pm 3$ s^{-1}, $K_5 = 1.80 \pm 0.07$ dm^3 mol^{-1}, $K_{R^+} = 14.7 \pm 0.8$ mol dm^{-3}, and $k_4 = 3200$ dm^3 mol^{-1} s^{-1}. These results are in good agreement with the ones obtained under conditions of constant hydronium ion concentration and varying perchlorate shown in Table 7.

Acknowledgements

We thank the Xunta de Galicia for a postdoctoral grant to J.C. and a referee for helpful comments.

References

1. N.C. Deno, J.J. Jaruzelski, and A. Schriesheim. J. Am. Chem. Soc. **77**, 3044 (1955); E.M. Arnett and R.D. Bushick. J. Am. Chem. Soc. **86**, 1564 (1964); M.J. Cook, N.L. Dassanayake, C.D. Johnson, A.R. Katritzky, and T.W. Toone. J. Am. Chem. Soc. **97**, 760 (1975).
2. N.C. Deno and A. Schriesheim. J. Am. Chem. Soc. **77**, 3051 (1955); R.A. Cox and K. Yates. Can. J. Chem. **61**, 2225 (1983).
3. T.W. Greene and P.G.M. Wuts. *In* Protecting groups in organic synthesis. 2nd ed. Wiley, New York. 1991.
4. M.J. Postle and P.A.H. Wyatt. J. Chem. Soc. Perkin Trans. 2, 474 (1972).
5. C.A. Bunton, J.H. Crabtree, and L. Robinson. J. Am. Chem. Soc. **90**, 1258 (1968).
6. P.A.H. Wyatt. J. Chem. Res. Synop. 297 (1980).
7. N.S. Zefirov, A.S. Koz'min, V.V. Zhdankin, V.N. Kirin, N.M. Yur'eva, and V.D. Sorokin. Chem. Scr. **22**, 195 (1983); N.S. Zefirov and A.S. Koz'min. Acc. Chem. Res. **18**, 154 (1985).
8. W.R. Longworth and C.P. Mason. J. Chem. Soc. A, 1164 (1966).
9. H. Maskill. *In* The physical basis of organic chemistry. Oxford University Press, Oxford. 1985.
10. J. Crugeiras and H. Maskill. J. Chem. Soc. Perkin Trans. 2, 1901 (1998).
11. C. Bleasdale, B.T. Golding, W.H. Lee, H. Maskill, J. Riseborough, and E. Smits. J. Chem. Soc. Chem. Commun. 93 (1994).
12. A. Finlay. *In* Practical physical chemistry. *Edited by* J.A. Kitchener. Longmans, London. 1960.
13. J.M. Masnovi and J.K. Kochi. J. Am. Chem. Soc. **107**, 7880 (1985).
14. J.R. Leis, J.C. Mejuto, and M.E. Peña. Langmuir, **9**, 889 (1993).
15. N.C. Deno and J.O. Turner. J. Org. Chem. **31**, 1969 (1966); E.M. Arnett, R.P. Quirk, and J.J. Burkit. J. Am. Chem. Soc. **92**, 1260 (1970).
16. R.A. Diffenbach, K. Sano, and R.W. Taft. J. Am. Chem. Soc. **88**, 4747 (1966).
17. R.A. McClelland, V.M. Kanagasabapathy, N.S. Banait, and S. Steenken. J. Am. Chem. Soc. **111**, 3966 (1989).

© 1999 NRC Canada

Strain in bicyclobutane: on the interpretation of quantitative data

Esther Rozental, Carmela Azran, Harold Basch, and Shmaryahu Hoz

Abstract: In small rings, strain energy is believed to be dominated by bond angles (Baeyer strain). However, it was found (Dill et al.) that, in bicyclobutane, bridgehead substitution effects on strain energy range from +10 to –30 kcal. Ab initio computation at the 6-31G and 6-31+G* levels have shown that the deformation caused by the bridgehead substitution is minimal and so are its energetic consequences.

Key words: bicyclobutane, strain energy, geometry distortion.

Résumé : Dans les petits cycles, on croit que l'énergie de tension est dominée par les angles de liaison (tension de Baeyer). Toutefois, il a été observé (Dill et al.) que, dans le bicyclobutane, des substitutions en tête de pont provoquent des changements dans l'énergie de tension qui vont de +10 à –30 kcal. Des calculs ab initio aux niveaux 6-1G et 6-31+G* ont permis de montrer que la déformation provoquée par une substitution au niveau de la tête de pont est minimale et qu'il en est de même pour ses conséquences énergétiques.

Mots clés : bicyclobutane, énergie de tension, distorsion de la géométrie.

[Traduit par la Rédaction]

Introduction

Mathematical formalism and intuition-based models are two approaches employed in scientific analysis. Oftentimes these two perceptions go hand in hand. However, there are cases where the mathematical formalism seems, at first sight, to contradict the intuitive understanding. An example of such a case, taken from first year chemistry course, is the pK_a of the hydronium ion H_3O^+. In aqueous solutions the proton is transferred to a water molecule leading to the identity reaction shown in eq. [1].

[1] $$H_3O^+ + H_2O \rightarrow H_2O + H_3O^+$$

This reaction is isoenthalpic and therefore should have a K = 1. However, the pK_a of H_3O^+ is –1.74, which corresponds to an equilibrium constant of 0.018 rather than to a K = 1, as expected on the basis of eq. [1]. The reason for the discrepancy between formalism and the intuitive model in this case is rather simple. In the formal language, the equilibrium constant for an acid HA is defined in eq. [2], which does not include the base (1).

[2] $$HA \rightarrow H^+ + A^-$$

For AH = H^+ = H_3O^+ where A = H_2O, this translates to K = [H_2O] = 55.5, which in turn leads into a pK_a = –1.74.

Strain energy of small ring compounds (Baeyer strain) (2) can, at the intuitive level, be pictured in simple geometrical terms such as deformation of bond lengths and bond angles. However, it also has its own formalism and definitions. In a their classical paper, Dill, Greenberg,and Liebman (DGL) (3) have shown in a variety of small ring compounds, that strain energy is affected by substitution. This point was neglected before, since the classical view "assumes electronic effects other than those resulting from angle bending to be unimportant". Because of our interest in the chemistry (4) and strain energy of bicyclobutane (5), we have examined to what extent the geometrical parameters of the bicyclobutane skeleton change due to bridgehead substitution.

Results and discussion

The list of substituents and their effect on the strain energy of bicyclobutane, as calculated by DGL (3), is given in Table 1. To see what are the structural changes caused by the substituents at the bridgehead position of bicyclobutane, we have optimized the geometries of the substituted systems at the RHF/6-31G basis set. Computations were performed with the Gaussian 94(6) package on IBM RS/6000 workstations. The energies and major geometrical parameters, defined in Fig. 1, are given in Table 2. The most important and sensitive structural parameter is the length of the central bond r1. Table 2 shows that, in general, r1 depends on the electronegativity of the atom bound to the bridgehead carbon. In the range of neutral substituents, r1 is shortest for

Received June 19, 1998.

This paper is dedicated to Jerry Kresge in recognition of his many achievements in chemistry.

E. Rozental, C. Azran, H. Basch, and S. Hoz.[1] Department of Chemistry, Bar-Ilan University, Ramat-Gan 52900, Israel.

[1]Author to whom correspondence may be addressed. Telephone: 972-3-5318822. Fax: 972-3-5353567.
e-mail: shoz@mail.biu.ac.il

 © 1999 NRC Canada

Table 1. Strain energy (kcal/mol) in substituted bicyclobutane.[a]

H	Li	CH_3	CN	CF_3	OH	F	BH_3^-	NH_3+	O^-
65.5	40.7	64.1	59.7	57.1	64.0	65.4	46.5	74.3	32.2

[a]Taken from ref. 3.

Table 2. Energies and structural parameters of bridgehead substituted bicyclobutanes calculated at the 6-31G level.

		Bond lengths (Å)						Angles (°)		
X	Energy (au)	r1	r2	R3	r4	r5	r(C1—X)	Φ	θ	α
H	–154.790 247 6	1.483	1.504	1.504	1.504	1.504	1.065	120.1	132.9	132.9
CH_3	–193.814 629 9	1.480	1.506	1.506	1.505	1.505	1.490	119.1	135.3	133.8
CF_3	–490.310 970 6	1.477	1.504	1.504	1.502	1.502	1.456	120.9	132.6	131.4
CN	–246.000 167 9	1.491	1.511	1.511	1.498	1.498	1.411	120.9	133.7	130.8
OH	–229.605 638 9	1.459	1.497	1.497	1.513	1.513	1.380	120.6	130.7	133.6
NH_3+	–210.150 906 6	1.465	1.503	1.503	1.508	1.508	1.461	121.2	135.0	135.2
F	–253.604 163 6	1.454	1.483	1.483	1.523	1.523	1.368	121.5	133.9	136.7
Li	–161.627 348 7	1.523	1.548	1.548	1.488	1.488	1.939	166.8	140.6	132.8
BH_3^-	–180.612 911 9	1.504	1.518	1.518	1.503	1.503	1.623	118.3	135.2	132.2
O^-	–228.996 298 3	1.568	1.513	1.513	1.513	1.513	1.301	121.4	140.1	141.0
Average[a]		1.473	1.501	1.501	1.508	1.508		120.6	133.4	133.5
SD		0.013	0.008	0.008	0.008	0.008		0.7	1.4	1.9

[a]Of values for X = H to F only.

Table 3. Deformation energies induced by bridgehead substitution on the skeleton of bicyclobutane.

X	H	CH_3	CF_3	CN	OH	NH_3+	F	Li	BH_3^-	O^-
E (kcal)	0.00	0.08	0.16	0.18	0.42	0.50	1.24	2.64	0.93	4.60

Table 4. Energies and structural parameters of some bridgehead substituted bicyclobutanes calculated at the 6-31+G* level.

		Bond lengths						Angles		
X	Energy (au)	r1	r2	r3	r4	r5	r(C1—X)	Φ	θ	α
H	–154.8747392	1.470	1.489	1.489	1.489	1.489	1.07	121.0	130.7	130.7
BH_3^-	–180.7181971	1.482	1.499	1.499	1.489	1.489	1.632	118.4	134.5	130.0
Li	–161.7140526	1.495	1.528	1.528	1.474	1.474	1.946	116.6	140.5	131.7
O^-	–229.1268996	1.529	1.498	1.498	1.499	1.499	1.282	121.5	138.6	135.1

Fig. 1. Schematic drawing of bridgehead substituted bicyclobutane.

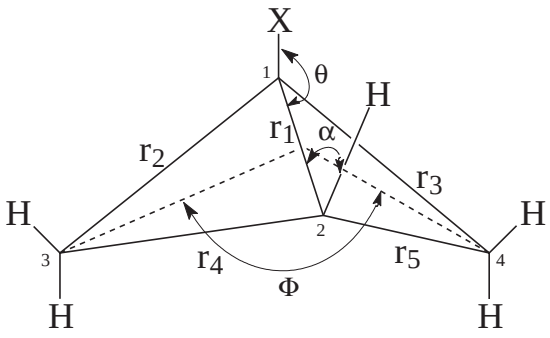

X = F (1.454 Å) and is the longest for Li (1.523 Å). This is probably due to the progressive contraction of the bonding orbitals of the substituted carbon atom, as X is more electronegative. At the bottom of the table, the average value of the geometrical parameters for X = H to X = F and the corresponding standard deviations are given. Examination of the data shows clearly that the variations in bond lengths and angles for most substituents is rather moderate. However, it is not clear what is the magnitude of the effect these changes inflict on the energy of the system. To answer this question we have performed the following calculations. The substituents were removed from the substituted bicyclobutanes, and the "distorted" geometry of the bicyclobutane moiety was kept frozen. To this geometry a hydrogen atom was added at the bridgehead position, replacing the removed substituent, and in each case, the three parameters defining the bonding of the hydrogen to the bicyclic system were fully optimized. This strategy enabled us to examine the energetic consequences of the geometrical changes induced by the various substituents. The results are given in Table 3. The data show that apart from the Li and the O^- substituents, the difference between the fully optimized bicyclobutane and the substituent – distorted systems is smaller than 1 kcal. Thus, the structural changes of the bicyclobutane system caused by the substituents are of no significant energetic consequences.

© 1999 NRC Canada

For the two negatively charged substituents O^- and BH_3^- as well as for H and Li, the computation was repeated at the RHF/ 6-31+G* level. The energies and the structural parameters are given in Table 4. The marked deviations of the structural parameters, from those of the unsubstituted system or from the averages of the data in Table 2, is largely diminished by using the 6-31+G* basis set. The energy changes after replacing the substituent by H, as described above, are also largely reduced to 2.61, 0.83, and 2.57 kcal for Li, BH_3^-, and O^-, respectively.

In conclusion, while the strain energy changes induced by bridgehead substitution covers roughly the range of +10 to –30 kcal, the energy changes associated with the net Baeyer strain (2) as conceived the intuitive way is negligible (with the exception of X = O^-, Li). The change in the strain energy observed by DGL indeed results from the electronic interaction of the substituent with the carbon framework of bicyclobutane. The distortion of the latter has a minimal effect on the energy of the system. The aforementioned enhanced interaction becomes possible due to the resemblance of the central bond to a π bond in olefin (4).

Acknowledgement

This work was supported by a grant from the Israel Science Foundation.

References

1. J. March. *In* Advanced organic chemistry: reactions, mechanisms, and structure. McGraw–Hill, New York. 1968. p. 219.
2. A. Greenberg and J.F. Liebman. *In* Strained organic molecules. Vol. 38. *Edited by* H.H. Wasserman. Academic Press, New York. 1978.
3. J.D. Dill, A. Greenberg, and J.F. Liebman. J. Am. Chem. Soc. **101**, 6814 (1979).
4. S. Hoz. *In* The chemistry of the cyclopropyl group. *Edited by* Z. Rappoport and S. Patai. John Wiley and Sons, New York. 1978. Chap. 19.
5. (*a*) A. Sella, H. Basch, and S. Hoz. J. Am. Chem. Soc. **118**, 416 (1996); (*b*) Tetrahedron Lett. **37**, 5573 (1996).
6. M.J. Frisch, G.W. Trucks, H.B. Schlegel, P.M.W. Gill, B.G. Johnson, M.A. Robb, J.R. Cheeseman, T. Keith, G.A. Petersson, J.A. Montgomery, K. Raghavachari, M.A. Al-Laham, V.G. Zakrzewski, J.V. Ortiz, J.B. Foresman, J. Cioslowski, B.B. Stefanov, A. Nanayakkara, M. Challacombe, C.Y. Peng, P.Y. Ayala, W. Chen, M.W. Wong, J.L. Andres, E.S. Replogle, R. Gomperts, R.L. Martin, D.J. Fox, J.S. Binkley, D.J. Defrees, J. Baker, J.P. Stewart, M. Head-Gordon, C. Gonzalez, and J.A. Pople. Gaussian 94, Revision C.2, Gaussian, Inc., Pittsburgh, Pa. 1995.

© 1999 NRC Canada

Facile formation of azines from reactions of singlet methylene and dimethylcarbene with precursor diazirines: theoretical explorations

Gennady V. Shustov, Michael T.H. Liu, and K.N. Houk

Abstract: The reactions of the singlet methylene (**1a**) and dimethylcarbene (**1b**), with their diazirine precursors, diazirine (**2a**), and dimethyldiazirine (**2b**), have been studied theoretically using ab initio and density functional theory. The reaction has no activation barriers for the parent system (**1a** + **2a**) and proceeds via a reactive complex and a transition state with a small negative enthalpy of activation ($\Delta H^{\neq}_{298}$ = –1.1 kcal mol^{-1}, $\Delta S^{\neq}_{298}$ = –34.4 cal mol^{-1} K^{-1}, ΔG°_{298} = 9.2 kcal mol^{-1}) for the dimethyl derivatives (**1b** + **2b**). The formation of *N*-methylene diazirinium ylides (**3a,b**) is exothermic by 64–80 kcal mol^{-1}. The isomer, 1,3-diazabicyclo[1.1.0]butane (**4a**), is more stable (5–12 kcal mol^{-1}) than isomer **3a**, but can neither be formed by direct thermal reaction of **1a** with **2a** nor undergo the direct rearrangement into formaldazine (**5a**). The rearrangement of ylides **3a,b** into azines **5a,b** proceeds by conrotatory C_3-N_1 ring opening. The predicted activation barrier of ca. 15 kcal mol^{-1} for the ring opening in ylide **3b** is in excellent agreement with experimental data. The formation of pyridinium ylides from carbenes and pyridine is also studied.

Key words: diazirinium ylide, ab initio MO (molecular orbital) theory, density functional theory, pyridinium ylide, CIS (singles configuration interaction) transition energies.

Résumé : Faisant appel à des calculs théoriques ab initio et à la théorie de la densité fonctionnelle, on a étudié sur une base théorique les réactions du méthylène singulet (**1a**) et du diméthylcarbène (**1b**) avec leurs précurseurs, la diazirine (**2a**) et la diméthyldiazirine (**2b**). Dans le cas du système parent (**1a** + **2a**), la réaction ne présente pas de barrières d'activation et elle se produit par le biais d'un complexe réactif alors que, pour les dérivés diméthylés (**1b** + **2b**), elle se produit par le biais d'un état de transition comportant une faible enthalpie d'activation négative ($\Delta H^{\neq}_{298}$ = –1,1 kcal mol^{-1}; $\Delta S^{\neq}_{298}$ = –34,4 cal mol^{-1}; ΔG° = 9,2 kcal mol^{-1}). La formation d'ylures de *N*-méthylène diazirinium (**3a,b**) est exothermique (64 à 80 kcal mol^{-1}). L'isomère **4a**, 1,3-diazabicyclo[1.1.0]butane, est plus stable que l'isomère **3a** par environ 5 à 12 kcal mol^{-1}; toutefois il ne peut être formé par réaction thermique directe de **1a** avec **2a** et il ne peut pas subir un réarrangement direct conduisant à la formaldazine (**5a**). Le réarrangement des ylures **3a,b** en azines **5a,b** se produit par une ouverture conrotatoire du cycle C_3-N_1. La barrière d'activation calculée, environ 15 kcal mol^{-1}, pour l'ouverture du cycle de l'ylure **3b** est en excellent accord avec les données expérimentales. On a aussi étudié la formation d'ylures de pyridinium à partir de carbènes et de pyridine.

Mots clés : ylure de diazirinium, théorie des orbitales moléculaires ab initio, théorie de la densité fonctionnelle, ylure de pyridinium, énergies de transition CIS.

[Traduit par la Rédaction]

Introduction

The generation of carbenes by thermolysis or photolysis of diazirines and diazoalkane precursors is a powerful method for preparative and mechanistic study. In the absence of alkenes, photolysis or thermolysis of diazirines (**2**) often results in the formation of azines (**5**) (1). Even in the presence of alkenes, this reaction may compete substantially with reactions of carbenes (1*a–c*); this side reaction can interfere with kinetic measurements on rates of carbene reactions (1*d*, *e*). The detailed mechanism of the reaction of carbenes with diazirines remains largely unknown. It has been suggested (1*a–c*) that an intermediate in the reaction can have a structure of diazirinium ylide (**3**) or 1,3-diazabicyclo[1.1.0]butane (**4**) (Scheme 1).

The measured rate constants for the reaction of singlet dialkyl- (2) and chlorosubstituted carbenes (3) with the corresponding diazirines lie within the range 10^5–10^8 M^{-1} s^{-1}.

Received October 21, 1998.

This paper is dedicated to Jerry Kresge in recognition of his many achievements in chemistry.

G.V. Shustov. Department of Chemistry, University of Calgary, Calgary, AB T2N 1N4, Canada.
M.T.H. Liu. Department of Chemistry, University of Prince Edward Island, Charlottetown, PE C1A 4P3, Canada.
K.N. Houk.[1] Department of Chemistry and Biochemistry, University of California, Los Angeles, CA 90095-1569, U.S.A.

[1]Author to whom correspondence may be addressed. Telephone: 310/206-0515. Fax: 310/206-1843.
e-mail: houk@chem.ucla.edu

© 1999 NRC Canada

Scheme 1.

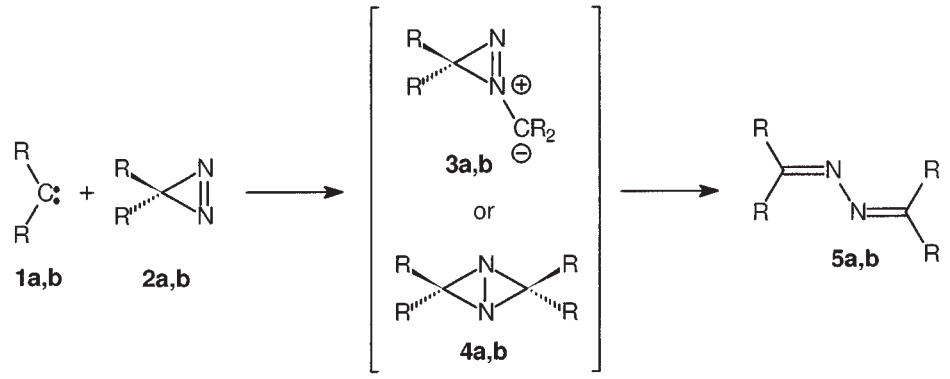

Table 1. Total energies (Hartrees) and zero-point vibrational energies[a] (kcal mol^{-1}) of $C_2H_4N_2$ stationary structures.

		B3LYP/6-31+G(d)		MP2(fc)/6-311+G(d,p)		G2
Species	PG	E_T	ZPVE	E_T	ZPVE	E_T
1a + **2a**	C_{2v} + C_{2v}	–187.861 25	31.5	–187.369 53	31.6	–187.551 69
3a	C_s	–188.000 27	38.7(0)	–187.5068	38.7(0)	–187.670 66
***E*-TS$_{rot}$-3a**	C_s	–187.915 89	36.3(1)	–187.424 85	36.6(1)	–187.591 49
***Z*-TS$_{rot}$-3a**	C_s	–187.908 93	36.6(1)	–187.450 77	36.9(1)	–187.585 86
TS(3a/4a)	C_1	–187.941 54	36.6(1)	–187.450 77	37.8(1)	–187.622 35
TS(3a/5a)	C_1	–187.969 59	37.4(1)	–187.470 99	37.5(1)	–187.640 24
4a	C_{2v}	–188.009 67	39.9(0)	–187.527 46	40.1(0)	–187.687 97
5a	C_{2h}	–188.059 31	38.6(0)	–187.562 90	38.5(0)	–187.730 04

[a]Number of imaginary frequencies in parentheses.

These values approximate those measured for reactions of the singlet carbenes with alkenes (1*b*), which in the absence of stabilizing substitutes lack an enthalpic barrier (4).

We have employed theoretical calculations at a high level of theory to answer the following questions.

(*i*) What are the activation energies for the reactions of the singlet carbenes with diazirines?

(*ii*) What intermediates are formed in these reactions?

(*iii*) What are the fates of intermediates formed in this reaction? Is the dissociation of intermediates possible? Can the intermediate be detected?

Our work represents the first attempt to address these questions of the mechanism of the reaction of carbenes with diazirines. We have studied theoretically the reactions of the singlet methylene (**1a**, R = H) and dimethylcarbene (**1b**, R = Me) with their diazirine precursors **2a** (R = H) and **2b** (R = Me), respectively, (Scheme 1), using both density functional and ab initio theory.

Computational methods

All calculations presented here were performed with Gaussian 94 (5). Geometry optimizations and frequency calculations were carried out at the B3LYP/6-31+G(d) theoretical level. For the parent system (**1a**–**5a**), MP2/6-311+G(d,p) (frozen core approximation) and standard G2 level calculations (5) were also performed. The G2 level (6) corresponds effectively to calculations at the QCISD(T)/6-311+G(3df,2p) //MP2(full)/6-31G(d) level with the incorporation of HF/6-31G(d) scaled zero-point vibrational energies (ZPE) and several higher level corrections. The harmonic frequency analysis verified the nature of the stationary points as minima (all real frequencies) or as transition structures (one imaginary frequency) and was used to provide an estimate of the ZPE values. Tables 1 and 2 show the total energies of reactants, products, and transition states along with the ZPE values. Schematic representations of the relative energies of the $C_2H_4N_2$ and $C_6H_{12}N_2$ isomers are drawn in Figs. 1 and 2.

Heat capacities and entropy corrections were made using scaled frequencies and standard statistical procedures (7) to determine enthalpies and free energies at 298 K. Zero-point

Table 2. Total energies (Hartrees) and zero-point vibrational energies[a] (kcal mol^{-1}) of $C_6H_{12}N_2$ and C_6H_7N stationary structures derived with B3LYP/6-31+G(d).

Species	PG	E_T	ZPVE
	$C_6H_{12}N_2$		
1b + **2b**	C_s + C_{2v}	–345.176 92	103.4
Complex (1b+2b)	C_1	–345.180 95	104.2(0)
TS(1b+2b/3b)	C_1	–345.179 96	104.4(1)
3b	C_s	–345.286 36	108.7(0)
***E*-TS$_{rot}$-3b**	C_s	–345.192 50	106.6(1)
TS(3b/5b)	C_1	–345.261 00	107.5(1)
5b	C_2	–345.351 61	108.9(0)
	C_6H_7N		
1 + **6**	C_s + C_{2v}	–287.430 31	66.2
7	C_{2v}	–287.544 68	72.2(0)
TS$_{rot}$-7	C_s	–287.500 50	71.5(1)

[a]Number of imaginary frequencies in parentheses.

© 1999 NRC Canada

Fig. 1. Schematic presentation of the relative energies (in kcal mol^{-1}) of the $C_2H_4N_2$ isomers, considered in the present work, at B3LYP/6-31+G(d) + ΔZPE, MP2(fc)/6-311+G(d,p) + ΔZPVE (in square brackets), and G2 (in braces); NIMAG = number of imaginary frequencies.

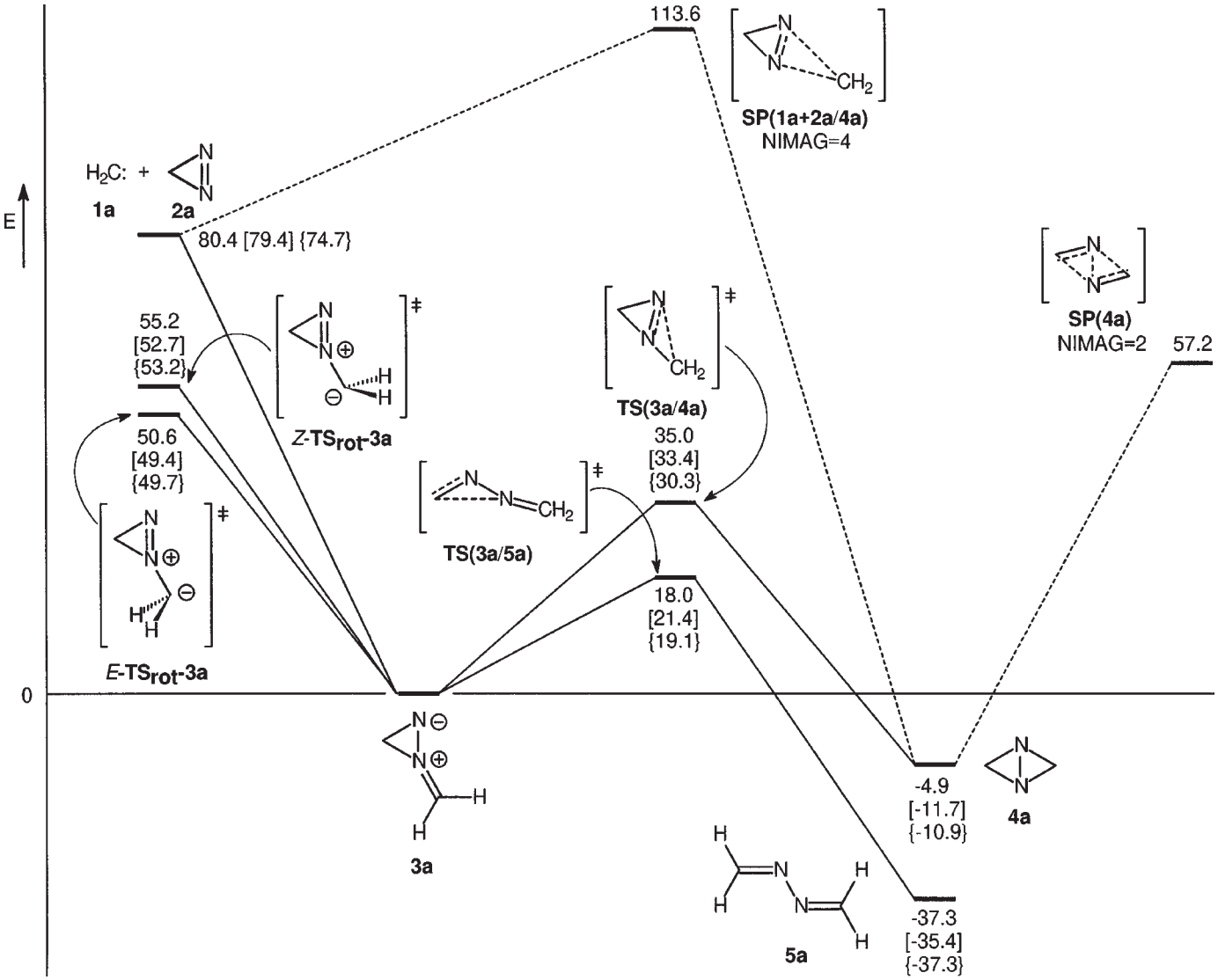

corrections (ΔZPE) and the frequencies were scaled by a 0.95 factor for the B3LYP/6-31+G(d) and MP2(fc)/6-311+G(d,p) levels and by a 0.89 factor for the G2 level.

A profile of the potential energy surface of the C_1 methylene–diazirine reaction to give ylide was calculated at the B3LYP/6-31+G(d) level by freezing the CN distance and optimizing all other geometrical parameters for each point. The CN distance was varied from 3.699 to 1.599 Å with a 0.3 Å step.

Charge distributions in ylide **3a** and its rotational transition states were computed based on HF/6-311+G(d,p)//MP2 (fc)/6-311+G(d,p) wave functions using the natural bond orbital (NBO) (5, 8)[2] analysis.

The intrinsic reaction coordinate (IRC) (9) connecting transition state **TS(3a/4a)** to the two associated minima **3a** and **4a** was computed at the B3LYP/6-31+G(d) level.

The energies of singlet excited states of diazirines **2a,b**, ylides **3a,b**, and azines **5a,b** were calculated by single point all singles configuration interaction (CIS) calculations (5) with the 6-311+G(d,p) basis set at the MP2/6-311+G(d,p) (for **2a**, **3a**, and **5a**) and B3LYP/6-31+G(d) optimized geometries (for **2b**, **3b**, and **5b**).

Results and discussion

Carbene–diazirine reaction

There are at least two probable approaches of carbenes **1a,b** to diazirines **2a,b**: the C_1 symmetrical approach leading to ylides **3a,b** and the C_s symmetrical one, which can afford in bicyclo[1.1.0] species, **4a,b**.

The C_s approach is an orbital symmetry forbidden reaction. Indeed, a saddle point **SP(1a+2a/4a)** (Figs. 1, 3) was

[2] E.D. Glendening, A.E. Reed, J.E. Carpenter, and F. Weinhold. NBO Version 3.1. For reviews, see ref. 8.

© 1999 NRC Canada

Fig. 2. Schematic presentation of the relative energies of the $C_6H_{12}N_2$ isomers, considered in the present work, at B3LYP/6-31+G(d) + ΔZPE in kcal mol^{-1}.

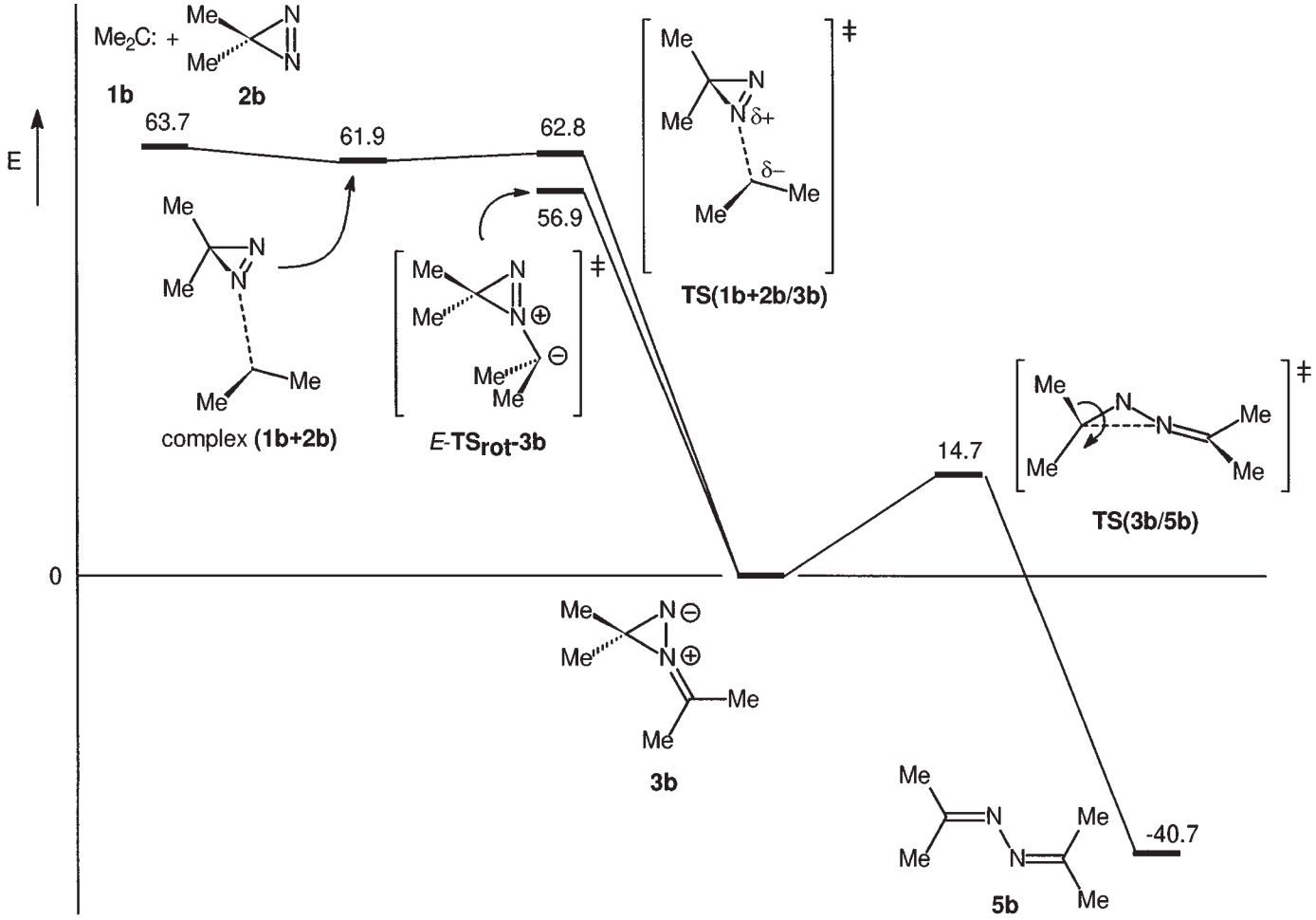

Scheme 2.

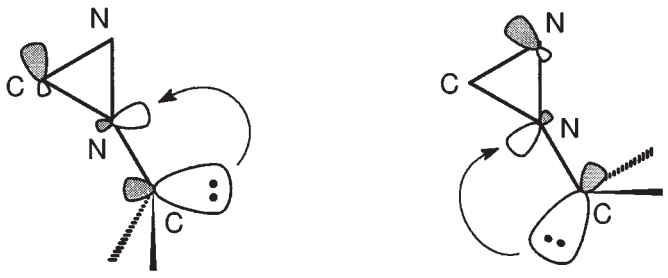

found on this pathway under a C_s symmetry constraint; it has *four* imaginary frequencies and is 33.5 kcal mol^{-1} higher in energy than the reactants. Any deviation from the C_s symmetrical approach of carbene **1a** to diazirine **2a** leads not to bicyclic product but to ylide **3a**. The formation of diazirinium ylide **3a** was simulated using the distance from the carbon atom of **1a** and one nitrogen of **2a** as a reaction coordinate. No local maxima and minima were found when the reaction coordinate was changed from 3.699 to 1.599 Å (Fig. 4).

The C_1 approach of carbene **1b** to diazirine **2b** proceeds via the formation of reaction complex **(1b+2b)**, which is a shallow minimum on the $C_6H_{12}N_2$ potential energy surface at 0 K (Table 2, Fig. 2). The transition state, **TS(1b+2b/3b)**, for conversion of complex to ylide product has an activation energy of only 0.9 kcal/mol, and a negative energy with respect to the reagents ($\Delta H^{\neq}_{298}$ = –1.1 kcal mol^{-1}). A substantial decrease of entropy upon formation of the reactive complex **(1b+2b)** ($\Delta S^{\neq}_{298}$ = –24.0 eu) and transition state **TS(1b+2b/3b)** ($\Delta S^{\neq}_{298}$ = –34.4 eu) leads to a free energy of formation ($\Delta G°_{298}$ = 5.9 kcal mol^{-1}) for the complex and a free energy of activation for the reaction of 9.2 kcal mol^{-1} at 298 K.

As shown in Fig. 3, carbenes **1a,b** attack diazirines **2a,b** from a direction which is substantially out of the plane of the diazirine ring. The empty *p* orbital of the carbenes interacts with the π orbital of the N=N bond and the out-of-phase combination of the nitrogen nonbonding orbitals as it approaches.

Structures and reactivities of diazirine ylide intermediate

The optimized C_s structures of ylides **3a,b** (Fig. 5) are true minima on the $C_2H_4N_2$ and $C_6H_{12}N_2$ potential energy

© 1999 NRC Canada

Fig. 3. B3LYP/6-31+G(d) geometries of the symmetrical (C_s, a saddle point of fourth order) and asymmetrical (C_1, an intermediate point) approaches of **1a** to **2a** and of reactive complex **(1b+2b)** and transition state **TS(1b+2b/3b)**; oop = out-of-plane angle; NIMAG = number of imaginary frequencies. The closed circles stand for nitrogen atoms. Distances in angstroms, angles in degrees.

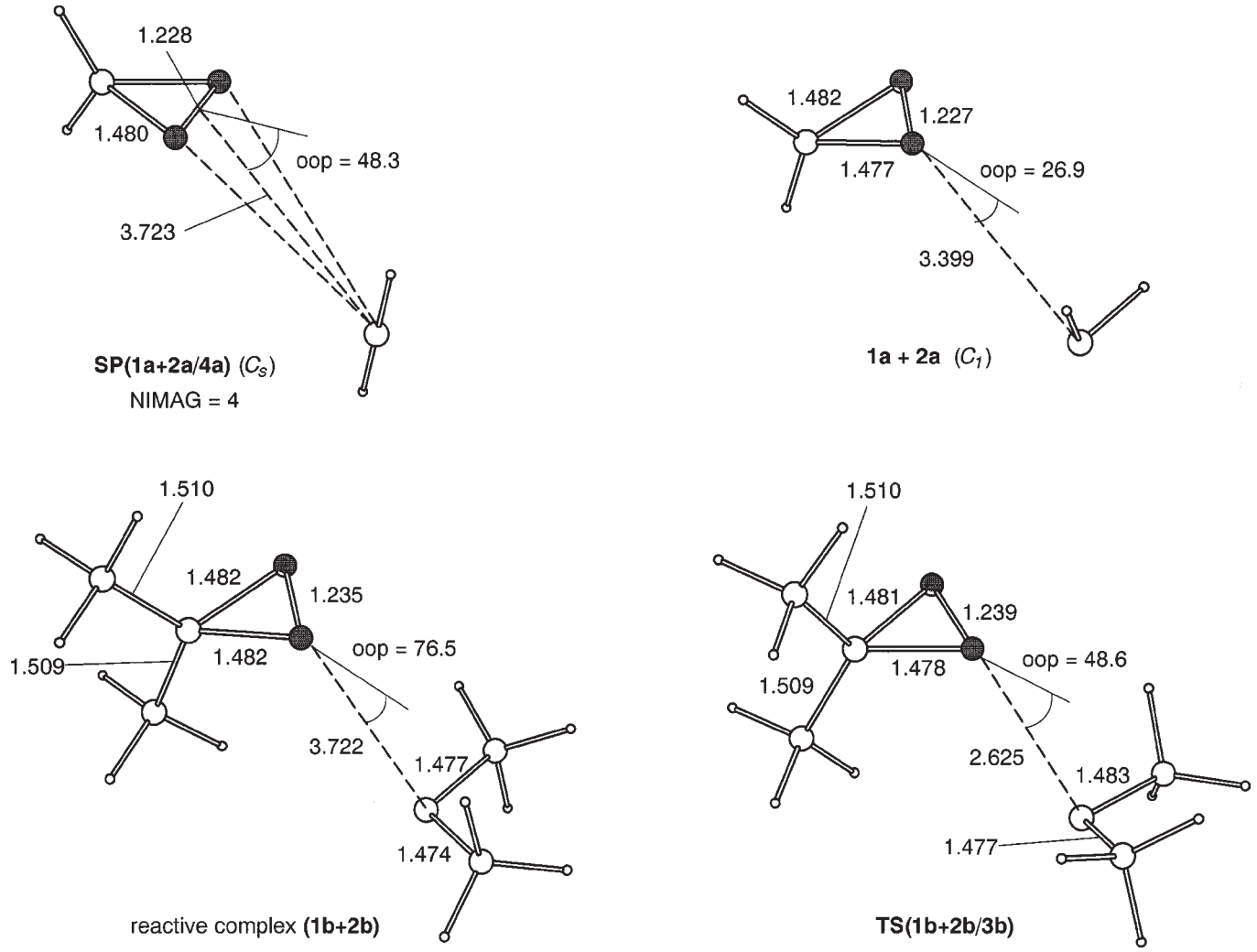

surfaces. The formation of ylides **3a,b** is very exothermic from carbenes **1a,b** and diazirines **2a,b** (Figs. 1, 2).

The planar configuration at N_1 and C_4, the N_1C_4 distance of ca. 1.3 Å (Fig. 5) indicates nearly complete double character of the C_4—N_1 exocyclic bond in ylides **3a,b**. High barriers to rotation about this bond, ca. 50 kcal mol^{-1} (Fig. 1, 2), confirms this double bonding.

Two isomers, *E*-$\mathbf{TS_{rot}}$-**3a** and *Z*-$\mathbf{TS_{rot}}$-**3a** (Fig. 5), of the rotational transition state of ylide **3a** were found. The lower energy of *E*-$\mathbf{TS_{rot}}$-**3a** in comparison to *Z*-$\mathbf{TS_{rot}}$-**3a** apparently caused by the interaction of the nonbonding (*n*) orbital of the C_4 atom with the anti-periplanar antibonding σ*-like orbital of the C_3—N_1 bond of the three-membered ring. In *Z*-$\mathbf{TS_{rot}}$-**3a**, the *n* orbital of the C_4 atom interacts with the σ*-like orbital of the N=N bond, which is a weaker internal σ acceptor due to its double-bond character (Scheme 2).

This is manifested by the shortening of the C_4—N_1 bond in *E*-$\mathbf{TS_{rot}}$-**3a** in comparison with *Z*-$\mathbf{TS_{rot}}$-**3b** (Fig. 5). In the case of ylide **3b**, only the *E*-isomer of the rotational transition state (Figs. 2, 5) was calculated.

The NBO analysis of **3a** confirms the presence of the C_4—N_1 double bond and the N—N double bonding in transition states *E*- and *Z*-$\mathbf{TS_{rot}}$-**3a**. Also, according to this analysis, a maximum negative charge is localized on the N_2 atom in the ground state **3a** and on the C_4 atom in the rotational transition states (Scheme 3).

It is of interest to compare the diazirinium ylide **3a** with the pyridinium ylide **7**.

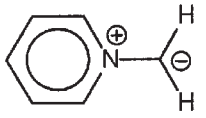

7 (C_{2v})

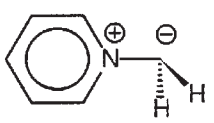

$\mathbf{TS_{rot}}$-**7** (C_s)

Pyridine (**6**) is a classical interceptor of singlet carbenes (10). According to earlier[3] MP2/6-311+G(d,p)//MP2/6-31G(d)

[3] M.W. Wong. Personal communication.

© 1999 NRC Canada

Scheme 3.

NBO HF/6-311+G(d,p)//MP2(fc)/6-311+G(d,p):

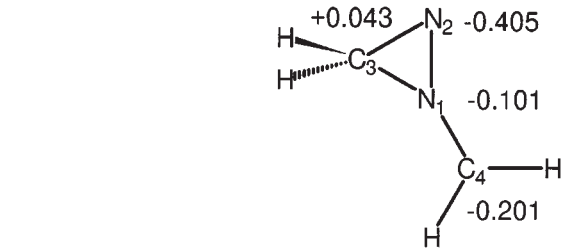

μ = 3.26 D

3a

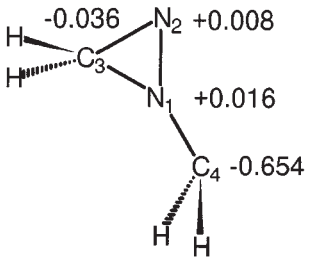

μ = 5.74 D

E-**TS$_{rot}$-3a**

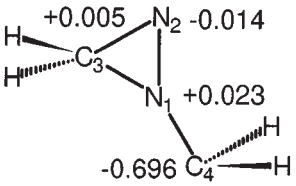

μ = 4.48 D

Z-**TS$_{rot}$-3a**

Fig. 4. A profile of the potential energy surface for the ylide **3a** formation (C_1 methylene–diazirine rapprochement) at the B3LYP/6-31+G(d) level of theory.

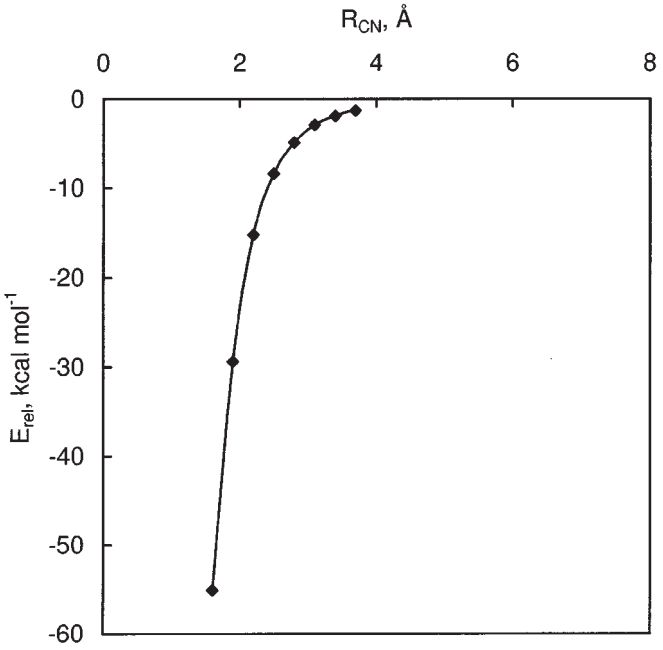

calculations, pyridinium ylide **7** is characterized by a stabilization energy of 69.7 kcal mol^{-1} with respect to carbene **1a** and pyridine **6**. Our B3LYP/6-31+G(d) calculations of pyridine and its ylide **6** yielded a similar value of the stabilization energy –66.1 kcal mol^{-1} (including ΔZPE). We also calculated a transition state (**TS$_{rot}$-7**, C_s symmetry) for rotation of the methylene group in ylide **7**.

The standard thermodynamic parameters of formation of the diazirinium ylide **3a** and the pyridinium ylide **7** are shown in Scheme 4. Both reactions are highly exothermic, but will be less so with carbene stabilizing substituents.

The exocyclic CN bond (1.342 Å) in pyridinium ylide **7** is appreciably longer, and the barrier to rotation (27.1 kcal mol^{-1}) is considerably lower than it is in the diazirinium ylides **3a,b** (1.30 Å, >50 kcal mol^{-1}) (Figs. 1, 2, 5). The localization of negative charge on the electronegative N_2 atom in diazirinium ylides **3a,b** substantially promotes double bonding.

For the parent system, we have also optimized an isomer of ylide **3a**–1,3-diazabicyclo[1.1.0]butane (**4a**) (Table 1, Figs. 1, 6). Compound **4a** is a true minimum on the $C_2H_4N_2$ potential energy surface. All three methods predict that **4a** is more stable then ylide **3a** (Table 1, Fig. 1). As shown above, bicycle **4a** is not be formed in the direct thermal reaction of carbene **1a** with diazirine **2a**. Moreover, the thermal rearrangement of **4a** into azine **5a** is also a forbidden reaction: a second-order saddle point **SP(4a)** (Figs. 1, 6) was found at an attempt to locate a transition state of the double ring opening in **4a** under C_2 symmetry constraint. Therefore, 1,3-diazabicyclo[1.1.0]butanes **4** are not likely intermediates in the thermal reactions of singlet carbenes with diazirines.

The cyclization of ylide **3a** into **4a**, **3**, was also studied. A transition state **TS(3a/4a)** (Fig. 6) is characterized by a high

© 1999 NRC Canada

Fig. 5. B3LYP/6-31+G(d) and MP2(fc)/6-311+G(d,p) (in square brackets) optimized structures of ylides **3a,b** and their rotational transition states. The closed circles stand for nitrogen atoms. Distances in angstroms, angles in degrees.

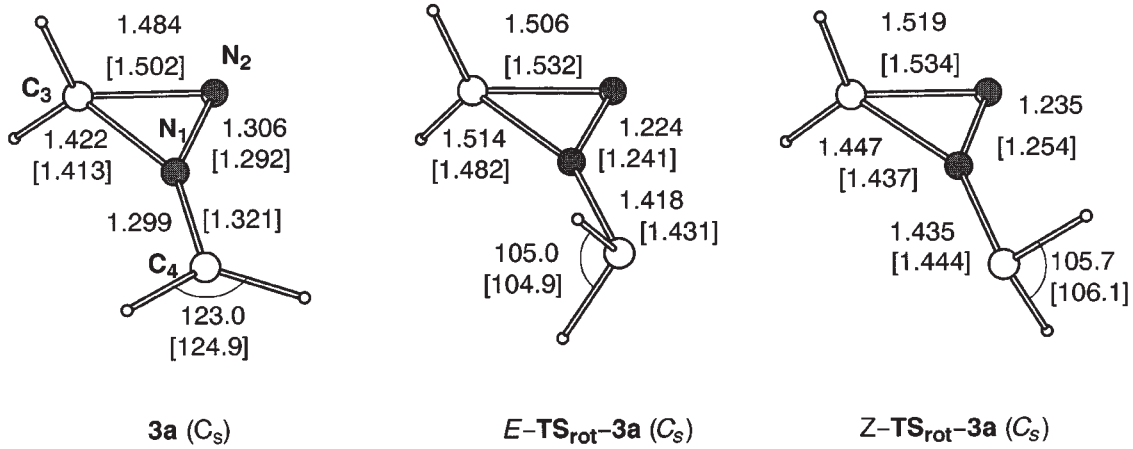

3a (C_s) *E*–**TS$_{rot}$–3a** (C_s) *Z*–**TS$_{rot}$–3a** (C_s)

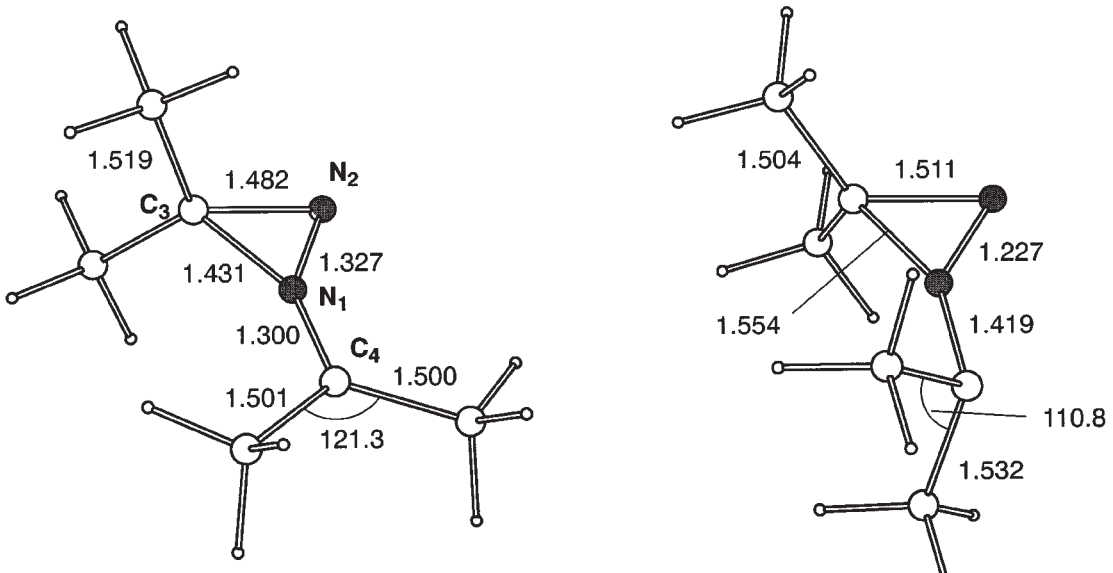

3b (C_s) *E*–**TS$_{rot}$–3b** (C_s)

relative energy (>30 kcal mol^{-1}, Fig. 1) and cannot compete with a transition state **TS(3a/5a)** (ca. 20 kcal mol^{-1}) for the rearrangement of ylide **3a** to formaldazine (**5a**).

The rearrangements of ylides **3a,b** into azines **5a,b** are exothermic conrotatory C_3-N_1 ring opening reactions (see the geometries of **TS(3a/5a)** and **TS(3b/5b)**, Fig. 6). With an activation barrier of ca. 15 kcal mol^{-1}, rearrangement of methylene diazirinium ylides like **3b** should proceed rapidly at temperatures >25°C. However, at low temperatures, a tetraalkyl ylide **3** can be detected by means of UV spectroscopy.

For comparison with experiment, the first two electronic transition energies of diazirines **2a,b**, ylides **3a,b**, and azines **5a,b**, calculated by the CIS method, are given in Table 3. The CIS method generally exaggerates the energies of electronic transitions, and the corresponding calculated wavelengths of these transitions are shorter than the experimental ones. In the case of diazirines **2a,b**, an average difference between the predicted wavelengths of the first transition and the experimental ones is ca. 23 nm, and for azines **5a,b**, this difference amounts to ca. 65 nm (Table 3). Taking into account these differences, the first electronic absorption bands of methylene diazirinium ylides **3** are expected to occur at 250–294 nm.

Recent experimental data on laser flash photolysis of adamantylidene diazirine confirm our predictions. Bonneau et al. (15) observed a transient absorption with λ_{max} = 290 nm,

© 1999 NRC Canada

Scheme 4.

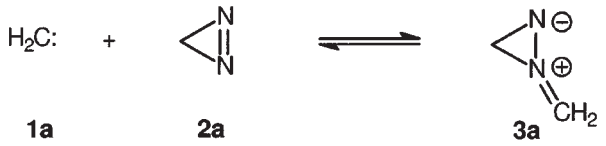

1a **2a** **3a**

	B3LYP/6-31+G	MP2(fc)/6-311+G(d,p)	G2
$\Delta S°_{298}$ (e.u.)	-37.2	-36.4	-37.4
$\Delta H°_{298}$ (kcal mol^{-1})	-81.7	-80.6	-76.4
$\Delta G°_{298}$ (kcal mol^{-1})	-70.6	-69.8	-65.3

1a **6** **7**

	B3LYP/6-31+G
$\Delta S°_{298}$ (e.u.)	-37.7
$\Delta H°_{298}$ (kcal mol^{-1})	-67.1
$\Delta G°_{298}$ (kcal mol^{-1})	-55.8

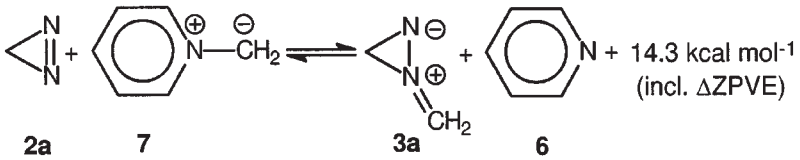

2a **7** **3a** **6**

which may be attributed to the formation of an ylide from the reaction of adamantylidene with the diazirine. The decay of this transient obeyed a first-order rate law with lifetime >150 ms in either air-saturated or nitrogen-flushed isooctane at room temperature. An activation energy of 15.5 kcal mol^{-1} and a pre-exponential factor of $10^{12.3}$ were obtained from the temperature dependence of the lifetime.

Conclusions

(*i*) The reactions of singlet methylene and dimethylcarbene with diazirines have no enthalpic barriers; the free energies of activation for these reactions of singlet carbenes with their diazirine precursors, like the reactions of singlet carbenes with alkenes, have mainly entropic origins.

(*ii*) *N*-Methylene diazirinium ylides (**3**) are the intermediates in the reactions of singlet carbenes (**1**) with their precursors diazirines (**2**). These ylides have a planar (C_s) equilibrium geometry with an exocyclic double CN bond and localization of the negative charge on the two-coordinated nitrogen atom of the ring. Although 1,3-diazabicyclo [1.1.0]butanes (**4**) are more stable than the corresponding methylene diazirinium ylides (**3**), they are not be formed by the direct reaction of carbene **1** with diazirine **2**.

(*iii*) *N*-Methylene diazirinium ylides (**3**) are much more stable than the reactants **1** and **2**, excluding the possibility of dissociation. The relatively high barrier (ca. 15–20 kcal mol^{-1}) for the rearrangement of ylides (**3**) to azines (**5**) offers an opportunity to detect these ylides through spectroscopic methods, or trapping by dipolarophiles.

© 1999 NRC Canada

Fig. 6. B3LYP/6-31+G(d) and MP2(fc)/6-311+G(d,p) (in square brackets) optimized structures of 1,3-diazabicyclo[1.1.0]butane (**4a**), a second-order saddle point **SP(4a)**, and transition states for the rearrangements of ylides **3a,b**; oop = out-of-plane angle; NIMAG = number of imaginary frequencies. The closed circles stand for nitrogen atoms. Distances in angstroms, angles in degrees.

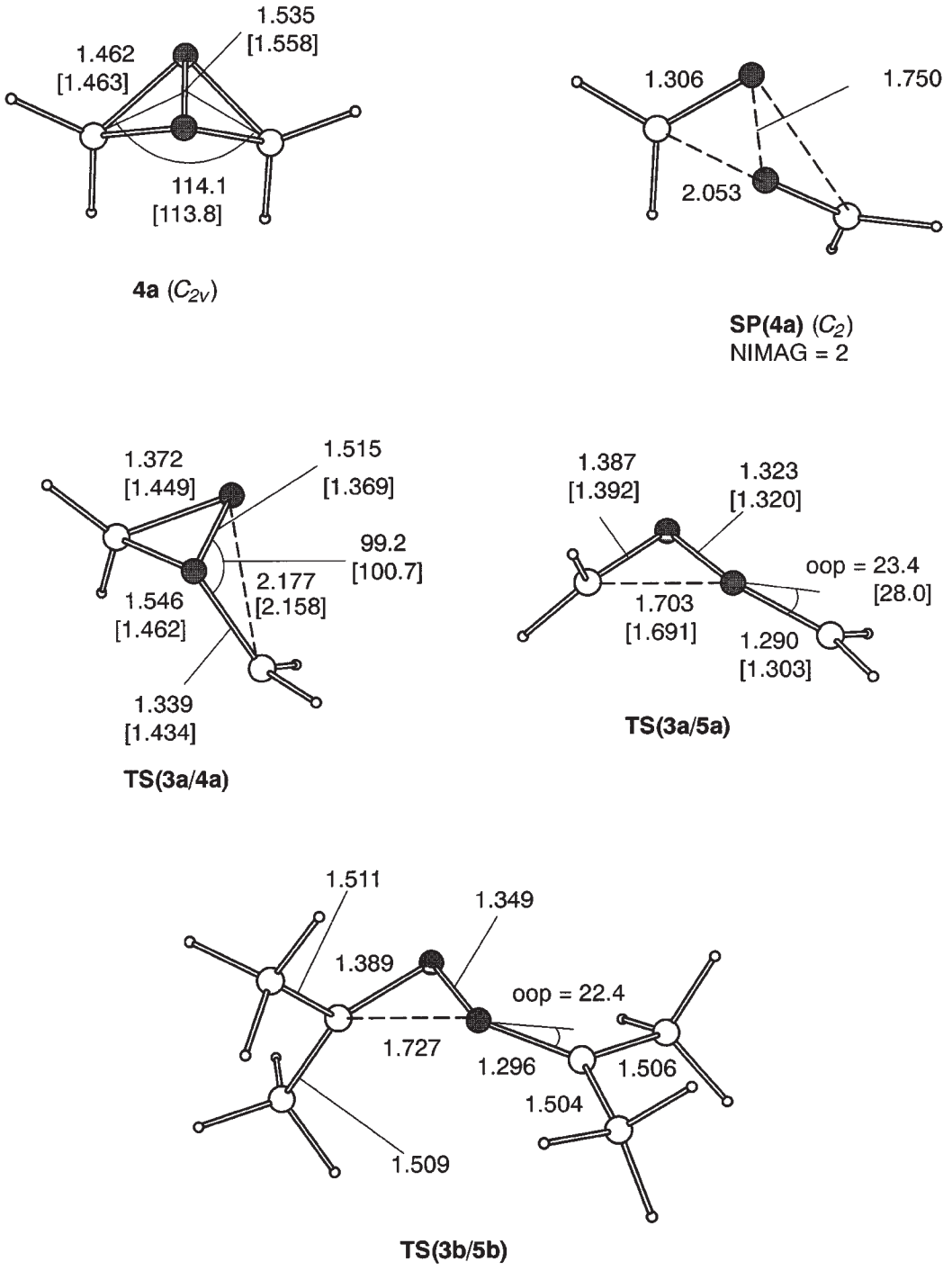

Since the reactions of carbons with diazirines is so facile, we assume that the low yields of the azines in carbene photolysis are due to secondary reactions. It has been reported (14) that the azines are unstable to photolysis. Also, the reactions of azines with carbenes may serve as an additional channel for azine disappearance. We simulated the reaction of the singlet methylene (**1a**) with formaldazine (**5a**) at the B3LYP/6-31+G(d) level of theory and found no enthalpic activation barrier.

Acknowledgements

G.V.S. thanks Professor Arvi Rauk for valuable comments and for providing access to the Gaussian 94 system of programs. We are grateful to the University of Calgary for providing computational facilities. We also grateful to Dr. Ming Wah Wong for sharing his results with us, prior to publication. M.T.H.L. acknowledges financial support from the Natural Sciences and Engineering Research Council of Canada,

© 1999 NRC Canada

Table 3. Calculated parameters[a] for two first electronic transitions of diazirines **2a,b**, ylides **3a,b**, and azines **5a,b**.

	$S_0 \rightarrow S_1$			$S_0 \rightarrow S_2$		
Species	ΔE	λ	f	ΔE	λ	f
Diazirine						
2a	4.06	305 (expt. 323)[b]	0.0035	7.14	174	0.0000
2b	3.75	331 (expt. 358)[c]	0.0017	7.28	170	0.0000
Ylide						
3a	5.35	232	0.4692	5.74	216	0.0367
3b	5.51	225	0.0097	5.64	220	0.5189
Azine						
5a	5.36	231 (expt. 294)[d]	0.0019	6.41	194	0.0000
5b	5.6	221 (expt. 288)[e]	0.0016	6.47	191 (expt. 227)[e]	0.2134

[a]CIS/6-311+G(d,p)//MP2(fc)/6-311+G(d,p) for **2a**, **3a**, and **5a**; CIS/6-311+G(d,p)//B3LYP/6-31+G(d) for **2b**, **3b**, and **5b**; transition energy (ΔE) in eV, wavelength (λ) in nm, oscillator strength (f) in cgs.

[b]Reference 11.

[c]Reference 12.

[d]Reference 13*d*.

[e]Reference 14.

and K.N.H. thanks the National Science Foundation for financial support of the research.

References

1. (*a*) M.T.H. Liu and I.D.R. Stevens. *In* Chemistry of diazirines. Vol. 1. *Edited by* M.T.H. Liu. CRC, Boca Raton. 1987. p. 112; (*b*) M.P. Doyle. *In* Chemistry of diazirines. Vol. 2. *Edited by* M.T.H. Liu. CRC, Boca Raton. 1987. p. 33; (*c*) M.P. Doyle, A.H. Devia, K.E. Basset, J.W. Terpstra, and S.N. Mahapatro. J. Org. Chem. **52**, 1619 (1987); (*d*) R.A. Moss and D.C. Merrer. J. Chem. Soc. Chem. Commun. 617 (1997).
2. S. Morgan, J.E. Jackson, and M.S. Platz. J. Am. Chem. Soc. **113**, 2782 (1991).
3. (*a*) R.A. Moss and G.J. Ho. J. Am. Chem. Soc. **112**, 5642 (1990); (*b*) M.T.H. Liu, R.G. Chapman, and R. Bonneau. J. Photochem. Photobiol. A: Chem. **63**, 115 (1992); (*c*) R.J. Bonneau and M.T.H. Liu. J. Photochem. Photobiol. A: Chem. **68**, 97 (1992); (*d*) M.T.H. Liu and J.E. Chateauneuf. Res. Chem. Intermed. **20**, 195 (1994); (*e*) E.J. Dix. Ph.D. thesis. University of Rochester, New York. 1994.
4. (*a*) K.N. Houk and N.G. Rondan. J. Am. Chem. Soc. **106**, 4293 (1984); (*b*) K.N. Houk, N.G. Rondan, and J. Mareda. Tetrahedron, **41**, 1555 (1985).
5. M.J. Frisch, G.W. Trucks, H.B. Schlegel, P.M.W. Gill, B.G. Johnson, M.A. Robb, J.R. Cheeseman, T. Keith, G.A. Petersson, J.A. Montgomery, K. Raghavachari, M.A. Al-Laham, U.G. Zakrewski, J.V. Ortiz, J.B. Foresman, J. Cioslowski, B.B. Stefanov, A. Nanayakkara, M. Challacombe, C.Y. Peng, P.Y. Ayala, W. Chen, M.W. Wong, J.L. Anders, E.S. Replogle, R. Gomperts, R.L. Martin, D.J. Fox, J.S. Binkley, D.J. Defrees, J. Baker, J.P. Stewart, M. Head-Gordon, C. Gonzalez, and J.A. Pople. Gaussian 94, Revision D.2. Gaussian, Inc., Pittsburgh, Pa. 1995.
6. L.A. Curtiss, K. Raghavachari, G.W. Trucks, and J.A. Pople. J. Chem. Phys. **94**, 7221 (1991).
7. D.A. McQuarrie. Statistical thermodynamics. Harper and Row, New York. 1973.
8. (*a*) A.E. Reed, L.A. Curtiss, and F. Weinhold. Chem. Rev. **88**, 899 (1988); (*b*) F. Weinhold and J.E. Carpenter. *In* The structure of small molecules and ions. *Edited by* R. Naaman and Z. Vager. Plenum, New York. 1988.
9. (*a*) C. Gonzalez and H.B. Schlegel. J. Phys. Chem. **94**, 5523 (1990); (*b*) C. Gonzalez and H.B. Schlegel. J. Phys. Chem. **95**, 5853 (1991).
10. (*a*) J.E. Jackson and M.S. Platz. *In* Advances in carbene chemistry. Vol. 1. *Edited by* U.H. Brinker. JAI Press Inc., Greenwich, Conn. 1994. p. 8; (*b*) R.A. Moss. *In* Advances in carbene chemistry. Vol. 1. *Edited by* U.H. Brinker. JAI Press Inc., Greenwich, Conn. 1994. p. 59.
11. W.H. Graham. J. Am. Chem. Soc. **84**, 1063 (1962).
12. H.M. Frey and I.D.R. Stevens. J. Chem. Soc. 3514 (1963).
13. (*a*) R.K. Brinton. J. Am. Chem. Soc. **77**, 842 (1955); (*b*) J.F.J. Ogilvie. Chem. Soc. Chem. Commun. 359 (1965); (*c*) J.F. Ogilvie and D.G. Horne. J. Chem. Phys. **48**, 2248 (1968); (*d*) D.G. Horne and R.G.W. Norrish. Proc. R. Soc. London Ser. A, **315**, 301 (1970).
14. V.V. Zverev, M.S. El'man, A.P. Stolyarov, A.V. Ermolaeva, and Yu.P. Kitaev. J. Gen. Chem. U.S.S.R. **43**, 2005 (1973).
15. R. Bonneau, M.T.H. Liu, B. Hellrung, and J. Wirz. J. Photochem. Photobiol. A: Chem. **116**, 9 (1998).

© 1999 NRC Canada

Synthesis and kinetics of decomposition of some novel *S*-nitrosothiols

Andrew P. Munro and D. Lyn H. Williams

Abstract: The *S*-nitrosothiols 2-acetamido-2-deoxy-*S*-nitroso-1-thio-β-D-glucopyranose 3,4,6-triacetate (GPSNO) and *S*-nitroso-*N*-carbamyl-D,L-penicillamine (SNCP) were synthesized by *S*-nitrosation of the corresponding thiols, isolated, and fully characterized. The nitrosothiol (TGSNO) from 1-thioglycerol was obtained as a red gelatinous liquid, which decomposed rapidly at room temperature and so was not characterized. The kinetics of decomposition of GPSNO showed that there is a surprisingly large thermal pathway overlaid with a Cu^{2+}/RS^{-} catalyzed reaction. The results strongly suggest that the product disulfide complexes Cu^{2+} (for which there is some spectral evidence), leading to incomplete conversion by that route. Ascorbate also acts as a Cu^{2+} reductant. Another *S*-nitroso sugar, *S*-nitroso-1-thio-β-D-glucose (SNTG), behaved very similarly from solutions generated and used in situ. The decomposition of TGSNO shows induction periods suggesting that slow initial generation of Cu^{+} (the true catalyst) is taking place. There appears to be also a significant alternative pathway (analogous to that found for GPSNO), where the rate appears to be independent of $[Cu^{2+}]$, but very unusually this pathway is effectively halted by addition of EDTA either at the start of the reaction or at a later time. Reaction schemes are put forward to account for these unusual reaction characteristics.

Key words: *S*-nitrosothiols, nitric oxide, ascorbate, copper catalysis.

Résumé : On a synthétisé les *S*-nitrosothiols, 3,4,6-triacétane de 2-acétamido-2-désoxy-*S*-nitroso-1-thio-β-D-glucopyranose (GPSNO) et *S*-nitroso-*N*-carbamyl-D,L-pénicillamine (SNCP), en procédant à la *S*-nitrosation des thiols correspondants, on les a isolés et caractérisés complètement. Le nitrosothiol (TGSNO) obtenu à partir du 1-thioglycérol est un liquide gélatineux rouge qui se décompose rapidement à la température ambiante et il n'a pas été caractérisé. La cinétique de décomposition du GPSNO montre qu'il existe une voie réactionnelle thermique importante qui est recouverte par une réaction catalysée par Cu^{2+}/RS^{-}. Les résultats suggèrent fortement que le disulfure formé se complexe avec le Cu^{2+} (quelques données spectrales supportent ces hypothèses); cette interaction provoque une conversion incomplète par cette voie. L'ion ascorbate agit aussi comme réducteur du Cu^{2+}. Un autre *S*-nitrososucre généré en solution et utilisé in situ, le *S*-nitroso-1-thio-β-D-glucose (SNTG), se comporte d'une façon très semblable. La décomposition du TGSNO présente des périodes d'induction qui suggèrent une génération initiale lente du Cu^{+} (le vrai catalyseur). Il semble exister une voie de réaction alternative importante (analogue à celle observée pour le GPSNO) dans laquelle la vitesse semble indépendante de $[Cu^{2+}]$; il est toutefois surprenant de réaliser que cette voie est effectivement interrompue par l'addition d'EDTA soit au début de la réaction soit plus tard. Des schémas réactionnels sont proposés pour expliquer ces caractéristiques réactionnelles inusitées.

Mots clés : *S*-nitrosothiols, oxyde nitrique, ascorbate, catalyse par le cuivre.

[Traduit par la Rédaction]

Introduction

One aspect of the continuing intense and widespread interest in the "nitric oxide story" concerns the chemistry of *S*-nitrosothiols, RSNO. Not only are these compounds under active consideration as possible nitric oxide donors for medical therapeutic use, but also currently there is much interest in establishing the part played by them in vivo, possibly in the storage and transport of NO in the body. *S*-Nitrosoglutathione GSNO (1), *S*-nitrosoproteins (2), and the *S*-nitroso derivative of hemoglobin (3) have been identified as naturally occurring compounds, and there are literature hypotheses regarding their role in the storage and transport of NO around the body (2, 4). A recent suggestion that the interconversion between the Fe-NO and side chain S-NO forms in nitrosated hemoglobin, in some way controls blood pressure (3), has attracted much interest. The biological (5) and chemical (6) properties of *S*-nitrosothiols have recently been reviewed.

Formerly, it was believed that most RSNO compounds (with a few exceptions, notably GSNO and *S*-nitroso-*N*-acetyl penicillamine, SNAP) were too unstable in the pure state to allow their isolation and characterization, but in recent years an increasing number have been shown to be stable at room temperatures, although others decompose during extraction. In general, the corresponding *O*-nitroso compounds, the alkyl nitrites, are much more widely stable and of course

Received February 16, 1998.

This paper is dedicated to Jerry Kresge in recognition of his many achievements in chemistry.

A.P. Munro and D.L.H. Williams.[1] Department of Chemistry, Durham University, South Road, Durham DH1 3LE, U.K.

[1]Author to whom correspondence may be addressed. Telephone: (44) 191 374 3125. Fax: (44) 191 384 4737. e-mail: D.L.H.Williams@durham.ac.uk

© 1999 NRC Canada

well known. Fairly dilute (1×10^{-3} to 1×10^{-4} M) solutions of all RSNO are easily generated from thiols and nitrous acid in an equilibrium process, which lies very much on the side of RSNO, and are usually sufficiently stable (even for those examples which cannot be obtained in the pure state) to allow experiments to be successfully carried out in situ.

For most RSNO compounds that have been studied, the thermal decomposition reaction is rather slow at room temperature, with half lives of many tens of hours. However, we have shown (7, 8) that in solution, in phosphate buffer at pH 7.4, RSNO species decompose giving NO and RSSR, in a copper-catalyzed process. The effective reagent is Cu^+, generated in situ by thiolate reduction of Cu^{2+} (eqs. [1]–[3]), which in many cases occurs when both RS^- and Cu^{2+} are present only at the trace impurity level. In contrast to the corresponding photochemical reaction, there is no EPR evidence for intermediate thiyl radical formation. There is a large reactivity range that results from the presence or otherwise of suitable substituents (e.g., $-NH_2$) which will allow bidentate binding by Cu^+ to occur. If the reactions are carried out aerobically then the ultimate fate of NO is NO_2^- after initial oxidation of NO, although at very low NO concentrations, such as those encountered in vivo, oxidation of NO by oxygen is very slow and probably will not compete with other NO reactions.

[1] $2Cu^{2+} + 2RS^- = 2Cu^+ + RSSR$

[2] $RSNO + Cu^+ = RS^- + Cu^{2+} + NO$

[3] $4NO + 4OH^- + O_2 = 4NO_2^- + 2H_2O$

[4] $RSNO + R'SH = R'SNO + RSH$

Added thiols can produce a variety of effects. If the thiol is structurally different from that from which RSNO is derived, then transnitrosation (eq. [4]) can occur, leading to the formation of a new R′SNO (9). If the added thiol is the same as that from which RSNO is derived, then at low concentration of added thiol, catalysis can occur (increasing the rate of Cu^+ formation), whereas at higher concentrations, thiol complexation of Cu^{2+} can occur, often resulting in the appearance of substantial induction periods, during which Cu^+ is being generated from very low concentrations of free Cu^{2+} (8, 10). The relative importance of each reaction (reduction and complexation) is governed by the thiol concentration and structure. At very much higher added thiol concentrations, a quite different reaction or series of reactions occurs, leading principally to ammonia formation, together with some nitrous oxide (11, 12).

Recently, we have shown that ascorbate ion can bring about two reactions with *S*-nitrosothiols (13): (*i*) at low ascorbate concentration, the copper catalyzed reaction is dominant in which ascorbate takes over the role of the thiolate and acts as a reducing agent for Cu^{2+} (this reaction can be completely halted by EDTA addition), and (*ii*) at much higher ascorbate concentration, a different reaction occurs, unaffected by the presence of Cu^{2+} or EDTA, and which leads to NO and *thiol* (and not diulfide) formation; under these conditions, all the evidence suggests that ascorbate acts as a nucleophile and undergoes electrophilic nitrosation in the same way as do nitrous acid and alkyl nitrites — the former being a very well known reaction.

In this paper we describe the synthesis and characterization of a *S*-nitrosothiol derived from a thio sugar and examine its decomposition together with that of the *S*-nitroso derivative of 1-thioglycerol (prepared in solution) to nitric oxide, both of which turn out to show some unusual features.

Experimental section

Materials

An aqueous solution of sodium nitrite (0.11 g in 1.65 cm^3) was added dropwise over 2 min with vigorous stirring to a solution of a commercial sample of 2-acetamido-2-deoxy-1-thio-β-D-glucopyranose 3,4,6-triacetate (0.30 g in 1:1 methanol: 1 M HCl, 3.3 cm^3, and containing concentrated sulfuric acid 0.17 cm^3). The mixture became pale red almost immediately, was stirred for 1 h, and the precipitate collected by filtration. The pink solid was washed with ice-cold water and air-dried for 24 h. (65% yield). The solid was stable at room temperature but decomposed on heating, so no melting point could be recorded. Elemental analysis calcd. for $C_{14}H_{20}N_2O_9S$: C 42.9, H 5.15, N 7.1%; found: C 43.0, H 5.03, N, 6.6%. The UV-visible spectrum showed λ_{max} (H_2O) 343 and 557 nm, ε 450 and 17 $dm^3\ mol^{-1}\ cm^{-1}$ respectively. The infrared spectrum included bands at 1572 cm^{-1} (NO stretch) and 654 cm^{-1} (CS stretch). The complex ^1H NMR spectrum was consistent with the expected structure **1**.

Attempts to prepare the *S*-nitroso derivative of 1-thioglycerol (3-mercapto-1,2-propanediol) TGSNO (structure **2**) resulted in the formation of a red gelatinous liquid, which decomposed rapidly at room temperature, but which could be kept for a short while below 4° in the dark. It was, however, too unstable to purify and characterize. However, a solution prepared from equimolar quantities of 1-thioglycerol and sodium nitrite gave a UV-visible spectrum with λ_{max} 333 and 544 nm, ε 881 and 21 $dm^3\ mol^{-1}\ cm^{-1}$, respectively. Similarly, the *S*-nitroso derivative of 1-thio-β-D-glucose SNTG (structure **4**) was too unstable to isolate, but we obtained the characteristic UV-visible spectrum with λ_{max} 342 and 557 nm with ε 436 and 14 $dm^3\ mol^{-1}\ cm^{-1}$, respectively. These spectral characteristics are very similar to those found for GPSNO.

The same synthetic procedure gave a 54% yield of the *S*-nitroso derivative SNCP (structure **3**) of *N*-carbamyl penicillamine (provided as a gift by the former Wellcome company). This was a stable green solid with red reflections, very similar in appearence to the closely related and very well known *S*-nitroso-*N*-acetyl penicillamine (SNAP). Elemental analysis calcd. for $C_6H_{11}N_3O_4S$: C 32.6, H 4.98, N 19.0%; found: C 32.3, H 4.86, N 18.4%. The UV-visible spectrum showed λ_{max} (H_2O) 340 and 590 nm, ε 853 and 20 $dm^3\ mol^{-1}\ cm^{-1}$. The infrared spectrum included bands at 1494 cm^{-1} (NO stretch) and 661 cm^{-1} (CS stretch). The ^1H NMR spectrum was in accord with the expected structure and included the characteristic (14) downfield shift of the proton signals in the vicinity of the sulfur atom upon nitrosation.

All other materials were commercial samples of the highest available purity grade.

© 1999 NRC Canada

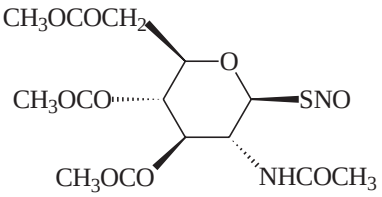

1 (GPSNO)

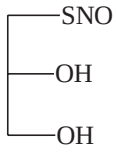

2 (TGSNO)

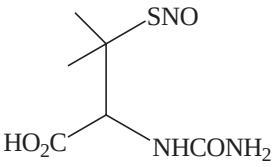

3 (SNCP)

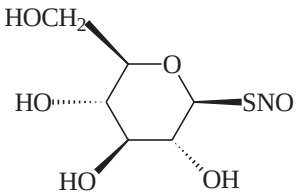

4 (SNTG)

Fig. 1. Absorbance–time plots for the decomposition of GPSNO (1×10^{-3} M) in the presence of Cu^{2+}: (*a*) no added Cu^{2+}; (*b*) [Cu^{2+}] 0.1×10^{-5} M; (*c*) [Cu^{2+}] 0.5×10^{-5} M; (*d*) [Cu^{2+}] 1.0×10^{-5} M; (*e*) 5.0×10^{-5} M.

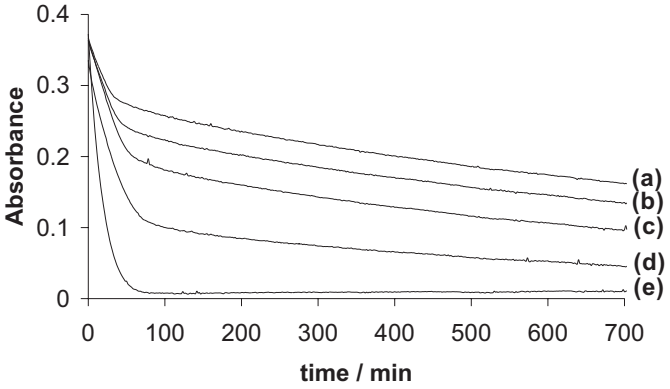

Spectral measurements

These were all carried out in aqueous phosphate buffer, pH 7.4, at 25° in a conventional spectrophotometer operating in the time-drive mode at around 340 nm or in the spectral scan mode. Typical concentrations of GPSNO were ~1×10^{-3} mol dm^{-3}. Solutions of TGSNO and SNTG were prepared at the same concentration by reaction of equimolar amounts of 1-thioglycerol or 1-thio-β-D-glucose and sodium nitrite in mildly acidic solution, immediately prior to investigations of the decomposition characteristics at pH 7.4.

Nitric oxide and nitrite ion analysis

Nitric oxide was determined in the reaction solutions, under nitrogen, using a commercial World-Precision ISO-NO specific electrode, calibrated with standard ascorbic acid-sodium nitrite solutions. Nitrite ion was determined by a modification of the Griess method (8).

Results

2-Acetamido-2-deoxy-*S*-nitroso-1-thio-β-D-glucopyranose 3,4,6-triacetate (GPSNO), 1

We have prepared GPSNO by direct *S*-nitrosation of the corresponding thiol, using a modification of the method used by Field et al. (15) for the first synthesis of SNAP. It was characterized by satisfactory elemental analyses and by the observation of the NO and CS stretching frequencies in the infrared spectrum and also by observation of the characteristic UV-visible absorbances at 343 and 557 nm. The pink solid is quite stable at room temperature. Analysis of an aqueous solution of GPSNO by Ellman's method (16) showed that the thiol level resulting from the equilibration of GPSNO in solution was 1.9% when the total GPSNO concentration was ~5×10^{-3} mol dm^{-3}.

In solution at pH 7.4, the decomposition of GPSNO showed the rather unusual absorbance–time plots shown in Fig. 1 for a series of solutions containing different concentrations of added Cu^{2+}. To separate any metal ion catalyzed process from any other reaction, we carried out two experiments with and without the addition of the general metal ion chelator EDTA, and these traces are given in Fig. 2. The faster reacting component of the reaction (which is Cu^{2+} catalyzed) is completely attenuated, leaving the other component unchanged. Addition of the specific Cu^{+} chelator neocuproine generated the same pattern of behaviour (not shown).

The effect of ascorbate in low concentration was also investigated, and the results are presented graphically in Fig. 3. Clearly ascorbate catalyzes the reaction, and also results in the quantitative decomposition of GPSNO observed now as a single process.

Repeat scans of the decomposition (shown in Fig. 4) at high concentration of added Cu^{2+} (5×10^{-5} mol dm^{-3}) showed the clear development of a small absorbance at around 280 nm, which can be interpreted as the Cu^{2+} complex of the

© 1999 NRC Canada

Fig. 2. Absorbance–time plots for the decomposition of GPSNO (1×10^{-3} M) in the presence of Cu^{2+} (1×10^{-5} M) (*a*) without EDTA, (*b*) with EDTA (1×10^{-3} M).

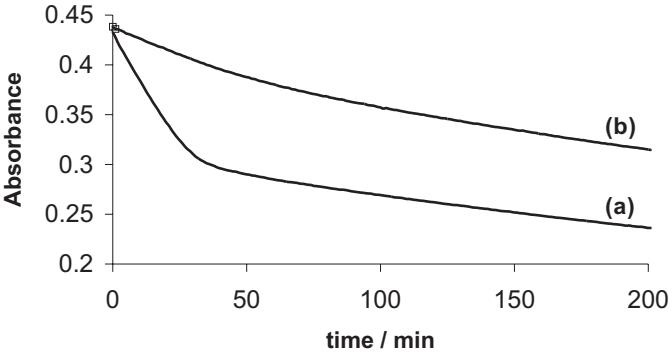

Fig. 3. Absorbance–time plots for the decomposition of GPSNO (1×10^{-3} M) in the presence of Cu^{2+} (1×10^{-5} M) with (*a*) no ascorbate, (*b*) ascorbate (5.0×10^{-5} M), (*c*) ascorbate (1.0×10^{-4} M).

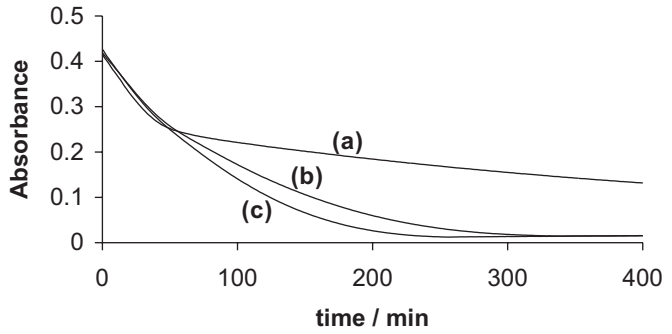

disulfide derived from GPSNO. When the reaction was carried out anaerobically, NO was detected using the NO–electrode system in the solution at ~30%. The same experiment carried out aerobically gave a value of 51% of the theoretical maximum of nitrite anion.

There was a very rapid reaction between GPSNO and sulfite ion at pH 7.4 in the presence of added EDTA, yielding a second-order rate constant of 8630 M^{-1} s^{-1}. No nitric oxide or nitrite ion were detected in these reaction products.

Attempts to isolate the *S*-nitroso derivative of 1-thio-β-D-glucose were unsuccessful, even though it was clear from the development of a red colour that *S*-nitrosation had occurred. The decomposition of solutions generated from the thiol and nitrous acid were examined spectrophotometrically at pH 7.4 and showed very similar behaviour to that shown in Fig. 1 for GPSNO. In the same way, the addition of EDTA completely suppressed the Cu^{2+}-catalyzed reaction leaving a significant thermal reaction.

S-Nitroso 1-thioglycerol (TGSNO), 2

All attempts to effect the nitrosation of 1-thioglycerol (3-mercapto-1,2-propanediol) using the known procedures generated an unstable red gelatinous liquid. It is almost certain that this is the *S*-nitroso derivative of 1-thioglycerol and solutions prepared from equimolar amounts of 1-thioglycerol and nitrous acid gave the expected UV-visible spectrum so characteristic of *S*-nitrosothiols.

The decomposition behaviour is shown in Fig. 5 and reveals a similar pattern of behaviour to that found earlier for

Fig. 4. Repeat scans (4 min intervals) for the decomposition of GPSNO (1×10^{-3} M) with added Cu^{2+} (5×10^{-5} M). Absorbance increases at 280 nm and decreases at 350 nm.

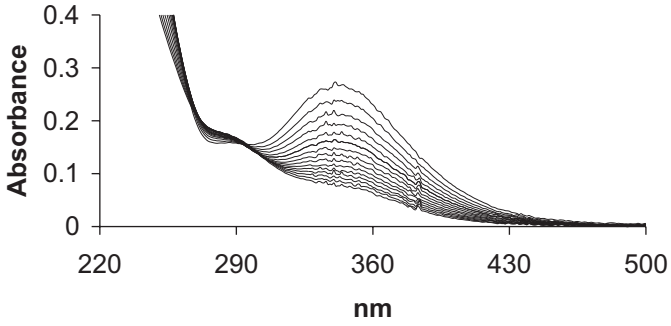

GPSNO in that it appears that there are two reactions: one catalyzed by added [Cu^{2+}] and the other not. In contrast, however, to the results for GPSNO, the spectral traces of the Cu^{2+}-dependent reaction show evidence of induction periods which are shorter as the [Cu^{2+}] and the concentration of the added 1-thioglycerol (not shown) is increased. In marked contrast to the behaviour of GPSNO, however, the effect of added metal ion chelator EDTA to solutions of TGSNO (Fig. 6) progressively halted *both* components of the reaction (the Cu^{2+}-dependent and Cu^{2+}-independent pathways), leaving a virtually stable solution of TGSNO over at least 12 h. Addition of neocuproine produced the same effect. When EDTA was added at various time points after the start of the reaction, decomposition was immediately halted at those time points. The NO-probe gave a value of ~45% for NO production and the nitrite analysis, and when the reaction was carried out aerobically, gave a figure of 97% of the theoretical maximum.

Ascorbic acid, added in low concentration (1×10^{-5} to 1×10^{-4} M) also catalyzed the decomposition of TGSNO and resulted in quantitative reaction, just as in the case of GPSNO. At much higher ascorbate concentration (0.04–0.24 M) and in the presence of EDTA, the reaction was fully first order in TGSNO concentration, and there was an excellent linear relationship between the observed first-order rate constant and ascorbate concentration, yielding a value of 1.59×10^{-3} M^{-1} s^{-1} for the second-order rate constant. Under these conditions NO (or NO_2^- if aerobic) is formed, together with the thiol product.

Repeat scans (not shown) of the reaction carried out in the presence of added Cu^{2+} (5×10^{-5} M) clearly showed the disappearence of the absorbance at around 340 nm, and there was some evidence of the development of a small absorbance in the 260 nm region, which disappeared during the course of the reaction.

S-Nitroso-*N*-carbamyl penicillamine (SNCP), 3

The *S*-nitroso derivative of *N*-carbamyl penicillamine (SNCP) was synthesized, fully characterized, and shown to be a stable solid at room temperature. In aqueous solution, 1.5% free thiol was determined by Ellman's method, reflecting again the equilibration in solution. The thiol was a gift from the former Wellcome company, and the quantity of SNCP synthesized did not allow enough material for the study of its decomposition characteristics. However, some rate measurements were carried out on the decomposition of

© 1999 NRC Canada

Fig. 5. Absorbance–time plots for the decomposition of TGSNO (1×10^{-3} M) with (*a*) no added Cu^{2+}, (*b*) Cu^{2+} (0.5×10^{-5} M), (*c*) Cu^2 (1×10^{-5} M).

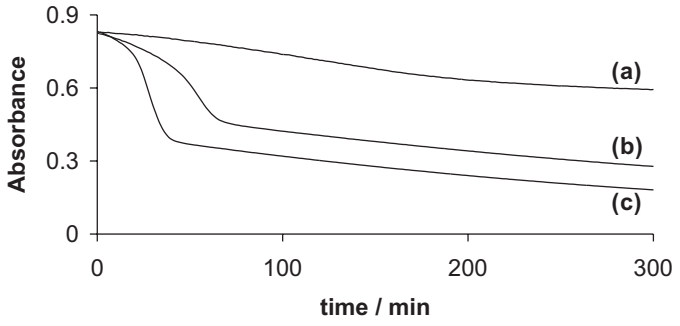

SNCP generated and used in situ from equimolar quantities of the thiol and nitrous acid. Good first-order plots were obtained for experiments with added Cu^{2+} in the range 0.3–1.0 $\times 10^{-5}$ M, and the measured first-order rate constants were linearly dependent on [Cu^{2+}].

Discussion

GPSNO (1)

The successful synthesis of GPSNO and and of SNCP together with the demonstration of their apparent indefinite stability in the solid state has added further examples to the small list of stable *S*-nitrosothiols. It is likely that it, along with all RSNO species tested, will show the general characteristics of vasodilation and inhibition of platelet aggregation in vivo. Testing is underway. It is possible that this sugar derivative may have significant advantages (e.g., of solubility in water) over SNAP and GSNO for in vivo administration in order to effect these properties. A related sugar derivative, which does not have the stability of GPSNO in the pure state, has been shown (17) to have vasodilatory properties, including when the application is made transdermally to human cutaneous vascular smooth muscle.

The characteristics of in vitro decomposition and NO release of GPSNO are somewhat unusual compared with those of other *S*-nitrosothiols, particularly those derived from cysteine and related compunds. Figure 1 shows the pattern. It is clear that there are two reactions here, an initial faster reaction which is Cu^{2+}-catalyzed (and which does not go to completion unless the [Cu^{2+}] is relatively high –5×10^{-5} M in this case), and a slower reaction which is unaffected by the [Cu^{2+}], shows no signs of stopping at incomplete conversion, and which appears to be a thermal reaction. This interpretation is supported by the evidence in Fig. 2 which shows the disappearance of the copper-promoted reaction when EDTA is present (7), leaving the thermal reaction unaffected. The same result was obtained (not shown) when the specific Cu^{+} chelator neocuproine was added, at the same concentration, instead of EDTA, confirming our earlier suggestions that in these copper ion catalyzed reactions, the true catalyst is Cu^{+} (8), generated by thiolate ion reduction of Cu^{2+}. Thiolate ion is likely to be present in all RSNO solutions because of the reversibility of the *S*-nitrosation process (18). In this case we have measured a thiol level of ~2% in a solution of GPSNO (~5×10^{-3} M), which is a fairly typical figure, and which is high enough to effect Cu^{2+} reduction.

Fig. 6. Absorbance–time plots for the decomposition of TGSNO (1×10^{-3} M) with added Cu^{2+} (1×10^{-5} M) (*a*) without EDTA, (*b*) with EDTA (1×10^{-5} M), (*c*) with EDTA (2×10^{-5} M), (*d*) with EDTA (5×10^{-5} M).

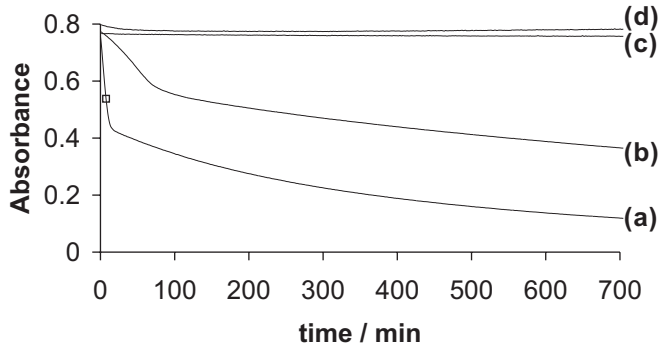

We estimate the first-order rate constant (assuming the decomposition to be a first-order process) for the decomposition of GPSNO by the thermal route to be ~3×10^{-5} s^{-1}, i.e., with a half life of about 6–7 h. This compares with a value for the half life for the thermal decomposition of *S*-nitroso cysteine (one of the more unstable nitrosothiols in the pure state) of ~55 h at the same temperature (8). Other related structures e.g., SNAP, behave similarly.

The copper-catalyzed part of the reaction shows an interesting feature in that reaction without added Cu^{2+} appears to cease after only less than 30% conversion. As the added Cu^{2+} increased so does the % conversion, until at 5×10^{-5} M added Cu^{2+} reaction is essentially quantitative and is so rapid as to effectively swamp the thermal reaction. We have not observed this pattern of behaviour with other *S*-nitrosothiols. Incomplete conversion, however, has been noted earlier in the glutathione (GSH)/Cu^{2+} promoted decomposition of GSNO, in the presence of added oxidized glutathione, GSSG (19), which was interpreted in terms of complexation of Cu^{2+} by the added GSSG. For the GSNO reaction, there was spectroscopic evidence of such a complex with a shoulder at 250 nm and at higher concentration, a peak of low extinction at 620 nm, characteristic of a Cu^{2+} complex, for which a 1:1 structure has been proposed (20). Here with GPSNO decomposition we find (Fig. 4) the development of a small absorbance at around 280 nm which could reasonably be ascribed to the formation of the Cu^{2+} complex of the disulfide.

The derivative from 1-thio-β-D-glucose (generated in situ) behaved in a very similar manner, suggesting that the basic sugar unit provides sites which are available in the product disulfides for coordination of Cu^{2+}, and which allows a significantly larger rate of thermal decomposition of *S*-nitroso sugars generally when compared with simpler cysteine derivatives.

We detected nitric oxide in the decomposition reaction when it was carried out anaerobically. With relatively long reaction times it is extremely difficult to determine NO quantitatively, because of its reactivity, particularly towards traces of oxygen. Under these circumstances a measured yield of ~30% NO is not unusual. A little more difficult to explain is the relatively low yield of nitrite anion (51%)

© 1999 NRC Canada

determined when the reaction was carried out aerobically. We have no obvious explanation at this stage.

When ascorbic acid was added at 5×10^{-5} and 1×10^{-4} M, reaction proceeds to completion, implying that Cu^{2+} bound to the disulfide product is accessible for reduction by ascorbate but not by thiolate.

As part of another study which is looking at reactions involving nucleophilic attack at the nitroso nitrogen atom,[2] we discovered that sulfite ion is generally very reactive towards *S*-nitrosothiols, bringing about complete decomposition in seconds or fractions of seconds in most cases. The reaction forms the thiol and not the disulfide product, and does not generate nitric oxide (or nitrite ion in the presence of air), and by analogy with the corresponding reaction of nitrous acid (21), probably forms hydroxylamine disulfonate.

GPSNO shows the same characteristics in reaction with sulfite ion with a second-order rate consant of 8630 M^{-1} s^{-1}, which means that for reaction of GPSNO (1×10^{-3} M) and sulfite (2×10^{-2} M), the half life of reaction is only 4×10^{-3} s. Since reaction is so rapid and thiol products are readily analysed by the Ellman procedure, this reaction could be the basis for a quantitative analytical procedure for the determination of *S*-nitrosothiols.

TGSNO (2)

Unfortunately, it appears that TGSNO is not sufficiently stable at room temperature to enable a complete characterization and to allow standard solutions to be prepared from it. The red liquid, which could be kept at 0° for some weeks, is almost certainly the *S*-nitroso compound, and the UV-visible spectrum supports this. TGSNO was chosen for this study because preliminary in vivo testing experiments with solutions generated and used in situ had shown some unusual results which could result in some beneficial therapeutic properties.[3]

The decomposition features shown in Fig. 5 are in some ways similar to those found for GPSNO, in that there appear to be two reactions, one copper ion catalyzed and the other not. The copper-catalyzed reaction, however, does show induction periods, not evident in the reactions of GPSNO. Induction periods of this kind have been observed on a number of previous occasions (8, 10), and have been interpreted as the relatively slow initial formation of Cu^{+} (from Cu^{2+} and RS^{-}) with the regeneration of both reactants (eq. [2]). As expected, the induction period is reduced as the $[Cu^{2+}]$ is increased. It is also effectively removed by addition of thioglycerol (RS^{-}), not shown. Nitrite ion was formed quantitatively when reactions were carried out aerobically, and a substantial amount of NO (45%) was measured when oxygen was excluded.

One major difference between the reactions of TGSNO and GPSNO is shown in Fig. 6, where it can be seen that the addition of EDTA effectively stops *both* reactions. Reaction can also be halted when the EDTA is added during the course of the reaction, rather than at the beginning. The non-Cu^{2+}-catalyzed reaction cannot therefore, for TGSNO, be a thermal reaction, if it is halted by the addition of EDTA. It is not immediately obvious what is going on here. There are clearly two reactions taking place, one catalyzed by "free" Cu^{2+} and the other not, yet both are stopped by EDTA addition. A possible explanation is that the slower reaction *is* a copper-promoted reaction, but the effective catalyst, Cu^{+}, is obtained by thiolate reduction of the RSSR–Cu^{2+} complex, which would be expected to be a slower process than the thiolate reduction of free Cu^{2+}, and which would lead to complete, rather than partial decomposition of TGSNO. Further work is needed to clarify this point.

Some evidence of RSSR–Cu^{2+} complex formation is evident from the repeat scan experiments (not shown), but the complex does not appear to be as stable as that generated from GPSNO. Ascorbate also acts as a reducing agent at low concentration, resulting in complete decomposition of TGSNO, implying that, as for GPSNO, Cu^{2+} bound to the disulfide product is accessible for reduction by ascorbate.

At higher concentrations of addded ascorbate, the role of ascorbate changes from that of a reducing agent to that of a nucleophile, which undergoes electrophilic nitrosation by TGSNO, resulting in the formation of NO (becoming NO_2^{-} if aerobic) and the thiol 1-thioglycerol (cf. the reaction of nitrous acid with ascorbic acid (22)). Its reactivity is comparable to that of SNAP and *S*-nitroso-*N*-acetylcysteine.[4] A similar reaction has been reported (13) for the reaction of TGSNO with 1-thioglycerol at high [1-thioglycerol], where RS^{-} now acts as a nucleophile, leading to ammonia formation.

SNCP (3)

Because of a shortage of material, we were unable to carry out a full kinetic analysis on the decomposition of SNCP. However, we found good first-order behaviour over a range of $[Cu^{2+}]$ and obtained a value of 780 dm^3 mol^{-1} s^{-1} for the second-order rate constant k_2 (defined by rate = $k_2[RSNO][Cu^{2+}]$), which compares with a value of 20 dm^3 mol^{-1} s^{-1} for the closely structurally related SNAP. It is tempting to account for the reactivity difference in terms of the relative abilities of the *N*-$COCH_3$ and *N*-$CONH_2$ groups to bind Cu^{+} in an intermediate leading to NO formation, but this does not take account of the relative thiolate concentrations in both cases, which can dramatically affect reactivity in the ability to generate Cu^{+} from Cu^{2+} (10).

Conclusions

We have prepared and characterized two new stable *S*-nitrosothiols, GPSNO and SNCP, and have examined the decomposition in aqueous buffer (pH 7.4) of GPSNO, TGSNO, and SNTG (the latter two generated and used in situ). All reactants decomposed by two pathways, (*i*) GPSNO by a significant thermal pathway in parallel with a Cu^{2+}-catalyzed reaction, which tends to stop at incomplete conversion, as the Cu^{2+} catalyst is tied up by complexation with the disulfide product, and (*ii*) TGSNO by a Cu^{2+} pathway, which also stops at incomplete conversion probably for the same reason, together with a component which may arise by copper

[2] A.P. Munro and D.L.H. Williams. To be published.
[3] A.R. Butler. Personnal communication.
[4] A.J. Holmes and D.L.H. Williams. To be published.

© 1999 NRC Canada

catalysis where the true catalyst Cu^{+} is generated from the product disulfide–Cu^{2+} complex. Both compounds showed the "normal" reactivity with relatively high concentrations of reactive nucleophiles such as ascorbate and sulfite.

Acknowledgement

We thank the EPSRC for a research studentship awarded to A.P.M.

References

1. B. Gaston, J. Reilly, J.M. Darzen, J. Fackler, P. Ramdev, D. Arnelle, M. Mullins, D.J. Sugarbaker, C. Chee, D.J. Singel, J. Loscalzo, and J.S. Stamler. Proc. Natl. Acad. Sci. U.S.A. **90**, 10 957 (1993).
2. J.S. Stamler, O. Jaraki, J. Osborne, D.I. Simon, J. Keaney, J. Vita, D. Singel, C.R. Valeri, and J. Loscalzo. Proc. Natl. Acad. Sci. U.S.A. **89**, 7674 (1992).
3. L. Jia, C. Bonaventura, J. Bonaventura, and J.S. Stamler. Nature (London), **380**, 221 (1996).
4. R.M. Clancy, D. Levartovsky, J. Leszczynska-Piziak, J. Yegudin, and S.B. Abramson. Proc. Natl. Acad. Sci. U.S.A. **91**, 3680 (1994).
5. A.R. Butler and P. Rhodes. Anal. Biochem. **249**, 1 (1997).
6. S. Oae, and K. Shinhama. Org. Prep. Proc. Int. **15**, 165 (1983).
7. J. McAninly, D.L.H. Williams, S.C. Askew, A.R. Butler, and C. Russell. J. Chem. Soc. Chem. Commun. 1758 (1993).
8. S.C. Askew, D.J. Barnett, J. McAninly, and D.L.H. Williams. J. Chem. Soc. Perkin Trans. 2, 741 (1995).
9. D.J. Barnett, A. Rios, and D.L.H. Williams. J. Chem. Soc. Perkin Trans. 2, 1279 (1995).
10. A.P. Dicks, P.H. Beloso, and D.L.H. Williams. J. Chem. Soc. Perkin Trans. 2, 1429 (1997).
11. S.P. Singh, J.S. Wishnock, M. Keshive, W.M. Deen, and S.R. Tannenbaum. Proc. Natl. Acad. Sci. U.S.A. **93**, 14 428 (1996).
12. A.P. Dicks, E. Li, A.P. Munro, H.R. Swift, and D.L.H. Williams. Can. J. Chem. **76**, 789 (1998).
13. A.J. Holmes and D.L.H. Williams. Chem. Commun. 1711 (1998).
14. B. Roy, A. du Moulinet d'Hardemare, and M. Fontcave. J. Org. Chem. **59**, 7019 (1994).
15. L. Field, R. Dilts, R. Ravichandran, P.G. Lenhert, and G.E. Carnahan. J. Chem. Soc. Chem. Commun. 249 (1978).
16. P.W. Riddles, R.L. Blakeley, and B. Zerner. Anal. Biochem. **94**, 75 (1979).
17. A.R. Butler, R.A. Field, I.R. Greig, F.W. Flitney, S.K. Bisland, F. Khan, and J.J.F. Belch. Nitric Oxide: Biol. Chem. **1**, 211 (1997).
18. P.H. Beloso and D.L.H. Williams. J. Chem. Soc. Chem. Commun. 89 (1997).
19. H.R. Swift. Ph.D. thesis. University of Durham, U.K. 1996. pp. 59–61.
20. K. Varnagy, I. Sovago, and H. Kozlowski. Inorg. Chim. Acta, **151**, 117 (1988).
21. S.B. Oblath, S.S. Markowitz, T. Novakov, and S.G. Chang. J. Phys. Chem. **86**, 4853 (1982).
22. C.A. Bunton, H. Dahn, and L. Loewe. Helv. Chim. Acta, **43**, 303 (1960); **43**, 317 (1960); **43**, 320 (1960); and earlier papers.

© 1999 NRC Canada

The secondary α-deuterium isotope effect at the site of the enzyme-catalyzed *cis-trans* isomerization of maleylacetone. Mechanistic implications

Michael S. Finnin and Stanley Seltzer

Abstract: An equal mixture of monodeuterated isotopomers of maleylacetone, viz., 4-hydroxy-6-oxo-2,4-heptadienoic-2-d_1 acid (**1**) and 4-hydroxy-6-oxo-2,4-heptadienoic-3-d_1 acid (**2**) was synthesized and subjected to catalyzed *cis-trans* isomerization by the maleylacetoacetate *cis-trans* isomerase–glutathione system. These studies were designed to probe the detailed mechanism of enzyme-catalyzed *cis-trans* isomerization about the C-2—C-3 bond of the substrate. In the competitive reaction, **2** accumulates with respect to **1** at high extent of reaction. ^{1}H NMR analysis indicates that **1** reacts 15% faster than **2** in line with a nucleophilic addition mechanism at C-2 rather than a conjugate addition mechanism at C-2 and C-3, to convert the C-2—C-3 double bond to a single bond to allow facile internal rotation.

Key words: enzyme-catalyzed *cis-trans* isomerization, secondary α-deuterium isotope effect, maleylacetoacetate *cis-trans* isomerase, *cis-trans* isomerization mechanism.

Résumé : On a synthétisé un mélange égal des isotopomères monodeutérés de la maléylacétone, soit l'acide 4-hydroxy-6-oxohepta-2,4-diénoïque-2-d_1 (**1**) et l'acide 4-hydroxy-6-oxohepta-2,4-diénoïque-3-d_1 (**2**) et on l'a soumis à une isomérisation *cis-trans* catalysée par le système glutathion–isomérase *cis-trans* du maléylacétoacétate. Ces études avaient pour but d'étudier en détail le mécanisme de l'isomérisation *cis-trans*, catalysée par les enzymes, autour de la liaison C-2—C-3 du substrat. Lors de réactions compétitives au cours desquelles on laisse aller la réaction pendant longtemps, le produit **2** s'accumule par rapport à **1**. Une analyse des spectres RMN du ^{1}H indique que le composé **1** réagit à une vitesse qui est de 15% supérieure à celle du composé **2**; ces résultats suggèrent que la conversion de la double liaison C-2—C-3 en liaison simple, qui permet une rotation interne facile, se fait par un mécanisme d'addition nucléophile en C-2 plutôt que par un mécanisme d'addition conjuguée en C-2 et en C-3.

Mots clés : isomérisation *cis-trans* catalysée par les enzymes, effet isotopique secondaire d'un deutérium en α, isomérase *cis-trans* de la maléylacétoacétonate, mécanisme de l'isomérisation *cis-trans*.

[Traduit par la Rédaction]

Introduction

The process of *cis-trans* isomerization about double bonds is an important reaction in biochemistry. Most notable is the visual process where light catalyzes the isomerization of opsin-bound 11-*cis*-retinal to the all-*trans* form thereby triggering, in a complex set of reactions, the transmission of the visual signal (1). While this reaction is photocatalytic, the regeneration of the 11-*cis*-retinal from the all-*trans*-isomer occurs in a series of dark reactions (2).

A similar reaction is found in the photocycle of the purple membrane which *Halobacteria salinarium* uses to capture and utilize sunlight as a source of energy (3). All-*trans*-retinal bound to the protein, bacterioopsin, is photoisomerized to the bound 13-*cis*-retinal, initiating structural changes which result in the active transport of a proton across the membrane. As part of the cycle, the 13-*cis*-bound retinal is reconverted to the bound all-*trans*-isomer in a dark reaction catalyzed by the protein in order to retrigger the system for the next cycle.

Another example of a biologically important *cis-trans* isomerization, and which this report is concerned with, is found in one of the enzymatic reactions necessary for the metabolic degradation of aromatic amino acids (4). Phenylalanine, for example,

Received May 27, 1998.

This paper is dedicated to Jerry Kresge in recognition of his many achievements in chemistry.

M.S. Finnin[1] and S. Seltzer.[2] Chemistry Department, Brookhaven National Laboratory, Upton, NY 11973, U.S.A.

[1]Present address: Cellular Biochemistry and Biophysics Program, Howard Hughes Medical Institute, Memorial Sloan–Kettering Cancer Center, 1275 York Ave., New York, NY 10021, U.S.A.

[2]Author to whom correspondence may be addressed. Telephone: (516) 344-4390. Fax: (516) 344-5815. e-mail: seltzer@bnl.gov

 © 1999 NRC Canada

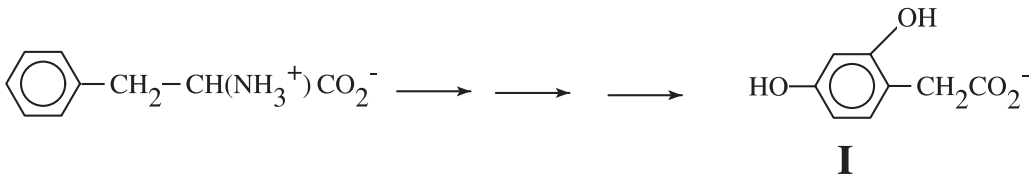

I

is converted through oxidation, deamination, and decarboxylation to homogentisic acid (**I**). The aromatic ring is then oxidatively cleaved to form maleylacetoacetate (**II**). This intermediate must first be *cis-trans* isomerized before the next enzyme can hydrolytically cleave it to fumarate and acetoacetate. The latter two compounds are then metabolized in the usual way.

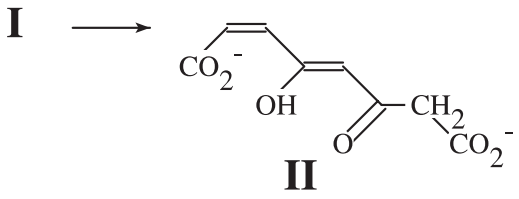

II

The mechanism of enzyme-catalyzed *cis-trans* isomerization of maleylacetoacetate has been the subject of continual research in our laboratory (5). Maleylacetoacetate, up to now, has been synthesized only through enzymatic oxidation of homogentisate, and it is formed in impure state. Early on we prepared maleylacetone (**III**), an analogue of **II**, with parallel functionality. The analogue can be prepared in pure state, and the enzyme, maleylacetoacetate *cis-trans* isomerase, readily catalyzes its *cis-trans* isomerization.

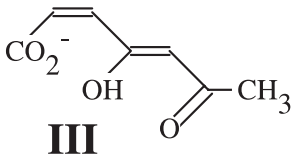

III

The enzymatic reaction requires a coenzyme, glutathione, a tripeptide of γ-glutamic–cysteine–glycine. It has been shown that the free sulfhydryl of cysteine is the catalytic site of the coenzyme in this reaction. Both the substrate and the coenzyme bind to the enzyme, and it is there where nucleophilic catalyzed isomerization takes place (6). Previous studies support the mechanism represented by eq. [1].

[1]

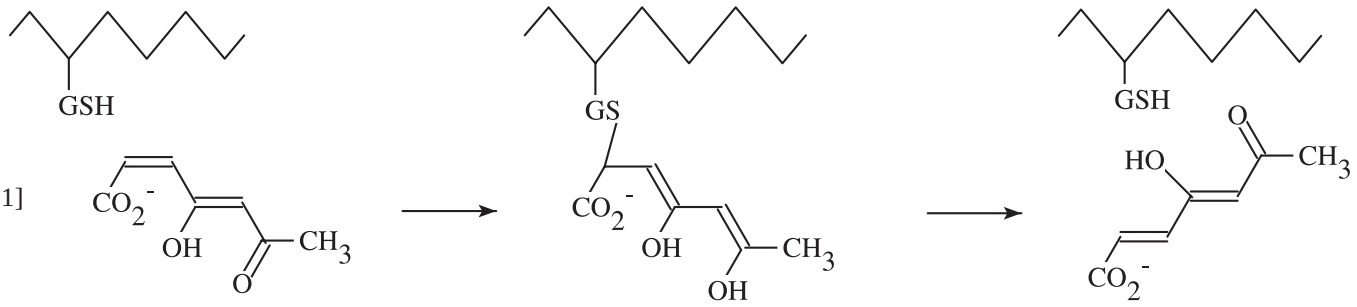

Recent studies with other analogues of maleylacetone, lacking the enolic hydroxyl have uncovered a concerted double *cis-trans* isomerization, presumably by a bicycle-pedal motion, catalyzed by the same enzyme system and proposed to follow the same mechanism (see eq. [2]) (7).

[2]

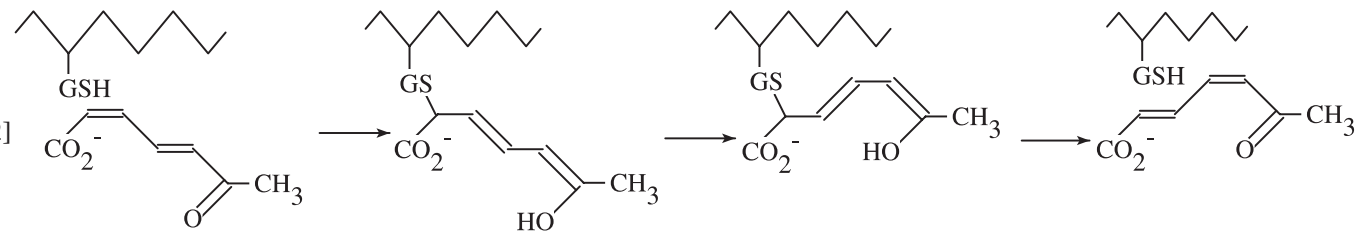

cis,trans ***trans,cis***

© 1999 NRC Canada

In this mechanism the reader should note that conjugate addition at C-2 and C-3 of the substrate is proposed not to take place. Instead, nucleophilic addition at C-2 with double bond migration is proposed, as supported by the lack of proton exchange at C-3 when the reaction is carried out in D_2O (8). This report is concerned with further evidence for nucleophilic addition at C-2 without concerted addition at C-3.

Several years ago the inverse secondary α-deuterium isotope effect in the thiocyanate-catalyzed *cis-trans* isomerization of maleic acid was reported (k_D/k_H = 1.16) (see ref. 9 in which the isotope effect given is for 40° but was measured from 15 to 80°). The isotope effect is consistent with the formation of an intermediate where one of the vinyl carbons becomes tetracoordinate while the other remains tricoordinate, allowing internal rotation about the central C—C bond. (Here, too, vinyl hydrogens do not exchange when the reaction is carried out in D_2O) (9). After rotation, loss of thiocyanate results in the formation of fumaric acid. A related α-deuterium isotope effect study in the enzyme-catalyzed *cis-trans* isomerization of maleylacetone is reported here, and the results are consistent with nucleophilic addition at C-2 of the substrate.

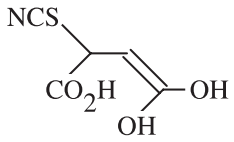

Results

Two deuterium-labeled isomers of maleylacetone (**1** and **2**) were prepared as a mixture. Monodeuterated maleic anhydride was first prepared by electrolytic reduction of monobromomaleic acid in D_2O, as described previously (10). The maleic-d_1 acid-d_2 was converted to its anhydride-d_1 and treated with isopropenyl acetate (11) to form the two deuterium-labeled butenolide isomers (**3** and **4**). Hydrolysis of the purified butenolides, as previously described (11), yielded a mixture of maleylacetone isotopomers. Mass spectral analysis of maleic-d_1 anhydride exhibits the following ion masses with their normalized intensities: 55(100.0), 98(1.18), 99(31.47), and 100(4.60). These data when compared with the data from the NBS library for maleic anhydride: 54(100.0), 98(50.4), and 99(2.4) suggest that there is 8.9% dideuterated maleic anhydride, and the remainder is the mono deuterated compound. Mass spectral analysis of the isotopically labeled butenolides exhibits the following important peaks: 96(44.31), 97(5.97), 123(4.65), 124(100.0), 125(13.88), 138(1.63), 139(21.36), and 140(4.10). The previously reported partial mass spectrum for the nondeuterated butenolide is 69(30), 95(31), 123(100), 138(33) (11). Correction for the ^{13}C and ^{17}O abundances to the 96–97 and the 123–125 mass regions result in an average content of 6.8% of dideuterated butenolide with the remainder represented by the monodeuterated species. We consider the content of the dideuterated maleylacetone to amount to between 6.8 and 8.9%.

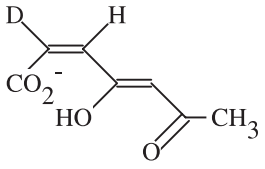

1

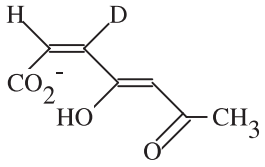

2

Fig 1. The ^1H NMR spectrum of the C-2-C-3 vinyl region of the initial methyl maleylacetone mixture of isotopomers.

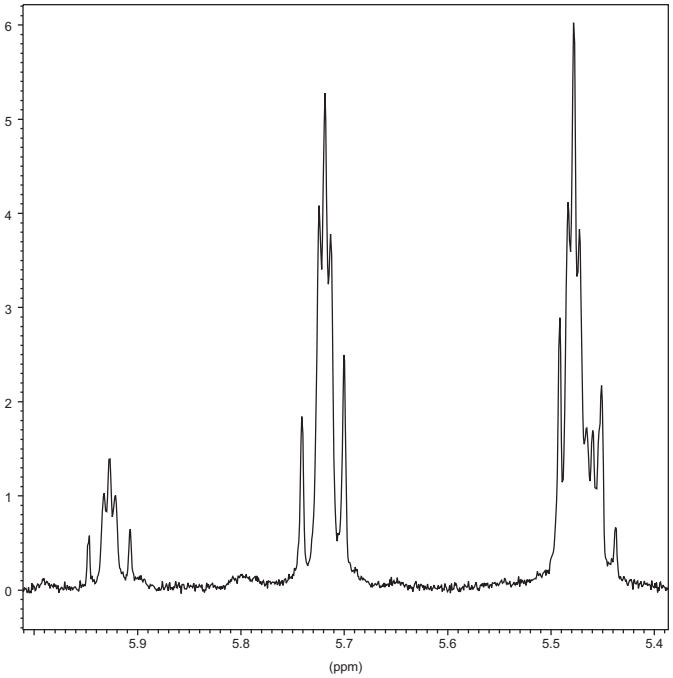

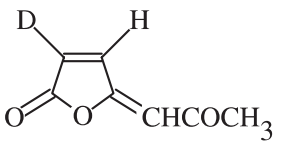

3

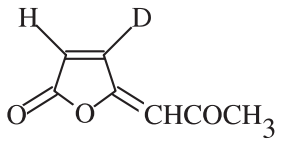

4

Quantitation of the isotope effect to be described below was accomplished by prolonged ^1H NMR signal acquisition. Consequently thermal isomerization of the unreacted labile substrate presented a problem. It was found, however, that conversion of the maleylacetone to its methyl ester with the Meerwein reagent, followed by extraction with chloroform and transfer to benzene-d_6 for ^1H NMR determination, resulted in a stable product with well-separated vinyl resonances.

© 1999 NRC Canada

Fig 2. NOE-difference spectrum for methyl maleylacetone of natural isotopic abundance. The FID, obtained from off-resonance irradiation, was subtracted from the FID, obtained from irradiation of H-5 at δ 5.03 with a decoupler power of 50 L. The FID difference was then Fourier transformed and phased.

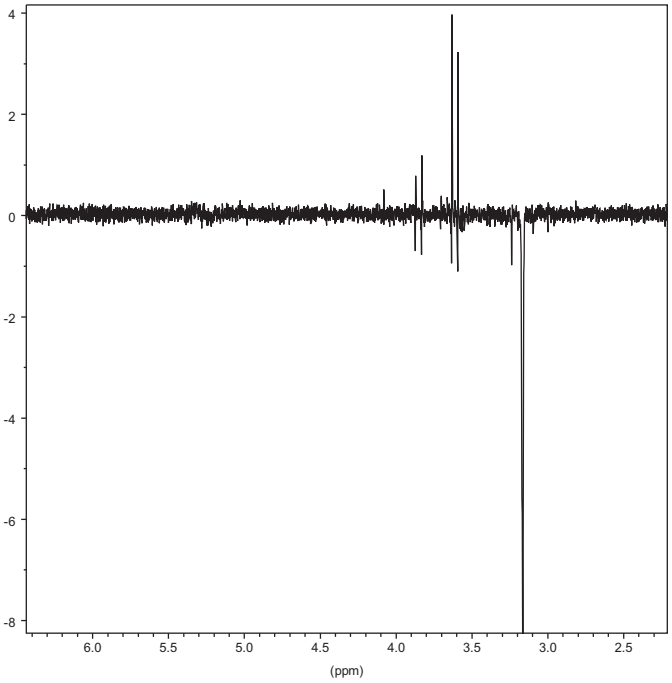

The C-2-C-3 vinyl region of the corresponding methyl ester of maleylacetone is shown in Fig 1. Any dideuterated species would, of course, be silent in this region. The major resonances at δ 5.72 and 5.48 each have a triplet in the approximate center of a doublet. The doublets each have a J = 12.2 Hz, representing an AB-quartet for nondeuterated maleylacetone methyl ester. The presence of the precursors of these isotopomers, viz., maleic anhydride-d_0 or the butenolide-d_0, was not obvious by mass spectrometry. The large triplets are expected for vinyl-H spin coupled to vinyl-D at the adjacent carbon. Each triplet represents one of the two following compounds.

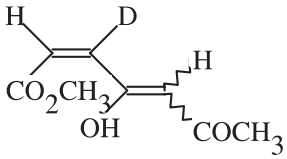

5

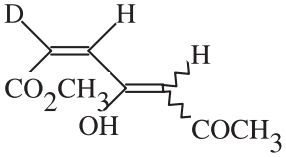

6

NOE-difference experiments were performed on the nondeuterated methyl ester. Irradiation of the methyl groups of the ester and of the acetyl groups produced no demonstrable changes in the intensity of the C-2-C-3 vinyl hydrogens. However, irradiation of H5 at δ 5.03 produced a small positive intensity difference in the downfield vinyl-H and a larger positive difference in the upfield vinyl-H (see Fig 2). Thus H-2 is the downfield vinyl-H, and H-3 is the upfield

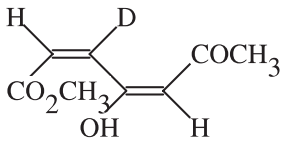

7 cis,cis-3-d$_1$

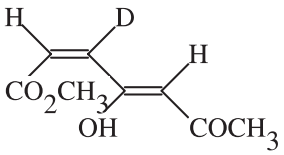

8 cis,trans-3-d$_1$

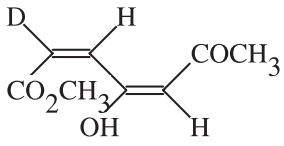

9 cis,cis-2-d$_1$

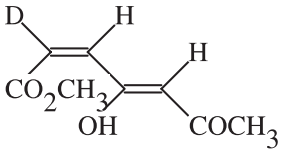

10 cis,trans-2-d$_1$

vinyl-H. Consequently, the area of the downfield vinyl triplet measures the amount of **5** present, while the area of the upfield vinyl triplet measures the amount of **6** present.

There are two smaller triplets centered in doublets at about δ 5.93 and 5.46. The low field doublet also has a J = 12.2 Hz; the low field peak of the minor high field doublet is under the major resonance and so its coupling constant was not determined. There are therefore four monodeuterated *cis*-2 isomers present which can be represented as **7**–**10**. As pointed out above the AB-quartets represent nondeuterated methyl ester isomers of maleylacetone: one being *cis,trans*, the other *cis,cis*. The major isomer has its C-5-vinyl proton at δ 5.03, while the corresponding C-5-vinyl proton of the minor isomer is at δ 6.12. Based on this the major isomer is tentatively assigned to the *cis,trans* structure. H-5 in the *cis,trans* structure is closer to the C-2—C-3 double bond and should feel its diamagnetic effect more strongly than H5 in the *cis,cis* structure. The diamagnetic effect of the ester carbonyl is at longer distance and consid-

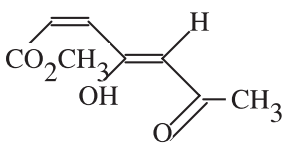

cis,trans

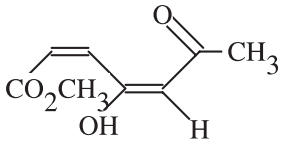

cis,cis

ered here to be smaller. Which is the minor and which is the major isomer, however, is of no consequence to the determination of the isotope effect (vide infra).

The individual resonances were deconvoluted and the areas measured to separate monodeuterated from nondeuterated species. The sum of the nondeuterated species is estimated to amount to about 9%. The areas of the separated minor and major low field triplets were summed and compared to the area of the high field sum of the major and coalesced minor triplet. As seen in Fig 1, half of the high field AB doublet of the minor nondeuterated species is under the coalesced high field triplet. It is assumed that the area of the half of the minor AB doublet under the triplet is equal to the half that is visible at δ 5.44. These peaks are

© 1999 NRC Canada

Table 1. Integrated vinyl NMR peak areas of remaining maleylacetone vs. fraction of remaining substrate.[a]

Run no.	VLF-D[b]	LF-D[c]	HF-D[d]	UF-H[e]	f[f]	R_f[g]
2	0.032	0.612	0.483	0.026	0.233	1.410
3	0.031	0.344	0.293	0.013	0.377	1.339
4	0.098	1.332	1.158	0.055	0.352	1.296
	0.661	2.632	3.468	0.134	1.0	0.988[h]

[a]Numbers given are in arbitrary units generated from integration and deconvolution by the Bruker WINNMR software package. Entries in the table are the averages of three successive integrations. Areas are for the methyl ester of maleylacetone.

[b]Very low field triplet; see text.

[c]Low field triplet; see text.

[d]High field multiplet representing two monodeuterated isomers plus half of an AB-doublet due to a nondeuterated species; see text.

[e]Upfield half of the separated AB-doublet due to a nondeuterated species; see text.

[f]The fraction of maleylacetone remaining.

[g]The ratio of maleylacetone isotopomers obtained from NMR integration after partial enzymatic reaction (VLF-D + LF-D)/(HF-D – UF-D), and designated as R_f.

[h]This is the initial ratio of maleylacetone isotopomers and designated as R_0.

Fig 3. Plot of ln (R_f/R_0) vs. ln $(f(R_0 + 1)/(R_f + 1))$. The least squares slope is equal to –0.133.

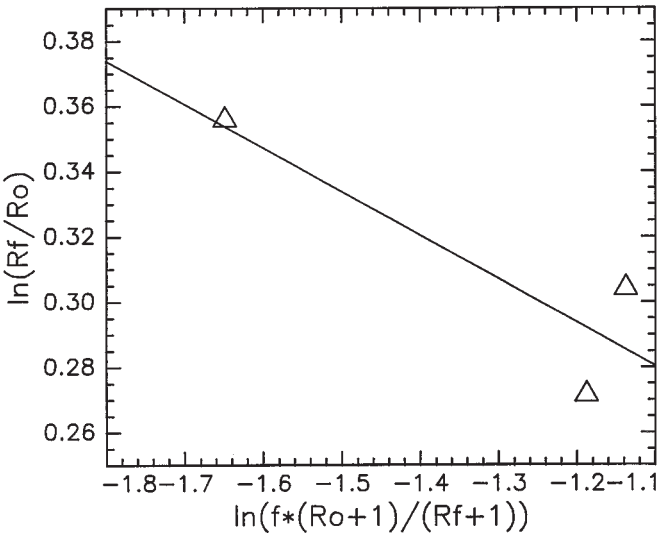

quite small, and any difference between the low and high field halves of this doublet will be quite small. Thus the area of the peak at δ 5.44 was subtracted from the sum of the major and minor coalesced triplets at high field.

Since these studies are highly dependent on the integrated areas of vinyl peaks, obtained from sequential pulsing, it is important to have fully relaxed protons from the previous pulse before a new pulse is applied. The T_1 values of the vinyls of the monodeuterated maleylacetone methyl ester were measured. They are 7.2 and 6.4 s for the protons at δ 5.72 and 5.48, respectively. The nondeuterated methyl ester exhibits T_1 values for the corresponding resonances of 3.9 and 2.2 s, respectively.

A relaxation delay of 60 s between pulses was chosen. Pulsing was generally for about 10 hs and was carried out in blocks of 64. Between each block the NMR was programmed to automatically reshim the Z and Z^2 coils to improve and maintain high resolution. The integrated areas of the peaks due to the vinyl proton of unreacted monodeuterated maleylacetone methyl ester together with the fraction of reaction are shown in Table 1.

The ratios of the vinyl ^{1}H NMR peak areas (see Fig. 1) of methyl ester isotopomers of maleylacetone, obtained from the four terms, viz., (VLH-D + LF-D)/(HF-D – UF-H), and defined as the areas of (*i*) the very low field monodeuterated species, (*ii*) the low field monodeuterated species, (*iii*) the highfield multiplet representing two monodeuterated isomers plus half of a nondeuterated isomer, and (*iv*) half of an AB-doublet representing half of the resonance due to the presence of a nondeuterated maleylacetone methyl ester species, respectively, are given in Table 1. These ratios are, in effect, the ratios of the amounts of **5** to **6**, remaining after enzymatic reaction where the quantity, f, refers to the fraction of initial reactant remaining after reaction and referred to as R_f. The initial ratio (no enzymatic reaction) of **5** to **6** is referred to as R_0 (see Table 1).

The relationship of the isotope effect to R_f, R_0, and f is given in Appendix as [A-10] and is previously derived in slightly different form in ref. 12. A plot of ln (R_f/R_0) vs. ln $(f(R_0 + 1)/(R_f + 1))$ is shown in Fig. 3. The slope, equivalent to $k_1/k_2 - 1$, is –0.133, leading to an inverse isotope effect, $k_D/k_H = 1.15$ at C-2.

Discussion

The *cis-trans* isomerization about a nonactivated carbon–carbon double bond, as in ethylene, requires an activation energy of about 60 kcal/mol (13). The energy can be reduced by formation of an intermediate where the double bond is converted to a single bond, thereby allowing facile rotation. This can be accomplished by addition of a nucleophile, an electrophile, or a radical to one of the sp^2 carbons of the double bond. In the case of nucleophilic addition, the negative charge generated in the intermediate can be delocalized in electron sinks if they are present in the molecule, thereby lowering the activation energy. If there are no groups available to stabilize a charged or a radical center, an alternative mechanism might be for the reactant to undergo conjugate addition at that carbon–carbon double bond to form a single bond to allow rotation after which the conjugate is expelled. To differentiate between the two types of mechanisms, a secondary α-deuterium isotope effect test can be applied.

The secondary α-deuterium isotope effect was first mechanistically rationalized by Streitwieser et al. (14) and later

© 1999 NRC Canada

theoretically justified by Wolfsberg and Stern (15). In simplest terms, a reaction at thermal equilibrium, involving a unimolecular conversion of a tetracoordinate carbon to a trigonal carbon will proceed approximately 15% more slowly when a deuterium atom is substituted for protium at that carbon atom. Many examples of this exist in the solvolysis literature. Conversely, conversion of a trigonal carbon to a tetracoordinate carbon will proceed at a comparable faster rate when a deuterium atom is substituted for protium at that carbon atom.

Maleylacetoacetate *cis-trans* isomerase requires the coenzyme, glutathione (GSH), for activity. The sulfhydryl group is the active site of the coenzyme, as shown by inhibition studies with *S*-methyl glutathione (6). Binding and affinity studies with glutathione analogues show that GSH binds to the enzyme along the backbone of the tripeptide, steering the sulfhydryl group away from the surface of the enzyme so that it is available to react with the maleylacetoacetate or maleylacetone substrate (6). GSH is itself a very good nucleophile (16), and judging from the model reaction of thiocyanate with maleic acid, a most reasonable mechanism would be for enzyme-bound GSH to add to the carbon–carbon double bond of the enzyme substrate. In fact in the absence of the enzyme, a conjugate addition product of GSH to maleylacetone has been identified where the sulfur has added to C-2 and a proton to C-3 (8). The question here is whether addition to only one carbon or concerted addition to both carbons, i.e., sulfur to C-2 and a proton to C-3, takes place in the enzymatic reaction in order to form an intermediate capable of facile internal rotation.

In previous studies it was shown that the enzymatic reaction when carried out in D_2O does not lead to D-exchange at C-3 of fumarylacetone, the product of maleylacetone *cis-trans* isomerization (8). Is it possible for the enzyme to catalyze concerted conjugate addition by putting a proton (deuteron) at C-3 and stereospecifically remove the same proton (deuteron) after rotation, masking this test for conjugate addition? To answer this question a secondary α-deuterium isotope effect at the carbon–carbon double bond undergoing rotation has been measured.

A mixture of equal amounts of isotopomers, **1** and **2**, and their minor isomers (vide supra), of maleylacetone has been synthesized and subjected to enzyme-catalyzed *cis-trans* isomerization. Substrate **1** has a deuterium label at C-2, while **2** has the label at C-3. If nucleophilic addition takes place at C-2 with double bond migration to form the intermediate shown in eq. [1] then one would expect **1** to react faster than **2**. That is to say that after a substantial extent of reaction an excess of **2** over **1** would be found in the remaining unreacted substrate. Only one of the two sp^2 carbons is converted to a tetracoordinate carbon. If, however, concerted conjugate addition takes place, both sp^2 carbons are converted to tetracoordinate carbons, and one would expect approximately equal isotope effects at each carbon, and the amounts of **1** and **2** in the remaining unreacted substrate would be expected to be equal.

The structures **1** and **2** and their minor isomers were converted to surrogates **6** and **5**, respectively, in order to stabilize maleylacetone against isomerization during the long periods necessary for NMR analysis. NOE experiments were performed on the undeuterated methyl ester of maleylacetone. These included irradiation of the OCH_3, and CH_3CO groups, and the vinyl proton at C-5, as well as off-resonance irradiation, under otherwise identical conditions. Figure 2 shows the difference spectrum for irradiation at H-5 minus that for off-resonance where the upfield vinyl doublet is enhanced relative to its partner at lower field. NOE enhancements are inversely proportional to the sixth power of the distance between two nuclei. Using standard bond angles and lengths, the distances between H-3 and H-5 in the *cis,cis* and *cis,trans* isomers are calculated to be 2.50 and 3.76 Å, respectively, while the distances between H-2 and H-5 for these isomers are 4.67 and 5.47 Å, respectively. While we have assigned the *cis,trans* conformation to the major isomer, H-3 is clearly closer to H-5 in either *cis,trans* or *cis,cis* isomers than is H-2 to H-5. Since the larger NOE enhancement is seen at the higher field vinyl doublet (δ 5.48), it is this doublet which represents H-3 and the lower field doublet at δ 5.72 which represents H-2. Thus the large triplet at δ 5.72 was assigned to compound **5** and the large triplet at δ 5.48 assigned to compound **6**. The assignment of which ^1H resonance is due to H-2 and which to H-3 is independent of the assignment of which conformational isomer, *cis,cis* or *cis,trans,* is the major isomer.

As shown in Fig. 1 and Table 1, the minor isotopomers with vinyl resonances at about δ 5.93 and δ 5.46 are low in concentration, relative to the major isomers in both the starting material and in the remaining substrate after extensive enzymatic reaction. While the interconversion of these *cis,cis* and *cis,trans* conformations is slow on the NMR time scale, the similar relative concentrations in starting material and remaining substrate indicates that either the enzyme is equally efficient in isomerizing minor and major conformations, the enzyme catalyzes interconversion of conformations, or that a nonenzymatic equilibration of conformations, slow on the NMR time scale but rapid before observation, occurs.

Secondary deuterium isotope effects, as the name implies, are considered to be small in magnitude, and one would hope that the precision in their measurements would be sufficient to demonstrate the absence or the presence of an isotope effect. In this study we examine the relative rates of isomerization of isotopomers in a competitive experiment by NMR integration. NMR allows one to study the relative rates of reaction of a mixture of isotopomers without prior separation of the individual components even if that were possible. Mass spectrometry, which is usually used in such studies, would likely be of little use in this competitive study unless the individual isotopomers were synthesized and isolated and their rates were measured against the natural compounds in separate experiments. In the past, NMR integration was considered to be a somewhat imprecise method to measure concentrations of solutes but the use of digital analysis instead of analog analysis has improved the precision of measurement. In this study we also resort to deconvolution of minor components of the spectrum. Because these are minor components and because this, too, is now done by digital analysis, the precision of deconvolution has also improved. This study, however, has less of a dependence on precision than most studies of secondary deuterium isotope effects. First, the reaction is taken to large extents of reaction so that an effect of 15% is magnified to

© 1999 NRC Canada

30–40% (see R_f and R_0 in Table 1). There is little doubt that **1** reacts faster than **2**. Second, as pertains to the mechanistic question posed in this study, this is essentially an all-or-none type of study. Either **1** or **2** reacts with equal rates, or one isotopomer reacts faster than the other. The results shown in Table 1 clearly show the latter. As for precision of the effect, which we determine to be $k_D/k_H = 1.15$ from Fig. 1, each R_f and R_0 are the averages of three determinations, each with an average deviation of ±0.7%. Using these apparent deviations and assuming a relative error of ±5% in f, an error analysis (17) of eq. [A-10] leads to a predicted relative error of 5% in $k_1/k_2 - 1$.

In conclusion, there is little doubt that **1** reacts faster than **2** by some 15%, inconsistent with an enzyme-catalyzed concerted conjugate addition but in line with a mechanism that proposes that rate-controlling addition at C-2 with double bond migration towards the acetyl group takes place. The results support the mechansism depicted in eqs. [1] and [2].

Experimental

General information

^{1}H NMR spectra were obtained with a Bruker AM-300 spectrometer. The vinyl region was deconvoluted and integrated using the Bruker WINNMR software package on a 486 PC. During data acquisition a relaxation delay of 60 s was used between 90° pulses. Data acquisition (4.2 s/fid) was generally carried out for about 10 hs for each kinetic isotope effect run. After each group of 64 fids was acquired, the NMR spectrometer, by previous programming, reshimed its Z and Z^2 coils to improve and maintain high resolution.

Enzyme preparation

Maleylacetoacetate *cis-trans* isomerase was obtained from *Vibrio O1* bacteria and purified as described previously (4*b*, 6). Isolation and purification included the following steps: (*i*) sonication of bacteria and centrifugation, (*ii*) protamine sulfate treatment, (*iii*) salt precipitation, (*iv*) hydroxyapatite chromatography, and (*v*) affinity chromatography on a GS-agarose column. The measured specific activity of the enzyme at this point was 13.4 μmol/min mg of protein (corrected for GSH and substrate saturation).

Maleylacetone-2 or -3-d_1 (4-hydroxy-6-oxo-2,4-heptadienoic-2 or-3-d_1 acid)

Maleic-d_1 acid-d_2 was prepared electrolytically from monobromomaleic acid (Aldrich) in D_2O as described previously (10). Maleic-d_1 acid-d_2 was converted to maleic anhydride-d_1 by distillation from P_2O_5 as previously described (see Results for mass spectrum) (10). Reaction of the anhydride with isopropenyl acetate in the presence of aluminum chloride, as previously described (11), yielded 4-acetonylidenebutenolide (Z) (see Results for its mass spectrum), which was hydrolyzed in H_2O (11), as previously described (11), to yield a mixture of maleylacetone isotopomers.

Methyl ester of maleylacetone-d_1 (methyl 4-hydroxy-6-oxo-2,4-heptadienoate-2 or -3-d_1)

Trimethyloxonium fluoroborate, obtained from Aldrich, was used to convert maleylacetone-d_1 in aqueous solution to its methyl ester with modification of the procedure previously published (5*a*). The enzyme reaction mixture was frozen in a dry ice – acetone bath and the solid lyophilized. The solid residue was taken up in 1 mL of water and transferred to a 10 mL beaker to which was added 170 mg of sodium bicarbonate and 550 mg of trimethyloxonium fluoroborate. Reaction was allowed to proceed for about 30 min while it was cooled in ice water. The ester was extracted into chloroform (4 × 0.5 mL) and the layers separated. The combined chloroform layers were dried over a few crystals of sodium sulfate, decanted, and evaporated. The residue was dissolved in benzene-d_6 for ^{1}H NMR analysis (see Fig. 1 for ^{1}H NMR of its C-2/C-3 vinyl region).

Kinetic isotope effect experiments

A computer program was written which used previously published rate constants (6, 8) for enzymatic and nonenzymatic reactions to calculate, by numerical integration, the instantaneous concentrations of substrate, GSH, and product to help predict the extent of reaction for given initial concentrations of reactants at various reaction times. GSH is not consumed in the enzymatic reaction, however, it is consumed in a nonenzymatic conjugate addition reaction with the isomerization product, which is 50 times faster than GSH conjugate addition with the starting material. As the GSH concentration is depleted through these nonenzymatic reactions, the enzymatic reaction is retarded, since the enzyme requires GSH for its action. The computer calculation proved to be a good predictor of the extent of reaction for a given specified time and specified initial concentration of reactants. Kinetic isotope effect experiments were carried out at ambient temperature.

Acknowledgments

This research was carried out under contract DE-AC02-76CH00016 with the U.S. Department of Energy and supported by its Division of Chemical Sciences, Office of Basic Energy Science. The authors thank Charles Hoogstraten for the preparation of maleic-d_1 acid-d_2 and Ms. Elinor Norton for mass spectral analysis.

References

1. (*a*) K.P. Hofmann. Photobiochem. Photobiophys. **13**, 309 (1986); (*b*) L. Stryer. Ann. Rev. Neurosci. **9**, 87 (1986).
2. (*a*) R.R. Rando. Angew. Chem. Int. Ed. Engl. **29**, 461 (1990); (*b*) R.R. Deigner, W.C. Law, F.J. Canada, and R.R. Rando. Science (Washington, D.C.) **244**, 968 (1989).
3. (*a*) J.K. Lanyi. Biochim. Biophys. Acta, **1183**, 241 (1993); (*b*) T.G. Ebrey. *In* Thermodynamics of membranes, receptors, and channels. *Edited by* M. Jackson. CRC Press, Boca Raton, Fla. 1993. pp. 353–387; (*c*) R.A. Mathies, S.W. Lin, J.B. Ames, and W.T. Pollard. Ann. Rev. Biophys. Biophys. Chem. **20**, 491 (1991).
4. (*a*) W.E. Knox. The Enzymes (Part A), **2**, 253 (1960); (*b*) S. Seltzer. J. Biol. Chem. **248**, 215 (1973); (*c*) The Enzymes, **6**, 381 (1972).
5. (*a*) R.A. Johnson and S. Seltzer. J. Am. Chem. Soc. **95**, 5700 (1973); (*b*) S. Seltzer. J. Labelled Compds. **9**, 643 (1974); (*c*) M. Lin and S. Seltzer. FEBS Lett. **124**, 169 (1981); (*d*) G. Wong and S. Seltzer. Brookhaven National Laboratory informal report no. 18123; (*e*) G. Struve and S. Seltzer. J. Org.

© 1999 NRC Canada

Chem. **47**, 2109 (1982); (*f*) H.E. Lee and S. Seltzer. Biochem. Intern. **18**, 91 (1989); (*g*) S. Seltzer and J. Hane. **16**, 394 (1988); (*h*) S. Seltzer. *In* Glutathione: chemical, biochemical, and medical aspects. Part A. *Edited by* D. Dolphin, R. Poulson, and O. Avramovic. John Wiley and Sons, New York. 1989. Chap. 17; (*i*) L. Angaw-Duguma, J. Maracek, and S. Seltzer. Bioorgan. Chem. **20**, 213 (1992).
6. W.S. Morrison, G. Wong, and S. Seltzer. Biochemistry, **15**, 4228 (1976).
7. (*a*) A.L. Feliu, K.J. Smith, and S. Seltzer. J. Am. Chem. Soc. **106**, 3046 (1984); (*b*) A.L. Feliu and S. Seltzer. J. Org. Chem. **50**, 447 (1985).
8. S. Seltzer and M. Lin. J. Am. Chem. Soc. **101**, 3091 (1979).
9. (*a*) S. Seltzer. Chem. Ind. (London), 1313 (1959); (*b*) J. Am. Chem. Soc. **83**, 1861 (1961).
10. S. Seltzer. J. Am. Chem. Soc. **87**, 1534 (1965).
11. J. Fowler and S. Seltzer. J. Org. Chem. **35**, 3529 (1970).
12. J. Bigeleisen and M. Wolfsberg. Adv. Chem. Phys. **1**, 15 (1958).
13. M.J.S. Dewar and W.J. Thiel. J. Am. Chem. Soc. **99**, 4907 (1977).
14. A. Streitwieser, R.H. Jagow, R.C. Fahey, and S. Suzuki. J. Am. Chem. Soc. **80**, 2326 (1958).
15. M. Wolfsberg and M.J. Stern. Pure Appl. Chem. **8**, 325 (1964); M.J. Stern and M. Wolfsberg. J. Chem. Phys. **45**, 4105 (1966).
16. P.C. Jocelyn. Biochemistry of the sulfhydryl group. Academic Press, New York. 1972. pp. 55, 63–70.
17. A.G. Worthing and J. Geffner. Treatment of experimental data. John Wiley and Sons, New York. 1946. Chap. 9.

Appendix

In a competitive reaction of two isotopic molecular species, A_1 and A_2, with nonisotopic reactants, B, C, etc., occurring with rate constants, k_1 and k_2, respectively, and which is unimolecular in A, the ratio of rate constants is given by[3]

[A-1] $k_1/k_2 = [\ln (a_1/a_1^0)]/[\ln (a_2/a_2^0)]$

where a_1 and a_2 are the amounts of remaining A_1 and A_2 reactants after a substantial amount of reaction, and a_1^0 and a_2^0 are the initial amounts of these reactants. The ratio, a_1/a_2, will differ more substantially from a_1^0/a_2^0 at high extents of reaction. The ratio, a_1^0/a_2^0 (= R_0), refers to the initial ratio of concentrations of malelyacetone-3-d_1 to maleylacetone-2-d_1 methyl esters. The ratio, a_1/a_2 (= R_f), refers to the corresponding ratio of unreacted species when the reaction is halted at fraction of substrate remaining, f, and defined as

[A-2] $f = (a_1 + a_2)/(a_1^0 + a_2^0)$

The fraction of substrate remaining is measured spectrophotometrically and consequently includes all maleylacetone species. This includes nondeuterated, monodeuterated, and dideuterated. Nondeuterated and dideuterated species are present in small concentrations. While eq. [A-2] is not exact, it is close to being exact in this system. From eq. [A-1] we get

$$[\text{A-3}] \quad \frac{a_1}{a_1^0} = \left(\frac{a_2}{a_2^0}\right)^{(k_1/k_2)}$$

and dividing by a_2/a_2^0, we get

$$[\text{A-4}] \quad \frac{\frac{a_1}{a_1^0}}{\frac{a_2}{a_2^0}} = \left(\frac{a_2}{a_2^0}\right)^{(k_1/k_2)-1}$$

But

$$[\text{A-5}] \quad \frac{R_f}{R_0} = \frac{\frac{a_1}{a_1^0}}{\frac{a_2}{a_2^0}}$$

Therefore,

$$[\text{A-6}] \quad \frac{R_f}{R_0} = \left(\frac{a_2}{a_2^0}\right)^{(k_1/k_2)-1}$$

Since

$$[\text{A-7}] \quad f = \frac{a_1 + a_2}{a_1^0 + a_2^0} = \frac{a_2 R_f + a_2}{a_2^0 R_0 + a_2^0} = \frac{a_2}{a_2^0} \times \frac{R_f + 1}{R_0 + 1}$$

and

$$[\text{A-8}] \quad \frac{a_2}{a_2^0} = f \times \frac{(R_0 + 1)}{(R_f + 1)}$$

Thus from eq. [A-6]

$$[\text{A-9}] \quad \frac{R_f}{R_0} = \left[\frac{f(R_0 + 1)}{(R_f + 1)}\right]^{(k_1/k_2)-1}$$

Therefore,

$$[\text{A-10}] \quad \frac{k_1}{k_2} - 1 = \frac{\ln\left(\frac{R_f}{R_0}\right)}{\ln f\frac{(R_0 + 1)}{(R_f + 1)}}$$

[3] L. Melander. Isotope effects on reaction rates. Ronald Press, New York. 1969. p. 48.

© 1999 NRC Canada

The problem of distinguishability of rate constants in the two-step consecutive sequence A → B → C

John Andraos

Abstract: A detailed analysis of the absorbance versus time functional forms of the chemical species in the consecutive two-step unimolecular reaction scheme is presented. Distinguishability of rate constants is discussed with respect to the characterization of growth–decay and decay–growth curves and the rate constant – reaction step ambiguity. A new method based on the functional form of the absorption extremum involving the intermediate B with catalyst concentration is proposed to overcome the problem of rate constant assignments.

Key words: reaction mechanism, kinetics analysis, physical organic chemistry.

Résumé : On présente une analyse détaillée de l'absorption en fonction du temps des formes fonctionnelles des espèces chimiques dans deux étapes consécutives d'une réaction unimoléculaire. On discute de la différentiation des constantes de vitesse par rapport à la caractérisation des courbes de croissance–décroissance et décroissance–croissance et de la difficulté d'identifier l'étape déterminante de la constante de vitesse de la réaction. On propose une nouvelle méthode basée sur la forme fonctionnelle de l'extremum d'absorption impliquant l'intermédiaire B avec une concentration du catalyseur pour surmonter le problème d'attribution des constantes de vitesse.

Mots clés : mécanisme réactionnel, analyse cinétique, chimie organique physique.

[Traduit par la Rédaction]

Introduction

The determination of rate laws and reaction mechanisms is of fundamental importance in chemistry. Indeed, the discipline of physical organic chemistry was born with these concepts at its centre and continues to be rich in this tradition in current pure and applied organic chemistry research. Most notably, the area of kinetic and spectroscopic characterization of reaction intermediates has benefitted greatly from reaction mechanism analysis. There exist cornerstone references on the subject of solution-phase chemical kinetics which describe in detail various kinetic systems and the time-dependent behaviour of their component chemical species (1–6).

One such reaction scheme is the two-step consecutive unimolecular transformation given in eq. [1] with associated rate constants k_1 and k_2. Note that the subscript labels for the rate constants, 1 and 2, refer to step 1 and step 2, respectively, in the sequence.

$$[1] \qquad A \xrightarrow{k_1} B \xrightarrow{k_2} C$$

This particular kinetic system is well known with several examples cited in the literature (1–14). The time-dependent absorbance functions of each of the chemical species, A, B, and C are given in eqs. [2*a*]–[2*c*] with initial conditions $A_A(0) = A_A^0$, $A_B(0) = 0$, and $A_C(0) = 0$ at time zero (1–6).

$$[2a] \qquad A_A = A_A^0 \exp[-k_1 t]$$

$$[2b] \qquad A_B = A_A^0 \left(\frac{\varepsilon_B}{\varepsilon_A}\right)\left(\frac{k_1}{k_1 - k_2}\right)\{\exp[-k_2 t] - \exp[-k_1 t]\}$$

$$[2c] \qquad A_C = A_A^0 \left(\frac{\varepsilon_C}{\varepsilon_A}\right)\left\{1 - \frac{1}{k_1 - k_2}(k_1 \exp[-k_2 t] - k_2 \exp[-k_1 t])\right\}$$

where A_A^0 represents the initial absorbance of A at time zero, and ε_A, ε_B, and ε_C represent the absorption coefficients of A, B, and C, respectively.

This paper presents a new detailed analysis of this kinetic system encompassing that found in the traditional works cited above. More importantly, the less well-documented experimental problem of assigning calculated rate constants, k_1 and k_2, obtained from nonlinear regression analysis to the appropriate steps in the reaction sequence is addressed. This problem has been documented by a few authors, and essentially two methods have been described which deal with the ambiguity of rate constant assignments (7–15). These methods rely either on inclusion of additional chemical knowledge or on analysis of the variation of absorption coefficients to remove the ambiguity. A method based only on the behaviour of the extremum absorption of the intermediate B is presented here. This method is universal and is particularly advantageous for cases where required additional

Received October 5, 1998.

This paper is dedicated to Jerry Kresge in recognition of his many achievements in chemistry.

J. Andraos.[1] Department of Chemistry, University of Toronto, Toronto, ON M5S 3H6, Canada.

[1]Telephone: 416–978–4344. Fax: 416–978–7259.

© 1999 NRC Canada

Fig. 1. Absorbance–time functions for species A, B, and C fitted according to eqs. [2*a*]–[2*c*]: (*a*) $k_1 = 10^5$ s^{-1}, $k_2 = 10^4$ s^{-1}, $A_A^0 = 1$, $\varepsilon_B/\varepsilon_A = 1$, $\varepsilon_C/\varepsilon_A = 1$; (*b*) $k_1 = 10^4$ s^{-1}, $k_2 = 10^5$ s^{-1}, $A_A^0 = 1$, $\varepsilon_B/\varepsilon_A = 1$, $\varepsilon_C/\varepsilon_A = 1$; and (*c*) fitted according to eqs. [5*a*]–[5*c*]: $k_1 = 10^4$ s^{-1}, $k_2 = 10^4$ s^{-1}, $A_A^0 = 1$, $\varepsilon_B/\varepsilon_A = 1$, $\varepsilon_C/\varepsilon_A = 1$.

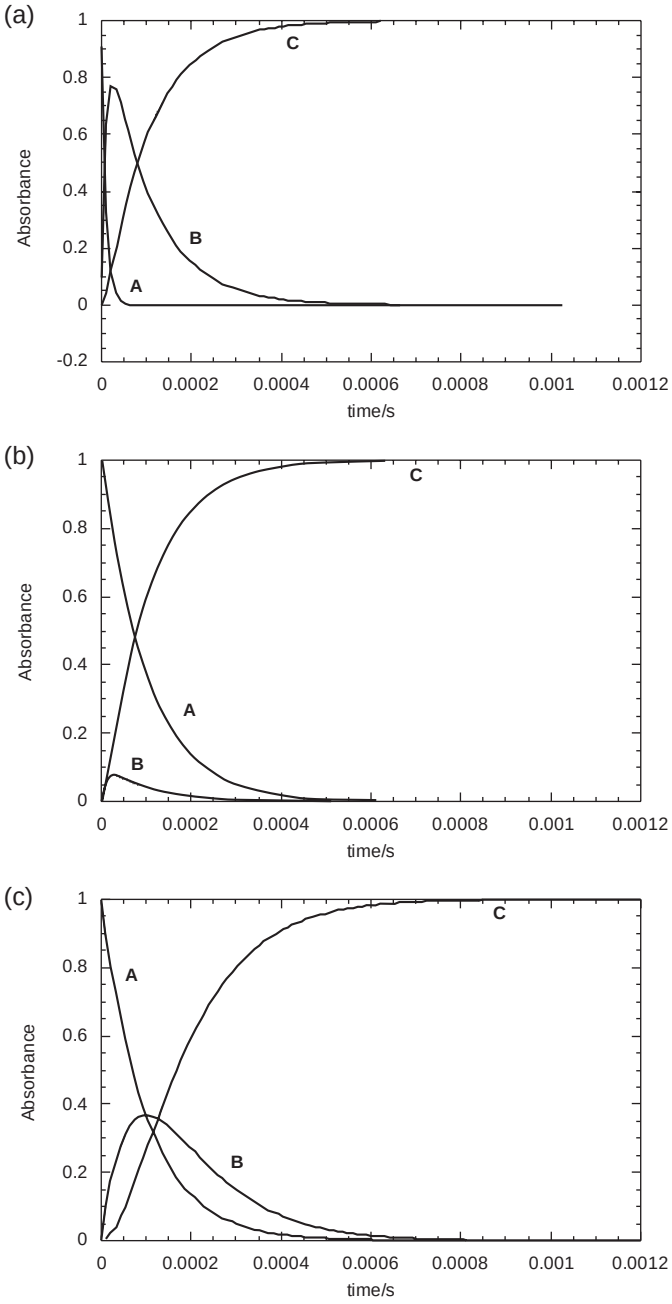

experimental information to overcome the problem may be difficult to obtain.

Explanations given in the literature of the apparent mathematical ambiguity in this kinetic scheme vary depending on the author and are either incomplete or somewhat cloaked in confusing language. In addition to presenting a new method, it is intended to also provide a unified analysis of the problem which ties all ideas together in a concise and clear fashion without sacrificing rigour.

Properties of the two-step consecutive sequence

We begin by reviewing the properties of the absorbance–time functions pertaining to eq. [1]. It is instructive to examine the following three cases: (*i*) $k_1 > k_2$, (*ii*) $k_2 > k_1$, and (*iii*) $k_1 = k_2 = k$. For case (*i*), eqs. [2*a*]–[2*c*] apply as written. For case (*ii*), eqs. [3*a*]–[3*c*] given below apply.

$$[3a] \quad A_A = A_A^0 \exp[-k_1 t]$$

$$[3b] \quad A_B = A_A^0\left(\frac{\varepsilon_B}{\varepsilon_A}\right)\left(\frac{k_1}{k_2 - k_1}\right)\{\exp[-k_1 t] - \exp[-k_2 t]\}$$

$$[3c] \quad A_C = A_A^0\left(\frac{\varepsilon_C}{\varepsilon_A}\right)\left\{1 - \frac{1}{k_2 - k_1}(k_2 \exp[-k_1 t] - k_1 \exp[-k_2 t])\right\}$$

It should be noted that the sets of eqs. [2*a*]–[2*c*] and [3*a*]–[3*c*] are identical. Multiplication of the numerator and denominator by –1 in the terms $k_1/(k_1 - k_2)$ and $1/(k_1 - k_2)$ in eqs. [2*b*] and [2*c*], respectively, leads immediately to eqs. [3*b*] and [3*c*]. For case (*iii*), setting $k_1 = k_2 = k$ in eqs. [2*a*]–[2*c*] results in indeterminate forms for A_B and A_C. A mathematical manipulation employed to overcome this problem is to express one rate constant as a multiple of the other and then to find the limiting expressions as this factor approaches unity. Hence, setting $k_2 = nk_1$ where $0 < n < \infty$ leads to the set of eqs. [4*a*]–[4*c*].

$$[4a] \quad A_A = A_A^0 \exp[-k_1 t]$$

$$[4b] \quad A_B = A_A^0\left(\frac{\varepsilon_B}{\varepsilon_A}\right)\left(\frac{1}{n-1}\right)\{\exp[-k_1 t] - \exp[-nk_1 t]\}$$

$$[4c] \quad A_C = A_A^0\left(\frac{\varepsilon_C}{\varepsilon_A}\right)\left\{1 - \frac{1}{n-1}(n \exp[-k_1 t] - \exp[-nk_1 t])\right\}$$

Taking the limit of eqs. [4*a*]–[4*c*] as $n \rightarrow 1$ and using l'Hôpital's rule (16) results in eqs. [5*a*]–[5*c*].

$$[5a] \quad A_A = A_A^0 \exp[-kt]$$

$$[5b] \quad A_B = A_A^0\left(\frac{\varepsilon_B}{\varepsilon_A}\right)kt \exp[-kt]$$

$$[5c] \quad A_C = A_A^0\left(\frac{\varepsilon_C}{\varepsilon_A}\right)\{1 - (1 + kt)\exp[-kt]\}$$

As is readily apparent, the set of eqs. [4*a*]–[4*c*] conveniently describes all three cases: case (*i*) occurs when $0 < n < 1$, case (*ii*) occurs when $1 < n < \infty$, and case (*iii*) occurs when $n = 1$. This manipulation of representing one rate constant as a multiple of the other is very useful and will become important in later analyses.

A detailed analysis of the forms of the functions describing the time-dependent absorbances of species A, B, and C reveals a number of important characteristics. Figs. 1*a–c* illustrate graphically the three absorbance–time functions for each of the cases given above. The absorbance–time func-

© 1999 NRC Canada

Table 1. Possible chemical species observed at a given monitoring wavelength.

Number of chemical species observed at given monitoring wavelength	Number of possible experimental outcomes	Possible chemical species observed at monitoring wavelength
1	3	A or B or C
2	3	A and B, or A and C, or B and C
3	1	A, B, and C

tion for species A is simply a first-order decay with an initial absorbance equal to A_A^0 and a limiting final absorbance ($t \to \infty$) equal to zero. The absorbance–time function for species B is characterized as concave down with a single maximum. The initial and limiting final absorbances are both equal to zero. The maximum point in the absorbance–time function for B has a value given by

$$[6a] \qquad A_B^{max} = A_A^0\left(\frac{\varepsilon_B}{\varepsilon_A}\right)\left(\frac{1}{n-1}\right)[n^{-1/(n-1)} - n^{-n/(n-1)}]$$

occurring at

$$[6b] \qquad t_m = \frac{1}{k_1}\left(\frac{\ln n}{n-1}\right)$$

where $k_2 = nk_1$, $0 < n < \infty$. Note that the co-ordinates of the maximum for each of the cases given above are

$$t_m = \frac{1}{k_1 - k_2}\ln\left(\frac{k_1}{k_2}\right)$$

and

$$A_B^{max} = A_A^0\left(\frac{\varepsilon_B}{\varepsilon_A}\right)\left(\frac{k_1}{k_1 - k_2}\right)\left[\left(\frac{k_1}{k_2}\right)^{-k_2/(k_1-k_2)} - \left(\frac{k_1}{k_2}\right)^{-k_1/(k_1-k_2)}\right]$$

when $k_1 > k_2$ ($0 < n < 1$) or $k_1 < k_2$ ($1 < n < \infty$), and $t_m = 1/k$ and $A_B^{max} = A_A^0(\varepsilon_B/\varepsilon_A)\exp(-1)$ when $k_1 = k_2$ ($n = 1$). It may be verified that the function in n in eq. [6*a*] approaches a limiting value of exp (–1) = 0.3679 as n approaches 1 (see Appendix A). Finally, the absorbance–time function for species C is a sigmoidal growth and is characterized as having an inflection point dividing the curve into a concave up portion before the inflection point and a concave down portion after it. The value of t corresponding to the inflection point is commonly referred to as the induction period. From eq. [4*c*] this inflection point occurs exactly at the value of t corresponding to the maximum of the absorbance–time function of B (see eq. [6*b*]), and has a corresponding absorbance value given by

$$[7] \qquad A_C^{inf} = A_A^0\left(\frac{\varepsilon_C}{\varepsilon_A}\right)\left\{1 - \frac{1}{n-1}(n^{(n-2)/(n-1)} - n^{-n/(n-1)})\right\}$$

The initial and limiting final absorbances are equal to zero and $A_A^0(\varepsilon_C/\varepsilon_A)$, respectively. The point (0, 0) corresponds to a minimum; whereas, the limiting absorbance of $A_A^0(\varepsilon_C/\varepsilon_A)$ corresponds to a maximum. Note also that the absorbance curve for C is invariant to the transposition of values for k_1 and k_2 (see Fig. 1).

Possible experimental outcomes

If a chemical system is described by the reaction mechanism of eq. [1], then there are several experimental possibilities for observing the chemical species depending on the number of species observed at any one time according to a particular property. For example, in the case of a kinetics experiment conducted using UV-vis spectrophotometry, if each chemical species has a characteristic monitoring wavelength unique to that species, then it is possible to observe the absorbance–time evolution of each component separately. In practice such an ideal situation is rarely encountered, and hence usually several combinations of species may be observed at once. Table 1 summarizes the various possible experimental situations, and Tables 2–4 list the possible absorbance–time functions for observing one, two, and three chemical species at a given monitoring wavelength, respectively. Note that the entries in Table 2 correspond to the equations and properties given in the previous section.

At this point it is important to examine the general case of observing three chemical species (A, B, and C) with respect to isobestic points. There are three cases of isobestic points to consider: (*i*) $\varepsilon_A = \varepsilon_B$, (*ii*) $\varepsilon_A = \varepsilon_C$, and (*iii*) $\varepsilon_B = \varepsilon_C$. The expression in Table 4 is simplified under these conditions and the possible functional outcomes are greatly reduced as is shown by the entries in Table 5.

Properties of growth–decay and decay–growth curves

Suppose that a kinetics experiment is performed in which the appearance and disappearance of B is monitored directly as a function of time. Typically, the array of data points (t_i, $A_{B,i}$) is fitted by means of a nonlinear regression algorithm to a model given by

$$[8] \qquad y = a[\exp(-bt) - \exp(-ct)]$$

where a, b, and c are parameters to be determined. Parameters b and c refer to the two rate constants and are thus always positively valued; whereas, parameter a is a pre-exponential factor that can be positively or negatively valued. Note that eq. [8] is the general form of eqs. [2*b*], [3*b*], and [4*b*]. It is worth examining in detail the functional behaviour of eq. [8] which will reveal information about the location of extrema (maxima, minima, and inflection points) and the directions of concavity of the curve between extrema.

Let us consider all parameters to be positively valued. We begin by taking first and second derivatives of y with respect to t

$$[9a] \qquad \frac{dy}{dt} = a[-b\exp(-bt) + c\exp(-ct)]$$

© 1999 NRC Canada

Table 2. Absorbance–time functions for observing one chemical species in eq. [1].

Case	Absorbance–time function and boundary conditions	Function type
A	$A_A(t) = A_A^0 e^{-k_1 t}$ $A_A(0) = A_A^0$ $A_A(\infty) = 0$	Decay
B	$A_B(t) = A_A^0\left(\frac{\varepsilon_B}{\varepsilon_A}\right)\left(\frac{k_1}{k_1 - k_2}\right)e^{-k_2 t} - A_A^0\left(\frac{\varepsilon_B}{\varepsilon_A}\right)\left(\frac{k_1}{k_1 - k_2}\right)e^{-k_1 t}$ $A_B(0) = 0$ $A_B(\infty) = 0$	Growth–decay if $k_1 > k_2$ or $k_2 > k_1$
C	$A_C(t) = A_A^0\left(\frac{\varepsilon_C}{\varepsilon_A}\right) - A_A^0\left(\frac{\varepsilon_C}{\varepsilon_A}\right)\left(\frac{k_1}{k_1 - k_2}\right)e^{-k_2 t} + A_A^0\left(\frac{\varepsilon_C}{\varepsilon_A}\right)\left(\frac{k_2}{k_1 - k_2}\right)e^{-k_1 t}$ $A_C(0) = 0$ $A_C(\infty) = A_A^0\left(\frac{\varepsilon_C}{\varepsilon_A}\right)$	Sigmoidal growth if $k_1 > k_2$ or $k_2 > k_1$

[9*b*] $$\frac{d^2y}{dt^2} = a[b^2 \exp(-bt) - c^2 \exp(-ct)]$$

and find that an extremum occurs at

[10] $$t = \frac{1}{c-b}\ln\left(\frac{c}{b}\right)$$

when $dy/dt = 0$. The value of y at this extremum is

$$y_m = a\left[\left(\frac{c}{b}\right)^{-b/(c-b)} - \left(\frac{c}{b}\right)^{-c/(c-b)}\right]$$

The identity of the extremum and the direction of concavity at this point are then found by substituting eq. [10] into the expression for the second derivative (eq. [9*b*]) and determining the sign of the value (16). Hence, eq. [8] exhibits a *minimum* (concave up) when $b > c$ and a *maximum* (concave down) when $c > b$. Figs. 2*a* and 2*b* illustrate the two possible curves: a positively valued growth–decay curve when $c > b$, and a negatively valued decay–growth curve when $b > c$. Note that if the pre-exponential factor a is negatively valued, the above analysis results only in the transposition of b and c in all equations; however, the conclusions of Theorems 1–3 (vide infra) remain unchanged. Table 6 summarizes the important conclusions of the above functional analysis on eq. [8].

From the above analysis we may then establish a simple inspection method to identify which rate constant corresponds to which part of the curve:

> *Theorem 1.* Given a growth–decay or decay–growth function of the form of eq. [8] with positively valued parameters a, b, and c, the rate constant corresponding to the growth part of the curve is the one associated with a minus sign preceding the exponential factor containing that rate constant.

Furthermore, from Table 6 we can also draw the following conclusions regarding the correspondence between the rate constant for the growth and its relative magnitude.

> *Theorem 2.* For a growth–decay function of the form of eq. [8] with positively valued parameters a, b, and c, the growth part of the curve corresponds to the larger rate constant; whereas, the decay part of the curve corresponds to the smaller rate constant.
>
> *Theorem 3.* For a decay–growth function of the form of eq. [8] with positively valued parameters a, b, and c, the growth part of the curve corresponds to the smaller rate constant; whereas, the decay part of the curve corresponds to the larger rate constant.

A similar analysis of the general expression in eq. [11] applicable to any

[11] $$y = a \exp(-\alpha t) - b \exp(-\beta t) + c$$

of the possible experimental growth–decay and decay–growth curves listed in Tables 3 and 4 reveals the same functional properties as summarized in Table 7.

The problem of distinguishability of rate constants

Consider the growth–decay curves for the intermediate B shown in Figs. 1*b* and 1*c*. Both curves are fitted to the expression given in eq. [2*b*] where the values $k_1 = 10^5$ s^{-1}and $k_2 = 10^4$ s^{-1} are applicable to Fig. 1*b*, and the values $k_1 = 10^4$ s^{-1}and $k_2 = 10^5$ s^{-1} are applicable to Fig. 1*c*. The subscripts 1 and 2 in the rate constant descriptors strictly refer to steps 1 and 2, respectively, in the reaction sequence. Comparison of the forms of these two growth–decay curves indicates that they have identical functional behaviours, *except that their amplitudes differ.* More precisely, the similarities are that the growth part in each curve corresponds to the faster rate, 10^5 s^{-1} (see Theorem 2), the decay part of each curve corresponds to the slower rate, 10^4 s^{-1} (see Theorem 2), and the occurrence of the maximum in each case is at $t = 2.56 \times 10^{-5}$ s (using eq. [6*b*]). The difference is that the amplitude of the maximum absorbance given by eq. [6*a*] is 0.77 for $k_2/k_1 = n = 0.1$ (Fig. 1*b*) and 0.077 for $k_2/k_1 = n = 10$ (Fig. 1*c*). From this example, it is evident that the faster rate constant associated with the growth in each curve corresponds to either the first *or* second steps in the reaction sequence. Likewise, the slower rate constant associated with the decay in each curve corresponds to either the first *or* second steps in the reaction sequence. The conclusion is that one cannot assign the two rate constants to their respective

© 1999 NRC Canada

Table 3. Absorbance–time functions for observing two chemical species in eq. [1].

Case	Absorbance–time function and boundary conditions	Function type
A and B	$A(t) = A_A^0\left(\frac{\varepsilon_B}{\varepsilon_A}\right)\left(\frac{k_1}{k_1 - k_2}\right)e^{-k_2 t}$	Sum of two decays if $\frac{\varepsilon_B}{\varepsilon_A} < \frac{k_1 - k_2}{k_1}$ and $k_1 > k_2$
	$+A_A^0\left[1 - \left(\frac{\varepsilon_B}{\varepsilon_A}\right)\left(\frac{k_1}{k_1 - k_2}\right)\right]e^{-k_1 t}$	Growth–decay if $\frac{\varepsilon_B}{\varepsilon_A} > \frac{k_1 - k_2}{k_1}$ and $k_1 > k_2$
	$A(0) = A_A^0$	N.B.: It is impossible to have a sum of two growths or a decay–growth curve.
	$A(\infty) = 0$	
A and C	$A(t) = A_A^0\left[1 + \left(\frac{\varepsilon_C}{\varepsilon_A}\right)\left(\frac{k_2}{k_1 - k_2}\right)\right]e^{-k_1 t}$	Sum of two decays if $\frac{\varepsilon_C}{\varepsilon_A} < \frac{k_2 - k_1}{k_2}$ and $k_2 > k_1$
	$-A_A^0\left(\frac{\varepsilon_C}{\varepsilon_A}\right)\left(\frac{k_1}{k_1 - k_2}\right)e^{-k_2 t} + A_A^0\left(\frac{\varepsilon_C}{\varepsilon_A}\right)$	Decay–growth if $\frac{\varepsilon_C}{\varepsilon_A} > \frac{k_2 - k_1}{k_2}$ and $k_2 > k_1$
	$A(0) = A_A^0$	N.B.: It is impossible to have a sum of two growths or a growth–decay curve.
	$A(\infty) = A_A^0\left(\frac{\varepsilon_C}{\varepsilon_A}\right)$	
B and C	$A(t) = A_A^0\left(\frac{k_2\varepsilon_C - k_1\varepsilon_B}{\varepsilon_A}\right)\left(\frac{1}{k_1 - k_2}\right)e^{-k_1 t}$	Sum of two growths if $\varepsilon_B > \varepsilon_C$, $k_2 > k_1$, and $\frac{k_2}{k_1} > \frac{\varepsilon_B}{\varepsilon_C}$
	$+ A_A^0\left(\frac{\varepsilon_B - \varepsilon_C}{\varepsilon_A}\right)\left(\frac{k_1}{k_1 - k_2}\right)e^{-k_2 t} + A_A^0\left(\frac{\varepsilon_C}{\varepsilon_A}\right)$	Growth–decay if $\varepsilon_B > \varepsilon_C$, $k_2 > k_1$, and $\frac{k_2}{k_1} < \frac{\varepsilon_B}{\varepsilon_C}$ or if $\varepsilon_B > \varepsilon_C$, $k_1 > k_2$, and $\frac{k_2}{k_1} < \frac{\varepsilon_B}{\varepsilon_C}$
	$A(0) = 0$	Sigmoidal growth if $\varepsilon_B < \varepsilon_C$, $k_1 > k_2$, and $\frac{k_2}{k_1} > \frac{\varepsilon_B}{\varepsilon_C}$ or if $\varepsilon_B < \varepsilon_C$, $k_1 < k_2$, and $\frac{k_2}{k_1} > \frac{\varepsilon_B}{\varepsilon_C}$
	$A(\infty) = A_A^0\left(\frac{\varepsilon_C}{\varepsilon_A}\right)$	N.B.: It is impossible to have a sum of two decays.

steps in the reaction sequence for either of these growth–decay curves when these curves are treated separately by data fits. The assignments can be made only when the results of the two data fits are compared. This apparent ambiguity has been stated by others (6, 14) in terms of two solutions satisfying an equation of the form of eq. [2*b*] and interchanging the values of the rate constants in eq. [2*b*]. It should be made clear that the operation of transposing k_1 and k_2 in eq. [2*b*] is different from and not to be confused with the functional analysis given previously in which the ratio of k_2 to k_1 in eq. [2*b*] is varied. In chemical terms, a given growth–decay kinetic curve may correspond to either of two situations: (*i*) a fast formation of a strongly absorbing intermediate in the first step followed by its slow decomposition in the second step, or (*ii*) a slow formation of a weakly absorbing intermediate in the first step followed by its rapid decomposition in the second step.

It can be shown that the same ambiguity holds true for decay–growth curves, and hence we are lead to the statement given in Theorem 4.

> *Theorem 4.* For growth–decay and decay–growth functions of the forms of eqs. [8] and [11] it is impossible to assign unambiguously the rate constant parameters to the particular steps in the reaction sequence solely on the basis of the results of a single data fit according to these equations.

Determining the rate constant – reaction step correspondence

External chemical information

An obvious method to relieve the ambiguity stated in Theorem 4 is to obtain one of the rate constants in eq. [1], either k_1 or k_2, from a separate experiment. The easier rate constant to obtain is k_1, since this is immediately derived from the single exponential decay of species A. However, as already noted, the methodology of conducting the time-resolved experiment may preclude such a solution. If all species in a given chemical system have overlapping absorptions, then it would be difficult to obtain unique absorbance–time functions for species A and B. This is especially true if species A and B either have similar structures so that they are not distinguishable by different monitoring absorption bands or have weak chromophores altogether. Only a fortuitous situation in which species A and B have unique UV-vis absorption bands will permit this method to work. Detection by infrared absorption spectroscopy, on the other hand, is more powerful in this regard, as it is more likely to distinguish chemical species from unique IR absorption bands than it is from UV-vis ones, particularly in solution-phase experiments.

Yamasaki et al. (7, 8) recently proposed a new integrated profiles method to handle simultaneous analysis of the absorbance–time functions for species A and B given in eq. [1],

© 1999 NRC Canada

Table 4. Absorbance–time functions for observing three chemical species in eq. [1].

Case	Absorbance–time function	Function type
A, B, and C	$A(t) = A_A^0\left[1 + \left(\frac{k_2\varepsilon_C - k_1\varepsilon_B}{\varepsilon_A}\right)\left(\frac{1}{k_1 - k_2}\right)\right]e^{-k_1 t}$ $+A_A^0\left(\frac{\varepsilon_B - \varepsilon_C}{\varepsilon_A}\right)\left(\frac{k_1}{k_1 - k_2}\right)e^{-k_2 t} + A_A^0\left(\frac{\varepsilon_C}{\varepsilon_A}\right)$ $A(0) = A_A^0$ $A(\infty) = A_A^0\left(\frac{\varepsilon_C}{\varepsilon_A}\right)$	Sum of two decays if $\varepsilon_B < \varepsilon_C,\ k_1 < k_2,\ \frac{\varepsilon_A}{\varepsilon_C} > \frac{\frac{k_2}{k_1} - \frac{\varepsilon_B}{\varepsilon_C}}{\frac{k_2}{k_1} - 1}$ Growth–decay if $\varepsilon_B > \varepsilon_C,\ k_1 > k_2$, and $\frac{\varepsilon_A}{\varepsilon_C} < \frac{\frac{k_2}{k_1} - \frac{\varepsilon_B}{\varepsilon_C}}{\frac{k_2}{k_1} - 1}$ or if $\varepsilon_B > \varepsilon_C,\ k_1 < k_2\ \ \frac{\varepsilon_A}{\varepsilon_C} > \frac{\frac{k_2}{k_1} - \frac{\varepsilon_B}{\varepsilon_C}}{\frac{k_2}{k_1} - 1}$ and $\frac{k_2}{k_1} > \frac{\varepsilon_B}{\varepsilon_C}$ Sum of two growths if $\varepsilon_B > \varepsilon_C,\ k_1 < k_2,\ \frac{\varepsilon_A}{\varepsilon_C} < \frac{\frac{k_2}{k_1} - \frac{\varepsilon_B}{\varepsilon_C}}{\frac{k_2}{k_1} - 1}$ and $\frac{k_2}{k_1} > \frac{\varepsilon_B}{\varepsilon_C}$ Decay–growth if $\varepsilon_B < \varepsilon_C,\ k_1 > k_2,\ \frac{\varepsilon_A}{\varepsilon_C} < \frac{\frac{k_2}{k_1} - \frac{\varepsilon_B}{\varepsilon_C}}{\frac{k_2}{k_1} - 1}$ and $\frac{k_2}{k_1} < \frac{\varepsilon_B}{\varepsilon_C}$ or if $\varepsilon_B < \varepsilon_C,\ k_1 > k_2,\ \frac{\varepsilon_A}{\varepsilon_C} > \frac{\frac{k_2}{k_1} - \frac{\varepsilon_B}{\varepsilon_C}}{\frac{k_2}{k_1} - 1}$ and $\frac{k_2}{k_1} < \frac{\varepsilon_B}{\varepsilon_C}$ Sigmoidal growth if $\varepsilon_B < \varepsilon_C,\ k_1 < k_2$, and $\frac{\varepsilon_A}{\varepsilon_C} < \frac{\frac{k_2}{k_1} - \frac{\varepsilon_B}{\varepsilon_C}}{\frac{k_2}{k_1} - 1}$ Sigmoidal decay if $\varepsilon_B > \varepsilon_C,\ k_1 > k_2$, and $\frac{\varepsilon_A}{\varepsilon_C} > \frac{\frac{k_2}{k_1} - \frac{\varepsilon_B}{\varepsilon_C}}{\frac{k_2}{k_1} - 1}$

© 1999 NRC Canada

Table 5. Absorbance–time functions for observing three chemical species in eq. [1] at isobestic points.

Isobestic point	Absorbance–time function	Function type
$\varepsilon_A = \varepsilon_B$	$A(t) = A_A^0\left[1 + \left(\frac{k_2\varepsilon_C - k_1\varepsilon_B}{\varepsilon_B}\right)\left(\frac{1}{k_1 - k_2}\right)\right]e^{-k_1 t}$	Sigmoidal decay if $\varepsilon_B > \varepsilon_C$ and $k_1 > k_2$ or if $\varepsilon_B > \varepsilon_C$ and $k_1 < k_2$
	$+ A_A^0\left(\frac{\varepsilon_B - \varepsilon_C}{\varepsilon_B}\right)\left(\frac{k_1}{k_1 - k_2}\right)e^{-k_2 t} + A_A^0\left(\frac{\varepsilon_C}{\varepsilon_B}\right)$	Sigmoidal growth if $\varepsilon_B < \varepsilon_C$ and $k_1 > k_2$ or if $\varepsilon_B < \varepsilon_C$ and $k_1 < k_2$
	$A(0) = A_A^0$	
	$A(\infty) = A_A^0\left(\frac{\varepsilon_C}{\varepsilon_A}\right)$	
$\varepsilon_A = \varepsilon_C$	$A(t) = A_A^0\left[1 + \left(\frac{k_2\varepsilon_C - k_1\varepsilon_B}{\varepsilon_C}\right)\left(\frac{1}{k_1 - k_2}\right)\right]e^{-k_1 t}$	Growth–decay if $\varepsilon_B > \varepsilon_C$ and $k_1 > k_2$ or if $\varepsilon_B > \varepsilon_C$ and $k_1 < k_2$
	$+ A_A^0\left(\frac{\varepsilon_B - \varepsilon_C}{\varepsilon_C}\right)\left(\frac{k_1}{k_1 - k_2}\right)e^{-k_2 t} + A_A^0$	Decay–growth if $\varepsilon_B < \varepsilon_C$ and $k_1 > k_2$ or if $\varepsilon_B < \varepsilon_C$ and $k_1 < k_2$
	$A(0) = A_A^0$	
	$A(\infty) = A_A^0$	
$\varepsilon_B = \varepsilon_C$	$A(t) = A_A^0\left[1 - \frac{\varepsilon_B}{\varepsilon_A}\right]e^{-k_1 t} + A_A^0\left(\frac{\varepsilon_B}{\varepsilon_A}\right)$	Growth if $\varepsilon_B > \varepsilon_C$ Decay if $\varepsilon_B < \varepsilon_C$
	$A(0) = A_A^0$	
	$A(\infty) = A_A^0\left(\frac{\varepsilon_B}{\varepsilon_A}\right)$	

provided that the condition of unique detection of the species is met. The strength of the method is that it is able to resolve nearly equally valued rate constants even when kinetic data may contain significant instrumentation noise.

Absorption coefficient method

A method based on the magnitude and variation of the absorption coefficient of intermediate B has been reported as a way of deciding which rate constant corresponds to which step in the reaction sequence (14). It is based on comparing the set of pre-exponential factors in an equation of the form of eq. [11] with that obtained when k_1 and k_2 are transposed. Taking the general case of observing all three species simultaneously, we have two forms of the absorbance–time equation given in Table 4. Equation [12] applies when k_1 is assigned to step 1 and k_2 is assigned to step 2.

[12] $A(t) = ae^{-k_1 t} + be^{-k_2 t} + c$

where $a = A_A^0[1 + (k_2\varepsilon_C - k_1\varepsilon_B)/\varepsilon_A(k_1 - k_2)]$, $b = A_A^0 k_1(\varepsilon_B - \varepsilon_C)/\varepsilon_A(k_1 - k_2)$, and $c = A_A^0(\varepsilon_C/\varepsilon_A)$. Equation [13] applies when k_1 is assigned to step 2 and k_2 is assigned to step 1.

[13] $A(t) = a' e^{-k_2 t} + b' e^{-k_1 t} + c'$

where $a' = A_A^0[1 + (k_1\varepsilon_C' - k_2\varepsilon_B')/\varepsilon_A'(k_2 - k_1)]$, $b' = A_A^0 k_2(\varepsilon_B' - \varepsilon_C')/\varepsilon_A'(k_2 - k_1)$, and $c' = A_A^0(\varepsilon_C'/\varepsilon_A')$. Since either of these expressions may describe a given experimental kinetic trace, the value of the absorbance, A(t), is the same in each case. Hence, equating eqs. [12] and [13] results in

[14a] $a = b'$

[14b] $b = a'$

[14c] $c = c'$

From eqs. [14a]–[14c] we have the following equalities relating absorption coefficients:

[15a] $\varepsilon_A' = \varepsilon_A$

[15b] $\varepsilon_B' = \varepsilon_A + \frac{k_1}{k_2}(\varepsilon_B - \varepsilon_A)$

[15c] $\varepsilon_C' = \varepsilon_C$

With prior knowledge of the values of the absorption coefficients of reactant A and product C, two possible values for the absorption coefficient of intermediate B, ε_B and ε_B', may be obtained corresponding to the two sets of rate constant assignments. As noted previously (6, 14), the "correct" value of the absorption coefficient for B may be decided immediately on the basis of structural assignments if a stable analogue of B is known. Otherwise, the assignment will be based on whether or not the absorption coefficient varies with the ratio k_1/k_2 as given by eq. [15b]. This necessarily means examining other kinetic traces of the form of eq. [11] recorded at different values of k_1/k_2. A correct value of the absorption coefficient is one that is independent of k_1/k_2 or k_2/k_1. As written, eq. [15b] implies that ε_B is the correct value, since it is independent of k_1/k_2; whereas ε_B' is the incorrect value, since it is linearly dependent on this ratio. The reverse statement is true if eq. [15b] is solved in terms of ε_B as the dependent variable so that in this case ε_B is linearly

© 1999 NRC Canada

Table 6. Summary of functional analysis on model equation $y = a[\exp(-bt) - \exp(-ct)]$.

Pre-exponential factor	Relative rate constant magnitude	Function type	First part of curve: Assigned rate constant	First part of curve: Function type	Second part of curve: Assigned rate constant	Second part of curve: Function type
$a > 0$	$c > b$	Growth–decay	c	Growth	b	Decay
$a < 0$	$b > c$	Growth–decay	b	Growth	c	Decay
$a > 0$	$b > c$	Decay–growth	b	Decay	c	Growth
$a < 0$	$c > b$	Decay–growth	c	Decay	b	Growth

Table 7. Summary of functional analysis on model equation $y = a \exp(-\alpha t) - b \exp(-\beta t) + c$.

Pre-exponential factor	Relative rate constant magnitude	Function type	First part of curve: Assigned rate function	First part of curve: Function type	Second part of curve: Assigned rate function	Second part of curve: Function type
$a > 0$ and $b > 0$	$\alpha > \beta$	Decay–growth	α	Decay	β	Growth
$a < 0$ and $b < 0$	$\beta > \alpha$	Decay–growth	β	Decay	α	Growth
$a < 0$ and $b > 0$	$\alpha > \beta$	Sum of two growths	α	Growth	β	Growth
$a < 0$ and $b > 0$	$\beta > \alpha$	Sum of two growths	β	Growth	α	Growth
$a > 0$ and $b < 0$	$\alpha > \beta$	Sum of two decays	α	Decay	β	Decay
$a > 0$ and $b < 0$	$\beta > \alpha$	Sum of two decays	β	Decay	α	Decay
$a < 0$ and $b < 0$	$\alpha > \beta$	Growth–decay	α	Growth	β	Decay
$a > 0$ and $b > 0$	$\beta > \alpha$	Growth–decay	β	Growth	α	Decay

Fig. 2. Plot of functions (*a*) $y = 0.1[\exp(-t) - \exp(-10t)]$ and (*b*) $y = 0.1[\exp(-10t) - \exp(-t)]$.

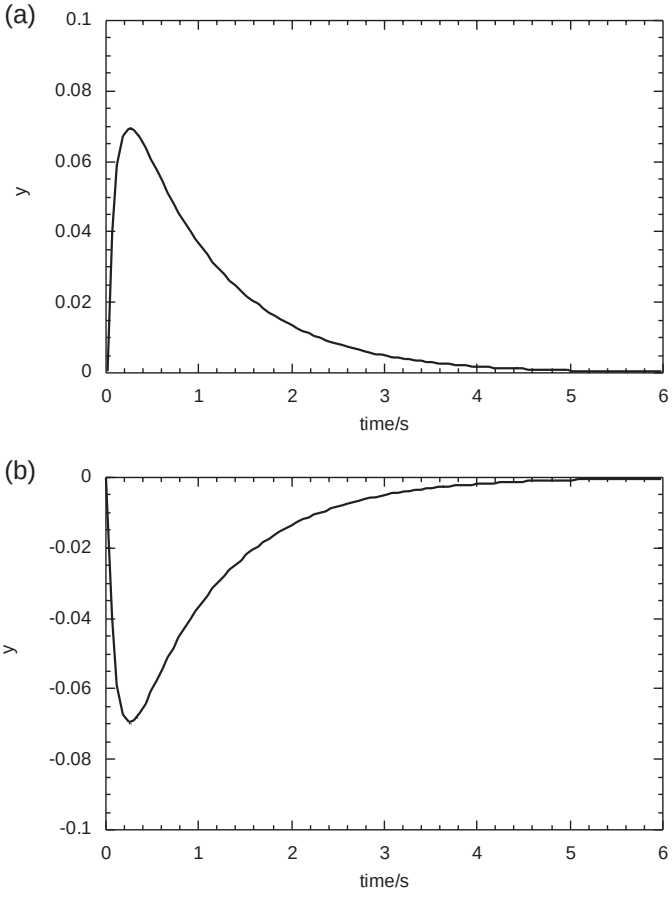

dependent on k_2/k_1 and ε_B' is not. An alternative formalism of distinguishing ε_B and ε_B', which is more practical, is to express each in terms of the pre-exponential coefficients *a*, *b*, and *c* that would be obtained from nonlinear least-squares analysis. The relationships are given by eqs. [16*a*] and [16*b*].

$$[16a] \quad \varepsilon_B = \frac{\varepsilon_A}{A_A^0}\left[b\left(1 - \frac{k_2}{k_1}\right) + c\right]$$

$$[16b] \quad \varepsilon_B' = \frac{\varepsilon_A}{A_A^0}\left[a\left(1 - \frac{k_1}{k_2}\right) + c\right]$$

It may be verified that eq. [16*a*] is invariant to the ratio of rate constants whereas eq. [16*b*] is not when ε_B is the correct absorption coefficient, and that the reverse is true when ε_B' is the correct absorption coefficient (see Appendix B).

Absorbance extremum method

If the transformations A to B and B to C in eq. [1] are catalyzed by some species Q such that the concentration of catalyst, [Q], is invariant with time during the course of the kinetic experiment, then the absorption–time functions for A, B, and C given by eqs. [4*a*]–[4*c*] still apply. Such an experimental constraint represents the well-documented pseudo-first-order condition. In general, the rate constants k_1 and k_2 will be some functions of the concentration of catalyst; for example, $k_1 = f([Q])$ and $k_2 = g([Q])$. The subscripts 1 and 2 refer to the first and second steps, respectively, so that the first step is associated with *f* and the second step is associated with *g*. Conversely, the functional assignments to the rate constants may be reversed so that $k_2 = f([Q])$ and $k_1 = g([Q])$. To resolve which assignment pertains to an experimental situation, the absorbance extremum is monitored as a function of catalyst concentration [Q]. The functional behaviour of the extremum with catalyst concentration will be

© 1999 NRC Canada

different for the two possible rate constant assignments. In the case of growth–decay curves the absorbance extremum is a maximum, and in the case of decay–growth curves it is a minimum. An important experimental criterion that must be met for this method to work is that the initial absorbance of species A must be kept constant in all experiments constituting the range of catalyst concentrations examined. This ensures that the correct values of the absorption maxima or minima are recorded from the collected growth–decay or decay–growth curves, respectively. Any artifacts or detractions from this criterion will result in spoiled data. Since growth–decay curves are more often encountered experimentally, we will now illustrate the method for these functions obtained under various experimental situations involving species B.

The case when B is observed uniquely

From eq. [6*a*], the absorption maximum of species B takes the form

$$[17] \qquad A_B^{max} = A_A^0\left(\frac{\varepsilon_B}{\varepsilon_A}\right)\left(\frac{f}{g-f}\right)\left[\left(\frac{g}{f}\right)^{-f/(g-f)} - \left(\frac{g}{f}\right)^{-g/(g-f)}\right]$$

where A_B^{max} is a function of [Q], when the assignments $k_1 = f([Q])$ and $k_2 = g([Q])$ are made. If the functional assignments of k_1 and k_2 are transposed so that $k_2 = f([Q])$ and $k_1 = g([Q])$, then the resultant analagous expression is given by

$$[18] \qquad A_B^{max} = A_A^0\left(\frac{\varepsilon_B}{\varepsilon_A}\right)\left(\frac{g}{f-g}\right)\left[\left(\frac{f}{g}\right)^{-g/(f-g)} - \left(\frac{f}{g}\right)^{-f/(f-g)}\right]$$

$$= A_A^0\left(\frac{\varepsilon_B}{\varepsilon_A}\right)\left(\frac{g}{g-f}\right)\left[\left(\frac{g}{f}\right)^{-f/(g-f)} - \left(\frac{g}{f}\right)^{-g/(g-f)}\right]$$

where the second step is associated with f and the first step is associated with g. A closer examination of eqs. [17] and [18] indicates that the expressions are distinguishable by the factors $f/(g-f)$ and $g/(g-f)$. Hence, it is possible to assign a rate constant to a particular step in the sequence on the basis of its functional dependence on catalyst concentration. This does *not* imply that the calculated rate constant parameters obtained from a *single* growth–decay curve may be assigned to a specific reaction step (see Theorem 4). To distinguish which rate constant is associated with which step in the reaction sequence, a *collective* analysis must be performed on all growth–decay curves obtained over the catalyst concentration range examined. The methodology is as follows. The $(t_i, A_{B,i})$ data points from a kinetic trace obtained at a given catalyst concentration are first fitted to the model eq. [8] using a nonlinear least-squares algorithm. Then, the absorption maximum of this trace is determined from the calculated parameters at $t = (1/(c-b))\ln(c/b)$ according to $y_m = a[(c/b)^{-b/(c-b)} - (c/b)^{-c/(c-b)}]$. Note that $y_m > 0$ when $a > 0$ and $c > b$, or when $a < 0$ and $b > c$. The process is repeated for other kinetic traces recorded at several catalyst concentrations until a set of data points $([Q]_i, y_{m,i})$ is obtained. The functions given by eqs. [17] and [18] can be constructed once the functional forms for f and g are known. The data points $([Q]_i, y_{m,i})$ are then plotted and matched with the appropriate curve. A match with eq. [17], for example, indicates that the first step in the reaction is associated with the rate constant having a catalyst dependence given by $f([Q])$, and the second step is associated with the rate constant having a catalyst dependence given by $g([Q])$.

We illustrate the method with two numerical examples. Suppose we have a chemical system described by eq. [1] such that the first step is invariant to catalyst concentration while the second step obeys a linear relationship with catalyst concentration. From our growth–decay curves for species B we obtain parameters b and c but cannot assign these to the particular steps in the reaction scheme on the basis of any one curve. Hence, we have either case (*i*) $b = f([Q]) = D_1$ and $c = g([Q]) = D_2 + D_3[Q]$ or case (*ii*) $c = f([Q]) = D_1$ and $b = f([Q]) = D_2 + D_3[Q]$, where the constants D_1, D_2, and D_3 would be known from separate experiments. To overcome the ambiguity, plots according to the forms of eqs. [17] and [18] are made and compared with the actual $y_{m,i}$ versus $[Q]_i$ plot to determine which of the above cases is applicable. Figures 3*a* and 3*b* illustrate the functions given by eqs. [17] and [18] using the definitions of f and g given in cases (*i*) and (*ii*). The method also works when the rate constants b and c are independent of catalyst concentration; i.e., we have either case (*iii*) $b = f([Q]) = D_1$ and $c = g([Q]) = D_2$ or case (*iv*) $c = f([Q]) = D_1$ and $b = g([Q]) = D_2$. Figures 4*a* and 4*b* illustrate the functions given by eqs. [17] and [18] using the definitions of f and g given in cases (*iii*) and (*iv*).

Cases when B and A, B, and C, and B, C, and A are observed together

From Tables 3 and 4 the functions describing growth–decay curves for these three cases may be conveniently described by the relation

$$[19] \qquad y = a\exp(-k_1 t) - b\exp(-k_2 t) + c$$

where

$$a = A_A^0\left[1 - \left(\frac{\varepsilon_B}{\varepsilon_A}\right)\left(\frac{k_1}{k_1 - k_2}\right)\right]$$

$$b = -A_A^0\left(\frac{\varepsilon_B}{\varepsilon_A}\right)\left(\frac{k_1}{k_1 - k_2}\right)$$

and $c = 0$ apply to observing B and A together;

$$a = A_A^0\left[\left(\frac{k_2\varepsilon_C - k_1\varepsilon_B}{\varepsilon_A}\right)\left(\frac{1}{k_1 - k_2}\right)\right]$$

$$b = A_A^0\left(\frac{\varepsilon_C - \varepsilon_B}{\varepsilon_A}\right)\left(\frac{k_1}{k_1 - k_2}\right)$$

and $c = A_A^0(\varepsilon_C/\varepsilon_A)$ apply to observing B and C together; and

$$a = A_A^0\left[1 + \left(\frac{k_2\varepsilon_C - k_1\varepsilon_B}{\varepsilon_A}\right)\left(\frac{1}{k_1 - k_2}\right)\right]$$

$$b = A_A^0\left(\frac{\varepsilon_C - \varepsilon_B}{\varepsilon_A}\right)\left(\frac{k_1}{k_1 - k_2}\right)$$

© 1999 NRC Canada

Fig. 3. Plot of (*a*) eq. [17] and (*b*) eq. [18] with $f([Q]) = D_1 = 10$, $g([Q]) = D_2 + D_3[Q] = 1 + 100[Q]$, and $A_A^0(\varepsilon_B/\varepsilon_A) = 1$. If the data fit this equation then (*a*) the function *f* corresponds to the first step, and the function *g* corresponds to the second step; (*b*) the function *g* corresponds to the first step, and the function *f* corresponds to the second step.

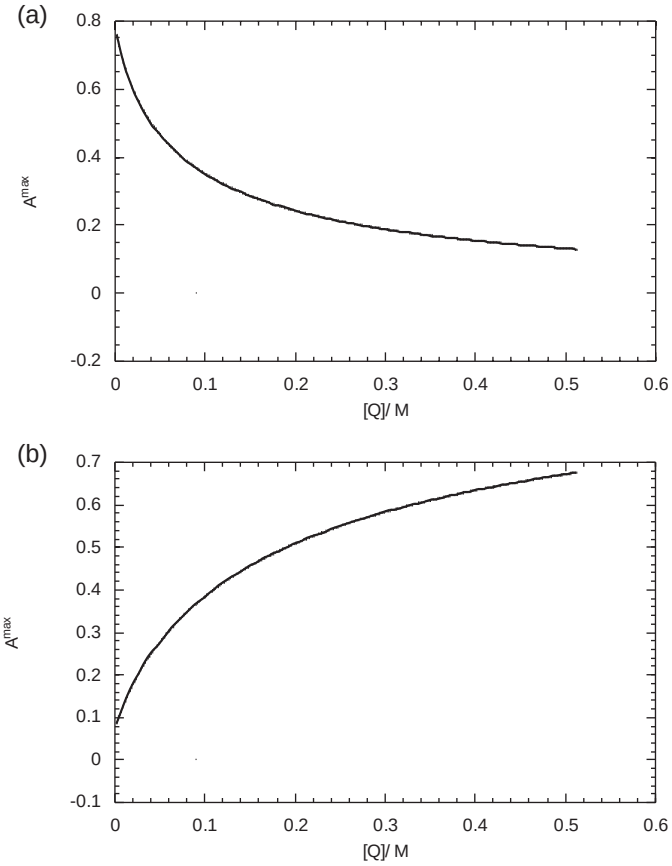

and $c = A_A^0(\varepsilon_C/\varepsilon_A)$ apply to observing B, C, and A together. The absorbance maximum occurs at

$$[20] \quad t = \frac{1}{k_2 - k_1} \ln\left(\frac{bk_2}{ak_1}\right)$$

and has a value given by

$$[21] \quad y_m = a\left(\frac{bk_2}{ak_1}\right)^{-k_1/(k_2-k_1)} - b\left(\frac{bk_2}{ak_1}\right)^{-k_2/(k_2-k_1)} + c$$

where the coefficients *a* and *b* are also functions of k_1 and k_2, as given by the relationships defined above depending on what chemical species are observed. The functional form of the absorbance maximum with catalyst concentration is given by

$$[22] \quad A^{max} = a\left(\frac{bg}{af}\right)^{-f/(g-f)} - b\left(\frac{bg}{af}\right)^{-g/(g-f)} + c$$

with the assignment $k_1 = f([Q])$ and $k_2 = g([Q])$ made in the appropriate expressions for the pre-exponential parameters; and by

Fig. 4. Plot of (*a*) eq. [17] and (*b*) eq. [18] with $f([Q]) = D_1 = 10$, $g([Q]) = D_2 = 1$, and $A_A^0(\varepsilon_B/\varepsilon_A) = 1$. If the data fit this equation then (*a*) the function *f* corresponds to the first step, and the function *g* corresponds to the second step; (*b*) the function *g* corresponds to the first step, and the function *f* corresponds to the second step.

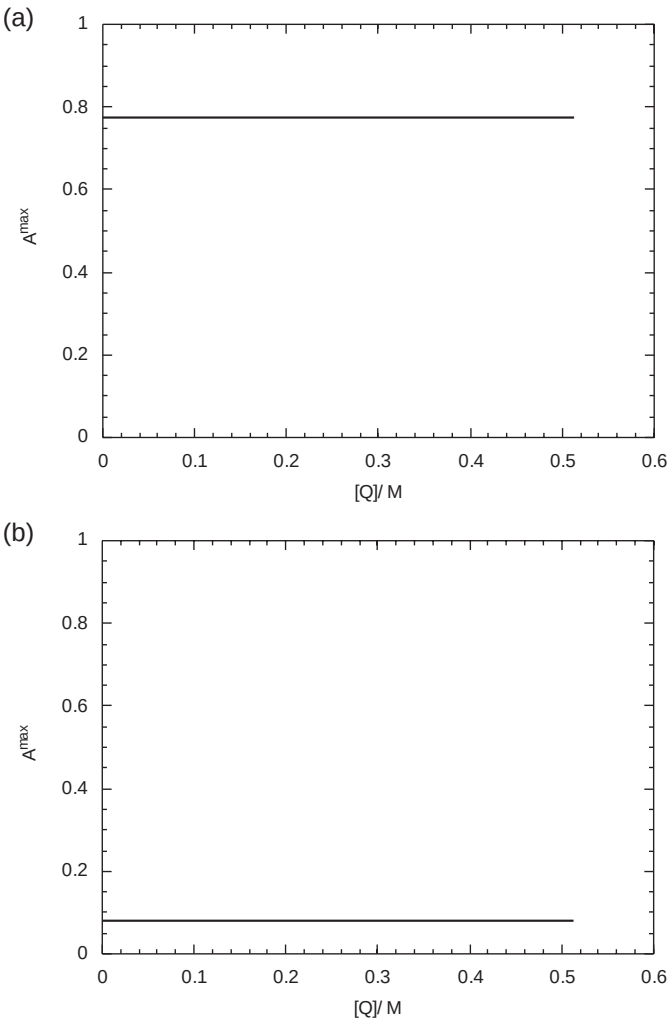

$$[23] \quad A^{max} = a\left(\frac{bf}{ag}\right)^{-g/(f-g)} - b\left(\frac{bf}{ag}\right)^{-f/(f-g)} + c$$

with the assignment $k_1 = g([Q])$ and $k_2 = f([Q])$.

Summary

A detailed account of the forms of the absorbance–time functions of the unimolecular consecutive two-step reaction sequence is given. The problem of distinguishability of rate constants is discussed with particular emphasis on the rate constant – reaction step ambiguity. A general method based on the functional form of the absorption extremum with catalyst concentration is proposed as a means to overcome this ambiguity in rate constant assignments. Of particular interest to biochemists, enzymologists, and medicinal chemists is the

© 1999 NRC Canada

application of this new method to the resolution of consecutive pseudo-first-order rate constants which are functions of pH. Chemical reactions obeying mechanisms of this type will then be described by simultaneous pH–rate profiles. Work is currently in progress on the theoretical and experimental verification of this new method for such chemical systems.

Acknowledgements

The author wishes to thank Prof. A.J. Kresge for stimulating discussions regarding this intriguing problem.

References

1. J.W. Moore and R.G. Pearson. Kinetics and mechanism. Wiley, New York. 1981.
2. B.K. Carpenter. Determination of organic reaction mechanisms. Wiley, New York. 1984.
3. K.J. Laidler. Chemical kinetics. Harper and Row Publishers, New York. 1987.
4. C. Capellos and B.H.J. Bielski. Kinetic systems: mathematical description of chemical kinetics in solution. Wiley, New York. 1972.
5. N.M. Rodiguin and E.N. Rodiguin. Consecutive chemical reactions: mathematical analysis and development. Van Nostrand, Toronto. 1964.
6. J.H. Espenson. Chemical kinetics and reaction mechanism. McGraw–Hill Book Company, New York. 1981.
7. K. Yamasaki and A. Watanabe. Bull. Chem. Soc. Jpn. **70**, 89 (1997).
8. K. Yamasaki, A. Watanabe, T. Kakuda, and I. Tokue. Int. J. Chem. Kinet. **30**, 47 (1998).
9. A.R. Fercht and W.P. Jencks. J. Am. Chem. Soc. **92**, 5432 (1970).
10. J. Andraos, Y. Chiang, A.J. Kresge, and V.V. Popik. J. Am. Chem. Soc. **120**, 8417 (1997).
11. R.H. Bisby and E.W. Thomas. J. Chem. Educ. **63**, 990 (1986).
12. R. Bonneau, J. Wirz, and A.D. Zuberbühler. Pure Appl. Chem. **69**, 979 (1997).
13. J.R. Chipperfield. J. Organomet. Chem. **137**, 355 (1977).
14. N.W. Alcock, D.J. Benton, and P. Moore. J. Chem. Soc. Faraday Trans. **66**, 2210 (1970).
15. A. Fersht. Enzyme structure and mechanism. W.H. Freeman, New York. 1985.
16. G.B. Thomas, Jr. Calculus and analytic geometry. Addison–Wesley, Reading. 1972.

Appendix A

In this appendix a proof is given for the relationship

$$[A1] \quad \lim_{n\to 1}\left\{\frac{1}{n-1}\left[n^{-1/(n-1)} - n^{-n/(n-1)}\right]\right\} = e^{-1}$$

Proof: Since substitution of $n = 1$ leads to an indeterminate form, the expression is rewritten as a rational function and l'Hôpital's rule (16) is applied as shown by the sequence of steps below.

$$[A2] \quad \lim_{n\to 1}\left\{\frac{1}{n-1}\left[n^{-1/(n-1)} - n^{-n/(n-1)}\right]\right\}$$

$$= \lim_{n\to 1}\left\{\frac{\left(\frac{1}{n}\right)^{-1/(n-1)} - \left(\frac{1}{n}\right)^{-n/(n-1)}}{n-1}\right\}$$

$$= \lim_{n\to 1}\left\{\frac{\left(\frac{1}{n}\right)^{-1/(n-1)}\left[\frac{\ln n + \frac{1}{n} - 1}{(n-1)^2}\right] - \left(\frac{1}{n}\right)^{-n/(n-1)}\left[\frac{\ln n + 1 - n}{(n-1)^2}\right]}{1}\right\}$$

$$= \lim_{n\to 1}\left\{\left(\frac{1}{n}\right)^{1/(n-1)}\left[\frac{\ln n}{n(n-1)}\right]\right\}$$

$$= \lim_{n\to 1}\left\{\left(\frac{1}{n}\right)^{1/(n-1)}\right\} \lim_{n\to 1}\left\{\frac{\ln n}{n(n-1)}\right\}$$

Each of the limits above is then evaluated separately. The left-hand limit is evaluated as follows. Letting $z = n^{-1/(n-1)}$ and taking natural logarithms of both sides leads to

$$\ln z = -\frac{\ln n}{n-1}$$

Then,

$$[A3] \quad \lim_{n\to 1} \ln z = -\lim_{n\to 1}\left\{\frac{\ln n}{n-1}\right\} = -\lim_{n\to 1}\left\{\frac{\frac{1}{n}}{1}\right\} = -1$$

after again applying l'Hôpital's rule, since substitution of $n = 1$ leads to an indeterminate form. Hence,

$$[A4] \quad \lim_{n\to 1} z = \lim_{n\to 1}\{n^{-1/(n-1)}\} = e^{-1}$$

The right-hand limit of eq. [A2] is evaluated with a final application of l'Hôpital's rule to yield

$$[A5] \quad \lim_{n\to 1}\left\{\frac{\ln n}{n(n-1)}\right\} = \lim_{n\to 1}\left\{\frac{\frac{1}{n}}{2n-1}\right\} = 1$$

Substitution of these results into eq. [A2] completes the proof.[2]

[2] A referee has suggested an alternative solution which involves substituting $n = 1 + \varepsilon$ in eq. [A1] and evaluating the limit as $\varepsilon \to 0$. The resultant limit is $\lim_{\varepsilon\to 0}(1+\varepsilon)^{-(1+\varepsilon)/\varepsilon}$ which can be evaluated to give e^{-1} using the same sequence of steps in arriving at eq. [A4] from eq. [A3].

© 1999 NRC Canada

Appendix B

Equations [16*a*]–[16*b*] are obtained by first rearranging the expressions for the pre-exponential factors *b* and *b*′, respectively, and then substituting *a* for *b*′ in the case of eq. [16*b*]. If ε_B is the correct absorption coefficient for the intermediate B then eq. [16*a*] becomes an identity upon substitution of the expression for *b*, thus making ε_B independent of k_1/k_2. On the other hand, eq. [16*b*] reduces to

$$[B1] \quad \varepsilon_B' = \varepsilon_A + (\varepsilon_B - \varepsilon_A)\frac{k_1}{k_2}$$

upon substitution of the expression for *a*, thus making ε_B' linearly dependent on k_1/k_2. Note that eq. [B1] is identical to eq. [15*b*]. An assignment of the absorption coefficient of B to ε_B implies that the first step in the sequential mechanism corresponds to rate constant k_1 and that the second step corresponds to rate constant k_2. If ε_B' is the correct absorption coefficient for the intermediate B, then eq. [16*a*] reduces to

$$[B2] \quad \varepsilon_B = \varepsilon_A + (\varepsilon_B' - \varepsilon_A)\frac{k_2}{k_1}$$

upon substitution of *b* with the expression for *a*′, thus making ε_B linearly dependent on k_2/k_1. On the other hand, eq. [16*b*] becomes an identity upon substitution of *a* with the expression for *b*′, thus making ε_B' independent of k_2/k_1. An assignment of the absorption coefficient of B to ε_B' implies that the first step in the sequential mechanism corresponds to rate constant k_2 and that the second step corresponds to rate constant k_1. It should be noted that eqs. [B1] and [B2] are identical upon rearrangement. Equation [B1] is written with ε_B' as the dependent variable while eq. [B2] is written with ε_B as the dependent variable.

In practice kinetic traces recorded at various k_1/k_2 ratios are fit to an expression of the form of eq. [11]. At this stage the rate constant subscript labels 1 and 2 are arbitrary. Having obtained the five parameters from nonlinear least-squares analysis, plots of $b(1 - k_2/k_1) + c$ versus k_1/k_2 and $a(1 - k_1/k_2) + c$ versus k_1/k_2 are then made. If the former plot shows no dependence on k_1/k_2 and the latter plot shows a linear dependence on k_1/k_2, then the absorption coefficient of B is ε_B and k_1 and k_2 are assigned to the first and second steps, respectively. If, on the other hand, the former plot shows a hyperbolic dependence on k_1/k_2 (linear dependence on k_2/k_1) and the latter plot shows no dependence on k_1/k_2, then the absorption coefficient of B is ε_B', and k_1 and k_2 are assigned to the second and first steps, respectively.

© 1999 NRC Canada

A theoretical study on the reactivity of vinyl iodonium ions

Tadashi Okuyama and Hiroshi Yamataka

Abstract: Reactions of methyl(vinyl)iodonium ion and the β-substituted derivatives as well as divinyliodonium ion with chloride ion were examined theoretically by ab initio MO (MP2) calculations at the double-zeta (DZ) + d level. Interaction of the iodonium ion **1** with Cl^- leads to chloro-λ^3-iodane **2**. Transition states for the S_N2, ligand-coupling substitution (LC), and β-elimination (βE) are found for reactions at the vinyl group. The barrier to LC is usually the lowest in the gas phase, but relative barriers to S_N2 and to βE change with the substituents. Effects of solvent were evaluated by a dielectric continuum model and found to be large on S_N2 but small on LC. The experimental observations in solution that the S_N2 is the most facile for the β-methyl-substituted **1** while it is retarded by the β-*tert*-butyl and β-chloro substitutions are reproduced by the calculations that take medium effects into account.

Key words: vinyliodonium salt, polyvalent iodine, vinylic S_N2 reaction, ligand coupling, ab initio MO calculation.

Résumé : Faisant appel à des calculs théoriques ab initio MO(MP2) au niveau DZ + d, on a étudié les réactions de l'ion chlorure avec l'ion méthyl(vinyl)iodonium, ses dérivés β-substitués ainsi que l'ion divinyliodonium. L'interaction de l'ion iodonium (**1**) avec Cl^- conduit au chloro-λ^3-iodane (**2**). Pour les réactions au niveau du groupe vinyle, on a trouvé des états de transition pour la réaction S_N2, la substitution de couplage du ligand (CL) et l'élimination β (Eβ). La barrière au CL est généralement la plus basse pour les réactions en phase gazeuse, mais les barrières relatives pour les réactions S_N2 et d'Eβ varient avec les substituants. On a évalué les effets de solvant par un modèle diélectrique continue et on a trouvé qu'ils sont importants pour les réactions S_N2, mais faibles pour le CL. Les calculs qui tiennent compte des effets de milieu permettent de reproduire les observations expérimentales pour les réactions en solution dans lesquelles les réactions S_N2 de l'ion **1** substitué par un groupe méthyle en β sont plus facilitées alors qu'elles sont ralenties par des substituants *tert*-butyle ou chloro.

Mots clés : sel vinyliodonium, iode polyvalent, réaction S_N2 vinylique, couplage de ligand, calculs d'OM ab initio.

[Traduit par la Rédaction]

Polyvalent organoiodine compounds have attracted the interest of organic chemists because of their diversity in reactivities, offering powerful synthetic tools as well as mechanistic challenges (1–4). Vinyl iodonium salts among others exhibit an intriguing mechanistic spectrum in the reaction with nucleophiles/bases.

First of all, vinyl iodonium salts are good precursors of vinyl cations. Simple α-alkyl substituted vinyliodonium salts cannot be isolated probably due to the ease of formation of the stable secondary vinyl cations. A 1-cyclohexenyliodonium salt is only moderately stable due to the angle strain in a 1-cyclohexenyl cation intermediate (5), and readily undergoes solvolysis (6). A styryliodonium salt gives a vinylenebenzenium intermediate in ionizing solvolytic media (7). A β,β-dialkylvinyliodonium salt also undergoes ionization to the secondary vinyl cation in polar solvents via participation of the β-alkyl group (8). By contrast, simple 1-alkenyliodonium salts do not show any sign of ionization even in a powerfully ionizing solvent like trifluoroacetic acid (9). Primary vinyl cation must be too unstable to be formed under these normal conditions.

A second easily occurring reaction when a hydrogen is present at the α position is α-elimination leading to alkylidenecarbene, eq. [1] (10, 11). Very weak bases like dichloroacetate can induce this reaction of 1-alkenyliodonium salts, and in neutral alcohols like methanol or ethanol, both substitution and α-elimination of these salts can compete with each other.[3]

[1]

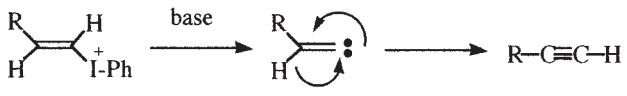

Received November 3, 1998.

This paper is dedicated to Professor A. Jerry Kresge on the occasion of his 70th birthday.

T. Okuyama.[1] School of Engineering Science, Osaka University, Toyonaka, Osaka 560-8531, Japan.
H. Yamataka.[2] Institute of Scientific and Industrial Research, Osaka University, Ibaraki, Osaka 567-0047, Japan.

[1] Present address: Himeji Institute of Technology, Faculty of Science, Kamigori, Ako-gun, Hyogo 678-1297, Japan. Telephone: +81-791-58-0169. e-mail: okuyama@sci.himeji-tech.ac.jp
[2] Telephone: +81-6-6879-8467. Fax: +81-6-6879-8469. e-mail: yamataka@isir1.sanken.osaka-u.ac.jp
[3] T. Okuyama, Y. Ishida, and M. Ochiai. Manuscript in preparation.

 © 1999 NRC Canada

Scheme 1.

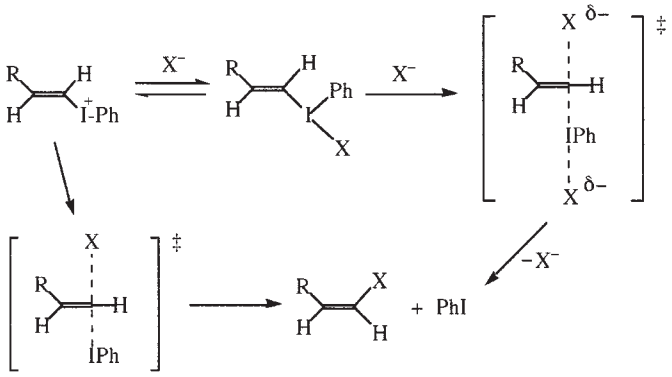

Reactions of 1-alkenyliodonium salts with nucleophiles like chloride, bromide, and iodide ions with extremely weak basicity lead to the in-plane vinylic S_N2 substitution with complete inversion of configuration, Scheme 1 (9, 11, 12). This is the first and definitive example of this kind of reaction, vinylic S_N2,[4] that has long been neglected as a possible mechanism (15). This reaction occurs both directly and via preequilibrium formation of halo-λ^3-iodane (Scheme 1). The accompanying reaction is intramolecular *syn* β-elimination (βE) within the λ^3-iodane intermediate, eq. [2]. The β-tertiary alkyl substitution seems to inhibit the S_N2 reaction of the vinyliodonium salts and leads exclusively to βE (12).

[2]

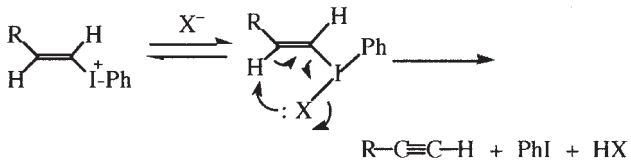

The β-alkyl,β-halogeno disubstitution retards the S_N2 substitution, while the β-elimination is impossible, and an alternative substitution reaction with complete retention of configuration was observed (16). This is concluded to occur through a ligand coupling (LC) within the halo-λ^3-iodane intermediate via an out-of-plane arrangement of the nucleophile. The accompanying formation of 1-iodo-1-alkene and halobenzene is consistent with this mechanism, Scheme 2. This reaction can show up even in the reaction of a simple 1-alkenyliodonium salt with halide ions when both the nucleophilic and basic reactions at the carbon (Scheme 1 and eq. [2]) are retarded in acidic media like trifluoroacetic acid (9).

To understand the variations of the closely related reactions of vinyl iodonium salts and the effects of β-substitution on these reactivities, theoretical investigations were carried out on the reactions of a series of β-substituted vinyliodonium ions with chloride ion by means of ab initio molecular orbital calculations. The results are summarized in this paper.

Calculation method

All calculations were carried out at the second-order Møller-Plesset perturbation (MP2) level (17) by using the

Scheme 2.

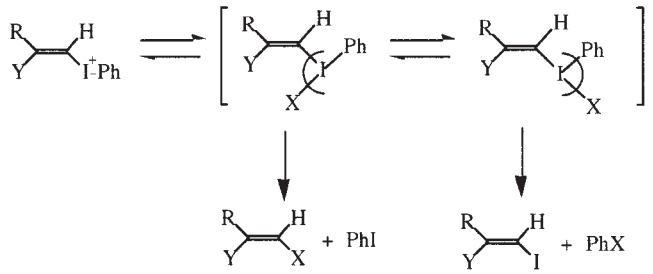

Gaussian 94 program (18). For carbon and hydrogen atoms, 6-31G(d) and 6-31G basis sets were used, respectively, while for other atoms the double-zeta (DZ) basis sets of Dunning and Hay (19) and effective core potentials (ECP) developed by Wadt and Hay (20) were employed. The DZ basis sets were augmented by a set of six *d*-type polarization functions for Cl and I (*d* exponents 0.75 (Cl) and 0.226 (I)) as well as a diffusion function for Cl. Reactants, complexes, and transition structures were fully optimized and were identified by means of a full analysis of the vibrational modes at those stationary points. Effects of solvation (acetonitrile, dielectric constant = 37.5) were evaluated by a dielectric continuum model using a self-consistent reaction field approximation (SCRF) (21). Free energy at 298 K was obtained on the basis of numerically calculated frequencies in the gas phase.

Results

We have chosen methyl(vinyl)iodonium ion, **1a**, as a model compound for phenyl(vinyl)iodonium ion, which is actually employed for reactions in solution, and studied the reaction at the vinyl group with the chloride ion as a reference reaction. Then, the effects of β-substitution on the structure and its reactivity were investigated for β-Me (**1b**), β-*t*-Bu (**1c**),

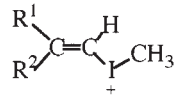

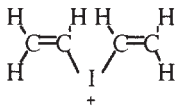

1a, $R^1 = R^2 = H$

b, $R^1 = CH_3$, $R^2 = H$

c, $R^1 = (CH_3)_3C$, $R^2 = H$

d, $R^1 = CH_3$, $R^2 = Cl$

1e

and β-Cl-β-Me (**1d**) derivatives.

The calculated geometry of **1a** is shown in Fig. 1. The interaction of **1a** with Cl^- leads to the formation of two complexes, **2a** and **3a** (Fig. 1). The location of the chloride ion in **2a** is characteristic of a hypervalent bonding of C_α-I-Cl with an angle of 170.3° and an elongated C_α—I bond (2.114 to 2.155 Å), while in **3a** Cl^- is located on the vinylic plane and is hydrogen-bonded to the α-hydrogen (2.202 Å). In **3a**, both C—H and C—I bonds at the α-position become longer than those in **1a** (Fig. 1). That is, **2a** is taken as a

[4] There are some experimental implications that the vinylic S_N2 reaction is possible (13), and some theoretical calculations on this subject have recently appeared (14).

© 1999 NRC Canada

Fig. 1. Optimized geometries of **1a** and derived states from its interaction with chloride ion. Numbers given are selected bond lengths (Å) and bond angles (°). Symbols: open circle, hydrogen; closed circle, carbon; dotted circle, iodine; hatched circle, chlorine.

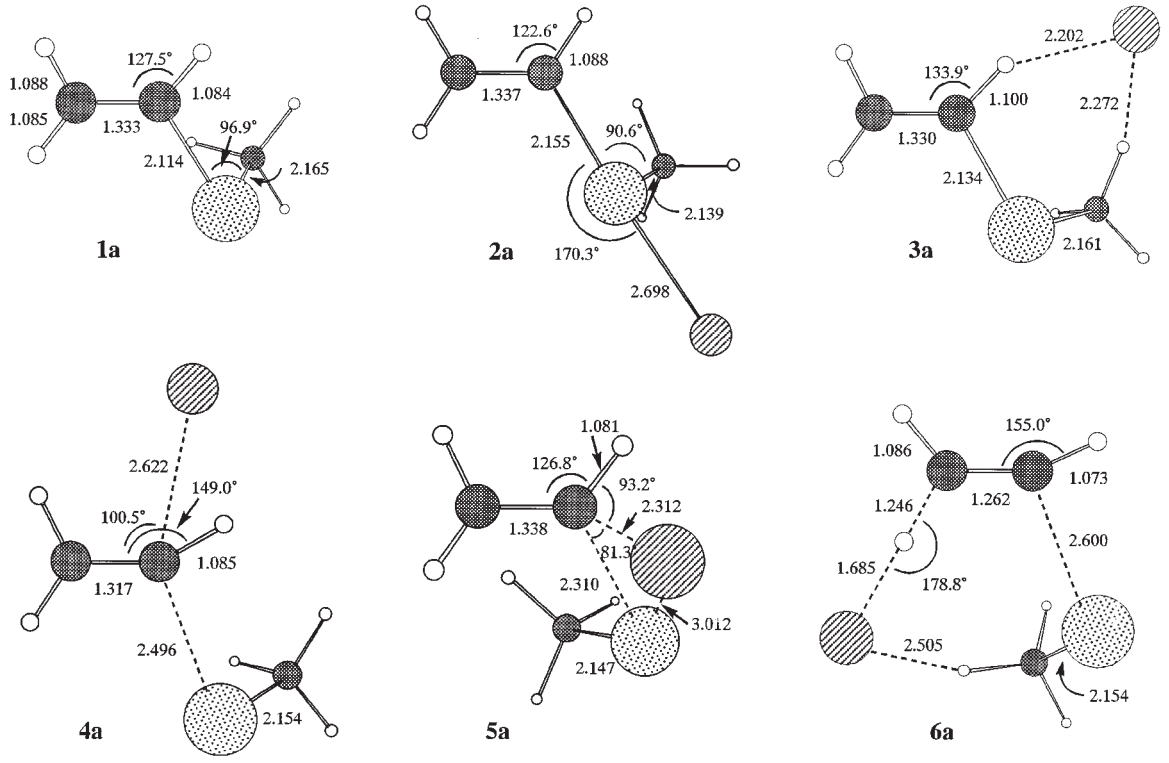

Table 1. Energies for the iodonium ions **1** and chloro-λ^3-iodanes **2**.

No.	R^1, R^2	$-E$ (au)	No.	$-E$ (au)	$-\Delta E$ (kcal mol^{-1})[a]	$-\Delta G$ (kcal mol^{-1})[a]
1a	H,H	128.413 50	**2a**	143.497 77	108.2	109.6
1b	CH_3,H	167.591 30	**2b**	182.670 66	105.1	106.5
1c	$(CH_3)_3C$,H	285.099 03	**2c**	300.175 14	103.1	104.1
1d	CH_3,Cl	181.861 66	**2d**	196.946 20	108.4	110.1
1e	H,H[b]	166.371 66	**2e**	181.455 80	108.2[c]	109.1
1e′	H,H[b]	166.370 99	**2e′**	181.454 26	107.2[c]	

[a]Stabilization energy for the formation of **2** from **1** and Cl^-.

[b]The divinyl model.

[c]Relative energy to **1e** + Cl^-.

hypervalent 10-I-3 species, chloro-λ^3-iodane, and **3a** is a hydrogen-bond complex. An alternative conformation of the λ^3-iodane **2a** with the apical methyl group could not be found as an energy-minimum species. The more electronegative vinyl group is favored in the apical position rather than methyl, as is generally referred to as apicophilicity (22). The β-substituted derivatives show similar behavior. In fact, the geometrical features of **1a–d** and of **2a–d** are essentially the same within each sets, irrespective of the β-substituents.

The total electronic energies of the iodonium ions **1a–d** and chloro-λ^3-iodanes **2a–d** are summarized in Table 1, together with the stabilization energies ($-\Delta E$) for formation of **2**. The energy levels for the low-lying vacant orbitals are given in Table 2. The formation of the hypervalent bond brings about stabilization of more than 100 kcal mol^{-1} in the gas phase. In contrast, the hydrogen bonding stabilization for **3a** is smaller (96.0 kcal mol^{-1}). The stability of λ^3-iodane decreases in the order, **2d** > **2a** > **2b** > **2c**. Clearly, the electronegative substituent on the apical ligand (vinyl group) stabilizes the λ^3-iodane (**2b** vs. **2d**), while the electron-donating β-alkyl group reduces this stability (22). The stability of λ^3-iodane **2** relative to iodonium ion **1** is similar both in terms of electronic energy and free energy.

Transition states (TS) for the substitutions with both inversion (**4a–d**) and retention (**5a–d**) of configuration were determined, and structures of those for the reference compound (**4a** and **5a**) are shown in Fig. 1. In TS **4**, the incoming chloride ion is located in a plane of the vinyl group and this is the TS for the in-plane vinylic S_N2 reaction of the iodonium ion **1**. In TS **5**, the chloride ion is located out-of-plane of the vinyl group and has interactions with both the α-carbon and iodine. The bond angle of Cl-C_α-I (81.3°) is smaller than that of Cl-C_α-H (93.2°), and TS **5** leads to substitution with retention of configuration. This retention TS may be regarded as the TS for LC within a halo-λ^3-iodane.

© 1999 NRC Canada

Table 2. Molecular orbital energy levels of the iodonium ions **1** and chloro-λ^3-iodanes **2**.[a]

No.	LUMO	LUMO + 1	LUMO + 2	No.	LUMO	LUMO + 1	LUMO + 2
1a	–3.09 (σ^*_M)	–1.77 (σ^*_V)	–0.78 (π^*)	**2a**	1.80 (σ^*_M)	3.21 (σ^*_V)	3.45 (π^*)
1b	–2.81 (σ^*_M)	–1.49 (σ^*_V)	–0.38 (π^*)	**2b**	1.91 (σ^*_M)	3.34 (σ^*_V)	3.65 (π^*)
1c	–2.65 (σ^*_M)	–1.34 (σ^*_V)	–0.15 (π^*)	**2c**	1.88 (σ^*_M)	3.43 (σ^*_V)	3.64 (π^*)
1d	–3.04 (σ^*_M)	–1.74 (σ^*_V)	–0.56 (π^*)	**2d**	1.53 (σ^*_M)	2.87 (σ^*_V)	3.06 (π^*)
1e	–2.88 (σ^*_V)	–1.82 (σ^*_V)	–0.96 (π^*)	**2e**	1.81 (σ^*_V)[b]	3.00 (σ^*_V)[c]	3.34 (π^*)[b]
1e′	–2.85 (σ^*_V)	–1.95 (σ^*_V)	–0.89 (π^*)	**2e′**	1.76 (σ^*_V)[b]	3.23 (σ^*_V)[c]	3.47 (π^*)[b]

[a]Energies are given in eV. Symbols in parentheses signify the symmetry of the orbital: σ^*_M, anti-bonding orbital of I-CH_3; σ^*_V, anti-bonding orbital of I-C_α; π^*, orbital of the vinyl group.

[b]Orbital localized on the apical vinyl group.

[c]Orbital localized on the equatorial vinyl group.

Fig. 2. Optimized geometries of **1e** and **2e** and their conformers.

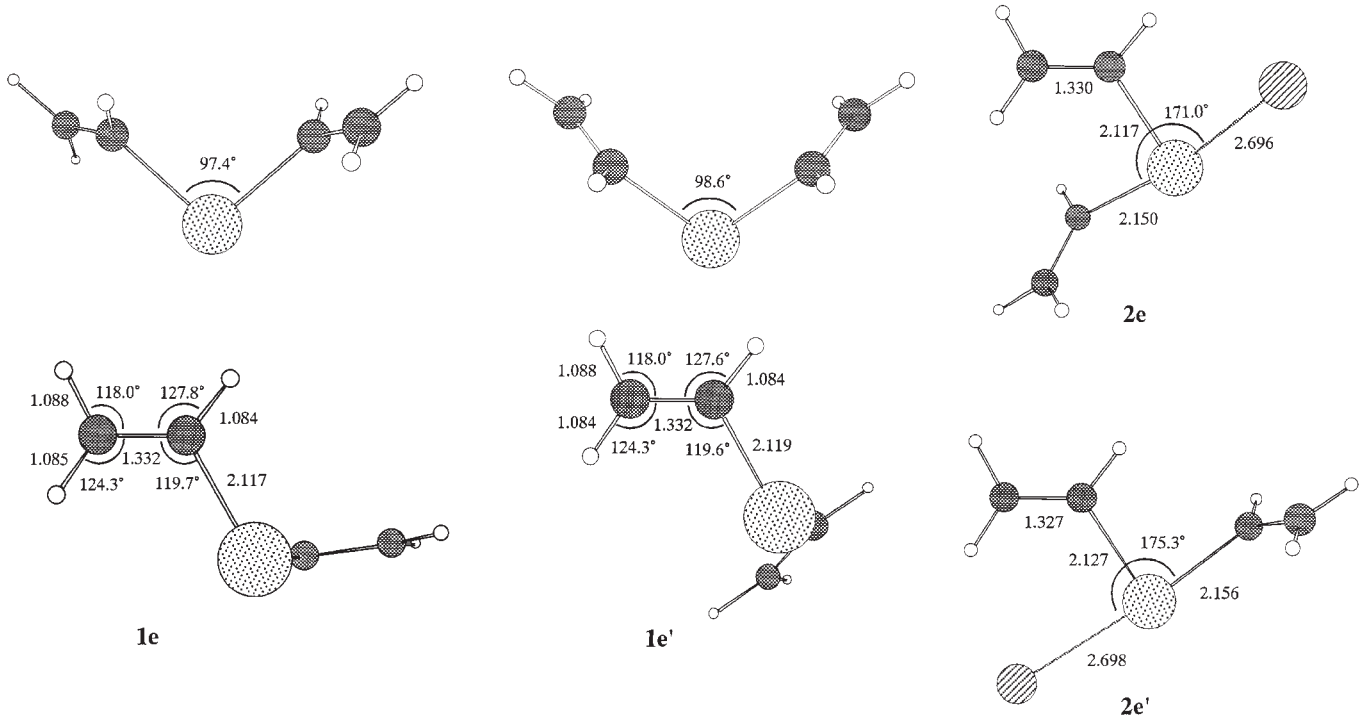

The TS values for βE (**6a–c**) were also determined (**6a** in Fig. 1). Here, the bond angle C_β-C_α-H becomes larger, and the C—C bond length shortens as compared to those in **2a**, exhibiting partial triple-bond nature. It is noted that the C_β—H—Cl bond is nearly linear (178.8°) in **6a**.

We have postulated previously that the LC substitution and βE occur both from the chloro-λ^3-iodane, which has a conformation with the vinyl group in an equatorial position (and the chlorine in the apical position) (9, 12). Since such a conformation could not be obtained as an energy minimum for the methyl(vinyl)iodonium model because of apicophilicity reasons (22), another model system closer to the actual phenyl(vinyl)iodonium ion was examined, i.e., the divinyliodonium ion (**1e**) and the species resulting from complexation with the chloride ion. We obtained two conformations of the ion; one with C_2 (**1e**) and one with C_s symmetry (**1e′**) as shown in Fig. 2. The former is only 0.42 kcal mol^{-1} more stable than the latter (Table 1). Figure 2 shows two views of each conformer with selected geometrical parameters. Interaction of **1e** (or **1e′**) with Cl^- results in the hypervalent intermediate of two different conformations, **2e** and **2e′**, with the former being more stable than the latter by 0.97 kcal mol^{-1} (Fig. 2 and Table 1). In **2e**, Cl is located near the α-hydrogen of the equatorial vinyl group, while Cl is near the β-hydrogen in **2e′**. The angles of the apical bonds are 171.0 and 175.3° for **2e** and **2e′**, respectively. It is also noted that the apical C_α—I bond length is 2.150–2.156 Å, while the equatorial bond length is 2.117–2.127 Å. The close similarity in Cl^- complexation energies of **2e** and **2a** shows that the difference in an equatorial ligand (i.e., methyl vs. vinyl) has little influence on the stability of the λ^3-iodane.

Optimized geometries of the TS values for the S_N2, LC, and βE obtained for **1e** + Cl^- are illustrated in Fig. 3. Geometrical features of these TS values **4e–6e** are similar to those obtained for the methyl vinyl species (**4a–6a**). The two views of **4e** and **5e** are shown to illustrate the stereochemistry of the substitutions in Fig. 3. The TS for βE, **6e**, is essentially in a plane except for the vinyl group of the nucleofuge.

The electronic and free energy of transition states **4–6** with respect to the stable iodane **2** are given in Table 3. Effects of solvation on these energies were evaluated for

© 1999 NRC Canada

Fig. 3. Transition state geometries for the reactions of **1e** and chloride ion.

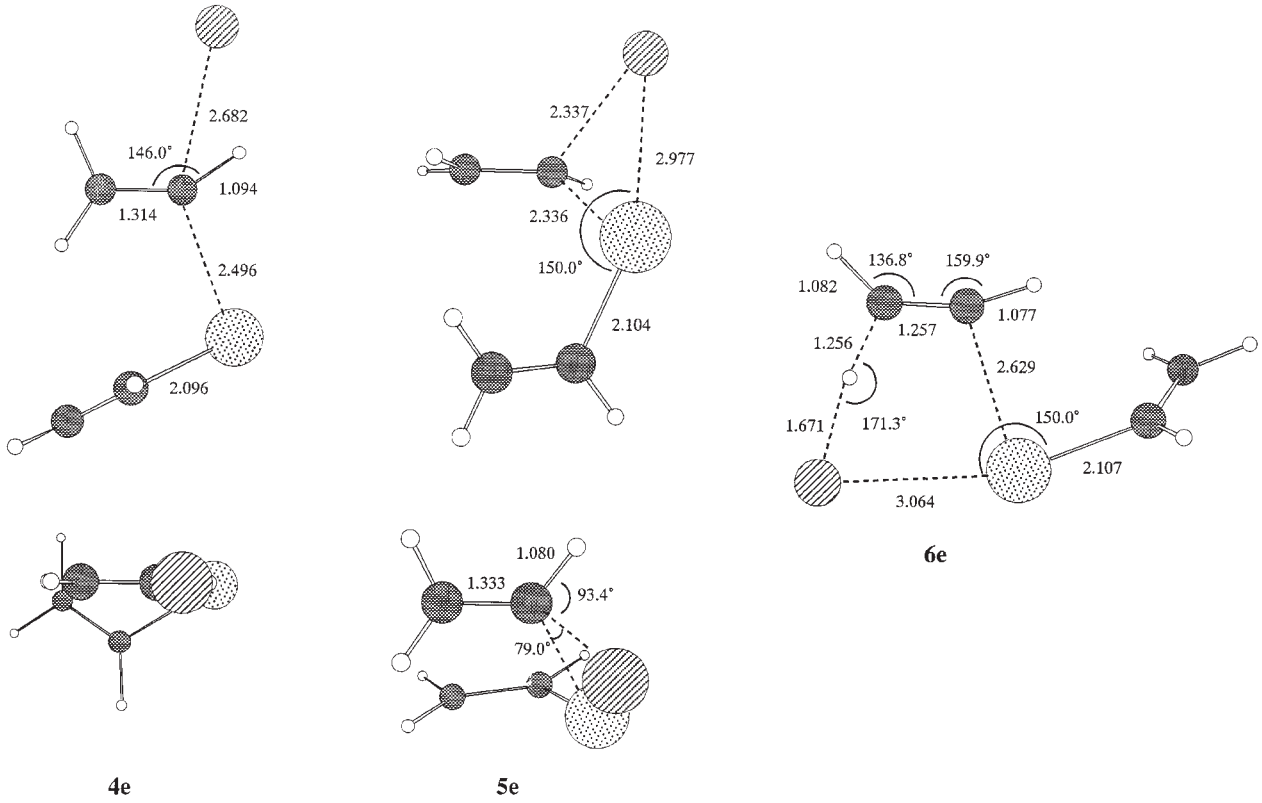

Table 3. Transition state energies, $\Delta E^{\ddagger}$ ($\Delta G^{\ddagger}$), for the reactions of iodonium ions **1** in the gas phase and solution.[a]

	4 (S_N2)		**5** (LC)		**6** (βE)	
Entry	Gas phase	Solution	Gas phase	Solution	Gas phase	Solution
a	28.6 (25.1)	23.6 (20.2)	22.9 (22.7)	24.5 (24.3)	29.2 (24.5)	32.1(27.4)
b	29.0 (25.4)	30.4 (26.6)	24.5 (24.4)	28.2 (28.1)	28.5 (24.3)	34.9 (30.7)
c	29.2 (27.5)	34.9 (33.2)	23.0 (22.6)	27.3 (26.9)	25.2 (21.2)	30.2 (26.2)
d	34.3 (31.2)	35.8 (32.7)	23.2 (23.6)	25.3 (25.7)		
e	30.5 (26.7)	17.1 (13.3)	23.7 (22.7)	24.4 (23.4)	24.6 (20.2)	25.3 (20.9)

[a]Energy differences, $\Delta E^{\ddagger}$ and $\Delta G^{\ddagger}$ in parentheses, between the transition state and the most stable chloro-λ^3-iodane **2** are given in kcal mol^{-1}. The values in acetonitrile solution (dielectric constant = 37.5) were calculated by the SCRF approximation.

acetonitrile solution by a dielectric continuum model using an SCRF approximation (21) at the gas phase geometries, and the results are included in Table 3.

Discussion

As described in the introduction section, the experimental results can be summarized as follows. (*i*) For simple 1-alkenyliodonium ions (modeled by **1a**, **1b**, or **1e**), S_N2 and βE are the competing reactions with LC being less favored. (*ii*) The β-*tert*-butyl substitution (modeled by **1c**) completely inhibits the S_N2 pathway, and the only reaction observed is βE. (*iii*) The 2-chloro substitution of 1-alkenyliodonium ion (modeled by **1d**) retards S_N2, makes βE impossible, and makes LC the only reaction observed (12). We will examine how the experimental observations of relative ease of the three reactions can be reproduced by the calculations.

Calculations in the gas phase

LUMO

Let us first examine what are the low-lying vacant orbitals of the vinyliodonium ion **1** and the λ^3-iodane **2** and how these orbitals are related to the reactivities toward nucleophiles. In Table 2 are summarized the lowest three vacant orbitals. For all the methyl iodonium salts (**1a**–**d**) and their λ^3-iodanes (**2a**–**d**), the LUMO is the anti-bonding orbital (σ^*_M) localized on the I—CH_3 bond even though this bond is in the equatorial position of **2**. This suggests that the most facile reaction to occur would be the S_N2 reaction at the methyl group; this is quite reasonable, although we do not examine reactions at this site. In the vinyl group portion of our interest, the σ* orbital (σ^*_V) for the C_α—I bond is lower than the π* orbital both for **1** and **2**. This feature that the σ* is lower than the π* orbital was recently pointed out by Modena and co-workers (14*b*) to suggest preference of

© 1999 NRC Canada

the in-plane vinylic S_N2 reaction of the methyl(vinyl)iodonium ion. In divinyl-λ^3-iodane **2e** the σ^* for the apical bonding is the LUMO, and the π^* orbital of the apical vinyl group is the third lowest vacant orbital (LUMO + 2); that is, the apical vinyl group would be a more reactive site than the equatorial one toward nucleophiles. The low-lying σ^* orbitals are characteristic of the vinyl iodonium ion and λ^3-iodane derivatives and contribute to make the in-plane nucleophilic attack at the vinyl group a facile pathway of these substrates.

S_N2 vs. LC

The calculated TS energies for the reactions of the vinyliodonium ions (Table 3) indicate that in the gas phase the in-plane S_N2 (**4**) is less favorable than the out-of-plane substitution (**5**) for all the compounds examined (**1a**–**1e**) both in terms of electronic energy and free energy. These results point out that the LUMO energy level is not the determining factor of the reactivity of the methyl(vinyl)iodonium ion (14*b*).

The above energetic order that predicts more favorable LC than S_N2 process is in marked contrast to arguments recently presented by Glukhovtsev et al. (14*a*), who carried out ab initio MO calculations on the reaction of vinyl chloride with chloride ion with the G2 procedure and found that the barrier to the in-plane S_N2 of inversion of configuration is lower (32.7 kcal mol^{-1}) than that to the out-of-plane substitution of retention of configuration (42.8 kcal mol^{-1}). The apparent discrepancy between the two computations are very likely due to the presence of a facile ligand coupling pathway for the iodonium salts (interaction of Cl with I at the transition state), which is absent in the reaction of vinyl chloride. Clearly the results on the reaction of vinyl chloride cannot be extrapolated to the vinyliodonium system.

Inclusion of the entropy term makes the energy difference between the S_N2 TS (**4**) and LC TS (**5**) smaller, as evident from $\Delta G^{\ddagger}$, but TS **4** is still consistently higher in energy than TS **5**. Thus, the gas-phase results differ from those observed experimentally in solution. Substituent effects on the barrier to LC (**5**) in the gas phase are rather small, but the β-chloro group raises the TS for S_N2 considerably (Table 3, **4d** vs. **4b**).

S_N2 vs. βE

The transition state for βE (**6a**), for the methyl(vinyl)iodonium system, does not seem to be a good model for the βE TS of the phenyl iodonium derivative (used in the actual reactions), because the chloride ion has a hydrogen-bonding interaction with the methyl hydrogen. By contrast, the chlorine keeps the interaction with the iodine in the divinyl system, **6e**, showing intramolecular reaction behavior within the hypervalent intermediate **2e′**. The TS values for S_N2 (**4a**) and βE (**6a**) were calculated to be similar in energy for the methyl(vinyl)iodonium system, while the former is considerably higher in energy than the latter for the divinyl system in the gas phase (cf. **4e** and **6e**, Table 3). Thus, the energetics obtained by the gas-phase calculations is again different from that deduced from the solution reactions (more facile S_N2 over βE).

Effects of the β-*tert*-butyl substitution are rather unexpected. The calculation results in the gas phase do not show appreciable retardation of S_N2 expected from the steric effect due to β-*tert*-butyl (**4c** vs. **4a**/**4b** in Table 3) either in terms of $\Delta E^{\ddagger}$ or $\Delta G^{\ddagger}$. Comparison of the S_N2 TS **4c** with **4b** (or more markedly with **4a**) shows that the angle C_β-C_α-Cl becomes larger from 110.3° to 115.0°, while the bond length C_α—Cl is shortened from 2.652 to 2.494 Å on going from **4b** to **4c**. That is, TS becomes considerably late by changing the β-methyl to the β-*tert*-butyl group. The steric bulk of the *tert*-butyl group is avoided by the wider angle of C_β-C_α-Cl. The late TS of **4c** results in its low polarity or a small TS dipole moment.

Table 4. Calculated dipole moments of the iodanes and transition states.[a]

Entry	**2**	**4** (S_N2)	**5** (LC)	**6** (βE)
a	9.303	11.331	8.767	8.754
b	10.117	9.949	9.064	8.555
c	10.629	7.683	8.924	8.195
d	9.959	7.906	8.875	
e	9.664 (8.797)[b]	14.610	9.147	8.969

[a] In debye.

[b] A value for **2e′**.

Medium effects

The calculations suggest that gas-phase reactivities, though the experimental data are not available, differ much from the trends observed on solution reactions. That is, medium effects are important in determining the reactivity of the iodonium/iodane substrates. Calculated dipole moments, μ, of the iodanes **2** and TS **4**–**6** are summarized in Table 4. The variation of μ is not uniform particularly in the case of S_N2 TS (**4**). All the μ of TS for LC (**5**) and βE (**6**) are somewhat smaller than those of the corresponding iodanes (**2**), and variation by the structure (**a**–**e**) is rather small. By contrast, the μ of **4** changes greatly with substituent: that for the β-*tert*-butyl derivative (**4c**) is much smaller than that of the iodane **2c**, while that of the unsubstituted vinyl system (**4a** or still markedly **4e**) is greater than that of **2a** (or **2e**). From these results we can expect different medium effects on different reactions, and thus we evaluated the medium effects by the SCRF calculations to examine how much those dipole moment variations affect the energetics in solution, even though the method is the simplest scheme that takes the effect of the dielectric constant of solvent into account and admittedly crude for quantitative energy evaluations.

The results listed in Table 3 in fact demonstrate that the medium effects dramatically change the energetics, and are as expected from the dipole moment differences, compared with the gas-phase results. First, the S_N2 TS is now lower in energy than the LC TS for **1a**, **1b**, and **1e**. It is also apparent that incorporation of medium effects results in a large stabilization of the TS for S_N2 (**4e**) but a small change in the energy barrier to βE (**6e**) for the divinyl system. The βE barriers for the other methyl systems are raised. Hence, the S_N2 reaction is now predicted to be the most facile reaction for **1a**, **1b**, and **1e**.

© 1999 NRC Canada

Second, although the gas-phase calculations do not show any appreciable adverse effects of the β-*tert*-butyl group on the S_N2 TS, the medium effect is large, and the free-energy difference for **4c** becomes greater than that for **4a** by 13.0 kcal mol^{-1}. This trend arises from a smaller μ of the late TS, **4c**, as discussed above. The S_N2 process is totally inhibited, and βE becomes the most feasible process of **1c** in solution. Finally, it is obvious that the S_N2 process is retarded by the β-chloro substitution, and LC becomes a more facile reaction for **1d**. In this case, the medium effects are rather small, and the observed effects of β-chloro substitution are intrinsic as reproduced by the gas-phase calculations (Table 3). Taking the medium effects into consideration, though crude, all the calculation results are consistent with the experimental observations in solution.

In summary, the major experimental preferences for the three product formation processes, namely, substitution with inversion of configuration (S_N2), substitution with retention of configuration (LC), and β-elimination (βE), are possible reaction pathways in the gas phase, but the relative ease of the three pathways can only be reproduced by the calculations with medium effects; that is, (*i*) the vinylic in-plane S_N2 reaction is demonstrated as a possible substitution pathway, and it is a more feasible pathway than LC, for **1a** and **1b** as well as **1e**; (*ii*) S_N2 is inhibited by the β-*tert*-butyl substitution (**1c**), and βE becomes the predominant pathway; (*iii*) S_N2 is disfavored, and LC is the predominant process for the β-Me–β-Cl system (**1d**); (*iv*) the experimental variation in the reactivity of a series of vinyliodonium salts are not only due to the intrinsic character of these species, but are modified by the medium effects. Finally, the present results fully support the previous idea that the substitution with inversion of configuration occurs via in-plane S_N2 TS, while that with retention and β-elimination occurs via the halo-λ^3-iodane intermediate.

Acknowledgments

The authors are grateful to Professor Shigeru Nagase for some preliminary calculations and advice and to Professor Masahito Ochiai for invaluable suggestions. Numerical calculations were in part carried out at the Computer Center of the Institute for Molecular Science, Okazaki, Japan.

References

1. G.F. Koser. *In* The chemistry of functional groups. Suppl. D. *Edited by* S. Patai and Z. Rappoport. Wiley–Interscience, Chichester. 1983. Chaps. 18 and 25.
2. A. Varvoglis. The organic chemistry of polycoordinated iodine. VCH, New York. 1992.
3. A. Varvoglis. Hypervalent iodine in organic synthesis. Academic Press, San Diego, Calif. 1997.
4. P.J. Stang and V.V. Zhdankin. Chem. Rev. **96**, 1123 (1996).
5. W.D. Pfeifer, C.A. Bahn, P.v.R. Schleyer, S. Bocher, C.E. Harding, K. Hummel, M. Hanack, and P.J. Stang. J. Am. Chem. Soc. **93**, 1513 (1971).
6. T. Okuyama, T. Takino, T. Sueda, and M. Ochiai. J. Am. Chem. Soc. **117**, 3360 (1995).
7. T. Okuyama and M. Ochiai. J. Am. Chem. Soc. **119**, 4785 (1997).
8. T. Okuyama, K. Sato, and M. Ochiai. Chem. Lett. 1177 (1998).
9. T. Okuyama, T. Takino, K. Sato, K. Oshima, S. Imamura, H. Yamataka, T. Asano, and M. Ochiai. Bull. Chem. Soc. Jpn. **71**, 243 (1998).
10. M. Ochiai, Y. Takaoka, and Y. Nagao. J. Am. Chem. Soc. **110**, 6565 (1988).
11. M. Ochiai, K. Oshima, and Y. Masaki. J. Am. Chem. Soc. **113**, 7059 (1991).
12. T. Okuyama, T. Takino, K. Sato, and M. Ochiai. J. Am. Chem. Soc. **120**, 2275 (1998).
13. (*a*) V. Lucchini, G. Modena, and L. Pasquato. J. Am. Chem. Soc. **115**, 4527 (1993); (*b*) B. A. Shainyan and Z. Rappoport. J. Org. Chem. **58**, 3421 (1993).
14. (*a*) M.N. Glukhovtsev, A. Pross, and L. Radom. J. Am. Chem. Soc. **116**, 5961 (1994); (*b*) V. Lucchini, G. Modena, and L. Pasquato., J. Am. Chem. Soc. **117**, 2297 (1995).
15. (*a*) D.R. Kelsey and R.G. Bergman. J. Am. Chem. Soc. **93**, 1953 (1971); (*b*) J. McMurry. Fundamentals of organic chemistry. 3rd ed. Brooks/Cole Pub. Co., Pacific Grove, Calif. 1994. p. 213.
16. (*a*) M. Ochiai, K. Oshima, and Y. Masaki. Chem. Lett. 871 (1994); (*b*) T. Okuyama, T. Takino, K. Sato, and M. Ochiai. Chem. Lett. 955 (1997).
17. C. Møller and M.S. Plesset. Phys. Rev. **46**, 618 (1934).
18. M.J. Frisch, G.W. Trucks, H.B. Schlegel, P.M.W. Gill, B.G. Johnson, M.A. Robb, J.R. Cheeseman, T. Keith, G.A. Petersson, J.A. Montgomery, K. Raghavachari, M.A. Al-Laham, V.G. Zakrzewski, J.V. Ortiz, J.B. Foresman, J. Cioslowski, B.B. Stefanov, A. Nanayakkara, M. Challacombe, C.Y. Peng, P.Y. Ayala, W. Chen, M.W. Wong, J.L. Andress, E.S. Replogle, R. Gomperts, R.L. Martin, D.J. Fox, J.S. Binkley, D.J. Defrees, J. Baker, J.P. Stewart, M. Head-Gordon, C. Gonzalez, and J.A. Pople. GAUSSIAN 94, Revision C.2. Gaussian, Inc., Pittsburgh, Pa. 1995.
19. T.H. Dunning and P.J. Hay. *In* Modern theoretical chemistry. Vol. 3. *Edited by* H.F. Schaefer. Plenum, New York. 1977. pp. 1–27.
20. W.R. Wadt and P.J. Hay. J. Chem. Phys. **82**, 284 (1985).
21. M.W. Wong, M.J. Frisch, and K.B. Wiberg. J. Am. Chem. Soc. **113**, 4776 (1991); M.W. Wong, K.B. Wiberg, and M.J. Frisch. J. Am. Chem. Soc. **114**, 1645 (1992).
22. (*a*) S. Tippett, Pure Appl. Chem. **40**, 595 (1974); (*b*) R.R. Holms. J. Am. Chem. Soc. **100**, 433 (1978); (*c*) R.S. McDowell and A. Streitwieser, Jr. J. Am. Chem. Soc. **107**, 5849 (1985); (*d*) P. Wang, Y. Zhang, R. Glaser, A.E. Reed, P.v.R. Schleyer, and A. Streitwieser. J. Am. Chem. Soc. **113**, 55 (1991).

© 1999 NRC Canada

Detection and kinetic characterization of S_NV intermediates. Reactions of thiomethoxybenzylidene Meldrum's acid with thiolate ions, alkoxide ions, OH^-, and water in aqueous DMSO

Claude F. Bernasconi, Rodney J. Ketner, Xin Chen, and Zvi Rappoport

Abstract: The reaction of thiomethoxybenzylidene Meldrum's acid (**5-SMe**) with thiolate and alkoxide ion nucleophiles is shown to proceed by the two-step addition–elimination S_NV mechanism in which the tetrahedral intermediate accumulates to detectable levels. For the reactions with thiolate ions, rate constants for nucleophilic addition (k_1^{RX}), its reverse (k_{-1}^{RX}), and for conversion of the intermediate to products (k_2^{RX}) were determined. For the reactions with alkoxide ions, only k_1^{RX} and k_{-1}^{RX} could be obtained; the intermediate in these reactions did not yield the expected substitution products, and hence no k_2^{RX} values could be determined. The reaction with OH^- and water are believed to follow the same mechanism, but the respective intermediates remain at steady-state levels, and only k_1^{OH} and $k_1^{H_2O}$ for nucleophilic attack on **5-SMe** were measurable. New insights regarding structure–reactivity behavior in S_NV reactions are gained from comparisons of rate and equilibrium constants in the reactions of **5-SMe** with the corresponding parameters in the reactions of methoxybenzylidene Meldrum's acid (**5-OMe**) and benzylidene Meldrum's acid (**5-H**). In particular, the relative importance of steric and π-donor effects of the MeS vs. MeO group in **5-SMe** and **5-OMe**, respectively, and their role in affecting the intrinsic rate constants for nucleophilic addition, has been clarified by these comparisons. Our results also add support to a previous suggestion that soft–soft type interactions tend to increase intrinsic rate constants for thiolate ion addition to vinylic substrates, especially **5-SMe** with the soft MeS group.

Key words: nucleophilic vinylic substitution, intrinsic rate constants, transition state imbalances, steric/π-donor/anomeric effects.

Résumé : On a démontré que la réaction du thiométhoxybenzylidène de l'acide de Meldrum (**5-SMe**) avec des nucléophiles comme les ions thiolate et alcoolate se produit par un mécanisme d'addition–élimination en deux étapes, S_NV, au cours duquel l'accumulation de l'intermédiaire tétraédrique est telle qu'il est possible de le détecter. Pour les réactions avec les ions thiolates, on a déterminé les constantes de vitesse de l'addition nucléophile (k_1^{RX}), de la réaction inverse (k_{-1}^{RX}) ainsi que celle de la conversion de l'intermédiaire en produits (k_2^{RX}). Pour les réactions avec les ions alcoolates, on n'a pu déterminer que les valeurs de k_1^{RX} et de k_{-1}^{RX}; dans ce cas, l'intermédiaire ne conduit pas aux produits de substitution attendus et on n'a donc pas pu déterminer les valeurs de k_2^{RX}. On suppose que les réactions avec l'eau et avec l'ion OH^- se produisent par le même mécanisme; toutefois, les intermédiaires respectifs se maintiennent aux niveaux de l'état stationnaire et, pour les réactions nucléophiles avec le **5-SMe** on ne peut mesurer que les valeurs de k_1^{OH} et $k_1^{H_2O}$. On a développé une meilleure compréhension du comportement structure–réactivité dans les réactions S_NV en procédant à des comparaisons des constantes de vitesse de réaction et d'équilibre dans les réactions du **5-SMe** avec les paramètres correspondants dans les réactions du méthoxybenzylidène de l'acide de Meldrum (**5-OMe**) et du benzylidène de l'acide de Meldrum (**5-H**). Ces comparaisons ont permis, en particulier, de clarifier l'importance des effets stériques et donneurs π des groupes MeS par rapport à MeO respectivement dans les composés **5-SMe** et **5-OMe** et de leur rôle sur les valeurs intrinsèques des constantes de vitesse de réaction de l'addition nucléophile. Nos résultats confirment une suggestion faite antérieurement à l'effet que les interactions de type mou-mou tendent à augmenter les constantes intrinsèques des vitesses de réactions pour les réactions d'addition de l'ion thiolate sur des substrats vinyliques, particulièrement le **5-SMe** comportant le groupe mou MeS.

Received November 5, 1998.

This paper is dedicated to Jerry Kresge in recognition of his many achievements in chemistry.

C.F. Bernasconi[1] and R.J. Ketner. Department of Chemistry and Biochemistry of the University of California, Santa Cruz, CA 95064, U.S.A.
X. Chen and Z. Rappoport. Department of Organic Chemistry, the Hebrew University of Jerusalem, Jerusalem 91904, Israel.

[1]Author to whom correspondence may be addressed. Telephone: (831) 459-2035. Fax: (831) 459-2935.
e-mail: bernasconi@chemistry.ucsc.edu

 © 1999 NRC Canada

Mots clés : substitution vinylique nucléophile, constantes intrinsèques de vitesses de réaction, déséquilibre dans état de transition, effets stériques/donneur-π/anomère.

[Traduit par la Rédaction]

Nucleophilic substitution at vinylic carbon (S_NV) is an important reaction that may proceed by a variety of different mechanisms (1–7). With substrates (**1**) moderately or strongly activated by electron withdrawing substituents (Y,Y′), the preferred mechanism involves two steps as shown in eq. [1] where Nu^- is an anionic nucleophile, and LG is the anionic leaving group.

[1] 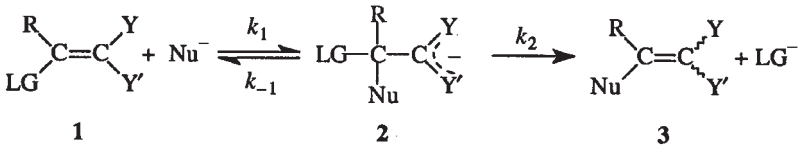

1 **2** **3**

Recent research in our laboratory has focused on reactions of strong nucleophiles with highly activated substrates that have a sluggish leaving group where the intermediate accumulates to detectable levels. Early examples include the reactions of β-methoxy-α-nitrostilbene, **4-OMe**, and β-thioalkoxy-α-nitrostilbene, **4-SR**, with thiolate ions (8, 9); for other examples see refs. 10–13. Recently, we have reported that in the reactions of thiolate and alkoxide ions with methoxybenzylidene Meldrum's acid, **5-OMe**, the respective intermediates are also directly observable (14).

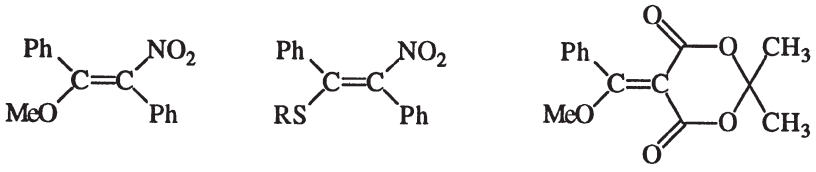

4-OMe **4-SR** **5-OMe**

Our main motivation in searching for systems that allow direct observation of the intermediate is that all rate constants in eq. [1] (k_1, k_{-1}, and k_2) can be determined. A systematic study of how these rate constants depend on the Nu^-, LG, and Y,Y′ is expected to help unravel the complex interplay of the various factors that affect reactivity in S_NV reactions. Apart from the basicities of nucleophile and leaving group, these factors include π-donor effects of the leaving group as well as the nucleophile (once attached to the substrate), anomeric, steric, polarizability, inductive/field, and resonance effects of the activating groups, and possibly others.

In the present paper we report on our study of the reactions of thiomethoxybenzylidene Meldrum's acid, **5-SMe**, with thiolate and alkoxide ions as well as OH^- and water in 50% Me_2SO – 50% water (v/v). Just as with **5-OMe**, the respective intermediates in the reactions of **5-SMe** with thiolate and alkoxide ions (but not with OH^-) were directly observable. However, the reactivity patterns with **5-SMe** show some important differences compared to those with **5-OMe**. Of particular interest are the insights gained not only from comparisons between **5-SMe** and **5-OMe** but also from those between **5-SMe** and the unsubstituted benzylidene Meldrum's acid, **5-H** (15), and especially from comparison of *intrinsic* rate constants[2] for the various compounds.

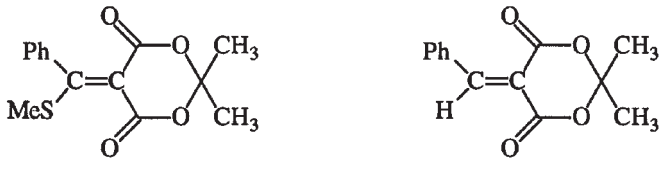

5-SMe **5-H**

Results

Reaction of 5-SMe with OH^- and water

The rate of hydrolysis of **5-SMe** conforms to eq. [2], as for the hydrolysis of **5-OMe** (14). The organic product is the same as in the hydrolysis of **5-OMe**, i.e., **5-OH**,[3] which under most conditions is present in the form of its anion

[2] The intrinsic rate constant of a reaction with a forward rate constant k_1 and a reverse rate constant k_{-1} is defined as $k_o = k_1 = k_{-1}$ when the equilibrium constant $K_1 = 1$ ($\Delta G° = 0$).

[3] The identification of **5-OH** has been described elsewhere (14).

© 1999 NRC Canada

Fig. 1. Reaction of **5-SMe** with $HOCH_2CH_2S^-$ at pH 10.58 in 50% DMSO – 50% water at 20°C. Pseudo-first-order rate constants of the second (slow) process according to eq. [6].

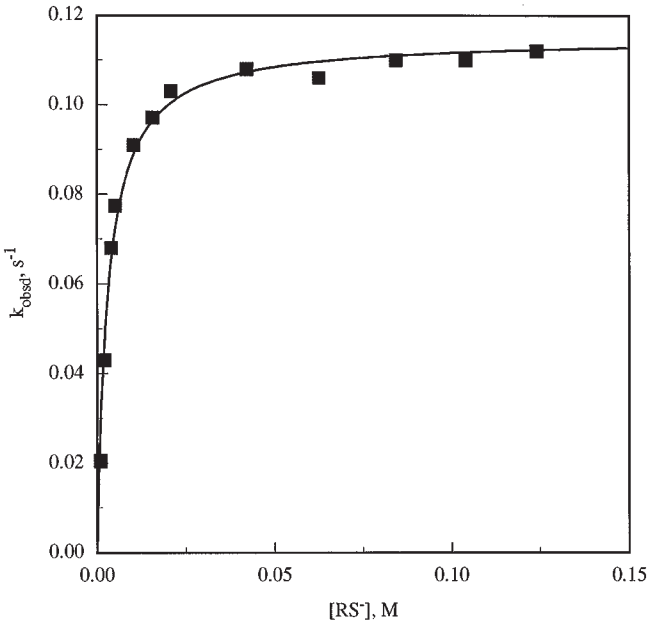

Fig. 2. Reaction of **5-SMe** with $CF_3CH_2O^-$ at pH 14.00 in 50% DMSO – 50% water at 20°C, $[\mathbf{5\text{-}SMe}]_o = 8.0 \times 10^{-5}$ M. Spectrum *a* represents **5-SMe** taken in a neutral solution in the absence of $CF_3CH_2O^-$; all other spectra are at pH 14.00 in the presence of 0.15 M $CF_3CH_2O^-$. Spectrum *b* taken approximately 5 s after mixing, spectrum *c* taken 5 s after *b*, and all other spectra taken at additional 5 s intervals for 120 s.

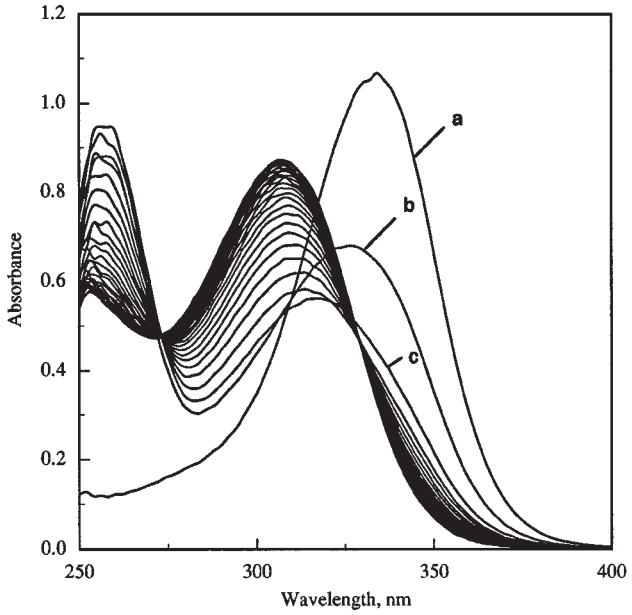

$\mathbf{6}^-$ (pK_a(**5-OH**) = 1.06) (14). The main difference between the hydrolysis of **5-SMe** and **5-OMe** is that the reaction of **5-SMe** is several orders of magnitude slower.

[2] $$k_{obsd} = k_{H_2O} + k_{OH}[OH^-]$$

Reaction of 5-SMe with thiolate ions

When **5-SMe** is mixed with a thiolate buffer two kinetic processes are observed. The first is on the stopped-flow time scale and leads to a loss of absorption at 335 nm, which is the λ_{max} of **5-SMe**. This is consistent with addition of RS^- to **5-SMe** according to eq. [3]. The spectrum of the intermediate, **5-(SMe,SR)**$^-$, which is expected to be similar to that of intermediates derived from the addition of thiolate or alkoxide ions to **5-OMe** (14) and **5-H** (15) or alkoxide in addition to **5-SMe** ($\lambda_{max} \approx 260$ nm, see below), could not be recorded. This is because at the relatively high thiolate ion concentrations (>10^{-2} M) required to push the equilibrium of eq. [3] to the right there is strong interference by the absorbance of RS^-. (In the reactions of **5-OMe** or **5-H** with thiolate ions, the spectra of the corresponding intermediates were easily obtained (14, 15) because the equilibrium constants for thiolate ion addition are much higher, so that much lower [RS^-] could be used.)

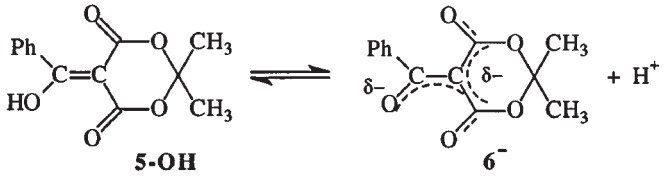

5-OH **6**$^-$

[3] 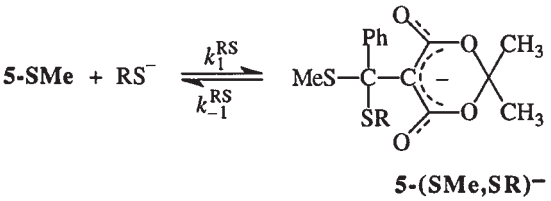

5-(SMe,SR)$^-$

The kinetic data conform to eq. [4]. Some of the plots of k_{obsd} vs. [RS^-] have measurable intercepts that yield an approximate value for k_{-1}^{RS}; k_1^{RS} and k_{-1}^{RS} values are reported in Table 1.

[4] $$k_{obsd} = k_1^{RS}[RS^-] + k_{-1}^{RS}$$

The second process is much slower, with k_{obsd} showing a nonlinear dependence on [RS^-] (Fig. 1). This is consistent with conversion of **5-(SMe,SR)**$^-$ to **5-SR** according to eq. [5].

[5] 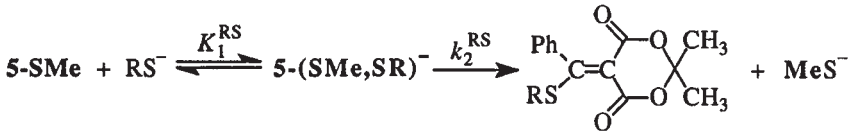

5-SR

© 1999 NRC Canada

Table 1. Summary of rate and equilibrium constants for the reactions of **5-SMe**, **5-OMe**, and **5-H** with various nucleophiles in 50% DMSO – 50% water (v/v) at 20°C, μ = 0.5 M.

RX^-	pK_a^{RXH}	k_1^{RX} (M^{-1} s^{-1})	k_{-1}^{RX} (s^{-1})	K_1^{RX} (M^{-1})	k_2^{RX} (s^{-1})	k_2^{RX}/k_{-1}^{RX}
			5-SMe[a]			
n-BuS^-	11.40	$(1.68 \pm 0.02) \times 10^3$	0.74 ± 0.10[b]	$(2.26 \pm 0.29) \times 10^3$	0.404 ± 0.01	0.55
$HOCH_2CH_2S^-$	10.56	$(9.22 \pm 0.12) \times 10^2$	2.78 ± 0.25[b]	$(3.32 \pm 0.27) \times 10^2$	0.115 ± 0.002	4.14×10^{-2}
$MeO_2CCH_2S^-$	8.83	$(7.17 \pm 0.15) \times 10^2$	22.3 ± 0.15[b]	$(3.21 \pm 0.17) \times 10^1$	$(2.69 \pm 0.01) \times 10^{-2}$	1.21×10^{-3}
$HC{\equiv}CCH_2O^-$	15.2	$(1.04 \pm 0.04) \times 10^1$[c]				
$CF_3CH_2O^-$	14.0	1.41 ± 0.12[c]	$(4.93 \pm 0.91) \times 10^{-2}$[b]	$(2.86 \pm 0.35) \times 10^1$	$\leq(2.30 \pm 0.10) \times 10^{-2}$[f]	<0.47
OH^-	17.33	$(6.43 \pm 0.06) \times 10^{-1}$				
H_2O	–1.44	$(2.80 \pm 0.40) \times 10^{-6}$[e]				
			5-OMe[d]			
n-BuS^-	11.40	6.70×10^4	0.395	1.70×10^5	1.11×10^{-4}	2.81×10^{-4}
$HOCH_2CH_2S^-$	10.56	4.40×10^4	1.71	2.57×10^4	2.16×10^{-4}	1.76×10^{-4}
$MeO_2CCH_2CH_2S^-$	10.40	4.43×10^4	2.00	2.22×10^4	1.98×10^{-5}	
$MeO_2CCH_2S^-$	8.83	2.40×10^4	14.0	1.71×10^3		
$HC{\equiv}CCH_2O^-$	15.2	4.61×10^3	1.06×10^{-3}	4.35×10^6		
$CF_3CH_2O^-$	14.0	1.09×10^3	1.60×10^{-2}	6.81×10^4		$<3.81 \times 10^{-4}$
OH^-	17.33	5.41×10^2				
H_2O	–1.44	2.98×10^{-2}[e]				
			5-H			
n-BuS^-	11.40	2.48×10^7	4.25×10^{-5}	5.89×10^{11}		
$HOCH_2CH_2S^-$	10.56	1.44×10^7	2.68×10^{-4}	5.38×10^{10}		
$MeO_2CCH_2S^-$	8.83	8.82×10^6	3.35×10^{-3}	2.63×10^9		
$HC{\equiv}CCH_2O^-$	15.2	3.93×10^4	4.71×10^{-4}	8.34×10^7		
$CF_3CH_2O^-$	14.0	2.06×10^4	3.25×10^{-3}	6.43×10^6		
OH^-	17.33	1.80×10^3	1.57×10^{-7}	1.15×10^{10}		

[a] This work.

[b] Calculated as $k_{-1}^{RX} = k_1^{RX}/K_1^{RX}$ with K_1^{RX} from eq. [6]; the k_{-1}^{RX} values based on eq. [4] are 0.48, 2.96, 26.4, and 0.041 s^{-1} for *n*-BuS^-, $HOCH_2CH_2S^-$, $MeO_2CCH_2S^-$, and $CF_3CH_2O^-$, respectively; the former values are considered more accurate.

[c] Average value based on determinations at 260 and 335 nm.

[d] Reference 14.

[e] In units of s^{-1}.

[f] The value 2.30×10^{-2} refers to k_u in eq. [9]; depending on which explanation holds for the reaction of **5-(SMe,OCH_2CF_3)$^-$**, k_2^{RX} is either k_u or $<k_u$, see text.

© 1999 NRC Canada

In this case, the nucleophilic addition step acts as a fast preequilibrium, and k_{obsd} is given by eq. [6].

$$[6] \qquad k_{obsd} = \frac{K_1^{RS} k_2^{RS}[RS^-]}{1 + K_1^{RS}[RS^-]}$$

K_1^{RS} and k_2^{RS} values determined by nonlinear squares fit to eq. [6] are summarized in Table 1.

The observed spectral changes call for comment. At low $[RS^-]$ ($K_1^{RS}[RS^-] << 1$) the change in absorbance at 355 nm (λ_{max} of **5-SMe**) is small. This is because the reaction represents conversion of **5-SMe** into **5-SR** with **5-(SMe,SR)**$^-$ acting as a steady-state intermediate, and the spectra of **5-SR** are similar to that of **5-SMe**. At intermediate $[RS^-]$ ($K_1[RS^-] \geq 1$), the changes in absorbance are large because the reaction refers mainly to conversion of **5-(SMe,SR)**$^-$ to **5-SR**, and **5-(SMe,SR)**$^-$ absorbs very little at 335 nm. As $[RS^-]$ is increased further, the observed changes in absorbance decrease again. This is because the product is a mixture of **5-SR** and the symmetrical adduct **5-(SR,SR)**$^-$ that is rapidly formed by addition of RS^- to **5-SR**. This adduct has a similar absorption spectrum as **5-(SMe,SR)**$^-$, which is the "reactant" under these conditions.

Reaction of 5-SMe with alkoxide ions

The reaction of **5-SMe** with a $CF_3CH_2O^-$ buffer at high $[CF_3CH_2O^-]$ is characterized by three kinetic processes. The fastest one leads to a rapid loss of **5-SMe**; it is accompanied by the formation of a new species at 260 nm. The spectrum of the latter is characteristic of a tetrahedral intermediate,[4] consistent with the formation of **5-(SMe,OR)**$^-$ (R = CF_3CH_2), eq. [7]. The spectral changes are shown in Fig. 2.

[7] **5-SMe** + RO^- $\underset{k_{-1}^{RO}}{\overset{k_1^{RO}}{\rightleftharpoons}}$ 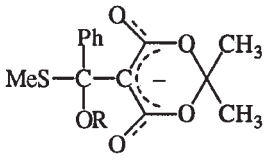

5-(SMe,OR)$^-$

The second process leads to a product with a λ_{max} = 306 nm (Fig. 2). It is unclear what this product is. It cannot be the substitution product **5-OCH$_2$CF$_3$** because its rate of hydrolysis is expected to be much faster than the rate of the transformation of **5-(SMe,OR)**$^-$ into the new species at 306 nm. (The hydrolysis of **5-OCH$_2$CF$_3$** can be expected to be at least as fast as hydrolysis of **5-OMe**. At pH 14.59 and 14.01, the conditions under which the second process was measured kinetically, k_{obsd}, for the hydrolysis of **5-OMe** is 27 and 7.2 s^{-1}, respectively, while the k_{obsd} values for the second process range from 1.06×10^{-3} to 1.80×10^{-2} s^{-1}, depending on $[CF_3CH_2O^-]$.) The spectrum of the new species is indeed inconsistent with **5-OCH$_2$CF$_3$** whose spectrum should be similar to that of **5-OMe** (λ_{max} = 278 nm) (14). But the spectrum is also inconsistent with the hydrolysis product **6**$^-$ (λ_{max} = 284 nm) (14); **6**$^-$ is eventually formed, but on a much slower time scale which corresponds to the third kinetic process mentioned earlier. Our results require one of two possible interpretations. (*i*) The intermediate, **5-(SMe,OCH$_2$CF$_3$)**$^-$, undergoes a reaction other than loss of MeS^-, leading to an unidentified product that eventually hydrolyzes to **6**$^-$. (*ii*) **5-(SMe,OCH$_2$CF$_3$)**$^-$ *is* converted to **5-OCH$_2$CF$_3$** but then rapidly reacts and forms an unidentified product that is eventually converted to **6**$^-$.

Fig. 3. Reaction of **5-SMe** with $CF_3CH_2O^-$ at pH 14.59 monitored at 260 nm or 335 nm in 50% DMSO – 50% water at 20°C. Pseudo-first-order rate constants of the second (slow) process according to eq. [9].

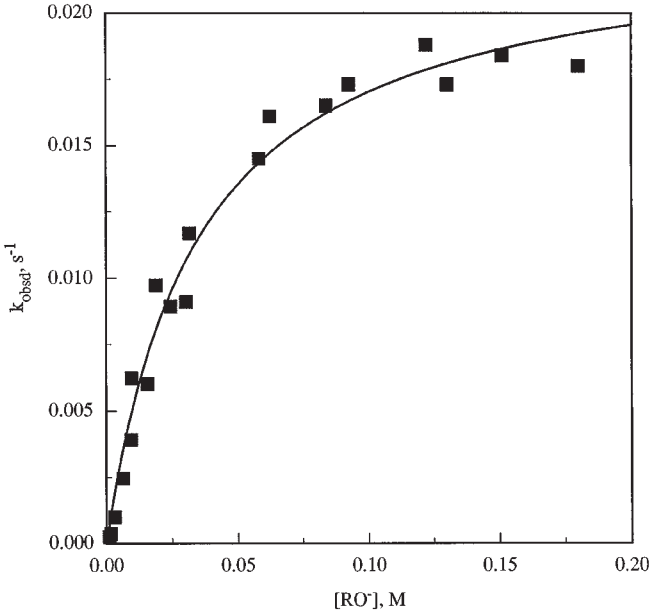

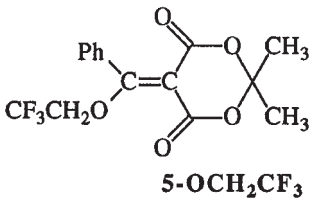

5-OCH$_2$CF$_3$

With respect to the kinetic determinations, the rates for the first process were measured at pH 14.59 by monitoring the reaction at 335 and 260 nm. The data are consistent with eq. [8].

$$[8] \qquad k_{obsd} = k_1^{RO}[RO^-] + k_{OH}[OH^-]$$

There is a contribution by the hydrolysis reaction ($k_{OH}[OH^-]$ term) that becomes significant at low $[RO^-]$; k_1^{RO} was determined from the slope of plots of $k_{obsd} - k_{OH}[OH^-]$ vs. $[RO^-]$ (not shown). ($[RO^-]$ was corrected for the homoassociation constant (K_{assoc} = 1.8 M^{-1}) (10) of $CF_3CH_2O^-$ with CF_3CH_2OH.) The reported k_1^{RO} value in Table 1 is the average of k_1^{RO} = 1.53 ± 0.04 M^{-1} s^{-1} at 335 nm and 1.28 ± 0.02 at 260 nm; k_{-1}^{RO} is too small to be obtained from these experiments.

The rates of the second process were measured at pH 14.59 (λ = 260 nm) and pH 14.01 (λ = 300 nm). A plot

[4] It is virtually identical to the spectra of **5-(OMe,SR)**$^-$ generated by the reaction of **5-OMe** with RS^- (14).

© 1999 NRC Canada

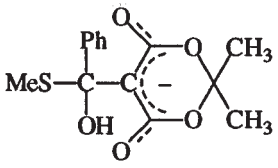

5-(SMe,OH)$^-$

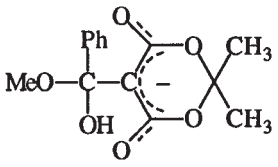

5-(OMe,OH)

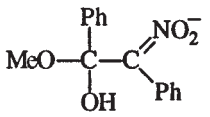

4-(OMe,OH)$^-$

of k_{obsd} vs. [RO$^-$] is shown in Fig. 3. It is consistent with eq. [9],

$$[9] \qquad k_{obsd} = \frac{K_1^{RO}[RO^-]}{1 + K_1^{RO}[RO^-]} k_u$$

with K_1^{RO} being the equilibrium constant for eq. [7], and k_u referring to the unknown reaction that depletes the intermediate. Least-squares analysis of the data according to eq. [9] yields $K_1^{RO} = (2.86 \pm 0.35) \times 10^1$ M^{-1} and $k_u = (2.30 \pm 0.10) \times 10^{-2}$ s^{-1}.

The kinetic behavior of the reaction of **5-SR** with HC≡CCH$_2$O$^-$ is similar to that for the reaction with CF$_3$CH$_2$O$^-$. However, the rate measurements for the second process gave irreproducible results which are not reported, and hence only k_1^{RO} could be determined.

Discussion

Detection of the intermediate

As is the case for **5-OMe**, the respective intermediates **5-(SMe,SR)**$^-$ in the reactions of **5-SMe** with *n*-BuS$^-$, HOCH$_2$CH$_2$S$^-$, and MeO$_2$CCH$_2$S$^-$, and the intermediates **5-(SMe,OR)**$^-$ in the reactions with HC≡CCH$_2$O$^-$ and CF$_3$CH$_2$O$^-$ all accumulate to detectable levels under the appropriate conditions. As has been discussed in detail elsewhere (8–13), the requirements for the intermediate to be detectable are that the equilibrium of the first step is favorable (k_1^{RX}[RX$^-$] > k_{-1}^{RX} or K_1^{RX}[RX$^-$] > 1) and that the rate of formation of the intermediate is faster than its rate of conversion to products (k_1^{RX}[RX] > k_2^{RX}). These conditions are evidently met in the reactions of **5-SMe** with RS$^-$ and RO$^-$.

The only intermediate that has remained elusive under all conditions is **5-(SMe,OH)**$^-$ in the hydrolysis reaction. The reasons for this are the same as why the corresponding intermediates such as **5-(OMe,OH)**$^-$ (14) and **4-(OMe,OH)**$^-$ (16) have not been detectable: their conversion to products via two pathways not available to intermediates lacking the OH group is faster than their formation and turns them into steady-state intermediates. One of these additional pathways is intramolecular acid catalysis of leaving-group departure by the OH group (10, 11, 16). The other involves rapid deprotonation of the OH group, generating the dianionic form of the intermediate which expels the leaving group much more rapidly than the monoanionic form (10, 11, 16). Note that the rapid conversion of **5-(SMe,OH)**$^-$ to products implies that attack by water and OH$^-$ is rate limiting in the hydrolysis reaction, i.e., $k_{H_2O} = k_1^{H_2O}$ and $k_{OH} = k_1^{OH}$, respectively (eq. [2]).

Structure–reactivity relationships

A. Equilibrium constants for nucleophilic addition

It is instructive to compare the equilibrium constants for nucleophilic addition to **5-SMe** with those for addition to **5-H** and **5-OMe**, which are included in Table 1. Irrespective of the nucleophile, the relative magnitude of these equilibrium constants follows the order K_1^{RX} (**5-SMe**) << K_1^{RX}(**5-OMe**) << K_1^{RX}(**5-H**). For example, for HOCH$_2$CH$_2$S$^-$ as the nucleophile, the ratios K_1^{RS}(**5-SMe**):K_1^{RS}(**5-OMe**):K_1^{RS}(**5-H**) are 6.2×10^{-9}:4.8×10^{-7}:1; for the other thiolate ions, these ratios are quite similar. For CF$_3$CH$_2$O$^-$ as the nucleophile, the ratios K_1^{RO}(**5-SMe**):K_1^{RO}(**5-OMe**): K_1^{RO}(**5-H**) are 4.5×10^{-6}:1.7×10^{-2}:1.

These trends result from an interplay of differences in steric, inductive/field, π-donor, and anomeric effects on the three reaction systems. These factors affect the K_1^{RX} values in the following way. (*i*) The increasing size in the order H << OMe << SMe leads to increasing steric crowding in the adduct and hence lowers K_1^{RX} for both **5-OMe** and **5-SMe** relative to **5-H**, and more so for **5-SMe**.[5] (*ii*) The electron-withdrawing inductive/field effect should enhance both K_1^{RX}(**5-OMe**) and K_1^{RX}(**5-SMe**) relative to K_1^{RX} (**5-H**), and somewhat more so for **5-OMe**.[6] (*iii*) The π-donor effect of the MeO and MeS groups that leads to resonance stabilization of **5-XMe** (see **5-XMe** $^{\pm}$) reduces K_1^{RX} for **5-OMe** and **5-SMe** relative to **5-H**, with the effect on K_1^{RX}(**5-OMe**) being the strongest.[7] (*iv*) The anomeric effect is an adduct stabilizing factor that mainly affects the dialkoxy intermediates in the reactions of **5-OMe** with RO$^-$ [8] and enhances K_1^{RO}(**5-OMe**) relative to K_1^{RO}(**5-SMe**) and K_1^{RO}(**5-H**).

For the thiolate ion reactions, the steric and π-donor effects appear to be the dominant factors, dramatically reducing K_1^{RS}(**5-OMe**) and K_1^{RS}(**5-SMe**) relative to K_1^{RS}(**5-H**), greatly offsetting the inductive/field effect. The fact that K_1^{RS}(**5-SMe**) is smaller than K_1^{RS}(**5-OMe**) indicates that the greater steric effect of the MeS group combined with the somewhat weaker inductive/field effect are dominant in this comparison and more than offset the weaker π-donor effect of the MeS group. Overall, when comparing the K_1^{RS} values of the three substrates, the steric effect emerges as the most important factor.

For the alkoxide ion reactions the K_1^{RO} values for **5-SMe** and **5-OMe** are not as strongly depressed relative to K_1^{RO} for

[5] Taft's steric substituent constants, E_s, are –0.55 for MeO and –1.07 for MeS, respectively (17), while Charton's (18) ν_{ef} values are 0.36 for MeO and 0.64 for MeS, respectively.
[6] σ_F = 0.30 and 0.20 for MeO and MeS, respectively (19).
[7] σ_R = –0.43 and –0.15 for MeO and MeS, respectively (19).
[8] In the present context, the anomeric effect (20, 21) refers to the stabilization exerted by geminal oxygen atoms (22–25), e.g., in dialkoxy adducts such as **5-(OMe,OR)**$^-$.

© 1999 NRC Canada

Table 2. Brønsted coefficients and intrinsic rate constants for the reactions of **5-SMe**, **5-OMe**, and **5-H** with thiolate and alkoxide ions.

Parameter	5-SMe[a]	5-OMe[b]	5-H[c]
	RS^- nucleophiles		
β_{nuc}[d]	0.13 ± 0.06	0.17	0.17
β_{lg}[e]	–0.57 ± 0.04	–0.59	–0.72
β_{eq}[f]	0.70 ± 0.09	0.76	0.89
β^n_{nuc}[g]	0.19 ± 0.06	0.22	0.19
β^n_{lg}[h]	–0.81 ± 0.06	–0.78	–0.81
log k_o^{RS}[i]	2.53 ± 0.14	3.66	5.17
β_{push}[j]	0.44 ± 0.07	0.75	
	RO^- nucleophiles		
β_{nuc}[d]	0.72[k]	0.51	0.23
β_{lg}[e]		–0.97	–0.81
β_{eq}[f]		1.48	1.03
β^n_{nuc}[g]	ca. 0.5[l]	0.34	0.22
β^n_{lg}[h]	–0.6	–0.66	–0.79
log k_o^{RO}[i]	ca. –0.9[l]	1.49	2.86

[a]This work.
[b]Reference 14.
[c]Reference 15.
[d]β_{nuc} = d log k_1^{RX}/dpK_a^{RXH}.
[e]β_{lg} = d log k_{-1}^{RX}/dpK_a^{RXH}.
[f]β_{eq} = d log K_1^{RX}/dpK_a^{RXH}.
[g]β^n_{nuc} = d log k_1^{RX}/d log K_1^{RX}.
[h]β^n_{lg} = d log k_{-1}^{RX}/d log K_1^{RX}.
[i]$k_o^{RX} = k_1^{RX} = k_{-1}^{RX}$ for $K_1^{RX} = 1$.
[j]β_{push}= d log k_2^{RS}/dpK_a^{RSH}.
[k]No standard deviation given (two points only).
[l]Estimated, see text.

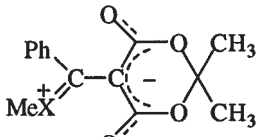

5-XMe± (X = O or S)

5-H as for the thiolate ion reactions. Here, the smaller size of the alkoxide ion nucleophiles reduces the steric crowding in the respective intermediates. On the other hand, K_1^{RO} (**5-OMe**) appears to be much more enhanced relative to K_1^{RO} (**5-SMe**) than is the case with thiolate ion nucleophiles. This demonstrates the importance of the anomeric effect, which stabilizes the dialkoxy but not the alkoxy–thioalkoxy complexes.

With respect to their absolute magnitude, the K_1^{RS} values are significantly larger than the K_1^{RO} for addition of alkoxide ion of comparable pK_a. For example, K_1^{RS} for *n*-BuS^- addition to **5-SMe** (2.26×10^3 M^{-1}) is 79-fold larger than K_1^{RO} = 28.6 M^{-1} for $CF_3CH_2O^-$ addition to the same substrate, even though the pK_a^{RSH} of *n*-BuSH is only 11.40, while that of $CF_3CH_2O^-$ is 14.0. The enhanced carbon basicity of sulfur

Fig. 4. Reaction of **5-SMe** with *n*-BuS^-, $HOCH_2CH_2S^-$, and $MeO_2CCH_2S^-$. Plots of log k_1^{RS} (●) and log k_{-1}^{RS} (○) vs. log K_1^{RS}. The point where the two lines intersect corresponds to log k_o^{RS}, see text.

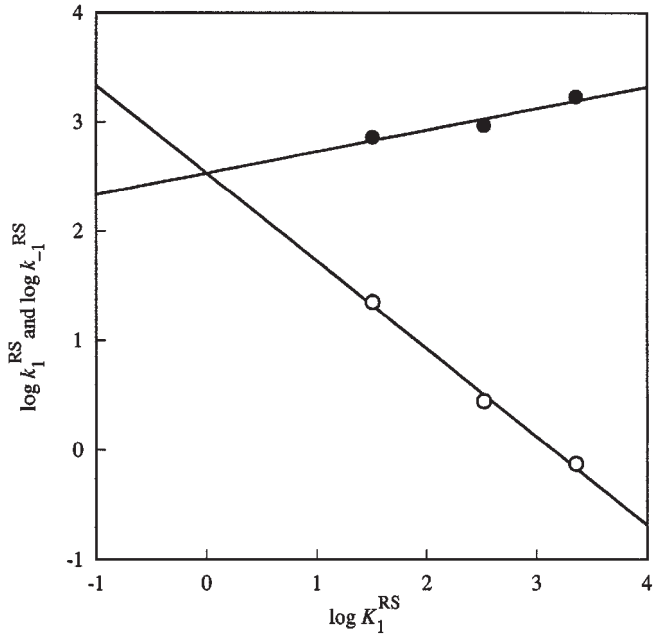

compared to oxygen nucleophiles manifests itself even more dramatically in the reactions of **5-H** where steric hindrance is less important: $K_1^{RS} = 5.89 \times 10^{11}$ M for *n*-BuS^- vs. $K_1^{RO} = 6.43 \times 10^6$ M^{-1} for $CF_3CH_2O^-$. On the other hand, in the reaction of **5-OMe** with alkoxide ions the anomeric effect reduces the advantage of the sulfur bases: $K_1^{RS} = 1.70 \times 10^5$ M (*n*-BuS^-) vs. $K_1^{RO} = 6.81 \times 10^4$ M ($CF_3CH_2O^-$).

The higher carbon basicity of sulfur compared to oxygen bases has been commonly attributed to stronger polarizability (26–28) or "softness" (29, 30) of the sulfur compounds, i.e., in the reaction of RS^- with polarizable electrophiles such as **5-H**, **5-OMe**, **5-SMe**, and other alkenes there is a favorable soft–soft interaction, while in the reactions of RO^- with the same electrophiles there is a less favorable hard–soft interaction. An additional factor, particularly important in aqueous media, is the weaker solvation of thiolate compared to that of alkoxide ions (31–33).

B. Rate constants for nucleophilic addition by RS^- and RO^-

The rate constants for nucleophilic attack on **5-SMe**, **5-OMe**, and **5-H** follow the same qualitative pattern as the equilibrium constants, i.e., k_1^{RX}(**5-SMe**) << k_1^{RX}(**5-OMe**) << k_1^{RX}(**5-H**). Specifically, the ratios k_1^{RS}(**5-SMe**):k_1^{RS}(**5-OMe**):k_1^{RS}(**5-H**) are 6.4×10^{-5}:3.1×10^{-3}:1 for $HOCH_2CH_2S^-$, which is representative for all thiolate ion nucleophiles. For the $CF_3CH_2O^-$ reaction the ratios k_1^{RO}(**5-SMe**):k_1^{RO}(**5-OMe**):k_1^{RO}(**5-H**) are 6.8×10^{-5}:5.3×10^{-2}:1. For the thiolate ion reactions the rate constant ratios are substantially smaller than the equilibrium constant ratios, consistent with the notion that the electronic and steric factors discussed above are only partially expressed at the transition state. On the other hand, for the alkoxide ion reactions the rate constant ratios are quite comparable to the equilibrium constant ratios, sug-

© 1999 NRC Canada

gesting that in moving from the reactants to the transition state, some or all the factors are nearly as strongly expressed as in moving from the reactants to the adducts. These results indicate that there must be significant differences in the *intrinsic* rate constants[2] of the various reactions.

The intrinsic rate constants are reported in Table 2. For the thiolate ion reactions they were obtained by suitable extrapolation of plots of log k_1^{RX} or log k_{-1}^{RX} vs. log K_1^{RX} (Fig. 4); they also yield the normalized Brønsted coefficients β_{nuc}^{n} and β_{lg}^{n}. For the alkoxide ion reactions, log k_o^{RX} was estimated as log k_1^{RO} – 0.5 log K_1^{RO} with k_1^{RO} and K_1^{RO} for $CF_3CH_2O^-$. (This is equivalent to applying the simplest version of the Marcus equation (34), $\Delta G^{\ddagger} = \Delta G_o^{\ddagger} + 0.5\Delta G° + (\Delta G°)^2/16\Delta G_o^{\ddagger}$ and neglecting the third term, which should be very small in our case. The factor 0.5 in front of $\Delta G°$ implies $\beta_n^{nuc} \approx 0.5$, which is a reasonable value in view of the trend in β_n^{nuc} for RO^- addition to **5-H** and **5-OMe** discussed below.)

There are large differences in the k_o^{RX} values for the various reactions. For a given type of nucleophile k_o^{RX}(**5-SMe**) << k_o^{RX}(**5-OMe**) << k_o^{RX}(**5-H**), while for a given substrate the intrinsic rate constant for the thiolate ion reactions is much higher than for the alkoxide ion reactions. To understand why such large differences in the k_o^{RX} values exist, we need to remind ourselves that intrinsic rate constants are purely kinetic quantities that have been corrected for differences in the equilibrium constants that arise from different degrees of steric, inductive/field, π-donor, anomeric, solvation, and polarizability effects. This means that if at the transition state these factors were being developed or lost in proportion to the degree of bond formation ("balanced" transition state), the k_o^{RX} values should be the same for all the reactions. The fact that they are different means that the transition states are imbalanced in several respects.

The rules of the principle of nonperfect synchronization (PNS) allow us to describe these effects as follows. (The PNS (35–37) states that if the development of a product stabilizing factor lags behind bond changes or charge transfer at the transition state, k_o is reduced. The same is true if the loss of a reactant stabilizing factor runs ahead of bond changes or charge transfer. For product stabilizing factors that develop early or reactant stabilizing factors that are lost late, k_o is enhanced. For product or reactant *de*stabilizing factors, the opposite relationships hold.)

(*i*) The π-donor resonance stabilization of **5-SMe** and **5-OMe** is expected to follow the generally observed pattern of resonance effects (35–37), and hence its loss should be more advanced than bond formation. This results in a reduction of the intrinsic rate constants and must be part of the reason why k_o^{RX} for both **5-OMe** and **5-SMe** are lower than for **5-H**.

(*ii*) The observation that the k_o^{RX}(**5-SMe**) values are more strongly reduced than the k_o^{RX}(**5-OMe**) values, despite the smaller π-donor effect of the MeS group compared to that of the MeO group, implies that an additional PNS effect is operative. We propose that this additional effect is the early development of the steric factor. (In the context of the PNS (35–37), steric crowding is a product destabilizing factor which depresses k_o if it is more advanced than bond formation.) This factor is stronger for the reactions with **5-SMe** than with **5-OMe** and should therefore depress k_o^{RX}(**5-SMe**) more than k_o^{RX}(**5-OMe**). This is a particularly significant conclusion because predictions as to whether development of steric effects is generally ahead of bond formation or lags behind it have been difficult to make (37). Specifically, in our earlier study (14) where only data on **5-OMe** and **5-H** were available, no definite conclusion regarding steric effects on the intrinsic rate constants could be drawn.

(*iii*) Following generally observed behavior (37–39), the partial desolvation of the nucleophiles that occurs as they enter the transition state should be more advanced than bond formation. This has the effect of reducing the intrinsic rate constant. Because the solvation of highly basic alkoxide ions is stronger than that of thiolate ions (31–33), k_o^{RO} decreases more than k_o^{RS}, which explains, at least in part, why k_o^{RS} >> k_o^{RO} for all substrates.

(*iv*) An additional PNS effect contributing to the high k_o^{RS} values in the thiolate ion reactions may come from the soft–soft interactions if these interactions developed ahead of bond formation. As has been discussed in more detail elsewhere (40), this is a reasonable possibility.

(*v*) The question whether the anomeric effect in the reactions of **5-OMe** with alkoxide ions develops early (increase in k_o^{RO}(**5-OMe**)) or late (decrease in k_o^{RO}(**5-OMe**)) is an interesting one. From the fact that for the alkoxide ion reactions log k_o^{RO}(**5-OMe**) – log k_o^{RO}(**5-SMe**) is large (≈2.39), while for the thiolate ion reactions log k_o^{RS}(**5-OMe**) – log k_o^{RS}(**5-SMe**) is small (1.13), one might conclude that the anomeric effect enhances log k_o^{RO}(**5-OMe**), implying that its development is ahead of bond formation of the transition state. However, an alternative interpretation of these differences is that it is log k_o^{RS}(**5-SMe**) for the thiolate ion reactions which is unusually large, making the difference log k_o^{RS}(**5-OMe**) – log k_o^{RS}(**5-SMe**) look small. An enhanced log k_o^{RS}(**5-SMe**) value could be the result of the MeS group making **5-SMe** softer than **5-OMe**, which would increase the soft–soft interactions and its k_o^{RS}(**5-SMe**) increasing PNS effect. (This may be similar to findings Bunnett has described 40 years ago (41).) Comparisons between **5-OMe** and **5-H** render this alternative interpretation more plausible: the difference log k_o^{RO}(**5-OMe**) – log k_o^{RO}(**5-H**) = –1.37 is, within experimental error, indistinguishable from log k_o^{RS}(**5-OMe**) – log k_o^{RS}(**5-H**) = –1.51, i.e., there is no enhancement of log k_o^{RO}(**5-OMe**) that could be attributed to early development of the anomeric effect.

C. Rate constants for the reactions with OH^- and water

The reactivity ratios for the OH^- reaction are k_1^{OH}(**5-SMe**):k_1^{OH}(**5-OMe**):k_1^{OH}(**5-H**) = 3.6 × 10^{-4}:0.3:1, which compares with k_1^{RO}(**5-SMe**):k_1^{RO}(**5-OMe**):k_1^{RO}(**5-H**) = 6.8 × 10^{-5}:5.3 × 10^{-2}:1 for the $CF_3CH_2O^-$ reactions. The smaller reductions in k_1^{OH} for the reactions with **5-SMe** and **5-OMe** relative to **5-H** must be the result of the smaller size of OH^- compared to $CF_3CH_2O^-$, which reduces the steric effect in the reactions with **5-SMe** and **5-OMe**. The fact that the absolute values of k_1^{OH} are all lower than for the corresponding alkoxide ion reactions can be attributed to the even stronger solvation of OH^- than that of the alkoxide ions (38, 39, 42), which reduces the intrinsic rate constant for OH^- addition (PNS effect) even more than for alkoxide ion addition.

For the water reaction only data for **5-SMe** and **5-OMe** are available; they yield $k_1^{H_2O}$(**5-SMe**)/$k_1^{H_2O}$(**5-OMe**) = 9.4 × 10^{-5}, which compares with k_1^{OH}(**5-SMe**)/k_1^{OH}(**5-OMe**) = 1.2

© 1999 NRC Canada

$\times 10^{-3}$ for the OH^- reaction. The greater selectivity in the water reaction may reflect a more intermediate-like transition state because the reaction is thermodynamically less favorable. As a result, $k_1^{H_2O}$(**5-SMe**) is more strongly reduced by the steric effect, and $k_1^{H_2O}$(**5-OMe**) is more strongly enhanced by the anomeric effect, consistent with the Hammond postulate (43–45).

D. Brønsted coefficients

Table 2 reports a variety of Brønsted coefficients such as β_{nuc}, β_{lg}, β_{eq}, β^n_{nuc}, and β^n_{lg}. For the thiolate ion reactions, β_{nuc} and β^n_{nuc} follow the well-known pattern of being very small (10, 11, 38, 40, 46–48) and $|\beta_{lg}|$ or $|\beta^n_{lg}|$ being quite large, implying little bond formation at the transition state. (This is the traditional view (43, 44, 49), although this view has been challenged (50–52) as well as defended (45).) It has been argued previously (15, 40) that the small β_{nuc} (β^n_{nuc}) values are not necessarily the result of a Hammond–Leffler effect (43, 44) arising from very large equilibrium constants for thiolate ion additions. Our results with **5-SMe** for which the K_1^{RS} values are much smaller than for **5-OMe** and particularly **5-H** support this view.

The finding that β_{eq} for the reaction of thiolate ions with **5-SMe** is smaller than 1 is again consistent with the results of **5-OMe** (14) and **5-H** (15) as well as with other examples (40, 46).

In contrast to the thiolate ion reactions β_{nuc} (β^n_{nuc}), alkoxide ion addition appears to follow the Hammond–Leffler (43, 44) trend towards larger values for thermodynamically less favored reactions. This is confirmed by the results for **5-SMe**. The unusually large β_{eq} value for alkoxide ion addition to **5-OMe** has been discussed elsewhere and attributed to the anomeric effect (14).

E. Rate constants for leaving group expulsion

Our data set for the k_2^{RX} process is not as complete as for the nucleophilic addition step. However, by including k_{-1}^{RX}, which also represents leaving group expulsion, into the discussion, several insights emerge.

(*i*) The k_{-1}^{RX} values indicate that there is moderate to strong inverse correlation between leaving group departure rate constants and the proton basicity of the leaving group. This is reflected in the relatively large β_{lg} values which range from –0.57 to –0.97 (Table 2).

(*ii*) The k_2^{RS} values for the reactions of thiolate ions with **5-SMe** and **5-OMe** increase significantly with increasing pK_a^{RSH}, indicating a substantial electronic push by the RS group left behind. This is reflected in the $\beta_{push} = d\log k_2^{RX}/dpK_a^{RXH}$ values of 0.44 (**5-SMe**) and 0.75 (**5-OMe**), respectively (Table 2). This push is the result of the developing resonance effect in the product **(5-SR)**$^{\pm}$.

(*iii*) Because a decrease in pK_a^{RSH} enhances k_{-1}^{RS} but lowers k_2^{RS}, the k_2^{RS}/k_{-1}^{RS} ratios in the reactions with thiolate ions increase strongly with decreasing pK_a^{RSH}($d(\log k_2^{RS}/k_{-1}^{RS})/dpK_a^{RSH}$ = 1.01 for **5-SMe** and 1.34 for **5-OMe**). ($d(\log k_2^{RS}/k_{-1}^{RS})/dpK_a^{RSH} = \beta_{push} - \beta_{lg}$, with β_{lg} referring to the k_{-1}^{RS} step.) For the reaction of *n*-BuS^- with **5-SMe**, the k_2^{RS}/k_{-1}^{RS} ratio is close to unity (0.55), reflecting the fact that $pK_a^{RSH} \approx pK_a^{MeSH}$.

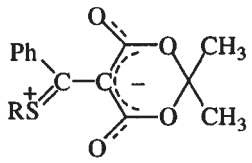

(5-SR)$^{\pm}$

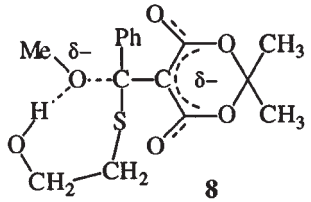

8

(*iv*) The k_2^{RS} value for the reaction of $HOCH_2CH_2S^-$ with **5-OMe** does not fit the correlation of log k_2^{RS} with the pK_a^{RSH} defined by *n*-BuS^- and $MeO_2CCH_2CH_2S^-$; it shows a strong positive deviation (14). This contrasts with k_2^{RS} for the reaction of $HOCH_2CH_2S^-$ with **5-SMe** which shows no deviation. The exalted k_2^{RS} value for **5-OMe** has been attributed to intramolecular hydrogen bonding assistance of methoxide ion departure by the OH group as shown in **8** (14). The absence of such assistance in the reaction of **5-SMe** is consistent with the weaker susceptibility to acid catalysis of thiolate ion departure compared to alkoxide ion departure (12, 13).

(*v*) The k_2^{RS} values for MeS^- departure from **5-(SMe,SR)**$^-$ are much higher than for MeO^- departure from **5-(OMe,SR)**$^-$. For example, k_2^{RS}(**5-SMe**)/k_2^{RS}(**5-OMe**) = 3.6×10^3 in the reaction with *n*-BuS^-. (The k_2^{RS}(**5-SMe**)/k_2^{RS}(**5-OMe**) ratio in the reaction with $HOCH_2CH_2S^-$ is approximately 5×10^3. This ratio is only approximate because for k_2^{RS}(**5-OMe**) the reaction with $MeO_2CCH_2CH_2S^-$ whose pK_a^{RSH} is very close to that of $HOCH_2CH_2S^-$ is used instead of the reaction with $HOCH_2CH_2S^-$; the reaction of **5-OMe** with $HOCH_2CH_2S^-$ is subject to intramolecular hydrogen bonding catalysis and has an exalted k_2^{RS} value (see (*iv*) above).) This is mainly the result of two factors. One is the superior leaving group ability of MeS^- compared to MeO^-, which is related to the lower proton basicity of the sulfur base ($pK_a^{MeSH} \approx 11.1$[9] vs. $pK_a^{MeOH} \approx 17.2$ (10)) but probably attenuated by its stronger carbon basicity. The other is the greater steric crowding in **5-(SMe,SR)**$^-$ compared to **5-(SMe,OR)**$^-$, which should enhance the k_2^{RS}(**5-SMe**)/k_2^{RS}(**5-OMe**) ratio. The steric effect on leaving group departure is also seen in the fact that k_2^{RS} for MeS^- departure from the more crowded **5-(SMe,SR)**$^-$ in the reaction of *n*-BuS^- with **5-SMe** is much larger than k_2^{RS} for MeS^- departure from the less crowded **5-(SMe,OR)**$^-$ in the reaction of $CF_3CH_2O^-$ with **5-SMe**. Without the steric effect, the expected stronger electronic push by the CF_3CH_2O group compared to that of the *n*-BuS group should render k_2^{RO} larger than k_2^{RS}. The same comments apply to the comparison of k_2^{RS} with k_2^{RO} in the reactions of **5-OMe** with *n*-BuS^- and $CF_3CH_2O^-$.

Experimental section

Materials

Thiomethoxybenzylidene Meldrum's acid, **5-SMe**, was synthesized as described by Huang and Chen (54); mp 160–162°C (lit. (54) 164°C). ^{1}H NMR ($CDCl_3$, 400 MHz) δ 1.77

[9] Estimated as 0.3 units lower than pK_a^{n-BuSH}, based on the fact that in pure water the pK_a difference between MeSH and *n*-BuSH is 0.3 units (53).

© 1999 NRC Canada

(s, 6H), 1.90 (s, 3H), 7.43–7.48 (m, 5H). All reagents were purified as described earlier (14).

Methodology

Preparation of solutions, pH measurements, in situ generation of intermediates, recording of spectra, and kinetic measurements were performed as described before (14).

Conclusions

(*i*) The conditions necessary for the direct observation of the S_NV intermediate, i.e., $K_1^{RX}[RX^-] > 1$ and $k_1^{RX}[RX^-] > k_2^{RX}$, are easily met for the reactions of **5-SMe** with all nucleophiles except for OH^-. In this latter reaction the acidic nature of the OH group in **5-(SMe,OH)**$^-$ leads to additional pathways that accelerate the conversion of the intermediate to products to the point of turning **5-(SMe,OH)**$^-$ into an undetectable steady state intermediate.

(*ii*) The ratios of the equilibrium constants for $HOCH_2CH_2S^-$ addition to **5-SMe**, **5-OMe**, and **5-H** are 6.2×10^{-9}:4.8×10^{-7}:1; they are representative for all thiolate ion reactions of this study. The strong reduction in K_1^{RS}(**5-SMe**) and K_1^{RS}(**5-OMe**) compared to K_1^{RS}(**5-H**) is mainly the result of the steric and π-donor effects. The fact that K_1^{RS}(**5-SMe**) < K_1^{RS}(**5-OMe**) indicates that the steric effect is, overall, the dominant factor. The corresponding ratios for $CF_3CH_2O^-$ addition are 4.5×10^{-6}:1.1×10^{-2}:1. They indicate less severe crowding in the intermediates derived from **5-SMe** and **5-OMe**. The smaller K_1^{RO}(**5-SMe**)/K_1^{RO}(**5-OMe**) ratio for the alkoxide ion reactions compared to the K_1^{RS}(**5-SMe**)/K_1^{RS}(**5-OMe**) ratio for the thiolate ion reactions shows the importance of the anomeric effect in **5-(OMe,OR)**$^-$.

(*iii*) Because of the greater polarizability and weaker solvation of thiolate compared to alkoxide ions, the equilibrium constants for thiolate addition to all substrates are much higher than for addition of alkoxide ions of the same proton basicity.

(*iv*) The rate constants for nucleophilic addition to **5-SMe**, **5-OMe**, and **5-H** are affected by the same factors as the equilibrium constants, but the relative importance of these factors is different because of multiple transition state imbalances that affect the intrinsic rate constants. For a given type of nucleophile the k_0^{RX} values follow the order **5-SMe** << **5-OMe** << **5-H**, which is mainly the result of early loss of the π-donor stabilization of **5-SMe** and **5-OMe** and early development of the steric effect at the transition state. For a given substrate, k_0^{RS} >> k_0^{RO}; this is a consequence of early desolvation of the nucleophile, probably combined with early development of the soft–soft interactions in the reactions with thiolate ions. These soft–soft interactions appear to be particularly beneficial in the reaction of **5-SMe** due to the softness of the MeS group.

(*v*) The fact that β_{nuc} is very low for thiolate ion addition to **5-SMe**, despite the relatively small equilibrium constants, confirms previous conclusions that in thiolate additions to electrophiles the generally observed low β_{nuc} values are not the result of a Hammond effect.

(*vi*) The leaving group departure rate constants depend on the following factors: the pK_a of the leaving group (increased rate with decreasing pK_a, moderate to large negative β_{lg} values), the pK_a of the remaining group (increased rate with increasing pK_a, moderate to large β_{push} values), leaving group atom (higher rate with S than with O), and steric effects (increased rate with bulkier leaving and (or) remaining groups).

(*vii*) In the reaction of **5-OMe** with $HOCH_2CH_2S^-$, the k_2^{RS} value is abnormally high because of intramolecular hydrogen bonding assistance of MeO^- departure by the OH group. In contrast, the k_2^{RS} value for the reaction of **5-SMe** with the same nucleophile is not enhanced, indicating that intermolecular assistance of MeS^- departure is not important.

Acknowledgments

This research was supported by grant CHE-9307659 from the National Science Foundation (C.F.B.) and a grant from the U.S.–Israel Binational Science Foundation (Z.R.).

References

1. Z. Rappoport. Adv. Phys. Org. Chem. **7**, 1 (1969).
2. G. Modena. Acc. Chem. Res. **4**, 73 (1971).
3. S.I. Miller. Tetrahedron, **33**, 1211 (1977).
4. Z. Rappoport. Acc. Chem. Res. **14**, 7 (1981).
5. Z. Rappoport. Recl. Trav. Chim. Pays-Bas, **104**, 309 (1985).
6. B.A. Shainyan. Usp. Khim. **55**, 942 (1986).
7. Z. Rappoport. Acc. Chem. Res. **25**, 474 (1992).
8. C.F. Bernasconi, J. Fassberg, R.B. Killion, Jr., and Z. Rappoport. J. Am. Chem. Soc. **111**, 6862 (1989).
9. C.F. Bernasconi, J. Fassberg, R.B. Killion, Jr., and Z. Rappoport. J. Am. Chem. Soc. **112**, 3169 (1990).
10. C.F. Bernasconi, D.F. Schuck, R.J. Ketner, M. Weiss, and Z. Rappoport. J. Am. Chem. Soc. **116**, 11 764 (1994).
11. C.F. Bernasconi, D.F. Schuck, R.J. Ketner, I. Eventova, and Z. Rappoport. J. Am. Chem. Soc. **117**, 2719 (1995).
12. C.F. Bernasconi, A.E. Leyes, Z. Rappoport, and I. Eventova. J. Am. Chem. Soc. **115**, 7513 (1993).
13. C.F. Bernasconi, A.E. Leyes, I. Eventova, and Z. Rappoport. J. Am. Chem. Soc. **117**, 1703 (1995).
14. C.F. Bernasconi, R.J. Ketner, X. Chen, and Z. Rappoport. J. Am. Chem. Soc. **120**, 7461 (1998).
15. C.F. Bernasconi and R.J. Ketner. J. Org. Chem. **60**, 6266 (1998).
16. C.F. Bernasconi, J. Fassberg, R.B. Killion, D.F. Schuck, and Z. Rappoport. J. Am. Chem. Soc. **113**, 4937 (1991).
17. S.H. Unger and C. Hansch. Prog. Phys. Org. Chem. **12**, 91 (1976).
18. M. Charton. Stud. Org. Chem. **42**, 629 (1991).
19. C. Hansch, A. Leo, and R.W. Taft. Chem. Rev. **91**, 165 (1991).
20. A.G. Kirby. The anomeric effect and related stereoelectronic effects of oxygen. Springer Verlag, Berlin, 1983.
21. P.v.R. Schleyer, E.D. Jemmis, and G.W. Spitznagel. J. Am. Chem. Soc. **107**, 6393 (1985).
22. J. Hine and A.W. Klueppl. J. Am. Chem. Soc. **96**, 2924 (1974).
23. K.B. Wiberg and R.R. Squires. J. Chem. Thermodyn. **11**, 773 (1979).
24. M.P. Harcourt and R.A. More O'Ferrall. J. Chem. Soc. Chem. Commun. 823 (1987).
25. M.P. Harcourt and R.A. More O'Ferrall. Bull. Soc. Chim. Fr. 407 (1988).
26. E.G. Sander and W.P. Jencks. J. Am. Chem. Soc. **90**, 6154 (1968).
27. J. Hine and R.D. Weimar, Jr. J. Am. Chem. Soc. **87**, 3387 (1965).

© 1999 NRC Canada

28. J. Hine. Structural effects on equilibria in organic chemistry. Wiley, New York. 1975. p. 225.
29. R.G. Pearson and J. Songstad. J. Am. Chem. Soc. **89**, 1827 (1967).
30. R.G. Pearson. Surv. Prog. Chem. **5**, 1 (1969).
31. A.J. Parker. Chem. Rev. **69**, 1 (1969).
32. F.G. Bordwell and D.L. Hughes. J. Org. Chem. **47**, 3224 (1982).
33. R.W. Taft. Prog. Phys. Org. Chem. **14**, 247 (1983).
34. R.A. Marcus. J. Chem. Phys. **43**, 679 (1965).
35. C.F. Bernasconi. Acc. Chem. Res. **20**, 301 (1987).
36. C.F. Bernasconi. Acc. Chem. Res. **25**, 9 (1992).
37. C.F. Bernasconi. Adv. Phys. Org. Chem. **27**, 119 (1992).
38. D.J. Hupe and W.P. Jencks. J. Am. Chem. Soc. **99**, 451 (1977).
39. W.P. Jencks, S.R. Brant, J.R. Gandler, G. Fendrich, and C. Nakamura. J. Am. Chem. Soc. **104**, 7054 (1982).
40. C.F. Bernasconi and R.B. Killion, Jr. J. Am. Chem. Soc. **110**, 7506 (1988).
41. J.F. Bunnett. J. Am. Chem. Soc. **79**, 5969 (1957).
42. A.J. Kresge. Chem. Soc. Rev. **2**, 475 (1973).
43. G.S. Hammond. J. Am. Chem. Soc. **77**, 554 (1955).
44. J.E. Leffler and E. Grunwald. Rates and equilibria of organic reactions. Wiley, New York. 1963. p. 156.
45. W.P. Jencks. Chem. Rev. **85**, 511 (1985).
46. C.F. Bernasconi and D.F. Schuck. J. Org. Chem. **57**, 2365 (1992).
47. H.F. Gilbert and W.P. Jencks. J. Am. Chem. Soc. **99**, 7931 (1977).
48. C.D. Ritchie and J.P. Gandler. J. Am. Chem. Soc. **101**, 7318 (1979).
49. A.J. Kresge. Acc. Chem. Res. **8**, 354 (1975).
50. A. Pross. J. Org. Chem. **49**, 1811 (1984).
51. F.G. Bordwell and D.L. Hughes. J. Am. Chem. Soc. **107**, 4737 (1985).
52. A. Pross and S.S. Shaik. New J. Chem. **13**, 427 (1989).
53. W.P. Jencks and J. Regenstein. *In* Ionization constants of acids and bases, CRC handbook of biochemistry and molecular biology. 3rd ed. *Edited by* G.D. Fasman. CRC Press, Cleveland. 1977. p. 305.
54. X. Huang and B.-C. Chen. Synthesis, 480 (1987).

© 1999 NRC Canada

Formation and behavior of intramolecular *N*-(styrylalkyl)aniline exciplexes

Frederick D. Lewis, Jill M. Wagner-Brennan, and Alan M. Miller

Abstract: The photophysical and photochemical behavior of several aniline spacer – styrene molecules in which the spacer is a short polymethylene chain has been investigated. Long wavelength excitation selectively excites the aniline chromophore which undergoes intramolecular quenching by the styrene to yield an intramolecular exciplex. Exciplex fluorescence is observed for both of the tertiary anilines investigated and for one of the three secondary anilines. More rapid exciplex formation in nonpolar vs. polar solvents is attributed to the necessity of desolvating the polar aniline singlet in polar solvents. Intramolecular adduct formation is the major photochemical process for the secondary anilines, but is highly inefficient for the tertiary anilines. The behavior of the intramolecular aniline–styrene exciplexes is compared to that of the styrene-amine exciplexes previously investigated in this laboratory.

Key words: intramolecular exciplex, fluorescence, aniline, styrene.

Résumé : On a étudié le comportement photophysique et photochimique de plusieurs molécules de type aniline écarteur – styrène dans lesquelles l'écarteur est une courte chaîne de polyméthylène. Une excitation de grande longueur d'onde excite sélectivement le chromophore aniline qui subit une désactivation intramoléculaire par le styrène pour donner un exciplexe intramoléculaire. On observe la fluorescence d'exciplexe dans les deux anilines tertiaires étudiées et dans l'une des trois anilines secondaires. La formation plus rapide de l'exciplexe dans les solvants non polaires par rapport aux solvants polaires est attribuée à la nécessité de désolvatation du singulet polaire de l'aniline dans les solvants polaires. La formation d'adduit intramoléculaire est le principal processus photochimique dans le cas des anilines secondaires, mais ce processus à toutes fins pratiques ne se produit pas dans le cas des amines tertiaires. On compare le comportement des exciplexes intramoléculaires aniline–styrène aux exciplexes styrène–amine étudiés antérieurement dans ce laboratoire.

Mots clés : exciplexe intramoléculaire, fluorescence, aniline, styrène.

[Traduit par la Rédaction]

N,*N*-Dialkylanilines are good electron donors and have been widely employed in studies of photoinduced electron transfer (1). Inter- and intramolecular quenching of singlet arenes by dialkylanilines in nonpolar solvents can result in the formation of charge-transfer stabilized fluorescent exciplexes (2–8). Increasing solvent polarity causes a red shift in the exciplex fluorescence and, in most cases, a decrease in fluorescence intensity. Complete electron transfer in polar solvents leads to the formation of the arene anion radical and aniline cation radical. Secondary *N*-alkylanilines are also good electron donors, however, exciplex fluorescence is generally not observed upon quenching of arenes by secondary anilines (9, 10). The absence of exciplex fluorescence has been attributed to rapid intersystem crossing or N-H proton transfer within the exciplex.

Received September 17, 1998.

This paper is dedicated to Jerry Kresge in recognition of his seminal contributions to the understanding of organic reaction mechanisms.

F.D. Lewis,[1] J.M. Wagner-Brennan, and A.M. Miller. Department of Chemistry, Northwestern University, Evanston, IL 60208-3113, U.S.A.

[1]Author to whom correspondence may be addressed. Telephone: (847) 491-3441. Fax: (847) 467-2184. e-mail: lewis@chem.nwu.edu

Quenching of singlet anilines by ground-state acceptors should also result in electron transfer. In comparison to quenching of singlet acceptors by ground-state anilines, quenching of singlet anilines by ground-state acceptors remains largely univestigated. The weak long-wavelength absorption and relatively short singlet lifetimes of the anilines restricts the choice of ground-state acceptors. Beens and Weller (2*a*) noted the failure of dimethylaniline and benzene to form an exciplex and suggested that the small extent of orbital overlap might be responsible. Fluorescence quenching of singlet anilines by chloromethanes (11) and chlorobenzenes (12) has been reported; however, exciplex fluorescence is not observed. Hansen and co-workers (13) reported that primary and secondary (but not tertiary) *o*-allylanilines undergo intramolecular addition reactions to yield indole derivatives. Electron transfer from the singlet aniline to the allyl group followed by proton transfer and radical pair combination was proposed as the mechanism for this reaction. Red-shifted fluorescence was observed for the secondary *o*-allylanilines compared to a saturated model compound; however, no exciplex fluorescence was observed for the tertiary *o*-allylanilines.

We previously observed that both secondary and tertiary (aminoalkyl)styrenes undergo intramolecular addition reactions (14). The observation of exciplex fluorescence supported the occurrence of electron transfer from ground-state tertiary alkyl amines to singlet styrene. We report here an in-

 © 1999 NRC Canada

Table 1. Fluorescence data for *N*,*N*-dimethylaniline (DMA), *N*-methylaniline (MA), and *trans*-β-methylstyrene (β-MS).

Compound	Solvent[a]	λ_f (nm)	τ_s (ns)	Φ_f	10^{-7} k_f (s^{-1})
DMA	Hexane	331	2.35	0.11	4.7
	Diethyl ether	339	2.25	0.11	4.9
	THF	342	2.70	0.12	4.4
	Acetonitrile	351	3.80	0.17	4.5
MA	Hexane	324	3.52	0.13	3.8
	Diethyl ether	332	3.73		
	Acetonitrile	355	4.35		
β-MS	Hexane	308	11.8	0.35	3.0
	Acetonitrile	307	10.9		

[a]Solvents deoxygenated by purging with nitrogen.

Chart 1.

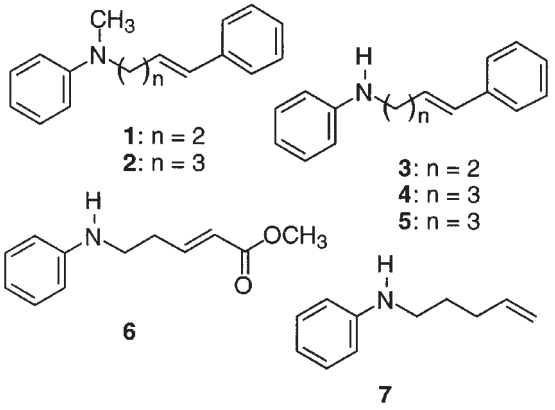

vestigation of the photochemical behavior of the covalently linked *N*-(styrylalkyl)anilines **1**–**5** and the *N*-alkenylanilines **6** and **7** (Chart 1). The lower singlet energy of the aniline vs. styrene chromophore permits investigation of electron transfer from the singlet aniline to the ground-state styrene in **1**–**5**. Intramolecular quenching of tertiary anilines by styrene in nonpolar solvent results in a single fluorescence band attributed to an intramolecular aniline–styrene exciplex. In moderately and highly polar solvents two fluorescence bands are observed and attributed to locally excited aniline and exciplex fluorescence. Exciplex fluorescence is also observed for the secondary styrylaniline **3**, but not its homologues **4** or **5**. Intramolecular adduct formation is observed for the secondary styrylanilines **3**–**5** and for the linked acrylate **6**, but not for tertiary styrylanilines **1** and **2** or for the linked alkene **7**. The pronounced differences in the behavior of arene–aniline and arene–alkylamine exciplexes are discussed.

Results

The *N*-alkenylanilines **1**–**7** were prepared by standard procedures, purified by column chromatography, and characterized by ^{1}H and ^{13}C NMR spectroscopy and mass spectrometry as well as by absorption and fluorescence spectroscopy (see Experimental). The alkenes in **1**–**6** possess the *E*-configuration, as determined by NMR, and contain <2% of the *Z*-isomer, as determined by gas chromatography.

The absorption spectrum of *N*,*N*-dimethylaniline (DMA) in hexane solution consists of a weak band at 296 nm (f = 0.04) and a stronger band at 250 nm (f = 0.28) (15). The

Fig. 1. Absorption spectra in acetonitrile solution. (*a*) *N*-Methylaniline (----) and β-methylstyrene (—); (*b*) styrylaniline **4**.

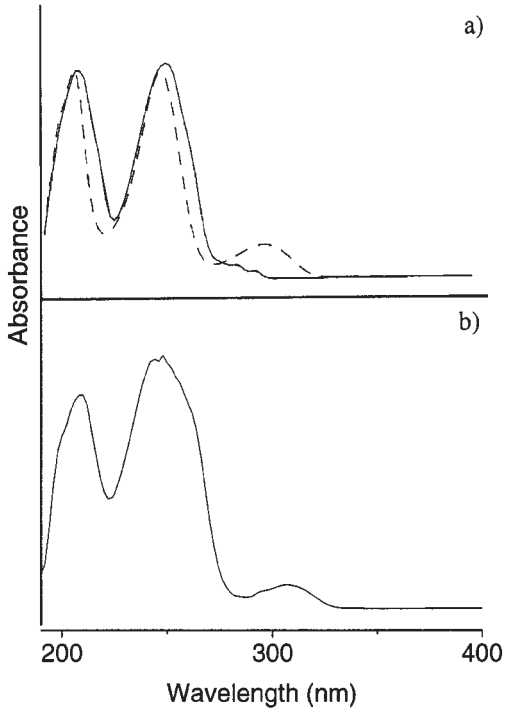

maxima for *N*-methylaniline (MA) are at slightly shorter wavelengths (294 and 243 nm). Increasing solvent polarity results in only small shifts in the band maxima. The absorption spectrum of β-methylstryene (β-MS) in hexane solution consists of a weak, structured band at long wavelength (284 nm, f = 0.008) and a stronger band at shorter wavelength (250 nm, f = 0.70) (15). The maxima change only slightly in more polar aprotic solvents. The spectra of MA and β-MS in acetonitrile solution are shown in Fig. 1*a*. The absorption spectra of the linked styrylanilines **1**–**5** are similar to the sum of the absorption spectra of DMA or MA and β-MS, as shown for **3** in Fig. 1b. Similarly, the spectra of **6** and **7** are similar to the sum of the spectra of the aniline and acrylate or alkene chromophores, respectively. At wavelengths >295 nm, the aniline chromophore in **1**–**7** absorbs essentially all of the incident light.

DMA, MA (16), and β-MS (17) are fluorescent in both polar and nonpolar solvents. Selected literature data for fluo-

© 1999 NRC Canada

Fig. 2. Fluorescence spectra of β-methylstyrene in acetonitrile (*A*), *N*-methylaniline in hexane (*B*), and *N*-methylaniline in acetonitrile solution (*C*).

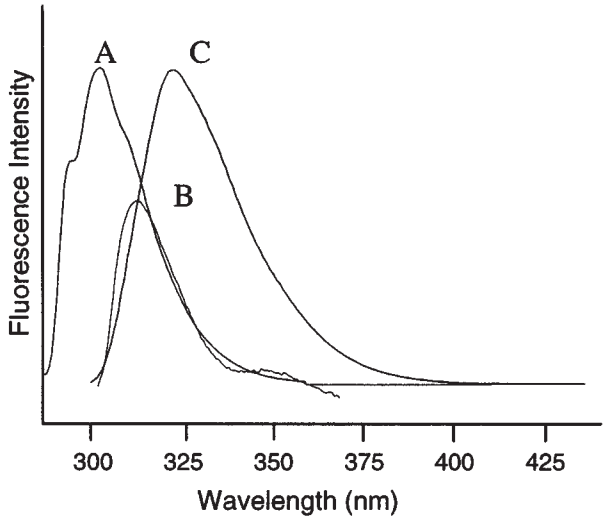

rescence maxima, lifetimes, and quantum yields are summarized in Table 1. The fluorescence maxima of DMA and MA display large solvent-induced shifts, whereas the maximum for β-MS is independent of solvent polarity. Spectra of MA in hexane and acetonitrile are shown in Fig. 2 along with the spectrum of β-MS in acetonitrile. The spectrum of DMA at 77 K in a methyltetrahydrofuran (MTHF) glass displays both fluorescence (λ_{max} = 336 nm) and phosphorescence (λ_{max} = 435 nm) with a ratio of ca. 1:10. Only fluorescence is observed under these conditions for β-MS.

The tertiary styrylanilines **1** and **2** and the secondary styrylaniline **3** display solvent-dependent dual emission (Fig. 3). In hexane solution only a single maximum is observed, however, it is red shifted and broadened with respect to the fluorescence of DMA or MA. In more polar solvents, dual emission is observed. For purposes of discussion, the single band observed in hexane and the shorter wavelength band in more polar solvents is designated F_1 and the longer wavelength band designated F_2. The alkenylanilines **4**–**7** display a single maximum designated F_1 in both nonpolar and polar solvents. The emission maxima, decay times, and fluorescence quantum yields for the F_1 and F_2 bands of **1**–**7** in several solvents are reported in Table 2. At 77 K in a MTHF glass, **1** and **2** display emission similar in appearance to the fluorescence of DMA with band maxima at 336 nm. No styrene-like fluorescence, aniline-like phosphorescence, or F_2 fluorescence is observed under these conditions.

Irradiation of the tertiary anilines **1** and **2** in acetonitrile solution results in rapid conversion to a 1:1 photostationary state of *trans* and *cis* styrene isomers which were isolated and characterized. Prolonged irradiation results in slow formation of other products which were not characterized. Product formation is more rapid in benzene vs. acetonitrile solution. The products were not isolated, however, GC–MS analysis of irradiated solutions is consistent with the formation of intramolecular adducts similar to those formed upon irradiation of tertiary (aminoalkyl)styrenes (14*b*).

Irradiation of the secondary anilines **3**–**6** in hexane or acetonitrile solution leads to the formation of products which

Fig. 3. Fluorescence spectra of styrylanilines in hexane (*A*), diethyl ether (*B*), and acetonitrile (*C*) solution. (*a*) Secondary styrylaniline **3**; (*b*) tertiary styrylaniline **2**.

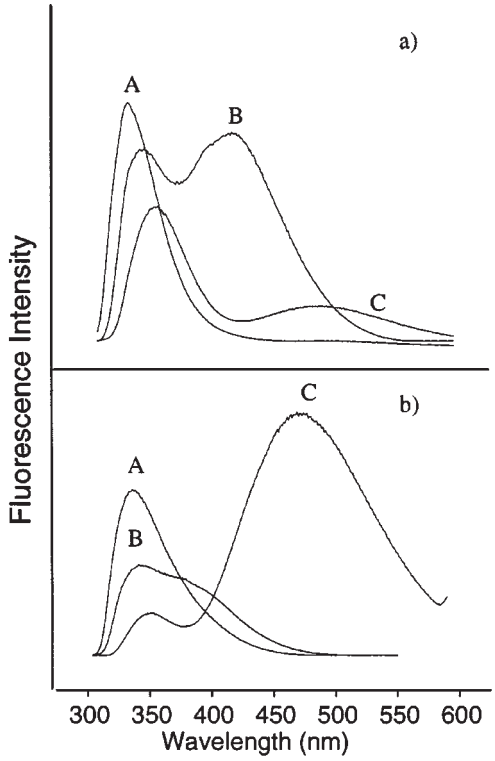

result from addition of the aniline N-H to the styrene or acrylate double bond (Chart 2). Formation of the *cis* isomers is also observed, but is a relatively minor photoprocess. Adducts **3a** and **4a** were obtained in 50 and 33% isolated yield, respectively, and were characterized as the pyrrolidine and piperidine derivatives by NMR and mass spectral fragmentation. The adducts are not stable under the conditions of irradiation, limiting the preparative yields. GC–MS analysis of the irradiated mixtures indicated that the regioisomeric adducts **3b** and **4b** were formed as minor products in acetonitrile solution. The acrylate **6** also forms mainly the pyrrolidine adduct **6a**. In the case of **5** the major product is piperidine derivative **5b**, rather than the azepine **5a**. Thus, the regioselectivity of adduct formation for **3**–**5** is analogous to that for the corresponding (aminoalkyl)styrenes (14*a*). No photoproducts are formed upon prolonged irradiation of the alkenylaniline **7**.

Discussion

The formation and behavior of intramolecular arene spacer – tertiary aniline exciplexes in which the spacer is a flexible polymethylene chain have been extensively investigated (5–9). The tertiary aniline chromophore has been connected to the spacer either at the para position (**8**, Ar = 9-anthryl or 1-pyrenyl) or via nitrogen (**9**, Ar = 9-anthryl) (Chart 3). Intramolecular quenching of the singlet arene by ground-state tertiary aniline in nonpolar solvents results in the formation of fluorescent exciplexes, which are proposed to have sandwich-type geometries. For exciplexes of largely charge-transfer character, Weller (2*c*, *d*) found the enthalpy

© 1999 NRC Canada

Table 2. Fluorescence data for *N*-alkenylaniline derivatives **1**–**7**.

Compound	Solvent[a]	λ_{f1} (nm)[b]	τ_{f1} (ns)[b]	Φ_{f1}[b]	λ_{f2} (nm)[c]	τ_{f2} (ns)[c]	Φ_{f2}[c]
1	Hexane	338[d]	0.6	0.04			
	Ether	332[e]	0.4	0.05	399	1.7	0.04
	CH_3CN	348[e]	0.1	0.002	456	13.1	0.49
2	Hexane	338[d]	0.6	0.09			
	Ether	343[e]	0.5	0.03	386	1.3	0.03
	CH_3CN	350[e]	0.3	0.007	472	8.8	0.18
3	Hexane	326[d]	0.4	0.02			
	Ether	334[e]	0.3	0.04	398	0.7	
	CH_3CN	344[e]	0.3	0.01	457	0.40	0.004
4	Hexane	331[d]	0.4	0.05			
	CH_3CN	346[e]	0.3	0.03			
5	Hexane	329[d]	0.6	0.15			
	CH_3CN	343[e]	0.6	0.03			
6	Hexane	329[d]	0.6	0.031			
	CH_3CN	341[e]	2.9	0.019			
7	Hexane	324[e]	1.5	0.22			
	CH_3CN	343[e]	3.9	0.31			

[a]Solvents deoxygenated by purging with nitrogen.

[b]Data for compounds with a single emission maximum or for the shorter wavelength emission for compounds with two emission maxima (F_1 fluorescence).

[c]Data for the longer wavelength emission for compounds with two emission maxima (F_2 fluorescence) assigned to the intramolecular exciplex.

[d]Assigned to the intramolecular exciplex.

[e]Assigned to the locally excited aniline singlet.

Chart 2.

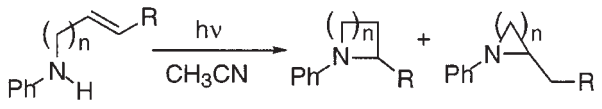

3: n = 2, R = Ph — **3a** (major) — **3b**
4: n = 3, R = Ph — **4a** (major) — **4b**
5: n = 4, R = Ph — **5a** (minor) — **5b**
6: n = 2, R = CO_2CH_3 — **6a** (major) — **6b**

Chart 3.

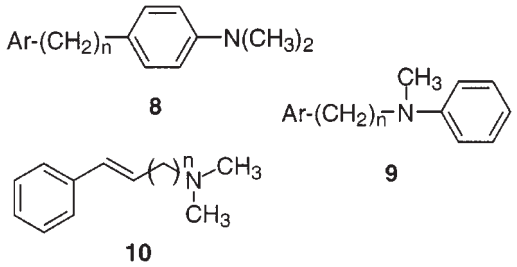

of exciplex formation could be related to the singlet energy of the excited molecule, E_S, and the reduction and oxidation potentials of the acceptor and donor, respectively, measured in acetonitrile solution, by the empirical relationship given in eq. [1],

$$[1] \qquad -\Delta H_{ex} = E_S + E_{red}(A) - E_{ox}(D) + C$$

where the constant term is the solvent-dependent Coulomb attraction energy. In polar solvents, arene spacer – aniline exciplexes are proposed to adopt "looser" or more extended geometries and fluoresce at longer wavelengths with diminished quantum yield or become totally nonfluorescent. We have observed similar solvent-dependent photophysical behavior for the tertiary (aminoalkyl)styrenes **10** (Chart 3), which also undergo intramolecular addition reactions via singlet exciplex intermediates (14).

The aniline spacer – styrene systems **1**–**5** differ from previously investigated systems such as **8** and **9** or the (aminoalkyl)styrenes **10** in that the singlet energy of the aniline chromophore is lower than that of the appended alkene. As seen in Fig. 1, MA and β-MS have similar absorption spectra, the lower energy band in MA extending to longer wavelength than that of β-MS. Thus the aniline chromophore in **1**–**5** can be selectively excited at wavelengths >290 nm. It is not possible to investigate bimolecular quenching of singlet anilines by ground-state styrenes due to competitive absorption by styrene at the higher concentrations needed in these experiments. The absorption spectra of **1**–**5** are similar to the sum of the spectra of the two chromophores. Thus, there appears to be no strong ground-state interaction between the two chromophores.

Behavior of tertiary anilines

The arene spacer – aniline systems **8** and **9** and the (aminoalkyl)styrenes **10** display both locally excited and exciplex fluorescence in hexane and moderately polar solvents. In contrast, the fluorescence spectra of the aniline spacer – styrene systems **1** and **2** in hexane consist of a single band, F_1, which is broadened and red-shifted by ca. 7 nm with respect to the fluorescence of DMA (Tables 1, 2). Identical spectra are obtained when the excitation is absorbed predominantly by aniline (294 nm) or equally by aniline and styrene (275 nm). The fluorescence of **1** and **2** (Fig. 3*b*) in

© 1999 NRC Canada

Fig. 4. Solvent polarity dependence of the emission maxima of *N*,*N*-dimethylaniline (▽), the styrylaniline locally excited aniline fluorescence in polar solvents (■), the styrylaniline exciplex fluorescence (□), and the exciplex fluorescence of ((*N*,*N*-dimethylamino)alkyl)styrenes (○). (*a*) Compounds with dimethylene linkers **1** and **10** (n = 2); (*b*) compounds with trimethylene linkers **2** and **10** (n = 3).

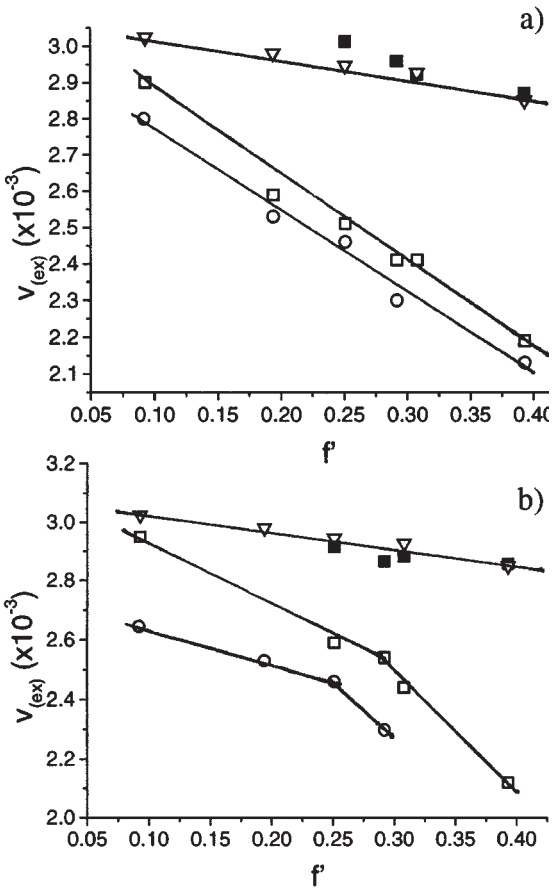

ethers and more polar solvents consists of two bands, F_1 and F_2. The higher energy F_1 band has similar maxima and band shape to that of DMA or MA in these solvents and is assigned to the locally excited aniline singlet. The lower energy F_2 band displays larger solvent-induced shifts and is assigned to the singlet aniline–styrene exciplex. The intensity of exciplex fluorescence for **1** and **2** increases with increasing solvent polarity, unlike the arene linker – aniline and (aminoalkyl)styrenes **8**–**10** for which the exciplex fluorescence intensity decreases in polar solvents. This difference suggests that the exciplexes from **1** and **2** retain a folded geometry even in acetonitrile solution.

Lippert–Mataga plots (18) of the fluorescence maxima for both the locally excited and exciplex bands of **1** and **2** vs. the solvent polarity parameter f', eq [2],

$$[2] \qquad f' = (\varepsilon - 1)/(2\varepsilon + 1) - (n^2 - 1)/(4n^2 + 2)$$

are shown in Fig. 4*a*, *b*, along with the data for DMA and the (aminoethyl)styrenes **10** (n = 2 and n = 3) (14*a*). The maxima for the F_1 bands of **1** and **2** in diethyl ether and more polar solvents are similar to those of DMA (Tables 1 and 2). However, the maximum for the single fluorescence

Scheme 1.

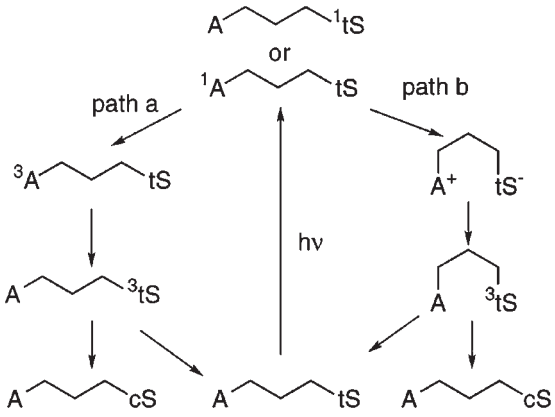

A: aniline, tS: *trans*-styrene, cS: *cis*-styrene

band F_1 observed for **1** and **2** in hexane solution lies below the maximum for DMA. In the case of **1**, inclusion of the hexane F_1 maximum with the exciplex maxima in more polar solvents provides a good fit to a straight line, which parallels the published data for **10** (n = 2) (Fig. 4*a*). The data for **2** and **10** (n = 3) is more limited, and there is an apparent change in slope for the Lippert–Mataga plot between solvents of moderate and high polarity (Fig. 4*b*).

Further evidence for the assignment of the single fluorescence band F_1 of **1** and **2** in hexane solution to an exciplex is provided by comparison of room temperature spectra with those obtained in frozen glasses at 77 K. In the moderately polar solvent MTHF, both locally excited and exciplex fluorescence are observed at room temperature in fluid solution. Cooling to 77 K results in disappearance of the exciplex fluorescence and a small shift in the locally excited fluorescence from 335 to 331 nm. The absence of exciplex fluorescence in 77 K glasses is commonly observed for donor spacer – acceptor systems with flexible polymethylene spacers and is attributed to their inability to adopt sandwich-type geometries in rigid media (6*b*, 19). The fluorescence spectrum of **2** at 77 K in a methylcyclohexane glass is similar to the fluorescence of DMA under the same conditions, however, the strong phosphorescence observed from DMA (20) is absent in the spectrum of **2**. Furthermore, no styrene-like fluorescence is observed upon excitation of **2** at 275 nm, at which the styrene and aniline chromophores have similar absorbance. The complete absence of both styrene fluorescence and aniline phosphorescence in the 77 K spectrum of **2** is indicative of efficient singlet–singlet energy transfer from styrene to aniline and triplet–triplet energy transfer from aniline to styrene, which does not phosphoresce. This singlet–singlet, triplet–triplet relay (Scheme 1, path a) is reminiscent of the benzophenone linker – naphthalene system investigated by Lamola et al. (21).

It is interesting to note that the emission maxima for the intramolecular exciplexes **1** and **2** lie at higher energy than those of the corresponding (aminoalkyl)styrenes (Fig. 4). The oxidation potential of DMA is lower than that of triethylamine, TEA, (0.78 vs. 0.98 V vs. SCE) (4*b*), and thus DMA would be expected to form a more stable exciplex with styrene. Since the singlet energy of DMA is lower than

© 1999 NRC Canada

that of β-MS (4.08 vs. 4.25 eV), similar enthalpies of exciplex formation are calculated using eq. [2] for the intermolecular quenching of singlet DMA by β-MS (E_{red} = –2.54 V (22), ΔH_{ex} = –0.61 eV) and for quenching of singlet β-MS by TEA (ΔH_{ex} = –0.58 eV). According to Weller (2), the exciplex emission maximum in hexane solution can be related to the donor and acceptor redox potentials by the empirical relationship given in eq. [3].

$$[3] \qquad h\nu_{ex} = E_{ox}(D) - E_{red}(A) - 0.15 \pm 0.10 \text{ eV}$$

Thus the emission maximum of the aniline exciplex should be lower than that of the corresponding (dimethylaminoalkyl)styrene by ca. 0.2 eV. However, the emission maxima of **2** and **10** (*n* = 3) in hexane solution are at 338 and 378 nm, respectively (14*b*). A similar difference is found upon comparison of the data of Yang et al. (8) for the intramolecular pyrene–aniline system **9** (*n* = 3) with the data of Swinnen et al. (23) for the analogous (dimethylaminopropyl) pyrene. A part of this difference can be accounted for by the larger ground-state repulsion energy for TEA vs. DMA intermolecular exciplexes, which has previously been noted by Knibbe et al. (2*b*), and recently examined in detail by Vauthey and Henseler (4*c*). An additional factor may be poor orbital overlap in the intramolecular arene–aniline exciplexes. While we do not have data for intermolecular aniline–styrene exciplexes, published data for pyrene–aniline exciplexes establish that the intermolecular exciplex (3) fluorescence maximum is at substantially lower energy than the intramolecular exciplex (8) with a trimethylene linker (460 vs. 430 nm). Much smaller differences in $h\nu_{ex}$ are observed for inter- vs. intramolecular arene–trialkylamine exciplexes (14*a*, 24).

The fluorescence quantum yields and decay times for the F_1 and F_2 fluorescence from **1** and **2** are reported in Table 2. The absence of locally excited fluorescence or dual exponential fluorescence decay in hexane solution indicates that exciplex formation is rapid ($>10^{10}$ s^{-1}) in this solvent. The exciplex fluorescence rate constants ($k_{fex} = \Phi_{fex}\tau_{ex}^{-1}$) for **1** and **2** are larger than that for DMA (Table 1), providing further support for the assignment of the F_1 emission in hexane to the intramolecular exciplex. The decay times of the locally excited fluorescence of **1** and **2** in ether and acetonitrile solution are between 0.1 and 0.6 ns, indicating that intramolecular quenching is slower in these solvents than in hexane solution. Desolvation of the moderately polar aniline chromophore must accompany formation of a sandwich-type exciplex and could account for the slower rates in more polar solvents. The decay times of the exciplexes in ether and acetonitrile are longer than those of the locally excited state, indicating that exciplex formation is irreversible. The exciplex fluorescence rate constants all are in the range 2.0–3.7 × 10^7 s^{-1}, similar to the values for (aminoalkyl)styrene exciplexes in nonpolar solvents (14).

The only photochemical reaction observed for **1** and **2** in acetonitrile solution is photoisomerization, which leads to a ca. 1:1 mixture of *trans* and *cis* isomers. Triplet sensitized irradiation of β-MS also yields a 1:1 photostationary state (25). Formation of the styrene triplet in **1** and **2** could occur either via intersystem crossing of the aniline chromophore followed by intramolecular triplet–triplet energy transfer from aniline to *trans*-styrene (Scheme 1, path a) or via intersystem crossing of the singlet exciplex to yield the locally excited *trans*-styrene triplet (Scheme 1, path b). In benzene solution, additional products are formed in low yield and tentatively identified as intramolecular stilbene–aniline adducts on the basis of their mass spectral fragmentation. In the case of the tertiary ((dimethylamino)ethyl)styrene **10** (*n* = 2), intramolecular addition is more efficient than isomerization (14*b*). The kinetic acidity of the more stable, delocalized, tertiary aniline cation radical is expected to be lower than that of a trialkylamine cation radical (26). Thus, it is not surprising that exciplex proton transfer is less efficient for the exciplex of **2** vs. **10** (*n* = 2).

Chart 4.

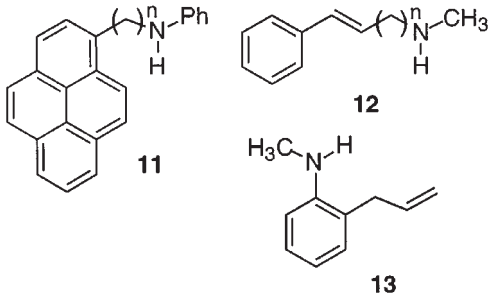

Behavior of secondary anilines

The behavior of arene spacer – secondary aniline systems has received relatively little attention. Okada et al. (9) reported that bimolecular quenching of singlet pyrene by MA results in the formation of a nonfluorescent exciplex that decays via both proton transfer and intersystem crossing processes. Proton transfer was not observed for the linked pyrene spacer – aniline systems **11** (*n* = 1–3) (Chart 4). Its absence was attributed to the high energy of conformations appropriate for its occurrence (10). Fast intersystem crossing was observed for **11** (*n* = 1) but not for *n* = 2 or 3, which were reported to have long exciplex lifetimes in ethyl ether solution. We have observed that the secondary (aminoalkyl) styrenes **12** (*n* = 1–5) form nonfluorescent exciplexes which undergo proton transfer, resulting in the formation of intramolecular adducts (14).

Dual fluorescence is observed for **3** in both ether and acetonitrile solution (Fig. 3*b*) and is attributed to locally excited aniline and intramolecular exciplex fluorescence. To our knowledge, this is the first reported observation of intramolecular exciplex fluorescence involving a secondary aniline. The exciplex emission maxima for **3** are essentially the same as those for **1**. In view of the higher oxidation potential of MA vs. DMA (1.03 vs. 0.79 V vs. SCE (4*b*)), the emission maximum for **3** would have been expected to be at higher energy than that of **1** (eq. [3]). Extra stabilization of the exciplex via intramolecular hydrogen bonding could account for this seeming anomaly. Exciplex stabilization could also account for the common observation of similar efficiencies of inter- and intramolecular quenching of singlet arenes by secondary and tertiary amines (1*c*, 14, 19). The exciplex fluorescence quantum yields and lifetimes for **3** are smaller or shorter than those of **1**, especially in acetonitrile solution (Table 2). The occurrence of proton transfer for **3** but not for

© 1999 NRC Canada

Scheme 2.

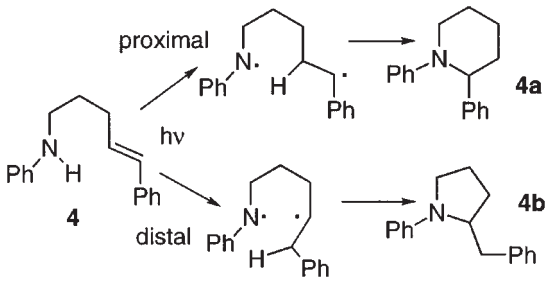

1 in polar solvents can account, at least in part, for this difference.

A single fluorescence band is observed for **4** and **5** in both nonpolar and polar solvents (Table 2). Their band maxima are red-shifted with respect to that of MA by 2–7 nm in hexane solution, and the fluorescence rate constants are larger than that of MA. These observations may reflect either perturbation (e.g., internal solvation) of the aniline locally excited state or the formation of an exciplex in nonpolar solvents. The band maxima and fluorescence rate constants in ether and acetonitrile are similar to those of MA, and thus these bands are assigned to locally excited aniline fluorescence. The decay times for the locally excited fluorescence of the secondary anilines **3** and **4** in ether and acetonitrile are similar to those of the tertiary anilines **1** and **2**. The longer singlet decay time for **5** is consistent with slower folding of the longer polymethylene spacer (14).

The photochemical behavior of **3**–**5** is qualitatively similar to that of the secondary (aminoalkyl)styrenes **12**. The formation of **3a**, **4a**, and **5b** as the major adducts is indicative of regioselective N-H transfer to the proximal end of the styrene double bond in **3** and **4** (Scheme 2) and the distal end in **5**. A similar pattern of regioselectivity was attributed in the case of **12** (n = 2–4) to least motion pathways for exciplex proton transfer (14*a*). The failure of styrene *trans*→*cis* isomerization to compete effectively with adduct formation for **3**–**5** indicates that neither aniline nor exciplex intersystem crossing (Scheme 1) competes effectively with proton transfer (Scheme 2). This result is consistent with the observation of slow intersystem crossing for the pyrene – secondary aniline exciplexes **11** (n = 2 or 3) (10).

The linked acrylate **6** and alkene **7** were investigated in order to determine the effect of changing the alkene acceptor upon exciplex formation and behavior. The reduction potential of methyl crotonate (–2.51 V vs. SCE) in acetonitrile solution (27) is similar to that of β-MS (–2.54 V vs. SCE) (22), and thus similar behavior might be anticipated. The photochemical behavior of the acrylate **6** is analogous to that of **3**, yielding an adduct tentatively identified as the pyrrolidine **6a** as the major product (Chart 2). The fluorescence parameters of **6** are also similar to those of **3** in nonpolar solvents (Table 2). However, no exciplex fluorescence is observed for **6** in ether or acetonitrile solution, and the lifetime of the locally excited aniline fluorescence from **6** in acetonitrile is much longer than that of **3**. These observations suggest that the more extensive π-orbital overlap for styrene vs. acrylate may result in the formation of a more stable exciplex.

The unactivated alkene **7** is a weaker electron acceptor than either the styrene or acrylate. Thus, it is not surprising that the aniline-like F_1 fluorescence maximum and lifetime of **7** are similar to those for MA in both hexane and aceonitrile solution (Tables 1, 2). The absence of intramolecular quenching of aniline by the terminal alkene is consistent with the observed absence of adduct formation. This result stands in contrast to the observation of red-shifted aniline fluorescence and intramolecular adduct formation reported by Hansen and co-workers (13) for the *o*-allylaniline **13**. The secondary anilines **7** and **13** differ both in the point of attachment of the alkene and the length of the spacer connecting the alkene to the aniline. We suspect the latter factor is most important, as much stronger through-bond coupling is expected for a single methylene vs. trimethylene spacer (10, 28).

Concluding remarks

In previous studies of arene linker – amine exciplex formation, the electronically excited arene interacts with a ground-state amine (5–10, 14, 19). The roles of the arene and amine have been reversed in the present investigation in which the singlet aniline interacts with a ground-state styrene. The styrylanilines **1**–**5** display photochemical behavior that differs in several important respects from that previously reported for the tertiary and secondary (aminoalkyl) styrenes **10** and **12** (14).

In the case of the tertiary anilines **1** and **2**, an increase in solvent polarity results in a decrease in the rate constant for intramolecular exciplex formation and an increase in the intensity of exciplex formation, precisely the opposite of the solvent effects observed for **10**. Since singlet aniline is much more polar than singlet styrene, the solvent reorganization energy for exciplex formation from singlet aniline but not singlet styrene is expected to increase with increasing solvent polarity. Once formed, the styrene–amine exciplexes undergo relaxation to a nonfluorescent extended geometry in polar solvents whereas the aniline–styrene exciplexes do not. Evidently, the localized alkylamine cation radical is more strongly solvated than is the delocalized aniline cation radical. The difference in charge delocalization can also explain the observation of more efficient proton transfer in the styrene–amine vs. aniline–styrene exciplexes in nonpolar solvents.

The photochemical behavior of the secondary anilines **3**–**5** (Scheme 2) is qualitatively similar to that of the analogous styrene–amines **12**. However, **3** provides the first example of exciplex fluorescence from an intramolecular arene–amine exciplex. The emission maxima of **3** is similar to that of **1** even though it should be less stable, based on the higher oxidation potential of MA vs. DMA. Similarly, the tertiary styrene–amine exciplexes have lower energy emission maxima than those of **1** or **2** in spite of the higher oxidation potential of trialkylamines vs. DMA. Clearly, factors other than amine oxidation potential influence the stability of the arene–amine intramolecular exciplexes.

Experimental

General methods

^{1}H NMR spectra were recorded on Varian VXR-300 and Varian Gemini 300 MHz spectrometers in $CDCl_3$ and methyl sulfoxide-d_6 solvents with TMS as an internal standard. In-

© 1999 NRC Canada

frared spectra of 0.005–0.02 M solutions of amines in dichloromethane or chloroform were recorded in 1 mm path-length NaCl cells using a Biorad FTS60 spectrometer. Mass spectra were obtained using a Hewlett–Packard 5985 GC/VG70-250E MS system using an ionizing voltage of 70 eV. UV-visible absorption spectra were measured with a Hewlett–Packard model 8452A diode array spectrophotometer in 1 cm path-length quartz cuvettes. Room temperature fluorescence emission and excitation spectra were recorded using a SPEX Fluoromax spectrophotometer. Solutions were approximately 10^{-4} M and were purged with nitrogen in a 1 cm path-length quartz cuvette fitted with a white rubber septum (Aldrich). Fluorescence quantum yields were determined using *trans*-1-phenylpropene (Φ_f = 0.35) (29) as a reference standard. Fluorescence decays were measured using a Photon Technology International LS-1 single photon counting apparatus with a gated hydrogen arc lamp using a scatter solution to obtain the lamp decay profile. The decays were analyzed using deconvolution and single or multiplex exponential least-squares fitting as described by James et al. (30). The reduced χ^2 values, randomness of residuals, and autocorrelation functions were used to determine the goodness of the fit.

Preparative scale irradiations were carried out under nitrogen in Pyrex test tubes using a Rayonet reactor fitted with RPR 3000 lamps. Acetonitrile solutions (0.01 M alkylstyrylaniline) were irradiated to >90% conversion of starting material, while monitoring the progress of the reaction by GC. The *cis* isomers of **1**–**6** have slightly shorter GC retention times than the *trans* isomers. Products were isolated by column chromatography. Product yields are based on either isolated yields or GC integration. Irradiations in hexane or benzene were done on a small scale and monitored by GC. The products from the small-scale photoreactions were characterized by mass spectral fragmentation.

Materials

All solvents used were spectral grade. Benzene (Aldrich) was refluxed over sodium metal and distilled prior to use. Acetonitrile (Fisher) was distilled over CaH_2 prior to use. Hexane (Aldrich), anhydrous diethyl ether (Fisher), acetonitrile (Aldrich), methanol (Fisher), chloroform (Fisher), and ethyl acetate (Fisher) were used without further purification. Aniline (Aldrich) was distilled over zinc powder prior to use.

trans-N-*Phenyl*-N-*methyl-4-phenyl-3-buten-1-amine (*trans-***1***)*

trans-Styrylacetic acid (Aldrich) was converted to the acid chloride by reaction with thionyl chloride followed by removal of excess thionyl chloride under reduced pressure. To a solution of the acid chloride in benzene was added a mixture of aniline, sodium methoxide, benzene, and ether. The resulting amide was isolated and purified by silica-gel chromatography (1:1 hexane/ether). Reduction of the amide with $LiAlH_4$ followed by silica-gel chromatography (1:3 hexane/dichloromethane) afforded *trans*-**1** (60%) as a colorless oil. ^{1}H NMR δ: 7.25–7.40 (m, 7H), 6.73–6.80 (m, 3H), 6.47–6.52 (d, 1H, *J* = 15.9 Hz), 6.23–6.31 (m, 1H), 3.49–3.54 (t, 2H, *J* = 7.4 Hz), 3.01 (s, 3H), 2.49–2.57 (q, 2H). ^{13}C NMR δ: 149.1, 137.6, 131.7, 129.3, 128.6, 127.8, 127.2, 126.1, 116.2, 112.3, 52.8, 38.6, 30.5. MS (*m*/*e*): 237 (M+), 120 (100). HRMS: 237.1517 (calcd.) and 237.1515 (obs.). Preparative irradiation of a 0.01 M solution of *trans*-**1** in acetonitrile followed by chromatography provided *cis*-**1** in an isolated yield of ca. 50%. ^{1}H NMR δ: 7.35–6.66 (m, 10H), 6.50–6.42 (d, 1H), 5.71–5.62 (m, 1H), 3.41–3.50 (m, 2H), 2.52–2.45 (m, 2H), 2.96 (s, 3H). ^{13}C NMR δ 149.03, 137.40, 130.78, 129.27, 128.60, 128.28, 127.74, 126.79, 116.17, 112.25, 52.78, 38.55, 26.04.

trans-N-*Phenyl*-N-*methyl-5-phenyl-4-penten-1-amine (*trans-***2***)*

Reaction of the lithium salt of phenylacetylene (Aldrich) with 1-bromo-3-chloropropane yielded 1-chloro-5-phenyl-4-pentyne, which was purified by vacuum distillation. Reaction of this chloroalkyne with *N*-methylaniline afforded the product of *N*-alkylation, which was purified by silica-gel chromatography (4:1 hexane/chloroform). Reduction with $LiAlH_4$ followed by purified by silica-gel chromatography (1:3 hexane/chloroform) afforded **2** as a colorless oil. ^{1}H NMR δ: 7.19–7.35 (m, 7H), 6.68–6.72 (m, 3H), 6.38–6.43 (d, *J* = 15.8 Hz, 1H), 6.19–6.25 (m, 1H), 3.34–3.39 (t, *J* = 7.4 Hz, 2H), 2.93 (s, 3H), 2.21–2.26 (q, *J* = 7.0 Hz, 2H), 1.73–1.78 (quintet, *J* = 7.4 Hz, 2H). ^{13}C NMR δ 149.3, 137.7, 130.4, 130.1, 129.3, 128.6, 127.0, 126.0, 116.0, 112.2, 52.3, 38.4, 30.6, 26.4. MS (*m*/*e*): 251 (M+), 120 (100). HRMS: 251.1674 (calcd.) and 251.1652 (obs.). Preparative irradiation of a 0.01 M solution of *trans*-**2** in acetonitrile followed by chromatography provided *cis*-**2** in an isolated yield of ca. 45%: ^{1}H NMR δ: 7.41–6.73 (m, 10H), 6.54–6.50 (d, 1H), 5.76–5.71 (m, 1H), 3.45–3.36 (m, 2H), 2.94 (s, 3H), 2.45–2.41 (q, 2H), 1.84–1.76 (m, 2H). ^{13}C NMR δ: 149.25, 137.61, 130.48, 129.56, 128.86, 128.28, 127.07, 126.71, 116.06, 112.21, 52.32, 38.49, 26.29, 26.97.

trans-N-*Phenyl-4-phenyl-3-buten-1-amine (**3**)*

Modification of the procedure used for the preparation of **1** by using aniline in place of *N*-methylaniline afforded **3** as a colorless oil. ^{1}H NMR ($CDCl_3$) δ: 7.19–7.41 (m, 7H), 6.64–6.76 (m, 3H), 6.50–6.55 (d, *J* = 16 Hz, 1H), 6.22–6.28 (m, 1H), 3.75 (bs, 1H), 3.27–3.32 (t, *J* = 6.7 Hz, 2H), 2.56–2.60 (q, *J* = 6.9 Hz, 2H). ^{13}C NMR δ: 148.2, 137.3, 132.3, 129.3, 128.6, 127.4, 127.3, 126.1, 117.5, 113.0, 43.3, 33.0. HRMS: 223.1361 (calcd.) and 223.1374 (obs.).

trans-N-*Phenyl-5-phenyl-4-penten-1-amine (**4**)*

Modification of the procedure used for the preparation of **2** by using aniline in place of *N*-methylaniline provided **3** as a colorless oil. ^{1}H NMR δ: 7.14–7.36 (m, 7H), 6.59–6.72 (m, 3H), 6.40–6.45 (d, *J* = 15.9 Hz, 1H), 6.20–6.28 (m, 1H), 3.65 (bs, 1H), 3.15–3.19 (t, *J* = 7.0 Hz, 2H), 2.29–2.36 (q, 2H), 1.76–1.84 (quintet, 2H). ^{13}C NMR δ: 148.4, 137.6, 130.6, 130.0, 129.3, 128.6, 127.1, 126.0, 117.3, 112.8, 43.5, 30.7, 29.2. MS (*m*/*e*): 237 (M+), 106 (100). HRMS: 237.1517 (calcd.) and 237.1518 (obs.).

trans-N-*Phenyl-6-phenyl-5-hexen-1-amine (**5**)*

Modification of the procedure used for the preparation of **4** by using 1-bromo-4-chlorobutane in place of 1-bromo-3-chloropropane provided **3** as a colorless oil in 15% overall yield. ^{1}H NMR δ: 7.19 (m, 3H), 6.97 (m, 2H), 6.47 (m, 2H), 5.80 (d, 2H), 3.68 (m, 2H), 3.25 (m, 2H), 2.50 (m, 2H). ^{13}C

© 1999 NRC Canada

NMR δ: 145.50, 129.67, 128.98, 125.49, 117.17, 112.70, 112.47, 26.88. HRMS: 251.1679 (calcd.) and 251.1674 (obs.).

*Ethyl-(*E*)-5-anilino-2-pentenoate (**6**)*

Ethyl-(*E*)-5-bromo-2-pentenoate was synthesized according to the procedure reported by Bunce and Irwin (31). Stirring at room temperature for 24 h with aniline afforded compound **6** as an oil (59%). ^{1}H NMR δ: 7.26 (t, 2H), 6.95 (m, 1H), 6.75 (t, 2H), 6.65 (d, 2H), 5.90 (m, 1H), 3.74 (s, 3H), 3.32 (t, 2H), 2.55 (m, 2H). ^{13} C NMR δ: 166.70, 147.26, 146.44, 145.64, 134.60, 132.44, 131.31, 129.79, 128.94, 113.51, 51.07, 42.51, 30.21. HRMS: 205.110 28 (calcd.) and 205.110 30 (obs.).

trans-N-*Phenyl-5-hexen-1-amine (**7**)*

Following the procedure of Ohsawa et al. (32), **7** was obtained as a colorless oil. ^{1}H NMR δ 7.27(m, 2H), 6.84 (m, 3H), 5.85 (m, 1H), 5.5 (bs, 1H), 5.11 (m, 2H), 3.20 (t, 2H), 2.17 (m, 2H), 1.81 (m, 2H). HRMS: 251.1674 (calcd.) and 251.1674 (obs.).

N-*Phenyl-2-phenylpyrrolidine (**3a**)*

A solution of compound **3** (0.1 g) in acetonitrile (36 mL) was bubbled with dry N_2 for 10–15 min in a Pyrex test tube and irradiated using a Rayonet reactor fitted with RPR 3000 lamps. The reaction was monitored by gas chromatography until >90% of starting material was converted to products (3 h). Evaporation of the solvent under reduced pressure and column chromatography (silica gel, 50% hexane in dichloromethane) yielded 0.05 g **3a**. ^{1}H NMR δ: 7.14–7.34 (m, 7H), 6.63–6.67 (dd, *J* = 7.3 Hz, 1H), 6.49–6.52 (d, *J* = 6.6 Hz, 2H), 4.72–4.76 (dd, J = 8.7 Hz, 1H), 3.69–3.74 (m, 1H), 3.38–3.46 (m, 1HO, 2.36–2.43 (m, 1H), 1.92–2.04 (m, 3H). ^{13}C NMR δ: 147.2, 144.6, 129.0, 128.5, 126.7, 126.0, 115.8, 112.3, 62.9, 49.1, 36.1, 23.1. HRMS: 223.1361 (calcd.) 223.1373 (obs.).

N-*Phenyl-2-phenylpiperdine (**4a**)*

Irradiation of **4** (0.15 g) in acetonitrile (60 mL) using the conditions described for **3** afforded 0.05 g **4a**: ^{1}H NMR δ: 6.72–7.28 (m, 10H), 4.48–4.52 (dd, *J* = 6.3 Hz, 1H), 3.36–3.42 (m, 1H), 3.23–3.29 (m, 1H), 1.92–2.00 (m, 2H), 1.52–1.73 (m, 2H); ^{13}C NMR δ: 151.9, 143.6, 128.8, 128.3, 127.3, 126.3, 119.6, 118.8, 61.0, 50.6, 33.5, 25.7, 22.1; HRMS: 237.1517 (calcd.) and 237.1500 (obs.). Small-scale irradiation **4** in hexane afforded **4a** as the major product and a second product tentatively identified as **4b**: MS-EI (*m*/*z*): 237, 222, 208, 194, 180, 167, 160 (100), 152, 146, 139, 132, 126, 117, 104, 97, 91, 83, 77, 65, 51.

5b

Small-scale irradiation of **5** in hexane or acetonitrile solution afforded a major product tentatively identified as **5b**. MS-EI (*m*/*z*): 251, 222, 208, 160, 146, 132, 119 (100), 106, 91, 77, 65, 51.

6a** and **6b

Small-scale irradiation of **6** in benzene solution afforded a major product tentatively identified as **6a**: MS-EI (*m*/*e*): 205, 146 (100), 130, 117, 104, 91, 77, 65, 51. Also detected was a minor product tentatively identified as **6b**: MS-EI (*m*/*e*): 205, 177, 144, 132 (100), 117, 104, 91, 77, 59, 51.

References

1. (*a*) N.J. Pienta. *In* Photoinduced electron transfer. Part C. *Edited by* M.A. Fox and M. Chanon. Elsevier, Amsterdam. 1988. pp. 421–486; (*b*) U.C. Yoon, P.S. Mariano, R.S. Givens, and B.W. Atwater III. *In* Advances in electron transfer chemistry. Vol. 4. *Edited by* P.S. Mariano. JAI Press Inc., Greenwich. 1994. pp. 117–205; (*c*) F.D. Lewis. *In* Advances in electron transfer chemistry. Vol. 5. *Edited by* P.S. Mariano. JAI Press Inc., Greenwich. 1996. pp. 1–39.
2. (*a*) H. Beens and A. Weller. Acta Physica Polonica, **34**, 593 (1968); (*b*) H. Knibbe, D. Rehm, and A. Weller. Ber. Bunsenges. Phys. Chem. **73**, 839 (1969); (*c*) A. Weller. *In* The exciplex. *Edited by* M. Gordon and W.R. Ware. Academic Press, New York. 1975. pp. 23–38; (*d*) Z. Phys. Chem. (Wiesbaden), **133**, 93 (1982).
3. S. Basu. J. Photochem. **9**, 539 (1978).
4. N. Ghoneim, C. Hammer, E. Haselbach, D. Pilloud, P. Suppan, and P. Jacques. J. Chem. Soc. Faraday Trans. **89**, 4271 (1993); (*b*) D. Burget, P. Jacques, E. Vauthey, P. Suppan, and E. Haselbach. J. Chem. Faraday Trans. I **90**, 2481 (1994); (*c*) E. Vauthey and A. Henseler J. Phys. Chem. **100**, 170 (1996).
5. (*a*) M.K. Crawford, Y. Wang, and K.B. Eisenthal. Chem. Phys. Lett. **79**, 529 (1981); (*b*) U. Werner and H. Staerk. J. Phys. Chem. **97**, 9274 (1993).
6. (*a*) S. Masaki, T. Okada, N. Mataga, Y. Sakata, and S. Misumi. Bull. Chem. Soc. Jpn. **49**, 1277 (1976); (*b*) T. Okada, T. Saito, N. Mataga, Y. Sakata, and S. Misumi. Bull Chem. Soc. Jpn. **50**, 331 (1977); (*c*) T. Okada, M. Migita, N. Mataga, Y. Sakata, and S. Misumi. J. Am. Chem. Soc. **103**, 4715 (1981); (*d*) N. Mataga, S. Nishikawa, T. Asahi, and T. Okada. J. Phys. Chem. **94**, 1443 (1990).
7. R. Ziebig and F. Pragst. Chem. Phys. Lett. **70**, 544 (1980).
8. (*a*) N.C. Yang, D.W. Minsek, D.G. Johnson, J.R. Larson, J.W. Petrich, R. Gerald, and M.R. Waselewski. Tetrahedron, **45**, 4669 (1989); (*b*) S. Zhang, M.J. Lang, S. Goodman, C. Durnell, V. Fidlar, G.R. Fleming, and N.C. Yang. J. Am. Chem. Soc. **118**, 9042 (1996).
9. T. Okada, T. Mori, and N. Mataga. Bull. Chem. Soc. Jpn. **49**, 3398 (1976); (*b*) T. Okada, I. Karaki, and N. Mataga. J. Am. Chem. Soc. **104**, 7191 (1982).
10. T. Okada, I. Karaki, E. Matsuzawa, N. Mataga, Y. Sakata, and S. Misumi. J. Phys. Chem. **85**, 3957 (1981).
11. (*a*) D. Goswami, R.S. Sarpal, and S.K. Dogra. Bull. Chem. Soc. Jpn. **64**, 3137 (1991); (*b*) S.K. Saha and S.K. Dogra. J. Luminescence, **75**, 117 (1997).
12. V. Avila, J.J. Cosa, C.A. Chesta, and C.M. Previtali. J. Photochem. Photobiol. A: Chem. **62,** 83 (1991).
13. (*a*) U. Koch-Pomeranz, H. Schmid, and H.-J. Hansen. Helv. Chim. Acta, **60**, 768 (1977); (*b*) S. Jolidon and H.-J. Hansen. Helv. Chim. Acta, **62**, 2581 (1979).
14. (*a*) F.D. Lewis, G.D. Reddy, S. Schneider, and M. Gahr. J. Am. Chem. Soc. **113**, 3498 (1991); (*b*) F.D. Lewis, G.D. Reddy, D.M. Bassani, S. Schneider, and M. Gahr. J. Am. Chem. Soc. **119**, 597 (1994); (*c*) F.D. Lewis, J.M. Wagner-Brennan, and J.M. Denari. J. Phys. Chem. A, **102**, 519 (1998).
15. H.H. Jaffë and M. Orchin. Theory and applications of ultraviolet spectroscopy. John Wiley and Sons, Inc, New York. 1962.
16. G. Köhler. J. Photochem. **38**, 217 (1987).
17. F.D. Lewis, D.M. Basssni, R.A. Caldwell, and D.J. Unett. J. Am. Chem. Soc. **116**, 10 477 (1994).
18. (*a*) E. Lippert. Z. Naturforsch. **109**, 541 (1955); (*b*) N. Mataga, Y. Kaifu, and M. Koizumi. Bull. Chem. Soc. Jpn. **28**, 690 (1955).

© 1999 NRC Canada

19. F.D. Lewis, D.M. Bassani, E.L. Burch, B.E. Cohen, J.A. Engleman, G.D. Reddy, S. Schneider, W. Jaeger, P. Gedeck, and M. Gahr. J. Am. Chem. Soc. **117**, 660 (1995).
20. E.C. Lim and S.K. Chakrabarti. J. Chem. Phys. **47**, 4726 (1967).
21. A.A. Lamola, P.A. Leermakers, G.W. Byers, and G.S. Hammond. J. Am. Chem. Soc. **87**, 2322 (1965).
22. J. Chodowski and T. Giovanoli-Jakubaczak. Rocz. Chem. **41**, 273 (1967).
23. A.M. Swinnen, M. Van der Auweraer, F.C. De Schryver, K. Nakatani, T. Okada, and N. Mataga. J. Am. Chem. Soc. **109**, 321 (1987).
24. M. Van der Auweraer, Z.R. Grabowski, and W. Rettig. J. Phys. Chem. **95**, 2083 (1991).
25. A.L. Lamola and G.S. Hammond. J. Chem. Phys. **43**, 2129 (1965).
26. S. Zhang, S.-R. Yeh, S. Hong, M. Freccero, A. Albini, D.E. Falvey, and P.S. Mariano. J. Am. Chem. Soc. **116**, 4211 (1994).
27. B.H. Lipshutz, R.S. Wilhelm, S.T. Nugent, R.D. Little, and M.M. Baizer. J. Org. Chem. **48**, 3306 (1983).
28. S. Schneider, H. Rehaber, W. Schüβlbauer, F.D. Lewis, and B.A. Yoon. J. Photochem. Photobiol. A: Chem. **99**, 103 (1996).
29. D.A. Considtron and J.D. Laposa. Chem. Phys. Lett. **64**, 313 (1979).
30. D.R. James, A. Siemiarczuk, and W.R. Ware. Rev. Sci. Instr. **64**, 1710 (1992).
31. R.A. Bunce and D.A. Irwin. Synth. Commun. **20**, 2979 (1990).
32. T. Ohsawa, M. Ihara, K. Fukumoto, and T. Kametani. J. Org. Chem. **48**, 3644 (1983).

© 1999 NRC Canada

Ketonization equilibria of phenol in aqueous solution[1]

Marco Capponi, Ivo G. Gut, Bruno Hellrung, Gaby Persy, and Jakob Wirz

Abstract: The two keto tautomers of phenol (**1**), cyclohexa-2,4-dienone (**2**) and cyclohexa-2,5-dienone (**3**), were generated by flash photolysis of appropriate precursors in aqueous solution, and the pH–rate profiles of their enolization reactions, **2** → **1** and **3** → **1**, were measured. The rates of the reverse reactions, **1** → **2** and **1** → **3**, were determined from the rates of acid-catalyzed hydron exchange at the *ortho*- and *para*-positions of **1**; the magnitude of the kinetic isotope effect was assessed by comparing the rates of hydrogenation of phenol-2*t* and -2*d*. The ratios of the enolization and ketonization rate constants provide the equilibrium constants of enolization, pK_E(**2**, aq, 25°C) = –12.73 ± 0.12 and pK_E(**3**, aq, 25°C) = –10.98 ± 0.15. Combination with the acidity constant of phenol also defines the acidity constants of **2** and **3** through a thermodynamic cycle. These ketones are remarkably strong carbon acids: pK_a(**2**) = –2.89 ± 0.12 and pK_a(**3**) = –1.14 ± 0.15. They disappear by proton transfer to the solvent with lifetimes, τ(**2**) = 260 μs and τ(**3**) = 13 ms, that are insensitive to pH in the range from 3–10.

Key words: proton transfer, tautomers, flash photolysis, kinetic isotope effect, pH–rate profiles.

Résumé : Opérant en solution aqueuse, on a généré les deux tautomères cétoniques du phénol (**1**), la cyclohexa-2,4-diénone (**2**) et la cyclohexa-2,5-diénone (**3**), par photolyse éclair de précurseurs appropriés et on a mesuré les profils pH de la vitesse pour leurs réactions d'énolisation, **2** → **1** et **3** → **1**. On a déterminé les vitesses des réactions inverses **1** → **2** et **1** → **3** à partir des vitesses d'échange d'hydron acidocatalysées dans les positions *ortho*- et *para*- de **1**; on a évalué l'amplitude de l'effet isotopique cinétique en comparant les vitesses d'hydrogénation du phénol-2*t* et -2*d*. Les rapports des constantes de vitesse d'énolisation et de cétonisation permettent d'arriver aux constantes d'équilibre d'énolisation, pK_E(**2**, aq, 25°C) = –12,73 ± 0,12 et pK_E(**3**, aq, 25°C) = –10,98 ± 0,15. Une combinaison avec la constante d'acidité du phénol permet de définir aussi les constantes d'acidité de **2** et de **3** à travers un cycle thermodynamique. Ces cétones sont des acides carbonés relativement forts: pK_a(**2**) = –2,89 ± 0,12 et pK_a(**3**) = –1,14 ± 0,15. Elles disparaissent par transfert de proton vers le solvant avec des temps de vie, τ(**2**) = 260 μs et τ(**3**) = 13 μs qui sont insensibles au pH entre 3 et 10.

Mots clés : transfert de proton, tautomères, photolyse éclair, effet isotopique cinétique, profils pH–vitesse.

[Traduit par la Rédaction]

Introduction

Twenty years ago, we reported on the observation of acetophenone enol by flash photolysis and determined the acidity constant of the enol from the pH–rate profile of its ketonization in aqueous solution (1). That work was a sideline of studies aimed primarily at the characterization of diradical intermediates in Norrish Type 2 reactions, and would not have been pursued, had Prof. A.J. Kresge not visited Basel and convinced us that the photochemical approach to study enol kinetics should be further exploited. Thus began a growing friendship and continued collaboration with the unbeatable research team of Jerry Kresge and his wife, Yvonne Chiang. On the scientific side, we were rewarded by participating in the kinetic and thermodynamic characterization of the enolization equilibria of a representative selection of carbonyl compounds over the last two decades (2).

The protomeric equilibria of thermodynamically stable enols have received less attention. Phenol (**1**) is much more stable than its keto tautomers cyclohexa-2,4-dienone (**2**) and cyclohexa-2,5-dienone (**3**), because proton transfer from oxygen to carbon disrupts π-conjugation of the phenyl ring. Nevertheless, keto tautomers of phenols are frequently invoked as reactive intermediates, e.g., in the Photo–Fries rearrangement, the Kolbe–Schmitt and Reimer–Tiemann reactions, in electrophilic substitutions of phenols, and in the oxidative metabolism of aromatic compounds ("NIH-shift"). In preliminary work (3), we generated cyclohexa-2,4-dienone (**2**) by flash photolysis and observed the kinetics of its enolization, **2** → **1**, in acidic and neutral aqueous solutions. The rate constant of ketonization, k^K(**1** → **2**), was estimated from the rate of deuteration of **1** in 1 N D_2SO_4 at 80°C. Combination with the rate constant of enolization, k^E(**2** → **1**), provided a preliminary estimate of the equilibrium constant of enolization of **2** in aqueous solution, $K_E \equiv [\mathbf{1}]/[\mathbf{2}] = k^E(\mathbf{2} \rightarrow \mathbf{1})/k^K(\mathbf{1} \rightarrow \mathbf{2}) \approx 10^{(13 \pm 1)}$. We now report the

Received January 12, 1999.

This paper is dedicated to Jerry Kresge in recognition of his many achievements in chemistry.

M. Capponi, I.G. Gut, B. Hellrung, G. Persy, and J. Wirz.[2] Institut für Physikalische Chemie der Universität Basel, Klingelbergstrasse 80, CH-4056 Basel, Switzerland.

[1]Tautomerization of phenols, part 2; see ref. 3 for part 1.

[2]Author to whom correspondence may be addressed. Telephone: +41 61 267 38 42. Fax: +41 61 267 38 55. e-mail: wirz2@ubaclu.unibas.ch

© 1999 NRC Canada

Scheme 1.

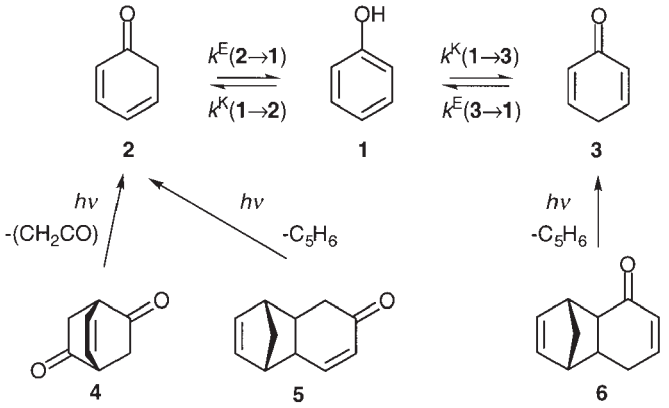

complete pH–rate profile of the enolization reaction **2** → **1** in aqueous solution and an accurate value for K_E. A brief study of the other keto tautomer of **1**, cyclohexa-2,5-dienone (**3**), is included. The photoreactions that were used to generate dienones **2** and **3** are shown in Scheme 1.

Results

Continuous irradiation of compounds 4–6

Direct irradiation of bicyclo[2.2.2]oct-2-ene-5,7-dione (**4**) eliminates ketene to yield **2** as a primary product that tautomerizes to phenol (3). Oxadi-π-methane rearrangement is the predominant reaction initiated by triplet sensitization of **4** (4). Irradiation of tricyclo[6.2.1.0^{2,7}]undeca-5,9-dien-4-one (**5**) or tricyclo[6.2.1.0^{2,7}]undeca-4,9-dien-3-one (**6**) also gave phenol as a major photoproduct that was identified by GC–MS analysis. The flash photolysis experiments described below provided direct evidence that phenol is formed via the primary photoproducts **2** and **3** after light-induced cycloelimination of cyclopentadiene from **5** and **6**, respectively, as indicated in Scheme 1.

Flash photolysis; rates of enolization of the keto tautomers 2 and 3

Aqueous solutions of compounds **4**–**6** were flashed with 25 ns pulses from an excimer laser operated on XeCl (200 mJ per pulse, 308 nm), or 20 μs pulses from a conventional electric discharge flashlamp of up to 1000 J electrical energy. The cycloadducts **4** and **5**, presumed to be photochemical precursors of **2**, both gave rise to weak transient absorption in the range of 280–330 nm. The decays of these transients obeyed first-order kinetics with rate constants depending on pH and buffer concentrations. Degassing had no influence on the yield or lifetime of the transient intermediates. Ketones **4** and **5** are sensitive to base, but decomposition was sufficiently slow to permit measurements in freshly prepared, weakly basic solutions. The decay rates of the 300 nm transients produced from **4** and **5** were equal, within the limits of error, in neutral water (k_{obs} = 3800 ± 300 s^{-1}) and faster, but again equal, in 2.0 mM aqueous KOH (7600 ± 800 s^{-1}).

Because **4** gave somewhat stronger transient signals and was available in larger quantity, this precursor was used to collect a more extensive set of data at various pH (25°C, ionic strength I = 0.1 M, Table 1). The resulting pH–rate profile of the enolization reaction **2** → **1** is shown in Fig. 1. As is well known from many studies of ketone enolization (2), the rate of enolization is accelerated by acid and by base, but, unlike the behavior of simple ketones, the pH-independent contribution dominates the overall reaction over a large range, 3 ≤ pH ≤ 10. The solid line corresponds to function [1], which was fitted to the observed rates of enolization by nonlinear least-squares adjustment of the parameters $k^E_{H^+}$ and $k^E_{OH^-}$, the rate coefficients for acid and base catalysis, and k^E_0 for the reaction catalyzed by the solvent (Table 2). The dissociation constant of water at ionic strength I = 0.1 M was taken as $K_w = 1.59 \times 10^{-14}$ M^2 (5). Weighting of the data was not required, because the relative errors of the observed rate constants, and hence, standard errors of log (k_{obs}) values, were approximately constant.

Fig. 1. pH–rate profile for the enolization of 2,4-cyclohexadienone (**2**) in aqueous solution at 25.0°C and I = 0.10 M.

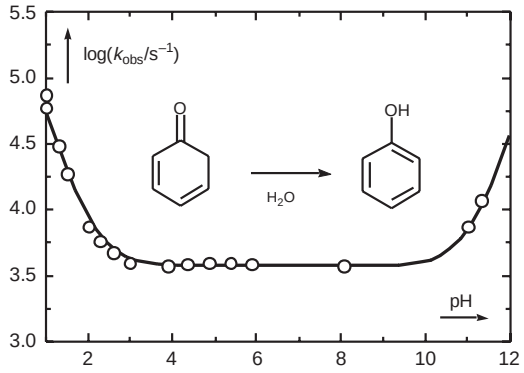

$$[1] \qquad \log (k^E_{obs}/s^{-1}) = \log \{(k^E_0 + k^E_{H^+}[H^+] + k^E_{OH^-}K_w/[H^+])/s^{-1}\}$$

Acetate and tris(hydroxymethyl)methyl amine (Tris) buffers were used to determine some rate constants at pH values around 5 and 8. The decay rates increased linearly with buffer concentration, and the intercepts obtained by least-squares fitting of these individual plots are given in Table 1. From the slopes of the buffer dilution plots only general base catalysis is detectable, $k_{Ac} = (9.5 \pm 0.4) \times 10^3$ M^{-1} s^{-1}, $k_{Tris} = (1.8 \pm 0.2) \times 10^5$ M^{-1} s^{-1}. Solvent isotope effects (Table 2) were found to be in the normal direction ($k_H > k_D$) for the decay rate constants k^E_0 of cyclohexa-2,4-dienone and of its 6,6-dideuterated derivative **2**-d_2, but strongly inverse on the coefficient $k^E_{H^+}$ of the acid-catalyzed reaction.

Flash photolysis of **6** gave very weak transient absorption around 250 nm, which is the wavelength expected for the absorption of 2,5-cyclohexadienone (**3**) (6). Eight traces were averaged for each measurement to improve the signal-to-noise ratio. Due to the instability of **6** to base, experiments were limited to acidic and neutral solution. The decay rates of **3** were more than an order of magnitude slower than those of **2** (Table 1). The rate coefficients k^E_0 and $k^E_{H^+}$ for **3** were determined by nonlinear least-squares fitting of eq. [1] (omitting the last term for base catalysis), and are also given in Table 2.

© 1999 NRC Canada

Table 1. Rates of enolization of **2** and **3** in aqueous solution at 25.0 ± 0.1°C.

Compound	Acid/base	Buffer ratio	Conc./M	log ([H$^+$]/M)	k^E_{obs}/(10^3 s^{-1})	No. of expts.
2	$HClO_4$		0.100	1.00	73.6 ± 1.9	[a]
2	HCl		0.100	1.00	60.8 ± 1.5	10
2	HCl		0.050	1.30	30.6 ± 0.7	10
2	HCl		0.032	1.50	18.5 ± 0.3	10
2	HCl		0.010	2.00	7.65 ± 0.08	10
2	HCl		0.005	2.30	5.80 ± 0.08	10
2	HCl		0.0025	2.60	4.80 ± 0.06	10
2	HCl		0.001	3.00	4.00 ± 0.06	10
2	HAc/NaAc	5.00	0.02–0.10	3.87[b]	3.82 ± 0.15[e]	18
2	HAc/NaAc	1.584	0.01–0.09	4.37[b]	3.90 ± 0.06[e]	23
2	HAc/NaAc	0.500	0.01–0.09	4.87[b]	3.98 ± 0.07[e]	24
2	HAc/NaAc	0.159	0.01–0.09	5.36[b]	3.99 ± 0.10[e]	18
2	HAc/NaAc	0.050	0.01–0.09	5.87[b]	3.95 ± 0.03[e]	23
2	HCl/Tris	1.12	0.01–0.10	8.07[c]	3.80 ± 0.15[e]	25
2	KOH		0.002	11.10[d]	7.59 ± 0.17	10
2	KOH		0.004	11.40[d]	12.0 ± 0.6	10
2	—		—	≈6	3.83 ± 0.04	5
2	—	(D_2O)	—	≈6	2.67 ± 0.02	6
2-d_2	—		—	≈6	0.58 ± 0.01	5
2-d_2	—	(D_2O)	—	≈6	0.40 ± 0.01	9
3	HCl		0.020	1.70	0.62 ± 0.07	8
3	HCl		0.005	2.30	0.224 ± 0.010	8
3	—		—	≈6	0.079 ± 0.004	8

[a]Value calculated from the regression line of an Arrhenius plot (data in Table 4).

[b]Calculated using the thermodynamic acidity constant $pK_a^{\ominus}$ = 4.76 (38), and activity coefficients recommended by Bates (5) to give the concentration quotient $pK_{a,c}(I = 0.1\ M) = 4.57$.

[c]Calculated from $pK_{a,c}(I = 0.1\ M) = 8.12$ (39).

[d]Calculated from the nominal base concentration with $K_w(I = 0.1\ M) \equiv [H^+][HO^-] = 1.59 \times 10^{-14}$ (ref. 5).

[e]Intercept of buffer dilution plot. From the slopes of the buffer dilution plots only general base catalysis is detectable, $k_{Ac} = (9.5 \pm 0.4)10^3\ M^{-1}\ s^{-1}$, $k_{Tris} = (1.8 \pm 0.2)10^5\ M^{-1}\ s^{-1}$.

Table 2. Rate constants of enolization and ketonization at 25 ± 0.1°C, I = 0.10 M.

Reaction	Rate coefficient	k/s^{-1}	$k(H_2O)/k(D_2O)$
2 → **1**	k^E_0	$(3.8 \pm 0.1)10^3$	1.43 ± 0.03[a]
2-d_2 → **1**	k^E_0	$(5.8 \pm 0.1)10^2$	1.45 ± 0.05[a]
2 → **1**	$k^E_{H^+}$	$(5.4 \pm 0.3)10^5\ M^{-1}$	0.50 ± 0.05[b]
2 → **1**	$k^E_{OH^-}$	$(2.0 \pm 0.3)10^6\ M^{-1}$	
3 → **1**	k^E_0	80 ± 8	
3 → **1**	$k^E_{H^+}$	$(2.8 \pm 0.9)10^4\ M^{-1}$	
1 → **2**	$k^K_{H^+}$	$(1.01 \pm 0.28)10^{-7}\ M^{-1}$	
1 → **3**	$k^K_{H^+}$	$(2.96 \pm 0.27)10^{-7}\ M^{-1}$	

[a]Average from ≥5 measurements each in H_2O and D_2O (no buffer); 25°C, I = 0.1 M.

[b]Average from 9 measurements each of HCl/H_2O and DCl/D_2O at matching nominal acid concentrations in the range of 0.02–0.1 N; 23°C, I = 0.1 M.

Isotope exchange kinetics; rates of ketonization

At room temperature the exchange of the aromatic hydrogen atoms of **1** is slow. Solutions of phenol-2*d* and phenol-2*t* in 0.1 N $HClO_4$ were kept at 80.0 ± 0.5°C, and the loss of their deuterium or tritium label to the solvent was monitored by 400 MHz ^{2}H NMR and by scintillation counting, respectively (Table 3). Details of the procedures are given in the experimental section. The analysis of these data to determine the isotope effect and to extrapolate to the rate constant $k^K_{H^+}$ for the acid-catalyzed ketonization reaction **1** → **2** is now described.

Acid-catalyzed exchange of aromatic hydrogen proceeds by a two-step reaction mechanism with a C-protonated intermediate (7), Scheme 2. Solutions of the substrate **2**-L in H_2O are assumed to be dilute, such that that the second step, **2**-L$^+$ → **1** + L$^+$, is practically irreversible. Following the notation

© 1999 NRC Canada

Table 3. Isotopic exchange rates of phenol.

Reaction	Symbol	k_{obs}/s^{-1}	Acid	Acid conc./M	*T*/K
1–2*t* → **1**	k^{-T}	(5.63 ± 0.03)10^{-7}	$HClO_4$	0.10	353.2
1–2*d* → **1**	k^{-D}	(9.04 ± 0.55)10^{-7}	$HClO_4$	0.10	353.2
1 → **1**-2*d*	k^{D_2}	(3.22 ± 0.03)10^{-5}	DCl	1.00	353.2
1 → **1**-2*d*	k^{D_2}	(1.11 ± 0.01)10^{-5}	DCl	1.00	343.2
1 → **1**-2*d*	k^{D_2}	(3.48 ± 0.03)10^{-6}	DCl	1.00	333.2
1 → **1**-4*d*	k^{D_4}	(5.39 ± 0.05)10^{-5}	DCl	1.00	353.2
1 → **1**-4*d*	k^{D_4}	(1.93 ± 0.02)10^{-5}	DCl	1.00	343.2
1 → **1**-4*d*	k^{D_4}	(7.02 ± 0.07)10^{-6}	DCl	1.00	333.2

Scheme 2.

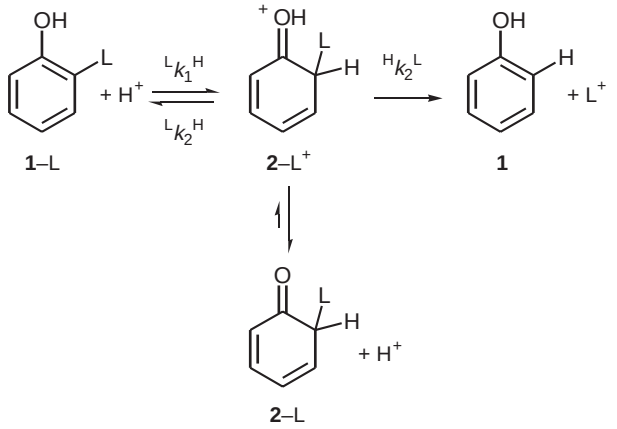

used by Kresge and Chiang (7), the rate coefficients shown in Scheme 2 carry two superscripts to facilitate the bookkeeping of isotope effects. The *right-hand superscript* designates the isotope involved in the hydron transfer reaction between C2 and the solvent (*primary isotope effect*). The *left-hand superscript* designates the spectator isotope remaining on C2 during this reaction (*secondary isotope effect*).

Dissociation equilibria of oxygen acids are, in general, established more rapidly than those of carbon acids (8). Accordingly, we assume that OH dissociation of **2**-L$^+$ (the vertical reaction shown in Scheme 2) is faster than hydron dissociation from carbon to form **1** or **1**-L (horizontal reactions). This assumption conforms to the accepted mechanism for hydronium-ion-catalyzed enolization of simple carbonyl compounds, which consists of rapid and reversible hydronation of the substrate on oxygen followed by rate-determining removal of a carbon-bound hydron by a molecule of water (9). Application to the present case might be questioned on the grounds that CH dissociation of **2**-L$^+$ is thermodynamically favored over OH dissociation by 2.3*RT* × pK_E which, as we shall see below, amounts to 72.6 ± 0.7 kJ mol^{-1}. However, we have recently shown that even larger thermodynamic bias is insufficient to overcome the kinetic preference for OH dissociation (10). Moreover, the inverse solvent isotope effect observed on the acid-catalyzed enolization of **2** (k_H/k_D = 0.5, Table 2, row 3) is strong evidence for pre-equilibrium protonation on oxygen.

If OH dissociation of **2**-L$^+$ is faster than CH dissociation, then carbon protonation is the rate-determining step in acid-catalyzed ketonization of **1** → **2**, and the rate constant of this process is given by eq. [2]. The statistical factor of 2 arises because the ketonization rate constant $k^K_{H^+}$ refers to protonation at either of the *ortho* positions C2 or C6, whereas $^{H}k_1^{H}$ refers to protonation at C2 only.

$$[2] \qquad k^K_{H^+} = 2\,{}^{H}k_1^{H}$$

Carbon protonation does, however, not fully determine the rate of isotopic exchange, because only a fraction of the protonated intermediate **2**-L$^+$ eventually loses the label by dissociating to **1** + L$^+$. The rates of the forward reaction (loss of label) and backward reaction (retention of label) are of the same order of magnitude, $^{H}k_2^{L} \approx {}^{L}k_2^{H}$. Since protonation of **1**–L is much slower than the subsequent steps, $^{L}k_1^{H}[H^+] << {}^{H}k_2^{L} + {}^{L}k_2^{H}$, the steady-state (Bodenstein) approximation is applicable to **2**-L$^+$, and the observed rate constant for acid-catalyzed loss of label L may be expressed as the product of the rate constant of C-protonation of **1**-L, the proton concentration, and the partitioning ratio of intermediate **2**-L$^+$, eq. [3].

$$[3] \qquad k^{-L}_{obs} = {}^{L}k_1^{H}[H^+]\frac{{}^{H}k_2^{L}}{{}^{H}k_2^{L} + {}^{L}k_2^{H}}$$

The ratio of the experimental rate constants of detritiation and dedeuteration in aqueous acid of a given concentration is then given by eq. [4].

$$[4] \qquad \frac{k^{-T}_{obs}}{k^{-D}_{obs}} = \frac{{}^{T}k_1^{H}}{{}^{D}k_1^{H}}\frac{{}^{H}k_2^{T}}{{}^{H}k_2^{T} + {}^{T}k_2^{H}}\frac{{}^{H}k_2^{D} + {}^{D}k_2^{H}}{{}^{H}k_2^{D}}$$
$$= \frac{{}^{T}k_1^{H}}{{}^{D}k_1^{H}}\frac{1 + {}^{D}k_2^{H}/{}^{H}k_2^{D}}{1 + {}^{T}k_2^{H}/{}^{H}k_2^{T}}$$

Our goal is to calculate the rate constant for acid-catalyzed ketonization of **1**, $k^K_{H^+}$, from the observed rates of dedeuteration and detritiation, k^{-D}_{obs} and k^{-T}_{obs}. Extrapolation from observed isotope exchange rates k_T and k_D to k_H is commonly done on the basis of the Swain relation (eq. [5]) (11). However, eq. [4] contains contributions from both primary and secondary kinetic isotope effects. In a detailed study of acid-catalyzed hydron exchange in 1,3,5-trimethoxybenzene, Kresge and Chiang (7) have established that the Swain relation gives reliable results when it is applied individually to primary and secondary isotope effects.

$$[5] \qquad (k_H/k_D)^{1.442} = k_H/k_T$$

The first factor on the right-hand side of eq. [4], $^{T}k_1^{H}/{}^{D}k_1^{H}$, is a purely secondary isotope effect: hybridization of carbon atom 2 changes from sp^2 to sp^3 upon protonation (step 1 in Scheme 2), which influences bonding to the isoto-

© 1999 NRC Canada

Table 4. Temperature dependence of the rate constants of enolization of **2** in 0.1 N $HClO_4$.

log (k^E_{obs}/s^{-1})	t/°C
4.85 ± 0.02	25.0 ± 0.1
5.05 ± 0.02	37.0 ± 0.1
5.21 ± 0.02	47.0 ± 0.1
5.37 ± 0.02	62.5 ± 0.2
5.49 ± 0.02	71.0 ± 0.2
5.59 ± 0.02	79.0 ± 0.3

pic label L. Such secondary isotope effects are known to be inverse, and to have a relatively constant value of about 12% per deuterium atom, i.e., ${}^{H}k_1^{H}/{}^{D}k_1^{H}$ = 0.88 ± 0.04 (7, 12). The factor ${}^{T}k_1^{H}/{}^{D}k_1^{H}$ can then be estimated using the Swain relation

$$[6]\qquad \frac{{}^{T}k_1^{H}}{{}^{D}k_1^{H}} = \frac{{}^{T}k_1^{H}}{{}^{H}k_1^{H}}\frac{{}^{H}k_1^{H}}{{}^{D}k_1^{H}} = \left(\frac{{}^{D}k_1^{H}}{{}^{H}k_1^{H}}\right)^{(1.442-1)}$$

$$= (0.88 \pm 0.04)^{-0.442} = 1.06 \pm 0.02$$

The fractions appearing in the second term of eq. [4] are a product of primary and secondary isotope effects. In the numerator we have ${}^{D}k_2^{H}/{}^{H}k_2^{D} \equiv x$. By application of the Swain relation we obtain ${}^{T}k_2^{H}/{}^{H}k_2^{T} = x^{1.442}$, and eq. [4] is replaced by eq. [7].

$$[7]\qquad \frac{k^{-T}_{obs}}{k^{-D}_{obs}} = (1.06 \pm 0.02)\frac{1+x}{1+x^{1.442}}$$

The experimental rate constants for detritiation and dedeuteration of **1**-2*l* at 80°C in 0.1 N $HClO_4$ are given in Table 3. Equation [7] can be solved for x by iterative approximation to give x = 4.1 ± 0.5. Insertion of x into eq. [3] (L = D) gives ${}^{D}k_1^{H} = k^{-D}_{obs}(1 + x)/[H^+]$ and using ${}^{H}k_1^{H} = {}^{D}k_1^{H}(0.88 \pm 0.04)$, we can replace eq. [2] by eq. [8], in which the desired rate constant of ketonization is expressed fully in terms of experimentally determined quantities

$$[8]\qquad k^{K}_{H^+} = 2k^{-D}_{obs}(x+1)(0.88 \pm 0.04)/[H^+]$$

We obtain $k^{K}_{H^+}$(353 K) = (8.1 ± 1.3)10^{-5} M^{-1} s^{-1} for the rate constant of acid-catalyzed ketonization, **1** → **2**. The error limits were determined by propagation of the standard errors of the experimental data and of the assumed range for the secondary isotope effect, taking account of the high covariance between x and k^{-D}_{obs} through eq. [7].

Temperature dependence of the kinetic data

Flash photolysis of **4** in 0.1 N aqueous $HClO_4$ was done at various temperatures from 25 to 80°C (Table 4). The rate constants accurately obeyed the Arrhenius equation, $k = A\exp(-E_a/RT)$, and linear regression of log (k^E_{obs}/s^{-1}) vs. 1/T gave the Arrhenius parameters log (A/s^{-1}) = 9.58 ± 0.11 and E_a = 27.0 ± 0.7 kJ mol^{-1}. The rate coefficient for the acid-catalyzed enolization of **2** at 80°C is calculated as $k^{E}_{H^+} = k^{E}_{obs}/[H^+]$ = (3.94 ± 0.06)10^6 M^{-1} s^{-1} from this regression. Combination with the rate constant of ketonization provides the equilibrium constant of enolization of **2** at this temperature, K_E(353 K) = $k^{E}_{H^+}/k^{K}_{H^+}$ = (3.94 ± 0.06)10^6/(8.1 ± 1.3)10^{-5} = (4.9 ± 0.8)10^{10}, pK_E(353 K) = –10.69 ± 0.07.

The temperature dependence of the isotopic exchange rates was determined by monitoring the deuteration of phenol in 1 N DCl/D_2O at 60.0, 70.0, and 80.0 ± 0.5°C by 300 MHz ^{1}H NMR. This was easier than repeating the dedeuteration of phenol-2*d* at several temperatures, and at the same time, provided exchange rates at C4 of phenol. Secondary isotope effects from isotopic substitution at positions remote from the site of protonation (C4 and C6 for deuteration at C2) have been demonstrated to be negligible (7). The resulting exchange rate constants k^{D_2} and k^{D_4} are given in Table 3. These values are two to three times higher than those obtained in preliminary work by deuteration of phenol in 1 N D_2SO_4 at the same temperature (3). The discrepancy may in part be attributed to incomplete dissociation of D_2SO_4 in 1 N solution. Linear least-squares regression of log (k/s^{-1}) vs. 1/T gave the Arrhenius parameters log (A/s^{-1}) = 11.61 ± 0.13 and E_a = 109 ± 1 kJ mol^{-1} for *ortho*-deuteration, and log (A/s^{-1}) = 10.47 ± 0.32 and E_a = 100 ± 2 kJ mol^{-1} for *para*-deuteration. The rate constants calculated for 25°C from these regressions are k^{D_2} = (3.47 ± 0.16)10^{-8} M^{-1} s^{-1} and k^{D_4} = (1.02 ± 0.12)10^{-7} M^{-1} s^{-1}.

The ratio between the rate constant of ketonization **1** → **2**, eq. [8], and the observed rate constant of *ortho*-deuteration amounts to $k^{K}_{H^+}/k^{D_2}$ = (8.1 ± 1.3)10^{-5}/(3.22 ± 0.03)10^{-5} = 2.5 ± 0.4 at 80°C. This factor is a compound of primary and secondary isotope effects of the substrate as well as ionic strength and isotope effects of the solvent. The temperature dependence of this factor is estimated from the formula $k^{K}_{H^+}/k^{D_2} = \exp(-\Delta E_0/RT)$, assuming that it may be attributed to a single dominant zero-point vibrational energy difference ΔE_0. That is an overly crude assumption, but the correction of +0.4 for extrapolation to room temperature is small; the ratio resulting for 25°C is $k^{K}_{H^+}/k^{D_2}$ = 2.9 ± 0.8 (the error margin was increased by 0.4, the amount of the above correction), and the rate constant for acid-catalyzed ketonization **1** → **2** at 25°C is then calculated as $k^{K}_{H^+}$ = (2.9 ± 0.8)(3.47 ± 0.16)10^{-8} = (1.01 ± 0.28)10^{-7} M^{-1} s^{-1}. The same factor was used to calculate the acid-catalyzed rate constant of ketonization **1** → **3**, $k^{K}_{H^+}$ = (2.9 ± 0.8)k^{D_4} = (2.96 ± 0.27)10^{-7} M^{-1} s^{-1}.

Discussion

Evidence for keto tautomers of phenol

In a review article on the theory of unsaturated and aromatic compounds, published in 1899, Thiele (13) speculated that the propensity of phenol (**1**) and its anion to undergo substitution and oxidation reactions might be attributed to rapid equilibration of **1** with the transient keto forms **2** and **3**. At that time, the concepts of protomerism, as in Scheme 3, and mesomerism, Scheme 4, were not clearly distinguished. From the present viewpoint, it is clear that the ketonization of phenol, Scheme 3, is much too slow to explain the reactivity of phenol towards, e.g., bromine, but mesomeric charge delocalization, as shown in Scheme 4, is still used to explain the enhanced reactivity of phenolate at the *ortho* and *para* positions.

Only 2 years later, Lapworth (14) put forth the hypothesis that bromocyclohexadienones are the primary products formed in the aqueous bromination of phenol to rationalize the exclusive bromination of **1** at the *o*- and *p*-positions.

© 1999 NRC Canada

Scheme 3.

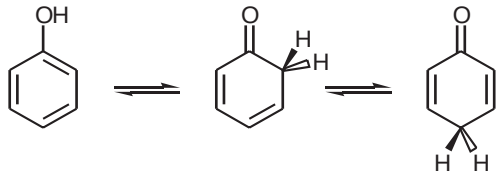

1 **2** **3**

Scheme 4.

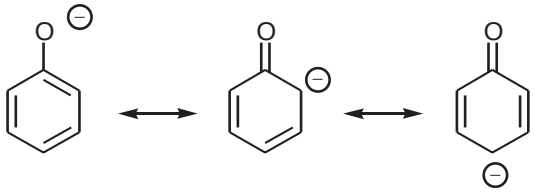

These bromocyclohexadienone intermediates were detected 15 years ago by Tee et al. (15) using the stopped-flow technique. Cyclohexadienones were also proposed (16) and later characterized (17, 18) as intermediates in the Photo–Fries rearrangement of aryl esters. 4-Benzylcyclohexa-2,5-dienone was identified by CIDNP as a transient intermediate in the photorearrangement of benzyl phenyl ether; it had a half-life of about 4 s in cyclohexane (19).

4*H*-Keto tautomers of heavily substituted phenols have been isolated in crystalline form (20). The tautomers of parent phenol, cyclohexa-2,4-dienone (**2**), and cyclohexa-2,5-dienone (**3**), were generated by flash vacuum pyrolysis of suitable Diels–Alder adducts, trapped at 77 K, and characterized by their IR and UV spectra (21). Pentaammineosmium complexes of **1**–**3** have been identified, and it was shown that all three tautomeric complexes are of comparable thermodynamic stability (22).

In the present work, cyclohexadienones **2** and **3** were formed by flash photolysis of suitable precursors (**4**–**6**, Scheme 1) in aqueous solution, which allowed their enolization rates to be measured directly. The transient formed by flash photolysis of **4** has previously been identified as cyclohexa-2,4-dienone (**2**) based on the observed decay kinetics, the position of its absorption (the first π,π^* absorption band of stable cyclohexa-2,4-dienones is around 300 nm, log $\epsilon \approx 3.7$ (6)), the identification of phenol as the final product, and the formation of 1,3,5-hexatrienone upon irradiation of **4** in a glassy matrix (3). The present finding that precursor **5** gives the same transient intermediate (absorption and pH-dependent decay rate) confirms that assignment. Formation of cyclohexa-2,5-dienone (**3**) from precursor **6** was assumed by analogy, and that is supported by the observed transient kinetics and the identification of phenol as the final product.

Thermochemistry of cyclohexadienone–phenol tautomerization

Several thermochemical estimates have been reported for the protomeric equilibria of phenol (**1**) with ketones **2** and **3** (Scheme 3): $\Delta_{(\mathbf{2}\text{ or }\mathbf{3})\rightarrow\mathbf{1}}G^{\ominus}$ (g, 298 K) = –18.6 kcal mol^{-1} was obtained from a bond additivity scheme (23), and $\Delta_{\mathbf{2}\rightarrow\mathbf{1}}G^{\ominus}$(aq, 298 K) = –13 ± 3 kcal mol^{-1} from estimates of the aqueous protonation equilibria for each tautomer to the common cation (24). $\Delta_{\mathbf{2}\rightarrow\mathbf{1}}H^{\ominus}$(g, 298 K) = –15.2 kcal mol^{-1} is obtained using Benson's group increments (25). Tee and Iyengar (15) predicted $\Delta_{\mathbf{3}\rightarrow\mathbf{1}}G^{\ominus}$(aq, 298 K) = –15 kcal mol^{-1} based on an earlier estimate of the p*K* for C-protonated phenol. Shiner et al. (26) generated the cyclohexadienones **2** and **3** by pyrolytic cycloreversion of their formal Diels–Alder adducts with cyclopentadiene, compounds **5** and **6**, and measured their gas phase acidities by the flowing afterglow technique. The derived heats of tautomerization, $\Delta_{\mathbf{2}\rightarrow\mathbf{1}}H^{\ominus}$ = – 6 ± 3 and $\Delta_{\mathbf{3}\rightarrow\mathbf{1}}H^{\ominus}$ = –10 ± 3 kcal mol^{-1} are, however, not compatible with present data.

Scheme 5.

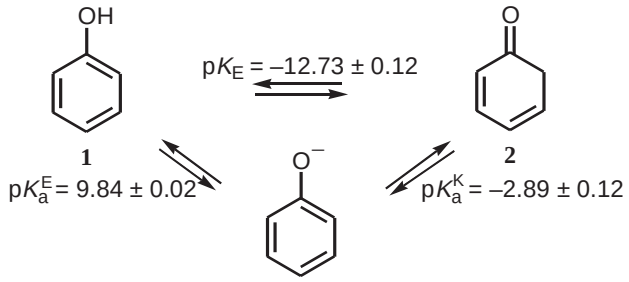

From the present data, the enolization constant of **2** at 25°C is determined as the ratio of the enolization and ketonization rate constants given in Table 2, K_E(**2**, aq, 298 K) = $k^E_{H^+}/k^K_{H^+}$ = (5.4 ± 0.3)10^5/(1.01 ± 0.28)10^{-7} = (5.4 ± 1.5)10^{12}, pK_E = –12.73 ± 0.12. This value, and the acidity constant of phenol, pK_a^E(**1**, 298 K) = 9.84 ± 0.02 (expt. sect.), form two legs of a thermodynamic cycle, from which the C–H acidity constant of ketone **2** can be calculated, pK_a^K = pK_E + pK_a^E = –2.89 ± 0.12 (Scheme 5). It turns out that ketone **2** is one of the strongest carbon acids known (27).

The enthalpy of enolization can be calculated by the second-law method from the temperature dependence of the enolization constant, d ln K_E/dT = $\Delta_E H^{\ominus}/RT^2$, $\Delta_E H^{\ominus}$ = 2.303R[pK_E(T_2 = 353 K) – pK_E(T_1 = 298 K)]/(1/T_2 – 1/T_1) = –74.8 ± 5.1 kJ mol^{-1}. The standard free energies of enolization are $\Delta_E G^{\ominus}$(aq) = 2.303RT × pK_E(353 K) = –72.3 ± 0.5 kJ mol^{-1} at 353 K and –72.7 ± 0.7 kJ mol^{-1} at 298 K. The entropy of enolization, $\Delta_E S^{\ominus}$(aq, 298 K) = –7 ± 16 J K^{-1} mol^{-1}, is very small, too small to be reliably determined from these values. In our preliminary communication (3), we had estimated the temperature dependence of the enolization constant by neglecting the temperature dependence of the free energy of enolization $\Delta_E G^{\ominus}$, i.e., by assuming $\Delta_E S^{\ominus} \approx 0$.

The enolization constant of 2,5-cyclohexadienone **3** is similarly obtained as the ratio of the corresponding acid-catalyzed rate constants of enolization and ketonization (Table 2), K_E(298 K) = $k^E_{H^+}/k^K_{H^+}$ = (9.5 ± 3.2)10^{10}, pK_E = –10.98 ± 0.15 (Scheme 6).

The thermochemical data obtained in this work are summarized in Table 5. Note that the acidity constants pK_a^E and pK_a^K reported here are concentration quotients determined at ionic strength I = 0.1 M. The experimental enolization constants are in reasonable, though not perfect, agreement with the results of density functional calculations given in Table 6. The (gas phase) enolization constants predicted by these calculations are pK_E(**2**) = –10.4 and pK_E(**3**) = –9.8.

© 1999 NRC Canada

Table 5. Thermochemical data (aq, 25°C, I = 0.1 N).

Reaction	pK_E	pK_a^K	pK_a^E	$\Delta_E H$/(kJ mol^{-1})	$\Delta_E S$/(J K^{-1} mol^{-1})[a]
2 → **1**	–12.73 ± 0.12	–2.89 ± 0.12	9.84 ± 0.02	–74.8 ± 5.1	–2.6
3 → **1**	–10.85 ± 0.29	–1.01 ± 0.30	9.84 ± 0.02	–61.9 ± 6.2[b]	–1.2

[a]Calculated B3LYP/6-31G* (g, 298 K), cf. Table 6.

[b]Calculated from pK_E assuming $|\Delta_E S(aq)| \leq 20$ J K^{-1} mol^{-1}.

Table 6. Results of ab initio calculations.[a]

Compound	Method	$-E_0$/hartree	Enthalpy/hartree[b]	$S^\ominus$/(J K^{-1} mol^{-1})
1	B3LYP/6-31G*	–307.464 865	0.111 231	74.55
2	B3LYP/6-31G*	–307.441 132	0.110 405	77.14
3	B3LYP/6-31G*	–307.442 838	0.110 618	75.76
1	6-31G*	–305.558 063	0.117 496	73.58
2	6-31G*	–305.538 575	0.117 177	75.63
3	6-31G*	–305.541 889	0.117 385	74.65

[a]Gaussian 94.

[b]Thermal correction to enthalpy including zero-point vibrational energy.

Scheme 6.

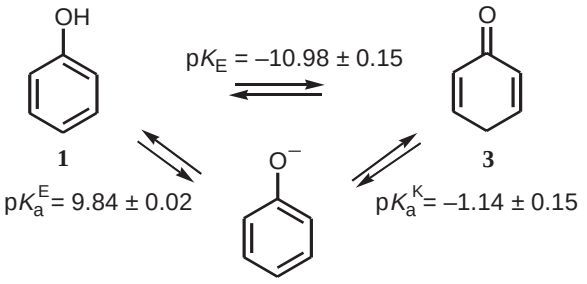

Exchange kinetics and kinetic isotope effects

Isotope exchange rates of phenol in aqueous sodium hydroxyde were already determined in 1936 by Ingold et al. (28). These authors used 2.2 M solutions of phenol and found that the exchange rate reached a maximum when the concentration of NaOH was about half that of phenol. Hydron transfer from phenol as a general oxygen acid to phenolate as a carbon base was identified as the dominant mechanism for exchange under these conditions. In the present work, hydron exchange experiments were done with dilute solutions and under acid catalysis. Note that, from the data given in Tables 2 and 5, base is predicted to *reduce* the rate of hydron exchange in dilute aqueous solutions. The rate of hydrogen exchange at carbon 2 of phenol in strong base, pH >> pK_a^E(**1**), is given by $k_0'^K = k_{OH}^E \cdot K_w / K_a^K = 4 \times 10^{-11}$ s^{-1} at 25°C. This is more than an order of magnitude less than the rate calculated for the same process in neutral solution, $k_0^K = k_0^E K_a^E / K_a^K = 7 \times 10^{-10}$ s^{-1}, because the reaction of protons with phenolate accelerates ketonization at pH < 12 until proton catalysis saturates at pH ≈ pK_a^E = 9.84.

The method used to assess the magnitude of the kinetic isotope effects and to determine the rate constants of ketonization from the observed rates of hydron exchange of phenol in aqueous acid closely follows previous work of Kresge and Chiang (7) and was described in the results section. Some of the observed kinetic isotope effects deserve mention. The four decay rates determined for **2** and **2**-d_2 in H_2O and D_2O (Table 2) give two closely similar values for the predominantly primary kinetic isotope effect, k(**2**-h_2)/k(**2**-d_2) = 6.6 ± 0.2, and for the compound (secondary and medium) solvent isotope effect, $k(H_2O)/k(D_2O)$ = 1.44 ± 0.03. Both of these values are consistent with the mechanism assigned to the pH-independent enolization of ketone **2**: rate-determining hydron transfer from carbon to solvent water. A crude a priori estimate for the solvent isotope effect, $k(H_2O)/k(D_2O) \approx 1.5$, is obtained by assuming $K_a^K(H_2O)/K_a^K(D_2O) \approx 1/l^3 = 3$ (l = 0.69 is the fractionation factor for the hydronium ion (29)) and application of the Brønsted equation $k(H_2O)/k(D_2O) = [K_a^K(H_2O)/K_a^K(D_2O)]^\alpha$ with $\alpha \approx 0.35$ (2*b*). Finally, the inverse isotope effect observed on the acid-catalyzed enolization of **2**-L (Table 2, row 3), shows that OH fission of **2**-L$^+$ (vertical reaction in Scheme 2) is faster than CH or CL fission, in spite of a strong thermodynamic bias for the latter.

The range covered by experimental data on keto–enol protomeric equilibria is nearly doubled by the present measurements of phenol ketonization: enolization constants now extend over a range of about 30 orders of magnitude, and the corresponding rate constants vary by about 20 orders of magnitude. The free-energy relationship between these quantities is clearly curved, and the curvature defines the intrinsic barrier of proton transfer to the β-carbon atom of enols $\Delta G_0^\ddagger$ = 57 kJ mol^{-1} (2*b*). Similar values have been determined previously from curvature in Brønsted plots (30, 31). The pH-independent, spontaneous dissociation of **2** as a carbon acid, $k_0^E = 3.8 \times 10^3$ s^{-1}, dominates the pH–rate profile of **2** (Fig. 1) from pH 3 to 10. On the other hand, the contribution of this mechanism to the pH–rate profiles for the enolization of simple ketones such as acetophenone is barely noticeable (31), because carbon protonation of enolates is so highly exergonic that these rates approach the diffusional limit.

Experimental

General

All concentrations are nominal values referring to 25°C. No corrections were applied for volume expansion at higher

© 1999 NRC Canada

temperatures. The required, small corrections would affect acid-catalyzed rate constants of enolization and ketonization by the same factor that would cancel in their ratio, the enolization constant.

Materials

Samples of tricyclo[6.2.1.$0^{2,7}$]undeca-5,9-dien-4-one (**5**) and tricyclo[6.2.1.$0^{2,7}$]undeca-4,9-dien-3-one (**6**) were obtained as a gift from Dr. C. Shiner, University of Colorado, Boulder (23), and samples of 5,7-dioxobicyclo[2.2.2]octane-2,3-dicarboxylic acid from Profs. M. Demuth, MPI Göttingen, and C.A. Grob, University of Basel.

Phenol-2*d* was synthesized from 2-bromophenol as described by Tashiro et al. (32). ^{1}H NMR indicated >90% deuteration at the 2-position. The same procedure was used to synthesize phenol-2*t*: NaOH (500 mg) was dissolved in 1 mL of tritium-enriched water and 520 mg of 2-bromophenolate (2.7 mmol) was added. CuAl catalyst (125 mg, Ventron, Karlsruhe) was added. The solution was stirred vigorously for 30 min. The catalyst was removed by filtration. The solution was acidified with 2 N HCl whereupon phenol precipitated. The aqueous solution was extracted with 10 mL of ether. The organic extract was dried with Na_2SO_4, and the solvent was evaporated at room temperature under a stream of N_2. The residue was sublimed in vacuo (<1 Pa) at room temperature. A sample containing 0.6 mg (6.4 μmol) of phenol-2*t* had an activity of 1750 Bq on a calibrated scintillation counter which corresponds to a tritium content of 0.25 ppm.

Bicyclo[2.2.2]oct-7-ene-2,5-dione (**4**) was prepared by oxidative bisdecarboxylation of 5,7-dioxobicyclo[2.2.2]octane-2,3-dicarboxylic acid, samples of which were obtained as gifts from Profs. Grob (33) and Demuth (5). The following, improved method was taken from the thesis of Weitemeyer (34). $Pb(OAc)_4$ (18 g) was added to a stirred solution of the diacid (4.48 g) in pyridine (60 mL) which was immersed in a water bath at 20°C. The yellow solution slowly turned orange to deep red under evolution of CO_2. After an hour, the solution was gently warmed to 40°C until the gas evolution ceased after 90 min. $CHCl_3$ (200 mL) was added and the mixture shaken with 40 mL of cold 20% HCl. The precipitate was removed and washed with $CHCl_3$. The combined organic phases were washed four times with 40 mL of 20% HCl until the color was removed, neutralized with $NaHCO_3$, and dried. Evaporation of the solvent left a brown–red solid residue which was chromatographed on silica with an 80:20 mixture of hexane and diethyl ether and sublimed at 90°C in vacuo to give 560 mg (20.6%) of **4** as colorless crystals.

A sample of **4** (50 mg) was deuterated in 2 mL of D_2O containing 0.1 g of NaOD. The solution turned yellow. After 10 min the diketone was extracted with ether. The organic phase was washed with D_2O, evaporated to dryness, and sublimed at 80°C in vacuo, giving off-white crystals of **4**-6,6,8,8-d_4 (40 mg). ^{1}H NMR (D_2O) δ: 2.8 (m, <0.01 H), 3.8 (m, 1 H, > CH-), 6.8 ppm (m, 1 H, -CH=); solvent peak (HDO) δ: 5.0 ppm. MS: 141 (8.8), 140 (100, M^+), 139 (9.1).

Isotopic exchange experiments

The samples of phenol-2*d* (7 NMR tubes containing 0.5 mL, 0.04 M) and phenol-2*t* (20 mL, 0.007 M) in 0.1 N $HClO_4$ were heated simultaneously in a thermostat bath that was kept at 80.0 ± 0.1°C. Deuterium loss from phenol-2*d* in samples removed periodically from the bath was determined by integration of the two peaks observed in the ^{2}H NMR spectra, at δ 1.13 (HDO) and at 1.28 ppm (phenol-2*d*). The first six samples covered two half-lives, the last was drawn after seven half-lives.

Deuteration rates of phenol in 1.0 N DCl in D_2O were determined by 300 MHz ^{1}H NMR. The NMR tubes (10 for each temperature) were heated in a water bath which was held at 80.0, 70.0, or 60.0 ± 0.1°C, removed at appropriate time intervals, and stored at in a refrigerator until all samples had been collected. The signal of the *meta* hydrogens (δ = 7.4 ppm; dd, $J_{2,3} = J_{3,4}$ = 7 Hz, 2H) was used as an internal standard. First-order exponential decays were fitted to the integrated signal intensities of the *ortho* (δ = 6.9 ppm; d, $J_{2,3}$ = 7 Hz, 2H) and *para* (δ = 7.1 ppm; t, $J_{3,4}$ = 7 Hz, 1H) hydrogens (Table 3).

The contents of phenol-2*t* were determined by liquid scintillation counting of 31 aliquots of 0.5 mL containing 7 mM of phenol which were drawn periodically over three half-lives of the exchange reaction. A final sample was measured after 10 half-lives. The aliquots were extracted with 4 mL of diethyl ether to separate the tritiated phenol from the tritium that had exchanged into water. To correct for variations (±10%) in the efficiency of the extraction, the absorbance of each extract was measured at 274 and 281 nm, and the radioactivity of the samples were normalized by these absorbances. In this way, the standard error of single measurements was reduced to about 3%. The activity of the samples was determined by scintillation counting on a Packard scintillation analyzer CA 2000 using 1,4-bis(5-phenyl-2-oxazolyl)benzene (POPOP) and Packard emulsifier 299 as scintillation reagents. Prior to the measurements, the instrument was calibrated with a standard of known activity.

Flash photolysis

All kinetic measurement were done with water-jacketed quartz cells which were kept at 25.0 ± 0.1°C unless stated otherwise. Temperature readings were taken from a thermoelement that was dipped into the sample solutions. Acid and base strength was adjusted with HCl in the range of 0.1 to 0.001 N or KOH in the range of 0.01 to 0.001 N. Values from buffered solutions quoted in this paper were obtained by extrapolation to zero buffer concentration and thus refer to wholly aqueous solutions. All solutions were adjusted to ionic strength I = 0.1 M by the addition of NaCl. Kinetic data determined by different persons using different experimental setups differed by up to 20%, much more than the standard error of sample means determined by a single person in a series of experiments (cf., e.g., the first two entries of Table 1).

Spectrophotometric titration of phenol

A 0.3 mM solution of phenol in water (3 mL) containing 0.010 M NH_4Cl and 0.09 M NaCl was titrated with 30 μL portions of 0.1 N NaOH in a quartz cell which was left untouched in the thermostatted (25 ± 0.1°C) sample holder of a Perkin–Elmer Lambda 9 UV spectrophotometer. The UV spectra were recorded and digitized (250–310 nm, 120 absorbance readings per spectrum, 16 spectra per titration) after each addition and the acid concentration was measured

© 1999 NRC Canada

with a calibrated (35) Metrohm 6.0236.100 micro glass electrode using a digital Metrohm pH meter 654. The spectra were analyzed using the program SPECFIT of Zuberbühler and co-workers (36). The original spectra were reproduced with a standard error of <0.002 absorbance units using the two dominant eigenvectors of the factor analysis. The loading coefficients fitted well to a titration curve (standard errors of single runs were <0.001 p*K* units). Three independent runs gave an average dissociation quotient of phenol, $pK_{a,c} = 9.84 \pm 0.02$ (ionic strength $I = 0.1$ M). Using activity coefficients for $I = 0.1$ M ($\gamma_{H^+} = 0.83$ and $\gamma_{\mathbf{1}^-} = 0.76$ (7)), the thermodynamic acidity constant of phenol is estimated as $pK_a^{\ominus} = 10.04 \pm 0.03$. This is about 0.05 units higher than the literature values commonly quoted (37).

Acknowledgements

This work was supported the Swiss National Science Foundation. Helpful advice for the analysis of isotope effects by Prof. A.J. Kresge is gratefully acknowledged.

References

1. P. Haspra, A. Sutter, and J. Wirz. Angew. Chem. Int. Ed. Engl. **18**, 617 (1979).
2. (*a*) J.R. Keefe and A.J. Kresge. *In* The chemistry of enols. *Edited by* Z. Rappoport. Wiley, New York. 1990. Chap. 7; (*b*) J. Wirz. Pure Appl. Chem. In press; (*c*) J. Wirz. Chem. unserer Zeit, **32**, 311 (1998).
3. M. Capponi, I. Gut, and J. Wirz. Angew. Chem. Int. Ed. Engl. **25**, 344 (1986).
4. M. Demuth, P. Ritterskamp, E. Weigt, and K. Schaffner. J. Am. Chem. Soc. **108**, 4149 (1986).
5. R.G. Bates. *In* Determination of pH. 2nd ed. *Edited by* P. de Mayo. Wiley, New York. 1973.
6. J. Derkosch and W. Kaltenegger. Monatsh. Chem. **88**, 778 (1957); K.L. Cook and A.J. Waring. J. Chem. Soc. 529 (1973); G. Quinkert, G. Dürner, E. Kleiner, E. Haupt, and D. Leinfritz. Angew. Chem. **91**, 584 (1979).
7. A.J. Kresge and Y. Chiang. J. Am. Chem. Soc. **89**, 4411 (1967), and refs. therein.
8. A.J. Kresge. Acc. Chem. Res. **8**, 354 (1975).
9. J.R. Keefe and A.J. Kresge. Can. J. Chem. **74**, 2481 (1996).
10. Y. Chiang, A.J. Kresge, B. Hellrung, P. Schünemann, and J. Wirz. Helv. Chim. Acta, **80**, 1106 (1997).
11. C.G. Swain, E.C. Stivers, J.F. Reuwer, Jr., and L.J. Schaad. J. Am. Chem. Soc. **80**, 5885 (1958).
12. A. Streitwieser, Jr., R.H. Jagow, R.C. Fahey, and S. Suzuki. J. Am. Chem. Soc. **80**, 2326 (1958); E.A. Halevi. Prog. Phys. Org. Chem. **1**, 109 (1963); S. Seltzer. J. Am. Chem. Soc. **83**, 2625 (1961).
13. J. Thiele. Liebigs Ann. Chem. **306**, 87 (1899); **306**, 129 (1899).
14. A. Lapworth. J. Chem. Soc. 1265 (1901).
15. O.S. Tee, N.R. Iyengar, and M. Paventi. J. Org. Chem. **48**, 759 (1983); O.S. Tee and N.R. Iyengar. J. Am. Chem. Soc. **107**, 455 (1985); J. Org. Chem. **51**, 2585 (1986).
16. J.W. Meyer and G.S. Hammond. J. Am. Chem. Soc. **94**, 2219 (1972).
17. C.E. Kalmus and D.M. Hercules. J. Am. Chem. Soc. **96**, 449 (1974); T. Arai, S. Tobita, H. Shizuka. J. Am. Chem. Soc. **117**, 3968 (1995).
18. S.M. Beck and L.E. Brus. J. Am. Chem. Soc. **104**, 1805 (1982).
19. R. Bausch, H.-P Schuchmann, C. von Sonntag, R. Benn, and H. Dreeskamp. J. Chem. Soc. Chem. Commun. 418 (1976).
20. V.V. Ershov and A.A. Volod'kin. Izv. Akad. Nauk. SSSR Otd. Khim. Nauk. 730 (1962); T. Matsuura and K. Ogura. J. Am. Chem. Soc. **89**, 3846 (1967).
21. M.-C. Lasne, J.-P. Ripoll, and J.-M. Denis. Tetrahedron Lett. **21**, 463 (1980); V.P. Vitullo. J. Org. Chem. **35**, 3975 (1970).
22. M.E. Kopach, W.G. Hipple, and W.D. Harman. J. Am. Chem. Soc. **114**, 1736 (1992).
23. J.B. Conant and G.B. Kistiakowsky. Chem. Rev. **20**, 181 (1937).
24. M.J. Cook, A.R. Katritzky, P. Linda, and R.D. Tack. Tetrahedron Lett. **49**, 5019 (1972).
25. S.W. Benson. Thermochemical kinetics. 2nd ed. J. Wiley, New York. 1976.
26. C.S. Shiner, P.E. Vorndam, and S.R. Kass. J. Am. Chem. Soc. **108**, 5699 (1986).
27. E.D. Laganis and D.M. Lemal. J. Am. Chem. Soc. **102**, 6633 (1980).
28. C.K. Ingold, C.G. Raisin, and C.L. Wilson. J. Chem. Soc. 1637 (1936).
29. A.J. Kresge, Y. Chiang, G.W. Koeppl, and R.A. More O'Ferrall. J. Am. Chem. Soc. **99**, 2245 (1977).
30. P. Pruszynski, Y. Chiang, A.J. Kresge, N.P. Schepp, and P.A. Walsh. J. Phys. Chem. **90**, 3760 (1986).
31. Y. Chiang, A.J. Kresge, J.A. Santabella, and J. Wirz. J. Am. Chem. Soc. **110**, 5506 (1988).
32. M. Tashiro, A. Iwasaki, and G. Fukata. J. Org. Chem. **43**, 196 (1978).
33. C.A. Grob and A. Weiss. Helv. Chim. Acta, **43**, 1390 (1960).
34. C. Weitemeyer. Dissertation. Universität Göttingen, Germany. 1976.
35. H. Sigel, A.D. Zuberbühler, and O. Yamauchi. Anal. Chim. Acta, **255**, 63 (1991).
36. H. Gampp, M. Maeder, C.J. Meyer, and A.D. Zuberbühler. Talanta, **32**, 95 (1985); **32**, 257 (1985).
37. H.M. Walborsky, R.M. Brownell, and E.C. Mayo. J. Am. Chem. Soc. **70**, 2493 (1948); A.J. Biggs. Trans. Fararay Soc. **52**, 35 (1956).
38. H.S. Harned and R.W. Ehlers. J. Am. Chem. Soc. **55**, 652 (1933).
39. R.G. Bates and H.B. Hetzer. J. Phys. Chem. **65**, 667 (1961).

© 1999 NRC Canada

Synthesis, characterization, and Cu(II) solution chemistry of dioxotetraazamacrocycles

Ramunas J. Motekaitis, Yizhen Sun, Arthur E. Martell, and Michael J. Welch

Abstract: The synthesis and characterization of four new dioxotetraazamacrocycles: 1,4,8,11-tetraazacyclotetradecane-3,9-dione; 1,4,7,10-tetraazacyclotridecane-2,9-dione; 1,4,7,10-tetraazacyclotridecane-3,8-dione; and 1,4,7,10-tetraazacyclododecane-2,9-dione are described. Two related, previously prepared macrocycles, are included in this study: 1,4,8,11-tetraazacyclotetradecane-5,7-dione and 1,4,7,10-tetraazacyclotridecane-11,13-dione. The protonation constants, stability constants with Cu^{2+} ions, as well as electronic spectra of the di-deprotonated copper(II) complexes are also reported. These results are discussed in terms of the suitability of this new class of ^{62}Cu, ^{64}Cu, ^{67}Cu complexes in PET imaging or radiotherapeutic applications. The synthetic schemes outlined provide a study of the relative Cu^{2+} behavior with a family of positional isomers of unsubstituted dioxotetraazamacrocycles.

Key words: multidentate ligand, tetraazamacrocyclic compound, dioxopolyaza macrocycles, cyclic amides, copper(II) complexes.

Résumé : On décrit la synthèse et la caractérisation de quatre nouveaux dioxotétraazamacrocycles: 1,4,8,11-tétraazacyclotétradécane-3,9-dione; 1,4,7,10-tétraazacyclotridécane-2,9-dione; 1,4,7,10-tétraazacyclotridécane-3,8-dione et 1,4,7,10-tétraazacyclododécane-2,9-dione. Dans cette étude, on a inclus deux macrocycles apparentés, préparés antérieurement: 1,4,8,11-tétraazacyclotétradécane-5,7-dione et 1,4,7,10-tétraazacyclotridécane-11,13-dione. On a déterminé les constantes de protonation, les constantes de stabilité avec les ions Cu^{2+} ainsi que les spectres électroniques des complexes diprotonés du cuivre(II). On discute de ces résultats en fonction de la possibilité d'utiliser cette nouvelle classe de complexes du ^{62}Cu, du ^{64}Cu et du ^{67}Cu dans l'imagerie PET ou dans des applications radiothérapeutiques. Les schémas de synthèse proposés permettent d'examiner le comportement relatif du Cu^{2+} avec celui d'une famille d'isomères de position de dioxotétraazamacrocyles non substitués.

Mots clés : ligand multidentate, composé tétraazamacrocyclique, dioxopolyazamacrocyles, amides cycliques, complexes du cuivre(II).

[Traduit par la Rédaction]

Introduction

Macrocyclic oxo polyamines are unique metal chelators, their structure bearing the dual features of macrocyclic polyamines and oligopeptides (1–5). They are capable of coordinating to certain transition metal ions, such as Cu^{2+}, Ni^{2+}, Co^{2+}, and Pd^{2+}, with simultaneous displacement of hydrogen ions from the amido groups. The imide anions may also stabilize the trivalent ions of Cu(III) and Ni(III) (6).

Our ultimate interest in macrocyclic oxo polyamines is the preparation and characterization of low molecular weight copper chelates possessing –2 to +2 net charge as potential radiopharmaceuticals and PET imagining candidates. Thus, depending on the ratio of amide groups to ligand, such a study is possible. Our initial focus, the subject of this research, is the study of six unsubstituted macrocyclic dioxotetraamines. To this end, two previously reported and four new macrocyclic ligands were synthesized with new and improved synthetic schemes. Previous studies were limited to compounds that may be obtained by direct methods. Herein are developed new schemes which will be helpful in the future synthesis of structural variants of these ligands.

Divalent transition metal ion complexes of macrocyclic dioxotetraamines have shown some interesting properties and important biological functions: copper(II) complexes have been used to model superoxide dismutase (7); cobalt(II) complexes to model methane monooxygenase (8*a*); and to carry oxygen reversibly (8*b*, *c*); nickel(II) complexes to oxidize olefins to cyclic alkoxyl compounds (9, 10) and to model methyl coenzyme-*M*-reductase (11). A novel application is the preparation of a chelating resin for copper based on the incorporation of a cyclic tetraazadione into a cross-linked polymer (12).

While more than thirty substituted macrocyclic dioxotetraamines have been synthesized, only a few methods have been used to prepare them. These methods are limited to the use of malonates (13) and other esters (14), diacid dichlorides under high-dilution conditions (15–17), and bis(α-chloroamides)

Received October 30, 1998.

This paper is dedicated to Jerry Kresge in recognition of his many achievements in chemistry.

R.J. Motekaitis, Y. Sun, and A.E. Martell.[1] Department of Chemistry, Texas A&M University, College Station, Texas 77842-3012, U.S.A.
M.J. Welch. The Edward Mallinckrodt Institute of Radiology, Washington University, School of Medicine, St. Louis, MO 63110, U.S.A.

[1]Author to whom correspondence may be addressed. Telephone: (409) 845-5055. Fax: (409) 845-4719. e-mail: martell@mail.chem.tamu.edu

© 1999 NRC Canada

Scheme 1.

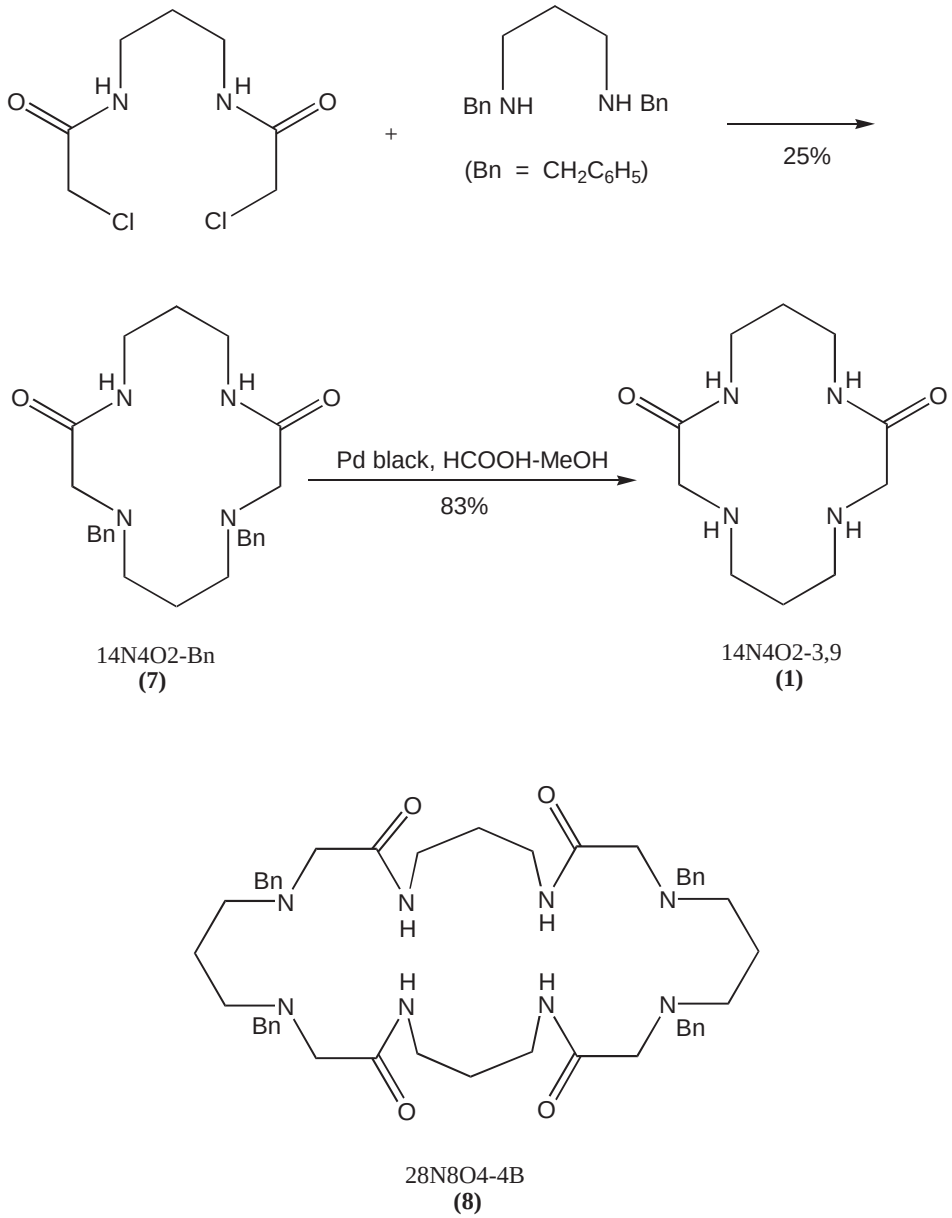

(18–20), which are reacted with various polyamines to form macrocyclic diamides from 1:1 cyclization reactions or macrocyclic tetraamides by 2:2 cyclization reactions.

Although the Richman–Atkins tosylamide procedure (21, 22) has been widely used for the preparation of polyaza macrocycles and crown ethers, it has not yet been exploited in the synthesis of macrocyclic dioxotetraamines. After trying the conventional methods (13–20), we found that the Richman–Atkins method is indeed superior to the others, and the fear that the amide bond would not survive the rather drastic detosylation conditions did not materialize. We now report the synthesis of four new dioxotetraamine macrocycles with this tosylation–detosylation procedure.

While many macrocyclic dioxotetraamines have been reported, only three unsubstituted dioxotetraazamacrocycles have been investigated potentiometrically for Cu^{2+} affinity. In this paper we report the protonation constants and stability constants with Cu^{2+} for all of the new ligands and compare these results with other polyaza oxo macrocycles studied with Cu^{2+}.

Results and discussion

Synthesis

Tabushi et al. (14) reported a convenient and general method for the synthesis of dioxopolyamine macrocycles through the cyclization of diamines and diesters of α,ω-dicarboxylic acids. Since then, most of the dioxotetraazamacrocycles were prepared by this method. This procedure requires neither high dilution nor nitrogen protection. However, the drawbacks of this method are that tedious chromatographic purification is needed, and the yield is usually very low. For the preparation of the four dioxotetraazamacrocycles mentioned in this paper, the Tabushi method is limited due to the different dioxo positions in these macrocyclic rings.

© 1999 NRC Canada

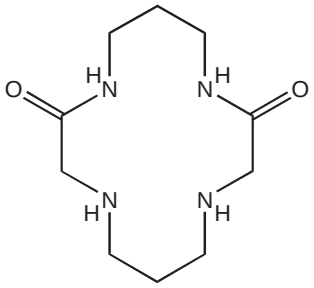

1,4,8,11-tetraazacyclotetradecane-3,9-dione

14N4O2-3 **(1)**

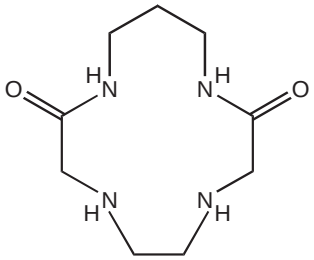

1,4,7,10-tetraazacyclotridecane-2,9-dione

13N4O2-2,9 **(2)**

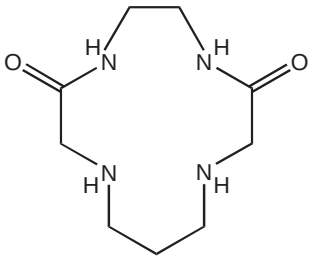

1,4,7,10-tetraazacyclotridecane-3,8-dione

13N4O2-3,8 **(3)**

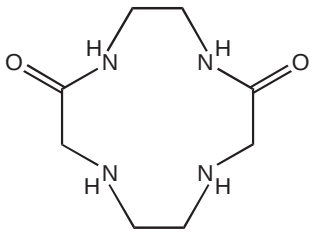

1,4,7,10-tetraazacyclododecane-2,9-dione

12N4O2-2,9 **(4)**

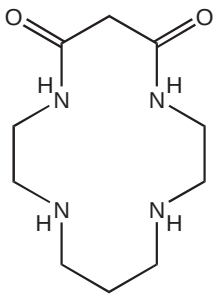

1,4,8,11-tetraazacyclotetradecane-5,7-dione

14N4O2-5,7 **(5)**

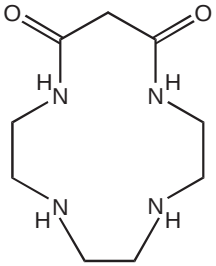

1,4,7,10-tetraazacyclotridecane-11,13-dione

13N4O2-11,13 **(6)**

Several *N*-substituted 1,4,8,11-tetraazacyclotetradecane-3,9-dione, 14N4O2-3,9 (1), were described by Bradshaw et al. (20). A bis(α-chloroamide) was used as starting material to react with a *N*,*N*′-dialkylated diamine to form the macrocyclic diamide. High-dilution conditions were not necessary, and the yields of the cyclization were about 40–50%. Adapted from this work, Scheme 1 was designed for the preparation of compound 1,4,8,11-tetraazacyclotetradecane-3,9-dione, 14N4O2–3,9 (**1**). The cyclization reaction was performed in refluxing acetonitrile, and the initial concentration of the reactants is 0.04 M. After chromatographic purification, an impure 14N4O2–3,9-Bn (**7**) and a nearly pure 28N8O4-Bn (**8**),which is the 2:2 condensation product, were obtained. The R_f values of compound **7** is 0.57 and of compound **8** is 0.48 (developed by CH_2Cl_2:MeOH = 9:1). After a second chromatographic purification, the yield of isolated 14N4O2–3,9-Bn (**7**) is 21%; and 7% of the 28-membered ring (28N8O4-Bn) (**8**) was also obtained. When the reaction was performed at the initial concentration of 0.007 M, the 2:2 cyclization reaction was nearly eliminated, and the yield of the 1:1 condensation product is about 25%. Another drawback of this synthetic route is the last step: debenzylation reaction. The activity of the catalyst, freshly prepared Pd black, is difficult to control, so that a good steady yield is difficult to obtain.

In Scheme 2, the Richman–Atkins tosylamide procedure was adopted. The initial concentrations of the reactants in the cyclization reaction are about 0.1 M, no 2:2 condensation product was found; thus chromatographic purification is unnecessary. Yield of the recrystallized products (tosylated) are about 40–50%. In the detosylation steps, the yields of 1,4,7,10-tetraazacyclotridecane-2,9-dione, 13N4O2–2,9 (**2**),

© 1999 NRC Canada

Scheme 2.

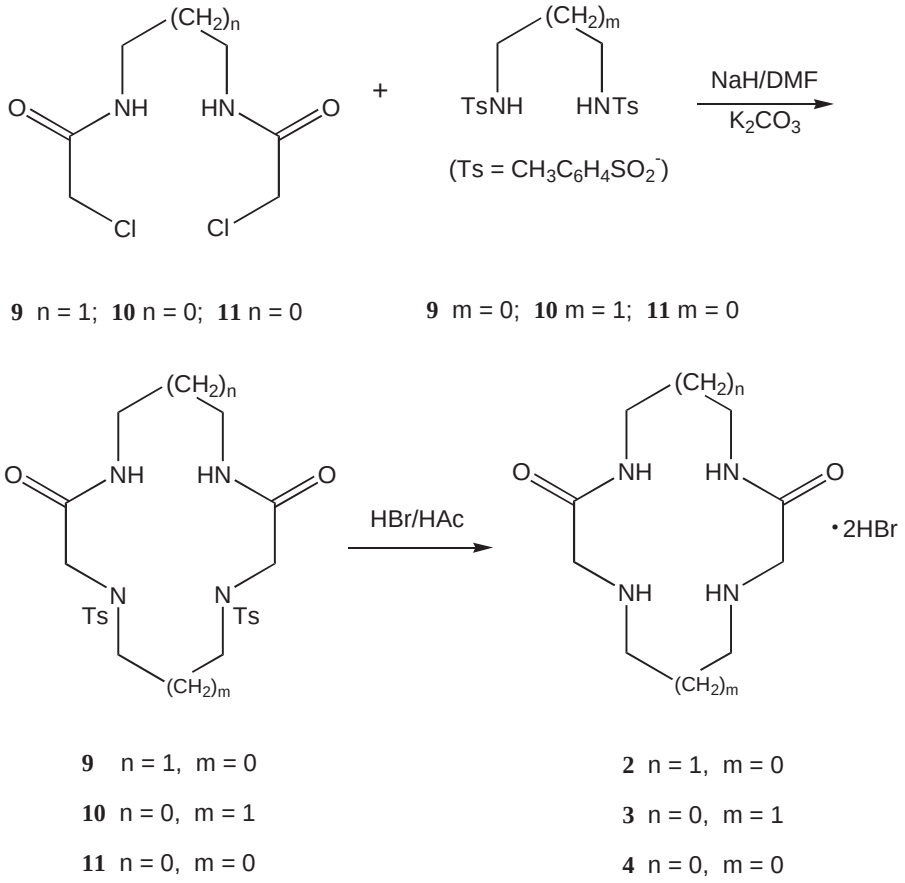

Table 1. Protonation constants of dioxotetraazamacrocycles at 25.0°C and μ = 0.100 (KCl).

	$\log K_1^H$	$\log K_2^H$	$\Delta \log K_{1-2}^H$
1	7.81 (1)	5.68 (2)	2.12
2	7.21 (2)	3.02 (2)	4.19
3	7.69 (1)	5.90 (1)	1.79
4	6.98 (1)	3.75 (2)	3.23
5	9.53[a] (1)	5.89[b] (8)	3.64
6	9.05[c] (1)	3.69[d] (6)	5.36

[a]Literature: 9.54.
[b]Literature: 5.80.
[c]Literature: 8.78 (NIST Database 46)[2].
[d]Literature: 4.12 (NIST Database 46)[2].

and 1,4,7,10-tetraazacyclotridecane-3,8-dione, 13N4O2–3,8 (**3**), are 47 and 87%, respectively; for the 12-membered ring 1,4,7,10-tetraazacyclododecane-2,9-dione, 12N4O2–2,9 (**4**), the isolated yield is 23%, probably due to the higher solubility of this compound in the reaction mixture.

Reactions of ligands in aqueous solution

Protonation constants

Each of the six macrocycles studied possesses two amino groups and two endocyclic amide groups. The amide group becomes a powerful coordinating group only upon loss of the nitrogen-bound proton. This has been discovered originally with various di-, tri-, and tetrapeptides (23) as well as with compounds such as diglycylethylenediamine (24) and its derivatives. The most notable metal ions found to participate in this kind of bonding in aqueous solution are Cu^{2+} and Ni^{2+}, but others are also possible. However, this deprotonation is always metal-ion assisted, and OH^- itself is too weak a base to remove this amidic proton.

The log protonation constants found for each ligand are listed in Table 1. In each case, the first protonation constant may be used to infer the relative basicity of its amino groups. Thus, depending on the ring size and isomer considered, the range of this basicity is from 6.98 to 9.53 log units. The ligands **5** and **6** possess the most basic amino groups, while the [12]aneN_4 ligand **4** is the weakest base. In compound **1**, the electropositive ends of the two keto groups are closer to the amino groups compared to its isomer **5**, and this proximity reduces the basicity from 9.52 to 7.88. A large reduction in basicity is observed in the comparison of isomeric ligands **6** and **2**: 9.05 to 7.21. As expected, the removal of a methylene between the amido nitrogens has very little effect on the basicities of the distal trimethylene diamine moieties in compounds **1** and **3**: 7.88 vs. 7.69. The basicity of the ethylenediamine moiety in ligand **4** is the lowest, since the two keto groups are closest and the ring size of the macrocycle is the smallest.

The relative magnitude of the second protonation constant is a measure of the difficulty of protonating near a protonated center. Thus, the tendency in the $\Delta \log K_{1-2}$ values is to be larger for the trimethylendiamine containing ligands and smaller for the ethylenediamine bridged compounds.

© 1999 NRC Canada

Table 2. Protonation constants of polyamines.[a]

Diaminodiamide	log K_1^H	log K_2^H	Δ log K_{1-2}^H
Ethylenediamine $NH_2CH_2CH_2NH_2$	9.92	7.10	2.82
Trimethylenediamine $NH_2CH_2CH_2CH_2NH_2$	10.54	8.76	1.78
N,N′-Diglycylethylenediamne $NH_2CH_2C(O)NHCH_2CH_2NH(O)CCH_2NH_2$	8.22	7.48	1.74
N,N′-Diglycylpropylendiamine $NH_2CH_2C(O)NHCH_2CH_2CH_2NH(O)CCH_2NH_2$	8.40	7.72	0.68
N,N′-Bis(2-aminoethyl)malonamide $NH_2CH_2CH_2NH(O)CCH_2C(O)NHCH_2CH_2NH_2$	9.40	8.68	0.72

[a]See footnote 2. All values at 25°C, μ = 0.1 M, except diglycylpropylenediamine which is at 25°C, μ = 0.5 M.

Table 3. Overall formation constants of dioxotetraazamacrocycles with Cu^{2+} at 25.0°C and μ = 0.100 M (KCl).

	log $\beta_{CuH_{-2}L}$	log β_{CuL}	log $\beta_{CuH_{-1}L}$	log β_{CuHL}	log $\beta_{CuH_{-3}L}$	pM[a]
1	1.86 (3)	8.33 (4)		11.72 (3)		16.1
2	–2.56 (4)	6.71 (4)				12.0
3	–3.47 (2)	6.08 (2)			–14.94 (2)	9.7
4[b]	–6.65 (6)	6.56 (5)	1.31 (2)		–16.00 (5)	8.4
5	0.56[c] (10)	8.99[d] (10)				13.2
6	–2.43[e] (2)	[f]	1.83 (8)		–13.76 (2)	10.7

[a]pM = –log $[Cu^{2+}]$ at 25°C and μ = 0.100 (KCl) with 100% excess ligand at pH 7.4.

[b]Also log $\beta(Cu^{2+} + 2\ L \rightleftarrows CuL_2^{2+})$ 12.18 (16) and log $\beta(Cu^{2+} + 3\ L \rightleftarrows CuL_3^{2+})$ 15.32 (10).

[c]Literature: 0.44 (NIST Database 46)[2].

[d]Literature: 8.75 (NIST Database 46)[2].

[e]Literature: –2.02 (NIST Database 46)[2].

[f]Literature: 7.73 (NIST Database 46)[2].

The very small Δ log K_{1-2} value of ligand **3** of 1.79 points to the existence of electronic independence of the two protonation steps, while the very large Δ log K_{1-2} value of 5.36 in ligand **6** is probably the highest difference observed in any ethylenediamine derivative and can be interpreted to mean that a second protonation requires a breakup of a favorably chelated single proton shared between the two amino nitrogens.

Several acyclic model compounds listed in Table 2 may be employed upon for assessing the absolute values of the protonation constants found in the macrocycles. Four rules may be derived from this list in Table 2:

(*i*) The first log protonation constant of ethylenediamine is ~9.9.

(*ii*) The first log protonation constant of a trimethylenediamine is ~10.5.

(*iii*) The second log protonation constant is <~2.0 units lower than the first, unless electrostatic interaction is a factor.

(*iv*) The presence of an amide group lowers the amino log protonation constant by >1 unit if the carbonyl side is closer to the amino group.

These rules, derived from the sterically free alicyclic compounds, suggest that when ΔpK values greater than 2 units are encountered in Table 1, the macrocyclic effects are such that the basic nitrogen groups are "forced" to be close to each other so that an H^+, initially chelated to two amino nitrogens, is actually displaced with difficulty to form a coulombic repulsive pair of contiguous N^+ species. The compounds containing a basic ethylenediamine moiety are **2**, **4**, and **6**. Rule 1 applies to **6** and Rule 4 applies to **2** and **4**. On the other hand, the compounds containing a basic trimethylenediamine moiety are **1**, **3**, and **5**. Rule 2 applies to **5** and Rule 4 applies to **1** and **3**. According to Rule 3, the second protonation constants imply that the nitrogens are very independent in **1** and **3** but a little more restricted in **5**.

Equilibrium constants of Cu^{2+} complexes

The expression of formation constants for systems that lose protons while forming the predominant complex in solution can be problematic with these H_2L^{2+} type ligands. The normal species ML^{2+} does not necessarily form. The convention used here uses the H_{-1} and H_{-2} notation to indicate that one and two protons were released, respectively, into solution during the formation of the metal complex. The negative subscripts –1 and –2 represent proton displacement from an amide, while any additional protons "lost" indicated by –3 imply a loss of one proton from a coordinated water molecule and 2 protons from amide groups. In this work, one or more of the following overall reactions were found to occur for Cu^{2+} with ligands **1**– **6**. These concentration constants are listed in Table 3.

[1] $Cu^{2+} + L \rightleftarrows CuH_{-2}L + 2\ H^+$ log $\beta_{CuH_{-2}L}$

[2] $Cu^{2+} + L \rightleftarrows CuH_{-1}L^+ + H^+$ log $\beta_{CuH_{-1}L}$

[3] $Cu^{2+} + L \rightleftarrows CuL^{2+}$ log β_{CuL}

© 1999 NRC Canada

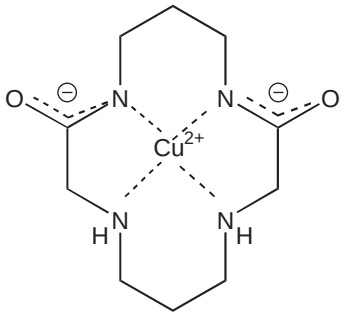

12 $CuH_{-2}L$ (L = 1)

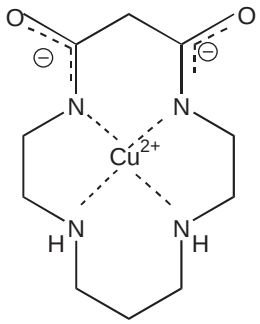

13 $CuH_{-2}L$ (L = 5)

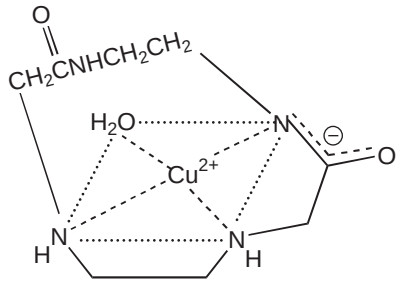

14

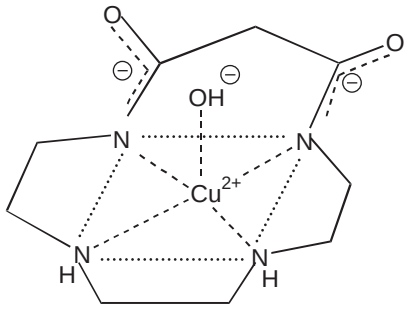

15

Fig. 1. Visible spectra of $CuH_{-2}L$ species where L = compounds **1** to **6**.

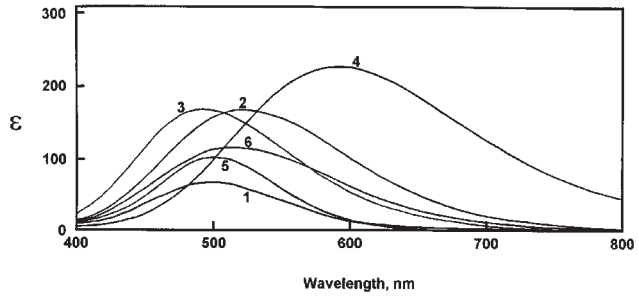

[4] $Cu^{2+} + L + H^+ \rightleftarrows CuHL^{3+}$ $\log \beta_{CuHL}$

[5] $Cu^{2+} + L \rightleftarrows CuH_{-3}L^- + 3\ H^+$ $\log \beta_{CuH_{-3}L}$

The most important species in all systems is $CuH_{-2}L$ in which Cu^{2+} is reasonably assumed to be tetracoordinated to four N donors as shown in **12** and **13**. The $CuH_{-2}L$ complexes of ligands **2**, **3**, **4**, and **6** would be similarly formulated. The normal chelate CuL^{2+} was found in five of the species, but in most cases it is not very important. The intermediate species $CuH_{-1}L^+$ was found only in two ligands, but is very important in the complexes found from compound **4**. It forms only to the extent of ~10% with ligand **6**. Drawing **14** illustrates the probable bonding arrangement in $CuH_{-1}L^+$. The proximity of the remaining amido N makes it statistically favorable to complete this reaction to give $CuH_{-2}L$. There probably is a very marked cavity size to metal ion diameter mismatch to make compound **4** the weakest ligand tested. The pentacoordinate axial hydroxo $CuH_{-3}L^{-1}$ species forms only at high p[H] and is of no interest at intermediate p[H] values. It is not surprising that for compound **4** this species is favored at lower p[H] than for the other compounds. The high p[H] pentacoordinate species for ligand **6** was previously not identified. Its suggested bonding is shown in drawing **15**. The other pentacoordinate complexes are probably similar.

Ligand **4** is somewhat special in its marked low affinity for Cu(II), since there was a tendency in 1:1 systems for $Cu(OH)_2$ precipitation just after initial formation of this complex. To prevent the onset of precipitation, advantage was taken of the larger than usual formation of the ML^{2+} type complex. Therefore, it was assumed that 1:2 Cu^{2+}/L complexes could form. The titration of a 1:2 ratio worked very well. The additional constants obtained are listed on the bottom of Table 3. This 1:2 M/L complex probably binds as indicated schematically by **16**.

One analog of **4** is found in the literature.[2] Perhaps not surprisingly 2,6-dioxo-1,4,7,10-tetraazacyclododecane, **17**, also exhibits unusual Cu^{2+} formation equilibria. It has similar protonation constants, 7.48 and 4.22, and forms stepwise amide complexes. Its formation constants[2] are lower than those of the Cu(II) complexes of **4**.

Visible spectra

During solution studies, distinct color development was noted as the titrations progressed. To compare these results, the visible spectra were obtained at p[H] values corresponding to the maximum concentration of species $CuH_{-2}L$ and

[2] NIST Standard Reference Database 46: NIST Critically Selected Stability Constants of Metal Complexes: Version 5.0. July, 1998.

© 1999 NRC Canada

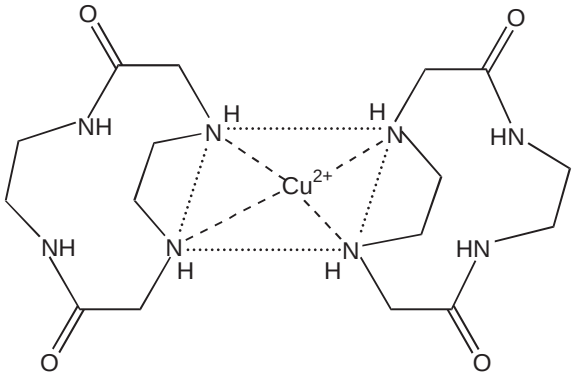

16 CuL_2^{2+} (L = 4)

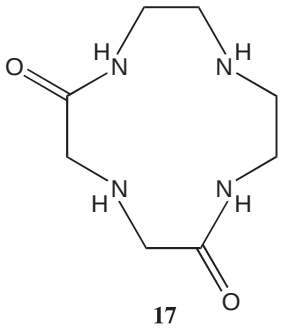

17

Fig. 2. Relative stability of the $CuH_{-2}Lx$ species where x = compounds **1** to **6**. All other species were omitted from the drawing to focus on the main species $CuH_{-2}L$.

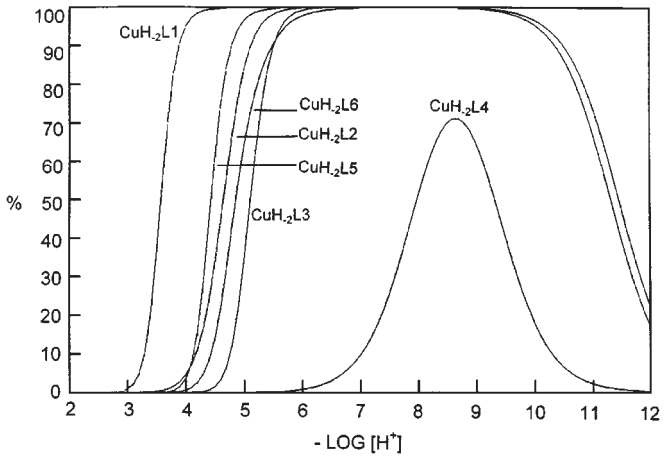

were normalized for concentration. From plots of the extinction coefficients vs. wavelength in Fig. 1, it becomes obvious that the solution structure of the copper complex with ligand **4** is fundamentally different from that of the remaining complexes. In fact, it is proposed that if the $CuH_{-2}L$ geometries are generally planar, then when L is **4**, the metal must be out of the plane. Support for this speculation can be gleaned from the spectrum of $CuH_{-2}L$ when L is the open-chain structural analog DGEN (*N*,*N*′-diglycylethylenediamine): $NH_2CH_2CH_2C(O)NH\text{-}CH_2CH_2\text{-}NHC(O)CH_2CH_2NH_2$ (24). Because there are no geometric restrictions, this species (DGEN-Cu) is planar as implied from its spectrum: λ_{max} 520, ε 170 $M^{-1}cm^{-1}$.

Suitability of Cu^{2+} complexes for applications

The pM values shown in Table 3 indicate that the copper complex with ligand **1** is the strongest from the concentration perspective. However, a deeper understanding may be seen in Fig. 2, which shows the relative behavior of all six Cu–L systems studied herein. By far the best ligand is **1**, both because it has the highest pM value and because it forms at the lowest pH as seen from the comparison in Fig. 2. It is noteworthy that **1** is an isomer of ligand **5** with a characteristic malonodiamide moiety that apparently is too restrictive for the best fit of a Cu^{2+} ion. A similar isomer pair may be found by comparison of compounds **2** and **6** of the [13] macrocycles. Apparently, by moving away from malonodiamide in the [13] macrocycles the ligand **2** is also somewhat better than ligand **6**.

Shrinking the macrocycle **1** by the removal of a methylene group produces ligand **3** or ligand **2**. Although both of these ligands have lower affinity for Cu(II), **2** gives the more stable complex.

However, one neutral complex studied here is found to be particularly ill-suited for in vivo application. Ligand **4** is so sterically unsuitable that it is reluctant to form its $CuH_{-2}L$ complex until above p[H] 7. The best candidate found is ligand **1**.

While there are several other ways of arranging two dioxo groups in the cyclam framework to form diamides, it is not known at this time whether they would outperform ligand **1**.

Experimental

Materials and methods

N,*N*′-Dibenzyl-1,3-diaminopropane (19), *N*,*N*′-bischloroacetyl-1,3-diaminopropane (25), *N*,*N*′-bischloroacetyl-1,2-

© 1999 NRC Canada

diaminoethane (25), *N,N′*-ditoluenesulfonyl-1,2-diaminoethane, and *N,N′*-ditoluenesulfonyl-1,3-diaminopropane were prepared by previously reported procedures (26). Hydrogen bromide, 30 wt.% in acetic acid and the ligand 1,4,8,11-tetraazacyclotetradecane-5,7-dione (**5**) were purchased from the Aldrich Chemical Company.

The ligand 1,4,7,10-tetraazacyclotridecane-11,13-dione (**6**) was kindly supplied by Dr. Ichiro Murase of Dojindo Chemical Company and prepared by Dr. Hidefumi Kato of Kurume Technical College. Although its direct synthesis had been published by Kimura and Machida (8*a*), the modification herein consists of refluxing a 1 L absolute ethanol solution of 16 g (0.1 mol) diethyl malonate and 14.6 g (0.1 mol) triethylenetetraamine for 72 h. It is important to reduce the volume substantially but not to remove the solvent completely. A few seeds were then added, and the crystallization was allowed to continue for 48 h at 25°C. The crystals collected were recrystallized from absolute ethanol for an overall yield of 6.4 g (~30%); mp 185–186°C. IR (KBr) 1660 cm^{-1} (strong, amide absorption). Mass (EI+) = 214 (calcd. 214.3).

The proton and carbon-13 NMR were recorded on a Varian XL-200 spectrometer operating at 200 MHz, and the chemical shifts are reported in ppm relative to tetramethylsilane. The mass spectra were obtained with the departmental VG analytical 70S high-resolution double focusing magnetic sector spectrometer with an attached VG analytical 11/250J data system. Measurements were made by the departmental mass spectrometry specialist, Dr. Lloyd W. Sumner. The C, H, N analyses were performed by Galbraith Laboratories, Inc., Knoxville, Tenn.

Synthetic routes and procedures

The route used for the synthesis of 14N4O2–3,9 (**1**) is shown in Scheme 1.

*1,11-Dibenzyl-1,4,8,11-tetraazacyclotetradecane-3,9-dione (**7**)*

N,N′-Dibenzyl-1,3-diaminopropane, 2.54 g (0.01 mol), *N,N′*-bischloroacetyl-1,3-diaminopropane, 2.27 g (0.01 mol), and powdered K_2CO_3, 25 g (0.18 mol) were added to 250 mL of acetonitrile, and this reaction mixture was heated to reflux for 20 h. It was filtered and washed with CH_3CN; from the filtrate 4.1 g of white residue was obtained. After chromatographic purification, 0.87 g of product was collected from an eluant of CH_2Cl_2:MeOH = 98:2. Another 0.57 g sample was also obtained (eluted by CH_2Cl_2:MeOH = 98:2). A pure sample of 0.71 g was obtained after a second flash chromatography from the 0.87 sample. ^{1}H NMR ($CDCl_3$): 7.29–7.14 (m, 12H, NH and arom.), 3.505 (s, 4H, -CH_2- of benzyl), 3.302–3.250 (m, 4H, -CH_2- of 5 and 7 position), 3.027 (s, 4H, -CH_2- of 2 and 10 position), 2.451 (t, 4H, -CH_2- of 12 and 14 position), 1.756 (quin. 2H, -CH_2- of 6 position), 1.641 (quin. 2H, -CH_2- of 13 position). ^{13}C NMR (in $CDCl_3$): 171.387 (-CO- of amido); 137.397 (C-1 of arom.); 128.984, 128.463, 127.508 (C-2,3,4 of arom.); 59.974 (-CH_2- of benzyl); 58.388 (-CH_2- of 5 and 7 positions); 52.845 (-CH_2- of 2 and 10 positions); 40.104 (-CH_2- of 12 and 14 positions); 28.432 (-CH_2- of 6 position); 27.277 (-CH_2- of 13 position). FABMS: [M + H^+] = 409. Anal. calcd. for $C_{24}H_{32}N_4O_2 \cdot 1/2H_2O$: C 69.06, H 7.91, N 13.43; found: C 69.28, H 7.87, N 13.31. R_f = 0.57 (developed by CH_2Cl_2:MeOH = 98:2); and the R_f value of the 28-membered ring (compound **6**) is about 0.48, developed by the same mixed solvents.

*1,4,8,11-Tetraazacyclotetradecane-3,9-dione (**1**)*

Compound **7**, 0.20 g (0.5 mmol), was dissolved in 12 mL of 4.4% HCOOH–CH_3OH solution containing about 0.2 g of freshly prepared palladium black catalyst (27). The mixture was stirred at room temperature under Ar atmosphere for 24 h. The crude product was recrystallized from 10:1 (v/v) of abs. EtOH:conc. HCl; 0.10 g of pure product was obtained, yield 83%. ^{1}H NMR (in D_2O *t*-BuOH as internal standard = 1.29 ppm): 3.711 (s, 4H, -CH_2- of 2 and 10 positions), 3.277 (t, 4H, -CH_2- of 5 and 7 positions), 3.063 (t, 4H, -CH_2- of 12 and 14 positions), 1.72 (m, 4H, -CH_2- of 6 and 13 positions). ^{13}C NMR (in D_2O; *p*-dioxane as internal standard: 67.400 ppm): 166.714 (-CO- of the amido), 47.577 (C-2 and C-10), 42.213 (C-5 and C-7), 40.480 (C-12 and C-14), 27.271 (C-6), 20.173 (C-13). FABMS: [M + H^+] = 229. Anal. calcd. for $C_{10}H_{20}N_4O_2 \cdot 2HCl$: C 39.88, H 7.31, N 18.60; found: C 39.70, H 7.42, N 18.41.

General procedure for the preparation of ditoluenesulfonyl dioxotetraazamacrocycles 9, 10, 11 (Scheme 2)

To a 500 mL three-necked flask, 120 mL of DMF, 4.5 g of K_2CO_3, 1.2 g of NaH (60% dispersion in mineral oil), and 0.015 mol of *N,N′*-ditoluenesulfonyl-1,2-diaminoethane or *N,N′*-ditoluenesulfonyl-1,3-diaminopropane were added in sequence. This reaction mixture was heated to 60°C to which a solution of 0.015 mol of *N,N′*-bischloroacetyl-1,3-diaminopropane or *N,N′*-bischloroacetyl-1,2-diaminoethane in 80 mL of DMF was added in about 15 min. The reaction mixture was then heated to 90–95°C for 18 h. The inorganic salts were removed by filtration, and the solvents were removed by vacuum distillation. The crude product was first boiled with 200 mL of 95% ethanol and then recrystallized in boiling glacial acetic acid; pure crystalline product was obtained.

*4,7-Ditoluenesulfonyl-1,4,7,10-tetraazacyclotridecane-2,9-dione (**9**)*

Compound **9** was obtained in 41% yield. ^{1}H NMR (in $CDCl_3$): 7.65 and 7.36 (d, 8H, arom.), 6.9 (b, 2H, -CONH-), 3.73 (s, 4H, -CH_2- 3 and 8 positions), 3.48 (t, 4H, -CH_2- 11 and 13 positions), 3.30 (s, 4H, ethylene), 2.46 (s, 6H, -CH_3), 1.8 (b, 2H, -CH_2- 12 position). ^{13}C NMR (in DMSO): 166.61 (-*C*ONH-); 134.63, 135.45, 129.94, 127.21, (arom.); 51.834 (-CH_2- of 3 and 8 positions); 45.941 (-CH_2- 11 and 13 positions); 33.382 (ethylene); 26.108 (-CH_2- 12 positions); 21.081 (-CH_3). FABMS: [M + Na^+] = 523. Anal. calcd. for $C_{23}H_{30}N_4O_6S_2 \cdot CH_3COOH$: C 51.55, H 5.84, N 9.62; found: C 51.55, H 6.01, N 9.65.

*1,10-Ditoluenesulfonyl-1,4,7,10-tetraazacyclotridecane-3,8-dione (**10**)*

Compound **8** was obtained in 36% yield. ^{1}H NMR (in DMSO-d_6): 7.69 and 7.38 (d, 8H, arom.), 3.52 (s, 4H, ethylene), 3.22 (t, 4H, -CH_2- 2 and 9 positions), 2.95 (t, 4H, -CH_2- 11 and 13 positions), 2.37 (s, 6H, -CH_3), 1.7 (b, 2H,

© 1999 NRC Canada

Table 4. Composition and molecular weights of tetraazacycloalkanedione ligands.

	Calc.	Found	Composition
1	301.3	302.9	$C_{10}H_{20}N_4O_2 \cdot 2HCl$
2	376.1	376.0	$C_9H_{18}N_4\ O_2 \cdot 2HBr$
3	376.1	378.3	$C_9H_{18}N_4\ O_2 \cdot 2HBr$
4	362.1	368.4	$C_8H_{16}N_4\ O_2 \cdot 2HBr \cdot 0.3H_2O$
5	228.3	225.5	$C_{10}H_{20}N_4O_2$
6	214.3	213.6	$C_9H_{18}N_4\ O_2$

-CH_2- 12 position). FABMS: [M + Na^+] = 545 and [M + H^+] = 523. Anal. calcd. for $C_{23}H_{30}N_4O_6S_2$: C 52.87, H 5.75, N 10.73; found: C 52.80, H 5.93, N 10.49.

*4,7-Ditoluenesulfonyl-1,4,7,10-tetraazacyclododecane-2,9-dione (**11**)*

Compound **11** was obtained in 53% yield. ^{1}H NMR (in DMSO-d_6): 8.285 (b, 2H, -CONH-), 7.65 and 7.46 (d, 8H, arom.), 3.56 (s, 4H, -CH_2- 3 and 8 positions), 3.21 (s, 4H, -CH_2- 5 and 6 positions), 2.96 (s, 4H, -CH_2- 11 and 12 positions), 2.416 (s, 6H, -CH_3). FABMS: [M + Na^+] = 531. Anal. calcd. for $C_{22}H_{28}N_4O_6S_2 \cdot H_2O$: C 50.19, H 5.70, N 10.65; found: C 50.32, H 5.783, N 10.04.

General procedure for the preparation of dioxotetraazamacrocycles 2, 3, 4 (Scheme 2)

Compound **9**, **10**, or **11** (2 mmol) and 1.2 g of phenol were dissolved in 20 mL of 30% HBr–CH_3COOH (30%), and this reaction solution was heated in a 90–95°C bath for 20 h. The solution became brown, and a large amount of white precipitate separated. It was cooled to room temperature. and was filtered, the crude product was washed with ether; a white precipitate was obtained. This crude product was dissolved in 12 mL of water and was extracted with 12 mL portions of ether. The separated ether phase was decolorized with charcoal. The colorless aqueous solution was evaporated to nearly dryness. The white residue was dissolved in 1 mL of water, then diluted with 25 mL of MeOH; after cooling at –10°C for 16 h, a pure product gradually crystallized.

*1,4,7,10-Tetraazacyclotridecane-2,9-dione (**2**)*

Compound **2** was obtained in 47% yield. ^{1}H NMR (in D_2O, MeOH as internal standard: 3.35 ppm): 3.925 (s, 4H, -CH_2- of 3 and 8 positions), 3.513 (s, 4H, ethylene), 3.454 (t, 4H, -CH_2- of 11 and 13 positions), 1.917 (quin. 2H, -CH_2- of 12 position). ^{13}C NMR (in D_2O, MeOH as internal standard: 49.00 ppm): 165.947 (-CONH-), 49.596 (-CH_2- of 11 and 13 positions), 42.458 (ethylene), 40.120 (-CH_2- of 11 and 13 positions), 27.167 (-CH_2- of 12 position). FABMS: [M + H] = 215. Anal. calcd. for $C_9H_{18}N_4O_2 \cdot 2HBr$: C 28.72, H 5.32, N 14.89; found: C 28.69, H 5.51, N 14.83.

*1,4,7,10-Tetraazacyclotridecane-3,8-dione (**3**)*

Compound **3** was obtained in 87% yield. ^{1}H NMR (in D_2O, MeOH as internal standard: 3.35 ppm): 3.882 (s, 4H, -CH_2- of 2 and 9 positions), 3.530 (s, 4H, ethylene), 3269 (t, 4H, -CH_2- of 11 and 13 positions), 2.05 (quin. 2H, -CH_2- of 12 position). ^{13}C NMR (in D_2O, MeOH as internal standard: 49.00 ppm): 167.757 (-CONH-), 47.688 (-CH_2- of 2 and 9 positions), 45.022 (ethylene), 39.005 (-CH_2- of 11 and 13 positions), 20.239 (-CH_2- of 12 position). FABMS: [M + H] = 215. Anal. calcd. for $C_9H_{18}N_4O_2 \cdot 2HBr$: C 28.72, H 5.32, N 14.89; found: C 28.71, H 5.70, N 14.66.

*1,4,7,10-Tetraazacyclododecane-2,9-dione (**4**)*

Compound **4** was obtained in 23% yield. ^{1}H NMR (in D_2O, *p*-dioxane as internal standard: 3.56 ppm): 3.739 (s, 4H, -CH_2- of 3 and 8 positions), 3.346 (s, 4H, -CH_2- of 11 and 12 positions), 3.306 (s, 4H, -CH_2- of 5 and 6 positions). ^{13}C NMR (in D_2O, *p*-dioxane as internal standard: 67.40 ppm): 166.38 (-CONH-), 48.22 (-CH_2- of 3 and 8 positions), 40.81 (-CH_2- of 11 and 12 positions), 39.543 (-CH_2- of 5 and 6 positions). FABMS: [M + Na^+] = 223. Anal. calcd. for $C_8H_{16}N_4O_2 \cdot 2HBr$: C 26.52, H 4.97, N 15.47; found: C 26.59, H 5.11, N 15.59.

Solution potentiometry

Standard solution

Carbon-dioxide-free, 0.10 M potassium hydroxide solution was prepared from Dilut-it® (Baker) Ampoules with doubly distilled water and standardized against KHP (potassium acid phthalate) to the phenolphthalein endpoint. Standard copper chloride solution 0.02 M was prepared from $CuCl_2$ (Fisher) and standardized by ion exchange methods (Dowex 50W X-8, strong acid resin).

Apparatus

The potentiometric apparatus consisted of a 100 mL capacity jacketed and capped glass cell provided with a magnetic stirrer, protective Ar inlets and outlets, a Metrohm 10 mL capacity incremental burette, and fitted with separate extension glass and reference (saturated calomel) electrodes for maximum accuracy and stability, connected to a Corning Model 150 pH meter.

Calibration

A small, known aliquot of standard 0.10 M HCl and a 5.000 mL aliquot of 1.000 M KCl were diluted to 50.00 mL with doubly distilled water in the thermostated (25.00 ± 0.05°C) titration cell. The p[H] ([H] = mol protons/L solution) was set on the meter to the calculated –log of the nominal H^+ molarity, and the standard KOH solution was added portionwise up to p[H] 11.0. Gran's plot showed the concentration of CO_2 to be <2.0% of KOH. From this it was also found that log K_w ($[H^+][OH^-]$) = –13.78 is suitable for reproducing the basic titration points.

Protonation constants

For each ligand studied, 0.1–0.2 mmol ligand was directly weighed and dissolved to make a 50.00 mL test solution at 25.0°C and μ = 0.100 (KCl). Usually, 0.050–0.100 mL aliquots of standard 0.10 M KOH were added to the test solution while the p[H] was noted. Generally, 10–20 points of data were collected for each *a* value (*a* = mol KOH added/mol of ligand present). The data collection was stopped at p[H] 11. The computation of the protonation constants was effected with Program BEST (28). The refinement process also yielded an exact molecular weight for each ligand (see Table 4).

© 1999 NRC Canada

Stability constants

To conserve ligand, each completed protonation titration solution was neutralized with standard 0.1 M HCl for reuse in copper determinations. A 1:1 molar ratio of copper to ligand was added, and a calculated portion of 1.000 M KCl was added to readjust the ionic strength back to 0.100. Usually, the copper-containing solution was treated with successive 0.100 mL aliquots of standard base until the recorded p[H] was near 11.0. The computations were made with the PC program BEST (28). The log β model developed for each Cu–ligand system was discovered by the systematic addition of required species until the titration curve was reproduced exactly. The initial species $MH_{-2}L$ was always the dominant form for most of the copper complexes, although, depending on the particular ligand, other species were also found, but in much lower concentrations. The computations on ligand **4** were carried out on three experiments, while all others were carried out on single experiments.

Electronic spectra

The UV-vis spectra of the complexes were obtained on a Perkin–Elmer Fast Scan model 553 spectrophotometer fitted with 1.000 cm matched cells and approximately 1.0 mM solution at p[H] corresponding to complete formation of $CuH_{-2}L$.

Acknowledgment

This research was supported by U.S. Public Health Service, National Cancer Institute, CA-42925. National Science Foundation grant CHE-8705697 supported the purchase of the mass spectrometers.

References

1. (*a*) Q.H. Luo, S.R. Zhu, M.C. Shen, S.Y. Yu, Z. Zhang, X.Y. Huang, and Q.J. Wu. J. Chem. Soc. Dalton Trans. 1873 (1994); (*b*) S.R. Zhu, H.K. Lin, C.C. Lin, F.P. Kuo, and Y.T. Chen. Inorg. Chim. Acta, **228**, 225 (1995).
2. (*a*) E. Kimura. J. Coord. Chem. **15**, 1 (1986); (*b*) R. Machida, E. Kimura. and Y. Kushi. **25**, 3461 (1986).
3. R.W. Hay, R. Bembi, and W. Sommerville. Inorg. Chim. Acta, **59**, 147 (1982).
4. Y.D. Lampeka and S.P. Gavrish. J. Coord. Chem. **21**, 351 (1990).
5. F.P. Kou, S.R. Zhu, H.K. Lin, Y.T. Chen, H.G. Wang, and X.K. Yao. J. Chem. Soc. Chem. Commun. 59 (1996).
6. G.L. Burce, E.B. Peniago, and D.W. Margerum. J. Chem Soc. Chem. Commun. 261 (1975).
7. E. Kimura, T. Yatsunami, A. Watanabe, R. Michida, T. Koike, H. Fujioka, Y. Kuramoto, M. Sumomogi, K. Kunimitsu, and A. Yamashita. Biochim. Biophys. Acta, **745**, 37 (1983).
8. (*a*) E. Kimura and R. Machida. J. Chem. Soc. Chem. Commun. 499 (1984); (*b*) R. Machida, E. Kimura, and M. Kodama. Inorg. Chem. **22,** 2055 (1983); (*c*) D. Chen, R.J. Motekaitis, and A.E. Martell. Inorg. Chem. **30**, 1396 (1991).
9. T.R. Wagler, Y. Fang, and C.J. Burrows. J. Org. Chem. **54**, 1584 (1989).
10. E. Kimura, Y. Lin, R. Machida, and H. Zenda. J. Chem. Soc. Chem. Commun. 1020 (1986).
11. Z. Zhang, J.L. Petersen, and A.M. Stolzenberg. Inorg. Chem. **35**, 4649 (1996).
12. A. Jyo, M. Sassa, and H. Egawa. J. Appl. Polym. Sci. **59**, 1049 (1996).
13. I. Tabushi, Y. Taniguchi, and H. Kado. Tetrahedron Lett. 1049 (1977).
14. I. Tabushi, H. Okino, and Y. Kuroda. Tetrahedron Lett. 4339 (1976).
15. J. Petranek and O. Ryba. Collect. Czech. Chem. Commun. **45**, 1567 (1980).
16. B. Dietrich, J.M. Lehn, J.P. Sauvage, and J. Blanzat. Tetrahedron, **29**, 1629 (1973).
17. J. Petranek and O. Ryba. Collect. Czech. Chem. Commun. **48**, 1944 (1983).
18. K.E. Krakowiak, J.S. Bradshaw, and R.M. Izatt. J. Heterocycl. Chem. **27**, 1585 (1990).
19. K.E. Krakowiak, J.S. Bradshaw, and R.M. Izatt. J. Org. Chem. **55**, 3364 (1990).
20. J.S. Bradshaw, K.E. Krakowiak, H.Y. An, and R.M. Izatt. J. Heterocycl. Chem. **27**, 2113 (1990).
21. J.E. Richman and T.J. Atkins. Org. Synth. **58**, 86 (1978).
22. M. Hediger and T.A. Kaden. Helv. Chim. Acta, **66**, 861 (1983).
23. M.K. Kim, A. Kaneda, and A.E. Martell. J. Coord. Chem. **4**, 159 (1975).
24. K.S. Bai and A.E. Martell. J. Am. Chem. Soc. **30**, 4412 (1969).
25. J.S. Bradshaw, K.E. Krakowiak, and R.M. Izatt. J. Heterocycl. Chem. **26**, 1431 (1989).
26. B. Dietrich, M.W. Hosseini, J.M. Lehn, and R.B. Sessions. Helv. Chim. Acta, **66**, 123 (1983).
27. J.P. Greenstein and M. Winitz. Chemistry of amino acids. Vol. 2. Wiley, New York. 1961. p. 1233.
28. A.E. Martell and R.J. Motekaitis. The determination and use of stability constants. 2nd ed. VCH Publishers, New York. 1992.

© 1999 NRC Canada

Organic reaction in water. Part 2[1]: Michael addition in water without phase transfer agents

Flavia Martins da Silva, Adriana Kniaseff Gomes, and Joel Jones, Jr.

Abstract: The Michael additions of dicarbonyl compounds, nitroalkanes, and thiols to 2-cyclohexen-1-one can be accomplished in water without phase transfer agents. The reaction is extremely sensitive to the pH of the reaction media, and therefore, the methodology can be optimized with the control of this variable. The best pH depends on the used nucleophile.

Key words: Michael addition, aqueous media, water, 2-cyclohexen-1-one, ketone.

Résumé : Les additions de Michael de composés dicarbonylés, de nitroalcanes et de thiols sur la cyclohexèn-2-one-1 peuvent être réalisées dans l'eau sans agents de transfert de charge. La réaction est extrêmement sensible au pH du milieu réactionnel et, en conséquence, la méthodologie peut être optimisée par le contrôle de cette variable. Le meilleur pH dépend du nucléophile utilisé.

Mots clés : addition de Michael, milieu aqueux, eau, cyclohexèn-2-one-1, cétone.

[Traduit par la Rédaction]

The use of water as the solvent in organic reactions has been uncommon for several reasons, among them the insolubility of the reactant (2), the incompatibility of the intermediates with water (2), and the competition of the desired reaction with hydrolysis (3). However, one of the main problems in the chemical industry is related with the use of organic solvents in its processes. The manufacture, transport, stock, handling, and disposal of solvents are aspects that demand great care and expense. For these reasons, the substitution of organic solvent as reaction media by water has great interest to organic synthesis because this minimizes the environmental impact, besides lowering the cost and decreasing operational danger.

In addition to the economic and human aspects, water presents many physical–chemical properties that can be useful in the reactions, such as high polarity, ion solvating capacity, and the ability to form hydrogen bonds, to form a structured liquid (4), and to aggregate apolar molecules dissolved in the water (hydrophobic effect) (2, 5–7).

Since 1980, when Breslow published his studies showing the importance of the use of water as solvent in Diels–Alder reactions (5), some studies have been made in this solvent in the sub- (2–31, 34–37) and superheated (31, 32) states. In the literature are examples of reactions such as hetero Diels–Alder (8, 9), dipolar cycloadditions (10), Claisen rearrangements (11), nucleophilic additions (12–23), and substitutions (3), Barbier reactions (24–31), autocatalytic cleavages (32, 33), oxidations (34, 35), reductions (36), photoreactions (37), among others.

The Michael addition reaction (38) is commonly applied in organic synthesis, and it has great importance in the formation of a new carbon–carbon bond and in the synthesis of polyfunctional compounds. Recently, examples of Michael reactions in aqueous media have appeared. Keller and Feringa (13) studied the 1,4-addition of several ketoesters with α,β-unsaturated aldehydes and ketones, and of α-nitroesters with methyl vinyl ketone (14). These reactions occur in aqueous media catalysed by ytterbium triflate.

Nitroalkanes give the same type reaction in aqueous media, catalyzed by sodium hydroxide in the presence of a phase transfer agent, as shown by Ballini and Bosica (15). Lubineaou and Augé (16) published the first example of Michael addition of nitroalkanes in water without catalyst. However, the method seems to be only effective when nitromethane and nitroethane are used as nucleophiles, and methyl vinyl ketone as electrophile.

The 1,4-addition of water-soluble phosphines (17, 18) and pyridines (19) were also studied in an aqueous media. Also in water or in double solvents systems, alkyl halides, in presence of zinc and copper, react with α,β-unsaturated ketones and aldehydes, leading to the addition products (20–23).

We have studied this reaction type in aqueous media, with basic catalysis, without phase transfer agents, to examine its

Received November 3, 1998.

This paper is dedicated to Jerry Kresge in recognition of his many achievements in chemistry.

F.M. da Silva, A.K. Gomes, and J. Jones, Jr.[2] Departamento de Química Orgânica, Instituto de Química, Universidade Federal do Rio de Janeiro, Rio de Janeiro 20910–240, Brazil.

[1]See ref. 1 for Part 1.

[2]Author to whom correspondence may be addressed. Telephone: (55)(21) 590–3544. Fax: (55)(21) 290–4740.
e-mail: jjones@iq.ufrj.br

 © 1999 NRC Canada

Table 1. pK_a values, reaction times, and yields of reaction products.

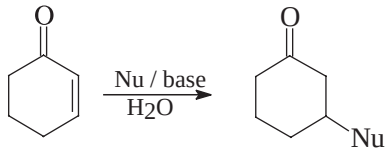

1 2

2	Nu	pK_a (Nu)	Base	Reaction time (h)	Purified yield (%)[a]
a	CH_3NO_2	10.21 (39)	NaOH (pH 14)	5	65
			Na_2CO_3 (pH 10)		40
			$NaHCO_3$ (pH 7.5)		20
b		8.5 (39)	NaOH (pH 14)	7.5	[b]
			Na_2CO_3 (pH 10)		20
			$NaHCO_3$ (pH 7.5)		25
c	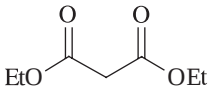	13 (40)	NaOH (pH 14)	5	20
			Na_2CO_3 (pH 10)		30
			$NaHCO_3$ (pH 7.5)		10
d	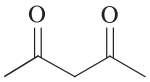	8.94 (3)	NaOH (pH 14)	1	[b]
			Na_2CO_3 (pH 10)		35
			$NaHCO_3$ (pH 7.5)		33
f	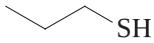	10.65 (41)	NaOH (pH 14)	2	30
			Na_2CO_3 (pH 10)		50
			$NaHCO_3$ (pH 7.5)		70
g	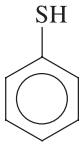	6.5 (42)	NaOH (pH 14)	0.75	30
			Na_2CO_3 (pH 10)		55
			$NaHCO_3$ (pH 7.5)		95

[a]Average of three reactions.
[b]Several products.

utility in organic synthesis and for preparation of polyfunctional intermediates.

Experimental

Materials

2-Cyclohexenen-1-one and thiophenol were purchased from Aldrich, nitromethane and 1-propanethiol from Merck, acetylacetone from Sigma, and diethyl malonate and nitroethane from Carlo Erba. The reagents were used as received. Reaction products were purified by radial chromatography in a Harrison Research Chromatotron. High-resolution gas chromatograph (HRGC) analyses were performed on a HP-5890-II gas chromatograph with FID by using a 30 m (length), 0.25 mm (i.d.), and 0.5 μm (phase thickness) RTX-5 silica capillary column; H_2 as gas carrier; and flow division of 1/20. NMR analyses were performed on a Brucker (300 or 200 MHz) in $CDCl_3$ solution with TMS as internal pattern. The FT-IR spectra were recorded on a Nicolet Magna-IR-FT (NaCl film).

Typical procedure

To 5 mmol of the nucleophile was added to a 10 mL of 0.5 M aqueous NaOH solution. Soon after, 5 mmol of 2-cyclohexenen-1-one were added. The reaction mixture was then stirred vigorously for the time indicated in the Table 1. Then the reaction mixture was neutralized with concentrated hydrochloric acid and extracted with chloroform. The organic extract was dried (anhydrous Na_2SO_4), and the solvent was evaporated under reduced pressure.

Products analysis

*3-Nitromethyl-1-cyclohexanone (**2a**)*: IR ν: 1713, 1551, 1384 cm^{-1}; ^{13}C NMR (75 MHz, $CDCl_3$) δ: 24.4, 29.6, 37.4, 41.0, 44.6, 80.2, 208.4; t_R = 6.3 min (column temperature: 50°C (2 min) to 280°C (min) (25°C/min); injector temperature: 200°C; detector temperature: 300°C); R_f = 0.27 (hexane:ethyl acetate 1:1).

*3-(1-Nitroethyl)-1-cyclohexanone – diastereomeric mixture (**2b**)*: ^1H NMR (300 MHz, $CDCl_3$) δ: 1.54 (m, 4H), 1.68 (m, 1H), 1.93 (m, 1H), 2.14 (m, 2H), 2.30 (m, 2H), 2.40 (m,

© 1999 NRC Canada

2H), 4.51 (m, 1H); ^{13}C NMR (75 MHz, $CDCl_3$) δ: 16.3, 16.4, 24.3, 24.5, 24.9, 27.0, 27.3, 27.6, 29.8, 41.0, 42.3, 42.4, 42.6, 43.3, 43.8, 50.9, 87.0, 87.1, 208.7, 208.9; t_R = 6.5; 6.7 min (column temperature: 50°C (2 min) to 280°C (1 min) (25°C/min); injector temperature: 200°C; detector temperature: 300°C); R_f = 0.28 (hexane:ethyl acetate 1:1).

*Diethyl 2-(3-oxocyclohexyl)malonate (**2c**)*: ^{13}C NMR (75 MHz, $CDCl_3$) δ: 14.1, 24.6, 28.8, 38.0, 41.0, 45.1, 56.9, 61.6, 167.9, 167.8, 209.7; t_R = 7.1 min (column temperature: 50°C (2 min) to 280°C (1 min) (30°C/min); injector temperature: 200°C; detector temperature: 300°C); R_f = 0.28 (hexane:ethyl acetate 1:1).

*3-(3-Oxocyclohexyl)-2,4-pentanedione (**2d**)*: IR ν: 3512, 3406, 1697 cm^{-1}; ^{13}C NMR (75 MHz, $CDCl_3$) δ: 24.5, 28.8, 29.7, 29.8, 38.4, 41.1, 45.2, 74.7, 202.8, 202.9, 209.2; t_R = 7.1 min (column temperature: 70°C (2 min) to 280°C (1 min) (25°C/min); injector temperature: 200°C; detector temperature: 300°C); R_f = 0.33 (hexane:ethyl acetate 1:1).

3-n-*Propylthio-1-cyclohexanone (**2e**)*: IR ν: 1713 cm^{-1}; ^{1}H NMR (300 MHz, $CDCl_3$) δ: 1.00 (t, 3H, J = 7.28), 1.60 (sextet, 2H, J = 7.28), 1.70 (m, 2H), 2.15 (m, 2H), 2.30 (m, 2H), 2.40 (d, 1H, J = 10.57), 2.53 (t, 2H, J = 7.28), 2.70 (dd, 1H, J = 10.57, J = 4.38), 3.05 (m, 1H); ^{13}C NMR (75 MHz, $CDCl_3$) δ: 13.6, 23.1, 24.3, 31.7, 32.6, 41.0, 42.8, 48.3, 209.0; t_R = 11.5 min (column temperature: 50°C (5 min) to 280°C (5 min) (25°C/min); injector temperature: 200°C; detector temperature: 300°C); R_f = 0.5 (hexane:ethyl acetate 3:1).

*3-Thiophenyl-1-cyclohexanone (**2f**)*: *IR* ν: 1712, 749, 693 cm^{-1}; ^{1}H NMR (200 MHz, $CDCl_3$) δ: 1.75 (m, 2H), 2.10 (m, 2H), 2.35 (m, 2H), 2.40 (d, 1H, J = 10.88), 2.70 (dd, 1H, J = 10.88, J = 4.41), 3.45 (m, 1H), 7.25 (m, 3H), 7.45 (m, 2H); ^{13}C NMR (75 MHz, $CDCl_3$) δ: 24.2, 31.4, 41.0, 47.9, 127.9, 129.2, 133.1, 133.4, 208.9; t_R = 11.5 min (column temperature: 70–280°C (2 min) (20°C/min); injector temperature: 220°C; detector temperature: 280°C); R_f = 0.43 (chloroform).

Results

In our experiments, we studied in aqueous media the Michael addition of dicarbonyl compounds, nitro compounds, and thiols to 2-cyclohexenen-1-one, without a phase transfer agent. As we know that in nucleophilic reactions in water one of the main problems is related to the competition with the hydrolysis process of the electrophile (3), we studied the reaction under three different conditions, where the main variant is the pH of the reaction media. The reaction was catalyzed by NaOH (pH 14), Na_2CO_3 (pH 10), or $NaHCO_3$ (pH 7.5). Yields of purified products obtained are reported in Table 1.

For the reactions of the dicarbonyl compounds, diethyl malonate, and acetylacetone, the best yields were reached in pH 10, leading to 30 and 35% yields, respectively.

In the case of the nitro compounds, the Michael addition of nitromethane leads to the product **2a** with 65% yield when the pH is 14. On the other hand, nitroethane leads to several products in this reaction condition. However, 1,4-addition products of the nitroethane to the 2-cyclohexenen-1-one can be obtained in pH 7.5 or 10 in 25 and 20% yields, respectively.

The tested thiols were 1-propanethiol and thiophenol. The best pH for the reaction is 7.5, leading to 70 and 95% yields, respectively.

Discussion

We verified that the Michael addition of dicarbonyl compounds, nitroalkanes, and thiols to the 2-cyclohexen-1-one can be carried in water without phase transfer agent. The reaction is sensitive to the pH of the reaction media, and therefore, the methodology can be optimized with this variable control. The best pH depends on the nucleophile used.

An important study for the understanding of the influence of pH in nucleophilic reactions is reported by King et al. (3), where it is shown that several nucleophilic reactions can be optimized with the pH control according to the equation: $pH_{max} = 1/2[\log (k_w/k_{OH}) + pK_w + pK_a]$, where k_w and k_{OH} are the hydrolysis rate of eletrophile promoted by the water and hydroxide, respectively, K_w is the autoprotolysis constant of water, and K_a is the acid dissociation constant of the nucleophile. However, this relationship has only been established in dilute solutions (10^{-4}–10^{-5} M).

As our work involves heterogeneous solutions, this equation does not apply to our system. This can be seen by comparison of the reactions of 1-propanethiol and nitromethane with 2-cyclohexen-1-one. In spite of using the same eletrophile and nucleophiles of similar pK_a, the best pH are very different.

In our opinion, the studied system is very complex. Several parallel reaction paths can occur depending on the nucleophile, the electrophile, and the used reaction media. The reaction can occur in solution where, probably, the hydrophobic effect will have an important weight, or in the interface of the aqueous solution with the organic reagents; besides, in some cases, retro-Michael is a possibility. For the mechanistic study, the dilute system seems to be less complex, since it is ideal solutions, presenting therefore fewer variables. However, in synthetic terms, the reaction in a heterogeneous media, even if it is of difficult understanding, it is more appropriate since it facilitates the scale-up because that would not have problems with a bigger reaction volume.

Conclusions

We believe that the present work contributes to the field of organic reactions in aqueous solution, demonstrating that Michael addition can be made in this solvent without phase transfer agents. The advantage of not using phase transfer agents is the emulsion absence in the extraction process. This simple fact is of extreme importance in wide scale (industrial production), reducing production costs and environmental pollution.

Acknowledgements

We are grateful to Conselho Nacional de Desenvolvimento Científico e Tecnológico for a fellowship to F.M.S. and

© 1999 NRC Canada

Fundação José Bonifácio for additional financial support of this work.

References

1. A.K. Gomes, F.M. da Silva, J. Jones, Jr. 21st Meeting of the Brazilian Chemical Society, Minas Gerais, Brazil, May 1998.
2. A. Lubineau and J. Augé. Synthesis, 741 (1994).
3. J.F. King, R. Rathore, J.Y.L. Lam, Z.R. Guo, and D.F. Klassen. J. Am. Chem. Soc. **114**, 3028 (1992).
4. S.W. Benson and E.D. Siebert. J. Am. Chem. Soc. **114**, 4269 (1992).
5. D.C. Rideout and R. Brelow. J. Am. Chem. Soc. **102**, 7816 (1980).
6. R. Breslow. Acc. Chem. Res. **24**,159 (1991).
7. G. Jenner. Tetrahedron Lett. **35**, 1189 (1994).
8. A. Lubineau and J. Augé. Tetrahedron Lett. **32**, 7529 (1991).
9. P.A. Grieco and S.D. Larsen. J. Org. Chem. **51**, 3553 (1986).
10. Y. Inoue, K. Araki, and S. Shiraishi. Bull. Chem. Soc. Jpn. **64**, 3079 (1991).
11. P.A. Grieco, E.B. Brandes, S. McCann, and J.D. Clark. J. Org. Chem. **54**, 5849 (1989).
12. R. Ballini and G. Bosica. J. Org. Chem. **62**, 425 (1997).
13. E. Keller and B.L. Feringa. Tetrahedron Lett. **37**, 1879 (1996).
14. E. Keller and B.L. Feringa. Synlett, 842 (1997).
15. R. Ballini and G. Bosica, Tetrahedron Lett, **37**, 8027 (1996).
16. A. Lubineau and J. Augé, Tetrahedron Lett. **33**, 8073 (1992).
17. C. Larpent and H. Pantin, Tetrahedron, **44**, 6107 (1988).
18. C. Larpent, G. Meignan, and Henri Pantin. Tetrahedron, **46**, 6381 (1990).
19. C.K. Heo and J.W. Bunting. J. Org. Chem. **57**, 3570 (1992).
20. C. Petrier, C. Dupuy, and J.L. Luche. Tetrahedron Lett. **27**, 3149 (1986).
21. J.L. Luche, C. Allavena, C. Petrier, and C. Dupuy. Tetrahedron Lett. **29**, 5373 (1988).
22. J.L. Luche and C. Allavena. Tetrahedron Lett. **29**, 5369 (1988).
23. C. Dupuy, C. Petrier, L.A. Sarandeses, and J.L. Luche. Synth. Commun. **21**, 643 (1991).
24. C.-J. Li. Tetrahedron, **52**, 5643 (1996).
25. C. Petrier, J. Einhorn, and J.L. Luche. Tetrahedron Lett. **26**, 1449 (1985).
26. S.R. Wilson and M.E. Guazzaroni. J. Org. Chem. **54**, 3087 (1989).
27. J.-y. Zhou, G.-di Lu, and S.-hui Wu. Synth. Commun. **22**, 481 (1992).
28. C.-J. Li and Y.-Q. Lu. Tetrahedron Lett. **36**, 2721 (1995).
29. C.-J. Li. Tetrahedron Lett. **36**, 517 (1995).
30. F. Rúbsam, S. Seck, and A. Giannis. Tetrahedron, **53**, 2823 (1997).
31. C.-J. Li and W.-C. Zhang. J. Am. Chem. Soc. **120**, 9102 (1998).
32. B. Kuhlmann, E.M. Arnett, and M. Siskin. J. Org. Chem. **59**, 3098 (1994).
33. A.R. Katritzky and S.M. Allin. Acc. Chem. Res. **29**, 399 (1996).
34. F. Fringuelli F. Pizzo, and R. Germani. Synlett, 475 (1991).
35. F. Fringuelli, R. Germani, F. Pizzo, F. Santinelli, and G. Savelli. J. Org. Chem. **57**, 1198 (1992).
36. C. Petrier and J.L. Luche. Tetrahedron Lett. **28**, 2351 (1987).
37. V. Ramamurthy. Tetrahedron, **42**, 5753 (1986).
38. A. Michael. J. Prakt. Chem. **35**, 349 (1887).
39. H. Feuer. *In* The chemistry of functional groups: the chemistry of the nitro and nitroso groups. *Edited by* S. Patai. Interscience Publishers, New York, London, Sydney, and Toronto. 1969. p. 366.
40. J. March. Advanced organic chemistry. Reactions, mechanisms, and structure. Wiley–Interscience Publication, New York, Chichester, Brisbane, Toronto, and Singapore. 1992. p. 251.
41. S. Patai. *In* The chemistry of functional groups: the chemistry of thiol groups. *Edited by* S. Patai. Interscience Publishers, New York, London, Sydney, and Toronto. 1974. p. 398.
42. G.H. Whitham. Organosulfur chemistry. Oxford Chemistry Primers, New York and Tokyo. 1995. p. 5.

© 1999 NRC Canada

Regioselective protonation of ferrocene in superacid and formation of a C—H—Fe bond. An experimental and theoretical study of the structure and dynamics of the ferrocenonium ion

Annika Karlsson, Anders Broo, and Per Ahlberg

Abstract: Protonation of ferrocene has been suggested to take place on carbon (*exo*-protonation) or iron (*endo*-protonation). However, experiments have not been conclusive because of interfering exchange reactions. Now low-temperature protonation of ferrocene and [$^2H_{10}$]-ferrocene in superacid and direct observation of the carbocation by ^1H NMR at low temperature shows only primary protonation and that it exclusively takes place in an *endo*-fashion. Studies by DFT calculations using B3LYP hybrid functional indicate the presence of an intramolecular nonlinear C—H—Fe bond and that the proton might be delocalized between carbon and iron. Potential energy barriers for degenerate rearrangements of the hydride bridged carbocation are low, suggesting that the proton might be delocalized between all 10 carbons and iron. The NMR results are consistent with such an interpretation.

Key words: regioselective, protonation, superacid, ferrocenonium ion.

Résumé : Il a été suggéré que la protonation du ferrocène puisse se faire sur le carbone (protonation-*exo*) ou sur le fer (protonation-*endo*). Toutefois, les expériences ne permettaient pas de tirer des conclusions à cause de réactions d'échange qui causaient des interférences. Il est maintenant possible d'opérer à basse température, dans un superacide, pour effectuer la protonation du ferrocène et du [$^2H_{10}$]-ferrocène; la RMN du ^1H à basse température permet d'observer le carbocation directement et de montrer que la protonation primaire se fait exclusivement de façon *endo*. Des calculs « DFT » à l'aide d'une fonction hybride B3LYP montrent qu'il existe une liaison intramoléculaire non linéaire C—H—Fe et que le proton pourrait être délocalisé entre le carbone et le fer. Les barrières d'énergie de potentiel pour les réarrangements dégénérés du carbocation ponté par un hydrure sont faibles; ceci suggère que le proton puisse être délocalisé entre les dix atomes de carbone et le fer. Les résultats de la RMN sont en accord avec une telle interprétation.

Mots clés : régiosélectif, protonation, superacide, ion ferrocénonium.

[Traduit par la Rédaction]

Introduction

Low-temperature protonation of ferrocene (**1**) and [$^2H_{10}$]-ferrocene ([$^2H_{10}$]-**1**) in superacid and direct observation of the carbocations formed by ^1H NMR at low temperature show that primary protonation in an *endo*-fashion exclusively takes place. Density functional theory (DFT) calculations using the B3LYP functional indicate that the proton is in a novel type of bond — an intramolecular nonlinear C—H—Fe bond.

The protonation and, more generally, the electrophilic substitution of the iron group metallocenes has been investigated many times. A focus has been the primary step in this reaction and whether or not the electrophile would first coordinate to the metal (*endo*-path in Fig. 1) or attach itself to one of the rings (*exo*-path in Fig. 1)(1).

Recent publications have adressed the protonation of **1** from the experimental and theoretical side (1*n*–*p*). These latest results again do not agree on the pathway. In this report, we present our results of a combined experimental and theoretical investigation that show that in superacid the primary process is exclusively *endo*-protonation and reveals the structure and dynamics of the protonated species, i.e., the ferrocenonium ion (**2**) which contains a C—H—Fe bond.

Received November 4, 1998.

This paper is dedicated to Jerry Kresge in recognition of his many achievements in chemistry.

A. Karlsson and P. Ahlberg.[1] Department of Chemistry, Göteborg University, S-412 96 Göteborg, Sweden.
A. Broo. Department of Physical Chemistry, Chalmers University of Technology, S-412 96 Göteborg, Sweden.

[1]Author to whom correspondence may be addressed. Telephone: 4631-772-2899. Fax: 4631-772-2908.
e-mail: Per.Ahlberg@oc.chalmers.se

© 1999 NRC Canada

Fig. 1. The *endo*- and *exo*-pathways for electrophilic substitution of ferrocene (**1**).

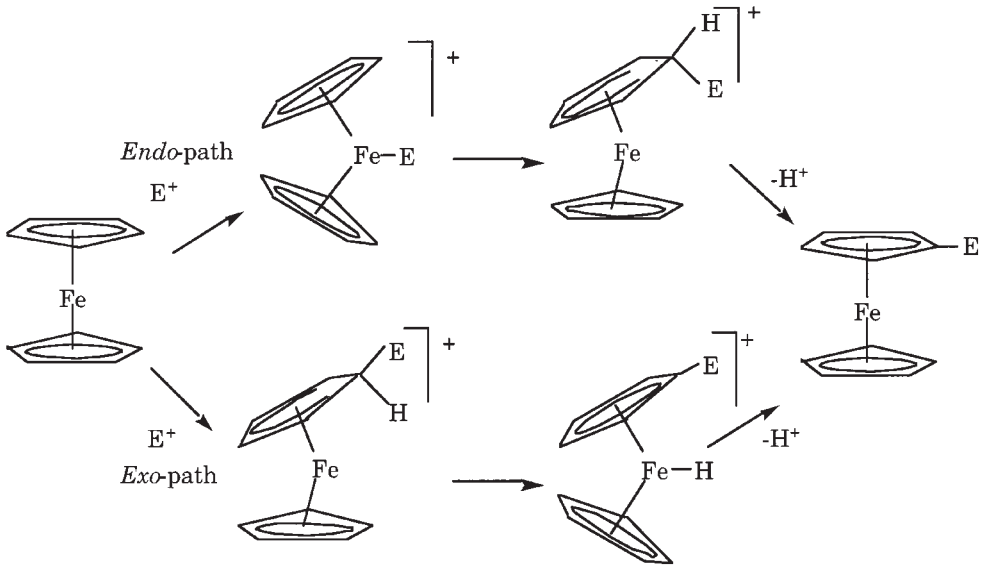

Fig. 2. (*a*) ^{1}H NMR spectrum at –122°C of ion **2** obtained by protonation of **1** in HSO_3F:SO_2ClF (1:10, v:v) at –125°C. (*b*) ^{1}H NMR spectrum at –109°C of deuterium labelled ion **2** obtained by protonation of [$^2H_{10}$-**1**] in HSO_3F:SO_2ClF:SO_2F_2 (1:6:1, v:v:v) at –115°C, showing that no protons have substituted ring-deuterons, i.e., that the protonation exclusively takes place in an *endo*-fashion. Chemical shifts are referenced to $CHDCl_2$ δ 5.32.

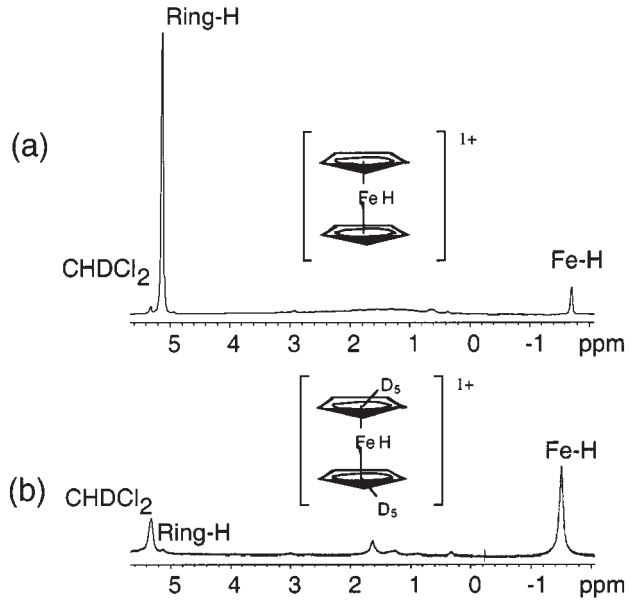

Previously, monoacylferrocenes have been protonated in superacid, yielding carbonyl oxygen protonation (2). Upon increasing the acidity of the superacid, both carbonyl oxygen and iron protonation have been reported to take place (3). However, there is no report on superacid protonation of the parent ferrocene **1** — an easily oxidized compound.

Results and discussion

Protonations of **1** and [$^2H_{10}$]-**1** in superacid were performed directly in NMR tubes using a special ion generation technique (4). A degassed solution of compound **1** (5 mg in 150 μL CD_2Cl_2) was mixed into a 0.5 mL degassed superacid solution with the composition HSO_3F:SO_2ClF (1:10, v:v) at –125°C, yielding a blue–green solution of ion **2** (0.025 M). The NMR tube was sealed and stored in liquid N_2 before spectroscopic investigation. The ^{1}H NMR spectrum of ion **2** at –122°C is shown in Fig. 2*a*.

The two singletts at δ 5.12 and δ –1.67 with the relative intensity 10:1 were assigned using ^{1}H,^{1}H NOESY to the ring C-H protons and the Fe-H proton, respectively. No spin–spin coupling between the ring hydrogens and Fe-H were resolved. That only two singletts were observed indicate that the ferrocenonium ion undergoes extensive fast degenerate rearrangements. The ^{1}H decoupled ^{13}C NMR spectrum showed only one signal at δ 77.82 ($CHDCl_2$ δ 54.00) ascribed to the ring carbons.

There are a number of previous reports on NMR studies of the ferrocenonium ion (**2**) in H_2O saturated with BF_3 (1). Compound **1** has been dissolved in H_2OBF_3 under anaerobic conditions. The ^{1}H NMR chemical shifts for ion **2** were similar to those obtained in superacid, i.e., δ 5.06 and δ –1.88 (relative to the acid peak set to δ 8.30) (1*p*).

When similarly compound **1** was dissolved in D_2O saturated with BF_3 and studied by NMR, it was found that the ferrocenonium ion formed contained essentially no protium. All protons had been exchanged for deuteriums. From this result it was concluded that ion **2** is formed by *exo*-protonation rather than *endo*-protonation. From the reaction mixture, compound [$^2H_{10}$]-**1** has been isolated (1*p*).

Compound [$^2H_{10}$]-**1** has been used in this work as a precursor for the preparation of deuterium labelled **2** in superacid. A degassed solution of compound [$^2H_{10}$]-**1** (5 mg in 150 μL CD_2Cl_2) was mixed into a 0.5 mL degassed superacid solution with the composition HSO_3F:SO_2ClF:SO_2F_2 (1:6:1, v:v:v) at –115°C, yielding a blue–green solution of deuterium labelled ion **2** (0.025 M). The NMR tube was sealed, and the ^{1}H NMR spectrum shown in Fig. 2*b* was obtained at –109°C. The singlett at δ –1.51 was ascribed to the Fe-H protons. Only traces (0.1 atom% ^{1}H) of ring hydrogens at δ 5.11

© 1999 NRC Canada

were observed. These results clearly show that the primary protonation is not *exo*-protonation, since such a protonation in Fig. 1 should have given a one proton signal at about δ 5.11 and no ^1H signal at δ –1.51 because in this mechanism deuterium ends up on iron. Rather, the results show that the protonation is highly regioselective in an exclusive *endo*-fashion, i.e., the protonation occurs directly on iron or *endo* on carbon.

Interestingly, the results in superacid also show that no $^1H/^2H$ exchange of the ferrocenonium ion takes place under these conditions. Obviously, the conjugate base of the superacid is too weak to yield reversible protonation. Thus, this irreversible protonation allowed for the resolution of the primary protonation step.

The previously reported extensive ring proton exchange observed in D_2OBF_3, which formed the basis for the conclusion that the primary protonation is *exo*-protonation, is presumably caused by reversible hydronation of compound **1**. The conjugate base of D_2OBF_3 is much stronger than the corresponding one for a superacid. As a consequence, D_2OBF_3 therefore yields protonation which is less complete and reversible. This makes it possible for a slower reaction with the *exo*-protonation mechanism to operate in combination with the faster reaction with the reversible *endo*-protonation mechanism, resulting in extensive exchange of the ring protons for deuteriums.

The "hydridic" shift of the *endo*-proton in the ferrocenonium ion has been assumed to indicate that the proton is bonded to iron (Fe-H) rather than to carbon (C-H). However, Mueller-Westerhoff et al. (1*p*) have recently resolved coupling between the *endo*-proton and all 10 ring protons. Furthermore, their results indicate the presence of an iron–proton coupling. These results have been interpreted as being due to the presence of both carbon protonated ferrocenonium ions and iron protonated ferrocenonium ions that are in rapid equilibrium with each other.

Computations

With the aim to further clarify the nature of **2**, we have carried out extensive calculations using density functional theory (DFT) with the B3LYP hybrid functional (5, 6). All DFT calculations were done with the Gaussian 94 program (7). The build in basis sets 6-311G(f), 6-311G(f,d,p), and 6-31G were used. Broo[2] has recently shown that at the B3LYP/6-311G(f), 6-31G level of theory the observed gas phase geometry of ferrocene is reproduced with high accuracy. The rather small basis set (6-31G) used for the ligands were demanded by the large computational cost to use a larger basis set in the geometry determination. Only minor changes in the geometrical parameters were found when the 6-311G(f,d) basis set were use for compound **1**. All molecules were fully optimized in the given point group. Recently, McKee (1*o*) has studied the energetics of the protonation reaction and the geometry of protonated ferrocene at the Hartree–Fock (HF) and second-order perturbation theory (MP2) level. Neither of these methods yields a reasonable geometry for **1**, as has been shown by several authors (8), as opposed to DFT calculations that reproduce the observed ferrocene geometry very well.[2] Consequently, the geometries reported by McKee differ much from the B3LYP/6-311G(f),6-31G geometries shown in Fig. 3.

Thus, it has been possible to locate the potential energy minima for both carbon protonated and iron protonated **1**, i.e., **3** and **4**, respectively (Fig. 3).

Structure **3** is 12 kJ mol^{-1} more stable than **4**. In **3** the protonated carbon is close to be sp^3 hybridized. The *endo*-C—H bond distance is 1.19 Å, and the corresponding *exo*-bond distance is 1.09 Å, i.e., 0.1 Å shorter. The *endo*-H—Fe distance is 1.785 Å.

In the iron protonated structure **4**, which has C_{2v} symmetry, the *endo*-H—Fe bond distance is 1.486 Å, and the *endo*-H—C proton distance to the nearest ring carbons is 1.891 Å. The ring-C-H bonds are 7° out of the plane made up of the ring carbons, i.e., the hydrogen-bonded carbons are slightly rehybridized towards sp^3.

These data clearly show that in both structure **3** and **4** the *endo*-proton participates in nonlinear bonds, i.e., C-H···Fe (agostic interaction (9) and C···H-Fe bonds, respectively. Formally, these bonds are hydride bridges. In the rearrangement of **3** to **4** the *endo*-H—C bond length increases by 0.701 Å and the H—Fe distance decreases 0.299 Å. The rearrangement is also accompanied by other structural changes than rehybridization, e.g., bond distances in the rings changes. The potential energy maximum on the reaction coordinate for the isomerization of **3** to **4** is only 13.6 and 1.7 kJ mol^{-1} above the minima for **3** and **4**, respectively. The structure (**5**) corresponding to the maximum is shown in Fig. 3*c*. In **5** the Fe—H bond is bent towards the hydride accepting ring carbon and slightly elongated to 1.498 Å. The *endo*-C—H bond distance is shorter than in **4** by 0.2 Å. The low barrier (1.7 kJ mol^{-1}) for the transfer of the hydride beween iron and carbon suggests that the first vibrational level may be in the vicinity of the potential energy maximum for the proton transfer, i.e., that the hydride might be delocalized between carbon and iron.

Other possible low-barrier processes in the ferrocenonium ion (**2**) have also been identified. The rotation of the non-hydride bridged ring relative to the hydrogen-bonded one reveals a shallow potential energy surface. The highest barrier is only 0.45 kJ mol^{-1}. Rotation of the Fe—H bond relative to the rings in **4** yields a barrier of 17.2 kJ mol^{-1}, and this barrier gives an indication that the Fe-H···C bond in **4** is quite strong. A lower barrier (3.1 kJ mol^{-1}) is obtained for the process in which one of the rings in **4** rotates relative to the Fe—H and the other hydrogen-bonded ring which are kept fixed.

Thus, our combined computational results indicate that the *endo*-proton, which is imbedded in the electron cloud from iron and the rings, might be delocalized between iron and all 10 carbons.

The ^1H chemical shifts for the ferrocenonium ions **3** and **4** and the reference CH_2Cl_2 have been calculated using the GIAO method (10). The 6-311G(f,d,p) basis set was used in the B3LYP-GIAO calculations. As a further test of the basis set dependency, the relatively large cc-pVTZ basis set were used on the carbon and hydrogen atoms. Only minor change of the relative shift was found with the larger basis set. To

[2] A. Broo. Submitted to J. Am. Chem. Soc.

© 1999 NRC Canada

Fig. 3. Calculated structures for carbon protonated **2**, i.e., **3** (*a*), iron protonated **2**, i.e., **4** (*b*), and for the transition state for the interconversion of the intramolecularly nonlinear hydrogen-bonded species **3** and **4**, i.e., **5** (*c*). Bond distances, selected bond angles, ^{1}H NMR, and ^{13}C NMR chemical shifts (in parentheses) are shown.

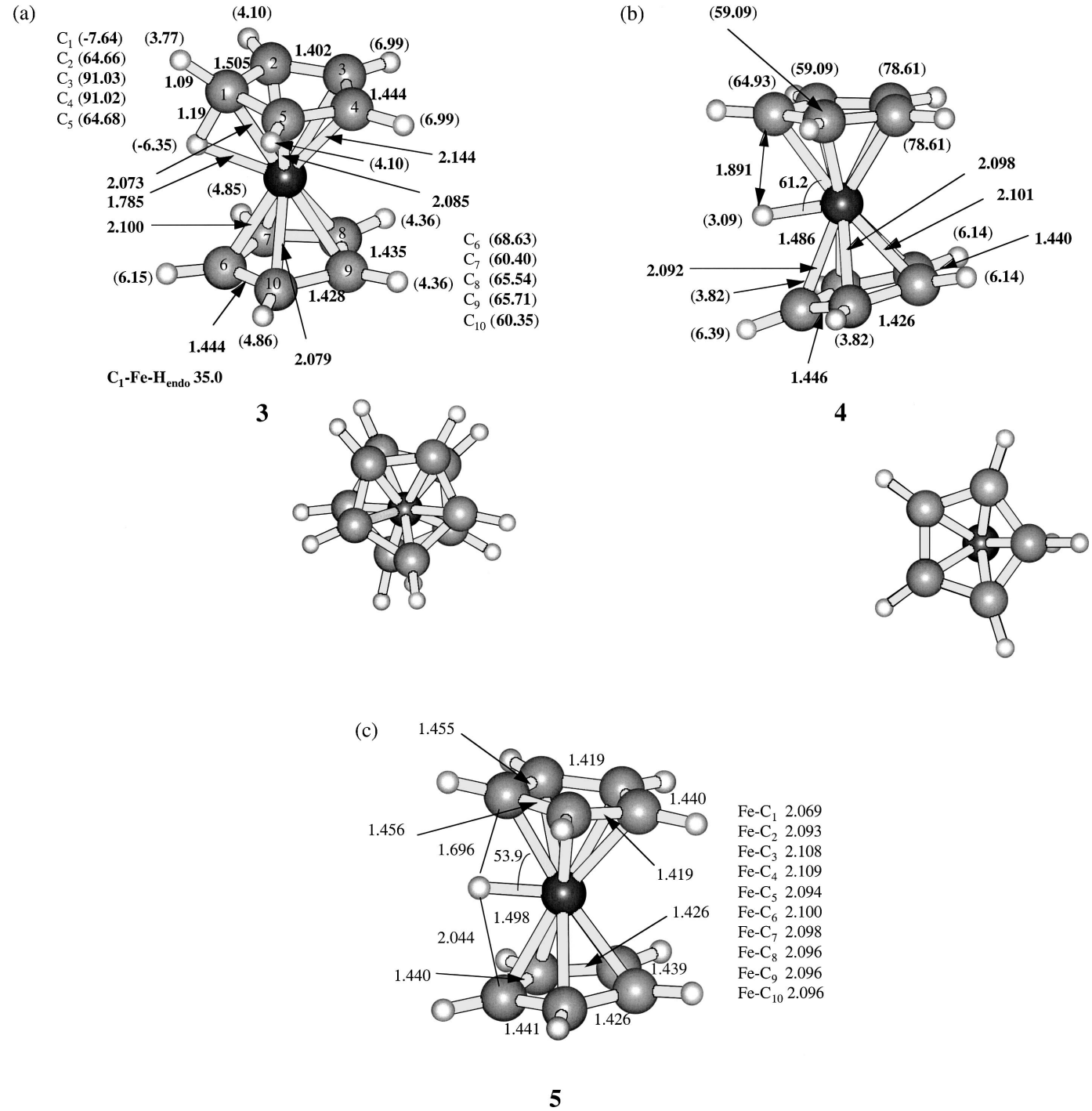

our surprise, it was the *endo*-proton in the carbon protonated species **3** rather than the proton in the iron protonated species **4** that showed a "hydrid" shift. The estimated *endo*-proton chemical shifts were δ –6.35 for **3** and δ 3.09 for **4**. The average value of the two shifts is –1.63, which is close to the observed value –1.67. The calculated average shift for the 10 ring protons (which show large shift variations) in **3** and **4** are similar, and the average of the averages is 5.16, which is close to the observed value 5.12.

At the B3LYP/6-311G(f),6-31G level of theory the calculated Mulliken group charges for the carbon protonated species **3** are for Fe 0.99, for the protonated cyclopentadienyl ligand 0.10, and for the cyclopentadienyl ligand –0.09. The *endo*-hydrogen in **3** has a charge of 0.10 and the *exo*-one

© 1999 NRC Canada

0.16, leaving the rest of the protonated cyclopentadienyl unit with a charge of –0.16, i.e., with a charge somewhat more negative than the other iron–ligand.

The iron-protonated species **4** has the following calculated group charges: Fe 0.69, each of the cyclopentadienyl rings 0.125, and the iron-bonded hydrogen 0.06.

Thus, the rearrangement from **3** to **4** results in charge redistribution. The iron charge becomes less positive by 0.3 units of charge, and the ligands (excluding the *endo*-hydrogen) become more positive by 0.34 charge units. The *endo*-hydrogen changes its charge from 0.10 to 0.06.

Experimental and computational section

Preparation of $[^2H_{10}]$-ferrocene ($[^2H_{10}]$-1)

A modified procedure described by Mueller-Westerhoff et al. (1*p*) was used to prepare $[^2H_{10}]$-**1**.

D_2OBF_3 was prepared from boron trifluoride and deuteriumoxide using an earlier described procedure (1*p*). Deuteriumoxide (5 mL, Glaser, >99.80 atom% D) was boiled in a flask while a stream of nitrogen was passed through the liquid for 1.5 h. The flask was then placed in an ice–methanol bath, and BF_3 gas (AGA gas, >99.994 vol.%) was bubbled through the liquid until saturation. The temperature was kept at ca. 0°C. The solution was used immediately after preparation.

Ferrocene (Aldrich, 98%, 206 mg, 1.1 mmol) was sublimated at 10^{-1} mbar (1 bar = 100 kPa) at 70°C. Under nitrogen, ferrocene was added into freshly prepared D_2OBF_3 (5 mL). The reaction mixture turned yellow–brown and was stirred for 40 min. Then, deuteriumoxide 50 mL was added and the mixture was stirred for another 15 min. The solution was then extracted with 10 × 25 mL methylene chloride. The methylene chloride phases were washed with water, dried over $MgSO_4$, and evaporated. To increase the deuterium content in $[^2H_{10}]$-ferrocene, the above procedure was repeated with the modification of a longer reaction time (2 h 20 min) The ^1H NMR spectrum in $CDCl_3$ with the internal reference CH_2Cl_2 at 19°C showed only traces of hydrogen (0.1% H) at 4.18 ppm.

Protonation of ferrocene (1) and $[^2H_{10}]$-1

To avoid oxidation side reactions, the reactions with the superacid have been conducted in an inert atmosphere and at low temperatures. The ions were generally prepared directly in 5 mm NMR tubes (Wilmad 503-PS) using a special ion generation technique (4). Typically, degassed solutions of (ca. 5 mg in ca. 150 μL CD_2Cl_2) were mixed into ca. 0.5 mL degassed superacid (HSO_3F:SO_2ClF, 1:10 v/v or HSO_3F:SO_2ClF:SO_2F_2, 1:6:1, v/v/v) at ca. –120°C, yielding ionic solutions ca. 0.025 M in ion. The CD_2Cl_2 used was from Cambridge isotope laboratories (>99.9% D), HSO_3F from Aldrich and SO_2F_2 from Matheson Gas Products, respectively. The SO_2ClF was freshly prepared from SO_2Cl_2 and NH_4F using an earlier described procedure.[3]

NMR spectroscopy

The spectra were recorded using a Varian Unity 500 instrument operating at 499.92 MHz and equipped with a 5 mm variable temperature ID500-5 indirect detection probe from Nalorac. ^1H chemical shifts were referenced to $CHDCl_2$ (δ 5.32). The spectra were obtained at ca. –120°C. One-dimensional ^1H spectra and ^{13}C spectra were recorded with standard parameters.

Computational methods and procedures

All calculations were done using density functional theory (DFT) with the Becke three-parameter hybrid functional with the Lee et al. (5) correlation functional, known as the B3LYP method (6). All the DFT calculations were done with the Gaussian 94 program (7). The build-in basis sets 6-311G(f), 6-311G(f,d,p), and 6-31G were used in this investigation. The 6-311G basis set generated the following contracted basis functions: Fe: [9s, 5p, 3d], C: [4s, 3p], and H: [3s]. The f, d, and p letters denotes additional polarization functions of the f-type for Fe, of d-type for C, and of p-type for hydrogen. In a recent work, Broo[2] showed that at the B3LYP/6-311G(f),6-31G level of theory the observed gas phase geometry of ferrocene and the crystallographic geometry of ferrocenophane were reproduced with high accuracy. The rather small basis set (6-31G) used for the ligands were demanded by the large computational cost to use a larger basis set in the geometry determination. Only minor changes in the geometrical parameters were found when the 6-311G(f,d) basis set were used for ferrocene.[2] All the molecules in this work were fully optimized in the given point group. All stationary points were verified by diagonalizing the Hess matrix. For the reported equilibrium geometries no negative eigenvalues were found. The reported transition states have one negative eigenvalue.

The chemical shift calculations were done with the GIAO method (10). The 6-311G(f,d,p) basis set was used in the B3LYP-GIAO calculations. All the shifts in Fig. 3 are relative to the experimental reference CH_2Cl_2 (^1H shift 5.32 ppm; ^{13}C shift 54.00 ppm). The geometry of reference compound CH_2Cl_2 was calculated at the B3LYP/6-31G and at the B3LYP/6-311G(d,p) levels of theory. The calculated shielding constants were C: 128.9536 and 111.1165 ppm and H: 27.7922 and 26.7781 ppm, respectively.

Acknowledgements

We are grateful for support from the Swedish Natural Science Research Council, the Center for Parallel Computers (PDC) at the Royal Institute of Technology, Stockholm, the Swedish Council for High Performance Computing (HPDR), and the Unix Numerically Intensive Center at Chalmers (UNICC).

References

1. (*a*) T. J. Curphy, J.O. Santer, M. Rosenblum, and J.H. Richards. J. Am. Chem. Soc. **82**, 5249 (1960); (*b*) M. Rosenblum, J.O. Santer, and W.G. Howells. J. Am. Chem. Soc. **85**, 1450 (1963); (*c*) B. Floris, G. Illuminati, and G. Ortaggi. Tetrahedron Lett. **4**, 269 (1972); (*d*) B. Floris, G. Illuminati, G. Ortaggi, and P.E. Jones. Coord. Chem. Rev. **8**, 39 (1972); (*e*) G. Cerichelli, G. Illuminati, G. Ortaggi, and A.M. Guiliani. J.

[3] J. Sommer. Personal communication.

© 1999 NRC Canada

Organomet. Chem. **127**, 357 (1977);, and refs. cited therein; (*f*) S.P. Gubin, S.A. Smiranova, L.I. Denisovich, and A.A. Lubovich. J. Organomet. Chem. **30**, 243 (1971); (*g*) T.E. Bitterwolf and A.C. Ling. J. Organomet. Chem. **57**, C15 (1973); (*h*) J. Organomet. Chem. **40**, 197 (1972); (*i*) J. Organomet. Chem. **141**, 355 (1977); (*j*) J. Organomet. Chem. **215**, 77 (1981); (*k*) T.E. Bitterwolf. Tetrahedron Lett. **22**, 2627 (1981); (*l*) C.A. Burton and W.E. Watts. J. Chem. Soc. Perkin Trans. 2, 1591 (1983); (*m*) W.E. Watts. *In* Comprehensive organometallic chemistry. *Edited by* G. Wilkinson, F.G.A. Stone, and E.N. Abel. Pergamon, New York. 1982; (*n*) A.F. Cunningham, Jr. J. Am. Chem. Soc. **113**, 4864 (1991); (*o*) M.L. McKee. J. Am. Chem. Soc. **115**, 2818 (1993); (*p*) U.T. Mueller-Westerhoff, T.J. Haas, G.F. Swiegers, and T.K. Leipert. J. Organomet. Chem. **472**, 229 (1994).

2. G.A. Olah and Y.K. Mo. J Organomet. Chem. **60**, 311 (1973).
3. P. Rimmelin, J. Sommer, J. Sandström, and J. Seita. J Organomet. Chem. **114**, 175 (1976).
4. C. Engdahl and P. Ahlberg. J. Am. Chem. Soc. **101**, 3940 (1979).
5. C. Lee, W. Yang, and R.G. Parr. Phys. Rev. **B37**, 785 (1988).
6. A.D. Becke. J. Chem. Phys. **98**, 1372 (1993); **98**, 5648 (1993).
7. M.J. Frisch, G.W. Trucks, H.B. Schlegel, P.M.W. Gill, B.G. Johnson, M.A. Robb, J.R. Cheeseman, T. Keith, G.A. Petersson, J.A. Montgomery, K. Raghavachari, M.A. Al-Laham, V.G. Zakrzewski, J.V. Ortiz, J.B. Foresman, C.Y. Peng, P.Y. Ayala, W. Chen, M.W. Wong, J.L. Andres, E.S. Replogle, R. Gomperts, R.L. Martin, D.J. Fox, J.S. Binkley, D.J. Defrees, J. Baker, J.P. Stewart, M. Head-Gordon, C. Gonzalez, and J.A. Pople. Gaussian 94. Gaussian Inc., Pittsburgh, Pa. 1995.
8. (*a*) H.P. Lüthi, J. Ammeter, J. Almlöf, and K. Korsell. Chem. Phys. Lett. **69**, 540 (1980); (*b*) H.P. Lüthi, J. Ammeter, J. Almlöf, and K. Faegri, Jr. J. Chem. Phys. **77**, 2002 (1982); (*c*) H.P. Lüthi, P.E.M. Siegbahn, J. Almlöf, K. Faegri, Jr., and A. Heiberg. Chem. Phys. Lett. **111**, 1 (1984).
9. (*a*) P. Muller (*Editor*). Glossary of terms used in physical organic chemistry. IUPAC commission on physical organic chemistry. Pure and Appl. Chem. **66**, 1077 (1994); (*b*) M. Brookhart and M.L.H. Green. J. Organomet. Chem. **250**, 395 (1983); (*c*) X.-L. Luo and R.H. Crabtree. J. Am. Chem. Soc. **111**, 2527 (1989).
10. (*a*) K. Wolinski, J.F. Hinton, and P. Pulay. J. Am. Chem. Soc. **112**, 8251 (1990); (*b*) R. Ditchfield. Mol. Phys. **27**, 789 (1974); (*c*) A. Bérces, T. Ziegler, and L. Fan. J. Phys. Chem. **98**, 1584 (1994).

© 1999 NRC Canada

Electronic effects on enol acidity and keto–enol equilibrium constants for ring-substituted 2-tetralones

Xudong Yao and Ralph M. Pollack

Abstract: Equilibrium constants for the ionization of a variety of phenyl-substituted 2-tetralones (pK_a^K), for the ionization of their enols (pK_a^E), and for keto–enol tautomerization (pK_E) were determined. Hammett plots of pK_a^K and pK_a^E vs. σ^- are linear with slopes ($-\rho$) of –1.66 ± 0.06 and –0.90 ± 0.03, respectively, except for deviations of the points corresponding to 6-nitro-2-tetralone (**1b**) and its enol. We have previously attributed the negative deviation of **1b** from the correlation for the acidities of the ketones obtained with the more limited set of data to the lack of a free electron pair on C-1 of the free tetralone (Nevy et al.). The negative deviation of the point for **1b** from the correlation for the acidities of the enols suggests that charge transfer from the hydroxyl group of the enol to the nitro group is less important than it is for phenols. This study represents the first systematic study of electronic effects on equilibria among ketone, enol, and enolate in aqueous solution.

Key words: enol, acidity, equilibrium, substituent, conjugation.

Résumé : On a déterminé les constantes d'équilibre pour l'ionisation d'un certain nombre de 2-tétralones substituées sur le noyau phényle (pK_a^K), pour l'ionisation de leurs énols (pK_a^E) et pour la tautomérisation cétoénolique (pK_E). Les courbes de Hammett pour les valeurs de pK_a^K et de pK_a^E en fonction de σ^- sont linéaires, avec des pentes ($-\rho$) respectives de –1,68 ± 0,06 et –0,90 ± 0,03 si l'on exclut les déviations du point correspondant à la 6-nitro-2-tétralone (**1b**) et son énol. En se basant sur une corrélation d'acidités de cétones obtenue avec un ensemble plus petit de données, on a antérieurement attribué la déviation négative de **1b** à l'absence d'une paire d'électrons libres en C-1 de la tétralone libre (Nevy et al.). La déviation négative du point pour **1b** pour les acidités des énols suggère que le transfert de charge à partir du groupe hydroxyle de l'énol vers le groupe nitro est beaucoup moins important que pour les phénols. Cette étude représente la première étude systématique d'effets électroniques sur l'équilibre entre une cétone, son énol et l'énolate en solution aqueuse.

Mots clés : énol, acidité, équilibre, substituant, conjugaison.

[Traduit par la Rédaction]

Introduction

The determination of equilibrium constants for the interconversion of aldehydes and ketones with their enols has been of interest since the early 1900s (1). Several methods have traditionally been used to detect enols in equilibrium with the corresponding carbonyl compounds, but these methods often gave conflicting results. In the early 1980s, Kresge and co-workers (2) and Capon et al. (3) sparked a resurgence in the area of enol chemistry by developing methods to generate enols in greater than equilibrium concentration. These kinetic approaches enabled the accurate measurement of keto–enol equilibrium constants for simple aldehydes and ketones, as well as rates of enolization and ketonization, and acidity constants for both the ketones and the enols. In parallel, Rappoport and co-workers investigated keto–enol equilibrium constants for sterically hindered aryl-substituted ketones, which produce enols that are kinetically and (or) thermodynamically stable relative to simple systems (4). Keto–enol equilibrium constants are now available for a variety of simple ketones, as well as for more complicated systems (1).

Studies of substituent effects on the keto–enol equilibrium have revealed several factors that govern these equilibria. For aryl aldehydes and ketones, the primary effect of the substituent on keto–enol tautomerization is on the stability of the ketone, rather than the enol (1). However, for α-aryl ketones, the effect of the aryl group on ketone stability is

Received September 30, 1998.

This paper is dedicated to Jerry Kresge in recognition of his many achievements in chemistry.

X. Yao and R.M. Pollack.[1] Laboratory for Chemical Dynamics and the Department of Chemistry and Biochemistry, University of Maryland, Baltimore County, 1000 Hilltop Circle, Baltimore, MD 21250, U.S.A., and the Center for Advanced Research in Biotechnology, 9600 Gudelsky Drive, Rockville, MD 20850, U.S.A.

[1]Author to whom correspondence may be addressed at the University of Maryland, Baltimore County. Telephone: (410) 455-2529. Fax: (410) 455-2608. e-mail: pollack@umbc.edu

 © 1999 NRC Canada

Scheme 1.

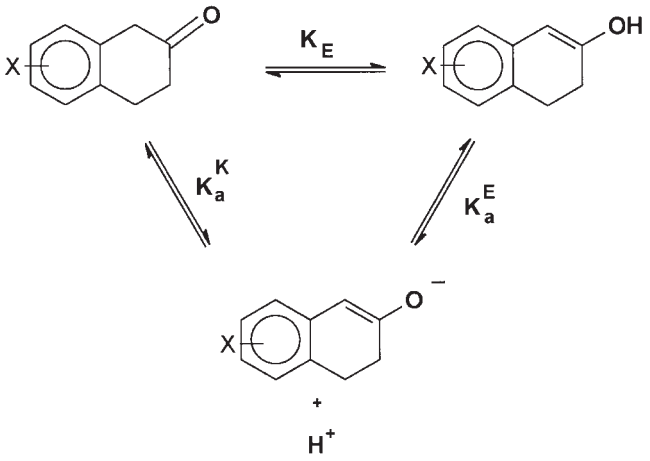

minimal (1), whereas enolization results in stabilization due to conjugation between the carbon–carbon double bond of the enol and the phenyl group. On the basis of the dependence of the enol content of ring-substituted 2-phenylpropionaldehydes in DMSO on σ^- (ρ = 0.72) (5), Toullec (1) suggested that the conjugation of the aryl ring with the double bond involves little π electron transfer (6). This conclusion is somewhat surprising considering the possibility of direct resonance interaction between the aryl ring and the hydroxyl group through the double bond. Rappoport, on the other hand, has interpreted the same data to suggest that there is "an important dipolar contribution to the enol ground state having a negative charge on the β-aryl group" (4*d*, 7). This system, however, is complicated by the potentially less than optimal coplanarity of the *p* orbitals of the phenyl ring with those of the double bond, which might cause a diminished interaction between the ring substituents and the OH group of the enol.

To isolate electronic effects on keto–enol equilibria and ionization of enols, we have examined the dependence of the equilibrium constants on substituent for substituted 2-tetralones (**1a**–**1j**) (Scheme 1). As a fused α-aryl ketone, 2-tetralone has no direct resonance between the phenyl ring and the carbonyl group, and therefore the electronic effect on the ketone stability is minimal. In addition, the carbon–carbon double bond and the phenyl ring of the enol should be almost coplanar (8), which allows maximal resonance and charge transfer. We report here the pK_a's of both the ketones (pK_a^K) and the enols (pK_a^E) of a variety of substituted 2-tetralones, from which the substituent effect on the keto–enol tautomerization can be derived. This study represents the first systematic study of electronic effects on equilibria among ketone, enol, and enolate in aqueous solution.

Experimental

Materials

Unless otherwise mentioned, all chemicals were reagent grade or better, purchased commercially and used without further purification. ^{1}H NMR spectra were recorded in $CDCl_3$ with TMS as an internal standard on a General Electric QE-300 spectrometer. Melting points were determined on a Mel-Temp apparatus and are uncorrected. 2-Tetralone (**1a**), 6-nitro-2-tetralone(**1b**), 6-methoxy-2-tetralone (**1d**), 7-nitro-2-tetralone (**1e**), 7-chloro-2-tetralone (**1f**), and 5,7-dinitro-2-tetralone (**1g**) were available from previous work (9). 6-Chloro-2-tetralone (**1c**) was synthesized as before, mp 67–68°C (lit. (9*a*) 67.0–67.5°C). Recrystallizations from mixed solvents were performed by adding cosolvent until the solution became cloudy, followed by heating until clarification.

*7-Methyl-2-tetralone (**1h**)*

A mixture of *m*-methylphenylacetic acid (3.40 g, 22.6 mmol) and 100 mL 2 M thionyl chloride in dichloromethane solution (200 mmol) was stirred overnight. The solvent and excess thionyl chloride were distilled off. The resulting *m*-methylphenylacetic chloride was vacuum distilled and dissolved in ca. 20 mL anhydrous dichloromethane. This solution was added dropwise under argon to a stirring suspension of anhydrous aluminum chloride (4 g, 30 mmol) in 120 mL anhydrous dichloromethane cooled at –15°C, while ethylene was bubbled through the reaction mixture. The reaction was stopped after 1.5 h. After work-up as for **1f** (9*a*), column chromatography (silica, Merck 60, 1:4 ethyl acetate:hexane) gave a 1:2 mixture of 5-methyl-2-tetralone and 7-methyl-2-tetralone (estimated from integration of protons on C-1 carbon from ^{1}H NMR), 1.76 g (combined yield 52.1%). 7-Methyl-2-tetralone was obtained from two recrystallizations of this mixture from methanol–water (1.03 g, 28%), mp 57.5–59.5°C (lit. (10) 57–59°C). ^{1}H NMR ($CDCl_3$) δ: 2.33 (s, 3H, CH_3), 2.57 (t, J = 6.0 Hz, 2H, H4), 3.03 (t, J = 6.0 Hz, 2H, H3), 3.55 (s, 2H, H1), 6.95 (s, 1H, H8), 7.03 (d, J = 7.5, 1H, H5), 7.13 (d, J = 7.5 Hz, 1H, H6). Anal. calcd. for $C_{11}H_{12}O$: C 82.46, H 7.55%; found: C 82.28, H 7.61%.

*6-Iodo-2-tetralone (**1i**)*

p-Iodophenylacetic chloride was obtained using a similar procedure as above, from *p*-iodophenylacetic acid (150 mg, 0.57 mmol) and 1.2 mL 2 M thionyl chloride in dichloromethane solution (2.3 mmol). With excess anhydrous aluminum chloride (3.0 g, 20 mmol), the acid chloride was reacted with ethylene to give 6-iodo-2-tetralone. Chromatography (hexane:ethyl acetate, 10:1.5) and recrystallization from hexane and ethyl acetate gave pure **1i** (58 mg, yield 37%), mp 60.5–62.0°C. UV (1 N NaOH): 312 nm. ^{1}H NMR ($CDCl_3$) δ: 2.53 (t, J = 6.6 Hz, 2H, H4), 3.02 (t, J = 6.6 Hz, 2H, H3), 3.53 (s, 2H, H1), 6.88 (d, J = 7.8, 1H, H8), 7.55 (d, J = 7.8 Hz, 1H, H7), 7.51 (s, 1H, H5). Anal. calcd. for $C_{10}H_9IO$: C 44.14, H 3.33%; found: C 44.22, H 3.38%.

*6-Chloro-7-nitro-2-tetralone **(1j)***

6-Chloro-2-tetralone (1.1 g, 6.1 mmol) was slowly added to 8 mL of 90% nitric acid at –25°C, with nitrogen bubbling through the solution. After addition was completed, the reaction mixture was stirred for 8 min, poured onto a mixture of sodium hydroxide (6.5 g) in water and ice (50 mL) and 200 mL ethyl acetate, and then shaken vigorously. Work-up followed the procedure for the preparation of **1e** (9*a*). The major product from chromatography was 6-chloro-7-nitro-2-tetralone, which was recrystallized from hexane – ethyl acetate (0.19 g, yield 14%), mp 130–132°C. UV (1 N NaOH): 317 nm. ^{1}H NMR ($CDCl_3$) δ: 2.60 (t, J = 6.6 Hz, 2H, H4), 3.14 (t, J = 6.6 Hz, 2H, H3), 3.63 (s, 2H, H1), 7.46 (s, 1H,

© 1999 NRC Canada

Table 1. Equilibrium constants for ionization of substituted 2-tetralones and their enols and for keto–enol equilibria.

Substituent	σ^{-a}	$pK_a^{K\,b}$	pK_a^{E}	pK_E
6-MeO (**1d**)	–0.27	13.27 (± 0.05) [c]	9.64 (± 0.05)	3.63 (± 0.10)
7-Me (**1h**)	–0.17	12.94 (± 0.01)	9.52 (± 0.01)	3.42 (± 0.02)
H (**1a**)	0	12.83 (± 0.01) [c]	9.44 (± 0.04)	3.39 (± 0.05)
6-Cl (**1c**)	0.19	12.51 (± 0.03) [c]	9.31 (± 0.02)	3.20 (± 0.05)
6-I (**1i**)	0.27	12.36 (± 0.02)	9.23 (± 0.02)	3.13 (± 0.04)
7-Cl (**1f**)	0.37	12.30 (± 0.07) [c]	9.09 (± 0.06)	3.21 (± 0.13)
7-NO_2 (**1e**)	0.71	11.76 (± 0.02) [c]	8.81 (± 0.01)	2.95 (± 0.03)
6-Cl-7-NO_2 (**1j**)	0.90	11.34 (± 0.03)	8.56 (± 0.01)	2.78 (± 0.04)
5,7-$(NO_2)_2$ (**1g**)	1.42	10.34 (± 0.06) [c]	8.14 (± 0.03)	2.20 (± 0.09)
6-NO_2 (**1b**)	1.23	10.09 (± 0.02) [c]	7.69 (± 0.02)	2.40 (± 0.04)

[a] σ^- for 5,7-$(NO_2)_2$ is calculated as twice the value of σ_m for a nitro group, σ^- for 6-Cl-7-NO_2 is taken as the sum of σ_m of a nitro group and σ_p of a chloro group. σ values are from reference 13.

[b] pK_a^K's are *concentration* pK_a's based upon the concentration of all species except for the pK_a^K of **1b**, which is a *mixed* pK_a based upon concentrations of solute and activity of hydronium ion. These constants are used in the same correlation since determinations of the pK_a^K under both conditions gave essentially the same value (9*a*).

[c] Reference 9*a*.

Fig. 1. Plot of the pK_a^K of substituted 2-tetralones vs. σ^-. The slope (–1.66 ± 0.06) was calculated *without* the inclusion of the point for **1b**.

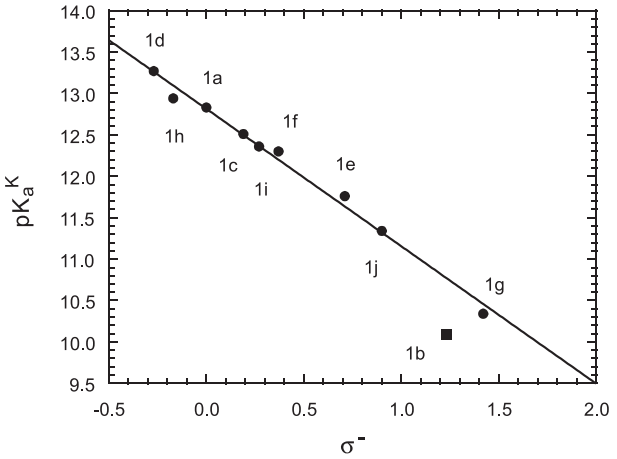

H5), 7.72 (s, 1H, H8). Anal. calcd. for $C_{10}H_8ClNO_3$: C 53.23, H 3.57, N 6.21%; found: C 53.26, H 3.63, N 6.19%.

Determination of the acidities of the ketones and the enols

Titration of the ketone was performed spectrophotometrically according to our previously described procedure (9*a*). For determination of the acidities of the enols, rapid quenching experiments were performed using a Hi-Tech QP/SF 53 stopped-flow spectrophotometer. Basic solutions of the respective tetralones were formed by mixing an aqueous solution of the tetralone (ca. 10 mM containing 6.6% v/v MeOH) with 0.1 N or 0.01 N NaOH solution in a 1:1 ratio. After a delay of 0.5–5 s, these solutions were then rapidly quenched in a 5:1 ratio with a range of buffers (containing 3.3% v/v MeOH), HOAc–NaOAc buffer (pH 4.0–6.0), KH_2PO_4–$Na_2B_2O_7$ buffer (pH 5.8–9.2), $NaHCO_3$–Na_2CO_3 (pH 9.2–11.0), or Na_2HPO_3–Na_3PO_4 (pH 11.0–12.0). The decay in the absorbance was recorded for more than 10 half-lives of a pseudo-first-order decay equation at 265 nm, except at 306 nm for **1j** and 340 nm for **1b**. The experimental temperature was 25.0 ± 0.1°C, and the ionic strength was 0.16, controlled by NaCl. The final pH of the quenching solution was determined by mixing equivalent solutions outside the stopped-flow. pH measurements were made with a Radiometer PHM85 pH meter, and were corrected for the concentration of sodium ion.

Results

Titration of substituted 2-tetralones

Substituted 2-tetralones are relatively acidic compared to most simple ketones, so that their pK_a's can be determined from direct titration in aqueous solution of hydroxide ion or buffer. We previously determined the pK_a's of compounds **1a–1g** (9*a*); in this work, pK_a's for **1h–1j** were determined similarly, and the combined results for **1a–1j** are given in Table 1. A plot of these pK_a's vs. σ^- (Fig. 1) is linear, except for the point corresponding to **1b**, with a slope ($-\rho$) of –1.66 ± 0.06, in agreement with the ρ value (1.72 ± 0.07) obtained previously with a more limited set of data from **1a**–**1g** (9*a*).

Titration of 2-tetralone enols

The relatively acidic nature of these ketones makes it possible to generate solutions of the enolate ions by mixing the ketones with solutions of sodium hydroxide. Since protonation of the enolate ion occurs more rapidly on oxygen than on carbon, the enols can be generated by quenching the enolate in an appropriate buffer. The absorbance of enol solutions of **1a**–**1j** generated in this manner was monitored at a wavelength (265 nm, except at 306 nm for **1j** and 340 nm for **1b**) where the enol has a stronger absorbance than the enolate ions. Conversion of the enol to the ketone results in a pseudo-first-order decay of the absorbance. However, the initial absorbance of the solution, obtained by extrapolation of the absorbance to the time of mixing,[2] can

[2] Since the half-life for these reactions are typically about 100 ms, and the mixing time is less than 5 ms, these extrapolations should have little error.

© 1999 NRC Canada

Fig. 2. Plot of the pK_a^E of substituted 2-tetralone enols vs. σ^-. The slope (–0.90 ± 0.03) was calculated *without* the inclusion of the point for **1b**.

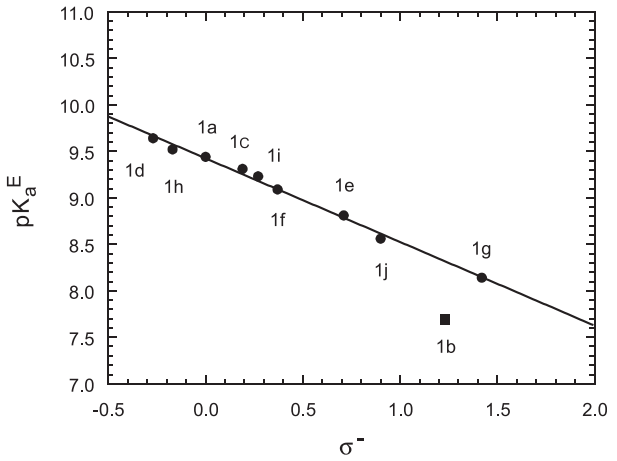

Fig. 3. Plot of the pK_E of substituted 2-tetralones vs. σ^-. The slope (–0.77 ± 0.05) was calculated *with* the inclusion of the point for **1b**.

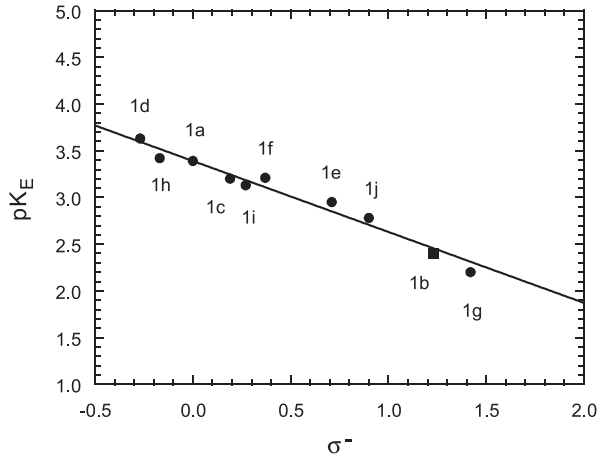

be used to determine the pK_a of the enol (pK_a^E). At this time, only the fast equilibrium between enol and enolate is observed. When this absorbance is plotted versus the pH of the final solution, a titration curve is obtained, which reflects the pK_a of the enol. These data were fit to eq. [1], where $[E]_t$ is the total concentration of enol and enolate, ε_E and ε_E^- are extinction coefficients for the enol and enolate, respectively, b is the light path length, and K_a^E is the acidity constant of the enol. The pK_a^E's for the 2-tetralone enols are summarized in Table 1. A plot of these pK_a^E's vs. σ^- is linear (ρ = 0.90 ± 0.03) with all points falling on the correlation, except the point for **1b** (Fig. 2).

$$[1] \qquad A_0 = b\,[E]_t\,(\varepsilon_E^- K_a^E + \varepsilon_E\,10^{-pH}) / (K_a^E + 10^{-pH})$$

Keto–enol equilibrium constants of 2-tetralones

The thermodynamic relationship among the ketone, enol, and enolate ion allows the equilibrium constants for the tautomerization of 2-tetralones (pK_E) in Table 1 to be calculated from the acidities of the ketones and the enols using eq. [2] (Table 1). The calculated pK_E for 2-tetralone obtained in this manner is 3.47 ± 0.04, in agreement with our previous result (3.64 ± 0.05) based on kinetics (8). A plot of pK_E vs. σ^- gives a slope (–ρ) of –0.77 ± 0.05, with all points including **1b** falling on the correlation line (Fig. 3).

$$[2] \qquad K_E = K_a^K / K_a^E$$

Discussion

Electronic effects on equilibria among 2-tetralones, their enolates and their enols

Electron-withdrawing substituents on the phenyl ring increase the acidities of both the ketones and the enols. The effect on the ketones is about twice that on the enols, with a ρ for pK_a^K of 1.66 compared to a ρ of 0.90 for pK_a^E. An instructive way to understand the decreased sensitivity to substitution of the enols compared to that of the ketones is to dissect the dissociation of the ketones into tautomerization from the ketones to the enols, followed by dissociation of the enols. Thus, a substantial portion of the electronic effect for ionization of the ketones (ca. 50%) is manifest in the enolization. The calculated ρ value of 0.76, $\rho(pK_E) = \rho(pK_a^K) - \rho(pK_a^E)$, for the tautomerization from ketone to enol shows that electron-withdrawing substituents enhance the tautomerization. Because the electron pair on the enol oxygen can be delocalized to the phenyl ring through resonance, electron-withdrawing substituents are expected to stabilize the enol more than the ketone. A similar result was obtained by Albrecht, who found a ρ value of 0.72 (with σ^-) for the enolization of 2-arylpropionaldehydes in DMSO (5). However, it is difficult to directly compare this value with the ρ for the tetralone series due to the difference in solvent composition in the two systems.

Keeffe and Kresge (11) have noted that there is a linear relationship between pK_a^K and pK_E, with a slope of 1.4, for a wide variety of simple aldehydes and ketones. This relationship demonstrates that structural effects on ketone acidity are due in large part to their effects on the keto–enol equilibria. Compounds with α-aryl substituents show deviations from this correlation in the direction of greater acidity of the carbonyl compound than predicted. Thus, 2-tetralone itself is approximately $10^{6.4}$-fold more acidic than acetone, but the relative acidities of the enols differ by only $10^{1.7}$-fold (8, 12). Therefore, the effect of the α-phenyl group on the dissociation of the ketone is predominantly due to an effect on the stability of the double bond, with little contribution from an effect on enol acidity. In contrast, electronic effects of ring substituents on enol acidity for the 2-tetralones are substantial, with the effect on ketone acidity due in almost equal parts to effects on enolization and enol acidity.

***p*-Nitro group as a probe for charge transfer**

For a Hammett plot of pK_a vs. σ^-, a negative deviation of *p*-nitro substituted compound means that the charge transfer for this specific equilibrium is larger than that upon ionization of phenol (the defining reaction), and zero deviation means a similar degree of charge transfer. From the plot of the pK_a's of both the ketone and the enol (Figs. 1 and 2), a negative deviation, or "enhanced" acidifying effect (9*a*), of 6-nitro-2-tetralone (**1b**) is observed. We previously attributed the enhanced effect of a 6-nitro group on the acidity of the 2-tetralone (10-fold) to the lack of a free electron pair on

© 1999 NRC Canada

the C-1 carbon (9*a*). Thus, no resonance stabilization for the 6-nitro group in the free tetralone is lost upon ionization. In contrast, in the ionization of phenol there is compensating resonance in the un-ionized acid.

Surprisingly, however, although direct resonance is possible for both the enol and the enolate, the acidity of the *enol* of 6-nitro-2-tetralone is also greater than predicted from the correlation with σ^- based on the other substituted enols (ca. 7-fold) (Fig. 2). Thus, relative to the ionization of *p*-nitrophenol, there is a greater increase in *direct* resonance interaction between the oxygen of the enol(ate) and the nitro group upon ionization. This result suggests that there is diminished stabilization of the enol by charge transfer from the hydroxyl group of the enol to the nitro group, consistent with the proposal of Toullec that the conjugation of the aryl ring with the double bond involves little π electron transfer for β-aryl enols (1).

The extent of charge transfer into the phenyl ring in the enol of 2-tetralone may also be probed by a consideration of the substituent effect on the enolization. A plot of pK_E vs. σ^- is linear, but in this case the point for 6-nitro-2-tetralone lies on the correlation line. If there were no direct resonance interaction between the hydroxyl group of the enol and the 6-nitro group, it would then be expected that this equilibrium would show a correlation with σ rather than with σ^-. Thus, this result suggests that there still is some direct resonance interaction between the hydroxyl group of the enol and the phenyl ring, although significantly less than there is in the enolate anion.

Acknowledgment

Acknowledgment is made to the donors of the Petroleum Research Fund, administered by the American Chemical Society, for support of this research.

References

1. J. Toullec. *In* The chemistry of enols. *Edited by* Z. Rappoport. Wiley, Chichester, U.K. 1990. Chap. 6
2. (*a*) Y. Chiang, A.J. Kresge, and P.A. Walsh. J. Am. Chem. Soc. **104**, 6122 (1982); (*b*) Y. Chiang, A.J. Kresge, Y.S. Tang, and J. Wirz. J. Am. Chem. Soc. **106,** 460 (1984); (*c*) Y. Chiang, A.J. Kresge, Y.S. Tang, and J. Wirz. J. Am. Chem. Soc. **106,** 6392 (1984).
3. (*a*) B. Capon, D.S. Rycroft, and T.W. Watson. J. Chem. Soc. Chem. Commun. 724 (1979); (*b*) B. Capon, D.S. Rycroft, T.W. Watson, and C. Zucco. J. Am. Chem. Soc. **103**, 1761 (1981); (*c*) B. Capon and A.K. Siddhanta. J. Org. Chem. **50,** 3580 (1985).
4. (*a*) S.E. Biali and Z. Rappoport. J. Am. Chem. Soc. **107**, 1007 (1985); (*b*) D.A. Nugiel and Z. Rappoport. J. Am. Chem. Soc. **107**, 3669 (1985); (*c*) E.B. Nadler and Z. Rappoport. J. Am. Chem. Soc. **109**, 2112 (1987); (*d*) H. Hart, Z. Rappoport, and S. Biali. *In* The chemistry of enols. *Edited by* Z. Rappoport. Wiley, Chichester, U.K. 1990. Chap. 8.
5. A. Ahlbrecht, W. Funk, and M.T. Reiner. Tetrahedron, **32**, 479 (1976).
6. (*a*) A. Pross and L. Radom. Prog. Phys. Org. Chem. **13**, 1 (1981); (*b*) R.D. Topsom. Prog. Phys. Org. Chem. **16**, 125 (1987).
7. E. Rochlin and Z. Rappoport. J. Am. Chem. Soc. **114**, 230 (1992).
8. S. Eldin, R.M. Pollack, and D.L. Whalen. J. Am. Chem. Soc. **113**, 1345 (1991).
9. (*a*) J.B. Nevy, D.C. Hawkinson, G. Blotny, X. Yao, and R.M. Pollack. J. Am. Chem. Soc. **119**, 12722 (1997); (*b*) G. Blotny and R.M. Pollack. Synth. Commun. **28**, 3865 (1998).
10. J.J. Sims, M. Cadoga, and L.H. Selman. Tetrahedron Lett. 951 (1971).
11. J.R. Keeffe and A.J. Kresge. *In* The chemistry of enols. *Edited by* Z. Rappoport. Wiley, Chichester, U.K. 1990. Chap. 7.
12. J.R. Keeffe, A.J. Kresge, and Y. Yin. J. Am. Chem. Soc. **110**, 8201 (1988).
13. C. Hansch, A. Leo, and R.W Taft. Chem. Rev. **91**, 165 (1991).

© 1999 NRC Canada

Electrophilic aromatic substitution in substituted anilines; kinetics of the reaction with 4,6-dinitrobenzofuroxan

Michael R. Crampton, Lynsey C. Rabbitt, and François Terrier

Abstract: Kinetic results are reported for reaction of aniline and six of its *N*- and ring-substituted derivatives with 4,6-dinitrobenzofuroxan (DNBF) in water – dimethyl sulfoxide mixtures. In acidic solution σ-adducts, the result of electrophilic substitution in the anilines, are formed with bonding between a ring-carbon atom of the anilines and the 7-position of DNBF. Reaction normally occurs at the 4-position of the aniline unless this carries a substituent, when reaction occurs at the 2-position. A value of 2.0 for k_H/k_D, the kinetic isotope effect, indicates that in the reaction with aniline bond formation is largely rate determining in the substitution pathway. The results allow estimates to be made for the pK_a values relating to carbon protonation of the anilines.

Key words: electrophilic substitution, σ-adducts, 4,6-dinitrobenzofuroxan, ambident reactivity of anilines.

Résumé : On rapporte les données cinétiques relatives à la réaction de l'aniline (et six de ses dérivés substitués sur l'azote et sur le noyau) avec le 4,6-dinitrobenzofuroxane (DNBF) dans des mélanges formés d'eau et de diméthylsulfoxyde. En solutions acides, il se forme des adduits-σ, résultant d'une substitution électrophile sur les anilines, qui lient un atome de carbone du noyau des anilines et la position 7 du DNBF. La réaction se fait généralement en position 4 de l'aniline, à moins que cette position porte un substituant; la réaction se fait alors en position 2. Une valeur de 2,0 pour l'effet isotopique cinétique, k_H/k_D, indique que, dans cette réaction la formation de la liaison avec l'aniline constitue l'étape cinétiquement déterminante de la réaction de substitution. Les résultats permettent d'évaluer les valeurs de pK_a associées à la protonation du carbone des anilines.

Mots clés : substitution électrophile, adduits-σ, 4,6-dinitrobenzofuroxane, réactivité ambidente des anilines.

[Traduit par la Rédaction]

Aniline and its substituted derivatives usually act as nitrogen nucleophiles. Thus, reaction with 1,3,5-trinitrobenzene (1, 2) in dimethyl sulfoxide (DMSO) in the presence of a strong base gives N-bonded σ-adducts, **1**; reaction with substrates carrying good leaving groups may result in substitution leading to diphenylamine derivatives (3–5).

Nevertheless, the ambident reactivity of aniline and its derivatives has been shown in reactions with 4,6-dinitrobenzofuroxan, DNBF. Here σ-adducts have been observed

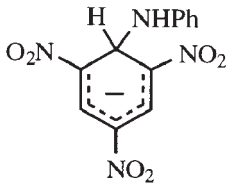

1

involving nucleophilic attack either through nitrogen or through a ring carbon atom *para*- or *ortho*- to the amino function (6–10).

The high electrophilic reactivity of DNBF is well known (5, 11, 12). In fact, it has been shown to be a more powerful electrophile than the 4-nitrobenzenediazonium ion (13) or the proton (14). Previously kinetic studies have been reported of electrophilic substitutions involving reactions of DNBF with pyrroles (14), 5-substituted indoles (13), 3,4-diaminothiophene (15), 3-methoxythiophene (16), and hydroxy- and methoxy-substituted benzenes (17). In the present work, we report kinetic studies of the reactions of aniline and some *N*-substituted or ring-substituted derivatives with DNBF in water–DMSO mixtures. Measurements were made in acidic solutions where the anilines are very largely protonated. Here the results are in accord with the reactions, shown in Scheme 1, leading to the formation of carbon bonded σ-adducts. In the case of anilines **2a**–**e**, reaction was found to occur *para* to the amino position. However,

Received November 22, 1998.

This paper is dedicated to Professor Jerry Kresge in recognition of his outstanding contributions to the study of physical organic chemistry.

M.R. Crampton[1] and L.C. Rabbitt. Chemistry Department, Durham University, Durham DH1 3LE, U.K.
F. Terrier. Université de Versailles, SIRCOB, Bâtiment Lavoisier, 45 avenue des Etats-Unis, 78035 Versailles Cedex, France.

[1]Author to whom correspondence may be addressed. Telephone: +44 191 374 3130. Fax: +44 191 384 4737.
e-mail: M.R.Crampton@durham.ac.uk

 © 1999 NRC Canada

Scheme 1.

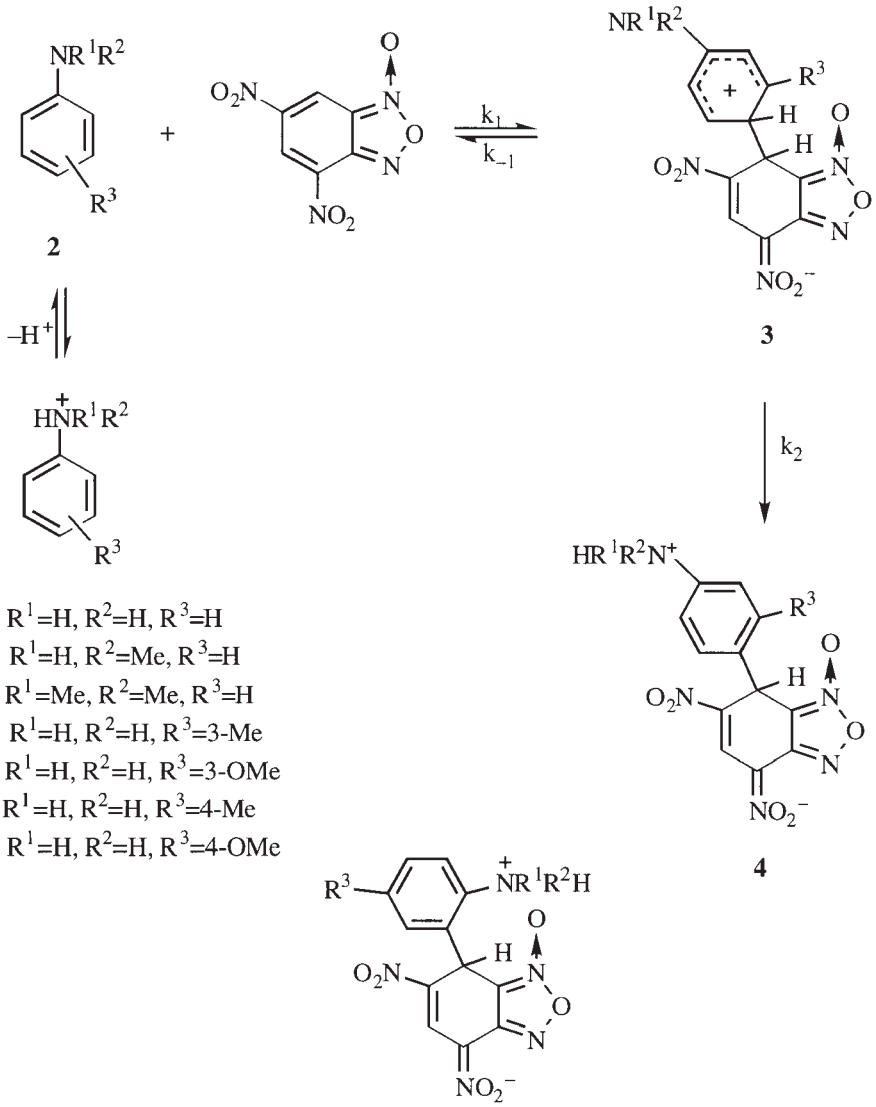

a R^1=H, R^2=H, R^3=H
b R^1=H, R^2=Me, R^3=H
c R^1=Me, R^2=Me, R^3=H
d R^1=H, R^2=H, R^3=3-Me
e R^1=H, R^2=H, R^3=3-OMe
f R^1=H, R^2=H, R^3=4-Me
g R^1=H, R^2=H, R^3=4-OMe

when the 4-position is blocked, reaction occurs *ortho* to the amino function to yield products **5f** and **5g**.

These reactions may be regarded as neutral nucleophile–electrophile combination reactions (18), and are examples of electrophilic substitution in the aniline ring. The powerful activating effect of the amino group towards electrophilic substitution in aromatic systems has been noted previously (19, 20). There are many examples of halogenation (21, 22) and of hydrogen exchange (23) in aniline derivatives. One of the aims of the present work was to use the reaction with DNBF to compare the reactivity of aniline with other aromatic systems.

Results and discussion

^{1}H NMR spectra have been reported previously for the products of reaction of DNBF and several amines (6–10). Our results relating to 1:1 mole ratio mixtures of DNBF and amines **2a**–**g** in [$^2H_6$] DMSO are given in Table 1. The spectra, showing bands at δ 5.3–5.6 and δ 8.7 for the hydrogens at the 7′ and 5′ positions of DNBF, are typical of C-adduct formation (5, 13, 14, 17), consistent with the production of **4a**–**e**. In 4-substituted anilines, the band due to the 7′ proton is at δ 5.8, consistent with the formation of **5f** and **g**. In solutions containing higher mole ratios of aniline to DNBF, there was NMR evidence for the kinetically controlled formation of N-bonded adducts followed by conversion to the thermodynamically more stable C-bonded adducts. In the case of aniline, **2a**, bands due to the N-bonded adduct were at δ 6.04 and 8.64, at positions similar to those reported previously (10).

Kinetic measurements were conveniently made in water–DMSO mixtures. Most data relate to a solvent composition of 30/70 (v/v) water/DMSO, although for comparison some measurements using aniline were made in 70/30 and 50/50 (v/v) water/DMSO mixtures. All measurements were made in the presence of excess hydrochloric acid. This had the effect of reducing the concentrations of free amines to very low levels, and under these conditions there was no evidence for nucleophilic attack via the nitrogen centre of the anilines.

© 1999 NRC Canada

Table 1. ^{1}H NMR shifts for σ-adducts, **4** or **5**, in [$^2H_6$] DMSO.

Compound	H7′	H5′	Aromatic[a]	Other
DNBF	8.94	9.27		
4a	5.36	8.74	7.19 (d), 7.33 (d), *J* 8	
4b	5.38	8.74	7.30 (d), 7.37 (d), *J* 8.5	2.90 (NMe)
4c	5.39	8.74	7.40 (m)	3.12 (NMe_2)
4d	5.60	8.72	7.08 (m)	2.58 (Me)
4e	5.56	8.66	6.89 (s), 6.87 (d), 7.34 (d), *J* 7.4	3.68 (OMe)
5f	5.84	8.74	6.92 (s), 7.10 (d), 7.16 (d), *J* 8	2.20 (Me)
5g	5.84	8.74	6.53 (s), 6.95 (d), 7.18 (d), *J* 8.5	3.67 (OMe)

[a] *J* in Hz.

[1] DNBF + H_2O $\rightleftharpoons$ (**6**) + H^+

(**6**)

A further beneficial effect of the acidic media was to reduce the equilibrium concentrations of the hydroxy adduct, **6**, of DNBF which is known to form in neutral media, as shown in eq. [1].

Spectrophotometric measurements, using the absorbance of **6** at 470 nm, gave values for K_{H_2O}, defined in eq. [1], of 0.0196 ± 0.0008 mol dm^{-3} in 70% DMSO and 0.0045 ± 0.0002 mol dm^{-3} in 50% DMSO. These values are in excellent agreement with literature values of 0.019, 0.0040, and 0.00080 mol dm^{-3} in media containing 70, 50, and 30% DMSO, respectively (24).

Reaction with aniline

The equilibrium between DNBF and **6** is established rapidly. Similarly, any adduct formation resulting from attack of aniline as a nitrogen nucleophile on DNBF will be a rapid process (3, 5). The UV/visible spectra in Fig. 1 show that in acidic solutions there is a slow reaction between DNBF and aniline, giving a band at 489 nm. In view of the NMR data, this is attributed to the C-bonded adduct **4a**. It has been reported (9, 10) that di-adducts may be formed by reaction of both N- and C-centres of an aniline molecule with two molecules of DNBF. There was no evidence for such 1:2 interaction in our systems, which contain very low, 4 × 10^{-5} mol dm^{-3}, concentrations of DNBF. Kinetic data, with concentrations of aniline hydrochloride and free hydrochloric acid in large excess of the DNBF concentration, indicated that adduct formation was an accurately first-order process. Values of k_{obs}, the measured rate constant, are in Table 2. The results show that at constant concentration of free acid, values increase linearly with the concentration of aniline hydrochloride. However, values decrease with increasing acid concentration. This observation indicates that reaction is likely to involve free aniline rather than its protonated form. Hence, we define by eq. [2] a rate constant *k*, which is related by eq. [3] to the constants for individual steps shown in the scheme. There is no evidence from NMR or UV/visible spectra of the accumulation of **3**, the intermediate in the substitution pathway. It may be shown that *k* is related to k_{obs} by eq. [4], where K_a is the acid dissociation constant of the anilinium ion. This equation allows for the small concentration of the hydroxy-adduct **6** in equilibrium with DNBF. In 70/30 (v/v) DMSO/water, the pK_a value for the anilinium ion is known to be 3.41 (25). Hence, at the acid concentrations used [H^+] >> K_a, allowing eq. [4] to be simplified to give eq. [5].

Fig. 1. UV-vis spectra for the reaction in 30/70 (v/v) water/DMSO of DNBF, 4 × 10^{-5} mol dm^{-3}, with aniline hydrochloride 0.05 mol dm^{-3} and hydrochloric acid 0.03 mol dm^{-3}. The absorbance at 489 nm increases with time.

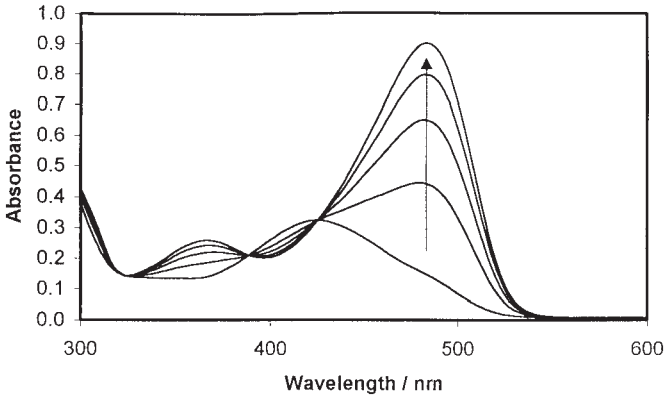

[2] $$\frac{-d[DNBF]}{dt} = k[DNBF][aniline]$$

[3] $$k = \frac{k_1 k_2}{k_{-1} + k_2}$$

© 1999 NRC Canada

Table 2. Rate data for reaction of DNBF[a] with aniline in acidic solutions in 30/70 (v/v) water/DMSO at 25°C.

[Aniline H^+Cl^-]/mol dm^{-3}	[HCl]/mol dm^{-3}	10^4 k_{obs}/s^{-1}[b]	k/dm^3 mol^{-1} s^{-1}[c]
0.050	0.059	8.28	3.3
0.050	0.117	5.15	3.6
0.050	0.146	4.30	3.7
0.050	0.200	3.58	4.0
0.050	0.242	3.10	4.2
0.050	0.30	2.44	4.0
0.020	0.033	4.76	3.2
0.040	0.033	9.60	3.2
0.10	0.033	23.1	3.1
0.10	0.31	5.12	4.3

[a]DNBF concentration is 4×10^{-5} mol dm^{-3}.

[b]Measured at 489 nm.

[c]Calculated from eq. [5] with K_a 3.89×10^{-4} mol dm^{-3} and K_{H_2O} 0.0196 mol dm^{-3}.

Table 3. Isotope and solvent effects on reaction of DNBF[a] and aniline.

Vol.% DMSO	$[C_6D_5NH_3^+Cl^-]$/mol dm^{-3}	$[C_6H_5NH_3^+Cl^-]$/mol dm^{-3}	[HCl]/mol dm^{-3}	10^4 k_{obs}/s^{-1}	k/dm^3 mol^{-1} s^{-1}[b]	k_H/k_D
70	0.050	—	0.30	1.31	2.13	
	0.100	—	0.30	2.22	1.85	2.1 ± 0.1
	—	0.050	0.30	2.51	4.10	
	—	0.100	0.30	5.12	4.27	
50	0.030	—	0.030	1.90	1.17	
	0.050	—	0.030	3.10	1.15	2.0 ± 0.1
	—	0.030	0.030	3.87	2.39	
	—	0.050	0.030	5.71	2.12	
30	0.030	—	0.030	0.45	0.55	
	0.050	—	0.030	0.70	0.52	2.1 ± 0.1
	—	0.030	0.030	0.91	1.13	
	—	0.050	0.030	1.54	1.14	

[a]All measurements were made with DNBF 4×10^{-5} mol dm^{-3} at 25°C.

[b]Calculated from eq. [5] with values for K_a 3.89×10^{-4} mol dm^{-3}, 70% DMSO, ref. 25; 1.86×10^{-4}, 50% DMSO, ref. 15; 8.3×10^{-5} mol dm^{-3}, 30% DMSO, ref. 15; and values of K_{H_2O} given in the text.

Table 4. Rate data for reaction of DNBF[a] with **2b**, *N*-methylaniline, in acidic solution in 30/70 (v/v) water/DMSO at 25°C.

[*N*-Methylaniline H^+Cl^-]/mol dm^{-3}	[HCl]/mol dm^{-3}	10^4 k_{obs}/s^{-1}[b]	k/dm^3 mol^{-1} s^{-1}[c]
0.050	0.014	136	10.6
0.050	0.025	104	10.6
0.050	0.036	85	10.8
0.050	0.102	42	11.4
0.050	0.150	26	9.9
0.050	0.200	19.6	9.8

[a]DNBF concentration is 4×10^{-5} mol dm^{-3}.

[b]Measured at 494 nm.

[c]Calculated from eq. [5] with K_a 8.7×10^{-4} mol dm^{-3} and K_{H_2O} 0.0196 mol dm^{-3}.

$$[4] \qquad k_{obs} = k[\text{aniline } H^+]\left(\frac{K_a}{K_a + [H^+]}\right)\left(\frac{[H^+]}{[H^+] + K_{H_2O}}\right)$$

$$[5] \qquad k = \frac{k_{obs}}{K_a}\frac{(K_{H_2O} + [H^+])}{[\text{aniline } H^+]}$$

The invariance of values, in Table 2, of k with acid concentration or aniline hydrochloride concentration confirms that reaction involves free aniline rather than the anilinium ion.

The availability of pentadeuterioaniline, $C_6D_5NH_2$, allowed the evaluation of the kinetic isotope effect, k_H/k_D, on the substitution reaction. Measurements were made in media containing 70, 50, and 30% DMSO by volume and are reported in Table 3. For accuracy of comparison, measurements were made simultaneously on deuteriated and nondeuteriated systems using the multicell facility in the

© 1999 NRC Canada

Table 5. Rate data for reaction of DNBF[a] with **2c**, *N*,*N*-dimethylaniline, in acidic solution in 30/70 (v/v) water/DMSO at 25°C.

[*N*,*N*-Dimethylaniline H^+Cl^-]/mol dm^{-3}	[HCl]/mol dm^{-3}	10^4 k_{obs}/s^{-1}[b]	k/dm^3 mol^{-1} s^{-1}[c]
0.020	0.024	30.6	6.5
0.020	0.044	20.5	6.4
0.020	0.055	15.8	5.8
0.020	0.108	9.3	5.8
0.020	0.200	5.3	5.8
0.020	0.230	5.0	6.2

[a]DNBF concentration is 4×10^{-5} mol dm^{-3}.

[b]Measured at 486 nm.

[c]Calculated from eq. [5] with K_a 1.02×10^{-3} mol dm^{-3} and K_{H_2O} 0.0196 mol dm^{-3}.

Table 6. Rate data for reaction of DNBF[a] with **2d**, 3-methylaniline, in acidic solution in 30/70 (v/v) water/DMSO at 25°C.

[3-Methylaniline H^+Cl^-]/mol dm^{-3}	[HCl]/mol dm^{-3}	10^4 k_{obs}/s^{-1}[b]	k/dm^3 mol^{-1} s^{-1}[c]
0.050	0.036	56	28
0.050	0.070	34	27
0.050	0.153	18.5	28
0.050	0.200	14.2	28
0.050	0.241	11.1	27
0.050	0.300	9.3	26

[a]DNBF concentration is 4×10^{-5} mol dm^{-3}.

[b]Measured at 485 nm.

[c]Calculated from eq. [5] with K_a 2.24×10^{-4} mol dm^{-3}, and K_{H_2O} 0.0196 mol dm^{-3}.

Table 7. Rate data for reaction of DNBF[a] with **2e**, 3-methoxyaniline, in acidic solution in 30/70 (v/v) water/DMSO at 25°C.

[3-Methoxyaniline H^+Cl^-]/mol dm^{-3}	[HCl]/mol dm^{-3}	10^4 k_{obs}/s^{-1}[b]	k/dm^3 mol^{-1} s^{-1}[c]
0.010	0.090	1100	1470
0.030	0.070	3700	1350
0.030	0.17	1660	1220
0.050	0.050	7170	1280

[a]DNBF concentration is 4×10^{-5} mol dm^{-3}.

[b]Measured by stopped-flow spectrophotometry at 487 nm.

[c]Calculated from eq. [5] with K_a 8.1×10^{-4} mol dm^{-3} and K_{H_2O} 0.0196 mol dm^{-3}.

Table 8. Rate data for reaction of DNBF[a] with **2f**, 4-methylaniline, in acidic solution in 30/70 (v/v) water/DMSO at 25°C.

[4-Methylaniline]/mol dm^{-3}	[HCl]/mol dm^{-3}	10^4 k_{obs}/s^{-1}[b]	k/dm^3 mol^{-1} s^{-1}[c]
0.050	0.0142	1.63	1.10
0.050	0.0249	1.28	1.14
0.050	0.0356	1.06	1.17
0.050	0.0570	0.75	1.15

[a]DNBF concentration is 4×10^{-5} mol dm^{-3}.

[b]Measured at 485 nm.

[c]Calculated from eq. [5] with K_a 1.0×10^{-4} mol dm^{-3} and K_{H_2O} 0.0196 mol dm^{-3}.

spectrophotometer. These values, rather than the value of 3.7 dm^3 mol^{-1} s^{-1} for k_H in 70% DMSO, were used in the calculation of the isotope effect. It is known that ring-deuteriation has only a small effect on the acidity of anilinium ions (26), thus in water values are 4.71 for $C_6H_5NH_3^+$ and 4.74 for $C_6D_5NH_3^+$. We have assumed that values for K_a are unaffected by deuteriation in the DMSO–water mixtures. The overall value of k contains contributions from k_1, k_2, and k_{-1} as indicated in eq. [3]. It is likely that the values of k_1 and k_{-1} will show only small changes with isotopic substitution, since these involve secondary isotope effects. However, the value of k_2 that involves carbon–hydrogen bond cleavage is likely to show a primary isotope effect of ca. 7. These assumptions, together with the observed value of k_H/k_D = 2.1, lead to a value for k_{-1}/k_2 of 0.2 for aniline with k_1 = 1.2k. This indicates that, as with most electrophilic substitution reactions (19), the k_1 step, the initial attack, is largely rate determining. A similar situation was reported in reactions of

© 1999 NRC Canada

Table 9. Rate data for reaction of DNBF[a] with **2g**, 4-methoxyaniline, in acidic solution in 30/70 (v/v) water/DMSO at 25°C.

[4-Methoxyaniline H^+Cl^-]/mol dm^{-3}	[HCl]/mol dm^{-3}	10^4 k_{obs}/s^{-1}[b]	k/dm^3 mol^{-1} s^{-1}[c]
0.050	0.0142	0.62	1.24
0.050	0.0356	0.47	1.54
0.050	0.0570	0.38	1.72

[a]DNBF concentration is 4×10^{-5} mol dm^{-3}.

[b]Measured at 490 nm.

[c]Calculated from eq. [5] with K_a 3.39×10^{-5} mol dm^{-3} and K_{H_2O} 0.0196 mol dm^{-3}.

Table 10. Summary of kinetic data for reaction of DNBF with substituted anilines in 30/70 (v/v) water/DMSO at 25°C.

Aniline		pK_a[a]	λ_{max}/nm[b]	k/dm^3 mol^{-1} s^{-1}
2a	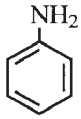	3.41	489	4.0 ± 0.7
2b	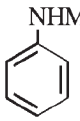	3.06	494	10.3 ± 0.6
2c	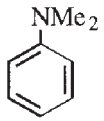	2.99	486	6.0 ± 0.8
2d	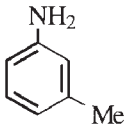	3.65	485	27 ± 1
2e	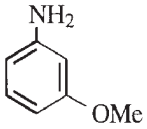	3.09	487	1300 ± 100
2f	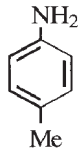	4.00	485	1.14 ± 0.03
2g	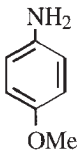	4.47	490	1.5 ± 0.2

[a]pK_a values of the anilinium ions in 30/70 (v/v) water/DMSO from ref. 25.

[b]Absorption maxima of adducts.

DNBF with substituted indoles (13, 14). However, in reactions with 1,3,5-trimethoxybenzene, a larger isotope effect was observed showing that here proton loss from the intermediate is more kinetically significant (17).

Our results show that for substitution in aniline, the value of the isotope effect is independent of the solvent composition in the range 30–70% DMSO. The small increase in k from 1.1 dm^3 mol^{-1} s^{-1} in 30% DMSO to 4.2 dm^3 mol^{-1} s^{-1} in 70% DMSO is thus likely to reflect a similar increase in value for k_1. This may indicate slightly better solvation by DMSO than by water of the charged polarizable intermediate **3**. The value of the rate constant for attack of water on DNBF shown in eq. [1] also increases with DMSO content of the solvent (24).

© 1999 NRC Canada

Table 11. Carbon nucleophilicity of some π-excessive aromatics towards DNBF in 50/50 (v/v) water/DMSO.

Compound[a]	k/dm^3 mol^{-1} s^{-1}	pK_a[a,b]
3-Methoxythiophene	0.5	–6.5
5-Cyanoindole	1.1	–6.0
Aniline	2.3	
N,*N*-Dimethylaniline[c]	3.5	(–6 to ~–5)
N-Methylaniline[c]	6.0	
3-Methylaniline[c]	16	(–5 to ~–4.5)
5-Bromoindole	46	–4.4
5-Chloroindole	52	–4.5
Pyrrole	520	–3.8
Indole	560	–3.5
3-Methoxyaniline[c]	750	(–3)
5-Methylindole	2100	–3.3
5-Methoxyindole	2600	–2.9
N-Methylindole	3500	–2.3
1,2,5-Trimethylpyrrole	24 000	–0.5
3,4-Diaminothiophene	9×10^5	1.5–2

[a]Data from ref. 16 or from present work.

[b]pK_a values in water for protonation on carbon

[c]Values of k in 30/70 water/DMSO were multiplied by 2.3/4.0.

Reaction with substituted anilines

Data analogous to that reported in Table 2 were obtained for reaction of DNBF with the substituted anilines **2b**–**g**. Results are given in Tables 4–9. Values of k calculated from eq. [5] using the value of K_a appropriate to the particular substituted anilinium ion are summarized in Table 10.

The results show that the value of k, the rate constant for adduct formation, increases on *N*-methylation. However, further methylation to give the *N*,*N*-dimethyl derivative results in a reduction in reactivity. Successive *N*-methylations might be expected to increase reactivity by increasing the electron releasing ability of the amino group. Thus σ^+ values (27, 28) are –1.30 for *para*-NH_2 and –1.70 for *para*-NMe_2, with the NHMe group showing intermediate behaviour (29). However these σ^+ values relate to largely aqueous media, while our results were obtained in media rich in DMSO. It is known that DMSO is an extremely good hydrogen-bond acceptor (30, 31), and in this solvent the stabilization of the cationic moiety of the intermediate, **3**, will be expected to increase as the number of NH bonds available for hydrogen-bonding increases. This effect may temper the increase in electron donation expected on *N*-methylation. A similar argument may be used (25) to explain the reduced acidity of the anilinium ion, pK_a = 3.41, in DMSO–water relative to the *N*,*N*-dimethyl derivative, pK_a = 2.99.

The values of k for reaction at the 4-positions of **2d** and **2e** are considerably higher than that for aniline. Here the electron releasing effect of the 3-substituent is dominant with σ^+ values reported as –0.31 for methyl and –0.78 for methoxy (32). There may be some steric retardation here, since the substituents are *ortho* to the reaction centre.

When the 4-position is blocked, reaction occurs at the 2-position, *ortho* to the amino function. Here the values for k are reduced relative to that for aniline. These reductions probably represent a steric effect to nucleophilic attack, although steric inhibition of solvation in the intermediates leading to the adducts **5** is a possibility.

Rate constants are available (17) for reaction, in 50/50 (v/v) water/DMSO, of DNBF at the 4-position of 1,3-dimethoxybenzene (0.52 dm^3 mol^{-1} s^{-1}) and with 1,3,5-trimethoxybenzene (205 dm^3 mol^{-1} s^{-1}). Comparison of these values with data in Table 10 shows that the 4-amino group is considerably more activating, in terms of carbon nucleophilicity, than the 4-methoxy group.

Comparison with other π-excessive aromatics

It is of interest to compare our results for the nucleophilicity of aniline derivatives towards DNBF with those for other arenes. Most of the literature data refer to a solvent system of 50/50 (v/v) water/DMSO, whilst our data generally refer to 30/70 (v/v) water/DMSO. However, for aniline we have data in both media and have assumed that the solvent effect will be similar for substituted derivatives. Data are in Table 11. It has been shown previously (16) that there is an approximately linear relationship between carbon nucleophilicities towards DNBF, and pK_a values in water for carbon protonation. On the assumption that the anilines obey the same relationship, the pK_a values for C-protonation may be estimated. For aniline and its N-methylated derivative values of ca. –6 to –5 are obtained, while values for 3-methylaniline and 3-methoxyaniline are ca. –4.7 and –3, respectively. The results clearly show that in water N-protonation of the anilines, with pK_a ca. 4, is strongly favoured over ring protonation.

Experimental

4,6-Dinitrobenzofuroxan was prepared by the Drost method (33); mp 172°C (lit. (16, 33) 172–174°C). All other reagents and solvents were the purest available commercial products.

^{1}H NMR spectra were recorded using a Varian Mercury 200 MHz spectrometer. UV-vis spectra and kinetic measurements were made at 25°C with a Perkin–Elmer Lambda 2 spectrophotometer, a Shimadzu UV-2101 PC spectrometer, or an Applied Photophysics SX-17 MV stopped-flow spectrophotometer. Reported rate constants are the means of several determinations and are precise to ±5%. Potassium chloride was used to maintain ionic strength I ($\equiv (1/2)\Sigma c_i z_i^2$) 0.1 mol dm^{-3} in those solutions with lower ionic concentrations.

Acknowledgements

Financial assistance for this project from Zeneca Fine Chemicals, Huddersfield, is gratefully acknowledged.

References

1. E. Buncel and J.G.K. Webb. Can. J. Chem. **50**, 129 (1972).
2. E. Buncel and W. Eggimann. J. Am. Chem. Soc. **99**, 5958 (1977).
3. M.R. Crampton and I.A. Robotham. Can. J. Chem. **76**, 627 (1998).

© 1999 NRC Canada

4. O. Banjoko and P. Otiono. J. Chem. Soc. Perkin Trans. 2, 399 (1981).
5. F. Terrier. Nucleophilic aromatic displacement. VCH, New York. 1991.
6. R.J. Spear, W.P. Norris, and R.W. Read. Tetrahedron Lett. **24**, 1555 (1983).
7. R.W. Read, R.J. Spear, and W.P. Norris. Aust. J. Chem. **37**, 985 (1984).
8. R.W. Read and W.P. Norris. Aust. J. Chem. **38**, 435 (1985).
9. M.J. Stauss, R.A. Renfrow, and E. Buncel. J. Am. Chem. Soc. **105**, 2473 (1983).
10. E. Buncel, R.A. Renfrow, and M.J. Strauss. J. Org. Chem. **52**, 488 (1987).
11. E. Buncel, R.A. Manderville, and J.M. Dust. J. Chem. Soc. Perkin Trans. 2, 1019 (1997).
12. J.-C. Hallé, D. Vichard, M.-J. Pouet, and F. Terrier. J. Org. Chem. **62**, 7178 (1997).
13. F. Terrier, M.-J. Pouet, J.-C. Hallé, S. Hunt, J.R. Jones, and E. Buncel. J. Chem. Soc. Perkin Trans. 2, 1665 (1993).
14. F. Terrier, E. Kizilian, J.-C. Hallé, and E. Buncel. J. Am. Chem. Soc. **114**, 1740 (1992).
15. F. Terrier, M.-J. Pouet, E. Kizilian, J.-C. Hallé, F. Outurquin, and C. Paulmier. J. Org. Chem. **58**, 4696 (1993).
16. E. Kizilian, F. Terrier, A.-P. Chatrousse, K. Gzoudi, and J.-C. Hallé. J. Chem. Soc. Perkin Trans. 2, 2667 (1997).
17. F. Terrier, M.-J. Pouet, J.-C. Hallé, E. Kizilian, and E. Buncel. J. Phys. Org. Chem. **11**, 707 (1998).
18. H. Mayr. Angew. Chem. Int. Ed. **33**, 938 (1994).
19. R.O.C. Norman and R. Taylor. Electrophilic substitution in benzenoid compounds. Elsevier, Amsterdam. 1965; R. Taylor. Electrophilic aromatic substitution. Wiley, New York. 1990.
20. P.W. Robertson, P.B.D. de la Mare, and B.E. Swedlund. J. Chem. Soc. 782 (1953).
21. E. Berliner. J. Am. Chem. Soc. **72**, 4003 (1950).
22. J. Berthelot, C. Guette, P.-L. Desbene, J.-J. Basselier, P. Chaquin, and D. Masure. Can. J. Chem. **67**, 2061 (1989).
23. S. Clementi and A.R. Katritzky. J. Chem. Soc. Perkin Trans. 2, 1076 (1973).
24. F. Terrier, H.A. Sorkhabi, F. Millot, J.-C. Hallé, and R. Schaal. Can. J. Chem. **58**, 1155 (1980).
25. K. Yates and G. Welch. Can. J. Chem. **50**, 474 (1972).
26. C.F. Bernasconi, W. Koch, and H. Zollinger. Helv. Chim. Acta, **46**, 1184 (1963).
27. H.C. Brown and Y. Okomoto. J. Am. Chem. Soc. **80**, 4979 (1958).
28. S. Clementi and A.R. Katritzky. J. Chem. Soc. Perkin Trans. 2, 1077 (1973).
29. M. Charton. Prog. Phys. Org. Chem. **13**, 211 (1981).
30. M.J. Kamlet and R.W. Taft. J. Am. Chem. Soc. **98**, 377 (1976)
31. M.R. Crampton and I.A. Robotham. J. Chem. Res. Synop. 22 (1997).
32. L.M. Stock and H.C. Brown. Adv. Phys. Org. Chem. **1**, 35 (1963).
33. P. Drost. Justus Liebigs Ann. Chem. **307**, 49 (1899).

© 1999 NRC Canada

^{15}N nuclear polarization in the reactions of diallyl ether with nitrogen dioxide

Robert P. Claridge, Ross W. Millar, and John H. Ridd

Abstract: The reaction of diallyl ether with nitrogen dioxide in organic solvents yields a mixture of *cis* and *trans* 2,3-bis(nitromethyl)-tetrahydrofurans, *cis* and *trans* 2-nitratomethyl-3-nitromethyl-tetrahydrofurans and a number of straight-chain compounds with one to four nitro groups. Under the conditions used, the cyclic compounds form the main products when the solution of nitrogen dioxide is slowly added to the solution of diallyl ether but not when the reverse mode of addition is used. When ^{15}N-nitrogen dioxide is used, the products show strong ^{15}N nuclear polarization: the 2,3-di(nitromethyl)-tetrahydofurans give an emission signal, and one straight-chain product with two nonequivalent nitro groups shows both an emission signal and an enhanced absorption signal. For both the cyclic and straight-chain products, the nuclear polarization is consistent with the successive reactions of diallyl ether with two nitrogen dioxide radicals with uncorrelated spins.

Key words: diallyl ether, nitrogen dioxide, ^{15}N nuclear polarization, CIDNP.

Résumé : La réaction de l'oxyde de diallyle avec le bioxyde d'azote dans des solvants organiques conduit à un mélange de *cis*- et *trans*-2,3-bis(nitrométhyl)tétrahydrofuranes, de *cis*- et *trans*-2-nitratométhyl-3-nitrométhyltétrahydrofuranes et d'un certain nombre de composés linéaires portant d'un à quatre groupes nitro. Dans les conditions utilisées, les composés cycliques sont les principaux produits lorsqu'on additionne le bioxyde d'azote lentement à la solution d'oxyde de diallyle; ce n'est toutefois pas le cas lorsqu'on fait l'addition inverse. Lorsqu'on utilise du bioxyde d'azote marqué au ^{15}N, les produits montrent une forte polarisation nucléaire du ^{15}N: les 2,3-di(nitrométhyl)tétrahydrofuranes donnent un signal d'émission et un produit linéaire portant deux groupes nitro non équivalents donne un signal d'émission ainsi qu'un signal d'absorption augmenté. Pour les produits tant cycliques que linéaires, la polarisation nucléaire est en accord avec les réactions successives de l'oxyde de diallyle avec deux radicaux de bioxyde d'azote ayant des spins n'ayant pas de corrélation.

Mots clés : oxyde de diallyle, bioxyde d'azote, polarisation nucléaire du ^{15}N, « CIDNP ».

[Traduit par la Rédaction]

Introduction

The reaction of electrophilic radicals with diallyl ether has been known for many years to lead both to addition to the double bonds and to cyclization to form derivatives of tetrahydrofuran (1). The cyclization reaction was first established in the free radical induced reaction of perfluoroalkyl iodides with diallyl ether (1) but similar results are obtained in the photochemical reaction of tosyl iodide and tosyl bromide with diallyl ether (2). The radical addition of tetrafluorohydrazine to diallyl ether is accompanied by about 50% cyclization to derivatives of tetrahydrofuran (3). The ready cyclization of diallyl ether following radical addition to one of the double bonds has been discussed by Beckwith and Schiesser (4). However, other products can be formed: thus, the reaction of diallyl ether with *tert*-butoxy radicals leads instead to H-abstraction (5).

The present work involves the reaction of diallyl ether with nitrogen dioxide in organic solvents.[2] This is an extension of our previous studies on the reactions of nitrogen dioxide with alkenes (6) and dienes (7) and offers the possibility of comparing the extent of ^{15}N nuclear polarization in the addition and cyclization reactions.

Results

To determine the product composition, the reactions were carried out by the mixing of solutions of nitrogen dioxide and diallyl ether in the same organic solvent. When reaction was complete, the solvent was removed under reduced pres-

Received November 4, 1998.

This paper is dedicated to Jerry Kresge in recognition of his many achievements in chemistry.

R.P. Claridge and J.H. Ridd.[1] Chemistry Department, University College, 20 Gordon Street, London WC1H 0AJ, England.
R.W. Millar. Defence Evaluation and Research Agency, Fort Halstead, Sevenoaks, Kent TN14 7BP, England.

[1]Author to whom correspondence may be addressed. Telephone: (0044) 1713877050. Fax: (0044) 1713807463. e-mail: j.h.ridd@ucl.ac.uk

[2]The term "nitrogen dioxide" without the qualification "molecular" is used here to specify both the molecular species and the various forms of the dimer in equilibrium with it.

© 1999 NRC Canada

Table 1. ^{13}C NMR chemical shifts for the products formed from the reaction of nitrogen dioxide with diallyl ether. The numbering for both cyclic and linear structures is as shown in Scheme 1. Calculated chemical shifts (8) are given in parentheses.

	δ_C ($CHCl_3$)					
Compound	1-C	2-C	3-C	1′-C	2′-C	3′-C
2	70.3	39.3	73.4	70.3	39.3	73.4
	(63.9)	(42.4)	(76.6)	(63.9)	(42.4)	(76.6)
3	70.7	40.8	76.7	70.7	40.8	76.7
	(63.9)	(42.4)	(76.6)	(63.9)	(42.4)	(76.6)
4	70.3	39.1	73.7	69.9	38.5	70.2
	(63.9)	(42.4)	(76.6)	(63.9)	(32.5)	(78.0)
5	70.8	40.5	76.8	70.0	40.5	72.9
	(63.9)	(42.4)	(76.6)	(63.9)	(32.5)	(78.0)
7	70.8	82.6	72.9	70.8	82.6	72.9
	(66.0)	(84.9)	(79.3)	(66.0)	(84.9)	(79.3)
8	72.5	67.7	78.0	70.2	133.7	118.0
	(72.2)	(71.6)	(79.3)	(72.1)	(135.1)	(116.5)
9	73.0	68.5	79.3	70.2	82.9	73.6
	(72.2)	(71.6)	(79.3)	(66.0)	(84.9)	(79.3)

Table 2. Product composition from the reaction of diallyl ether (DAE) with nitrogen dioxide in organic solvents.

			%						
Solvent	$[NO_2]$	[DAE]	**2**	**3**	**4**	**5**	**7**	**8**	**9**
C_6H_{14}	0.29[a]	0.11	17	30	14	26	—	—	—
CH_2Cl_2	0.30[b]	0.11	44	15	20	6	—	4	—
CH_2Cl_2	1.12[c]	0.11	11		4		13	—	28

[a]Addition of the solution of nitrogen dioxide to the solution of diallyl ether over a period of 30 min at 0–5°C.

[b]Addition of the solution of nitrogen dioxide to the solution of diallyl ether over a period of 30 min at room temperature.

[c]Addition of the solution of diallyl ether to the solution of nitrogen dioxide over a period of 30 min at 0–5°C.

Scheme 1.

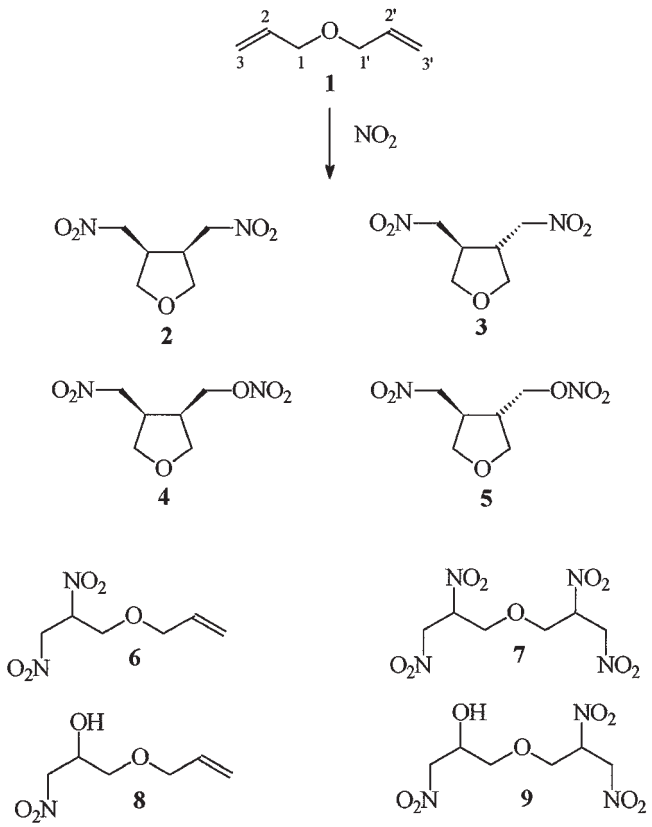

sure, and after separation by HPLC, the products were identified by a combination of ^1H and ^{13}C NMR spectroscopy and CI mass spectrometry; with some labelled compounds, ^{15}N NMR spectroscopy was also used. Plots of the NMR spectra are available elsewhere (7). The products identified are shown in Scheme 1. In this identification, the ^{13}C NMR spectra were of particular value for the high field signal at ca. 40 δ_C was characteristic of the cyclic compounds (1), and the patterns of signals from combinations of the $CH_2NO_2CHNO_2$-, CH_2NO_2CHOH-, and CH_2 = CH– groups were easy to recognize. The ^{13}C signals are compared with those calculated from an empirical program (8) in Table 1. In the identification of the *cis* and *trans* cyclic compounds, we have relied on earlier arguments (1*b*) that the ^{13}C signals in related *trans* compounds are slightly downfield to those in the *cis* compounds.

The product composition is very sensitive to the order of mixing of the reagents. The results for the runs in Table 2 show that, when the solution of nitrogen dioxide is added to the solution of diallyl ether, the major products are the cyclic tetrahydrofuran derivatives **2**–**5**, but when the solution of diallyl ether is added to the solution of nitrogen dioxide, the major products are the open-chain derivatives **7** and **9**. The combined yields in Table 2 show that a considerable amount of material remained unidentified in each run, and the small yields of the cyclic compounds in the third run were not separated into the *cis* and *trans* compounds.

The studies of ^{15}N nuclear polarization were carried out using ^{15}N labelled nitrogen dioxide (99% ^{15}N). Because of

© 1999 NRC Canada

Table 3. ^{15}N NMR chemical shifts for the main products formed in the low-temperature reactions of nitrogen dioxide with diallyl ether. The numbering of the nitrogen atoms indicates their position on the carbon chain in the substrate. The chemical shifts are given on the liquid ammonia scale based on δ_N 370.3 for $Ph^{15}NO_2$.

	Product			
	2	**3**	**6**	**8**
3-N	381.0	381.5	373.7	380.9
2-N			377.9	

Fig. 1. The final ^{15}N NMR spectrum of the products formed in the reaction of diallyl ether with nitrogen dioxide in deuterochloroform. The ppm measurements are taken from the signal for ^{15}N-nitrobenzene as an external standard.

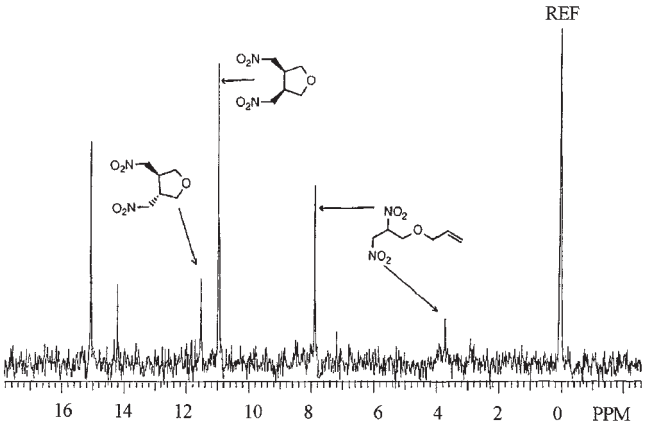

the speed of the reaction, the solution of diallyl ether in an NMR tube was very rapidly mixed with rather more than 2 equiv. of labelled nitrogen dioxide in the same solvent ($CDCl_3$); the tube was then frozen with liquid nitrogen and allowed to thaw out in the cavity of the NMR machine. Analysis of the products formed under these conditions, including some experiments on a somewhat larger scale, showed that the main products are the tetrahydrofuran derivatives **2**, **3** and the open-chain derivatives **6** and **8**. These were isolated from the reaction mixtures, and the ^{15}N NMR chemical shifts are listed in Table 3. The distinction between the ^{15}N signals in the dinitro compound **6** was based on the complexity of the coupling, for the nitrogen atom on C^3 is coupled to three protons but that on C^2 is coupled to five protons.

The ^{15}N NMR spectrum of the products taken after complete reaction in deuterochloroform is shown in Fig. 1 together with the identification of a number of the peaks. The *cis* dinitro compound **2** is the predominant cyclic product; this accords with the results obtained in dichloromethane (Table 2). The very different ^{15}N NMR spectra obtained during reaction are shown in Fig. 2: both cyclic dinitro compounds give emission signals and, for the open-chain dinitro compound **6**, the signal of one nitro group appears in emission and that for the other appears in enhanced absorption (compare with the signal for nitromethane present as a reference).

Discussion

The formation of the straight-chain products listed in Scheme 1 is consistent with what is known concerning the

Fig. 2. ^{15}N NMR spectra taken during the reaction of diallyl ether with nitrogen dioxide in deuterochloroform. Times: *A*, 1 min; *B*, 3 min; *C*, 5 min.

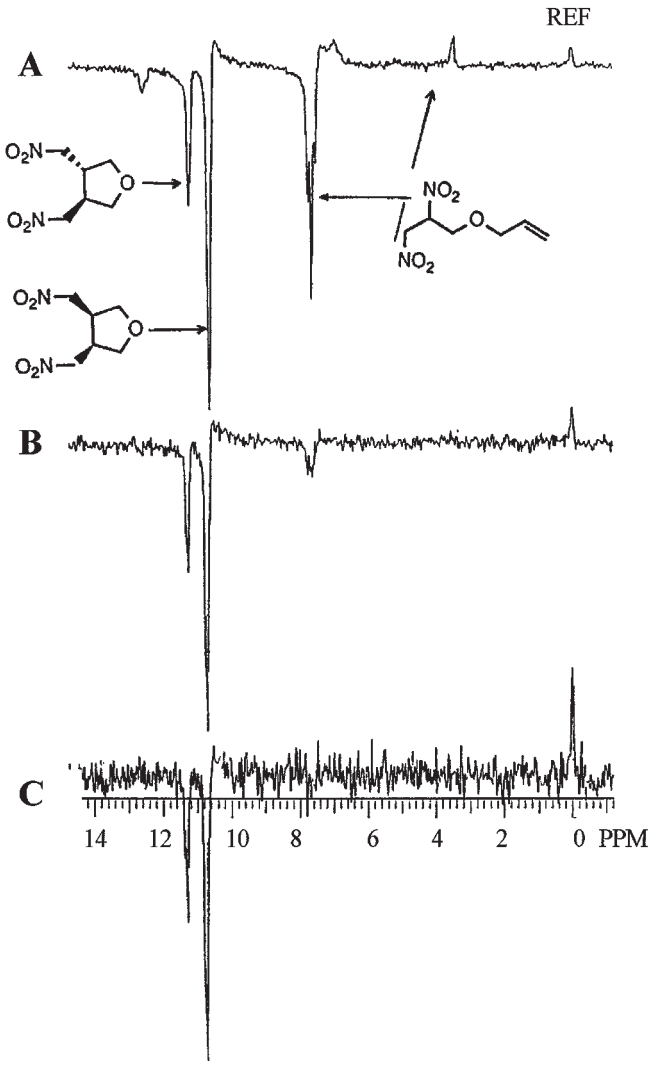

addition of nitrogen dioxide to unsaturated systems (6). The first nitrogen dioxide molecule appears always to add via a C—N bond and at the position that gives rise to the most stable radical; the subsequent reaction of this radical with a second nitrogen dioxide molecule gives a mixture of products resulting from addition via the nitrogen or via the oxygen. The nitroalcohols are presumably formed from the ready hydrolysis of the initial nitronitrites. It is also entirely reasonable that the addition of the solution of nitrogen dioxide to that of diallyl ether should give mainly the cyclic products, while the reverse mode of addition should give mainly the open-chain products, for the presence of excess nitrogen dioxide in the solution should favour addition (Scheme 2, Path B) rather than cyclization (Scheme 2, Path A).

The formation of the cyclic nitronitrates **4** and **5** rather than the corresponding nitroalcohols was unexpected but when the major part of the reaction follows the cyclization pathway, there must be excess nitrogen dioxide left in the solution, and this may lead to the oxidation of any cyclic nitronitrites to nitronitrates. This formation of nitronitrates in the reaction of phenanthrene with nitrogen dioxide has

© 1999 NRC Canada

Scheme 2.

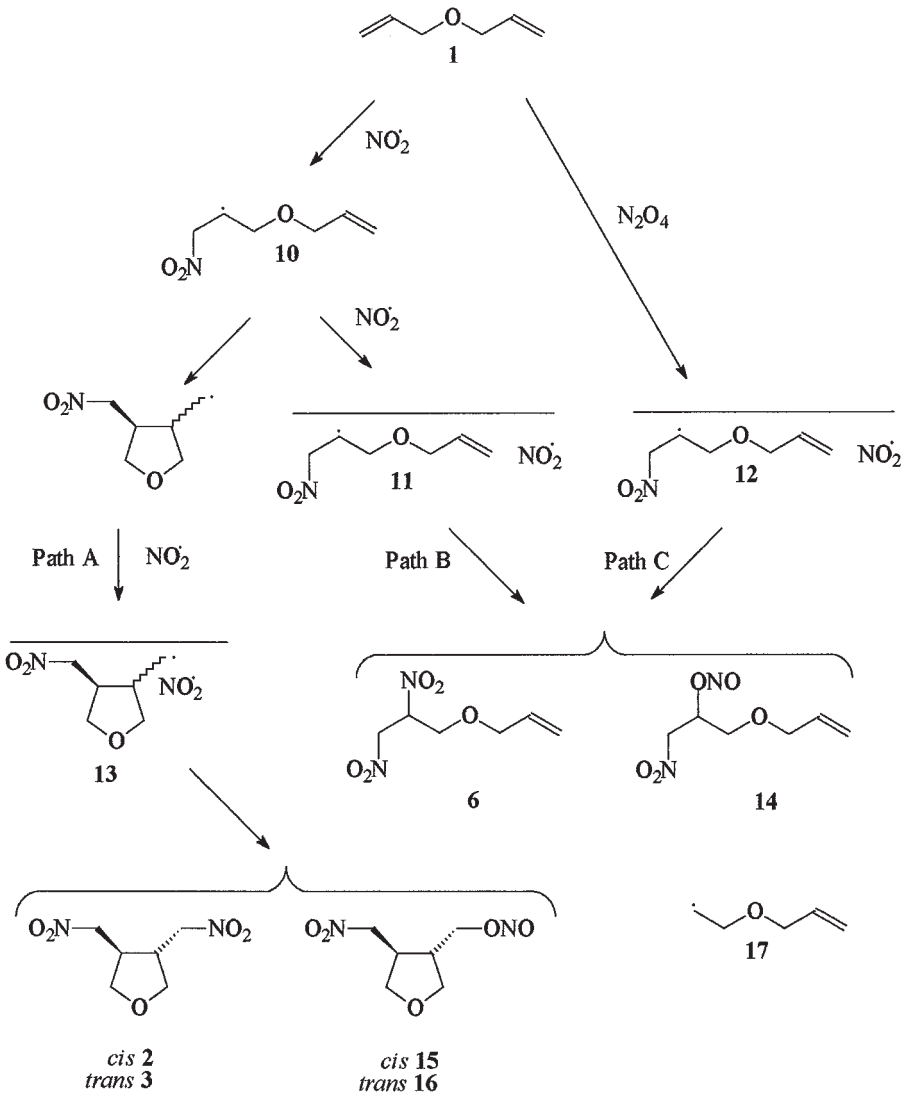

been ascribed to the reaction of the first-formed nitronitrites with nitrogen dioxide (9). The absence of a corresponding nitronitrate from the open-chain products identified (Scheme 1) is curious but there may not be a problem here for the ratio of products formed in these reactions of diallyl ether depends very much on the conditions and ca. 10–30% of the products were unidentified (Table 2).

In considering the ^{15}N polarization observed during reaction (Fig. 2), it is simplest to look first at the open-chain product **6**. Here the nitrogen atom at C^3 gives an absorption signal and that at C^2 gives an emission signal. This is as expected from Kaptein's rules (10) as applied to the ^{15}N nucleus (11) for the reaction of the radical **11** with molecular nitrogen dioxide on the reaction path shown in Scheme 2, Path B. Following earlier discussions (12, 13), the *g*-value of the NO_2 radical has been taken (14) to be 2.0000 and the *g*-values of the organic radicals to be >2.0000; this is in agreement with the listed *g*-values for a wide range of related carbon radicals (15). In this argument, the radical pair **11** is considered to be formed by the diffusion together of the radicals; the radical pair has therefore uncorrelated spins and (in the terminology of Kaptein (10)) is an F-precursor. With the cyclic dinitro compounds, the ^{15}N NMR signals of the two nitro groups are superimposed, but since the signal from the second nitro group should be the stronger,[3] the overall signal should be in emission, as observed.

The above observations accord with those found in the addition of nitrogen dioxide to alkenes (13), but in one respect, the present observations provide further evidence on the reaction mechanism. Although the previous studies of ^{15}N nuclear polarization were consistent with the reaction of the alkene with two separate nitrogen dioxide molecules, the earlier work left open the possibility that the major part of the product was formed through the reaction of the alkene with molecular dinitrogen tetraoxide (Scheme 2, Path C); a possibility given some support from kinetic studies of re-

[3] In the radical pair **13**, the ^{15}N hyperfine coupling constant of the nitrogen dioxide radical should be greater than that of the nitro group attached to the organic radical.

© 1999 NRC Canada

lated reactions (16, 17). Since the radical pair **12** shown in Scheme 2, Path C, is necessarily formed in a singlet state (an S-precursor (10)), the resulting ^{15}N nuclear polarization for each nitrogen atom in the product should be of opposite phase to that formed in Scheme 2, Path B, and probably also considerably weaker, since none of the radical pairs on Path C requires a triplet–singlet transition for combination to occur. Hence, the signals observed previously, and for the dinitro compound **6** in the present work, could also be the resultant polarization from the combination of the reaction Paths B and C in Scheme 2.

However, in the present work, the cyclic dinitro compounds can hardly be formed by a direct reaction with dinitrogen tetraoxide because of the time required for cyclization to occur. The presence of the nuclear polarization implies that the reaction of such singlet radical pairs as **12** occurs within approximately the time of a molecular encounter, and although the time required for the radical **10** to undergo cyclization is probably very short,[4] it must still be long in comparison with the lifetime of the singlet radical pair **12**. Hence, the nuclear polarization observed in the formation of the cyclic structures **2** and **3** must reflect simply the path involving successive reactions with two separate nitrogen dioxide molecules. It is then significant that the comparison of the signals during and after reaction shows that the enhancement of the signals is approximately the same for the cyclic and straight-chain structures. The relative intensities of the signals for the two cyclic structures and that for the "second" nitro group of **6** (also initially in emission) are very similar in the first polarized spectrum (spectrum **A**, Fig. 2) and the final spectrum (Fig. 1). For the straight-chain structure **6**, there is therefore no indication here of any major contribution from the separate reaction path (Scheme 2, Path C) involving attack by dinitrogen tetraoxide and leading to the opposite phase of ^{15}N nuclear polarization. The greater persistence with time of the emission signals for the cyclic structures (Fig. 2, spectra B and C) can be understood if, in the final stages of the reaction, cyclization predominates over the addition of nitrogen dioxide to the double bonds. This is, of course, the expected consequence of the fall in the concentration of nitrogen dioxide in the solution.

We conclude therefore that, under the conditions used, the reaction of diallyl ether with nitrogen dioxide occurs predominantly by the successive reactions of the substrate with two nitrogen dioxide radicals with uncorrelated spins.

Experimental

Materials

The nitrogen dioxide was obtained from ARGO International. It was purified by distillation over phosphorus pentoxide in a stream of dry oxygen using an all glass apparatus. The resulting white solid was kept over phosphorus pentoxide in a deep freeze at –16°C. ^{15}N-labelled nitric acid (99.5% ^{15}N) was obtained from MSD isotopes. Diallyl ether (99% purity) was obtained from Aldrich and was used without further purification. Dichloromethane and hexane were high-purity solvents obtained from Romil; they were refluxed over calcium hydride and under nitrogen for an hour before use and then distilled and collected over preactivated 3 Å molecular sieves and degassed using ultrasound.

^{15}N-nitrogen dioxide was prepared by heating lead ^{15}N-nitrate in an all glass apparatus flushed with argon before and after reaction. The product (yield 83%) was collected as white crystals in a trap at –80°C. The labelled lead nitrate was obtained from the reaction of a suspension of lead oxide (Aldrich) with aqueous ^{15}N-nitric acid. After stirring for 3 h, the solution was filtered and the solvent removed under reduced pressure to yield ^{15}N-labelled lead nitrate (yield 100%).

Experimental procedure

The preparation of the solutions and the reactions were carried out under nitrogen. In the experiments carried out to identify the products formed, a solution of nitrogen dioxide was added to a stirred solution of diallyl ether in the same solvent using a syringe pump. The reactions were carried out either at room temperature or at 0–5°C. In some experiments, the order of addition was reversed. The usual time of addition was 30 min.

After addition was complete, stirring was continued for ca. 3 h, and the solvent was then removed under reduced pressure. The reaction mixture was passed down a "flash" silica column eluting with ethyl acetate, and the products were then separated by HPLC using 2 × 25 cm × 1 cm silica columns (particle size 0.005 mm) and refractive index detection. When the molar ratios of diallyl ether:nitrogen dioxide were 1:2, the mobile phase employed was ethyl acetate:hexane (1:4 vol/vol), but when the corresponding molar ratios were 1:4, a mobile phase of ethyl acetate:hexane (1:1 vol/vol) was used first to remove the more polar components; the remaining components were then separated as before. The apparatus used included a Waters M6000 pump, a Waters R401 refractive index detector, a Rheodyne injection valve, and a Hewlett Packard integrator HP 3396a. The yields were estimated from the weights of material isolated or the relative areas of the HPLC peaks after calibration.

The ^{1}H, ^{13}C, and ^{15}N NMR spectra of the separated products were carried out in deuterochloroform or acetone-d_6 using a 400 MHz Varian VXR400 spectrometer. The CIMS measurements were carried out at the London University School of Pharmacy using ammonia as the ionizing gas.

Reactions and products

Compounds **2**–**9** appear to be new but, unfortunately, it has not been possible to characterize them completely. The experiments were carried out on a small scale partly because of the possible danger of explosions with the polynitro compounds and partly because of the cost of the ^{15}N labelled nitrogen dioxide. The ^{13}C NMR chemical shifts are given in Table 1, the ^{15}N NMR chemical shifts are given in Table 3, and the details of the ^{1}H NMR spectra and CIMS spectra are given below.

The first run described below is an example of the "normal" mode of addition (adding the solution of nitrogen dioxide to the solution of diallyl ether); the second run is an example of the reverse mode of addition. The product yields are those listed for the second and third runs in Table 2.

[4] The rate coefficient for the cyclization of the related radical **17** has been given as 8.5×10^6 s^{-1} (4).

© 1999 NRC Canada

A solution of nitrogen dioxide (0.139 g) in dichloromethane (10 mL) was added dropwise over 30 min to a stirred solution of diallyl ether (0.104 g) in dichloromethane (10 mL) at room temperature. The solution was stirred for a further 3 h, and then the solvent was removed under reduced pressure yielding a yellow oil. Separation of the components as described above gave the following.

trans-*2,3-Bis(nitromethyl)-tetrahydrofuran* ***3***: ^{1}H NMR ($CDCl_3$) δ: 2.78 (m, 2H), 3.63 (dd, 4.96, 9.68 Hz, 2H), 4.05 (dd, 6.78, 9.68 Hz, 2H), 4.45 (dd, 7.77, 13.75 Hz, 2H), 4.53 (dd, 6.71, 13.75 Hz, 2H); CIMS *m/z*: 208 ($M.NH_4^+$), 161($M.NH_4^+ - 47$), 113 ($M.NH_4^+ - 95$).

cis-*2,3-Bis(nitromethyl)-tetrahydrofuran* ***2***: ^{1}H NMR ($CDCl_3$) δ: 3.24 (m, 2H), 3.71 (dd, 5.08, 9.48 Hz, 2H), 4.02 (dd, 6.53, 9.48 Hz, 2H), 4.41 (dd, 6.21, 13.29 Hz, 2H), 4.51 (dd, 8.14, 13.29 Hz, 2H); CIMS *m/z*: 208 (M, NH_4^+), 190 (M^+).

trans-*2-Nitratomethyl-3-nitromethyl-tetrahydrofuran* ***5***: ^{1}H NMR ($CDCl_3$) δ: 2.4 (m, 1H), 2.8 (m, 1H), 3.62 (m, 5.25, 5.32, 9.62 Hz, 2H), 3.98 (dd, 7.39, 9.67 Hz, 1H), 4.05 (dd, 7.19, 9.67 Hz, 1H), 4.45 (m, 4H); CIMS *m/z*: 224 ($M.NH_4^+$), 206 (M^+), 179 ($M.NH_4^+ - 45$), 113 ($M^+ - 91$), 82 ($M^+ - 124$).

cis-*2-Nitratomethyl-3-nitromethyl-tetrahydrofuran* ***4***: ^{1}H NMR ($CDCl_3$) δ: 2.85 (m, 4.8, 6.94, 7.08, 7.54 Hz, 1H), 3.20 (m, 6.56, 6.68, 7.24, 7.49, 8.88 Hz, 1H), 3.68 (dd, 6.68, 9.26 Hz, 1H), 3.75 (dd, 4.80, 9.33 Hz, 1H), 3.98 (dd, 6.94, 9.33 Hz, 1H), 4.03 (dd, 7.24, 9.27 Hz, 1H), 4.43 (dd, 8.88, 13.57 Hz, 1H), 4.46 (d, 7.08 Hz, 2H), 4.57 (dd, 6.56, 13.59 Hz, 1H); CIMS *m/z*: 224 ($M.NH_4^+$), 206 (M^+), 179 ($M.NH_4^+ - 45$), 113 ($M^+ - 91$), 82 ($M^+ - 124$).

Allyl 2-hydroxy-3-nitropropyl ether ***8***: ^{1}H NMR ($CDCl_3$) δ: 2.72 (d, 4.83 Hz, 1H), 3.53 (m, 2H), 4.01 (m, 1.44, 5.75 Hz, 2H), 4.49 (m, 3H), 5.21 (dq, 1.44, 2.4, 10.39 Hz, 1H), 5.26 (dq, 1.40, 1.44, 17.22 Hz, 1H), 5.86 (m, 5.74, 10.39, 17.22 Hz, 1H).

A solution of diallyl ether in dichloromethane at 0°C was added dropwise over a period of 30 min to a stirred solution of nitrogen dioxide in dichloromethane at the same temperature. The reaction mixture was stirred for a further 2 h at 0°C, and the solvent was then removed under reduced pressure yielding a yellow oil. After a product analysis as described above, the reaction yielded a mixture of the two 2,3-bis(nitromethyl)-tetrahydrofurans **2** and **3**, a mixture of the two 2-nitratomethyl-3-nitromethyl-tetrahydrofurans **3** and **4**, and the following.

Bis*(2,3-dinitropropyl) ether* ***7***: ^{1}H NMR (CD_3COCD_3) δ: 4.12 (dd, 4.21, 11.09 Hz, 2H), 4.34 (dd, 3.62, 11.09 Hz, 2H), 5.18 (dd, 2.39, 16.57 Hz, 2H), 5.38 (dd, 9.69, 16.56 Hz, 2H), 5.67 (m, 2.29, 3.62, 4.21, 9.69 Hz, 2H); this compound decomposed before a CIMS spectrum could be obtained.

2,3-Dinitropropyl 2′-hydroxy-3′-nitropropyl ether ***9***: ^{1}H NMR ($CDCl_3$) δ: 3.64 (dd, 7.66, 17.16 Hz, 1H), 3.67 (dd, 8.99, 17.16 Hz, 1H), 4.15 (dd, 4.11, 11.05 Hz, 1H), 4.33 (dd, 3.62, 11.05 Hz, 1H), 4.48 (m, 2H), 4.68 (dd, 5.15, 10.05 Hz, 1H), 4.88 (bs, 1H), 5.20 (dd, 9.90, 16.45 Hz, 1H), 5.45 (dd, 2.31, 16.45 Hz, 1H), 5.63 (m, 1H); CIMS *m/z*: 271 ($M.NH_4^+$), 253 (M^+), 224 ($M.NH_4^+ - 47$), 204 ($M^+ - 47$), and 179 ($M.NH_4^+ - 96$).

Experiments with ^{15}N-nitrogen dioxide

For the study of CIDNP effects, ^{15}N-lead nitrate (0.061 g) was heated in a small flask with a tapped gas inlet and sidearm. The system was then purged with dry argon, and the evolved ^{15}N-nitrogen dioxide was collected in deuterochloroform (0.25 mL) in an acetone–cardice bath. The process was repeated three times, and the solution of nitrogen dioxide was then added by syringe to a solution of diallyl ether (0.0153 g) in deuteriochloroform (0.25 mL) within an NMR tube containing ^{15}N-nitrobenzene in an inner reference tube. The tube was briefly shaken (2 s) and immediately immersed in liquid nitrogen. Then the tube, while still frozen, was placed in the preshimmed and locked Varian 400 MHz NMR spectrometer, and acquisitions started immediately. The spectra taken during reaction were recorded using 10 pulses with an acquisition time of 5 s and a pulse delay of 12 s; the times quoted refer to the midpoint of the acquisitions. The final spectrum was taken after 24 h using 6000 pulses.

The reaction mixtures from this and related experiments on a larger scale were analyzed as described above and yielded the ^{15}N-labelled derivatives of **2**, **3**, and **8** each of which gave one signal in the ^{15}N NMR spectrum (Table 3). An additional product gave two ^{15}N NMR signals (δ_N 373.7, 377.9) in the range for nitro groups and close to the signals given by the dinitro compound formed by the addition of nitrogen dioxide to 2-ethylbut–1-ene (δ_N 373.3, 385.3) (13). From this and from the analysis of the ^{1}H NMR spectrum, the product was identified as the dinitro compound **6**: ^{1}H NMR ($CDCl_3$) δ: 3.87 (m, 10.70, 4.58 Hz, J_{HN} 3.55 Hz, 1H), 3.99 (m, 5.78, 2.56, 1.25 Hz, 2H), 4.11 (m, 10.7, 4.1 Hz, J_{HN} 1.7 Hz, 1H), 4.70 (m, 13.25, 4.96 Hz, J_{HN} 2.47 Hz, 1H), 5.21–5.35 (m, 4H), 5.78 (m, 16.56, 11.01, 5.78 Hz, 1H).

Acknowledgements

This work forms part of the UK MOD Corporate Research Program, © British Crown Copyright 1998/DERA Farnborough, Hants., U.K.; published with the permission of the Controller of Her Britannic Majesty's Stationery Office.

References

1. (*a*) N.O. Brace. J. Am. Chem. Soc. **86**, 524 (1964); (*b*) J. Org. Chem. **44**, 212 (1979).
2. A.C. Serra and C.M.M. da Silva Corrêa. J. Chem. Res. Synop. 85 (1989).
3. S F. Reed. J. Org. Chem. **32**, 3675 (1967).
4. A.L.J. Beckwith and C. H. Schiesser. Tetrahedron, **41**, 3925 (1985).
5. K.W. Busfield, I.D. Jenkins, S.H. Thang, E. Rizzardo, and D.H. Solomon. J. Chem. Soc. Perkin Trans. 1, 485 (1988).
6. P. Golding, J.L. Powell, and J.H. Ridd. J. Chem. Soc. Perkin Trans. 2, 813 (1996), and refs. there listed.
7. R.P. Claridge. Ph.D. thesis. University of London, London. 1993.

© 1999 NRC Canada

8. D.A. Fletcher, R.F. McMeeking, and D.J. Parkin. Using the SpecInfo package of the United Kingdom chemical database service. Chem. Inf. Comput. Sci. **36**, 746 (1996).
9. M.C. Judd, M.P. Hartshorn, R.J. Martyn, W.T. Robinson, G.J. Wright, and R.W. Vannoort. Aust. J. Chem. **43**, 125 (1990).
10. R. Kaptein. Chem. Commun. 732 (1971).
11. N.A. Porter, G.R. Dubay, and J.G. Green. J. Am. Chem. Soc. **100**, 920 (1978).
12. A.H. Clemens, J.H. Ridd, and J.P.B. Sandall. J. Chem. Soc. Perkin Trans. 2, 1659 (1984).
13. J.L. Powell, J.H. Ridd, and J.P.B. Sandall. Appl. Mag. Res. **5**, 151 (1993).
14. J.R. Morton, K.F. Preston, and S.J. Strach. J. Phys. Chem. **83**, 533 (1979).
15. K.-H. Hellwege and H. Fischer (*Editors*). Landolt-Børnstein: Numerical data and functional relationships in science and technology. Vol 96. Springer-Verlag, Berlin. 1977. p. 204.
16. D.H. Giamalava, G.B. Kenion, D.F. Church, and W.A. Pryor. J. Am. Chem. Soc. **109**, 7059 (1987).
17. J. Chatterjee, R.G. Coombes, J.R. Barnes and M.J. Fildes. J. Chem. Soc. Perkin Trans. 2, 1031 (1995).

© 1999 NRC Canada

Aggregation and ion pair acidity in THF: lithium and cesium enolates of α-phenylcyclohexanone[1]

Daniel Ze-Rong Wang and Andrew Streitwieser

Abstract: The lithium (**1**) and cesium (**2**) enolates of α-phenylcyclohexanone, PCH, have been studied in THF at 25°C. Both form monomer–dimer equilibria with $K_{1,2}$ = 2.8 × 10^3 M^{-1} for **1** and 1.8 × 10^3 M^{-1} for **2**. The ultraviolet-visible (UV-vis) spectra of the monomers and dimers were derived from the spectra of the enolates at a series of concentrations by singular value decomposition. Measurements of the ion pair p*K* values gave p*K* = 12.7 for **1** and 19.8 for **2**. The monomers of **1** and **2** are alkylated by benzyl halides faster than are the dimers.

Key words: carbon-acid ionization, enolate ions, ion pairs, ion pair acidity, aggregation, dimerization constants, alkylation.

Résumé : On a étudié les énolates de lithium (**1**) et de césium (**2**) de l'α-phénylcyclohexanone (PCH) en opérant à 25°C, dans le THF. Les deux sels donnent des équilibres monomère–dimère avec des $K_{1,2}$ = 2,8 × 10^3 M^{-1} pour le composé **1** et 1,8 × 10^3 M^{-1} pour le composé **2**. En procédant à une décomposition à une valeur particulière, on a déduit les spectres ultraviolet-visible (UV-vis) des monomères et des dimères à partir des spectres des énolates à une série de concentrations. Des mesures des p*K* de la paire d'ion permettent de déduire les valeurs de p*K* des composés **1** (12,7) et **2** (19,8). Sous l'influence des halogénures de benzyle, les monomères des produits **1** et **2** sont alkylés plus rapidement que des dimères.

Mots clés : ionisation d'un acide carboné, ions énolates, paires d'ions, acidité d'une paire d'ions, agrégation, constantes de dimérisation, alkylation.

[Traduit par la Rédaction]

Introduction

Keto–enol equilibrium constants and their pK_a values are now known for a number of simple carbonyl compounds in aqueous solution and in DMSO, in large part through the work of Kresge (1) and Bordwell (2), respectively. A selected set of values is summarized in Table 1. For several years, we have determined the ion pair acidities of a number of ketones in THF solution. In this solvent, the enolates are ion-paired and frequently aggregated (3). It is as ion pairs that these metal enolates in THF are used in synthesis; thus, we have referred to the corresponding equilibria between such enolates and ketones as "ion pair acidities" generally in reference to a scale of ion-paired indicators (4). Some of these results are summarized in Table 2. The p*K* values in this table are defined by eq. [1] in terms of the equilibria in eq. [2] in which InH is a suitable indicator and M is either lithium or cesium.

[1] $$pK(RH) - pK(Ind\text{-}H) = -\log K$$

Received November 11, 1998.

This paper is dedicated to Jerry Kresge in recognition of his many achievements in chemistry.

D.Z. Wang and A. Streitwieser.[2] Department of Chemistry, University of California, Berkeley, CA 94720–1460, U.S.A.

[1]Carbon acidity. 106.

[2]Author to whom correspondence may be addressed. Telephone: (510) 642-2204. Fax: (510) 643-6232. e-mail: astreit@socrates.berkeley.edu.

[2] $$RH + In^-M^+ \overset{K}{\Leftrightarrow} R^-M^+ + InH$$

The p*K* values are given absolute numbers by assigning to fluorene its pK_a in DMSO, 22.9 (per hydrogen) (2, 4). Extensive tables of p*K* values for the indicators are now available for both the lithium (5, 6) and cesium (7) scales. To the previously determined results in Table 2, we add the results from the present work on the lithium **1** and cesium **2** enolates of 2-phenylcyclohexanone.

Spectral analyses

Treatment of 2-phenylcyclohexanone (PCH) with diphenylmethylcesium gave the conjugated cesium enolate **2** directly. Treatment of PCH with a lithium base gave a small absorption for the enolate **1** followed by a slower increase in this absorption. This behavior is interpreted as shown in Scheme 1 by initial formation predominantly of the unconjugated enolate, **3**, which does not absorb in the UV region studied, followed by gradual rearrangement to the conjugated lithium enolate. The mixture of **1** and **3** is stable in the absence of ketone.

Accordingly, the reaction mixture of ketone with lithium base was allowed to stand for at least 2 days to ensure complete conversion to **1** before the spectral measurements. In each of several runs, the enolate solution was diluted with known amounts of THF to obtain spectra as a function of concentration. For both **1** and **2**, λ_{max} varies with concentration. Over a concentration range of about 10^{-3}–10^{-5} M, λ_{max} for **1** ranges from 316.5 to 332 nm, for **2** from 345.5 to

© 1999 NRC Canada

Table 1. pK_a values of some ketones in water and DMSO.

Ketone	pK_a (aqueous)	pK_a (DMSO)[a]
Acetophenone	18.31[b]	24.7
Isobutyrophenone	18.25[c]	26.25
1-Indanone	16.96[d]	23.0
2-Indanone	12.2[e]	16.95
Cyclohexanone	18.09[f]	26.4
Dibenzyl ketone		18.7

[a]Reference 2.
[b]References 20–22.
[c]Reference 23.
[d]Reference 24.
[e]Reference 25.
[f]Reference 1.

Table 2. Ion pair acidities of some ketones in THF.

Ketone	Cesium pK	Lithium pK
Dibenzyl ketone	18.07[a,b]	11.62[a]
Di-*p*-biphenylylmethyl ketone	17.10[b]	
p-Phenylisobutyrophenone	25.08[c]	15.86[d]
2-Phenylcyclohexanone[e]	19.82	12.69

[a]Reference 26.
[b]Reference 8.
[c]Reference 11.
[d]Reference 10.
[e]This work.

354 nm. This result indicates that different aggregates have significantly different spectra (8). In both cases, normalized spectra showed an isosbestic point, at 320.5 nm for **1** and 349.0 nm for **2**, indicating that only two components make significant contributions in both cases. These were shown as detailed below to be the monomer and dimer. The absorbance at the isosbestic points varied linearly with concentration; ε = 18 392 ± 91 for **1** and 16 602 ± 38 for **2**.

The spectra were analyzed by singular value decomposition (SVD) (9); the composite results of several runs are given in Fig. 1. In agreement with previous results, the dimer absorbs at shorter wavelength than the monomer, and the lithium enolate absorbs at shorter wavelength than the cesium enolate (10, 11). The latter result shows that both the lithium and cesium enolates are contact ion pairs.

The monomer and dimer spectra were used to deconvolute the spectral mixtures for determining the compositions of each spectrum. The concentration of dimer was plotted against the square of the monomer concentration in order to obtain the dimerization constant, $K_{1,2}$, as given by eq. [3]. For **1** the results of three runs are in good mutual agreement over a range of total enolate concentration up to 10^{-3} M with $K_{1,2}$ = 2988 ± 17 M^{-1}; this result has high *precision* but the *accuracy* is expected to be much less. The results for four runs with **2** show more variation with $K_{1,2}$ = 1627 ± 13, 1945 ± 9, 1974 ± 12, 2328 ± 11 M^{-1}; each run by itself has good precision as indicated by the errors given as standard deviations, but the variation from the average value of 1969 M^{-1} among them is almost 10%. Nevertheless, the linearity of the plots for **1** and **2** confirms that these are monomer–dimer species; if significant amounts of higher aggregates were involved a higher order function would be required and these plots would curve upward.

Scheme 1.

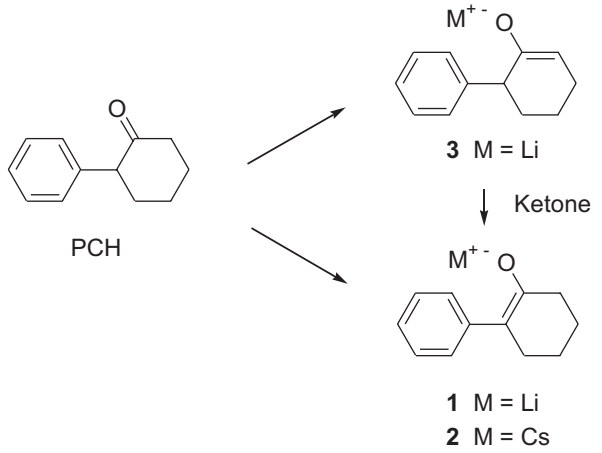

Fig. 1. Spectra of dimer (D) and monomer (M) of **1** and **2** as determined by SVD; λ_{max} are 327.5, **1**(M); 314.5, **1**(D); 356.5, **2**(M); 344.5 nm, **2**(D).

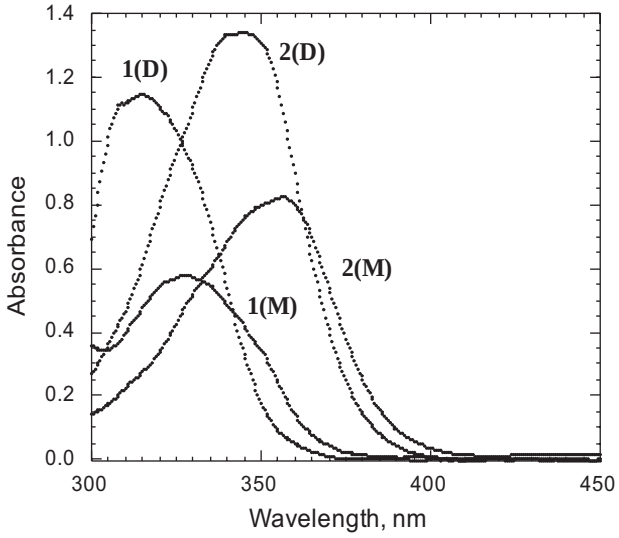

$$[3] \qquad 2M \overset{K_{1,2}}{\Leftrightarrow} D, \qquad K_{1,2} = [D]/[M]^2$$

Once the extinction coefficient of **1** was known, it was possible to do kinetic measurements of the conversion of **3** to **1**. Treatment of known amounts of the ketone with known amounts of the deprotonating reagent 9-lithio-9,9,10-trimethyl-9,10-dihydroanthracene gave initially and rapidly a 0.16 ratio of **1** to **3**. This was followed by a slow conversion of **3** to **1**, as shown by a gradual increase in the spectrum of **1**. The rate of this increase was determined for the first 10% reaction as an initial rate; since **3** has no useful spectrum, its concentration was determined as the difference between that of the deprotonating agent used and **1**. A series of eight runs with initial concentrations of [**1**] = 1.66 × 10^{-4} M and [**3**] = 8.60 × 10^{-4} M, and with [PCH] varying from 6.6 × 10^{-5} M to 3.8 × 10^{-4} M, gave the result in eq. [4].

© 1999 NRC Canada

Scheme 2.

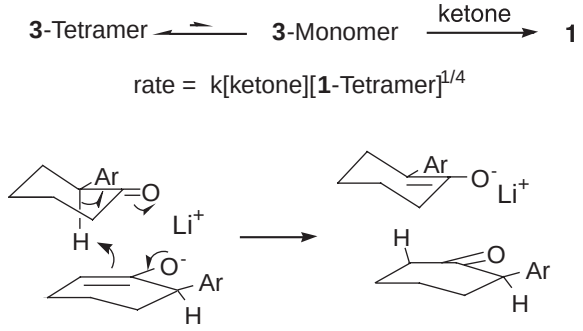

[4] log rate ($M\ s^{-1}$) = –3.02 ± 0.28
+ (0.941 ± 0.076) log [PCH], R^2 = 0.962

This result shows that the reaction is first order in the added ketone. A second series of 10 runs was carried out with [PCH] held constant at 2.74×10^{-4} M and [**3**] varying from 8.9×10^{-4} M to 2.9×10^{-3} M to give the result in eq. [5], which shows that the reaction is 1/4 order in [**3**].

[5] log rate ($M\ s^{-1}$) = –5.72 ± 0.02
+ (0.250 ± 0.008) log [**3**], R^2 = 0.991

These kinetic results indicate that **3** is present predominantly as a tetramer but that the small amount of monomer in equilibrium reacts with ketone to produce **1** and the ketone (Scheme 2). Kinetically favored deprotonation of the less hindered nonconjugated hydrogen is not new. Beutelman et al. (12) and Xie and Saunders (13), for example, have found that deprotonation of several ketones with LDA in THF at 0°C gives predominantly the less substituted lithium enolate. What is new is the present demonstration that proton transfer from the ketone is much faster with the enolate monomer than with an aggregate at 25°C. This result is relevant to recent interest in enantioselective protonations of lithium enolates with chiral protonating agents (14), because it is a rare example of a demonstrated kinetic protonation of a coordinated lithium enolate monomer in equilibrium with an aggregate. The other point of interest is that the less stable **3** forms a monomer–tetramer mixture compared to the monomer–dimer of **1**, in agreement with the generalization that aggregation is lower for more stable alkali enolates (8).

Acidity measurements

Equilibria were measured (eq. [2]) for the enolates with suitable indicators. A suitable indicator is one for which λ_{max} is sufficiently different from that of the enolate to permit facile determination of both and an equilibrium constant sufficiently close to unity so that accurately measurable amounts of both are present at equilibrium. 1,3-Diphenylindene (DPI, pK = 12.32 (6)) was used for **1**; two indicators, 9-*p*-(dimethylaminophenyl)fluorene (DMAPhFl, pK = 19.28)[3] and phenyl-2,3-benzofluorene (Ph-2,3-BF, pK = 18.92 (7)) were used for **2**. From the known amounts of ketone and indicator used and the amounts of the ion pairs from the spectral analyses, the equilibrium constants for eq. [2] were calculated. For lithium enolates, however, a correction is required because at the high dilutions used ([Li-Ind] = 10^{-4} to 10^{-5} M) significant amounts of the lithium salts of the indicators are dissociated to free ions. The free-ion spectra are close to those of the solvent-separated indicator ion pairs, and the concentrations were corrected using $K_{dissoc} = 10^{-5}\ M^{-1}$ (4). The lithium enolate contact ion pairs are not significantly dissociated. The cesium salts of the indicators have dissociation constants 10^{-2}–10^{-3} that of the lithium salts (4), and no correction is necessary.

Fig. 2. Plot of observed equilibrium constant (eq. [2]) from pK measurements of LiPCH (**1**) and CsPCH (**2**) vs. {MPCH}/K_{ob}. Closed circles and squares are two runs of **1** with the same indicator, 1,3-diphenylindene (DPI). The equation of the LiPCH line shown is K_{ob} = (0.43 ± 0.02) + (993 ± 42){**1**}/K_{ob}. Two indicators were used with CsPCH: open squares with 9-*p*-(dimethylaminophenyl)fluorene (DMAPhFl), K_{ob} = (0.268 ± 0.006) + (252 ± 9){**2**}/K_{ob}; open circles with phenyl-2,3-benzofluorene (Ph-2,3-BF), K_{ob} = (0.133 ± 0.002) + (66.5 ± 3.6){**2**}/K_{ob}.

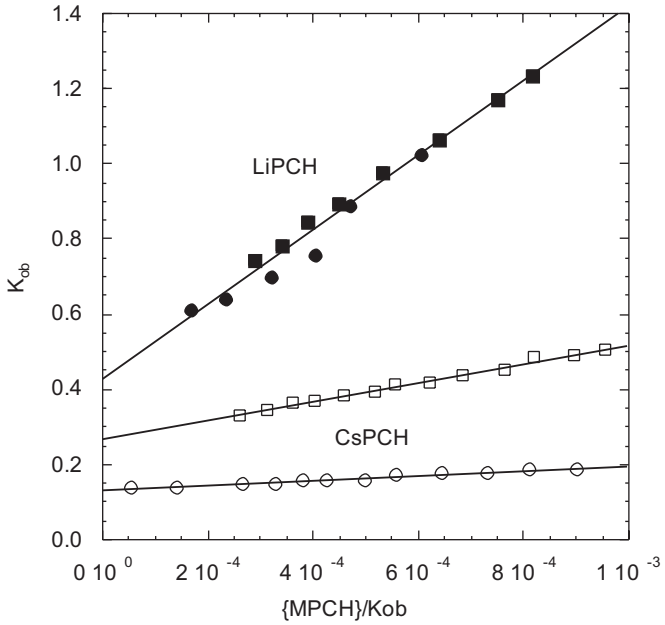

The effect of aggregation is to increase the observed equilibrium constant, K_{ob}, in eq. [2] as the enolate concentration is increased; the equilibrium is displaced to the right as monomer is converted to the aggregate. The corresponding equilibrium constant defined for the monomer enolate defines pK_o and can be obtained from a plot of K_{ob} vs. {MPCH}/K_{ob} (9) in which {MPCH} is the formal concentration of the metal enolate as determined, for example, from its absorbance at $\lambda_{isosbestic}$. Such plots are shown for the equilibrium constants of LiPCH, **1**, and CsPCH, **2**, in Fig. 2. For LiPCH, the intercept gives K_o = 0.43 and the slope = $2K_{1,2}K_o^2$ (9) from which pK of **1** (monomer) = 12.69 ± 0.02 and $K_{1,2}$ = 2710 M^{-1}. The latter number is close to that obtained from the SVD analysis and is probably somewhat

[3] This value differs slightly from that (19.23) given in ref. 7 because of additional measurements.

© 1999 NRC Canada

Fig. 3. Rates/[RX] (s^{-1}) vs. monomer concentrations (M) for reaction of **1** (squares, [RX] = 0.006 97 M, k_2 = 1.34 ± 0.02 M^{-1} s^{-1}) and **2** (circles, [RX] = 0.00708 M, k_2 = 0.546 ± 0.013 M^{-1} s^{-1}) with *m*-chlorobenzyl bromide and *p*-*t*-butylbenzyl chloride, respectively, in THF at 25°C.

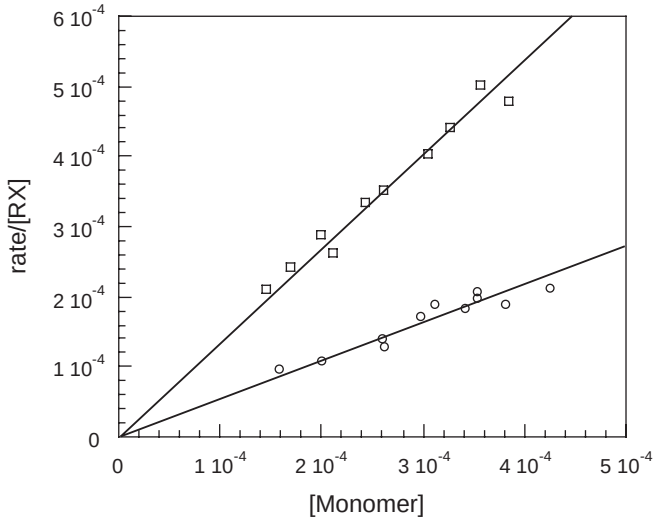

more accurate. We take $K_{1,2}$ = 2.8 × 10^3 as the best value. The results for CsPCH with two different indicators gave mutually consistent results. With DMAPhFl (open squares in Fig. 2), the intercept is 0.27 (from which p*K* = 19.85) and the slope gives $K_{1,2}$ = 1725 ± 63. With Ph-2,3-BF (open circles in Fig. 2), the intercept of 0.13 gives p*K* = 19.80 and the slope gives $K_{1,2}$ = 1868 ± 123. The $K_{1,2}$ values are in the range given by the SVD treatment above. We take as average values, p*K* = 19.82, $K_{1,2}$ = 1.8 × 10^3 M^{-1}. The fact that the plots in Fig. 2 are linear also shows that only monomers and dimers contribute significantly in this concentration range; if higher aggregates were important, a higher power of {MPCH}/K_{ob} would be required (9) and the plots would curve upward.

With these acidities added to Table 2, some relationships can be made even though no one compound has been studied in all three solvent systems, water, DMSO, and THF. Several comparisons between water and DMSO in Table 1 follow the well-known phenomenon that aqueous p*K* values of species involving oxide ion conjugate bases are lower than the corresponding p*K* values in DMSO undoubtedly because of hydrogen-bond stabilization of the anions in water. For the ketones in Table 1 this difference ranges from about 5 to 8 p*K* units. Two comparisons can be made between DMSO and THF, since the p*K* of *p*-phenylisobutyrophenone is expected to be quite close to that for isobutyrophenone (10, 11). The cesium ion pair p*K* values thus differ from the DMSO values by no more than 1 p*K* unit. The slightly greater acidity in THF indicates that cesium cation is bound electrostatically to the vinyloxide ion slightly more than to the delocalized carbanions used as indicators. The lithium p*K* values, however, are about 7–9 p*K* units lower than those of the cesium enolates and, indeed, are in the same range as the aqueous values if not even lower. Lithium cation as the smallest alkali cation is bound tightly to the enolate oxide anion. Since the free-ion acidities must be the same, these differences mean that the corresponding dissociation constants of lithium enolates are several orders of magnitude less than the cesium enolates (4).

The role of conjugation is shown not only by the comparison of 2-indanone with 1-indanone in Table 1 but also by comparison of conjugation with phenyl and with *p*-biphenylyl. The *p*-phenyl substituent decreases the p*K* of dibenzyl ketone by 1 unit on the cesium scale. The conjugated enolate systems **1** and **2** are, as expected, less basic than the nonconjugated enolates of *p*-phenylisobutyrophenone but the difference for lithium, 3.1 p*K* units, is substantially less than that for cesium, 5.3 p*K* units. A simple interpretation is that the tighter lithium ion pair electrostatically impedes delocalization of charge.

Alkylation kinetics

Previous kinetic studies with other lithium and cesium enolates reacting with alkyl halides and sulfonates have shown that the rate constants for the enolate monomers are much greater than for the aggregates (10, 11, 15) These results are extended to reactions of **1** and **2**. Convenient rates were found for the reaction of **1** with *m*-chlorobenzyl bromide and for **2** with *p*-*t*-butylbenzyl chloride. The alkyl halide concentrations were used in large excess so that the reactions are pseudo first order in enolate, but only initial rates (about 10% reaction) were used to avoid possible complications with mixed aggregates from the products. Rates at fixed concentrations of the enolate and varying [RX] show the reactions to be, as expected, first order in alkyl halide. For 7.79 × 10^{-4} M **1** and *m*-chlorobenzyl bromide varying from 7.4 × 10^{-3} to 2.4 × 10^{-2} M, log rate = –3.55 + (1.07 ± 0.07) log [RX] and for **2** = 8.02 × 10^{-4} M and *p*-*tert*-butylbenzyl chloride varying from 5.6 × 10^{-3} to 1.5 × 10^{-2} M, log rate = –3.82 + (0.95 ± 0.03) log [RX]. Similar log–log plots at constant [RX] and varying enolate concentrations give fractional slopes; for example, 0.58 for **1** and 0.57 for **2**. More meaningful are direct comparisons of the initial rates divided by [RX] with the concentrations of monomer as shown in Fig. 3. The plots are those of straight lines with no apparent curvature and show that the reactions are first order in monomer. In the points at the righthand side of the plots, the amount of enolate present as dimer is substantially greater than that present as monomer; thus, if there were any significant contribution by reaction with dimer, the plots would show an upward curvature. We conclude that $k_{monomer} >> k_{dimer}$ in agreement with the other cases we have studied.

This relative reactivity is rationalized on the basis of **4** as a reasonable structure for the dimer (16). In the monomer, the enolate oxygen is coordinated to a single metal cation; in the dimer, it is coordinated to two cations and is accordingly effectively less nucleophilic.

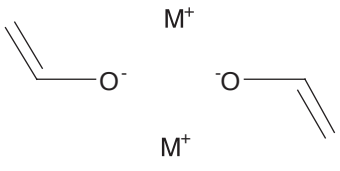

4

© 1999 NRC Canada

Experimental section

2-Phenylcyclohexanone was purified by sublimation, mp 61°C (lit. 59–60°C (17), 56–58°C (18), 59.5–60°C (19)) and was >99% pure by GC. The indicators and bases used were available from previous studies. Solutions of the cesium enolate **2** were prepared by adding solutions of diphenylmethylcesium to the ketone and using *p*-biphenylyldiphenylmethane as an endpoint indicator; the cesium salt is bright red compared to the greenish yellow of **2**. The initial solutions were diluted with THF to produce a series of solutions of varying concentration for spectral analysis. Spectra were taken with a thermostated cell block in the floor of a glovebox and connected to an external spectrometer by fiber optics cables (9). Because of the formation of **3**, spectra of **1** were more difficult to obtain. A sample procedure follows: to a 1 mm UV cell was weighed 0.485 g of THF and 0.113 mg of PCH. Then, 4.0 μL (an excess) of the lithium base (9-lithio-9,10,10-trimethyl-9,10-dihydroanthrance), ca. 0.2 M in THF, was added to deprotonate the PCH. To a small vial was added 0.418 g of THF and 0.514 mg of PCH ([PCH] = 6.2×10^{-3} M). Varying amounts (2–5 μL) of this PCH solution were added to the UV cell to titrate the base, until the endpoint was reached. Small additional amounts of the PCH solution were added, mixed well, and allowed to stand in order to ensure that all of the unconjugated enolate had converted into the conjugated enolate. This procedure took several days. At this point, the solution was diluted with varying amounts of THF for spectral analysis.

Alkylation kinetics at fixed enolate concentrations utilized previously prepared enolate solutions which were added to several 1 mm cells. Each cell was equilibrated in the cell block for several minutes, and varying known amounts of benzylic halide were weighed into the cell, mixed quickly, and the initial rate of loss of absorbance of enolate was measured. For fixed concentrations of alkylating agent, a stock solution was added to a cell, equilibrated, and an aliquot of a batch solution of enolate was added by micro syringe such that the volume change was less than 5%.

Acknowledgement

This research was supported in part by National Science Foundation grant no. 9528273.

References

1. A.J. Kresge. Pure Appl. Chem. **63**, 213 (1991).
2. F.G. Bordwell. Acc. Chem. Res. **21**, 456 (1988).
3. L.M. Jackman and J. Bortiatynski. Adv. Carbanion Chem. **1**, 45 (1992).
4. M.J. Kaufman, S. Gronert, and A. Streitwieser, Jr. J. Am. Chem. Soc. **110**, 2829 (1988).
5. S. Gronert, and A. Streitwieser, Jr. J. Am. Chem. Soc. **108**, 7016 (1986).
6. A. Streitwieser, D.Z. Wang, M. Stratakis, A. Faccetti, R. Gareyev, A. Abbotto, J.A. Krom, and K.V. Kilway. Can. J. Chem. 1998. In press.
7. A. Streitwieser, J.C. Ciula, J.A. Krom, and G. Thiele. J. Org. Chem. **56**, 1074 (1991).
8. J.C. Ciula and A. Streitwieser. J. Org. Chem. **57**, 431 (1992); correction p. 6686.
9. J.A. Krom, J.T. Petty, and A. Streitwieser. J. Am. Chem. Soc. **115**, 8024 (1993).
10. A. Abbotto, S.S.-W. Leung, A. Streitwieser, and K.V. Kilway. J. Am. Chem. Soc. **120**, 10 807 (1998).
11. A. Streitwieser, J.A. Krom, K.A. Kilway, and A. Abbotto. J. Am. Chem. Soc. **120**, 10 801 (1998).
12. H.P. Beutelman, L. Xie, and W.H. Saunders. J. Org. Chem. **54**, 1703 (1989).
13. L. Xie and W.H. Saunders, Jr. Z. Naturforsch. **44a**, 413 (1989).
14. C. Fehr. Angew. Chem. Int. Ed. Engl. **35**, 2566 (1996).
15. F. Abu-Hasanayn, M. Stratakis, and A. Streitwieser J. Org. Chem. **60**, 4688 (1995).
16. A. Abbotto, A. Streitwieser, P.v.R. Schleyer. J. Am. Chem. Soc. **119**, 11 255 (1997).
17. A.S. Hussey and R.R. Herr. J. Org. Chem. **24**, 843 (1959).
18. A.J. Sisti. J. Org. Chem. **33**, 453 (1968).
19. W.E. Bachmann, G.I. Fujimoto, and L.B. Wick. J. Am. Chem. Soc. **72**, 1995 (1950).
20. Y. Chiang, A.J. Kresge, and J. Wirz. J. Am. Chem. Soc. **106**, 6392 (1984).
21. P. Haspra, A. Sutter, and J. Wirz. Angew. Chem. Int. Ed. Engl. **18**, 617 (1979).
22. J.R. Keeffe, A.J. Kresge, and J. Toullec. Can. J. Chem. **64**, 1224 (1986).
23. J.R. Keeffe and A.J. Kresge. Can. J. Chem. **74**, 2481 (1996).
24. E.A. Jefferson, J.R. Keeffe, and A.J. Kresge. J. Chem. Soc. Perkin Trans. 2, 2041 (1995).
25. J.R. Keeffe, A.J. Kresge, and Y. Yin. J. Am. Chem. Soc. **110**, 8201 (1988).
26. R. Gareyev, J.C. Ciula, and A. Streitwieser. J. Org. Chem. **61**, 4589 (1996).

© 1999 NRC Canada

Structure–reactivity correlations in the reaction of 2,4-dinitrophenyl X-substituted benzoates with alicyclic secondary amines

Ik-Hwan Um, Ji-Sook Min, and Hye-Won Lee

Abstract: Apparent second-order rate constants (k_{app}) have been measured spectrophotometrically for the reaction of 2,4-dinitrophenyl X-substituted benzoates with a series of alicyclic secondary amines in H_2O containing 20 mol% DMSO at 25°C. The microconstants involved in the reaction (k_{-1}/k_2, k_1, and k_1k_2/k_{-1}) have also been calculated. The magnitude of k_{app}, k_1, and k_1k_2/k_{-1} values increases with increasing amine basicity and with increasing acid strengthening ability of the acyl substituent X. The k_{-1}/k_2 value decreases from ca. 6.5 to 0.3 with increasing the amine basicity, but remains almost constant upon changing the acyl substituent X for a given amine, indicating that the rate-determining step is governed by the basicity of amine but not by the electronic nature of the acyl substituent X. The Brønsted-type plots for k_{app} show a break at pK_a = 9.1, supporting the assumption that a change in the rate-determining step occurs from rate-limiting breakdown to formation of the addition intermediate as amine basicity increases. The corresponding Brønsted-type plots for k_{-1}/k_2, k_1, and k_1k_2/k_{-1} are linear but their β values are different. σ^+ constants show better correlation with log k_{app}, log k_1 and log k_1k_2/k_{-1} for the reaction with low basic amines (pK_a < 9.1), while σ constants exhibit better correlation for the reaction with highly basic amines (pK_a > 9.1). The magnitude of ρ_1 is identical to that of ρ_{app} and ρ_{eq} for a given amine.

Key words: aminolysis, Brønsted-type plot, structure–reactivity correlations, rate-determining step.

Résumé : Faisant appel à la spectrophotométrie et opérant à 25°C dans H_2O contenant 20 mol% de DMSO, on a mesuré les constantes de vitesse apparentes du deuxième ordre de benzoates (portant un substituant X) de 2,4-dinitrophényle avec une série d'amines alicycliques secondaires. On a calculé les microconstantes impliquées dans la réaction (k_{-1}/k_2, k_1 et k_1k_2/k_{-1}). L'amplitude des valeurs de k_{app}, k_1, k_1k_2/k_{-1} augmente avec une augmentation de la basicité de l'amine et avec une augmentation de l'habilité du substituant acyle X à augmenter l'acidité. Les valeurs de k_{-1}/k_2 diminuent d'environ 6,5 à 0,3 avec une augmentation de la basicité de l'amine, mais elles demeurent pratiquement constantes pour un changement de substituant acyle X pour une amine donnée; ceci indique que l'étape cinétiquement déterminante est fixée par la basicité de l'amine, mais pas par la nature électronique du substituant acyle X. Les courbes de type Brønsted pour k_{app} présentent un bris à un pK_a = 9,1; ce résultat supporte l'hypothèse selon laquelle il se produit un changement dans l'étape cinétiquement limitante à cause d'un bris cinétiquement limitant dans la formation de l'intermédiaire lorsque la basicité de l'amine augmente. Les courbes de type Brønsted correspondantes pour $k_{-1}k/_2$, k_1 et k_1k_2/k_{-1} sont linéaires, mais leurs valeurs β sont différentes. Pour les amines de faible basicité (pK_a < 9,1), les constantes σ^+ donnent une meilleure corrélation avec log k_{app}, log k_1 et log k_1k_2/k_{-1} alors que les constantes σ conduisent à une meilleure corrélation pour la réaction avec les amines plus fortement basiques (pK_a > 9,1). Pour une amine donnée, l'amplitude de ρ_1 est identique à celle de ρ_{app} et de ρ_{eq}.

Mots clés : aminolyse, courbe de type Brønsted, corrélations structure-activité, étape cinétiquement déterminante.

[Traduit par la Rédaction]

Introduction

The aminolysis reaction of carbonyl compounds is one of the most intensively investigated reactions due to the interest in biology as well as in chemistry (1–6). The reactions of carboxylic acid derivatives with amines have been suggested to proceed through a stepwise mechanism with an addition intermediate or through a concerted mechanism without an intermediate (1–6). Linear free energy relationships such as Hammett and Brønsted-type correlations have been most frequently used to investigate the reaction mechanism (7). Aminolyses of carboxylic esters with a good leaving group have often shown a break or a curvature in Brønsted-type plots from a large slope (β_{nuc} = 0.8 ± 0.1) to a small one (β_{nuc} = 0.2 ± 0.1) as the basicity of the attacking amine increases (3, 4). Such a break or a curvature in Brønsted-type plots has been attributed to a change in rate determining step (RDS) of a stepwise reaction. Generally, the RDS of aminolysis of carboxylic esters has been suggested to be depend-

Received November 9, 1998.

This paper is dedicated to Professor A.J. Kresge in recognition of his numerous contributions to physical organic chemistry.

I.-H. Um,[1] J.-S. Min, and H.-W. Lee. Department of Chemistry, Ewha Womans University, Seoul 120–750, Korea.

[1]Author to whom correspondence may be addressed. Telephone: 822) 3277-2349. Fax: 822) 3277-2844. e-mail: ihum@mm.ewha.ac.kr

© 1999 NRC Canada

Scheme 1.

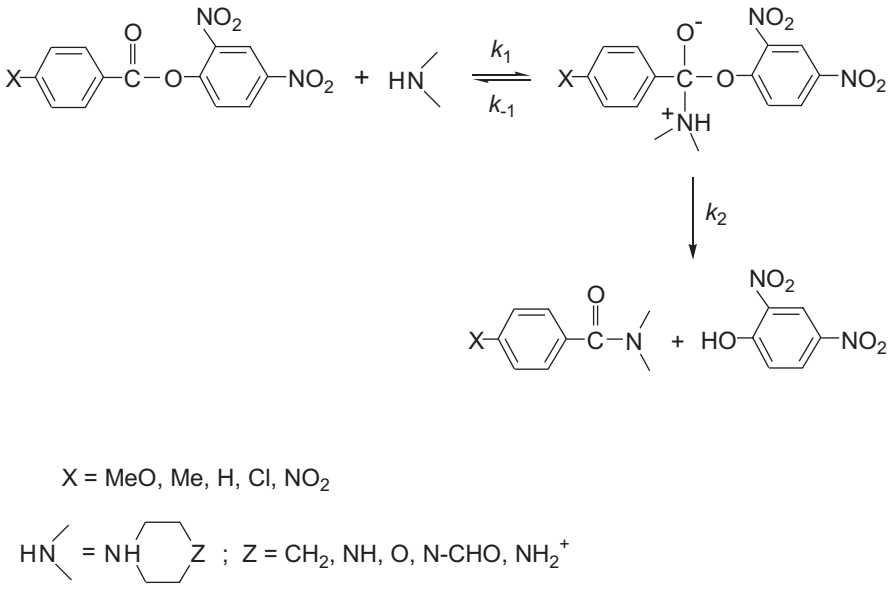

Table 1. Summary of apparent second-order rate constants (k_{app}) for the aminolysis reaction of 2,4-dinitrophenyl X-substituted benzoates with secondary alicyclic amines in H_2O containing 20 mol% DMSO at 25°C.

		k_{app} (M^{-1} s^{-1})				
Amine (Z)	p*Ka*[a]	X = 4-NO_2	4-Cl	H	4-Me	4-MeO
Piperidine (CH_2)	11.02	2880	371	174	100	56.2
Piperazine (NH)	9.85	974	157	82.1	49.8	27.4
Morpholine (O)	8.65	138	32.7	19.6	11.2	5.77
1-Formyl piperazine (NCHO)	7.98	28.2	7.58	5.43	2.94	1.49
Piperazinium ion (NH_2^+)	5.95	1.83	0.675	0.467	0.306	0.162

[a]pK_a of the conjugate acid of amine taken from ref. 20.

ent on the basicity of the leaving group and the attacking amine, i.e., the RDS changes from the rate-determining breakdown of the addition intermediate to the rate-determining formation of the intermediate as the basicity of amines increases (3, 4).

However, until recently, most studies were directed to investigate the reaction mechanism by changing the basicity of the leaving or attacking groups. The effect of the acyl group on reaction rates as well as on reaction mechanisms has been rarely investigated (8–10). We have carried out a systematic study as shown in Scheme 1, and evaluated all the microconstants involved in the aminolysis reactions to obtain further information about the reaction mechanism.

Results and discussion

All the reactions in the present study obeyed pseudo-first-order kinetics up to over 90% of the total reaction. Pseudo-first-order rate constants (k_{obs}) were obtained from the equation, $\ln (A_\infty - A_t) = -k_{obs}t + c$. The correlation coefficients of the linear regressions were always higher than 0.9995. The plots of k_{obs} vs. [>NH] were linear, indicating that general base catalysis by a second amine molecule is absent. Therefore, one can derive a rate equation, as eq. [1], where [S] and [>NH] represent the concentration of the substrate and the amines used, respectively. Apparent second-order rate constants (k_{app}) were determined from the slope of the plots of k_{obs} vs. [>NH]. The k_{app} values obtained in this way are summarized in Table 1. It is estimated from replicate runs that the error in any particular measured rate constants is less than ± 3%. Under pseudo-first-order conditions, eq. [1] can be simplified into eqs. [2] and [3].

$$[1] \qquad \text{Rate} = \frac{k_1 k_2}{k_{-1} + k_2}[\text{S}][>\text{NH}]$$

$$[2] \qquad \text{Rate} = k_{obs}[\text{S}], \qquad \text{where } k_{obs} = \frac{k_1 k_2}{k_{-1} + k_2}[>\text{NH}]$$

$$[3] \qquad k_{app} = \frac{k_1 k_2}{k_{-1} + k_2}$$

Reaction mechanism

As shown in Table 1, the k_{app} value increases with increasing the basicity of amines and with increasing acid strengthening ability of the acyl substituent X. In Fig. 1 is demonstrated the effect of amine basicity on reactivity, which was statistically corrected by using *p* and *q*, i.e., $p = 2$ (except $p = 4$ for piperazinium ion) and $q = 1$ (except $q = 2$ for piperazine) (11). The Brønsted-type plots in Fig. 1 are nonlinear for all the acyl substituents. Such a nonlinear Brønsted-type plot has often been observed in aminolyses of esters with a good leaving group, and used as evidence of a change in the rate determining step, i.e., the RDS changes

© 1999 NRC Canada

Fig. 1. Plots of logarithm of k_{app} versus pK_a of the conjugate acid of amines for the reaction of 2,4-dinitrophenyl X-substituted benzoates with secondary alicyclic amines (Z) in H_2O containing 20 mol% DMSO at 25°C.

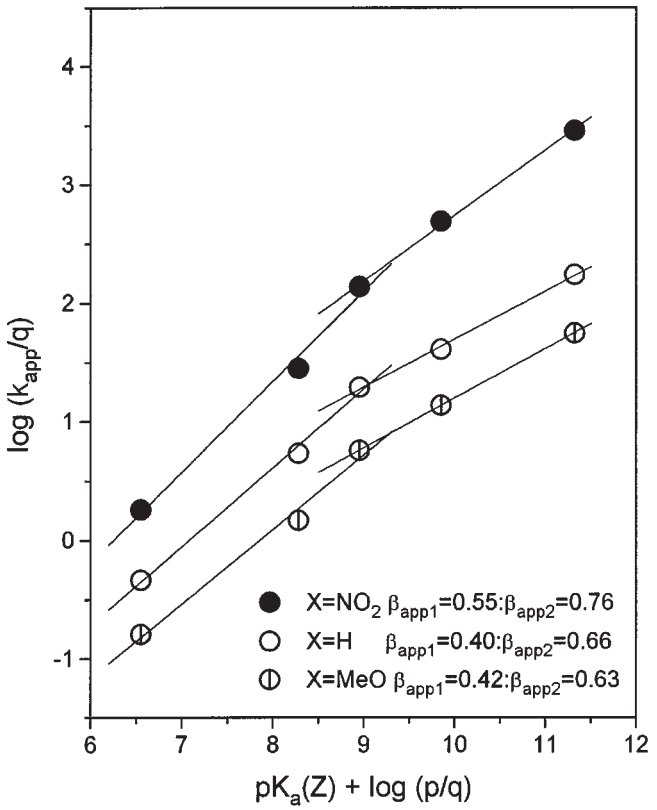

Fig. 2. Plots of logarithm of k_{app} versus σ_X (or σ_X^+) constants for the reaction of 2,4-dinitrophenyl X-substituted benzoates with secondary alicyclic amines (Z) in H_2O containing 20 mol% DMSO at 25°C.

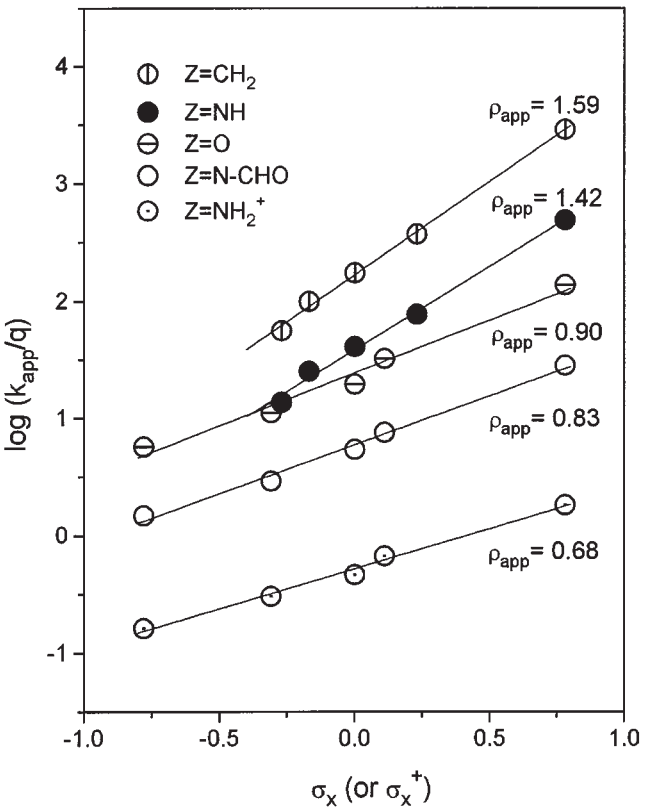

from breakdown of the addition intermediate to formation of the intermediate as the attacking amine becomes more basic than the leaving group by 4~5 pK_a units (12). Figure 1 shows that the position of the break is about 9.1, which is 5 pK_a units higher than the pK_a of the conjugate acid of the leaving group (pK_a of 2,4-dinitrophenol = 4.1). Therefore, one can suggest that the RDS in the present aminolysis changes from the k_2 step to the k_1 step in Scheme 1 as the amine becomes more basic than morpholine (pK_a > 9.1).

It is noted that the position of the break in Fig. 1 is nearly unchanged although the electronic nature of the acyl substituent X varies significantly, suggesting that the RDS change is governed by the basicity of amines but not by the acyl moiety. The β_{app2} (the slope in Fig. 1 for the low basic amines, pK_a < 9.1) has been calculated to be 0.63, 0.66, and 0.76 for the acyl substituent X = MeO, H, and NO_2, respectively. The β_{app1} value (the slope in Fig. 1 for the highly basic amines, pK_a > 9.1) is 0.42, 0.40, and 0.55 for X = MeO, H, NO_2, respectively. Therefore, the electronic nature of the acyl substituents X affects the magnitude of the slopes in the Brønsted-type plots (both β_{app1} and β_{app2}).

Figure 2 demonstrates the effect of acyl substituent on reactivity. Good linear Hammett plots are observed for all the amines studied. However, interestingly, log k_{app} shows good linear correlation with σ constants for the reactions with highly basic amines (pK_a > 9.1) but with σ^+ constants for the ones with low basic amines (pK_a < 9.1). σ^+ constants were derived from the solvolysis of $ArCMe_2Cl$ in 90% acetone–water mixture at 25°C, and used for reactions in which a positive charge is developed at the reaction centre which can resonate with an electron-donating group (EDG) (13). Accordingly, negative ρ values have generally been obtained when σ^+ constants were used. However, as shown in Fig. 2, the slope of the Hammett plots (ρ_{app}) is positive. Therefore, the present result is quite unusual and suggests that the ground-state stabilization by resonance or hyperconjugation is significant for the reactions with the low basic amines as shown in Scheme 2.

The ρ_{app} values of the Hammett plots in Fig. 2 are much larger for the reactions with the highly basic amines (ρ_{app} = 1.42~1.59) than for the ones with the low basic amines (ρ_{app} = 0.68~0.90). Since the attack of amines to the carbonyl carbon to form an addition intermediate would be accelerated by an electron withdrawing group (EWG) but retarded by an EDG in the acyl moiety, one would expect a large ρ value for the reactions where the RDS is the first step (k_1) in Scheme 1. On the contrary, the departure of the leaving group from the addition intermediate would be disfavoured by an EWG but favoured by an EDG in the acyl moiety. Accordingly, the ρ value has been suggested to be small when the RDS is the k_2 step due to the opposite substituent effect, and the magnitude of ρ values has often been used to determine the RDS for two step reactions (8–10). Based on the magnitude of the ρ_{app} values in the present system, one can suggest that the RDS is the k_2 step for the reactions with the low basic amines (small ρ_{app}) and the k_1 step for the ones with the highly basic amines (large ρ_{app}).

© 1999 NRC Canada

Scheme 2.

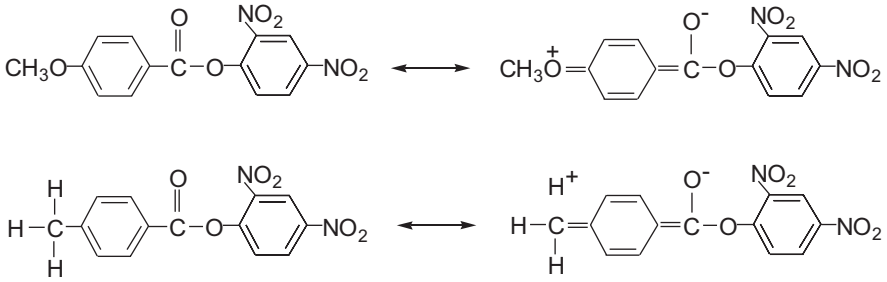

Table 2. Summary of k_{-1}/k_2 values for the aminolysis reaction of 2,4-dinitrophenyl X-substituted benzoates with secondary alicyclic amines in H_2O containing 20 mol% DMSO at 25°C.

	k_{-1}/k_2				
Amine (Z)	X = 4-NO_2	4-Cl	H	4-Me	4-MeO
Piperidine (CH_2)	0.397	0.364	0.316	0.364	0.397
Piperazine (NH)	0.694	0.671	0.637	0.671	0.694
Morpholine (O)	1.24	1.27	1.31	1.27	1.24
1-Formyl piperazine (NCHO)	1.72	1.81	1.96	1.81	1.72
Piperazinium ion (NH_2^+)	4.61	5.29	6.58	5.29	4.61

Recently, we reported a ρ value of 2.4 for the reaction of 4-nitrophenyl X-substituted benzoates with phenoxide ion under the same reaction conditions in which the nucleophilic attack by phenoxide ion was proposed to be the RDS (14). The ρ_{app} value for the present aminolysis with the highly basic amines is 1.5 ± 0.1, which is much smaller than the one for the reaction with the anionic nucleophile. However, the difference in the ρ value between the two systems is considered not to be due to any difference in the reaction mechanism, but due to the difference in the type of nucleophiles (phenoxide anion vs. neutral amine). Since phenoxide anion would donate electrons more significantly to the acyl moiety in the transition state (TS) than the neutral amines, it would be natural to observe a larger ρ value for the former system than the latter one.

Evaluation of microconstants

To get insight into the reaction mechanism, it is necessary to determine all the microconstants involved in the present aminolysis reactions. The method used to calculate the microconstants is based on Castro's procedure (12*c*) as follows.

As suggested in the preceding section, the RDS is considered to change from the k_2 to k_1 step as the amine becomes more basic than morpholine (or pK_a > 9.1). Therefore, eq. [3] can be simplified into eqs. [4] and [5].

$$[4] \qquad k_{app} = k_1k_2/k_{-1} = Kk_2, \qquad \text{when } k_2 << k_{-1}$$

$$[5] \qquad k_{app} = k_1, \qquad \text{when } k_2 >> k_{-1}$$

Let β_{app2} and β_{app1} represent the slope for the Brønsted plots in Fig. 1 for the reactions with the low and the highly basic amines, respectively. Then, one can express β_{app1} and β_{app2} as eqs. [6] and [7], respectively.

$$[6] \qquad \beta_{app1} = d(\log k_1)/d(pK_a)$$

$$[7] \qquad \beta_{app2} = d(\log k_1k_2/k_{-1})/d(pK_a) = \beta_{app1} + d(\log k_2/k_{-1})/d(pK_a)$$

Equation [7] can be rearranged as eq. [8]. Integral of eq. [8] from pK^0 to pK_a results in eq. [9], where pK^0 represents the position of the break in Fig. 1.

$$[8] \qquad \beta_{app2} - \beta_{app1} = d(\log k_2/k_{-1})/d(pK_a)$$

$$[9] \qquad (\log k_2/k_{-1})_{pKa} - (\log k_2/k_{-1})_{pK^0} = (\beta_{app2} - \beta_{app1})(pK_a - pK^0)$$

The values of β_{app1} and β_{app2} for the reaction of 2,4-dinitrophenyl benzoate (X = H) were calculated to be 0.66 and 0.40, respectively, and pK^0 is 9.1. Since $k_2 = k_{-1}$ at pK^0, the term $\log (k_2/k_{-1})_{pK^0}$ is zero. Therefore, one can simplify eq. [9] as eq. [10], which allows one to calculate the k_2/k_{-1} values for all the amines studied in the present system.

$$[10] \qquad \log (k_2/k_{-1})_{pKa} = 0.26(pK_a - 9.1)$$

In a similar manner, the k_2/k_{-1} values for the other systems (X = NO_2, Cl, Me, MeO) have been calculated and summarized in Table 2.

The k_2 value has been suggested to be constant upon changing the basicity of amines for aminolysis reactions of a given substrate (15, 16). However, the k_{-1} value would be inversely proportional to the basicity of amines. Therefore, one can expect that the k_{-1}/k_2 values become larger with decreasing amine basicity. In fact, as shown in Table 2, k_{-1}/k_2 values increase from ca. 0.3–6.5 as amine basicity decreases. The magnitude of k_{-1}/k_2 values is larger than 1 for the low basic amines (pK_a < 9.1) and smaller than 1 for the highly basic amines (pK_a > 9.1), indicating that the RDS changes from the k_2 to k_1 step as the amine becomes more basic than morpholine (or pK_a > 9.1). This is consistent with the preceding suggestion based on the nonlinear Brønsted-type

© 1999 NRC Canada

Table 3. Summary of k_1 values for the aminolysis reaction of 2,4-dinitrophenyl X-substituted benzoates with secondary alicyclic amines in H_2O containing 20 mol% DMSO at 25°C.

	k_1 (M^{-1} s^{-1})				
Amine (Z)	X = 4-NO_2	4-Cl	H	4-Me	4-MeO
Piperidine (CH_2)	4020	506	229	136	78.5
Piperazine (NH)	1650	263	134	83.3	46.5
Morpholine (O)	310	74.2	45.3	25.4	12.9
1-Formyl piperazine (NCHO)	76.7	21.3	16.1	8.26	4.05
Piperazinium ion (NH_2^+)	10.2	4.25	3.55	1.93	0.907

Fig. 3. Plots of logarithm of k_{-1}/k_2 versus pK_a of the conjugate acid of amines for the reaction of 2,4-dinitrophenyl X-substituted benzoates with secondary alicyclic amines (Z) in H_2O containing 20 mol% DMSO at 25°C.

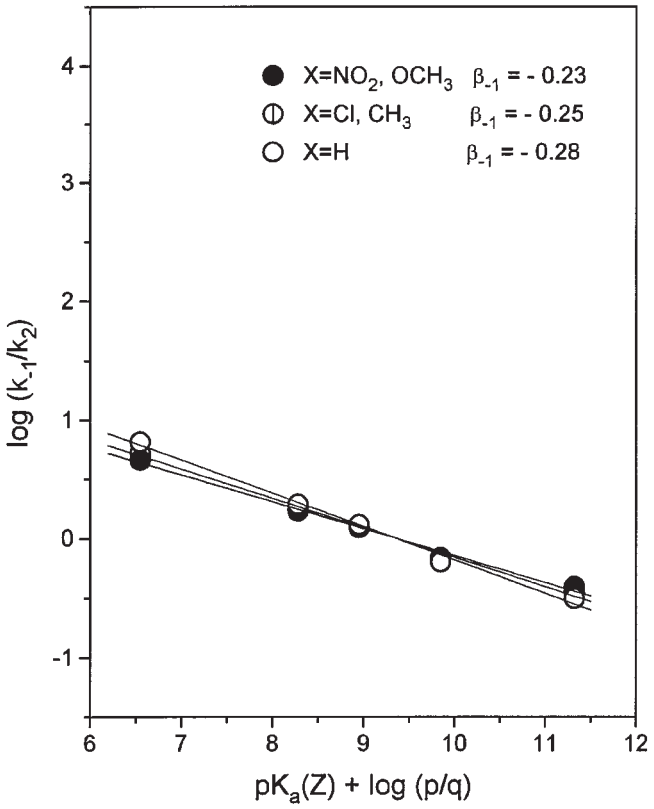

plots shown in Fig. 1 and the difference in the magnitude of the ρ values shown in Fig. 2.

Figure 3 demonstrates the effect of amine basicity on the k_{-1}/k_2 values. Linear Brønsted-type plots are observed for all the acyl substituents X. Since the k_2 value has been suggested to be constant upon changing the basicity of amines (15, 16), the magnitude of the slope in Fig. 3 (β_{-1}) would be governed mainly by k_{-1}. The β_{-1} value was calculated to be about 0.25, indicating that log k_{-1} is little sensitive toward the basicity of the amines used. Such a small β_{-1} value obtained in the present system is consistent with the recent suggestion by Colthurst and Williams (9*b*), that k_{-1} would not be sensitive to the basicity of nucleophiles.

Both the k_{-1} and k_2 steps would be accelerated by an EDG but retarded by an EWG in the acyl moiety for a given amine. Accordingly, k_{-1}/k_2 values would be expected to be constant upon changing the acyl substituent X. In fact, as shown in Table 2, the magnitude of k_{-1}/k_2 values appears to be nearly constant although the acyl substituent changes from a strong EDG to a strong EWG for a given amine, clearly supporting the preceding argument that the position of the RDS change (pK^0) would not be influenced by the electronic nature of the acyl substituents but governed by the basicity of the leaving group and the attacking amines. However, it has been recently suggested that pK^0 and the k_{-1}/k_2 ratio increase with increasing electron-withdrawing ability of the acyl moiety in aminolyses of aryl carbonates and thionocarbonates, which is inconsistent with our present result (15, 16).

$$[11] \quad k_1 = k_{app} (k_{-1}/k_2 + 1)$$

Equation [3] can be rewritten as eq. [11], which allows the calculation of the k_1 values using the known values of k_{app} and k_{-1}/k_2 from Tables 1 and 2. The k_1 values calculated in this way are summarized in Table 3. One can see that the magnitude of k_1 decreases with decreasing the basicity of amines and with decreasing acid strengthening ability of the acyl substituent X. The data in Tables 1 and 3 reveal that k_1 is always larger than the corresponding k_{app}. However, the difference in the magnitude of k_1 and k_{app} becomes small as amine basicity increases for a given acyl substituent X, because the k_{-1}/k_2 values decrease with increasing amine basicity.

Figure 4 shows the effect of amine basicity on the magnitude of k_1 value. One can notice that log k_1 is linearly correlated with the basicity of amines for all the acyl substituent X. The magnitude of the slopes in Fig. 4 (β_1) was calculated to be 0.55, 0.38, and 0.41 for X = NO_2, H, and MeO, respectively. The β_1 value is about twice the value of β_{-1}, indicating that the k_1 step is about twice more sensitive than the k_{-1} step toward the basicity of amines for a given acyl substituent X.

Figure 5 demonstrates linear Hammett plots for all the amines studied. One can see that log k_1 is better correlated with σ constants for the reactions with the highly basic amines (pK_a > 9.1) and with σ^+ constants for the low basic amines (pK_a < 9.1). Besides, the magnitude of the slopes in Fig. 5 (ρ_1) is much larger for the reactions with the highly basic amines than for the ones with the low basic amines. One can notice that the magnitude of ρ_1 and ρ_{app} values is same. However, this is not so surprising if one analyses eq. [11]. Since the k_{-1}/k_2 value has been shown to be almost constant upon changing the acyl substituent X for a given amine, log k_{app} = log k_1 + constant. Consequently, the slopes in the plots of log k_1 vs. σ (or σ^+) and log k_{app} vs. σ (or σ^+) should be identical each other for a given amine.

© 1999 NRC Canada

Table 4. Summary of Kk_2 (= k_1k_2/k_{-1}) values for the aminolysis reaction of 2,4-dinitrophenyl X-substituted benzoates with secondary alicyclic amines in H_2O containing 20 mol% DMSO at 25°C.

	Kk_2 (M^{-1} s^{-1})				
Amine (Z)	X = 4-NO_2	4-Cl	H	4-Me	4-MeO
Piperidine (CH_2)	10100	1390	723	375	198
Piperazine (NH)	2370	390	211	124	66.6
Morpholine (O)	249	58.5	34.5	20.0	10.4
1-Formyl piperazine (NCHO)	44.7	11.8	8.22	4.56	2.36
Piperazinium ion (NH_2^+)	2.22	0.801	0.537	0.363	0.197

Fig. 4. Plots of logarithm of k_1 versus pK_a of the conjugate acid of amines for the reaction of 2,4-dinitrophenyl X-substituted benzoates with secondary alicyclic amines (Z) in H_2O containing 20 mol% DMSO at 25°C.

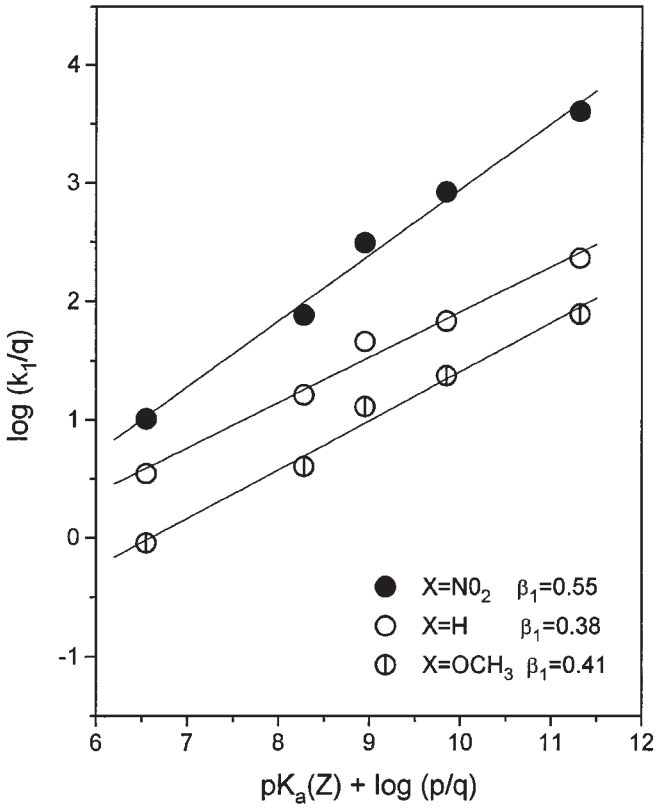

Fig. 5. Plots of logarithm of k_1 versus σ_X (or σ_X^+) constants for the reaction of 2,4-dinitrophenyl X-substituted benzoates with secondary alicyclic amines (Z) in H_2O containing 20 mol% DMSO at 25°C.

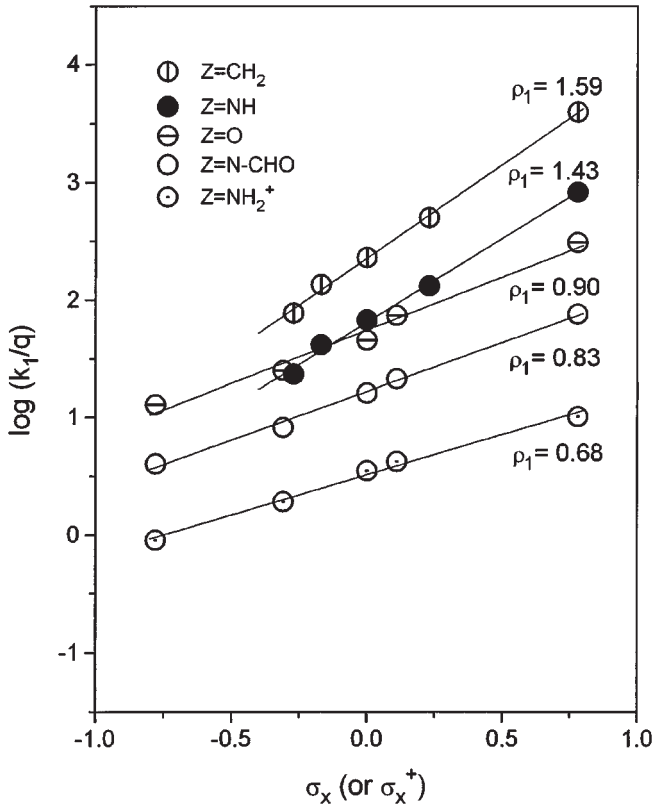

The Kk_2 (= k_1k_2/k_{-1}) values have been calculated from the known values of k_1 and k_{-1}/k_2, and summarized in Table 4. The Kk_2 value decreases with decreasing amine basicity and with increasing acid weakening ability of the acyl substituent X, as expected. Comparison of the data in Tables 3 and 4 reveals that the magnitude of Kk_2 is larger than the corresponding k_1 for the highly basic amines but smaller than k_1 for the low basic amines. However, this is not so surprising either, since $k_2/k_{-1} > 1$ for the reactions with the highly basic amines (pK_a > 9.1) and $k_2/k_{-1} < 1$ for the low basic amines (pK_a < 9.1), as shown in Table 2.

Figure 6 exhibits the effect of amine basicity on Kk_2. One can see linear Brønsted-type plots. The magnitude of the slopes in Fig. 6 (β_{eq}) has been calculated to be 0.78, 0.66, and 0.64 for X = NO_2, H, and MeO, respectively. Since the magnitude of k_2 values has been suggested to be constant upon changing the basicity of amines (16, 17), the slope in the plots of log Kk_2 vs. pK_a (e.g., β_{eq}) and log k_1/k_{-1} vs. pK_a (e.g., $\beta_1 - \beta_{-1}$) should be same. In fact, it has been calculated that $\beta_{eq} = \beta_1 - \beta_{-1}$ for all the acyl substituents.

Figure 7 demonstrates the effect of acyl substituent X on Kk_2. Good linear Hammett plots are obtained for all the amines used. Interestingly, as observed in Figs. 2 and 5, log Kk_2 shows good linear correlation with σ constants for the reactions with the highly basic amines but with σ^+ constants for the low basic amines. Besides, the slopes in Fig. 7 (ρ_{eq}) are much larger for the highly basic amines than for the low basic ones, as observed in Figs. 2 and 5.

Since the magnitude of k_{-1}/k_2 values are almost constant upon changing the acyl substituent X for a given amine, the slopes of the plots of log Kk_2 vs. σ (or σ^+) and log k_1 vs. σ (or σ^+) should be same for a given amine. In fact, one can notice that the magnitude of ρ_{eq} and ρ_1 is identical for a

© 1999 NRC Canada

Fig. 6. Plots of logarithm of Kk_2 versus pK_a of the conjugate acid of amines for the reaction of 2,4-dinitrophenyl X-substituted benzoates with secondary alicyclic amines (Z) in H_2O containing 20 mol% DMSO at 25°C.

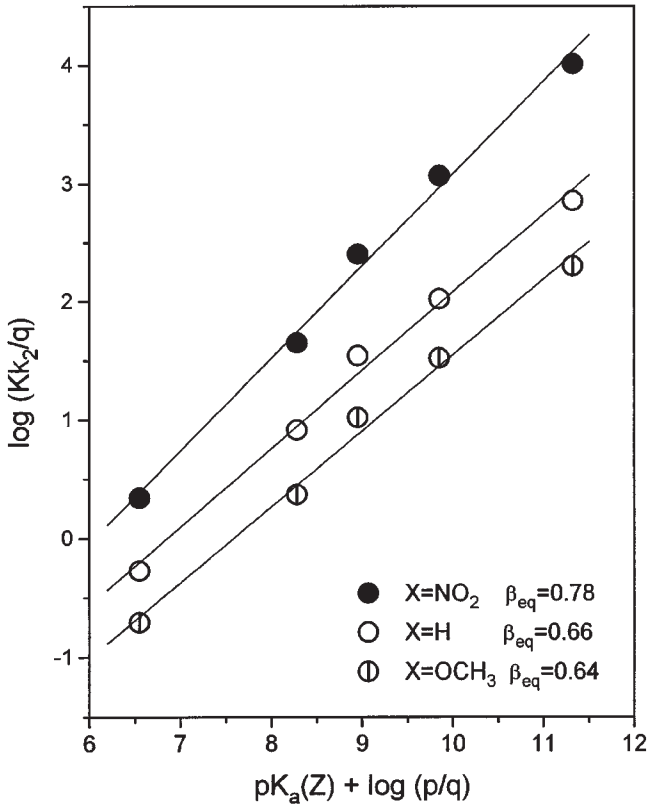

Fig. 7. Plots of logarithm of Kk_2 versus σ_X (or σ_X^+) constants for the reaction of 2,4-dinitrophenyl X-substituted benzoates with secondary alicyclic amines (Z) in H_2O containing 20 mol% DMSO at 25°C.

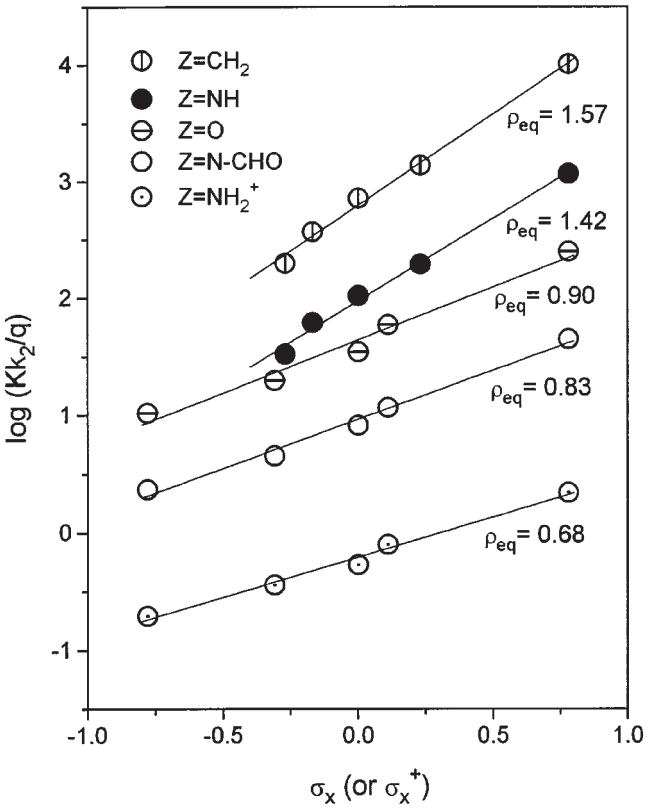

given amine. The present study clearly shows that the ρ_{app} and ρ_{eq} values are identical to the ρ_1 value for a given amine, and the magnitude of ρ_1 dominates that of ρ_{app} and ρ_{eq} (see Figs. 2, 5, and 7).

As mentioned in the preceding section, the magnitude of ρ_{app} and ρ_{eq} has been generally suggested to be small for the reactions in which the leaving group departure occurs in the RDS (9, 10), since the effect of acyl substituents on the k_1 and k_2 steps would be opposite. In fact, the magnitude of ρ_{app}, ρ_{eq}, and ρ_1 has been shown to be much smaller for the reactions with the low basic amines (pK_a < 9.1) in which the leaving group departure is the RDS than for the ones with the highly basic amines (pK_a > 9.1) in which the leaving group departure occurs after the RDS. However, the present result clearly suggests that the small ρ_{app} and ρ_{eq} values for the low basic amines are not due to the opposite substituent effect on the k_1 and k_2 steps, but due to small ρ_1 value for the low basic amines.

Experimental

Materials

2,4–Dinitrophenyl X-substituted benzoates (X-$C_6H_5CO_2C_6H_3$-$(NO_2)_2$-2,4) were easily prepared from the reactions of X-substituted benzoyl chlorides with 2,4-dinitrophenol in the presence of triethylamine in methylene chloride (18). Their purity was checked by means of melting points and spectral data such as IR and ^{1}H NMR characteristics. The amines and other chemicals used were of the highest quality available. To eliminate a solubility problem, 20 mol% dimethyl sulfoxide (DMSO) – H_2O mixture was used as the reaction medium. DMSO was distilled over calcium chloride at a reduced pressure (bp 64~66°C at 6~7 mmHg) (1 mmHg = 133.3 Pa) and stored under nitrogen. Doubly glass distilled water was further boiled and cooled under a nitrogen atmosphere just before use.

Kinetics

The kinetic studies were performed with a Hitachi U-2000 model UV-vis spectrophotometer for slow reactions ($t_{1/2}$ = 10 s) or with an Applied Photophysics SX-17MV stopped-flow spectrophotometer for fast reactions ($t_{1/2}$ < 10 s) equipped with a Neslab RTE-110 constant temperature circulating bath to keep the reaction mixture at 25.0 ± 0.1°C. The reactions were followed by monitoring the appearance of the leaving 2,4-dinitrophenoxide at 410 nm. All the reactions were carried out under pseudo-first-order conditions in which the amine concentrations were at least 20 times greater than the substrate concentration. The amine stock solution of ca. 0.2 M was prepared in a 25.0 mL volumetric flask under nitrogen atmosphere by adding 2 equiv. of amine to 1 equiv. of standardized HCl solution in order to obtain a self-buffered solution. All the solutions were transferred by Hamilton gas-tight syringes. Other details of kinetic methods were reported previously (19).

© 1999 NRC Canada

Conclusions

The present study has allowed us to conclude the following. (*i*) The RDS of the present aminolysis reactions changes from the k_2 step to the k_1 step as the amine becomes more basic than the leaving group by ca. 5 pK_a units. (*ii*) σ^+ constants give better correlation with log k_{app}, log k_1, and log Kk_2 when the k_2 step is the RDS (e.g., the reactions with the low basic amine, pK_a < 9.1). However, σ constants show better correlation when the k_1 step is the RDS (e.g., the reactions with highly basic amines, pK_a > 9.1). (*iii*) The magnitude of k_{-1}/k_2 is nearly constant upon changing the acyl substituent for a given amine, indicating that the RDS is not governed by the electronic nature of the acyl substituent X. (*iv*) The magnitude of ρ_1 is identical to that of ρ_{app} and ρ_{eq} for a given amine. (*v*) The magnitude of ρ_{app}, ρ_1, and ρ_{eq} is much smaller for the reactions with the low basic amines (pK_a < 9.1) than for the ones with the highly basic amines (pK_a > 9.1). (*vi*) The small values of ρ_{app} and ρ_{eq} for the reactions in which the RDS is the k_2 step is not because the effect of the acyl substituents on the k_1 and k_2 step is opposite, but because the corresponding ρ_1 value is small.

Acknowledgements

The authors are grateful for the financial support from the Korean Science and Engineering Foundation (KOSEF-981-0303-017-2) and the MOST through the Women's University Research Fund (97-N6-01-01-A-14).

References

1. W.P. Jencks. *In* Catalysis in chemistry and enzymology. McGraw–Hill Book Company, New York. 1969. pp. 463–554.
2. (*a*) D.J. Hupe, and W.P. Jencks. J. Am. Chem. Soc. **99**, 451 (1977); (*b*) W.P. Jencks, S.R. Brant, J.R. Gandler, G. Fendrich, and C. Nakamura. J. Am. Chem. Soc. **104**, 7045 (1982); (*c*) D. Stefanidis, S. Cho, S. Dhe-Paganon, and W.P. Jencks. J. Am. Chem. Soc. **115**, 1650 (1993).
3. (*a*) H.K. Oh, S.Y. Woo, C.H. Shin, Y.S. Park, and I. Lee. J. Org. Chem. **62**, 5780 (1997); (*b*) H.J. Koh, J.W. Lee, H.W. Lee, and I. Lee. New J. Chem. **21**, 447 (1997); (*c*) H.J. Koh, S.I. Kim, B.C. Lee, and I. Lee. J. Chem. Soc. Perkin Trans. 2, 1353 (1996); (*d*) H.K. Oh, C.H. Shin, and I. Lee. J. Chem. Soc. Perkin Trans. 2, 1169 (1995).
4. (*a*) E.A. Castro, M.I. Pizzaro, and J.G. Santos. J. Org. Chem. **61**, 5982 (1996); (*b*) E.A. Castro, F. Ibanez, J.G. Santos, and C. Ureta. J. Org. Chem. **58**, 4908 (1993); (*c*) E.A. Castro, M. Cubillos, and J.G. Santos. J. Org. Chem. **61**, 3501 (1996); (*d*) E.A. Castro and C.A. Araneda. J. Org. Chem. **62**, 126 (1997).
5. (*a*) A. Williams. Chem. Soc. Rev. **23**, 93 (1994); (*b*) S. Ba-Saif, A.K. Luthra, and A. Williams. J. Am. Chem. Soc. **111**, 2647 (1989).
6. (*a*) D.F. DeTar. J. Am. Chem. Soc. **104**, 7205 (1982); (*b*) T. Okuyama, H. Takano, and K. Senda. Bull. Chem. Soc. Jpn. **69**, 2639 (1996).
7. N.B. Chapman and J. Shorter (*Editors*). *In* Advances in linear free energy relationships. Plenum, London. 1972.
8. (*a*) I.H. Um, E.K. Chung, and S.M. Lee. Can. J. Chem. **76**, 729 (1998); (*b*) I.H. Um, Y.J. Hong, and D.S. Kwon. Tetrahedron, **53**, 5073 (1997); (*c*) I.H. Um, E.S. Yeom, H.J. Kwon, and D.S. Kwon. Bull. Korean Chem. Soc. **18**, 865 (1997); (*d*) I.H. Um, M.J. Kim, J.S. Min, and D.S. Kwon. Bull. Korean Chem. Soc. **18**, 523 (1997); (*e*) I.H. Um, E.K. Chung, and D.S. Kwon. Tetrahedron Lett. **38**, 4787 (1997).
9. (*a*) F.M. Menger and J.H. Smith. J. Am. Chem. Soc. **94**, 3824 (1972); (*b*) M.J. Colthurst and A. Williams. J. Chem. Soc. Perkin Trans. 2, 1493 (1997); (*c*) E.A. Castro and G.B. Steinfort. J. Chem. Soc. Perkin Trans. 2, 453 (1983); (*d*) E.A. Castro and C.L. Santander. J. Org. Chem. **50**, 3595 (1985); (*e*) E.A. Castro and J.L. Valdivia. J. Org. Chem. **51**, 1668 (1986); (*f*) J.F. Kirsch and A. Kline. J. Am. Chem. Soc. **91**, 1841 (1969).
10. (*a*) J.F. Kirsch, W. Clewell, and A. Simon. J. Org. Chem. **33**, 127 (1968); (*b*) M. Caplow and W.P. Jencks. Biochemistry, **1**, 883 (1962); (*c*) V.R. Correia, I.M. Cuccovia, and H. Chaimovich. J. Phys. Org. Chem. **4**, 13 (1991).
11. R.P. Bell. *In* The proton in chemistry. Methuen, London. 1973. p. 159.
12. (*a*) W.P. Jencks and M. Gilchrist. J. Am. Chem. Soc. **90**, 2622 (1968); (*b*) E.A. Castro, M. Salas, and J.G. Santos. J. Org. Chem. **56**, 4919 (1991); (*c*) E.A. Castro and C. Ureta. J. Org. Chem. **54**, 2153 (1989); (*d*) I.H. Um, H.J. Kwon, D.S. Kwon, and J.Y. Park. J. Chem. Res. Miniprint, 1801 (1995); J. Chem. Res. Synop. 301 (1995).
13. H.C. Brown and Y. Okamoto. J. Am. Chem. Soc. **80**, 4979 (1958).
14. I.H. Um, E.K. Chung, and D.S. Kwon. Tetrahedron Lett. **38**, 4787 (1997).
15. E.A. Castro, M. Cubillos, J.G. Santos, and J. Tellez. J. Org. Chem. **62**, 2512 (1997).
16. M.J. Gresser and W.P. Jencks. J. Am. Chem. Soc. **99**, 6963 (1977); **99**, 6970 (1977).
17. E.A. Castro, F. Ibanez, J.G. Santos, and C. Ureta. J. Org. Chem. **12**, 93 (1991).
18. C.D. Hubbard and J.F. Kirsch. Biochemistry, **11**, 2483 (1972).
19. E. Buncel, I.H. Um, and S. Hoz,. J. Am. Chem. Soc. **111**, 971 (1989).
20. I.H. Um, E.S. Yeom, H.J. Kwon, and D.S. Kwon. Bull. Korean Chem. Soc. **18**, 865 (1997).

© 1999 NRC Canada

The effect of metal ions on the reaction of hydrogen peroxide with Kraft lignin model compounds

Yujun Sun, Michael Fenster, Annie Yu, Richard M. Berry, and Dimitris S. Argyropoulos

Abstract: Peroxide bleaching is significantly affected by transition and alkaline earth metals. Isolating the effects of different transition and alkaline earth metals on the reactions of peroxide with different representative lignin structures allows the separation of the positive from the negative contributions of these metal ions. In this work, five monomeric or dimeric phenolic lignin model compounds were treated with alkaline hydrogen peroxide in the absence or presence of Mn^{2+}, Cu^{2+}, Fe^{3+}, and Mg^{2+}. We followed the disappearance of the starting material and the progress of demethylation, radical coupling and oxalic acid formation were followed. Transition metals increased the reactivities of all the lignin model compounds with hydrogen peroxide in the order $Mn^{2+} > Cu^{2+} > Fe^{3+}$, which is the same as the order of activity toward peroxide decomposition while Mg^{2+} stabilized the system. Demethylation, radical coupling, and oxalic acid formation were all increased by the presence of transition metals in the system and decreased by the addition of Mg^{2+}. The acceleration of the total degree of reaction and of the demethoxylation reactions improves peroxide bleaching, but the increase in the radical coupling reactions can affect the further bleachability of pulp while the increase in the formation of oxalic acid could lead to a greater probability of scaling.

Key words: lignins, hydrogen peroxide, peroxide bleaching, reactivity, chemical pulps, metal compounds, alkali treatment, transition metals, delignification.

Résumé : Le blanchiment au peroxyde est affecté d'une façon significative par les métaux de transition et alcalinoterreux. En isolant les effets des divers métaux de transition et alcalinoterreux sur les réactions du peroxyde avec diverses structures représentatives de lignine, on peut séparer les contributions positives et négatives de ces ions métalliques. Dans ce travail, cinq composés modèles de lignine phénolique monomère ou dimère ont été traités par du peroxyde d'hydrogène en milieu alcalin, en présence ou en l'absence de Mn^{2+}, Cu^{2+}, Fe^{3+} et Mg^{2+}. On a suivi la disparition du produit de départ et le progrès de la déméthylation, du couplage radicalaire ainsi que de la formation d'acide oxalique. Les métaux de transition augmentent les réactivités de tous les composés modèles de la lignine avec le peroxyde d'hydrogène et l'ordre de cet effet est $Mn^{2+} > Cu^{2+} > Fe^{3+}$, le même que celui de l'ordre d'activité vis-à-vis de la décomposition du peroxyde; le Mg^{2+} stabilise le système. En présence de métaux de transition dans le système, les vitesses de déméthylation, de couplage radicalaire et de formation d'acide oxalique sont toutes augmentées; l'addition de Mg^{2+} les diminue. L'accélération du degré total de réaction et des réactions de déméthoxylation améliore le blanchiment au peroxyde, mais l'augmentation des réactions de couplage radicalaire peut éventuellement affecter la possibilité de pousser le blanchiment de la pulpe alors que l'augmentation de la formation d'acide oxalique peut éventuellement conduire à une plus grande probabilité de d'encrassement.

Mots clés : lignines, peroxyde d'hydrogène, blanchiment par le peroxyde, réactivité, pulpes chimiques, composés métalliques, traitement alcalin, métaux de transition, délignification.

[Traduit par la Rédaction]

Received November 11, 1998.

This paper is dedicated to Jerry Kresge in recognition of his many achievements in chemistry.

Y. Sun and D.S. Argyropoulos.[1] PAPRICAN and Department of Chemistry, Pulp and Paper Research Centre, McGill University, 3420 University St., Montreal, PQ H3A 2A7, Canada.
R.M. Berry. PAPRICAN, McGill University, 3420 University St., Montreal, PQ H3A 2A7, Canada.
M. Fenster and A. Yu. Department of Chemistry, Pulp and Paper Research Centre, McGill University, 3420 University St., Montreal, PQ H3A 2A7, Canada.

[1]Author to whom correspondence may be addressed. Telephone: (514) 398-6178. Fax: (514) 398-8254.
e-mail: dimitria@shared1.lan.mcgill.ca

 © 1999 NRC Canada

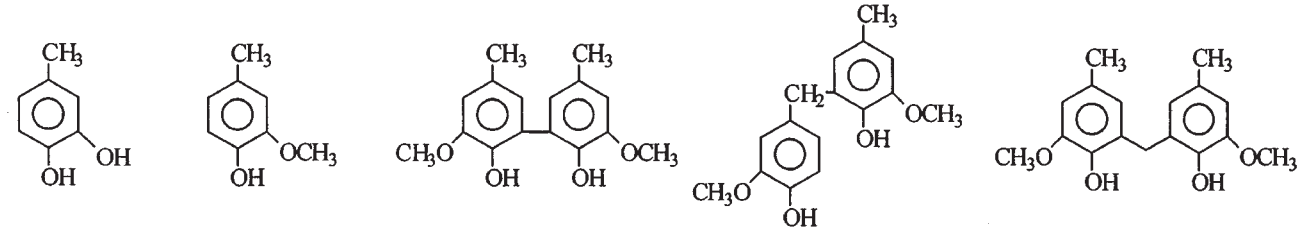

Introduction

Hydrogen peroxide interacts with lignin via two different sets of reactions; perhydroxyl anions nucleophilically attack and eliminate lignin chromophores, while free radical species, formed through the decomposition of hydrogen peroxide, cause the oxidative degradation of phenolic lignin structures converting them to carboxylic acids (1). Free-radical species have also been claimed to participate in chromophore elimination reactions (2–5). During hydrogen peroxide bleaching of chemical pulps, the presence of transition metal ions and in particular manganese, copper, and iron is known to catalyze peroxide decomposition. In contrast, magnesium is known to stabilize peroxide. In the absence of transition metal ions, the decomposition of hydrogen peroxide proceeds via a homogeneous, pH dependent, bimolecular reaction involving hydroperoxy anions (6, 7). Earlier efforts aimed at revealing the reaction details between lignin model compounds and alkaline hydrogen peroxide in the absence of transition metal ions have shown that hydrogen peroxide degrades phenolic units to low molecular weight aliphatic carboxylic acids (8–14). However, Gierer and Imsgard (15) have shown that phenolic units are stable to alkaline peroxide but are reactive to hydroxy radicals arising from the decomposition of hydrogen peroxide. Abbot et al. (6, 7, 16) have also demonstrated that differences exist in the catalytic action of manganese, copper, iron, and magnesium ions toward peroxide decomposition in the presence and absence of pulp. Despite the fact that chelation and even an acid wash is frequently used to remove the transition metal ions from the pulp prior to bleaching, it is undeniable that traces of such species still remain in the system contributing to the complexity of the reaction sequences. The large variety of highly reactive species present in such reactions coupled with the complex structural features of residual Kraft lignin has made it difficult to define the interaction of alkaline peroxide with residual Kraft lignin and transition metal ions.

The continued international effort toward implementing environmentally benign bleaching sequences, which now often include pressurized (17, 18) and high-temperature (19, 20) peroxide warrants closer attention to be paid at the fundamentals of the reactions of alkaline hydrogen peroxide with residual Kraft lignins and its model compounds. Residual Kraft lignin contains significant amounts of condensed structures such as 5-5′, α-5, diphenylmethane, and stilbene units (21–23). Despite such structures being abundant in residual Kraft lignin, to date there have been no studies dealing with their reactions with alkaline hydrogen peroxide and the effect of transition metals in such a system. The aim of this work is to evaluate the reactivity of residual Kraft lignin moieties with alkaline hydrogen peroxide in the presence and absence of transition metals. In particular, a series of model compounds representing typical structures found in residual Kraft lignin were allowed to react with alkaline hydrogen peroxide in the presence and absence of manganese, iron, copper, and magnesium ions.

Experimental

Materials

The model compounds used during this investigation were 4-methylcatechol (**1**), 3-methoxy-4-hydroxytoluene or creosol (**2**), the condensed dimer containing a 5-5′ linkage (**3**), the condensed dimer containing an α-5 linkage (**4**), and the condensed dimer containing a methylene linkage (**5**). Catechol (**1**) and creosol (**2**) were purchased from Aldrich Chemicals and used without further purification. Model compounds **3**, **4**, and **5** were synthesized following literature procedures (24, 25). Hydrogen peroxide (30%) and magnesium sulfate (98.0%) were purchased from ACP Chemicals, and iron(III) sulfate (97.0%), sodium hydroxide of semiconductor purity (99.99%) were purchased from Aldrich Chemical Co. Copper(II) sulfate (98.4%) was purchased from Baker Chemicals, while manganese sulfate (99.8%) was purchased from Fisher Scientific Co. The remaining reagents and solvents were of analytical grade or better. The water used in this study was first distilled and then passed through a nanopure analytical deionization system (Barnstead).

Reactions of model compounds with peroxide

The precise reagent stoichiometry was established by considering a benzene ring as one unit. As such the ratio of model compound/peroxide/NaOH was 1/3/2 (on molar basis) for mononuclear models **1** and **2** and 1/6/4 for dinuclear models **3**, **4**, and **5**. The concentration of metal ions used during this study was 0.5% for compounds **1** and **2** and 1% for compounds **3**, **4**, and **5**. This concentration was in excess of the solubility limit of the hydroxides under the alkaline conditions used in this work. Therefore, the metal ions present should be considered as being present as their hydrous oxide precipitates in equilibrium with the oxidation mixture.

The model compound (100 mg) was mixed with a known volume of deionized water, never exceeding 20 mL. The pH was adjusted to 12 by adding a predetermined amount of 1 N NaOH, and then the solution of the metal ion (0.01 N) was added. Hydrogen peroxide was then added using a 100 mL syringe. Finally, the total volume was made up to 25 mL with water. All reactions were carried out in stainless steel bombs equipped with a glass liner immersed in a hot water bath maintained at 80°C for 2 h.

© 1999 NRC Canada

Table 1. The calculated H_2O_2 consumption (%) and the general product profiles as obtained using quantitative GC analyses for the treatment of various model compounds with alkaline peroxide in the presence or absence of metal ions.

			Product weights determined by GC (wt.%)			
Model compound	Metal ion added	H_2O_2 % consumed	Starting material	Total identified products[a]	Unidentified products	Undetected products
Catechol (**1**)	No metal	95.3	40.5	42.9	6.8	9.8
	Mn^{2}+	98.3	14.5	22.4	2.8	58.3
	Cu^{2}+	99.2	12.5	43.2	6.1	38.4
	Fe^{3}+	98.3	22.1	63.3	6.0	8.6
	Mg^{2}+	91.2	47.9	36.5	13.2	2.4
Creosol (**2**)	No metal	91.3	42.1	45.9	5.8	6.2
	Mn^{2}+	98.3	20.9	19.7	7.4	52.0
	Cu^{2}+	98.0	18.6	33.7	5.4	42.3
	Fe^{3}+	97.2	25.2	26.7	5.2	42.9
	Mg^{2}+	83.1	48.5	22.5	5.8	23.2
5-5′ Dimer (**3**)	No metal	81.8	57.8	33.9	0.5	7.8
	Mn^{2}+	93.7	41.9	5.5	0.6	52.0
	Cu^{2}+	94.3	46.2	12.5	0.4	40.9
	Fe^{3}+	91.5	49.4	37.9	1.9	10.8
	Mg^{2}+	45.8	84.9	7.8	0.4	6.9
α-5′ Dimer (**4**)	No metal	80.3	45.5	32.9	2.2	19.4
	Mn^{2}+	91.5	13.3	23.8	8.8	54.1
	Cu^{2}+	88.6	33.6	29.2	6.6	30.6
	Fe^{3}+	94.3	38.5	35.4	3.9	22.2
	Mg^{2}+	47.7	54.5	24.2	0.9	20.4
5-CH_2-5′ dimer (**5**)	No metal	82.6	53.3	13.3	3.8	29.6
	Mn^{2}+	92.8	32.3	9.2	4.3	54.2
	Cu^{2}+	93.4	35.5	9.5	1.9	53.1
	Fe^{3}+	92.8	41.2	14.8	2.9	41.1
	Mg^{2}+	49.4	66.8	6.9	1.6	24.7

[a]Total identified products excluding starting material.

Reaction work-up procedure

At the end of the reaction a 2.0 mL aliquot of reaction mixture was withdrawn, and the concentration of residual peroxide was determined using an iodometric titration. The pH of the reaction mixtures was then adjusted to 2 using 10% HCl, and the acidified mixture was extracted with ethyl acetate (3 × 50 mL) and chloroform (3 × 50 mL). The organic extracts were stirred over anhydrous magnesium sulfate, filtered, and concentrated using a rotary evaporator with the water bath set at 25°C. The aqueous phase was freeze-dried, and the resulting solid was extracted with acetone. The extracts from the organic and aqueous phases were combined, dried at room temperature, and subjected to GC/MS analyses. The H_2O_2 consumption data and reaction yields are tabulated in Table 1.

Analytical methods

GC/MS analyses were carried out on a Hewlett Packard 5972 mass spectrometer interfaced to a Hewlett Packard 5890-A gas chromatograph equipped with a DB-5 30 m × 0.25 mm packed silica capillary column. The injection port temperature was 280°C, and the oven temperature was raised from 70 to 250°C with a gradient of 15°C/min. The products were analyzed after being silylated using N,O-bis(trimethylsilyl)acetamide. The compounds were identified by comparing their fragmentation patterns with those of commercially available or independently synthesized authentic samples.

Product quantification was carried out by using a gas chromatograph coupled to a flame ionization detector under conditions identical to those described previously. The product ratios were evaluated by using 4-methoxyphenol as the internal chromatographic standard. The GC response factors relative to the standard were determined using one of two methods. For commercially available compounds, their response factors were obtained by mixing known volumes of the compound with standard solutions, followed by GC area measurements. For compounds that were not available, their relative response factors were calculated by using the Effective Carbon Number (ECN) concept (26, 27). The contributions to ECN for specific functional groups are shown in Appendix.

The major MS fragmentation patterns for trimethylsilylated compounds discussed in this work are as follows: –*m/z* (relative intensity %): product **1**: 268 (M, 35%), 253(6), 180(10), 165(6), 149(6), 73(100); 1.01: 219 (M – 15, 3%), 190(5), 147(81), 133(4), 73(100); 1.02: 233 (M – 15, 30%), 147(100), 117(23), 73(45); 1.03: 260 (M, 9%), 245(4), 147(29), 143(79), 73(100); 1.04: 356 (M, 26%), 341(2), 267(50), 179(40), 147(15), 73(100); 1.05: 534 (M, 16%),

© 1999 NRC Canada

343(7), 305(8), 205(8), 147(10), 73(100); **2**: 210 (M, 24), 195(14), 180(100), 165(8), 149(8), 73(13); 2.02: 205 (M – 15, 12), 177(9), 147(81), 73(100); 2.03: 261 (M – 15, 7%), 186(3), 147(100), 129(7), 73(79); 2.04: 259 (M – 15, 9%), 184(4), 147(100), 97(8), 73(41); 2.06: 418 (M, 37%), 403(16), 388(23), 314(4), 287(8), 179(6), 165(3), 73(100); 2.07: 476 (M, 15%), 461(2), 358(13), 299(4), 207(3), 179(4), 147(8), 73(100); 2.08: 346(43%), 331(29), 316(56), 287(15), 241(47), 213(13), 165(11), 147(11), 73(100); 2.09: 404 (M, 46%), 389(11), 374(13), 300(8), 193(21), 73(100); 3.03: 238 (M, 5%), 223(100), 208(34), 179(8), 165(7), 151(7), 73(14); 3.04: 311 (M – 15, 75%), 281(8), 238(10), 207(11), 179(11), 151(12), 133(14), 73(100); 3.05: 436 (M, 4%), 305(100), 215(4), 188(6), 115(5), 73(39); **4**: 418 (M, 100%), 403(35), 388(79), 373(10), 358(23), 193(8), 179(14), 73(74); 4.02: 247 (M – 15, 15%), 147(100), 73(73); 4.03: 245 (M – 15, 100%), 147(58), 143(17), 115(9), 73(98); 4.06: 335 (M – 15, 7%), 245(13), 233(24), 147(63), 133(10), 73(100); 4.07: 312 (M, 67%), 297(100), 282(35), 267(64), 253(41), 223(53), 193(20), 126(24), 73(76); 4.08: 396 (M, 25%), 338(34), 308(11), 209(90), 179(40), 147(9), 73(100); 4.09: 346 (M, 20%) 331(12), 316(48), 301(16), 241(13), 179(13), 115(11), 73(100); **5**: 432 (M, 68%), 417(27), 402(35), 329(8), 299(7), 193(16), 179(7), 73(100); 5.03: 490 (M, 16%), 475(3), 372(15), 360(9), 195(19), 180(13), 147(6), 73(100); 5.04: 410 (M, 17%), 352(6), 277(15), 220(11), 208(13), 193(31), 147(19), 73(100); 5.05: 450 (M, 17%), 435(14), 390(10), 243(14), 217(10), 251(26), 147(11), 73(100); 5.06: 538 (M, 3%), 404(17), 263(32), 231(29), 147(14), 73(100).

Results and discussion

Table 1 shows the H_2O_2 consumption, the total amounts of identified products (excluding any remaining starting materials), the amounts of unidentified compounds, and those that could not be detected by GC. The yields of products recovered after the reaction varied between 67 and 92%. Severe degradation of model compounds with the formation of volatile and highly water soluble products likely accounts for the unrecovered material.

Effect of metal ions on the reactivity of hydrogen peroxide with residual Kraft lignin model compounds

The mechanism of alkaline hydrogen peroxide delignification of chemical pulps is complicated due to the complexity of the lignin structure and the large variety of reactive species formed during the process. Figures 1*a* and 1*b* display the reactivities of the examined lignin model compounds toward alkaline H_2O_2 in the presence or absence of metal ions. By presenting the same data in different ways, two sets of evaluations and comparisons can be made: one addressing the reactivity of the various lignin models in the presence (or absence) of the same metal ion (Fig. 1*a*) and the other the influence of the various metal ions on the same model compound (Fig. 1*b*).

The plots of Fig. 1*a* show that, in general, the reactivities of the five model compounds examined was of the following order: catechol (**1**) > creosol (**2**) > α-5′ dimer (**4**) > 5-CH_2-5′ dimer (**5**) > 5–5′ dimer (**3**). This reactivity order is what one would expect by considering the degree of activation caused

Fig. 1. The reactivity (reflected by the amount of remaining starting material) of the various residual Kraft lignin model compounds examined during this work, in the presence and absence of various metal ions: (*a*) displays the data as a function of the individual metal ions added; (*b*) displays the data as a function of the individual model compounds examined.

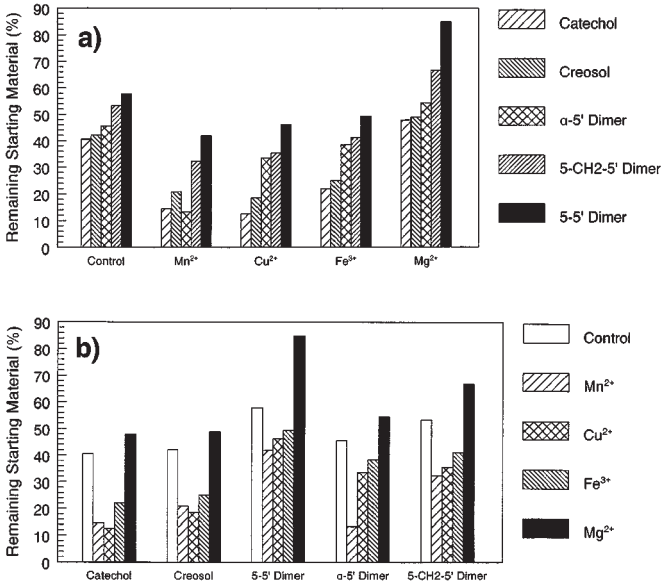

by the groups present on the aromatic rings, i.e., OH > OCH_3 > CH_3 > C_6C_5. The high reactivity of catechol moieties is in accord with the finding of Francis and Reeve (28). Our data also show that the more activated the aromatic structure, the greater its reactivity toward alkaline hydrogen peroxide, irrespective of the metal ion being added. The presence of metal ions did not significantly alter the above reactivity order but did change the extent of reactions.

Johansson and Ljunggren (29) have demonstrated, using model compounds, that during oxygen delignification the presence of two phenolic hydroxyl groups on an aromatic ring considerably increases its reactivity toward oxygen; methylcatechol was found to be more reactive than creosol. In addition, Johansson and Ljunggren (29) have shown that the reactivity of a mononuclear aromatic structure is greater than its dinuclear analogue. Similarly, using critical oxidation potential data, Kratzl et al. (30) have arrived at the same conclusions. In these respects, our findings are in complete agreement with the literature claims despite different systems having been examined. Since hydroxyl and superoxide anion radicals are the two major radical species produced from the stepwise reduction of oxygen and from the decomposition of hydrogen peroxide (31) and since these radicals are more reactive toward phenolic compounds than peroxide or oxygen, it is not surprising that the data that emerges from the present study parallels the mechanistic information already described for oxygen delignification.

Compared to our control runs, the addition of metal ions dramatically affected the reactivities of the examined model compounds toward alkaline hydrogen peroxide (Fig. 1*b*). The transition metals increased the extent of reaction between hydrogen peroxide and the model compounds, as evidenced by the decreased amounts of remaining starting material present after the reaction (compared to the control).

© 1999 NRC Canada

The presence of magnesium ions, however, protected all model compounds from being decomposed as evidenced by the increase of the remaining starting material (Fig. 1*b*).

Of the transition metals evaluated in most cases, the manganese ions caused the greatest increase in reactivity, while iron caused the least. The range of reactivity was particularly large for the dinuclear model compounds. Similar conclusions describing the effect of these ions toward decomposing peroxide have appeared in the literature (16, 32). Smith and McDonough (33) have demonstrated that the oxidation of compound **5** and the decomposition of peroxide was aided by transition metals in the following order: $Mn^{2+} > Cu^{2+} > Fe^{3+}$, their results being somewhat different at longer reaction times.

Our data are also in agreement with the speculation of Brown and Abbot (16) that transition metals decompose peroxide with the subsequent formation of a number of reactive species and that these species in turn react with lignin considerably faster than alkaline peroxide itself. The transition metals can also affect the reactivity of alkaline peroxide with phenolic moieties in lignin. Transition metal ions such as Mn^{2+}, Cu^{2+}, and Fe^{3+} may act as electron acceptors catalyzing phenoxy radical formation. The formation of such radicals is thought to be the rate-determining step in the oxidation of phenols, with copper ions being particularly effective (33, 34). This increase in reactivity caused by copper ions is seen in this present work. Catechol **1** and creosol **2** were oxidized more efficiently in the presence of copper ions than in the presence of any other metals (Fig. 1*b*).

The mechanism of action of magnesium salts in peroxide and oxygen delignification has been the subject of considerable literature discussions (7, 32, 35–37). In general, magnesium ions are thought to stabilize alkaline hydrogen peroxide either by deactivating the transition metals, by forming protective Mg-metal complexes around them (37), or by stabilizing superoxide anion radicals via the formation of stable magnesium superoxide complexes, thereby disrupting free-radical chain decomposition reactions (32). The stabilizing action of magnesium ions is clearly reflected in the data of Fig. 1*b*, since in its presence, the reactivity of all model compounds with alkaline hydrogen peroxide was significantly reduced.

Radical coupling reactions

Literature accounts have documented that aqueous hydrogen peroxide decomposes to yield molecular oxygen and water via various free-radical intermediates, particularly when the process is catalyzed by transition metal ions (38, 39), i.e.,

$$H_2O_2 + OH^- \leftrightarrow HO_2^- + H_2O$$

$$H_2O_2 + HO_2^- \rightarrow HO^\cdot + O_2^{\cdot -} + H_2O$$

$$HO^\cdot + O_2^{\cdot -} \rightarrow OH^- + O_2$$

The various radical species formed interact with phenolic compounds, giving rise to phenoxyl radicals, which then become involved in coupling and (or) rearrangement reactions. Gierer et al. (40) who have examined the detailed chemistry that operates between lignin model compounds and hydroxyl radicals have arrived at the conclusion that under alkaline conditions coupling is the dominant reaction.

In an effort to examine the role of the different transition metal ions in inducing the formation of radical coupling products in phenolic residual Kraft lignin moieties, particular attention was paid to accurately quantifying the fraction of products which were of high molecular weight. Such compounds could not be volatilized and consequently could not be detected by gas chromatography. To these values the amount of identified and (or) rearranged products was then added, yielding the total amount of radical coupling products formed. More specifically, the following identified products (Table 2) were considered the result of radical coupling reactions: for compound **1**: 1.05; for compound **2**: 2.06–2.09; for compound **3**: 3.05, 3.06; for compound **4**: 4.09; for compound **5**: 5.05 and 5.06.

The data of Fig. 2 show that of transition metal ions induced the formation of considerable amounts of coupling products. Manganese ions caused the highest formation of radical coupling products for all examined model structures.

Of the three transition metal ions examined in this effort, Fe^{3+} ions were found to generate the least amount of radical coupling products. This is consistent with the data of Landucci (34) who reported that, in alkaline media, Fe^{3+} ions cannot abstract an electron from a phenol or a phenolate anion. The beneficial effects of Mg^{2+} ions are once again apparent in the data of Fig. 2. The presence of Mg^{2+} significantly reduced the amount of radical coupling products being formed, except for creosol, which was also particularly sensitive to all of the transition metals.

In summary, the data presented in this section suggest that the negative effects of transition metals in peroxide bleaching are not only due to peroxide decomposition reactions which reduce its efficiency, but also to the formation of stable structures through radical coupling reactions which also make residual Kraft lignin harder to oxidize. The radical coupling data of Fig. 2 can explain the relatively poor response of Kraft pulp toward chlorine dioxide after oxygen or peroxide delignification (41). Radical coupling products formed in residual Kraft lignin during an oxygen and a peroxide stage are more susceptible to reaction with chlorine or ozone rather than chlorine dioxide (42). Since the role of magnesium ions in the presence of different transition metal ions has not been addressed in detail, the focus of a subsequent investigation in our laboratory will be precisely this, with emphasis on radical coupling product formation.

Reaction product profiles

Scheme 1 shows the structures of the main reaction products detected for all examined model compounds, while Table 2 depicts the determined amounts for each product. However, some minor identified products and certain intermediates are not shown. The following discussion will be focused on the effect of the various metal ions on product profiles without delving into the detailed reaction mechanisms responsible for the formation of these products, since such efforts have been adequately covered by other authors (9, 40, 43).

If the main reactive species during alkaline hydrogen peroxide bleaching was the hydroperoxide anion, enone and carbonyl containing moieties would react while phenolic or

© 1999 NRC Canada

Table 2. The determined amounts of products formed from the interaction of model compounds **1**–**5** when treated with alkaline hydrogen peroxide in the presence or absence of various transition metal ions.[a]

Model	Metal ion	Product profiles (%)								
Catechol (**1**)		**1.01**	**1.02**	**1.03**	**1.04**	**1.05**				
	None	4.4	10.6	8.2	10.7	2.8				
	Mn^{2}+	7.1	2.0	2.3	3.4	6.5				
	Cu^{2}+	16.5	7.2	8.4	5.4	3.9				
	Fe^{3}+	19.7	8.1	17.5	8.7	3.4				
	Mg^{2}+	1.6	10.0	9.3	10.3	0.5				
Creosol (**2**)		**2.01**	**2.02**	**2.03**	**2.04**	**2.05**	**2.06**	**2.07**	**2.08**	**2.09**
	None	2.9	2.6	16.4	14.2	0.5	0	2.6	0.5	0
	Mn^{2}+	5.1	1.9	1.0	0.6	3.0	1.0	5.9	3.1	1.0
	Cu^{2}+	8.0	2.1	1.4	4.3	2.9	0.7	6.3	7.2	1.4
	Fe^{3}+	6.8	3.5	1.6	4.9	2.2	0.5	5.5	1.5	1.0
	Mg^{2}	1.9	2.2	5.7	3.8	1.5	0.9	0.5	0	0
5-5′ Dimer (**3**)		**3.01**	**3.02**	**3.03**	**3.04**	**3.05**	**3.06**			
	None	1.0	1.9	0.0	31.1	0	0			
	Mn^{2}+	0	0	0	4.6	0.9	0.0			
	Cu^{2}+	0.5	0.5	0.0	10.0	1.5	0.0			
	Fe^{3}+	2.0	2.4	1.7	29.1	1.0	1.7			
	Mg^{2}+	0	0	2.4	5.4	0	0			
α-5′ Dimer (**4**)		**4.01**	**4.02**	**4.03**	**4.04**	**4.05**	**4.06**	**4.07**	**4.08**	**4.09**
	None	6.1	3.0	4.7	1.6	4.1	9.1	0.9	0.6	2.6
	Mn^{2}+	7.8	0.6	1.1	1.0	1.4	2.6	1.0	1.5	6.6
	Cu^{2}+	8.5	0	4.2	2.2	2.1	4.0	0	1.2	5.3
	Fe^{3}+	9.3	2.6	4.3	1	4.1	6.5	1	1.7	3.5
	Mg^{2}+	2.3	1.3	2.0	3.1	1.4	11.4	0.8	0.7	1.1
5-CH_2-5′ dimer (**5**)		**5.01**	**5.02**	**5.03**	**5.04**	**5.05**	**5.06**			
	None	1.5	3.9	0.5	3.0	3.9	0.5			
	Mn^{2}+	0	0.7	6.0	1.7	0.4	0.4			
	Cu^{2}+	1.4	3.3	1.1	1.8	1.8	0			
	Fe^{3}+	0.9	3.9	4.9	2.8	1.7	0			
	Mg^{2}+	2.3	1.2	0.6	0.8	2.0	0			

[a]Product numbering corresponds to the structures shown in Scheme 1.

Fig. 2. The amounts of radical coupling products formed during the reaction of alkaline hydrogen peroxide with various residual Kraft lignin model compounds in the presence or absence of various metal ions.

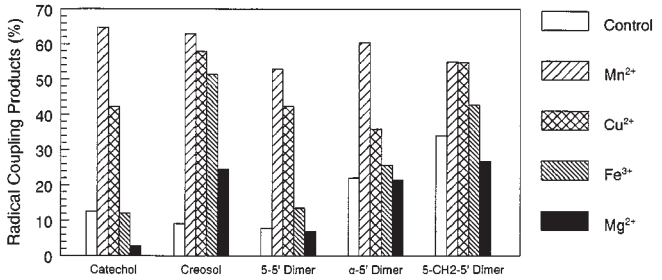

catecholic centres would not (15). The structures of the detected products, however (Scheme 1), show that significant degradation and radical coupling reactions have occurred. Such products are formed from the interaction of the decomposition products of hydrogen peroxide with model compounds **1**–**5**.

The reaction products detected from the interaction of catechol **1** and creosol **2** with alkaline hydrogen peroxide in the presence and absence of the various transition metal ions indicate that the primary route for the breakdown of such phenolic moieties consists of ring opening followed by more severe fragmentation (9). In addition, 5-5′ and 5-O-4′ coupling products were present (products 1.05 and 2.06–2.09) as a consequence of carbon- and oxygen-centred radical coupling reactions. As well, the detected radical coupling products were found to increase in the presence of Mn^{2+}, Cu^{2+}, and Fe^{3+} ions (Table 2). Carbon-centred radicals are thought to efficiently recombine, since the resulting dimers have lower critical oxidation potentials (COP) than the original monomers (30).

Oxalic acid (entries 1.01, 2.01, and 4.01; Table 2) is of particular significance to peroxide bleaching operations, since oxalate salts are known to form detrimental deposits on bleach plant process equipment. Table 2 and Fig. 3 show that compounds **1**, **2**, and **4** generated a large amount of oxalic acid, and catechol **1** produced the most. The amount of formed oxalic acid increased in the presence of transition metal ions, while the presence of magnesium ions significantly suppressed the formation of oxalic acid, bringing it to levels lower to those of the control experiments.

© 1999 NRC Canada

Scheme 1. The main identified products obtained from the interaction of model compounds **1**–**5** when treated with alkaline hydrogen peroxide in the presence and absence of various transition metal ions. The product numbering corresponds to the amounts shown in Table 2.

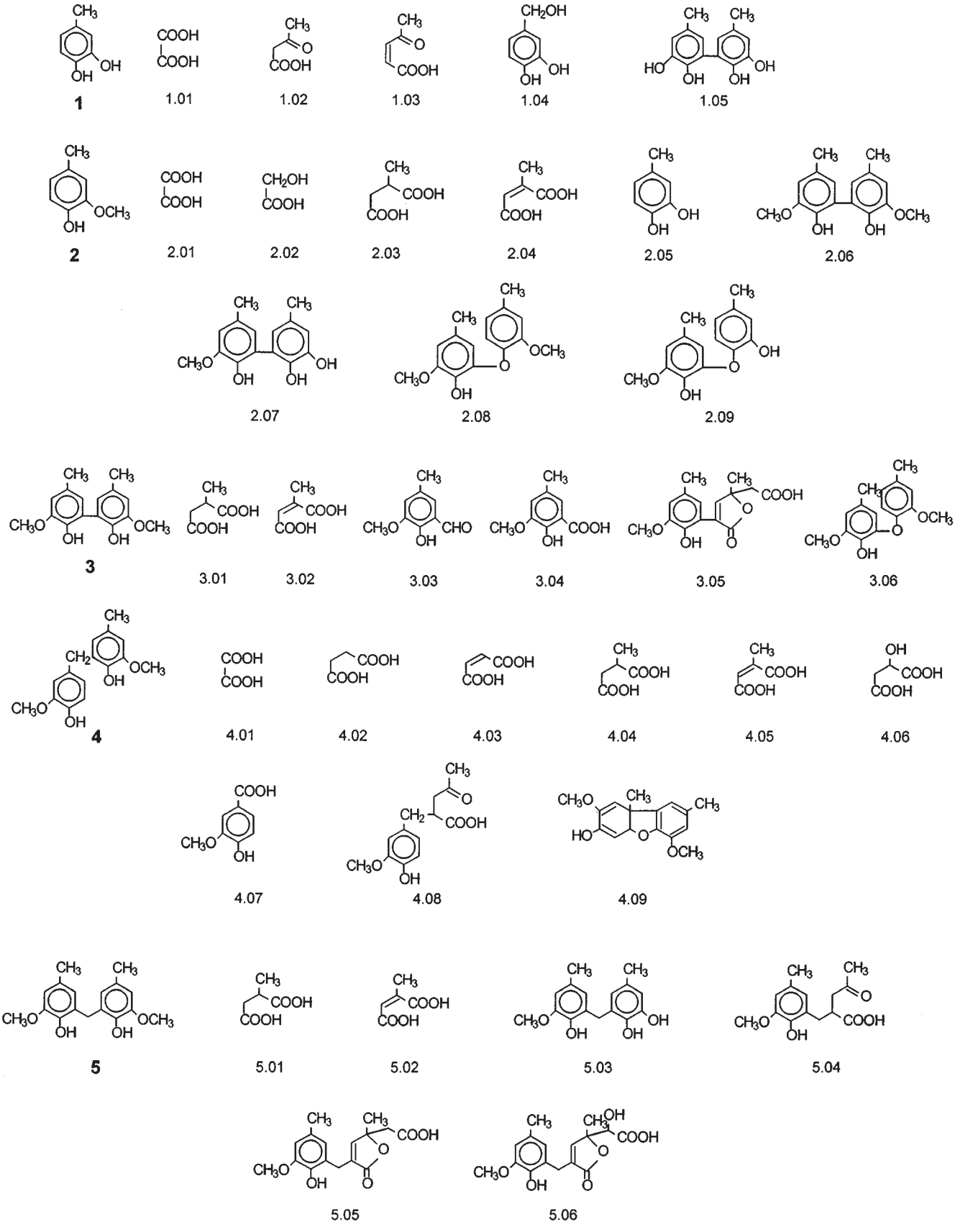

© 1999 NRC Canada

Fig. 3. The amounts of oxalic acid formed during the reaction of alkaline hydrogen peroxide with three Kraft lignin model compounds in the presence and absence of various metal ions.

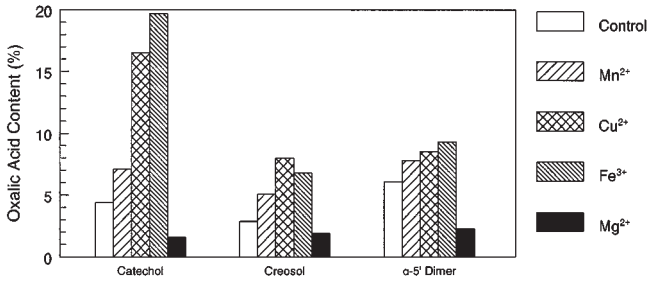

Products 2.05, 2.07, and 2.09 show the occurrence of demethoxylation reactions. These are significant reactions, since free phenolic hydroxyl groups predispose the structure of lignin to further oxidation. The sum of product 2.05, 2.07, and 2.09 shows the scale of demethoxylation reaction; product 2.05 is likely the precursor of products 2.07 and 2.09. The sum of 2.05, 2.07, and 2.09 shows that demethoxylation reactions prevail in the presence of transition metal complexes. Hydroxyl radicals forming from the decomposition of hydrogen peroxide are known to induce demethoxylation (14, 40). Copper ions caused the greatest degree of demethoxylation, while the presence of magnesium ions significantly suppressed demethoxylation reactions, bringing them to levels lower than those of the control experiments.

During the 60's, Kartzl's team (30, 44) investigated the fundamentals of the interaction of oxygen with phenols under delignification conditions. Their research efforts, amongst others, led to a comprehensive qualitative understanding of radical coupling reactions that cause the formation of biphenolic structures and their eventual degradation to 1-methyl-3-methoxy-4-hydroxy benzoic acid, acetone, and carbon dioxide. Since the underlying chemistry of oxygen and peroxide delignification stages are similar, it was not surprising to discover that the dominant degradation product arising from the interaction of alkaline hydrogen peroxide with the biphenolic 5-5′ dimer was 1-methyl-3-methoxy-4-hydroxy benzoic acid (compound 3.04, Table 2). Residual traces of the corresponding aldehyde (compound 3.03) were also apparent in some cases, signifying that the aldehyde is the precursor to the acid during the oxidation. The small amounts of the aldehyde also signified that the oxidation of aldehyde 3.03 to acid 3.04 is a very rapid reaction under alkaline peroxide delignification conditions.

Since it is conceivable that the radical coupling product 2.06 (which is model compound **3**) would convert to acid 3.04 and traces of aldehyde 3.03, it is interesting to note that no 1-methyl-3-methoxy-4-hydroxy benzoic acid (3.04) was detected amongst the degradation products of compound **2**. This may indicate that under alkaline peroxide delignification conditions the formation of radical coupling products is faster than their further degradation. The precise determination of the energies of activation for these reactions may further substantiate such a conclusion.

Amongst the three dimers examined, the α-5′ dimer **4** was found to be the most reactive followed by dimer **5**, as evidenced by the amount of remaining starting materials after the reaction (Fig. 1*a*). This is not surprising when one considers that these compounds contain a benzylic carbon which is known to be relatively labile. That the α-5′ dimer **4** was slightly more reactive than dimer **5** may be explained on the basis of spin density considerations, taking into account the stability of the resulting radicals after cleavage at the benzylic centre. It is also worth noting that compound **4** yielded the rearrangement product 4.09 (Scheme 1), which is formed by the coupling of a phenoxy and a benzyl radical followed by rearomatization. Similar reaction products were found by Gierer et al. (40) when they treated creosol with hydroxyl radicals. The presence of lactonic acids 5.05, 5.06, amongst the degradation products of model **5**, provides evidence that the muconic acid pathway was also operational. This pathway involves the initial formation of catechols possibly via an initial, radically induced, demethylation reaction followed by their oxidation to *ortho*-quinones. Such moieties may then be attacked by hydroperoxide anions, forming dioxetanes, followed by carbon–carbon bond scission of the dioxetane ring, giving rise to the corresponding carbonyl-containing fragments (15). Structures of similar nature were also present amongst the degradation products of dimers **3** and **4**, i.e., products 3.05 and 4.08.

Concluding remarks

(*i*) Transition metals have the positive effects of accelerating the total degree of reaction and the demethoxylation reactions. They also have the negative effects of increasing the rate of radical coupling reactions, which can affect the further bleachability of pulp, and significantly increasing the amount of oxalic acid generated by peroxide bleaching reactions. (*ii*) Magnesium ions have exactly the opposite effects probably because of the deactivation of the small quantities of transition metals present in even control samples. (*iii*) Oxygen and peroxide delignification reactions are very similar. (*iv*) The order of reactivity of the phenolic lignin models towards hydrogen peroxide was determined by the degree of activation of the aromatic ring by the various ring substituents. The presence of metal ion did not alter this reactivity order. (*v*) The addition of metal ions induced the formation of radical species by initiating the decomposition of hydrogen peroxide to radicals and (or) catalyzing the formation of phenoxy radical directly. In this work, the overall catalytic ability of the transition metals toward increasing the reactivity of phenolic models was found mostly to be $Mn^{2+} > Cu^{2+} > Fe^{3+}$, which is the same as the order of activity toward peroxide decomposition.

Acknowledgements

The authors would like to acknowledge Mr. Luc Lapierre of Paprican for his input while reviewing the manuscript. This research was supported by the Government of Canada in the form of a Strategic Grant.

References

1. G. Gellerstedt and I. Pettersson. J. Wood Chem. Technol. **2**(3), 231 (1982).
2. G.C. Hobbs and I. Abbot. J. Wood Chem. Technol. **11**(2), 225 (1991).
3. C.W. Dence and S. Omori. TAPPI, **69**(9), 120 (1986).

© 1999 NRC Canada

4. W.G. Strunk. *In* Pulp and paper manufacture. Mechanical pulping. Vol. 2. *Edited by* R.A. Leask. 1987. p. 238.
5. J. Gierer, K. Jansbo, and T. Reitberger. J. Wood Chem. Technol. **13**(4), 561 (1993).
6. J. Abbot. J. Pulp Paper Sci. **17**(1), J10 (1991).
7. J. Abbot and D.G. Brown. Can. J. Chem. **68**, 1537 (1990).
8. R.H. Reeves and I.A. Pearl. TAPPI, **48**(2), 121 (1965).
9. C.W. Bailey and C.W. Dence. TAPPI, **52**(3), 491 (1969).
10. A.W. Kempf and C.W.Dence. TAPPI, **58**(6), 104 (1975).
11. R. Agnemo and G. Gellerstedt. Acta Chem. Scand. **B33**, 337 (1979).
12. G. Gellerstedt and R. Agnemo. Acta Chem. Scand. **B34**, 275 (1980).
13. S. Omori and C.W. Dence. Wood Sci. Technol. **15**, 113 (1981).
14. A.J. Nonni and C.W. Dence. Holzforschung, **42**(1), 37 (1988).
15. J. Gierer and F. Imsgard. Svensk Papperstidn. **80**(16), 510 (1977).
16. D.G. Brown and J. Abbot. J. Wood Chem. Technol. **15**(1), 85 (1995).
17. U. Germgard and S. Nordén. Int. Pulp Bleaching Conf. TAPPI Proc. 1994. p. 53.
18. B. Stromberg and R. Szopinski. Int. Pulp Bleaching Conf. TAPPI Proc. 1994. p. 199.
19. B.P. Roy, B. Van Lierop, and A. Audet. TAPPI Pulp. Conf. Proc. 1995. p. 771.
20. B. Van Lierop, B.P. Roy, R. Berry, A. Audet and L. Shackford. Int. Pulp Bleaching Conf. TAPPI Proc. 1996. p. 303.
21. T. Eriksson and J. Gierer. J. Wood Chem. Technol. **5**(1), 53 (1985).
22. A. Granata and D.S. Argyropoulos. J. Agric. Food Chem. **43**(6), 1538 (1995).
23. B. Ahvazi, G. Pageau, and D.S. Argyropoulos. Can. J. Chem. **76**, 506 (1998).
24. F.X. Douglas, W. Reeve, and A.B. McKague. J. Wood Chem. Technol. **16**(1), 35 (1996).
25. K. Kratzl and F.W. Virhopper. Monatsh. Chem. **102**, 425 (1971).
26. J.T. Scanlon and D.E. Willis. J. Chrom. Sci. **23**, 333 (1985).
27. W.A. Dietz. J. Gas Chrom. 68 (1967).
28. R.C. Francis and W.D. Reeve. J. Pulp Paper Sci. **13**(6), 171 (1987).
29. E. Johansson and S. Ljunggren. J. Wood Chem. Technol. **14**(4), 507 (1994).
30. K. Kratzl, P. Claus, W. Lonsky, and J.S. Gratzl. Wood Sci. Technol. **8**, 35 (1974).
31. J. Gierer. Holzforschung, **51**, 34 (1997).
32. J.L. Colodette, S. Rothenberg, and C.W. Dence. J. Pulp Paper Sci. **15**(2), J45 (1989).
33. P.K. Smith and T.J. McDonough. Svensk Papperstid. **12**, R106 (1985).
34. L.L. Landucci. Trans. Tech. Sect. Can. Pulp. Pap. Assoc. **4**, 25 (1978).
35. J. Basta, L. Holtinger, and J. Hook. 6th Int. Symp. Wood Pulping Chem. 237 (1991).
36. M. Yasumoto, Y. Matsunoto, and A. Ishizu. J. Wood Chem. Technol. **16**(1), 95 (1996).
37. H.S. Isbell, E.W. Parks, and R.G. Naves. Carbohydr. Res. **45**, 197 (1975).
38. R.C. Francis. TAPPI Press Anthol. 418 (1989).
39. J.W. Weaver, L.R. Schroeder, and N.S. Thompson. Pap. Puu. **1**, 31 (1979).
40. L. Gierer, E. Yang, and T. Reitberger. Holzforschung, **46**(6), 495 (1992).
41. K.R. Kumar, C. Jacobs, H. Jameel, and H.-M.Chang. Int. Pulp Bleaching Conf. TAPPI Proc. 147 (1996).
42 Y. Sun and D.S. Argyropoulos. Holzforschung, **50**(2), 175 (1996).
43. M. Holocher-Ertl, P. Fricko, and K. Kratzl. SPCI Int. Symp. Wood Pulp. Chem. Vol. 2. Preprints, Stockholm. June, 1981. pp. 83–89.
44. K. Kratzl, J. Gratzl, and P. Claus. Adv. Chem. Ser. **59**, 157 (1966).

Appendix

Contributions to the effective carbon number.

Atom	Type	ECN contribution
C	Aliphatic	1
C	Aromatic	1
C	Olefinic	0.95
C	Acetylenic	1.3
C	Carbonyl	0
C	Carboxyl	0
C	Ether	–1
C	Primary alcohol	–0.5
C	Secondary alcohol	–0.75
TMS-derivatives:		
H-C-O-TMS		3.70
CO_2-TMS		3.0

© 1999 NRC Canada

Reactivity of aminyl radicals in radical nucleophilic substitution reactions with diphenylphosphide anion

Gabriela S. Foray, Alicia B. Peñéñory, and Roberto A. Rossi

Abstract: The photostimulated reactions of *N*-cyclopropyl-*N*-ethyl *p*-toluensulfonamide (**4**) with diphenylphosphide ions (**2**) in liquid ammonia gave 1,3-bis(diphenylphosphinyl)-1-(*N*-ethyl)propylamine, isolated as the oxide **5**, and 1,3-bis(diphenylphosphinyl)-1-propanol, isolated as the oxide **6**, all of them corresponding to the aperture of the cyclopropylaminyl radical intermediate. The reaction of **4** with **2** in excess and longer reaction times gave only **5** (73% yield). The photostimulated reactions of *N*-(*n*-butyl)-*N*-cyclobutyl *p*-toluensulfonamide (**13**) with **2** in liquid ammonia gave, after oxidation, *N*-(*n*-butyl)-*N*-cyclobutyl diphenylphosphonamide (**14**) in 94% yield. All these reactions occur by the radical nucleophilic substitution in which aminyl radicals are intermediates. The order of the magnitude of the rate constant for the coupling reaction of a dialkylaminyl radical with **2** could be intermediate between those of the rearrangements of the cyclopropyl and cyclobutylaminyl radicals.

Key words: aminyl radicals, $S_{RN}1$ reactions, radical clocks, photochemistry.

Résumé : Les réactions photostimulées du *N*-cyclopropyl-*N*-éthyl *p*-toluènesulfonamide (**4**) avec les ions diphénylphosphure (**2**), dans l'ammoniac liquide, conduisent à la 1,3-bis(diphénylphosphinyl)-1-(*N*-éthyl)propylamine, isolé sous la forme d'oxyde (**5**), et de 1,3-bis(diphénylphosphinyl)-propan-1-ol, isolé sous la forme d'oxyde (**6**); tous ces produits correspondent à l'ouverture du radical cyclopropylaminyle intermédiaire. La réaction du produit **4** avec **2** en excès et l'utilisation de temps de réaction plus longs conduisent à la formation exclusive du produit **5** (rendement de 73%). Les réactions photostimulées du *N*-(butyl)-*N*-cyclobutyl *p*-toluènesulfonamide (**13**) avec **2** dans l'ammoniac liquide conduit, après oxydation, au *N*-(butyl)-*N*-cyclobutyl diphénylphosphonamide (**14**) avec un rendement de 94%. Toutes ces réactions se produisent par le biais d'une réaction de substitution radicalaire nucléophile dans laquelle les intermédiaires sont des radicaux aminyles. L'ordre de grandeur de l'amplitude de la constante de vitesse de la réaction de couplage d'un radical dialkylaminyle avec le composé **2** se situerait à une valeur intermédiaire entre celles des réarrangements des radicaux cyclopropyl- et cyclobutyl-aminyles.

Mots clés : radicaux aminyles, réactions $S_{RN}1$, horloges radicalaires, photochimie.

[Traduit par la Rédaction]

Nucleophilic substitution by electron transfer is an area of great interest which has increased considerably in the last 20 years (for reviews on $S_{RN}1$ see ref. 1). Several substrates have been described to react by a chain radical mechanism of nucleophilic substitution or $S_{RN}1$. The mechanism of the reaction is a chain process, and the propagation steps are shown in Scheme 1.

According to this mechanism the radical anion of the substrate $(RX)^{-\cdot}$ is formed, in the initiation step, by an electron transfer (ET) from a suitable electron source. The $(RX)^{-\cdot}$ formed fragments to give a radical and the anion of the leaving group (eq. [1]). The radical can react with the nucleophile to afford the radical anion of the substitution product (eq. [2]), which by ET to the substrate (eq. [3]), affords the substitution product and $(RX)^{-\cdot}$ to continue the chain process.

All of the examples known imply the reaction of a carbon-centered radical with an appropriate nucleophile. We are interested in the study of the reactivity of heterocentered radicals with nucleophiles, and more specifically, the study of aminyl radicals.

Recently, we have reported the first example of an $S_{RN}1$ reaction involving a nitrogen-centered radical (2). Thus, *N*,*N*-di-(*n*-butyl)-*p*-toluensulfonamide (**1**) reacts under irradiation with diphenylphosphine ion (**2**) in liquid ammonia, giving, after oxidation, the corresponding phosphonamide (**3**) in good yields (79%). This reaction proceeds by an $S_{RN}1$ mechanism in which the aminyl radicals are intermediates ([eq. 4]).

Received November 4, 1998.

This paper is dedicated to Jerry Kresge in recognition of his many achievements in chemistry.

G.S. Foray, A.B. Peñéñory, and R.A. Rossi.[1] INFIQC, Departamento de Química Orgánica, Facultad de Ciencias Químicas, Universidad Nacional de Córdoba – Ciudad Universitaria, 5000 Córdoba, Argentina.

[1]Author to whom correspondence may be addressed. Telephone: 54-351-4334170/4334173. Fax: 54-351-4333030. e-mail: rossi@dqo.fcq.unc.edu.ar

© 1999 NRC Canada

Scheme 1.

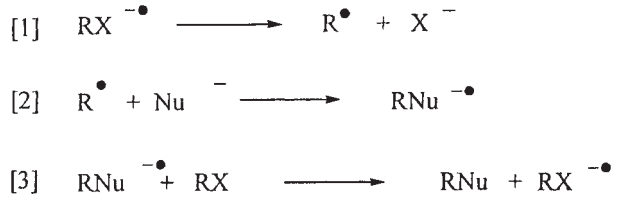

In this reaction, the reduction of the dibutylaminyl radical to di-*n*-butylamine is a competitive process. This result led us to suppose that the coupling reaction was not as fast as in the case of aromatic radicals.[2] It has been suggested that the coupling of **2** with 2-quinolyl radicals is diffusional (4).

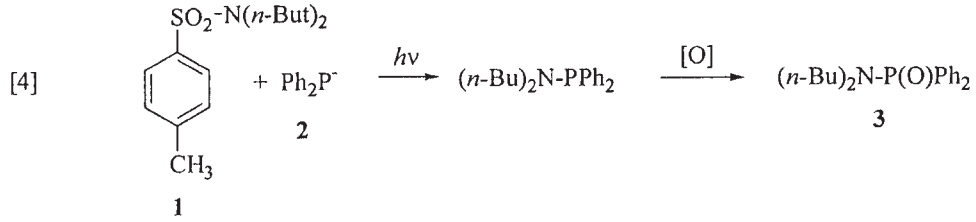

Rate constants for the rearrangement of different aminyl radicals, like the ring opening of cyclopropyl and cyclobutyl aminyl radicals are known (5). Substrates that give cyclopropyl and cyclobutyl aminyl radicals could, in principle, be used as clock reactions (6), and it could be possible to estimate the order of the rate constant for the coupling reaction between the dialkylaminyl radical and **2**.

Results and discussion

The photostimulated reaction of *N*-cyclopropyl-*N*-ethyl *p*-toluensulfonamide (**4**) with **2** in liquid ammonia gave, after oxidation, compounds containing the diphenylphosphinyl group, identified as **5** and **6** in 8 and 20% yield, respectively (eq. [5]) (Table 1, expt. 1).[3]

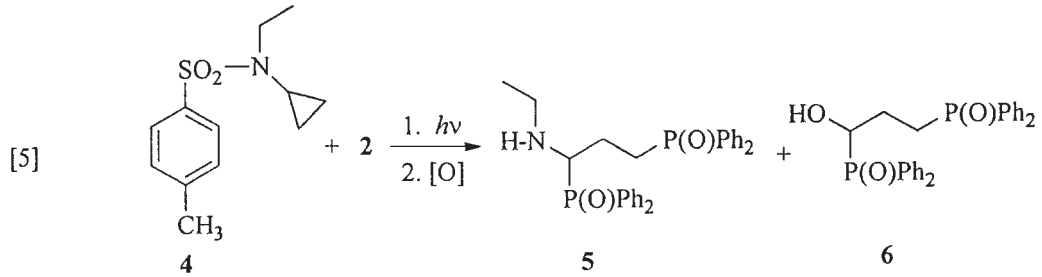

The yields of these products increase as does the concentration of **2**. Thus, when the molar relation was 1:2.6, 69% of **5** and 24% of **6** were quantified. No products containing the cyclopropyl aminyl moiety were detected. There was no reaction in the dark, and the substrate was recovered in high yield (Table 1, expt. 4). When the time of irradiation was reduced to 5 min, 18% of **5** and 12% of **6** were produced. This photoinduced reaction was inhibited by the presence of *p*-dinitrobenzene and di-*tert*-butylnitroxide, a strong electron acceptor and a radical trap, respectively (Table 1, expts. 5–7). When the photostimulated reaction was treated with DMSO, the liquid ammonia was allowed to evaporate, and the reaction was kept during 4 days, **5** was the only product isolated (73% yield).

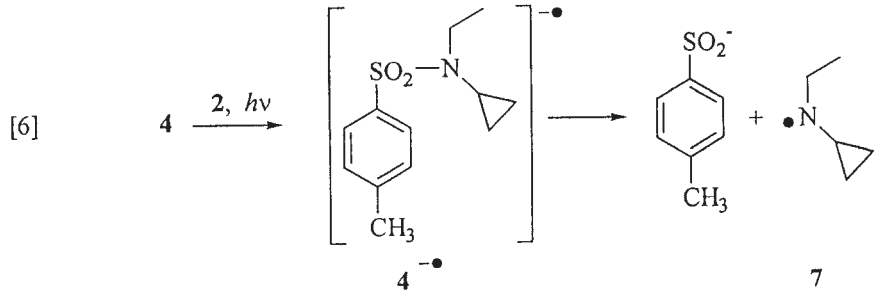

[2] Coupling rate constants for aromatic radicals with nucleophiles have been determined, and most of them are in the order of 10^7–10^{10} (see ref. 3).

[3] Small amounts of 3-(diphenylphosphinyl) propanal, isolated as the oxide, was detected (<2% yield).

© 1999 NRC Canada

Table 1. Photostimulated reactions of *N*-alkyl-*N*-cycloalkyl *p*-toluensulfonamide (**4** and **13**) with **2** in liquid ammonia.[a]

			Products distribution (%)[c]		
			On nitrogen[d]	On carbon[e]	
Expt.	Substrate (mmol)[b]	**2** (mmol)	**14**	**5**	**6**
1	**4** (0.5)	0.8	—	8	20
2	**4** (0.5)	1	—	15	32
3	**4** (0.5)	1.3	—	69	24
4[f]	**4** (1.0)	2.5	—	—	—
5[g]	**4** (1.0)	2.5	—	18	12
6[g,h]	**4** (1.0)	2.5	—	2	4.5
7[g,i]	**4** (1.0)	2.5	—	4	<1
8	**4** (1.0)	2.5	—	73[j]	—
9	**13** (1.0)	1.5	66[k]	—	—
10	**13** (1.0)	2.6	94	—	—

[a]Performed in ca. 350 mL of liquid ammonia under nitrogen atmosphere, irradiation time 30 min with two 400 W lamps.

[b]**4** and **11** were dissolved in ca. 2 mL of anhydrous diethyl ether prior addition to the reaction flask.

[c]Determined by GC or HPLC using the internal standard method, based on the concentration of the substrates.

[d]Products coming from the coupling reaction of **2** with a nitrogen centered radical.

[e]Products coming from coupling reaction of **2** with a carbon-centered radical.

[f]Dark reaction.

[g]5 min of irradiation.

[h]*p*-Dinitrobenzene (20 mol%) was added.

[i]Di-*tert*-butylnitroxide (20 mol%) was added.

[j]After 30 min of irradiation DMSO was added to the reaction mixture and was stirred for 4 days under nitrogen atmosphere.

[k]Quantified after isolation from silica-gel chromatography.

From all these results, it is concluded that **4** reacts under irradiation with **2** by the $S_{RN}1$ mechanism, with aminyl radicals as intermediates. Under irradiation, anion **2** transfers one electron to **4**, giving the radical anion $\mathbf{4}^{-\cdot}$, which after fragmentation yields *p*-toluensulfonate ion and the cyclopropylethylaminyl radical **7** (eq. [6]).

Radical **7** can undergo two possible reactions, i.e., it can couple with **2**, giving radical anion $\mathbf{8}^{-\cdot}$ (vide infra), which after electron transfer affords the substitution product **8** (eq. [7]), or it can rearrange to a carbon-centered radical, **7′**, which is able to react with the anion **2** to yield, finally, the substitution product **9** ([eqs. [8] and [9]).

[7] 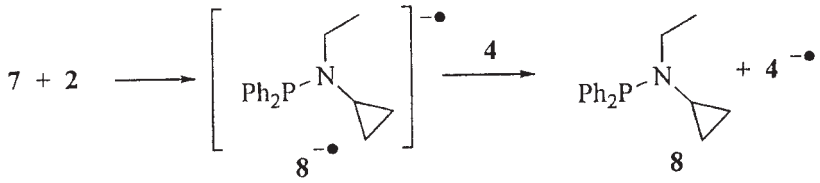

[8] 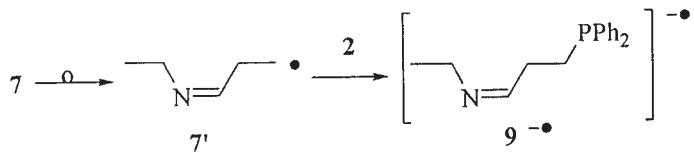

[9] 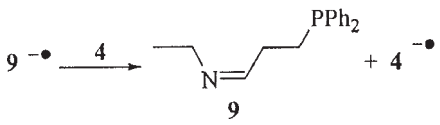

The amount of products **8** and **9** depends on the rate for the coupling of **7** with nucleophile **2** as well as on the concentration of **2** (eq. [7]), and on the rate of ring opening of the cyclopropylaminyl radical **7** to yield the radical **7′**. The rate constant for rearrangement of **7** was determined in benzene at 50°C and is ca. 10^9 s^{-1} (5). From the relation of products **8** to **9**, and taking into account the rate constant for ring opening of **7**, it would be possible to estimate the rate constant for coupling of cyclopropylalkylaminyl radical **7** with **2**. Unfortunately, **8** was not observed experimentally, and the reaction gave only products coming from the ring opening of the aminyl radical **7**.

© 1999 NRC Canada

[10] 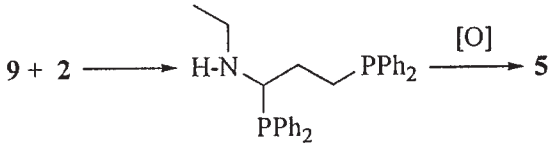

10

[11] 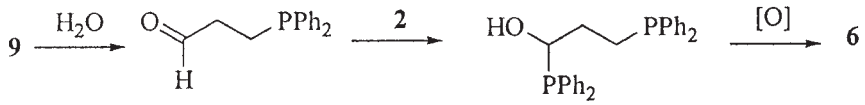

11 12

Product **9** was not isolated as such, since the imine group can react further with **2** to yield the addition product **10**, which upon oxidation affords **5** (eq. [10]). Product **9** can also yield, as a result of aqueous work-up, the aldehyde **11** (hydrolysis of the imine group), which also adds **2** or diphenylphosphine to the carbonyl group, giving the addition product **12**, which after oxidation renders **6** (eq. [11]).

The relation **5**/**6**, depends on the concentration of **2** and on the rate of the addition reaction to the imine group. Thus, the amount of **5** increases as the concentration of **2** increases. Upon treatment of a liquid ammonia photostimulated solution of **4** and excess of **2** with DMSO, the liquid ammonia allowed to evaporate, and the reaction mixture kept for 4 days under a nitrogen atmosphere (to avoid hydrolysis of the imine), only product **5** was obtained in 73% (Table 1, expt. 8).

The fact that only open chain products were obtained means that the rearrangement of **7** is faster than the coupling with anion **2** (the product from coupling of the aminyl radical with **2** is not observed).

To establish the extent to which the rate of the coupling reaction competes favourably with the rate of rearrangement of the *N*-cycloalkylaminyl radicals, we synthesized *N*-(*n*-butyl)-*N*-cyclobutyl *p*-toluensulfonamide (**13**), which upon photostimulated reaction with the nucleophile (electron transfer), and ulterior fragmentation could afford *N*-(*n*-butyl)-*N*-cyclobutyl aminyl radicals, which, in term, are known to ring open in a slower fashion than the cyclopropyl analogue **7** (5).

Thus, the photostimulated (30 min) reaction of **13** with anion **2** in liquid ammonia gives, after oxidation, *N*-(*n*-butyl)-*N*-cyclobutyl-*P,P*-diphenylphosphonamide (**14**) (66% of isolated product) (eq. [12]),[4] (Table 1, expt. 9).[5] When the molar relation was 1:2.6, 94% of **14** was quantified (Table 1, expt. 10).

[12] 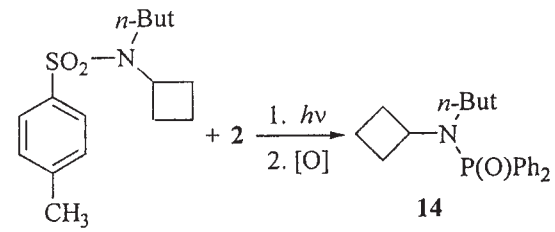

13 14

From these results, we can conclude that the rate constant for the coupling reaction of a dialkylaminyl radical with **2** is not diffusional as in the case of aryl radicals, and its order of magnitude could be estimated to be intermediate between that for the rearrangement of the cyclopropyl and that of the cyclobutylaminyl radicals (2×10^9 and 1.6×10^6 s^{-1} at 50°C in benzene, respectively) (5). On the other hand, aminyl radicals are unequivocally intermediates in these reactions.

Experimental section

General methods

^1H and ^{13}C NMR spectra were recorded on a Bruker AC-200 spectrometer, and all spectra are reported in δ (ppm) relative to Me_4Si, with $CDCl_3$ as solvent. ^{31}P NMR were performed on a Bruker AC-300 spectrometer, using H_3PO_4 as external reference and $CDCl_3$ as solvent. The IR spectra were recorded on a Nicolet FT 5-SXC spectrometer, and the mass spectra were obtained with a Finnigan Model 3300 mass spectrometer. Gas-chromatographic analyses were performed on a Hewlett Packard 5890 Series II with a flame-ionization detector and the data system Spectra Physics 4290, on a HP-1 capillary column (methyl silicone gum, 5 m × 0.53 mm, 2.65 μm film thickness). High-performance liquid chromatography (HPLC) was performed on an LKB Model 2249 instrument with a LKB Model 2122 UV-visible detector, Spherisorb ODS-2 column (5 μm, 250 × 4 mm i.d.) and a Spectra Physics SP-2400 data system. Column chromatography was performed on silica gel (70–230 mesh ASTM). Irradiation was conducted in a reactor equipped with two 400-W UV lamps emitting maximally at 350 nm (Philips Model HPT, water-refrigerated).

Materials

N-Cyclopropyl-*N*-ethyl *p*-toluensulfonamide (**4**) (^1H NMR δ: 0.70 (m, 2H), 0.84 (m, 2H), 1.14 (m, H), 2.43 (s, 3H), 3.28 (q, 2H, *J* = 7.3 Hz), system A2B2 7.24 (d, 2H, *J* = 8.25 Hz), 7.74 (d, 2H, *J* = 8.25 Hz)) and *N*-(*n*-butyl)-*N*-cyclobutyl *p*-toluensulfonamide (**13**) (^1H NMR δ: 0.93 (t, 3H, *J* = 7.3 Hz), 1.31 (m, 2H), 1.6 (m, 4H), 2.03 (m, 4H), 2.41 (s, 3H), 3.09 (m, 2H), 4.12 (q, H, *J* = 8.4 Hz), system A2B2 7.28 (d, 2H, *J* = 8.28 Hz), 7.74 (d, 2H, *J* = 8.28 Hz)) were synthesized from the alkylation of the cyclopropyl or cyclobutyl *p*-toluensulfonamide (7) with iodoethane or *n*-bromobutane under phase-transfer conditions in good

[4] Only mere traces of a possible product from the rearranged carbon-centered radical was observed.
[5] NMR spectra data have been deposited as supplementary material and may be purchased from: The Depository of Unpublished Data, Document Delivery, CISTI, National Research Council Canada, Ottawa, Canada, K1A 0S2.

© 1999 NRC Canada

yields (75–83%) (8). Diphenylphosphide ions (**2**) were prepared from the reaction of triphenylphosphine (Fluka) with 2 equiv. of sodium metal in liquid ammonia. The sodium amide formed was neutralized with *tert*-butyl alcohol. DMSO (Carlo Erba) was distilled under vacuum and stored over molecular sieves (4 A).

Photostimulated reaction of *N*-cyclopropyl-*N*-ethyl *p*-toluensulfonamide (4) with 2

The following procedure is representative of all the reactions. Into a three-necked, 500 mL round-bottom flask equipped with a cold finger condenser charged with dry ice – ethanol, a nitrogen inlet, and a magnetic stirrer were distilled 350 mL of ammonia. Triphenylphosphine (0.8 mmol) and sodium metal (1.6 mmol) were added to form **2**, and then *tert*-butyl alcohol (0.8 mmol) was added. Substrate **4** (0.5 mmol) was dissolved in ca. 2 mL of anhydrous diethyl ether prior addition to the reaction flask. After 30 min of irradiation the reaction was quenched by the addition of ammonium nitrate. Ammonia was allowed to evaporate. Water (50 mL) was added to the residue and the mixture extracted with diethyl ether. The ether extract was analyzed by HPLC (petroleum ether:methylene chloride:acetone:ethyl acetate:methanol: 1:1:1:1:0.3), and the substitution products **5** and **6** were quantified using *N*,*N*-dibutyl *p*-toluensulfonamide as internal standard.

1,3-Bis(diphenylphosphinyl)-1-(*N*-ethyl)propylamine (5)

It was isolated by silica-gel chromatography with petroleum ether/diethyl ether (25:75). IR (KBr) (cm^{-1}): 3414.9, 3286.7, 3058.2, 2963.5, 2935.6, 2868.7, 1665, 1436.5, 1274.9, 1118.9. ^{1}H NMR δ: 0.92 (t, 3H), 1.8 (m, 2H), 2.4 (m, 4H), 3.52 (m, 1H), 7.6 (m, 20H).^{13}C NMR δ: 15.44 (s, CH_3), 24.65 (dd, CH_2, $J_{C–P}$ = 8.14 Hz, $J_{C–P}$ = 12.21 Hz), 25.78 (dd, CH_2, $J_{C–P}$ = 5.42 Hz, $J_{C–P}$ = 17.6 Hz), 42.77 (d, CH_2, $J_{C–P}$ = 8.14 Hz), 57.6 (dd, CH, $J_{C–P}$ = 12.2 Hz, $J_{C–P}$ = 78.7 Hz). The aromatic signals without assignment due to the high complexity of the system. ^{31}P NMR δ (H_3PO_4 85%): 31.73, 33.58.[5]

1,3-Bis(diphenylphosphinyl)propanol (6)

It was isolated by silica-gel chromatography with petroleum ether/diethyl ether (25:75). IR (KBr) (cm^{-1}): 3300, 1433, 1176, 1124, 729, 696. ^{1}H NMR δ: 1.8 (m, 1H), 2.5 (m, 4H), 4.6 (m, 1H), 7.6 (m, 20H).^{13}C NMR δ: 24.2 (d, CH_2, $J_{C–P}$ = 4.1 Hz), 27.9 (dd, CH_2, $J_{C–P}$ = 13.6 Hz, $J_{C–P}$ = 70.5 Hz), 70.7 (dd, CH, $J_{C–P}$ = 4.1 Hz, $J_{C–P}$ = 89.5 Hz), aromatic signals without assignment due to the high complexity of the system. ^{31}P NMR δ (H_3PO_4 85%): 31.78, 36.09.[5]

***N*-*n*-Butyl-*N*-cyclobutyl-*P*,*P*-diphenylphosphonamide (14)**

It was isolated by silica-gel chromatography with diethyl ether. ^{1}H NMR δ: 0.70 (t, 3H), 1.05 (m, 2H), 1.44 (m, 4H), 1.89 (m, 2H), 2.16 (m, 2H), 2.94 (m, 2H), 3.82 (m, 1H), 7.42 (m, 6H), 7.76 (m, 4H).^{13}C NMR δ: 13.56 (s, CH_3), 14.72 (s, CH_2), 20.05 (s, CH_2), 29.96 (d, CH_2, $J_{C–P}$ = 4.07 Hz), 34.07 (d, CH_2, $J_{C–P}$ = 2.71 Hz), 43.19 (d, CH_2, $J_{C–P}$ = 4.07 Hz), 52.09 (d, CH, $J_{C–P}$ = 4.07 Hz), 128.2 (d, $^3J_{C–P}$ = 13.57 Hz), 131.4 (d, $^4J_{C–P}$ = 2.71 Hz), 132.2 (d, $^2J_{C–P}$ = 9.49 Hz), 132.9 (d, $^1J_{C–P}$ = 127.5 Hz). MS, *m*/*z* (rel. intensity): 327 (0.26), 299 (3.59), 284 (11.69), 244 (9.53), 243 (11.41), 215 (3.28), 202 (43.37), 201 (98.84), 126 (16.22), 125 (15.4), 98 (100), 97 (83.5), 84 (13.85), 83 (8.32), 77 (4.33), 70 (6.9), 69 (5.3), 57 (12.19), 56 (13.45), 55 (11.4), 43 (3.31), 42 (2.97), 41 (3.34).

Reaction of 4 with 2 in the dark

The described procedure was followed. In this case, however, the reaction flask was wrapped with aluminum foil.

Acknowledgments

This work was supported in part by the SECYT, National University of Córdoba, Consejo de Investigaciones de la Provincia de Córdoba (CONICOR), and the Consejo Nacional de Investigaciones Científicas y Técnicas (CONICET), Argentina. G.F. gratefully acknowledges receipt of a fellowship from the SECYT, Universidad Nacional de Córdoba.

References

1. (*a*) R.A. Rossi and R.H. de Rossi. *In* Aromatic substitution by the $S_{RN}1$ mechanism. ACS 178, Washington D.C. 1983; (*b*) W.R. Bowman. Chem. Soc. Rev. **17**, 283 (1988); (*c*) J.M. Savéant. Adv. Phys. Org. Chem. **26**, 1 (1990); (*d*) R.K. Norris. *In* Comprehensive organic synthesis. Vol. 4. *Edited by* B.M. Trost. Pergamon, Oxford. 1991. p. 451. (*e*) R.A. Rossi, A.B. Pierini, and A.B. Peñéñory. *In* The chemistry of halides, pseudo-halides and azides. Suppl. D2. Part. 2. Chap. 24. *Edited by* S. Patai and Z. Rappoport. J. Wiley and Sons, Chichester. 1995. pp. 1395–1485, and refs. cited therein.
2. G.S. Foray, A.B. Peñéñory, and R.A. Rossi. J. Phys. Org. Chem. **8**, 356 (1995).
3. J.M. Savéant. Tetrahedron, **50**, 10 117 (1994); Acc. Chem. Res. **26**, 455 (1993).
4. R.A. Alonso, A. Bardon, and R.A. Rossi. J. Org. Chem. **49**, 3584 (1984).
5. O.M. Musa, J.H. Horner, H. Shahin, and M. Newcomb. J. Am. Chem. Soc. **118**, 3862 (1996).
6. M. Newcomb. Adv. Detailed React. Mech. **1**, 1 (1991); N.A. Porter, B. Giese, and D.P. Curran. Acc. Chem. Res. **24**, 296 (1991); A.L.J. Beckwith. Chem. Soc. Rev. **22**, 143 (1993); B. Giese. *In* Radicals in organic synthesis: formation of C-C bonds. Pergamon, Oxford. 1986.
7. A.I. Vogel. *In* Vogel's textbook of practical organic chemistry. 5th ed. Longman Scientific and Technical, New York. 1989. p. 1275.
8. T. Gajda and A. Zwierzak. Synthesis, **12**, 1005 (1981).

© 1999 NRC Canada

Redox switching of carbohydrate binding to ferrocene boronic acid[1]

Andrew N.J. Moore and Danial D.M. Wayner

Abstract: The redox properties of ferrocene boronic acid in aqueous buffers from pH 4 to pH 12 have been investigated using cyclic voltammetry. It is shown that the proton transfer equilibrium is under thermodynamic control over the range of scan rates employed (20–5000 mV/s), leading to pK_a values of 10.8 and 5.8 for the ferrocene and ferrocenium forms, respectively. In the presence of sorbitol, fructose, or glucose, the voltammetric behaviour of ferrocene boronic acid at pH 7 is consistent with reversible formation of a carbohydrate – boronic acid complex. However, in all cases, the complexation–dissociation is under kinetic control. Analysis of the voltammetric response as a function of scan rate and carbohydrate concentration, together with an independent spectroscopic determination of the binding constant to the ferrocene form, allows all of the kinetic and thermodynamic constants for each system to be determined. In general, it is found that the binding constants ferrocenium form are about two orders of magnitude greater than those for the ferrocene form. It is possible that this redox dependent switching of the carbohydrate binding can be exploited in amperometric or potentiometric sensing devices.

Key words: electrochemistry, boronic acid, binding constants, pK_a.

Résumé : Faisant appel à la voltampérométrie cyclique, on a étudié les propriétés redox de l'acide ferrocène boronique dans des solutions aqueuses tampon à partir d'un pH de 4 jusqu'à un pH de 12. On montre que l'équilibre du transfert de proton est sous contrôle thermodynamique dans tout l'intervalle de vitesse de balayage utilisé (20–5000 mV/s), conduisant à des valeurs de pK_a de 10,8 et de 5,8 respectivement pour les formes ferrocène et ferricinium. En présence du sorbitol, du fructose ou du glucose le comportement voltampérométrique de l'acide ferrocène boronique à pH 7 est en accord avec la formation réversible d'un complexe hydrate de carbone – acide boronique. Cependant, dans tous les cas, la complexation–dissociation est sous contrôle cinétique. L'analyse des réponses voltampérométriques en fonction de la vitesse de balayage et de la concentration en hydrate de carbone, ainsi qu'une détermination indépendante par spectroscopie de la constante de jonction de la forme ferrocène, permet de déterminer toutes les constantes cinétiques et thermodynamiques de chaque système. On a trouvé, en général, que la constante de jonction de la forme ferricinium est de deux ordres de grandeur supérieure à celle de la forme ferrocène. Il est possible que cette réaction redox qui dépend de la commutation du point de jonction de l'hydrate de carbone, peut-être exploité dans des senseurs ampérométrique ou potentiométrique.

Mots clés : électrochimie, acide boronique, constantes de jonction, pK_a.

[Traduit par la Rédaction]

Introduction

Although complexation of diols by boronic acids has been well known for a number of years (1) it has been shown, recently, that these complexes may be used for the molecular recognition of carbohydrates for sensors (2–9) for transportation across biological membranes (10–13) or for racemic resolution of free sugars (14). While the structures of these complexes are not well understood (15), the kinetics and thermodynamics of complex formation and dissociation have been shown to involve a number of proton – hydroxide ion equilibria in aqueous solution (Scheme 1) (16–20). From the observed pH dependence of the rates of complex formation and dissociation it has been shown that (*i*) for a given boronic acid, as the pK_a of the diol decreases the stability constant of the complex increases (18), (*ii*) for a given diol, as the pK_a of the boronic acid decreases, the stability constant of the complex increases (18), and (*iii*) the kinetics of complex dissociation is dominated by hydroxide ion addition to the trigonal form (19). Thus, the formation of the complexes are believed to follow the mechanism indicated by the large arrows in Scheme 1.

With these guidelines in mind, it then follows that, in principle, one electron oxidation of either the boronic acid or the diol can be used to modulate the binding properties of the system, since it is well known that this results in a decrease (often dramatic) in the pK_a of the acidic protons. This would then form the basis of a redox switchable complexing agent that can form the basis of a simple chemical sensor. The thermodynamic and kinetic criteria for the design (or selection) of a boronic acid is straight forward: both the oxi-

Received September 16, 1998.

This paper is dedicated to Jerry Kresge in recognition of his many achievements in chemistry.

A.N.J. Moore and D.D.M. Wayner.[2] Steacie Institute for Molecular Sciences, National Research Council of Canada, Ottawa, ON K1A 0R6, Canada.

[1]Issued as NRCC Publication No. 40915.
[2]Author for correspondence. Telephone: 613-990-9953. Fax: 613-991-4278. e-mail: dan.wayner@nrc.ca

© 1999 NRC Canada

Scheme 1.

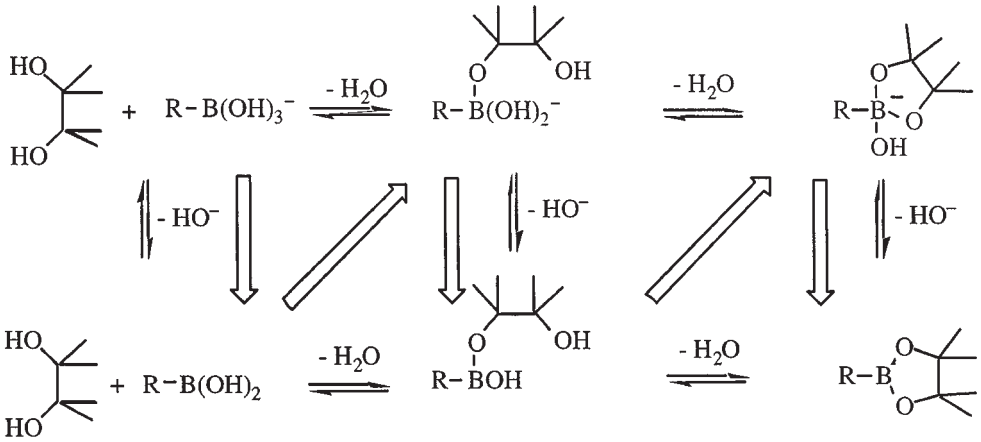

dized and reduced forms must be chemically stable, the redox process must occur in close proximity to the boronic acid group in order to maximize the change in pK_a, and the complexation must be reversible on the time scale of the measurement. We have chosen to study ferrocene boronic acid as a model for a redox switchable complexing agent for sugars. Cyclic voltammetric analysis allows the determination of the pK_a values of both oxidized and reduced forms as well as the determination of the kinetics and thermodynamics of binding of sorbitol, fructose, and glucose.

Experimental

Materials

All materials were purchased from Aldrich. Ferrocene boronic acid was synthesized by lithiation of ferrocene in THF (21), addition of the lithioferrocene in solution to a solution of trimethylborate in THF (8), followed by acidic work-up.

Cyclic voltammetry

Cyclic voltammetry was performed with a PAR model 273A Potentiostat interfaced to a 386 base PC using the EG&G model 270 software package. The cell was a standard three-electrode setup using a 3 mm diam. glassy carbon working electrode, a platinum coil counter electrode, and a Ag/AgCl reference electrode. Potentials reported are with respect to this reference which gave a standard potential for potassium ferricyanide of 0.231 V at pH 7.6.

Volammetric experiments were carried out in aqueous buffers. All buffers were prepared using distilled deionized water, with 1 M KCl as supporting electrolyte. For the titration of ferrocene boronic acid the following buffers (0.1 M) were used: potassium hydrogen phthalate (pH 4.0–6.0), potassium phosphate, dibasic (pH 6.0–8.0), sodium tetraborate decahydrate (pH 7.0–10.0), and sodium carbonate (pH 10.0–12.5). Sodium hydroxide or hydrochloric acid were added to adjust to the desired pH. The pH of the solutions was measured using a Cole–Parmer Chemcadet 5986-25 pH/mV meter.

Cyclic voltammetry in the presence of sugars

Varying amounts of sugar were added to a 90 μM solution of ferrocene boronic acid in phosphate buffer (0.1 M, pH 7.6, 1 M KCl). Voltammograms were recorded between –0.25 and 0.5 V at scan rates of 100, 200, 500, 1000, and 2000 mV/s. Alternatively, the potential was held for 20 s at 0.5 V before being cycled between 0.5 and –0.25 V. Digital simulation of the voltammograms was performed using DigiSim 2.0 software (Bioanalytical Systems Inc., W. Lafayette, Indiana). The two adjustable parameters (see text) were optimized manually by overlaying the experimental and calculated voltammograms. The estimated errors represent the limits outside of which the fit the experimental data is unacceptable based on relative peak currents for the anodic and cathodic waves.

UV-vis titrations with sugars

A 60 μM solution of ferrocene boronic acid in phosphate buffer (0.1 M pH 7.6) was prepared. An amount of sugar sufficient to prepare a solution of the desired concentration was placed in a volumetric flask, and a small amount of the Ferrocene boronic acid solution was added. After complete dissolution of the sugar, the solution was diluted to volume. Complexation of the sugar and ferrocene boronic acid was measured by determining the absorbance increase at 622 nm, using a Cary 3 UV-visible spectrophotometer. Errors in the binding constants are based on the average of three independent determinations.

Results and discussion

Determination of pK_a values

As far as we are aware, only one report of the electrochemistry of ferrocene boronic acid has appeared (22). In this study, a standard potential, $E°$, of 0.250 V vs. Ag/AgCl in water/methanol (1:1, v/v) containing 0.1 M $NaClO_4$ was obtained. The pH of the solution was not reported. We have studied the ferrocene–ferrocenium boronic acid couple over a pH range between 4 and 12. Under these conditions and at all pH values, the redox process remained quasireversible (i.e., $E_p^a - E_{pc} \approx 75$ mV), indicating that the redox system is under thermodynamic control with respect to proton transfer. Thus, the apparent standard potential ($E°_{expt}$) is determined by the pK_a values of the oxidized and reduced forms of the boronic acid (eq. [1]). The $E°_{expt}$ values (estimated as the midpoint between the anodic and cathodic waves) as a function of the pH are shown graphically in Fig. 1 along with the

© 1999 NRC Canada

Scheme 2.

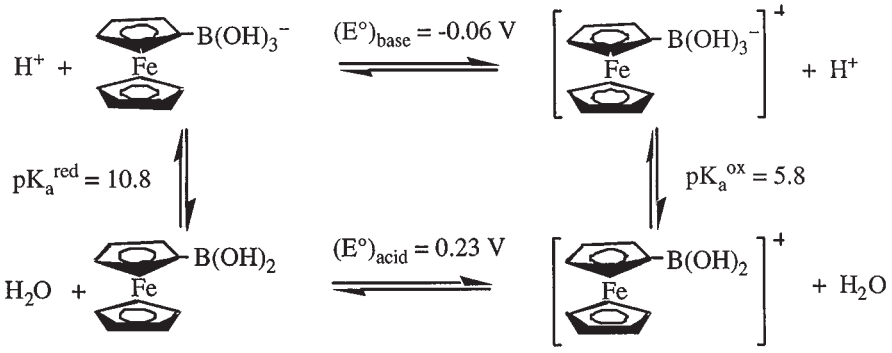

Fig. 1. The pH dependence of the apparent standard potential, $E°_{expt}$, of ferrocene boronic acid (90 μM) in various buffers (see Experimental).

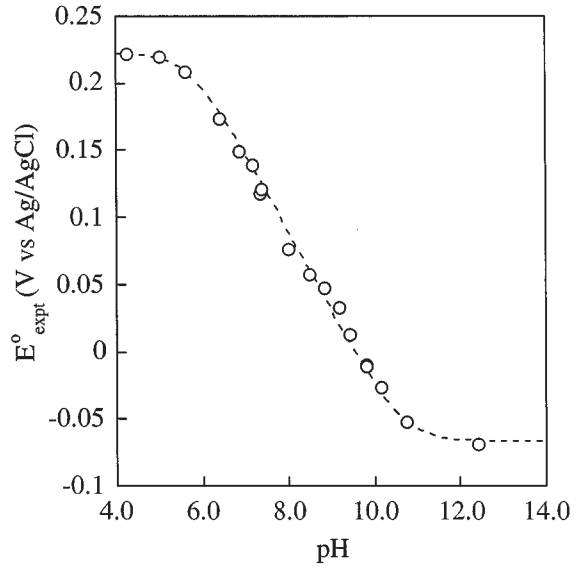

nonlinear least-squares fit to eq. [1]. To cover the pH range, four different buffer systems were employed (see Experimental). The fact that the standard potentials were the same within experimental errors for the points where the buffer systems overlap confirmed that any interaction of the boronic acid with the buffer was too weak to influence the standard potential. The analysis allowed the evaluation of the standard potentials of the trigonal (acid) and tetrahedral (conjugate base) forms of ferrocene boronic acid as well as the pK_a values of the ferrocene and ferrocenium forms. These results are shown in Scheme 2.

$$[1] \qquad (E°)_{app} = (E°)_{acid} - 0.059 \log\left(\frac{[H^+] + K_a^{ox}}{[H^+] + K_a^{red}}\right)$$

As expected, oxidation of the ferrocene resulted in a decrease in the pK_a of the boronic acid. In this case the change is about 5 pK units. The pK_a of the ferrocene form is typical of those values reported for simple alkyl or aryl boronic acids (18). Oxidation of the ferrocene results in a modest decrease in pK_a, since the electron transfer is predominantly associated with changing the oxidation state of the iron center. Nevertheless, the pK_a of the ferrocenium boronic acid is one of the lowest reported for a substituted boronic acid (e.g., 4-nitrophenyl boronic acid has a pK_a of 6.96 (18) and 3-pyridinium boronic acid has a pK_a of only 4.0 (23)).

Table 1. Thermodynamic and kinetic data for the binding of some sugars to ferrocene and ferrocenium boronic acid.

	Sugar		
Constant	Sorbitol	Fructose	Glucose
K_1 (M^{-1})[a,b]	11	4	0.05[c]
k_1 ($M^{-1}s^{-1}$)[d]	165	8	0.05
k_{-1} (s^{-1})[e]	15	2	1
K_2 (M^{-1})[f]	1900	1600	20
k_2 ($M^{-1}s^{-1}$)[d]	3100	2700	20
k_{-2} (s^{-1})[e]	1.6	1.7	1

[a]Determined spectrophotometrically at pH 7.6 (see text).
[b]Errors are ±10%.
[c]Error is ±20%.
[d]Determined by digital simulation of the voltammetric waves. The error in these values is approximately ±10%.
[e]This is not an independent variable: $k_{-1} = k_1K$.
[f]Determined by cyclic voltammetry, see Scheme 4. The error in this value is determined by the error in $\Delta E° \approx \pm 10$ mV leading to an error in the equilibrium constant of ±30%.

Spectrophotometric determination of sugar binding to ferrocene boronic acid

The addition of a sugar to a solution (pH 7.6) of ferrocene boronic acid resulted in the appearance of a broad visible absorption with a maximum at 622 nm which depended on the concentration of the sugar. The apparent equilibriium contant for the complexation was determined by fitting the concentration dependence of this absorption to eq. [2], where A_{622} is the optical density at 622 nm, ε_{free} and $\varepsilon_{complex}$ are the respective extinction coefficients of the free and complexed ferrocene boronic acid and K_c^{obs} is the observed equilibrium constant. Values determined for sorbitol, fructose, and glucose are given in Table 1.

$$[2] \qquad A_{622} = \varepsilon_{free}[FcB(OH)_2]_{tot} + (\varepsilon_{complex} - \varepsilon_{free})\left(\frac{K_c^{obs}[FcB(OH)_2]_{tot}[S]}{1 + K_c^{obs}[S]}\right)$$

The observed equilibrium constants are actually composite values that represent the complexation of the sugar with both the trigonal (K_c^{acid}) and tetrahedral (K_c^{base}) forms of the boronic acid. The relationship between the observed equilib-

© 1999 NRC Canada

Scheme 3.

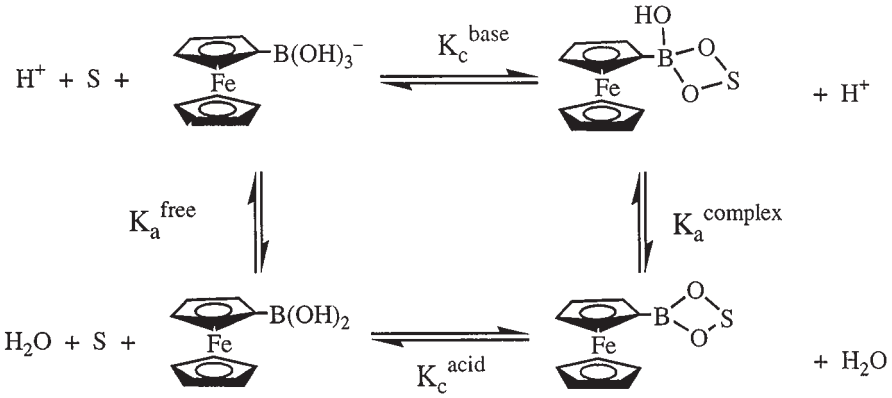

rium constant (K_c^{obs}) and the independent proton transfer equilibria is shown graphically in Scheme 3 (where S represents a sugar) and by eq. [3].

$$[3] \qquad K_c^{obs} = K_c^{base}\left(\frac{[H^+] + K_a^{complex}}{[H^+] + K_a^{free}}\right)\frac{K_a^{free}}{K_a^{complex}}$$

Thus, at low pH, $K_{csup}^{obs} = K_c^{acid}$ and at high pH, $K_c^{obs} = K_c^{base}$. In general, it has been found from potentiometric titrations, i.e., measuring the pH of a solution of boronic acid as a function of concentration of sugar, that the complexed boronic acid is more acidic than the uncomplexed form. In these cases, complexation results in a decrease in pH. However, in the present case, we have use buffered solutions so the addition of a sugar is expected to lead to an increase in the overall equilibrium concentration of the total boronic acid that exists in the tetrahedral form. In this analysis, we have assumed a 1:1 boronic acid to sugar stoichiometry. In nonaqueous solution, it has been shown that glucose forms a weak 1:1 complex and a more well-defined 2:1 complex (15). However, in that study the concentration of the boronic acid was high (about 100 mM and a concentration ratio acid:sugar of 2:1) compared to the concentration in this study (about 0.1 mM and an acid:sugar ratio of 1:50). Thus, it is reasonable to expect only a 1:1 complex to form under our conditions.

Voltammetry in the presence of sugars

Cyclic voltammograms were measured between 100 and 2000 mV/s both in the absence and presence of added sugars. The pH chosen for these experiments of 7.6 was conveniently between the pK_a values of the ferrocene and ferrocenium forms (see above). Unlike the voltammetry as a function of pH, in the presence of the sugars it was clear that the complexation was not under thermodynamic control. Rather than observing a monotonic change in the apparent $E°$ with increasing concentration of sugar, a very different picture emerged. Voltammetry, initially in the direction of oxidation, had a small effect on the anodic wave (Fig. 2). However, the cathodic wave was clearly split into two closely spaced waves, separated by ca. 130–150 mV, which integrated to a total of one electron. Increasing the concentration of sugar increased the contribution of this new cathodic wave (Fig. 2). At a fixed concentration of sugar, variations in the scan rate were consistent with rates of complexation–dissociation be-

Fig. 2. Cyclic voltammogram (background substracted) of ferrocene boronic acid at 100 mV s^{-1} with (*a*) 0.0 mM sorbitol, (*b*) 1.0 mM sorbitol, and (*c*) 5 mM sorbitol.

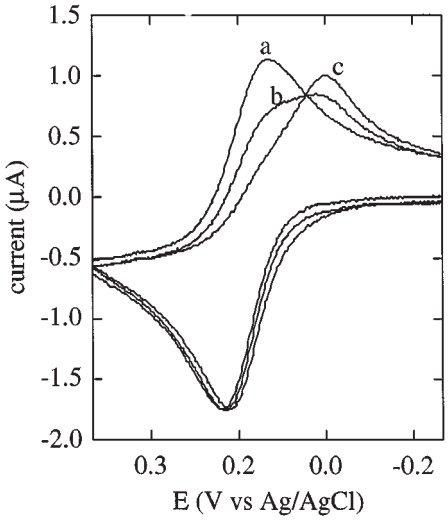

ing competitive with the time scale of the experiment (Fig. 3). This behaviour is typical of a square scheme (24) under chemical kinetic control and is consistent in this case with the fast complexation and slow dissociation of the ferrocenium form on the time scale of the voltammetric experiment. These results are in contrast to fluoride binding studies reported by Shinkai and co-workers (22) who studied the complexation of fluoride to ferrocene boronic acid. In this case, similar to protonation redox couple appears reversible at all fluoride concentrations and scan rates (i.e., under thermodynamic control). There was a clear preference for binding to the ferrocenium form (i.e., the $E°$ shifted to more negative potentials in the presence of fluoride ion).

It is possible to make a rough guess at the relevant equilibrium constants from Fig. 2. A shift in standard potential by 140 mV for the complexed versus uncomplexed boronic acid requires that the binding constant in the oxidized (ferrocenium) form be larger than in the reduced (ferrocene) form by a factor of about 250 (Scheme 3). Under slow scan conditions the ratio of bound to unbound ferrocenium is about 1:1 when the concentration of sorbitol is about 1 mM. Thus, an estimate for the equilibrium constant in the oxidized form is [oxidized complex]/([sugar][free ferrocenium]). Since at this

© 1999 NRC Canada

Scheme 4.

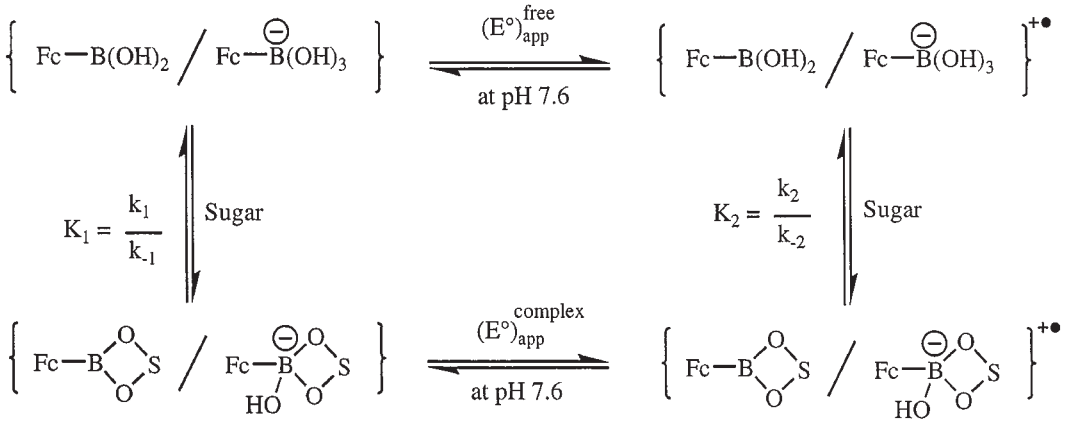

Fig. 3. Cyclic voltammograms (background substracted) of ferrocene boronic acid (90 μM) in a phosphate buffer (0.1 M) with KCl (1 M) with 1 mM sorbitol at a scan rate of (*a*) 100 mV s^{-1}, (*b*) 500 mV s^{-1}, (*c*) 1000 mV s^{-1}, and (*d*) 2000 mV s^{-1}. The corresponding simulations in the same order using the parameters in Table 1 are shown in (*e*)–(*h*). The voltammograms were initially scanned from –0.25 V to 0.5 V.

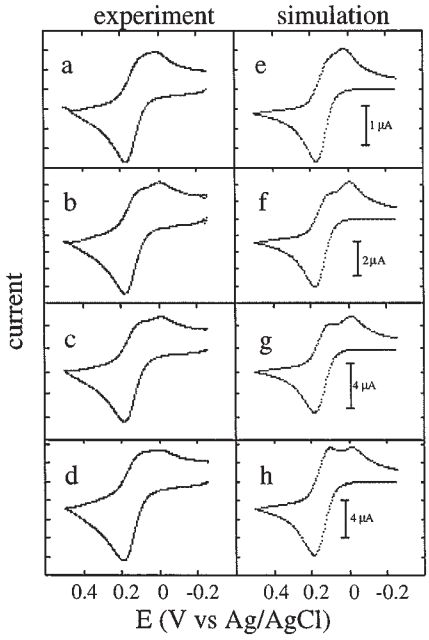

Fig. 4. Cyclic voltammograms (background substracted) of ferrocene boronic acid (90 μM) in a phosphate buffer (0.1 M) with KCl (1 M) with 1 mM sorbitol at a scan rate of (*a*) 100 mV s^{-1}, (*b*) 500 mV s^{-1}, (*c*) 1000 mV s^{-1}, and (*d*) 2000 mV s^{-1}. The corresponding simulations in the same order using the parameters in Table 1 are shown in (*e*)–(*h*). In these experiments, the potential was held at 0.5 V for 20 s, and the voltammograms were initially scanned from 0.5 V to –0.25 V.

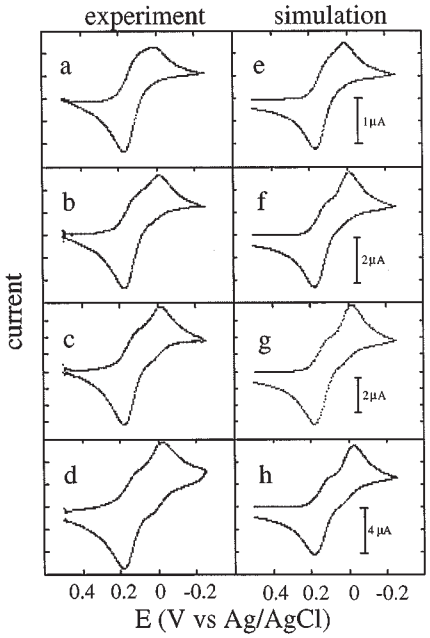

concentration the [oxidized complex] ≈ [free ferrocenium], an equilibrium constant on the order of 1000 M^{-1} is obtained. A more precise value can be extracted by examining the scan rate dependence of the voltammogram as function of sugar concentration (see below).

The second cathodic wave begins to be chemically reversible at scan rate greater than 2 V/s (Fig. 4). This can be clearly observed by holding potential for 20 s at 0.5 V (to build up the concentration of the oxidized form) then recording the voltammogram by scanning initially in the direction of reduction. Under these conditions, it is possible to use digital simulation methods to extract the kinetic and thermodynamic parameters for the complexation of the sugars with both the ferrocene and ferrocenium forms. In fact, only there are only two independent parameters that must be fit to the experimental data. At the high scan rates, the standard potential of the complex can be measured directly. The $E°$ of the uncomplexed ferrocene boronic acid and the apparent equilibrium constant for the complexation of ferrocene boronic acid were determined independently (see above) so the equilibrium constant for complexation to the ferrocenium boronic acid is fixed by a thermochemical cycle (Scheme 4). The data are given in Table 1. Since the equilibrium constants are known, only two rate constants are required to complete the scheme (Scheme 4). These rate constants were determined by iterative fitting of the experimental voltammograms. The rate and equilibrium constants

© 1999 NRC Canada

are given in Table 1, and a comparison of the experimental and simulated voltammograms are shown in Figs. 3 and 4.

There are a number of interesting features of the data in Table 1. Oxidation of the ferrocene moiety results in a decrease in the pK_a of the boronic acid which, not unexpectedly, leads to an increase in the apparent binding constant. It should be reiterated that the extracted equilibrium constants are composite values (eq. [3]) that apply only to the pH of the experiment (7.6). We have not attempted to separate the kinetic and thermodynamic parameters for the individual acid and conjugate base. However, the decrease in the apparent $E°$ value, which is close to the $E°$ of ferrocene boronate (Scheme 2), is consistent with the complexed ferrocene boronic acid being almost entirely in the tetrahedral form. It is this significant decrease in the pK_a of the complexed ferrocene boronic acid (1) that is likely responsible for the change in the apparent standard potential at this pH.

It is interesting to compare the equilibrium constants obtained with those reported recently by Ori and Shikai (25) for a chiral ferrocene boronic acid derivative. In this derivative, which contains an adjacent *N*,*N*-dimethyl-1-aminoethyl group, modest chiral selectivity for sugars was observed. Interestingly, while the equilibrium constants for complexation with the ferrocene form were similar to those reported in our work (Table 1), the equilibrium constants for complexation with the ferrocenium form were only one order of magnitude larger. This was evident from the only 50 mV decrease in the apparent $E°$ for the complexed versus uncomplexed form. Although Ori and Shikai (25) suggested that the ferrocenium boronic acid derivative was more acidic (and thus had a higher affinity for the saccharides), the pK_a of neither oxidation state was determined, nor was the pH dependence of the reported constants considered. Rate constants for complexation and dissociation were not determined. The only modest change in the standard potential and the equilibrium constants may be related to a subtle change in steric demand upon oxidation.

The fact that oxidation of the ferrocene moiety leads to an increase in the equilibrium constant for binding with a sugar by about two orders of magnitude may be useful in the design of chemical sensors based on potentiometric or amperometic detection. On one hand, the binding event can be used to induce current flow at constant potential by maintaining the electrode potential between the standard potential for the free and complexed forms. On the other hand, the electrode potential can be used to switch binding on or off for detection by other nonelectrochemical means. In both cases, the advantage of such a system is that a reversible redox process of a group that in itself is a "spectator" vis-a-vis the binding process can be used to modulate or switch the reversible chemical reactivity at a remote site.

An important criterion for use in chemical sensors is the long-term stability of the ferrocene–ferrocenium species. Simple ferrocenium derivatives (especially those with electron deficient substituents) are unstable in the presence of nucleophilic species (including water). In some cases, the stability can be improved by encapsulation as guest–host complexes such as cyclodextrins (26). While it may seem surprising that the ferrocenium boronic acid complexes are stable for several minutes at pH 7.6 (i.e., the time scale of the measurements), the long term stability of these complexes have not yet been determined. The fact that the complex exists in the tetrahedral form at neutral pH (i.e., the boron has a formal negative charge) undoubtedly contributes to the apparent enhanced stability, much in the same way that ferrocenium carboxylate is less reactive in water than the methyl ester. Futher studies are underway to determine the long term stability and explore applications of this system.

References

1. J.P. Lorand and J.O. Edwards. J. Org. Chem. **24**, 769 (1959), and refs. cited therein.
2. S. Shinkai. *In* Chemosensors of ion and molecule recognition. *Edited by* J.P. Desvergne and A.W. Czarnik. Kluwer Academic Publishers, Amsterdam. 1997. pp. 37–59.
3. T.D. James, K.R.A. Samankumara Sandanayake, and S. Shinkai. Nature (London), **374**, 345 (1995).
4. I. Hamachi, Y. Taijiri, and S. Shinkai. J. Am. Chem. Soc. **116**, 7437 (1994).
5. H. Murakami, T. Nagasaki, I. Hamachi, and S. Shinkai. J. Chem. Soc. Perkin Trans. 2, 975 (1994).
6. R. Ludwig, T. Harada, K. Ueda, T.D. James, and S. Shinkai. J. Chem. Soc. Perkin Trans. 2, 697 (1994).
7. H. Murakami, T. Nagasaki, I. Hamachi, and S. Shinkai. Tetrahedron Lett. **34**, 6273 (1993).
8. J. Yoon and A.W. Czarnik. J. Am. Chem. Soc. **114**, 5874 (1992).
9. K. Tsukagoshi and S. Shinkai. J. Org. Chem. **56**, 4089 (1991).
10. G.T. Morin, M.P. Hughes, M. Paugam, and B.D. Smith. J. Am. Chem. Soc. **116**, 8895 (1994).
11. G.T. Morin, M. Paugam, M.P. Hughes, and B.D. Smith. J. Org. Chem. **59**, 2724 (1994).
12. M. Paugam, L.S. Valencia, B. Boggess, and B.D. Smith. J. Am. Chem. Soc. **116**, 11 203 (1994).
13. P.R. Westmark and B.D. Smith. J. Am. Chem. Soc. **116**, 9343 (1994).
14. G. Wulff and S. Schauhoff. J. Org. Chem. **56**, 397 (1991).
15. J.C. Norrild and H. Eggert. J. Am. Chem. Soc. **117**, 1479 (1995).
16. S. Friedman, B. Pace, and R. Pizer. J. Am. Chem. Soc. **96**, 5381 (1974).
17. R. Pizer and L. Babcock. Inorg. Chem. **16**, 1677 (1977).
18. L. Babcock and R. Pizer. Inorg. Chem. **19**, 56 (1980).
19. R.E. London and S.A. Gabel. J. Am. Chem. Soc. **116**, 2562 (1994).
20. R.E. London and S.A. Gabel. J. Am. Chem. Soc. **116**, 2570 (1994).
21. F. Rebiere, O. Samuel, and H.B. Kagan. Tetrahedron Lett. **31**, 3121 (1990).
22. C. Dusemund, K.R.A. Samankumara Sandanayake, and S. Shinkai. J. Chem. Soc. Chem. Commun. 333 (1995).
23. L.K. Mohler and A.W. Czarnik. J. Am. Chem. Soc. **115**, 2998 (1993).
24. C. Amatore. *In* Organic electrochemistry. *Edited by* H. Lund and M.M. Baizer. Marcel Dekker, New York. 1991. pp. 11–119.
25. A. Ori and S. Shinkai. J. Chem. Soc. Chem. Commun. 1771 (1995).
26. R.S. Brown and J.H.T. Luong. Electroanalysis, **6**, 391 (1994).

© 1999 NRC Canada

The electrochemical reduction of α-nitrocumene in a protic and basic medium on large surface area (porous) electrodes: electronation–protonation or electrocatalytic hydrogenation?

Elisa Soazara Chan-Shing, Denys Boucher, and Jean Lessard

Abstract: The electrochemical reduction of α-nitrocumene (**1**) has been investigated under controlled potential, at a mercury pool cathode and at Raney metal (Raney nickel, Raney cobalt and Devarda copper) and fractal nickel electrodes in basic aqueous ethanol. A comparison of the product distribution from the reduction at Hg (electronation–protonation (EP) mechanism) and that from the reduction at Raney metals and fractal nickel has shown that both the electrocatalytic hydrogenation (ECH) and EP mechanisms can be involved at large surface area (porous) transition metal electrodes in a basic protic medium. Cyclic voltammetry was used to determine the reduction potential of **1** at Hg and at bright polycrystalline nickel, cobalt, and copper cathodes in the same medium.

Key words: electrocatalytic hydrogenation, electroreduction, 2-nitro-2-phenylpropane, Raney metal cathodes, mechanism.

Résumé : La réduction électrochimique, à potentiel controlé, de l'α-nitrocumène (**1**) a été étudiée, en milieu hydroéthanolique basique, sur Hg, sur des électrodes de métaux de Raney (nickel de Raney, cobalt de Raney et cuivre de Devarda) et sur des électrodes de nickel fractal. Une comparaison de la distribution de produits obtenue par réduction sur Hg (mécanisme d'électronation–protonation (EP)) avec celles obtenues par réduction sur les électrodes de métaux de Raney et sur l'électrode de nickel fractal démontre que les deux mécanismes, celui d'électronation–protonation (EP) et celui d'hydrogénation électrocatalytique (HEC), interviennent sur les électrodes de métaux de transition à grande surface spécifique (poreuses) en milieu basique protique. La voltamétrie cyclique a été utilisée pour déterminer le potentiel de réduction de **1,** dans le même milieu, sur des électrodes de Hg et des électrodes de nickel, cobalt et cuivre polycristallins.

Mots clés : hydrogénation électrocatalytique, électroréduction, 2-nitro-2-phénylpropane, cathodes de métaux de Raney, mécanisme.

Introduction

Unprotonated hydroxylamines are not reducible by electron transfer (1). As a consequence, the electrochemical reduction of aromatic nitro compouds (2–4) and tertiary nitroalkanes (5, 6) at a mercury electrode in neutral and basic (pH > 5) protic media, which proceeds by successive electron and proton transfer steps (electronation–protonation (EP) mechanism), stops at the hydroxylamine. At a mercury electrode, primary and secondary nitroalkanes are not reducible at pH > 13 because they exist as nitronate anions which are not reducible by electron transfer (EP mechanism) (1) but are reducible in neutral protic media and the reduction stops at the hydroxylamine (5, 6). In contrast, the electrochemical reduction of nitro compounds at Raney metal electrodes (Raney nickel (R-Ni), Raney cobalt (R-Co), and Devarda copper (D-Cu)), in basic and neutral aqueous methanolic solutions, gives the corresponding amine in high yields and current efficiencies, both for nitroaryl (7–9) and nitroalkyl (10) compounds. Therefore, in basic and neutral protic media, the electrochemical reduction, at Raney metal electrodes, of arylhydroxylamines and alkylhydroxylamines to the corresponding amines must involve an electrocatalytic hydrogenation (ECH) mechanism, that is, reaction with chemisorbed hydrogen, M(H) (reactions [2]–[4]), generated by reduction of water (reaction [1]) (7–10).

[1] $2\ H_2O(H_3O^+) + 2e^- + M \xrightarrow{\text{Volmer}} 2M(H) + 2OH^-(H_2O)$

[2] $RNHOH + M \longrightarrow M(RNHOH)$

[3] $M(RNHOH) + 2M(H) \longrightarrow M(RNH_2) + H_2O$

[4] $M(RNH_2) \longrightarrow RNH_2 + M$

Received November 3, 1998.

This paper is dedicated to Jerry Kresge in recognition of his many achievements in chemistry.

E.S. Chan-Shing, D. Boucher, and J. Lessard.[1] Centre de Recherche en Électrochimie et Électrocatalyse, Département de Chimie, Université de Sherbrooke, Sherbrooke, PQ J1K 2R1, Canada.

[1]Author to whom correspondence may be addressed. Telephone: (819) 821–7091. Fax: (819) 821–8017. e-mail: jlessard@courrier.usherb.ca

© 1999 NRC Canada

Scheme 1.

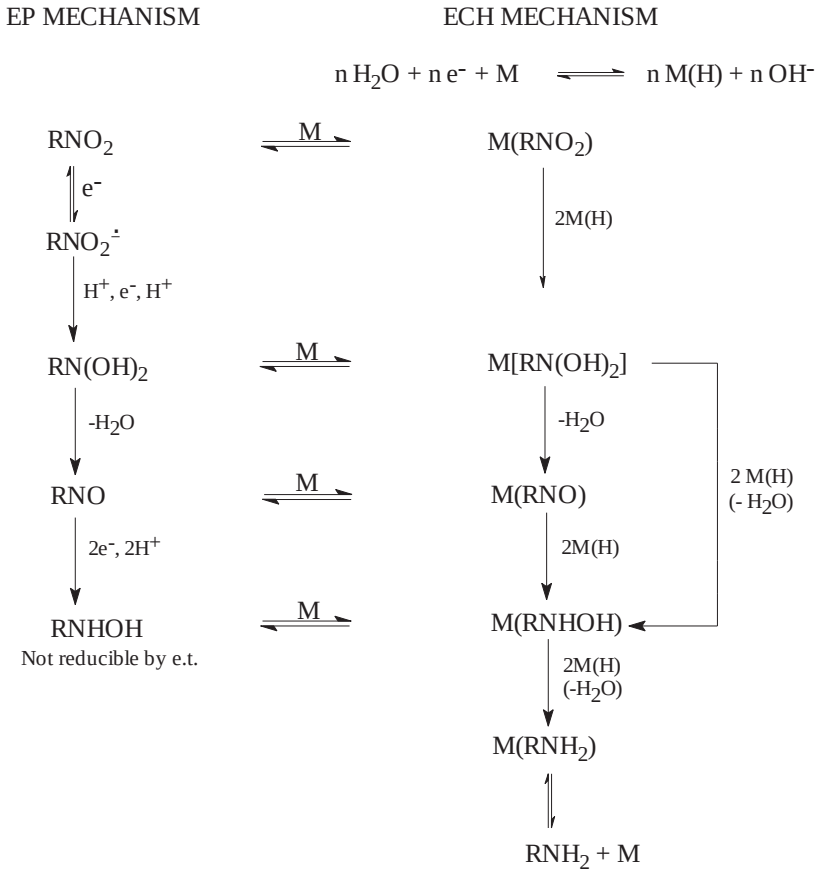

Since the reduction potential of water to chemisorbed hydrogen M(H) is very close to that of nitro groups, their reduction to the corresponding hydroxylamines ($RNO_2 \rightarrow$ RNHOH), at Raney metal electrodes and in neutral and basic media, could involve an ECH or an EP mechanism or both (see Scheme 1) (7–10). The electrochemical reduction of primary and secondary nitroalkanes at Raney metal electrodes and pH > 13 must involve the reaction of the nitronate anion with chemisorbed hydrogen (ECH mechanism) (Scheme 2) (10). Interestingly, at Raney metal electrodes, if dehydration of the intermediate dihydroxylamine is slower than its reaction with chemisorbed hydrogen, the hydroxylamine could be formed directly by electrocatalytic hydrogenolysis of the dihydroxylamine which could be formed by an EP or an ECH mechanism (see Schemes 1 and 2).

One way to distinguish between an EP and an ECH mechanism for the electrochemical reduction of nitro compounds to hydroxylamines at Raney metal electrodes would be to use a molecule, the reduction of which would give a different product distribution depending on the reduction mechanism. Coté et al. (11) reported that 2-iodonitrobenzene was not effective to distinguish between the EP and ECH mechanisms, since the product distribution was similar for its electrochemical reduction at mercury (EP mechanism), for its catalytic hydrogenation at Raney metals (involving reaction with chemisorbed hydrogen as in ECH) and for its electrochemical reduction at Raney metal electrodes.

In this paper, we report that, in the electrochemical reduction of α-nitrocumene (**1**), at electrodes with a large surface area (porous electrodes) and in basic hydroorganic solutions, both the EP and ECH mechanisms can participate and compete.

Experimental

^{1}H and ^{13}C Nuclear Magnetic Resonance (NMR) spectra were obtained on a Brucker AC-300 MHz instrument. IR spectra were taken with a Perkin Elmer 1600 series FTIR. Mass spectra and exact masses were obtained with a ZAB-2F model VG instrument.

α-Nitrocumene (**1**) (Scheme 3) was prepared as described by Kornblum et al. (12) and its ^{1}H NMR spectrum was identical with that reported. IR ($CHCl_3$) cm^{-1}: 1543 and 1349 (NO_2); ^{13}C NMR ($CDCl_3$) δ: 140.5 (C3), 129.0 (C4, C5), 125.2 (C6), 90.0 (C2), 27.5 (C1); HRMS, *m*/*z*: 119.0863; calcd. for C_9H_{11} ($M^+ - NO_2$): 119.0861.

α-Aminocumene (**3**) was prepared by preparative electrolysis of **1** at a Raney nickel (R-Ni) electrode in EtOH/H_2O 40:60 w/w + KOH 0.15 M or preparative electrolysis of α-azidocumene at a R-Ni electrode in MeOH/H_2O 93:7 w/w + NaCl 0.2 M. IR ($CHCl_3$) cm^{-1}: 3446 and 3621 (NH_2); ^{1}H NMR ($CDCl_3$) δ: 7.4 (m, 4H, arom), 1.5 (s, 6H, CH_3), 1.25 (s, 2H, NH_2) (lit. (12): 7.1–7.2 (m, 5H), 1.41 (s, 8H)); HRMS, *m*/*z*: 136.1129; calcd. for $C_9H_{14}N$ $(MH)^+$: 136.1126.

Bicumyl (**6**) was prepared by preparative electrolysis at a mercury pool in EtOH/H_2O 40:60 w/w + KOH 0.15 M: mp 117–118°C, white powder (lit. (13): 115–117°C); ^{1}H NMR ($CDCl_3$) δ: 7.1 (m, 10H, arom), 1.3 (s, 12H, CH_3); ^{13}C NMR

© 1999 NRC Canada

Scheme 2.

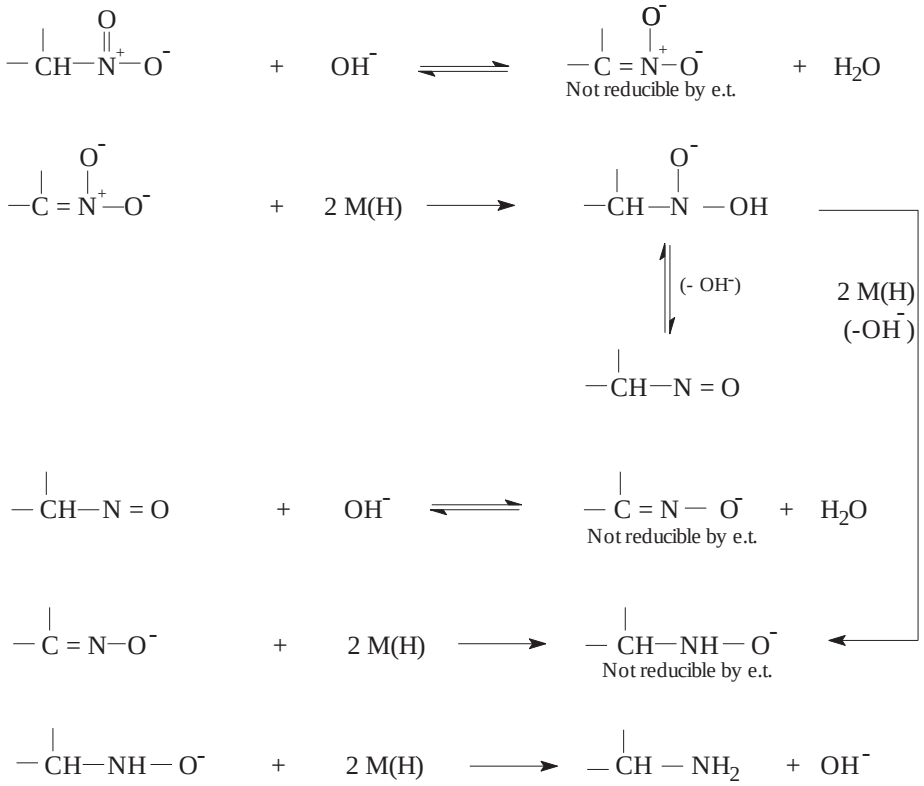

($CDCl_3$) δ: 146.4 (C3), 129.0 (C5), 127.0 (C6), 125.6 (C4), 43.4 (C2), 30.0 (C1); HRMS, *m*/*z*: 238.1709; calcd. for $C_{18}H_{22}$: 238.1721.

Distilled ethanol and distilled water were used to prepare solutions of KOH 0.15 M in ethanol–water 40:60 w/w. Solutions for all voltammetric analyses and preparative electrolyses were deoxygenated by bubbling through dry and oxygen-free argon saturated with ethanol. An argon atmosphere was maintained throughout the experiments which were carried out at room temperature.

The cyclic voltammetry experiments were performed using a Princeton Applied Research (PAR) 173 potentiostat and a single-compartment cell with three electrodes containing 5 mL of a 5×10^{-4} M solution of α-nitrocumene (**1**). A carbon rod was used as counter-electrode. An Ag/AgCl/Cl^- electrode whose potential was adjusted to that of an SCE served as reference. The working electrode was a hanging mercury drop or a metal disc (polycrystalline Ni, Co, or Cu) having a geometric area of 3.14 mm^2. The solid electrodes were polished with 0.05 mm micropolish alumina (Buehler) before each use. The controlled-potential preparative electrolyses were carried out using an Electrosynthesis Company (ESC) 410 potentiostat with an ESC 640 coulometer and an amperometer connected in series within the auxiliary circuit. For the electrolyses at a mercury pool, a vertical glass cell with two concentric compartments (cathodic compartment: 40 mL; anodic compartment: 10 mL) and a platinum grid as counter electrode were used. For the electrolyses at a Raney metal (R-M) electrode, a two-compartment glass H-cell (40 mL for each compartment) with a Nafion-324 (E-I du Pont de Nemours and Co.) membrane as separator and a counter electrode consisting of two carbon rods placed side by side were used. The same reference electrode as above was used and positioned near the surface of the mercury pool or, for the Raney metal electrodes, near the surface of the electrode facing the counter electrode.

The R-Ni alloy (Ni-Al 50:50 w/w) powder was purchased from Aldrich, the R-Co alloy (Co-Al 31:69 w/w) powder from Alfa AESAR, the Devarda copper (D-Cu) alloy (Cu-Al-Zn 50:45:5 w/w) powder from BDH, and Co and Cu powders were purchased from Fisher. The Raney alloy precursory electrodes were prepared by pressing, at room temperature, 5 g of R-Ni alloy powder (R-Ni electrodes) or 5 g of a mixture of Raney metal alloy powder (4 g) and particles (1 g) of the corresponding transition metal (Co or Cu for R-Co and D-Cu electrodes, respectively) at a pressure of 14.5×10^7 kg m^{-2}. The pressed electrodes were activated by leaching in 10% aqueous NaOH for 2 h at 50°C. If not used immediately, the electrode was kept in a 0.1 M aqueous solution of NaOH. The fractal nickel powder was purchased from INCO (filamentary nickel powder type 255), and the electrodes were prepared by pressing 5 g of powder as above.

The controlled-potential electrolyses at R-M electrodes were run at the so-called zero-current potential. The procedure was as follows. After leaching, the electrode was washed with distilled water and rinsed with EtOH/H_2O 40:60 w/w and placed in the cathodic compartment containing the deoxygenated electrolyte. A steady current of 100 mA was maintained until a charge of 100 C was passed (hydrogen evolution). Then the potential was increased slowly until the current reached zero (zero-current potential: –1.1 V for R-Ni and for R-Co electrodes and –1.2 V for D-Cu electrodes). The substrate (33 mg, 0.2 mmol, 5 mM solution) was added,

© 1999 NRC Canada

Scheme 3.

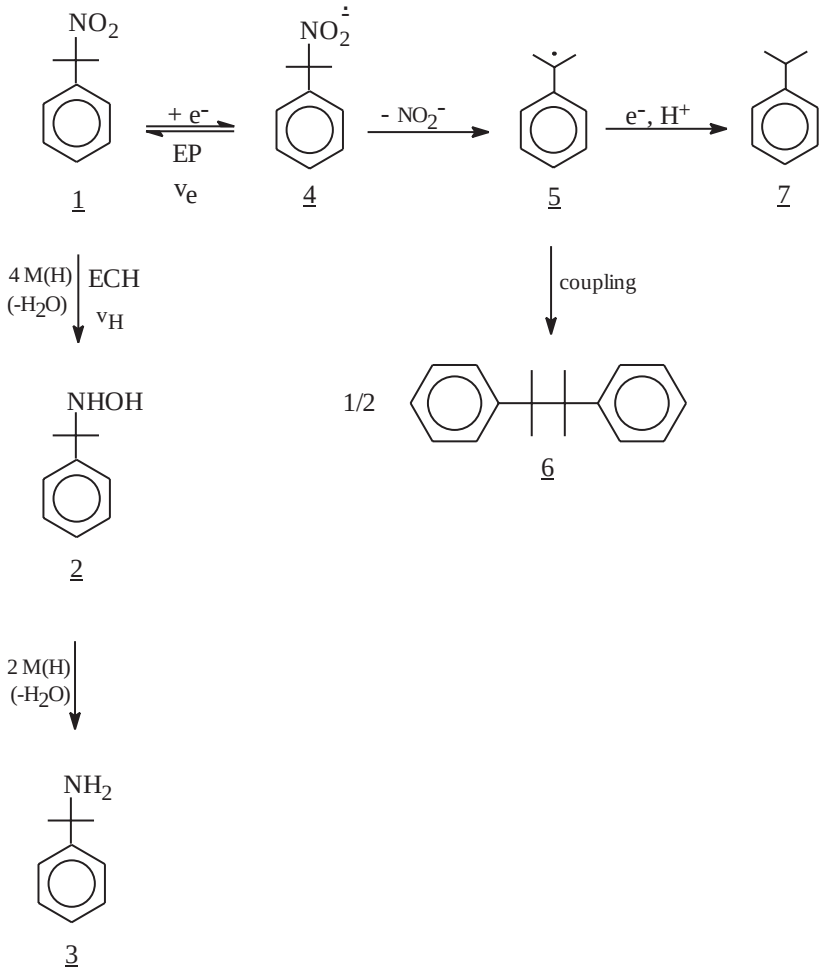

the current increased suddenly and then decreased steadily and slowly until reaching a near-zero value when the substrate was almost completely consumed. Aliquots of 0.3 mL were taken and analyzed by VPC using a DB-5 column (30 m, 0.25 μ) with a Hewlett Packard (HP) 5790 chromatograph equipped with an FID detector and an HP 3390A integrator. The products were identified by comparing their retention times with those of authentic samples. When the electrolysis was completed, the electrode was rinsed (EtOH then ether) and the products were extracted from the catholyte and the mass balance and yield of products were determined by VPC using the internal standard method.

Catalytic hydrogenations on nonpolarized electrodes were performed in the same cell as that used above. The electrode (catalyst) was placed in the cathodic compartment containing the deoxygenated solution. Its potential was lowered in order to reach a steady current of 100 mA and was kept at this value until 100 C had passed. Then, the circuit was opened and the electrode put to ground in order to depolarize it. The counter and reference electrodes were removed. The organic substrate was added, and aliquots of 0.3 mL were taken for analysis as above. Catalytic hydrogenations were also performed with the Raney metal powder obtained by leaching the commercial alloy powder. After leaching, the Raney metal particles were washed with water and transferred into a round-bottomed flask containing the deoxygenated solution. The substrate was added under a hydrogen atmosphere which was maintained throughout the reaction.

Results and discussion

Cyclic voltammetry was used to determine the reduction potential of α-nitrocumene (**1**) in basic (KOH 0.15 M) aqueous ethanol (ethanol–water 40:60 w/w). At a hanging mercury drop electrode (HMDE), two reduction peaks were observed on the cathodic sweep, the first peak at –1.13 V vs. SCE, corresponding to the one-electron reduction to the radical anion **4**, and the second cathodic peak at –1.45 V, to the reduction of **4** to the hydroxylamine **2** (see Scheme 3 for the structures of **4** and **2**). On the reverse scan: (*i*) no anodic peak corresponding to the oxidation of the radical anion **4** appeared even when the potential was inverted immediately after the first cathodic peak and the sweep rate was increased from 100 to 500 mV s^{-1}, thus showing that the cleavage and (or) the protonation of the radical anion were faster than its oxidation to **1** on the voltammetric time scale as observed before in aprotic medium (13); and (*ii*) there was one oxidation peak at –0.46 V corresponding to the oxidation of hydroxylamine **2** to nitrosocumene (not shown in Scheme 3), the reduction of which gave a cathodic peak at –0.60 V on the second cathodic scan. At a polycrystalline bright Ni electrode, no cathodic peak was observed because

© 1999 NRC Canada

Table 1. Preparative electroreduction of α-nitrocumene **1** (5 mM) at Hg and room temperature in basic ethanol–water (40:60 w/w) solutions.

			Yield of products (%)[c]		
pH[a]	*E* (V)[b]	Conversion (%)	Bicumyl **6**	Cumene **7**	Current efficiency (%)
>13	–1.13	100	85	2	71
10	–1.15	98	75	2	56

[a]pH >13, KOH 0.15 M; pH = 10: Britton–Robinson buffer.

[b]Reference electrode: $Ag/AgCl/Cl^-$ with $E = E_{SCE}$; counter electrode: platinum.

[c]Determined by gas chromatography using an internal standard. The other products were α-methylstyrene and α-hydroxycumene (see text). The material balance was 94% at pH >13 and 96% at pH 10.

Table 2. Preparative electrolysis of α-nitrocumene **1** (5 mM) at porous metal electrodes and room temperature in basic (KOH 0.15 M, pH > 13) ethanol–water (40:60 w/w) solutions.

				Yield of products (%)[c]		
Entry	Cathode[a]	Potential (V)[b]	Conversion (%)	Amine **3**	Dimer **6**	Current efficiency (%)[d]
1	R-Ni	–1.1[e]	100	97	2	72
2		–1.2	97	75	20	19
3	R-Co	–1.1[e]	100	66–73	24 –31	26–58
4	D-Cu	–1.2[e]	100	19	76	9

[a]See Experimental for electrode preparation. The electrode was charged with chemisorbed hydrogen by applying a current of 100 mA until a charge of 100 C was passed.

[b]Reference electrode: $Ag/AgCl/Cl^-$ with $E = E_{SCE}$; counter electrode: vitreous carbon.

[c]Determined by gas chromatography using an internal standard. Average value from two to three experiments. The range is indicated for variations larger than ±2%.

[d]Computed current efficiencies do not take into account the initial charge 100 C used for charging the electrode.

[e]Zero-current potential (see Experimental).

the reduction of nitrocumene (**1**) was hidden by the reduction of water (hydrogen evolution) at ca. –1.1 V. At polycrystalline bright Co and Cu electrodes, only one cathodic peak appeared in the cathodic sweep at –1.3 and –1.15 V, respectively. No anodic peak was seen on the reverse scan at any of the polycrystalline metal electrodes. Thus, the reduction of nitrocumene (**1**) occurs at similar potentials at mercury and at polycrystalline metal electrodes, and these reduction potentials are also similar to the so-called zero-current potential (potential at which no current flows at an electrode charged with chemisorbed hydrogen, see Experimental) used for the electrolyses at Raney metal and fractal nickel electrodes (–1.07 to –1.2 V vs. SCE). Thus, electron transfer to (electronation of) α-nitrocumene (**1**) generating the radical anion **4** could occur at Raney metal and fractal Ni electrodes at the zero-current potential in basic medium, and it does occur, as will be seen below.

The results of bulk electroreduction of α-nitrocumene (**1**) at a mercury pool and at ca. –1.15 V vs. SCE in basic (pH > 13 and pH 10) ethanol–water (40:60 w/w) solutions are recorded in Table 1. The main product was bicumyl (dimer **6**), resulting from the cleavage of radical anion **4** to cumyl radical (**5**) and nitrite anion followed by coupling of two cumyl radicals (**5**) (Scheme 3). Cumene (**7**), the product of reduction of radical **5**, was formed in small amounts (~2%). The other products not shown in Scheme 3 were α-methylstyrene (7% at pH > 13, 1% at pH 10) and cumyl alcohol (<1% at pH > 13, 19% at pH 10). The yield of dimer **6** was higher at pH > 13 than at pH 10. This is due to a faster protonation of radical anion **4** at pH 10 competing with its cleavage. The resulting neutral radical (not shown in Scheme 3) was then reduced rapidly to the hydroxylamine **2** which is unstable and decomposed to α-methylstyrene and cumyl alcohol (14).[2] The results of Table 3 clearly show that reduction of α-nitrocumene (**1**) by electron transfer in basic medium gives bicumyl (**6**) as the main product. The current efficiencies were lower than 100% and were lower at pH 10 than at pH > 13. This is most probably due to the reduction of water competing with the reduction of **1**.

The results of the controlled-potential reduction of α-nitrocumene (**1**) at Raney metal electrodes in basic (pH > 13) aqueous ethanol are summarized in Table 2. As shown in entry 1, at a R-Ni electrode and at the zero-current potential (–1.1 V), which corresponds to the potential of formation of radical anion **4** at a Hg cathode as already pointed out, α-aminocumene (**3**) was formed in a 97% yield (Table 2, entry 1). Only 2% of bicumyl (**6**) was formed. This shows that, under the conditions used, both the reduction of water to chemisorbed hydrogen (M(H)) and the reaction of α-nitrocumene (**1**) with M(H) were about 50 times faster than the electronation of **1** (see Scheme 1). Therefore, at the zero-current potential and at pH > 13, 98% of the electrochemical reduction of α-nitrocumene (**1**) at a R-Ni electrode proceeds via an ECH mechanism.

At a potential more negative than the zero-current potential (–1.2 V, see Table 2, entry 2), the amount of dimer (**6**) increased to 20%, the amount of amine having decreased accordingly to 75%. This can be readily explained by an in-

[2]Details of a study, as a function of pH, of the electroreduction of α-nitrocumene, *p*-cyano-α-nitrocumene, and *p*-methoxy-α-nitrocumene at mercury and in aqueous ethanol will be reported in a subsequent paper.

© 1999 NRC Canada

Table 3. Results of catalytic hydrogenation of α-nitrocumene **1** (5 mM) at Raney Ni, Raney Co, and Devarda Cu cathodes at room temperature in basic (KOH 0.15 M, pH > 13) ethanol–water (40:60 w/w) solutions.

				Yield of products (%)[a]		
Entry	Catalyst	Conditions	Conversion (%)	Amine **3**	Dimer **6**	Time (h)[b]
1	R-Ni	Electrode[c,d]	100	91–86	7–4	20
2		Electrode[e]	100	88	5	24
3		Electrode[f]	100	91	4	19
4		Powder/H_2[g]	100	98	2	16
5		Powder/H_2[h]	100	100	0	13
6	R-Co	Electrode[c,d]	100	79	7	22
7		Powder/H_2[h]	0	0	0	24
8	D-Cu	Electrode[c,d]	100	57–54	31–20	23
9		Electrode/H_2[c,i]	100	63	10	20
10		Powder/H_2[h]	0	0	0	24

[a]See footnote *c* of Table 2.

[b]Reaction time.

[c]Electrode: the electrode was prepared as for the ECH experiments except that it was connected to the ground after being polarized at a current of 100 mA for 100 C.

[d]Electrode activated by leaching in 10% NaOH at 50°C.

[e]Electrode activated by leaching in 10% NaOH at 50°C for 1 h but not polarized before adding the substrate.

[f]Same conditions as in footnote *c*, except the time of leaching was 2 h.

[g]Powder activated by leaching in 10% NaOH at 50°C for 1 h.

[h]Powder activated by leaching in 30% NaOH at 70°C for 8 h.

[i]Same conditions as in footnote *d* but a hydrogen atmosphere was maintained in the cathodic compartment instead of an argon atmosphere.

Table 4. Preparative electrolysis of α-nitrocumene **1** (5 mM) at a fractal nickel[a] electrode and room temperature in basic (KOH 0.15 M, pH > 13) ethanol–water (40:60 w/w) solutions.

			Yield of products (%)[c]		
Entry	Potential (V)[b]	Conversion (%)	Amine **3**	Dimer **6**	Current efficiency (%)
1	–1.07[d]	96	53	38	26
2	–1.2	97	15	56	5

[a]Fractal nickel from INCO Type 255 (5 g of powder pressed at $p = 14.5 \times 10^4$ kg m^{-2}) washed and kept in ethanol–water (40/60 w/w) before use.

[b]See footnote *b* of Table 2.

[c]See footnote *c* of Table 2.

[d]Zero-current potential (see Experimental).

crease of the rate of electronation of α-nitrocumene (**1**), v_e (Scheme 3), due to an increase of k_e, as the potential becomes more negative, the rate of reaction of **1** with M(H), v_H (Scheme 3), increasing less rapidly.

At a R-Co electrode (Table 2, entry 3), the electrochemical reduction of α-nitrocumene (**1**) at the zero-current potential, under the same conditions as those used for reduction at R-Ni, gave a much larger proportion of dimer **6** (24–31%) than the reduction at R-Ni (2%, entry 1) and less amine **3** accordingly (73–66%). Thus, on a R-Co electrode, the reaction of α-nitrocumene (**1**) with M(H) (ECH mechanism) competes less effectively with its electronation than on a R-Ni electrode: $(v_H/v_e)_{R\text{-}Ni} \approx 48.5 >> (v_H/v_e)_{R\text{-}Co} \approx 2.5$ (Scheme 3). This is in agreement with the fact that R-Co is less efficient than R-Ni as catalyst for catalytic hydrogenation (CH) (15–17). Copper catalysts are still less efficient than cobalt catalysts for CH (17), and as result, the electrochemical reduction of α-nitrocumene (**1**) at a D-Cu electrode, again at the zero-current potential and under the same solvent and pH conditions, gave the dimer **6** as the major product (75–77%) and the amine **3** as the minor product (15–20%). Thus, at a D-Cu electrode, the reaction of α-nitrocumene (**1**) with M(H) was now slower than its electronation: $(v_H/v_e)_{D\text{-}Cu} \approx 0.25$. It is noteworthy that, as the ECH process becomes less efficient with respect to the EP process (v_H/v_e becomes smaller), the desorption of M(H) to give molecular hydrogen (reaction [5] and (or) reaction [6]), which competes with its reaction with the adsorbed organic substrate, becomes more important as shown by the decrease in current efficiency from 72% with a R-Ni electrode to about 10% with a D-Cu electrode. The electrochemical desorption of M(H) (reaction [5]) competes also with the electronation of α-nitrocumene (**1**). So, the situation is quite complex.

$$[5] \quad M(H) + H_2O + e^- \xrightarrow{\text{Heyrovsky}} H_2 + M + OH^-$$

$$[6] \quad M(H) + M(H) \underset{\leftarrow - - - -}{\xrightarrow{\text{Tafel}}} H_2 + M$$

The hydrogenation steps in the ECH mechanism shown in Scheme 1 are exactly the same as in the classical catalytic hydrogenation (CH) (reaction of the adsorbed organic substrate with M(H) followed by desorption of the product(s) (7–9)). The main differences between ECH and CH are two-

© 1999 NRC Canada

fold: (*i*) M(H) is generated in situ by reduction of water in the former (reaction [1]) and by thermal dissociation of molecular hydrogen in the latter (reverse of reaction [6]); (*ii*) the catalyst is negatively polarized in the former and is not polarized in the latter. Since the catalyst is not polarized in CH, the sole product formed by CH of α-nitrocumene (**1**) should be the amine **3** assuming that the nonpolarized catalyst cannot transfer an electron to nitrocumene (**1**). Then, CH constitutes the best model of an ECH mechanism. We therefore studied the CH of α-nitrocumene (**1**) under the same solvent and pH conditions and on the same catalysts as those used for the ECH experiments, that is on Raney metal "electrodes" which had been initially charged with chemisorbed hydrogen by reduction of water in the absence of α-nitrocumene (**1**) but then, after opening the circuit, had been connected to the ground. These CH experiments were carried out under an argon atmosphere as for the electrolyses. The product distribution was compared with that obtained by carrying CHs on a freshly leached Raney catalyst powder under a H_2 atmosphere at atmospheric pressure and room temperature. The results are summarized in Table 3.

The most striking feature of Table 3 is the formation of some bicumyl (**6**) in all the CH experiments with the nonpolarized electrodes as catalysts (entries 1–3, 6, and 8). Thus, some electronation of α-nitrocumene (**1**) did occur on the nonpolarized Raney metal electrodes and, in the case of D-Cu electrode (entry 8), to a nonnegligible extent (20–31%). Such electronation is not due to reduction of nitrocumene (**1**) by the transition metal (Ni, Co, or Cu) but to its reduction by the residual aluminum left after leaching (18). This was confirmed by the following experiments. (*i*) α-Nitrocumene (**1**) was quantitatively recovered when treated with fractal Ni particles or with a Cu metallic powder in the same basic medium. (*ii*) No bicumyl (**6**) was formed when CH of α-nitrocumene (**1**) was carried out on a Raney metal powder which was prepared by extensive leaching of the Raney alloy (leaching for 8 h at 70°C in 30% aqueous NaOH; see Table 3, entries 5, 7, and 10). (*iii*) Bicumyl (**6**) was formed only when residual aluminum was still present in the catalyst (according to eq. [7], 0.6 mg of Al would reduce up to 33 mg of **1**), that is, in all experiments performed with the

$$[7] \qquad Al + 3RNO_2 + 4OH^- \longrightarrow Al(OH)_4^- + 3RNO_2$$

nonpolarized electrodes (entries 1–3, 6, 8, and 9) leached under milder conditions (2 h at 50°C in 10% aqueous NaOH), in order to effect leaching of the surface layers of the disc only (more vigorous leaching conditions led to complete disintegration of the disc). (*iv*) Finally, bicumyl (**6**) and cumene (**7**) were formed in 28–39 and 1% yields, respectively, together with 7–3% of amine **3** and 25–28% of products (α- methylstyrene and α-hydroxycumene) resulting from decomposition of hydroxylamine **2** (15, 16) when α-nitrocumene (**1**) was reduced with metallic aluminum (powder) always in the same basic medium. So, on a nonpolarized catalyst containing residual aluminum, there is a competition between reaction of adsorbed α-nitrocumene (**1**) with chemisorbed hydrogen present on the catalyst (as in Scheme 1) and its reduction by electron transfer from aluminum according to eq. [7] (19). The fact that, with the less active hydrogenation catalysts R-Co and D-Cu, much more bicumyl (**6**) was formed on the polarized catalysts (24–31 and 76%, respectively; see Table 2, entries 3 and 4) than on the nonpolarized catalyst (7 and 20–31%, respectively; see Table 3, entries 6 and 8), shows that direct electron transfer from a negatively polarized electrode was faster as would be expected. It is noteworthy that, when there was no residual aluminum present in the R-Co and D-Cu catalysts, not only electronation of nitrocumene (**1**) did not occur but there was no CH either (see Table 3, entries 7 and 10). This was not the case with R-Ni free of residual aluminum (Table 3, entry 5). This suggests that in the the case of R-Co and D-Cu, the presence of residual aluminum would favor the CH process possibly by influencing the adsorption energies of hydrogen and of the organic substrate. The catalytic activity of the catalyst in CH, that is, the rate of reaction of the adsorbed organic substrate with M(H), must depend on the energy of adsorption of hydrogen as well as on the energy of adsorption of the organic substrate (M-H and M-substrate bond energies), and the same should hold for the electrocatalytic activity of large surface area electrodes in ECH of organic substrates. These energies of adsorption depend on the metal itself (Ni, Co, or Cu in this work), and for a given metal, for instance, R-Ni and fractal Ni, on the nature of the adsorption sites as noted by Bockris and Minevski (20) and Lasia (21). The nature of the adsorption site depends on (*i*) the type of crystallographic structure (the crystal plane, a step, or an edge) exposed for adsorption; (*ii*) irregularities in the crystallographic surface structure; (*iii*) impurities strongly bound to the surface; (*iv*) a small amount of a second metal, such as aluminum, forming alloy (17). For instance, the nature of the M—H bond may vary from a nearly covalent bond (22, 23), an adsorbed state producing a large increase in the free electron density in the metal surface (23), to a hydridic bond (22). So, the knowledge of the various factors and forces involved is as yet insufficient to be able to pinpoint the exact reasons of the differences in electrocatalytic activity observed in this work.

The results presented and discussed so far show that α-nitrocumene (**1**) can be used to evaluate the competition between the ECH and EP processes (the ratio v_H/v_e) in Scheme 3) for the electrochemical hydrogenation at porous electrodes. This competition can be used to compare the activity of various electrode materials for the ECH process at zero-current potential. The results of Table 2 show clearly that the activity of Raney metals decreases in the order R-Ni (entry 1) > R-Co (entry 3) > D-Cu (entry 4) as already discussed. The activity of fractal Ni was evaluated also. The results of entry 1, Table 2, show that fractal Ni ($v_H/v_e \approx 1.4$) is more active than D-Cu ($v_H/v_e \approx 0.25$) but somewhat less active than R-Co ($v_H/v_e \approx 2.53$). Upon decreasing the potential to –1.2 V (entry 2, Table 2), the rate of electronation (v_e) increases, and the ratio of v_H/v_e decreases accordingly ($v_H/v_e \approx 0.27$) as was observed with R-Ni electrodes (compare entry 1 ($v_H/v_e \approx 48.5$) and entry 2 ($v_H/v_e \approx 3.8$) and of Table 4).

Fractal Ni was found to be completely inactive for CH of α-nitrocumene (**1**) in basic aqueous ethanol either using fractal Ni particles under a hydrogen atmosphere or pressed fractal Ni electrodes initially charged with M(H) and put to ground. α-Nitrocumene (**1**) was quantitatively recovered as in the attempted CH on R-Co and D-Cu catalysts free of residual aluminum.

© 1999 NRC Canada

Conclusions

In the electrochemical reduction of α-nitrocumene (**1**) in basic aqueous ethanol, at solid electrodes with large specific surface areas (porous electrodes), two mechanisms of electrohydrogenation can be operative: namely, an ECH mechanism giving α-aminocumene (**3**) and an EP mechanism giving products derived from the cumyl radical (**5**), itself resulting from a rapid elimination of the nitrite anion from the α-nitrocumyl radical anion (**4**) (Scheme 3). The relative rates of the ECH and EP processes depend on the potential imposed, the rate of electronation (EP process) increasing upon decreasing the potential. These relative rates depend also on the nature of the transition metal (Ni, Co, Cu) and, for a porous metal, on the surface structure of the electrode (R-Ni, fractal Ni). Thus, α-nitrocumene (**1**) can be used to evaluate the electrocatalytic activity of an electrode for the ECH process. The following order of electrocatalytic activity was determinated at the so-called zero-current potential (potential at which no current flows at an electrode charged with chemisorbed hydrogen): R-Ni > R-Co > fractal Ni > D-Cu.

It is noteworthy that R-Co, fractal Ni, and D-Cu were completely inactive for catalytic hydrogenation of α-nitrocumene (**1**) at an atmospheric pressure of molecular hydrogen. On the other hand, when residual aluminum was present on the catalyst charged with chemisorbed hydrogen, both catalytic hydrogenation at atmospheric pressure and reduction by metallic aluminum (electron transfer) occurred on D-Cu in a ratio close to 70/30. This suggests that the presence of residual aluminum favors the catalytic hydrogenation process.

Acknowledgements

We gratefully acknowledge financial support from the Agence Canadienne de Developpement International (ACDI) (E.S. Chan-Shing), the Natural Sciences and Engineering Research Council of Canada (NSERC), the Fonds pour la Formation de Chercheurs et l'Aide à la Recherche (FCAR) du Québec and l'Université de Sherbrooke. We are thankful to Dr. Jean Marc Chapuzet for helpful discussions and to Mr. Gaston Boulay for the mass spectra.

References

1. H. Lund. *In* Organic electrochemistry. *Edited by* M.M.Baizer and H. Lund. Marcel Dekker, Inc., New York. 1991. Chap. 9.
2. F. Haber. Z. Electrochem. **4**, 506 (1898).
3. G. Pezzatini and R. Guidelli. J. Electroanal. Chem. **102**, 205 (1979).
4. A. Cyr, E. Laviron, and J. Lessard. J. Electroanal. Chem. **263**, 69 (1989).
5. P.E. Iversen and H. Lund. Acta Chem. Scand. **19**, 2303 (1965).
6. P.E. Iversen and H. Lund. Tetrahedron Lett. 4027 (1967).
7. A. Cyr, P. Huot, G. Belot, and J. Lessard. Electrochim. Acta, **35**, 147 (1990).
8. A. Vélin-Prikidanovics and J. Lessard. J. Appl. Electrochem. **20**, 527 (1990).
9. J. M. Chapuzet, A. Lasia, and J. Lessard. *In* Electrocatalysis. *Edited by* J. Lipkowski. Wiley–VCH, Inc., Pennington, N.J. 1998. pp. 155–196.
10. P. Delair, A. Cyr, and J. Lessard. *In* Electroorganic synthesis. Festchrift for M.M. Baizer. *Edited by* R.D. Little and N.L. Weinberg. Marcel Dekker, Inc. New York. 1991. p.129.
11. B.J. Côté, D. Després, R. Labrecque, J. Lamothe, J.M. Chapuzet, and J. Lessard. J. Electroanal. Chem. **355**, 219 (1993).
12. N. Kornblum, S.C. Carlson, J. Widmer, M.J. Fifolt, B.N. Newton, and R.G. Smith. J. Org. Chem. **43**, 1394 (1978).
13. A.K. Hoffmann, W.G. Hodgson, D.L. Maricle, and W.H. Jura. J. Am. Chem. Soc. **86**, 631 (1964).
14. E.S. Chan-Shing. Ph.D. thesis. Université de Sherbrooke, Sherbrooke. 1999.
15. B.V. Aller. J. Appl. Chem. **8**, 163 (1959).
16. B.V. Aller. J. Appl. Chem. **8**, 492 (1958).
17. R.L. Augustine. Catalytic hydrogenation. Marcel Dekker, Inc., New York. 1965. pp. 23–56.
18. Y. Choquette, L. Brossard, and H. Ménard. J. Appl. Electrochem. **20**, 855 (1990).
19. U. Birkenstock, R. Holm, B. Reinfandt, and S. Storp. Catalysis, **93**, 55 (1985).
20. J.O'M. Bockris and Z.S. Minevski. Electrochim. Acta, **39**, 1471 (1994).
21. A. Lasia. Can. J. Chem. **75**, 1615 (1997).
22. D.J. Barclay. Electroanal. Chem. Interfacial Electrochem. **44**, 47 (1973).
23. R.J. Nichols and A. Bewick. J. Electroanal. Chem. **243**, 445 (1988).

© 1999 NRC Canada

Classical variational rate theory portraits of the dynamical stereochemistry of the F + H_2 → FH + H reaction

Irina Rutenburg and Gerald W. Koeppl

Abstract: A general classical variational theory of reaction rates is applied to the F + H_2 → FH + H reaction. The variational theory gives the rate as the equilibrium flux of phase points through a trial surface which divides reactants from products and is varied to obtain a least upper bound for the rate. This dividing surface (DS) is defined by a power-series expansion of the H-H internuclear separation (r) in internal coordinates R and θ, i.e., r = F(R, θ) where R is the approach coordinate and θ is the orientation angle. The downhill simplex algorithm is used to search the space of 6 and 10 variational parameters of second- and third-order expansions of the DS and obtain minimum values for the canonical rate constant or, in the microcanonical formulation of the theory, the energy-dependent mean reaction cross section. The presence of angle-dependent terms in the DS makes it possible to describe the dynamical stereochemistry of atom–diatom reactions in a new and useful manner. Portraits of the dynamical stereochemistry are obtained by plotting contours of the density of reaction systems on the DS; such plots are reactivity relief maps of the DS. Reactivity relief maps show how the field of reactivity which surrounds the diatomic reactant molecule expands with increasing temperature and energy. Results are presented here for a new power series formulation of the DS which obeys a condition: $\partial F(R, \theta)/\partial\theta = 0$ at $\theta = \pi/2$ which is appropriate for reaction of a homonuclear diatomic molecule. The relationship between reactivity relief maps obtained using quadratic and cubic formulations of the new DS and the locations of angle-dependent energy barriers for reaction is described. Variational and classical mechanical trajectory results are used to show how energy-dependent factors, which correct the variational mean reaction cross section for trajectories which cross and recross the DS, depend on the orientation angle.

Key words: variational, transition, rate, dividing, surface.

Résumé : On applique la théorie variationnelle générale classique des vitesses de réaction à la réaction F + H_2 → FH + H. Selon la théorie variationnelle, la vitesse est donnée par le flux à l'équilibre des points de phase à travers une surface de référence qui divise les réactifs des produits et que l'on fait varier pour obtenir une valeur limite de la vitesse. Cette surface de division (SD) est définie par une expansion en série de puissance de la distance internucléaire H-H (r) dansles coordonnées internes R et θ, c'est-à-dire r = F(R, θ) dans laquelle R est la coordonnée d'approche et θ est l'angle d'orientation. On utilise l'algorithme simplex de descente de la pente pour rechercher l'espace de 6 et de 10 paramètres variationnels des expansions des deuxième et troisième ordre de la SD et pour obtenir les valeurs minimales de la constante de vitesse canonique ou, dans un formulation microcanonique de la théorie, la section droite moyenne qui dépend de l'énergie. La présence de termes qui dépendent de l'angle dans la SD fait qu'il est possible de décrire la stéréochimie dynamique des réactions atome–diatome d'une manière nouvelle et utile. On obtient des portraits de la stéréochimie dynamique en traçant des contours de la densité des systèmes réactionnels sur la SD; de tels tracés sont des cartes en relief de la réactivité sur la SD. Les cartes en relief de la réactivité montrent comment s'effectue l'expansion du champ de la réactivité qui entoure la molécule de réactif diatomique avec une augmentation de la température et de l'énergie. Les résultats sont présentés ici pour une nouvelle formulation de la série de puissance de la SD qui obéit à la condition: $\partial F(R, \theta)/\partial\theta = 0$, à $\theta = \pi/2$ qui est approprié pour la réaction d'une molécule diatomique homonucléaire. On décrit la relation entre les cartes de relief de réactivité obtenues à l'aide de formulations quadratique ou cubine de la nouvelle SD et les positions des barrières d'énergie de la réaction qui dépendent de l'angle. On utilise les résultats de trajectoires mécanique variationnelle et classique pour montrer

Received December 18, 1998.

This paper is dedicated to Jerry Kresge in recognition of his many achievements in chemistry.

I. Rutenburg[1] and G.W. Koeppl.[2] Department of Chemistry and Biochemistry, Queens College of The City University of New York, Flushing, NY 11367, U.S.A.; Graduate School and University Center of The City University of New York, 33 West 42nd St., New York, NY 10036, U.S.A.

[1]Present address: Department of Chemistry, Queensborough Community College of The City University of New York, Bayside, NY 11364, U.S.A.

[2]Author to whom correspondence may be addressed at the Graduate School and University Center of The City University of New York. Telephone: (212) 642-2450. Fax: (212) 642-2290. e-mail: gkoeppl@gc.cuny.edu

© 1999 NRC Canada

comment, des facteurs qui dépendent de l'énergie et qui corrigent la section droite moyenne variationnelle de la réaction pour les trajectoires qui croisent et recroisent la SD, dépendent de l'angle d'orientation.

Mots clés : variationnel, transtion, vitesse, division, surface.

[Traduit par la Rédaction]

Introduction

The classical variational theory of chemical reaction rates gives the rate as the equilibrium flux of reaction systems through a trial surface. This theory was introduced by Pelzer and Wigner (1), and developed and generalized further by Horiuti (2), Keck (3, 4), Marcus (5), Koeppl (6, 7), Pechukas (8–10), and Pollak (11), Truhlar et al. (12–14), and others (15–17). The study and development of this theory in its various forms continues to be an active area of research (18–35). In the most general development of the theory by Keck, the trial surface divides the phase space of the reaction system into reactant and product regions. The trial surface is usually referred to as a dividing surface (DS). In practice, the theory is nearly always applied using a DS which is a function of internal coordinates of the reaction system. The transition state theory (TST) of chemical reaction rates is a special case of the variational theory. The conventional version of TST, developed by Eyring and co-workers (36, 37) and Evans and Polanyi (38), gives the reaction rate for a particular DS (4, 39). This DS passes through a saddle point of the potential-energy surface and is perpendicular to the unbound normal coordinate of the transition state.

The variational rate, i.e., the equilibrium flux of reaction systems through a particular DS, is an upper bound because phase points which start in the reactant region of configuration space can cross and recross the DS regardless of whether they proceed ultimately to the product region. Furthermore, phase points which do not originate in the reactant region, but are present in the equilibrium flux, can cross and recross the DS. The DS can be varied to obtain a minimum upper bound for the reaction rate. The variational rate will equal the actual rate of reaction if the DS is crossed only once by all reactive trajectories. For a classical microcanonical formulation of the variational theory, the reaction rate corresponds to an ensemble of reaction systems of fixed total energy E. It is possible to find DSs at energies up to some value E' which give the actual rate (40). For the classical canonical formulation of the variational theory, the rate corresponds to an ensemble of reaction systems for temperature T which contains trajectories with energies above E'; hence, it is impossible to find a DS which gives the actual rate.

The accuracy of the classical variational theory for a given DS can be determined by comparing variational values of the canonical rate constant at a given temperature or energy-dependent mean reaction cross section at a given energy with corresponding values calculated by executing a Monte Carlo sample of classical mechanical trajectories. The same Born–Oppenheimer potential-energy function (PEF) must be used for the variational and trajectory calculations. Morokuma and Karplus (41) and Koeppl and Karplus (42) were the first to determine the accuracy of TST in this unequivocal manner for collinear reactions and reactions in three-dimensional space, respectively. In a theory versus experiment test of the accuracy of TST, one cannot be sure whether error is caused by failure of the variational theory or inaccuracy of the PEF.

The Born–Oppenheimer PEF for a given electronic state of the chemical reaction system is often referred to as a potential-energy surface (PES). For a collinear atom–diatom reaction, a trajectory can be plotted as a mass point moving on the potential-energy surface (43). In most applications of classical variational and trajectory theories, it is assumed that reaction takes place on the PES for the electronic ground state of the reaction system, i.e., the electronic state does not change during chemical reaction.

Koeppl (7) developed a general classical variational treatment for atom–diatom reactions. The Koeppl formulation of the variational theory is based on a method developed by Martin and Raff (44). Expressions were derived for the microcanonical and canonical formulations of this theory which give the energy-dependent mean reaction cross section and canonical rate constant, respectively, for the most general DS defined by configuration space coordinates. A numerical method which uses the downhill simplex algorithm was developed to evaluate these quantities by determining constants (variational parameters) of terms in first, second, and third-order expansions of the DS in the internal coordinates of the reaction system. Sverdlik and Koeppl (45) applied this treatment to the $H' + HH \rightarrow H'H + H$ and $H + I_2 \rightarrow HI + I$ reactions.

Rutenburg and Koeppl (46) applied this treatment to the $F + H_2 \rightarrow FH + H$ reaction for a series of three PEFs in which an important feature of the interaction potential was varied in a systematic manner. The steepness of the profile of the angle-dependent barrier for chemical reaction increased in the PEF series. The $F + H_2$ reaction was chosen for this study because it has been the subject of many theoretical and experimental studies. Many attempts have been made to calculate an accurate potential-energy function for this reaction (47–59). Rutenburg and Koeppl showed how the angle-dependent terms, i.e., terms containing the angle θ which the H_2 internuclear axis makes with a line from atom F to the center-of-mass of H_2, in the power series formulation of the DS made it possible to characterize the dynamical stereochemistry of atom–diatom reactions in a new and useful way. This was done by plotting contours of the variational flux density of reaction systems through the DS. Flux density contours were plotted in the space of internal coordinates θ and R where R is the distance between atom F and the center-of-mass of H_2; at each point on the DS, the value of the H_2 internuclear separation is defined by the function which defines the DS. They also characterized the dynamical stereochemistry in a less detailed manner by dividing the full range of orientation angle θ (0–π) into equal intervals and calculating the contribution to the canonical rate constant or energy-dependent mean reaction cross section for each interval to show how this quantity varies with θ.

© 1999 NRC Canada

Levine and co-workers (60, 61) and others (62, 63) have used the concept of an orientation-dependent critical configuration for reaction and other concepts to characterize the dynamical stereochemistry of atom–diatom reactions. Although their work does not make explicit use of a DS, for certain reactions including the F + H_2 reaction, the DS implied by their approach must pass through angle-dependent potential-energy barriers for chemical reaction. The barriers are located at saddle points in the *r*–*R* space defined by fixing the orientation angle θ. For the F + H_2 reaction, Rutenburg and Koeppl obtained contour plots of the variational flux density on the DS for quadratic DSs which showed that regions of large flux density on the DS did not follow the path of the angle-dependent barriers for chemical reaction over the entire range in θ from 0 to π. Regions of large flux density were expected to follow the positions of the barriers because the barriers correspond to the minimum energy for chemical reaction at each value of the orientation angle. This unexpected behavior, found for all three of the PEFs studied, could be caused by a DS function which was not flexible enough to pass through the angle-dependent barriers for chemical reaction and follow the path of steepest ascent from them and (or) because entropic as well as enthalpic factors determine the path of regions of large flux density.

The present work is concerned in part with studying this unexpected behavior. Reactivity relief maps are calculated using a cubic expansion of the DS to learn whether a more flexible function would yield the expected behavior. Variational searches were also performed using a new expansion which contains $\sin^2\theta$ factors; these factors ensure that the function which defines the DS has a continuous derivative with respect to θ at $\theta = \pi/2$, a condition which should be satisfied for a homonuclear diatomic reactant. We performed classical variational calculations for two potential-energy functions developed by Truhlar et al. (49) (designated T1 and T2).

We are not concerned with comparing theoretical and experimental rate constants in the present work. The T1 and T2 PEFs cited above yield variational rate and semiclassical trajectory rate constants which are in reasonable agreement with experiment. We are concerned instead at this stage of our work with the relationship between classical variational results and features of reasonable PEFs for the F + H_2 reaction, and using the variational theory to characterize the dynamical stereochemistry for these PEFs. We are also interested in the relationship between the accuracy of the classical variational theory, i.e., the accuracy of the no-recrossing assumption of transition state theory, for a given reasonable PEF and the temperature for a canonical ensemble and energy for a microcanonical ensemble of reaction systems. We determine this accuracy in the present work by comparing variational and classical mechanical trajectory results for the same PEF. Our ultimate goal is a semiclassical formulation of the general variational theory which makes theory and experiment comparisons meaningful.

We are also concerned here with the characterization of the difference between the variational flux through the DS and the accurate flux determined by calculating classical mechanical trajectories. Variational and trajectory results are used to show how energy-dependent factors which correct the variational mean reaction cross section for trajectories which cross and recross the DS depend on the orientation angle.

Finally, we show how variational values of the energy-dependent mean reaction cross section can be used to calculate the canonical rate constant and how the effect of such a complete optimization of the canonical rate constant depends on temperature.

The equations for the canonical rate constant and microcanonical mean reaction cross section for a general configuration space DS are presented in Sect. 1. The derivation of these equations is given in ref. 7. Expressions for DSs used in the present work and corresponding expressions for the canonical rate constant are given in Sect. 2.

Canonical variational results are presented in Sect. 3. The determination and significance of DSs which pass through angle-dependent saddle points and follow the path of steepest ascent from them are described.

In Sect. 4, variational and trajectory energy-dependent differential (angle-dependent) mean reaction cross sections are used to show how energy-dependent transmission and product factors which correct the variational mean reaction cross section for the error of the no-recrossing approximation of transition state theory depend on the orientation angle. The effect of microcanonical optimization on the canonical rate constant at three temperatures is described.

Concluding remarks are given at the end.

1. General expressions for the canonical rate constant and microcanonical mean reaction cross section

A. Canonical rate constant for general dividing surface

We consider chemical reactions of the type

[1] $$A + BC \rightarrow AB + C$$

between an atom and a diatomic molecule (7). We assume that electronic transitions do not occur during the reaction and treat the motion of the nuclei classically. The exact classical rate constant is given by (4, 8, 40, 64–67)

[2] $$k^{\text{exact}}(T) = Q_{\rho_s}(T)^{-1} \times \int d\tau\, \mathbf{v}\cdot\mathbf{n}_S \chi_S(\mathbf{q}, \mathbf{p})\, \delta[S(\mathbf{q}, \mathbf{p})] \times \exp[-\beta H(\mathbf{q}, \mathbf{p})]$$

where $\int d\tau$ is an integral operator which sums the flux over the 12 internal (center-of-mass) degrees of freedom of the phase space of the reaction system, $\mathbf{q}$ and $\mathbf{p}$ are the coordinates and momenta of phase space, the delta function $\delta(S)$ restricts the integration to the 11-dimensional phase space surface defined by $S(\mathbf{q}, \mathbf{p}) = 0$, $\mathbf{v}$ is the generalized velocity of a phase point, $\mathbf{n}_S$ is the unit vector normal to the surface, $\chi_S(\mathbf{q}, \mathbf{p})$ (8, 64–66) is the characteristic function, $H(\mathbf{q}, \mathbf{p})$ is the classical Hamiltonian of the reaction system, $\beta = (k_B T)^{-1}$ where k_B is Boltzmann's constant and T the Kelvin temperature, and $Q_{\rho_s}(T)$ is the classical partition function per unit volume for the internal degrees of freedom of the reactants times Planck's constant (h) to the sixth power. The characteristic function $\chi_S(\mathbf{q}, \mathbf{p})$ for the surface is +1 for phase points which cross the surface in the direction of products

© 1999 NRC Canada

Fig. 1. Values of R and r at angle-dependent saddle point of the T2 potential-energy function versus orientation angle.

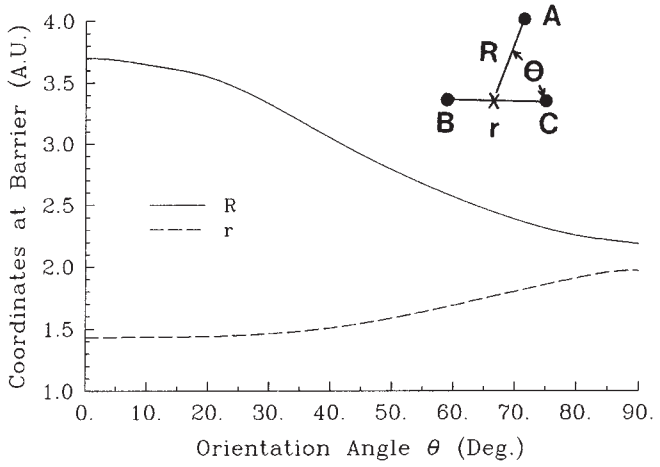

and were on the reactant side of the surface in the asymptotic past, –1 for phase points which cross the surface in the direction of reactants and were on the reactant side in the asymptotic past, and zero otherwise. The critical assumption of variational TST may be expressed as

$$[3] \qquad \chi_S(\mathbf{q}, \mathbf{p}) = \chi_S^{TST}(\mathbf{q}, \mathbf{p}) = \hbar(\mathbf{v}\cdot\mathbf{n_S})$$

where χ_S^{TST} is the characteristic function of TST, and $\hbar(x)$ is the Heaviside step function. All phase points moving in the direction of products at the dividing surface contribute to the rate. Since the integral operator $\int d\tau\ \delta(S)$ equals $\int d\sigma$ where $d\sigma$ is the 11-dimensional element of reduced phase space of the surface, substitution of eq. [3] in eq. [2] gives the Keck (4) expression for the variational rate constant of transition state theory (TST):

$$[4] \qquad k^{TST}(T) = Q_{\rho_s}(T)^{-1} \times \int d\sigma\ \mathbf{v}\cdot\mathbf{n_S}\ \hbar(\mathbf{v}\cdot\mathbf{n_S})\ \exp\ [-\beta H(\mathbf{q}, \mathbf{p})]$$

The most general dividing surface may be defined by

$$[5] \qquad S(\mathbf{q}, \mathbf{p}, \Omega) = 0$$

where S depends on both configuration (**q**) and momentum (**p**) coordinates of phase space and a set of constants and arbitrary variational parameters (Ω). We consider the case where the surface depends only on configuration coordinates, i.e., the internal coordinates of the reaction system, and is therefore independent of constants of motion in the canonical formulation of the variational theory (4). A surface defined by internal coordinates depends on the total energy of the reaction system in the microcanonical formulation of the variational theory. The most general surface of this type for the reaction considered here may be expressed as

$$[6] \qquad S = r - F(R, \theta) - C = 0$$

where r is the internuclear separation between atoms B and C, R is the distance between atom A and the center of mass of atoms B and C, C is a variational parameter, and the defining function $F(R, \theta)$ depends on additional variational parameters. See the inset of Fig. 1. Function $F(R, \theta)$ defines a surface which provides an unambiguous division of configuration space into reactant and product regions; i.e., a surface which is crossed by all reactive trajectories. It is convenient to choose a set of generalized coordinates (**q**) which makes S a coordinate surface for one of them. Hence, we take

$$[7] \qquad q_1 = r - F(R, \theta) = q_*$$

Coordinate q_* is the generalized reaction coordinate of transition state theory; i.e., $q_* = C$ defines transition state configurations of the reaction system. The integrals of eq. [4] were evaluated using spherical polar coordinates which correspond to the relative Cartesian coordinates of atom C with respect to atom B, and atom A with respect to the center-of-mass of atoms B and C. The rate constant may be expressed as

$$[8] \qquad k^{TST}(T) = (2\pi/\beta)^{1/2}(\sigma_{BC}/\sigma_*)[N_*^C(T)/D_{BC}^C(T)]$$

where σ_{BC} and σ_* are the symmetry numbers of reactant BC and reaction system configuratons on the DS (4, 68, 69), respectively.

The DS function $N_*^C(T)$ is given by

$$[9] \qquad N_*^C(T) = \int_0^\pi \exp\ \{-\beta V[r(\Omega, R, \theta), R, \theta]\} \sin\theta\ d\theta \times \int_0^{R_{max}^{S=0}} r(\Omega, R, \theta)^2 R^2 dR \times [\mu_{BC}^{-1}\{1 + [F_\theta(R, \theta)/r(\Omega, R, \theta)]^2\} + \mu_{A,BC}^{-1} F_R(R, \theta)^2]^{1/2}$$

where $V[r(\Omega, R, \theta), R, \theta]$ is the potential energy for configurations on the DS, $F_R(R, \theta)$ and $F_\theta(R, \theta)$ are partial derivatives of function $F(R, \theta)$ with respect to R and θ, respectively, μ_{BC} and $\mu_{A,BC}$ are reduced masses of atom groups (B, C) and (A, BC), respectively, and $R_{max}^{S=0}$ is a practical limit for the integration over R which is required due to the finite limit for the potential energy as $R \to \infty$ on the dividing surface (44, 70, 71).

The reactant function $D_{BC}^c(T)$ is given by

$$[10] \qquad D_{BC}^c(T) = \int_0^{r_{max}^{BC}} r^2\ \exp\ [-\beta V_{\rho_s}(r)]dr$$

where $V_{\rho_s}(r)$ is the potential energy of BC with atom A on the reaction shell radius, i.e., $R = \rho_S$, and r_{max}^{BC} is a practical limit for r which is required due to the finite limit for the potential energy of reactant BC at dissociation.

B. Energy-dependent mean reaction cross section for general DS

Koeppl (7) used the collisional theory of chemical reactions (72–74) and the appropriate inverse Laplace transform (75) to derive an expression for the energy-dependent mean reaction cross section defined by Morokuma et al. (76) for the reaction A + BC → AB + C:

© 1999 NRC Canada

[11] $$\bar{S}_r(E)^{TST} = (\pi\mu_{A,BC}{}^{1/2}/2)\,(\sigma_{BC}/\sigma_*)[N^{\mu}_*(E)/D^{\mu}_{BC}(E)]$$

The DS function $N^{\mu}_*(E)$ is given by

[12] $$N^{\mu}_*(E) = \int_0^{\pi} \sin\theta\, d\theta \int_0^{\infty} r(\Omega, R, \theta)^2 R^2 \{E - V[r(\Omega, R, \theta), R, \theta]\}^{5/2} \times \hbar\{E - V[r(\Omega, R, \theta), R, \theta]\}\, dR \times [\mu_{BC}{}^{-1}\{1 + [F_\theta(\Omega, R, \theta)/r(\Omega, R, \theta)]^2\} + \mu_{A,BC}{}^{-1} F_R(\Omega, R, \theta)^2\ ]^{1/2}$$

The reactant function $D^{\mu}_{BC}(E)$ is given by

[13] $$D^{\mu}_{BC}(E) = \int_0^{\infty} r^2[E - V_{\rho_s}(r)]^{5/2} \quad \hbar[E - V_{\rho_s}(r)]\, dr$$

The relationship between $\bar{S}_r(E)^{TST}$ and the canonical rate constant is given by

[14] $$k^{TST}(T) = (8\pi\mu_{A,BC})Q_{\rho_s}(T)^{-1}\int_0^{\infty} \epsilon_{BC}(E)\bar{S}_r(E)^{TST} \exp(-\beta E)\, dE$$

where $\epsilon_{Bc}(E) = (64/15)(2)^{1/2}\pi^2\mu_{Bc}^{3/2}\sigma_{Bc}^{-1}D^{\mu}_{BC}(E)$.

2. Dividing surfaces, expressions for canonical rate constant and microcanonical mean reaction cross section, and numerical methods

A. Dividing surface functions used in this work

1. Functions expressed in powers of R *and* θ
Quadratic (Q) DS

[15] $$r = AR + B\theta + C + 1/2(DR^2 + 2ER\theta + F\theta^2)$$

where *A*, *B*, *C*, *D*, *E*, and *F* are variational parameters. This DS was introduced by Sverdlik and Koeppl (45). It is designated linear θ function in figures and tables to distinguish it from the quadratic $\sin^2\theta$ function given below.

Cubic (C) DS

[16] $$r = AR + B\theta + C + 1/2(DR^2 + 2ER\theta + F\theta^2) + 1/6(GR^3 + 3HR^2\theta + 3IR\theta^2 + J\theta^3)$$

where *A*, *B*, *C*, *D*, *E*, *F*, *G*, *H*, *I*, and *J* are variational parameters. This DS was introduced by Sverdlik and Koeppl (45). It is designated linear θ function in figures and tables to distinguish it from the cubic $\sin^2\theta$ function given below.

2. Functions expressed using powers of R *and* $\sin^2\theta$
Quadratic DS

[17] $$r = AR + B\sin^2\theta + C + 1/2(DR^2 + 2ER\sin^2\theta + F\sin^4\theta)$$

where *A*, *B*, *C*, *D*, *E*, and *F* are variational parameters. This DS is introduced here. It is designated $\sin^2\theta$ function in figures and tables to distinguish it from the quadratic function of powers of θ.

Cubic DS

[18] $$r = AR + B\sin^2\theta + C + 1/2(DR^2 + 2ER\sin^2\theta + F\sin^4\theta) + 1/6(GR^3 + 3HR^2\sin^2\theta + 3IR\sin^4\theta + J\sin^6\theta)$$

where *A*, *B*, *C*, *D*, *E*, *F*, *G*, *H*, *I*, and *J* are variational parameters. This DS is introduced here. It is designated $\sin^2\theta$ function in figures and tables to distiniguish it from the cubic function of powers of θ.

B. Expressions for the canonical rate constant

Expressions for the rate constant $[k^{TST}(T)]$ for the $F + H_2 \rightarrow FH + H$ reaction for the DS formulations of Sect. 2A are given below. To simplify our notation, the variational rate constant is henceforth designated $k(T)$. $V[r(\Omega, R, \theta), R, \theta]$ is the PEF for

© 1999 NRC Canada

configurations on the DS. The symmetry numbers σ_{H_2} and σ_* are both two (4). The integration over θ is from 0 to π/2; a factor of 2 is introduced to obtain the rate for reaction at both ends of the symmetrical H_2 reactant.

1. Dividing surface functions expressed using powers of R *and* θ
*Quadratic dividing surface (*θ *function)*

$$[19]\quad k(T) = 2(2\pi/\beta)^{1/2}[D^{c}_{HH}(T)]^{-1}\int_0^{\pi/2}\int_0^{R_{max}^{S=0}}[r(\Omega, R, \theta)R]^2 \sin\theta\, dR\, d\theta \times [\mu_{HH}{}^{-1}\{1+[(B+ER+F\theta)/r(\Omega, R, \theta)]^2\} + \mu_{F,HH}{}^{-1}(A+DR+E\theta)^2]^{1/2} \times \exp\{-\beta V[r(\Omega, R, \theta), R, \theta]\}$$

where *A*, *B*, *C*, *D*, *E*, and *F* are variational parameters.

*Cubic dividing surface (*θ *function)*

$$[20]\quad k(T) = 2(2\pi/\beta)^{1/2}[D^{c}_{HH}(T)]^{-1}\int_0^{\pi/2}\int_0^{R_{max}^{S=0}}[r(\Omega, R, \theta)R]^2 \sin\theta\, dR\, d\theta \times [\mu_{HH}{}^{-1}\{1+[(B+ER+F\theta+(1/2)(HR^2+2IR\theta+J\theta^2))/r(\Omega, R, \theta)]^2\} + \mu_{F,HH}{}^{-1}\{A+DR+E\theta + (1/2)(GR^2+2HR\theta+I\theta^2)\}^2]^{1/2} \times \exp\{-\beta V[r(\Omega, R, \theta), R, \theta]\}$$

where *A*, *B*, *C*, *D*, *E*, *F*, *G*, *H*, *I*, and *J* are variational parameters.

2. Dividing surface functions expressed using powers of R *and sin*^{2} θ
Quadratic dividing surface (sin^2 θ *function)*

$$[21]\quad k(T) = 2(2\pi/\beta)^{1/2}[D^{c}_{HH}(T)]^{-1}\int_0^{\pi/2}\int_0^{R_{max}^{S=0}}[r(\Omega, R, \theta)R]^2 \sin\theta\, dR\, d\theta \times [\mu_{HH}{}^{-1}\{1+[(B+ER+F\sin^2\theta)(2\sin\theta\cos\theta)/r(\Omega, R, \theta)]^2\} + \mu_{F,HH}{}^{-1}(A+DR+E\sin^2\theta)^2]^{1/2} \times \exp\{-\beta V[r(\Omega, R, \theta), R, \theta]\}$$

where *A*, *B*, *C*, *D*, *E*, and *F* are variational parameters.

Cubic dividing surface (sin^2 θ *function)*

$$[22]\quad k(T) = 2(2\pi/\beta)^{1/2}[D^{c}_{HH}(T)]^{-1}\int_0^{\pi/2}\int_0^{R_{max}^{S=0}}[r(\Omega, R, \theta)R]^2 \sin\theta\, dR\, d\theta \times [\mu_{HH}{}^{-1}\{1+[((B+ER+F\sin^2\theta)(2\sin\theta\cos\theta) + (\sin\theta\cos\theta)(HR^2+2IR\sin^2\theta+J\sin^4\theta))/r(\Omega, R, \theta)]^2\} + \mu_{F,HH}{}^{-1}\{A+DR+E\sin^2\theta + (1/2)(GR^2+2HR\sin^2\theta+I\sin^4\theta)\}^2]^{1/2} \times \exp\{-\beta V[r(\Omega, R, \theta), R, \theta]\}$$

where *A*, *B*, *C*, *D*, *E*, *F*, *G*, *H*, *I*, and *J* are variational parameters.

C. Expressions for the microcanonical mean reaction cross section

These expressions may be readily obtained using eqs. [11]–[13] and the DS functions of Sect. 2A. See also refs. 7 and 46.

D. Numerical methods and computational details

The searches performed to determine the 6 and 10 variational parameters of the second and third-order expansions of the DS were made using the downhill simplex algorithm (77–79). See refs. 45 and 46 for a description of the methods used to generate the initial vertices for the searches.

Variational calculations were performed on a VAX 6420 minicomputer. The integrals of functions $N_*^c(T)$ and $D^c_{BC}(T)$ were evaluated using Simpson's rule. The two-dimensional integral which gives $N_*^c(T)$ requires integration over *R* and θ. θ was integrated over the range 0–π/2; the resulting value of the integral was doubled to obtain the flux for reaction at both ends of the H_2 molecule. Appropriate limits for *R* were found by trial and error; the integration range for *R* was usually from 1 to 7 au. A grid of 280 (*R*) by 180 (θ) points was usually used to calculate $N_*^c(T)$. The quantity $D^c_{BC}(T)$ in the denominator of the expression for $k(T)$ was usually calculated using 500 points. The value used for r_{max}^{BC} was usually 7 au.

The simplex method can be readily applied with constraints on the parameter space which is searched. Because

© 1999 NRC Canada

Fig. 2. T2 potential-energy surface for θ = 0°. Contours are shown as solid lines for energies of –1.25, –0.75, –0.25, 0.0, 0.05, 0.10, 0.25, 0.5, 1.0, 2.0, 3.0, and 4.0 eV. Distances are in au. Broken curves show intersections of canonical dividing surfaces at 300 K with the (*r, R*) plane. Broken curves show cubic dividing surfaces obtained using different methods: linear θ expansion, slope-restriction variational DS (—); $\sin^2$ θ expansion, slope restriction variational DS (·····); linearθ expansion, steepest ascent DS (-----); $\sin^2$ θ expansion, steepest ascent DS (– – –).

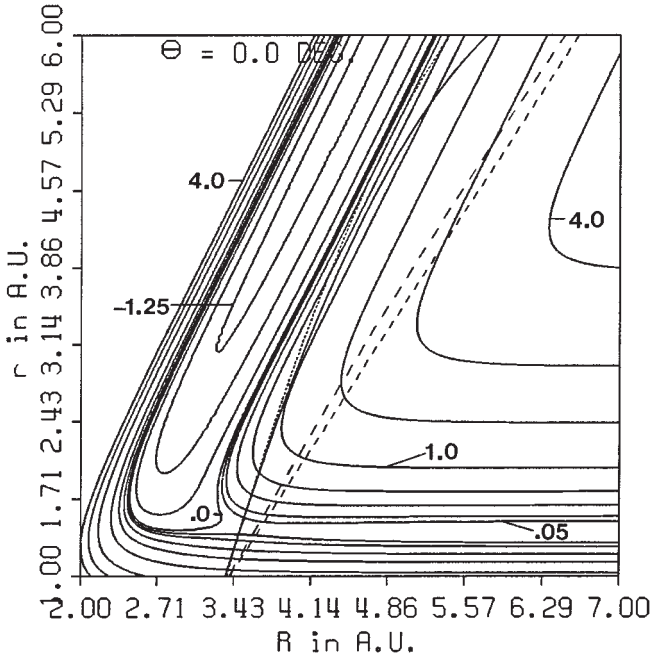

Fig. 3. Contours of canonical reactive flux density at 300 K through the cubic, $\sin^2$ θ function, slope-restriction dividing surface for T2 potential-energy function. Contours are shown for 10^{10}, 10^{11}, 10^{12}, and 10^{13} arbitrary units. The broken line *p* shows the path of angle-dependent saddle points.

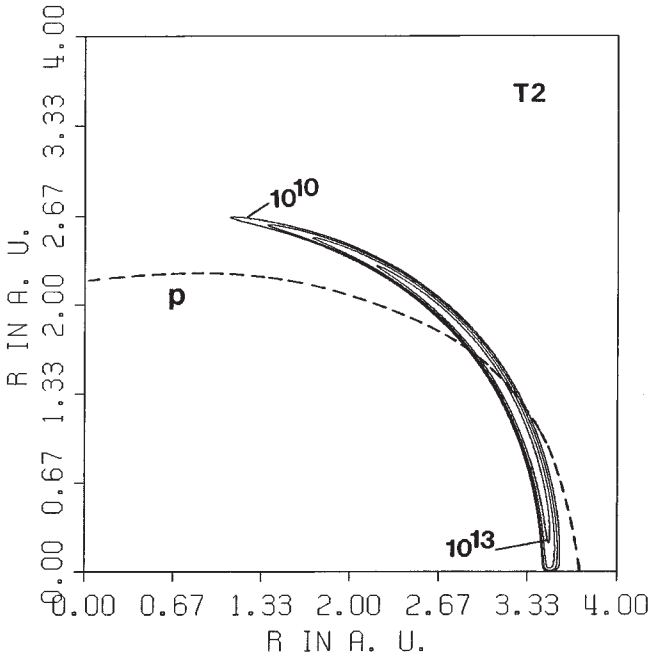

variational searches for quadratic and cubic functions can produce unusual results, restrictions are sometimes imposed on the parameters (see refs. 45 and 46). In the present work, some results are reported for the restrictions: $\partial r/\partial R > 0$ for $0 < \theta < \pi/2$ (denoted *S* for slope restriction) and $V(r^*, R, \theta) > 4.0$ eV at R_{max} where *V* is the potential energy on the DS (denoted *E* for energy limit restriction). Note that r^* is the value of *r* on the DS.

Note that the simplex search algorithm finds a local minimum, not the absolute minimum. Hence, many searches which started with different sets of trial parameters were often made in attempts to find the global minimum for a given DS and PEF.

E. Potential-energy functions

Variational calculations were performed for two PEFs developed by Truhlar et al. (49) designated by them as T1 and T2.

Plots of potential-energy contours for fixed θ in *r* and *R* coordinate space show a single saddle point and no basins for $0 \le \theta \le \pi/2$ for these PEFs. The energy at the saddle point varies with θ. The saddle point energy at θ is the minimum potential energy required for chemical reaction at θ.

The variation of *R* and *r* with θ for the T2 PEF is shown in Fig. 1. This figure shows why the PEFs used in this work present a challenge to the variational theory; the values of *R* and *r* at the angle-dependent saddle point vary markedly with θ. The DS must be flexible enough to span regions of configuration space near angle-dependent saddle points over the θ range where the reaction flux is large in order to minimize the variational rate.

4. Canonical results and discussion

Quadratic and cubic searches for linear θ and $\sin^2$ θ functions

Reactivity relief maps for the F + H_2 reaction for restricted and unrestricted searches showed that high reactive flux contours do not "follow" the path of angle-dependent saddle points over the entire range in θ. For example, the path of angle-dependent saddle points is shown as a broken line on the reactivity relief map for the T2 PEF at 300 K for the Q(*S*) DS in Fig. 6 of ref. 46. The maximum value of the variational flux lies on the small *R* side of the path of angle-dependent saddle points for $\theta \le 28°$ and on the large *R* side for $\theta > 28°$. The integrand of $N^{S}_{*}(T)$ contains the factor exp $\{-\beta V(r^*, R, \theta)\}$; hence, if potential energy alone determines the variational DS, the DS will pass through angle-dependent saddle points where the lowest potential energy on the DS for a specified θ has the highest value and follow the path of steepest ascent from the saddle points over the full range of θ. The maximum value of the flux may not follow the path of angle-dependent saddle points because the location of the variational DS is determined by entropic as well as energetic factors and (or) the formulation of the DS may not be flexible enough to follow the angle-dependent saddle points. We elected to learn whether the quadratic and cubic formulations of the DS used in our studies are capable

© 1999 NRC Canada

Table 1. Cubic canonical rate constants and variational parameters. Variational results for linear θ and $\sin^2$ θ formulations of the slope restriction (*S*) dividing surface for the T2 potential-energy function at 300 K and results for dividing surfaces determined by a least-squares fit of angle-dependent saddle points (SA fit).

	Variational parameters[a]					
	A	B	C	D	E	F
$k(T)$ cm^3/mol s × 10^{12}	(G)	(H)	(I)	(J)		
8.908	7.309 670	–2.663 466	–16.441 117	–1.358 521	0.136 348	0.105 112
(θ var. DS)	(0.089 795 8)	(0.294 703)	(1.424 943)	(0.039 938 2)		
13.67	1.586 843	3.075 645	–4.358 422	–0.004 448 63	–0.502 935	–0.014 727 1
(θ SA fit DS)	(–0.001 017 8)	(–0.001 147 3)	(–0.000 392 3)	(0.001 247 07)		
8.962	7.027 809	–0.245 490	–16.505 48	–1.124 055	0.021 366 2	–0.061 400 2
($\sin^2$ θ var. DS)	(0.034 338 6)	(0.210 295 9)	(1.485 553)	(1.487 029)		
11.80	2.121 372	5.247 149	–5.593 206	–0.103 556	–0.922 324	–0.075 352 4
($\sin^2$ θ SA fit DS)	(0.000 021 487)	(0.000 102 18)	(0.007 863 1)	(0.005 424)		

[a]DS type in parentheses.

Fig. 4. Contours of *r* for the dividing surface of Fig. 3. Contours for 1.0, 1.2, 1.4, 1.6, 1.8, and 2.0 au are shown.

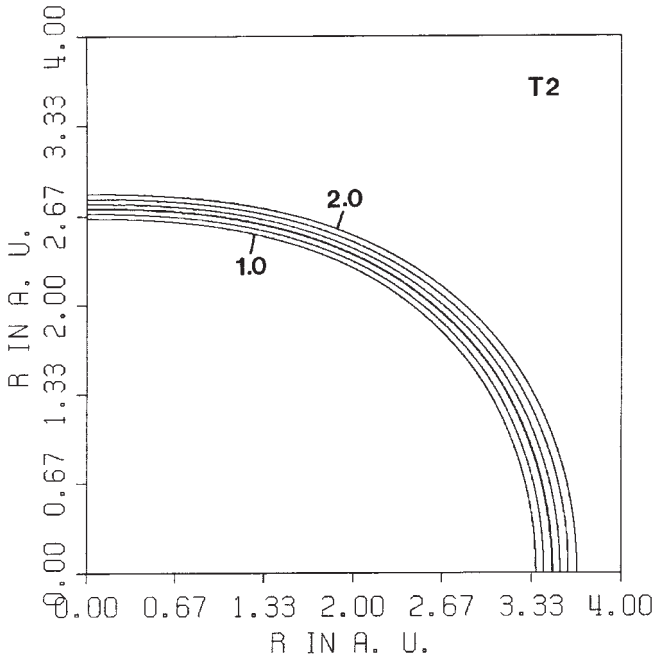

Fig. 5. Contours of canonical reactive flux density at 300 K through the cubic, $\sin^2$ θ function, steepest ascent dividing surface for the T2 potential-energy function. Contours are shown for 10^{10}, 10^{11}, 10^{12}, and 10^{13} arbitrary units. The broken line *p* shows the path of angle-dependent saddle points.

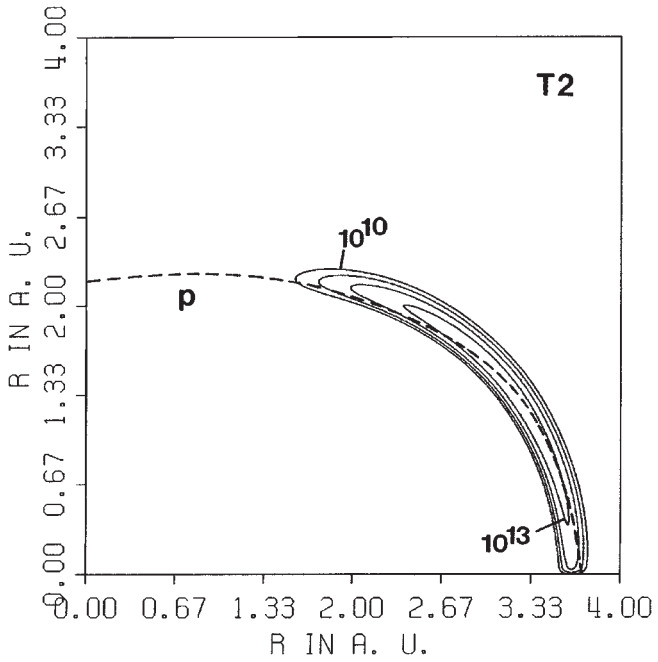

of following the paths of steepest ascent from angle-dependent saddle points.

We developed a least-squares method to find such a steepest ascent (SA) DS to compare with the variational DS. Potential-energy contour plots for the T2 PEF were made for a set of θ values. On each plot, a line was drawn through the saddle point which followed the path of steepest ascent from it. Points were read from the line and in this way sets of points were found at each θ which lie on the path of the steepest ascent. The downhill simplex algorithm together with a least-squares criterion was used to find the parameters of a quadratic DS (designated SA DS) which fits the points so generated, i.e., variational parameters were found which minimize the sum of the squares of the difference between the value of *r* for points determined as explained above and the value of *r* given by the SA DS function.

This work met with limited success. By assigning large weights for the fit at saddle points, we were able to find a least-squares SA DS which did a good job of passing close to saddle points over the full range in θ; however, this DS did not do a good job of following the path of steepest ascent from angle-dependent saddle points. We elected to examine an alternative quadratic DS in which θ is replaced with $\sin^2$ θ in the Q DS function. See Sect. 2.A.2. The partial derivative $(\partial r/\partial\theta)_\theta$ is zero at π/2 for this function; this requirement recognizes the symmetry of the F + H_2 interaction potential. Note that the partial derivative of the overlap parameter for HF with respect to θ is also zero at π/2 for the T2 PEF. See ref. 46. The alternative ($\sin^2$ θ) function gave a least-squares DS which did a marginally better job of pass-

© 1999 NRC Canada

Fig. 6. Contours of several variational theory functions for the T2 PEF: variational flux density for the linear θ C(*S*) DS at 300 K (10^{13} arbitrary units), *f* (·····); potential-energy contour for this DS at 0.15 eV, *V* (-----); and three contours of the configuration factor in arbitrary units, *c* (—). The path of angle-dependent saddle points is also shown, *P* (— - — -).

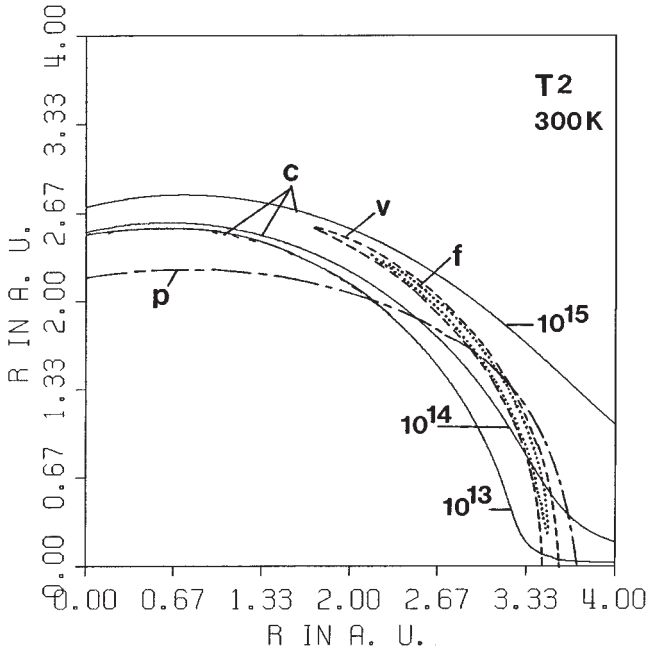

ing through the saddle points; nevertheless, the alternative quadratic DS did not do a good job of following the path of steepest ascent from the angle-dependent saddle points.

In our earlier study of the H + H_2 and H + I_2 reactions, we found that canonical rate constants calculated using the cubic expansion of the DS (C DS) were close in value to those obtained using the quadratic expansion, i.e., the improvement was negligible. We decided to learn whether this was also true for the F + H_2 reaction and also whether a least-squares SA DS obtained using the more flexible cubic function would do a better job of following the path of steepest ascent from angle-dependent saddle points.

Variational calculations were performed for both the usual (linear θ function) and alternative ($\sin^2$ θ function) formulations of the slope restriction cubic (C(*S*)) DS at 300 K. Rates were also calculated for the least squares SA DSs obtained using both the θ and $\sin^2$ θ cubic functions. Figure 2 shows the collinear potential-energy surface for the T2 PEF. Contours of the potential energy and intersections of four cubic DSs with the (*r*, *R*) plane are shown. Linear θ and $\sin^2$ θ slope restriction variational DSs for 300 K and linear θ and $\sin^2$ θ least-squares SA DSs are shown. The cubic variational and least squares SA parameters are given in Table 1.

The rate constants for the linear θ and $\sin^2$ θ C(*S*) DS at 300 K are 8.908 and 8.960 × 10^{12} cm^3 mol^{-1} s^{-1}, respectively. Figure 3 shows the reactivity relief map for the $\sin^2$ θ C(*S*) DS at 300 K. Figure 4 shows contours of *r* on the DS for the $\sin^2$ θ DS. The rate constants for the cubic DSs are nearly the same, and the reactivity relief maps are very similar; the contours for the highest flux can be superimposed to a good approximation. Contours for lower values of the flux

Table 2. Comparison of classical mechanical trajectory (CMT) and variational theory (VT) mean reaction cross sections ($\langle S_r(E)\rangle$).

		$\langle S_r(E)\rangle^{VT}$ (au)		
E (eV)	$\langle S_r(E)\rangle^{CMT}$ (au)	d*r*/d*R* > 0	Unrestricted	*E* limit
0.10	1.043 ± 0.057	1.249		1.215
0.25	5.62 ± 0.32	6.316	6.185	6.185
0.50	11.83 ± 0.33	13.109	12.956	12.956
0.75	15.82 ± 0.57	18.567	18.500	18.500
1.0	19.74 ± 0.45	23.397		23.362
1.5	25.49 ± 0.63	31.812		31.700

are tipped more toward the path of angle-dependent saddle points as θ increases for the cubic than for the quadratic DSs. The variation of the *r* contours with θ for the two cubic functions is very similar for values of θ where the contribution to the flux is large. The reactivity relief maps for the cubic DS functions closely resemble that for the Q(*S*) DS. The rate constant for the quadratic DS, 9.178 × 10^{12} cm^3 mol^{-1} s^{-1}, is only slightly larger than the values for the cubic DSs. For the F + H_2 reaction as well as others we have studied, rate constants for the quadratic DS are close to the converged value for a power series DS.

Figure 5 shows the reactivity relief map for the $\sin^2$ θ cubic SA DS at 300 K. The rate constants for the linear θ and $\sin^2$ θ SA DSs are 13.67 and 11.80 × 10^{12} cm^3 mol^{-1} s^{-1}, respectively. Although both SA DSs pass closer to the angle-dependent saddle points than the variational DSs, the rate constants are significantly larger than the variational values. Contours of the same value in reactivity relief maps span larger areas and are thicker in the direction of increasing *R* for SA than for variational DSs. Variational DSs follow the path of steepest ascent from points which are near angle-dependent saddle points better than least-squares SA DSs over the θ range where the reactive flux is large; consequently, the rates are significantly lower. Sets of simplex vertices based on SA DSs were used to initiate variational searches with and without restrictions on variational parameters. These searches converged to smaller variational rate constants and values of DS parameters which were found using other methods to generate initial vertices for simplex searches.

Figure 6 shows that the region of high flux on reactivity relief maps does not cross from the small to the large *R* side of the path of angle-dependent saddle points at intermediate θ because of an entropic effect. This figure shows results for the linear θ C(*S*) DS for the T2 PEF at 300 K. The contour for a large variational flux (marked *f*) is shown with a potential-energy contour for 0.15 eV (marked *v*). Three contours of the configuration factor (marked *c*) of the integrand for $N_*^c(T)$ are also shown.

$$[23] \quad c = \sin\theta\, r(\Omega, R, \theta)^2 R^2 \times [\mu_{BC}^{-1}\{1 + [F_\theta(R,\theta)/r(\Omega,R,\theta)]^2\} + \mu_{A,BC}^{-1} F_R(R,\theta)^2]^{1/2}$$

See eqs. [8] and [9]. This factor excludes only the potential-energy factor exp {$-\beta V(r^*, R, \theta)$}. The path of the angle-dependent saddle points is also shown. The minimum poten-

© 1999 NRC Canada

Fig. 7. T1 potential-energy surface for θ = 30°. Contours are in eV relative to F + H_2 at infinite separation. Contours are shown as solid lines for energies of –1.0, –0.75, –0.5, –0.25, 0.0, 0.05, 0.10, 0.15, 0.20, 0.25, 0.5, 0.75, 1.0, 1.25, 1.5, 2.0, and 2.5 eV. Distances are in au. Solid curves show intersections of microcanonical unrestricted (*E*) dividing surfaces at energies 0.1, 0.15, 0.25, 0.5, 0.75, 1.0, and 1.5 eV with the (*r, R*) plane. The broken curve shows the cubic slope-restriction dividing surface.

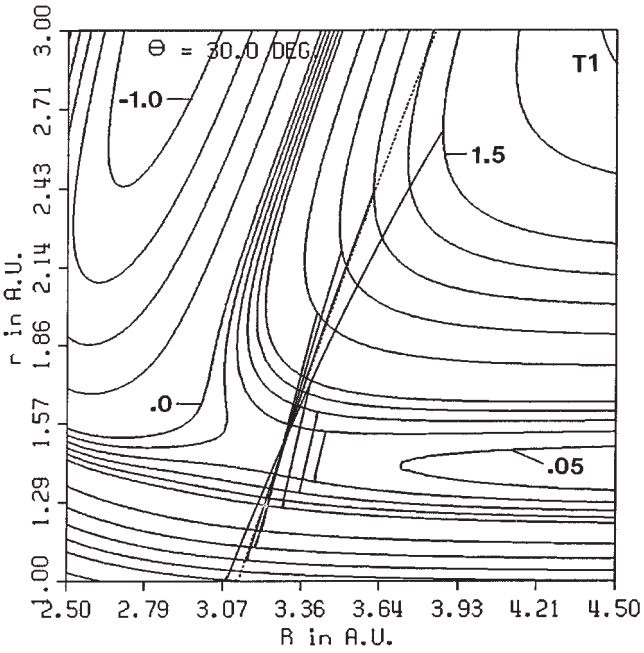

tial energy lies within the 0.15 eV contour; and this minimum corresponds to a good approximation to the maximum of the variational flux. It is the potential-energy factor, not the entropic (configuration) factor, which is responsible for the location of the large flux region on the DS.

We conclude that the large flux region crosses the path of angle-dependent saddle points because the DS can not pass through the angle-dependent saddle points over the entire range in θ where the flux is large and take the path of steepest ascent from them. The variational DS passes from the small *R* side of the saddle point path to the large *R* side as θ increases to stay as close to the saddle points and the path of steepest ascent as possible over the θ range where the flux is large.

It is possible that another DS function exists which does a better job of following the path of steepest ascent from angle-dependent saddle points over the full range of θ, yields rate constants which are significantly lower than values for the quadratic and cubic linear θ and $\sin^2\theta$ DS functions, and gives reactivity relief maps with high flux contours which follow angle-dependent saddle points more closely than the functions studied here. This possibility could be investigated by formulating more DS functions and studying them as we did with the $\sin^2\theta$ DS function. We chose instead to address this point by comparing variational and classical mechanical trajectory results for the Q DS functions used in our earlier studies (45, 46). If variational rate constants, energy-dependent mean reaction cross sections, and angular distributions of reactivity are in good agreement with Monte Carlo trajectory results for the Q linear θ DS, then these DSs are flexible enough to give accurate rate constants and mean reaction cross sections and provide an accurate description of the dynamical stereochemistry of the F + H_2 reaction.

5. Accuracy of variational results

A. Comparison of variational and classical mechanical trajectory mean reaction cross sections

The accuracy of the classical variational theory was studied by comparing values of the energy-dependent mean reaction cross section with classical mechanical trajectory values. Quadratic rather than cubic formulations of the DS were used because of the small cubic versus quadratic gain in accuracy and the relative ease of a quadratic variational search. Calculations were performed for the T1 PEF. The accuracy of the variational theory was determined by comparing variational and trajectory mean reaction cross sections rather than rate constants because the former could be calculated with a much smaller error than the latter in Monte Carlo calculations of the same number of trajectories. The accuracy of the variational theory was also studied by comparing angular distributions of contributions to the energy-dependent mean reaction cross section with corresponding trajectory distributions.

Variational values of the mean reaction cross section were calculated for the slope (*S*) restriction, energy limit (*E*) restriction, and unrestricted (*N*) quadratic DSs for energies of 0.1, 0.25, 0.5, 0.75, 1.0, and 1.5 eV using eq. [11]. The results are compared with classical trajectory values in Table 2. Note that the energy limit and unrestricted values of the mean reaction cross section are the same. The energy limit used was not 4.0 eV, the value used for the canonical calculations, but rather the energy of the microcanonical ensemble. This restriction is easy to satisfy; three variational searches performed with this restriction converged to results obtained for unrestricted searches. We therefore refer to the energy limit results of Table 2 as unrestricted in the text which follows. The value of R_{max} used in the microcanonical calculations was the same as that used for canonical calculations, i.e., 7 au. Values of the mean reaction cross section calculated using the slope restriction are slightly larger than the unrestricted values as expected. The errors cited for the trajectory results correspond to a confidence level of 68%. The difference between the unrestricted variational and trajectory mean reaction cross sections increases with energy as expected; however, the difference at 1.0 and 1.5 eV amounts to only 18 and 25%, respectively. These energies are very high in the sense that the probability that reaction systems have these energies at temperatures commonly used in the study of gas phase reactions is extremely small. Figure 7 shows potential-energy contours for the T1 PEF at orientation angle 30°. The intersections of microcanonical unrestricted quadratic DSs for the energies cited above with the (*r, R*) plane are also shown.

B. Conversion, transmission, and product correction factors

The difference between variational theory ($\langle S_r(E)\rangle^{VT}$) and classical mechanical trajectory ($\langle S_r(E)\rangle^{CMT}$) values can be ex-

© 1999 NRC Canada

Table 3. Classical mechanical trajectory (CMT) results.

E (eV)	b_{max} (au)	Number of traj.	$\langle S_r \rangle^{CMT}$ (au)	$\langle S_{R\ddagger} \rangle^{CMT}$ (au)	κ	ρ	χ
0.10	3.0	24 000	1.043 ± 0.057	1.065 ± 0.058	0.979 ± 0.070	0.877 ± 0.047	0.858 ± 0.047
0.25	4.0	6000	5.62 ± 0.32				0.909
0.50	4.5	18 000	11.83 ± 0.33	12.35 ± 0.34	0.958 ± 0.031	0.953 ± 0.026	0.913 ± 0.025
0.75	4.5	6000	15.82 ± 0.57				0.855
1.0	4.5	18 000	19.74 ± 0.45	21.44 ± 0.48	0.921 ± 0.021	0.918 ± 0.020	0.845 ± 0.019
1.5	5.0	12 000	25.49 ± 0.63	27.74 ± 0.67	0.919 ± 0.024	0.875 ± 0.021	0.804 ± 0.020

Fig. 8. Differential mean reaction cross section for quadratic unrestricted DS versus orientation angle for energy 1.0 eV.

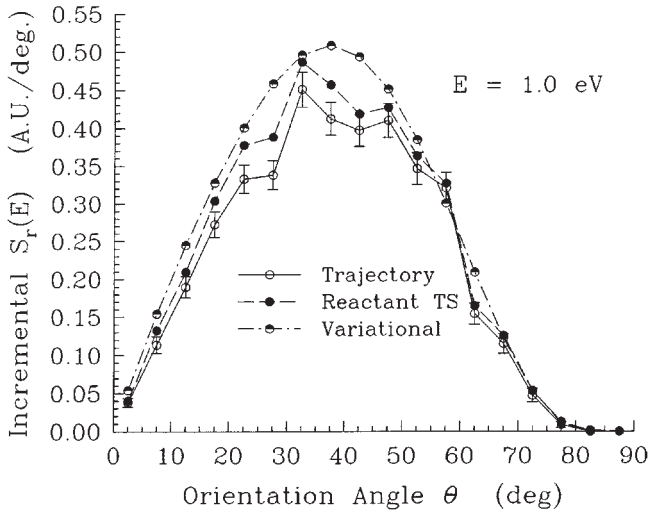

Fig. 9. Average transmission, product, and conversion coefficient versus θ for energy 0.1 eV.

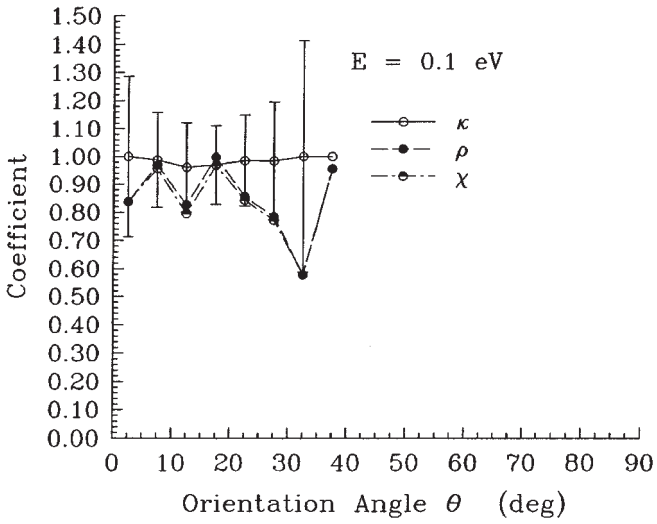

pressed as a fraction ($\chi(E)$) which is referred to as the conversion coefficient (67).

$$[24] \quad \chi(E) = \frac{\langle S_r(E) \rangle^{CMT}}{\langle S_r(E) \rangle^{VT}}$$

The correction factor $\chi(E)$ may be applied to the variational mean reaction cross section to obtain the trajectory mean reaction cross section, i.e., the actual value of this quantity.

Fig. 10. Same as Fig. 9 for energy 0.5 eV.

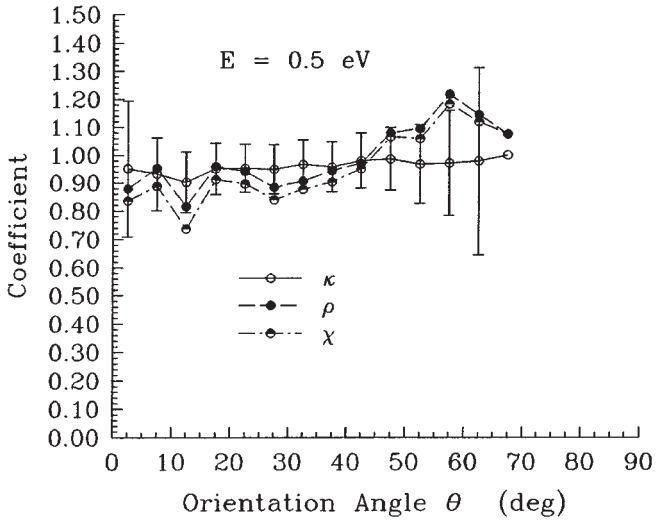

Fig. 11. Same as Fig. 9 for energy 1.0 eV.

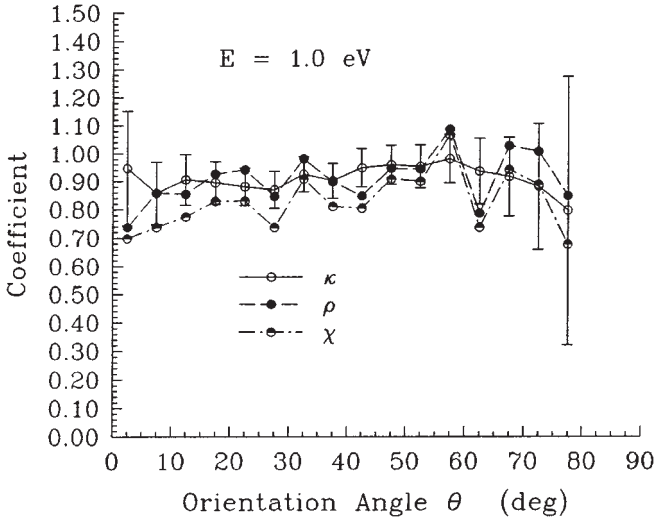

We further describe the difference between variational and trajectory values of the mean reaction cross section by expressing the conversion coefficient as the product of two factors, the transmission coefficient ($\kappa(E)$) and product coefficient ($\rho(E)$):

$$[25] \quad \chi(E) = \kappa(E)\rho(E)$$

where these factors are defined by

$$[26] \quad \kappa(E) = \frac{\langle S_r(E) \rangle^{CMT}}{\langle S_r(E) \rangle^{R\ddagger}}$$

© 1999 NRC Canada

Table 4. Microcanonical optimization of the canonical rate constant.

	Temperature (K)		
	300	900	1500
Variational rate constant for Q(S) linear θ DS in units of 10^{12} cm^3 mol^{-1} s^{-1}	5.021	44.07	93.78
Rate constant calculated using microcanonical variational parameters (Q(N) linear θ DS)	4.813	42.52	91.72
Rate constant ratio	0.958	0.965	0.978
Variational rate constant for C(S) linear θ DS			93.77

Fig. 12. Variational mean reaction cross section for the quadratic unrestricted (E) dividing surface versus energy (solid curve). The broken curve shows the energy dependent integrand for the canonical rate constant at 1500 K in arbitrary units.

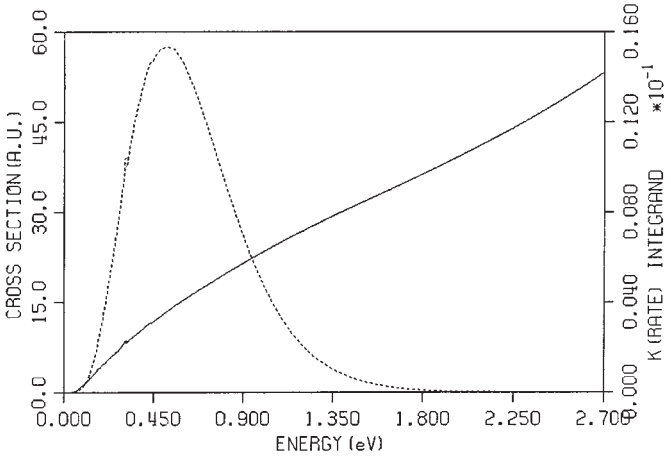

and

$$[27] \qquad \rho(E) = \frac{\langle S_r(E)\rangle^{R\ddagger}}{\langle S_r(E)\rangle^{VT}}$$

The quantity $\langle S_r(E)\rangle^{R\ddagger}$ is defined below.

Many chemists believe that a correction, the transmission coefficient, must be applied to transition state theory because some trajectories which originate in the reactant region cross the DS and subsequently recross it and return to the reactant region. The quantity $\langle S_r(E)\rangle^{R\ddagger}$ is the energy-dependent mean reaction cross section for all reaction systems on the DS that correspond to trajectories which originate in the reactant region and are moving toward products at the DS, regardless of whether the reaction system ultimately reaches the product region. All crossings of the DS from the reactant to the product side which correspond to trajectories which originate in the reactant region contribute to $\langle S_r(E)\rangle^{R\ddagger}$. The factor $\kappa(E)$ provides a correction for multiple crossings of the DS by trajectories which originate in the reactant region. This factor corrects for trajectories which are reflected after crossing the DS and return to the reactant region and for trajectories which are ultimately reactive but cross and recross the DS an odd number of times on their way to the product region.

Another factor, the product factor ($\rho(E)$), must be applied to correct the variational value of the mean reaction cross section. Transition state theory must also be corrected because trajectories which originate in the product region, which are present in the equilibrium flux of reaction systems through DS, can cross and recross the DS and contribute (incorrectly) to the reaction rate, i.e., $k(T)$ and $\langle S_r(E)\rangle^{VT}$ should correspond to the rate of reaction in the absence of products. Hence, the variational theory must also be corrected by applying the factor $\rho(E)$. Note that the product factor is unity if trajectories which originate in the product region do not contribute to the variational flux.

Trajectory and variational results for the unrestricted quadratic DS are summarized in Table 3. The quantity $\langle S_r(E)\rangle^{R\ddagger}$ is determined by calculating the function that defines configurations on the DS ($r - F(R, \theta) - C = 0$) for each time step of each trajectory to detect crossings of the DS by trajectories which contribute to this quantity. The values of the coefficients are given in Table 3. Note that the deviation between variational and trajectory values of the mean reaction cross section at the lowest energy (0.1 eV) caused by trajectories that start in the reactant region and cross the DS more than once appears to be smaller than the deviation caused by trajectories that originate in the product region, i.e., $\kappa(E) > \rho(E)$ for this energy, although there is some overlap of the error ranges. For the energies from 0.5 to 1.5 eV, $\kappa(E)$ is equal to $\rho(E)$ within numerical error for 68% confidence.

C. Accuracy of the no-recrossing approximation of transition state theory

The accuracy of the no-recrossing assumption of transition state theory for collinear atom–diatom reactions has been the subject of many studies (42, 71, 80–85). The application of a DS formulation which includes terms in θ makes it possible to determine how the accuracy of the no-recrossing assumption depends on the orientation angle. One way to do this is illustrated in Fig. 8. This figure shows a plot of both variational and trajectory differential mean reaction cross sections versus θ for energy 1.0 eV. The variational distributions correspond to the Q(N) DS. The results labeled "reactant ‡" correspond to all reaction systems on the DS for trajectories which originate in the reactant region and are moving toward the products at the DS. Alternately, the 5° increments for the mean reaction cross sections $\langle S_r(E)\rangle^{CMT}$, $\langle S_r(E)\rangle^{R\ddagger}$, and $\langle S_r(E)\rangle^{VT}$ and eqs. [25]–[27] may be used to calculate average values of $\kappa(E)$, $\rho(E)$, and $\chi(E)$ for each 5° range of θ. Figures 9–11 show average values of these coefficients versus θ for energies of 0.1, 0.5, and 1.0 eV. For collinear atom–diatom reactions, the correction factors decline more rapidly with increasing energy than for reaction in three-dimensional space. On this basis, one expects deviations from the variational flux to be skewed toward low values of θ. This does not appear to be the case at the lowest energy studied but the overall coefficent χ does appear to show an increasing trend for the energies 0.5 and 1.0 eV. Figure 9 shows that at 0.1 eV the deviation from the variational flux is due more to trajectories which originate in the product region and cross and recross the DS than from those which originate in the reactant region ($\rho < \kappa$) and that

© 1999 NRC Canada

this holds over the entire range of the orientation angle. At the energies 0.5 and 1.0 eV, deviations from the variational flux are due as much to trajectories which originate in the product region and contribute incorrectly to the rate as the reactant region, i.e., $\kappa \simeq \rho$ over the entire range of θ. Finally, although the overall coefficient χ does not show marked variation with θ at any of the energies studied, the failure of the no-recrossing assumption is most significant at intermediate values of θ because the variational flux peaks here.

D. Calculation of the canonical rate constant using energy-dependent mean reaction cross sections

Variational parameters for 13 energy-dependent Q(*N*) DSs at energies of 0.1, 0.125, 0.15, 0.20, 0.25, 0.375, 0.5, 0.625, 0.75, 0.875, 1.0, 1.25, and 1.5 eV were used to calculate the canonical rate constant at temperatures 300, 900, and 1500 K. The DSs at energies of 0.1, 0.15, 0.25, 0.5, 0.75, 1.0, and 1.5 eV are plotted on the potential-energy contour map for 30° in Fig. 7. Energy-dependent mean reaction cross sections were calculated for a range of energies centered on each of the values cited above using an increment of 0.001 eV. The rate constant was calculated using simple quadrature with an energy increment of 0.001 eV to evaluate the integral of eq. [14]. Figure 12 shows the variational mean reaction cross section calculated using the 13 sets of variational parameters and the integrand of the integral of eq. [14] at 1500 K versus energy. The maximum value of the integrand occurs at 0.5 eV. In Table 4, canonical variational rate constants for the Q(*S*) DS at 300, 900, and 1500 K are compared with values calculated using the 13 sets of Q(*N*) energy-dependent variational parameters described above. The improvement obtained by microcanonical optimization is small; the ratios of the microcanonical variational and canonical variational values of the canonical rate constant at 300, 900, and 1500 K are 0.958, 0.965, and 0.978, respectively. The effect of microcanonical optimization decreases with increasing temperature.

Concluding remarks

The general variational theory of chemical reaction rates will help chemists understand transition state theory in a new and richer way. If a chemist is asked to identify the transition state for a collinear reaction on a plot of potential-energy surface, he or she will probably point to the saddle point. A more informed chemist will draw a line or curve through the saddle point that follows the path of steepest ascent from it. A still more informed chemist will draw a curve that misses the saddle point and corresponds to a periodic orbit dividing surface. A variational DS defines a generalized transition state. A generalized variational DS for an atom–diatom reaction in three-dimensional space that depends on the orientation angle provides a description of the dynamical stereochemistry of the reaction. The reactivity relief map shows how the reactive flux through the DS depends upon the location on it. Reactivity relief maps can also be used to show how the field of reactivity that surrounds the reactant expands with increasing temperature and energy. Finally, reactivity relief maps can be used to show how the field of reactivity that surrounds a reactant depends on the identity of the attacking atom and how the field depends on the identity of the diatomic reactant for the same attacking atom. There is more work to be done.

Acknowledgements

This work was supported by grants from the PSC-BHE Research Award Program of the City University of New York.

References

1. H. Pelzer and E. Wigner. Z. Physik. Chem. B, **15**, 445 (1932).
2. J. Horiuti. Bull. Chem. Soc. Jpn. **13**, 210 (1938).
3. J.C. Keck. J. Chem. Phys. **29**, 410 (1958); **32**, 1035 (1960).
4. J.C. Keck. Adv. Chem. Phys. **13**, 85 (1967).
5. R.A. Marcus. J. Chem. Phys. **41**, 2614 (1964); **41**, 2624 (1964); **43**, 1598 (1965).
6. G.W. Koeppl. J. Am. Chem. Soc. **96**, 6539 (1974); D.I. Sverdlik and G.W. Koeppl. Chem. Phys. Lett. **59**, 449 (1978); G.P. Stein. Ph.D. dissertation, The City University of New York, New York. 1977; I. Rutenburg. Ph.D. dissertation, The City University of New York, New York. 1995.
7. G.W. Koeppl. J. Chem. Phys. **87**, 5746 (1987).
8. P. Pechukas. *In* Dynamics of molecular collisions. Part B. Edited by W.H. Miller. Plenum, New York. 1976. p. 239.
9. P. Pechukas. Ann. Rev. Phys. Chem. **32**, 159 (1981).
10. P. Pechukas. Ber. Bunsenges. Phys. Chem. **86**, 372 (1982).
11. E. Pollak. *In* The theory of chemical reaction dynamics. *Edited by* M. Baer. Chemical Rubber, Boca Raton, Fla. 1984.
12. D.G. Truhlar, W.L. Hase, and J.T. Hynes. J. Phys. Chem. **87**, 2664 (1983).
13. D.G. Truhlar and B.C. Garrett. Ann. Rev. Phys. Chem. **35**, 159 (1984).
14. D.G. Truhlar, A.D. Isaacson, and B.C. Garrett. *In* The theory of chemical reaction dynamics. *Edited by* M. Baer. Chemical Rubber, Boca Raton, Fla. 1984.
15. W.J. Chesnavich and M.T. Bowers. *In* Gas-phase ion chemistry. *Edited by* M.T. Bowers, Academic, New York. 1979. p. 119.
16. W.J. Chesnavitch and M.T. Bowers. Prog. React. Kinet. **11**, 137 (1982).
17. R.B. Walker and J.C. Light. Ann. Rev. Phys. Chem. **31**, 401 (1980).
18. M. Menendez, L. Banares, J. Alonso, and G. Urena. Chem. Phys. **120**, 273 (1988).
19. R.D. Levine. Chem. Phys. Lett. **175**, 331 (1990).
20. D.G. Truhlar and B.C. Garrett. J. Phys. Chem. **96**, 6515 (1992).
21. R.J. Frost and I.W.M. Smith. J. Chem. Soc. Faraday Trans. **84**, 1825 (1988).
22. G.A. Voth, D. Chandler, and W.H. Miller. J. Chem. Phys. **91**, 7749 (1989).
23. R. Hernandez and W.H. Miller. Chem. Phys. Lett. **214**, 129 (1993).
24. W.H. Miller. Acc. Chem. Res. **26**, 174 (1993).
25. E. Pollak and D. Proselkov. Chem. Phys. **170**, 265 (1993).
26. W.H. Miller. Ber. Bunsenges. Phys. Chem. **95**, 389 (1991).
27. S.H. Robertson, A.F. Wagner, and D.M. Wardlaw. J. Chem. Phys. **103**, 2917 (1995).
28. S.C. Smith. J. Phys. Chem. **98**, 6496 (1994).
29. D.G. Truhlar, Y.P. Liu, G.K. Schenter, and B.C. Garrett. J. Phys. Chem. **98**, 8396 (1994).
30. K.F. Lim and R.I. Kier. J. Chem. Phys. **97**, 1072 (1992).
31. N.F. Hansen and H.C. Andersen. J. Chem. Phys. **101**, 6032 (1994).
32. G.K. Shenter, G. Mills, and H. Jonsson. J. Chem. Phys. **101**, 8964 (1994).

© 1999 NRC Canada

33. N.F. Hansen and H.C. Andersen. J. Phys. Chem. **100**, 1137 (1996).
34. J.G. Muga, V. Delgado, R. Sala, and R.F. Snider. J. Chem. Phys. **104**, 7015 (1996).
35. D.H. Zhang and J.C. Light. J. Chem. Phys. **104**, 6184 (1996).
36. H. Eyring. J. Chem. Phys. **3**, 107 (1935).
37. S. Glasstone, K.J. Laidler, and H. Eyring. Theory of rate processes. McGraw–Hill, New York. 1941.
38. M.C. Evans and M. Polanyi. Trans. Faraday Soc. **31**, 875 (1935).
39. G.W. Koeppl. J. Am. Chem. Soc. **96**, 6539 (1974).
40. P. Pechukas and F.J. McLafferty. J. Chem. Phys. **58**, 1622 (1973).
41. K. Morokuma and M. Karplus. J. Chem. Phys. **55**, 63 (1971).
42. G.W. Koeppl and M. Karplus. J. Chem. Phys. **55**, 4667 (1971).
43. J.O. Hirschfelder. Int. J. Quant. Chem. IIIS, 17 (1969).
44. D.L. Martin and L.M. Raff. J. Chem. Phys. **77**, 1235 (1982).
45. D.I. Sverdlik and G.W. Koeppl. J. Chem. Phys. **91**, 250 (1989).
46. I. Rutenburg and G.W. Koeppl. J. Chem. Phys. **110**, 3842 (1999).
47. C.F. Bender, B.J. Garrison, and H.F. Schaefer. J. Chem. Phys. **62**, 1188 (1975).
48. M.J. Frisch, B. Liu, J.S. Binkley, H.J. Schaefer, and W.H. Miller. Chem. Phys. Lett. **114**, 1 (1985).
49. D.G. Truhlar, B.C. Garrett, and N.C. Blais. J. Chem. Phys. **80**, 232 (1984).
50. D.W. Schwenke, R. Stekler, F.B. Brown, and D.G. Truhlar. J. Chem. Phys. **84**, 5706 (1986).
51. F. Brown, R. Stekler, D.W. Schwenke, D.G. Truhlar, and B.C. Garrett. J. Chem. Phys. **82**, 188 (1985).
52. R. Stekler, D.G. Truhlar, and B.C. Garrett. J. Chem. Phys. **82**, 5499 (1985).
53. C.W. Bauschlicher, Jr., S.P. Walch, S.R. Langhoff, P.R. Taylor, and R.L. Jaffe. J. Chem. Phys. **88**, 1743 (1988).
54. G.C. Lynch, R. Stekler, D.W. Schwenke, A.J.C. Varandas, D.G. Truhlar, and B.C. Garrett. J. Chem. Phys. **94**, 7136 (1991).
55. T. Takayanagi and S. Sato. Chem. Phys. Lett. **144**, 191 (1988).
56. D.W. Schwenke. Chem. Phys. Lett. **213**, 10 (1993).
57. K. Stark and H.-J. Werner. J. Chem. Phys. **104**, 6515 (1996).
58. S.L. Mielke, G.C. Lynch, D.G. Truhlar, and D.W. Schwenke. Chem. Phys. Lett. **213**, 10 (1993).
59. J.T. Muckerman. J. Chem. Phys. **54**, 1155 (1971).
60. I. Schecter, R.D. Levine, and R.B. Bernstein. J. Phys. Chem. **91**, 5466 (1987).
61. I. Schecter, M.G. Prisant, and R.D. Levine. J. Phys. Chem. **91**, 5472 (1987).
62. J.N.L. Connor, J.C. Whitehead, and W. Jakubetz. J. Chem. Soc. Faraday Trans. **83**, 1703 (1987).
63. J.N.L. Connor and W. Jakubetz. J. Chem. Soc. Faraday Trans. **89**, 1481 (1993).
64. W.H. Miller. J. Chem. Phys. **61**, 1823 (1974).
65. B.C. Garrett and D.G. Truhlar. J. Chem. Phys. **70**, 1593 (1979).
66. W.H. Miller. J. Chem. Phys. **65**, 2216 (1976); Acc. Chem. Res. **9**, 306 (1976).
67. J.B. Anderson. J. Chem. Phys. **58**, 4684 (1973); **60**, 2566 (1974); **67**, 2446 (1975).
68. E. Pollak and P. Pechukas. J. Am. Chem. Soc. **100**, 2984 (1978).
69. D.R. Coulson. J. Am. Chem. Soc. **100**, 2992 (1978).
70. R.N. Porter, D.L. Thompson, L.M. Raff, and J.M. White. J. Chem. Phys. **62**, 2429 (1975).
71. B.C. Garrett and D.G. Truhlar. J. Phys. Chem. **83**, 1052 (1979).
72. M.A. Eliason and J.O. Hirschfelder. J. Chem. Phys. **30**, 1426 (1959).
73. J. Ross and P. Mazur. J. Chem. Phys. **35**, 19 (1961).
74. M. Karplus, R.N. Porter, and R.D. Sharma. J. Chem. Phys. **43**, 3259 (1965).
75. L.A. Pipes. Applied mathematics for engineers and physicists. McGraw–Hill, New York. 1946.
76. K. Morokuma, B.C. Eu, and M. Karplus. J. Chem. Phys. **51**, 5193 (1969).
77. W. Spendley, G.R. Hext, and F.R. Himsworth. Technometrics, **4**, 441 (1962).
78. J.A. Nelder and R. Mead. Computer J. **7**, 308 (1965).
79. W.H. Press, B.P. Flannery, S.A. Tevkolsky, and W.T. Vetterling. Numerical recipes. Cambridge University Press, Cambridge. 1986.
80. E. Pollak and P. Pechukas. J. Chem. Phys. **69**, 1218 (1978).
81. D.I. Sverdlik, G.P. Stein, and G.W. Koeppl. Chem. Phys. Lett. **67**, 87 (1979).
82. G.P. Stein. Ph.D. dissertation. The City University of New York, New York. 1977.
83. B.C. Garett and D.G. Truhlar. J. Am. Chem. Soc. **101**, 4534 (1979).
84. B.C. Garett, D.G. Truhlar, and R.S. Grev. J. Phys. Chem. **85**, 1569 (1981).
85. W.J. Chesnavich. Chem. Phys. Lett. **53**, 300 (1978).

© 1999 NRC Canada

Styrene hydration and stilbene isomerization in strong acid media. An excess acidity analysis[1]

Robin A. Cox

Abstract: Rate constants obtained for the hydration of some ring-substituted styrenes, $YC_6H_4CR{=}CH_2$ (R = H, CH_3, CF_3) (**1**–**3**), and for the isomerization of some *cis*-stilbenes substituted in both rings, $YC_6H_4CH{=}CHC_6H_4Z$ (**4**), in aqueous H_2SO_4, D_2SO_4, and $HClO_4$ media at 25°C and, in some cases, at other temperatures, have been subjected to an excess acidity analysis. Data obtained by different groups and in different media for the same substrates agree very well. The $m^{\ddagger}$ values obtained show that all the substrates react via the A-S_E2 mechanism, rate-determining proton transfer to carbon; the transition state is late, with the proton transfer being about three-quarters complete. The reactivities of **1**–**3** in the aqueous standard state are obtained by extrapolation; they are $1{:}10^3{:}10^{-7}$, respectively. The stilbenes are relatively unreactive; log k_0 values for compounds with substituents in the ring adjacent to the developing positive charge show a good correlation with σ^+ with a large negative ρ^+ value, but those for compounds with substituents in the other ring correlate with σ with a small negative ρ. Extrapolated log k_0 values for **1** and **3** show a good correlation with σ^+, but those for **2** correlate with neither σ^+ nor σ, because the α-CH_3 group twists the molecule and reduces the resonance interaction of ring substituents with the developing positive charge. On the other hand, this effect is not seen in **3**, when the strongly deactivating α-CF_3 group is present, meaning that the transition state is forced to be planar in this case. The activation parameters, solvent isotope effects, and excess acidity slope parameters $m^{\ddagger}m^*$ obtained in the analysis are tabulated and discussed. The parameters obtained for the parent styrenes **1** are very similar to those previously obtained for the phenylacetylenes $YC_6H_4C{\equiv}CH$, meaning that reactions with vinyl cation intermediates and reactions with benzyl cation intermediates can be quite similar.

Key words: styrenes, stilbenes, hydration, excess acidity, LFER, mechanism.

Résumé : Opérant à 25°C (et, dans quelques cas, à d'autres températures), dans des solutions aqueuses de H_2SO_4, D_2SO_4 et $HClO_4$, on a mesuré les constantes de vitesse de réaction pour l'hydratation de styrènes substitués sur le noyau, $YC_6H_4CR{=}CH_2$ (R = H, CH_3, CF_3) (**1**–**3**) et pour l'isomérisation de quelques *cis*-stilbènes substitués sur chacun des noyaux, $YC_6H_4CH{=}CHC_6H_4Z$ (**4**) et on a soumis ces valeurs à une analyse par d'acidité en excès. Les données obtenues par divers groupes et dans divers milieux pour la même substance sont généralement en bon accord. Les valeurs obtenues pour $m^{\ddagger}$ montrent que tous les substrats réagissent par le biais d'un mécanisme A-S_E2 impliquant un transfert de proton vers le carbone dans l'étape cinétiquement déterminante. Les réactivités des composés **1**–**3** dans l'état aqueux standard ont été obtenues par extrapolation; elles sont respectivement égales à $1{:}10^3{:}10^{-7}$. Les stilbènes sont relativement peu réactifs; les valeurs de log k_0 pour les composés portant des substituants sur le noyau adjacent à la charge positive qui se développe donnent une bonne corrélation avec σ^+, avec une valeur négative élevée pour ρ^+; toutefois, pour les composés portant des substituants sur l'autre cycle, la corrélation se fait avec σ et la valeur de ρ est négative et faible. Les valeurs extrapolées du log k_0 des composés **1** et **3** présentent une bonne corrélation avec σ^+, mais celles extrapolées pour le composé **2** ne donnent pas de corrélation soit avec σ soit avec σ^+ en raison du fait que le groupe CH_3 déforme la molécule et réduit l'interaction de résonance des substituants du noyau avec la charge positive qui se développe. Toutefois, on n'observe pas cet effet avec le composé **3** qui comporte le groupement CF_3 fortement désactivant; ce résultat implique que, dans ce cas, une structure planaire est imposée à l'état de transition. On présente les paramètres d'activation, les effets isotopiques du solvant ainsi que les paramètres ($m^{\ddagger}m^*$) relatifs à la pente de l'excès d'activité sous forme de tableau et on les discute. Les paramètres obtenus pour les styrènes parents (**1**) sont très semblables à ceux obtenus antérieurement pour les phénylacétylènes, $YC_6H_4C{\equiv}CH$; ceci signifie que les réactions impliquant des intermédiaires vinylcationiques et celles impliquant des intermédiaires benzylcationiques peuvent être très semblables.

Mots clés : styrènes, stilbènes, hydratation, acidité en excès, « LFER », mécanisme.

[Traduit par la Rédaction]

Received November 12, 1998.

This paper is dedicated to Professor Jerry Kresge in recognition of his major contributions to physical organic chemistry.

R.A. Cox.[2] Department of Chemistry, University of Toronto, 80 St. George St., Toronto, ON M5S 3H6, Canada.

[1]Mechanistic studies in strong acids, part 25; parts 23 and 24 are refs. 25 and 20, respectively.

[2]Author to whom correspondence may be addressed. Telephone: (416) 978-4581. Fax: (416) 978-8775.
e-mail: rcox@alchemy.chem.utoronto.ca

 © 1999 NRC Canada

Introduction

Rate-determining proton transfer in strong acid media, the A-S_E2 [or Ad-E2, or A(E)+A(N)] mechanism, has until recently been difficult to distinguish from the case in which the proton transfer involved in an acid-catalyzed reaction is a pre-equilibrium process, the A1 mechanism. Rate-determining proton transfer involves general acid catalysis, and Jerry Kresge was one of the first to exploit rate differences in aqueous sulfuric and perchloric acid mixtures (1), later expanded to also include aqueous nitric and phosphoric acids (2), to make this mechanistic distinction. Slightly later, I pointed out that these mechanisms could also be distinguished in sulfuric acid by working at acidities high enough that catalysis by H_3O^+, undissociated H_2SO_4, and $H_3SO_4^+$ as individual species is visible (3).

Jerry Kresge was also among the first to point out, in 1971, that alkene hydration followed an A-S_E2 mechanism rather than the A1 π-complex formation process that had been in vogue until then (4). Many different alkene hydrations in strong acid have been studied since that time, for instance, of vinyl ethers in a series of papers by the Kresge group (5), and of norbornene derivatives by the Lajunen group (6). Kresge has also studied the hydration of various alkenes (7), and thus it seemed appropriate in this paper to analyze the rates of hydration of a number of simple phenyl-substituted alkenes, to compare them among themselves and also with a previous study of the hydrations of a number of different phenylacetylenes (8).

The alkenes chosen for study were a series of phenyl-substituted styrenes **1** for which hydration rate constants as a function of acid concentration at 25°C are available in aqueous H_2SO_4 (9–11), D_2SO_4 (12), and $HClO_4$ (13) media, some compounds having also been studied at other temperatures (9, 13); some phenyl-substituted α-methylstyrenes **2** at 25°C, with data in H_2SO_4 (12, 14) and D_2SO_4 (12); some phenyl-substituted α-trifluoromethylstyrenes **3** in H_2SO_4 at 25°C (15); and a series of *cis*-stilbenes **4** with varying substituents in both rings, for which rate constants for isomerization to the *trans* form as a function of acid concentration are available in aqueous H_2SO_4 at 25°C and some other temperatures (16).

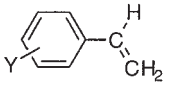

1*a* Y = 4-OCH_3
1*b* Y = 4-SCH_3
1*c* Y = 4-CH_3
1*d* Y = 4-F
1*e* Y = 3-CH_3
1*f* Y = H
1*g* Y = 4-Cl
1*h* Y = 4-Br
1*i* Y = 3-Cl
1*j* Y = 3-Br
1*k* Y = 3-CF_3
1*l* Y = 3-NO_2
1*m* Y = 4-NO_2
1*n* Y = 3-$^+NH_3$

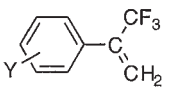

3*a* Y = 4-OCH_3
3*b* Y = 4-CH_3
3*c* Y = H
3*d* Y = 4-Cl
3*e* Y = 3-Cl

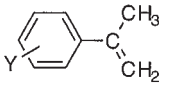

2*a* Y = 4-OCH_3
2*b* Y = 4-CH_3
2*c* Y = 3-CH_3
2*d* Y = H
2*e* Y = 4-Cl
2*f* Y = 3-Cl
2*g* Y = 4-CO_2H
2*h* Y = 4-NO_2

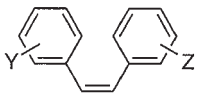

4*a* Y = 4-OCH_3 Z = 4'-OCH_3
4*b* Y = 4-OCH_3 Z = 4'-CH_3
4*c* Y = 4-OCH_3 Z = H
4*d* Y = 4-OCH_3 Z = 3'-NO_2
4*e* Y = 4-OCH_3 Z = 4'-NO_2
4*f* Y = 4-SCH_3 Z = 4'-NO_2
4*g* Y = 4-CH_3 Z = H
4*h* Y = 4-CH_3 Z = 4'-NO_2
4*i* Y = H Z = H
4*j* Y = H Z = 3'-OCH_3
4*k* Y = H Z = 4'-NO_2
4*l* Y = 3-Cl Z = 3'-Cl

Results

[1] 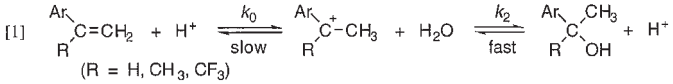

The mechanism that applies to the hydrations of the styrenes **1**–**3** is given in eq. [1] (4, 8–13, 15). The hydration of **1** in strong acids is a process that comes to equilibrium, with some unhydrated styrene almost always being present at the end of the reaction, and so the measured rate constants are the sum of those for the forward reaction and for the reverse dehydration. All the rate constants used in this work are for the forward reaction only, having been corrected for the reverse process (9–13); here they are called k_ψ, since they are all pseudo-first-order.

$$[2] \qquad \log k_\psi - \log C_{H^+} = \log k_0 + m^\ddagger m^* X$$

The rate equation that applies to all of the reactions in this paper is eq. [2] (17), where C_{H^+} is the proton concentration, simply the acid molarity for $HClO_4$ solutions. Available operationally defined values are used for H_2SO_4 media, ones which account for the variable extent of dissociation of bisulfate ion at different acidities (30). The excess acidity X for both media is also available (30), and can be easily modified to temperatures other than 25°C if necessary (31). The intercept log k_0 values refer to the rate constant for the reaction in the standard state, which is the same hypothetical ideal 1 M acid solution as that used for pH measurements (30), allowing easy comparison with k_{H^+} values obtained from buffer media, etc. (17). Of the slope parameters, $m^\ddagger$ and m^*, the former depends on the reaction mechanism, being >1 for A1 reactions and <1 for A-S_E2 processes (17), allowing the easy distinction of these two mechanisms; in fact, in the latter case (which applies to the reactions in this paper) it is identical to the term α_A previously defined for these reactions by Kresge et al. (32). However, here $m^\ddagger$ is multiplied by m^*, which refers to the type of substrate present, being ~1 for primary nitroanilines, ~0.6 for carbonyl compounds, ~1.3 for thio-compounds, and so on (30). For

© 1999 NRC Canada

Table 1. Standard-state hydration rate constants for **1** in aq H_2SO_4.

Substrate	Y	log $k_0^{H_2SO_4}$ [a]	log $k_0^{D_2SO_4}$	Reference[b]
1*a*	4-OCH_3	–4.221 ± 0.011	–4.662 ± 0.022	9, 10, 12
1*b*	4-SCH_3	–4.96 ± 0.14	—	11
1*c*	4-CH_3	–5.662 ± 0.026	–6.022 ± 0.038	9, 10, 12
1*d*	4-F	–6.519 ± 0.032	—	11
1*e*	3-CH_3	–6.465 ± 0.023	–6.847 ± 0.048	9, 10, 12
1*f*	H	–6.769 ± 0.052	–7.138 ± 0.057	9, 10, 12
1*g*	4-Cl	–7.518 ± 0.048	—	9, 10
1*h*	4-Br	–7.369 ± 0.080	—	9
1*i*	3-Cl	–8.163 ± 0.075	–8.432 ± 0.097	9, 10, 12
1*j*	3-Br	–8.278 ± 0.098	—	9
1*k*	3-CF_3	–8.82 ± 0.27	—	11
1*l*	3-NO_2	–9.83 ± 0.11	–10.18 ± 0.13	9, 10, 12
1*n*	3-$^+NH_3$	–9.465 ± 0.041	—	9

[a]Intercepts of Fig. 1.

[b]Source of the original rate constant data.

Table 2. Slopes, activation parameters, solvent isotope effects, and statistical data for **1** in aq H_2SO_4.[a]

Substrate	$m^{\ddagger}m^{*}$[b]	$\Delta H^{\ddagger}$[c]	$\Delta S^{\ddagger}$[d]	SIE[e]	$\pm\sigma_y$[f]	N[g]
1*a*	1.444 ± 0.015	—	—	2.76 ± 0.15	0.033	36(2)
1*b*	1.406[h]	—	—	—	0.135	4
1*c*	1.377 ± 0.021	—	—	2.30 ± 0.24	0.083	39
1*d*	1.406[h]	—	—	—	0.006	3
1*e*	1.377 ± 0.015	21.4 ± 1.6	–16.4 ± 5.3	2.41 ± 0.30	0.057	36(2)
1*f*	1.370 ± 0.024	24.0 ± 2.2	– 9.2 ± 7.2	2.34 ± 0.42	0.080	35(2)
1*g*	1.490 ± 0.021	26.6 ± 1.3	–3.8 ± 4.5	—	0.079	31(1)
1*h*	1.406[h]	—	—	—	0.082	5(2)
1*i*	1.332 ± 0.028	27.7 ± 2.8	–2.9 ± 9.5	1.86 ± 0.52	0.104	33(1)
1*j*	1.406[h]	—	—	—	0.049	5(1)
1*k*	1.406[h]	—	—	—	0.115	3
1*l*	1.398 ± 0.031	32.0 ± 2.4	+3.9 ± 7.9	2.23 ± 0.88	0.120	39(2)
1*n*	1.406[h]	—	—	—	0.032	4

[a]Experimental data sources as given in Table 1.

[b]Slopes of Fig. 1.

[c]In kcal mol^{-1}.

[d]In cal mol^{-1} K^{-1}.

[e]Solvent isotope effect; $k_0^{H_2SO_4}/k_0^{D_2SO_4}$.

[f]Root-mean-square deviation between the experimental points and the fitted lines in Fig. 1, in log k units.

[g]Number of points. Any rejected by the regression programs used as not being part of the same data set as the rest, to 95% confidence, are in parentheses here and in Fig. 1.

[h]Fixed; taken as the average of the experimentally determined values in this column.

the carbocations formed here this number is quite large, ~1.8 (8, 33, 34), and the combined $m^{\ddagger}m^{*}$ slopes may well be larger than one because of this.

Application of eq. [2] to the available rate constants for **1***a–l* and **1***n* in sulfuric acid (9–12) leads to the intercept log k_0 values given in Table 1 and the $m^{\ddagger}m^{*}$ slopes given in Table 2; some of the very good straight lines obtained according to eq. [2] are illustrated in Fig. 1. This figure also shows that data obtained by different groups for the same compound (9, 10) are in fact equivalent. For clarity the D_2SO_4 results are not shown; preliminary work showed that the $m^{\ddagger}m^{*}$ slopes in H_2SO_4 and D_2SO_4 are identical, and so from then on both were constrained to be the same. Throughout this work data were analyzed using statistics programs modified from those given by Bevington (35). For simplicity, in cases where only a few data points were available (**1***b*, **1***d*, **1***h*, **1***j*, **1***k*, **1***n*) the $m^{\ddagger}m^{*}$ slopes for them were taken as being the average value for those compounds with plenty of data points, as preliminary work showed this to be statistically valid. Table 2 also contains the derived solvent isotope effect values, enthalpies and entropies of activation based on the standard-state intercepts for those substrates with rate constants at different temperatures available ($m^{\ddagger}m^{*}$ slopes are independent of temperature (31)), and relevant statistical information. In Tables 1 and 2 and throughout this paper the errors quoted are standard deviations.

Some styrenes have also been studied in aqueous perchloric acid (13), and the results of applying eq. [2] to the available rate constants are given in Table 3 and Fig. 2. Comparison with Tables 1 and 2 shows that the log k_0 values for the same compounds in the different media (**1***a*, **1***c*, **1***f*, **1***g*), and the $\Delta H^{\ddagger}$ and $\Delta S^{\ddagger}$ values for **1***f*, agree very well. The

© 1999 NRC Canada

Table 3. Standard-state hydration rate constants and other data for **1** in aq $HClO_4$.[a]

Substrate	Y	log k_0[b]	$m^{\ddagger}m^{*}$[c]	$\pm\sigma_y$[d]	N[d]
1*a*	4-OCH_3	–4.0845 ± 0.0068	1.132 ± 0.010	0.0091	7
1*c*	4-CH_3	–5.586 ± 0.031	1.152 ± 0.019	0.016	6
1*f*	H	–7.008 ± 0.052[e]	1.297 ± 0.021	0.031	10
1*g*	4-Cl	–7.367 ± 0.031	1.246 ± 0.012	0.015	5
1*m*	4-NO_2	–10.60 ± 0.16[f]	1.266 ± 0.031	0.057	12

[a]Experimental data from ref. 13.
[b]Intercepts of Fig. 2.
[c]Slopes of Fig. 2.
[d]See footnotes to Table 2.
[e]$\Delta H^{\ddagger}$ = 23.54 ± 0.66 kcal mol^{-1}; $\Delta S^{\ddagger}$ = –11.7 ± 2.2 cal mol^{-1} K^{-1}.
[f]$\Delta H^{\ddagger}$ = 28.1 ± 1.1 kcal mol^{-1}; $\Delta S^{\ddagger}$ = –12.8 ± 3.8 cal mol^{-1} K^{-1}.

Fig. 1. Excess acidity plots of log k_{ψ} – log C_{H^+} against X for the hydration of some styrenes **1** in aqueous sulfuric acid at 25°C. Closed symbols, data of Coussemant's group (9); open symbols, data of Ellis and Johnson (10). For clarity, only the data for the seven compounds shown are plotted, and results obtained in D_2SO_4 (12) are not included.

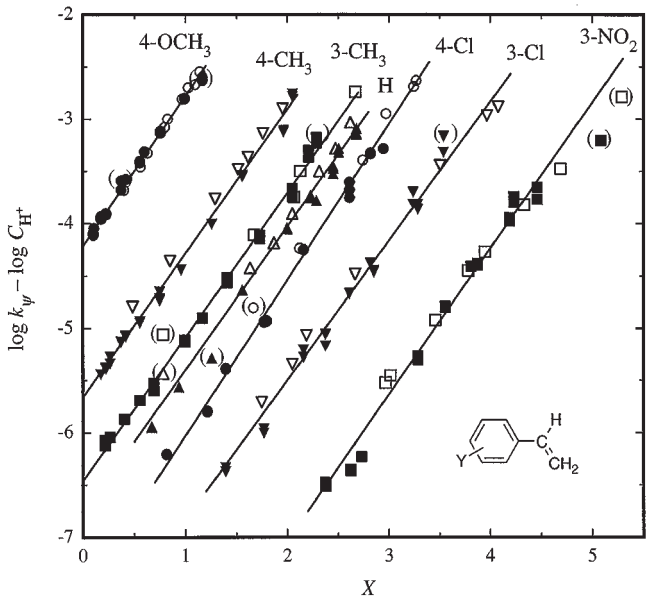

$m^{\ddagger}m^{*}$ slopes, however, do not, averaging 1.41 in H_2SO_4 and 1.19 in $HClO_4$. Many groups prefer to use the X_0 scale (based on primary nitroaniline indicators only) (33) rather than X (based on a wide variety of indicators of different types (30)) in aqueous $HClO_4$ media (5–7, 23), since Kresge et al. (36) showed that this offered the best connection between the concentrated aqueous $HClO_4$ and dilute aqueous acid media. In this work, I tried both X and X_0 for **1** in $HClO_4$; X offered the better correlation coefficient in five cases and X_0 in two, although the differences were marginal. X was chosen for this reason and because the comparison with the results obtained using the X scale in H_2SO_4 is more valid. The slopes found using X_0 were smaller in dilute acid and larger in concentrated acid than those obtained using X, and the overall average was much the same (1.22 vs. 1.19), still quite different from the H_2SO_4 value of 1.41.

When eq. [2] is applied to the available rate constants for **2***a–h* in sulfuric acid (12, 14), the intercept log k_0 values given in Table 4 and the $m^{\ddagger}m^{*}$ slopes in Table 5 result. The

Fig. 2. Excess acidity plots of log k_{ψ} – log C_{H^+} against X for the hydration of five styrenes **1** in aqueous perchloric acid at 25°C (13).

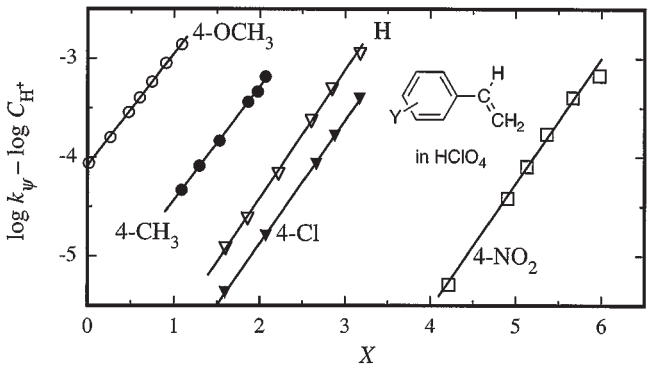

data are illustrated in Fig. 3; again for clarity the D_2SO_4 results are not shown. In two cases where only one or two data points were available (**2***b*, **2***g*), there was no choice but to take the $m^{\ddagger}m^{*}$ slopes as being the average value for the remaining compounds. Table 5 also contains the derived solvent isotope effect values and relevant statistical information.

Table 6 contains the results of applying eq. [2] to the available data for **3***a–e* (15), and the data fit is illustrated in Fig. 4. Here, preliminary work showed that the $m^{\ddagger}m^{*}$ slopes for all five compounds were, within experimental error, the same, and so, since few data points were available overall, the slope was constrained to be the same for all the compounds. This worked very well, as can be seen from Fig. 4; the low error on the calculated overall slope, 1.16 ± 0.05, amply justifies this simplification.

[3] 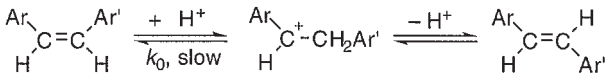

The A-S_E2 mechanism that applies to **4** is given in eq. [3] (16). This is very similar to eq. [1] for the styrenes, and the same rate equation, eq. [2], applies. This is illustrated for **4***a–l* in aqueous H_2SO_4 at 25°C in Fig. 5 (16), again omitting rate constants obtained in D_2SO_4 and those obtained at other temperatures for clarity. The log k_0 intercepts are given in Table 7 and the $m^{\ddagger}m^{*}$ slopes in Table 8, together with the activation parameters calculated from the different log k_0 intercepts obtained at different temperatures, the solvent isotope effects and statistical information. To enable direct

© 1999 NRC Canada

Table 4. Standard-state hydration rate constants for **2** in aq H_2SO_4.

Substrate	Y	log $k_0^{H_2SO_4}$ [a]	log $k_0^{D_2SO_4}$	Reference[b]
2*a*	4-OCH_3	–2.076 ± 0.044	—	14
2*b*	4-CH_3	–3.189[c]	—	14
2*c*	3-CH_3	–3.568 ± 0.045	–4.014 ± 0.041	12
2*d*	H	–3.751 ± 0.031	–4.206 ± 0.028	12, 14
2*e*	4-Cl	–4.486 ± 0.032	–4.870 ± 0.033	12, 14
2*f*	3-Cl	–5.067 ± 0.023	–5.459 ± 0.022	12, 14
2*g*	4-CO_2H	–5.774[c]	—	14
2*h*	4-NO_2	–6.46 ± 0.13	—	14

[a]Intercepts of Fig. 3.

[b]Source of the original rate constant data.

[c]Based on only one or two data points; see Table 5.

Table 5. Slopes, solvent isotope effects, and statistical data for **2** in aq H_2SO_4.[a]

Substrate	$m^{\ddagger}m^{*b}$	SIE[c]	$\pm\sigma_y$[c]	N[c]
2*a*	1.33 ± 0.19	—	0.037	4
2*b*	1.38[d]	—	—	1
2*c*	1.208 ± 0.069	2.79 ± 0.39	0.076	14
2*d*	1.248 ± 0.039	2.85 ± 0.27	0.049	14(1)
2*e*	1.660 ± 0.045	2.42 ± 0.26	0.042	17(1)
2*f*	1.405 ± 0.022	2.47 ± 0.18	0.026	13
2*g*	1.38[d]	—	—	2
2*h*	1.154 ± 0.058	—	0.098	4

[a]Experimental data sources as given in Table 4.

[b]Slopes of Fig. 3.

[c]See footnotes to Table 2.

[d]Fixed; taken as the average of the experimentally determined values in this column.

Table 6. Standard-state hydration rate constants and other data for **3** in aq H_2SO_4.[a]

Substrate	Y	log k_0[b]	N[c]
3*a*	4-OCH_3	–10.21 ± 0.25	7
3*b*	4-CH_3	–11.81 ± 0.32	6
3*c*	H	–13.31 ± 0.37	6
3*d*	4-Cl	–14.10 ± 0.40	6
3*e*	3-Cl	–15.09 ± 0.44	6(1)

[a]Data from ref. 15. The calculated $m^{\ddagger}m^{*}$ was 1.159 ± 0.054, which applies to all five compounds; see text. The overall σ_y value was ±0.144.

[b]Intercepts of Fig. 4.

[c]See footnotes to Table 2.

Fig. 3. Excess acidity plots of log k_ψ – log C_{H^+} against X for the hydration of some α-methylstyrenes **2** in aqueous sulfuric acid at 25°C. Closed symbols, data of Coussemant's group (12); open symbols, data of Deno's group (14). For clarity, results obtained in D_2SO_4 (12) are not included.

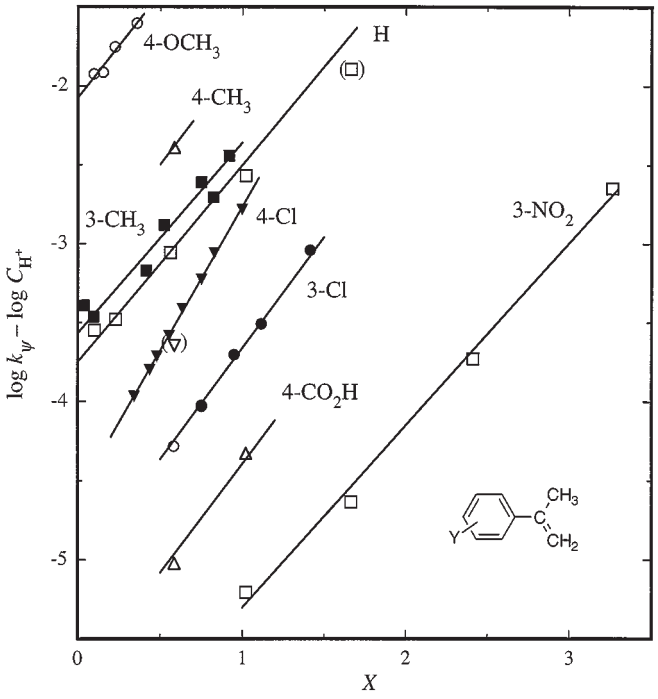

comparison, the log k_0 values obtained for the compounds that have two equivalent reaction sites (**4***a*, **4***i*, **4***l*) are statistically corrected by subtracting log 2 from them.

The intercept log k_0 values for **1**–**3** are plotted as linear free energy relationships (LFERs) in Fig. 6. Preliminary work showed that the slopes were within experimental error the same for the values obtained in H_2SO_4 and those obtained in D_2SO_4, and so for simplicity these were constrained to be the same, with different intercepts. The values obtained for **1** in $HClO_4$ were not included in the LFER, but they are shown in Fig. 6 for comparison with the H_2SO_4 ones; as can be seen they agree very well. For **1** and for **3** the log k_0 values were accurately linear in σ^+, but for **2** they were linear in neither σ nor σ^+. A double linear regression in σ and σ^+ according to Yukawa and Tsuno (37) gave an r value of ~0.4, and thus the plot of log k_0 for **2** against $\sigma + 0.4(\sigma^+ - \sigma)$ shown in Fig. 6 is linear. Individual results were weighted according to their standard deviations, so the more precise values contribute more than the less precise ones to the linear fit. Values of σ and σ^+ were obtained from a standard source (38), and those not listed there from a newer compilation (39). The ρ^+ values and other summary information is given in Table 9. The solvent isotope effects listed in Table 9 are obtained from the log k_0 values in H_2SO_4 and D_2SO_4 given there, and are the same as the averages of the individual numbers in Tables 2, 5, and 8. Included in Table 9 are the equivalent results previously

© 1999 NRC Canada

Table 7. Standard-state isomerization rate constants for **4** in aq H_2SO_4.[a]

Substrate	Y	Z	$\log k_0^{H_2SO_4}$ [b,c]	$\log k_0^{D_2SO_4}$ [b]
4*a*	4-OCH_3	4′-OCH_3	–6.502 ± 0.080	–7.09 ± 0.12
4*b*	4-OCH_3	4′-CH_3	–6.40 ± 0.11	–6.94 ± 0.13
4*c*	4-OCH_3	H	–6.521 ± 0.046	–7.092 ± 0.062
4*d*	4-OCH_3	3′-NO_2	–7.013 ± 0.070	–7.657 ± 0.077
4*e*	4-OCH_3	4′-NO_2	–7.094 ± 0.070	–7.730 ± 0.092
4*f*	4-SCH_3	4′-NO_2	–7.18 ± 0.10	—
4*g*	4-CH_3	H	–8.364 ± 0.065	–8.883 ± 0.071
4*h*	4-CH_3	4′-NO_2	–8.777 ± 0.078	–9.389 ± 0.086
4*i*	H	H	–9.552 ± 0.038	–10.001 ± 0.043
4*j*	H	3′-OCH_3	–9.48 ± 0.10	–9.92 ± 0.12
4*k*	H	4′-NO_2	–9.86 ± 0.10	–10.47 ± 0.10
4*l*	3-Cl	3′-Cl	–11.55 ± 0.18	—

[a]Data from ref. 16.
[b]Symmetrical compounds (**4***a*, **4***i*, and **4***l*) are corrected by having log 2 subtracted from their log k_0 values.
[c]Intercepts of Fig. 5.

Table 8. Slopes, activation parameters, solvent isotope effects, and statistical data for **4** in aq H_2SO_4.[a]

Substrate	$m^{\ddagger}m^{*b}$	$\Delta H^{\ddagger c}$	$\Delta S^{\ddagger d}$	SIE[e]	$\pm\sigma_y$[f]	N[f]
4*a*	1.317 ± 0.059	21.06 ± 0.96	–16.3 ± 3.2	3.9 ± 1.3	0.054	18(1)
4*b*	1.261 ± 0.055	—	—	3.4 ± 1.3	0.049	10
4*c*	1.299 ± 0.024	19.74 ± 0.56	–22.2 ± 1.9	3.73 ± 0.66	0.037	16
4*d*	1.251 ± 0.032	20.57 ± 0.59	–21.6 ± 2.0	4.4 ± 1.1	0.028	10
4*e*	1.262 ± 0.031	22.01 ± 0.81	–17.2 ± 2.7	4.3 ± 1.2	0.049	18
4*f*	1.053 ± 0.037	17.70 ± 0.85	–32.0 ± 2.9	—	0.053	20(1)
4*g*	1.474 ± 0.022	24.75 ± 0.49	–13.8 ± 1.7	3.30 ± 0.73	0.028	14
4*h*	1.318 ± 0.023	24.34 ± 0.68	–17.1 ± 2.3	4.1 ± 1.1	0.032	13
4*i*	1.466 ± 0.012	25.95 ± 0.33	–13.8 ± 1.1	2.81 ± 0.37	0.026	22
4*j*	1.463 ± 0.030	26.62 ± 0.62	–12.6 ± 2.1	2.76 ± 0.98	0.031	17
4*k*	1.298 ± 0.023	—	—	4.0 ± 1.3	0.023	7
4*l*	1.479 ± 0.038	—	—	—	0.024	3

[a]Data from ref. 16.
[b]Slopes of Fig. 5.
[c]In kcal mol^{-1}.
[d]In cal mol^{-1} K^{-1}.
[e]Solvent isotope effect; $k_0^{H_2SO_4}/k_0^{D_2SO_4}$.
[f]See footnotes to Table 2.

obtained from the phenylacetylenes **5**–**9** (8), for purposes of comparison.

The LFER for **4** is given in Fig. 7 (for clarity only the values measured in H_2SO_4 are plotted); the slopes and intercepts are in Table 9. The individual compounds form a number of different series, resulting in the six different lines shown, and Fig. 7 is the result of a double linear regression of the log k_0 values with σ^+ and σ. Here, the Y substituents are assumed to be on the phenyl group attached to the carbon with the developing positive charge (σ^+ values, large negative slope) and the Z substituents on the phenyl group attached to the other one (σ values, small negative slope).

Discussion

As can be seen from Figs. 1–5, eq. [2] fits the rate constant data for all of the substrates exceptionally well. Deriving it is straightforward; if we call the substrate in eq. [1] or eq. [3] S and the initial protonation is rate-determining, absolute rate theory requires eq. [4] to be true:

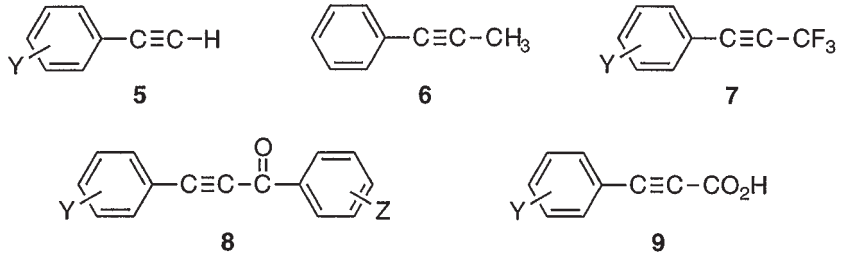

© 1999 NRC Canada

Fig. 4. Excess acidity plots of log k_ψ – log C_{H^+} against X for the hydration of five α-trifluoromethylstyrenes **3** in aqueous sulfuric acid at 25°C (13).

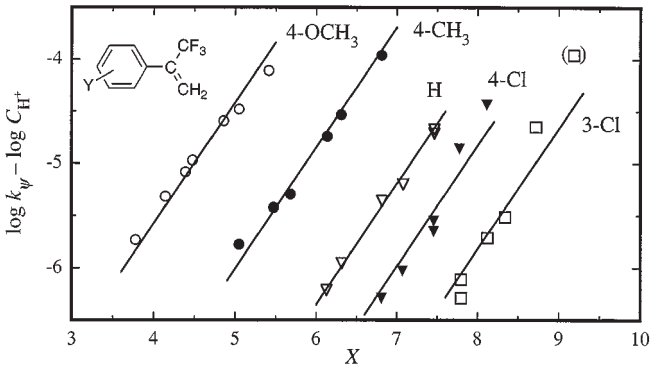

Fig. 5. Excess acidity plots of log k_ψ – log C_{H^+} against X for the isomerization of the *cis*-stilbenes **4** in aqueous sulfuric acid at 25°C (16). For clarity, the results obtained in D_2SO_4 are not included.

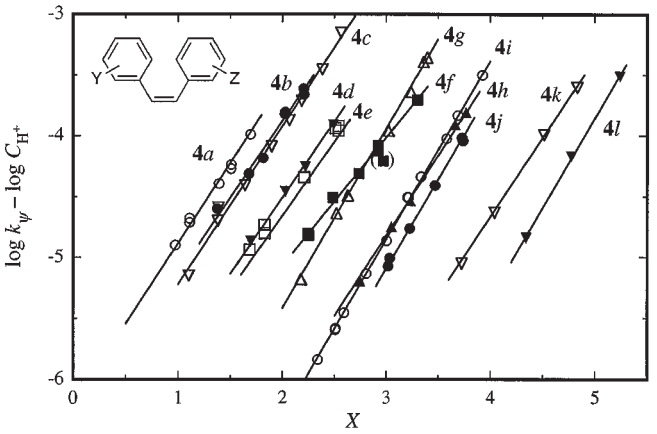

$$[4] \qquad k_\psi C_S = k_0 \frac{a_S a_{H^+}}{f_\ddagger} = k_0 C_S C_{H^+} \frac{f_S f_{H^+}}{f_\ddagger}$$

$$[5] \qquad \log k_\psi - \log C_{H^+} = \log k_0 + \log \frac{f_S f_{H^+}}{f_\ddagger}$$

$$[6] \qquad \log \frac{f_S f_{H^+}}{f_\ddagger} = m^\ddagger \log \frac{f_S f_{H^+}}{f_{SH^+}} \left(= \alpha_A \frac{f_S f_{H^+}}{f_{SH^+}} \right) = m^\ddagger m^* X$$

Canceling and taking logs then gives eq. [5], and eq. [2] results when the activity coefficient ratio term is subjected to the by now very well tested excess acidity assumption of eq. [6] (17). For A-S_E2 mechanisms like eqs. [1] and [3] the terms $m^\ddagger$ and α_A (32) are equivalent, see above. If the k_2 step in eq. [1] were rate-determining, rather than the k_0 step, the water activity or the bisulfate ion concentration would have to be taken into account, and plots like Figs. 1–5 would be curved, as has been amply demonstrated before (22, 24, 28).

It is readily apparent from a comparison of **1**–**3** in Fig. 6 or Table 9 that the activating methyl group in **2** causes it to react three orders of magnitude faster than the unsubstituted **1**, and the deactivating CF_3 group in **3** slows the reaction down by nearly seven powers of 10. (The errors are worse

Fig. 6. Linear free energy relationship plots of standard-state rate constants, log k_0, for the hydrations of **1**–**3**. Open circles, **1** in H_2SO_4 (intercepts of Fig. 1, Table 1); closed circles, **1** in $HClO_4$ (intercepts of Fig. 2, Table 3); open triangles, **1** in D_2SO_4 (Table 1); closed triangles, **2** in H_2SO_4 (intercepts of Fig. 3, Table 4); open squares, **2** in D_2SO_4 (Table 4); closed squares, **3** in H_2SO_4 (intercepts of Fig. 4, Table 6). Plots against σ^+ except for **2**, which is a Yukawa–Tsuno plot against $\sigma + 0.4(\sigma^+ - \sigma)$.

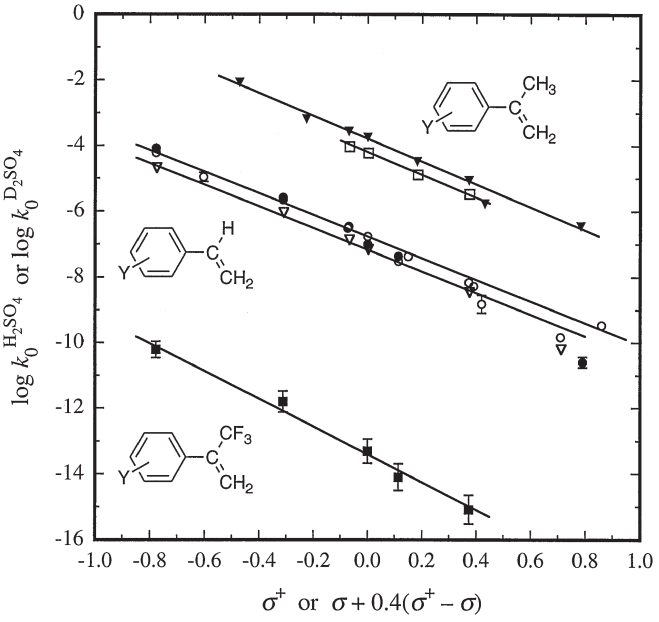

for **3** because the extrapolation to $X = 0$ is longer for these compounds; being deactivated they require much stronger acid to achieve reaction in a reasonable period of time.) This is what would be expected; it contrasts with the situation in the phenylacetylenes in Table 9, where any sort of substituent slows the reaction down. This probably has a steric component, since the carbon with the substituent is the one being protonated, rather than the one without it in **1**–**3**.

Interestingly, the stilbenes are also deactivated, **4** reacting nearly three orders of magnitude more slowly than **1**. This effect has been seen before; for instance, it has been found that the presence of a mesityl group attached at the functional group slows ketene hydration by a factor of 2200, acid catalysis of the reaction only being observable in strong acid media (41). Presumably, this deactivation is due to ground-state stabilization by the second phenyl ring, and to the inductive electron-withdrawing effect of the phenyl group (40), but there may be a steric component too.

Steric effects certainly show up in the fact that **2** requires a Yukawa–Tsuno plot involving σ and σ^+ to give an LFER, rather than giving a straightforward correlation with σ^+ as all the other substrates do. This must be due to the α-CH_3 twisting the molecule and causing a decrease of conjugation of the double bond with the ring; resonance-effect substituents cannot exert their full influence if this is so (an r value of 0.4 means that they exert only ≈40% of it). The ring does not need to provide so much stabilization with the methyl group also stabilizing the positive charge inductively. This effect does not show up with a strongly electron-withdrawing α-CF_3 substituent present; like it or not, the

© 1999 NRC Canada

Table 9. Summarized results for **1**–**4** and some phenylacetylenes in aq H_2SO_4.[a]

Substrate	ρ+	log k_0 for Y = H[b]	$k_0^{H_2SO_4}/k_0^{D_2SO_4}$[c]	$m^{\ddagger}m^{*}$[d]
Styrenes:				
1	–3.287 ± 0.061	–6.771 ± 0.040	2.52 ± 0.44	1.406 ± 0.050[e]
2	–3.480 ± 0.093[f]	–3.793 ± 0.032	2.54 ± 0.28	1.38 ± 0.15
3	–4.23 ± 0.24	–13.41 ± 0.12	—	1.159 ± 0.053[g]
4	–3.762 ± 0.074[h]	–9.498 ± 0.046	3.55 ± 0.56	1.33 ± 0.11
Phenylacetylenes:				
5	–4.03 ± 0.06	–6.63 ± 0.03	2.9 ± 0.2	1.37 ± 0.07
6	—[i]	–8.31 ± 0.06	—	1.56 ± 0.02
7	–5.28 ± 0.41	–8.69 ± 0.19	—	1.21 ± 0.10
8	–3.54 ± 0.21[j]	–9.05 ± 0.09	2.0 ± 0.2	1.06 ± 0.08
9	–3.85 ± 0.09	–8.26 ± 0.07	4.0 ± 0.2	[k]

[a]Data for compounds **5**–**9** from ref. 8.
[b]Intercepts of the LFERs in Figs. 6 and 7.
[c]Average values obtained from the LFER intercepts.
[d]Averages of values in Tables 2, 3, 5, and 8.
[e]1.191 ± 0.070 in $HClO_4$.
[f]ρ value. Yukawa–Tsuno $r \approx 0.4$.
[g]Value calculated for all five compounds.
[h]For the Z substituents, ρ = –0.583 ± 0.072.
[i]Only data for the phenyl compound in aq H_2SO_4 available (8).
[j]Variation of Z with Y constant gives ρ = –0.1 ± 0.6 (8).
[k]A variable function of σ^+ (8).

Fig. 7. Linear free energy relationship plots of standard-state rate constants, log k_0, for the isomerizations of the *cis*-stilbenes **4** (intercepts of Fig. 5, Table 7). Plots against σ^+ for the Y substituents and against σ for the Z substituents.

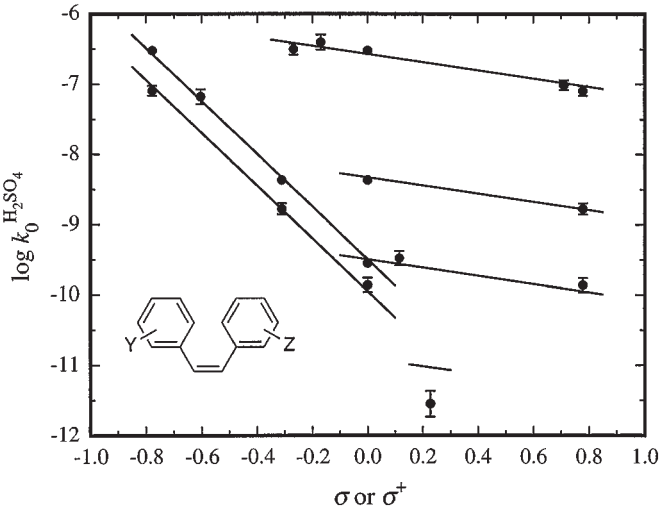

ring must provide all of the stabilization, and this forces the ring and the substituent to be in the same plane, for maximum resonance interaction between the developing positive charge and the ring.

In Fig. 6 the log k_0 values obtained for **1** in $HClO_4$ (closed circles) are plotted for comparison with the values obtained in H_2SO_4. The comparison is in general very good, with the exception of the 4-NO_2 derivative **1***m*, which falls somewhat below the correlation line. However, the error for this compound is much higher than it is for the others. It is gratifying that results obtained in different acid media agree so well; this is what would be expected, since proton transfer is from H_3O^+ in both of the relatively dilute aqueous acid media used in this work (3). Thus, extra justification is provided for the excess acidity approach, and the faith that can be placed in the extrapolated log k_0 values is increased. The $m^{\ddagger}m^{*}$ slopes, however, are not the same in the two media, and for all the substrates there is some variability in the values for individual compounds from the averages in Table 9 (Tables 2, 3, 5, and 8; Figs. 1–5); the author feels that the difference between the H_2SO_4 and $HClO_4$ values for **1**, and other individual differences from the Table 9 averages, are due to differences in m^{*} rather than in $m^{\ddagger}$, but there is no evidence for or against this view at present.

The distinction between A1 and A-S_E2 [or Ad-E2, or A(E)+D(E)] mechanisms depends on the magnitude of $m^{\ddagger}$ (17). All of the values of $m^{\ddagger}m^{*}$ in the Tables are >1, but these have to be divided by m^{*}. Values of this quantity for **1**–**4** are not available, but it is known that typical carbocations such as are produced in the reactions under consideration here have $m^{*} \approx 1.8$ (8, 33, 34), and in all cases division by this leads to $m^{\ddagger} < 1$, demonstrating that all of the substrates in fact react by the A-S_E2 pathway shown in eqs. [1] and [3]. The $m^{\ddagger}$ (or α_A) value can be interpreted like a Brønsted α as being roughly the extent of proton transfer at the transition state (32). If the 1.8 value applies, the extent of proton transfer is 78% for **1** (66% in $HClO_4$), 77% for **2**, 64% for **3**, and 74% for **4** (all values ±~10%). Thus, we have a late transition state in all cases, with the proton being three-quarters transferred for all except **3**, where it is only two-thirds transferred. (However, it must be pointed out that this interpretation differs from the results of very recent theoretical calculations, which compare 1-phenylethanol dehydration with styrene hydration via the same carbocation intermediate, and indicate that whereas the S_N1 transition state for the former reaction is halfway between reactant and

© 1999 NRC Canada

product, in the latter case it is earlier than this (42).) Thus, the slowest reaction has the least advanced transition state, as was observed previously for the phenylacetylenes (8); this counter-intuitive result indicates that a reaction surface such as that used by Chokotho and Johnson (43), rather than a linear profile, is probably necessary for a complete analysis of these reactions.

For some of the phenylacetylenes $m^{\ddagger}m^{*}$ was observed to be a variable function of σ^{+}, which means that the observed ρ^{+} values would be different at different acidities (8). The same effect (but in the opposite direction) had previously been observed for some acylal and thioacylal hydrolyses (44). For the styrenes and stilbenes in this paper, however, the $m^{\ddagger}m^{*}$ values are approximately the same for all the substituents, which means that the ρ^{+} values would be the same at any given acidity as they are in the standard state (values quoted in Table 9). This can be interpreted as indicating that the reactivity–selectivity principle does not apply to **1**–**4** (10, 42, 45).

The ρ^{+} values for **1**–**9** are all approximately the same, quite reasonable numbers between –3.3 and –4.0, except for the compounds with CF_3 substituents, **3** and **7**, where ρ^{+} is significantly more negative (Table 9). This would be expected, because the presence of the strongly electron-withdrawing CF_3 puts much more demand on the ring to supply electrons. Figure 7 for the stilbenes is interesting; for substituents on the ring adjacent to the developing positive charge the log k_0 values follow σ^{+} with a large negative ρ^{+}, but for substituents on the other ring they follow σ, with a small negative ρ value. Thus, the ring on the second carbon plays little part in stabilizing the transition state.

For **1** and **2**, reaction in D_2SO_4 is about 2.5 times slower than it is in H_2SO_4, which seems reasonable, but for the stilbenes, **4**, this factor is 3.6 (Table 9). This would imply a later transition state for **4**, which in terms of the arguments given above means that the m^{*} values for the stilbenes would be smaller than they are for the styrenes. Evidence, however, is lacking.

Activation parameters for some of the substrates are given in Tables 2 and 8. For **4**, $\Delta H^{\ddagger}$ averages 22.5 ± 2.9 kcal mol^{-1} and $\Delta S^{\ddagger}$ –16.8 ± 5.0 cal mol^{-1} K^{-1}. Thus, at 25°C the entropy term contributes only –5 kcal mol^{-1}, so the protonation of **4** is largely an enthalpy-controlled process. The same probably applies to **1** and **5**. The values for **1** in H_2SO_4 are not as reliable as those for **4**, being based on very few data points obtained at temperatures other than 25°C (9): $\Delta H^{\ddagger}$ = 25.6 ± 3.6 kcal mol^{-1}; $\Delta S^{\ddagger}$ = –7.0 ± 7.5 cal mol^{-1} K^{-1}; entropy contribution = –2.1 kcal mol^{-1}. Probably the values obtained in $HClO_4$ are better (Table 3), but there are only two of them (13). Phenylacetylene **5** is very similar to **4**, the averages being $\Delta H^{\ddagger}$ = 19.2 ± 2.2 kcal mol^{-1} and $\Delta S^{\ddagger}$ = –16.3 ± 3.8 cal mol^{-1} K^{-1}, so at 25°C the entropy term contributes –4.9 kcal mol^{-1} (8). The variations in the individual $\Delta H^{\ddagger}$ and $\Delta S^{\ddagger}$ values in Tables 2 and 8 are not quite random; there is a tendency for $\Delta H^{\ddagger}$ to increase and for $\Delta S^{\ddagger}$ to become less negative, or even positive, as the ring substituents become more deactivating, particularly for **1**. Thus, the effect of substituents in the benzene ring would seem to be mainly an effect on the enthalpy of reaction, with the well-known tendency of $\Delta S^{\ddagger}$ to be correlated with $\Delta H^{\ddagger}$ (46) counteracting it.

Comparison of the styrenes and stilbenes **1**–**4** with the phenylacetylenes **5**–**9** in Table 9 is instructive more in terms of the similarities than the differences. For instance, $k_{H^{+}}$ in the standard state for styrene itself is 1.7×10^{-7} M^{-1} s^{-1}, and for phenylacetylene, 2.3×10^{-7} M^{-1} s^{-1}. In other words, the latter is marginally more reactive than the former. Insofar as styrenes and stilbenes react via a benzyl carbocation and phenylacetylenes via a vinyl cation, this result might perhaps not have been anticipated, although it has been shown that substituents can have a greater effect on alkyne protonation than they have on alkene protonation, due to the shorter bond from the substituent to carbon, and thus some alkynes are significantly more reactive than the corresponding alkenes are (47). In Table 9, it can also be seen that in this work the phenylacetylenes are found to be more substituent-sensitive than the styrenes (larger negative ρ^{+} value).

The overall conclusion of the work in this paper is that both sets of substrates are reacting in the same way by initial rate-determining carbon protonation, subsequent product-forming reactions being fast. The numerical information given here all refers to the aqueous standard state, and should provide trustworthy data for comparison with the more reactive compounds which can have their reaction rates determined in aqueous solution or aqueous buffer media.

Acknowledgments

I would like to thank Dr. C.D. Johnson for providing rate constant data from a thesis, members of Professor A.J. Kresge's group for information and advice, and Professor T.T. Tidwell for helpful suggestions and discussion, and for reading the manuscript.

References

1. A.J. Kresge, L.E. Hakka, S. Mylonakis, and Y. Sato. Disc. Faraday Soc. 75 (1965).
2. A.J. Kresge, S.G. Mylonakis, and L.E. Hakka. J. Am. Chem. Soc. **94**, 4197 (1972).
3. R.A. Cox. J. Am. Chem. Soc. **96**, 1059 (1974).
4. A.J. Kresge, Y. Chiang, P.H. Fitzgerald, R.S. McDonald, and G.H. Schmid. J. Am. Chem. Soc. **93**, 4907 (1971).
5. A.J. Kresge and D. Ubysz. J. Phys. Org. Chem. **7**, 316 (1994), and earlier papers.
6. M. Lajunen, J. Jantunen, and P. Koiranen. Acta Chem. Scand. **52**, 728 (1998), and earlier papers.
7. Y. Chiang, A.J. Kresge, P.A. Obraztsov, and J.B. Tobin. Croat. Chem. Acta, **65**, 615 (1992), and earlier papers.
8. R.A. Cox, E. Grant, T. Whitaker, and T.T. Tidwell. Can. J. Chem. **68**, 1876 (1990).
9. J.-P. Durand, M. Davidson, M. Hellin, and F. Coussemant. Bull. Soc. Chim. Fr. 43 (1966).
10. G.W.L. Ellis and C.D. Johnson. J. Chem. Soc. Perkin Trans. 2, 1025 (1982); G.W.L. Ellis. Ph.D. thesis. University of East Anglia, Norwich, England. 1982.
11. A.D. Allen, M. Rosenbaum, N.O.L. Seto, and T.T. Tidwell. J. Org. Chem. **47**, 4234 (1982).
12. J.-C. Simandoux, B. Torck, M. Hellin, and F. Coussemant. Bull. Soc. Chim. Fr. 4402 (1972).
13. W.M. Schubert, B. Lamm, and J.R. Keeffe. J. Am. Chem. Soc. **86**, 4727 (1964); W.M. Schubert and B. Lamm. J. Am. Chem.

© 1999 NRC Canada

Soc. **88**, 120 (1966); W.M. Schubert and J.R. Keeffe. J. Am. Chem. Soc. **94**, 559 (1972).
14. N.C. Deno, F.A. Kish, and H.J. Peterson. J. Am. Chem. Soc. **87**, 2157 (1965).
15. K.M. Koshy, D. Roy, and T.T. Tidwell. J. Am. Chem. Soc. **101**, 357 (1979).
16. D.S. Noyce, D.R. Hartter, and F.B. Miles. J. Am. Chem. Soc. **90**, 4633 (1968); J. Org. Chem. **33**, 4260 (1968).
17. R.A. Cox. Acc. Chem. Res. **20**, 27 (1987); R.A. Cox and K. Yates. Can. J. Chem. **57**, 2944 (1979).
18. J.-P. Bégué, F. Benayoud, D. Bonnet-Delpon, A.D. Allen, R.A. Cox, and T.T. Tidwell. Gazz. Chim. Ital. **125**, 399 (1995).
19. R.A. Cox. J. Phys. Org. Chem. **4**, 233 (1991).
20. R.A. Cox, K.-S. Cheon, S.-R. Keum, and E. Buncel. Can. J. Chem. **76**, 896 (1998).
21. E. Buncel and K.-S. Cheon. J. Chem. Soc. Perkin Trans. 2, 1241 (1998).
22. K.-S. Cheon, R.A. Cox, S.-R. Keon, and E. Buncel. J. Chem. Soc. Perkin Trans. 2, 1231 (1998).
23. M. Lajunen, R. Laine, and M. Aaltonen. Acta Chem. Scand. **51**, 1155 (1997), and earlier papers.
24. R.A. Cox, D.B. Moore, and R.S. McDonald. Can. J. Chem. **72**, 1910 (1994).
25. R.A. Cox. Can. J. Chem. **76**, 649 (1998).
26. M. Ali and D.P.N. Satchell. J. Chem. Soc. Perkin Trans. 2, 167 (1995); J. Chem. Soc. Perkin Trans. 2, 1825 (1993).
27. R.A. Cox. J. Chem. Soc. Perkin Trans. 2, 1743 (1997).
28. R.A. Cox. Can. J. Chem. **74**, 1774 (1996); Can. J. Chem. **74**, 1779 (1996).
29. R.A. Cox. Can. J. Chem. **75**, 1093 (1997).
30. R.A. Cox and K. Yates. J. Am. Chem. Soc. **100**, 3861 (1978).
31. R.A. Cox, M.F. Goldman, and K. Yates. Can. J. Chem. **57**, 2960 (1979); R.A. Cox and K. Yates. Can. J. Chem. **62**, 2155 (1984).
32. A.J. Kresge, R.A. More O'Ferrall, L.E. Hakka, and V.P. Vitullo. J. Chem. Soc. Chem. Commun. 46 (1965); A.J. Kresge, S.G. Mylonakis, Y. Sato, and V.P. Vitullo. J. Am. Chem. Soc. **93**, 6181 (1971).
33. R.A. Cox and K. Yates. Can. J. Chem. **59**, 2116 (1981).
34. F. Dorion and R. Gaboriaud. J. Chim. Phys. **77**, 1057 (1980); A. Bagno and G. Scorrano. Gazz. Chim. Ital. **126**, 365 (1996).
35. P.R. Bevington. Data reduction and error analysis for the physical sciences. 1st. ed. McGraw–Hill, New York. 1969.
36. A.J. Kresge, H.-J. Chen, G.L. Capen, and M.F. Powell. Can. J. Chem. **61**, 249 (1983).
37. Y. Yukawa and T. Tsuno. Bull. Chem. Soc. Japan, **32**, 965 (1959); Bull. Chem. Soc. Japan, **32**, 971 (1959); Y. Yukawa, Y. Tsuno, and M. Sawada. Bull. Chem. Soc. Japan, **39**, 2274 (1966).
38. L.M. Stock and H.C. Brown. Adv. Phys. Org. Chem. **1**, 35 (1963).
39. F. Ruff and I.G. Csizmadia. Organic reactions: equilibria, kinetics and mechanism. Elsevier, Amsterdam. 1994. p. 164.
40. P. Knittel and T.T. Tidwell. J. Am. Chem. Soc. **99**, 3408 (1977).
41. J. Andraos, A.J. Kresge, and N.P. Schepp. Can. J. Chem. **73**, 539 (1995).
42. M. Mishima and H. Yamataka. Bull. Chem. Soc. Jpn. **71**, 2427 (1998).
43. N.C.J. Chokotho and C.D. Johnson. Isr. J. Chem. **26**, 409 (1985).
44. R.A. Cox and K. Yates. Can. J. Chem. **51**, 3619 (1986).
45. C.D. Johnson. The Hammett equation. Cambridge University Press, Cambridge. 1973; Chem. Rev. **75**, 755 (1975).
46. J.E. Leffler and E. Grunwald. Rates and equilibria of organic reactions. Wiley, New York. 1963. Chap. 9.
47. A.D. Allen, Y. Chiang, A.J. Kresge, and T.T. Tidwell. J. Org. Chem. **47**, 775 (1982).

© 1999 NRC Canada

Keto ⇄ enol equilibria for and oxidative cyclization to benzofurans of 2,2-ditipyl-1-R-ethenols. Comparison with dimesityl analogs

Joseph Frey and Zvi Rappoport

Abstract: 2,2-Ditipyl-1-R-ethenols (R = H, Me, *t*-Bu; tipyl (Tip) = 2,4,6-triisopropylphenyl) were equilibrated in hexane with their carbonyl isomers. The equilibration was accompanied by an oxidative cyclization of the enols to substituted 2-R-3-tipyl-4,6-diisopropylbenzofurans, which became more facile with the increase in the bulk of R. At 77.5°C in hexane the K_{Enol} values were 90, 0.11, and 0.0011 for R = H, Me, *t*-Bu, respectively. Comparison with K_{Enol} values for the 2,2-dimesityl analogs indicate a higher value for the 2,2-ditipyl derivative with R = H, but lower values for R = Me and *t*-Bu. The factors affecting this difference are discussed.

Key words: 2,2-ditipyl-1-R-ethenols, keto ⇄ enol equilibria, enols oxidative cyclization.

Résumé : Opérant dans l'hexane, on a équilibré les 2,2-ditypyl-1-R-éthénols (R = H, Me, *t*-Bu; tipyle (Tip) = 2,4,6-triisopropylphényle) avec leurs isomères carbonylés. L'équilibre est accompagné par une cyclisation oxydante des énols en 2-R-3-tipyl-4,6-diisopropylbenzofuranes qui devient plus facile avec une augmentation de l'encombrement du groupe R. À 77,5°C, dans l'hexane, les valeurs de $K_{énol}$ sont respectivement 90, 0,11 et 0,0011 pour R = H, Me et *t*-Bu. Une comparaison des valeurs de $K_{énol}$ avec celles des analogues 2,2-dimésityle permet d'observer que, pour R = H, la valeur est plus élevée pour le dérivé 2,2-ditipyle; toutefois, elles sont plus faibles pour R = Me et *t*-Bu. On discute des facteurs qui affectent cette différence.

Mots clés : 2,2-ditipyl-1-R-éthénols, équilibre céto ⇄ énolique, cyclisation oxydante des énols.

[Traduit par la Rédaction]

Introduction

In our previous work on the keto (**1**) ⇄ enol (**2**) equilibria of aryl-substituted stable simple enols (eq. [1]) (1), two trends

[1] $$\underset{\mathbf{1}}{R'ArCHCR}(=O) \underset{}{\overset{K_{Enol}}{\rightleftharpoons}} \underset{\mathbf{2}}{R'ArC{=}C(OH)R}$$

were observed. For the 2,2-dimesityl-substituted series **3** (**1**/**2**, Ar = R′ = Mes = mesityl), the increase in the bulk of an *aliphatic* 1-R substituent reduced K_{Enol} (= [**4**]/[**3**] at equilibrium) in hexane at 80°C in a monotonic way, e.g., from 20 ± 1 for R = H (**3a**/**4a**) to 0.006 for R = *t*-Bu (**3c**/**4c**) (eq. [2]) (2). With R being an aromatic substituent the opposite was observed, i.e., K_{Enol} increased with the increase of the bulk

Received October 9, 1998.

This paper is dedicated to Jerry Kresge in recognition of his many achievements in chemistry.

J. Frey and Z. Rappoport[1]. Department of Organic Chemistry, The Hebrew University of Jerusalem, Jerusalem 91904, Israel.

[1]Author to whom correspondence may be addressed. Telephone: (972) 2-658-5278. Fax: (972) 2-658-5345. e-mail: zr@vms.huji.ac.il

[2] $$\underset{\mathbf{3}}{Mes_2CHCR}(=O) \underset{}{\overset{K_{Enol}}{\rightleftharpoons}} \underset{\mathbf{4}}{Mes_2C{=}C(OH)R}$$

3	**4**
a: R = H	**a**: R = H
b: R = Me	**b**: R = Me
c: R = *t*-Bu	**c**: R = *t*-Bu
d: R = Ph	**d**: R = Ph
e: R = Mes	**e**: R = Mes

of R, e.g., from 1 for R = Ph (**3d**/**4d**) to 79 for R = Mes (**3e**/**4e**) (3, 4). Increase in the electron-withdrawal ability of R by *m*- and *p*-substituents also increased K_{enol} (4).

The corresponding change in K_{Enol} on changing the 2-substituents was much less studied. For 2-alkyl-1,2-dimesityl-substituted systems **1**/**2**, R = Ar = Mes, R′ = H, alkyl, the carbonyl compound predominates in the equilibria, and although K_{Enol} values could not be measured, since the reaction is too slow (5), $K_{Enol} < 10^{-2}$. Several equilibrium constants were measured for **1**/**2**, R′ = Ar. For the *Z*-1,2-dimesityl-2-phenyl system, **1**/**2**, R = R′ = Mes, Ar = Ph, K_{Enol} = 0.67 (6), a value slightly higher than for its isomers **3d**/**4d**.

It is therefore of interest to use constant 2-substituents bulkier than phenyl or mesityl and to learn how K_{Enol} changes with the change of the 1-substituent. Aryl groups bulkier than mesityl with identical *o*,*o*′-substituents, which

© 1999 NRC Canada

Table 1. K_{Enol} values for $Ar_2C{=}C(OH)R$ systems in hexane.

	Ar					
	Tip[a]		Mes[b,c]		Me_5C_6[d,e]	
R	% enol[f]	K_{Enol}	% enol[f]	K_{Enol}	% enol[f]	K_{Enol}
H	98.9 ± 0.5[g]	89.9 ± 0.3	95 ± 2	20 ± 1	99.5 ± 0.1	185 ± 3
Me	10 ± 2	0.11 ± 0.02	39 ± 1	0.64 ± 0.02	78.4 ± 0.2	3.6 ± 0.1
t-Bu	0.1 ± 0.05	0.001 ± 0.0005	0.6 ± 0.06	0.0059 ± 0.0005	2.04 ± 0.07	0.021 ± 0.007

[a]At 77.5°C.
[b]At 80.6°C.
[c]Reference 2.
[d]At 80 ± 1°C.
[e]Reference 7.
[f]At equilibrium.
[g]From the vinylic CH:aldehyde CH integration ratio.

facilitate the study of the equilibria by NMR, are 2,4,6-triisopropylphenyl (tipyl, Tip) and 2,4,6-tri-*tert*-butylphenyl (supermesityl, Sup), or pentamethylphenyl. However, since no Sup_2C-substituted system was so far prepared, the pentamethylphenyl and the tipyl groups are a convenient choice.

2,2-Bis(pentamethylphenyl)ethenols **1**/**2** (Ar = R′ = Me_5C_6) were equilibrated with their carbonyl analogs. The K_{Enol} values given in Table 1, which were higher than with the mesityl analogs (7), were ascribed to electronic and buttressing effects.

The effect of a tipyl group was compared previously with that of a mesityl group. Fuson et al. (8) prepared 2,2-ditipylethenol in order to "bring the amount of hindrance to a maximum" and compared the kinetic stability of 1,2-ditipylethenediol with that of the corresponding mesityl derivative (for a summary see ref. 9). A quantitative comparison is also available: K_{Enol} in DMSO of 2-tipyl-1-acenaphthyl enol is 2.6 compared with 0.3 for the 2-mesityl analog (10). The major source for the relative stability of the enol was attributed to the relief of steric strain on isomerization to the isomeric ketone. The strain arises from the interaction of the *o*-alkyl group and the *p*-electron cloud of the acetonaphthenone system, and that in the enol is regarded to be much smaller (10).

The compounds *E*- and *Z*-1-phenyl-2-tipylethenols and an indanol were formed in a 15:1 ratio from the photoenolization of α-tipylacetophenone, whereas the α-mesityl analog afforded only the indanone (11). This was ascribed to greater stability of the tipyl-substituted enols due to higher steric hindrance of tipyl compared with mesityl.

We had used the greater steric bulk of tipyl compared with mesityl to kinetically stabilize enols of ditipylacetic acid derivatives more than the mesityl derivatives (12). Also, the rotational barriers of the 1- and 2-rings flips for 2,2-ditipylethenol are higher than for the dimesityl analog (13).

Consequently, in order to further evaluate the 2-aryl group effect on K_{Enol} values, several 2,2-ditipyl-1-R-ethenols (**6**) and their carbonyl isomers (**5**) were prepared and equilibrated (eq. [3]). The equilibrations and the accompanying oxidative cyclization reactions are described below.

Results

[3] $Tip_2CHC(=O)\text{-}R \rightleftharpoons Tip_2C{=}C(OH)R$ (K_{Enol})

5: a: R = H; b: R = Me; c: R = *t*-Bu

6: a: R = H; b: R = Me; c: R = *t*-Bu

Synthesis of 2,2-ditipylethanones (5) and 2,2-ditipylethenols (6)

The precursor for compounds **6** and **5** was ditipylketene, which was prepared by us previously (12). Its reduction by $LiAlH_4$ (13) gave 2,2-ditipylethenol (**6a**), which was prepared earlier by Fuson et al. (8). Grignard reactions with MeLi and *t*-BuLi gave 1,1-ditipyl-1-propen-2-ol (**6b**) and 1,1-ditipyl-3,3-dimethyl-1-buten-2-ol (**6c**) as described earlier (13).

In the synthesis of **5c**, three other compounds were formed and identified by NMR, (*i*) ditipylacetic acid, (*ii*) the oxidative-cyclization product, 2-*tert*-butyl-3-tipyl-4,6-di (isopropyl) benzofuran, **7c**, which was described earlier (13), and (*iii*) the ketone, 1,1-ditipyl-3,3-dimethyl-2-butanone (**5c**). Indeed, when the ketene was reacted with *t*-BuLi in refluxing THF, **6c** comprises <5% of the product, and the main products were the acid, **5c** and **7c** (eq. [4]). However, at 0°C, >95% of **6c** was formed, but on work-up, which involved evaporation of the solvent by heating in vacuo on a steam bath, **6c** and **5c** were formed in different ratios, depending

[4] $Tip_2C{=}C{=}O \xrightarrow{t\text{-BuLi}} Tip_2C{=}C(OH)Bu\text{-}t \longrightarrow$ *i*-Pr, Tip, Bu-*t* + $Tip_2CH\text{-}C(=O)\text{-}Bu\text{-}t$

6c **7c** **5c**

© 1999 NRC Canada

on the length of the heating time. Formation of the side products was avoided by conducting the reaction in ether and evaporation of the solvent at room temperature.

Ketones **5b** and **5c** were prepared by TFA-catalyzed ketonization of their isomeric enols **6b** and **6c** in hexane (eq. [5]). To avoid a competing facile oxidative cyclization to benzofurans **7b** and **7c** in air, especially at higher temperatures, the isomerization of **6b** was performed at room temperature and that of **6c** in vacuum-sealed ampoules. The yields of the ketones were affected by the competitive oxidative cyclization.

[5] $\underset{\textbf{6b}\ \textbf{6c}}{Tip_2C{=}C(OH)R} \underset{}{\overset{TFA,\ hexane}{\rightleftharpoons}} \underset{\textbf{5b}\ \textbf{5c}}{Tip_2CHC(=O)\text{-}R}$

Ditipylethanal **5a** could not be isolated from an equilibrium mixture with 2,2-ditipylethenol **6a**, since **6a** comprises >98% of the mixture. This also provides a mechanistic rationalization for Fuson's method (8) for the formation of **6a**, which involves dehydration of 1,2-ditipylethanediol. A pinacol rearrangement probably generates **5a**, which rapidly isomerizes under the acidic conditions to the more stable **6a**. A similar behavior was observed with 2,2-dimesitylethanal, which was defined as "elusive" (14). The latter was then prepared by pyridinium dichromate (PDC) oxidation of 2,2-dimesitylethanol, which proceeds at neutral pH and which presumably does not involve an enolic intermediate.

An attempt was made to form **5a** by a similar oxidation of 2,2-ditipylethanol **8**. A LAH reduction of ditipylacetyl chloride ($Tip_2CHCOCl$) failed, and ditipylketene rather than the required **8** was obtained by spontaneous elimination of HCl. LAH reduction of methyl ditipylacetate at room temperature in THF gave directly ethenol **6a**. This is probably due to reduction of the ester to the desired **5a**, which, however, isomerized to **6a** under the strongly basic conditions (eq. [6]). In refluxing diglyme, the LAH reduction gave 1,1-ditipylethylene, presumably by elimination of water from the intermediate **8** (eq. [6]). This is interesting, since the method used to prepare 1,1-dimesitylethylene (15) failed in attempted preparation of 1,1-ditipylethylene.

We succeeded in synthesis of **8** in 72% yield by bubbling formaldehyde vapor into a solution in which the ditipylmethyl anion Tip_2CH^- was generated by ultrasonic irradiation of a solution of Tip_2CHOMe in the presence of a Na/K alloy (eq. [7]).

However, when **8** was oxidized with PDC, both **5a** and **6a** were formed (eq. [8]). This is attributed to isomerization of **5a** to **6a** under the mild reaction conditions. Consequently, long reaction times have to be avoided, and the oxidation has to be stopped before completion of the reaction when some **8** still unreacted and **5a** was formed in a low amount, i.e., the **8**:**5a**:**6a** ratio is 5:5:1. Attempted purification of **5a** by chromatography or crystallization was unsuccessful, since both processes led to isomerization to **6a**. Nevertheless, **5a** could be detected by NMR using the characteristic formyl doublet at δ 10.20 (J = 2 Hz) and the CH doublet at δ 6.15. These signals were used in evaluating K_{Enol} for **5a**/**6a**.

Equilibrations and K_{Enol} values

The K_{Enol} values for the **5a**–**5c**/**6a**–**6c** pairs were measured semiquantitatively and compared with values previously measured for the dimesityl (2) and pentamethylphenyl (7) analogs. An accurate determination of K_{Enol} at 80°C, where K_{Enol} values for **3a**–**c** were determined, was not performed due to the easy oxidation–cyclization to benzofurans **7a**–**c**.

Samples of the enol were dissolved in hexane and TFA was added. From the light-protected ampoules kept at 77.5°C, samples were withdrawn, the solvent was evaporated at room temperature, and the **5** to **6** ratios were determined by integration of well-separated signals (usually Tip-H) of the two species in the ^{1}H NMR spectrum of the equilibrium mixture. When the **5**/**6** ratios were identical for two samples taken at sufficiently different reaction times, the ratio was regarded as the equilibrium ratio. However, even in vacuum-sealed pressure ampoules, presumably oxygen-free conditions, the benzofurans were still observed and in up to 5% in the reaction of **6a**. This reduces the accuracy of the measurements. The percentage of enol at equilibrium, the derived K_{Enol} values and K_{Enol} values for the corresponding 1-R-2,2-dimesityl and 2,2-bis(pentamethylphenyl) derivatives are given in Table 1.

Oxidation–cyclization of 2,2-ditipylethenols to 3-tipylbenzofurans

As noted above, during the preparation of **5c**, we observed the formation of benzofuran **7c**, especially at high temperature. In addition, in the course of variable-temperature NMR experiments (13), pure samples of enols

[6] $Tip_2CH\text{-}C(=O)\text{-}OMe \xrightarrow[THF]{(a)\ LiAlH_4} [\underset{\textbf{5a}}{Tip_2CH\text{-}C(=O)\text{-}H}] \rightleftharpoons \underset{\textbf{6a}}{Tip_2C{=}CHOH}$

$[Tip_2CHCH_2OH]_{\textbf{8}} \xrightarrow{-H_2O} Tip_2C{=}CH_2$ (b) $LiAlH_4$, diglyme, reflux

[7] $Tip_2CHOMe \xrightarrow[)))]{K/Na} [Tip_2CH^-] \xrightarrow{CH_2O} \underset{\textbf{8}}{Tip_2CHCH_2OH}$

[8] $\underset{\textbf{8}}{Tip_2CHCH_2OH} \xrightarrow{PDC} \underset{\textbf{5a}}{Tip_2CHCHO} + \underset{\textbf{6a}}{Tip_2C{=}CHOH}$

© 1999 NRC Canada

6a and **6b** in $C_6D_5CD_3$ or in DMSO-d_6 became contaminated by side products formed at >80°C, after 1–2 h. When samples of **6a** and **6b** in the same solvents were kept for 18 h at 110°C, the ^{1}H NMR spectra of pure benzofurans **7a** and **7b** (identical with the side products mentioned above) were obtained, whereas the transformation of **6c** to **7c** was much faster and required only 2–3 h (eq. [9]). We ascribe the enol to benzofuran transformation to air oxidation of the enols, which becomes easier when R is bulkier so that **6c** cyclizes even at room temperature.

[9] $Tip_2C{=}C(OH)R \xrightarrow{\Delta}$ 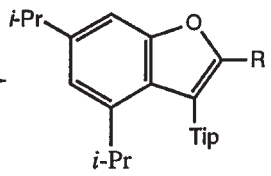

6a R = H
6b R = Me
6c R = *t*-Bu

7a R = H
7b R = Me
7c R = *t*-Bu

Discussion

The effect of β-substituents on K_{Enol} values

We have now three short sets of K_{Enol} values in hexane for β,β-diaryl-1-R carbonyl–enol systems for R = H, Me, *t*-Bu and Ar = Tip, Mes, and Me_5C_6 under nearly similar conditions (Table 1). The qualitative behavior is the same, for R the K_{Enol} values follow the order H >> Me >> *t*-Bu, where the percentage of enol is ≥95% for R = H, 10–78% for R = Me, and 2–0.1% for R = *t*-Bu.

Comparison of the data of Table 1 with the dimesityl systems was already discussed for the pentamethylphenyl system, where the increase in bulk is due to buttressing effect. In the case of the ditipyl system, the effect is related to the increased bulk of the 2,6-substituents, assuming that the difference in the electronic effect of Mes and Tip will be small.

However, before making comparisons, a comment on the accuracy of the data is in order. The advantage of "observing" directly both the carbonyl and the enol species at equilibrium by NMR (excellent data reliability) is also a disadvantage, since only in a relatively narrow range of the equilibrium constants, K_{Enol} values, is the error rather low, i.e., when both species are formed in appreciable quantities (between ca. 10% to ca. 90%). Due to NMR integration, when the concentration of either the carbonyl compound or the enol is ≤2–3%, the relative errors in the concentration and in the derived K_{Enol} value are rather high. This should be taken into account when comparing K_{Enol} values for relatively high or relatively low enol concentration in our systems.

Two interesting points arise from comparison of the dimesityl and the ditipyl systems. First, the α-H-β,β-ditipyl enol **6a** is relatively more stabilized than the α-H-β,β-dimesityl enol **4a**, whereas the relative stability is inversed with the α-alkyl (Me, *t*-Bu) systems. The K_{Enol} values for **5a**/**6a** is even higher than for trimesitylethenol (14), but it is lower than for the pentamethylphenyl system (7). Considering the errors in the values, the higher value for **5a**/**6a** compared with **3a**/**4a** is real. Second, qualitatively, we found that the equilibration rates are affected by the bulk of the α-ring. Whereas for **3b** and **3c** equilibration was achieved after 14 and 8 h, respectively, longer times, i.e., 8 and 4 days were required for the tipyl analogs for reaching equilibrium under almost identical conditions. When **6b** was equilibrated with **5b** at room temperature, the changes in the keto:enol ratios were <2% during several months.

The factors influencing the stability of 2,2-diaryl-1-R-ethenols were previously discussed (1). They involve mainly the extent of Ar-C=C conjugation and steric effect on it. Ph-C=C conjugation at full planarity was estimated as 4.5 kcal mol^{-1} per completely coplanar single ring, and the effect of a change to a mesityl ring was estimated to be small (fully planar Mes-C=C, 4.8 kcal mol^{-1}) (4). This interaction lacks a counterpart in the ketone where the CH is sp^3-hybridized. Steric effects in the aryl group, e.g., by 2,6-alkyl substituents affect the K_{Enol} values in two ways. First, they increase the Ar-C=C dihedral angle and, consequently, decrease the conjugation. Second, the steric repulsion between two geminal bulky aryl groups is better accommodated in the enols with a "formal" 120° angle between these groups than in the carbonyl system with 109° angle. This interpretation suggests that this factor will increase K_{Enol} with the increased bulk of the β-aryl. Moreover, the decrease of K_{Enol} with the increased bulk of R for the **3**/**4** series (2) is accounted for by the sensitivity of the Ar-C=C interaction to steric hindrance. Since the interaction will be larger with the bulkier α-tipyl ring, it explains why enols **6b** and **6c** are destabilized relatively to their mesityl analogs. Unfortunately, supporting crystallographic data for this assumption is not available due to the difficulty in getting good crystals.

On the other hand, the higher stability of **6a** compared with **4a** is puzzling, since the repulsion should distort the bulkier tipyl rings from planarity with the double bond even more than in **4a**. The solid-state structure show that the Ar-C=C torsion angles for **6a** (56.7 and 50.2°) (13) are close to those of **4a** (54.5 and 58.9°) (16). We note that electronic effect resulting from the change Me → *i*-Pr could not account for the observed difference. We conclude that the increase of steric effect and in K_{Enol} values by *m*-Me buttressing is higher than by the change *o*-Me → *o*-*i*-Pr.

Oxidation of 2,2-ditipylethenols to the benzofurans

The oxidation of enols is a known reaction (1*b*), and it was even stated that the acid-catalyzed oxidation of some carbonyl compounds occurs via their enol tautomers (17). The ozonation of ethenols **4a** and **4e** have been investigated by Bailey et al. (18) who suggested that **4e** and ozone produce at –78°C a radical by hydrogen abstraction from the enolic OH group and isolated a benzofuran as the only product in 2–3% yield.

In studying the reactions of cation radicals derived from enols **4a** and **4c**, Schmittel et al. (19) observed the facile oxidation of the enols, which led to substituted benzofurans. In their proposed mechanism, the cation radical is first deprotonated and then oxidized to the α-carbonyl carbocation (eq. [10]). This in turn cyclizes intramolecularly to form cation **10**, which upon [1,2] methyl shift and subsequent deprotonation affords the benzofuran **9**.

© 1999 NRC Canada

[10]

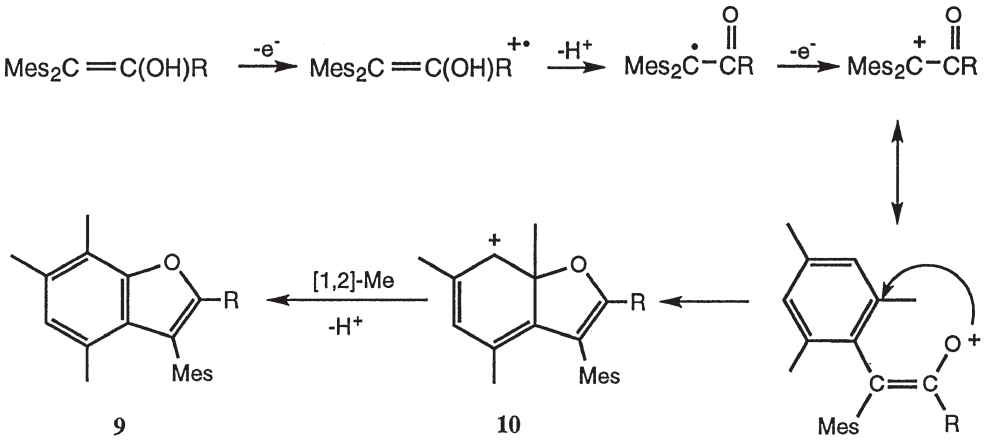

9 10

The main difference between the benzofurans **9**, derived from enols **4**, and benzofurans **7** lies in the fate of the alkyl substituent on the bridging carbon atom in the intermediate cation. With enols **4**, when Ar = Mes, a [1,2] methyl shift occurs in **10** resulting in a triaalkyl-substituted benzofuran (**9**), after a loss of a proton. When Ar = Tip, expulsion of an isopropyl cation from cation **11** is apparently more favourable energetically than its [1,2] shift, and the product is the substituted benzofuran (**7**) (eq. [11]). This is easily accounted for by the higher stability of the *i*-Pr^+ cation compared with the Me^+ cation.

[11]

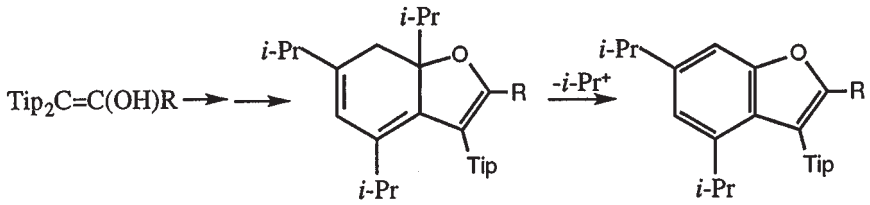

6 7 11

Another difference is that the oxidation–cyclization process, reported by Schmittel et al. (19) for enols **4**, occurs only upon addition of one-electron oxidants, and a similar thermal-induced process has not been reported. Thus, the oxidative cyclization of **4a** and **4c** occurs at room temperature but needs a one electron oxidant (e.g., $(4\text{-}BrC_6H_4)_3N^{+\cdot}SbCl_6$) as initiator whereas enols **6a**–**c** undergo a similar process without additional oxidant at a higher temperature for **6a** and **6b** and at room temperature for **6c**. These differences may indicate different stabilities of the radical cations or they may only reflect different relative rates for the [1,2] alkyl shift vs. loss of the alkyl cations.

Experimental section

General methods

Melting points were measured on a Thomas–Hoover apparatus and are uncorrected. FT infrared spectra were measured with a Nicolet Impact 400 spectrometer, and NMR spectra were recorded on Bruker WP 200 SY, Bruker WH 300, and AMX 400 pulsed FT spectrometers operating at 200.13, 300.13, and 400.13 MHz for ^1H and 50.32, 75.48, and 100.62 MHz for ^{13}C, respectively. Low-resolution mass spectra were recorded on a MAT-311 mass spectrometer, and some electron impact (EI) and chemical ionization (CI) mass spectra were recorded on a Finnigan Mat 4600 apparatus. High-resolution mass spectral analyses (HRMS) were conducted at the Mass Spectrometry Center at the Technion, Haifa, on a Finnigan Mat 711 apparatus. Microanalysis was performed at the Hebrew University.

Solvents and materials

Tetrahydrofuran (THF) was distilled from sodium benzophenone ketyl, ether from $LiAlH_4$, and benzene from P_2O_5 immediately before use. All purchased reagents were the best commercial samples and were used without purification. Polydeuteriated solvents for NMR spectroscopy (Aldrich), were dried over 4 or 3Å molecular sieves. Solvents used for chromatography were used without purification.

Equilibration studies

Solutions of the enol (10 mg) in spectroscopic hexane (Merck, 5 mL) and TFA (0.025 mL) were sealed in vacuo in pressure ampoules. The ampoules were wrapped in aluminum foil and kept at 77.5 ± 0.1°C for different time spans after which the samples were withdrawn, the solvent was evaporated at room temperature (to avoid oxidation–cyclization), and the ^1H NMR spectra in $CDCl_3$ were recorded. Samples already measured were not reused for further equilibration experiments in order to avoid interference of the formed benzofurans with the equilibration process. Hence, a separate sample was used for each time measurement. Nevertheless, some oxidation products were observed, especially in the case of **6c** but they comprised ≤5% of the equilibrium mixture. The relative ratios of the **5**/**6** species were determined by integration of the Tip-H signals of each

© 1999 NRC Canada

of the keto–enol pairs for **6b** and **6c** and of the vinylic CH and aldehyde CH doublets for **6a**. The integration values, based on these signals, were corroborated by comparing them with integration ratios of additional well-separated signals (e.g., *i*-Pr Me doublets at 0.1–0.3 ppm). To obtain reliable integration, complete relaxation of the various protons was ensured.

2,2-Bis(2,4,6-triisopropylphenyl)ethanol (8)

To a solution of ditipylmethyl methyl ether (860 mg, 1.9 mmol) in dry ether (100 mL) in a three-necked round-bottomed flask fitted with a reflux condenser, an argon inlet, and a closed gas bubbler, about 1.5 g of 4:1 potassium–sodium alloy were added, and the resulting suspension was sonicated in a dry argon atmosphere. After 6 h, formaldehyde vapours were allowed through the deep red solution until a total decolouration was achieved. Isopropanol (50 mL) was added to neutralize the unreacted alloy, and the solution was acidified to pH 2 with 10% HCl. Additional ether (100 mL) was added, the phases were separated, and the organic phase was washed with water (50 mL), dried ($MgSO_4$), and the solvent was evaporated in vacuo. The crude mixture was chromatographed on silica gel using a petroleum ether – ether gradient as eluent. The first fraction was ditipylmethane (180 mg, 22%), mp 73°C (lit. 69.5–70°C) (20). It was followed by 2,2-bis(2,4,6-triisopropylphenyl)ethanol **8** (620 mg, 72%), mp 121–123°C, after recrystallization from hexane.

^{1}H NMR (400 MHz, $CDCl_3$) δ: 0.96 (12H, d, J = 6.7 Hz, *o*-*i*-Pr-Me), 1.03 (12H, d, J = 6.7 Hz, *o*-*i*-Pr-Me), 1.20 (12H, d, J = 6.9 Hz, *p*-*i*-Pr-Me), 2.82 (2H, m, J = 6.9 Hz, *p*-*i*-Pr-CH), 3.33 (4H, m, J = 6.7 Hz, *o*-*i*-Pr-CH), 3.55 (1H, d, J = 5.6 Hz, OH), 4.33 (2H, d, J = 5.6 Hz, CH_2), 5.09 (1H, t, J = 5.7 Hz, Tip_2CH), 6.95 (4H, s, Tip-H). ^{13}C NMR (100.64 MHz, $CDCl_3$) δ: 23.94, 23.97 (2 *p*-*i*-Pr-Me), 24.53, 24.66 (2 *o*-*i*-Pr-Me), 29.08(*o*-*i*-Pr-CH), 33.81 (*p*-*i*-Pr-CH), 46.41 (Tip_2CH), 65.50 (CH_2), 122.60 (*m*-Tip-C), 134.33 (*ipso*-Tip-C), 146.70 (*p*-Tip-C), 147.83 (*o*-Tip-C). FTIR: ν_{max} (Nujol): 3277 (br, OH), 1610 (m, C=C) cm^{-1}. MS (EI) *m*/*z* (relative abundance, assignment): 450 (7%, M), 419 (36%, Tip_2CH), 377 (6%, Tip_2CH – $MeCH{=}CH_2$), 335 (66%, Tip_2CH – $2MeCH{=}CH_2$), 293 (B, Tip_2CH – $3MeCH{=}CH_2$), 251 (67%, Tip_2CH – $4MeCH{=}CH_2$), 246 (11%, $TipCH_2CHO$), 231 (18%, TipCO), 215 (21%, TipC), 209 (21%, Tip_2CH – $5MeCH{=}CH_2$). Microanalysis: calcd. for $C_{32}H_{50}O$: C 85.27, H 11.18; found: C 85.46, H 11.07.

2,2-Bis(2,4,6-triisopropylphenyl)ethanal

To a solution of 2,2-bis(2,4,6-triisopropylphenyl)ethanol (**8**) (430 mg, 0.95 mmol) in dry CH_2Cl_2 (20 mL) was added pyridinium dichromate (PDC) (537 mg, 1.43 mmol). The light-protected mixture was stirred in an argon atmosphere at room temperature for 42 h, the salts were filtered through a $MgSO_4$ coated scintered glass filter, and the filtrate was centrifuged at 1200 rpm for 3 min. The supernatant liquid was decanted, and the solvent was evaporated. The ^{1}H NMR of the crude product displayed a spectrum of a 5:5:1 mixture of **8**, aldehyde **5a**, and 2,2-ditipylethenol **6a**. The mixture was chromatographed on a slurry-packed silica column and eluted with a petroleum ether (60–80°C) – ether gradient. Aldehyde **5a** could not be isolated, since it tautomerizes completely to **6a** during the chromatographic separation.

1,1-Bis(2,4,6-triisopropylphenyl)acetone (5b)

1,1-Bis(2,4,6-triisopropylphenyl)-1-propen-2-ol (**6b**) (20 mg, 0.04 mmol) was dissolved in hexane (5 mL), and trifluoroacetic acid (TFA) (1 mL, 20%) was added. The mixture was allowed to stand at room temperature for 24 h, and TFA (1 mL) was again added. After standing at room temperature for 24 additional hours, the solvent was evaporated to dryness, and the mixture was chromatographed on a small slurry-packed silica gel column using a petroleum ether – ether gradient as eluent. Benzofuran **7b** (7 mg, 41%) and ketone **5b** (5 mg, 25%) were isolated and characterized without further purification.

5b: ^{1}H NMR (400 MHz, $CDCl_3$, 240 K) δ: 0.88 (12H, d, J = 6.5 Hz, *o*-*i*-Pr-Me), 1.02 (12H, d, J = 6.5 Hz, *o*-*i*-Pr-Me), 1.20 (12H, d, J = 6.8 Hz, *p*-*i*-Pr-Me), 2.25, 2.42 (2 × 1.5 H, 2 s, 1 Me), 2.75, 2.82 (6H, 2 overlapping m, J = 6.8 Hz, *o*,*p*-*i*-Pr-CH), 5.51, 5.53 (2 × 0.5 H, 2 s, Tip_2CH), 6.87 (4H, s, Tip-H). ^{13}C NMR (100.64 MHz, $CDCl_3$, 273 K) δ: 24.48 (*p*-*i*-Pr-Me), 24.56 (*o*-*i*-Pr-Me), 24.80 (*o*-*i*-Pr-Me), 30.54 (*p*-*i*-Pr-CH), 31.36, 32.87 (2 halves of 1 Me), 34.33 (*o*-*i*-Pr-CH), 57.60, 58.33 (2 halves of 1 Tip_2CH), 65.50 (CH_2), 122.81, 123.02 (*m*-Tip-C), 123.29 (*ipso*-Tip-C), 132.92 (*p*-Tip-C), 147.74, 147.95 (*o*-Tip-C), 210.99, 212.06 (2 halves of 1 C=O). FTIR: ν_{max} (Nujol): 1697 (s, C=O), 1610 (m, C=C) cm^{-1}. MS (EI) *m*/*z* (relative abundance, assignment): 462 (9%, M), 419 (B, M – COMe), 377 (1%, M – COMe – $MeCH{=}CH_2$), 375 (3%, M – MeCO – *i*-Pr – H), 335 (39%, M – COMe – 2 $MeCH{=}CH_2$), 293 (55%, M – COMe – 3 $MeCH{=}CH_2$), 251 (45%, M – COMe – 4 $MeCH{=}CH_2$), 215 (22%), 173 (29%, 215 – $MeCH{=}CH_2$), 131 (90%, $C_{10}H_{11}$), 119 (23%). HRMS, *m*/*z*: 462.3905; requires 462.3861 calcd. for $C_{33}H_{50}O$.

7b: ^{1}H NMR (300 MHz, $CDCl_3$) δ: 1.00 (6H, d, J = 6.9 Hz, *i*-Pr-Me), 1.01 (6H, d, J = 6.8 Hz, *i*-Pr-Me), 1.09 (6H, d, J = 6.9 Hz, *i*-Pr-Me), 1.30 (6H, d, J = 6.9 Hz, *i*-Pr-Me), 1.31 (6H, d, J = 6.9 Hz, *i*-Pr-Me), 2.15 (3H, s, Me), 2.71 (4H, m, J = 6.9 Hz, *i*-Pr-CH), 2.97 (2 × 1H, 2 overlapping m, J = 6.9 Hz, *i*-Pr-CH), 6.93 (1H, d, J = 0.8 Hz, benzofuran Ar-H), 7.04 (2H, s, Tip-H), 7.15 (1H, d, J = 0.8 Hz, benzofuran Ar-H). ^{13}C NMR (100.64 MHz, $CDCl_3$, 273 K) δ: 13.20 (C=C-*Me*), 23.38, 24.08, 24.34, 24.50, 24.99 (5 *i*-Pr-Me), 30.63, 34.21 (*i*-Pr-CH), 105.80 (C=C-Me), 113.75, 118.16, 120.57, 125.89, 127.95, 143.10, 144.68, 146.80, 146.85, 148.31, 151.83 (10 Tip-C + C=*C*-Me). MS (EI) *m*/*z* (relative abundance, assignment): 418 (B, M), 403 (21%, M – Me), 375 (16%, M – *i*-Pr), 345 (7%, M – *i*-Pr – MeOH), 216 (11%, TipCH).

1,1-Bis(2,4,6-triisopropylphenyl)-3,3-dimethyl-2-butanone (5c)

In a pressure ampoule, enol **6c** (10 mg, 0.02 mmol) was dissolved in hexane (5 mL), and TFA (0.025 mL) was added. The ampoule was vacuum-sealed and kept at 77.5°C for 6 days after which the solvent was evaporated. The ^{1}H NMR of the crude product displayed a spectrum of almost pure **5c** with some (<5%) benzofuran **7c**. The mixture was chromatographed on a small slurry-packed silica gel column using a petroleum ether – ether gradient as eluent. **5c** was isolated and characterized by ^{1}H and ^{13}C NMR.

© 1999 NRC Canada

FTIR, ν_{max} (Nujol): 1692 (s, C=O), 1610 (m, C=C) cm^{-1}. ^1H NMR (400 MHz, $CDCl_3$) δ: 0.84 (12H, d, *J* = 6.7 Hz, *o*-*i*-Pr-Me), 1.00 (12H, d, *J* = 6.7 Hz, *o*-*i*-Pr-Me), 1.16 (2 × 6H, 2 overlapping d, *J* = 6.8 and 6.9 Hz, *p*-*i*-Pr-Me),1.37 (9H, s, *t*-Bu), 2.78 (2H, m, *J* = 6.9 Hz, *p*-*i*-Pr-CH), 3.00 (4H, m, *J* = 6.7 Hz, *o*-*i*-Pr-CH), 6.22 (1H, s, Tip_2CH), 6.87 (4H, s, Tip-H). ^{13}C NMR (100.64 MHz, $CDCl_3$, 273 K) δ: 14.11 (*t*-Bu-Me), 22.65, 23.88 (*p*-*i*-Pr-Me), 24.65, 28.44 (*o*-*i*-Pr-Me), 29.98 (*p*-*i*-Pr-CH), 31.58, 33.71 (*o*-*i*-Pr-CH), 46.40 (*t*-Bu-*C*Me_3), 51.77 (Tip_2CH), 122.59 (*m*-Tip-C), 134.89 (*ipso*-Tip-C), 146.65 (*p*-Tip-C), 147.27 (*o*-Tip-C), 218.07 (C=O). MS (DCI, *i*-C_4H_{10}) *m*/*z* (relative abundance, assignment): 505 (9%, MH), 419 (7%, M – *t*-BuCO or M – 2 *i*-Pr), 371 (8%), 301 (B, M – Tip), 259 (18%, M – Tip – MeCH=CH_2), 203 (13%).

3-(2,4,6-Triisopropylphenyl)-4,6-diisopropylbenzofuran (7a)

A solution of 2,2-ditipylethenol (**6a**) (20 mg, 0.045 mmol) in diglyme (5 mL) was refluxed for 18 h. The solution was cooled to room temperature, and water (10 mL) was added. The solution was extracted twice with ether (20 mL), and the combined organic phase was washed thrice with water (20 mL), dried ($MgSO_4$), and the solvent was evaporated to dryness. Chromatography on silica gel using petroleum ether as eluent afforded 3-(2,4,6-triisopropylphenyl)-4,6-diisopropylbenzofuran (**7a**) (5 mg, 27%) as a colourless oil, which was identified by ^1H and ^{13}C NMR.

FTIR, ν_{max} (Nujol): 1620, 1611 (w, C=C) cm^{-1}. ^1H NMR (400 MHz, $CDCl_3$) δ 1.01 (6H, d, *J* = 6.8 Hz, *i*-Pr-Me), 1.05 (6H, d, *J* = 6.8 Hz, *i*-Pr-Me), 1.13 (6H, d, *J* = 6.8 Hz, *i*-Pr-Me), 1.32 (12H, dd, *J* = 6.8 Hz, *i*-Pr-Me), 2.75 (2H, m, *J* = 6.8 Hz, *i*-Pr-CH), 2.78 (1H, m, *J* = 6.8 Hz, *i*-Pr-CH), 2.95 (1H, m, *J* = 6.8 Hz, *i*-Pr-CH), 3.03 (1H, m, *J* = 6.8 Hz, *i*-Pr-CH), 7.00 (1H, d, *J* = 0.8 Hz, benzofuran Ar-H), 7.05 (2H, s, Tip-H), 7.24 (1H, d, *J* = 0.8 Hz, benzofuran Ar-H), 7.33 (1H, s, vinylic H). ^{13}C NMR (100.64 MHz, $CDCl_3$, 273 K) δ 22.61, 23.94, 24.06, 24.16, 24.31, 25.94, 27.56 (*i*-Pr-Me), 30.61, 34.27, 34.30 (*i*-Pr-CH), 106.06 (H-*C*=C), 118.30, 118.43, 120.45, 126.92, 141.96, 143.86, 145.99, 148.38, 148.63, 155.71 (10 Ar-C + C=*C*-Tip). HRMS, *m*/*z*: 404.3138; requires 404.3079 calcd. for $C_{29}H_{40}O$. MS (EI) *m*/*z* (relative abundance, assignment): 404 (48%, M), 361 (B, M – *i*-Pr).

References

1. (*a*) Z. Rappoport and S.E. Biali. Acc. Chem. Res. **21**, 442 (1998); (*b*) H. Hart, Z. Rappoport, and S.E. Biali. *In* The chemistry of enols. *Edited by* Z. Rappoport. Wiley, Chichester. 1990. Chap. 8. p. 481.
2. D.A. Nugiel and Z. Rappoport. J. Am. Chem. Soc. **107**, 3669 (1985).
3. S.E. Biali and Z. Rappoport. J. Am. Chem. Soc. **106**, 477 (1984).
4. E.B. Nadler and Z. Rappoport. J. Am. Chem. Soc. **109**, 2112 (1987).
5. E.B. Nadler and Z. Rappoport. J. Org. Chem. **55**, 2673 (1990).
6. S.E. Biali and Z. Rappoport. Bull. Soc. Chim. Belg. **91**, 388 (1982).
7. I. Eventova, E.B. Nadler, E. Rochlin, J. Frey, and Z. Rappoport. J. Am. Chem. Soc. **115**, 1290 (1993).
8. R.C. Fuson, D.H. Chadwick, and M.L. Ward. J. Am. Chem. Soc. **68**, 389 (1946).
9. H. Hart, Z. Rappoport, and S.E. Biali. *In* The chemistry of enols. *Edited by* Z. Rappoport. Wiley, Chichester. 1990. Chap. 8. pp. 524–528.
10. A.R. Miller. J. Org. Chem. **41**, 3599 (1976).
11. P.J. Wagner and M.A. Meador. J. Am. Chem. Soc. **106**, 3684 (1984).
12. J. Frey and Z. Rappoport. J. Am. Chem. Soc. **118**, 5169 (1996).
13. J. Frey and Z. Rappoport. J. Org. Chem. **62**, 8372 (1997).
14. S.E. Biali and Z. Rappport. J. Am. Chem. Soc. **107**, 1007 (1985).
15. R.M. Roberts, A.M. El-Khawaga, and S. Roengsumran. J. Org. Chem. **49**, 3180 (1984).
16. M. Kaftory, D.A. Nugiel, S.E. Biali, and Z. Rappoport. J. Am. Chem. Soc. **111**, 8181 (1989).
17. H.S. Verter. *In* The chemistry of the carbonyl group. Vol. 2. *Edited by* J. Zabicky. Wiley, New York. 1970. p. 71.
18. (*a*) P.S. Bailey, F.E. Potts III, and J.W. Ward. J. Am. Chem. Soc. **92**, 230 (1970); (*b*) P.S. Bailey, J.W. Ward, R.E. Hornish, and F.E. Potts III. Adv. Chem. Ser. **112**, 1 (1970); (*c*) P.S. Bailey, J.W. Ward, F.E. Potts III, Y.-G. Chang, and R.E. Hornish. J. Am. Chem. Soc. **96**, 7228 (1974).
19. (*a*) M. Schmittel and U. Baumann. Angew. Chem. Int. Ed. Engl. **29**, 541 (1990); (*b*) M. Schmittel and M. Röck. Chem. Ber. **125**, 1611 (1992); (*c*) M. Schmittel, G. Gescheidt, and M. Röck. Angew. Chem. Int. Ed. Engl. **33**, 1961 (1994); (*d*) M. Schmittel, J. Heinze, and H. Trenkle. J. Org. Chem. **60**, 2726 (1995).
20. C.M. Welch and H.A. Smith. J. Am. Chem. Soc. **73**, 4391 (1951).

© 1999 NRC Canada

Intermolecular proton transfer in catalysis by carbonic anhydrase V

J. Nicole Earnhardt, Chingkuang Tu, and David N. Silverman

Abstract: The dehydration of bicarbonate catalyzed by carbonic anhydrase is accompanied by the transfer of a proton from solution to the zinc-bound hydroxide. We have investigated the properties of proton transfer from donors in solution, mostly derivatives of imidazole and pyridine, to a truncated mutant of carbonic anhydrase V with replacements that render the active site cavity less sterically constrained, Tyr 64 → Ala and Phe 65 → Ala. Catalysis was measured by determining the rate of exchange of ^{18}O between the CO_2–HCO_3^- system and water, and rate constants for proton transfer were estimated as the rate-limiting step in the release of $H_2{}^{18}O$ from the enzyme to solution. Each proton donor enhanced catalytic activity in a saturable manner. The resulting rate constants for proton transfer when compared with the values of pK_a of the donor and acceptor gave a Brønsted plot of high curvature. These data could also be described by Marcus theory which showed an intrinsic barrier for intermolecular proton transfer near 0.8 kcal/mol and a work term or thermodynamic contribution to the free energy of reaction near 10 kcal/mol. This low intrinsic kinetic barrier for proton transfer is very similar to nonenzymic bimolecular proton transfer between nitrogen and oxygen acids and bases in solution. However, the significant thermodynamic contribution suggests appreciable involvement of solvent and active-site organization prior to proton transfer. These Marcus parameters are very similar to those describing intramolecular proton transfer from His 64 in carbonic anhydrase, suggesting similarities in the intra- and intermolecular proton transfer processes.

Key words: carbonic anhydrase, proton transfer, Marcus theory, carbon dioxide.

Résumé : La déshydratation du bicarbonate catalysée par l'anhydrase carbonique est accompagnée par le transfert d'un proton de la solution à l'hydroxyde lié au zinc. Nous avons étudié les propriétés du transfert de protons de donneurs en solution, principalement de dérivés de l'imidazole et de la pyridine, vers un mutant tronqué de l'anhydrase carbonique V avec des remplacements qui rendent la cavité du site actif stériquement moins encombrée, Tyr 64 → Ala et Phe 65 → Ala. On a mesuré la catalyse en déterminant la vitesse d'échange du ^{18}O entre le système CO_2–HCO_3^- et l'eau et on a évalué les constantes de vitesse pour le transfert de proton en faisant l'hypothèse qu'il s'agit de l'étape cinétiquement limitante dans le transfert du $H_2{}^{18}O$ de l'enzyme à la solution. Chaque donneur de proton augmente l'activité catalytique d'une façon saturable. Quand on compare les constantes de vitesse pour le transfert de proton avec les valeurs de pK_a du donneur et de l'accepteur, on obtient une courbe de Brønsted qui comporte une grande courbure. Ces données peuvent aussi être décrites par la théorie de Marcus qui met en évidence une barrière intrinsèque pour le transfert intermoléculaire de proton près de 0,8 kcal/mol et un terme de travail ou une contribution thermodynamique à l'énergie libre de la réaction près de 10 kcal/mol. Cette faible barrière cinétique intrinsèque pour le transfert de proton est très semblable au transfert de proton bimoléculaire non enzymatique entre l'azote et l'oxygène d'acides et de bases en solution. Toutefois, la contribution thermodynamique significative suggère une implication appréciable du solvant et une organisation du site actif avant le transfert de proton. Ces paramètres de Marcus sont très semblables à ceux qui décrivent le transfert intramoléculaire de proton à partir du His 64 de l'anhydrase carbonique; ceci suggère l'existence de similarités entre les processus de transfert de proton intra- et intermoléculaires.

Mots clés : anhydrase carbonique, transfert de proton, théorie de Marcus, bioxyde de carbone.

[Traduit par la Rédaction]

Small buffers in solution such as imidazole and derivatives can act as proton donors and acceptors to enhance the maximal rate of catalysis by carbonic anhydrase (CA) (1–3). Such enhancement is also observed in mutants of isozyme II in which the predominant intramolecular proton shuttle residue His 64 is replaced with Ala (2). The rate enhancement occurs in the second stage of catalysis shown in eq. [2] for the dehydration direction. A series of proton transfer steps

Received November 18, 1998.

This paper is dedicated to Jerry Kresge in recognition of his many achievements in chemistry.

J.N. Earnhardt, C.K. Tu, and D.N. Silverman.[1] Department of Biochemistry and Molecular Biology and Department of Pharmacology, University of Florida College of Medicine, Gainesville, FL 32610-0267, U.S.A.

[1]Author to whom correspondence may be addressed. Telephone: (352) 392-3556. Fax: (352) 392-9696. e-mail: silvrmn@nervm.nerdc.ufl.edu

 © 1999 NRC Canada

reestablishes the zinc-bound water form of the enzyme following the conversion of HCO_3^- into CO_2, eq. [1]. Here, BH represents buffer in solution or a proton donor that is part of the enzyme itself.

$$[1] \quad HCO_3^- + E\text{-}ZnH_2O \rightleftarrows CO_2 + E\text{-}ZnOH^- + H_2O$$

$$[2] \quad E\text{-}ZnOH^- + BH \rightleftarrows E\text{-}ZnH_2O + B^-$$

These buffer enhancements have been observed in steady-state experiments and in ^{18}O exchange at chemical equilibrium and are saturable and consistent with proton transfer to the zinc-bound hydroxide (3–5). The maximal rate constants of catalysis by variants of CA lacking His 64 but enhanced by proton transfer from these buffers often are similar to their counterparts containing His 64. The introduction of proton shuttles through site-directed mutagenesis or buffers in solution both are capable of achieving proton transfer rates nearly as rapid as in the most efficient carbonic anhydrase II.

In this study, a series of structurally homologous imidazole, pyridine, and morpholine buffers were used as proton donors in catalysis by a truncated mutant of CA V lacking a single predominant proton shuttle. The buffers met several criteria: a small size, a heterocyclic ring with nitrogen atoms, and only methyl substitutions on the ring. In using not only more proton donors but also donors of a more extended range of pK_a values, we extend earlier work on proton transfer to CA II (6). For the enzyme, we chose a truncated mutant of the well-studied murine CA V in which the active site was made less sterically constrained by the double replacements Tyr 64 → Ala and Phe 65 → Ala (Y64A/F65A CA V). This also has the advantage that intermolecular proton transfer from external donors can be compared with intramolecular proton transfer in Y64H/F65A CA V containing the proton shuttle His 64 (7).

Rates of catalysis were measured by ^{18}O exchange at chemical equilibrium, offering the advantage that measurements can be made in the absence of buffer or in the presence of large amounts of buffer. Such measurements are difficult using steady-state methods that depend on changes in absorbance of a pH indicator. The exchange of ^{18}O between CO_2 and water was measured by mass spectrometry to determine rate-limiting proton transfer from these buffers to the zinc-bound hydroxide in the dehydration direction of catalysis.

Rate constants for proton transfer are presented in a free-energy plot, similar to previous studies of intramolecular proton transfer in mutants of human CA III containing a histidine as a proton shuttle (8). A curvature was found in this free-energy plot that is characteristic of a fast and efficient proton transfer. Application of Marcus rate theory shows that this proton transfer has the small intrinsic energy barrier (near 0.8 kcal/mol), which is also characteristic of nonenzymic rapid proton transfer between nitrogen and oxygen acids and bases in solution. The Marcus parameters yield a thermodynamic component of the free energy of reaction (near 10 kcal/mol), indicating that there is a significant involvement of energy requiring processes such as solvent reorganization or enzyme conformational change, similar to intramolecular counterparts in catalysis by carbonic anhydrase.

Methods

Enzymes

Bacterial expression vectors optimized for efficient site-directed mutagenesis and protein synthesis as described by Tanhauser et al. (9) were used to prepare murine carbonic anhydrase V and mutants. Mutant forms of murine CA V were created using a mutating oligonucleotide (10) in the pET31 expression vector system. All mutations were confirmed by DNA sequencing of the expression vector used to produce the mutant protein. All of the expressed enzymes in this work were truncated forms lacking the first 51 amino-terminal residues. In a sequence numbering scheme consistent with CA II, the expressed CA V variants began at residue 22, Ser. This truncated form of murine CA V (denoted mCA Vc by Heck et al. (11)) has been shown to have identical catalytic properties to CA V expressed from both a full-length coding sequence and a 30 residue truncation of murine CA V (11).

Mutants of carbonic anhydrases V were purified by affinity chromatography on a gel containing *p*-aminomethylbenzenesulfonmamide coupled to agarose beads as described by Heck et al. (11). The resulting enzymes were greater than 95% pure, determined by polyacrylamide gel electrophoresis. Concentrations of wild-type murine CA V and mutants were determined from the molar absorptivity of 4.3×10^4 M^{-1} cm^{-1} at 280 nm (11). The concentration of enzyme was also determined by titration with the inhibitor ethoxzolamide using a Henderson plot (12).

Oxygen-18 exchange

Mass spectrometry was used to measure the rate of catalyzed and uncatalyzed exchange of ^{18}O between CO_2 and water.

$$[3] \quad HCOO^{18}O^- + EZnH_2O \rightleftarrows EZn^{18}OH^- + CO_2 + H_2O$$

$$[4] \quad BH + EZn^{18}OH^- \overset{k_B}{\rightleftarrows} B^- + EZn^{18}OH_2 \overset{H_2O}{\rightleftarrows} B^- + EZnH_2O + H_2{}^{18}O$$

This method is based on experiments of Mills and Urey (13) and is described in its application to carbonic anhydrase by Silverman (14). The kinetic equations for the redistribution of ^{18}O from the CO_2–HCO_3^- system to water were solved to obtain two rates in the ^{18}O exchange catalyzed by carbonic anhydrase (15, 16). The first is R_1, the rate of exchange of HCO_3^- and CO_2, as shown in eq. [3]. The substrate dependence of R_1 is given by

$$[5] \quad R_1/[E] = k_{cat}^{ex}[S]/(K_{eff}^{S} + [S])$$

in which k_{cat}^{ex} is a rate constant for maximal interconversion of CO_2 and HCO_3^-, K_{eff}^{S} is an apparent substrate binding constant, and [S] is the concentration of substrate, CO_2 or HCO_3^- or both (17). In theory and in practice, $k_{cat}^{ex}/K_{eff}^{CO_2}$ is equal to k_{cat}/K_m for hydration obtained by steady-state methods (17). The second rate is R_{H_2O}, the rate of release from the active site of water bearing substrate oxygen, as shown in eq. [4] (14). In this mechanism, a proton converts

© 1999 NRC Canada

Table 1. Constants of eqs. [6] and [7] for the enhancement of catalysis by buffers in Y64A/F65A CA V.

Entry in Fig. 4	Donor	pK_a(donor)[a]	ΔpK_a[b]	k_B ($\times 10^{-5}$ s^{-1})[c]	K_{eff}^B (mM)[c]
a	Morpholine	8.6	–1.5	0.6 ± 0.1	16 ± 14
b	2-Methyl imidazole	8.1	–1.0	1.3 ± 0.3	105 ± 40
c	4(5)-Methyl imidazole	7.7	–0.6	1.8 ± 0.2	32 ± 9
d	1-Methyl imidazole	7.3	–0.2	3.7 ± 1.0	110 ± 61
e	3,4-Dimethyl pyridine	6.7	0.4	4.5 ± 0.5	24 ± 7
f	3,5-Dimethyl pyridine	6.3	0.8	3.5 ± 0.2	20 ± 3
g	3-Methyl pyridine	5.9	1.3	5.4 ± 0.6	35 ± 10
h	Pyridine	5.4	1.7	3.0 ± 0.7	2.4 ± 1.1
1	2,4-Dimethyl pyridine	6.9	0.2	1.9 ± 0.2[d]	
2	2,6-Dimethyl pyridine	6.9	0.2	1.2 ± 0.2	19 ± 16
3	2,5-Dimethyl pyridine	6.7	0.4	1.4 ± 0.2	15 ± 6
4	2-Methyl pyridine	6.1	1.0	2.3 ± 0.2	18 ± 5
	Imidazole	7.3	–0.2	9.6 ± 2.0	82 ± 41
z	CA V Y64H/65A[e]	6.2	–0.1	3.7 ± 0.7	

[a] pK_a(donor) is equal to –log K_B in eq. [7]. pK_a values were determined from pH titration of 10 mM solutions of buffers with the ionic strength maintained near 0.2 M with the addition of Na_2SO_4. Standard errors in pK_a were less than 1%.

[b] pK_a(zinc-bound water) – pK_a(donor), the pK_a(zinc-bound water) was 7.1 ± 0.2 in Y64A/F65A CA V in the absence of buffer.

[c] k_B^{obs} and K_{eff}^B were determined from the dependence of R_{H_2O}/[E] as a function of the concentration of protonated buffer in catalysis by Y64A/F65A CA V at pH values equal to pK_a of buffer and under the experimental conditions described in the legend of Fig. 1. Where applicable the data for R_{H_2O}/[E] were corrected for the apparent inhibition manifested in R_1/[E]. Values of k_B^{obs} and pK_a for the donor and acceptor were then applied to eq. [7] to determine the k_B values listed for each buffer.

[d] Experimental conditions are described in the legend to Fig. 1. For this buffer, the data are means and standard errors of four measurements of R_{H_2O}/[E] using a saturating concentration of buffer. The value of k_B was determined from eq. [7].

[e] Data was obtained from the difference in R_{H_2O}/[E] determined from a pH profile of CA V Y64H/F65A (C.K. Tu, unpublished data) and Y64A/F65A CA V, the experimental conditions are described in the legend of Fig. 2.

Fig. 1. The dependence of R_{H_2O}/[E] (●) and R_1/[E] (□) on concentration of 3,5-dimethyl pyridine at pH 6.3 and 25°C. The total concentration of all species of CO_2 was 25 mM, and the total ionic strength of solution was maintained at a minimum of 0.2 M by addition of Na_2SO_4. Values of R_{H_2O}/[E] were fit to eq. [6], yielding a value for k_B^{obs} of (1.7 ± 0.1) × 10^4 s^{-1} represented by the solid line. The broken line is a fit to the same equation for R_{H_2O}/[E] when corrected for the apparent inhibition in R_1/[E].

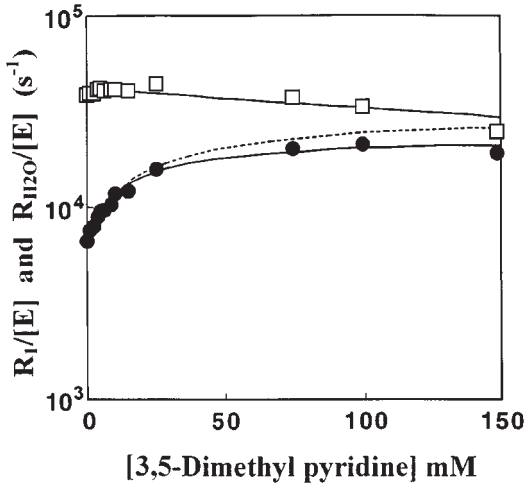

zinc-bound hydroxide into zinc-bound water which then allows rapid exchange with solvent water. The steps measured by R_{H_2O} are separate and distinct from those of the interconversion of CO_2 and HCO_3^- in eq. [3].

Measurements of the isotopic content of CO_2 were made using an Extrel EXM-200 mass spectrometer with a membrane inlet probe (14). Solutions contained 25 mM total substrate ([CO_2] + [HCO_3^-]). Total ionic strength of solution was maintained at a minimum of 0.2 M with Na_2SO_4, and the temperature was 25°C unless otherwise noted. For determination of solvent hydrogen isotope effects, all pH measurements are presented as uncorrected pH meter readings. This procedure causes the approximate cancellation of the effects of D_2O on both the pH meter and the ionization constant of titratable groups. Solvent hydrogen isotope effects for catalysis by Y64A/F65A CA V were determined for several of the buffers of Table 1 by measuring the pH profiles for R_{H_2O}/[E] in 99.8% D_2O.

Results

Saturable enhancement of catalysis by buffers

We have determined the effect of imidazole, pyridine, and morpholine, and some of their methylated derivatives as proton donors to Y64A/F65A CA V in catalysis of ^{18}O exchange. These proton donors enhance R_{H_2O}/[E] in a saturable manner with relatively little effect on R_1/[E], the rate of interconversion of CO_2 and HCO_3^-. These effects are demonstrated in Fig. 1 for the activation of R_{H_2O}/[E] by 3,5-dimethyl pyridine. Note that there is a very slight inhibition of the catalysis of R_1/[E] caused by this addition. Similar results were reported for the saturable activation of R_{H_2O}/[E] by imidazole also catalyzed by this mutant (18). The data for Y64A/F65A CA V enhanced by 3,5-dimethyl pyridine and each buffer listed in Table 1 can be described by eq. [6], which assumes proton transfer from buffers, designated BH, to the zinc-bound hydroxide (3).

© 1999 NRC Canada

Fig. 2. Variation with pH of $R_{H_2O}/[E]$, the proton-transfer dependent rate constant for the release from the enzyme of ^{18}O-labeled water, catalyzed by Y64A/F65A CA V in the (●) absence of buffer, and in the presence of (□) 100 mM 3,5-dimethyl pyridine, and (▲) 100 mM imidazole at 25°C. For Y64A/F65A in the absence of buffer, the solid line represents a nonlinear least-squares fit of eq. [7] to the data with the pK_a of the donor >9 and acceptor equal to 6.9 ± 0.3 and the rate constant for proton transfer, $k_B = (3.7 \pm 0.4) \times 10^{-4}$ s^{-1}. The total ionic strength of solution was maintained at 0.2 M by addition of Na_2SO_4; the total concentration of all species of CO_2 was 25 mM; at 25°C.

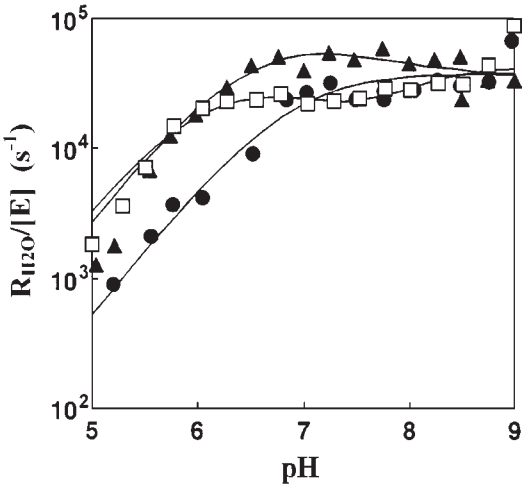

[6] $$R_{H_2O}/[E] = k_B^{obs}[BH]/(K_{eff}^{B} + [BH]) + R_{H_2O}^{0}$$

Here, k_B^{obs} is the observed rate constant for the exchange of ^{18}O to water that is enhanced by the buffers as proton donors, and K_{eff}^{B} is an apparent binding constant of the buffer to the enzyme. [E] and [BH] are the concentrations of total enzyme and total buffer. $R_{H_2O}^{0}$ is the rate of release of ^{18}O into solvent water in the absence of buffer and represents the contribution to proton transfer from the enzyme and other sources such as solvent water. Equation [6] was fit to the experimental values of $R_{H_2O}/[E]$ using least-squares methods to determine k_B^{obs} and K_{eff}^{B}. Listed in Table 1 are the values K_{eff}^{B} for each buffer.

pH dependence of buffer enhancement

The pH dependence of $R_{H_2O}/[E]$ catalyzed by Y64A/F65A CA V was determined in the absence and presence of saturating concentrations of two buffers, 3,5-dimethyl pyridine and imidazole (Fig. 2). Although it was not determined that these buffers were saturating at all pH values of Fig. 2, each of the homologous buffers of Table 1 was tested over a range of pH from 5.4 to 8.6. In these experiments, concentrations of each buffer were sufficient to saturate even the buffer of weakest binding. A difference plot of $R_{H_2O}/[E]$ for the data in Fig. 2 is shown in Fig. 3. This analysis is similar to previous pH profiles of $R_{H_2O}/[E]$ catalyzed by human CA III and mutants of human CA III in the presence of large concentrations of small buffers (3, 5, 19).

The maximal, pH-independent rate constant k_B for proton transfer from the donor group to the zinc-bound hydroxide and the corresponding pK_a values of the donor and acceptor

Fig. 3. The difference in $R_{H_2O}/[E]$, the proton-transfer dependent rate constant for the release from the enzyme of ^{18}O-labeled water, between Y64A/F65A CA V in the absence and presence of (□) 100 mM 3,5-dimethyl pyridine and (▲) 100 mM imidazole at 25°C. Experimental conditions are described in the legend to Fig. 2. The solid lines are nonlinear least-squares fits of eq. [7]. For 3,5-dimethyl pyridine, the donor pK_a = 6.2 ± 0.1, acceptor pK_a = 6.9 ± 0.1, and $k_B = (2.5 \pm 0.8) \times 10^5$ s^{-1}. For imidazole, the solid lines describe the donor pK_a = 6.4 ± 0.1, acceptor pK_a = 7.5 ± 0.1, and $k_B = (7.2 \pm 1.6) \times 10^5$ s^{-1}. The fit to the data points for the difference between Y64A/F65A in the absence and presence of 100 mM 3,5-dimethyl pyridine at pH >7.0 was not considered.

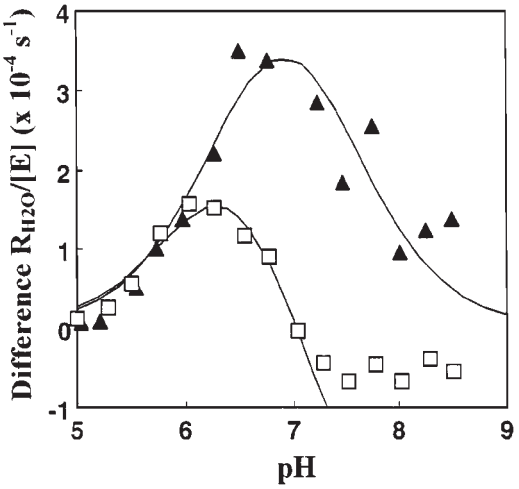

were determined from the fit of the data in Figs. 2 and 3 to eq. [7]

[7] $$R_{H_2O}/[E] = k_B/\{(1 + K_B/[H^+])(1 + [H^+]/K_E)\}$$

in which $R_{H_2O}/[E]$ can be interpreted in terms of the rate constant from a predominant donor group to the zinc-bound hydroxide (8). Here, K_B is the ionization constant for the donor group, and K_E is the ionization constant of the zinc-bound water molecule. The values of k_B and pK_a for the donor and acceptors determined for the difference between Y64A/F65A in the absence of buffer and Y64A/F65A in the presence of saturating amounts of buffer are given in the legend of Fig. 3 and are described in more detail in the following sections. In the absence of buffer, $R_{H_2O}/[E]$ determined for Y64A/F65A CA V has a maximum near 4×10^4 s^{-1} at high pH (Fig. 2). This can be interpreted as the contribution to k_B from proton shuttles of high pK_a on the enzyme (18).

The maximum near pH 6.5 in the pH profile for 100 mM 3,5-dimethyl pyridine (Fig. 2) is due to the capacity of 3,5-dimethyl pyridinium to act a proton donor. This is supported by the difference between the pH profile for $R_{H_2O}/[E]$ for Y64A/F65A CA V in the presence and absence of 3,5-dimethyl pyridine shown in Fig. 3. This difference plot shows the bell-shaped pH dependence consistent with a single proton shuttle and corresponding to a proton transfer capacity ($R_{H_2O}/[E]$) of $(2.5 \pm 0.8) \times 10^5$ s^{-1} in the presence of saturating 3,5-dimethyl pyridine. Similar results were obtained upon addition of imidazole to Y64A/F65A (Figs. 2 and 3).

© 1999 NRC Canada

pK_a of zinc-bound water

The pH dependence of k_{cat}/K_m for the hydration of CO_2 is dependent on the ionization state of the zinc-bound water and therefore yields its pK_a (1, 20). The pK_a 7.1 ± 0.2 for the zinc-bound water in the double mutant Y64A/F65A CA V was determined from the pH dependence of k_{cat}/K_m obtained from ^{18}O-exchange methods. This value of pK_a for the zinc-bound water agrees within experimental error with the pK_a 6.9 ± 0.3 determined from the pH profiles of R_{H_2O}/[E] (Fig. 2). As a control, these pK_a values were compared to those determined in the experiment shown in Fig. 3 in which saturating amounts of two buffers, 3,5-dimethyl pyridine and imidazole, were added to Y64A/F65A CA V. In each case, the pK_a of the zinc-bound water determined from R_{H_2O}/[E] was not greatly changed from that of the mutant Y64A/F65A CA V determined in the absence of buffer (Fig. 2). This finding supports the assumptions used in Table 1 that the pK_a of the zinc-bound water remains relatively unchanged upon addition of buffer to the enzyme.

pK_a of buffers

The pK_a values of the buffers listed in Table 1 were determined by pH titration of each buffer in solution (see legend of Table 1). The pH profile of R_{H_2O} catalyzed by Y64A/F65A CA V was also carefully determined in the presence of saturating amounts of two buffers, 3,5-dimethyl pyridine and imidazole (Figs. 2, 3). The value of the pK_a for 3,5-dimethyl pyridine measured from R_{H_2O} was nearly identical to that determined from titration of the buffer in solution, (Table 1, Fig. 3). However, the buffer imidazole had its pK_a decreased by 0.8 pH units in measurements of R_{H_2O}/[E]; but as will be described in the coming sections, imidazole behaves differently compared with the other buffers tested.

Solvent hydrogen isotope effects

The solvent hydrogen isotope effects (SHIE) were measured for catalysis by Y64A/F65A CA V in the presence of three buffers with values of pK_a near the pK_a of the zinc-bound water. At concentrations of buffer that saturated R_{H_2O}, the SHIE on k_B were 3.4 ± 0.1 for 3,5-dimethyl pyridine; 2.0 ± 0.4 for 3,4-dimethyl pyridine; and 1.8 ± 0.2 for 1-methyl imidazole. Values for solvent hydrogen isotope effects were determined to be near unity on k_{cat}/K_m for the steps of the interconversion of CO_2 and HCO_3^-, a stage separate and distinct from the proton transfer steps in catalysis.

Discussion

The enhancement of catalysis by carbonic anhydrase caused by introduction of proton donors in solution has been well documented (1–3, 6) In this study, we have extended this previous work to a group of homologous buffers to investigate rate–equilibria relationships in intermolecular proton transfer to the active site of carbonic anhydrase. Our goal is to understand this proton transfer process at the level described for nonenzymic bimolecular proton transfers as described by Kresge (21). This ultimately involves application of Marcus theory to proton transfer in an enzyme's active site (22).

Fig. 4. Dependence of the logarithm of k_B (s^{-1}) on ΔpK_a ($pK_{a(ZnH_2O)} - pK_{a\ (donor)}$). Values of k_B are listed in Table 1, and the experimental conditions are described in the legend of Table 1. The value of pK_a for each buffer and the zinc-bound water are determined as described in Table 1. The solid line is a nonlinear least-squares fit of eq. [9] to the Marcus equation for points *a* through *h*. This fit yielded values of $\Delta G^{\ddagger}_0$ of 0.8 ± 0.5 kcal/mol, w^r of 10.0 ± 0.2 kcal/mol, and w^p of 8.2 ± 1.0 kcal/mol.

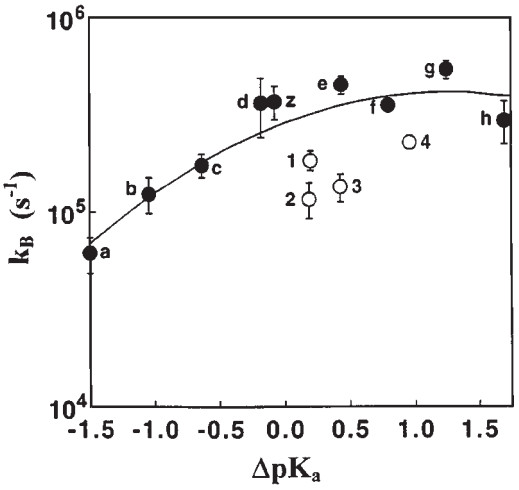

Enhancement of catalysis

As depicted in eqs.[3] and [4], R_{H_2O}/[E] measures a proton transfer dependent step of catalysis that is separate and distinct from the interconversion of CO_2 and HCO_3^-. The addition of each buffer listed in Table 1 to Y64A/F65A CA V increased R_{H_2O}/[E] in a saturable manner (Fig. 1). This is consistent with the role of buffer as a second substrate and the formation of an enzyme–substrate complex involving buffer. Several arguments suggest that the rate constant for proton transfer to the zinc-bound hydroxide, k_B, is measuring the rate-determining step of catalysis. First, previous work from ^{18}O-exchange and steady-state experiments, pH profiles, and solvent hydrogen isotope effects has demonstrated that the high values of k_B and k_{cat} found for CA V represent the rate-determining step in catalysis (7, 11). Second, these measures of maximal rates of catalysis yield solvent hydrogen isotope effects for k_B from 1.8 to 3.4 for three buffers with values of pK_a near that of the zinc-bound water. This is consistent with rate-limiting proton transfer for k_B. Therefore, the activation of R_{H_2O}/[E], as well as k_{cat}, upon increasing concentrations of buffer, is a significant measure of the effect of buffer on proton transfer. The contribution from proton shuttle residues on the enzyme itself has been reported earlier (18).

Brønsted analysis

The buffers studied in Table 1 were found to fall into three classes. The first class consists of buffers *a* through *h* that are methyl-substituted imidazoles, pyridine, and methyl-substituted pyridines at the 3, 4, and 5 positions, and morpholine. The rate constants determined for proton transfer in Y64A/F65A CA V in the presence of the buffers *a* through *h* correlated with the difference in pK_a of the zinc-bound water as acceptor group and the buffer as donor

© 1999 NRC Canada

Table 2. Marcus theory parameters for proton transfer in isozymes of carbonic anhydrase.

System	Proton donor	$\Delta G^{\ddagger}_0$ (kcal/mol)	w^r (kcal/mol)	w^p (kcal/mol)
CA V	Buffers[a]	0.8 ± 0.5	10.0 ± 0.2	8.2 ± 1.0
CA III	His 64[b]	1.4 ± 0.3	10.0 ± 0.2	5.9 ± 1.1
	His 67[c]	1.3 ± 0.3	10.9 ± 0.1	5.9 ± 1.1
	Glu or Asp 64[d]	2.2 ± 0.5	10.8 ± 0.1	4.0 ± 1.6
Nonenzymic	Buffer to buffer[e]	2.0	3.0	

[a]The data were obtained by a least-squares fit of eq. [9] to rate constants for proton transfer for points *a* to *h* given in Fig. 4 and Table 1. For this calculation, $\Delta G^{\ddagger} = -RT \ln (hk_B/kT)$ and $\Delta G^{\circ} = RT \ln [(K_a)_{ZnH_2O}/(K_a)_{donor}]$.

[b]See ref. 8.

[c]See ref. 29.

[d]See ref. 30.

[e]See ref. 25.

(Fig. 4). Such Brønsted relationships are described by eq. [8] (23–25):

$$[8] \qquad \log (k_B) = \beta[pK_a(\text{acceptor}) - pK_a(\text{donor})] + \text{constant}$$

The slope β of a Brønsted plot provides information on the transition-state structure in terms of the degree of charge transfer between reactants and products in the transition state (21). Proton transfer reactions involving carbon acids or bases usually yield slow rates and result in linear Brønsted relationships whereas fast proton transfer reactions between nitrogen and oxygen acids and bases are characterized by an observed variation in slope β over a relatively small range of pK_a values (3–5 pK_a units). This curvature is also observed in Fig. 4 for the buffers *a* through *h*. This observation establishes that the intermolecular proton transfer involving carbonic anhydrase (Fig. 4) shares an intrinsically low kinetic barrier with these nonenzymic proton transfers; that is, this conclusion is independent of the application of Marcus theory to proton transfer in an enzyme's active site that is described below.

The second class of buffers are also methyl-substituted pyridines, however, these pyridines have a methyl substitution at the 2 or 6 position (designated "1" through "4" in Table 1). The rate constants for proton transfer, k_B, from these buffers to the zinc-bound hydroxide showed greater scatter from the Brønsted plot than the previous class of buffers (Fig. 4). An explanation for this observation is that methyl groups at carbons 2 or 6 may sterically hinder access to the nitrogen and its general acid and base properties in substituted pyridines (26), in contrast to the buffers *a* through *h*.

Finally, the buffer imidazole is in a class by itself in that it has a greater rate constant for proton transfer to Y64A/F65A CA V than any buffer listed in Table 1. Its small size, similar pK_a to the conjugate acid of the proton acceptor zinc-bound hydroxide, and lack of steric hindrance in the active site may all be factors in the enhancements of proton transfer observed for Y64A/F65A CA V in the presence of this buffer.

Marcus rate theory

The curvature in Brønsted plots, similar to that found in Fig. 4, can be interpreted quantitatively through Marcus theory which provides an intrinsic energy barrier for proton transfer and work terms that correspond to the energy required to align the reactants into the reaction complex for both forward and reverse directions (25, 27). In analogy with nonenzymic transfers, w^r is the energy required to arrange the acceptor and donor groups and the surrounding water structure in the active site appropriate for the proton transfer in the dehydration direction (8). The work term w^p is the energy required for the same reorganization in the reverse direction of catalysis. $\Delta G^{\ddagger}_0$ is then the intrinsic kinetic barrier with the appropriate active site orientation. The measured overall free energy for the reaction is given by $\Delta G^{\circ} = w^r + \Delta G_R^{\circ} - w^p$, where ΔG_R° is the standard free energy of reaction in the complex with appropriate orientation for proton transfer.

The Marcus rate theory for proton transfer relates the observed overall activation barrier for proton transfer, $\Delta G^{\ddagger}$, to the intrinsic energy barrier $\Delta G^{\ddagger}_0$

$$[9] \qquad \Delta G^{\ddagger} = w^r + \{1 + \Delta G_R^{\circ}/4\Delta G^{\ddagger}_0\}^2 \Delta G^{\ddagger}_0$$

The intrinsic energy barrier $\Delta G^{\ddagger}_0$ is the value of $\Delta G^{\ddagger}$ when ΔG_R°, the standard free energy of reaction with the required active-site orientation, is zero. $\Delta G^{\ddagger}_0$ is then the barrier to reaction when the proton transfer is free of any thermodynamic constraints (25, 27). The slope of the Brønsted plot, β in eq. [8], is identified in terms of the Marcus parameters as $d\Delta G^{\ddagger}/d\Delta G^{\circ}$ and provides the connection between the curvature of the Brønsted plot and the Marcus theory.

A least-squares fit of the Marcus equation to the free-energy plot representing the rate constants for proton transfer from buffers *a* through *h* of Table 1 to the zinc-bound hydroxide of the mutant CA V were found to fit the Marcus equation (Fig. 4). The values for the intrinsic energy barrier and work terms are given in Table 2 and legend to Fig. 4. The intrinsic energy barrier for the proton transfer was found to be low with large work functions in both the forward and reverse directions (Table 2). These values determined for the contribution of external proton donors to catalysis are very similar in magnitude to the Marcus parameters describing intramolecular proton transfer from His 64 and His 67 to the zinc-bound hydroxide in mutants of human CA III (Table 2). This low intrinsic energy barrier for proton transfer is also very similar to nonenzymic proton transfer between nitrogen and oxygen acids and bases in solution (Table 2; 25). However, the large energy barrier present in the work terms of this and previous studies is large compared to work terms of 3 kcal/mol for nonenzymic reactions (24, 25). This has been interpreted as a requirement for water reorganization and possible conformation change in the active site to provide a hydrogen-bonded water pathway for proton transfer between the proton shuttle and the zinc-bound hydroxide (8). Some of

© 1999 NRC Canada

the uncertainties in the Marcus parameters derived from Fig. 4 may be due to the use of the solution values of the pK_a values of the buffers. These were measured more precisely than the pK_a of the buffers bound to the enzyme and determined from the pH profile of R_{H_2O}.

Conclusions

It is significant that proton transfer to carbonic anhydrase from external donors as quantitated by the Marcus theory is similar to proton transfer from His 64 or His 67 in the active site itself. This suggests that the water structure and possibly protein conformation appropriate for proton transfer is about equally well formed to support catalysis by buffers or by His 64, and is probably reflecting the great flexibility of many different water structures of approximately equal energy in the active site. The Marcus theory indicates that the formation of the required water structure and (or) conformational change requires considerable energy (~10 kcal/mol), but when it occurs the proton shuttles in a facile manner, similar to nonenzymic bimolecular proton transfers. The Marcus parameters obtained for His 64 and His 67 required the use of mutants of carbonic anhydrase with replacements at position 198. These replacements of Phe 198 in human CA III altered the pK_a of the zinc-bound water and allowed the construction of a Brønsted plot by varying the pK_a of the proton acceptor in dehydration. All of the data of Fig. 4 were obtained with one enzyme. Therefore, the Marcus parameters that characterize proton transfer in this study are not predominately due to the changes in the structure at the active site of the mutants.

The similarity between intermolecular proton transfer from external donors and proton transfer from His 64 is emphasized by the position of point *z*, representing Y64H/F65A murine CA V, on the same line of Fig. 4 that represents intermolecular transfer. This supports the hypothesis that proton transfer involving His 64 and external donors utilize intervening water structures of similar free energy. Such a water structure is observed in the active site in the crystal structure of CA V (28), but of course this need not be the catalytically relevant water structure. This comment about proton donors does not extend to imidazole which is a more efficient proton donor in catalysis than the other buffers of Table 1. Imidazole also had a rate constant for proton transfer in catalysis greater than that observed for Y64H/F65A CA V which contains the internal proton donor His 64 (Table 1); however, the value of k_B for imidazolium as a proton donor in catalysis by Y64A/F65A CA V is comparable to catalysis in the absence of external buffers by CA II which has His 64 as proton donor (30).

Acknowledgments

We thank Professor Philip J. Laipis for his guidance and encouragement throughout the course of this work. This work was supported by a grant (GM25154) from the NIH.

References

1. D.N. Silverman and S. Lindskog. Acc. Chem. Res. **21**, 30 (1988).
2. C.K. Tu, D.N. Silverman, C. Forsman, B.-H. Jonsson, and S. Lindskog. Biochemistry, **28**, 7913 (1989).
3. C.K.Tu, S.R. Paranawithana, D.A. Jewell, S.M. Tanhauser, P.V. LoGrasso, G.C. Wynns, P.J. Laipis, and D.N. Silverman. Biochemistry, **29**, 6400 (1990).
4. C.K.Tu, G. Sanyal, G.C. Wynns, and D.N. Silverman. J. Biol. Chem. **258**, 8867 (1983).
5. S.R. Paranawithana, C.K. Tu, P.J. Laipis, and D.N. Silverman. J. Biol. Chem. **265**, 22 270 (1990).
6. S. Taoka, C.K.Tu, K.A. Kistler, and D.N. Silverman. J. Biol. Chem. **269**, 17 988 (1994).
7. R.W. Heck, P.A. Boriack-Sjodin, M.Z. Qian, C.K. Tu, D.W. Christianson, P.J. Laipis, and D.N. Silverman. Biochemistry, **35**, 11 605 (1996).
8. D.N. Silverman, C.K. Tu, X. Chen, S.M. Tanhauser, A.J. Kresge, and P.J. Laipis. Biochemistry, **32**, 10 757 (1993).
9. S.M.Tanhauser, D.A Jewell, C.K. Tu, D.N. Silverman, and P.J. Laipis. Gene, **117**, 113 (1992).
10. T.A. Kunkel. Proc. Natl. Acad. Sci. U.S.A. **82**, 488 (1985).
11. R.W. Heck, S.M. Tanhauser, R. Manda, C.K. Tu, P.J. Laipis, and D.N. Silverman. J. Biol. Chem. **269**, 24 742 (1994).
12. I.H. Segel. Enzyme kinetics. John Wiley and Sons, New York. 1975. p. 150.
13. G.A. Mills and H.C. Urey. J. Am. Chem. Soc. **62**, 1019 (1940).
14. D.N. Silverman. Methods Enzymol. **87**, 732 (1982).
15. D.N. Silverman, C.K. Tu, S. Lindskog, and G.C. Wynns. J. Am. Chem. Soc. **101**, 6734 (1979).
16. S.H. Koenig and R.D. Brown. Biophys. J. **35**, 59 (1981).
17. I. Simonsson, B.-H. Jonsson, and S. Lindskog. Eur. J. Biochem. **93**, 409 (1979).
18. J.N. Earnhardt, M.Z. Qian, C.K. Tu, P.J. Laipis, and D.N. Silverman. Biochemistry, **37**, 7649 (1998).
19. D.A. Jewell, C.K. Tu, S.R. Paranawithana, S.M. Tanhauser, P.V. LoGrasso, P.J. Laipis, and D.N. Silverman. Biochemistry, **30**, 1484 (1991).
20. S. Lindskog. *In* Zinc enzymes. *Edited by* T.G. Spiro. John Wiley and Sons, New York. 1983. p. 78
21. A.J. Kresge. *In* Proton-transfer reactions. *Edited by* E. Caldin and V. Gold. John Wiley and Sons, New York. pp. 179–199. 1974.
22. A.J. Kresge and D.N. Silverman. Methods Enzymol. In press.
23. J.N. Brønsted and K. Pedersen. Z. Phys. Chem. 108 (1924).
24. A.J. Kresge. Chem. Soc. Rev. **2**, 475 (1973).
25. A.J. Kresge. Acc. Chem. Res. **8**, 354 (1975).
26. W.P. Jencks. *In* Catalysis in chemistry and enzymology. McGraw–Hill Book Co., New York. 1969. pp 96–97.
27. R.A. Marcus. J. Phys. Chem. **72**, 891 (1968).
28. P.A. Boriack-Sjodin, R.W. Heck, P.J. Laipis, D.N. Silverman, and D.W. Christianson. Proc. Natl. Acad. Sci. U.S.A. **92**, 10 949 (1995).
29. X. Ren, C.K. Tu, P.J. Laipis, and D.N. Silverman. Biochemistry, **34**, 8492 (1995).
30. C.K. Tu, M.Z. Qian, J.N. Earnhardt, P.J. Laipis, and D.N. Silverman. Biophys. J. **74**, 3182 (1998).

© 1999 NRC Canada

Geometric isotope effects in crystalline sodium hydrogen bis(4-nitrophenoxide) dihydrate

Maurice M. Kreevoy and Victor G. Young, Jr.

Abstract: The crystal structure of sodium hydrogen bis(4-nitrophenoxide) dihydrate, **1**, with deuterium replacing hydrogen in the bridge and the structural water molecules, has been determined crystallographically at 113, 173, and 295 K. The structure of **1** had previously been determined at similar temperatures (Kreevoy et al.). The O,O distances are 1.5–1.7 pm greater in the deuterated compound than in the undeuterated, at all three temperatures, providing another example of an Ubbelohde effect in a Speakman–Hadži compound. The temperature invariance of the Ubbelohde effect at temperatures up to room temperature is evidence against centralization of the hydron within this temperature range. It has previously been suggested (Kreevoy et al.) that simplification of the IR spectrum of **1** with increasing temperature is due to an increase in the rate of the hydron shift between the two basic oxygens. This suggestion is strengthened by the elimination of hydron centralization as an alternative. The O,O distance in **1** also increases with temperature, and the dihedral angle between the mean planes of the two aromatic rings decreases. Similarly, the increase in the O,O distance with isotopic substitution is accompanied by a small decrease in the dihedral angle; another geometric isotope effect. Ubbelohde effects in Speakman–Hadži compounds make the geometric isotope effects found computationally in the critical complexes for hydron, hydrogen atom, or hydride transfer more credible.

Key words: low-barrier hydrogen bond, Speakman–Hadži compound, geometric isotope effect, Ubbelohde effect.

Résumé : Opérant à 113, 173 et 295 K, on a déterminé la structure cristalline du dihydrate du bis(4-nitrophénolate) de sodium et d'hydrogène, **1**, dans lequel du deutérium remplace l'hydrogène dans le pont et dans les molécules structurales. La structure de **1** a été déterminée antérieurement à des températures semblables (Kreevoy et al.). À ces trois températures, les distances O,O sont de 1,5–1,7 pm plus grandes dans le composé deutéré que dans le produit non deutéré; ce résultat fournit un autre exemple d'un effet Ubbelohde dans un composé Speakman–Hadži. L'invariance avec la température de l'effet Ubbelohde à des températures allant jusqu'à la température ambiante prouve qu'il n'y a pas de centralisation de l'hydron dans cette plage de température. Il a été suggéré antérieurement (Kreevoy et al.) que la simplification du spectre IR du composé **1** avec une augmentation de la température est due à une augmentation dans la vitesse de déplacement de l'hydron entre les deux oxygènes basiques. Cette suggestion est corroborée par l'élimination de la centralisation de l'hydron comme alternative. La distance O,O dans **1** augmente aussi avec la température et l'angle dièdre entre les plans moyens des deux noyaux aromatiques diminue. De la même manière, l'augmentation de la distance O,O avec la substitution isotopique est accompagnée par une faible diminution de l'angle dièdre; un autre effet isotopique géométrique. Les effets Ubbelohde dans les composés Speakman–Hadži rendent plus plausibles les effets isotopiques géométriques calculés d'une façon théorique dans les complexes critiques pour les transferts d'hydron, d'atome d'hydrogène ou d'hydrure.

Mots clés : liaison hydrogène avec faible barrière, composé Speakman–Hadži, effet isotopique géométrique, effet Ubbelohde.

[Traduit par la Rédaction]

Introduction

The infrared spectrum of crystalline sodium hydrogen bis(4-nitrophenoxide) dihydrate (**1**) becomes simpler as the temperature is raised from 14 K to room temperature (1). A number of bands, which are separate below about 200 K, merge above 250 K. The changes are reminiscent of the changes with temperature in the NMR spectra of substances in which isomeric structures are interconverting reversibly (2). As the temperature is increased, the isomerization rate increases. When the isomerization frequency exceeds the frequency difference between a pair of related bands, those bands merge, and only their average is observed. The changes in the IR spectrum of **1** were interpreted like similar changes in NMR spectra.

The hydrogen bis(4-nitrophenoxide) ion is a Speakman–Hadži anion (3) with the two 4-nitrophenoxide groups bridged by a very short hydrogen bond. The bridging proton appears to be distributed between two sites (1). The estimated

Received December 12, 1998.

This paper is dedicated to Jerry Kresge in recognition of his many achievements in chemistry.

M.M. Kreevoy[1] and V.G. Young, Jr. Department of Chemistry, University of Minnesota, 207 Pleasant St. S.E., Minneapolis, MN 55455-0431, U.S.A.

[1]Author to whom correspondence may be addressed. Telephone: (612) 624-2501. Fax: (612) 626-7541. e-mail: kreevoy@chemsun.chem.umn.edu

© 1999 NRC Canada

isomerization rate constant was close to kT/h at temperatures around 225 K (1). The transfer of the bridging proton between the basic oxygen sites provides an intuitively attractive structural interpretation for the isomerization. The transfer exchanges the roles of a 4-nitrophenoxide ion and a 4-nitrophenol. The ^{13}C NMR spectrum shows only one kind of 4-nitrophenoxide carbon, even at 12 K (4). This confirms that the proton transfer frequency is at least 10^4 s^{-1} even at that temperature (1, 4).

However, the interpretation of such observations in IR spectra is much less secure than the interpretation of the corresponding phenomena in NMR spectra. In the absence of chemical changes, the width, position, and splitting of bands in NMR spectra are not expected to change much with temperature. But the increased population of vibrationally excited levels may change these features significantly in an IR spectrum, even in the absence of isomerization (5). In the present case, progressive centralization of the bridging proton with increasing temperature could be responsible for all or part of the effect. Centralization has been suggested as a major reason for similar changes in the IR spectrum of a carboxylic acid – carboxylate complex in a noncrystalline phase (6). Centralization has been discounted in the present case (1) because the results of rotational-echo, double-resonance ^{13}C NMR experiments at room temperature appear incompatible with a centralized proton (4).

In addition, the neutron diffraction pattern of **1** at 105 K is more satisfactorily analyzed if the bridging hydrogen is treated as two half-hydrogens (1). Also, the distance between the basic oxygens increases steadily with temperature, whereas it would be expected to decrease if the hydrogen became centralized (1). Nevertheless, further evidence on this point is desirable.

In the present paper, we add the observation that the distance between the basic oxygens increases when deuterium is substituted for hydrogen in the short hydrogen bond at all temperatures between about 110 K and room temperature. (The deuterium compound is designated **1-d**. It is deuterated in the water molecules as well as in the bridging position.) This sort of secondary geometric isotope effect was first observed by Ubbelohde and Gallager (7). It is expected if the bridging hydron is distributed between two sites in **1** and **1-d** (8). The O,O distance is shortened because this allows better delocalization of the hydron between the two sites, thereby reducing the requirement for zero-point energy to satisfy the uncertainty principle. The bond is shortened more in the hydrogen compound because its lower mass makes its zero-point energy requirement larger. If the hydron were centralized, delocalization would be complete, and very little further shortening would occur.

We also note that the dihedral angle formed by the planes of the two aromatic rings appears to decrease systematically as the O,O distance increases, in response both to temperature changes and isotopic substitution.

It seems likely that the barrier separating the two sites is very low, because delocalization would be negligible for both **1** and **1-d** otherwise. Therefore, **1** and **1-d** resemble critical configurations for hydron transfer (9, 10).[2] The present observations strengthen the argument for geometric isotope effects on the critical configurations for hydrogen (hydron, hydrogen atom, or hydride) transfer (9–11).

Experimental

Material

The compound **1-d** was prepared from **1** by recrystallization from D_2O. This exchanges the bridging hydrogen and also the hydrogens of the waters for deuterium, but does not introduce deuterium into the aromatic groups (3). Past experience (4) indicates that exchange in the bridging position is negligible in the solid state.

Crystallography

The present paper reports results taken from the crystal structure of **1-d** at 113 and 173 K and at room temperature. Comparable data has been previously reported for **1** (1, 3). The cryostat, which permitted us to obtain a crystal structure of **1** at 103 K, would not maintain a constant temperature below 113 K during the present work. Fortunately, none of the quantities of interest appears to be sharply temperature dependent, so we have treated the 103 and 113 K results as comparable, and both as comparable with the neutron diffraction results obtained at 105 K.

Crystals with dimensions between 0.09 and 0.5 mm and volumes between 6×10^{-3} and 2×10^{-2} mm^3 were mounted on glass fibers and used for structure determination. Nitrogen evaporating from liquid nitrogen was used for cooling. Monitoring of standard reflections indicated no need to correct for sample decay or instrumental drift. Direct methods, supplemented by full-matrix least-squares difference Fourier cycles, gave preliminary structures containing all the atoms except the hydrogens (12). In the final refinement, all the hydrogens except the bridging hydrogen and the water hydrogens were placed in ideal locations and treated as riding atoms (12). The water hydrogens were individually refined (12). The bridging hydrogen was treated as two half-hydrogens, one of which was refined, and the other located by symmetry. Hydrogens were assumed to be isotropic, and each was assigned a single, isotropic displacement parameter, because there was insufficient information in the diffraction patterns to assign two displacement parameters to each. The heavier atoms were refined with individual, anisotropic displacement parameters (12).

A Siemens SMART system was used to collect data. An initial set of cell constants was calculated for each from reflections harvested from three sets of 20 frames. Final cell constants were calculated from large sets of strong reflections from the data collections. Random hemispheres of reciprocal space were surveyed to about 7.1 pm, and space groups were determined from systematic absences and intensity statistics (12). Structures were determined using the SHELXTL V5.0 suite of programs (12).

[2] The critical configuration has been defined as the most probable structure for crossing the hardest-to-attain dividing surface that separates reactants from products (9). This definition reserves the term "transition state" for the structure at the highest point (the saddle point) on the minimum energy path from reactants to products.

© 1999 NRC Canada

Table 1. Isotopically sensitive geometric parameters.[a,b]

T/K[c]	RO1,O1′/pm, **1**[d]	$R_{O1,O1'}$/pm, **1-d**	Ø/deg, **1**	Ø/deg, **1-d**	$R_{O1,O1W}$ /pm, **1**	$R_{O1,O1W}$ /pm, **1-d**
295[e]	248.5(3)	250.0(3)	49.09(5)	48.94(5)	278.5(2)	279.1(2)
173	246.5(2)	248.2(2)	49.34(6)	49.28(3)	278.6(2)	277.8(1)
113		247.3(3)		49.38(4)		278.0(2)
103	245.8(2)		49.49(5)		277.5(2)	

[a] $R_{X,Y}$ is the distance between atom X and atom Y.

[b] The quantities in parentheses after the numerical values are the standard deviations of the values (1, 3, 12).

[c] All temperatures are uncertain by 2–3 K.

[d] Taken from ref. 1.

[e] The original data for **1** at 295 K was rerefined using the SHELXTL program suite (12) so as to make all the reported parameters and their uncertainties comparable. The rerefinement resulted in only very minor changes.

Fig. 1. An ORTEP structure of **1** based on X-ray diffraction at 103 K (1), showing the identification system for atoms discussed in the text. The primed and unprimed atoms are related by a rotational axis of symmetry. H1 and H1′ are half-hydrogens, which implies that each of the two sites is occupied half of the time. Structures based on X-ray diffraction at other temperatures, or based on diffraction by **1-d** instead of **1**, are indistinguishable by inspection. The structure based on neutron diffraction shows the half-hydrogens closer together, but they remain off of the O,O line (1). Otherwise, the structure based on neutron diffraction is also indistinguishable by inspection from the one shown.

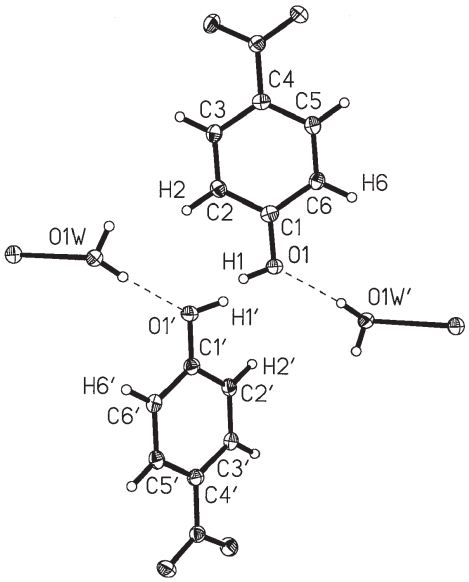

The crystallographic parameters of **1-d** at the three temperatures are similar to those which have previously been reported for **1** (1, 3).

Results

The Ubbelohde effect

Figure 1 shows the structure of **1** and establishes a numbering system to identify the atoms. The distance between two atoms, X and Y, is indicated by $R_{X,Y}$. The dihedral angle formed by the mean least-squares planes (12) of the two aromatic rings is Ø. The structure in Fig. 1 is based on the X-ray diffraction pattern of **1** at 103 K. Its general appearance is not changed either by changing the temperature or by substituting deuterium for the readily exchangeable hydrogens. However, $R_{O1,O1'}$ and Ø show small changes both with temperature and isotopic substitution. These changes are shown in Table 1. For comparison, Table 1 also shows $R_{O1,O1W}$, which seems to show very slight variation with temperature, and only random variation with isotopic substitution, so that the magnitude of the scatter can be judged.

At each temperature, $R_{O1,O1}$(D) is greater than $R_{O1,O1}$(H). The average difference is 1.6 pm. The standard deviation of these distances is 0.2–0.3 pm. The $R_{O1,O1W}$ are sometimes larger for **1**, and sometimes larger for **1-d**. The average difference between them is 0.6 pm. Thus, there is little doubt that the geometric isotope effect (Ubbelohde effect) is real. The effect does not appear to be very temperature sensitive. The uncertainties preclude any further conclusion about systematic variation of the Ubbelohde effect, but the effect does not disappear at temperatures up to room temperature.

Another geometric isotope effect

The average standard deviation of Ø is 0.05°. On going from room temperature to around 110 K, Ø increases by 0.4° in both **1** and **1-d**. At the same time, $R_{O1,O1'}$ decreases by 2.7 pm, for both isotopic variants. The dihedral angle decreases with isotopic substitution at all three temperatures, but the average decrease is only 0.11°. If this were a single, isolated observation, we would not regard it as significant. However, in each case, both for temperature change and for isotopic substitution, Ø decreases when $R_{O1,O1'}$ increases. Because of their consistency, we believe that these changes are real. The changes in response to isotopic substitution are another geometric isotope effect.

Apart from $R_{O1,O1'}$ and Ø, the structures of **1** and **1-d** were not notably different.

Discussion

Origin of the Ubbelohde effect

Ground vibrational states are the minimum energy states that satisfy the uncertainty principle. To meet this requirement, both **1** and **1-d** have expectation values of $R_{O1,O1'}$ smaller than the value at the potential energy minimum, because reducing $R_{O1,O1'}$ permits more delocalization of the hydron. The increased uncertainty in the hydron coordinate value reduces the required uncertainty in momentum, thereby reducing the energy requirement. Because the mass of hydrogen is less than that of deuterium, the effect is larger in **1** than in **1-d**.

© 1999 NRC Canada

Fig. 2. A two-dimensional cartoon attempting to show the relation of potential energy, plotted perpendicular to the page, as a function of the O,O distance, $R_{O,O}$, and the O,H distance, $R_{O,H}$. The vertical lines show the suggested hydrogenic stretching oscillations at the expectation values of $R_{O,O}$ in **1** and **1-d**. The potential energy minima are the small closed figures to the right of the $R_{O,D}$ line. Even though the same potential surface is used for **1** and **1-d** (following Born–Oppenheimer), the one-dimensional potential functions for hydrogenic stretching are different. The figures off to the right of the potential surface attempt to show the squares of the vibrational wave functions. None of this is based on calculation. It attempts to illustrate the ideas described in the text.

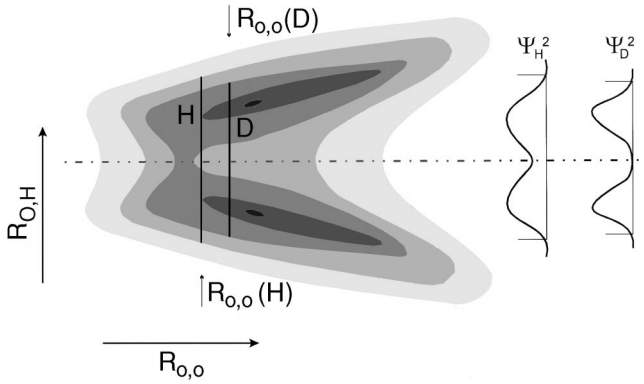

Such changes in structure must not cost more in potential energy than they save in vibrational energy. Ordinarily, they are very small. If the motions of the atoms near the potential energy minimum are governed by steep, approximately harmonic forces, structural changes are expensive, yield little delocalization, and, therefore, little reduction in the required vibrational energy. However, the antisymmetric stretch of the bridging hydron in a Speakman–Hadži compound is governed by a low-barrier double minimum potential function (13). The central barrier can be reduced, so that it ultimately falls below the lowest vibrational eigenvalue, by reducing the bridged O,O distance (8, 13–16).[3] When the lowest vibrational eigenvalue is slightly below the top of the central barrier, a small decrease in the O,O distance can yield a considerable delocalization of the hydron, with a corresponding decrease in the vibrational energy requirement. As noted, these effects are less pronounced in **1-d** than in **1**. These ideas are illustrated by a cartoon in Fig. 2.

Tunneling results in a progressive increase in hydron delocalization as the O,O distance decreases. Without tunneling, the hydron would either be completely delocalized, if the vibrational eigenvalue was above the central barrier, or insignificantly delocalized, if it was below. An Ubbelohde effect would occur if hydrogen could achieve delocalization by shortening the O,O distance, but deuterium could not. But the effect would be rare, since the eigenvalues of substances differing only by isotopic substitution are similar. In fact, the effect always appears to occur in Speakman–Hadži compounds, for a considerable range of O,O distances (14).[4] Thus, the concept of tunneling is supported by these observations on stable substances.

Recent theoretical studies have generally concluded that the lowest allowed eigenvalues of the O,H asymmetric stretch in Speakman–Hadži compounds is above the central barrier (17–19),[5] contrary to our present conclusions, and contrary to the results obtained with the same and related substances in solution (13, 20). We believe that the most important cause for the discrepancy is the use of the harmonic oscillator approximation by theoreticians to evaluate the zero-point energy, with a force constant obtained from the curvature at the potential energy minimum. This procedure considerably overestimates the zero-point energy for a shallow double-minimum potential function (13, 21). The condensed phase results may also be influenced by the permittivity of the condensed media.

The Ubbelohde effect does not imply a breakdown of the Born–Oppenheimer approximation (22).

Implications for IR spectra

The observation of the Ubbelohde effect at all three temperatures is additional, strong evidence that the hydron is not centralized in its vibrational ground state, and does not become centralized at temperatures up to room temperature. This, taken together with the NMR observations (4) and the monotonous increase with temperature of $R_{O1,O1'}$, removes the possibility that the simplification of the IR spectrum of **1** with increasing temperature (1) is mainly due to the centralization of the hydron.

Increasing temperature leads to increases in the population of low-lying excited vibrational states. When a molecule in one of these low-lying excited states is excited in one of its valence vibrations, its excitation frequency may be slightly different from that of a molecule in the vibrational ground state. As a result, valence vibration bands in the mid-IR tend to broaden as temperature increases. Such broadening might lead to the apparent merging of some bands as the temperature increases. This is the only remaining alternative to the kinetic explanation of the observed changes in the IR spectrum of **1** that we are aware of. However, the changes in the spectrum of **1** are more dramatic than those which are usually observed, and they appear to affect only a limited number of bands, while others remain distinct and sharp (1). We therefore conclude that an increase in the rate of prototropic isomerization is the main cause of the merging of the IR bands (1). The rate constants calculated (1) should be valid, though quite inexact.

Thermal and isotopic variation of Ø

The decrease in Ø with increasing temperature is well outside of its standard deviation, and very probably real. It is correlated with the increase in $R_{O1,O1'}$, which probably increases with temperature due to excitation of the O,O stretching vibration (23). It seems intuitively likely that Ø is increased by nonbonded atom repulsions. The impression that the structure incorporates nonbonded atom repulsions is

[3] Additional references on this point can be found in refs. 15 and 16.
[4] Ubbelohde effects appear to have been found wherever they have been sought among Speakman–Hadži compounds. The largest effect we are aware of is 2.7 pm (14).
[5] References 17–19 are merely a selection of recent, relevant papers that came to hand. A systematic search would yield a much longer list.

© 1999 NRC Canada

strengthened by the fact that the two half-hydrogens do not lie on the O,O line in the neutron structure (1). Repulsions between atoms of one ring and those of the other could be relieved either by increasing $R_{O1,O1'}$ or by increasing Ø so the increase in $R_{O1,O1'}$ would allow a decrease in Ø. However, we are not able to identify the specific atoms involved, and we do not dismiss the possibility that these characteristics are intrinsic to the hydrogen bond itself.

Substitution of deuterium in the bridging position also increases $R_{O1,O1}$, but the effect is only about half as big as the effect of increasing the temperature from about 110 K to room temperature. Isotopic substitution also decreases Ø. These effects are similar in size to the standard deviations, but they are consistent, and consistent with the effect of temperature, so we believe they are real. The isotope effect on Ø seems to be a result of the isotope effect on $R_{O1,O1}$, which is, itself, a secondary isotope effect.

The Ubbelohde effect and critical configurations

Within the Born–Oppenheimer approximation (22), the conventional transition states for a hydrogen (hydron, hydrogen atom, or hydride) transfer and the corresponding deuterium transfer are the same (9, 10). However, computational studies indicate that such reactions probably occur most commonly by barrier penetration at donor–acceptor distances slightly larger than those in the corresponding transition states (corner-cutting tunneling) (9, 10, 24).[2] Since this effect is more important when the transfered mass is smaller, there are geometric isotope effects on the structures of the critical configurations.[2]

The criteria by which the critical configuration is found are different from those that are at work to give the structures that are observed in stable Speakman–Hadži anions, but the bases of the effects are the same. The calculated isotope effect on the heavy atom separation in the critical configuration for hydrogen transfer is about 5 pm (10). This is about twice the larger observed Ubbelohde effects (14). The existence of a related effect in stable structures is strong support for a geometric isotope effect in critical configurations.

References

1. M.M. Kreevoy, S. Marimanikkuppam, V.G. Young, J. Baran, M. Szafran, A.J. Schultz, and F. Trouw. Ber. Bunsenges. Phys. Chem. **102**, 370 (1998).
2. H. Strehlow. *In* Investigation of rates and mechanisms of reaction. Part 2. *Edited by* S.L. Friess, E.S. Lewis, and A. Weissberger. John Wiley and Sons, New York. 1963. pp. 865–893.
3. S.H. Marimanikkupam, I-S.H. Lee, D.A. Binder V.G. Young, and M.M. Kreevoy. Croatica Chem. Acta, **69**, 1661 (1996).
4. C.A. Klug, P.L. Lee, I-S.H. Lee, M.M. Kreevoy, R. Yaris, and J. Schaefer. J. Phys. Chem. B, **101**, 8086 (1997).
5. K.A. Wood and H.L. Strauss. J. Phys. Chem. **94**, 5677 (1990).
6. V. Doan, R. Köppe, and P.H. Kasai. J. Am. Chem. Soc. **119**, 9810 (1997).
7. A.R. Ubbelohde and K.G. Gallager. Acta Crystallogr. **8**, 71 (1955).
8. H. Benedict, H.-H. Limbach, M. Wehlan, W.-P. Fehlhammer, N.S. Golubev and R. Janoschek. J. Am. Chem. Soc. **120**, 2039 (1998).
9. M.M. Kreevoy, D. Ostovic, D.G. Truhlar, and B.C. Garrett. J. Phys. Chem. **90**, 3766 (1987).
10. Y. Kim, D.G. Truhlar, and M.M. Kreevoy. J. Am. Chem. Soc. **113**, 7837 (1991).
11. Y. Kim and M.M. Kreevoy. J. Am. Chem. Soc. **114**, 7116 (1992).
12. Users manual, SHELXTL-Plus V5.0. Siemans Industrial Automation, Madison, Wisconsin. 1994.
13. M.M. Kreevoy and T.M. Liang. J. Am. Chem. Soc. **99**, 3315 (1980).
14. (*a*) M. Ichikawa. Acta Cryst. **B34**, 2074 (1978); (*b*) Ferroelectrics, **168**, 177 (1995).
15. P. Gilli, V. Bertolasi, V. Ferretti, and G. Gilli. J. Am. Chem. Soc. **116**, 909 (1994).
16. Th. Steiner and W. Saenger. Acta Cryst. **B50**, 348 (1994).
17. M. Garcia-Viloca, A González-Lafont, and José M. Lluch. J. Am. Chem. Soc. **119**, 1081 (1997).
18. M.A. McAllister. Can. J. Chem. **75**, 1195 (1997).
19. J. Chen, M.A. McAllister, J.K. Lee, and K.N. Houk. J. Org. Chem. **63**, 4611 (1998).
20. C.L. Perrin, J.B. Nielson, and Y-J. Kim. Ber. Bunsenges. Phys. Chem. **102**, 403 (1998).
21. J.E. Del Bene and M.J.T. Jordan. J. Chem. Phys. **108**, 3205 (1998).
22. I.N. Levine. Physical chemistry. 3rd ed. McGraw–Hill Book Company, New York. 1988. pp. 656–659.
23. A. Rabold and G. Zundel. J. Phys. Chem. **99**, 12 158 (1995).
24. Y. Kim and M.M. Kreevoy. J. Am. Chem. Soc. **114**, 7116 (1992).

© 1999 NRC Canada

New chloride anion receptors: trifluoromethyl sulfonylated polyamines

H.S. Lee, X.Q. Yang, J. McBreen, D. Vyprachticky, and Y. Okamoto

Abstract: A new chloride anion receptor, derivatized oligoethylene oxide CF_3SO_2 substituted tetraamine (**3**), was synthesized. This compound exhibited strong Cl^{-1} ion binding properties in nonpolar solvents such as benzene. Neutral red and Nile blue chloride dye molecules do not dissolve in benzene. However, when compound (**3**) was added to a benzene solution containing the solid dye compounds, the color of the solution immediately turned to dark blue, and the intensity of the color proportionally increased with the concentration of (**3**). The phenomena indicated that the Cl^- ions of Neutral red or Nile blue chloride are complexed with (**3**), thereby resulting in an increase in the solubility of the Neutral red or Nile blue cations in benzene. The dissociation of chloride anions from 4,4′,4′′-trimethoxytriphenyl chloromethane in a benzene solution proceeded with addition of compound (**3**) and increased with increasing time at room temperature. In contrast, another tetraamine compound (**4**) which was substituted with a less electron withdrawing group, CH_3SO_2, did not complex with Cl^- anions in a benzene solution.

Key words: Cl^- anion receptor, trifluoromethyl sulfonated tetraamine, ion pair dissociation.

Résumé : On a synthétisé un nouveau récepteur de l'anion chlorure, une trifluorométhylsulfonyltétraamine dérivatisée par de l'oligooxyde d'éthylène (**3**). Dans des solvants non polaires comme le benzène, ce composé donne lieu à une forte fixation de l'ion Cl^{-1}. Les molécules des colorants chlorés, rouge neutre et bleu Nil, ne se dissolvent pas dans le benzène. Toutefois, lorsqu'on ajoute du composé (**3**) à une solution benzénique contenant les colorants solides, la couleur de la solution passe immédiatement au bleu foncé et l'intensité de la couleur augmente d'une façon proportionnelle à la concentration de (**3**). Le phénomène indique que les ions Cl^- du rouge neutre et du bleu Nil sont complexés par (**3**) et qu'il en résulte une augmentation dans la solubilité des cations du rouge neutre et du bleu Nil dans le benzène. Lors de l'addition du composé (**3**) à une solution benzénique de 4,4′,4′-triméthoxytriphénylchlorométhane à la température ambiante, il se produit une dissociation des anions chlorures qui augmente avec le temps. Par ailleurs, une autre tétraamine (**4**) substituée par un groupe moins électroaffinitaire, le CH_3SO_3, ne donne pas de complexes avec les anions Cl^- en solution dans le benzène.

Mots clés : réception de l'anion Cl^-, tétraamine trifluorométhylsulfonée, dissociation en paire d'ions.

[Traduit par la rédaction]

Introduction

Host–guest molecular systems have attracted much attention during the past two decades (1). Although various compounds, which are cation receptors, have been investigated widely, the number of host molecules for anion complexation is very small (2). To accomplish anion binding, most of the reported host molecules have positively charged sites (3), Lewis acid metal centers (4), or hydrogen bond forming moieties (5–8).

Recently, we have synthesized a family of polyamine compounds as anion receptor molecules (9). A strong electron withdrawing CF_3SO_2 group was substituted on the nitrogen atoms of linear and cyclic tetramines (Fig. 1). When the amine hydrogen atoms are substituted by CF_3SO_2 groups, the nitrogen becomes electropositive and expedites the complexation with an anion. Therefore, the CF_3SO_2 substituted polyamine compounds exhibit an anion binding property. The degree of the anion complexation depends on the number of CF_3SO_2 groups substituted, the structure of amine compounds, and the nature of the complexed anions (9).

We have used Near Edge X-ray Absorption Fine Structure (NEXAFS) spectroscopy at the Cl K edge to elucidate the formation of the complexes between the Cl^- ions and the amine compounds; NEXAFS is a useful tool for the study of the coordination symmetry of the Cl^- ions both in solution and in the solid state. Detailed NEXAFS spectroscopy studies showed that the Cl^- ions of LiCl in THF were complexed strongly with the nitrogen atoms of compounds (**1**) and (**2**) of Fig. 1 (9).

Received November 3, 1998.

This paper is dedicated to Jerry Kresge in recognition of his many achievements in chemistry.

H.S. Lee, X.Q. Yang, and J. McBreen. Brookhaven National Laboratory, Upton, NY 11973, U.S.A.
D. Vyprachticky and Y. Okamoto.[1] Department of Chemistry, Polytechnic University, Brooklyn, NY 11201, U.S.A.

[1]Author to whom correspondence may be addressed. Telephone: (718) 260-3638. Fax: (718) 260-3125.
e-mail: yokamoto@duke.poly.edu

© 1999 NRC Canada

Fig. 1. CF_3SO_2 substituted tetraamines, R = CF_3SO_2.

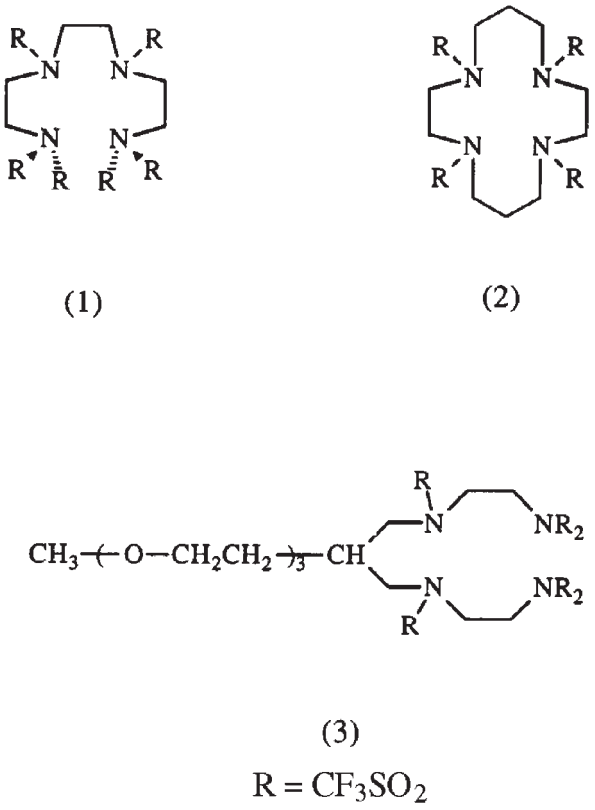

Fig. 3. UV-vis spectra of the reaction products of Nile blue chloride (NB) (1.7×10^{-5} mol), and compounds (**3**) or (**4**) in benzene solutions (10 mL) at room temperature: (*a*) NB (saturated solution); (*b*) NB + 3.4×10^{-5} mol of (**4**); (*c*) NB + 1.7×10^{-5} mol of (**3**); (*d*) NB + 3.4×10^{-5} mol of (**3**). The UV-vis spectra were taken 24 h after mixing.

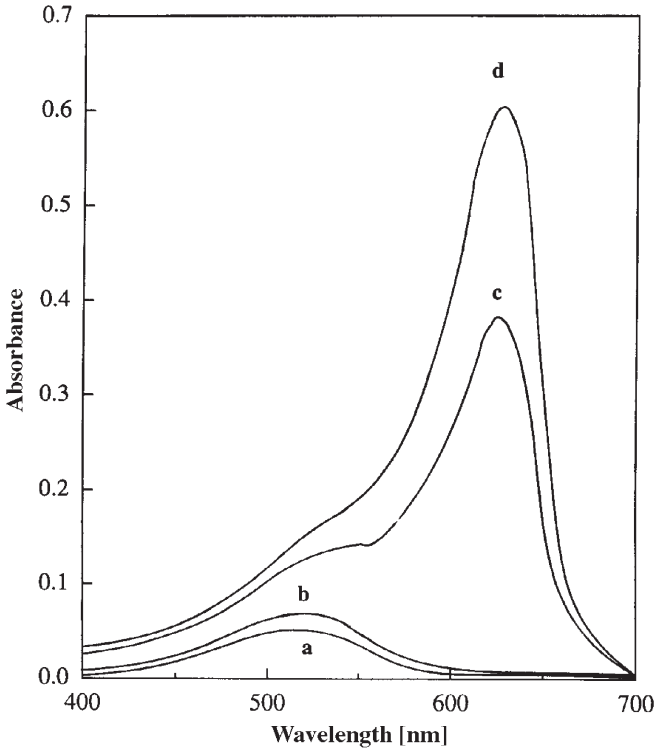

Fig. 2. UV-vis spectra of the reaction products of Neutral red (NR) (1.7×10^{-5} mol), and compounds (**3**) or (**4**) in benzene solutions (10 mL) at room temperature: (*a*) NR (saturated solution); (*b*) NR + 1.7×10^{-5} mol of (**3**); (*c*) NR + 3.4×10^{-5} mol of (**3**); (*d*) NR + 5.1×10^{-5} mol of (**3**); (*e*) NR + 3.4×10^{-5} mol of (**4**). The UV-vis spectra were taken 24 h after mixing.

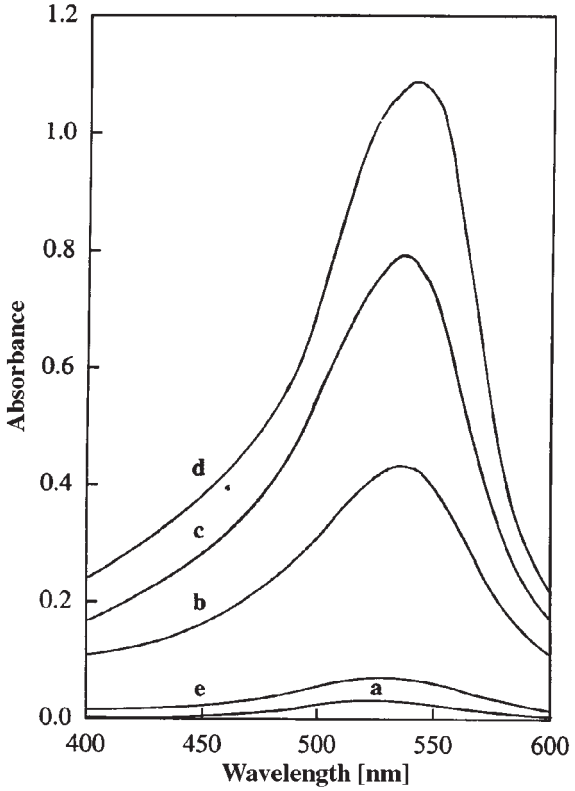

We have also found that the addition of compounds (**1**) or (**2**) to THF solutions of LiCl increased the ionic conductivity by two to three orders of magnitude compared to solutions without an amine compound. This effect can be ascribed to the formation of complexes of Cl^- ions with the nitrogen atoms of the amine compounds, thereby resulting in an increased concentration of free Li^+ ions, which in turn increase the ionic conductivity.

Results and discussion

The tetraamine compounds (**1**) and (**2**) are not soluble in nonpolar solvents such as benzene. Thus, to solubilize the amine compound and its anion complex, we have synthesized an oligoethylene oxide derivative of CF_3SO_2 substituted tetraamine (**3**).

The ^{35}Cl NMR spectrum of LiCl in THF showed a single sharp peak for ^{35}Cl. Upon the addition of the amine compound (**3**) to the THF solution (1:2 molar ratio), the peak corresponding to Cl^- became very broad, presumably the result of average quadruple coupling which would occur as a result of bound chloride (10). In this study, we report examples of the Cl^- receptive behavior by compound (**3**) in benzene solution.

Neutral red dye does not dissolve in benzene at room temperature. However, when the tetraamine compound (**3**) was added to a benzene solution containing solid Neutral red

© 1999 NRC Canada

Fig. 4. Structures of Neutral red and Nile blue chloride. The reaction scheme with compound (**3**) is also shown.

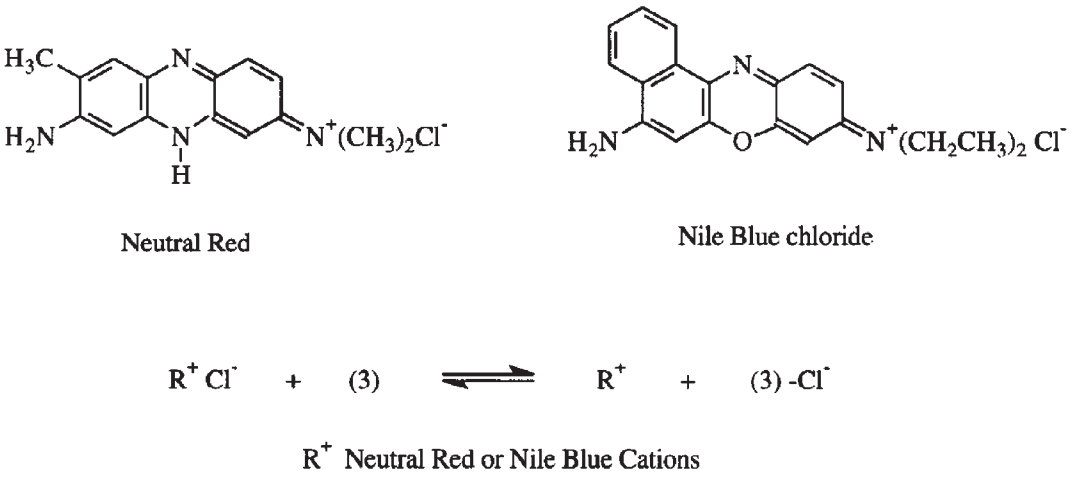

Fig. 5. UV-vis spectra of the reaction products of equimolar reactions (2.7×10^{-5} mol) of 4,4′,4″-trimethoxytriphenyl chloromethane and compounds (**3**) or (**4**) in benzene (40 mL) at room temperature as a function of time: (*a*) $(MeOC_6H_4)_3C$-Cl; (*b*) $(MeOC_6H_4)_3C$-Cl + (**3**) after 5 min; (*c*) $(MeOC_6H_4)_3C$-Cl + (**3**) after 12 h; (*d*) $(MeOC_6H_4)_3C$-Cl + (**3**) after 10 days; (*e*) $(MeOC_6H_4)_3C$-Cl + (**4**) after 10 days.

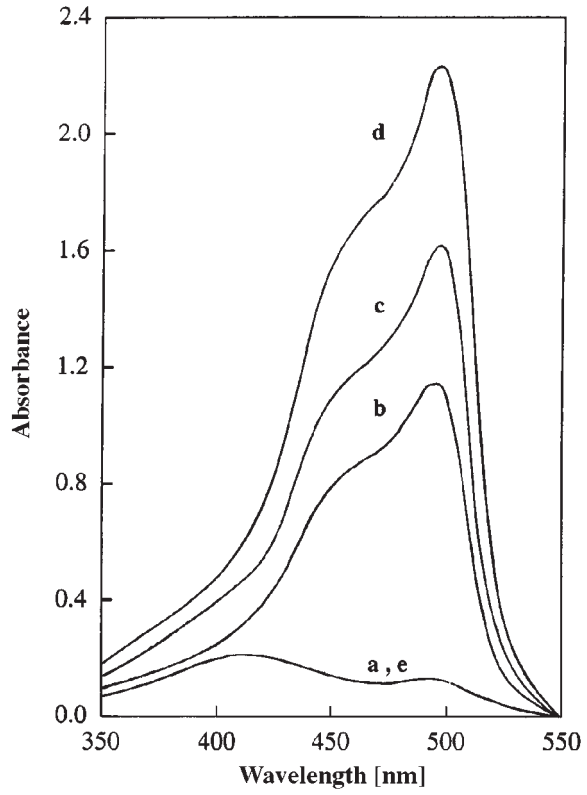

compound at room temperature, the color of the solution immediately turned to dark blue, and the intensity of the color was proportionally increased with increasing concentrations of (**3**) (Fig. 2). The Cl^- ion of Neutral red was complexed with the amine compound (**3**), resulting in an increased solubility of the dissociated Neutral red cation moiety in benzene solution. Similar phenomena were also observed with other dye molecules such as Nile blue chloride (Fig. 3). Figure 4 shows the structures for both Neutral red and Nile blue chloride.

Additionally, a compound where CH_3SO_2 instead of CF_3SO_2 groups were substituted on the nitrogen atoms of the tetraamine was synthesized (**4**). When compound (**4**) was added to benzene solutions containing dye molecules, the dye compounds did not dissolve, and the color of the solutions remained unchanged. These results indicated that the weaker electron withdrawing group, CH_3SO_2, did not create a sufficiently strong electropositivity on the nitrogen atoms to form a complex with the Cl^- ions.

The chloride anion of 4,4′,4″-trimethoxytriphenyl chloromethane has little dissociation in benzene at room temperature. However, with addition of the Cl^- ion receptor (**3**), the dissociation of chloride anion proceed in yielding the trimethoxytriphenylmethyl cation,

$$(CH_3OC_6H_4)_3CCl + (\mathbf{3}) \rightarrow (CH_3OC_6H_4)_3C^+ + (\mathbf{3})\text{-}Cl^-$$

whereas compound (**4**) has no effect on the dissociation of the chloride anion (Fig. 5). The data in Fig. 5 also indicate a long-term effect on the degree of complexation. However, this was not studied in detail.

Under similar conditions, the chloride ion of triphenyl chloromethane did not react with compound (**3**). Without the electron-donating para methoxy groups, the C—Cl bond is stronger and does not dissociate in the presence of compound (**3**).

To summarize, these results show that CF_3SO_2 substituted polyamine compounds form complexes with Cl^- ions and enhances ion pair dissociation in nonpolar solvents such as benzene. Further studies are needed to elucidate the stoichiometry and kinetics of these processes.

Experimental

Materials

Neutral red (~90%), Nile blue chloride (~90%), trimethoxytriphenyl chloromethane, trifluoromethanesulfonic anhydride, triphenyl chloromethane, and organic solvents were

© 1999 NRC Canada

Scheme 1. Reaction scheme for preparation of compound (**3**).

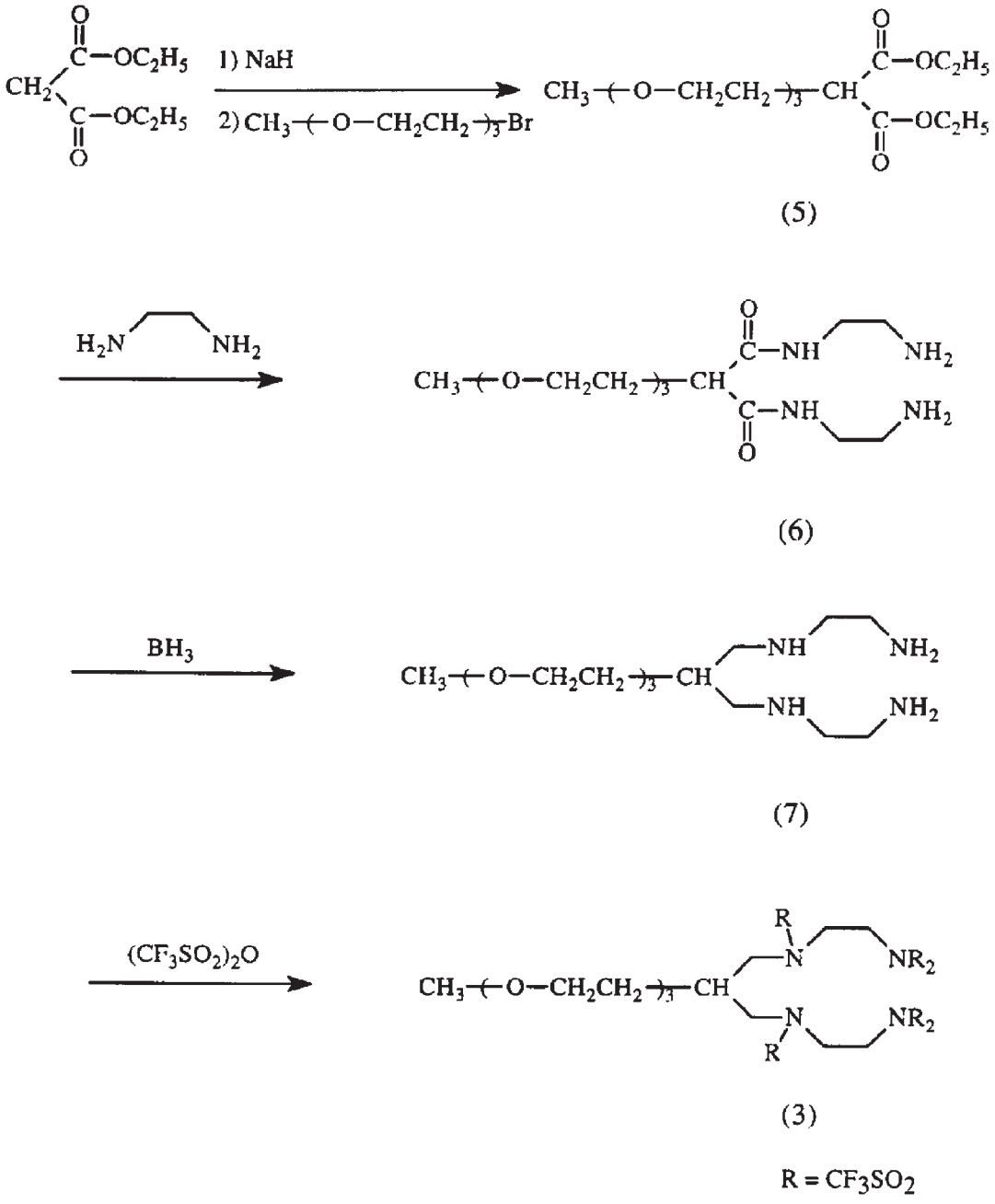

purchased from Aldrich Chemical Co. and used without further purification.

Characterization

A Varian U-plus 300 MHz instrument was used for ^{1}H NMR spectroscopy. UV-vis absorption spectra were obtained by means of Varian Cary 2300 UV-vis spectrometer. IR data were obtained on an Analect FX 6260 Fourier transform infrared spectrometer.

Synthesis

*6-(3,6,9-Trioxadecyl)-1,1,4,8,11,11-hexatrifluoromethylsulfonyl-1,4,8,11-tetraazaundecane (**3**)*

The compound (**3**) was prepared by the route shown in Scheme 1.

*Diethyl 3,6,9-trioxadecyl malonate (**3**)*

Diethyl malonate, 80 g (0.05 mol), was added dropwise to a suspension of 12.0 g (0.5 mol) of sodium hydride in 600 mL of anhydrous tetrahydrofuran at room temperature. After the evolution of gas was completed, 114 g (0.5 mol) of 3,6,9-trioxadecyl bromide was added, and the solution was heated at 80° for 5 h. The precipitate was filtered off, and the solvent was evaporated. The residue was dissolved in ether, washed with water, and dried over magnesium sulfate. The ether was evaporated, and the crude product was distilled, bp 120–125°/0.05 mmHg (1 mmHg = 133.3 Pa). The yield

© 1999 NRC Canada

Scheme 2. Reaction scheme for preparation of compound (**4**).

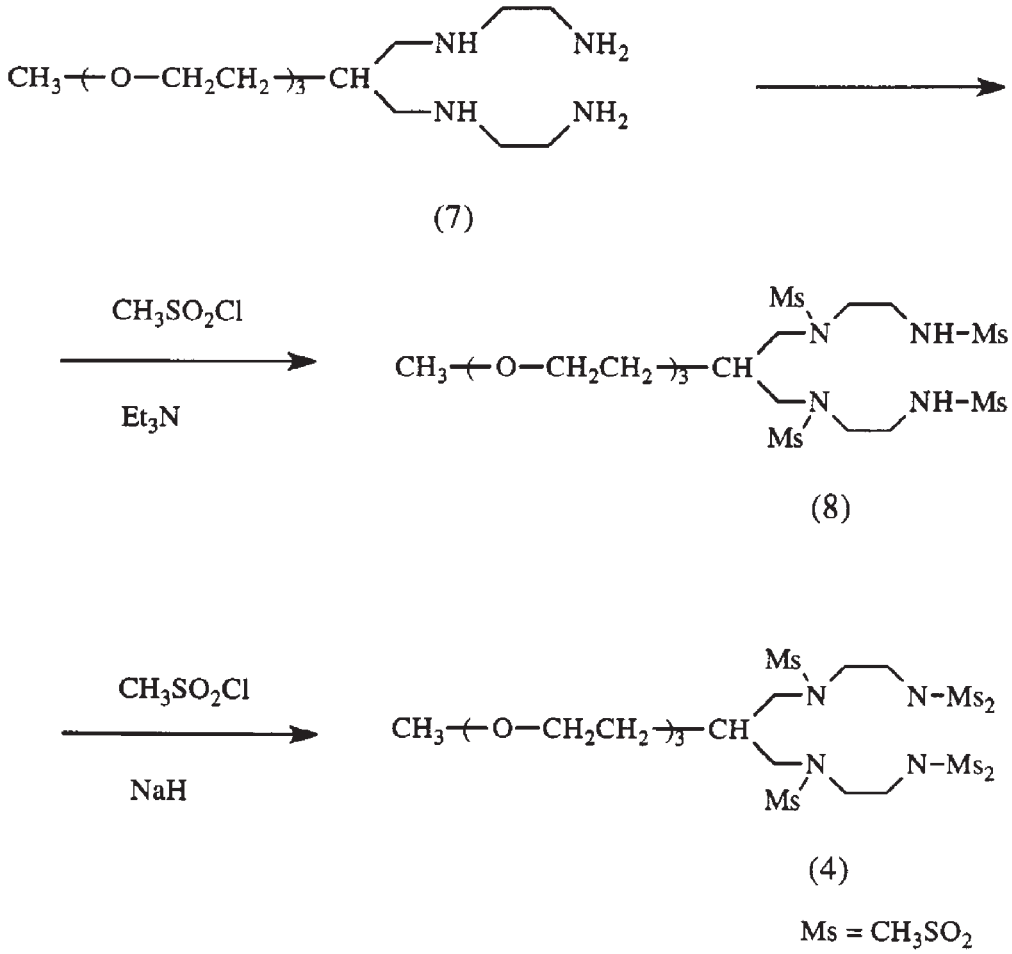

was 122 g (80%). NMR ($CDC1_3$) δ 1.30 (t, 6H), 2.15 (q, 2H), 3.40 (s, 3H), 3.45~3.70 (m, 11 H), 4.20 (q, 4H) ppm.

N,N′-*Bis(2-aminoethyl)-3,6,9-trioxadecyl malonodiamide (**6**)*

A mixture of 58.6 g (0.19 mol) of compound (**5**) and 200 mL (3 mol) of ethylene diamine was heated at 90° for 15 h. The solution was evaporated to dryness, tetrahydrofuran was added to the residue, and the insoluble material was removed by filtration. The solvent was removed under vacuum, and the residue was dried at 60°/0.05 mmHg. The yield was 56.1 g (88%). NMR ($CDC1_3$) δ 1.75 (s, 6N-H), 2.20 (q, 2H), 2.80 (q, 4H), 3.10~3.80 (m, 18H) ppm.

*6-(3,6,9-Trioxadecyl)-1,4,8,11-tetraazaundecane (**7**)*

Compound (**6**), 53 g (0.16 mol), was dissolved in anhydrous tetrahydrofuran, and the solution was added dropwise to 800 mL of 1 M borane in tetrahydrofuran at 0°. The reaction mixture was heated for 24 h. The solvent was evaporated, the residue was dissolved in water, and then the basicity of the solution was adjusted with sodium hydroxide to pH = 13. Water was removed under reduced pressure, and the residue was treated with ethanol. The ethanol upper layer was decanted from the lower sticky layer. The ethanol solution was then evaporated to dryness. The residue was dissolved in tetrahydrofuran, and any insoluble material was removed by filtration. After removing the solvent, the product was distilled, bp 160–165°/0.05 mmHg. The yield was 38.2 g (78%). NMR (CD_3OD) δ 1.40~1.90 (m, 3H), 2.40~2.60 (m, 12H), 3.40 (s, 3H), 3.50–3.80 (m, 10H), 4.00 (s, 6H) ppm.

*6-(3,6,9-Trioxadecyl)-1,1,4,8,11,11-hexatrifluoromethyl-1,4,8,11-tetraazaundecane (**3**)*

Compound (**7**), 6.12 g (0.02 mol), and triethylamine (12.5 g, 0. 12 mol) were dissolved in 160 mL of anhydrous chloroform and cooled to –20°. Trifluoromethanesulfonic anhydride (34.9 g, 0. 12 mol) was added into the solution under a nitrogen atmosphere. The addition was carried out over 3 h, and the solution was stirred 1 h at room temperature. The reaction mixture was washed with water, and the solution was dried over magnesium sulfate. Chloroform was evaporated, and a solid product was recrystallized from methanol. The yield was 17.2 g (78%) of pure needle crystals, mp 93-95°. NMR ($CDCl_3$): δ 1.50~1.90 (m, 3H), 3.40 (s, 5H), 3.50~3.90 (m, 18H), 4.00~4.50 (m, 4H) ppm. Elemental analysis for $C_{20}H_{28}O_{15}N_4S_6F_{18}$ (**3**), calcd.: C 21.85, H 2.55, N 5.10, S 17.49, and F 31.16; found: C 21.97, H 2.74, N 5.01, S 17.42, and F 30.72.

*6-(3,6,9-Trioxadecyl)-1,1,4,8,11,11-hexamethylsulfonyl-1,4,8,11-tetraazaundecane (**4**)*

The compound was synthesized by a similar method as described for the preparation of (**3**) using methanesulfonyl chloride instead of trifluoromethanesulfonic anhydride (Scheme 2).

© 1999 NRC Canada

*6-(3,6,9-Trioxadecyl)-1,4,8,11-tetramethylsulfonyl-1,4,8,11-tetraazaundecane (**8**)*

Compound (**7**), 4.30 g (0.015 mol), and triethylamine (6.7 g, 0.065 mol) were dissolved in 50 mL of anhydrous chloroform, and the solution was cooled with an ice bath. Methanesulfonyl chloride, 7.5 g (0.065 mol), was added dropwise to the solution over a period of a half hour, and the mixture was stirred for another half hour. The solution was washed with water and dried over anhydrous magnesium sulfate. Chloroform was evaporated to give 8.2 g (88%) of viscous liquid product (**8**). NMR ($CDCl_3$–CD_3OD) δ 1.5~2.0 (m, 3H), 2.8~3.0 (m, 12H), 3.3~3.5 (m, 15H), 3.55~3.7 (m, 10 H), 3.8 (s, 2H) ppm. IR (neat): 3289, 3020, 2934, 2878, 1453, 1325, 1148, 1096, 971, 920, 765 cm^{-1}.

*6-(3,6,9-Trioxadecyl)-1,1,4,8,11,11-hexamethylsulfonyl-1,4,8,11-tetraazaundecane (**4**)*

Compound (**8**), 8.2 g (0.013 mol) in 50 mL of anhydrous tetrahydrofuran was added dropwise into a suspension of 0.7 g (0.029 mol) of sodium hydride in 80 mL of tetrahydrofuran. Methanesulfonyl chloride, 3.7 g (0.033 mol), was then added to the solution. The mixture was heated at 60° for 1 h. The inorganic salt was filtered off, and the filtrate was stirred with diluted aqueous sodium hydroxide. After extraction with chloroform, a pure semisolid product (**4**) was obtained. The yield was 7.5 g (75%). NMR ($CDCl_3$) δ 1.5~2.0 (m, 3H), 2.8~3.0 (m, 8H), 3.35 (s, 21H), 3.45~3.7 (m, 10H), 3.8~4.1 (m, 4H) ppm. IR (neat): 3016, 2953, 2879, 1456, 1333, 1154, 1086, 966, 853, 764, 533 cm^{-1}.

Acknowledgements

We are grateful to L.S. Choi at the Naval Research Laboratory for doing the ^{35}Cl NMR. This work was supported partly by the U.S. Department of Energy, Division of Material Science, the Office of Basic Energy Sciences under contact number DE-AC02-98CH10886.

References

1. J.M. Lehn. Angew. Chem. **102**, 1347 (1990).
2. (*a*) B. Dietrich. Pure Appl. Chem. **65**, 1457 (1993); (*b*) D.E. Kaufmann and A. Otten. Angew. Chem. Int. Ed. Engl. **33**, 1832 (1994).
3. (*a*) F.P. Schmidtchen. Chem. Ber. **113**, 864 (1980); (*b*) F.P. Schmidtchen and G. Müller. J. Chem. Soc. Chem. 1115 (1984); (*c*) F.P. Schmidtchen and G. Müller. Pure Appl. Chem. **61**, 1535 (1989); (*d*) K. Worm, F.P. Schmidtchen, A. Schier, A. Schäfer, and M. Hesse. Angew. Chem. Int. Ed. Engl. **33**, 327 (1994).
4. (*a*) Y. Azuma and M. Newcomb. Organometallics, **3**, 9 (1984); (*b*) M. Newcomb, M.T. Blanda, Y. Azuma, and T.J. Delord. J. Chem. Soc. Chem. Commun. 1159 (1994); (*c*) M.T. Blanda, J.H. Horner, and M. Newcomb. J. Org. Chem. **54**, 4626 (1989); (*d*) X. Yang, C.B. Knobler, and M.F. Hawthorne. Angew. Chem. Int. Ed. Engl. **30**, 1507 (1991); (*e*) Z. Zheng, C.B. Knobler, and M.F. Hawthorne. J. Am. Chem. Soc. **117**, 5105 (1995).
5. E. Graf and J.M. Lehn. J. Am. Chem. Soc. **98**, 6403 (1976).
6. W.B. Famham, D.C. Roe, D.A. Dixon, J.C. Calabrese, and R.L. Harlow. J. Am. Chem. Soc. **112**, 7707 (1990).
7. S. Valiyaveettil, J.F.J. Engbersen, W. Verboom, and D.N. Reinhoudt. Angew. Chem. Int. Ed. Engl. **32**, 900 (1993).
8. Y. Morzherin, D.M. Rudkevich, W. Verbom, and D.N. Reinhoudt. J. Org. Chem. **58**, 1602 (1993).
9. H.S. Lee, X.Q. Yang, J. McBreen, L.S. Choi, and Y. Okamoto. J. Electrochem. Soc. **143**, 3825 (1966).
10. J.J. Falke. R.J. Pace, and S.I. Chan. J. Biol. Chem. **259**, 6472 (1984).

© 1999 NRC Canada

Acid-catalyzed decomposition of diazodiphenylmethane in dimethylsulfoxide

Robert Eliason

Abstract: Acid-catalyzed decomposition of diazodiphenylmethane (DDM) has been studied in DMSO containing varying amounts of water. The reaction was found to be first-order in DDM and first-order in acid. The Brønsted plot for a series of carboxylic acids is curved with the H^+ point falling below the curve defined by the carboxylic acids. In near-anhydrous DMSO, kinetic hydrogen isotope effects (KIEs) are 1.7 and 1.6 for acetic acid and chloroacetic acid, respectively. The chloroacetic acid KIE increases with increasing water concentration, rising to 2.9 at 3.6 M water. As a function of $[H_2O]$, k_{HA} for chloroacetic acid shows a sharply defined minimum occurring at 1 M water. This behavior and the water effect on KIE suggest that the carboxylic acid-catalyzed reactions in near-anhydrous DMSO do not use the AS_E-2 mechanism attributed to the reaction of DDM in hydroxylic solvents. A mechanism, leading to an azoalkane, is suggested. Either directly or indirectly, this may lead to diphenylcarbene, which would account for the observed products: benzophenone, benzhydrol, and benzhydryl esters. For the H^+ catalyzed decomposition of DDM in near-anhydrous DMSO, benzophenone is not found among the products, and we suggest that this reaction does not undergo a change in mechanism and continues to use the AS_E-2 mechanism.

Key words: decomposition mechanism, kinetics, solvent effect, reaction with carboxylic acids.

Résumé : On a étudié la décomposition acidocatalysée du diazodiphénylméthane (DDM) dans le DMSO contenant des quantités variables d'eau. On a trouvé que la réaction est du premier ordre en DDM et du premier ordre en acide. La représentation graphique de Brønsted pour une série d'acides carboxyliques est incurvée et le point pour H^+ se trouve en dessous de la droite définie par les acides carboxyliques. Dans le DMSO pratiquement anhydre, les effets cinétiques de l'hydrogène (EICs) sont de 1,7 et 1,6 respectivement pour l'acide acétique et l'acide chloroacétique. L'EIC de l'acide chloroacétique augmente avec une augmentation de la concentration en eau lorsqu'on passe de 2,9 à 3,6 M en eau. Le graphique représentant $[H_2O]$ en fonction de k_{HA} de l'acide chloroacétique présente un minimum bien défini se produisant à 1 M. Ce comportement et l'effet de l'eau sur l'EIC suggèrent que les réactions catalysées par les acides carboxyliques dans le DMSO pratiquement anhydre ne font pas appel au mécanisme AS_E-2 que l'on attribue généralement à la réaction du DDM dans les solvants hydroxyliques. On suggère un mécanisme pour la réaction conduisant à un azoalcane. Ceci peut conduire directement ou indirectement au diphénylcarbène qui pourrait expliquer la formation des produits observés: benzophénone, benzhydrol et esters benzhydryles. Pour la décomposition catalysée par H^+ du DDM dans le DMSO pratiquement anhydre, on n'observe pas de benzophénone parmi les produits et on suggère que cette réaction n'est pas soumise à un changement de mécanisme et qu'elle continue à faire appel au mécanisme AS_E-2.

Mots clés : mécanisme de décomposition, cinétiques, effet de solvant, réaction avec des acides carboxyliques.

[Traduit par la Rédaction]

The reaction of diazodiphenylmethane (DDM) with acid has long been a kineticist's favorite (1–11). Its mechanism in hydroxylic solvents is well established as AS_E-2 (Scheme 1) and is characterized by kinetic isotope effects (KIEs) between 2.5 and 4, depending on solvent and catalyzing acid.

In near-anhydrous acetonitrile, a KIE of 3.3 was obtained when the reaction was catalyzed by perchloric acid, suggesting that the reaction occurs by the AS_E-2 mechanism (3). In contrast, when the reaction is carried out in aprotic solvents with low concentrations of sulfonic or carboxylic acids, the KIE falls to values ~1 (4, 5). It has also been reported that the reaction becomes zeroth-order in DDM in anhydrous acetonitrile with *p*-toluenesulfonic acid as the catalyst (4). This behavior was not noted in a study of the reaction in 19 dipolar, aprotic solvents (including acetonitrile), with either benzoic or acetic acid as catalyst (5). Instead, it was found that the reaction is kinetically first-order in diazodiphenylmethane and that the rate law contains both a first-order and second-order term in acid. Dimethylsulfoxide and *N*,*N*-dimethylformamide solvents were two notable exceptions in which only the first-order term in acid was observed. The study also determined the KIEs for benzoic and acetic acids

Received October 26, 1998.

This paper is dedicated to Jerry Kresge in recognition of his many achievements in chemistry.

R. Eliason.[1] Contribution from the Chemistry Department, Southwest State University, Marshall MN 56258, U.S.A.

[1]Telephone: (507) 537-6144. Fax: (507) 537-7154. e-mail: eliason@ssu.southwest.msus.edu

 © 1999 NRC Canada

Scheme 1.

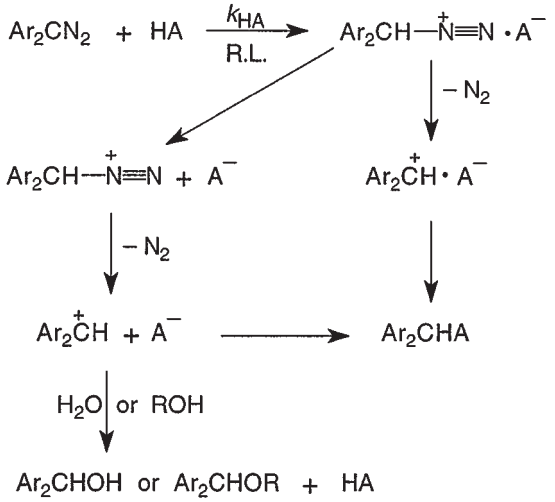

in ethyl acetate and acetone. The KIEs for the second-order term (first-order in both diazodiphenylmethane and acid) were in the range of 0.6–1.8, and for the third-order term (first-order in diazodiphenylmethane and second-order in acid) the KIEs ranged from 4.2 to 7.3. To account for these observations, it was suggested that for the second-order reaction the first step of Scheme 1 becomes reversible, and one of the subsequent steps becomes largely rate-limiting (4, 5). The third-order reaction was accounted for by reaction of an acid dimer with DDM (5).

Given the behavior in DMSO compared to the other aprotic solvents, we undertook an investigation of the reaction in DMSO containing varying amounts of water. Isotope effects, products, the effect of acid strength on reactivity, and the effect of water concentration up to 12 M are reported. For carboxylic acid induced reactions, but not for those induced by H^+, a change in mechanism does appear to occur. The mechanistic change appears to involve the opening of a new pathway rather than just a shift to a later rate-limiting step within the general framework of Scheme 1. A candidate mechanism is proposed.

Experimental section

Materials

Dimethylsulfoxide (Aldrich Chemical Co.), dried as described previously (12), was used for all kinetic experiments; DMSO containing 0.01% water was later purchased commercially (Burdick and Jackson Laboratories, Inc.) and was used directly for product analysis experiments. Diazodiphenylmethane was prepared by the method of Nenitzescu and Solomonica (13) and was purified by recrystallization from methanol and then from petroleum ether (bp 30–60°C). Acetic acid-*d* was a gift from Dr. B. Spencer Meeks, Jr., was prepared by him (14), and was assumed to contain the same isotopic purity as the deuterium oxide (99.8 atom% D) from which it was prepared. Trifluoromethanesulfonic acid was distilled prior to use (bp 162–164°C; lit. (12) 162°C). Chloroacetic acid-*d* was prepared by reaction of freshly distilled (bp 103–104°C) chloroacetyl chloride (0.31 mol; Matheson Colman and Bell; practical grade) with deuterium oxide (0.27 mol; Bio-Rad Laboratories; specified 99.87 atom% D). The reaction mixture was fractionally distilled, and the middle fraction (bp 183.5°C) was used. The isotopic purity was assumed to be the same as that of the deuterium oxide.

Bis(triphenylphosphonium)nitrogen(1+) trifluoroacetate (PNP trifluoroacetate) was prepared after the method of Martinsen and Songstad (15). The white solid was recrystallized from methanol–water solution (mp 184.5–185.5°C).

Anal. calcd. for $C_{38}H_{38}O_2NP_2F_3$: C 70.02, H 4.64, N 2.15, P 9.51; found: C 70.20, H 4.63, N 2.02, P 9.76.

All other reagents were commercial products of the highest available purity and were used as received.

Procedures

The kinetic procedures have been previously described (2). All kinetic measurements were performed in a spectrophotometer cell holder, at constant temperature, 25.0 ± 0.2°C. Except for trifluoroacetic acid, the k_{HA} values in DMSO were determined in unbuffered carboxylic acid solutions. The k_{HA} for trifluoroacetic was determined in solutions containing enough PNP trifluoroacetate to produce a 1:1 buffer ratio.

The water content of the DMSO used in all experiments was determined from the intensity of its absorption at 3400 cm^{-1} (12). The adventitious water content never exceeded 0.048 M for product analysis experiments, 0.045 M for kinetic experiments, or 0.18 M for experiments in which the water concentration was varied when trifluoromethanesulfonic acid was used as the catalyst.

Five mmol of DDM were used in each product determination. When either chloroacetic acid or trifluoromethanesulfonic acid was added to the DDM, 11 mmol of the acid were used. Thermal decomposition was accomplished by dissolving the DDM in 20 mL DMSO and heating this solution for 3 h in a boiling water bath. Acid-catalyzed decomposition was done by dissolving the DDM in 10 mL of DMSO and the acid in 10 mL of DMSO. Both solutions were cooled in an ice bath until the DMSO began to freeze. Then the acid solution was added, dropwise, to the stirred DDM solution while cooling it in the ice bath. All the acid-catalyzed reaction mixtures were kept overnight in the dark before workup. In one experiment, the chloroacetic acid solution was heated to 110°C in an oil bath. The DDM solution was placed in the hot oil bath, and the hot acid solution was added dropwise with stirring to the DDM solution. This mixture was kept in the oil bath for 3 h before workup. In every experiment, the reaction mixture turned yellow. The following workup procedure was used for all experiments. The reaction mixture was poured into 80 mL water. The resulting solution was extracted four times with 20 mL diethyl ether. The combined ether extracts were washed four times with 20 mL of 5% aqueous sodium bicarbonate; then three times with 20 mL water. The ether solution was dried over anhydrous magnesium sulfate. The ether was removed from the products under reduced pressure (water aspirator). In each case, an oily residue was left after the ether removal. An IR spectrum was taken of each product mixture, and the products were identified by comparison with known spectra. In those experiments that were heated, crystals formed in the product mixture. The crystals were separated and identified by IR spectroscopy.

© 1999 NRC Canada

Table 1. Rates of reaction of DDM with trifluoromethanesulfonic acid in near-anhydrous DMSO at 25°C.

$[CF_3SO_3H]/10^{-3}$ M	$k_{obs}/10^{-4}$ s^{-1}
12.7	76.7, 79.2, 75.5
8.52	54.4, 53.6, 54.9
4.87	30.0, 30.0, 30.4
1.22	9.05, 9.09, 9.02
$k_{obs}/s^{-1} = (7.84 \pm 6.36) \times 10^{-5} + (6.26 \pm 0.08) \times 10^{-1}$ $[CF_3SO_3H]$	

Table 2. Rates of reaction of DDM with trifluoroacetic acid in near-anhydrous DMSO at 25°C.

$[CF_3CO_2H]/10^{-4}$ M	$k_{obs}/10^{-4}$ s^{-1}
117.0	59.1, 57.6
81.9	41.3, 40.9, 39.8
45.3	20.6, 24.7, 22.8
9.52	5.62, 5.89, 6.03
$k_{obs}/s^{-1} = (1.11 \pm 0.62) \times 10^{-4} + (4.82 \pm 0.09) \times 10^{-1}$ $[CF_3CO_2H]$	

Table 3. Rates of reaction of DDM with dichloroacetic acid in near-anhydrous DMSO at 25°C.

$[Cl_2CHCO_2H]/10^{-2}$ M	$k_{obs}/10^{-4}$ s^{-1}
12.6	87.6, 91.2, 90.6
8.80	62.7, 63.2, 62.9
5.03	34.8, 35.1, 34.7
1.26	8.63, 8.68, 8.36
$k_{obs}/s^{-1} = (-7.85 \pm 65.3) \times 10^{-5} + (7.21 \pm 0.01) \times 10^{-2}$ $[Cl_2CHCO_2H]$	

Table 4. Rates of reaction of DDM with chloroacetic acid in near-anhydrous DMSO at 25°C.

$[ClCH_2CO_2H]/10^{-2}$ M	$k_{obs}/10^{-5}$ s^{-1}
12.5	53.7, 57.0, 57.0
8.74	40.3, 42.8, 40.5
4.99	22.0, 22.7, 21.6
1.25	5.62, 5.51, 5.53
$k_{obs}/s^{-1} = (-8.84 \pm 821) \times 10^{-8} + (4.55 \pm 0.10) \times 10^{-3}$ $[ClCH_2CO_2H]$	

Results

Pseudo first-order rate constants, k_{obs}, were determined from plots of log $(A_t - A_\infty)$ versus time. (See Tables 1–8 for k_{obs} values of DDM in various acids.) The reactions were followed for about three half-lives (>75% completion), and these plots were completely rectilinear, showing no systematic deviations. Figures 1 and 2 show that reactions of DDM with both chloroacetic and trifluoromethanesulfonic acids are first-order in DDM. In Fig. 1, the DDM concentration between the curves differs by a factor of 2.2 as determined by the initial absorbance. The observed rate constant, k_{obs}, for curve A was 5.37×10^{-4} s^{-1} and for curve B 5.70×10^{-4} s^{-1}. The reaction in curve B was followed to about 90% completion, which represents 3.2 half-lives. The plot shows no indication of curvature over that extent of reaction. If the first 10% of reaction of curve A is compared with the last 10% of reaction in curve B, there is over a 10-fold difference in DDM concentration, and yet the slopes of the two curves are essentially equivalent. A similar argument can be made using the data in Fig. 2. In this case, there is slightly less than

Table 5. Rates of reaction of DDM with acetic acid in near-anhydrous DMSO at 25°C.

$[CH_3CO_2H]/10^{-2}$ M	$k_{obs}/10^{-6}$ s^{-1}
23.8	7.77, 8.14, 7.14
19.0	6.65, 6.57, 6.20
14.2	4.68, 4.87, 4.55
9.50	3.08, 3.10, 3.12
4.75	1.54, 1.59, 1.56
$k_{obs}/s^{-1} = (2.4 \pm 15.7) \times 10^{-8} + (3.28 \pm 0.10) \times 10^{-5}$ $[CH_3CO_2H]$	

Table 6. Rates of reaction of DDM with acetic acid-d[a] in near-anhydrous DMSO[b] at 25°C.

$[CH_3CO_2L]/10^{-2}$ M[c]	$k_{obs}/10^{-6}$ s^{-1}[d]
23.2	5.96, 6.09, 6.13
18.6	4.65, 5.00, 5.21
13.9	3.96, 3.89, 3.92
9.28	3.00, 2.79, 2.88
4.64	1.50, 1.85, 1.42
$k_{obs}{}^{d}/s^{-1} = (5.79 \pm 1.03) \times 10^{-7} + (2.37 \pm 0.07) \times 10^{-5}$ $[CH_3CO_2L]$	

[a]See experimental section for isotopic purity.

[b]The DMSO contained 0.045 M adventitious H_2O.

[c]The symbol L represents an atom that may be either hydrogen or deuterium.

[d]Not corrected to 100 atom% D.

Table 7. Rates of reaction of DDM with 0.103 M chloroacetic acid in DMSO–water mixtures at 25°C.

$[H_2O]$[a]	$k_{obs}/10^{-4}$ s^{-1}	$k_{HA}/10^{-3}$ M^{-1} s^{-1}
0.045	4.82, 5.26, 4.92	4.69, 5.11, 4.78
0.161	7.42, 7.22, 7.22	7.21, 7.02, 7.01
0.443	10.7, 10.2, 8.19	10.4, 9.91, 7.96
0.768	10.8, 10.0, 9.82	10.5, 9.72, 9.54
1.09	6.42, 6.38, 5.84	6.24, 6.20, 5.67
1.55	8.48, 8.35, 8.60	8.31, 8.18, 8.42
2.06	11.0, 10.7, 11.3	10.7, 10.4, 11.0
3.55	10.6, 10.0, 10.7	10.3, 9.82, 10.4

[a]The DMSO contained 0.045 M adventitious water.

Table 8. Rates of reaction of DDM with 0.105 M chloroacetic acid-d[a] in DMSO–D_2O mixtures at 25°C.

$[L_2O]$[b]	$k_{obs}/10^{-4}$ s^{-1}[c]	$k_{LA}/10^{-3}$ M^{-1} s^{-1}[c]
0.045	4.15, 4.05, 4.06	3.99, 3.89, 3.91
0.155	4.11, 4.86, 4.32	3.95, 4.67, 4.16
0.476	6.10, 6.47, 5.97	5.86, 6.22, 5.74
0.798	5.43, 5.13, 5.36	5.22, 4.93, 5.15
1.05	2.30, 2.00, 2.38	2.21, 1.92, 2.29
1.59	3.44, 3.44, 3.49	3.28, 3.28, 3.33
2.12	5.23, 4.98, 5.10	5.03, 4.79, 4.91
3.55	3.83, 3.74, 3.81	3.66, 3.56, 3.63

[a]See experimental section for isotopic purity.

[b]The DMSO contained 0.045 M adventitious H_2O. The added deuterium oxide contained 99.87 atom% D. The symbol L represents an atom that may be either hydrogen or deuterium.

[c]Not corrected to 100 atom% D.

© 1999 NRC Canada

Fig. 1. Adherence to the first-order rate law by chloroacetic acid-catalyzed decomposition of DDM. From the beginning of experiment A to the end of experiment B, there is ~20-fold change in DDM concentration, but no significant change in the pseudo first-order rate constant. The circles are not error circles; they merely identify the points.

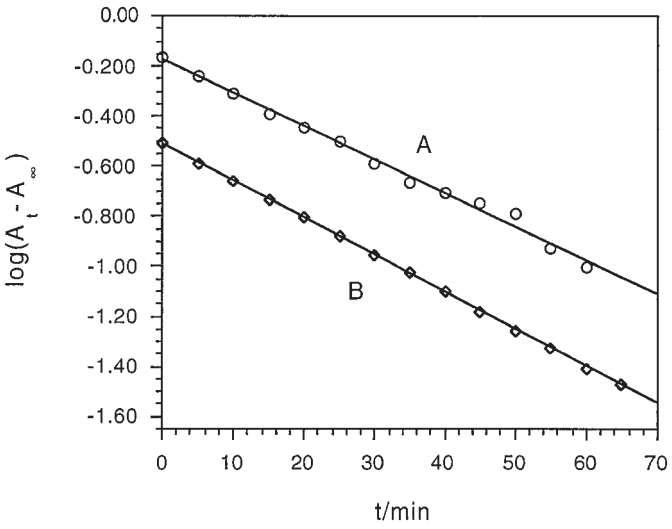

Fig. 2. Adherence to the first-order rate law by trifluoromethylsulfonic acid-catalyzed decomposition of DDM. From the beginning of experiment C to the end of experiment D, there is ~10-fold change in DDM concentration, but no significant change in the pseudo first-order rate constant. The circles are not error circles; they merely identify the points.

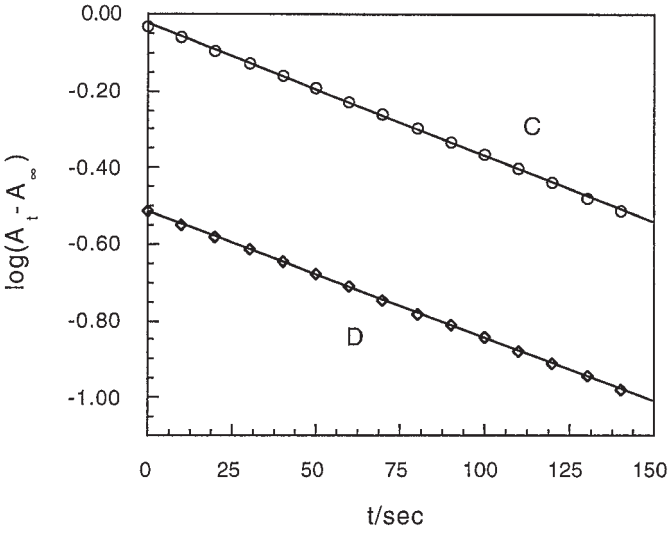

a 10-fold difference in DDM concentration between the first part of curve C and curve D, but the slopes of these curves are similar. If the reaction were actually zeroth-order in DDM, there would be a corresponding 10-fold increase in the slopes of the plots shown in Figs. 1 and 2. No such increase is apparent. Since reactions like these are also first-order in DDM when the solvent is 12 M water in DMSO (7), we concluded that this was true throughout our range of interest. We also concluded that the reaction was first-order in DDM for both strong and weak acids.

Table 9. Dissociation constants and catalytic coefficients for reaction with DDM in near-anhydrous DMSO at 25°C.

Acid	K_{HA}/M[a]	k_{HA}/M^{-1} s^{-1}[b]
H+	15.1[c]	$6.26 \pm 0.08 \times 10^{-1}$
CF_3COOH	3.55×10^{-4} [d]	$4.73 \pm 0.09 \times 10^{-1}$
$Cl_2CHCOOH$	4.36×10^{-7}	$7.21 \pm 0.01 \times 10^{-2}$
$ClCH_2COOH$	1.0×10^{-9}	$4.55 \pm 0.10 \times 10^{-3}$
$ClCH_2COOD$		$2.81 \pm 0.10 \times 10^{-3}$
PhCOOH	1.0×10^{-11}	5.26×10^{-4}[e]
CH_3COOH	2.51×10^{-13}	$3.28 \pm 0.10 \times 10^{-5}$
CH_3COOD		$2.37 \pm 0.07 \times 10^{-5}$

[a]From ref. 20, unless otherwise noted.

[b]Reported uncertainties are standard errors as determined by least-squares regression analysis.

[c]Based on the molar concentration of the solvent and of questionable significance.

[d]Reference 39.

[e]From ref. 5. The value given, 1.2×10^{-3} M^{-1} s^{-1}, was measured at 37°C. An activation energy of 12.5 kcal mol^{-1} was assumed in order to estimate the 25°C value.

A catalytic coefficient for H^+, k_H, was obtained from dilute (<0.13 M) trifluoromethanesulfonic acid solutions. At such concentrations in DMSO, trifluoromethanesulfonic acid has been considered to be completely dissociated (16), and we have also made this assumption. The slope of a plot of k_{obs} as a function of $[H^+]$ is k_H.

Table 9 lists the carboxylic acid dissociation constants, K_{HA}, and the catalytic coefficients, k_{HA}. Trifluoroacetic acid is significantly dissociated in DMSO. So the reactions were run with 1:1 buffer solutions, and the catalytic coefficient was determined from a plot of the quantity, $k_{obs} - k_H[H^+]$, against $[CF_3COOH]$. Dichloroacetic acid is the next most strongly dissociated. In the most dilute solution used, 0.0125 M, it is 0.6% dissociated, and the resulting $k_H[H^+]$ term contributes 5% to k_{obs}. The remaining carboxylic acids were assumed to be undissociated, and in these other cases the fractional contribution of $k_H[H^+]$ to k_{obs} was smaller still. Thus, the carboxylic acid coefficients, k_{HA}, were the slopes of plots of k_{obs} as a function of the acid concentration, [HA]. The slopes of all these linear plots were evaluated by the method of least squares. The average deviation of points from the lines was ~2%, and the intercepts were indistinguishable from zero. The range of [HA] studied was typically 0.01–0.1 M, and the experimental points defined linear relations. We concluded that contributions to the rate from terms higher than first order in acid were not present. The benzoic catalytic coefficient was estimated from the value at 37°C given by Chapman et al. (5). An activation entropy of –35 cal mol^{-1} deg^{-1} was assumed. This seemed appropriate for a bimolecular reaction producing ions in a nonaqueous solvent (17). This leads to an activation energy of 12.5 kcal mol^{-1}.

The variation of k_H with water concentration is shown in Fig. 3. The water concentration was varied from under 0.1 M to over 8 M. Each point represents the average of triplicate determinations. The point at 12 M water is from a previous study (7).

The effect of water concentration on the catalytic coefficient for chloroacetic acid and for chloroacetic acid-d_1 was also determined. All the measurements were made with

© 1999 NRC Canada

Fig. 3. The H^+ catalytic coefficient (trifluoromethanesulfonic acid) as a function of water concentration. The point at 12 M H_2O is from a previous study (7). The solid line is merely a smooth curve through the points, and it has no theoretical significance.

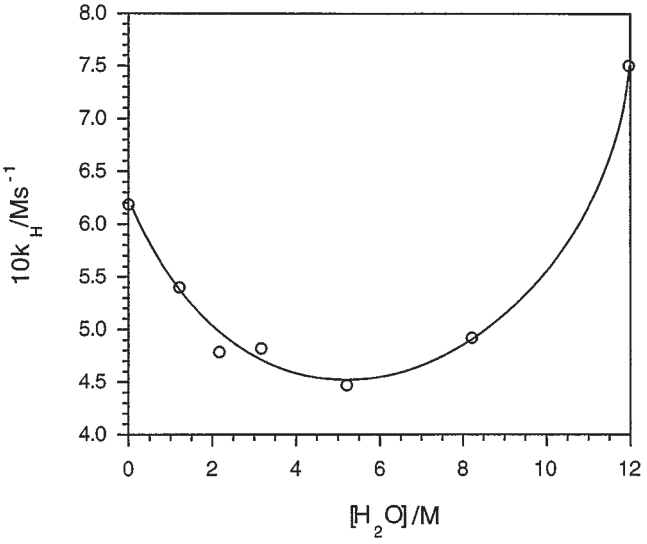

Fig. 4. Chloroacetic acid catalytic coefficients, k_{HA}, as a function of water concentration. The error bars indicate estimated uncertainities in measurements. The solid line is a plausible smooth curve through the circles.

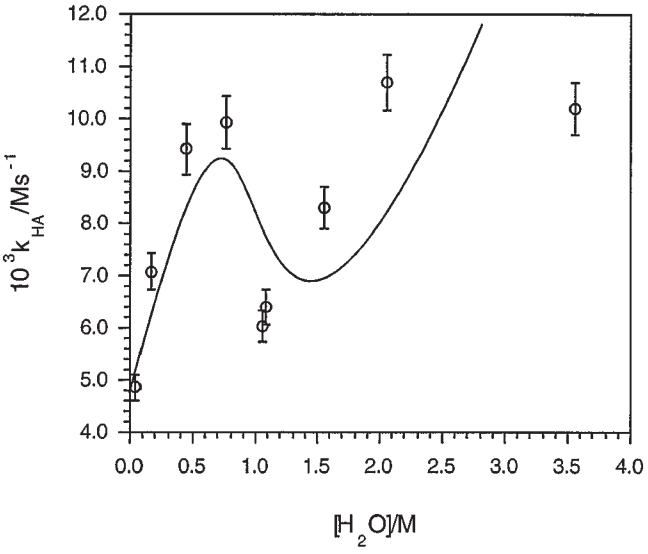

Fig. 5. Chloroacetic acid catalytic coefficients, k_{HA}, divided by the benzoic acid dissociation constants, K_{HA}, as a function of water concentration. The error bars indicate estimated uncertainties in measurements. The solid line is a plausible smooth curve through the circles.

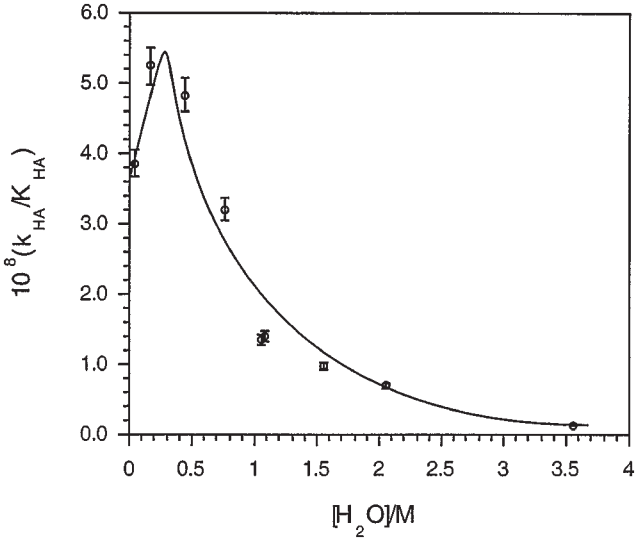

~0.1 M acid. The catalytic constants are shown in Figs. 4 and 5, and the isotope effects in Fig. 6. They have not been corrected for a $k_H[H^+]$ contribution. The pK_{HA} for chloroacetic acid drops from 9.00 in DMSO to 5.69 in a water–DMSO mixture of mole fraction DMSO, X_{DMSO}, of 0.445 (18). Assuming that pK_{HA} is a linear function of X_{DMSO} (18), a pK_{HA} of 7.5 is obtained by interpolation at a water concentration of 3.55 M. This leads to a $k_H[H^+]$ contribution to k_{obs} of 0.3% at 0.1 M. At lower water concentrations, the $k_H[H^+]$ contribution would be lower still. The isotopic purity of the chloroacetic acid-d_1 was assumed to be equal to that of the deuterium oxide from which it was prepared, which was specified as 99.87% atom percent D. Since the near-anhydrous DMSO contained 0.045 M water, k_{LA}[2] was extrapolated to 100% D by assuming a linear function of the atom fraction D. The probable errors of the experimental k_{LA} values were ~5%, and the extrapolation to 100% D adds to the uncertainty of the k_{DA} values, which we estimated to be ~10%. The uncertainty of the isotope effects is, then, ~15%.

For acetic acid, a value of k_{DA}, 1.97×10^{-5} M^{-1} s^{-1}, and an isotope effect, 1.7, were also obtained, in the same manner as described above.

Reaction products were determined by comparing the IR spectra of product mixtures with published standards[3] and with the IR spectrum of an authentic sample of benzhydryl chloroacetate that was prepared for this purpose. At or below 25°C with trifluoromethanesulfonic acid in DMSO containing 0.045 M water, the sole product was benzhydrol. It is likely that any benzhydryl trifluoromethanesulfonate formed in the original reaction would have been converted to benzhydrol during the work-up. Less than 2% of benzophenone can have been present, since its very strong and distinctive carbonyl band would have been easily detected, and it was not. The same experiment was conducted using chloroacetic acid, and in this case the product mixture consisted of benzhydryl chloroacetate, benzhydrol, and benzophenone in comparable quantities. No other products could be detected. When the same reactants were allowed to react at 110°C, ~3% of solid tetraphenylethene separated from the rest of the product mixture that proved to be benzhydrol and benzophenone in about equal proportions. Because of coincidences in the IR spectra, we cannot be certain that a small amount of tetraphenylethene was not present among the

[2] L is used for an atom that may be either hydrogen or deuterium.
[3] Grating infrared spectra nos. 326, 382, 10 404, and 16 434. Satler Research Laboratories.

© 1999 NRC Canada

Fig. 6. Isotope effects on chloroacetic acid catalytic coefficients as a function of water concentration. (L may be either H or D.) The point at 12 M L_2O is from a previous study (7). The error bars indicate estimated uncertainties in measurements. The point marked with a question mark is substantially removed from the curve defined by other points, including points at essentially the same L_2O concentration, and although no error was identified the point is discounted. The solid line is a plausible smooth curve through the circles.

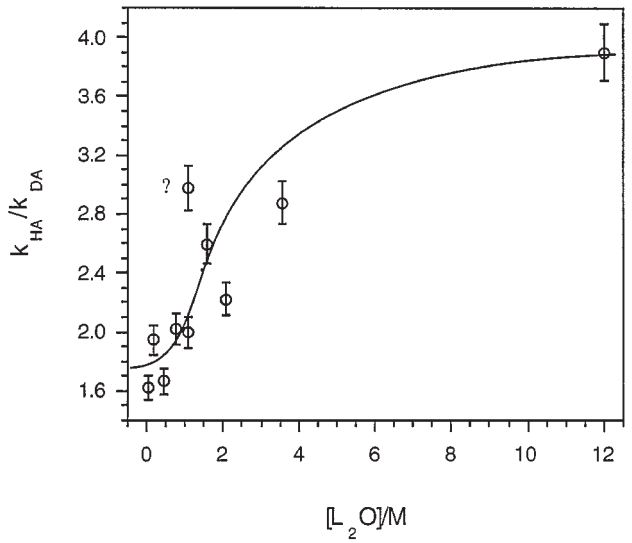

products of the lower-temperature reaction. When DDM was heated in the same DMSO without any added acid, about 40% of the product crystallized spontaneously. This proved to be mostly benzophenoneazine with a small amount of tetraphenylethene. The remaining 60% consisted of benzophenone and benzhydrol.

Discussion

There are two general ways in which a reaction can change under a change in reaction conditions. Without changing the sequence of steps, a new step may become rate-limiting. Alternately, a new reaction channel may open up: that is, a new sequence of steps, which was uncompetitive under the old conditions, may become competitive under the changed conditions. Earlier workers (4, 5) have favored the first alternative based, in part, on the behavior of the reaction rate on changing the water concentration. As the water concentration was decreased from 11 to 2 M, the reaction rate increased to a maximum after which the rate decreased sharply (4). We believe our results favor the second alternative.

A plot of k_{HA} for chloroacetic acid versus $[H_2O]$ produces an interesting bimodal curve (Fig. 4). The general trend of increasing k_{HA} with increasing $[H_2O]$ can be rationalized. Addition of water to DMSO would increase the dielectric constant of the solvent mixture and, specifically, would increase its solvation power for anions, since DMSO cannot act as an H-bond donor. A solvent with increased water would be better able to stabilize a charged transition state relative to the uncharged reactants. The activation free energy would be lowered, and the reaction rate increased. Thus, we concluded that the reaction probably involves charge formation in the transition state. The minimum which

Scheme 2.

$$Ar_2CN_2 + HA \underset{k_{-1}}{\overset{k_1}{\rightleftharpoons}} Ar_2CHN_2^+ + A^-$$

$$Ar_2CHN_2^+ \xrightarrow{k_2} \text{Products}$$

occurs at approximately 1 M water could be explained as due to a change in reaction mechanism. A mechanistic change from rate-limiting proton transfer (AS_E-2) to a pre-equilibrium step followed by a rate-limiting step (A-1) on going from high to low water concentration has been previously proposed (Scheme 2) (4, 5). The k_1 step will be rate-limiting if $k_2 >>> k_{-1}[A^-]$, which is apparently the case at high $[H_2O]$. Decreasing the water content of the solvent would decrease the solvation of the carboxylic anion and increase the free energy of this species. The resulting activation free energy decrease would cause the $k_{-1}[A^-]$ term to become larger than k_2 at some point. When $k_{-1}[A^-] >>> k_2$, then the mechanism would have become A-1 at low $[H_2O]$. If this general picture is true that the decrease in k_{HA} is a result of a decrease in the solvation of the incipient carboxylate anion in the transition state, then k_{HA} should be some function of K_{HA} at various $[H_2O]$. The decrease in K_{HA} with decreasing $[H_2O]$ is a reflection of the inability of the solvent to solvate the anion. A plot of k_{HA}/K_{HA} versus $[H_2O]$ should give a curve that breaks downward at the point where the mechanism changes from AS_E-2 to A-1 because decreased anion solvation would greatly increase $k_{-1}[A^-]$ term. The hypothesis is tested in Fig. 5 in which K_{HA} is that for benzoic acid obtained from data of Kolthoff et. al. (19, 20) and Fiordiponti et. al. (21), since similar data for dichloroacetic acid was unavailable. As can be seen, the curve breaks sharply upward upon going below 1 M water. We take this to indicate that there has not been a simple shift in the rate-limiting step of the mechanism of Scheme 1 but that an entirely new mechanistic pathway is being employed.

This alternative pathway must account for the reduction of the isotope effect on the carboxylic acid catalytic coefficient but must still provide for general acid catalysis by carboxylic acids and must account for the alteration of the product distribution to include a substantial amount of benzophenone. We believe the mechanism shown in Scheme 3 meets these requirements. The first step consists of reversible proton transfer to nitrogen with the carboxylate group still strongly associated (intermediate **1**). It has been shown that for diazomethane in super acid media protonation can occur on nitrogen (22). The second step involves rate-limiting internal attack by the carboxylate anion on carbon to produce intermediate **2**. These two steps lead to kinetics that conform to general-acid-catalysis. The KIE for the reaction would depend on the isotope effect of the reversible equilibrium step. It is expected that the zero-point separation for H and D going from OH to NH bonds would be similar, and this would result in an isotope effect around unity. Calculations of equilibrium isotope effects from OH and NH stretching frequencies predict a K_H/K_D of ~1 for non-hydrogen-bonded NH and 1.4 for hydrogen-bonded NH (23). This suggests that the association of the carboxylate anion with the hydrogen in **1** may give a KIE of about 1.4, which is close to the values observed for acetic and chloroacetic acids.

© 1999 NRC Canada

Scheme 3.

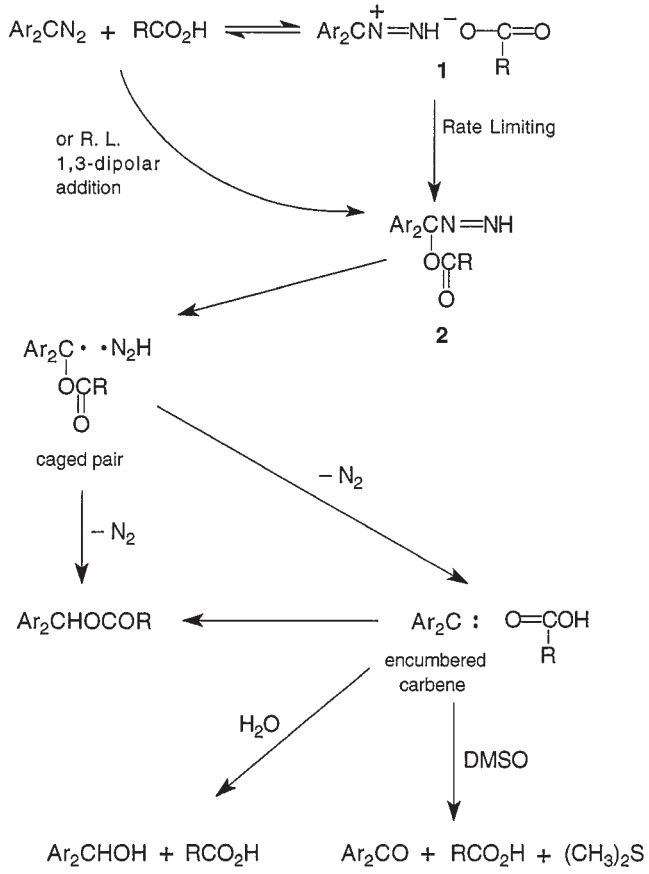

An alternative to the two-step mechanism outlined above is a rate-limiting 1,3 dipolar addition of the carboxylic acid to DDM (shown in Scheme 3). Dipolar additions to diazoalkanes are common (24). Although addition of carboxylic acids to diazoalkanes has not been previously recognized, 1,3-dipolar additions of a thiol to a nitrile imine and methanol to an azomethine imine (25) have been. Since the molecular acid is involved, it would give rise to general-acid-catalysis. The transition state of this 1,3-dipolar addition would involve heavy atom motions in the reaction coordinate as well as hydrogenic motion. It is reasonable, therefore, that the isotope effect should be small.

Both these pathways should depend on the nucleophilicity of the A fragment in HA. They would, then, become uncompetitive if the acid is perchloric or trifluoromethanesulfonic acid and would become more competitive for carboxylic acids in non-hydroxylic solvents. Since either pathway is basically a proton transfer reaction, the reaction might, quite reasonably, produce the curved Brønsted plot shown in Fig. 7 (26). The H^+ point would fall below the plot because it is structurally different from the carboxylic acids (27, 28). In fact, we believe that H^+ catalysis provided by trifluoromethanesulfonic acid occurs via the AS_E-2 mechanism (Scheme 1). A plot of k_{H+} versus [H_2O] (Fig. 3) follows the same pattern obtained for the hydrolysis of ethyl vinyl ether in DMSO occurring by the AS_E-2 mechanism (29).

Fig. 7. A log–log plot of the data from Table 9 of catalytic coefficients as a function of dissociation constants. The solid line has no theoretical significance. It is merely a smooth curve through the carboxylic acid points.

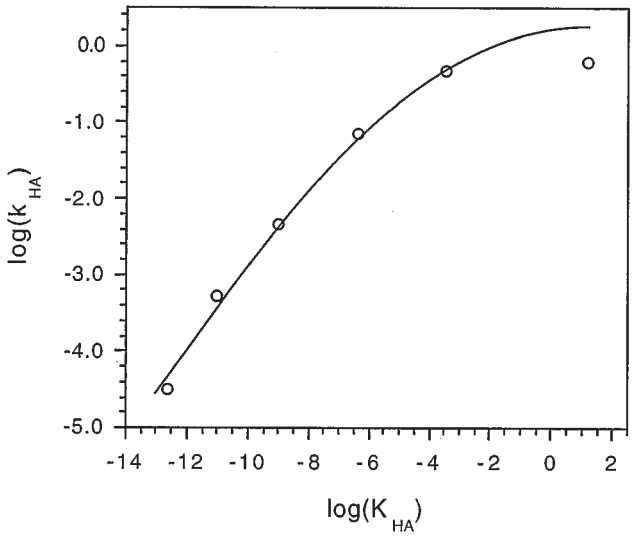

The fragmentation of diazoalkanes is well documented (30). It may be symmetrical if the reactant is symmetrical but is unsymmetrical if the reactant is unsymmetrical (31). In the present case, the cleavage of the N—C bond of **2** is energetically much easier than the cleavage of the N—H bond,[4] and we suggest, therefore, the one-bond cleavage shown giving a caged radical pair. Cage recombination gives benzhydryl chloroacetate if the hydrogen is transferred to carbon or gives diphenylmethylene plus chloroacetic acid if the hydrogen is transferred to one of the carboxyl oxygens. In both cases, N_2 is liberated. We envision that the diphenylmethylene produced is an encumbered carbene. Diphenylcarbene is known to insert into the OH bond of methanol (34).[5] This carbene could then react with chloroacetic acid, with which it is associated, to give benzhydryl chloroacetate, and with water, present in small amounts, to give benzhydrol. Oda et al. (36) found that diphenylcarbene is oxidized by DMSO to benzophenone; thus, this reaction could produce the benzophenone found in our product mixtures. The benzhydrol could also arise from hydrolysis of benzhydryl chloroacetate in the product analysis workup and (or) from a residual contribution from the AS_E-2 mechanism. Since benzhydryl chloroacetate and benzhydrol are also the products of the AS_E-2 mechanism (Scheme 1), they could also be produced in simple variants of that scheme. However, we believe that benzophenone is most easily explained with the aid of a carbene precursor. Benzophenone could also be produced by reaction of triplet diphenylmethylene with O_2 (37). Closs and Goh (38) have previously observed ~50% yields of stereospecific cyclopropane formation in the acid-promoted reactions of aryldiazomethanes with olefins, and they suggested a carbenoid mechanism.

In this way, the mechanism shown in Scheme 3 can account for all our observations on the carboxylic acid pro-

[4] The CH_3—NH_2 bond has bond energy of 79 ± 3 kcal mol^{-1}, while the H—NH_2 bond has energy of 103 ± 3 kcal mol^{-1} (32). In addition, the acetoxydiphenylcarbinyl radical would be stabilized by over 10 kcal mol^{-1} of resonance energy (33).

[5] This reaction can apparently occur with either the singlet or triplet state (35).

© 1999 NRC Canada

moted breakdown of DDM in near-anhydrous DMSO. While we cannot prove that scheme is unique in doing so, we have shown that all the steps have precedent, and we believe it is correct. We also believe that this is essentially the mechanism for the reaction of DDM with low concentrations of carboxylic acids in other non-hydroxylic solvents.

References

1. R. Eliason. Acta Chem. Scand. Ser. A, **33**, 343 (1979).
2. A.I. Hassid, T.-M. Liang, R. Eliason, and M.M. Kreevoy. Croat. Chem. Acta, **49**, 757 (1977).
3. D. Bethell and J.D. Callister. J. Chem. Soc. 3801 (1963).
4. D. Bethell and J.D. Callister. J. Chem. Soc. 3808 (1963).
5. N.B. Chapman, M.R.J. Dack, D.J. Newman, J. Shorter, and R. Wilkinson. J. Chem. Soc. Perkin Trans. 2, 962 (1974).
6. M.H. Aslam, N.B. Chapman, J. Shorter, and M. Charton. J. Chem. Soc. Perkin Trans. 2, 720 (1981).
7. A.I. Hassid, M.M. Kreevoy, and T.-M. Liang. Faraday Symp. Chem. Soc. **10**, 69 (1975).
8. N.B. Chapman, M.R.J. Dack, D.J. Newman, and J. Shorter. J. Chem. Soc. B, 834 (1971).
9. R.A. More O'Ferrall. Adv. Phys. Org. Chem. **5**, 331 (1967).
10. J.D. Roberts and W. Watanabe. J. Am. Chem. Soc. **72**, 4869 (1950).
11. D. Bethell and R.D. Howard. Chem. Commun. 94 (1966).
12. L.M. Abts, J.T. Langland, and M.M. Kreevoy. J. Am. Chem. Soc. **87**, 3181 (1975).
13. C.D. Nenitzescu and E. Solomonica. Org. Syn. Coll. **2**, 496 (1943).
14. B.S. Meeks, Jr., and M.M. Kreevoy. Inorg. Chem. **18**, 2185 (1979).
15. A. Martinsen and J. Songstad. Acta Chem. Scand. Ser. A, **27**, 645 (1977).
16. C. McCallum and A.D. Pethybridge. Electrochim. Acta, **20**, 815 (1975).
17. M.M. Kreevoy. *In* Technique of organic chemistry. Vol. 8. Part 2. *Edited by* A. Wiessberger. Wiley, New York. 1967. p. 1361.
18. E.H. Baughman and M.M. Kreevoy. J. Phys. Chem. **78**, 421 (1974).
19. I.M. Kolthoff and M.K. Chantooni, Jr. J. Am. Chem. Soc. **93**, 3843 (1971).
20. I.M. Kolthoff and M.K. Chantooni, Jr. J. Am. Chem. Soc. **98**, 5063 (1976).
21. P. Fiordiponti, F. Rallo, and F. Rodante. Gazz. Chim. Ital. **104**, 649 (1974).
22. J.F. McGarrity and D.P. Cox. J. Am. Chem. Soc. **105**, 3961 (1983).
23. R.P. Bell. The proton in chemistry. Cornell Univ. Press, Ithaca, N.Y. 1973. Chap. 11.
24. L.I. Smith. Chem. Rev. **23**, 193 (1938).
25. R. Huisgen. Angew. Chem. Int. Ed. Engl. **2**, 565 (1963).
26. A.J. Kresge. Chem. Soc. Rev. **2**, 475 (1973).
27. J.M. Williams, Jr., and M.M. Kreevoy. Adv. Phys. Org. Chem. **90**, 63 (1968).
28. A.J. Kresge and Y. Chiang. J. Am. Chem. Soc. **95**, 803 (1973).
29. J.M. Williams, Jr., and M.M. Kreevoy. J. Am. Chem. Soc. **90**, 6809 (1968).
30. P.T. Krueger. *In* The chemistry of the hydrazo, azo, and azoxy groups. *Edited by* S. Patai. Wiley, New York. 1975. p. 153.
31. R.J. Crawford and K. Takagi. J. Am. Chem. Soc. **94**, 7406 (1972).
32. J.A. Dean. Lange's handbook of chemistry. 12th ed. McGraw–Hill, New York. 1979. pp. 3-128 and 3-310.
33. P.D. Bartlett and R.R. Hiatt. J. Am. Chem. **80**, 1398 (1958).
34. W.J. Baron, M.R. DeCamp, M.E. Hendrick, M. Jones, Jr., R.H. Levin, and M.B. Sohn. *In* Carbenes. Vol. 1. *Edited by* M. Jones, Jr., and R.A. Moss. Wiley, New York. 1973. p. 77.
35. D. Griller, A.S. Nazran, and J.C. Scaiano. J. Am. Chem. Soc. **106**, 198 (1984).
36. R. Oda, M. Mieno, and Y. Hayashi. Tetrahedron Lett. 2365 (1967).
37. P.D. Bartlett and T.G. Traylor. J. Am. Chem. Soc. **84**, 3408 (1962).
38. G.L. Closs and S.H. Goh. J. Org. Chem. **39**, 1717 (1974).
39. R.L. Benoit and C. Buisson. Electrochim. Acta, **18**, 105 (1973).

© 1999 NRC Canada

An ab initio study on the magnetic susceptibility and magnetically induced current density distribution of the bicyclo[3.2.1]octa-3,6-dien-2-yl anion

Nick Henry Werstiuk and Jiangong Ma

Abstract: The molecular susceptibility and the atomic contributions including the basin and surface components calculated at the RHF/6-31+G(d)//6-31+G(d) level of theory along with vector current densities obtained at the 6-31++G(d,p)//6-31+G(d) and 6-31+G(d)//6-31+G(d) levels are reported for benzene (**1**) and correlated — the agreement is excellent — with the results obtained by Keith and Bader with the 6-311++G(2d,2p) basis. This validates our similar studies on the bicyclo[3.2.1]octa-3,6-dien-2-yl anion (**2**) — initially considered to be a bishomoaromatic species — its parent hydrocarbon bicyclo[3.2.1]octa-2,5-diene (**3**), the bicyclo[3.2.1]oct-3-ene-2-yl anion (**4**), and **5**, the lithium complex of **2**. While a magnetic susceptibility exhalation is found in going from **4** to **2**, the increase in atomic surface contribution to $\Delta\chi$ arises predominately (42.6%) from the ethenyl bridge carbons C6 and C7, with C2 + C4 and C3 exhibiting substantially smaller increases (27.4 and 8.3%, respectively). This result, in conjunction with the nature of the vector current density maps of **2** and **4,** provides further evidence that **2** does not possess a ring current as depicted in **2-bh**, the usual representation of "bishomoaromatic" **2**.

Key words: ab initio calculations, IGAIM, CSGT, magnetic susceptibility, induced current density distributions, bicyclo[3.2.1]octa-3,6-dien-2-yl anion.

Résumé : On a calculé la susceptibilité moléculaire et les contributions atomiques, y compris les composants du bassin et de la surface (en opérant au niveau RHF/6-31+G(d)//6-31+G(d) de la théorie) ainsi que les densités de courant vectoriel (obtenues au niveaux 6-31++G(d,p)//6-31+G(d) et 6-31+G(d)//6-31+G(d)) du benzène (**1**) et on a établi une corrélation — pour laquelle l'accord est excellent — avec les résultats obtenus par Keith et Bader avec la base 6-311++G(2d,2p). Cet accord valide notre étude semblable sur l'anion bicyclo[3.2.1]octa-3,6-dién-2-yle (**2**) (considéré initialement comme une espèce bishomoaromatique) et son hydrocarbure parent, le bicyclo[3.2.1]octa-2,5-diène (**3**), sur l'anion bicyclo[3.2.1]oct-3-én-2-yle (**4**) et sur **5**, le complexe lithié de **2**. Alors qu'on observe une exaltation de la susceptibilité magnétique en allant de **4** à **2**, l'augmentation dans la contribution de la surface atomique jusqu'à $\Delta\chi$ provient principalement (42,6%) des carbones C6 et C7 du pont éthényle alors que les augmentations dues à C2 + C4 et C3 sont substantiellement plus faibles (27,4 et 8,3% respectivement). Ce résultat, pris de concert avec la nature des cartes de densité du courant vecteur de **2** et **4** confirme que **2** ne possède pas de courant de cycle tel que montré par **2-bh**, la représentation habituelle du produit « bishomoaromatique » **2**.

Mots clés : calculs ab initio, « IGAIM », « CSGT », susceptibilité magnétique, distributions de densité du courant induit, anion bicyclo[3.2.1]octa-dién-2-yle.

[Traduit par la Rédaction]

Introduction

The key quantity related to the response of a molecule (or atom) to a magnetic field is the induced current density which gives rise to additional fields at the nuclei. A clockwise circulating (diamagnetic) current generates a field which weakens the applied external field and is said to shield nuclei leading to a shift of ^{1}H and ^{13}C resonances to higher frequencies. On the other hand, an anticlockwise circulating (paramagnetic) current produces a field which strengthens the applied field at the nuclei; the resonances shift to lower frequencies. The induced diamagnetic and paramagnetic currents are of two types. They can be localized or atom-like as in the case of CO_2, or they can have significant components which involve fluxes through interatomic surfaces. Maps of these magnetically induced first-order current density distributions were first illustrated in the pioneering calculational studies of Lipscomb and co-workers (1–3). In following studies, Lazzeretti and Zanasi (4, 5) calculated and analysed the magnetically induced current densities of two Huckel

Received January 7, 1999.

This paper is dedicated to Jerry Kresge in recognition of his many achievements in chemistry.

N.H. Werstiuk[1] and J. Ma. Department of Chemistry, McMaster University, Hamilton, ON L8S 4M1, Canada.

[1]Author to whom correspondence may be addressed. Telephone (905) 525-9140. Fax: (905) 522-2509. e-mail: werstiuk@mcmaster.ca

© 1999 NRC Canada

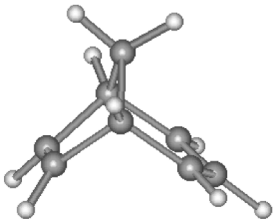

2

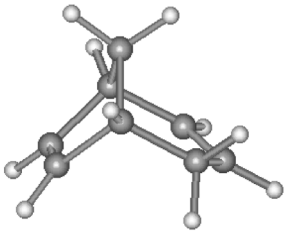

3

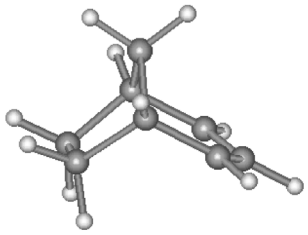

4

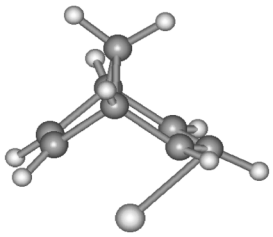

5

aromatic systems, benzene (**1**) and the cyclopropenyl cation $C_3H_3^+$, in an attempt to define a physical basis of the ring-current model. Their analyses were based on relatively inaccurate $\mathbf{J}^{(1)}(\mathbf{r})$ distributions which were calculated using the conventional single gauge origin CPHF method. Several incorrect conclusions were drawn in their studies, conclusions which were corrected by Keith and Bader (6, 7). Using their newly developed IGAIM (individual gauges for atoms in molecules) and CSGT (continuous set of gauge transformations) methods, Keith and Bader established that benzene exhibits inner-core paramagnetic and outer diamagnetic ring currents, the latter contributing significantly to the flux of $\mathbf{J}^{(1)}$ through the interatomic surfaces of the ring atoms. In fact, this interatomic flux — the ring current — is responsible for 77% of the parallel component of the molecular magnetic susceptibility. The results of IGLO calculations on benzene and other hydrocarbons have been published (8), and the π and total current densities of a group of monocyclic π-electron systems have been mapped (9).

Experimentally determined ^{1}H and ^{13}C shifts of π-system-containing neutral molecules, carbocations, and carbanions have been used for many years to probe the aromaticity of these species on the assumption that the shifts derive from induced ring currents (10). This was the case for the bicyclo[3.2.1]octa-3,6-dien-2-yl anion (**2**) which attracted the attention of chemists for over 30 years and was the object of a considerable number of studies beginning with the work of Brown and Occolowitz (11). The goal of the research (11–15) was to establish whether the enhanced kinetic and thermodynamic acidities of the methylene hydrogens at C4 of the parent diene **3** and the unusual shifts of selected ^{1}H and ^{13}C resonances of **2** (the ^{1}H resonances of H6 and H7 are shielded by an average of 2.3 ppm relative to the corresponding hydrogen atoms of **3**, and the C6 and C7 of **2** (14) are shielded by an average of 44.0 ppm relative to the corresponding carbons of **3**) derive from the bishomoaromaticity of **2**. It was concluded that **2** is a bishomocyclopentadienide ion (the usual representation is displayed as **2-bh**) possessing a ring current. Yet, the results of calculational studies (16–18), except for those obtained by Brown et al. (19), provided no support that the bicyclo[3.2.1]octa-3,6-dien-2-yl anion was a bishomoaromatic species. For example, the results of calculations at the MCSCF ab initio level led Lindh et al. (18) to conclude that **2** is not bishomoaromatic. In their view, interaction between unoccupied and occupied orbitals necessary to achieve the bicycloaromaticity does not take place due to the large distance between the interacting bridges. They also suggested that stabilization of **2** at the calculated equilibrium internuclear distances is due to an electrostatic interaction between the allylic anion fragment and the remote polarizable double bond. In their view, it is the considerable redistribu-

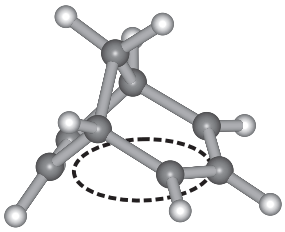

2-bh

© 1999 NRC Canada

Table 1. Molecular magnetic susceptibilities and anisotropies. Units in cgs ppm.

Compound	$\chi^{\perp}$	$\chi^{\parallel}$	χ(M)	$\Delta\chi$
1	–30.66 (–37.18)[a]	–99.54 (–104.83)	–53.58 (–59.73)	–68.88 (–67.65)
2	–60.47 (χ_{xx}–58.26, χ_{yy}–62.68)[b]	–78.98 (χ_{zz})	–66.64	–18.51
	–64.05 (χ_{xx}–65.91, χ_{yy}–62.68)[c]	–71.34 (χ_{zz})	–66.64	–7.29
	–63.73 (χ_{xx}–64.77, χ_{yy}–62.68)[d]	–72.48 (χ_{zz})	–66.64	–8.75
3	–56.13 (χ_{xx}–60.41, χ_{yy}–51.86)	–62.50 (χ_{zz})	–58.25	–6.37
4	–64.87	–61.91	–63.88	2.96
5	–67.46	–80.29	–72.08	–12.83

[a]The values in parentheses for **1** were obtained at the HF/6-311++G(2d,2p)//HF/6-311++G(2d,2p) level (6): $\chi^{\perp} = (\chi_{xx} + \chi_{yy})/2$.

[b]Field applied perpendicular to the plane defined by C3, C6, and C7.

[c]Field applied perpendicular to the plane defined by C1, C2, C3, C4, and C5.

[d]Field applied perpendicular to the plane defined by C1, C5, C6, and C7.

tion of charge, not benzene-like induced diamagnetic and paramagnetic ring currents, which are responsible for the unusual NMR chemical shifts of **2**. Our interest in exploring the chemistry of carbanions experimentally and calculationally coupled with the availability of the IGAIM and CGST suite of programs at McMaster led us to a computational study of **2**, the parent hydrocarbon of **2**, 2,5-bicyclo[3.2.1]-octadiene (**3**), the bicyclo[3.2.1]octen-2-yl anion (**4**) — the dihydro analogue of **1** — and **5** — the lithium complex of **2**. We showed in an earlier study that IGAIM calculations at the HF/6-31+G(d) level of theory give ^{1}H and ^{13}C chemical shifts of unsaturated hydrocarbons (including benzene which is the archetypal aromatic system) and unsaturated organolithium compounds including **2** that correlate well with experimental data (20). We also obtained the atom electron populations of **2** and its lithium complex with AIM calculations, but found no obvious correlation between the charges on the carbon atoms and the experimental ^{13}C shifts. In this case, our goals were (*i*) to extend our studies on the magnetic response properties of **2** by calculating and analysing the magnetic susceptibility tensors and the current flux through the interatomic surfaces and (*ii*) to obtain information on the induced current flow by calculating the current density maps of **2** and **4**. This paper documents the results of our study.

Computational methods

All the current distributions and susceptibilities were obtained with either IGAIM or CSGT calculations as described by Keith and Bader (6, 7). In a perturbation expansion of the magnetic field induced current $\mathbf{J}(\mathbf{r})$ with respect to the field strength $\mathbf{B}$ as shown in eq. [1],

$$[1]\qquad \mathbf{J}^{(1)}(\mathbf{r}) = -(eN/m)\int d\tau'\{\psi^{(0)*}\hat{\mathbf{p}}\psi^{(1)} + \psi^{(1)*}\hat{\mathbf{p}}\psi^{(0)}\} - (e^2/mc)\mathbf{A}(\mathbf{r})\rho^{(0)}(\mathbf{r}) = \mathbf{J}_{\rho}^{(1)}(\mathbf{r}) + \mathbf{J}_{d}^{(1)}(\mathbf{r})$$

the first-order term in the expansion (1–3, 21) is where $\rho^{(0)}(\mathbf{r})$ is the unperturbed electron density, $\hat{\mathbf{p}}$ is the linear momentum operator, $\mathbf{A}(\mathbf{r})$ is a vector potential (assumed first-order in $\mathbf{B}$), describing $\mathbf{B}$ through Maxwell's equation, $\psi^{(1)}$ is the first-order correction to the unperturbed molecular wave function due to the presence of the magnetic field, and separate terms $\mathbf{J}_{\rho}^{(1)}(\mathbf{r})$ and $\mathbf{J}_{d}^{(1)}(\mathbf{r})$ are called the paramagnetic and diamagnetic contributions to $\mathbf{J}^{(1)}(\mathbf{r})$, respectively. The induced current density distribution $\mathbf{J}^{(1)}(\mathbf{r})$ is related to the measurable magnetic susceptibility tensor χ and to the nuclear magnetic shielding tensor σ^N (for a nucleus with magnetic dipole moment μ^N) according to eqs. [2] and [3], respectively (1).

$$[2]\qquad \mathbf{B}\chi = (\mathbf{1}/2c)\int d\mathbf{r}\{\mathbf{r} \times \mathbf{J}^{(1)}(\mathbf{r})\}$$

$$[3]\qquad \mu^N\sigma^N\mathbf{B} = (-1/c)\,\mu^N\int d\mathbf{r}_N\{\mathbf{r}_N \times \mathbf{J}^{(1)}(\mathbf{r})/\mathbf{r}_N{}^3\}$$

The molecular magnetic susceptibility tensor χ is expressible as a sum of atomic or group contributions ($\chi(\Omega)$). An atomic contribution consists of a basin $\chi_b(\Omega)$ and a surface flux $\chi_f(\Omega)$ component; the former is given by the integral of a magnetization density over the basin of the atom, and the latter by the integral of the flux in the position weighted current density through the interatomic surfaces that the atom shares with its bonded neighbours. The detailed derivations and descriptions of the magnetically induced current density distribution $\mathbf{J}^{(1)}(\mathbf{r})$ and magnetic susceptibility tensor χ are available (22). The coupled-perturbed Hartree–Fock procedure was used for calculating $\mathbf{J}^{(1)}\mathbf{r}$ as coded in CADPAC (23). Geometry optimizations were carried out with Gaussian 92 at the RHF/6-31+G(d) level of theory (24) because ^{1}H and ^{13}C chemical shifts of unsaturated hydrocarbons including benzene, **2**, and **5** are calculated with good accuracy with these geometries (20), and our calculations were subject to hardware limitations. The wave functions obtained with CADPAC were used in IGAIM and CSGT calculations within PROAIMV (25) to obtain the magnetic susceptibilities χ. CURDENDAMP4 and CURDEN (22) were used to obtain the plots of $\mathbf{J}^{(1)}(\mathbf{r})$.

Results and discussion

Molecular susceptibility of benzene

To determine whether IGAIM and CSGT calculations at the HF/6-31+G(d)//HF/6-31+G(d) level of theory give molecular susceptibilities and anisotropies as well as the atomic susceptibilities and their basin and surface components with good accuracy, benzene was studied, and the results correlated with the data obtained by Keith and Bader (6) at the HF/6-311++G(2d,2p) level. The magnetic susceptibility of benzene χ(M) (χ(M) = 1/3($\chi_{xx} + \chi_{yy} + \chi_{zz}$)) and the tensors $\chi^{\perp}$ ($\chi^{\perp} = 1/2(\chi_{xx} + \chi_{yy})$) and $\chi^{\parallel}(\chi_{zz})$ as well as the anisotropy

© 1999 NRC Canada

Table 2. Atomic contributions to the magnetic susceptibility of benzene obtained at the HF/6-31+G(d)// HF/6-31+G(d) level. Units are cgs ppm.[a]

Atom/molecule	$\chi^{\perp}(\Omega)$	$\chi^{\parallel}(\Omega)$	$\chi(\Omega)_{av}$	$\Delta\chi$(M)
C	*–2.35*^{B} *(–2.23)*	*–3.66 (–3.56)*	*–2.79 (–2.67)*	
	–0.27^{H} (–0.56)	–1.25 (–1.35)	–0.60 (–0.82)	
	–1.13^{R} (–1.79)	–9.71 (–10.48)	–3.99 (–4.68)	
	–1.40^{T} (–2.35)	–10.96 (–11.83)	–4.59 (–5.51)	
	–3.75^{S} (–4.57)	–14.62 (–15.39)	–7.37 (–8.18)	–65.22 (–64.92)
H	–1.20^{B} (–1.29)	*–1.26 (–1.29)*	*–1.22 (–1.29)*	
	–0.16^{H} (–0.33)	–0.71 (–0.79)	–0.34 (–0.48)	
	–1.36^{S} (–1.62)	–1.97 (–2.08)	–1.56 (–1.77)	
C_6H_6	*–21.30*^{BM} *(–21.10)*	*–29.52 (–29.11)*	*–24.06 (–23.77)*	
	–9.36^{TM} (–16.08)	–70.02 (–75.72)	–29.58 (–35.96)	
	–30.66^{SM} (–37.18)	–99.54 (–104.83)	–53.58 (–59.73)	–68.88 (–67.65)

[a]The symbol $\perp$ refers to the axes perpendicular to the principle rotation axis, and the corresponding values are averaged over both $\perp$ field directions. The symbol $\parallel$ refers to the principle rotation axis. The values in parentheses were obtained at the HF/6-311++G(2d,2p)//HF/6-311++G(2d,2p) level (6). The superscript B indicates the basin contributions shown in italics. The superscript H refers to the flux through the C|H surface. The superscript R refers to the flux through the C|C surface. The superscript T refers to the total current flux contribution. The superscript S (M indicates the molecule) refers to the sum of the basin and total flux contributions.

$\Delta\chi(\chi^{\parallel} - \chi^{\perp})$ are collected in Table 1. The corresponding values obtained by Keith and Bader with the 6-311++G(2p,2d) basis set are given in parentheses. It is seen that the 6-31+G(d) basis set yields values of χ(M) and $\Delta\chi$ for benzene, which are remarkably close to values obtained at the 6-311++G(2d,2p) level of theory and the experimental values. In fact, χ(M) (–53.6 cgs ppm) obtained at the 6-31+G(d) level is closer to the experimental value (–54.8) (26) than the χ(M) (–59.7) obtained with the 6-311++G(2d,2p) basis set. The $\Delta\chi$ of –68.88 calculated at the 6-31+G(d)//6-31+G(d) level of theory — it differs by 1.1 cgs ppm from the value of –67.65 obtained with the 6-311++G(2d,2p) basis set — also agrees well with the experimental value of –59.7 (27). These results are in accord with the findings of Keith and Bader who showed that there is a lack of a serious basis set dependence of the current and its derived properties obtained with the IGAIM and CSGT methods.

That molecular calculations yield the magnetic susceptibility χ(M) of benzene — and its anisotropy $\Delta\chi$ — with good accuracy at the 6-31+G(d)//6-31+G(d) level is an indication that the atomic susceptibilities — and the basin and surface components — should correlate with the values obtained by Keith and Bader with the 6-311++G(2d,2p) basis set. That this is the case is seen in Table 2 where our results along with the Keith–Bader data shown in parentheses are collected. At the 6-31+G(d)//6-31+G(d) level of theory, 95% of the value of $\Delta\chi$ (–65.22/–68.88 × 100) comes from carbon atom contributions, 75% having its origin in a current flowing from the basin of one carbon into that of its neighbour (((–9.71 – (–1.13) × 6)/–68.88) × 100); the values are 96% (–64.92/–67.65 × 100) and 77% (((–10.48 – (–1.79) × 6)/–67.55) × 100), respectively, at the 6-311++G(2p,2d) level. For a field aligned parallel to the principle axis — the ring atoms occupy the *x–y* plane — the surface terms are calculated to be 3.0 and 3.3 times the magnitude of the basin terms obtained at the 6-31+G(d) and 6-311++G(2d,2p) levels of theory, respectively. These surface terms (–9.71 at 6-31+G(d) and –10.48 at 6-311++G(2d,2p)) arise from the flux in the induced current through the interatomic surface separating the basins of the ring carbon atoms. These C|C surface terms exhibit a large anisotropy (Table 1); 8.58 and 8.69 ppm for a single carbon atom at the 6-31+G(d) and 6-311++G(2d,2p) levels of theory, respectively. That the atomic contributions calculated at the 6-31+G(d) level compare well with the data obtained with the larger basis set in our view establishes that calculations on the bicyclic compounds at the 6-31+G(d)//6-31+G(d) level will yield χ(M)

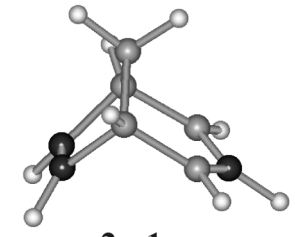
2-a1

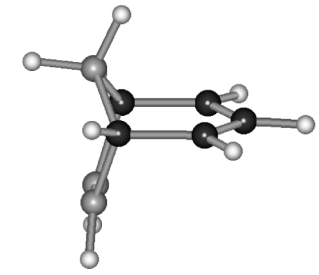
2-a2

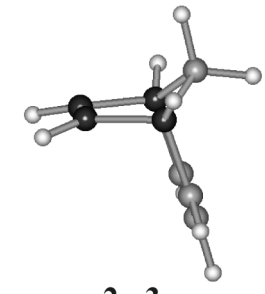
2-a3

© 1999 NRC Canada

Table 3. Carbon atom contributions to the magnetic susceptibilities of **2** and **4**.[a]

	2				**4**			
Atom	$\chi^{\perp}(\Omega)$	$\chi^{\parallel}(\Omega)$	$\chi(\Omega)_{av}$	$\Delta\chi(\Omega)$	$\chi^{\perp}(\Omega)$	$\chi^{\parallel}(\Omega)$	$\chi(\Omega)_{av}$	$\Delta\chi(\Omega)$
C1	*–2.43*^{B}	*–2.55*	*–2.47*	*–0.12*	*–2.53*	*–2.65*	*–2.57*	*–0.12*
	–0.55^{H}	–0.64^{H}	–0.58^{H}	–0.10^{H}	–0.59	–0.70	–0.63	–0.11
	–1.24^{R}	–1.99^{R}	–1.49^{R}	–0.75^{R}	–1.36	–1.43	–1.38	–0.07
	–1.79^{T}	–2.63^{T}	–2.07^{T}	–0.85^{T}	–1.95	–2.13	–2.01	–0.18
	–4.22^{S}	–5.18^{S}	–4.54^{S}	–0.97^{S}	–4.48	–4.78	–4.58	–0.30
C2	*–5.46*^{B}	*–4.09*	*–5.00*	*1.37*	*–5.09*	*–3.62*	*–4.60*	*1.47*
	–0.57^{H}	–1.06^{H}	–0.74^{H}	–0.49^{H}	–0.55	–1.09	–0.73	–0.54
	–0.54^{R}	–4.45^{R}	–1.84^{R}	–3.91^{R}	–0.41	–1.97	–0.92	–1.56
	–1.11^{T}	–5.51^{T}	–2.58^{T}	–4.40^{T}	–0.96	–3.06	–1.65	–2.10
	–6.57^{S}	–9.60^{S}	–7.58^{S}	–3.03^{S}	–6.05	–6.68	–6.25	–0.63
C3	*–1.71*^{B}	*–2.08*	*–1.62*	*–0.37*	*–1.28*	*–1.18*	*–1.24*	*0.1*
	–0.42^{H}	–0.86^{H}	–0.57^{H}	–0.44^{H}	–0.43	–0.81	–0.55	–0.38
	–1.53^{R}	–3.00^{R}	–2.02^{R}	–1.47^{R}	–1.68	–1.73	–1.69	–0.05
	–1.95^{T}	–3.86^{T}	–2.59^{T}	–1.84^{T}	–2.11	–2.54	–2.24	–0.43
	–3.69^{S}	–5.94^{S}	–4.21^{S}	–2.21^{S}	–3.39	–3.72	–3.48	–0.33
C6	*–3.06*^{B}	*–3.31*	*–3.14*	*–0.25*	*–3.04*	*–2.75*	*–2.94*	*0.29*
	–0.75^{H}	–0.64^{H}	–0.71^{H}	+0.11^{H}	–1.50	–0.72	–1.24	0.78
	–1.79^{R}	–5.84^{R}	–3.14^{R}	–4.06^{R}	–1.15	–1.54	–1.28	–0.40
	–2.54^{T}	–6.48^{T}	–3.85^{T}	–3.95^{T}	–2.65	–2.26	–2.52	0.38
	–5.60^{S}	–9.79^{S}	–6.99^{S}	–4.20^{S}	–5.69	–5.01	–4.46	0.67
C8	*–2.84*^{B}	*–2.97*	*–2.88*	*–0.13*	*–2.91*	*–2.94*	*–2.92*	*–0.03*
	–1.17^{H}	–1.11^{H}	–1.15^{H}	+0.06^{H}	–1.25	–1.12	–1.20	0.13
	–3.05^{R}	–4.17^{R}	–3.42^{R}	–1.12^{R}	–4.17	–2.89	–3.74	1.28
	–4.22^{T}	–5.28^{T}	–4.57^{T}	–1.06^{T}	–5.42	–4.01	–4.94	1.41
	–7.06^{S}	–8.25^{S}	–7.45^{S}	–1.19^{S}	–8.33	–6.95	–7.86	1.38
$\Sigma\Delta\chi^{R}$			–20.03				–2.83	
χ(M)	–60.48	–79.00	–66.66	–18.52	–64.87	–61.91	–63.88	2.96

[a]The symbol $\perp$ refers to axes perpendicular to the field direction perpendicular to the plane defined by C3, C6, and C7. The symbol $\parallel$ refers to the principal rotation axes that is perpendicular to the plane defined by C3, C6, and C7. $\chi(\Omega)_{av} = \chi_b(\Omega)_{av} + \chi_f(\Omega)^{H}_{av} + \chi_f(\Omega)^{R}_{av} = (2 \times \chi^{\perp}(\Omega) + \chi^{\parallel}(\Omega))/3$; $\Delta\chi(\Omega) = \chi^{\parallel}(\Omega) - \chi^{\perp}(\Omega)$. The superscripts B, H, R, T, and S are described in Table 2. χ(M) is the sum of the hydrogen and carbon atom basin and flux contributions.

and $\Delta\chi$ and the atomic contributions to these parameters with the accuracy seen for benzene provided that a suitable separation scheme can be written.

Magnetic susceptibilities of bicyclic compounds

The tensors $\chi^{\perp}$ ($\chi^{\perp} = 1/2(\chi_{xx} + \chi_{yy})$) and $\chi^{\parallel}$ (χ_{zz})) along with the χ(M) values, and $\Delta\chi$ values of the bicyclo[3.2.1]-octa-3,6-dien-2-yl anion (**2**), the parent diene **3,** the bicyclo-[3.2.1]octa-3-en-2-yl anion (**4**), and **5**, the lithium complex of **2**, calculated with the 6-31+G(d) basis set are collected in Table 1. Three sets of calculations were carried out on **2** to determine the variation of χ_{zz} as a function of the orientation of the applied field. The field was set (*i*) perpendicular to the plane defined by C3, C6, and C7 (the highlighted atoms of **2-a1**), (*ii*) perpendicular to the plane defined by C1, C2, C3, C4, and C5 (see **2-a2**), and (*iii*) perpendicular to the plane defined by C1, C5, C6, and C7 (see **2-a3**). While the molecular susceptibilities are identical as expected, the anisotropies of **2-a2** and **2-a3** are in the region of 10 cgs ppm less than in the case of **2-a1**. In the case of benzene, the large anisotropy (67.65 cgs ppm) was taken by Bader (7) and Fleischer (8) as evidence in support of the ring current model. Because **2**, **3**, **4**, and **5** are nonplanar species and their $\Delta\chi$s cannot be compared directly with $\Delta\chi$ of benzene, our analysis is based on the variation in $\Delta\chi$ in going from **4** to **2** and **3**. It is seen that $\Delta\chi$ increases from –6.6 to –18.5 cgs ppm when the parent diene **3** is converted into **2**, and it is largest when the field is applied perpendicular to the plane defined by C3, C6, and C7. When an ethano bridge is replaced with an ethenyl bridge in going from **4** to **2**, $\chi^{\parallel}$ increases by –17.3 cgs ppm and $\Delta\chi$ increases by –21.3 cgs ppm. Given that $\Delta\chi$ is –6.7 cgs ppm ($\chi^{\perp} = -14.4$ and $\chi^{\parallel} = -21.1$) for ethene, the enhancement of the susceptibility could be taken as evidence for the existence of a ring current in **2**. When **2** complexes with Li^{+}, $\chi^{\parallel}$ increases marginally to 80.3 cgs ppm, but $\Delta\chi$ decreases to –12.8 because $\chi^{\perp}$ decreases by 7.1 cgs ppm.

To interpret the variations in the magnitudes of the tensors and $\Delta\chi$, we calculated and analysed the atomic susceptibilities partitioned into basin and surface components. Only the atomic contributions arising from the carbon atoms of **2** and **4** and the molecular parameters obtained as sums of the hydrogen and carbon atom contributions calculated with the 6-31+G(d) basis set are given in Table 3. A separation scheme, which may be obtained from the author as supplementary material, was used to obtain the basin and surface contributions. That the scheme is valid is seen in the fact that the molecular tensors obtained by summing the atomic contributions are virtually identical to the ones obtained by the standard molecular calculations. In both cases, the field is aligned parallel to the principle axis that is perpendicular to

© 1999 NRC Canada

Fig. 1. Display of the vector current density of benzene: (*a*) in the molecular plane obtained at the 6-31+G(d)//6-31+G(d) level; (*b*) 0.8 au above the molecular plane obtained at the 6-31+G(d)//6-31+G(d) level; (*c*) in the molecular plane obtained at the 6-31++G(d,p)//6-31+G(d) level; (*d*) 0.8 au above the molecular plane obtained at the 6-31++G(d,p)//6-31+G(d) level.

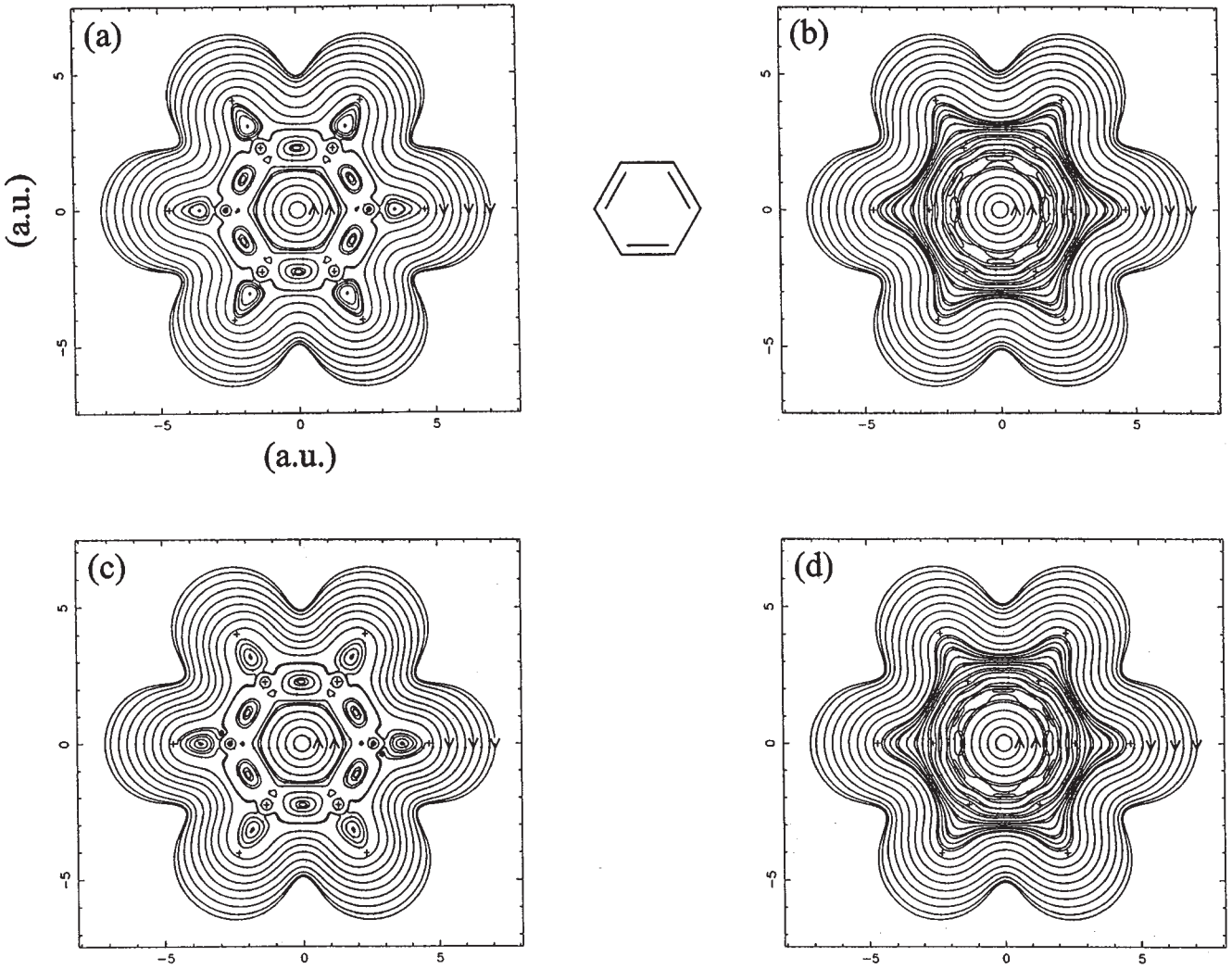

the plane defined by C3, C6, and C7. Overall, $\Delta\chi$ and the surface flux contributions to $\Delta\chi$ ($\Sigma\Delta\chi^R$(**2**) – $\Sigma\Delta\chi^R$(**4**) = –20.03 – (–2.83) = –17.20) increase when the ethano bridge of **4** is replaced with the ethenyl bridge of **2**. The percentage contribution of the various carbon atoms to the change in the atomic surface component of χ in going from **4** to **2** are $\Delta\chi^R$(**4** to **2**)(C1 + C5)/$\Delta\Sigma\Delta\chi^R$(**4** to **2**), 7.9% (2 × (–0.75 – (–0.07))/–17.2); $\Delta\chi^R$(C2 + C4)/$\Delta\Sigma\Delta\chi^R$, 27.3% (2 × (–3.91 – (–0.05))/–17.2); $\Delta\chi^R$(C3)/$\Delta\Sigma\Delta\chi^R$, 8.3% (–1.47 – (–1.56))/–17.2); $\Delta\chi^R$(C6 + C7)/$\Delta\Sigma\Delta\chi^R$, 42.6% (2 × (–3.91 – (–1.56))/–17.2); $\Delta\chi^R$(C8)/$\Delta\Sigma\Delta\chi^R$, 13.9% ((–1.12 – (1.28))/–17.20). That the increase in the atomic surface contribution to $\Delta\chi$ in going from **4** to **2** arises predominantly from C6 + C7 (42.6%), with C2 + C4 and C3 exhibiting substantially smaller increases of 27.4 and 8.3%, respectively, establishes that a through-space ring current, usually represented as illustrated in **2-bh**, does not exist in **2** even though there is a significant exaltation of the magnetic susceptibility. The enhanced magnetic susceptibility of **2** does not arise from current flowing from the basin of one ring atom into that of a neighbour.

Current maps

To validate the current maps of **2** obtained at the 6-31+G(d)//6-31+G(d) and 6-31++G(d,p)//6-31+G(d) levels of theory, in-plane and above-the-plane (0.8 au) maps of benzene (Fig. 1) were calculated at these levels of theory and compared with those generated with the 6-311++G(2d,2p) basis by Keith and Bader (7). It is seen that both levels of theory — in this study, we plotted fewer trajectories—reproduce the important features of the in-plane and above-the-plane (0.8 au) maps of benzene obtained at the higher level of theory (7); the in-plane maps (Figs. 1(*a*) and 1(*c*)) exhibit a paramagnetic current flow inside the benzene ring, a diamagnetic flow outside the ring, and diamagnetic current loops located in the C—C and C—H bonded regions. As found at the 6-311++G(2d,2p) level of theory, for a plane displaced 0.8 au (Figs. 1(*b*) and 1(*d*)) there is an inner paramagnetic current flow bounded by an outer diamagnetic flow. Consequently, calculations at the HF/6-311++G(d,p)//HF/6-31+G(d) and HF/6-31+G(d)//HF/6-31+G(d) levels of theory can be used to map the current densities of aromatic

© 1999 NRC Canada

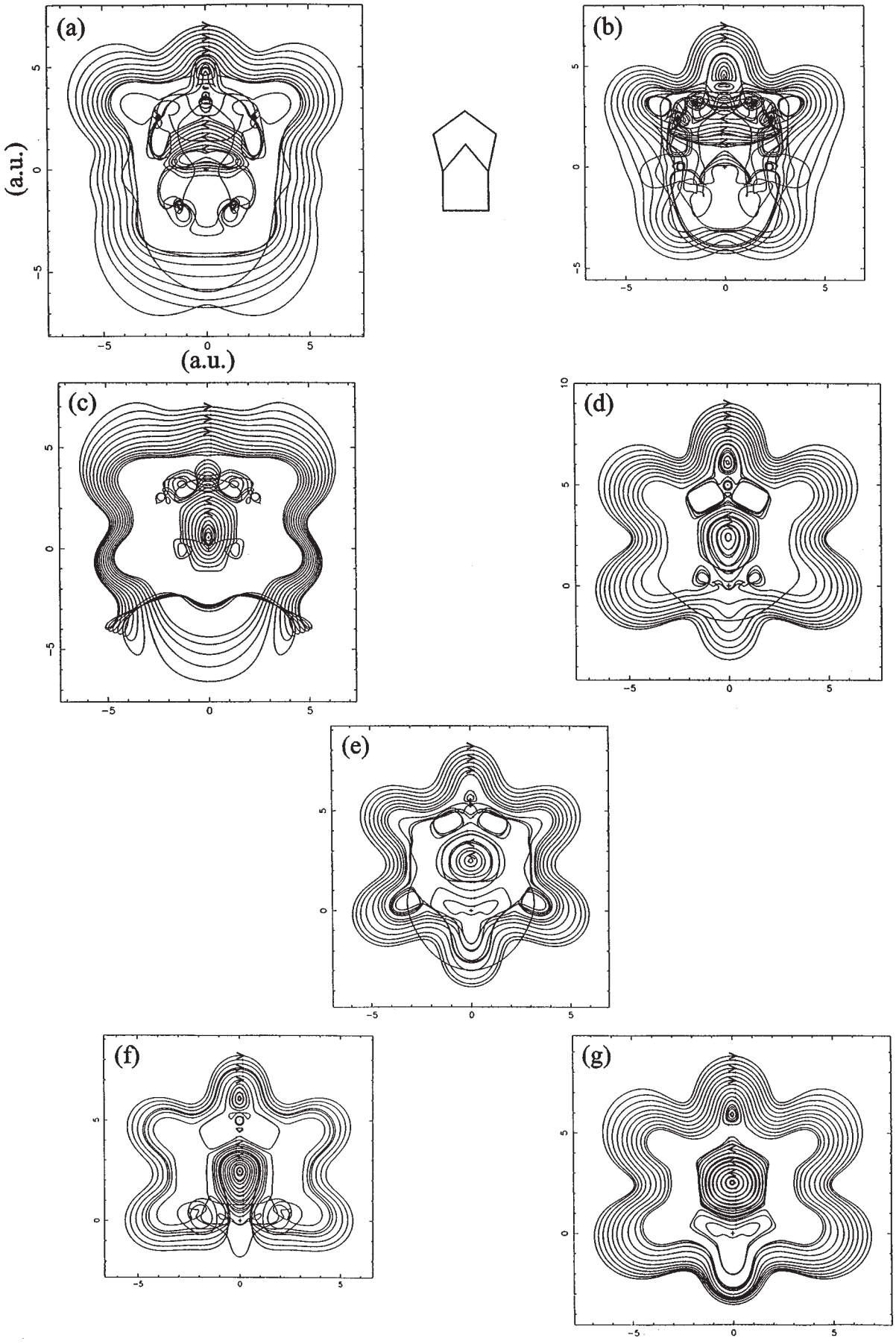

© 1999 NRC Canada

Fig. 2. Display of the vector current density of **2** obtained at the 6-31++G(d,p)//6-31+G(d) level: (*a*) intersecting the plane defined by C3, C6, and C7; (*b*) intersecting the plane 0.8 au below the plane defined by C3, C6, and C7; (*c*) intersecting the plane 0.8 au above the plane defined by C3, C6, and C7; level; (*d*) intersecting the plane defined by C1, C2, C3, C4, and C5; (*e*) intersecting the plane 0.8 au above the plane defined by C1, C2, C3, C4, and C5; (*f*) intersecting the plane defined by C1, C2, C3, C4, and C5 of 4; (*g*) intersecting the plane 0.8 au above the plane defined by C1, C2, C3, C4, and C5 of 4.

species. Because **2** is nonplanar and the induced current density depends on the orientation of the applied field, current maps were obtained with the field applied perpendicular to the plane defined by C3, C6, and C7 (see **2-a1**) and perpendicular to the plane defined by C1,C2, C3, C4, and C5 (see **2-a2)** at the HF/6-31++G(d,p)//HF/6-31+G(d) level. Owing to the complexity of the maps, partial plots are provided. Figure 2(*a*) is a plot of the vector current density of **2** intersecting the plane defined by C3, C6, and C7; Figure 2(*b*) is a display of the vector current density of **2** intersecting the plane 0.8 au below the plane defined by C3, C6, and C7, and 2(*c*) is a display of the vector current density of **2** intersecting the plane 0.8 au above the plane defined by C3, C6, and C7. Figures 2(*a*) and 2(*b*) show clearly that there is no benzene-like ring current in the C3, C6, and C7 plane or 0.8 au below it as would be expected if **2** is a bishomoaromatic species represented by **2-bh**. Figure 2(*d*) is a display of the vector current density of **2** intersecting the plane defined by C1, C2, C3, C4, and C5, and Fig. 2(*e*) is a display of the vector current density of **2** intersecting a plane 0.8 au above the plane defined by C1, C2, C3, C4, and C5. While Figs. 2(*c*–*e*) exhibit a paramagnetic circulation within C1, C2, C3, C4, and C5, this feature appears to be common to the bicyclo[3.2.1]octyl ring system as seen in the displays of the vector current densities of **4** which is not homoaromatic: Figure 2(*f*) is a display of the vector current density in the plane defined by C1, C2, C3, C4, and C5, and Fig. 2(*g*) is the vector current density intersecting the plane 0.8 au above the plane defined by C1, C2, C3, C4, and C5.

Conclusions

That the molecular susceptibility, atomic contributions (RHF/6-31+G(d)//6-31+G(d) level), and vector current densities (6-31++G(d,p)//6-31+G(d) and 6-31+G(d)//6-31+G(d) levels) calculated for benzene correlate well with the results obtained by Keith and Bader (6, 7) with the 6-311++G(2d,2p) basis indicates that these magnetic response properties can be obtained with good accuracy for aromatic compounds at a modest level of theory. Studies on the bicyclo[3.2.1]- octa-3,6-dien-2-yl anion (**2**) and bicyclo[3.2.1]oct-3-ene-2-yl anion (**4**) show that the magnetic susceptibility exaltation found in going from **4** to **2** is due primarily to an increase in atomic surface contributions to $\Delta\chi$ of the ethenyl bridge carbons C6 and C7 (42.6%) with C2 + C4 and C3 exhibiting substantially smaller increases (27.4 and 8.3%, respectively). This result, in conjunction with the nature of the vector current density maps of **2** and **4**, provide evidence that **2** does not possess a ring current as depicted in the usual representation of "bishomoaromatic" **2**.

Acknowledgements

Financial support by the Natural Sciences and Engineering Research Council of Canada is gratefully acknowledged.

References

1. R.M. Stevens, R.M. Pitzer, and W.N. Lipscomb. J. Chem. Phys. **38**, 550 (1963).
2. W.N. Lipscomb. Adv. Magn. Res. **2**, 137 (1966).
3. W.N. Lipscomb. MTP Int. Rev. Sci. **1**, 167 (1972).
4. P. Lazzeretti and R.J. Zanasi. Chem. Phys. **77**, 3129 (1982).
5. P. Lazzeretti and R.J. Zanasi. Chem. Phys. Lett. **80**, 533 (1981).
6. T.A. Keith and R.F.W. Bader. Chem. Phys. Lett. **194**, 1 (1992).
7. T.A. Keith and R.F.W. Bader. J. Chem. Phys. **99**, 3683 (1993).
8. U. Fleischer, W. Kutzelnigg, P. Lazzeretti, and V.J. Mühlenkamp. J. Am. Chem. Soc. **116**, 5298 (1994).
9. P.W. Fowler and E. Steiner. J. Phys. Chem. **101**, 1409 (1997).
10. C.W. Haigh and R.B. Mallion. Prog. Nucl. Magn. Reson. Spectrosc. **13**, 303 (1980).
11. J.M. Brown and J.L. Occolowitz. Chem. Commun. **376** (1965).
12. J.M. Brown. Chem. Commun. **638** (1967).
13. S. Winstein, M. Ogliaruso, M.Sakai, and J.M. Nicholson. J. Am. Chem. Soc. **89**, 3656 (1967).
14. F.H. Köhler and N. Hertkorn. Chem. Ber. **116**, 3274 (1983).
15. M. Christl, H. Leininger, and D.J. Bruckner. J. Am. Chem. Soc. **109**, 4843 (1983).
16. J.B. Grutzner and W.L. Jorgensen. J. Am. Chem. Soc. 1981, **103**, 1372.
17. E. Kaufmann, H. Mayr, J. Chandrasekhar, and P.v.R. Schleyer. J. Am. Chem. Soc. **103**, 1375 (1981).
18. R. Lindh, B.O. Roos, G. Jonsall, and P.J. Ahlberg. Am. Chem. Soc. **108**, 6554 (1986).
19. J.M. Brown, R.J. Elliott, and W.G. Richards. J. Chem. Soc. Perkin Trans. 2, 485 (1982).
20. N.H. Werstiuk and J. Ma. Can. J. Chem. **74**, 875 (1996).
21. S.T. Epstein. *In* The variation method in quantum chemistry. Academic Press, New York. 1974.
22. T.A. Keith. Molecules in magnetic fields. Ph.D. thesis. McMaster University, Hamilton. 1993.
23. R.D. Amos and J.E. Rice. CADPAC: the Cambridge analytic derivatives package. Cambridge, U.K.
24. M.J. Frisch, M. Head-Gordon, G.W. Trucks, J.B. Foresman, H.B. Schlegel, K. Raghavachari, M.A. Robb, J.S. Binkley, C. Gonzalez, D.J. De Frees, D.J. Fox, K.A. Whiteside, R. Seeger, G.F. Melius, J. Baker, R.L. Martin, L.R. Kahn, J.J.P. Stewart, S. Topiol, and J.A. Pople. Gaussian 92. Gaussian, Inc., Pittsburgh, Pa. 1992.
25. F.W. Biegler-Konig, R.F.W. Bader, and T.-H. Tang, Comput. Chem. **13**, 317 (1982).
26. T.G. Schmalz, C.L. Norris, and W.H. Flygare. J. Am. Chem. Soc. **95**, 7961 (1973).
27. J. Hoarau, N. Lumbroso, and A. Pecault. C.R. Acad. Sci. **242**, 1702 (1956).

© 1999 NRC Canada

General acid-catalyzed addition of methanol to (*E*)-*N*-benzylideneanilines

Sadjia Bennour and Jean Toullec

Abstract: The reaction of equilibrium addition of methanol (α-amino ether formation) to benzylideneanilines ($C_6H_5CH{=}NC_6H_4Y$, with Y = H (**1a**), 3-Cl (**1b**), 3-NO_2 (**1c**), 4-CN (**1d**), and 4-NO_2(**1e**)) in methanol is shown to be general acid-catalyzed in carboxylic acid buffers. The mechanism involves fast iminium ion formation followed by base-assisted addition of methanol. The α Brønsted exponents are in the 0.67–0.88 range, and α increases with the electron-withdrawing ability of Y. The same mechanism is valid for $MeOH_2^+$-catalysis, meaning that two solvent molecules are involved in the addition process, one of them playing the role of base. The equilibrium constant, *K*, is increased by electron-withdrawing substituents, log *K* depending linearly on the σ^- substituent parameters. The substituent effects on the forward and reverse catalytic rate constants are analyzed by means of the log $k = \rho^n\sigma^n + \rho^r(\sigma^- - \sigma^n)$ + constant (Young–Jencks) equation. For carboxylic acid catalysis, the ρ^n and ρ^r parameters are in keeping with ca. half C—O bond forming or breaking at the transition state. The catalytic rate constants and α exponent for elimination of $ClCH_2CH_2OH$ in methanol from the $C_6H_5CH(OCH_2CH_2Cl)NH(4\text{-}CNC_6H_4)$ chloroethyl adduct are compared with those for the elimination of methanol from $C_6H_5CH(OCH_3)NH(4\text{-}CNC_6H_4)$. The chloromethyl group makes the reaction slower and α lower. This indicates that proton transfer is a little ahead of C—O bond cleavage at the transition state. Y substituent effects, α values, and the effects of the CH_2Cl group are interpreted on the basis of a More O'Ferrall – Jencks diagram.

Key words: imine, free energy linear relationship, nucleophilic addition, More O'Ferrall – Jencks diagram, Schiff base.

Résumé : On montre qu'en milieu méthanolique la réaction équilibrée d'addition du méthanol sur les benzylidèneanilines ($C_6H_5CH{=}NC_6H_4Y$, avec Y = H (**1a**), 3-Cl (**1b**), 3-NO_2 (**1c**), 4-CN (**1d**) et 4-NO_2(**1e**)) est soumise à une catalyse acide générale lorsqu'elle s'effectue en présence de tampons d'acides carboxyliques. Le mécanisme implique la formation d'ions iminium dans un prééquilibre rapide suivi d'une addition du méthanol assistée par la base conjuguée de l'acide. Les exposants α de Brønsted sont compris entre 0.67 et 0.88 et augmentent avec le caractère électroattracteur de Y. Le même mécanisme est opérant pour la catalyse par les ions $MeOH_2^+$; ceci signifie que deux molécules de solvant sont impliquées dans le processus d'addition, l'une jouant le rôle de base. La constante d'équilibre *K* augmente avec le caractère électroattracteur de Y, ceci se traduisant par une corrélation linéaire entre log *K* et les paramètres de substituant σ^-. Les effets de substituant sur les constantes catalytiques pour les réactions directes et inverses sont analysés au moyen de l'équation de Young et Jencks: log $k = \rho^n\sigma^n + \rho^r(\sigma^- - \sigma^n)$ + constante. Pour la catalyse par les acides carboxyliques, les paramètres ρ^n et ρ^r sont en accord avec un degré de formation ou de coupure de la liaison C—O environ moitié à l'état de transition. Les constantes de vitesse catalytiques ainsi que l'exposant α de Brønsted observés pour l'élimination de $ClCH_2CH_2OH$ dans le méthanol à partir de l'adduit chloroéthylique $C_6H_5CH(OCH_2CH_2Cl)NH(4\text{-}CNC_6H_4)$ sont comparés à ceux de l'élimination du méthanol à partir de l'adduit méthylique $C_6H_5CH(OCH_3)NH(4\text{-}CNC_6H_4)$. Le groupe chlorométhyle provoque un ralentissement de la réaction et une diminution de α, ce qui indique que le transfert du proton à l'état de transition est légèrement en avance par rapport à la coupure de la liaison C—O. Les effets du substituant Y, les valeurs de α et les effets du groupe CH_2Cl sont interprétés sur la base d'une diagramme de More O'Ferrall – Jencks.

Mots clés : imine, relation linéaire d'enthalpie libre, addition nucléophile, diagramme de More O'Ferrall – Jencks, base de Schiff.

Received October 26, 1998.

This paper is dedicated to Jerry Kresge in recognition of his many achievements in chemistry.

S. Bennour.[1] Institut de Topologie et de Dynamique des Systèmes (C.N.R.S., UPRESA 7086), Université Denis Diderot, 1 rue Guy de la Brosse, 75005 Paris, France.
J. Toullec.[2] Laboratoire S.I.R.C.O.B. (C.N.R.S., UPRESA 8086), Université de Versailles, 45 Avenue des Etats-Unis, 78035 Versailles Cedex, France.

[1]Present address: Institut de Chimie, Université des Sciences et de la Technologie Houari Boumediene, B.P. 32, El-Alia, 16111 Bab-Ezzouar, Alger, Algeria.
[2]Author to whom correspondence may be addressed. Telephone: (33) 01 39 25 44 57. Fax: (33) 01 39 25 44 52.
e-mail address: toullec@chimie.uvsq.fr

 © 1999 NRC Canada

Introduction

Schiff bases and their derivatives play an important role in many fields of organic chemistry, including biological systems and liquid crystals. However, except studies of Schiff base formation (1, 2) and hydrolysis (1, 3), there is relatively little work dealing with the mechanism of reactions involving these compounds, especially with nucleophilic addition to the imino group. Although the C=N group is isoelectronic with the carbonyl group, the shortage of data for alcohol addition (α-amino ether (α-AE) formation), eq. [1], a reaction similar to the well-documented hemiacetal formation, eq. [2], is striking.

[1] 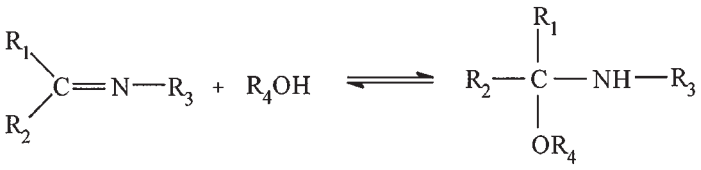

[2]

Until 1974, only a few reports had paid attention to α-AE formation (4, 5). At that time, Ogata and Kawasaki (6) examined the addition of methanol and other aliphatic alcohols to benzylideneanilines, **1**, and to *N*-(4-nitrobenzylidene)-anilines, **2**, both essentially substituted at the aniline residue. These authors showed that this reaction is induced by alkoxide attachment to the C=N group and, for *meta* and π-electron-releasing Y substituents, that the logarithm of the equilibrium constant, *K* (eq. [3]) depends linearly on the σ^+ Brown and Okamoto parameters (7), this because of the conjugation between the π orbitals of C=N and the π system of C_6H_4Y.

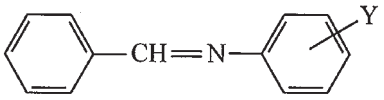

1

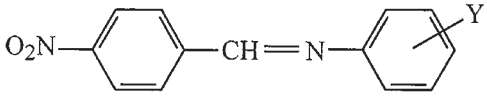

2

[3] 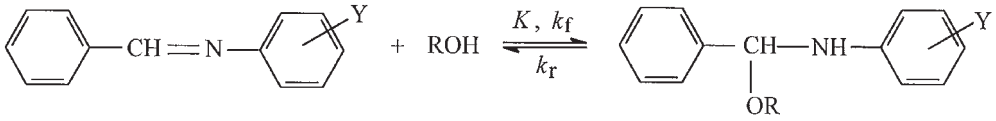

In contrast, the second-order rate constant for the forward reaction depends on Hammett's σ constants with a large and positive ρ value. These data and inverse kinetic solvent isotope effects were interpreted in terms of the mechanism shown in Scheme 1.

Scheme 1.

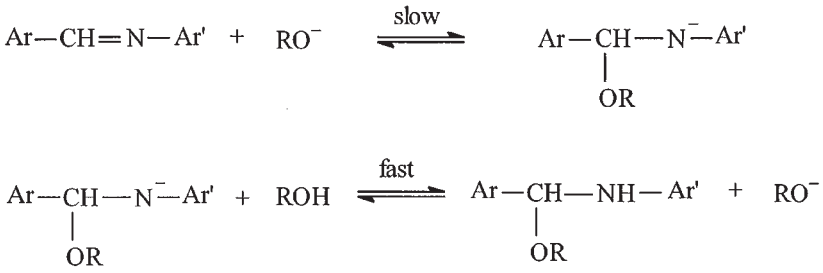

In a fairly recent paper (8), we examined the substituent effects on the equilibrium and rate and rate constants for methoxide ion-catalyzed methanol addition to **3**. This work was mainly focussed on a dissection of the polar and resonance substituent effects in terms of two-parameter free energy relationships.

© 1999 NRC Canada

Scheme 2.

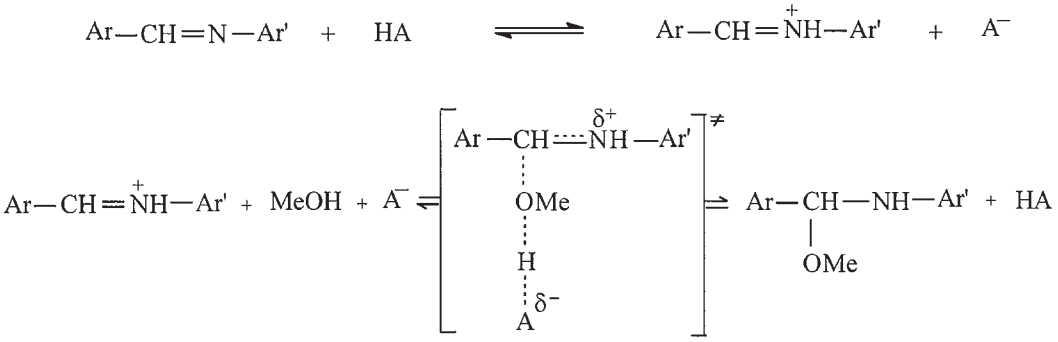

Scheme 3.

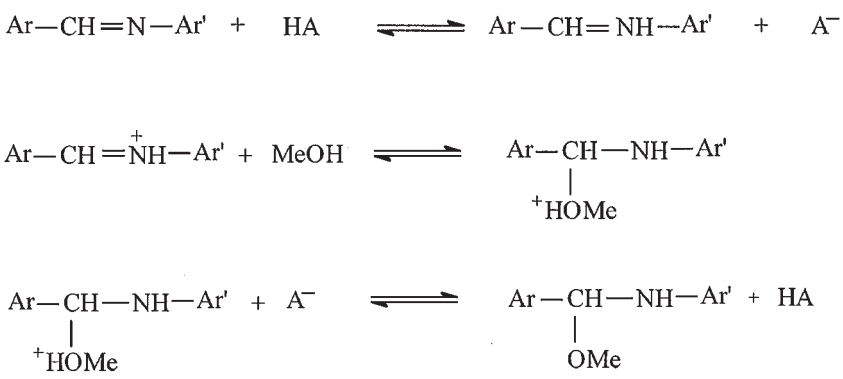

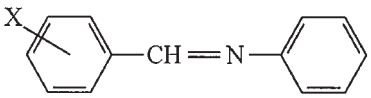

3

Studies of general acid- and base-catalyzed hemiacetal formation and hydrolysis have played an important role in the development of the theories dealing with concerted mechanisms (9–20). In view of the analogy of Schiff bases (and corresponding iminium ions) with carbonyl compounds, we thought that a general acid-catalyzed mechanism according to Scheme 2 can occur for alcohol addition to the former compounds. This mechanism can be energetically more favorable than the more straightforward specific acid-catalysis mechanism shown in Scheme 3 because of the short lifetimes of the *O*-protonated α-AE intermediates. We therefore examined the rates of methanol addition to **1** in methanolic buffer solutions.

One of the interesting aspects of the reaction of alcohol addition to **1** lies in the possibility of changing substrate electrophilicity by substituents within the aniline residue. Moreover, studies of the effects of Y on the rate constants make it possible to examine the changes in the nitrogen charge on going from the starting materials to the transition states. Since the changes in substrate electrophilicity are expected to be large when Y is a π-electron-withdrawing group, we examined the kinetic behavior with Y = H (**1a**), 3-Cl (**1b**), 3-NO_2 (**1c**), 4-CN (**1d**), and 4-NO_2 (**1e**) in formic, acetic, benzoic, chloroacetic, and cyanoacetic buffers.

Since the equilibrium constants are not known (except for **1a** in methanol (8) and for **1b** and **1c** in methanol–acetonitrile mixture (90:10 v/v) (6)), the values of *K* were measured for **1a**–**e**. As in Ogata and Kawasaki's (6) work, the measurements were carried out in sodium methoxide solutions. The data on *K* are interesting, since the π-electron-withdrawing substituents can be thought to cause large variations of the equilibrium constant by stabilization of the α-AE form. The free energy relationships are expected to include π-electron-withdrawing resonance contributions instead of the π-electron-donating resonance contributions accounted for by Ogata and Kawasaki (log $K - \sigma^+$ plot) in the absence of π-electron-withdrawing substituents, but in the presence of π-electron-donating groups.

Combination of rate and equilibrium data for acid-catalyzed α-AE formation provides a way to calculate the rate constants for acid-catalyzed α-AE cleavage. In this latter process, the charge on the oxygen atom at the transition state depends on the relative degrees of *O*-protonation and C—O bond cleavage: it is positive if *O*-protonation is ahead of C—O bond breaking; it is negative in the reverse situation. It follows that replacing the methyl group by an electron-withdrawing group is highly relevant for mapping the charges of the transition state. By analogy with previous work in the case of hemiacetal breakdown (12, 13), we ex-

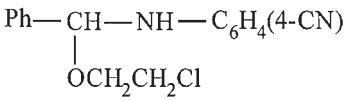

4

© 1999 NRC Canada

Scheme 4.

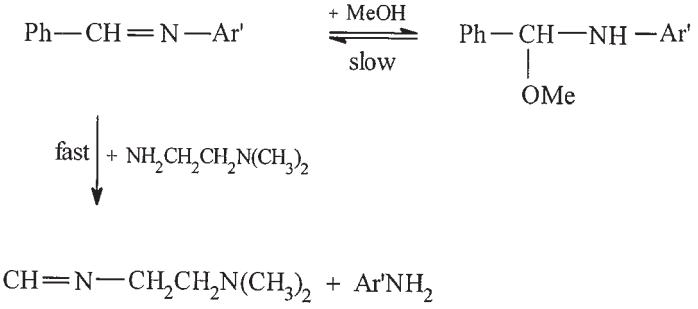

6

amined the rates of decomposition of **4** in methanol buffer solutions (**4** being preformed in 2-choroethanol), by comparison with those for the breakdown of **5**.

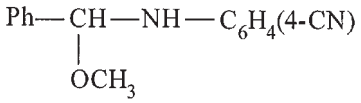

5

Results

Equilibrium constants

The equilibrium constants for the addition of methanol to **1a** has been previously reported (8). For **1b**, K was calculated by eq. [4] (where $[\alpha\text{-AE}]_{eq}$ and $[\text{imine}]_{eq}$ are the equilibrium molarities of α-AE and imine, respectively, at equilibrium) from the absorbances at 325 nm before (A_0) and after (A_∞) equilibration in sodium methoxide solutions [(0.4–3.2) × 10^{-2} M].

$$[4] \qquad K = [\alpha\text{-AE}]_{eq}/a_m[\text{imine}]_{eq} = (A_0 - A_\infty)/a_m A_\infty$$

Under these conditions, the α-AE formed is expected not to absorb, because its absorbance spectrum should roughly correspond to the sum of those for 3-chloroaniline and benzene, and A_∞ and $A_0 - A_\infty$ are proportional to concentrations of free imine and α-AE, respectively. The activity of methanol a_m (a_m = 1 for pure methanol) was taken as the mole fraction of methanol (ca. 0.99) after addition of small amounts of a dioxane solution of **1b**. Since the above method cannot be used for **1c** and **1e** because the spectra of the α-AEs and benzylideneanilines should overlap, we used an indirect method which consists in measuring (at 318 and 325 nm, respectively) the initial, A'_0, and final, A'_∞, absorbances after addition of small amounts of an equilibrated solution of **1c** or **1e** in methanolic acetic acid buffer (ca. 10^{-2} M) to a solution of *N*,*N*-dimethylethylenediamine (DMEDA) (0.04 M) and its monohydrochloride salt (0.04 M). Under these conditions, free imine is quantitatively transformed in **6** (21) by the transimination process shown in Scheme 4. Since the transimination reaction is ca. 10^3 times faster (intramolecular catalysis) than the imine–AE equilibration process in DMEDA buffer, and since **6** does not absorb at the wavelengths at which the measurements were conducted, A'_0 and A'_∞ can be expressed by eqs. [5] and [6], and K is given by eq. [7].

$$[5] \qquad A'_0 = [\varepsilon_{Im}(1 - x_\infty) + \varepsilon_{Add}x_\infty][\text{Im}]_0$$

Table 1. Substituent effects on α-amino ether formation equilibrium constants from **1a**–**e**.[a]

Y in **1**	Temp./°C	K in MeOH[b]	K in MeOH/MeCN[c]
H (**1a**)	25.0	0.047 ± 0.003	0.036 ± 0.001[d]
3-Cl (**1b**)	25.0	0.211 ± 0.004	0.207 ± 0.005[d]
3-NO_2 (**1c**)	25.0	0.855 ± 0.057	0.55 ± 0.02[d]
4-CN (**1d**)	10.0	5.59 ± 0.25	
	15.0	4.54 ± 0.29	
	20.0	3.71 ± 0.20	
	25.0	3.19 ± 0.10	3.34 ± 0.08[b]
	30.0	2.76 ± 0.15	
	35.0	2.34 ± 0.15	
4-NO_2 (**1e**)	25.0	7.33 ± 0.46	

[a]Figures after the sign ± are standard deviations.
[b]This work.
[c]By reference to pure methanol (a_m = 1).
[c]Ogata and Kasawaki data (6).

$$[6] \qquad A'_\infty = [\varepsilon_{An}(1 - x_\infty) + \varepsilon_{Add}x_\infty][\text{Im}]_0$$

$$[7] \qquad K = \frac{[\text{Im}]_0(\varepsilon_{Im} - \varepsilon_{An}) - (A'_0 - A'_\infty)}{(A'_0 - A'_\infty)a_m}$$

In these equations, x_∞ is the mole fraction of imine transformed to adduct, $[\text{Im}]_0$ is the initial concentration of **1c** or **1e**; ε_{Im}, ε_{Add}, and ε_{An} are the molar absorption coefficients of imine, α-AE, and aniline, respectively. The K values were calculated as the slopes of the plots of $[\text{Im}]_0(\varepsilon_{Im} - \varepsilon_{An}) - (A'_0 - A'_\infty)$ vs. $(A'_0 - A'_\infty)a_m$ from the absorbances measured for various initial imine concentrations. The two methods (at 340 and 330 nm, respectively) were used in the case of **1d**; the same results were obtained. Table 1 lists the values of K as well as those calculated from data in methanol–acetonitrile (90:10 v/v) (a_m = 0.92) either from Ogata and Kawasaki's paper (**1a**–**c**) or from new measurements (**1d**). The value of 0.55 calculated for **1c** from Ogata and Kawasaki's data is obviously much too small because of errors due to neglecting the absorbance of the adduct. The equilibrium constants have been confirmed by ^{1}H NMR spectroscopy in CD_3OD solutions containing ca. 10^{-3} M CD_3ONa. For instance, for **1d** the ^{1}H NMR spectrum shows a peak at δ 5.61 ppm, corresponding to the proton of the -C*H*(OMe)- group, which is about three times larger than the -C*H*=N- peak at δ 8.54 ppm.

© 1999 NRC Canada

Fig. 1. Dependence of the forward ($k_{\psi f}$) and reverse ($k_{\psi r}$) first-order rate constants on 1:1 sodium acetate – acid buffer concentration (buffer ratio = 1) for α-AE formation by addition of methanol to **1d** at 25°C.

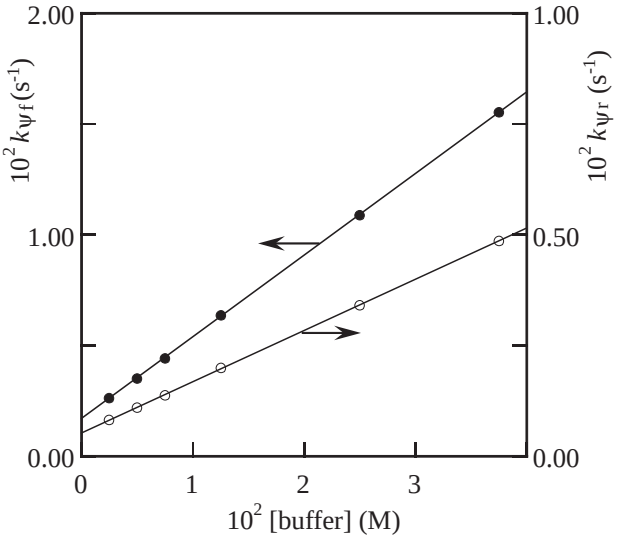

In the case of **1d**, the ΔH^0 and ΔS^0 values were calculated from eq. [8],

$$[8] \quad \ln (K/[\mathrm{MeOH}]^*) = -\Delta H^0/RT + \Delta S^0/R$$

where [MeOH]* is the concentration in pure solvent at 25°C (24.49 M), by plotting ln (K/[MeOH]*) against 1/*T*. The results obtained (ΔH^0 = –6.06 kcal mol^{-1} (stand. dev. = 0.15 kcal mol^{-1}) and ΔS^0 = 24.4 cal mol^{-1} K^{-1} (stand. dev. = 0.5 cal. mol^{-1} K^{-1}) are in disagreement with Ogata and Kawasaki's data (e.g., ΔH^0 = 1.5 kcal mol^{-1} and ΔS^0 = 0 for **2** with Y = 3-NO_2), but are in excellent agreement with those expected by reference to hemiacetal formation (22) (e.g., ΔH^0 = –5.7 kcal mol^{-1} and ΔS^0 = 23 cal mol^{-1} K^{-1} for 4-nitrobenzaldehyde hemiacetal formation for which the equilibrium constant is 3.2 at 25°C). Because of the strong analogy between the two reactions, it can be thought that the ΔS^0 and ΔH^0 values for α-AE and hemiacetal formation should approximately be the same for similar reaction driving forces.

Equilibrium rate constants for methanol addition

Kinetic runs were observed spectrophotometrically for **1a**–**e** at wavelengths of 330, 325, 318, 330, and 325 nm, respectively, in buffer methanolic solutions for various RCOOH and RCOONa concentrations (R = H, CH_3, C_6H_5, CH_2Cl, and CH_2CN). The experimental curves agree with eq. [9],

$$[9] \quad A_t - A_\infty = (A_0 - A_\infty)e^{-k_\psi t}$$

where k_ψ is the sum of the forward, $k_{\psi f}$, and reverse, $k_{\psi r}$, pseudo-first order rate constants for incomplete α-AE formation and breakdown. Whatever Y in **1**, the observed rate constants $k_{\psi f}$ [= $k_\psi Ka_m/(1 + Ka_m)$] and $k_{\psi r}$ [= $k_\psi/(1 + Ka_m)$] were observed to increase linearly with buffer concentration at constant buffer ratio (*r*) and constant ionic strength (I_c = 0.0375 M; NMe_4Br) (see Fig. 1 in the case of **1d** for [sodium acetate]/[acetic acid] = 1)). The $k_{\psi f}$ and $k_{\psi r}$ rate constants were also observed to depend linearly on [RCOOH] at constant carboxylate ion concentration, with slope decreasing when [$RCOO^-$] increased. Such a behavior is typical of general-acid catalysis involving RCOOH and lyonium ion. The rate constants $k_{\psi f}$ and $k_{\psi r}$ can be expressed by eq. [10] (*j* = f or r),

Fig. 2. Plots of the slopes of $k_{\psi f}$ (●) and $k_{\psi f}$ (○) vs. acetic acid concentration against the reciprocal of sodium acetate concentration for formation and breakdown of **1d** methanol adduct.

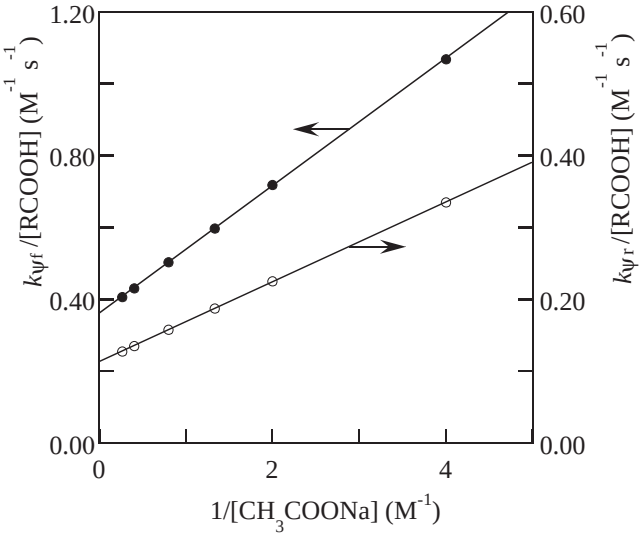

$$[10] \quad k_{\psi j} = k_j^{\mathrm{MeOH_2^+}}[\mathrm{MeOH_2^+}] + k_j^{\mathrm{RCOOH}}[\mathrm{RCOOH}] + k_0$$

where k_0 is the rate constant in the absence of buffer, $k_j^{\mathrm{MeOH_2^+}}$ and k_j^{RCOOH} are the catalytic rate constants relative to $MeOH_2^+$ and RCOOH, respectively. [$MeOH_2^+$] can be expressed by eq. [11],

$$[11] \quad [\mathrm{MeOH_2^+}] = \frac{K_a[\mathrm{RCOOH}]}{[\mathrm{RCOO^-}]y_\pm^2}$$

where K_a is the acidity constant of RCOOH at I_c = 0; $y_\pm$ is the mean activity coefficient for the $RCOO^-$ and Na^+ ions at I_c = 0.0375 M. Since ion pairs are not expected to be formed in significant amounts under the conditions used (23), $y_\pm$ can be expressed by the Debye–Hückel equation, eq. [12],

$$[12] \quad -\log y_\pm = \frac{A\sqrt{I_c}}{1 + Bq\sqrt{I_c}}$$

where *A* = 1.901 and *B* = 5.1 M^{-1} nm^{-1} (the Debye–Hückel parameters for methanol at 25°C), and *q* is the Bjerrum critical distance ($e^2/2Dk_BT$), which has the value 0.858 nm in this system (24). At I_c = 0.0375 M, $y_\pm$ = 0.632. Since the k_0 constants were observed to be negligible, in agreement with previous data (8), eq. [10] can be written as in eq. [13].

$$[13] \quad k_{\psi j} = \left(\frac{K_a}{[\mathrm{RCOO^-}]y_\pm^2} k_j^{\mathrm{MeOH_2^+}} + k_j^{\mathrm{RCOOH}} \right)[\mathrm{RCOOH}]$$

As illustrated by Fig. 2, the $K_a k_j^{\mathrm{MeOH_2^+}}/y_\pm^2$ and k_j^{RCOOH} coefficients were determined by plotting $k_{\psi j}$/[RCOOH] against 1/[$RCOO^-$]. The k_j^{RCOOH} data are listed in Table 2 as well as

© 1999 NRC Canada

Table 2. Catalytic rate constants (M^{-1} s^{-1}) for formation and breakdown of α-amino ethers formed by addition of methanol to *N*-benzylideneanilines substituted at the aniline moiety at 298 K.

Y in **1**	k_f^{HA}	k_r^{HA}	$10^{-6}k_f^{MeOH_2^+}$	$10^{-6}k_r^{MeOH_2^+}$
		Acetic acid (pK_a = 9.58)		
H (**1a**)	0.96	20.45	7.0	148
3-Cl (**1b**)	0.50	2.36	5.3	25.2
3-NO_2 (**1c**)	0.295	0.344	4.12	4.8
4-CN (**1d**)	0.350	0.109	7.04	2.2
4-NO_2 (**1e**)	0.288	0.0393	6.6	0.9
		Benzoic acid (pK_a = 9.35)		
3-Cl (**1b**)	0.86	4.09	5.3	25.2
3-NO_2 (**1c**)	0.497	0.582	4.1	4.8
4-CN (**1d**)	0.633	0.199	7	2.2
4-NO_2 (**1e**)	0.558	0.076	6.6	0.90
		Formic acid (pK_a = 8.38)		
3-Cl (**1b**)	3.40	16.1	5.5	25.9
3-NO_2 (**1c**)	1.82	2.13	3.9	4.6
4-CN (**1d**)	2.56	0.802	7.2	2.2
4-NO_2 (**1e**)	2.18	0.298	6.3	0.86
		Chloroacetic acid (pK_a = 7.84)		
3-NO_2 (**1c**)	8.15	9.54	4.35	5.1
4-CN (**1d**)	8.76	2.75	7.3	2.3
4-NO_2 (**1e**)	7.61	1.04	7.1	0.97
		Cyanoacetic acid (pK_a = 7.43)		
4-CN (**1d**)	23.7	7.43	6.7	2.1
4-NO_2 (**1e**)	20.0	2.73	6.4	0.86

the $k_j^{MeOH_2^+}$ rate constants, calculated when K_a and the estimated value of $y_\pm$ are accounted for. The acidity constants K_a were measured by UV-visible absorption spectroscopy, as described in Experimental Section, by reference to 2,4-dinitrophenol and (or) 2,5-dinitrophenol.

When deriving the catalytic rate constants, it was implicitely assumed that the contribution of the catalytic terms associated with H_3O^+ is negligible, even though the H_3O^+ ions are formed — even in fairly dry methanol — in significant amounts as the result of the proton exchange equilibrium (eq. [14] where K_r = 4.94 M^{-1} at 25°C (25)) between methanol and water.

[14] $$MeOH_2^+ + H_2O \underset{}{\overset{K_r}{\rightleftharpoons}} H_3O^+ + MeOH$$

As already done in similar situations (26), it can be easily shown that the presence of H_3O^+ should not make any significant influence on k_ψ. It was checked that additions of water until concentrations as large as 0.22 M (0.5% w/w) do not cause not any change in the observed rate constants.

Figure 3 shows the Brønsted plot of log k_r^i and log k_f^i (with i = RCOOH or $MeOH_2^+$; statistically corrected by a factor of 2 in the case $MeOH_2^+$) against pK_a^i for **1d**, either (*i*) for carboxylic acids only or (*ii*) including the $MeOH_2^+$ points. Similar Brønsted plots have been plotted for **1b** (4 points), **1c** (5 points), and **1e** (6 points). Table 3 lists the α Brønsted coefficients derived for carboxylic acid general catalysis. Since $k_f^i = Kk_r^i$ similar Brønsted coefficients can be calculated from the k_f^i rate constants.

Fig. 3. Brønsted plots for general acid-catalyzed equilibrium addition of methanol to **1d** in methanol; (●) carboxylic acids; (■) lyonium ion; (*a*) not including the points corresponding to the lyonium ion; (*b*) including the lyonium ion points.

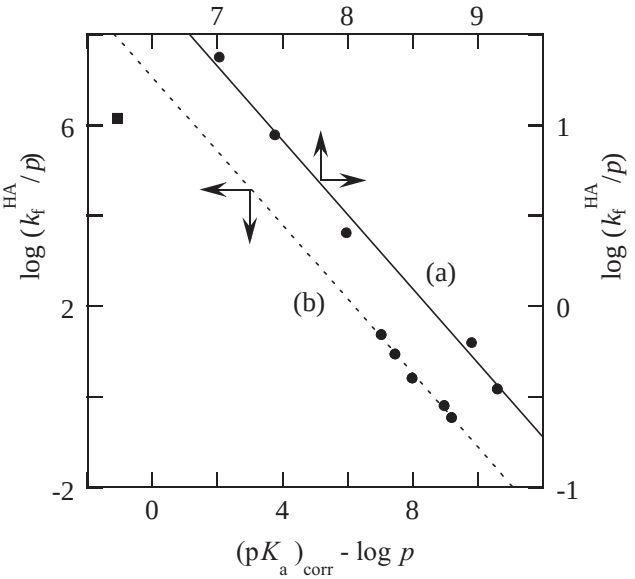

Rate constants for the breakdown of 4 in methanol

Figure 4 shows the variations of absorbance at 330 nm when 25 μL of an equilibrated solution of **4** (formed by allowing a mixture of **1d** (10^{-2} M), sodium acetate (0.05 M), and sodium acetate (0.05 M) to equilibrate at 5°C for 12 h in

© 1999 NRC Canada

Scheme 5.

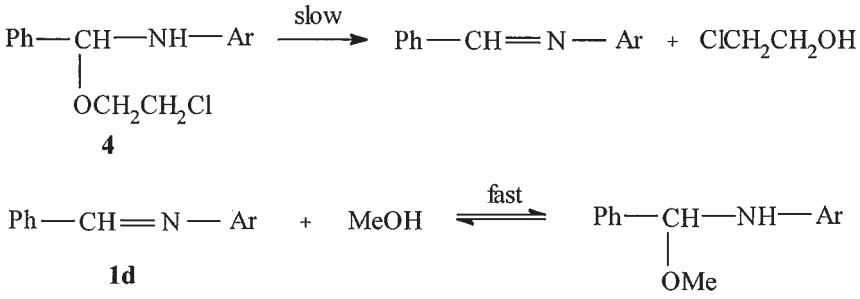

4 **1d**

Table 3. Brønsted exponents for α-amino ether formation or breakdown (lyonium ion omitted).

Y in **1**	α[a]	*r*
3-Cl (**1b**)	0.67 ± 0.07	0.995
3-NO_2 (**1c**)	0.78 ± 0.07	0.987
4-CN (**1d**)	0.81 ± 0.05	0.995
4-NO_2 (**1e**)	0.88 ± 0.06	0.993

[a]Figures after the sign ± are standard deviations.
[b]Correlation coefficients.

Table 4. Catalytic rate coefficients for the breakdown in methanolic buffers of α-amino ether **4**, formed by addition of 2-chloroethanol to *N*-benzylidene-(4-cyano)aniline.

Catalyst	pK_a	k_b^{HA} (M^{-1} s^{-1})	Lg effect[a]
$MeOCH_2COOH$	8.58	0.665	
HCOOH	8.38	0.627	0.78
$ClCH_2COOH$	7.84	1.85	0.67
$CNCH_2COOH$	7.43	3.59	0.48
$MeOH_2^+$	–1.38	3.6×10^5	0.16

[a]Leaving group effects corresponding to the ratios of the rate constants k_b^{HA} for the breakdown of **4** to the k_r^{HA} backward rate constants for methanol addition to **1d**.

2-chloroethanol) are injected in methanolic acetic acid buffer. The initial absorbance is significantly lower than that expected (ca. 5.9) if **1d** were completely on the imino form. This means that ca. 80% of **1d** had been converted to the 2-chloroethanol adduct in the bulk solution. The initial decreasing curve corresponds to methanol addition to the remaining amounts of free **1d**. The rate constant for this process is close to that observed for the addition of methanol to **1d** under similar conditions. The second process, corresponding to exponential increase of absorbance, is attributed to slow breakdown of the chloroethanol adduct followed by more rapid formation of the methanol adduct according to Scheme 5. The final absorbance corresponds to the free imino form in equilibrium with the α-amino methoxy ether.

The rate constants $k_{\psi b}$ for the breakdown of **4** in methanolic carboxylic buffer solutions (I_c = 0.0375 M; Me_4NBr) were calculated from the two-exponential absorbance curves as described previously in the case of methanol addition to α-methoxystyrenes followed by acetal breakdown (26). The constant $k_{\psi b}$ was observed to agree with eq. [15],

Fig. 4. Kinetic behavior for beakdown of preformed 2-chloroethanol adduct **4**. Methanol; [HCOOH] = 0.025 M; [HCOONa] = 0.025 M. 25°C.

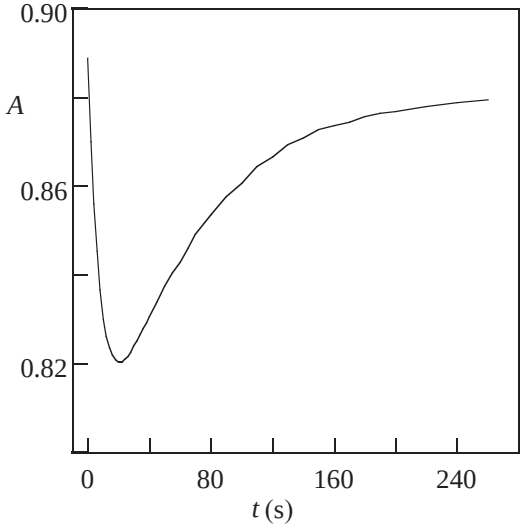

$$[15] \quad k_{b\psi} = \left(\frac{K_a}{[RCOO^-]y_\pm} k_b^{MeOH_2^+} + k_b^{RCOOH} \right) [RCOOH]$$

where $k_b^{MeOH_2^+}$ and k_b^{RCOOH} are the catalytic constants relative to $MeOH_2^+$ and RCOOH, respectively, for the breakdown of the chloroethyl adduct. The $k_b^{MeOH_2^+}$ and k_b^{RCOOH} are listed in Table 4. The slope of the Brønsted plot between log k_b^{RCOOH} and pK_a^{HA} is 0.58.

Discussion

Substituent effects on the equilibrium constant

Figure 5 shows the plot of log *K* against the σ^n parameters (27). The large positive deviations observed for Y = 4-CN (**1d**) and 4-NO_2 (**1e**) from the straight line defined by the other substituents can be attributed to stabilization of the adducts by conjugation of the lone pair of the nitrogen atom with the substituted ring. Such a conjugation is represented by Scheme 6 in the case of **1d** derivative. Figure 5 also shows that a good straight line is observed when the σ^- parameters (28) are used to account for the π-electron-withdrawing effects. The ρ^- value is 1.81 ± 0.10 (correlation coefficient = 0.9994).

As thoroughly discussed in previous papers (8, 29), "direct resonance effects" of substituted aromatic rings and ring

© 1999 NRC Canada

Scheme 6.

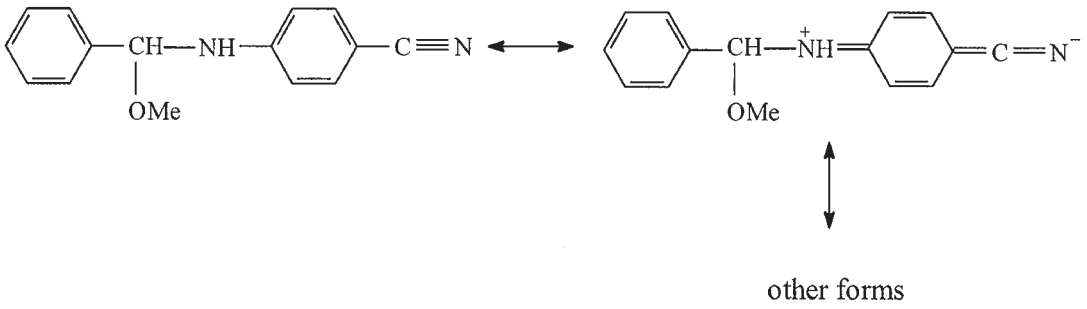

Fig. 5. Plots of the decimal logarithm of the equilibrium constant for the addition of methanol to **1a–e** against σ^n (●) and σ^- (○) substituent parameters.

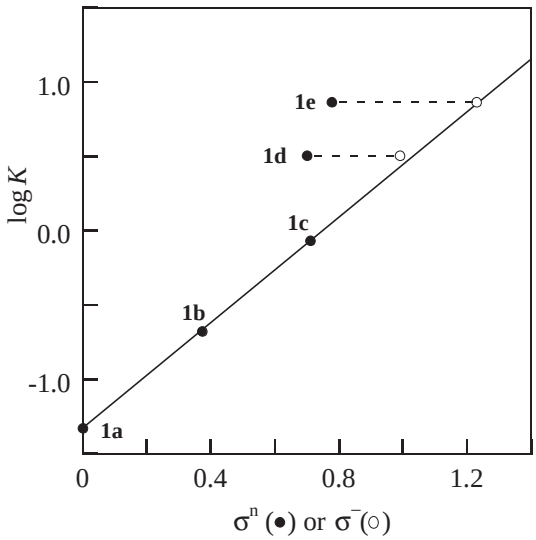

polar effects (including the "resonance-induced polar effect") can be conveniently separated by using eq. [16].

[16] $\log K$ (or $\log k$) = $\rho^n\sigma^n + \rho^r(\sigma^- - \sigma^n)$ + constant

This equation is similar to that suggested by Young and Jencks (30) (and advocated by various authors (17, 29, 31)) in the case of π-electron-donating stabilization of one of the states of the reaction (starting materials, products, or transition state) and is strongly analogous to the Yukawa–Tsuno–Sawada equation (eq. [17]) (32), where the σ parameters are adjusted to account for the duality of the substituent effects.

[17] $\log K$ (or $\log k$) = $\rho^n[\sigma^n + r^-(\sigma^- - \sigma^n)]$ + constant

As also emphasized by Young and Jencks, eq. [16] is preferable because the ratios of the ρ^n or ρ^r values for forward and reverse rate constants correspond to the ρ^n or ρ^r values for full equilibrium. The r^- parameter in eq. [17] equals ρ^r/ρ^n, but its interpretation for the forward and reverse reactions is less straightforward.

For α-AE formation, the $\log K - \sigma^-$ relationship means that ρ^n and ρ^r are approximately equal (a two-parameter treatment gives $\rho^n = 1.79 \pm 0.20$ and $\rho^r = 1.86 \pm 0.36$). These values are lower than for anilinium ion deprotonation ($\rho^n = \rho^r = 2.8$ in water (23); $\rho^n = 3.5$ and $\rho^r = 2.8$ in nitromethane if only the electron-withdrawing substituents are taken into account (33)). The relatively low ρ^r value is probably due to some compensation of the effects on α-AE energy by π-electron-withdrawing substituents effects on the stability of the imino form. It is well-accepted from IR and Raman data (34), UV-visible absorption spectra (35), X-ray diffraction (36), electron-diffractron spectroscopy (37), NMR data (38), and calculations (39) that the aniline ring in (*E*)-benzylideneanilines is twisted (Fig. 6) by a dihedral angle θ (usually significantly larger than 45° when Y is π-electron-demanding) because of a balance between resonance and steric effects, this geometry allowing some interactions of the π orbitals of the aniline ring with the nitrogen lone pair. In contrast, ρ^n looks rather high in view of the charge neutrality of the species involved. These high polar effects stem probably from the large dipole–dipole interactions between the aniline ring and the C=N group.

Fig. 6. Twisted conformation of (*E*)-*N*-benzylideneanilines.

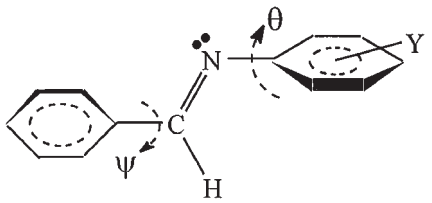

More O'Ferrall – Jencks diagram

The α Brønsted exponents and the substituent effects observed on general acid-catalyzed breakdown (or formation) of α-AEs in methanol can be examined on the basis of the More O'Ferrall – Jencks diagram (40, 41) shown in Fig. 7*a*. This diagram, which is similar to those suggested for general acid- and base-catalyzed breakdown (or formation) of hemiacetals (12–20), shows the different possibilities of mechanism for iminium ion intermediate formation from starting materials, depending on the sequence of C—O bond cleavage and O—H bond formation (proton transfer) in the presence of acids. If the reaction route follows the left edge and top of the diagram, via the upper left corner, protonation of the oxygen atom of the adduct occurs first in a fast preequilibrium, and the reaction is expected to be specific acid-catalyzed. If the reaction follows the bottom and the right edge of the diagram, C—O bond breaking occurs first, and the reaction is not expected to be acid-catalyzed, since proton transfer from acids to the methoxide ion would be fast. General acid-catalysis should occur when the mechanism corresponds to that shown in Scheme 2 with C—O bond breaking and proton transfer occuring concertedly.

© 1999 NRC Canada

Fig. 7. More O'Ferrall – Jencks diagram for the acid-catalyzed breakdown of α-AEs. (*a*) Free energy labelling for acetic acid-catalyzed methanol addition. (*b*) Changes in reaction coordinates associated with a change (acidity increase) in general acid catalyst. (*c*) Changes reaction coordinates associated with a change in aniline ring substituent (increase in electron-withdrawing ability). (*d*) Changes reaction coordinates induced by substitution of the methyl group of methyl α-AE **5** by the chloroethyl group. Broken arrows parallel to the rp and ih diagonals represent Hammond and perpendicular effects, respectively. Upward and downward bold arrows correspond, respectively, to free energy increase and decrease.

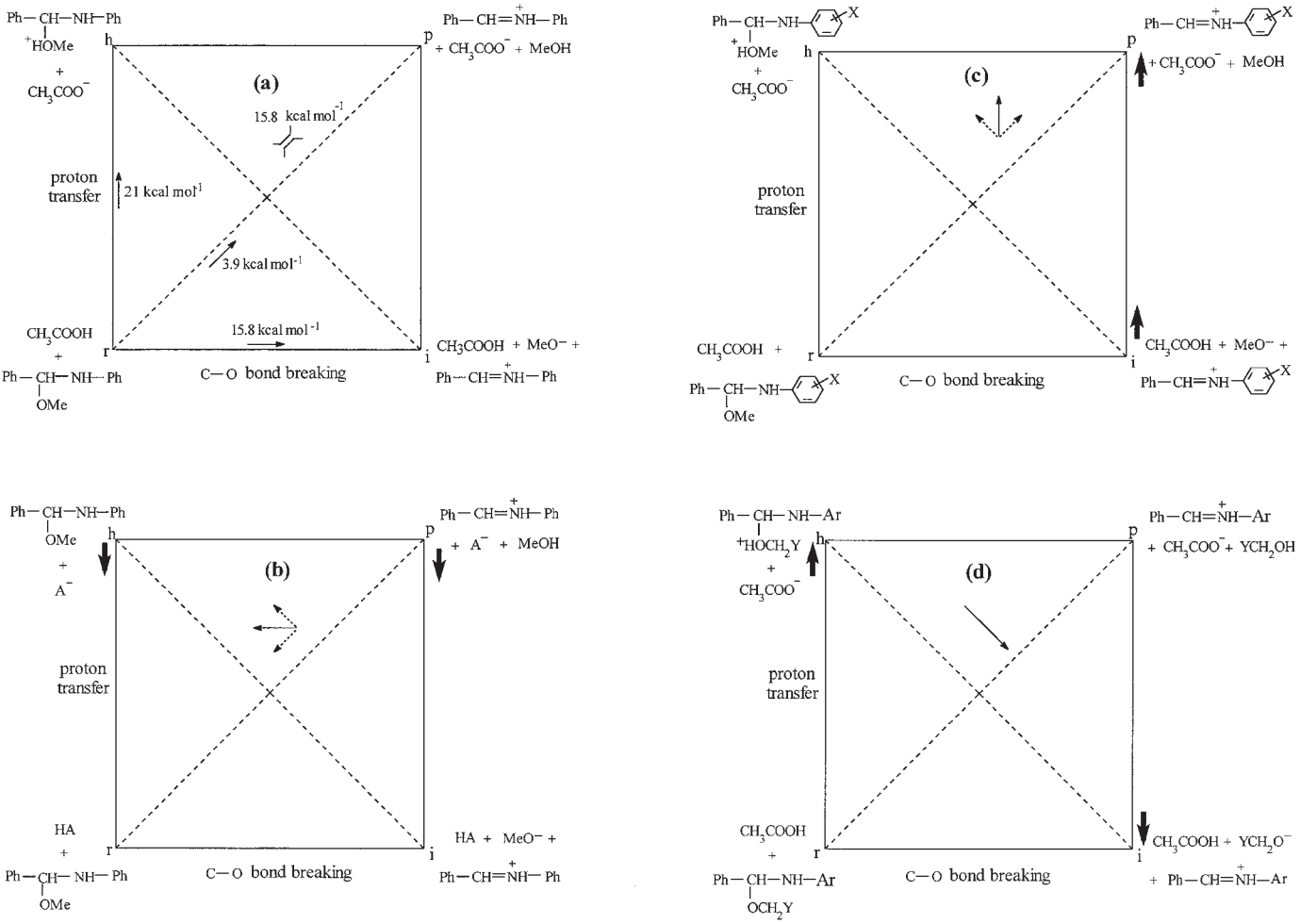

This mechanism is energetically more favorable than the two stepwise mechanisms because the formation of the h or i high energy intermediates is avoided.

In a way similar to that described previously in the case of hemiacetal breakdown (20), the standard Gibbs free energy differences, $G_h^0 - G_r^0$, $G_i^0 - G_r^0$, and $G_p^0 - G_r^0$ between corners h, i, and p, and starting materials can be calculated by combining the free energy changes for α-EA formation, iminium ion and α-EA protonation, carboxylic acid dissociation, and methanol autoprotolysis. In the case of **1a**, the pK_a value of the corresponding iminium ion (ca. 4) was taken as 4.0 from (8), and that for the protonated methanol adduct was estimated as –6 on the basis of literature data (measured or estimated) on the pK_a of protonated ethers or hemiacetals in water. (For doing so, the pK_a for protonated ethers (42) and hemiacetals (20*b*) were plotted against the Charton σ_I values (43) of the groups attached to the oxygen atom, the σ_I value for the PhCH(NHPh) was estimated as 0.13, and the difference in solvants was neglected, since it is usually observed that the pK_a of unit-charged acids do not differ much on going from water to methanol.) For the acetic acid-catalyzed addition of methanol to **1a**, the $G_h^0 - G_r^0$, $G_i^0 - G_r^0$, and $G_p^0 - G_r^0$ free energy differences were calculated as 21, 15.8, and 3.9 kcal mol^{-1}, respectively. Since, $\Delta G^{\neq}$ = 15.8 kcal mol^{-1}, the transition state for α-AE breakdown lies below corner h and at about the same energy as corner i. The concerted mechanism is obviously more favorable than the two-step mechanism corresponding to specific acid catalysis (sequence r → h → p). It is enforced because of the high energy of the protonated α-AE intermediate **7** in the specific acid-catalysis pathway would make its lifetime too short for this species to be involved as an intermediate. The

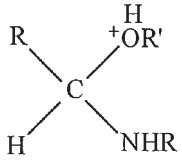

7

© 1999 NRC Canada

Scheme 7.

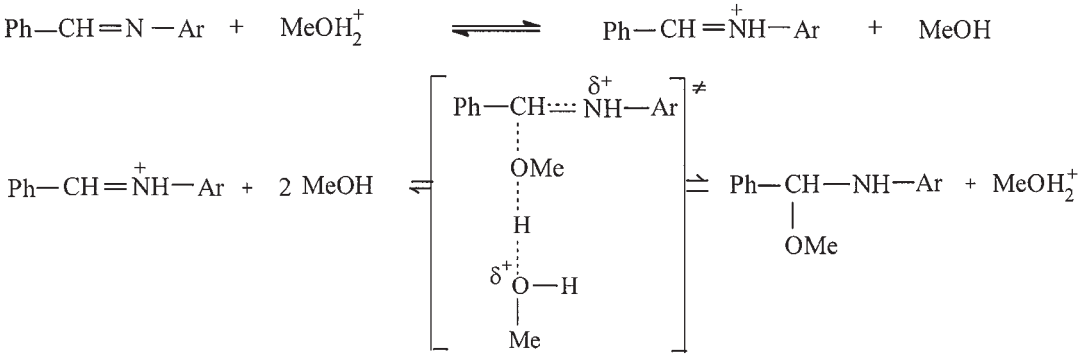

situation is analogous to that found in the case of acid-catalyzed hemiacetal breakdown (12–20), for which the conjugate acid (**8**) is too short-lived for being intermediately formed. The concerted mechanism is also more favorable than that corresponding to the r → i → p sequence, since the i → p step would require a small but nonnegligible energy of activation.

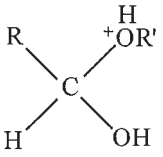

8

Similar estimates can also be done for $MeOH_2^+$ catalysis. In the case of **1a**, the $G_h^0 - G_r^0$, $G_i^0 - G_r^0$, and $G_p^0 - G_r^0$ free energy differences are 6.3, 15.8, and –11.0 kcal mol^{-1}, respectively. The transition state ($\Delta G^{\neq}$ = 6.3 kcal mol^{-1}) lies at about the same energy level as the protonated α-AE + methanol system (corner h), but the stepwise mechanism is not plausible since, in view of $k_r^{MeOH_2^+} = 1.46 \times 10^8$ M^{-1} s^{-1}, the ΔG^0 = 6.3 kcal mol^{-1} figure for the r → h step — corresponding to an equilibrium constant of $10^{-4.6}$ — would require the intermediate to have a lifetime as low as 10^{-13}–10^{-12} s. Such a lifetime is too short even if the h → p and h → r steps are diffusion-controlled.

α Brønsted exponents

The α values observed for α-AE breakdown (α = 0.67–0.88 for the methoxy adduct and ca. 0.6 for the chloroethyl adduct) suggest that the proton is more than half transferred at the transition state. This is roughly what is expected from theory (12, 20) for an endergonic process with a transition state lying not far from the diagonal because corners h and i of the More O'Ferrall – Jencks diagram have roughly similar high energies. The fact that corner i lies below corner h (this suggesting that the transition state is closer to i than to h) is not probably a matter of concern, since the termolecular diagonal i → h transformation (the "disparity reaction" (20)) would require to go through a relatively high-free energy (low entropy) transition state. Grunwald (20) pointed out that the free energies of the encounter complexes would need to be considered instead of those of systems of separate molecular entities.

It has been suggested in the case of acid- and base-catalyzed hemiacetal breakdown (12, 20) that the observation of linear Brønsted plots requires that changes in the catalyst make the transition state move along a direction roughly parallel to the horizontal edges of the diagram. Figure 7*b* shows the expected displacement of the transition state associated with an increase in catalyst acidity. This displacement is the result of longitudinal (Hammond) and perpendicular effects which are of similar amplitude if, according to Grunwald (20), the intrinsic energy well and the intrinsic energy barrier are equal.

It has been shown above that the points associated with catalysis by $MeOH_2^+$ do not deviate much from the Brønsted plot based on carboxylic acids. This behavior is in line with what is expected if one assumes that the concerted mechanism is still valid. Since such a mechanism is energetically plausible, we conclude that the mechanism of α-AE formation involves two methanol molecules, one playing the role of nucleophile, the other acting as a general base catalyst (Scheme 7).

Table 3 shows that α increases with electron-withdrawing substituent effects. These variations are is in keeping with what is expected. The stronger the withdrawing substituent, the lower the stability of the iminium ion and the upper are corners p and i. In contrast, the effect on corner h is expected to be small because the positive charge in *O*-protonated α-AE lies on the oxygen atom, i.e., far from the substituent. As Fig. 7*c* shows, these relative energy variations should result in large variations in the degree of proton transfer, but in small variations of the degree in C—O bond breaking.

Change in the alkoxy group

As stressed in Introduction, a comparison of the rate constants for the breakdown of **4** and **5** is expected to provide valuable information about the relative extents the concerted proton transfer and C—O bond breaking have progressed at the transition state. Table 4 lists the ratios of the catalytic rate constants on α-AE breakdown (CH_2Cl group effects). Since they are lower than unity, it can be concluded that the oxygen atom is positively charged at the transition state and that proton-tranfer is ahead of C—O bond breaking. As Fig. 7*d* shows, since CH_2Cl makes the *O*-protonated ether much less stable and the alkoxide ion more stable, the change in transition state location should almost exclusively

© 1999 NRC Canada

Table 5. Coefficients of the Young–Jencks equation calculated from rate and equilibrium constants for acid-catalyzed α-amino ether formation and breakdown.[a]

Catalyst	ρ^n	ρ^r	ρ^r/ρ^r	r^b
		Rates of α-amino formation		
$MeOH_2^+$	–0.31 ± 0.10	0.55 ± 0.15	–1.77 ± 0.70	0.934
CH_3COOH	–0.71 ± 0.05	0.23 ±0.08	–0.32 ± 0.12	0.996
C_6H_5COOH	–0.71 ± 0.12	0.24 ± 0.09	–0.33 ± 0.15	0.987
HCOOH	–0.80 ± 0.19	0.33 ± 0.15	–0.41 ± 0.23	0.974
		Rates of α-amino ether breakdown		
$MeOH_2^+$	–2.10 ± 0.02	–1.30 ± 0.03	0.62 ± 0.02	0.999 97
CH_3COOH	–2.50 ± 0.03	–1.73 ± 0.04	0.69 ± 0.03	0.999 96
C_6H_5COOH	–2.51 ± 0.11	–1.61 ± 0.08	0.64 ± 0.06	0.9998
HCOOH	–2.61 ± 0.05	–1.51 ± 0.04	0.58 ± 0.02	0.999 96
		α-Amino ether formation equilibrium		
	1.79 ± 0.08	1.86 ± 0.12	1.04 ± 0.03	0.9995

Fig. 8. Plot of decimal logarithm of the forward catalytic rate constants for acetic acid-catalyzed addition of methanol to **1a–e** against σ^n (●) and σ^- (○) substituent parameters.

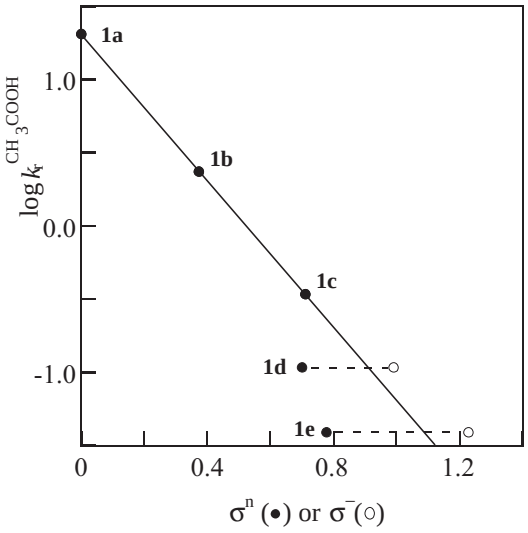

Fig. 9. Plot of decimal logarithm of the forward catalytic rate constants for lyonium ion-catalyzed addition of methanol to **1a–e** against σ^n (●) and σ^- (○) substituent parameters.

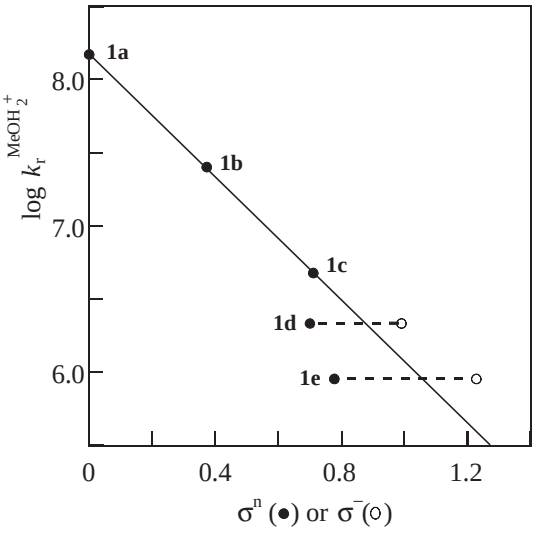

result from perpendicular effects. The large decrease in α, from 0.81 to 0.58 is in line with what is predicted.

Ring substituent effects on the catalytic rate constants

Figure 8 shows the plot of log $K_r^{CH_3COOH}$ against σ^n. The points corresponding to the π-electron-withdrawing substituents deviate negatively from the lines defined by the other points, but data fit eq. [16] very nicely. The same behavior is observed for the other catalysts, including the lyonium ion (Fig. 9). The ρ^n and ρ^r data are given in Table 5. These are fairly independent of R in RCOOH, but both coefficients are a little smaller for catalysis by the lyonium ions. The values ρ^n and ρ^r are thought to be related to the degree of C—O bond breaking at the transition and a comparison with those expected for full bond breaking is worthwhile.

The ρ^n and ρ^r coefficients for the α-AE to iminium ion (r → p) full transformation can be estimated according to the thermodynamical cycle of Scheme 8. These coefficients correspond to the sums of the ρ^n and ρ^r values for iminium ion deprotonation and methanol addition to the Schiff bases. The $(\rho^n)_{eq}$ (4.1) and $(\rho^r)_{eq}$ (2.8) values shown on Scheme 8 for iminium ion deprotonation are those calculated from literature data in nitromethane. It is assumed that the change in solvent is not too much a matter of concern as far as pK_a differences are considered.

The ratios of the ρ^n and ρ^r values between rate and equilibrium constants ((–2.5)/(–4.1) = 0.61 and (–1.50)/(–2.8) = 0.54) for carboxylic acid catalysis are close one another and are in agreement with what is expected on the basis of the energy diagrams. The transition state is closer to p than to r, since the adduct-to-iminium ion transformation is endergonic. For $MeOH_2^+$ catalysis, the ρ^n and ρ^r ratios are smaller ((–2.09)/(–4.1) = 0.51 and (–1.33)/(–2.8) = 0.47, respectively), this being in line with the prediction (Fig. 7*b*) that an increase in the acidity of the catalyst causes an approximately horizontal shift of the transition state, with less C—O bond breaking. It is noteworthy that the ρ^n and ρ^r variations

© 1999 NRC Canada

Scheme 8.

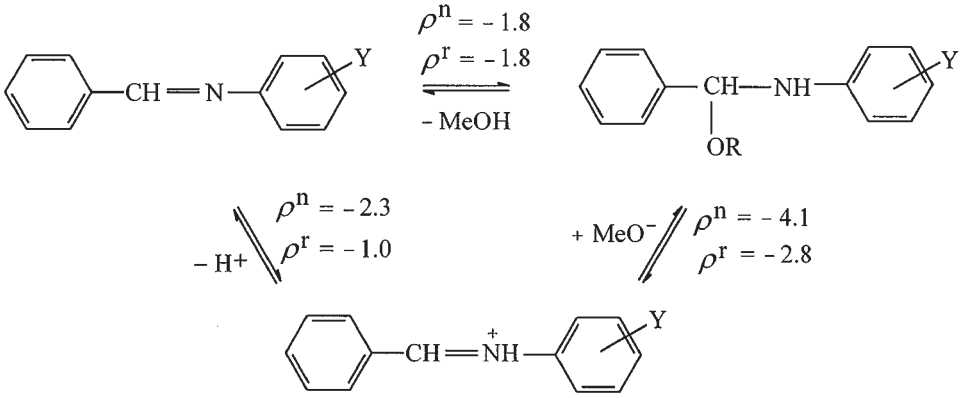

Fig. 10. Plot of decimal logarithm of the catalytic rate constants for acetic acid-catalyzed breakdown of **1a**–**e** methanol adducts against σ^n (●) and σ^- (○) substituent parameters.

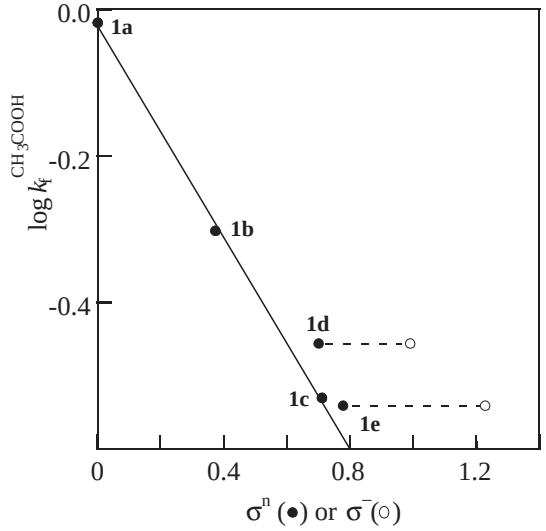

Fig. 11. Plot of the decimal logarithm of the catalytic rate constants for lyonium ion-catalyzed breakdown of **1a**–**e** methanol adducts against σ^n and σ^- substituent parameters.

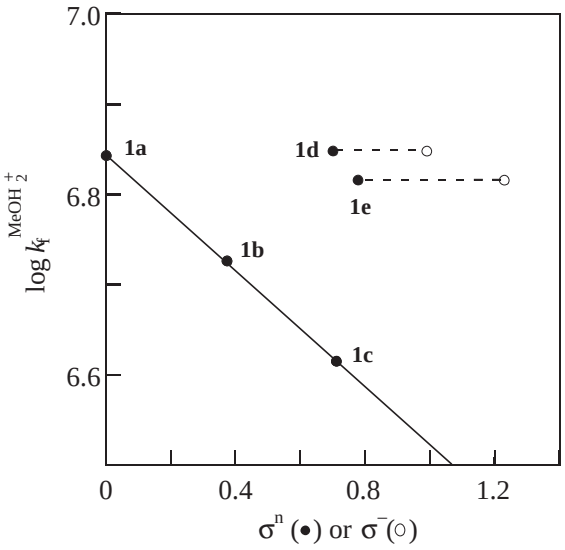

are parallel, this suggesting that there is no imbalance between polar and resonance effects.

Figure 10 shows the plot of log $k_f^{CH_3COOH}$ versus σ^n. The points associated with the π-electron-withdrawing substituents lie above the straight line. This means that –M effects cause the rate increase whereas –I effects make it decrease. This uncommon situation is due to the fact that a σ-electron-withdrawing group *increases* the energy of the transition state because of the positive charge on nitrogen, but that the π-electron withdrawing contribution *decreases* it because the conjugation with the nitrogen lone pair is enhanced by the sp^2-to-sp^3 change in carbon hybridization. As shown in Fig. 11, the phenomenon of inversion between polar and resonance effects is much more pronounced in the case of lyonium ion catalysis. This is because the C—O bond is more formed at the transition state than in the case of carboxylic acid catalysis. The ρ^n coefficient is lower because of less positive charge on nitrogen; ρ^r is larger because of more resonance contribution to the energy of later transition state. Table 5 also lists the values of the ρ^n and ρ^r coefficients on the forward catalytic rate constants. Standard deviations are rather poor probably because the deviations from the straight lines of the **1e** points in Figs. 10 and 11 are smaller than what is expected in view of the data for **1d**. This is probably be due to the fact that the gain in resonance on going from imine to α-AE is less because of more resonance contribution to the energy of the starting material. The θ angle (Fig. 6) has been reported to be close to 90° for Y = 4-NO_2 (36*a*, 38, 39*a*, *b*); this angle is probably lower for Y = 4-CN.

It is interesting to note that the ρ^n values are much smaller when considering the α-AE formation rate constants than those for the reverse reaction. This clearly stems from the large substituent effects on the stability of the imino form. There is compensation between substituent effects on the starting materials and on the transition state. We would like to emphasize the fact that consistent conclusions about bond breaking or formation at the transition state have been reached here through a detailed analysis of the substituent effects on the equilibrium constants and on the rate constants for both directions. A discussion on the substituents only on the basis of α-AEs would have been misleading since the low ρ values could wrongly suggest that C—O bond is almost completely formed at the transition state.

© 1999 NRC Canada

Experimental section

Reagents

1a–**e** were prepared by the previously described condensation of benzaldehyde (ALDRICH) with freshly distilled or recrystallized (from ethanol) anilines (from ALDRICH or ACROS) dissolved in heptane (8). Water was removed by azeotropic distillation by means of a Dean Stark tube. Crystallization was usually observed on cooling and **1a**–**e** were recrystallized twice from ethanol (**1a**), pentane (**1b**), diethyl ether (**1c**), pentane and cyclohexane (**1d**), and cyclohexane and ethanol (**1e**). The melting points were observed to correspond, when available, to literature data (all melting points (uncorrected) in °C): **1a**, 51.5–52 (lit. 52 (44), lit. 52–53 (44), lit. 50.5–51.5 (45), lit. 51–52 (46)); **1b**, 38 ; **1c**, 73 (lit. 71–71.5 (47)); **1d**, 70, and **1e**, 118 (lit. 119.7–121.2 (47), lit. 117–118 (48), lit. 114–117 (49)). Methanol ("Analyzed Baker Reagent") was used as received. Sodium methoxide solutions, prepared by the addition of sodium to methanol, were protected against moisture and carbon dioxide. Acetic acid (reagent ACS, ACROS), methoxyacetic acid (98%, ACROS), benzoic acid (p.a., ACROS), formic acid (reagent ACS, 96%, ACROS), chloroacetic acid (p.a., ACROS), and cynoacetic acid (99%, ACROS) were used as received and the methanolic solutions were pH-metrically titrated (after 1:10 dilution in water). Sodium acetate (anhydrous, reagent ACS, ACROS), benzoate (99+%, ACROS), and formate (99+%, ACS Reagent, ALDRICH) were used as received. Sodium methoxyacetate, chloroacetate, and cyanoacetate solutions in methanol were prepared by mixing equal volumes of freshly prepared equimolecular solutions of the corresponding acid and of sodium methoxide. The solutions obtained were titrated according to an original double-titration method, which consists in titrating two equal amounts of the same solution by HCl 0.1 M and NaOH 0.1 M successively and in recording the pH titration curves. The two pH curves were plotted on the same graph with positive and negative abscissa, respectively, for the volumes of HCl and NaOH solutions added, the inflexion of the whole curve corresponding the perfect neutralization of the small excess in acid or base. Small amounts in acid or in sodium methoxide were added to the bulk solution until getting perfectly neutral solutions. To avoid any acid esterification, the methanolic buffer solutions were prepared directly in the spectrophotometer cells just before the kinetic runs. The required amounts (weighted) of acid were added by a microsyringe to the carboxylate + tetramethylammonium bromide solutions.

Kinetic and equilibrium measurements

Rate and equilibrium measurements at I_c = 0.0376 M (Me_4NBr) and 25 ± 0.1°C were performed as described in (8).

Acidity constant determinations

The acidity constants of the carboxylic acids measured spectrophotometrically by using 2,4-dinitrophenol (pK_a = 7.9 (50)) and 2,5-dinitrophenol as indicators at 400 nm and 436 nm, respectively. The apparent molar extinction coefficients, defined as $\varepsilon_{obs} = A/[phenol]_{st}$, where $[phenol]_{st}$ is the stoichiometric concentration of phenol, were determined for various sodium carboxylate/carboxylic acid concentration ratios. Since ε_{obs} can be expressed by eq. [18],

$$[18] \qquad \varepsilon_{obs} = \varepsilon_{phenate} \frac{K_{ArOH/HA}}{K_{ArOH/HA} + \{[RCOO^-]/[RCOOH]\}}$$

where $K_{ArOH/HA}$ is the ratio of the acidity constants of the indicator and carboxylic acid, K was taken as the value of $[RCOO^-]/[RCOOH]$ at which $\varepsilon_{obs} = \varepsilon_{phenate}/2$. The absorption molar coefficients of the phenoxide ions, $\varepsilon_{phenate}$, was measured as 11 200 M^{-1} cm^{-1} and 4270 M^{-1} cm^{-1} in 1.5 × 10^{-3} M NaOMe, for 2,4-dinitrophenol and 2,5-dinitrophenol, respectively. The pK_a values at I_c = 0.0376 M [$(Me)_4NBr$] for acetic acid, methoxyacetic acid, benzoic acid, and formic acid were measured against 2,4-dinitrophenol and those for chloroacetic acid and cyanoacetic acid against 2,5-dinitrophenol. The pK_a value (9.09) for 2,5-dinitrophenol was determined against formic acid.

References

1. W.P. Jencks. Catalysis in chemistry and enzymology. McGraw–Hill, New York. 1969.
2. M. Brezina and P. Zuman. Chem. Listy, **47**, 975 (1953); J. Hine and C.Y. Yeh. J. Am. Chem. Soc. **89**, 2669 (1967); J. Hine, C.Y. Yeh, and F.C. Schmalstieg. J. Org. Chem. **35**, 340 (1970); A. Williams and M.L. Bender. J. Am. Chem. Soc. **88**, 2508 (1966); B.M. Anderson and W.P. Jencks. J. Am. Chem. Soc. **82**, 1773 (1960); R. Rosenberg, S.M. Silver, J.M. Sayer, and W.P. Jencks. J. Am. Chem. Soc. **96**, 7986 (1974); J.M. Sayer and C. Edman. J. Am. Chem. Soc. **101**, 3010 (1979); J. Hine, J.P. Ziegler, and M. Johnston. J. Org. Chem. **44**, 3540 (1979).
3. E.H. Cordes and W.P. Jencks. J. Am. Chem. Soc. **85**, 2843 (1963); R.H. Kayser and R.M. Pollack. J. Am. Chem. Soc. **99**, 3379 (1977); T. Okuyama, H. Shibuya, and T. Fueno. J. Am. Chem. Soc. **104**, 730 (1982).
4. W. von Miller and J. Plöchl. Ber. **31**, 2699 (1898).
5. T.I. Crowell, D.H. O'Brien, and M. Neveu. J. Org. Chem. **29**, 2043 (1964); R.L. Reeves. J. Org. Chem. **30**, 3129 (1965).
6. Y. Ogata and A. Kawasaki. J. Org. Chem. **39**, 1058 (1974).
7. H.C. Brown and Y. Okamoto. J. Am. Chem. Soc. **80**, 4947 (1958).
8. J. Toullec and S. Bennour. J. Org. Chem. **59**, 2831 (1994).
9. R.P. Bell and W.C.E. Higginson. Proc. R. Soc. London Ser. A, **197**, 141 (1949); R.P. Bell. Adv. Phys. Org. Chem. **4**, 1 (1966).
10. W.P. Jencks. Prog. Phys. Org. Chem. **2**, 63 (1964).
11. T.J. Pryztas and T.H. Fife. J. Am. Chem. Soc. **103**, 4884 (1981).
12. L.H. Funderburk, L. Aldwin, and W.P. Jencks. J. Am. Chem. Soc. **100**, 5444 (1978).
13. P.E. Sørensen and W.P. Jencks. J. Am. Chem. Soc. **109**, 4675 (1987).
14. P.E. Sørensen, K.J. Pedersen, P.R. Pedersen, V.M. Kanagasabapathy, and R.A. McClelland. J. Am. Chem. Soc. **110**, 5118 (1988).
15. B.G. Cox, A.J. Kresge, and P.E. Sørensen. Acta. Chem. Scand. **42A**, 202 (1988).
16. P.E. Sørensen, T. Løgager, V.M. Kanagasabapathy, and R.A. McClelland. Bull. Soc. Chim. Fr. 313 (1988).
17. R.A. McClelland, K.M. Engel, T.S. Larsen, and P.E. Sørensen. J. Chem. Soc. Perkin Trans. 2, 2199 (1994).

© 1999 NRC Canada

18. (*a*) C.A. Coleman and C.J. Murray. J. Am. Chem. Soc. **113**, 1677 (1991); (*b*) C.J. Murray and T. Webb. J. Am. Chem. Soc. **113**, 1684 (1991).
19. N. Buckley and N.J. Oppenheimer. J. Org. Chem. **61**, 8048 (1996).
20. (*a*) E. Grunwald. J. Am. Chem. Soc. **107**, 125 (1985); (*b*) J. Am. Chem. Soc. **107**, 4710 (1985); (*c*) J. Am. Chem. Soc. **107**, 4715 (1985); (*d*) Prog. Phys. Org. Chem. **17**, 55 (1990).
21. J. Toullec and R. Razafindralambo. J. Org. Chem. **52**, 1646 (1987).
22. M. Arota, B.G. Cox, and P.E. Sørensen. J. Chem. Soc. Perkin Trans. 2, 103 (1979).
23. J. Barthel, M. Knerr, and G. Engel. Z. Phys. Chem. (Frankfurt/Main), **69**, 283 (1970).
24. V. Gold and J. Toullec. J. Chem. Soc. Perkin Trans. 2, 596 (1979).
25. R. de Lisi, M. Goffredi, and V.T. Liveri. J. Chem. Soc. Faraday Trans. 1, **74**, 1096 (1978).
26. J. Toullec, M. El-Alaoui, and R. Bertrand. J. Chem. Soc. Perkin Trans. 2, 167 (1989).
27. (*a*) H. Van Bekkum, P.E. Verkade, and B.M. Wepster. Rec. Trav. Chim. Pays-Bas, **78**, 815 (1959); (*b*) A.J. Hoefnagel and B.M. Wepster. J. Am. Chem. Soc. **95**, 7357 (1973).
28. A.I. Biggs and R.A. Robinson. J. Chem. Soc. 388 (1961).
29. J. Toullec and D. Milin. J. Org. Chem. **59**, 2840 (1994).
30. (*a*) P.R. Young and W.P. Jencks. J. Am. Chem. Soc. **99**, 8238 (1977); (*b*) J. Am. Chem. Soc. **100**, 1228 (1978); (*c*) P.R. Young and P.E. McMahon. J. Am. Chem. Soc. **101**, 4678 (1979).
31. J.E. Dubois, M. El-Alaoui, and J. Toullec. J. Am. Chem. Soc. **103**, 5393 (1981); J. Toullec, M. El-Alaoui, and P. Kleffert. J. Org. Chem. **48**, 4808 (1983); J. Org. Chem. **50**, 4928 (1985); J. Toullec and M. El-Alaoui. J. Org. Chem. **51**, 4054 (1986).
32. Y. Yukawa, Y. Tsuno, and M. Sawada. Bull. Chem. Soc. Jpn. **39**, 2274 (1966).
33. B.A. Korolev, N.A. Rozanel'skaya, and B.I. Stepanov. Zh. Obshch. Khim. **39**, 1161 (1968); J. Genet. Chem. U.S.S.R. **39**, 1128 (1969).
34. (*a*) Z. Meic and G. Baronovic. Pure Appl. Chem. **61**, 61 (1989); (*b*) J.T. Rafalko and E.W. Choe. Appl. Spectrosc. **39**, 1065 (1985); (*c*) Z. Meic, G. Baranovic, and T. Suste. J. Mol. Struct. **296**, 163 (1993).
35. (*a*) R. Akaba, T. Tokumaru, and T. Kobayashi. Bull. Chem. Soc. Jpn. **53**, 1993 (1980). (*b*) A. Mehlhorn and J. Juergen. J. Prakt. Chem. **324**, 267 (1982).
36. (*a*) H.B. Burgi and D.D. Dunitz. Helv. Chim. Acta, **53**, 1747 (1970); (*b*) H. Nakai, M. Shiro, K. Ezumi, S. Sakata, and T. Kubota. Acta Cryst. **B32**, 1827 (1976).
37. (*a*) M. Traettenberg, I. Himo, R.J. Abraham, and S. Ljunggren. J. Mol. Struct. **48**, 395 (1978); (*b*) R. Akaba, K. Tokumaru, T. Kobahashi, and C. Utsunomiya. Bull. Chem. Soc. Jpn. **53**, 2002 (1980).
38. (*a*) S.B. Bulgarevich, S.I. Adamova, A.A. Polunin, V.A. Kogan, and O.A. Osipov. Zh. Obshch. **47**, 1144 (1977); J. Genet. Chem. U.S.S.R. **47**, 1050 (1977); (*b*) R. Akaba, H. Sakuragi, and K. Tokumaru. Bull. Chem. Soc. Jpn. **58**, 1186 (1985); (*c*) R. Gawinecki. Z. Phys. Chem. (Leipzig), **271**, 863 (1990).
39. (*a*) P. Jacques and J. Faure. Theoret. Chim. Acta (Berlin), **46**, 307 (1977); (*b*) U. Norinder. Mol. Cryst. Liq. Cryst. **149**, 195 (1987); (*c*) N. Russo. THEOCHEM, **41**, 403 (1988). (*d*) M. Kontoylanni, A.J. Hoffman, and J.P. Bowen. J. Comput. Chem. **13**, 57 (1992).
40. (*a*) R.A. More O'Ferrall. J. Chem. Soc. B, 274 (1970); (*b*) W.P. Jencks. Chem. Rev. **72**, 705 (1972); (*c*) Chem. Rev. **85**, 511 (1985).
41. Glossary of terms used in physical organic chemistry (UIPAC recommendations 1994). Pure Appl. Chem. **66**, 1077 (1994).
42. G. Perdoncin and G. Scorrano. J. Am. Chem. Soc. **99**, 6983 (1977).
43. M. Charton. Prog. Phys. Org. Chem. **13**, 131 (1981).
44. A. Roe and J.A. Montgomery. J. Am. Chem. Soc. **75**, 910 (1953).
45. K. Tabei and E. Saitou. Bull. Chem. Soc. Jpn. **42**, 2693 (1969).
46. C. Yijima, T. Tsujimoto, K. Suda, and M. Yamauchi. Bull. Chem. Soc. Jpn. **59**, 2165 (1986).
47. A. Echevaria, J. Miller, and M. Nascimento. Magn. Reson. Chem. **23**, 809 (1985).
48. (*a*) E. Walker and M. Latif. Chem. Ind. (London), **2**, 51 (1969); (*b*) G.F. D'Alelio, J.W. Crivello, R.K. Shoenig, and T.H. Hulmmer. J. Microanal. Sci. Chem. **1**, 1251 (1967).
49. Y. Ogata and A. Kawasaki. J. Chem. Soc. B, 325 (1971).
50. B.W. Clare, D. Cook, E.C.F. Ko, Y.C. Mac, and A.J. Parker. J. Am. Chem. Soc. **88**, 1911 (1966).

© 1999 NRC Canada

Oxidative dealkylation of aromatic amines by "bare" FeO^+ in the gas phase

Mark Brönstrup, Detlef Schröder, and Helmut Schwarz

Abstract: The gas-phase oxidations of aniline, *N*-methylaniline, and *N*,*N*-dimethylaniline by FeO^+ cation are examined by using mass spectrometric techniques. Although bare FeO^+ is capable of hydroxylating aromatic C—H bonds, the fate of the oxidation of arylamines is determined by docking of the FeO^+ unit at nitrogen. The major reactions of the metastable aniline/FeO^+ complex are losses of molecular hydrogen, ammonia, and water, all involving at least one N-H proton. N-alkylation results in a complete shift of the course of the reaction. The unimolecular processes observed can be regarded as initial steps of an oxidative dealkylation of the amines mediated by FeO^+. More detailed mechanistic insight is obtained by examining the C—H(D) bond activation of *N*-methyl-*N*-([D_3]-methyl)aniline by bare and ligated FeO^+ species. The gas-phase reactions of FeO^+ with methylanilines show some similarities to the enzymatic dealkylation of amines by cytochrome P-450. The kinetic isotope effects observed experimentally suggest an electron transfer mechanism for the gas-phase reaction.

Key words: mass spectrometry, gas-phase chemistry, iron, dealkylation, *N*,*N*-dimethylaniline.

Résumé : L'oxidation d'aniline, *N*-méthylaniline et *N*,*N*-diméthylaniline par l'ion FeO^+ dans la phase gazeuse est suivie par spectrométrie de masse. Tant que FeO^+ est capable d'activer des liaisons C—H aromatiques, l'oxidation d'anilines est determinée par la fixation du fer sur l'azote. Les complexes metastabiles d'aniline/FeO^+ expulsent l'hydrogène moléculaire, l'ammoniac et l'eau, qui contiennent toujours au moins d'un proton N-H. La N-alkylation provoque un changement complet dans la réaction. Ainsi, les décompositions unimoléculaires ressemblent aux premiers pas de la dégradation oxidative d'alkylamines. L'activation des liaisons C—H(D) en *N*-méthyl-*N*-([D_3]-méthyl)-aniline par FeO^+ sans ou avec ligands permet d'améliorer la compréhension mécanistique. La réaction de FeO^+ avec les *N*-méthylanilines s'apparente à la désalkylation oxidative des amines par l'enzyme cytochrome P-450. Dans la phase gazeuse, les effets cinétiques des isotopes proposent un mécanisme avec transfert d'un seul electron.

Mots clés : spectrométrie de masse, phase gazeuse, fer, désalkylation, *N*,*N*-diméthylaniline.

Introduction

Whereas alkylation of amines can be achieved easily by simple nucleophilic substitution reactions, N-dealkylation is much more difficult. As evolution led to heme-containing enzymes like cytochrome P-450 or peroxidases fulfilling this purpose under physiological conditions, there has been a continuous interest in revealing the molecular mechanisms of the biochemical N-dealkylation reactions (1–4).

In the literature (2), a long and controversial discussion about the N-dealkylation of aromatic amines **1** by cytochrome P-450 has focused on the sequence of elementary steps (Scheme 1): Dinnocenzo and co-workers (3) have provided support for a radical-type H-atom abstraction ($H^{\bullet}_T$) as a key step (**1** → **2**, path (a)), while Guengerich et al. (4) have argued that initial electron transfer (ET) is rate determining (**1** → $\mathbf{1}^{+\bullet}$, path (b)). Both pathways collapse to the same intermediates en route to C—N bond cleavage, i.e., either the imminium ion $\mathbf{2}^+$ or the α-aminoalcohol **3**, which is formed by a "rebound" of the hydroxyl group from [FeOH] to the substrate. Under physiological conditions, these intermediates undergo hydrolysis to yield the dealkylated amine and the corresponding aldehyde. The most recent studies seem to agree upon initial electron transfer from the amine (5). In essence, the debate concerns two fundamental questions: (*i*) is the transfer of a hydrogen atom (**1** → **2**) a real $H^{\bullet}_T$ or in fact a sequence of ET and deprotonation? (*ii*) does a formal hydride ion transfer (**1** → $\mathbf{2}^+$) occur in a single step (H^-_T), as a combination of $H^{\bullet}_T$ and ET, or even as sequence of two ETs and a deprotonation?

Cytochrome P-450 is commonly believed to involve a high-valent iron oxo species in the active site (2). The most simple model system for this reactive entity is the bare FeO^+ cation in the gas phase (6), which can be generated and studied using mass spectrometry (7). The extreme simplification of the complexity of the biological system permits investigation of the intrinsic chemical behavior of the reactive core under rigorous exclusion of many complicating parameters such as solvent and aggregation effects, counterions, or ligands. For example, the problem that the intrinsic isotope effect might be "masked" due to the chirality of the enzyme

Received December 3, 1998.

This paper is dedicated to Jerry Kresge in recognition of his many achievements in chemistry.

M. Brönstrup, D. Schröder,[1] and H. Schwarz. Institut für Organische Chemie der Technischen Universität Berlin, Straße des 17. Juni 135, D-10623 Berlin, Germany.

[1]Author to whom correspondence may be addressed. Telephone: +49 30 314 26546. Fax: +49 30 314 21102. e-mail: df@www.chem.tu-berlin.de

© 1999 NRC Canada

Scheme 1.

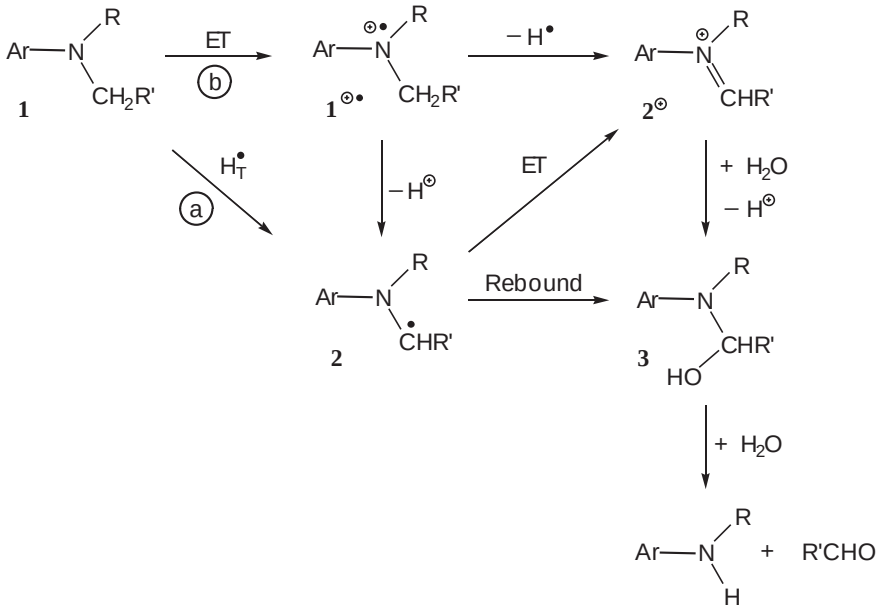

Chart 1.

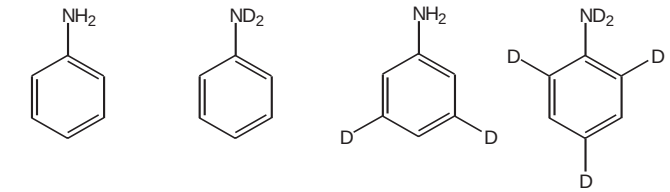

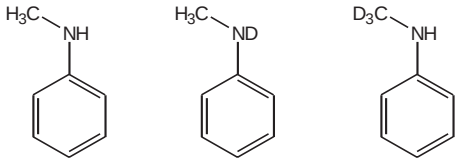

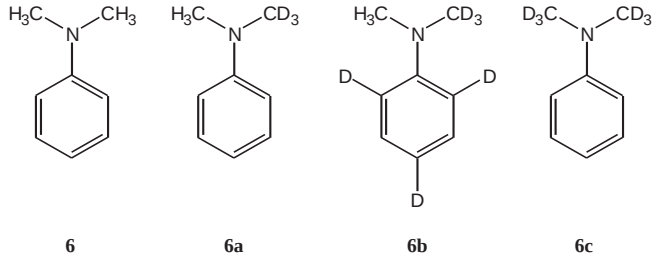

backbone (3*a*, 8) does not exist for the simple model system FeO^+. Further, the role of electronic structure effects can be probed in detail (7, 9). Previous studies have demonstrated that FeO^+ is capable of oxidizing a large number of substrates (7), ranging from simple hydrocarbons such as methane (10), benzene (11), or norbornane (12) to more oxidation-resistant compounds like acetonitrile (13) or hexafluorobenzene (14). Thus, efficient oxidation of aromatic amines by FeO^+ is expected to take place as well. To this end, we used two different mass spectrometric techniques (see experimental section) to investigate the gas-phase reactions of phenylamines C_6H_5-NRR′ **4**–**6** (R, R′ = H, D, CH_3, CD_3; see Chart 1) with the FeO^+ cation. In spite of many differences, the present experiments are entirely complementary to biochemical studies; in addition, they basically address the same fundamental problem. While the present study cannot resolve the above mechanistic controversy, our results may provide valuable new insight into the problem.

Results

First, we describe separately the results obtained with a four-sector mass spectrometer (sector MS) and with an ion cyclotron resonance mass spectrometer (ICR MS). This is followed by a discussion of the mechanistic insight gained from these studies with respect to fundamental aspects of amine dealkylation in the condensed phase.

Sector MS

Metastable aniline/FeO^+ complexes undergo unimolecular losses of molecular hydrogen, ammonia, water, and carbon monoxide (Table 1). Unfortunately, for some of the isotopomers losses of isobaric ammonia and water overlap, thereby preventing a strictly quantitative analysis of the labeling distribution. However, the data of the labeled complexes reveal that the major pathways involve the N—H(D) bonds with a high preference. Thus, for the [*N*,*N*-D_2]-labeled complex **4a**/FeO^+, loss of NH_3 is no longer detected, and the water molecules lost contain preferentially one deuterium atom (-HDO). Losses of H_2O and D_2O are observed to a smaller extent. Complementing this, the label is almost completely retained in the ions for the [3,5-D_2]-labeled species **4b**/FeO^+. The prevailing generations of HDO from **4a**/FeO^+ and D_2O from **4c**/FeO^+ suggest that dehydration preferentially involves cleavages of one N—H(D) and one of the

© 1999 NRC Canada

Table 1.. Intensities[a] of the neutrals lost in the unimolecular dissociation of metastable arylamine complexes **4**/FeO^+–**6**/FeO^+ and their isotopologues (see Chart 1).

	-H_2	-HD	-D_2	-NH_3[b]	-NH_2D[c] -H_2O[c]	-NHD_2[c] -HDO[c]	-ND_3[c] -D_2O[c]	-CO	-FeOH	-FeOD
4/FeO^+	8			9	82			1		
4a/FeO^+		9			7	61	21	2		
4b/FeO^+	4	2		10	78	4		2		
4c/FeO^+		4	2		5	16	72	1		
5/FeO^+					100					
5a/FeO^+						100				
5b/FeO^+						100				
6/FeO^+					39				61	
6a/FeO^+					33	3	9		42	13
6b/FeO^+					27	5	10		43	15
6c/FeO^+							38			62

[a]Normalized to a sum of fragments of 100%; intensities <1% are omitted.

[b]Loss of hydroxy radical was excluded by ICR experiments with high mass resolution in which $[Fe,C_6,H_4,O]^+$ but not $[Fe,C_6,H_6,N]^+$ (both 148 amu) is observed.

[c]These losses are isobaric.

Scheme 2.

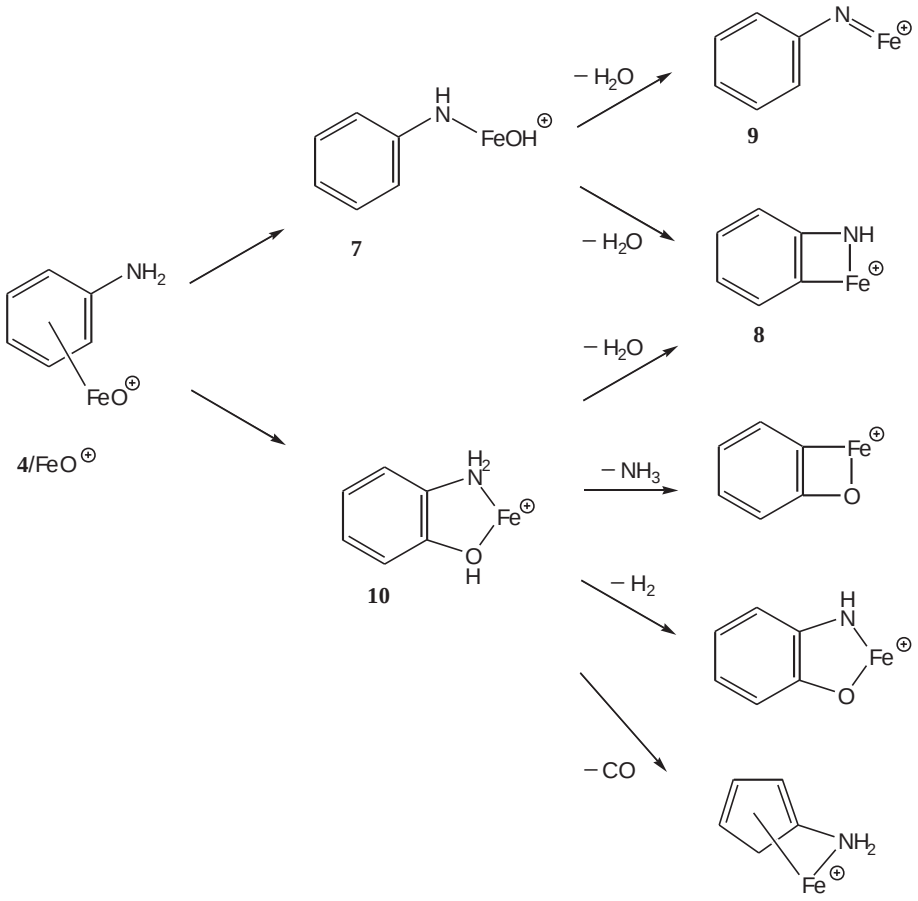

arene's *ortho* C—H(D) bonds. A possible mechanistic scenario is depicted in Scheme 2.

Accordingly, initial N—H bond activation (**4**/$FeO^+ \rightarrow$ **7**) is followed by cleavage of the aromatic C—H bond and loss of water, thus affording the metallacyclic species **8**. In analogy to the formation of $FeNH^+$ from FeO^+ and ammonia (15, 16), the significant loss of D_2O from **4a**/FeO^+ can be rationalized by the formation of iron phenylimine **9**. Considering the fact that bare FeO^+ cation is also capable of activating aromatic C—H bonds (11), it is obvious from the product distribution that coordination of FeO^+ at the hetero substitutent governs the reactivity. By reference to previous studies (11, 17, 18), we suggest that oxidation of the aromatic ring competes with attack at the amino group to yield

© 1999 NRC Canada

Scheme 3.

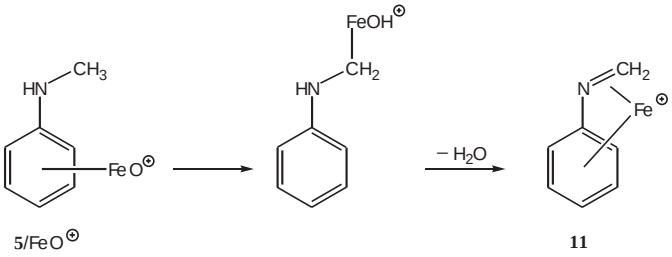

10, which is presumably the intermediate for the minor losses of CO, NH_3, and H_2. **10** may also contribute to dehydration (**10** → **8**).

Unimolecular dissociation of metastable **5**/FeO^+ is even more specific and affords loss of water exclusively. Clean shifts from H_2O to HDO losses for the labeled complexes **5a**/FeO^+ and **5b**/FeO^+ further reveal that dehydration can be ascribed to a formal 1,2-elimination of two hydrogen atoms by FeO^+, leading to formation of the imine/Fe^+ complex **11** concomitant with water (Scheme 3).

Thus, N-alkylation dramatically changes the overall course of the reaction compared to aniline/FeO^+ in that activation of aromatic C—H bonds is completely suppressed. Formation of **11** can indeed be regarded as the key step for the oxidative dealkylation of amines considering that aldimines readily hydrolyze in an aqueous environment.

Dehydration is also observed with the *N*,*N*-dimethylaniline complex **6**/FeO^+, but the major reaction corresponds to a loss of neutral FeOH. The expulsions of neutral D_2O and FeOD from **6c**/FeO^+ demonstrate that both reactions involve only the methyl groups. Formation of the imminium ion **12** (Scheme 4) can again be considered as the first step in the oxidative dealkylation of **7**.

Valuable mechanistic insight is obtained from the intramolecular kinetic isotope effect (k_H/k_D) associated with C—H(D) bond activation of **6**. For **6a**/FeO^+ the losses of FeOH and FeOD imply $k_H/k_D = 3.2 \pm 0.3$; similarly, dissociation of **6b**/FeO^+ leads to $k_H/k_D = 2.9 \pm 0.3$. Isotope effects of similar sizes are indicated by the ratio of H_2O and D_2O losses from **6a**/FeO^+ and **6b**/FeO^+; however, the formation of HDO from these complexes indicates some H–D equilibration and (or) competing mechanisms preceding dehydration. It is not our aim to unravel the mechanism of dehydration but, for the sake of consistency, a plausible scenario is included in Scheme 4, which assumes a formally dyotropic (19) rearrangement of an inserted species to a benzylmethylamide/$FeOH^+$ complex **13**, followed by β-hydride elimination. The H_2O:HDO:D_2O ratio obtained from **6a**/FeO^+ and **6b**/FeO^+ reflects the preference of H- over D-bond activation, followed by preferred formation of the internal conjugated double bond **14** rather than **15**.

With respect to the mechanistic debate outlined in the introduction, it is also useful to consider the isotope effect for the metal – free cation radical **6**$^{+\bullet}$. Thus, unimolecular losses of H$^\bullet$ and D$^\bullet$ comprise >95% of the total metastable ion decompositions of **6a**$^{+\bullet}$. Interestingly, the experimentally measured $k_H/k_D = 3.0 \pm 0.3$ associated with loss of H(D) atom is close to that found for **6a**/FeO^+ (vide supra).

Table 2. Branching ratios[a] of the neutrals lost in the ion–molecule reactions of (L)FeO^+ cations (L = none, benzene,

	-FeO	-FeOH	-FeOD	-L
6a + FeO^+	70	20	10	
6a + $(C_6H_6)FeO^+$	56	18	6	20
6a + $(C_6H_5CN)FeO^+$	58	21	8	13

[a]Normalized to a sum of 100%.

ICR MS

To examine the kinetic isotope effect for C—H(D) bond activation of **6** in more detail, the reactions of **6a** with bare and ligated (L)FeO^+ (L = none, C_6H_6, C_6H_5CN) were studied using the ICR technique. Unfortunately, all our attempts to generate (L)FeO^+ complexes with L being a donor-substituted arene have so far been unsuccessful. For example, while the reactions of N_2O with $(C_6H_6)Fe^+$ and $(C_6H_5CN)Fe^+$ can be used to form the corresponding (L)FeO^+ complexes (20), the same procedure results in oxidation of the substrates for L = C_6H_5OH and $C_6H_5OCH_3$.

Three types of reactions are observed in the ICR experiments (Table 2), as follows:

(*i*) Electron transfer from the amine to (L)FeO^+ to afford the cation radical **6a**$^{+\bullet}$. This process can be attributed to the low ionization energy, IE(**6**) = 7.1 eV as compared to IE(FeO) = 8.9 eV (unless noted otherwise, all thermochemical data are taken from ref. 21). Although the arene ligands C_6H_6 and C_6H_5CN in (L)FeO^+ are expected to lower the IE of iron oxide, ligation can obviously not compensate the intrinsic difference of the IEs.

(*ii*) The process of interest is the formal hydride (deuteride) transfer to afford the correspondingly labeled imminium ions via H^-_T and D^-_T, respectively, and neutral FeOH (FeOD).

(*iii*) For the ligated species, a formal ligand exchange of L against **6a** is observed. These processes can be rationalized by the higher binding energy of the electron-rich ligand **6a** compared to C_6H_6 and C_6H_5CN (22). Note, however, that the ions formed may not be intact **6a**/FeO^+, but rearranged species according to Scheme 4.

The kinetic isotope effects associated with formal H^-_T and D^-_T from **6a** to FeO^+ show an interesting trend, i.e., an increase from $k_H/k_D = 2.0 \pm 0.2$ for bare FeO^+, to $k_H/k_D = 2.6 \pm 0.2$ for L = C_6H_5CN, and $k_H/k_D = 3.0 \pm 0.2$ for L = C_6H_6. This trend indicates that the size of the isotope effect can be varied by tuning the electronic properties of the ligand (C_6H_6 vs. C_6H_5CN) and also depends on the overall size of the system (FeO^+ vs. (L)FeO^+).

Discussion

In this section, let us try to interpret the gas-phase data with respect to the mechanistic controversy on amine dealkylation by cytochrome P-450 as outlined in the introduction. Compared to the reactions of FeO^+ with other arenes (7, 11, 14–18), the chemistry of aniline and its N-methyl derivatives is governed by coordination of the metal oxide to nitrogen ("docking"). In contrast to the enzymatic reactions, no hint for N—O bond formation is found in the gas-phase model system. Upon N-methylation, only these alkyl groups are attacked specifically by FeO^+. For *N*-methylaniline and

© 1999 NRC Canada

Scheme 4.

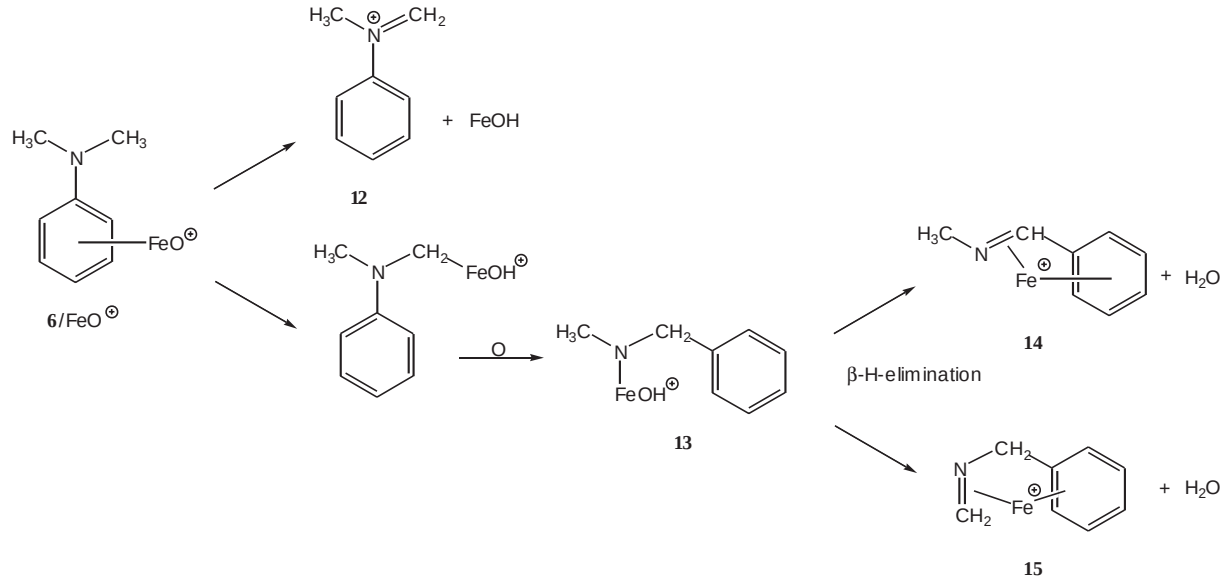

N,*N*-dimethylaniline, the reaction intermediates can be ascribed to the key steps towards the oxidative dealkylation of the amines.

Interestingly, the kinetic isotope effects associated with C—H(D) bond activation of metastable **6a**/FeO^+ and **6b**/FeO^+ are lower than or equal to that of unimolecular hydrogen atom loss from the radical cation $\mathbf{6a}^{+\bullet}$ itself. This result indicates that in the gas phase, the reaction most likely follows path (b) in Scheme 1, i.e., initial electron transfer from the amine to the iron oxo unit followed by C—H bond cleavage in the amine cation radical. This interpretation is further corroborated by the fact that electron transfer from the amine to (L)FeO^+ is observed as an efficiently competing process. In this comparison, it has to be kept in mind that the gas-phase reactions sample species generated with quite a different internal energy content than reactions occurring in the condensed phase. Thus, in the diluted gas phase any energy transfer to media is impossible. Moreover, the species under study carry real Coulomb charges that are not shielded by solvation, additional ligands, counterions, etc. Let us illustrate these fundamental aspects by referring to the differences in the reactions of metastable **6a**/FeO^+ in the sector instrument compared to the ion–molecule reaction of bare FeO^+ with **6a** under ICR conditions. For metastable **6a**/FeO^+ and **6b**/FeO^+, losses of FeOH and FeOD with an average isotope effect of $k_H/k_D = 3.0 \pm 0.3$ are observed, as well as loss of water. In contrast, reaction of bare FeO^+ with **6a** gives rise to the amine cation radical via electron transfer along with losses of neutral FeOH and FeOD, having a smaller isotope effect of $k_H/k_D = 2.0 \pm 0.2$. Dehydration is not observed under these conditions. The reason for these seemingly inconsistent results is simply the different starting conditions in both experiments (23). Thus, under ICR conditions bare FeO^+ interacts with the substrate thereby deliberating the full complexation energy $D(\mathbf{6} - FeO^+)$; we use $D(\mathbf{6} - FeO^+) \approx D(\mathbf{4} - Fe^+) = 54$ kcal/mol (22) for lack of other data. In contrast, metastable **6**/FeO^+ examined in sector MS is formed in a chemical ionization plasma, which allows for some collisional cooling. Moreover, in the experiments only those metastable ions are sampled which undergo unimolecular decay in the microsecond (μs) regime. Therefore, it is fair to anticipate that the metastable ions formed upon chemical ionization in the sector MS have a lower average internal energy than the encounter complexes formed under ICR conditions. Consequently, the lifetimes of the encounter complexes and the isotope effects are larger with sector MS. Increase of ion lifetimes also explains why loss of water is observed for the metastable ions, because this obviously requires a more complex mechanism than simple ET or hydrogen atom abstraction occurring under ICR conditions. This line of reasoning is nicely corroborated by the increase of the isotope effects for the ligated (L)FeO^+ ions under ICR conditions. Thus, the high excess energy gained upon complexation of **6a** with (L)FeO^+ can be distributed over various degrees of freedom for L = C_6H_6 and C_6H_5CN, resulting in a higher H/D selectivity than for bare FeO^+. The fact that the KIE is larger for L = C_6H_6 than for L = C_6H_5CN and unligated FeO^+ further suggests a dependence on the electronic properties of the ligands. Thus, the size of the KIE is proportional to the ability to compensate the electron deficiency of bare FeO^+ by a donating ligand. However, the small KIE of bare FeO^+ results from a combination of size and electronic effects. Moreover, as the range of systems studied is very limited, the interpretation outlined above should only be regarded as a qualitative orientation.

Finally, it is worth considering the stability of the putative aminoalkyl radical **2** in somewhat more detail. Unfortunately, not many thermochemical data for α-aminoalkyl radicals are available (24). However, the ionization energy of the *N*,*N*-dimethylaminomethyl radical is rather low (IE = 5.2 eV) (24*e*). The IE of the corresponding *N*-methyl-*N*-phenylaminomethyl radical **2** (Scheme 1) may be even lower due to stabilization by the aromatic substituent. Note, however, that there exists a subtle balance of radical and ion stabilization in this case that has not been examined so far. Notwithstanding, the mere range of the IE of the putative

© 1999 NRC Canada

radical **2**, in the order of 5 eV, questions whether this particular radical is stable in aqueous media at all,[2] with respect to ionization to the imminium ion.

Conclusions

The reactions of FeO^+ with aniline and its N-methyl derivatives are governed by initial docking at the nitrogen atom. A feature of the gas-phase reaction of *N*,*N*-dimethylaniline with bare and ligated FeO^+ is a formal hydride transfer to yield neutral FeOH and the *N*-methyl-*N*-phenylformimine cation, which is a central intermediate in an N-dealkylation process in the condensed phase. The fact that the intramolecular KIE associated with hydride transfer to FeO^+ is smaller than or equals that for unimolecular $H^\bullet$ loss from the *N*,*N*-dimethylaniline cation radical under various experimental conditions suggests that an electron transfer might be the initial elementary step in our gas-phase model system. Besides, the present study demonstrates that the KIE of a given substrate is affected by the electronic environment of the iron oxide core, implying that the interpretation of KIEs for *N*-dealkylation processes derived from certain enzymes or model systems is not necessarily valid for others.

Experimental

In this study, two different mass spectrometric approaches were used. (*i*) Unimolecular reactions of metastable arylamine/FeO^+ complexes were examined by sector mass spectrometry. (*ii*) Ion–molecule reactions of bare and ligated $(L)FeO^+$ ions (L = none, C_6H_6, and C_6H_5CN) were studied with Fourier transform ion cyclotron resonance (ICR) mass spectrometry. This combined approach was chosen for two major reasons. At first, arylamines have a significant memory effect in high-vacuum devices due to adsorption in the device itself as well as in the inlet systems. The ICR instrument is particularly sensitive to this effect and even overnight bakeout does not suffice to completely remove the substrates. Secondly, some of the deuterium-labeled compounds applied in this study are sensitive to H–D exchange with themselves, upon contact with the walls of the inlet systems or the machinery, as well as with background gases (i.e., moisture). For example, pure N-[D_2]-labeled aniline can easily be prepared in large quantities, but once a micromole (μmol) sample is introduced into the machinery, it can undergo H–D exchange with surface protons or intra-/intermolecular exchange with the labile ring protons in *ortho* and *para* positions catalyzed by acidic surfaces. Again, the ICR is more sensitive to this effect. The superior performance of the sector MS in both respects is basically due to a mass-flow effect, because the operating pressure (ca. 10^{-4} mbar; 1 bar = 100 kPa) is about four orders of magnitude higher than the typical ICR conditions (ca. 10^{-8} mbar). Thus, the reactions of aniline, its N-methylated derivatives, and the corresponding deuterium-labeled substrates were screened using sector MS, and only the reactions of the most decisive *N*-methyl-*N*-([D_3]-methyl)aniline with bare and ligated FeO^+ were examined with the ICR technique. The prime advantages of ICR MS compared to chemical ionization in sector MS are that it provides full control of the ions' history and a narrow distribution of their internal energy, i.e., the reactions occur under well-defined conditions at ambient temperature.

Sector MS

Most experiments were performed with a modified VG ZAB/HF/AMD four-sector mass spectrometer of BEBE configuration (B stands for magnetic and E for electric sector), which has been described previously (25). Briefly, the metal complexes were generated in a chemical ionization source (CI, repeller voltage ca. 0 V) by 100 eV electron bombardment of an approximately 20:1:1 mixture of N_2O, $Fe(CO)_5$, and the corresponding arylamine. The ions were accelerated to 8 keV kinetic energy and mass selected by means of B(1)/E(1) at a resolution of $m/\Delta m \approx 4000$. Unimolecular fragmentations of metastable ions occurring in the field-free region preceding B(2) were recorded by scanning this sector. All spectra were accumulated and processed on-line with the AMD–Intectra data system; 10–30 scans were averaged to improve the signal-to-noise ratio. Kinetic isotope effects were determined from the peak ratios for isotopologous losses (e.g., loss of FeOH versus loss of FeOD) and are reported as the average of at least three independent measurements with an error of ±10%. Due to the relatively high pressure that prevails in the CI source, efficient collisional cooling of the ions can be assumed, such that excited states of the metal species (26) are not likely to participate in the reactions observed (27).

ICR MS

The experiments were performed with a Spectrospin CMS 47X FT ICR mass spectrometer, which has been described previously (ref. 28; for an introduction to FT ICR mass spectrometry, see ref. 29). Briefly, Fe^+ ions were generated via laser desorption/laser ionization by focusing the beam of a Nd:YAG laser (Spectron Systems, λ = 1064 nm) onto an iron target. The ions were extracted from the source, transferred into the analyzer cell by a system of electrostatic potentials and lenses, decelerated, and trapped in the field of a superconducting magnet (maximum field strength 7.05 T). Prior to ion–molecule reactions, the $^{56}Fe^+$ isotope was mass selected using the FERETS technique (30). FeO^+ was generated by pulsing in N_2O, thermalized with pulsed-in argon, and subsequently mass selected (31). Ligated $(L)FeO^+$ ions were generated by the following sequence (20). At first, mass-selected Fe^+ was reacted with a pulsed-in ca. 10:1 mixture of argon and the desired ligand L (L = C_6H_6, C_6H_5CN). Subsequently, an excess of N_2O was pulsed in to yield the corresponding $(L)FeO^+$ species, which were then mass selected using FERETS and reacted with the substrate. Note that the inverse sequence, i.e., ligating FeO^+ with pulsed-in L does not work, because the reactive FeO^+ cation simply oxidizes the ligands (7). As neutral substrate, only *N*-methyl-*N*-([D_3]-methyl)aniline was used in this study with typical pressures of $(5–15) \times 10^{-9}$ mbar. Ionic reaction products were monitored as a function of reaction time and reactant pressure. The data were accumulated and processed by

[2] The related *N*,*N*-dimethylaminomethyl radical is only observed as a transient intermediate in aqueous solution (24*b* and 24*c*).

© 1999 NRC Canada

means of an ASPECT 3000 minicomputer. Product branching ratios are reported within experimental errors of ±10%.

Substrates

The unlabeled arylamines were commercially available and used without further purification. N-[D_3]-Methylation was achieved by treatment of the corresponding anilines with [D_3]-methyliodide. [*N*,*N*-D_2]-Aniline and [*N*-D]-methylaniline were made by repeated H–D exchange of the undeuterated compounds with CH_3OD at room temperature. [*N*,*N*-2,4,6–D_5]-Aniline was prepared by subsequent H–D exchange of aniline with D_2O catalysed by D_3PO_4 at 100°C, followed by liberation of the base with concentrated NaOH solution (32). [3,5-D_2]-Aniline was made by D–H exchange of [2,3,4,5,6-D_5]-aniline in an excess of water catalyzed by diluted H_2SO_4 (32). [2,3,4,5,6-D_5]-Aniline was obtained in two steps via nitration of [D_6]-benzene and reduction of [2,3,4,5,6-D_5]-nitrobenzene with $NaBH_4$ (33). All labeled compounds were purified by chromatography and characterized by ^{1}H NMR.

Acknowledgements

We are grateful to the Volkswagen Stiftung, the Deutsche Forschungsgemeinschaft, and the Fonds der Chemischen Industrie for continuous financial support. M.B. acknowledges the Stiftung Stipendien – Fonds des Verbandes der Chemischen Industrie for a Kékulé scholarship. We thank Professor J.P. Dinnocenzo, Rochester, for his support and C. Trage, Berlin, for the synthesis of [3,5-D_2]-aniline.

References

1. (*a*) F.P. Guengerich. FASEB J. **6**, 667 (1992); (*b*) P.R. Ortiz de Montellano (*Editor*). Cytochrome P-450; structure, mechanism, and biochemistry. 2nd ed. Plenum Press, New York. 1995.
2. (*a*) W.-D. Woggon. Top. Curr. Chem. **184**, 39 (1996); (*b*) M. Sono, M.P. Roach, E.D. Coulter, and J.H. Dawson. Chem. Rev. **96**, 2841 (1996).
3. (*a*) J.P. Dinnocenzo, S.B. Karki, and J.P. Jones. J. Am. Chem. Soc. **115**, 7111 (1993); (*b*) S.B. Karki and J.P. Dinnocenzo. Xenobiotica, **25**, 711 (1995); (*c*) S.B. Karki, J.P. Dinnocenzo, J.P. Jones, and K.R. Korzekwa. J. Am. Chem. Soc. **119**, 5069 (1997).
4. F.P. Guengerich, O. Okazaki, Y. Seto, and T.L. MacDonald. Xenobiotica, **25**, 689 (1995).
5. (*a*) Y. Goto, Y. Watanabe, S. Fukuzumi, J.P. Jones, and J.P. Dinnocenzo. J. Am. Chem. Soc. **120**, 10762 (1998); (*b*) M. Bietti, A. Cuppoletti, C. Dagostin, C. Florea, C. Galli, P. Gentili, H. Petride, and C.R. Caia. Eur. J. Org. Chem. 2425 (1998).
6. S. Shaik, M. Filatov, D. Schröder, and H. Schwarz. Chem. Eur. J. **4**, 193 (1998).
7. D. Schröder and H. Schwarz. Angew. Chem. **107**, 2023 (1995); Angew. Chem. Int. Ed. Engl. **34**, 1973 (1995).
8. B.K. Hawkins and J.H. Dawson. J. Am. Chem. Soc. **114**, 3547 (1992).
9. (*a*) M.F. Ryan, D. Stöckigt, and H. Schwarz. J. Am. Chem. Soc. **116**, 9565 (1994); (*b*) A. Fiedler, D. Schröder, S. Shaik, and H. Schwarz. J. Am. Chem. Soc. **116**, 10734 (1994).
10. D. Schröder and H. Schwarz. Angew. Chem. **102**, 1468 (1990); Angew. Chem. Int. Ed. Engl. **29**, 1433 (1990).
11. D. Schröder and H. Schwarz. Helv. Chim. Acta, **75**, 1281 (1992).
12. (*a*) J. Schwarz and H. Schwarz. Helv. Chim. Acta, **78**, 1013 (1995); (*b*) J. Schwarz, R. Wesendrup, D. Schröder, and H. Schwarz. Chem. Ber. **129**, 1463 (1996).
13. D. Schröder. Dissertation D83, Technische Universität, Berlin. 1992.
14. D. Schröder, J. Hrušák, and H. Schwarz. Helv. Chim. Acta, **75**, 2215 (1992).
15. S.W. Buckner, J.R. Gord, and B.S. Freiser. J. Am. Chem. Soc. **110**, 6606 (1988).
16. M. Brönstrup, I. Kretzschmar, D. Schröder, and H. Schwarz. Helv. Chim. Acta, **81**, 2348 (1998).
17. H. Becker, D. Schröder, W. Zummack, and H. Schwarz. J. Am. Chem. Soc. **116**, 1096 (1994).
18. D. Schröder, W. Zummack, and H. Schwarz. Organometallics, **12**, 1449 (1993).
19. (*a*) M.T. Reetz. Tetrahedron, **29**, 2189 (1973); (*b*) H. Schwarz, C. Wesdemiotis, and M.T. Reetz. J. Organomet. Chem. **161**, 153 (1978); (*c*) B. Ciommer, H. Schwarz, A. Maaroufi, M.T. Reetz, and K. Levsen. Z. Naturforsch. B: Anorg. Chem. Org. Chem. **36B**, 771 (1981).
20. (*a*) D. Stöckigt and H. Schwarz. Chem. Ber. **127**, 2499 (1994); (*b*) Liebigs Ann. 429 (1995).
21. S.G. Lias, J.F. Liebmann, J.L. Holmes, R.D. Levin, and W.G. Mallard. J. Phys. Chem. Ref. Data, **17**, 695 (1988).
22. K. Schroeter, R. Wesendrup, and H. Schwarz. Eur. J. Org. Chem. 565 (1998).
23. C.A. Schalley, R. Wesenrup, D. Schröder, T. Weiske, and H. Schwarz. J. Am. Chem. Soc. **117**, 7711 (1995).
24. (*a*) Y.L. Chow, W.C. Danen, S.F. Nelsen, and D.H. Rosenblatt. Chem. Rev. **78**, 243 (1978); (*b*) S. Das and C. v. Sonntag. Z. Naturforsch. B: Anorg. Chem. Org. Chem. **41B**, 505 (1986); (*c*) S. Das, M.N. Schuchmann, H.-P. Schuchmann, and C. v. Sonntag. Chem. Ber. **120**, 319 (1987); (*d*) D.A. Armstrong, A. Rauk, and D. Yu. J. Am. Chem. Soc. **115**, 666 (1993); (*e*) S.A. Shaffer, F. Tureček, and R.L. Cerny. J. Am. Chem. Soc. **115**, 12117 (1993); (*f*) G.H. Loew and Y.-T. Chang. Int. J. Quantum Chem. Quantum Chem. Symp. **27**, 815 (1993).
25. (*a*) R. Srinivas, D. Sülzle, T. Weiske, and H. Schwarz. Int. J. Mass Spectrom. Ion Processes, **107**, 369 (1991); (*b*) R. Srinivas, D. Sülzle, W. Koch, C.H. DePuy, and H. Schwarz. J. Am. Chem. Soc. **113**, 5970 (1991).
26. P.B. Armentrout. Science (Washington, D.C.), **251**, 175 (1991).
27. (*a*) C. Schulze and H. Schwarz. Chimia, **42**, 297 (1988); (*b*) K. Eller, W. Zummack, H. Schwarz, L.M. Roth, and B.S. Freiser. J. Am. Chem. Soc. **113**, 833 (1991); (*c*) C.A. Schalley, D. Schröder, and H. Schwarz. J. Am. Chem. Soc. **116**, 11 089 (1994).
28. (*a*) K. Eller, W. Zummack, and H. Schwarz. J. Am. Chem. Soc. **112**, 621 (1990); (*b*) K. Eller and H. Schwarz. Int. J. Mass Spectrom. Ion Processes, **93**, 243 (1989).
29. A.G. Marshall, C.L. Hendrickson, and G.S. Jackson. Mass Spectrom. Rev. **17**, 1 (1998).
30. R.A. Forbes, F.H. Laukien, and J. Wronka. Int. J. Mass Spectrom. Ion Processes, **83**, 23 (1988).
31. D. Schröder, H. Schwarz, D.E. Clemmer, Y. Chen, P.B. Armentrout, V.I. Baranov, and D.K. Böhme. Int. J. Mass Spectrom. Ion Processes, **161**, 175 (1997).
32. A.F. Thomas. *In* Deuterium labeling in organic chemistry. Appleton–Century–Crofts, New York. 1971. p. 131.
33. T. Neilson, H.C.S. Wood, and A.G. Wylie. J. Chem. Soc. 371 (1962).

© 1999 NRC Canada

The role of the medium in solvent isotope effects on serine protease action

Jiaher Tian, Jue Tan, K. Barbara Schowen, and Richard L. Schowen

Abstract: The hydrolysis of *N*-carbobenzyloxyaminoacyl-*O*-*p*-nitrophenyl esters derived from L-leucine, L-phenylalanine, and L-tryptophan, with catalysis by bovine pancreatic α-chymotrypsin at pH 7.00 at 25.00°C in water containing acetonitrile from 15.0% to 60% (v/v), exhibits values of k_{cat}/K_m that decrease as the 34th to 36th power of the activity of water and values of k_{cat} that are essentially constant. Solvent isotope effects $k_{cat}(H_2O)/ k_{cat}(D_2O)$ range from 2.1 to 3.0 with proton inventories (dependences of $k_{cat}(n)$ on n, the atom fraction of deuterium in the water component of the solvent) that are linear, regardless of the amount of acetonitrile in the medium. The isotope effect on k_{cat} thus appears to arise from a single transition-state site and to be little affected by the medium. Contributions from the medium to solvent isotope effects on enzymic reactions clearly exist but appear not to be detectable in the deacylation reactions of acyl chymotrypsins.

Key words: solvent isotope effects, proton inventories, medium effects, enzyme catalysis, α-chymotrypsin.

Résumé : Pour les réactions d'hydrolyse des esters *N*-carbobenzyloxyaminoacyl-*O*-*p*-nitrophénylés dérivés de la L-leucine, de la L-phénylalanine et du L-tryptophane catalysées par l'α-chymotrypsine pancréatique bovine, à un pH de 7,0, à 25,00°C, dans de l'eau contenant de l'acétonitrile à des concentrations allant de 15,0 à 60% (v/v), les valeurs de k_{cat} sont pratiquement constantes alors que celles de k_{cat}/K_m diminuent en fonction de l'activité de l'eau portée à des puissances allant de 34 à 36. Les effets isotopiques de solvant, $k_{cat}(H_2O)/k_{cat}(D_2O)$ vont de 2,1 à 3,0 avec des inventaires de proton (dépendances de $k_{cat}(n)$ sur n, la fraction atomique de deutérium dans la composante aqueuse du solvant) qui sont linéaires, quelle que soit la quantité d'acétonitrile dans le milieu. Il semble donc que les effets isotopiques sur k_{cat} découlent d'un seul site de l'état de transition et qu'ils ne sont pas très affectés par le milieu. Il est évident qu'il existe des contributions du milieu sur les effets isotopiques du solvant sur des réactions enzymatiques; ils ne semblent toutefois pas décelables dans les réactions de désacylations des acyl chymotrypsines.

Mots clés : effets isotopiques du solvant, inventaires de proton, effets de solvant, catalyse enzymatique, α-chymotrypsine.

[Traduit par la Rédaction]

Introduction

Professor A.J. Kresge is one of a small number of scientists who contribute to the shaping of research fields not only through original creations, but also through their role as critics of their own and other work. Kresge has written a number of reviews that often incorporate original work and have had great influence. A review on solvent isotope effects in mixtures of protium and deuterium oxides (1) was the subject of a seminar presented to our research group by Cherie Behn in mid-1967. Its clarity, particularly in illustrating the applications of a form of the Gross–Butler equation developed by Kresge, was so appealing that we immediately set about using the technique in studies of reactions of small molecules (2) and later of enzymes (3). In the vastly simplified version favored by us, the technique has come to be called the *proton-inventory method* (3).

The first application of the method to catalysis by an enzyme, the hydrolysis of *p*-nitrophenyl acetate by α-chymotrypsin, showed that a plot of k_{cat} against the atom fraction, n, of deuterium in mixed isotopic solvents was linear (4). We took this result to indicate that the solvent isotope effect of 2.4 arose from a single site and that the then-fashionable "charge-relay system" was therefore not in operation in the transition state **1** for the rate-limiting deacylation of acetyl-α-chymotrypsin (no change in binding at the question mark as reactant state becomes transition state).

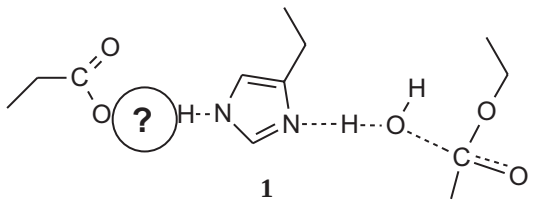

1

The entire isotope effect was therefore taken to arise from the single protonic site bridging between water and histidine. Although structure **1** portrays the transition state for forma-

Received November 17, 1998.

This paper is dedicated to Jerry Kresge in recognition of his many achievements in chemistry.

J. Tian, J. Tan, K.B. Schowen,[1] and R.L. Schowen. Department of Chemistry and Higuchi Biosciences Center, University of Kansas, Lawrence, KS 66045, U.S.A.

[1]Author to whom correspondence may be addressed. Telephone: (785) 864-4614. Fax: (785) 864-5349. e-mail: bschowen@ukans.edu

© 1999 NRC Canada

Fig. 1. Dependence of the logarithm of the rate constant k_{cat}/K_m on the logarithm of the activity of water in aqueous acetonitrile solutions for the action of α-chymotrypsin on three substrates. Open squares represent data for *Z*-Phe-ONp at 25.00 ± 0.05°C, pH 7.00 (0.100 M phosphate buffer) in mixtures from 15.1% (v/v) acetonitrile to 60.0% (v/v) acetonitrile. Open circles represent data for *Z*-Trp-ONp at 25.00 ± 0.05°C, pH 7.00 (0.100 M phosphate buffer) in mixtures from 15.0% (v/v) acetonitrile to 49.8% (v/v) acetonitrile. Both data sets can be described by the same linear function, suggesting that the rate in pure water, $a_w = 1$, is diffusional and that the rate decreases in acetonitrile–water mixtures as the 34th power of the activity of water. Filled circles represent data for *Z*-Leu-ONp under the same conditions (mixtures from 15.2% (v/v) acetonitrile to 59.9% (v/v) acetonitrile. They are described by a similar function with a smaller rate constant in pure water and a slightly larger exponent for the activity of water.

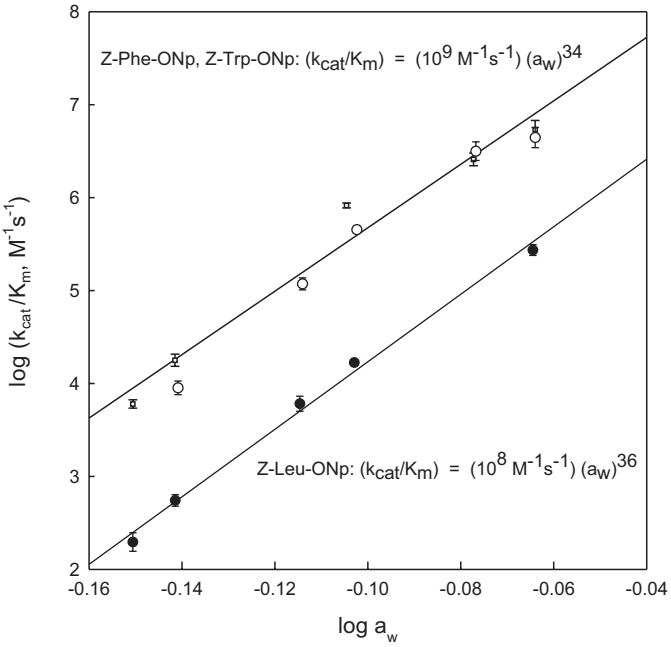

tion of the tetrahedral intermediate, that for decomposition may also contribute to determining the rate. The question of which of these steps is rate limiting does not influence the isotope-effect arguments.

Kresge immediately pointed out (5) the ambiguity of this interpretation, and later expanded on the point with the inclusion of experimental measurements on an enzyme-catalyzed reaction and on host–guest complexation (6, 7). A linear dependence such as we observed (eq. [1]) and attributed to transition-state fractionation of magnitude ϕ_1 at the histidine–water bridge could in fact (eq. [2]) be the result of cancellation between a second-site contribution (of magnitude ϕ_2, for example, at the question mark in **1**) and a medium effect Z^n in the opposite direction.

$$[1] \qquad k_n = k_0 (1 - n + n\phi_1)$$

$$[2] \qquad k_n = k_0 (1 - n + n\phi_1) (1 - n + n\phi_2) Z^n$$

Fig. 2. Dependence of the logarithm of the rate constant k_{cat} on the logarithm of the activity of water in aqueous acetonitrile solutions for the action of α-chymotrypsin on three substrates. Conditions are the same as in Fig. 1. The lines are drawn through the mean values (41 s^{-1} for the Phe substrate, 14 s^{-1} for the Trp substrate, 2.5 s^{-1} for the Leu substrate).

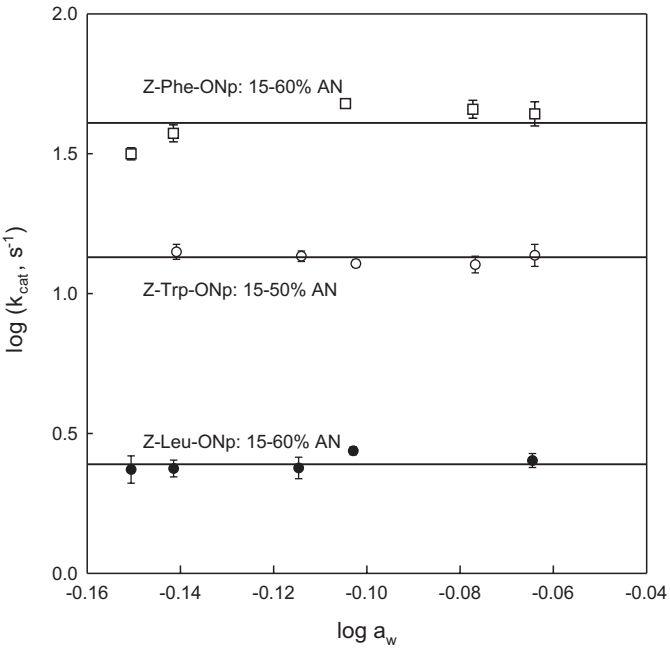

We have now returned to this matter and present herein measurements in which acetonitrile is used to perturb the environment in which deacylation of various acyl-α-chymotrypsins is occurring. The use of organic solvents in the perturbation of enzyme systems is now a well-developed field in terms of both structural and dynamic information (8). The information now presented enables further consideration of the number of sites that are likely to contribute to stabilization of the transition state for enzymic deacylation.

Results

Kinetics of α-chymotrypsin-catalyzed hydrolysis of *N*-carbobenzyloxy-L-aminoacyl-*p*-nitrophenoxides (*Z*-L-aminoacyl-ONp) in mixtures of acetonitrile and protium oxide

The hydrolysis (eq. [3]) of the activated L-amino-acid esters *Z*-Leu-ONp, *Z*-Phe-ONp, and *Z*-Trp-ONp, where Leu means L-leucyl (R = $CH_2CH(CH_3)_2$ in eq. [3]), Phe means L-phenylalanyl (R = $CH_2C_6H_5$ in eq. [3]), and Trp means L-tryptophanyl (R = CH_2-indolyl in eq. [3]), *Z* means $C_6H_5CH_2OCO$, and ONp means O-*p*-nitrophenyl, in aqueous solutions containing from 15.0 to 60% (v/v) acetonitrile at pH 7.00 (phosphate buffer) and 25.0°C obeys the Michaelis–Menten kinetic law (eq. [4], where *v* is the initial velocity, e_0 is the total enzyme concentration, and [S] is the concentration of substrate). The values of the two rate constants k_{cat} and k_{cat}/K_m have been tabulated and are available as Supplementary Material.[2] The values are presented graphically in

[2] Supplementary material may be purchased from: The Depository of Unpublished Data, Document Delivery, CISTI, National Research Council of Canada, Ottawa, ON K1A 0S2, Canada.

© 1999 NRC Canada

Fig. 3. Proton inventories (rate constant vs. atom fraction of deuterium in mixed isotopic solvents) for k_{cat}, effectively the rate constant for deacylation of each of the three acyl α-chymotrypsins indicated. Conditions are the same as in Fig. 1. The symbols indicate the percentage (v/v) of acetonitrile in the medium: circles (15.1 for the Phe case, 14.8 for Trp, 15.9 for Leu); squares (20.1 for Phe, 19.8 for Trp, 20.0 for Leu); triangles (35.4 for Phe, 35.3 for Trp, 30.3 for Leu); and inverted triangles, 50.1 for Trp. The straight lines are the linear least-squares fits of all data on each plot.

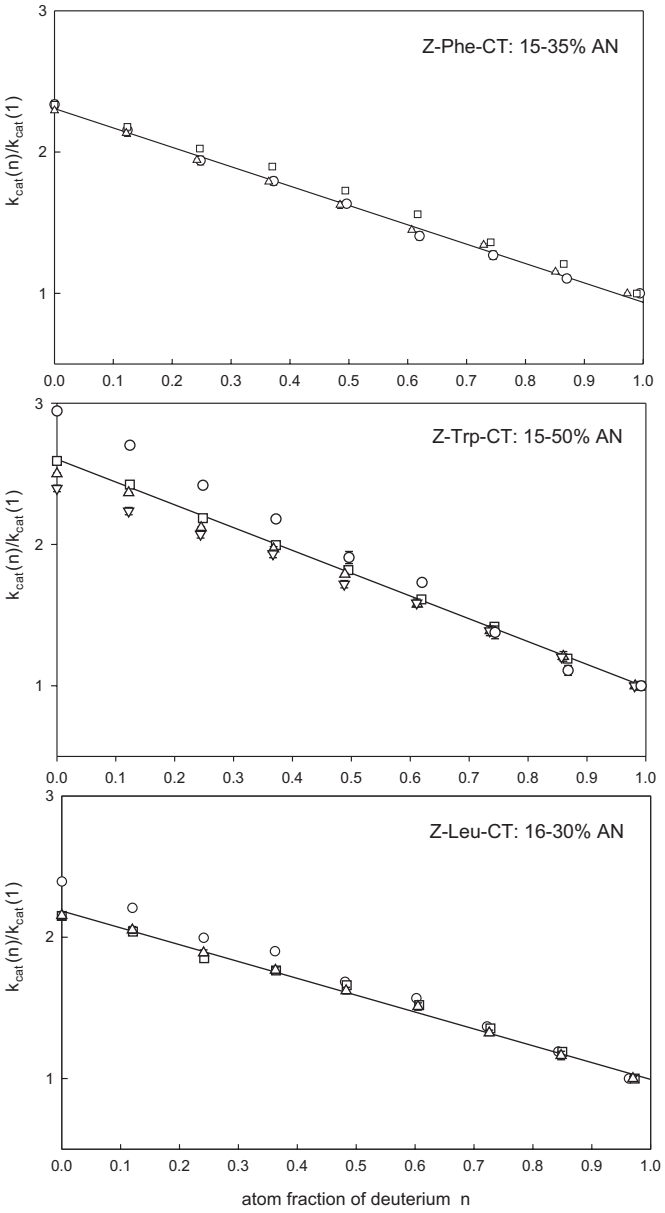

Figs. 1 and 2 as plots versus the activity of water in acetonitrile–water mixtures. Values of the activity of water were obtained as described in the experimental section. Generally consistent results were obtained for *Z*-Phe-ONp in aqueous solutions containing 20%, 50%, and 80% (v/v) acetonitrile at pH 8.00 (triethylamine buffer) at 25.2°C. The values of k_{cat} (s^{-1}) were 59 ± 3 (20%), 48 ± 2 (50%), and 12 ± 1 (80%).

[3] $C_6H_5CH_2OCONHCHRCOONp + H_2O \rightarrow C_6H_5CH_2OCONHCHRCOO^- + {}^-ONp + 2\ H^+$

[4] $v/e_0 = k_{cat}\ [S] / (K_m + [S])$

Isotope effects and proton inventories for k_{cat} in the α-chymotrypsin-catalyzed hydrolysis of *N*-carbobenzyloxy-L-aminoacyl-*p*-nitrophenoxides (*Z*-L-aminoacyl-ONp) in mixtures of acetonitrile and protium oxide and deuterium oxide

The values of the rate constants at saturating concentrations of the substrate in binary mixtures of protium and deuterium oxide are given in the Supplementary Material.[2] The values are presented graphically in Fig. 3 as plots versus *n*, the atom fraction of deuterium in the isotopic solvent mixtures. In mixtures of acetonitrile and water, *n* refers to the atom fraction of deuterium in the aqueous component alone.

Discussion

Dependence of k_{cat} and k_{cat}/K_m on the water content of acetonitrile–water mixtures

The results of Figs. 1 and 2 show that the rate constant k_{cat}/K_m is greatly dependent on the activity of water in acetonitrile mixtures in the range of 15–60% acetonitrile, while the rate constant k_{cat} is unaffected by the activity (or the molarity) of water in these mixtures. This result seems counterintuitive in terms of the well-established mechanism of action of the serine proteases (9), as shown in Fig. 4. The overall reaction has two stages, acylation of the enzyme by the substrate to form an acyl–enzyme intermediate, and deacylation of the acyl–enzyme intermediate by water to regenerate free enzyme, completing the catalytic cycle. The kinetics, also illustrated in Fig. 4, can be described by the two rate constants k_{cat}/K_m and k_{cat}.

The overall second-order rate constant k_{cat}/K_m leads from free reactants through the transition state for acylation of the enzyme, and can thus be considered the rate constant for the acylation reaction. Although the stoichiometry of this reaction is not explicitly dependent on the amount of water in the medium, the rate constant k_{cat}/K_m nevertheless is a sharp function of the amount of water, decreasing as the 34th to the 36th power of the activity of water. From 15% acetonitrile to 60% acetonitrile, the value of k_{cat}/K_m falls by a factor of 900 (Phe substrate), 500 (Trp substrate, not studied at 60% acetonitrile — the ratio given is for 50% acetonitrile), and 1400 (Leu substrate).

The first-order rate constant k_{cat} leads in principle from either or both of the enzyme complexes E:RCOX (enzyme–substrate complex) and ECOR (acyl–enzyme) to the transition state(s) following them. However, with such reactive esters as the *p*-nitrophenyl species used here, acylation of the enzyme (rate constant k_3) tends to be much faster than acyl transfer to water (rate constant k_5), so that k_{cat} is approximately equal to k_5 and is thus the rate constant for the deacylation reaction. The stoichiometry of this reaction is explicitly dependent on the first power of the water concentration, yet the rate constant varies little and unsystematically over the range 15–60% acetonitrile. The molarity of water varies from 46.9 M in 15% acetonitrile to 22.2 M in 60% acetonitrile, or by a factor of 2.1. The values of k_{cat} in

© 1999 NRC Canada

Fig. 4. Simple mechanistic scheme for the serine proteases, including α-chymotrypsin. The kinetics is shown in the center. The reaction proceeds through an initial acylation stage (right side), the effective rate constant for which is k_{cat}/K_m. The acyl enzyme (bottom) then reacts with water to go through the deacylation stage (left side) for which (in the case of reactive esters where $k_3 >> k_5$) the effective rate constant is k_{cat}.

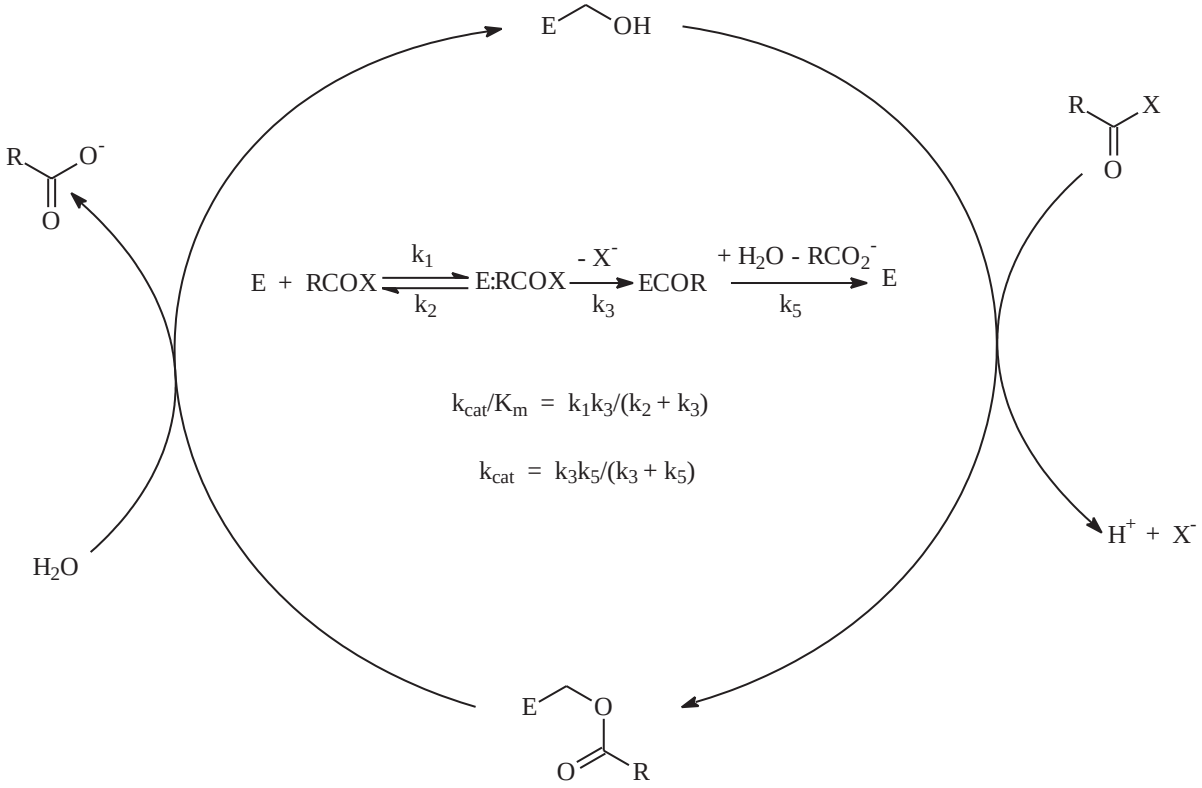

these limiting solvents are 44 and 32 s^{-1} (Phe substrate); 14 and 14 s^{-1} (Trp substrate, not studied at 60% acetonitrile — the last value is thus for 50% acetonitrile); 2.5 and 2.4 s^{-1} (Leu substrate). For the Phe substrate at pH 8, k_{cat} is 59 s^{-1}at 50% acetonitrile but does decline to 12 s^{-1} at 80% acetonitrile. Clearly the variation in k_{cat} is much smaller than even the stoichiometric first-power prediction (at least below 60% acetonitrile) and greatly smaller than the factors of 500–1400 seen for k_{cat}/K_m.

Simple, speculative explanations of the results can be given. The large factor by which the value of k_{cat}/K_m decreases may be a result of two contributing causes. First, organic solvents such as acetonitrile can compete for the recognition sites of serine proteases and thus may act as competitive inhibitors that increase the work required for binding of the substrate and passage through the transition state for acylation. Second, considerable hydration of the enzyme structure may be required to maintain the flexibility necessary for admission of the substrate to the active site and subsequent reaction.

The fact that k_{cat} is independent of the water content of the medium may result from the strong binding of a nucleophilic water molecule in the active site, thus assuring that all enzyme molecules possess the nucleophilic water regardless of the composition of the external medium.

Proton inventories in mixtures of water and acetonitrile

The data plotted in Fig. 3 show that, with two exceptions, the solvent isotope effects and proton inventories for deacylation of the acyl enzymes formed from the Phe, Trp, and Leu substrates are very similar in various acetontrile–water mixtures. For media from 15 to 35% acetonitrile, the *Z*-Phe enzyme undergoes deacylation with solvent isotope effects of 2.3–2.5 and nearly identical, linear, proton inventories. For media from 20 to 50% acetonitrile, the Z-Trp enzyme undergoes deacylation with solvent isotope effects of 2.4–2.6 and identical, linear, proton inventories. However, for 15% acetonitrile a larger isotope effect (around 3.0) is seen, although the proton inventory remains linear. For 20 and 30% acetonitrile, the *Z*-Leu enzyme undergoes deacylation with solvent isotope effects of 2.1–2.2 and identical, linear, proton inventories. However, for 16% acetonitrile a larger isotope effect (around 2.4) is seen, although the proton inventory remains linear.

The linearity of the proton inventories appears to indicate that, with possible exceptions, the solvent isotope effects arise almost entirely from a single site in the deacylation transition state. This is presumably the protonic bridge between His 57 and the oxygen center of either the water molecule (if generation of the tetrahedral intermediate through attack of water is largely rate limiting) or the serine residue (if decomposition of the tetrahedral intermediate through expulsion of serine is largely rate limiting). The magnitude of the solvent isotope effects (2–3) is consistent with general experience in general acid–base catalyzed reactions (10). The effect does not distinguish between a proton that is "in flight" (i.e., participates in the reaction-coordinate motion) and one engaged in what is currently called a low-barrier hydrogen bond. In agreement with Eliason and Kreevoy (11)

© 1999 NRC Canada

and earlier views we expressed (12), we suspect that a low-barrier hydrogen bond stabilizes the transition state here.

Conclusions

The fact that the proton inventories and solvent isotope effects generally remain linear over a considerable range of solvent compositions suggests that the medium plays no role in controlling the magnitude or character of the *largest contribution* to the solvent isotope effects and proton inventories (see below for smaller contributions). If there were actually multiple contributions to the major part of the isotope effect from generalized medium effects, then it would seem likely that strong variations in the composition of the medium would lead to non-linearity in the proton inventories as the medium-dependent part of the isotope effect was changed. The conclusion that the secondary site (at the question mark in **1** does not generate an isotope effect or participate in catalysis for these deacylation reactions therefore seems justifiable.

There are two exceptions to the observation of constant isotope effect and identical proton inventory in different media. These exceptions are the shifts from an isotope effect of 2.5 to an isotope effect of 3.0 as the acetonitrile content falls from higher values to 15% for the Trp acyl enzyme and from an isotope effect of 2.2 to one of 2.5 as the acetonitrile content falls from higher values to 16% for the Leu acyl enzyme. Both changes in the isotope effect are relatively small (factors of 1.2 and 1.1, respectively) and may in fact signal the incursion of medium effects of the order of 10–20% as the medium approaches pure water. However, the effects are in the same direction as the single-site effect and would therefore not conceal any normal isotope effect from a secondary-site contribution. Thus the absence of a secondary-site contribution appears a reasonable conclusion.

Although there seem to be no generalized medium effects at work in the enzymic deacylation reactions examined here, they certainly exist. Stein et al. (13) and Kresge and coworkers (7) found such effects, for example, in the acylation reactions of the serine proteases. Therefore, Kresge's critique (5) is in general one that requires attention.

Experimental

Materials

Buffer salts and spectranalyzed acetonitrile were obtained from Fisher Scientific Co. Deuterium oxide (99.9%) was obtained from Aldrich Chemical Co. Substrates were obtained from Sigma Chemical Co. and stored in a desiccator below 0°C. Bovine pancreatic α-chymotrypsin (EC 3.4.21.1) was obtained from Sigma Chemical Co. as a salt-free, lyophilized, three-times recrystallized powder with an activity of 42 BTEE units/mg of solid and was stored in a desiccator below 0°C. Distilled water was deionized on an ion-exchange column before use.

Solutions

Buffers were prepared in mixtures of protium oxide, deuterium oxide, and acetonitrile with constant weights of buffer acid and buffer base. Densities of water–acetonitrile mixtures were determined pycnometrically and found to be within 1.2–1.7% of the densities estimated as the weighted average of the densities of the pure solvents. To obtain the activities of water a_w in mixtures of acetonitrile and water, the data of Vierk (14) and of Maslan and Stoddard (15) at 20 and 30°C were fitted to third-order polynomial functions in the mole fraction of acetonitrile. Values at other temperatures were interpolated or extrapolated assuming a linear relation between ln a_w and $1/T$. The effective pH in mixtures of acetonitrile and water, pH*, was estimated by the method of Perrin and Dempsey (16) according to which $pH^* = R - \delta$, where R is the apparent pH as read from a pH-meter equipped with a glass electrode. Values of δ were available from the work of Douheret (17) for some mixtures of acetonitrile and water. These values were fitted to a third-order polynomial in the mole fraction of acetonitrile so that δ could be obtained for other mixtures by interpolation or extrapolation. The magnitude of δ never exceeded 0.1–0.4. The effective pH in mixtures of protium and deuterium oxides was obtained from the customary correction to the glass-electrode reading (3*c*).

Kinetics

Initial rates of enzyme-catalyzed hydrolysis were determined as slopes of absorbance at 400 nm vs. time. Reaction solutions of 3 mL volume in a quartz cuvette, lacking only enzyme, were thermally equilibrated in the cell compartment of an HP 8542A diode-array spectrophotometer and reaction was initiated by injection of 10 μL of enzyme stock solution. After manual mixing, data collection was initiated. Initial rates in absorbance units were converted to molar units on the basis of measured extinction coefficients for acetonitrile–water mixtures. For the range 0–30% (v/v) acetonitrile, the extinction coefficients were constant within 0.1%, so that the average value of 9830 M^{-1} cm^{-1} was used for all cases. Values of k_{cat} and k_{cat}/K_m were obtained by weighted least-squares fitting of specific initial velocities (initial rate/total enzyme concentration) to substrate concentrations in a double-reciprocal (Lineweaver–Burk) formulation.

References

1. A.J. Kresge. Pure Appl. Chem. **8**, 243 (1964).
2. C.R. Hopper, R.L. Schowen, K.S. Venkatasubban, and H. Jayaraman. J. Am. Chem. Soc. **95**, 3280 (1973).
3. (*a*) K.B. Schowen. *In* Transition states of biochemical processes. *Edited by* R.D. Gandour and R.L. Schowen. Plenum Press, New York. 1978. Chap. 6. pp. 225–283; (*b*) K.S. Venkatasubban and R.L. Schowen. Crit. Rev. Biochem. **17**, 1 (1984); (*c*) K.B. Schowen and R.L. Schowen. Methods Enzymol. **87C**, 551 (1982); (*d*) D.M. Quinn and L.D. Sutton. *In* Enzyme mechanisms from isotope effects. *Edited by* P.F. Cook. CRC Press, Boca Raton, Fla. 1991. pp. 73–126.
4. E. Pollock, J.L. Hogg, and R.L. Schowen. J. Am. Chem. Soc. **95**, 968 (1973).
5. A.J. Kresge. J. Am. Chem. Soc. **95**, 3065 (1973).
6. Y. Chiang, A.J. Kresge, T.K. Chang, M.F. Powell, and J. Wells. J. Chem. Soc. Chem. Commun. 1587 (1995).
7. T.K. Chang, Y. Chiang, H.-X. Guo, A.J. Kresge, L. Mathew, M.F. Powell, and J.A. Wells. J. Am. Chem. Soc. **118**, 8802 (1996).
8. (*a*) T. Ke and A.M. Klibanov. J. Am. Chem. Soc. **120**, 4259 (1998); (*b*) K. Kawashiro, W.J. Moree, P. Sears, K. Witte, and

© 1999 NRC Canada

C.-H. Wong. J. Am. Chem. Soc. **119**, 3942 (1997); (*c*) A.M. Klibanov, J.L. Schmitke, and L.J. Stern. Proc. Natl. Acad. Sci. U.S.A. **94**, 4250 (1997); (*d*) K. Griebenow and A.M. Klibanov. J. Am. Chem. Soc. **118**, 11695 (1996); (*e*) G.K. Farber, R.D. Kidd, P. Sears, C.-H. Wong, and H.P. Yennawar. J. Am. Chem. Soc. **118**, 1645 (1996).

9. C. W. Wharton. *In* Comprehensive biological catalysis. Vol. 1. *Edited by* M.L. Sinnott. Academic Press, London. 1998. p. 345.
10. F.J. Alvarez and R.L. Schowen. Isot. Org. Chem. **7**, 1 (1987).
11. R. Eliason and M.M. Kreevoy. J. Am. Chem. Soc. **100**, 7037 (1978).
12. R.L. Schowen. *In* Mechanistic principles of enzyme activity. *Edited by* J.F. Liebman and A. Greenberg. VCH Publishers, New York. 1988. pp. 119–168.
13. (*a*) R.L. Stein, H. Hori, J.C. Powers, and A.M. Strimpler. Biochemistry, **26**, 1305 (1987); (*b*) R.L. Stein and D.A. Trainor. Biochemistry, **25**, 5414 (1986); (*c*) R.L. Stein. J. Am. Chem. Soc. **107**, 6039 (1985); (*d*) J. Am. Chem. Soc. **107**, 7768 (1985); (*e*) R.L. Stein and M.S. Matta. Fed. Proc. **46**, 1519 (1985).
14. A.L. Vierk. Z. Anorg. Chem. **261**, 283 (1950).
15. F.D. Maslan and E.A. Stoddard. J. Phys. Chem. **60**, 1146 (1956).
16. D.D. Perrin and B. Dempsey. *In* Buffers for pH and metal ion control. Chapman & Hall, London. 1974. pp. 77–82.
17. G. Douheret. Bull. Soc. Chim. Fr. **8**, 3122 (1968).

© 1999 NRC Canada

Photoinduced electron transfer chemistry of 2,3-dicyanonaphthalene[1]

Lorenzo Brancaleon, Darryl Brousmiche, and Linda J. Johnston

Abstract: The electron transfer photochemistry of 2,3-dicyanonaphthalene has been studied by a combination of fluorescence and transient absorption spectroscopy. The singlet excited state has a lifetime of 26 ns in acetonitrile and reacts with aromatic and alkene donors with oxidation potentials less than ~1.8 V with rate constants that are close to the diffusion-controlled limit. Transient absorption measurements demonstrate that the fluorescence quenching leads to efficient formation of free-radical ions. The radical ion yields have been measured for several donors and are compared to those for the more commonly used sensitizer, 1.4-dicyanonaphthalene. In the absence of added donors, direct excitation of 2,3-dicyanonaphthalene provides evidence for photoionization at high laser energy, in addition to triplet formation. The results illustrate the utility of this sensitizer for photoinduced electron transfer reactions.

Key words: photoinduced electron transfer, laser flash photolysis, fluorescence, photosensitizers.

Résumé : Faisant appel à la fluorescence et à la spectroscopie d'absorption des espèces transitoires, on a étudié la photochimie du transfert d'électron dans le 2,3-dicyanonaphtalène. L'état excité singulet possède un temps de vie de 26 ns dans l'acétonitrile et il réagit avec les donneurs aromatiques et alcéniques ayant des potentiels d'oxydation inférieurs à environ 1,8 V, avec des constantes de vitesse qui se rapprochent de la limite sous contrôle de la diffusion. Les mesures d'absorption par les espèces transitoires démontrent que la désactivation de la fluorescence conduit à des ions radicaux libres. Les rendements en ion radical ont été mesurés pour plusieurs donneurs et on les a comparés à ceux du sensibilisateur le plus couramment utilisé, le 1,4-dicyanonaphtalène. En absence de donneurs ajoutés, l'excitation directe du 2,3-dicyanonaphtalène fournit des données qui suggèrent la présence, en plus de la formation d'un triplet, d'une photoionisation à énergie de laser élevée. Les résultats illustrent l'utilité de ce sensibilisateur pour les réactions de transfert d'électron photoinduites.

Mots clés : transfert d'électron photoinduit, photolyse laser éclair, fluorescence, photosensibilisateurs.

[Traduit par la Rédaction]

Introduction

Photoinduced electron transfer (PET) reactions are of increasing utility in synthetic chemistry (1) and of significant importance in areas as diverse as biology and materials science (2). In particular, the use of zeolites as a medium for carrying out PET reactions has potential advantages in minimizing the back electron transfer that limits the efficiency of singlet PET in solution and in controlling product distributions (3, 4). Our recent work in this area (5) has established that 2,3-dicyanonaphthalene (2,3-DCN) is a useful sensitizer, since it is more readily included in X and Y zeolites than other dicyanoaromatics. This work has prompted us to examine the photochemistry of 2,3-DCN in solution and to compare it to other more commonly used cyanoaromatics. We report herein the solution characterization of the photoinduced electron transfer and photoionization behavior of this sensitizer using fluorescence and transient absorption spectroscopies. The results demonstrate that 2,3-DCN has some advantages over certain other cyanoaromatic sensitizers since it has a relatively long fluorescence lifetime and gives reasonably high radical-ion yields. Photoionization of the sensitizer is also observed at high laser energies.

Received November 5, 1998.

This paper is dedicated to Jerry Kresge in recognition of his many achievements in chemistry.

L. Brancaleon, D. Brousmiche, and L.J. Johnston.[2] Steacie Institute for Molecular Sciences, National Research Council, Ottawa, ON K1A 0R6, Canada.

[1]Issued as NRCC No. 42174.

[2]Author to whom correspondence may be addressed. Telephone: (613) 990-0973. Fax: (613) 952-0068. e-mail: linda.johnston@nrc.ca

Experimental section

2,3-Dicyanonaphthalene was sublimed and recrystallized from acetonitrile before use. 1,4-Dicyanonaphthalene was prepared according to a literature procedure (6) and purified by chromatography on alumina followed by recrystallization. Donors were purified by recrystallization or passage through a small alumina column. Solvents were spectrograde and were used as received.

Steady state and time-resolved fluorescence measurements were carried out using a PTI spectrometer equipped with single-photon counting capabilities. The laser flash photolysis system has been described in detail (7). For these experiments either a Lumonics EX-530 excimer laser (XeCl, 308 nm, 6 ns/pulse, <40 mJ/pulse), a Molectron UV-24 nitrogen laser (337 nm, 10 ns/pulse, <10 mJ/pulse), or a Lumonics HY750 Nd:YAG laser (355 nm, 10 ns/pulse,

© 1999 NRC Canada

Fig. 1. Fluorescence spectrum obtained by 310 nm excitation of 20 mM 2,3-DCN in acetonitrile. The inset shows a plot of the observed rate constant for fluorescence decay as a function of the concentration of *trans*-anethole in acetonitrile.

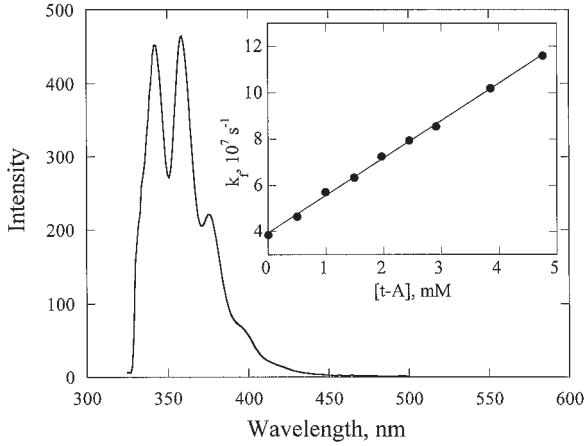

<40 mJ/pulse) was used for sample excitation. Samples were contained in 7 × 7 mm^2 static or flow-through quartz cuvettes and were purged with either oxygen or nitrogen for at least 10 min before use.

Results and discussion

Fluorescence spectroscopy

Fluorescence spectra and lifetimes for 2,3-DCN were measured in a number of organic solvents. The fluorescence spectrum exhibits a structured emission with maxima at 342, 359, and 376 nm in acetonitrile (Fig. 1) that shows a good mirror image relationship with the ground state absorption. The spectrum is independent of the excitation wavelength between 280 and 345 nm and shows no evidence for the broad long-wavelength emission that has been observed in hydrocarbon matrices at low temperature (8). A fluorescence quantum yield of 0.3 for 2,3-DCN in acetonitrile was measured using anthracene in cyclohexane as a standard (Φ = 0.30) (9).

Fluorescence lifetimes for 2,3-DCN in nitrogen-purged solutions were measured by single-photon counting; values obtained ranged from 35.5 ns in cyclohexane to 14.4 ns in dichloromethane, with an intermediate value of 26.0 ns in acetonitrile (Table 1). The latter is somewhat longer than a previous estimate of 13.2 ns (10). The fluorescence of 2,3-DCN is efficiently quenched by oxygen with a measured lifetime of 7 ns for oxygen-saturated acetonitrile. The fluorescence lifetime is unaffected by the ground state concentration over the range 20–80 μM in acetonitrile. For comparison, the fluorescence lifetime for 1,4-dicyanonaphthalene (1,4-DCN) in acetonitrile is 12 ns, in good agreement with literature data (11). Fluorescence lifetimes of 14.9 and 16.6 ns in acetonitrile have been reported for 9,10-dicyanoanthracene and 2,6,9,10-tetracyanoanthracene, respectively (12).

Bimolecular rate constants for quenching of 2,3-DCN fluorescence by a number of aromatic donors were determined by measuring the fluorescence decay as a function of the concentration of added quencher. The data were plotted according to eq. [1] where k_f is the reciprocal of the fluorescence lifetime in the presence of a given concentration of quencher, k_0 is the reciprocal of the fluorescence lifetime in the absence of quencher, and k_q is the quenching rate constant.

Table 1. Fluorescence lifetimes for 2,3-DCN in nitrogen-purged solutions at room temperature.

Solvent	τ_F, ns
Cyclohexane	35.5
Diethyl ether	32.0
Benzene	28.8
Acetonitrile	26.0
Methanol	25.5
Carbon tetrachloride	18.7
Chloroform	15.8
Dichloromethane	14.4

[1] $$k_f = k_0 + k_q(\text{donor})$$

A typical plot for *trans*-anethole (*t*-A) is shown in the inset of Fig. 1, and the quenching rate constants for a series of donors with varying oxidation potentials are listed in Table 2. No change in the 2,3-DCN fluorescence spectrum was observed at the highest concentration of donor used for determining the rate constants. The rate constant for biphenyl quenching is 2.1 × 10^8 M^{-1} s^{-1}, whereas tetramethylbenzene, 1,4-dimethoxybenzene, 4-vinylanisole, and *t*-A all have rate constants at or close to the diffusion-controlled limit. Data for fluorescence quenching of 1,4-DCN by the same series of donors are also included in Table 2. In this case rate constants in excess of 10^{10} M^{-1} s^{-1} were measured for all five donors. These results are consistent with the estimated singlet energies (82.8 and 85.9 kcal from absorption spectra) and reduction potentials (–1.67, –1.28 V vs. SCE in acetonitrile) for 2,3-DCN and 1,4-DCN (13). The Rehm–Weller equation can be used to estimate that electron transfer will be exergonic by ~5 kcal for donors with oxidation potentials of <1.7 V for 2,3-DCN and <2.1 V for 1,4-DCN (15). This is in good agreement with our observations of diffusion-controlled rate constants for quenching of singlet 1,4-DCN with all the donors in Table 1 and with the reduction by two orders of magnitude in the rate constant for quenching of singlet 2,3-DCN by biphenyl, which has E_{ox} of 1.96 V (12). For comparison, the singlet excited state of 9,10-dicyanoanthracene reacts with biphenyl with a rate constant of ~1 × 10^8 M^{-1} s^{-1}, which is very similar to that measured herein for 2,3-DCN (16).

Laser flash photolysis

Excitation of 2,3-DCN (60 μM) in nitrogen-saturated acetonitrile at 308 or 337 nm at low laser energy (<5 mJ/pulse) generates the transient absorption spectrum shown in Fig. 2, with λ_{max} at 410 and 430 nm. The transient decays with mixed kinetics over a period of 50–100 μs, with the observed decay increasing with increasing laser energy, and reacts with oxygen with an observed decay rate constant of 7 × 10^6 s^{-1} in oxygen-saturated acetonitrile. The 430 nm transient is assigned to triplet 2,3-DCN based on its reactivity toward oxygen and the similarity of the observed spectrum

© 1999 NRC Canada

Table 2. Rate constants and radical cation yields for fluorescence quenching of 2,3-DCN and 1,4-DCN by a series of donors in acetonitrile.

		k_q (M^{-1} s^{-1})		Φ	
Quencher	$E_{1/2}^{ox}$ (V)[a]	2,3-DCN	1,4-DCN	2,3-DCN	1,4-DCN
Biphenyl	1.96	2.1×10^8	1.1×10^{10}	0.90	0.49
Tetramethylbenzene	1.8	8.7×10^9	2.0×10^{10}	—	—
Vinyl anisole	1.49	1.6×10^{10}	2.1×10^{10}	—	—
trans-Anethole	1.39	1.6×10^{10}	1.9×10^{10}	0.57	0.14
1,4-Dimethoxybenzene	1.35	1.6×10^{10}	1.9×10^{10}	0.24	0.028

[a]Data from refs. 12–14.

Fig. 2. Transient absorption spectra measured 0.3 (●) and 2 (◆) μs after 337 nm (5 mJ/pulse) excitation of 60 μM 2,3-DCN in nitrogen-saturated acetonitrile.

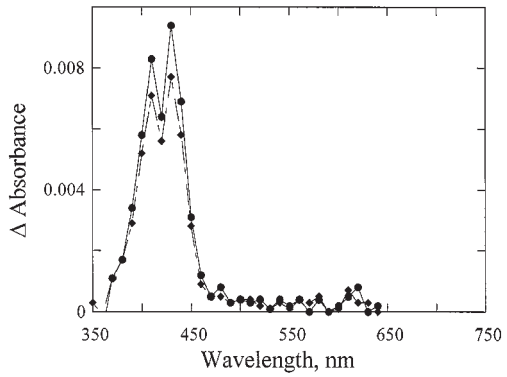

Fig. 3. Transient absorption spectra measured 0.8 (●), 5.2 (◆), and 29 (■) μs after 308 nm (35 mJ/pulse) excitation of 60 μM 2,3-DCN in nitrogen-saturated acetonitrile.

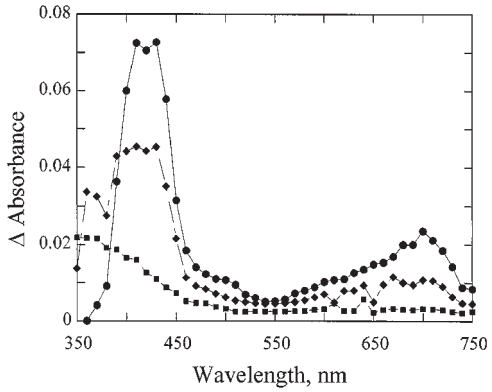

to those for a number of substituted naphthalene triplets (17). Similar spectra are observed in less polar solvents such as diethyl ether and dichloromethane–hexane mixtures.

Excitation of 2,3-DCN in nitrogen-saturated acetonitrile with higher laser energy (>10 mJ/pulse) at either 337 or 308 nm gives more complex transient spectra that show new bands at 700 and 370 nm in addition to the triplet (Fig. 3). There is also a small shoulder at 490 nm. There are clearly two new species, since the lifetime of the 700 nm species (and the shoulder at 490 nm) decreases substantially for oxygen-saturated solutions, whereas the decay kinetics at 380 nm are very similar for oxygen and nitrogen. The yield of both species is lower in oxygen-saturated solution, consistent with reduction of the transient yields via oxygen quenching of singlet 2,3-DCN. These results can be explained by photoionization of 2,3-DCN (eq. [2]) to give a radical cation (380 nm, insensitive to oxygen) and a solvated electron that is trapped by the ground state to give a radical anion (eq. [3], 700 nm absorption). In agreement with this assignment, the 2-cyanonaphthalene radical anion has absorption bands between 650 and 740 nm and 410 and 470 nm in a matrix at low temperature and the corresponding radical cation has a sharper absorption at approximately 700 nm and a broad band at 400 nm (18). Transient spectra obtained at high laser energy in dichloromethane–hexane mixtures also show the formation of the 380 nm transient but the 700 nm absorption is not detected, presumably due to rapid scavenging of the electron or radical anion by the chlorinated solvent.

[2] $$\text{2,3-DCN} \xrightarrow{h\nu} \text{2,3-DCN}^{\bullet+} + e^-_{solv}$$

[3] $$\text{2,3-DCN} \xrightarrow{e^-_{solv}} \text{2,3-DCN}^{\bullet-}$$

The yield of the additional long-wavelength signals in acetonitrile was measured as a function of the 308 nm laser energy. Plots of signal intensity at 680 nm vs. laser energy were reasonably linear, except for an induction period at low energies. By contrast, the triplet signal at 430 nm showed pronounced negative curvature over the same range of laser energies, indicative of saturation effects due to either ground state depletion or competitive absorption of the excitation pulse by both ground and triplet states. The difference between the intensity dependence for the triplet and radical ions, in combination with the fact that only the triplet is observed at low energies using 337 nm excitation, suggest that the photoionization – electron trapping process that generates the observed radical cation–anion signals has a two-photon component. It is also possible that electron transfer interactions between singlet 2,3-DCN and the ground state give rise directly to the radical cation–anion pair. However, the laser energy dependence of the transient phenomena and the fact that the singlet lifetime is not dependent on the 2,3-DCN concentration are inconsistent with this hypothesis.

Excitation (337 nm) of 2,3-DCN in the presence of 0.01 M *t*-A in acetonitrile generates the transient spectrum shown in Fig. 4. This concentration of *t*-A does not absorb significantly at the excitation wavelength and, based on the fluorescence data, will result in approximately 75% singlet quenching. Consistent with this, triplet 2,3-DCN is not observed. However, there are strong absorptions at both 600 and 390 nm, in agreement with the reported spectrum for *t*-$A^{\bullet+}$, (19), as well as weaker bands beyond 650 nm, between

© 1999 NRC Canada

Fig. 4. Transient absorption spectra measured 320 ns after 337 nm excitation of 55 μM 2,3-DCN plus 0.01 M *trans*-anethole in nitrogen (◆)and oxygen (●) saturated acetonitrile.

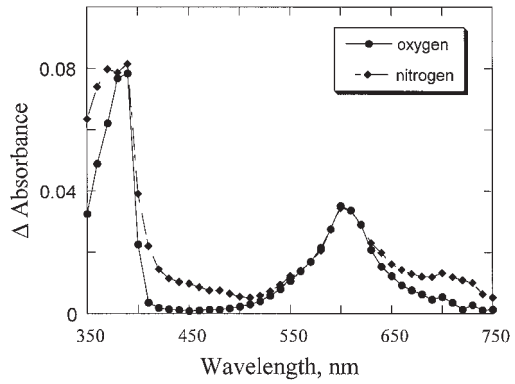

420 and 520 nm and at 365 nm. Spectra recorded for oxygen-saturated solutions are clearly due solely to *t*-A$^{\bullet+}$ (Fig. 4). The additional weaker absorptions that are removed by oxygen can be more readily characterized by excitation of a nitrogen-saturated solution containing tetrabutylammonium chloride as a selective radical-cation scavenger (19). Under these conditions the radical anion (2,3-DCN$^{\bullet-}$) expected as the other product of electron transfer quenching of singlet 2,3-DCN by *t*-A (eq. [4]) should be readily visible. The spectrum obtained, although weak, indicates that 2,3-DCN$^{\bullet-}$ absorbs between 650 and 730 nm, with additional absorption between 420 and 500 nm and at ~365 nm. These results are consistent with the assignment of the weak absorption in the 700 nm region obtained by excitation of 2,3-DCN alone to the radical anion.

[4] $$2,3\text{-DCN}^* + t\text{-A} \rightarrow 2,3\text{-DCN}^{\bullet+} + t\text{-A}^{\bullet+}$$

Triplet 2,3-DCN was also quenched by *t*-A, $k_q = 1.8 \times 10^{10}$ M^{-1} s^{-1}. However, triplet quenching is not accompanied by the formation of *t*-A$^{\bullet+}$, based on the lack of radical-cation signal upon excitation of 2,3-DCN in the presence of 0.4 mM *t*-A. Under these conditions there is approximately 90% triplet quenching and <1% singlet quenching by *t*-A. These results are consistent with the large decrease in available excitation energy for the triplet as compared to the singlet excited state of 2,3-DCN (20).[3]

Transient spectra measured in the presence of sufficient donor to quench >80% of 2,3-DCN singlets were also recorded for biphenyl, 4-vinylanisole, and 1,4-dimethoxybenzene. For both biphenyl and 1,4-dimethoxybenzene, absorptions due to the respective radical cations at 670 and 460 nm were readily detected (18). The 4-vinylanisole radical cation with λ_{max} at 600 nm was also observed; however, the radical cation decayed quite rapidly, with an observed rate constant of ~3×10^6 s^{-1} for 1.7 mM substrate. This short lifetime is due to rapid reaction of the radical cation with the precursor alkene, for which a quenching rate constant of 1.4×10^9 M^{-1} s^{-1} has been reported in acetonitrile (21).

The yields of radical cations obtained by quenching singlet 2,3-DCN and 1,4-DCN were measured for biphenyl, *t*-A, and 1,4-dimethoxybenzene. The required molar absorption coefficients for the radical cations for the latter two donors were estimated by electron transfer quenching of biphenyl radical cation in the following manner. The biphenyl radical cation was generated by electron transfer quenching of singlet 1,4-DCN in the presence of 0.21 M biphenyl in oxygenated acetonitrile. The signal intensity due to biphenyl radical cation was then measured. Either *t*-A or 1,4-dimethoxybenzene was added to an identical aliquot of the same stock solution of 1,4-DCN plus biphenyl. The concentration of donor used was sufficient to quench >99% of the biphenyl radical cations, assuming a diffusion-controlled rate constant, without competing with biphenyl for quenching of the initial 1,4-DCN singlet. The intensity of the donor radical cations at their respective maxima was then measured. By making the reasonable assumption that quenching of the biphenyl radical cation occurs exclusively by electron transfer, the ratio of the secondary donor/biphenyl signal intensities (for an average of three determinations) can be used in combination with the reported molar absorption coefficient of 14 500 M^{-1} cm^{-1} for biphenyl$^{\bullet+}$ (12) to calculate molar absorption coefficients for the donor radical cations. Values of 10 960 and 12 200 M^{-1} cm^{-1} were estimated for the *t*-A and dimethoxybenzene radical cations at 600 and 470 nm, respectively. Note that although these numbers may contain absolute errors due to the biphenyl radical-cation molar absorption coefficient, they provide a consistent set of numbers to use for estimation of the quantum yields, as outlined below.

The yield of the donor radical cations was estimated by measuring the radical-cation signal intensity as a function of laser energy for samples of both the naphthalene plus donor and the benzophenone actinometer. The slopes of these plots, along with the molar absorption coefficients for the radical cation and benzophenone triplet (7800 M^{-1} cm^{-1} at 525 nm in benzene) and a value of 1 for the yield of benzophenone triplet, were then used to calculate the donor radical-cation yields, according to eq. [5]. The values are listed in Table 2. The measured yields were corrected, where necessary, for incomplete quenching of the singlet naphthalene by the donor. To eliminate any contribution from naphthalene radical anions, the radical-cation intensities were measured for oxygenated solutions for cases where a sufficiently high donor concentration could be used to prevent competitive quenching of the singlet naphthalene by oxygen rather than the donor.

[5] $$\Phi(\text{donor}^{\bullet+}) = [\text{slope (donor}^{\bullet+})/\text{slope (^{3}Bp)}]\ [\varepsilon(^3\text{Bp})/\varepsilon(\text{donor}^{\bullet+})]\ [\Phi(^3\text{Bp})]$$

For each of the naphthalene sensitizers the measured radical-ion yield decreases dramatically with decreasing oxidation potential of the donor. For example, for 2,3-DCN the yields are 0.90, 0.57, and 0.24 for biphenyl, *t*-A, and 1,4-dimethoxybenzene. These results are to be expected on the basis of the decrease in the back electron transfer rate with

[3] The singlet energy of 2,3-DCN is estimated at 82.8 kcal/mol as compared to triplet energies for substituted naphthalenes, which range from 58 to 61 kcal/mol (20).

© 1999 NRC Canada

increasing reaction exothermicity in the Marcus inverted region, as studied in detail by Farid and Gould for a variety of singlet sensitizers (12, 22). The measured radical-ion yields for each donor are higher for 2,3-DCN than for 1,4-DCN, consistent with formation of a higher-energy ion pair for the former sensitizer. Note that the difference in reduction potential for the two naphthalenes means that back electron transfer for the initial radical-ion pair is approximately 0.4 V more exothermic for 2,3-DCN than for 1,4-DCN for any given donor. The very high radical-ion yields for biphenyl, particularly for 2,3-DCN, are in good agreement with literature data; for example, a quantum yield for free-radical ion formation for 9,10-dicyanoanthracene/ biphenyl of 0.83 has been reported (15).

Conclusions

A combination of fluorescence and transient absorption spectroscopies demonstrates that singlet 2,3-dicyanonaphthalene undergoes efficient electron transfer quenching by a variety of aromatic and arylalkene donors. Both the radical cations and the 2,3-DCN radical anion have been characterized and their yields compared to those obtained with 1,4-DCN. In both cases the radical-ion yields show the expected increase with increasing oxidation potential of the donor. Our results demonstrate that 2,3-DCN provides a useful alternative to other cyanoaromatic sensitizers, particularly since it has a relatively long singlet lifetime that minimizes the amount of donor required for complete singlet quenching. Although it can be used to oxidize a similar range of donors to the widely used 1,4-dicyanonaphthalene, it has the added advantage of giving substantially higher free radical-ion yields. Surprisingly, laser excitation of 2,3-DCN also leads to photoionization but this appears to be predominantly a biphotonic process that is unlikely to play a role in steady state photoinduced electron transfer reactions.

References

1. J. Mattay. Synthesis, 233 (1989); N.J. Bauld. Adv. Electron Transfer Chem. **2**, 1 (1992); U.C. Yoon and P.S. Mariano. Acc. Chem. Res. **25**, 233 (1992); J. Cossy and J.-P. Pete. Adv. Electron Transfer Chem. **5**, 141 (1996).
2. M.A. Fox and M. Chanon (*Editors*). Photoinduced electron transfer. Elsevier, Amsterdam. 1988.
3. K.B. Yoon, S.M. Hubig, and J.K. Kochi. J. Phys. Chem. **98**, 3865 (1994); E.H. Yonemoto, Y.I. Kim, R.H. Schmehl, J.O. Wallin, B.A. Shoulders, B.R. Richardson, J.F. Haw, and T.E. Mallouk. J. Am. Chem. Soc. **116**, 10557 (1994).
4. V. Ramamurthy (*Editor*). Photochemistry in organized and constrained media. VCH Publishers, New York. 1991.
5. L. Brancaleon, D. Brousmiche, V.J. Rao, L.J. Johnston, and V. Ramamurthy. J. Am. Chem. Soc. **120**, 4926 (1998).
6. R.W. Bayer and E.J. O'Reilley, Jr. J. Org. Chem. **23**, 311 (1958); M.S. Newman. Org. Synth. Collect. Vol. **3**, 631 (1995).
7. S. Kazanis, A. Azarani, and L.J. Johnston. J. Phys. Chem. **95**, 4430 (1991).
8. S. Matsuzawa and Y. Shimizu. Polycyclic Aromat. Compd. **5**, 95 (1994).
9. D.F. Eaton. *In* Handbook of organic photochemistry. Vol. I. *Edited by* J.C. Scaiano. CRC Press, Boca Raton, Fla. 1989. Chap. 8.
10. T. Nishiyama, K. Mizuno, Y. Otsuji, and H. Inoue. Tetrahedron, **51**, 6695 (1995).
11. D.R. Arnold and A. Maroulis. J. Am. Chem. Soc. **98**, 5931 (1976).
12. I.R. Gould, D. Ege, J.E. Moser, and S. Farid. J. Am. Chem. Soc. **112**, 4290 (1990).
13. D.D.M. Wayner. *In* Handbook of organic photochemistry. Vol. II. *Edited by* J.C. Scaiano. CRC Press, Boca Raton, Fla. 1989. Chap. 18.
14. N.P. Schepp and L.J. Johnston. J. Am. Chem. Soc. **118**, 2872 (1996).
15. D. Rehm and A. Weller. Isr. J. Chem. **8**, 259 (1970).
16. I.R. Gould, D. Ege, S.L. Mattes, and S. Farid. J. Am. Chem. Soc. **109**, 3794 (1987).
17. I. Carmichael and G.L. Hug. J. Phys. Chem. Ref. Data, **15**, 1 (1986).
18. T. Shida. Electronic absorption spectra of radical ions. Elsevier, Amsterdam. 1988.
19. L.J. Johnston and N.P. Schepp. J. Am. Chem. Soc. **115**, 6564 (1993).
20. S.L. Murov. Handbook of photochemistry. Marcel Dekker, New York. 1973.
21. N.P. Schepp and L.J. Johnston. J. Am. Chem. Soc. **116**, 6895 (1994).
22. I.R. Gould, R.H. Young, R.E. Moody, and S. Farid. J. Phys. Chem. **95**, 2068 (1991).

© 1999 NRC Canada

A mechanism for efficient proton-transfer catalysis. Intramolecular general acid catalysis of the hydrolysis of 1-arylethyl ethers of salicylic acid

Sarah E. Barber, Kathryn E.S. Dean, and Anthony J. Kirby

Abstract: The *tert*-butyl (**1**) and 1-arylethyl ethers (**2**) of salicylic acid are hydrolyzed with efficient general acid catalysis by the ortho-COOH group. The half-life of the neutral COOH form of the *tert*-butyl ether is 15.2 min at 39°, and the estimated acceleration by the COOH group of **2**, X = Me, Y = H is 2.13×10^5. The salicylate leaving group from **2** (X = Me, Y = H) has an effective pK_a of 2.9, compared with a nominal pK_a of 8.52. Analysis of substituent effects in both arylethyl and leaving groups provides the most detailed available mechanistic insight into a reaction involving efficient intramolecular proton-transfer catalysis. The mechanism is very different from classical general acid–base catalysis. Proton transfer takes place very rapidly within a developing strong hydrogen bond, and though an integral part of the C—O cleavage process is practically uncoupled from it. "Strategic delay" of the proton-transfer step, relative to C—O cleavage, makes a significant contribution to efficiency by setting up the conditions for the formation of the strong, intramolecular hydrogen bond.

Key words: catalysis, carboxyl, hydrogen bond, proton transfer, enzyme mechanism.

Résumé : L'hydrolyse des éthers *tert*-butyle (**1**) et 1-aryléthyle (**2**) de l'acide salicylique se fait avec une catalyse acide générale efficace par le groupe -COOH en ortho. La demi-vie de la forme COOH neutre de l'éther *tert*-butyle est de 15,2 min à 39° et l'accélération évaluée de groupe COOH de **2**, X = Me, Y = H, est de $2{,}13 \times 10^5$. Le pK_a effectif du groupe salicylate partant de **2** (X = Me, Y = H) est égal à 2,9 par rapport à un pK_a nominal de 8,52. L'analyse des effets de substituants du groupe arylméthyle et des groupes partants fournit la compréhension mécanistique la plus détaillée possible pour une réaction impliquant une catalyse efficace par transfert intramoléculaire de proton. Le mécanisme est très différent de la catalyse générale acide–base classique. Le transfert de proton se produit très rapidement dans la forte liaison hydrogène qui se développe et, même s'il fait partie intégrale du processus de clivage de la liaison C—O, il n'existe pratiquement pas de couplage avec lui.

Mots clés : catalyse, carboxyle, liaison hydrogène, transfert de proton, mécanisme enzymatique.

[Traduit par la Rédaction]

We are interested in the efficiency and thus the detailed mechanism of intramolecular general acid–base catalysis, as a simple model for the myriad of proton-transfer processes involved in catalysis by enzymes (1). General acid–base catalysis may be presumed to be efficient in enzyme reactions: but effective molarities (EM) for intramolecular proton-transfer catalysis are generally lower by many orders of magnitude than those for intramolecular nucleophilic (cyclization) reactions, rising above 1–10 M only in special cases (2). We have recently reported systems showing intramolecular general acid catalysis with EMs as high as 10^6 M, (3) and have identified as a key factor the development of a strong intramolecular hydrogen bond as the reaction proceeds. For optimum catalytic efficiency this H-bond should be absent in the ground state and strongest in the transition state, a state of affairs that depends critically on geometry and the extent and timing of charge development during the reaction. We report an in-depth investigation of general acid catalysis by the carboxyl group of nucleophilic substitution at carbon (S_N1 and S_N2), a reaction that is particularly well understood. The leaving group is the salicylate monoanion, known to be stabilised by a strong H-bond of well-defined geometry, and the substrates its methyl, *tert*-butyl **1**, and substituted 1-phenylethyl ethers **2**. We can vary the degree of charge development on the leaving group oxygen by varying the carbon centre from which it leaves systematically in the series **2**, by changing the pattern of substitution on both the salicylate leaving group and on the aromatic ring of the 1-phenylethyl group (4).

Received December 2, 1998.

This paper is dedicated to Professor A. Jerry Kresge on the occasion of his 70th birthday.

S.E. Barber, K.E.S. Dean, and A.J. Kirby.[1] University Chemical Laboratory, Cambridge CB2 1EW, U.K.

[1]Author to whom correspondence may be addressed. Telephone:+44 1223 336370 (direct). Fax: +44 1223 336913. e-mail: ajk1@cam.ac.uk

Kinetic methods and results

The *tert*-butyl ether **1** was made directly, by carboxylation of the *ortho*-lithiated *tert*-butyl phenyl ether: it disappeared

© 1999 NRC Canada

Table 1. Kinetic data for hydrolysis of *tert*-butyl salicyl ether **1** and its methyl ester, in 10% (v/v) dioxan–water, ionic strength 1.0 M (KCl).

T (°C)	pK_{app}	10^3k_H (dm^3 mol^{-1} s^{-1})	10^4k_0 (s^{-1})	k_0^H/k_0^D
25	4.05	10.9 ± 0.4	1.04 ± 0.07	
39	4.16	85.0 ± 3.0	7.6 ± 0.3	1.36 ± 0.16
50	4.27	365 ± 8.5	30.9 ± 0.9	
65[a]	4.29	2022 ± 73	122 ± 4	
		Methyl ester		
39		90.0 ± 0.3		

[a]Variable temperature data give for k_0: $\Delta H^{\ddagger}$ = 98 ± 3 kJ mol^{-1}, $\Delta S^{\ddagger}$ = 8 ± 9 J K^{-1} mol^{-1}; for k_H: $\Delta H^{\ddagger}$ = 107 ± 3kJ mol^{-1}, $\Delta S^{\ddagger}$ =77 ± 8 J K^{-1} mol^{-1}.

rapidly in organic solvents, but was stable in aqueous solution as the anion. Compounds of the 1-phenylethyl series **2** were generated from the stable methyl esters (**3**): the esters were made by the Williamson ether synthesis, as described in the experimental section. Stock solutions of the stable carboxylate anions of ethers **2** were prepared by hydrolysing the esters **3** with 1.1 equiv. of KOH in 50% dioxan–water. For all but the most reactive esters, hydrolysis required an overnight reflux. The resulting solutions were diluted, and used directly in kinetic studies (final concentration 10^{-4}–10^{-5} mol dm^{-3}).

Table 1 shows kinetic data for the hydrolysis of the *tert*-butyl ether **1**, and Table 2 summarizes results for the series of 16 1-arylethyl ethers **2** studied in this work. Rates are very sensitive to substitution in the aromatic ring of the 1-arylethyl derivatives, and pH–rate profiles were measured conveniently at 25, 39, and 65°C, respectively, for compounds with X = 4-Me, H, and 3-Br. (In the case of the very reactive compound **2**, X = 4-MeO, Y = 5-NO_2, hydrolysis was too fast to follow below pH 4, even at 1°C, and we could only estimate the plateau rate constant.) Derived rate constants were extrapolated to a common 39°C for the 4-Me and 3-Br systems from variable temperature measurements, which gave the thermodynamic parameters also shown in Table 2.

The reactions of all the salicylic acid derivatives show the same basic features, illustrated in Fig. 1 for the hydrolysis of **1** and **2** (X = H, Y = H, and X = H, Y = NO_2); namely, rapid acid-catalysed hydrolysis at low pH, a plateau between pH 2–4 corresponding to the pH-independent hydrolysis of the COOH form, and no significant reaction above pH 6. The plateau reaction is of primary interest for this work, and derived kinetic data in the tables refer to rate constants k_0 for this process. Rate constants and apparent carboxyl-group pK_a values were calculated from eq. [1]:

$$[1] \qquad k_{obs} = \frac{k_0 + k_H a_H}{1 + (K_a/a_H)}$$

where k_H is the rate constant for the acid-catalysed hydrolysis of the neutral acid form and k_0 the first-order rate constant calculated for its spontaneous hydrolysis. (The alternative interpretation as the kinetically equivalent acid-catalysed hydrolysis of the carboxylate anion has been ruled out in many similar cases.) The pK_{app} values agree with the values expected for the pK_a values of salicylic acid derivatives.

For comparison with the reactions of the salicylic acid derivatives **2,** we measured rates of hydrolysis under the same conditions for a series of simple sterically comparable aryl 1-phenylethyl ethers **4**, with good leaving groups and a 2-NO_2 in place of the *o*-COOH group. These compounds are less reactive than the corresponding salicyl ethers and were mostly studied at 80°C. The data appear in Table 3. The 2,4-dinitrophenyl ethers (**4**, Y = NO_2, X = H, and 4-Me) show pH-independent hydrolysis between pH 4.5 and 9. These reactions are not catalysed by added buffer. (Some amine buffers are an exception, but HPLC examination of the products showed that the products were anilines, and thus that the amines had attacked the aromatic ring, rather than the benzylic centre.) The addition of the strongly nucleophilic thiosulphate (Swain–Scott (5) *n* value –6.4) had no effect on the rate of hydrolysis of **4** (Y = NO_2, X = H), and in the case of **4** (Y = NO_2, X = 4-Me) a six-fold increase in the concentration of thiosulphate gave only a 20% increase in the rate constant. This increase is so small that it is reasonable to suppose that less powerful nucleophiles would have little or no effect on the rates for these compounds. In other cases, a small *negative* effect of increasing buffer concentration could be ascribed to specific salt effects.

In only one case was there convincing evidence for buffer catalysis, and thus for an S_N2 reaction at the benzylic centre. The least reactive 2,4-dinitrophenyl ether **4** (Y = NO_2, X = 3-Br) also showed a pH-independent reaction between pH 4.5 and pH 6.3, at 80°C. Pseudo-first-order behaviour could be observed only at buffer concentrations of 0.08 M or less, but at these concentrations the reaction was catalysed by the free-base form of the buffer (linear dependence on acetate or phosphate concentration, 52% acceleration for 0.08 M phosphate, 50% free base). Extrapolation of the observed rate constants to zero buffer gave the same intercept for both phosphate and acetate buffers (and second-order rate constants of 3.04×10^{-4} and 5.66×10^{-5}, respectively). It seems clear that in this case, against the slowest spontaneous reaction, acetate and phosphate anions do provide some nucleophilic catalysis.

This result suggested that the 1-(3-bromophenyl)ethyl salicyl ethers would be the most likely to show second-order reactions with nucleophiles, but the addition of bromide (Swain–Scott *n* value –3.9) had no effect on the rate of hydrolysis of (**2**, Y = H, X = 3-Br), and the reaction was not catalysed to a measurable extent by the base component of added buffers. The reactions of (**2**, Y = 5-NO_2, X = 3-Br) were studied in the presence of substituted pyridines. These were of particular interest because they catalyse the hydrolysis of salicyl phosphate (6), and we would be able to compare the two β_{nuc} values obtained. However, the rate of reaction was independent of the concentration of cyanopyridine, and a slight rate retardation was seen in the presence of increasing concentrations of nicotinamide.

It is difficult to observe S_N2 reactions with the 1-arylethyl ethers **2** because of the dominant S_N1 reactions of these systems, so we searched carefully for reactions of nucleophiles with the methyl ether **5**. A UV study in water (0.1 M HCl and formate buffer) showed no detectable reaction with 0.9 M iodide or thiocyanate (we should have detected a reaction with a first-order rate constant $\geq 10^{-8}$ s^{-1}), and we could detect no reaction by ^{1}H NMR with iodide in acetonitrile,

© 1999 NRC Canada

Table 2. Kinetic data for hydrolysis of 1-phenylethyl salicyl ethers **2** at various temperatures, in 10% (v/v) dioxan–water, ionic strength 1.0 M (KCl).

Compound **2**									
X	Y	T (°C)	pK_{app}	k_0^H/k_0^D	10^4k_0 (s^{-1})	10^3k_H ($dm^3\ mol^{-1}\ s^{-1}$)	k_0(39) (s^{-1})[a]	$\Delta H^{\ddagger}$ (kJ mol^{-1})	$\Delta S^{\ddagger}$ (J $K^{-1}\ mol^{-1}$)
4-Me	5-Me	25	4.53 ± 0.11	0.96	0.24	—	$1.55 \pm 0.15 \times 10^{-2}$	—	—
4-Me	H	25	4.12 ± 0.03		0.36	0.27	$2.57 \pm 0.15 \times 10^{-2}$	105 ± 6	63 ± 10
4-Me	4-MeO	25	4.83 ± 0.07		0.42	0.28	$2.49 \pm 0.30 \times 10^{-2}$	96 ± 7	32 ± 23
4-Me	5-Cl	25	3.79 ± 0.06		0.67	—	$6.21 \pm 1.00 \times 10^{-2}$	120 ± 10	116 ± 20
4-Me	5-NO_2	25	3.36 ± 0.06		1.51	—	0.160 ± 0.03	129 ± 9	156 ± 30
H	5-Me	39	4.17 ± 0.08		2.35	9.54	$2.35 \pm 0.23 \times 10^{-4}$	—	—
H	H	39	3.94 ± 0.02	0.97	3.44	4.56	$3.44 \pm 0.17 \times 10^{-4}$	—	—
H	4-MeO	39	4.53 ± 0.05		4.30	8.66	$4.30 \pm 0.21 \times 10^{-4}$	—	—
H	5-Cl	39	3.40 ± 0.05		8.10	3.46	$8.10 \pm 0.40 \times 10^{-4}$	—	—
H	5-NO_2	39	2.92 ± 0.03		33.6	—	$3.36 \pm 0.17 \times 10^{-3}$	—	—
3-Br	5-Me	65	4.16 ± 0.05		0.97	11.6	$3.0 \pm 1.0 \times 10^{-6}$	114 ± 6	14 ± 30
3-Br	H	65	3.83 ± 0.07		1.33	4.63	$9.0 \pm 1.5 \times 10^{-6}$	88 ± 6	–59 ± 17
3-Br	4-MeO	65	4.43 ± 0.07		2.16	9.63	$2.1 \pm 0.5 \times 10^{-5}$	76 ± 10	–91 ± 29
3-Br	5-Cl	65	3.44 ± 0.06		3.60	—	$1.20 \pm 0.13 \times 10^{-5}$	110 ± 6	12 ± 12
3-Br	5-NO_2	65	3.13 ± 0.07	1.36	13.4	—	$1.05 \pm 0.09 \times 10^{-4}$	83 ± 10	–53 ± 4
4-MeO	5-NO_2	1–26	2.93[b]				55 ± 10[b]	—	—

[a]Rate constant measured at (X = H and X = Y = Me) or extrapolated to 39°C from measurements over a range of temperatures.

[b]Estimate based on measurements between 1 and 26°C (too fast to measure below pH 4). Extrapolation of the data to 39°C allowed the construction of a partial pH–rate profile.

© 1999 NRC Canada

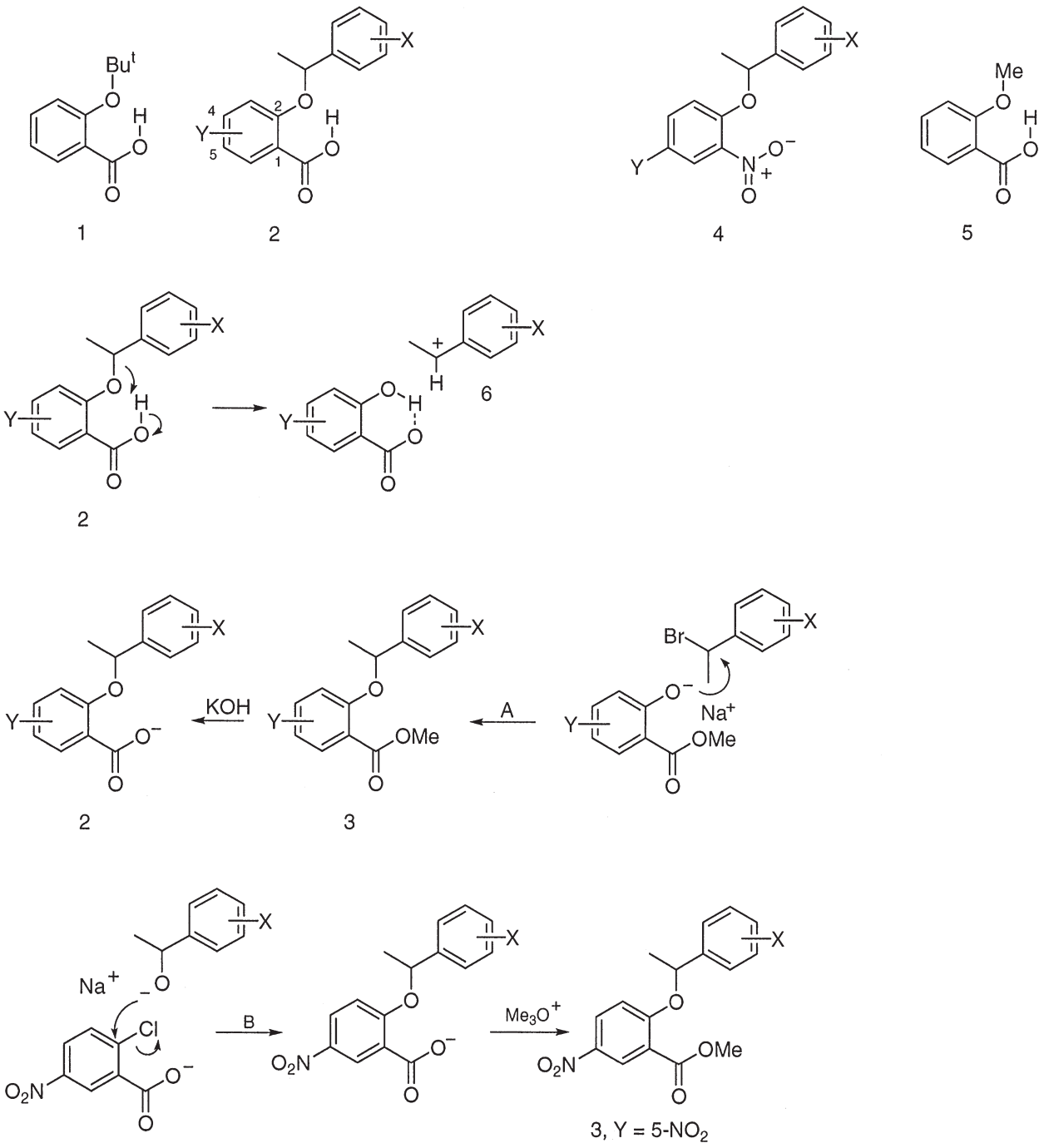

DMSO (both run for 2 weeks at 40°C) or water (5 days at 60°). We find no measurable nucleophilic catalysis for any of the salicyl ethers **1** and **2**.

Discussion

Ethers **1** and **2** were designed to show intramolecular general acid-catalysed hydrolysis at a measurable rate.[2] A phenol oxygen is not normally a viable leaving group in the S_N1 or S_N2 reaction in the absence of very strongly electron-withdrawing substituents on the aromatic ring, and the rapid cleavage of the ether C—O bonds confirms that catalysis by the *o*-COOH group is efficient in these systems.

Figure 1 shows pH–rate profiles for the hydrolysis of three representative alkyl salicyl ethers, the unsubstituted *tert*-butyl (**1**) and 1-phenylethyl derivatives and the 5-nitro-

[2] The terms general acid and general base catalysis are commonly used to denote either or both of (*i*) a kinetic dependence on the concentration of the general acid or base, and (*ii*) the *mechanism* of this catalysis, involving rate-determining proton transfer from or to the general acid or base. The intramolecular reaction in the salicylic acid system is so efficient that catalysis by external general acids is not significant.

© 1999 NRC Canada

Table 3. Kinetic data for hydrolysis of aryl 2-nitro-4-substituted-phenyl ethers **4** at various temperatures, in 10% (v/v) dioxan–water, ionic strength 1.0 M (KCl).

Compound **4**					
X	Y	T (°C)	k_0 (s^{-1})	$\Delta H^{\ddagger}$ (kJ mol^{-1})	$\Delta S^{\ddagger}$ (J K^{-1} mol^{-1})
4-Me	CF_3	80	6.2×10^{-3}		
4-Me	H	80	1.7×10^{-4}		
4-Me	Cl	80	7×10^{-4}		
4-Me	NO_2	39	1.87×10^{-3}	91 ± 9	–6.68 ± 3.7
H	NO_2	65	3.84×10^{-4}		
3-Br	NO_2	80	4.22×10^{-5}	98.4 ± 1	–49.5 ± 2

Fig. 1. pH–rate profiles (at 39°C) for the hydrolysis of *tert*-butyl (**1**, circles) and salicyl and 5-nitrosalicyl 1-phenylethyl ethers (**2**, Y = H and NO_2: squares and diamonds, respectively).

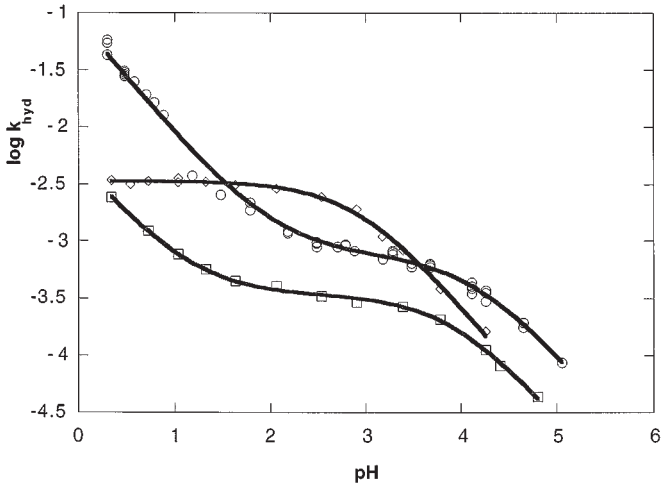

salicyl 1-phenylethyl ether (**2**, X = H, Y = NO_2), with the nitro group *para* to the leaving group oxygen. The salicylic acid derivatives **2** studied in this work all showed similar behaviour: more or less well-defined pH-independent regions between pH 2–4, with rates falling off at high pH with the fraction of COOH form present. The presence of this feature for the salicylic acid derivatives, and its absence for their methyl esters is prima facie evidence for catalysis by the carboxylic acid group. The half-life of the neutral COOH form of *tert*-butyl ether **1** is 15.2 min at 39°, less than half that of the unsubstituted 1-phenylethyl ether **2** (X = Y = H, in 10% dioxan:water); which is itself accelerated by a factor of 10 by the introduction of the 5-nitro group.

At low pH specific acid catalysis is observed, for all except the ethers derived from 5-nitrosalicylic acid. (This latter effect is the simple consequence of a high rate of spontaneous hydrolysis combined with a lower k_H for the compounds with the most electronegative leaving groups.)

These rapid hydrolysis reactions are an indication of the efficiency of intramolecular catalysis by the *o*-COOH group in the reactions of salicylic acid derivatives **1** and **2**. The corresponding intermolecular reaction, general acid catalysis of the hydrolysis of similar ethers by carboxylic acids, is too slow to measure, so we cannot estimate effective molarities (EM) (2). As an alternative. we can quantify efficiency by the comparison with the spontaneous reactions of simple ethers **4**. The slope of the linear free energy relationship (β_{LG}) relating the rates of hydrolysis of the series of four compounds **4**, with X = 4-Me to the pK_a of the leaving group is –0.95 ± 0.03 at 80°C. This allows us to estimate an acceleration of 2.13×10^5 by the COOH group of **2**, X = Me, Y = H (at 39°C, based on an estimated pK_a of 8.52 (7) for the phenol OH of salicylic acid). The observed rate of the COOH-catalysed reaction of this compound is equivalent to that expected for the spontaneous departure of the anion derived from a phenol of pK_a = 2.9. The effective pK_a of the leaving group is close to 3 for similar reactions of salicyl acetals (8, 9) and of salicyl phosphate (6).

The effect of nucleophiles on the expulsion of salicylate

The evidence indicates that the enhanced salicylate leaving group departs in a simple S_N1 reaction, and we discuss the details of this process below. We looked also for evidence of catalysis of the attack of nucleophiles (the S_N2 reaction). We could find no detectable reaction at the methyl group of salicylic acid methyl ether **5**; and would expect none for the reaction of the *tert*-butyl ether **1**.

The work of Richard and Jencks (10, 11) has defined the point at which the nucleophilic substitution reactions of 1-phenylethyl derivatives become coupled concerted. No reactions of 1-(4-methylphenyl) ethyl derivatives are concerted: unsubstituted 1-phenylethyl derivatives show a coupled concerted reaction only with azide, but 1-(3-bromophenyl)ethyl chloride shows coupled concerted reactions with azide and with acetate ion, though not with solvent. Consistently, we find evidence for weak catalysis by acetate and phosphate anions of the cleavage of 1-(3-bromophenyl)ethyl 2,4-dinitrophenylether **4** (Y = NO_2, X = 3-Br) at 80°C, but for no other derivative **4**.

Thus, our 1-(3-bromophenyl)ethyl salicyl ethers **2** (Y = 3-Br) are the most likely to show second-order reactions with nucleophiles. We found no evidence of such reactivity. The thermodynamic activation parameters for the cleavage reaction (Table 2) similarly offer no evidence to support nucleophilic participation by water in the transition state for hydrolysis: entropies of activation for the most reactive compounds **2**, X = 4-Me are generally large and positive. Those for the least reactive systems (**2**, Y = 3-Br) are significantly more negative, consistent with more ordering of solvent in the transition states for hydrolysis. Nevertheless, we do not consider that these reactions are solvent assisted, since far better nucleophiles than water show no effect.

These activation parameters can be compared with those obtained for the spontaneous hydrolyses of two 2,4-dinitrophenyl ethers **4** (Table 3). Here also the entropy of activation for the hydrolysis of (**4**, X = 3-Br, Y = NO_2), which shows

© 1999 NRC Canada

Table 4. Linear free energy relationships for 1-phenylethyl salicyl ethers **2**.

Compound **2**					
X	Y	*T* (°C)		ρ_{phenol}[c]	ρ_{COOH}[c]
			Hydrolysis reactions		
			ρ^{+}[a]		
Varied	5-Me	39	–5.27 ± 0.1		
Varied	H	39	–4.91 ± 0.5		
Varied	4-MeO	39	–4.34 ± 0.7		
Varied	5-Cl	39	–5.29 ± 0.4		
Varied	5-NO_2	39	–4.53 ± 0.4		
			$\rho_{I.G.}$[b] (OAr)		
4-Me	Varied	25	0.84 ± 0.08	0.97 ± 0.10	–0.08 ± 0.15
H	Varied	39	1.25 ± 0.08	0.96 ± 0.10	0.23 ± 0.14
3-Br	Varied	65	1.23 ± 0.09	0.89 ± 0.30	0.08 ± 0.40
			Ionization of COOH group[d]		
Salicylic acids			ρ_{COOH}[d]		
	Varied[e]	25	0.89 ± 0.06	0.10 ± 0.05	0.82 ± 0.04
	Varied[f]	25	0.96 ± 0.04	0.25 ± 0.11	1.04 ± 0.07
4-Me	Varied	25	1.45 ± 0.19	0.03 ± 0.44	1.31 ± 0.30
H	Varied	39	1.63 ± 0.09	0.50 ± 0.38	1.96 ± 0.26
3-Br	Varied	65	1.32 ± 0.16	0.26 ± 0.57	1.82 ± 0.38

[a]Based on standard Hammett equation using substituent constants σ^{+}.

[b]Based on standard Hammett equation using substituent constants σ, relative to leaving group phenol O.

[c]Based on extended Hammett equation (17) $\log (k_Y/k_H) = \rho_{COOH}\sigma_{COOH} + \rho_{phenol}\sigma_{phenol}$, using substituent constants σ relative to COOH and leaving group phenol O, respectively. All substituent constants are taken from Jaffé's compilation.

[d]Based on standard Hammett equation using substituent constants σ, relative to the COOH group.

[e]Correlation for pK_a values of 17 substituted acids (28).

[f]Correlation using pK_a values of the five substituents used in this work (28).

evidence of nucleophilic participation with nucleophiles, is more negative than that for the hydrolysis of 4 (X = 4-Me, Y = NO_2), which does not. However, the differences are small and entropies of activation are unreliable mechanistic indicators, particularly in the borderline region which we are considering. It seems clear that the cleavage of the C—O bond of the salicyl ethers 2 generally involves — at the carbon centre — simple, uncoupled S_N1 mechanisms.

The effect of changing cation lifetime

As the substituent X becomes less electron-donating, the lifetime of the 1-phenylethyl cation (**6**) decreases. From the work of Richard et al. (11–13), we know the lifetimes of such cations in 1:1 trifluoroethanol:water. These lifetimes were determined by competition experiments between solvent and azide, or for short-lived cations, by extrapolation of the data obtained for long-lived cations. In water, the lifetimes are reduced by a factor of two.[3] Thus, we can study the effect of the substituent X on the rate of hydrolysis of 1-phenylethyl salicyl ethers and relate this to the cation lifetime.

For a fixed salicylate leaving group (**2**, constant Y) the plateau rate constants, corrected to 39°C, are correlated by the Hammett equation using substituent constants σ^{+} (Table 4). The plots are linear over a range of cation lifetimes, from 10^{-8} s (4-MeO substituent) to 5×10^{-13} s (3-Br substituent). There is no evidence of a change in catalytic mechanism as the cation lifetimes gets close to the point at which its existence may be called into question.

The correlations are generally good and give values of ρ^{+} from –4.5 to –5.3. A number of literature values of ρ^{+} are available for comparison, for the solvolysis of various 1-phenylethyl derivatives. For substituted 1-phenylethyl chlorides in 80% aqueous acetone, $\rho^{+} = -5.5$ (14); for 1-phenylethylacetates in 30% aqueous ethanol, ρ^{+} is –5.7 (15); and for 1-phenylethyl diphenylphosphinates in 80% ethanol–water, ρ^{+} is –5.1 (16). Also Richard et al. (13) correlated rate constants for the acid-catalysed cleavage of 1-phenylethyl alcohols to form the corresponding cations in 1:1 trifluoroethanol:water), obtaining $\rho^{+} = -4.5$. Similar values were observed in this work for the hydrolyses of simple 2,4-dinitrophenyl ethers **4** (Table 3). These are correlated by the Hammett equation with $\rho^{+} = -4.9 \pm 0.5$.

These large, negative values of ρ^{+} indicate similar, substantial charge development on carbon. The fact that the values obtained for the hydrolysis of 1-phenylethyl salicyl ethers are close to those obtained for the solvolyses of other 1-phenylethyl derivatives show that charge development on carbon is also similar.

A more meaningful estimate of the extent of charge development on carbon is obtained by comparing ρ^{+} with the equilibrium value of for complete C—O cleavage, i.e., for the formation of 1-phenylethyl carbocations, ρ^{+}_{eq}. Richard et al. (13) determined ρ^{+} not only for the acid-catalysed cleav-

[3]J.P. Richard. Personal communication.

© 1999 NRC Canada

Fig. 2. More O-Ferrall – Jencks potential energy diagram for the intramolecular general acid-catalysed cleavage of 1-arylethyl ethers (**2**) of salicylic acid to salicylate anion and the 1-arylethyl cation **6**. A and B represent, respectively, the approximate locations of the transition state for the reverse reaction, the general base-catalysed hydrolysis of the cations (21), and the forward reaction studied in this work. For details see the text.

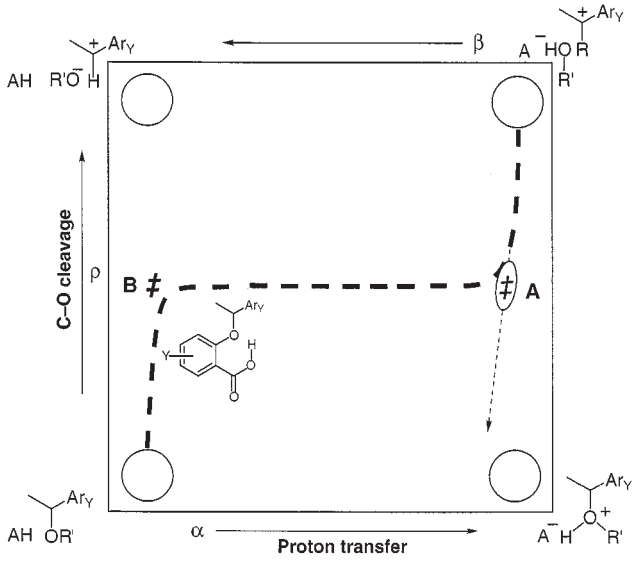

age of substituted 1-phenylethyl alcohols, but also for the reverse reaction, the addition of water to the cations, for which ρ^+ is +4.5. The equilibrium value ρ^+_{eq} ($\rho^+_{forward} - \rho^+_{reverse}$) is therefore –9. Using this as an estimate for ρ^+_{eq} for the formation of phenylethyl cations from our ethers suggests that the cleavage of the C—O bond in our salicyl ethers **2** has proceeded about halfway towards the cation in the transition state.[4]

The effect of changing leaving group

When the substituent Y on the aromatic ring of salicylate is varied, both the leaving group capability of the phenol and the strength of the catalytic carboxylic acid group change. Jaffé's simple extension of the Hammett equation (17) (eq. [2]) allows the two effects to be separated.

$$[2] \quad \log (k_H/k_Y)/\sigma_{carboxyl} = \rho_{carboxyl} + (\rho_{phenol} \times \sigma_{phenol})/\sigma_{carboxyl}$$

Values of σ_{phenol} and $\rho_{carboxyl}$ obtained from the Jaffé plots are also given in Table 4. It is evident that in the transition state for the hydrolysis of these 1-phenylethyl salicyl ethers, there is extensive bond cleavage to the leaving group oxygen. The values of ρ_{phenol} may be converted to β_{LG} values by dividing by ρ for the ionization of a phenol, –2.28 (18). The values obtained should be close to normalized β_{LG}, since substituent effects on the carbon basicity of phenolate anions are the same, within experimental error, as those on their proton basicity (19, 20). They are also close to those (0.4–0.5) reported for other salicylic acid acetals (9). So too are the very low values of $\rho_{carboxyl}$, indicating that substantial bond cleavage to oxygen is accompanied by very little proton transfer from the COOH group in the transition state for C—O cleavage. These data complement those for charge development at carbon: rather less than half a full negative charge appears to have developed on the leaving group oxygen in the transition state, as expected if the bond is about half broken, with an apparently very small amount of the developing charge neutralized by proton transfer.

Further evidence that proton transfer in the transition state is not far advanced comes from the solvent deuterium isotope effects. These were measured for four compounds, and are presented in Tables 1 and 2. The values of k^0_H/k^0_D are similar to those obtained for other salicylate derivatives (6, 9), and lead, as before, to the conclusion that proton transfer in the transition state is not as far developed as in a classical general acid-catalysed reaction.

The $\rho_{carboxyl}$ values could be converted into α-values by dividing them by ρ for the ionization of the carboxylic acid, but in this case the operation is of little significance since the ρ values are already close to zero. (The apparent pK_a values for the five substituted compounds are correlated reasonably well by the simple Hammett equation but, surprisingly, give ρ values substantially greater than 1, especially for the set with X = H (Table 4). The value ρ for the ionization of benzoic acids is 1 by definition, and generally close to 1 for substituted benzoic acids.)

There is no evidence for any change in α as the stability of the cation changes (X is varied), indicating that the interaction coefficient P_{xy} is zero. It is not possible to assess whether α changes with changing pK_a of the phenol, because the Jaffé treatment assumes ρ_{phenol} and $\rho_{carboxyl}$ to be constant over the range of compounds studied. If this assumption were not valid the Jaffé equation would not give linear plots. In fact, for one subset of ethers (with X = 3-Br) the plot does not give a good straight line (see the data in Table 3). However, if the extent of proton transfer to the leaving group oxygen were changing over this series, we would not expect the simple Hammett plot (which assumes that the substituent Y affects the phenol oxygen *only*) to give a good straight line; but it does (r = 0.992). We conclude that the nonlinear Jaffé plot is not indicative of varying extents of proton transfer, but rather reflects experimental error.

A final question is whether the extent of bond cleavage to the leaving group in the transition state changes with the stability of the cation. For values of ρ_{phenol} obtained from the simple Hammett correlation (Table 4), ρ_{phenol} is significantly smaller for X = 4-Me than for X = H and X = 3-Br. However, the difference disappears when the Jaffé treatment is applied, and we conclude that this variation also is unlikely to be significant. Our general conclusion is that, as far as C—O cleavage is concerned, the expulsion of salicylate closely resembles the spontaneous expulsion of good leaving groups.

The mechanism for efficient general acid catalysis

The detailed mechanism which emerges for proton-transfer catalysis appears to be very different from the mechanism proposed by Jencks and his co-workers (21, 22) for

[4] There is some variation in the values of ρ^+ as the leaving group changes (Table 4), but the variation is not systematic, and the errors too large to convince us that the effect is significant.

© 1999 NRC Canada

Scheme 1.

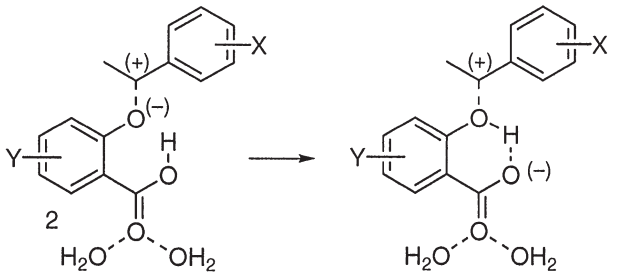

the reverse reaction, the general base-catalysed addition of alcohols to 1-phenylethyl cations. The contrast is illustrated in Fig. 2, a More O-Ferrall – Jencks diagram based on the published plot of Richard and Jencks (21). These authors found that addition of alcohols and phenols to moderately stable arylethyl cations **6** is general base catalysed, and shows very small β values: corresponding to large α-values, close to unity, for general acid catalysis of ether cleavage. We by contrast observe very *small* α-values for the cleavage of the salicyl ethers **2**. Richard and Jencks proposed a reaction coordinate close to vertical, and thus very close to the pathway for specific acid catalysis (broken arrow, transition state A in Fig. 2) for the reaction of the 1-(4-methoxyphenyl)ethyl cation with trifluoroethanol, suggesting that general base catalysis will not be observed at all for the addition of alcohols to less stable carbocations. Thus, the evidence indicates that the expulsion of the phenol oxygen catalysed by the *ortho*-carboxylic acid group of salicylate, for which the transition state (B) appears to be located on the opposite side of Fig. 2, is quite different from the same reaction catalysed by external general acids.

This apparent divergence can be resolved if the (vertical) C—O cleavage and (horizontal) proton-transfer processes (Fig. 2) are only very weakly coupled, as indicated by the bold, broken reaction coordinate, with the transition state at B. We have pointed out previously, for the similar departure of salicylate from salicyl phosphate (6), that in the ground state of salicylic acid derivatives in aqueous solution the carboxyl group is likely to be rotated out of the plane of the aromatic ring (as it is in crystal structures of salicylic acid derivatives), while proton transfer takes place most efficiently in the plane, within a developing strong hydrogen bond. At a given stage of the C—O cleavage process of a reactive system **2**, the COOH group must rotate into plane to form the hydrogen bond to the developing oxyanion. If this happens at, or close to, the point where proton transfer becomes thermodynamically favourable, it marks the transition state for the overall process. The apparent contradiction between the observation of efficient proton-transfer catalysis and the evidence that there is little proton transfer from the COOH group in the transition state arises because the proton transfer itself takes place within a strong intramolecular — and thus low barrier (23–25) — hydrogen bond. Because the proton-transfer step is so fast it (*i*) does not contribute significantly to the free energy barrier to reaction, and (*ii*) takes place faster than the solvation shell can respond (Scheme 1). In this situation (related to the "imperfect synchronisation of resonance" identified by Bernasconi (26) in reactions involving proton transfer to carbon), substituent effects (here, the Bronsted α coefficient) lag behind changes in local bond order.

Mechanism and efficiency in intramolecular general acid catalysis

This mechanism in which a rapid proton-transfer step forms an integral part of C—O cleavage, yet is largely uncoupled from it, is the most detailed available for a reaction involving efficient intramolecular proton-transfer catalysis. An important question is whether it is peculiar to the salicylic acid leaving group: the potential delocalization of the developing negative charge of the leaving group oxygen into the COOH group is a relevant special feature of the salicylate system. Comparisons of ρ values for the leaving group suggest that this is not a major factor.

This mechanism also differs significantly from a classical general acid catalysis mechanism. Most well-characterized general species catalysed reactions appear to involve proton transfers strongly coupled to bond making or breaking processes, as indicated by Bronsted coefficients in the region 0.5 ± 0.2. However, intramolecular versions of these reactions are characteristically inefficient. Features of the proposed mechanism which clearly favour efficient catalysis are the development of a strong hydrogen bond in the transition state, and its absence in the ground state (1). This makes possible the horizontal section of the pathway (Fig. 2) for efficient catalysis.

This strategic delay in setting up the hydrogen bond that is central to efficient proton-transfer catalysis is incidental to the salicylate system, but could clearly make an important contribution to catalysis in an enzyme active site, where distance and geometry are under much closer control. The preliminary stages of C—O bond breaking, not a problem in reactive model systems, require separate, perhaps nucleophilic assistance in the case of the poor leaving groups involved in most enzyme-catalysed cleavages of C—OR and P—OR bonds, so details of systems where the two modes of catalysis might work together are of great potential interest. In this context, we find no evidence for catalysis of nucleophilic attack on any ether of salicylic acid. Such negative evidence is not strong, but the leaving group is good enough for nucleophilic attack to be expected for simple 1-(3-bromophenyl)ethyl ethers, on the basis of its observation for the 2,4-ditrophenyl derivative. We can speculate that the timing of the proton-transfer step may be too critical to be coupled with the attack of an outside nucleophile in this very simple model.

Experimental

Materials

Dry THF used in anion reactions was refluxed over sodium before use. Substituted methyl salicylates were obtained commercially (Aldrich) or prepared by esterification of the corresponding salicylic acid (BF_3–methanol). Substituted acetophenones and chlorobenzenes were obtained commercially (Aldrich or Fluka).

Column chromatography was performed on Merck Kieselgel 60 (7734) and flash chromatography on Merck Kieselgel 60 (9385). NMR spectra were recorded on a Varian EM390 instrument and IR spectra on a Perkin–Elmer 297 spectro-

© 1999 NRC Canada

Table 5. Summary of synthesis and characterization of substrate methyl esters **3**.

Compound **2**					
X	Y	Method	Yield (%)	Found, M^+	Required; for
4-Me	5-Me	A	66	253.1233	253.1229; $C_{17}H_{17}O_2$
4-Me	H	A	58	270.1252[a]	270.1256; $C_{17}H_{18}O_3$
4-Me	4-MeO	A	67	300.1347	300.1362; $C_{18}H_{20}O_4$
4-Me	5-Cl	A	63	304.0863	304.0866; $C_{17}H_{17}ClO_3$
4-Me	5-NO_2	B	38	284.0965[a]	284.0944; $C_{16}H_{14}NO_4$
H	5-Me	A	66	270.1262	270.1255; $C_{17}H_{18}O_3$
H	4-MeO	A	17	286.1218	286.1205; $C_{17}H_{18}O_4$
H	5-Cl	A	23	259.0548[a]	259.0526; $C_{17}H_{17}ClO_2$
H	5-NO_2	B	30	301.0957[b]	301.09501; $C_{16}H_{15}NO_5$
3-Br	5-Me	A	84	348.0343	348.0360; $C_{16}H_{15}BrO_3$
3-Br	H	A	79	334.0129	334.0144; $C_{16}H_{15}BrO_3$
3-Br	4-MeO	A	15	364.0327	364.0310; $C_{17}H_{17}BrO_4$
3-Br	5-Cl	A	77	371.9756	371.9767; $C_{16}H_{14}BrClO_3$
3-Br	5-NO_2	B	40	379.0031	379.0056; $C_{16}H_{14}BrNO_5$

[a]Largest fragment, $[M - Ome]^+$.

[b]Crystallized from ether–hexane as cubes, mp 95–96°C. Found: C 64.0, H 5.20, N 4.6; $C_{16}H_{15}NO_5$ requires C 63.8, H 5.05, N 4.6%.

photometer. Mass spectra were determined on a Kratos MS 30 instrument. Melting points (uncorrected) were determined on a Kofler hot stage apparatus.

1-Phenyl ethyl salicyl ethers **2** were prepared in situ by the alkaline hydrolysis of their methyl esters **3**. The esters **3** (Table 5) were in most cases made by the Williamson synthesis, by alkylation of the sodium salt of the methyl salicylate (Method A). Details follow for a representative example.

1-Phenylethyl (2-carbomethoxy)phenyl ether (3, X = H, Y = H)

Methyl salicylate (4 mL) was added to a suspension of sodium hydride (1.36 g) in THF. When effervescence had ceased the mixture was refluxed for 30 min, then cooled. 1-Phenylethyl bromide (5.73 g) and tetrabutyl ammonium bromide (0.97 g) were added and the mixture refluxed for 24 h. THF was removed under reduced pressure and water and ether added. The ether layer was separated and the water layer washed twice more with ether. The combined organic extracts were dried over sodium sulphate and solvent removed under reduced pressure. The residue was purified by column chromatography on silica gel under pressure using 10% ether–hexane as eluant, to give the ether (**3**, X = H, Y = H; 5.68 g, 71%) as an oil. ν_{max}: 1730, 1610, 1580, and 1500 cm^{-1}. δ_H (90 MHz, $CDCl_3$): 7.77 (IH, dd, 8, 2 Hz), 7.5–7.2 (6H, m), 7.0–6.7 (2H, m), 5.37 (lH, q, 6 Hz), 3.91 (3H, s), 1.61 (3H, d, 6 Hz). *m*/*z*: 256 (5%, M^+), 105 (100%, 1-phenylethyl cation) (found: M 256.1095; $C_{16}H_{16}O_3$ requires 256.1099).

Ethers of 5-nitrosalicylic acids were made by aromatic nucleophilic substitution reactions, of the substituted 1-phenylethanolate anion on the 2-chloro-5-nitrobenzoate (method B). For example:

1-(4-Methoxyphenyl)ethyl (2′-carboxymethyl-4′-nitrophenyl) ether 2 (X = OMe, Y = 5-NO_2)

Sodium hydride (0.14 g of a 60% slurry in oil) was suspended in dry THF and 1-(4-methoxyphenyl) ethanol (0.46 g) added. The mixture was refluxed for 30 min, then cooled. Sodium 2-chloro-4-nitrobenzoate was prepared separately by treating 2-chloro-4-nitro benzoic acid (0.61 g) with sodium hydride (0.12 g) in dry THF to give a white slurry of the sodium salt. Tetrabutylammonium bromide (0.1 g) was added and the slurry poured quickly into the solution of alcoholate anion. The mixture was stirred at 50°C for 24 h. Trimethyloxonium tetrafluoroborate (0.89 g) was then added and the mixture stirred for 1 h longer. During this time, the cloudy solution of the acid salt clarified as the carboxylate ion was methylated. The THF was removed under reduced pressure and dichloromethane added. The dichloromethane was extracted three times with 1 M HC1, three times with 1 M potassium bicarbonate, and once with saturated brine. The organic layer was dried over sodium sulphate and the solvent removed under reduced pressure to leave a brown oil. The oil was purified by column chromatography on silica gel under pressure using 25% ether–hexane as eluant to give **2** (X = 4-OMe, Y = 5-NO_2, 0.46 g, 47%) as an oil. ν_{max}: 1740 (C=O), 1620, 1600, 1500, 1520, and 1360 cm^{-1}. δ_H (90 MHz, $CDCl_3$): 8.71 (1H, d, 3Hz), 8.20 (lH, dd, 9, 3Hz), 7.37 (2H, d, 7.5 Hz), 6.95 (1H, d, 9 Hz), 6.91 (2H, d, 7.5 Hz), 5.50 (1H, q, 6Hz), 4.00 (3H, s), 3.81 (3H, s), 1.70 (3H, d, 6Hz). *m*/*z*: 331 (10%, M + 1), 135 (100%, 1-(4-methoxyphenyl)ethyl cation) (found: M^+ 331.1056; $C_{17}H_{17}NO_6$ requires 331.1056).

Aryl 1-phenylethyl ethers **4** were prepared by the same method, by S_NAr substitution on the chloro- or fluoronitrobenzene (e.g., by 1-(4-methylphenyl)ethoxide on 2,4-dinitrofluorobenzene for **4**, X = 4-Me, Y = 4-NO_2). Details are summarized in Table 6.

Kinetic measurements

Stock solutions (5 mM in dioxan) of aryl acetals were injected into buffer solutions in 10% (v/v) dioxan–water (up to 0.4 M total buffer) made up with KCl to ionic strength 1.0 M. Rates of hydrolysis were measured by monitoring the appearance of the aryloxide anion over time, at 39.2°C. Reactions were followed in 10% (v/v) dioxan–water, ionic strength 1.0 M (KCl), for at least three half-lives and end points taken after at least 10. Ether hydrolysis could in most

© 1999 NRC Canada

Table 6. Summary of synthesis and characterization of ethers **4**.

Compound **4**					
X	Y	Yield (%)	Found, M^+	Required; for	mp
4-Me	CF_3	67	278.09335	278.0925; $C_{16}H_{13}F_3O$	Oil
4-Me	H[a]	20	257.1062	257.1052; $C_{15}H_{15}NO_3$	Oil
4-Me	Cl[a]	16	291.0663	291.0673; $C_{15}H_{14}ClNO_3$	Oil
4-Me	NO_2	60	184 (5%), 119 (100%)	$C_6H_4NO_5$; C_9H_{11}[b]	Oil
H	NO_2	40[a]	184 (51%), 105 (100%)	$C_6H_4NO_5$; C_8H_9[b,c]	103–104°C
3-Br	NO_2	50	M^+, 365.9870	365.9862; $C_{14}H_{11}BrN_2O_5$	108–109°C

[a]The chloronitrobenzene was used.

[b]No molecular ion observed. Correct by IR, ^{1}H NMR, and fragmentation pattern.

[c]Found: C 58.2, H 4.1, N 9.6; $C_{14}H_{12}N_2O_4$ requires C 58.3, H 4.2, N 9.7%.

cases be followed directly by measuring the increase in UV absorbance as the salicylate anion was released, but for most 5-nitrosalicylic acid derivatives the change in absorbance was too small, so a simple pH jump technique was used. Reactions were initiated by injecting a sample of stock solution into 2 mL of buffer to give a final substrate concentration of about 5×10^{-4} mol dm^{-3}: aliquots were taken at intervals and injected into 2 mL portions of pH 10.5 buffer. This quenched the reaction and converted all the 5-nitrosalicylate into the dianion. All pH measurements were made under the conditions of the kinetic experiments using a Radiometer PHM82 pH meter fitted with a Russell CTWL electrode. Activities at pH < 2 were calculated by adding the appropriate activity coefficient correction (e.g., 0.18 at 39°, ionic strength 1.0 M with KCl) to –log [H^+]. The pD of solutions in D_2O was measured by adding 0.4 to the meter reading obtained using the same electrode standardized against H_2O buffers (27).

References

1. A.J. Kirby. Acc. Chem. Res. **30**, 290 (1997).
2. A.J. Kirby. Adv. Phys. Org. Chem. **17**, 183 (1980).
3. C.J. Brown and A.J. Kirby. J. Chem. Soc. Perkin Trans. 2, 1081 (1997).
4. S.E. Barber and A.J. Kirby. Preliminary communication: J. Chem. Soc. Chem. Commun. 1775 (1987).
5. C.G. Swain and C.B. Scott. J. Am. Chem. Soc. **75**, 141 (1953).
6. R.H. Bromilow and A.J. Kirby. J. Chem. Soc. B, 149 (1972).
7. R.H. Bromilow, S.A. Khan, and A.J. Kirby. J. Chem. Soc. B, 911 (1972).
8. C. Buffet and G. Lamaty. Rec. Trav. Chim. Pays-Bas, **95**, 1 (1976).
9. G.-A. Craze and A.J. Kirby. J. Chem. Soc. Perkin Trans. 2, 61 (1974).
10. J.P. Richard and W.P. Jencks. J. Am. Chem. Soc. 1383 (1984).
11. J.P. Richard. In Advances in carbocation chemistry. *Edited by* X. Creary. JAI Press, London. 1989. pp. 121–169.
12. J.P. Richard and W.P. Jencks. J. Am. Chem. Soc. **104**, 4689 (1982).
13. J.P. Richard, M.E. Rothenberg, and W.P. Jencks. J. Am. Chem. Soc. **106**, 1361 (1984).
14. Y. Tsuno, Y. Kusuyama, M. Sawada, T. Fujii, and Y. Yukawa. Bull. Chem. Soc. Jpn. **48**, 3337 (1975).
15. E.A. Hill, M.L. Gross, M. Stasiewicz, and M. Manion. J. Am. Chem. Soc. **91**, 7381 (1969).
16. D.S. Noyce and J.A. Virgilio. J. Org. Chem. **37**, 2643 (1972).
17. H.H. Jaffé. Chem. Rev. **53**, 191 (1953).
18. P.D. Bolton, F.M. Hall, and J. Kudrynski. Aust. J. Chem. **21**, 1541 (1968).
19. C.F. Bernasconi and G.D. Leonarduzzi. J. Am. Chem. Soc. **104**, 5133 (1984).
20. A. Williams. Adv. Phys. Org. Chem. **27**, 1 (1992).
21. J.P. Richard and W.P. Jencks. J. Am. Chem. Soc. **106**, 1396 (1984).
22. R. Ta-Shma and W.P. Jencks. J. Am. Chem. Soc. **108**, 8040 (1986).
23. J.A. Gerlt and P.G. Gassman. J. Am. Chem. Soc. **115**, 11 552 (1993).
24. W.W. Cleland, P.A. Frey, and J.A. Gerlt. J. Biol. Chem. **273**, 25 529 (1998).
25. S. Scheiner. Acc. Chem. Res. **28**, 402 (1995).
26. C.F. Bernasconi. Tetrahedron, **41**, 3219 (1985).
27. P.K. Glasoe and D.A. Long. J. Phys. Chem. **64**, 188 (1960).
28. G.E. Dunn and F.L. Kung. Can. J. Chem. **44**, 1261 (1966).

© 1999 NRC Canada

Ring opening of cyclobutene-1,2-dione and 3-trimethylsilylcyclobutene-1,2-dione. Dimerization/decarbonylation of a bisketene to a ketenylbutenolide

Annette D. Allen and Thomas T. Tidwell

Abstract: Hydrolysis of 3-trimethylsilyl-4,4-dichlorocyclobut-2-ene-1-one (**4**) in H_2SO_4 gave small amounts of cyclobutene-1,2-dione (**2a**) and 3-trimethylsilylcyclobutene-1,2-dione (**2d**). Photolysis of **2a** gave evidence for the formation of the bisketene ($CH{=}C{=}O_2$) (**1a**) in solution for the first time, as identified by the IR band at 2120 cm^{-1} and the ^1H NMR signal at δ 3.20. Thermolysis of **2d** gave evidence for the intermediacy of $O{=}C{=}CHC(SiMe_3){=}C{=}O$ (**1d**), with an ^1H NMR signal at δ 3.43, and the isolation of the unusual ketenyl lactone **6**, which could arise by formation of an unsymmetrical [2+2] ketene dimer from **1d**, followed by rearrangement and decarbonylation.

Key words: bisketenes, cyclobutenediones, ketene dimerization.

Résumé : L'hydrolyse de la 3-triméthylsilyl-4,4-dichlorocyclobut-2-ène-2-one (**4**) dans du H_2SO_4 fournit de faibles quantités de cyclobutène-1,2-dione (**2a**) et de 3-triméthylsilylcyclobutène-1,2-dione (**2d**). La photolyse du produit **2a** fournit des données suggérant pour la première fois qu'il peut y avoir formation du biscétène $(CH{=}C{=}O)_2$ (**1a**) en solution, identifié par la bande IR à 2120 cm^{-1} et du signal en RMN du ^1H à δ 3,20. La thermolyse du produit **2d** fournit des données suggérant la formation, comme intermédiaire, de la $O{=}C\text{-}CHC(SiMe_3){=}C{=}O$ (**1d**) qui présente un signal en RMN du ^1H à δ 3,43; elle permet aussi d'isoler la lactone céténylе inhabituelle **6** qui pourrait provenir de la formation, à partir de **1d**, de la formation d'un cétène dimère non symétrique [2+2] qui serait suivie d'un réarrangement et d'une décarbonylation.

Mots clés : biscétènes, cyclobutènediones, dimérisation de cétène.

[Traduit par la Rédaction]

The parent 1,2-bisketene 1,4-dioxo-1,3-butadiene (**1a**) is calculated at the MP2/6-31G*//MP2/6-31G* level to be most stable in the twisted structure shown, which is only 2.9 kcal/mol less stable than cyclobutenedione **2a** (1). The SiH_3, H, and bis(SiH_3) substituted bisketenes **1b** and **1c** are calculated at the MP2/6-31G*//HF/6-31G* level to be more stable than the corresponding cyclobutenedione **2b**,**c** by 0.5 and 4.9 kcal/mol, respectively (1). The preparation of **1a** by photolysis of the bis(diazoketone) **3** in an Ar matrix at 10 K has been reported (eq. [2]), as characterized by an IR band at 2125 cm^{-1} (2). The formation of **1a** as an unobserved intermediate from the pyrolysis of 4-cyclopentene-1,2,3-trione that gave the observed formation of **2a** has also been proposed (3). Because of our interest in the 1,2-bisketene–cyclobutenedione interconversion (4), it was attractive to attempt to observe **1a** and the Me_3Si analogue **1d** of **1b** in solution.

[1] 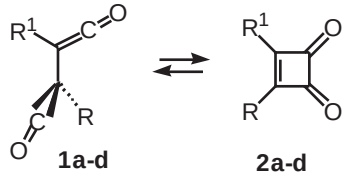

where R = R^1 = H (**a**); R = SiH_3, R^1 = H (**b**); R = R^1 = SiH_3 (**c**); R = $SiMe_3$, R^1 = H (**d**).

[2] 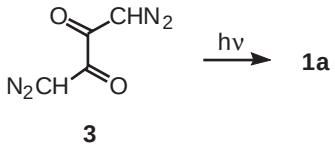

Results

Two syntheses of **2a** have been reported (5, 6), but because we had noticed that the desilylation of trimethylsilyl substituted cyclobutenones occurred in acid, it was decided to attempt the preparation of **2a** and **2d** in a one-pot procedure. To form a suitable precursor, the reaction of trimethylsilylacetylene with dichloroketene, generated in situ from zinc dechlorination of trichloroacetyl chloride, gave predom-

Received November 27, 1998.

This paper is dedicated to Jerry Kresge in recognition of his many achievements in chemistry.

A.D. Allen and T.T. Tidwell.[1] Department of Chemistry, University of Toronto, Toronto, ON M5S 3H6, Canada.

[1]Author to whom correspondence may be addressed. Telephone: (416) 287-7217. Fax: (416) 287-7279. e-mail: ttidwell@chem.utoronto.ca

© 1999 NRC Canada

inant dichlorocylobutenone **4** (eq. [3]) as the major product, as reported by Danheiser and Sard (7).

[3] $CCl_3COCl + Me_3SiC{\equiv}CH \xrightarrow{Zn}$ 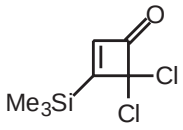

[4] 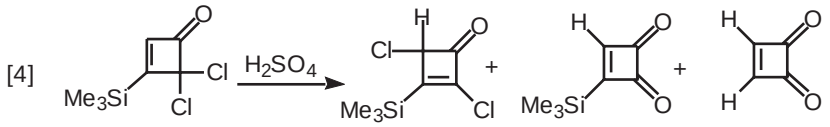

4 **5** **2d** **2a**

Hydrolysis of **4** at 60–65°C with concentrated H_2SO_4 for various times followed by quenching in ice water and extraction with ether resulted in the gradual disappearance of **4** with the formation of three new products, identified as described below as the rearranged chloride **5**, **2d**, and **2a**, in the relative yields shown, as measured by ^{1}H NMR (eq. [4], Table 1).

Chromatrographic separation of the product from 260 min reaction time gave **5** (obtained in 95% purity, containing 5% **4**, after three-fold rechromatography) and **2d** (8%). Each of these was fully characterized by spectroscopic means, with distinctive ^{1}H NMR signals in $CDCl_3$ for **5** (δ 0.37, 5.39) and **2d** (δ 0.35, 9.61). After extraction of the reaction mixture from another preparation with ether and evaporation of the solvent, crystallization from pentane gave crystals of **2a**, identified spectroscopically, in good agreement with literature values (5, 6).

The ^{17}O NMR chemical shift of **2a** was also measured as δ 514.5 ppm. Previous (8) ab initio calculations of ^{17}O chemical shifts of 1,2-cyclobutenediones gave values that deviated by 51 ppm downfield from experimentally available values (for the Cl, Cl and CH_3, CH_3 substituted derivatives), and application of this correction factor to that calculated for **2a** gives a prediction of δ 511 for **2a**, in close agreement to that observed experimentally. This ^{17}O shift is the lowest that has been reported for a cyclobutenedione (8), and is comparable to that of the $SiMe_3$, $SiMe_3$ derivative (499.1 ppm). The low-field shifts of these two compounds are consistent with the observed trend in which electron donor groups cause ^{17}O shifts to higher fields (8).

Upon photolysis of **2a** in isooctane with 300 and 350 nm light at 0°C, partial conversion to the bisketene **1a** was observed, as detected by the IR band at 2120 cm^{-1}, compared to the reported (2) absorption at 2125 cm^{-1} in an Ar matrix. The ^{1}H NMR spectrum showed a signal at δ 3.20 that disappeared with time, which is attributed to the bisketene, and which may be compared to the value for the ketenyl proton of $CH_2{=}CHCH{=}C{=}O$ of δ 4.0 (9). Efforts to observe the ^{13}C NMR spectrum were unsuccessful due to the lack of material.

Other signals appeared and their possible assignments included δ 8.90 (cyclopropenone, reported (10) 9.1 in CH_2Cl_2), 7.04 (maleic anhydride, identical to an authentic sample), 3.01 (succinic anhydride, identical to an authentic sample), and 1.91 (HC≡CH, identical to an authentic sample). These products correspond to the matrix observed products from mono- and bisdecarbonylation (2), the reaction with O_2 (previously (11) observed for $[Me_3SiC{=}C{=}O]_2$), and hydration.

Attempts to observe a UV band which could be reliably ascribed to **1a** and to measure a rate of reformation of **2a** were unsuccessful. From our published correlation (4) of the rates of bisketene ring closure with ketenyl substituent stabilizing parameters SE (log k = –0.292 Σ SE – 2.02), a predicted rate constant is 5.0 × 10^{-5} s^{-1} at 25°C, based on the SE value of 3.9 kcal/mol for H.

Photolysis of degassed solutions **2d** in $CDCl_3$ with 300–350 nm light resulted in the formation of a yellow color and complex ^{1}H NMR spectra, and so these were not pursued further. Thermolysis of **2d** in $CDCl_3$ for 6.7 h at 100°C gave ^{1}H NMR signals attributed to **1d** (^{1}H NMR signal at δ 3.43) and the ketenyl lactone **6** (Scheme 1). Evaporation of the solvent and chromatographic separation (silica gel, 3/2 CH_2Cl_2/hexane) gave **6** as a yellow solid that was identified by its IR spectrum (C=C=O at 2089 cm^{-1}, C=O at 1754, 1738 cm^{-1}, C=C at 1632 cm^{-1}), ^{1}H NMR ($CDCl_3$) δ 0.24 (Me_3Si), 0.28 (Me_3Si), 4.97 (CHC=C=O), and 7.31 (CH=CTMS), the correct M^+ peak (280) using EIMS or FAB, and the expected ^{13}C NMR spectrum. The *Z*-stereochemistry of the exocyclic double bond in **6** is tentatively assigned by analogy with *Z*-5-ethylidene-2(5*H*)-furanone (**7**) for which as in the case of **6** no coupling was detected between H_4 and H_6 in the ^{1}H NMR, whereas for *E*-**7** a coupling of 0.8 Hz was observed (12). Also, the chemical shift of H_4 in **6** (7.31 ppm) is similar to that of H_4 in *Z*-**7** (7.25 ppm).

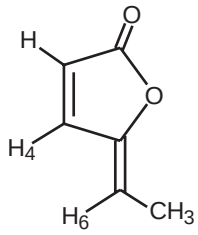

Z–**7**

A possible mechanism for the formation of **6** from the bisketene **1d** is shown in Scheme 1. In this process, either an intermediate zwitterion **8** may be formed or there may be concerted formation of an unsymmetrical ketene dimer **9**. Either of these species may form the epoxide intermediate **10**, or the cyclopropanone **11**, which could then undergo decarbonylation to **6**. The interconversion of allene oxides analogous to **10** and cyclopropanones has been suggested (13, 14) to occur through oxyallyl species (15), and the reaction of bisketenes with dienes to form ketenylcyclobutan-

© 1999 NRC Canada

Scheme 1.

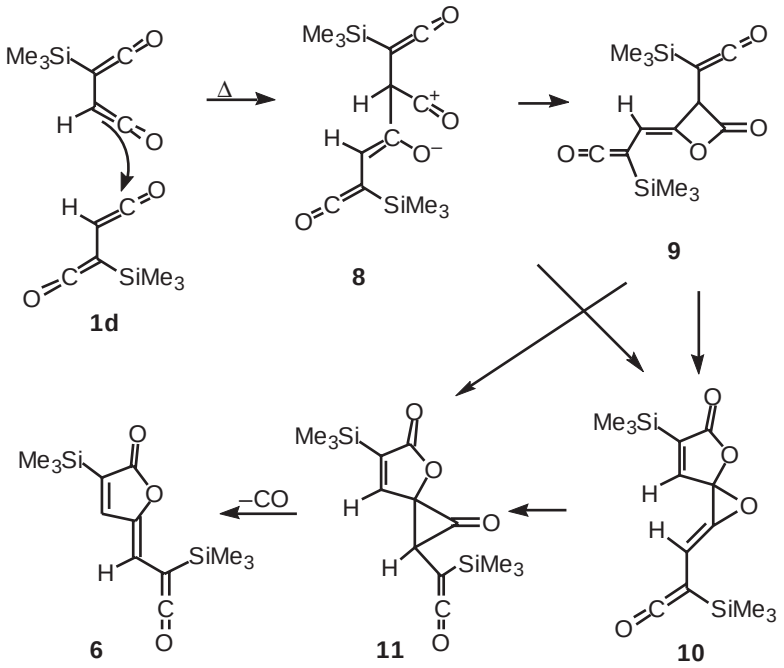

Table 1. Hydrolysis of **4** with H_2SO_4 at various times and relative yields of the products, **5**, **2d**, and **2a**.

	% yield (rel.)			
Time (min)	**4**	**5**	**2d**	**2a**
100	62	17	8	13
160	38	31	15	16
260	14	46	18	19

ones, which are analogous to the β-lactone **9** and which rearrange to spirocyclopropylbutenolides resembling **11**, has been demonstrated (16, 17). The intermediate **8** resembles those proposed as occurring in the mixed dimerizations of ketenes (18).

In summary, the cyclobutenediones **2a** and **2d** serve as precurors for the first solution phase observation of the bisketenes **1a** and **1d**. The latter is the first bisketene observed to undergo intermolecular self-reaction, eventually forming after decarbonylation the unusual ketenyl lactone **6**.

Experimental

General procedures

All reactions were carried out in oven-dried glassware under an atmosphere of N_2 or Ar. NMR spectra were measured with Varian Gemini 200 and XL-400 spectrometers. Infrared spectra were measured using a Nicolet DX FT-IR instrument. Mass spectra were obtained on a VG 70-2505 instrument by Dr. A. Young. Photolyses were carried out with a Rayonet RPR-100 photoreactor.

3-Trimethylsilylcyclobutene-1,2-dione (2d)

Cyclobutenone **4** (0.277 g, 1.3 mmol) was added to 6 mL conc. H_2SO_4 in a round-bottom flask, and the mixture was stirred while heating at 60–65°C for various times. The reaction mixture was added to 20 mL ice water and extracted 10 times with 10 mL portions of ether, and the combined ether layers were dried over $CaSO_4$ with small amounts of K_2CO_3 and evaporated, yielding a yellow oil, and the composition of the product was analyzed by ^{1}H NMR. Chromatography on Me_3SiCl treated silica gel with hexane gave **4** and **5**, and further chromatography (3% EtOAc in hexane) gave **2d** (0.016 g, 8%) as a yellow liquid. IR ($CDCl_3$): 1780 cm^{-1}; ^{1}H NMR ($CDCl_3$) δ 0.35 (s, 9, Me_3Si), 9.61 (s, 1); ^{13}C NMR ($CDCl_3$) δ –2.52, 192.6, 197.7, 201.8, 214.4; UV (isooctane) λ_{max}: 214 nm; EIMS *m/z*: 154 (M^+, 54), 126 (M^+ – CO, 18), 111 (M^+ – CO, CH_3, 12), 98 (M^+ – 2CO, 42), 83 (M^+ – 2CO, CH_3, 97), 73 (Me_3Si^+, 100); HRMS *m/z* calcd. for $C_7H_{10}O_2Si$: 154.0450; found: 154.0456.

2,4-Dichloro-3-trimethylsilylcyclobut-2-ene-1-one (5)

Threefold rechromatography of the hexane eluant from preparation of **2d** (5/95 EtOAc/hexane) gave **5** containing 5% **4**. ^{1}H NMR ($CDCl_3$) δ 0.37 (s, 9, Me_3Si), 5.39 (s, 1, CHCl); ^{13}C NMR ($CDCl_3$) δ –2.21, 69.27, 143.43, 179.64, 180.38; EIMS *m/z*: 208 (M^+, 12), 193 (M^+ – CH_3, 24), 165 (12), 145 (17), 93 (56), 73 (Me_3Si^+, 100); HRMS *m/z* calcd. for $C_7H_{10}Cl_2OSi$: 207.9878; found: 207.9868.

Cyclobutene-1,2-dione (2a)

Cyclobutenone **4** (0.936 g, 4.5 mmol) was stirred with 21 mL conc. H_2SO_4 at 52–67°C for 1.5 h and was worked up as before, and the ether extract was shown by ^{1}H to contain residual **4** (23%), **2a** (35%), and **5** (41%). After evaporation of the ether, the product was crystallized from pentane at –5°C to yield pale yellow crystals of **2a** (ca. 0.01 g, 0.15 mmol, 3%). ^{1}H NMR ($CDCl_3$) δ 9.65 (s, 1, $^1J_{C–H}$ = 185.1 Hz, $^3J_{H,H}$ = 2.9 Hz); lit. (CCl_4) δ 9.73 (5); ($CDCl_3$) δ 9.70, $^1J_{CH}$ = 185.8 Hz (6).

© 1999 NRC Canada

Thermolysis of 2d

A sample of **2d** in Ar degassed $CDCl_3$ in a sealed NMR tube was heated in a boiling water bath for 6.7 h, and the ^1H NMR spectrum was measured at intervals. A signal of δ 3.43 was observed, possibly due to the bisketene **1d**, along with signals assigned to ketenyl lactone **6**. The tube was opened, and the solvent evaporated, and chromatography on silica gel (6/4 CH_2Cl_2/hexane) gave **6**. ^1H NMR ($CDCl_3$) δ 0.24 (s, 9, Me_3Si), 0.28 (s, 9, Me_3Si), 4.97 (s, 1, CHC=C=O), 7.31 (s, 1, CH=CTMS); ^{13}C NMR ($CDCl_3$) δ –2.02, –0.82, 22.31, 104.35, 128.49, 148.04, 148.89, 178.65, 181; IR ($CDCl_3$): 2089 (C=C=O), 1754, 1738 (C=O), 1632 (C=C) cm^{-1}; EIMS *m/z*: 280 (M^+, 44), 265 ($M^+ - CH_3$, 53), 252 (M^+ – CO, 8), 237 (36), 73 (Me_3Si^+, 100).

Photolysis of 2a

A sample of **2a** in isooctane was degassed by a flow of Ar in an NMR tube and then was irradiated for 30 min using a combination of 300 and 350 nm lamps at 5°C. Measurement of the IR showed a band at 2120 cm^{-1} attributed to **1a** which disappeared with a 6 min half-life. Similar photolysis in $CDCl_3$ at –56°C and observation of the ^1H NMR spectra gave a signal at δ 3.20, possibly due to **1a**, and other signals with possible assignments: δ 8.96 (cyclopropenone lit. (10) 9.1 in CH_2Cl_2, δ 7.04 (maleic anhydride, identical to an authentic sample), δ 3.01 (succinic anhyride, identical to an authentic sample), δ 1.91 (acetylene, identical to an authentic sample).

Acknowledgements

Financial support by the Natural Sciences and Engineering Research Council is gratefully acknowledged.

References

1. M.A. McAllister and T.T. Tidwell. J. Am. Chem. Soc. **116**, 7233 (1994).
2. G. Maier, H.P. Reisenauer, and T. Sayrac. Chem. Ber. **115**, 2192 (1982).
3. M. Kasai, M. Oda, and Y. Kitahara. Chem. Lett. 217 (1978).
4. A.D. Allen, J.D. Colomvakos, F. Diederich, I. Egle, X. Hao, R. Liu, J. Lusztyk, J. Ma, M.A. McAllister, Y. Rubin, K. Sung, T.T. Tidwell, and B.D. Wagner. J. Am. Chem. Soc. **119**, 12 125 (1997).
5. J.C. Hinshaw. Chem. Commun. 630 (1971).
6. H.-D. Martin, A. Oftring, and R. Iden. Tetrahedron Lett. **23**, 841 (1982).
7. R.L. Danheiser and H. Sard. Tetrahedron Lett. **24**, 23 (1983).
8. G. Cerioni, R. Janoschek, Z. Rappoport, and T.T. Tidwell. J. Org. Chem. **61**, 6212 (1996).
9. W.S. Trahanovsky, B.W. Surber, M.C. Wilkes, and M.W. Preckel. J. Am. Chem. Soc. **104**, 6779 (1982).
10. R. Breslow, G. Ryan, and J.T. Groves. J. Am. Chem. Soc. **92**, 988 (1970).
11. D. Zhao, A.D. Allen, and T. T. Tidwell. J. Am. Chem. Soc. **115**, 10 097 (1993).
12. J. Font, R.M. Ortuno, F. Sanchez-Ferrando, C. Segura, and N. Terris. Synth. Commun. **19**, 2977 (1989).
13. D. Lim, D.A. Hrovat, W.T. Borden, and W.L. Jorgensen. J. Am. Chem. Soc. **116**, 3494 (1994).
14. B. A. Hess, Jr., U. Eckart, and J. Fabian. J. Am. Chem. Soc. **120**, 12 310 (1998).
15. T.S. Sorensen and F. Sun. J. Am. Chem. Soc. **119**, 11 327 (1997).
16. D. Miller, W. Theis, G. Heilig, and S. Kirchmeyer. J. Org. Chem. **56**, 1453 (1991).
17. R.D. Miller and S. Kirchmeyer. J. Org. Chem. **58**, 90 (1993).
18. H.W. Moore and D.S. Wilbur. J. Org. Chem. **45**, 4483 (1980).

© 1999 NRC Canada

Addition of the nitroxyl radical TEMPO to 1-naphthylketene: formation of an unusual adduct

Jennifer Carter, Michael H. Fenwick, Wen-wei Huang, Vladimir V. Popik, and Thomas T. Tidwell

Abstract: 1-Naphthylketene (**2**), generated by thermal Wolff-rearrangement, is trapped in situ by 2,2,6,6-tetramethylpiperidinyloxy radical (TEMPO, TO·) to form the adduct 1-naphthCH(OT)CO_2T (**4**), whose structure is confirmed by an X-ray determination. The ^{1}H NMR spectrum of **4** displays three CH_3 groups with very high field chemical shifts (δ 0.10–0.47), and this is attributed to the location of these groups in the shielding region above the π system of the naphthyl ring. At –40°C, doubling of most of the ^{1}H NMR signals occurs, and this is attributed to a freezing out of two conformations differing by rotation around the naphthyl—CH bond.

Key words: ketene, TEMPO, restricted rotation, ^{1}H NMR, conformational analysis, free radicals.

Résumé : Le 1-naphtylcétène (**2**) généré par un réarrangement de Wolff thermique peut être piégé in situ par le radical 2,2,6,6-tétraméthylpipéridinyloxy (TEMPO, TO·) pour former l'adduit 1-naphtylCH(OT)CO_2T (**4**) dont la structure a été confirmée par diffraction des rayons X. Le spectre RMN du ^{1}H du composé **4** comporte trois groupes CH_3 avec des déplacements chimiques à très haut champ (δ 0,10–0,47); ce résultat est attribué à la localisation de ces groupes dans la région de blindage au-dessus du système π du noyau naphtyle. À –40°C, la plupart des signaux de la RMN du ^{1}H sont dédoublés; cette observation pourrait être attribuée au fait que deux conformations ne différant que par une rotation autour de la liaison naphtyl—CH sont figées.

Mots clés : cétène, TEMPO, rotation restreinte, RMN du ^{1}H, analyse conformationnelle, radicaux libres.

[Traduit par la rédaction]

Diazoketones are useful sources of ketenes by Wolff-rearrangements, and this reaction has been utilized in a variety of mechanistic and theoretical studies of these intermediates (1). Both thermal and photochemical reactions of diazoketones lead to ketenes which can be trapped by nucleophiles such as H_2O, alcohols, and amines (1). In some cases, the reaction of the diazoketone is proposed to proceed through ketocarbenes, and in the case of photosensitized reactions, evidence for the intermediacy of these species has been provided by trapping of the carbenes with alcohols and amines (1).

Nitroxyl radicals (2) are powerful trapping agents for free radicals, but there has been little utilization of nitroxyls for the reaction with other functional groups and reactive intermediates. Recent reports have appeared of the addition of 2,2,6,6-tetramethylpiperidinyloxy (TEMPO, TO·) to styrene forming PhCH(OT)CH_2OT (3), of hydrogen abstraction from methylbenzenes (3, 4), and of TEMPO reaction with *t*-BuOO· radicals to form the unstable trioxide *t*-BuOOOT (5), but to our knowledge there are no reports of reactions of nitroxyl radicals with diazoketones.

Recently, we have made the first observations of the reactions of a nitroxyl radical with ketenes (6). Thus, TEMPO reacted with $Ph_2C{=}C{=}O$ at room temperature to give, after exposure to air, a peroxide interpreted as arising from TO· attachment to the carbonyl carbon forming a diphenylmethyl radical which combined with O_2 to give a peroxide whose structure was confirmed by X-ray crystallography (eq. [1]). Also, the bisketene $(Me_3SiC{=}C{=}O)_2$ reacted with TEMPO at 90°C to give the maleic anhydride derived from net oxygen atom donation, with expulsion of the piperidinyl radical (eq. [2]).

[1] $Ph_2C{=}C{=}O \xrightarrow{TO\bullet} Ph_2\dot{C}CO_2T \xrightarrow{O_2} TO_2CCPh_2OOCPh_2CO_2T$

[2] 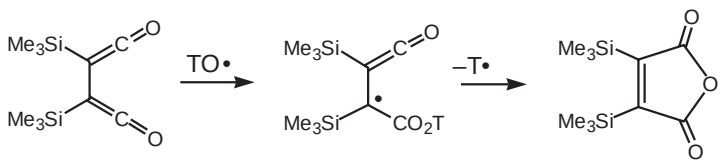

Received December 3, 1998.

This paper is dedicated to Jerry Kresge in recognition of his many achievements in chemistry.

J. Carter, M.H. Fenwick, W.-w. Huang, V.V. Popik, and T.T. Tidwell.[1] Department of Chemistry, University of Toronto, Toronto, ON M5S 3H6, Canada.

[1]Author to whom correspondence may be addressed. Telephone: (416) 287-7217. Fax: (416) 287-7279. e-mail: ttidwell@chem.utoronto.ca

 © 1999 NRC Canada

Fig. 1. X-ray structure of **4**.

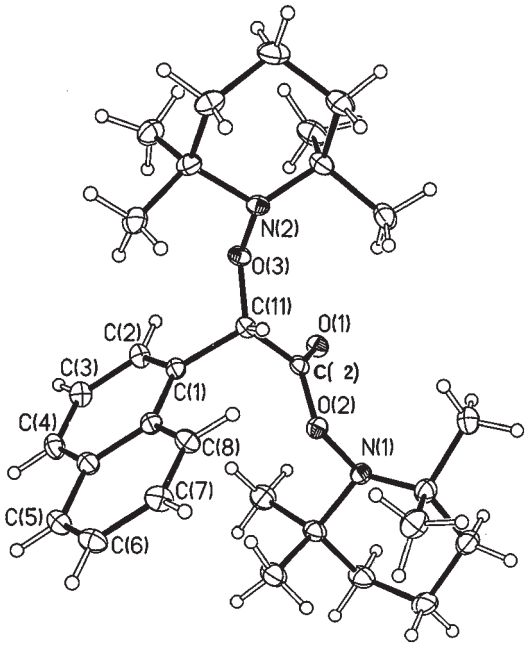

We now report the utilization of the stable nitroxyl radical 2,2,6,6-tetramethylpiperidinyloxy (TEMPO, TO·) for the examination of the Wolff-rearrangement of 1-naphthyl diazomethyl ketone (**1**), which is known to form ketene **2** upon thermolysis (7). No reaction was observed between **1** and TEMPO in solution at room temperature, but upon heating in refluxing toluene, reaction of **1** occurred and a new product **4** was found in 41% yield (eq. [3]). This was identified as the product of 1,2-addition of two molecules of TEMPO to **2** on the basis of the spectral properties and X-ray structure (Fig. 1). A pathway involving attack of TEMPO at the carbonyl carbon of the ketene forming the radical **3** is proposed by analogy with eq. [1] (6), with subsequent capture of **3** by TEMPO. Recent reports of trapping of α-carbonyl radicals by TEMPO have appeared (8).

Chemical ionization mass spectroscopy shows the expected MH^+ peak for **4** at *m*/*z* 481, and the ester IR peak appeared at 1772 cm^{-1}. The ^1H NMR spectrum, measured at 500 mHz, is, however, extraordinary. At 30°C (Fig. 2*a*) the eight CH_3 groups are nonequivalent because of the slow chair–chair inversion of the piperidinyl ring and also because of the chiral center. The barriers to bond rotation and ring inversion in *N*-alkoxy-2,2,6,6-tetramethylpiperidines have been investigated in detail by Anderson et al. (9, 10), who also report an example of four nonequivalent CH_3 groups in $TOCH_2CH(OH)Ph$ (10). In **4**, each of the CH_3 groups gives rise to a distinct signal, and three of these methyls appear at very high field, δ 0.10, 0.32 (broad), and 0.47, while the others are at δ 1.00, 1.06, 1.07, 1.34, and 1.36. A broad signal at δ 5.9 is assigned to the CHOT proton (at C(11) in Fig. 1). The seven naphthyl protons appear as a two-proton triplet at δ 7.45, a one-proton triplet at δ 7.52, two one-proton doublets at 7.78 and 7.82, and two broad one-proton signals at 7.63 and 8.42. At 60°C (Fig. 2*b*), the naphthyl peaks sharpen while the signals between δ 0.0 and 2.0 become very broad, evidently indicative of enhanced ring inversion of the piperidinyl groups, and the CH(OT) proton at δ 5.89 becomes sharper. At higher temperatures, decomposition of **4** becomes noticeable, and the details of this process are under investigation.

At –40°C (Fig. 2*c*), there is a doubling of many of the ^1H NMR signals of **4** visible at 30°C, with CH_3 signals at –0.03, 0.02, 0.06, 0.37, 0.40, 0.50, 0.88, 1.00, 1.03, 1.05, 1.06 (2 CH_3), 1.29, 1.30 (2 CH_3), and 1.36. The CH_2 signals are spread between δ 1.0 and 2.0, the CH(OT) proton appears as two sharp singlets at δ 5.63 and 6.14 (relative intensity 0.47 and 0.53, respectively), and the naphthyl protons appear as doublets (δ 7.88, 8.29, 8.51), triplets (δ 7.41, 7.59), and multiplets at 7.5 and 7.8.

The doubling of the signals was confirmed by a ^{13}C DEPT spectrum at –40°C (supplementary information)[2], which showed the presence of 16 CH_3 signals between δ 19.97 and 35.14, 7 CH_2 signals, 2 signals for C(11) at δ 83.03 and 90.44, and 11 aryl CH signals. Evidently, three of the CH and one of the CH_2 signals expected for doubling of the resonances were not resolved. In the room-temperature ^{13}C spectrum, no signal for C(11) is visible between δ 80–90 ppm, indicating that this signal is broadened by the coalescence phenomenon observed in the ^1H NMR spectrum. From the observed difference in frequency of 255.8 Hz of the signals for the C(8) proton at –40°C, a rate constant for interconversion of the two conformers of 7.9×10^2 s^{-1} may be esti-

[3]

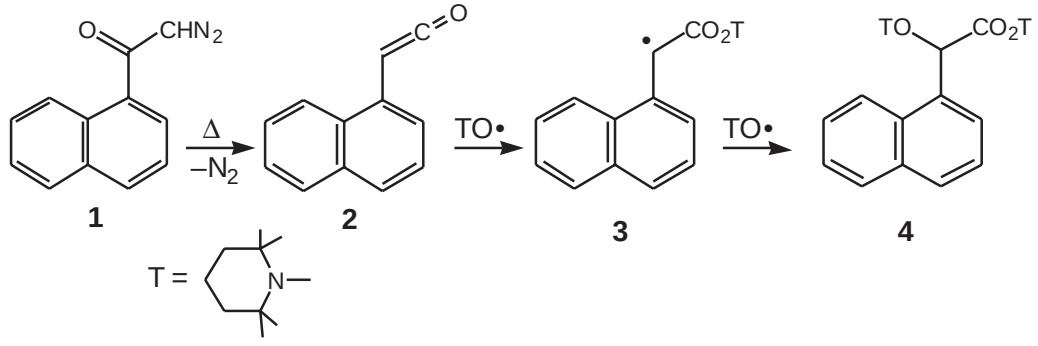

[2] X-ray crystallographic data and NMR spectra have been deposited as supplementary material and may be purchased from: The Depository of Unpublished Data, Document Delivery, CISTI, National Research Council Canada, Ottawa, Canada, K1A 0S2. Crystallographic data have also been deposited with the Cambridge Crystallographic Data Centre and can be obtained on request from: The Director, Cambridge Crystallographic Data Centre, University Chemical Laboratory, 12 Union Road, Cambridge, CB2 1EZ, U.K.

© 1999 NRC Canada

Fig. 2. ^{1}H NMR spectra of **4**. (*a*) 30°C; (*b*) 60°C; (*c*) –40°C.

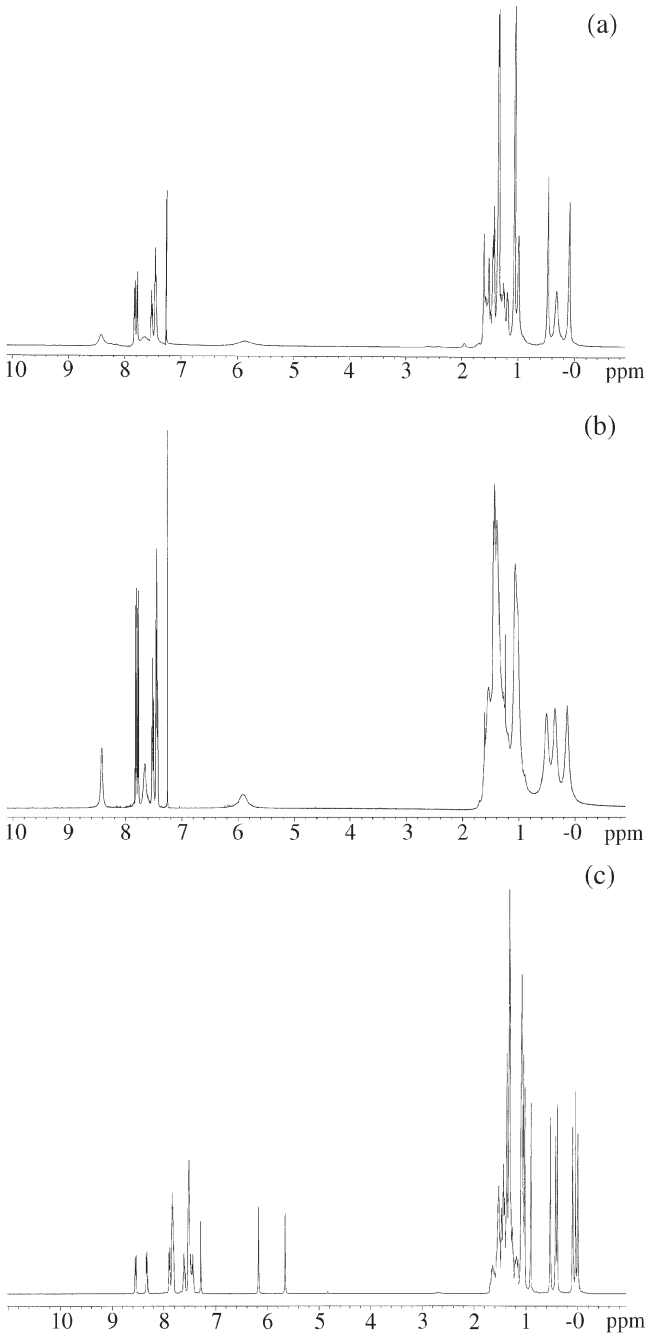

mated at the coalescence temperature near 25°C, using the formula $T_{1/2} = \sqrt{2}/2\pi\Delta\nu$ (11).

The high field shift of three methyl groups in the ^{1}H NMR spectrum of **4** (Fig. 2) may be explained from the conformation shown in the X-ray structure (Fig. 1), which places two CH_3 groups from one of the piperidinyl moieties and one CH_3 from the other in the shielding regions on either side of the naphthalene ring. As seen in the view from above the naphthalene ring (Fig. 3), these three methyls are in the shielding region along the periphery of the substituted aryl ring.

Fig. 3. View of **4** perpendicular to the naphthyl ring.

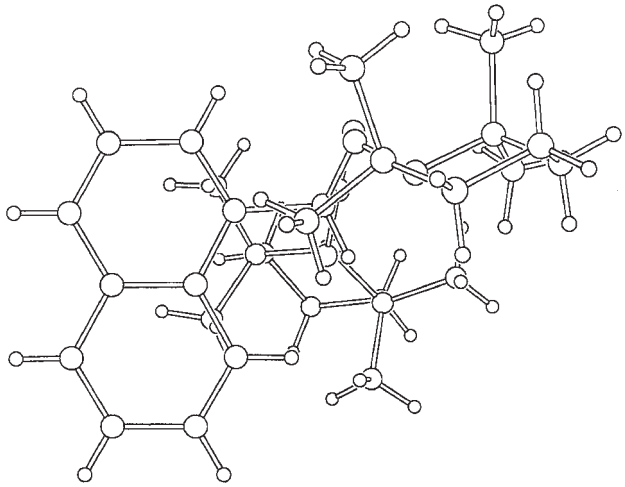

The doubling of the NMR signals indicates that two observable conformations are frozen out at low temperatures in near equal amounts, leading to the observation of separate signals for each. To elucidate the structures, semiempirical AM1 molecular orbital calculations (12) were performed using MOPAC 93 (13). The starting geometry for the optimization was taken from the X-ray data, and a series of geometries varying by 20° rotations around the C(2)—C(1)—C(11)—C(12) bond (Fig. 1) were fully optimized. The resulting plot of energy versus the rotation angle is shown in Fig. 4.

The lowest energy conformation calculated is similar to that shown in Fig. 1, with a C(2)-C(1)-C(11)-C(12) torsion angle of –88.8°, as compared to –78.1° in the X-ray structure. In the next most stable conformation, this angle is 111.1°, and the naphthyl ring has undergone a near 180° rotation relative to the side chain. This second conformation differs from the first by $\Delta\Delta H$ of 0.62 kcal/mol, $\Delta\Delta S$ of –1.84 cal K^{-1} mol^{-1}, and $\Delta\Delta G$ of 1.17 kcal/mol. The lowest energy barrier connecting the two is 6.76 kcal/mol.

Although these calculations are not expected to be quantitatively reliable for this large system, there is good qualitative agreement with the experimental observations of two conformations of similar energies and a significant barrier for interconversion in solution. Based on the AM1 calculations, these may be assigned as one resembling the structure found by X-ray, and one with the opposite rotational disposition of the naphthyl ring relative to the side chain.

Density functional calculations (B3LYP/6-31G*//B3LYP/6-31G*) indicate that the attachment of the H_2NO radical to the CH_2 group of $CH_2{=}CH_2$ or $CH_2{=}C{=}O$ is endothermic, by 7.5 and 8.5 kcal/mol, respectively, whereas attachment to the carbonyl carbon of $CH_2{=}C{=}O$ to produce $\cdot CH_2CO_2NH_2$ is exothermic by 18.7 kcal/mol (6). These reactions are much less favorable than the attachment of the much more reactive HO radical for which exothermicities of 35.4 (14), 44.2, and 39.5 kcal/mol, respectively, to the CH_2 termini of $CH_2{=}CH_2$ and $CH_2{=}C{=}O$, and the $C{=}O$ group of latter, have been calculated (15). The naphthylketene **2** is quite reactive toward nucleophiles (16), and the reactivity for radical attachment to the carbonyl carbon should be significantly

© 1999 NRC Canada

Fig. 4. Enthalpy of formation of **4** versus C(2)-C(1)-C(12)-C(11) torsion angle (calculated at 20° intervals).

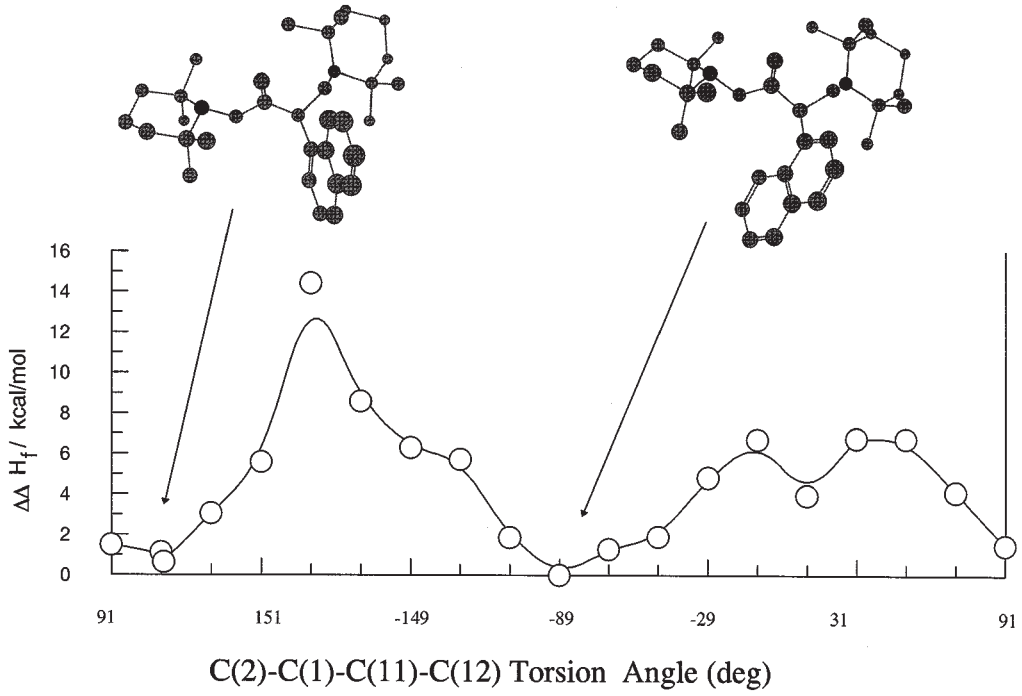

enhanced due to delocalization of the unpaired spin by the naphthyl group.

Experimental

2,2,6,6-Tetramethylpiperidinyl 2-(1-naphthyl)-2-(2′-2′,6′,6′-tetramethylpiperidinyloxy)-acetate (4)

A solution of 72.1 mg (0.368 mmol) 1-naphthyl diazomethyl ketone (**1**) and TEMPO (141 mg, 0.903 mmol) was refluxed in 1 mL of toluene for 48 h. The solvent was evaporated, and the resulting solid purified by flash chromatography on silica gel (1/5 EtOAc/hexane) to give **4** (73 mg, 0.15 mmol, 41%), which was further purified by recrystallization from ether–pentane, mp 147–148°C. IR ($CDCl_3$) 1772 cm^{-1} (C=O). ^1H NMR ($CDCl_3$) δ 0.10, 0.35, 0.47, 1.00, 1.06, 1.07, 1.34, 1.36 (each s, 3, CH_3), 1.0–2.0 (m, 12, CH_2), 5.9 (bs, 1, CHOT), 7.4–7.9 (m, 7, Ar), 8.42 (bs, 1, Ar). ^{13}C NMR ($CDCl_3$) δ 16.6, 16.8, 19.18, 19.91, 20.00, 20.32, 30.22, 31.73, 32.94, 34.47 (b), 38.76, 38.89, 39.88, 40.07, 59.24, 59.49, 59.85, 60.21, 124.77 (b), 125.30, 125.76, 128.01 (b), 133.46, 135.55, 170.61. CIMS (isobutane) *m/z*: 481 (MH^+, 4), 326 (9), 156 (TO^+, 100), 140 (55), 126 (29).

Conclusions

The thermal Wolff-rearrangement forming 1-naphthylketene may be conducted in the presence of the stable free-radical TEMPO with efficient trapping of the ketene as a benzylic acid derivative. The adduct **4** has a remarkable ^1H NMR spectrum arising from the unique structure involved.

Acknowledgements

Financial support by the Natural Sciences and Engineering Research Council of Canada is gratefully acknowledged.

References

1. M. Regitz and G. Maas. Diazo compounds. Academic Press, New York. 1986; H. Zollinger. Diazo Chemistry II. VCH, Weinheim. 1994; T.T. Tidwell. Ketenes. John Wiley, New York. 1995.
2. L.B. Volodarsky, V.A. Reznikov, and V.I. Ovcharenko. Synthetic chemistry of stable nitroxides. CRC Press, Boca Raton. 1994.
3. T.J. Connolly, and J.C. Scaiano. Tetrahedron Lett. **38**, 1133 (1997).
4. I.A. Opieda, A.G. Matrienko, and O.Z. Ostrovskaya. Kinet. Catal. **36**, 441 (1995); Chem. Abstr. **123**, 169 037m (1995).
5. D.H.R. Barton, V.N. Le Gloahec, and J. Smith. Tetrahedron Lett. **39**, 7483 (1998).
6. W. Huang, H. Henry-Riyad, and T.T. Tidwell, J. Am. Chem. Soc. **121**, 3939 (1999).
7. L.H. Dao, A.C. Hopkinson, and E. Lee-Ruff. Tetrahedron Lett. 1413 (1978); V. Lee and M.S. Newman. *In* Organic synthesis. Coll. vol. 6. *Edited* by W.E. Noland. John Wiley, New York. 1988. pp. 613–615.
8. U. Jahn. J. Org. Chem. **63**, 7130 (1998); R. Braslau, L.C. Burrill II, M. Siano, N. Naik, R.K. Howden, and L.K. Mahal. Macromolecules, **30**, 6445 (1997).
9. J.E. Anderson and J.E.T. Corrie. J. Chem. Soc. Perkin Trans. 2, 1027 (1992).
10. J.E. Anderson, D. Casarini, J.E.T. Corrie, and L. Lunazzi. J. Chem. Soc. Perkin Trans. 2, 1299 (1993).
11. R.S. Drago. Physical methods for chemists. 2nd ed. Saunders Publishing, New York. 1992.
12. M.J.S. Dewar, E.G. Zoebisch, E.F. Healy, and J.J.P. Stewart. J. Am. Chem. Soc. **107**, 3902 (1985).
13. J.J.P. Stewart. MOPAC 93 manual. Fujitsu Ltd., Tokyo. 1993.
14. M. Guerra. J. Am. Chem. Soc. **114**, 2077 (1992).
15. K. Sung and T.T. Tidwell. J. Org. Chem. **63**, 9690 (1998).
16. Y. Chiang, A.J. Kresge, and V.V. Popik. J. Am. Chem. Soc. **117**, 9165 (1995).

© 1999 NRC Canada

Identity-reaction proton transfers from oxygen acids yielding localized vs. delocalized conjugate bases. An ab initio study

James E. Van Verth and William H. Saunders, Jr.

Abstract: Identity-reaction proton transfers from a series of oxygen acids to the corresponding conjugate bases have been studied by ab initio methods at the MP2/6-31+G*//MP2/6-31+G* level. The acids are H_3O^+, $CH_3OH_2^+$, $CH_2=OH^+$, $HC(O)OH_2^+$, $CH_2=CHOH_2^+$, H_2O, CH_3OH, HOOH, $HOCH_2OH$, FOH, FCH_2OH, HC(O)OH, and $CH_2=CHOH$. Gas-phase acidities were calculated at the G2(MP2) level in order to have benchmark values for all acidities regardless of whether experimental values were available. Barriers to proton transfer relative to the separated reactants, ΔH_{TS}, show a straight-line relation to acidity for all but two of the neutral acids and for all but one of the cationic acids. Two neutral acids, HOOH and FOH, show negative deviations that can be attributed to polarizability of the atoms attached to the proton donor oxygens. The cationic acid $HC(O)OH_2^+$ shows a large positive deviation, which probably arises from substantial heavy-atom reorganization from reactant to TS. Charges provide evidence of a lag in delocalization in the reaction of $CH_2=CHOH_2^+$, though it does not show an elevated ΔH_{TS}.

Key words: ab initio, oxygen acids, proton transfer, acidity.

Résumé : Faisant appel à des méthodes théoriques ab initio aux niveaux MP2/6-31+G*//MP2/6-31+G*, on a étudié les réactions d'identité des transferts de proton d'une série d'acides oxygénés vers les bases conjuguées correspondantes. Les acides sont H_3O^+, $CH_3OH_2^+$, $CH_2=OH^+$, $HC(O)OH_2^+$, $CH_2=CHOH_2^+$, H_2O, CH_3OH, HOOH, $HOCH_2OH$, FOH, FCH_2OH, HC(O)OH et $CH_2=CHOH$. Afin d'avoir des valeurs de référence pour toutes les acidités, on a calculé les acidités en phase gazeuse au niveau G2(MP2) pour lequel il n'existe pas de valeurs expérimentales. Pour tous les acides neutres, à l'exception de deux, et pour tous les acides cationiques, à l'exception d'un, les barrières au transfert de proton relatives aux réactifs séparés, ΔH_{ET}, présentent une relation de ligne droite par rapport à l'acidité. Deux acides neutres présentent des déviations négatives, HOOH et FOH; celles-ci peuvent être attribuées à la polarisabilité des atomes attachés aux atomes d'oxygène donneurs de proton. L'acide cationique $HC(O)OH_2^+$ présente une forte déviation positive qui découle probablement d'une réorganisation substantielle des l'atomes lourds du réactif à l'état de transition (ET). Les charges indiquent un décalage dans la délocalisation pour la réaction du $CH_2=CHOH_2^+$; toutefois, elle ne présente pas de valeur élevée pour le ΔH_{ET}.

Mots clés : calculs ab initio, acides oxygénés, transfert de proton, acidité.

[Traduit par la Rédaction]

Introduction

Proton transfers to or from "normal" or Eigen acids usually occur at a diffusion-controlled (or close to diffusion controlled) rate when the proton transfer is exoergic (1). Slower deprotonation results when the reaction is endoergic, but essentially the only barrier is the endoergicity. Eigen acids are those in which the proton is bound to an electronegative atom such as nitrogen or oxygen. In contrast, carbon acids often deprotonate at much slower rates than Eigen acids of similar acidity. The factors contributing to these barriers have been examined in recent years by means of quantum–chemical calculations as well as experiment.

A clear distinction can be made between carbon acids that yield localized vs. delocalized conjugate bases. Although both, unlike Eigen acids, show significant barriers, the carbon acids yielding delocalized bases deprotonate more slowly than acids of similar acidity yielding localized bases. In general terms, the need for heavy-atom reorganization during proton transfer is considered to raise the barrier to the reaction (2, 3). In a seminal contribution, Kresge (2) argues that the heavy-atom reorganization is only partly complete in the transition structure. The ability of the TS to delocalize the partial negative charge transferred from the base is thus limited, and delocalization lags behind the extent of proton transfer. A more quantitative treatment called the principle of nonperfect synchronization (PNS) has been proposed by Bernasconi (4–6). He presents methods for evaluating the intrinsic barrier, the magnitude of the lag in delocalization, and the contribution of various factors to the lag. More re-

Received December 3, 1998.

This paper is dedicated to Jerry Kresge in recognition of his many achievements in chemistry.

J.E. Van Verth. Department of Chemistry, Canisius College, Buffalo, NY 14208, U.S.A.
W.H. Saunders, Jr.[1] Department of Chemistry, University of Rochester, Rochester, NY 14627, U.S.A.

[1]Author to whom correspondence may be addressed. Telephone: (716) 275-4235. Fax: (716) 473-6889. e-mail: saunders@chem.chem.rochester.edu

© 1999 NRC Canada

Table 1. Observed and calculated enthalpies[a] for $HA^+ \rightarrow H^+ + A$ and $HA \rightarrow H^+ + A^-$.

		ΔH(acid)		
	Expt./G2(MP2)[a]	MP2/6-31+G*//6-31+G*	MP2/6-31+G*//MP2/6-31+G*	MP4/6-31+G*//MP2/6-31+G*
HA^+				
H_3O^+	—/164.5	161.6	161.7	162.5
$CH_3OH_2^+$	—/180.4	177.0	177.0	178.0
$CH_2{=}OH^+$	—/170.4	163.5	162.9	164.5
$HC(O)OH_2^+$	—/157.7	152.2	154.5	156.1
$CH_2{=}CHOH_2^+$	—/171.7	168.3	168.3	169.9
HA				
H_2O	390.7/390.3	383.3	383.8	385.2
CH_3OH	380.6/382.8	376.4	376.8	378.0
HOOH	375.6/376.9	367.5	369.8	369.8
$HOCH_2OH$	—/367.3	359.4	359.2	360.5
FOH	362.5/362.0	350.4	353.8	351.9
FCH_2OH	—/359.4	349.2	348.6	349.0
HCOOH	345.3/342.9	335.0	335.5	337.0
$CH_2{=}CHOH$	—/357.0	349.1	349.4	350.9

[a]In kcal mol^{-1} at 298 K. Experimental values are given where available. G2(MP2) calculated values are given in all cases.

cently, it has been shown by means of VBSCF calculations that the lag results from a balance between the stabilization resulting from resonance and the energy lowering from preservation of as much C---H---C bonding as possible (7).

The validity of the PNS can be most easily tested if contributions from solvent reorganization can be eliminated and the intrinsic barrier determined directly by employing identity reactions. It is not easy to accomplish experimentally, but ab initio calculations are ideally suited to this end. Pioneering work by Scheiner and his co-workers (8–11) on simple systems was followed by studies that treated mainly carbon acids yielding delocalized conjugate bases (12–16). From these studies, it was clear that even in the absence of solvent intrinsic barriers to proton transfers from such carbon acids are higher than expected from their acidity. Furthermore, the charge distributions in the transition structures show that charge delocalization lags well behind proton transfer.

With these results in mind, we became interested in whether the PNS would apply to Eigen acids as well as carbon acids. Until our recent work on nitrogen acids, no computational results in the literature addressed this question. We examined a series of identity reaction proton transfers involving nitrogen acids and their conjugate bases, including both neutral and cationic acids (17). As expected, all of the acids yielding localized conjugate bases showed small or nonexistent barriers to proton transfer. Among the neutral acids, even those yielding delocalized conjugate bases showed negligible barriers. These acids were OCNH, $OCHNH_2$, and $HNCHNH_2$. The reason was shown to be that the transition structures preferred conformations such that the C=O and C=N π bonds attached to nitrogen conjugated with the unshared pairs on the proton-donating nitrogen rather than with the N---H bonding electrons. In the case of the corresponding cationic acids, $OCNH_2^+$, $OCHNH_3^+$, and $HNCHNH_3^+$, there are no unshared pairs on the proton-donating nitrogens, so the only conjugation that can occur is with the N---H bonding electrons. Consequently, as with carbon acids that yield delocalized anions, lags in delocalization and appreciable barriers are observed.

In the case of oxygen acids, even acids of the type ROH_2^+ still have a single unshared pair remaining on oxygen with which a π bond could conjugate. We wished to find out whether the oxygen acids would behave in a manner analogous to the nitrogen acids, or whether they would now all show negligible barriers. Again, the literature provided no guidance. Proton transfers in the simplest systems, OH^- + HOH and HOH + HOH_2^+, have been extensively studied from the early days of molecular orbital computations. It is not the purpose of this paper to provide an exhaustive bibliography, but mention should be made of key early work (18–20) and recent applications of density functional methods (21–23). All of the calculations agree that barriers are small, and in some cases, stable symmetrically hydrogen bonded structures were found rather than a transition structure. The only other proton transfer involving a system similar to those we had studied with carbon and nitrogen acids was the CH_3OH to CH_3O^- reaction (24). Here again, the barriers were quite small when the geometry of the transition structure was optimized.

Computational procedures[2]

Ab initio calculations utilized the Gaussian 92 (25) and Gaussian 94 (26) programs with the standard basis set 6-31+G* (27). Correlation corrections utilized the Møller–Plesset method (28). The enthalpies (ΔH) in the tables (Tables 1, 2) are corrected to constant pressure and for zero-point-energy differences from MP2/6-31+G*//MP2/6-31+G* calculations scaled to 0.95 to account for the overestimation of frequencies by Hartree-Fock methods (29). Enthalpies were further corrected to 298 K for the contributions of the translational, rotational, and vibrational partition functions (30). The vibrational correction is not based on scaled frequencies, for it

[2]Cartesian coordinates and *z*-matrices have been deposited as supplementary material and may be purchased from: The Depository of Unpublished Data, Document Delivery, CISTI, National Research Council Canada, Ottawa, Canada, K1A 0S2.

© 1999 NRC Canada

Table 2. Enthalpies[a] of stationary points in $AH^+ + A$ and $AH + A^-$ identity proton transfers at MP2/31+G*//MP2/6-31+G*.

	ΔH_{well}	$\Delta H^{\neq b}$ ($\Delta E^{\neq}$)	ΔH_{TS}[c]	$\nu^{\neq}_i$
AH^+				
H_3O^+	–35.95	—[d]	—[d]	0
$CH_3OH_2^+$	–34.10	–0.86 (0.005)	–34.96	82*i*
$CH_2{=}OH^+$	–30.96	–1.20 (0.03)	–32.16	83*i*
$HC(O)OH_2^+$	–17.97	–0.86 (2.05)	–18.82	687*i*
$CH_2{=}CHOH_2^+$	–28.72	–1.23 (0.04)	–29.95	73*i*
AH				
H_2O	–27.89	–1.61 (0.73)	–29.50	816*i*
CH_3OH	–27.49	–1.60 (0.51)	–29.09	677*i*
HOOH	–36.16	–1.06 (1.46)	–37.23	522*i*
$HOCH_2OH$	–32.04	1.58 (4.33)	–30.46	874*i*
FOH	–37.92	—[d]	—[d]	0
FCH_2OH	–27.73	–1.60 (0.85)	–29.34	664*i*
HCOOH	–28.66	–1.66 (0.35)	–30.31	596*i*
$CH_2{=}CHOH$	–27.90	–1.66 (0.34)	–29.56	625*i*

[a]In kcal mol^{-1} at 298 K.

[b]$H_{TS} - H_{complex}$.

[c]$H_{TS} - H_{reactants}$.

[d]No central barrier was found.

[e]Ion–dipole complex not determined.

is doubtful that low-lying frequencies (the only ones that contribute significantly to the vibrational partition function) bear a predictable relation to experimental values (31). Although many of the calculations were done up to the MP4SDTQ(frozen core)/6-31+G*//MP2/6-31+G* level, the results did not differ much from the complete set done at MP2/6-31+G*//MP2/6-31+G*, so only the latter are reported in Table 2. Where different stable conformations of a species are possible, the most stable one is listed in the tables. All reasonable conformations of reactants and transition structures were, however, optimized. In nearly all cases, the energy difference between the most stable and the next most stable conformation was large enough that the latter should make no significant contribution. No effort was made to locate all possible conformations of the ion-dipole complexes. Our experience with carbon acids has been that the complexes have several conformations very close in energy and easily interconvertible (11, 14). Since the energies of the complexes in the present context are useful only for establishing the magnitude of the central barrier, they were usually not explored exhaustively.

Results and discussion

A comparison of experimental (32)[3] and calculated gas-phase acidities was used to test the adequacy of the levels of our calculations. The results are given in Table 1. Because experimental values are missing for some of the neutral and all of the cationic acids, G2(MP2) (33) calculated values were used as benchmarks. The second column of the table records both experimental and G2(MP2) values, while the remaining three columns record values at three levels of increasing computational flexibility. None of the three had a clear advantage with respect to the other two, so MP2/6-31+G*//MP2/6-31+G* was chosen for subsequent calculations so as to facilitate comparison with the earlier results on nitrogen acids (17).

Where comparisons are possible the G2(MP2) values agree very well with experiment, the difference exceeding 2 kcal in only one case. The same cannot be said for a comparison of the benchmark values and the values in the last three columns, where the MP2/6-31+G*//MP2/6-31+G* acidities are frequently lower by 5 kcal or more, and in one case by more than 10 kcal, than the benchmark values. The situation is a little better for the cationic acids, where the differences are in the range of 2.9–6.9 kcal. Relative values, however, look much better. Linear least-squares correlations of the G2(MP2) values as dependent variable and the MP2/6-31+G*//MP2/6-31+G* values as independent variable show that the latter predict the former with a standard deviation of 1.1 kcal for the neutral and 2.2 kcal for the cationic acids (correlation coefficients 0.998 and 0.974, respectively). Because our analyses do not depend on often unavailable experimental data, these good relative values are deemed adequate.

Table 2 records the stationary points for the identity-reaction proton transfers at MP2/6-31+G*//MP2/6-31+G*. The reactions of $OH^- + H_2O$ and $H_2O + H_3O^+$ have been the subject of experimental studies. Our well depths are in reasonable agreement with experiment (–32 and –26.8 kcal for the former, –31.8 kcal for the latter) (34). The only other experimental results on our systems are alcohol–alkoxide reactions studied by ICR (35). Our methanol–methoxide well

[3]Reference 32, as updated by NIST databases 19*a* and *b*, National Institute of Standards and Technology, Gaithersburg, Md., 20889. The most up-to-date version of these databases is available at the web site http://webbook.nist.gov/chemistry.

© 1999 NRC Canada

Fig. 1. Calculated barriers, ΔH_{TS}, vs. calculated acidity at MP2/6-31+G*//MP2/6-31+G* for neutral acids reacting with their anionic conjugate bases. Open squares, points included in least-squares fit; closed diamonds, outlying points.

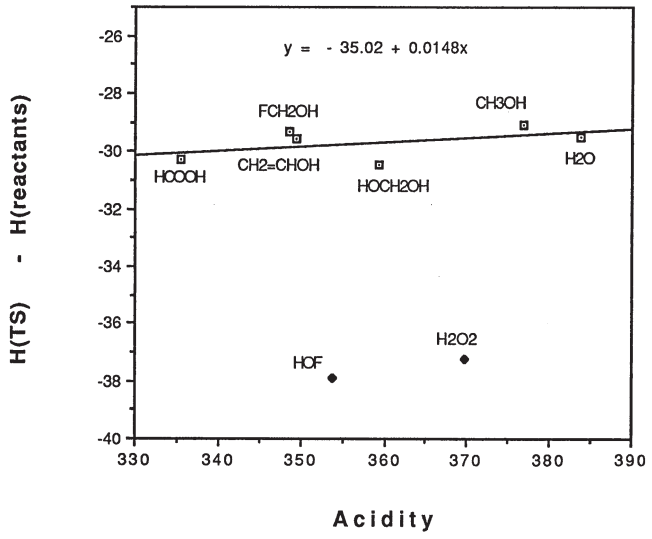

Fig. 2. Calculated barriers, ΔH_{TS}, vs. calculated acidity at MP2/6-31+G*//MP2/6-31+G* for cationic acids reacting with their neutral conjugate bases. Open squares, points included in least squares fit; closed diamond, outlying point.

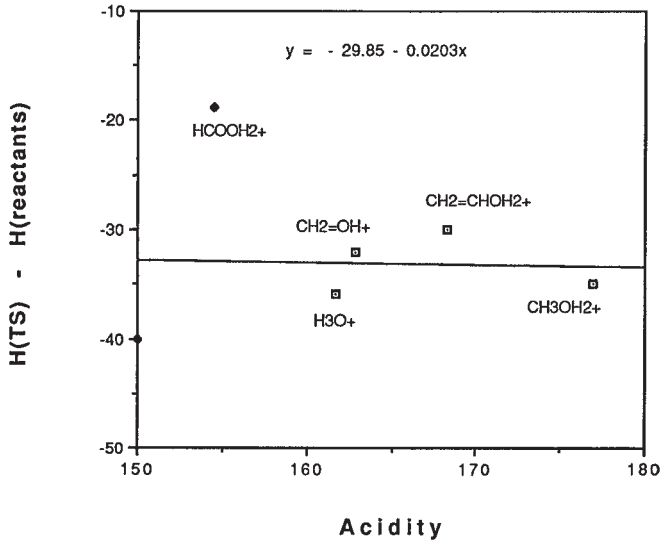

depth is in good agreement with the stabilization energy of –29.3 kcal reported in this paper. Interestingly, the efficiency of the reaction was only 26% rather than the 50% expected for an essentially barrierless process. By the conventional RRKM treatment, this would indicate a significant central barrier, but the authors present computational evidence that the low efficiency is the result of dynamic constraints rather than a potential barrier (36).

Only two of our reactions, those of HOF and H_3O^+, show a symmetrically hydrogen bonded minimum. The others show small potential energy barriers that are, except for $HOCH_2O^-$ + $HOCH_2OH$, below the zero point energy levels of the transition structures. In fact, the very low barriers led us to wonder whether they represented torsional barriers rather than true proton transfer processes. The eigenvectors of the reaction coordinate modes did show significant motion of the proton in all cases, but some also involved motions of other atoms, particularly hydrogens. Animation of the vibrational modes by means of GaussView[4] showed that the highest amplitude motion was proton transfer, but often accompanied by torsional or rocking motion of other atoms. The $CH_2{=}CHOH_2^+$ + $CH_2{=}CHOH$ reaction in particular gave an eigenvector in which most atoms were moving. The animation of the reaction coordinate motion showed that the proton transfer was coupled with disrotatory torsions of the $CH_2{=}CHOH$ fragments moving as units.

At first glance, it would appear that all of these oxygen acids behave as Eigen acids in the sense of showing no significant barriers to proton transfer. Closer examination shows that the situation is a little more complicated. In our previous work (15, 17), we have used plots of ΔH_{TS} vs. acidity as a measure of unusual values of ΔH_{TS}. Acids that showed a lag in charge delocalization were found to have ΔH_{TS} values that fell well above the correlation line. By this measure the neutral acids in Fig. 1 all behave as normal Eigen acids. Two of them, HOF and HOOH, fall well below the line. This is an example of the α-effect. The origins of the α-effect are not entirely clear (37). In the present case, it is probably a consequence of the polarizability of the unshared pairs on the atoms (F and O, respectively) attached to the proton-donor oxygen atoms (15*b*). The slope of the plot is very shallow (slope 0.015) — so much so that all but two of the acids have ΔH_{TS} values within a few kilocalories of each other.

The cationic acids (Fig. 2) show more scatter. Leaving out the point for $HC(O)OH_2^+$, the correlation line actually has a very slightly negative slope (–0.02). That point, however, is above the correlation line by more than 10 kcal. In common with all the other acids, there is no enthalpic central barrier for this reaction, though it does show the highest potential barrier, 2.05 kcal, of all the cationic reactions. We have pointed out previously (15, 17) that ΔH_{TS} is more reliable than $\Delta H^{\neq}$ as a measure of barrier height because it avoids complications arising from special effects on stability of the ion–dipole complex, which have no effect on the rate of product formation relative to return to reactants. A particularly instructive illustration of this point is the reaction $HOCH_2O^-$ + $HOCH_2OH$. This should be a normal Eigen acid, and its ΔH_{TS} is even a little below the correlation line in Fig. 1, but it still shows the highest central barrier of all the oxygen acid reactions. We believe this arises from high stabilization of the ion–dipole complex by hydrogen bonding, which occurs from the oxide oxygen of $HOCH_2O^-$ to both oxygen-bound protons of $HOCH_2OH$. Consequently, we should focus on ΔH_{TS}, not the central barrier, to explore whether a reaction is unusually slow. Apart from details such as the above, the overall picture remains essentially the same whether $\Delta H^{\neq}$ or ΔH_{TS} is plotted in Figs. 1 and 2.

To consider further the reactions that may involve lags in charge delocalization, we chose to compare the way group

[4] GaussView 1.0. Gaussian Inc., Pittsburgh, Pa. 1997.

© 1999 NRC Canada

Table 3. Group charges (NPA) at MP2/6-31+G*.

Species	X/q_x	Δq(acid→TS)	Δq(TS→base)
	HCO		
HC(O)OH	0.2693		
TS^- (**3b**)	0.1022	–0.1671	–0.1912
$HC(O)O^-$	–0.0890		
$HC(O)OH_2^+$	0.7824		
TS^+ (**3a**)	0.4611	–0.3213	–0.1918
	CH_2=CH		
CH_2=CHOH	0.2750		
TS^- (**4b**)	0.1153	–0.1597	–0.1864
CH_2=CHO^-	–0.0711		
CH_2=$CHOH_2^+$	0.5330		
TS^+ (**4a**)	0.4402	–0.0928	–0.1652

charges changed from acid to the TS and from the TS to the base just as we had done for the nitrogen acids (17). The appropriate data, calculated from NPA charges (38), are recorded in Table 3. These must not be taken as quantitatively accurate reflections of the π-electron shifts we are interested in, for they include σ-electron contributions to the total atomic charges. Nonetheless, they should at least show trends because the π electrons tend to be more mobile. Even the two neutral acids, HC(O)OH and CH_2=CHOH, show Δq(TS→base) to be slightly larger than Δq(acid→TS), as expected for systems following the PNS, but the changes are so small that no positive conclusion is warranted.

The one case where ΔH_{TS} is unusually large offers a surprise: Δq(acid→TS) exceeds Δq(TS→base) by a substantial margin, the reverse of the behavior expected from operation of the PNS! There is, however, a very logical reason for this anomaly. $HC(O)OH_2^+$ has a structure that might better be regarded as a complex between $HC(O)^+$ and OH_2, for the C—OH_2 bond is 1.845 Å long, compared to 1.453 Å in TS **3a** and 1.354 Å in HC(O)OH for the same bond (Table 4). Thus, HC(O) has a large positive charge in the acid, which decreases markedly at the TS and undergoes a much smaller decrease from the TS to the product.

Since this behavior overwhelms any electron shifts that might result from operation of the PNS, is there any explanation of the high ΔH_{TS}? We believe an explanation can be found in a suggestion made by Hine (39) more than 20 years ago. He noted that reactions resulting in substantial electronic and concomitant geometric reorganization usually show high barriers. He utilized the Principle of Least Nuclear Motion to argue that a contributor to the transition structure resonance hybrid that possessed a reactant-like electron distribution would be of unusually high energy at the TS because this electron distribution would have to be "squeezed" into the substantially different TS geometry. Since the transition structure results to a first approximation from the intersection of reactant-like and product-like contributors, the result would be a higher energy TS than that for an analogous system that underwent less geometric reorganization.

This leaves the last set of data in Table 3, that for the reaction of CH_2=$CHOH_2^+$ and CH_2=CHOH. Here Δq(TS→base) is almost twice as large as Δq(acid→TS), which would normally be taken as clear evidence for the operation of the PNS. The point for CH_2=$CHOH_2^+$, however, is above the correlation line in Fig. 2 by scarcely more than the scatter of the data. Thus, one normally expected consequence of nonperfect synchronization is not evident in the reaction. Possible further evidence of PNS behavior is afforded by changes in the C—O bond distances (Table 4). For **4a** the change from reactant to TS (–0.057) is smaller than the change from TS to base (–0.071). A reexamination of C—N bond-distance changes in the reactions of the cationic nitrogen acids (17) also reveals lags in Δr(reactant→TS) for the three reactions that show high barriers, those of O=$CHNH_3^+$, HN=$CHNH_3^+$, and O=CH=NH_2^+. For **3b** and **4b**, as in the reactions of the neutral nitrogen acids, none of which display elevated reaction barriers, no such lag is observed.

Table 4. C—O bond distances at MP2/6-31+G*.

Species	r_{CO}	Δr(acid→TS)	Δr(TS→base)
HC(O)OH	1.354		
TS^- (**3b**)	1.304	–0.050	–0.036
$HC(O)O^-$	1.268		
$HC(O)OH_2^+$	1.845		
TS^+ (**3a**)	1.453	–0.392	–0.099
CH_2=CHOH	1.372		
TS^- (**4b**)	1.324	–0.048	–0.039
CH_2=CHO^-	1.285		
CH_2=$CHOH_2^+$	1.500		
TS^+ (**4a**)	1.443	–0.057	–0.071

Fig. 3. Transition structures optimized at MP2/6-31+G*//MP2/6-31+G* for $HC(O)OH_2^+$ reacting with HC(O)OH (**3a**) and HC(O)OH reacting with $HC(O)O^-$ (**3b**).

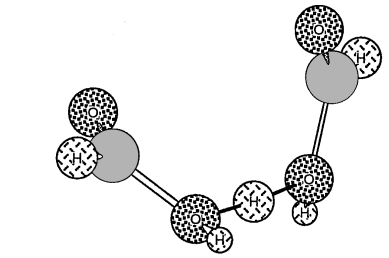

3a

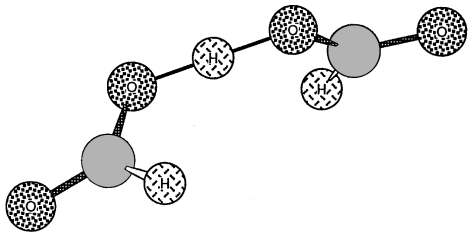

3b

The geometries of the transition structures in Figs. 3 and 4 offer some further enlightenment. As with the similar nitrogen acids (17), the transition structures from the neutral oxygen acids, **3b** and **4b**, exist in conformations that appear to

© 1999 NRC Canada

Fig. 4. Transition structures optimized at MP2/6-31+G*//MP2/ 6-31+G* for $CH_2{=}CHOH_2^+$ reacting with $CH_2{=}CHOH$ (**4a**) and $CH_2{=}CHOH$ reacting with $CH_2{=}CHO^-$ (**4b**).

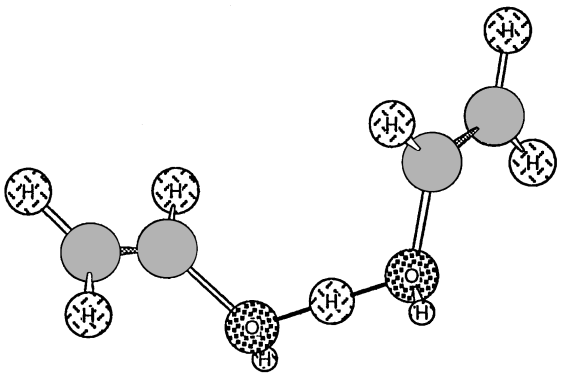

4a

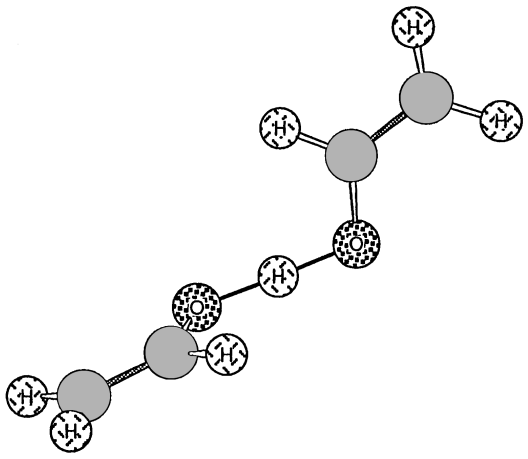

4b

exclude overlap of the π systems with the O---H bonding electrons (H---O-C-O and H---O-C-C dihedral angles of 180°). In these cases, the tendency is to maximize overlap with the unshared pairs on oxygen. Indeed, it has been argued that carboxylate ions are only slightly more resonance stabilized than the corresponding carboxylic acids (40). Cationic transition structure **3a** has its π system oriented so as to overlap mainly with the remaining unshared pair on oxygen (H---O-C-O dihedral angle 22°). In **4a**, there is extensive overlap of the π system with the O---H bonding electrons, but also some overlap with the unshared pair (H---O-C-C dihedral angle 95°). The fact that the cationic oxygen acids have one unshared pair still remaining on oxygen makes it possible that changes in resonance stabilization between the proton donor, the TS, and the product may not be as large as in the reactions of carbon acids and cationic nitrogen acids.

In the present results, the association between delocalization and a high barrier is not as clear as with the carbon and nitrogen acid reactions (15, 17). Nonetheless, the data indicate that when delocalization does occur there is a lag in transfer of charge (**4b**). The results of the VBSCF calculations (7) provide an explanation for this, namely, that in the TS some resonance stabilization must be sacrificed so that as much X---H---X bond energy as possible can be conserved.

An obvious difference between the carbon, nitrogen, and oxygen acid systems is the increasing electronegativity of the donor/acceptor atoms along the series. This should result in increasing importance of contributors such as **1** for the neutral and **2** for the cationic systems to the transition structure resonance hybrid.

$$\underset{\mathbf{1}}{R^-\ H^+\ R^-} \qquad \underset{\mathbf{2}}{RXH\ H^+\ HXR}$$

1 is already an important contributor in the case of the carbon acids as shown by VBSCF calculations on the allyl anion + propene reaction (7). The proton in transit in the carbon acid transition structures has an NPA charge in the range 0.29–0.34 (15*a*). This figure rises to 0.44–0.51 for the neutral nitrogen acids, and to 0.55–0.58 for the neutral oxygen acids. For the cationic acids, the NPA charges are 0.51–0.52 for the nitrogen acids and 0.60–0.63 for the oxygen acids. These numbers cannot be translated directly into contributions from **1** and **2** because they include σ as well as π electron effects, but they certainly should be reliable in showing trends. Thus the contribution of **1** to the neutral acid transition structures must increase in the order carbon < nitrogen < oxygen, and the contribution of **2** to the cationic acid transition structures in the order nitrogen < oxygen. The O---H---O bonding in all of the transition structures we have studied must have a great deal of ionic character.

References

1. M. Eigen. Angew. Chem. Int. Ed. Engl. **3**, 1 (1964).
2. A.J. Kresge. Chem. Soc. Rev. **2**, 475 (1973).
3. W.J. Albery, C.F. Bernasconi, and A.J. Kresge. J. Phys. Org. Chem. **1**, 29 (1988).
4. C.F. Bernasconi. Acc. Chem. Res. **20**, 301 (1987).
5. C.F. Bernasconi. Acc. Chem. Res. **25**, 9 (1992).
6. C.F. Bernasconi. Adv. Phys. Org. Chem. **27**, 119 (1992).
7. N. Harris, W. Wei, W.H. Saunders, Jr., and S. Shaik. J. Phys. Org. Chem. **12**, 259 (1999).
8. Z. Latajka and S. Scheiner. Int. J. Quantum Chem. **29**, 285 (1986).
9. S.M. Cybulski and S. Scheiner. J. Am. Chem. Soc. **109**, 4199 (1987).
10. S. Scheiner and L. Wang. J. Am. Chem. Soc. **114**, 3650 (1992).
11. S. Scheiner. J. Mol. Struct. (Theochem), **307**, 65 (1994).
12. W.H. Saunders, Jr. J. Am. Chem. Soc. **116**, 5400 (1994).
13. C.F. Bernasconi and P.J. Wenzel. J. Am. Chem. Soc. **116**, 5404 (1994).
14. C.F. Bernasconi and P.J. Wenzel. J. Am. Chem. Soc. **118**, 10 494 (1996).
15. (*a*) W.H. Saunders, Jr. and J.E. Van Verth. J. Org. Chem. **60**, 3452 (1995); (*b*) J.E. Van Verth and W.H. Saunders, Jr. J. Org. Chem. **62**, 5743 (1997).
16. C.F. Bernasconi, P.J. Wenzel, J.R. Keeffe, and S. Gronert. J. Am. Chem. Soc. **119**, 4008 (1997).
17. J.E. Van Verth, W.H. Saunders, Jr., and T.W. Kermis. Can J. Chem. **76**, 821 (1998).

© 1999 NRC Canada

18. W. Meyer, W. Jakubetz, and P. Schuster. Chem. Phys. Lett. **21**, 97 (1973).
19. B.O. Roos, W.P. Kraemer, and G.H.F. Diercksen. Theor. Chim. Acta, **42**, 77 (1976).
20. S. Scheiner, M.M. Szczesniak, and L.D. Bigham. Int. J. Quantum Chem. **23**, 739 (1983).
21. V. Barone, L. Orlandini, and C. Adamo. Chem. Phys. Lett. **231**, 295 (1994).
22. D. Wei and D.R. Salahub. J. Chem. Phys. **101**, 7633 (1994).
23. R.V. Stanton and K.M. Merz, Jr. J. Chem. Phys. **101**, 6658 (1994).
24. S. Wolfe, S. Hoz, C.K. Kim, and K. Yang. J. Am. Chem. Soc. **112**, 4186 (1990).
25. M.J. Frisch, G.W. Trucks, M. Head-Gordon, P.M.W. Gill, M.W. Wong, J.B. Foresman, B.G. Johnson, H.B. Schlegel, M. Robb, E.S. Replogle, R. Gomperts, J.L. Andres, K. Raghavachari, J.S. Binkley, C. Gonzalez, R.L. Martin, D.J. Fox, D.J. Defrees, J. Baker, J.J.P. Stewart, and J.A. Pople. Gaussian 92. Gaussian Inc., Pittsburgh, Pa. 1992.
26. M.J. Frisch, G.W. Trucks, H.B. Schlegel, P.M.W. Gill, B.G. Johnson, M.A. Robb, J.R. Cheeseman, T. Keith, G.A. Petersson, J.A. Montgomery, K. Raghavachari, M.A. Al-Laham, V.G. Zakrzewski, J.V. Ortiz, J.B. Foresman, J. Cioslowski, B.B. Stefanov, A. Nanayakkara, M. Challocombe, C.Y. Peng, P.Y. Ayala, W. Chen, M.W. Wong, J.L. Andres, E.S. Replogle, R. Gomperts, R.L. Martin, D.J. Fox, J.S. Binkley, D.J. Defrees, J. Baker, J.J.P. Stewart, M. Head-Gordon, C. Gonzalez, and J.A. Pople. Gaussian 94. Gaussian Inc., Pittsburgh, Pa. 1995.
27. (*a*) W.J. Hehre, R. Ditchfield, and J.A. Pople. J. Chem. Phys. **56**, 2257 (1972); (*b*) T. Clark, J. Chandrasekhar, G.W. Spitznagel, and P.v.R. Schleyer. J. Comput. Chem. **4**, 294 (1983).
28. (*a*) C. Møller and M.S. Plesset. Phys. Rev. **46**, 618 (1934); (*b*) M.J. Frisch, M. Head-Gordon, and J.A. Pople. Chem. Phys. Lett. **166**, 281 (1990); (*c*) J.A. Pople, R. Seeger, and R. Krishnan. Int. J. Quantum Chem. Symp. **11**, 149 (1978); (*d*) R. Krishnan and J.A. Pople. Int. J. Quantum Chem. **14**, 91 (1978); (*e*) R. Krishnan, M.J. Frisch, and J.A. Pople. J. Chem. Phys. **72**, 4244 (1980).
29. (*a*) J.A. Pople, H.B. Schlegel, R. Krishnan, D.J. Defrees, J.S. Binkley, M.J. Frisch, R.A. Whiteside, R.F. Hout, and W.J. Hehre. Int. J. Quantum Chem. Symp. **15**, 269 (1981); (*b*) D.J. Defrees and A.D. McLean. J. Chem. Phys. **82**, 333 (1985).
30. K.B. Wiberg. Physical organic chemistry. Wiley, New York. 1964. p. 218.
31. W.J. Hehre, L. Radom, P.v.R. Schleyer, and J.A. Pople. Ab initio molecular orbital theory. Wiley–Interscience, New York. 1986. p. 228.
32. S.G. Lias, J.E. Bartmess, J.L. Liebman, R.D. Holmes, R.D. Levin, and W.G. Mallard. J. Phys. Chem. Ref. Data Suppl. 17 (1988).
33. L.A. Curtiss, K. Raghavachari, and J.A. Pople. J. Chem. Phys. **98**, 1293 (1994).
34. (*a*) P. Kebarle, Annu. Rev. Phys. Chem. **28**, 445 (1977); (*b*) M.J. Meot-Ner. J. Am. Chem. Soc. **108**, 6189 (1986).
35. J.A. Dodd, S. Baer, C.R. Moylan, and J.A. Brauman. J. Am. Chem. Soc. **113**, 5942 (1991).
36. (*a*) K.F. Lim and J.A. Brauman. Chem. Phys. Lett. **177**, 326 (1991); (*b*) J. Chem. Phys. **94**, 7164 (1991).
37. S. Hoz and E. Buncel. Isr. J. Chem. **26**, 313 (1985).
38. (*a*) E.D. Glendenning, A.E. Reed, E. Carpenter, and F. Weinhold. NBO version 3.1 in Gaussian 92 and 94; (*b*) A.E. Reed, L.A. Curtiss, and F. Weinhold. Chem. Rev. **88**, 899 (1988).
39. J. Hine. Adv. Phys. Org. Chem. **15**, 1 (1977).
40. (*a*) M.R. Siggel and T.D. Thomas. J. Am. Chem. Soc. **108**, 4360 (1986), (*b*) M.R. Siggel, A. Streitwieser, and T.D. Thomas. J. Am. Chem. Soc. **110**, 8022 (1988).

© 1999 NRC Canada

The hydration mechanism of ketene: 15 years later

Minh Tho Nguyen and Greet Raspoet

Abstract: New insights into the detailed mechanism of the hydration of ketene yielding acetic acid ($H_2C=C=O + H_2O \rightarrow CH_3COOH$) were obtained by theoretical methods in both gas phase and solution. While gas phase calculations were performed using ab initio molecular orbital theory, bulk solvent effects were included using the self-consistent reaction field method (SCRF) and the polarizable continuum model (PCM). The hydration modeled by attack of water clusters containing two, three, and four water molecules confirms that a two-step addition of water to the ketene C=O bond, yielding a 1,1-enediol intermediate as initially demonstrated in 1984, is energetically, slightly but consistently, preferred over a concerted addition across the C=C bond leading directly to the acid product. Attempts to locate a zwitterion intermediate in solution were not successful. At least a cluster of three hydrogen-bonded water molecules is present in the gas phase supersystem to facilitate the proton transfer. Further incorporation of active water molecules in the catalytic water chain induces rather minor energetic improvements on the proton relay, which indicates a certain saturation of the cluster when reaching 3–4 water molecules. Effects of the surrounding solvent bulk do not change qualitatively the facts found in gas phase. The C=O addition mechanism is in better agreement with recent experimental developments in identifying enols of carboxylic acids than other mechanisms involving either a zwitterion or a direct C=C addition, as proposed for years in the literature.

Key words: ketene, ketene hydration, hydration mechanism, solvent effect, ab initio calculations.

Résumé : On a été amené à mieux comprendre le mécanisme détaillé de l'hydratation du cétène conduisant à l'acide acétique ($H_2C=C=O + H_2O \rightarrow CH_3COOH$) grâce à des calculs théoriques tant en phase gazeuse qu'en solution. Alors que les calculs en phase gazeuse ont été effectués en faisant appel à des calculs ab initio basés la théorie des orbitales moléculaires, on a introduit les effets de solvant en utilisant la méthode du champ de réaction autocohérent (MCRA) et le modèle du continuum polarisable (MCP). Comme on l'avait démontré initialement en 1984, l'hydratation modélisée par l'attaque d'agrégats d'eau contenant deux, trois et quatre molécules d'eau confirme qu'une addition d'eau (en deux étapes) à la liaison C=O du cétène conduisant à un intermédiaire ène-1,1-diol est toujours le modèle légèrement préféré d'un point de vue énergétique par rapport à un mécanisme d'addition concertée sur la double liaison C=C qui conduirait directement au produit acide. Les essais faits en vue de localiser un intermédiaire zwitterion en solution se sont avérées infructueux. Dans le supersystème en phase gazeuse, un agrégat d'au moins trois molécules d'eau reliées par des liaisons hydrogènes facilite le transfert d'hydrogène. L'incorporation d'un plus grand nombre de molécules d'eau dans la chaîne catalytique de l'eau induit ne donne lieu qu'à de faibles améliorations énergétiques sur le relais du proton; ceci indique que l'on atteint une certaine saturation de l'agrégat avec 3 ou 4 molécules d'eau. Les effets de l'ensemble du solvant environnant ne changent pas de façon significative les faits observés en phase gazeuse. Le mécanisme d'addition sur le C=O est en meilleur accord avec les développements expérimentaux récents puisqu'il permet d'identifier des énols des acides carboxyliques plutôt que d'autres mécanismes impliquant un zwitterion ou une addition directe sur la double liaison C=C, tel qu'il avait été proposé dans la littérature pendant des années.

Mots clés : cétène, hydratation du cétène, mécanisme d'hydratation, effet de solvant, calculs ab initio.

[Traduit par la Rédaction]

Introduction

Owing to the fact that ketenes are structurally interesting functional groups and basic building blocks in organic synthesis, they have been the subject of intensive study throughout this century and their chemistry has frequently been reviewed (1–7). In the preface of his recent book, Tidwell (7) summarized well the historical development: "The study of ketene chemistry has been marked from the beginning by scientific controversy, disagreement and uncertainty.... Even today, the mechanisms of ketene cycloadditions and ketene hydration are not agreed upon." In fact, the hydration is one of the earliest known reactions of ketenes (eq. [1]). To have a global view on the problems, it seems necessary to briefly

Received November 13, 1998.

This paper is dedicated to Professor Jerry Kresge on the occasion of his 65th birthday.

M.T. Nguyen[1] and G. Raspoet. Department of Chemistry, University of Leuven, Celestijnenlaan 200F, B-3001 Leuven, Belgium.

[1]Author to whom correspondence may be addressed. Fax: 32-16-327992. e-mail: minh.nguyen@chem.kuleuven.ac.be

 © 1999 NRC Canada

summarize the literature results on two important topics, namely the hydration mechanism and the existence of enols of carboxylic acids.

[1] 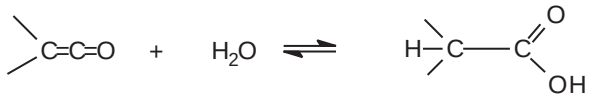

Summary of earlier results

Hydration mechanism

In neutral aqueous solution (pH = 4–9), the hydration was shown to be pH-independent, indicating that it is a nucleophilic reaction of water molecules (8, 9). In solvents other than water, such as dioxane or acetonitrile, no specific effect of the solvents has been observed (9). A solvent kinetic isotope effect $k(H_2O)/k(D_2O)$ lies in the range of 1.7–2.3 for most systems studied, whereas the rate constants are rather dependent on the ketene substituents (10, 11). In the parent ketene ($H_2C{=}C{=}O$), an activation enthalpy and entropy of 43 kJ mol^{-1} and –16 eu, respectively, were measured in pure water (9). Regarding the mechanism, there have been mainly three distinct propositions to account for the course of acid formation.

(1) Tidwell's mechanism: polar transition state

Earlier studies of hydration kinetics of arylketenes (4-$RC_6H_4CH{=}C{=}O$) in pure water performed by Bothe et al. (8) showed that the 4-NO_2 derivative was 13 times more reactive than the 4-CH_3 derivative. These authors (8) did not propose a mechanism at that time but Tidwell and co-workers (10, 12, 13) have subsequently interpreted these data in terms of rate-determining nucleophilic attack at C_α followed by rapid proton transfer (eq. [2]).

[2] 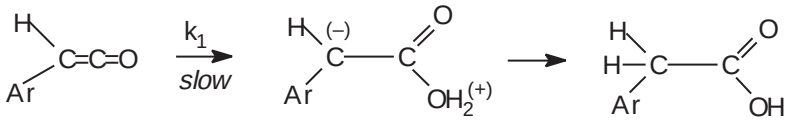

The possibility of a ketene hydrate intermediate **1**, $H_2C{=}C(OH)_2$, was mentioned by Bothe et al. (9). Subsequently, Tidwell and co-workers studied the hydration of a series of alkylketenes including **2**–**5** (13, 14). The order of the reactivity was found to be **2** < **5** < **4** < **3**.

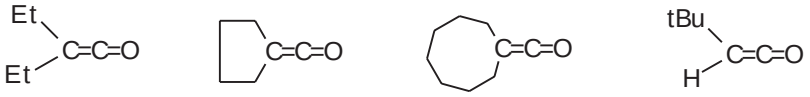

2 **3** **4** **5**

From these results, the latter authors (13) proposed a mechanism involving an in-plane nucleophilic attack at C yielding a polar transition state **6**, with more negative charge on oxygen than carbon.

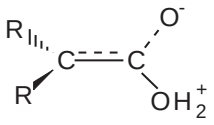

6

This mechanism accounts for the large rate depression when there are two bulky groups on both sides of the plane, as in **4**. The similar reactivity of ketene, **2**, and **5** led to the suggestion that in alkyl ketenes, electronic effects are small whereas steric effects are large. Overall, this group has not taken any advocacy position on the possible intermediates (cf. ref. 7, p. 577).

(2) Satchell's mechanism: C=C addition

Satchell and co-workers (11, 15–21) extensively investigated the hydration kinetics and were the first group to propose a global mechanism for solvolysis of cumulenes. In particular, they (11–15) measured the rates of hydration of dimethylketene and diphenylketene in ether solution containing up to 0.35 M H_2O. The neutral hydration of diphenylketene was found to be 40 times faster than that of dimethylketene over the range studied. The spontaneous hydration of diphenylketene was found to be first-order in ketene concentration and third-order in stoichiometric water concentration, and that of dimethylketene was second-order in water concentration. Based on these data, Satchell and co-workers (15–21) proposed a concerted nucleophilic

© 1999 NRC Canada

addition of a water dimer perpendicular to the ketene plane across the C=C bond involving a cyclic transition state **7**. However, these authors did not suggest why diphenylketene requires a higher-order in water concentration. The open transition state **8** was mentioned but discarded (15).

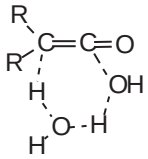

7

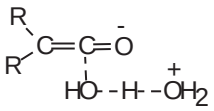

8

Later, this group favoured a mechanism involving a cyclic, multimolecular, H-bonded transition state across the C=C bond **9** that is similar to **7** but implies larger water clusters (eq. [3]). It was also suggested that the hydration mechanism may differ in a medium of higher dielectric constants (15–21).

[3]

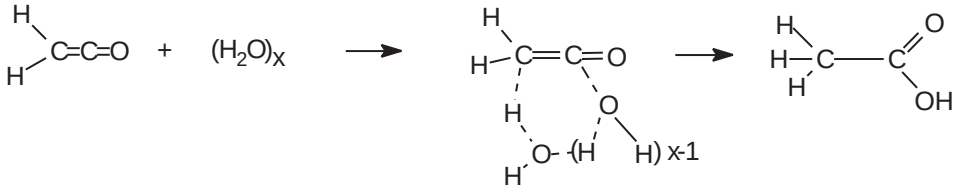

9

(3) Nguyen–Hegarty's mechanism: C=O addition

In 1984, Nguyen and Hegarty (22) suggested a novel mechanism for ketene hydration that differs fundamentally from the previous ones. Perhaps the most interesting fact was that our proposition was solely based on ab initio molecular orbital calculations. Indeed, we calculated transition state structures for the addition of monomeric and dimeric water across both ketene C=C and C=O bonds. Even though the levels of theory employed at that time were rather low, as compared with today's state-of-the-art methods, two essential results were reported (22): (*i*) the presence of an additional water in the supermolecule is a crucial factor in facilitating the proton transfer within a cyclic transition state and thereby reducing substantially the energy barriers (23–26). In other words, the hydration reaction is better modeled by the attack of a water dimer rather than a water monomer; and (*ii*) addition of a water dimer across the C=O bond giving rise to an 1,1-enediol **1** is energetically favoured over the C=C addition. The compact transition structure **10** is consistent with a negative activation entropy found earlier for the hydration of ketene (9). The preference for C=O addition of water is in contrast with the thermodynamic preference for C_β protonation **11** over O-protonation **12**.

We also suggested that the transformation of an enediol to an acid should be rapid in aqueous solution, and this would probably be the reason for their nonobservation. Indeed, a number of authors have subsequently rejected the possibility of such an initial C=O attack due to the lack of evidence for the existence of enols of carboxylic acids.

Evidence for enediol intermediates in ketenes hydration

There were cases where the presence of an enediol intermediate in ketene hydration has been implied. However, it was not before the nineties that the existence of enediols could be established (27). We refer to a recent review by Kresge (42) for details. Aumann and Worman (28) suggested that an iron–ketene complex reacted reversibly with water giving a primary enediol. Ried and Junker (29) mixed diphenyl and dimethylketenes with various alcohols in the presence of an aryldiazonium electrophile and explained the results by the initial formation of an ester enol.

Hegarty and O'Neill (30) reported in 1987 the first detection of acid and ester enols by using very hindered substituents, such as pentamethylphenyl, that slow down the ketonization. In 1990, the groups of Kresge and Wirz (31, 32) demonstrated that the hydration of a fulvene ketene proceeds via a 6,6-fulvenediol, based on the formation and subsequent decay of a transient intermediate absorbing in the range 280–320 nm. They were also able to generate the unhindered acid enol as a result of the hydration of the hydroxyketene, itself formed by a photochemical route. In the mean time, Hegarty and co-workers (33) studied the hydration of hindered diarylketenes and provided strong kinetic evidence

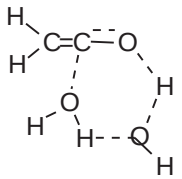

10

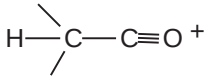

11

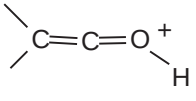

12

© 1999 NRC Canada

Fig. 1. Selected optimized structures of stationary points along a ketene hydration path with one water molecule across both C=O and C=C bonds. The entries are HF, HF-SCRF (in italics), and MP2 (in bold). The MP2 values are taken from ref. 53 and given for purpose of comparison.

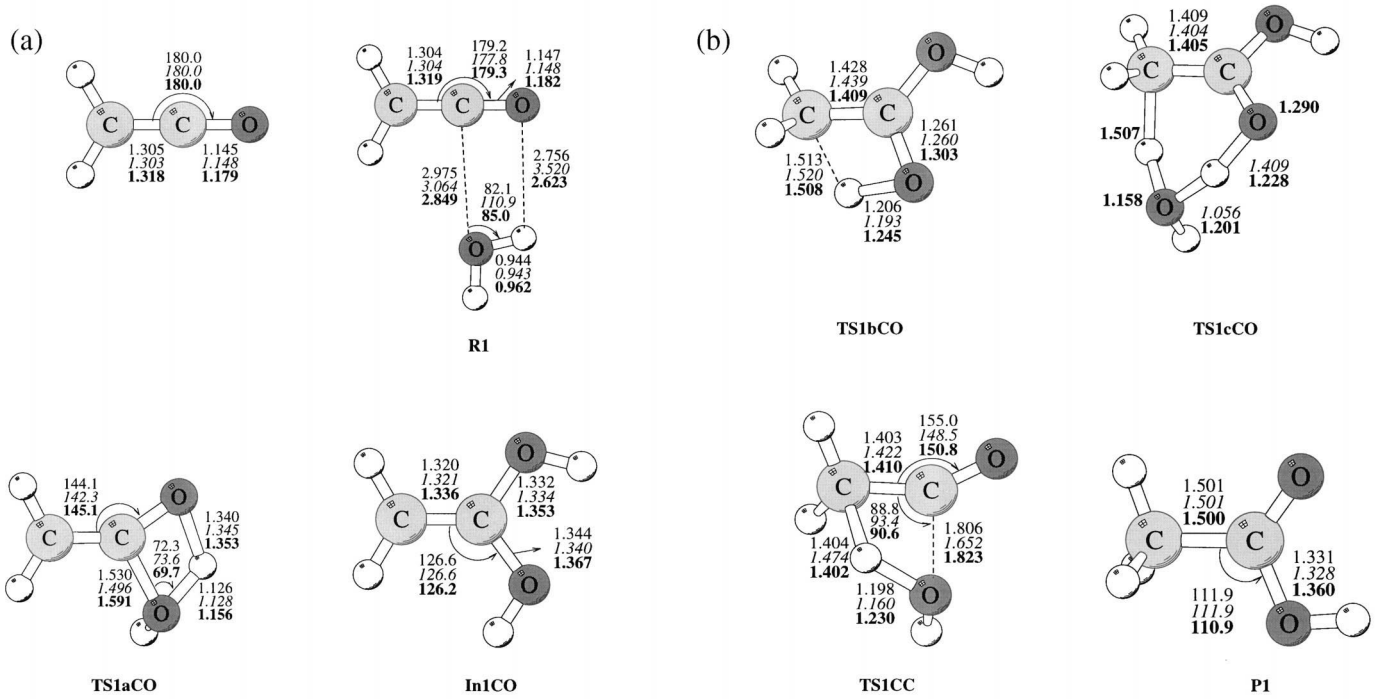

for the intermediacy of 1,1-enediols. Furthermore, they substantiated the fact that the less hindered enediols ketonise rapidly and are insufficiently long lived to be observed by conventional methods. In 1995, the enediol–acid reversibility has been demonstrated by Frey and Rappoport (34) in the hydration of arylketenes by carrying out the reaction in ^{18}O labeled water. The latter authors (35) argued that application of the most recent techniques to detect the enol isomers of simple carboxylic acids, however, remains difficult, because the latter are very much more unstable (34, 35). Recently, Kresge et al. (36–42), Wirtz et al. (43), Guthrie et al. (44, 45), and Hegarty and co-workers (46–48) have produced a massive body of results that constitute a valuable set of detailed information on the chemistry of sterically hindered as well as nonhindered carboxylic acid enols.

From a theoretical point of view, subsequent ab initio calculations by various groups (49–54) have consistently pointed out the kinetic preference for a two-step ketene hydration. Nevertheless, the calculated energy barriers even with a two-water cluster remains larger than the experimental estimate of 43 kJ mol^{-1} reported in ref. 9. This suggests the participation of additional water molecules in the transition state structures (55–57). More recently, the assistance of a cluster of water or reactant molecules is clearly demonstrated in the amination of ketenes (58, 59) or alcoholysis of isocyanates (60). On the one hand, the question of the zwitterion mechanism has not been properly adressed. On the other hand, recent ab initio MO studies (61) on the cycloaddition of ketenes with imines have suggested an initial formation of zwitterionic intermediates in polar solvents. In this context, it seems necessary to reinvestigate the ketene hydration mechanism employing on the one hand larger water clusters as models, and on the other hand, theoretical methods treating appropriately the solvent effect. This is the main purpose of the present study. Concretely, both C=O and C=C additions are considered using progressively larger water clusters from one to four water molecules. The bulk solvent effect is treated by the continuum methods.

Methods of calculation

Ab initio molecular orbital calculations were carried out using the GAUSSIAN 94 (62) set of programs. The stationary points of interest were initially located and characterized by harmonic vibrational analysis employing Hartree Fock (HF) calculations with the dp-polarized 6-31G(d,p) basis set. The relevant structures were then reoptimized at second-order Møller–Plesset perturbation theory (MP2) level with the same basis set. Improved relative energies between stationary points were finally estimated using the quadratic configuration interaction method (QCISD(T)) also with the same basis at MP2 optimized geometries. These relative values were also corrected for zero-point vibrational energies (ZPE) derived from HF/6-31G(d,p) calculations and uniformly scaled by 0.9. The influence of the bulk solvent on the hydration reaction has been tackled employing two different approaches. The solvent is in general represented by a dielectric continuum characterized by its dielectric constant (ε). First, we used a self-consistent reaction field method (SCRF) (63) in which the electrostatic expansion is truncated at the dipole level and a spherical cavity is used. All relevant gas phase stationary structures including water clusters up to four water molecules were reoptimized in aqueous solution (ε = 78.3) using this approach (HF-SCRF/6-31G(d,p)). Furthermore, single-point calculations were done including electron correlation (MP2-SCRF) using both 6-31G(d,p) and

© 1999 NRC Canada

Table 1. Calculated total (hartree) and zero-point vibrational (ZPE) (kJ mol^{-1}) energies for the hydrolysis of ketene ($H_2C=C=O$).

	HF[a]	MP2[b]	MP2[b]	QCISD(T)[b]	ZPE[c]
	6-31G**	6-31G**	6-311++G**	6-31G**	
$H_2C=C=O$	–151.728 76	–152.176 29	–152.235 18	–152.195 28	81
H_2O	–76.023 61	–76.222 45	–76.274 91	–76.231 65	55
$H_2C=C=O + H_2O$	–227.752 38	–228.398 74	–228.510 09	–228.426 93	136
$H_2C=C=O\cdots H_2O$ **R1**	–227.757 67	–228.405 82	–228.514 36	–228.433 99	140
TS C=O **TS1aCO**	–227.672 54	–228.341 77	–228.445 90	–228.368 78	143
$H_2C_2(OH)_2$ **In1CO**	–227.771 50	–228.415 63	–228.520 07	–228.445 13	156
CH_3COOH **P1**	–227.822 17	–228.469 33	–228.568 15	–228.497 13	158
TS C=C **TS1CC**	–227.659 96	–228.338 51	–228.444 54	–228.362 27	135
$H_2C=C=O + 2H_2O$	–303.776 00	–304.621 19	–304.785 00	–304.658 58	191
$H_2C=C=O\cdots 2H_2O$ (C=O) **R2CO**	–303.794 53	–304.645 38	–304.802 37	–304.682 23	205
TS C=O **TS2CO**	–303.736 22	–304.610 95	–304.762 02	–304.644 87	207
$H_2C_2(OH)_2\cdots H_2O$ **In2CO**	–303.807 48	–304.656 04	–304.808 06	–304.693 87	219
$CH_3COOH\cdots H_2O$ **P2CO**	–303.862 57	–304.695 50	–304.858 74	–304.750 31	222
$CH_3COOH + H_2O$	–303.845 79	–304.691 78	–304.843 06	–304.728 78	212
$H_2C=C=O\cdots 2H_2O$ (C=C) **R2CC**	–303.792 11	–304.645 05	–304.802 20	–304.680 64	205
TS C=C **TS2CC**	–303.727 42	–304.609 14	–304.759 62	–304.639 90	207
$CH_3COOH\cdots H_2O$ **P2CC**	–303.851 55	–304.701 34	–304.849 62	–304.737 92	218
$H_2C=C=O + 3H_2O$	–379.799 59	–380.843 64	–381.059 91	–380.890 23	246
$H_2C=C=O\cdots 3H_2O$ (C=O) **R3CO**	–379.832 60	–380.864 69	–381.093 40	–380.931 38	268
TS C=O **TS3CO**	–379.781 85	–380.836 92	–381.058 71	–380.899 54	277
$H_2C_2(OH)_2\cdots 2H_2O$ **In3CO**	–379.845 04	–380.876 57	–381.098 91	–380.944 02	284
$CH_3COOH\cdots 2H_2O$ **P3CO**	–379.903 98	–380.937 57	–381.152 74	–381.003 21	286
$CH_3COOH + 2H_2O$	–379.869 39	–380.914 23	–381.117 97	–380.960 43	267
$H_2C=C=O\cdots 3H_2O$ (C=C) **R3CC**	–379.830 57	–380.865 47	–381.093 92	–380.930 54	269
TS C=C **TS3CC**	–379.773 81	–380.835 94	–381.056 39	–380.895 84	275
$CH_3COOH\cdots 2H_2O$ **P3CC**	–379.887 47	–380.918 86	–381.138 10	–380.985 22	282
$H_2C=C=O + 4H_2O$	–455.823 20	–457.066 09	—	—	301
$H_2C=C=O\cdots 4H_2O$ (C=O) **R4CO**	–455.875 89	–457.113 31	—	—	336
TS C=O **TS4CO**	–455.825 66	–457.084 42	—	—	340
$H_2C_2(OH)_2\cdots 3H_2O$ **In4CO**	–455.885 32	–457.118 96	—	—	348
$CH_3COOH\cdots 3H_2O$ **P4CO**	–455.941 73	–457.174 52	—	—	349
$CH_3COOH + 3H_2O$	–455.893 00	–457.136 68	—	—	323
$H_2C=C=O\cdots 4H_2O$ (C=C) **R4CC**	–455.867 38	–457.113 45	—	—	332
TS C=C **TS4CC**	–455.811 73	–457.073 78	—	—	336
TS 1,3-H-shift **TS1bCO**	–227.677 49	–228.342 04	–228.447 15	–228.368 43	144
TS 1,3-H-shift **TS1cCO**	–303.752 57	–304.607 11	–304.775 54	–304.658 47	208

[a]Based on HF/6-31G(d,p) geometries.

[b]Based on MP2/6-31G(d,p) geometries.

[c]Zero-point energies from HF/6-31G(d,p) and scaled by 0.9.

6-311++G(d,p) basis sets. Another technique, namely the polarizable continuum model (PCM) developed by Tomasi and co-workers (64), has also been applied; this constitutes a more realistic method, using a cavity adapting the molecular shape instead of a sphere. Thus, single-point calculations were performed at the MP2-PCM/6-31G(d,p) level using the gas phase MP2/6-31G(d,p) optimized geometries. In the discussion, the gas phase relative energies quoted refer to the QCISD(T) values, whereas those in solution are obtained from MP2-PCM. Geometrical parameters mentioned are, unless otherwise stated, the gas phase MP2-values.

Results and discussion

Ketene plus one water molecule

While Fig. 1 shows the optimized geometries of the stationary points along the pathway involving one water molecule, Tables 1 and 2 list the corresponding energetic parameters. This system has been examined in previous papers (52, 53), but for the purpose of comparison, parameters optimized at three distinct levels of theory are reported, including the gas phase HF and MP2 as well as the HF-SCRF level using the 6-31G(d,p) basis set. It seems useful to recall the main features. The addition occurs through an initial interaction of weak nature involving an oxygen lone pair and the ketene LUMO which has a dominant contribution from C_α. Due to the weak intermolecular force resulting in **R1**, where the stabilization energy amounts to only –11 kJ mol^{-1}, the energy surface relevant to the orientation of the H_2O molecule in this plane is rather shallow. With this weakly bound complex **R1** as the starting point, the reaction may proceed along two different planes, the one representing an addition to the ketene C=O bond and the other to its C=C bond. Both transition structures characterizing these addi-

© 1999 NRC Canada

Table 2. Calculated relative energies (kJ mol^{-1}) for the hydrolysis of ketene ($H_2C=C=O$), all corrected by zero-point vibrational energies (ZPE) (kJ mol^{-1}).

	HF[a] 6-31G**	MP2[b] 6-31G**	MP2[b] 6–311++G**	QCISD(T)[b] 6-31G**
$H_2C=C=O + H_2O$	0	0	0	0
$H_2C=C=O\cdots H_2O$ **R1**	–10	–15	–7	–15
TS C=O **TS1aCO**	217	157	176	161
$H_2C_2(OH)_2$ **In1CO**	–29	–23	–5	–27
CH_3COOH **P1**	–161	–163	–130	–161
TS C=C **TS1CC**	242	158	172	170
$H_2C=C=O + 2H_2O$	0	0	0	0
$H_2C=C=O\cdots 2H_2O$ (C=O) **R2CO**	–34	–49	–31	–47
TS C=O **TS2CO**	121	44	77	53
$H_2C_2(OH)_2\cdots H_2O$ **In2CO**	–54	–62	–31	–64
$CH_3COOH\cdots H_2O$ **P2CO**	–196	–163	–162	–209
$CH_3COOH + H_2O$	–161	–163	–130	–162
$H_2C=C=O\cdots 2H_2O$ (C=C) **R2CC**	–28	–48	–30	–43
TS C=C **TS2CC**	144	48	83	66
$CH_3COOH\cdots H_2O$ **P2CC**	–170	–182	–141	–180
$H_2C=C=O + 3H_2O$	0	0	0	0
$H_2C=C=O\cdots 3H_2O$ (C=O) **R3CO**	–64	–32	–65	–85
TS C=O **TS3CO**	78	49	28	7
$H_2C_2(OH)_2\cdots 2H_2O$ **In3CO**	–80	–47	–63	–102
$CH_3COOH\cdots 2H_2O$ **P3CO**	–233	–205	–202	–256
$CH_3COOH + 2H_2O$	–161	–163	–130	–162
$H_2C=C=O\cdots 3H_2O$ (C=C) **R3CC**	–57	–33	–65	–82
TS C=C **TS3CC**	98	51	40	15
$CH_3COOH\cdots 2H_2O$ **P3CC**	–194	–161	–168	–212
$H_2C=C=O + 4H_2O$	0	0	—	—
$H_2C=C=O\cdots 4 H_2O$ (C=O) **R4CO**	–103	–89	—	—
TS C=O **TS4CO**	33	–9	—	—
$H_2C_2(OH)_2\cdots 3H_2O$ **In4CO**	–116	–92	—	—
$CH_3COOH\cdots 3H_2O$ **P4CO**	–263	–237	—	—
$CH_3COOH + 3H_2O$	–161	–163	—	—
$H_2C=C=O\cdots 4H_2O$ (C=C) **R4CC**	–85	–93	—	—
TS C=C **TS4CC**	65	15	—	—
TS 1,3-H-shift **TS1bCO**	205	157	174	163
TS 1,3-H-shift **TS1cCO**	79	53	42	17

[a]Based on HF/6-31G(d,p) geometries.

[b]Based on MP2/6-31G(d,p) geometries.

tions, **TS1aCO** and **TS1CC**, respectively, are shown in Fig. 1. As expected, both four-membered TSs are not planar, due to the fact that the additions are not pseudo-pericyclic. The optimized geometry of **TS1aCO** reveals a compact structure with a significant bending of ketene at this stage of the reaction (the CCO angle being 145.1°). The hydrogen transfer to the ketene oxygen giving the enediol **In1CO** occurs, but the O—H distance in water remains shorter than that to ketene oxygen; in fact, the O(water)–H and O(ketene)–H distances amount to 1.156 and 1.353 Å, respectively. The newly formed C—O bond is quite short in this TS, its length being 1.591 Å. An imaginary frequency of 1947*i* cm^{-1} is associated with mainly two motions, namely, the oxygen attack and the hydrogen transfer. In **TS1CC**, leading immediately to acetic acid **P1**, the deformation of the attacking water molecule has proceeded to a larger extent (the O—H bond distance being 1.230 Å), whereas the formation of the new C—H bond is also noticeable (1.402 Å). Furthermore, the C—C bond has lost an appreciable amount of its π-contribution, having now a distance of 1.410 Å due no doubt to the distortion of the CH_2 group. This occurs at a quite larger C—O (water) distance of 1.823 Å. The nature of **TS1CC** is confirmed by the imaginary vibrational frequency (ν_i = 2106*i* cm^{-1}) in which the normal mode is a pure migration of hydrogen from the attacking water to the β-carbon.

Relative energies given in Table 3 confirm that the C=O addition is slightly preferred over the C=C. At the highest level of theory, QCISD(T)/6-31G(d,p)+ZPE, the energy barrier for C=O addition amounts to 172 kJ mol^{-1}, which is 9 kJ mol^{-1} lower than that for C=C addition. In spite of intensive attempts, search for a stationary point on the potential surface describing an open zwitterion of the type **6** failed, either in gas phase or in aqueous solution. Inclusion of bulk solvent effects by both SCRF and PCM models does not affect the fact that both C=C and C=O additions have energy

© 1999 NRC Canada

Table 3. Energy barriers (kJ mol^{-1}) for the hydrolysis of ketene ($H_2C=C=O$), including different numbers of water molecules.

	HF[a]	MP2[b]	MP2[b]	QCISD(T)[b]
	6-31G**	6-31G**	6-311++G**	6-31G**
$H_2C=C=O$ + **1**H_2O				
TS C=C	252	173	179	185
TS C=O	227	172	183	176
$H_2C=C=O$ + **2**H_2O				
TS C=C	172	96	114	109
TS C=O	155	92	108	100
$H_2C=C=O$ + **3**H_2O				
TS C=C	155	84	104	97
TS C=O	142	81	93	92
$H_2C=C=O$ + **4**H_2O				
TS C=C	150	108	—	—
TS C=O	136	80	—	—
1,3-H-shift				
TS1bCO	205	157	174	163
TS1cCO (active H_2O)	79	53	42	17

[a]Based on HF/6-31G(d,p) geometries.
[b]Based on MP2/6-31G(d,p) geometries.

Table 4. Energy barriers[a] (kJ mol^{-1}) of the considered stationary points, both in gas phase and solvent (ε = 78.3).

	Gas phase		Solution	
	MP2	MP2-SCRF	MP2-SCRF	MP2-PCM
	6-31G**	6-31G**	6-311++G**	6-31G**
$H_2C=C=O$ + **1**H_2O				
TS C=C	173	166	173	180
TS C=O	172	162	174	167
$H_2C=C=O$ + **2**H_2O				
TS C=C	96	90	107	110
TS C=O	92	84	100	97
$H_2C=C=O$ + **3**H_2O				
TS C=C	84	63	82	81
TS C=O	81	69	95	73
$H_2C=C=O$ + **4**H_2O				
TS C=C	108	89	96	99
TS C=O	80	73	85	87
1,3-H-shift				
TS1bCO	157	183	185	186
TS1cCO (active H_2O)	53	22	60	29

[a]Based on gas phase MP2/6-31G(d,p) optimized geometries.

barriers that are too large to be realistic. As reported in Table 4, energy barriers of 160 and 173 kJ mol^{-1} are found in aqueous solution (MP2-PCM/6-31G(d,p), ε = 78.3) for C=O and C=C additions, respectively. It is likely that use of larger basis set will not affect significantly these quantities.

Intramolecular hydrogen shift

The 1,3-hydrogen shift connecting both adducts enediol **In1CO** and acetic acid **P1** has been examined in previous papers (49–54). Here, we wish to add some comments regarding the process in aqueous solution. Note that a significant change in the structure around C_β has taken place as the reaction passes through **TS1bCO**. The carbon atom has changed from a planar to a tetrahedral arrangement of bonds, and the C—C bond has changed from 1.336 Å in **In1CO** via 1.409 Å in **TS1bCO** to 1.500 Å in **P1**. The **TS1bCO** has one imaginary frequency of 2405*i* cm^{-1} whose normal mode is a pure H-atom migration. It is well known that 1,3-sigmatropic shifts in hydrocarbons are orbital symmetry forbidden; the presence of a single orthogonal orbital in the present case seems to be sufficient to make it pseudopericyclic, and thereby more allowed by the same reason, reducing thus the barrier to migration (65). However, due to the strained four-membered ring geometry of the transition structure in which the hydrogen is being transfered from the molecular plane to a *p*-orbital above the plane, and the C-H-

© 1999 NRC Canada

Fig. 2. Selected optimized structures of stationary points along a ketene hydration path with two water molecules across both C=O and C=C bonds. The entries are HF, HF-SCRF (in italics), and MP2 (in bold). The HF values are taken from ref. 52 and given for purpose of comparison.

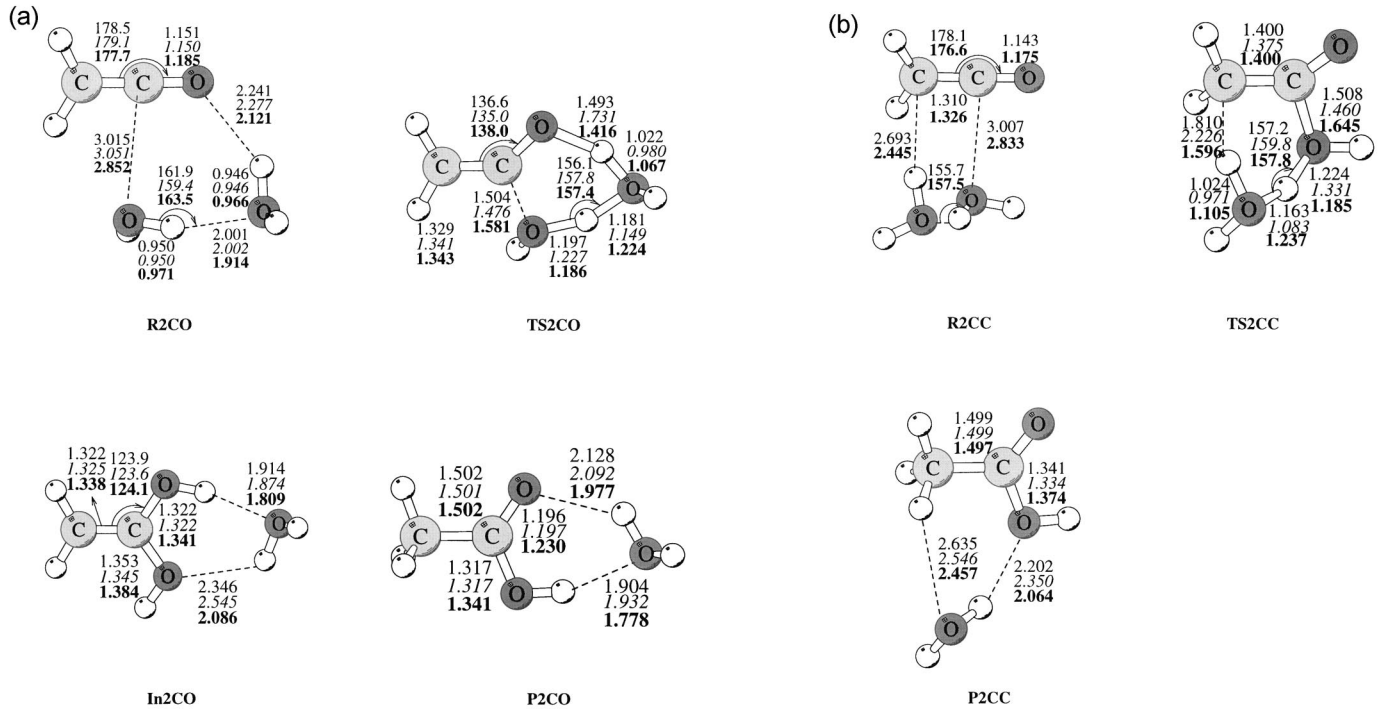

Fig. 3. Contour map of the Fukui function $f^{(+)}$ for ketene in both perpendicular *xy* (*a*) and molecular *yz* (*b*) planes. The solid isocontours correspond to positive values and the broken lines to negative values of the $f^{(+)}$ functions.

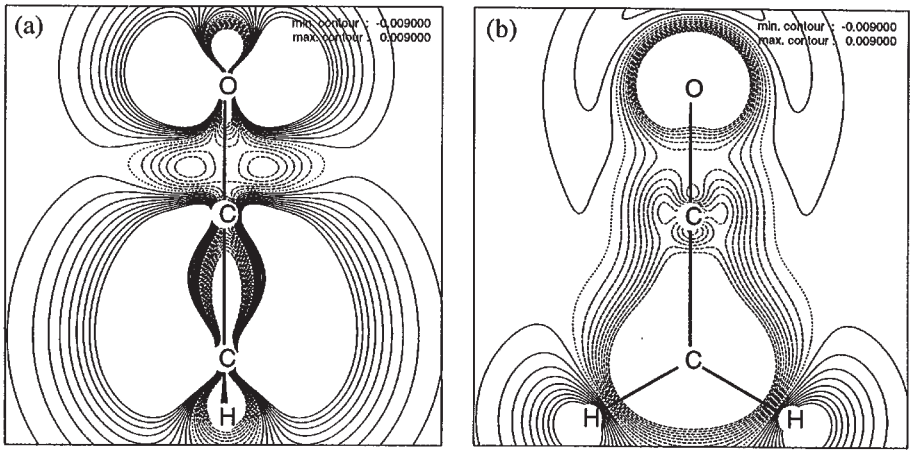

O bond angle is far away from the ideal linearity, the energy barrier remains high. As a matter of fact, the energy of **TS1bCO** relative to **In1CO** amounts to 163 kJ mol^{-1}, at the QCISD(T)/6-31G(d,p)+ZPE level of theory.

This result indicates that a 1,3-H-shift from enediol to acetic acid is not competing energetically with the direct production of acetic acid via **TS1CC**. However, the interconversion is greatly accelerated with the aid of an extra water molecule assisting the 1,3-H-shift. Inclusion of a second water molecule through **TS1cCO** reduces the energy barrier for 1,3-H-shift by an amount as large as 146 kJ mol^{-1}. Such lowering gives rise to an almost barrierless process, having now an activation energy of only 17 kJ mol^{-1} relative to the separated water and ketene species. As a consequence, the conversion of an enediol to an acid in the presence of water is a fast process, in agreement with experimental observations (27). Accordingly, the 1,3-H-shift will be omitted in the further discussion and only the rate-determining attack of water across the ketene C=O bond will be compared to that across the C=C bond.

Ketene plus two water molecules

While Table 3 emphasizes a dramatic decrease of activation energy when an extra water molecule is added in the water chain, Fig. 2 shows the relevant geometrical features. As found in earlier studies (49–53), each of the two additions begins with a preassociative complex, **R2CO** or **R2CC**, overcomes a transition structure, **TS2CO** or **TS2CC**,

© 1999 NRC Canada

Fig. 4. Contour map of the Fukui function $f^{(-)}$ for ketene in both perpendicular *xy* (*a*) and molecular *yz* (*b*) planes. The solid isocontours correspond to positive values and the broken lines to negative values of the $f^{(-)}$ functions.

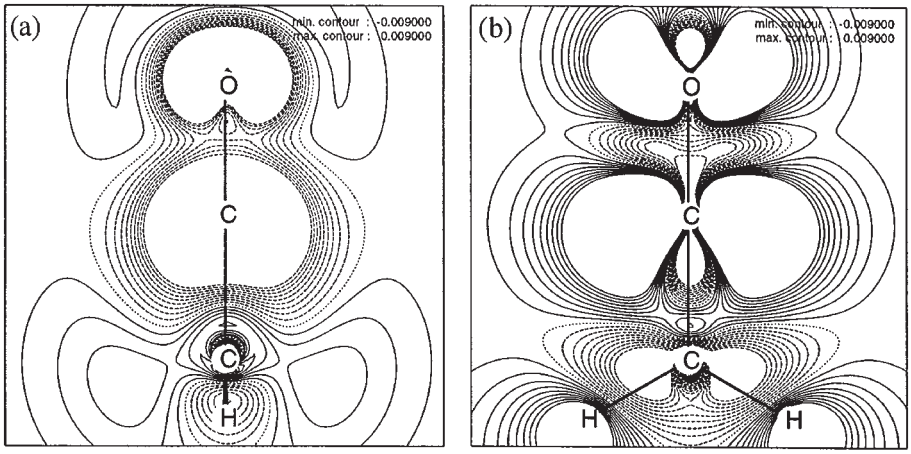

and gives a product complex, **In2CO** or **P2CC**. **P2CO** is another complex between acetic acid and water involving the carboxylic functional and therefore more stable than **P2CC**. At the highest QCISD(T) level of calculation, both energy barriers for attack across C=O via **TS2CO** and C=C via **TS2CC** are lowered by 72 kJ mol^{-1}, as compared with those involving one water. The resulting energy barriers turn out to be 100 and 109 kJ mol^{-1}, respectively, with respect to the corresponding initial complexes (Table 2). In a simple view, the addition of one water molecule to ketene via **TS1aCO** and **TS1CC** can be regarded as allowed pseudopericyclic reactions with strained transition state geometries. When the second water is added, the TS geometries are improved, and as a consequence, the barriers drop. As the additions are pseudo-pericyclic, the size of the water chain is not expected to have a large electronic effect on the barrier.

The difference of both additions depends on the plane of attack and can be rationalized in terms of Fukui functions (f) that are the descriptors of reactivity based solely on the properties of the reactants (66). Depending on the type of attack, different sites are indicated as the most reactive site for $H_2C{=}C{=}O$, i.e., the site for which f is largest. Attack of the water system can occur either in the molecular plane (C=O) or in the perpendicular plane (C=C). While Fig. 3 displays contour maps of the Fukui function $f^{(+)}$ for ketene in both *xz* (Fig. 3*a*) and *yz* plane (Fig. 3*b*), Fig. 4 shows contour maps of the Fukui function $f^{(-)}$ (*xz* plane (Fig. 4*a*); *yz* (Fig. 4*b*)). These terms are defined as follows:

$$f_K^+ = [\rho_K(N + 1) - \rho_K(N)]$$

relevant for nucleophilic attack, and

$$f_K^- = [\rho_K(N) - \rho_K\ (N - 1)]$$

relevant for electrophilic attack, where ρ_K is the electron density at the atom K, and N is the number of electrons.

The preferred attack in the *yz* plane proceeds via a nucleophilic attack of O on C_α ($f^{(+)}$ being largest for C_α), while an electrophilic attack occurs by H^+ at oxygen ($f^{(-)}$ being largest for O). This indicates that the ability of the O atom to accept and redistribute a positive charge is of considerable importance, such that attack on O is preferred over attack on C_β. In the *xz* plane, however, the opposite is observed. Electrophilic attack occurs by H^+ at the β-carbon and no longer at oxygen ($f^{(-)}$ being largest for C_β). Thus, the Fukui functions predict that while C=O addition is preferred in the molecular plane of ketene, C=C addition is, as would be expected, preferred in the perpendicular plane.

Ketene plus three water molecules

As in the two previous cases, interaction between ketene and a three-water cluster is initiated by strong cyclic intermolecular interactions. Two such eight-membered ring complexes are found, the one **R3CO** involving the ketene C=O bond and the other **R3CC** the C=C bond. While geometrical parameters are displayed in Fig. 5, calculated total and relative energies are given in Tables 1 and 2. Both complexes are characterized by long C_α-oxygen distances, 2.766 and 2.924 Å, respectively. In the latter, the C_β-hydrogen distance is found to be 2.507 Å. The energy lowering by complex formation, obtained at the QCISD(T)+ZPE level, is found to be substantial, –85 and –82 kJ mol^{-1} for **R3CO** and **R3CC**, respectively, with respect to the separated reactants, $H_2C{=}C{=}O + 3H_2O$. Inclusion of an extra water molecule increases further the stabilization upon complex formation by a significant amount. While the complex **R1** is only –15 kJ mol^{-1} below the separated reactants, in the two-water system, a lowering was calculated of –47 kJ mol^{-1} for **R2CO** and –43 kJ mol^{-1} for **R2CC**. The larger the water cluster, the stronger the hydrogen bonds in the corresponding complexes and the more extended the stabilization.

From each of the complexes, the reaction proceeds through the TSs **TS3CO** and **TS3CC** depicted in Fig. 5. The geometry of **TS3CC** indicates that the forming of the new carbon–oxygen bond precedes the establishing of the C—H bond at the C_β carbon. While the former has virtually taken shape, the O—H bond remains unchanged. Nevertheless, the spatial arrangement of the three hydrogen atoms around this carbon is roughly tetrahedral at this stage of the reaction. The electronic reorganisation is also reflected by the elongation of the C=C bond to 1.400 Å in **TS3CC**. The hydrogen atoms linking the water molecules shifted their position and are approximately midway between the neighbouring oxygen atoms. **TS3CC** is characterized by a smaller imaginary

© 1999 NRC Canada

Fig. 5. Selected optimized structures of stationary points along a ketene hydration path with three water molecules across both C=O and C=C bonds. The entries are HF, HF-SCRF (in italics), and MP2 (in bold).

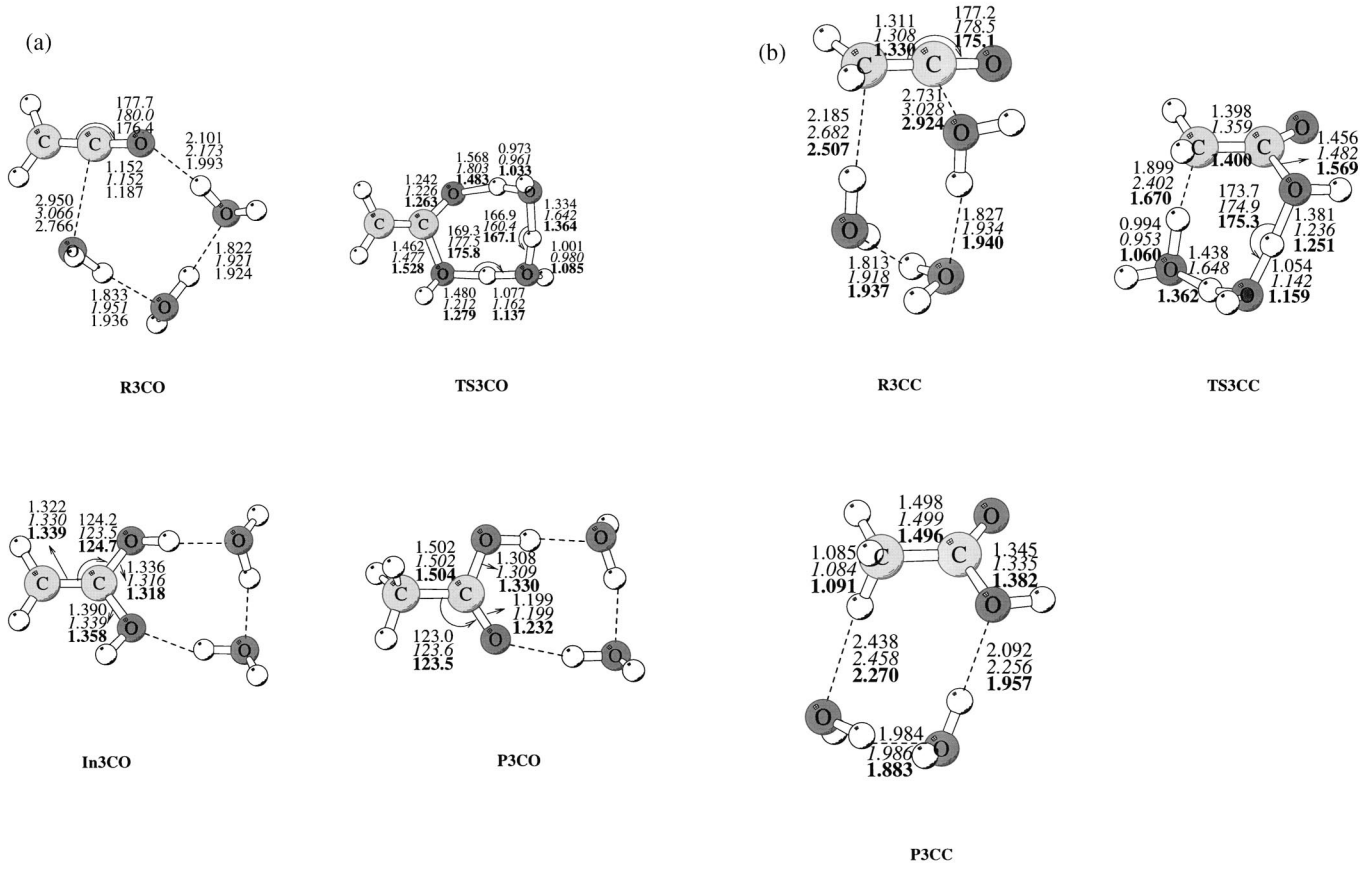

frequency of 292*i* cm^{-1}. The dominant contribution to the associated normal mode is a shift of the attacking hydrogen towards the C_β atom, and concomitant migration of the hydrogen atoms linking the water molecules. Similarly, in **TS3CO**, the imaginary frequency of 201*i* cm^{-1} is associated with a transfer of the hydrogen atom between both water and ketene oxygens.

TS3CO appears to be more compact than **TS3CC**; the hydrogen transfer to O is much more advanced. While HF calculations tend to a ($H_2OH_2OH^+.OH^-$) ionic structure within the water cluster, both MP2 and HF-SCRF levels suggest a less polar form. It is also worth noting that in both TSs, the oxygen attack and the hydrogen transfer take place in two quasi perpendicular planes, a situation similar to hydrogen transfer that in the CO_2 + $(H_2O)_3$ supersystem (56). As revealed by Table 3, the activation energies are 92 and 97 kJ mol^{-1} for attacks across C=O and C=C of ketene, respectively, relative to the reactant complexes. Again, the barriers towards addition to these bonds are virtually of the same magnitude, but with a slight preference for attack on C=O. Regarding the adducts, the complex **P3CC** is far more stable than **In3CO**.

Regarding the entropic contributions to the activation parameters, the difficulty lies rather in the starting point to be taken. If the completely separated system was considered, the activation entropy should be large; if the complex was considered, then the entropy variation was much smaller. In either case, the calculated values do not match well the experimental one mentioned above.

Ketene plus four water molecules

Having established a significant effect in going from two to three water molecules in the water chain, it is interesting to see what happens when the chain is further increased by another water molecule. It is needless to say that in reality, there are several cluster forms of water tetramer, and as a consequence, other addition TSs are expected to exist. Nevertheless, it is not our purpose to explore all the possible approaches. We consider rather the case where the water molecules form a chain in which a successive proton relay occurs; only in this case, the results could best be compared with those of the two and three water chains discussed above.

Optimized geometries of the stationary points including four water molecules are shown in Fig. 6. Again, each addition starts with a preassociative complex (**R4CO** and **R4CC**), passes through a TS (**TS4CO** and **TS4CC**), and finally gives rise to an adduct complex (**In4CO** and **P4CO**). A **P4CC** complex, analogous to **P3CC**, could not be located. The calculations show that as both transition states **TS4CO** and **TS4CC** are approached, the four water molecules move in the form of a compact chain tetramer towards the ketene. At the transition states, the deformation of ketene is an important nuclear motion, involving a significant bending of

© 1999 NRC Canada

Fig. 6. Selected optimized structures of stationary points along a ketene hydration path with four water molecules across both C=O and C=C bonds. The entries are: HF, HF-SCRF (in italics), and MP2 (in bold). The arrows indicate either bond distances (straight lines) or bond angles (bent arrows connecting two bonds).

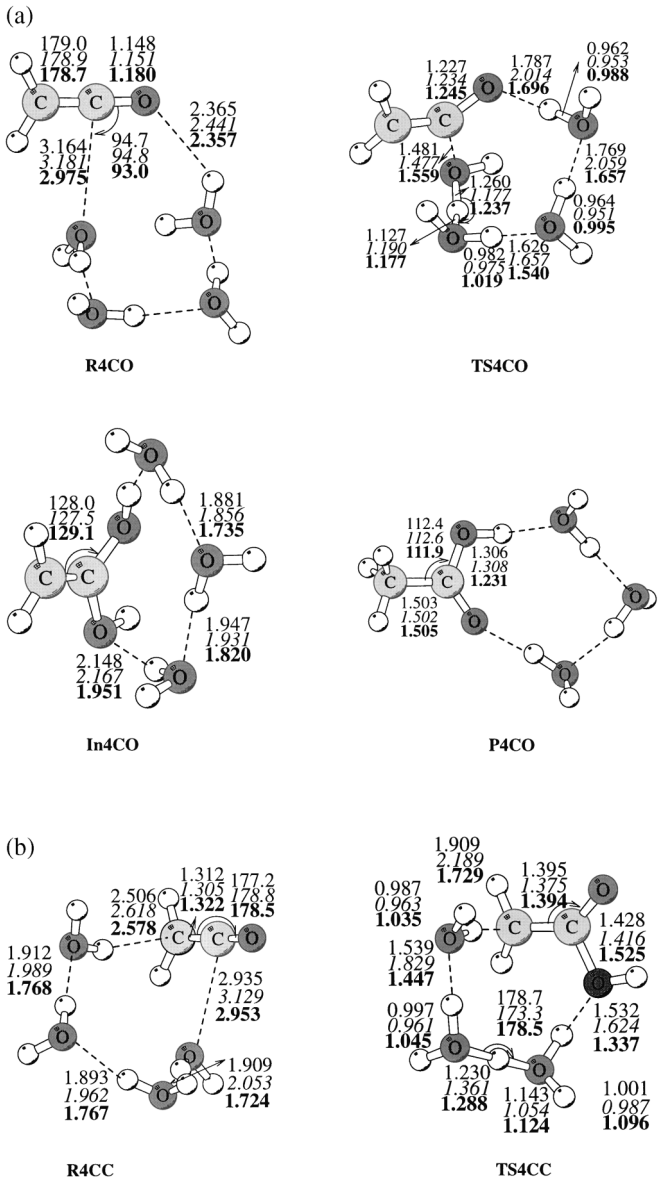

Fig. 7. Schematic energy profiles showing the energy barriers for ketene hydration paths including different chains of water molecules, ($H_2C{=}C{=}O + nH_2O$, n = 1, 2, 3, 4), calculated in gas phase at the MP2/6-31G(d,p)+ZPE level of theory. All barriers are with respect to the corresponding preassociative complexes.

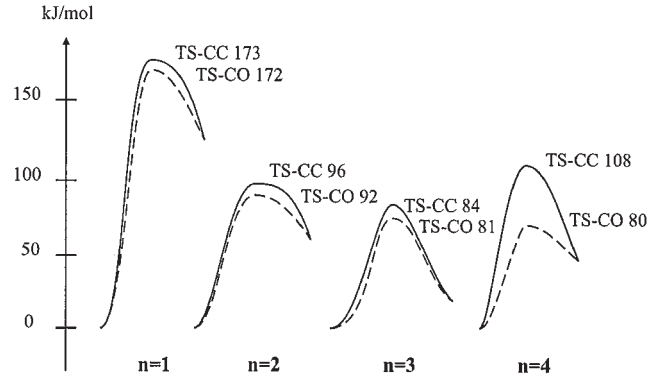

Fig. 8. Schematic energy profiles showing the energy barriers for ketene hydration paths including different chains of water molecules ($H_2C{=}C{=}O + nH_2O$, n = 1, 2, 3, 4), calculated in aqueous solution (ε = 78.3) at the MP2-PCM/6-31G(d,p)+ZPE level of theory. All barriers are relative to the corresponding preassociative complexes.

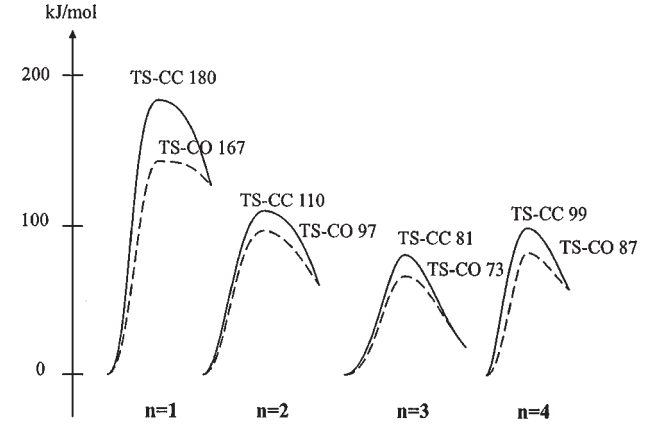

the C=C=O angle. The preference for addition across C=O over C=C can be understood by the extra distortion of the CH_2 group present in **TS4CC**, which makes it energetically less favoured. The results in Table 3 indicate that some saturation of the length of the water chain is reached for C=O attack. The activation energy is only changed by 1 kJ mol^{-1} at the MP2/6-31G(d,p) level of theory. This saturation suggests that the bridging effect is no longer important in chain lengths in the gas phase with more than three water molecules. For C=C addition, the energy barrier is found to be even increased, relative to the three water case, being 28 kJ mol^{-1} higher than the barrier for C=O addition by now. This fact is a further proof for the hydration of ketene occurred by addition of chains of water across the ketene C=O bond rather than the C=C.

Bulk solvent electrostatic influence

Having established the catalytic effect of increasing water clusters during the hydration reaction, we now turn to that of the bulk solvent. Results when the supermolecules are put in a cavity in a dielectric continuum (ε = 78.3) are summarized in Table 4. Gas phase geometries are re-optimized incorporating a continuum by means of a reaction field method (SCRF), and energetic parameters are obtained using single-point calculations with SCRF geometries and both SCRF and PCM models. While the SCRF results show some fluctuations, in particular for the three-water system, the more reliable PCM results give a consistent picture. That is, compared with the reaction pathways of the gas phase system, a trend emerges showing a small change in the energy barrier of, at most, 14 kJ mol^{-1}. A comparison between the energy

© 1999 NRC Canada

barriers in gas phase and aqueous solution is made in Figs. 7 and 8 for both additions across C=O and C=C, including increasing number of water molecules. For the sake of uniformity, only values based on MP2 calculations are employed. We note that the barriers for the four-water cluster with bulk solvation, are higher than the three-water ones. This is presumably due to the use of single-point MP2 energies. Usually, energy barriers obtained from single-point energies are consistent, thanks to the fact that the geometries do not change appreciably in going from one to another level, or that the energy surface is shallow in the saddle region. In this case, the bulk solvation is likely to distort the geometries in different ways in the MP2 level, as compared with that in the HF.

By and large, a passive, nonspecific solvation of the medium does not change the found preference for C=O addition when going from gas phase to liquid phase. Concerning the geometrical parameters of the transition structures, however, a significant difference can be noted between gas phase and continuum. As shown in Figs. 1, 2, 5, and 6, the proton transfer to the ketene oxygen in the various transition structures for water addition is far more completed in gas phase than in aqueous solution. This results in a longer H—O distance in solution, being elongated by at least 0.3 Å relative to the gas phase values. As mentioned above, a zwitterion could not be found, neither in gas phase, nor in solution using different reaction field models.

Concerning the size of the energy barrier, a point of concern, however, remains. Our estimates for this quantity using three-water and four-water clusters amount to about 70–80 and 80–90 kJ mol^{-1}, respectively, which are much larger than the experimental estimate (9) of 43 kJ mol^{-1}. Three possible reasons for this difference can be noted: (*i*) the first is that the atomic basis set employed in this work remains of moderate quality; (*ii*) the second reason, perhaps more importantly, is the fact that the point of references may be not the same. In our evaluation, the preassociation complexes involving ketene and water clusters are taken as the references. Probably, this is not the case in experimental studies. We note that in the four-water cluster case, both TSs actually lie below the separated system $H_2C=C=O + 4H_2O$; an energy barrier only exists when considering the complexes as stationary points; and (*iii*) the third reason is that the treatment of the solvent effect is also far from complete. Treatments using more advanced simulation techniques are certainly necessary for a more quantitative picture of the solvation phenomenon.

Although the reality of a hydration process is far more complex than the model calculations reported here, the proposal of a two-step reaction across the ketene C=O bond involving a chain of three or four water molecules appears overall in better agreement with recent experimental developments in identifying enols of carboxylic acids.

Concluding remarks

In the present paper, the reaction mechanism of the ketene hydration by increasing water clusters has been probed by theoretical methods in both gas phase and aqueous solution. Our calculations provide further evidence that a two-step addition of water across the carbon–oxygen double bond of ketene, yielding first an enediol intermediate is energetically preferred over a concerted addition across the carbon–carbon double bond leading immediately to the carboxylic acid product. Chains of two or three hydrogen-bonded water molecules are expected to be present in the hydration supersystem. A further incorporation of active water molecules induces rather small improvements of the energy barrier. Effects of the surrounding bulk do not change qualitatively the gas phase findings. These results, together with the recent experimental developments in identifying enols of carboxylic acids, do not support either a direct C=C addition or an ionic mechanism involving a zwitterion intermediate.

Fifteen years have passed since we reported the first theoretical results pointing out the preference for a C=O hydration of ketene (22). Thanks to the effort of several groups, there is now compelling experimental and theoretical results supporting this hydration mechanism. The existence of enols of carboxylic acids appears now to be a fact of life. This story also illustrates, once more, the necessary and beneficial symbiosis between theory and experiment in which simple but reliable theoretical predictions may lead to far reaching experimental research. It is interesting to note that in earlier textbooks of organic chemistry (see for example ref. 67), up to the fifties, the ketene hydration was explained as a two-step reaction with the intermediacy of 1,1-enediols. Due to the total lack of evidence, this mechanism was progressively discarded from the sixties. It is now hoped that the enols of carboxylic acids will occupy again their own place in future textbooks.

Acknowledgments

The authors are grateful to the Flemish Science Organisations (FWO-Vlaanderen, IWT, and GOA program) and the KULeuven Computing Centre for continuing support.

References

1. H. Staudinger. *In* Die Ketene. Enke, Stuttgart. 1912.
2. W.E. Hanford and J.C. Sauer. Org. React. **3**, 108 (1946).
3. R.N. Lacey. *In* The chemistry of the alkenes. Interscience, New York. 1964. pp. 1161–1227.
4. D. Borrmann. *In* Methoden der organische chemie. Vol. 7. Part 4. Georg Thieme Verlag, Stuttgart. 1968.
5. S. Patai. The chemistry of ketenes and related compounds. Parts 1 and 2. Wiley, New York. 1980.
6. W.T. Brady. Tetrahedron, **37**, 2949 (1981).
7. T.T. Tidwell. Ketenes. Wiley, New York. 1995.
8. E. Bothe, H. Meier, D. Schulte-Frohlinde, and C. von Sonntag. Angew. Chem. Int. Ed. Engl. **15**, 380 (1976).
9. E. Bothe, A.M. Dessouki, and D. Schulte-Frohlinde. J. Phys. Chem. **84**, 3270 (1980).
10. S.H. Kabir, H.R. Seikaly, and T.T. Tidwell. J. Am. Chem. Soc. **101**, 1059 (1979).
11. D.P.N. Satchell and R.S. Satchell. Chem. Soc. Rev. **4**, 231 (1975).
12. A.D. Allen and T.T. Tidwell. J. Am. Chem. Soc. **109**, 2774 (1987).
13. H.R. Seikaly and T.T. Tidwell. Tetrahedron, **42**, 2587 (1986).
14. T.T. Tidwell. Acc. Chem. Res. **23**, 273 (1990).
15. P.J. Lillford and D.P.N. Satchell. J. Chem. Soc. B, 889 (1968).

© 1999 NRC Canada

16. N.L. Poon and D.P.N. Satchell. J. Chem. Soc. Perkin Trans. 2, 1381 (1983).
17. N.L. Poon and D.P.N. Satchell. J. Chem. Soc. Perkin Trans. 2, 1083 (1984).
18. N.L. Poon and D.P.N. Satchell. J. Chem. Soc. Perkin Trans. 2, 1551 (1985).
19. N.L. Poon and D.P.N. Satchell, J. Chem. Soc. Perkin Trans. 2, 1485 (1986).
20. G. Donohoe, D.P.N. Satchell, and R.S. Satchell. J. Chem. Soc. Perkin Trans. 2, 1671 (1990).
21. D.P.N. Satchell and R.S. Satchell. Z. Naturforsch. B, **46**, 391 (1991).
22. M.T. Nguyen and A.F. Hegarty. J. Am. Chem. Soc. **106**, 1552 (1984).
23. I.H. Williams, D. Spangler, D.A. Femec, G.M. Maggiora, and R.L. Schowen. J. Am. Chem. Soc. **102**, 6619 (1980); **105**, 31 (1983).
24. T. Oie, G.H. Loew, S.K. Burt, J.S. Binkley, and R.D. Mac Elooy. J. Am. Chem. Soc. **104**, 6169 (1982).
25. M.T. Nguyen and A.F. Hegarty. J. Am. Chem. Soc. **105**, 3811 (1983).
26. M.T. Nguyen and T.K. Ha. J. Am. Chem. Soc. **106**, 599 (1984).
27. A.F. Hegarty and P. O'Neill. *In* The chemistry of enols. *Edited by* S. Patai. Wiley, New York. 1990. Chap. 10.
28. R. Aumann and H. Wormann. Chem. Ber. **112**, 1233 (1979).
29. W. Ried and P. Junker. Liebigs Ann. Chem. **709**, 85 (1979)
30. A.F. Hegarty and P. O'Neill. J. Chem. Soc. Chem. Commun. 744 (1987).
31. B. Urwyler and J. Wirz. Angew. Chem. Int. Ed. Ingl. **29**, 790 (1990).
32. Y. Chiang, A.J. Kresge, P. Pruszynski, N.P. Schepp, and J. Wirz. Angew. Chem. Int. Ed. Engl. **29**, 792 (1990),
33. B.M. Allen, A.F. Hegarty, P. O'Neill, and M.T. Nguyen. J. Chem. Soc. Perkin Trans. 2, 927 (1992).
34. J. Frey and Z. Rappoport. J. Am. Chem. Soc. **117**, 1161 (1995); **118**, 5182 (1996).
35. Z. Rappoport, J. Frey, M. Sigalov, and E. Rochlin. Pure Appl. Chem. **69**, 1933 (1997).
36. Y. Chiang, A.J. Kresge, V.V. Popik, and N.D. Schepp. J. Am. Chem. Soc. **119**, 10 203 (1997).
37. Y. Chiang, A.J. Kresge, V.A. Nikolaev, and V.V. Popik. J. Am. Chem. Soc. **119**, 11 183 (1997).
38. J. Androas, Y. Chiang, C.G. Huang, A.J. Kresge, and J.C. Scaiano. J. Am. Chem. Soc. **115**, 10 605 (1993).
39. J. Androas, Y. Chiang, A.J. Kresge, I.G. Pojarlieff, N.P. Schepp, and J. Wirz. J. Am. Chem. Soc. **116**, 73 (1994).
40. J. Androas, A.J. Kresge, and V.V. Popik. J. Am. Chem. Soc. **116**, 961 (1994).
41. J. Androas, Y. Chiang, A.J. Kresge, and V.V. Popik. J. Am. Chem. Soc. **169**, 8417 (1997).
42. A.J. Kresge. Chem. Soc. Rev. **275** (1996).
43. J.I.K. Almstead, B. Hrwyler, and J. Wirz. J. Am. Chem. Soc. **116**, 954 (1994).
44. J.P. Guthrie. Can. J. Chem. **71**, 2123 (1993).
45. J.P. Guthrie and Z. Liu. Can. J. Chem. **73**, 1395 (1995).
46. P. O'Neill and A.F. Hegarty. J. Org. Chem. **57**, 4421 (1992).
47. A.F. Hegarty, J.G. Kelly, and C.M. Rehilan. J. Chem. Soc. Perkin Trans. 2, 1175 (1997).
48. B.M. Allen, A.F. Hegarty, and P. O'Neill. J. Chem. Soc. Perkin Trans. 2, 2733 (1997).
49. M.T. Nguyen and P. Ruelle. Chem. Phys. Lett. **138**, 786 (1987).
50. J. Androas, A.J. Kresge, M.R. Peterson, and I.G. Csizmada, J. Mol. Struct. (Theochem), **232**, 155 (1991).
51. J. Androas and A.J. Kresge. J. Mol. Struct. (Theochem), **233**, 165 (1991).
52. P.N. Skancke. J. Phys. Chem. **96**, 8065 (1992).
53. M.T. Nguyen, D. Sengupta, G. Raspoet, and L.G. Vanquickenborne. J. Phys. Chem. **99**, 11 883 (1995).
54. X. Duan and M. Page. J. Am. Chem. Soc. **117**, 5114 (1995).
55. A.D. Allen, J. Androas, A.J. Kresge, M.A. McAllister, and T.T. Tidwell. J. Am. Chem. Soc. **114**, 1878 (1992).
56. M.T. Nguyen, G. Raspoet, L.G. Vanquickenborne, and P.Th. Van Duijnen. J. Phys. Chem. **101**, 7379 (1997).
57. G. Raspoet, M.T. Nguyen, M. McGarraghy, and A.F. Hegarty. J. Org. Chem., **63**, 6867 (1998).
58. K. Sung and T.T. Tidwell. J. Am. Chem. Soc. **120**, 3043 (1998).
59. G. Raspoet, M.T. Nguyen, S. Kelly, and A.F. Hegarty. J. Org. Chem., **63**, 9969 (1998).
60. G. Raspoet, M.T. Nguyen, M. McGarraghy, and A.F. Hegarty. J. Org. Chem. **63**, 6878 (1998).
61. B. Lecea, I. Arrastia, A. Arrieta, G. Roa, X. Lopez, M.I. Arriortua, J.M. Ugalde, and F.P. Cossio. J. Org. Chem. **61**, 3070 (1996).
62. M.J. Frisch, G.W. Trucks, H.B. Schlegel, P.M.W. Gill, B.G. Johnson, M.A. Robb, J.R. Cheeseman, T. Keith, G.A. Petersson, J.A. Montgomery, K. Raghavachari, M.A. Al-Laham, V.G. Zakrzewski, J.V. Ortiz, J.B. Foresman, J. Cioslowki, B.B. Stefanov, A. Nanayakkara, M. Challacombe, C.Y. Peng, P.H. Ayala, W. Chen, M.W. Wong, J.L. Andres, E.S. Replogle, R. Comperts, R.L. Martin, D.J. Fox, J.S. Binkley, D.J. DeFrees, J. Baker, J.J.P. Stewart, M. Head-Gordon, C. Gonzalez, and J.A. Pople. GAUSSIAN 94, Revision C.3. Gaussian Inc., Pittsburgh, Pa. 1995.
63. M.W. Wong, M.J. Frisch, and K.B. Wiberg. J. Am. Chem. Soc. **113**, 4776 (1991).
64. S. Miertus, E. Scrocco, and J. Tomasi. Chem. Phys. **55**, 117 (1981).
65. D. M. Birney, S. Ham, and G.R. Unruth. J. Am. Chem. Soc. **119**, 4509 (1997).
66. R.G. Parr and W. Yang. *In* Density functional theory of atoms and molecules. Oxford University Press, New York. 1989.
67. J.B. Conant and A.A. Blatt. *In* The chemistry of organic compounds. 3rd ed. 1948. p. 213.

© 1999 NRC Canada

Theoretical simulation of Brønsted correlations for proton transfer and methyl transfer: the significance of the Brønsted coefficient β

Ian H. Williams and Paul A. Austin

Abstract: Brønsted correlations for proton transfer and methyl transfer between pairs of mimicked 4-substituted pyridines have been simulated by means of AM1 molecular orbital calculations. The enthalpies of activation and of reaction are well correlated by the Marcus relation. The Brønsted correlation is markedly curved for proton transfer for which the Marcus intrinsic barrier is very low (~5 kJ mol^{-1}). Conversely, the Brønsted correlation is almost imperceptibly curved for methyl transfer for which the Marcus intrinsic barrier is very high (~152 kJ mol^{-1}). The slope of the Brønsted correlation provides an approximate measure of the position of the transition structure along the reaction coordinate between the reactant and product encounter complexes. Primary kinetic isotope effects for proton transfer show a broad maximum, centered on $\Delta H_{rxn} = 0$, when plotted against reaction exo/endothermicity only if computed with respect to isolated acids and bases, but intracomplex kinetic isotope effects show a maximum displaced significantly towards the endothermic proton transfers.

Key words: Brønsted correlation, rate–equilibrium relationship, transition state, isotope effect.

Résumé : Faisant appel à des calculs d'orbitales moléculaires AM1, on a simulé des corrélations de Brønsted pour le transfert de proton et pour le transfert de méthyle entre des paires simulées de pyridines substituées en position 4. On a établi une bonne corrélation de Marcus entre les enthalpies d'activation et de réaction. La corrélation de Brønsted est fortement incurvée pour le transfert de proton pour laquelle la barrière intrinsèque de Marcus est très faible (environ 5 kJ mol^{-1}). Inversement, la corrélation de Brønsted est à peine incurvée pour le transfert de méthyle pour laquelle la barrière de Marcus est très élevée (environ 152 kJ mol^{-1}). La pente de la corrélation de Brønsted donne une mesure approximative de la position de la structure de transition sur les coordonnées de la réaction qui se situe entre le réactif et les complexes de rencontre. Lorsqu'on trace une courbe des effets isotopiques cinétiques primaires pour le transfert de proton en fonction de exo/endothermicité de la réaction, ces effets ne présentent un large maximum, centré autour de $\Delta H_{exn} = 0$, que lorsqu'on les calcule par rapport aux acides et aux bases isolés; toutefois, les effets isotopiques cinétiques intracomplexes présentent un maximum qui est fortement déplacé vers les transferts de proton endothermiques.

Mots clés : corrélation de Brønsted, relation vitesse–équilibre, état de transition, effet isotopique.

[Traduit par la Rédaction]

Introduction

The existence of linear free-energy relationships, implying the complete interchangeability of equilibrium and rate constants, was from the very earliest days (1) taken to be one of the simplest and strongest supports of transition state (TS) theory (2). Moreover, it was noted on the basis of simple energy profiles that the more thermodynamically favoured a member of a family of related reactions is, the faster it should proceed, and the earlier its TS should occur along the reaction coordinate; conversely, a thermodynamically unfavourable reaction would be slower and its TS would occur later (cf. Hammond's postulate) (3). Leffler (4) proposed that the slope of a linear correlation between log k and log K (i.e., of $\Delta G^{\ddagger}$ vs. ΔG_{rxn}) could be identifed as a parameter measuring the degree of resemblance of the TS to the products as compared with its resemblance to the reagents. Thus, for a proton transfer from an acid to a series of related bases, the value of the Brønsted coefficient β obtained from the linear correlation $\Delta G^{\ddagger} = \beta \Delta G_{rxn}$ would be interpreted as a measure of the degree of transfer of the proton in the TS. A value of $\beta \approx 0$ would indicate a reactant-like TS in which essentially no proton transfer had occurred from the acid to the base, $\beta \approx 1$ would indicate a product-like TS in which proton transfer was essentially complete, and $\beta \approx 0.5$ would indicate a TS in which the proton was about half transferred (5).

The use of slopes of structure–reactivity correlations (particularly the Brønsted β) as measures of TS structure has come under severe criticism (6) in recent years, but has also been thoughtfully defended with appropriate cautionary notes (7). It has long been recognised that there is a fundamental incompatibility within the corpus of ideas which

Received November 18, 1998.

This paper is dedicated to Jerry Kresge in recognition of his many achievements in chemistry.

I.H. Williams[1] and P.A. Austin. Department of Chemistry, University of Bath, Bath BA2 7AY, U.K.

[1]Author to whom correspondence may be addressed. Telephone: +44-1225-826625. Fax: +44-1225-826231. e-mail: i.h.williams@bath.ac.uk

© 1999 NRC Canada

Fig. 1. Positioning of dipoles and ammonia moieties for mimicking of (*a*) proton transfer and (*b*) methyl transfer between substituted pyridines.

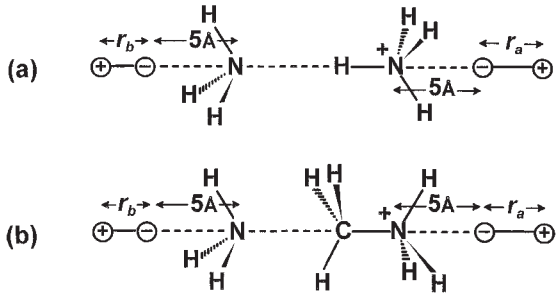

arise from TS theory: if the slope of a linear rate–equilibrium relationship is interpreted as some index of TS structure, it must reflect some *constant* property of the TS for the entire family of reactions used to construct the correlation; however, the Leffler principle (4), Hammond postulate (3), and related notions (8) all suggest that changing the reaction energetics should cause *variation* in TS structure within this same family. Modern computational chemistry offers a means by which this paradox may be resolved. For a particular reaction of a series of substituted compounds, the energetics and geometries of reactants, TSs, and products may be obtained from calculated potential energy surfaces. Rate–equilibrium relationships may be constructed from plots of calculated $\Delta G^{\ddagger}$ vs. ΔG_{rxn} (or $\Delta H^{\ddagger}$ vs. ΔH_{rxn}) values. The merit of this approach is that the TS structure, deduced indirectly from the slopes of these plots, may be compared with those determined directly (9). A simulation in this manner for an acyl-transfer process established (10) that (*i*) variation in basicity of the nucleophile led to variation in TS structure but also to a linear extended Brønsted correlation, and that (*ii*) bond-order changes, angular changes, and charge development occurred more-or-less concertedly but bore no obvious relation to the magnitude of the (extended) Brønsted coefficient β_{nuc}. Thus, there was no fundamental incompatibility between the notion of TS variation and the observation of a linear structure–reactivity correlation, but it was concluded that β_{nuc} did not provide a direct measure of TS structure.

We now report results of analogous gas-phase theoretical simulations for families of proton-transfers (eq. [1], R = H) and S_N2 methyl transfers (eq. [1], R = Me) between mimicked pyridine bases (11).

Methods

The MOPAC 6.0 program (12) was used to perform semiempirical RHF molecular orbital calculations with the AM1 Hamiltonian (13). We chose to simulate *only* the polar effect of substituents X and Y modifying the gas-phase basicity of the nucleophiles and nucleofuges in eq. [1], and to consider only 4-substituted pyridines. It was assumed that the contributions from entropy and from the steric component of the enthalpy to the standard Gibbs energies of activation $\Delta G^{\circ\ddagger}$ and the standard Gibbs energies of reaction ΔG°_{rxn} throughout this series would be essentially constant and would not sensibly affect the *relative* values of $\Delta H^{\ddagger}$ and ΔH_{rxn} as determined directly from the AM1 calculated enthalpies of formation. Optimized geometries for the reactant and product ion–dipole complexes and transition structures for proton transfer (R = H) and methyl transfer (R = CH_3) in eq. [1] were obtained within the constraint of a three-fold axis of symmetry. This allowed two important simplifications to be made. First, the rate–equilibrium correlations were constructed as plots of $\Delta H^{\ddagger}$ vs. ΔH_{rxn} only. Second, the pyridine nucleophiles and nucleofuges were *mimicked* by ammonia molecules whose proton affinities were modulated to reproduce the experimental proton affinity (PA) of each base relative to that of ammonia; this enabled the computations to be performed economically (as an undergraduate research project) by avoiding repetitious and uninformative calculation upon the large and constant aryl portions of the nitrogen bases.

Table 1. Dipolar charges, separations, and proton affinities relative to ammonia for mimicked 4-X-substituted pyridines.

X	$\|q\|$	r_b/Å	ΔPA/kJ mol^{-1}
CN	1	0.245	10.5
Cl	2	0.503	41.4
H	2	0.678	54.4
CH_3	2	0.919	71.2
$(CH_3)_2N$	2	1.657	115.5

The mimicking was accomplished (as previously described (10)) by placing a pair of oppositely charged MOPAC "sparkles" (constituting a dipole) on the three-fold axis of ammonia, on the same side as the hydrogens, with the negative charge a constant distance of 5 Å from the nitrogen atom, as shown in Fig. 1. By adjustment of the charge ($|q|$ = 1 or 2) and dipolar separation (in the range 0.2–1.7 Å), the basicity of the ammonia could be suitably tuned. A sparkle is an integral charge at the centre of a spherical repulsive potential (14); if the separation between oppositely charged sparkles is less than 1.0 Å, the energy due to the dipole on its own is subtracted from the total energy. Appropriate variation of the dipole lengths r_a and r_b thus allowed the NH_3 groups a and b to mimic pyridines with 4-CN, 4-Cl, 4-H, 4-CH_3, and 4-$(CH_3)_2N$ substituents; the calculated ΔPA values shown in Table 1 are exactly equal to the proton affinities relative to ammonia as determined experimentally (10). This resulted in 25 pairs of $\Delta H^{\ddagger}$ and ΔH_{rxn} values for each transferring group R = H or CH_3, except that no accurately determined transition structures could be located for proton transfer between the protonated pyridines 4-CN-PyH^+ and 4-Cl-Py H^+ (with the most strongly electron withdrawing substituents) and 4-$(CH_3)_2$N-Py (with the most strongly electron donating substituent). Sparkles have been employed in a similar fashion in AM1 calculations for S_N2 methyl transfer from methyl halides to 2-methylpyridine to represent a solvent effect upon the leaving group (15).

Our earlier theoretical simulation of a rate–equilibrium correlation for transfer of the methoxycarbonyl group between isoquinoline and substituted pyridines, in which the

[1] 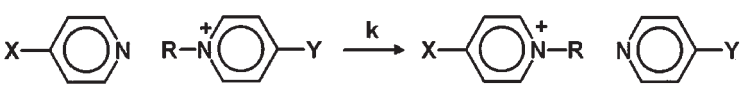

© 1999 NRC Canada

Table 2. AM1 calculated enthalpies (kJ mol^{-1}) of proton transfer between separated (sparkle-mimicked) acid and base (ΔH_{PT}), enthalpies of formation ($\triangle H_f$) for reactant complexes and enthalpies of association (ΔH_{rc}) relative to separated acid and base, intracomplex enthalpies of activation ($\Delta H^{\ddagger}$) and reaction (ΔH_{rxn}) for proton transfer, and enthalpies of association (ΔH_{pc}) for product complexes relative to separated conjugate base and conjugate acid.

Base 4-XPy	Acid 4-YPyH$^+$		Reactant complex XPy···HPyY$^+$		Transition structure [XPy···H$^+$···PyY]‡	Product complex $^+$XPyH··· PyY	
X	Y	ΔH_{PT}	ΔH_f	ΔH_{rc}	$\Delta H^{\ddagger}$	ΔH_{rxn}	ΔH_{pc}
CN	CN	0.0	508.06	–83.00	5.58	0.00	–83.00
Cl		–30.94	486.96	–101.79	2.16	–7.57	–78.41
H		–43.89	476.86	–109.95	1.12	–10.55	–76.61
CH_3		–60.61	463.68	–120.76	0.19	–14.21	–74.37
$(CH_3)_2N$		–105.09	–1923.70	–146.88	~0.01	–22.91	–64.71
CN	Cl	30.94	479.39	–78.41	9.73	7.57	–101.79
Cl		0.0	459.38	–96.12	5.32	0.00	–96.12
H		–12.95	449.78	–103.78	3.83	–3.06	–93.89
CH_3		–29.66	437.30	–113.89	2.20	–6.88	–91.10
$(CH_3)_2N$		–74.14	–1952.32	–142.32	~0.01	–16.00	–84.11
CN	H	43.89	466.31	–76.61	11.68	10.54	–109.95
Cl		12.95	446.73	–93.89	6.88	3.06	–103.78
H		0.0	437.31	–101.35	5.22	0.00	–101.35
CH_3		–16.72	425.10	–111.20	3.37	–3.85	–98.32
$(CH_3)_2N$		–61.20	–1963.60	–138.65	0.21	–13.28	–90.73
CN	CH_3	60.61	449.68	–74.37	14.41	14.21	–120.76
Cl		29.66	427.95	–91.10	9.08	6.88	–113.89
H		16.72	421.45	–98.32	7.22	3.85	–111.20
CH_3		0.0	409.56	–107.84	5.11	0.00	–107.84
$(CH_3)_2N$		–44.48	–1979.27	–134.29	1.07	–9.61	–99.41
CN	$(CH_3)_2N$	105.09	–1946.61	–64.71	~22.92	22.91	–146.88
Cl		74.14	–1968.32	–84.11	~16.01	16.00	–142.32
H		61.20	–1977.83	–90.73	13.50	13.28	–138.65
CH_3		44.48	–1988.88	–99.41	10.68	9.61	–134.29
$(CH_3)_2N$		0.0	–4375.30	–123.44	4.60	0.00	–123.44

same range of nucleophiles and the nucleofuge were also mimicked by sparkle-modulated ammonia molecules, has recently been reinvestigated (16) using explicit nucleophiles and nucleofuge in the gas phase and in water (modelled as a continuum). None of the earlier conclusions was altered in the slightest. The mimicking procedure is a convenient and valid approximation, and may be considered as a simple type of hybrid quantum–classical method. Moreover, we may note that there is a good linear correlation between gas-phase proton affinities and aqueous pK_a values for 4-substituted pyridines (10), which suggests that the qualitative trends described in this work may also apply to reactions in solution.

Results and discussion

Brønsted correlations for proton transfer

The relevant AM1 calculated gas-phase enthalpic data for the mimicked reaction series with R = H in eq. [1] are shown in Table 2. The calculated enthalpies of the ion–molecule reactant and product complexes, XPy···HPyY$^+$ and $^+$XPyH···PyY, respectively, and of the transition structures [XPy···H$^+$···PyY]‡ for proton transfer in the double-well potential (Fig. 2) are consistently lower than those of the separated reactant or product species. The enthalpy change ΔH_{PT} for proton transfer between the separated acid and base species, HPyY$^+$ and XPy, becomes more exothermic, or less endothermic, with increasing proton affinity PA of the base (relative to ammonia) from X = CN to X = $(CH_3)_2N$. A similar trend is found for the enthalpy change ΔH_{rxn} for proton transfer between the acid and base within the encounter complex, although the magnitudes are smaller. The most exothermic proton transfer (–22.91 kJ mol^{-1}) is from the

Fig. 2. Double-well enthalpy profile for proton transfer between mimicked pyridine bases.

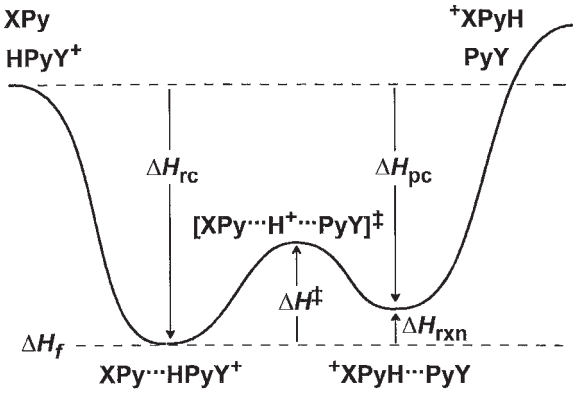

© 1999 NRC Canada

Fig. 3. Simulated Brønsted correlations for intracomplex proton transfers: $-\Delta H^{\ddagger}$ (solid lines) and $-\Delta H_{rxn}$ (broken lines) vs. proton affinities ΔPA of mimicked pyridine bases relative to ammonia.

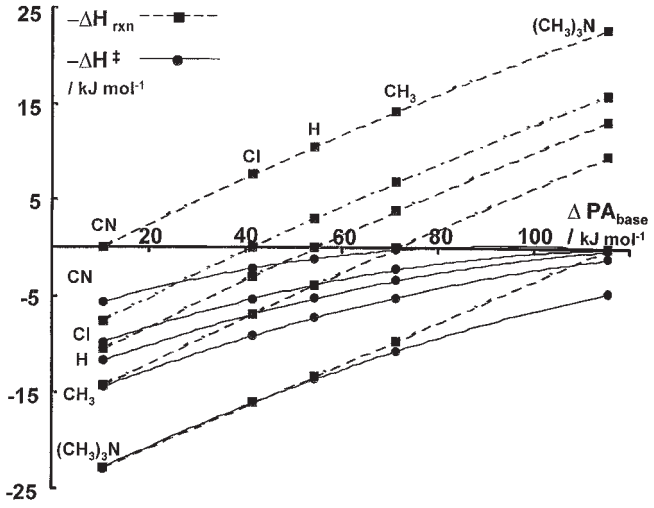

strongest acid 4-CN-PyH$^+$ and the strongest base 4-$(CH_3)_2$N-Py: for this combination ΔH_{PT} is –105.09 kJ mol^{-1} between the separated species but ΔH_{rxn} is only –22.91 kJ mol^{-1} for the intracomplex reaction. The most endothermic process is the reverse reaction for this system.

Families of Brønsted correlations may be generated by plotting the (negatives of the) enthalpies of activation and of reaction for intracomplex proton transfer ($-\Delta H_{rxn}$ and $-\Delta H^{\ddagger}$) against the relative proton affinity as the base is varied whilst keeping constant the identity of the acid. The five (very slightly curved) parallel dashed lines in Fig. 3 are the set of correlations of $-\Delta H_{rxn}$ vs. ΔPA; the value of about 0.22 for their slopes reflects the attenuation factor for intracomplex proton transfer as compared with proton transfer between separated acids and bases. The solid lines in Fig. 3 are the correlations $-\Delta H^{\ddagger}$ vs. ΔPA; these curves have slopes tending to zero as the proton affinity of the base is increased in combination with the strongest acid (exothermic proton transfer), but tending to equal the slope of $-\Delta H_{rxn}$ vs. PA as the proton affinity of the base is decreased in combination with the weakest acid (endothermic proton transfer).

However, it is more instructive to plot $-\Delta H^{\ddagger}$ vs. $-\Delta H_{rxn}$ directly for all the reactions on a single graph (Fig. 4); the slope of such a correlation is a normalized Brønsted coefficient β. The circles in Fig. 4 refer to AM1 calculated points. There is only a very small variation in $\Delta H^{\ddagger}$ for the five identity reactions, from 4.60 kJ mol^{-1} for X = Y = $(CH_3)_2$N to 5.58 kJ mol^{-1} for X = Y = CN. The squares in Fig. 4 refer to points calculated according to the Marcus eq. [2] with an intrinsic barrier $\Delta H^{\ddagger}_{int}$ of 5.22 kJ mol^{-1} (= $\Delta H^{\ddagger}$ for X = Y = H); the Marcus equation provides a satisfactory fit to the AM1 calculated data. The slope of the curved Brønsted correlation for proton transfer approaches 0 for the most exothermic and 1 for the most endothermic reactions in accord with expectation (17, 18).

$$[2] \qquad \Delta H^{\ddagger} = \Delta H^{\ddagger}_{int} + \Delta H_{rxn}/2 + (\Delta H_{rxn})^2/16\Delta H^{\ddagger}_{int}$$

The energy differences ΔH_{rc} and ΔH_{pc} (Table 2) represent the strengths of hydrogen bonding between acid and base

Fig. 4. Simulated Brønsted rate–equilibrium correlation $-\Delta H^{\ddagger}$ vs. $-\Delta H_{rxn}$ for proton transfer: circles denote AM1 calculated enthalpies, diamonds denote Marcus-equation calculated values; broken lines show slopes of +1 (endothermic limit) and 0 (exothermic limit).

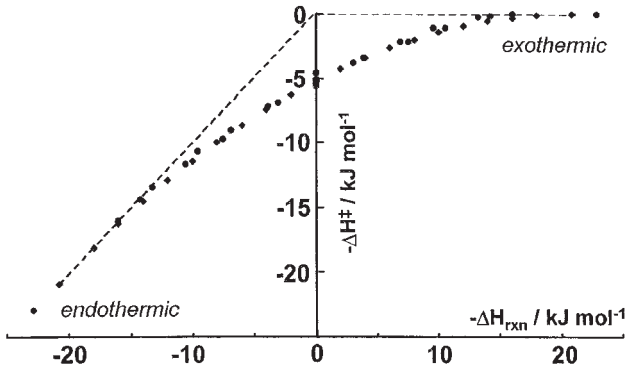

and between conjugate base and conjugate acid. Increasing the proton affinity of the base increases the hydrogen-bond strength ΔH_{rc} with a given acid and decreases the hydrogen-bond strength ΔH_{pc}. The most exothermic proton transfers are therefore associated with the strongest reactant–complex hydrogen bonds but the weakest product–complex hydrogen bonds. The most endothermic proton transfers are associated with the weakest reactant–complex hydrogen bonds but the strongest product–complex hydrogen bonds.

Bond length and bond-order changes for proton transfer

The bond lengths presented in Table 3 show that strongly hydrogen-bonded complexes have shorter $N_b\cdots H$ distances to the base and longer $H—N_a$ distances in the acid. The $H—N_a$ distance is 1.023 Å in the isolated acid 4-H-PyH$^+$ but is 1.305 Å in the transition structure [HPy$\cdots$H$^{\ddagger}\cdots$PyH‡]; assigning Pauling bond orders (19) *n* of 1.0 and 0.5 to these bonds allows the coefficient *c* in eq. [3] to be determined as 0.407.

$$[3] \qquad n = \exp\,[(R_1 - R_n)/c]$$

A consequence of this definition is that the sums of the bond orders for the intracomplex $N_b\cdots H$ and $H—N_a$ bonds are, respectively, about 1.2 and 0.9 for the strongest and weakest hydrogen bonds; bond orders n_b for $N_b\cdots H$ vary in magnitude from about 0.18 to about 0.34, whereas those for $H—N_a$ range from about 0.73 to about 0.89. In the transition structures, n_b varies from <0.378 for the most exothermic reactions to >0.629. (Note that when the activation energy for either the forward or reverse reaction approaches zero, as in the case of X = $(CH_3)_2$N and Y = Cl or CN, we were unable to determine the transition structures accurately.) This result accords with the Hammond postulate (3): the more exothermic members of this family of related reactions have more reactant-like transition structures, while the more endothermic have more product-like transition structures. Clearly, variation in the exo/endothermicity of proton transfer causes variation in the geometry of the transition structure.

It is important to bear in mind that the absolute accuracy of the bond lengths reported in Table 3 is not the issue of prime concern, but rather the manner in which they change

© 1999 NRC Canada

Table 3. AM1 calculated bond lengths (Å) for reactant complexes, transition structures and product complexes for proton transfer, Pauling bond orders n_b for making bond between base and transferring proton, and normalized TS bond orders $n^{\ddagger}$.

Acid 4-YPyH$^+$	Base 4-XPy	Reactant complex XPy···HPyY$^+$			Transition structure [Xpy···H$^+$···PyY]‡			Product complex $^+$XPyH···PyY			
Y	X	N_b···H/Å	n_b	H–N_a/Å	N_b···H/Å	n_b	H···N_a/Å	N_b–H/Å	n_b	H···N_a/Å	$n^{\ddagger}$
CN	CN	1.630	0.225	1.103	1.308	0.496	1.308	1.103	0.822	1.630	0.454
	Cl	1.581	0.254	1.121	1.355	0.442	1.263	1.091	0.846	1.659	0.318
	H	1.562	0.266	1.130	1.378	0.418	1.243	1.087	0.854	1.670	0.259
	CH_3	1.522	0.293	1.148	1.419	0.378	1.212	1.082	0.865	1.682	0.149
	$(CH_3)_2N$							1.071	0.889	1.712	
Cl	CN	1.659	0.210	1.091	1.263	0.555	1.355	1.121	0.786	1.581	0.599
	Cl	1.622	0.230	1.103	1.306	0.499	1.306	1.103	0.822	1.622	0.454
	H	1.605	0.239	1.110	1.325	0.476	1.287	1.098	0.832	1.635	0.400
	CH_3	1.581	0.254	1.119	1.350	0.448	1.264	1.092	0.844	1.649	0.329
	$(CH_3)_2N$							1.079	0.871	1.683	
H	CN	1.670	0.204	1.087	1.243	0.582	1.378	1.130	0.769	1.562	0.669
	Cl	1.635	0.222	1.098	1.287	0.523	1.325	1.110	0.808	1.605	0.514
	H	1.619	0.231	1.103	1.305	0.500	1.305	1.103	0.822	1.619	0.455
	CH_3	1.598	0.243	1.111	1.329	0.471	1.282	1.096	0.836	1.636	0.384
	$(CH_3)_2N$	1.518	0.296	1.147	1.412	0.385	1.212	1.082	0.865	1.671	0.156
CH_3	CN	1.682	0.198	1.082	1.212	0.629	1.419	1.148	0.736	1.522	0.801
	Cl	1.649	0.215	1.092	1.264	0.553	1.350	1.119	0.790	1.581	0.588
	H	1.636	0.222	1.096	1.282	0.529	1.329	1.111	0.806	1.598	0.526
	CH_3	1.616	0.233	1.103	1.304	0.501	1.304	1.103	0.822	1.616	0.455
	$(CH_3)_2N$	1.553	0.272	1.129	1.371	0.425	1.242	1.087	0.854	1.654	0.263
$(CH_3)_2N$	CN	1.712	0.184	1.071							
	Cl	1.683	0.198	1.079							
	H	1.671	0.203	1.082	1.212	0.629	1.412	1.147	0.737	1.518	0.798
	CH_3	1.654	0.212	1.087	1.242	0.584	1.371	1.129	0.771	1.553	0.669
	$(CH_3)_2N$	1.608	0.238	1.103	1.303	0.503	1.302	1.103	0.822	1.608	0.454

in response to the polar influence of a substituent. Furthermore, since the point of interest is change in the transition state relative to reactants and products, it is useful to consider the *normalized* Pauling bond order $n^{\ddagger}$ for each transition structure, as given by eq. [4].

$$[4] \qquad n^{\ddagger} = [(n_b)^{\ddagger} - (n_b)_{rc}]/[(n_b)_{pc} - (n_b)_{rc}]$$

This quantity is a Leffler index which measures the degree of progress of the transition structure along the reaction coordinate between the reactant and product complexes according to a geometrical criterion for bonding of the transferring proton to the base. Figure 5 shows the value of $n^{\ddagger}$ (triangles) plotted as a function of the exo/endothermicity of the reaction, along with the normalized Brønsted coefficient β (diamonds). The plot of vs. $-\Delta H_{rxn}$ is a straight line, whereas that of $n^{\ddagger}$ vs. $-\Delta H_{rxn}$ is somewhat sigmoidal in nature. Nonetheless, the two quantities do have similar magnitudes across the full range of exo/endothermicities, such that for any particular reaction the value of β does provide a rough estimate for the degree of bonding between the proton and the base in the transition structure.

Fig. 5. Variation in normalized values of Brønsted β (diamonds), charge on basic moiety $q^{\ddagger}$ (squares), and Pauling bond order $n^{\ddagger}$ (triangles) in transition structures for proton transfer with respect to $-\Delta H_{rxn}$.

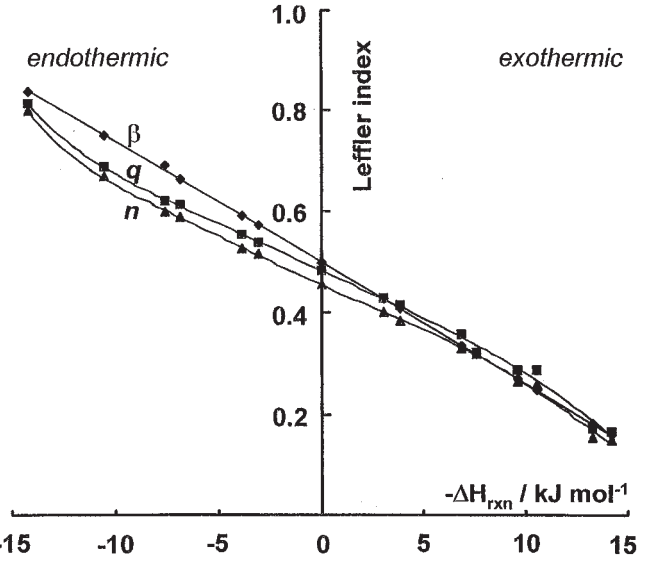

Charge changes for proton transfer

The value of a normalized Brønsted coefficient is sometimes interpreted as a measure of effective charge in the transition state (20). The formal charge on the nitrogen atom of the basic moiety in this series of proton transfers between (mimicked) substituted pyridines changes from zero to +1 in

© 1999 NRC Canada

Table 4. AM1 calculated charges for basic moiety in reactant complexes, transition structures, and product complexes for proton transfer, normalized TS charges $q^{\ddagger}$, semiclassical kinetic isotope effects for intracomplex proton transfer, equilibrium isotope effects for hydrogen bonding, and overall kinetic isotope effects for proton transfer between separated (sparkle-mimicked) acids and bases at 298 K.

Acid Y	Base X	$(q_b)_{rc}$	$(q_b)^{\ddagger}$	$(q_b)_{pc}$	$q^{\ddagger}$	KIE	$(EIE)_{hb}$	KIE × $(EIE)_{hb}$
CN	CN	0.135	0.338	0.555	0.483	3.443	1.964	6.762
	Cl	0.160	0.293	0.574	0.321	2.930	2.290	6.710
	H	0.171	0.287	0.581	0.285	2.674	2.469	6.602
	CH_3	0.194	0.259	0.589	0.165	2.053	2.904	5.962
Cl	CN	0.120	0.373	0.527	0.622	3.761	1.800	6.770
	Cl	0.138	0.339	0.555	0.482	3.416	1.995	6.815
	H	0.146	0.324	0.562	0.428	3.238	2.102	6.806
	CH_3	0.159	0.306	0.572	0.356	2.967	2.280	6.765
H	CN	0.115	0.390	0.514	0.689	3.822	1.748	6.681
	Cl	0.131	0.353	0.544	0.538	3.563	1.917	6.830
	H	0.139	0.339	0.553	0.483	3.406	2.007	6.836
	CH_3	0.150	0.321	0.564	0.413	3.174	2.149	6.821
	$(CH_3)_2N$	0.195	0.262	0.587	0.171	2.069	2.922	6.046
CH_3	CN	0.109	0.419	0.489	0.816	(3.585)	1.690	6.059
	Cl	0.123	0.372	0.529	0.613	3.715	1.835	6.817
	H	0.130	0.357	0.540	0.554	3.591	1.908	6.852
	CH_3	0.140	0.339	0.553	0.482	3.393	2.022	6.861
	$(CH_3)_2N$	0.174	0.290	0.578	0.287	2.660	2.515	6.690
$(CH_3)_2N$	CN	0.095					1.574	
	Cl	0.107					1.678	
	H	0.112	0.419	0.490	0.812	3.550	1.728	6.134
	CH_3	0.120	0.390	0.514	0.685	3.754	1.800	6.757
	$(CH_3)_2N$	0.143	0.340	0.551	0.483	3.364	2.058	6.923

going from reactants to products, and in the transition structure it is reasonable to suppose it has some intermediate value. In this study, the net charge q_b on basic moiety was calculated as the sum of the Mulliken charges on all the atoms of the NH_3 group used to mimic the pyridine bases. Values of these group charges in each reactant complex, transition structure, and product complex are given in Table 4. As with the bond lengths considered above, the reliability of the absolute values of these group charges is not the issue of prime concern, but rather the manner in which they change in response to the polar influence of a substituent.

Increasing the proton affinity of the base leads to greater positive charge on the basic moiety in both the reactant and product complexes. The magnitude of the charge mirrors the strength of hydrogen bonding. The values range from 0.095 to >0.194 in the reactant complexes and from <0.489 to 0.609 in the product complexes. In these AM1 calculations the charge on the transferring proton is always about +0.3; thus complete intracomplex proton transfer raises this group charge from between +0.1 and +0.2 (in NH_3) to between +0.8 and +0.9 (in NH_4^+).

A normalized charge $q^{\ddagger}$ may be obtained for each transition structure as the fractional change in the total charge on the basic moiety from its value in the reactant complex to its value in the product complex, as given by eq. [5]; these are indicated by squares in Fig. 5.

$$[5] \qquad q^{\ddagger} = [(q_b)^{\ddagger} - (q_b)_{rc}]/[(q_b)_{pc} - (q_b)_{rc}]$$

This quantity is a Leffler index which measures the degree of progress of the transition structure along the reaction coordinate between the reactant and product complexes according to a criterion of developing charge on the basic moiety. The plot of $q^{\ddagger}$ vs. $-\Delta H_{rxn}$ gives a curve of similar shape to that for $n^{\ddagger}$ vs. $-\Delta H_{rxn}$., which roughly tracks the value of. Strongly exothermic reactions have very low values of $q^{\ddagger}$, strongly endothermic reactions have very high values of $q^{\ddagger}$, and thermoneutral identity reactions have values of $q^{\ddagger}$ rather close to 0.5. Thus, for any particular reaction the value of the normalized Brønsted coefficient also provides a rough estimate for the degree of charge development on the base in the transition structure.

Primary isotope effects for proton transfer

Table 4 also contains semiclassical kinetic isotope effects (KIE = k_H/k_D) for replacement of the transferring proton by a deuteron, within the hydrogen-bonded encounter complex, at a temperature of 298 K. The KIEs are calculated from the vibrational zero-point energies and the partition functions for translation, rotation, and vibration using standard procedures (21); the AM1 method has been shown to reproduce experimental primary KIEs for hydrogen transfer to within 13% (22). These values, plotted as circles in Fig. 6, range from 2.0 for strongly exothermic hydron transfers to a maxi-

© 1999 NRC Canada

Table 5. AM1 calculated stretching force constants (mdyn Å^{-1}) for reactant complexes, transition structures, and product complexes for proton transfer.

Acid 4-YPyH$^+$	Base 4-XPy	Reactant complex XPy···HPyY$^+$		Transition structure [XPy···H$^+$···PyY]‡		Product complex $^+$XPyH···PyY	
Y	X	F(N$_b$···H)	F(H—N$_a$)	F(N$_b$···H)	F(H···N$_a$)	F(N$_b$—H)	F(H···N$_a$)
CN	CN	0.828	4.270	1.698	1.698	4.270	0.828
	Cl	0.919	3.921	1.460	2.029	4.531	0.779
	H	0.950	3.757	1.365	2.211	4.624	0.760
	CH_3	1.016	3.436	1.233	2.549	4.734	0.736
	$(CH_3)_2N$	1.104	3.013			4.978	0.679
Cl	CN	0.779	4.531	2.029	1.460	3.921	0.919
	Cl	0.851	4.278	1.721	1.721	4.278	0.851
	H	0.881	4.153	1.613	1.847	4.392	0.829
	CH_3	0.922	3.967	1.486	2.033	4.523	0.803
	$(CH_3)_2N$	1.125	3.002			4.811	0.742
H	CN	0.760	4.624	2.211	1.365	3.757	0.950
	Cl	0.829	4.392	1.847	1.613	4.153	0.881
	H	0.857	4.280	1.727	1.727	4.280	0.857
	CH_3	0.895	4.117	1.590	1.891	4.424	0.829
	$(CH_3)_2N$	1.030	3.470	1.257	2.558	4.732	0.767
CH_3	CN	0.736	4.734	2.549	1.233	3.436	1.016
	Cl	0.803	4.523	2.033	1.486	3.967	0.922
	H	0.829	4.424	1.891	1.590	4.117	0.895
	CH_3	0.865	4.282	1.735	1.735	4.282	0.865
	$(CH_3)_2N$	0.972	3.785	1.396	2.235	4.624	0.798
$(CH_3)_2N$	CN	0.679	4.978			3.013	1.104
	Cl	0.742	4.811			3.002	1.125
	H	0.767	4.732	2.558	1.257	3.470	1.030
	CH_3	0.798	4.624	2.235	1.396	3.785	0.972
	$(CH_3)_2N$	0.883	4.286	1.753	1.753	4.286	0.883

Fig. 6. Semiclassical kinetic isotope effects KIE for intracomplex proton transfer, equilibrium isotope effects (EIE)$_{hb}$ for hydrogen bonding, and overall kinetic isotope effects KIE × (EIE)$_{hb}$ for proton transfer between separated acids and bases, with respect to $-\Delta H_{rxn}$.

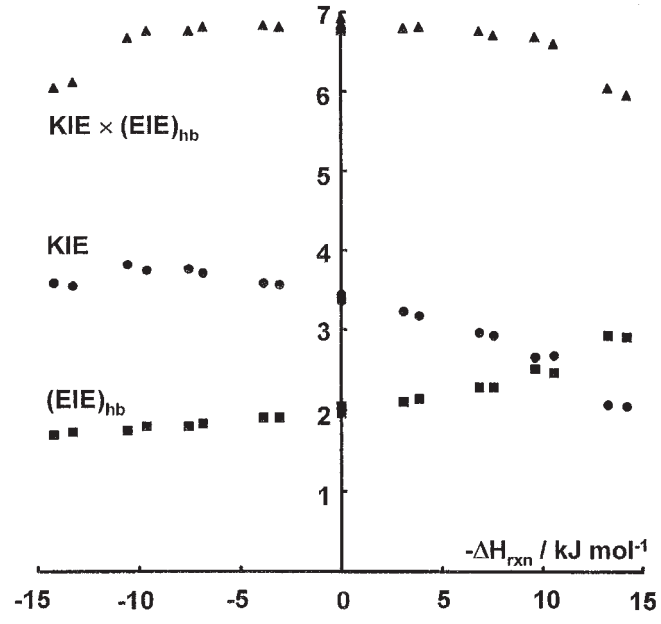

mum of about 3.8 for reactions endothermic by about 10 kJ mol^{-1}. Unfortunately, transition structures for hydron transfers between the most strongly basic and acidic groups could not be determined with sufficient reliability to enable us to extrapolate with confidence for processes with $\Delta H_{rxn} > +15$ kJ mol^{-1}, but there is certainly a clear indication that the magnitude of the KIE diminishes for reactions with endothermicities greater than 10.5 kJ mol^{-1}. The identity reactions have KIEs of about 3.4.

It is often thought that the maximum in a plot of the primary kinetic isotope effect against base strength in a series of hydron transfer reactions occurs when the force constants for the making and breaking bonds are equal in the transition state (23, 24). Stretching force constants for the bonds N$_b$···H and H—N$_a$ are presented in Table 5. The transition structures for the identity reactions do indeed each have equal force constants (of about 1.7 mdyn Å^{-1}) (1 dyn = 10 μN) for these bonds. However, the maximum KIE occurs for hydron transfer from 4-H-PyH$^+$ to 4-CN-Py for which F(N$_b$···H) = 2.211 and F(H—N$_a$) = 1.365 in the transition structure. The reason for the apparent anomaly is that the strength of hydrogen bonding in the reactant and product complexes is isotopically sensitive. In other words, there are significant equilibrium isotope effects upon formation of these gas-phase ion–molecule complexes from separated acids and bases. These isotope effects (EIE)$_{hb}$ are largest (>3)

© 1999 NRC Canada

Table 6. AM1 calculated enthalpies (kJ mol^{-1}) of formation (ΔH_f) for reactant complexes, intracomplex enthalpies of activation ($\Delta H^{\ddagger}$), and reaction (ΔH_{rxn}) for methyl transfer.

Electrophile	Nucleophile	Reactant complex	Transition structure	Product complex
4-YPyMe$^+$	4-XPy	XPy···MePyY$^+$	[XPy···Me···PyY]‡	$^+$XPyMe···PyY
Y	X	ΔH_f	$\Delta H^{\ddagger}$	ΔH_{rxn}
CN	CN	549.15	152.88	0.00
	Cl	534.87	144.56	–16.11
	H	527.72	141.21	–22.76
	CH_3	518.47	136.94	–31.17
	$(CH_3)_2N$	–1861.99	126.06	–52.72
Cl	CN	518.74	160.71	16.11
	Cl	505.01	152.30	0.00
	H	498.10	148.91	6.63
	CH_3	489.16	144.56	–15.02
	$(CH_3)_2N$	–1890.44	133.60	–36.61
H	CN	504.98	163.93	22.76
	Cl	491.47	155.52	6.61
	H	484.66	152.09	0.00
	CH_3	467.44	147.74	–8.41
	$(CH_3)_2N$	–1903.36	136.69	–30.00
CH_3	CN	487.32	168.07	31.17
	Cl	474.12	159.62	15.02
	H	475.86	156.15	8.41
	CH_3	458.82	151.80	0.00
	$(CH_3)_2N$	–1919.91	140.71	–21.59
$(CH_3)_2N$	CN	–1914.71	178.78	52.72
	Cl	–1927.06	170.21	36.61
	H	–1933.37	166.73	30.00
	CH_3	–1941.51	162.30	21.59
	$(CH_3)_2N$	–4318.85	151.08	0.00

Fig. 7. Simulated Brønsted rate–equilibrium correlation $-\Delta H^{\ddagger}$ vs. $-\Delta H_{rxn}$ for S_N2 methyl transfer.

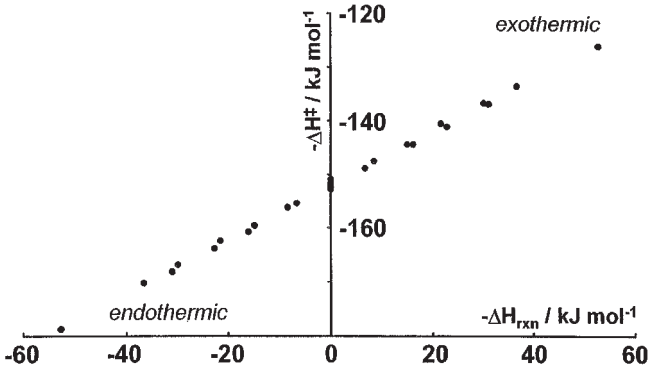

for the most exothermic reactions and diminish smoothly to <1.7 for the most endothermic processes, as shown by the squares in Fig. 6. The overall primary kinetic isotope effect for hydron transfer between separated acids and bases is given by the product KIE $(EIE)_{hb}$, plotted in Fig.6 as triangles. These isotope effects display a very broad maximum centred on the thermoneutral reactions, with KIE $(EIE)_{hb} \approx 6.8$ for all reactions for which $-10 \leq \Delta H_{rxn} \leq +10$ kJ mol^{-1}, but falling to lower values for the most exothermic and endothermic reactions.

Brønsted correlations for methyl transfer

AM1 calculated gas-phase enthalpic data for the mimicked reaction series with R = CH_3 in eq. [1] are shown in Table 6. The enthalpies of activation ($\Delta H^{\ddagger}$) and of reaction (ΔH_{rxn}) for intracomplex methyl transfer are given relative to enthalpies of formation (H_f) of the reactant complexes XPy···MePyY$^+$. Increasing the proton affinity of the nucleophile causes the methyl transfer to be more exothermic or less endothermic. Plots of $-\Delta H^{\ddagger}$ and $-\Delta H_{rxn}$ vs. ΔPA for methyl transfer (not shown) are less interesting than those for proton transfer (Fig. 3): there are two sets of imperceptably curved parallel lines, those for ΔH_{rxn} having larger slopes than those for $\Delta H^{\ddagger}$. Three clear differences may be noted for methyl transfer as compared with proton transfer: the individual plots are scarcely distinguishable from straight lines; the range of values for both $\Delta H^{\ddagger}$ and ΔH_{rxn} is twice as wide; the absolute values for the barrier heights $\Delta H^{\ddagger}$ are very much larger.

Figure 7 shows a plot of $-\Delta H^{\ddagger}$ vs. $-\Delta H_{rxn}$ for methyl transfer. Linear and second-order polynomials regressions may be achieved with equal confidence; in each case the slope of the linear term is exactly 0.5. The enthalpies of activation for the five identity reactions vary from 151.08 kJ mol^{-1} for X = Y = $(CH_3)_2N$ to 152.88 kJ mol^{-1} for X = Y = CN. A Marcus relation, eq. [2], with an intrinsic barrier $\Delta H^{\ddagger}_{int}$ of 152.09 kJ mol^{-1} (= $\Delta H^{\ddagger}$ for X = Y = H) provides an excel-

© 1999 NRC Canada

lent correlation for the AM1 calculated points. Differentiation of eq. [2] (at constant $\Delta H^{\ddagger}_{int}$) yields an expression for the Leffler index, $\partial\Delta H^{\ddagger}/\partial\Delta H_{rxn}$, which is also the slope of a normalized Brønsted correlation (17, 18).

$$[6] \qquad \partial\Delta H^{\ddagger}/\partial\Delta H_{rxn} = \beta_{Marcus} = 0.5 + \Delta H_{rxn}/8\Delta H^{\ddagger}_{int}$$

With $\Delta H^{\ddagger}_{int}$ = 152.09 kJ mol^{-1}, the value for this Marcus-derived Brønsted coefficient varies from 0.50 by only ±0.04 over the entire range of $-52.72 \le \Delta H_{rxn} \le 52.72$ kJ mol^{-1}. However, the curvature of the Marcus correlation ($1/8\Delta H^{\ddagger}_{int} = 8 \times 10^{-4}$) is five times as great as for the second-order polynomial regression to the AM1 calculated points in Fig. 7.

Bond length and bond-order changes for methyl transfer

As the data in Table 7 show, better nucleophiles and electrophiles give slightly shorter $N_{nu}\cdots C$ but slightly longer $C—N_{el}$ distances in the reactant complexes $XPy\cdots MePyY^{+}$, although the magnitude of variation is only small. The $C—N_{el}$ distance is 1.476 Å in the isolated electrophile 4H-$PyMe^{+}$ but is 1.843 Å in the transition structure $[4HPy\cdots Me^{\ddagger}\cdots 4HPy]^{\ddagger}$; assigning Pauling bond orders n_{nu} of 1.0 and 0.5 to these bonds allows the coefficient c in eq. [3] to be determined as 0.529. The bond orders n_{nu} in the transition structures vary only a little, but in accord with the Hammond postulate. The sums of the bond orders vary between 1.053 and 1.068 for both the reactant and product complexes, and between 0.968 and 1.034 for the transition structures; there is therefore a high degree of conservation of bond order.

The normalized transition-structure bond orders $n^{\ddagger}$ vary between 0.429 for the most exothermic and 0.509 for the most endothermic intracomplex reactions. Figure 8 shows the values of $n^{\ddagger}$ (triangles) plotted against $-\Delta H_{rxn}$ for methyl transfer; the resulting straight line is parallel with and close to the gently sloping line drawn through the values of β determined by the Marcus relation with $\Delta H^{\ddagger}_{int}$ of 152.09 kJ mol^{-1}. Clearly for any particular methyl transfer reaction the value of does provide a good estimate for the degree of bonding between the nucleophile and the electrophile in the transition structure.

Charge changes for methyl transfer

The small variations in bond orders are mirrored by correspondingly small changes in net charges q_{nu} on the nucleophilic moiety in the methyl transfers (Table 8). The formal charge on the nitrogen atom of the nucleophile changes from 0 to +1 in each reaction, just as for proton transfer. The values of $(q_{nu})_{rc}$ are indeed very close to zero in the reactant complexes for methyl transfer. The overall charge on the XPyMe moiety in the product complexes is the sum of $(q_{nu})_{pc}$ and the net charge on the transferring methyl group; since the latter varies between +0.27 and +0.30, this overall charge is very close to unity. In the transition structures, the value of $(q_{nu})^{\ddagger}$ varies from +0.27 and +0.29, but the net charge on the transferring methyl group has a larger value, of between +0.43 and +0.46. Since the normalized charge is determined solely as the fractional change in q_{nu} and does not consider the effect of the changing charge on the methyl group, the value of $q^{\ddagger}$ underestimates the progress of methyl transfer as compared with $n^{\ddagger}$ and β (Fig. 8).

Fig. 8. Variation in normalized values of Brønsted β (diamonds), charge on basic moiety $q^{\ddagger}$ (squares), and Pauling bond order $n^{\ddagger}$ (triangles) in transition structures for S_N2 methyl transfer with respect to $-\Delta H_{rxn}$.

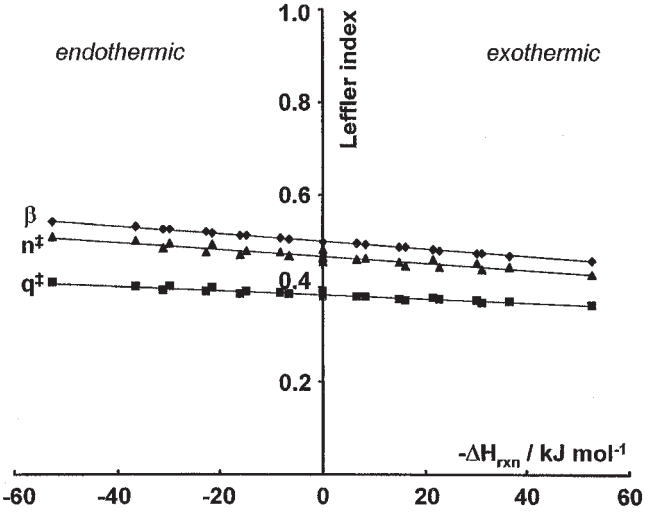

Brønsted curvature, intrinsic barrier height, and the significance of β

The proton transfers considered in this study are characterized by a very low and essentially constant Marcus intrinsic barrier of just over 5 kJ mol^{-1} and manifest a curved Brønsted correlation, the slope of which varies between 0 and 1 over the range for which the simple Marcus eq. [2] is valid (17, 18, 25), i.e., $-4\Delta H^{\ddagger}_{int} \le \Delta H_{rxn} \le +4\Delta H^{\ddagger}_{int}$; the extent of this range is 21 kJ mol^{-1}. The analogous methyl transfers are characterized by a rather high but still essentially constant Marcus intrinsic barrier of 152 kJ mol^{-1} and manifest what appears to be a linear Brønsted correlation. Very slight curvature may be detected by regression to a second-order polynomial, but a range of enthalpies of reaction extending over 1216 kJ mol^{-1} ($-4\Delta H^{\ddagger}_{int} \le \Delta H_{rxn} \le +4\Delta H^{\ddagger}_{int}$) would be required in order for the slope to change from 0 to 1.

Proton transfer yields a markedly curved Brønsted correlation, and there is a correspondence between the value of β (the instantaneous slope) and the degree of proton transfer in the TS. A similar conclusion was reached in an ab initio MO study of proton transfer between ammonia and a range of alkylamines: calculated energy changes fit the Marcus relation well, and fair agreement was obtained between the Marcus-derived Brønsted coefficient and the position of the transition structure along the reaction coordinate (26).

Methyl transfer yields an apparently linear, but actually very slightly curved, Brønsted correlation whose slope also corresponds to degree of bonding of the nucleophile to the transferring group in the TS, as measured by the Pauling bond order. However, it should be noted here that this correspondence between β and $n^{\ddagger}$ depends upon the value adopted for the coefficient c in eq. [3] for the Pauling bond order. In this study, we have made the assumption that the bond order of the $N_{nu}\cdots C$ and $N_b\cdots H$ partial bonds in the transition structures for methyl transfer and proton transfer is exactly one-half, and have accordingly determined the values of c as

© 1999 NRC Canada

Table 7. AM1 calculated bond lengths for reactant complexes, transition structures, and product complexes for methyl transfer, Pauling bond orders n_{nu} for making bond between (sparkle-mimicked) nucleophile and electrophile, and normalized TS bond orders $n^{\ddagger}$.

Electrophile 4-YPyMe$^+$	Nucleophile 4-XPy	Reactant complex XPy···MePyY$^+$			Transition structure [XPy···Me‡···PyY]‡			Product complex $^+$XPyMe··· PyY			
Y	X	N_{nu}···C/Å	n_{nu}	C–N_{el}/Å	N_{nu}···C/Å	n_{nu}	C···N_{el}/Å	N_{nu}–C/Å	n_{nu}	C···N_{el}/Å	$n^{\ddagger}$
CN	CN	2.931	0.064	1.482	1.860	0.484	1.860	1.482	0.989	2.931	0.454
	Cl	2.907	0.067	1.482	1.864	0.481	1.844	1.480	0.992	2.938	0.448
	H	2.898	0.068	1.482	1.866	0.479	1.838	1.479	0.994	2.941	0.444
	CH_3	2.886	0.070	1.482	1.868	0.477	1.830	1.478	0.996	2.945	0.440
	$(CH_3)_2N$	2.857	0.074	1.483	1.875	0.471	1.810	1.476	1.000	2.955	0.429
Cl	CN	2.938	0.063	1.480	1.844	0.499	1.864	1.482	0.989	2.907	0.471
	Cl	2.915	0.066	1.480	1.848	0.495	1.848	1.480	0.992	2.915	0.463
	H	2.906	0.067	1.480	1.850	0.493	1.842	1.479	0.994	2.918	0.460
	CH_3	2.894	0.069	1.480	1.852	0.492	1.834	1.478	0.996	2.922	0.456
	$(CH_3)_2N$	2.866	0.072	1.481	1.859	0.485	1.814	1.476	1.000	2.932	0.445
H	CN	2.941	0.063	1.479	1.838	0.505	1.866	1.482	0.989	2.898	0.477
	Cl	2.918	0.066	1.479	1.842	0.501	1.850	1.480	0.992	2.906	0.470
	H	2.909	0.067	1.479	1.843	0.500	1.843	1.479	0.994	2.909	0.467
	CH_3	2.897	0.068	1.480	1.845	0.498	1.835	1.479	0.994	2.913	0.464
	$(CH_3)_2N$	2.869	0.072	1.480	1.852	0.492	1.816	1.476	1.000	2.924	0.453
CH_3	CN	2.945	0.062	1.478	1.830	0.512	1.868	1.482	0.989	2.886	0.485
	Cl	2.922	0.065	1.478	1.834	0.509	1.852	1.480	0.992	2.894	0.479
	H	2.913	0.066	1.479	1.835	0.508	1.845	1.480	0.992	2.897	0.477
	CH_3	2.902	0.068	1.479	1.837	0.506	1.837	1.479	0.994	2.902	0.473
	$(CH_3)_2N$	2.874	0.071	1.479	1.844	0.499	1.818	1.476	1.000	2.913	0.461
$(CH_3)_2N$	CN	2.955	0.061	1.476	1.810	0.532	1.875	1.483	0.987	2.857	0.509
	Cl	2.932	0.064	1.476	1.814	0.528	1.859	1.481	0.991	2.866	0.501
	H	2.924	0.065	1.476	1.816	0.526	1.852	1.480	0.992	2.869	0.497
	CH_3	2.913	0.066	1.476	1.818	0.524	1.844	1.479	0.994	2.874	0.494
	$(CH_3)_2N$	2.886	0.070	1.477	1.825	0.517	1.825	1.477	0.998	2.886	0.482

© 1999 NRC Canada

Table 8. AM1 calculated group charges for nucleophilic moiety in reactant complex, transition structure, and product complex for methyl transfer, and normalized TS charge $q^{\ddagger}$.

Electrophile	Nucleophile				
Y	X	$(q_{nu})_{rc}$	$(q_{nu})^{\ddagger}$	$(q_{nu})_{pc}$	$q^{\ddagger}$
CN	CN	0.0027	0.2706	0.7055	0.381
	Cl	0.0033	0.2688	0.7024	0.374
	H	0.0035	0.2683	0.7010	0.377
	CH_3	0.0036	0.2678	0.6990	0.369
	$(CH_3)_2N$	0.0045	0.2665	0.6943	0.362
Cl	CN	0.0026	0.2742	0.7128	0.388
	Cl	0.0030	0.2738	0.7094	0.383
	H	0.0032	0.2736	0.7081	0.381
	CH_3	0.0034	0.2730	0.7064	0.378
	$(CH_3)_2N$	0.0041	0.2715	0.7017	0.371
H	CN	0.0026	0.2765	0.7156	0.392
	Cl	0.0029	0.2760	0.7123	0.387
	H	0.0029	0.2758	0.7110	0.385
	CH_3	0.0031	0.2753	0.7093	0.383
	$(CH_3)_2N$	0.0038	0.2737	0.7044	0.375
CH_3	CN	0.0024	0.2791	0.7191	0.397
	Cl	0.0028	0.2789	0.7158	0.392
	H	0.0028	0.2784	0.7145	0.390
	CH_3	0.0031	0.2781	0.7129	0.387
	$(CH_3)_2N$	0.0038	0.2764	0.7083	0.380
$(CH_3)_2N$	CN	0.0019	0.2864	0.7279	0.411
	Cl	0.0025	0.2857	0.7247	0.405
	H	0.0025	0.2854	0.7234	0.403
	CH_3	0.0028	0.2850	0.7217	0.400
	$(CH_3)_2N$	0.0034	0.2831	0.7172	0.392

0.529 and 0.407, respectively. A different choice for c would lead to a different conclusion: indeed, Pauling bond orders n_{nu} calculated for these same methyl transfer TSs using $c = 0.3$ led us previously to conclude that β did *not* provide a measure of the degree of bonding to the nucleophile in the TS (27). The normalized charge $q^{\ddagger}$ for methyl transfer, defined as the fractional change in the net charge on the nucleophilic NH_3 moiety, suffers the problem (described above) of not accounting for the variable charge on the transferring methyl itself, and therefore of underestimating the position of the TS along the intracomplex reaction coordinate.

Hori et al. (28) have very recently shown the existence of a linear correlation between calculated barrier heights and relative proton affinities for gas-phase S_N2 methyl transfer reactions of 4-X-substituted pyridines (X = NO_2, H, OCH_3, $N(CH_3)_2$) with chloromethane. Ab initio MP2/6-31+G*//HF/6-31+G* potential energies were employed to evaluate the activation energy with respect to isolated reactants for reaction of each nucleophile relative to reaction of ammonia with chloromethane; the proton affinities were also calculated relative to ammonia (just as in the present work). The slope of the linear correlation was not — and indeed cannot — be interpreted directly as a measure of the position of the TS along the reaction coordinate, in the way that a normalized Brønsted coefficient may be, because the ion–molecule reactant and product complexes were not considered by these workers. However, their calculated trends in bond lengths and charges involving the nucleophile in the TS are completely in accord with the Hammond postulate and with the trends we have reported in the present study. Although we have not only used a semiempirical MO method but also a very simple trick to mimic the substituted pyridines instead of treating the full molecules, the results of Hori et al. do provide welcome evidence (further to our own (16)[2]) to suggest that our approximate procedures are indeed quite reasonable.

Summarizing remarks

We have performed simple MO calculations to simulate intracomplex proton transfer and methyl transfer between series of 4-substituted pyridines. The enthalpies of activation and of reaction are well correlated by the Marcus relation. The Brønsted correlation is markedly curved for proton transfer, for which the Marcus intrinsic barrier is very low (~5 kJ mol^{-1}). The range of validity of the Marcus relation, $-4\Delta H^{\ddagger} \leq \Delta H_{rxn} \leq +4\Delta H^{\ddagger}$, is completely spanned by the range of substituents, strongly electron-withdrawing to strongly electron-donating, available to experiment and simulation.

[2] G.D. Ruggiero and I.H. Williams. Unpublished work.

© 1999 NRC Canada

Thus, the full change in slope from 0 to 1 of the curved Brønsted may be sampled. Conversely, the Brønsted correlation is almost imperceptibly curved for methyl transfer, for which the Marcus intrinsic barrier is very high (~152 kJ mol^{-1}), and the range of ΔH_{rxn} spanned by the substituents considered represents only the central 10% or so of the full range over which the slope changes from 0 to 1. It would be physically impossible to find nucleophiles and (or) leaving groups which could allow the full extent of Brønsted curvature to be expressed. A similar result was obtained by Kreevoy and co-workers (29) in simulations for families of hydride transfer reactions: an essentially linear Brønsted correlation was found for a reaction series with a high Marcus intrinsic barrier of ~87 kJ mol^{-1}.

Nearly a quarter of a century ago, Kresge contributed to a book dedicated to R.P. Bell; his chapter was entitled "The Brønsted relation: significance of the exponent" (5). That article, together with his slightly earlier *Chemical Society Reviews* paper (17), are remarkable for their insight. The present theoretical study, contributed to this issue dedicated to Jerry Kresge, achieves little more than to confirm the correctness of his ideas.

References

1. L.P. Hammett. Chem. Rev. **17**, 125 (1935).
2. H. Eyring. J. Chem. Phys. **3**, 107 (1935); Chem. Rev. **17**, 65 (1935).
3. G.S. Hammond. J. Am. Chem. Soc. **77**, 334 (1955).
4. J.E. Leffler. Science (Washington, D.C.) **117**, 340 (1953); J.E. Leffler and E. Grunwald. Rates and equilibria of organic reactions. Wiley, New York. 1963.
5. A.J. Kresge. *In* Proton-transfer reactions. *Edited by* E.F. Caldin and V. Gold. Chapman and Hall, London. 1975. pp. 179–199.
6. A. Pross and S. Shaik. Nouv. J. Chim. **13**, 427 (1989).
7. W.P. Jencks. Bull. Soc. Chim. Fr. 218 (1988).
8. E.K. Thornton and E.R. Thornton. *In* Transition states of biochemical processes. *Edited by* R.D. Gandour and R.L. Schowen. Plenum, New York. 1978; W.P. Jencks. Chem. Rev. **85**, 511 (1985).
9. I.H. Williams. Bull. Soc. Chim. Fr. 192 (1988).
10. R.B. Hammond and I.H. Williams. J Chem. Soc. Perkin Trans. 2, 59 (1989).
11. I.H. Williams. 11th IUPAC Conf. Phys. Org. Chem. Ithaca, N.Y. 1992. Abstr. IA-5.
12. J.J.P. Stewart. QCPE Bull. **10**, 86 (1990).
13. M.J.S. Dewar, E.G. Zoebisch, E.F. Healy, and J.J.P. Stewart. J. Am. Chem. Soc. **107**, 3902 (1985).
14. J.J.P. Stewart. User Guide to MOPAC 6.0. Sect. 6.12. Frank J. Seiler Research Laboratory, U.S. Air Force Academy, Colo. 1990.
15. U. Berg, M. Chanon, R. Gallo, and M. Rajzmann. J. Org. Chem. **60**, 1975 (1995).
16. G.D. Ruggiero. Ph.D. thesis. University of Bath, Bath. 1999.
17. J. Kresge. Chem. Soc. Rev. **2**, 475 (1973).
18. J.R. Murdoch. J. Am. Chem. Soc. **94**, 4410 (1972).
19. L. Pauling. J. Am. Chem. Soc. **69**, 542 (1947).
20. A. Williams. Acc. Chem. Res. **17**, 425 (1984); Adv. Phys. Org. Chem. **27**, 1 (1991).
21. I.H. Williams. J. Am. Chem. Soc. **106**, 7206 (1984).
22. Y.P. Liu, G.C. Lynch, T.N. Truong, D.H. Lu, D.G. Truhlar, and B.C. Garrett. J. Am. Chem. Soc. **115**, 2408 (1993).
23. A.J. Kresge. *In* Isotope effects on enzyme catalyzed reactions. *Edited by* W.W. Cleland, M.H. O'Leary, and D.B. Northrop. University Park Press, Baltimore. 1977.
24. J.P. Klinman. *In* Transition states of biochemical processes. *Edited by* R.D. Gandour and R.L. Schowen. Plenum, New York. 1978.
25. S.S. Shaik, H.B. Schlegel, and S. Wolfe. Theoretical aspects of physical organic chemistry: the S_N2 mechanism. Wiley, New York. 1992. pp. 33–41.
26. S. Scheiner and P. Redfern. J. Phys. Chem. **90**, 2969 (1986).
27. I.H. Williams. Chem. Soc. Rev. **22**, 277 (1993).
28. K. Hori, J.-L.M. Abboud, C. Lim, M. Fujio, and Y. Tsuno. J. Org. Chem. **63**, 4228 (1998).
29. Y. Kim, D.G. Truhlar, and M.M. Kreevoy. J. Am. Chem. Soc. **113**, 7837 (1991).

© 1999 NRC Canada

Acid–base chemistry in high-performance lubricating oils

Duncan C. Hone, Brian H. Robinson, David C. Steytler, Roger W. Glyde, and John A. Cleverley

Abstract: We have used stopped-flow kinetic studies to conduct an investigation into the acid neutralization reaction between overbased detergent additives and aqueous acid dispersed as w/o microemulsion droplets. Water-soluble pH indicators have been used to monitor the change in pH during the reaction. The acid neutralization rate was found to be dependent on the concentration of overbased additive, the temperature of the system, and the hydrocarbon chain length of the solvent. The systems are of importance in relation to the mechanism of acid neutralization by engine lubricants.

Key words: overbased detergent additive, acid neutralization, pH indicator, stopped flow.

Résumé : On a fait appel à des études cinétiques à flux stoppé pour étudier la réaction de neutralisation acide d'additifs de détergents surbasiques et de l'acide aqueux dispersé dans des gouttelettes d'une microémulsion e/h. On a utilisé des indicateurs de pH solubles dans l'eau pour évaluer le changement de pH au cours de la réaction. On a trouvé que la vitesse de neutralisation acide dépend de la concentration de l'additif surbasique, de la température du système et de la longueur de la chaîne de l'hydrocarbure agissant comme solvant. Les systèmes sont importants pour le mécanisme de neutralisation acide des lubrifiants de moteur.

Mots clés : additif de détergent surbasique, neutralisation acide, indicateur de pH, flux stoppé.

[Traduit par la Rédaction]

Introduction

Acid–base chemistry in aqueous-based media has, over the 60 years since the pioneering work of Brønsted and Bell, been an important and well-studied area of physical chemistry. By contrast, acid–base chemistry in nonpolar aprotic solvents has received rather less attention. This is particularly true of kinetic studies. In general, it can be stated that the products of a reaction between an organic acid (RH) and a base (B) can be either a hydrogen-bonded complex (RH–B) or a hydrogen-bonded ion pair (R^-–HB^+). Separation of the product components is prevented by the strong attraction between oppositely charged ions in the low-dielectric medium. The product formed will depend primarily on the relative acid–base strength of the reacting partners, as illustrated in the structures (following page).

In both reactions, the association rate constant k_f is close to diffusion controlled (~10^9 dm^3 mol^{-1} s^{-1}).

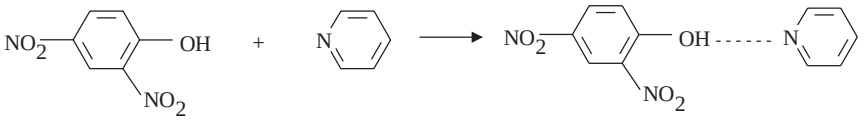

Weak base — Hydrogen-bonded complex

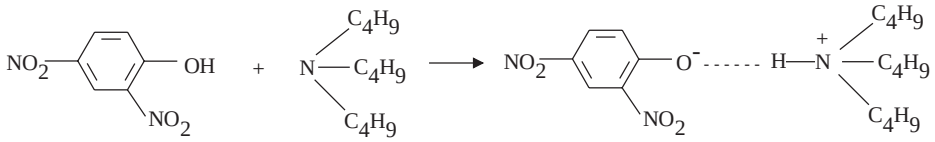

Strong base — Hydrogen-bonded ion pair

Received September 29, 1998.

This paper is dedicated to Jerry Kresge in recognition of his many achievements in chemistry.

D.C. Hone,[1] B.H. Robinson, and D.C. Steytler. School of Chemical Sciences, University Of East Anglia, Norwich, Norfolk. NR4 7TJ, U.K.
R.W. Glyde and J.A. Cleverley. Paramins, Exxon Chemical Ltd. Abingdon, U.K.

[1]Author to whom correspondence may be addressed. e-mail: d.hone@uea.ac.uk

 © 1999 NRC Canada

Fig. 1. Schematic diagram of an overbased additive particle.

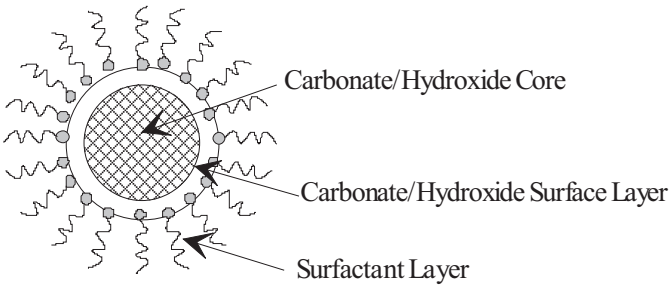

In lubricating oils, for example, in automobile engines, a range of carbon-based acids (e.g., RCOOH) can be produced as a result of oxidative degradation of the hydrocarbon base oil. In addition, gases that are formed in the combustion process can react with water to produce acidic species such as H_2SO_4, HCl, and HNO_3. For example, fuel supplied for marine diesel engines is normally rich in sulphur, leading to the production of sulphuric acid. Unless neutralized, these acids will attack metal surfaces and this will subsequently lead to corrosion of engine components and to polymerization of organic species, resulting in resin formation and the buildup of deposits. Consequently there is a requirement to continuously neutralize these acids, which form during the operation of an engine. Since large amounts of acid are required to be neutralized it is convenient to supply "basicity" to the oil by means of an overbased additive (or detergent) formulation. This class of additive enables large amounts of sterically stabilized, colloidally dispersed, base to be present in the oil, and is found in nearly all modern oil formulations involving crankcase applications (automobile, truck, marine, etc.).

High-performance oils are now an essential component in modern engines. In addition to the fundamental role of providing a protective film for the metal, and dissipating the heat generated in an engine, such oils have a variety of other tasks. Preventing acid-induced metal corrosion and lubricant degradation is just one of these tasks. Others include, for example, the dispersion of considerable quantities of soot generated in diesel engines and the control of friction to improve the fuel efficiency of the engine. Crankcase lubricants are therefore formulated with a number of different chemical additives (1), in addition to the overbased detergents. Correctly formulated, these additives provide optimum engine performance over a wide range of operating conditions.

Detergent additives are generally surfactant-stabilized colloidal particles of metal carbonates. Their structure is generally believed to fit the model shown in Fig. 1 (2). This consists of a core of basic metal carbonate or a mixture of metal carbonate and metal hydroxide, depending on the cation and the process employed in their production. The core is stabilized by a monolayer skin of surfactant. Both the type of surfactant and the metal used depend on the application required. Surfactants used include sulphonates, phenates, and salicylates. The cation is typically calcium, magnesium, or sodium. The core radius of the overbased particle is usually in the range 15–100 Å. The overall dimension is determined by the additional contribution of the alkyl chain length of the stabilizing surfactant (approx. 10–25 Å, depending on the surfactant employed). Because the particles are small, a large proportion of the core molecules will be located at the surface layer. Size-related measurements are readily made using Small Angle Neutron Scattering (SANS) (3), Dynamic Light Scattering (DLS), Ultracentrifugation, and viscosity studies.

The final product is defined by its Total Base Number (TBN). TBN is the equivalent milligrams KOH per gram of sample and is usually determined by method ASTM D-2896. For example, an overbased additive with a TBN of 300 contains basic material equivalent to 300 mg KOH/g. The synthetic route to an overbased product is summarized by Marsh (4). A typical procedure is as follows: firstly, the acidic form of the surfactant is neutralized by the addition of metal hydroxide to form the neutral metal salt of the surfactant. The system is then carbonated in the presence of excess metal hydroxide and a polar solvent to give the metal carbonate core stabilized by the metal surfactant. The polar solvent is then removed to give the final additive.

The aim of this study is to obtain fundamental kinetic information about the acid-neutralization process occurring in a high-performance engine lubricant. To this end, one mineral acid only has been investigated for the work described in this paper, namely, HCl (although similar results are obtained with other strong acids). The acid has been studied in a microemulsion medium because, in an engine, excess free surfactant and water are often present, which can lead to microemulsification of the acid/water in the oil.

To simplify the base conditions, a model-overbased system, which was prepared by Exxon Chemical, U.K., has been used. This has the essential properties of a commercial detergent additive. In an engine, buildup of acid will not generally occur while sufficient base additive is present, since neutralization is a continuous process. However, to test the ability of the additive to neutralize acid we typically used millimolar (mM) overall concentrations of acid. In an engine, the neutralization reaction will occur over a wide range of operating conditions, e.g., shear rate, temperature, etc. We have studied the neutralization reaction in low alkane chain length (C_7, C_{10}, C_{12}) solvents, which are representative of the solvent viscosity for neutralization in an oil at operational temperatures (100–120°C in the sump).

The neutralization process is found to be rapid and so the stopped-flow method is appropriate to follow its rate. Using this technique, reactions are studied in the ms–s time range. We have devised a spectrophotometric assay, based on pH-responsive dye indicators, to monitor the neutralization process.

Experimental

The overbased additive used in this study as a model system was supplied by Exxon Chemical as a concentrate in a base oil (TBN = 300 mg KOH g^{-1}) and was used without further purification. It contains an amorphous calcium carbonate/hydroxide core stabilized by a high molecular weight alkylbenzene sulphonate surfactant. All additive solutions were diluted in hydrocarbon solvents, supplied by Fisher, before use in kinetic studies. We have estimated the basicity of these solutions by means of a newly defined parameter TBN*, which is effectively the base equivalent (OH^-) molarity of the dispersion. A typical calculation shows how

© 1999 NRC Canada

Fig. 2. (*a*) pH indicator methyl orange in unprotonated form (pK_a^{me} = 1.3). (*b*) pH indicator PNPS shown in unprotonated form (pK_a^{me} = 5.1).

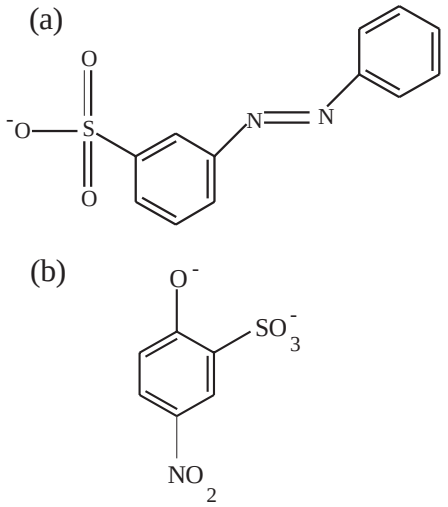

the TBN* value is obtained from the TBN for a *y*% w/v solution.

Fig. 3. Schematic diagram of the acid-neutralization reaction taking place between an overbased additive particle and an acidified w/o microemulsion droplet.

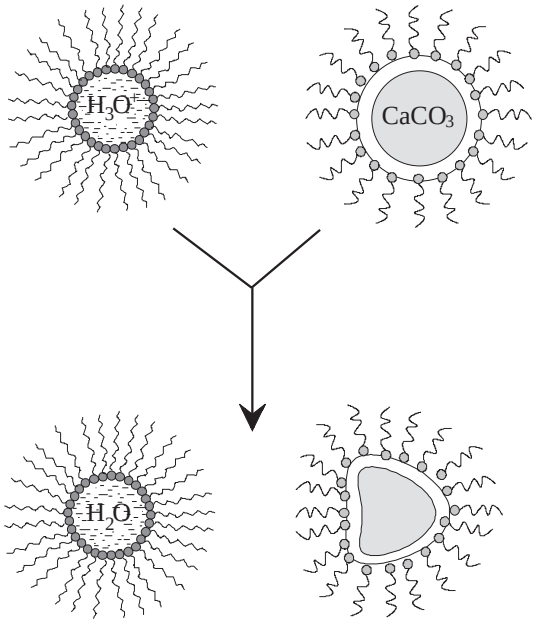

$$TBN^* = 10^{-2} \times y\ (g/100\ mL) \times TBN\ (mg/g)/MW\ KOH\ (g\ mol^{-1})\ (MW\ KOH = 56.11\ g\ mol^{-1})$$

For example, for a dilution factor leading to y = 0.5 g/100 mL, TBN* ($[OH^-]$) = 0.0267 mol dm^{-3}.

Water-in-oil (w/o) microemulsion droplets were prepared by dispersing an acidified aqueous solution (typically $[H^+]_{aq}$ = 0.1 mol dm^{-3}) into a surfactant–hydrocarbon mixture. Microemulsions form spontaneously on gentle shaking. The overall hydrogen ion concentration $[H^+]_{ov}$ is given by $[H^+]_{aq}\ \phi$ where ϕ is the volume fraction of the dispersed droplet phase and is typically 0.01–0.03. In our experiments ϕ was kept constant at 0.018. In these systems the basic component is in excess over the microemulsified acid, so that only a small part of the overbased system is neutralized (~10%). The percentage extent of additive neutralization (%N) is given by

$$\%N = ([H^+]^{initial} - [H^+]^{final} / TBN^*) \times 100$$

where $[H^+]^{initial}$ and $[H^+]^{final}$ refer to $[H^+]_{ov}$ and $[H^+]^{final}$ can be readily obtained from analysis of the stopped-flow transient (1/2 amplitude) and the pK_a^{me} of the indicator, where pK_a^{me} is the pK_a of the pH indicator measured in the microemulsion system. (Note that this will be different from the pK_a in water as a result of charge/partitioning effects (5).)

The surfactant used in this work was the sodium salt of sulfosuccinic acid bis(2-ethylhexyl) ester (Sigma), commonly known as Na-AOT (AOT), and was used throughout at an overall concentration $[AOT]_{ov}$ of 0.1mol dm^{-3} and w = 10, where $w = [H_2O]_{ov} / [AOT]_{ov}$. This system forms spherical droplets of well-defined water core, radius r, and it has been shown that the radius, measured in nm, is given for this system, by r/nm = 0.175w (6).

The concentration of droplets is given by [Droplets] = $[AOT]_{ov} \times w^{-2} \times 1.331$. Thus for a microemulsion system in which $[AOT]_{ov}$ = 0.1 mol dm^{-3} and w = 10, [Droplets] = 1.331 × 10^{-3} mol dm^{-3}. HCl (BDH) and AnalaR water (BDH) were used throughout and the pH values were measured with a Radiometer Copenhagen PHM82 standard pH meter. For the measurements reported in this paper the aqueous phase before dispersion was essentially pH 1. Stock solutions of the pH indicators, methyl orange (BDH) (Fig. 2*a*) and 4-nitrophenyl-2-sulphonate (PNPS) (Fluka) (Fig. 2*b*), were prepared in AnalaR water. Spectrophotometric data were obtained at 25°C on an HP8452A diode array spectrophotometer with a resolution of 2 nm. Acid-neutralization data were acquired by mixing microemulsion and overbased solutions in a HiTech stopped-flow apparatus with a dead time of <10 ms. The unit was thermostated to ±0.1°C using a Haake water bath.

Small-angle neutron scattering (SANS) data were recorded on the LOQ instrument at the Rutherford–Appleton Laboratory (RAL), Harwell, U.K. Ultracentrifuge experiments were performed by means of a Beckmann L5-50 ultracentrifuge.

Results and discussion

(*a*) pH indicators

Figure 3 is a schematic diagram of the acid-neutralization reaction taking place between an overbased particle and aqueous acid that is solubilized inside a w/o microemulsion droplet.

The time for neutralization to occur was typically of the order of a few seconds. Due to the difference in sedimentation coefficients between the two product species (i.e., particles and droplets in Fig. 3), the droplets could be separated from the particles after the neutralization reaction had taken place. This was achieved by means of selective sedimentation of the particles using an analytical ultracentrifuge (40 000 rpm for 1.5 h). SANS data on the non-sedimented

© 1999 NRC Canada

Fig. 4. (*a*) UV–VIS spectrum of methyl orange solubilized in an Na-AOT microemulsion, $[AOT]_{ov}$ = 0.10 mol dm^{-3}, [methyl orange]$_{aq}$ = 5.0 × 10^{-4} mol dm^{-3}. (*b*) Stopped-flow trace for the reaction between 0.2% w/v overbased additive in *n*-heptane and methyl orange – acid droplets. $[AOT]_{ov}$ = 0.10 mol dm^{-3}, [methyl orange]$_{aq}$ = 5.0 × 10^{-4} mol dm^{-3}, $[HCl]_{aq}$ = 1.0 × 10^{-1} mol dm^{-3}.

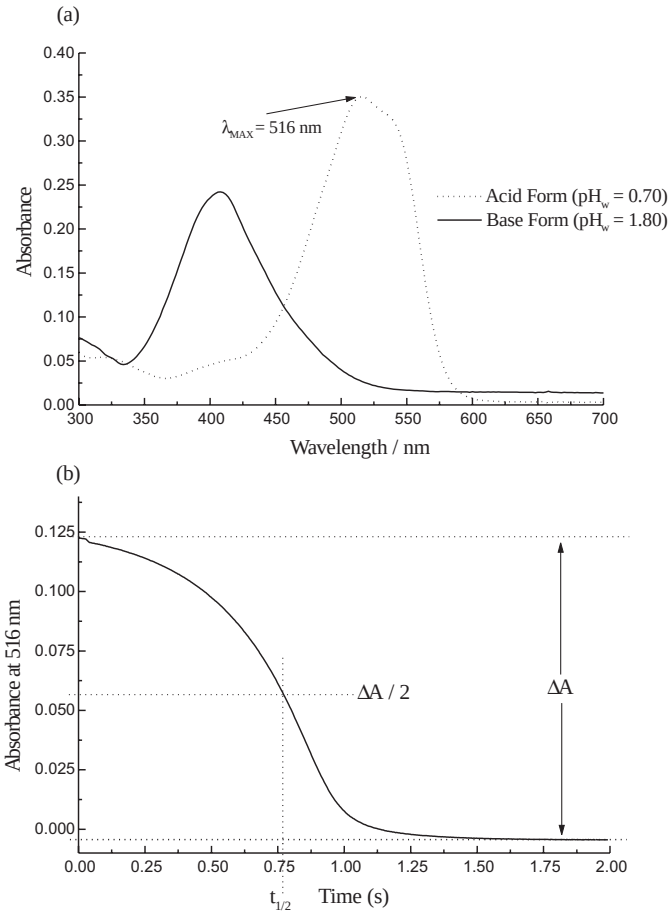

part of the system (after centrifugation) indicated that the microemulsion water droplets remain the same size after the reaction and that no indicator or water, initially located in the core of the droplets, is transferred to the particles. However, this does not discount the possibility that surfactant molecules are exchanged to some extent between the droplets and particles. Other experiments we carried out using nile blue as the pH indicator show that the water pools of the microemulsion droplets (initially at pH ~7) increase further in pH when mixed with the overbased particles. This leads us to conclude that the preferred mechanism of neutralization involves base transfer from the overbased additive into the water pools of the microemulsion where the acid-neutralization reaction occurs.

Solubilization of water-soluble pH indicators inside the water pools of w/o microemulsions allows any change in pH of the water to be monitored spectrophotometrically (7, 8). The main indicators used were methyl orange (MO) and 4-nitrophenyl-2-sulphonate (PNPS). Figure 4*a* shows the UV–VIS spectrum of MO dispersed in a w/o microemulsion stabilized by the surfactant Na-AOT. In aqueous solution as the ionic strength → 0, MO has a pK_a of 3.44 at 25°C but on solubilization in the microemulsion (pK_a^{me}) this value is lowered by approximately 2 pK_a units.

The state of the water present in the microemulsion droplets studied is quite different from that of the bulk aqueous solution due to the high concentration of sodium ions provided by the AOT. This leads to an increase in ionic strength and the indicator behaviour is affected by the so-called salt error (9). λ_{max} for the acid form of the indicator when solubilized inside the microemulsion is 516 nm. When a diluted solution of overbased additive is mixed with a microemulsion solution, in which the water pool is acidified and hence contains methyl orange in the acid form, there is an observed colour change (red to yellow) as the acid is neutralized and the indicator is converted to the base form. This process is taken to relate to base being released from the overbased particles into the acidified water pools of the microemulsion where neutralization of the acid occurs. The colour change can be monitored by recording the change in absorbance of the acid or base form of the indicator with time.

Using the stopped-flow method, a solution of overbased additive is mixed in equal volumes with the acid – methyl orange microemulsion solution. The absorbance is recorded at λ_{max} for the acid form of the indicator, 516 nm. As acid neutralization occurs there is a decrease in the measured absorbance as shown in Fig. 4*b*.

The reaction is recorded until the absorbance levels off and the indicator has been converted to the base form. The total change in absorbance, ΔA, is recorded and the time taken to reach $\Delta A/2$ is designated as $t_{1/2}$ (s). From knowledge of the pK_a^{me} and $\Delta A/2$, the extent of neutralization (%N) at $t_{1/2}$ can be determined.

Replacing MO with PNPS allows the acid-neutralization reaction to be monitored at a later stage since pK_a^{me} is increased from 1.3 to 5.1. Figure 5*a* shows the UV–VIS spectrum of PNPS dispersed in a w/o microemulsion stabilized by the surfactant Na-AOT. In aqueous solution the pK_a is 6.5 but this is lowered to 5.1 (pK_a^{me}) for the w = 10 microemulsion system.

When the overbased particle is mixed with the acid – PNPS microemulsion the observed colour change is from colourless to yellow. This corresponds to an increase in the base form of the indicator inside the water pools of the microemulsion for which λ_{max} = 398 nm. Figure 5*b* shows the stopped-flow trace recorded at 398 nm using PNPS as the indicator but under the same conditions as Fig. 4*b*.

The observed colour change ($t_{1/2}$) is longer using PNPS. This is as expected due to the higher pK_a^{me} value and, therefore, lower value of $[H^+]^{final}$, since more base must be released from the particle in order that the acid is sufficiently neutralized to convert the indicator to its base form. Therefore the indicator to be used depends on the "pH window" one wishes to observe during neutralization. Table 1 shows the difference in $t_{1/2}$ values obtained using the two different pH indicators under otherwise identical conditions.

It should be noted that in recording the absorbance at the other λ_{max} positions, the base form of methyl orange (λ_{max} = 406 nm) and the acid form of PNPS (λ_{max} = 302 nm) give the same value for $t_{1/2}$ and the expected increase and decrease in absorbance, respectively.

© 1999 NRC Canada

Fig. 5. (*a*) UV–VIS spectrum of PNPS solubilized in an Na-AOT microemulsion, $[AOT]_{ov}$ = 0.10 mol dm^{-3}, w = 10, $[PNPS]_{aq}$ = 1.6 × 10^{-3} mol dm^{-3}. (*b*) Stopped-flow trace for the reaction between 0.2% w/v overbased additive in *n*-heptane and PNPS–acid droplets. $[AOT]_{ov}$ = 0.10 mol dm^{-3}, $[HCl]_{aq}$ = 1.0 × 10^{-1} mol dm^{-3}.

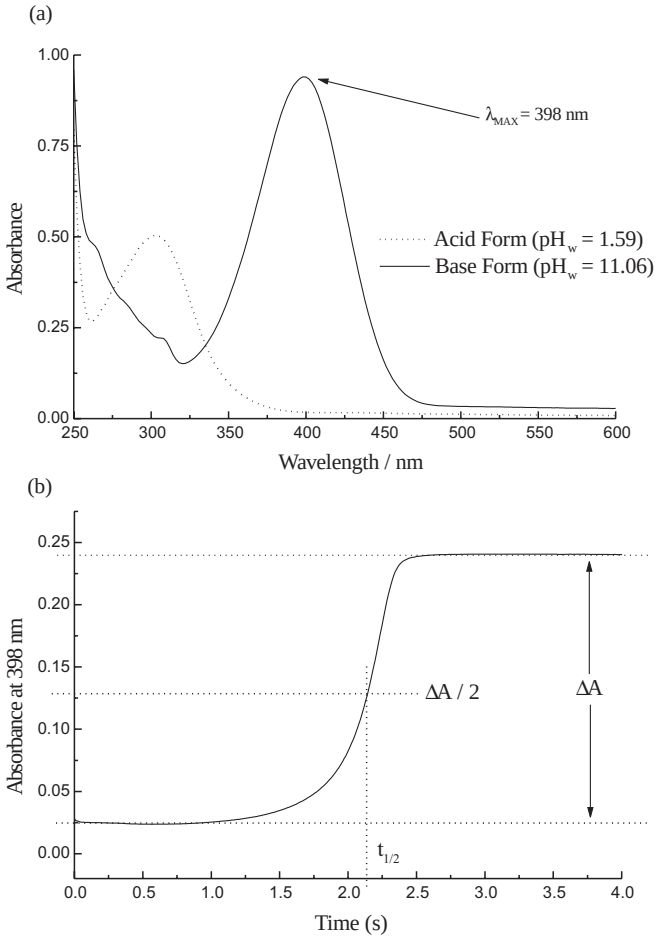

Table 1. Stopped-flow data for the reaction between overbased additive particles and acid/pH indicator microemulsion droplets.[a]

	$t_{1/2}$ (s)	
Temperature (°C)	Methyl orange	PNPS
30	0.54	1.69
25	0.76	2.14
20	1.09	2.64
15	1.62	3.55
10	2.57	4.96
%N	8.39%	16.82%

[a]Additive concentration = 0.2% w/v in *n*-heptane, $[Na\text{-}AOT]_{ov}$ = 0.10 mol dm^{-3}, w = 10, $[methyl\ orange]_{aq}$ = 5.0 × 10^{-4} mol dm^{-3}, $[PNPS]_{aq}$ = 1.0 × 10^{-3} mol dm^{-3}, $[HCl]_{aq}$ = 0.10 mol dm^{-3}, TBN* = 0.0107 mol dm^{-3}, $[H^+]_{initial(ov)}$ = 1.8 × 10^{-3} mol dm^{-3}.

Table 2. Stopped-flow data for the reaction between overbased additive particles and acid/methyl orange microemulsion droplets.[a]

Additive concentration (% w/v)	$t_{1/2}$ (s)	Temperature (°C)
0.2	0.54	30
	0.76	25
	1.09	20
	1.62	15
	2.57	10
0.4	0.34	30
	0.51	25
	0.74	20
	1.07	15
	1.84	10
0.8	0.22	30
	0.31	25
	0.45	20
	0.66	15
	1.04	10

[a]Additive diluted in *n*-heptane, $[Na\text{-}AOT]_{ov}$ = 0.10 mol dm^{-3}, w = 10, $[methyl\ orange]_{aq}$ = 5.0 × 10^{-4} mol dm^{-3}, $[HCl]_{aq}$ = 0.10 mol dm^{-3}.

(*b*) Effect of particle concentration on the neutralization process

Table 2 shows the effect of increasing the concentration of overbased carbonate particles in the hydrocarbon solvent. As the concentration is increased, more base has effectively been added to the system and hence the value of $t_{1/2}$ becomes shorter, i.e., the neutralization becomes faster. Over the particle concentration range investigated, there is a linear relationship between $(t_{1/2})^{-1}$ and [particles] but interestingly there is not a direct proportionality and so a second-order rate constant cannot be derived.

(*c*) Effect of temperature on the neutralization process

The technique outlined has been applied to study the effect of temperature on acid neutralization by overbased additive particles in these systems. As the temperature of the system is increased the value of $t_{1/2}$ decreases, i.e., the reaction becomes faster, as shown in Table 2. The values of $t_{1/2}$ were analysed using a modified Arrhenius plot in which the rate is given by the reciprocal of $t_{1/2}$. This procedure assumes that the pK_a^{me} is essentially independent of temperature. Figure 6 shows that the activation energy, E_A, for these reactions is approximately 55 kJ mol^{-1}.

(*d*) Effect of change of solvents on the neutralization process

Various systems were studied in which the hydrocarbon solvent was systematically changed. Data using the methyl orange system to monitor the change in absorbance are shown in Table 3.

As the chain length of the oil solvent is increased from C_7 to C_{10} to C_{12} using *n*-heptane, *n*-decane, and *n*-dodecane, respectively, the value of $t_{1/2}$ decreases. It is well established, using SANS, that the size (and hence concentration) of droplets is independent of the solvent for these low w systems. However, the upper temperature phase boundary, which leads to clustering of droplets, is lowered as the solvent chain length is increased. This means that interpenetration of the tail groups of the surfactant surrounding the water cores is facilitated. This results in the reaction rate being faster in the higher molecular weight (higher viscosity) solvent.

© 1999 NRC Canada

Fig. 6. Arrhenius-type plots for the reaction between overbased additive particles and methyl orange – acid microemulsion droplets in *n*-heptane. E_A = 55 (± 1) kJ mol^{-1}.

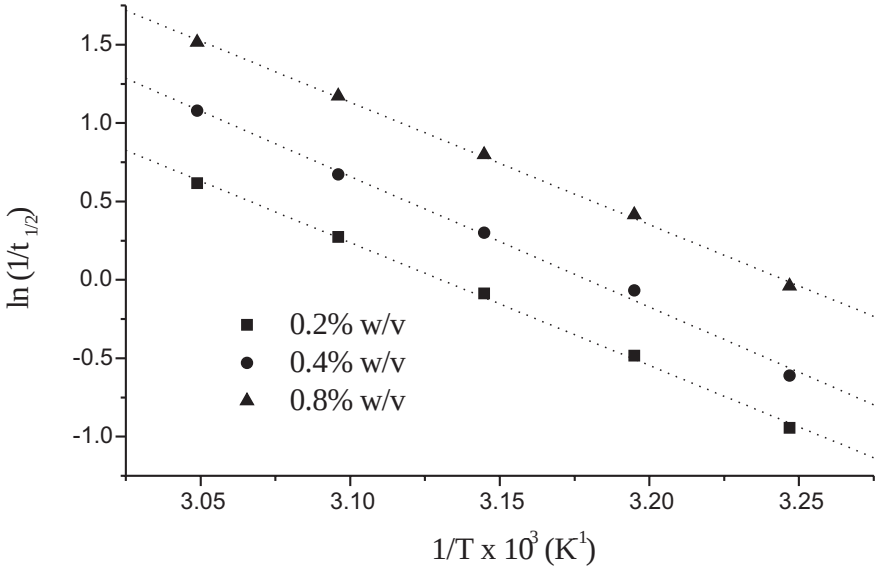

Table 3. Stopped-flow data for the reaction between overbased additive particles and acid/methyl orange microemulsion droplets.[a]

Hydrocarbon solvent	$t_{1/2}$ (s)	Temperature (°C)
n-Heptane	0.54	30
	0.76	25
	1.09	20
	1.62	15
	2.57	10
n-Decane	0.13	30
	0.17	25
	0.24	20
	0.33	15
	0.53	10
n-Dodecane	0.04	30
	0.07	25
	0.09	20
	0.13	15
	0.20	10

[a] Additive concentration = 0.2% w/v, $[Na\text{-}AOT]_{ov}$ = 0.10 mol dm^{-3}, w = 10, $[methyl\ orange]_{aq}$ = 5.0 × 10^{-4} mol dm^{-3}, $[HCl]_{aq}$ = 0.10 mol dm^{-3}.

The results for droplet/particle neutralization can be interpreted if we consider the neutralization reaction occurring as a result of the interaction of two types of colloidal assemblies, the microemulsion droplet and the overbased particle. The surfactant configuration is tightly packed and so interactions between the droplet and particle can be considered as an interaction between two reasonably "hard" spheres. However, the shorter the chain length of the solvent acting as the dispersion medium (e.g., *n*-heptane), the easier it becomes to interpenetrate the surfactant layers stabilizing the overbased particle and the microemulsion droplet, as has indeed been previously shown from kinetic studies of the interactions between two microemulsion droplets in hydrocarbon solvents (10). Likewise, as we move to the longer-chain solvent the interactions become more "sticky" as the longer-chain alkanes penetrate less effectively into the surfactant layer. This type of interaction means that collisions between the particle and droplet will last longer and therefore lead to a higher probability of base transfer and hence acid neutralization. The activation energy is independent of concentration of overbased particles, as would be expected. The relatively high value (E_A = 55 kJ mol^{-1}) clearly indicates that the reactions are not diffusion controlled since the E_A values should then reflect the lower values for the temperature dependence of the viscosity of the solvent.

Summary

The methodology outlined in this paper has been used to study the neutralization behaviour of model overbased detergent additive systems. It is thought that the free excess surfactant present in engine oil formulations disperses the aqueous acid present in a similar way to that of the model w/o microemulsion droplets. The use of water-soluble pH indicator molecules allows the change in pH of the water to be monitored for these reactions in a facile way. More complex additive systems of commercial importance have also been investigated. These systems are those in which a number of other additves (e.g., dispersant) are blended with the overbased detergent additive. Using the technique described in this paper, it has been possible to investigate the effect these additional additves have on the acid-neutralization properties, and the approach provides a new simple diagnostic test of the performance efficiency of lubricant detergent additives.

References

1. R.W. Glyde. Chem. Br. **7**, 39 (1997).
2. J.-P. Roman, P. Hoornaert, D. Faure, C. Biver, F. Jacquet, and J.-M. Martin. J. Colloid Interface Sci. **144**, 324 (1991).
3. I. Markovic, R.H. Ottewill, D.J. Cebula, I. Field, and J.F. Marsh. J. Colloid Polym. Sci. **262**, 648 (1984).
4. J.F. Marsh. Chem. Ind. **14**, 470 (1987).

© 1999 NRC Canada

5. C.J. Drummond, F.Grieser, and T.W. Healy. J. Chem. Soc. Faraday Trans. 1, **85**, 561 (1989).
6. P.E. Zinsli. J. Phys. Chem. **83**, 3323 (1979).
7. O.A. Seoud and R.C. Viera. J. Colloid Interface Sci. **93**, 289 (1983).
8. O.A. Amire. J. Colloid Interface Sci. **126**, 508 (1987).
9. R.G. Bates. *In* Determination of pH. Wiley, New York. 1964.
10. P.D.I. Fletcher, A.M. Howe, and B.H. Robinson. J. Chem. Soc. Faraday Trans. 1, **83**, 985 (1987).

© 1999 NRC Canada

Multiple changes in rate-determining step in the acid and base catalyzed cyclizations of ethyl *N*-(*p*-nitrophenyl)hydantoates caused by methyl substitution

Iva B. Blagoeva, Anthony J. Kirby, Asen H. Koedjikov, and Ivan G. Pojarlieff

Abstract: The slopes of the pH–rate profiles for the cyclization of 2-methyl- and 2,3-dimethyl hydantoates **1**-NPU and **2**-NPU between pH 1 and 7 change from 1 to 0 and then back to 1. A reaction first order in H^+ was observed with the latter compound. The 2,2,3-trimethyl derivative **3**-NPU showed only one reaction first order in OH^-, but complex acid catalysis is described by slopes 0, –1, 0, and finally –1 again. The cyclizations were general base catalyzed, with Brønsted β values of 0.5–0.6. The OH^- catalysis at higher pH for **1**-NPU and **2**-NPU showed inverse solvent kinetic isotope effects and deviated from the Brønsted relationships, while that for **3**-NPU showed a normal effect and complied with the Brønsted relationship. The accelerations due to the *gem*-dimethyl effect were lost with the OH^- and general base-catalyzed reactions of **3**-NPU. This behaviour is due to a change from the rate-determining formation of the tetrahedral intermediate with **1**-NPU and **2**-NPU to the rate-determining breakdown with **3**-NPU, due to steric hindrance to protonation of the leaving ethoxy group. The OH^- reaction at higher pH involves attack of the ureide anion with **1**-NPU and **2**- NPU, becoming concerted with deprotonation when catalyzed by general bases and changing to acid inhibition of the anion of the tetrahedral intermediate at low pH. With **3**-NPU at higher pH, T^- is in equilibrium and the conjugate acids of the general bases accelerate its breakdown by protonating the ethoxy group. Acid catalysis of the cyclization of **3**-NPU at higher pH is also protonation of the leaving group from T^0 changing to the rate-determining formation of T at lower pH. The latter mechanism is preferred for the cyclization of **2**-NPU.

Key words: *gem*-dimethyl effect, mechanism, general base catalysis, proton transfer, steric hindrance.

Résumé : Les pentes des profils pH–vitesse pour la cyclisation des 2-méthyl- et 2,3-diméthylhydantoates **1**-NPU et **2**-NPU entre les pH 1 et 7 passe de 1 à 0 avant de revenir à 1. Avec le dernier composé, on observe que la réaction est du premier ordre en H^+. Le dérivé 2,2,3-triméthylé **3**-NPU ne donne qu'une réaction du premier ordre en OH^-, mais une catalyse acide complexe décrite par des pentes de 0, –1, 0 et finalement –1 encore une fois. Les cyclisations sont soumises à une catalyse générale par les bases avec des valeurs β de Brønsted qui vont de 0,5 à 0,6. Les **1**-NPU et **2**-NPU soumis à une catalyse par OH^-, à des pH plus élevés, mettent en évidence l'existence d'effets isotopiques cinétiques inverses du solvant et des déviations des relations de Brønsted. Avec OH^-, les accélérations provoquées par l'effet *gem*-diméthyle sont perdues ainsi que les réactions soumises à une catalyse générale par les bases. Ce comportement est dû au fait que dans les cas des **1**-NPU et **2**-NPU l'étape cinétiquement déterminante est la formation d'un intermédiaire tétraédrique alors que dans le cas du **3**-NPU l'étape déterminante est son bris qui est dû à l'empêchement stérique à la protonation du groupe éthoxy partant. La réaction OH^-, à un pH plus élevé, implique une attaque de l'anion uréide par les **1**-NPU et **2**-NPU qui devient concertée avec la déprotonation lorsqu'elle est soumise à une catalyse générale par les bases et qui change à une inhibition acide de l'anion de l'intermédiaire tétraédrique à pH plus bas. Avec le **3**-NPU, à des pH plus élevés, T^- est en équilibre et les acides conjugués des bases générales accélère son bris en protonant le groupe éthoxy. La catalyse acide de la cyclisation du **3**-NPU à des pH plus élevés est aussi la protonation du groupe partant de T^0 qui se change en formation cinétiquement limitante de T à des pH plus faibles. Ce dernier mécanisme est préféré pour la cyclisation du **2**-NPU.

Mots clés : effet *gem*-diméthyle, mécanisme, catalyse générale par les bases, transfert de proton, empêchement stérique.

[Traduit par la Rédaction]

Received December 2, 1998.

This paper is dedicated to Jerry Kresge in recognition of his many achievements in chemistry.

I.B. Blagoeva, A.H. Koedjikov, and I.G. Pojarlieff.[1] Institute of Organic Chemistry, Bulgarian Academy of Sciences, ul. Acad. G. Bonchev block 9, Sofia 1113, Bulgaria.
A.J. Kirby. University Chemical Laboratory, Cambridge CB2 1EW, U.K.

[1]Author to whom correspondence may be addressed. Telephone: +359-2-7334-116. Fax: 359-2-700-225. e-mail: ipojarli@orgchm.bas.bg

 © 1999 NRC Canada

Introduction

The hydroxide ion catalyzed cyclization of ethyl 2,2,3-trimethyl-5-phenyl hydantoate, **3**-PUE, is slower than that of the dimethyl compound **2**-PUE (1). This result is surprising because the reaction of **3**-PUE should be subject to the *gem*-dimethyl effect (2): indeed, a normal *gem*-dimethyl effect operates on the acid-catalyzed cyclizations of these compounds (**1**-PUE–**3**-PUE) (3, 4). Data on the general acid-base catalysis and solvent kinetic isotope effects (SKIE) on PUE and their 5-methyl analogues (**1**-MUE–**3**-MUE) led us to the conclusion that the loss of the *gem*-dimethyl effect was due to steric hindrance to proton transfer of the leaving ethoxide group, resulting in a change in the rate-determining step (r.d.s.) from formation to breakdown of the tetrahedral intermediate (3). The balance of evidence as to which r.d.s. is preferred, with the less heavily substituted compounds changing into an alternate one in the fully methylated derivatives, was delicate and thus further evidence was sought for these systems. The improved leaving group ability of the *p*-nitrophenylureido group was intended to bias the system towards rate-determining departure of the ethoxy group, thus allowing a simpler evaluation of the various effects. Grounds for such reasoning were the alternative cyclizations of dicarbamoylglycine **4**: the specific base-catalyzed (SBC) ring closure with the *N*-isopropylcarbamoyl moiety was attributed to r.d. attack of the anion while the GBC reaction involved the end aryl group to r.d. departure of the hydroxy group (5).

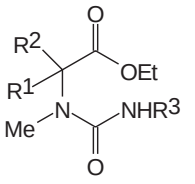

	R^1	R^2		R^3
1	H	H	MUE	Me
2	Me	H	PUE	Ph
3	Me	Me	NPU	4-nitrophenyl

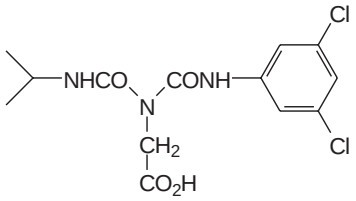

4

Unexpectedly, the hydroxide-catalyzed reaction of the *p*-nitrophenyl esters mirrored the behaviour of the ureido esters with less negative ω-substituents, showing only a small increase in rate with **3**-NPU compared to a large one under acid catalysis, and a normal SKIE opposed to the inverse one with **1**-NPU and **2**-NPU. In contrast to MUE and PUE, however, the *p*-nitrophenyl derivatives showed highly complex rate profiles, varying extensively upon methyl substitution.

We now report how this interplay of the *gem*-dimethyl effect and reaction mechanism can be understood from an analysis of the reaction profiles, general base catalysis, and SKIE. The results obtained support our previous interpretation of the loss of the *gem*-dimethyl effect in the HO^--catalyzed cyclization in esters **3** and allow further insight into the workings of the *gem*-dimethyl effect in reactions through tetrahedral intermediates.

Experimental

Materials

Inorganic reagents and buffer components were of analytical grade and were used without further purification. Potassium hydroxide and buffer solutions were prepared with CO_2-free distilled water. D_2O and DCl (20 wt.% in D_2O), 99 at.% were from Aldrich.

Ethyl esters of methyl substituted 5-(4-nitrophenyl)hydantoic acids were prepared by reaction of the corresponding amino acid esters with 4-nitrophenyl isocyanate. The amino acid esters were converted into the free base form and distilled prior to use. The typical experimental procedure consisted in addition of 10% excess of 4-nitrophenyl isocyanate (3.3 mmol in 5 mL dry benzene) to an ice-cooled solution of the amino acid ester (3 mmol in 5 mL dry benzene). A heavy precipitate was formed immediately and the reaction mixture was left for 20 min at room temperature. The precipitated product was filtered, washed with dry benzene, and dried in a vacuum desiccator with P_2O_5. The products could not be heated or recrystallized due to their fast cyclization at higher temperatures. **3**-NPU cyclized readily in the presence of traces of moisture and was best stored in sealed ampoules at low temperatures. The purity of the products was checked by NMR and the yields of pure esters were 62–64%.

*Ethyl 3-methyl-5-(4-nitrophenyl)hydantoate (**1**-NPU)*: mp 124–125°C. IR $\nu_{max}(CHCl_3)/cm^{-1}$: 1727 (CO ester), 1676 (CO ureido). ^1H NMR ($CDCl_3$) δ (ppm): 1.31 (t, *J* 7.1 Hz, 3H, CH_3CH_2), 4.15 (s, 2H, N-CH_2), 3.16 (s, 3H, CH_3N), 4.25 (q, *J* 7.1 Hz, 2H, CH_2O), 7.08 (s, 1H, HN), 7.54–8.19 (m, 4H, Ar).

*Ethyl 2,3-dimethyl-5-(4-nitrophenyl)hydantoate (**2**-NPU)*: mp 130–131°C. IR $\nu_{max}(CHCl_3)/cm^{-1}$: 1727 (CO ester), 1672 (CO ureido).^1H NMR (CDCl) δ (ppm): 1.30 (t, *J* 7.2 Hz, 3H CH_3CH_2), 1.49 (d, *J* 7.35 Hz,, 3H CH_3CH), 3.04 (s, 3H, CH_3N), 4.23 (q, *J* 7.2 Hz, 2H, -CH_2O), 5.04 (q, *J* 7.35 Hz 1H,-CHN), 6.99 (s, 1H, HN), 7.56–8.20 (m, 4H, Ar).

*Ethyl 2,2,3-trimethyl-5-(4-nitrophenyl)hydantoate (**3**-NPU)*: mp 125–127°C. IR $\nu_{max}(CHCl_3)/cm^{-1}$: 1725 (CO ester), 1670 (CO ureido). ^1H NMR (CDCl) δ (ppm): 1.29 (t, *J* 7.1 Hz, 3H, CH_3CH_2), 1.51 (s, 6H, $(CH_3)_2C$), 3.07(s, 3H, CH_3N), 4.21 (q, *J* 7.1 Hz, 2H, CH_2O), 7.28 (s, 1H, HN), 7.49–8.34 (m, 4H, Ar).

Product analysis

The cyclizations of the ethyl hydantoates studied in this paper proceeded quantitatively to the corresponding hydantoins. Good isosbestic points were obtained for all three compounds studied and the end-point absorbances for the kinetic runs were identical within experimental error with the absorbances of model solutions of the respective hydantoins described previously (6).

Kinetic measurements

Rate constants were determined at 25.0 ± 0.01°C under pseudo-first-order conditions in the thermostatted cell com-

© 1999 NRC Canada

Fig. 1. Rate profiles for the cyclization of **1**-NPU (○) and **2**-NPU (△).

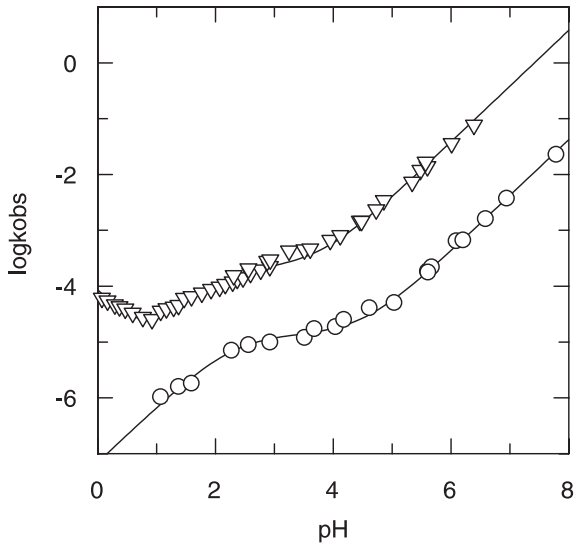

partment of a Unicam SP-800 spectrophotometer. The rates of cyclization of the substituted esters were followed by monitoring the decrease of the absorbance at 330 nm due to the 4-nitrophenylureido group. Reactions were initiated by injecting 20 mL of 1×10^{-2} M stock solutions of the substrates in dry THF into 2.7 cm^3 of preheated buffer solution. Ionic strength was maintained constant (1.0 M) with KCl. Measurements of pH values and calculations of the observed pseudo-first-order rate constants (k_{obs}) were as previously described (7). Good linear plots ($r > 0.999$) of $\ln(A_t - A_\infty)$ against time were obtained over three half-lives and k_{obs} values were reproducible to within 3% with the exception of the slow ring closure of **1**-NPU in hydrochloric acid below pH 2 where the hydrolysis of the ester group was significant. Since the product acids cyclized more rapidly than the esters, plots of $\ln(A_t - A_\infty)$ against time sloped downwards with time. In this case the rate constants were obtained from the initial part of the reaction where linearity was preserved: initial rates in 0.1 M Hcl up to ca. 20% conversion in 0.01 M HCl.

Solvent kinetic isotope effects

The solvent kinetic isotope effects (SKIE) for k_H were determined by comparison of k_{obs} values measured in solutions of HCl or DCl of the same concentration. The k_{OH} values for calculation of SKIE were determined by extrapolation to zero buffer concentrations of k_{obs} in phosphate or cacodylate buffers both in H_2O and D_2O. For the hydroxide-catalyzed reaction k_0 values were divided by the activity of HO^- or DO^- to obtain k_{OH} or k_{OD}. pD values were obtained by adding 0.4 to the pH-meter readings and the a_{OD} values were calculated using $pK_w = 14.86$ (8).

Results and discussion

Rate profiles

1. Base catalysis

With ureido ester **1**-NPU the slope of the plot of log k_{obs} versus pH changes from 1 to 0 and then back again to 1 (Fig. 1).

Fig 2. Rate profile for the cyclization of **3**-NPU.

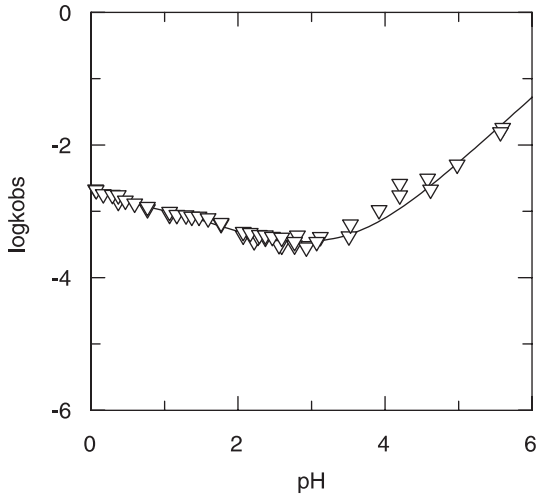

Scheme 1.

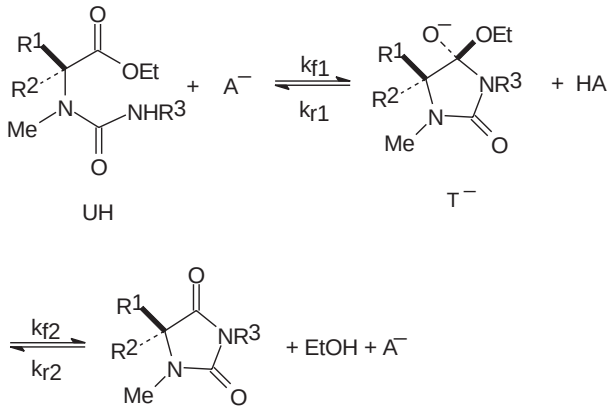

Below pH = 1, hydrolysis of the ester group was observed and acid catalysis could not be detected. With the faster cyclization of compound **2**-NPU the reaction could be studied up to 1 M HCl and an acid-catalyzed region could be registered in addition to base catalysis. The latter is also best described by equations leading to the same changes of slopes against pH, from 1 to 0 and back again to 1. The minimum between the acid-catalyzed and base-catalyzed regions occurs around pH = 1, illustrating the very poor nucleophilicity of the neutral *p*-nitrophenylureido group. The same minimum occurs around pH 3 with **2**-PUE (3).

The behaviour of ester **3**-NPU, presented separately in Fig. 2 to avoid overlap in the base-catalyzed region, is distinctly different: only one segment, first order in $[OH^-]$, is observed, while the acid catalysis region is complex.

The rate law for base catalysis can be derived from Scheme 1, depicting the main steps in the reorganization of bonds from reactants to products.

The steady state solution is

$$[1] \qquad k_{obs} = \frac{k_{f1}[A^-]k_{f2}[HA]}{(k_{r1} + k_{f2})[HA]}$$

When the bases are water and hydroxide ion this becomes

© 1999 NRC Canada

Table 1. Kinetic solvent isotope effects for ring closure of methyl substituted ethyl 5-(4-nitrophenyl)hydantoates at 25°C

Substrate	[LCl] mol dm^{-3}	$(k_H / k_D)_{obs}$	pH (H)	k_{OH} / k_{OD}
1-NPU	0.002	2.9	5.60[a]	0.78
	0.005	2.4		
	0.01	1.8		
2-NPU	0.005	3.0	5.57[b]	0.6
	0.01	2.9		
	0.90	0.8		
3-NPU	0.005	2.5	5.62[b]	1.8
	0.01	2.6	5.82[c]	1.9
	0.90	1.1		

[a]Cacodylate buffer 20% base.
[b]Phosphate 10% base.
[c]Phosphate 15% base.

$$[2] \qquad k_{obs} = \frac{(k_{f1w} + k_{f1OH}[OH^-])(k_{f2w} + k_{f2H}[H^+])}{k_{r1w} + k_{f2w} + (k_{r1H} + k_{f2H})[H^+]}$$

*1(a). Ethyl hydantoates **1**-NPU and **2**-NPU*: Various limiting conditions lead to simplified forms of eq. [2], describing rate profiles with slopes changing from 1 to 0 and then back to 1. In the following discussion[2] we designate the apparent second-order constant at lower pH as $k_{OH}{}^a$ and the one at higher pH as $k_{OH}{}^b$. Two conditions have to be met (9) in order that two different k_{OH} are observed in situations described by eq. [2]. The first is that the two forward fractions for breakdown of T^-, $k_{f2}/(k_{r1} + k_{f2})$, for H_2O and H^+ catalysis, respectively, have to be different. The first one will operate at higher pH and the second one at lower pH. Two different reactions of the same order are usually associated with a change in the rate-determining step; in the case under discussion, when $k_{r1w} < k_{f2w}$ then $k_{r1H} > k_{f2H}$ or vice versa. The second condition for two reactions of the same order to be observed is that the intermediates involved should not equilibrate. In such a case the reactions go simply by the lowest energy path available to, for example, T^-, which in turn corresponds to single first order in the $[OH^-]$ region in the rate profile. In our case two different k_{OH} can be observed when one or both processes are general acid–base catalyzed.

As is generally the case for kinetically equivalent mechanisms, the preference must be based on non-kinetic evidence. Comparison of the rate profiles of Figs. 1 and 2 with the SKIE data listed in Table 1 shows that the $k_{OH}{}^a$ values for **1**-NPU and **2**-NPU, as well as the single k_{OH} constant for **3**-NPU, exhibit normal isotope effects ($k_H > k_D$) These allow a choice between various possible mechanisms. The similarity in the p*K*'s of the *p*-nitrophenylureido group and water, the conjugate acid of OH^-, could give rise to a normal SKIE (10) for proton removal from nitrogen (a p*K* of 14 has been reported for *p*-nitrophenylurea (11)). However, if this step was rate determining, a Brønsted β value of 1 is expected, contrary to the observed values of 0.5–0.6 (vide infra Table 6). Such a deprotonation would be diffusion controlled and would certainly be much faster than the overall rates in at least two of the cases; second-order constants of ca. 10^6–10^7 dm^3 mol^{-1} s^{-1} are observed for the $k_{OH}{}^a$ of **1**-NPU and for the k_{OH} of **3**-NPU (Table 2). Participation of OH^- in a concerted process in which the N—C bond is formed while the NH proton is pulled off (formula **5**, B = OH^-) is also unlikely because, according to the libido rule of Jencks (12), the base has to be of strength intermediate between that of the proton-donating group in the ground and product states. The alternative SB-GAC mechanism for N—C formation, i.e., attack of the ureide anion concerted with proton transfer

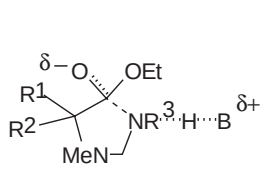

5

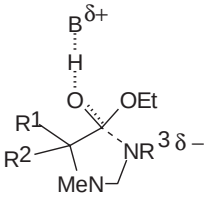

6

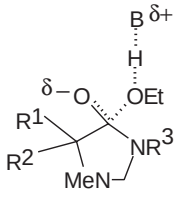

7

to the ester carbonyl leading to T^0 (formula **6**, B = OH^-) was refuted (3) for the ω-methyl and ω-phenyl analogues MUE and PUE as it contradicts Jencks' requirement for T^- to be an unstable intermediate (13); this apparently applies also for NPU to permit the SBC catalyzed reaction of **1**-NPU and **2**-NPU presented by $k_{OH}{}^b$, discussed below. We are thus left with the last possible proton transfer as the cause of the normal SKIE, that is, water donating a proton to the ethoxy group cleaving from T^- (formula **7**, B = OH^-). As discussed before (3), a concerted mechanism is possible with a late C—O bond cleavage. In terms of Scheme 1 and eq. [2], this mechanism requires $k_{r1} > k_{f2}$. The process $k_{OH}{}^a$ is observed at low pH when $k_{r1w} + k_{f2w} < (k_{r1H} + k_{f2H})[H^+]$ so the inequality $k_{r1H} > k_{f2H}$ will apply. When $k_{f1w} > k_{f1OH}[OH^-]$ and if $k_{f2w} > k_{f2H}[H^+]$ in the region for base catalysis, the observed rate constant becomes

$$[3] \qquad k_{obs} = \frac{k_{f1w}k_{f2w}}{k_{r1H}[H^+]}$$

The rate constant first order in $[OH^-]$ at low pH can be then be presented as

$$[4] \qquad k_{OH}^a = \frac{K_{T^-}k_{f2w}}{K_w}$$

where k_{T^-} is the equilibrium constant for formation of T^- when $A^- = H_2O$. Thus at low pH the first order in $[OH^-]$ behaviour is determined by the equilibrium concentration of T^-, and the rate-determining step is the water-catalyzed decomposition of T^-. Such a mechanism is referred to as acid inhibition of T^- (14).

[2]For the sake of brevity exhaustive consideration of the various cases afforded by eq. [2] will be avoided.

© 1999 NRC Canada

Table 2. Rate constants for H^+, OH^-, and H_2O catalyzed ring closure of ethyl 5-(4-nitrophenyl)hydantoates at 25°C and ionic strength 1.0 M.

Compound	k_{OH}[b] $dm^3\ mol^{-1}\ s^{-1}$	k_{OH}[a] $dm^3\ mol^{-1}\ s^{-1}$ [b]	$k_w\ s^{-1}$	$k_{2H}\ dm^3\ mol^{-1}\ s^{-1}$	$k_{1H}\ dm^3\ mol^{-1}\ s^{-1}$
1-NPU[a]	(4.23±0.22) × 10^4	(6.94±0.69) × 10^6	(1.36±0.11) × 10^{-5}	196±30	
2-NPU[c]	(3.85±0.20) × 10^6	(2.07±0.019) × 10^8	(2.18±0.16) × 10^{-4}	107±16	(8.34±0.61) × 10^{-5}
	k_{OH}	$k_{1w}\ s^{-1}$	$k_{2w}\ s^{-1}$		
3-NPU[d]	(5.20±0.37) × 10^6	(1.10±0.18) × 10^{-3}	(2.46±0.37) × 10^{-1}	35.2±16.9	(1.21±0.36) × 10^{-3}

[a]Equation [5].
[b]$k_w / k_{2H}K_w$.
[c]Equation [6].
[d]Equation [12].

Scheme 2.

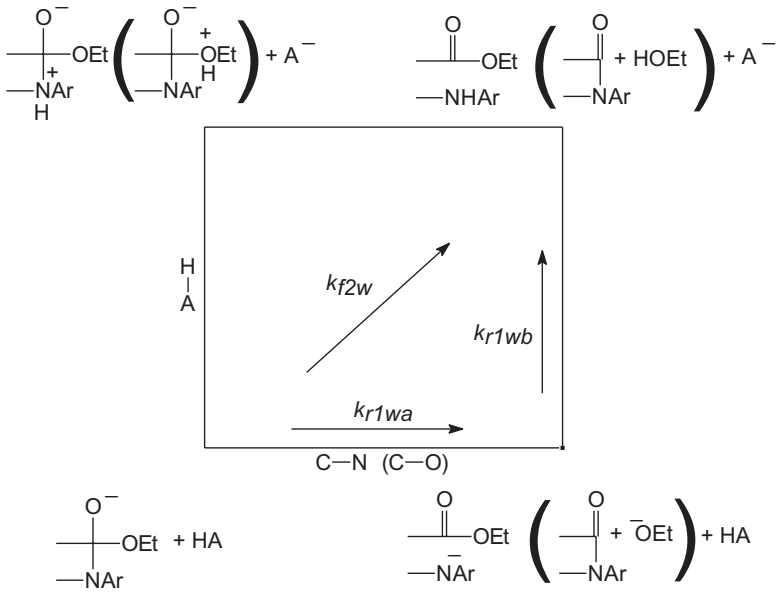

Upon increasing the pH, the plateau is reached with **1**-NPU and **2**-NPU when the $[H^+]$ term in the denominator can be neglected. Now $k_{obs} = k_{f1w}$ because, as discussed above, $k_{r1w} < k_{f2w}$ in order for the second slope of 1 in the rate profile to be observed at higher pH. Then $k_{obs} = k_{f1OH}[OH^-]$. With the above limitations eq. [2] can be simplified to

$$[5] \qquad k_{obs} = \frac{k_w + k_{OH}[OH^-]}{1 + k_{2H}[H^+]}$$

where $k_{OH} = k_{OH}^b = k_{f1OH}$, $k_w = k_{f1w}$, $k_{2H} = k_{r1H}/k_{f2w}$, and $k_{OH}^a = k_w/(k_{2H}K_w)$. The rate constants for **1**-NPU in Table 2 were obtained by fitting the rate data to eq. [5]. In the case of **2**-NPU the equation was expanded with a term for acid catalysis.

$$[6] \qquad k_{obs} = \frac{k_w + k_{OH}[OH^-]}{1 + k_{2H}[H^+]} + k_{1H}[H^+]$$

The $k_{OH}{}^b$ constants for **1**-NPU and **2**-NPU refer to an SBC process as evidenced by the inverse isotope effect at pH = 5.6 where, according to Fig. 1, the second first order in $[OH^-]$ process dominates. Because, as already discussed, $k_{r1w} < k_{f2w}$, this is r.d. formation of T^- taking place by preliminary ionization of the ureido esters.

The crossover of reactivities for H_2O and H_3O^+ catalysis of partitioning of the intermediate is an interesting problem. The inequality $k_{r1w} < k_{f2w}$ means that *p*-nitrophenylureido leaves less readily than ethoxide at high alkalinity against expected fugacities while the opposite is true at low pH ($k_{r1H} > k_{f2H}$). The reason for the former inequality can be sought in reactivities of stepwise vs. concerted processes (15). The acid-catalyzed breakdown of T^- can be described by the alternate route diagram (16) shown in Scheme 2. When HA = H_2O, the leaving of the ureido group is a two-step process along the edges of the diagram: splitting off of the ureide anion, $k_{r1w}{}^a$, followed by proton transfer from H_2O to the nitrogen atom, $k_{r1w}{}^b$. This is not a concerted process for reasons discussed above explaining why OH^- cannot act as a general base in the reverse reaction and, in terms of the alternate route diagram, this happens because the energy of the bottom right-hand corner is considerably lower than that of the top-left corner. On the other hand, as discussed above for **3**-NPU, the ethoxy group cleaves along the diagonal in a one-step process with both bonds changing simultaneously, k_{f2w}. This occurs because the energy of the bottom-right corner is raised, ethanol being a weaker acid by more than two p*K* units, and that of the top-left corner is lowered because of the greater basicity of the ethoxy group. Thus a valley along the diagonal is created, with the energy of the transition state apparently lower than that for the attack of the ureide anion.

When HA = H_3O^+ the relationships in the diagram change significantly. Considered in the reverse direction, the

© 1999 NRC Canada

Scheme 3.

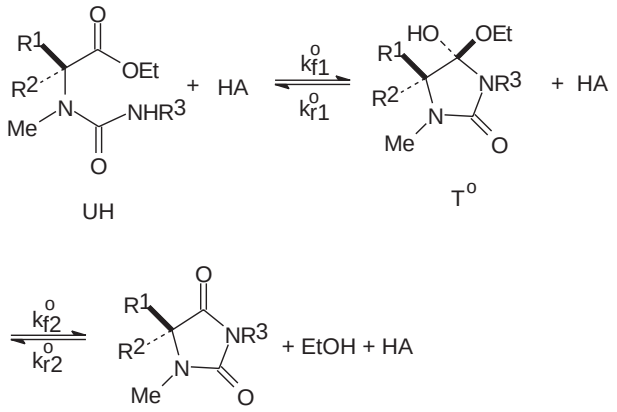

deprotonation by water along the right-hand edge is now quite an uphill reaction, offering no easy bypassing of the zwitterions at the top-left corner. These are highly unstable and so will enforce general catalysis. This applies to both reactions, k_{r1H} and k_{f2H} and, when the mechanism is the same, the intrinsically better fugacity of the *p*-nitrophenylureido group determines reactivity.

*1(b). Ethyl hydantoate **3**-NPU*: In contrast to **1**-NPU and **2**-NPU, the rate profile of **3**-NPU (Fig. 2) is characterized by a single rate constant first order in [OH^-]. This implies that the partitioning ratios for water and H^+ catalyzed breakdown of T^- of **3**-NPU are biased in the same way, i.e., no change in the r.d.s. takes place. Why **3**-NPU is different can be understood by comparing with previous results on MUE and PUE (3). The inverse SKIE observed with the $k_{OH}{}^b$ constants for **1**-NPU and **2**-NPU and the normal effect with the k_{OH} constant for **3**-NPU repeat the pattern of **1**–**3**-MUE and PUE. Significant also is the disappearance of the *gem*-dimethyl effect with the k_{OH} of **3**-NPU: in contrast to acid catalysis, where **3**-NPU reacts 15 times faster than **2**-NPU, the rates in the higher pH region are almost the same (Table 2). The change of mechanism brought about by the introduction of the extra methyl group in **3**-MUE or **3**-PUE was explained by steric hindrance to protonation of the oxygen atom of the ethoxy group. The ester ethyl group will adopt the least crowded conformation, blocking easy protonation of the ethoxy oxygen because its lone pairs are effectively shielded in a half-chair conformation by the methyl groups on C-5 and the aryl ring on N-2 (see **8**; for clarity, one of the methyl groups at C-5 in the formula is represented by a single bond).

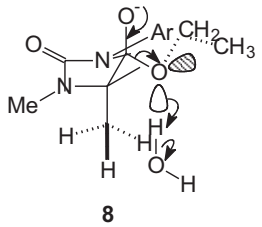

8

Thus there is good reason to believe that, for **3**-NPU, steric hindrance to protonation determines r.d. breakdown of T^-, concerted with catalysis by water. When the ethyl group is replaced by hydrogen, as is the case with the respective hydantoic acids, the intermediate becomes less crowded and slowing down is no longer observed.[3] The GBC cyclization of thioureido esters (17) and the above-mentioned (5) GBC cyclization of the aryl moiety of the *N*,*N*-dicarbamoylglycine **4** are also believed to be limited by breakdown of T^-.

2. Acid catalysis

The complex course for acid catalysis of the cyclization of **3**-NPU can be accommodated by an equation predicting four regions of slopes 0, –1, 0, and –1 in the rate profile on decreasing pH. Such an equation can be derived from Scheme 3, similar to Scheme 1, involving H^+ and water-catalyzed formation and decomposition of T^0.[4] This would then yield an equation in the format of eq. [2], the superscripts 0 denoting that they are related to T^0.

$$[7] \qquad k_{obs} = \frac{(k^0_{f1w} + k^0_{f1H}[H^+])(k^0_{f2w} + k^0_{f\,2H}[H^+])}{(k^0_{r1w} + k^0_{f\,2w}) + (k^0_{r1H} + k^0_{f\,2H})[H^+]}$$

To describe the rate profile for acid catalysis we chose the combination $k^0_{r1w} > k^0_{f\,2w}$ and $k^0_{r1H} < k^0_{f2H}$ because when [T^-] reaches equilibrium (as assumed in the preferred mechanism for k_{OH} of **3**-NPU) so should [T^0] and the constants for water catalysis are important in the overlapping region. So when all the [H^+] terms are small one gets

$$[8] \qquad k_{obs} = \frac{k^0_{f1w}k^0_{f\,2w}}{k^0_{r1w} + k^0_{f\,2w}} \approx K_{T^0}k^0_{f\,2w}$$

Equation [8], the water-catalyzed decomposition of T^0, is kinetically equivalent to another pathway: the H^+-catalyzed decomposition of T^-, $k_{obs} = K_{T-}\,k_{f2H}$, and the latter is most probably a more efficient one.

After the plateau described by eq. [8], most likely the adjoining slope of –1 is due to acid-catalyzed decomposition of T^0:

$$[9] \qquad k_{obs} = K_{T^0}k^0_{f2H}[H^+]$$

followed by a change in the rate-determining step when $(k^0_{r1w} + k^0_{f2w}) < (k^0_{r1H} + k^0_{f2H})[H^+]$:

$$[10] \qquad k_{obs} = k^0_{f1w}$$

This formally acid-catalyzed reaction according to Scheme 3 is also most likely the kinetically equivalent general base catalysis by water.

Finally, when $k_{f1w} < k_{f1H}[H^+]$

$$[11] \qquad k_{obs} = k^0_{f1H}[H^+]$$

The rate profile can then be described by eq. [12]:

$$[12] \qquad k_{obs} = \frac{(k_{1w} + k_{1H}[H^+])(k_{2w} + k_{2H}[H^+])}{1 + k_{2H}[H^+]} + k_{OH}[OH^-]$$

$$k_{OH} = \frac{k_{T^-}k_{f2w}}{K_w};\ k_{2w} = K_{T^-}k_{f2H} \text{ or } = K_{T^0}k^0_{f2w};\ k_{2H} = K_{T^0}k^0_{f2H};$$
$$k_{1w} = k^0_{f1w};\ k_{1H} = k^0_{f1H}.$$

[3] To be published.

[4] Catalysis by H^+ can be formally assumed to produce T^o as T^+ loses proton to bulk water under diffusion control.

© 1999 NRC Canada

Fig. 3. Plot of k_{buf} against fraction base in acetate buffers for **2**-NPU.

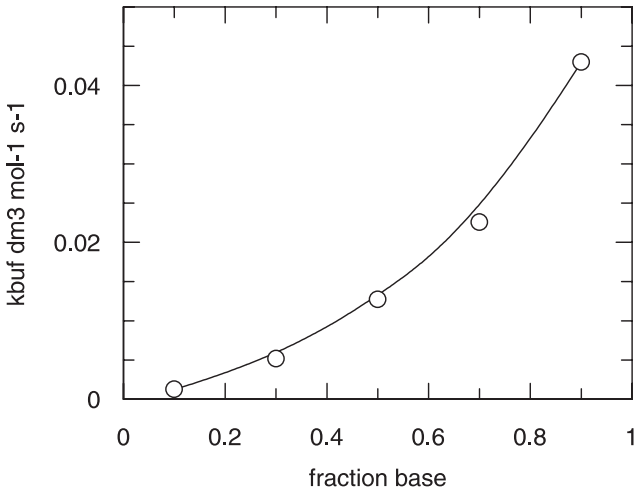

The above assignments of mechanism agree well with the SKIE values listed in Table 1. In 0.90 M LCl it is 0.8 for **2**-NPU. This value applies for a "clean" reaction and is the same as the values of 0.7–0.8 found for ω-phenylhydantoic esters.(4) This and other evidence with the latter (4) supported rate-determining formation of T via the transition state **9**:

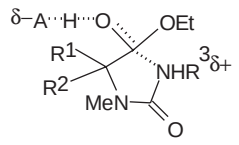

9

The somewhat larger SKIE value of 1.1 for **3**-NPU does not contradict the conclusion for k_{f1H} as rate determining at the highest acidity because it is most probably enlarged by contribution from the water-catalyzed reaction. According to Table 1, effects of about 2.5–3 are observed at lower [LCl] with **2**-NPU and **3**-NPU.

3. General base catalysis

In contrast to the case of ω-phenylureido esters where GC was clearly expressed only in the case of **3**-PUE and difficult to establish with the remaining compounds, the effect of buffer catalysis was significant and could be readily monitored with all three *p*-nitrophenylureido derivatives.

Corrections for buffer failure were carried out as pH varied strongly at low fractions of base in acid phosphate and glycine buffers. Changes in pH were satisfactorily reproduced by solving the equation for the ionization

$$K_{AH} = \frac{(C_A - a_H)a_H}{(C_{AH} + a_H)}$$

where K_{AH} is the dissociation constant at I = 1 M KCl according to ref. 7, C_A and C_{AH} are the concentrations as weighed, and the actual concentration of the buffer components may be approximated as $[A^-] = C_A - a_H$, and $[AH] = C_{AH} + a_H$.

Fig. 4. Plot of k_{buf} against fraction base for **1**-NPU in neutral phosphate. Insert excluding data for 0.9 fraction base.

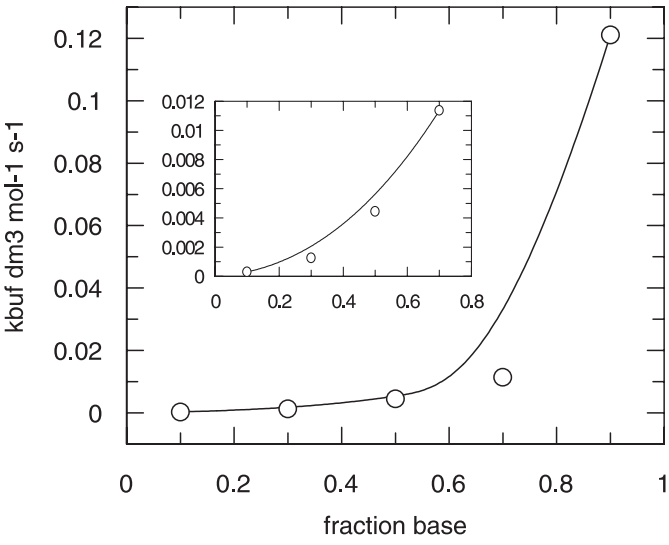

Plots of k_{buf} vs. fraction (of) base were convex to a varying degree. The "nonlinear" behaviour is illustrated by the examples in Figs. 3 and 4.

This nonlinearity is appreciable when a wide range of buffer ratios are studied. With narrow ranges it is indicated by the negative intercepts in plots of k_{buf} vs. fraction base. A solution was sought by means of equations derived from Scheme 1. When a general base is included in Scheme 1, the full steady state treatment yields a complex solution that can reasonably be analyzed only under simplifying assumptions. The constants for general base catalysis were obtained by nonlinear regression curve fitting of the equations shown below. The parameters describing the rate profile as a function of pH were fed in as known constants. A series of equations were tried: only those that gave good fits will be discussed. Unless stated otherwise, all equations used have a $1 + k_{2H}[H^+]$ term in the denominator; k_{2H} from the rate profiles (Table 2) varies from around 200 in **1** to 30 in **3**, which means that at pH > 3 its influence becomes negligible.

In cases when the general base is HPO_4^{2-} we found previously (3) that upward trends at high buffer ratios are described well by the addition of a $k_{BOH} \times [B] \times [OH^-]$ term interpreted as PO_4^{3-} catalysis. An extensive series of data in neutral phosphate for ester **1** was treated by means of eq. [13]:

$$[13] \qquad k_{obs} = \frac{k_w + k_{OH}[OH^-] + k_B[B] + k_{BOH}[OH^-][B]}{1 + k_{2H}[H^+]}$$

(The k_H term is negligible in neutral phosphate.) This equation gave the very good fit as illustrated in Fig. 5, which compares the experimental with the calculated points (eq. [14] is a multivariable function and cannot be presented as a two-dimensional graph).

The rate constant for catalysis for PO_4^{3-} is obtained as $k_{PO_4^{3-}} = k_{BOH}K_w/K_{HPO_4^{2-}}$.

Alternately the deviations from linearity could be described by equations including a k_{BH} term in the denominator. The following two equations proved most useful with

© 1999 NRC Canada

Table 3. Buffer catalysis data for the cyclization of ethyl 3-methyl-5-(4-nitrophenyl)-hydantoate, **1**-NPU, at 25°C and ionic strength 1.0 M.

Buffer acid	pK_{AH}[a,b]	Conc. range mol dm^{-3}	Runs	% base	10^4 k_B dm^3 mol^{-1} s^{-1}[b]	10^4 $k_{2BH}(k_{1BH})$ dm^3 mol^{-1} s^{-1}
H_3O^+	–1.74				0.136 ± 0.011[c]	
	(–1.26)					
$H_3N^+CH_2CO_2H$	2.45	0.1–0.5	3	30	0.274 ± 0.067[d]	27 000 ± 18 000
		0.1–0.5	3	50		(0.32 ± 0.17)
		0.1–0.5	3	70		
		0.1–0.5	3	90		
HCO_2H	3.57	0.01–0.5	4	50	2.77 ± 0.13[d]	21 500 ± 2600
		0.01–0.5	4	70		(0.432 ± 0.189)
CH_3CO_2H	4.62	0.1–0.5	4	30	7.28 ± 0.19[e]	5000 ± 2.9800
		0.1–0.5	4	50		
		0.1–0.5	4	70		
$(CH_3)AsO_2H$	6.19	0.01–0.3	4	20	56.7 ± 2.8[f]	
		0.01–0.3	4	30		
		0.01–0.4	5	50		
$H_2PO_4^-$	6.48	0.016–0.2	4	10	42.7 ± 3.1[g] (21.3)	
		0.016–0.5	4	30		
		0.016–0.5	9	50		
		0.016–0.4	8	70		
		0.016–0.35	5	90		
HPO_4^{2-}	12.32				978 000[h]	
	(11.84)				(326 000)	
H_2O	15.74				(4.23 ± 0.22) × 10^8	
	(16.04)					

[a] pK_{AH} values from ref. 7.
[b] Statistically corrected values in parentheses.
[c] First-order rate constant.
[d] Equation [15].
[e] Equation [14].
[f] Equation [5] + k_B[B].
[g] Equation [13].
[h] Calculated from k_{BOH}.

compounds **1**-NPU and **2**-NPU. They derive from eq. [1] under certain conditions.

$$[14] \quad k_{obs} = \frac{k_w + k_{OH}[OH^-] + k_B[B]}{1 + k_H[H^+] + k_{2BH}[BH^+]}$$

$$[15] \quad k_{obs} = \frac{k_w + k_{OH}[OH^-] + k_B[B] + k_{1BH}[BH^+]}{1 + k_H[H^+] + k_{2BH}[BH^+]}$$

In the case of ester **2**-NPU the term for H^+ catalysis was added as in eq. [6].

Equation [14] is an extension of eq. [5], derived by assuming that k_{BH} behaves as k_{2H} in the case of **1** and **2**, that is, $k_{r1BH} > k_{f2BH}$ and $k_{f2BH}[BH^+] < k_{f2w}$ in the range studied. Then $k_B = k_{f1B}$ and $k_{2BH} = k_{r1BH}/k_{f2w}$ ($k_{f2w} > k_{r1w}$). The increase of $k_{2BH}[BH^+]$ with the decrease of fraction base will cause at the same time $_{kbuf}$ to decrease faster than demanded by a linear function. These assumptions mean that k_B is involved in the formation of T^- and can be measured directly as long as formation of T^- is r.d. for the overall reaction. When k_{2BH} $[BH^+]$ becomes greater than $1 + k_H[H^+]$ there is a change in the r.d.s.; actually eq. [14] predicts reaching the situation determined by eqs. [3] and [4], the first step becoming an equilibrium and T^- giving products by k_{f2w}.

Fig. 5. Logarithms of the first-order rate constants for cyclization of **1**-NPU in neutral phosphate: (○) experimental data, (●) theoretical points obtained by means of eq. [14] and parameters in Tables 2 and 3.

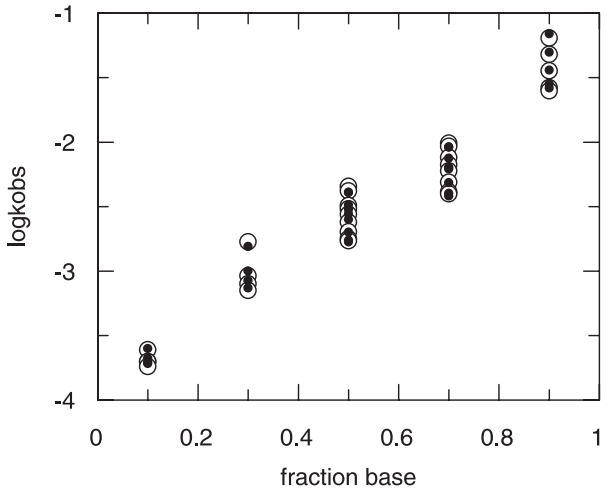

Equation [15] improves the fit further in some cases. The term k_{1BH} $[BH^+]$ in the numerator could either be due to

© 1999 NRC Canada

Table 4. Buffer catalysis data for the cyclization of ethyl 2,3-dimethyl-5-(4-nitrophenyl)-hydantoate, **2**-NPU, at 25°C and ionic strength 1.0 M.

Buffer acid	pK_{AH} [a,b]	Conc. range mol dm^3	Runs	% base	10^4 k_B dm^3 mol^{-1} s^{-1} [a,b]	10^4 k_{2BH} dm^3 mol^{-1} s^{-1}
H_3O^+	–1.74				2.18 ± 0.16[c]	
	(–1.26)					
H_3PO_4	1.78	0.01–1	6	30	16.1 ± 2.0[d]	120 000 ± 21 300
	(2.26)	0.01–1	6	50		
		0.1–1	5	70		
		0.1–1	5	90		
$H_3N^+CH_2CO_2H$	2.45	0.1–1	3	50	12.7 ± 1.3[d]	22 400 ± 5500
		0.1–1	3	70		
		0.1–1	3	90		
HCO_2H	3.57	0.01–0.2	4	30	65.9 ± 5.6[e]	
		0.01–0.2	4	50		
		0.01–0.2	4	70		
		0.01–0.2	4	90		
CH_3CO_2H	4.62	0.05–0.2	3	10*	533 ± 64[d]	78 800 ± 19 100
		0.01–0.2	4	30		
		0.01–0.2	4	50		
		0.01–0.2	4	70		
		0.05–0.2	3	90		
$(CH_3)AsO_2H$	6.19	0.01–0.15	4	10	1930 ± 170[e]	
		0.01–0.15	4	20		
		0.01–0.15	4	30		
		0.01–0.15	4	50		
		0.01–0.15	4	70		
H_2O	15.74				(3.85 ± 0.20) × 10^{10}	
	(16.04)					

[a] pK_{AH} values from ref. 4.
[b] Statistically corrected values in parentheses.
[c] First-order rate constant.
[d] Equation [14].
[e] Equation [6] + k_B[B].

$k_{f2BH}[BH^+]$ not being negligible in eq. [1] and result from $k_{f1w} \times k_{f2BH}$. Independent GAC is another possibility.

However, within the experimental data available for compounds **1** and **2**, a definite choice cannot be made between eqs. [14] and [15]. Equation [15] performed better with **1**-NPU but there is no considerable improvement over eq. [14]. In contrast,with ureido ester **2**-NPU eq. [14] is definitely the better choice as eq. [15] fails. With the stronger buffer bases, acid catalysis becomes unimportant. In acetate and cacodylate buffers, either a straightforward equation for GBC (adding kB × [B] to eqs. [5] or [12]) best described the results or the more complex equations gave insignificant improvement together with unrealistic additional constants.[5]

For compound **3**-NPU the following modification of eq. [12] was preferred in the case of the more acidic buffers such as acid phosphate, glycine, and formate (the latter gave large errors for the BH constants):

$$[16]\quad k_{obs} = \frac{(k_{1w} + k_{1H}[H^+])(k_{2w} + k_{2H}[H^+]) + k_B[B] + k_{1BH}[BH^+]}{1 + k_{2H}[H^+] + k_{2BH}[BH^+]} + k_{OH}[OH^-]$$

The data obtained in acetate were best described by an equation assuming independent GBC. In cacodylate and neutral phosphate only a few measurements at low fraction base could be taken due to the fast reaction and the rate constants were obtained by assuming independent GBC.

The rate constants for GBC listed in Tables 3–5 yield the Brønsted plots shown in Fig. 6. The lines drawn are linear fits obtained from the data for the general bases with pK's between 2 and 6.5. The data for ureido ester **3**-NPU in acid phosphate and glycine buffers deviate strongly from the Brønsted plot and the β-value was determined from the remaining four data points. The slopes of the lines are presented in Table 6. As observed before for the cyclization of ethyl 5-phenylhydantoates, the points for water catalysis fall on the correlation lines. It is noteworthy that the data for OH^- catalysis repeat the pattern observed with the ω-methyl and ω-phenyl analogues of compounds **1**-NPU–**3**-NPU. Esters **1**-NPU and **2**-NPU exhibit strong positive deviations while the point for **3**-NPU fits the line, a behaviour parallel to the SKIE results.

The present series of Brønsted linear relationships for three NPU hydantoates with increasing numbers of methyl groups revealed an unexpected feature: the *gem*-dimethyl effect on

[5] It should be noted also that eq. [13] on the one hand and eqs. [14] and [15] on the other give different k_B constants in principle. With eq. [13] k_B is approached at low [OH^-], while with eqs. [14] and [15] k_B is approached at high [OH^-] (low [BH^+]).

© 1999 NRC Canada

Table 5. Buffer catalysis data for the cyclization of ethyl 2,2,3-trimethyl-5-(4-nitrophenyl)-hydantoate, **3**-NPU, at 25 °C and ionic strength 1.0 M.

Buffer acid	pK_{AH} [a,b]	Conc. range mol dm^3	Runs	% base	$10^4 k_B$ dm^3 mol^{-1} s^{-1} [b]	$10^4 k_{2BH}(k_{1BH})$ dm^3 mol^{-1} s^{-1}
H_3O^+	–1.74 (–1.26)				11.0 ± 1.8[c]	
H_3PO_4	1.78 (2.26)	0.01–1	6	30	492 ± 104[d]	73 700 ± 44 200
		0.01–1	6	50		(992 ± 426)
		0.1–1	5	70		
		0.1–1	5	90		
$H_3N^+CH_2CO_2H$	2.45	0.1–1	3	30	759 ± 134[d]	60 100 ± 26 100
		0.1–1	3	50		(518 ± 258)
		0.1–1	3	70		
		0.01–1	4	90		
HCO_2H	3.57	0.1–0.5	4	30	165 ± 7.2[d]	3350 ± 2880
		0.1–0.5	4	50	172[e]	(16.3 ± 6.2)
		0.1–0.5	4	70		
CH_3CO_2H	4.62	0.01–0.5	9	30	1190 ± 40[e]	
		0.01–0.5	9	50		
		0.01–0.2	4	70		
$(CH_3)AsO_2H$	6.19	0.01–0.3	4	20	17 500 ± 1500 [f]	
$H_2PO_4^-$	6.48	0.008–0.2	8	10	14 900 ± 5100 [f]	
		0.008–0.048	4	15	(7450)	
H_2O	15.74 (16.04)				(5.20 ± 0.37) × 10^{10}	

[a] pK_{AH} values from ref. 4.
[b] Statistically corrected values in parentheses.
[c] First-order rate constant
[d] Equation [16].
[e] Equation [12] + k_B[B].
[f] See text.

Table 6. Brønsted β values for general base catalysis of the cyclization of ethyl *p*-nitrophenylhydantoates.

Compound	β	No. of points	*r*
1-NPU	0.50 [a]	5	0.9559
2-NPU	0.58	5	0.9866
3-NPU	0.63	4	0.9638

[a] If the data for neutral phosphate are discarded, a slope of 0.60 is obtained in which case the point for alkaline phosphate falls on the correlation line.

Fig. 6. Brønsted plots of the rates GBC for the cyclization of **1**-NPU (△), **2**-NPU (●), and **3**-NPU (□). See text for linear relationships.

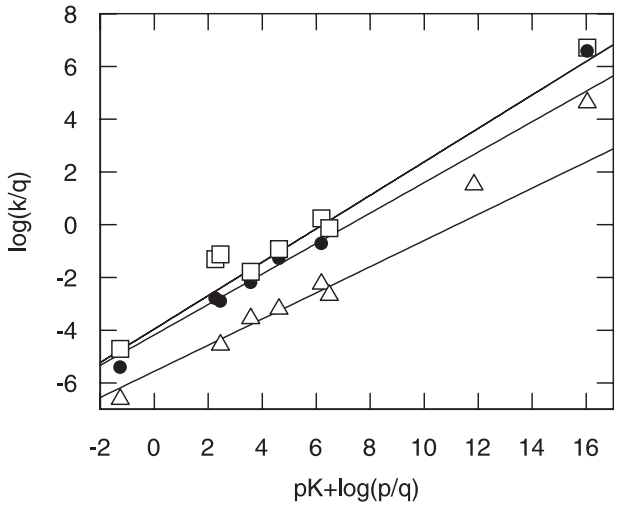

the rates for GBC showed the same saturation behaviour as observed with the OH^- catalysis. Figure 6 demonstrates how, except for the deviating points acid phosphate and glycine, the k_B values for **3**-NPU are insignificantly larger than those for **2**-NPU, though the increases for **2**-NPU over **1**-NPU amount to almost two orders of magnitude. This fact indicates that our previous conclusion (3) on the mechanism of GBC of the cyclization of ω-phenylhydantoic esters is incorrect. No data could be obtained for **1**-PUE. The similarity in the β values of ca. 0.6 for **2**-PUE and for **3**-PUE was interpreted as evidence of the same mechanism and the close catalytic constants as due to an early transition state with respect to ring formation, namely r.d. formation of T^- concerted with deprotonation of the ureido group. If the same mechanism applies to NPU, obviously it does not fit the large *gem*-dimethyl effect observed between **1**-NPU and **2**-NPU. The latter is compatible with two other possibilities. Either GBC of **3**-NPU involves a different mechanism than that of **1**- and **2**-NPU and the similar β values are accidental or all three involve GAC of the breakdown of T^-, the loss of

© 1999 NRC Canada

the *gem*-dimethyl effect with **3**-NPU being caused by steric hindrance to protonation. Actually the question can be answered within the framework of the mechanisms accepted for the rate profiles. GBC must comply with the rate-determining step of the reaction as a whole. Thus under conditions where formation of T^- is rate determining, the GBC reaction cannot proceed with r.d. breakdown unless the r.d.s. for the whole reaction is changed, a situation discussed above in relation to the curvature of the k_{obs} against fraction base plots. In the particular case of NPU, the r.d.s. in the various regions of the rate profiles are established above with a fair degree of certainty. The rate profiles (Fig. 1) indicate that the in whole region above pH 2.5 for esters **1**-NPU and **2**-NPU (the plateau and $k_{OH}{}^b$) where GBC was actually measured the reaction proceeds with rate-determining formation of T. Alternatively, under conditions where an equilibrium between reactant and T^- is established, as assumed for **3**-NPU above pH ca. 4, GBC formation of T^- cannot accelerate the reaction because the $[T^-]/[UH]$ ratio becomes time independent. Thus we have to conclude the **3**-NPU on the one hand and **1**-NPU–**2**-NPU on the other react by different mechanisms and that the similarity in β values is coincidental. Supporting evidence is the fact that the data for GBC by $H_2PO_4^{2-}$ and glycine with **3**-NPU deviate from the log k_B / p*K* correlation; in the low pH region a change in the r.d.s. is indicated by the rate profile.

Thus the best explanation for the loss of the *gem*-dimethyl effect in the GBC cyclizations of **3** appears once again to be a change to r.d. breakdown of the tetrahedral intermediate caused by steric hindrance to proton transfer as assumed by us for the OH^- catalysis of other ureido esters. Thus GBC with **1**-NPU and **2**-NPU has to be attributed to rate-determining formation of T^- concerted with deprotonation of the ureido group, structure **5**, while that with **3**-NPU to the general acid-catalyzed breakdown of T^-, structure **7**.[6]

Acknowledgments

We thank the National Foundation for Scientific Research of Bulgaria for funding this research and the Royal Society of Chemistry for a Journals Grant for International Authors (to I.G.P.).

References

1. I.B. Blagoeva, D.T. Tashev, and A.J. Kirby. J. Chem. Soc. Perkin Trans. 1, 1157 (1989).
2. C.K. Ingold. J. Chem. Soc. **119**, 305 (1921); C.K. Ingold, S. Sako, and J.F.Thorpe. J. Chem. Soc. 1117 (1922); N.L. Allinger and V. Zalkow. J. Org. Chem. **25**, 701 (1960); I.B. Blagoeva, B.J. Kurtev, and I.G. Pojarlieff. J. Chem. Soc. Perkin Trans. 2, 1115 (1979); A.J. Kirby. Adv. Phys. Org. Chem. **17**, 183 (1980); L. Mandolini. Adv. Phys. Org. Chem. **22**, 17 (1986).
3. E. Atay, I.B. Blagoeva, A.J. Kirby, and I.G. Pojarlieff. J. Chem. Soc. Perkin Trans. 2, 2289 (1998).
4. E. Atay, I.B. Blagoeva, and I.G. Pojarlieff. Dokl. Bolg. Akad. Nauk, **52**, No. 2, (1999). In press.
5. O. Belafdal, M. Bergon, M. Calmon, and J.P. Calmon. J. Org. Chem. **54**, 4193 (1989).
6. A.H. Koedjikov, I.B. Blagoeva, I.G. Pojarlieff, and A.J. Kirby. J. Chem. Soc. Perkin Trans. 2, 2479 (1996).
7. I.B. Blagoeva. J. Chem. Soc. Perkin Trans. 2, 127 (1987).
8. A.K. Covington, R.A. Robinson, and R.G. Bates. J. Phys. Chem. **70**, 3820 (1966); J.C. Fishbein and W.P. Jencks. J. Am. Chem.Soc. **110**, 5075 (1988).
9. D.F. Detar. J. Am. Chem. Soc. **104**, 7205 (1982).
10. F. Hibbert. Adv. Phys. Org. Chem. **22**, 113 (1986).
11. J. Kavalek, V. Sterba, and S. El Bahaie. Collect. Czech. Chem. Commun. **48**, 1753 (1983).
12. W.P. Jencks. Chem. Rev. **72**, 702 (1972).
13. W.P. Jencks. Acc. Chem. Res. **9**, 425 (1976).
14. K.J. Davies and M.I. Page. J. Chem. Soc. Chem. Commun. 1448 (1990).
15. T.C. Bruice. Annu. Rev. Biochem. **45**, 331 (1976).
16. R.A. More O'Ferrall. J. Chem. Soc. B: 274 (1970).
17. J. Kavalek, V. Machacek, G. Svobodova, and V. Sterba. Collect. Chech. Chem. Commun. **51**, 375 (1986).

[6] Tables of observed rate coefficients for 1-, 2-, and 3-NPU have been deposited as supplementary material (6 pages), which may be purchased from: The Depository of Unpublished Data, Document Delivery, CISTI, National Research Council Canada, Ottawa, Canada, K1A 0S2.

© 1999 NRC Canada

Effect of cyclodextrin on elimination reactions

Luis Viola and Rita H. de Rossi

Abstract: The reaction of 1-bromo-2-X-2-(Y-phenyl) ethane derivatives (**1**: X = Y = H; **2**: X = Ph, Y = H; **3**: X = H, Y = 4-Ac; **4**: X = H, Y = 3-NO_2; **5**: X = H, Y = 4-NO_2; **6**: X = H, Y = 3-Me; **7**: X = H, Y = 4-Me) in basic solution was studied, and in most cases, only the elimination product is formed. Only (2-bromo-1-phenylethyl)benzene, **2**, yielded significant substitution product, and this yield decreased with the concentration of HO^-. Addition of cyclodextrin (β-CD) diminished (about half for 0.02 M cyclodextrin concentration) the reaction rate of all substrates but **4** and **5**. In the latter two cases, the rate rises. The observed rate-constant value at 0.5 M NaOH is 6.78×10^{-4} s^{-1} (at 40°C) and 1.80×10^{-3} s^{-1} (at 25°C) for **4** and **5**, respectively. Under the same reaction conditions but with 0.01 M β-CD, the corresponding rates were 7.70×10^{-4} s^{-1} and 5.20×10^{-3} s^{-1}. The elimination yield for **2** increased from 64 to 98% when the β-CD changed from zero to 0.02 M at 0.5 M NaHO. Also, there was an increase in the relative elimination products of 20–40% for compounds **6** and **7**. The Hammet ρ values were 1.3 and 2.3 for the reaction in pure solvent and in the presence of β-cyclodextrin, indicating an increase in the negative character of the transition state for the reactions in the latter conditions. The results are interpreted in terms of the formation of an inclusion complex whose structure depends on the substrate.

Key words: cyclodextrin, elimination reactions, inhibition, catalysis.

Résumé : On a étudié la réaction de dérivés du 1-bromo-2-X-2-(Y-phényl)éthane (**1**, X = Y = H; **2**, X = Ph, Y = H; **3**, X = H, Y = 4-Ac; **4**, X = H, Y = 3-NO_2; **5**, X = H, Y = 4-NO_2; **6**, X = H, Y = 3-Me; **7**, X = H, Y = 4-Me) en solution basique et, dans la plupart des cas, il ne se forme que le produit d'élimination. Le (2-bromo-1-phényléthyl)benzène, **2**, est le seul à donner des quantités significatives de produit de substitution et ce rendement diminue avec une augmentation de la concentration de OH^-. L'addition de cyclodextrine (β-CD) diminue (environ de moitié pour une concentration égale à 0,02 M en cyclodextrine) la vitesse de réaction pour chacun des substrats, à l'exception des produits **4** et **5**. Dans ces deux derniers cas, la vitesse augmente. Les valeurs des constantes de vitesse observée, pour une concentration de 0,5 M de NaOH, sont de $6{,}78 \times 10^{-4}$ s^{-1} (à 40°C) et de $1{,}80 \times 10^{-3}$ s^{-1} (à 25°C) pour les composés **4** et **5** respectivement. Dans les mêmes conditions de réaction, mais en présence de 0,01 M de β-CD, les vitesses correspondantes sont de $7{,}70 \times 10^{-4}$ s^{-1} et $5{,}20 \times 10^{-3}$ s^{-1}. Pour une concentration de NaOH égale à 0,5 M, le rendement en élimination pour le produit **2** augmente de 64 à 98% lorsque la concentration en β-CD passe de zéro à 0,02 M. Avec les composés **6** et **7**, on a aussi observé une augmentation des produits d'élimination de 20 à 40%. Les valeurs ρ de Hammett sont égales respectivement à 1,3 et 2,3 pour les réactions dans un solvant pur et celles en présence de β-cyclodextrine; ces valeurs signalent une augmentation du caractère négatif de l'état de transition pour les réactions dans ces dernières conditions. On interprète les résultats en fonction de la formation d'un complexe d'inclusion dont la structure dépend du substrat.

Mots clés : cyclodextrine, réactions d'élimination, inhibition, catalyse.

[Traduit par la Rédaction]

Introduction

Cyclodextrins are cyclic oligomers of α-D-glucose that are produced by enzymatic degradation of starch (1). The more common cyclodextrins have six, seven, and eight glucose units and are called α, β, and γ cyclodextrins, respectively. They have a cavity formed by two rings of CH group of the glucose units and one ring of the glycosidic oxygens. The secondary OH groups are located in the wider rim of the cavity and the primary in the smaller one. Since the cavity is relatively apolar compared with water, it provides a favorable environment for the location of many organic compounds, and the formation of inclusion complexes leads to many interesting changes in the properties of the included compound which result in changes in their reactivity (2). One of the properties of cyclodextrins that has been exploited considerably is the possibility of induction of selectivity in reactions that lead to more than one product. Inclusion of the substrate and (or) the reagent in the cavity leads to different distribution of products when the reactions are compared with the same reaction in the bulk solvent. For example, the iodination of phenol (3) and the photochemical rearrangement of phenyl acetate give an increase in the *para*/*ortho* and *ortho*/*para* ratio of products, respectively, in

Received November 4, 1998.

This paper is dedicated to Jerry Kresge in recognition of his many achievements in chemistry.

L. Viola and R.H. de Rossi.[1] Instituto de Investigaciones en Físico Química de Córdoba, Facultad de Ciencias Químicas, Departamento de Química Orgánica, Universidad Nacional de Córdoba, Ciudad Universitaria, 5000 Córdoba, Argentina.

[1]Author to whom correspondence may be addressed. Telephone: 54-351-4334170. Fax: 54-351-4333030. e-mail: ritah@dqo.fcq.unc.edu.ar

 © 1999 NRC Canada

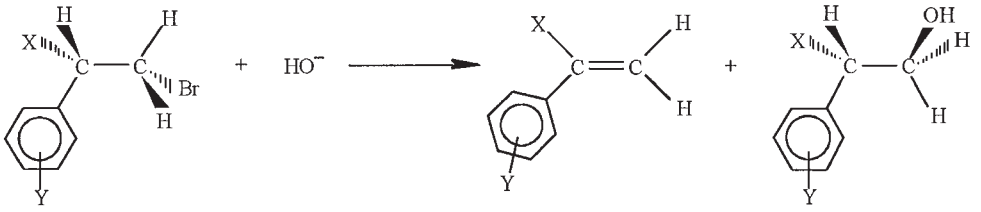

1. X = H Y = H (2-Bromoethyl) benzene
2. X = Ph Y = H (2-Bromo-1-phenylethyl) benzene
3. X = H Y = 4-Ac 1-(2-Bromoethyl)-4-acetyl benzene
4. X = H Y = 3-NO_2 1-(2-Bromoethyl)-3-nitro benzene
5. X = H Y = 4-NO_2 1-(2-Bromoethyl)-4-nitro benzene
6. X = H Y = 3-Me 1-(2-Bromoethyl)-3-methyl benzene
7. X = H Y = 4-Me 1-(2-Bromoethyl)-4-methyl benzene

the presence of β-CD (4). More recent examples that are important for synthetic applications can be found in the literature (5). The changes in product selectivity may be the result of a different stabilization of the transition state for the formation of the various products.

The elimination mechanism of 2-bromoethylbenzenes is well established, and it proceeds by an E_2 type of mechanism. The transition state for this mechanism has severe stereoelectronic requirements; moreover, competition by substitution often occurs (6). We considered of interest to study this type of reactions in the presence of cyclodextrin to determine the effect of inclusion on the reaction rates and the elimination/substitution ratio. Thus, we studied the reaction of compounds **1**–**7** in basic water solution and the effect of cyclodextrins on their relative yield of elimination and substitution in the cases were the two reactions compete. Compounds with substituents at 3- or 4-position were chosen because it is known that the orientation of the ring in the inclusion complex is quite dependent on the position of the substituent on the ring (7).

Results

(2-Bromoethyl)benzene (1)

Substrate **1** is very insoluble in water, so dioxane/water 1:9 was used as solvent. Under all our reaction conditions, the only product formed was styrene. The addition of 1.5×10^{-2} M of β-CD produced no changes in the rate. The observed rate constants at 0.5 M OH^- are 1.27×10^{-4} and 1.24×10^{-4} s^{-1}, respectively. The fact that the rate was not affected by β-CD can be attributed to competitive binding by the solvent. Since it is known that dioxane forms inclusion complexes with β-CD (K_{Ass} = 9 M^{-1}) (8), and the association constant of **1** with β-CD should be in the order of 200 M^{-1} (see below), only 10% of the substrate would be bound at the maximum β-CD used.

Ethanol also binds to β-CD but the association equilibrium constant is lower, i.e., 1.2 M^{-1} (9); besides, its smaller size may allow the co-inclusion of ethanol and the substrate as was found in other systems (10).

Fig. 1. k_{obs} vs. β-CD concentration for the reaction of **1**. [HO] = 0.5 M. Temperature, 40°C; solvent, ethanol/water (1:9 v/v); ionic strength, 0.5 M (NaCl as compensating electrolyte). The line was calculated fitting the data to eq. [3].

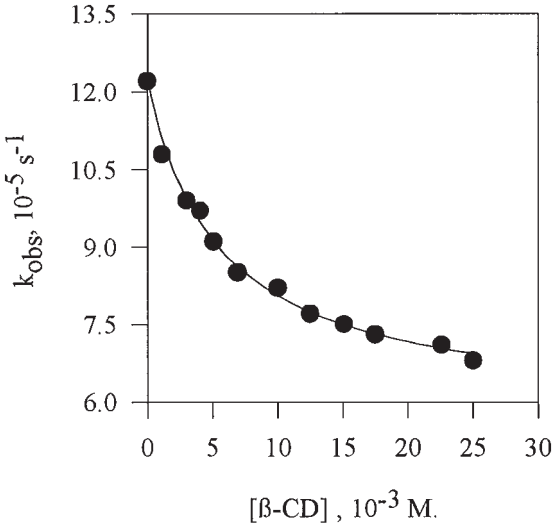

In ethanol/water 1:9 v/v, the only product formed was styrene, and the observed pseudo-first-order rate constant is linearly dependent of HO^- concentration (Table S1).[2] The slope of a plot of k_{obs} vs. HO^- concentration (not shown) gave the second-order rate constant 2.49×10^{-4} M^{-1} s^{-1} in good agreement with the literature values, i.e., 3.01×10^{-4} M^{-1} s^{-1} (11). At constant HO^- concentration, the reaction was inhibited by the addition of β-CD and showed a saturation effect (Fig. 1). GC analysis of the products showed that the major product formed was styrene, although a small (<5%) amount of the substitution product was also formed but no significant changes in the relative yield of the elimination and substitution products could be detected.

At constant β-CD concentration (0.01 M), there was linear dependence of k_{obs} on HO^-, and the slope was 1.49×10^{-4} M^{-1} s^{-1}, which is about 60% of the value in the absence of

[2] Copies of material on deposit may be purchased from: The Depository of Unpublished Data, Document Delivery, CISTI, National Research Council Canada, Ottawa K1A 0S2, Canada.

© 1999 NRC Canada

Fig. 2. k_{obs} vs. β-CD concentration for the reaction of **2**. [HO] = 0.5 M. Temperature, 40°C; solvent, ethanol/water (1:9 v/v); ionic strength, 0.5 M (NaCl as compensating electrolyte). The line was calculated fitting the data to eq. [3].

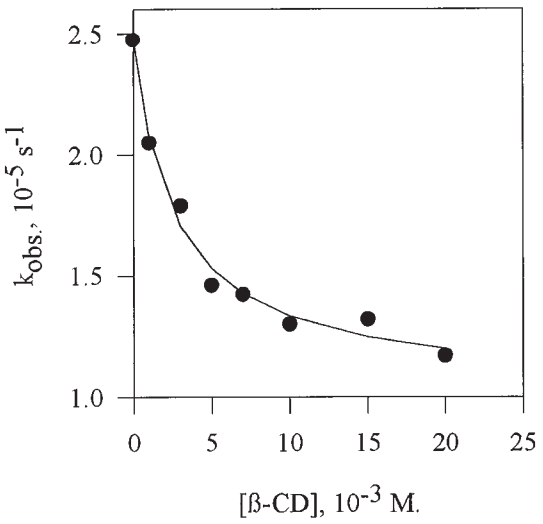

Table 1. Effect of β-CD on the observed rate constant and the elimination yield for the reaction of **2** in basic solution.[a]

β-CD (10^{-3} M)	k_{obs} (10^{-5} M)	Elimination yield (%)
0	24.8	64
1.0	20.3	75
3.0	17.9	79
5.0	14.6	78
7.0	14.2	85
10.0	13.0 (26.2)[b]	79
15.0	13.2	83
20.0	11.7	98

[a]Temperature, 25°C; solvent, ethanol/water (1:9 v/v); ionic strength, 0.5 M (NaCl as compensating electrolyte) unless otherwise indicated; NaOH, 0.5 M. Substrate concentration 2×10^{-5} M.

[b]Soluble starch instead of cyclodextrin.

β-CD. On the other hand, the addition of α-CD did not affect the rate in the range 1×10^{-4}–2.5×10^{-2} M.

(2-Bromoethyl-1-phenylethyl)benzene (2)

This reaction gave substitution as well as elimination products, although the latter is predominant. The concentration of the elimination products increased with that of HO^- in agreement with the known effect of base concentration on the competition between substitution and elimination reactions (6). The observed pseudo-first-order rate is linearly dependent on HO^- concentration with a second-order rate constant of 4.95×10^{-4} M^{-1} s^{-1} (Table S1).[2] The addition of β-CD produces a decrease on the observed rate and shows saturation effect (Fig. 2, Table 1). The yield of the elimination product increases as the amount of CD increases (Table S2).[2] At constant β-CD concentration, there is an increase in the observed rate with HO^- concentration, which is linear but at low concentration the values are somewhat smaller than expected. The elimination yield is higher than in the absence of CD and increases as the OH concentration increases but in a somewhat scattered form (Table S1).[2]

1-(2-Bromoethyl)-4-acetylbenzene (3)

The second-order rate constant obtained from the slope of the linear plot (not shown) of k_{obs} vs. HO^- concentration (Table S1)[2] is 3.3×10^{-3} M^{-1} s^{-1}. There is a modest (~20%) but out of experimental error decrease in the observed rate in the presence of β-CD. The ratio of elimination/substitution products is not affected (Table S2).[2]

1-(2-Bromoethyl)-3-nitrobenzene (4) and 1-(2-bromoethyl)-4- nitrobenzene (5)

The reactions of **4** were measured at 40°C and those of **5** at 25°C. There is linear dependence of the observed rate constant with the HO^- concentration (Table S1)[2] from which a second-order rate constant of 1.33×10^{-3} and $(3.65 \pm 0.17) \times 10^{-3}$ M^{-1} s^{-1} are calculated, respectively, for **4** and **5**. The second-order rate constants for **5** is somewhat higher than the reported values 2.61×10^{-3} (12) and 3.47×10^{-3} M^{-1} s^{-1} (11). The discrepancy may be attributed to the presence of ethanol.

In contrast with the behavior of the substrates described before (**1**–**3**), the addition of cyclodextrin produces an increase in the observed rate constant for both substrates, although for **4** it is at most 10%, with α- or β-cyclodextrin at 0.01 M (Table S2).[2] On the other hand, the increase is more significant for **5**, and saturation effect is observed at three concentrations of HO^- (Fig. 3). The relative increase in rate is higher at lower HO^- concentration, i.e., the ratio of the rate at β-CD = 0.015 M and zero is 3.2, 12.7, and 22.2 for HO^- concentrations 0.49, 0.04, and 0.01 M, respectively. In all cases, only the elimination product is formed.

At constant β-CD concentration, there is nonlinear dependence of the observed rate constant for **5** with HO^- concentration (Fig. 4).

The addition of 3×10^{-2} M concentration of α- or γ-cyclodextrin with HO^- = 0.5 M gives rate constants 3.28×10^{-3} and 3.08×10^{-3} s^{-1}, indicating that both receptors accelerate the reaction in approximately the same amount but less than β-CD, since the value of the observed rate constant in the presence of 0.015 M β-CD is 5.75×10^{-3} s^{-1}.

1-(2-Bromoethyl)-3-methylbenzene (6) and 1-(2-bromoethyl)-4-methylbenzene (7)

The reactions of these substrates were studied at 40°C, there is first-order dependence on the HO^- concentration (Table S1) and the second-order rate constant obtained from the slope of the linear plot (not shown) is 2.23×10^{-4} and 1.84×10^{-4} M^{-1} s^{-1} for **6** and **7**, respectively. The addition of β-CD produces a decrease in the rate and an increase in the relative elimination yield (see Experimental) of about 20% for **6** and 40% for **7** at the higher cyclodextrin concentration used (Table S2). The decrease in the yield of substitution product was confirmed by HPLC.

Discussion

Effect of cyclodextrin on reaction rates

All the reactions studied were affected by the addition of β-CD. To determine whether the effect was due to a medium effect, the observed rate constants were determined in the presence of soluble starch in similar weight concentration as that of β-CD. In Table 2, the data are collected, and it can be

© 1999 NRC Canada

Fig. 3. k_{obs} vs. β-CD concentration for the reaction of **5**. Temperature, 25°C; solvent, ethanol/water (1:9 v/v); ionic strength, 0.5 M (NaCl as compensating electrolyte). [HO] = 0.5 M, A; 0.04 M, B; and 0.01 M, C. The line was calculated adjusting the data to eq. [4].

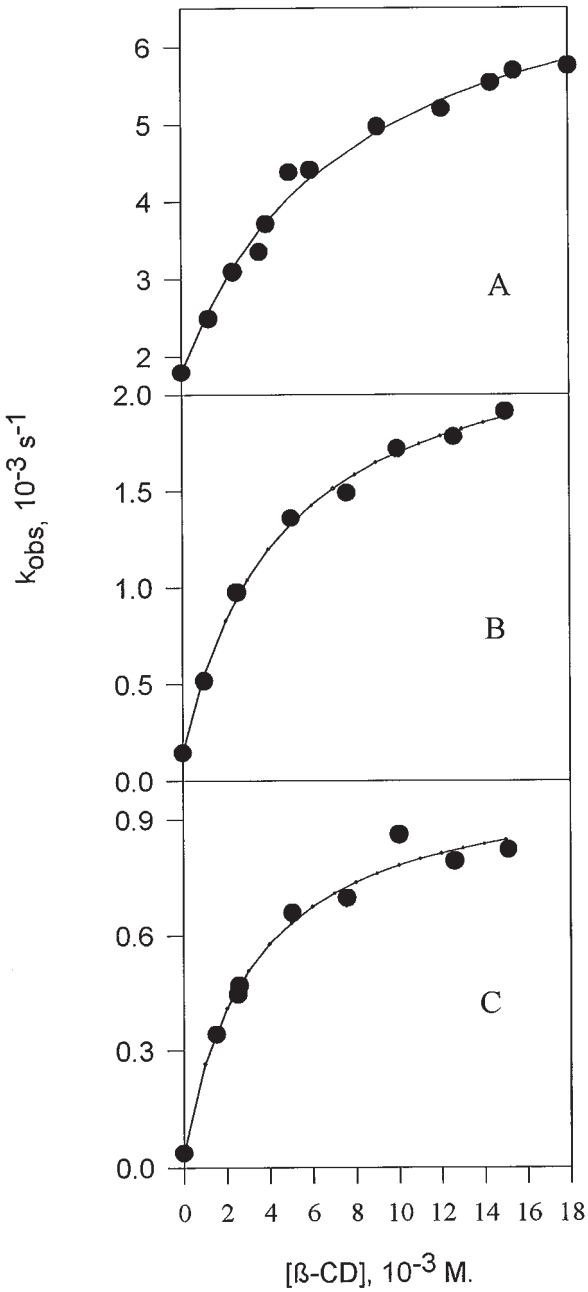

seen that within experimental error, starch produces no changes in the observed rate constant, which indicates that the effect of β-CD should be attributed to specific interactions. Besides, the addition of β-CD produces a decrease in the absorption at the maximum wavelength for 1-(2-bromoethyl)-4-acetylbenzene and 1-(2-bromoethyl)-4-nitrobenzene. These results indicate that the substrate may form some type of inclusion complex with the β-CD. For the 1:1 inclusion

Fig. 4. Change in k_{obs} with HO^- concentration for the reaction of **5**. [β-CD] = 0.01 M. Temperature, 25°C; solvent, ethanol/water (1:9 v/v); ionic strength, 0.5 M (NaCl as compensating electrolyte). The line was calculated using eq. [9].

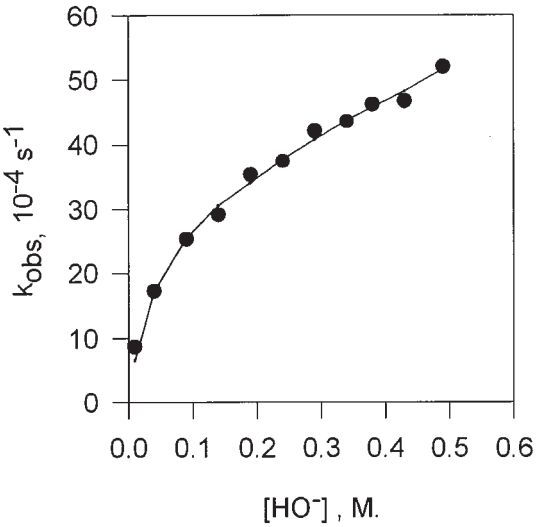

complex, there are two possible modes of inclusion, with the aliphatic chain inside the cavity (Fig. 5*A*) and with the aromatic part of the molecule inside (Fig. 5*B*).

The pK_a of β-CD is 12.2 (13), so we suggest that the reaction takes place as indicated in Scheme 1 where k_0, k_1, and k_2 represent the reactions of the free substrate, the substrate complexed with neutral β-CD (CDOH), and the reaction with anionized β-CD (CDO^-), respectively.

The observed rate constant for Scheme 1 is given by eq. [1] where f represents the fraction of ionized β-CD as defined in eq. [2]. Under the conditions of constant HO^- concentration, 0.5 M, $f \approx 1$, then eq. [1] simplifies to eq. [3]:

$$[1] \qquad k_{obs} = \frac{k_0[HO^-] + k_1K_1[HO^-](1-f)[CD] + k_2K_2\,f[CD]}{1 + K_1(1-f)[CD] + K_2\,f[CD]}$$

$$[2] \qquad f = \frac{[HO^-]}{[HO^-] + K_b}$$

$$[3] \qquad k_{obs} = \frac{k_0[HO^-] + k_2K_2[CD]}{1 + K_2[CD]}$$

Fitting the experimental data to eq. [3],[3] k_2 and K_2 were calculated, and the data are collected in Table 3.

The reactions of substrate **5** in the presence of β-CD were studied at three HO^- concentrations, i.e., 0.01, 0.04, and 0.49 M. For each HO^- concentration, the observed rate constant was fitted to an equation of the form of eq. [4] with $a = k_0[HO^-]$ and b and c adjustable parameters given in eqs. [5] and [6]. The calculated parameters are given in Table 4.

$$[4] \qquad k_{obs} = \frac{a + b[\beta\text{-CD}]}{1 + c[\beta\text{-CD}]}$$

[3] Sigmaplot, DOS version 6.0. Handel Scientific. 1986–1993.

© 1999 NRC Canada

Table 2. Effect of β-CD and soluble starch on the pseudo-first-order observed rate constant for the reaction of compounds **1**–**7** with hydroxide ion.[a]

Substrate	k_{obs} (10^{-4} s^{-1})[b]	k_{obs}^{CD} (10^{-4} s^{-1})[c]	k_{obs}^{Alm} (10^{-4} s^{-1})[d]
1	1.22	0.82	1.26
2[e]	2.48	1.30	2.62
3	16.2	13.0	
4	6.78	7.58	
5[e]	18.0	52.0	21.0
6	1.14	0.91	1.18
7	0.94	0.65	0.96

[a]Temperature, 40°C; unless otherwise indicated, solvent, ethanol/water (1:9 v/v); ionic strength, 0.5 M (NaCl as compensating electrolyte); NaOH, 0.5 M.

[b]Observed rate constant.

[c]Observed rate constant in the presence of 0.01 M β-CD.

[d]Observed rate constant in the presence of 11.35 mg/mL of soluble starch.

[e]Temperature, 25°C.

Fig. 5. Schematic representation of the inclusion complexes of compounds **1**–**7**.

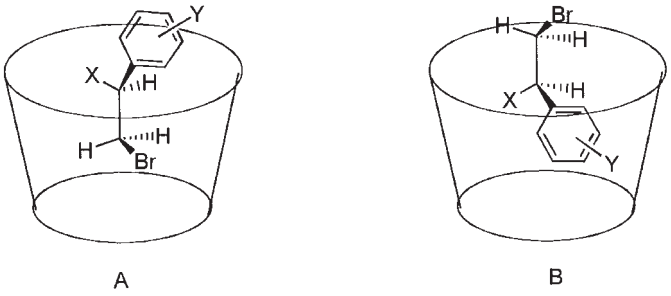

Scheme 1.

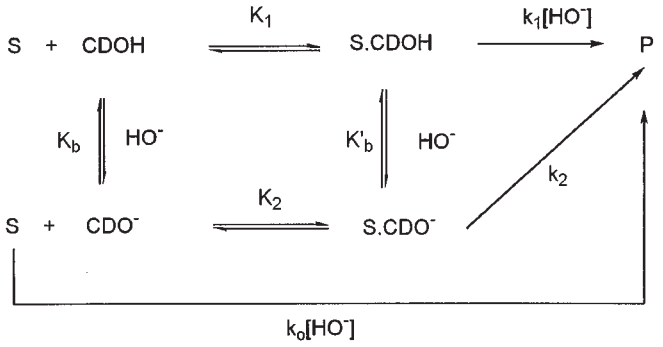

[5] $$b = (k_1K_1[HO^-](1 - f) + k_2K_2 f)[CD] = (k_1K_1K_b + k_2K_2) f[CD]$$

[6] $$c = K_1(1 - f) + K_2 f$$

The decrease in c as the HO^- concentration increases indicates that the association constant of cyclodextrin anion with the substrate, K_2, is smaller than the corresponding value of the neutral cyclodextrin, K_1. Using the value of c at 0.5 M HO^- as K_2, K_1 can be calculated from the value of c at 0.01 and 0.04 M giving 370 ± 10 M^{-1}. The parameter b divided by f should be constant (see eq. [5]). It can be seen in the last column of Table 4 that similar values are obtained at the two lower concentrations of HO^-, but the value increases considerably at high HO^- concentration. This might indicate that at this high concentration there is some contribution to the overall catalyzed reaction from a pathway involving the substrate complexed with cyclodextrin anion and HO^- (eq. [7]).

[7] $$SCDO^- + HO^- \xrightarrow{k_3} P$$

If reaction [7] takes place, a term $k_3K_2[HO^-]$ should be included in parameter c. Using the average value of b/f for the two lowest concentrations of HO^-, namely, 0.769, k_3K_2 is calculated as 0.777 M^{-1} s^{-1}.

Equation [1] can be rearranged as shown in eq. [8]:

[8] $$\frac{k_{obs}(1 + K_1(1 - f)[CD] + K_2 f[CD]) - k_0[HO^-]}{f} = (k_1K_1K_b + k_2K_2)[CD]$$

Since K_1 and K_2 were calculated as indicated above, the left hand side of eq. [8] can be obtained for each concentration of HO^- using the data at constant β-CD and varying HO^- (Table S1);[2] these values were calculated and are not constant as eq. [8] requires but they show a linear dependence with HO^- concentration with slope 3.86×10^{-3} and intercept 4.87×10^{-3} (plot not shown). From the last two values, k_3K_2 and $k_1K_1K_b + k_2K_2$ can be calculated and are in fair agreement with the values obtained from another set of data, namely, the change in rate with β-CD at constant HO^- (see above). From the results just discussed, it follows that a pathway involving the reaction of the substrate complexed with cyclodextrin anion and HO^- (eq. [7]) is playing some role in the catalyzed pathway. The observed rate constant is then given by eq. [9]:

[9] $$k_{obs} = \frac{k_0[HO^-] + (k_1K_1K_b + k_2K_2 + k_3K_2[HO^-]) f[CD]}{1 + K_1(1 - f)[CD] + K_2[CD] f}$$

The value of k_3K_2 is of the same order of magnitude as that corresponding to the reaction involving the cyclodextrin anion acting as a base, k_2K_2, so it is likely that k_1K_1 is also

© 1999 NRC Canada

Table 3. Rate and equilibrium constants for the substrates **1**–**7** and transition state and changes in Gibbs free energy.

Substrate	k_2 (10^{-4} s^{-1})	K_2 (M^{-1})	$-\Delta G_o$ (kcal M^{-1})	K^*_{TS} (M^{-1})	$-\Delta G^*_o$ (kcal M^{-1})
1[a]	58	184	324	87	277
2[b]	100	380	351	153	298
3[a]	120	292	353	216	334
5[b]	760	156	299	658	384
6[a]	67	95	283	56	250
7[a]	53	261	346	147	310

[a]Temperature, 40°C.

[b]Temperature, 25°C.

Table 4. Parameters of eq. [4] calculated with the data of compound **5**.

b	*c*	HO^- (M)	*b*/*f*
0.311 ± 0.034	304 ± 46	0.01	0.808
0.522 ± 0.035	216 ± 21	0.04	0.731
1.167 ± 0.099	154 ± 19	0.49	1.150

similar. Therefore, in the sum the term $k_1K_1K_b$ is probably negligible.

Following Kurz treatment (14), which was adapted by Tee (15) to reactions catalyzed by cyclodextrins, we calculated the formal equilibrium constant for the association of the transition state (TS) with β-CD, and the corresponding free energy using eq. [10]:

$$[10] \qquad K^*_{TS} = \frac{[TS.CDO^-]}{[TS][CDO^-]} = \frac{k_2K_2}{k_0[HO^-]}$$

K^*_{TS} is an apparent association constant for the formation of the transition state of the CD-mediated reaction (symbolized as $TS.CDO^-$) from the transition state of the normal reaction (TS) and the β-CD. The logarithm of this quantity is related to the differences in free energy of the transition state of the catalyzed and uncatalyzed reactions under standard conditions. The value of K^*_{TS} is obtained from experimentally measured quantities, so it gives a measure of the binding energy of the transition state to the catalyst for those conditions regardeless of the mechanism. (16) Therefore, K^*_{TS} and its variation can be taken as a criterium of mechanism in similar way as other kinetic parameters such as Bronsted β or Hammett ρ values. According to eq. [10], the change in rate is determined by the strength of binding of the transition state relative to that of the substrate, i.e., $k_2/k_0 = K^*_{TS}/K_2$.

Cyclodextrins may show two basic forms of catalysis: "noncovalent" and "covalent" (1). In the former case, the cyclodextrin binds to the substrate (S) and provides an environment for the reaction that is different from the bulk solvent; in this case, the effect of CD arises from the less polar nature of the cavity (a microsolvent effect) and (or) from the conformational restrains imposed on the substrate by the geometry of inclusion. Another factor that may be important for noncovalent catalysis may be differential solvation effects at the interface of the cyclodextrin cavity with the external aqueous enviroment (17). In the covalent catalysis, there is some type of covalent interactions between the substrate (S) and functional groups on the CD in the rate-limiting step of the reaction. For instance, the anion of CD may function as simply basic catalyst towards acidic substrates included in their cavity (18).

Considering the less polar microenvironment of the cavity of β-CD, and that elimination reactions are faster in less polar solvents, one would expect that all elimination reaction were catalyzed by cyclodextrin. Contrary to the above expectations, all the reactions studied except for compounds **4** and **5** are retarded.

There is no correlation between K^*_{TS} and K_S, which is an evidence that the transition state of the catalyzed or retarded reaction does not correspond to the inclusion complex of the substrate. There are two possible types of 1/1 inclusion complex: one with the aromatic ring inside the cavity and another with the aliphatic chain inside the cavity (Fig. 5). Since all the compounds have the same aliphatic chain, the differences in stability of the two types of complexes should depend on the nature and position of the substituent. The compounds having nitro and acetyl groups are those that have the more hydrophilic moieties, therefore, it is more likely that the major type of interaction is the one represented by *A* in Fig. 5.

When the transition state for the included compound is more stable than that for the free compound, the reaction will be accelerated by cyclodextrin and vice versa (eq. [10]). When the stabilization of the included transition state is higher than that of the substrate, the barrier for the reaction will be lower and consequently the overall rate faster.

The affinity for the substrate is stronger than that for the transition state for all the substrates but **5**, consequently, the reaction is catalyzed as shown in Table 3. This can be associated with a change in the nature of the transition state for this compounds. Several authors (19) have proposed that in these systems the increased withdrawing effect of the substituent changes the transition state from a classic E_2 mechanism towards one with some E_{1cb} character.

The second-order rate constant can be correlated by the Hammet equation, and a value of 1.3 and 2.3 is obtained for k_0 and k_2, respectively, indicating an increase in the carbanionic character of the transition state for the reactions in the presence of CD. The mechanism of the catalyzed step is kinetically indistinguishable from one in which the substrate complexed with neutral cyclodextrin reacts with HO^- (K_1k_1 step in Scheme 1). Then, the increase in the carbanionic character of the transition state may indicate that the base, HO^-, is stronger in the cavity. However, for this pathway to be kinetically significant under our reaction conditions, K_1k_1 should be about 100 times higher than k_2K_2, which seems unlikely considering the values that have been estimated for these two rate constants for compound **5**, so the increase in

© 1999 NRC Canada

carbanionic character of the included transition state may be attributed to esteric constrain in the cavity for a truly E_2 type of mechanism.

Similar effect was observed by Tagaky and co-workers (20) for elimination reactions in micelles. They also found an important increase in the ρ value, which was attributed to a change of the transition state toward a more negative character although the results of isotopic exchange indicated that the mechanism was not E_{1cb}.

Comparing the values of K_2 and K^*_{TS} for substrates **6** and **7** (Table 3), which have the same substituent but in different position, it can be seen that the *meta* substituted compound has a significatively lower equilibrium constant than the *para*. This result indicates that the inclusion of the substrate takes place with the aromatic ring inside the cavity, which is characteristic of benzene derivatives (21). The unfavorable forces that lead to a weaker interaction of the *meta* substituted compound remain in the transition state for the reaction with β-CD because the ratio of K_2 and K^*_{TS} for **6** and **7** are about the same, namely, 0.36 and 0.37, respectively.

Effect of β-CD on the reaction selectivity

In the presence of β-CD, the relative yield of elimination (see Experimental) increases for substrates **6** and **7** by 20 and 39%, respectively. In the case of substrate **2**, the elimination yield increases from 64 to 98% when β-CD increases from 0 to 0.02 M at constant HO^- concentration (Table S2). The free activation energy of the elimination reaction for substrates **1** and **3**–**5** is lower than that of the substitution reaction, and it is possible that β-CD changes the relative energy of these two transition states, however, the change is not big enough, and the substitution product is not formed in detectable amount. On the other hand, the compounds having electron donor substituents produce a decrease in the relative acidity of the hydrogen of the β-carbon increasing the free energy for the elimination reaction, but the substitution is less affected, therefore, the two reactions compete, and the effect of β-CD can be experimentally determined.

The relative yield of elimination products increase with the β-CD concentration, which may be a consequence of microsolvent effect, since elimination reaction are favored over substitution in solvents of low polarity.

Experimental section

The kinetic measurements were carried out on the thermostated cell of a Beckman 24 spectrophotometer connected to a personal computer that was used to acquire and process the kinetic data.

UV-vis spectra were done on a Shimadzu 260 spectrophotometer. RMN were done on a Bruker AD-C 200.

Water was purified in a Millipore aparatus. Dioxane was dried with Na metal and distilled before use over lithium aluminum hydride. Ethanol was distilled and the purity controlled by UV-vis spectrometry. The α- and γ-cyclodextrin (Aldrich), β-cyclodextrin (Roquette),[4] and soluble starch (Mallinkcrodt) were used as received. Inorganic salts were analytical grade and (2-bromo-1-phenyl)ethylbenzene were used as received. 4-Acetyl-1-(2-bromoethyl)benzene was prepared from (2-bromoethyl)benzene and acetyl chloride and $AlCl_3$ in S_2C (22). The purity of the compound was controlled by mass spectrometry, NMR, IR, and thin layer chromatograpy.

1-(2-Bromoethyl)-3-nitrobenzene was obtained from (3-nitrophenyl)ethanol (Sigma) and PBr_3 in benzene (23). The product was identified by NMR.

1-(2-Bromoethyl)-4-nitrobenzene was obtained from (2-bromoethyl)benzene and nitric acid in acetic anhydride as described in the literature (22). 1-(2-Bromoethyl)-3-methylbenzene was obtained according to the literature from (3-methylphenyl)ethanol and PBr_3 in benzene solution (23). The product had 5% of the starting alcohol as determined by NMR. 1-(2-Bromoethyl)-4-methylbenzene was obtained as described in the literature (23) from (4-methylphenyl)ethanol and PBr_3 in benzene. NMR analysis indicated that it contains 20% of the starting alcohol.

Kinetic procedures

Reactions were initiated by adding 10 μL of a concentrated solution of the substrate dissolved in ethanol to 3 mL of a water solution containing all the other constituents. The cell was flashed with nitrogen and stopped. The change in absorption with time was measured at the maximum of the corresponding styrene derivative, namely, styrene 248 nm, diphenylethene 247 nm, *p*-acetylstyrene 282 nm, *m*-nitrostyrene 241 nm, *p*-nitrostyrene 308 nm, *m*-methylstyrene 250 nm, *p*-methyl styrene 249 nm. The yield of products for (2-bromoethyl)- and (2-bromo-1-phenylethyl)benzene was determined from eq. [11]:

$$[11] \quad \%\ \text{elimination} = \frac{(A_\infty - A_0)100}{\varepsilon [S]_0}$$

where A_∞ and A_0 represent the initial and final absorbance at the wavelength of the measurement, S represents the initial substrate concentration, and ε the extinction coefficient of the product.

For all the other compounds, the relative elimination yields (REY) was determined by using eq. [12] were the subscript x and y stand for the reactions in the presence and absence of cyclodextrin, respectively.

$$[12] \quad \text{REY} = \frac{\%E_x}{\%E_y} = \frac{(A_\infty - A_0)_x [S]_{oy}}{(A_\infty - A_0)_y [S]_{ox}}$$

Product analysis

The reactions of (2-bromoethyl)benzene, 1-(2-bromoethyl)-3-methylbenzene, and 1-(2-bromoethyl)-4-methylbenzene were analyzed by HPLC and CGL and the reaction of 1-(2-bromoethyl)-3-nitrobenzene by H^1 NMR using a MCH-5-n cap column of 150 × 4 mm with UV-vis detection. The solvent was water/methanol 4:6 v/v and 0.5 mL/min flow rate. Retention times were 5.69, 21.94, and 24.32 for 2-phenyl ethanol, styrene, and **1**, respectively. GC analyses were carried out in a Konik KNK 3000 HRGC with a column CPSIL 19 CV 6 m long and 0.75 mm diameter.

[4] α- and β-cyclodextrin were generous gift of Ferromet SA, Buenos Aires, Argentina.

© 1999 NRC Canada

Acknowledgements

This research was supported in part by the Consejo Nacional de Investigaciones Científicas y Técnicas (CONICET), Consejo de Investigaciones de Córdoba (CONICOR), and Universidad Nacional de Córdoba, Secretaría de Ciencia y Técnica (SECYT UNC). Luis Viola was a grateful recipient of a fellowship from the CONICET.

References

1. M.L. Bender and M. Komiyama. Cyclodextrin chemistry. Springer-Verlag, New York. 1977.
2. (*a*) W. Saenger. Angew. Chem. Int. Ed. Engl. **19**, 344 (1980); (*b*) I. Tabushi and Y. Kuroda. *In* Advances in catalysis. Vol. 32. *Edited by* D.D. Eley, H. Pines, and P.B. Weisz. Academic Press, London. 1983. pp. 417–462; (*c*) D.R. Smith. Chem. Ind. London. 14 (1994).
3. A. Veglia and R.H. de Rossi. J. Org. Chem. **53**, 5281(1988).
4. A.V. Veglia, A.M. Sanchez, and R.H. de Rossi. J. Org. Chem. **55**, 4083 (1990).
5. (*a*) G. Westman, O. Wennerström, and I. Raston. Tetrahedron, **49**, 483 (1993); (*b*) E. Monflier, E. Blouet, Y. Barbaux, and A. Mortreux. Angew. Chem. Int. Ed. **33**, 2100 (1994); (*c*) A. Guy, J. Doussot, A. Dallamaggiore, and R. Garreau. Can. J. Chem. **73**, 599 (1995); (*d*) C.J. Easton, C.M. Hughes, E.R.T. Tiekink, G.P. Savage, and G.W. Simpson. Tetrahedron Lett. **36**, 629 (1995).
6. J. March. *In* Advanced organic chemistry, reactions, mechanisms, and structure. 4th ed. John Wiley and Sons, New York. 1992. p. 1003.
7. (*a*) M. Sakura, M. Kitagawa, H. Hoshi, Y. Inoue, and R. Chujo. Carbohydr. Res. **198**, 181 (1990); (*b*) D. Mentzafos, I.M. Mavridis, G. Le Bas, and G. Tsoucaris. Acta Cryst. **B47**, 746 (1991).
8. M. Barra. Ph.D. thesis. Facultad de Ciencias Químicas, Universidad Nacional de Córdoba, Cordoba. 1988.
9. M.V. Rekharsky, F.P. Schwarz, Y.B. Tewari, and R.N. Goldberg. J. Phys. Chem. **98**, 10 282 (1994).
10. (*a*) O.S. Tee and M. Bozzi. J. Am. Chem. Soc. **112**, 7815 (1990); (*b*) O.S. Tee, M. Bozzi, J.J. Hoeven, and T.A. Gadosy. J. Am. Chem. Soc. **115**, 8990 (1993).
11. S. Alumni and W.P. Jencks. J. Am. Chem. Soc. **102**, 2052 (1980).
12. K.A. Wilk. J. Phys. Chem. **95**, 3405 (1991).
13. (*a*) R.L. Van Etten, G.A. Clowes, J.F. Sebastian, and M.L. Bender. J. Am. Chem. Soc. **89**, 3253 (1967); (*b*) R.I. Gelb, M.L. Schwartz, J.J. Bradshaw, and D.A. Laufer. Biorg. Chem. **9**, 299 (1980).
14. J.L. Kurz. J. Am. Chem. Soc. **85**, 987 (1963).
15. (*a*) O.S. Tee. Carbohydr. Res. **192**, 181 (1989); (*b*) *In* Advances in physical organic chemistry. Academic Press Limited, New York. 1994. pp. 1–85.
16. R.L. Schowen, *In* Transition stated in biochemical processes. *Edited by* R.D. Gandour and R.L. Schowen. Plenun, New York. Chap. 2.
17. O.S. Tee and J.M. Bennett. J. Am. Chem. Soc **110**, 269 (1988).
18. V. Daffe and J. Fastrez. J. Chem. Soc. Perkin Trans 2, 789 (1983).
19. (*a*) J.R. Gandler, J.W. Storer, and D.A. Ohlberg. J. Am. Chem. Soc. **112**, 7756 (1990); (*b*) L.F. Blackwell, P.D. Buckley, K.W. Jolley, and A.K.H. MacGibbon. J. Chem. Soc. Perkin Trans. *2*, 169 (1973); (*c*) S. Alunni, E. Bacciocchi, P. Perrucci, and R. Ruzziconi. J. Org. Chem. **43**, 2414 (1978).
20. Y. Yano, Y. Yosida, A. Kurashima, Y. Tamura, and W. Tagaki. J. Chem. Soc. Perkin Trans. 2, 1128 (1979).
21. (*a*) J.A. Hamiltonn and L. Chen. J. Am. Chem. Soc. **110**, 5833 (1988); (*b*) Y. Kotake and E.G. Jansen. J. Am. Chem. Soc. **111**, 5138 (1989).
22. E.L. Foreman and S.M. Mc Elvain. J. Am. Chem. Soc. **62**, 1435 (1940).
23. J.H. Speer and A.J. Hill. J. Org. Chem. **139**, 139 (1937).

© 1999 NRC Canada

Contrasting behaviour in the photosolvolysis of 1- and 2-hydroxy-9-fluorenols in aqueous solution

Maike Fischer, Yijian Shi, Bao-ping Zhao, Victor Snieckus, and Peter Wan

Abstract: The photosolvolysis of 1- and 2-hydroxy-9-fluorenols **4**–**6** has been studied in aqueous solution. All of these 9-fluorenols photosolvolyze efficiently in 1:1 H_2O–CH_3OH, to give the corresponding methyl ether products in high chemical and quantum yields. Whereas the photosolvolysis of the parent 9-fluorenol (**2**, R = H) is known to proceed via the very short-lived and formally ground-state antiaromatic 9-fluorenyl cation (**1**, R = H), the photosolvolysis of 1-hydroxy-9-fluorenol (**4**) proceeds via a much longer-lived (≈5–10 s) fluorenyl quinone methide **9**, which is trappable by ethyl vinyl ether via a [4+2] cycloaddition reaction to give a chroman derivative. Interestingly, 2-hydroxy-9-fluorenol (**5**) photosolvolyzes via a very short-lived intermediate with similar lifetimes as observed for the 9-fluorenyl cation (**1**, R = H), although a corresponding fluorenyl quinone methide intermediate is accessible for this compound. This study demonstrates that the mechanism of photosolvolysis of these types of compounds can be dramatically altered when an aryl hydroxy group is present.

Key words: photosolvolysis, 9-fluorenyl cation, quinone methide, carbocation, antiaromatic.

Résumé : Opérant en solution aqueuse, on a étudié la photosolvolyse des 1- et 2-hydroxy-9-fluorénols (**4**–**6**). Tous ces 9-fluorénols se photosolvolysent d'une façon efficace dans un mélange 1:1 H_2O–CH_3OH; ils conduisent aux éthers méthyliques correspondants avec des rendements chimiques et quantiques élevés. Alors qu'il est bien connu que la photosolvolyse du 9-fluorénol parent (**2**, R = H) se fait par le biais du cation 9-fluorényle (**1**, R = H) qui est formellement un état fondamental antiaromatique de temps de vie très court, la photosolvolyse du 1-hydroxy-9-fluorénol (**4**) se fait par le biais d'un méthide de quinone du fluorényle (**9**) de temps de vie beaucoup plus long (environ 5–10 s) que l'on peut piéger par l'oxyde d'éthyle et de vinyle, par une réaction de cycloaddition [4+2], qui fournit un dérivé chromane. Il est intéressant de noter que le 2-hydroxy-9-fluorénol (**5**) se photosolvolyse par le biais d'un intermédiaire de temps de vie très court, semblable à celui observé pour le cation 9-fluorényle (**1**, R = H) même si l'intermédiaire méthide de quinone de fluorényle correspondant est accessible pour ce composé. Cette étude démontre que le mécanisme de photosolvolyse de ces types de composés peut être dramatiquement modifié lorsqu'un groupe hydroxyaryle est présent.

Mots clés : photosolvolyse, cation 9-fluorényle, méthide de quinone, carbocation, antiaromatique.

[Traduit par la Rédaction]

Introduction

Our first report and subsequent mechanistic studies (1) of the efficient *photo*generation of the *formally* antiaromatic 9-fluorenyl cations (**1**) from 9-fluorenol derivatives (**2**) (eq. [1]) in aqueous solution resulted in renewed interest in the study of the dynamics of highly reactive carbocations of this type (2). Using laser flash photolysis (LFP), it is now established (2*a*) that the lifetime of the parent 9-fluorenyl cation (**1**, R = H) is very short in aqueous solution, in the order of 20 ps, consistent with its destabilized nature, although recent calculations indicate that it is probably not antiaromatic (3). Lifetimes can be extended considerably (to the microsecond range) in the non-nucleophilic but polar 1,1,1,3,3,3-hexafluoro-2-propanol (HFIP) (2*b*, *c*).

[1]

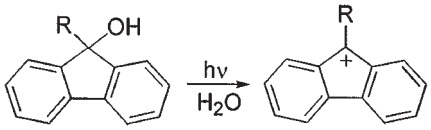

2 R = H
3 R = Ph

1

Received September 16, 1998.

This paper is dedicated to Jerry Kresge in recognition of his many achievements in chemistry.

M. Fischer, Y. Shi, and P. Wan.[1] Department of Chemistry, University of Victoria, Victoria, BC V8W 3V6, Canada.
B.-p. Zhao and V. Snieckus.[2] Guelph–Waterloo Centre for Graduate Work in Chemistry, Department of Chemistry, University of Waterloo, Waterloo, ON N2L 3G1, Canada.

[1]Author to whom correspondence may be addressed. Telephone: (250) 721-7150. Fax (250) 721-7147. e-mail: pwan@uvic.ca
[2]Present address: Department of Chemistry, Queen's University, Kingston, ON K7L 3N6, Canada.

© 1999 NRC Canada

More recently, we have reported on the photosolvolytic reactivity of hydroxy-substituted benzyl alcohols in aqueous solution and found that for the *o*- and *p*-substituted isomers, long-lived ($\tau >> 10^{-3}$ s) *o*- and *p*-quinone methides (QMs) were efficiently formed (eq. [2]), which are responsible for the observed photosolvolysis of these compounds (4).[3] These results

[2] 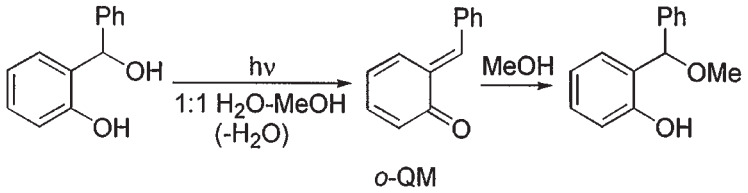

o-QM

indicate that an aromatic hydroxy group can readily alter the photosolvolytic mechanism of benzyl derivatives. We therefore embarked on a study of the photosolvolysis of readily available hydroxy-9-fluorenols **4**–**6**, to investigate the possibility that a similar change in photosolvolytic mechanism can occur for these compounds and whether the corresponding longer-lived fluorenyl-type QMs are formed as intermediates. Such information would be useful in light of the interest in the photosolvolysis of these types of compounds.

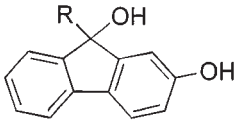

5 R = H
6 R = Ph

Results and discussion

Materials

The hydroxy-9-fluorenols **4** and **5** were readily made from a $NaBH_4$ reduction of the corresponding hydroxy-9-fluorenone, which are known compounds. Treatment of 2-hydroxy-9-fluorenone with phenyl magnesium bromide afforded **6**. A new and more versatile method for the synthesis of 1-hydroxy-9-fluorenone was employed, which was based on remote metalation/Suzuki cross coupling methodology developed by Snieckus and co-workers (5).

Product studies

Photolysis of **4**–**6** (argon purged; ~10^{-3} M; 1:1(v/v) H_2O–CH_3OH; RPR-100 photochemical reactor; ~15°C) gave the corresponding methyl ether (e.g., **7**) in high yield in low-conversion experiments (<30%) (e.g., eq. [3]). Control experiments

[3] 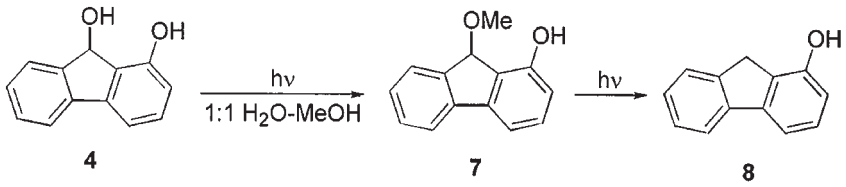

4 **7** **8**

showed no reaction in the absence of irradiation. High-conversion experiments for **4** resulted in formation of low yields of a secondary photoreduction product **8**, which is believed to arise via homolysis of the C-OMe bond (1*b*). Quantum yields for methyl ether formation (Φ_p) for **4**–**6** were determined relative to that of the parent **2** (Φ_p = 0.14 (1*b*)) using ^{1}H NMR. Fluorenols **4** and **5** gave significantly higher Φ_p (Φ_p = 0.48 and 0.24, respectively) compared to the parent **2**, suggesting that both *o*- and *m*-hydroxy substituents aid the photosolvolysis reaction. The presence of a phenyl group at the 9-position in fluorenol **6** further increased the quantum efficiency (Φ_p = 0.44).

We have previously shown that photogenerated *o*-QMs from *o*-hydroxybenzyl alcohols (4)[3] are readily trappable by ethyl vinyl ether (EVE) and other alkoxy alkenes in a [4+2] cycloaddition reaction, to give chroman derivatives. To test for the possibility that the photosolvolysis of **4** might be proceeding via an *o*-QM intermediate (i.e., **9**), photolysis was carried out in the presence of EVE (0.2 M in 3:7 H_2O–CH_3CN), which gave predominantly the *cis*-chroman **10a** (>70% yield), consistent with *endo* attack of EVE on the *o*-QM **9** (eq. [4]). The high diastereoselectivity of this reaction as well as its high efficiency are consistent with a concerted cycloaddition mechanism involving *o*-QM rather than a stepwise mechanism involving a carbocation (4).[3] Attempts to purify *cis*-**10a** on silica gel resulted in substantial isomerization to *trans*-**10b**, presumably via acid-catalyzed epimerization of the acetal carbon. Molecular models of *cis*-**10a** and *trans*-**10b** show that only the former has a

[3] L. Diao and P. Wan. Unpublished results.

© 1999 NRC Canada

[4]

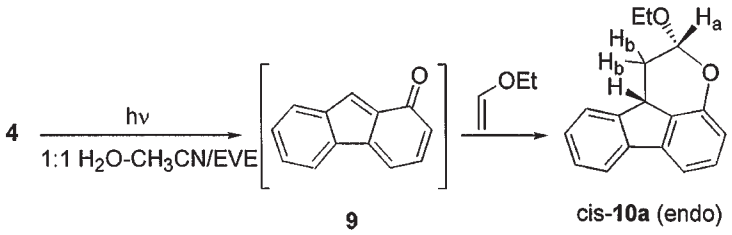

Fig. 1. Absorption spectra of transients generated in neat H_2O via LFP of **4**, monitored ~3 μs after the laser pulse (the insert is a decay measured at pH 1 with τ = (125 ± 2) μs, monitored ~80 ns after the laser pulse).

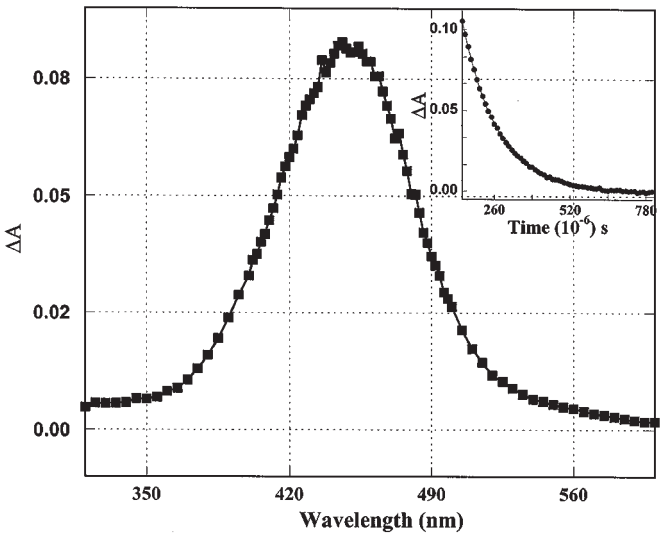

dihedral angle approaching 180° between H_a and one of the H_b protons. Therefore, the *cis*-**10a** adduct was assigned, based on a larger coupling constant observed for H_a coupling with H_b (*cis*-**10a**: δ 5.67 (dd, *J* = 9.6, 3.0 Hz); *trans*-**10b**: δ 5.51 (dd, *J* = 3.0, 1.5 Hz)). Both isomers are susceptible to hydrolysis leading to the aldehyde **10c**.

Laser flash photolysis

Laser flash photolysis (LFP) of **4** (266 nm; YAG laser; <35 mJ; 20°C) in neat H_2O resulted in a strongly absorbing and very long-lived transient (τ > > 1 ms, λ_{max} = 450 nm) (Fig. 1), similar to that reported previously for other QMs (4).[3] A lifetime of about 5–10 s was measured using a standard spectrophotometer in aqueous CH_3CN. This long lifetime implies an *o*-QM intermediate (i.e., **9**) rather than a carbocation. This same transient was produced in water throughout the pH 1–12 range. Also, relative quantum yields (as measured by monitoring absorbance change at 450 nm for production of *o*-QM **9**) showed no dependence on pH within this range. However, the lifetime decreased at low pH consistent with acid quenching of the *o*-QM and was eventually measurable by LFP at pH 1 (τ = (125 ± 2) μs).

LFP of **5** yielded no observable transient in aqueous solution. This suggested possible formation of the carbocation **11**, which would be too short-lived for detection. To confirm this, we used the solvent HFIP, since McClelland and coworkers (2*b*, *c*) were able to observe a large number of short-lived carbocations including 9-fluorenyl cations in this polar yet weakly nucleophilic solvent. The resulting transient spectrum observed for **5** was similar to that previously reported for **1** generated from the parent **2** in HFIP (λ_{max} = 515 nm) (2*b*). Transient lifetimes measured for **1** (R = H) and the proposed **11** in the same HFIP solvent (lifetimes can vary significantly according to the amount of trace water present in HFIP (2*b*)) were similar (~2 μs), which supports that **5** generates the carbocation **11** rather than the *m*-QM which would be longer lived. It is unlikely that the transient is the radical cation, since the radical cation of **2** has been reported as absorbing at 395, 595, and 645 nm and shown to have a complex decay with lifetimes in the microsecond range in aqueous solution (2*b*). Our transient shows simple first exponential decay with a short lifetime in aqueous solution. This would be consistent with a carbocation, since the parent fluorenyl cation **1** (R = H) has been shown to have a lifetime of less than 20 ps in 9:1 H_2O:CH_3OH (2*a*).

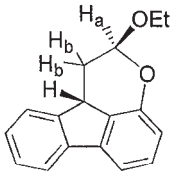

trans-**10b** (exo)

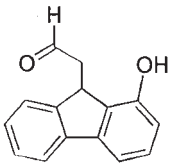

10c

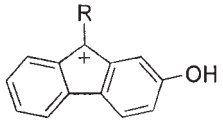

11 R = H
12 R = Ph

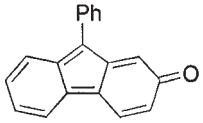

13

To study the kinetics of decay of **11** in aqueous solution, a phenyl group at position 9 was added (i.e., compound **6**). LFP of **6** resulted in a transient absorbing broadly at 480 nm with a lifetime of 47.0 ± 0.4 ns in 100% water (Fig. 2). For comparison, LFP of **3**, whose transient was assigned as the carbocation, gave λ_{max} = 355, 490 nm with τ = 66 ns in 1:4 CH_3CN:H_2O (6). The lifetime observed for **3** in 1:4 CH_3CN:H_2O is comparable to ours in 100% H_2O. Hence, we assign this transient as **12**. An additional absorption band observed at 320 nm (τ = 0.54 μs) is probably due mostly to the radical cation, although a shorter lived component due to a shorter wavelength band of **12** cannot be excluded. As was observed for **3**, the radical cation (weak absorption at 380 nm) can arise from photoionization within the laser pulse (6).

Transient spectra of **12** were taken as a function of pH. At pHs 1 and 7, the single-exponential decay rates were similar,

© 1999 NRC Canada

Fig. 2. Absorption spectra of transients generated via LFP of **6** at pH 6–7 (*a*), 1 (*b*), and 12 (*c*), monitored ~0.1–1 μs after the laser pulse.

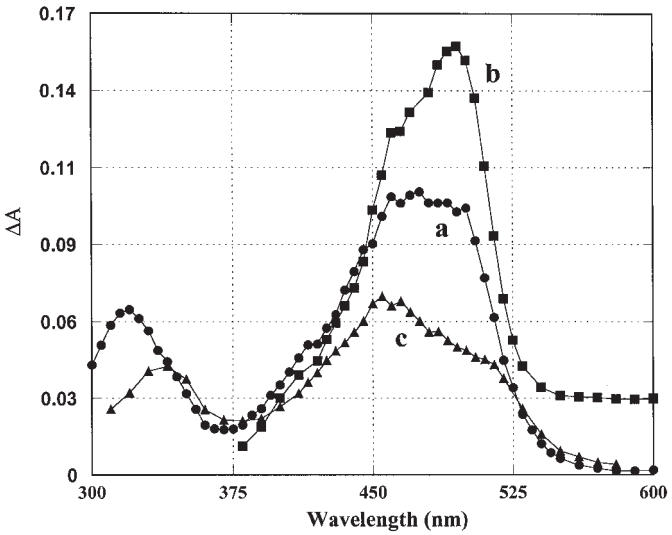

which is consistent with a carbocation whose lifetime would be unaffected by acid. At pH 12, the spectral shape changed considerably (Fig. 2), and its decay was best fitted to the sum of two single exponentials (i.e., two species absorbing in the same region each undergoing single exponential decay). The long lifetime ((0.27 ± 0.03) μs) of the major component (~80%) suggests that *m*-QM **13** rather than carbocation **12** is produced under basic conditions. The minor component (τ = 0.60 μs) is probably due to the aryoxyl radical. At pH 13.7, a similar spectrum and decay were observed as at pH 12. *m*-QM **13** may also be present to a small extent even at pH 7 (pK_a of the ArOH moiety of **12** is probably significant less than 10, due to the electron-withdrawing effect of the positive charge) around since the spectral bandshape observed here is not identical to that observed at pH 1. However, the decay can be fitted to a single exponential. Slight variations in bandshapes may be due to the function of other minor transients that cannot be resolved in the kinetic analysis.

Mechanism of photosolvolysis

Although all of **4**–**6** photosolvolyze efficiently in aqueous solution, as shown by the high quantum yields for methyl ether formation measured in 1:1 H_2O–CH_3OH, it is clear that substantial differences exist with respect to their mechanism of photosolvolysis. The mechanism of photosolvolysis of **2** and **3** is now understood (1) to involve simple heterolytic C—OH bond cleavage from the singlet excited state, to give the corresponding 9-fluorenyl cations **1**. The driving force for forming fluorenyl cations **1** is believed to be due to an inherently stabilized cyclically conjugated 4*n*π system in the excited state (1). Although this driving force is inherent in all of **2**–**6**, the presence of a potentially electron-donating hydroxy substituent, which can also deprotonate in both the ground and excited states, results in the observed complexity in mechanistic behaviour.

It would appear that the observed quantum yields for methyl ether formation measured for **4** and **5** are consistent

Scheme 1.

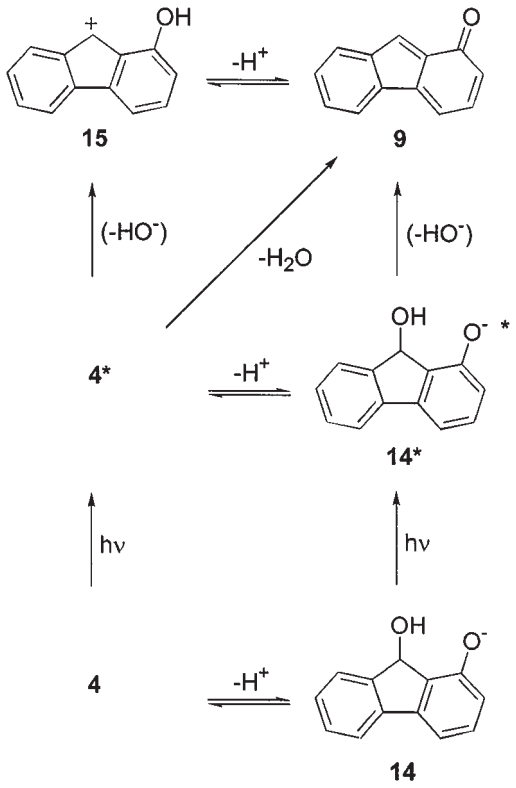

with the simple heterolytic C—OH cleavage mechanism. Based on Zimmerman's "*ortho-meta*" effect (7), compounds **4** and **5**, which have an *ortho* and a *meta* hydroxy substituent, respectively (relative to the benzylic centre), would both be expected to be more reactive with respect to cleavage of the C—OH bond compared to the parent **2**. Indeed, quantum yields for methyl ether formation for **4** (0.48) and **5** (0.24) are significantly higher than that observed for **2** (0.14), with the "*ortho*" compound **4** having the highest quantum yield. However, LFP results do not support this simple mechanistic view. Rather, LFP results indicate that only **5** and **6** (at pH 7) react via initial C—OH bond heterolysis, to give the corresponding 9-fluorenyl cations **11** and **12** as primary intermediates. The high reactivity of **11** with solvent is such that deprotonation of the phenol proton does not compete whereas the lower reactivity of **12** allows for competition by deprotonation, which gives rise to QM **13**. Indeed, only **13** is generated on direct photolysis of the phenolate of **6**. The formation of the *m*-QM is also expected upon excitation of the phenolate of **5**; however, it was not observable in aqueous basic solution in our experiments. Based on recent work from our group on analogous systems (4*a*), its predicted lifetime in aqueous solution would be below the detection limit of our ns–LFP system.

LFP results for **4** indicate that *o*-QM **9** is observed at all pHs. Three possible pathways may be envisoned for its formation (Scheme 1): (*i*) adiabatic deprotonation of the phenol proton of **4*** to give **14*** followed by loss of hydroxide ion to give **9** (this pathway is identical to that proposed for the photochemistry of hydroxybenzyl alcohols which give rise to QMs (4)[3]); (*ii*) C—OH bond heterolysis to give initially 9-fluorenyl cation **15** followed by deprotonation of the phe-

© 1999 NRC Canada

nol; (*iii*) concerted loss of H_2O from **4*** directly giving **9**. If mechanism (*i*) were operative, it would be difficult to envisage why such a mechanism cannot also operate for **5** and **6**. Mechanism (*ii*) should also be equally applicable to 9-fluorenyl cations **11** and **12**. Thus, the most reasonable mechanism for **4** is a concerted but probably not synchronous loss of water from **4***. This is reasonable considering that both the hydroxy group and the phenolic proton are labile in the excited state, and their close proximity would promote a concerted process. Such a mechanism cannot operate for either **5** or **6**, since the hydroxy group and the phenolic proton are too far apart; therefore, only C—OH cleavage can occur below pH 10. In addition, this pathway would also be consistent with the lack of a pH dependence in the 1–7 range where one would have been expected if deprotonation were required first. No increase in quantum yield for **4** was observed in the 8–12 range, which suggests that excitation of the phenolate results in no further enhancement in QM formation, indicating that the process at lower pH is as efficient.

Experimental section

General

^{1}H NMR spectra were recorded on a Bruker AC-300 (300 MHz) instrument. UV-vis spectra were obtained using a Philips PU 8740 UV-vis scanning spectrophotometer, and the fluorescence spectra were taken on a Photon Technology International A-1010 (PTI) QuantaMaster™ luminescence spectrometer. High-resolution mass spectra were obtained on a Kratos Concept H (EI) instrument and the uncorrected melting points on a Koefler hot stage microscope. IR spectra were recorded on a Bruker IFS25 FTIR spectrometer using a KBr pellet. Photolyses were carried out in 100 mL quartz tubes using a Rayonet RPR 100 photochemical reactor. THF was dried over K and distilled before use.

Materials

2-Hydroxy-9-fluorenone was purchased from Aldrich Chemical Co. 1-Hydroxy-9-fluorenol (**4**) was synthesized according to the multi-step procedure described below.

*2-(*N,N-*diisopropylcarboxamido)phenylboronic acid*

A solution of *N*,*N*-diisopropyl benzamide (6.15 g, 30.0 mmol) in anhydrous THF (30 mL), was added dropwise to a solution of *s*-BuLi (26.8 mL of 1.23 M solution, 33.0 mmol) and *N*,*N*,*N*,*N*-tetramethylethylenediamine (TMEDA) (4.87 mL, 33 mmol) in THF (90 mL) at –78°C. The resulting mixture was stirred at –78°C for 1 h, and $B(OMe)_3$ (7.07 mL, 60.0 mmol) was added dropwise by syringe, then slowly warmed to room temperature over 4 h. Saturated aqueous NH_4Cl was added and THF was removed in vacuo. The residue was subjected to standard work-up (addition of water, extraction with CH_2Cl_2, washing of the organic with saturated brine solution, drying (Na_2SO_4), filtration, and evaporation to dryness in vacuo) to afford the crude product, which was directly used for the cross coupling reaction without purification.

N,N-*Diisopropyl-3′-methoxybiphenyl-2-carboxamide*

A mixture of $Pd(PPh_3)_4$ (0.342 g, 0.296 mmol) and 3-bromoanisole (1.85 g, 9.9 mmol) in dimethoxyethane (45 mL) was stirred at room temperature for 5 min. To this mixture was added dropwise in sequence a solution of 2-(*N*,*N*-diisopropylcarboxamido)phenylboronic acid (3.45 g, 13.8 mmol) in EtOH (7 mL) and a 2 M aqueous Na_2CO_3 solution (7 mL). The resulting mixture was heated to reflux for 12 h, cooled down to room temperature, and the catalyst was removed by filtration. The filtrate was evaporated to dryness. Standard work-up followed by flash chromatography afforded the coupled product (2.61 g, 85%); mp 81–82°C (hexane–EtOAc); IR ($CHCl_3$) (cm^{-1}): 1619; ^{1}H NMR ($CHCl_3$) δ 7.1–7.26 (m, 5H), 7.14–7.08 (m, 2H), 6.88 (ddd, *J* = 8.1, 2.4, 1.0 Hz, 1H), 3.82 (s, 3H), 3.43 (sept, *J* = 6.6 Hz, 1H), 3.23 (sept, *J* = 6.8 Hz, 1H), 1.52 (d, *J* = 6.8 Hz, 3H), 1.29 (d, *J* = 6.8 Hz, 3H), 0.90 (d, *J* = 6.6 Hz, 3H), 0.40 (d, *J* = 6.6 Hz, 3H); MS *m*/*z* (rel. intensity): 311 (M^+, 48), 268 (10), 211 (100), 168 (40).

1-Methoxyfluorenone

To a solution of LDA (4.0 mmol) in THF (10 mL) was added a solution of *N*,*N*-Diisopropyl 3′-methoxybiphenyl-2-carboxamide (0.566 g, 2.0 mmol) in THF (2 mL) at 0°C. The resulting mixture was stirred at room temperature for 10 h to give a purple color. A saturated solution of NH_4Cl was added and THF was removed in vacuo. The residue was extracted with CH_2Cl_2. Standard work-up followed by flash chromatography afforded the product (0.387 g, 92%); mp 140–142°C (EtOH) (lit. (8*a*, *b*) 142–143°C); IR ($CHCl_3$) (cm^{-1}): 1699; ^{1}H NMR ($CHCl_3$) δ: 7.59 (dd, *J* = 7.3, 0.7 Hz, 1H), 7.45–7.37 (m, 3H), 7.25 (td, *J* = 7.3, 2.2 Hz, 1H), 6.98 (d, *J* = 7.3 Hz, 1H), 6.80 (d, *J* = 8.5 Hz, 1H), 3.85 (s, 3H); ^{13}C NMR ($CDCl_3$) δ: 191.8, 158.2, 146.4, 143.1, 136.7, 134.4, 133.8, 129.1, 123.8, 120.1, 113.0, 112.8, 55.8.

1-Hydroxy-9-fluorenone

To a solution of 1-methoxyfluorenone (0.120 g, 0.57 mmol) in CH_2Cl_2 (5 mL), BBr_3 (0.1 mL, 0.85 mmol) was added dropwise at –78°C. The mixture was slowly warmed up to room temperature and stirred for 12 h. Standard work-up followed by flash chromatography afforded the product (0.106 g, 95%); mp 115–117°C (EtOH) (lit. (8*a*–*c*) 117–118°C); IR ($CHCl_3$) (cm^{-1}): 3407, 1688; ^{1}H NMR ($CHCl_3$) δ: 8.41 (s, 1H, OH), 7.59 (d, *J* = 7.3 Hz, 1H), 7.46–7.22 (m, 4H), 6.98 (d, *J* = 7.2 Hz, 1H), 6.73 (d, *J* = 8.4 Hz, 1H); ^{13}C NMR ($CDCl_3$) δ: 196.3, 157.3, 144.1, 137.4, 134.2, 129.0, 124.0, 121.0, 118.1, 117.4, 112.8.

*1-Hydroxy-9-fluorenol (**4**)*

To a stirred solution of 1-hydroxy-9-fluorenone (0.50 g, 2.5 mmol) in 95% EtOH (30 mL) in an ice bath, a solution of $NaBH_4$ (0.29 g, 7.7 mmol) in 95% EtOH was added dropwise. After stirring for 1 h at room temperature, the mixture was heated at 30–35°C for 2 h. Work-up (addition of NH_4Cl, extraction with CH_2Cl_2, drying with $MgSO_4$, filtration, and evaporation to dryness in vacuo) yielded **4** quantitatively. Recrystallization with a two-solvent system of Et_2O and hexanes gave a white solid; mp 152–153 °C; IR (cm^{-1}): 3450 (broad), 3161(very broad); ^{1}H NMR ($(CD_3)_2CO$) δ: 4.50 (s, 1H, OH), 5.76 (s, 1H, Ar_2CH), 6.76

© 1999 NRC Canada

(dd, *J* = 6.5, 2.5 Hz, 1H, arom.), 7.19–7.39 (m, 4H, arom.), 7.59 (d, *J* = 7.4 Hz, 1H, arom.), 7.68 (d, *J* = 7.4 Hz, 1H, arom.), 8.09 (s, 1H, OH); HRMS calcd. for $C_{13}H_{10}O_2$: 198.0681; observed: 198.0679.

*2-Hydroxy-9-fluorenol (**5**)*

To a stirred solution of 2-hydroxy-9-fluorenone (1.50 g, 7.6 mmol) in 95% EtOH (150 mL) in an ice bath, $NaBH_4$ (2.31 g, 61.1 mmol) in 95% EtOH (50 mL) was added dropwise. After stirring for 1 h, the reaction mixture was heated at ~40°C for 1 h. Work-up (addition of $NH_4OC(O)CH_3$, extraction with CH_2Cl_2, drying with $MgSO_4$, filtration, and evaporation to dryness in vacuo) yielded **5** quantitatively. Recrystallization with either toluene or ligroines gave a white solid; mp 193–194°C (lit. (9) 188–189°C); IR (cm^{-1}): 3387 (broad), 3136 (very broad); ^1H NMR ($(CD_3)_2CO$) δ: 4.68 (d, *J* = 7.7 Hz, 1H, OH), 5.47 (d, *J* = 7.7 Hz, 1H, Ar_2CH), 6.84 (dd, *J* = 8.2, 2.3 Hz, 1H, arom.), 7.12 (d, *J* = 2.3 Hz, 1H, arom.), 7.18 (t, *J* = 7.4 Hz, 1H, arom.), 7.29 (t, *J* = 7.4 Hz, 1H, arom.), 7.50–7.55 (m, 2H, arom.), 7.58 (d, *J* = 7.4 Hz, 1H, arom.), 8.54 (s, 1H, OH); HRMS calcd. for $C_{13}H_{10}O_2$: 198.0681; observed: 198.0679.

*2-Hydroxy-9-phenyl-9-fluorenol (**6**)*

The Grignard reagent was prepared by adding dropwise PhBr (43 mL, 0.41 mol) in THF (50 mL) to Mg (10 g, 0.41 mol) in THF (200 mL) under nitrogen. The reaction was initiated by adding an I_2 crystal and applying heat. An aliquot of the resulting PhMgBr (11 mL of the above solution, 15 mmol) was added dropwise via a syringe to a stirred solution of 2-hydroxy-9-fluorenone (1.00 g, 5.10 mmol) dissolved in THF (100 mL) under nitrogen. The reaction was stirred for 1 h and refluxed for 1 h. Work-up (addition of NH_4Cl, extraction with CH_2Cl_2, drying with $MgSO_4$, filtration, and evaporation to dryness in vacuo) yielded ~84% of **6**. Recrystallization with $CHCl_3$ gave a white solid; mp 181–182°C; IR (cm^{-1}): 3369 (broad), 3193 (very broad); ^1H NMR ($(CD_3)_2CO$) δ: 5.10 (s, 1H, OH), 6.77 (d, *J* = 2.4 Hz, 1H, arom.), 6.83 (dd, *J* = 8.2, 2.4 Hz, 1H, arom.), 7.07–7.38 (m, 8H, arom.), 7.59 (d, *J* = 8.2 Hz, 1H, arom.), 7.62 (d, *J* = 7.3 Hz, 1H, arom.), 8.50 (s, 1H, OH); HRMS calcd. for $C_{19}H_{14}O_2$: 274.0994; observed: 274.0992.

Product studies

In a typical photolysis, ~10^{-3} M of substrate in 1:1 (v/v) H_2O–CH_3OH (100 mL) was purged with argon for 15 min before and during irradiation at 254 nm in a Rayonet RPR-100 photochemical reactor equipped with a cooling finger (~15°C). After photolysis, work-up involved extraction with CH_2Cl_2 and drying with $MgSO_4$. The conversion to product was calculated by ^1H NMR. The product quantum yields (Φ_p) were measured relative to that of the parent **2**, using the same number of moles and irradiation times (4 lamps, 1.5 or 3 min). The percent conversion was kept ≤30% to minimize production of the secondary product, the fluorene derivative (≤3%). After isolation by preparative silica gel TLC (solvent: 10% ethyl acetate in CH_2Cl_2), the methyl ether product was characterized by ^1H NMR and HRMS.

*Photolysis of **4***

Photolysis of **4** in 1:1 H_2O–CH_3OH (~10^{-3} M, 1.5 min, 4 lamps, 254 nm) led to 30% methyl ether product and 3% fluorene product. Extended irradiation (2 min, 8 lamps) yielded 51 and 9%, respectively. Methyl ether product: ^1H NMR ($(CD_3)_2CO$) δ: 3.03 (s, 3H, OCH_3), 5.85 (s, 1H, Ar_2CH), 6.12 (s, 1H, OH), 6.81 (d, *J* = 7.6 Hz, 1H, arom.), 7.21–7.43 (m, 4H, arom.), 7.58 (d, *J* = 7.4 Hz, 1H, arom.), 7.65 (d, *J* = 7.4 Hz, 1H, arom.); HRMS calcd. for $C_{14}H_{12}O_2$: 212.0838; observed: 212.0836.

Photolysis of **4** in 3:7 H_2O–CH_3CN (~10^{-3} M, 10 min, 16 lamps, 254 nm) was also carried out in the presence of ethyl vinyl ether (2 mL, 0.2 M). The [4+2] cycloaddition resulted in 73% *endo* adduct (*cis*-**10a**), 8% *exo* adduct (*trans*-**10b**) and 19% hydrolysis product (**10c**). On silica gel (mild acidic conditions), the *cis*-**10a** rearranged to *trans*-**10b** and more of **10c** formed. Silica preparative TLC with CH_2Cl_2:hexanes as solvent was used to isolate all products; *cis*-**10a**: ^1H NMR ($CDCl_3$) δ: 1.31 (t, *J* = 7.0 Hz, 3H, CH_3CH_2), 1.49–1.60 (m, 1H, H_b), 2.76–2.83 (m, 1H, H_b), 3.69–3.80 (m, 1H, CH_3CH_2), 3.93 (dd, *J* = 5.0, 13.0 Hz, 1H, Ar_2CH), 4.07–4.19 (m, 1H, CH_3CH_2), 5.67 (dd, *J* = 9.6 Hz, 3.0 Hz, 1H, H_a), 6.76 (m, 1H, arom.), 7.23–7.32 (m, 3H, arom.), 7.38 (tm, *J* = 7.6 Hz, 1H, arom.), 7.51 (dm, *J* = 7.6 Hz, 1H, arom.), 7.74 (dm, *J* = 7.6 Hz, 1H, arom.); HRMS calcd. for $C_{17}H_{16}O_2$: 252.1151; observed: 252.1144; *trans*-**10b**: ^1H NMR ($CDCl_3$) δ: 1.27 (t, *J* = 7.4 Hz, 1H, CH_3CH_2), 1.38–1.58 (m, 1H, H_b), 2.71 (ddd, *J* = 13.0, 5.2, 1.5 Hz, 1H, H_b), 3.68–3.82 (m, 1H, CH_3CH_2), 4.02–4.18 (m, 2H, CH_3CH_2, Ar_2CH), 5.51 (dd, *J* = 3.0, 1.5 Hz, 1H, H_a), 6.74 (dd, *J* = 7.5, 1.5 Hz, 1H, arom.), 7.16–7.41 (m, 4H, arom.), 7.52 (d, *J* = 7.5 Hz, 1H, arom.), 7.74 (d, *J* = 7.5 Hz, 1H, arom.); HRMS calcd for $C_{17}H_{16}O_2$: 252.1151; observed: 252.1146; **10c**: ^1H NMR ($CDCl_3$) δ: 3.03 (dd, *J* = 19.2, 7.6 Hz, 1H, $C(O)CH_2$), 3.25 (dd, *J* = 19.2, 4.2 Hz, 1H, $C(O)CH_2$), 4.46 (dd, *J* = 7.6, 4.2 Hz, 1H, Ar_2CH), 5.24 (s, 1H, OH), 6.62–6.79 (m, 2H, arom.), 7.18–7.42 (m, 3H, arom.), 7.45 (d, *J* = 7.2 Hz, 1H, arom.), 7.71 (d, *J* = 7.2 Hz, 1H, arom.), 9.84 (s, 1H, C(O)H); HRMS calcd. for $C_{15}H_{12}O_2$: 224.0838; observed: 224.0838. ^1H COSY NMR was used above to show the correlations between signals.

*Photolysis of **5***

Photolysis of **5** in 1:1 H_2O–CH_3OH (~10^{-3} M, 3 min, 4 lamps, 254 nm) led to 27% methyl ether product and 3% fluorene product. Upon extended photolysis (15 min, 16 lamps), the methyl ether product led to a large amount of the secondary fluorene product (17 and 46%, respectively). ^1H NMR ($CDCl_3$) δ: 3.07 (s, 3H, OCH_3), 5.45 (s, 1H, Ar_2CH), 6.89 (dd, *J* = 8.2, 2.3 Hz, 1H, arom.), 7.07 (d, *J* = 2.3 Hz, 1H, arom.), 7.22 (t, *J* = 7.5 Hz, 1H, arom.), 7.35 (t, *J* = 7.5 Hz, 1H, arom.), 7.51 (d, *J* = 7.5 Hz, 1H, arom.), 7.59 (d, *J* = 8.2 Hz, 1H, arom.), 7.62 (d, *J* = 7.5 Hz, 1H, arom.), 8.58 (s, 1H, OH); HRMS calcd. for $C_{14}H_{12}O_2$: 212.0838; observed: 212.0835.

*Photolysis of **6***

Photolysis of **6** in 1:1 H_2O–CH_3OH (~10^{-3} M, 1.5 min, 4 lamps, 254 nm) led to 28% methyl ether product. Also upon extended photolysis (2 min, 8 lamps), the methyl ether product led to some secondary fluorene product (53 and 8%, re-

© 1999 NRC Canada

spectively). An even longer irradiation time (15 min, 16 lamps) resulted in 2 and 84%, respectively. ^{1}H NMR ($(CD_3)_2CO$) δ: 2.91 (s, 3H, OCH_3), 6.70 (d, J = 2.3 Hz, 1H, arom.), 6.89 (dd, J = 8.2, 2.3 Hz, 1H, arom.), 7.13–7.38 (m, 8H, arom.), 7.65 (d, J = 8.2 Hz, 1H, arom.), 7.68 (d, J = 7.3 Hz, 1H, arom.), 8.55 (s, 1H, OH); HRMS (EI) calcd. for $C_{20}H_{16}O_2$: 288.1151; observed: 288.1153.

Laser flash photolysis (LFP)

All transient spectra and lifetimes were obtained using a Nd:YAG laser (Spectra Physics Quanta-Ray GCR-12, <30 mJ) with pulse width of ~10 ns and excitation wavelength of 266 nm. Signals were digitized with a Tektronix TDS 520 recorder. Samples were prepared with OD ≈ 0.3 at 266 nm. Static cells were used for the solvent HFIP, otherwise flow cells for the aqueous solutions. The solutions were purged with oxygen for ~10 min before excitation.

Summary

New insights into the mechanism of photosolvolysis of 9-fluorenols have been obtained by studying simple hydroxy-substituted derivatives whose mechanism of photosolvolysis is more complex than that of the parent compounds. Although the parent 9-fluorenol system is intrinsically highly reactive towards photosolvolysis, we have shown that the quantum efficiency can be further enhanced by hydroxy substitution, *ortho* and *meta* to the benzylic position. It is proposed that the mechanism for **5** and **6** at neutral pH involves simple C–OH heterolysis, to generate the corresponding 9-fluorenyl cations, which in the case of **12**, can form the *m*-QM **13** via deprotonation. The mechanism for **4** probably involves a concerted loss of water to give *o*-QM **9** in one step from the singlet excited state. The structural rigidity and planarity inherent in fluorenyl quinone methides of this type may be useful as photogenerated electrophiles for use in biological systems.

Acknowledgments

We thank the Natural Sciences and Engineering Research Council (NSERC) of Canada for supporting this research in the form of research grants (to P.W. and V.S.) and a post-graduate scholarship (to M.F.). We also thank L. Diao for some lifetime measurements.

References

1. (*a*) P. Wan and E. Krogh. J. Chem. Soc. Chem. Commun. 1207 (1985); (*b*) J. Am. Chem. Soc. **114**, 4887 (1989); (*c*) E. Krogh and P. Wan. Can. J. Chem. **68**, 1725 (1990); (*d*) A. Blazek, M. Pungente, E. Krogh, and P. Wan. J. Photochem. Photobiol. A, **64**, 315 (1992).
2. (*a*) S.L. Mecklenburg and E.F. Hilinski. J. Am. Chem. Soc. **111**, 5471 (1989); (*b*) R.A. McClelland, N. Mathivanan, and S. Steenken. J. Am. Chem. Soc. **112**, 4857 (1990); (*c*) R.A. McClelland. Tetrahedron, **52**, 6823 (1996); (*d*) L.J. Johnston, P. Kwong, A. Shelemay, and E. Lee-Ruff. J. Am. Chem. Soc. **115**, 1664 (1993); (*e*) C.S.Q. Lew, B.D. Wagner, M.P. Angelini, E. Lee-Ruff, J. Lusztyk, and L.J. Johnston. J. Am. Chem. Soc. **118**, 12 066 (1996); (*f*) C.S.Q. Lew, D.F. Wong, L.J. Johnston, M. Bertone, A.C. Hopkinson, and E. Lee-Ruff. J. Org. Chem. **61**, 6805 (1996).
3. H. Jiao, P. von R. Schleyer, Y. Mo, M.A. McAllister, and T.T. Tidwell. J. Am. Chem. Soc. **119**, 7075 (1997).
4. (*a*) L. Diao, C. Yang, and P. Wan. J. Am. Chem. Soc. **117**, 5369 (1995); (*b*) P. Wan, B. Barker, L. Diao, M. Fischer, Y. Shi, and C. Yang. Can. J. Chem. **74**, 465 (1996).
5. J.-M. Fu, B.-P. Zhao, M.J. Sharp, and V. Snieckus. J. Org. Chem. **56**, 1683 (1991).
6. F.L. Cozens, N. Mathivanan, R.A. McClelland, and S. Steenken. J. Chem. Soc. Perkin Trans. 2, 2083 (1992).
7. (*a*) H.E. Zimmerman. J. Am. Chem. Soc. **117**, 8988 (1995); (*b*) H.E. Zimmerman and V.R. Sandel. J. Am. Chem. Soc. **85**, 915 (1963).
8. (*a*) L. Horner and D.W. Baston. Justus Lieb. Ann. Chem. 910 (1973); (*b*) J. Buckingham (*Editor*). Dictionary of organic compounds. Vol. 3. 5th ed. Chapman and Hall, New York. 1982. p. H-01815; (*c*) C.J. Pouchert. The Aldrich library of infrared spectra. Aldrich Chemical Co., Inc., Milwaukee. 1970. p. 660D.
9. C.L. Arcus and M.M. Coombs. J. Am. Chem. Soc. **76**, 3977 (1954).

© 1999 NRC Canada

Ab initio test of the usefulness of the Redlich–Teller product rule in computing kinetic isotope effects

L.J. Schaad, Laimutis Bytautas, and K.N. Houk

Abstract: It has been known since the early work of Bigeleisen that incorporating the Redlich–Teller product rule into isotope-effect equations minimizes the importance of low-frequency vibrations. Similar analysis suggests that errors in low frequencies especially are minimized by the use of the Redlich–Teller rule, though its use improves accuracy at all frequencies. However, in the computation of isotope effects, cancellation between isotopomers caused this advantage to vanish exactly in the case of diatomic reactants or products. It does not do so for all polyatomics, and computational experiments again show use of the Redlich–Teller rule to be preferred.

Key words: isotope effect, Bigeleisen equation, Redlich–Teller product rule, formamide, *Z*-1,3-pentadiene.

Résumé : On sait depuis les travaux originaux de Bigeleisen que l'incorporation de la règle du produit de Redlich–Teller dans les équations d'effets isotopiques minimise l'importance des vibrations de basse fréquence. Une analyse similaire suggère que les erreurs dans les basses fréquences sont particulièrement minimisées par l'utilisation de la règle de Redlich–Teller, même si son utilisation améliore la précision à toutes les fréquences. Toutefois, dans le calcul des effets isotopiques, une annulation entre isotopomères a fait disparaître complètement cet avantage dans le cas de réactifs ou des produits diatomiques. Ce n'est toutefois pas le cas pour tous les produits polyatomiques et les expériences de calcul montrent à nouveau que l'utilisation de la règle de Redlich–Teller est préférable.

Mots clés : effet isotopique, équation de Bigeleisen, règle de produit de Redlich–Teller, formamide; *Z*-penta-1,3-diène.

[Traduit par la Rédaction]

Introduction

In a study of secondary kinetic isotope effects (KIEs) in the internal rotation of formamide (1), small differences were found between KIEs computed using eqs. [1]–[3] and using Bigeleisen's (2) modification, eq. [4].

[1] $\mathrm{KIE} = k_H/k_D = \mathrm{MMI} \times \mathrm{VIB}$

The factors in eq. [1] are

[2] $$\mathrm{MMI} = \left(\frac{M_H^{\ddagger} M_D}{M_D^{\ddagger} M_H}\right)^{3/2} \left(\frac{I_{H1}^{\ddagger} I_{H2}^{\ddagger} I_{H3}^{\ddagger} I_{D1} I_{D2} I_{D3}}{I_{D1}^{\ddagger} I_{D2}^{\ddagger} I_{D3}^{\ddagger} I_{H1} I_{H2} I_{H3}}\right)^{1/2}$$

[3] $$\mathrm{VIB} = \left(\prod_{i=1}^{3N^{\ddagger}-7} \frac{e^{u_i^{\ddagger}(D)/2} - e^{-u_i^{\ddagger}(D)/2}}{e^{u_i^{\ddagger}(H)/2} - e^{-u_i^{\ddagger}(H)/2}}\right)\left(\prod_{i=1}^{3N-6} \frac{e^{u_i(H)/2} - e^{-u_i(H)/2}}{e^{u_i(D)/2} - e^{-u_i(D)/2}}\right)$$

and I_1, I_2, I_3 are the principal moments of inertia, M is the total mass of the system, $u_i = h\nu_i/kT$ where ν_i is the vibrational frequency of ith normal mode, h is Planck's, and k is Boltzmann's constant. Bigeleisen incorporated the Redlich–Teller product rule (3) to give

[4] $$\mathrm{KIE} = \left(\frac{\nu_H^*}{\nu_D^*}\right)\left(\prod_{i=1}^{3N^{\ddagger}-7} \frac{\nu_{Hi}^{\ddagger}}{\nu_{Di}^{\ddagger}}\right)\left(\prod_{i=1}^{3N-6} \frac{\nu_{Di}}{\nu_{Hi}}\right) \times \mathrm{VIB}$$

where the first factor in eq. [4] is the ratio of imaginary frequencies in the transition structure.

With perfect computational accuracy, the two expressions must give identical KIEs, but with errors in computed frequencies or force constants, which gives the better result?

A preliminary analysis

The differences in computed KIEs (1) were traced back to small differences of 1–5 cm^{-1} in computed vibrational fre-

Received November 3, 1998.

This paper is dedicated to Jerry Kresge in recognition of his many achievements in chemistry.

L.J. Schaad[1] and L. Bytautas.[2] Department of Chemistry, Vanderbilt University, Box 1575, Station B, Nashville, TN 37235, U.S.A.
K.N. Houk. Department of Chemistry and Biochemistry, University of California, Los Angeles, CA 90095, U.S.A.

[1]Author to whom correspondence may be addressed. Telephone (615) 322-2684. e-mail: SchaadLJ@Ctrvax.Vanderbilt.edu
[2]Current address: Department of Oceanography, Marine Sciences Program, Texas A. and M. University at Galveston, Galveston, TX 77553, U.S.A. On leave from the Institute of Theoretical Physics and Astronomy, Gostauto 12, Vilnius 2600, Lithuania.

 © 1999 NRC Canada

Fig. 1. The ratio of contribution to the isotope effect of frequency ν + Δν to that of frequency ν. The top two curves are for Δν = +5 cm^{-1} and the lower two for –5 cm^{-1}. The top and lowest curves show Φ of eq. [5], which does not use the Redlich–Teller product rule; the two middle curves show Φ′ of eq. [6], which does.

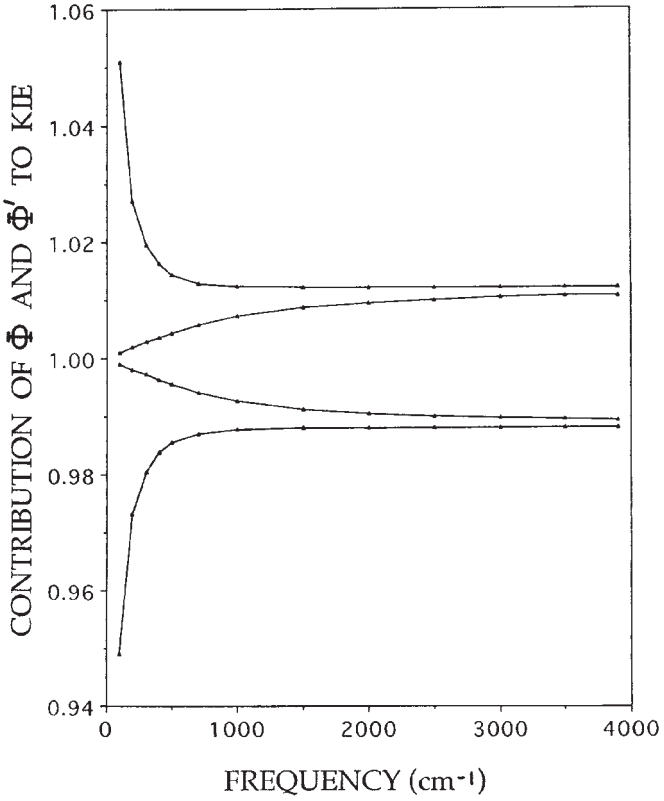

quencies. As Saunders et al. (4) point out, it has long been known that the Bigeleisen eq. [4] is less sensitive to low-frequency vibrations and hence is to be used if these are inaccurately known. To examine this in more detail, we begin by factoring out the contribution of a particular vibrational frequency ν of the H isotopomer of the reactant to the KIE computed from eq. [1]. Next imagine replacing ν by ν + Δν (i.e., a frequency in error by Δν) and factoring out its contribution to the modified KIE. Then dividing the contribution of the incorrect frequency by that of the correct gives the ratio

$$[5] \qquad \Phi(\nu + \Delta\nu) = \frac{e^{h(\nu+\Delta\nu)/2kT} - e^{-h(\nu+\Delta\nu)/2kT}}{e^{h\nu/2kT} - e^{-h\nu/2kT}}$$

In a similar way, one gets the contribution of frequency ν

$$[6] \qquad \Phi'(\nu + \Delta\nu) = \frac{\nu}{\nu + \Delta\nu}\Phi$$

to a KIE computed using using eq. [4] from the Redlich–Teller rule. Equations [5] and [6] are convenient to represent the error in KIE caused by an error Δν in the frequency ν, since multiplying the KIE computed using ν by Φ(ν + Δν) gives the KIE computed using ν + Δν. Equations [5] and [6] are for the H isotopomer of the reactant or for the D isotopomer of the TS. For the D isotopomer of the reactant or the H isotopomer of the TS, the reciprocals of Φ and Φ′ are used.

The factors Φ and Φ′ are shown in Fig. 1 with Δν = ±5 cm^{-1}. The most dramatic effect is, as expected, at low frequencies where eq. [5] goes to +∞ as ν goes to 0 for Δν = 5 cm^{-1} and –∞ for Δν = –5 cm^{-1}. Equation [6] approaches $(e^{h\Delta\nu/2kT} - e^{-h\Delta\nu/2kT})(kT/h\Delta\nu) = 1.000\,024$ at the same limit for both values of Δν. As ν → ∞, eqs. [5] and [6] both approach $e^{h\Delta\nu/2kT} = 1.012$ for Δν = 5 cm^{-1}. and 0.988 for Δν = –5 cm^{-1}. Since Φ′ is closer than Φ to 1 for all ν, it might appear that eq. [4] is obviously the better computational formula.

However, in computing isotope effects there may be error cancellation between the factors Φ or Φ′ for the H and D isotopomers. The errors in the numerator and denominator of these ratios are not independent, since the force constants in which the computational errors occur are the same for both isotopomers, while the masses vary from one to the other but are more accurately known. Consider any chemical reaction involving the diatomic AH as a reactant. Replace AH by the isotopomer AD, and consider the relative rates or equilibria of the two in this reaction. The single frequency of the two isotopomers contributes $\Phi'(\nu + \Delta\nu)_D/\Phi'(\nu + \Delta\nu)_H$ or $\Phi(\nu + \Delta\nu)_D/\Phi(\nu + \Delta\nu)_H$ to errors in relative rates or equilibria, depending upon whether or not one uses the Redlich–Teller formula [4]. From eq. [6], it is seen that these error contributions to the Φ and Φ′ ratios differ by a factor of

$$[7] \qquad \frac{\nu_D}{\nu_H} \times \frac{(\nu + \Delta\nu)_H}{(\nu + \Delta\nu)_D} = \left(\frac{k}{\mu_D} \times \frac{\mu_H}{k}\right)^{1/2} \left(\frac{k + \Delta k}{\mu_H} \times \frac{\mu_D}{k + \Delta k}\right)^{1/2} = 1$$

where the reduced masses $\mu_{H(D)} = m_A m_{H(D)}/(m_A + m_{H(D)})$. Therefore, in this special case, use of the Redlich–Teller product rule gives no better computed value of the isotope effect than do formulas [1]–[3].

In more complicated cases, reduced masses will not cancel in this way; and we do not see how to generalize this result. It is thus not clear whether the Redlich–Teller formula will or will not be of advantage in calculating isotope effects of polyatomics. We have therefore carried out computational studies of the problem in the next two sections.

Secondary KIE in formamide isomerization

Isomerization of formamide occurs by internal rotation of the molecule about the C—N bond (1). RHF/6-31G* optimization of formamide and its transition structure using GAUSSIAN 92 (5) gave energies and geometries in close agreement with Wiberg and Laidig (6). There are two possible transition structures, and the one of lower energy (**A** of ref. 6.) was used. Frequencies were calculated for reactant and transition structure and for their isotopomers with the two Hs of the amide group replaced by Ds. These and principal moments of inertia were then used in a small program to compute KIEs at 321.15 K of 1.132 42 from eq. [1] and 1.129 00 from eq. [4]. The optimizations used the default accuracy of the GAUSSIAN programs.

At first sight, one cannot say which of these values of the isotope effect is more accurate. Fortunately, in addition to the default optimization accuracy, *tight* and *very tight* options are available. Using *tight* optimization gave KIE =

© 1999 NRC Canada

Fig. 2. Error = (computed KIE) – 1.129 17 for 25 sets of computations of the secondary isotope effect in formamide isomerization. Errors are shown by the vertical bars where the dark bar uses the Redlich–Teller product rule and the light bar does not. Each set of a dark bar followed by an adjacent light bar uses the same set of Gaussian random errors between ± 0.000 05 Hartree/(Bohr)^2 added to the Cartesian force constants. The same errors are used for both isotopomers. Here and in the following figures, the errors are sometimes too small to show on the graph.

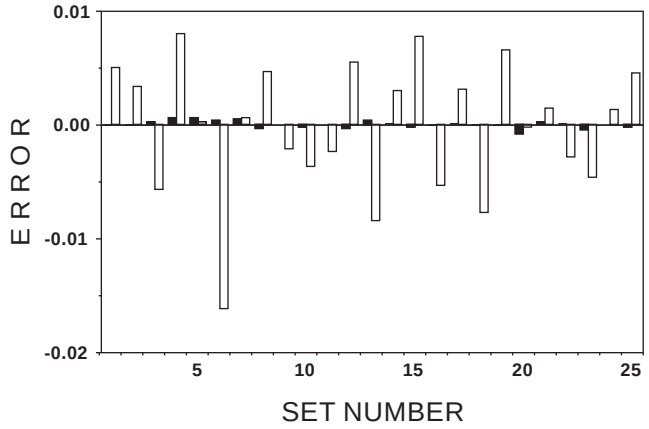

Fig. 3. Calculations are like those of Fig. 2, but with a uniform, rather than Gaussian, error distribution in the range 0 to 0.000 05 Hartree/(Bohr)^2.

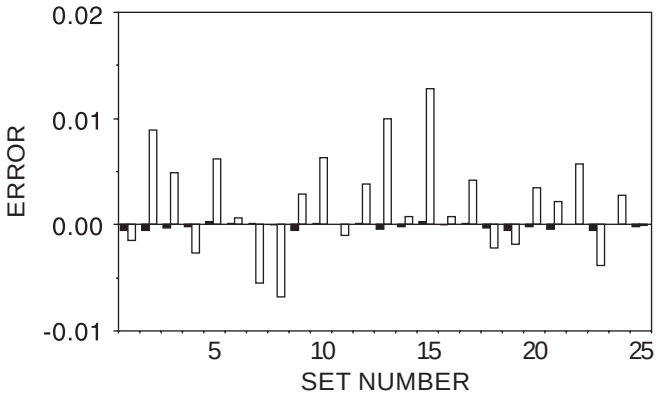

1.129 19 and 1.129 16, respectively, from eq. [1] and eq. [4], while the *very tight* option gave KIE = 1.129 17 from both. Here, the limiting value from the *very tight* optimization lies between the eq. [1] and eq. [4] values in both looser optimizations, and in both of these the Redlich–Teller value of eq. [4] is closer to the limiting value.

Although the geometry and hence the principal moments of inertia vary from *default* to *very tight* optimization, the resulting change in KIE is insignificant and can be ignored. It is sufficient to study the effect of errors in frequencies alone without concern for those in MMI. More exactly, the errors are in force constants, which are the same for both isotopomers, rather than directly in the frequencies themselves. We therefore added random errors to the Cartesian force constants from the *very tight* optimization, then computed the resulting frequencies and KIEs to see whether eq. [1] or eq. [4] is less affected by these errors.

Fig. 4. Calculations are like those of Fig. 2, but different Gaussian random errors are used for isotopomers.

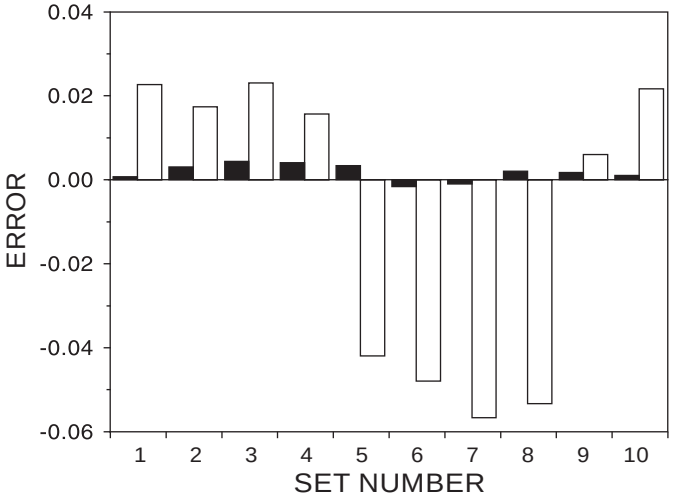

The results of 25 such computer experiments are displayed across the horizontal axis in Fig. 2 for a Gaussian distribution of random errors between ±0.000 05 Hartrees/(Bohr)^2, generated by standard random error programs (7), in the Cartesian force constants, and in Fig. 3 for a uniform random distribution of errors in the range 0 to 0.000 05 Hartrees/(Bohr)^2. The vertical axis shows the difference between each computed KIE and the exact value of 1.129 17. Results are in pairs with a dark bar showing the error in KIE computed using eq. [4] followed by a light bar showing the error using eq. [1]. For each such pair, the same set of force constant errors was used. In a few cases, e.g., the dark bar in the eighth run and the light bar in the last run of Fig. 3, KIE errors are too small to show. In both figures, KIE errors using the Redlich–Teller rule are usually, but not always, considerably smaller. Whether the error in force constants is Gaussian or uniform does not appear to make a large difference in the KIE error.

We also considered the artificial case with Gaussian errors as above, but where different errors were added independently to the same Cartesian force constant of the H and the D isotopomer. Results are in Fig. 4 for 10 computer runs and show considerably larger errors than in Figs. 2 and 3. There thus appears to be some canceling of errors between isotopomers in the real case. Here, too, eq. [4] gives the better result.

Figures 2 and 3 are specific to errors in force constants that are common to both isotopomers so that frequency errors in the two isotopomers are correlated. This is appropriate to the case of an ab initio calculation of KIE. It is also worth considering uncorrelated frequency errors as in the determination of equilibrium isotope effects from experimental frequencies. This can scarcely apply to KIEs, since transition structure frequencies are not experimentally available, but we can use a computed KIE to see whether the effect of uncorrelated frequency errors is very different from what was seen in Figs. 2 and 3. Accordingly, random errors from a uniform distribution over the range between –2.5 and +2.5 cm^{-1} were added to all frequencies from the *very tight* calculation of both isotopomers of reactant and product in the formamide isomerization. Results are in Fig. 5. The larg-

© 1999 NRC Canada

Fig. 5. Calculations are like those of Fig 3, but with a uniform distribution of random errors in the range –2.5 cm^{-1} to +2.5 cm^{-1} added to all frequencies independently.

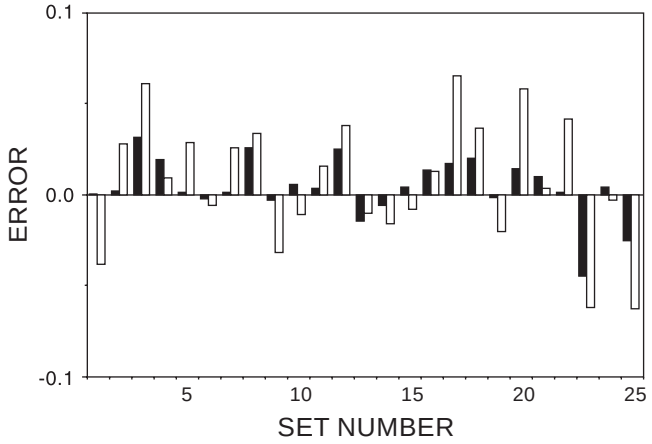

est errror here is four times the largest in Figs. 2 and 3. Again eq. [4] gives better results than eq. [1], but the advantage appears slightly less than in Figs. 2 and 3.

Primary KIE for H-transfer reaction in *Z*-1,3-pentadiene

To see whether the superiority of the Redlich–Teller expression for the small secondary isotope effect above also holds for larger primary effects, we examined the hydrogen transfer in *Z*-1,3-pentadiene (8–11). The *s-trans* conformer is the lowest energy conformation, but it is in rapid equilibrium with the *s-cis* conformer in which the H transfer occurs.[3] This justifies the use of the *s-trans* conformer as reactant in calculations which give KIE = 2.796. As for formamide, errors from a uniform distribution up to 0.000 05 Hartrees/(Bohr)^2 were added to the Cartesian force constants, and the 25 computer runs in Fig. 6 were carried out. The results show that use of the Redlich–Teller product rule again gives the better accuracy.

Conclusions

Ab initio calculations strongly indicate that eq. [4], which incorporates the Redlich–Teller product rule, is more reliable than eq. [1], which does not, for computing both primary and secondary KIEs in the presence of various kinds of random errors in force constants and frequencies.

Acknowledgment

L.J.S. has known and worked with Professor Kresge for over 40 years and is honored to contribute to this memorial issue. K.N. Houk thanks Professor Jerry Kresge for collaboration and inspiration on many occasions. We thank Professor P.L. Polavarapu for the use of his program VOA to transform Cartesian force constants to frequencies.

Fig. 6. Calculations are like those of Fig. 3, but for the primary KIE of H transfer in pentadiene. Here, error = (computed KIE) – 2.796.

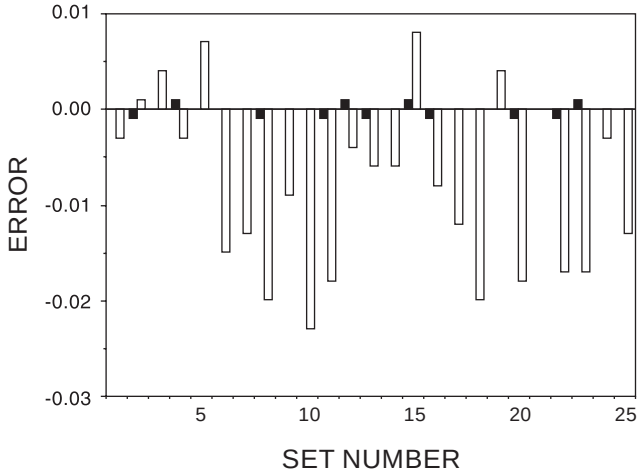

References

1. L.P. Olson, Y. Li, K.N. Houk, A.J. Kresge, and L.J. Schaad. J. Am. Chem. Soc. **117**, 2992 (1995).
2. J. Bigeleisen. J. Chem. Phys. **17**, 675 (1949).
3. O. Redlich. Z. Phys. Chem. B, **28**, 371 (1935).
4. M. Saunders, K.E. Laidig, and M. Wolfsberg. J. Am. Chem. Soc. **111**, 8989 (1989).
5. M.J. Frisch, G.W. Trucks, M. Head-Gordon, P.M.W. Gill, M.W. Wong, J.B. Foresman, B.G. Johnson, H.B. Schlegel, M.A. Robb, E.S. Replogle, R. Gomperts, J.L. Andres, K. Raghavachari, J.S. Binkley, C. Gonzales, R.L. Martin, D.J. Fox, D.J. DeFrees, J. Baker, J.J.P. Stewart, and J.A. Pople. GAUSSIAN 92, Revision C.4. Gaussian, Inc., Pittsburgh, Pa. 1992.
6. K.B. Wiberg and K.E. Ladig. J. Am. Chem. Soc. **109**, 5935 (1987).
7. W.H. Press, B.P. Flannery, S.A. Teukolsky, and W.T. Vetterling. Numerical recipes: the art of scientific computing. Cambridge University Press, Cambridge. 1986. pp. 195–203.
8. W.R. Roth and J. König. Liebigs Ann. Chem. **699**, 24 (1966).
9. S.D. Kahn, W.J. Hehre, N.G. Rondan, and K.N. Houk. J. Am. Chem. Soc. **107**, 8291 (1985).
10. F. Jensen and K.N. Houk. J. Am. Chem. Soc. **109**, 3139 (1987).
11. L. Chantranupong and T.A. Wildman. J. Am. Chem. Soc. **112**, 4151 (1990).

[3] L.J. Schaad and L. Bytautas. Unpublished results.

© 1999 NRC Canada

Isotope effects in nucleophilic substitution reactions XI. The effect of ion-pairing, substituents, and the solvent on S_N2 transition states

Kenneth Charles Westaway and W. Jiang

Abstract: The secondary alpha deuterium and primary leaving group nitrogen KIEs and Hammett ρ values found for the free ion and ion-pair S_N2 reactions between benzyldimethylphenylammonium ion and sodium *para*-substituted thiophenoxides in methanol at 20.000°C show how (*i*) ion-pairing of the nucleophile, (*ii*) a change in substituent in the nucleophile, and (*iii*) a change in solvent alters the structure of a Type II S_N2 transition state. Ion-pairing shortens the weaker sulfur – alpha carbon (S—C_α) transition state bond significantly but does not alter the stronger alpha carbon – leaving group (C_α—N) transition state bond as the bond strength hypothesis predicts. However, the effect of ion pairing, i.e., the decrease in the S—C_α bond on ion-pairing, decreases as a more electron-withdrawing substituent is added to the nucleophile, and the S—C_α bond actually increases when the nucleophile is the *p*-chlorothiophenoxide ion. The identical Hammett ρ values of –0.85 and –0.84 for the free ion and ion-pair reactions, respectively, may be observed because, *on average*, the S—C_α bonds are identical in the free ion and ion-pair transition states. When a more electron-donating substituent is added to the nucleophile, an earlier transition state is found in both the ion-pair and free ion reactions. However, the substituent effect is smaller in the ion-pair reactions, presumably because the change in the negative charge on the sulfur atom with substituent is greater in the free ion than in the ion-pair. The substituent effect on transition state structure suggested by the KIEs is not predicted by any of the theories that are used to predict substituent effects on S_N2 reactions. Both the secondary alpha deuterium and primary leaving group nitrogen KIEs and the Hammett ρ values indicate that the transition state is earlier when the solvent is changed from DMF to methanol as the "solvation rule for S_N2 reactions" predicts. This probably occurs because an earlier, more ionic, transition state is more highly solvated (more stable) in methanol.

Key words: nucleophilic substitution, S_N2, isotope effect, transition state, substituent, ion-pair.

Résumé : Les effets isotopiques cinétiques (EIC) secondaires du deutérium en alpha et primaire du groupe partant azoté ainsi que les valeurs de ρ trouvées pour les réactions S_N2 de l'ion libre et de la paire d'ion entre l'ion benzyldiméthylphénylammonium et les thiophénolates de sodium *para*-substitués, dans le méthanol à 20,000°C, montrent comment (*i*) la formation d'une paire d'ions du nucléophile; (*ii*) un changement de substituant dans le nucléophile et (*iii*) un changement dans le solvant peuvent altérer la structure d'un état de transition S_N2 du Type II. Tel que le prédit l'hypothèse de la force de liaison, la formation d'une paire d'ions raccourcit d'une façon significative la liaison d'état de transition soufre – carbone en alpha (S—C_α) qui est plus faible, mais qu'elle ne modifie pas la liaison d'état de transition carbone alpha – groupe partant (C_α—N) qui est plus forte. Toutefois, l'effet de la formation d'une paire d'ions (c'est-à-dire la diminution dans la longueur de la liaison S—C_α lors de la formation de la paire d'ions) diminue lorsqu'on ajoute au nucléophile un substituant plus électroaffinitaire; en fait, la liaison S—C_α s'allonge avec l'ion *p*-chlorothiophénolate. Dû au fait que les longueurs *moyennes* des liaisons S—C_α sont identiques dans les états de transition de l'ion libre et de la paire d'ions, les valeurs ρ de Hammett sont identiques, –0,85 et –0,84 respectivement, pour les réactions de l'ion libre et de la paire d'ions. Quand on ajoute un substituant électrodonneur au nucléophile, on observe un état de transition qui se produit plus tôt pour les réactions tant de l'ion libre que de la paire d'ions. Toutefois, l'effet de substituant est plus faible pour les réactions de la paire d'ions, probablement parce que le changement dans la charge négative sur l'atome de soufre en fonction du substituant est plus grand dans l'ion libre que dans la paire d'ions. L'effet de substituant sur la structure de l'état de transition qui est suggéré par les EIC n'est pas prédit par aucune des théories utilisées pour prédire les effets de substituant sur des réactions S_N2. Tel que le prédit la règle de solvatation des réactions S_N2, les EIC tant secondaire du deutérium en alpha que primaire de l'azote

Received December 17, 1998.

This paper is dedicated to Jerry Kresge in recognition of his many achievements in chemistry.

K.C. Westaway[1] and W. Jiang. Chemistry Department, Laurentian University, Sudbury, ON P3E 2C6, Canada.

[1]Author to whom correspondence may be addressed. Telephone: (705) 675-1151 (ext. 2105). Fax: (705) 675-4844. e-mail: KWestawa@Nickel.Laurentian.CA

 © 1999 NRC Canada

du groupe partant ainsi que les valeurs de ρ de Hammett indiquent que l'état de transition se produit plus tôt quand on change le solvant de DMF à méthanol. Ceci se produit vraisemblablement parce qu'un état de transition rapide, plus ionique, est plus solvaté (plus stable) dans le méthanol.

Mots clés : substitution nucléophile, S_N2, effet isotopique, état de transition, substituant, paire d'ions.

[Traduit par la Rédaction]

Introduction

The secondary alpha deuterium and primary nitrogen leaving group KIEs for the S_N2 reactions (1, 2) between benzyldimethylphenylammonium nitrate and sodium *para*-substituted thiophenoxides, eq. [1],

[1]

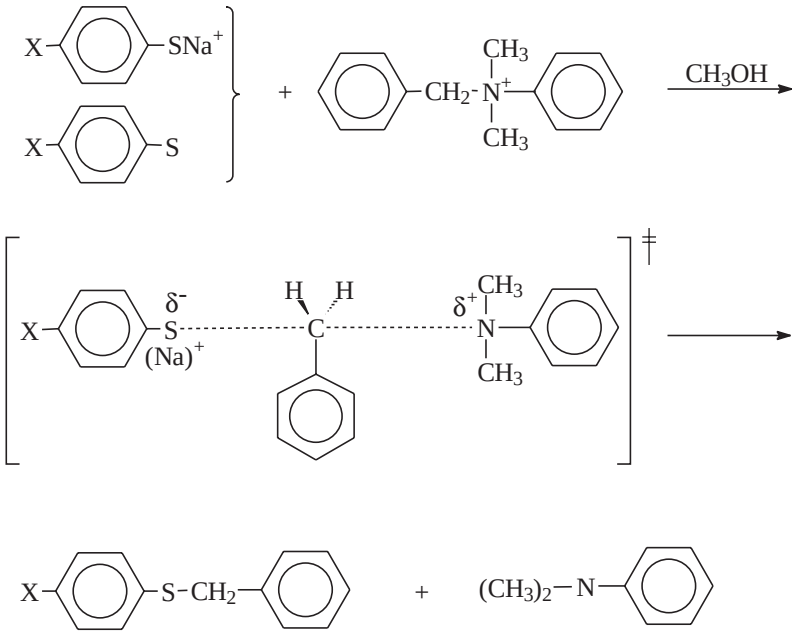

were measured in methanol at 20.000 ± 0.002°C when the reacting nucleophile existed as a solvent-separated ion-pair complex and as a free ion (3) to determine how (*i*) ion-pairing of the nucleophile, (*ii*) a change in substituent in the nucleophile, and (*iii*) a change in solvent alters the structure of the S_N2 transition state.

Results and discussion

Form of the reacting nucleophile

Since one of the objectives of this study was to determine the effect of ion-pairing on the structure of the S_N2 transition state, the form of the reacting nucleophile must not change throughout the reaction. The ion-pair/free ion absorbance ratio at a concentration of approximately 3.5×10^{-4} M, Table 1, increases from 0.74 to 1.72 when a more electron-withdrawing group is added to the benzene ring of the sodium *para*-substituted thiophenoxide. This suggests that ion-pairing begins at a lower concentration when a more electron-withdrawing substituent is used. This presumably occurs because the more negative sulfur ion of the *para*-methoxythiophenoxide ion is more strongly solvated by hydrogen bonding to methanol and is, therefore, not able to form an ion-pair as easily as the less strongly solvated *para*-chlorothiophenoxide ion. However, the difference between the salts is small, and all three salts begin ion-pairing near the same concentration. For instance, sodium thiophenoxide begins forming ion-pairs at 1×10^{-4} M (3), and both the sodium *para*-methoxy- and *para*-chlorothiophenoxide salts exist partly as a free ion and partly as an ion-pair at 3×10^{-4} M. The important observation, however, is that all three salts exist completely as the ion-pair at concentrations $\geq 1 \times 10^{-3}$ M. The initial concentration of the sodium *para*-substituted thiophenoxide in every reaction in this study was approximately 5×10^{-3} M and the nucleophile/substrate ratio was 2/1. Therefore, even at 100% reaction, the concentration of the sodium *para*-substituted thiophenoxide solution was still 2.5×10^{-3} M, or approximately three times the concentration (1×10^{-3} M) where the sodium *para*-substituted thiophenoxides exist completely as the ion-pair. This ensured that the nucleophile is the solvent-separated sodium *para*-substituted thiophenoxide ion-pair complex (3) in all the reactions in this study.

The free *para*-substituted thiophenoxide ion required for this study was generated by adding a 2.6 molar excess of 15-crown-5 ether, which complexes the sodium ion in the ion-pair complex converting it into a free *para*-substituted thiophenoxide ion (3, 4). The data in Table 2 show that the amount of ion-pair decreases when 15-crown-5 ether is added to each sodium *para*-substituted thiophenoxide solution. Although only the free ion was observed when the (15-crown-5 ether/thiophenoxide ion) ratio was 0.5 for sodium *para*-

© 1999 NRC Canada

Table 1. The λ_{max} and absorbance for sodium *para*-substituted thiophenoxide solutions in methanol at 20°C.

		Free ion		Ion-pair		
para-Substituent	Conc. (M)	λ_{max}	Abs.	λ_{max}	Abs.	$(Abs.)_{Ion\text{-}pair}/(Abs.)_{Free\ ion}$
CH_3O	1×10^{-5}	235	0.15	265	—	0
	1×10^{-4}	238	1.10	265	0.40	0.36
	4×10^{-4}	238	1.95	265	1.45	0.74
	1×10^{-3}	238	—	Wide	2.80	∞
H	7×10^{-6}	238	0.08	265	—	0
	3×10^{-4}	238	1.56	267	1.74	1.12
	8×10^{-4}	238	—	Wide	2.70	∞
Cl	2×10^{-5}	248	0.16	273	0.11	0.69
	3×10^{-4}	250	1.10	275	1.90	1.72
	7×10^{-4}	250	—	Wide	2.60	∞

Table 2. The effect of adding 15-crown-5 ether on λ_{max} and the absorbance of sodium *para*-substituted thiophenoxide solutions in methanol at 20°C.

		Free ion		Ion-pair		Mole ratio
para-Substituent	Conc. (M)	λ_{max} (nm)	Abs.	λ_{max} (nm)	Abs.	15-crown-5/*p*-X-C_6H_4SNa
CH_3O	1×10^{-4}	238	1.10	265	0.40	0
		238	1.13	—	—	0.50
H	4×10^{-5}	237	0.34	266	0.16	0
		237	0.44	—	—	0.50
Cl	2×10^{-4}	250	1.08	275	1.70	0
		246	1.10	275	1.46	0.40
		246	1.16	275	1.27	1.0
		244	1.36	—	—	2.0

methoxythiophenoxide and sodium thiophenoxide, a (15-crown-5 ether/thiophenoxide ion) ratio of >1.0 was required to convert all the sodium *para*-chlorothiophenoxide into the free ion. The higher (15-crown-5 ether/thiophenoxide ion) ratio required for the sodium *para*-chlorothiophenoxide is presumably needed because this salt is the most prone to ion-pairing. A (15-crown-5 ether/sodium *para*-substituted thiophenoxide) ratio of 2.6 was used in all the free ion reactions in this study to ensure that all of the reacting nucleophile existed as a free ion. It is interesting that increasing the (15-crown-5 ether/sodium *para*-substituted thiophenoxide) mole ratio from 0 to 2.6 does not change the λ_{max} for the free thiophenoxide ion significantly. This suggests that the 15-crown-5 ether does not affect the nucleophile significantly.

Secondary alpha deuterium and primary nitrogen leaving group KIEs

The secondary alpha deuterium and primary nitrogen (leaving group) KIEs for the S_N2 reactions between benzyldimethylphenylammonium nitrate and sodium *para*-substituted thiophenoxides were measured in methanol at 20.000 ± 0.002°C when the reacting nucleophile existed as a solvent-separated ion-pair complex and as a free ion to learn how (*i*) changing the nucleophile from a solvent-separated ion-pair complex to a free ion, (*ii*) changing the *para*-substituent on the nucleophile, and (*iii*) changing the solvent affect the structure of the S_N2 transition state.

The nitrogen KIEs, Table 3, were measured by reacting the nucleophile with both isotopically labelled substrates in the same reaction. Two kinds of the reactions, completes (taken to 100% of completion, 14 half-lives) and partials (stopped at approximately 12.5% of completion) were carried out. The products, a benzyl-*para*-substituted phenyl sulfide and *N*,*N*-dimethylaniline were separated and analyzed by HPLC and a Kjeldahl analysis, respectively. Then, the ammonium sulphate obtained from the Kjeldahl analysis was oxidized quantitatively into nitrogen gas and purified on a high vacuum line. Finally, the $^{14}N/^{15}N$ ratio of the nitrogen gas obtained from the partial and complete reactions was determined on an isotope ratio mass spectrometer, and the primary nitrogen leaving group KIE was calculated from these ratios and the average fraction of reaction from the Kjeldahl and HPLC analyses (1, 2). The secondary alpha deuterium KIEs, Table 4, were obtained by dividing the average rate constants from between three and five kinetic runs using the deuterated and undeuterated substrates, respectively (4).

The effect of ion-pairing on the structure of the S_N2 transition state

A comparison of the secondary alpha deuterium and primary nitrogen KIEs for the free ion and ion-pair reactions between benzyldimethylphenylammonium nitrate and sodium *para*-substituted thiophenoxides in methanol, Table 4, illustrate how ion pairing affects the structure of the S_N2 transition state. The leaving group nitrogen KIEs for the free ion

© 1999 NRC Canada

Table 3. The percent reaction based on the Kjeldahl and HPLC analyses, the average fraction of reaction, the δ value, the $^{14}N/^{15}N$ ratio (R_f) for partial reactions and the nitrogen KIE for the S_N2 reactions between benzyldimethylphenylammonium nitrate and several solvent-separated sodium *para*-substituted thiophenoxide ion-pair complexes and free *para*-substituted thiophenoxide ions in methanol at 20.000°C.

Sample number	% reaction Kjeldahl	% reaction HPLC	Average f[a]	δ[b]	R_f	k^{14}/k^{15}
			Solvent-separated ion-pair complex			
MeO-1	12.03	11.89	0.1196 ± 0.0007[c]	–21.057	282.606	1.0168
MeO-2	12.03	11.91	0.1197 ± 0.0006	–19.852	282.272	1.0155
MeO-3	11.99	11.91	0.1195 ± 0.0004	–20.516	282.456	1.0162
MeO-4	12.03	11.94	0.1198 ± 0.0004	–20.330	282.405	1.0160
						Average 1.0161 ± 0.0005[d]
H-1	12.49	12.61	0.1255 ± 0.0006	–19.729	282.238	1.0155
H-2	12.93	12.66	0.1279 ± 0.0014	–20.411	282.427	1.0162
H-3	12.47	12.60	0.1253 ± 0.0007	–19.469	282.166	1.0151
H-4	12.57	12.39	0.1248 ± 0.0009	–20.617	282.484	1.0164
H-5	12.48	12.52	0.1250 ± 0.0002	–21.781	282.806	1.0176
						Average 1.0162 ± 0.0010[d]
Cl-1	13.48	13.46	0.1347 ± 0.0001	–20.717	282.512	1.0165
Cl-2	13.14	12.70	0.1292 ± 0.0022	–21.157	282.634	1.0170
Cl-3	12.73	12.43	0.1258 ± 0.0015	–20.546	282.465	1.0163
Cl-4	12.88	12.68	0.1278 ± 0.0010	–20.844	282.547	1.0166
Cl-5	12.94	12.56	0.1275 ± 0.0019	–20.642	282.491	1.0164
						Average 1.0166 ± 0.0003[d]
			Free ion			
MeO-6	12.61	12.04	0.1233 ± 0.0029	–21.121	282.624	1.0169
MeO-7	12.48	12.21	0.1235 ± 0.0014	–20.659	282.496	1.0164
MeO-8	12.26	11.92	0.1209 ± 0.0017	–20.270	282.388	1.0159
MeO-9	12.70	12.03	0.1237 ± 0.0034	–20.025	282.320	1.0157
MeO-10	12.12	12.01	0.1207 ± 0.0006	–20.638	282.490	1.0163
						Average 1.0162 ± 0.0005[d]
H-6	12.65	12.54	0.1259 ± 0.0005	–21.936	282.849	1.0177
H-7	12.26	12.56	0.1241 ± 0.0015	–20.852	282.549	1.0166
H-8	12.51	12.95	0.1273 ± 0.0022	–20.592	282.477	1.0163
H-9	13.33	13.14	0.1323 ± 0.0009	–21.067	282.609	1.0168
H-10	13.57	13.31	0.1344 ± 0.0013	–19.919	282.291	1.0156
						Average 1.0166 ± 0.0008[d]
Cl-6	12.53	12.31	0.1242 ± 0.0011	–20.718	282.512	1.0165
Cl-7	12.54	12.18	0.1236 ± 0.0018	–20.711	282.510	1.0164
Cl-8	12.34	12.21	0.1227 ± 0.0007	–20.427	282.708	1.0172
Cl-9	12.10	11.93	0.1202 ± 0.0009	–21.049	282.604	1.0169
Cl-10	12.39	12.06	0.1222 ± 0.0016	–21.705	282.785	1.0176
						Average 1.0169 ± 0.0005[d]

[a]The fraction of reaction, *f*, is based on the average of the percent reaction found in the Kjeldahl and the HPLC analyses.

[b]The average δ value for five complete samples was –5.257 ± 0.255, and the average $^{14}N/^{15}N$ was 278.23 ± 0.065.

[c]Standard deviation for *f*.

[d]Standard deviation for the KIE.

and ion-pair reactions are clearly identical within the experimental error of the method. For example, even for the sodium thiophenoxide reactions with the greatest $[(k^{14}/k^{15})_{\text{free ion}} - (k^{14}/k^{15})_{\text{ion-pair}}] = 0.0004$, the difference between the KIEs is much smaller than the experimental error in either isotope effect.[2]

One can deduce how the S—C_α bond changes on ion-pairing by combining the information provided by the secondary alpha deuterium and nitrogen KIEs. The identical nitrogen KIEs for the free ion and ion–pair reactions show that the C_α—N transition state bond is not changed by ion-pairing. Therefore, the change in the secondary alpha deute-

[2]A student "*t*" test (5) indicates that the nitrogen KIEs for the free ion and ion-pair reactions are only different at the 61% confidence level when the nucleophile is the *para*-methoxythiophenoxide ion, at the 23% confidence level when the nucleophile is the thiophenoxide ion, and at the 9% confidence level when the nucleophile was the *para*-chlorothiophenoxide ion.

© 1999 NRC Canada

Table 4. The secondary alpha deuterium and primary nitrogen leaving group KIEs and the Hammett ρ values for the ion-pair and free ion S_N2 reactions between benzyldimethylphenylammonium nitrate and sodium *para*-substituted thiophenoxides in methanol at 20.000°C.

para-Substituent on the nucleophile	Free ion	Ion-pair
	k^{14}/k^{15}	k^{14}/k^{15}
CH_3O-	1.0162 ± 0.0005[a]	1.0161 ± 0.0005[a]
H-	1.0166 ± 0.0008	1.0162 ± 0.0010
Cl-	1.0169 ± 0.0005	1.0166 ± 0.0003
	$(k_H/k_D)_\alpha$[b]	$(k_H/k_D)_\alpha$[b]
CH_3O-	1.271 ± 0.013[c]	1.216 ± 0.012[c]
CH_3-	1.237 ± 0.008	1.213 ± 0.013
H-	1.222 ± 0.013	1.207 ± 0.008
Cl-	1.121 ± 0.014	1.150 ± 0.009
Hammett ρ[d]	–0.85 ± 0.14[e]	–0.84 ± 0.11[e]

[a]Standard deviation for the average KIE.

[b]Several of these isotope effects were remeasured when the nitrogen KIEs were measured to ensure that they were correct under the conditions used to measure the nitrogen KIEs. The KIEs that were checked were identical to those in ref. 4. The KIEs from the more complete study (4) are quoted in this table.

[c]The error in the isotope effect is $1/k_D[\Delta(k_H)^2 + (k_H/k_D)^2 \times \Delta(k_D)^2]^{1/2}$ where Δk_H and Δk_D are the standard deviations for the rate constants for the reactions of the undeuterated and deuterated substrates, respectively.

[d]The Hammett ρ values were obtained by changing the *para*-substituent in the nucleophile.

[e]The standard error of coefficient of the ρ value.

rium KIE on ion-pairing must be due to a change in the S- -N distance (6, 7) and the S—C_α transition state bond. Although ion-pairing affects the secondary alpha deuterium KIE (the S—C_α bond), the effect is different for each nucleophile. The $(k_H/k_D)_\alpha$ decreases on ion-pairing by 5% (from 1.27 to 1.22), by 3% (from 1.24 to 1.21), and by 1% (from 1.22 to 1.21) when the *para*-substituent on the nucleophile is methoxy, methyl, and hydrogen, respectively, but increases by 3% (from 1.12 to 1.15) when the *para*-substituent is chlorine. This means the S- -N distance and therefore, the S—C_α bond, is much longer (6, 7) in the free *p*-methoxythiophenoxide ion reaction, longer in the *p*-methylthiophenoxide ion reaction, slightly longer in the free thiophenoxide ion reaction, but shorter in the free *p*-chlorothiophenoxide ion reaction than the S—C_α bonds in the corresponding ion-pair reactions, Fig. 1.

One explanation for the longer S—C_α bond in the free ion transition state is that the sodium ion reduces the electron density on the sulfur atom (4). As a result, the sulfur has to be closer to the alpha carbon to distort the C_α—N bond and cause the reaction. Three out of four cases are consistent with this suggestion. Unfortunately, this is not true for the *para*-chlorothiophenoxide ion reaction, which has a shorter S—C_α bond in the free ion transition state.

The effect of ion pairing becomes smaller as a more electron-withdrawing substituent is added to the nucleophile. Since the electron density on the sulfur atom decreases when a more electron-withdrawing substituent is added to the nucleophile, the strength of the ionic bond between the sodium and sulfur ions would also decrease. This suggests that the difference between the electron density on the sulfur atom of a free ion nucleophile and an ion-pair nucleophile will be smaller when a more electron-withdrawing substituent is on the nucleophile. As a result, the difference between the free ion and the ion-pair secondary alpha deuterium KIEs should be smaller when a more electron-withdrawing group is on the nucleophile. We cannot explain why the effect of ion pairing for the *para*-chlorothiophenoxide ion reaction does not follow this trend.

The identical Hammett ρ values found by changing the *para*-substituent on the nucleophile for the free ion and ion-pair S_N2 reactions, Table 4, suggest that the change in charge on the nucleophilic sulfur atom on going to the transition state is identical for the free ion and ion-pair reactions and, therefore, that the S—C_α transition state bond is not altered significantly when the nucleophile changes from a free ion to an ion-pair. The identical ρ values for the free ion and ion-pair reactions may be observed because, *on average*, the S—C_α bond of the free ion reactions is identical to the S—C_α bond of the ion-pair reactions, Fig. 1.

Another observation is that the major change on ion-pairing occurs in the S—C_α bond, and there is no change in the C_α—N bond. This is predicted by the bond strength hypothesis (8). If ion-pairing can be treated like a substituent effect, changing a free ion to an ion-pair nucleophile lowers the electron density on the nucleophilic sulfur atom, making it a poorer nucleophile. According to the bond strength hypothesis, the weaker S—C_α reacting bond in the S_N2 transition state will change significantly, and little or no change will occur in the stronger C_α—N reacting bond when the nucleophile is changed. Unfortunately, the bond strength hypothesis does not predict how the two transition state bonds will change on ion-pairing.

Substituent effects on the structure of the S_N2 transition state

Although several studies have attempted to determine how a change in substituent in the substrate (9–11) and the leaving group (2, 12, 13) affect the structure of an S_N2 transition state, no study has shown how a change of substituent in the nucleophile changes *both* the nucleophile – alpha carbon *and* the alpha carbon – leaving group bond in an S_N2 transi-

© 1999 NRC Canada

Fig. 1. The relative transition state structures for the free ion and ion-pair S_N2 reactions between sodium *para*-substituted thiophenoxides and benzyldimethylphenylammonium ion in methanol at 20.000°C.

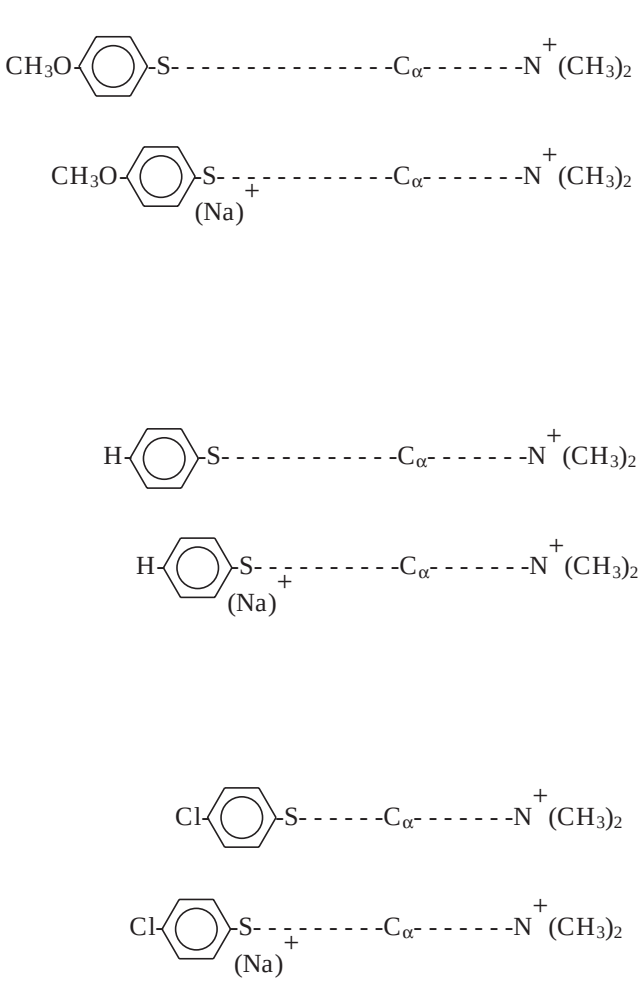

tion state. The secondary alpha deuterium and nitrogen KIEs for the S_N2 reactions between benzyldimethylphenylammonium nitrate and sodium *para*-substituted thiophenoxides show how changing a substituent on the nucleophile affects both reacting bonds in the S_N2 transition state. The $(k_H/k_D)_\alpha$, Table 4, decreases from 1.271 to 1.121 when the *para*-substituent on the free thiophenoxide ion changes from methoxy to chloro. Since the secondary alpha deuterium KIEs are directly related to the S- -N distance in the S_N2 transition state (6, 7), adding a more electron-withdrawing substituent to the nucleophile leads to a transition state with a shorter S- -N distance. The nitrogen leaving group KIEs, Table 4, on the other hand, increase very slightly when a more electron-withdrawing substituent is added to the nucleophile. For instance, the k^{14}/k^{15} increases by 0.0007 when the *para*-substituent on the free thiophenoxide ion changes from methoxy to chloro.[3] This means the C_α—N transition state bond length increases slightly as a more electron-withdrawing substituent is added to the nucleophile.

The relative length of the S—C_α transition state bond can be deduced from the primary nitrogen and the secondary alpha deuterium KIEs. When a more electron-withdrawing substituent is added to the nucleophile, the C_α—N transition state bond becomes slightly longer and the S- -N distance shorter. Therefore, the S—C_α transition state bond must be much shorter when a more electron-withdrawing substituent is added to the nucleophile, Fig. 2.

The substituent effects on the secondary alpha deuterium and nitrogen KIEs for the ion-pair reactions are the same as those for the free ion reactions, Table 4. The $(k_H/k_D)_\alpha$ decreases from 1.216 to 1.150 and there is a small increase[4] (0.0005) in the nitrogen leaving group nitrogen KIE when the *para*-substituent on the ion-pair nucleophile changes from methoxy to chloro. This means that the S- -N transition state distance decreases and the C_α—N bond is slightly longer when a more electron-withdrawing substituent is added to the nucleophile. Again, the nitrogen KIEs indicate that the C_α—N transition state bond length increases very slightly,

[3] A student "*t*" test (5) showed that the nitrogen KIEs for the reactions with the free *p*-methoxythiophenoxide ion and the free *p*-chlorothiophenoxide ion are different at the 97% confidence level.

[4] A student "*t*" test (5) showed the primary nitrogen KIEs for the ion-pair reactions where the nucleophile is the sodium *para*-methoxythiophenoxide ion-pair and the sodium *p*-chlorothiophenoxide ion-pair are different at the 92% confidence level.

© 1999 NRC Canada

Fig. 2. The relative transition state structures for the S_N2 reactions between benzyldimethylphenylammonium ion and free *para*-substituted thiophenoxide ions in methanol at 20.000°C.

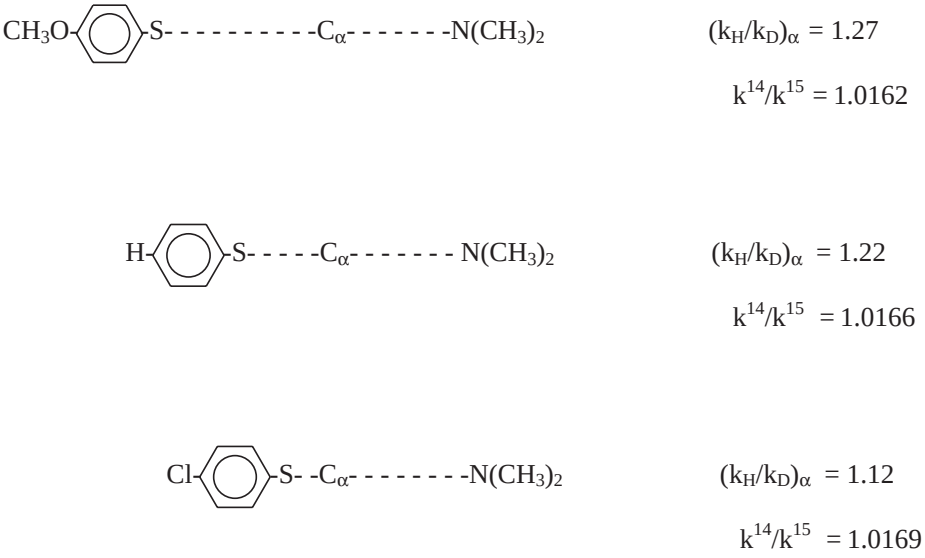

and the secondary alpha deuterium KIEs show that the S- -N distance decreases when a more electron-withdrawing group is added to the nucleophile. Since the S- -N distance decreases when the C_α—N bond becomes longer, the S—C_α bond must be shorter when a more electron-withdrawing substituent is added to the nucleophile in the ion-pair reactions.

The results indicate that both the free ion and ion-pair S_N2 reactions between benzyldimethylphenylammonium nitrate and sodium *para*-substituted thiophenoxides have a later transition state with a shorter S—C_α bond and a slightly longer C_α—N bond when a more electron-withdrawing substituent is added to the nucleophile. This may occur because adding a more electron-withdrawing substituent to the nucleophile pulls electron density away from the nucleophilic sulfur atom, making it a poorer nucleophile. As a result, the nucleophile has to come closer to the alpha carbon to distort the C_α—N bond (cause the reaction), and a later transition state should be observed.

The greater change in the S—C_α bond with substituent can be understood in terms of the bond strength hypothesis (8), which predicts that the weaker S—C_α bond will change significantly but that there will be little or no change in the stronger C_α—N bond when the *para*-substituent on the nucleophile is changed. The decrease in the S—C_α transition state bond length is greater than the increase in the C_α—N transition state bond because the energy obtained by increasing the bond order of the weak S—C_α bond will only lengthen the stronger C_α—N slightly.

The substituent effect is greater in the free ion reactions than in the ion-pair reactions. The $(k_H/k_D)_\alpha$ decreases by 15% in the free ion reactions but only by 7% in the ion-pair reactions when the *para*-substituent on the nucleophile changes from a methoxy to a chloro group. The corresponding change in the k^{14}/k^{15} is 0.0007 in the free ion reactions but only 0.0005 in the ion-pair reactions. A possible explanation for this is that the change in charge on the nucleophilic sulfur atom with substituent is greater in the free ions than in the ion-pairs. A CNDO/2 calculation (4) showed that the decrease in charge on the sulfur is 0.0208 for the free ions but is only 0.0171 for the ion-pairs when the *para*-substituent on the nucleophile changes from methoxy to chloro. Since the substituent effect on the negative charge on the sulfur atom is 22% greater for the free ions, it is not surprising that the greatest substituent effect is found in these reactions.

The substituent effect on transition state structure found in this study can be used to test the theories that predict the substituent effect on transition state structure. The Bell–Evans–Polanyi (BEP) principle (Hammond's thermal postulate) (14) predicts that adding an electron-withdrawing group to the nucleophile makes a poorer nucleophile and increases the free energy of activation for the reaction. This leads to a more product-like transition state with a shorter S—C_α and a longer C_α—N bond. This theory predicts correctly the substituent effect on transition state structure but does not predict the different magnitude of the changes in the two reacting bonds. Thornton's reacting bond rule (15) and the More O'Ferrall – Jencks energy surface method (16, 17) predict that adding a more electron-withdrawing substituent to the nucleophile will lead to a transition state with an unchanged S—C_α bond and longer C_α—N bond. Neither Thornton's rule nor the energy surface method predict the change in the S_N2 transition state that is observed. The Harris–Kurz modification of Thornton's reacting bond rule (18) predicts the transition state will have a longer S—C_α and a shorter C_α—N bond when a more electron-withdrawing substituent is added to the nucleophile. Although the Harris–Kurz theory predicts the change in transition state structure correctly, it does not indicate the relative magnitude of the changes in the two transition state bonds. The Pross–Shaik method (19), which predicts that adding a more electron-withdrawing substituent to the nucleophile will lead to a transition state with a longer S—C_α bond and a shorter C_α—N transition state bond, is clearly not consistent with the experimental results. Critchlow (20) predicted that a change in substituent on the nucleophile will only change the remote C_α—N transition state bond and will not affect

© 1999 NRC Canada

Table 5. The secondary alpha deuterium and primary leaving group nitrogen KIEs for the ion-pair S_N2 reactions between sodium thiophenoxide and benzyldimethylphenylammonium nitrate in DMF at 0°C and in methanol at 20.000°C.

Solvent	Temp. (°C)	$(k_H/k_D)_\alpha$	k^{14}/k^{15}	Hammett ρ value[a]
Methanol	20	1.207 ± 0.008[b]	1.0162 ± 0.0010[c]	–0.84 ± 0.11[d]
DMF	0	1.179 ± 0.010	1.0200 ± 0.0007	–1.70 ± 0.05
DMF	20	1.17[e]	1.018[e]	

[a]The Hammett ρ value was obtained by changing the *para*-substituent on the nucleophile.

[b]The error in the isotope effect is $1/k_D[(\Delta k_H)^2 + (k_H/k_D)^2 \times (\Delta k_D)^2]^{1/2}$ where Δk_H and Δk_D are the standard deviations for the rate constants for the reactions of the undeuterated and deuterated substrates, respectively.

[c]Standard deviation of the average KIE.

[d]Standard error of the ρ value.

[e]This KIE is estimated at 20°C.

the S—C_α transition state bond significantly. However, the major change in transition state structure is at the S—C_α bond and Critchlow's theory is not correct. Finally, Westaway's bond strength hypothesis (8) predicts that changing a substituent in the nucleophile, in the leaving group, or at the alpha carbon will change the weaker (S—C_α) reacting bond markedly but that the stronger (C_α—N) reacting bond will not change significantly. This is what is observed for both the ion-pair and free ion reactions. However, the bond strength hypothesis does not predict how the transition state bonds will change when a more electron-withdrawing substituent is added to the nucleophile.

The change in the S—C_α and C_α—N bonds observed in this study is only predicted by Hammond's postulate and the Harris–Kurz theory. However, neither theory predicts that the S—C_α bond order increases significantly while the C_α—N bond order decreases very slightly. While the bond strength hypothesis predicts the relative changes in the two reacting bonds, it does not predict how the reacting bonds will change.

The failure of these rules to predict the substituent effects on the structure of S_N2 transition states is not unique to this study. Westaway and Ali (2) reported that the predictions based on the BEP principle, Thornton's reacting bond rule, the More O'Ferrall – Jencks energy surface method, Critchlow's method, and the Harris–Kurz theory were not consistent with the experimental changes found in transition state structure when the leaving group was altered in the S_N2 reactions between *para*-substituted phenylbenzyldimethylammonium nitrates and sodium thiophenoxide in DMF at 0°C. In another study, Pham and Westaway (21) found that only the bond strength hypothesis was consistent with the change in transition state structure that was observed when the nucleophile was changed in the S_N2 reactions between benzyldimethylphenylammonium nitrate and sodium *para*-substituted thiophenoxide ions at high ionic strength in DMF at 0°C. Finally, Westaway and Waszczylo (10) observed that the change in the transition state structure found when a substituent on the alpha carbon was changed in the S_N2 reactions between sodium thiophenoxide and *para*-substituted benzyl chlorides in methanol at 20°C, was only predicted by the Harris–Kurz theory, the Pross–Shaik method, and the bond strength hypothesis. In fact, the only theory that is consistent with all the experimental substituent effects that have been found in S_N2 reactions where the *total* transition state structure has been determined is the bond strength hypothesis, and it is only partially successful because it only predicts the relative magnitudes of the changes in the two reacting bonds and does not indicate how these bonds change.

Solvent effect on the structure of the S_N2 transition state

The "solvation rule for S_N2 reactions" (22) suggests that the transition state for a Type II S_N2 reaction (with a neutral and a negatively charged nucleophile in the transition state) will change significantly when the solvent is changed. A comparison of the secondary alpha deuterium and primary leaving group nitrogen KIEs and Hammett ρ values found for the S_N2 reaction between benzyldimethylphenylammonium nitrate and a solvent-separated sodium thiophenoxide ion-pair complex in methanol at 20°C and in DMF at 0°C, Table 5, can be used to test this rule.

Unfortunately, the KIEs in the two solvents were measured at different temperatures. However, the temperature dependence for both these KIEs is small. Shiner et al. (23) found that increasing the temperature by 20°C decreased the $(k_H/k_D)_\alpha$ for several S_N2 reactions by approximately 0.01, and Koshy and Robertson (24) found that increasing the temperature of several S_N2 reactions by 20°C decreased the $(k_H/k_D)_\alpha$ by between 0.002 and 0.014. Applying the average temperature dependence of 0.008 per 20°C to the secondary alpha deuterium KIE of 1.179, found at 0°C in DMF, suggests that this KIE would be approximately 1.17 at 20°C. Therefore, the secondary alpha deuterium KIE in methanol ($(k_H/k_D)_\alpha$ = 1.215 at 20°C) is significantly larger than the $(k_H/k_D)_\alpha$ = 1.179 at 0°C (approximately 1.17 at 20°C) in DMF. No temperature effect has been reported for primary nitrogen leaving group KIEs. However, Turnquist et al. (25) found the chlorine leaving group KIE for the solvolysis of *tert*-butyl chloride decreased from 1.010 87 at 10°C to 1.010 58 at 20°C and that the chlorine KIE for the S_N2 reaction between butyl chloride and sodium thiophenoxide in methanol decreased from 1.009 64 at 0°C to 1.008 95 at 20°C. Thus, the chlorine KIE decreases by 0.000 58 and 0.000 69, respectively, (by an average of 0.0006) when the reaction temperature is increased by 20°C. If one assumes that the temperature effect of a nitrogen KIE can be estimated from the temperature dependence of the chlorine KIE and the maximum chlorine and nitrogen KIEs of 1.0141 and 1.0436, respectively, at 25°C (26), the nitrogen KIE should decrease by approximately 0.0019 when the temperature increases by 20°C. This suggests the leaving group nitrogen

© 1999 NRC Canada

Fig. 3. The relative transition state structures for the ion-pair S_N2 reactions between sodium thiophenoxide and benzyldimethylphenylammonium nitrate in DMF and in methanol.

In methanol:

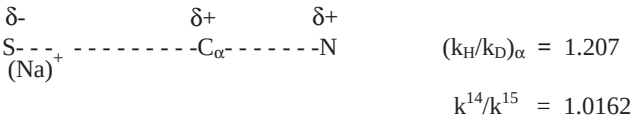

In DMF:

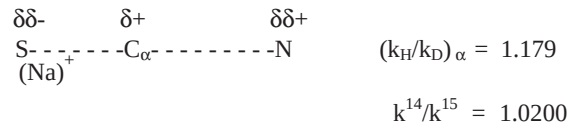

KIE of 1.0200 in DMF at 0°C would be approximately 1.018 in DMF at 20°C and that the nitrogen KIE is significantly larger in DMF than in methanol.

The larger secondary alpha deuterium KIE of 1.215 in methanol ($(k_H/k_D)_\alpha$ = 1.17 in DMF), Table 5, indicates that the S- -N transition state distance is greater in methanol than it is in DMF. The nitrogen KIE, on the other hand, is smaller in methanol than in DMF. This indicates the C_α—N transition state bond is considerably shorter in methanol than in DMF. Because the transition state in methanol has a longer S- -N distance but a shorter C_α—N bond, the S—C_α bond must be much longer in methanol than in DMF. Therefore, an earlier transition state, with a much longer S—C_α and a shorter C_α—N bond, is found in methanol.

The Hammett ρ values measured by changing the *para*-substituent on the nucleophile in DMF and methanol, Table 5, support this conclusion. The greater magnitude of the ρ value in DMF indicates that the change in charge on the nucleophilic sulfur atom is greater on going from the initial state to the transition state in DMF than it is in methanol. Therefore, the S—C_α transition state bond must be shorter in DMF than in methanol. This supports the conclusions based on the KIEs, and it is safe to conclude that an earlier, more highly charged, transition state is found in methanol, Fig. 3.

The earlier transition state in methanol can be rationalized if two assumptions are valid. First, solvation of the S_N2 transition state will occur primarily at the partial negative charge on the sulfur atom, and there will be little or no solvation of the partial positive charges on the alpha carbon and the nitrogen atom because these charges are sterically hindered to solvation, Fig. 4. This means the transition state is solvated by hydrogen bonding to the sulfur atom in methanol whereas it is only solvated by a weaker ion–dipole interaction in DMF. A second assumption is that a more ionic transition state, which would be more highly solvated (more stable) in a hydrogen bonding solvent, would be found in a hydrogen bonding solvent and that a less ionic (polar) transition state would be found in a less ionic (dipolar aprotic) solvent, i.e., the structure of the transition state found in a particular solvent will depend on its stability in that solvent. This means

Fig. 4. The structure of the transition state showing the solvation of the S_N2 transition state by methanol.

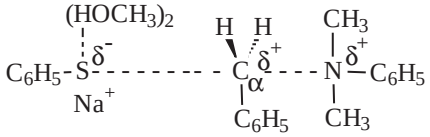

that an early, more ionic, transition state would be found in methanol where it is more stable because solvation of the negatively charged sulfur atom is greater. DMF, on the other hand, cannot form hydrogen bonds to the sulfur atom in the transition state and only stabilizes the transition state by a weak ion–dipole interaction. Therefore, a late, less ionic (dipolar) transition state, which would be more strongly solvated in DMF, should be observed in DMF. It is worth noting that this explanation of the solvent effect is supported by the secondary alpha deuterium and nitrogen KIEs found for the S_N2 reactions between sodium thiophenoxide and benzyldimethylphenylammonium nitrate at two different ionic strengths in DMF (21).

Finally, the different transition state structures suggested by the secondary alpha deuterium and nitrogen KIEs measured in methanol and in DMF are consistent with the "solvation rule for S_N2 reactions" (22), which predicts that the transition state for a Type II S_N2 reaction will be very solvent dependent. While the solvation rule does not indicate how the transition state bonds will change when the solvent changes, the results for this system show how a change in solvent will affect a Type II S_N2 transition state.

Conclusions

The secondary alpha deuterium and primary leaving group nitrogen KIEs and Hammett ρ values for the free ion and ion-pair S_N2 reactions between benzyldimethylphenylammonium nitrate and sodium *para*-substituted thiophenoxides in methanol at 20.000°C have shown that ion-pairing of the nucleophile does not affect the alpha carbon – leaving group (C_α—N) transition state bond but changes the nucleophile – alpha carbon (S—C_α) transition state bond significantly. The change in transition state structure on ion pairing is predicted by the bond strength hypothesis because the only change in transition state structure is in the weaker S—C_α bond, and no change occurs in the stronger C_α—N bond. The free ion S—C_α bond is much longer than the ion-pair S—C_α bond in the *para*-methoxythiophenoxide ion reaction, longer than the ion-pair S—C_α bond in the *para*-methylthiophenoxide ion reaction, slightly longer than the ion-pair S—C_α bond in the thiophenoxide ion reaction, but is shorter than the ion-pair S—C_α bond for the *para*-chlorothiophenoxide ion reaction. Thus, the effect of ion pairing (the difference between the S—C_α bond in the free ion and ion-pair reactions) decreases in three out of four comparisons as a more electron-withdrawing substituent is added to the nucleophile. The opposite effect, found with *para*-chlorothiophenoxide ion, cannot be explained. Finally, the identical Hammett ρ values of –0.85 and –0.84 for the free ion and ion-pair reactions, respectively, may be observed because, *on average*, the S—C_α bonds are identical in the free ion and ion-pair transition states.

© 1999 NRC Canada

Table 6. The conditions used for the HPLC analyses of the various benzyl *para*-substituted phenyl sulfides.

Substance analyzed	Benzyl *p*-methoxyphenyl sulfide	Benzyl phenyl sulfide	Benzyl *p*-chlorophenyl sulfide
Internal standard	Nitrobenzene	Nitrobenzene	Nitrobenzene
Solvent (v/v)% ($MeOH:H_2O$)	60:40	65:35	75:25
Flow rate (mL/min)	1.0	1.5	2.0
Detector wavelength (nm)	260	256	260
Volume of the 9.879×10^{-3} M nitrobenzene solution added to each 50 mL sample (mL)	4.00	6.00	12.00
Slope of the calibration curve	1.832 ± 0.006[a]	1.216 ± 0.007[a]	0.490 ± 0.002[a]
Correlation coefficient for the calibration curve	0.9998	0.9998	0.9999

[a]Standard error of the slope.

When a more electron-withdrawing substituent is added to the nucleophile, a later transition state with a much shorter S—C_α bond and a slightly longer C_α—N bond is found in both the ion-pair and free ion reactions. The later transition state found with the poorer nucleophile is expected because the less negative sulfur has to come closer to the alpha carbon to distort the C_α—N bond and cause reaction. Another discovery is that the substituent effect is smaller in the ion-pair reactions than in the free ion reactions. This may be observed because the change in the negative charge on the sulfur atom with substituent is greater in the free ion than in the ion-pair. The change in transition state structure suggested by the KIEs is not predicted by Thornton's reacting bond rule, the More O'Ferrall – Jencks energy surface method, the Critchlow method, or the Pross–Shaik method but the BEP principle, the Harris–Kurz method, and the bond strength hypothesis partially predict the experimental results. The BEP principle and the Harris–Kurz theory do not predict the very different magnitudes of the changes in the two reacting bonds, and the bond strength hypothesis does not indicate how the transition state bonds will change when a more electron-withdrawing substituent is added to the nucleophile. Thus, none of the theories predict the substituent effects on transition state structure that were found in this study.

A comparison of the secondary alpha deuterium and nitrogen leaving group KIEs in the S_N2 reactions between sodium *para*-substituted thiophenoxide ions and benzyldimethylphenylammonium ion in methanol and in DMF has shown that a change in solvent affects the structure of a Type II S_N2 transition state as the "solvation rule for S_N2 reactions" predicts. Both the KIEs and the Hammett ρ values indicate that an earlier transition state, with a longer S—C_α bond and a shorter C_α—N bond, is found in methanol. This probably occurs because an earlier, more ionic, transition state is more highly solvated (more stable) in methanol.

Experimental

Four liters of methanol (Caledon Laboratories) were dried over 50 g of anhydrous sodium sulfate, then refluxed over 4.0 g of sodium hydroxide (BDH) and 3.4 g of silver nitrate (BDH) for 1 h to remove any aldehyde or acid. Then, the methanol was distilled under a nitrogen atmosphere and stored in a cool, dark place until it was used in a kinetic run. The preparation of the sodium *para*-substituted thiophenoxide salts has been published (6). The synthesis of the deuterated and undeuterated substrates (2) and the procedure used for determining the rate constants (4) have been described previously.

The procedure used to measure the rate constant for the free ion reactions was the same as that used for the ion-pair complex reactions except that approximately 0.20 mL (0.001 mol) of 15-crown-5 ether (Aldrich) was injected into the QAS(H) and QAS(D) stock solutions using a 1 mL Hamilton syringe before the temperature equilibration. This means the free thiophenoxide ion was generated when the nucleophile was injected into the QAS(H) and QAS(D) solutions at the beginning of the reaction. The concentration of the 15-crown-5 ether was approximately 1.26×10^{-2} M (2.6 times the initial concentration of the nucleophile) to ensure that all of the nucleophile was the free ion.

The secondary alpha deuterium KIEs were obtained by dividing the average rate constants from between three to five separate kinetic runs of the undeuterated and of the deuterated substrates. The reactions were followed to between 65 and 70% of completion, and the correlation coefficient for the least-squares line that was used to calculate the second-order rate constant was ≥0.999. The procedure for determining the nitrogen KIEs is identical to that in ref. 2 except that the analysis of the *para*-substituted phenyl benzyl sulfide was done by HPLC rather than by gas chromatography. The $^{14}N/^{15}N$ ratios that were needed to calculate the KIE, were obtained by analyzing nitrogen gas samples from partial and complete reactions on a Micromass Sira 9 dual inlet isotope ratio mass spectrometer at the University of Waterloo.

The HPLC analysis of benzyl *para*-substituted phenyl sulfides

The amount of benzyl *para*-substituted phenyl sulfide formed in each complete and partial reaction was determined by an HPLC analysis using the internal standard technique (27). The analysis involved removing most of the ether from the solution containing the benzyl *para*-substituted phenyl sulfide (2), diluting the sample and the required amount of the 9.879×10^{-4} M nitrobenzene (the internal standard) solution, Table 6, to 50 mL in a volumetric flask with HPLC grade methanol. Then, three 10 μL samples of the solution were injected into the HPLC, and the average (benzyl *para*-substituted phenyl sulfide/internal standard) peak area ratio was determined. The amount of benzyl

© 1999 NRC Canada

para-substituted phenyl sulfide was calculated using the calibration curve.

The HPLC system consisted of a 100 × 5 mm Waters 5PAH 10 μm Radical Pak column, a Waters model 600 multisolvent delivery system, a Waters 490 programmable multiwavelength detector, and a Hewlett Packard model HP3396A integrator. The amount of internal standard, the eluting solvent, the flow rate, and the detector wavelengths for each analysis are given in Table 6. All the calibration curves were straight lines passing through the origin. The slope, correlation coefficient, and the error for each calibration curve are also given in Table 6.

The HPLC analyses of complete reactions showed no trace of methyl phenyl sulfide, and the average percent reaction at the benzyl carbon was 99.3 ± 0.4% when the nucleophile was sodium thiophenoxide and sodium *para*-methoxythiophenoxide. The Kjeldahl analyses of the *N*,*N*-dimethylaniline indicated the complete reactions were 99.8 ± 0.2% complete.

Acknowledgements

The authors gratefully acknowledge the financial support provided by the Natural Sciences abnd Engineering Research Council of Canada (NSERC).

References

1. K.C. Westaway and R.A. Poirier. Can. J. Chem. **53**, 3216 (1975).
2. K.C. Westaway and S.F. Ali. Can. J. Chem. **57**, 1354 (1979).
3. K.C. Westaway and Z.G. Lai. Can. J. Chem. **66**, 1263 (1988).
4. Z.G. Lai and K.C. Westaway. Can. J. Chem. **67**, 21 (1989)
5. W.J. Dixon and F.J. Massey, Jr. Introduction to statistical analysis. 2nd ed. McGraw Hill Book Company Inc., New York. 1957. pp. 117–118.
6. R.A. Poirier, Y. Wang, and K.C. Westaway. J. Am. Chem. Soc. **116**, 2526 (1994).
7. J.A. Barnes and I.H. Williams. J. Chem. Soc. Chem. Commun. 1286 (1993).
8. K.C. Westaway. Can. J. Chem. **71**, 2084 (1993).
9. O. Matsson, J. Persson, B.S. Axelsson, B. Langstrom, Y. Fang, and K.C. Westaway. J. Am. Chem. Soc. **118**, 6350 (1996).
10. K.C. Westaway and Z. Waszczylo. Can. J. Chem. **60**, 2500 (1982).
11. M. Ashan, R.E. Robertson, M.J. Blandamer, and J.M.W. Scott. Can. J. Chem. **58**, 2142 (1980).
12. K.C. Westaway, Y. Fang, J. Persson, and O. Matsson. J. Am. Chem. Soc. **120**, 3340 (1998).
13. I. Lee, H.J. Koh, B.-S. Lee, D.S. Sohn, and B.C. Lee. J. Chem. Soc. Perkin Trans. 2, 1741 (1991).
14. M.J. Dewar and R.C. Dougherty. The PMO theory of organic chemistry. Plenum Pub. Corp., New York. 1975. pp. 219–220.
15. E.R. Thornton. J. Am. Chem. Soc. **89**, 2915 (1967).
16. R.A. More O'Ferrall. J. Chem. Soc. B, 274 (1970).
17. W.P. Jencks. Chem. Rev. **72**, 705 (1972).
18. J.C. Harris and J.L. Kurz. J. Am. Chem. Soc. **92**, 349 (1970).
19. A. Pross and S.S. Shaik. J. Am. Chem. Soc. **103**, 3702 (1981).
20. J.E. Critchlow. J. Chem. Soc. Faraday Trans. 1, **68**, 1774 (1972).
21. T.V. Pham and K.C. Westaway. Can. J. Chem. **74**, 2528 (1998).
22. K.C. Westaway. Can. J. Chem. **56**, 2691 (1978).
23. V.J. Shiner, Jr., W. Dowd, R.D. Fisher, S.R. Hartshorn, M.A. Kessick, L. Milakofsky, and M.W. Rapp. J. Am. Chem. Soc. **91**, 4838 (1969).
24. K.M. Koshy and R.E. Robertson. J. Am. Chem. Soc. **96**, 914 (1974).
25. C.R. Turnquist, J.W. Taylor, E.P. Grimsrud, and R.C. Williams. J. Am. Chem. Soc. **95**, 4133 (1973).
26. A. Maccoll. Ann. Rep. Chem. Soc. Sect. A, **71**, 77 (1974).
27. L.R. Snyder and J.J. Kirkland. Introduction to modern liquid chromatography. 2nd ed. Wiley–Interscience, New York. 1987. p. 144.

© 1999 NRC Canada

The phosphoryl and the carbonyl group as hydrogen bond acceptors

Agnes M. Modro and Tom A. Modro

Abstract: Formation constants for the hydrogen-bonded complexes between phenol (donor) and selected carbonyl or phosphoryl compounds (acceptors) were determined from IR $\Delta\nu$ shifts. The P=O group is about two orders of magnitude stronger as an acceptor than the C=O group, but no evidence for the enolization of a β-diphosphoryl system was found. The IR absorption band of the phosphoryl group ($\nu_{P=O}$) showed weak response to the involvement in the hydrogen bonding, and the shifts of the donor molecule (ν_{OH}) provide a better measure of the formation constants.

Key words: carbonyl and phosphoryl groups as hydrogen bond acceptors, enolization of a β-difunctional system, determination of K_{assoc} from the IR $\Delta\nu$ shifts.

Résumé : Faisant appel aux déplacements, $\Delta\nu$, de l'IR, on a déterminé les constantes de formation de complexes à liaison hydrogène entre le phénol (donneur) et des composés carbonylés ou phosphorylés choisis (accepteurs). Par opposition au groupe C=O, le groupe P=O donne des complexes qui sont environ deux fois plus forts; on n'a toutefois pas rien observé qui pourrait laisser croire qu'il y a énolisation d'un système β-diphosphoryle. La bande d'absorption IR du groupe phosphoryle ($\nu_{P=O}$) présente une faible réponse à l'implication dans la liaison hydrogène, et les déplacements de la molécule donneur (ν_{OH}) donnent une meilleure mesure des constantes de formation.

Mots clés : groupes carbonyle et phosphoryle comme accepteurs de liaison hydrogène, énolisation d'un système β-bifonctionnel, détermination des K_{assoc} à partir des déplacements ($\Delta\nu$) dans l'infrarouge.

[Traduit par la Rédaction]

Introduction

One of the fundamental concepts in chemistry is that of hydrogen bonding and the carbonyl, as well as the phosphoryl, functionalities are among the most important hydrogen bond acceptor groups in organic molecules. The bibliography of the subject is enormous and spans a long period of time; we mention, for example, a comprehensive study on the relationship between vibrational frequencies and bond distances in the O—H···O H-bonded systems (1), or an excellent introduction to the topic published 30 years later (2). The involvement of the carbonyl group in the intramolecular bonding of the O—H···O=C type is related to the keto–enol tautomerism of dicarbonyl compounds, and this topic is now discussed in various textbooks (see, for example, ref. 3). The ability of the phosphoryl (P=O) and the phosphate (PO_2^-) groups to act as strong hydrogen bond acceptors is also well recognized (4). Much less is known, however, about the relative hydrogen-bonding abilities of the C=O and the P=O groups, both of them playing a key role in many biomolecules. In our earlier work on the 2-hydroxy-3-benzoylpropylphosphonate system, $PhC(O)CH_2CH(OH)CH_2P(O)(OR)_2$, ^1H NMR spectroscopy and X-ray diffraction demonstrated complete regioselectivity in the intramolecular interactions between the β-OH group and the potential acceptor phosphoryl or carbonyl functions in favor of the former (5). In this work we applied IR spectroscopy to investigate the hydrogen-bonding properties of some systems with two acceptor groups linked via the methylene bridge. In two cases (acetylacetone **1** and diethyl malonate **la**) both groups are carbonyl, in one (tetraethyl methylenebisphosphonate **2**) both are phosphoryl, and in the last (triethyl phosphonoacetate **3**) the acceptors are mixed (Scheme 1). Each system is, in principle, capable of tautomerism leading to an enol form stabilized by intramolecular hydrogen bonding to the remaining X=O (X = C, P) group. This effect should, in turn, affect the donor properties of the whole molecule with respect to an external hydrogen bond donor in the formation of an intermolecular H-bonded complex. Phenol **4** was selected as such donor and the interactions of **4** with substrates **1**, **2**, **3**, as well as with some model carbonyl and phosphoryl compounds were studied.

Received October 22, 1998.

This paper is dedicated to Jerry Kresge in recognition of his many achievements in chemistry.

A.M. Modro and T.A. Modro.[1] Centre for Heteroatom Chemistry, Department of Chemistry, University of Pretoria, Pretoria 0002, South Africa.

[1]Author to whom correspondence may be addressed. Telephone: 27-12-420-2512. Fax: 27-12-362-5297. e-mail: tamodrofaiscientia.up.ac.za

Results and discussion

The hydrogen-bonding ability of the phosphoryl compounds was extensively studied by Norwegian and Russian workers about 30 years ago, and a large number of association constants and enthalpies of complexation were obtained. In most cases the IR spectroscopy was applied and the shifts in the vibrational frequency of the *donor* group (usually, the

 © 1999 NRC Canada

Scheme 1.

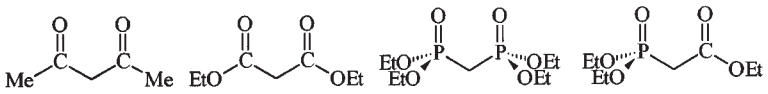

1 **1a** **2** **3**

Table 1. Data on the hydrogen bonding of phenol to carbonyl and phosphoryl compounds in CCl_4 at 25°C.

	$\nu_{X=O}$ (cm^{-1})	$\Delta\nu_{X=O}$[a] (cm^{-1})	K_{assoc} (M^{-1})	ν_{OH} (cm^{-1})	$\Delta\nu_{OH}$[a] (cm^{-1})	K_{assoc} (M^{-1})	Lit. K_{assoc} (M^{-1})
1b	1723.0	54.0	11.8 ± 0.5				12.3[b]
1c	1664.4	21.1	7.4 ± 0.8				7.8[b]
1d	1710.7	67.0	12.8 ± 0.4				16.8[b]
1e	1741.3	33.6	12.1 ± 0.2				9.8[b]
2a	1200.6	22.8	182 ± 13	3600	434	552 ± 35[d]	627[e]
2b	1250.0	35.8	34 ± 3[c]	3600	412	605 ± 11[d]	[f]
2c	1249.0	24.6	26 ± 5[c]	3600	420	354 ± 14[d]	325[e]
2d	1267.6	41.9	8.6 ± 0.5[c]	3600	344	345 ± 15[d]	351[b]
2e	1271.5	61.2	10.8 ± 0.7[c]	3600	306	271 ± 9[d]	[f]

[a]Maximum shift observed for the formation of the hydrogen-bonded complex.
[b]Taken from ref. 8; $\Delta\nu_{OH}$ was used for the determination of K_{assoc}
[c]Obtained from the $\Delta\nu_{P=O}$ shift of the acceptor.
[d]Obtained from the $\Delta\nu_{O-H}$ shift of the donor.
[e]Taken from ref. 6*d*; $\Delta\nu_{OH}$ was used for the determination of K_{assoc}.
[f]Not available.

Scheme 2.

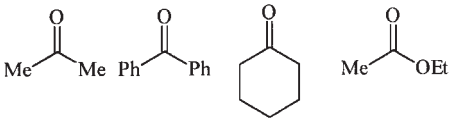

1b **1c** **1d** **1e**

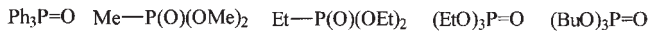

2a **2b** **2c** **2d** **2e**

OH group of a phenol or an alcohol) was used to measure the bonding effects (6). In only one case the association of phosphoryl compounds with proton donors was determined on the basis of the shift in the $\nu_{P=O}$ value (7). Similarly, an extensive study on the hydrogen bond association of phenols with carbonyl compounds was based on the measurements of the IR frequency shifts, $\Delta\nu_{OH}$ (8). Since the $\Delta\nu_{OH}$ could not be applied to the study of the hydrogen bonding of **3**, as the effect would not identify the acceptor group (C=O vs. P=O), we first investigated the problem of the agreement between the data obtained from the frequency shift of the donor ($\Delta\nu_{OH}$), as well as the acceptor ($\Delta\nu_{CO}$, $\Delta\nu_{PO}$) groups. To this purpose, the association between **4** and four simple carbonyl (**1b**–**1e**) and five simple phosphoryl (**2a**–**2e**) compounds (Scheme 2) was studied using the values of the frequency shifts $\Delta\nu_{X=O}$. In case of disagreement with the literature values, another set of K_{assoc} values was determined from the $\Delta\nu_{OH}$ shifts of the donor. The results obtained for those reference compounds are given in Table 1.

Two important conclusions emerge from Table 1. First, for the carbonyl substrates, there is a good agreement between our values of K_{assoc}, obtained from the $\Delta\nu_{C=O}$ shifts, and the literature values, which were obtained by measuring the $\Delta\nu_{OH}$ shifts of the phenol OH group in the carbonyl substrate – **4** hydrogen-bonded complexes. It means that in the C=O···H—O bonding system there is a good (and linear) correlation between the stretching frequencies (hence the bond orders) of the donor, as well as the acceptor group. Second, the correlation fails in the case of the phosphoryl substrates. While the K_{assoc} values obtained from the $\Delta\nu_{OH}$ shifts show good agreement with the reported data (also obtained from the same shifts), using the $\Delta\nu_{P=O}$ frequency shifts led to much lower values of the association constants with the K_{assoc} smaller by a factor between 3 and 40 (!) relative to the values obtained from the $\Delta\nu_{OH}$ shifts. The observed discrepancy is particularly intriguing in view of the fact that both shifts give curves of similar quality when plotted versus concentration changes of the donor or the acceptor, respectively. Figure 1 shows such two plots for the **2a**–**4** hydrogen-bonding system. This result, although complicating the IR spectroscopic studies of the hydrogen bonding by the P=O group, is in general agreement with the properties and bonding characteristics of the phosphoryl function. Solid-state studies demonstrated that although the P=O linkage can accept up to three H-bonds from such donors as P-OH, C-OH, or N-H groups, its length seems to be little affected by acting as the acceptor (ref. 4, p. 963). The IR spectra of compounds with the C=C—P=O moiety show no lowering in $\nu_{P=O}$ of the kind found in the analogous α,β-un-

© 1999 NRC Canada

Fig. 1. (*a*) Plot of the $\Delta\nu_{P=O}$ value for **2a** (0.005 M) as a function of the concentration of **4**. (*b*) Plot of $\Delta\nu_{O\text{-}H}$ for **4** (0.005 M) as a function of the concentration of **2a**.

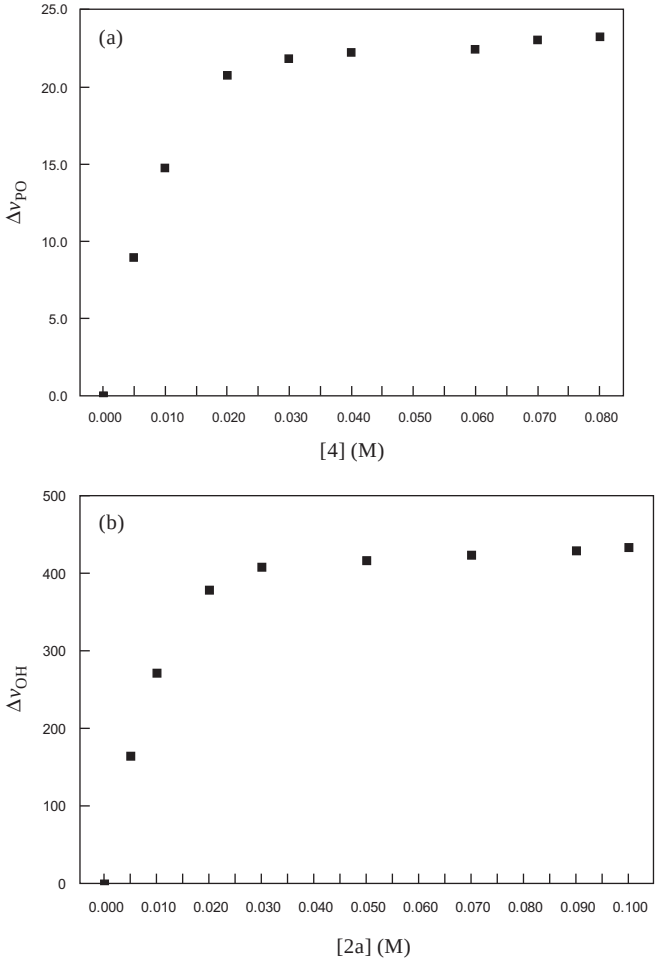

saturated carbonyl compounds (9). The phosphoryl group is a highly polar function and its vibration always produces a strong band in the IR spectrum (10). It seems, however, that the change in the $\nu_{P=O}$ values resulting from the involvement in hydrogen bonding should be used as a qualitative rather than a quantitative measure of the complexation equilibrium. A similar situation exists in the ^{31}P NMR spectroscopy. The ^{31}P NMR chemical shifts (δ_P) reflect direct protonation of the P=O group in phosphine oxides, $R_3P{=}O$ (11), but the change in the δ_P values upon protonation decreases with the number of oxygen ligands and was found to be zero for trialkyl phosphates, $(RO)_3P{=}O$ ("compensating" effect of oxygen atoms) (12).

The IR spectrum of a dilute (0.05 M) solution of acetoacetone **1** in CCl_4 exhibits the absorption band of the carbonyl group at 1616 cm^{-1}. The bathochromic shift of 107 cm^{-1} relative to acetone (**1b**) reflects the effect of the intramolecular hydrogen bonding of the enolic form of **1** (Scheme 3). Recent studies on the keto–enol tautomerism of β-dicarbonyl compounds demonstrated that in CCl_4 approximately 98% of **1** exists in the enolic form (13). In agreement with this result, we have found that the addition of increasing amounts of **4** to solutions of **1** (up to the molar ratio [**4**]/[**1**] = 50) had almost negligible effect on the ν_{CO} value

Scheme 3.

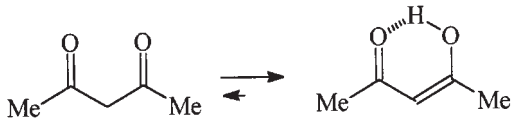

(maximum of $\Delta\nu_{CO}$ = 5 cm^{-1}). The only significant effect observed at higher concentrations of **4** was the shift in the ν_{OH} value, resulting from self-association of phenol (14) and independent of the presence of **1**. It can be concluded that an external donor like **4** does not significantly disturb the intramolecular hydrogen bonding existing in **1**.

Contrary to the situation existing for **1**, it is known that diethyl malonate **la** contains only negligible quantities of its enol form (15). Consequently, **1a** exhibits a strong carbonyl absorption band at 1746.0 cm^{-1}, only 4.7 cm^{-1} greater than that of **1e**; the difference can be explained by an electronic effect of the second ester group in **1a.** The addition of **4** to solutions of **1a** led to a systematic shift of the ν_{CO} value (maximum shift $\Delta\nu_{CO}$ = 31.0 cm^{-1}) from which the association contant, K_{assoc} = 2.5 ± 0.2 M^{-1} was calculated for **1a**. It can be seen that although acetone (**1b**) and ethyl acetate (**1e**) yield very similar values of K_{assoc} with respect to **4**, their "enolizable" analogues, **1** and **1a** behave very differently. While for the highly enolic **1** no K_{assoc} could be obtained, poorly enolic **1a** gave a lower value, but comparable to that obtained for its simple model, **1e**.

If the concept of tautomerism is applied to the substrate **2**, the "enolic" form analogous to that of **1** can be formulated, stabilized by intramolecular hydrogen bonding, as well as by the formation of the "conjugate" C=C—P=O system. Literature reports do not, however, provide support for such an effect. IR studies of a series $Et_2O_3P\text{-}(CH_2)_n\text{-}PO_3Et_2$ show no difference in the $\nu_{P=O}$ and $\nu_{P\text{-}C}$ values for n = 1 and n > 1 members (16). Similarly, a structural study on the bisphosphine oxide, $Ph_2P(O)\text{-}CH_2\text{-}P(O)Ph_2$, showed that the P=O and P—C bond lengths are perfectly within the range observed for other, "non-enolizable," phosphine oxides (17). Our results support the conclusion about the "non-enolizability" of **2**. The IR spectrum of **2** contains a strong band at 1258 cm^{-1}, typical for the "free" P=O group observed for phosphoryl substrates and similar to the values obtained for **2b** and **2c**. The effect of the addition of **4** on the IR spectra of **2** and the effect of the addition of **2** on the ν_{OH} of **4** are identical to those obtained for **2b** and **2c**, indicating independent complexation of both P=O groups in **2** with two molecules of **4** (Scheme 4). As before, the K_{assoc} for the reaction shown in Scheme 4, determined using the $\nu_{P=O}$ shifts (maximum $\Delta\nu_{P=O}$ = 44.6 cm^{-1}) gave a markedly low value of K_{assoc} = 6.8 ± 0.2 M^{-1}. When the ν_{OH} shift of **4** was, however, used for the calculations, a much more acceptable value of K_{assoc} = 398 ± 3 M^{-1} was obtained. This value compares well with the K_{assoc} = 354 M^{-1} obtained for **2c**, supporting the conclusion about viewing the molecule of **2** as a system of two non-interacting P=O functions.

For triethyl phosphonoacetate **3** the behavior of both donor groups was studied. The ester carbonyl group gives rise to a strong band at 1740.2 cm^{-1}, similar to that observed for **1a** and **1e**, thus indicating that there is little, if any, of the enol form present.When increasing proportions of **4** were

© 1999 NRC Canada

Table 2. Data on the hydrogen bonding of phenol to difunctional compounds in CCl_4 at 25°C.

	$\nu_{C=O}$ (cm^{-1})	$\Delta\nu_{C=O}$ [a] (cm^{-1})	K_{assoc} (M^{-1})	$\nu_{P=O}$ (cm^{-1})	$\Delta\nu_{P=O}$ [a] (cm^{-1})	K_{assoc} (M^{-1})	$\Delta\nu_{OH}$ [a] (cm^{-1})	K_{assoc} (M^{-1})	Remarks
1	1616.0	5.0	[b]				[c]		Exists as intramolecularly bonded enol. Not an acceptor to an external donor
1a	1746.0	31.0	2.5 ± 0.2				[c]		Exists as a dicarbonyl compound and forms hydrogen bonds with PhOH. Weaker acceptor than **1e**
2				1257.9	44.6	6.8 ± 0.2	346.0	398 ± 3	No evidence for enolization. Strong hydrogen bond acceptor. $\Delta\nu_{PO}$ not a good measure of bonding
3	1740.2	21.4	3.4 ± 0.7	1296.6	57.2	11.5 ± 1.6	334.0	381 ± 2	Exists as a non-enolized carbony/phosphoryl compound. Both groups can act as acceptors, P=O group being ca. 100-fold stronger

[a]Maximum shift observed for the formation of the hydrogen-bonded complex.
[b]Could not be calculated; the shift of 5.0 cm^{-1} occurs upon the addition of small quantities of **4** and does not increase upon further addition.
[c]Not determined in a separate experiment of the effect of the increase of the concentration of a donor on the IR spectrum of **4**.

Scheme 4.

added to the solutions of **3**, the carbonyl group band underwent bathochromic shift to a maximum value of $\Delta\nu_{C=O}$ = 21.4 cm^{-1}. The shift allowed the calculation of the association constant, K_{assoc} = 3.4 M^{-1}, a value that locates **3** in the same group of carbonyl acceptors of the hydrogen bond as **1a**, and not much weaker than the simple ester **1e**. The phosphoryl absorption band in free **3** is $\nu_{P=O}$ = 1269.6 cm^{-1} and upon the addition of **4** it moves to lower wave numbers with the maximum shift of $\Delta\nu_{P=O}$ = 57.2 cm^{-1}. It is clear that the phosphoryl group in the molecule of **3** is not involved in any significant intramolecular hydrogen bonding and with respect to an external donor behaves as its other "nonenolizable" analogues, **2b**, **2c**, and **2**. As with other phosphoryl substrates, the determination of the association constant from the $\Delta\nu_{P=O}$ shift gave an abnormally low value (11.5 ± 1.6 M^{-1}), while the value obtained using the $\Delta\nu_{OH}$ shifts of the donor, K_{assoc} = 381 ± 3 M^{-1}, remains in excellent agreement with the association constants obtained for other phosphoryl substrates. The hydrogen-bonding properties of four bifunctional compounds studied are summarized in Table 2. The results of this study led us to the following conclusions about the hydrogen-bonding properties of the phosphoryl group. (*i*) The P=O group is a strong hydrogen bond acceptor and, with respect to phenol, it is approximately 100-fold more effective than the carbonyl group in a similar molecular structure. (*ii*) Although it acts as a strong acceptor, its involvement in the bonding does not produce great changes in the IR absorption of the phosphoryl group. Spectroscopic changes taking place for the donor molecule offer a more correct measure of the association constants. (*iii*) In the 1,3-diphosphoryl system there is no evidence for tautomerization to the analogue of the enolic form observed for some 1,3-dicarbonyl substrates.

Experimental section

Tetrachloromethane (Aldrich, 99.9%, A.C.S. reagent) was distilled over P_4O_{10} and stored over 4Å molecular sieves. Commercially available substrates **1**, **2**, **3**, and **4** were purified by conventional methods immediately before use. **2c** was prepared according to the literature procedure (18). IR spectra were recorded on a Bomen Michelson 100 spectrometer in CCl_4 solutions using sodium chloride cells of 1 mm thickness and thermostated at 25.0 ± 0.2°C. The formation constants for the hydrogen-bonded complexes, K_{assoc}, were calculated on the assumption that each donor function forms a 1:1 complex with **4**:

© 1999 NRC Canada

[1] $K_{assoc} = [acceptor]_{bonded}/[acceptor]_{free}\ [donor]_{free}$

Solutions (0.005 M) of an acceptor in CCl_4 were prepared and the IR spectra were recorded in order to determine the $\nu_{X=O}$ value for the "free" acceptor. Solutions containing acceptor (0.005 M) and increasing amounts (usually 0.005–0.10 M) of **4** were then prepared and the shifts in the X=O absorption band, $\Delta\nu_{X=O}$ were measured as a function of [**4**]. For all systems in which the hydrogen bonding occurred, smooth curves were obtained, leveling-off at a given concentration of **4**. The $\nu_{X=O}$ value was then taken as that of the absorption for the fully bonded acceptor, $\Delta\nu_{X=O}$ (max), and used for the calculations. The concentrations of the hydrogen-bonded acceptor (and donor) ($[acceptor]_{bonded}$, $[donor]_{bonded}$) were calculated as: $[acceptor]_{bonded} = 0.005\ M \times \Delta\nu_{X=O}/\Delta\nu_{X=O}$ (max), and substituted into eq. [1]. For the K_{assoc} calculated from the IR shift of the donor, the reverse procedure was applied and the IR spectra of **4** (0.005 M) and of its mixtures with increasing concentrations of the acceptor were recorded. The shifts in the ν_{OH} values of the donor were then measured and the K_{assoc} values were calculated as above. Good reproducibility of the formation constants was obtained and the values induded in the tables represent the average of three independent experiments.

Acknowledgments

Financial support from the University of Pretoria and the Foundation for Research Development is gratefully acknowledged.

References

1. H. Ratajczak and W.J. Orville-Thomas. J. Mol. Struct. **1**, 449 (1967).
2. G.A. Jeffrey. An introduction to hydrogen bonding. Oxford University Press, New York. 1997.
3. (*a*) F.A. Carey and R.J. Sundberg. Advanced organic chemistry. Part A. 3rd ed. Plenum Press, New York. 1990. Chap. 7.3; (*b*) J. March. Advanced organic chemistry. 4th ed. J. Wiley, New York. 1992. Chaps. 2, 3.
4. D.E.C. Corbridge. Phosphorus. An outline of its chemistry, biochemistry and technology. 4th ed. Elsevier, Amsterdam. 1990. Chap. 14.1.
5. (*a*) M.P. Belciug, T.A. Modro, and P.L. Wessels. J. Phys. Org. Chem. **6**, 523 (1993); (*b*) S. Bourne, A.M. Modro, and T.A. Modro. Phosphorus, Sulfur Silicon, **102**, 83 (1995).
6. (*a*) G. Aksnes. Acta Chem. Scand. **14**, 1475 (1960); (*b*) G. Aksnes and T. Gramstad. Acta Chem. Scand. **14**, 1485 (1960); (*c*) T. Gramstad. Spectrochim. Acta, **19**, 1363 (1963); (*d*) G. Aksnes and P. Albriktsen. Acta Chem. Scand. **22**, 1866 (1968); (*e*) T. Gramstad and H.J. Storesund. Spectrochim. Acta, Part A: **26A**, 426 (1970); (*f*) V.E. Bel'skii, R.F. Bakeeva, L.A. Kudryavtseva, A.M. Kurguzova, and B.E. Ivanov. Zh. Obshch. Khim. (Engl. Transl.), **43**, 2568 (1975); (*g*) O.A. Raevskii, M.M. Gilyazov, and Ya. A. Levin. Zh. Obshch. Khim. **48**, 1053 (1978).
7. V.E. Bel'skii and L.Kh. Ashrabullina. Zh. Obshch. Khim. (Engl. Transl.), **49**, 1968 (1979).
8. T. Gramstad. Spectrochim. Acta. **19**, 497 (1963).
9. J. Emsley and D. Hall. The chemistry of phosphorus. Harper and Row, London. 1976. p. 95.
10. R.A. Nyquist and W.J. Potts. *In* Analytical chemistry of phosphorus compounds. *Edited by* M. Halman. Wiley–Interscience, New York. 1972. Chap. 5.
11. N.K. Skvortsov, A.V. Dogadina, G.F. Treshchenko, N.V. Morkovin, B.I. Ionin, and A.A. Petrov. J. Gen. Chem. (USSR), Engl. Transl. **41**, 2839 (1971).
12. N.K. Skvortsov, B.I. Ionin, and A.A. Petrov. J. Gen. Chem. (USSR), Engl. Transl. **44**, 209 (1974).
13. M. Moriyasu, A. Kato, and Y. Hashimoto. J. Chem. Soc. Perkin Trans. 2, 515 (1986).
14. R.M. Silverstein, G.C. Bassler, and T.C. Morril. *In* Spectroscopic identification of organic compounds. J. Wiley, New York. 1981. p. 112.
15. (*a*) K.H. Meyer. Ber. Dtsch. Chem. Ges. **45**, 2864 (1912); (*b*) A. Gero. J. Org. Chem. **19**, 1960 (1954).
16. K. Moedritzer and R.R. Irani. J. Inorg. Nucl. Chem. **22**, 297 (1961).
17. D.G. Gilheany. *In* The chemistry of organophosphorus compounds. Vol. 2. *Edited by* F.R. Hartley. J. Wiley, Chichester. 1992. p. 10.
18. T.C. Myers, S. Preis, and E.V. Jensen. J. Am. Chem. Soc. **76**, 4172 (1954).

© 1999 NRC Canada

Reactions of aryl sulfides and phosphorus(V) esters of thiols with acidic hydrogen peroxide

Clifford A. Bunton, Houshang J. Foroudian, Nicholas D. Gillitt, and Anurag Kumar

Abstract: Oxidations of sulfides and phosphorus(V) esters of thiols by H_2O_2 are catalyzed by H_2SO_4 and $HClO_4$. Sulfides are 4-ZC_6H_4SMe, **1a**–**1e**, respectively, Z = MeO, Me, H, Cl, NO_2; $PhSCH_2CH_2Cl$, **2**, Ph_2S, **3**, and the esters are Ph(R)PO·SEt, **4a**, **4b**, R = Ph, EtO. Electron donation by Z moderately accelerates reaction, but the sulfides are much more reactive than the esters. Reactions are first order in H_2O_2 and substrate, and second-order rate constants, k_2, in H_2SO_4 are related to excess acidity, *X*. Plots of log k_2 against *X* have slopes in the range 0.61–0.85. Rate constants are similar for given concentrations of H_2SO_4 and $HClO_4$, except that with greater than 50 wt.% H_2SO_4 peroxymonosulfuric acid is formed and the observed rate constants then increase. Methanesulfonic acid is a less effective catalyst than the mineral acids. Oxidations of the sulfides are also catalyzed by strongly acidic ion-exchange resins.

Key words: sulfide oxidation, hydrogen peroxide, acid catalysis, excess acidity.

Résumé : Les oxydations sulfures et des esters phosphorés(V) de thiols par le H_2O_2 sont catalysées par le H_2SO_4 et le $HClO_4$. Les sulfures sont 4-ZC_6H_4SMe (**1a–1e** qui portent respectivement Z = MeO, Me, Cl et NO_2), $PhSCH_2CH_2Cl$ (**2**) et Ph_2S (**3**); les esters sont Ph(R)PO·SEt (**4a**, **4b**, R = Ph, EtO). Un groupe Z électrodonneur accélère la réaction d'une façon modérée, mais les sulfures sont beaucoup plus réactifs que les esters. Les réactions sont du premier ordre en H_2O_2 et en substrat et les constantes de vitesse du deuxième ordre, k_2, dans H_2SO_4 sont reliées à l'excès d'acidité, *X*. Les pentes des courbes du log k_2 en fonction de *X* vont de 0,61 à 0,85. Les constantes de vitesse sont semblables pour des concentrations données de H_2SO_4 et de $HClO_4$; toutefois, si la concentration en H_2SO_4 est supérieure à environ 50%, il se forme de l'acide peroxymonosulfurique et les constantes de vitesse observées sont alors plus élevées. L'acide méthanesulfonique est un catalyseur moins efficace que les acides minéraux. Les oxydations des sulfures sont aussi catalysées par les résines échangeuses d'ions fortement acides.

Mots clés : oxydation de sulfure, peroxyde d'hydrogène, catalyse acide, excès d'acidité.

[Traduit par la Rédaction]

Introduction

Oxidations of two important chemical warfare agents, "Mustard Gas," HD, and *O*-ethyl *S*-[2-diisopropylamino]ethyl methylphosphonothioate, VX, are potentially useful methods for their detoxification (1, 2) (Scheme 1).

Reaction of VX and related compounds probably involves formation of an S-oxide, which rapidly undergoes P—S cleavage and further oxidation at sulfur (2). In reactions with peroxymonosulfate as OXONE ($2KHSO_5 \cdot KHSO_4 \cdot K_2SO_4$), oxygen in the final phosphonate is derived from water rather than the oxidant (3).

Received November 9, 1998.

This paper is dedicated to Jerry Kresge in recognition of his many achievements in chemistry.

C.A. Bunton,[1] H.J. Foroudian, N.D. Gillitt, and A. Kumar. Department of Chemistry, University of California, Santa Barbara, CA 93106, U.S.A.

[1] Author to whom correspondence may be addressed. Telephone: (805) 893-2605. Fax: (805) 893-4120. e-mail: bunton@ultra.chem.ucsb.edu

Typical oxidants are OCl^- and peroxyacids (1, 2) but alkaline H_2O_2, as HO_2^-, rapidly detoxifies VX and other phosphorus(V) nerve agents (3) by nucleophilic attack, although it is relatively ineffective against chlorosulfides, e.g., HD. The high molecular weight of peroxyacids, including OXONE, and extensive oxidation of the amino group of VX by OCl^-, makes these reagents relatively uneconomical. In contrast, H_2O_2 is an economical oxidant, but its oxidative reactions typically require activation, e.g., by an acylating agent or the hydrogen ion (4–6).

Many nucleophiles, e.g., halide ions, are oxidized by H_2O_2 with acid catalysis (5), and oxidations of sulfides are catalyzed by $HClO_4$ (6). We have examined acid-catalyzed oxidations of sulfides by H_2O_2 (Scheme 2). These sulfides react rapidly with HSO_5^-, giving sulfoxides and, more slowly, sulfones (7, 8). These oxidations have very low activation enthalpies and negative activation entropies and are modestly accelerated by electron-donating substituents, Z (Scheme 2). Rate constants are strongly increased by polar, aqueous, solvents (8), as for other oxidations of sulfides (9, 10). These observations are consistent with "early" polar transition states.

The esters (Scheme 3) are much less reactive than the sulfides (8, 11) and, as with VX, oxidation by HSO_5^- is fol-

© 1999 NRC Canada

Scheme 1.

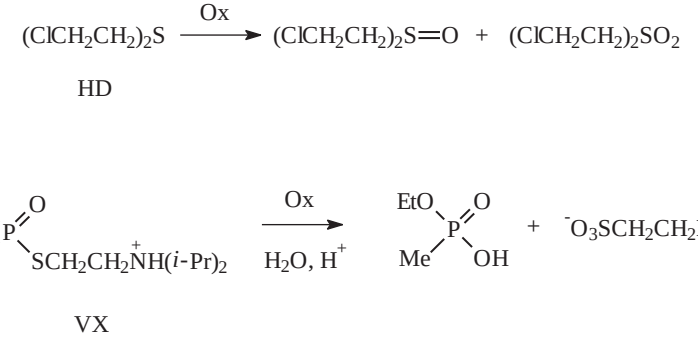

Scheme 2.

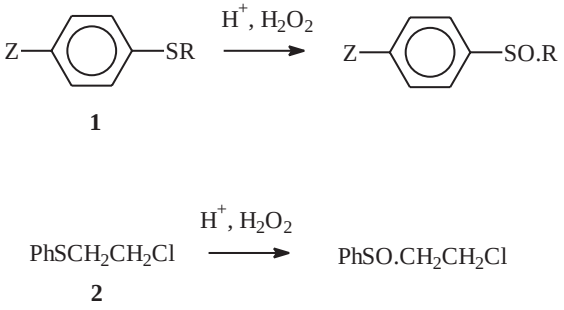

Scheme 3.

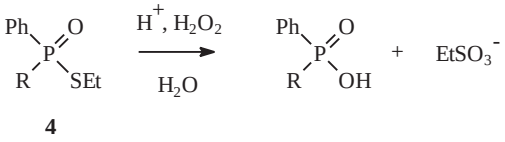

lowed by P—S cleavage (1, 2) Sensitivities of rate constants to solvent and temperature are similar to those of the sulfides (8, 11).

Substrates used in the present work are 4-ZC_6H_4SMe, **1**, **a–e**, respectively: Z = MeO, Me, H, Cl, NO_2; $Ph_2SCH_2CH_2Cl$, **2**; Ph_2S, **3**; Ph(R)PO·SEt, **4**, **a**, **b**, R = Ph, EtO. These compounds are nontoxic models for HD and VX.

Reactions of sulfides and esters of thiols by HSO_5^- are modestly accelerated by moderately concentrated H_2SO_4 (12) but it appears that acid catalysis is unimportant. Bentley et al. (13) found that moderately concentrated H_2SO_4 accelerates S_N1 reactions due to its high polarity. They fitted their rate data to the Bentley–Schleyer eq. [1] (14), which is an extension of the Grunwald–Winstein eq. [2] (15).

$$[1] \quad \log (k/k_0) = mY_{OTs} + l N_{OTs}$$

$$[2] \quad \log (k/k_0) = mY$$

The terms Y and Y_{OTs} relate to polarities based, respectively, on solvolyses of *tert*-butyl chloride and sulfonic esters, respectively, and N_{OTs} describes solvent nucleophilicity. The reference solvent is 80% EtOH – H_2O and m and l are reaction parameters (14).

Oxidations of sulfides by IO_4^- and HSO_5^- follow the Grunwald–Winstein equation with $m = 1$, based on Y values in aqueous organic solvents (8, 10, 11) and Y_{OTs} in aqueous H_2SO_4 (12). Values of m are typical of reactions with high sensitivities to solvent ionizing power and polarity (14, 15).

Catalysis by aqueous H_2SO_4 of oxidations by H_2O_2 could involve: (*i*) protonation that generates $H_3O_2^+$ (5, 6); (*ii*) formation of peroxymonosulfuric acid (7, 16); (*iii*) a kinetic solvent effect of aqueous H_2SO_4 (11, 12). The behaviour could be different for catalysis by $HClO_4$ (6), because the aqueous acid probably does not form a peroxy acid with H_2O_2.

Table 1. Oxidation of 4-$NO_2C_6H_4SMe$.[a]

H_2SO_4, wt.%	$[H_2O_2]$, M	$10^3\ k_{obs}$, s^{-1}	$10^3\ k_2$, $M^{-1}\ s^{-1}$
0.184	0.791	0.765	0.97
0.525	1.15	2.63	2.29
0.525	1.91	4.69[b]	2.46
9.62	0.119	0.641	5.39
9.90	0.119	0.706	5.93
9.90	0.178	1.05	5.90
9.90	0.306	1.81	5.92
10.3	0.292	1.88	6.44
25.0	0.0492	5.94	120
40.8	0.0258	17.5	678
48.3	0.0061	7.71	1270
50.0	0.0115	25.7	2230
50.0	0.0391	82.0	2100

[a]At 25.0°C with 1.4×10^{-5} M substrate.

[b]Mean of values (±2%) with 0.8 and 1.4×10^{-5} M substrate.

Rate constants of hydrogen ion catalyzed reactions typically have integral orders with respect to H^+ in dilute acid, with deviations at higher concentrations, because protonating power increases more steeply than concentration. These increases are treated by using acidity functions based on selected indicators (17–19) or in terms of excess acidity scales (20).

Results

Reactions were followed at 25.0°C (unless specified), with H_2O_2 in excess over substrate. First-order rate constants, k_{obs}, with respect to substrate varied linearly with H_2O_2, i.e., $k_{obs} = k_2[H_2O_2]$ (Tables 1 and 2 and Fig. 1). A range of $[H_2O_2]$ was used, depending on the reactivity of the substrate and the acid concentration.

Second-order rate constants, k_2, increased steeply with increasing concentration of H_2SO_4, but without affecting the

© 1999 NRC Canada

Fig. 1. Dependence of k_{obs} on $[H_2O_2]$ at 25.0°C. (▲), 4-$MeOC_6H_4SMe$ in 9.9 wt.% H_2SO_4; (●), 4-MeC_6H_4SMe in 17.7 wt.% H_2SO_4; (□) and (○), 4-ClC_6H_4SMe in 24.5 and 51.1 wt.% $HClO_4$, respectively.

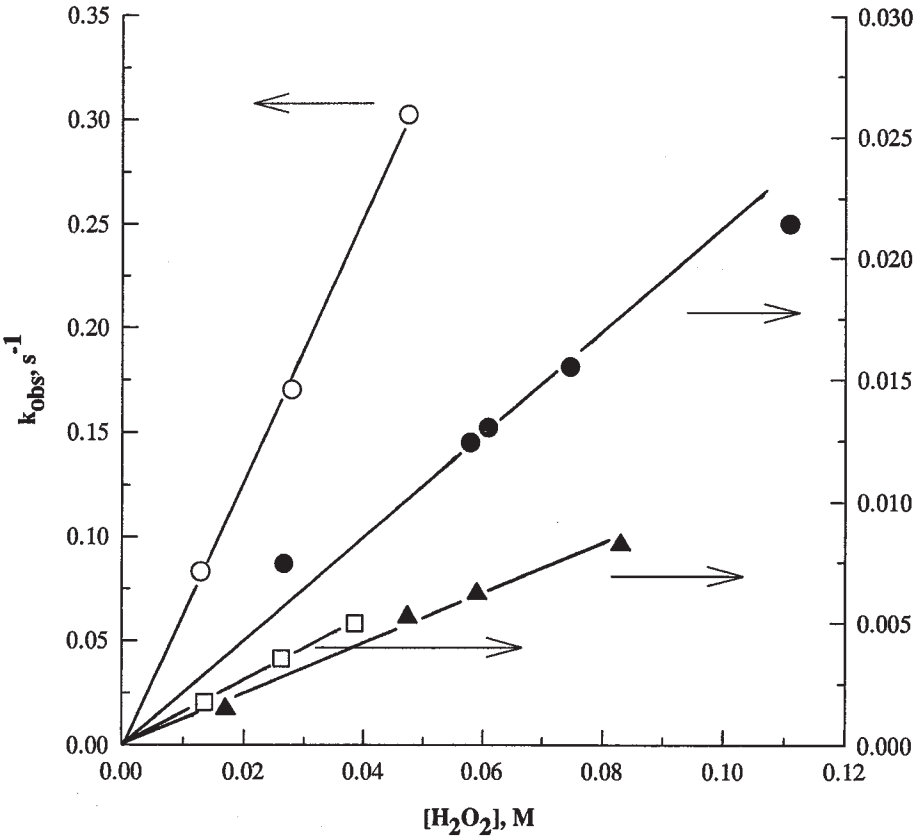

Table 2. Oxidation of $PhSCH_2CH_2Cl$.

H_2SO_4, wt.%	10^2 $[H_2O_2]$, M	10^3 k_{obs}, s^{-1}	10^3 k_2, M^{-1} s^{-1}
11.3	3.40	0.558	16.4
11.3	7.23	1.12	15.5
20.2	7.43	4.33	58.3
39.0	7.91	44.8	566
51.6	1.53	92.1	6020
51.6	3.06	189	6180

order with respect to H_2O_2 (Tables 1–3 and Fig. 1). Sulfonation of the more reactive sulfides, and the rapidity of the oxidations, limits the concentration of H_2SO_4 that can be used. In addition, formation of peroxymonosulfuric acid in more concentrated H_2SO_4 introduces a new reaction path (16). There is, however, no indication of complete protonation of H_2O_2 and, based on the data of Evans and Uri (21), Edwards (6) estimated $pK_a \approx -4.7$ for $H_3O_2^+$.

Substituent effects

Electron-donating substituents in the 4-position increase k_2 (Table 4) and the Hammett equation is obeyed with σ_p parameters and $\rho = -1.15$. This value is similar to that for oxidation by HSO_5^- where $\rho = -1.0$ (8). Similar substituent effects are reported for oxidation of sulfides by IO_4^- (10).

The esters are very much less reactive than the sulfides, by factors of ca. 10^4 (Tables 3 and 5). These structural effects on reactivity are also qualitatively similar to those observed for reactions with HSO_5^-, and can be rationalized on the same basis (9, 11).

Temperature effects

Oxidations of some sulfides were followed over a range of temperature (Table 6). These oxidations, like those by HSO_5^- (9, 11) and IO_4^- (10), have relatively low activation energies and low pre-exponential terms. These low activation energies (or enthalpies) and low pre-exponential terms (or negative activation entropies) are typical of oxygen transfers (9–11, 21). Activation energies are, however, higher for these oxidations than for those with HSO_5^- (9, 11), in part because of the contribution of the equilibrium protonation of H_2O_2 (5, 22).

Time dependence of rate constants

Except at the higher concentrations of H_2SO_4, values of k_2 were unaffected by leaving mixtures of H_2O_2 and H_2O–H_2SO_4 before addition of the substrate, but with the less reactive substrates, which could be studied in the more acidic solutions, there was a time dependence of k_2 (Table 7).

We assume that the rate increases are due to a relatively slow equilibration with peroxymonosulfuric acid (16). In confirmation, we observed a second-order rate constant of 2.2 M^{-1} s^{-1} for the reaction of Ph(EtO)PO·SEt and peroxymonosulfuric acid in 65.3 wt.% H_2SO_4 (extrapolated to the time of making up the solution) and over 10 h it decreased to ca. 0.5 M^{-1} s^{-1}, which is close to the value obtained by using a mixture of H_2O_2 and H_2SO_4 (Table 7).

© 1999 NRC Canada

Table 3. Oxidations of sulfides in H_2SO_4–H_2O_2.

$MeOC_6H_4SMe$	H_2SO_4, wt.%	9.90	16.7	25.2	30.6			
	k_2, M^{-1} s^{-1}	0.100	0.243	0.688	1.19			
Me C_6H_4SMe	H_2SO_4, wt.%	10.1	14.1	17.7	21.2	21.7	24.7	28.2
	k_2, M^{-1} s^{-1}	0.074	0.138	0.209	0.441	0.495	0.592	0.886
	H_2SO_4, wt.%	32.4	35.2	38.2	40.3	41.0		
	k_2, M^{-1} s^{-1}	1.37	2.89	3.37	5.43	5.30		
C_6H_5SMe	H_2SO_4, wt.%	9.90	14.6	20.9	21.7	30.6	32.2	
	k_2, M^{-1} s^{-1}	0.054	0.118	0.315	0.289	0.767	0.934	
	H_2SO_4, wt.%	35.2	37.6					
	k_2, M^{-1} s^{-1}	1.26	2.15					
ClC_6H_4SMe	H_2SO_4, wt.%	9.70	9.90	18.5	31.5	40.8	47.9	53.9
	k_2, M^{-1} s^{-1}	0.029	0.031	0.092	0.511	1.72	4.50	11.8
Ph_2S	H_2SO_4, wt.%	16.1	30.9	40.9	51.6			
	k_2, M^{-1} s^{-1}	0.017	0.117	0.410	3.34			

Table 4. Substituent effects on oxidation of 4-ZC_6H_4SMe.[a]

Z	MeO	Me	H	Cl	NO_2
k_2, M^{-1} s^{-1}	0.100	0.0767	0.054	0.0307	0.0060

[a]At 25.0°C in 9.9 wt.% H_2SO_4.

Table 5. Oxidative hydrolyses in H_2SO_4–H_2O_2.

$Ph_2PO{\cdot}SEt$	H_2SO_4, wt.%	37.5	47.3	51.7
	10^4 k_2, M^{-1} s^{-1}	4.07	22.3	34.6
Ph(EtO)PO·SEt	H_2SO_4, wt.%	38.7	49.6	52.6
	10^4 k_2, M^{-1} s^{-1}	6.31	36.0	64.2

There was almost no change in the value of k_2 for reaction of peroxymonosulfuric acid in 52.6 wt.% H_2SO_4 over a period of 4 h. Therefore equilibration of H_2O_2 and peroxymonosulfuric acid is kinetically important only in the more concentrated H_2SO_4.

Reactions in $HClO_4$ and $MeSO_3H$

We followed a few reactions in $HClO_4$–H_2O_2 (Table 8 and Fig. 1). As in H_2SO_4–H_2O, k_{obs} varied linearly with $[H_2O_2]$ (Fig. 1) and second-order rate constants, k_2, increased sharply with increasing acid. These values are similar to those in corresponding wt.% compositions of H_2SO_4, as expected from the protonating power of the two acids (17–20), and consistent with our conclusion that formation of peroxymonosulfuric acid is not essential for oxidation.

Methanesulfonic acid catalyzes the oxidation of **1e** (Table 9) although it is considerably less effective than H_2SO_4 or $HClO_4$ (Tables 7, 8, and 9), as expected in view of the differences in protonating power as given by values of H_0, e.g., with 5 M acid H_0 is more negative by 0.82 for H_2SO_4 than for $MeSO_3H$ (23). However, rate constants are only approximately comparable because the data for $MeSO_3H$ are at 22°C and in 20 vol.% MeCN. There is no indication of formation of a peroxysulfonic acid. Oxidation was also catalyzed by sulfonic acid ion-exchange resins. Qualitative evidence is given in the experimental section.

Discussion

Oxidation of sulfides by H_2O_2 is acid catalyzed, and rate constants increase more steeply than does stoichiometric acidity, as for many acid-catalyzed reactions (17–20).

Several factors can be responsible for this catalysis; e.g., equilibrium protonation of H_2O_2 (5), a kinetic solvent effect of H_2SO_4, and formation of peroxymonosulfuric acid (16). In principle, the ester **4a**, **b** could be initially hydrolyzed, followed by rapid oxidation of the thiol (8), but this reaction would be zero order in H_2O_2.

Formation of peroxymonosulfuric acid (16) is the probable reaction path in more concentrated H_2SO_4, 52 wt.%, (Table 7). Conversely, for reaction with HSO_5^-, k_2 decreases if solutions are left standing. These observations indicate that interconversion of H_2O_2 and HSO_5^- is relatively slow and unimportant with less than ca. 52 wt.% H_2SO_4. Catalysis by $HClO_4$ (Table 8 and ref. 6) confirms that protonation of H_2O_2 can increase the rate of oxidation without formation of a peroxyacid. It appears that, except in the more concentrated H_2SO_4, $H_3O_2^+$ is the oxidant because OH^+ is excluded as an intermediate (5).

Except at the higher concentrations the relation between k_2 and the concentration of H_2SO_4 depends on the equilibrium protonation of H_2O_2 (5, 6) and the kinetic solvent effect upon the reaction of $H_3O_2^+$ with substrate. The problem of separating these medium effects of strong acids is general for reactions in moderately concentrated acids, although most emphasis has been given to hydrolyses, where the role of water in the rate-limiting step has to be considered (12, 19, 24).

Relation between reactivity and acid concentration

Rate constants of A-1 reactions, i.e., hydrogen ion catalyzed reactions in which water is not involved nucleophilically, or as a base, increase more rapidly than stoichiometric acidity. For many of these reactions plots of log k_{obs} against Hammett's acidity function, $-H_0$, are linear with slopes close to unity (17, 18). However, this scale of acidity is based on the protonation of aromatic primary amines, and acidity functions have been evaluated by using a variety of indicator types, including the $-H_A$ scale for protonation of amides (24).

© 1999 NRC Canada

Table 6. Temperature effects on sulfide oxidations.[a]

Temp.°C	25.0	35.0	45.0	50.0	*E*, kcal mol^{-1}	log *A*
MeC_6H_4SMe	1.00	1.64	2.80	3.63	9.87	6.24
C_6H_5SMe	0.54	0.81	1.42	1.93	9.76	5.89
$O_2NC_6H_4SMe$	0.060	0.130	0.229	0.31	12.4	6.88

[a]Values of 10 k_2, M^{-1} s^{-1} in 9.90 wt.% H_2SO_4.

Table 7. Time dependence of reactions in H_2SO_4–H_2O_2.[a]

	4-$O_2NC_6H_4SMe$: 48.2 wt.% H_2SO_4[b]			
Time, min	10	40		
10^3 k_2, M^{-1} s^{-1}	1.26	1.28		
	4-$O_2NC_6H_4SMe$: 63.4 wt.% H_2SO_4[c]			
Time, min	11	28	40	69
10^3 k_2, M^{-1} s^{-1}	151	229	279	365
	Ph(EtO)PO·SEt: 52.6 wt.% H_2SO_4[d]			
Time, min	10	60	1080	
10^3 k_2, M^{-1} s^{-1}	6.42	6.50	29.1	
	Ph(EtO)PO·SEt: 65.3 wt.% H_2SO_4[e]			
Time, min	24	100	210	330
10^3 k_2, M^{-1} s^{-1}	106	282	489	447
	Ph_2S: 59.0 wt.% H_2SO_4[f]			
Time, min	29	53	106	
k_2, M^{-1} s^{-1}	24	35	66	

[a]At 25.0°C.
[b]6.09×10^{-3} M H_2O_2.
[c]3.41×10^{-3} M H_2O_2.
[d]0.26 M H_2O_2.
[e]0.0309 M H_2O_2.
[f]7.49×10^{-3} M H_2O_2.

Table 8. Oxidations of sulfides in $HClO_4$–H_2O_2.

MeC_6H_4SMe[a]	$HClO_4$, wt.%	16.0	50.6	
	k_2, M^{-1} s^{-1}	0.14	10.2	
C_6H_5SMe[b]	$HClO_4$, wt.%	16.0	36.2	51.0
	k_2, M^{-1} s^{-1}	0.054	0.78	8.50
ClC_6H_4SMe[c]	$HClO_4$, wt.%	24.5	51.1	
	k_2, M^{-1} s^{-1}	1.28	6.25	

[a]$[H_2O_2]$ = 0.006–0.036 M.
[b]$[H_2O_2]$ = 0.026–0.081 M.
[c]$[H_2O_2]$ = 0.014–0.048 M.

Plots of log k_{obs} against either $-H_0$ (17) or $-H_A$ (24) are linear, with slopes that are, respectively, lower or higher than unity. They depend slightly upon the substrate, i.e., they depend not only upon protonation of H_2O_2 but also upon the medium effects of moderately concentrated H_2SO_4 upon the reaction of $H_3O_2^+$ and the substrates.

Various extensions of the original relationships between log k_{obs} and acidity functions have been suggested (17–20, 22) For example, Bunnett and Olsen (18) wrote protonation of weak bases, B, in the form of eq. [3], and applied eq. [4] to acid-catalyzed reactions (19).

$$[3] \qquad \log \frac{[B]}{[BH^+]} = H_0 - \phi(H_0 + \log[H^+]) - pK_a$$

$$[4] \qquad \log k + H_0 = \phi(H_0 + \log [H^+]) + \text{constant}$$

Table 9. Oxidation of **1e** in $MeSO_3H$–H_2O_2.[a]

$[MeSO_3H]$, M	2.0	3.0	4.0	5.0
10^3 k_2, M^{-1} s^{-1}	0.67	1.56[b]	3.54	8.50

[a]At 22°C in H_2O:MeCN 80:20 v/v.
[b]Mean of values from 10^4 k_{obs}, s^{-1} = 4.71, 5.05, 6.76, 9.19, and 10.2 with $[H_2O_2]$, M = 0.031, 0.031, 0.047, 0.06, and 0.06, respectively.

They showed that values of ϕ are characteristic of reaction mechanism, but their treatment involves selection of primary amines as indicators.

An alternative approach involves estimation of "excess acidity," *X*, above that predicted by stoichiometry, and independent of the selected indicators (eq. [5]) (20). Both eqs. [3] and [5] fit protonation data (25), $m^* \approx 1 - \phi$ (19), and m^* is a function of the base.

$$[5] \qquad \log \frac{[B]}{[BH^+]} = -\log[H^+] - {}^* X - pK_a$$

For a reaction catalyzed by a hydrogen ion the relation becomes (25):

$$[6] \qquad \log k_2 - \log[H^+] = m^* m^{\ddagger} X + \text{constant}$$

where, for the present reaction, m^* describes protonation of H_2O_2, and $m^{\ddagger}$ includes the activity coefficients of the transition state and substrate (26). As a result, slopes of plots of log k_2 – log$[H^+]$ against *X* (Table 10) depend modestly upon the nature of the substrate. The Bunnett–Olsen eq. [4] also

© 1999 NRC Canada

Table 10. Variation of rate constants with excess acidity of H_2SO_4.[a]

Substrate	$MeOC_6H_4SMe$	MeC_6H_4SMe	C_6H_5SMe	ClC_6H_4SMe
$m^*m^‡$	0.61 (–1.26)	0.80 (–1.45)	0.66 (–1.49)	0.72 (–1.80)
Substrate	$O_2NC_6H_4SMe$	Ph_2S	$PhSCH_2CH_2Cl$	$Ph_2PO.SEt$
$m^*m^‡$	0.80 (–2.45)	0.82 (–2.52)	0.81 (–2.22)	0.79 (–5.33)
Substrate	Ph(EtO)PO·SEt			
$m^*m^‡$	0.85 (–5.34)			

[a]Calculated with values of X and $[H^+]$ interpolated from data in ref. 20. Values in parentheses are log k_3 obtained from eq. [6] by extrapolation.

Scheme 4.

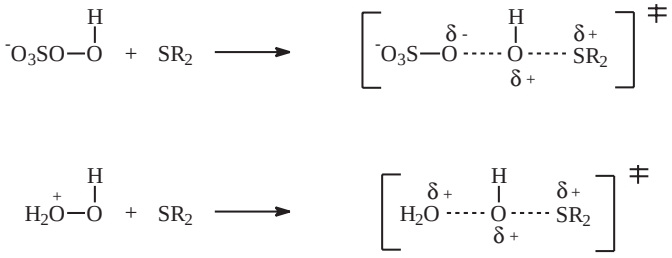

fits the rate data (not shown), with modest dependence of ϕ on substrate, consistent with the analysis of protonation equilibria (25). The excess acidity method has also been used to treat hydrolysis of acyl imidazoles where protonation inhibits reaction by forming dead-end species (27).

Values of m^* are less than 1 for protonations of amides and benzophenones on oxygen (20); this generalization should apply to protonation of H_2O_2, and therefore values of $m^‡$ should be close to 1, based on data in Table 10. For some substrates few data points were used in estimating $m^*m^‡$, but the mean value is 0.76 and most are within 0.1 of this value (Table 10), even though concentrations of H_2O_2 and H_2SO_4 differ for the more, and less, reactive substrates. The constant term in eq. [6] is the logarithm of the third-order rate constant, k_3, with respect to substrate, H_2O_2 and H^+ estimated by extrapolation by a linear regression to dilute acid where $X \rightarrow 0$ (Table 10). These values are least reliable for the unreactive substrates where there is a long extrapolation, based on few data points.

Protonation of H_2O_2 is the most important factor in controlling overall rate constants. To the extent that these oxygen transfers to sulfur involve "early" transition states (8, 9, 11, 21) and limited charge redistribution, we would not expect large solvent effects upon these reactions of $H_3O_2^+$. Oxidations by HSO_5^-or IO_4^- are sensitive to medium polarity (8, 10, 11), and rate constants follow values of Y (15) or Y_{OTs} (14) in mixed solvents and aqueous H_2SO_4, respectively (8, 10–12), with high sensitivities to medium polarities. Differences in kinetic medium effects upon oxygen transfers from HSO_5^- and $H_3O_2^+$ are understandable in terms of differences in charge redistributions in transition state formation, especially as regards the numbers of hydrogen-bonding centers (Scheme 4), consistent with $m^‡ \approx 1$ for oxygen transfers from $H_3O_2^+$ (δ indicates partial charge and has no quantitative significance). The marked solvent effect on oxidations by HSO_5^- is consistent with development of positive charge on both sulfur and the transferred oxygen, and the similar values of ρ in oxidations by IO_4^-, HSO_5^-, and H_2O_2 point to modest charge development on sulfur (Table 5 and refs. 8 and 10).

A problem in separating medium effects upon proton transfers from those on subsequent kinetic steps is that the parameters are often related. Bentley et al. (13) found that Y_{OTs} is linearly related to Hammett's acidity function, H_0 (in up to 60 wt.% H_2SO_4), with $H_0 = -3.76\ Y_{OTs} + 15.2$. There is also a linear relation between N_{OTs} and Y_{OTs} (or H_0), and variations of N_{OTs} and Y_{OTs} approximately follow changes in log a_{H_2O} in H_2O–H_2SO_4 (13). These relations indicate the dependence of these medium parameters upon hydration changes in the processes under consideration (17–20).

A plot of Y_{OTs} (13) against X (20) is linear in up to 60 wt.% H_2SO_4 and follows eq. [7].

$$[7] \qquad Y_{OTs} = 4.08 + 0.37\ X$$

(The value of Y_{OTs} in water ($X \equiv 0$) is uncertain within ±0.1 (13)). Values of log k for oxidations of sulfides and related esters by HSO_5^- in aqueous H_2SO_4 are linearly related to Y_{OTs} (12), and we expected to find a corresponding relation between log k and X. Slopes of plots of log k against X for reaction with HSO_5^- in H_2SO_4 (12) are as follows: 4-$O_2NC_6H_4SMe$, 0.40 (1.3); Ph_2S, 0.57 (1.4); $PhCO{\cdot}SC_6H_4Me$, 0.48 (1.6); PhCO·SPh, 0.46 (1.5); $Ph_2PO{\cdot}SPh$, 0.41 (1.5); Ph(EtO)PO·SEt, 0.37 (1.1). Slopes of plots of log k against Y_{OTs} (13) are in parentheses, and there is an approximate correspondence between these two sets of slopes.

These correlations between X and log k for both non-acid-catalyzed S_N1 reactions (13) and oxygen transfers (12) are not unexpected, and they illustrate the problem in separating the factors that control rate constants of acid-catalyzed reactions in aqueous media. The decrease in protonating power due to hydration of the hydronium ion is well recognized and explains the approximate correlations between water activity and acidity functions, e.g., H_0 (17, 23, 28). Hydration and solvent polarity are key factors in reactions of polar or ionic reactants in aqueous media, even though water may not be involved covalently. It is therefore difficult to separate parameters such as m^* and $m^‡$ (eq. [6]) (25), unless m^* can be measured directly, or estimated, based on data for protonation of structurally similar, but unreactive, bases (20, 25–27). The relation between structure and values of m^* has been analyzed (29). However, relations between rate constants and acidity functions provide valuable mechanistic information (17–20, 26), especially as regards the covalent involvement of water in reactions. Recent work by Marziano et al. (30) extends studies of protonation by analyzing the solvent–solute interactions, which are of particular importance in concentrated acids.

© 1999 NRC Canada

Table 11. Catalysis by ion-exchange resins.[a]

Resin	mg	$t_{1/2}$, h
Dowex	100	1.5
Dowex	100	1.0[b]
Dowex	200	1.5
Dowex	500	0.5
CGC	100	1.3
CGC	100	1.0[b]
CGC	500	0.5
C-350	100	1.5
C-350	100	1.0[b]

[a]With 0.094 M H_2O_2, unless otherwise specified.
[b]0.19 M H_2O_2.

Experimental

Materials

Substrates were materials used earlier (8, 11). Solutions of moderately concentrated acids were made up by weight with redistilled deionized water. Except as noted, kinetic solutions of H_2O_2 were used promptly. Ion-exchange resin in the acid form was washed with H_2O, then with 3% H_2O_2, and finally with H_2O. It was air dried.

Kinetics

Reactions were followed spectrophotometrically by the decreasing absorbance in HP 8450 double-beam or 8451 single-beam diode array spectrometers as described for reactions with HSO_5^- (8, 11). In earlier experiments with HSO_5^- (as OXONE) we had erratic results with some substrates when reactions were followed in the single-beam spectrometer. We did not have this problem in oxidations by H_2O_2 and we followed reactions of the sulfides in the single-beam spectrometer and reaction of $Ph_2PO{\cdot}SEt$ in the double-beam spectrometer. Reaction of Ph(EtO)PO·SEt was followed in both instruments and results agreed.

Reactions were followed at the following wavelengths (nm) (wavelengths at isobestic points are in parentheses): $MeOC_6H_4SMe$, 260–265 (253); MeC_6H_4SMe, 256–270 (242); PhSMe, 250–260 (235); ClC_6H_4SMe, 260–280 (245); $O_2NC_6H_4SMe$, 340–360 (305); Ph_2S, 270–280 (240); $PhSCH_2CH_2Cl$, 255–265; $Ph_2PO{\cdot}SEt$, 240; Ph(EtO)PO·SEt, 240–245.

Substrate concentrations were in the range of (0.75–1.5) × 10^{-5} M (cf. Table 1) and $[H_2O_2]$ was varied between ca. 10^{-2} and 0.26 M depending on the reactivity of the substrate and the acid concentration. Substrates were added in MeCN and the kinetic solution contained 0.5 vol.% MeCN. Sulfonation of the more reactive thiols limited the usable concentration of H_2SO_4.

Catalysis by acidic ion-exchange resins

The reaction of **1e** with H_2O_2 was catalyzed by several ion-exchange sulfonate resins in their acidic forms. The resins were Dowex 50 W-4 (20–50 mesh), Baker CGC-241 (200–400 mesh), and Baker C-350 (16–50 mesh). We used 2 × 10^{-5} M **1e** in 10 mL of unstirred water at room temperature (ca. 22°C). Reaction was followed by the decreasing absorbance at 340 nm, which reached final values similar to those with reactions in aqueous H_2SO_4, and approximate half-lives were obtained by inspection (Table 11). These half-lives decrease with increasing amounts of resin and $[H_2O_2]$, but are apparently not very sensitive to the brand of resin. Control experiments showed that the decreases in absorbance were not due to uptake of **1e** by the resins. Due to the heterogeneity of the system these results are qualitative and merely show that acidic resins catalyze these oxidations by H_2O_2. We also used ^{1}H NMR spectroscopy at 200 MHz to demonstrate reaction of 2 × 10^{-3} **1a** with 0.5 M H_2O_2 in 2.6 mL of D_2O with 6 vol.% CD_3CN and 0.051 g Dowex 5O W-4. After 35 min, with shaking at room temperature, signals of the sulfide had disappeared, and we observed the signal of the sulfoxide ($SO{\cdot}CH_3$) at 2.86 ppm. The corresponding signal of **1a** at 2.45 ppm had disappeared and there was no signal of the sulfone. Oxidation by HSO_5^- gives both sulfoxide and sulfone (8); the SCH_3 ^{1}H signal of the latter is at 3.15 ppm, referred to δ = 4.80 ppm for HOD. Control tests showed that **1a** is not significantly bound by the resin.

Acknowledgements

Support by the US Army Office of Research is gratefully acknowledged. We thank Christina Villareal for help in preparing the manuscript.

References

1. Y.-C. Yang, J.A. Baker, and J.R. Ward. Chem. Rev. **92**, 1729 (1993); Y.-C. Yang. Chem. Ind. (London), 334 (1995).
2. Y.-C. Yang, L.L. Szafraniec, W.T. Beaudry, and D.K. Rohrbaugh. J. Am. Chem. Soc. **112**, 6621 (1990).
3. Y.-C. Yang, F.J. Berg, L.L. Szafraniec, W.T. Beaudry, C.A. Bunton, and A. Kumar. J. Chem. Soc. Perkin Trans. 2, 607 (1997).
4. G.J. Hignett. Tenside Deterg. **23**, 69 (1986); D.M. Davis and M.E. Deary. J. Chem. Soc. Perkin Trans. 2, 559 (1992).
5. J.O. Edwards. Peroxide reaction mechanisms. Interscience, New York. 1962. p. 67; J. Phys. Chem. **56**, 279 (1952); E.J. Behrman and J.O. Edwards. Prog. Phys. Org. Chem. **4**, 93 (1967).
6. G. Modena and L. Maioli. Gazz. Chim. Ital. **87**, 1306 (1957).
7. R.J. Kennedy and A.M. Stock. J. Org. Chem. **25**, 1901 (1960); K.S. Webb. Tetrahedon Lett. **35**, 3457 (1994).
8. C.A. Bunton, H.J. Foroudian, and A. Kumar. J. Chem. Soc. Perkin Trans. 2, 33 (1995).
9. R.P. Hanzlik and G.O. Shearer. J. Am. Chem. Soc. **97**, 5231 (1975).
10. F. Ruff and A. Kucsman. J. Chem. Soc. Perkin Trans. 2, 683 (1985).
11. A. Blasko, C.A. Bunton, and A. Kumar. J. Phys. Org. Chem. **10**, 427 (1997).
12. C.A. Bunton and A. Kumar. J. Phys. Org. Chem. **11**, 803 (1998).
13. T.W. Bentley, S. Jurczyk, K. Roberts, and D.J. Williams. J. Chem. Soc. Perkin Trans. 2, 293 (1987).
14. T.W. Bentley and P.v.R. Schleyer. Adv. Phys. Org. Chem. **14**, 1 (1977).
15. A.H. Fainberg and S. Winstein. J. Am. Chem. Soc. **78**, 2770 (1956).
16. R.E. Hall. Encyclopedia of chemical technology. Vol. 17. 3rd ed. Wiley–Interscience, New York. 1982. p. 14.

© 1999 NRC Canada

17. C.H. Rochester. Acidity functions. Academic Press, London. 1970; M. Liler. Reaction mechanisms in sulphuric acid. Academic Press, London. 1971.
18. J.F. Bunnett and F.P. Olsen. Can. J. Chem. **44**, 1899 (1966).
19. J.F. Bunnett and F.P. Olsen. Can. J. Chem. **44**, 1917 (1966).
20. R.A. Cox and K. Yates. J. Am. Chem. Soc. **100**, 3861 (1978).
21. R.W. Murray. Chem. Rev. **89**, 1187 (1989); W. Adam, C. Curci, and J.O. Edwards. Acc. Chem. Res. **22**, 205 (1989).
22. M.G. Evans and N. Uri. Trans. Faraday Soc. **45**, 224 (1949).
23. R.H. Boyd. *In* Solute–solvent interactions. *Edited by* J.F. Coetzee and C.D. Ritchie. Dekker, New York. 1969. Chap. 3.
24. K. Yates, J.B. Stevens, and A.R. Katritzky. Can. J. Chem. **42**, 1957 (1964).
25. V. Lucchini, G. Modena, G. Scorrano, R.A. Cox, and K. Yates. J. Am. Chem. Soc. **104**, 1958 (1982).
26. R.A. Cox. Acc. Chem. Res. **20**, 27 (1987).
27. R.A. Cox. Can. J. Chem. **75**, 1093 (1997).
28. K.N. Bascombe and R.P. Bell. Discuss. Faraday Soc. **24**, 158 (1957); P.A.H. Wyatt. Discuss. Faraday Soc. **24**, 162 (1957).
29. A. Bagno, G. Scorrano, and R.A. More O'Ferrall. Rev. Chem. Intermed. **7**, 313 (1987).
30. N.C. Marziano, A. Tomasin, C. Tortato, and P. Isandelli. J. Chem. Soc. Perkin Trans. 2, 2535 (1998).

© 1999 NRC Canada

Quantitative investigations of the aggregation behaviour of hydrophobic anilino squaraine dyes through UV/vis spectroscopy and dynamic light scattering

James Wojtyk, Andrew McKerrow, Peter Kazmaier, and Erwin Buncel

Abstract: In continuing studies of the aggregation behaviour of squaraine dyes in DMSO–water mixtures, we have examined a series of symmetrical anilino-based squaraines with increasing *N*-alkyl chain length (*n*-butyl, *n*-octyl, and *n*-dodecyl). The aggregation behaviour was assessed through UV/vis spectroscopic and Dynamic Light Scattering (DLS) studies with quantitative interpretation based on exciton theory. This class of *N*-alkyl squaraines forms two distinct solution aggregates, Type J and Type H, depending on the composition of the DMSO–water medium. DLS measurement of the aggregates in the Type J and Type H morphologies showed that (*i*) the particle diameter increased with increasing hydrophobicity; (*ii*) DMSO has a large effect on the aggregate size; (*iii*) Type J aggregates are of equal dimensions with Type H aggregates. Moreover, even though as the DMSO–water solvent composition is varied the UV/vis spectra of Type H and Type J aggregates remained unchanged, the number of molecules comprising each aggregate varies widely. It is proposed that the dynamic conversion (J → H) results from intramolecular reorganization of individual molecules within the aggregate. Quantification of aggregation through DLS has further developed the "kinetic" versus "thermodynamic" control model of dye aggregation.

Key words: squaraine, dynamic light scattering, DMSO–water mixtures, self-assembly, kinetic/thermodynamic control.

Résumé : Dans le cadre de nos études sur le comportement d'agrégation des colorants de la squaraïne dans des mélanges DMSO–eau, on a étudié une série de squaraïnes symétriques à base anilino portant des chaînes *N*-alkyles de longueur variable (*n*-butyle, *n*-octyle et *n*-décyle). On a évalué le comportement d'agrégation par le biais de la spectroscopie UV/visible et d'études de diffusion dynamique de la lumière (DDL) avec interprétation quantitative basée sur la théorie de l'exciton. Cette classe de squaraïnes *N*-alkylées forme deux types distincts d'agrégats en solution, Type J et Type H, suivant la composition du milieu DMSO–eau. L'étude des morphologies des agrégats de Type J et de Type H par des mesures de DDL montrent que: (*i*) le diamètre des particules augmente avec une augmentation de l'hydrophobicité; (*ii*) le DMSO a un effet prononcé sur la taille des agrégats et (*iii*) les dimensions des agrégats de Type J sont égales à celles des agrégats de Type H. De plus, même si l'on fait varier la composition du solvant DMSO–eau, les spectres UV/visible des agrégats de Type H et de Type J demeurent inchangés; le nombre de molécules formant chaque agrégat varie considérablement. On suggère que la conversion dynamique (J → H) résulte d'une réorganisation intramoléculaire des molécules individuelles dans l'agrégat. La quantification de l'agrégation à l'aide de la DDL a permis de mieux développer le modèle de contrôle « cinétique » / « thermodynamique » de l'agrégation du colorant.

Mots clés : squaraïne, diffusion dynamique de la lumière, mélanges DMSO–eau, auto-assemblage, contrôle cinétique/thermodynamique.

[Traduit par la Rédaction]

Introduction

Advancement of squaraine chemistry has resulted in highly efficient photoconductive dyes that have promise of substitution into technological applications which are currently based on inorganic systems. Using various precursors,

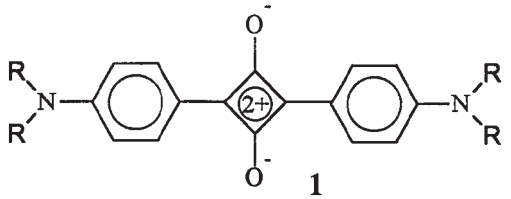

1

Received November 12, 1998.

This paper is dedicated to Jerry Kresge in recognition of his many achievements in chemistry.

J. Wojtyk, A. McKerrow, and E. Buncel.[1] Department of Chemistry, Queen's University, Kingston, ON K7L 3N6, Canada.
P. Kazmaier. Xerox Research Centre of Canada, 2660 Speakman Drive, Mississauga, ON L5K 2L1, Canada.

[1]Author to whom correspondence may be addressed. Telephone: (613) 533-2653. Fax: (613) 533-6669. e-mail: duncelea@chem.queensu.ca

© 1999 NRC Canada

a variety of these symmetrical and unsymmetrical dyes have been synthesized; those that absorb in the near-IR region of the spectrum have potential applications in xerography, organic solar cells and optical recording media (1).

Symmetrical anilino-squaraines, **1**, are characterized by having an intense, long-wavelength absorption (620–680 nm, $\varepsilon \approx 300\,000\ M^{-1}\ cm^{-1}$) as a result of an intramolecular charge transfer occurring in both the ground and excited states (2). The squaraine chromophore provides the essential properties for photoconduction in the solution state. In the solid state, the assembly of squaraine molecules into aggregates causes a misalignment of the donor and acceptor moieties within the aggregate. As a result, the efficiency of the intermolecular charge transfer is severely hindered, and the photophysical properties are severely depleted.

Detailed understanding of the relationship of photophysical properties to structure has in the past focused primarily on the role of the molecular chromophore and not on the role of crystal packing. More recently, studies have shown that there exists a large dependence of color on crystal packing, i.e., crystallochromy (3). In particular, photoconductive dyes such as squaraines, phthalocyanines, perylenes, azobenzenes, and stilbenes which exhibit polymorphism have also been labeled as crystallochromic (4). Studies of these crystallochromic dyes have shown that through understanding of the interrelationship between crystal packing and the wavelength shift relative to solution, it is possible to correlate the change in electronic structure with the photoconductive behaviour of the pigments.

Previously, detection of squaraine aggregates was accomplished through single-crystal studies (5) and through the formation of Langmuir–Blodgett (LB) films (6). However, a novel method of observing aggregates of squaraine dyes in the solution state was developed in our laboratory using binary DMSO–water mixtures, which allowed detection of aggregates through UV/vis spectroscopy and facilitated examination of the relationship of molecular structure to aggregation behaviour (7). Depending on solvent composition, two different aggregate types with characteristic spectral features were observed for symmetrical anilinosquaraine dyes that varied in the *N*-alkyl substituents. In a subsequent study, Whitten and co-workers (8) investigated the aggregation behaviour of unsymmetrical surfactant squaraine dyes in DMSO–water mixtures and bilayer vesicles. The aggregates were found to be blue-shifted and circular dichroism measurements showed the aggregate to be chiral; the basic aggregate unit was proposed as a chiral "pin-wheel" structure.

In the present study of squaraines **2**–**4**, the aggregation behaviour as observed by UV/vis spectroscopy has been combined with Dynamic Light Scattering (DLS) in order to determine aggregate size and thereby examine the effect of hydrophobicity of the squaraine as well as the effect of solvent composition on the aggregate size. DLS studies of photoactive pigments enable the determination of the aggregate size and the relationships between particle size, solvent, temperature, and electrolyte concentration (9–11).

A higher order hydrophobic squaraine has been synthesized, **4**, and a study of the effect of hydrophobicity on aggregation behaviour is reported. Spectrophotometric study of **4** in DMSO–water solutions has shown that two specific aggregate types are formed, and a dynamic conversion between the two can be followed using UV/vis spectroscopy. DLS measurement of the dyes was performed in solutions of specific percentages of DMSO where Type J or the Type H aggregates were dominant and where the Type J $\rightarrow$ H aggregate interconversion could be monitored. The DLS measurements permitted quantification of all squaraine aggregates including estimation of the number of molecules/aggregate of each aggregate in various DMSO–water compositions.

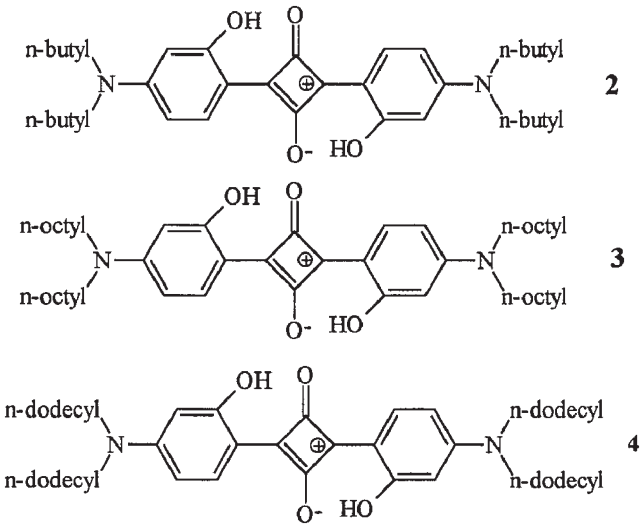

Experimental

Synthesis and procedures

Squaraine dyes were prepared using the method of Sprenger and Ziegenbien (12) in which 2 equiv. of aromatic dialkylamine were condensed with 1 equiv. of squaric acid in a toluene–1-butanol solvent system. Preparation of the dialkylanilines was accomplished through the reaction of the appropriate dialkylamine with resorcinol. A representative procedure for the synthesis of these class of squaraines is described.

*3-(*N,N-*Dialkylamino)phenol*

A mixture of dialkylamine (0.03 mol) and resorcinol (0.06 mol) was sealed and heated in a teflon-lined acid digestion bomb with an internal temperature of 185°C. The reaction was followed through TLC (10:1 hexanes/EtOAc) and was complete after 3 days. The bomb was then opened, the mixture dissolved in CH_2Cl_2 and washed with (3 × 250 mL) water, followed by evaporation to a yellow oil. Flash chromatography of the oily liquid (20:1 hexanes/EtOAc) yielded a clear yellow oil which was stored under nitrogen at 0°C.

*3-(*N,N-*Dioctylamino)phenol*: Yield: 67%. ^{1}H NMR (400.1 MHz) in $CDCl_3$, δ: 6.92 (1H, d, J = 8.5), 6.18 (3H, m), 3.16 (4H, t, J = 7.5), 1.54 (4H, br,), 1.24 (20H, br), 0.85 (6H, t, J = 6.1).

*3-(*N,N-*Didodecylamino)phenol*: Yield: 67%. ^{1}H NMR (400.1 MHz) in $CDCl_3$, δ: 6.90 (1H, d, J = 8.5), 6.16 (3H, m), 3.10 (4H, t, J = 7.5), 1.45 (4H, br,), 1.24 (36H, br), 0.84 (6H, t, J = 6.1).

© 1999 NRC Canada

Table 1. UV/vis characteristics of the monomeric and Type H and J aggregate forms of squaraines **2**, **3**, and **4**.

Squaraine	Aggregate form	λ_{max} (nm)	ε (M^{-1} cm^{-1})
2 R = *n*-butyl	Monomer	642	342 000
	H	533	78 300
	J	658	82 300
3 R = *n*-octyl	Monomer	648	348 000
	H	530	78 000
	J	659	83 500
4 R = *n*-dodecyl	Monomer	644	310 000
	H	530	76 200
	J	650	82 900

Bis(4-di-n-*alkyl-2-hydroxyphenyl)squaraine*

A 250 mL three-necked round bottom flask was fitted with a Dean–Stark apparatus, thermometer, stirbar, N_2 inlet, and dropping funnel. The flask was charged with 50 mL toluene, 20 mL *n*-butanol, and squaraic acid (1.44 g, 0.013 mol) and heated to 110°C. Once the squaric acid was dissolved, 3-(*N*,*N*-dialkylamino)phenol (0.03 mol) in 10 mL toluene was added dropwise over a period of 30 min, and the mixture was refluxed for 3 h. After cooling, the dark green precipitate that formed was filtered and washed with EtOAc. The crystals were recrystallized twice from EtOH, giving metallic-green crystals.

*Bis(4-di-octyl-2-hydroxyphenyl)squaraine (**3**)*: Yield: 57%, mp: 128.5–130.0°C. ^{1}H NMR (400.1 MHz, $CDCl_3$), δ: 7.76 (1H, d, *J* = 9.3), 6.50 (1H, d, *J* = 9.3), 6.12 (1H, s), 3.43 (4H, t, *J* = 7.1,-NCH_2-), 1.60 (4H, m, -CH_2-), 1.30 (10H, m, -$(CH_2)_5$-), 0.86 (6H, t, *J* = 7.1, -CH_3). Anal. calcd. for $C_{48}H_{76}O_4N_2$: C 77.37, H 10.28, N 3.76; found: C 77.70, H 10.24, N 3.76.

Bis(4-di-n-*dodecyl-2-hydroxyphenyl)squaraine (**4**)*: Yield: 65%, mp: 96.5–98.0°C. ^{1}H NMR (400.1 MHz, $CDCl_3$), δ: 7.80 (1H, d, *J* = 9.3), 6.53 (1H, d, *J* = 9.3), 6.18 (1H, s), 3.45 (4H, t, *J* = 7.1,-NCH_2-), 1.60 (4H, m, -CH_2-), 1.30 (36H, m, -$(CH_2)_5$-), 0.86 (6H, t, *J* = 7.1, -CH_3). Anal. calcd. for $C_{64}H_{108}O_4N_2$: C 79.33, H 11.15, N 2.89; found: C 79.50, H 11.20, N 2.85.

Spectrophotometric method

Preparation of solutions used in the aggregation spectrophotometric and DLS studies followed the procedure described previously (7*b*). The appropriate DMSO–water mixture (2 mL) was injected directly into the UV/vis quartz cuvette fitted with a rubber septum under nitrogen. An aliquot (20 μL) of the dye stock solution (1.0×10^{-3} M) in the organic solvent (2,2,2-trifluoroethanol:*n*-butyl, acetone:*n*-octyl, *n*-dodecyl; max. final composition 0.5% v/v) was injected into the mixture, which was stirred for 30 s and then sonicated for 60 s. The solution was placed in a Hewlett–Packard 8452A Diode Array UV-vis spectrophotometer, and the absorption spectrum was recorded immediately (ca. 1 min after mixing) and at intervals of 12 min for a minimum of 1 h or until there was no visible change. Spectra were then recorded at intervals of 1 and 3 days. These experiments were performed in triplicate. Use of the above protocol ensured consistent results, although neither the stirring time nor the sonication time was found to have an effect on the aggregation behaviour.

Dynamic light scattering

Particle sizing experiments were performed using a NICOMP Dynamic Light Scattering instrument that used a He/Ne laser as the light source (λ = 628 nm). The statistical treatment used to measure the diameter of solid particles was Gaussian volume-weighted distributions. All measurements were performed in manual mode with the number of photons of scattered light averaging 300 000 per second (300 kHz). Measurements of the stable aggregate forms were carried out for 20 min, and the dynamic interconversion was monitored for 2 h. Prior to each measurement in the DMSO–water mixtures, the appropriate refractive index and viscosity of the solution at ambient temperature was determined to ensure that correct diffusion coefficient data was obtained.

An aliquot of each UV/vis sample (0.6 mL) was placed in a NICOMP particle size analyzer fitted with thermostatted cell compartment (*T* = 298 K). The particle size was determined in tandem with the solution state of aggregation through UV/vis spectroscopy. This ensured that the DLS measured particle size corresponded to the correct aggregate type as determined by UV/vis spectroscopy. The aggregate size was unaffected by concentration of the dye solution or the incident laser wavelength.

Two latex standards (91 and 248 nm diam.) were used to calibrate the analyzer. Solutions of the standards were diluted until a significant amount of scattered-light intensity was observed, nominally 300 kHz. The observed particle diameter for each standard, using Gaussian analysis volume-weighted distribution, was 90.5 ± 9 and 245 ± 25 nm. On this basis, values reported for aggregate diameters are believed to be accurate to ±10%.

For all acquired particle sizing data, the distribution of diameters was narrow. Based on the latex calibration standards used, a 10% deviation is inherently incorporated into the NICOMP DLS instrument for monodisperse samples. In addition, the observation of particle size distribution is facilitated by the Gaussian volume-weighted statistical treatment performed to acquire the actual diameter. The use of Gaussian treatments is valid for monodisperse and polydisperse samples, but the presence of a polydisperse sample increases the "chi-squared" value to >3. Polydispersity broadens the Gaussian curve over a wider range and significantly alters the ability of the treatment to adequately fit all the data. All of the samples that were analyzed by DLS had χ^2-values less than unity, indicating a true Gaussian fit to the data and a monodisperse sample.

Molecular modelling calculations

Molecular modelling calculations were performed to determine the physical dimensions of the monomeric squaraines using Spartan 3.0. Semi-empirical calculations were done using PM3 and all geometrical optimizations performed with MM2+ restrictions.

Results

1. Spectrophotometric study

As listed in Table 1, the squaraines in organic media exhibit long wavelength, intense absorptions (λ_{max} ca. 640 nm, ε ca. 3×10^5 M^{-1} cm^{-1}) with a limited positive solvatochromism (637 nm in Et_2O; 642 nm in DMF). When

© 1999 NRC Canada

Table 2. Observed aggregate forms (UV/vis) of the three squaraine dyes as a function of percentage DMSO.

Squaraine	Type J aggregate	Type J → Type H % DMSO	Type H aggregate
2 R = *n*-butyl	0–20	30–50	50–70
3 R = *n*-octyl	0–70	80	N/A[a]
4 R = *n*-dodecyl	0–80	90	N/A[a]

[a]Solution was not stable in high percentages of DMSO due to degradation of squaraine chromophore (see text).

Fig. 1. Overlay spectra comparing the absorption properties of **4**: (*A*) monomer; (*B*) Type J aggregate; (*C*) Type H aggregate.

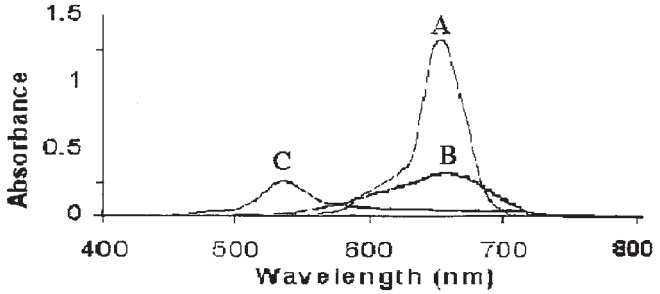

injected into solutions of varying DMSO–water content, two aggregate species are formed instantly; these have been classified as Type H and J, with characteristic spectroscopic properties that are markedly different from the monomer spectrum (Fig. 1).

The aggregation behaviour for the three squaraine dyes was investigated by injection of a 10^{-3} M stock solution (20 μL) to DMSO–water mixtures, giving final concentrations of 10^{-5}–10^{-6} M. The aggregation behaviour of squaraines **2** and **3** has been reported previously, and the solvent compositions in which each aggregate species is formed are listed in Table 2 (7*b*). In solutions ranging from 0–80% DMSO, the self-association of squaraine **4** resulted in a spectrum with a broad absorption (λ = 650 nm, ε = 80 000 M^{-1} cm^{-1}) relative to the monomer, identifying the aggregate as Type J (Fig. 2*a*), which was stable over a 3 day monitoring period. In contrast, addition of the monomer **4** stock solution to 90% DMSO produced a spectrum that corresponded initially to a Type J aggregate. Over the 3 h time period, there was a decrease in the absorption at 650 nm and an increase in the absorption at 530 nm corresponding to a dynamic conversion to the Type H aggregate, with an isobestic point at 560 nm (Fig. 2*b*). After the dynamic conversion was complete, a stable Type H aggregate (Fig 2*c*) was observed to be hypsochromically shifted relative to Type J by 120 nm (λ = 530 nm, ε = 80 000 M^{-1} cm^{-1}).

Injection of the monomeric forms of squaraine **4** into 100% DMSO, resulted initially in a broad absorption and a bathochromic-shift relative to the monomer, characteristic of the Type J aggregate. However, instead of dynamically converting to the Type H aggregate, the absorption corresponding to the Type J aggregate decreased over time until no optical absorption remained. This behaviour was related to the slow precipitation of the dye and hydroxide attack on the squaric ring that becomes more reactive on increasing the DMSO content.

Fig. 2. (*a*) Spectra of **4**, Type J aggregate, in 0–80% DMSO–water mixtures. (*b*) Overlay spectra of **4** acquired every 12 min in 90% DMSO–water, depicting the dynamic conversion of Type J aggregate to Type H aggregate. (*c*) Spectra of **4** as Type H aggregate following completion of dynamic conversion from Type J form in 90% DMSO–water.

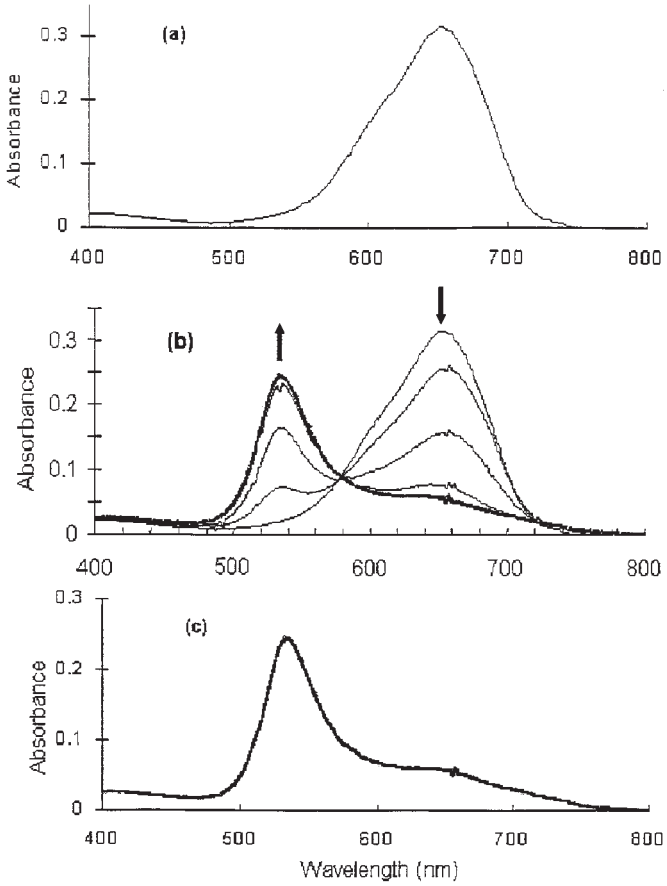

2. Particle sizing data

In DLS, the frequency spectrum of scattered light from particular species in solution is determined. The relaxation time for fluctuation in the scattered light depends solely on the diffusion behaviour of the aggregates. For aggregates, the translational diffusion constant, D, is given by the Stokes–Einstein relation

$$[1] \qquad D = kT/6\pi\eta r$$

where k is Boltzmann's constant, T is the absolute temperature, η is the viscosity of the solution, and r is the hydrodynamic radius of the aggregate. The relaxation time, τ, is then given by

$$[2] \qquad \tau = (2Dq^2)^{-1}$$

© 1999 NRC Canada

Table 3. The hydrodynamic diameter (nm) measured by dynamic light scattering (DLS) for each aggregate in various DMSO–water media as characterized by UV/vis spectroscopy.

Squaraine aggregate type	*n*-Butyl, **2**		*n*-Octyl, **3**		*n*-Dodecyl, **4**	
% DMSO	Type H	Type J	Type H	Type J	Type H	Type J
10	—	67.4	—	101	—	127
		81.8	—	99.9	—	127
50			—	153	—	111
			—	153	—	
70			145	151	—	102
90					101	100
					100	

Table 4. Particle size diameter (nm) and corresponding aggregate number calculated for squaraines exhibiting Type J morphology in 10% DMSO solution.

	Squaraine		
	n-Butyl	*n*-Octyl	*n*-Dodecyl
Diameter (nm)[a]	74.6	101	127
Aggregate number[a]	213	290	365

[a]Infers 10% error in measurement and the average value of three runs.

Table 5. Comparison of the aggregate size and aggregate number for Type J aggregate of *n*-dodecyl squaraine, **4**, in solutions of varying DMSO compositions.

	% DMSO			
	10	50	70	90
Diameter (nm)[a]	127	111	102	100
Aggregate number[a]	365	318	290	286

[a]Infers 10% error in measurement and the average value of three runs.

Table 6. DLS measurements of the dynamic conversion of *n*-octyl, **3**, Type J to Type H aggregate in 80% DMSO.

	n-Octyl, **3**	
	Type J	Type H
Diameter (nm)[a]	151	145
Aggregate number[a]	440	416

[a]Infers 10% error in measurement and the average value of three runs.

Table 7. DLS measurements of the dynamic conversion of *n*-dodecyl, **4**, Type J to Type H aggregate in 90% DMSO.

	n-Dodecyl, **4**	
	Type J	Type H
Diameter (nm)[a]	100	100
Aggregate number[a]	286	286

[a]Infers 10% error in measurement and the average value of three runs.

where $q = 2k_m \sin(\theta/2)$ and θ is the scattering angle, and measurement of τ therefore determines the hydrodynamic radius of the aggregates, which is the largest dimension of the aggregate present in this solution that is developing a sphere through rotational and translational motion.

Solutions of aggregates for squaraines **2**, **3**, and **4** in 10, 50, 70, and 90% DMSO–water were analyzed by Dynamic Light Scattering. Since the UV/vis measurements carried out simultaneously characterized the aggregates in solution as Type J or Type H, the particle size of each aggregate type in the different solvent media could be determined from the DLS measurements. The results are presented in Table 3.

DLS analysis of **2** in 10% DMSO where the aggregate is known to be Type J, gave a particle size of 67.4 and 81.8 nm. Measurements in higher DMSO content solutions were not attempted as the Type H aggregate was not stable for the time period required for accurate measurements to be taken.

For **3** in 10 and 50% DMSO where UV/vis results show the Type J aggregate to be present, the measured size in 10% DMSO was ~100 nm, while in 50% DMSO the size was 153 nm. For **3** in 70% DMSO, where the Type J aggregate is initially present, the DLS measurement gave a diameter of 151 nm. After the dynamic conversion had occurred to the Type H aggregate, the diameter for the Type H aggregate was found to be 146 nm.

Squaraine **4** was analyzed by DLS in 10, 50, 70, and 90% DMSO, since the Type J aggregates of **4** have been found to be the most stable over the widest range of solvent compositions used in this study. In 10% DMSO, the diameter of the aggregate was determined to be 128 nm, corresponding to the Type J aggregate. In 50 and 70% DMSO, the Type J aggregate was still the only form present and was found to have a diameter of 111 and 145 nm, respectively. The last set of measurements taken was in 90% DMSO where the Type J aggregate converts dynamically to Type H from the UV/vis studies. As with squaraine **3,** the DLS at the onset of the dynamic conversion identified the aggregate as Type J. After the conversion was complete and there was no further increase in Type H aggregate absorption, the particle size was again determined. In this way, the dimensions for the Type J and Type H aggregates obtained in 90% DMSO were found to be 100 and 106 nm, respectively.

The aggregate number was then calculated from DLS measured diameter. Based on single crystal studies and X-ray diffraction patterns of squaraine aggregates, the intermolecular spacing between aggregates was calculated to be 0.35 nm (5, 6, 13, 14). Hence, the aggregate number is simply given by the measured diameter of the particle divided by the interplanar distance, 0.35 nm. Results are given in Tables 4–7.

© 1999 NRC Canada

Fig. 3. (*a*) Schematic illustration of the stabilization effect of intermolecular charge-transfer interactions between adjacent molecules in a Type J squaraine solution aggregate.
(*b*) Schematic illustration of the face–face stacking of molecules resulting from alignment of the transition dipole moment in the Type H squaraine aggregate.

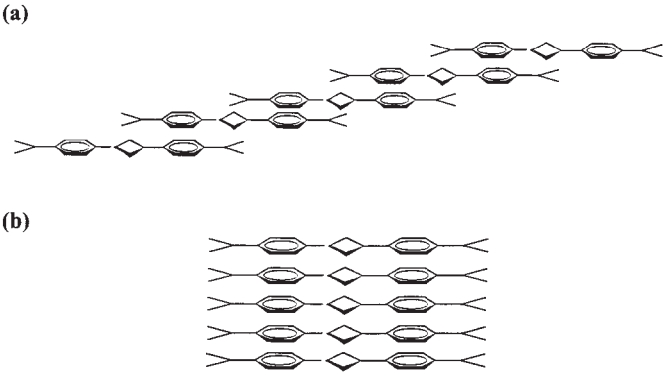

Discussion

1. Dye aggregation

In this work, we have investigated the aggregation of squaraine dyes through the dual approaches of UV/vis spectroscopy and Dynamic Light Scattering (DLS). These two approaches provide information, respectively, on the type of aggregate that is formed and on the degree of aggregation (particle size). Our study pertains to aggregation in solution (DMSO–water mixtures) as contrasted from the traditional studies of aggregation on the surface of a liquid as in Langmuir–Blodgett (LB) films or in a crystalline matrix (6, 15).

Several studies have examined the molecular orientations of squaraine aggregates with two predominant morphologies occurring (6, 15). Through studies of crystalline solids, it was found that formation of specific aggregates with "red-shifted" spectra — characteristic of a J aggregate — were stabilized by intermolecular charge-transfer interactions between adjacent molecules that were 3.5 Å apart (13). These interactions were the result of a specific alignment of the electron-deficient squarylium moieties with the electron-rich dialkylamino phenyl groups (Fig. 3*a*). Conversely, the aggregates exhibiting hypsochromic shifts — characteristic of an H aggregate — resulted from the alignment of the transition dipole moments, enforcing a "face–face" stacking of the molecules that are 3.5 Å apart (14). This particular geometry of the aggregate (Fig. 3*b*) leads to very poor photoconduction due to inefficient intermolecular charge transfer, which is observed in both UV/vis studies and LB films.

In our previous studies, the squaraine aggregates that were formed in solution were classified as "Class A" and "Class B." However, these aggregates exhibit similar spectral characteristics that can be more appropriately described through the adaptation of Exciton theory (16). Even though classical exciton treatments relay qualitative explanations of the spectral trends observed in dimers with equal interchromophore distances, the solution aggregates formed in this study can also be described as Type H and J because of the following common features: (*i*) bathochromic shift of λ_{max} relative to the monomer due to the effects of intermolecular charge-transfer stabilization and proper donor–acceptor alignment in the Type J (B) aggregate; (*ii*) hypsochromic shift of λ_{max} relative to the monomer due to the face–face alignment of transition dipole moments in the Type H (A) aggregate; (*iii*) large decrease in molar absorptivity coefficient for both aggregate forms (300 000 M^{-1} cm^{-1} → 80 000 M^{-1} cm^{-1}); and (*iv*) similar intermolecular spacing within the aggregates.

Limitations of exciton theory are that it only explains the observation of single bands equally spaced from the monomer absorption that arise from the formation of dimers, whereas the Type H and Type J aggregates being described in the present study are of a much higher order with a large increase in number of transitions that are dependent on the relative spatial orientation of the molecules (6, 7). Thus, exciton theory is too simplistic to provide a thorough theoretical understanding of the aggregation described herein but is in accord with spectral evidence that the molecules that comprise the aggregate in our systems have similar intermolecular spacing and defined intermolecular interactions.

2. Effects of increasing hydrophobicity on squaraine aggregation

Comparison of the aggregation behaviour of the three squaraines in this study shows that the main determining factor is the length of the *N*-alkyl substituent. Since the hydroxyphenyl functionality and squaraine ring remain constant throughout the series, the difference in aggregation characteristics can be attributed to the increase in hydrophobic interactions resulting from the increasing chain length of the alkyl substituent.

The results of the spectrophotometric studies for the *n*-butyl, *n*-octyl, and *n*-dodecyl substituents are shown in Table 2 and reveal the role of hydrophobic interactions on aggregation of the squaraine dyes. It is seen that the expected increase of hydrophobic interactions that would attend increasing the alkyl substituent chain length significantly alters the aggregation states present in different DMSO compositions. Thus, upon lengthening the alkyl chain, the Type J aggregates that are formed in water-rich media become the dominant form in solutions with increasing percentages of DMSO and conversion from Type J to Type H does not occur until much higher DMSO compositions. For all the squaraines studied, it was found that the Type J aggregate was formed initially. The two main driving forces for formation of the Type J aggregate are (*i*) intermolecular charge-transfer interactions between the donor and acceptor moieties and (*ii*) the hydrophobic interactions associated with the *N*-alkyl chains. These two types of interactions stabilize the Type J aggregate and prevent the dynamic conversion to the Type H form.

In assessing the relative contribution of each interaction for squaraines **2**, **3**, and **4**, it is considered that the intermolecular charge-transfer interaction remains constant while the hydrophobic interactions become increased along this series. Since the dynamic conversion to Type H is observed when the concentration of DMSO is increased, this must destabilize the aggregate to reorganize to a more energetically favourable form; i.e., in solutions of high DMSO con-

© 1999 NRC Canada

Fig. 4. Illustration of the individual monomer length measurement for **2** using molecular mechanics (Spartan 3.0).

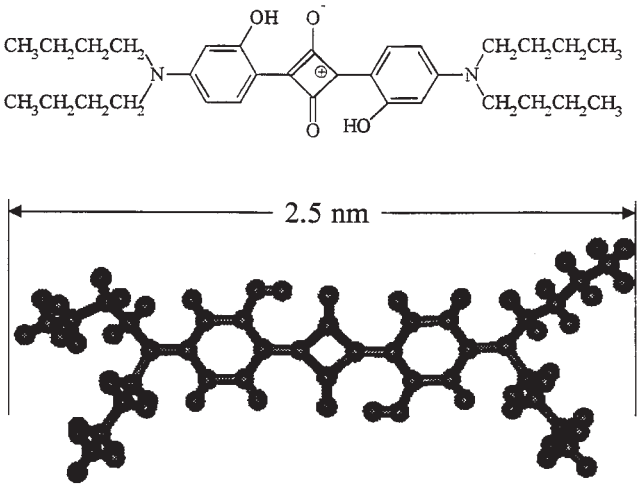

tent, the most favorable aggregate is the Type H. However, with the increase in the hydrophobic interactions on going from *n*-butyl to *n*-dodecyl, it becomes much more difficult for the solvent to destabilize the Type J aggregate for it to convert to the Type H form. This is the main reason that the Type J aggregates formed from squaraines **3** and **4** persist in solutions with a wider range of DMSO percentages compared to the *n*-butyl case. The UV/vis results show that the decrease in hydrophobic interactions in the squaraine monomer facilitates the formation of Type H aggregates.

3. Particle sizing

The use of UV/vis spectroscopy to study aggregation phenomena in a quantitative fashion is not definitive, as it is difficult to differentiate new bands that correspond to dimers or higher order aggregates (17). Hence, dynamic light scattering measurements were performed in parallel with the spectrophotometric study to: (*i*) quantify the aggregate size; (*ii*) calculate the number of molecules associated with each aggregate; (*iii*) determine the influence of solvent on aggregation; and (*iv*) provide further evidence for the kinetic versus thermodynamic product control associated with each aggregate type.

In Table 3 is presented a summary of the DLS measurements. However, in the ensuing discussion, for clarity, the data is broken down so as to highlight the different factors that control aggregation, such as *N*-alkyl chain length, the DMSO–water solvent composition, and the dynamic conversion from Type J to Type H. Combined with these measurements is the actual aggregate number, calculated by dividing the hydrodynamic diameter by the intermolecular spacing within the aggregate.

(a) Effect of increasing hydrophobic interactions

The first trend observed in the DLS data is the effect of increasing hydrophobic interactions on the measured diameter for the Type J aggregate. Table 4 lists the particle size measurements for each of the squaraines in 10% DMSO solution. In this solution, all of the squaraines have aggregated to form the Type J species, as indicated by the UV/vis study. The trend apparent in comparing the DLS data of each Type J aggregate is the increase in particle size while traversing the *n*-butyl to *n*-dodecyl series. It is interesting that whereas the individual monomer lengths vary only modestly, *n*-butyl = 2.5 nm, *n*-dodecyl = 4.8 nm (Fig. 4), yet the hydrodynamic diameter of these species is widely different. The *n*-butyl aggregate in 10% DMSO solution has an aggregate number of ~210 molecules; evidently, in this aggregate comprising ~200 molecules, efficient charge-transfer interactions are occurring and give rise to the observed spectral characteristics.

It is further shown in Table 4 that the aggregate numbers for the *n*-octyl and *n*-dodecyl Type J aggregate, 290 and 365, respectively, increase in the 10% DMSO solution relative to the *n*-butyl Type J aggregate. The *n*-octyl has an aggregate number of ~290 molecules, i.e., almost 100 more molecules than for the *n*-butyl case. Similarly, the *n*-dodecyl Type J aggregate has an aggregate number of ~365 molecules, much larger than the values calculated for both the *n*-butyl and the *n*-octyl systems. Clearly, there is a relationship between the degree of aggregation and hydrophobicity; i.e., the hydrophobic effect increases the degree of self-association along the series *n*-butyl, *n*-octyl to *n*-dodecyl.

The formation of aggregates in DMSO–water media by the squaraine monomers is driven by the hydrophobic effect (18). Squaraine dyes are aggregated in water-rich media but self-association is expected to be entropically unfavorable, since a considerable degree of translational, vibrational, and rotational freedom is lost. However, the loss in energy resulting from association of the dye molecules is offset by the release of solvent molecules surrounding the dye molecule. A specific type of aggregate is formed that is dependent on the degree of hydrophobic interactions that influence monomer aggregation. As the level of hydrophobic interactions increases in the system so does the degree of association.

(b) Effect of solvent composition on aggregate size

Typically, the absorption spectra of dyes are a function of dye concentration resulting from the formation of dimers and higher order aggregates. However, in the present systems the spectral characteristics are determined by the DMSO–water solvent composition, since the dye concentration remains constant. Table 5 shows the DLS results obtained for the *n*-dodecyl squaraine Type J aggregate as observed through UV/vis spectroscopy in 10, 50, 70, and 90% DMSO–water mixtures. The effect of solvent composition on aggregate particle size is best exemplified with *n*-dodecyl, since this exists in the Type J aggregate form throughout the largest range of solvent media and where the UV/vis results indicate dynamic conversion from Type J to Type H occurring only at 90% DMSO.

It is noted that the effect of solvent on the Type J aggregate size can not be deduced from the UV/vis data, but rather from the corresponding DLS measurements, since the spectral properties of the Type J aggregate remain constant throughout the solvent range in which it is observed. However, the DLS results exhibit a marked effect on the aggregate size depending on the region of DMSO composition even though the UV/vis spectra are identical. Thus, the results in Table 5 show that the particle size of the *n*-dodecyl aggregate decreases steadily as the percentage of DMSO is

© 1999 NRC Canada

increased from 10 to 70%, and then remains constant at 90%.

Studies of DMSO–water mixtures have demonstrated that their properties deviate considerably from those that would be expected on the basis of additive relative contributions from both pure solvents (19). There are two distinct regions of behaviour for these binary solvent systems, a water-rich zone and a DMSO-rich zone. The break point between these regions occurs at approximately 60% (v/v) (33 mol%) DMSO. Up to 60% DMSO, the DMSO and water act as a structure-maker resulting in the strengthening of the hydrogen bond network. This unusual extension of the hydrogen-bonding network orders the solution and decreases the aggregate number as the DMSO percentage increases. As the DMSO content is increased, water molecules are forming hydrogen bonds with DMSO that are stronger than the hydrogen-bonding between water molecules themselves. The increase in structure of the solvent places limitations on the number of molecules that form the Type J species. The ordering of the solvent restricts the formation of higher order aggregates due to a decrease in the release of solvent molecules to offset the energetically unfavourable association of these dyes.

The maximum structure in this binary mixture occurs at 60% DMSO (v/v) (33 mol%) and corresponds roughly to two molecules of water binding with one molecule of DMSO (20). Beyond 60% DMSO, deviations from ideal behaviour are not observed. This is believed to be the result of a relatively consistent solvent structure as the majority of water molecules are involved in strong hydrogen bonding interactions with DMSO. The results from the DLS study indicate that there is no further change in the particle size beyond the 60% v/v breakpoint. Thus, once DMSO becomes the predominant solvent component, the ordered nature of the solvent molecules is not as profound and results in aggregates of the same number of molecules being formed.

(c) DLS measurement of Type J to Type H conversion

The dynamic conversion of squaraines **3** and **4** from the Type J aggregate to the Type H aggregate forms was examined, and each form was quantified through DLS. In DMSO–water media where the UV/vis studies showed that dynamic conversion was occurring from Type J to Type H aggregate, the DLS method was unable to follow the rate process. In the procedure adopted to circumvent the problem, DLS measurements were made immediately after injection of the dye solution into the given solvent mixture, and then again once the dynamic conversion was complete. Prior to each DLS measurement, the UV/vis spectrum was recorded to ascertain the particular Type J and Type H aggregates formed. In this way, the particle size could be obtained initially for the Type J aggregate and finally for the Type H aggregate.

Tables 6 and 7 show the DLS results for the dynamic conversion from Type J to Type H aggregate forms. Table 6 presents the dynamic conversion of the *n*-octyl squaraine in 70% DMSO solution. The DLS calculated aggregate number for both the *n*-octyl Type J and Type H system was found to be ~430, i.e., interconversion between the two forms resulted in the same aggregate number being calculated. Measurement of each aggregate type by DLS showed no change in the aggregate size or in the aggregate number. This was further apparent on measurement of the *n*-dodecyl dynamic J $\rightarrow$ H conversion where the DLS calculated aggregate number was found to be ~300 for each form. It follows from these results that the number of molecules in the Type J and the Type H aggregate is the same in these systems.

The UV/vis spectra accompanying the dynamic conversion show that there is an hypsochromic shift of the absorption maximum. Previously, it was thought that the hypsochromic shift arises from higher orders of aggregates being formed, but it appears from the above results that the spectroscopic behaviour is due to a realignment of the charge-transfer moieties within the associated form. Thus, the interactions between the aggregate and the DMSO cosolvent provides the driving force to form a more stable aggregate form.

One can explain the effect of DMSO on the interconversion of Type J aggregate to Type H on the basis of the properties inherent to DMSO–water media and interactions with the nonpolar solute. Essentially, the Type J aggregate is being destabilized to the Type H aggregate as the percentage of DMSO in solution increases.[2] The actual percentage of DMSO where this occurs is directly related to the hydrophobic interactions associated with the aggregation. The destabilization by DMSO must overcome the stability produced by hydrophobic interactions to ensure that the conversion does occur. This is the primary reason that squaraine **4** forms Type J aggregates that predominate over the largest range of solvent. Once the destabilization effect of the DMSO overcomes the hydrophobic interactions, the alignment of the dipole–dipole interactions of the solvent with the C-O squaraine ring becomes the driving force to form the Type H aggregate. The dipole moment of DMSO is much larger than that of water (3.9 D vs. 1.8 D). In single crystal studies of DMSO, it has been shown that the structure of DMSO molecules is the face–face alignment of the dipoles (21). The DMSO molecules exert the same effect on the squaraine aggregates by forcing the alignment of the squaraine molecules such that the major dipole moments located along the C–O axis of the squaric acid moiety are coincidental, as in Type H aggregate (Fig. 3*b*).

3. Kinetic vs. thermodynamic control of aggregation

In our previous paper concerned with structure–property relationships of squaraine dyes, a model of aggregation behaviour was proposed in which the basis for formation of Type J and Type H aggregates was the thermodynamic relationship between these two forms: the Type J aggregate is a product of "kinetic" control, while the Type H aggregate is a product of "thermodynamic" control.

The results are consistent with Type J aggregates being a product of kinetic control because this aggregate type is initially formed upon injection of squaraine solution in an organic solvent into DMSO–water media As the percentage of

[2] It has been suggested by a referee that increased DMSO concentration may alternatively shift the equilibrium by stabilizing the H-aggregate. Differentiation between these alternatives will await studies now in progress with other binary solvent systems. We thank the referee for the suggestion.

© 1999 NRC Canada

DMSO in the system increases, the Type H aggregate becomes the product of thermodynamic control, as it is only formed following the dynamic interconversion. Even though the Type J species has not been observed for the *n*-butyl squaraine in media >50% DMSO, the conversion to Type H from Type J may be so rapid in this system that the experimental protocol can not detect the short-lived kinetic species. Also, the conversion of Type J to Type H aggregate can be induced on the addition of DMSO to a 10% DMSO solution of *n*-butyl squaraine. However, the opposite is not observed, i.e., dilution of the Type H aggregate in 50% DMSO with water does not result in the conversion to Type J aggregate. Thus, the irreversibility of this process is a direct result of the more thermodynamically favored aggregate–solution interaction.

Type J aggregates are formed in water-rich media immediately upon injection into the solvent. The UV/vis studies show that the stability of these aggregate types is increased as the alkyl chain length is increased. The DLS measurements readily support this as the aggregation number is found to increase in the order *n*-butyl < *n*-octyl < *n*-dodecyl. Being a product of kinetic control, the effect of the hydrophobic interactions is to increase the size of the aggregate formed as well as hindering the dynamic conversion to the Type H form. However, the Type H aggregate is ultimately formed in higher percentages of DMSO as the thermodynamic product, as the result of more favorable interaction with solvent molecules.

Importantly, the DLS measurements have shown that the Type H aggregates are formed with the same number of molecules in the aggregate as for the Type J. It has been found (Table 2) that for both the *n*-octyl and *n*-dodecyl substrates, the dynamic conversion results from the solvent molecules overcoming the hydrophobic interactions within the aggregate, since DMSO compositions of 80 and 90%, respectively, are required to bring about the change. In solutions of high DMSO content, the most energetically favorable form is the Type H, but this is only formed over time. Hence, the Type H aggregate is not formed from the combination of a number of Type J aggregates; rather, the molecules in the aggregate undergo an intramolecular reorganization of the individual molecules. The driving force for the formation of Type H is attributed to the dipole–dipole interactions between solvent and aggregate; alignment of the molecules in Type H formation minimizes the energy within the system.

Conclusions

Our DLS analysis of squaraine aggregates has given further insight into the mechanism of aggregation, the effect of hydrophobic interactions on the size of aggregate as observed spectroscopically, and the effect of solvent stabilization/destabilization on aggregates. From the UV/vis studies, it was concluded that the *n*-dodecyl squaraine aggregate had the most persistent formation of Type J aggregate in the widest range of DMSO–water mixtures due to the increase in hydrophobic interactions associated with the aggregate. Our results indicate that the nature of the squaraine aggregate is markedly affected by the tailored substituents and also by the effect of solvent. Hydrophobic interactions and the interactions of the aggregate with the solvent molecules further dictate the size of the aggregate that is formed in various DMSO–water media. In addition, the transition between aggregate forms, Type J and Type H, is a direct result of intramolecular reorganization, as there is no change in aggregate size during this process.

These studies provide an informative view on the structure and photophysical properties that may be applicable to incorporation of these dyes into technology. The knowledge gained from this study, plus the fact that squaraine application to technology is hindered by the formation of Type H aggregates, reiterates the importance of optimizing the molecular architecture to form solely the Type J aggregate in the solid state; the Type J has the most beneficial photophysical properties. The DLS has shown that the more efficient charge transfer is not a result of the aggregate size being smaller, but that the intermolecular charge transfer which is essential for photoconduction will occur in extended forms of the aggregate. Based on the UV/vis data and the DLS results, it is envisaged that an efficient model will be developed to aid in the understanding of the aggregation of photoconductors; optimization of the Type J aggregate through molecular engineering may result in a superior photoconductor applicable to technology. This in turn will lead to a better design and molecular engineering strategy to optimize the physical properties of photoconductors in the solid-state, using solution-state experiments.

Acknowledgements

Financial support of this research by the Natural Sciences and Engineering Research Council of Canada is gratefully acknowledged. The authors express warm appreciation to Professor Robert Pasternack for discussions and counsel concerning dye interactions and Dynamic Light Scattering.

References

1. (*a*) J. Treibs and K. Jacob. Angew. Chem. Int. Ed. Engl. **4**, 694 (1965); (*b*) K.Y. Law, F.C. Bailey, and L.J. Blusett. Can. J. Chem. **64**, 1607 (1986); (*c*) K.Y. Law and F.C. Bailey. Dyes Pigm. **9**, 85, (1988); (*d*) P.M. Kazmaier, R. Burt, G. DiPaolo-Baranyi, C.K. Hsiao, R.O. Loutfy, T.I. Martin, G.K. Hamer, T.L. Bluhue, and M.G. Taylor. J. Imaging Sci. **32**, 1 (1988).
2. R.W. Bigelow and H.J. Freund. J. Chem. Phys. **107**, 159 (1986).
3. (*a*) R. Hoffman and P.M. Kazmaier. J. Am. Chem. Soc. **116**, 9684 (1994); (*b*) F. Nuesch, J.E. Moser, V. Shklover, and M. Gratzel. J. Am. Chem. Soc. **118**, 5420 (1996); (*c*) F. Neusch and M. Gratzel. Chem. Phys. **193**, 1 (1995).
4. (*a*) A.J. McKerrow, E. Buncel, and P.M. Kazmaier. Can. J. Chem. **71**, 390 (1993); (*b*) P.M. Kazmaier, A.J. McKerrow, and E. Buncel. J. Imag. Sci. **36**, 373 (1992).
5. R.E. Wingard. IEEE Ind. Appl. **37**, 1251 (1982).
6. K.Y. Law and C.C. Chen. J. Phys. Chem. **93**, 2533 (1989).
7. (*a*) E. Buncel, A.J. McKerrow, and P.M. Kazmaier. J. Chem. Soc. Chem. Commun. 1242, (1992); (*b*) A.J. McKerrow, E. Buncel, and P.M. Kazmaier. Can. J. Chem. **73**, 1605 (1995).
8. H. Chen, M.S. Farahat, K.Y. Law, and D.G. Whitten. J. Am. Chem. Soc. **118**, 2584 (1996).
9. (*a*) R.F. Pasternack and P.J. Collings. Science (Washington, D.C.) **269**, 935 (1995); (*b*) R.F. Pasternack, C. Bustamante, P.J. Collings, A. Gianetto, and E.J. Gibbs. J. Am. Chem. Soc.

© 1999 NRC Canada

115, 5393 (1993); (*c*) R.F. Pasternack, E.J. Gibbs, P.J. Collings, Julio C. DePaula, L. Christine Turzo, and Antonio Terracina. J. Am. Chem. Soc. **120**, 24, 5873 (1998).
10. R. Fusy. Adv. Colloid Interface Sci. **52**, 79 (1994).
11. (*a*) A. Daytner and M.T. Pailthrope. J. Colloid Interface Sci. **76**, 557 (1980); (*b*) A. Daytner, A.G. Flovers, and M.T. J. Phailthorpe. Colloid Interface Sci. **74**, 71 (1980).
12. H.E. Sprenger and W. Ziegenbein. Angew. Chem. Int. Ed. Engl. **5**, 894 (1966).
13. M. Tristani-Kendra and C.J. Eckhardt. J. Chem. Phys. **81**, 1160 (1984).
14. D.G. Farnum, M.A. Neuman, and W.T. Suggs. J. Cryst. Mol. Struct. **4**, 199 (1974).
15. (*a*) K. Liang, K.Y. Law, and D.G. Whitten. J. Phys. Chem. **98**, 13379 (1994); (*b*) S. Das, T.L. Thanulingam, K.G. Thomas, G.V. Kamat, and M.V. George. J. Phys. Chem. **98**, 13379 (1994).
16. M. Kasha. *In* Molecular processes in radiation biology. *Edited by* L. Augenstein and R. Mason. Academic Press, New York. 1964.
17. H. Chen, K.Y. Law, J. Perlstein, and D. Whitten. J. Am. Chem. Soc. **117**, 7257 (1995).
18. (*a*) S.B. Singham and C.F. Bohren. Langmuir, **9**, 1431 (1993); (*b*) X.K. Jiang. Acc. Chem. Res. **21**, 362 (1988); (*c*) O. Valdes-Aguilera and D.C. Neckers. Acc. Chem. Res., **22**, 171 (1989).
19. (*a*) E. Buncel and H. Wilson. Adv. Phys. Org. Chem. **14**, 133 (1977); (*b*) E. Buncel, I.H. Um, and S. Hoz. J. Am. Chem. Soc. **111**, 971 (1989); (*c*) R.M. Tarkka, W.K.C. Park, P. Liu, E. Buncel, and S. Hoz. J. Chem. Soc. Perkin Trans. 2, 2439 (1994); (*d*) P. Liu, S. Hoz, and E. Buncel. Gazz. Chim. Ital. **126**, 31 (1996).
20. E.A. Symons. Can. J. Chem. **49**, 3940 (1978).
21. S.W. Jacob, E.E. Rosenbaum, and D.C. Wood. *In* Basic concepts of DMSO. Academic Press, New York. 1971.

© 1999 NRC Canada

Vicinal–diaryl interactions in stilbenoid hydrocarbons as observed in the through-space charge delocalization of their cation radicals

Rajendra Rathore and Jay K. Kochi

Abstract: The conformational preference of vicinal or 1,2-phenyl groups is probed in two classes of ring-substituted 1,2-diphenylbicyclooctene (stilbenoid) hydrocarbons **1a**–**1d** and **2a**–**2c.** UV–vis spectroscopy reveals, and X-ray crystallography verifies, the intramolecular (edge-to-face) orientation for the phenyl–phenyl interaction in stilbenoids **1a**–**1d.** Most importantly, when two pairs of *ortho*-methyl substituents are present, the cofacial phenyl groups in the stilbenoid donors are established by X-ray crystallography and spectrally observed in the cation radicals (**2a**$^{+\bullet}$–**2c**$^{+\bullet}$) by the appearance of new bands with strong absorptions in the near IR with λ_{max} = 1100–1315 nm, analogous to those previously observed in intermolecular (aromatic) interactions of aromatic cation radicals.

Key words: stilbenoid hydrocarbon, cation radical, aryl–aryl interaction.

Résumé : On a étudié la préférence conformationnelle de groupes phényles vicinaux (ou en positions 1,2) de deux classes d'hydrocarbures, des 1,2-diphénylbicycloocènes (stilbénoïdes) substitués sur le cycle, **1a–1d** et **2a–2c**. La spectroscopie UV-visible révèle, et la diffraction des rayons X permet de confirmer, l'orientation intramoléculaire (arête vers la face) de l'interaction phényle-phényle dans les stilbénoïdes, **1a-1d**. La diffraction des rayons X a permis d'établir un fait encore plus important, à savoir que, lorsque deux paires de substituants *ortho*-méthyles sont présents, les groupes phényles des stilbénoïdes donneurs sont coaxiaux et on peut les observer spectralement dans les cations radicaux (**2a**$^{+\bullet}$–**2c**$^{+\bullet}$) par l'apparition de nouvelles bandes de forte intensité dans le proche infrarouge, avec un λ_{max} de 1100–1315 nm, analogues à celles observées antérieurement dans les interactions intermoléculaires (aromatiques) des cations radicaux aromatiques.

Mots clés : hydrocarbure stilbénoïde, cation radical, interaction aryle–aryle.

[Traduit par la Rédaction]

Introduction

The through-space interaction between a pair of vicinal aromatic π-systems is known to decrease the ionization potential in a variety of aromatic hydrocarbons such as 1,1,2,2-tetraphenylethane, 1,2-diarylethanes, triptycenes, cyclophanes, benzpinacols, etc. (1–3). In the latter, Penn et al. (4) noted that such cofacial aryl–aryl interactions can explain the increased electron-transfer reactivity in carbon–carbon bond cleavage. Recently, Gano et al. (5) pointed out that similar 1,2-diaryl interactions are also responsible for the observed decrease in the ionization potentials in (*Z)*-stilbenes as compared to the corresponding (*E)* isomers. Since these findings suggest that the cation-radical intermediates resulting from 1-electron oxidation of such systems may be unusually stable species, a detailed (UV–vis) spectroscopic analysis of these cationic intermediates must be carried out to further explore the structural requirements of aryl–aryl interactions. As such, the observation of new electronic transitions in multichromophoric assemblies would provide valuable information regarding the spatial (electronic) interactions amongst the various chromophores. For example, *intermolecular* interactions of aromatic hydrocarbons (ArH) have been previously observed by the presence of new broad absorption bands in the near-IR region in the electronic absorption spectra of a variety of dimeric aromatic cation radicals (6, 7), and the broad NIR absorption bands have been assigned to charge-resonance transitions within the dimeric cation radicals $(ArH)_2^{+\bullet}$ arising from the favorable π, π-orbital overlap between the two coplanar arene moieties arranged in a sandwich-like structure (also compare ref. 8).

In this study, we report the preparation of cation-radical salts of various stilbenoid donors with cofacially juxtaposed aryl groups, and show how analysis of the electronic absorption spectra provides spectroscopic evidence for direct 1,2-diaryl interactions. The two series of stilbenoid donors in Chart 1 are readily synthesized by an efficient palladium-catalyzed synthetic method (9). The spatial arrangements of the neighboring aryl groups in these stilbenoid donors are evaluated by monitoring the UV–vis spectra (and chemical reactivity) and further confirmed by X-ray crystallography. Moreover, the spectral comparison of the cation radical de-

Received November 24, 1998.

This paper is dedicated to Professor A.J. Kresge in recognition of his many seminal contributions to physical organic chemistry.

R. Rathore and J.K. Kochi.[1] Department of Chemistry, University of Houston, Houston, TX 77204-5641, U.S.A.

[1]Author to whom correspondence may be addressed. Telephone: (713) 743-3290. e-mail: jkochi@pop.uh.edu

 © 1999 NRC Canada

Chart 1. Stilbenoid donors.

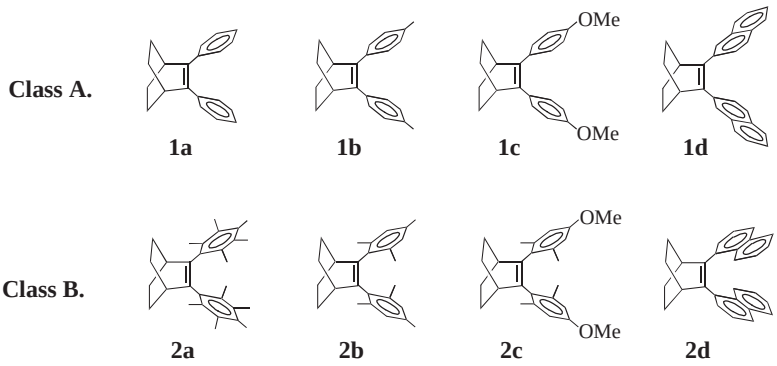

rived from other cofacial π-systems oriented at different dihedral angles (such as *m*-cyclophane and a cofacially oriented phenylene donor) sheds additional light on the angular requirements for such cofacial aryl–aryl interactions.

Results and discussion

1. Synthesis of stilbenoid donors

The various stilbenoid donors in Chart 1 were readily prepared by the palladium-catalyzed coupling of aryl Grignard reagents with a dibromoalkene, e.g.

[1] 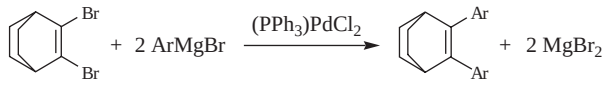

In a typical example, a freshly prepared solution of phenylmagnesium bromide (2.1 equiv.) was mixed with a solution of 2,3-dibromobicyclo[2.2.2]oct-2-ene in anhydrous tetrahydrofuran containing a catalytic amount of bis(triphenylphosphine)palladium(II) chloride (10) under an argon atmosphere at 25°C. The resulting pale-yellow solution was refluxed for 8 h, and a standard aqueous work-up, followed by recrystallization, afforded 2,3-diphenylbicyclo[2.2.2]oct-2-ene (**1a**) in essentially quantitative yield. The generality of the procedure was demonstrated by coupling various arylmagnesium bromides (with increasing substitution) with dibromobicyclooctene to afford the diarylbicyclooctenes listed in Table 1 in excellent yields.

Table 1. Synthesis of various stilbenoid donors by the Pd-catalyzed coupling of arylmagnesium bromides with 1,2-dibromobicyclooctene in tetrahydrofuran.[a]

Stilbenoid hydrocarbon	Time[b] (h)	% Yield[c]
1a	8	96
1b	6	94
1c	12	92
1d	12	91
2a	18	94
2b	18	94
2c	24	91
2d	24	82

[a]See the experimental section for the general procedure.
[b]The course of the reaction monitored by GC.
[c]Isolated yields.

2. Conformational analysis of stilbenoid donors

Owing to the rigid backbone structure, the various stilbenoid donors can attain one of the two stable (idealized) conformations, i.e., face-to-face (cofacial) (11) or edge-to-face (perpendicular) (12), as diagrammatically presented in Chart 2. Optimum π–π interactions between aryl groups in various stilbenoid donors are expected to arise from the cofacial arrangement of the aryl groups, and we will determine how such a preferred conformation can be achieved by varying the substituents on the aryl groups as follows.

Chart 2. Aromatic–aromatic orientations.

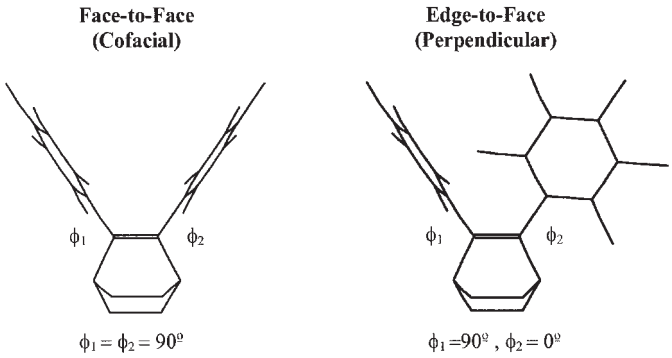

X-ray crystallography

Single crystal structure analysis was performed on **1a** in class A and **2a**/**2b** in class B in order to ascertain the molecular structures and conformations of the stilbenoid donors. For the sake of simplicity, we identify the structural parameters used for the comparison of all three structures as *d*, the olefinic C=C bond length; *l*, the C–C bond length to the aryl group; θ, the twist of the olefinic C=C bond; and ϕ_1/ϕ_2, the coplanarity of aryl groups with the C=C bond (as designated in the generic structure in Table 2). (Note that equal values of $\phi_1$and ϕ_2 indicate that the aryl groups are cofacial.)

Comparison of the various parameters *d*, *l*, θ, ϕ_1, and ϕ_2 for **1a**, **2a**, and **2b** in Table 2 shows that the stilbenoid donors (**2a** and **2b**), that contain *ortho*-methyl groups have essentially the same molecular structure that is characterized by the presence of *cofacial* aryl groups. It is clear that steric hindrance of the *ortho*-methyl groups forces both aryl groups to lie parallel to each other and (almost) orthogonal to the ethylenic bond with $\phi_1 = \phi_2 = 65°$, and the rotations of the aryl groups (around the C_1–C_3 and the C_2–C_5 bonds) are strongly coupled (i.e., mutually dependent), as indicated by the identical values of ϕ_1 and ϕ_2 in **2a** and **2b**. By contrast, the absence of *ortho*-methyl groups in the parent analog **1a**

© 1999 NRC Canada

Table 2. Comparison of selected structural parameters for various stilbenoid donors.

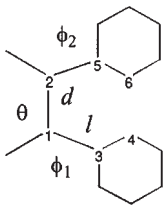

Parameter	1a	2a	2b
d	1.351(1)	1.328(5)	1.352(1)
l^a	1.484(1)	1.51(2)	1.496(1)
θ^b	6.6°	4.9°	4.5°
$\phi_1{}^c$	45.6°	64.8°	59.9°
$\phi_2{}^d$	60.1°	65.5	62.1°

[a]Average of two bonds (C_1–C_3 and C_2–C_5).
[b]Torsional angle C_3-C_1-C_2-C_5.
[c]Torsional angle C_2-C_1-C_3-C_4.
[d]Torsional angle C_1-C_2-C_5-C_6.

allows a greater degree of rotational freedom around the C_1–C_3 or the C_2–C_5 bond, as indicated by the different torsion angles ϕ_1 (46°) and ϕ_2 (60°).[2] Furthermore, an arbitrary superposition of the molecular structures of **1a** and **2b** (such as that illustrated in Fig. 1[3]) shows that at least one of the phenyl groups in **1a** can readily acquire a coplanar conformation with the olefinic bond.

Electronic (UV–vis) spectra

Structural analysis (vide supra) reveals that the presence of four *ortho*-methyl groups in various stilbenoid donors in class B forces both aryl groups to lie orthogonal to the olefinic bond, and thus effectively prevents π-conjugation with the olefinic bond. As such, the UV–vis spectral data show that all donors in class B absorb at $\lambda_{max} < 260$ nm, whereas the class A derivatives show well-defined absorption bands that are relatively red-shifted to $\lambda_{max} \geq 260$–310 nm (see Experimental). Importantly, the UV–vis absorption spectra of various derivatives in class A are strongly reminiscent of those of the parent stilbenes (14). In contrast, the cofacial stilbenoid donors in class B show absorption spectra that closely resemble those of the *isolated* (non-conjugated) aryl groups.

Reactivity and steric crowding

The olefinic carbons in class B donors are completely entombed due to the presence of four *ortho*-methyl groups (as well as the bicyclooctene framework), as shown by the space-filling representation of **2a** in Fig. 2. Such steric crowding around the olefinic bonds makes these donors completely inert to hydrogenation and epoxidation reactions. (Note that the

Fig. 1. The superimposition of the molecular structures of diphenyl- (**1a**, light lines) and dimesityl- (**2b**, dark lines) bicyclooctenes to show the coplanarity of a single phenyl group with the olefinic bond in **1a**.

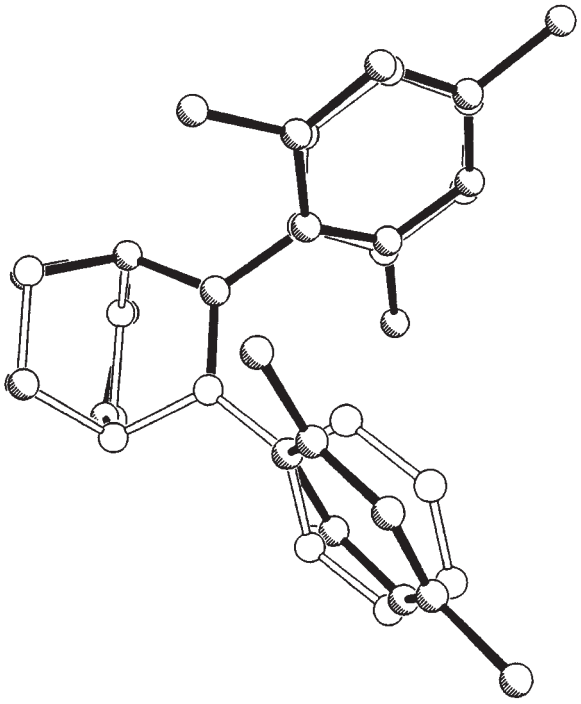

Fig. 2. Space-filling representation of **2a** to show the complete entombment of the olefinic carbons (darkened spheres) by four *ortho*-methyl groups and the bicyclooctene framework.

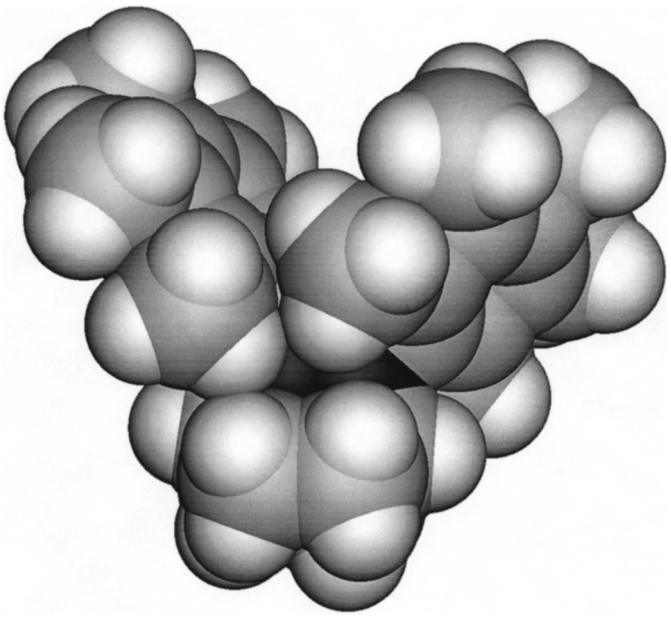

[2] Such a restricted rotation around the C–Ar single bond can lead to atropisomers as observed in a variety of biphenyls (ref. 13). For example, spectral (NMR) analysis of naphthyl derivative **1d** showed the presence of two isomers (see Experimental) that could not be separated or interconverted by heating up to 180°C. A (molecular mechanics) minimization of the molecular structure of **2d** with the aid of the QUANTA graphics (Molecular Simulation Inc., 16 New England Executive Park, Burlington, MA 081803) confirmed the presence of two (*syn* and *anti*) atropisomers. An X-ray structural study (in progress) should establish this point.
[3] All eight of the carbon atoms of the bicyclooctene moiety in **1a** were superimposed on those of **2a** for Fig. 1.

© 1999 NRC Canada

1-naphthyl derivative **2d** is similarly unreactive.[4]) In contrast, the class A derivatives (which lack *ortho*-methyl groups) readily undergo hydrogenation and epoxidation reactions owing to a greater rotational freedom of the aryl groups.[4, 5]

3. Cation radicals of the stilbenoid donor

Methods of oxidation

All the stilbenoid donors in Chart 1 undergo reversible electrochemical oxidation in the range E^0_{ox} = 0.98–1.45 V vs. SCE[6] (see Table 3). The electrochemical reversibility in such an easily accessible potential range allows the ready preparation of the corresponding cation radicals by either chemical or electrochemical oxidation in dichloromethane solution. For example, the chemical oxidation can be readily carried out by electron exchange with stable aromatic cation-radical salts $\mathbf{MA}^{+\bullet}$ and $\mathbf{EA}^{+\bullet}$, as selective organic oxidants with reversible reduction potentials that differ by only 190 mV, as listed in Chart 3 (16). Similarly, a mixture of

Chart 3. Cation-radical oxidants.

	$\mathbf{MA}^{+\cdot}$	$\mathbf{EA}^{+\cdot}$	
E^o_{red}	1.11	1.30	(V *vs* SCE)

chloranil and methanesulfonic acid (15) can also serve as an effective oxidant for the preparation of dichloromethane solutions of the cation radicals of the various stilbenoid donors in Chart 1. Moreover, the isolation of crystalline cation-radical salts from a number of stilbenoid donors can be effected with triethyloxonium hexachloroantimonate (17) as the 1-electron oxidant (see Experimental). Alternatively, the stable cation-radical solutions from stilbenoid donors in Chart 1 can be obtained by anodic oxidation in anhydrous dichloromethane containing tetrabutylammonium hexafluorophosphate as the supporting electrolyte (see Experimental).

Electronic absorption spectra

A solution of stilbenoid derivative **1c** when mixed with 1 equiv. of $\mathbf{MA}^{+\bullet}SbCl_6^-$ in dichloromethane (under an argon atmosphere at 25°C) immediately turned red, and the UV–vis absorption spectrum showed the characteristic twin absorption bands, at λ_{max} = 546 nm (band I) and 880 nm (band II), of dianisylbicycloctene cation radical $\mathbf{1c}^{+\bullet}$, as shown in Fig. 3*a*. Quantitative spectral analysis of the magenta solution (log ε_{546} = 4.16) indicated that the electron exchange in eq. [2] was displaced completely to the right, i.e.,

$$[2] \qquad \mathbf{1c} + \mathbf{MA}^{+\cdot} \rightarrow \mathbf{1c}^{+\cdot} + \mathbf{MA}$$

The same exchange procedure was used for the preparation of the UV–vis absorption spectra of the other stilbenoid cation radicals in Fig. 3*a*. It is important to emphasize, however, that the spectra were not dependent on the method of oxidation of the neutral donors, i.e., either electrochemical or chemical oxidation (vide supra). Thus the absorption spectra for the various stilbenoid cation radicals presented in Figs. 3 and 4 were obtained by at least three independent methods of oxidation and found to be the same, as follows.

Class A stilbenoid cation radicals

The class A stilbenoid cation radicals showed the characteristic (UV–vis) absorption spectra (in Fig. 3*a*) with twin absorption bands I and II (consisting of similar band shapes and fine structure in the high-energy band). These spectra are strongly reminiscent of the absorption spectrum previously observed for the transient cation radical of the parent (*Z*)-stilbene in frozen matrices (18) (see Fig. 3*b*). Interestingly, a change of the aryl group from phenyl to tolyl to anisyl in class A stilbenoid cation radicals leads to a monotonic red shift in the absorption maxima of both bands I and II as well as a hyperchromic increase in the (relative) intensity of band II. Such an observation is in accord with the increasing stabilization of the cationic charge by a coplanar aryl group containing a *para* substituent (19) in the order: H < CH_3 < OCH_3.

Class B stilbenoid cation radicals

In marked contrast, the various class B stilbenoid cation radicals in Fig. 4*a* showed an intense new (broad) absorption band (band III) in near-IR region (1100–1315 nm) in addition to the twin absorption bands I and II in the UV–vis region. It is important to reemphasize that the NIR absorption band III was completely absent in all the class A stilbenoid cation radicals, as shown in Fig. 4*b*.

Such a remarkable difference in the electronic absorption spectra of class A and B stilbenoid cation radicals can be ascribed to the steric effects of the *ortho*-methyl groups. Thus, in class A derivatives, the absence of *ortho*-methyl groups allows ready attainment of a conformation (edge-to-face) in which one of the aryl groups is coplanar with the ethylenic bond. However, such a coplanar conformation is strongly discouraged in class B derivatives due to the presence of *ortho*-methyl groups, and leads to only a face-to-face (cofacial) conformation (for example, see Chart 4). The observation of new electronic absorption bands in the NIR region (band III in Fig. 4*a*) is thus ascribed to charge-resonance transitions between the rigidly held cofacial aryl groups in **2a–2d** cation radicals. Such a spectral assignment is in accord with the observations of Badger and Brocklehurst (6) and Rodgers (7), who showed the presence of in-

[4] A palladium-catalyzed hydrogenation of **2d** under high pressure led to a partial reduction of the naphthyl moiety. For the hydrogenation procedures, see R. Rathore et al. (9)

[5] A standard epoxidation procedure using *m*-chloroperbenzoic acid was employed, see ref. 15.

[6] (*a*) Reversible electrochemical oxidation potentials (E^0_{ox} in V vs. SCE) were measured for the various stilbenoid donors (5 mM) by cyclic voltammetry in dichloromethane (containing 0.2 M tetra-*n*-butylammonium hexafluorophosphate as supporting electrolyte). Note that the naphthyl derivative **1d** was irreversibly oxidized even at a scan rate of v = 2 V s^{-1}. (*b*) It is noteworthy that E^0_{ox} values of the class B donors are not significantly less positive than those of the class A analogues, despite the presence of additional electron-releasing methyl groups (24). No doubt part of the discrepancy lies in the orthogonal aromatic rings, which completely remove them from ethylene conjugation. We hope to develop other qualitative methods for determining the stabilization energy of the through-space delocalized cation radicals $\mathbf{2a}^{+\bullet}$–$\mathbf{2c}^{+}$.

© 1999 NRC Canada

Table 3. Cation radicals of various stilbenoid donors in solution.[a]

Donor (D)	E^0_{ox}[b]	Cation radical: UV–vis band λ_{max} (I)[c]	UV–vis band λ_{max}(II)[c]	IR band λ_{max}(III)[c]	log ε
1a	1.47	493, 472(sh)	722	[d]	[d]
1b	1.36	518, 478(sh)	781	[d]	[d]
1c	0.98	547, 506(sh)	880	[d]	[d]
1d	1.28[e]	[f]	[f]	[f]	[f]
2a	1.28	426	740	1162	3.87
2b	1.40	410	681	1100	3.73
2c	1.21	428	700	1315	3.98
2d	1.33	534	782	1294	[g]
3	0.80	440	460	1200	3.98
4	1.41	475	—	1180	[g]

[a]For the oxidation procedures, see Experimental.
[b]V vs. SCE at 25°C. In dichloromethane containing 0.2 M *n*-tetrabutylammonium hexafluorophosphate at 100 mV s^{-1}.
[c]λ_{max} in nm.
[d]No absorption band observed in NIR region.
[e]Peak potential, irreversible cyclic voltammogram at v = 1000 mV s^{-1}.
[f]Transient cation radical.
[g]Not determined.

Fig. 3. (*a*) The UV–vis absorption spectra of various cation radicals from class A stilbenoid donors (as indicated) obtained by oxidation with $\mathbf{EA}^{+\bullet}$ $SbCl_6^-$ in dichloromethane at 22°C. (*b*) Comparison of the UV–vis absorption spectra of the cation radicals of parent (*Z*)-stilbene (18) and 2,3-diphenylbicyclooctene **1a** (as indicated).

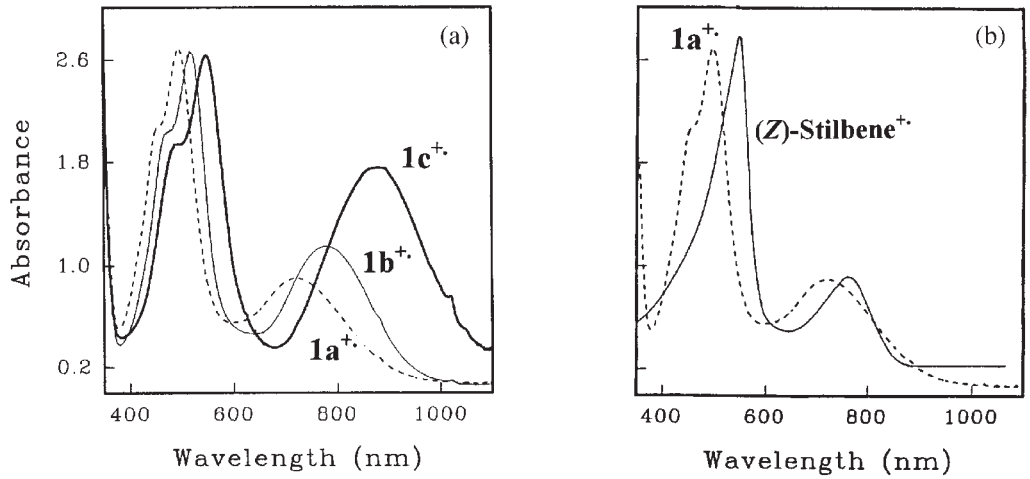

Fig. 4. (*a*) The pronounced NIR absorption band III in the electronic spectra of the cation radicals from class B stilbenoid donors (as indicated) in the region between λ_{max} = 1100–1315 nm in dichloromethane at 22°C. (*b*) For comparison, the UV–vis absorption spectra of the cation radicals $\mathbf{1b}^{+\bullet}$ and $\mathbf{1c}^{+\bullet}$ showing the absence of the NIR band.

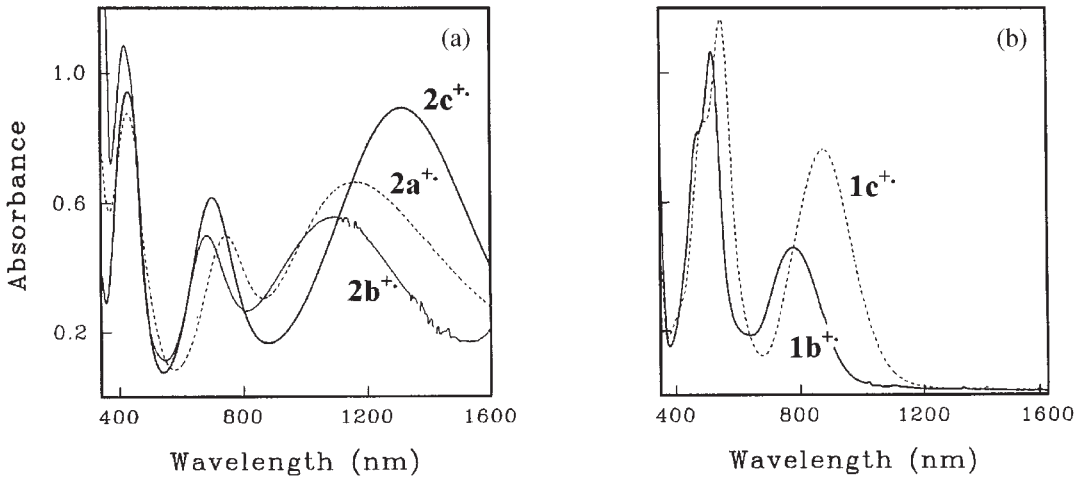

© 1999 NRC Canada

Chart 4. Interplanar dihedral angles.

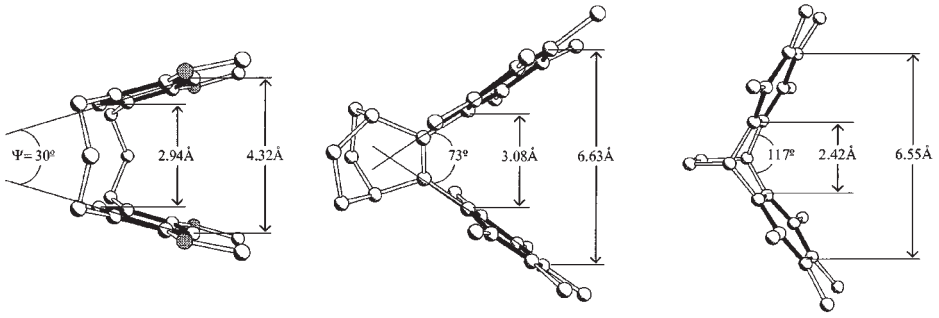

3 **2a** **4**

tense NIR absorption bands in the electronic spectra of a variety of (intermolecular) dimeric aromatic cation radicals. They further suggested that the efficient orbital overlap between the parallel aromatic π-systems (in a sandwich-like structure) is the structural basis for the observed charge-resonance transitions (i.e., NIR absorption bands). Note that a sandwich-like arrangement of the dimeric aromatic cation radicals (of naphthalene and its derivatives) has been verified by isolation of single crystals and their X-ray crystallographic characterization (for a review, see ref. 20).

Angular requirements for the charge-resonance transitions

Intense charge-resonance absorption bands of the stilbenoid cation radicals **2a**–**2d** are observed despite the fact that the interplanar (dihedral) angle of Ψ > 70° between the two aryl π-systems deviates significantly from that of a parallel arrangement (see Chart 4). To address the question of the angular requirements for observation of charge-resonance transitions in the cation radicals, we extend the donors to a cyclophane (2,4,2′,4′-tetramethoxy-*m*-cyclophane, **3** (21)) and a phenylene donor (octamethyl-9,10-dihydro-9,10-ethanoanthracene **4** (22)) in which the cofacial π-systems are oriented at different interplanar Ψ angles as established by X-ray crystallography (see Chart 4). (Also note that the closest interplanar contacts between two aromatic π-systems in **2a**, **3**, and **4** are 3.08, 2.94, and 2.42 Å, which are much shorter than the sum of van der Waals thickness 2*r* = 3.4 Å.)

Cyclophane **3** and the phenylene donor **4** undergo reversible electrochemical oxidation in dichloromethane at potentials of E^0_{ox} = 0.80 V and 1.41 V vs. SCE, respectively, which are lower by 380 and 230 mV than those of the parent 4,6-dimethyl-1,3-dimethoxybenzene (E^0_{ox} = 1.18 V vs. SCE) (23) and hexamethylbenzene (E^0_{ox} = 1.64 V vs. SCE) (24). Furthermore, the cofacial donors **3** and **4** were both readily oxidized to the corresponding cation radicals by electron exchange with $\mathbf{MA}^{+\bullet}$ and chloranil – methanesulfonic acid mixture (vide supra), and the UV–vis spectral analysis of the yellow-green solutions in both cases showed intense charge-resonance absorption bands at 1200 and 1180 nm, respectively (see Fig. 5). Such an observation of the NIR absorption bands in **2a**, **3**, and **4**, with drastically varied interplanar angles from Ψ = 30°–117°, suggests that minimal orbital overlap between interacting π-systems is sufficient for charge-resonance transitions to occur. Thus, a close, but not necessarily complete, cofacial approach of π-systems in various cation radicals (see Chart 4) leads to strong electronic interactions between the two aryl moieties, and results in

Fig. 5. The NIR bands in the UV–vis absorption spectra of the cation radicals from cofacial donors **3** and **4** (as indicated) showing the presence of intense charge-resonance bands in the 1200-nm region.

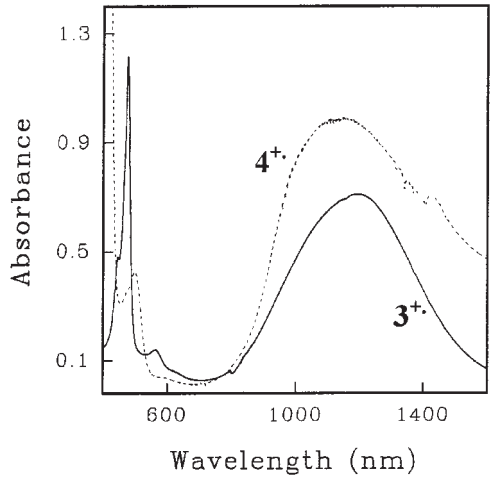

charge-resonance transitions in the UV–vis–NIR absorption spectra similar to those observed for the dimeric cation radicals. Theoretical analysis and quantitative comparison of the (NIR) charge-resonance absorption bands with changes in various structural parameters in a variety of mixed-valence cation-radical salts are currently under investigation.

Summary and conclusions

The efficient synthesis of the stilbenoid donors in Chart 1 allows the steric requirement for the cofacial interaction of aromatic groups to be established. Thus the presence of *ortho*-methyl substituents in the class B donors **2a**–**2c** forces the aromatic rings to lie parallel and orthogonal to the ethylenic bond (Fig. 1). As a result, the electronic (UV–vis) transitions in the cation radicals $\mathbf{2a}^{+\bullet}$–$\mathbf{2c}^{+\bullet}$ show strong new absorption bands in the near-IR region (1100 –1315 nm) arising from the charge-resonance interaction between cofacial aromatic rings. However, the energy of such a through-space charge delocalization is not sufficient to overcome the through-bond conjugation inherent to stilbene cation radicals, and the UV–vis spectra of the cation radicals of the class A donors **1a**–**1d** (with no *ortho* substituents) are singularly bereft of the near-IR absorption. We believe, however, that 1,2-diaryl interactions of the type described for stilbenoids **2a**–**2c** in this study will also pertain to the saturated analogues such as

© 1999 NRC Canada

vicinal diarylalkanes, etc. (1–3), in which restricted (single) bond rotations and through-bond conjugation will be less restrictive.

Experimental

Materials

The synthesis of 2,3-dibromobicyclo[2.2.2]oct-2-ene (25), *2*, 4, 2′, 4′-tetramethoxy-[3.3]-*m*-cyclophane (**3**) (21), and 1,2,3,4,5,6,7,8-octamethyl-9,10-dihydro-9,10-ethanoanthracene (**4**) (22) have been described previously. Bis(triphenylphosphine) palladium(II) chloride and triethyloxonium hexachloroantimonate (Aldrich) were stored in a Vacuum Atmosphere HE-493 dry box kept free of oxygen. The cation radicals $\mathbf{MA}^{+\bullet}$ and $\mathbf{EA}^{+\bullet}$ were readily obtained as the stable hexachloroantimonate salts in quantitative yields from the reaction of corresponding neutral hydroquinone ethers **MA** (9,10-dimethoxy-1,4:5,8-dimethano-1,2,3,4,5,6,7,8-octahydroanthracene) and **EA** (9,10-dimethoxy-1,4:5,8-dimethano-1,2,3,4,5,6,7,8-octahydroanthracene), respectively, with antimony pentachloride (16) or triethyloxonium hexachloroantimonate (17).

Synthesis of 2,3-diarylbicyclo[2.2.2]oct-2-enes

General procedure

An approximately 0.4 M solution of pentamethylphenylmagnesium bromide was prepared from bromopentamethylbenzene (5.0 g, 22 mmol) and excess magnesium turnings (2.4 g, 100 mmol) in tetrahydrofuran, under an argon atmosphere by refluxing for 3 h. The Grignard solution thus obtained was transferred via a cannula to a Schlenk flask containing a solution of 2,3-dibromobicyclo[2.2.2]oct-2-ene (25) (2.66 g, 10 mmol) and a catalytic amount of bis(triphenylphosphine)palladium(II) chloride (0.10 g, 0.15 mmol) in anhydrous tetrahydrofuran (20 mL). The resulting yellow mixture was refluxed for 18 h, cooled to room temperature, and quenched with saturated aqueous ammonium chloride (100 mL). The organic layer was separated and the aqueous phase was further extracted with diethyl ether (3 × 50 mL). The combined organic extracts were washed with water, followed by brine solution, and dried over anhydrous magnesium sulfate. Evaporation of the solvent afforded a pale yellow residue that was filtered through a short pad of silica gel with ether:hexanes (1:1) as the eluent. The resultant product was further purified by recrystallization from ethanol to afford bis(pentamethylphenyl) bicyclooctene **2a** as colorless prisms (3.7 g).

The characteristic spectral data for the various diarylbicyclooctenes obtained using the above general procedure are given as follows.

*2,3-Diphenylbicyclo[2.2.2]oct-2-ene (**1a**)*: Yield 96%, mp 126–127°C (ethanol); UV–vis (CH_2Cl_2) λ_{max}: 228, 280 nm; ^{1}H NMR ($CDCl_3$) δ: 1.68 (sym m, 4H), 1.82 (sym m, 4H), 3.03 (s, 2H), 7.14–7.28 (m, 10H); ^{13}C NMR ($CDCl_3$) δ: 26.20, 37.49, 125.85, 127.83, 124.83, 140.23, 141.02; GC–MS *m*/*z*, calcd. for $C_{20}H_{20}$: 260; found (M^+): 260. Anal. calcd. for $C_{20}H_{20}$: C 92.26, H 7.74; found: C 91.98, H 7.78.

*2,3-Bis(4-methylphenyl)bicyclo[2.2.2]oct-2-ene (**1b**)*: Yield 92%, oil; UV–vis (CH_2Cl_2) λ_{max}: 227, 283 nm; ^{1}H NMR ($CDCl_3$) δ: 1.70 (d, *J* = 7.5 Hz, 4H), 1.81 (d, *J* = 7.5 Hz, 4H), 2.40 (s, 6H), 3.04 (br s, 2H), 7.10 (d, *J* = 8.4 Hz, 4H), 7.14 (d, *J* = 8.4 Hz, 4H); ^{13}C NMR ($CDCl_3$) δ: 21.10, 26.23, 37.52, 128.28, 128.56, 135.26, 138.23, 139.52; GC–MS *m*/*z*, calcd. for $C_{22}H_{24}$: 288; found (M^+): 288. Anal. calcd. for $C_{22}H_{24}$: C 91.61, H 8.39; found: C 91.45, H 8.35.

*2,3-Bis(4-methoxyphenyl)bicyclo[2.2.2]oct-2-ene (**1c**)*: Yield 94%, mp 72–73°C (ethanol); UV–vis (CH_2Cl_2) λ_{max}: 237, 291 nm; ^{1}H NMR ($CDCl_3$) δ: 1.62 (br d, 4H), 1.74 (br d, 4H), 2.94 (s, 2H), 3.79 (s, 6H), 6.77 (d, *J* = 8.7 Hz, 4H), 7.09 (d, *J* = 8.7 Hz, 4H); ^{13}C NMR ($CDCl_3$) δ: 26.23, 37.44, 54.97, 113.23, 129.44, 133.63, 138.60, 157.59; GC–MS *m*/*z*, calcd. for $C_{22}H_{24}O_2$: 320; found (M^+): 320. Anal. calcd. for $C_{22}H_{24}O_2$: C 82.46, H 7.55; found: C 82.38, H 7.53.

*2,3-Bis(2-naphthyl)bicyclo[2.2.2]oct-2-ene (**1d**)*: Yield 91%, mp 195–196°C (ethanol); UV–vis (CH_2Cl_2) λ_{max}: 270, 315 nm; ^{1}H NMR ($CDCl_3$) δ: 1.73 (d, *J* = 8.7 Hz, 4H), 1.83 (d, *J* = 8.7 Hz, 4H), 3.16 (s, 2H), 7.18–7.78 (m, 14 H); ^{13}C NMR ($CDCl_3$) δ: 26.48, 38.01, 125.44, 125.81, 126.66, 127.20, 127.59, 127.82, 132.07, 133.60, 138.73, 140.85; GC–MS *m*/*z*, calcd. for $C_{28}H_{24}$: 360; found (M^+): 360. Anal. calcd. for $C_{28}H_{24}$: C 93.29, H 6.71; found: C 93.12, H 6.54.

*2,3-Bis(pentamethylphenyl)bicyclo[2.2.2]oct-2-ene (**2a**)*: Yield 94%, mp 239–240°C (ethanol); UV–vis (CH_2Cl_2) λ_{max}: 227, 251 nm; ^{1}H NMR ($CDCl_3$) δ: 1.77 (br d, *J* = 7.4 Hz, 4H), 1.91 (br d, *J* = 7.4 Hz, 4H), 2.14 (s, 12H), 2.18 (s, 6H), 2.19 (s, 12H), 2.63 (br s, 2H); ^{13}C NMR ($CDCl_3$) δ: 16.63, 16.81, 19.83, 27.28, 37.79, 131.96, 132.08, 132.05, 139.45, 142.71; GC–MS *m*/*z*, calcd. for $C_{30}H_{40}$: 400; found (M^+): 400. Anal. calcd. for $C_{30}H_{40}$: C 89.94, H 10.06; found: C 89.77, H 10.01.

*2,3-Bis(2,4,6-trimethylphenyl)bicyclo-[2.2.2]oct-2-ene (**2b**)*: Yield 94%, mp 134–136°C (ethanol); UV–vis (CH_2Cl_2) λ_{max}: 225, 258 nm; ^{1}H NMR ($CDCl_3$) δ: 1.49 (sym m, 8H), 2.16 (s, 12H), 2.20 (s, 6H), 2.64 (s, 2H), 6.74 (s, 4H); ^{13}C NMR ($CDCl_3$) δ: 20.71, 21.90, 26.84, 36.65, 128.88, 135.20, 136.23, 138.43, 141.67; GC–MS *m*/*z*, calcd. for $C_{26}H_{32}$: 344; found (M^+): 344. Anal. calcd. for $C_{26}H_{32}$: C 90.64, H 9.36; found: C 90.49, H 9.19.

*2,3-Bis(2,6-dimethyl-4-methoxyphenyl)bicyclo[2.2.2]oct-2-ene (**2c**)*: Yield 91%, mp 129–130°C (ethanol); UV–vis (CH_2Cl_2) λ_{max}: 221, 260 nm; ^{1}H NMR ($CDCl_3$) δ: 1.79 (br s, 8H), 2.23 (s, 12H), 2.67 (s, 2H), 3.76 (s, 6H), 6.54 (s, 4H); ^{13}C NMR ($CDCl_3$) δ: 22.41, 27.03, 36.91, 54.98, 113.45, 134.20, 137.98, 141.64, 157.30; GC–MS *m*/*z*, calcd. for $C_{26}H_{32}O_2$: 376; found (M^+): 376. Anal. calcd. for $C_{26}H_{32}O_2$: C 82.94, H 8.57; found: C 82.69, H 8.73.

2,3-Bis(1-naphthyl)bicyclo[2.2.2]oct-2-ene (2d), a mixture of atropoisomers:[2] Yield 82%, mp 186–188°C (ethanol); UV–vis (CH_2Cl_2) λ_{max}: 231, 296 nm; ^{1}H NMR ($CDCl_3$) δ: 1.75–2.00 (m) and 2.13 (d, *J* = 7.2 Hz, 8H), 2.96 and 3.03 (two singlets, 2H), 7.00–8.12 (m, 14H); ^{13}C NMR ($CDCl_3$) δ: 26.12, 26.64, 27.55, 28.28, 37.49, 38.37, 125.21, 1225.45, 125.53, 125.68, 126.35, 126.46, 126.60, 126.68, 126.78, 128.83, 128.29, 12.56, 132.14, 133.78, 133.84, 140.04, 140.38, 142.23, 143.88; GC–MS *m*/*z*, calcd. for $C_{28}H_{24}$: 360; found (M^+): 360. Anal. calcd. for $C_{28}H_{24}$: C 93.29, H 6.71; found: C 93.04, H 6.64.

Dichloromethane (Mallinckrodt analytical reagent) was repeatedly stirred with fresh aliquots of concentrated sulfuric acid (~20% by volume) until the acid layer remained colorless. After separation, it was washed successively with wa-

© 1999 NRC Canada

ter, aqueous sodium bicarbonate, water, and aqueous sodium chloride, and dried over anhydrous calcium chloride. The dichloromethane was distilled twice from P_2O_5 under an argon atmosphere and stored in a Schlenk flask equipped with a Teflon valve fitted with Viton O-rings. The hexane and toluene were distilled from P_2O_5 under an argon atmosphere and then refluxed over calcium hydride (~12 h). After distillation from CaH_2, the solvents were stored in the Schlenk flasks under an argon atmosphere.

Instrumentation

The UV–vis absorption spectra were recorded on HP 8453 diode array and Varian CARY 5 (UV–vis–NIR) spectrometers. The ^1H and ^{13}C NMR spectra were obtained on a General Electric QE-300 FT NMR spectrometer. Electrochemical apparatus and the procedures for the determination of oxidation potentials and for the preparation of cation radicals have been described elsewhere (9).

Oxidation of various stilbenoid donors

General procedure

A stock solution of $\mathbf{EA}^{+\bullet}$ (λ_{max} = 486 nm, log ε_{486} = 3.66 M^{-1} cm^{-1}) was obtained by dissolving a known quantity of $\mathbf{EA}^{+\bullet}SbCl_6^-$ (4.25 mg, 6.92 × 10^{-5} mmol) in anhydrous dichloromethane (50 mL) at 22°C and under an argon atmosphere. A 5 mL aliquot of the red-orange solution was transferred to a 1 cm quartz cuvette equipped with a Schlenk adapter (under an argon atmosphere). A solution of the stilbenoid donor **2c** (1 equiv.) was added at 25°C. The reaction mixture immediately turned bright green and the UV–vis spectral analysis confirmed the formation of $\mathbf{2c}^{+\bullet}$ (λ_{max} = 428, 700, and 1315 nm, log ε_{1315} = 3.98 M^{-1} cm^{-1}). In a similar manner, various stilbenoid donors in Chart 1 were quantitatively oxidized to corresponding cation radicals, and the UV–vis absorption maxima are compiled in Table 3. Various donors with E^0_{ox}<1.2 V vs. SCE were readily oxidized with $\mathbf{MA}^{+\bullet}$ (λ_{max} = 518 nm, log ε_{518} = 3.86 M^{-1} cm^{-1}, whereas donors with E^0_{ox} >1.2 V were oxidized with $\mathbf{EA}^{+\bullet}$ (λ_{max} = 518 nm, log ε_{486} = 3.66 M^{-1} cm^{-1}). Oxidation procedures with chloranil – methanesulfonic acid (method B) (15) and triethyloxonium hexachloroantimonate (method C) (17) have been described in detail.

Preparative isolation of stilbenoid cation radical salts using Et_3O^+ $SbCl_6^-$

A 200 mL flask equipped with a Schlenk adapter was charged with triethyloxonium hexachloroantimonate (657 mg, 1.5 mmol), and a solution of **1c** (320 mg, 1 mmol) in anhydrous dichloromethane (25 mL) was added under an argon atmosphere at –20°C. The heterogeneous mixture immediately took on magenta coloration, which intensified with time. The dark-red mixture was stirred for 1 h to yield a magenta-red solution of $\mathbf{1c}^{+\bullet}$ (λ_{max} (nm) = 546, 880; see Fig. 3*a*). The dark magenta solution was cooled to –50°C in an Dry Ice – acetone bath, and anhydrous toluene (100 mL) was added to precipitate the dissolved salt. The dark-red precipitate was filtered under an argon atmosphere, washed with hexane (3 × 25 mL), and dried in vacuo. The cation radical $\mathbf{1c}^{+\bullet}$ $SbCl_6^-$ (vide infra) was obtained in essentially quantitative yield (550 mg, 0.84 mmol).

The purity of the isolated cation radical $\mathbf{1c}^{+\bullet}$ $SbCl_6^-$ was determined by iodometric titration as follows. A solution of $\mathbf{1c}^{+\bullet}$ $SbCl_6^-$ (65.5 mg, 0.01 M) in dichloromethane was added to a dichloromethane solution containing excess tetra-*n*-butylammonium iodide (1 mmol, 0.1 M) at 22°C, under an argon atmosphere, to afford a dark-brown solution. The mixture was stirred for 5 min and was titrated (with rapid stirring) by slow addition of a standard aqueous sodium thiosulfate solution (0.005 M) in the presence of a starch solution as internal indicator. Based on the amount of thiosulfate solution consumed (57.4 mL), purity of the cation radical was determined to be >97%. With the same procedure, the crystalline cation radical salts of **2a** and **2c** were also isolated in 76 and 81% yields, respectively.

X-ray crystallography

The intensity data for all the compounds were collected with the aid of a Siemens SMART diffractometer equipped with a CCD detector using Mo-Kα radiation (λ = 0.71073 Å), at –150°C unless otherwise specified. The structures were solved by direct methods (26) and refined by full-matrix least-squares procedure with IBM Pentium and SGI Indigo computers. The details of the X-ray structure of the various compounds have been deposited.[7]

*2,3-Diphenylbicyclo[2.2.2]oct-2-ene (**1a**) ($C_{20}H_{20}$)*

An X-ray quality crystal (0.20 × 0.20 × 0.20 mm) of diphenylbicyclooctene was obtained from an ethanol–dichloromethane mixture at –30°C. MW = 260.36, orthorhombic, space group $P2_12_12_1$, a = 6.0645(1), b = 12.1491(3), and c = 19.4396(5) Å, D_c = 1.207 Mg m^{-3}, V = 1432.28(6) $Å^3$, Z = 4. The total number of reflections measured were 6492, of which 6492 reflections were symmetrically non-equivalent. Final residuals were $R1$ = 0.0477 and $wR2$ = 0.1017 for 6492 reflections with $I > 2\sigma(I)$.

*2,3-Bis(pentamethylphenyl)bicyclo[2.2.2]oct-2-ene (**2a**) ($C_{30}H_{40}$)*

An X-ray quality crystal (0.3 × 0.2 × 0.1 mm) of **2a** was obtained from an ethanol–dichloromethane mixture at –30°C. MW = 400.62, monoclinic, space group $P2_1/n$, a = 8.6608(7), b = 13.223(1), and c = 20.401(2) Å, β = 91.519(2)°, D_c = 1.139 Mg m^{-3}, V = 2335.6(3) $Å^3$, Z = 4. The total number of reflections measured were 8416, of which 3237 reflections were symmetrically non-equivalent. Final residuals were $R1$ = 0.0730 and $wR2$ = 0.1259 for 3073 reflections with $I > 2\sigma(I)$.

[7] Supplementary material, including tables of crystal data and structure refinement, atomic coordinates, isotropic and anisotropic displacement parameters, and bond lengths and angles for 2,3-diphenylbicyclo[2.2.2]oct-2-ene (**1a**), bis(pentamethylphenyl)bicyclooct-2-ene (**2a**), bis(2,4,6-trimethyl-phenyl)bicyclooct-2-ene (**2b**), and 2,4,2′,4′-tetramethoxy-*m*-cyclophane (**3**)·chloranil molecular complex may be purchased from: The Depository of Unpublished Data, Document Delivery, CISTI, National Research Council Canada, Ottawa, Canada, K1A 0S2. With the exception of the anisotropic displacement parameters, this material has also been deposited with the Cambridge Crystallographic Data Centre and can be obtained on request from: The Director, Cambridge Crystallographic Data Centre, University Chemical Laboratory, 12 Union Road, Cambridge, CB2 1EZ, U.K.

© 1999 NRC Canada

*2,3-Bis(2,4,6-trimethylphenyl)bicyclo-[2.2.2]oct-2-ene (**2b**) ($C_{26}H_{32}$)*

An X-ray quality crystal (0.5 × 0.4 × 0.2 mm) of **2b** was obtained from an ethanol–dichloromethane mixture at –30°C. MW = 344.52, orthorhombic, space group *Pbcn*, a = 21.6486(1), b = 8.7822(1), and c = 21.7995(2) Å, D_c = 1.104 Mg m^{-3}, V = 4144.57(6) Å^3, Z = 8. The total number of reflections measured were 50 440, of which 9646 reflections were symmetrically non-equivalent. Final residuals were $R1$ = 0.0584 and $wR2$ = 0.1342 for 9638 reflections with $I > 2\sigma(I)$.

2,4,2′,4′-Tetramethoxy-[3.3]-m-*cyclophane (**3**)–chloranil molecular complex ($C_{22}H_{28}O_4{\cdot}C_6Cl_4O_2$).*

X-ray quality crystals (0.35 × 0.30 × 0.20 mm) of the charge-transfer complex of **3**·chloranil were obtained by slow evaporation of a equimolar solution of **3** and chloranil in dichloromethane at 25°C. MW = 602.30, orthorhombic, space group *Pnma*, a = 13.464(3), b = 20.144(4), and c = 10.033(2) Å, D_c = 1.470 Mg m^{-3}, V = 2721.1(9) Å^3, Z = 4. The total number of reflections measured were 6618, of which 2161 reflections were symmetrically non-equivalent. Final residuals were $R1$ = 0.0388 and $wR2$ = 0.0948 for 2153 reflections with $I > 2\sigma(I)$. (Note that the molecular structure of the cyclophane moiety in the **3**·chloranil complex is quite similar to that previously observed for the uncomplexed cyclophane (21).)

Acknowledgments

We thank S.V. Lindeman and J. Hecht for the X-ray crystallography and the National Science Foundation and Robert A. Welch Foundation for financial support.

References

1. (*a*) S.J. Crystal and D.C. Lewis. J. Am. Chem. Soc. **89**, 1476 (1967); (*b*) W.M. MacIntyre and A.H. Tench. J. Org. Chem. **38**, 130 (1973); (*c*) K.B. Wiberg, M. Matturo, and R. Adams. J. Am. Chem. Soc. **103**, 1600 (1981); (*d*) H. Lange, W. Schafer, R. Gleiter, P. Camps, and S. Vazquez. J. Org. Chem. **63**, 3478 (1998), and refs. therein.
2. (*a*) F. Vögtle. Cyclophane chemistry. Wiley, New York. 1993, and refs. therein; (*b*) T. Kobayashi, T. Kubota, and K. Ezumi. J. Am. Chem. Soc. **105**, 2172 (1983); (*c*) T. Nakazawa and I. Murata. J. Am. Chem. Soc. **99**, 1996 (1977); (*d*) S. Mataka, K. Takahashi, T. Hirota, K. Takuma, H. Kobayashi, and M.J. Tashiro. J. Chem. Soc. Chem. Commun. 983 (1985); (*e*) S. Mataka, K. Takahashi, T. Mimura, T. Hirota, K. Takuma, H. Kobayashi, and M.J. Tashiro. J. Org. Chem. **52**, 2656 (1987).
3. (*a*) W. Grimme, H.T. Kämmeerling, J. Lex, R. Gleiter, J. Heinze, M. Dieterich, and W.R. Roth. Angew. Chem. Int. Ed. Engl. **30**, 205 (1991); (*b*) H. Prinzbach, G. Sedelmeier, C. Krüger, R. Goddard, H.-D. Martin, and R. Gleiter. Angew. Chem. **90**, 297 (1978); (*c*) Y.-S. Chen, J.W. Kampf, and R.C. Lawton. Tetrahedron Lett. **38**, 7815 (1997); (*d*) S. Mataka, Y. Mitoma, T. Sawada, and M. Tashiro. Tetrahedron Lett. **37**, 65 (1996), and refs, therein; (*e*) S. Pignataro, V. Mancini, J.N.A. Ridyard, and H.J. Lempka. J. Chem. Soc. Chem. Commun. 142 (1971).
4. (*a*) J.H. Penn, Z. Lin, and D.-L. Deng. J. Am. Chem. Soc. **113**, 1001 (1993); (*b*) J.H. Penn and J.H. Duncan. J. Org. Chem. **58**, 2003 (1993).
5. J.E. Gano, B.-S. Park, G. Subramaniam, D. Lenoir, and R. Gleiter. J. Org. Chem. **56**, 4806 (1991).
6. B. Badger and B. Brocklehurst. Trans. Faraday Soc. **65**, 2582 (1969); **65**, 2588 (1969).
7. M.A.J. Rodgers. J. Chem. Soc. Faraday Trans. 1, **68**, 1278 (1972).
8. I.C. Lewis and L.S. Singer. J. Chem. Phys. **43**, 2712 (1965).
9. R. Rathore, U. Weigand, and J.K. Kochi. J. Org. Chem. **61**, 5246 (1996).
10. K. Kumada. Pure Appl. Chem. **52**, 669 (1980).
11. (*a*) C.A. Hunter and J.K.M. Sanders. J. Am. Chem. Soc. **112**, 5527 (1990); (*b*) G.R. Desiraju and A. Gavezzotti. J. Chem. Soc. Chem. Commun. 621 (1989); (*c*) I. Dance and M. Scudder. New J. Chem. 481 (1998).
12. (*a*) J.F. Malone, C.M. Murry, M.H. Charlton, R. Docherty, and A.J. Lavery. J. Chem. Soc. Faraday Trans. **93**, 3429 (1997); (*b*) J.E. Cochran, T.J. Parrott, B.J. Whitlock, and H.W. Whitlock. J. Am. Chem. Soc. **114**, 2269 (1992).
13. M. Oki. Top. Stereochem. **14**, 1 (1983).
14. (*a*) A.J. Gordon and R.A. Ford. The chemist's companion. Wiley, New York. 1972. p. 211; (*b*) D.J. Cram, N.L. Allinger, and H. Steinberg. J. Am. Chem. Soc. **76**, 6132 (1954).
15. R. Rathore and J.K. Kochi. Acta. Chem. Scand. **52**, 114 (1998).
16. R. Rathore and J.K. Kochi. J. Org. Chem. **60**, 4399 (1995).
17. R. Rathore, A.S. Kumar, S.V. Lindeman, and J.K. Kochi. J. Org. Chem. **63**, 5847 (1998).
18. T. Shida. Electronic absorption spectra of radical ions. Elsevier, New York. 1988. p. 112; T. Majima, S. Tajo, A. Ishida, and S. Takamatu. J. Phys. Chem. **100**, 13615 (1996).
19. R. Rathore, S.V. Lindeman, A.S. Kumar, and J.K. Kochi. J. Am. Chem. Soc. **120**, 6931 (1998); H. Suzuki, K. Koyano, T. Shida, and A. Kira. Bull. Chem. Soc. Jpn. **52**, 2794 (1979).
20. V. Enkelmann. *In* Polynuclear aromatic compounds. *Edited by* L.B. Eshert. ACS, Washington, D.C. 1988. p. 177.
21. J. Zhang, R.L. Hertzler, E.M. Holt, T. Vickstrom, and E.J. Eisenbraun. J. Org. Chem. **58**, 556 (1993).
22. R. Rathore and J.K. Kochi. J. Org. Chem. **63**, 8630 (1998).
23. T.C. Jempty, K.A.J. Gogins, Y. Mazur, L.L. Miller. J. Org. Chem. **46**, 4545 (1981).
24. J.O. Howell, J.M. Gonclavez, C. Amatore, L. Klasinc, R.M. Wightman, and J.K. Kochi. J. Am. Chem. Soc. **106**, 3968 (1984).
25. K. Kamatsu, S. Aonuma, Y. Jinbu, R. Tsuji, C. Hirosawa, and K. Takeuchi. J. Org. Chem. **56**, 196 (1991).
26. G.M. Sheldrick. SHELX-86. Program for structure solution. University of Göttingen, Göttingen, Germany. 1986.

© 1999 NRC Canada

How does organic structure determine organic reactivity? The effect of *ortho*-dimethyl groups on the nucleophilic substitution and alkene-forming elimination reactions of ring-substituted cumyl derivatives

Tina L. Amyes, Tadeusz Mizerski, and John P. Richard

Abstract: The addition of a pair of *ortho*-methyl groups to ring-substituted cumyl derivatives to give the corresponding 2,6-dimethylcumyl derivatives X-**1**-Y leads to modest (<5-fold) changes in the observed rate constant for reaction in 50:50 (v:v) trifluoroethanol–water (I = 0.50, $NaClO_4$). The reactions of X-**1**-Y proceed by a stepwise mechanism through the liberated 2,6-dimethylcumyl carbocations X-**2** that partition between nucleophilic addition of solvent and deprotonation to give good yields (≥ 67%) of the corresponding 2-(2,6-dimethylaryl)propenes X-**3**. The carbocations X-**2** are also trapped by nucleophilic addition of azide ion to give good yields (≥ 68% at $[N_3^-]$ = 0.50 M) of the corresponding 2,6-dimethylcumyl azides X-**1**-N_3. In the presence of high concentrations of azide ion there are constant limiting yields of the alkenes X-**3,** which shows that X-**2** also undergo significant reactions with azide ion as a Brønsted base. The product rate constant ratios for partitioning of the 2,4,6-trimethylcumyl carbocation Me-**2** between reaction with azide ion as a Lewis and a Brønsted base, k_{az}/k_B, the nucleophilic addition of azide ion and solvent, k_{az}/k_s (M^{-1}), and deprotonation by solvent, k_{az}/k_e (M^{-1}), were combined with $(k_{az} + k_B) = 5 \times 10^9$ M^{-1} s^{-1} for the diffusion-limited reaction of azide ion to give absolute rate constants for the reactions of Me-**2**. The data show that the addition of a pair of *ortho*-methyl groups to the 4-methylcumyl carbocation to give the sterically hindered Me-**2** results in a 70-fold decrease in the rate constant for nucleophilic addition of solvent to the benzylic carbon, but a 60-fold *increase* in the rate constant for deprotonation of the carbocation by solvent.

Key words: carbocation, *ortho*-substituent effects, steric effects, solvolysis, elimination.

Résumé : L'addition d'une paire de groupes méthyles en *ortho* de dérivés cumyles substitués sur le cycle donne les dérivés 2,6-diméthylcumules X-**1**-Y; leurs vitesses de réaction dans un mélange 50 : 50 (v : v) de trifluoroéthanol–eau (I = 0,50, $NaClO_4$) sont légèrement augmentées (par un facteur d'environ 5). Les réactions des produits X-**1**-Y se produisent par un mécanisme par étapes, par le biais des carbocations 2,6-diméthylcumyles libérés, X-**2**, qui réagissent en partie par une addition nucléophile du solvant ou par une déprotonation conduisant à des bons rendements (≥ 67%) des 2-(2,6-diméthylaryl)propènes correspondants, X-**3**. Les carbocations X-**2** peuvent aussi être piégés par l'addition nucléophile de l'ion azoture qui fournit de bons rendements (≥ 68%, à des $[N_3^+]$ = 0,50 M) des azotures de 2,6-diméthylcumyle correspondants, X-**1**-N_3. En présence d'une concentration élevée d'ion azoture, on observe la formation des alcènes X-**3** avec des rendements limites constants; ceci démontre que les ions X-**2** subissent aussi des réactions significatives avec l'ion azoture agissant comme base de Brønsted. Dans le but de déterminer les constantes de vitesse absolue des réactions de Me-**2**, on a combiné la constante de vitesse de réaction de l'ion azoture limitée par la diffusion ($(k_{az} + k_B) = 5{,}0 \times 10^9$ M^{-1} s^{-1}) avec les rapports de constante de vitesse des réactions du carbocation 2,4,6-triméthylcumyle, Me-**2**, avec l'ion azoture comme base de Lewis et comme base de Brønsted, k_{az}/k_B, par addition nucléophile de l'ion azoture et du solvant, k_{az}/k_s (M^{-1}), et par déprotonation par le solvant, k_{az}/k_e (M^{-1}). Les données montrent que l'addition d'une paire de groupes méthyles en *ortho* du carbocation 4-méthylcumyle provoque un empêchement stérique qui engendre une diminution (par un facteur de 70) de la constante de vitesse d'addition nucléophilique du solvant sur le carbone benzylique et une augmentation (par un facteur de 60) de la constante de vitesse de déprotonation du carbocation par le solvant.

Mots clés : carbocation, effets de substituants en *ortho*, effets stériques, solvolyse, élimination.

[Traduit par la Rédaction]

Received November 13, 1998.

This paper is dedicated to Jerry Kresge in recognition of his many achievements in chemistry.

T.L. Amyes, T. Mizerski, and J.P. Richard.[1] Department of Chemistry, University at Buffalo, SUNY, Buffalo, NY 14260–3000, U.S.A.

[1]Author to whom correspondence may be addressed. Telephone: (716) 645-6800, ext. 2194. Fax: (716) 645-6963. e-mail: jrichard@acsu.buffalo.edu

© 1999 NRC Canada

Scheme 1.

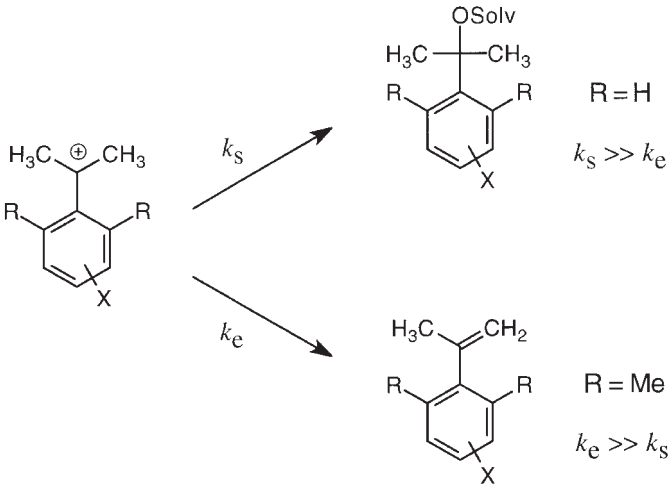

Introduction

We are interested in the effects of changing substrate structure on the stepwise reactions of simple α-methylbenzyl derivatives $XC_6H_4CMe(R)Y$ in nucleophilic solvents. These studies have shown that changes in the α-substituent R result in large changes in the thermodynamic stability of the carbocation intermediates $XC_6H_4CMe(R)^+$ (1, 2), but that the usual fate of these carbocations is their almost exclusive capture at the benzylic carbon by solvent and (or) added nucleophiles. For example, in 50:50 trifluoroethanol–water, liberated ring-substituted cumyl carbocations $XC_6H_4CMe_2^+$, generated from the ionization of cumyl 4-nitrobenzoates or the acid-catalyzed cleavage of cumyl methyl ethers, partition to give >99% of the products of solvolysis and <1% of the α-methylstyrene product of elimination (R = H, $k_s >> k_e$, Scheme 1) (3, 4). This stands in sharp contrast with the report of Creary et al. that in acetic acid or trifluoroethanol, 2,6-dimethylcumyl trifluoroacetate (H-**1**-(trifluoroacetate)) undergoes stepwise reaction through the 2,6-dimethylcumyl carbocation H-**2** to give the alkene H-**3** as the sole product (5). This is a dramatic example of an "*ortho* effect" (6–8), and it suggests that the addition of a pair of *ortho*-methyl groups results in a fundamental change in the partitioning of cumyl carbocations, from the almost exclusive nucleophilic addition of solvent to the benzylic carbon (R = H, $k_s >> k_e$, Scheme 1) to the exclusive loss of a proton to give the corresponding α-methylstyrene (R = Me, $k_e >> k_s$, Scheme 1).

We report here a study of the nucleophilic substitution and elimination reactions of a series of ring-substituted 2,6-dimethylcumyl derivatives X-**1**-Y (X = MeO, Me, H) in 50:50 (v:v) trifluoroethanol–water. The results show that X-**1**-Y undergo stepwise reactions through the liberated carbocations X-**2** that are trapped by the nucleophilic addition of solvent and azide ion to the benzylic carbon. To the best of our knowledge, these reactions represent the first examples of the conversion of a disubstituted sp^2-hybridized carbon attached to a 2,6-disubstituted aryl moiety into a stable tetrahedral adduct. The carbocations X-**2** also undergo proton transfer to solvent and azide and acetate ions to give the alkenes X-**3**. The data provide relative and absolute rate constants for the formation and reaction of the sterically hindered carbocations X-**2** with Brønsted and Lewis bases.

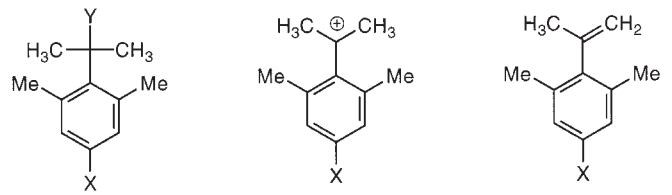

X-**1**-Y X-**2** X-**3**

Experimental section

Materials

2-Bromo-*m*-xylene, 2-bromomesitylene, 3,5-dimethylanisole, 4-methoxybenzoyl chloride, 4-nitrobenzoyl chloride, butyllithium, acetone, and 2,2,2-trifluoroethanol were purchased from Aldrich. Sodium azide was purchased from Fluka. 9-Methyl-9-fluorenol was available from a previous study (9). Tetrahydrofuran was distilled from sodium–benzophenone. All other chemicals were reagent grade and were used without further purification. Water for HPLC analysis and kinetic studies was distilled and then passed through a Milli-Q purification system.

Synthesis

^{1}H NMR spectra were recorded in $CDCl_3$ on Varian spectrometers. Chemical shifts are reported downfield of an internal tetramethylsilane standard at 0 ppm. Melting points were determined using a Mel-Temp apparatus and are uncorrected.

4-Bromo-3,5-dimethylanisole (10), 2-(2,6-dimethylphenyl)-2-propyl alcohol [H-**1**-OH] (5) and 2-(2,4,6-trimethylphenyl)-propene [Me-**3**] (11) were prepared by literature procedures.

2-(2,4,6-Trimethylphenyl)-2-propyl alcohol

Me-**1**-OH was prepared from 2-bromomesitylene by the literature procedure (5) used for the preparation of 2-(2,6-dimethylphenyl)-2-propyl alcohol. Purification by column chromatography on silica gel, eluting with 1:3 ethyl acetate – hexanes, gave the alcohol in 23% yield as a white solid: mp 111–112°C (lit. (12) 111–112°C); ^{1}H NMR (200 MHz) δ: 6.83 (2H, s, Ar), 2.51 (6H, s, $(CH_3)_2Ar$), 2.23 (3H, s, CH_3Ar), 1.72 (6H, s, $(CH_3)_2$), 1.67 (1H, s, OH).

2-(4-Methoxy-2,6-dimethylphenyl)-2-propyl alcohol

MeO-**1**-OH was prepared from 4-bromo-3,5-dimethylanisole by the literature procedure (5) used for the preparation of 2-(2,6-dimethylphenyl)-2-propyl alcohol. Purification by column chromatography on silica gel, eluting with 1:3 ethyl acetate – hexanes, gave the alcohol in 22% yield as a white solid: mp 96–97°C; ^{1}H NMR (400 MHz) δ: 6.55 (2H, s, Ar), 3.77 (3H, s, OCH_3), 2.52 (6H, s, $(CH_3)_2Ar$), 1.71 (6H, s, $(CH_3)_2$), 1.66 (1H, s, OH).

2-(2,6-Dimethylphenyl)-2-propyl 4-methoxybenzoate

H-**1**-(4-methoxybenzoate) was prepared by adaptation of a literature procedure (13). Butyllithium (4.4 mL of a 1.6 M solution in hexanes, 7.0 mmol) was added to a solution of 2-(2,6-dimethylphenyl)-2-propyl alcohol (1.06 g, 6.5 mmol) in dry tetrahydrofuran (8 mL) at room temperature under argon and the mixture was stirred for 0.5 h. 4-Methoxybenzoyl chloride (1.2 g, 7.0 mmol) in dry tetrahydrofuran (5 mL)

© 1999 NRC Canada

was added and the mixture was heated under reflux for 2 h. The solvent was removed by evaporation and the residue was dissolved in dichloromethane (50 mL), washed with water (50 mL), dried with $MgSO_4$, and evaporated. The resulting yellow crystals were decolorized with activated charcoal and recrystallized twice from hexane to give the ester (0.65 g, 34%) as white crystals: mp 86–87°C; ^{1}H NMR (200 MHz) δ: 8.00 (2H, d, J = 9 Hz, Ar), 6.98 (3H, m, Ar), 6.92 (2H, d, J = 9 Hz, Ar), 3.87 (3H, s, OCH_3), 2.44 (6H, s, $(CH_3)_2Ar$), 2.00 (6H, s, $(CH_3)_2$).

2-(2,4,6-Trimethylphenyl)-2-propyl 4-methoxybenzoate

Me-**1**-(4-methoxybenzoate) was prepared from 2-(2,4,6-trimethylphenyl)-2-propyl alcohol by the procedure described above for 2-(2,6-dimethylphenyl)-2-propyl 4-methoxybenzoate. Recrystallization from hexane gave the ester in 50% yield: mp 106–107°C; ^{1}H NMR (200 MHz) δ: 8.00 (2H, d, J = 9 Hz, Ar), 6.92 (2H, d, J = 9 Hz, Ar), 6.80 (2H, s, Ar), 3.87 (3H, s, OCH_3), 2.41 (6H, s, $(CH_3)_2Ar$), 2.21 (3H, s, CH_3Ar), 1.99 (6H, s, $(CH_3)_2$).

2-(4-Methoxy-2,6-dimethylphenyl)-2-propyl 4-methoxybenzoate

MeO-**1**-(4-methoxybenzoate) was prepared from 2-(4-methoxy-2,6-dimethylphenyl)-2-propyl alcohol by the procedure described above for 2-(2,6-dimethylphenyl)-2-propyl 4-methoxybenzoate. Purification by column chromatography on silica gel, eluting with 1:1 ethyl acetate – hexanes, followed by recrystallization from hexane gave the ester in 22% yield as plates: mp 86–87°C; ^{1}H NMR (400 MHz) δ: 7.99 (2H, d, J = 9 Hz, Ar), 6.91 (2H, d, J = 9 Hz, Ar), 6.52 (2H, s, Ar), 3.86 (3H, s, OCH_3), 3.74 (3H, s, OCH_3), 2.43 (6H, s, $(CH_3)_2Ar$), 1.98 (6H, s, $(CH_3)_2$).

2-(2,4,6-Trimethylphenyl)-2-propyl 4-nitrobenzoate

Me-**1**-(4-nitrobenzoate) was prepared from 2-(2,4,6-trimethylphenyl)-2-propyl alcohol and 4-nitrobenzoyl chloride by the procedure described above for 2-(2,6-dimethylphenyl)-2-propyl 4-methoxybenzoate. Recrystallization from ether gave the ester in 18% yield as needles: mp 232–233°C (sl. dec.); ^{1}H NMR (400 MHz) δ: 8.28 (2H, d, J = 9 Hz, Ar), 8.20 (2H, d, J = 10 Hz, Ar), 6.81 (2H, s, Ar), 2.39 (6H, s, $(CH_3)_2Ar$), 2.22 (3H, s, CH_3Ar), 2.03 (6H, s, $(CH_3)_2$).

2-(4-Methoxy-2,6-dimethylphenyl)propene

MeO-**3** was prepared by dehydration of 2-(4-methoxy-2,6-dimethylphenyl)-2-propyl alcohol by the literature procedure (11) for the preparation of 2-(2,4,6-trimethylphenyl)propene. Purification by distillation gave the alkene in 96% yield: bp 82°C (1 Torr (= 133.3 Pa)); ^{1}H NMR (400 MHz) δ: 6.60 (2H, s, Ar), 5.27 (1H, broad, CH_2), 4.75 (1H, br, CH_2), 3.78 (3H, s, OCH_3), 2.25 (6H, s, $(CH_3)_2Ar$), 1.94 (3H, s, CH_3).

Product studies

Unless stated otherwise, product studies were carried out in 50:50 (v:v) trifluoroethanol–water at 25°C and I = 0.50 ($NaClO_4$). Reactions were initiated by making a 100-fold dilution of a solution of substrate in acetonitrile into the appropriate reaction mixture and product distributions were determined by HPLC analysis. For reactions at $[N_3^-] \leq 0.05$ M the solutions were buffered with 25 mM cacodylate, 80% anion, which prevented acid-catalyzed breakdown of the solvolysis products. Aqueous solutions containing sodium azide were adjusted to pH ≈ 7 with concentrated $HClO_4$ before use.

The products of the reactions of Me-**1**-(4-methoxybenzoate) ([S] = 2 mM) in the absence of azide ion were analyzed after 2–30 halftimes for reaction of the substrate and were shown to be stable during this time. For reactions in the presence of azide ion the products were analyzed after 30–40 halftimes, because the substrate and the azide ion adduct Me-**1**-N_3 coeluted from the HPLC column. At these long reaction times there was slight (≤5%) breakdown of Me-**1**-N_3 that resulted in significant increases in the relatively small fractional yields of the solvent adducts Me-**1**-OSolv. For the reactions in the presence of 0.05 M azide ion and increasing concentrations of acetate ion the solutions were buffered with acetate, 95% anion. UV spectroscopy showed that under these conditions more than 97% of the azide is in the anionic form. In all cases the HPLC peak area for the elimination product Me-**3** was corrected for the 7.0% of this alkene that was present as a contaminant of the substrate.

The products of the reactions of Me-**1**-(4-nitrobenzoate) ([S] = 1 mM) were analyzed after 5–20 halftimes for reaction of the substrate and were shown to be stable during this time.

Product studies for the relatively fast reactions of MeO-**1**-(4-methoxybenzoate) ([S] = 0.1–0.5 mM) were carried out at room temperature, 22 ± 2°C. It has been shown in previous work that there is no detectable difference between product ratios determined at room temperature and at 25°C (1, 14). For reactions in the absence of azide ion the products were analyzed after 20–70 halftimes for reaction of the substrate and were shown to be stable during this time. For reactions in the presence of azide ion the substrate concentration was at least 10-fold smaller than that of azide ion, in order to maintain pseudo-first-order conditions. For reactions at $[N_3^-]$ = 1–5 mM the azide ion adduct MeO-**1**-N_3 was unstable and the products were analyzed within the first 3 halftimes for reaction of the substrate, during which breakdown of MeO-**1**-N_3 is insignificant. For reactions at $[N_3^-] \geq 0.05$ M, the azide ion adduct Me-**1**-N_3 was stabilized by a common ion effect and the products were analyzed after 10–20 halftimes for reaction of the substrate. The substrate and the trifluoroethyl ether solvolysis product MeO-**1**-OCH_2CF_3 coeluted from the HPLC column. Therefore, for reactions that were analyzed before complete disappearance of the substrate, the total HPLC peak area for the solvent adducts was calculated with the assumption that the ratio of the HPLC peak areas for the solvolysis products MeO-**1**-OH and MeO-**1**-OCH_2CF_3 is the same as that determined in the absence of azide ion. In all cases, the HPLC peak area for the elimination product MeO-**3** was corrected for the 1.6% of this alkene that was present as a contaminant of the substrate.

HPLC analyses

Unless noted otherwise, the products of the reactions of X-**1**-Y were cleanly separated by reverse-phase HPLC as described previously (14, 15), with peak detection by a Waters 996 diode array detector. The products were detected by their UV absorbance at 280 nm for MeO-**1**-Y and at 269 nm for Me-**1**-Y and H-**1**-Y. These wavelengths are λ_{max} for the corresponding alcohols X-**1**-OH. The products of solvolysis

© 1999 NRC Canada

and nucleophilic substitution by azide ion were identified as described previously (14, 15). The products of the elimination reactions of MeO-**1**-Y and Me-**1**-Y were identified as MeO-**3** and Me-**3**, respectively, by showing that their retention times were identical with those for authentic samples.

Ratios of product yields, $[P_1]/[P_2]$, were calculated using eq. [1], where A_1/A_2 is the ratio of the HPLC peak areas for the two products, and $\varepsilon_2/\varepsilon_1$ is the ratio of the molar extinction coefficients of the two products at the wavelength of the analysis.

$$[1] \qquad [P_1]/[P_2] = (A_1/A_2)(\varepsilon_2/\varepsilon_1)$$

Ratios of $\varepsilon_{alkene}/\varepsilon_{ROH}$ = (220 M^{-1} cm^{-1})/(210 M^{-1} cm^{-1}) = 1.0 at 269 nm for Me-**3** and Me-**1**-OH and $\varepsilon_{alkene}/\varepsilon_{ROH}$ = (1270 M^{-1} cm^{-1})/(860 M^{-1} cm^{-1}) = 1.5 at 280 nm for MeO-**3** and MeO-**1**-OH in 50:50 (v:v) methanol–water were determined using authentic materials. The extinction coefficients of the azide ion adduct Me-**1**-N_3 and the alkene Me-**3** at 269 nm were shown to be identical by comparison of the decrease in the HPLC peak area for the alkene and the increase in the sum of the peak areas of the solvent and azide ion adducts for reaction of a constant amount of substrate when the concentration of azide ion was increased from zero to 0.50 M. The extinction coefficients of the azide ion adduct MeO-**1**-N_3 and the alcohol MeO-**1**-OH at 280 nm were assumed to be identical because the extinction coefficients of the solvent and azide ion adducts to a wide range of α-substituted 4-methoxybenzyl carbocations are identical at λ_{max} for the corresponding alcohol (1). The extinction coefficients of the alcohols X-**1**-OH and trifluoroethyl ethers X-**1**-OCH_2CF_3 were assumed to be identical because it has been shown in previous work that the extinction coefficients of ring-substituted cumyl alcohols and trifluoroethyl ethers are identical at λ_{max} for the alcohols (4).

Calculation of product yields and rate constant ratios

Fractional yields of the solvolysis and elimination products of the reactions of X-**1**-Y were calculated as the ratio of the HPLC peak area for the product divided by the sum of the peak areas for all products, with correction where necessary for differences in the extinction coefficients of the various products (see above).

Dimensionless product rate constant ratios for the nucleophilic substitution reactions of water and trifluoroethanol with X-**1**-Y were calculated from the ratio of the yields of the corresponding alcohols and trifluoroethyl ethers using eq. [2]. Dimensionless product rate constant ratios for the partitioning of X-**1**-Y between solvolysis and elimination were calculated directly as the ratio of the yields of the products of these reactions using eq. [1].

$$[2] \qquad k_{HOH}/k_{TFE} = [\text{X-}\mathbf{1}\text{-OH}][CF_3CH_2OH]/[\text{X-}\mathbf{1}\text{-}OCH_2CF_3][HOH]$$

Rate constant ratios k_{az}/k_s (M^{-1}) for the partitioning of Me-**1**-(4-nitrobenzoate) and MeO-**1**-(4-methoxybenzoate) between nucleophilic substitution by azide ion and solvent were calculated from the ratio of the yields of the azide ion and solvent adducts using eq. [3]. The values of k_{az}/k_s (M^{-1}) determined at five or more values of $[N_3^-]$ agreed within the experimental error of ±10%.

$$[3] \qquad k_{az}/k_s\ (M^{-1}) = [\text{X-}\mathbf{1}\text{-}N_3]/(\sum\ [\text{X-}\mathbf{1}\text{-OSolv}][N_3^-])$$

Kinetic methods

Kinetic studies were carried out in 50:50 (v:v) trifluoroethanol–water at 25°C and I = 0.50 ($NaClO_4$). Reactions were initiated by making a 100-fold dilution of a solution of substrate in acetonitrile into the appropriate reaction mixture. For reactions in the absence of azide ion, the solutions were buffered with 25 mM cacodylate, 80% anion, which prevented acid-catalyzed breakdown of the solvolysis products. Aqueous solutions containing sodium azide were adjusted to pH ≈7 with concentrated $HClO_4$ before use.

Rate constants for the reaction of MeO-**1**-(4-methoxybenzoate) ([S] = 0.1 mM) were determined spectrophotometrically by following the disappearance of the substrate at 270 nm or at 280 nm for reactions in the presence of azide ion. Rate constants for the reactions of Me-**1**-(4-nitrobenzoate) ([S] = 0.2 mM) were determined spectrophotometrically by following the increase in absorbance at 297 nm.

Rate constants for the reactions of Me-**1**-(4-methoxybenzoate) ([S] = 2 mM) and H-**1**-(4-methoxybenzoate) ([S] = 1 mM) were determined by following the disappearance of the substrate by HPLC, with peak detection at 285 nm. For Me-**1**-(4-methoxybenzoate) the reaction mixtures contained 9-methyl-9-fluorenol (1.7×10^{-5} M) as an internal HPLC injection standard. For H-**1**-(4-methoxybenzoate) the solution was unbuffered and contained 3-(4-methoxyphenyl)-1-propanol (4×10^{-4} M) as an internal HPLC injection standard.

In all cases, good first-order kinetics were observed over at least three reaction halftimes. First-order rate constants, k_{obsd}, were determined from the slopes of semilogarithmic plots of reaction progress against time. Rate constants determined spectrophotometrically were reproducible to ±5% and those determined by HPLC were reproducible to ±10%.

Results

Table 1 gives observed first-order rate constants, k_{obsd}, for the reactions of 4-substituted 2,6-dimethylcumyl derivatives X-**1**-Y in 50:50 (v:v) trifluoroethanol–water at 25°C and I = 0.50 ($NaClO_4$) that were determined by monitoring the reaction progress by UV spectroscopy or HPLC analysis, as described in the Experimental section. There was no significant change in k_{obsd} for the reactions of MeO-**1**-(4-methoxybenzoate), Me-**1**-(4-methoxybenzoate), and Me-**1**-(4-nitrobenzoate) when the concentration of azide ion was increased from zero to 0.50 M (I = 0.50, $NaClO_4$) (Table 1). The reactions of these substrates in the presence of 0.50 M azide ion result in the following good yields of the corresponding azide ion adducts: MeO-**1**-(4-methoxybenzoate), 93%; Me-**1**-(4-methoxybenzoate), 67%; Me-**1**-(4-nitrobenzoate), 68%.

Table 2 gives the yields of the solvolysis and elimination products of the reactions of MeO-**1**-Y and Me-**1**-Y in 50:50 (v:v) trifluoroethanol–water at I = 0.50 ($NaClO_4$) that were determined by HPLC analysis. The reaction mixtures were buffered with 25 mM cacodylate, 80% anion, which prevented acid-catalyzed breakdown of the solvolysis products X-**1**-OSolv to the alkenes X-**3**. In a control experiment, the yields of the products of the reaction of Me-**1**-(4-methoxybenzoate) in the absence of buffer determined during 10

© 1999 NRC Canada

Table 1. Observed first-order rate constants, k_{obsd} (s^{-1}), for the reactions of 4-substituted 2,6-dimethylcumyl derivatives X-**1**-Y in 50:50 (v:v) trifluoroethanol–water at 25°C and I = 0.50 ($NaClO_4$).[a]

	Leaving group Y	
Ring substituent X	4-Methoxybenzoate	4-Nitrobenzoate
MeO	5.8×10^{-3} [b]	
	(5.5×10^{-3}) [c,d]	
Me	3.3×10^{-4} [e]	3.2×10^{-3} [f]
	(3.0×10^{-4}) [e,d]	(2.9×10^{-3}) [f,d]
H	2.2×10^{-5} [e,d]	

[a]Determined in the presence of 25 mM cacodylate buffer, 80% anion, unless noted otherwise. Values in parentheses are for reaction in the presence of 0.50 M azide ion.

[b]Determined spectrophotometrically by following the disappearance of the substrate at 270 nm.

[c]Determined spectrophotometrically by following the disappearance of the substrate at 280 nm.

[d]Determined in unbuffered solution.

[e]Determined by following the disappearance of the substrate by HPLC.

[f]Determined spectrophotometrically by following the increase in absorbance at 297 nm.

Table 2. Yields of solvolysis and elimination products from the reactions of 4-substituted 2,6-dimethylcumyl derivatives X-**1**-Y in 50:50 (v:v) trifluoroethanol–water at I = 0.50 ($NaClO_4$).[a]

		Yield of product		
Ring substituent X	Leaving group Y	X-**1**-OH	X-**1**-OCH_2CF_3	X–**3**
MeO	4-Methoxybenzoate [b]	31.0%	1.8%	67.2%
Me	4-Methoxybenzoate [c]	13.1%	1.2%	85.7%
	4-Nitrobenzoate [d]	13.0%	1.3%	85.7%

[a]Determined in the presence of 25 mM cacodylate buffer, 80% anion, which prevented acid-catalyzed conversion of the solvent adducts to the alkenes. Product yields were determined by HPLC analysis.

[b]Product yields were determined at room temperature, 22 ± 2°C, after 20–70 halftimes for reaction of the substrate, and were stable during this time.

[c]Product yields were determined at 25°C after 2–30 halftimes for reaction of the substrate and were stable during this time.

[d]Product yields were determined at 25°C after 5–20 halftimes for reaction of the substrate and were stable during this time.

halftimes for reaction of the substrate were extrapolated to zero time. The absolute difference between the yields of Me-**1**-OSolv (14.6%) and Me-**3** (85.4%) obtained from this extrapolation and those determined in the presence of 25 mM cacodylate buffer (Table 2) is only 0.3%. The reaction of H-**1**-(4-methoxybenzoate) in 50:50 (v:v) trifluoroethanol–water at I = 0.50 ($NaClO_4$) gave a high yield of the alkene H-**3** along with the alcohol H-**1**-OH. The yield of H-**3** was not quantified, but this alkene represented ca. 94% of the total HPLC peak area of the products.

Table 3 gives the dimensionless product rate constant ratios k_{HOH}/k_{TFE} for partitioning of X-**1**-Y between nucleophilic substitution by water and trifluoroethanol in 50:50 (v:v) trifluoroethanol–water that were calculated from the ratio of the yields of the corresponding alcohols X-**1**-OH and trifluoroethyl ethers X-**1**-OCH_2CF_3 using eq. [2]. The dimensionless product rate constant ratios k_s/k_e for partitioning of X-**1**-Y between solvolysis and elimination (Table 3) were calculated directly as the ratio of the yields of the products of these reactions using eq. [1].

The products of the reactions of X-**1**-Y in 50:50 (v:v) trifluoroethanol–water in the presence of increasing concentrations of azide ion (I = 0.50, $NaClO_4$) were determined by HPLC analysis. Table 3 gives the rate constant ratios k_{az}/k_s (M^{-1}) for partitioning of MeO-**1**-(4-methoxybenzoate) and Me-**1**-(4-nitrobenzoate) between nucleophilic substitution by azide ion and solvent that were calculated from the ratio of the yields of the azide ion adducts X-**1**-N_3 and the solvent adducts X-**1**-OSolv using eq. [3]. For Me-**1**-(4-methoxybenzoate) the reaction products had to be analyzed at long reaction times, during which the azide ion adduct was unstable and broke down to give exalted yields of the solvolysis products (see Experimental section). Therefore, the value of k_{az}/k_s (M^{-1}) determined by direct product analysis was unreliable and this rate constant ratio was obtained from nonlinear least-squares analysis of the product data (see Discussion).

Figure 1 shows the effect of increasing concentrations of azide ion on the fractional yields of the nucleophilic substitution and elimination products of the reaction of MeO-**1**-(4-methoxybenzoate) in 50:50 (v:v) trifluoroethanol–water (I = 0.50, $NaClO_4$).

Figure 2 shows the effect of increasing concentrations of azide ion on the fractional yields of the nucleophilic substitution and elimination products of the reaction of Me-**1**-(4-nitrobenzoate) in 50:50 (v:v) trifluoroethanol–water (I = 0.50, $NaClO_4$). The yields of the azide ion adduct Me-**1**-N_3 and the alkene Me-**3** from these reactions agreed with those from the reaction of Me-**1**-(4-methoxybenzoate) under the same conditions, within the experimental error of ±10%.

Figure 3 shows the effect of increasing concentrations of acetate ion on the fractional yields of the nucleophilic substitution and elimination products of the reaction of Me-**1**-(4-methoxybenzoate) in the presence of 0.05 M azide ion in 50:50 (v:v) trifluoroethanol–water (I = 0.50, $NaClO_4$). In these experiments, the solutions were buffered with acetate, 95% anion, and there was no detectable formation of the acetate ion adduct.

© 1999 NRC Canada

Table 3. Rate constant ratios for partitioning of 4-substituted 2,6-dimethylcumyl carbocations X-**2** between nucleophilic addition and deprotonation in 50:50 (v:v) trifluoroethanol–water (Scheme 4).[a]

Ring substituent X	Leaving group[b]	k_{HOH}/k_{TFE}[c]	k_s/k_e[d]	k_{az}/k_s[e] (M^{-1})	k_{az}/k_e[f] (M^{-1})	k_{az}/k_B[g]
4-MeO	4-Methoxybenzoate	4.2	0.49	6200[h]	3000[i]	15.9[j]
4-Me	4-Methoxybenzoate	2.6	0.17	250[j]	42[j]	2.2[j]
	4-Nitrobenzoate	2.5	0.17	250[k]	42[i]	2.4[j]

[a]Determined in the presence of 25 mM cacodylate buffer, 80% anion, at 25°C and I = 0.50 ($NaClO_4$), unless noted otherwise. Product yields for MeO-**1**-(4-methoxybenzoate) were determined at room temperature, 22 ± 2°C.

[b]Leaving group at X-**1**-Y that was used to generate the corresponding carbocation X-**2**.

[c]Dimensionless ratio of second-order rate constants, calculated from the ratio of the yields of the alcohol and the trifluoroethyl ether using eq 2.

[d]Dimensionless ratio of first-order rate constants, calculated as the ratio of the yields of the solvent adducts X-**1**-OSolv and the alkene X-**3** in the absence of azide ion (Table 2) using eq. [1].

[e]Rate constant ratio for partitioning of the carbocation between nucleophilic addition of azide ion and solvent, calculated from the ratio of the yields of the azide ion and solvent adducts using eq. [3], unless noted otherwise.

[f]Rate constant ratio for partitioning of the carbocation between nucleophilic addition of azide ion and deprotonation by solvent.

[g]Dimensionless ratio of second-order rate constants for reaction of the carbocation with azide ion as a Lewis and a Brønsted base.

[h]Average of values determined at five concentrations of azide ion in the range 0.001–0.005 M.

[i]Calculated as $(k_{az}/k_s)(k_s/k_e)$.

[j]Determined from the nonlinear least-squares fit of the product data to eqs. [4] and [5], see text.

[k]Average of values determined at eight concentrations of azide ion in the range 0.005–0.300 M.

Fig. 1. Dependence of the fractional yields of the azide ion adduct MeO-**1**-N_3 (●), the solvent adducts MeO-**1**-OSolv (▼), and the alkene MeO-**3** (■) from the reaction of MeO-**1**-(4-methoxybenzoate) on the concentration of azide ion in 50:50 (v:v) trifluoroethanol–water at room temperature, 22 ± 2°C, and I = 0.50 ($NaClO_4$). For $[N_3^-] \leq 0.05$ M the solutions were buffered with 25 mM cacodylate, 80% anion. The solid lines show the nonlinear least-squares fits of the data to eqs. [4]–[6] (see text).

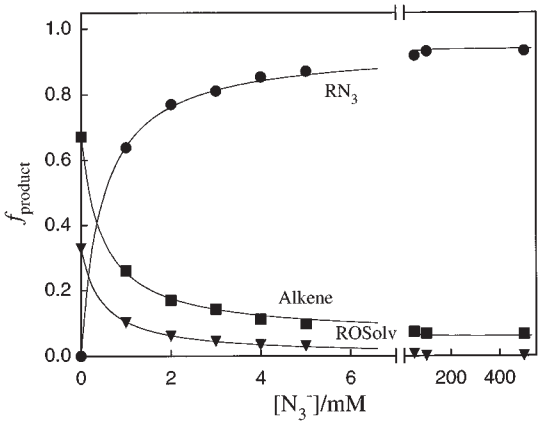

Fig. 2. Dependence of the fractional yields of the azide ion adduct Me-**1**-N_3 (●), the solvent adducts Me-**1**-OSolv (▼), and the alkene Me-**3** (■) from the reaction of Me-**1**-(4-nitrobenzoate) on the concentration of azide ion in 50:50 (v:v) trifluoroethanol–water at 25°C and I = 0.50 ($NaClO_4$). For $[N_3^-] \leq 0.05$ M the solutions were buffered with 25 mM cacodylate, 80% anion. The solid lines show the nonlinear least-squares fits of the data to eqs. [4]–[6] (see text).

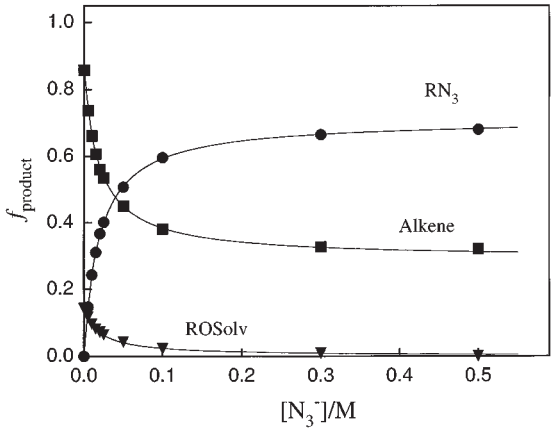

Discussion

In 50:50 (v:v) trifluoroethanol–water (I = 0.50, $NaClO_4$) the ring-substituted 2,6-dimethylcumyl derivatives X-**1**-Y undergo nucleophilic substitution by solvent to give the corresponding alcohols X-**1**-OH and trifluoroethyl ethers X-**1**-OCH_2CF_3 (Table 2). However, the major products of the reactions of X-**1**-Y are those of elimination, the alkenes X-**3** (Table 2). The yield of the alkene X-**3** increases as the ring substituent at X-**1**-Y is made more electron withdrawing, from 67% for MeO-**1**-(4-methoxybenzoate) to 86% for Me-**1**-(4-methoxybenzoate) and Me-**1**-(4-nitrobenzoate) (Table 2).

Reaction mechanism

We have shown previously that the nucleophilic substitution reactions of ring-substituted cumyl 4-nitrobenzoates ($XC_6H_4CMe_2$(4-nitrobenzoate)) and the acid-catalyzed reactions of ring-substituted cumyl alcohols ($XC_6H_4CMe_2OH$) in 50:50 (v:v) trifluoroethanol–water proceed by a stepwise mechanism through cumyl carbocation intermediates, $XC_6H_4CMe_2^+$. The reactions of the 2,6-dimethylcumyl derivatives MeO-**1**-Y and Me-**1**-Y in 50:50 (v:v) trifluoroethanol–water in the presence of 0.50 M azide ion give good yields (≥67%) of the azide ion adducts X-**1**-N_3 at the expense of both the solvent adducts X-**1**-OSolv and the alkenes X-**3** (Figs. 1 and 2). The absence of any increases in k_{obsd} for these reactions in the presence of azide ion (Table 1), and the identical yields of the substitution and elimination products from the reactions of Me-**1**-(4-methoxybenzoate) and

© 1999 NRC Canada

Scheme 2.

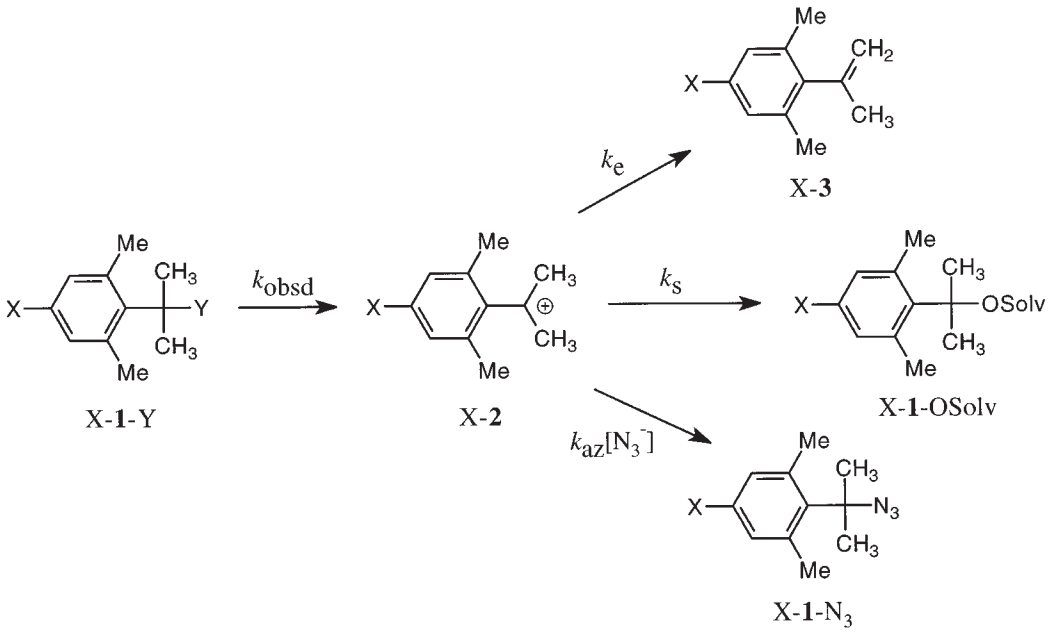

Fig. 3. Dependence of the fractional yields of the alkene Me-**3** (■), the azide ion adduct Me-**1**-N_3 (●), and the solvent adducts Me-**1**-OSolv (▼) from the reaction of Me-**1**-(4-methoxybenzoate) on the concentration of acetate ion in the presence of 0.05 M azide ion in 50:50 (v:v) trifluoroethanol–water at 25°C and I = 0.50 ($NaClO_4$). The solutions were buffered with acetate, 95% anion.

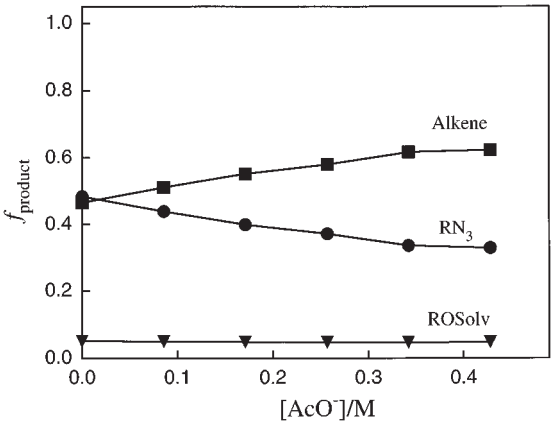

Me-**1**-(4-nitrobenzoate), which have different leaving groups, provide strong evidence that X-**1**-Y also react by a stepwise $D_N + A_N$ (S_N1) (16) mechanism through the liberated 2,6-dimethylcumyl carbocations X-**2** (Scheme 2). Similarly, the elimination reactions of H-**1**-(trifluoroacetate) in acetic acid and trifluoroethanol have been reported to proceed by a stepwise mechanism through the 2,6-dimethylcumyl carbocation H-**2**, which undergoes proton loss to give the alkene H-**3** as the sole product (5). Therefore, the rate constant ratios k_{az}/k_s (M^{-1}) and k_s/k_e for the reactions of X-**1**-Y that were determined by product analysis (Table 3) represent rate constant ratios for partitioning of the 2,6-dimethylcumyl carbocation intermediates X-**2** between nucleophilic addition of azide ion and solvent to the benzylic carbon, and nucleophilic addition of solvent and deprotonation, respectively (Scheme 2).

Effect of *ortho*-methyl groups on the formation of cumyl carbocations

The effects of *ortho* substituents on the reactivity of aromatic substrates are difficult to interpret because their close proximity to the reaction site may result in gross changes in the energy of the ground state and (or) the transition state that are not related to the polar and resonance effects of these substituents (6–8).

Table 4 gives relative rate constants for the stepwise reactions of ring-substituted cumyl 4-nitrobenzoates (data from previous work (1)[2]) and the corresponding 2,6-dimethylcumyl 4-nitrobenzoates (data from this work) in 50:50 (v:v) trifluoroethanol–water. The data show that the addition of a pair of *ortho*-methyl groups to $XC_6H_4CMe_2Y$ results in relatively small (<5-fold) changes in the rate constant for cleavage of the substrate to give the corresponding carbocation. This is surprising, because the simple expectation is that *ortho*-methyl substituents should result in large increases in the rate constant for carbocation formation, as a result of both electron donation from the *ortho* methyl groups and increased steric crowding at the sp^3-hybridized benzylic carbon in the ground state that is relieved on moving towards sp^2-hybridization in the transition state. A crude analysis, based on the assumption that the effect of each *ortho*-methyl group is the same as that of a 4-Me group at $XC_6H_4CMe_2Y$, suggests that formation of the 2,4,6-trimethylcumyl carbocation Me-**2** from Me-**1**-Y should be ca. $(40)^2$ = 1600-fold faster than the formation of 4-$MeC_6H_4CMe_2^+$ from 4-$MeC_6H_4CMe_2Y$. However, although the solvolyses of both benzyl chloride and 1-phenylethyl chloride are accelerated by the addition of an *ortho*-methyl group, for both compounds the effect is ca. 2-fold smaller than the effect of a 4-Me group (17). This suggests that any steric or other un-

[2] T.L. Amyes. Unpublished results.

© 1999 NRC Canada

Table 4. Relative rate constants, k_{rel}, for the reactions of ring-substituted cumyl 4-nitrobenzoates and the corresponding 2,6-dimethylcumyl 4-nitrobenzoates in 50:50 (v:v) trifluoroethanol–water.[a]

Ring substituent	k_{rel} Cumyl	k_{rel} 2,6-Dimethylcumyl	2,6-Me_2/2,6-H_2[b]
4-MeO	1840[c]	1150[d]	0.63
4-Me	39[e]	65[f]	1.7
4-H	1	4.4[d]	4.4

[a]At 25°C and I = 0.50 ($NaClO_4$). Relative rate constants are normalized to k_{obsd} = 4.9 × 10^{-5} s^{-1} for the reaction of cumyl 4-nitrobenzoate that was determined by interpolation of the data in Fig. 4 (T. L. Amyes. Unpublished results).

[b]Ratio of rate constants for reaction of 2,6-dimethylcumyl and cumyl 4-nitrobenzoates with the same aromatic ring substituent.

[c]k_{obsd} = 0.09 s^{-1} (1).

[d]Calculated from data for 2,6-dimethylcumyl 4-methoxybenzoates (Table 1) with the assumption that the change to a 4-nitrobenzoate leaving group results in the same 9.7-fold increase in k_{obsd} as that observed for Me-**1**-(4-methoxybenzoate) (Table 1).

[e]k_{obsd} = 1.9 × 10^{-3} s^{-1} (T.L. Amyes. Unpublished results).

[f]Calculated from data in Table 1.

usual *ortho* effects (6–8) associated with the addition of a single *ortho*-methyl group to 1-phenylethyl chloride are small. Therefore, if the effects of *ortho*-methyl groups at $XC_6H_4CMe_2Y$ are additive, the cleavage of Me-**1**-Y to give Me-**2** is expected to be $(40/2)^2$ = 400-fold faster than the cleavage of 4-$MeC_6H_4CMe_2Y$ to give 4-$MeC_6H_4CMe_2^+$. The observation that the formation of Me-**2** is only 1.7-fold faster than the formation of 4-$MeC_6H_4CMe_2^+$ (Table 4) suggests there is an offsetting 240-fold *decrease* in the rate of carbocation formation due to an *ortho* effect. Similar analyses for the formation of MeO-**2** and H-**2** suggest that the cleavage reactions of MeO-**1**-Y and H-**1**-Y are 630-fold and 90-fold slower, respectively, than expected on the basis of additivity of the effects of *ortho*-methyl groups. The origin of these large effects is undoubtedly adverse steric interactions between the *ortho*-methyl groups and the α-methyl groups at the benzylic carbon in the carbocations X-**2** and in the transition state leading to their formation. These steric interactions are expected to lead to significant decreases in coplanarity and overlap of the π-orbitals of the aromatic ring with the empty *p*-orbital at the benzylic carbon of X-**2**, resulting in a decrease in the resonance stabilization of X-**2** and increases in the energy of both these carbocations and the transition state leading to their formation. Such effects have long been recognized and termed "steric inhibition of resonance" (11, 18). Consistent with this, the addition of a pair of *ortho*-methyl groups to the less sterically congested 1-phenylethyl derivatives should result in a smaller degree of "steric inhibition," and the solvolysis of 1-(2,4,6-trimethylphenyl)ethyl chloride is only 5-fold slower than expected on the basis of additivity of the effects of *ortho*-methyl groups at 4-$MeC_6H_4CH(Me)Cl$ (17).

Structure–reactivity correlations

The data in Table 4 show that there is a 7-fold decrease in the *relative* rate constant for cleavage of X-**1**-Y and the corresponding $XC_6H_4CMe_2Y$ in 50:50 (v:v) trifluoroethanol–water as the aromatic substituent X is made more electron donating. In fact, the addition of two electron-donating *ortho*-methyl groups to 4-$MeOC_6H_4CMe_2Y$ to give MeO-**1**-Y actually leads to a 1.6-fold *decrease* in the rate constant for cleavage of the substrate to give the corresponding carbocation! Figure 4 shows the Hammett correlation of k_{obsd} for the reaction of ring-substituted cumyl 4-nitrobenzoates in 50:50 (v:v) trifluoroethanol–water (data from previous work (1)[2]) with σ^+ substituent constants (19) and the correlation of the more limited set of data from this work for the reactions of 2,6-dimethylcumyl 4-methoxybenzoates in the same solvent (Table 1). The data are correlated by ρ^+ = –4.3 for the reactions of $XC_6H_4CMe_2$(4-nitrobenzoate) and by a somewhat smaller value of ρ^+ = –3.0 for the reactions of X-**1**-(4-methoxybenzoate). Decreased Hammett ρ values and small Yukawa–Tsuno *r* values have been observed for the solvolysis reactions of benzyl derivatives substituted with very bulky alkyl groups at the α-carbon (20).

Fig. 4. Logarithmic correlations of observed first-order rate constants, k_{obsd} (s^{-1}), for the reactions of ring-substituted cumyl 4-nitrobenzoates (●, data from previous work (1)[2]) and 4-substituted 2,6-dimethylcumyl 4-methoxybenzoates (■, data from Table 1) in 50:50 (v:v) trifluoroethanol–water at 25°C and I = 0.50 ($NaClO_4$) with Hammett σ^+ substituent constants (19). The slopes of the plots give ρ^+ = –4.3 for cumyl 4-nitrobenzoates and ρ^+ = –3.0 for 2,6-dimethylcumyl 4-methoxybenzoates.

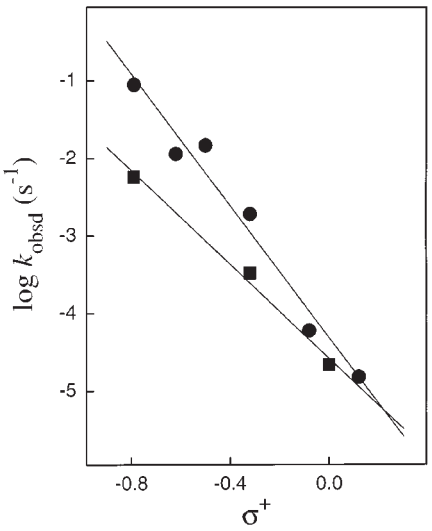

The substantial negative value of ρ^+ = –3.0 for the reactions of X-**1**-Y shows that, despite the above estimated 630-fold decrease in the rate constant for formation of MeO-**2** resulting from decreased overlap between the π-orbitals of the aromatic ring and the developing empty p-orbital at the benzylic carbon, the 4-MeO group results in a significant 3.3 kcal/mol stabilization of the transition state for carbocation formation from X-**1**-Y (Table 4). For the corresponding simple cumyl system, the addition of a 4-MeO group results in stabilization of the transition state for carbocation formation by 4.4 kcal/mol (Table 4). Therefore, only 25% of the stabilization of the transition state for formation of $XC_6H_4CMe_2^+$ from $XC_6H_4CMe_2Y$ by resonance delocalization of positive charge at the benzylic carbon onto the 4-MeO group is lost as a result of the increased steric requirements of the *ortho*-methyl groups in the transition state for formation of X-**2** from X-**1**-Y. The crystal structure of

© 1999 NRC Canada

Scheme 3.

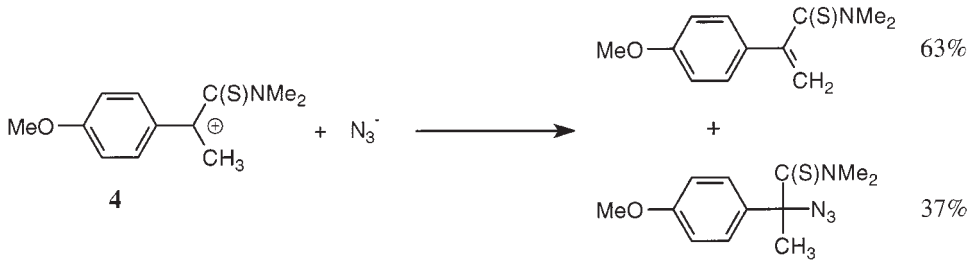

$C_6H_5CMe_2^+ \cdot SbF_6^-$ shows that the cumyl carbocation is almost completely planar: the aromatic ring is twisted out of the plane of the benzylic carbon by only 8° (21). By contrast, the small value of λ_{max} for the 2,4,6-trimethylcumyl carbocation suggests that there is considerable twisting about the bond between the aromatic ring and the benzylic carbon in this carbocation (11). Our results suggest that, despite the nonplanar structures of X-**2**, electron-donating aromatic substituents can provide substantial resonance stabilization of these carbocations.

Mechanism of elimination reactions of *ortho*-dimethylcumyl derivatives

Figures 1 and 2 show that the addition of azide ion results in the formation of good yields of the azide ion adducts X-**1**-N_3 from the stepwise reactions of MeO-**1**-(4-methoxybenzoate) and Me-**1**-(4-nitrobenzoate) in 50:50 (v:v) trifluoroethanol–water (I = 0.50, $NaClO_4$). At high concentrations of azide ion, the yields of the solvent adducts X-**1**-OSolv approach zero, as required by the mechanism shown in Scheme 2. By contrast, the yields of the alkenes decrease to essentially constant limiting values of 7% MeO-**3** from the reaction of MeO-**1**-(4-methoxybenzoate) (Fig. 1) and 32% Me-**3** from the reactions of Me-**1**-(4-nitrobenzoate) (Fig. 2) and Me-**1**-(4-methoxybenzoate) (data not shown). The simple mechanism shown in Scheme 2, in which the solvent and azide ion adducts and the alkenes are formed by partitioning of a common carbocation intermediate, requires that, like the solvent adducts, the yields of the alkenes also approach zero in the presence of high concentrations of azide ion. However, the results show that only 93% of the reaction of MeO-**1**-Y and 68% of the reaction of Me-**1**-Y proceed through the liberated carbocation intermediate X-**2** that can be trapped by nucleophilic addition of azide ion. The remainder proceeds through an additional pathway that results in formation of the alkenes X-**3**. There are several mechanistic possibilities for this additional pathway for the elimination reactions of X-**1**-Y to give the alkenes X-**3**.

Mechanism 1: The substrates X-1-Y undergo concerted elimination

The constant limiting yields of the alkenes X-**3** in the presence of high concentrations of azide ion may result from a concerted elimination reaction of X-**1**-Y that bypasses the carbocation intermediate of the stepwise reaction and has an observed rate constant that is independent of the concentration of added azide ion (3). This possibility can be excluded because the quantitative elimination reaction of H-**1**-(trifluoroacetate) in acetic acid has been shown to proceed by a stepwise mechanism through the carbocation H-**2** (5). The change in solvent from acetic acid (Y = –1.64) (22) to the more ionizing solvent of 50:50 (v:v) trifluoroethanol–water ($Y \approx 2.0$)[3] used in this work is expected to increase rather than decrease the importance of the stepwise reaction pathway through the carbocations X-**2**.[4]

Mechanism 2: The carbocations X-2 undergo proton transfer to the leaving group within an ion pair intermediate

The carbocation-leaving group ion-pair intermediates of the reactions of ring-substituted cumyl derivatives are too shortlived to undergo trapping by azide ion because they undergo fast diffusional separation to give the free ions (24, 25). Therefore, any proton transfer from the carbocation to the leaving group within the ion pairs X-**2**$\cdot Y^-$ would provide a pathway for formation of the alkenes X-**3** that is insensitive to added azide ion. The yields of α-methylstyrenes from the ion-pair intermediates of the reactions of ring-substituted cumyl 4-nitrobenzoates with electron-donating substituents are negligible (3). Therefore, this possibility would require that the addition of a pair of *ortho*-methyl groups to ring-substituted cumyl derivatives result in a large increase in the rate constant for proton transfer from the carbocation to the leaving group within an ion pair, relative to that for diffusional separation of the ion pair to give the free carbocation. It is difficult to exclude rigorously the formation of small amounts of the alkenes X-**3** from deprotonation within an ion-pair intermediate. However, the observation of identical limiting yields of 32% Me-**3** from the reactions of Me-**1**-(4-nitrobenzoate) and Me-**1**-(4-methoxybenzoate) with leaving groups of different basicities provides strong evidence against the formation of large amounts of Me-**3** from proton transfer to the leaving group within an ion-pair intermediate.

Mechanism 3: The carbocations X-2 react with azide ion as both a Brønsted and a Lewis base

Azide ion usually undergoes reaction with α-methylbenzyl carbocations exclusively as a nucleophile (Lewis base). However, we have recently shown that the α-thioamide substituted 4-methoxybenzyl carbocation **4** reacts with azide ion in 50:50 (v:v) methanol–water predominantly as a Brønsted

[3] Calculated by linear interpolation of the values of Y = 2.23 and 1.89 for 50:50 (w:w) and 60:40 (w:w) trifluoroethanol–water, respectively (23), to 58:42 (w:w) trifluoroethanol–water which corresponds to 50:50 (v:v) trifluoroethanol–water.

[4] A change to a more ionizing solvent results in a smaller increase in the rate constant for concerted pericyclic elimination of simple cumyl derivatives with electron-withdrawing ring substituents than in the rate constant for the concurrent solvolysis reaction (3).

© 1999 NRC Canada

Scheme 4.

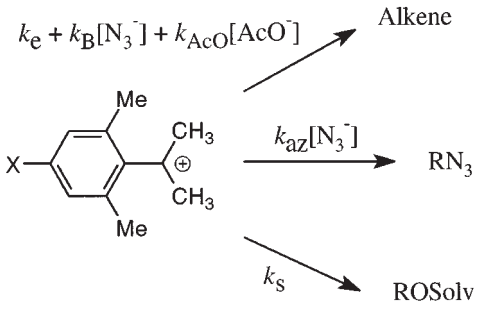

base (63% deprotonation) rather than a Lewis base (37% nucleophilic addition, Scheme 3) (2). In the absence of azide ion, **4** undergoes loss of a proton to solvent to give the corresponding alkene as the only detectable product ($k_s/k_e \leq 0.01$) (2). This surprising reactivity of azide ion as a Brønsted base was attributed to the large stability of the corresponding α-thioamide substituted alkene relative to the nucleophile adducts, and the resulting strong tendency of **4** to undergo loss of a proton rather than nucleophilic capture (2).

The values of $k_s/k_e = 0.49$ for partitioning of MeO-**2** and $k_s/k_e = 0.17$ for partitioning of Me-**2** in 50:50 (v:v) trifluoroethanol–water (Table 3) are much smaller than $k_s/k_e > 100$ for the partitioning of simple cumyl carbocations $XC_6H_4CMe_2^+$ between addition of solvent to the benzylic carbon and deprotonation in the same solvent (3, 4). Therefore, the 2,6-dimethylcumyl carbocations X-**2** also show an unusual tendency to undergo loss of a proton to solvent rather than nucleophilic capture at the benzylic carbon. We propose that the constant limiting yields of the alkenes X-**3** observed in the presence of high concentrations of azide ion result from reaction of azide ion with the carbocations X-**2** as a Brønsted rather than a Lewis base (k_B, Scheme 4).

The solid lines in Figs. 1 and 2 show that there is a good fit of the observed product yields for the reactions of MeO-**1**-(4-methoxybenzoate) and Me-**1**-(4-nitrobenzoate) to eqs. [4]–[6], which were derived for the mechanism shown in Scheme 4, using the values of k_s/k_e and k_{az}/k_e (M^{-1}) = $(k_{az}/k_s)(k_s/k_e)$ that were determined directly from product analysis (Table 3). The nonlinear least-squares fits of the product data to eqs. [4] and [5] gave $k_B/k_e = 191 \pm 12$ M^{-1} and 17.4 ± 0.2 M^{-1} for the partitioning of MeO-**2** and Me-**2** between deprotonation by azide ion and by solvent, respectively. These rate constant ratios were combined with the values of k_{az}/k_e (M^{-1}) to give values of $k_{az}/k_B = (k_{az}/k_e)(k_e/k_B)$ for partitioning of X-**2** between reaction with azide ion as a nucleophile and as a Brønsted base (Table 3). For the reactions of Me-**1**-(4-methoxybenzoate), the value of k_{az}/k_s (M^{-1}) determined directly from product analysis was unreliable (see Results). Therefore the product data were fitted to eqs. [4] and [5] using the only the observed value of k_s/k_e (Table 3) to give values of $k_{az}/k_e = 42$ M^{-1}, $k_B/k_e = 19$ M^{-1}, and $k_{az}/k_s = (k_{az}/k_e)(k_e/k_s) = 250$ M^{-1}, which are in good agreement with those for partitioning of Me-**2** generated from the cleavage of Me-**1**-(4-nitrobenzoate) (Table 3).

$$[4] \qquad f_{alk} = \frac{1 + (k_B/k_e)[N_3^-]}{1 + (k_s/k_e) + (k_B/k_e + k_{az}/k_e)[N_3^-]}$$

$$[5] \qquad f_{az} = \frac{(k_{az}/k_e)[N_3^-]}{1 + (k_s/k_e) + (k_B/k_e + k_{az}/k_e)[N_3^-]}$$

$$[6] \qquad f_{solv} = \frac{(k_s/k_e)}{1 + (k_s/k_e) + (k_B/k_e + k_{az}/k_e)[N_3^-]}$$

The rate constant ratio for partitioning of the α-thioamide substituted 4-methoxybenzyl carbocation **4** between reaction with azide ion as a nucleophile and a Brønsted base, $k_{az}/k_B = 0.59$ (2), is 27-fold smaller than $k_{az}/k_B = 15.9$ for the presumably much more hindered carbocation MeO-**2**. This suggests that the unusual reactivity of azide ion as Brønsted base for deprotonation of X-**2** is not due simply to steric hindrance to nucleophilic attack at the benzylic carbon, because this should be less favored for MeO-**2** than for **4**.

The pK_a's of acetic acid (4.76) and hydrazoic acid (4.72) are similar (26), so that acetate and azide ions would be expected to show similar reactivities as Brønsted bases for deprotonation of X-**2**. We determined the relative reactivity of azide and acetate ions as general bases for the deprotonation of Me-**2** from the effect of increasing concentrations of acetate ion (0.086–0.430 M) on the product distribution for the reaction of Me-**1**-(4-methoxybenzoate) in 50:50 (v:v) trifluoroethanol–water in the presence of a fixed concentration of azide ion (0.05 M) at $I = 0.50$ ($NaClO_4$). Figure 3 shows that increases in the concentration of acetate ion result in increases in the fractional yield of the alkene Me-**3** at the expense of the azide ion adduct Me-**1**-N_3. The constant yields of the solvent adducts Me-**1**-OSolv in the presence of increasing concentrations of acetate ion is not expected on the basis of the mechanism of Scheme 4, but it can be attributed to general base catalysis by acetate ion of the nucleophilic addition of solvent to the carbocation (27, 28). Acetate ion is less nucleophilic towards carbocations than azide ion (14) and there was no detectable formation of the acetate ion adduct in these experiments. Conversely, the very high reactivity of azide ion as a nucleophile towards unstable carbocations (29, 30) precludes the observation of general base catalysis by azide ion of the addition of solvent to Me-**2**. Figure 5 shows that the *ratio* of the fractional yields of the alkene Me-**3** and the azide ion adduct Me-**1**-N_3 formed in these experiments, f_{alk}/f_{az}, shows a linear dependence on the concentration of added acetate ion, according to eq. [7], derived for the mechanism shown in Scheme 4. The solid line through the data in Fig. 5 is the least-squares fit to eq. [7] with slope $(k_{AcO}/k_{az}[N_3^-]) = 2.29$ M^{-1} ($r = 0.992$), which gives $k_{AcO}/k_{az} = (2.29\ M^{-1} \times 0.05\ M) = 0.115$. This was combined with the average value of $k_{az}/k_B = 2.3$ from Table 3 to give $k_B/k_{AcO} = 3.8$ as the relative reactivities of azide and acetate ions as Brønsted bases for deprotonation of Me-**2**. A very similar 4.5-fold greater reactivity of azide than of acetate ion was determined for deprotonation of the α-thioamide substituted 4-methoxybenzyl carbocation **4** (2).

$$[7] \qquad f_{alk}/f_{az} = \left(\frac{k_B[N_3^-] + k_e}{k_{az}[N_3^-]}\right) + \left(\frac{k_{AcO}}{k_{az}[N_3^-]}\right)[AcO^-]$$

© 1999 NRC Canada

Table 5. Rate constants for nucleophilic addition and proton transfer reactions of 4-substituted 2,6-dimethylcumyl carbocations X-**2** and the 4-methylcumyl carbocation in 50:50 (v:v) trifluoroethanol–water at 25°C and I = 0.50 ($NaClO_4$) (Scheme 4).

Carbocation	k_{az} (M^{-1} s^{-1})	k_B (M^{-1} s^{-1})	k_s (s^{-1})	k_e (s^{-1})
MeO-**2** [a]	$\leq 4.7 \times 10^9$	$\leq 3.0 \times 10^8$	$\leq 7.6 \times 10^5$	$\leq 1.6 \times 10^6$
Me-**2** [b]	3.5×10^9	1.5×10^9	1.4×10^7	8.3×10^7
4-$MeC_6H_4CMe_2$+	5.0×10^9		1×10^9 [c]	1.4×10^6 [d]

[a]At room temperature 22 ± 2°C. Rate constants are upper limits calculated from the rate constant ratios in Table 3 using values of $(k_{az} + k_B) \leq 5 \times 10^9$ M^{-1} s^{-1} and k_{az}/k_B = 15.9, see text.

[b]Calculated from the rate constant ratios in Table 3 using $(k_{az} + k_B) = 5 \times 10^9$ M^{-1} s^{-1} and the average value of k_{az}/k_B = 2.3, see text.

[c]Calculated from k_{az}/k_s = 5 M^{-1} (31) and $k_{az} = 5 \times 10^9$ M^{-1} s^{-1} for the diffusion limited reaction of azide ion with unstable carbocations, see text.

[d]Calculated from k_e/k_s = 0.0014 determined from product analysis of the acid-catalyzed cleavage of 4-methylcumyl methyl ether (T. L. Amyes. Unpublished results).

Fig. 5. Dependence of the ratio of the fractional yields of the alkene Me-**3** and azide ion adduct Me-**1**-N_3 from the reaction of Me-**1**-(4-methoxybenzoate), f_{alk}/f_{az}, on the concentration of acetate ion in the presence of 0.05 M azide ion in 50:50 (v:v) trifluoroethanol–water at 25°C and I = 0.50 ($NaClO_4$). The solutions were buffered with acetate, 95% anion. The solid line shows the least-squares fit of the data to eq. [7]. The slope of this line is $k_{AcO}/k_{az}[N_3^-]$ = 2.29 M^{-1} (r = 0.992) for partitioning of the carbocation Me-**2** between deprotonation by acetate ion and nucleophilic addition of azide ion (see text).

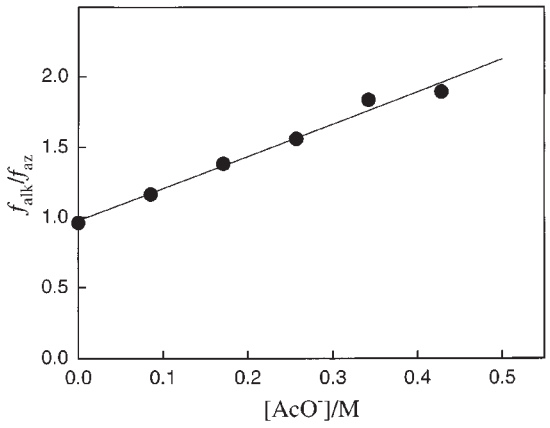

Effect of *ortho*-methyl groups on the reactions of cumyl carbocations

The azide ion selectivities k_{az}/k_s (M^{-1}) for nucleophilic capture of the 2,6-dimethylcumyl carbocations MeO-**2** and Me-**2** by azide ion and a solvent of 50:50 (v:v) trifluoroethanol–water (Table 3) are significantly larger than the corresponding values of k_{az}/k_s = 380 M^{-1} (1, 31) and 5 M^{-1} (31) for the corresponding simple cumyl carbocations 4-$MeOC_6H_4CMe_2^+$ and 4-$MeC_6H_4CMe_2^+$, respectively, which shows that X-**2** are moderately selective carbocations. The reaction of azide ion with a range of unstable α-substituted 4-methoxybenzyl carbocations in 98:2 (v:v) trifluoroethanol–water is diffusion controlled, with $k_{az} = 5 \times 10^9$ M^{-1} s^{-1} (29), and the rate constant for reaction of azide ion with ring-substituted triarylmethyl carbocations in 1:2 (v:v) acetonitrile–water does not drop significantly below this value until the azide/solvent selectivities become larger than $k_{az}/k_s \approx 10^4$ M^{-1} (30). This diffusion-limited reaction of azide ion with carbocations acts as a "clock" for other reactions of the carbocation (15, 32, 33). Therefore, the values of k_{az}/k_B, k_{az}/k_s (M^{-1}), and k_{az}/k_e (M^{-1}) for the partitioning of Me-**2** (Table 3) can be combined with $(k_{az} + k_B) = 5 \times 10^9$ M^{-1} s^{-1} for the diffusion-controlled reaction of azide ion (29, 30) to give the absolute values of k_B, k_s, and k_e for the reactions of Me-**2** given in Table 5. The large value of k_{az}/k_s = 6200 M^{-1} for partitioning of MeO-**2** is approaching the azide/solvent selectivity at which the reactions of triarylmethyl carbocations with azide ion drop below the diffusion limit, and a value of $k_{az} = 4 \times 10^9$ M^{-1} s^{-1} has been determined for the reaction of azide ion with 4-$MeOC_6H_4CMe_2^+$ (29). Therefore, the partitioning ratios for MeO-**2** (Table 3) were combined with $(k_{az} + k_B) \leq 5 \times 10^9$ M^{-1} s^{-1} to give the upper limits on the absolute rate constants for the reactions of MeO-**2** given in Table 5.

Scheme 5.

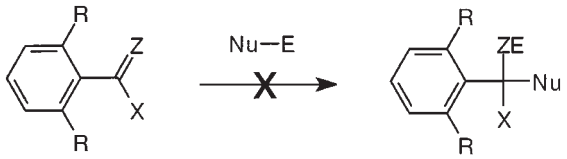

5 **6**

The data in Table 5 show that the effect of the pair of *ortho*-methyl groups on the *overall* reactivity of Me-**2** is small: a 10-fold decrease in $(k_s + k_e)$ compared with the simple 4-methylcumyl carbocation. However, the addition of a pair of *ortho*-methyl groups to 4-$MeC_6H_4CMe_2^+$ to give Me-**2** results in a larger 70-fold decrease in k_s for nucleophilic capture by solvent of the carbocation at the benzylic carbon (Table 5) and a 60-fold *increase* in k_e for deprotonation of the carbocation by solvent. The steric requirements of proton transfer from the β-carbon of Me-**2** should be similar to those for deprotonation of 4-$MeC_6H_4CMe_2^+$. Therefore, the greater reactivity of Me-**2** than of 4-$MeC_6H_4CMe_2^+$ towards proton transfer suggests that, relative to the corresponding alkenes, 2,6-dimethylcumyl carbocations are intrinsically less stable than simple cumyl carbocations. This decreased stability of X-**2** relative to X-**3** is very likely due to a nonplanar conformation of these species in which overlap between the π-orbitals of the aromatic ring and the *p*-orbital at the sp^2-hybridized benzylic carbon is decreased relative to that at $XC_6H_4CMe_2^+$ and ring-substituted α-methylstyrenes. This would tend to increase the energy of X-**2** relative to X-**3**, because there is more demand for resonance stabilization of the positive charge at the benzylic carbon of X-**2** than of the alkene double bond at X-**3**. The very low extinction coefficient of Me-**3** (220 M^{-1} cm^{-1}, this work) provides strong

© 1999 NRC Canada

evidence that the alkene double bond is twisted out of the plane of the aromatic ring by a considerable amount (34), and the UV spectrum of Me-**3** resembles that of benzene rather than an α-methylstyrene (11).

Formation of *ortho*-methyl cumyl derivatives

The very large yield of 93% of the products of nucleophilic substitution from the reaction of MeO-**1**-(4-methoxybenzoate) in the presence of high concentrations of azide ion (Fig. 1) represents, to the best of our knowledge, the first example of the formation of stable products of the addition of nucleophiles to disubstituted sp^2-hybridized carbon attached to a 2,6-disubstituted aryl moiety. Compounds of general structure **5** are known to be extremely unreactive (35) and 2,6-disubstituted α-methylstyrenes (**5**, X = CH_3, Z = CH_2) are inert to addition across the olefinic double bond (11, 12) (Scheme 5). For example, Me-**3** reacts with bromine to give the products of electrophilic substitution rather than addition (36, 37), and it does not undergo polar addition of hydrogen chloride (12) or radical addition of 1-butanethiol (34). The observations that the basic hydrolysis of methyl 2,4,6-trimethylbenzoate proceeds by the usual attack of hydroxide ion at the carbonyl carbon (38), and that the acid-catalyzed hydrolysis of methyl α-(2,6-dimethoxyphenyl)vinyl ether proceeds by the normal mechanism involving nucleophilic attack of water at the benzylic carbon of the oxocarbenium ion intermediate (39), show that nucleophilic attack at the benzylic carbon of species of general structure **5** is not prohibited. However, in both of these cases, the ultimate product is itself of general structure **5** rather than the more sterically congested **6**. Our results suggest that the apparent inaccessibility of species of general structure **6** results primarily from their much smaller thermodynamic stability relative to **5**, so that **6** can be formed only when the reaction conditions do not permit for its rapid conversion to the more stable and sterically less congested **5**.

Acknowledgment

This work has been supported by the National Institutes of Health (Grant GM 39754).

References

1. T.L. Amyes, I.W. Stevens, and J.P. Richard. J. Org. Chem. **58**, 6057 (1993).
2. J.P. Richard, S.-S. Lin, J.M. Buccigross, and T.L. Amyes. J. Am. Chem. Soc. **118**, 12 603 (1996).
3. T.L. Amyes and J.P. Richard. J. Am. Chem. Soc. **113**, 8960 (1991).
4. J.P. Richard, V. Jagannadham, T.L. Amyes, M. Mishima, and Y. Tsuno. J. Am. Chem. Soc. **116**, 6706 (1994).
5. X. Creary, V.P. Casingal, and C.E. Leahy. J. Am. Chem. Soc. **115**, 1734 (1993).
6. R. Taft, Jr. *In* Steric effects in organic chemistry. *Edited by* M.S. Newman. John Wiley and Sons, New York. 1956. pp. 556–675.
7. J. Shorter. *In* Advances in linear free energy relationships. *Edited by* N.B. Chapman and J. Shorter. Plenum Press, London. 1972. pp. 71–117.
8. M. Charton. *In* Progress in physical organic chemistry. Vol. 8. *Edited by* A. Streitwieser, Jr. and R.W. Taft. Wiley–Interscience, New York. 1971. pp. 235–317.
9. T.L. Amyes, J.P. Richard, and M. Novak. J. Am. Chem. Soc. **114**, 8032 (1992).
10. J.D. Edwards, Jr. and J.L. Cashaw. J. Am. Chem. Soc. **78**, 3821 (1956).
11. M.S. Newman and N.C. Deno. J. Am. Chem. Soc. **73**, 3644 (1951).
12. H.C. Brown and M. Grayson. J. Am. Chem. Soc. **75**, 20 (1953).
13. E.M. Kaiser and R.A. Woodruff. J. Org. Chem. **35**, 1198 (1970).
14. J.P. Richard. J. Am. Chem. Soc. **111**, 1455 (1989).
15. J.P. Richard, M.E. Rothenberg, and W.P. Jencks. J. Am. Chem. Soc. **106**, 1361 (1984).
16. R.D. Guthrie and W.P. Jencks. Acc. Chem. Res. **22**, 343 (1989).
17. J.C. Charlton and E.D. Hughes. J. Chem. Soc. 850 (1956).
18. G.W. Wheland. Resonance in organic chemistry. John Wiley and Sons, New York. 1955; E.L. Eliel. *In* Steric effects in organic chemistry. *Edited by* M.S. Newman. John Wiley and Sons, New York. 1956. pp. 61–163.
19. J. Hine. Structural effects on equilibria in organic chemistry. Wiley, New York. 1975.
20. Y. Tsuno and M. Fujio. Chem. Soc. Rev. 129 (1996).
21. T. Laube, G.A. Olah, and R. Bau. J. Am. Chem. Soc. **119**, 3087 (1997).
22. A.H. Fainberg and S. Winstein. J. Am. Chem. Soc. **78**, 2770 (1956).
23. V.J. Shiner, Jr., W. Dowd, R.D. Fisher, S.R. Hartshorn, M.A. Kessick, L. Milakofsky, and M.W. Rapp. J. Am. Chem. Soc. **91**, 4838 (1969).
24. T.L. Amyes and W.P. Jencks. J. Am. Chem. Soc. **111**, 7900 (1989).
25. J.P. Richard. J. Org. Chem. **57**, 625 (1992).
26. W.P. Jencks and J. Regenstein. *In* Handbook of biochemistry and molecular biology (physical and chemical data). Vol. 1. *Edited by* G.D. Fasman. CRC Press, Cleveland, Ohio. 1976. pp. 305–351.
27. J.P. Richard and W.P. Jencks. J. Am. Chem. Soc. **106**, 1396 (1984).
28. R. Ta-Shma and W.P. Jencks. J. Am. Chem. Soc. **108**, 8040 (1986).
29. R.A. McClelland, F.L. Cozens, S. Steenken, T.L. Amyes, and J.P. Richard. J. Chem. Soc. Perkin Trans. 2, 1717 (1993).
30. R.A. McClelland, V.M. Kanagasabapathy, N.S. Banait, and S. Steenken. J. Am. Chem. Soc. **113**, 1009 (1991).
31. J.P. Richard, T.L. Amyes, and T. Vontor. J. Am. Chem. Soc. **113**, 5871 (1991).
32. J.P. Richard and W.P. Jencks. J. Am. Chem. Soc. **104**, 4689 (1982).
33. T.L. Amyes and W.P. Jencks. J. Am. Chem. Soc. **111**, 7888 (1989).
34. E.S. Huyser and L. Kim. J. Org. Chem. **33**, 94 (1968).
35. M.S. Newman. *In* Steric effects in organic chemistry. *Edited by* M.S. Newman. John Wiley and Sons, New York. 1956. p. 201–248.
36. E.S. Huyser and L. Kim. J. Org. Chem. **33**, 1243 (1968).
37. R.F. Evilia, D. Pan, J.W. Timberlake, and S.L. Whittenburg. Tetrahedron Lett. **32**, 871 (1991).
38. M.L. Bender and R.S. Dewey. J. Am. Chem. Soc. **78**, 317 (1956).
39. J. Jones and A.J. Kresge. Can. J. Chem. **71**, 38 (1993).

© 1999 NRC Canada

The hydration of ketene and carbon dioxide: an examination of the kinetics in terms of No Barrier Theory

J. Peter Guthrie

Abstract: Rate constants for hydration of carbon dioxide and ketene can be calculated by applying No Barrier Theory, which needs only equilibrium constants and distortion energies, the latter calculated using molecular orbital theory. The calculated free energies of activation are in satisfactory agreement with experiment: the rms error in free energy of activation is 2.38 kcal/mol. These compounds can also be described using Marcus Theory or Multidimensional Marcus Theory using the transferable intrinsic barrier appropriate to simple carbonyl compounds; in this case the rms error in free energy of activation is 2.19 kcal/mol. The two methods agree on preferred mechanistic path except for uncatalyzed hydration of ketene where Multidimensional Marcus Theory leads to a lower activation free energy for addition to the C=O, while No Barrier Theory leads to a lower free energy of activation for addition to the $C=CH_2$. A rate constant for hydroxide ion catalyzed hydration of ketene can be calculated and is in accord with preliminary experimental results.

Key words: ketene, carbon dioxide, hydration, Marcus Theory, No Barrier Theory.

Résumé : On a calculé les constantes de vitesse d'hydratation du dioxyde de carbone et du cétène en utilisant la théorie sans barrière qui ne nécessite que les constantes d'équilibre et les énergies de distorsion; ces dernières sont calculées par la théorie des orbitales moléculaires. Les énergies libres d'activation calculées sont en bon accord avec les valeurs expérimentales : l'erreur sur l'énergie libre d'activation est de 2,38 kcal/mol. On peut aussi décrire ces composés à l'aide de la théorie de Marcus ou de la théorie multidimensionnelle de Marcus en utilisant la barrière intrinsèque transférable appropriée aux composés carbonylés simples; dans ce cas, l'erreur sur l'énergie libre d'activation est de 2,19 kcal/mol. À l'exception de l'hydratation non catalysée du cétène pour laquelle la théorie multidimensionnelle de Marcus conduit à une énergie libre d'activation plus faible pour l'addition au groupe C=O alors que la théorie sans barrière conduit à une énergie d'activation plus faible pour l'addition sur le $C=CH_2$, les deux méthodes sont concordantes en ce qui a trait à la voie mécanistique préférée. On peut calculer une constante de vitesse pour l'hydratation du cétène catalysée par l'ion hydroxyde et elle est en accord avec les résultats expérimentaux préliminaires.

Mots clés : cétène, dioxyde de carbone, hydratation, théorie de Marcus, théorie sans barrière.

[Traduit par la Rédaction]

Introduction

Ketene is a highly reactive molecule, which undergoes very facile hydration. It has only recently become possible to measure the rate constants for this reaction in aqueous solution (1, 2). Carbon dioxide, a closely analogous molecule, has long been studied because of its biological importance (3, 4). We have recently reported an analysis of the hydration of carbonyl compounds in terms of No Barrier Theory (5). I wish now to report an application of this theory to the hydration of ketene and carbon dioxide. Ketene shows an interesting switch in mechanism from C-protonation in acidic or neutral solution to carbonyl hydration in basic solution. This paper will demonstrate that both the mechanistic path, and the absolute value of the free energies of activation, follow directly from application of No Barrier Theory to these reactions. The rate constant for the hydroxide-catalyzed hydration of ketene will also be predicted.

No Barrier Theory is a recent development (6, 7), following in the spirit of Marcus Theory (8–10), but requiring no intrinsic barrier. The idea is that if only one thing happens in a reaction, then there is no kinetic barrier: the common observation of an intrinsic kinetic barrier is a consequence of almost all reactions requiring more than one thing to happen in the rate- determining step to produce an observable chemical change. For additions of a nucleophile to a simple carbonyl compound, the two simple things are formation of a bond between nucleophile and carbon and change in geometry at carbon from sp^2 to sp^3.

Received November 17, 1998.

This paper is dedicated to Jerry Kresge in recognition of his many achievements in chemistry.

J.P. Guthrie.[1] Department of Chemistry, University of Western Ontario, London ON N6A 5B7, Canada.

[1]Telephone: (519) 679-2111, ext. 6352. Fax: (519) 661-3022. e-mail: peter.guthrie@uwo.ca

 © 1999 NRC Canada

Table 1. Thermodynamic quantities for compound discussed in this paper.[a]

(*a*) Compounds for which ΔG_f(aq) has not previously been reported.

Compound	ΔH_f(g)	$S°$(g)	ΔG_f(g)[b]	ΔG_t	ΔG_f(aq)
CH_2=C=O	–11.40 ± 0.60[c]	59.18 ± 0.06[c]	–11.59 ± 0.60[c]	+1.95 ± 1.00	–9.64 ± 1.16
$CH_3C{\equiv}O^+$					–14.10 ± 3.00[d]

(*b*) Compounds for which ΔG_f(aq) has previously been reported.

Compound	ΔG_f(aq)	Compound	ΔG_f(aq)	+Compound	ΔG_f(aq)
H_2O	–56.69 ± 0.01[c]	CH_3COOH	–94.35 ± 0.06[e]	CO_2	–92.25 ± 0.06[c]
HO^-	–37.58 ± 0.01[c]	CH_2=$C(OH)_2$	–67.90 ± 1.67[f]	$CO(OH)_2$	–145.13 ± 0.09[g]
				HCO_3^-	–140.24 ± 0.06[c]

[a]All at 25°C; enthalpies and free energies are in kcal/mol, entropies are in cal deg^{-1} mol^{-1}, standard states are the ideal gas at 1 atm and 1 M aqueous solution with an infinitely dilute reference state. Unless otherwise noted, enthalpies of formation are from ref. 12, entropies are from ref. 13, free energies of formation in the gas phase are calculated from the corresponding enthalpies of formation and the standard entropies, and free energies of formation in aqueous solution are calculated from the corresponding free energies of formation in the gas and free energies of transfer.

[b]Free energy of transfer from the gas at 1 atm to 1 M aqueous solution.

[c]Reference 14; errors are stated to be between 8 and 80 in the last figure given in these tables (in kJ/mol). The geometric mean, 25, was used to calculate numerical values of these limits.

[d]Calculated as described in the text.

[e]Reference 15.

[f]Reference 16.

[g]Calculated from the free energy of formation of aqueous CO_2, and the equilibrium constant for hydration (3).

It was found in this work that Multidimensional Marcus Theory (11), using the average intrinsic barriers that worked well for all but the most reactive carbonyl compounds, led to satisfactory predictions for ketene or CO_2. No Barrier Theory also permitted calculation of the rate constants for these reactions with similar precision and no empirical parameters.

No Barrier Theory requires molecular orbital calculations to evaluate distortion energies, but gives satisfactory results at much lower levels of theory than are required for direct calculation of transition state structures and energies.

Results

First, Multidimensional Marcus Theory will be applied to the hydration reactions of ketene and carbon dioxide. Then No Barrier Theory in the form that successfully described simple carbonyl compounds (5) will be employed. For both of these treatments we require equilibrium constants for the overall reactions and for various proton transfer equilibria involved in the mechanisms. For No Barrier Theory we will also require various distortion energies.

We first require free energies of formation for the various species involved. For CO_2 these are readily available: see Table 1. For ketene, the enthalpy of formation (14) and the standard entropy (14) have been reported for the molecule in the ideal gas standard state. Naturally enough there is no value for the free energy of transfer of ketene from the gas phase to aqueous solution, so we must estimate this quantity. We do so starting with the free energies of transfer from the gas phase to aqueous solution of carbon dioxide, ΔG_t = 2.00 kcal/mol (14), and allene, for which the value was assumed to be the same as that for acetylene, ΔG_t = 1.89 kcal/mol (15), since the solubilities of acetylene and allene in propylene carbonate (which is the only solvent for which solubility data for allene could be found) are very similar (17), and more similar than the solubilities of allene and propyne, which might have been assumed to be isosteric. Thus the approach is to use the hypothetical disproportionation reaction [1], for which it is assumed that the total free energies of transfer for the products and reactants are the same.

[1] $O{=}C{=}O + H_2C{=}C{=}CH_2 \rightleftharpoons H_2C{=}C{=}O + H_2C{=}C{=}O$

From the free energies of transfer of carbon dioxide, 2.00 kcal/mol, and allene, 1.89 kcal/mol, a value of 1.95 kcal/mol for ketene was estimated, and assigned an uncertainty of ±1.0 kcal/mol.

This estimated free energy of transfer leads to a value of –9.64 ± 1.16 kcal/mol[2] for the free energy of formation of aqueous ketene. We previously reported (18) the free energy of formation of ketene hydrate (acetic acid enol) in aqueous solution as –67.90 ± 1.67 kcal/mol (16). Thus the free energy change upon covalent hydration of ketene to form ketene hydrate is $\Delta G°$ = –1.57 ± 2.03 kcal/mol, and the free energy change for hydration of ketene to acetic acid is $\Delta G°$ = –28.02 ± 1.16 kcal/mol.

The free energy of formation of acetylium ion was estimated from that of acetic acid (15) with the pK_R value calculated (19) from data of Deno et al. (20). The extrapolation involved was long and consequently uncertainties are large but it is not clear how to estimate them. In the hope of being conservatively pessimistic, an uncertainty of ±3.0 kcal/mol was assigned.

To carry out Multidimensional Marcus Theory or No Barrier Theory calculations we require pK_a values for various intermediates or potential intermediates in the hydrolysis pathways. These have been estimated using analogy and linear free energy relationships. The values that we estimated are found in Table 2. In the gas phase, ketene has a proton

[2]Thermodynamic quantities are normally given to two decimal figures in this paper; these are in many cases only guard figures to ensure reproducibility of calculations. The error limits will indicate how many figures are significant.

© 1999 NRC Canada

Table 2. pK_a values for compounds discussed in this paper.[a]

Compound	pK_a	Compound	pK_a
CH_2=C=OH^{+}[b]	–23	CH_2=C(O-)(OH_2^{+})[b]	–5.11
CH_2=C(OH)(OH_2^{+})[b,c]	–9.0	CH_3-CO^{+}[b,d]	3.27
CH_2=C(OH)(OH_2^{+})[b,e]	4.21	CH_3-CO-OH_2^{+}[b]	–13.0
CH_2=C(OH)$_2$[b]	8.10	O=C(OH)$_2$ [b]	3.49
O=C(OH)(OH_2^{+})[b,f]	–13.49	O=C(O-)(OH_2^{+})[b]	–9.60
O=C(OH)(OH_2^{+})[b,g]	–0.40		

[a]All in aqueous solution at 25°C.

[b]Estimated as described in the text.

[c]For loss of a proton to give the zwitterion.

[d]For loss of a proton to give ketene.

[e]For loss of a proton to give the neutral hydrate.

[f]For loss of a proton to give the zwitterion.

[g]For loss of a proton to give the neutral hydrate.

affinity of 198 kcal/mol (21), similar to that of acetone, 202 kcal/mol (21). Kebarle and co-workers concluded that the proton affinity of ketene referred to acetylium formation (22). To estimate the proton affinity of ketene for protonation on oxygen we calculated the energies of the isomeric cations by ab initio MO methods (23) at the B3LYP/3-21+G* level. The difference in energy was such that O-protonation is 38.17 kcal less favorable than C-protonation, implying a proton affinity of 160 kcal/mol.

The aqueous solution pK_a of O-protonated ketene was estimated by comparison with N-protonated acetonitrile, which has a very similar shape and overall size.

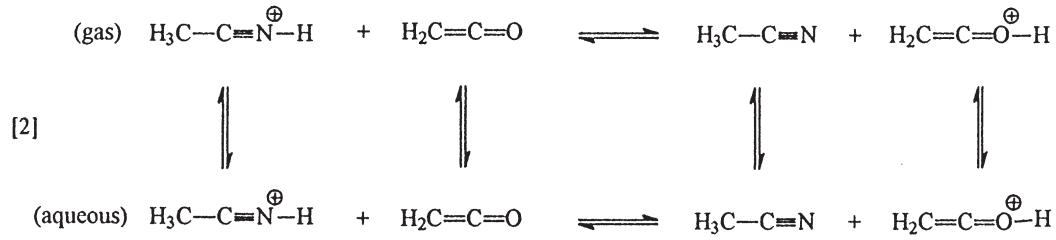

A correlation has been reported between the difference in free energies of transfer of acids and the corresponding methyl esters, and was believed to be dominated by hydrogen bond formation by the acid. This will now be used as a measure of hydrogen bond strength to solvent, and it will be assumed that the difference in free energy of transfer for protonated ketene and protonated acetonitrile will be estimated by this correlation. One can then deduce that the free energy change in water for process [2] is given by:

$$-1.366*(pK_a^{\text{protonated acetonitrile}} - pK_a^{\text{protonated ketene}} = -\Delta G_t^{\text{ketene}} + \Delta G°_{\text{gas}} + \Delta G_t^{\text{acetonitrile}} + 0.732(pK_a^{\text{protonated ketene}} - pK_a^{\text{protonated acetonitrile}})$$

The pK_a of protonated acetonitrile has been reported as –12 (24). Substituting values and solving leads to a very approximate value of $pK_a^{\text{protonated ketene}} = -23$.

Ketene hydrate, CH_2=C(OH)$_2$, has not yet been studied in aqueous solution; its pK_a may be estimated by analogy with the enol of mandelic acid, which has been studied (25): pK_a 6.6. The enol of acetaldehyde has a pK_a of 10.5 (26). We will estimate the effect of a second OH on the same carbon as the first by comparing ethanol, pK_a 15.9 (27), and acetaldehyde hydrate, pK_a 13.48 (28); the difference, 2.4 pK_a units, will be assumed to apply to the change from acetaldehyde enol to acetic acid enol as well; the pK_a so predicted for acetic acid enol is 8.1. The enol of *trans*-phenylacetaldehyde enol is 9.46 (26), for a pK_a shift of 1.0 from the addition of a phenyl; this leads to a predicted pK_a of 7.1 for the enol of phenylacetic acid. Finally, the pK_a of catechol is 9.48 (28), symmetry corrected 9.78, while that of phenol is 9.95 (28), for a pK_a shift of 0.17. Thus we arrive at a pK_a of 6.96 for the enol of mandelic acid. The approximate agreement suggests that the procedure is reasonable. We will take the pK_a of acetic acid enol as 8.1. This differs from a previous suggestion (16, 18) that was based on the pK_a of *o*-phenylphenol, 9.93 (28), implying that the phenyl would have a very small effect. There remains the question of why a phenyl substitutent has such different effects depending on environment.

To estimate pK_a values for O-protonated ketene hydrate, CH_2=C(OH)(OH_2^{+}), protonated phenol was used as a model, assuming that ΔpK_a for Ph-OH_2^{+}, pK_a = –7.04 (29) vs. PhOH, pK_a = 9.95 (28), will be the same, with suitable symmetry corrections, as for CH_2=C(OH)(OH_2^{+}) vs. CH_2=C(OH)$_2$. This leads to a pK_a of –9. The pK_a for conversion to a zwitterion was estimated by analogy with the corresponding pK_a values previously estimated for acetone hydrate (30), i.e., assuming Δ pK_a for CH_2=C(OH)(OH_2^{+}) vs. CH_2=C(OH)$_2$ is the same as for $(CH_3)_2$C(OH)(OH_2^{+}), pK_a=10.34 (31) vs. $(CH_3)_2$C(OH)$_2$, 14.19 (31). This leads to a pK_a of 4.2. Now the pK_a of CH_2=C(O^{-})(OH_2^{+}) is defined by the values already estimated, as –5.1.

© 1999 NRC Canada

C-Protonated ketene is acetylium ion, for which the pK_a can be calculated as 3.27 from the free energies of the species involved, a rather strong carbon acid, though a rather weakly acidic carbocation (which it could be considered to be: CH_3-C≡O^+ ↔ CH_3-C^+=O).

Finally, we need a pK_a for acetic acid protonated on the OH, CH_3-CO-OH_2^+. This value can be estimated following the procedure suggested by Fastrez (32) (for estimating hydration energies), i.e., by using the barrier to rotation about the HO—CO bond to estimate the cost of losing conjugation, and then treating the acyl substituent as an electron-withdrawing group perturbing the pK_a of the protonated OH. $\rho^* = -0.89$ will be used as for protonated alcohols (31) and σ^* for $CH_3CO = 1.81$ (33). The barrier for rotation is taken as that in methyl acetate, 13 kcal/mol (34). These values lead to a pK_a for CH_3-CO-OH_2^+ of –13.

It is also necessary to estimate analogous pK_a values for carbonic acid. For carbonic acid itself, the true pK_a is 3.49; this is derived from the apparent pK_a, 6.35 (28), and the equilibrium constant for covalent hydration of CO_2, 720 (3). For hydroxyl protonated carbonic acid, a procedure analogous to that for hydroxyl protonated acetic acid was used: the barrier to rotation of the OH was taken as that in methyl acetate. This led to a pK_a for HO-CO-OH_2^+ of –13.5. It was assumed that ΔpK_a for O=C(OH)(OH_2^+) vs. O=C$(OH)_2$ is the same as for $(CH_3)_2$C(OH)(OH_2^+) vs. $(CH_3)_2$C$(OH)_2$ (30); this led to a pK_a of –0.40 for HO-CO-OH_2^+ going to the zwitterion. Now the pK_a of O=C(O^-)(OH_2^+) is defined, by the values already estimated, as –9.6.

In calculating the energies of various encounter complexes involved in the mechanisms it is necessary to consider partial desolvation processes. Hydroxide ion in contact with a carbon must have lost one of its solvating waters. As before (35), this was estimated as 7.1 kcal/mol. When the carbon is the *sp* hybridized carbon of an acylium ion, which will bear significant positive charge, it is assumed that electrostatic and other interactions will compensate for the loss of hydrogen bonding. It is less clear what should be assumed for hydroxide in contact with ketene or carbon dioxide bent into the geometry for addition of water leading to acetic acid or carbonic acid. In this geometry the C=O π-bond is relatively undisturbed, but the central carbon has changed from *sp* to sp^2 geometry, and consequently overlap with the neighboring carbon or oxygen is drastically impaired. To the extent that this new sp^2 hybrid orbital is unoccupied, interaction with a nonbonded hydroxide would be more favorable than unfavorable. Two assumptions were tested: one that the standard desolvation applies for hydroxide in contact with such a carbon; the other that there is no desolvation cost for such contact. The calculations were insensitive to these assumptions, so it seems best for the moment only to assume a desolvation cost for bringing hydroxide into contact with linear ketene or carbon dioxide. Water molecules in liquid water are extensively hydrogen bonded, as shown by the remarkably high boiling point for such a small molecule, even though they are no longer in the perfect array of four hydrogen bonds per molecule found in ice. The energetics of partially desolvating water, by removing one face of the tetrahedron (two H faces, two lone-pair faces) from contact with appropriately polarized neighbors and bringing it into contact with something of the opposite polarity is taken as one quarter of the hydrogen-bonding energy of an average water molecule at 25°C. This in turn is taken as the difference in free energies of transfer (gas at 1 atm (101.3 kPa) to 1 M aqueous solution) between water and methane. This desolvation energy is 2.08 kcal/mol. Water molecules are of course in contact with any molecule fully dissolved in water, but will be oriented to optimize polarity matching. In the C-protonation of ketene there is a necessary initial mismatch if the final ion is to be appropriately solvated. In view of the much larger solvation energies for ions than for neutrals, it seems plausible to assume that the needs of the ion take precedence. The oxygen of ketene has partial negative character, but in acetylium the oxygen becomes strongly positive. Thus the initial orientation of water at equilibrium for ketene will be all wrong for acetylium ion. If the initial orientation of the waters is correct for acetylium ion, this initial state will have three partially desolvated waters, oriented with lone pairs directed at the oxygen of ketene in order to be in place to solvate the developing positive charge. If the oxygen of ketene has approximately four nearest neighbors, as seems appropriate for a small atom, then there would be three such waters; if this oxygen acted as if it had two lone pairs that might have attracted very weak hydrogen bonds, then there would be two. In the calculations that follow, a total of three partially desolvated molecules was used, though the calculations are not extremely sensitive to the number.

A serious problem in applying Marcus theory, either in its traditional one-dimensional form or as Multidimensional Marcus Theory, is that one requires intrinsic barriers as well as thermodynamic barriers in order to predict rate constants. In a case such as the present one, where ketene is distinctly different from almost any model reaction, this is a serious problem. Although intrinsic barriers are approximately transferable within families of "similar" reactions, they cannot be expected to remain independent of major changes in structure. The closest available values are the intrinsic barrier for addition of water (or hydroxide) to carbonyl compounds, for which a value of 7.36 was found to be a good average value (36), and the intrinsic barrier for protonation of an enol ether, for which a value of 12.3 was found (18).

Nonetheless, Multidimensional Marcus Theory was applied to the hydration of ketene and carbon dioxide. The results, see Table 3, were free energies of activation for water attack that were too high, implying that the effective intrinsic barriers for ketene or CO_2 would be lower than for simple carbonyl compounds. On the other hand the calculated free energy of activation for the hydroxide reaction of CO_2 was too low, implying that the intrinsic barrier was too small. Since these compounds are structurally different from the sp^2 hybridized carbonyl compounds used to determine the intrinsic barrier, and are quite reactive, it is not very surprising that a model appropriate to simple carbonyl compounds did not fit well.

Fortunately, No Barrier Theory, which requires no intrinsic barriers, has been developed (6, 7, 36), and can be applied to the present reactions. This theory assumes that for simple reaction processes there is no kinetic barrier, but simply a quadratic potential. The kinetic barrier commonly encountered for real reactions results from the need for more than one simple reaction process for almost any real chemi-

© 1999 NRC Canada

Table 3. Observed and calculated free energies of activation for hydration of CO_2 and ketene.[a]

Reactant	Catalyst	ΔG^*obsd.	ΔG^*calcd. NBT	MMT
CO_2	None	19.41[b]	21.63 cyc[d]	22.45 cyc[d]
		19.55[c]	23.35 gbc[e]	22.45 gbc[e]
	HO^-	12.09[b]	13.49	10.52
		12.29[c]		
Ketene	None	15.32[f]	21.68 cyc[d]	18.11 cyc[d]
			20.79 gbc[e]	18.11 gbc[e]
			18.82 CH_2[g]	20.35 CH_2[g]
	HO^-	11.00[h]	13.89	10.47
	H_3O+	11.98[f]	10.28 CH_2[g]	14.12 CH_2[g]
			25.77 CO[i]	20.87 CO[i]

[a]All in aqueous solution at 25°C. Free energies of activation are in kcal/mol and are based on rate constants with dimensions of s^{-1} or M^{-1} s^{-1}.

[b]Reference 3.

[c]Reference 4.

[d]Cyclic path for hydrationinvolving three water molecules.

[e]General base path for hydration involving two water molecules.

[f]Reference 2.

[g]Protonation at carbon by a water molecule.

[h]Preliminary value: personal communication from A.J. Kresge.

[i]Acid catalysis of carbonyl hydration.

cal transformation. In the case of ketene hydration, there will be both bond-making processes and geometry-changing processes.

To apply No Barrier Theory we require distortion energies corresponding to only one of the possible dimensions into which the overall chemical transformation is resolved: see Fig. 1. Thus for addition to a carbonyl the dimensions are bond formation and geometry change at the carbonyl carbon. The energy costs of these distortions were calculated by ab initio quantum mechanics at the B3LYP/3-21+G* level. In calculating the distortion energies of the ketene hydrate or its anion, or of carbonic acid or its anion, the angles and dihedrals specifying geometry about the central carbon were locked. For the anions, the bond length of the bond to the perpendicular OH had to be locked to prevent dissociation. In calculating the distortion energies of ketene or CO_2 the angle at the central carbon was locked.

The distortions needed for C-protonation of ketene are shown in Fig. 2. For these distortions, it was found that direct calculation using ketene and acetylium gave surprisingly small distortion energies. This was attributed to the fact that the calculations are done for the gas phase where these small, relatively unstable, molecules or ions are in severe need of stabilization by whatever means they can find. Thus relative to solution, the importance of some resonance-contributing forms is enhanced.

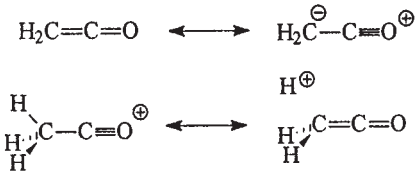

This is reminiscent of the situation encountered in calculating distortion energies for enolate ions, where gas phase calculations for the distortion of the CR_2 of an enolate, CH_2=C(O-)R, gave unreasonably low distortion energies, and distortion energies based on the enols were used instead in a treatment of rates of protonation/deprotonation of enolates/carbonyl compounds (6).

In the present case the most similar possible models have been used, lacking only the charge or tendency for charge separation, i.e., allene, CH_2=C=CH_2, as a model for ketene, CH_2=C=O, and acetonitrile, CH_3-C≡N, as a model for acetylium, CH_3-C≡O^+. With these model compounds distortion energies more in accord with naive expectation were obtained, and led to successful calculation of the rates of reaction. The problem appears to be general and requires that care be taken in transferring gas phase calculations to solution.

A number of possible mechanisms were examined for each term in the rate law for the hydration reactions, and for every case it was necessary to calculate the energies of each of the hypothetical corner intermediates where only one (or two or...) of the possible simple processes had occurred. The energies so calculated are found in the supplementary material.[3] In carrying out these calculations allowance was made for the entropic cost of bringing species together, any hydrogen-bonding interactions, any electrostatic interactions, any proton transfer equilibria, any desolvations required to bring a reactive lone pair into contact with a nonpolar center, and the strain energies required for geometrical distortion.

The reactions of carbon dioxide were examined as possible models for the ketene reactions. The advantage is that the solution thermodynamics are well established, as are the pK_a values for carbonic acid.

For the uncatalyzed reaction of carbon dioxide with water two models were examined: see Fig. 3. The first involved attack of water with a second water acting as general base (to

[3]Copies of the supplementary material (Excel table, 14 pages; Appendix S1, 2 pages) may be purchased from: The Depository of Unpublished Data, Document Delivery, CISTI, National Research Council Canada, Ottawa, ON K1A 0S2. Canada.

© 1999 NRC Canada

Fig. 1. Distortions required for addition to carbonyl compounds or to ketene/CO_2.

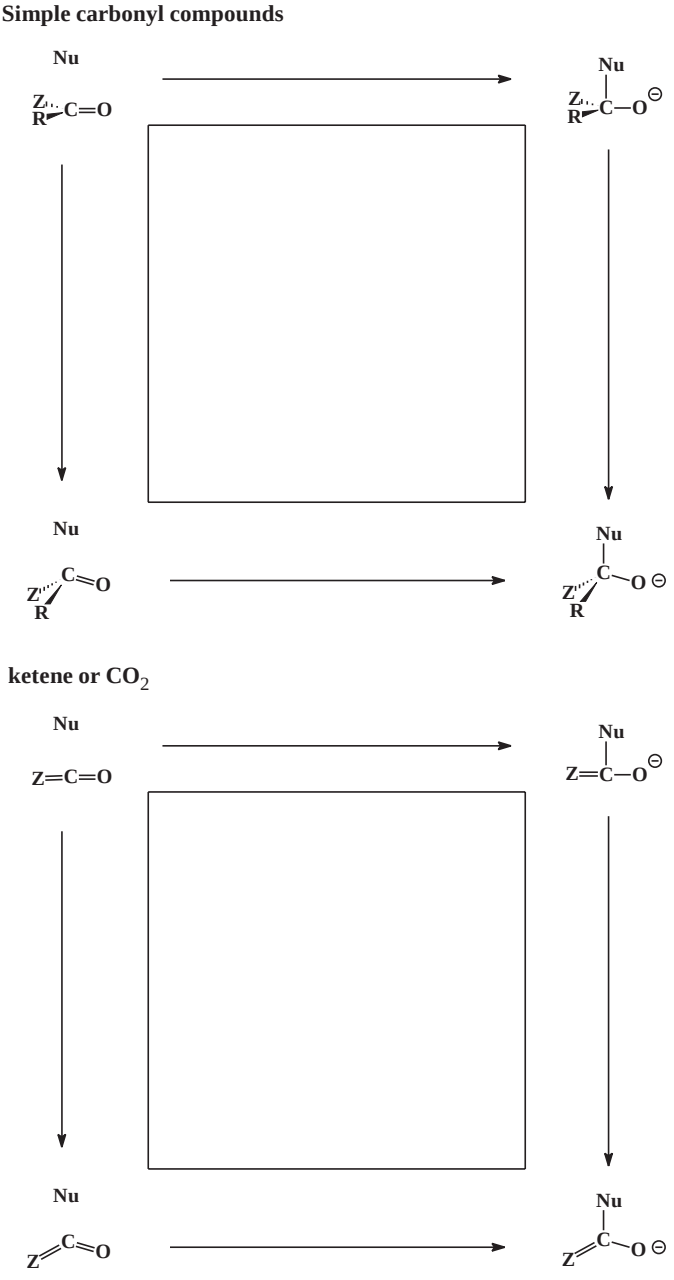

avoid formation of the zwitterion of carbonic acid), leading to a hydronium bicarbonate ion pair. The second involved a cyclic reaction with three waters leading directly to carbonic acid. For carbon dioxide the cyclic process led to the lower activation barrier, with an energy of 21.63 kcal/mol: see Table 3. This is in good agreement with the observed 19.60 kcal/mol. The barrier to these reactions comes from the extremely high distortion energies for carbonic acid. The conclusion that the hydration processes involves a cyclic array of three water molecules is in complete accord with the conclusions from a high-level ab intitio molecular orbital study (37).

For the hydroxide-catalyzed hydration of CO_2, the model used begins with hydroxide separated from CO_2 by one water, see Fig. 3. The final diffusional step bringing OH^- into

Fig. 2. Distortions required for the C-protonation of ketene.

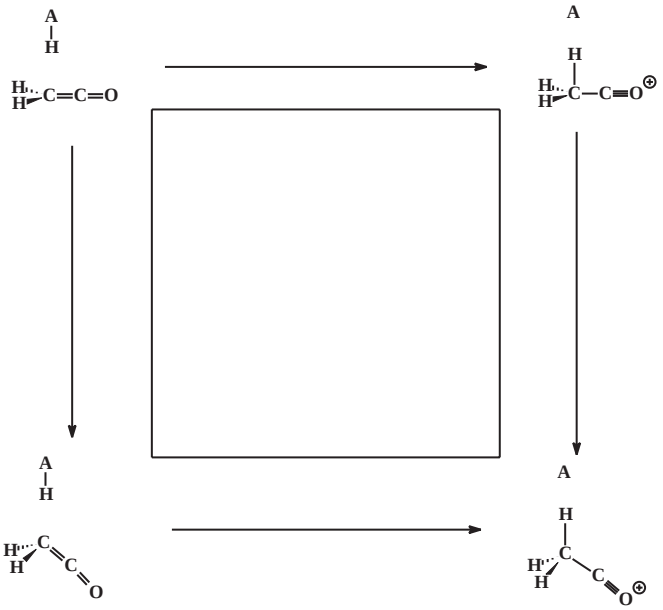

Fig. 3. Mechanistic possibilities for the hydration of carbon dioxide.

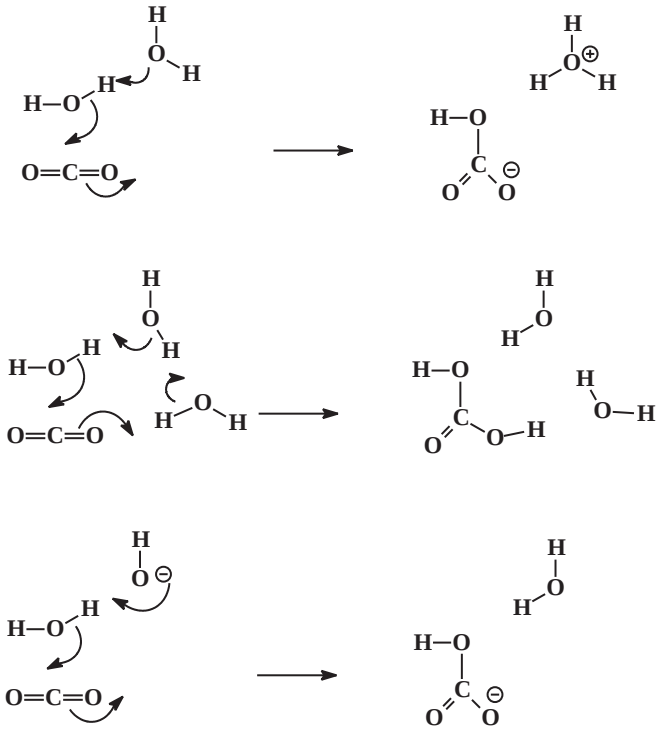

contact with CO_2 imposes a severe desolvational barrier, and thus is expected to occur only as part of a concerted reaction process. For this path the calculated barrier is in very satisfactory agreement with experiment.

Four models were examined for the uncatalyzed hydration of ketene: see Fig. 4. The first was a cyclic mechanism with three water molecules in a potentially concerted path, attacking the carbonyl carbon and ultimately transferring a proton to the carbonyl oxygen. The second mechanism involved attack of water on the carbonyl with general base catalysis

© 1999 NRC Canada

Fig. 4. Mechanistic possibilities for hydration of ketene.

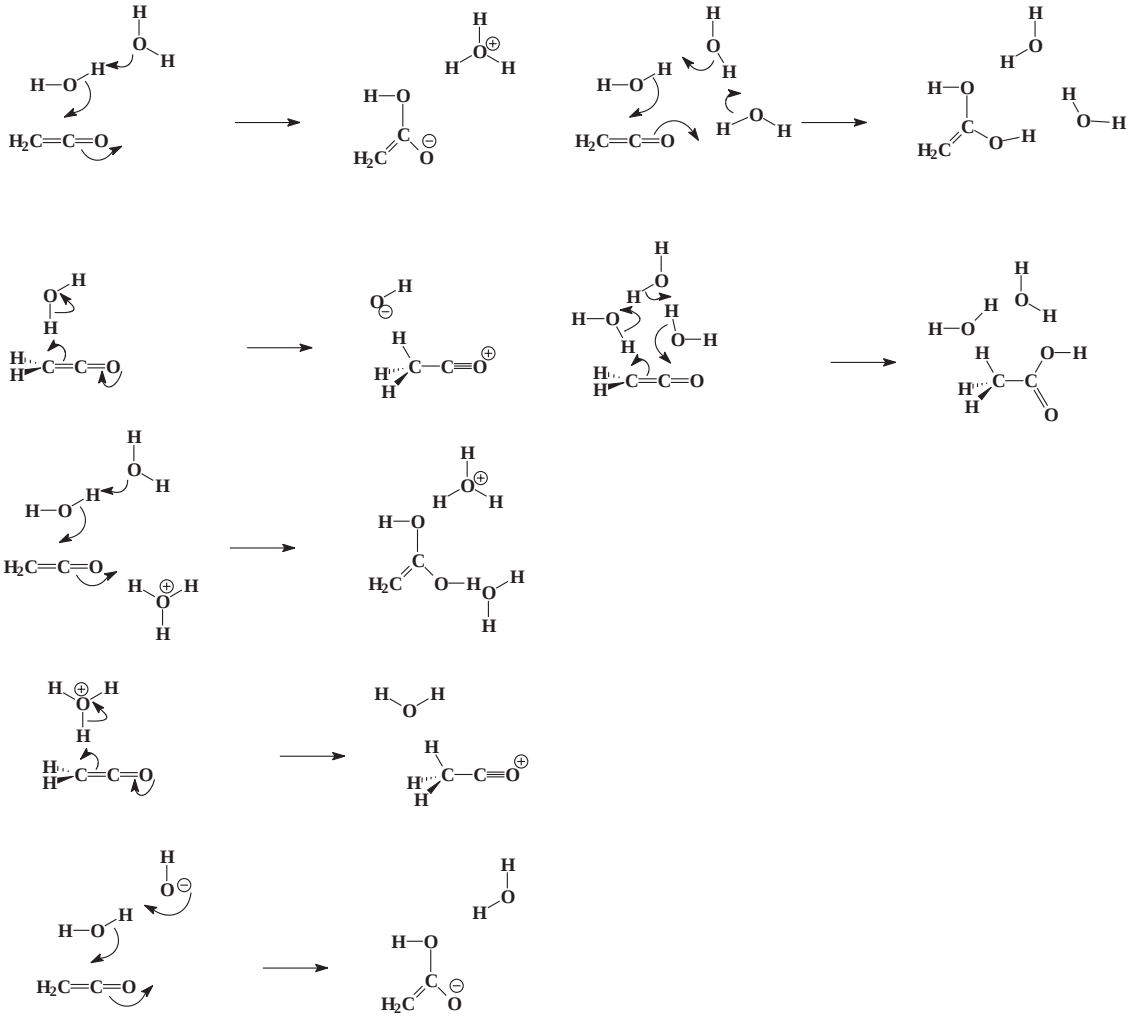

by a second water. The third involved attack of water acting as a general acid, protonating ketene at carbon, to give a short-lived hydroxide–acetylium ion pair. The fourth was a cyclic mechanism with three water molecules in a potentially concerted path, with a proton transferred to the CH_2, and oxygen of a water attacking the carbonyl carbon. This path, with three proton transfer dimensions, one C—O bond formation, and two carbons undergoing geometry changes, involves a six-reaction dimension hypercube model.

Although the general base catalyzed path is predicted to be lower energy than the cyclic path for hydration of ketene, both are 5–6 kcal/mol higher than the observed free energy of activation: see Table 3. By contrast, the C-protonation path gives a reasonable match to the observed value. This path leads to a hydroxide–acetylium ion pair, which after a short lateral diffusion bringing the charges closer together can collapse to acetic acid. However, the calculated transition state for formation of acetylium ion is very close to the product, so that there is essentially no barrier to reversion to starting material. By consideration of the cyclic mechanism we can calculate the barrier for conversion of the hydroxide–acetylium ion pair to acetic acid (since this is another section of the cyclic reaction path) and find that the barrier for this path is 3.40 kcal/mol, for a total reaction barrier of 18.82 kcal/mol. Although we examined the full six-dimensional potentially cyclic concerted path for addition of water to the $C{=}CH_2$ of ketene, we were unable to find the lowest energy fully concerted path through this hypercube; this is apparently a defect in the algorithm currently being used, because various paths involving successively lower dimensional stages could be found, using the same corner energies, which corresponded to lower barriers than the best six-dimensional transition state that could be found (which had a transition state free energy of 19.85 kcal/mol). Better algorithms are being sought. The lowest energy path found so far is the one mentioned above, with a free energy of activation of 18.82 kcal/mol. This is in fair agreement with the observed value of 15.32 kcal/mol.

For acid-catalyzed hydration we considered two possibilities: attack of hydronium ion at the CH_2 and at the carbonyl oxygen. The preferred transition state had the hydronium ion attack the CH_2, and led to a calculated free energy of activation in good agreement with the observed value.

Finally, we examined the hydroxide-catalyzed reaction. We consider the possibility that the hydroxide may act directly as a nucleophile or indirectly as a general base, removing a proton from water as it attacks. It was found that the general base path leads to the lower free energy of

© 1999 NRC Canada

activation. The predicted free energy of activation is 13.89, corresponding to a rate constant of $10^{2.6}$ M^{-1} s^{-1}.

Discussion

The conclusion that uncatalyzed hydration of ketene occurs by initial C-protonation followed by rate-limiting hydroxide attack on acetylium ion flies in the face of the accepted mechanism for this reaction, namely, that it occurs by nucleophilic attack on the carbonyl (1, 2, 38–45). The strongest evidence for this path was the small normal isotope effect of k_H/k_D=1.9 (1). However, this is actually in reasonable accord with initial C-protonation and rate- determining attack of hydroxide.[4] Plausible values of fractionation factors for the protons involved in the transition state lead to a predicted isotope effect of 1.4; there are enough unusual features involving imperfect solvation that this could be consistent with the observed value. If the reaction path were water attack on the carbonyl, leading initially to the zwitterion of ketene hydrate, proton transfer from the cationic site to water would be expected to be superfast, and indeed to have happened before the zwitterion was fully formed. This implies a primary kinetic isotope effect; however, the calculations reported here suggest that the proton transfer will be very little advanced at the transition state and so the primary isotope effect will be very small. Secondary solvent isotope effects could give rise to an effect somewhat larger than that observed; a plausible estimate leads to a value of 2.6. Estimation of kinetic isotope effects is found in Appendix S1.[3] No model could be found, even with rather extreme assumptions about solvation requirements, which could overcome the high barriers to distortion of the rigid ketene and ketene hydrate structures and allow nucleophilic attack on the carbonyl as rate-limiting process to have a lower free energy of activation than attack on CH_2. It should be noted that Multidimensional Marcus Theory, using the average intrinsic barrier for attack on carbonyls, predicted that nucleophilic attack would be competitive with protonation by water (again using an average intrinsic barrier, derived from enol ether protonation reactions) and actually would be the preferred path. Other than this one case, the conclusions from the present study are in full agreement with those reached by other workers.

In a number of cases Kresge and co-workers (46–50) have shown that substituted ketones do add water to give enols of carboxylic acids. These are strongly perturbed systems, with substituents known to stabilize enols, and might well have reversals in relative rates of the two modes of reaction. The two modes of reaction of water with ketene are found to be competitive by both theories employed in the present work.

Gas phase calculations on the uncatalyzed hydration of ketene favor the carbonyl attack option rather that $C{=}CH_2$ attack (39, 51, 52). However, the calculated preference depends on the basis set used; the transition state for C=O addition is lower than that for $C{=}CH_2$ addition by 11 kcal at STO-3G (39), 10 kcal at RHF 3-21G (51), and by only 1.9 kcal at MP4(SDTQ)/6-31G*//RHF/6-31G* (52). In solution the situation appears to be reversed, and the No Barrier Theory calculations reported here show $C{=}CH_2$ attack favored over C=O attack. This seems reasonable enough because ionic intermediates or very polar transition states are much less unfavorable in polar solvent than in the gas phase. In the case of very highly hindered ketenes, bis(pentamethylphenyl)ketene and bismesitylketene, the initial products were shown to be the ene-1,1-diols. It does not seem surprising that crowding in these very hindered compounds should have caused a switch in the relative rates of the two modes of reaction.

The conclusion from the calculations reported in this work concerning acid-catalyzed hydration of ketene, namely, that the mechanism involves protonation at carbon, leading initially to acetylium ion, is in full accord with the accepted mechanism (2, 40, 41).

In constructing models for these reactions it was assumed that water is in contact with reactants, and that, at negligible cost in free energy, it will at least part of the time have H's directed at even weakly negative atoms, so that hydrogen bonding can develop as reaction proceeds, to yield fully solvated products. It was also assumed that the Stahl–Jencks equation (53) can be used to estimate the strengths of hydrogen bonds, even those involving hydrogen acids, provided vertical pK_a's are used, corresponding to the hypothetical dissociation of H^+ with no geometry change at carbon. This assumption has been used in a treatment of enolate-forming reactions (6). In the present context it means that acetylium ion is solvated to a significant extent by hydrogen bonding to the CH's, for which the vertical pK_a is 15.7 (the equilibrium pK_a is 3.3).

The rates of hydration reactions of these two unusual compounds, CO_2 and ketene, have been successfully calculated by No Barrier Theory, which uses no kinetic information in the calculation of $\Delta G^{\neq}$. These reactions could also be treated by Marcus Theory or Multidimensional Marcus Theory even though it seemed unlikely that the intrinsic barriers determined for simple carbonyl compounds would also apply to these *sp* hybridized carbon centers.

The enol content of acetic acid has been determined by indirect thermodynamic calculations (16, 18) and by molecular orbital calculations (54). The two approaches are in good agreement.

There are two problems with the No Barrier Theory treatment for the reactions of ketene. The calculations on the uncatalyzed reaction did not lead to a value in satisfactory agreement with experiment; the error was 3.5 kcal/mol, where normally the theory leads to values within 2 kcal/mol of the observed value. Since the best algorithm that we have devised so far for searching hyperspace did not lead to a value for the full six-reaction coordinate system as low as could be found by manual search of lower dimensional subsections, it seems clear that the algorithm is failing in this high-dimensional space. Thus it is still possible that there is a concerted path through the reaction hyperspace that has not yet been found. There is also a problem with the hydroxide-catalyzed reaction where the disagreement is also disappointingly large. One possibility that must be considered is that the assumption of a desolvation cost for bringing a

[4] I thank a referee for suggesting that rate-limiting attack of hydroxide on acetylium could lead to the observed solvent deuterium isotope effect.

© 1999 NRC Canada

hydroxide ion into contact with a carbonyl group may not be correct. On general principles this had seemed a valid assumption but direct evidence is hard to find. It may be that the polar nature of C=O is such that there is no such desolvation cost, and other interactions balance the missing hydrogen bond. If the calculations are carried out with no such desolvation cost, the only significant changes are in the free energies of activation for the reaction of hydroxide with CO_2 and ketene, which become 10.84 and 10.98 kcal/mol, respectively. Both are in good agreement with experiment. Clearly a reexamination of the assumption concerning desolvation of hydroxide is in order.

Despite these difficulties, No Barrier Theory permits calculation of free energies of activation with useful precision, and requires only calculation of some distortion energies, which demand only relatively low levels of molecular orbital theory. Direct attack on the problem, by calculating transition state structures and energies by ab initio methods with full incorporation of solvation effects, is far more demanding of CPU time. For example, Nguyen et al. (37) were able to come within a few kcal of the transition state energy (23.8 calcd., vs. 19.6 expt.), but this required QCISD(T)/6-31G**//MP2/6-31G** calculations combined with Monte Carlo and reaction field simulations.

Acknowledgments

I thank the Natural Sciences and Engineering Research Council of Canada for financial support of this work. I thank Professor A.J. Kresge, University of Toronto, for communicating a preliminary value of the rate constant for the reaction of hydroxide with ketene prior to its publication.

References

1. E. Bothe, A.M. Dessouki, and D. Schulte-Frohlinde. J. Phys. Chem. **84**, 3270 (1980).
2. J. Andraos and A. Kresge. J. Photochem. Photobiol. A: **57**, 165 (1991).
3. F. Roughton. Harvey Lect. 96 (1943).
4. Y. Pocker and D. Bjorkquist. J. Am. Chem. Soc. **99**, 6537 (1977).
5. J.P. Guthrie and V. Pitchko. Submitted for publication.
6. J.P. Guthrie. J. Phys. Org. Chem. **11**, 632 (1998).
7. J.P. Guthrie. J. Am. Chem. Soc. **120**, 1688 (1997).
8. A.O. Cohen and R.A. Marcus. J. Phys. Chem. **72**, 4249 (1968).
9. R.A. Marcus. Annu. Rev. Phys. Chem. **15**, 155 (1964).
10. R.A. Marcus. J. Am. Chem. Soc. **91**, 7224 (1969).
11. J.P. Guthrie. J. Am. Chem. Soc. **118**, 12878 (1996).
12. J.B. Pedley, R.D. Naylor, and S.P. Kirby. Thermochemical data of organic compounds. Chapman and Hall, London. 1986.
13. D.R. Stull, E.F. Westrum, and G.C. Sinke. The chemical thermodynamics of organic compounds. Wiley, New York. 1967.
14. D.D. Wagman, W.H. Evans, V.B. Parker, R.H. Schumm, I. Halow, S.M. Bailey, K.L. Churney, and R.L. Nuttall. J. Phys. Chem. Ref. Data 11, Suppl. 2, (1982).
15. J.P. Guthrie. Can. J. Chem. **70**, 1042 (1992).
16. J.P. Guthrie and Z. Liu. Can. J. Chem. **73**, 1395 (1995).
17. V.G. Bova, D.A. Kuznetsov, I.E. Furmer, and V.I. Sasov. Zh. Prikl. Khim. (S.-Peterburg), **47**, 701 (1974).
18. J.P. Guthrie. Can. J. Chem. **71**, 2123 (1993).
19. J.P. Guthrie and D.C. Pike. Can. J. Chem. **65**, 1951 (1987).
20. N.C. Deno, C.U. Pittman, and M.J. Wisotsky. J. Am. Chem. Soc. **86**, 4370 (1964).
21. J. Long and B. Munson. J. Am. Chem. Soc. **95**, 2427 (1973).
22. W.R. Davidson, Y.K. Lau, and P. Kebarle. Can. J. Chem. **56**, 1016 (1978).
23. M.J. Frisch, G.W. Trucks, H.B. Schlegel, P.M.W. Gill, B.G. Johnson, M.A. Robb, J.R. Cheeseman, T. Keith, G.A. Petersson, J.A. Montgomery, K. Raghavachari, M.A. Al-Laham, V.G. Zakrzewski, J.V. Ortiz, J.B. Foresman, J. Cioslowski, B.B. Stefanov, A. Nanayakkara, M. Challacombe, C.Y. Peng, P.Y. Ayala, W. Chen, M.W. Wong, J.L. Andres, E.S. Replogle, R. Gomperts, R.L. Martin, D.J. Fox, J.S. Binkley, D.J. Defrees, J. Baker, J.P. Stewart, M. Head-Gordon, C. Gonzalez, and J.A. Pople. Gaussian 94. Revision E.1. Gaussian, Inc., Pittsburgh, Pa. 1995.
24. N.C. Deno, R.W. Gaugler, and M.J. Wisotsky. J. Org. Chem. **31**, 1967 (1966).
25. Y. Chiang, A.J. Kresge, P. Pruszynski, N.P. Schepp, and J. Wirz. Angew. Chem. Int. Ed. Engl. **29**, 792 (1990).
26. J.R. Keeffe and A.J. Kresge. *In* The chemistry of enols. *Edited by* Z. Rappoport. Wiley, Chichester. 1990. pp. 399–480.
27. P. Ballinger and F.A. Long. J. Am. Chem. Soc. **81**, 1050 (1959).
28. W.P. Jencks and J. Regenstein. *In* Handbook of biochemistry and molecular biology. Vol. 1. *Edited by* G. Fassman. Chemical Rubber Company, Cleveland, ohio. 1976. pp. 305–351.
29. E.M. Arnett and C.Y. Wu. J. Am. Chem. Soc. **82**, 5660 (1960).
30. J.P. Guthrie. J. Am. Chem. Soc. **100**, 5892 (1976).
31. J.P. Guthrie. J. Am. Chem. Soc. **100**, 5892 (1978).
32. J. Fastrez. J. Am. Chem. Soc. **99**, 7004 (1977).
33. D.D. Perrin, B. Dempsey, and E.P. Serjeant. pK_a prediction for organic acids and bases. Chapman and Hall, London. 1981.
34. S.W. Benson. Thermochemical kinetics. Wiley, New York. 1976.
35. J.P. Guthrie. J. Am. Chem. Soc. **113**, 3941 (1991).
36. J.P. Guthrie. Submitted.
37. M. Nguyen, G. Raspoet, L. Vanquickenborne, and P.T. VanDuijnen. J. Phys. Chem. A, **101**, 7379 (1997).
38. H.R. Seikaly and T.T. Tidwell. Tetrahedron, **42**, 2587 (1986).
39. M.T. Nguyen and A.F. Hegarty. J. Am. Chem. Soc. **106**, 1552 (1984).
40. T. Tidwell. Acc. Chem. Res. **23**, 273 (1990).
41. A.D. Allen and T.T. Tidwell. J. Am. Chem. Soc. **109**, 2774 (1987).
42. A.D. Allen, A.J. Kresge, N.P. Schepp, and T.T. Tidwell. Can. J. Chem. **65**, 1719 (1987).
43. S.H. Kabir, H.R. Seikaly, and T.T. Tidwell. J. Am. Chem. Soc. **101**, 1059 (1979).
44. A.D. Allen, A. Stevenson, and T.T. Tidwell. J. Org. Chem. **54**, 2843 (1989).
45. J. Andraos, A.J. Kresge, M.R. Peterson, and I.G. Csizmadia. J. Mol. Struct. (Theochem), **232**, 155 (1991).
46. A. Kresge. Chem. Soc. Rev. **25**, 275 (1996).
47. Y. Chiang, A.J. Kresge, P. Pruszynski, N.P. Schepp, and J. Wirz. Angew. Chem. Int. Ed. Engl. **29**, 792 (1990).
48. J. Andraos, Y. Chiang, A. Kresge, I. Pojarlieff, N. Schepp, and J. Wirz. J. Am. Chem. Soc. **116**, 73 (1994).
49. J. Andraos, Y. Chiang, C. Huang, A. Kresge, and J. Scaiano. J. Am. Chem. Soc. **115**, 10 605 (1993).
50. J. Almstead, B. Urwyler, and J. Wirz. J. Am. Chem. Soc. **116**, 954 (1994).
51. B. Allen, A. Hegarty, P. Oneill, and M. Nguyen. J. Chem. Soc. Perkin Trans. 2, 927 (1992).
52. P. Skancke. J. Phys. Chem. **96**, 8065 (1992).
53. N. Stahl and W.P. Jencks. J. Am. Chem. Soc. **108**, 4196 (1986).
54. S. Sklenak, Y. Apeloig, and Z. Rappoport. J. Am. Chem. Soc. **120**, 10 359 (1998).

© 1999 NRC Canada

Exploring zero-point energies and hydrogen bond geometries along proton transfer pathways by low-temperature NMR

Sergei N. Smirnov, Hans Benedict, Nikolai S. Golubev, Gleb S. Denisov, Maurice M. Kreevoy, Richard L. Schowen, and Hans-Heinrich Limbach

Abstract: We have followed by NMR the zero-point energy changes of the hydrogen bond proton in 1:1 acid–base complexes AHB ≡ {A—H···B ↔ $A^{\delta-}$···H···$\overset{\delta+}{B}$ ↔ A^{-}···H—B^{+}} as a function of the proton position between A and B. For this purpose, the isotopic fractionation factors *K* between the acid–base complexes AHB + Ph_3COD···B ⇆ ADB + Ph_3COH···B, where AH represents a variety of acids and B represents pyridine-^{15}N, were measured around 110 K, using a 2:1 mixture of liquefied $CDClF_2$–CDF_3 as solvent. As under these conditions the slow hydrogen bond exchange regime is reached, the values of *K* could be obtained directly by integration of appropriate proton NMR signals. Using the valence-bond order concept established previously by crystallography, the fractionation factors and corresponding zero-point energy changes (ΔZPE) are related in a quantitative way to the hydrogen bond geometries, the ^{1}H chemical shift of the hydrogen bond proton, and the pyridine-^{15}N chemical shift. The *K* values are related in a quasi-linear way to the chemical shifts of the hydrogen bond proton, where the slope depends on whether the proton is closer to oxygen or nitrogen. In the region of the strongly hydrogen-bonded quasi-symmetric complexes, which are characterized by a strong hydrogen bond contraction, the variation of *K* is very small in spite of substantial proton displacements.

Key words: NMR, isotopic fractionation, hydrogen bonding, acid–base complexes, proton transfer, geometric isotope effects.

Résumé : Faisant appel à la RMN, on a suivi les changements d'énergie du point zéro du proton de la liaison hydrogène de complexes acide–base 1 : 1 AHB ≡ {A—H···B ↔ $A^{\delta-}$···H···$\overset{\delta+}{B}$ ↔ A^{-}···H—B^{+}} en fonction de la position du proton entre A et B. À cette fin, opérant à environ 110 K et utilisant un mélange 2 : 1 liquéfié de $CDClF_2$: CDF_3 comme solvant, on a mesuré les facteurs de fractionnement isotopiques, *K*, entre les complexes acide–base, AHB + Ph_3COD···B ⇆ ADB + Ph_3COH···B, dans laquelle AH représente une variété d'acides et B correspond à pyridine-^{15}N. Dans de telles conditions, on atteint un régime d'échange lent de la liaison hydrogène et il est possible de déduire les valeurs de *K* directement par intégration des signaux RMN des protons appropriés. Utilisant le concept d'ordre de la liaison de valence mis au point antérieurement par cristallographie, on peut établir une corrélation quantitative entre les facteurs de fractionnement ou les changements correspondants dans les énergies de point zéro (« ΔZPE ») et les géométries de la liaison hydrogène, le déplacement chimique ^{1}H du proton de la liaison hydrogène et le déplacement chimique de la pyridine-^{15}N. On peut établir une corrélation pratiquement linéaire entre les valeurs de *K* et les déplacements chimiques du proton de la liaison hydrogène; la pente dépend de la distance entre le proton et l'oxygène ou l'azote. Dans la région de forte liaison hydrogène où les complexes sont pratiquement symétriques et qui est caractérisée par une forte contraction de la liaison hydrogène, la variation de *K* est très faible malgré le fait que les déplacements de proton soient importants.

Mots clés : RMN, fractionnement isotopique, liaison hydrogène, complexes acide–base, transfert de proton, effets isotopiques géométriques.

[Traduit par la Rédaction]

Received January 9, 1999.

This paper is dedicated to Jerry Kresge in recognition of his many achievements in chemistry.

S.N. Smirnov and N.S. Golubev. Institut für Organische Chemie, Freie Universität Berlin, Takustrasse 3, D-14195 Berlin, Germany, and the Institute of Physics, St. Petersburg State University, 198904 St. Petersburg, Russian Federation.
H. Benedict, and H.-H. Limbach.[1] Institut für Organische Chemie, Freie Universität Berlin, Takustrasse 3, D-14195 Berlin, Germany.
G.S. Denisov. Institute of Physics, St. Petersburg State University, 198904 St. Petersburg, Russian Federation.
M.M. Kreevoy. Department of Chemistry, University of Minnesota, Kolthoff & Smith Halls, 207 Pleasant Street, Minneapolis, MN 55455, U.S.A.
R.L. Schowen. Departments of Chemistry and Biochemistry, University of Kansas, Lawrence, KS 66045, U.S.A.

[1]Author to whom correspondence may be addressed. Fax: 49 30 838-5310. e-mail: limbach@chemie.fu-berlin.de

 © 1999 NRC Canada

Introduction

It has been known for a long time that H/D isotopic fractionation between different proton donor sites is mainly caused by zero-point energy changes between the sites (1). The measurement of fractionation factors using a variety of methods is, therefore, an established tool of isotopic research (2). On the other hand, fractionation factor theory in combination with transition state theory constitutes the classical theory of kinetic H/D isotope effects of proton transfer reactions (1, 3). However, proton tunneling through the reaction barrier is another source of kinetic isotope effects (4), and it is thus often difficult from an experimental standpoint to decide which effect causes the observed kinetic H/D isotope effects. As proton transfer is an elementary step of many organic and biochemical reactions (5–7) and is interesting from a theoretical standpoint, it would be desirable if one could follow directly the proton transfer pathways and the associated zero-point energy changes. Since this is experimentally very difficult, the study of model hydrogen-bonded systems is of great help where each system models a typical point or region of the reaction coordinate. For example, using a series of hydrogen-bonded anions, Kreevoy and Liang (2*a*) determined fractionation factors as a function of the hydrogen bond geometry using UV spectroscopy. However, using this method it is difficult to follow, at the same time, changes in the hydrogen bond geometries.

Recently some of us (8) have proposed a model series for the pathway of a proton from an acid (AH) to a base (B) that can conveniently be studied by low-temperature liquid state NMR (9) around 110 K using liquefied deuterated gases as solvents. This method allows one to distinguish different hydrogen-bonded species $(AH)_nB_m$ in the slow-exchange regime, in contrast to the usual NMR spectroscopy where only average signals are observed. Thus, the NMR properties of simple neutral 1:1 complexes of the type AHB ≡ {A—H···B ↔ $A^{\delta-}\cdots H\cdots B^{\delta+}$ ↔ $A^-\cdots H$—B^+} could be studied, in which the proton was gradually displaced from the acid AH to the acceptor B, ≡ pyridine-^{15}N, by changing the proton-donating power of AH. The optical spectroscopy of such complexes is well known (for references concerning properties of pyridine – carboxylic acid complexes, see ref. 10). During this displacement, characteristic changes of NMR chemical shifts and coupling constants were observed, including H/D isotope effects in the former that were qualitatively related to associated changes of the hydrogen bond geometries (8*d*). Such effects were quantified in other model systems using solid state NMR and theoretical methods (11).

In this paper we extend the low-temperature NMR technique to the measurement of the equilibrium constants *K* of isotopic fractionation between AHB with respect to a reference XH or XHB. Therefore, the fractionation factors measured here are defined by the equations

$$[1] \qquad AHB + XDB \overset{K}{\rightleftarrows} ADB + XHB$$

$$[2] \qquad K = \frac{x_{XHB}\, x_{ADB}}{x_{XDB}\, x_{AHB}} \approx \exp\left(-\Delta ZPE/RT\right)$$

R is the gas constant, *T* the temperature, *x* the mole fractions or concentrations, and ΔZPE the zero-point energy difference given by

$$[3] \qquad \Delta ZPE = ZPE(XHB) - ZPE(XDB) + ZPE(ADB) - ZPE(AHB)$$

The idea was that using the low-temperature NMR technique it should be possible to determine *K* directly by integration of appropriate NMR signals as the slow hydrogen bond and proton exchange regime can be reached. However, as this concept had not yet been realized, the setup of the technique was not trivial. Especially difficult was the choice of the reference proton donor XH. We tried out different acids and found that acetic acid (AcOH) is a good choice from the standpoint of the experimental technique. In a later stage of this study we found that triphenylmethanol is a reference that is more closely related than AcOH to the usual standard, water, because the fractionation factor of Ph_3COH in acetonitrile with respect to water is unity; moreover, this alcohol shows little evidence of self-association (2*a*). Thus we succeeded in measuring *K* for a number of AHB complexes with respect to the 1:1 complex of Ph_3COH with pyridine.

In the following, after a short experimental section, the results are presented and discussed qualitatively in terms of an appropriate hydrogen bond geometry correlation analysis.

Experimental section

All NMR experiments reported in this paper were performed on a Bruker NMR AMX 500 instrument operating at 500.13 MHz for ^{1}H. The details of these experiments have been reported previously (8*d*). Pyridine-^{15}N (95% enriched) was purchased from Chemotrade, Leipzig, Germany. CH_3COOD was purchased from Aldrich; the other acids were deuterated using either D_2O or CH_3OD. The deuterated freon solvent mixture $CDClF_2$:CDF_3 (2:1) freezes below 90 K. It was synthesized, as described previously (9), at 100°C and elevated pressures (between 30 and 60 bar (1 bar = 100 kPa)) from $CDCl_3$ via fluorination with $SbF_3/SbCl_5$. The solvent was handled on a vacuum line and stored over basic alumina in order to remove traces of acids and water. The vacuum line also served to prepare the samples using well-established techniques (4*d*). No special effort was made to remove water from the solutes employed as water traces precipitate in freons at low temperature. Each sample consisted of comparable amounts of the partially deuterated acid for which the fractionation factor was to be determined, of acetic acid-*d*, of a small excess of pyridine-^{15}N with respect to both acids, and of about 0.5 mL of the solvent. The concentrations of the solutes refer to room temperature and were determined prior to the sample preparation either by weighing, in the case of solids, or by volumetric measurements on the vacuum line in the case of liquid components as described previously (4*d*). The fractionation factors *K* for a given complex AHB referring to $Ph_3COH\cdots B$ were determined from the low-temperature ^{1}H NMR spectra using the equation

$$[4] \qquad K' = K/K'(Ph_3COH) = \frac{I_{CH}\left(I_{CH} - I_{AHB}\right)}{I_{AHB}\left(I_{CH3}/3 - I_{AcHB}\right)}$$

© 1999 NRC Canada

which can easily be derived from eq. [2]. $K'(Ph_3COH)$ is the H/D-fractionation factor for $Ph_3COH\cdots B$ with respect to the acetic acid – pyridine complex, I_{CH3} the intensity of the methyl group signal of acetic acid, I_{CH} the sum of the intensities of the CH proton signals for AHB and ADB, I_{AcHB} the intensity of the H-bonded proton signal for the 1:1 acetic acid – pyridine complex, I_{AHB} the intensity of the H-bonded proton signal for AHB. The relative solute mole fractions determined by signal integration of the low-temperature spectra were slightly different from those calculated from the total concentrations determined as described above. However, as the absolute concentrations do not enter eq. [4] and as small variations of the concentrations do not affect the intrinsic chemical shifts of the acid–base complexes, no attempt was made to determine the correct concentrations, which are also temperature dependent because of the temperature dependence of the solvent density.

Results

Typical low-temperature ^1H NMR spectra of equilibrated solutions containing a partially deuterated acid, AL (L = H, D), a comparable amount of CH_3COOL (AcOL), and of pyridine-^{15}N in small molar excess over both acids combined, dissolved in a 2:1 mixture of liquefied $CDClF_2$:CDF_3, are shown in Figs. 1*a* and 1*b*. Under these conditions the acids form only 1:1 complexes with pyridine, B (8*d*), and the complexation of the acids is essentially complete. Each solution gives rise to two low-field signals in its ^1H NMR spectrum: one for AHB and one for the complex with acetic acid, AcOHB. As the slow hydrogen bond regime is reached, the chemical shifts observed are the intrinsic values referring to the 1:1 complexes and are not affected by small concentration variations. As discussed previously (8*e*, 8*h*), the intrinsic chemical shifts depend on temperature because of a temperature-dependent solvent ordering causing changes in the hydrogen bond geometries. The mobile protons in the two sites exchange slowly on the timescale of seconds, as shown by a differential NOE experiment depicted in Fig. 1*c*, where the acetic acid peak at 17.65 ppm was irradiated and a positive formic acid – pyridine peak at 21 ppm indicated a slow magnetization transfer by chemical exchange between the two mobile proton sites. However, the exchange is complete on the timescale of many minutes, as shown by the invariance with time of the relative integrated areas. The fractionation factors are easily obtained by signal integration using eq. [4]. The results of the measurements are assembled in Table 1 and Fig. 2, which contain also the ^1H and ^{15}N chemical shifts reported previously (8d); the shifts of triphenylmethanol, methylaniline, and 4-*tert*-butylphenol were determined in this study.

Discussion

We have measured the H/D fractionation factors *K* of 1:1 hydrogen-bonded complexes of various proton donors with pyridine by low-temperature NMR spectroscopy in the slow hydrogen bond exchange regime, using Ph_3COH with an excess of pyridine as a reference. We note from Table 1 that the OH chemical shift of this donor is around 10 ppm at 112 K, as compared to the neat compound exhibiting an OH

Fig. 1. Partial 500 MHz ^1H NMR spectra of solutions of pyridine-^{15}N (B)/acetic acid (AcOH)/variable acid AH in a 2:1 mixture of $CDClF_2$:CDF_3 at non-zero deuterium fractions *D* in the mobile proton sites. (*a*) AH ≡ dichloroacetic acid, uncorrected concentrations at room temperature C_B = 0.058, $C_{AH} + C_{AD}$ = 0.011 mol L^{-1}, $C_{AcOH} + C_{AcOD}$ = 0.038 mol L^{-1}, *T* = 107 K. (*b*) AH ≡ formic acid, uncorrected concentrations at room temperature C_B = 0.033 mol L^{-1}, $C_{AH} + C_{AD}$ = 0.019 mol L^{-1}, $C_{AcOH} + C_{AcOD}$ = 0.011 mol L^{-1}, *T* = 109 K. (*c*) NOE difference spectrum of the sample in Fig. 1*b*, where the hydrogen-bonded proton of acetic acid at 17.65 ppm was irradiated.

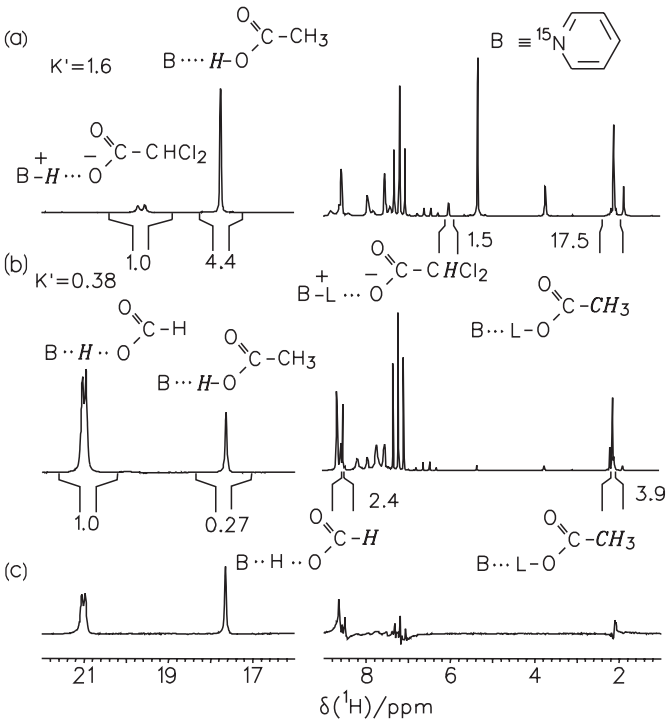

chemical shift of about 5 ppm at room temperature. The ^{15}N chemical shift of pyridine in the presence of Ph_3COH is slightly shifted upfield, indicating that Ph_3COH forms a weak 1:1 hydrogen bond with pyridine. Therefore, we conclude that the complex $Ph_3COH\cdots B$ is the true reference for the fractionation factors *K*, as indicated by eqs. [1] and [2]. As the fractionation factor between Ph_3COH and water in acetonitrile is close to unity (2*a*), the fractionation factors reported here are good estimates for those referring to water.

To facilitate the discussion of our results we first review the concept of the valence bond order for the estimation of hydrogen bond geometries. This concept goes back to the valence bond – length relationship developed by Pauling and Brown (14). It states that one can associate with any bond between two atoms *i* and *j* an empirical valence bond order p_{ij}, which decays exponentially with the bond distance r_{ij}, i.e.,

$$[5] \qquad p_{ij} = \exp\{-(r_{ij} - r_{ij}^0)/b_{ij}\}$$

where b_{ij} is a decay parameter and r_{ij}^0 the distance where $p_{ij} = 1$. A hydrogen-bonded system, e.g., an O—H···N hydrogen bond (Scheme 1), is then characterized by two bond orders p_{OH} and p_{HN} involving the hydrogen-bonded proton. As the total valency of hydrogen is unity,

© 1999 NRC Canada

Table 1. Fractionation factors and chemical shifts of 1:1 hydrogen-bonded complexes of acids AH with pyridine-^{15}N (B) dissolved in a 2:1 mixture of $CDClF_2$:CDF_3.[a]

AH	pK_a (ref.)	C_{AL}	C_{AcOL}	C_B	T/K	δ(^{1}H)	δ(^{15}N)	K'[c]	K
Triphenylmethanol	12.9 (13*a*)	0.025	0.018	0.045	112	9.95	–7.0[b]	2.8	1.0
4-*tert*-Butylphenol	10.23 (13*b*)	0.013	0.014	0.032	108	13.264	–16.0	1.94	0.69
Acetic acid	4.75 (13*c*)	0.037	0.037	0.07	111	17.65	–27.9	1.00	0.36
o-Toluic acid	3.91 (13*c*)	0.012	0.011	0.027	107	19.202	–33.7	0.66	0.24
3-Br-propionic acid	3.89 (13*d*)	0.014	0.014	0.030	108	19.949	–41.6	0.52	0.19
Formic acid	3.75 (13*c*)	0.019	0.011	0.033	109	21.009	–59.0	0.38	0.14
2-Furoic acid	3.17 (13*e*)	0.020	0.036	0.064	107	21.467	–70.8	0.52	0.19
Chloroacetic acid	2.85 (13*c*)	0.017	0.020	0.048	107	20.824	–79.5	0.76	0.27
Dichloroacetic acid	1.48 (13*c*)	0.011	0.038	0.058	107	19.637	–89.4	1.6	0.57
N-Methylaniline	29.5 (13*f*)	0.017	0.015	0.037	111	3.95	–0.01	2.8	1.0

[a] $C_{AL} = C_{AH} + C_{AD}$ and C_B total concentrations (uncorrected, see experimental section) of the acid AH and of pyridine–^{15}N in mol L^{-1} determined at room temperature. AcOH ≡ acetic acid. The chemical shifts δ(^{1}H) and δ(^{15}N) are taken from ref. 8*d*, with the exception of those of *N*-methylaniline, triphenylmethanol, and 4-*tert*-butylphenol (this study).

[b] 1:1 Ph_3COH:pyridine-^{15}N complex in CD_2Cl_2, 170 K. The δ(^{15}N) are referenced to internal or free pyridine, where δ(CH_3NO_2) = δ(C_5H_5N) – 69.2 ppm, and δ(NH_4Cl) = δ(CH_3NO_2) – 338 ppm (12). The pK_a values were taken from ref. 13 and refer to aqueous solutions at 298 K.

[c] *K'*: fractionation factor referred to the 1:1 complex of acetic acid with pyridine and *K:* fractionation factor referred to the triphenylmethanol–pyridine complex. The errors in the fractionation factors could not be determined precisely, but are estimated in the region of 10–20%.

Fig. 2. (*a*) Hydrogen bond correlation curve for (dotted line) 1:1 hydrogen-bonded acid–base complexes according to refs. 8*d* and 11*b*. $q_2 = r_1 + r_2$ represents the heavy atom distance for the case of a linear hydrogen bridge, $q_1 = 1/2(r_1 - r_2)$ the proton transfer coordinate. The filled circles represent the geometries of the corresponding chemical shift data points in Fig. 2*b*. (*b*) Low-temperature NMR chemical shifts of the hydrogen bond proton in 1:1 complexes between acids and pyridine-^{15}N dissolved in a 2:1 CDF_2Cl:CDF_3 mixture as a function of the ^{15}N chemical shifts. Reference: solid NH_4Cl, where δ(NH_4Cl) = δ(CH_3NO_2) – 353 ppm (12). In the initial measurement (8*d*) internal pyridine-^{15}N was used as a reference, where δ(CH_3NO_2) = δ(C_5H_5N) – 69.2 ppm. (*c*) Corresponding fractionation factors *K* (circles) and zero-point energy differences ΔZPE (squares) as a function of the ^{15}N chemical shifts. (*d*) Fractionation factors *K* as a function of the proton chemical shifts. The dotted lines in (*b*) to (*c*) were calculated as described in the text. The broken limits correspond to infinite values of q_1 and q_2.

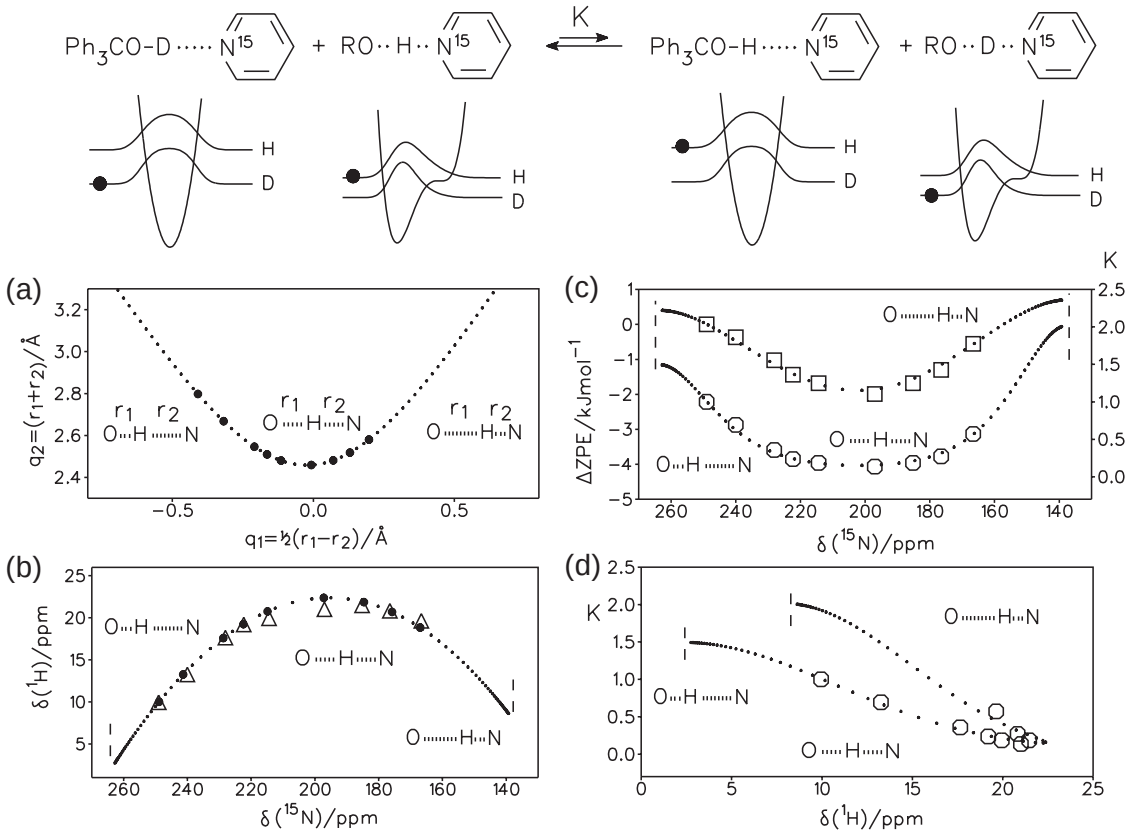

© 1999 NRC Canada

Scheme 1.

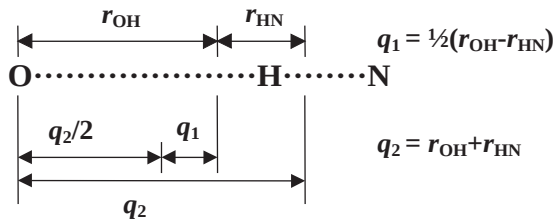

$$[6] \quad p_{OH} + p_{HN} = 1 = \exp\{-(r_{OH} - r_{OH}^0)/b_{OH}\} + \exp\{-(r_{HN} - r_{HN}^0)/b_{HN}\}$$

it follows that the two bond distances r_{OH} and r_{HN} cannot be varied independently. Naturally, this prediction implies at the same time a correlation between q_1 and q_2, defined in Scheme 1. For a linear hydrogen bond, q_1 corresponds to the distance of the proton or deuteron from the center of the hydrogen bond, i.e., it represents the proton transfer coordinate, and q_2 is equal to the A···B distance (11*b*) The dependence of q_1 as a function of q_2 can be obtained easily from the definition in Scheme 1 and eq. [6].

Hydrogen bond correlations have been established by crystallography (15) by comparing the neutron crystal structures of a large number of systems exhibiting hydrogen bonds of weak and medium strength. The curves depend only on the type of donor and acceptor atoms, i.e., OHO, OHN, and NHN bonds exhibit different parameters in eq. [6]. The NHN bond correlation has been verified by some of us (11*b*) using solid state NMR and theoretical calculations. In conclusion, the valence bond order model does not distinguish qualitatively but only quantitatively between the covalent bond and the hydrogen bond.

For the case of O—H···N bonds, Steiner (15*d*) has proposed the parameter set $r_{OH}^0 = 0.942$ Å, $r_{HN}^0 = 0.992$ Å, $b_{OH} = 0.371$ Å, $b_{HN} = 0.385$ Å. Using these values, we have calculated the correlation curve $q_1 = f(q_2)$ depicted in Fig. 2*a*. The curve indicates that when the proton is transferred from O to N the O···N distance first shortens, then reaches a minimum in the quasi-symmetric complex, and finally widens again as the zwitterionic complex is approached.

Figure 3 shows in more detail, in a qualitative way, what exactly may happen during the transfer process. Two limiting cases are represented. In Fig. 3*a* the proton exhibits a medium barrier for proton transfer at the quasi-symmetric midpoint whereas such a barrier is absent in Fig. 3*b*. In the case of Fig. 3*a* the solute–solvent interaction may easily break the symmetry of the potential, leading to a proton transfer equilibrium between two strongly hydrogen-bonded states, characterized by a common value of q_2 but different values $-q_1$ and $+q_1$, i.e., q_2 will not reach the minimum value. Generally, deuteration leads to a primary geometric H/D isotope effect on q_1 and to a secondary effect on q_2 (8*d*, 11*b*). The latter effect was found by Ubbelohde and Gallagher (16) and is also called the Ubbelohde Effect. If there is a barrier to the proton motion, the secondary isotope effect is always directed in such a way that the A···B distance increases after deuteration. On the other hand, the primary geometric isotope effect implies a larger distance to the hydrogen bond center for the deuteron than for the proton (11*b*). The primary and secondary geometric isotope effects are similar in the no-barrier case of Fig. 3*b*, as well as around the quasi-symmetric midpoint where the A···B distance can contract slightly after deuteration because of the smaller width of the deuteron wave function in the vibrational ground state (12*b*).

Fig. 3. One-dimensional hydron (L = H, D) potentials and geometric changes during the transfer of a hydron from A to B characterized by the reaction coordinate $q_1 = 1/2(r_1 - r_2)$. The squares of the wave functions of the vibrational ground states for H and D, i.e., the proton and deuteron distribution functions, are included. (*a*) Case involving a medium proton transfer barrier at the quasi-symmetric midpoint. (*b*) Case involving a very small or no barrier at the quasi-symmetric midpoint. For further explanation see text. Adapted from ref. 8*d*.

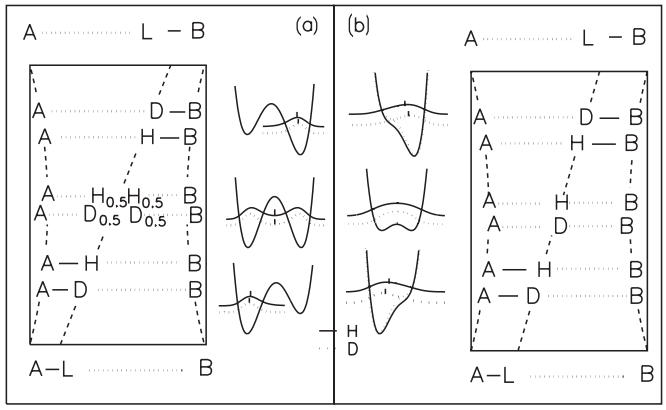

In the latter paper, the hydrogen bond correlation concept was extended to other hydrogen bond properties. Thus, empirical equations were presented relating the geometric H/D isotope effects, zero-point energy changes, ^{1}H and ^{15}N chemical shifts to derivatives, or combinations of various derivatives of the correlation of eq. [7]. However, the equations presented referred only to the symmetric case of NHN hydrogen bonds. Here, we had to treat the unsymmetrical NHO case. During this work we found that it is possible to expand all correlations directly in terms of the valence bond orders, which constitutes a considerable simplification. For example, we observe that the ^{15}N chemical shifts can be expressed by

$$[7] \quad \delta_N = \delta_N^\infty - (\delta_N^\infty - \delta_{HN}^0)p_{HN}$$

$$\delta_N^\infty = 264 \text{ ppm and } \delta_{HN}^0 = 138 \text{ ppm}$$

where the parameters δ_N^∞ and δ_{HN}^0 are the values of free pyridine and of the isolated pyridinium where $r = r_{HN}^0 = 0.992$ Å. For the ^{1}H chemical shifts we find empirically that

$$[8] \quad \delta(^1H) = 4\Delta_H\, p_{OH}\, p_{HN} + \delta_{OH}^0\, p_{OH} + \delta_{HN}^0\, p_{HN}$$

$$\Delta_H = 17.25 \text{ ppm}, \ \delta_{OH}^0 = 2 \text{ ppm, and } \delta_{HN}^0 = 8 \text{ ppm}$$

Δ_H is the excess chemical shift of the quasisymmetric complex and δ_{OH}^0 and δ_{HN}^0 the limiting chemical shifts corresponding to the distances $r_{OH}^0 = 0.942$ Å and $r_{HN}^0 = 0.992$ Å. It is clear that, because of eq.[6], $\delta(^1H)$ must be correlated with $\delta(^{15}N)$, which is indeed the case as depicted by the dotted line in Fig. 2*b*. This curve was generated by calculating

© 1999 NRC Canada

$\delta(^1H)$ and $\delta(^{15}N)$ from an arbitrary grid of q_1 values. The parameters in eqs. [7] and [8] were adjusted by "eye-fitting" the calculated dotted line in Fig. 2*b* to the experimental values taken from ref. 8*d*. The agreement is very satisfactory. We note that the $\delta(^1H)$ vs. $\delta(^{15}N)$ correlation curve exhibits a principal difference from the q_1 vs. q_2 curve of Fig. 2*a* because the distance between the separate residues AH and B can be varied in an infinite number of ways during which their chemical shifts remain constant. Therefore, the dotted correlation line in Fig. 2*b* ends at the left and the right sides as illustrated by the vertical bars. Finally, we note that the experimental chemical shift data of Fig. 2*b* can be easily converted into distances as indicated by the filled circles of Figs. 2*a* and 2*b*.

Let us now discuss the graph of Fig. 2*c* where we have plotted the fractionation factors *K* of Table 1 (lower graph) and the corresponding values of ΔZPE (upper graph), as defined in eq. [2], as a function of $\delta(^{15}N)$. Previously (11*b*), we had noted for the NHN case that ΔZPE is proportional to the square of the second derivative of q_2. Here, we find a simpler equation, valid also in the unsymmetric NHO case, i.e.,

$$[9]\qquad \Delta ZPE = \Delta ZPE^{o}(4p_{OH}p_{HN})^2 + \Delta ZPE(OH)^0 p_{OH} + \Delta ZPE(HN)^0 p_{NH}$$

$$\Delta ZPE^0 = -2.44 \text{ kJ mol}^{-1},$$

$$\Delta ZPE(OH)^0 = +0.4 \text{ kJ mol}^{-1},$$

$$\Delta ZPE(HN)^0 = +0.7 \text{ kJ mol}^{-1}$$

Here, $\Delta ZPE(OH)^0$ and $\Delta ZPE(HN)^0$ are the zero-point energy differences of the limiting states where $r_{OH}{}^0 = 0.942$ Å and $r_{HN}{}^0 = 0.992$ Å with respect to our reference complex $Ph_3COH\cdots B$. ΔZPE^0 determines the total drop of the zero-point energy at the quasi-symmetric midpoint with respect to the limiting states. Again, the parameters of eq. [9] were adapted by eye-fitting the calculated values of ΔZPE as a function of $\delta(^{15}N)$ to the experimental values reported in Table 1, leading to the upper dotted line in Fig. 2*c*. We find that the reference $Ph_3COH\cdots B$ exhibits a small drop in the zero-point energy of 0.4 kJ mol^{-1} with respect to the hypothetical free proton donor ROH. Moreover, the experimental value of ΔZPE^0 is smaller than the value of –4 kJ mol^{-1} calculated previously (11*b*) for the anion $[C{\equiv}N\cdots H\cdots N{\equiv}C]^-$. In this case the situation corresponds to Fig. 3*b*. The lower graph in Fig. 2*c* is the straightforward extension of the upper graph, considering eq. [2] and the average temperature of about 120 K at which the experiments were performed. The fractionation factor of 0.2 at 110 K would correspond to about 0.5 at 298 K. The experimental finding of a reduced isotopic fractionation as compared to $[C{\equiv}N\cdots H\cdots N{\equiv}C]^-$ is then consistent with the situation depicted in Fig. 3*a*, where solute–solvent interactions, however, destabilize the quasi-symmetric configurations, hence leading to a smaller extent of the maximum zero-point energy losses. On the other hand, it could also be that the real drop of the hydrogenic stretching frequency in $[C{\equiv}N\cdots H\cdots N{\equiv}C]^-$ is smaller than was calculated and is partly compensated for by an increased in-plane and (or) out-of-plane bending vibrational frequency that was not included in the calculations of ref. 11*b*.

In any case, Fig. 2*c* indicates a quite flat central region in which the fractionation factors *K* do not exhibit major changes although the proton is displaced by about 0.3–0.4 Å in this region, as estimated from Fig. 2*a*. If we take the series of complexes presented in this paper as models of transition states of proton transfer and the fractionation factors as classical kinetic H/D isotope effects, this result would mean that proton motions in strong hydrogen bonds may fail to appear to be contributing substantially to the overall observed kinetic isotope effect, as discussed recently by some of us (5*m*).

Finally, we have plotted in Fig. 2*d* the experimental fractionation factors as a function of the ^1H chemical shifts. The calculated dotted line was here obtained from eqs. [8] and [9]. We find that, in addition to some curvature, *K* is an almost linear function of $\delta(^1H)$, exhibiting, however, a different slope on both sides of the quasi-symmetric complex characterized by the lowest value of *K* and the largest value of $\delta(^1H)$. The slopes are different depending on whether the proton is closer to oxygen or nitrogen. Thus, $\delta(^1H)$ is a qualitative measure, not only of the A···B distance but also of the fractionation factor.

Conclusions

In conclusion, the development of low-temperature NMR makes it possible not only to obtain information on the geometries and on geometric H/D isotope effects but also of isotopic H/D fractionation in a series of intermolecular low-barrier hydrogen-bonded 1:1 acid–base complexes because the slow hydrogen bond exchange regime is reached. Thus, interesting information can be obtained about zero-point energy changes along the reaction pathways of proton transfer. A task of the future will be to study experimentally the hydrogen bond vibrations in this series and to provide a full theoretical treatment of the experimental findings.

Acknowledgements

We thank the Stiftung Volkswagenwerk, Hannover, the Deutsche Forschungsgemeinschaft, Bonn – Bad Godesberg, the Fonds der Chemischen Industrie, Frankfurt, and the Russian Foundation for Fundamental Research for financial support. R.L.S. thanks the Alexander von Humboldt Foundation, Bonn – Bad Godesberg, for a Humboldt award.

References

1. (*a*) J. Bigeleisen and M. Wolfsberg. Adv. Chem. Phys. **1**, 15 (1958); (*b*) R.A. More O'Ferrall. *In* Proton transfer reactions. *Edited by* E.F. Caldin and V. Gold. Chapman and Hall, London. 1975. Chap. 8. pp. 201–262.
2. (*a*) M.M. Kreevoy and T.M. Liang. J. Am. Chem. Soc. **102**, 361 (1980); (*b*) R. Bone and R. Wolfenden. J. Am. Chem. Soc. **107**, 4772 (1985); (*c*) Y. Chiang, A.J. Kresge, T.K. Chang, M.F. Powell, and J.A. Wells. J. Chem. Soc. Chem. Commun. 1587 (1995); (*d*) S.N. Loh and J.L. Markley. Biochemistry, **33**, 1029 (1994); (*e*) C.H. Arrowsmith, H.X. Guo, and A.J. Kresge. J. Am. Chem. Soc. **116**, 8890 (1994); (*f*) V.J. Shiner, Jr. and T.E. Neumann. Z. Naturforsch. A: Phys. Sci. **44**, 337 (1989);

© 1999 NRC Canada

(*g*) R.M. Jarret and M. Saunders. J. Am. Chem. Soc. **107**, 2648 (1985); (*h*) L. Baltzer and N.A. Bergman. J. Chem. Soc. Perkin Trans. 2, 313 (1982); (*i*) V. Gold and S. Grist. J. Chem. Soc. B: 1665 (1971); (*j*) V. Gold and C. Tomlinson. J. Chem. Soc. B, 1707 (1971); (*k*) J.M.A. Al-Rawi, J.P. Bloxsidge, J.A. Elvidge, J.R. Jones, and R.A. More O'Ferrall. J. Chem. Soc. Perkin Trans. 2, 1593 (1979); (*l*) P. Salomaa. Acta Chem. Scand. **23**, 2095 (1969); (*n*) W.P. Jencks and K. Salvesen. J. Am. Chem. Soc. **93**, 4433 (1971).

3. (*a*) L. Melander. Isotope effects on reaction rates. Ronald, New York. 1960. p. 24; (*b*) F.H. Westheimer. Chem. Rev. **61**, 265 (1961).
4. (*a*) R.P. Bell. The tunnel effect. Chapman and Hall, London. 1980; (b) E. Caldin and V. Gold. Proton transfer. Chapman and Hall, London. 1975; (*c*) L. Melander and W.H. Saunders. Reaction rates of isotopic molecules. John Wiley & Sons, New York, Toronto. 1980; (*d*) H.H. Limbach. NMR, **26**, 66 (1991); (*e*) J. Braun, R. Schwesinger, P.G. Williams, H. Morimoto, D.E. Wemmer, and H.H. Limbach. J. Am. Chem. Soc. **118**, 11101 (1996); (*f*) Ch. Hoelger, B. Wehrle, H. Benedict, and H.H. Limbach. J. Phys. Chem. **98**, 843 (1994).
5. (*a*) C.G. Swain, D.A. Kuhn, and R.L. Schowen. J. Am. Chem. Soc. **87**, 1553 (1965); (*b*) R. Eliason and M.M. Kreevoy. J. Am. Chem. Soc. **100**, 7037 (1978); (*c*) W.W. Cleland and M.M. Kreevoy. Science, **264**, 1887 (1994); (*d*) C.L. Perrin. Science, **266**, 1665 (1994); (*e*) D.M. Blow, J.J. Birktoft, and B.S. Hartley. Nature, **221**, 337 (1969); (*f*) D.M. Blow and T.A. Steitz. Annu. Rev. Biochem. **39**, 63 (1970); (*g*) D. Hadzi. J. Mol. Struct. **177**, 1 (1988); (*h*) R.L. Schowen. *In* Mechanistic principles of enzyme activity. *Edited by* J.F. Liebman and A. Greenberg. VCH Publishers, New York. 1988. p. 119; (*i*) K.B. Schowen and R.L. Schowen. Methods Enzymol. **87**, 551 (1982); (*j*) K.S. Venkatasubban and R.L. Schowen. CRC Crit. Rev. Biochem. **17**, 1 (1984); (*k*) P.F. Cook. Enzyme mechanisms from isotope effects. CRC Press, New York. 1992; (*l*) P.A. Frey, S.A. Whitt, and J.B. Tobin. Science, **264**, 1927 (1994); (*m*) J.A. Bibbs, M.P. Garoutte, B. Wang, P.D. Tittel, K.B. Schowen, and R.L. Schowen. Ber. Bunsen-Ges. Phys. Chem. **102**, 573 (1998).
6. A. Staib, D. Borgis, and J.T. Hynes. J. Chem. Phys. **102**, 2487 (1995), and references cited therein.
7. (*a*) P. Schuster, G. Zundel, and C. Sandorfy (*Editors*). The hydrogen bond. North Holland Publ. Co., Amsterdam. 1976; (*b*) J. Emsley, D.J. Jones, and J. Lucas. Rev. Inorg. Chem. **3**, 105 (1981); (*c*) B.S. Ault. Acc. Chem. Res. **15**, 103 (1982); (*d*) D. Mootz and K. Bartmann. Angew. Chem. **100**, 424 (1988); Angew. Chem. Int. Ed. Engl. **27**, 391 (1988); (*e*) H.J. Berthold, E. Preibsch, and E. Vonholdt. Angew. Chem. **100**, 1581 (1988); Angew. Chem. Int. Ed. Engl. **27**, 1527 (1988); (*f*) F. Hibbert and J. Emsley. Adv. Phys. Org. Chem. **26**, 255 (1990); (*g*) A. Novak. Struct. Bonding (Berlin), **18**, 177 (1974).
8. (*a*) G.S. Denisov, N.S. Golubev, V.A. Gindin, H.H. Limbach, S.S. Ligay, and S.N. Smirnov. J. Mol. Struct. **322**, 83 (1994); (*b*) N.S. Golubev, V.A. Gindin, S.S. Ligay, and S.N. Smirnov. Biochemistry (Moscow), **59**, 447 (1994); (*c*) N.S. Golubev, S.N. Smirnov, V.A. Gindin, G.S. Denisov, H. Benedict, and H.H. Limbach. J. Am. Chem. Soc. **116**, 12055 (1994); (*d*) S.N. Smirnov, N.S. Golubev, G.S. Denisov, H. Benedict, P. Schah-Mohammedi, and H.H. Limbach. J. Am. Chem. Soc. **118**, 4094 (1996); (*e*) N.S. Golubev, G.S. Denisov, S.N. Smirnov, D.N. Shchepkin, and H.H. Limbach. Z. Phys. Chem. **196**, 73 (1996); (*f*) N.S. Golubev, S.N. Smirnov, P. Schah-Mohammedi, I.G. Shenderovich, G.S. Denisov, V.A. Gindin, and H.H. Limbach. Russ. J. Gen. Chem. **67**, 1082 (1997); (*g*) I.G. Shenderovich, S.N. Smirnov, G.S. Denisov, V.A. Gindin, N.S. Golubev, A. Dunger, R. Reibke, S. Kirpekar, O.L. Malkina, and H.H. Limbach. Ber. Bunsen-Ges. Phys. Chem. **102**, 422 (1998); (*h*) N.S. Golubev, I.G. Shenderovich, S.N. Smirnov, G.S. Denisov, and H.H. Limbach. Chem. Eur. J. **5**, 492 (1999).
9. (*a*) G.S. Denisov and N.S. Golubev. J. Mol. Struct. **75**, 311 (1981); (*b*) N.S. Golubev, S.F. Bureiko, and G.S. Denisov. Adv. Mol. Relaxation Interact. Processes, **24**, 225 (1982); (*c*) N.S. Golubev, G.S. Denisov, and E.G. Pushkareva. J. Mol. Liq. **26**, 169 (1983); (*d*) N.S. Golubev and G.S. Denisov. J. Mol. Struct. **270**, 263 (1992).
10. (*a*) Th. Zeegers-Huyskens and P. Huyskens. Mol. Interact. **2**, 1 (1980); (*b*) G. Zundel and J. Fritsch. The Chemical Physics of Solvation, **2**, 21 (1986); (*c*) Z. Dega-Szafran and M. Szafran. Heterocycles, **37**, 627 (1994); (*d*) R. Lindemann and G. Zundel. J. Chem. Soc. Faraday Trans. 2, **68**, 979 (1972); (*e*) J. Chem. Soc. Faraday Trans. 2, **86**, 301 (1990); (*f*) Z. Dega-Szafran, A. Hrynio, and M. Szafran. J. Mol. Struct. **240**, 159 (1990); (*g*) G.V. Gusakova, G.S. Denisov, A.L. Smolyanski, and V.M. Schreiber. Dokl. Akad. Nauk SSSR, **193**, 1065 (1970); (*h*) Z. Dega-Szafran, M. Grunwald-Wyspianska, and M. Szafran. Spectrochim. Acta, Part A: **47A**, 125 (1991); (*i*) L. Sobczyk. J. Mol. Struct. **177**, 111 (1988); (*j*) Z. Dega-Szafran and E. Dulewicz. J. Chem. Soc. Perkin Trans. 2, 345 (1983); (*k*) Z. Dega-Szafran, M. Grunwald-Wyspianska, and M. Szafran. J. Chem. Soc. Faraday Trans. **87**, 3825 (1991); (*l*) S.E. Odinokov, A.A. Mashkovsky, V.P. Glazunov, A.V. Iogansen, and B.V. Rassadin. Spectrochim. Acta, **32A**, 1355 (1976); (*m*) V.P. Glazunov, A.A. Mashkovsky, and S.E. Odinokov. Spectrosc. Lett. **9**, 391 (1976); (*n*) S.E. Odinokov, A.A. Nabiullin, A.A. Mashkovsky, and V.P. Glazunov. Spectrochim. Acta, Part A: **39A**, 1055 (1983); (*o*) L.B. Jerzykiewicz, T. Lis, Z. Malarski, and E. Grech. J. Crystallogr. Spectrosc. Res. **23**, 805 (1993).
11. (*a*) H. Benedict, Ch. Hoelger, F. Aguilar-Parrilla, W.P. Fehlhammer, M. Wehlan, R. Janoschek, and H.H. Limbach. J. Mol. Struct. **378**, 11 (1996); (*b*) H. Benedict, H.H. Limbach, M. Wehlan, W.P. Fehlhammer, N.S. Golubev, and R. Janoschek. J. Am. Chem. Soc. **120**, 2939 (1998); (*c*) M. Ramos, I. Alkorta, J. Elguero, N.S. Golubev, G.S. Denisov, H. Benedict, and H.H. Limbach. J. Phys. Chem. A, **101**, 9791 (1997).
12. (*a*) M. Witanowski, L. Stefaniak, and G.A. Webb. Annu. Rep. NMR Spectrosc. **11** (1981); **(***b*) G. Martin, M.L. Martin, and J.P. Gouesnard. NMR, **18** (1989), and references cited therein.
13. (*a*) W. Saffioti and W.A. Bueno. J. Chim. Phys. Phys.-Chim. Biol. **73**, 731 (1976); (*b*) C.H. Rochester and S.A. Sclosa. J. Chem. Soc. Faraday Trans. 1, **75**, 2781 (1979); (*c*) Handbook of chemistry and physics. 62nd ed. CRC Press Inc., Boca Raton, Fla. 1981–1982. p. D.142; (*d*) K.L. Brown and E. Zahonyi-Budo. Inorg. Chem. **20**, 1264 (1981); (*e*) G. Kortüm, W. Vogel, and K. Angrussow. Dissociation constants of organic acids in aqueous solution. Butterworths, London. 1961; (*f*) In DMSO: F.G. Bordwell, X.M. Zhang, and J.P. Cheng. J. Org. Chem. **58**, 6419 (1993).
14. (*a*) L. Pauling. J. Am. Chem. Soc. **69**, 542 (1947); (*b*) I.D. Brown. Acta Crystallogr. Sect. B: Struct. Sci. **B48**, 553 (1992).
15. (*a*) P. Gilli, V. Bertolasi, V. Ferretti, and G. Gilli. J. Am. Chem. Soc. **116**, 909 (1994); (*b*) Th. Steiner and W. Saenger. Acta Crystallogr. Sect. B: Struct. Sci. **B50**, 348 (1994); (*c*) Th. Steiner. J. Chem. Soc. Chem. Commun. 1331 (1995); (*d*) J. Phys. Chem. A, **102**, 7041 (1998).
16. A.R. Ubbelohde and K.G. Gallagher. Acta Crystallogr. **8**, 71 (1955).

© 1999 NRC Canada

Aminolysis of naphthyl acetates catalyzed by cyclodextrins

Oswald S. Tee and Michael J. Boyd

Abstract: The effects of cyclodextrins (CDs) on the rate of nucleophilic attack on 1- and 2-naphthyl acetates (1-NA and 2-NA) in aqueous solution have been investigated. Analysis of the variation of the pseudo-first-order rate constants with [nucleophile] and [CD] affords rate constants for reaction of the nucleophiles with free ester (k_N) and with ester bound to the CD (k_{cN}). The reaction of 1-NA and 2-NA with the trifluoroethoxide anion is slowed down by β-CD as the ratios k_{cN}/k_N are 0.11 and 0.30, respectively. For reaction with the anion of 2-mercaptoethanol in the presence of α-CD, β-CD, "hydroxypropyl-β-CD" (hp-β-CD) and γ-CD, the reactivity ratios k_{cN}/k_N vary between 0.04 and 2.4, ranging from strong retardation to modest catalysis; the retardations arise with β-CD and hp-β-CD, which bind the esters strongly. By contrast, the attack of primary alkylamines is generally accelerated, and in many cases substantially so. For the aminolysis of 1-NA in the presence of β-CD, values of k_{cN}/k_N range from 7 to 460, assuming that free amine reacts with CD-bound ester. Alternatively, if the CD-catalyzed reaction involves free ester reacting with CD-bound amine, with rate constant k_{Nc}, the ratios k_{Nc}/k_N vary from 43 to 140. *Either way, there is appreciable catalysis of the aminolysis of 1-NA by β-CD*. For the aminolysis of 2-NA, the effects are less dramatic: the ratios k_{cN}/k_N range from 0.19 to 17, and values of k_{Nc}/k_N vary from 17 to 110. The reaction of 1-NA with *n*-hexylamine is also catalyzed by γ-CD. The variations of kinetic parameters with alkylamine chain length suggest that the CD-catalyzed aminolysis basically takes place by the attack of CD-bound amine on the free ester. However, there must be some stabilizing interactions between the aryl group of the ester and the CD during the reaction, since the transition state stabilization is different for 1-NA and 2-NA, as well for other esters.

Key words: aminolysis, catalysis, cyclodextrin, ester cleavage, kinetics.

Résumé : On a étudié les effets de cyclodextrines (CD) sur la vitesse d'attaque nucléophile sur les acétates de 1- et 2-naphtyle (1-NA et 2-NA) en solution aqueuse. Une analyse de la variation des constantes de vitesse de pseudo-ordre un avec les concentrations de nucléophile et de CD permet de déterminer les constantes de vitesse pour la réaction de nucléophiles avec l'ester libre (k_N) et avec l'ester lié à la CD (k_{cN}). La réaction des 1-NA et 2-NA avec l'anion trifluoroéthanolate est ralentie par la β-CD alors que les rapports k_{cN}/k_N sont égaux respectivement à 0,11 et 0,30. Pour la réaction avec l'anion du 2-mercaptoéthanol, en présence d'α-CD, de β-CD, d'hydroxypropyl-β-CD (hp-β-CD) et de γ-CD, les rapports k_{cN}/k_N varient entre 0,04 et 2,4, qui correspondent à des influences qui vont d'un ralentissement important à une catalyse modeste; les retards se produisent avec la β-CD et la hp-β-CD qui lient fortement les esters. Par opposition, l'attaque des alkylamines primaires est généralement accéléré et, dans plusieurs cas, d'une façon importante. Pour l'aminolyse du 1-NA en présence de β-CD, les valeurs de k_{cN}/k_N vont de 7 à 460 si l'on fait l'hypothèse que l'amine libre réagit avec l'ester lié à la CD. Par ailleurs, si la réaction catalysée par la CD implique un ester libre qui réagit avec une amine liée à la CD et une constante de vitesse k_{Nc}, les rapports k_{Nc}/k_N varient de 43 à 140. *Quelle que soit le type de liaison avec la CD, la β-CD provoque une accélération importante de la réaction d'aminolyse du 1-NA.* Pour l'aminolyse du 2-NA, les effets sont moins dramatiques: les rapports k_{cN}/k_N vont de 0,19 à 17 alors que les valeurs de k_{Nc}/k_N varient de 17 à 110. La réaction du 1-NA avec l'hexylamine est aussi catalysée par la γ-CD. Les variations des paramètres cinétiques avec la longueur de la chaîne suggèrent que l'aminolyse catalysée par la CD se produit essentiellement par une attaque de l'acétate libre par une amine liée à la CD. Toutefois, lors de la réaction, il doit exister des interactions entre le groupe aryle de l'ester et la CD puisque la stabilisation de l'état de transition est différente pour les 1-NA, 2-NA et d'autres esters.

Mots clés : aminolyse, catalyse, cyclodextrine, clivage d'esters, cinétiques.

[Traduit par la Rédaction]

Received November 3, 1998.

This paper is dedicated to Jerry Kresge in recognition of his many achievements in chemistry.

O.S. Tee[1] and M.J. Boyd. Department of Chemistry and Biochemistry, Concordia University, Montréal, PQ H3G 1M8, Canada.

[1]Author to whom correspondence may be addressed. Telephone: (514) 848-3348. Fax: (514) 848-2868.
e-mail: ostee@vax2.concordia.ca

 © 1999 NRC Canada

Introduction

Recently, we embarked on a series of studies of the effects of cyclodextrins (1) on the reactions of aryl esters with amines and other nucleophiles (2–4).[2] In the first instance, we wished to find out if esters bound to cyclodextrins (CDs) are more or less reactive towards nucleophiles, which do not bind to CDs, and to ascertain how the reactivities vary with the ester, the CD, and the nucleophile (2). Accordingly, we studied the reaction of *p*-nitrophenyl acetate and hexanoate with hydroxylamine, imidazole, and the anions of trifluoroethanol (TFE) and 2-mercaptoethanol (2-ME), in the presence of three CDs (2). It was established that the free and CD-bound esters have quite similar reactivities towards the nucleophiles, implying that when the esters are bound to CDs, their carbonyl groups are reasonably exposed to the bulk medium and accessible to nucleophiles in it.

From our initial study, it was not possible to tell the orientation of the ester during the attack by the nucleophile (Nuc), which could occur with the aryl group of the ester included in the CD cavity, as in **1**, or with the acyl group in the cavity, as in **2**. To address this question, we carried out a second study on the effects of CDs on the reaction of the TFE and 2-ME anions with *p*-nitrophenyl alkanoates having acyl chain length from C_2 to C_{10} (3).[2] Broadly speaking, it was found that the CD-bound esters are somewhat less reactive than the free esters. However, from the biphasic variation in the reactivities of the CD-bound esters with acyl chain length, we concluded that there is a change in the mode of transition state binding at about C_6: shorter esters reacting with aryl group inclusion (**1**), whereas longer esters react with acyl group inclusion (**2**).

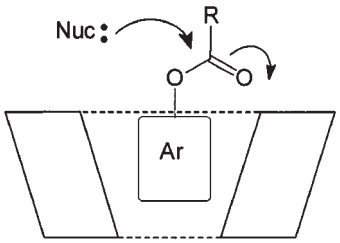

1

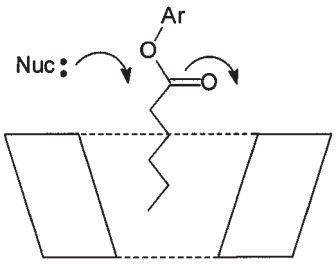

2

We have also carried out a detailed study of the reaction of primary alkylamines (C_3 to C_8) with *p*-nitrophenyl alkanoates (C_2 to C_7) in the presence of CDs.[2] Inherently, the situation is more complicated because binding of both the esters (5, 6) and the amines (7) to CDs must be accounted for in the data analysis. Overall, it appears that short amines react with short esters by the attack of free amine on aryl-bound ester (cf. **1**), whereas with longer amines, the ester is free and the alkylamine is CD-bound (**3**). The reaction of long esters with long amines, which is catalyzed by β-CD and γ-CD, also takes place with inclusion of the amine (**3**), but there may be partial inclusion of either the acyl group (β-CD) or the aryl group (γ-CD) of the ester, as well. For none of the ester–amine–CD combinations studied, did reaction of acyl-bound ester with free amine (cf. **2**) appear to be important.[2]

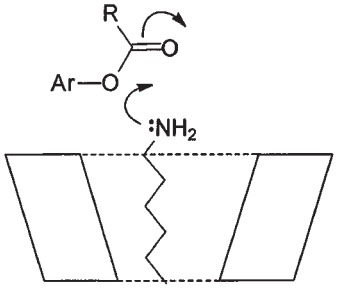

3

In a related study of the effect of β-CD on the reaction of amino acid anions with *p*-nitrophenyl acetate, we concluded that free and CD-bound ester have similar reactivities towards the nucleophiles (4), unlike an earlier report (8). Rate ratios for the two species ranged from 0.76 to 3.5, with ratios greater than one only arising with amino acid anions that bind significantly to β-CD. In such cases, the CD-catalyzed aminolysis may entail reaction of free ester with CD-bound nucleophile, comparable to the depiction in **3**.

The present paper reports investigations of the reactions of 1- and 2-naphthyl acetate (1-NA and 2-NA) with two nonbinding nucleophiles, and with several alkylamines, in the presence of cyclodextrins. The reactivities of these two esters towards hydroxide ion are very similar, but they show subtle differences in their cleavage by CDs, due to differences in their initial state and transition state binding (9). Consequently, it was natural for us to wonder how binding of the two naphthyl esters to CDs would influence their attack by other nucleophiles.

Results

We first measured the kinetics of the cleavage of the reaction of 1-NA and 2-NA with the anions of 2,2,2-trifluoroethanol (TFE) and 2-mercaptoethanol (2-ME), with and without added CDs. Following the methodology established in previous work (2–4), pseudo-first-order rate constants (k_{obs}) determined at various [Nuc] and [CD] were analyzed to yield rate constants for reaction of the nucleophiles with

[2] T.A. Gadosy, M.J. Boyd, and O.S. Tee. Manuscript submitted for publication.

© 1999 NRC Canada

Fig. 1. Rate constants for the cleavage of 1-naphthyl acetate as a function of [2-ME], at pH 10.60, in the absence and presence of cyclodextrins, plotted as follows: ■, no CD; △, 5.0 mM α-CD; ▽, 2.0 mM β-CD; □, 5.0 mM hp-β-CD; ◆, 5.0 mM γ-CD. From eq. [5], the slopes of the straight lines are $(k_N K_S + k_{cN}[CD])/(K_S + [CD])$, at fixed [CD].

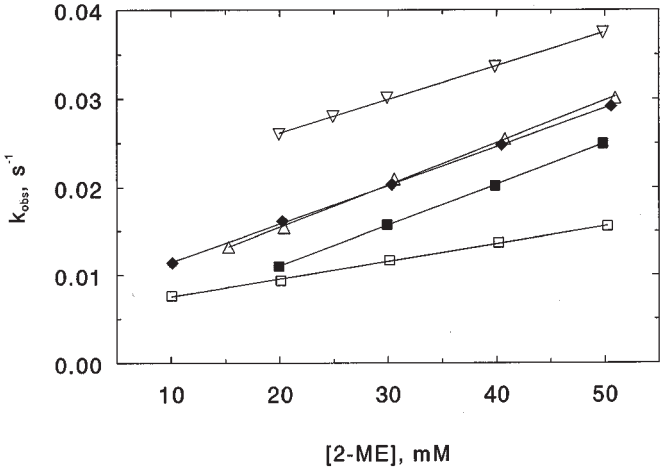

free and CD-bound ester. In the analysis, allowance is made for four processes: hydrolysis of the ester (S) in basic medium (eq. [1]); ester cleavage through an {ester·CD} complex (eq. [2]); reaction of the free (unbound) ester with the nucleophile (Nuc) (eq. [3]); and reaction of the CD-bound ester complex with the nucleophile (eq. [4]). For these four processes in competition, the expected variation of k_{obs} with [Nuc] and [CD] is given by eq. [5], assuming that [S] is low enough that it does not significantly alter [CD].

[1] $$S \xrightarrow{k_u} \text{products}$$

[2] $$S + CD \underset{K_s}{\rightleftharpoons} S \cdot CD \xrightarrow{k_c} \text{products}$$

[3] $$S + Nuc \xrightarrow{k_n} \text{products}$$

[4] $$S \cdot CD \xrightarrow{k_{cN}} \text{products}$$

[5] $$k_{obs} = \frac{(k_u K_S + k_c[CD]) + (k_N K_S + k_c N[CD])[Nuc]}{(K_s + [CD])}$$

Figure 1 shows plots of k_{obs} against [Nuc] for the reaction of 1-NA with the anion of 2-ME in the absence and presence of four CDs: α-CD, β-CD, hp-β-CD,[3] and γ-CD (1); Fig. 2 has comparable data for the analogous reaction of 2-NA. The experiments were carried out at pH 10.60 where 2-ME is largely ionized (pK_a = 9.5) (10), and competition from the background reactions (eqs. [1] and [2]) is not large.

The plots in Fig. 1 show linear dependences of k_{obs} on [Nuc], at fixed [CD], as required by eq. [5], with slopes (in M^{-1} s^{-1}) as follows: no CD, 0.46; α-CD, 0.48; β-CD, 0.38; hp-β-CD, 0.20; γ-CD, 0.44. According to eq. [5], these slopes

Fig. 2. Rate constants for the cleavage of 2-naphthyl acetate as a function of [2-ME], at pH 10.60, in the presence and absence of cyclodextrins, with symbols as in Fig. 1.

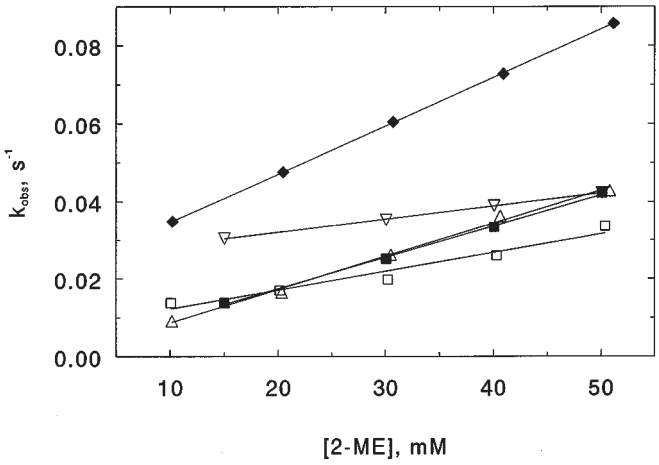

are equal to $(k_N K_S + k_{cN}[CD])/(K_S + [CD])$, and so variations in them reflect the relative magnitudes of k_{cN} and k_N. In the case of α-CD and γ-CD, the slopes imply that $k_{cN} \sim k_N$, whereas for β-CD and especially for hp-β-CD $k_{cN} < k_N$. Similar considerations apply to the plots for 2-NA in Fig. 2, but the trends are slightly different, and in particular, the slope is greater with γ-CD present, meaning that $k_{cN} > k_N$ in that case. These trends are quantified by analysis of the data in terms of eq. [5], using an approach that has been thoroughly tested in previous studies (2–4).[2]

To simplify the data analysis, eq. [5] is linearized by dividing it by the fraction of free substrate, $f_S = K_S/(K_S + [CD])$, to produce eq. [6].[4] According to this equation, k_{obs}/f_s varies linearly with [Nuc], at fixed [CD], and from the slope of $(k_N + k_{cN}[CD]/K_S)$, we can estimate k_{cN}, knowing k_N from experiments with no added CD, and taking K_S from earlier work (9). In the case of 2-ME, the first two terms of eq. [6], which comprise the intercept at fixed CD, are sensitive to pH, but the second two terms in [Nuc] are not, since the 2-ME is largely ionized at pH 10.6. Thus, errors from small variations in pH are minimized, and the rate constants k_N and k_{cN}, and especially the ratio k_{cN}/k_N, can be obtained with good reliability from the slopes of the plots k_{obs} vs. [2-ME] at zero CD and fixed CD, respectively.

[6] $$k_{obs}/f_S = k_u + k_c[CD]/K_S + k_N[Nuc] + k_{cN}[CD][Nuc]/K_S$$

Application of the above approach gave the rate constants k_N and k_{cN} for reaction with 2-ME (see Table 1), which justify the statements made about them, above. Table 1 also contains constants for the effects of β-CD on the reaction of 1-NA and 2-NA with TFE at pH 11.6, where TFE is about 14% ionized (pK_a = 12.4) (11); the actual data are shown in Fig. 3. In both cases, the CD-bound ester is less reactive than the free naphthyl ester towards the anion of TFE.

[3] The hydroxypropyl-β-cyclodextrin (hp-β-CD) used was β-CD in which about six of the seven primary hydroxyl groups are substituted with 2-hydroxypropyl groups (1*c*, *d*).

[4] The form of f_S assumes that $[CD] >> [S \cdot CD] \leq [S]_0$, which was valid for the ester concentrations used. The requisite values of K_S were taken from our previous study of the cleavage of 1-NA and 2-NA by CDs under basic conditions (9).

© 1999 NRC Canada

Table 1. Constants for the reaction of nonbinding nucleophiles with 1-naphthyl and 2-naphthyl acetate (1-NA and 2-NA) in the presence of cyclodextrins.[a]

Reaction	CD	K_S (mM)	k_N (M^{-1} s^{-1})	k_{cN} (M^{-1} s^{-1})	k_{cN}/k_N
1-NA + 2-ME	None		0.464 ± 0.004[b]		
	α	38.7		0.580 ± 0.090	1.25
	β	6.29		0.111 ± 0.025	0.24
	hp-β	3.13		0.0360 ± 0.0083	0.08
	γ	10.7		0.378 ± 0.015	0.81
2-NA + 2-ME	None		0.810 ± 0.021[c]		
	α	25.1		1.09 ± 0.20	1.35
	β	1.32		0.029 ± 0.010	0.04
	hp-β	0.729		0.437 ± 0.072	0.54
	γ	7.92		1.91 ± 0.01	2.40
1-NA + TFE	None		1.18 ± 0.01		
	β	6.29		0.251 ± 0.068[d]	0.21
2-NA + TFE	None		2.00 ± 0.06		
	β	1.32		0.607 ± 0.224[e]	0.30

[a]At 25°C, in aqueous solution; TFE = 2,2,2-trifluoroethanol; 2-ME = 2-mercaptoethanol. Values of K_S are taken from an earlier study (9). Experiments with TFE (pK_a = 12.4) were carried out at pH 11.60 (0.20 M phosphate buffer) whereas those with 2-ME (pK_a = 9.5) employed a lower pH of 10.60 (0.10 M carbonate buffer) to reduce competition from the background reactions (eqs. [1] and [2]). For the experiments to find k_{cN} for 2-ME, the solutions contained 5.0 mM of α-CD, 2.0 mM of β-CD, 5.0 mM of hp-β-CD, or 5.0 mM of γ-CD. The actual data are shown in Figs. 1 and 2.

[b]Initial experiments in the phosphate buffer at pH 11.60 gave k_N = 0.519 ± 0.019 M^{-1} s^{-1}.

[c]Initial experiments in the phosphate buffer at pH 11.60 gave k_N = 0.847 ± 0.008 M^{-1} s^{-1}.

[d]From experiments with [β-CD] = 2.0 mM and varying [TFE] (see Fig. 3).

[e]From experiments with [β-CD] = 1.0 mM and varying [TFE] (see Fig. 3).

Fig. 3. Rate constants for the cleavage of 1-naphthyl and 2-naphthyl acetate (1-NA and 2-NA) as a function of [TFE], at pH 11.60, in the presence and absence of β-CD. The symbols are for 1-NA: ■, no CD; ▽, 2.0 mM β-CD; for 2-NA: ▲, no CD; △, 1.0 mM β-CD.

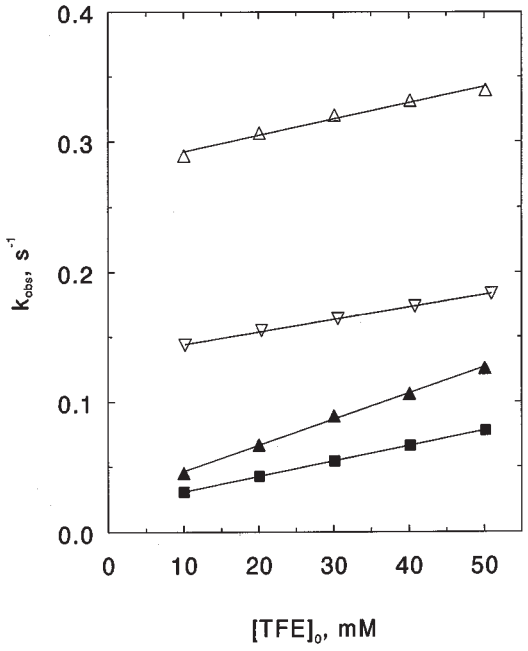

The major part of the present work entailed with studies of the effects of β-CD on the reactions of 1-NA and 2-NA with *n*-alkylamines (C_3 to C_7), cyclopentylamine, and cyclohexylamine. These studies were more demanding for three main reasons. First and foremost, because there is CD-amine binding (eq. [7]), as well as CD-ester binding (9), a more elaborate data analysis is required, and both [CD] and [amine] (= [Nuc]) must be corrected for the CD-amine binding (4).[2] Second, with the larger amines there comes a point where one cannot get enough of the amine into solution for aminolysis to compete effectively with the background processes (eqs. [1] and [2]). Third, in cases where the CD-mediated aminolysis makes only a small contribution, it can be hard or even impossible to quantitate. The reaction medium was buffered at pH 11.6 in which the amines are largely present as their reactive, free base forms ($pK_a \approx 10.6$) (12).

$$[7] \qquad \text{CD} + \text{amine} \underset{K_N}{\rightleftharpoons} \text{CD} \cdot \text{amine}$$

In the absence of a cyclodextrin, the kinetics of aminolysis of 1-NA and 2-NA are simple, with $k_{obs} = k_u + k_N[\text{amine}]_o$, as shown by the linear plots in Fig. 4, and as reported earlier by Bruice et al. (13) for the reaction of *n*-butylamine with 1-NA.[5] Rate constants, k_N, obtained from such plots, are collected in Table 2, along with dissociation constants (K_N) for β-CD·amine complexes, determined previously (7).[2]

For aminolysis in the presence of a CD, the variation of k_{obs} with $[\text{amine}]_o$ is not simple (e.g., Fig. 5) because the amine binds to the CD. In two previous studies (4),[2] our analysis made use of multiple linear regression (14) of the

[5]Ester aminolysis in nonaqueous solvents generally shows both first- and second-order dependence on [amine], but the reactions of "activated" esters in aqueous solution do not. Background references can be found in our previous paper.[2]

© 1999 NRC Canada

Fig. 4. Rate constants for the cleavage of 1-NA (open symbols) and 2-NA (closed symbols), as a function of $[amine]_o$. The slopes afford k_N values for aminolysis. The amines are *n*-butylamine, ■, □; *n*-pentylamine, ▼, ▽; cyclopentylamine, ▲, △.

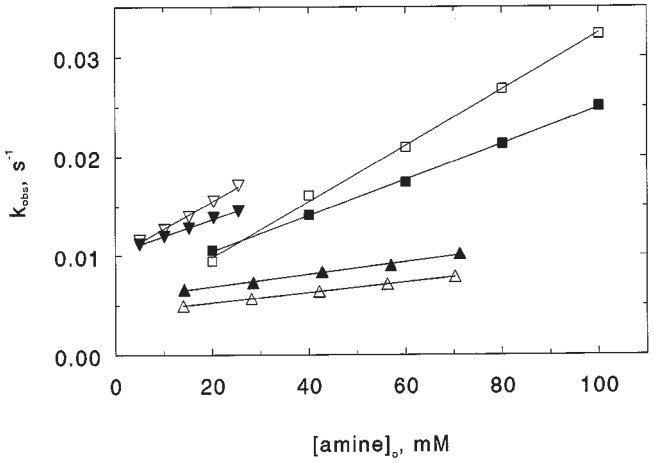

Table 2. Rate constants for the reaction of amines with 1- and 2-naphthyl acetate (1-NA and 2-NA), and dissociation constants of amine.β-CD complexes.[a,b]

	k_N (M^{-1} s^{-1})		
Amine	1-NA	2-NA	K_N, mM
n-Propyl	0.172 ± 0.003	0.349 ± 0.002	108
n-Butyl	0.181 ± 0.003	0.282 ± 0.007	35.6
n-Pentyl	0.166 ± 0.007	0.273 ± 0.013	11.4
n-Hexyl	0.194 ± 0.009	0.225 ± 0.018	2.62[c]
n-Heptyl	0.194[d]	0.225[d]	0.955
Cyclopentyl	0.0621 ± 0.0034	0.0515 ± 0.0002	13.5
Cyclohexyl	0.0415 ± 0.0015	—	1.83

[a]At 25°C, in aqueous solution at pH 11.60. At this pH, the amines are ~91% ionized ($pK_a \approx 10.6$) (12).

[b]The rate constants k_N were determined in this work (e.g., Fig. 4); the dissociation constants K_N are taken from earlier studies (7).[2]

[c]For *n*-hexylamine binding to γ-CD, K_N = 9.29 mM.[2]

[d]Not easily determined and so taken to be the same as for *n*-hexylamine.

variation of k_{obs}/f_s with [CD], [amine], and [amine][CD] (eq. [6]), to obtain their coefficients k_c/K_S, k_N, and k_{cN}/K_S, and from the last of these a value of k_{cN} was extracted.[6] The procedure worked well in the earlier work, but in the present work it is not satisfactory because in most cases there is a considerable disparity between the contributions of the two aminolysis terms to k_{obs} (see later). To circumvent the problem, we adopted a slightly different approach that separates the four terms in eq. [6] into two pairs. Since the rate constants k_u and k_N are readily available (e.g., from Fig. 4), it is feasible to subtract away the first two terms of [6], due to the reactions of the free ester ([1] and [3]), and to isolate the terms due to the two processes involving the CD ([2] and [4]). Thus, eq. [6] is transformed into eq. [8], which requires a linear variation of k_{corr} with [amine].

Fig. 5. Rate constants for the cleavage of 1-NA in the presence of amines and β-CD. The closed symbols (and solid curves) are for the observed rate constants, while the open symbols (and broken curves) are rate constants, calculated assuming that $k_{cN} = k_N$. The four amines are *n*-butylamine, ■, □; *n*-pentylamine, ▼, ▽; cyclopentylamine, ▲, △; cyclohexylamine, ◆, ◇. The concentrations of β-CD are given in Table 3.

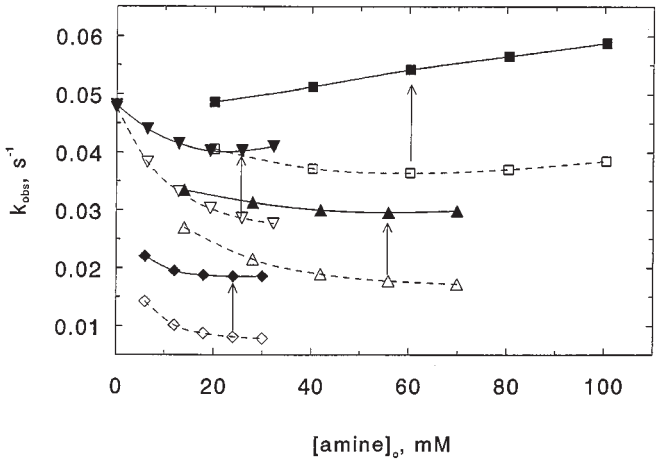

Fig. 6. Analysis for CD-catalyzed aminolysis, with data plotted according to eq. [8], and against [amine] corrected for CD-amine binding. The slopes of the linear plots provide estimates of the rate constants k_{cN}. The symbols are *n*-butylamine, ■; *n*-pentylamine, ▼; cyclopentylamine, ▲; cyclohexylamine, ◆; *n*-hexylamine, ●. The raw data for the first four cases are displayed in Fig. 5.

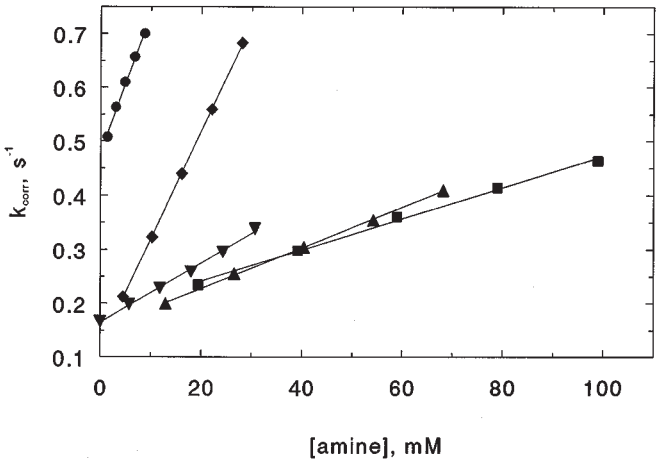

[8] $$k_{corr} = (k_{obs}/f_S - k_u - k_N[amine])K_S/[CD]$$
$$= k_c + k_{cN}[amine]$$

Figure 6 shows five examples of data plotted in accord with eq. [8], which include the four cases in Fig. 5. The

[6]The combined kinetic data from two or more sets of experiments (one without CD and one or more with CD) were analyzed to obtain the coefficients of [CD], [amine], and [amine][CD] in eq. [6], where both [CD] and [amine] were corrected for CD-amine binding (4).[2] For the purposes of further analysis, a more accurate value of k_N was taken from the experiments where $[CD]_o = 0$.

© 1999 NRC Canada

Table 3. Constants relating to the aminolysis of 1- and 2-naphthyl acetate, catalyzed by β-cyclodextrin.[a,b]

Amine	k_{cN} (M^{-1} s^{-1})	k_{cN}/k_N	k_3 (M^{-2} s^{-1})	k_{Nc} (M^{-1} s^{-1})	k_{Nc}/k_N	K_{TS} (mM)
			(*a*) 1-Naphthyl acetate			
n-Propyl	1.23 ± 0.05	7.1	195	21	120	0.88
n-Butyl	2.89 ± 0.10	16	460	16	90	0.40
n-Pentyl	5.48 ± 0.16	33	870	9.9	60	0.19
n-Hexyl	25.8 ± 1.1	130	4100	11	55	0.047
	33.1 ± 1.0[c]	170	5300	14	71	0.037
n-Heptyl	40.2 ± 0.6[d]	210	6400	6.1	32	0.030
Cyclopentyl	3.76 ± 0.05	61	600	8.1	130	0.10
Cyclohexyl	20.0 ± 0.1	480	3200	5.8	140	0.013
	18.2 ± 0.4[e]	440	2900	5.3	130	0.014
	19.0 ± 2.4[f]	460	3000	5.5	130	0.014
n-Hexyl	31.1 ± 0.4[g]	160	2900	27	140	0.067
	25.2 ± 0.9[h]	130	2400	22	110	0.082
			(*b*) 2-Naphthyl acetate			
n-Propyl[i]	0.067 ± 0.008	0.19	51	5.5	16	6.9
n-Butyl	0.175 ± 0.031	0.62	130	4.7	17	2.1
n-Pentyl	1.58 ± 0.06	5.8	1200	14	50	0.23
n-Hexyl	3.86 ± 0.18	17	2900	7.7	34	0.077
n-Heptyl	—[i]					
Cyclopentyl	0.534 ± 0.052	10	400	5.5	110	0.13
Cyclohexyl	—[j]					

[a]As in Table 2.

[b]Values of K_S for the esters and CDs are in Table 1. Values of k_{cN} were obtained by the variation of k_{corr} with [amine] (eq. [8]), for data from experiments with $[\beta\text{-CD}]_o$ = 2.00 mM, and varying $[\text{amine}]_o$ (e.g., Figs. 5 and 6), except where noted otherwise.

[c]$[\beta\text{-CD}]_o$ = 1.00 mM.

[d]$[\beta\text{-CD}]_o$ = 4.00 mM. For an experiment with $[\beta\text{-CD}]_o$ = 2.00 mM, the analysis was poorer, and it gave k_{cN} = 55.1 ± 2.3 M^{-1} s^{-1}.

[e]$[\beta\text{-CD}]_o$ = 4.00 mM.

[f]Obtained from experiments with constant $[\text{amine}]_o$ = 14.82 mM and varying $[\beta\text{-CD}]_o$ (2.00–10.00 mM). The analysis was poorer because k_{corr} and [amine] did not vary greatly under these conditions. Nevertheless, the value of k_{cN} agrees well with those from the other two experiments.

[g]$[\gamma\text{-CD}]_o$ = 2.50 mM.

[h]$[\gamma\text{-CD}]_o$ = 5.00 mM.

[i]CD-mediated aminolysis was barely detectable.

[j]Experiments unsuccessful because aminolysis barely competes with ester cleavage by β-CD at the amine concentrations accessible.

good linearity of the plots strongly support the model used,[7] and the significant slopes, which equal k_{cN}, imply appreciable catalysis of aminolysis by β-CD. Values of k_{cN} obtained in this way are presented in Table 3, along with the rate constants k_3 and k_{Nc} for the processes [9] and [10], which will be used in Discussion. Because the processes [4], [9], and [10] are kinetically equivalent, the three relevant rate constants are related through the expression: $k_3 = k_{cN}/K_S = k_{Nc}/K_N$.

[9] $\text{S} + \text{CD} + \text{Nuc} \xrightarrow{k_3} \text{products}$

[10] $\text{S} + \text{CD} \cdot \text{Nuc} \xrightarrow{k_{Nc}} \text{products}$

For the purposes of subsequent discussion, Table 3 also contains "dissociation constants," K_{TS}, which provide a measure of the strength of CD-binding in the transition states of CD-mediated reactions (15). In the present case, K_{TS} is defined as in eq. [11] to be the apparent dissociation constant of the transition state of the CD-mediated aminolysis (TS·CD) into the transition state of normal aminolysis (TS) and the CD. Analogous constants were used in our previous discussions of the effects of CDs on the reactions of nucleophiles with *p*-nitrophenyl esters (2–4),[2] as well as in much of our other recent work (6, 9, 15).

[11] $$K_{TS} = [\text{TS}][\text{CD}]/[\text{TS}\cdot\text{CD}] = k_N/k_3 = k_N K_S/k_{cN} = k_N K_N/k_{Nc}$$

Discussion

Even a cursory viewing of the results presented in Figs. 1–6 and Tables 1–3 reveals that cyclodextrins retard or have little effect on cleavage of the naphthyl acetates by the anions of TFE and 2-ME but they significantly catalyze ester cleavage by alkylamines. The extent of the CD-catalyzed aminolysis can be estimated using the rate constants obtained by experiment, as outlined below.

[7]The linearity of the plots in Fig. 6 also means that our values of K_N and K_S are not seriously in error.

© 1999 NRC Canada

Fig. 7. Variation of the first-order contributions of the pathways [1]–[4] to k_{obs} with $[amine]_o$ for the cleavage of 1-NA in the presence of cyclohexylamine and β-CD, with $[\beta\text{-CD}]_o$ = 2.00 mM. At the highest $[amine]_o$, the contribution of CD-catalyzed pathway reaches 58%. See Table 4 for this case and several others.

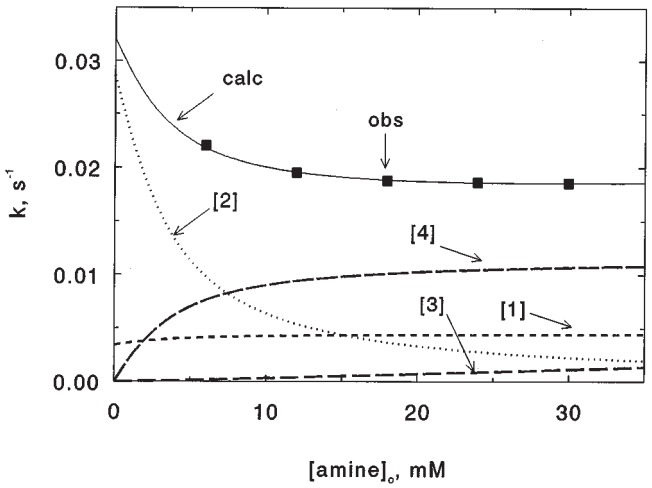

Table 4. Contributions from the processes [1]–[4] to k_{obs} for the cleavage of 1-naphthyl acetate in the presence of β-CD and amines.[a]

Amine	$[Amine]_{max}$ (mM)	$[CD]_o$ (mM)	Contribution (%) [1]	[2]	[3]	[4]
n-Propyl	267	2.00	12	19	41	27
n-Butyl	100	2.00	11	24	28	37
n-Pentyl	32	2.00	23	32	12	33
n-Hexyl	10.3	1.00	34	37	4	25
n-Hexyl	10.3	2.00	22	52	2	24
n-Heptyl	5.70	4.00	14	68	1	17
Cyclopentyl	69.8	2.00	18	26	13	43
Cyclohexyl	29.9	2.00	24	12	6	58
Cyclohexyl	29.9	4.00	15	14	4	67
n-Hexyl	10.8	2.50[b]	24	19	3	55
n-Hexyl	10.8	5.00[b]	15	28	2	55

[a]$[Amine]_{max}$ is the highest amine concentration used in the experiments (e.g., Fig. 5). The CD-catalyzed aminolysis pathway is designated as process [4], but it should be remembered that the processes [9] and [10] are kinetically equivalent.

[b]Experiments with γ-CD (see Table 3).

The curved plots of k_{obs} vs. $[amine]_o$, such as those in Fig. 5, arise from the varying contributions of four cleavage pathways [1]–[4],[8] and the shapes of the curves are understandable when one works out how these contributions vary with $[amine]_o$. For example, Fig. 7 shows the contributions to k_{obs} for 1-NA reacting with cyclohexylamine in the presence of β-CD.[9] As $[amine]_o$ is increased, the amount of free CD drops quickly, due to CD-amine binding, causing a sharp decline in the CD-mediated ester cleavage (eq. [2]) and a modest increase in background hydrolysis of free ester, [1]. At the same time, the contributions of the two aminolysis pathways ([3] and [4]) increase with $[amine]_o$, especially that due to CD-catalyzed aminolysis ([4]), which levels off at high $[amine]_o$ as the CD becomes saturated with the amine. Overall, k_{obs} decreases with $[amine]_o$ but much less than if the CD-catalyzed aminolysis was small or negligible.

The same features apply to the other amines, but the shapes of their curves (e.g., Fig. 5) vary somewhat because of the different rate constants, the dissociation constants for CD-amine binding, and the ranges of $[amine]_o$ used. This point is emphasized in Table 4, which shows the percentage contributions made by the four kinetic processes, at the highest amine concentration used, for 1-NA reacting with the various amines in the presence of β-CD and, in two cases, γ-CD. In the most favourable case, which involves reaction with cyclohexylamine, the percentage contribution of CD-catalyzed aminolysis exceeds 65%.

Substrate reactivity (k_N)

Before discussing CD-catalyzed aminolysis in detail, it is necessary to remark upon the reactivities of the esters towards nucleophiles in the absence of CDs. Towards hydroxide ion, the two naphthyl acetates, 1-NA and 2-NA, have very similar reactivities: k_{OH} = 2.03 and 1.85 M^{-1} s^{-1}, respectively (9). However, with the other nucleophiles (TFE anion, 2-ME anion, and *n*-alkylamines), 2-NA is 1.2–2.0 times as reactive as 1-NA (k_N, Tables 1 and 2), except with cyclopentylamine where 1-NA is slightly more reactive. For the *n*-alkylamines (C_3 to C_6), there is little variation of k_N for both naphthyl esters, but the two cyclic amines are appreciably less reactive because they have branching next to the reacting amino group. These observations were anticipated, since similar behaviour had been observed for the aminolysis of *p*-nitrophenyl alkanoates.[2] Overall, the two naphthyl esters have fairly similar reactivities towards nucleophiles, so that any appreciable differences seen for their reactions in the presence of CDs must be attributable to differences in substrate binding and (or) the transition state binding.[10]

Reactivity ratios (k_{cN}/k_N and k_{Nc}/k_N)

The ratio k_{cN}/k_N measures the relative reactivities of the bound and free forms of the ester towards the nucleophile, assuming the CD-mediated reaction takes place between bound ester and free nucleophile (eq. [4]). The reactions of the two naphthyl acetates with the anions of TFE and 2-ME, both nonbinding nucleophiles (2, 3), are slowed down appreciably (k_{cN}/k_N = 0.04–0.5, Table 1) by ester binding to β-CD and hp-β-CD. By contrast, reactions of the esters with the 2-ME anion are hardly affected by α-CD (k_{cN}/k_N = 1.25 and 1.35) and in different ways by γ-CD (k_{cN}/k_N = 0.81 for 1-NA, and 2.4 for 2-NA). Roughly speaking, there is an in-

[8]The CD-catalyzed aminolysis pathway is designated as process [4], but it should be remembered that the processes [9] and [10] are kinetically equivalent.

[9]To calculate the contributions to k_{obs}, we have taken the rate constants k_u and k_N from the variation of k_{obs} with $[amine]_o$ (e.g., Fig. 4), and k_c and k_{cN} from the linear dependence of k_{corr} on [amine], corresponding to eq. [8] (e.g., Fig. 6).

[10]For the most part, 2-NA *reacts* faster than 1-NA with CD anions, but there is considerable variation in the rate ratio because of binding of the 1- and 2-naphthyl groups to the CDs in the initial state and the transition state (9).

© 1999 NRC Canada

Fig. 8. Variation of transition state stabilization (pK_{TS}) with the strength of amine binding (pK_N) for the aminolysis of 1-naphthyl acetate, 2-naphthyl acetate, and *p*-nitrophenyl acetate (1-NA, ■; 2-NA, □; pNPA, ○) catalyzed by β-cyclodextrin. Additional points are for 1-NA reacting with cyclopentylamine and cyclohexylamine (▼), and for 2-NA reacting with cyclopentylamine (△). The dotted lines are to aid the eye; the solid lines are the correlation lines for 1-NA and 2-NA. The data for pNPA are taken from ref. 3.

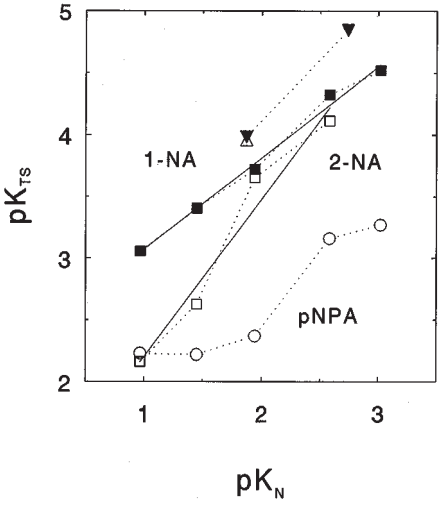

verse relationship between the strength of binding of the ester and the reactivity ratio: the stronger the binding, the lower the ratio. The relationship is not exact, of course, because of differences in the sizes of the CD cavities (1) and in the modes of inclusion of the two esters (9).

The effects of β-CD on aminolysis of the two esters are much more dramatic than those on the reactions with the TFE and 2-ME anions, since most of the ratios k_{cN}/k_N *are much greater than one* (Table 3), ranging from 0.2 all the way up to 460.[11] Moreover, since alkylamines bind to CDs (7),[2] we also consider reaction between free ester and CD-bound amine (eq. [10]) for which the relevant ratios are all significantly greater than one (k_{Nc}/k_N = 17–140, Table 3). Thus, regardless of whether the reaction takes place as in eq. [4] or in eq. [10], *the aminolysis of the two naphthyl acetates is catalyzed by the* β*-CD in almost all cases*.[12]

It will be noted that the ratios k_{cN}/k_N increase appreciably with the amine chain length, and they are large for the two cyclic amines, suggesting a sensitivity to the ability of the amine to bind to β-CD (see K_N in Table 2), which seems inconsistent with reaction taking place as in eq. [4]. At the same time, the ratios k_{Nc}/k_N vary much less (only from 30 to 140 for 1-NA; 16 to 50 for 2-NA), as one would expect if the reaction proceeded more or less as in eq. [10], and through a transition state structure like that in **3**.

One further point to be noted is that for a given amine, both reactivity ratios are larger for 1-NA than for 2-NA (Table 3), indicating stronger catalysis for 1-NA, and implying some difference in the interactions of the two naphthyl groups with β-CD in the transition state for CD-catalyzed aminolysis, even though it mainly involves alkylamino group binding (**3**).

Third-order reactivity (k_3)

An unbiased view of the CD-mediated ester aminolysis is afforded by the rate constants evaluated for the third-order process in eq. [9]. Values of k_3 for 1-NA and 2-NA reacting with the primary *n*-alkylamines in the presence of β-CD increase appreciably with the chain length of the amine, and they are comparatively large for cyclopentylamine and cyclohexylamine (Table 3), especially since these two amines are inherently less reactive (see k_N in Table 2). All of the values are consistent with the third-order reaction (eq. [9]) taking place with the alkylamino group in the CD cavity and the naphthyl group of the ester more or less outside (**3**).

Transition state binding (pK_{TS})

The quantity $pK_{TS} = -\log K_{TS}$ is a measure of the stabilization of a transition state afforded by the CD and its variations with structure can provide information about transition state binding (15). Figure 8 shows values of pK_{TS} for the two naphthyl esters, reacting with amines in the presence of β-CD, plotted against pK_N for the binding of the amines to β-CD.

The first thing to note is that pK_{TS} increases steeply with pK_N, and for both esters the slopes are near one (0.74 for 1-NA and 1.27 for 2-NA). Thus, both sets of data are quite consistent with a transition state structure in which binding of the alkylamino group in the CD cavity is most important, with the ester moiety being largely outside (**3**), as suggested above. However, since there are large differences between the values of pK_{TS} for the two naphthyl esters when the amine is relatively short, there must be differences between the interactions of the 1- and 2-naphthyl groups with the edge or rim of the β-CD cavity, in the transition state.

A clear indication that there are significant *favorable* interactions between the naphthyl groups of the esters and the β-CD cavity (or its rim) in the transition state is given by the larger pK_{TS} values for aminolysis of the two naphthyl acetates (3.06–4.85 for 1-NA; 2.16–4.11 for 2-NA), as compared to those for *p*-nitrophenyl esters reacting with the same amines (pK_{TS} = 2.23–3.15 for the acetate; 2.30–3.76 for the hexanoate).[13] Correspondingly, the rate ratios, k_{cN}/k_N and k_{Nc}/k_N, are generally much higher for the naphthyl esters than for the *p*-nitrophenyl ester,[2] and so the evidence for catalysis of aminolysis by β-CD is more clear-cut in this present work.

Conclusions

Binding of 1-naphthyl and 2-naphthyl acetates to CDs affects their reactivities to nonbinding nucleophiles to different extents, depending on the CD. Reactions of the esters with the anions of TFE and 2-ME are slowed down appreciably by β-CD and hp-β-CD, both of which bind the esters strongly. By contrast, their reactions with the 2-ME anion

[11]The largest ratio was obtained for the reaction of 1-NA with cyclohexylamine, catalyzed by β-CD. For this case, three different experiments gave essentially the same value of k_{cN} and, hence, of this ratio (Table 3).
[12]Additionally, it was shown in two experiments that the reaction of *n*-hexylamine with 1-NA is catalyzed by γ-CD (Table 3).
[13]From K_{TS} values in Table 3 of ref. 3.

© 1999 NRC Canada

are hardly affected by α-CD and γ-CD, which bind the esters less strongly.

Aminolysis of both esters by alkylamines is catalyzed by β-CD. The catalysis appears to arise primarily from binding of the alkylamino group in the CD cavity in the transition state (**3**), since the extent of the catalysis increases strongly with the ability of the alkylamine to bind to β-CD (Fig. 8). However, there must be additional factors involving the aryl groups of the esters, which contribute to transition state stabilization, since pK_{TS} values are not the same for the two naphthyl esters reacting with short amines, and these values are generally greater than those for *p*-nitrophenyl acetate and hexanoate reacting with the same amines, under the same reaction conditions.[2]

Experimental

The alkylamines, naphthyl esters, and most of the other required chemicals were the best grades available from the Aldrich Chemical Co. Cyclodextrins were obtained from Aldrich and from Wacker Chemie (Munich, Germany). To be compatible with earlier studies (2, 3, 6, 7, 9), the "hydroxypropyl-β-cyclodextrin" used had an average molecular weight of 1500, consistent with alkylation of about six of the seven primary hydroxyl groups of β-CD by 2-hydroxypropyl groups (1*c*, *d*).[14] Aqueous buffers were made from the requisite reagents and water that had been ion-exchanged and doubly distilled from glass.

Kinetics procedures were basically the same as those used in previous, related work (2–4, 9). Reactions were initiated by mixing equal volumes of a solution of the nucleophile in buffer with a solution of the ester (with or without a CD), in a stopped-flow apparatus. The ester concentrations used were 50 or 100 μM, after mixing.

The reactions of the esters with TFE and with amines were carried out at pH 11.60, to be compatible with previous studies (2, 3, 7, 9). Initial experiments with 2-ME were also performed at pH 11.60, but the results were unsatisfactory due to the small change in k_{obs}. Consequently, most of the experiments with 2-ME were executed at pH 10.60, in a 0.10 M carbonate buffer, where competition from the background reactions (eqs. [1] and [2]) is less significant (Figs. 1 and 2), and k_N and k_{cN} are more easily evaluated. The range of [TFE] and [2-ME] used can be judged from Figs. 1–3.

For aminolysis, the amine solutions were all set to pH 11.60 in a buffer, as in the previous studies (3). For the less soluble *n*-hexylamine and *n*-heptylamine, a phosphate buffer (0.40 M before mixing) was used; for the others, the buffer was made using the amine itself. The range of amine concentrations used was the same as previously,[2] as can be seen in Figs. 4 and 5. The concentrations of CDs used are noted in Tables 1 and 3.

The kinetics of naphthyl ester cleavage were followed by monitoring the first-order appearance of the naphthoxide ion at 330–350 nm (9), using an Applied Photophysics SX17MV stopped-flow spectrophotometer, with the cell temperature maintained at 25.0 ± 0.1°C. In general, 5–10 good absorbance traces, each containing 400 data points, were averaged, and the pseudo-first-order rate constant k_{obs} was estimated from the average trace by nonlinear least-squares fitting of an exponential increase to the data.

Analyses of the kinetic data based on eqs. [5], [6], and [8], as outlined in the text and detailed elsewhere (2–4), require the use of known values of K_S and K_N for binding between CDs and the reactants. These values were available from earlier studies (7, 9),[2] as indicated in the Tables 1 and 2. The use of eqs. [6] and [8] for the analysis of aminolysis requires values of [CD] and [amine] to be corrected for binding of the amine to the CD (eq. [7]). Details of the calculation of such corrected concentrations have been given already (4).

Acknowledgements

We are grateful to the Natural Sciences and Engineering and Research Council of Canada for an operating grant and an equipment grant towards the purchase of the stopped-flow spectrophotometer. We also thank Dr. T.A. Gadosy for helpful discussions.

References

1. (*a*) M. Bender and M. Komiyama. Cyclodextrin chemistry. Springer Verlag, New York, 1978; (*b*) W. Saenger. Angew. Chem. Int. Ed. Engl. **19**, 344 (1980); (*c*) J. Szejtli. Cyclodextrins and their inclusion complexes. Akademiai Kiado, Budapest. 1982; (*d*) Carbohydr. Polym. **12**, 375 (1990); (*e*) G. Wenz. Angew. Chem. Int. Ed. Engl. **33**, 803 (1994); (*f*) V.T. D'Souza and K.B. Lipkowitz. Chem. Rev. **98**, 174 (1998), and other reviews in the same issue.
2. O.S. Tee and T.A. Gadosy. J. Chem. Soc. Perkin Trans. 2, 2307 (1994).
3. T.A. Gadosy and O.S. Tee. J. Chem. Soc. Perkin Trans. 2, 71 (1995).
4. O.S. Tee, T.A. Gadosy, and J.B. Giorgi. Can. J. Chem. **75**, 83 (1997).
5. G.M. Bonora, R. Fornasier, P. Scrimin and U. Tonellato. J. Chem. Soc. Perkin Trans 2, 367 (1985).
6. (*a*) O.S. Tee, C. Mazza, and X.-X. Du. J. Org. Chem. **55**, 3603 (1990); (*b*) O.S. Tee and X.-X. Du. J. Am. Chem. Soc. **114**, 620 (1992); (*c*) T.A. Gadosy and O.S. Tee. J. Chem. Soc. Perkin Trans. 2, 715 (1994); (*d*) O.S. Tee and T.A. Gadosy. J. Chem. Soc. Perkin Trans. 2, 2191 (1994).
7. O.S. Tee, T.A. Gadosy, and J.B. Giorgi. Can. J. Chem. **74**, 736 (1996).
8. M. Barra and R.H. de Rossi. Can. J. Chem. **69**, 1124 (1991).
9. O.S. Tee and M.J. Boyd. J. Chem. Soc. Perkin Trans. 2, 1237 (1995).
10. W.P. Jencks and J. Carriuolo. J. Am. Chem. Soc. **82**, 1778 (1960).
11. C.H. Arrowsmith, A.J. Kresge, and Y.C. Tang. J. Am. Chem. Soc. **113**, 179 (1991).
12. (*a*) G.D. Fasman (*Editor*). Handbook of biochemistry and molecular biology, Vol. 1. 3rd ed. CRC Press, Cleveland, Ohio. 1976; (*b*) J.A. Dean (*Editor*). Handbook of organic chemistry. McGraw–Hill, New York. 1987.
13. T.C. Bruice, A.Donzel, R.W. Huffmman, and A.R. Butler. J. Am. Chem. Soc. **89**, 2106 (1967).

[14]This formulation has been checked using electrospray mass spectroscopy (see footnote 2).

© 1999 NRC Canada

14. L.M. Mezei. Practical spreadsheet statistics and curve-fitting for scientists and engineers. Prentice–Hall, Englewood Cliffs, N.J. 1990.

15. (*a*) O.S. Tee. Carbohydr. Res. **192**, 181 (1989); (*b*) Adv. Phys. Org. Chem. **29**, 1 (1994); (*c*) A.J. Kirby. Angew. Chem. Int. Ed. Engl. **35**, 707 (1996).

© 1999 NRC Canada

The surprising formation of structurally distorted *ap*-9-(*o-tert*-butylphenyl)-9-methylthiofluorene and its facile homolysis into *sp*-9-(*o-tert*-butylphenyl)-3-methylthiofluorene and *sp*-9-(*o-tert*-butylphenyl)fluorene

Yuqing Hou and Cal Y. Meyers

Abstract: The continued study of rotationally restricted 9-(*o-tert*-butylphenyl)fluorenes has provided surprising results. Treatment of *sp*-9-(*o-tert*-butylphenyl)-9-fluorenol (**1**) with ethanol or methanol under acidic conditions affords *sp*-9-(*o-tert*-butylphenyl)-9-ethoxyfluorene (**2b**) and *sp*-9-(*o-tert*-butylphenyl)-9-methoxyfluorene (**3b**), respectively, but similar treatment with methanethiol converts **1** into the rotamerically opposite *ap*-9-(*o-tert*-butylphenyl)-9-methylthiofluorene (**4a**). While all three products reflect reaction with inversion at C-9, **2b** and **3b** reflect subsequent rotation, which is not the case with **4a**. X-ray diffraction shows **4a** to be highly distorted and strained, but apparently favored thermodynamically over its *sp* rotamer. Homolysis of **4a** is observed at room temperature, and at elevated temperatures accounts for the formation of *sp*-9-(*o-tert*-butylphenyl)fluorene (**6b**) and *sp*-9-(*o-tert*-butylphenyl)-3-methylthiofluorene (**7c**) as major products. X-ray diffraction shows **6b** and **7c** to be virtually devoid of distortion. Methylation of **6b** via its anion also proceeds with inversion without rotation to form *ap*-9-(*o-tert*-butylphenyl)-9-methylfluorene (**4c**). Dynamic NMR unexpectedly showed that in these *ap* configurations 9-CH_3 (of **4c**) has a greater bulk effect than 9-CH_3S (of **4a**) in forcing the *o-tert*-butyl group into the fluorene plane.

Key words: fluorene, rotamer, distortion, homolysis, carbanion, carbocation, radical.

Résumé : La suite de nos études sur les 9-(*o-tert*-butylphényl)fluorènes à rotation empêchée a fourni des résultats surprenants. Les réactions du *sp*-9-(*o-tert*-butylphényl)-9-fluorénol (**1**) avec l'éthanol et le méthanol dans des conditions acides conduisent respectivement au *sp*-9-(*o-tert*-butylphényl)-9-éthoxyfluorène (**2b**) et *sp*-9-(*o-tert*-butylphényl)-9-méthoxyfluorène (**3b**); toutefois, une réaction avec le méthanethiol transforme le composé **1** au rotamère opposé, le *ap*-9-(*o-tert*-butylphényl)-9-méthylthiofluorène (**4a**). Même si les trois produits sont le reflet d'une inversion en C-9, les produits **2b** et **3b** reflètent une rotation subséquente, ce qui n'est pas le cas avec **4a**. La diffraction des rayons X montre que le composé **4a** est tendu et très déformé, mais qu'il est apparemment thermodynamiquement favorisé par rapport à son rotamère sp. On observe de l'homolyse du produit **4a** à la température ambiante et, à des températures plus élevées, elle peut expliquer la formation des *sp*-9-(*o-tert*-butylphényl)fluorène (**6b**) et *sp*-9-(*o-tert*-butylphényl)-3-méthylthiofluorène (**7c**) comme produits majeurs. La diffraction des rayons X montre que les composés **6b** et **7c** sont pratiquement sans distorsion. La méthylation du produit **6b** par le biais de son anion se produit avec inversion, sans rotation, pour former le *ap*-9-(*o-tert*-butylphényl)-9-méthylfluorène (**4c**). La RMN dynamique a montré d'une façon inattendue que, dans des configurations *ap*, le 9-CH_3 (du composé **4c**) présente un effet stérique plus important que celui du 9-CH_3S (du composé **4a**) pour forcer le groupe *o-tert*-butyle dans le plan du fluorène.

Mots clés : fluorène, rotamère, distorsion, homolyse, carbanion, carbocation, radical.

[Traduit par la Rédaction]

Introduction

As part of our recent studies of rotationally restricted 9-substituted fluorenes (1), we reported that the parent structure in our series, 9-(*o-tert*-butylphenyl)fluorene (**6b**), as well as 9-(*o-tert*-butylphenyl)-9-fluorenol (**1**), exists only in their *sp* form in solution at ambient temperatures and crystalline state (2).[2] While treatment of **1** with CH_3CH_2OH or

Received November 18, 1998.

This paper is dedicated to Jerry Kresge in recognition of his many achievements in chemistry.

Y. Hou and C.Y. Meyers.[1] Department of Chemistry and Biochemistry, Southern Illinois University-4409, Carbondale, IL 62901, U.S.A.

[1]Author to whom correspondence may be addressed. Telephone: (618) 453-6474. Fax: (618) 453-6408. e-mail: cal@chem.siu.edu

[2]The designations *sp* (*syn* periplanar) and *ap* (*anti* periplanar) for these conformations are in accord with Rule E-6.6 (see ref. 14).

© 1999 NRC Canada

Scheme 1.

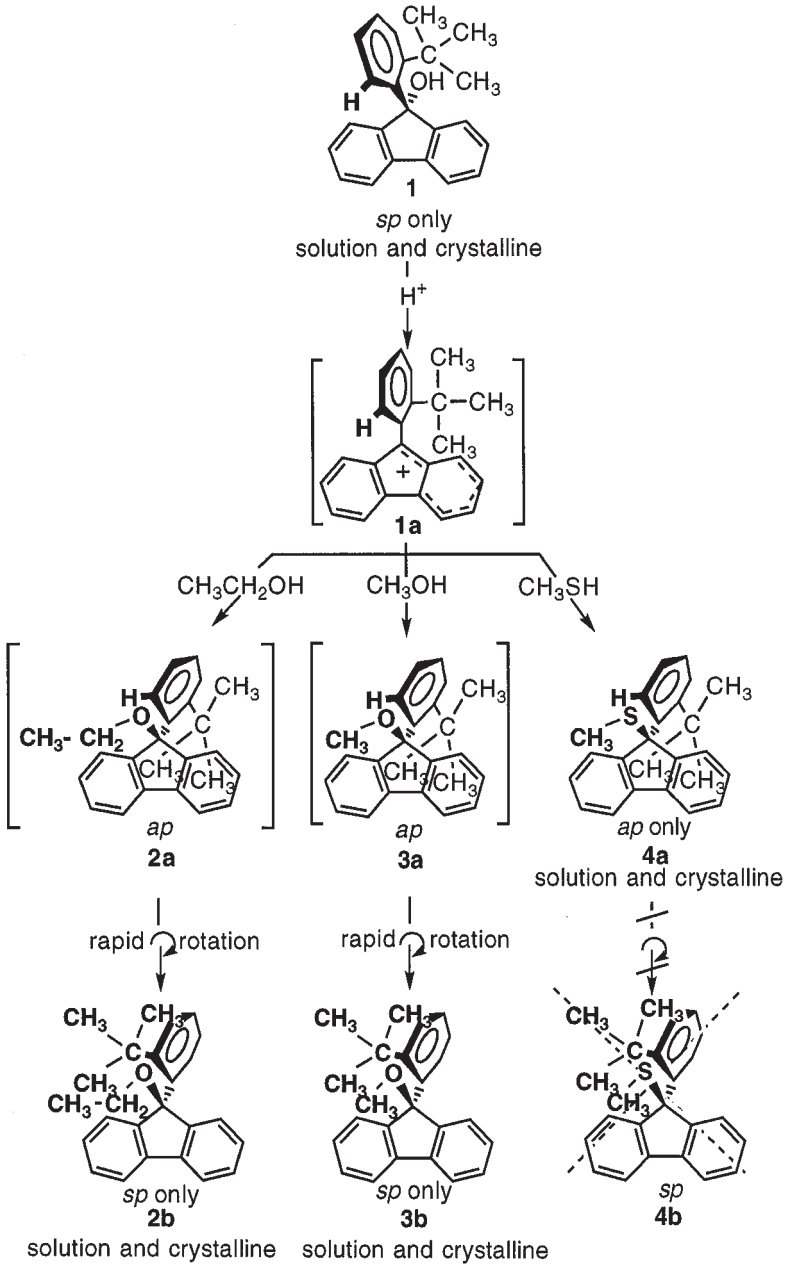

CH_3OH in the presence of strong acid also provided only the corresponding *sp*-9-alkoxy rotamers, *sp*-9-(*o-tert*-butylphenyl)-9-ethoxyfluorene (**2b**), and *sp*-9-(*o-tert*-butylphenyl)-9-methoxyfluorene (**3b**), respectively, similar treatment of **1** with CH_3SH unexpectedly provided only the rotamerically opposite *ap*-9-methylthio derivative, *ap*-9-(*o-tert*-butylphenyl)-9-methylthiofluorene (**4a**), in solution and crystalline form (3, 4) (Scheme 1).

The *ap* conformation in the series of 9-(*o-tert*-butylphenyl)fluorenes provokes a strong steric repulsion between the *tert*-butyl group and the fluorene π cloud, which raises the ground-state energy making it, in most cases, highly unstable relative to the *sp* conformation (3, 5–7). This strong shielding of the *tert*-butyl methyls by the fluorene-ring *p* electrons in the *ap* conformation accounts for their correspondingly high upfield ^{1}H NMR resonance, near 0.6 ppm. In contrast, in the *sp* conformation these methyls are maintained in the deshielding zone of the fluorene ring, giving rise to a much lower field resonance, near 1.8 ppm. This distinction has provided a ready means to differentiate between the two rotameric configurations of these fluorene derivatives in solution (3, 5–7). For the rotameric structure characterization of their solid states and the corresponding bonding parameters, we have relied on X-ray crystallography (2, 4, 8–10).

Results and discussion

Highly distorted/strained structure of *ap*-9-(*o-tert*-butylphenyl)-9-methylthiofluorene (4a)

The X-ray structure of **4a** (Fig. 1), whose geometric parameters have been reported in detail (4), clearly displays

© 1999 NRC Canada

Fig. 1. X-ray structure of **4a**.

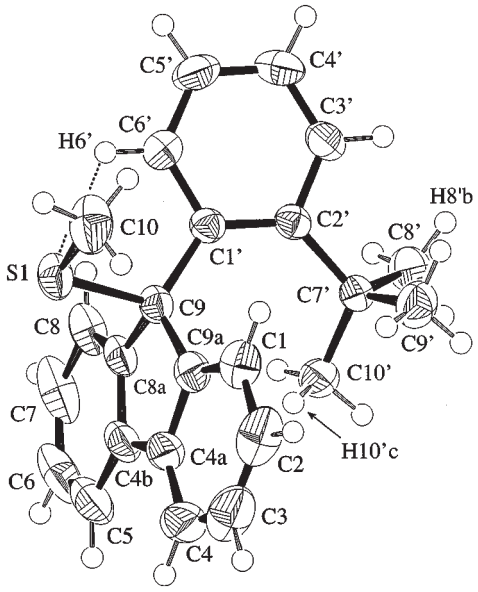

extensive distortions. Our finding that **4a** exists exclusively in its *ap* conformation tells us that the 9-methylthio group enforces this conformation, which, although highly energetic per se, is thermodynamically favored over the *sp* conformation *in this case*.[3] Nonetheless, *ap* **4a** is highly distorted, provoking the strain that is clearly responsible for its unusual instability, which promotes its facile homolytic decomposition at room temperature, in contrast to the thermal stability of the *sp* compounds, e.g., **1**, **2b**, **3b**, and **6b** (2, 3). The major source of the strain emanates from the enforced impinging of a methyl of the *tert*-butyl group on the face of the fluorene ring. As a result, the bond between the *tert*-butyl group and phenyl, C2′—C7′, is considerably bent, angle C1′-C2′-C7′ being almost 18° larger than the corresponding angle C3′-C2′-C7′. In turn, angle C2′-C7′-C10′ is greatly distorted relative to the corresponding angles C2′-C7′-C9′ and C2′-C7′-C8′. For the same reason, the bond between the phenyl and fluorene rings, C1′—C9, is bent, making the angle C2′-C1′-C9 some 13° larger than the corresponding angle C6′-C1′-C9 and forcing the S1—C9 bond more towards perpendicularity with the fluorene plane, the angle between the S1-C9 vector and the fluorene ring plane being 99.09 (7)°. In turn, torsion angle C4b-C8a-C9-C1′ is almost 53° larger than its counterpart S1-C9-C9a-C4a. These enforced strains provoke an unusual distortion from planarity of the phenyl ring, the average deviation of the atoms of the C1′-to-C6′ ring from the least-squares plane being 0.028 (2) Å, while the corresponding values for the fluorene C1-to-C9a and C4b-to-C8a phenyl rings are 0.010 (2) and 0.005 (2) Å, respectively. The molecular distortion is manifested in unusually intimate intramolecular nonbonding contacts, e.g., C9a···C10′, C1···C10, C9a···H10′c, C8′···H3′, C3′····H8′b, and C4a···H10′c, all of whose distances are smaller than the sum of their respective van der Waals radii.

In this regard, the very close contact of S1···H6′, 2.42 Å, and S1···C6′, 2.96 Å (4), could give rise to a "hydrogen bond" reflected in the unusually low field signal of H6′, near δ 9.0, in its ^{1}H NMR spectrum (1, 3). Similar aromatic-H downfield shifts have been previously reported but were not associated with hydrogen bonding (11; cf. 12). While hydrogen bonding involving an aromatic H is unusual, it has been suggested from time to time (for related studies see ref. 13) and is supported in **4a** by comparison to a related structure, 9-(*o*-*tert*-butylphenyl)-9-methylfluorene (**4c**), in which such a possibility is absent. Compound **4c** is the only other 9-substituted 9-(*o*-*tert*-butylphenyl)fluorene we have so far prepared that exists solely in its *ap* conformation in solution, eq. [1]. While the *tert*-butyl group of **4c**, like that of **4a**, impinges onto the face of the fluorene ring (viz. the upfield ^{1}H NMR resonance of these methyls, δ 0.63 and 0.65, respectively) and thereby forces the 9-methyl and H6′ into close proximity, the ^{1}H NMR resonance of H6′, δ 8.0, is normal for an aromatic H held in the deshielding zone of the fluorene moiety. In comparing the thermodynamic favorability of the *ap* rotamer over the *sp* rotomer of both **4a** and **4c**, it is important to note that the 9-S atom and 9-CH_3 group exert a similar steric influence, which is not exerted by the 9-O atom in related structures whose *sp* rotamers are thermodynamically preferred (vide infra).

Facile homolysis of 4a into *sp*-9-(*o*-*tert*-butylphenyl)fluorene (6b) and *sp*-9-(*o*-*tert*-butylphenyl)-3-methylthiofluorene (7c)

It was not unexpected that such a highly strained molecule like **4a** would undergo facile decomposition. Such a consequence indeed was initially exhibited by the appearance of a blue cast taken on by the originally colorless crystals on standing in a sealed vial at room temperature over the period of a day or two. In attempting a dynamic ^{1}H NMR study of **4a** in DMSO-d_6 to examine the effect of temperature on the rotation of the sterically encumbered *tert*-butyl group (vide infra), little change was observed between 20 and 100°C. Slightly above this temperature, however, the resonances of **4a** began to deteriorate as other resonances appeared. Subsequently, a sample from the NMR tube was examined by TLC, which indicated the absence of **4a** but the presence of two new compounds. In a larger scale study, a DMSO solution of crystalline **4a**, heated for 30 min in a 155°C oil bath, afforded the same TLC results. The two products were identified as *sp*-9-(*o*-*tert*-butylphenyl)fluorene (**6b**, 24%) and *sp*-9-(*o*-*tert*-butylphenyl)-3-methylthiofluorene (**7c**, 48%), suggesting that the decomposition of **4a** was homolytic (Scheme 2). In contrast to **4a**, both products have the *sp* conformation, and their X-ray diffraction parameters (**6b** (2); **7c** (8)) show them to be nearly free of distortion and strain, as illustrated in Figs. 2 and 3.

Mechanisms

Our recent studies with the enantiomers of 9-(*o*-*tert*-butylphenyl)-2-methylfluorenes show that the 9-anion, -cation, and -radical of 9-(*o*-*tert*-butylphenyl)fluorene are

[3] That the *ap* conformation is thermodynamically preferred is supported by energy minimization calculations of both the *ap* (**4a**) and *sp* (**4b**) conformations using the AM1 method with a closed-shell (restricted) wave function and then comparing the energies of the heats of formation. The results showed that the *ap* conformation is favored over the *sp* conformation by 21.3 kJ/mol. We are indebted to a referee of our X-ray paper (4) for performing these calculations and transmitting them to us.

© 1999 NRC Canada

Scheme 2.

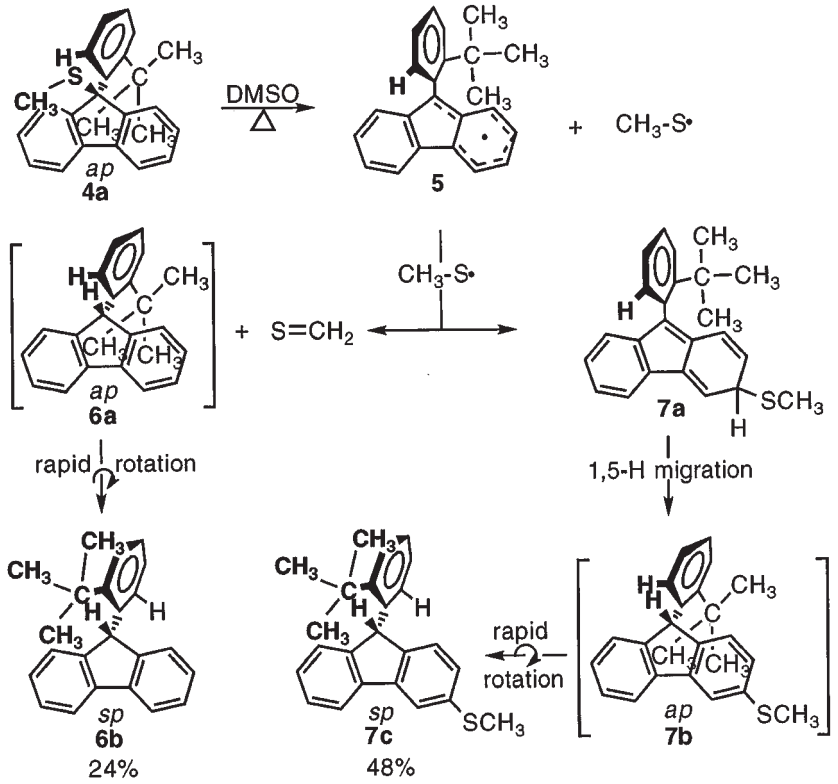

Fig. 2. X-ray structure of **6b.**

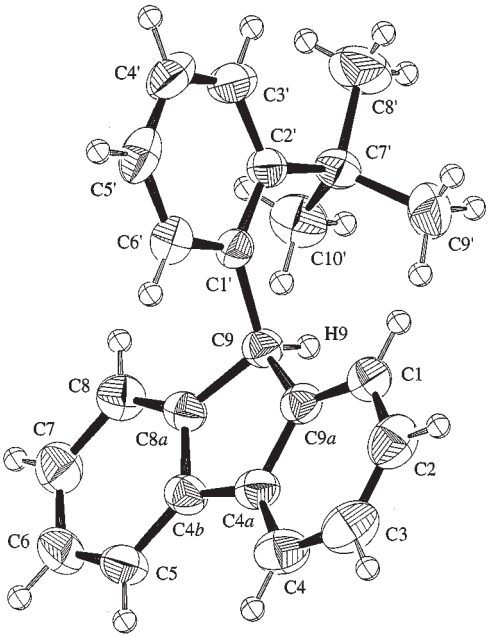

Fig. 3. X-ray structure of **7c**.

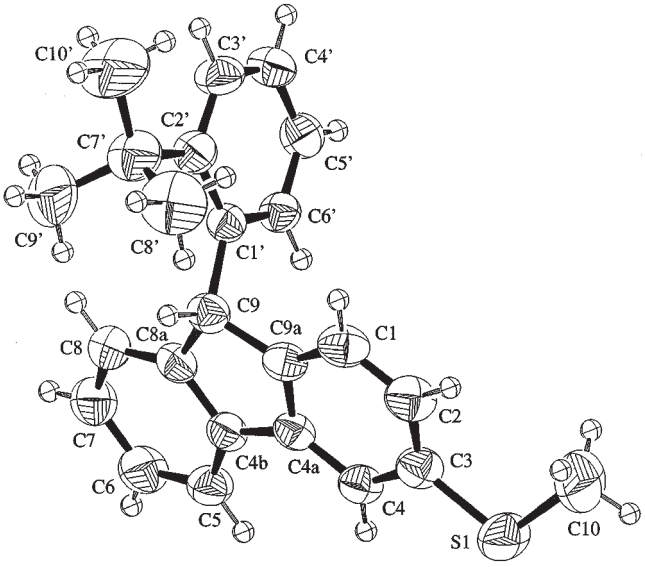

largely sp^2 hybridized and are generally attacked from the less hindered face of the fluorene plane (1, 3). It follows, and we indeed found, that *sp*-9-(*o*-*tert*-butylphenyl)fluorenes that undergo 9-substitution reactions involving the respective 9-anion, -cation, or -radical will produce the products of *inversion* and *ap* conformation. In most cases, however, these products undergo rapid rotation to the energetically favored *sp* rotamers. In rare instances, the initially formed *ap* rotamer is thermodynamically preferred and is the one isolated.

Shown in Scheme 1 is the conversion of *sp*-**1** into cation **1a** and its subsequent reaction with ethanol, methanol, or methanethiol leading to the respective *ap* products, **2a**, **3a**, and **4a**. The former two quickly undergo rotation to their more stable *sp* isomers, **2b** and **3b**, while *ap*-**4a**, being thermodynamically preferred over its *sp* rotamer, **4b**, remains

© 1999 NRC Canada

Scheme 3.

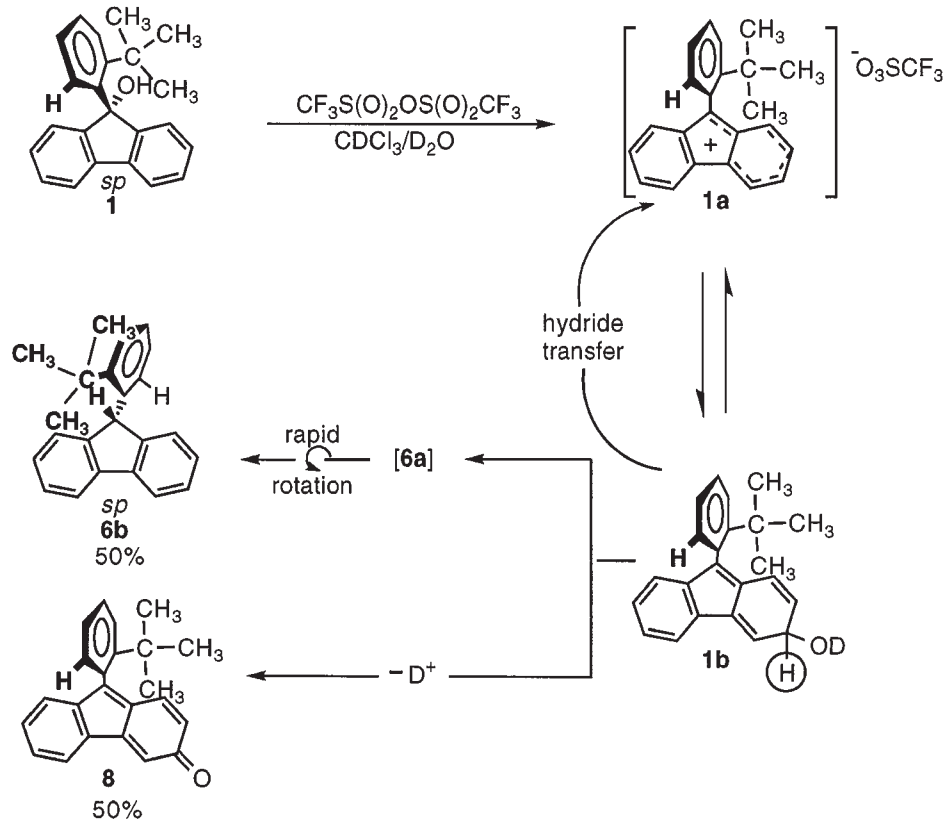

the exclusive product. In a similar manner, but via anion **1b**, *sp*-**6b** is methylated with inversion into *ap*-**4c**, which, like **4a**, does not undergo rotation and consequently is the exclusive product, eq. [1].

As illustrated in Scheme 2, the concurrent formation of **6b** and **7c** is homolytically initiated. This is the consequence of the highly distorted and strained structure of **4a**, the low C—S bond strength, and the formation of the relatively stable methylthio free radical and free radical **5**, whose formation greatly relieves the distortion and strain characterizing **4a**. Hydrogen-atom transfer from $CH_3S\cdot$ to **5** produces *ap*-**6a**, which undergoes rapid rotation to *sp*-**6b** (24% yield). Concurrently, $CH_3S\cdot$ also adds to **5** at its unhindered 3-position forming **7a**; 1,5-H migration provides *ap*-**7b**, which undergoes rotation to the more stable *sp*-**7c** (48% yield).

Via a similar but heterolytic pathway shown in Scheme 3, **1** is converted to cation **1a** by treatment with triflic anhydride. We utilized $CDCl_3$ containing some D_2O as the solvent to determine the mechanism more precisely. Addition of D_2O to **1a** provides **1b** reversibly and permits a hydride transfer from **1b** to **1a**, converting the latter into **6a**, which undergoes rapid rotation to **6b**. The transfer of hydride from **1b** is followed by loss of D^+ from the residual cation, thereby providing 9-(*o*-*tert*-butylphenyl)-3*H*-fluorenone (**8**). Both products were formed in 50% yield, which supports the suggested disproportionation mechanism. Moreover, the fact that **6b** was formed exclusively bearing 9-H and not 9-D proves that the H transfer emanated solely from the fluorene 3-H even when the solvent was $CHCl_3$–H_2O.

Dynamic NMR study

As already noted, in the *ap* conformation of these structures, the *o*-*tert*-butyl is forced into the fluorene plane, an effect which is amplified with 9-methylthio and 9-methyl substituents. Surprisingly, a dynamic NMR study showed that 9-methyl exerts a larger effect than 9-methylthio. ^1H NMR spectra of **4a** in CD_2Cl_2 taken between 20 and –85°C and in DMSO-d_6 between 20 and 100°C consistently exhibited one sharp singlet for the *tert*-butyl methyls, showing that rotation of the *tert*-butyl group was faster than NMR acquisition time, even at –85°C, and therefore was not sterically impeded. The 6′-H remained a doublet within this temperature range. However, a similar study with **4c** in $CDCl_3$ showed at 20°C, after a broad singlet of nine protons for the *tert*-butyl methyls, but whose signal height was similar to that of the three protons for the 9-methyl. The 6′-H ap-

[1]

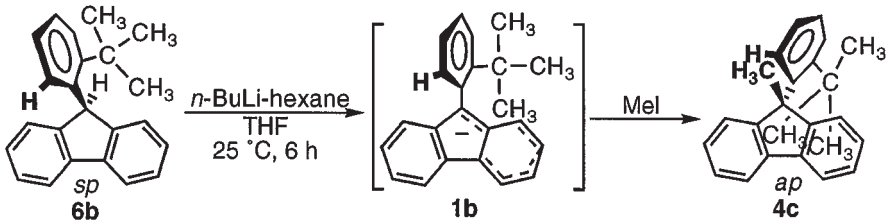

© 1999 NRC Canada

peared to be a broad doublet. At 50°C, the *tert*-butyl signal had narrowed, and its height was commensurate with nine protons relative to that for three protons of the 9-methyl, and the 6′-H became a much sharper doublet. These results indicate that, at 20°C, rotation of the *tert*-butyl group of **4c** is noticeably impeded by steric encumbrance, becoming close to or slower than NMR acquisition time, so that the methyls are detected as being "almost" nonequivalent.

Experimental

Melting points are corrected. NMR spectra were taken on a Varian VXR-300 spectrometer, 300 MHz for ^{1}H and 75 MHz for ^{13}C, in $CDCl_3$ with TMS as internal standard, except for the dynamic NMR studies, which were carried out in CD_2Cl_2, $CDCl_3$, or DMSO-d_6, as described in the discussion.

sp-9-(*o*-*tert*-Butylphenyl)-9-fluorenol (1)

Following the method recently reported for the X-ray study (2), **1** was prepared from the reaction of *o*-*tert*-butylphenylmagnesium bromide with fluorenone in 76% yield, 97% conversion based on unrecovered fluorenone; colorless crystals (from isooctane), mp 158–159°C (lit. (5) mp 156.5–158°C).

sp-9-(*o*-*tert*-Butylphenyl)-9-ethoxyfluorene (2b)

To a colorless solution of 9-(*o*-*tert*-butylphenyl)-9-fluorenol (1) (50.2 mg, 0.16 mmol) and 5 mL of ethanol in a 10 mL round-bottomed flask, 2 g of 48% HBr (9.9 mmol) was added. The reaction mixture, which became light yellow, was stirred overnight at room temperature and then extracted with hexanes (20 mL × 3). The combined extracts were washed with water, aq $NaHCO_3$, and again with water, dried (anhyd $MgSO_4$), and rotary evaporated to give a sticky oil that slowly crystallized (53.6 mg, 98.5%); colorless crystals, mp 100.5–101.5°C. ^{1}H NMR showed them to be almost pure (**2b**), δ: 1.08 (t, 3 H, *J* = 6.9 Hz), 1.81 (s, 9 H), 2.92 (q, 2 H, *J* = 6.9 Hz), 6.41 (dd, 1 H, *J* = 8.1, 1.5 Hz), 6.71 (ddd, 1 H, *J* = 1.5, 8.1, 7.2 Hz), 7.01 (ddd, 1 H, *J* = 1.5, 7.2, 8.1 Hz), 7.20 (ddd, 2 H, *J* = 1.2, 7.5, 7.2 Hz), 7.27 (dd, 2 H, *J* = 1.2, 7.5 Hz), 7.33 (ddd, 2 H, *J* = 1.5, 7.2, 7.5 Hz), 7.55 (dd, 1 H, *J* = 8.1, 1.5 Hz), 7.67 (dd, 2 H, *J* = 7.5, 1.2 Hz). ^{13}C NMR, δ: 15.06, 34.16, 37.61, 58.48, 92.74, 119.62, 124.95, 125.48, 126.01, 127.72, 128.46, 132.09, 140.37, 140.61, 149.31, 151.15. Anal. calcd. for $C_{25}H_{26}O$: C 87.68, H 7.65; found: C 87.37, H 7.62.

sp-9-(*o*-*tert*-Butylphenyl)-9-methoxyfluorene (3b)

To an Erlenmeyer flask containing a colorless solution of **1** (500 mg, 1.6 mmol) in methanol (10 mL), 1 mL of 9 M sulfuric acid (9 mmol) was added. After the flask was swirled at room temperature for 10 min, TLC showed that all the starting material was consumed; only one spot, reflecting a less polar compound, was observed. The reaction mixture was transferred to a separatory funnel with the aid of 40 mL of hexanes to rinse the flask. The mixture was washed with water, aq $NaHCO_3$, and water again. The organic layer was separated, dried over anhyd $MgSO_4$, and evaporated in vacuo, leaving a colorless oil (**3b**) (510 mg, 97.6%) that slowly crystallized at room temperature; mp: 87–89°C. Recrystallization from methanol provided crystals mp 89.5–90.5°C. ^{1}H NMR, δ: 1.76 (s, 9 H); 2.76 (s, 3 H), 6.43 (dd, 1 H, *J* = 8.1, 1.5 Hz), 6.72 (ddd, 1 H, *J* = 1.5, 8.4 Hz), 7.02 (ddd, 1 H, *J* = 1.5, 7.2, 8.1 Hz), 7.18–7.27 (m, 4 H), 7.31–7.37 (m, 2 H), 7.52 (dd, 1 H, *J* = 8.1, 1.5 Hz), 7.67 (dd, 2 H, *J* = 7.5, 0.9 Hz). ^{13}C NMR, δ: 33.93, 37.66, 49.62, 93.05, 119.59, 124.88, 125.56, 125.99, 127.72, 128.39, 128.54, 131.93, 140.36, 140.53, 141.16, 150.26. Anal. calcd. for $C_{24}H_{24}O$: C 87.76, H 7.36, found: C 87.86, H 7.32.

ap-9-(*o*-*tert*-Butylphenyl)-9-methylthiofluorene (4a)

A stoppered 10 mL round-bottomed flask containing **1** (33.6 mg, 0.107 mmol) was kept in the freezer (–15°C) for 2 h. Methanethiol (–15°C, 3 mL) was then added with a precooled pipet; the solution remained colorless. Precooled 48% HBr solution (ca. 1 mL, 8.8 mmol) was added, and the reaction mixture immediately turned light yellow. This mixture was maintained at –15°C overnight, the residual methanethiol was then evaporated in the hood and the residue extracted with hexanes (3 × 20 mL). The combined extracts were washed with water, dilute aq $NaHCO_3$, and water again. Rotary evaporation left a light yellow solid (36 mg, ca.100% yield); mp 110–113.5°C (dec., bubbling, probably MeSSMe or CH_2=S; color deepens at 90°C). ^{1}H NMR showed the solid was essentially pure **4a**, δ: 0.65 (s, 9 H), 1.70 (s, 3 H), 7.14 (d, 2 H, *J* = 7.5 Hz), 7.27 (ddd, 2 H, *J* = 7.5, 1.2 Hz), 7.30 (ddd, 1 H, *J* = 1.8, 8.1 Hz), 7.37 (ddd, 1 H, *J* = 1.8, 7.5 Hz), 7.39 (ddd, 2 H, *J* = 7.5, 1.2 Hz), 7.59 (dd, 1 H, *J* = 7.8, 1.8 Hz), 7.80 (dd, 2 H, *J* = 7.5, 0.6 Hz), 8.92 (d, 1 H, *J* = 8.4 Hz). ^{13}C NMR, δ: 16.69, 32.81, 37.42, 67.60, 120.64, 123.79, 125.36, 127.08, 127.30, 127.49, 131.43, 134.78, 133.47, 139.27, 150.71, 150.79. Recrystallization from hexanes provided colorless single crystals for X-ray analysis (4). During X-ray diffraction, the crystal became yellow. Within a few days standing on the desktop under normal fluorescent lighting, crystalline **4a** developed a deep blue coloration suggestive of homolytic decomposition.

ap-9-(*o*-*tert*-Butylphenyl)-9-methylfluorene (4c)

A 10 mL round-bottomed flask containing **6b** (2) (140 mg, 0.47 mmol) was flushed with argon and sealed with a rubber septum. Freshly distilled THF (3 mL) was syringed into the flask and to this colorless solution an *n*-BuLi solution (1.0 mL, 1.6 M, 1.6 mmol) was added via syringe. The mixture, which turned red immediately, was stirred at room temp for 6 h after which time iodomethane (0.10 mL, 1.6 mmol) was syringed dropwise into the flask. The red solution became colorless within 5 min. TLC produced two spots, the minor one matching that of the starting material. The solvent was removed in vacuo leaving a pale yellow solid. Water (5 mL) was added, the resulting slurry was extracted with hexanes, and the combined extracts were concentrated in vacuo to give a white solid, 135 mg, shown by ^{1}H NMR to be essentially **4c** and a small amount of residual **6b**. Purification via column chromatography (silica gel, hexanes) yielded colorless crystalline *ap*-**4c**, 120 mg (82% yield), mp 89.5–90.5°C. ^{1}H NMR, δ: 0.63 (bs, 9 H), 1.72 (s, 3 H), 7.10 (d, 2 H, *J* = 7.5 Hz), 7.12 (ddd, 2 H, *J* = 7.5, 1.5 Hz), 7.30 (m, 2 H), 7.33 (ddd, 2 H, *J* = 7.5, 1.2 Hz), 7.59

© 1999 NRC Canada

(m, 1 H), 7.77 (d, 2 H, J = 7.8 Hz), 8.05 (br d, 1 H, J = 6.3 Hz). ^{13}C NMR, δ: 32.92, 37.46, 38.62, 56.89, 120.61, 123.12, 125.23, 126.56, 126.74, 127.33, 130.85, 131.45, 138.73, 139.23, 150.74, 156.42. ^{1}H NMR at 50°C: the chemical shifts of the peaks were essentially the same, but the peaks at δ 0.63, 1.72, and 8.05 were much sharper. Anal. calcd. for $C_{24}H_{24}$: C 92.26, H 7.74; found: C 92.21, H 7.46.

Homolysis of 4a. Formation of *sp*-9-(*o*-*tert*-butylphenyl)fluorene (6b) and *sp*-9-(*o*-*tert*-butylphenyl)-3-methylthiofluorene (7c)

A solution of **4a** (115 mg, 0.334 mmol) in 5 mL of DMSO in a 25 mL round-bottomed flask was magnetically stirred for 30 min while heated in an oil bath maintained at 155°C. The reaction mixture was cooled to room temperature and transferred to a separatory funnel, the residue was transferred by several washings with ether, and the combined solution was washed with water to remove DMSO. The ethereal solution was dried (anhyd $MgSO_4$) and evaporated in vacuo, leaving a black sticky oil. ^{1}H NMR showed the presence of two major products, and only a trace amount of **4a**. The two products were separated and isolated by "dry-column chromatography" (silica gel; hexane). From the first fraction **6b** (24 mg, 24.1% yield) was isolated and identified by mp (179.5–180.5°C), NMR, and X-ray crystallography (2). Evaporation of the second fraction produced **7c** (55 mg, 47.8% yield), which had almost the same R_f value as **4a** in TLC (10:1 hexanes:ether). Recrystallization from hexanes gave almost colorless crystals of **7c**, mp 156.5–157.5°C (no dec.), which were used for X-ray analysis (8). ^{1}H NMR, δ: 1.70 (s, 9 H), 2.58 (s, 3 H), 5.83 (s, 1 H), 6.22 (dd, 1 H, J = 7.8, 1.5 Hz), 6.87 (ddd, 1 H, J = 7.8, 7.2, 1.2 Hz), 7.11 (ddd, 1 H, J = 8.1, 7.2, 1.8 Hz), 7.14 (d, 2 H, J = 1.2 Hz), 7.23 (m, 2 H), 7.38 (m, 1 H), 7.48 (dd, 1 H, J = 8.1, 1.5 Hz), 7.73 (dd, 1 H, J = 1.2 Hz), 7.81 (dd, 1 H, J = 7.5, 1.2 Hz). ^{13}C NMR, δ: 16.51, 32.57, 35.62, 50.62, 118.37, 119.88, 125.21, 125.43, 125.79, 126.19, 126.34, 126.42, 127.10, 127.70, 130.82, 137.09, 139.76, 140.47, 141.89, 147.32, 148.14, 150.39.

Reaction of 1 with triflic anhydride in $CDCl_3$–D_2O. Formation of equimolar quantities of 6b and 9-(*o*-*tert*-butylphenyl)-3*H*-fluorenone (8)

To a stirred colorless solution of **1** (63.2 mg, 0.20 mmol) in 1.0 mL of $CDCl_3$, three drops of D_2O followed by 0.1 mL of triflic anhydride (0.059 mmol) were added. The reaction mixture turned deep red immediately. The reaction flask was glass-stoppered and the mixture stirred at room temperature for 6 h during which time it gradually turned brown. TLC (9:1 hexanes:ether) showed mainly the presence of **1**, **6b**, and a red compound. The mixture was put on a silica-gel column through which $CDCl_3$ was passed, leaving the triflic acid and D_2O on the column. The first fraction collected provided a slightly off-white solid, 42 mg, shown by ^{1}H NMR to be composed only of **1** and **6b** (with no D atom on C-9). The second fraction yielded a red solid, 18 mg; recrystallization from hexanes provided red crystals, mp 142.5–143.5°C, identified as **8**. The yield (by NMR) of **6b** as well as **8** was 29%, or close to 50% of each, based on unrecovered starting material. IR (film on salt plate): 3055 (w), 2962 (m), 2930 (m), 2865 (w), 1640 (m), 1620 (s), 1597 (m), 1562 (m), 755 (m), 740 (s) cm^{-1}. ^{1}H NMR of **8**, δ: 1.32 (s, 9 H), 6.03 (dd, 1 H, J = 1.8, 9.6 Hz), 6.61 (d, 1 H, J = 1.8 Hz), 6.77 (dd, 1 H, J = 1.5, 6.9 Hz), 6.84 (d, 1 H, J = 9.9 Hz), 7.00 (dd, 1 H, J = 1.8, 7.5 Hz), 7.12 (ddd, 1 H, J = 1.2, 7.5 Hz), 7.17 (ddd, 1 H, J = 1.5, 7.8 Hz), 7.26 (ddd, 1 H, J = 1.2, 7.5 Hz), 7.39 (dd, 1 H, J = 1.8, 8.1 Hz), 7.42 (ddd, 1 H, J = 1.2, 7.5 Hz), 7.62 (dd, 1 H, J = 1.2, 8.1 Hz). ^{13}C NMR, δ: 32.30, 36.58, 121.53, 121.94, 124.36, 125.63, 127.27, 127.64, 128.79, 129.09, 129.71, 130.03, 130.51, 131.99, 134.10, 136.40, 146.67, 149.25, 150.92, 157.05, 189.03. Anal. calcd for $C_{23}H_{20}O$: C 88.43, H 6.45; found: C 88.59, H 6.47.

Acknowledgments

Partial support of this research from Southern Illinois University through doctoral fellowship (Y.H.) and Distinguished Professorship (C.Y.M.) funding and from the University Research Foundation – La Jolla is graciously acknowledged.

References

1. Y. Hou. A stereochemical and mechanistic study of reactions of rotationally restricted 9-substituted fluorenes and brief study of factors responsible for the chirality of crystalline urazoles. Ph.D. dissertation. Southern Illinois University at Carbondale, Carbondale. 1997.
2. P.D. Robinson, Y. Hou, H.G. Lutfi, and C.Y. Meyers. Acta Crystallogr. **C54**, 73 (1998).
3. C.Y. Meyers, Y. Hou, H.G. Lutfi, P.D. Robinson, H.E. Dunn, and J.W. Seyler. 213th Am. Chem. Soc. Natl. Meet. San Francisco, April 1997. Abstract ORGN 351.
4. C.Y. Meyers, Y. Hou, and P.D. Robinson. Acta Crystallogr. **C55**, 626 (1999).
5. M. Nakamura, N. Nakamura, and M. Ōki. Bull. Chem. Soc. Jpn. **50**, 1097 (1977).
6. M. Ōki. The chemistry of rotational isomers. *Edited by* K. Hafner, J.-M. Lehn, C.W. Rees, P. von R. Schleyer, B.M. Trost, and R. Zahradník. Springer–Verlag, New York. 1993.
7. C.Y. Meyers, Y. Hou, H.G. Lutfi, and P.D. Robinson. 210th Am. Chem. Soc. Natl. Meet. Chicago, August 1995. Abstract ORGN 297.
8. P.D. Robinson, Y. Hou, and C.Y. Meyers. Acta Crystallogr. **C54**, CIF access, Oct. DVN IUC 9800051 (1998).
9. C.Y. Meyers, Y. Hou, D. Scott, and P.D. Robinson. Acta Crystallogr. **C53**, 1149 (1997).
10. P.D. Robinson, Y. Hou, and C.Y. Meyers. Acta Crystallogr. **C54**, 1173 (1998).
11. H. Suzuki, T. Murafuji, and N. Azuma. J. Chem. Soc. Perkin Trans. 1, 1169 (1993); L.J. Adjima, C.C. Chiang, I.C. Paul, and J.C. Martin. J. Am. Chem. Soc. **100**, 953 (1978); J.C. Martin and T.M. Balthazor. J. Am. Chem. Soc. **99**, 152 (1977); T.M. Balthazor and J.C. Martin. J. Am. Chem. Soc. **97**, 5634 (1975).
12. Z. Berkovitch-Yellin and L. Leiserowitz. Acta Crystallogr. **B40**, 159 (1984).
13. R. Thaimattam, D.S. Reddy, F. Xue, T.C.W. Mak, A. Nangia, and G.R. Desiraju. J. Chem. Soc. Perkin Trans. 2, 1783 (1998); C.J. Marjo, M.L. Scudder, D.C. Craig, and R. Bishop. J. Chem. Soc. Perkin Trans. 2, 2099 (1997); M.C. Wahl and M. Sundaralingam. TIBS, **22**, 97 (1997); G.R. Desiraju. Acc. Chem. Res. **29**, 441 (1996); R. Taylor and O. Kennard. J. Am. Chem. Soc. **104**, 5063 (1982).
14. IUPAC tentative rules, Sect. E. Fundamental stereochemistry. J. Org. Chem. **35**, 2861 (1970).

© 1999 NRC Canada

^{13}C, ^{15}N, and ^{18}O equilibrium isotope effects and fractionation factors[1]

Mark A. Rishavy and W.W. Cleland

Abstract: A listing of ^{13}C, ^{15}N, and ^{18}O equilibrium isotope effects and fractionation factors for atoms in specific positions is provided. Empirical factors that can be used to adjust these fractionation factors for more complex structures are presented and discussed. While much work needs to be done to determine equilibrium isotope effects for these heavy atoms, the values tabulated here should be useful to anyone working with isotope effects involving these atoms.

Key words: equilibrium isotope effects, fractionation factors, ^{13}C, ^{15}N, ^{18}O.

Résumé : On présente une liste des effets isotopiques d'équilibre et des facteurs de fractionnement du ^{13}C, du ^{15}N et du ^{18}O relatifs à des atomes dans des positions spécifiques. On présente et on discute des facteurs empiriques qui peuvent être utilisés pour ajuster ces facteurs de fractionnement dans les cas de structures plus complexes. Même si beaucoup de travail reste à faire pour déterminer les effets isotopiques d'équilibre pour ces atomes lourds, les valeurs rapportées ici devraient s'avérer utiles pour quiconque s'intéresse aux effets isotopiques impliquant ces atomes.

Mots clés : effets isotopiques d'équilibre, facteurs de fractionnement, ^{13}C, ^{15}N et ^{18}O.

[Traduit par la Rédaction]

Substitution of a heavier isotope for a lighter one not only affects the rates of chemical reactions, but also changes equilibrium constants if the isotopic atom is more stiffly bonded in the reactant than in the product or vice versa. Since the equations for kinetic isotope effects include the equilibrium isotope effect in one of the numerator terms (1), it is important for anyone trying to interpret kinetic isotope effects to know these values.

Equilibrium isotope effects are commonly expressed as the ratio of K_{eq} for the light isotope to K_{eq} for the heavy one. A leading superscript indicates the isotope involved. Thus, $^{13}K_{eq}$ is $K_{eq\ C\text{-}12}/K_{eq\ C\text{-}13}$. $^{14}K_{eq}$, $^{15}K_{eq}$, and $^{18}K_{eq}$ are equilibrium isotope effects caused by replacement of ^{12}C, ^{14}N, or ^{16}O by ^{14}C, ^{15}N, or ^{18}O, respectively. Values greater than unity show that the heavy isotope is enriched in the reactant, while values less than unity show enrichment in the product. The equilibrium isotope effect in the back reaction is the reciprocal of that in the forward reaction. For comparison of ^{14}C and ^{13}C equilibrium isotope effects (2),

$$[1] \qquad {}^{14}K_{eq} = 1 + 1.9({}^{13}K_{eq} - 1)$$

When a chemical reaction has sat long enough for both chemical and isotopic equilibrium to be reached (we usually allow 10 times longer for the latter to ensure that true isotopic equilibrium has been reached), the equilibrium isotope effect is readily measured by determining the mass ratio at the atom of interest in both the reactant and product. This is particularly simple for enzyme-catalyzed reactions, as the enzyme can be denatured or filtered off with an ultrafiltration apparatus to leave a mixture of reactant and product that can be separated and analyzed at one's leisure. Isotope ratio mass spectrometry is the usual method of analysis used for ^{13}C, ^{15}N, and ^{18}O because of the precision that can be obtained (3). Radioactive counting to determine ^{14}C isotope ratios is generally an order of magnitude less precise. Other methods such as NMR may also be used. The effect of ^{18}O substitution on the acid dissociation constant of any carboxylic acid, phenol, or alcohol containing ^{13}C attached to the oxygen, or in any phosphate group, is readily determined by titrating a 50–50 mixture of ^{16}O and ^{18}O-containing species and determining the separation between the ^{13}C or ^{31}P signals for the ^{16}O and ^{18}O species (the latter resonating slightly upfield) as the chemical shift changes with pH (4). If there is an ^{18}O equilibrium isotope effect on the pK, the ^{16}O species ionizes at a slightly lower pH than the ^{18}O one, and this separation in signals will increase to a

Received September 24, 1998.

This paper is dedicated to Professor Jerry Kresge in honor of his many contributions to physical organic chemistry.

M.A. Rishavy and W.W. Cleland.[2] Institute for Enzyme Research and Department of Biochemistry, University of Wisconsin–Madison, 1710 University Ave, Madison, WI 53705, U.S.A.

[1]Supported by NIH grant 18938.

[2]Author to whom correspondence may be addressed. Telephone: (608) 262-1373. Fax: (608) 265-2904.
e-mail: Cleland@enzyme.wisc.edu

© 1999 NRC Canada

maximum at the average of the p*K* values and then decrease again as the titration is continued. The method gives excellent values because the separation between the ^{16}O and ^{18}O-containing species is so small compared with the change in chemical shift seen during the titration. NMR has also been used to determine equilibrium isotope effects in carbenium ions where the hydride shift between adjacent atoms is fast (5).

It is convenient for many purposes to tabulate fractionation factors, which are equilibrium isotope effects for exchange of heavy isotope between the compound of interest and a reference molecule. Hartshorn and Shiner (6) originally used acetylene as the reference for deuterium and ^{13}C isotope effects, but biochemists have found it more convenient to use H_2O as the reference for deuterium and ^{18}O isotope effects and aqueous CO_2 and NH_3 for ^{13}C and ^{15}N isotope effects, respectively, and these reference molecules will be used in our tabulations.[3] A fractionation factor greater than unity means the heavy isotope becomes enriched in the compound of interest rather than in the reference molecule, while a value less than unity indicates that the heavy isotope becomes enriched in the reference molecule.

Several tabulations of fractionation factors for deuterium are available (7, 8), but the data for ^{13}C, ^{15}N, and ^{18}O are scattered. In the present article, we tabulate those values known to us, including several previously unpublished numbers. We also show how several empirical rules can be used to extend the usefulness of the experimental or calculated fractionation factors for small molecules to ones with more complex structures. Hopefully, we will stimulate research in this field, since there are still numerous fractionation factors that are not well known, and the empirical rules for extending them need further verification.

^{13}C equilibrium isotope effects and fractionation factors

Table 1 shows a number of experimental ^{13}C equilibrium isotope effects. Most were measured enzymatically using isotope ratio mass spectrometry. These should be reasonably accurate, but except for decarboxylations, where CO_2 is one component of the reaction, the actual fractionation factors of the carbons involved expressed relative to aqueous CO_2 are less certain. By using the data in Table 1 and fractionation factors calculated by Hartshorn and Shiner (6) for various small molecules (see Table 2), however, certain empirical rules based on these values can be used to calculate approximate ^{13}C fractionation factors for other molecules.

Replacing a hydrogen on the isotopic carbon with a CH_3 group multiplies the fractionation factor by 1.013 (compare ethane and methane in Table 2), while replacing it with OH multiplies it by 1.019 (methanol vs. methane). Replacement of H by NH_2 and NH_3^+ raises fractionation factors by 1.012 and 1.016, respectively (neutral or protonated methylamine vs. methane). These increases are largely due to effects on the stretching vibrations. A C-H stretch is not very ^{13}C-sensitive because most of the motion is by the lighter hydrogen atom, but C-C, C-N, and C-O stretches are ^{13}C-sensitive. While these increases in fractionation factors apply to modifications of methane, they will be smaller for changes to more stiffly bonded atoms. For example, the increase in fractionation factor for replacing H with C drops to 1.010 for replacement on a carbon of ethane to give propane with the center atom the isotopic one.

When we consider the effects of replacing hydrogen with a heavier atom on a carbon (or other heavy atom) attached to the isotopic one, the major effects will be on bending vibrations. A [C]-C-H bending vibration is not very sensitive to ^{13}C in the bracketed carbon because the lighter hydrogen undergoes most of the motion. Note the small equilibrium isotope effect of 0.9986 (1/1.0014) in Table 1 for protonating benzoic acid, which adds a [C]-O-H bending vibration. A [C]-C-C bending vibration, however, *is* ^{13}C-sensitive. The increase in fractionation factor for replacing H with CH_3 in this situation appears to be 1.004 (terminal carbon of propane (0.960) vs. that of ethane (0.956)), at least for the first replacement.

The increase in fractionation factor should be somewhat higher for replacement by oxygen or nitrogen because of their increased mass. For example, 6-phosphogluconate has a CHOH group at C-2, while malate has a CH_2 group at C-3. Both have a CHOH group at the next carbon (C-3 of 6-phosphogluconate; C-2 of malate). The fractionation factor of C-1 of 6-phosphogluconate is higher than that of C-4 of malate by a factor of 1.008 ± 0.001 (second and third entries of Table 2). This is bigger than the factor of 1.004 for replacement of hydrogen by CH_3, but may be a valid indication of the greater effect of oxygen than carbon in stiffening vibrational modes.

The effect of replacing hydrogen with a heavier atom on the second carbon from the isotopic one will largely be on the torsional vibrations. Again, a [C]-C-C-H torsional vibration is not very sensitive to ^{13}C in the bracketed carbon, but a [C]-C-C-C one will be. Shiner and co-workers (6, 8) did not include any four carbon molecules in their calculations, but we can get some estimate of this effect by comparing the fractionation factors of two of the carboxylic acids which have been equilibrated with CO_2.

The structure of isocitrate differs from that of malate by having a carboxymethyl group attached to C-3 of malate (the carbon next to the isotopic carboxyl). The CH_2 group of this addition is expected to raise the fractionation factor of the carboxyl removed by isocitrate dehydrogenase by 1.004, but the overall increase in fractionation factor from C-4 of malate to the carboxyl of isocitrate is a factor of 1.015 ± 0.001 (first and third entries in Table 2). While some of the increase in fractionation factor of 1.015/1.004 = 1.011 is certainly caused by the added torsional [C]-C-C-C vibration, some may come from other effects such as steric crowding as the isotopic carbon is now secondary, not primary, and some may represent experimental error. This example illustrates the effect that torsional vibrations can have on fractionation factors. Changes in torsional frequencies have been invoked to explain ^{15}N isotope effects on carbamyl-*P* hydrolysis (9) and the differing fractionation factors of the two cysteine SH protons in the active site of proline racemase (10).

[3] The deuterium fractionation factors of Shiner are readily converted to the H_2O reference by division by his fractionation factor of water (see ref. 7, footnote *c*, p. 109), while the ^{13}C ones are corrected by division by his fractionation factor for CO_2 (see footnote *r*, p. 110, of ref. 7).

© 1999 NRC Canada

Table 1. ^{13}C equilibrium isotope effects.

Reaction[a]	$^{13}K_{eq}$ at 25°C	Reference
($^{-}$OOC-CHOH-)($^{-}$OOC-CH_2)-CH-[C]OO^{-} (isocitrate) === α-ketoglutarate + $[C]O_{2aqueous}$	1.0027 ± 0.0005	18
$^{=}O_3POCH_2$-$(CHOH)_4$-[C]OO^{-} (6-phosphogluconate) === ribulose-5-*P* + $[C]O_{2aqueous}$	0.996 ± 0.001	19
$^{-}$OOC-CHOH-CH_2-[C]OO^{-} (malate) === pyruvate + $[C]O_{2aqueous}$	0.988 ± 0.0003	20
$^{-}$OOC-C=O-CH_2-[C]OO^{-} (oxaloacetate) === H[C]O_3^{-}	0.9985 ± 0.0001	21
H[C]O_3^{-} === $[C]O_{2aqueous}$	1.009	22
—— $(CHOH)_3$-[C]HOH === —— $(CHOH)_3$-[C]=O | | | | $CH(CH_2OPO_3^{=})$-O $CH(CH_2OPO_3^{=})$-O	0.992 ± 0.001	23
—— $(CHOH)_3$-[C]HOH === —— $(CHOH)_3$-[C]=O | | | | $CH(CH_2OPO_3^{=})$-S $CH(CH_2OPO_3^{=})$-S	0.9941 ± 0.0004	17
CH_3-[C]=O-SCoA === CH_3-[C]=O-$OPO_3^{=}$	0.997 ± 0.001	17
$^{=}O_3PO$-CH_2-CHOH-[C]$H(OH)_2$ === $^{=}O_3PO$-CH_2-CHOH-[C]=O-$OPO_3^{=}$	0.995 ± 0.001	17
$^{=}O_3PO$-CH_2-CHOH-[C]$H(OH)_2$ === $^{=}O_3PO$-CH_2-CHOH-[C]H=O	1.003[b] ± 0.001	17
$^{=}O_3PO$-CH_2-CHOH-[C]H=O === $^{=}O_3PO$-CH_2-CHOH-[C]HOH-SCH_2-CH_2OH	1.004[b] ± 0.001	17
φ-[C]OOH === φ-[C]OO^{-} + H^{+}	1.0014	24
$[C]O_{2gas}$ === $[C]O_{2aqueous}$	1.0011	22
$[C]O_{2gas}$ === $[C]O_{2dioxane}$	1.0017	21
$(CH_3)_2$-[C^{+}]-CH-$(CH_3)_2$ === $(CH_3)_2$-[C]H-C^{+}-$(CH_3)_2$	1.0073[c]	5
ϕ_3-[C]Cl === ϕ_3-[$C]^{+}$ + Cl^{-}	0.983[d] ± 0.003	25
$^{-}$OOC-[C]HOH-CH_2-COO^{-} === $^{-}$OOC-[C]=O-CH_3 + CO_2	1.0102 ± 0.0001	20
$^{-}$OOC-CHOH-[C]H_2-COO^{-} === $^{-}$OOC-C=O-[C]H_3 + CO_2	1.0113 ± 0.0001	20
$^{-}$OOC-[C]=O-CH_2-COO^{-} === $^{-}$OOC-[C]HOH-CH_2-COO^{-}	1.0091 ± 0.0003	*e*
$^{-}$OOC-C=O-[C]H_2-COO^{-} === $^{-}$OOC-CHOH-[C]H_2-COO^{-}	0.9964 ± 0.0003	*e*
$^{-}$OOC-[C]=O-CH_2-COO^{-} === $^{-}$OOC-[C]HNH_3^{+}-CH_2-COO^{-}	1.0074 ± 0.0010	*e*
$^{-}$OOC-C=O-[C]H_2-COO^{-} === $^{-}$OOC-$CHNH_3^{+}$-[C]H_2-COO^{-}	0.9965 ± 0.0004	*e*
$^{-}$OOC-[C]=O-CH_3 === $^{-}$OOC-[C]HNH_3^{+}-CH_3	1.012 ± 0.001	*e*
$^{-}$OOC-C=O-[C]H_3 === $^{-}$OOC-$CHNH_3^{+}$-[C]H_3	0.9987 ± 0.0006	*e*
$^{-}$OOC-[C]=O-CH_3 === $^{-}$OOC-[C]HOH-CH_3	1.008 ± 0.001	*e*
$^{-}$OOC-C=O-[C]H_3 === $^{-}$OOC-CHOH-[C]H_3	0.9980 ± 0.0005	*e*
φ-[C]H_2OH === φ-[C]H=O	0.9847 ± 0.0005	26
NH_2-[C]O_2^{-} === $[C]O_3H^{-}$	1.0024 ± 0.0001	27
NH_2-[C]O_2^{-} === NH_2-[C]=O-$OPO_3^{=}$	0.9983 ± 0.0005	27
CH_2-CH_2-N-[C]O_2^{-} === CO_2 gas | | CH_2-CH_2–	1.0112 ± 0.0007	21

[a]The atom in brackets is the isotopic one, the replacement of which with ^{13}C gives the equilibrium isotope effect. $^{13}K_{eq}$ is the K_{eq} for ^{12}C divided by that for ^{13}C.

[b]Maximum value; true value could be as low as halfway to unity.

[c]In SbF_5/SO_2ClF; value extrapolated to 25°C.

[d]In liquid SO_2 at 0°C.

[e]This work (see Experimental).

© 1999 NRC Canada

Table 2. ^{13}C fractionation factors relative to aqueous CO_2.

Group[a]	Fractionation factor	Reference
Experimentally determined:		
(C-CHOH)(C-CH_2)-CH-[C]OO^-	1.003	18
C-$(CHOH)_2$-[C]OO^-	0.996	19
C-CHOH-CH_2-[C]OO^-	0.988	20
$^-$OOC-C=O-CH_2-[C]OO^-	1.0075	21
[C]O_{2gas}	1.001	22
[C]O_3H^-	1.009	22
NH_2-[C]O_2^-	1.011	27
NH_2-[C]=O-$OPO_3^=$	1.013	27
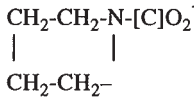	1.0123	21
Calculated from full force fields (gas phase):		
Acetylene	0.939	6
Methane	0.944	6
Ethylene	0.955	6
Cyclopropane	0.955	6
Ethane	0.956	6
[C]H_3-CH_2-CH_3	0.960	6
CH_3-[C]H_2-CH_3	0.966	6
Methyl iodide	0.935	6
Methyl bromide	0.942	6
Methyl chloride	0.945	6
Methyl fluoride	0.964	6
[C]H_3-CN	0.955	6
[C]H_2=CBr_2	0.950	6
[C]H_2=CF_2	0.953	6
Methyl mercaptan	0.943	8
[C]H_3-Li	0.906	8
[C]H_3-SnH_3	0.938	8
[C]H_3-SiH_3	0.940	8
[C]H_3-SeH	0.947	8
[C]H_3-AsH_2	0.948	8
[C]H_3-PH_2	0.949	8
[C]H_3-Cd-CH_3	0.928	8
[C]H_3-Zn-CH_3	0.930	8
[C]H_3-Hg-CH_3	0.933	8
[C]O	0.923	[b]
Methylamine	0.955	[b]
Methylazide	0.957	[b]
Protonated methylamine	0.959	[b]
Methanol	0.962	[b]
Nitromethane	0.966	[b]
Formaldehyde	0.971	[b]
[C]H_3-CH=O	0.959	[b]
CH_3-[C]H=O	0.985	[b]
[C]H_3O-CH=O	0.964	[b]
CH_3O-[C]H=O	0.987	[b]

[a]The fractionation factor is for the atom in brackets.

[b]W.E. Buddenbaum and V.J. Shiner, Jr. Unpublished results.

Calculated fractionation factors for keto acids

In the cases of oxaloacetate and pyruvate, corrections have to be made to the equilibrium isotope effects in Table 1 for the degree of hydration and enolization of these molecules. Pyruvate is 6% hydrated at 25°C (11), while the dianion of oxaloacetate is 18% hydrated and 8% enolized (12). In calculating the fractionation factors for the keto structures, we can use the empirical rules above to apportion the observed equilibrium isotope effect among the various structures.

© 1999 NRC Canada

As an example of this procedure, consider C-2 of L-malate. Relative to C-2 of propane (fractionation factor 0.966), a hydrogen is replaced by OH at C-2, three hydrogens are replaced by two oxygens at C-1, and a hydrogen is replaced by a carboxyl group at C-3. To evaluate the fractionation factor of C-2, we multiply 0.966 by 1.019 for the hydroxyl at C-2, by 1.008 twice for the oxygen replacements at C-1, by 1.004 for the addition of C-4, and by 1.011 twice for the two oxygens attached to C-4 to give 1.026.[4]

For the hydrate of oxaloacetate, we multiply 1.026 by 1.019 for the extra hydroxyl at C-2 to get 1.046. For the enol form of oxaloacetate, we start with ethylene (0.955) and multiply by the same factors as for malate, except that we must also multiply by 1.010 for the addition of C-1, giving 1.013. Since the apparent fractionation factor of C-2 of oxaloacetate is higher than that of malate by 1.009 (third and fourth entries in Table 2), we can write:

$$[2] \qquad 1.026 \times 1.009 = 1.0352$$

$$= 0.18 \times 1.046 + 0.08 \times 1.013 + 0.74X$$

where X is the fractionation factor of the keto form, which is 74% of the total, the rest being 18% hydrate and 8% enol. Solution of this equation gives 1.035 for C-2 of the keto form, so the fractionation factor for the keto carbon is higher than that for a CHOH carbon (1.026) by 1.009. The fact that a keto carbon is more stiffly bonded than a CHOH one by 0.8–0.9% is born out by the equilibrium isotope effect for the conversion of glucose-6-*P* to 6-*P*-gluconolactone, which is 0.992 (Table 1). In comparison, the aldehyde carbon of benzaldehyde is more stiffly bonded than the CH_2OH carbon of benzyl alcohol by 1.5% (Table 1). Thus, the stiffening effect of replacing H with C on the carbonyl carbon diminishes the difference between carbonyl and hydroxyl-bound carbons. This is clear evidence that the empirical factors are not fully multiplicative. However, the $^{13}K_{eq}$ value of 1.003 for dehydration of glyceraldehyde hydrate is only slightly less than the value of 1.004 predicted from a value of 1.015 for reduction of an aldehyde to a CH_2OH group, divided by 1.019 for subsequent replacement of H with OH to give the hydrate.

Application of this method to C-2 of lactate involves replacing H with OH at C-2 of propane and replacing three hydrogens with two oxygens at C-1. For the fractionation factor of C-2 we get $0.966 \times 1.019 \times 1.008 \times 1.008 = 1.000$. The hydrate of pyruvate will then have a fractionation factor 1.019 times this or 1.019. Since the observed fractionation factor of C-2 of pyruvate is less than that of C-2 of malate (calculated above as 1.026) by a factor of 1.01 (Table 1), we can write:

$$[3] \qquad 1.026/1.01 = 1.0158 = 0.06 \times 1.019 + 0.94X$$

where X is the fractionation factor of the keto form, which makes up 94% of the mixture at 25°C, the rest being hydrate. Solution of this equation gives 1.016 as the fractionation factor for C-2 of ketopyruvate.

We can compare this value with the one computed above for oxaloacetate by mutiplying the value of 1.016 for pyruvate by 1.004 for adding C-4 and twice by 1.011 for adding the two oxygens at C-4. The resulting value of 1.042 is higher than the value of 1.035 computed above, suggesting that the correction factors being used may be too large, especially when two of them are being applied at the same time. Thus, the torsional correction may be 1.011 for the first added atom, but smaller for the second, or the value is too high for experimental reasons. Clearly, more experimental equilibrium isotope effects are needed to clarify how these empirical rules should be applied and to pin down their values more accurately.

It is of interest to note that the keto carbon of pyruvate has a higher fractionation factor than the $CHNH_3^+$ carbon of alanine by 1.012 (Table 1). This implies that a CHOH carbon, which we have estimated above to have a fractionation factor lower than a keto carbon by 1.009, has a higher fractionation factor than a $CHNH_3^+$ one by 1.012/1.009 = 1.003. The calculated fractionation factor for methanol is higher than that for protonated methylamine by the same ratio (Table 2).

A similar analysis can be carried out for C-3 of malate and oxaloacetate. Applying the correction factors discussed above gives 1.0153 for the fractionation factor of C-3 of malate, 1.0234 for C-3 of the hydrate, and 1.0008 for the enol. With the equilibrium isotope effect of 0.996 for the reduction of oxaloacetate to malate, solution of the equations gives 1.0094 for the fractionation factor of C-3 of the keto form, or 0.6% lower than the estimate of 1.0153 for C-3 of malate. This difference, if real, may represent the effect of hyperconjugation.

However, when the same analysis is applied to C-3 of lactate, one estimates that the fractionation factor should be 0.989, while comparison of pyruvate with malate (Table 1) suggests a value of 1.005 for C-3 of pyruvate. The difference here is in the opposite direction from that for malate and oxaloacetate, suggesting that some of the empirical factors may not be correct, or the experimental numbers are off. The near equivalence of the fractionation factors for C-3 of pyruvate and alanine (Table 1) suggests that the latter is probably correct, and the effect of hyperconjugation is less than 0.5%.

Other ^{13}C fractionation factors

Replacement of H or O with S has some interesting results on ^{13}C fractionation factors. Methyl mercaptan actually has a lower fractionation factor (0.943) than methane (0.944 in Table 2), so replacement of H with S does not stiffen the bonding in this case.

The fractionation factor of an aldehyde carbon is less than that of its hydrate by a maximum of 1.003, while the thiohemiacetal is less stiffly bonded than the free aldehyde by a maximum value of 1.004, for an overall ratio of 1.007 between hydrate and thiohemiacetal. Since a thioester is only stiffer than a hydrated aldehyde by 1.002 (compare re-

[4] It is not clear that it is valid to multiply these factors together in this way. For ^{15}N equilibrium isotope effects (see below) the effect of a second substitution is diminished. In the present calculation, errors will largely cancel out, however, as many of the same factors are applied to both of the molecules being considered. Thus, the calculated fractionation factors for the individual molecules may be too high, but the difference between two molecules is likely to be more accurate.

© 1999 NRC Canada

Table 3. ^{15}N equilibrium isotope effects.

Reaction		$^{15}K_{eq}$ at 25°C	Reference
$NH_{3aqueous}$ === NH_{3gas}		1.007 ± 0.002	28
NH_4^+ === $NH_{3aqueous}$		1.0192 ± 0.0001	13
ND_4^+ === $ND_{3aqueous}$		1.0246 ± 0.0001	13
Aspartate$^{=+}$ === fumarate$^=$ + NH_4^+		1.0138 ± 0.0001	13
Phenylalanine$^-$ === cinnamate$^-$ + NH_3		1.0163 ± 0.0001	13
$^-$OOC-C(R)=NH_2^+ === NH_4^+		1.00	13
$^-$OOC-C(R)=ND_2^+ === ND_4^+		0.99	13
Dihydrophenylalanine- + E=CH_2 === E-CH_2-NH_2^+-R		0.979	13
Acetylpyridine-NAD === acetylpyridine-NADH (N-1 of pyridine)		1.0042 ± 0.0007	29
Aspartate$^{+=}$ === *N*-carbamyl-aspartate$^=$ (amino N)	in H_2O	0.9990 ± 0.0002	14
	in D_2O	1.0071 ± 0.0002	14
pNO_2-C_6H_4-O-C=O-CH_3 === *p*NO_2- C_6H_4-O^-		1.0016 ± 0.0006	30
NO_3^- === HNO_2	(0°C)	1.057 ± 0.001	31
NO_2^- === NO_{gas}	(0°C)	1.024 ± 0.002	32
NO_3^- === NO_{gas}	(0°C)	1.086 ± 0.001	33
Other deprotonation reactions:			
Pyridinium ion (in H_2O)		1.0211 ± 0.0003	34
Pyridinium ion (in D_2O)		1.0250 ± 0.0003	35
p-Nitrophenol		1.0023 ± 0.0001	36
Phenylalanine (NH_3^+)		1.016 ± 0.002	13
Anilinium ion		1.019	37
N,*N*-Dimethylanilinium ion		1.014	38

actions of both to give an acyl phosphate), we might expect that the ^{13}C equilibrium isotope effect for oxidation of a thiohemiacetal to a thioester would be less inverse than that for oxidation of a hemiacetal by 1.005. The actual ratio is 1.002 (compare glucose-6-*P* and 5-thioglucose-6-*P* oxidations), suggesting that the difference between hydrated aldehyde and a thiohemiacetal is only 1.004, rather than 1.007. In any case, S replacement for O makes much less difference in these molecules than it does between methanol and methyl mercaptan, where the ratio is 1.02. The small difference between acetyl-CoA and acetyl-*P* is another example.

Two at first surprising entries in Table 1 are those for the hydride shift in the dimethyl-*tert*-butylcarbenium ion and for the ionization of triphenylmethyl chloride (in contrast to the other entries that relate to aqueous solution, these equilibria were measured in SbF_5/SO_2ClF or liquid SO_2). Opposite to intuition, ^{13}C is enriched in the carbenium ion carbon, rather than in the neighboring sp^3 carbon. The explanation is the high degree of hyperconjugation that increases the bond order of the bonds to the carbenium ion carbon. Similarly, ^{13}C is enriched in the ionized triphenylmethyl carbenium ion, rather than in triphenylmethyl chloride, as the result of conjugation with the phenyl rings.

^{15}N equilibrium isotope effects and fractionation factors

Table 3 shows ^{15}N equilibrium isotope effects that have been determined experimentally. The value for NH_3 in the gas phase was determined from the mass ratio of ammonia gas in equilibrium with aqueous ammonia. The NH_4^+–NH_3 equilibrium isotope effect was determined by letting ammonia equilibrate between two compartments separated by a membrane that will pass NH_3 and not NH_4^+, with one compartment containing excess NH_4^+. O'Leary (unpublished) tried to determine this value by sampling the first portion of ammonia passing through such a membrane from a compartment containing ammonia and excess NH_4^+, but his unpublished value of 1.039 included the kinetic isotope effect on diffusion through the membrane, which could easily be 2%.

When ammonium ion is deuterated, the ^{15}N equilibrium isotope effect on deprotonation is 0.5% greater, and a similar increase of 0.4% is seen for deprotonation of pyridinium ion in D_2O. This effect depends on the numbers of deuterons on each side of the reaction. Thus when a positively charged imine (=ND_2^+) is hydrolyzed to ND_4^+, there are four deuterons attached to nitrogen on the right side and two on the left

© 1999 NRC Canada

Table 4. ^{15}N fractionation factors relative to aqueous NH_3.

Group[a]	Fractionation factor	Reference
Experimentally determined:		
NH_{3gas}	0.993	28
NH_4^+	1.0192	13
Amino acid (unprotonated NH_2)	1.0163	13
Amino acid (protonated NH_3^+)	1.0333	13
Protonated imine	1.0192	13
Protonated secondary amine	1.038	13
Calculations from full force fields (gas phase):		
NO	0.9615	[b]
HCN	0.995	[b]
$H_2C(CN)_2$	0.997	[b]
CH_3-CN	0.9983	[b]
[N]NO	0.9996	[b]
N[N]O	1.0527	[b]
$CH_3NN[N]$	1.0013	[b]
$CH_3[N]NN$	1.0096	[b]
$CH_3N[N]N$	1.0428	[b]
N_2	1.0029	[b]
CH_3NH_2	1.0060	[b]
$CH_3NH_3^+$	1.0296	[b]
NO_2	1.0115	[b]
CH_3-NC	1.0208	[b]
CH_3NO_2	1.0590	[b]
NO_3^-	1.0817	[b]

[a]The fractionation factor is for the nitrogen atom in brackets.
[b]W.E. Buddenbaum and V.J. Shiner, Jr. Unpublished results.

side of the equation, so the equilibrium isotope effect is 0.99, or a 1% change in this case (13). Similarly, a difference of 0.8% in the ^{15}N equilibrium isotope effect is seen for the aspartate transcarbamylase reaction in D_2O where two protons are lost during the conversion of aspartate to carbamylaspartate (14). Similar changes should apply to other reactions run in D_2O where the number of deuterium atoms attached to nitrogen is different on the two sides of the reaction.

Table 4 shows ^{15}N fractionation factors relative to aqueous NH_3. The experimentally determined ones can be used with some confidence, but the calculated ones must be treated with caution, since they are gas-phase calculations and do not take into account the effects of hydration in aqueous solution. For example, the ratio of calculated fractionation factors for NO_3^- and NO is 1.125, while the ratio of the experimental values in Table 3 is only 1.086. Still, these calculated values can be used as a rough guide to the stiffness of bonding of nitrogen in different molecules.

Just as with ^{13}C, we can use empirical factors to correct the fractionation factor of a small molecule to one with a more complicated structure. The ratio of fractionation factors for methylamine and ammonia in the gas phase is 1.013, which is slightly higher than the value of 1.011 for replacing H with CH_3 for ^{13}C isotope effects. We do not have good numbers on which to base the effects of replacing H with C on a carbon attached to nitrogen, although the ratio of fractionation factors for CH_3CN and HCN is 1.0033. This is a reasonable value, since a C-C-N bend should be slightly less sensitive to ^{15}N substitution than a C-C-C bend is to ^{13}C substitution, because nitrogen is heavier than carbon. The effects of replacing H with C on the second carbon from a nitrogen, which will generate an ^{15}N-sensitive torsional mode, cannot be estimated at this time, although the effects should be present.

What can be noted is that while an unprotonated amino acid has a fractionation factor higher than NH_3 by 1.0163, the factor between a protonated amino acid and NH_4^+ is only 1.0138. Thus, the empirical factors for adjusting fractionation factors are less when the nitrogen is already strongly bonded than when it is more weakly bonded, and thus these factors cannot be used in a completely mutiplicative sense. If we take 1.013 for the first carbon of the amino acid and 1.0033 for the ones attached to it, the predicted fractionation factor of an unprotonated amino acid nitrogen would be 1.0197, which exceeds the observed value of 1.0163 before any allowance is made for torsional effects of atoms further removed. With a protonated amino acid nitrogen, the discrepancy is even larger. The failure of the empirical correction factors to be multiplicative with ^{15}N suggests that they probably are not so for ^{13}C, either. Clearly, more experimental equilibrium isotope effects need to be measured to put all of this analysis on a sounder footing.

We draw attention to the equilibrium ^{15}N isotope effect in Table 3 at the N-1 position during reduction of acetylpyridine-NAD to acetylpyridine-NADH. It was thought originally on the basis of poorly defined kinetic isotope effects that there might be a sizeable equilibrium isotope effect caused by N-1 of the pyridine ring changing from trigonal to tetrahedral during reduction and the bond order dropping

© 1999 NRC Canada

Table 5. ^{18}O equilibrium isotope effects.

Reaction[a]	$^{18}K_{eq}$ at 25°C	Reference
$H_2[O]$ (gas) === $H_2[O]$ (liq)	0.991	39
$C[O]_2$ (aqueous) === $C[O]_2$ (gas)	1.001	40
$C[O]_2$ (gas) === $H_2[O]$ (liq)	1.0412	41
$HC[O]_2H$ === H_2O (liq)	1.0345 ± 0.0003	16
$^{-}$OOC-CH[O]H-CH_2-COO^{-} === $H_2[O]$ (liq) + fumarate	1.033 ± 0.003	42
$^{-}$OOC-C=[O]-CH_2-CH_2-COO^{-} === $H_2[O]$ (liq)	1.031 ± 0.006	43
$p$$NO_2$-$C_6H_4$-[O]-C=O-$CH_3$ === $p$$NO_2$-$C_6H_4$-$[O]^{-}$	1.0277 ± 0.0007	30
$(NH_3)_5$Co(III)-$[O]H_2$ === $H_2[O]$ (liq)	1.0196 ± 0.0004	44
$(NH_3)_5$Co(III)-$[O]H^{-}$ === $H_2[O]$ (liq)	1.008 ± 0.001	44
Cyclen-Co(III)-[O]-$P[O]_2$-O-C_6H_4-NO_2 === $p$$NO_2$-$C_6H_4$-$OP[O]_3^{=}$	1.0081 ± 0.0006	45
Proton or deuteron dissociations:		
$p$$NO_2$-$C_6H_4$-[O]H	1.0153 ± 0.0002	30
$HP[O]_4^{=}$	1.019 ± 0.001	46
$H_2P[O]_4^{-}$	1.019 ± 0.001	46
$D_2P[O]_4^{-}$	1.0248 ± 0.0007	46
Glucose-6-$OP[O]_3H^{-}$	1.0147 ± 0.0006	46
Glycerol-3-$OP[O]_3H^{-}$	1.0145 ± 0.0005	46
Glycerol-3-$OP[O]_3D^{-}$	1.022 ± 0.001	46
$HC[O]_2H$	1.0222 ± 0.0002	4
$HC[O]_2D$	1.0291 ± 0.0001	4
ϕ-$C[O]_2H$	1.020 ± 0.002	47

[a]The atom in brackets is the isotopic one, the replacement of which with ^{18}O gives the equilibrium isotope effect. $^{18}K_{eq}$ is the K_{eq} for ^{16}O divided by that for ^{18}O.

from 4 to 3. The small value of 1.0042 shows, however, that dipolar resonance forms contribute heavily to the structure of the reduced nucleotide, and N-1 remains largely planar with bond order close to 4.

^{18}O equilibrium isotope effects and fractionation factors

Table 5 includes a number of experimental ^{18}O equilibrium isotope effects. A number of these are for ionization of phenols, phosphates, or carboxylic acids. These vary from 1.5–2.0%, with lower values seen for substituted phosphates, or for *p*-nitrophenol, where the quinonoid resonance form that contributes to the structure of the ion provides double bond character to the phenoxide oxygen. Deuteration increases the equilibrium isotope effect by ~0.5%, as is the case with ^{15}N isotope effects.

There are several values in Table 5 for inert coordination of water or *p*-nitrophenyl phosphate to Co(III). Clearly, the inert coordination bonds result in stiffening of the bonding to the coordinated oxygen. This is in contrast to coordination by Mg^{2+} or similar ions, which seems not to affect the fractionation factor of coordinated oxygens (15).

Only a few ^{18}O equilibrium isotope effects have been determined experimentally for other reactions. The known ^{18}O fractionation factors (Table 6), however, are sufficient for many purposes, especially the ones for H_3O^{+} and OH^{-}. Table 6 includes a number of values calculated from the force fields of small molecules. These allow empirical rules to be developed for the effects of substitution, as was done above for ^{13}C and ^{15}N. The effect on the ^{18}O fractionation factor of replacing H with CH_3 on the isotopic oxygen is 1.022, which is double the effect seen with ^{13}C. Likewise, the effect of replacing H with CH_3 on a carbon attached to the oxygen (1.008) is twice the value seen with ^{13}C. Application of these factors accurately predicts the sequence from methane to methanol to ethanol to malate.

Only one fractionation factor is known for a carboxylic acid; 1.0345 for formic acid. While carboxylic acids exchange their oxygens with water at low pH, it is only the fact that I_2 in dimethyl sulfoxide oxidizes anhydrous sodium formate to CO_2 without oxygen exchange that permitted the determination of this fractionation factor. One might expect that going from formic to acetic acid might raise the fractionation factor by ~1.008, but this needs experimental verification. It is interesting to note that the experimental fractionation factor of 1.0345 for formic acid is close to the average of the calculated gas phase fractionation factors in Table 6 for the two types of oxygen in formic acid (1.037 for the -OH and 1.030 for the =O).

When one applies the ^{18}O equilibrium isotope effect for deprotonation for formic acid, one calculates the formate fractionation factor as 1.0124. This is higher than the value from the force field (1.008), suggesting a problem with the latter. It is interesting to note that the fractionation factor of formate is higher in the crystal by 1.0016, and when ion paired on Dowex-1 by 1.0042. In an ion pair with tetrabutylammonium ion in $CHCl_3$, the increase is 1.0040 (16). The ion pair effect is thought to be a stiffening caused by vibration in an electric field of opposite charge.

A number of ^{18}O fractionation factors are not known, however. Thus, we do not have values for bicarbonate, phosphates, or phenols, although these can all be equilibrated with water under appropriate conditions or in the presence

© 1999 NRC Canada

Table 6. ^{18}O fractionation factors relative to liquid water.

Group[a]	Fractionation factor	Reference
Experimentally determined:		
$C[O]_2$ (gas)	1.0412	41
$H_2[O]$ (gas)	0.991	39
$H_3[O]^+$	1.023	48
$[O]H^-$	0.960	49
$^-OOC\text{-}CH[O]H\text{-}CH_2\text{-}COO^-$	1.033	42
$^-OOC\text{-}C{=}[O]\text{-}CH_2\text{-}CH_2\text{-}COO^-$	1.031	43
$HC[O]_2H$	1.0345	16
$HC[O]_2^-$	1.0124	16
Na formate (solid)	1.0140	16
Formate on Dowex-1	1.0167	16
Formate, Bu_4N^+ salt in $CHCl_3$	1.0165	16
$(NH_3)_5Co(III)\text{-}[O]H_2$	1.0196	44
$(NH_3)_5Co(III)\text{-}[O]H^-$	1.008	44
Calculations from full force fields (gas phase):		
$CH_3[O]H$	1.017	[b]
$CH_3\text{-}CH_2\text{-}[O]H$	1.025	[b]
$CH_3\text{-}[O]\text{-}CH_3$	1.040	[b]
$[O]_2$	1.008	[b]
$HC[O]_2^-$	1.008	[b]
$HC{=}O\text{-}[O]H$	1.037	[b]
$HC{=}[O]\text{-}OH$	1.030	[b]
$HC{=}O\text{-}[O]CH_3$	1.058	[b]
$HC{=}[O]\text{-}OCH_3$	1.029	[b]
$H_2C{=}[O]$	1.023	[b]
$CH_3\text{-}CH{=}[O]$	1.016	[b]
$N[O]_3^-$	1.017	[b]
$N[O]_2$	1.023	[b]
$N[O]$	1.027	[b]
$N\text{-}N[O]$	1.027	[b]
$CH_3\text{-}N[O]_2$	1.026	[b]

[a]The fractionation factor is for the oxygen atom in brackets.
[b]W.E. Buddenbaum and V.J. Shiner, Jr. Unpublished work.

of appropriate enzymes. The difficulty is in designing sufficiently accurate methods for determining ^{18}O mass ratios in the equilibrated species.

Experimental

Materials

Malic, α-ketoglutaric, glutamic, and aspartic acids were from Aldrich. Oxaloacetic acid, sodium pyruvate, glucose-6-*P*, NADP, NAD, NADH, malic enzyme, malate dehydrogenase, glutamic-pyruvic transaminase, glutamic-oxaloacetic transaminase, lactate dehydrogenase, and *n*-octane were from Sigma. Oxidized glutathione was from Acros. *n*-Octane was washed with concentrated sulfuric acid and then 5% sodium carbonate prior to use.

Equilibrium isotope effects between oxaloacetate and malate

A solution containing 400 μmol each of oxaloacetic and L-malic acids, 80 μmol of NAD, and 2 mmol of sodium pyrophosphate in 40 mL 50 mM potassium phosphate, pH 7, was titrated to pH 9.0, and 10 mL of the solution was set aside. To the remainder at 4°C was added 800 units of malate dehydrogenase. At 40 min intervals, 10 mL aliquots were withdrawn and passed through an Amicon filter with a 10 000 MW cutoff. Each deproteinized sample, as well as the initial one from before the enzyme addition, was titrated to pH 4.0 with conc. sulfuric acid, and 1 mL of 10 mM aluminum sulfate was added to degrade the oxaloacetate to pyruvate. After 12 h at 22°C, the samples were titrated to pH 7, loaded onto a 3 × 50 cm anion exchange column (AG 1-X8-Cl, 200–400 mesh), and eluted with a linear gradient from 0 to 0.1 N HCl.

Fractions containing malate were located with an assay containing 2 mL of 100 mM potassium phosphate, pH 7.0, 0.3 mL of 30 mM $MgCl_2$, 0.3 mL of 1 mM NADP, 0.1 units of malic enzyme, and 0.1 mL of column eluent. The pooled malate fractions were evaporated to dryness, taken up in 10 mL of water, acidified with three drops of concentrated sulfuric acid, and subjected to continuous extraction with ethyl acetate for 48 h. The ethyl acetate solutions were evaporated to dryness, taken up in 20 mL of 0.01 N HCl, and evaporated to dryness again. This process was repeated three times to eliminate contamination with acetic acid. The malic acid samples were then dissolved in a solution containing 150 μmol of oxidized glutathione, 2 mg of NADP, and

© 1999 NRC Canada

3 mM $MgCl_2$ in 15 mL of 50 mM potassium phosphate, pH 7. These solutions were titrated to pH 7.2, and 5 units of malic enzyme and 18 units of glutathione reductase were added. After 3 h, 0.3 mL of 3% H_2O_2 was added to oxidize the pyruvate to acetate.

After overnight reaction at room temperature, the samples were acidified to pH 2 with conc. sulfuric acid and placed in a 1 L flask with 500 mL of *n*-octane. Acetic acid was removed by azeotropic distillation until the vapor temperature remained at 124°C for several minutes, with four drops of 5 N KOH placed in the receiving flasks. The aqueous portion of the distillate was neutralized to pH 6.0 with HCl and the samples sparged overnight with N_2 scrubbed with Ascarite to remove CO_2. The samples were then evaporated to dryness and the acetate salt analyzed as described below.

Fractions from the original anion exchange column containing pyruvate were located with an assay containing 2 mL of 100 mM potassium phosphate, pH 7.0, 0.3 mL of 1 mM NADH, 1 unit of lactate dehydrogenase, and 0.1 mL column eluent. The pooled pyruvate fractions were loaded onto a 3 × 25 cm desalting column (AG 11-A8 ion retardation resin), which was then washed with deionized water until all of the pyruvate was eluted. To each sample was added 5 mL of 100 mM potassium phosphate, pH 7.0, and the samples were reduced to 10 mL by evaporation. Then, 0.3 mL of 3% H_2O_2 was added, and after overnight reaction, the samples were acidified to pH 2, and the acetic acid was recovered by azeotropic distillation with *n*-octane as described above.

Equilibrium isotope effects between pyruvate and alanine

A solution containing 700 μmol each of glutamic acid and sodium pyruvate in 35 mL of 50 mM potassium phosphate was titrated to pH 7.5 with KOH and a 5 mL portion removed. The concentration of pyruvate in the remainder was determined by an endpoint assay containing 1 unit of lactate dehydrogenase, 1 mL of 100 mM potassium phosphate, pH 7, 1.69 mL of water, 0.3 mL of 1 mM NADH, and 0.01 mL of sample containing pyruvate. Glutamic-pyruvic transaminase (100 units) was then added, and the concentration of pyruvate was determined by endpoint assay until equilibrium was reached (2 h). The alanine concentration was determined by difference between the initial and final pyruvate concentrations. At 2 h and at 1 h intervals after this, 10 mL aliquots were filtered through an Amicon filter (10 000 MW cutoff) and set aside. When all samples had been collected, each was loaded on a 3 × 50 cm anion exchange column (AG 1-X8-Cl, 200-400 mesh) and eluted with a linear gradient from 0 to 0.1 N HCl. Fractions containing pyruvate were located with the lactate dehydrogenase assay and oxidized to acetate as described above. The mass ratios of C-2 or C-3 of alanine were calculated from the corresponding mass ratios of initial and final pyruvate and the pyruvate/alanine ratio at equilibrium.

Equilibrium isotope effects between oxaloacetate and aspartate

A solution containing 400 μmol each of aspartic and oxaloacetic acids in 40 mL of 50 mM potassium phosphate, pH 7.0, was titrated to pH 7.5, and 10 mL was set aside. To the remainder at 4°C was added 250 units of glutamic-oxaloacetic transaminase. At 20 min intervals, 10 mL aliquots were withdrawn and passed through an Amicon filter with a 10 000 MW cutoff. Each deproteinized sample, as well as the initial one from before enzyme addition, was titrated to pH 4.0 with conc. sulfuric acid and loaded onto a 3 × 1.5 cm column of AG50W-X2-H^+ cation exchange resin, and the columns were washed with water until 25 mL had been collected. These samples were titrated to pH 4.0 with KOH, and to each was added 2 mL of 10 mM aluminum sulfate to degrade the oxaloacetate to pyruvate. After 10 h the pyruvate was purified and analyzed as described above to give the mass ratios from oxaloacetate.

The cation exchange columns were then eluted with 50 mL of 0.4 N ammonia. The eluates were evaporated to dryness, and the residual aspartate samples were each taken up in a solution contining 120 μmol α-ketoglutaric acid, 120 μmol of glucose-6-*P*, and 5 mg of NADH in 10 mL of potassium phosphate, pH 7. These solutions were titrated to pH 7.5 with KOH, and to each was added 40 units of malate dehydrogenase, 25 units of glucose-6-*P* dehydrogenase, and 20 units of glutamic-oxaloacetic transaminase. After 16 h at 22°C, the malate product of these reactions was purified and analyzed as described above to give the mass ratios in aspartate.

Equilibrium isotope effects between pyruvate and lactate

A solution was prepared containing 700 μmol of sodium pyruvate, 350 μmol of glucose-6-*P*, 1750 μmol of sodium pyrophosphate, and 100 mg NAD in 35 mL of water. The solution was titrated to pH 9.0 with KOH, and 5 mL were set aside. The concentration of pyruvate in the remainder was determined by a lactate dehydrogenase assay as described above. Lactic dehydrogenase (2000 units) and 100 units of glucose-6-*P* dehydrogenase were then added. The concentration of pyruvate was followed until equilibrium was reached after 2 h. At intervals of 1, 5, and 9 h following attainment of chemical equilibrium, 10 mL aliquots were passed through an Amicon filter with a 10 000 MW cutoff. The pyruvate in these and the initial sample from before enzyme addition was purified and analyzed as above. The mass ratios in lactate at equilibrium were calculated from the initial and final mass ratios in pyruvate and the pyruvate/lactate ratio at equilibrium.

Analysis of the isotopic content of acetate

Each acetate sample was divided into two parts. One part was oxidized totally to CO_2 by being placed in a quartz tube (25 cm × 9 mm, 2 mm thick) with a layer of 0.5 g diatomaceous earth followed by 10 g of CuO. The tubes were evacuated, sealed with a torch, and heated to 850°C for 2 h. The cooled tubes were cracked on the vacuum line and the CO_2 distilled through two dry ice – isopropanol traps and collected in a trap cooled with liquid nitrogen. The $^{13}C/^{12}C$ mass ratio in the CO_2 samples was determined with a Finnegan Delta E isotope ratio mass spectrometer.

The second portion of the acetate was degraded to produce methane from C-2 (17). The acetate was placed in a 2.5 × 25 cm pyrex tube with 0.3 g of NaOH. The tube was evacuated and heated to 200°C for 15 min with two dry ice – isopropanol traps between the tube and the vacuum pump to remove water. The pump was disconnected (but the vacuum

© 1999 NRC Canada

maintained), a liquid nitrogen trap was added to trap CO_2, and the tube was heated to 400°C for 5 min with the methane produced collected on molecular sieves cooled with liquid nitrogen. The methane was later allowed to expand into an evacuated 1 m combustion tube. The bottom 30 cm of this tube contained 20 g CuO and was composed of quartz. The middle 30 cm was a quartz to glass gradient and the final 40 cm was glass equipped with a stopcock. The quartz portion was placed in an oven and heated to 850°C for 12 h. The CO_2 gas produced in this combustion was analyzed in similar fashion to that from the oxidation of acetate. Since this CO_2 is from C-2 of acetate, the mass ratio of C-1 was calculated from this value and the average value of both carbons determined in the total oxidation of acetate.

Data analysis

The isotopic composition of C-2 and C-3 of malate and oxaloacetate at equilibrium were both measured directly and compared to determine the equilibrium isotope effect. This reaction reached isotopic equilibrium before the first time point was taken, as shown by the equivalence of compositions at C-2 and C-3 of both malate and oxaloacetate at all three time points. The equilibrium isotope effects between aspartate and oxaloacetate were determined in the same manner. The isotopic composition of C-2 and C-3 of pyruvate was measured directly, and the isotopic composition of C-2 and C-3 of alanine was determined by calculation. Since all of the alanine was formed by the transamination of pyruvate, the isotopic composition at C-2 or C-3 of alanine was calculated from the known isotopic composition of the pyruvate starting material. This reaction also reached isotopic equilibrium before the first time point was taken. The equilibrium isotope effects between pyruvate and lactate were determined in the same manner.

Acknowledgements

We would like to thank V.J. Shiner, Jr., for permission to include previously unpublished fractionation factors.

References

1. P.F. Cook and W.W. Cleland. Biochemistry, **20**, 1790 (1981).
2. L. Melander and W.H. Saunders, Jr. Reaction rates of isotopic molecules. John Wiley and Sons, New York. 1980.
3. M.H. O'Leary. Methods Enzymol. **64**, 83 (1980).
4. L.R. Ellison and M.J.T. Robinson. J. Chem. Soc. Chem. Commun. 745 (1983).
5. M. Saunders, M.R. Kates, and G.E. Walker. J. Am. Chem. Soc. **103**, 4623 (1981).
6. S.R. Hartshorn and V.J. Shiner, Jr. J. Am. Chem. Soc. **94**, 9002 (1972).
7. W.W. Cleland. Methods Enzymol. **64**, 104 (1980).
8. V.J. Shiner, Jr., and T.E. Neumann. Z. Naturforsch. **44a**, 337 (1989).
9. G.L. Waldrop, J.L. Urbauer, and W.W. Cleland. J. Am. Chem. Soc. **114**, 5911 (1992).
10. W.W. Cleland. Bioorg. Chem. **15**, 283 (1987).
11. Y. Pocker, J.E. Meany, B.J. Nist, and C. Zadorojny. J. Phys. Chem. **73**, 2879 (1969).
12. M. Emly, and D.L. Leussing. J. Am. Chem. Soc. **103**, 628 (1981).
13. J.D. Hermes, P.M. Weiss, and W.W. Cleland. Biochemistry, **24**, 2959 (1985).
14. L.E. Parmentier, P.M. Weiss, M.H. O'Leary, H.K. Schachman, and W.W. Cleland. Biochemistry, **31**, 6577 (1992).
15. J.P. Jones, P.M. Weiss, and W.W. Cleland. Biochemistry, **30**, 3634 (1991).
16. J.D. Hermes, S.W. Morrical, M.H. O'Leary, and W.W. Cleland. Biochemistry, **23**, 5479 (1984).
17. P.F. Canellas and W.W. Cleland. Biochemistry, **30**, 8871 (1991).
18. M.H. O'Leary and C.J. Yapp. Biochem. Biophys. Res. Commun. **80**, 155 (1978).
19. A.R. Rendina, J.D. Hermes, and W.W. Cleland. Biochemistry, **23**, 6257 (1984).
20. W.A. Edens, J.L. Urbauer, and W.W. Cleland. Biochemistry, **36**, 1141 (1997).
21. P.V. Attwood, P.A. Tipton, and W.W. Cleland. Biochemistry, **25**, 8197 (1986).
22. W.G. Mook, J.C. Bommerson, and W.H. Staverman. Earth Plan. Sci. Lett. **22**, 169 (1974).
23. J.D. Hermes, C.A. Roeske, M.H. O'Leary, and W.W. Cleland. Biochemistry, **21**, 5106 (1982).
24. J.W. Bayles, J. Bron, and S.O. Paul. J. Chem. Soc. Faraday Trans. 1, **72**, 1546 (1976).
25. A.J. Kresge, N.N. Lichtin, K.N. Rao, and R.E. Weston, Jr. J. Am. Chem. Soc. **87**, 437 (1965).
26. M. Scharschmidt, M.A. Fisher, and W.W. Cleland. Biochemistry, **23**, 5471 (1984).
27. P.A. Tipton and W.W. Cleland. Arch. Biochem. Biophys. **260**, 273 (1988).
28. H.G. Thode, R.L. Graham, and J.A. Ziegler. Can. J. Res. Sect B, **23**, 40 (1945).
29. N.S. Rotberg and W.W. Cleland. Biochemistry, **30**, 4068 (1991).
30. A.C. Hengge and R.A. Hess. J. Am. Chem. Soc. **116**, 11 256 (1994).
31. L.L. Brown, and J.S. Drury. J. Chem. Phys. **48**, 1399 (1968).
32. L.L. Brown, and J.S. Drury. J. Chem. Phys. **48**, 1400 (1968).
33. M.J. Stern, L.N. Kauder, and W. Spindel. J. Chem. Phys. **34**, 333 (1961).
34. J.L. Kurz, M.W. Daniels, K.S. Cook, and M.M. Nasr. J. Phys. Chem. **90**, 5357 (1986).
35. J.L. Kurz and M.M. Nasr. J. Phys. Chem. **93**, 937 (1989).
36. A.C. Hengge and W.W. Cleland. J. Am. Chem. Soc. **112**, 7421 (1990).
37. N. Tanaka, A. Yamaguchi, M. Araki, and K. Kimata. J. Am. Chem. Soc. **107**, 7781 (1985).
38. N. Tanaka, K. Hosoya, K. Nomura, T. Yoshimura, T. Ohki, R. Yamaoka, K. Kimata, and M. Araki. Nature (London), **341**, 727 (1989).
39. S. Szapiro and F. Steckel. Trans. Faraday Soc. **63**, 883 (1967).
40. J.C. Vogel, P.M. Grootes, and W.G. Mook. Z. Physik. **230**, 225 (1970).
41. J.R. O'Neil, L.H. Adami, and S. Epstein. J. Res. U.S. Geol. Surv. **3**, 623 (1975).
42. J.S. Blanchard and W.W. Cleland. Biochemistry, **19**, 4506 (1980).
43. J.E. Rife and W.W. Cleland. Biochemistry, **19**, 234 (1980).
44. H.R. Hunt and H. Taube. J. Phys. Chem. **63**, 124 (1959).
45. J. Rawlings, A.C. Hengge, and W.W. Cleland. J. Am. Chem. Soc. **119**, 542 (1997).
46. W.B. Knight, P.M. Weiss, and W.W. Cleland. J. Am. Chem. Soc. **108**, 2759 (1986).
47. N. Tanaka and M. Araki. J. Am. Chem. Soc. **107**, 7780 (1985).
48. E.R. Thornton. J. Am. Chem. Soc. **84**, 2474 (1962).
49. M. Green and H. Taube. J. Phys. Chem. **67**, 1565 (1963).

© 1999 NRC Canada

The decomposition of methyl hemiacetals of benzaldehyde in aqueous solution: a study of the effect of aromatic substitution

Karen M. Engell, Robert A. McClelland, and Poul E. Sørensen

Abstract: The acid–base catalysed decomposition of hydrates and hemiacetals of carbonyl compounds are classical examples of reactions where (slow) proton transfer is coupled with heavy atom reorganization, i.e., C—O bond breaking and solvent reorganization. We have studied the influence of *m*- and *p*-substitution in the carbonyl electrophile on the kinetics of the acid and base catalysis of the decomposition of methyl hemiacetals of benzaldehyde. The experimental data are well described by three-dimensional More O'Ferrall – Jencks energy contour diagrams according to principles developed by Jencks (the BEMA HAPOTHLE). Thus, for acid catalysis, a Cordes cross-interaction coefficient $p_{xy'} = \partial\rho/\partial \mathrm{p}K_a = 0.15$ indicates the coupled nature of the rate-limiting step in a *class e* mechanism, similar to conclusions reached from systematic substitution in the nucleophile. Our more extensive set of data for base catalysis permits a more rigorous analysis according to the BEMA HAPOTHLE. The data are consistent with a *class n* mechanism as also suggested earlier on the basis of substitution in the nucleophile. A slight upward curvature observed in the Hammett plots for the various catalysts is described by the direct correlation parameter $p_y = -\partial\rho/\partial\sigma = -0.11$. This second derivative demonstrates the concerted nature of the C—O bond cleavage and O-H formation in the transition state, which changes with changing substituent. A *class n* mechanism for base catalysis is also supported by the observation of a Cordes cross-interaction parameter $p_{xy} = -\partial\rho/\partial \mathrm{p}K_a = -\partial\beta/\partial\sigma = 0.03$, which describes the experimentally observed decrease in Hammett ρ with increasing $\mathrm{p}K_a$ of the catalyst. This change may be rationalized by the movement of a saddle point on a diagonal reaction coordinate in the energy contour diagram, as a resultant of shifts parallel and perpendicular to the coordinate, when the energy along one side of the diagram is changed. It is concluded that observed rate changes as a result of substitution in the electrophile are consistent with and present further confirmation of earlier suggested mechanisms of hemiacetal decomposition reactions.

Key words: methyl hemiacetals of benzaldehydes, acid–base catalysed breakdown, Hammett plots, More O'Ferrall – Jencks diagrams.

Résumé : La décomposition, catalysée par les acides et les bases, des hydrates et des hémiacétals de composés carbonylés fourni des exemples classiques de réactions dans lesquelles le transfert (lent) d'un proton est couplé à une réorganisation des atomes lourds, comme le bris de la liaison C—O et la réorganisation du solvant. Nous avons étudié l'influence des substituants en m et en *p* du carbonyle électrophile sur la cinétique des décompositions catalysées par les acides et les bases d'hémiacétals de méthyle du benzaldéhyde. Les données expérimentales sont bien décrites par les diagrammes tridimensionnels de contour d'énergie de More O'Ferrall – Jencks selon les principes de Jencks (BEMA HAPOTHLE). Ainsi, pour la catalyse acide, un coefficient d'interaction croisée de Cordes, $p_{xy'} = \partial\rho/\partial \mathrm{p}K_a = 0{,}15$, est une indication de la nature couplée de l'étape cinétiquement limitante dans un mécanisme de *classe e* et ceci est semblable aux conclusions découlant d'une substitution systématique dans le nucléophile. Le large ensemble de nos données rend possible une analyse rigoureuse en fonction de BEMA HAPOTHLE. Les données sont en accord avec un mécanisme de *classe n*, tel qu'il avait été suggéré antérieurement sur la base de substitutions dans le nucléophile. Une observation directe du paramètre $p_y = -\partial\rho/\partial\sigma = -0{,}11$, nous permet aussi de décrire une courbe légèrement remontante dans les droites de Hammett pour les diverses catalyses. Cette deuxième dérivée démontre la nature concertée du clivage de la liaison C—O et de la formation de la liaison O-H dans l'état de transition qui est accompagnée de changements lors de changements de substituants. Un mécanisme de *classe n* pour la catalyse basique est aussi supporté par l'observation d'un paramètre d'interaction croisée de Cordes, $p_{xy} = -\partial\rho/\partial \mathrm{p}K_a = -\partial\beta/\partial\sigma = 0{,}03$, qui décrit la diminution observée expérimentalement de la constante ρ de Hammett avec une augmentation du $\mathrm{p}K_a$ du catalyseur. On peut rationaliser ce changement par le mouvement d'un point de selle sur une coordonnée de réaction en diagonale dans le diagramme de contour d'énergie, qui serait le résultat de déplacements parallèle et perpendiculaire à la

Received January 7, 1999.

This paper is dedicated to Jerry Kresge in recognition of his many achievements in chemistry.

K.M. Engell and P.E. Sørensen.[1] Department of Chemistry, Technical University of Denmark, DK-2800 Lyngby, Denmark.
R.A. McClelland. Department of Chemistry, University of Toronto, Toronto, ON M5S 1A1, Canada.

[1]Author to whom correspondence may be addressed. Telephone: +45 45 25 24 14. Fax: +45 45 88 31 36. e-mail: pes@kemi.dtu.dk

 © 1999 NRC Canada

coordonnée, lorsqu'on modifie l'énergie sur un côté du diagramme. On conclut que les changements de vitesse observés lors de substitutions dans l'électrophile sont en accord avec, et confirment, les mécanismes suggérés antérieurement pour les réactions de décomposition des hémiacétals.

Mots clés : hémiacétals de méthyle des benzaldéhydes, décomposition catalysée par les acides et les bases, courbes de Hammett, diagrammes de More O'Ferrall – Jencks.

[Traduit par la Rédaction]

The importance of proton transfer reactions in elementary chemistry and the life sciences is indisputable. Our present knowledge of the nature of these reactions and their coupling with other (heavy atom) processes or relocations is originally based on some careful and now almost historical experimental studies of acid–base catalysis. J.N. Brønsted (1879–1947) and R.P. Bell (1907–1996), who created a school with a large number of pupils, are commonly regarded as two of the scientific fathers of this discipline. In relation to the present paper, it is appropriate to focus on two of the pupils by mentioning the outstanding contributions by W.P. Jencks, and by A.J. Kresge, the former through his studies of the O—H bond, the latter, the C—H bond.

Protons and hydrogen continue to fascinate scientists. Recently, proton flips in thin silica discs have been suggested as memory units in future "molecular computers" with a 1000-fold enhancement in memory capacity (1). In addition, our steadily growing interest in biology (enzymology) keeps putting a strong demand on the need for knowledge of the basic nature of proton transfer reactions.

The mechanisms of acid–base catalysed reactions have been roughly defined in many cases, and our continuous goal is to improve the understanding of the more intimate details of all the parameters involved. In (classical) carbonyl addition reactions like the formation/decomposition of hemiacetals, one way of doing this is to introduce small but systematic variations in the various reactive sites and to observe the resulting effect on chemical rates. Thus, in a series of papers published during the period 1960–1990, Jencks has taught and convinced us that such studies are relevant in relation to understanding and visualizing reaction mechanisms, especially in coupled systems. Jencks has introduced the acronym BEMA HAPOTHLE — from the names of some key physical organic chemists — to characterize the principle of applying three-dimensional energy contour diagrams (More O'Ferrall – Jencks diagrams) in explaining complex chemical mechanisms (2).

In relation to Scheme 1, several (relatively easy) studies of changing R_3 in the nucleophile/leaving group, combined with systematic series of acid–base catalysts, have been performed and analysed according to the BEMA HAPOTHLE (2–5). However, very few extensive and systematic substitutions in the carbonyl electrophile have been reported so far, although as for carbon acids (6) such (supplementary) studies might also bring about important information on transition state structures.

In continuation of earlier work and as an attempt to fill this gap, we report in the present paper results from studies of the decomposition of methyl hemiacetals of a series of *m*- and *p*-substituted benzaldehydes.

It will be obvious from below that our results may be treated according to the BEMA HAPOTHLE. The fact that earlier suggestions concerning the reaction mechanisms are confirmed by our data give further support to the general validity of the principle.

Experimental section

Materials

Benzaldehyde dimethyl acetal and all benzaldehydes needed for the synthesis of corresponding acetals and hemiacetals were commercially available. Solids were sublimed before use. The *dimethyl acetals* of the substituted benzaldehydes were made as described by Davis et al. (7) apart from for 3- and 4-fluoromethylbenzaldehyde, where a method of Langvad (8) using dimethyl sulphate was applied. Solid acetal products were recrystallized from methanol, and liquids were purified by fractional spinning band distillation. In a few cases for aldehydes of low reactivity, we were not able to isolate the pure dimethyl acetal, i.e., an equilibrium mixture of acetal, and the benzaldehyde builds up in methanol. However, samples from these mixtures could still be used to initiate reaction, although a higher background absorption was present in these cases from unreacted benzaldehyde.

The various dimethyl acetals were typically checked and identified in two ways: (*i*) verification of the ^{1}H NMR spectrum from a solution in $CDCl_3$ run on a Bruker AD-250 instrument at 250 MHz (Me_4Si internal reference). In the NMR spectra of all acetals, a singlet appears at $\delta = 5.35 \pm 0.05$, typical of the aldehyde proton, which is shifted from around $\delta = 9.94$. For the dimethyl acetal type, the identity is further supported by a singlet at $\delta = 3.31 \pm 0.05$, six times the intensity of the aldehyde proton peak. (*ii*) Verification of the UV spectrum of the corresponding benzaldehyde after a hydrolysis of the acetal in weak HCl. Details are as follows:

Benzaldehyde dimethyl acetal (1,1-dimethoxy-1-phenylmethane): δ_H ($CDCl_3$): 5.39 (1 H, s, $HC(OMe)_2$), 3.31 (6 H, s, OMe), 7.3–7.5 (5 H, m, ArH) (lit. (9), δ_H ($CDCl_3$): 5.40, 3.32, 7.20–7.70, respectively); λ_{max} (H_2O)/nm 250 (lit. (9), λ_{max} (C_6H_{12})/nm 241).

4-Methylbenzaldehyde dimethyl acetal (1,1-dimethoxy-1-(4-methylphenyl)methane): bp 102–103°C at 18 Torr (1 Torr = 133.3 Pa) (lit. (7), bp 54°C at 1.1 Torr); δ_H ($CDCl_3$): 5.35 (1 H, s, $HC(OMe)_2$), 3.31 (6 H, s, OMe), 2.33 (3 H, s, ArMe), 7.1–7.2 (2 H, br d, half of AB system, 2 × ArH), 7.35–7.45 (2 H, br d, half of AB system, 2 × ArH); λ_{max} (H_2O)/nm: 261.6 (lit. (7, 9), λ_{max}/nm: 262, λ_{max} (MeOH)/nm: 255).

3-Methylbenzaldehyde dimethyl acetal (1,1-dimethoxy-1-(3-methylphenyl)methane): bp 95.5–96.5°C at 12 Torr; δ_H ($CDCl_3$): 5.32 (1 H, s, $HC(OMe)_2$), 3.32 (6 H, s, OMe), 2.35 (3 H, s, ArMe), 7.1–7.3 (4 H, m, ArH); λ_{max} (H_2O)/nm: 254.9, 297.3 (lit. (9), λ_{max} (MeOH)/nm: 249, 289).

© 1999 NRC Canada

4-Methoxybenzaldehyde dimethyl acetal (1,1-dimethoxy-1-(4-methoxyphenyl)methane): bp 125–126°C at 15 Torr (lit. (7), bp 86°C at 1.6 Torr); δ_H ($CDCl_3$): 5.32 (1 H, s, $HC(OMe)_2$), 3.32 (6 H, s, OMe), 3.80 (3 H, s, ArOMe), 6.85–6.95 (2 H, br d, half of AB system, 2 × ArH), 7.3–7.4 (2 H, br d, half of AB system, 2 × ArH); λ_{max} (H_2O)/nm: 285.8 (lit. (7, 9), λ_{max}/nm: 283.5, λ_{max} (MeOH)/nm: 273).

3-Methoxybenzaldehyde dimethyl acetal (1,1-dimethoxy-1-(3-methoxyphenyl)methane): bp 127–128°C at 15 Torr; δ_H ($CDCl_3$): 5.32 (1 H, s, $HC(OMe)_2$), 3.32 (6 H, s, OMe), 3.80 (3 H, s, ArOMe), 6.8–7.5 (4 H, m, ArH); λ_{max} (H_2O)/nm: 257.1, 314.3 (lit. (9), $\lambda\lambda_{max}$ (MeOH)/nm: 218.5, 251.5, 310).

3-Bromobenzaldehyde dimethyl acetal (1,1-dimethoxy-1-(3-bromophenyl)methane): bp 121–121.5°C at 14 Torr; δ_H ($CDCl_3$): 5.36 (1 H, s, $HC(OMe)_2$), 3.32 (6 H, s, OMe), 7.2–7.7 (4 H, m, ArH); λ_{max} (H_2O)/nm: 254.5 (lit. (9), $\lambda\lambda_{max}$ (MeOH)/nm: 244.5, 291).

4-Dimethylaminobenzaldehyde dimethyl acetal (1,1-dimethoxy-1-(4-dimethylaminophenyl)methane): bp 163.5–164.5°C at 18 Torr; δ_H ($CDCl_3$): 5.30 (1 H, s, $HC(OMe)_2$), 3.32 (6 H, s, OMe), 3.10 (6 H, s, ArNMe), 6.65–6.75 (2 H, d triplet, half of AB system, 2 × ArH), 7.7–7.8 (2 H, d triplet, half of AB system, 2 × ArH); λ_{max} (H_2O)/nm: 245.9, 353.2 (lit. (9), λ_{max} (MeOH)/nm: 242, 340).

4-Trifluoromethylbenzaldehyde dimethyl acetal (1,1-dimethoxy-1-(4-trifluorophenyl)methane): bp 60–62°C at 10 Torr; δ_H ($CDCl_3$): 5.46 (1 H, s, $HC(OMe)_2$), 3.32 (6 H, s, OMe), 7.6–7.75 (4 H, dd, AB system, 2 × 2 × ArH); λ_{max} (H_2O)/nm: 240.

3-Chlorobenznzaldehyde dimethyl acetal (1,1-dimethoxy-1-(3-chlorophenyl)methane): λ_{max} (H_2O)/nm: 251.5 (lit. (9), λ_{max} (MeOH)/nm: 243, 289.5).

4-Bromobenzaldehyde dimethyl acetal (1,1-dimethoxy-1-(4-bromophenyl)methane): λ_{max} (H_2O)/nm: 264.2 (lit. (7, 9), λ_{max}/nm: 258, λ_{max} (MeOH)/nm: 245.5).

4-Nitrobenzaldehyde dimethyl acetal (1,1-dimethoxy-1-(4-nitrophenyl)methane): λ_{max} (H_2O)/nm: 270.2 (lit. (9), λ_{max} (MeOH)/nm: 265).

4-Hydroxybenzaldehyde dimethyl acetal (1,1-dimethoxy-1-(4-hydroxyphenyl)methane): λ_{max} (H_2O)/nm: 244.4, 340.0 (lit. (9), λ_{max} (MeOH)/nm: 218.5, 253, 314.5).

Two *mixed acetals* were synthesized according to prescriptions by Anderson and Capon (10) where the respective benzaldehyde dimethyl acetals are initially converted by thionyl chloride to the corresponding α-chlorobenzyl methyl ether, which is then reacting with methyl salicylate. The final products were purified by HPLC and (or) fractional distillation: the compounds so prepared were benzaldehyde 2-(carbomethoxy)phenyl methyl acetal (1-methoxy,1-(2-carbomethoxyphenoxy)-1-phenyl-methane) and 4-methylbenzaldehyde 2-(carbomethoxy)phenyl methyl acetal (1-methoxy, 1-(2-carbomethoxyphenoxy)-1-(4-methylphenyl)methane). Spectroscopic and kinetic specifications were as described by Anderson and Capon (10).

Methyl hemiacetals of the various benzaldehydes are too unstable to be isolated. However, sufficient concentrations of the hemiacetals with substituents more electron withdrawing than 4-methyl can be obtained by simply dissolving the appropriate benzaldehyde in methanol and leaving the solution for about 1 h. Addition of small amounts of base (sodium carbonate or calcium hydride) shifts the equilibrium towards the hemiacetal even further and at the same time prevents the formation of acetal.

Kinetics

The decomposition of acetals and hemiacetals of the various substrates can be easily followed spectrophotometrically because of the benzaldehyde reaction product, which has distinct UV absorption maxima deriving from the aromatic aldehyde group. Three spectrophotometric techniques have been applied:

(a) Conventional spectrophotometry

For reactions with half-lives >30 s. A small sample of the substrate — usually about a microliter of a methanolic solution of acetal or hemiacetal was transferred by a micro syringe to a thermostatted quartz cell containing the aqueous reaction medium (Shimadzu UV-150-02 spectrophotometer). The reaction was initiated by quick stirring with a small Teflon stirrer before data collection.

(b) Conventional stopped-flow spectrophotometry

For reactions with half-lives <30 s. This technique was primarily used in our study of the specific acid-catalysed reaction, through the stepwise decomposition of the full acetal. This produced s-shaped absorbance–time traces for the benzaldehyde appearance that could be analysed to give simultaneously H^+-catalytic constants for hemiacetal and acetal decomposition. A slightly alkaline aqueous solution of the acetal was mixed in the instrument (Durrum or HiTech Scientific stopped-flow spectrophotometer) with varying concentrations of excess HCl, followed by measuring the pH in the final mix after each experiment. This stopped-flow technique was also used in studying the decomposition of the mixed acetals. A slightly alkaline, aqueous solution of the substrate was mixed in the apparatus usually with a buffer containing enough HCl to neutralize the "alkalinity" of the substrate solution.

(c) Double-mixing stopped-flow spectrophotometry

(HiTech Scientific PQ/SF-53 instrument). As shown earlier for equivalent studies of acetophenones (11, 12), this technique, which is essentially a fast pH jump method, offers an advantage in the (fast) recording of absorbance–time traces for the buffer-catalysed decomposition of aromatic hemiacetals. As suggested in Scheme 1, a certain percentage (depending on aromatic substituent) of hemiacetal intermediate builds up during acetal hydrolysis in acid. The time of maximum buildup may be calculated, and if the pH of the reaction mixture is jumped to a higher value at that time, further acetal breakdown will stop, and we are left with a situation where the decomposition of accumulated hemiacetal can be studied separately. In a typical double-mixing experiment an aqueous solution of 5×10^{-4} M acetal in 0.002 M NaOH was first mixed (1:1) with 0.004 M aqueous HCl. After "incubation" for 2–30 s (depending on the substrate), this mixture was then jumped to a higher pH by a second mixing in the instrument (1:1) with an appropriate

© 1999 NRC Canada

Scheme 1.

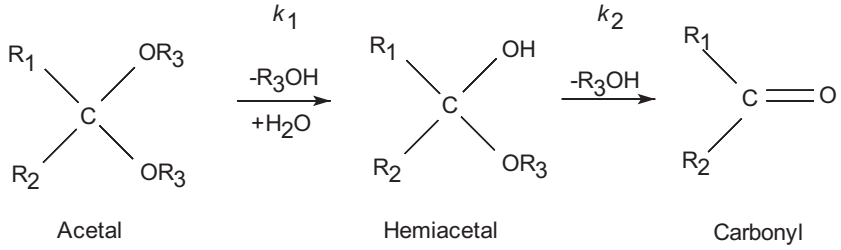

Fig. 1. S-shaped absorbance–time trace (λ_{max} = 250 nm) of the hydrolysis of the dimethyl acetal of benzaldehyde in weak hydrochloric acid.

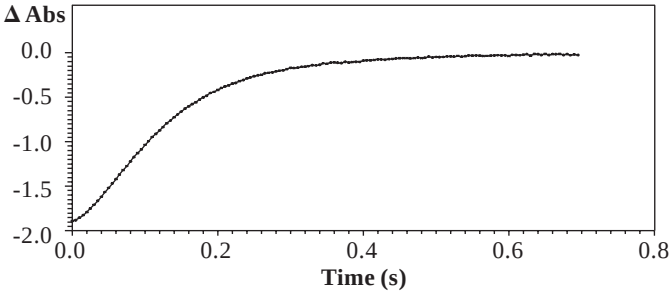

buffer (acetate, cacodylate, phosphate, or TRIS), and the increase in absorbance with time was recorded.

All experiments are carried out in such a way that ionic strengths of 1.0 M (KCl) are obtained in the reaction medium. Temperatures were kept at 25.0 ± 0.2°C.

Results and discussion

Specific acid catalysis

The consecutive reaction in Scheme 1 leads to s-shaped absorbance–time plots when the appearance of the final (aldehyde) product is followed spectrophotometrically. The exception to this are cases where the rate constant $k_1 >> k_2$ or vice versa, where the reaction will approach a single exponential nature. This is generally what is observed for the (acidic) hydrolysis of acetals ($k_1 << k_2$). However, as pointed out by Jensen and Lenz (13) and Finley et al. (14), for certain symmetric acetals like the diethyl and dimethyl acetals of benzaldehydes and of acetophenones, the rate constants k_1 and k_2 are sufficiently close to cause a detectable accumulation of hemiacetal, and an s-shaped kinetic trace.

An example is shown in Fig. 1 for the hydrolysis of the dimethyl acetal of benzaldehyde, the absorbance recorded for the appearance of the aromatic carbonyl peak at λ_{max} = 250 nm. The trace is an average of six single runs of 600 points per run. The solid line derives from a least-squares computer fit (MINSQ)[2] based on a double exponential expression of the type $\Delta A = Me^{-k_1 t} + Ne^{-k_2 t} + P$. This procedure produces two first-order rate constants, k_1 and k_2, of which one is approximately 10 times bigger than the other. We know from experience and from a single (slow) acetal hydrolysis experiment at about pH 6 ($t_{1/2} \approx 10^4$ s) that the smaller rate constant can be assigned to acetal hydrolysis, i.e., the first step in Scheme 1. At pH 6, this step is solely rate-limiting because the hemiacetal step is accelerated by hydroxide catalysis (vide infra).

Fig. 2. Specific acid catalysis of the hydrolysis of benzaldehyde dimethylacetal (closed squares) and methyl hemiacetal (closed circles).

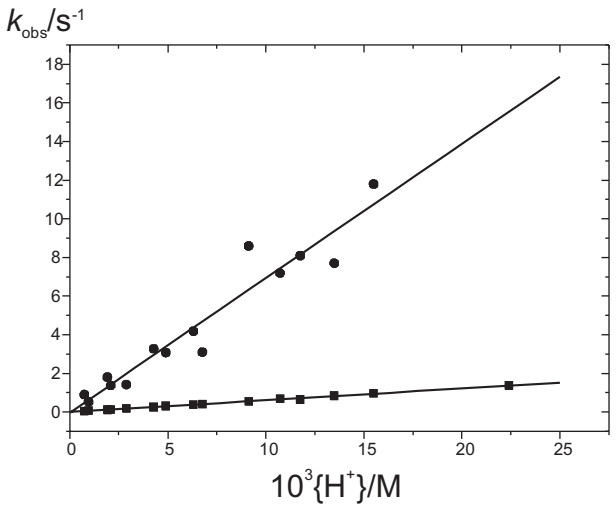

Figure 2 shows a plot of results from experiments at 15 different pH values in the range pH = 1.65–3.13 for the hydrolysis of benzaldehyde dimethyl hemiacetal ($\{H^+\}$ taken as 10^{-pH}). It is clear that the (faster) hemiacetal rate constants (k_2) are not as well defined as the corresponding k_1 values. The observed relative standard deviation on k_2 being 5–10%, while it is less than 0.5% for k_1. Nevertheless, in both cases, catalytic constants (k_H) for H^+ catalysis may be derived from Fig. 2 as indicated by the least-squares lines based on $k_{obs} = k_H\{H^+\} + k_w$. In these plots, the water values k_w are too small to be determined with certainty.

Table 1 summarizes all the results from the acid catalysis experiments for 11 aromatic substituents (primary data in the supplementary Table S1).[3]

The aromatic substituent effects on the H^+-catalysed breakdown of benzaldehyde acetals and hemiacetals in Table 1 are conveniently visualized in a Hammett plot. We have applied the Young and Jencks (19) version in eq. [1] where the contributions from polar and resonance effects are separated where possible, i.e., σ (Table 1) are taken for σ^n or σ^+ if no specific values are available for those parameters.

[2] MicroMath scientific software. P.O. Box 21550, Salt Lake City, UT 84121.

[3] Tables S1–S3 (kinetic data) have been deposited as supplementary material and may be purchased from: The Depository of Unpublished Data, Document Delivery, CISTI, National Research Council Canada, Ottawa, Canada, K1A 0S2.

© 1999 NRC Canada

Table 1. Summary of data for the H^+-catalyzed decomposition of some *meta*- and *para*-substituted benzaldehyde dimethyl acetals. Temperature 25°C, ionic strength = 1.0 M.

	Hammett σ			Acetal	Hemiacetal	t_{max}[c]	Hemiacetal[d]
Substituent	σ[a]	σ^+[a]	σ^n[b]	k_H (M^{-1} s^{-1})	k_H (M^{-1} s^{-1})	(s)	(%)
4-Nitro	0.778	0.79		0.176[e]	23.7 ± 0.5[e]	208	0.72
3-Nitro	0.71			0.294[e]	30.4 ± 0.6[e]	154	0.92
3-Bromo	0.391	0.405		4.84 ± 0.11	137 ± 6	25.3	3.1
3-Chloro	0.373			4.04 ± 0.05	125 ± 8	28.4	2.9
4-Bromo	0.232	0.15	0.265	16.9 ± 0.2	255 ± 12	11.4	5.5
3-Methoxy	0.115	0.047		29.7 ± 0.3	430 ± 15	6.67	5.7
Parent	0	0		60.5 ± 0.9 (54)[f]	690 ± 60	3.85	6.9
3-Methyl	–0.1	–0.066		99.4 ± 1.3	870 ± 30	2.81	8.6
4-Methyl	–0.17	–0.31	–0.13	252 ± 5	1850 ± 100	1.24	9.9
4-Methoxy	–0.27	–0.78	–0.18	1614 ± 16	3600 ± 400	0.405	23
4-Hydroxy	–0.37	–0.92	–0.2	957 ± 13	5500 ± 300	0.384	12

[a]Reference 15.

[b]Reference 16.

[c]t_{max} is the time of maximum buildup of hemiacetal B (d[B]/dt = 0) in the reaction scheme A → B → C, calculated as t_{max} = (ln (k_1[H^+]) – ln (k_2[H^+]))/(k_1[H^+] – k_2[H^+]) where [H^+] is taken as 0.001 M.

[d]B_{max} (%) at t_{max}, calculated as 100[B]/A_0 = 100(k_1[H^+]/((k_2[H^+]) – (k_1[H^+]))(exp (–(k_1[H^+]t_{max}) – exp (–(k_2[H^+]t_{max})).

[e]Reference 17 (T = 298 K, μ = 1.25 M).

[f]Reference 18 (T = 298 K, μ = 0.5 M).

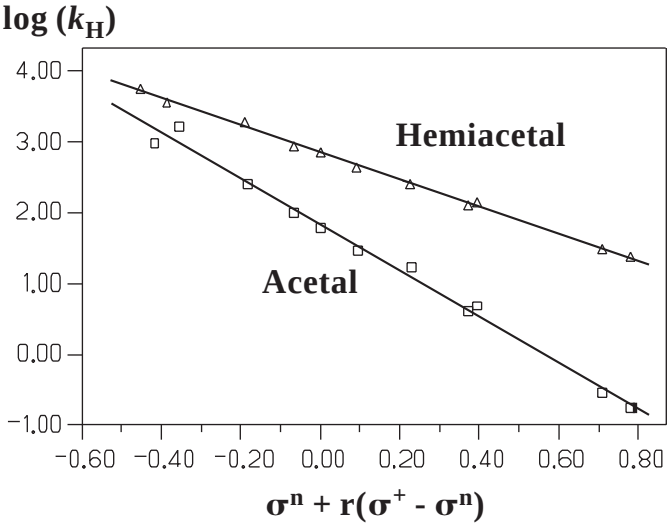

Fig. 3. Modified Hammet plots (Young and Jencks (19)) for the H^+-catalysed decomposition of some *m*- and *p*-substituted benzaldehyde dimethyl acetals and methyl hemiacetals. Data taken from Table 1.

[1] $$\lg (k/k_0) = \rho\sigma^n + \rho^r(\sigma^+ - \sigma^n) = \rho[\sigma^n + r(\sigma^+ - \sigma^n)]$$

where r (= ρ^r/ρ) is a parameter ranging from 0 (no resonance) to 1 (full resonance).

The resulting two Hammett plots are shown in Fig. 3 as two straight lines. A least-squares analysis according to eq. [1] $(MINSQ)^2$ gives the following results: acetal hydrolysis, ρ = –3.24 ± 0.16 with r = 0.30 ± 0.06 (correlation coefficient 0.996); hemiacetal hydrolysis, ρ = –1.89 ± 0.04 with r = 0.35 ± 0.04 (correlation coefficient 0.999). For a corresponding study of benzaldehyde *ethyl* acetals, Jensen et al. (20) found ρ(acetal) = –3.16 ± 0.02 with r = 0.34 ± 0.01 (T = 298 K, μ = 0.25 M, correlation coefficient 0.9998). Similarly, Przystas and Fife (21) found in a less extensive study for the hemiacetal breakdown of benzaldehyde *ethyl* hemiacetals ρ (hemiacetal) = –1.90 ± 0.05 (correlation coefficient 0.9997).

The observed change in hemiacetal buildup (%B_{max} in Table 1, last column) with the aromatic substituent clearly has its origin in the differing slopes in Fig. 3, a fact that was also observed for acetophenone acetal and hemiacetal breakdown (11, 12).

Buffer catalysis

Kinetics of the breakdown of a number of substituted benzaldehyde methyl hemiacetals were studied rather extensively for general catalysis by buffers. This section describes measurements in acetate buffer where catalysis can be seen from both Hac and ac. Experiental techniques (*a*) and (*b*) were applied. The double-mixing experimental technique (*c*) was employed where there was primarily only catalysis by the basic buffer components. These results are presented in the next section.

Each substrate was typically studied at three different buffer ratios. As usual, the observed first order rate constants are given as $k_{obs} = k_w + k_H\{H^+\} + k_{Hac}[Hac] + k_{ac}[ac] + k_{OH}\{OH\}$. As an alternative to classical plotting procedures, we have applied a least-squares multiparameter fitting procedure by $MINSQ^2$ based on this equation and leading to the "best" values for all catalytic constants involved. Detailed results from such a calculation for the decomposition of 3-methylbenzaldehyde methyl hemiacetal are shown in Table 2, where the derived catalytic constants are given at the bottom of the table. The pH of the acetate buffers are low enough to prevent any catalysis of the reaction by hydroxide ion (vide infra). The value in the table of k_H = (7.9 ±

© 1999 NRC Canada

Table 2. Kinetic data for the buffer-catalysed decomposition of 3-methylbenzaldehyde methyl hemiacetal. Acetate buffer, r = fraction of acid = [HA]/([HA]+[A$^-$]). Temperature 25°C, ionic strength = 1.0, λ_{max} = 255 nm.[a]

Total buffer concentration (M)	pH	k_2 (obs.) (s^{-1})	k_2 (calcd.) (s^{-1})
r = 0.250			
0.10	5.04	0.0496 ± 0.0019	0.0523
0.20	5.04	0.080 ± 0.005	0.084
0.30	5.04	0.113 ± 0.003	0.117
0.40	5.05	0.147 ± 0.006	0.149
0.50	5.07	0.180 ± 0.006	0.181
r = 0.500			
0.10	4.59	0.060 ± 0.002	0.061
0.20	4.56	0.088 ± 0.014	0.090
0.30	4.59	0.120 ± 0.011	0.116
0.40	4.57	0.152 ± 0.008	0.145
0.50	4.58	0.179 ± 0.006	0.173
r = 0.750			
0.10	4.08	0.101 ± 0.002	0.102
0.20	4.07	0.134 ± 0.005	0.127
0.30	4.04	0.159 ± 0.018	0.155
0.40	4.04	0.182 ± 0.008	0.178
0.50	3.99	0.196 ± 0.013	0.210

[a] k_W = (0.013 ± 0.008) s^{-1}; k_{OH} = 0.0 M^{-1} s^{-1} (fixed); k_H = (7.9 ± 1.1) × 10^2 M^{-1} s^{-1}; k_A = (0.37 ± 0.04) M^{-1} s^{-1}; k_{HA} = (0.19 ± 0.04) M^{-1} s^{-1}; correlation coefficient = 0.993.

Scheme 2.

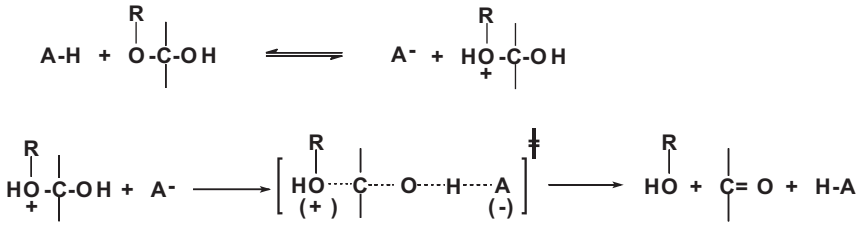

1.1) × 10^2 M^{-1} s^{-1} compares well with k_H = (8.7 ± 0.3) × 10^2 M^{-1} s^{-1} from the experiments reported previously in more acidic solution (Table 1).

The supplementary Table S2 contains results for the remaining 12 substituents (acetate catalysis), and the final results are summarized in Table 3.

Base catalysis

Catalysis by the buffers cacodylate, phosphate, and TRIS were studied by the double-mixing technique (*c*) described in the experimental section. The buildup to a maximum of hemiacetal takes place in the first mix at a pH around 3 and at a speed that varies from compound to compound. After the second mix, the base-catalysed breakdown of the acetal is followed spectrophotometrically. A drifting infinity line in most cases is due to a slight background reaction from continued hydrolysis of acetal even at higher pH. As before, the observed first-order rate constants depend on the concentration of the various catalysts as described by equation k_{obs} = k_w + k_H{H^+} + k_{Hac}[Hac] + k_{ac}[ac] + k_{OH}{OH}. In almost all cases, however, only contributions from k_A and k_{OH} were relevant in the pH range studied, and this equation reduces to k_{obs} = k_{ac}[ac] + k_{OH}{OH}. Again, a MINSQ[2] procedure was used to evaluate the best values of the catalytic constants. Primary results are contained in the supplementary Table S3, and final results are summarized in Table 3 together with other relevant data from the literature.

Acid catalysis and the BEMA HAPOTHLE

The specific as well as general acid-catalysed breakdown of carbonyl adducts such as hemiacetals and hydrates is believed to take place by a so-called class e mechanism (24), where the (concerted) proton transfer takes place from the electrophile (carbonyl group) in the transition state of the rate-limiting (second) step as shown in Scheme 2.

According to Jencks and Jencks (4), the mathematical description of the saddle point in a More O'Ferrall – Jencks energy contour diagram visualizing this rate-limiting concerted step is given in eq. [2], the primes referring to the fact that "diagonal" substituent effects are involved, i.e., effects of substituents on the central carbonyl oxygen atom.

$$[2] \quad -\log (k/p) = 1/2p_x(pK_a)^2 + 1/2p_{y'}(\sigma)^2 - p_{xy'}(pK_a)\sigma + x_o(pK_a) - y_o\sigma + F$$

The chemical interpretation of p_x, $p_{y'}$, and $p_{xy'}$ is as follows:

$$p_x = \partial\alpha/\partial pK_a$$

direct correlation expressing curvature in the Brønsted plot.

© 1999 NRC Canada

Table 3. Collected catalytic constants for the base-catalyzed decomposition of some *meta*- and *para*-substituted benzaldehyde methyl and ethyl hemiacetals, and benzaldehyde hydrates. Numbers in bold are from this work. Temperature 25°C, ionic strength = 1.0.

				Water	Acetate	Acetic acid	Cacodylate	HPO_4^{2-}	$H_2PO_4^-$	TRIS base	Hydroxide
	Hammett σ			pK_A = –1.74	pK_A = 4.65	pK_A = 4.65	pK_A = 6.29	pK_A = 6.49	pK_A = 6.49	pK_A = 8.36	pK_A = 15.74
Substituent	σ	σ^+	σ^n	*p*, *q* = 3, 1 (s^{-1})	*p*, *q* = 1, 2	*p*, *q* = 1, 2	*p*, *q* = 1, 2	*p*, *q* = 2, 3	*p*, *q* = 2, 3	*p*, *q* = 3, 1	*p*, *q* = 2, 1 ($10^{-6}k_{OH}$)
3,5 Dinitro	1.42			**0.055 ± 0.009**	**1.21 ± 0.04**	**–0.10 ± 0.03**		3.1[a]	0.097[a]	**5.2**	**1.98 ± 0.07**
					0.30[a]	0.03[a]					0.77[a]
3-Nitro, 4-chloro	0.94	0.82	0.95		0.42[a]	0.11[a]		4.4[a]	0.36[a]		0.41[a]
4-Nitro	0.778	0.79		**0.014 ± 0.004**	**0.51 ± 0.02**	**0.08 ± 0.02**		**7.1 ± 0.5**	0.39[a]		**3.72 ± 0.09**
					0.42 ± 0.01	0.12[a]		4.4[a]			4.07 ± 0.07[e]
					0.40[a]						0.49[a]
											1.42[f]
3-Nitro	0.71			**0.08 ± 0.08**	**0.63 ± 0.03**	**–0.02 ± 0.03**	1.55[b]	**7.1 ± 0.3**	0.10 ± 0.05[c]	**9.2**	**4.00 ± 0.07**
					0.39[a]	0.16[a]		4.2[a]	0.46[a]		0.75[c]
					0.24[b]			2.2[b]			0.43[a]
											0.54[g]
											4.01 ± 0.07[e]
3,4-Dichloro	0.6	0.49	0.6		0.25[b]	0.04 ± 0.01[c]	1.45[b]	2.3[b]	0.15 ± 0.05[c]		0.78[g]
											0.46[g]
3-Cyano	0.56										**2.97 ± 0.06**
											0.97[d]
4-Trifluormethyl	0.54			**0.033 ± 0.004**	**0.32 ± 0.02**	**0.11 ± 0.01**		**7.0 ± 0.3**	0.63[a]	**13**	**2.13 ± 0.05**
					0.39[a]	0.21[a]		4.3[a]			1.19[d]
											0.33[a]
3-Trifluormethyl	0.43							**7.1 ± 0.2**			**2.0 ± 0.1**
3-Bromo	0.391	0.405					**4.44**	**6.5**		**13**	3.6 ± 0.1
3-Chloro	0.373			**0.026 ± 0.009**	**0.44 ± 0.04**	**0.12 ± 0.04**	**3.67**	**6.7**	0.98 [a]	**13**	3.5 ± 0.1
					0.37[a]	0.31[a]		4.6[a]			2.0 [f]
											0.75[d]
					0.224[b]			2.74[b]			0.40[b]
											0.30[a]
3-Fluoro	0.337			**0.033 ± 0.009**	**0.32 ± 0.04**	**0.04 ± 0.04**					
4-Bromo	0.232	0.15	0.3	**0.011 ± 0.008**	**0.50 ± 0.04**	**0.07 ± 0.04**	**3.61**	**7.6**		**16**	**2.4 ± 0.1**
4-Chloro	0.227	0.114	0.2	**0.049 ± 0.013**	**0.24 ± 0.07**	**0.18 ± 0.06**		5.2[a]	1.1[d]		2.99[d]
											2.34[f]
					0.33[a]	0.47[d]		3.22[b]			0.59[d]
											0.29[b]
											0.20[a]
3-Methoxy	0.115	0.05		**0.008 ± 0.011**	**0.40 ± 0.04**	**0.15 ± 0.04**	**3.22**	**6.8 ± 0.2**	**–0.1 ± 0.2**	**15**	**2.0 ± 0.1**
4-Fluoro	0.06	–0.07		**0.008 ± 0.012**	**0.43 ± 0.04**	**0.26 ± 0.04**					

© 1999 NRC Canada

Table 3 (*concluded*).

	Hammett σ			Water	Acetate	Acetic acid	Cacodylate	HPO_4^{2-}	$H_2PO_4^-$	TRIS base	Hydroxide
				pK_A = –1.74	pK_A = 4.65	pK_A = 4.65	pK_A = 6.29	pK_A = 6.49	pK_A = 6.49	pK_A = 8.36	pK_A = 15.74
Substituent	σ	σ^+	σ^n	*p*, *q* = 3, 1 (s^{-1})	*p*, *q* = 1, 2	*p*, *q* = 1, 2	*p*, *q* = 1, 2	*p*, *q* = 2, 3	*p*, *q* = 2, 3	*p*, *q* = 3, 1	*p*, *q* = 2, 1 ($10^{-6}k_{OH}$)
Parent	0	0	0	**0.012 ± 0.007**	**0.26 ± 0.04**	**0.17 ± 0.03**	**3.36**	**6.25 ± 0.15**	**0.23 ± 0.09**	**20**	**1.7 ± 0.2**
				0.016 ± 0.010	**0.29 ± 0.03**	**0.21 ± 0.04**	1.41[b]	2.76[b]	0.51 ± 0.17[c]		3.07[d]
											2.47[f]
					0.170[b]			2.54[b]			0.72[d]
											0.34[b]
3-Methyl	–0.067	–0.066		**0.013 ± 0.008**	**0.37 ± 0.04**	**0.19 ± 0.04**	**3.09**	**6.6 ± 0.2**	**0.1 ± 0.2**	**15**	**2.0 ± 0.1**
4-Methyl	–0.17	–0.31	–0.129	**0.029 ± 0.011**	**0.23 ± 0.05**	**0.35 ± 0.05**	**4.17**	**7.7 ± 0.3**	**0.8 ± 0.2**	**19**	**2.8 ± 0.4**
								3.18[b]			
											1.04[d]
											0.31[b]
4-Methoxy	–0.27	–0.78	–0.175				**4.75**	**9.1 ± 0.3**	**1.0 ± 0.2**	**28**	**3.4 ± 2.0**
											1.37[d]
											0.49[b]
4-Hydroxy	–0.37	–0.92					**4.20**	**10.6**		**35**	**4.0 ± 1.1**
4-Dimethylamino	–0.63	–1.7	–0.219				**5.56**	**11 ± 1**	**2 ± 1**	**42**	**5.24 ± 0.05**

[a]Reference 22, benzaldehyde hydrate.
[b]Ethyl hemiacetal (J.L. Jensen. Private communication. Unpublished results. 1991.).
[c]Reference 23, ethyl hemiacetal.
[d]Reference 14, ethyl hemiacetal
[e]Reference 17, methyl hemiacetal.
[f]Reference 21, ethyl hemiacetal.
[g]Reference 23, benzaldehyde hydrate.

© 1999 NRC Canada

Scheme 3.

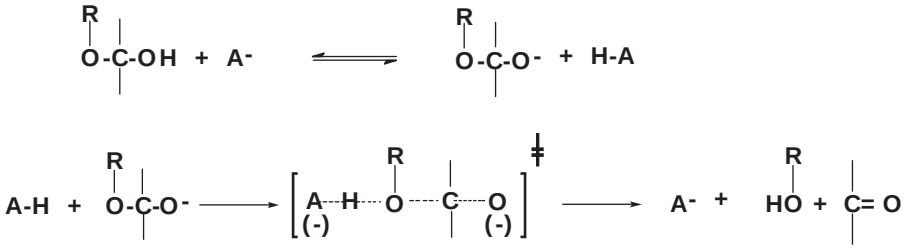

Fig. 4. A More O'Ferrall – Jencks diagram for the rate-limiting step in the acid-catalysed breakdown of benzaldehyde methyl hemiacetal (step 2 in Scheme 2) in a class e mechanism (24). The actual value of Hammett ρ throughout the diagram is a compromise between the values of ρ indicated at the corners of the diagram. These corner values represent the experimentally observed or estimated sensitivity of the various carbonyl forms to aromatic substitution with reference to the upper left corner (22). The location of the saddle point (transition state) is shown with horizontal and vertical level lines (i.e., a diagonal reaction coordinate). The bold arrow indicates the expected direction of movement of the transition state for a weaker acid catalyst, i.e., toward higher ρ values ($p_{xy'}$ positive, see text).

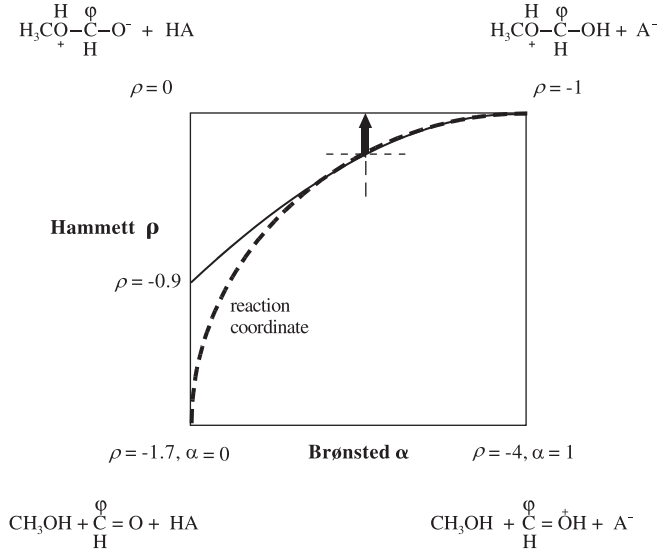

$$p_{y'} = -\partial\rho/\partial\sigma$$

direct correlation expressing curvature in the Hammett plot.

$$p_{xy'} = \partial\rho/\partial pK_a = -\partial\alpha/\partial\sigma$$

Cordes cross-interaction coefficient.

The values x_0 and y_0 are fixpoints defined as $x_0 = \alpha_0$ (α extrapolated to σ = 0, i.e., for the parent compound); $y_0 = \rho_0$ (ρ extrapolated to $pK_a = 0$ for the catalyst). The value of F is taken to fit the absolute value of the observed rate constants.

No detailed data for a reliable Brønsted plot analysis is carried out in this work, but in a similar study by Cox et al. (23), no curvature was observed within experimental error in the Brønsted plots for acid catalysis. Similarly, the Hammett plots, as discussed above, are linear, implying that p_x and $p_{y'}$ are both equal to zero. The two "level lines" of the saddle point are therefore perpendicular to each other and parallel to the x and y axes in the More O'Ferrall – Jencks diagram, leading to a diagonal reaction coordinate. In this case, a value of $p_{xy'} > 0$ is required to produce a saddle point in the diagram in the right direction (4).

A diagram based on data in the present paper for the acid-catalysed breakdown of hemiacetals is illustrated in Fig. 4. A value of $\rho_0 = -1.6$ is estimated from an interpolation based on the data in Table 3. A value of $\alpha_0 = 0.55$ is estimated from Brønsted $\alpha = 0.47 \pm 0.01$ for 3-nitro- and $\alpha = 0.50 \pm 0.01$ for 3,4-dichlorobenzaldehyde ethyl hemiacetal breakdown, based on a series of carboxylic acids (23). The coordinates of the saddle point in Fig. 4 are taken as $\rho = -1.9 - (-1) = -0.9$ (for H^+-catalysis) and $\alpha = 0.55$ (for the parent compound). Based on Hammond and anti-Hammond effects, the bold arrow represents the expected resulting movement of the transition state when a weaker acid catalyst is introduced, i.e., an increase in ρ as observed experimentally and in accordance with a positive value of $p_{xy'}$ (see next paragraph).

The result from a statistical treatment, based on eq. [1] $(MINSQ)^2$ of our (limited) set of experimental data for acid catalysis (Tables 1 and 3), is that a small positive value of $p_{xy'}$ is obtained, but with a large standard deviation. Alternatively, a rather crude plot of ρ versus pK_a for the three acids H_3O^+, HAc, and $H_2PO_4^-$, according to $p_{xy} = \partial\rho/\partial pK_a$, leads to a value of $p_{xy'} = 0.15$ for the methyl hemiacetals of benzaldehyde. This value is in good agreement with a value of $p_{xy'} = 0.12$ found by McClelland and Coe (22) and by Cox et al. (23) for dehydration of benzaldehyde hydrates.

The literature contains many studies where the effect of systematic substitution in the nucleophile/leaving group has been investigated and analysed (2). However, there are not many equivalent studies dealing with the electrophile. While we realise that our body of experimental data for acid catalysis is too incomplete to perform a rigorous statistical analysis according to the Jencks formalism, it does show that a systematic variation by substitution in the *electrophile* leads to experimentally observable effects that follow the rules stated by this formalism.

Base catalysis and the BEMA HAPOTHLE

In this section, we are dealing with a more complete set of catalytic data (Table 3) and a rather detailed mechanistic analysis is therefore possible.

Figure 5 shows Hammett plots where all bases are included. Rate constants are plotted against σ^+ throughout as a result of the fact that a (perhaps) more rigorous plot against $\sigma^n + r(\sigma^+ - \sigma^n)$ leads to values of $r \geq 1$, indicating a predominant influence of resonance effects by the substituents, as

© 1999 NRC Canada

Fig. 5. Hammett plots for the base-catalysed decomposition of benzaldehyde hemiacetals. Solid lines are simulated by a least-squares procedure on the basis of eq. [3] and data from Table 3.

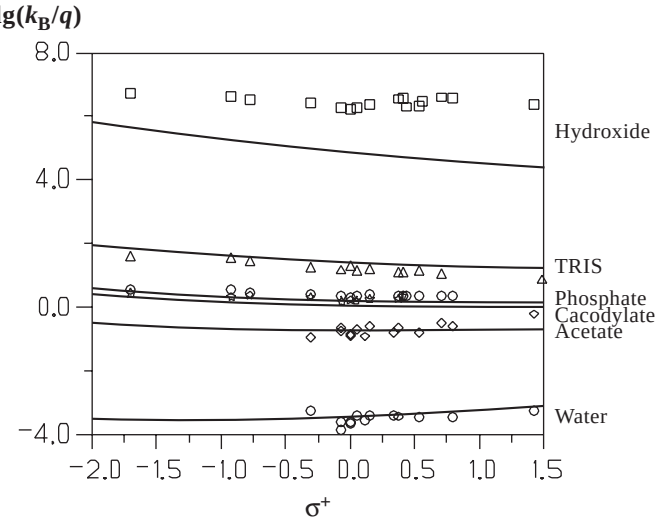

best reflected by σ^+. The curves drawn in the figure are simulated based on the statistical analysis reported below.

According to Jencks, the general base-catalysed breakdown of hemiacetals is believed to take place by a *class n* mechanism, where the concerted proton transfer in the transition state occurs to the leaving nucleophile as shown in Scheme 3 (24).

As for acid catalysis, the saddle point in an energy contour diagram for the rate-limiting (second) step may be characterized by an equation of the type (4):

$$[3] \quad -\log (k/q) = 1/2p_x(\mathrm{p}K_a)^2 + 1/2p_y(\sigma)^2 + p_{xy}(\mathrm{p}K_a)\sigma + x_o(\mathrm{p}K_a) - y_o\sigma + F$$

where again the chemical interpretation of p_x, p_y, and p_{xy} is as follows:

$$p_x = -\partial\beta/\partial \mathrm{p}K_a$$

direct correlation expressing curvature in the Brønsted plot.

$$p_y = -\partial\rho/\partial\sigma$$

direct correlation expressing curvature in the Hammett plot.

$$p_{xy} = -\partial\rho/\partial \mathrm{p}K_a = -\partial\beta/\delta\sigma$$

Cordes cross-interaction coefficient.

The values x_0 and y_0 are fixpoints defined as $x_0 = \beta_0$ (β extrapolated to $\sigma = 0$, i.e., for the parent compound); $y_0 = \rho_0$ (ρ extrapolated to $\mathrm{p}K_a = 0$ for the catalyst). The value of F is taken to fit the absolute value of the observed rate constants. No primes are assigned here because the central oxygen atom of the transition state is not involved in substitution.

The limited number of catalyst bases implied in this work means that no reliable Brønsted analysis could be performed, but from the rather extensive investigations by Jensen (see reference in footnote *b*, Table 3) and by Cox et al. (23), including the breakdown of benzaldehyde ethyl hemiacetals, we are convinced that there is no observable curvature in Brønsted plots, i.e., $p_x = 0$, and eq. [3] reduces to eq. [4]

$$[4] \quad -\log (k/q) = 1/2p_y(\sigma)^2 + p_{xy}(\mathrm{p}K_a)\sigma + x_o(\mathrm{p}K_a) - y_o\sigma + F$$

where $y_0 = \rho_o$ is the slope in the Hammett plot for a theoretical base with $\mathrm{p}K_a = 0$. It may be clear from a quick inspection of Fig. 5 that all the Hammett plots have slopes around zero, but with a tendency of ρ to increase with decreasing $\mathrm{p}K_a$ (p_{xy} positive). Thus, a good starting guess of ρ_o in eq. [4] will be $\rho_o \approx 0$; β_o is Brønsted β for the unsubstituted benzaldehyde methyl hemiacetal. Cox et al. (23) found $\beta = 0.52 \pm 0.02$ for 3-nitro- and $\beta = 0.50 \pm 0.02$ for 3,4-dichlorobenzaldehyde ethyl hemiacetal based on carboxylic acids. Therefore, a good starting guess of β_o is expected to be $\beta_o \approx 0.5$.

All our data for the methyl hemiacetal decomposition, catalysed by the five general bases in Table 3 (incl. water) were now fitted to eq. [4] by a least-squares procedure (MINSQ)[2] and the following results were obtained, with a correlation coefficient of 0.993:

$$p_x = 0.0 \text{ (fixed)}, \; p_y = -0.11 \pm 0.08, \; p_{xy} = 0.03 \pm 0.02$$

$$\beta_o = 0.48 \pm 0.01, \; \rho_o = 0.10 \pm 0.10, \; F = 2.84 \pm 0.05$$

The direct correlation coefficient p_y was found to be small and negative in consequence of a slight upward curvature of the Hammett plots. Experiments on leaving-group effects (substitution in the nucleophile) for formaldehyde and acetaldehyde (3, 5) lead to a value of $p_{y'} = -0.20$. The U-shaped curvature characterized by negative values of p_y and $p_{y'}$ represent the balance between the amount of C—O bond cleavage and O—H bond formation in the transition state, which changes with changing substituents. This is strong evidence for a concerted mechanism that involves both processes in the transition state (2, 4).

A positive value of $p_{xy} = 0.03$ is in accordance with a *class n* mechanism and has been observed in several studies before, as a result of the fact that when the carbonyl electrophile becomes less stable the observed Brønsted β value for base catalysis decreases (2). This phenomenon may be rationalized from and visualized in Fig. 6, which shows a energy contour diagram for a *class n* mechanism corresponding to step two in eq. [3]. A decrease in stability of the electrophile (carbonyl) by introducing a more electronegative substituent, as illustrated by an increase in energy of the electrophile at the bottom of the diagram, leads to a shift of the transition state toward the upper left corner, perpendicular to the the reaction coordinate, and towards the lower left corner, parallel to the reaction coordinate. The resultant of these effects moves the transition state to the left in the diagram, leading to a decrease in Brønsted β, as observed. The same diagram may be used to demonstrate the increase in ρ with decreasing $\mathrm{p}K_a$ of the catalyst, as observed in the present study. A decrease in $\mathrm{p}K_a$ due to introducing a weaker base raises the energy of the right-hand site of the diagram, leading to a shift of the transition state toward the upper right corner, parallel to the reaction coordinate, and toward the upper left corner, perpendicular to the

© 1999 NRC Canada

Fig. 6. More O'Ferrall – Jencks diagram for the rate-limiting step in the base-catalysed breakdown of benzaldehyde methyl hemiacetal (step 2 in Scheme 3) in a class n mechanism (24). The actual value of Hammett ρ throughout the diagram is a compromise between the values of ρ indicated at the corners of the diagram. These corner values represent the experimentally observed or estimated sensitivity of the various carbonyl forms to aromatic substitution with reference to the upper left corner (22). The location of an actual saddle point (transition state) is shown in the diagram with one vertical level line parallel to the *y*-axis ($p_x = 0$) and one turned 151° clockwise from vertical. This angle may be calculated according to Jencks and Jencks (4) when the the parameters p_x, p_{xy}, and p_y are known. The bold arrow indicates the expected shift in the transition state for a less stable carbonyl electrophile, i.e., toward lower Brønsted β values (p_{xy} positive, see text).

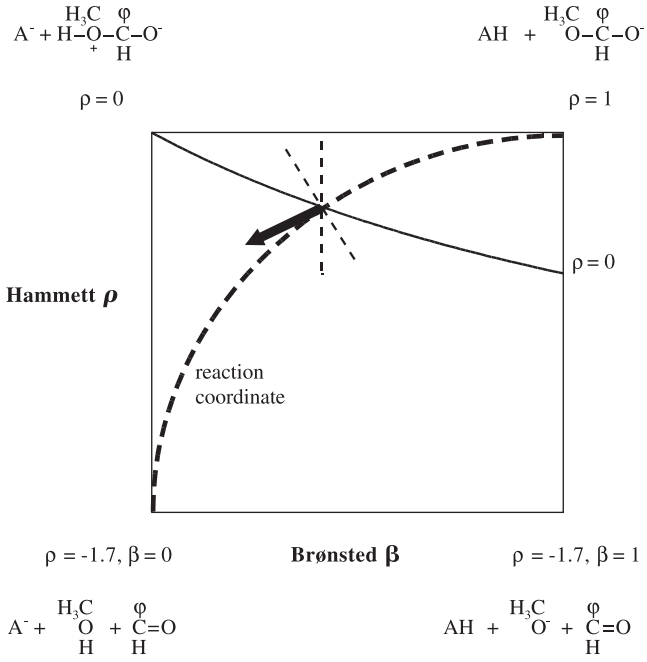

the reaction coordinate. The resulting effect is a vertical movements of the transition state toward higher ρ values.

In catalysis by the *hydroxide ion* (specific base catalysis), the points in Fig. 5 (Table 3) are seen to lie remarkably above the simulated curve, and the points are not included in the statistical analysis above. This seems to be a generally observed phenomenon in this type of chemical system (12, 22, 23, 25), presumably predicting a different mechanism with direct expulsion of the leaving group with no assistance from the conjugated acid (water) in step two. In Fig. 6, this situation may be described by a reaction coordinate running along the right hand edge of rather than across the diagram. It was observed by Cox et al. (23) that the positive deviation for the OH^- point on a Brønsted plot decreases with increasing Brønsted β, indicating that the Hammett plot for specific base catalysis will be less steep than expected from the general bases. This effect seems to be a general one and is confirmed from inspection of the data in the present work (Fig. 5). The disappearance of a positive deviation for k_{OH} for Hammett as well as Brønsted plots, when more electron-donating substituents are introduced in the electrophile, may be the result of a change in rate-limiting step for specific base catalysis. If Scheme 3 is considered, it is plausible that the pre-equilibrium step (step one) gradually becomes rate-limiting under such circumstances.

In conclusion, we can state that our experimental data for general base catalysis show all the essential elements expected for a concerted class n mechanism. The observation of a negative value of the direct interaction coefficient p_y — as a result of upward curvature in the Hammett plots — is new and represents a further confirmation of this mechanism. It also confirms the general validity of the More O'Ferrall – Jencks energy contour diagram as a useful tool in describing a complex chemical system.

Acknowledgements

This paper is dedicated to Professor A. Jerry Kresge for his many contributions to understanding the mechanisms of proton transfer reactions and for his friendship over the years. The paper is also dedicated to the memory of Professor James L. Jensen for his interest in our work and support over the years. This work was supported by a NATO collaborative research grant, CRG no. 900990. We also wish to thank Statens naturvidenskabelige Forskningsraad og Forskerakademiet for grants (K.M.E.).

References

1. U.J. Quaade, K. Stokbro, C. Thirstrup, and F. Grey. Surf. Sci. **415**, L1037 (1998).
2. W.P. Jencks. Chem. Rev. **85**, 511 (1985).
3. L.H. Funderburk, L. Aldwin, and W.P. Jencks. J. Am. Chem. Soc. **100,** 5444 (1978).
4. D.A. Jencks and W.P. Jencks. J. Am. Chem. Soc. **99**, 7948 (1977).
5. P.E. Sørensen and W.P. Jencks. J. Am. Chem. Soc. **109**, 4675 (1987).
6. (*a*) R.P. Bell and S. Granger. J. Chem. Soc. Perkin Trans. 2, 1367 (1976); (*b*) F.G. Bordwell. Faraday Symp. Chem Soc. **10**, 100 (1975); (*c*) C.F. Bernasconi. Adv. Phys. Org. Chem. **27**, 119 (1992).
7. T.S. Davis, P.D. Feil, D.G. Kubler, and D.J. Wells, Jr. J. Org. Chem. **40**, 1478 (1975).
8. T. Langvad. Acta Chem. Scand. **8**, 336 (1954).
9. Sadtler standard spectra. Sadtler Research Laboratory, Philadelphia. 1980, 1989.
10. E. Anderson and B. Capon. J. Chem. Soc. B, **8**, 1033 (1969).
11. R.A. McClelland and P.E. Sørensen. Acta Chem. Scand. **44**, 1082 (1990).
12. R.A. McClelland, K.M. Engell, T.S. Larsen, and P.E. Sørensen. J. Chem Soc. Perkin Trans. 2, 2199 (1994).
13. J.L. Jensen and P.A. Lenz. J. Am. Chem. Soc. **100**, 1291 (1978).
14. R.L. Finley, D.G. Kubler, and R.A. McClelland. J. Org. Chem. **45**, 644 (1980).
15. H. Maskill. The physical basis of organic chemistry. Oxford University Press, Oxford. 1993.
16. J. Hine. Physical organic chemistry. McGraw–Hill Book Co., N.Y. 1962.
17. L. Hansen. Internal report. Technical University of Denmark, Lyngby. 1994.
18. J.L. Jensen, A.B. Martinez, and C.L. Shimazu. J. Org. Chem. **48**, 4174 (1983).

© 1999 NRC Canada

19. P.R. Young and W.P. Jencks. J. Am. Chem. Soc. **99**, 8238 (1977); **101**, 3288 (1979).
20. J.L. Jensen, L.R. Herold, P.A. Lenz, S. Trusty, V. Sergi, K. Bell, and P. Rogers. J. Am. Chem. Soc. **101**, 4672 (1979).
21. T.J. Przystas and T.H. Fife. J. Am. Chem. Soc. **103**, 4884 (1981).
22. R.A. McClelland and M. Coe. J. Am. Chem. Soc. **105**, 2718 (1983).
23. B.G. Cox, A.J. Kresge, and P.E. Sørensen. Acta Chem. Scand. **A42**, 202 (1988).
24. W.P. Jencks. Acc. Chem. Res. **9**, 425 (1976).
25. P.E. Sørensen, K.J. Pedersen, P.R. Pedersen, V.M. Kanagasabapathy, and R.A. McClelland. J. Am. Chem. Soc. **110**, 5118 (1988).

© 1999 NRC Canada

Versatility of helix–loop–helix catalysts — cooperative $HisH^+$–His sites that span both helices

Jonas Nilsson, Kerstin S. Broo, Richard S. Sott, and Lars Baltzer

Abstract: Peptides with 42 amino acid residues have been designed to fold into helix–loop–helix motifs that dimerize to form four-helix bundles and catalyze the hydrolysis of *p*-nitrophenyl esters. Their reactivities depend on nucleophilic and general-acid catalysis by cooperative $HisH^+$–His pairs. The peptide catalyst MNV with the $HisH^+$–His pair separated by three residues within the helical segment catalyzes the hydrolysis of *p*-nitrophenyl fumarate with a second-order rate constant of 0.034 M^{-1} s^{-1} at pH 5.1 and 290 K. This *i*, *i*+3 site is a factor of three more efficient than the corresponding *i*, *i*+4 site. Helix–loop–helix peptides having histidines situated at opposing helices were designed and exhibited cooperative $HisH^+$–His catalytic pairs. The peptide H11,34K hydrolyzed *p*-nitrophenyl acetate and *p*-nitrophenyl valerate with second-order rate constants of 0.044 and 0.15 M^{-1} s^{-1}, respectively, at pH 5.1 and 290 K, indicating that the hydrophobic substituent was recognized by the catalyst.

Key words: de novo design, helix–loop–helix, four-helix bundle, histidine, catalysis.

Résumé : Des peptides à 42 résidus d'acides aminés ont été conçus pour se replier et former des motifs à hélice–boucle–hélice qui pourraient se dimériser pour former des faisceaux à quatre hélices et catalyser l'hydrolyse des esters *p*-nitrophényle. Leurs réactivités dépendent d'une catalyse nucléophile et acide générale par coopération de paires $HisH^+$–His. Le catalyseur peptidique MNV comportant une paire $HisH^+$–His séparée par trois résidus dans le segment hélicoïdal catalyse l'hydrolyse du fumarate de *p*-nitrophényle avec une constante de vitesse du deuxième ordre de 0,034 M^{-1} s^{-1}, à un pH de 5,1 et une température de 290 K. Ce site *i*, *i* +3 est plus efficace par un facteur de trois que le site correspondant *i*, *i* +4. Les peptides à hélice–boucle–hélice comportant des résidus histidines situés dans des hélices opposées ont été conçus et les paires catalytiques $HisH^+$–His donnent lieu à de la coopération. Le peptide H11,34K permet d'hydrolyser les acétate et valérate de *p*-nitrophényle avec des constantes de vitesse respectives de 0,044 M^{-1} s^{-1} et 0,15 M^{-1} s^{-1}, à un pH de 5,1 et une température de 290 K; ces résultats indiquent que le substituant hydrophobe est reconnu par le catalyseur.

Mots clés : conception de novo, hélice–boucle–hélice, faisceau à quatre hélices, histidine, catalyse.

[Traduit par la Rédaction]

Introduction

De novo designed folded polypeptides provide model systems of sufficient size and complexity to test intricate reaction mechanisms and to allow the construction of novel catalysts that perform enzyme-like reactions. The ultimate goal is the elucidation of the principles that control the functions of the natural enzymes and the understanding of how to design new enzymes for reactions not catalyzed by nature. Polypeptide supersecondary structures can now be constructed using nonnatural sequences that approach 100 residues in size as demonstrated by the successful design of folded polypeptides with well-defined tertiary structures such as helix–loop–helix motifs (1, 2), monomeric triple-stranded β-sheets (3, 4), a ββα motif (5), a triple helix collagen mimic (6), and coiled coils (7). Some of these motifs, which can all be produced by solid-phase techniques on automated synthesizers, have sufficient inherent stability to withstand the decreased free energy of unfolding that is a consequence of introducing several reactive residues. Others are readily repacked to regain the conformational stability that may be lost upon modification. These motifs are therefore suitable as scaffolds or templates for the construction and systematic modification of reactive sites in the engineering of new catalysts. So far, a small number of designed catalysts have been reported that are capable of rate enhancements of three orders of magnitude over those of the uncatalysed reactions (8–10) with at least partial understanding of their function. While the complexity of natural enzymes has been demonstrated in these designed catalysts,

Received January 6, 1999.

This paper is dedicated to Jerry Kresge in recognition of his many achievements in chemistry.

J. Nilsson, K.S. Broo, R.S. Sott, and L. Baltzer.[1] Department of Chemistry, Göteborg University, 412 96 Göteborg, Sweden.

[1]Author to whom correspondence may be addressed. Telephone: 46-31-772 2894. Fax: 46-31-772 3840. e-mail Lars.Baltzer@oc.chalmers.se

 © 1999 NRC Canada

the efficiencies and selectivities are far from those of their natural role models. It is therefore timely to address the issue of optimization of reactive site geometries to explore the scope and limitations of polypeptide catalysts. We have previously reported on histidine-based helix–loop–helix motifs that catalyse hydrolysis, transesterification, and amidation reactions of *p*-nitrophenyl esters (10). Their reactivities are due to cooperative nucleophilic and general-acid catalysis by unprotonated and protonated His residues four positions apart in a helical segment (11). We now wish to report on a systematic investigation of the reactive site geometries in helix–loop–helix motifs and the conditions required for cooperativeness between His residues. Such studies form the basis for the further development of designed polypeptide catalysts with tailored specificities and, eventually, for the engineering of artificial enzymes.

Experimental

The peptides were synthesized on a PerSeptive Biosystems Pioneer peptide Synthesizer using PerSeptive Biosystems standard Fmoc protocols, and the N-terminals were acetylated using acetic anhydride (0.3 mM in DMF). A PAL-PEG-PS polymer (PerSeptive Biosystems) was used that gave the C-amidated peptide upon cleavage by a mixture of TFA (13.5 mL), anisole (0.15 mL), thioanisole (0.35 mL), and ethanedithiol (0.20 mL) for 2 h at room temperature. The crude peptides were precipitated and washed with cold diethylether, and then lyophilized. They were purified isocratically by reversed phase HPLC on a semipreparative C-8 Kromasil column using 35–42% 2-propanol in 0.1% TFA with a flow rate of 7 mL/min and UV-detection at 229 nm. The identity and purity of the peptides were checked using electro-spray mass spectrometry, and the molecular weights were within 1 au from the theoretical values. No high molecular weight impurities were detected for the HPLC-purified peptides, and they are estimated to be more than 95% pure.

Kinetic measurement

The rate of hydrolysis of the *p*-nitrophenyl esters were measured on Varian Cary 100 or Cary 500 spectrophotometers equipped with Varian temperature controllers. The release of *p*-nitrophenol was followed at 320 nm and 290 K using 1 mm cuvettes. Stock solutions of the peptides were prepared by weighing (0.4 mM in 100 mM acetate buffer, pH 5.1), assuming that the peptides contain 25% water, and the concentrations of the stock solutions were determined by quantitative amino acid analysis. The pH was adjusted to 5.1 and readjusted after centrifugation if necessary. Solutions at concentrations of 0.2 and 0.3 mM were prepared by diluting the stock solution, and the same peptide solutions were used for all substrates. The peptide solutions (270 μL) were transferred by pipette to three cuvettes and temperature equilibrated for at least 20 min at 290 K in the temperature-controlled sample compartment of the spectrometer. The substrate (5 μL, 7.15 mM) was added to give a total substrate concentration of 0.13 mM. The poorly water-soluble substrates *p*-nitrophenyl acetate and *p*-nitrophenyl valerate were dissolved in acetonitrile, and mono-*p*-nitrophenyl fumarate was dissolved in 50% buffer 50% acetonitrile. The reactions were followed for more than two half-lives, and a single exponential function was fitted to the experimental data using Igor Pro software. The resulting pseudo-first-order rate constants were plotted as a function of the peptide concentrations, and the second-order rate constants were obtained by linear regression analysis. The error limits in the reported rate constants are probably ±10% due to possible errors in the amino acid analysis and the linear regression analysis.

CD and NMR spectroscopy

CD spectra were recorded on a JASCO-720 spectropolarimeter, routinely calibrated with (+)-camphor-10-sulfonic acid. The peptide solutions from the kinetic experiments were used, in 0.1 mm cuvettes, and the spectra were recorded in the wavelength interval 260–200 nm. The ^{1}H-NMR spectra of 0.4 mM peptide solutions in D_2O at 319 K were recorded at 400 or 500 MHz using Varian Unity spectrometers. The chemical shifts of the histidine ring protons were measured versus pH, under the usual assumption that the isotope effect on the electrode potential is cancelled by the isotope effect on the dissociation constant of the histidinium ion. A function describing the dissociation of a monoprotonic acid was fitted to the experimental result using Igor Pro software.

Results and discussion

The reactivity of histidine catalysts

Recently, we reported on histidine-based polypeptide catalysts, their reaction mechanisms, and their capacity for substrate recognition and discrimination (10–12). They were all derived from KO-42 (Fig. 1, Table 1, entry *b*), a 42-residue peptide that catalyzes the hydrolysis, transesterification, and amidation reactions of *p*-nitrophenyl esters (10). The hydrolysis of mono-*p*-nitrophenyl fumarate (**I**) was catalyzed by KO-42 with a second-order rate constant that is more than three orders of magnitude larger than that of the 4-methyl imidazole catalyzed reaction in aqueous solution at 290 K and pH 4.1. The catalyst was designed to fold into a helix–loop–helix supersecondary structure and dimerize to form a four-helix bundle. Its catalytic efficiency was based on six histidine residues His-11, His-15, and His-19 in helix **I**, and His-26, His-30, and His-34 in helix **II**. Histidine residues can function as nucleophiles and general base catalysts in their unprotonated form, and as general acid catalysts and

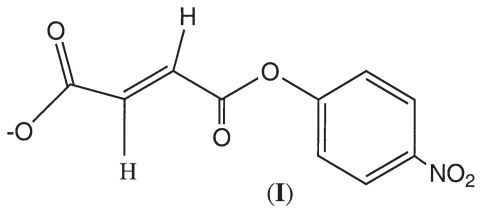

(**I**)

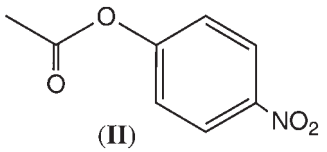

(**II**)

© 1999 NRC Canada

Table 1. The amino acid substitutions and second-order rate constants at pH 5.1 and 290 K of catalytically active polypeptides derived from KO-42. Positions not shown in the peptides are the same as those in KO-42.

Entry	Peptide	8	11	14	15	17	19	26	30	34	k_2(**I**) (M^{-1} s^{-1})	k_2(**II**) (M^{-1} s^{-1})	k_2(**III**) (M^{-1} s^{-1})
a	SA-42[a]	A	A	E	H	A	K	Q	Q	A	—	—	—
b	KO-42[b]	A	H	E	H	A	H	H	H	H	0.310	0.290	0.535
c	JNI[c]	A	A	E	Q	A	K	H	H	A	0.010	—	0.027
d	JNII[c]	A	A	E	Q	A	K	Q	H	H	0.054	0.048	0.186
e	JNIII[c]	A	A	E	Q	A	K	H	Q	H	0.007	—	0.097
f	JNIIHR	A	H	E	Q	A	K	Q	H	H	0.140	0.053	0.140
g	JNIIRH	A	R	E	H	A	K	Q	H	H	0.120	0.080	—
h	MNI[c]	A	H	E	H	A	Q	Q	Q	A	0.011	—	—
i	MNIV	H	H	E	Q	A	Q	Q	Q	A	0.015	—	0.015
j	MNV	A	H	H	Q	A	Q	Q	Q	A	0.034	—	0.032
k	MNKV	K	H	H	Q	K	Q	Q	K	R	0.033	—	0.066
l	MNKI[d]	A	H	K	H	A	Q	Q	Q	A	0.044	—	—
m	H15,30	A	A	E	H	A	K	Q	H	A	0.018	0.023	0.021
n	H11,34K	A	H	K	Q	A	K	Q	Q	H	0.018	0.044	0.150

[a]Reference 13.
[b]Reference 10.
[c]Reference 11.
[d]Reference 17.

Fig. 1. The modelled structure of KO-42, and its amino acid sequence, showing only the sidechains of the histidine residues together with their measured pK_a values. Only the monomer is shown for reasons of clarity.

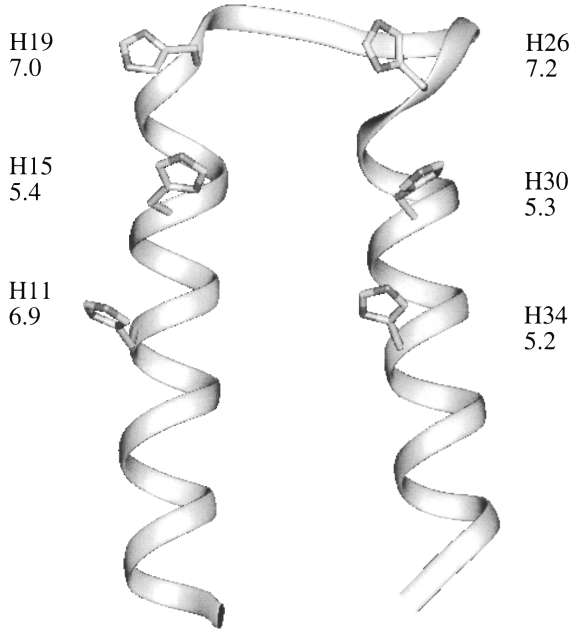

1
Ac-N-A-A-D-Nle-E-A-A-I-K-**H**-L-A-E-**H**-Nle-A-A-**H**-
20 23
-G-P-V-D-
42
NH_2-G-A-R-A-F-A-E-F-**H**-K-A-L-**H**-E-A-Nle-**H**-A-A-

hydrogen-bond donors in their protonated form. The versatility of histidine is due to its pK_a that is typically in the range of 5–7 in a helix–loop–helix motif, depending on the nature of the flanking residues. The design principle in the engineering of the KO-42 catalyst was that unprotonated His residues should be flanked by protonated His residues, and that these residues should be four residues apart in the sequence.

The histidine residues in KO-42 were assigned by NMR spectroscopy, and the pK_a values measured and found to be 6.9, 5.4, 7.0, 7.2, 5.3, and 5.2 for His-11, His-15, His-19, His-26, His-30, and His-34, respectively (Table 2, entry *b*). The pH dependence of the second-order rate constant and the kinetic solvent isotope effect showed that the catalysis was due to cooperative reactive sites formed from protonated and unprotonated $HisH^+$–His pairs.

To elucidate the reaction mechanism of KO-42, seven 42-residue polypeptides with two or three histidine residues in positions occupied by histidine residues in KO-42 were synthesized (11), and the positions formerly occupied by histidines were replaced by the "unreactive" amino acids found in the template peptide SA-42 (13). The sequences of the peptides in this report were based on those of SA-42 (13) and KO-42 (10) that were thoroughly investigated by NMR spectroscopy, CD spectroscopy, and equlibrium sedimentation ultracentrifugation. They were shown to fold into the designed hairpin motifs and dimerize to form antiparallel four-helix bundles. The CD spectra showed the negative maxima at 222 and 208 nm that are characteristic of helical peptides. The mean residue ellipticities at 222 nm are –25 000 ± 1000 deg cm^2 $dmol^{-1}$ for KO-42 and –24 000 ± 1000 deg cm^2 $dmol^{-1}$ for SA-42, which corresponds to helical contents of 60–70% (14, 15). The sequences of the peptides reported here differ from those of SA-42 or KO-42 by less than 5 residues, and the measured mean residue ellipticities at 222 nm are in the range from –17 000 to –25 000 deg cm^2 $dmol^{-1}$. We therefore conclude that these peptides also fold into antiparallel four-helix bundles, although complete structural analyses have not been carried out for all peptides.

© 1999 NRC Canada

Table 2. The measured pK_a values of catalytically active polypeptides derived from KO-42. pK_a values of individual histidines have not been determined for MNV.

Entry	Peptide	8	11	14	15	19	26	30	34
a	SA-42[a]	A	A	E	Q (6.5)	K	Q	Q	A
b	KO-42[b]	A	H (6.9)	E	H (5.4)	H (7.0)	H (7.2)	H (5.3)	H (5.2)
c	JNI[c]	A	A	E	Q	K	H (6.9)	H (5.6)	A
d	JNII[c]	A	A	E	Q	K	Q	H (5.6)	H (5.6)
e	JNIII[c]	A	A	E	Q	K	H (6.8)	Q	H (5.4)
f	MNI[c]	A	H (6.5)	E	H (6.1)	Q	Q	Q	A
g	MNIV[d]	H (5.5)	H (6.6)	E	Q	Q	Q	Q	A
h	MNV[d]	A	H (6.1/6.3)	H (6.1/6.3)	Q	Q	Q	Q	A
i	MNKV	A	H (5.8)	H (5.8)	Q	Q	Q	K	R
j	MNKI[d]	A	H (5.6)	K	H (5.6)	Q	Q	Q	A
k	H15,30	A	A	E	H (6.2/6.3)	K	Q	H (6.2/6.3)	A
l	H11,34K	A	H (5.4/5.5)	E	Q	K	Q	Q	H (5.4/5.5)

[a]Reference 13.

[b]Reference 10.

[c]Reference 11.

[d]Reference 17.

The efficiency of the histidine sites varied by almost an order of magnitude. For example, the second-order rate constants were 0.010 M^{-1} s^{-1} (JNI, His-26, His-30), 0.054 M^{-1} s^{-1} (JNII, His-30, His-34), and 0.007 M^{-1} s^{-1} (JNIII, His-26, His-34) for the hydrolysis of **I** at pH 5.1 and 290 K (Table 1, entries *c*–*e*).

The considerable difference in reactivity between JNII and JNI that both have His residues separated by four positions in the sequence could be explained by a model where the catalytic efficiency depends on the pK_a values of the histidine residues that determine their degree of protonation and intrinsic nucleophilicity. The second-order rate constant (k_2) for nucleophilic catalysis depends on the pK_a of the corresponding acid of the nucleophile and that for general-acid catalysis depends on the pK_a of the acid according to the Brønsted eqs. [1] and [2].

$$[1] \qquad \log k_2 = A + \beta pK_a$$

$$[2] \qquad \log k_2 = A - \alpha pK_a$$

The Brønsted coefficient β is 0.8 for imidazole catalysis of *p*-nitrophenyl acetate hydrolysis (16). Under the assumption that this value is valid also for histidine catalysis, a histidine with a low pK_a is more reactive than a histidine with a high pK_a if the reaction is carried out at a pH that is lower than its pK_a. This is because the nucleophilicity decreases with pK_a as $10^{0.8pKa}$, but the concentration of unprotonated histidine residues increases as 10^{pKa}. A His residue with a low pK_a is also a more efficient general acid catalyst than a residue with a high pK_a, under the same conditions. To test this model, the reactivities of histidine sites with different pK_a values were compared at a single pH. In the polypeptide JNI, the pK_a values of the reactive histidine residues are 6.9 (His-26) and 5.6. (His-30), and in the peptide JNII, the pK_a values are 5.6 for both His-30 and His-34 (Table 2, entries *c*–*d*). By comparing the rates of the JNII catalyzed reaction with that of JNI, it was shown that the relative catalytic efficiencies of JNI and JNII fitted this model if His-34 is the nucleophile and His-30 is the proton donor, and that the lower the pK_a values of both residues, the better the catalytic efficiency at a pH below the pK_a values. The comparison of reactivities using the Brønsted equations is therefore a good measure of cooperativity in His-based catalysis.

Transition-state binding of the carboxylate residue of *p*-nitrophenyl fumarate was accomplished by introducing basic amino acids in helix **I** of JNII(12) to supplement the His site in helix **II**. The most efficient catalyst for the hydrolysis of **I** at pH 5.1 and 290 K was JNIIRK (k_2 = 0.134 M^{-1} s^{-1}), where His-30 and His-34 were supplemented with an arginine in position 11 and a lysine in position 15. The hydrolysis of *p*-nitrophenyl acetate (**II**) (k_2 = 0.088 M^{-1} s^{-1}) is less efficient, which shows that there is significant binding of the fumaryl anion in the transition state of the hydrolysis reaction.

The peptide catalyst JNIII contains the histidine residues, His-26 and His-34, and hydrolyzes **I** with a k_2 of 0.007 M^{-1} s^{-1} but *p*-nitrophenyl valerate (**III**) with a k_2 of 0.097 M^{-1} s^{-1} (Table 1, entry *e*). The rate enhancement of a factor of 14 shows that there is considerable binding of the aliphatic substituent. The recognition of a substrate that has both a negatively charged and hydrophobic substituent, such as the monoester of a dicarboxylic acid that has an aliphatic substituent, should therefore give rise to a rate enhancement of more than a factor of 70 if the binding is cooperative. This has not yet been accomplished perhaps because of the transition state geometry imposed by the structure of the helix.

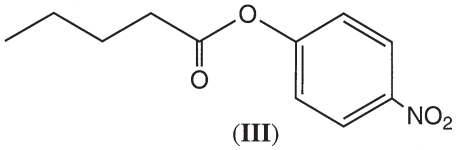

(**III**)

To reach a higher level of efficiency and selectivity in $HisH^+$–His catalysis, the requirements for cooperativity in substrate binding must be defined, something that has not yet been accomplished with the *i*, *i*+4 sites of the KO-42 derived catalysts. We tried therefore to elucidate if other

© 1999 NRC Canada

$HisH^+$–His sites could be employed in four-helix bundle motifs where cooperative binding of two or more substituents of a single substrate could be achieved. In particular, the possibility of having each residue in separate secondary structures should provide the most flexibility for optimization because the helical segments can be moved in very small steps, whereas the distance between two residues in a helical conformation is comparatively long and well defined.

In this study, we have therefore inspected the possibilities of designing new reactive site geometries based on histidine pairs three positions apart in the sequence of a helix and histidine pairs where there is one His residue in each helix of a helix–loop–helix motif.

The reactivity of the $HisH^+$–His site *i, i*+3

To test the reactivity of a catalyst with a $HisH^+$–His pair where the residues are separated by three positions in the sequence within a helical segment, i.e., in positions *i, i*+3, we synthesized MNV with His-11 and His-14 in helix **I**. MNV catalyzed the hydrolysis of **I** with a second-order rate constant of 0.034 M^{-1} s^{-1} at pH 5.1 and 290 K. Previously, it was shown that MNI, with His-11 and His-15, catalyzed the hydrolysis of **I** with a second-order rate constant of 0.011 M^{-1} s^{-1} (11) (Table 1, entries h and *j*). The pK_a values of the histidine residues of MNV are 6.1 and 6.3 (17), but due to spectral overlap, they could not be unequivocally assigned by NMR spectroscopy. For MNI, the pK_a values are 6.5 and 6.1 for His-11 and His-15, respectively (Table 2, entries *f* and h).

The pK_a values of the histidine residues of MNI and MNV are similar but the reactivities differ, and the $HisH^+$–His pair *i, i*+3 is a factor of three more efficient than the *i, i*+4 pair in hydrolysis of **I** at pH 5.1 and 290 K. The kinetic solvent isotope effect for the MNV catalysed reaction has now been determined, and the ratio $k_2(H_2O)/k_2(D_2O)$ found to be 2.6. A value larger than one is indicative of strong hydrogen bonding in the transition state, and general-acid catalysis by the protonated flanking His is therefore suggested. The $HisH^+$–His pair *i, i*+3 is thus a promising template reactive site for cooperative nucleophilic and general-acid catalysis. The increased reactivity of the *i, i*+3 site over that of the *i, i*+4 can be of general use in the design of new polypeptide catalysts.

If the pK_a values of the histidine residues in MNV can be depressed, the catalysis is expected to be even more efficient in comparison with that of the 4-methylimidazole catalyzed reaction at pH 5.1. The Brønsted equations can be used to calculate that a decrease of both pK_a values by 0.5 units gives rise to a relative increase in reactivity by a factor of 1.3 for nuclophilic catalysis and by a factor of 2.1 for general-acid catalysis. The overall reactivity increase thus amounts to a factor of 2.7 in favor of the low-pK_a peptide at low pH. The reactivity of the MNI peptide was previously successfully enhanced by replacing Glu-14 by Lys-14. The resulting peptide, MNKI, had pK_a values of 5.6 for both His-11 and His-15 (Table 2, entry *j*), and k_2 for the hydrolysis of **I** was 0.041 M^{-1} s^{-1}, (Table 1, entry *l*) a factor of four larger than that of MNI (17).

To lower the pK_a of His-11 and of His-14 of MNV, we introduced Lys-8 and Lys-17 to depress the pK_a values of His-11 and His-14, respectively, and form the peptide MNKV according to the procedure outlined in ref. 16. In addition, Lys-30 and Arg-34 were added in helix **II** to provide further binding of the fumaryl anion. The pK_a values were measured and found to be 5.8 for both of the histidine residues (Table 2, entry *i*). Surprisingly, the reactivity towards **II** did not increase but remained the same (Table 1, entry *k*). The reason may be that the transition-state geometry along the most efficient pathway cannot be adopted because substituents of the substrate are too close proximity to amino acid side chains of the catalyst. For the MNKV catalyzed reactions, k_2 is 0.033 M^{-1} s^{-1} for the hydrolysis of **II** and 0.066 M^{-1} s^{-1} for the hydrolysis of **I**. A rate constant ratio of 2 due to the binding of the fumarate anion was accomplished, which is in good agreement with those observed for the catalysis by the JNII series of peptides that have basic residues in positions 11 and 15, with the ratio k_2(**I**)/k_2(**II**) in the range of 1.5–2.5. The $HisH^+$-11–His-14 site is also cooperative in both peptides.

A second *i, i*+3 site was designed with His-8 and His-11 (MNIV), and this peptide catalyzed the hydrolysis of **I** with a second-order rate constant of 0.015 M^{-1} s^{-1} (Table 1, entry *i*). The pK_a values were measured and found to be 5.5 for His-8 and 6.6 for His-11 (Table 2, entry g). In this polypeptide, the pK_a value of His-11 is somewhat elevated but it could probably be depressed by the incorporation of a Lys-10 to make a more efficient catalyst in analogy with the modifications undertaken with MNKI. Nevertheless, it too forms a cooperative site as the reactivity is higher than that calaculated from the reactivity of 4-methylimidazole. The relative reactivities of 4-methylimidazole and the peptide catalysts at that pH are calculated from the pK_a of the reference catalyst and the pK_a values of the two histidines as described above.

The reactivity of the interhelical $HisH^+$–His site

To test the possibility of obtaining a cooperative interhelical $HisH^+$–His pair, we synthesized the peptide H15,30 that contains His-15 and His-30, i.e., one His in each helix but in positions that are close in space in the four-helix bundle. We have previously shown by measurements of reactivity that residues in positions 15 and 30 are close in space as are those in positions 11 and 34 (18). The pK_a values of the histidine residues were measured and found to be 6.2 and 6.3 (Table 2, entry *k*), and the second-order rate constant for the hydrolysis of **I** was 0.018 M^{-1} s^{-1} (Table 1, entry m). Although the value is low, the rate is larger than those of two independent nucleophilic histidine residues, and there is clearly cooperativeness between His-15 and His-30. To construct a peptide with an interhelical $HisH^+$–His site with depressed pK_a values, we synthesized H11,34K (Fig. 2) that contained His-11 and His-34. Position 34 is known to be close to the hydrophobic core, and a histidine in this position has a low pK_a. Furthemore, the pK_a of His-11 of H11,34K was depressed by the introduction of a lysine residue at position 14, and the pK_a values for His-11 and His-34 were measured and found to be 5.4 and 5.5 (Table 2, entry *l*).

This reactive site of H11,34K may be directly compared to that of JNII, since the pK_a values of the two peptides are very similar. H11,34K catalyzed the hydrolysis of **II** with a second-order rate constant of 0.044 M^{-1} s^{-1} (Table 1, entry *n*), which is similar to that of the JNII catalyzed hydrolysis of **II** (k_2 = 0.048 M^{-1} s^{-1}). The rate of hydrolysis of **I** was somewhat lower. The hydrolysis of **III** (k_2 = 0.15 M^{-1} s^{-1})

© 1999 NRC Canada

Fig. 2. The modelled structure of H11,34K showing only the sidechains of the histidine residues and Lys14. Only the monomer is shown for reasons of clarity.

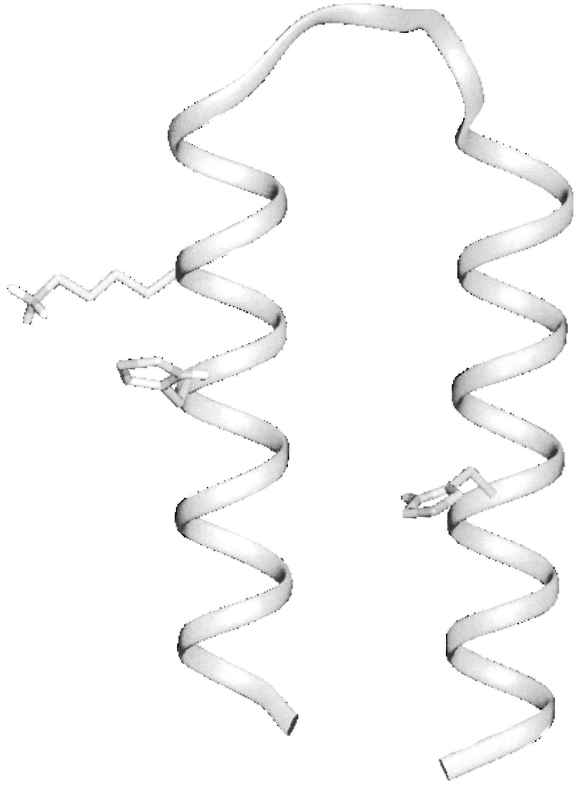

shows that there is recognition of the aliphatic side chain by the hydrophobic residues of the core. The increase by a factor of 3.4 is similar to the value obtained for JNII, which is 3.9. These results show for the first time that cooperative reactive sites can be constructed in the "enzyme-like" way by introducing residues in separate secondary structures and is an important step forward towards the engineering of optimized polypeptide catalysts.

Protonated His residues provide transition state binding of oxyanions and carboxylate anions

To identify the detailed functions of His-based catalysts, it must also be clarified to what extent the protonated residues can provide transition-state binding of anionic substituents in addition to general-acid catalysis. We have therefore investigated if histidine residues can also function as hydrogen-bond donors in the transition state of the acyl transfer reaction of **I**. The "length" of the His side chain is similar to that of the ornithine although its geometry is more constrained due to its ring structure. We have previously shown that ornithine enhances the reactivity of $HisH^+$–His sites in the adjacent helix, and the idea that protonated His residues can function in the same way is therefore a reasonable one and compatible with the diverse reactivity of the imidazoyl residue.

We synthesized the peptides JNIIHR and JNIIRH with a nucleophilic histidine residue in position 34 and a proton donating histidine in position 30. For binding of the fumaryl anion, the peptides were supplemented with His-11 and Arg 15 in JNIIHR and Arg 11 and His-15 in JNIIRH. These polypeptides catalyzed the hydrolysis of **I** with second-order rate constants of 0.14 M^{-1} s^{-1} and 0.12 M^{-1} s^{-1} at pH 5.1 and 290 K (Table 1, entries *f–g*), respectively, whereas the second-order rate constant of the JNII catalyzed reaction is 0.054 M^{-1} s^{-1}. The reactivities thus increase by factors of 2.2 and 2.6, however, these enhancements are only slightly larger than what is expected from the sum of the individual $HisH^+$–His pairs in peptides such as JNII, His15,30, and His11,34. A protonated histidine residue may thus bind the fumaryl anion during the course of the reaction without giving rise to any further enhancement to binding relative to that furnished by the other basic residues. His-15 is known to have a pK_a value of approximately 5.4 in KO-42 and the MN series of peptides. Since JNIIRH has a similar rate constant as JNIIHR and other JNII derived peptides, which have been supplemented by Arg or Lys side chains in positions 11 and 15, it can be assumed that the protonated form of His-15 can also function as a binding residue in combination with histidine residues 30 and 34. However, a nucleophilic contribution from this residue probably also occurs. If this is the case, it will probably form cooperative sites with residues in positions 30 or 34, which is an efficient interhelical His–$HisH^+$ site in the catalysis of hydrolysis reactions, in comparison with other $HisH^+$ –His pairs.

Conclusions

We have shown that the $HisH^+$–His reactive sites provide efficient catalysis also in the *i, i*+3 configuration and most gratifyingly also when the site is interhelical. The residues are far from each other in the primary structure but are brought together as the helix–loop–helix is formed. This demonstration implies that reactive sites can be fine tuned also in motifs that are small in comparison with the naturally occurring ones. Yet, another function of the His residue has been identified in these motifs as it has been shown, in its protonated form, to bind anionic substituents of substrates in catalytic reactions. The *i, i*+3 site and the interhelical $HisH^+$–His pair is of general interest in the design of new polypeptide catalysts. An interhelical reactive site in a helix–loop–helix is more easily fine-tuned than an intrahelical one, since secondary structures are readily repositioned in small increments than single residues in helical segments. The reactive sites may now be introduced into cavities and crevices of natural proteins where the hydrophobic environment is expected to enhance peptide–substrate interactions and where the positioning of flanking residues is more precise and controllable.

Acknowledgments

Financial support from the Swedish Natural Science Research Council and Carl Tryggers Foundation is gratefully acknowledged.

References

1. L. Brive, G.T. Dolphin, and L. Baltzer. J. Am. Chem. Soc. **119**, 8598 (1997).
2. B. R. Hill and W.F. DeGrado. J. Am. Chem. Soc. **120**, 1138 (1998).

© 1999 NRC Canada

3. T. Kortemme, M. Ramirez-Alvarado, and L. Serrano. Science (Washington, D.C.) **281**, 253 (1998).
4. H.L. Schenck and S.H. Gellman. J. Am. Chem. Soc. **120**, 4869 (1998).
5. M.D. Struthers, R.P. Cheng, and B. Imperiali. Science (Washington, D.C.) **271**, 342 (1996).
6. E.A. Jefferson, E. Locardi, and M. Goodman. J. Am. Chem. Soc. **120**, 7420 (1998).
7. S.F. Betz and W.F. DeGrado. Biochemistry, **35**, 6955 (1996).
8. K. Johnsson, R.K. Allemann, H. Widmer, and S.A. Benner. Nature (London), **365**, 530 (1993).
9. K. Severin, H.D. Lee, A.J. Kennan, and M.R. Ghadiri. Nature (London), **389**, 706 (1997).
10. K.S. Broo, L. Brive, P. Ahlberg, and L. Baltzer. J. Am. Chem. Soc. **119**, 11 362 (1997).
11. K.S. Broo, H. Nilsson, J. Nilsson, A. Flodberg, and L. Baltzer. J. Am. Chem. Soc. **120**, 4063 (1998).
12. K.S. Broo, H. Nilsson, J. Nilsson, and L. Baltzer. J. Am. Chem. Soc. **120**, 10 287 (1998).
13. S. Olofsson, G. Johansson, and L. Baltzer. J. Chem. Soc. Perkin Trans. 2, 2047 (1995).
14. Y.-H. Chen, J.T. Yang, and K.H. Chau. Biochemistry, **13**, 3350 (1974).
15. M. Engel, R.W. Williams, and B.W. Erickson. Biochemistry, **30**, 3161 (1991).
16. T.C. Bruice and R.J. Lapinski. J. Am. Chem. Soc. **80**, 2265 (1958).
17. K.S. Broo, L. Brive, R.S. Sott, and L. Baltzer. Fold. Des. **3**, 303 (1998).
18. L. Baltzer, K.S. Broo, H. Nilsson, and J. Nilsson. Bioorg. Med. Chem. **7**, 83 (1999).

© 1999 NRC Canada

Solvent isotope effects in the oxidation of dipeptides by aqueous chlorine

X.L. Armesto, M. Canle L., V. García, and J.A. Santaballa

Abstract: A kinetic study of the mechanism of oxidation of Ala-Gly and Pro-Gly by aqueous chlorine has been carried out. Among other experimental facts, the deuterium solvent isotope effects were used to clarify the mechanisms involved. In a first stage, *N*-chlorination takes place, and then the (*N*-Cl)-dipeptide decomposes through two possible mechanisms, depending on the acidity of the medium. The initial chlorination step shows a small isotope effect. In alkaline medium, two consecutive processes take place: first, the general base-catalyzed formation of an azomethine (β ca. 0.27), which has an inverse deuterium solvent isotope effect (k_{OH^-}/k_{OD^-} ~ 0.8). In a second step, the hydrolysis of the azomethine intermediate takes place, which is also general base-catalyzed, without deuterium solvent isotope effect, the corresponding uncatalyzed process having a normal deuterium solvent isotope effect (k_{H2O}/k_{D2O} ~ 2). In acid medium, the (*N*-Cl)-dipeptide undergoes disproportionation to a (*N*,*N*)-di-Cl-dipeptide, the very fast decomposition of the latter in deuterium oxide preventing a reliable estimation of the solvent isotope effect.

Key words: chlorination, deuterium isotope effects, fractionation factors, peptide oxidation, water treatment.

Résumé : On a effectué une étude cinétique du mécanisme d'oxydation des peptides Ala-Gly et Pro-Gly par le chlore en milieu aqueux. Parmi les résultats expérimentaux, on a utilisé les effets isotopiques du deutérium du solvant pour clarifier les mécanismes impliqués. La première étape implique une *N*-chloration qui est suivie d'une décomposition du (*N*-Cl)-dipeptide par le biais de deux mécanismes possibles suivant l'acidité du milieu. L'étape de chloration initiale ne présente qu'un faible effet isotopique. En milieu alcalin, il se produit deux processus consécutifs: le premier, la formation d'un azométhine sous catalyse basique générale (β d'environ 0,27) qui présente un effet isotopique inverse pour le deutérium du solvant (k_{OH^-}/k_{OD^-} ~ 0,8). La deuxième étape correspond à l'hydrolyse de l'intermédiaire azométhine sous catalyse basique générale, sans effet isotopique du deutérium du solvant alors que le processus non catalysé présente un effet isotopique du deutérium du solvant qui est normal (k_{H20}/k_{D2O} ~ 2). En milieu acide, le (*N*-Cl)-dipeptide subit une réaction de disproportionation conduisant à un (*N*,*N*)-di-Cl-dipeptide dont la décomposition dans l'oxyde de deutérium est tellement rapide qu'il n'est pas possible d'obtenir une évaluation fiable de l'effet isotopique du solvant.

Mots clés : chloration, effets isotopiques du deutérium, facteurs de fractionnement, oxydation de peptides, traitement des eaux.

[Traduit par la Rédaction]

Introduction

Although well-developed countries are looking for safe and inexpensive water and wastewater treatment methods, water halogenation, and mainly chlorination, is still nowadays a world-wide used disinfection method. During this process, the different organic compounds present in natural water undergo different chemical processes, giving rise to a number of intermediate species that are relatively unstable or reactive (1). The time of residence of such intermediates in the medium depends mainly on the structure of the compound itself and the physico-chemical conditions of the medium (2). Notwithstanding this fact, humanity is somehow indebted to chlorine, since after its adoption as a common water disinfectant, most water-transmitted diseases were beaten. The disinfection power of chlorine relies on its ability to penetrate the cell membrane and thus kill pathogens (3) (with some known exceptions, like Cryptosporidium) (4), the resulting water being suitable for drinking and domestic use.

All the mentioned facts make desirable to understand as best as possible the different reactions taking place during such industrial process.

Different studies have analyzed the risks associated to water chlorination, the main danger coming from the byproducts, some of which have been demonstrated to be carcinogenic and (or) mutagenic (5). Despite the fact that the last two decades have seen an important effort toward clarification of the pathways through which byproducts of water chlorination are generated, the topic is still far from an end (1). The oxidation of amines and amino acids by aqueous halogen solutions have been extensively studied (1). In turn,

Received November 24, 1998.

This paper is dedicated to Jerry Kresge in recognition of his many achievements in chemistry.

X.L. Armesto, M. Canle L., V. García, and J.A. Santaballa.[1] Departamento de Química Fundamental e Industrial. Facultade de Ciencias, Universidade da Coruña, A Zapateira, s/n, E-15071 A Coruña, Galicia, Spain.

[1]Author to whom correspondence may be addressed. Telephone: +34 981 167000, ext. 2195, 2200. Fax: +34 981 167065. e-mail: arturo@udc.es

© 1999 NRC Canada

Scheme 1.

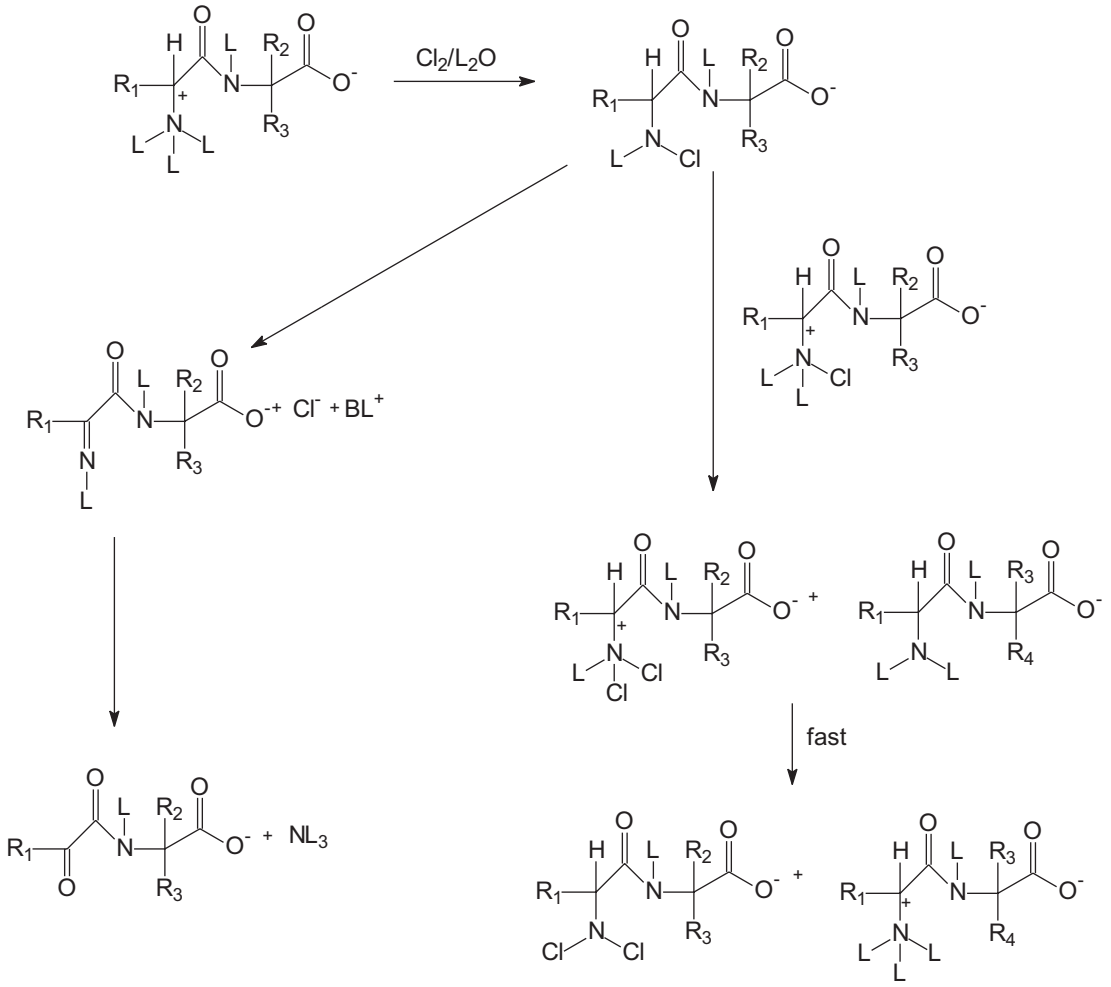

dipeptides received much less attention, assuming they had similar behaviour. Aqueous chlorine oxidants are intracellularly available by the action of the myeloperoxidase–H_2O_2–Cl^- system (6), and the action of such oxidants is of most relevance for biological phenomena like oxidative stress and aging (7).

The mechanism of chlorination of dipeptides is, therefore, of biochemical relevance and should be studied in depth.

Different authors have contributed to the application and establishment of solvent isotope effects (SIE) as a powerful tool to the elucidation of reaction mechanisms. Between his many fundamental contributions to physical organic chemistry, Kresge (8*b*) showed the way to describe the dependence of reaction rates at equilibrium with the isotopic composition of the solvent in terms of fractionation factors.

Here, we present a kinetic study of the oxidation of the dipeptides Alanyl-Glycine (Ala-Gly), **1**, and Prolyl-Glycine (Pro-Gly), **2**, by aqueous chlorine, using the D_2O SIE as a tool for the elucidation of the corresponding reaction mechanisms.

The processes under study are shown in Scheme 1 (through the paper, L is used to represent any of the used isotopic forms of hydrogen, i.e.: H or D). The generation of the corresponding (*N*-Cl)-dipeptides **3** and **4** is discussed first, and then the reactivity of such (*N*-Cl)-dipeptides under different conditions of acidity.

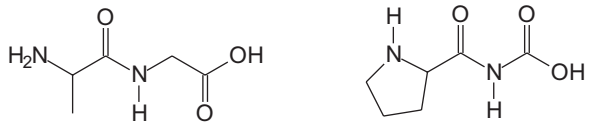

1

2

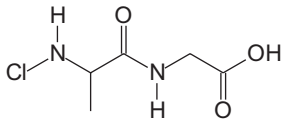

3

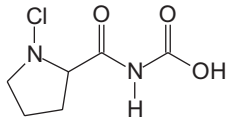

4

Results and discussion

(*i*) Generation of (*N*-Cl)-dipeptides

The chlorination of **1** and **2** to yield, respectively, (*N*-Cl)-Ala-Gly (**3**) and (*N*-Cl)-Pro-Gly (**4**) follows a second-order kinetic law, order one relative to both the dipeptide and the chlorinating agent. The so-obtained second-order rate constants show an inverse dependence with hydroxide ion concentration (Fig. 1).

© 1999 NRC Canada

Fig. 1. Dependence of the rate of chlorination of peptides to (*N*-Cl)-dipeptides with the acidity of the medium. $[Dipeptide]_0 = [LOCl]_0 = 5.0 \times 10^{-4}$ mol dm^{-3}; I = 1.0 mol dm^{-3}; T = 298.0 K.

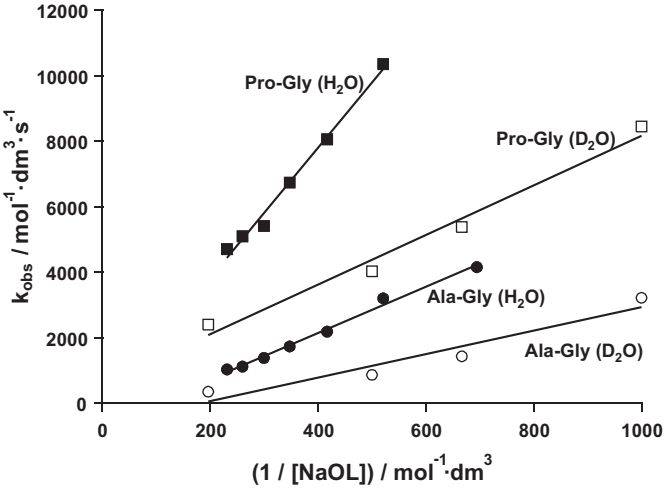

The following rate equation accounts for the observed behaviour:

$$r = k_{obs}\,[\text{dipeptide}][\text{chlorinating agent}]$$

$$= \frac{a\,[\text{dipeptide}][\text{chlorinating agent}]}{OL^-}$$

Such result is consistent with the mechanism shown in Scheme 2, which has been previously proposed to explain the chlorination of amines and amino acids to, respectively, (*N*-Cl)-amines and (*N*-Cl)-amino acids (9). $R_1R_2NL_2^+/R_1R_2NL$ refers to the amino group of the peptide. Chlorination of the peptidic nitrogen linkage does not take place under the working conditions (10). From Scheme 2, the following theoretical rate equation can be obtained:

$$r = \frac{kK_{a2}[L_3O^+]}{(K_{a2} + [L_3O^+](K_c + [L_3O^+])}\,[\text{dipeptide}][LOCl]$$

Kinetic runs have been performed at pH >>11, such that $K_{a2} >> [L_3O^+]$ and $K_C >> [L_3O^+]$. Hence, the previous equation simplifies to

$$r = \frac{kK_w}{K_c[OL^-]}\,[\text{dipeptide}][LOCl]$$

This equation is formally similar to the one empirically found, where the parameter a equals (kK_w/K_C). The values for the bimolecular rate constant k are compiled in Table 1. For H_2O, we use pK_w = 13.997 and pK_C = 7.26, whereas for D_2O, pK_w = 14.873 (11) and pK_C = 7.76, the latter value being proposed assuming $\Delta pK_a \approx 0.50$ on going from H_2O to D_2O (12).

The obtained bimolecular chlorination rate constants for **1** and **2** (Table 1) are in agreement with those previously found for amines and amino acids, whose pK_{a2} is close to that of the studied dipeptides. The deuterium secondary SIE found for **1** and **2** are close to unity, which is expected in this fast process, where the transition state should be reactant-like. These values could increase by ca. 10% if $(pK_C(D_2O) - pK_C(H_2O)) > 0.50$.

Scheme 2.

$$LOCl \rightleftharpoons ClO^- + L_3O^+ \qquad K_C$$

$$R_1R_2NL_2^+ \rightleftharpoons R_1R_2NL + L_3O^+ \qquad K_{a2}$$

$$R_1R_2NL + LOCl \longrightarrow R_1R_2NL + L_2O \qquad k$$

The magnitude of the observed SIE is in agreement with the currently accepted reaction mechanism, the slow step being the bimolecular reaction between the free amino nitrogen of the peptide and LOCl. However, the observed SIE does not allow to distinguish between direct *Cl* transfer from the *O* of LOCl to the amino *N* of the peptide and the possible involvement of a number of water molecules in the transition state (TS), like in structure (**5**) (12). In both cases, an early TS would imply a secondary SIE close to unity.

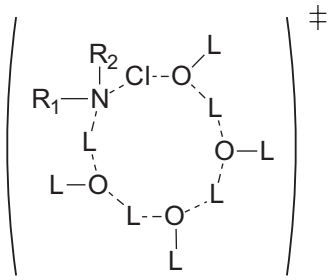

5

(*ii*) Decomposition of (*N*-X)-dipeptides in alkaline medium. Generation of *N*-(2-azomethino, 1-oxoalkyl)-amino acids

It is known from kinetic studies on the base-promoted decomposition of (*N*-X)-amines and (*N*-X)-amino acids that once the (*N*-X)-derivatives have been formed, they decompose through two consecutive processes (13): a base-promoted elimination of X^- to yield the corresponding azomethines, and a subsequent very fast hydrolysis of such azomethines to produce α-keto derivatives, chloride, and ammonia (or the corresponding amine).

For (*N*-X)-dipeptides, the intermediate azomethines lifetime is long enough to allow their observation, contrary to the case of (*N*-X)-amines. A plot of absorbance at the working wavelength (ca 237 nm) vs. time shows a maximum (14). Using Cl^- and NH_4^+ selective electrodes, it was shown that at such maximum Cl^- has been almost quantitatively released from **3** and **4**, while no NH_4^+ has been yet formed. In what follows, the mechanism of elimination to yield the azomethine intermediates is discussed.

The base-promoted elimination of X^- from (*N*-X)-dipeptides to *N*-(2-azomethino, 1-oxoalkyl)-amino acids is of first order, relative to both the (*N*-Cl)-dipeptide and the used base (Fig. 2), i.e.,

$$r = k\,[(N - X) - \text{dipeptide}][\text{base}]$$

Table 1 shows the rate constant values so-obtained, both in H_2O and D_2O. Table 1 compiles, as well, the observed values of k for the corresponding (*N*-Br)-dipeptides.

© 1999 NRC Canada

Table 1. Observed rate constants for the different processes taking place during the oxidation of dipeptides by aqueous chlorine at 298 K.

Process	λ (nm)	k_{H2O} (mol^{-1} dm^3 s^{-1})	k_{D2O} (mol^{-1} dm^3 s^{-1})	k_{H2O}/k_{D2O}
Chlorination of the dipeptides to the corresponding *N*-Cl-dipeptides				
1 + LOCl	292	3.88×10^7	4.64×10^7	85
2 + LOCl	292	1.10×10^8	9.81×10^7	112
Decomposition of (*N*-X)-dipeptides: (1,2)-elimination of X^- from (*N*-X)-dipeptides to yield the corresponding *N*-(2-azomethino, 1-oxoalkyl)-amino acid derivatives				
3 + OL^-	237	236	277	85
4 + OL^-	235	283	383	74
(*N*-Br)-**1** + OL^-	240	110		
(*N*-Br)-**2** + OL^-	235	137		
Decomposition of *N*-halo-dipeptides: hydrolysis of the corresponding *N*-(2-azomethino, 1-oxoalkyl)-amino acid derivatives				
3 + OL^-	237	2.39×10^{-3}	2.37×10^{-3}	101
3 + L_2O	237	2.08×10^{-3}[a]	1.07×10^{-3}[a]	194
3 + CF_3-CH_2O^-[b]	237	1.5×10^{-3}		
Decomposition of (*N*-Cl)-dipeptides in acid medium: disproportionate to the corresponding (*N*,*N*)-di-Cl-peptides				
		b_{H2O}[c]	b_{D2O}	b_{H2O}/b_{D2O}
3 + $\mathbf{3L}^+$	303	4424	—	—

[a] Rate constant units: s^{-1}.

[b] pK_a of CF_3-CH_2OH: 12.43.

[c] Parameter *b* is given in units of mol^{-2} dm^6 s^{-1}.

Fig. 2. Influence of the concentration of sodium hydroxide on the rate of generation of *N*-(2-azomethino, 1-oxoalkyl)-amino acids during the decomposition of (*N*-X)-dipeptides. [*N*-Cl-Ala-Gly]$_0$ = 1.0×10^{-3} mol dm^{-3}; I = 1.0 mol dm^{-3}; T = 298.0 K.

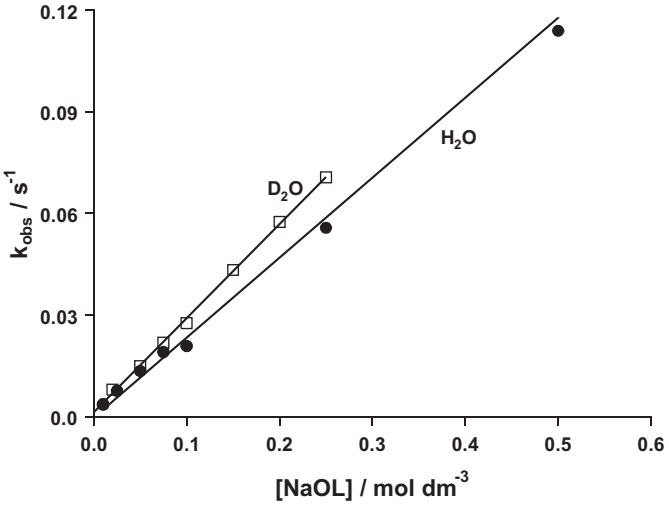

Brønsted plots for **3** and **4** are linear, with slopes of, respectively, β = 0.27 (15, 16) and 0.29. Such values of β are in agreement with the magnitude of the observed deuterium isotope effect: $[k(OH^-)/k(OD^-)]$ = 0.74 for **3** and $[k(OH^-)/k(OD^-)]$ = 0.84 for **4**. These values can be explained using fractionation factors (17).

$$\frac{k_{OH^-}}{k_{OD^-}} = \frac{\Phi_{OL^-}\,\Phi_{NCIL}}{\Phi^{\pm}_{OL^-}\,\Phi^{\pm}_{NCIL}}$$

In this kind of process, the main contribution to the isotope effect is due to the transformation of OL^- into L_2O, the OL^- fractionation factor changing from 0.41 to 1.

The deuterium secondary isotope effect, due to the hydrogen attached to the nitrogen, has almost no effect. In fact, in the case of the azomethine formed from **4**, the deuterium SIE comes only from the conversion of OL^- into L_2O:

$$\frac{k_{OH^-}}{k_{OD^-}} = \frac{\Phi_{OL^-}}{\Phi^{\pm}_{OL^-}} \rightarrow \Phi^{\pm}_{OL^-} = \frac{0.41}{0.74} = 0.55$$

By definition, the fractionation factor for water is 1. This means that OL^- retains most of its character at the TS, i.e.: the TS is reactant-like and the proton is slightly transferred to OL^-. Assuming very small change in the fractionation factor of the hydrogen attached to the *N*, 0.48 is estimated for the OL^- fractionation factor at the TS in the case of **3**. Such value is close to the typical value of 0.41 for the fractionation factor of the OL^-, which, in practice, means that L^+ is less transferred when the reactant is **3**. The same conclusion is drawn from the Brønsted β values: β (**4**) >> β (**3**).

From the results with (*N*-Br)-derivatives, the influence of the nucleofuge can be expressed in terms of β_{lg} (0.33 and 0.34, respectively, for (*N*-X)-**1** and (*N*-X)-**2**).

Using both parameters, it is possible to locate the TS in a More O'Ferrall – Jencks diagram (16). Figure 3 shows clearly that the process is concerted ($A_{xh}D_hD_n$), and slightly imbalanced (ca. 5%) (18), the *N—Cl* bond breaking going slightly ahead of the *C—H* bond breaking (see Scheme 3). However, no information is available about the process of carbon–nitrogen double bond formation.

(*iii*) Decomposition of (*N*-X)-dipeptides in alkaline medium: hydrolysis of *N*-(2-azomethino, 1-oxoalkyl)-amino acids to *N*-(1,2-dioxo-alkyl)-amino acids

The compounds **3** and (*N*-Br)-**1** decomposed with different rates to the corresponding *N*-(2-azomethino, 1-oxoalkyl)-amino acids (vide supra), but they have the same time of decay for such intermediate. In both cases, the process was of

© 1999 NRC Canada

Fig. 3. More O'Ferrall – Jencks plot for the base-promoted decomposition of (*N*-X)-dipeptides (□, (*N*-X)-**1**; ●, (*N*-X)-**2**).

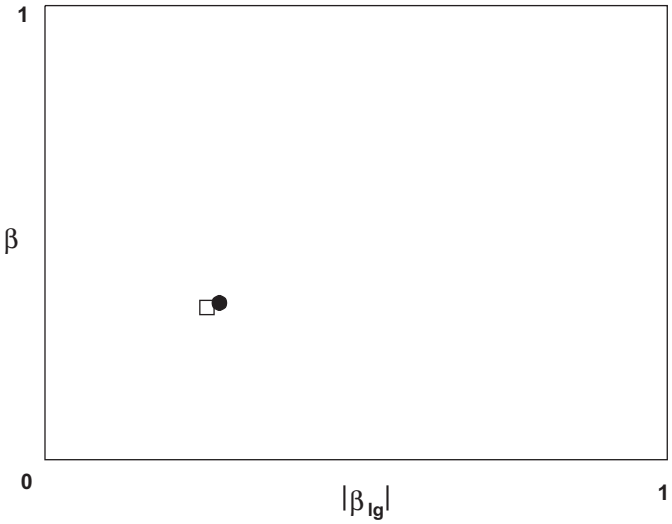

Scheme 3.

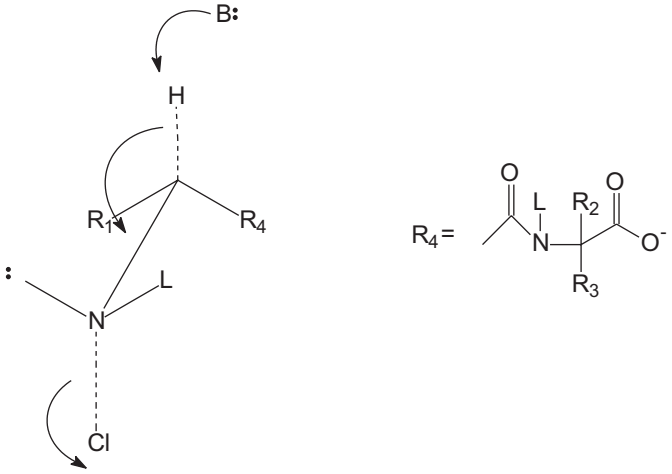

first order, relative to both the *N*-(2-azomethino, 1-oxoalkyl)-amino acid, and to OL^-. The dependence k_{obs} vs. [OL^-] was in all cases linear, showing an intercept statistically different from zero (Fig. 4).

Much work has been done on the hydrolysis of imines (19), the mechanism being satisfactorily known under different conditions. In the discussion ahead, we will take the established mechanism as a starting point.

The rate equation includes a base-catalyzed pathway and an uncatalyzed one, the corresponding values of the rate constants for those routes being compiled in Table 1.

$$r = (k_0 + k_{Base}[\text{base}])[N\text{-(2-azomethino, 1-oxoalkyl)-amino acid}]$$

The rate constants obtained for the base-catalyzed azomethine hydrolysis allow to estimate a zero value for the Brønsted β. This process shows no SIE ($k_{OH}/k_{OD} \approx 1$).

Fig. 4. Decomposition of *N*-halo-dipeptides. Influence of the [OL^-] on the rate of hydrolysis of the *N*-(2-azomethino, 1-oxoalkyl)-amino acids. [*N*-Cl-Ala-Gly]$_0$ = 1.0×10^{-3} mol dm^{-3}; I = 1.0 mol dm^{-3}; T = 298.0 K.

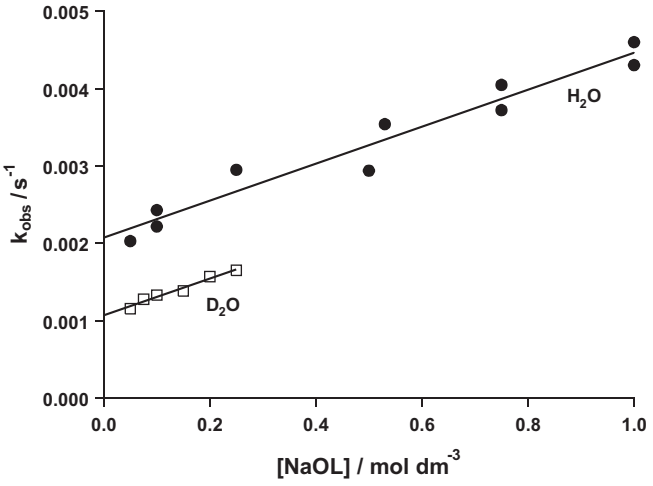

The fact β = 0 is consistent with a mechanism in which no proton transfer takes place, but at first sight, the absence of the deuterium SIE is not easily explained. An inverse deuterium SIE would be expected for a step in which the OL^- (ϕ = 0.41) joins the azomethine to form a carbinolamine ($\phi_{COL} \approx 1$).

These results can be accounted for in terms of the reaction pathway depicted in Scheme 4: one water molecule provides assistance in the formation of the carbinolamine. In this case, there are two contributions to the isotope effect: primary and secondary deuterium isotope effects:

$$\frac{k_{OH^-}}{k_{OD^-}} = \left(\frac{k_H}{k_D}\right)_{primary} \frac{\Phi_{OL^-}\Phi_{NL}}{\Phi^{\pm}_{OL^-}\Phi^{\pm}_{NL}\Phi^{\pm}_{L_2O}}$$

The primary deuterium isotope effect is due to the proton being transferred between the water molecule and the azomethine (Scheme 4). The absence of isotope effect is explained in terms of a reactant-like TS, where the proton is only slightly transferred, so that the magnitude of the primary isotope effect cancels with the contribution of the secondary ones. The latter involves the rest of interchangeable hydrogens whose bonds are not formed or broken at the TS.

The uncatalyzed hydrolysis of the azomethine is typically explained in terms of two kinetically indistinguishable pathways: one is shown in Scheme 5, and the other consists in the attack of OL^- to the protonated azomethine (iminium ion).

As in the previous processes where a OL^- is lost, an inverse isotope effect would be expected. However, this is not the case. The value of the solvent isotope effect (k_{H2O}/k_{D2O} = 1.96) is in support of the pathway depicted in Scheme 5.

By using typical fractionation factors for the species involved in the pre-equilibrium, a minimum value of 2.1 is predicted for the deuterium SIE. Most likely, this value is an overestimation, since in addition to the formation of OL^-, the force constants for the interchangeable hydrogens are bigger for the reactants than for the products (see Scheme 5) (20).

© 1999 NRC Canada

Scheme 4.

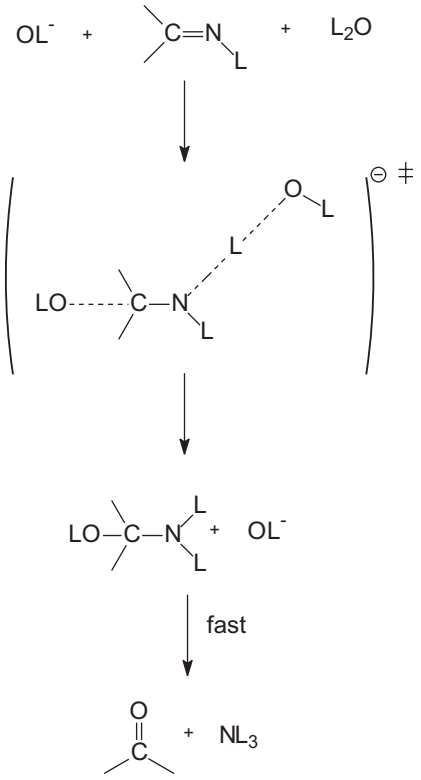

Considering now the rate-determining step, the value of the observed deuterium SIE would imply a reactant-like TS, where the OL^- mostly retains its character.

(*iv*) Decomposition of *N*-halo-dipeptides in acid medium: disproportionation

Although (*N*-X)-dipeptides are fairly stable under mild acidic conditions, they decompose in acid medium to give the (*N*,*N*)-di-Cl-dipeptide (see Scheme 1), the process follows a second-order kinetic law, and shows a linear dependence on proton concentration (Fig. 5), i.e.,

$$r = k_{obs}[\text{N-Cl-Ala-Gly}]^2 = b[L_3O^+][\text{N-Cl-Ala-Gly}]^2$$

The mechanism shown in Scheme 6 has been proposed to explain the observed behaviour of *N*-Cl compounds in acid media (21).

From this mechanism, the following theoretical rate equation is derived:

$$r = \frac{kK_{aN\text{-Cl}}[L_3O^+]}{(K_{aN\text{-Cl}} + [L_3O^+])^2}[N\text{-Cl-Ala-Gly}]^2$$

The experimental rate dependence matches the theoretical one when $K_{aN\text{-Cl}} >> [L_3O^+]$, where the empirical parameter b equals $(k/K_{aN\text{-Cl}})$, the different obtained values being collected in Table 1. In a rough estimation for **3**, fitting the full equation to our kinetic data, gives $pK_{aN\text{-Cl}} = -1.42 \pm 0.70$ (see Scheme 6), which is within the order of magnitude of other values previously obtained for this type of compounds. In general, the pK_a of *N*-Cl compounds is ca. 9 units lower than that of the parent amine (22). Since $pK_a(1) = 8.27$, a value lower than zero is expected for $pK_{aN\text{-Cl}}$.

Fig. 5. Influence of the acidity in the decomposition of *N*-Cl-Ala-Gly. $[N\text{-Cl-Ala-Gly}]_0 = 5.0 \times 10^{-4}$ mol dm^{-3}; I = 1.0 mol dm^{-3}; T = 298.0 K.

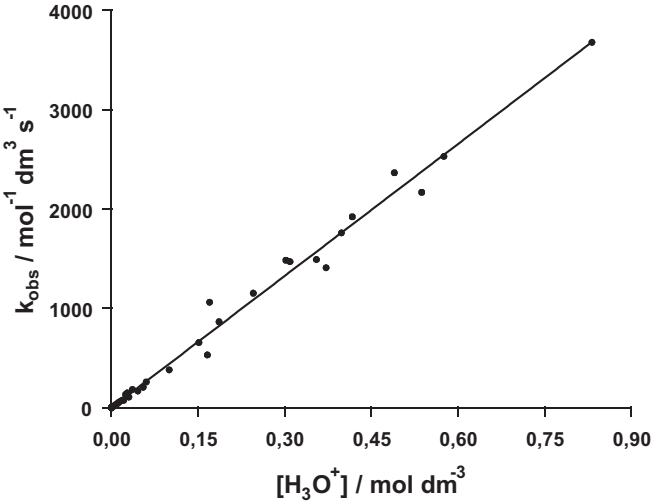

Obviously, a better value of the $pK_{aN\text{-Cl}}$ could be obtained working at higher acidities, but the decomposition of the so-formed (*N*,*N*)-di-Cl-dipeptide, which is also acid catalyzed, interferes. On the other hand, the decomposition process is very fast in D_2O. As a consequence, it is very difficult to get reliable values of the rate equation parameters, and the corresponding value given in Table 1 should be taken with caution. Since this processes are not of special interest from a biochemical or environmental point of view, we do not try any discussion on the magnitude of the deuterium SIE for them.

Further work is under progress with more stable (*N*,*N*)-di-Cl-dipeptides. The interest of such experiments relies on the possibility of estimating secondary deuterium isotope effects when the species isotopically substituted is attached to a nitrogen (see Scheme 6), since commonly secondary deuterium isotope effect are measured for reactions involving carbon centers (23).

Conclusions

The deuterium solvent isotope effect has proved to be a very useful tool in the investigation of the mechanisms involved in the oxidation of dipeptides by aqueous chlorine solutions. Fractionation factors have successfully explained the observed deuterium solvent isotope effects on the different mechanisms involved in such oxidation.

Experimental section

Materials, reagents

Deuterium oxide (99.9%), Ala-Gly, and Pro-Gly were purchased from Sigma®, and used without further purification. Aqueous chlorine solutions were prepared weekly by bubbling Cl_2 (g) through NaOH (aq) and spectrophotometrically titrated daily ($\lambda_{max}(H_2O) \simeq 292$ nm, $\varepsilon \simeq 350$ mol^{-1} dm^3 s^{-1} when pH >12) (22). Aqueous bromine solutions were prepared daily by dissolving Br_2 (l) in NaOH (aq) and spectrophotometrically titrated ($\lambda_{max}(H_2O) \simeq 331$ nm, $\varepsilon \simeq 326$ mol^{-1} dm^3 s^{-1} when pH > 12) (23). (*N*-X)-compounds were

© 1999 NRC Canada

Scheme 5.

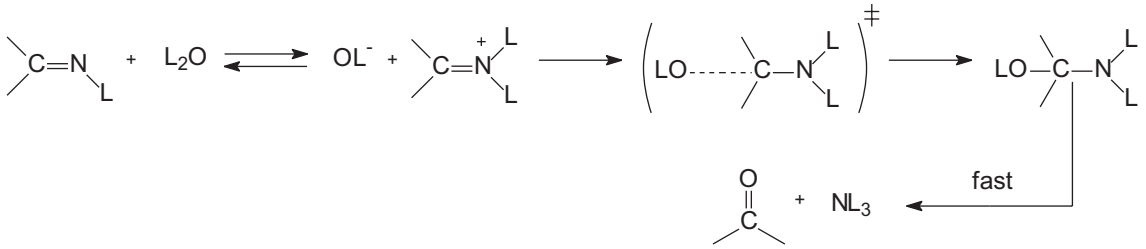

Scheme 6.

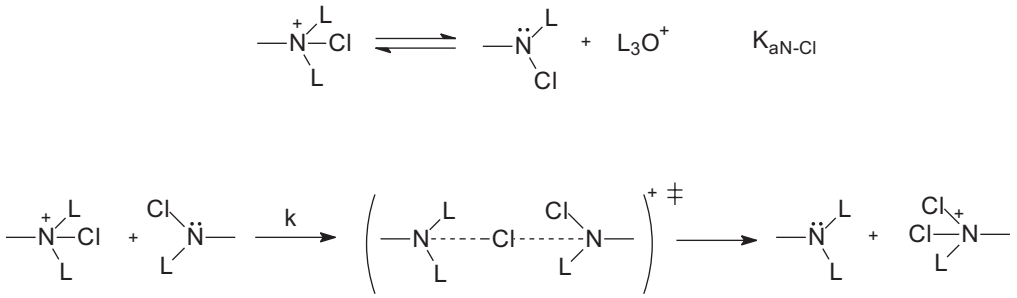

generated in the reaction cell by mixing appropriate amounts of aqueous halogen and dipeptide solutions so the ratio of the final concentrations were one. $(CF_3)_2CHOH/(CF_3)_2CHO^-$ was used as a buffer solution, HCl (aq), and NaOH (aq) were, respectively, used to get acid and alkaline media. $NaClO_4$ was used in general to control the ionic strength (I = 1 mol dm^{-3}), but KCl was used when buffering with $CF_3CH_2OH/CF_3CH_2O^-$. All other chemicals used were of the best quality commercially available.

Equipment

Conventional UV-vis (Beckman®, Cary®) and single- and multi-mixing Hi-Tech Scientific® stopped-flow spectrophotometers were used to monitor the reactions. An Ingold® Cl^- selective electrode and an Ingold® NH_3 (g) selective electrode were also used.

pH measurement and control

pH and pD measurements were carried out with combined glass electrodes. When buffer solutions of $CF_3CH_2OH/CF_3CH_2O^-$ were employed, the pH-meter was calibrated by using standardized KOH solutions, KCl being used as internal electrolyte for the reference electrode. Due to the slow response of the electrode in KOH solutions (24), ca. 5 min were allowed to elapse before any measurement.

Kinetics

Reactions were carried out at 298.0 ± 0.1 K. Reaction mixtures were prepared as described elsewhere (25). For the study on the chlorination of dipeptides to (*N*-Cl)-dipeptides, equimolar concentrations of both reagents or, at most, 1–2% excess of dipeptide were used. Unless in the study of the generation of (*N*-Cl)-dipeptides, chlorination was always carried out at a pH ca. 9, while bromination was carried out at pH ca. 11. Following this procedure, the halogenation was always finished in less than a tenth of a second (12). The solution used to achieve the acidity or basicity conditions was added only after halogenation had taken place. There was no evidence of simultaneous or partial chlorination on the nitrogen of the peptidic bond (26).

The reactions were followed at the wavelengths shown in Table 1. Kinetic data treatment was done by means of the DSC (27) or Marquardt (28) algorithms for nonlinear optimization. All reported rate constants are an average of, at least, five different runs, and their accuracy is better than 5%.

Products

The final products of the reported elimination reaction are always *N*-(2-imino-1-oxo-alkyl)-amino acids, halide, and ammonia, proofs of which have been given elsewhere (20, 29). The product of elimination reaction for *N*-Cl-Pro-Gly is *N*-[1-oxo-2-(4,5-dihydro-3H-pyrrole)]-glycine was identified using a Fisons Instruments VG quattro mass spectrometer (m/e = 171.1) (2.09%). One hundred percent chlorine loss in the reported process has been proved using a chloride selective electrode, and ammonia formation was followed using an ammonia selective electrode.

Acknowledgments

J.A. Santaballa wish to thank to Dr. R.A. McClelland for the opportunity to participate in this homage to Prof. Dr. A.J. Kresge. The research described in this paper was financed by the Xunta de Galicia (project XUGA 10307B95) and the Universidade da Coruña.

References

1. X.L. Armesto, M. Canle L., M.V. García, and J.A. Santaballa. Chem. Soc. Rev. **27**, 453 (1998), and refs. therein.
2. (*a*) W.H. Glaze. AWWA Research Foundation workshop report. Denver. 1993; (*b*) E.A Bryant, G.P. Fulton, and G.C. Budd. Disinfection alternatives for safe drinking water. Van Nostrand Reinhold, New York. 1992; (*c*) R.P. Martin, G.J. Martens, G. Porter, T.E. Graedel, W.C.Keene, G.W. Gribble,

© 1999 NRC Canada

J. Fauvarque, K.R. Solomon, H. Galal-Gorchev, J. Miyamoto, M.J. Molina, H.W. Sidebottom, J.A. Franklin, K. Ballschmiter, Ch. Rappe, A. Hanberg, R. Papp, G. Menges, and A.E. Fischli. Pure and Appl. Chem. **68**, 1683 (1996).
3. (*a*) M.B. Grisham, M.M. Jefferson, D.F. Melton, and E.L. Thomas. J. Biol. Chem. **259**, 10 404 (1984); (*b*) E.L. Thomas, M.B. Grisham, and M.M. Jefferson. J. Clin. Invest. **72**, 441 (1983); (*c*) E.L. Thomas. Infect. Inmmun. **23**, 522 (1979).
4. W.R. Mac Kenzie, N.J. Hoxie, and M.E. Proctor. New England J. Med. **331**, 161 (1994).
5. (*a*) R.J. Bull, L.S. Birnbaum, K.P. Cantor, J.B. Rose, B.E. Butterworth, R. Pegram, and J. Tuomisto. Fundam. Appl. Toxicol. **28**, 155 (1995); (*b*) D. Henschler. Angew. Chem. Int. Ed. Engl. **33**, 1920 (1994); (*c*) T. Soldi, V. Riganti, A. Profumo, and O. Conio. Microbiol. Alim. Nutr. **12**, 371 (1994).
6. (*a*) K. Agner. *In* Structure and function of oxidation-reduction enzymes. *Edited by* A. Akeson and A. Ehrenberg. Pergamon Press, London, 1972; (*b*) S.T. Test and S.J. Weiss. Adv. Free Radical Biol. Medicine, **2**, 91 (1986).
7. (*a*) B.S. Berlett and E.R. Stadtman. J. Biol. Chem. **272**, 20 313 (1997); (*b*) M.C.M. Vissers and C.C. Winterbourn. Arch. Biochem. Biophys. **285**, 53 (1991); (*c*) I.U. Schraufstätter, K.Browne, A. Harris, P.A. Hyslop, J.H. Jackson, O. Quehenberger, and C.G. Cochrane. J. Clin. Invest. **85**, 554 (1990); (*d*) S.J. Weiss. New England J. Med. **320**, 365 (1989).
8. (*a*) V. Gold. Trans. Faraday Soc. **56**, 255 (1960); (*b*) A.J. Kresge. Pure Appl. Chem. **8**, 243 (1964).
9. L. Abia, X.L. Armesto, M. Canle L., M.V. García, and J.A. Santaballa. Tetrahedron, **54**, 521 (1998), and refs. therein.
10. R.C. Ayotte and T. Gray, Jr. Water chlorination: chemistry, environmental impact and health effects. Vol. 5. Lewis Publishers Inc., Chelsea, Mich. 1973. p. 797.
11. Handbook of chemistry and physics. 79th ed. CRC Press Inc., Boca Raton, Fla. 1998.
12. W.J. Albery. Solvent-isotope effects. *In* Proton-transfer reactions. *Edited by* E. Caldin and V. Gold. Chapman and Hall, London. 1975.
13. X.L. Armesto, M. Canle L., M.V. García, M. Losada, and J.A. Santaballa. J. Phys. Org. Chem. **9**, 552 (1996), and refs. therein.
14. X.L. Armesto, M. Canle L., M.V. García, and J. A. Santaballa. Tetrahedron, **53**, 12 615 (1997).
15. A.J. Kresge. The Brønsted relation. Significance of the exponent. *In* Proton-transfer reactions. *Edited by* E. Caldin and V. Gold. Chapman and Hall, London. 1975.
16. H. Maskill. The physical basis of organic chemistry. Oxford University Press, Oxford. 1993.
17. W.J. Albery and M.H. Davies. Trans. Faraday Soc. **65**, 1059 (1969).
18. C.F. Bernasconi. Adv. Phys. Org. Chem. **27**, 119 (1992).
19. A. Bruylants and E. Feytmants-de Medicis. *In* The chemistry of the carbon-nitrogen double bond. *Edited by* S. Patai. Interscience Publishers. 1970. Chap. 10.
20. O. Matsson and K.C. Westaway. Adv. Phys. Org. Chem. **31**, 143 (1998).
21. (*a*) J.M. Antelo, F. Arce, M.C. Castro, J. Crugeiras, J.C. Pérez Moure, and P. Rodríguez. Int. J. Chem. Kinet. **27**, 703 (1995); (*b*) X.L. Armesto, M. Canle L., A.M. Gamper, M. Losada, and J.A. Santaballa. Tetrahedron, **50**, 10 509 (1994).
22. J.R. Gandler and W.P. Jencks.J. Am. Chem. Soc. **104**, 1937 (1982).
23. C.H. Cheek and V.J. Linnenbom. J. Phys. Chem. **67**, 1856 (1963).
24. J.C. Morris. J. Phys. Chem. **70**, 3798 (1966).
25. X.L. Armesto, M. Canle L., M. Losada, and J.A. Santaballa. Int. J. Chem. Kinet. **25**, 331 (1993).
26. L. Hureiki, J.P. Croué, and B. Legube. Wat. Res. **28**, 2521 (1994).
27. J. Casado, M. Mosquera, A. Rivas, M.F. Rodríguez Prieto, and J.A. Santaballa. Comput. Chem. **7**, 209 (1983).
28. D.W. Marquardt. J. Soc. Ind. Math. **11**, 431 (1963).
29. (*a*) L.I. Abia, X.L. Armesto, M. Canle L., M.V. García, M. Losada, and J.A. Santaballa. Bull. Soc. Chim. Belg. **105**, 349 (1996); (*b*) J.M. Stelmaszyńska and J.M. Zgliczyński. Eur. J. Biochem. **92**, 301 (1978).

© 1999 NRC Canada

Strong Zn^{2+} and Co^{2+} catalysis of the methanolysis of acetyl imidazole and acetyl pyrazole

Ayla Khan, Alexei A. Neverov, Anatoly K. Yatsimirsky, and R.S. Brown

Abstract: The kinetics of methanolysis of acetyl imidazole (**1**) and acetyl pyrazole (**2**) have been investigated under anhydrous conditions in the presence of $Zn(ClO_4)_2$, $Co(ClO_4)_2$, and $HClO_4$ at 25°C. In all cases, the plots of the pseudo-first-order rate constant for methanolysis (k_{obs}) vs. [metal ion] or [$HClO_4$] show saturation behavior indicative of equilibrium binding of the M^{2+} or H^+ to the amide. Relative to the spontaneous methanolysis rate constant (k_o), the catalytic rate constant obtained at saturation, k_{cat}, is larger for metal-ion catalysis than for H^+ catalysis. The (k_{cat}^{H+}/k_o) ratio is 10.7 and 1.25 for **1** and **2**, respectively, while the (k_{cat}^{M2+}/k_o) for these divalent metals varies from 150-fold for **1** to between 700 and 5700-fold for **2**. By contrast, in water, proton is far more effective at promoting the hydrolysis of **1** than are metals, the aqueous (k_{cat}^{H+}/k_o) ratio being 560, while the (k_{cat}^{Zn2+}/k_o) and (k_{cat}^{Ni2+}/k_o) ratios are 15 and 3.2, respectively.

Key words: methanolysis, kinetics, metal-ion catalysis, acetyl imidazole, acetyl pyrazole.

Résumé : Opérant dans des conditions anhydres, à 25°C, en présence de $Zn(ClO_4)_2$, $Co(ClO_4)_2$ et de $HClO_4$, on a étudié la cinétique de la méthanolyse de l'acétyl imidazole (**1**) et de l'acétyl pyrazole (**2**). Les courbes de la constante de vitesse de pseudo-ordre un de la méthanolyse (k_{obs}) en fonction de [ion métallique] ou de [$HClO_4$] présentent toutes un comportement de saturation qui suggère l'implication d'une fixation en équilibre de M^{2+} ou H^+ par l'amide. Si on la compare à la constante de vitesse de méthanolyse spontanée (k_o), la constante de vitesse catalytique obtenue à saturation (k_{cat}) est supérieure pour la catalyse par les ions métalliques que pour la catalyse par les ions H^+. Le rapport k_{cat}^{H+}/k_o est égal à 10,7 et 1,25 pour les composés **1** et **2** respectivement alors que le rapport k_{cat}^{M2+}/k_o pour ces métaux bivalents varie de 150 pour **1** à 700–5700 pour **2**. En comparaison, dans l'eau, les protons sont beaucoup plus efficaces que les métaux pour favoriser l'hydrolyse de **1**; le rapport k_{cat}^{H+}/k_o est égal à 560 alors que les rapports k_{cat}^{Zn2+}/k_o et k_{cat}^{Ni2+}/k_o sont de 15 et 3,2.

Mots clés : méthanolyse, cinétiques, catalyse par les ions métalliques, acétyl imidazole, acétyl pyrazole.

[Traduit par la Rédaction]

The catalytic effect of metal ions on the hydrolyses of simple amides is usually small for the HO^- reactions (1) and generally nonexistent for the H_2O reactions. There are notable exceptions, but these involve situations where M^{2+}-ions are intramolecularly chelated to enforce proximity to the scissile C=O unit (2–5), or with ligand exchange inert Co(III) complexes (6). Some systems using M^{2+} are intermolecularly catalytic for amides not having proximal binding sites, the most important of these being Cu^{2+} complexes that probably exhibit bimodal catalysis with the Cu^{2+} acting transiently as both a Lewis acid activator of the C=O and the source of a nucleophilic Cu^{2+}-OH^- (7). Notably, M^{2+}-catalysis of the hydrolysis of simple N-acyl imidazoles devoid of a suitably positioned chelating site is, to our knowledge, relatively weak (8), and metal ions are not as good as H^+ is in promoting the hydrolysis of these, and normal, amides. As pointed out by Sigel and Martin (9), solvent H_2O provides a potent oxygen donor for binding the metal ion in competition with the weakly basic amide oxygen (or even more weakly basic N of normal amides), so the equilibrium position for binding lies well to the side of the solvated metal. Based on previous work of Deiko et al. (10) on the methanolysis of acetyl imidazole, we reasoned that metal-ion solvation in methanol might be sufficiently weakened that the equilibrium position for binding to amides might lie further to the side of the M^{2+}-amide com-

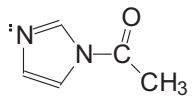

1

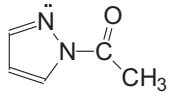

2

Received February 9, 1999.

This paper is dedicated to Jerry Kresge in recognition of his many achievements in chemistry.

A. Khan, A.A. Neverov, and R.S. Brown.[1] Department of Chemistry, Queen's University, Kingston, ON K7L 3N6, Canada.
A.K. Yatsimirsky. Facultad de Quimica, Universidad Nacional Autónoma de México, México D.F. 04510, México.

[1]Author to whom correspondence may be addressed. Telephone: (613) 533-2426. Fax: (613) 533-6669.
e-mail: rsbrown@chem.queensu.ca

© 1999 NRC Canada

Table 1. Kinetic (k_{cat}) and metal or proton dissociation constants (K_M, K_{H+}) for the methanolysis of acetyl imidazole (**1**) and acetyl pyrazole (**2**) in the presence of $M^{2+}(ClO_4)_2$ salts or $HClO_4$, T = 25°C.

M^2+	k_{cat} (s^{-1})	K_M (M)	k_{cat}/K_M (M^{-1} s^{-1})	k_{cat}/k_o
		Acetyl imidazole (**1**)[a,b]		
Zn^2+	(5.3 ± 0.3) × 10^{-2}	(1.2 ± 0.2) × 10^{-3}	44	138 ± 11
Zn^{2+}(MeOD)	9.0 × 10^{-3}	(5.6 ± 0.5) × 10^{-4}	16	97 ± 5
Co^2+	(6.10 ± 0.1) × 10^{-2}	(2.8 ± 0.2) × 10^{-3}	22	158 ± 3
H+	(4.12 ± 0.09) × 10^{-3}	(1.2 ± 0.2) × 10^{-4}[e] [3.9]	k_{cat}/K_{H+} = 34	10.7
		Acetyl pyrazole (**2**)[c,d]		
Zn^2+	2.22 ± 0.05	(2.8 ± 0.2) × 10^{-3}	793	700 ± 20
Zn^{2+}(MeOD)	(8.1 ± 0.2) × 10^{-1}	(1.2 ± 0.1) × 10^{-3}	675	324 ± 20
Co^2+	17.9 ± 0.3	(2.6 ± 0.1) × 10^{-3}	6884	5700 ± 100
H+	~4 × 10^{-3}	~1 × 10^{-3}[e] [3.0]	k_{cat}/K_{H+} = 4	1.25

[a] k_o = 3.85 × 10^{-4} s^{-1} in MeOH; 9.3 ± 0.4 × 10^{-5} s^{-1} in MeOD, $k_o^{(MeOH)/(MeOD)}$ = 4.1.
[b] k_{cat}^{Zn}(MeOH/MeOD) = 5.9.
[c] k_o = 3.16 ± 0.02 × 10^{-3} s^{-1} in MeOH; 2.5 ± 0.1 × 10^{-3} in MeOD; $k_o^{(MeOH)/(MeOD)}$ = 1.26.
[d] k_{cat}^{Zn}(MeOH/MeOD) = 2.74.
[e] K_{H+}; pK_{H+} in square brackets.

[1] 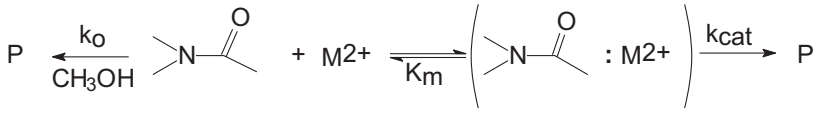

plex (11) with concomitant catalytic enhancement of the cleavage of the N—C(O) bond. Herein, we report preliminary results of a study of the Zn^{2+}- and Co^{2+}-catalyzed methanolysis of acetyl imidazole **1** (12) and acetyl pyrazole **2** (13), indicating that there is saturation metal-ion binding and great acceleration of the methanolysis.

The plots shown in Fig. 1 illustrate that the observed pseudo-first-order rate constants for methanolysis (k_{obs}) exhibit saturation behavior at increasing [$M^{2+}(ClO_4^-)_2$], indicative of the process given in eq. [1] where P indicates the products of amine and methyl acetate, and for which can be written the kinetic expression given in eq. [2]. Given in Table 1 are the various rate (k_o, k_{cat}) and kinetic metal-dissociation (K_M) constants determined from NLLSQ fits of

[2] $$k_{obs}=(k_oK_M + (k_{cat}[M^{2+}]))/(K_M + [M^{2+}])$$

the k_{obs} vs. [$M^{2+}(ClO_4^-)_2$] data to eq. [2].[2] Also included are the rate and H^+-dissociation constants for the acid-catalyzed methanolysis of **1** and **2**, these being obtained by fits of the k_{obs} vs. [$HClO_4$] data to eq. [2] where [M^{2+}] is replaced by [$HClO_4$].

There are several features of note in the data contained in the table. First, the k_{cat}, K_M, and K_{H+} constants for metal- and acid-catalyzed methanolysis allow comparison of the relative catalytic and binding abilities of the two divalent metal ions and H^+ for each amide. The rate enhancements afforded by these, given as k_{cat}/k_o where k_o is the rate constant for the spontaneous methanolysis, are larger for the metal ions than for proton. This is unusual considering that in water, proton is far more effective at promoting the hydrolysis of **1** than are metal ions, the aqueous (k_{cat}^{H+}/k_o) ratio being 560 (12*b*), while the (k_{cat}^{Zn2+}/k_o) and (k_{cat}^{Ni2+}/k_o) ratios are 15 and 3.2.[3] Even for the exchange inert Co^{3+} complex ($(NH_3)_5Co^{3+}ImC(O)CH_3$) where the Co^{3+} is fixed at the distal N, the reaction is accelerated by only 24-fold (8). By contrast, in methanol the (k_{cat}^{H+}/k_o) ratio is 10.7 and 1.25 for **1** and **2**, respectively, while the enhancement by metals varies from 150-fold for **1** to between 700 and 5700-fold for **2**.

Second, the metal-dissociation constants (K_M) vary only by a factor of 2 in MeOH, irrespective of the amide structure and nature of the metal, and the H^+-dissociation constants vary by ~10-fold. Acetyl pyrazole, **2**, is less basic (toward H^+) than **1** by 10-fold. However, the similarity of its K_M data to those of **1**, which certainly binds the metal ion through the distal sp^2-N, indicates that association of the metal with the proximal carbonyl oxygen of the former (14) contributes to the stability of the complex in methanol to some extent. In MeOD, the Zn^{2+}-K_M values for **1** and **2** decrease by about

[2] UV kinetics were monitored under anhydrous conditions by observing in duplicate or triplicate the rate of loss of **1** and **2** at 235 and 240 nm in methanol under pseudo-first-order conditions of excess 0 < [$M^{2+}(ClO_4)_2$] < 0.01 M, [amide] = 6.7 × 10^{-5} M, ionic strength not held constant. Pseudo-first-order rate constants (k_{obs}) were evaluated by fitting the abs. vs. time traces to a standard exponential model. Values of k_{cat} and K_M given in Table 1 are derived from NLLSQ fits of the k_{obs} vs. [M^{2+}] or [H^+] plots to eq. [2].

[3] A.A. Neverov (18), reports that for the reaction of acetyl imidazole in water containing $Zn^{2+}$and Ni^{2+}, the respective k_{cat} and K_M values in the neutral hydrolysis region are (1.25 ± 0.2) × 10^{-3} s^{-1}; 3.5 × 10^{-2} M ([Zn^{2+}] = 0.1 M, $ZnCl_2$) and (2.7 ± 0.3) × 10^{-4} s^{-1}; 7.3 × 10^{-3} M ([Ni^{2+}] = 0.2 M, $NiCl_2$). These can be compared with the k_o value for water attack on the protonated species at μ = 0.2, 4.7 × 10^{-2} s^{-1}, pK_a = 3.5 (*b*). The spontaneous rate constant for neutral hydrolysis of acetyl imidazole in water is reported to be 3 × 10^{-4} s^{-1}, μ = 0 (10), 8.3 × 10^{-5} s^{-1} at μ = 0.2 (*b*), or 4.6 × 10^{-5} s^{-1} at μ = 1.0 (8*b*). For the sake of consistency, we used the available Zn^{2+}, Ni^{2+}, and H^+ data at μ = 0.2 for our comparisons.

© 1999 NRC Canada

Fig. 1. Plot of pseudo-first-order rate constants for the methanolysis of acetyl pyrazole (**2**) as a function of $[M^{2+}(ClO_4^-)_2]$ at 25°C, (■) Zn^{2+}, (●) Co^{2+}. Lines are the nonlinear least-squares fits of the data to eq. [**2**].

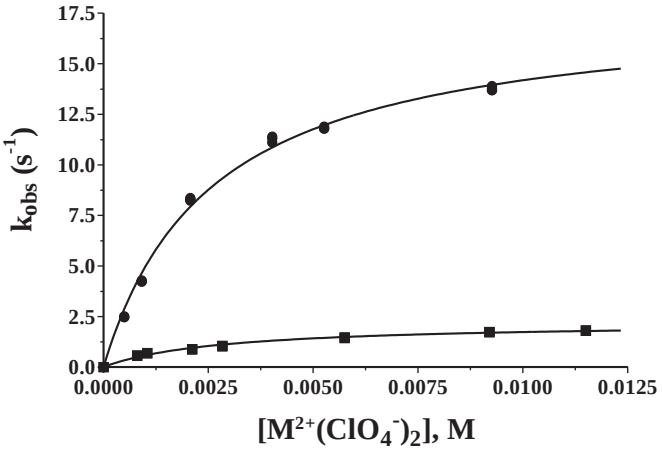

2–3-fold from their values in MeOH, perhaps suggestive of a decreased solvation of the metal ion in MeOD and (or) the possibility that the K_M value may be a more complex term involving multiple equilibria.

The solvent deuterium kinetic isotope effects for the spontaneous methanolysis (k_o) and the Zn^{2+}-reaction (k_{cat}) of **1** are 4.1 and 5.9, while those for **2** are 1.25 and 2.74, respectively. Proton inventories (15) of the Zn^{2+}-catalyzed reactions indicates that the plots of k_{cat}^{Zn2+} vs. *n*, where *n* is the atom fraction of deuterium in the solvent, are significantly bowed downwards. This is suggestive of a transition state for the metal-catalyzed reaction where there are two or more protons from multiple methanol molecules undergoing changes in bonding.

It is difficult to rationalize the unusual observation that Zn^{2+} and Co^{2+} are more effective than H^+ in catalyzing methanolysis of **1** and **2**, but the converse is true for hydrolysis. The effect is not small, since for **1**, the change in the ($k_{cat}^{H+}/k_{cat}^{Zn2+}$) ratio is roughly 500-fold. It seems reasonable that if the same acyl-transfer mechanisms and distribution of metal–H^+-bound species are operative in each solvent, then the relative greater effectiveness of the proton would be maintained. In the case of acetyl imidazole, the catalysis by proton must occur through its binding to the distal N and accelerating the rate-limiting attack of water or methanol on the remote C=O as in **3** (16). Fife and co-workers' studies (3) showed that strong acceleration of the hydrolyses of various acyl imidazoles by divalent metal ions is expected only when the metal ion can be coordinated to the C=O. In such cases, the metal ion can act as a strong electrophilic catalyst to enhance nucleophilic attack of solvent or SO^- on the polarized C=O, or to deliver a metal bound SO^-. For acyl imidazoles where there is no additional chelating group present to hold the metal ion in proximity to the C=O, modest or no catalysis of hydrolysis is observed. Chelation of the metal to the pyrazole N and C=O as in **4** can occur with acetyl pyrazole in methanol, accounting for the enhancement of methanolysis. However, metal association with the C=O cannot occur in complexes of **1** unless there is a translocation of the metal ion from the favored binding site of the distal N to the carbonyl oxygen. Subsequent to such a translocation, methanolysis would be strongly catalyzed. One might speculate that the medium effect produced by methanol alters the equilibrium between N and C=O bound metal ion to a more favourable distribution than in water with concomitant acceleration of methanolysis.

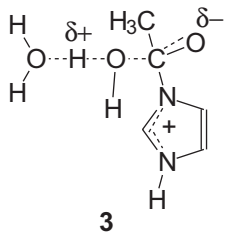

3

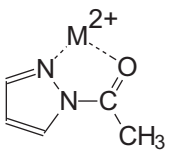

4

More work is necessary to clarify the factors responsible for the metal-ion catalysis and the effect of the medium. What we have shown here is that methanolysis of acetyl pyrazole is strongly accelerated by the presence of Zn^{2+} and Co^{2+} as is the methanolysis of acetyl imidazole, contrasting the poor metal-ion catalysis of its hydrolysis. It is often considered that the microenvironment existing in the active sites of enzymes more closely resemble alcohols or other reduced polarity media so the methanolysis results reported here may be relevant to the mechanism of acyl transfer mediated by metallo-proteases such as carboxypeptidase (17). The intriguing possibility that the medium alters the equilibrium distribution between solvated, N, and C=O bound metal ions begs the question of whether methanolysis of more normal amides is subject to metal-ion catalysis, a question we are actively investigating.

Acknowledgements

The authors gratefully acknowledge the financial assistance of the Natural Sciences and Engineering Research Council of Canada, and Queen's University.

References

1. (*a*) L. Meriwether and F.H. Westheimer. J. Am. Chem. Soc. **78**, 5119 (1956); (*b*) I.J. Grant and R.W. Hay. Aust. J. Chem. **18**, 1189 (1965).
2. (*a*) J.T. Groves and R.M. Dias. J. Am. Chem. Soc. **101**, 1033(1979); (*b*) J.T. Groves and R.R. Chambers, Jr. J. Am. Chem. Soc. **106**, 630 (1984); (*c*) J.T. Groves and J.R. Olsson. Inorg. Chem. **24**, 2717 (1985); (*d*) J. Suh. Acc. Chem. Res. **25**, 273 (1992); (*e*) L.M. Sayre, K.V. Reddy, A.R. Jacobson, and W. Tang. Inorg. Chem. **31**, 935 (1992).
3. T.H. Fife. Acc. Chem. Res. **26**, 325 (1993), and refs. therein.
4. T.N. Parac and N.M. Kostic'. J. Am. Chem. Soc. **118**, 51 (1996), and refs. therein.
5. L. Singh and R. Ram. J. Org. Chem. **59**, 710 (1994).
6. (*a*) P.A. Sutton and D.A. Buckingham. Acc. Chem. Res. **20**, 357 (1987), and refs. therein; (*b*) A. Schepartz and R. Breslow. J. Am. Chem. Soc. **109**, 1814 (1987), (*c*) B.K. Takasaki, J.H. Kim, E. Rubin, and J. Chin. J. Am. Chem. Soc. **115**, 1157 (1993); (*d*) J.A. Connolly, J.H. Kim, M. Banaszczyk, M. Drouin, and J. Chin. Inorg. Chem. **34**, 1094 (1995).
7. (*a*) J. Chin, V. Jubian, and K. Mrejen. J. Chem. Soc. Chem. Commun. 1326 (1990); (*b*) L.M. Sayre, K.V. Reddy, A.R Ja-

© 1999 NRC Canada

cobson, and W. Tang. Inorg. Chem. **31**, 935 (1992); (*c*) E.L. Hegg and J.N. Burstyn. J. Am. Chem. Soc. **117**, 7015 (1995).
8. (*a*) J. MacB. Harrowfield, V. Norris, and A.M. Sargeson. J. Am. Chem. Soc. **98**, 7282 (1976); (*b*) D.A. Buckingham and C.A Clark. J. Chem. Soc. Dalton Trans. 1757 (1979).
9. H. Sigel and R.B. Martin. Chem. Rev. **82**, 385 (1982).
10. S.A. Deiko, A.A. Neverov, and A.K Yatsimirsky. Kinet. Catal. **30**, 694 (1989); original Russian version Kinet. Katal. **30**, 793 (1989).
11. K.-K. Mui, W.A.E. McBryde, and E. Nieboer. Can. J. Chem. **52**, 1821 (1974).
12. (*a*) J.H. Boyer. J. Am. Chem. Soc. **74**, 6274 (1952); (*b*) W.P Jencks and J. Carriuolo. J. Biol. Chem. **234**, 1272 (1959).
13. (*a*) L. Knorr. Chem. Ber. **28**, 714 (1895); (*b*) R. Hüttel and J. Kratzer. Chem. Ber. **92**, 2014 (1959); (*c*) J. Barthel and G. Schmeer. Ann. Chem. **738**, 195 (1970).
14. W.L. Driessen and P.L.A. Everstijn. Inog. Chim. Acta, **41**, 179 (1980).
15. (*a*) R.L. Schowen. *In* Isotope effects on enzyme-catalyzed reactions. *Edited by* W.W. Cleland, M.H. O'Leary, and D.B. Northrop. University Park Press, Baltimore. 1977; (*b*) F.J. Alvarez and R.L. Schowen. *In* Isotopes in organic chemistry. *Edited by* E. Buncel and C.C. Lee. Elsevier, Amsterdam. 1987, Vol. 7, pp. 1–60; (*c*) A.J. Kresge, R.A. More-O'Ferrall, and M.F. Powell. *In* Isotopes in organic chemistry. *Edited by* E. Buncel and C.C. Lee. Elsevier, Amsterdam, 1987, Vol. 7, pp.177–274.
16. (*a*) D.G. Oakenfull, K. Salvesen, and W.P. Jencks. J. Am. Chem. Soc. **93**, 188 (1971); (*b*) J.L. Hogg, M.K. Phillips, and D.E. Jergens. J. Org. Chem. **42**, 2459 (1977).
17. J. Suh, B.K. Hwang, and Y.H. Koh. Bioorg. Chem. **18**, 207 (1990), and refs. therein.
18. A.A. Neverov. Ph.D. dissertation. Moscow State University, Moscow. 1991.

© 1999 NRC Canada

Reactivity in acid-catalyzed carbon–carbon heterolysis

Weiguo Cao, Ihsan Erden, Richard H. Grow, James R. Keeffe, Jiangao Song, Mary B. Trudell, Teri L. Wadsworth, Fu-Pei Xu, and Ji-Bin Zheng

Abstract: Equilibrium and rate constants have been determined for the acid-catalyzed heterolysis of two alcohols, 9-xanthydrol and *p*-anisyldiphenylmethanol, and two sulfides, (9-xanthyl) methyl sulfide and (7-tropyl) methyl sulfide. These data together with literature information are compared with rate constants for acid-catalyzed C-C heterolysis of several (9-xanthyl) compounds, (7-tropyl) compounds, a set of 3-arylcyclobutanones, and two 2-arylnitrocyclopropanes, all of which fragment to carbocations plus a carbon-centered nucleofuge. The fragmentation mechanisms are shown to be A1 or A1(ion pair) except for the 2-arylnitrocyclopropanes which cleave in trifluoroacetic acid by a concerted mechanism. Rate comparisons among several unstrained substrate sets indicate that *O*-centered nucleofuges undergo acid-catalyzed heterolysis ca. 10^3–10^4 faster than *S*-centered nucleofuges and ca. 10^9–10^{14} faster than the *C*-centered nucleofuges used here. Factors assisting C-C heterolysis (and their effectiveness) include the acidity of the medium (strong); the basicity and nucleofugality of the nucleofuge (moderate); the stability of the electrofugic carbocation (strong); and relief of ring strain (enormous). Compared with acyclic cleavages, rate accelerations worth ca. 15 kcal/mol (for cyclobutanones) and ca. 27 kcal/mol (for nitrocyclopropanes) are found. These effects are discussed in terms of transition-state structure, aided by computational evidence.

Key words: C-C heterolysis, fragmentation, acid catalysis, carbocation, ring strain.

Résumé : On a déterminé les constantes d'équilibre et les constantes de vitesse des réactions d'hétérolyse acidocatalysée de deux alcools, le 9-xynthydrol et le *p*-anisyldiphénylméthanol, et de deux sulfures, le sulfure de 9-xanthyle et de méthyle et le sulfure de 7-tropyle et de méthyle. Ces données et d'autres tirées de la littérature ont été comparées aux constantes de vitesse d'hétérolyse C-C acidocatalysée de plusieurs dérivés du 9-xanthyle, du 7-tropyle, d'un ensemble de 3-arylcylobutanones et de deux 2-arylnitrocyclopropanes qui se fragmentent tous pour donner des carbocations en plus d'un nucléofuge centré sur le carbone. On a montré que tous les mécanismes de fragmentation sont A1 ou A1(paire d'ions), à l'exception des 2-arylnitrocyclopropanes qui se clivent dans l'acide trifluoroacétique par un mécanisme concerté. Une comparaison des vitesses de plusieurs ensembles de substrats non tendus indiquent que les nucléofuges centrés sur l'oxygène subissent des hétérolyses acidocatalysées environ 10^3–10^4 fois plus rapides que celles impliquant des nucléfuges centrés sur le soufre et environ 10^9–10^{14} fois plus rapides que celles impliquant les nucléfuges centrés sur le carbone utilisés ici. Les facteurs qui favorisent l'hétérolyse C-C (et leur efficacité) incluent l'acidité du milieu (forte); la basicité et la nucléofugacité du nucléofuge (modérée); la stabilité du carbocation électrofuge (forte) et l'élimination de la contrainte de cycle (énorme). Comparés avec les clivages acycliques, les accélérations de vitesses correspondent à environ 15 kcal/mol (pour les cyclobutanones) et environ 27 kcal/mol pour les nitrocyclopropanes. On discute de ces effets en fonction de la structure de l'état de transition en s'appuyant sur des résultats de calculs théoriques.

Mots clés : hétérolyse C-C, fragmentation, catalyse acide, carbocation, tension de cycle.

[Traduit par la Rédaction]

Introduction

A large number of synthetically important reactions occur with the formation of one or more carbon–carbon bonds by polar mechanisms. Some of the more obvious of these are the aldol condensation and its large family, Michael additions, Friedel–Crafts chemistry, and acid-catalyzed polymerizations. A number of cationic cyclizations (1, 2) and cycloadditions (3, 4) also fall into this category, as does the biosynthesis of squalene (5), and the subsequent cyclization of squalene oxide to lanosterol (6). Heterolytic C-C cleavage is also well known; retroversions of some of the reactions

Received November 3, 1998.

This paper is dedicated to a good friend and associate, A.J. Kresge, on the occasion of his choice.

W. Cao, I. Erden,[1] R.H. Grow, J.R. Keeffe,[1] J. Song, M.B. Trudell, T.L. Wadsworth, F.-P. Xu, and J.-B. Zheng. Department of Chemistry and Biochemistry, San Francisco State University, 1600 Holloway Ave., San Francisco, CA 94132, U.S.A.

[1]Authors to whom correspondence may be addressed. Telephone: (415) 338-1117. Fax: (415) 338-2384. e-mail: ierden@sfsu.edu or keeffe@sfsu.edu

© 1999 NRC Canada

cited above sometimes occur. Such reactions offer, in principle, opportunities to study mechanism and structure–reactivity patterns by microscopic reversibility. Polycyclic cage compounds comprise a substantial group able to undergo rearrangement and cleavage by C-C heterolysis (7, 8). Relief of strain and enforced geometries render these transformations synthetically and mechanistically interesting.

One category of heterolytic C-C cleavages is known as β-fragmentations. Early examples include the important work of Whitmore (9) on acid-catalyzed reactions of some highly branched aliphatic systems in which substitution, elimination, rearrangement, and fragmentation competed under thermodynamic control. Shiner and Meier (10) extended this work providing rate constants and partitioning ratios for competing pathways under kinetic control. (These authors also review much of the earlier work on branched aliphatic compounds.) Meanwhile, Grob (11) had generalized cationic β-fragmentations as shown in eqs. [1] and [2]. In these systems, a-C_γ^+ is an electrofuge which, depending on its stability and reaction conditions, might depart assisted only by donor a, or might be helped to leave by a base or nucleophile. Atom or group X is a nucleofuge, i.e., an adequate electron acceptor, perhaps aided by acid. In addition to these specifications, Grob proposed that for fragmentation to be concerted, a stereochemical requirement must be met, namely that the *sigma* bond skeleton linking C_γ with X should be *anti* and coplanar, as shown in eq. [1], for optimal reactivity. This analysis is analogous to one given earlier by Nesmeyanov (12). These requirements are identical to those preferred for the E2 elimination reaction where H^+ takes the role of a-C_γ^+. Also in this category are a number of synthetically useful β-elimination reactions of silanes and stannanes in which the place of the γ-carbon is taken by Si (13) or Sn (14). Of course, whenever the fragmentation mechanism is stepwise, the stereochemical restrictions can be relaxed.

[1] 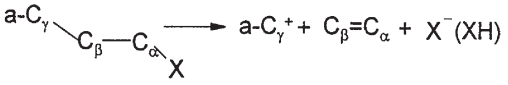

[2] 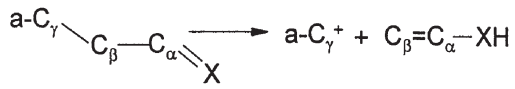

Grob also proposed that, in general, fragmentation of simple a-C–X systems would be faster than otherwise analogous a-C-C-C-X compounds. This prediction has been confirmed by Conrow (15) and by Shiner and Meier (10). Conrow, studying reactions [3] and [4] (among others), was able to obtain evidence that direct nucleophilic substitution at C_α is faster than fragmentation (eq. [3]), and that protonation at oxygen plus nucleophilic addition are also faster than fragmentation (eq. [4]), even with so stable an electrofuge as tropylium (Tr^+).

[3] 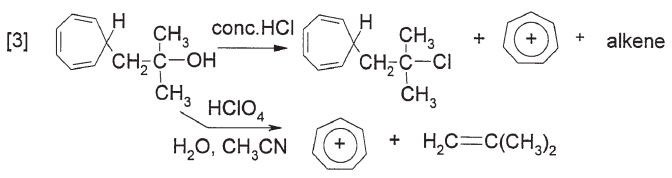

[4] 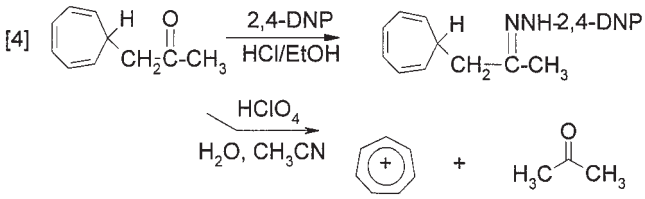

Conrow's results indicate that direct observation of a carbon-centered, cationic electrofuge should be a general result for suitable fragmentation reactions. Indeed, Fosse (16), in 1906, reported acid-promoted fragmentation of certain 9-xanthyl compounds. Deno and Sacher (17) extended these studies observing reactions [5] and [6]. Attempted cleavages of the corresponding triphenylmethyl compounds were completely unsuccessful, even in 96% H_2SO_4 at 100°C. This result indicates the powerful influence of the stability of the electrofuge in this particular case; triphenylmethyl$^+$ (pK_{R+} = –6.6) (18) is almost 10^6 less stable than xanthyl$^+$, both relative to their respective alcohols.

[5] 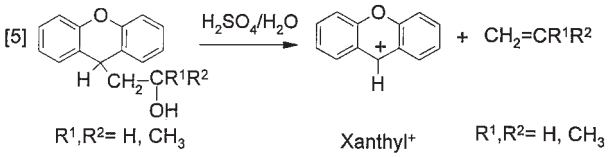

[6] 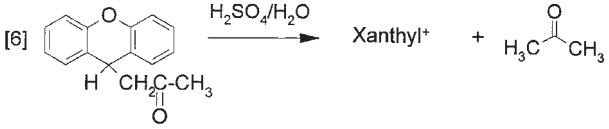

More recently, Arnett et al. (19) have determined the enthalpies of fragmentation, ΔH_{het}, for heterolytic C-C cleavage to form highly resonance stabilized carbocations and carbanions. These extensive data have allowed formulation of highly precise "master equations," which should be useful predictors of heterolysis enthalpies provided the ions formed are stabilized by resonance. Others have provided examples of measurable equilibria between covalent precursors and unusually stable, all hydrocarbon cations and anions (20). Arnett has noted that "there is increasing interest in developing low temperature processes for the cleavage of carbon–carbon bonds … especially as applied to the fossil fuel industries, where pyrolytic processes waste thermal energy and lead to tars. Heterolysis by treatment with strong acids and bases to yield ionic products are a promising alternative" (19*a*). Partly for this reason and partly because of its intrinsic interest, we set out to quantify the more general circumstances that make C-C heterolysis kinetically viable. Among these circumstances are the structures of the fragments formed in reactions [1] and [2], the efficacy of acid or base catalysis, and the influence of strain in the reactant. Also, we wished to probe for details of reaction mechanisms in the

© 1999 NRC Canada

catalyzed reactions (21, 22). Additionally, we present a useful synthetic sequence, involving regiospecific C-C cleavage in the final step, in which alkenes are acylated leading to dichloro-α,β-unsaturated ketones in two steps or to the dechlorinated analogues in three steps.

Experimental section

Materials

The following compounds were synthesized according to the literature procedures cited. NMR data are given in each case.

9-Xanthydrol (XanOH), ***1*** *(23)*: ^{1}H NMR (60 MH_3, CCl_4), δ: 7.6 (8H, m), 5.7 (1H, d, *J* = 8 Hz), 2.2 (1H, d, *J* = 8 Hz).

*9-Xanthydrol-9-*d *(XanOH-9-*d): Synthesized in the same way as **1**, but using CH_3CH_2OD in place of CH_3CH_2OH: ^{1}H NMR (60 MHz, $CDCl_3$), δ: 7.2 (8H, m), 5.2 (very low intensity), 2.2 (1H, s).

(7-Tropyl)acetone (TrAc), ***4*** *(24)*: ^{1}H NMR (300 MHz, $CDCl_3$), δ: 6.60 (2H, t), 6.14 (2H, dt), 5.11 (2H, dd), 2.75 (2H, d), 2.20 1H, m), 2.10 (3H, s).

(9-Xanthyl)acetone (XanAc), ***6*** *(25)*: ^{1}H NMR (60 MHz, $CDCl_3$), δ: 7.13 (8H, m), 4.62 (1H, t), 2.80 (2H, d), 1.96 (3H, s).

*(9-Xanthyl)acetone-9-*d *(XanAc-9-*d): Synthesized in the same way as **6**, but using XanOH-9-*d* in place of XanOH: ^{1}H NMR (60 MHz, CDCl3), δ: 7.15 (8H, m), 2.80 (2H, s), 1.97 (3H, s).

α*-(9-Xanthyl)acetophenone (XanAp),* ***7*** *(25)*: ^{1}H NMR (60 Mhz, $CDCl_3$), δ: 7.20 (13H, m), 4.85 (1H, t), 3.35 (2H, d).

α*-(9-Xanthyl)-4-nitroacetophenone (Xan-4-*NO_2*Ap),* ***8*** *(25)*: mp 139–140°C; ^{1}H NMR (300 MHz $CDCl_3$), δ: 8.15 (2H, d), 7.85 (2H, d), 7.21 (8H, m), 4.83 (1H, t), 3.39 (2H, d); ^{13}C NMR (75 MHz, $CDCl_3$), δ: 202.1, 129.2, 128.7, 128.2, 122.5, 116.5, 44.9, 35.1.

2-Methyl-1-(9-xanthyl)-2-propanol (Xantba), ***9*** *(17)*: ^{1}H NMR (300 MHz, $CDCl_3$), δ: 7.20 (8H, m), 4.22 (1H, t), 1.89 (2H, d), 1.65 (1H, s), 1.20 (6H, s).

*2-Methyl-1-(9-xanthyl)-2-propanol-9-*d (*Xantba-9-*d): Prepared in the same way as **9**, but using XanAc-9-*d* in place of XanAc: ^{1}H NMR (300 MHz, $CDCl_3$), δ: 7.22 (8H, m), 1.85 (2H, s), 1.55 1H, s), 1.15 (6H, s).

(7-Tropyl)nitromethane (TrCH_2NO_2*),* ***11a*** *(24)*: ^{1}H NMR (300 MHz, $CDCl_3$), δ: 6.68 (2H, t, *J* = 3.0 Hz), 6.31 (2H, dt, *J* = 9.6 Hz, 3.0 Hz), 5.31s (2H, dd, *J* = 9.0 Hz, 6.6 Hz), 4.46 (2H, d, *J* = 7.5 Hz), 2.98 (1H, q, 7.2 Hz).

1-(7-Tropyl)nitroethane (Tr$CH(NO_2)CH_3$*),* ***11b*** *(24)*: ^{1}H NMR (300 MHz, $CDCl_3$), δ: 6.68 (2H, m), 6.31 (2H, m), 5.30 (2H, m), 4.67 (1H, dq, *J* = 9.6 Hz, 6.6 Hz), 2.58 (1H, dt, *J* = 9.6 Hz, 6.9 Hz), 1.58 (3H, d, *J* = 6.6 Hz).

2-(7-Tropyl)-2-nitropropane (Tr$C(CH_3)_2NO_2$*),* ***11c*** *(24)*: mp 43–44°C; ^{1}H NMR (300 MHz, $CDCl_3$), δ: 6.72 (2H, t, *J* = 3.0 Hz), 6.27 (2H, m), 5.26 (2H, dd, *J* = 9.0 Hz, 5.7 Hz), 2.05 (1H, t, *J* = 6.0 Hz), 1.73 (6H, s).

trans*-2-Phenylnitrocyclopropane (PhNc),* ***12*** *(26)*: ^{1}H NMR (300 MHz, $CDCl_3$), δ: 7.22 (5H, m), 4.41 (1H, m), 3.14 (1H, m), 2.24 (1H, m), 1.67 (1H, m); ^{13}C NMR (75 MHz, $CDCl_3$), δ: 327.0, 129.5, 128.3, 127.3, 62.3, 30.0, 19.4; MS, *m*/*z*: 163 (M^+), 117 ($M^+ - NO_2$), 116, 115 (phenylcyclopropenium$^+$), 91 (tropyl$^+$).

trans*-2-(4-Methoxyphenyl)nitrocyclopropane (AnNc),* ***13*** *(26)*: mp 66–68°C; ^{1}H NMR (300 MHz, $CDCl_3$), δ: 6.98 (2H, d, *J* = 8.7 Hz), 6.78 (2H, d, *J* = 8.7 Hz), 4.27 (1H, m), 3.72 (3H, s), 3.02 (1H, m), 2.13 (1H, m), 1.56 (1H, m); ^{13}C NMR (75 MHz, $CDCl_3$), δ: 159.8, 128.9, 128.6, 114.9, 62.3, 56.0, 29.7, 19.3.

4-Methoxyphenyldiphenylmethanol (AnPh_2COH*),* ***5*** *(18)*: ^{1}H NMR (60 MHz, CCl_4), δ: 7.1 (14H, m), 3.7 (3H, s), 2.7 (1H, s).

*2,2-Dichloro-3-arylcyclobutanones,****14a–g****, and 3-arylcyclobutanones,* ***15a–g***: A procedure for synthesis of cyclobutanones has been developed by Erden (27) following results reported by Krepski and Hassner (28) and Bak and Brady (29). The method requires two steps: the regio- and stereospecific cycloaddition of dichloroketene to alkenes, then dechlorination of the resultant 2,2-dichlorocyclobutanones with activated zinc. A general procedure is described here followed by ^{1}H NMR data for **14** and **15**.

Cycloaddition

A dried, nitrogen-filled, three-necked flask equipped with a reflux condenser, constant-pressure addition funnel, and nitrogen inlet is charged with 50 mmol of alkene, 75 mmol of activated zinc powder, and 100 mL of anhydrous ether, then placed in a sonication water bath. To the agitated suspension is added a solution containing 50 mmol of $POCl_3$ (distilled from anhydrous K_2CO_3), 75 mmol of trichloroacetyl chloride, and 25 mL of anhydrous ether over a 0.5 h period. The reaction mixture is maintained at 15–20°C (or refluxed) for 1–22 h. After being quenched with wet ether, the reaction mixture is filtered through Celite, and the filtrate is washed with water, sat. $NaHCO_3$, and sat. NaCl, then dried over anhydrous $MgSO_4$. Removal of ether gives a crude product that is purified by vacuum distillation (Kugelrohr) or by column chromatography or by TLC (silica gel, pet. ether/ethyl acetate, 80/20).

Dechlorination

In a flask equipped with a reflux condenser are placed a saturated methanolic NH_4Cl solution, the dichloroketene cycloadduct from the previous procedure, and an excess of activated zinc powder. The suspension is refluxed for 4–19 h, then cooled and filtered through Celite. The methanol is removed under reduced pressure, and the residue dissolved in ether. The ethereal solution is washed with water, then saturated NaCl, and dried over anhydrous $MgSO_4$. Removal of the ether gives a crude product which is purified by Kugelrohr distillation or by column and (or) thin layer chromatography (silica gel, pet. ether/ethylacetate, 80/20).

2,2-Dichloro-3-methyl-3-phenylcyclobutanone, ***14a***: ^{1}H NMR (300 MH_3, $CDCl_3$), δ: 7.46–7.26 (5H, m), 4.00 (1H, d, *J* = 17.5 Hz), 3.08 (1H, d, *J* = 17.5 Hz), 1.66 (3H, s).

© 1999 NRC Canada

*2,2-Dichloro-3-phenyl-4-*trans*-methylcyclobutanone,* ***14b***: ^{1}H NMR (300 MHz, $CDCl_3$), δ: 7.45–7.16 5H, m), 4.03 (1H, m), 3.81 (1H, d, *J* = 12.0 Hz), 1.44 (3H, d, *J* = 7.2 Hz).

*2,2-Dichloro-3-(*p*-tolyl)cyclobutanone,* ***14c***: ^{1}H NMR (300 MHz, $CDCl_3$), δ: 7.26–7.18 (4H, m), 4.18 (1H, m), 3.70 (1H, dd), 3.52 (1H, dd), 2.38 (3H, s).

*2,2-Dichloro-3-(*m*-tolyl)cyclobutanone,* ***14d***: ^{1}H NMR (300 MHz, $CDCl_3$), δ: 7.35–7.10 (4H, m), 4.18 (1H, m), 3.70 (1H, dd), 3.51 (1H, dd), 2.40 (3H, s).

2,2-Dichloro-3,3-diphenyl-4-methylcyclobutanone, ***14e***: mp 131–133°C; ^{1}H NMR (300 MHz, $CDCl_3$), δ: 7.52–6.84 (10H, m), 4.61 (1H, q, *J* = 6.0 Hz), 1.14 (3H, d, *J* = 6.0 Hz).

2,2-Dichloro-3,3-diphenylcyclobutanone, ***14f***: ^{1}H NMR (300 MHz, $CDCl_3$), δ: 7.37–7.26 (10H, m), 4.07 (2H, s).

2,2-Dichloro-3-phenylcyclobutanone, ***14g***: ^{1}H NMR (300 MHz, $CDCl_3$), δ: 7.37–7.15 (5H, m), 4.19 (1H, m), 3.70 (1H, dd), 3.54 (1H, dd).

3-Methyl-3-phenylcyclobutanone, ***15a***: ^{1}H NMR (300 MHz, $CDCl_3$), δ: 7.40–7.22 (5H, m), 3.47 (2H, d, *J* = 18 Hz), 3.11 (2H, d, *J* = 18 Hz), 1.60 (3H, s).

trans*-2-Methyl-3-phenylcyclobutanone,* ***15b***: ^{1}H NMR (300 MHz, $CDCl_3$), δ: 7.40–7.25 (5H, m), 3.42–3.14 (4H, m), 1.29 (3H, d, *J* = 7.2 Hz).

*3-(*p*-Tolyl)cyclobutanone,* ***15c***: ^{1}H NMR (300 MHz, $CDCl_3$), δ: 7.22–7.15 (4H, m), 3.62 (1H, m), 3.47 (2H, m), 3.21 (2H, m), 2.35 (3H, s).

*3-(*m*-Tolyl)cyclobutanone,* ***15d***: ^{1}H NMR (300 MHz, $CDCl_3$), δ: 7.25–7.08 (4H, m), 3.62 (1H, m), 3.46 (2H, m), 3.23 (2H, m), 2.38 (3H, s).

2-Methyl-3,3-diphenylcyclobutanone, ***15e***: ^{1}H NMR (300 MHz, $CDCl_3$), δ: 7.44–6.96 (10H, m), 4.08 (1H, m), 3.80 (1H, dd, *J* = 17.4 Hz, 1.2 Hz), 3.65 (1H, dd, *J* = 17.4 Hz, 2.9 Hz), 0.94 (3H, d, *J* = 7.2 Hz).

3,3-Diphenylcyclobutanone, ***15f***: ^{1}H NMR (300 MHz, $CDCl_3$), δ: 7.37–7.20 (10H, m), 3.82 (4H, s).

3-Phenylcyclobutanone, ***15g***: ^{1}H NMR (300 MHz, $CDCl_3$), δ: 7.40–720 (5H, m), 3.67 (1H, m), 3.48 (2H, m), 3.24 (2H, m).

Cyclobutanone cleavage products: α, β-*unsaturated ketones,* ***16a–g,*** *and dichloro-*α, β-*unsaturated ketones,* ***17a***, ***c***, ***e***, ***f***: In an acidic medium, the 3-arylcyclobutanones isomerize to acyclic α,β-unsaturated ketones (**16**), while the 2,2-dichloro-3-arylcyclobutanones isomerize to dichloro-α,β-unsaturated ketones (**17**). Several of the unchlorinated ketones were synthesized independently for comparison purposes. The others were synthesized by treatment of the 3-arylcyclobutanones with CF_3CO_2H (this work). The dichloro-α,β-unsaturated ketones were observed by ^{1}H NMR upon treatment of the 2,2-dichlorocyclobutanones with CF_3CO_2H, but not further investigated. ^{1}H NMR data are given below.

*(*E*)-4-Phenylpent-3-en-2-one,* ***16a****:* Synthesized according to Hughes (30): mp 38°C, lit. (31) 37.5–38.5°C; ^{1}H NMR (300 MHz, $CDCl_3$), δ: 7.51–7.37 (5H, m), 6.51 (1H, broad), 2.54 (3H, s), 2.30 (3H, s). A NOESY experiment established the stereochemistry. In particular, the vinyl hydrogen was strongly coupled to the *ortho* and the acyl methyl protons, while the vinyl methyl hydrogens were also strongly coupled to the *ortho* and the acyl methyl protons.

*(*E*)-5-Phenylpent-4-en-3-one,* ***16b***: ^{1}H NMR (300 MHz, $CDCl_3$), δ: 7.57 (1H, d, *J* = 16.2 Hz), 7.59–7.38 (5H, m), 6.75 (1H, d, *J* = 16.2 Hz), 2.71 (2H, q, *J* = 7.5 Hz), 1.17 (3H, t, *J* = 7.5 Hz).

*(*E*)-4-(*p*-Tolyl)but-3-en-2-one,* ***16c***: To a stirred solution of 20 mmol of *p*-tolualdehyde in 20 mL of acetone was added 20 mL of 10% NaOH in H_2O over a 30 min period. After another 1.5 h of stirring, the yellow mixture was extracted twice with ether and the combined ethereal solutions dried over anhydrous $MgSO_4$. Removal of ether left a liquid which was fractionally distilled, a pure fraction boiling at 80–85°C, 0.02 Torr (1 Torr = 133.3 Pa); ^{1}H NMR (300 MHz, $CDCl_3$), δ: 7.54 (1H, d, *J* = 16.2 Hz), 7.45–7.19 (4H, m), 6.61 (1H, d, *J* = 16.2 Hz), 2.38 (3H, s), 2.37 (3H, s).

*(*E*)-4-(*m*-Tolyl)but-3-en-2-one,* ***16d***: Prepared in the same way as **16c**, using *m*-tolualdehyde: ^{1}H NMR (300 MHz, $CDCl_3$), δ: 7.58 (1H, d, *J* = 16.2 Hz), 7.36–7.22 (4H, m), 6.71 (1H, d, *J* = 16.2 Hz), 2.37 (6H, s).

5,5-Diphenylpent-4-en-3-one, ***16f***: ^{1}H NMR (300 MHz, $CDCl_3$), δ: 7.44–7.18 (10H, m), 7.00 (1H, s), 2.31 (1H, q, *J* = 7.4 Hz), 1.00 (3H, t, *J* = 7.4 Hz).

4,4-Diphenylbut-3-en-2-one, ***16f***: ^{1}H NMR (300 MHz, $CDCl_3$), δ: 7.49–7.18 (10H, m), 6.72 (1H, s), 1.98 (3H, s).

*(*E*)-4-Phenylbut-3-en-2-one,* ***16g***: Prepared in the same way as **16c** using benzaldehyde: mp 38–39°C; ^{1}H NMR (300 MHz, $CDCl_3$), δ: 7.57–7.41 (5H, m), 7.52 (1H, d, *J* = 16.2 Hz), 6.73 (1H, d, *J* = 16.2 Hz), 2.39 (3H, s).

*(*E*)-1,1-Dichloro-4-phenylpent-3-en-2-one,* ***17a***: ^{1}H NMR (300 MHz, CF_3CO_2H), δ: 7.55–7.30 (5H, m), 7.01 (1H, broad), 6.13 (1H, s), 2.23 (3H, s); the singlet at δ 6.13, assigned to the proton on C-1, slowly undergoes isotopic exchange in CF_3CO_2D.

*(*E*)-1,1-Dichloro-4-(*p*-tolyl)but-3-en-2-one,* ***17c***: ^{1}H NMR (300 MHz, CF_3CO_2H, δ: 8.05 (1H, d, *J* = 16.2 Hz), 7.56 (1H, d, *J* = 16.2 Hz), 7.25–7.18 (4H, m), 6.18 (1H, s), 2.38 (3H, s).

1,1-Dichloro-3-methyl-4,4-diphenylbut-3-en-2-one, ***17c***: ^{1}H NMR (300 MHz, CF_3CO_2H), δ: 7.67–7.28 (10H, m), 6.25 (1H, s), 1.85 (3H, s).

1,1-Dichloro-4,4-diphenylbut-3-en-2-one, ***17f***: ^{1}H NMR (300 MHz, CF_3CO_2H), δ 7.50–7.28 (10H, m), 7.12 (1H, s), 5.92 (1H, s).

4-Hydroxy-4-phenyl-2-pentanone, ***18*** *(32)*: ^{1}H NMR (300 MHz, $CDCl_3$), δ: 7.38–7.09 (5H, m), 4.38 (1H, s), 3.07 (1H, d, *J* = 18.Hz), 2.72 (1H, d, *J* = 18 Hz), 1.94 (3H, s), 1.41 (3H, s).

© 1999 NRC Canada

*4-Hydroxy-4-(*p*-tolyl)-2-pentanone, **19** (32)*: ^{1}H NMR (300 MHz, $CDCl_3$), δ: 7.21–7.01 (4H, m), 4.38 (1H, s), 3.06 (1H, d, *J* = 18 Mz), 2.71 (1H, d, *J* = 18 Hz), 2.21 (3H, s), 1.96 (3H, s), 1.39 (3H, s).

*(9-Xanthyl)methylsufide, (XanSMe), **2***: To a prechilled roundbottom flask were added 15 mmol of 9-xanthydrol and 10 mL (0.36 mol) of methanethiol, both prechilled. The flask was kept in an ice-water bath, topped with a Dry Ice condenser, and connected to a trap containing 6 M NaOH to capture evaporated CH_3SH. To the stirred solution was added one drop of conc. H_2SO_4. After the vigorous reaction subsided, another drop of acid was added and stirring continued for 3 h. Then a final drop of acid was added. After two more hours of stirring, the ice-water bath was removed, and the excess CH_3SH allowed to evaporate into the trap. The white residue was neutralized with 6 M NaOH, then taken up in ethanol. After removal of ethanol the product was recrystallized from ethanol or hexane: yield 57%; mp 64.5–66.5°C; ^{1}H NMR (60 MHz, $CDCl_3$), δ: 7.2 (8H, m), 5.1 (1H, s), 1.7 (3H, s); ^{13}C NMR (25 MHz, $CDCl_3$); δ 129.7, 128.4, 123.5, 116.4, 42.5, 11.0. Elemental analysis (%), calcd. for $C_{14}H_{12}OS$: C 73.65, H 5.30, S 14.04; found: C,73.70, H 5.42, S 13.95.

*(7-Tropyl)methylsulfide, (TrSMe), **3** (33)*: ^{1}H NMR (60 MHz, $CDCl_3$), δ: 7.0–5.1 (6H, complex), 3.2 (1H, t), 2.0 (3H, s). The compound was not very stable and was stored under N_2 at 6°C. It was distilled before use: 74°C, 4.5 Torr. After distillation, the tropylium$^+$ content was determined by adding a weighed amount to 25 mL of 2 M H_2SO_4 and determining the apparent molar absorptivity at λ_{max} = 274 nm. This value was compared with a literature value, $\varepsilon_{273.5}$ = 4350 cm^{-1} M^{-1} (34), to establish purity.

*2-Methyl-3-(9-xanthyl)propene, (xanthylisobutylene, XanIb), **10***: Six grams of triphenylmethylphosphonium bromide (Aldrich) was slowly added to a mixture of 3 g of potassium *tert*-butoxide and 75 mL of dry benzene, refluxed under argon,, over a 1.5 h period. To this solution was added a solution of 2.45 g of (9-xanthyl)acetone (**6**). The resulting solution was refluxed for 5.5 h, then cooled and quenched with ice water. The benzene layer was washed with NH_4Cl–H_2O, then H_2O. Distillation of the benzene left a residue which was recrystallized from ethanol: yield 31%; mp 80–81°C; ^{1}H NMR (300 MHz, $CDCl_3$), δ: 7.23 (8H, m), 4.80 (1H, s), 4.40 (1H, s), 4.15 (1H, t), 2.45 (2H, d), 1.68 (3H, s); ^{13}C NMR (75 Mz, $CDCl_3$), δ: 152.5, 142.0, 128.8, 127.5, 125.4, 122.9, 116.3, 114.3, 49.6, 38.3, 22.8.

3,3-Diphenylcyclopentanone: Prepared by treatment of 3,3-diphenylcyclobutanone with diazomethane following Greene and Deprés (35): ^{1}H NMR (300 MHz, $CDCl_3$), δ 7.26 (10H, m), 3.00 (2H, s), 2.69 (2H, t, *J* = 7.5 Hz), 2.29 (2H, t, *J* = 7.5 Hz).

Reaction media for C-C heterolysis reactions

Concentrated sulfuric and perchloric acids were the best available commercial products. They were diluted with doubly distilled water and standardized by titration. Sulfuric acid-d_2 (99.5 atom% D) and perchloric acid-d_2 (99 + atom% D) were purchased as concentrated solutions from Aldrich. They were diluted with D_2O (Aldrich, 99.8 atom% D) and standardized by titration.

Trifluoroacetic acid (TFA) and trifluoroacetic anhydride (TFAA) were purchased from Aldrich. TFA was distilled before use. For determination of solvent kinetic hydrogen isotope effects, TFA and TFA-*d* were prepared in two ways. For kinetics by ^{1}H NMR, equal weights of TFAA were added to 0.98 equiv of H_2O or D_2O. NMR analysis showed the media to contain < 2% protium. Substrate concentration was 0.45 M in both isotopic media. For kinetics by UV spectroscopy equal weights of TFAA were added to 0.98 equiv. of H_2O or D_2O (as above), or to 1.02 equiv. of H_2O or D_2O in order to avoid large absorbance readings caused by TFAA. Stock solutions of substrate were made in CH_3OH or CH_3OD to be ca. 1.4–1.8 × 10^{-2} M. Reaction was initiated by addition of one drop of substrate solution to 3.0 mL of reaction medium for the UV experiments resulting in initial substrate concentrations of ca. 2.5–3.0 × 10^{-4} M. Kinetic runs were made in a pairwise fashion: TFA followed immediately by TFA-*d*, then vice versa.

Equilibrium methods

In aqueous acid media 9-xanthydrol (**1**), (9-xanthyl) methylsulfide (**2**), (7-tropyl)methylsulfide (**3**), and 4-methoxyphenyldiphenylmethanol (**5**) all undergo heterolysis to an extent governed by the acidity of the medium. The equilibrium ratios of carbocation product to starting material were determined by UV-vis spectroscopy according to eq. [7] where R^+ represents a carbocation, xanthyl$^+$ (Xan^+), or tropyl$^+$ (Tr^+), R-X is the substrate precursor, and ε_{ST} is the molar absorptivity of the equilibrium mixture in a given acidic medium.

$$[7] \qquad [R^+]/[RX] = (\varepsilon_{ST} - \varepsilon_{RX})/(\varepsilon_{R^+} - \varepsilon_{ST})$$

Absorbance measurements were made at absorbance maxima for the carbocations: 374 nm (ε = 3.97 × 10^4 cm^{-1} M^{-1}) for Xan^+ (this work), and 274 nm (ε = 4350 cm^{-1} M^{-1}) for Tr^+ (34). For compound **3**, TrSMe, it was necessary to account for substrate absorbance at 274 nm: ε = 2300 cm^{-1} M^{-1} (this work). For the two sulfides, **2** and **3**, the acid solutions used were concentrated enough that the corresponding alcohols, XanOH and TrOH, had negligible concentration. For compounds **1** and **2**, 10–15 acid concentrations were used, for **3** and **4**, 5 concentrations.

For XanSMe, measurements were made using sulfuric acid solutions, perchloric acid solutions, and more dilute perchloric acid solutions at constant ionic strength, μ = 5.00 M ($NaClO_4$). For compound **5**, measurements were made both in $HClO_4$ and H_2SO_4 solutions.

Kinetic methods

Acid-promoted heterolysis of compound **1** in $HClO_4$–H_2O solution, [H^+] = 0.12–2.66 M, was monitored by the temperature jump method. The same method was used to follow heterolysis of **2** in aq. $HClO_4$ ([H^+] = 2.18–3.29 M) and H_2SO_4 ([H_2SO_4] = 3.61–6.35 M). Likewise, the heterolysis rates of **5** were determined in $HClO_4$ ([H^+] = 2.36–4.17 M) and H_2SO_4 ([H_2SO_4] = 3.97–4.70 M) solutions. Good first-order relaxation curves were obtained and

© 1999 NRC Canada

analyzed using the "small perturbation" approximation according to Bernasconi (36). The experimental first-order rate constants found in this way are, when both reactant and products have significant equilibrium concentrations, sums of pseudo first-order forward rate constants, k_f (s^{-1}) and reverse rate constants, $k_r[R^+]$ (s^{-1}) for the alcohols and $k_r([R^+]+[CH_3SH])$ (s^{-1}) for the sulfides, where k_r is a second-order constant. Equilibrium concentration ratios, $[R^+]/[RX]$, were obtained over the same range of acidity, usually at identical acid concentrations. Since these data can be written as a function of k_f/k_r, all the information needed to evaluate k_f and k_r was available.

Compound **2** was also studied by the stopped-flow method using $HClO_4$ solutions ranging from 0.73–2.00 M. Ionic strength was held constant at 5.0 M ($NaClO_4$) in both drive syringes in order to overcome optical artifacts caused by mixing solutions of different ionic strength. Compound **3** was also examined by the stopped-flow method using H_2SO_4 solutions ($[H_2SO_4]$ = 0.0133–0.0860 M). It can be shown that when the concentration of the observed species are small, hence the change in its concentration is small, that acceptably first-order behavior is obtained even though the reverse reaction is bimolecular (36). Hence, the small perturbation analysis was used in these two instances as well. For the concentration changes observed over the number of halflives used to gather data, it can be shown that the average error in k_{exp} incurred by treating the data in the first-order fashion as no greater than 10% (36).

The cleavages of the 3-arylcyclobutanones (**14a**, **15a**, **c**, **d**, **f**, **g**) were studied in CF_3CO_2H (TFA) solvent, taking advantage of the strong UV absorbance maxima (310–325 nm) shown by the cleavage products, β-aryl-α,β-unsaturated ketones. Rate constants for **15b** and **15e** were obtained by integration of the ^1H NMR signals as a function of time in reacting solutions (CF_3CO_2H). Compound **15a** was also studied in aqueous $HClO_4$ ($[H^+]$ = 6.69–8.89 M). In aqueous acid, **15a** cleaves first to 4-phenylpent-3-en-2-one (**16a**), but this material undergoes a retroaldol condensation leading to acetone and acetophenone. For this reason, the behavior of **16a** and of the aldol addition products, **18** and **19**, were also studied. These processes were monitored at 347 nm, λ_{max} for the protonated form of enone **16a**. This form is prominent in the acid solutions used for these measurements. All the reactions in TFA gave excellent first-order kinetics. The reaction of **15a** in $HClO_4$–H_2O gave biphasic behavior, an exponential rise in absorbance followed by an overlapping exponential loss of absorbance. The latter stages of the reaction gave sequential UV spectra with excellent isosbestic points. The late-stage behavior was accurately reproduced by starting with **16a**. With the alcohols **18** and **19** acid-catalyzed dehydration to the enones, **16a** and its *p*-methyl analogue, is relatively rapid and accurately first-order, and is followed by a well-separated first-order retroaldol cleavage.

The C-C cleavages of the (7-tropyl)nitroalkanes, **11a**–**c**, were also studied by UV spectroscopy using the λ_{max} for the product tropylium ion: 272 nm in TFA and 274 nm in $HClO_4$–H_2O. These kinetics were accurately first order (37). (7-Tropyl)acetone (**4**) was studied using TFA solvent.

Carbon–carbon cleavage of the 9-xanthyl compounds, **6**–**10**, was monitored in H_2SO_4–H_2O solutions, and in the case of **6** in TFA as well, by observing the intense absorption of xanthyl cation (Xan^+) at 375 nm ($\varepsilon = 3.97 \times 10^4$, this work). The reactions in aqueous sulfuric acid were strongly acid-promoted. All reactions showed excellent first-order kinetics except that for 2-methyl-3-(9-xanthyl)propene (**10**). In this case, production of Xan^+ showed a slight induction period. The data were best fit by a double exponential equation providing first-order rate constants for the earlier and later stages of the reaction.

Finally, the ring-opening C-C cleavage reactions of 2-arylnitrocyclopropanes, **12** and **13**, were studied in TFA by ^1H NMR spectroscopy. Good first-order behavior was again observed, as previously reported (38).[2]

Computational studies

All molecular orbital calculations were performed using the SPARTAN modeling software, versions 3.0, 4.0, 5.0, and MacSpartan Plus (Wavefunction, Inc., 18401 Von Karman Ave., Suite 370, Irvine, Calif., 92612), AM1 (40) and PM3 (41) semiempirical methods were used. These showed results for *series of related compounds* that were in good agreement. However, AM1 did a better job at reproducing the heat of protonation for nitromethane, the heat of formation of cyclobutanone, and the heat of the ring-opening isomerization of cyclobutanone to but-3-en-2-one. Therefore, it is these values that are reported here. Conformational enthalpies were investigated systematically. Transition-state structures were all characterized by a single imaginary frequency corresponding to the pertinent reaction coordinate.

Ab initio calculations at the HF/3-21G and HF/6-31G* levels were carried out for several smaller model compounds. Conformational minima and maxima for rotations about specific bonds were determined by systematic variation at the 3-21G level, and these conformations were further optimized at the 6-31G* level.

Results

Product studies

The alcohols, 9-xanthydrol (XanOH, **1**) and 4-*p*-methoxyphenyldiphenylmethanol ($AnPh_2COH$, **5**), could be completely heterolyzed to the carbocations, Xan^+ and $AnPh_2C^+$, in sufficiently acidic media. The UV-vis spectra of these cations agreed well with published data (18, 42). Basification of the carbocation solutions permitted recovery of the alcohols.

The sulfides, XanSMe (**2**) and TrSMe (**3**), gave the spectra of Xan^+ and tropylium (Tr^+), respectively, in sufficiently concentrated acid. It requires significantly higher acid concentrations to effect complete formation of the cations from their sulfide precursors than from the alcohols. At acidities high enough to negate the presence of XanOH or TrOH, the sulfides produced greater or lesser conversion to Xan^+ or Tr^+ depending on the acidity. The reactions of **1**, **5**, **2**, and **3** are

[2] In our original communication, we noted that rate-determining proton transfer between heteroatoms requires a close match of pK_a values between the acid (TFA) and the protonated base (RNO_2H^+) and that this match does not appear evident at first glance. Our explanation was that ring-opening electron release from the Cl—C2 bond, concurrent with protonation, greatly increases the basicity of the oxygens at the transition state, allowing the pK_a match. We neglected to point out that this idea is an application of Jencks (38*b*) "libido rule."

© 1999 NRC Canada

Table 1. Reaction conditions and yields for dichloroketene (DCK) cycloadditions, dechlorinations, and ring-opening isomerizations. See eqs. [11] and [13].

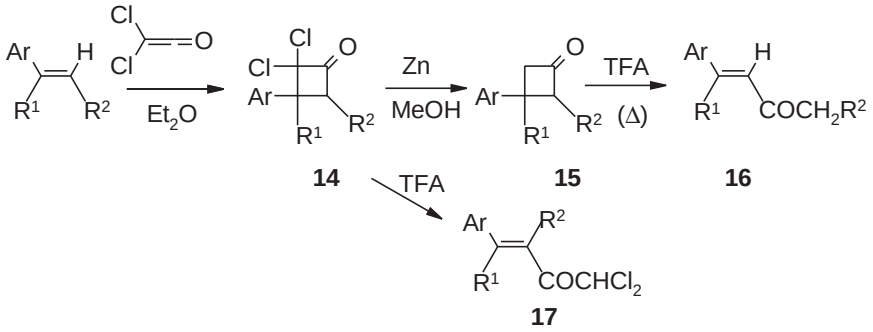

Substrate	Adduct **14** (temp., time, % yield)	Adduct **15** (reflux, time, % yield)	Adducts **16**, **17** (temp., time, % yield by NMR)
a	15–20°C, 1, 59	4 h, 47	rt, 22 h, 90 (**16**) Reflux, 5 h, 100 (**16**)
b	Reflux, 2 h, 38	19 h, 46	rt, 56 days, 82 (**16**) Reflux, 5 h, 52 (**16**)
c	Reflux, 2 h, 68	4 h, 42	rt, 145 h, 100 (**16**) Reflux, 5 h, 100 (**16**) rt, 20 days, 50 (**17**)
d	Reflux, 2 h, 66	4 h, 52	rt, 19 days, 90 (**16**) Reflux, 5 h, 100 (**16**)
e	Reflux, 20 h, 3	4 h, 48	rt, 7 h, 87 (**16**) rt, 15.6 days, 71 (**17**)
f	Reflux, 2 h, 55	4 h, 67	rt, 9 h, 80 (**16**) rt, 20 h, 100 (**17**)

therefore formulated as reversible, acid-promoted heterolyses, eq. [8] and [9].

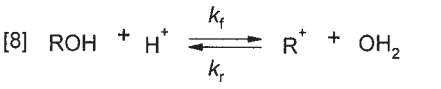

1: $R^+ = Xan^+$ **5**: $R^+ = AnPh_2C^+$

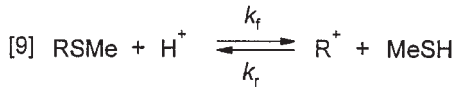

2: $R^+ = Xan^+$ **3**: $R^+ = Tr^+$

The acid-catalyzed carbon–carbon heterolyses of compounds **4**, **6**–**15**, **16a**, **18**, and **19** proceeded with irreversible production of an electrofugic carbocation (or a product derived therefrom) and a carbon-centered nucleofuge. For compound **4**, $TrCH_2COCH_3$, Conrow (15) showed the nucleofuge to be acetone, presumably as its enol. Deno and Sacher (17) did the same for **6**, $XanCH_2COCH_3$. The product UV spectrum of **7**, $XanCH_2COPh$, exactly matches that of an equimolar mixture of Xan^+ and acetophenone (this work). We have assumed therefore that *p*-nitroacetophenone is the nucleofugic product from **8**. Deno and Sacher (17) have shown that 2-(9-xanthyl)ethanol and 1-(9-xanthyl)-2-propanol fragment in acid solution to yield Xan^+ and either ethylene or propene. In our work, cleavage of 2-methyl-1-(9-xanthyl)-2-propanol (**9**, Xantba) as well as 2-methyl-3-(9-xanthyl)propene (**10**, $XanCH_2C(CH_3)=CH_2$, XanIb) lead quantitatively to Xan^+; we assume the nucleofuge to be isobutylene (subsequently, *tert*-butyl alcohol). In the few kinetic runs in which the "infinite time" spectrum differed from expectation by more than 2%, the runs were discarded.

Ring-opening cleavage of 3-arylcyclobutanones (**15a**–**g**) in trifluoroacetic acid (TFA) leads to β-aryl-α, β-unsaturated ketones, **16a**–**g**. These were identified by comparison with authentic samples. The cleavage products of the 2,2-dichloro-3-arylcyclobutanones were not synthesized independently, but were characterized by their ^1H NMR spectra as 1,1-dichloro-4-aryl-3-en-2-ones (**17a**, **c**, **e**, **f**), also in TFA. Yields and reaction conditions are found in Table 1.

Compound **15a**, 3-methyl-3-phenylcyclobutanone, was also studied in aqueous $HClO_4$ solution. In this medium, the initial product is **16a** (partly protonated at higher acidities). Subsequently, the characteristic UV spectrum of this compound is replaced by that of acetophenone, with acetone as the presumed byproduct. 4-Hydroxy-4-aryl-2-pentanones, **18** and **19**, also yield the UV spectrum of β-aryl-α,β-unsaturated ketones in aqueous $HClO_4$: **16a** from **18** and 4-(*p*-tolyl)pent-3-en-2-one from **19**. These spectra are eventually replaced by those of acetophenone and *p*-methylacetophenone, respectively. These changes over time are accompanied by good isosbestic points in the spectra.

The acid-catalyzed cleavages of the (7-tropyl)nitroalkanes, **11** (37) and the 2-arylnitrocyclopropanes, **12** and **13** (38*a*) have been previously characterized.

© 1999 NRC Canada

A summary of the C-C cleavage reactions studied by us is presented in the following equations.

[10] 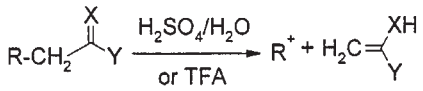

where

	R	X	Y
4	Tr	O	CH_3
6	Xan	O	CH_3
7	Xan	O	Ph
8	Xan	O	4-nitrophenyl
9	Xan	O	$-C(CH_3)_2OH$
10	Xan	CH_2	CH_3

[11] 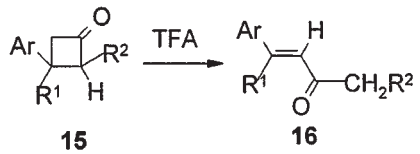

15 **16**

where

	R^1	Ar	R^2
15a	CH_3	Ph	H
b	H	Ph	*trans*-CH_3
c	H	*p*-tolyl	H
d	H	*m*-tolyl	H
e	Ph	Ph	CH_3
f	Ph	Ph	H
g	H	Ph	H

[12]

15a **16a**

[13] 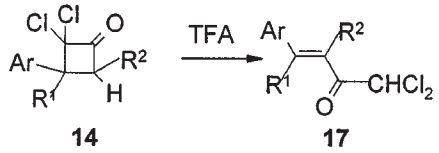

14 **17**

where

	R^1	Ar	R^2
14a	CH_3	Ph	H
b	H	Ph	*trans*-CH_3
c	H	*p*-tolyl	H
d	H	*m*-tolyl	H
e	Ph	Ph	CH_3
f	Ph	Ph	H
g	H	Ph	H

[14] 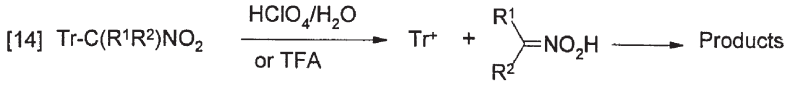

11a: $R^1=R^2=H$; **11b**: $R^1=H$, $R^2=CH_3$; **11c**: $R^1=R^2=CH_3$

[15] 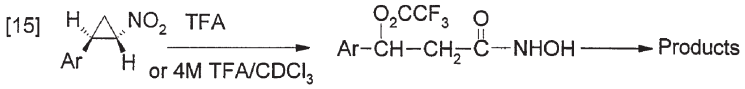

12: Ar=Ph; **13**: Ar=*p*-anisyl

Equilibrium studies

Equilibrium production of carbocations from alcohol precursors, **1** and **5**, was analyzed as a function of acidity according to Deno's (18, 43) H_R acidity function and also using Cox and Yates (44, 45) "excess acidity" functions, X (for H_2SO_4 solutions) and X_o (for $HClO_4$ solutions), as recommended by Kresge et al. (46). Xanthydrol (**1**) was not one of the alcohols used to establish the H_R function, yet its ionization follows H_R acceptably well, giving $pK_{R+} = -0.90$ in $HClO_4$–H_2O; Deno and Evans (42) reported $pK_{R+} = -0.84$ in H_2SO_4–H_2O. The Cox and Yates correlation is given as eq. [16] (47).[3] For xanthydrol ($HClO_4$–H_2O), eq. [16] gives $pK_{R+} = -0.85 \pm 0.03$, $m^* = 2.6$ with $r^2 = 0.992$.

The other alcohol, *p*-anisyldiphenylmethanol (**5**), was one of the original H_R indicators. Deno et al. (18) reported $pK_{R+} = -3.40$ (H_2SO_4–H_2O), while we find, using the H_R function, $pK_{R+} = -3.65$ (H_2SO_4) and -3.60 ($HClO_4$). Treated according to eq. [16], $AnPh_2COH$ gives $pK_{R+} = 3.55$ in H_2SO_4

$$[16] \quad \log\left(\frac{[R^+]\, a_{OH_2}}{[ROH]\,[H^+]}\right) = m^*X + pK_{R^+}$$

[3] Values for the activity of water in H_2SO_4–H_2O solutions were taken from a compilation made by R.A. Cox (personal communication); see also ref. 47*a*. For $HClO_4$–H_2O solutions, water activities were taken from ref. 47*b*.

© 1999 NRC Canada

Table 2. Equilibrium constants for reversible ionization of alcohols **1** and **5** and concentration equilibrium quotients for sulfides **2** and **3** at 25°C.

Compound	pK_{R+} [a]	pK^s_{R+} [b]	log K_c^s [c]
1	–0.85 ± 0.03 ($HClO_4$–H_2O)		
5	–3.51 ($HClO_4$–H_2O) –3.55 (H_2SO_4–H_2O)		
2		–7.36 ± 0.14 ($HClO_4$–H_2O)	–4.67 ± 0.07 (($HClO_4$)H_2O/5.0 M ClO_4^-) ~–5.3[d] (H_2SO_4–H_2O)
3			–1.8[e] (H_2SO_4–H_2O)

[a]Obtained using eq. [16] and the X function for H_2SO_4–H_2O, the X_o function for $HClO_4$–H_2O. The standard state is 1.00 M H^+, activity coefficients unity.

[b]Obtained using eq. [17] and the X_o function.

[c]Obtained using eq. [18].

[d]The use of eq. [17] gave severe curvature. See text.

[e]Dilute H_2SO_4: 0.013 – 0.086 M. Use of an acidity function is unnecessary.

solution and –3.51 in $HClO_4$ solution, in good agreement with our H_R result and in fair agreement with Deno's original result. These and other equilibrium constants are listed in Table 2.[4] The slope parameter in eq. [16], m^*, was found for **5** to be 2.2 in H_2SO_4 and 3.3 in $HClO_4$ solution. Large values of m^* are to be expected for alcohol–carbocation equilibria (45).

Adaptation of the excess acidity correlation to the reversible heterolysis of the sulfides leads to eq. [17]. The equilibrium constant indicated as K^s_{R+} is unitless as defined here.

$$[17]\quad \log\left(\frac{[R^+]\,[MeSH]}{[RSMe]\,[H^+]}\right) = m^*X + pK^s_{R^+}\ ;\ K^s_{R^+} = \frac{a_{RSMe}\,a_{H^+}}{a_{R^+}\,a_{MeSH}}$$

In perchloric acid solution, the data for XanSMe (**2**) are fairly well behaved with some scatter but no curvature: pK^s_{R+} = –7.36 ± 0.14, m^* = 2.5, r^2 = 0.968. The difference between the ionizations of XanOH and XanSMe is very large and perhaps best revealed by the fact that whereas XanOH is half-ionized in ca. 1 M $HClO_4$, XanSMe requires over 3 M $HClO_4$ for half-ionization despite the tiny concentration of methanethiol in these solutions, ca. 10^{-5} M or less. In sulfuric acid solution, the plot of eq. [17] was badly curved. Rather than speculate about this result, we report the correlation suggested by eq. [18] where K^s_c is a concentration ratio. This plot produced $K^s_c = 5.5 \times 10^{-6}$ with r^2 = 0.970.[5]

$$[18]\quad \frac{[Xan^+]\,[MeSH]}{[XanSMe]} = K^s_c\,[H^+]$$

We also studied the fragmentation of XanSMe in perchloric acid solutions of constant ionic strength, μ = 5.00 M, maintained with $NaClO_4$. Medium effects appear to be insensitive to $[H^+]$ in these media, dominated by total $[ClO_4^-]$. The concentration quotient from eq. [18] is approximately constant against $[H^+]$, leading to a value for $K^s_c = 2.1 \times 10^{-5}$ (r^2 = 0.986) in this medium. The corresponding value in ordinary $HClO_4$–H_2O solutions obtained by the X_o function correlation is $1/K^s_{R+} = 4.3 \times 10^{-8}$, amounting to a 500-fold diminution of ionization in the standard state of 1.0 M acid, all activity coefficients at unity, compared with the 5.0 M perchlorate state. Bunton and Huang (48) found that the ionization of trianisylmethanol in dilute aqueous acid is enhanced by a number of salts, especially $LiClO_4$ and $NaClO_4$. They found further that the rate of carbocation formation is enhanced, and the rate of its reaction with water decreased by these salts. Johnston, Scaiano, and their co-workers (49) observed reduced rates of reaction of some diarylmethyl cations with azide and other anionic nucleophiles in the presence of $LiClO_4$. Bunton and Huang's analysis of activity coefficient behavior indicates that perchlorate strongly stabilizes carbocations relative to the solvated proton, and also stabilizes the fragmentation transition state though by a lesser amount. An attractive interaction between the large, nonspecifically solvated carbocation and the large, low-charge-density perchlorate ion is proposed as the cause. The overall result resembles Winstein's special salt effect on S_N1 solvolyses (50).

(7-Tropyl)methylsulfide (TrSMe, **3**) was studied in dilute H_2SO_4 solutions with poor success owing to irreproducibility of equilibrium measurements. The quantity K^s_c, defined as in eq. [18] but with tropylium$^+$ replacing xanthyl$^+$,

[4]Primary equilibrium and rate constants are available as supplemental material. Copies of material on deposit may be purchased from: The Depository of Unpublished Data, Document Delivery, CISTI, National Research Council Canada, Ottawa, Canada, K1A 0S2.

[5]$K^s_c(\gamma_{R+}\gamma_{MeSH}/\gamma_{RSMe}\gamma_{H+}) = 1/K^s_{R+}$. Thus, the approximate insensitivity of K^s_c to changes in sulfuric acid concentrations tells us that the ratio of activity coefficients is also approximately constant in these media. The value of this ratio is not known but is probably much less than 1, since γ_{R+}/γ_{H+} decreases with increasing acidity. Therefore, multiplication of K^s_c by the activity coefficent ratio would reduce K^s_c, bringing it closer to the value of $1/K^s_{R+}$ found in $HClO_4$ solutions.

© 1999 NRC Canada

Table 3. Medium-independent rate constants and kinetic solvent isotope effects for reversible ionization processes: eqs. [8] and [9], 25°C.[a]

Compound	$k_f°$ (M^{-1} s^{-1})		$k_r°$		$k_f(H_2O)/k_f(D_2O)$[c]	$k_r(H_2O)/k_r(D_2O)$[c]
	Cox–Yates[a]	Kresge[b]	Cox–Yates[a]	Kresge[b]		
1						
($HClO_4$–H_2O)	(1.70 ± 0.08) × 10^3	(1.9 ± 0.2) × 10^3 α_K = 0.63	(1.2 ± 0.2) × 10^4 s^{-1}	(1.3 ± 0.2) × 10^4 s^{-1}	0.51 ± 0.04[d]	1.27 ± 0.09[c]
5						
($HClO_4$–H_2O)	0.42	0.49 α_K = 0.54	1.5 × 10^3 s^{-1}	1.6 × 10^3 s^{-1}	—	—
2						
($HClO_4$–H_2O)	0.35	0.45 ± 0.13 α_K = 0.71	8.1 × 10^6 M^{-1} s^{-1}	1.0 ± 0.4 × 10^7 M^{-1} s^{-1}	—	—
($HClO_4$–H_2O) ([ClO_4^-] = 5.0 M)[e]	19.5		9.2 × 10^5 M^{-1} s^{-1}		—	—
(H_2SO_4–H_2O)	0.08	—	—	—	0.6 ± 0.2[f]	0.9 ± 0.5[f]
3[e]						
(H_2SO_4–H_2O)	—	6.6	—	4.4 × 10^2 M^{-1} s^{-1}	0.7 ± 0.2[g]	0.5 ± 0.2[h]

[a]Obtained using eq. [19] and the X function for H_2SO_4–H_2O, the X_o function for $HClO_4$–H_2O. The standard state is 1.00 M H^+, activity coefficients unity.
[b]Obtained using eq. [20] for alcohols **1** and **5** or eq. [21] for sulfides **2** and **3**.
[c]Ratios of pseudo first-order rate constants determined in isotopic media of equal formal concentrations of sulfuric acid, L_2SO_4.
[d]Average of two values, 0.802 and 1.22 F L_2SO_4.
[e]Values obtained from a linear plot of k_f (s^{-1}) vs. [H^+]; $k_r^o = k_f^o \times K_c^s$.
[f]Average of two values, 3.43 and 4.54 F L_2SO_4.
[g]Average of two values, 0.0245 and 0.980 F L_2SO_4.
[h]Determined in 0.0245 F L_2SO_4.

is approximately a constant, however. Its value is ca. 1.5 × 10^{-2}. The ratio of these ionization "constants" is 2.7 × 10^3 favoring production of Tr^+ over Xan^+. Fot comparison, the ratio of the K_{R+} values derived from ionization of the corresponding alcohols is ~4 × 10^5, taking pK_{R+} = 4.75 for Tr^+ (51, 52).

We had two reasons for determining equilibrium ionization constants for compounds **1**–**3** and **5**. First, because values for **1** and **5** had already been reported (42, 18), it was important to see how well we reproduced those results. Second, we shall employ the pK_{R+} and pK^s_{R+} values in some of the analyses made of kinetic data in the next section.

Kinetic studies

*Rate constants for the reversible ionization of compounds **1**–**3** and **5***

Experimental first-order rate constants for the reversible ionization of alcohols **1** and **5** and sulfide **2** were measured as a function of acidity in aqueous acid. These could be separated into first-order constants for the fragmentation (forward) reaction, k_f, and for the recombination (reverse) direction, k_r, using the equilibrium (product/reactant) concentration ratios. The k_r values for sulfide **2** are, to a good approximation, second-order constants (see Experimental section). The k_f and k_r values depend in turn on the acidity and electrolyte properties of the media in which they were measured. Conversion of these into medium-independent second-order constants with a defined standard state required additional analysis.

We have used two methods to obtain second-order rate constants for compounds **1**, **2**, and **5**. One is the application of the excess acidity function treatment to kinetic equations developed by Cox and Yates (53). Equation [19] is the relationship to be plotted when substrate is predominately unprotonated. Equation [19*a*] is appropriate when water is used as a reactant.

$$[19]\quad \log (k_f/[H^+]) = m^{\ddagger} m^*X + \log k_f^o$$

$$[19a]\quad \log (k_f/[H^+]) - \log a_{OH_2} = m^{\ddagger} m^*X + \log k^o_f$$

The intercept provides the medium-independent second-order rate constant in the forward (fragmentation) direction for these reactions. Knowledge of K_{R+} (or K^s_{R+}) for the reaction permits calculation of $k°_r$ from the relationship $k°_r = k°_f/K_{R+}$. The slope parameters given in eq. [19] contain a factor, m^*, which is the slope of an X-plot made for *equilibrium* protonation of the substrate, similar to eq. [16]. The other factor, $m^{\neq}$, is characteristic of the way the log of the activity coefficient of the transition state behaves relative to that of the protonated substrate as X is varied.

An alternative analysis is possible for acid-catalyzed reactions for which both rate and equilibrium data are available over the same range of acid concentrations. Kresge et al. (54) proposed a linear free energy rate–equilibrium correlation for such processes. As applied to the ionization of the alcohols, the Kresge analysis uses eq. [20]; for the sulfides it is eq. [21]. In these equations, the symbols have the same

$$[20]\quad \log (k_f/[H^+]) = \alpha_K \log\left(\frac{[R^+]\, a_{OH_2}}{[ROH][H^+]}\right) + (\log k_f^o + \alpha_K \log K_{R^+})$$

© 1999 NRC Canada

$$[21]\quad \log(k_f/[H^+]) = \alpha_K \log\left(\frac{[R^+][MeSH]}{[RSMe][H^+]}\right) + (\log k^\circ_f + \alpha_K \log K^s_{R^+})$$

significance as above except that the slope coefficient, labeled α_A by Kresge (54*b*), is here denoted α_K in his honor. This coefficient relates the medium dependence of log $\gamma^{\neq}$ to that of log ($\gamma_{R+}a_{H2O}$) or log ($\gamma_{R+}\gamma_{MeSH}$). Since log γ is proportional to free energy, α_K has the significance of a normalized Brønsted coefficient, α, indicating the medium sensitivity of $G^{\ddagger}$ relative to G(products). A caveat is in order for reactions that are mechanistically general-acid or -base catalyzed, and are carried out in H_2SO_4 solutions. This is because HSO_4^- (or SO_4^{2-}) could be catalytically active, thereby having an effect on k_f (or k_r) but not on the [product]/[reactant] equilibrium ratio (53, 55).

For 9-xanthydrol (**1**) the Cox–Yates correlation was good, $r^2 = 0.990$, yielding $k^\circ_f = (1.70 \pm 0.08) \times 10^3$ M^{-1} s^{-1}. Combined with the value determined by us for K_{R+}, we obtain $k^\circ_r = (1.2 \pm 0.2) \times 10^4$ s^{-1}. This value is in reasonably good agreement with a value, $k^\circ_r = 2.3 \times 10^4$ s^{-1}, obtained by McClelland et al. (56) in 1:4 acetonitrile/water. The slope parameter, $m^{\ddagger}m^*$, is 1.9 ± 0.1. Use of the Kresge correlation also gave good linearity, $r^2 = 0.993$, with slope, $\alpha_K = 0.63 \pm 0.03$. Equation [20] (intercept) leads to $k^\circ_f = (1.9 \pm 0.2) \times 10^3$ M^{-1} s^{-1}, thence $k^\circ_r = 1.3 \times 10^4$ s^{-1}. These and other rate constants for the reversible acid-catalyzed reactions are collected in Table 3.

For $AnPh_2COH$ (**5**) in $HClO_4$ solutions, the Cox–Yates plot was accurately linear for three of the five data points only; of the other two, one was above, the other below the line. By accepting this line, we obtain $k^\circ_f = 0.42$ M^{-1} s^{-1}, $k^\circ_r = 1.5 \times 10^3$ s^{-1}, with $m^*m^{\neq} = 1.9$. The Kresge plot was excellent with $\alpha_K = 0.54 \pm 0.01$, $k^\circ_f = 0.49$ M^{-1} s^{-1}, and $k^\circ_r = 1.60 \times 10^3$ s^{-1}. The recombination rate constant for **5** has previously been measured by Diffenbach et al. (57), $k^\circ_r = (1.0 \pm 0.7) \times 10^3$ s^{-1}, and by McClelland et al. (58), in 1:2 acetonitrile/water at 20°, $k^\circ_r = 1.4 \times 10^3$ s^{-1}. In sulfuric acid, the Cox–Yates plot suffered from an insufficient range of data points though it did extrapolate to approximately the same intercept as for perchloric acid. Interestingly, a fairly good Kresge plot ($r^2 = 0.951$) could be made from the combined $HClO_4$ and H_2SO_4 data. This gave $\alpha_K = 0.56$, $k^\circ_f = 0.44$ M^{-1} s^{-1}, and $k^\circ_r = 1.5 \times 10^3$ s^{-1}. As for 9-xanthydrol, the two methods of analysis give convergent results.

For 9-xanthylmethylsulfide (**2**), the Cox–Yates plots were fairly good ($HClO_4$) and good (H_2SO_4), however, the slopes and intercepts of these plots did not agree. For $HClO_4$ solutions, $k^\circ_f = 0.35$ M^{-1} s^{-1}, the slope $m^{\neq}m^* = 1.9$, and $r^2 = 0.944$. In H_2SO_4, the same parameters were $k^o_f = 7.9 \times 10^{-2}$ M^{-1} s^{-1}, $m^{\neq}m^* = 1.1$ with $r^2 = 0.987$. A value for the recombination rate constant in $HClO_4$–H_2O is obtained using $pK^s_{R+} = -7.36$ found for that medium: $k^\circ_r = 8.1 \times 10^6$ M^{-1} s^{-1}. For H_2SO_4–H_2O, the calculation of k°_r is hampered by lack of a reliable K^s_{R+} value (see above). We report only that the experimental k_r is insensitive to [H_2SO_4] over the range 3.6–5.1 M. This suggests a value for $k^\circ_r \cong 2.5 \times 10^5$ M^{-1} s^{-1} in this medium, but it should, perhaps, not be given much quantitative weight. The Kresge plot for $HClO_4$–H_2O was accurately linear over the range 2.2–3.2 M ($r^2 = 0.999$) and led to $\alpha_K = 0.71 \pm 0.01$. This result allows from eq. [21] calculation of $k^\circ_f = 0.45 \pm 0.13$ M^{-1} s^{-1} and $k^\circ_r = (1.0 \pm 0.4) \times 10^7$ M^{-1} s^{-1}. These results are in satisfactory agreement with the Cox–Yates numbers. In H_2SO_4–H_2O, the Kresge plot was markedly curved, concave upward, allowing no further calculations. There do not appear to be any measurements of recombination rate constants for Xan^+ and neutral thiols in the literature. Ritchie and Gandler (59) report $k^\circ_r = 3.4$ M^{-1} s^{-1} for the reaction of 2-mercaptoethanol with trianisylmethyl cation, An_3C^+. The difference between that constant and the one reported here for Xan^+ plus CH_3SH is large, but is influenced by at least three factors: methanethiol is expected to be a better nucleophile than 2-mercaptoethanol; σ^* for the $-CH_2OH$ group is 0.56 (60). An_3C^+, with $pK_{R+} = 0.82$ (18, 58*a*), is almost two orders of magnitude more stable than Xan^+. Finally, triarylmethyl cations are known to combine with nucleophiles more slowly than does xanthyl$^+$. For example, An_2PhC^+, $pK_{R+} = -1.24$ (18), is less stable than Xan^+, yet reacts with water 160 times more slowly (58).

As we did with equilibrium studies, the rates of fragmentation of XanSMe (**2**) were also studied in $HClO_4$–H_2O solutions of constant ionic strength, $\mu = 5.00$ M ($NaClO_4$). Once again, medium effects appear to be dominated by the large perchlorate concentration. A simple plot of k_f vs. [H^+] was linear, $r^2 = 0.986$, giving a k^o_f value for this medium of 19.5 M^{-1} s^{-1}, which, combined with the equilibrium constant determined in this medium, provides a value for $k^\circ_r = 9.2 \times 10^5$ M^{-1} s^{-1}. Compared with the results from ordinary $HClO_4$–H_2O solutions, we see that k°_f has increased by a factor of about 50 while k°_r has decreased 10-fold. The likely cause of these effects was discussed above in the Equilibrium studies section.

(7-Tropyl)methylsulfide (TrSMe, **3**) was studied in dilute H_2SO_4 solutions, 0.013–0.086 M. A simple plot of k_f vs. [H^+] was linear, $r^2 = 0.989$, with slope = 6.6 M^{-1} s^{-1} = k°_f. Combined with the equilibrium value for dissociation, this value gives $k^\circ_r \cong 4.4 \times 10^2$ M^{-1} s^{-1}. These values are ca. 80-fold larger and 550-fold smaller, respectively, than the corresponding values for XanSMe derived from more concentrated H_2SO_4 solutions (see above). We are not aware of any previous reports of rate constants for reactions of neutral thiols with tropylium ion.

Rate constants and related data presented in this section are listed in Table 3. We estimate that for quantities without listed error limits the experimental uncertainties range from ±10 to ±20%.

*Rate constants for irreversible fragmentation of 9-xanthyl compounds **6**–**10***

Compounds **6**–**10** undergo irreversible fragmentation in acid media giving Xan^+ (xanthyl cation) and a carbon-centered nucleofuge. The tropylium compound, **4**, behaves analogously, see eq. [10]. The rates of these reactions were studied in H_2SO_4–H_2O solution. Medium-independent, second-order rate constants were obtained using the method of Cox and Yates (53) (eq. [19]) as described above. In two cases, compounds **4** and **6**, we also determined rate constants in trifluoroacetic acid. The second-order fragmentation rate constant taken from the intercept of the Cox–Yates plot has a significance that depends on the mechanism of the fragmentation reaction. If, for example, the first step is rate controlling, then one may infer that k°_f has to do with protonation of the substrate, regardless of whether or not

© 1999 NRC Canada

Table 4. Medium-independent rate constants and other parameters for the fragmentations of compounds **4**, **6**–**10** in H_2SO_4–H_2O, 25°C, eq. [10].[a]

Compound	$k_f°/10^{-8}$ (M^{-1} s^{-1})	k_{TFA} (s^{-1})	$m^{\ddagger}m^*$	k_{frag} (s^{-1})[b]	$k_f(H_2O)/k_f(D_2O)$[c]
4	—	~0.2	—	—	—
6	1.6 ± 0.2	1.86×10^{-2}	1.27	$(1.9 \pm 0.4) \times 10^{-5}$	0.56
7	31.6 ± 0.7	—	1.41	$(9.1 \pm 2.5) \times 10^{-4}$	0.55
8	40.0 ± 0.9	—	1.36	$(4.0 \pm 1.8) \times 10^{-2}$	0.55
9	42.6 ± 0.7	—	1.37	$\sim 5 \times 10^{8}$	0.59
10[d]	ca. 5000 (stage 1)	—	~0.9	$\sim 5 \times 10^{8}$	~6
	ca. 80 (stage 2)	—	~1.2		~0.6

[a]Obtained using eq. [19]. The standard state is 1.00 M H^+, activity coefficients unity.

[b]Obtained as $k_{frag} = k_{rds} = k_f°/K_{eq}$ for reactions wherein unimolecular fragmentation succeeds an acid-promoted equilibrium, as assumed for compounds **6**–**9** (see text). The value of k_{frag} depends critically on K_{eq}. For **6**–**8** K_{eq} is $1/K_{BH+}$, and for **9** we take $K_{eq} = 1/K_{R+}$. Values for K_{BH+} are taken from refs. 61 (**6**, **7**) and 62 (**8**). K_{R+} for tertiary alcohol **9** is taken as ca. 10^{15} M^{-1} (see text).

[c]Determined in 7.41 M L_2SO_4 for compounds **6**–**8,** and in 5.50 M L_2SO_4 for **9** and **10**. Quoted values are averages of 3–5 ratios. Estimated uncertainty in the ratio is ±10% for **6**–**9** and ±30% for **10**.

[d]Parameters are for the two rate constants obtained by fitting the absorbance vs. time data to a double exponential expression, while k_{frag} is taken from data for **9**.

Table 5. Rate constants for the ring opening isomerizations of 3-arylcyclbutanones, **15** and **14**, in trifluoroacetic acid, 25°C, eq. [11] and [13].

Compound	Ar	R1	R2	k_{TFA} (s^{-1})[a]	$k°_{TFA}/k°_{TFA\text{-}d}$
15a	Ph	CH_3	H	1.41×10^{-3}	1.7 ± 0.1
b[b]	Ph	H	*trans*-CH_3	$\sim 1.2 \times 10^{-5}$	
c	*p*-Tolyl	H	H	4.17×10^{-4}	
d	*m*-Tolyl	H	H	2.34×10^{-5}	
e[b]	Ph	Ph	CH_3	$\sim 2.5 \times 10^{-2}$	
f	Ph	Ph	H	1.24×10^{-2}	
g	Ph	H	H	7.88×10^{-6}	
14a	Ph	CH_3	H	2.22×10^{-6}	

[a]Obtained at 25.0°C by UV spectroscopy except for compounds **15b** and **e**.

[b]These were measured at room temperature (23–24°C) by ^1H NMR spectroscopy, and compared with rates for **15g** and **f**, respectively, obtained in the same way, to estimate the rate constants listed here.

fragmentation is concerted with protonation. If the role of acid is to cause an equilibrium to be established, this followed by a rate-determining fragmentation step, i.e., the A1 mechanism, then $k°_f = K_{eq}k_{rds}$. Knowledge of the equilibrium constant enables an estimate of the rate constant for the rate-determining step, $k_{rds} = k_{frag}$. For **6** and **7**, we have used pK_{BH+} values for acetone and acetophenone, respectively (61). For **8**, a pK_{BH+} value for *p*-nitroacetophenone was used (62). For compound **9**, we required a pK_{R+} value for a 3° alcohol having assumed that fragmentation occurs from a 3° carbocation. Values for pK_{R+} ranging from –14.7 to –16.4 are found in the literature for *tert*-butyl alcohol (63, 64). The latter appears to be suitable for aqueous solution. However, the results of Arnett and Hofelich (63) for four 3° alcohols larger than *t*-BuOH show an average pK_{R+} less negative by ca. 1.5 units. We have applied this correction and estimate $pK_{R+} \approx -15$ for **9**. The Cox–Yates parameters and related quantities are collected in Table 4.

*Rate constants for ring opening isomerizations of 3-arylcyclobutanones (**15**) and 2,2-dichloro-3-arylcyclobutanones (**14**)*

In trifluoroacetic acid solutions, all the cyclobutanones studied by us undergo acid-catalyzed ring cleavage of the C2—C3 bond to yield β-aryl-α, β-unsaturated ketones, eq. [11] and [13]. Compound **15a** was also examined in $HClO_4$–H_2O solution wherein biphasic behavior is seen: ring opening isomerization is followed by a retroaldol condensation, eq. [12], and is marked by a rise in absorbance vs. time followed by an overlapping decrease. First-order rate constants for the ring opening reactions in TFA are given in Table 5. Rate constants for the reactions of **15a** in $HClO_4$–H_2O, and for the related compounds **16a**, **18a**, and **19** (see eq. [12]) are found in Table 6. These rate constants are those obtained from the Cox–Yates X_o extrapolation (eq. [19] or [19*a*]). The rate of the retroaldol reaction of compound **16a** was determined from three different sources: (*i*) from the latter stages of the ring opening reaction; (*ii*) directly from the enone, **16a**; (*iii*) from the latter stages of the dehydration of ketol, **18**. All three reactions include the retroaldol reaction of **16a**. The slope and intercept parameters of the X_o plots were in satisfactory agreement with one another, given the fact that from source (*i*), the cyclobutanone, the ring opening, and retroaldol stages were only moderately well separated. The preferred values for $k°_{retro}$ reported in Table 6 are therefore those obtained from the enone and ketol sources.

In the course of investigating the retroaldol reaction of **16a**, it was found useful to compare the rates of dehydration of ketol **18** and its *p*-methyl analog, **19**. Additional comparisons required the use of literature data for dehydration of some ring substituted α-arylacetophenones. These data are assembled in Table 7.

© 1999 NRC Canada

Table 6. Medium-independent rate constants and other parameters for the ring opening isomerization and subsequent reactions of 3-methyl-3-phenylcyclobutanone (**15a**) in $HClO_4$–H_2O, 25°C. eq. [12].[a]

Compound	$k_f°$ (M^{-1} s^{-1})	$m^{\ddagger}m^*$	$k°_{retro}$ (M^{-1} s^{-1})	$m^{\ddagger}m^{*b}$	$k°_{dehyd}$ (M^{-1} s^{-1})
15a	9.3×10^{-9}	1.19	1.55×10^{-7}	0.54	—
16a	—	—	3.03×10^{-7}	0.48	—
18	—	—	3.19×10^{-7}	0.47	2.13×10^{-7}

[a]Obtained using eq. [19]. The standard state is 1.00 M H^+, activity coefficients unity.

[b]Obtained using eq. [19*a*] for the reaction starting from enone **16a**, or the second stage of reactions starting from **15a** or **18**. Combined data from **16a** and **18** give $k_{retro} = 3.13 \times 10^{-7}$ M^{-1} s^{-1}, slope = 0.47, $r^2 = 0.996$.

Table 7. Relative rates for several reactions pertinent to the mechanism of the retroaldol reaction of 4-phenylpent-3-en-2-one (**16a**), 25°C.

Reactant pair	Acid-catalyzed reaction	Relative rate (k_x/k_H)
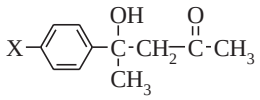	Dehydration	$k_{CH_3}/k_H = 11.1$,[a] 11.6[b]
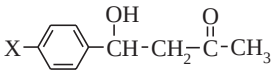	Dehydration	$k_{CH_3}/k_H = 1.00$[c]
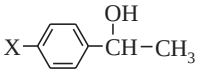	Dehydration	$k_{CH_3}/k_H = 14.6$,[d] $k_{NO_2}/k_H = 0.0026$[d]
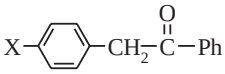	Enolization	$k_{CH_3}/k_H = 1.15$[e]

[a]In 7.39 M $HClO_4$–H_2O, this work.

[b]In 7.72 M $HClO_4$–H_2O, this work.

[c]Reference 117*d*.

[d]Reference 39. Data from this source were reprocessed using eq. [19].

[e]Reference 94.

Table 8. Rate constants for acid-catalyzed cleavage of (7-tropyl)nitroalkanes (**11a**–**c**) in trifluoroacetic acid and $HClO_4$–H_2O, 25°C, eq. [14].

Compound	$k_{TFA}/10^{-5}$ (s^{-1})	$k°_f/10^{-9}$ (M^{-1} s^{-1})[a]	$m^{\ddagger}m^*$	$k_{TFA\text{-}d}$[b]
11a	3.35	0.752	1.34	1.25 ± 0.10
11b	59.0	304	0.94	1.44 ± 0.05
11c	1180	4720	1.05	1.51 ± 0.05

[a]Obtained using eq. [19]. The standard state is 1.00 M H^+, activity coefficients unity.

[b]Measured at 23–24°C.

*Rate constants for acid-catalyzed cleavage of (7-tropyl)nitroalkanes (**11**), eq. [14], and 2-arylnitrocyclopropanes (**12**, **13**), eq. [15]*

Tropylium compounds, **11a**–**c**, fragment in TFA or in $HClO_4$–H_2O to give tropylium ion, Tr^+ (quantitatively), and products expected from reaction of the other fragment, a nitronic acid, in acid media, namely, hydroxamic acids (Victor Meyer reaction) or acetone, the Nef reaction product from **11c** (37). Rate constants and solvent isotope effects for these reactions are presented in Table 8. The data for **12** and **13** are found in Table 9.

Discussion

Synthesis of β-aryl-α,β-unsaturated ketones, 16 and 17

The sequence of reactions in which olefins (styrenes) are converted to 2,2-dichlorocyclobutanones (**14**), which are then (optionally) dechlorinated to cyclobutanones (**15**), which in turn undergo acid-catalyzed ring opening leading to enones **16** and **17**, is suggested by us to be a simple and useful preparative method for such enones. A similar sequence has also been recommended by Doyle et al. (65). A particularly useful feature of the sequence is that the final step is regiospecific and (in the cases investigated by us) stereospecific. As discussed below, ring opening occurs to produce the enol in which the double bond is more highly substituted. Ketonization then takes place so that the resulting acyl group is *trans* to the larger group on the other double bond carbon, see eqs. [11] and [13]. The ring opening step appears to be virtually quantitative, but its rate is highly dependent on the substitution pattern, especially at C3 (see Tables 1 and 5). More convenient rates in the slower cases could doubtless be achieved by using more powerfully acidic conditions, for example CF_3SO_3H–TFA or $HClO_4$–TFA. Other aspects of the electrophilic cleavage of cyclobutanones are discussed below.

Mechanisms: fragmentation of the alcohols (1, 5) and sulfides (2, 3)

In this section, we propose that hydronium ion promoted cleavage of the alcohols and sulfides occurs by the two-step

© 1999 NRC Canada

Scheme 1.

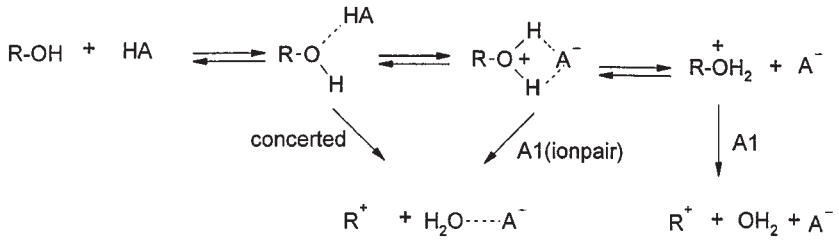

Table 9. Rate constants for acid-catalyzed ring cleavage of 2-arylnitrocyclopropanes (**12**, **13**) in trifluoroacetic acid, 18–20°C, eq. [15].

Compound	$k_{TFA}/10^{-3}$ (s^{-1})	$k_{TFA}(CDCl_3)/10^{-3}$ (s^{-1})[a]	$k_{TFA}/k_{TFA\text{-}d}$
12	1.08	0.0117	2.1±0.1
13	—	>23	—

[a]4 M TFA in $CDCl_3$.

A1 mechanism in which the leaving group, water or methanethiol, is strongly hydrogen bonded to a water cluster in the rate-determining transition state. Slopes of the Kresge plots for **1**, **5**, and **2** are α_K = 0.63, 0.54, and 0.71, respectively. These results tell us that the sensitivity of the free energy of the transition states of these cleavages toward added $HClO_4$ is not as great as is the sensitivity of the free energy of the separated cleavage products. It is thus permissible to view α_K values like classic Brønsted α values. Indeed, Kresge (66) has shown that for a number of general-acid catalyzed proton transfers, experimental α and α_K values have similar magnitudes. Although providing information about the transition states, the Kresge correlations do not, unfortunately, tell us whether the reaction mechanisms are stepwise A1 processes, with equilibrium protonation followed by rate-determining fragmentation, or are concerted, with protonation accompanied by cleavage.

It has been established that nucleophilic attack by water on carbocations as unstable as 1-(*p*-anisyl)ethyl is catalyzed by general bases (67). Likewise, general base catalysis is observed for capture by water of a host of more stable carbocations including triarylmethyl, aryltropylium, and some highly stabilized xanthyl cations. Ritchie et al. (68) has argued that the reactions of water with carbocations covering the pK_{R+} range from –7 to +9.4 are all subject to general base catalysis. With the inclusion of 1-(*p*-anisyl)ethyl, $pK_{R+} \cong -8.5$, this range extends close to the limit of any carbocations capable of existence in aqueous solution. General base catalysis of attack by nucleophilic water implicates general acid catalysis for departure of nucleofugic water from the corresponding alcohols.

Catalytic assistance by general bases does not guarantee that in the absence of these bases attack of water is similarly assisted by other water molecules. Gandler (69) has given a simple but persuasive argument that, in general, the "water reaction will be stepwise, passing through the oxonium ion, ROH_2^+, rather than concerted"; (very similar arguments have been given by Jensen and Jencks (79)). In the fragmentation direction, this is the A1 mechanism. Gandler's argument compares estimated, but reasonable, values of $\Delta G°$ for the equilibrium protonation of alcohols with the overall free energies of activation for their acid-catalyzed heterolyses. Significant free energy barriers to heterolysis (8–10 kcal/mol at 25°C) remain following the protonation step. Likewise, one may estimate a residual barrier to heterolysis of at least 8 kcal/mol for $XanOH_2^+$ and a barrier of 6 kcal/mol or more even for protonated tropyl alcohol.

Gandler's conclusion does not of course negate hydrogen-bonding assistance to the departure of water by neighboring water molecules; an oxonium ion will be well hydrated. In this connection, Wolfe et al. (70) have recently reported experimental and computational results on the uncatalyzed hydration of acetone. The experimental free energy of activation is well modeled by a transition state containing four molecules of water. Further, their computations indicate that a major component of bulk water is a cyclic tetramer. Insofar as a ketone can represent a carbocation for this purpose, it seems logical that the uncatalyzed addition of water to a cationic center involves a water cluster, polarized by the cation's positive charge. The constituent water molecules in the cluster, already hydrogen-bonded in the bulk, will be even more firmly linked in the transition state and in the product oxonium ion. In the fragmentation direction, nucleofugic water is welcomed, joining, or helping to form a stable cluster.

We have observed inverse solvent isotope effects for the fragmentations of XanOH (**1**), XanSMe (**2**), and TrSMe (**3**), see Table 3. Solvent isotope effects, k_{H3O+}/k_{D3O+}, were once thought to be diagnostic for distinguishing the A1 mechanism from rate-determining protonation: the former would display an inverse rate ratio favoring reaction in D_2O by a factor of 2.5 or more, while the latter would show normal primary isotope effects being faster.

However, there now exist many examples of reactions that show both general acid catalysis *and* inverse solvent isotope effects. Just a few examples are formation of An_3C^+ from An_3COH (71), the hydrolysis of ethylorthocarbonate (72), hydrolysis of a number of acetals (73, 74), and the fragmentation of *N*-*p*-nitrophenylcarbamate (75). The magnitudes of these inverse effects range from $k_{H3O+}/k_{D3O+} \cong 0.3$ to just under unity. In such cases, the large inverse effect associated with the nonreacting hydrogens in the protonation event is more or less mitigated by a variable and normal primary effect associated with the transferred hydrogen. This partly compensating primary effect can arise if the transferred hy-

© 1999 NRC Canada

drogen is part of the reaction coordinate motion, or if for any reason, for example, strong hydrogen bonding, the zero-point vibrational energy associated with this hydrogen is reduced in the transition state relative to the reactant state (74–77).[6] It is quite conceivable that a slight variation of the A1 mechanism, one in which the transferred hydrogen remains strongly associated with the atom from which it left rather than being solvationally equilibrated, provides the necessary set of zero-point energy changes, giving rise to solvent isotope effects that are inverse, but not maximally so. Note that this variant, when employed by general acid catalysts, has the transferred proton (and (or) a geminal partner) hydrogen bonded to the conjugate base of the general acid in the rate-determining transition state. Further, in the reverse or recombination direction, one has general base catalysis by preassociation (74, 75; Wann and Kreevoy (78) present a more detailed scheme for the mechanistic possibilities of acid-catalyzed heterolyses, including diffusional events). Scheme 1 presents some of the possibilities discussed in this section.

There is much less information available about the reactions of carbocations with neutral thiols than with water. We are unaware of unequivocal evidence for general catalysis of reaction [3] or its reverse (79, 80). Perdoncin and Scorrano (81) report a pK_a = –7.0 for the conjugate acid of dimethyl sulfide. Borrowing this value for sulfides **2** and **3**, and comparing the free energy of protonation, $\Delta G°$, with the free energy of activation governing $k_f°$, $\Delta G^‡$, one finds that $\Delta G^‡$ exceeds $\Delta G°$ by 8.5–9.5 kcal/mol for XanSMe and ca. 7 kcal/mol for TrSMe. Since an error of ± 1 pK_a unit in the protonation equilibrium alters the difference between $\Delta G^‡$ and $\Delta G°$ by only ± 1.4 kcal/mol, estimates such as these leave plenty of room for the two-step A1 mechanism. Compared with alcohols **1** and **5**, the equilibrium constants for protonation of the sulfides are smaller, but so are the overall rate constants, $k_f°$.

There is no thermodynamic imperative for avoiding the conjugate acids of alcohols and sulfides in hydronium ion promoted fragmentations. Therefore, we propose the simplest mechanistic interpretation of the data: the A1 mechanism or the ion-pair variant described above.

Mechanisms: carbon–carbon cleavage of xanthyl compounds 6–10, and of (7-tropyl)acetone

The xanthylketones, **6**–**8**, and the related tropyl compound, **4**, all appear to undergo fragmentation by the classical A1 mechanism, eq. [22]. It is possible that reversible enolization of the ketones occurs prior to fragmentation, however, we have no direct evidence on the matter.

The medium-independent rate constants for the fragmentations (Table 4) are ca. 10^2 smaller than typical values (82) for acid-catalyzed enolization. However, the fragmentation rates have *much* greater dependencies on acidity than do enolizations (62, 83[7]). For the moderately concentrated acid solutions used by us, we can estimate that fragmentation rates exceed enolization rates by a factor of at least 30, thus we exclude an enolization side reaction in these media.

The evidence for the A1 mechanism is threefold. First, the thermodynamic rationale used in the previous section permits a large barrier for fragmentation of the substrate conjugate acid to be estimated, ~19–24 kcal/mol for **8**, **7**, and **6**; see listings for k_{frag} in Table 4. The solvent isotope effects, $k_f(H_2O)/k_f(D_2O)$, are about 0.55 for these substrates, allowing interpretation by the A1 mechanism. A related and important point is the solvent isotope effect measured for **6** in trifluoroacetic acid: $k_{TFA\text{-}d}$ = 0.78 ± 0.04. Acids with only one acidic hydrogen have no nonreacting hydrogens, hence any primary isotope effect will not be concealed by an inverse secondary effect. Johnson and co-workers (84) have shown that an inverse solvent isotope effect in TFA is to be expected for an A1 pathway. Less diagnostic but consistent with this assignment is the secondary isotope effect observed with compound **6** deuterated at the 9-position: k_H/k_D = 1.10 ± 0.03 in 62% H_2SO_4. This result is consistent with a rate-determining step involving a hybridization change, $sp^3 \rightarrow sp^2$ at C-9. We assume in these arguments that the reaction mechanism in TFA is the same as that in water. This seems likely; the dielectric constant of TFA is low, only 8.22 (85). The A1 (ion pair) mechanism (or conjugate acid – conjugate base pair in water) is much more likely in a medium of this sort than in water. Yet, the solvent isotope effect in TFA tells us that this does not occur. A small *normal* effect would be predicted for the ion pair mechanism (75).

Computational evidence supports the thermodynamic argument given above. The enthalpic barrier to fragmentation of the conjugate acid of **6** is calculated by the semiempirical AM1 method to be 19.3 kcal/mol, in reasonable accord with the experimentally estimated free energy barrier of 23.9 kcal/mol. For the tropyl analogue, **4**, the fragmentation barrier is computed at a healthy 14.4 kcal/mol. For this reason and because **4** fragments in TFA only 10–20 times faster than **6**, we do not imagine a different, "improved" mechanism for **4**.

For compound **9**, 2-methyl-1-(9-xanthyl)-2-propanol or Xantba, we propose that acid-promoted heterolysis to a 3° carbocation occurs reversibly and that fragmentation of this cation to xanthyl$^+$ and isobutylene is rate determining, eq. [23]. As described in Results we estimate a pK_{R+} for the intermediate 3° carbocation of ~–15. With this value, a unimolecular fragmentation constant of ca. 5×10^8 s^{-1} may be estimated for the rate-determining step. This rate is smaller than that estimated for combination of *t*-butyl$^+$ with water by about

[22] 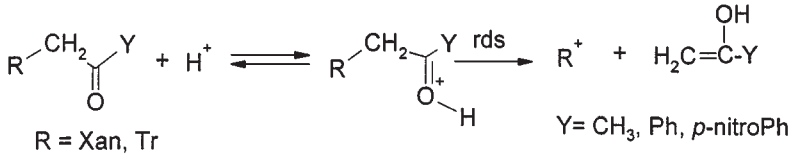

[6] A model for proton transfer along a hydrogen bond has the proton moving in a stable well, not part of the reaction coordinate: see ref. 76. Kreevoy and Liang (77) have presented evidence for reduced fractionation factors for protons in some hydrogen-bonded complexes.

[7] The very small dependence of k_{exp} (s^{-1}) on *X* is anticipated by the original Zucker–Hammett hypothesis that an A2 mechanism such as enolization should be correlated with [H$^+$], not requiring an excess acidity function: ref. 83*b*.

© 1999 NRC Canada

Table 10. Comparison of rates of C-C cleavages in trifluoroacetic acid and in $HClO_4$–H_2O at a common H_o = –2.71, 25°C.

Compound	k_{TFA} (s^{-1})	k_{HClO4} (s^{-1})[a]	H_o value required to make $k_{HClO4} = k_{TFA}$
6, XanAc	1.86×10^{-2}[b]	3.7×10^{-5}[b]	–5.2[c]
11a, $TrCH_2NO_2$	3.35×10^{-5}	1.4×10^{-6}	–3.8
11b, $TrCH(CH_3)NO_2$	5.90×10^{-4}	8.1×10^{-5}	–3.6
11c, $TrC(CH_3)_2NO_2$	1.18×10^{-2}	2.8×10^{-3}	–3.4
15a, 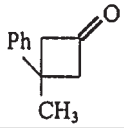	1.41×10^{-3}	1.0×10^{-5}	–4.5

[a]Calculated using linear correlations between log k_{exp} (s^{-1}) and H_o.

[b]Calculated for 43.7% (5.93 M) H_2SO_4.

[c]Corresponding to 66.0% (10.5 M) H_2SO_4.

[23] 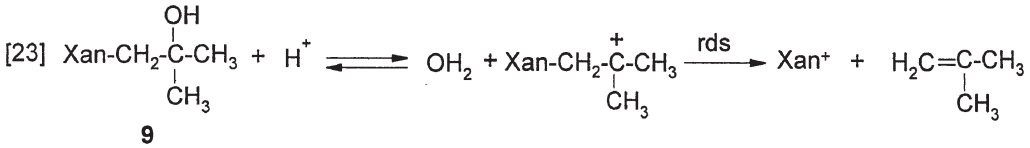

9

5000 (64*a*) and smaller than that for reaction of 1-methycyclooctyl cation with water by a factor of ca. 12 (64*b*). Hence, we believe that the 3° cation in the present case is formed reversibly. A supporting piece of evidence is the secondary kinetic isotope effect, k_H/k_D = 1.07 ± 0.03, measured by use of Xantba-9-*d* in 50.4% H_2SO_4–H_2O, a result consistent with a hybridization change from sp^3 to sp^2 at C-9 in the rate-determining step.

Compound **10**, 2-methyl-3-(9-xanthyl)propene or XanIb, fragments quantitatively to Xan^+ and isobutylene but by a more complex mechanism than for the other xanthyl compounds. Data from biphasic time courses were fit to a double exponential equation. This allowed rate constants to be estimated for both phases (Table 4). Data from the later part of the reaction (stage 2) could be approximated by a single exponential equation, yielding a rate constant similar to that for the fragmentation of **9**. The solvent isotope effect for this stage was inverse and close to that obtained with **9**. Data from stage 1 gave a normal solvent isotope effect of approximately 6. We characterize this stage as protonation of the olefin. All results including the requirement of a double exponential fit are satisfied by mechanism [24] (86).

Trifluoroacetic acid appears to be an excellent medium for these fragmentations as well as others, see Table 10. An *X*-function value for TFA is not known, but the H_o value has been determined to be –2.71 (87). The H_o value for an H_2SO_4–H_2O medium, which would bring about fragmentation of **6** at the same rate as in TFA, is –5.2! To put it another way, the rate of fragmentation in a sulfuric acid solution of H_o = –2.71 (44% H_2SO_4) is 500 times slower than in TFA. A part of the superiority of TFA in these carbocation-forming reactions may lie in the fact that the H_R value for TFA is –11.3 (87), a value reached by H_2SO_4–H_2O solutions only at 69% H_2SO_4. Tidwell and co-workers (88) have observed that rates of protonation of a number of aliphatic olefins are slightly elevated in TFA compared with 44% H_2SO_4 and that, as a class, substituted styrenes are even more reactive in TFA. The relatively large value of $-H_R$ suggests that TFA might be particularly hospitable to delocalized carbocations (as well as to water and to other oxygen-centered leaving groups).

Mechanisms: carbon–carbon cleavage of tropylnitroalkanes, 11

In our earlier report, we identified the reaction of eq. [14] as the first example of acid-catalyzed conversion of a nitroalkane to a nitronic acid (37). The reactions differ from a tautomerization process in that instead of proton loss from the carbon next to the nitro group, we see loss of the tropylium carbocation. Not only is tropylium a superior electrofuge, its loss occurs unimolecularly with no requirement for covalent participation by a base, H_2O or TFA.

Ordinary nitroalkane-to-nitronic acid tautomerization has never been demonstrated to be acid catalyzed unlike the otherwise similar keto–enol transformations of carbonyl compounds. The extremely low basicity of nitroalkanes must be a major part of the reason for the lack of observed acid catalysis. Rather, tautomerization occurs through deprotonation by water, then reprotonation by H_3O^+. In fact, the basicity of nitroalkanes is not well quantitated, though it is known that

[24] 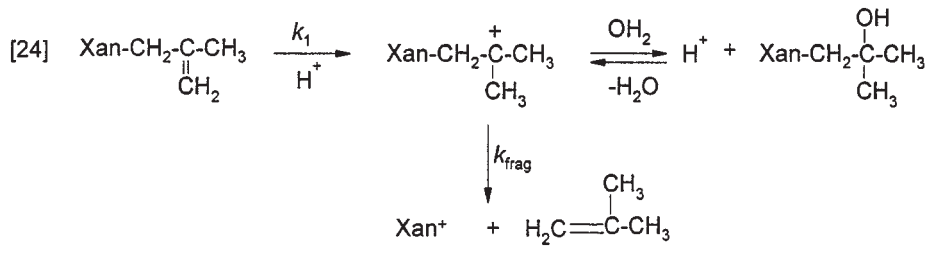

© 1999 NRC Canada

nitromethane is not significantly protonated in 99–100% H_2SO_4 (89). Gillespie and Solomons (90) have reported conductometric measurements giving $K_b \cong 2.5 \times 10^{-3}$ M in H_2SO_4 solvent, and Arnett (91) provides an estimated $pK_a \cong -12$ for the conjugate acid of nitromethane. The latter value allows a calculation of $\Delta G° \cong 16$ kcal/mol for protonation of CH_3NO_2. The known rate constant for deprotonation of nitromethane by water (92) provides $\Delta G^{‡} \cong 27.5$ kcal/mol for that reaction. These results require that the tautomerization of nitromethane have a rate constant, $k \cong 5 \times 10^4$ s^{-1}, for deprotonation of $CH_3NO_2H^+$ at carbon in order for the A1 mechanism to compete with the water reaction. This does not seem an extraordinary requirement, but it must be kept in mind that the pK_a value for $CH_3NO_2H^+$ could be even more negative than assumed here.

In our original communication, we proposed that the tropylnitroalkanes fragment by the A1 mechanism (37). Since then, we have determined the solvent isotope effects, $k_{TFA}/k_{TFA\text{-}d}$, reported in Table 8. These ratios are small but normal, and stand in contrast to the inverse effect found for fragmentation of (9-xanthyl)acetone. The ratios, ranging from 1.25–1.51, are too small to represent rate-determining proton transfer, but of the right size for the A1 (ion pair) mechanism. Good precedent for this assignment comes from the studies by Ewing et al. (75) and by Johnson and Morrison (93) on the acid-catalyzed decomposition of *N*-arylcarbamates. These groups found, respectively, $k_{HCO3-}/k_{DCO3-} = 1.6$ for Ar = *p*-nitrophenyl and 1.4 for Ar = phenyl. By contrast, the lyonium-catalyzed reactions showed an inverse solvent isotope effect, 0.59 for *N*-phenylthiocarbamate and 0.67 for *N*-*p*-nitrophenylcarbamate (75). Equation [25] gives the A1 (ion pair) mechanism for tropylnitroalkane cleavage in trifluoroacetic acid. We did not determine the solvent isotope effect for H_3O^+ catalysis in water, but we speculate that the ion pair mechanism used in the low dielectric TFA medium might become the more typical A1 pathway in water.

Semiempirical (AM1 and PM3) calculations are in accord with our mechanistic assignments. Protonation of (7-tropyl)- nitromethane (**11a**) has an enthalpy change equal, within 0.25 kcal/mol, to that calculated for a model compound, 3-nitromethyl-1,4-cycloheptadiene. This result indicates that the tropyl group confers no unusual basicity upon the nitro moiety, and that the success of reactions [14] is therefore due to a subsequent step, namely, fragmentation to yield Tr^+. The computed barriers for the fragmentation of the conjugate acids are in the 11–12 kcal/mol range, smaller than that for (9-xanthyl)acetone and (7-tropyl)acetone (see above), suggesting a shorter lifetime toward fragmentation for compounds **11**-$\mathbf{H}^+$ compared with **6**-$\mathbf{H}^+$ and **4**-$\mathbf{H}^+$. This outcome permits the postulate that **11** fragments via the ion pair intermediate of eq. [25], which does not survive long enough to diffuse apart in contrast to the longer lived conjugate acids of **6** and **4**.

Computed geometries are also of interest. AM1 calculations show that ground state (7-tropyl)nitroalkanes prefer the pseudoequatorial conformation whereas their conjugate acids and fragmentation transition states are pseudoaxial: a weak preference is shown by the conjugate acids and a strong preference by the transition states. Bond lengths (C-7—C8 and C8—N) and bond orders are barely changed upon protonation. At the transition state the C7—C8 bond order has fallen to ~20% of the reactant state value while that of the C8—N bond has grown to 45–50% of the value for the product nitronic acid. Flattening at C7 has outpaced that at C8 by 52–34%. Bond order changes and flattening progress both show that cleavage of the C7—C8 bond runs ahead of the development of nitronic acid character.

Mechanisms: ring-opening addition of trifluoroacetic acid to 2-arylnitrocyclopropanes, 12 and 13

Recently, we reported that *trans*-2-phenyl- and *trans*-2-*p*-anisylnitrocyclopropanes, **12** and **13**, are easily cleaved at room temperature and below, giving rise to products derived from the intermediacy of nitronic acids, eq. [15] (38*a*). The reaction shows a strong dependence on the aryl substituent: $k_{13}/k_{12} > 2000$ in 4 M TFA/$CDCl_3$ equivalent to a reaction constant, $-\rho(\sigma^+) > 4$. Additionally, compound **12** exhibited a solvent kinetic isotope effect, $k_{TFA}/k_{TFA\text{-}d} = 2.1 \pm 0.1$. Reaction by protonation of the three-membered ring, known to occur for phenylcyclopropane, was ruled out. These pieces of evidence led us to formulate the mechanism as eq. [26] wherein the initial protonation step is concerted with cleavage of the C1—C2 bond.

This assignment is supported by several kinds of computational evidence at the AM1 level: first, the gap between the computed enthalpies of the *O*-protonated conjugate acids and the ring cleavage transition states has fallen to 3.9 kcal/mol for **12** and 2.5 kcal/mol for **13**. These numbers are significantly smaller than those found for the other C-C cleavages in this study, and make it easy to imagine that there exists no substantial barrier either to deprotonation or to cleavage. In other words, concerted proton-assisted ring opening is enforced by the vanishingly short lifetime of the conjugate acid.

In addition to the energetics, the computed geometries provide useful information. Protonation of **12** and **13** is accompanied by lengthening of the C1—C2 bond by 0.04 Å (**12**) and 0.05 Å (**13**) and reduction of the C1—N distance by 0.03 Å in each case. These changes represent at least 15–18% of the ultimate change in bond order for the C1-C2 cleavage and at least 18–24% of the increase in C1—N bond order that occurs upon completion of nitronic acid formation. These changes are much greater than those found for the tropylium series, **11**, and are made possible by an inter-

[25] $Tr\text{-}C(R)_2NO_2 \overset{TFA}{\rightleftharpoons} Tr\text{-}C(R)_2\overset{+}{N}O_2H\cdots TFA^- \xrightarrow{rds} Tr^+ + R_2C{=}NO_2H\cdots TFA^-$

[26] 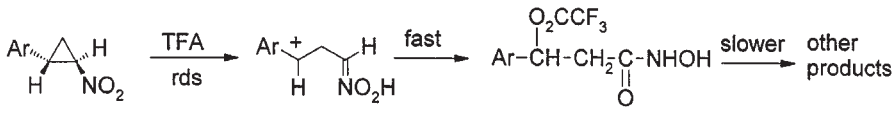

© 1999 NRC Canada

Table 11. Calculated enthalpies of activation for fragmentation of substrate conjugate acids and experimental solvent kinetic isotope effects, $k_{TFA}/k_{TFA\text{-}d}$.

Substrate	Calculated $(H^{\ddagger} - H_{SH}^{+})^a$	$k_{TFA}/k_{TFA\text{-}d}$
XanAc, **6**	19.3	0.78 ± 0.04[b]
$TrCH_2NO_2$, **11a**	11.5	1.25 ± 0.10
$TrCH(CH_3)NO_2$, **11b**	12.2	1.44 ± 0.05
$TrC(CH_3)_2NO_2$, **11c**	<12.0	1.51 ± 0.05
3-Methyl-3-phenylcyclobutanone, **15a**	19.1	1.7 ± 0.1[c]
2-Phenylnitrocyclopropane, **12**	3.5	2.1 ± 0.1[c]

[a]25°C, calculated by the semiempirical AM1 method (40).
[b]Measured at 23°C.
[c]Measured at 18–20°C.

esting feature of the calculated conjugate acid structures: the plane of the $-NO_2H^+$ group bisects that of the three-membered ring just as in the preferred conformation of a cyclopropylcarbinyl cation; this allows efficient electronic interaction between the two moieties.[8]

The solvent isotope effect obtained for **12** completes a spectrum of $k_{TFA}/k_{TFA\text{-}d}$ values ranging from inverse (for compound **6**) to weakly normal (for **11** and also for **15a**, see below) to a value for **12**, which we class as a small, but primary isotope effect (96).[9] Unencumbered by an inverse secondary effect of uncertain magnitude as found with k_{H3O+}/k_{D3O+} measurements, these results allow finer mechanistic distinctions to be made than would otherwise be possible. Table 11 compares calculated enthalpies of activation for fragmentation of the conjugate acids of compounds for which we have measured solvent isotope effects in TFA. The data show that with the exception of the cyclobutanone, **15a**, smaller $\Delta H^{\neq}$ values are accompanied by small, but regular increases in the isotope effect, a mechanistically useful result. A disadvantage in the use of TFA as a reaction medium is that many reactions of interest will be too fast to be studied at room temperature by conventional means. At the other end of the reactivity range, it is possible to increase the acidity of TFA solutions, thereby accelerating sluggish reactions, by including small amounts of $HClO_4$ or CF_3SO_3H in the medium ($HClO_4$/TFA and H_2SO_4/TFA: ref. 97*a*; CF_3SO_3H/TFA: ref. 97*b*). The utility of these media for solvent isotope effect determinations has yet to be established.

In closing this section, we call attention to the acid catalyzed cleavage of some cyclopropyl ketones. Equation [27] summarizes some of the experimental results with this class of compounds. The cleavage has been interpreted as occurring via protonation of the ring by D_2SO_4 (98), but a more straightforward explanation, consistent with our mechanism [26], is that first the carbonyl oxygen is protonated, then (subsequently or in concert) cleavage of C1-C2 occurs, leading to an enol which gives rise to the observed products. Ring-opening enolization of this type was first suggested by Kohler and Conant (100), and later by Deno et al. (101) and deMeijere (102). Mechanistic details such as the question of whether ring cleavage is stepwise or concerted with protonation have not been investigated.

Mechanisms: ring-opening isomerization of 3-arylcyclobutanones, 14 and 15

Ring-opening as well as ring-expansion and ring-contraction reactions of cyclobutanones have been known for some time. Many of these reactions have synthetic value and have been reviewed by Trost (103), Wong et al. (104), and by Lee-Ruff (105). The thermodynamic driving force behind such transformations is relief of ring strain. Rocek

[27] 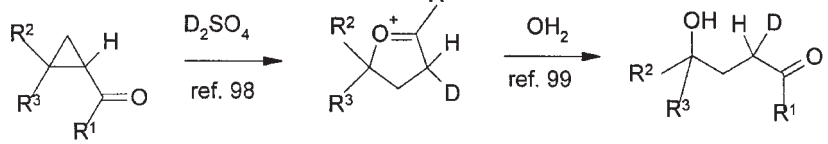

[28] 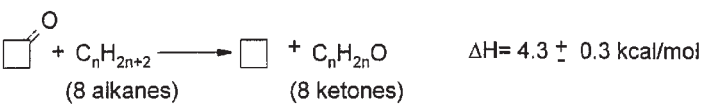

[8]This geometric feature persists at the HF/6-31G* level of computation for protonated nitrocyclopropane but is *not* found, for example, in protonated 2-nitropropane or protonated nitrocyclobutane, which show a twist of 40–45°. A corollary prediction is that rotation about the exocyclic bond will be more difficult for protonated nitrocyclopropane and cyclopropylcarbinyl cation than for the other protonated nitro compounds. At HF/6-31G* dimethylcyclopropylcarbinyl$^+$ has a calculated $\Delta H^{\neq}$ = 13.9 kcal/mol, whereas the experimental value (95) for E_a is 13.7 ± 0.4 kcal/mol. Rotation is accompanied, computationally, by a lengthening of the C$^+$—C1 bond at the transition state of 0.07 Å. Similarly, but less dramatically, protonated nitrocyclopropane has a rotational barrier calculated at 5.7 kcal/mol with a C—N lengthening of 0.05 Å. By contrast, the rotational barriers and C-N distensions for protonated 2-nitropropane and nitrocyclobutane are calculated to be 1.3 kcal/mol (0.02 Å) and 1.2 kcal/mol (0.01 Å), respectively, all at the HF/6-31G* level.

[9]For example, Anderson and Fife (96) have observed $k(CH_3CO_2H)/k(CH_3CO_2D)$ = 2.1 for the general-acid catalyzed hydrolysis of diethylphenylorthoformate, a reaction for which Brønsted's α = 0.47, a value indicative of rate-determining proton transfer: ref. 96.

© 1999 NRC Canada

Table 12. Calculated (AM1) relative enthalpies of activation and selected bond length changes at the transition state for the ring-opening isomerizations of 3-arylcyclobutanones, 25°C.

Compound	$\Delta G^{\ddagger}_{exp}$(TFA) (kcal/mol)[a]	$\Delta H^{\ddagger}_{rel}$[b]	Bond lengths (‡) and bond length changes (Δ)[c] (Å)		
			C2—C3	C1—C2	C1—O
15a	21.4	195.8	2.048/0.484	1.416/–0.105	1.318/0.099
b[a]	24.2	193.4	2.035/0.471	1.429/–0.100	1.317/0.099
c	22.1	196.8	2.035/0.471	1.429/–0.108	1.319/0.100
d	23.8	199.2	2.053/0.497	1.413/–0.109	1.320/0.100
e[a]	19.7	187.4	2.032/0.450	1.429/–0.098	1.316/0.097
f	20.1	194.0	2.044/0.476	1.420/–0.099	1.320/0.100
g	24.4	199.9	2.056/0.500	1.414/–0.109	1.320/0.100
14a	25.2	198.7	2.052/0.459	1.471/–0.077	1.305/0.092

[a]See Table 5 for rate constant information.

[b]Calculated as the difference, $\Delta H_f°$ (‡) – $\Delta H_f°$ (ketone). $\Delta H^{\ddagger}_{rel} = 1.37\Delta G^{\ddagger}_{exp} + 166.6$, $r^2 = 0.999$. This correlation excludes C2-substituted compounds, **15b**, **15e**, and **14a**.

[c]The difference between the bond length in the transition state and the ketone.

Scheme 2.

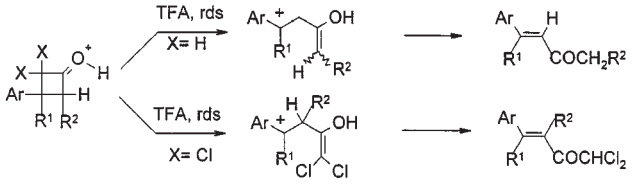

Scheme 3.

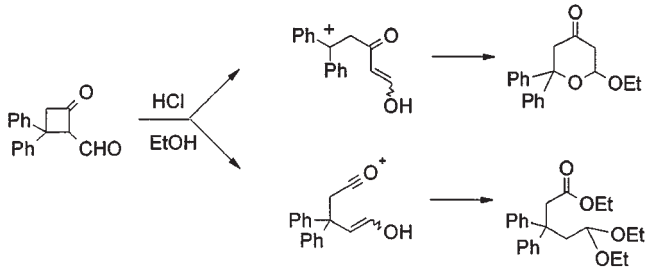

Scheme 4.

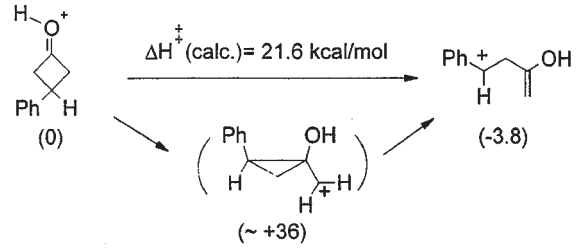

and Radkowsky (106) have estimated the strain energy for cyclobutanone at 24.5 kcal/mol. Another estimate arises from the set of homodesmotic reactions shown as eq. [28].

The average heat of reaction for these processes is 4.3 ± 0.3 kcal/mol. This indicates that cyclobutanone is less strained than cyclobutane by ca. 4.3 kcal/mol, and therefore has a strain energy of about 22 kcal/mol (107).[10]

Electrophilic activation by acids permits at least five different cleavage or rearrangement paths to occur, the result depending on the substitution pattern on the four-membered ring, the presence and location of basic sites other than the cyclobutanone oxygen, the nucleophilic properties (if any) of the medium, and the nature of the acid catalyst: strong or weak, protic or Lewis. At least four different cationic intermediates have been implicated (or merely suggested). The reactions studied by us (see eqs. [11]–[13]) are most easily understood as cleavage of the C2—C3 bond producing the most stable of the possible enols (65) along with a carbocation center at C3, see Scheme 2. This pathway is encouraged by electron donation at C3. Normally, there must be two alkyl groups at C3 (108–110), or at least one group must be aryl (110–113)[11] or vinyl (113, 114). Sufficiently good electron donors at C3 (e.g., RO, Ph; RO, RO; or R_2N) allow cleavage at moderate temperatures *without* acid catalysis (115). A relatively good nucleofuge, a conjugated enol, for example, will also help as in Scheme 3, upper path (111).[11]

A reasonable alternative to Scheme 2 is that proposed for the acetolysis of three-substituted cyclobutyl tosylates by Wiberg et al. (116). Their results were rationalized as proceeding through a bridged cyclobutyl cationic transition state to a cyclopropylcarbinyl intermediate from which the products are ultimately formed. However, this path is not tenable for our reactions, principally because the reactivity patterns for the two series are opposed. The solvolysis reactions are *retarded* by alkyl and phenyl groups at C3 in contrast to the cyclobutanone ring openings. Two phenyl groups at C3 caused further retardation of the solvolyses. All these substitutions accelerate our reaction, see Table 5. A final difference: solvolysis of the 3-aryl tosylates produced a Hammett ρ value (σ) of –1.55. From compounds **15c**, **d**, and **g**, we obtain a much larger effect, ρ = –5.5, requiring the use of σ^+ for the *p*-methyl substituent.

A further detail is revealed by the solvent isotope effect for cleavage of **15a** in trifluoroacetic acid. The rate ratio,

[10]The heat of formation of cyclobutanone was taken from Bouchoux and Houriet (107); heats of formation for the other compounds are from Pedley et al. (107); the strain energy of cyclobutane is 26.4 ± 0.2 kcal/mol: Wiberg (107).

[11]I. Erden and R.D. Miller. Unpublished results.

© 1999 NRC Canada

Scheme 5.

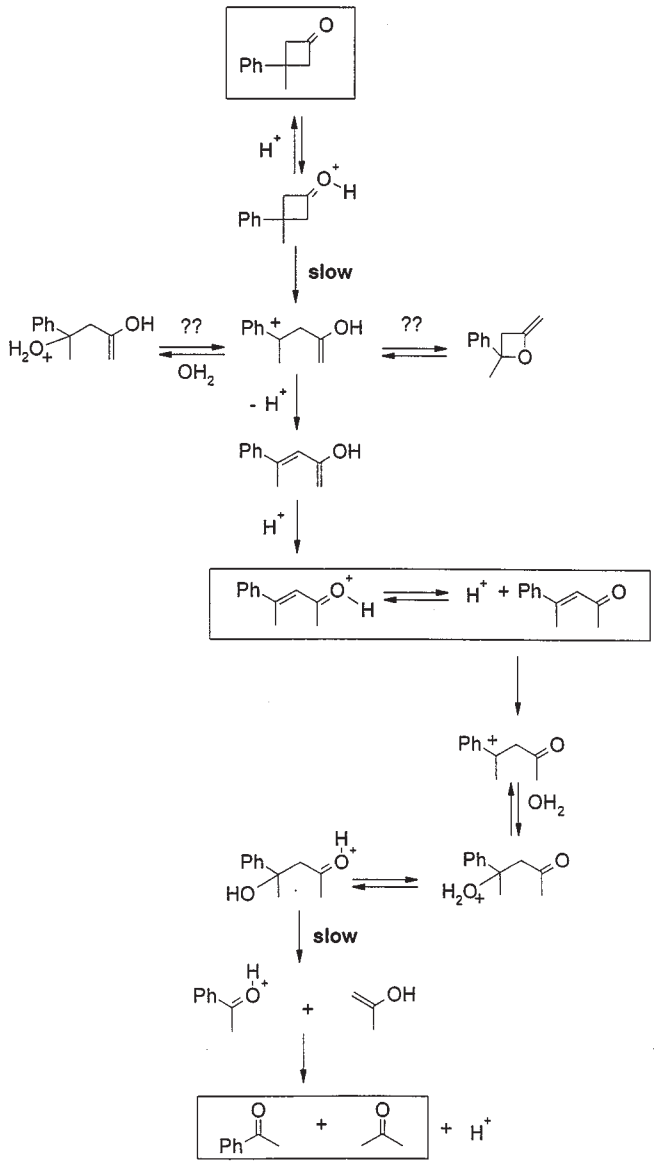

$k_{TFA}/k_{TFA\text{-}d}$ = 1.7 ± 0.1, allows placement of this reaction into the A1 (ion pair) category, although the possibility that proton transfer from TFA to substrate is at least partly rate controlling cannot be rigorously excluded.

The ring-opening isomerizations of 3-arylcyclobutanones were studied computationally using the semiempirical AM1 method, chosen because it reproduces the experimental heat of formation for cyclobutanone and its heat of isomerization to but-3-en-2-one better than do PM3 and MNDO. These calculations confirm that protonated 3-phenylcyclobutanone prefers to undergo C2-C3 cleavage forming the enolic carbocation rather than ring contraction to a cyclopropylcarbinyl cation. In fact, the ring-contracted cation is not stable toward rearrangement to the ring-opened product. This information is summarized by Scheme 4 in which relative AM1 enthalpies are given in kcal/mol.

Additionally, the computed relative enthalpies of activation for the ring-opening path, $\Delta H^{\ddagger}_{rel} = (\Delta H_f^{\ddagger} - \Delta H_f^{K})$, correlate very well with the experimental $\Delta G^{\neq}$ values for all of the ketones (K) which are unsubstituted at C2: $\Delta H^{\ddagger}_{rel}$ = 1.37 $\Delta G^{\neq}_{exp}$ + 166.6, r^2 = 0.999 (see data in Table 12). Experimentally, the replacement of H by CH_3 at C2 causes a very modest 1.5–2-fold rate enhancement (compare **15b** with **15g** and **15e** with **15f**, Table 5) even though the intramolecular regioselectivity is strong, favoring formation of the more highly substituted, more stable (82) enol intermediate. The small rate increases are likely due to a combination of opposing effects: some relief of torsional strain due to elongation of the C2—C3 bond and concomitant flattening at both termini; development of some enol character at the transition state; but both factors countered by steric inhibition of solvation. Computationally, alkylation at C2 delivers much larger rate enhancements (see Table 12), but these values are calculated for the gas phase where stabilization of a nearby positive charge by polarizable groups is an important factor, generally masked in solution.

A few calculated transition-state bond lengths are also given in Table 12 along with the differences between these lengths and those in the reactant ketone. As expected, the C2—C3 bond is considerably lengthened, while C1—C2 and C1—CO are somewhat shortened and lengthened, respectively, upon reaching the transition state. A trend can be discerned, especially for the five compounds not substituted at C2. The more reactive the ketone the less change in C2—C3 and C1—C2 lengths has occurred between the reactant and transition states — a Hammond effect. The C1—O lengthening was almost constant through the series except for the 2,2-dichloro compound, **14a**. All its bond length changes are smaller than for the other entries.

One of the cyclobutanones, 3-methyl-3-phenylcyclobutanone (**15a**), was examined in aqueous $HClO_4$ solutions. An initial ring-opening isomerization to (*E*)-4-phenylpent-3-en-2-one is overlapped in time by a retroaldol reaction leading to acetophenone and acetone: see eq. [12] and Table 6.

Taking the ring-opening reaction to have an A1 mechanism, we wished to establish the remainder of the pathway: hydration of the double bond and the final cleavage step. The hydration–dehydration equilibrium connecting enones with ketols can, in general, proceed by either of two paths: via the enol of the ketol, or by the standard carbocation mechanism. Noyce et al. (117) have shown that β-aryl-β-hydroxyketones, without sufficiently good donors at the β-carbon, use the enol mechanism. Acid-catalyzed, rate-determining enolization is followed by dehydration to the enone. With good donors at C_β, however, the mechanism passes through a carbocation at the β-carbon. The distinction is easily tested by determining the effects on the dehydration reaction rate caused by β-aryl substituents. Dehydration via the enol shows almost no substituent effect, nor does directly studied enolization. The carbocation mechanism is expected to have a large substituent effect as does the dehydration of 1-arylethanols. The relevant comparisons are found in Table 7 where it is seen that compound **18**, the ketol derived from enone **16a**, undergoes dehydration 11–12 times slower than its *p*-methyl analogue; this establishes the carbocation mechanism.

It is still possible to argue that enolization is involved for this conversion, but that enol formation is not rate determining. We argue, however, that the enol is not a competent intermediate because its rate of formation would be too

© 1999 NRC Canada

Table 13. Comparison of the nucleofugalities of some O-, S-, and C-centered leaving groups, 25°C. Solvent is H_2O unless otherwise indicated.

Reactant	Leaving group	Approximate pK_{BH}^+ of reactant[a]	k (M^{-1} s^{-1}) or relative k
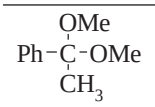	CH_3OH	–3	1.6×10^3[b]
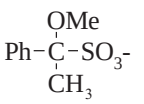	HSO_3^-	–1.2	0.15[c]
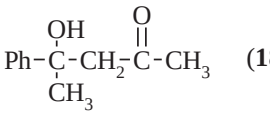 (**18**)	$H_2C{=}C(CH_3)OH$	–3.06[d], –5.37[e]	3.1×10^{-7}[f]
XanOH (**1**)	OH_2	–3	1.7×10^3[f]
XanSMe (**2**)	CH_3SH	–7	0.45[f]
$XanCH_2$-$COCH_3$	$H_2C{=}C(CH_3)OH$	–3.06[d], –5.37[e]	1.6×10^{-8}[f]
TrOH	OH_2	–3	1.5×10^5[g]
TrSMe (**3**)	CH_3SH	–7	~6.6[f]
$TrCH_2NO_2$ (**11a**)	$CH_2{=}NO_2H$	–12	7.5×10^{-10}[h]
$PhSO_2\bar{C}HCH_2OPh$	PhO^-	10[j]	1[i]
$PhSO_2\bar{C}HCH_2SPh$	PhS^-	7.8[j]	0.06[i]
$PhSO_2\bar{C}HCH_2C(CH_3)_2NO_2$	$(CH_3)_2CNO_2^-$	7.7[j]	1.2×10^{-8}[i]

[a]Reference 129.
[b]Reference 130.
[c]Reference 131.
[d]Reference 61.
[e]Reference 62.
[f]This work.
[g]Calculated from data in refs. 51 and 52.
[h]Reference 37.
[i]Relative rates taken from ref. 132. The solvent is ethanol.
[j]The quoted pK_{BH}^+ refers to the leaving group in these cases.

slow to account for the dehydration rate. Acid-catalyzed enolization rates are remarkably insensitive to structure (82); it is unlikely that the second-order enolization rate constant for **18** is larger than 2.5×10^{-5} M^{-1} s^{-1} (118). Additionally, the dependence of the rate of enolization upon the acidity of the medium is not great, and has been carefully investigated (83).[7] A representative example of eq. [19] quantified for acid-catalyzed enolization is log (k_{exp} (s^{-1})/[H^+]) = $0.1X$ – 4.6. With this equation, we can estimate the experimental rate constants for enolization of **18** in the $HClO_4$–H_2O media used by us for the dehydration reaction, 7.39–8.89 M $HClO_4$. Enolization is estimated to be ca. 5–40 times *slower* than the observed dehydration rates. It remains possible that at lower acidities enolization could become competitive.

Scheme 5 shows the complete mechanism for eq. [12] proposed by us. Starting from the cyclobutanone ring-opening, isomerization to the enone is the slower of the two observable stages. The retroaldol reaction then occurs, passing through the ketol. The ketol reverts to the enone faster than the retroaldol reaction, hence the rate-determining step for the latter is the C-C cleavage producing acetophenone and acetone enol. In Scheme 4, boxes enclose observable entities.

Some uncertainty remains regarding the precise state of the enone in our reaction media: how much of it is in the protonated state? In 4.30 M $HClO_4$, the UV spectrum shows λ_{max} at 283 nm. In 8.05 M $HClO_4$, this maximum shifts to 347 nm with a shoulder visible near 280 nm. We did not determine the pK_a of **16a**-H^+. Since plots of the retroaldol kinetic data using eq. [19*a*] were accurately linear over the entire acidity range used by us, we conclude that substrate protonation is a minor perturbation.

Structure and reactivity: the electrofuge

The stability of the departing electrofuge has a huge effect on the rates of C-C heterolyses; a few examples make the point clearly. As mentioned in the Introduction, neither triphenylmethylacetone nor derived alcohols cleave even in hot 100% H_2SO_4, yet the corresponding xanthyl compounds do (16, 17), see eq. [5] and [6]. Xan^+ is ca. 10^6 more stable than Ph_3C^+ in K_{R+} units. As expected, (7-tropyl)acetone (**4**) is even more reactive than (9-xanthyl)acetone (**6**), see Table 4. A second comparison involves nitroalkanes. Acid-catalyzed deprotonation at the C-N carbon is not observed, but unimolecular loss of tropylium cation from protonated (7-tropyl)nitroalkanes (**11**) is relatively facile, see Table 8.

© 1999 NRC Canada

Table 14. Comparison of fragmentation rate constants and substrate basicities for xanthyl compounds **1**, **2**, and **6**–**9** in H^+–H_2O at 25°C. See eq. [29].

Substrate	pK_{SH^+} of compound	log k_{frag} (s^{-1})[a]
1, XanOH	–3[b]	6.2
2, XanSMe	–7[b]	6.5
6, $XanCH_2COCH_3$	–3.06[c]	–4.7
7, $XanCH_2COPh$	–3.46[c]	–3.0
8, $XanCH_2COAr$[d]	–5.0[e]	–1.4
9, $XanCH_2C(CH_3)_2OH_2$	–12.5[f]	8.7

[a]Calculated as $k_{frag} = k_f°/K_{eq}$, where rate controlling fragmentation is assumed to follow equilibrium protonation of substrate (K_{eq}), except for **9**, where $K_{eq} = 1/K_{R+}$. See Table 4.

[b]Estimated using data from ref. 129.

[c]Reference 61. These are K_{BH+} values for the keto forms of the leaving groups.

[d]Ar = *p*-nitrophenyl.

[e]Reference 62. This is the K_{BH+} value for the keto form of the leaving group.

[f]Calculated from $pK_{R+} = -16.4$ for *tert*-butyl alcohol (ref. 64*a*) and log $K_{eq} = 3.9$ for the isobutylene – *tert*-butyl alcohol equilibrium: ref. 133.

Tr^+ is a more stable electrofuge than H^+ as shown by the reaction $H^+ + TrOH \rightarrow H_2O + Tr^+$, $K_{eq} = 10^{4.7}$ (51).

Less dramatic, but still large effects can be caused by tuning the stability of the carbocationic electrofuge within a series. The relative rates of cleavage of cyclobutanones **15c**, **d**, and **g** are correlated with a $\rho(\sigma^+)$ value of –5.5. Replacement at C3 of H by CH_3 or Ph produces accelerations of 180-fold and 1500-fold, respectively. The pair of 2-arylnitrocyclopropanes, **12** and **13** show that a *p*-methoxy group on the aryl ring brings about a rate enhancement greater than 2000-fold (Table 9). Other examples from cyclobutanone chemistry are found in references 110–115.

Structure and reactivity: carbon-centered nucleofuges are relatively poor

Data in Table 13 show that in general *O*-centered nucleofuges are better than *S*-centered ones, which are much better than *C*-centered nucleofuges. The entries in Table 13 are arranged in four groups; within each group the electrofuge is held constant. The basicity of the reactant is another variable that affects nucleofugality for acid-catalyzed reactions, but the effect is complex. The substrate must be protonated in order for the leaving group to depart, and this thermodynamic barrier adds to the total free energy of activation. However, the less basic the leaving group is, the greater should be its ability to leave, once protonated, other factors being equal. This reduced kinetic barrier will attenuate the thermodynamic disadvantage.

Among the first three groups in Table 13, all acid-catalyzed reactions, only in the comparison between XanOH and XanSMe does the basicity ratio, perhaps 10^4, approach or match the rate constant ratio. But if CH_3SH were a better nucleofuge than H_2O (owing to its diminished basicity), then the observed rate constant ratio favoring XanOH would be much smaller than it is. We conclude that, in this case, as in the other groups, the sulfur-centered nucleofuge is poorer than the oxygen-centered one. Further examples in support of this conclusion are given by Jensen and Jencks (79). As for the C-centered nucleophiles, it is clear from the entries that poor basicity cannot explain the greatly reduced rate constants. The final set, a group of unimolecular fragmentations, makes the same case unencumbered by the necessity to consider protonation.

Another comparison can be made using unimolecular fragmentation rate constants (calculated as described in Table 4, footnote *b*) and normalizing for substrate basicity. The process considered here is eq. [29], and the form of the comparison is a linear free energy relationship between log k_{frag} (s^{-1}) and $pK_a(SH^+)$. The data for this comparison are collected in Table 14. Although the examples are few, the data for the carbon-centered nucleofuges (compounds **6**–**9**) produce the linear correlation shown below eq. [29]. The points for the *O*-centered and *S*-centered leaving groups lie above the correlation line by 10.4 and 5.3 log *k* units, respectively. Uncertainties in the estimation of the pK_a values preclude any but a semiquantitative conclusion, but it is clear that when the basicities of the substrates are normalized, the nucleofugic reactivity order is *O*-centered > *S*-centered > *C*-centered.

[29] $$\text{Xan-XH}^+ \xrightarrow{k_{frag}} \text{Xan}^+ + \text{XH}$$

$$\log k_{frag} = 1.36\, pK_a(SH^+) - 8.30 \qquad r^2 = 0.994$$

Why is C-C heterolysis intrinsically slow? Compared with C-O heterolysis, part of the disadvantage may be thermodynamic. Heats of heterolysis (in sulfolane at 25°C) measured and compiled by Arnett et al. (19*b*–*d*) show that, on average, C-O heterolysis of xanthyl substrates is 8–9 kcal/mol (ca. 6 log units) less endothermic than C-C heterolysis for leaving groups of identical basicity. The thermodynamic influence on the relative rates of C-O heterolysis may therefore be significant, although even if fully expressed at the transition state, it does not account for the observed superiority described above. The same comparison with *S*-centered leaving groups shows *no* thermodynamic advantage favoring C-S over C-C cleavage.

To address the purely kinetic factors, we adopt a simple, but useful, electrostatic point of view. We model the transition states for two processes as structures **20** and **21**. Structure **20** represents heterolysis of a neutral reactant producing carbocation R^+ and nucleofuge X^-. Structure **21** shows heterolysis of a protonated reactant in which B is a basic site and X=BH is the nucleofuge. In the first instance, **20b** will have an importance determined by the electronegativity and polarizability of X. The contribution of **20b** will be stabilizing, just as it is in strengthening a bond against homolysis. The more electronegative is X, the greater the electrostatic stabilization imparted by the contribution of **20b**. This is, of course, the idea used by Pauling (119) in establishing his electronegativity scale. Under acid catalysis, a negligible or poor leaving group can become a better one. Transition state **21** shows that the BH^+ moiety can accelerate heterolysis by increasing the importance of contributor **21b**. In addition, resonance delocalization of negativity into the BH^+ might be possible, shown by **21c**. While this effect can strongly stabi-

$$[\text{R-X} \longleftrightarrow \text{R}^+\text{X}^-]^{\ddagger}$$

20a **20b**

© 1999 NRC Canada

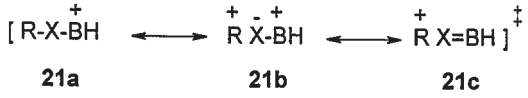

lize the product nuclofuge, X=H, its contribution to the transition state *diminishes* the favorable electrostatic interaction represented by **21b**. As in **20**, when X is carbon rather than oxygen, contributor **21b** will be less important, and compensation by **21c** does not, as just described, fully remedy this deficiency. This sort of argument was first made by Bell (120) in discussing proton transfer at carbon (slow) relative to that at heteroatoms. (Note that Bell's analysis offers one way of viewing the "nitroalkane anomaly" and other examples of "transition state imbalance" (see ref. 121)). The importance of electrostatic stabilization by triple-ion contributors analogous to **21b** has been predicted by computation (122) and inferred from experiment (123) for gas phase S_N2 reactions. It has also recently been confirmed by high level computations of the transition states for identity proton transfer reactions between a variety of first- and second-row nonmetal hydrides and their conjugate bases (124*a*; additional relevant calculations involving proton transfer between carbons are found in Bernasconi et al. (124*b*)).

Structure and reactivity: ring strain and stereoelectronic effects

Previous discussion has demonstrated the very large influence of acid catalysis and the stability of the electrofuge in determining the success or failure of C-C heterolysis. In this section, we address the even greater potential for reactivity made possible by relief of ring strain. First, a qualitative observation: Although 3,3-diphenylcyclobutanone (**15f**) opens at 25°C in TFA with a half life of about 1 min, 3,3-diphenylcyclopentanone remains unchanged in TFA for at least a month. This represents a rate factor of more than 50 000. Next, two quantitative comparisons are given. One is the comparison between 1-(7-tropyl)nitroethane (**11b**) and *trans*-2-phenylnitrocyclopropane (**12**). These two cleave in TFA, each yielding a monoalkylnitronic acid, $RCH{=}NO_2H$, at virtually the same rate despite the enormous difference in stability between the electrofugic moieties. Tropyl cation has pK_{R+} = 4.75 (51, 52), while $PhCHR^+$, modeled by $PHCHCH_3^+$, has $pK_R^+ \cong -15.3$ (125). The ΔpK_R^+ of approximately 20 units corresponds to 27 kcal/mol at room temperature. As noted before (38*a*), this corresponds to the strain energy of a cyclopropane ring. Fractional development of carbocation character at the transition state, a factor favoring cleavage of **11b**, is almost exactly balanced by fractional relief of ring strain! The second example compares the cleavages of (9-xanthyl) acetone (**6**) and 3-methyl-3-phenylcyclobutanone (**15a**), both of which produce an enol, $CH_2{=}C(OH)R$, and a carbocation. They do so at identical rates in H_2O and at rates differing only by a factor of 13 in TFA. The pK_{R+} of xanthyl$^+$ found in this work is –0.85, while that for $PhC(CH_3)R^+$, modeled by $PhC(CH_3)_2^+$, is estimated to be –11.8 using the correlation of Arnett and Hofelich (63). This difference amounts to almost 15 kcal/mol worth of stability in favor of xanthyl$^+$, but which is matched by relief of ring strain.

Both three- and four-membered rings provide huge rate accelerations for C-C cleavage, but the greater effect is seen with opening of cyclopropanes. Many examples of the comparative reactivity of three- and four-membered rings have been documented and discussed (126). Often, the examples are of ring-closure reactions, but since the two rings have almost the same strain energies (107),[10] the ease of closing a three-membered ring (relative to a four-membered ring) corresponds to the same relative ease of opening a three-membered ring.[12]

In the present case, we are dealing with acid-catalyzed reactions, and it is pertinent to ask whether the basicities of the nitrocyclopropane and cyclobutanone compounds are unusual enough to contribute either to the acceleration of the C-C cleavages or to the different acceleration produced by the two differently sized rings. Lacking experimental information on the basicities of nitrocompounds, we have performed semiempirical (AM1) and ab initio calculations of the proton affinities of some nitroalkanes. Compounds **11b** and **12** have, by the AM1 method, proton affinities of 189.5 and 187.1 kcal/mol, respectively. That is, the tropyl compound is the *more* basic. At the HF/6-31G* level (including corrections for zero point vibrational energy and thermal energy), we find proton affinities (298 K) for 2-nitropropane and nitrocyclopropane of 189.5 and 188.8 kcal/mol, respectively. Again, the acyclic example is more basic; that is, increased basicity for the nitrocyclopropanes is not evident and cannot, therefore, contribute to a rate acceleration. Our evidence, in fact, indicates that the protonated nitrocyclopropanes are avoided: protonation is concerted with C-C cleavage, and is accompanied by release of ring strain and an increase in basicity at the NO_2 oxygens (38*a*). All these factors combine to produce a remarkable activating effect. The story is only slightly different for the cyclobutanones. Cyclobutanone itself has an experimental proton affinity of 191.8 kcal/mol; it is 5.9 kcal/mol *less* basic than 2-butanone.[13] By the AM1 method 3-methyl-3-phenylcyclobutanone is *less* basic than (9-xanthyl)acetone by 14.9 kcal/mol. Accelerated C-C cleavage occurs despite a sizeable disadvantage in apparent basicity at the carbonyl oxygen. Again other factors, for example, relief of ring strain, more than compensate.

With regard to the comparison between the ring openings of cyclopropanes and cyclobutanes, computational evidence offers some insights. Gronert et al. (127) have reported high level calculations of nucleophilic ring closures leading to three- and four-membered rings. Cyclization to three-membered rings is characterized by unusually low enthalpies of activation — lower than for the bimolecular S_N2 analogue. Two factors were highlighted. One is that the reactant state is destabilized by a nonbonding 1,3-interaction between the nucleophilic and electrophilic centers, an interaction that has no counterpart in the intermolecular case. It is as though the reactant is already partly activated by this "proximity effect." The second factor is that the transition state comes early in the closure, before bond angle strain (the only major

[12]The homodesmotic reaction, cyclopropane + butane → cyclobutane + propane, has ΔH_{RXN} = –1 kcal/mol (107).
[13]Cited in the NIST standard reference database, http://webbook.nist.gov/chemistry/ (May 1999).

© 1999 NRC Canada

strain element at that point on the reaction coordinate) has increased very much. In terms of a ring-*opening* process, most of the ring strain has vanished at the transition state. Both effects are less important for four-membered than for three-membered rings (127*a*), and less of the ring strain energy is released at the ring-opening transition state.

There is another computational difference between the ring openings of three- and four-membered rings that we wish to note. This difference focuses on the torsional (dihedral) angle containing the breaking C—C bond, the forming C=C bond (cyclobutanone cleavages) or C=N bond (nitrocyclopropane cleavages), and the C=O (or N=O) bond of the electron-withdrawing group (see structures **22** and **23**; the starred atoms define the dihedrals). AM1 calcu-

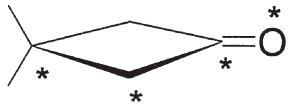

22

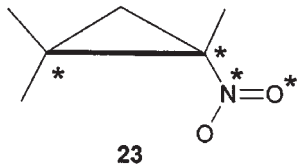

23

lations on 2-phenylnitrocyclopropane (**12)** and cyclobutanones **15a** and **15g** show that the three-membered ring undergoes but a 7.5° change in this angle as the opening proceeds from reactant to protonated transition state. Moreover, the torsion occurs about an *exo*cyclic bond. The four-membered rings however must twist approximately 35° about an *endo*cyclic bond to reach the transition state. We propose that torsional stress, a costly condition in a small, relatively rigid ring, contributes significantly to the activation barrier for opening the four-membered rings, but much less for the three-membered rings. That is, we invoke the principle of least nuclear motion (128).

Conclusions

Acid-catalyzed C-C cleavages, eqs. [1] and [2], can be made conveniently fast by varying a number of structural and environmental factors. These include:

(*i*) The acidity of the medium. Enormous variation is possible, especially when nonleveling solvents are used.

(*ii*) The basicity of the nucleofuge, X, and the nucleofugality of its conjugate acid, XH, or C=C-XH. These two influences can oppose each other; the more basic is X, the less nucleofugic tends to be XH. Even substrates so weakly basic as alkenes and nitroalkanes can be induced to fragment if other factors are made favorable.

(*iii*) The stability of the electrofuge. Sufficient stability on the part of the carbocation moiety can change a failed reaction into a successful one.

(*iv*) Relief of strain. Strain release associated with opening small rings can produce spectacular rate increases. Appropriately substituted cyclopropanes can be made particularly reactive, undergoing C-C cleavage in concert with a protonation event. The cleavage of cyclobutanones, themselves easily prepared, is useful for the preparation of conjugated enones.

Additionally, we advocate the use of trifluoroacetic acid, neat or diluted with a nonbasic solvent, for the investigation of mechanistic detail through determination of solvent kinetic isotope effects on acid-catalyzed reactions. The isotope effect caused by the transferred hydrogen is uncontaminated by the inverse secondary effects which occur when H_3O^+ and D_3O^+ are used.

Acknowledgements

We are pleased to acknowledge Dr. Robert G. Bergstrom and Professor Claude Bernasconi for help with the use of the temperature-jump equipment at University of California, Santa Cruz. We also thank Professor Scott Gronert of San Francisco State University for valuable discussions. We are grateful for financial support from the NSF (no. CHE-9729001), and The Petroleum Research Fund, administered by the American Chemical Society. This research was partially supported by a Research Infrastructure in Minority Institutions award from the National Center for Research Resources with funding from the Office of Research on Minority Health, National Institutes of Health no. 5 P20RR11805.

References

1. W.S. Johnson. Acc. Chem. Res. **1**, 1 (1968).
2. H.W. Whitlock, Jr., and A.H. Olson. J. Am. Chem. Soc. **92**, 5383 (1970).
3. R. Huisgen. Acc. Chem. Res. **10**, 117, 199 (1977); **10**, 199 (1977).
4. P.G. Gassman and D.B. Gorman. J. Am. Chem. Soc. **112**, 8624 (1990), and refs. therein.
5. B. Jarstfer, B.S.J. Blagg, D.H. Rogers, and C.D. Poulter. J. Am. Chem. Soc. **118**, 13 089 (1996).
6. E.J. Corey, S.C. Virgil, H. Cheng, C.H. Baker, S.P.T. Matsuda, V. Singh, and S. Sarshar. J. Am. Chem. Soc. **117**, 11 819 (1995), and refs. therein.
7. A.P. Marchand. Aldrichim. Acta, **28**, 95 (1995).
8. S.A. Godleski, P.V.R. Schleyer, E. Osawa, and W.T. Wipke. Prog. Phys. Org. Chem. **13**, 63 (1981).
9. F.C. Whitmore. J. Am. Chem. Soc. **54**, 3274 (1932); F.C. Whitmore and E.E. Stahly. J. Am. Chem. Soc. **55**, 4153 (1933); J. Am. Chem. Soc. **67**, 2158 (1945).
10. V.J. Shiner, Jr., and G.F. Meier. J. Org. Chem. **31**, 137 (1966).
11. (*a*) C.A. Grob and P.W. Schiess. Angew. Chem. Int. Ed. Eng. **6**, 1 (1967), and refs. to earlier work by Grob; (*b*) K.B. Becker and C.A. Grob. *In* Chemistry of functional groups. Suppl. A. Part 2. *Edited by* S. Patai. John Wiley and Sons, London. 1976.
12. A.N. Nesmeyanov. Proc. Moscow Univ. **132**, 5 (1950); cited and quoted by V.I. Maksimov. Tetrahedron, **21**, 687 (1965).
13. E.W. Colvin. Silicon in organic synthesis. Butterworths, London. 1981.
14. M. Pereyre, J.-P. Quintard, and A. Rahm. Tin in organic synthesis. Butterworths, London. 1987.
15. K. Conrow. J. Am. Chem. Soc. **81**, 5461 (1959).
16. R. Fosse. Bull. Soc. Chim. Fr. **35**, 1005 (1906).
17. N.C. Deno and E. Sacher. J. Am. Chem. Soc. **87**, 5120 (1965).
18. N.C. Deno, J.J. Jaruzelski, and A. Schriesheim. J. Am. Chem. Soc. **77**, 3044 (1955).

© 1999 NRC Canada

19. (*a*) E.M. Arnett, B. Chawla, K. Molter, K. Amarnath, and M. Healy. J. Am. Chem. Soc. **107**, 5288 (1985); (*b*) E.M. Arnett, B. Chawla, K. Amarnath, and L.G. Whitesell, Jr. Energy Fuels, **1**, 17 (1987); (*c*) E.M. Arnett, K. Amarnath, N.G. Harvey, and J.-P. Cheng. J. Am. Chem. Soc. **112**, 344 (1990); (*d*) E.M. Arnett, L.G. Whiteswell, Jr., K. Amarnath, J.-P. Cheng, and E. Marchot. Makromol. Chem. Macromol. Symp. **13**/**14**, 21 (1988).
20. (*a*) K. Komatsu, A. Aonuma, K. Takeuchi, and K. Okamoto. J. Org. Chem. **54**, 2039 (1989), and refs. therein; (*b*) S. Nakamura, S. Yamago, S. Ejiri, A.E. Dorigo, and K. Morokuma. J. Am. Chem. Soc. **113**, 3183 (1991).
21. Toronto Int. Conf. Org. React. Intermed., Toronto, July 30–August 1, 1992; 22nd Ont.–Que. Phys. Org. Minisymp., Toronto, November 11–13, 1994.
22. T.L. Wadsworth. M.S. thesis. San Francisco State University, San Francisco. 1981; R.H. Grow. M.S. thesis. San Francisco State University, San Francisco. 1986; M.B. Trudell. M.S. thesis. San Francisco State University, San Francisco. 1988.
23. A.F. Holleman. Org. Synth. **1**, 554 (1941).
24. I.D. Reingold, H.A. Trujillo, and B.E. Kahr. J. Org. Chem. **51**, 1627 (1986).
25. R. Fosse. Bull. Soc. Chim. Fr. **35**, 1005 (1906).
26. J. Asunskis and H. Schecter. J. Org. Chem. **33**, 1164 (1968).
27. I. Erden. Tetrahedron Lett. **25**, 1535 (1984).
28. L.R. Krepski and A. Hassner. J. Org. Chem. **43**, 2879 (1978).
29. D.A. Bak and W.T. Brady. J. Org. Chem. **44**, 107 (1979).
30. L.J. Hughes. Chem. Abstr. **67**, 53893h, (1967); U.S. Patent 3,322,831 (1967).
31. C.L. Areus and T.J. Howard. J. Chem. Soc. 670 (1961).
32. T.J. Leitereg and D.J. Cram. J. Am. Chem. Soc. **90**, 4019 (1968).
33. K. Okamoto, K. Komatsu, M. Fujiori, and S. Yasuda. Bull. Chem. Soc. Jpn. **47**, 2431 (1974).
34. H.J. Dauben, Jr. J. Am. Chem. Soc. **79**, 4557 (1957).
35. A.E. Greene and J.-P. Deprés. J. Am. Chem. Soc. **101**, 4003 (1979).
36. C.F. Bernasconi. Relaxation kinetics. Academic Press, New York. 1976, p. 180; (*b*) *In* Techniques of chemistry. Vol. 6. Part 1. 4th ed. *Edited by* C.F. Bernasconi. Wiley–Interscience, New York. 1986. Chap. 6.
37. I. Erden, J.R. Keeffe, F.-P. Xu, and J.-B. Zheng. J. Am. Chem. Soc. **115**, 9834 (1993).
38. (*a*) W. Cao, I. Erden, and J.R. Keeffe. Angew. Chem. Int. Ed. Engl. **34**, 1091 (1995); (*b*) W.P. Jencks. J. Am. Chem. Soc. **94**, 4731 (1972); see also W.P. Jencks. Chem. Rev. **72**, 705 (1972).
39. W.M. Schubert and J. R. Keeffe. J. Am. Chem. Soc. **94**, 559 (1972).
40. M.J.S. Dewar, E.G. Zoebisch, E.F. Healy, and J.J.P. Stewart. J. Am. Chem. Soc. **107**, 3902 (1985).
41. J.P. Stewart. J. Comput. Chem. **10**, 221 (1989).
42. N.C. Deno and W.L. Evans. J. Am. Chem. Soc. **79**, 5804 (1957).
43. N.C. Deno, H.F. Berkheimer, W.L. Evans, and H.J. Peterson. J. Am. Chem. Soc. **81**, 2344 (1959).
44. R.A. Cox and K. Yates. J. Am. Chem. Soc. **100**, 3861 (1978); see also V. Lucchini, G. Modena, G. Scorrano, R.A. Cox, and K. Yates. J. Am. Chem. Soc. **104**, 1958 (1982).
45. R.A. Cox and K. Yates. Can. J. Chem. **59**, 2116 (1981).
46. A.J. Kresge, H.J. Chen, G.L. Capen, and M.F. Powell. Can. J. Chem. **61**, 249 (1983).
47. W.F. Giauque, E.W. Hornung, J.E. Kunzler, and T.R. Rubin. J. Am. Chem. Soc. **82**, 62 (1960); (*b*) J.F. Bunnett. J. Am. Chem. Soc. **83**, 4956 (1961).
48. C.A. Bunton and S.K. Huang. J. Am. Chem. Soc. **94**, 3536 (1972).
49. E.O. Alonso, L.J. Johnston, J.C. Scaiano, and V.G. Toscano. J. Am. Chem. Soc. **112**, 1270 (1990).
50. S. Winstein and G.C. Robinson. J. Am. Chem. Soc. **80**, 169 (1958).
51. W.v.E. Doering and L.H. Knox. J. Am. Chem. Soc. **76**, 3203 (1954).
52. C.D. Ritchie and H. Fleischauer. J. Am. Chem. Soc. **94**, 3481 (1972).
53. R.A. Cox and K. Yates. Can. J. Chem. **57**, 2944 (1979).
54. (*a*) A.J. Kresge, R.A. More O'Ferrall, L.E. Hakka, and V.P. Vitullo. J. Chem. Soc. Chem. Comm. 46 (1965); (*b*) A.J. Kresge, S.G. Mylonakis, Y. Sato, and V.P. Vitullo. J. Am. Chem. Soc. **93**, 6181 (1971).
55. A.J. Kresge, S.G. Mylonakis, and L.E. Hakka. J. Am. Chem. Soc. **94**, 4197 (1972).
56. R.A. McClelland, N. Banait, and S. Steenken. J. Am. Chem. Soc. **111**, 2929 (1989).
57. R.A. Diffenbach, K. Sano, and R.W. Taft. J. Am. Chem. Soc. **88**, 4747 (1966).
58. R.A. McClelland, V.M. Kanagasabapathy, N.S. Banoit, and S. Steenken. J. Am. Chem. Soc. **111**, 3966 1989); (*b*) J. Am. Chem. Soc. **113**, 1009 (1991).
59. C.D. Ritchie and J. Gandler. J. Am. Chem. Soc. **101**, 7318 (1979).
60. R.W. Taft. *In* Steric effects in organic chemistry. *Edited by* M.S. Newman. Wiley, New York. 1956. Chap. 13.
61. A. Bagno, G. Scorrano, and R.A. More O'Ferrell. Rev. Chem. Int. **7**, 313 (1987).
62. R.A. Cox, C.R. Smith, and K. Yates. Can. J. Chem. **57**, 2952 (1979).
63. E.M. Arnett and T.C. Hofelich. J. Am. Chem. Soc. **105**, 2889 (1983).
64. (*a*) M.M. Toteva and J.P. Richard. J. Am. Chem. Soc. **118**, 11 434 (1996); (*b*) Y. Chiang, W.K. Chwang, A.J. Kresge, M.F. Powell, and S. Szilagyi. J. Org. Chem. **49**, 5218 (1984).
65. P. Doyle, R.H.B. Galt, and R.J. Pearce. Tetrahedron Lett. 2903 (1973).
66. A.J. Kresge. *In* Proton transfer reactions. *Edited by* E.F. Caldin and V. Gold. Chapman and Hall, London. 1975. Chap. 7.
67. J.P. Richard and W.P. Jencks. J. Am. Chem. Soc. **106**, 1373 (1984).
68. C.D. Ritchie, D.J. Wright, D.-S. Huang, and A.A. Kamego. J. Am. Chem. Soc. **97**, 1163 (1975).
69. J.R. Gandler. J. Am. Chem. Soc. **107**, 8218 (1985).
70. S. Wolfe, Z. Shi, K. Yang, S. Ro, N. Weinberg, and C.-K. Kim. Can. J. Chem. **76**, 114 (1998).
71. C.D. Ritchie. J. Am. Chem. Soc. **94**, 3275 (1972).
72. A.J. Kresge and R.J. Preto. J. Am. Chem. Soc. **87**, 4593 (1965).
73. T.H. Fife. Acc. Chem. Res. **5**, 264 (1972), and refs. therein.
74. J.L. Jensen and K.S. Yamaguchi. J. Org. Chem. **49**, 2613 (1984).
75. S.P. Ewing, D. Lockshon, and W.P. Jencks. J. Am. Chem. Soc. **102**, 3072 (1980).
76. C.G. Swain, D.A. Kuhn, and R.L. Schowen. J. Am. Chem. Soc. **87**, 1553 (1965); R. Eliason and M.M. Kreevoy. J. Am. Chem. Soc. **100**, 7037 (1978).
77. M.M. Kreevoy and T.M. Liang. J. Am. Chem. Soc. **102**, 3315 (1980).
78. S.R. Wann and M.M. Kreevoy. J. Org. Chem. **46**, 419 (1981).
79. J.L. Jensen and W.P. Jencks. J. Am. Chem. Soc. **101**, 1476 (1979).
80. T.H. Fife and T.J. Przystas. J. Am. Chem. Soc. **102**, 292 (1980).
81. G. Perdoncin and G. Scorrano. J. Am. Chem. Soc. **99**, 6983 (1977).

© 1999 NRC Canada

82. J.R. Keeffe and A.J. Kresge. *In* The chemistry of enols. *Edited by* Z. Rappoport. J. Wiley and Sons, Chichester. 1990. Chap. 7.
83. (*a*) Y. Chiang, A.J. Kresge, R.A. More O'Ferrall, B.A. Murray, and J. Wirz. Can. J. Chem. **68**, 1653 (1990); (*b*) L. Zucker and L.P. Hammett. J. Am. Chem. Soc. **61**, 2791 (1939).
84. C.M. Brennan, I. Hunt, T.C. Jarvis, C.D. Johnson, and P.D. McDonnell. Can. J. Chem. **68**, 1780 (1990).
85. G.P. Nilles and R.D. Schuetz. J. Chem. Educ. **50**, 267 (1973).
86. K.B. Wiberg. *In* Investigation of rates and mechanisms of reactions. 4th ed. Part 1. *Edited by* C.F. Bernasconi. Wiley–Interscience, New York. 1986. Chap. 16.
87. V.A. Spizer, T.W. Toone, and R. Stewart. Can. J. Chem. **54**, 440 (1976).
88. (*a*) A.D. Allen and T.T. Tidwell. J. Am. Chem. Soc. **104**, 3145 (1982); (*b*) A.D. Allen, M. Rosenbaum, N.O.L. Seto, and T.T. Tidwell. J. Org. Chem. **47**, 4234 (1982).
89. A. Hantzsch. Z. Phys. Chem. **61**, 257 (1907).
90. R.J. Gillespie and C. Solomons. J. Chem. Soc. 1796 (1957).
91. E.M. Arnett. Prog. Phys. Org. Chem. **1**, 223 (1963).
92. D. Turnbull and S.H. Maron. J. Am. Chem. Soc. **65**, 212 (1943).
93. S.L. Johnson and D.L. Morrison. J. Am. Chem. Soc. **94**, 1323 (1972).
94. A. Fischer, J. Packer, and J. Vaughan. J. Chem. Soc. 3318 (1962).
95. D.S. Kabakoff and E. Namanworth. J. Am. Chem. Soc. **92**, 3234 (1970).
96. E. Anderson and T.H. Fife. J. Org. Chem. **37**, 1993 (1972).
97. (*a*) G. Dallinga and G. TerMaten. Rec. Trav. Chim. **79**, 737 (1960); (*b*) S. Saito, S. Saito, T. Ohwada, and K. Shudo. Chem. Pharm. Bull. **39**, 2718 (1991).
98. C.U. Pittman, Jr., and S.P. McManus. J. Am. Chem. Soc. **91**, 5915 (1969).
99. T. Nakai, E. Wada, and M. Okawara. Tetrahedron Lett. 1531 (1975).
100. E.P. Kohler and J.B. Conant. J. Am. Chem. Soc. **39**, 1404 (1917).
101. N.C. Deno, W.E. Billups, D. LaVietes, P.C. Scholl, and S. Schneider. J. Am. Chem. Soc. **92**, 3700 (1970).
102. A. de Meijere. Angew. Chem. Int. Ed. Engl. **18**, 809 (1979).
103. B. Trost. Top. Curr. Chem. **133**, 3 (1986).
104. H.N.C. Wong, K.-L. Lau, and K.-F. Tam. Top. Curr. Chem. **133**, 83 (1986).
105. E. Lee-Ruff. *In* Advances in strain in organic chemistry. Vol. 1. *Edited by* B. Halton. JAI Press, Ltd., London. 1991. Chap. 5.
106. J. Rocek and A.E. Radkowsky. J. Am. Chem. Soc. **95**, 7123 (1973).
107. G. Bouchoux and R. Houriet. Tetrahedron Lett. **25**, 5755 (1984); J.B. Pedley, R.D. Naylor, and S.P. Kirby. Thermochemical data of organic compounds. 2nd ed. Chapman and Hall, London. 1986; K.B. Wiberg. Angew. Chem. Int. Ed. Engl. **25**, 312 (1986).
108. W.F. Erman, R.S. Treptow, P. Bakuzis, and E. Wenkert. J. Am. Chem. Soc. **93**, 657 (1971).
109. (*a*) F. Bourelle-Wargnier. Tetrahedron Lett. 1589 (1974); (*b*) F. Bourelle-Wargnier and R. Jeanne-Carlier. Tetrahedron, **32**, 2725 (1976).
110. R. Huisgen and L.A. Feiler. Chem. Ber. **102**, 3391 (1969).
111. I. Erden. Int. Chem. Congr. Pac. Basin Soc. Honolulu, Dec. 19, 1989.
112. R. Huisgen and P. Koppitz. Chem. Ztg. **98**, 461 (1974).
113. V.P. Abegg, A.C. Hopkinson, and E. Lee-Ruff. Can. J. Chem. **56**, 99 (1978).
114. K.E. Hine and R.F. Childs. Can. J. Chem. **54**, 12 (1976).
115. (*a*) R. Huisgen, L.A. Feiler, and P. Cho. Chem. Ber. **102**, 3405 (1969); (*b*) L.A. Feiler and R. Huisgen. Chem. Ber. **102**, 3428 (1969); see also R.H. Hasek and J.C. Martin. J. Org. Chem. **26**, 4775 (1961).
116. K.B. Wiberg, D. Shobe, and G.L. Nelson. J. Am. Chem. Soc. **115**, 10 645 (1993).
117. (*a*) D.S. Noyce and W.L. Reed. J. Am. Chem. Soc. **80**, 5539 (1958); (*b*) D.S. Noyce, W.A. Pryor, and P.A. King. J. Am. Chem. Soc. **81**, 5423 (1959); (*c*) D.S. Noyce and W.L. Reed. J. Am. Chem. Soc. **81**, 624 (1959); (*d*) D.S. Noyce and M.J. Jorgenson. J. Org. Chem. **28**, 3208 (1963).
118. J.R. Keeffe, A.J. Kresge, and N.P. Schepp. J. Am. Chem. Soc. **112**, 4862 (1990).
119. L. Pauling. The nature of the chemical bond. 2nd ed. Cornell University Press, Ithaca. 1940. pp. 58–69.
120. R.P. Bell. The proton in chemistry. Cornell University Press, Ithaca. 1959. pp. 172–174.
121. C.F. Bernasconi. Adv. Phys. Org. Chem. **27**, 116 (1992).
122. (*a*) A. Dedieu and A. Veillard. J. Am. Chem. Soc. **94**, 6730 (1972); (*b*) R.F.W. Bader, A. Duke, and R.R. Messer. J. Am. Chem. Soc. **95**, 7715 (1973).
123. (*a*) M.L. Chabinyc, S.L. Craig, C.K. Regan, and J.I. Brauman. Science (Washington, D.C.) **279**, 1882 (1998); (*b*) M.J. Pellerite and J.I. Brauman. J. Am. Chem. Soc. **105**, 2672 (1983).
124. (*a*) S. Gronert. J. Am. Chem. Soc. **115**, 10 258 (1993); (*b*) C.F. Bernasconi, P.J. Wenzel, J.R. Keeffe, and S. Gronert. J. Am. Chem. Soc. **119**, 4008 (1997).
125. J.P. Richard, M.E. Rothenberg, and W.P. Jencks. J. Am. Chem. Soc. **106**, 1361 (1984).
126. C.J.M. Stirling. Tetrahedron report no. 183. Tetrahedron, **41**, 1613 (1985).
127. (*a*) S. Gronert and J.M. Lee. J. Org. Chem. **60**, 6731 (1995); (*b*) S. Gronert, K. Azizian, and M.A. Friedman. J. Am. Chem. Soc. **120**, 3220 (1998).
128. J.A. Altman, O.S. Tee, and K. Yates. J. Am. Chem. Soc. **98**, 7133 (1976), and refs. therein.
129. A. Streitwieser, C.H. Heathcock, and E.M. Kosower. Introduction to organic chemistry. 4th ed. Macmillan, New York. 1992. App. 4.
130. P.R. Young and W.P. Jencks. J. Am. Chem. Soc. **99**, 8238 (1977).
131. P.R. Young and W.P. Jencks. J. Am. Chem. Soc. **100**, 1228 (1978).
132. C.J. Stirling. Acc. Chem. Res. **12**, 198 (1977).
133. W.F. Eberz and H.J. Lucas. J. Am. Chem. Soc. **56**, 1230 (1934).

© 1999 NRC Canada

Formation of a cyclic tetrahedral intermediate by the addition of water to 2-methyl-4H-3,1-benzoxazine followed by ring opening to 2-aminobenzyl acetate and 2-acetylaminobenzyl alcohol; pH-dependence of rate of reaction and product ratio

Wendy J. Dixon and Frank Hibbert

Abstract: Kinetic studies have shown that addition of water to protonated 2-methyl-4H-3,1-benzoxazine occurs to give a cyclic tetrahedral carbonyl addition intermediate. At pH <5, the intermediate is protonated and reacts to 2-aminobenzyl acetate, whereas at pH >7.5, the unprotonated intermediate collapses to give 2-acetylaminobenzyl alcohol. The former reaction is catalysed by buffer base but the latter is uncatalysed. At pH 9–12, reaction of hydroxide ion with protonated 2-methyl-4H-3,1-benzoxazine to give 2-acetylaminobenzyl alcohol becomes important, and at pH >12, the same product is formed by reaction of hydroxide ion with unprotonated 2-methyl-4H-3,1-benzoxazine.

Key words: mechanism, addition, tetrahedral intermediate, hydrolysis, pH profile.

Résumé : Des études cinétiques ont montré que l'addition d'eau à la 2-méthyl-4*H*-3,1-benzoxazine protonée se produit pour donner un intermédiaire d'addition au carbonyle de nature tétraédrique et cyclique. À un pH <5, l'intermédiaire est protoné et réagit vers l'acétate du 2-aminobenzyle alors qu'à pH >7,5, l'intermédiaire non protoné se décompose pour donner l'alcool 2-acétylaminobenzylique. La première réaction est catalysée par une base tampon, mais la dernière n'est pas catalysée. À des pH allant de 9–12, la réaction de l'ion hydroxyde avec la 2-méthyl-4*H*-3,1-benzoxazine protonée conduisant à l'alcool 2-acétylaminobenzylique devient important et à un pH >12, le même produit se forme par réaction de l'ion hydroxyde avec 2-méthyl-4*H*-3,1-benzoxazine non protonée.

Mots clés : mécanisme, addition, intermédiaire tétraédrique, hydrolyse, profil de pH.

[Traduit par la Rédaction]

Introduction

In the pH range 1–5, 2-methyl-4H-3,1-benzoxazine undergoes addition of water and ring opening to give 2-aminobenzyl acetate, eq. [1] (1). The form of the rate coefficient – pH profile and the observation of rectilinear plots of rate coefficient against the concentration of buffer base have identified the mechanism shown in Scheme 1. The collapse of the cyclic tetrahedral intermediate to product involves uncatalysed and buffer base (B) catalysed pathways, and the variation of the observed first-order rate coefficient with concentration of buffer base is given by eq. [2]. At low buffer concentrations, buffer base catalysed collapse of the tetrahedral intermediate to 2-aminobenzyl acetate is rate-limiting, but at high buffer concentrations, addition of water to protonated 2-methyl-4H-3,1-benzoxazine becomes rate-limiting. In previous studies, measurements were limited to pH <5, under which conditions reaction occurs to give 2-aminobenzyl acetate in greater than ca. 95% yield. At higher pH values, it was noted (1) that increasing amounts of 2-acetylaminobenzyl alcohol were formed, eq. [3]. It was also found that at fixed pH the proportion of 2-aminobenzyl ace-

[1] 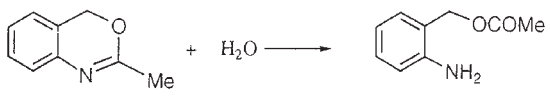

[2] $$k_{obs} = \frac{[H_3O^+]}{K_{SH^+} + [H_3O^+]} \times \frac{k_1(k_2 + k_B[B])}{k_{-1} + k_2 + k_B[B]}$$

[3] 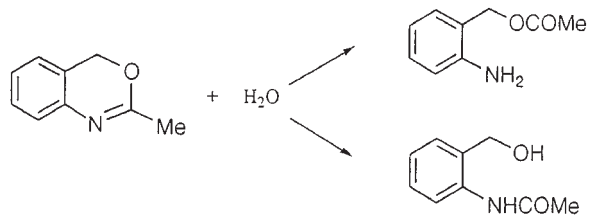

Received November 11, 1998.

This paper is dedicated to Jerry Kresge in recognition of his many achievements in chemistry.

W.J. Dixon and F. Hibbert.[1] Department of Chemistry, King's College London, Strand, London WC2R 2LS, U.K.

[1]Author to whom correspondence may be addressed. Telephone: 44 0171 873 2284. Fax: 44 0171 873 2810. e-mail: frank.hibbert@kcl.ac.uk

© 1999 NRC Canada

Scheme 1.

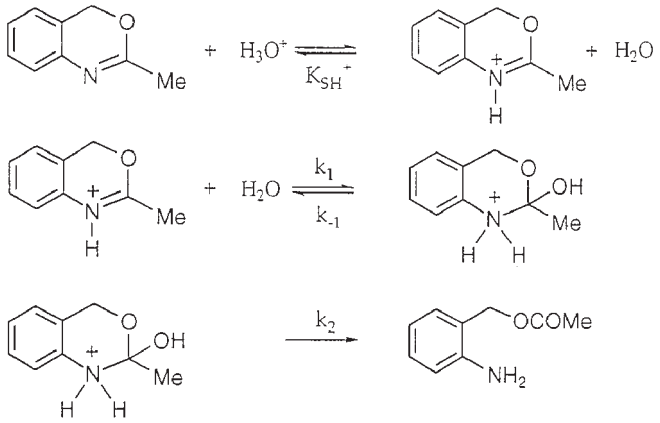

tate formed as product compared with 2-acetylaminobenzyl alcohol increased as the concentration of buffer base was increased, implying that reaction to the amide is less susceptible to buffer catalysis than formation of the ester. We have now investigated the factors influencing the formation of ester and amide and the kinetics of the formation of the amide in detail over the whole of the pH range. The reaction of acyclic imidates is known to give amides and esters depending on the reaction conditions and evidence is available to support the participation of tetrahedral carbonyl addition intermediates (2, 3). The tetrahedral carbonyl addition intermediates involved in the present work are cyclic, and their stability relative to reactants and products compared with that of acyclic intermediates is of particular interest.

Experimental

Materials

The preparations of 2-methyl-4H-3,1-benzoxazine, 2-aminobenzyl acetate, and 2-acetylaminobenzyl alcohol have been described previously (1). Carboxylic acid buffer solutions were made up by partial neutralization of a standardized solution of the carboxylic acid with a standard solution of potassium hydroxide. Buffer solutions of dihydrogen orthophosphate monoanion and monohydrogen orthophosphate dianion were made up by partial neutralization of a solution of potassium dihydrogen orthophosphate with a standard solution of potassium hydroxide. Buffer solutions of tris(hydroxymethyl)aminomethane and 2-amino-2-methyl-1,3-propanediol with the corresponding protonated amine were made up by partial neutralization of a standardized solution of the amine with standard hydrochloric acid solution. The ionic strength of all solutions was maintained at 0.25 mol dm^{-3} by addition of a weighed quantity of potassium chloride. Double distilled water was used for the preparation of solutions. Reactions under various conditions were begun by injecting 0.01 cm^3 of a concentrated solution of 2-methyl-4H-3,1-benzoxazine in Me_2SO into the reaction medium (3 cm^3).

Product analysis

The products of hydrolysis of 2-methyl-4H-3,1-benzoxazine were identified from the changes in UV spectrum accompanying the reaction. In the range pH 1–5, the final

Fig. 1. Reaction of 2-methyl-4H-3,1-benzoxazine to 2-acetylaminobenzyl alcohol and 2-aminobenzylacetate; variation with pH of the percentage of 2-acetylaminobenzyl alcohol.

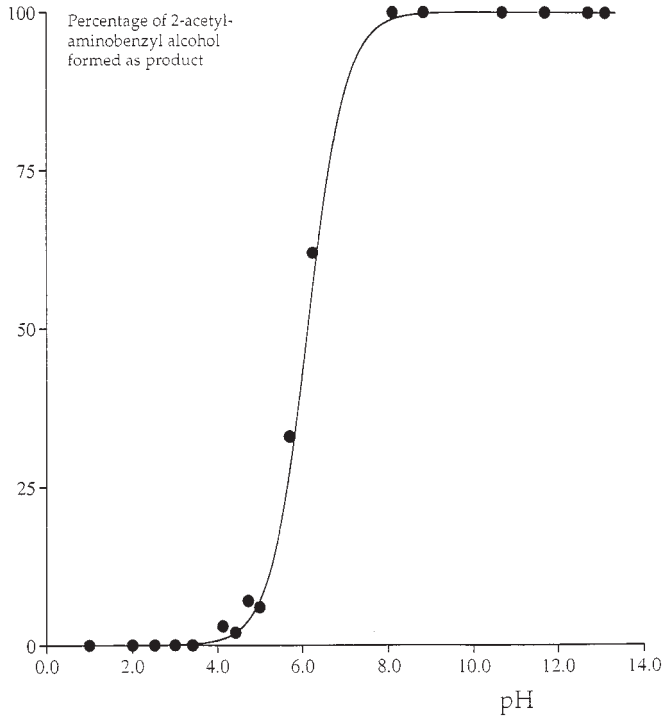

spectrum following reaction was found to be quantitatively identical with the spectrum of an authentic sample of 2-aminobenzyl acetate, and at pH 7.5–13, the spectrum of the product was identical with that of 2-acetylaminobenzyl alcohol. At intermediate pH values of 5–7.5, hydrolysis of 2-methyl-4H-3,1-benzoxazine results in a mixture of 2-aminobenzyl acetate and 2-acetylaminobenzyl alcohol, depending on the pH and buffer concentration. In acetate, pivalate, and phosphate buffers, the exact composition of the product mixture was calculated from the measured absorbance at 284 nm using the known absorbance of 2-aminobenzyl acetate and 2-acetylaminobenzyl alcohol at this wavelength. Results for the variation with pH of the fraction of 2-acetylaminobenzyl alcohol compared with 2-aminobenzyl acetate formed as product are shown in Fig. 1. The results were obtained at a buffer concentration of ca. 0.01 mol dm^{-3} in the basic component of the buffer. The points in Fig. 1 are experimental values, and the solid line is a best fit predicted from the mechanism in Scheme 2 (see below). It was also found that the percentage of 2-aminobenzyl acetate formed increased with buffer base concentration, indicating that reaction to 2-aminobenzyl acetate was more susceptible to catalysis by buffer than reaction to 2-acetylaminobenzyl alcohol. This was confirmed in kinetic studies (see below).

Kinetic measurements

The methods used to study the kinetics of the ring opening of 2-methyl-4H-3,1-benzoxazine to 2-aminobenzyl acetate in the pH range 1–5 have been described previously (1). In the present work, kinetic measurements of the reaction of 2-methyl-4H-3,1-benzoxazine to 2-aminobenzyl acetate and

© 1999 NRC Canada

Scheme 2.

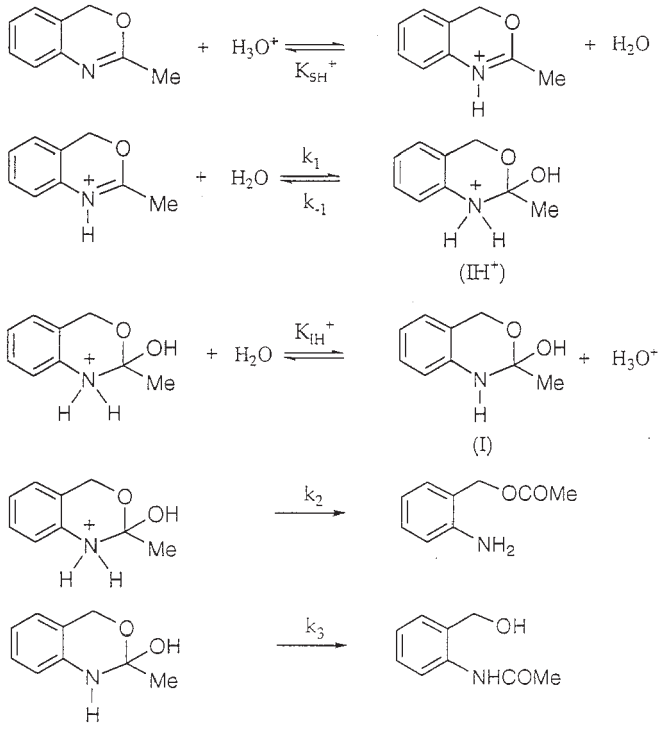

to 2-acetylaminobenzyl alcohol were made at pH values 5–13 at 298.2 K and ionic strength 0.25 mol dm^{-3}. Studies in the range pH 6–9 were made in buffers of orthophosphate monanion and dianion (pK_a 6.52) (4)[2] and of tris(hydroxymethyl)aminomethane (pK_a 8.07) (5)[3] and 2-amino-2-methyl-1,3-propanediol (pK_a 8.80) (5)[3] with the corresponding protonated amines at various buffer ratios. The dependence of the rate of reaction on buffer concentration was also investigated. Solutions of potassium hydroxide with concentrations in the range 0.001–0.25 mol dm^{-3} were used for studies at higher pH. Reactions were begun by injecting a concentrated solution of 2-methyl-4H-3,1-benzoxazine in Me_2SO into the reaction mixture to give an initial concentration of ca. 1.0×10^{-4} mol dm^{-3}. The concentration of 2-methyl-4H-3,1-benzoxazine was always kept in at least 10-fold deficit compared with buffer species or hydronium ion or hydroxide ion. Hydrolysis was followed by observing the UV spectral change with time. In a buffer of tris(hydroxymethyl)aminomethane (buffer ratio 1.0, pH 8.07 at a buffer concentration of 0.25 mol dm^{-3} in each buffer component), the spectral changes with time occurred to give clean isosbestic points at 242 and 308 nm. Reactions were usually followed by measuring the decrease in absorbance at 261 nm and were found to be accurately of first order. The value of the first-order rate coefficient (k_{obs}) was determined from an exponential fit to the variation of absorbance with time over at least three half lives. Reactions were followed for a sufficient time to allow the determination of an absorbance value corresponding to complete reaction except in the case of some of the slowest reactions. Correlation coefficients were typically 0.9999, and standard deviations of the calculated first-order rate coefficients were typically less than 1% The reactions occurred with half-lives in the range ca. 40 – 3.5×10^3 s.

Fig. 2. Dependence on pH of the rate coefficient ($\log_{10}$ k/s^{-1}) for the ring opening of 2-methyl-4H-3,1-benzoxazine in aqueous solution.

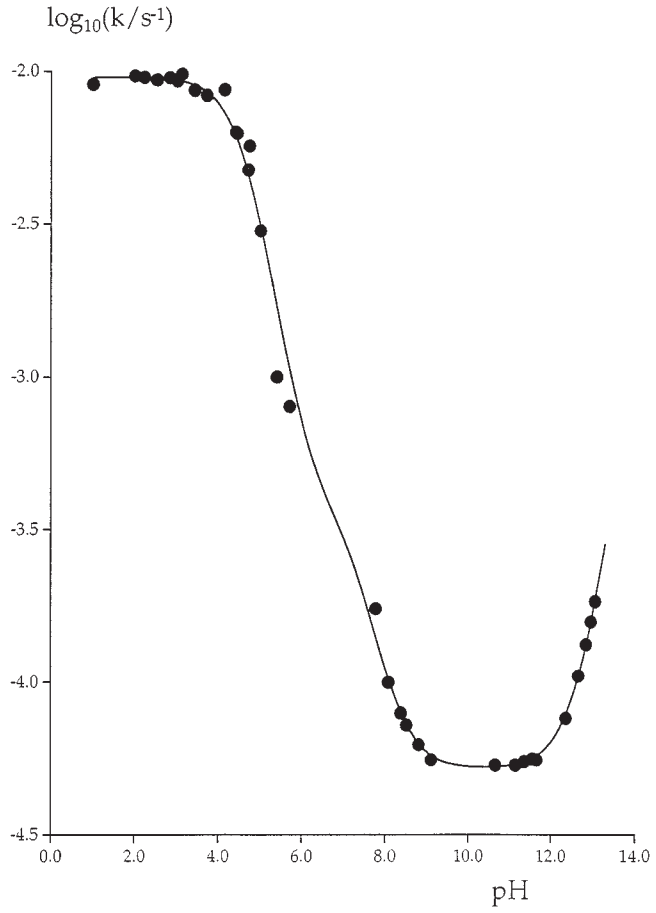

Results and discussion

Rate–pH profile

The pH dependence of the rate coefficient (k) for the hydrolysis of 2-methyl-4H-3,1-benzoxazine is shown in Fig. 2. The data were obtained from studies in solutions of hydrochloric acid and potassium hydroxide or in the presence of buffers. The value of the rate coefficient (k) given for hydrolysis in buffer solutions was obtained by extrapolation of the observed rate coefficient (k_{obs}) to zero buffer concentration and hence refers to reaction involving species derived from the solvent (water). In the range pH 1–5 the product of reaction at high buffer concentrations is exclusively 2-aminobenzyl acetate, and at pH 7.5–13, 2-acetylaminobenzyl alcohol is the sole product. In the region 5–7.5, hydrolysis of 2-methyl-4H-3,1-benzoxazine yields a mixture of 2-

[2] The pK_a value (7.20) (ref. 4) for dihydrogen orthophosphate monoanion at infinite dilution was adjusted to ionic strength (I) 0.25 mol dm^{-3} using the Debye–Huckel expression $-\log \gamma_{\pm} = 0.51 Z_i^2 \sqrt{I}/(1 + \sqrt{I})$.

[3] The value of pK_a at infinite dilution (5) was used uncorrected for the present conditions of ionic strength 0.25 mol dm^{-3}.

© 1999 NRC Canada

Table 1. Values of equilibrium constants and rate coefficients for the best fit of eq. [12] to the rate coefficient – pH profile.

K_{SH^+} (mol dm^{-3})	$k_1k_2/(k_{-1} + k_2)$ (s^{-1})	k_1 (s^{-1})	$k_2/k_3K_{1H^+}$ (mol dm^{-3})	k_0 (s^{-1})	k_{OH} (dm^3 mol^{-1} s^{-1})
$2.4 \pm 0.5 \times 10^{-5}$	$9.5 \pm 1 \times 10^{-3}$	0.17	$1.29 \pm 0.1 \times 10^{6}$	$5.1 \pm 0.5 \times 10^{-5}$	$5.3 \pm 0.5 \times 10^{-4}$

aminobenzyl acetate and 2-acetylaminobenzyl alcohol depending on the reaction conditions. The results in each of these pH regions will be considered in turn.

Reaction to 2-aminobenzyl acetate at pH 1–5

Data for hydrolysis in the range pH 1–5 have been published (1). Reaction occurs by addition of water to the protonated form of 2-methyl-4H-3,1-benzoxazine to give a cyclic tetrahedral addition intermediate which collapses to 2-aminobenzyl acetate, Scheme 1. Evidence for the involvement of a tetrahedral addition intermediate on the reaction pathway was provided by the observation of rectilinear plots of the observed rate coefficient against buffer base concentration as described earlier. According to the mechanism in Scheme 1, the rate coefficient for hydrolysis of 2-methyl-4H-3,1-benzoxazine extrapolated to zero buffer concentration is given by eq. [4] in which K_{SH^+} is the acid dissociation

$$[4] \qquad k = k_1k_2[H_3O^+]/(k_{-1} + k_2)(K_{SH^+} + [H_3O^+])$$

constant of protonated 2-methyl-4H-3,1-benzoxazine and the rate coefficients k_1, k_{-1}, and k_2 refer to the steps in Scheme 1. The solid line in Fig. 2 through the data points in the region pH 1–5 is a best-fit of eq. [4] to the experimental results (1) using the values shown in Table 1 for K_{SH^+}, k_1, and $k_2/(k_{-1} + k_2)$. The observed rectilinear dependence of the first-order rate coefficient (k_{obs}) on buffer concentration, eq. [2], was used to deduce values for the ratio $k_B/(k_{-1} + k_2)$ where k_B is the value of the second-order rate coefficient for catalysis of the collapse of the tetrahedral intermediate to 2-aminobenzyl acetate by chloroacetate, formate, acetate, and pivalate ions. The value of the rate coefficient ratio $k_B/(k_{-1} + k_2)$ was found to increase with increase in base strength of the catalysing buffer, giving a Brønsted plot with a value of β ca. 0.8 for the Brønsted exponent. It was also found that the value of the rate coefficient ratio $k_2/(k_{-1} + k_2)$ for spontaneous collapse of the intermediate with k_2 corrected to a second-order rate coefficient for reaction with water fitted the Brønsted plot for catalysis by buffers. This is compatible with the solvent acting as a base in catalysing the collapse of the tetrahedral intermediate.

Reaction to 2-aminobenzyl acetate and 2-acetylaminobenzyl alcohol at pH 5–9

In the present work, kinetic studies have been extended above pH 5, and the hydrolysis of 2-methyl-4H-3,1-benzoxazine gives a mixture of 2-aminobenzyl acetate and 2-acetylaminobenzyl alcohol, depending on the reaction conditions. Measurements were made in pivalate, phosphate, and in amine buffers.

In buffers of 2-amino-2-methyl-1,3-propanediol and of tris(hydroxymethyl)aminomethane (pH 7.8–9.1) where the reaction occurs to give exclusively 2-acetylaminobenzyl alcohol, there is a shallow dependence of k_{obs} on buffer concentration. Data for the reaction in buffers of 2-amino-2-methyl-1,3-propanediol buffer at different buffer ratios (r = [B]/[BH$^+$]) are shown in Fig. 3. The increase in k_{obs} with buffer concentration up to a concentration of the buffer cation of 0.125 mol dm^{-3} amounts to ca. 10, 8, and 9% at buffer ratios of r = 0.5, 1.0, and 2.0, respectively. Similar effects are observed in buffers of tris(hydroxymethyl)aminomethane. The shallow dependence on buffer concentration could be due to a salt effect as the inert salt (potassium chloride) is replaced by the buffer cation at constant ionic strength. A similar effect was previously observed in the reaction of 2-methylnaphth[1,8-de]-1,3-oxazine to 1-hydroxy-8-acetylaminonaphthalene in acetate buffers and was attributed to a salt effect (6). However, the possibility of weak buffer catalysis cannot be ruled out.

Fig. 3. Variation of the rate coefficient (k_{obs}/s^{-1}) with concentration for buffers of 2-amino-2-methyl-l,3-propanediol at different buffer ratios (r).

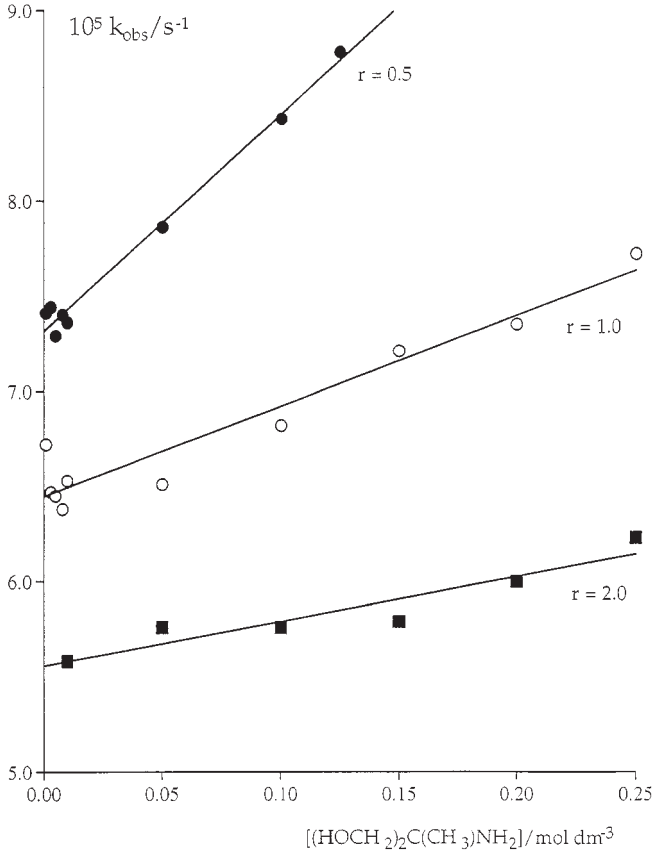

In the lower pH range, measurements were made in the presence of buffers of dihydrogen orthophosphate monoanion and monohydrogen orthophosphate dianion at buffer ratios r ($HPO_4^{2-}/H_2PO_4^-$) 0.5, 1.0, and 2.0, corresponding to pH values 6.22, 6.52, and 6.82. The change in k_{obs} with buffer concentration was small. For example, at a buffer ratio r = 1.0, the value of k_{obs} increased from 0.114 to 0.230 s^{-1} as the

© 1999 NRC Canada

buffer base concentration was increased from 0.001 to 0.05 mol dm^{-3}. At buffer ratios of r = 0.5 and 2.0, the values of k_{obs} increased from 0.213 to 0.447 s^{-1} and from 0.0671 to 0.107 s^{-1}, respectively. Extrapolation to zero buffer concentration gave values of k that did not fit the rate–pH profile determined in other buffers. At these pH values, the reaction of 2-methyl-4H-3,1-benzoxazine occurs to give both 2-aminobenzyl acetate and 2-acetylaminobenzyl alcohol. Although the latter reaction is not susceptible to strong catalysis by buffer, the reaction to 2-aminobenzyl acetate is catalysed by buffer. Details of the catalysis of the reaction to 2-aminobenzyl acetate by carboxylic acid buffers can be used to predict the behaviour in orthophosphate buffers. The variation of k_{obs} with buffer concentration for reaction of 2-methyl-4H-3,1-benzoxazine to 2-aminobenzyl acetate is given by eq. [2]. Extrapolation of the Brønsted plot for the variation of the value of $k_B/(k_{-1} + k_2)$ with base strength for carboxylic acid buffers (1) gives the result $k_B/(k_{-1} + k_2)$ = 1.92 × 10^3 dm^3 mol^{-1} for catalysis by monohydrogen orthophosphate dianion. This value can be used to predict that for the reaction of 2-methyl-4H-3,1-benzoxazine to 2-aminobenzyl acetate in a phosphate buffer, catalysis will be close to the upper limiting value of the rectilinear dependence of k_{obs} against buffer concentration for most of the concentrations of monohydrogen orthophosphate dianion studied. At a buffer ratio r = 1.0 and a buffer concentration of 0.001 mol dm^{-3}, catalysis will have reached ca. 66% of the limiting rate. It follows that extrapolation of values of k_{obs} obtained in the range $[HPO_4^{2-}]$ 0.001–0.05 mol dm^{-3} to zero buffer concentration is unreliable, and the results are not included in the rate–pH profile in Fig. 2.

A mechanism that is compatible with the effect of pH on product ratio and with the dependence of the rate coefficient extrapolated to zero buffer concentration on pH in the range 0–9 is shown in Scheme 2. The mechanism differs from that in Scheme 1 used to explain the kinetics and formation of 2-aminobenzyl acetate in acidic solution by the inclusion of a route for collapse of an unprotonated form of the cyclic tetrahedral intermediate to 2-acetylaminobenzyl alcohol. It is assumed that collapse of the intermediate IH^+ to 2-aminobenzyl acetate is catalysed by buffer base but that collapse of the unprotonated intermediate (I) to 2-acetylaminobenzyl alcohol is uncatalysed by buffer species. If the proton transfer steps in Scheme 2 are assumed to occur rapidly and the intermediates IH^+ and I are present in low concentration, the expression in eq. [5] is obtained for the pH dependence of the rate coefficient for disappearance of 2-methyl-4H-3,1-benzoxazine.

$$[5] \qquad k = \frac{k_1[H_2O][H_3O^+](k_2[H_3O^+] + k_3K_{1H^+})}{(K_{SH^+} + [H_3O^+])\{k_3K_{1H^+} + (k_{-1} + k_2)[H_3O^+]\}}$$

$$[6] \qquad \frac{100[A]}{([E] + [A])} = \frac{100k_3K_{1H^+}}{(k_3K_{1H^+} + k_2[H_3O^+])}$$

According to the mechanism in Scheme 2, the percentage of 2-acetylaminobenzyl alcohol (A) formed as product compared with 2-aminobenzyl acetate (E) is given by the expression in eq. [6]. The results obtained for the percentage of 2-acetylaminobenzyl alcohol formed as product compared with 2-aminobenzyl acetate were plotted in the reciprocal form of eq. [6], and linear regression analysis gave a value for $k_2/k_3K_{1H^+}$ of 1.29 × 10^6 mol^{-1} dm^3. This result was used in eq. [6] to calculate the solid line in Fig. 1 for the pH dependence of the percentage of 2-acetylaminobenzyl alcohol formed as product.

Fig. 4. Variation of the rate coefficient (10^5 k/s^{-1}) for ring opening of 2-methyl-4H-3,1-benzoxazine with hydroxide ion concentration.

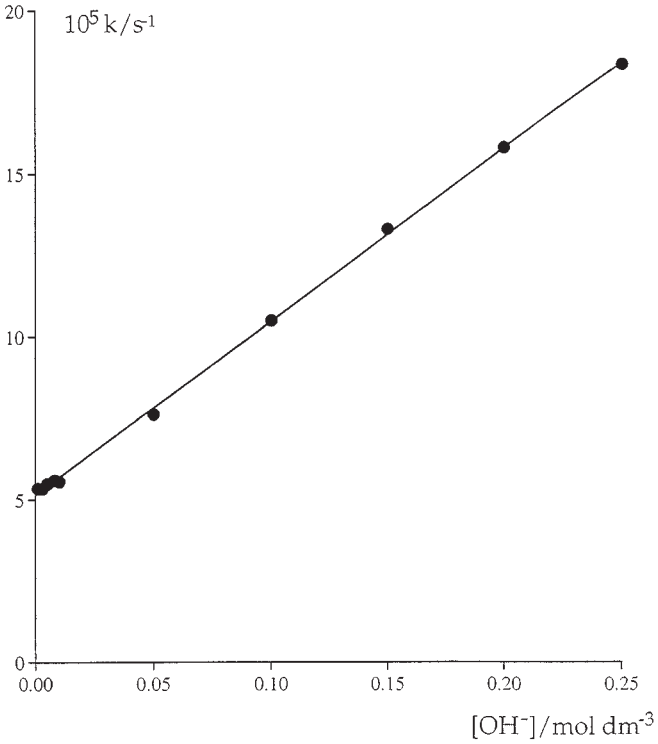

At pH <5 where 2-aminobenzyl acetate is the exclusive product, the terms involving k_3 can be neglected, and eq. [5] reduces to eq. [4]. In the pH region 8–9 where 2-acetylaminobenzyl alcohol is the only product, the terms involving k_2 can be neglected, and eq. [5] reduces to eq. [7]. If it is further assumed that $k_3K_{1H^+} > k_{-1}[H_3O^+]$, eq. [8] is obtained, which further reduces to eq. [9] on the assumption that $K_{SH^+} > [H_3O^+]$. Equation [9] predicts a direct dependence of k against $[H_3O^+]$. The experimental values of k in the range pH 7.8–9.1 were plotted against $[H_3O^+]$. However, a linear plot with gradient 7.1 × 10^3 dm^3 mol^{-1} s^{-1} and intercept 4.9 × 10^{-5} s^{-1} was obtained from linear regression analysis rather than the direct dependence of k against $[H_3O^+]$ predicted by eq. [9]. It was therefore necessary to modify the rate expression to include a pH-independent rate term k_0 as in eq. [10]. Thus, eq. [10] is compatible with the experimental results with values of k_1/K_{SH^+} = 7.1 × 10^3 dm^3 mol^{-1} s^{-1} and k_0 = 4.9 × 10^{-5} s^{-1}.

$$[7] \qquad k = k_1[H_2O][H_3O^+]k_3K_{1H^+}/(K_{SH^+} + [H_3O^+])(k_3K_{1H^+} + k_{-1}[H_3O^+])$$

$$[8] \qquad k = k_1[H_2O][H_3O^+]/(K_{SH^+} + [H_3O^+])$$

$$[9] \qquad k = (k_1/K_{SH^+})[H_2O][H_3O^+]$$

© 1999 NRC Canada

Scheme 3.

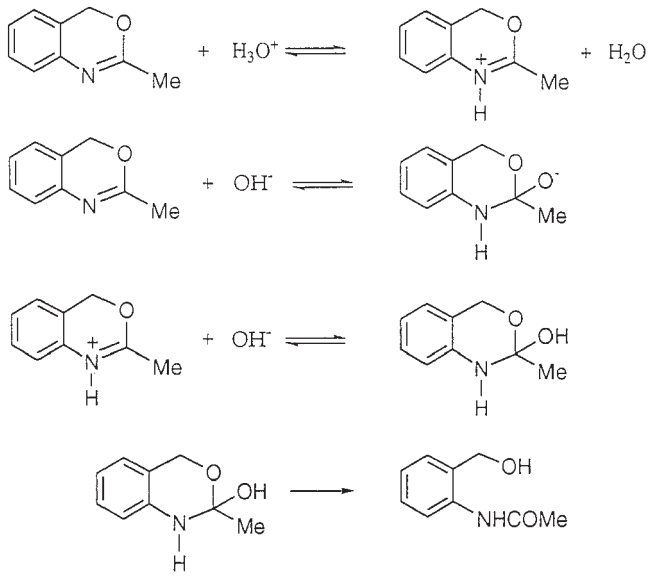

$$[10] \quad k = k_0 + (k_1/K_{SH^+})[H_2O][H_3O^+]$$

Reaction to 2-acetylaminobenzyl alcohol at pH 10–13

In the range pH 10–13, the product of reaction is 2-acetylaminobenzyl alcohol. Kinetic studies in this region were made in solutions of potassium hydroxide at concentrations in the range 0.001–0.25 mol dm^{-3}. The dependence of the measured first-order rate coefficient on hydroxide ion concentration is linear as shown in Fig. 4 with linear regression gradient $k_{OH} = 5.3 \times 10^{-4}$ dm^3 mol^{-1} s^{-1} and intercept $k_0 = 5.2 \times 10^{-5}$ s^{-1}. Hence, a pH-independent term and a term that is of first order in hydroxide ion contribute to the rate in this region, eq. [11]. The pH-independent term with a slightly

$$[11] \quad k = k_0 + k_{OH}[OH^-]$$

different value $k_0 = 4.9 \times 10^{-5}$ s^{-1} was also found from the variation of k with $[H_3O^+]$ in the range 7.8–9.1, eq. [10]. The average of these two values leads to k_o 5.1×10^{-5} s^{-1}.

A mechanism that is compatible with the formation of 2-acetylaminobenzyl alcohol as the sole product and with the experimentally observed dependence of k against $[OH^-]$ shown in Fig. 4 involves addition of hydroxide ion to protonated and unprotonated forms of 2-methyl-4H-3,1-benzoxazine to give a tetrahedral intermediate which collapses to product, Scheme 3.

In Scheme 3, it can be assumed that the tetrahedral intermediates are present in low concentration. The pH-independent term and the first-order term in hydroxide ion are explained by reaction of hydroxide ion with the protonated and unprotonated forms of 2-methyl-4H-3,1-benzoxazine, respectively. An alternative mechanism that will explain the pH-independent term involves reaction of the unprotonated form of 2-methyl-4H-3,1-benzoxazine with solvent. The relative importance of these two possibilities for the pH-independent term can be assessed by comparison of the value of the rate coefficient k_0 with the values of the other rate coefficients in the mechanism. If the pH-independent term arises from reaction of hydroxide ion with protonated 2-methyl-4H-3,1-benzoxazine, the result k_0 5.1×10^{-5} s^{-1} corresponds to a second-order rate coefficient for reaction with hydroxide ion of 5.7×10^4 dm^3 mol^{-1} s^{-1} using the values of K_{SH^+} 2.4×10^{-5} mol dm^{-3} for the acid dissociation constant of protonated 2-methyl-4H-3,1-benzoxazine and $K_w = 2.19 \times 10^{-14}$ mol^2 dm^{-6} for the ionic product of water under the reaction conditions. This is to be compared with the value $k_1 = 3.1 \times 10^{-3}$ dm^3 mol^{-1} s^{-1} obtained for the reaction of water with protonated 2-methyl-4H-3,1-benzoxazine. The 1.8×10^7-fold difference seems reasonable in view of the very large difference in nucleophilicity of hydroxide ion and water. If the pH-independent term arises from rate-limiting attack of water on unprotonated 2-methyl-4H-3,1-benzoxazine, the result k_0 5.1×10^{-5} s^{-1} corresponds to a second-order rate coefficient of 9.2×10^{-7} dm^3 mol^{-1} s^{-1} for reaction with water. This is to be compared with the value k_{OH} 5.3×10^{-4} dm^3 mol^{-1} s^{-1} found for reaction of hydroxide ion with unprotonated 2-methyl-4H-3,1-benzoxazine. This 600-fold difference is smaller than would have been anticipated from the very large difference in nucleophilicity of water and hydroxide ion. For this reason, the preferred explanation of the pH-independent term in the rate law, eqs. [10] and [11], is a reaction involving addition of hydroxide ion to protonated 2-methyl-4H-3,1-benzoxazine.

Dependence of *k* in the range pH 0–13

The pH dependence of the rate coefficient (k) for hydrolysis of 2-methyl-4H-3,1-benzoxazine involving species derived from the solvent over the whole of the pH range 0–13 is fitted by eq. [12], which is obtained by combining eq. [5] with eq. [11]. The solid line in Fig. 2 is a plot of eq. [12] using the values of the rate coefficients and equilibrium

$$[12] \quad k = \frac{k_1[H_2O][H_3O^+](k_2[H_3O^+] + k_3K_{1H^+})}{(K_{SH^+} + [H_3O^+])\{k_3K_{1H^+} + (k_{-1} + k_2)[H_3O^+]\}} + k_0 + k_{OH}[OH^-]$$

constants given in Table 1. At low pH, reaction of protonated 2-methyl-4H-3,1-benzoxazine with solvent occurs through a protonated tetrahedral intermediate, leading to 2-aminobenzyl acetate as product. As the pH is raised, reaction of protonated 2-methyl-4H-3,1-benzoxazine leads to 2-acetylaminobenzyl alcohol, since the tetrahedral intermediate that is common to both pathways is present in the unprotonated form. In the protonated form, the intermediate leads to 2-aminobenzyl acetate because departure of an aromatic amine as leaving group is facile. Collapse of the unprotonated intermediate to 2-aminobenzyl acetate would involve departure of an amine anion, and reaction to 2-acetylaminobenzyl alcohol involving an aliphatic alkoxide as leaving group is preferred. The change in pathway that occurs between pH ca. 6 and 7 leads to an inflexion point in the rate coefficient against pH profile. The relative amount of the two products is determined by the fraction of the tetrahedral intermediate that is protonated and the relative rates of collapse of the protonated intermediate to 2-aminobenzyl acetate and the unprotonated intermediate to 2-acetylaminobenzyl alcohol, eq. [6]. At pH 9, reaction of protonated

© 1999 NRC Canada

2-methyl-4H-3,1-benzoxazine with hydroxide ion becomes important, and above pH 12, reaction of unprotonated 2-methyl-4H-3,1-benzoxazine with hydroxide ion predominates. Both of these reactions result in the formation of 2-acetylaminobenzyl alcohol, presumably through the unprotonated form of the tetrahedral intermediate.

It was found that collapse of the protonated intermediate to 2-aminobenzyl acetate is catalysed by buffer base. This presumably occurs by assistance of removal of the hydroxy proton as the carbonyl group of the product is formed. In contrast, collapse of the unprotonated tetrahedral intermediate to 2-acetylaminobenzyl alcohol is not assisted by buffer base. The absence of catalysis in this case could indicate that addition of water to protonated 2-methyl-4H-3,1-benzoxazine is rate-limiting (that is, collapse of the intermediate to product occurs more rapidly than collapse to protonated 2-methyl-4H-3,1-benzoxazine). Alternatively, if the value of the Brønsted exponent for base catalysis of the collapse of the unprotonated tetrahedral intermediate was close to zero, buffer catalysis would be undetectible compared with solvent catalysed collapse.

References

1. W.J. Dixon, F. Hibbert, and J.F. Mills. J. Chem Soc. Perkin Trans. 2, 1503 (1997).
2. R.H. De Wolfe and D.G. Neilson. *In* The chemistry of amidines and imidates. *Edited by* S. Patai. Wiley, New York. 1975.
3. A.C. Satterthwait and W.P. Jencks. J. Am. Chem. Soc. **96**, 7031 (1974).
4. D.D. Perrin. *In* Dissociation constants of inorganic acids and bases in aqueous solution. 2nd ed. Butterworths, London. Pergamon Press, London. 1982.
5. D.D. Perrin. *In* Dissociation constants of organic bases in aqueous solution. Butterworths, London; Pergamon Press, Oxford. (1st ed.) 1965; (supplement) 1972.
6. W.J. Dixon and F. Hibbert. J. Chem. Soc. Perkin Trans. 2, 795 (1994).

© 1999 NRC Canada

Kinetic study of the reactions of various types of C-acids with amine bases in acetonitrile. An unusual effect of common BH^+ cation on the rate constants

Wlodzimierz Galezowski, Iwona Grzeskowiak, and Arnold Jarczewski

Abstract: The rates of proton transfer reactions between C-acids of different types such as 1-(4-nitrophenyl)-1-nitroalkanes, 4-nitrophenylcyanomethanes, and 2,4,6-trinitrotoluene, and organic bases such as 1,1,3,3-tetrametylguanidine, 7-methyl-1,5,7-triazabicyclo[4.4.0]dec-5-ene (MTBD), and tri-*n*-butylamine have been measured in acetonitrile at pseudo-first-order conditions. A general equation for the rates of proton transfer reactions between C-acids and bases with product existing in two forms, ions and ion pairs, has been derived and its applicability tested. The equation works well except for reactions of 1-(4-nitrophenyl)-1-nitroalkanes with guanidines for which the second-order rate constant is diminished with concentration of guanidinium cation, while tetrabutylammonium salts accelerate the reactions. Possible reasons for this are discussed.

Key words: proton transfer, kinetic study, ion pairs, C-acids, organic bases, acetonitrile, salt effect.

Résumé : Opérant dans l'acétonitrile, dans des conditions de pseudo-premier ordre, on a mesuré les vitesses des réactions de transfert de proton entre divers types d'acides-C, comme les 1-(4-nitrophényl)-1-nitroalcanes, les 4-nitrophénylcyanométhanes et le 2,4,6-trinitrotoluène, et des bases organiques, comme la 1,1,3,3-tétraméthylguanidine, le 7-méthyl-1,5,7-triazabicyclo[4.4.0]déc-5-ène (MTBD) et la tri-*n*-butylamine. On a développé une équation générale pour les vitesses de réactions de transfert de proton entre les acides-C et les bases comportant des produits existant sous deux formes, ionique et paire d'ions, et on en a vérifié le domaine d'application. L'équation donne de bons résultats, excepté pour le cas des réactions des 1-(4-nitrophényl)-1-nitroalcanes avec les guanidines pour lesquelles on observe une diminution de la constante de vitesse du deuxième ordre avec la concentration du cation guanidinium alors que les sels de tétrabutylammonium accélère les réactions. On discute des causes de ces divergences.

Mots clés : transfert de proton, étude cinétique, paire d'ions, acides-C, bases organiques, base, acétonitrile, effet de sel.

[Traduit par la Rédaction]

Introduction

The proton transfer reactions between C-acids of various structures and amine bases in solution have been extensively studied for many years (1–6). The fascination with this research results from the relative simplicity of the mechanism of the reaction even though the multistep mechanism should be considered (1).

In our previous papers, we found that the products of reactions between various C-acids and strong amine bases in acetonitrile are largely dissociated into free ions (7–9). This was evident from conductometric measurements (7, 8), but went undetected in earlier spectrophotometric equilibrium studies (10–15) in which the Benesi–Hildebrand formalism indicated an ion-pair product. Kinetics of these reactions was also consistent with the concept of associated product. The pitfall was additional amount of common BH^+ cation resulting from side reactions of acidic contaminants with amine base. The concentration of BH^+ cation appeared to be larger than that formed in deprotonation of C-acid. Therefore, the rates of proton transfer reactions from C-acids to amine bases in acetonitrile of not very large equilibrium constant should be measured in $B–BH^+$ buffer solutions to maintain reversible pseudo-first-order conditions (5, 8). However, the disadvantage of measuring in buffers is that some anions, especially nitronates, tend to show appreciable ion association at large $[BH^+]$, which is easily seen as blue shifts in electronic spectra (5). This ion association brings on undesired complexity to the supposedly simple proton transfer reactions, which makes kinetic isotope effects studies

Received November 24, 1998.

This paper is dedicated to Jerry Kresge in recognition of his many achievements in chemistry.

W. Galezowski, I. Grzeskowiak, and A. Jarczewski.[1] Faculty of Chemistry, A. Mickiewicz University, Grunwaldzka 6, 60-780 Poznan, Poland.

[1]Author to whom correspondence may be addressed. Telephone: 00-4861-8659-562. Fax: 00-4861-8658008. e-mail: arnold@main.amu.edu.pl

 © 1999 NRC Canada

bases:

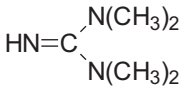

TMG

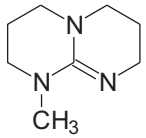

MTBD

Bu_3N

C-acids:

Nitroalkanes:

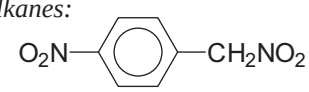

1

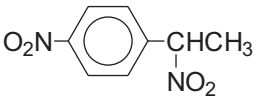

2

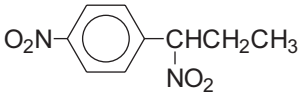

3

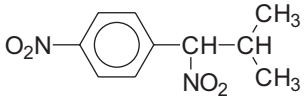

4

Cyanomethanes:

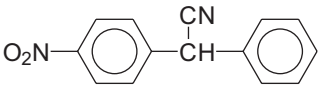

5

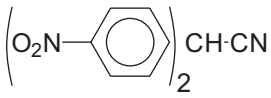

6

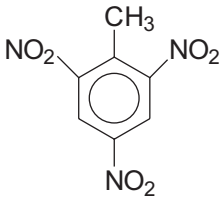

7

more difficult. Another problem arising from using buffers is salt effects. Actually, in our earlier kinetic measurements in buffered media, we found an example of unexpected negative salt effect (8). Therefore, we decided to measure kinetics of reactions of various C-acids with amine bases in buffer solutions in acetonitrile to see if reliable second-order rate constants can be obtained, particularly for deprotonations of nitroalkanes where the product is split into two forms of ions and ion pairs. To avoid further complications, amine bases like tributylamine (16) and MTBD (17) that do not form homoconjugated complexes or bases characterized by low homoconjugation constant such as TMG (17) were chosen.

© 1999 NRC Canada

Scheme 1. The two kinetically indistinguishable mechanisms of proton transfer reactions between a C-acid and an amine base.

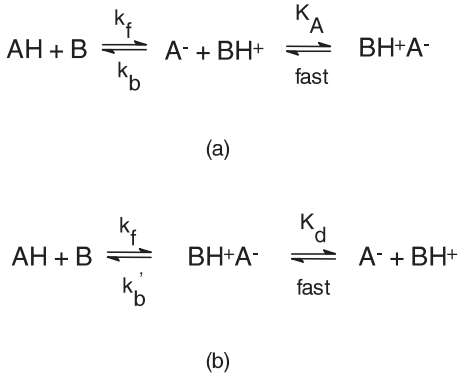

Results and discussion

The reactions of C-acids with amine bases give colored products. With **5**, **6**, and **7**, spectra of the products are insensitive to $[BH^+]$, and the reactions were followed at λ_{max}. With nitroalkanes **1**, **2**, **3**, and **4**, a blue shift resulting from ion association is observed, and measurements were done at maximum absorbance and occasionally at λ_{max} of ion, λ_{max} of ion pair, and at isosbestic point. The observed rate constants k_{obs} were wavelength independent. For most proton transfer reactions in acetonitrile solvent, the reaction product exists predominantly as free ions (7, 8), but with alkanenitronates, ion association cannot be neglected if an amine salt is added (5).

If the equilibrium constant is not very large, the rates of proton transfer from C-acids to amine bases in acetonitrile should be measured in buffer solutions to maintain reversible pseudo-first-order conditions (8). The visible spectra of ions and ion pairs differ significantly (5), which gives an opportunity to test the assumption that ion association/dissociation is much faster than proton transfer. Inasmuch as the rates proved to be wavelength independent, the ion association/dissociation must be much faster than proton transfer, as expected. Consequently, mechanisms (*a*) and (*b*) shown in Scheme 1 could not be distinguished from our stopped-flow kinetic data. In both cases, as long as ion association/dissociation is much faster than proton transfer, eq. [1] is fulfilled.

$$[1] \qquad k_{obs} = k_f[B] + \frac{k_b f^2[BH^+]}{1 + K_A f^2[BH^+]}$$

where k_b is a second-order rate constant for proton transfer between ions at zero ionic strength (Scheme 1*a*) or is equal to a product of a first-order rate constant of proton transfer within ion pair k_b' and ion association constant K_A (Scheme 1*b*); $K_d = 1/K_A$; f is the ion activity coefficient (18). Should both mechanisms (*a*) and (*b*) operate simultaneously, then eq. [1] would retain its form with the sum of two second-order constants instead of k_f and $k_b + k_b'K_A$ instead of k_b. The second term in eq. [1] has a summation in the denominator, which is characteristic for reactions with the substrate split into two forms (19). Provided the dependence of intercept (itcp) of k_{obs} vs. [B] plot on $[BH^+]$ is known, k_b and K_A can be easily found from a double reciprocal plot:

Fig. 1. Plots of observed rate constants versus $[Bu_3N]$ for the reaction of 4-nitrophenylnitromethane with Bu_3N measured at various concentrations of Bu_3NHClO_4 in acetonitrile at 25°C. (○ 0, □ 0.0001, △ 0.0002, ◇ 0.0004, ◆ 0.001, ▲ 0.002, ■ 0.004, ⬡ 0.01 M Bu_3NHClO_4).

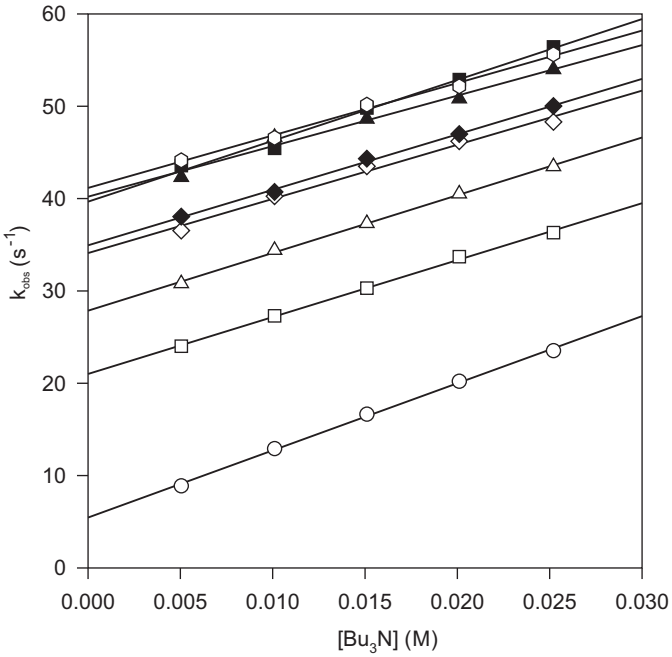

$$[2] \qquad 1/\text{itcp} = K_A/k_b + 1/(k_b f^2[BH^+])$$

One reason for measuring rates at constant $[BH^+]$ is to prevent changes in $[BH^+]$ during a kinetic run, thus avoiding a relatively complicated analysis. Deviations from first-order kinetics might have gone undetected in many kinetic studies performed without addition of BH^+, especially when a very strong base such as an amidine or guanidine have been used (9–13, 20, 21). Since [B] is much larger than the concentration of C-acid to ensure pseudo-first-order kinetics, some BH^+ is brought to the system with the base. The concentration of the adventitious BH^+ can be comparable to the concentration of C-acid of ca. 1×10^{-5} M. Under such conditions, a plot of k_{obs} vs. [B] may be close to a straight line, despite that initial $[BH^+]$ is unknown and it changes with base concentration, and it may give a distorted k_f and an intercept of no physical meaning. If $[BH^+]$ is kept constant by means of addition of a well-dissociated salt, the slope of the plot should give the correct value of k_f, while the second term in eq. [1] can be found as an intercept of the plot, and it has a definite physical meaning. For several reactions, all the plots of relation [1] are parallel except ones with no BH^+ salt added, some of which have markedly larger slopes (Fig. 1). However, as follows from our computer simulations of the kinetic curves, those enlarged slopes cannot be accounted for by variable concentration of BH^+ during a kinetic run.

The approach outlined above works well for many reactions of C-acids with amine bases in acetonitrile. The reaction of **1** (pK_a = 20.7) (18) with tributylamine (pK_a = 18.1) (16) is an illustrative example of a reaction of a relatively small equilibrium constant and considerable ion association

© 1999 NRC Canada

Table 1. Rate constants for proton transfer reactions of 4-nitrophenylnitromethane **1** and bis(4-nitrophenyl)cyanomethane **6** with tributylamine measured at various concentrations of tributylammonium cation in acetonitrile at 25°C.

$10^3[Bu_3NHClO_4]$ (M)	$10^2[Bu_3N]$ (M)	k_{obs} (s^{-1})	k_f (M^{-1} s^{-1})	itcp (s^{-1})[a]
		1		
0	0.505–2.515	8.89–23.53	720 ± 20	5.5 ± 0.3
0.1	0.505–2.515	24.01–36.31	617 ± 14	21.0 ± 0.2
0.2	0.505–2.515	30.8–43.47	625 ± 14	27.9 ± 0.2
0.4	0.505–2.515	36.54–48.31	590 ± 40	34.1 ± 0.6
1	0.505–2.515	38.04–50.02	600 ± 20	34.9 ± 0.3
2	0.505–2.515	42.31–53.98	550 ± 40	44.5 ± 0.7
4	0.505–2.515	43.56–56.42	660 ± 40	39.7 ± 0.6
10	0.505–2.515	44.14–55.63	570 ± 30	41.2 ± 0.4
		6		
0	0.505–2.515	14.50–70.02	2660 ± 150	0.8 ± 2
0.093	0.505–2.515	13.78–54.34	1990 ± 40	4.2 ± 0.7
0.2	0.505–2.515	15.40–58.95	2070 ± 130	5 ± 2
0.4	0.505–2.515	18.70–59.61	1950 ± 100	9 ± 2
1	0.505–2.515	27.45–65.11	1880 ± 90	18 ± 2
2	0.505–2.515	35.82–73.67	1830 ± 70	27 ± 1
4	0.505–2.515	53.30–91.92	1880 ± 70	44 ± 1
10	0.505–2.515	92.08–129.7	1860 ± 20	82.7 ± 0.3
1[b]	0.505–2.515	22.43–63.29	1950 ± 110	12 ± 2

[a]Intercept.

[b]Adjusted to ionic strength of $I = 0.01$ with tetrabutylammonium perchlorate.

of the product. Unlike with guanidine or amidine bases, the product is roughly half-associated at $[BH^+]$ as low as 1×10^{-4} M. The distance between the parallel straight lines in Fig.1 decreases with $[BH^+]$ as the second term in eq.[1] approaches its limiting value of k_b/K_A. The dissociation constant of 9×10^{-5} M and k_b of 4.6×10^5 M^{-1} s^{-1} were obtained from the double reciprocal plot [2]. The values of k_f are independent of the concentration of tributylammonium cation (Table 1) except the one for $[BH^+] = 0$.

Equation [1] is fulfilled also for the reaction of **6** (pK_a = 19) (18) with tributylamine. The equilibrium constant is still not very large, so intercepts are significant. However, since the anions of cyano C-acids do not associate with ammonium cation as easily as nitronates do, the second term in eq. [1] can be approximated by $k_b f^2[BH^+]$, and in the ranges of $[BH^+]$, the plot [1] does not converge to the limiting straight line. The value of k_b calculated by dividing the intercepts by $f^2[BH^+]$ is (15 800 ± 1400) M^{-1} s^{-1}. The values of k_f are insensitive to the concentration of tetrabutylammonium perchlorate (Table 1). Similarly, in the reaction of **5** with TMG, the second-order rate constants do not change with $[TMGH^+]$ (Table 2). As in the preceding case, ion association constant of the product is too small to be found from eq. [2] with a reasonable accuracy; k_b is 1800 ± 200 M^{-1} s^{-1}. The reaction of **7** (pK_a = 23.2) (18) with MTBD (pK_a = 25.4) (22) has a fairly large equilibrium constant, so reverse reaction is not visible, i.e., intercepts of the plots [1] are 0 (Table 3). Again, the $MTBDH^+$ cation has no impact on k_f values (Table 3).

Quite different response of phenomenological value of k_f to increased BH^+ concentration is observed for reactions of nitroalkanes with guanidines in acetonitrile. A decrease in k_f for the reaction of **3** with TMG (Table 2), which is evident for $TMGH^+$ concentration larger than 5×10^{-3} M, could only in part be explained by a weak homoconjugation of $TMGH^+$. Our computer simulations show that at a homoconjugation constant K_{HOMO}[17] = 5 M^{-1} and in the ranges of TMG base used, a 3.7% drop in k_f value could be observed for 0.01 M BH^+ and a 7.2 % drop for 0.02 M BH^+. In fact, k_f is reduced by at least 17 and 28 % for 0.01 M and 0.02 M BH^+, respectively (Table 2). Although the equilibrium constant is not very large as indicated by intercepts increasing with $[TMGH^+]$, these intercepts do not give exact value of the second term in eq.[1].

The situation is yet clearer with MTBD base that has a negligible homoconjugation constant (17) and very large basicity (22), which allows for neglect of the second term in eq. [1]. The values of k_f for reactions of this base with **2**, **3** (pK_a = 23.9) (18), and **4** (pK_a = 25.9) (8) show considerable decrease with $MTBDH^+$ concentration (Table 3). A typical k_f at 0.01 M $MTBDH^+$ is 20–30% lower than at 0.001 M $MTBDH^+$. The extent of this reduction increases with the bulk of alkyl substituent in the C-acid. The phenomenon described above is not a typical salt effect. For a reaction with transition state more polar than substrates, one would expect rather an increase than a decrease in rates with ionic strength (23). In a relevant study of deprotonation of arylnitroalkanes by benzoate in DMSO, no salt effect was found using lithium and potassium counterions for total salt concentration up to 2×10^{-2} M (24). However, unlike with amine bases, in the reactions with anionic bases, charge separation does not take place and simple comparisons of salt effects are impossible.

The deprotonations of nitroalkanes with MTBD are in line with concept of positive salt effect. When ionic strength is increased by means of tetrabutylammonium perchlorate, k_f values actually increase with ionic strength (Table 4 and some entries in Tables 1 and 5). As already mentioned, k_f values for the reaction of MTBD with **7** are constant unless the concentration of $MTBDH^+$ is unreasonably high

© 1999 NRC Canada

Table 2. Rate constants for proton transfer reactions of (4-nitrophenyl)phenylcyanomethane **5** and 1-(4-nitrophenyl)-1-nitropropane **3** with TMG measured at various concentrations of $TMGH^+$ in acetonitrile at 25°C.

10^3[TMGHPi] (M)	10^3[TMG] (M)	k_{obs} (s^{-1})	k_f (M^{-1} s^{-1})	itcp (s^{-1})[a]
		5		
0	1–5	8.34–36.55	7000 ± 200	1.7 ± 0.7
0.1	1–5	7.848–38.78	7600 ± 100	0 ± 0.2
0.2	1–5	8.03–38.54	7500 ± 100	0.4 ± 0.2
0.4	1–5	8.164–39.16	7500 ± 100	0.38 ± 0.06
1	1–5	9.124–39.31	7400 ± 100	1.7 ± 0.3
2	1–5	10.23–41.0	7500 ± 100	2.6 ± 0.2
4	1–5	12.34–42.57	7400 ± 100	4.8 ± 0.2
0.1[b]	1–5	7.99–38.70	7600 ± 100	0.2 ± 0.2
0.2[b]	1–5	7.90–38.80	7600 ± 100	0.2 ± 0.1
0.4[b]	1–5	8.01–38.47	7500 ± 100	0.4 ± 0.1
1[b]	1–5	8.61–38.61	7400 ± 100	1.2 ± 0.2
2[b]	1–5	9.41–39.71	7400 ± 100	1.9 ± 0.1
4[b]	1–5	10.85–41.14.	7500 ± 100	3.2 ± 0.2
10[b]	1–5	12.01–42.50.	7500 ± 300	5.1 ± 0.9
		3		
0	1.09–5.46	0.03842–0.0998	13.9 ± 0.4	0.024 ± 0.002
1.01	1.09–5.46	0.03467–0.0815	10.7 ± 0.1	0.0227 ± 0.0005
2.02	1.09–5.46	0.04274–0.0883	10.3 ± 0.2	0.032 ± 0.001
4.04	1.09–5.46	0.0517–0.09744	10.56 ± 0.2	0.040 ± 0.001
10.01	1.09–5.46	0.06753–0.1066	8.91 ± 0.3	0.058 ± 0.001
19.5	1.09–5.46	0.06412–0.0970	7.76 ± 0.6	0.056 ± 0.002

[a]Intercept.
[b]$TMGHClO_4$.

(Table 3), indicating that any changes in the base such as homoconjugation cannot provide a reasonable explanation for the decrease of k_f with concentration of $MTBDH^+$. Stabilization of the nitroalkane by $MTBDH^+$ seems unlikely. Nevertheless, we studied effect of concentrated (0.1 M) $MTBDH^+$ on ^1H NMR spectra of **4** in CD_3CN, and no shifts were found.

Looking for a possible explanation of the negative salt effect, we considered that very strong amine bases such as guanidines can produce small quantities of another base, which is stronger than the guanidine, but has small steric demands. This base could deprotonate some C-acids, like sterically hindered nitroalkanes, while with others, say **7**, the other route would be unimportant. Should this be the case, the alternative deprotonation reaction could be separated by switching from constant BH^+ concentration to buffers of a constant $[B]/[BH^+]$ ratio. In such buffers, the concentration of the competing base would be kept constant, and the slopes of k_{obs} vs. [MTBD] should be parallel, giving the true k_f value. The results of such an experiment are shown in Table 5. Again, for the reaction of **7**, there is little change in k_f, but for **4** there are large variations. The smallest k_f values were found for the buffers of the lowest $[B]/[BH^+]$ ratio. Hence, this proposal had to be rejected.

Additional opportunities for explanation are open when an unstable intermediate is assumed, a natural candidate for which would be a pyramidal carbanion (Scheme 2). The lifetime of this intermediate would have to be long enough that it could not only turn into nitronate ion but also reprotonate to the nitroalkane. If the steady-state approach is applied to this mechanism, eq. [3] is derived:

$$[3]\qquad k_{obs} = \frac{k_1(k_3 f^2[BH^+] + k_2)}{(k_{-1} + k_3) f^2[BH^+] + k_2}[B] + \frac{k_{-1}(k_{-2} + k_{-3}K_A)}{(k_{-1} + k_3) f^2[BH^+] + k_2} \times \frac{f^2[BH^+]}{1 + K_A f^2[BH^+]}$$

As follows from eq. [3], the coefficient at [B] can decrease with $[BH^+]$ if only k_{-1} is not much smaller than k_3, or k_2 is not much larger than $(k_{-1} + k_3)f^2[BH^+]$ in which cases the slope would be equal k_1, and BH^+ salts would have no effect on the slope of k_{obs} vs. [B].

The existence of the intermediate, although plausible, has not been supported by independent evidence. However, the concept of the two-anion mechanism is not new. The mechanism including the carbanionic intermediate is consistent with anomalous Brönsted α values for deprotonations of nitroalkanes (25), which were explained by large electron density on the carbon atom in the transition state (26), in contrast to the nitronate ion. Formation of such a pyramidal nitro carbanion as an intermediate was postulated by Bordwell and Boyle (27). According to them, the two-anion mechanism for deprotonation of nitroalkanes could account for the kinetic isotope effects observed equally well, and perhaps better than the one-step mechanism. Probably, it would suffice to assume that the transition state has some character of a pyramidal carbanion, so our negative salt effects on rates of proton transfer could actually provide the evidence for a true carbanionic intermediate.

In conclusion, experimental evidence for fast ion association/dissociation has been provided and a general equation for the rates of proton transfer reactions with product exist-

© 1999 NRC Canada

Table 3. Rate constants for proton transfer reactions of 1-(4-nitrophenyl)-1-nitroalkanes **2**, **3**, **4**, and TNT **7** with MTBD measured at various concentrations of $MTBDH^+$ in acetonitrile at 25°C.

10^3[MTBDHPi] (M)	10^2[MTBD] (M)	k_{obs} (s^{-1})	k_f (M^{-1} s^{-1})	itcp (s^{-1})[a]
		2		
0	1–5	3.379–18.44	378 ± 5	–0.6 ± 0.2
1.035	1–5	3.076–17.55	360 ± 10	–0.8 ± 0.4
2.07	1–5	3.078–16.79	342 ± 8	–0.5 ± 0.3
4.14	1–5	3.013–15.89	324 ± 6	–0.4 ± 0.2
10	0.99–4.97	2.566–14.498	300 ± 9	–0.6 ± 0.3
		3		
0	1–5	0.7174–3.982	83 ± 1	–0.14 ± 0.05
1.0	1–5	0.6036–3.706	78 ± 3	–0.26 ± 0.09
2.0	1–5	0.5972–3.468	72 ± 1	–0.17 ± 0.05
4.0	1–5	0.5701–3.279	68 ± 2	–0.15 ± 0.05
10.08	1–5	0.5526–2.987	60 ± 1	–0.06 ± 0.03
20.2	1–5	0.5279–2.7810	56.5 ± 0.5	–0.05 ± 0.01
		4		
0	1–5	51.5–285.6	5.8 ± 0.1	–0.007 ± 0.005
0.2	1–5	50.53–310.7	6.3 ± 0.3	–0.002 ± 0.001
1	1–5	45.56–280.3	5.6 ± 0.4	0.01 ± 0.02
2	1–5	45.62–254.43	5.0 ± 0.3	0.01 ± 0.01
4	1–5	45.58–232.8	4.6 ± 0.3	0.004 ± 0.01
10	1–9	42.39–379.3	4.0 ± 0.2	–0.004 ± 0.01
100[b]	1–5	42.8–148.8	2.6 ± 0.1	0.01 ± 0.004
		7		
0	1–5	1.231–6.225	126 ± 2	–0.07 ± 0.06
1	1–5	1.242–6.161	124 ± 2	0.04 ± 0.07
2	1–5	1.225–6.266	126 ± 2	–0.08 ± 0.06
4	1–5	1.265–6.122	123 ± 1	0.03 ± 0.04
5	1–5	1.248–6.3647	127.8 ± 0.3	–0.08 ± 0.06
10	1–5	1.154–6.1015	123.8 ± 0.5	–0.01 ± 0.02
100	1–5	0.58–4.6215	104 ± 4	–0.5 ± 0.1

[a]Intercept.
[b]$MTBDH^+ClO_4$.

Table 4. Effect of ionic strength on the rates of the reaction of 2-methyl-1-(4-nitrophenyl)-1-nitropropane **4** with MTBD in acetonitrile at 25°C.

10^3[Bu_4NClO_4] (M)	10^2[MTBD] (M)	k_{obs} (s^{-1})[b]	k_f (M^{-1} s^{-1})	itcp (s^{-1})[a]
0	1–5	5.15–28.56	5.8 ± 0.1	–0.007 ± 0.005
0.5	1–5	4.52–28.6	6.1 ± 0.2	–0.022 ± 0.007
1	1–5	4.88–30.09	6.4 ± 0.2	–0.02 ± 0.006
2	1–5	5.05–31.67	6.6 ± 0.3	–0.02 ± 0.01

[a]Intercept.
[b][$MTBDHClO_4$] = 1×10^{-4} M.

ing in two forms, ions and ion pairs, has been derived. This equation is fulfilled except for reactions of nitroalkanes with guanidine bases. The decrease in second-order rate constant up to 30% with concentration of BH^+ is not caused by ionic strength or by a side reaction with a base produced by the buffer. The kinetic scheme involving carbanionic intermediate is a possible explanation for these salt effects.

Guanidines are very strong bases and are characterized by low homoconjugation constants, which makes them potentially suitable for kinetic studies in acetonitrile. Unfortunately, the rates of their reactions with nitroalkanes show, as described above, relatively strong dependence on guanidinium cation concentration.

Experimental

Acetonitrile

Spectroscopic grade solvent from Romil was stored over CaH_2, distilled over P_2O_5, and finally fractionally distilled from CaH_2. The middle fraction was collected and stored under nitrogen free from moisture and CO_2. Solutions of C-acids and the bases as well as B/BH^+ buffer were prepared freshly before each kinetic or equilibrium experiments.

The B/BH^+ buffer of needed concentration was made using appropriate base and its perchlorate or picrate. The picrates and perchlorates were prepared as described earlier (5, 28).

© 1999 NRC Canada

Table 5. Rate constants for proton transfer from 2-methyl-1-(4-nitrophenyl)-1-nitropropane **4** and TNT **7** to MTBD measured in buffers of constant [MTBD]/[MTBDH$^+$] ratio in acetonitrile at 25°C.

[B]/[BH$^+$][a]	10^2[MTBD] (M)	k_{obs} (s^{-1})	k_f (M^{-1} s^{-1})	itcp (s^{-1})[b]	I[c]
		4			
5	1–5	0.0436–0.1785	3.36 ± 0.12	0.014 ± 0.004	0.01
10	1–5	0.0515–0.2245	4.35 ± 0.05	0.009 ± 0.002	0.1
10	1–5	0.0491–0.2126	4.04 ± 0.06	0.01 ± 0.002	0.01
50	1–5	0.073–0.2976	5.6 ± 0.2	0.022 ± 0.007	0.01
		7			
5	1–5	1.170–5.651	112 ± 1	0.05 ± 0.03	0.01
10	1–5	1.258–6.217	124.3 ± 0.7	–0.005 ± 0.024	0.1
10	1–5	1.187–5.703	112 ± 1	0.1 ± 0.04	0.01
50	1–5	1.258–5.85	115 ± 1	0.13 ± 0.04	0.01

[a]$MTBDHClO_4$.

[b]Intercept.

[c]Ionic strength adjusted with tetrabutylammonium perchlorate.

Scheme 2. Mechanism of the reaction of a nitroalkane with amine base including a carbanionic intermediate.

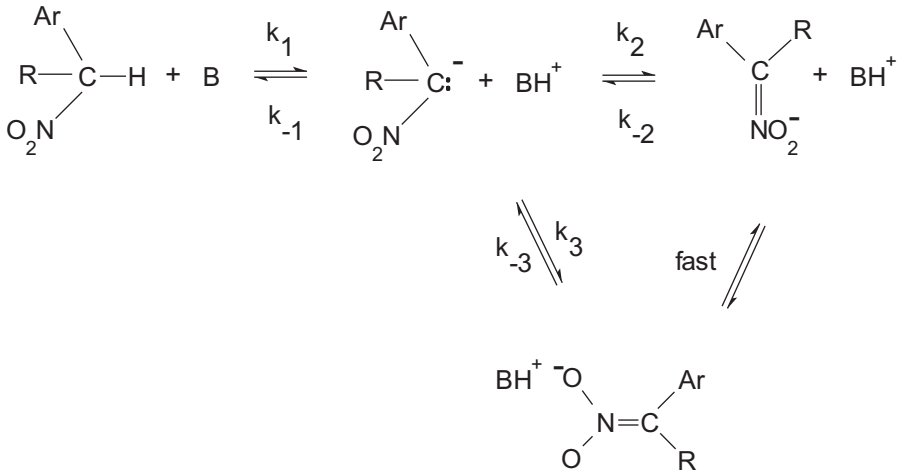

C-acids

4-Nitrophenylnitromethane **1** (8), 1-(4-nitrophenyl)-1-nitroethane **2** (7), 1-(4-nitrophenyl)-1-nitropropane **3** (7), 2-methyl-1-(4-nitrophenyl)-1-nitropropane **4** (7), 4-nitrophenylphenylcyanomethane **5** (29), and bis(4-nitrophenyl)cyanomethane **6** (8) were prepared according to procedures already published. The melting points and spectra after recrystallization from ethanol were in accordance with the literature. 2,4,6-Trinitrotoluene **7**, a commercial product, was purified by repeated crystallization from ethanol (mp 81°). The purity parameters were in agreement with the literature (30).

Bases

1,1,3,3-Tetramethylguanidine (TMG), commercial product from Aldrich, was stored over KOH pellets, then distilled under vacuum in an atmosphere of argon. 7-Methyl-1,5,7-triazabicyclo[4.4.0]dec-5-ene (MTBD) base, a commercial product from Aldrich, was used. The purity of the base was satisfactory as tested by NMR and titration (31). Tributylamine (Bu_3N), the commercial product from Fluka, p.a. (≥99.0% GC) was used. The purity of the sample was in agreement with FT NMR spectra published by Poucher and Behnke (32). All the operations were accomplished with protection from atmospheric carbon dioxide and moisture. The results of titration of base solutions were consistent with gravimetric concentrations within 1%. Kinetic measurements were performed with a stopped-flow spectrophotometer (Applied Photophysics) using a C-acid concentration of ca. 2.5×10^{-5} M and base concentrations shown in Tables 1–5. The values of k_{obs} were measured for typically five concentrations of base in a large excess over C-acid. Since different [BH$^+$] were used, in Tables 1–3, the ionic strength changes from one series to another and was not adjusted to a constant value with a neutral salt. In Table 5, results in buffers of a constant [B]/[BH$^+$] ratio are reported, and the ionic strength is adjusted with tetrabutylammonium perchlorate to 0.01 except for two entries where it is 0.1.

The value of spectrophotometric equilibrium constant K of 0.352 for the reaction between **4** and MTBD was calculated using the following equation: $K = f^2[BH^+][A^-]/[B][AH]$. [A$^-$] was found from the absorbance at $\lambda = 600$ nm, where the absorption of ion pair is negligible, [AH] was calculated as a difference of an analytical C-acid concentration and the sum of ([A$^-$] + [ion pair]). The K_d used for calculation of ion pair concentration is 0.0024 (5).

Acknowledgements

We gratefully acknowledge the financial support from KBN grant no. 3 TO9A 06914.

© 1999 NRC Canada

References

1. M. Eigen. *In* Proc. Nobel Symp. *Edited by* S. Claessen. Almquist and Wiksell, Stockholm. 1967. p. 245.
2. R.P. Bell. The proton in chemistry. 2nd ed. Chapman and Hall, London. 1973.
3. R.P. Bell. Chem. Soc. Rev. **3**, 513 (1974).
4. A. Müller, H. Ratajczak, W. Junge, and E. Diemann. Electron and proton transfer in chemistry and biology. Elsevier, Amsterdam. 1992.
5. W. Galezowski, M. Stanczyk, I. Grzeskowiak, and A. Jarczewski. J. Chem. Soc. Perkin Trans. 2, 2647 (1996).
6. W. Galezowski, I. Grzeskowiak, and A. Jarczewski. J. Chem. Soc. Perkin Trans. 2, 1607 (1998).
7. W. Galezowski and A. Jarczewski. J. Chem. Soc. Perkin Trans. 2, 1647 (1989).
8. W. Galezowski and A. Jarczewski. Can. J. Chem. **70**, 935 (1992).
9. P. Pruszynski and A. Jarczewski. J. Chem. Soc. Perkin Trans. 2, 1117 (1986).
10. E.F. Caldin, A. Jarczewski, and K.T. Leffek. Trans. Faraday Soc. **67**, 110 (1971).
11. E.F. Caldin and S. Mateo. J. Chem. Soc. Faraday Trans. 1, **72**, 112 (1976).
12. E.F. Caldin, S. Mateo, and P. Warrick. J. Am. Chem. Soc. **103**, 202 (1981).
13. K.T. Leffek and P. Pruszynski. Can. J. Chem. **66**, 1454 (1988).
14. M. Hojatti and K.T. Leffek. Can. J. Chem. **62**, 2653 (1984).
15. N. Sugimoto and M. Sasaki. J. Chem. Soc. Faraday Trans. 1, **81**, 1441 (1985).
16. J.F. Coetzee and G.R. Padmaanabhan. J. Am. Chem. Soc. **87**, 5005 (1965).
17. W. Galezowski, A. Jarczewski, M. Stanczyk, B. Brzezinski, F. Bartl, and G. Zundel. J. Chem. Soc. Faraday Trans. 1, **93**, 2515 (1997).
18. W. Galezowski, M. Stanczyk, and A. Jarczewski. Can. J. Chem. **75**, 285 (1997).
19. J.F. Bunnett. *In* Techniques of chemistry. *Edited by* E.S. Lewis. Vol. 6. Part 1. Wiley, New York, London, Sydney, Toronto. 1974. Chap. 8.
20. O. Rogne. Acta Chem. Scand. Ser. A, **32**, 559 (1978).
21. A.J. Kresge and M.F. Powell. J. Am. Chem. Soc. **103**, 201 (1981).
22. R. Schwesinger, J. Willaredt, H. Schlemper, M. Keller, D. Schmitt, and H. Fritz. Chem. Ber. **127**, 2235 (1994).
23. C.L. Perrin and J. Pressing. J. Am. Chem. Soc. **93**, 5705 (1971).
24. J.R. Keeffe, J. Morey, C.A. Palmer, and J.C. Lee. J. Am. Chem. Soc. **101**, 1295 (1979).
25. A.J. Kresge. Can. J. Chem. **52**, 1897 (1974).
26. F.G. Bordwell, W.J. Boyle, Jr., and K.C. Yee. J. Am. Chem. Soc. **87**, 3879 (1970).
27. F.G. Bordwell and W.J. Boyle, Jr. J. Am. Chem. Soc. **97**, 3447 (1975).
28. K.T. Leffek, P. Pruszynski, and K. Thanapaalasingham. Can. J. Chem. **67**, 590 (1989).
29. M. Hojatti and K.T. Leffek. Can. J. Chem. **64**, 2365 (1986).
30. P. Pruszynski and A. Jarczewski. Ann. Soc. Chim. Polonorum. **51**, 2171 (1977).
31. G. Schroeder, B. Leska, A. Jarczewski, B. Nowak-Wydra, and B. Brzezinski. J. Mol. Struct. **344**, 77 (1995).
32. C.J. Poucher and J. Behnke. The Aldrich library of ^{13}C and ^{1}H FT-NMR spectra. Vol. 1. 484 A.

© 1999 NRC Canada

Hydrolysis and aminolysis of alkyl xanthate esters and cellulose analogues

Eduardo Humeres, Valdir Soldi, Marilene Klug, Mauricéa Nunes, Célia M.S. Oliveira, and Patrick J. Barrie

Abstract: The hydrolysis and aminolysis of a series of S-substituted *O*-alkylxanthate esters was studied in 20% v/v aqueous methanol at 35°C. The pH–rate profiles of the hydrolyses showed water and hydroxide-ion-catalyzed reactions. The reaction of 2,4-dinitrophenyl cellulose xanthate (CelXDNP) and *p*-nitrobenzyl cellulose xanthate (CelXNB) with polyalanine and lysozyme produced a covalent bond between the polypeptide and the cellulose matrix, as shown by solid-state ^{13}C NMR. However, the nature of the bonding could not be identified. The reaction of nucleophiles (H_2O, OH^-, RNH_2) and xanthic esters was consistent with an addition–elimination mechanism through a tetrahedral intermediate. Brønsted plots against the pK_a of the nucleophile (β_{nu}) or the nucleofuge of the substrate (β_{lg}) were used to characterize the rate-determining step. The pK_a values of the nucleophiles ranged between –1.74 and 15.74, and for the nucleofuges, they were in the range of 10.50–0.92. For nucleophiles with pK_a values up to about 10, β_{lg} was 0.10–0.15, and β_{nu} changed from 0.48 to 0.35 for the strongest electron-withdrawing nucleofuge. It was concluded that the water-catalyzed hydrolyses, and also aminolyses with moderately basic amines, occur with rate-determining formation of the tetrahedral intermediate. For strong bases such as hydroxide ion, the disappearance of the intermediate becomes the slowest step. The reaction of cellulose xanthic esters with external nucleophiles as hydroxide ion and amines shows simple first-order kinetics and is slower than alkyl or sugar xanthates, probably due to the diffusion effect through the tight cybotactic region of cellulose.

Key words: hydrolysis, aminolysis, alkyl xanthic esters, cellulose xanthic esters, sugar xanthic esters.

Résumé : Opérant à 35°C, dans un mélange à 20% v/v de méthanol aqueux, on a étudié l'hydrolyse et l'aminolyse d'une série d'esters *O*-alkylxanthiques S-substitués. Les profils pH–vitesse de réaction d'hydrolyse montrent que l'eau et l'ion hydroxyde catalysent les réactions. Les réactions du cellulose xanthate de 2,4-dinitrophényle (CeIXDNP) et du cellulose xanthate de *p*-nitrophényle (CelXNB) avec la polyalanine et la lysosyme conduisent à la formation d'une liaison covalente entre le polypeptide et la matrice de cellulose, comme on a pu le montrer par RMN du ^{13}C à l'état solide. Toutefois, il n'a pas été possible de déterminer la nature de la liaison. La réaction des nucléophiles (H_2O, OH^-, RNH_2) avec les esters xanthiques est en accord avec un mécanisme d'addition–élimination impliquant un intermédiaire tétraédrique. On a utiliser les courbes de Brønsted en fonction du pK_a du nucléophile (β_{nu}) ou du nucléofuge du substrat (β_{lg}) pour caractériser l'étape cinétiquement limitante. Les valeurs de pK_a des nucléophiles s'étalent de –1,74 et 15,74 alors que celles des nucléofuges vont de 10,50 à 0,92. Pour les nucléophiles de valeurs de pK_a allant jusqu'environ 10, les valeurs de β_{lg} va de 0,10 à 0,15 alors que pour β_{nu} elles vont de 0,48 à 0,35 pour le nucléofuge portant le groupe électroattracteur le plus fort. On en conclut que l'hydrolyse catalysée par l'eau et l'aminolyse à l'aide d'amines de basicité modérée se produisent avec formation cinétiquement limitante de l'intermédiaire tétraédrique. Pour des bases fortes, telles que l'ion hydroxyde, la disparition de l'intermédiaire devient l'étape la plus lente. La cinétique de la réaction des esters xanthiques de la cellulose avec des nucléophiles externes, tels que l'ion hydroxyde et les amines, est du premier ordre simple et ces réactions sont plus lentes que celles des xanthates d'alkyles ou de sucres; ce résultat est probablement dû à l'effet de diffusion à travers la région cybotactique compacte de la cellulose.

Mots clés : hydrolyse, aminolyse, esters xanthiques d'alkyles, esters xanthiques de la cellulose, esters xanthiques de sucres.

[Traduit par la Rédaction]

Received December 2, 1998.

This paper is dedicated to Jerry Kresge in recognition of his many achievements in chemistry.

E. Humeres,[1] V. Soldi, M. Klug, M. Nunes, and C.M.S. Oliveira. Departamento de Química, Universidade Federal de Santa Catarina, Florianópolis, SC, 88040-900, Brazil.
P.J. Barrie. Department of Chemistry, University College London, 20 Gordon Street, London WC1H OAJ, U.K.

[1]Author to whom correspondence may be addressed. Telephone: 55 48 331 9219. Fax: 55 48 331 9711.
e-mail: humeres@mbox1.ufsc.br

 © 1999 NRC Canada

Introduction

Xanthic esters have been used in the synthesis of trithiocarbonates (1), in Friedel–Crafts reaction (2), Chugaev's reaction (3), and in the synthesis of thiols (4, 5), and also as derivatives for the isolation of carbohydrates (6). The hydrolysis of xanthic esters occurs as shown in eq. [1], and they react with amines displacing the thiol and forming a thioncarbamate ester (5). Thioncarbamates have shown high specificity as collectors in the flotation of sulfide minerals (7).

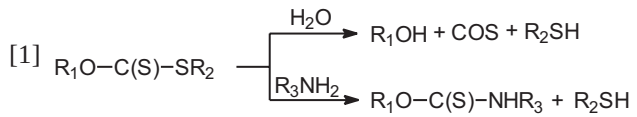

The study of the reactivity of xanthate ester moieties covalently bound to cellulose showed that the reaction of water was much faster compared to small analogue molecules (8). The water-catalyzed hydrolysis of *p*-nitrobenzyl (CelXNB) and 2,4-ditrophenyl cellulose xanthate (CelXDNP) occurs through two parallel processes (9, 10). The faster hydrolysis was ascribed to the reaction of the C-2 + C-3 isomers, whereas the slower hydrolysis corresponds to the C-6 isomer. The fast hydrolysis is due to an entropic effect of a well-oriented water molecule catalyzed by a second molecule that acts as a general base, as shown by proton inventory. Nucleophiles such as hydroxide ions and amines do not discriminate between the isomers, and the kinetics are first order (9).

In this paper, we seek to extend a previous study of the hydrolysis and aminolysis of a series of S-substituted *O*-ethylxanthate esters (11), to include sugar analogues and 2,4-dinitrophenyl cellulose xanthate, CelXDNP, a cellulose ester with a better leaving group, in order to get an insight into the mechanism of nucleophilic attack on cellulose xanthate esters and small molecule analogues.

Experimental

All reagents were of analytical grade and were used without further purification except the amines that were previously distilled in a high efficiency distilling column and kept under nitrogen atmosphere at low temperature.

The solid-state ^{13}C CP/MAS TOSS NMR measurements were performed using a Bruker MSL-300 spectrometer. All xanthate esters were identified by ^{1}H NMR and IR spectra.

S-Ethyl *O*-ethylxanthate (EXE)

Potassium *O*-ethylxanthate (EXK) was obtained using the classical procedure (12), adding carbon disulfide to a cooled solution of potassium hydroxide in ethanol. The product was recrystallized twice in ethanol; λ_{max} (ethanol) 301 nm. *S*-ethyl *O*-ethylxanthate was obtained after refluxing for 4 h, using an equimolar amount of EXK and ethyl bromide in ethanol. The product was washed with water, dried over anhydrous sodium sulfate, and distilled under vacuum: bp 76°C/10 mmHg (1 mmHg = 133.3 Pa) (lit. (13) 78°C/18 mmHg); λ_{max} 283 nm.

S-Benzyl *O*-ethylxanthate (EXB)

EXK and benzyl bromide (1:1 mol) were refluxed for 6 h in ethanol. The product was washed with water, dried over anhydrous sodium sulfate, and distilled under vacuum: bp 160°C/8 mmHg (lit. (14) 143°C/3 mmHg); λ_{max} (ethanol) 280 nm.

S-*p*-Nitrobenzyl *O*-ethylxanthate (EXNB)

EXK (2.2 g) dissolved in 10% aqueous EtOH, was allowed to react at room temperature with a solution of 2.1 g of *p*-nitrobenzyl bromide (acetone–ethanol). The reaction was followed by the appearance of the maximum at 280 nm. KBr was eliminated by filtration, and the solvent was evaporated in a rotatory evaporator. The product was recrystallized in ethanol: mp 61.6°C.

S-Phenyl *O*-ethylxanthate (EXP)

A solution of sodium ethoxide prepared from 2.3 g of sodium in 50 mL of dried ethanol was slowly added to a solution of 12 g of thiophosgene dissolved in 100 mL of chloroform at 0°C, and it was allowed to react for 3 h to obtain a solution of ethyl chlorothionoformate that was washed with water and dried over anhydrous magnesium sulfate. The solvent was stripped off in a rotatory evaporator, and the product was used without further purification (15*a*, *b*). The reaction of 1 g of sodium thiophenolate in 5 mL of dried ethanol with 1 g of ethyl chlorothionoformate produced EXP after 15 min of reaction at room temperature. Crystals of NaCl were filtered off, and the solution was treated with an aqueous solution of phosphate buffer at pH 8, the product then being extracted with diethyl ether and dried over anhydrous magnesium sulfate. Evaporation of diethyl ether left a yellow oil that was identified as EXP:TLC, alumina, hexane:ethyl acetate (1:1), one spot; λ_{max} 285 nm; after reaction with NaOH, λ_{max} 265 nm (thiophenol); after reaction with ethylamine, λ_{max} 245 nm (thioncarbamate) (15*c*).

S-*p*-Nitrophenyl *O*-ethylxanthate (EXNP)

Ethyl chlorothionoformate (3.5 g), obtained as described above, was added to 1.45 g of *p*-nitrothiophenol in 1.0 mL of pyridine, and then the temperature was raised to 60°C for 1 h. The precipitate was dissolved in 30 mL of chloroform and washed with water, subsequently being dried and then concentrated in a rotatory evaporator. Crystals were obtained after 8 h in the refrigerator: mp 51°C (lit. (16) 50°C).

S-2,4-Dinitrophenyl *O*-ethylxanthate (EXDNP)

EXK (9.2 g) dissolved in 30 mL of water was mechanically shaken with a solution of 10.1 g of 1-fluoro-2,4-dinitrobenzene in 300 mL of methylene chloride, for 64 h at room temperature. The methylene chloride phase was washed with water and dried over anhydrous magnesium sulfate. The solvent was stripped off in a rotatory evaporator, and the residue was crystallized in methanol: mp 43.0°C; λ_{max} 267 nm; ms, mol. wt. 288 g mol^{-1}. Anal. (calculated values for $C_9H_8N_2O_5S_2$ in parentheses): C 37.5 (37.5), H 2.7 (2.8), N 9.7 (9.7), S 21.5 (22.0).

Methyl α-D-glucopyranoside 6-(*S*-benzyl xanthate) (MGXB)

CS_2 (2.5 mL) was added to a solution of 22.9 g of α-methyl-D-glucopyranoside in 23.6 mL of water, with magnetic stirring at room temperature, and then, slowly, 6 mL of 20 M NaOH was also added. After being allowed to react

© 1999 NRC Canada

for 5 h, the solution was neutralized with acetic acid cooled to 10°C. Benzyl bromide, 11.0 g, in 20 mL of methylene chloride, was then put in slowly, and the stirring was kept up for 2 h. The product was extracted with chloroform, and the solution was dried over anhydrous sodium sulfate. The solvent was evaporated under vacuum. The product was purified by column chromatography using alumina and eluted with hexane–CCl_4–ethanol: R_f 0.66; λ_{max} 284 nm; $[\alpha]_D^{25}$ = +80.3° (lit. +79.8°) (6).

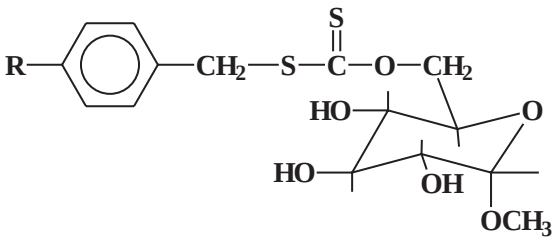

R = H (MGXB), NO_2 (MGX–6)

The preparation of methyl α-D-glucopyranoside 6-(*S*-*p*-nitrobenzyl xanthate) (MGX-6) has been already reported (10).

2,4-Dinitrophenyl cellulose xanthate (CelXDNP) and *p*-nitrobenzyl cellulose xanthate (CelXNB) were obtained from commercial cotton tissue as described previously (9, 10), and were characterized from the degree of substitution DS (number of xanthate ester groups per 100 glucoanhydropyranose units) and the solid-state ^{13}C NMR spectra.

Reaction of CelXDNP and CelXNB with polypeptides

The reaction of cellulose esters with polyalanine (mol. wt. 1000–5000) and lysozyme was studied in dried acetone and in water saturated at pH 10, with the polypeptide at room temperature under nitrogen atmosphere. The product was exhaustively washed with water, ethanol, and diethyl ether, and finally dried under vacuum. The modified celluloses were analyzed by solid-state ^{13}C NMR.

Kinetics

The hydrolyses and aminolyses were carried out in 20% v/v aqueous methanol, at 35°C. The kinetics were followed spectrophotometrically by the disappearance of the xanthate at appropriate wavelengths during at least three half-lives and were always pseudo-first order. The pH and pK_a values were corrected to the appropiate temperature (17).

In the range of pH 3–11, the hydrolyses were carried out in the presence of buffers at 10–30 mM concentrations, and the value of k_{obs} was extrapolated to zero buffer concentration.

For the aminolyses, the amine itself acted as buffer. For each ester and amine, the reaction was measured at three pH values in the range of pK_a ±1 of the amine. For each amine, the second-order rate constant k_N for the aminolysis by the free amine was obtained from a plot of k_2, the second-order rate constant at each pH, against the molar fraction of the free amine. The ester concentration was ca. 10^{-4} M, and the amine concentration was 0.03–0.1 M. The ionic strength was maintained at 0.1 (KCl).

Fig. 1. pH–rate profile of the hydrolysis of *S*-phenyl *O*-ethylxanthate at 35°C in 20% v/v aqueous methanol, μ = 0.1 (KCl).

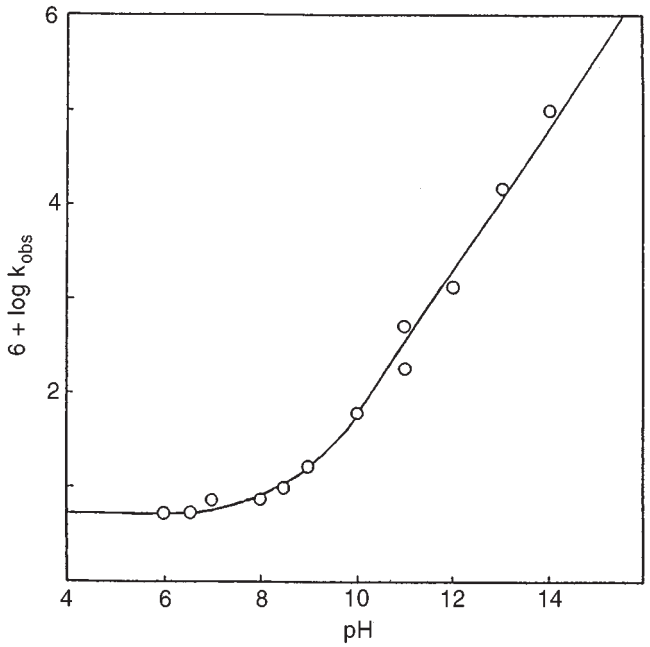

Results

pH–rate profiles

The pH–rate profiles of the series of S-substituted *O*-ethyl xanthates were obtained in 20% v/v aqueous methanol at 35°C. They are all similar to the example shown in Fig. 1, where k_{obs} is the rate constant extrapolated to zero buffer concentration, and can be expressed by eq. [2]. There is

$$[2] \qquad k_{obs} = k_{H2O} + k_{OH}[OH^-]$$

a pH-independent region with rate constant k_{H2O} of the water-catalyzed reaction, followed at high pH by a hydroxide-catalyzed reaction with second-order rate constant k_{OH}. Table 1 shows the rate constants obtained, including those of some cellulose and sugar xanthate esters. The continuous line in Fig. 1 was drawn using the rate constant values of Table 1.

For the water-catalyzed hydrolysis of CelXNB and CelXDNP, there are two parallel reactions with rate constants k'_{H2O} for the fast hydrolysis and k''_{H2O} for the slower one. We have included these values in order to compare them with those of the series of S-substituted *O*-ethylxanthates and methylglucose xanthates analogues.

Aminolyses

The aminolyses were carried out in 20% aqueous methanol and at low ionic strength (0.1 M KCl), because the low solubility of xanthate esters produces plots of k_{obs} vs. N_T, total amine concentration, that deviate from linearity due to changes in the activity coefficients of the species involved (18).

The aminolyses were carried out with ethylenediamine (EDA, pK_1), ethanolamine (EA), and *n*-butylamine (BA).

© 1999 NRC Canada

Table 1. Rate constants for the hydrolysis of some xanthate esters in 20% v/v aqueous methanol at 35°C.[a]

Ester	pK_a(RSH)		k_{H2O} (s^{-1})	k_{OH} (M^{-1} s^{-1})
EXE	10.50		3.26×10^{-6}	2.27×10^{-3}[b,c]
EXB	9.43		1.57×10^{-6}	3.83×10^{-2}
EXNB	8.60		1.35×10^{-6}	13.7×10^{-2}
EXP	6.43		5.20×10^{-6}	10.5×10^{-2}[c]
EXNP	4.50		2.54×10^{-6}	92.9×10^{-2}[c]
EXDNP	0.92		3.70×10^{-5}	13.8[c]
MGXB	9.43		1.33×10^{-6}	2.84
MGX-6[d]	8.60		4.57×10^{-7}	5.39
CelXNB	8.60	k'_{H2O}	2.97×10^{-3}[e]	2.65×10^{-2}[c]
		k''_{H2O}	4.29×10^{-5}[e]	
CelXDNP	0.92	k'_{H2O}	1.37×10^{-2}	37.5×10^{-2}[c]
		k''_{H2O}	6.52×10^{-5}	

[a]μ = 0.1 (KCl).
[b]20% aqueous dioxane.
[c]μ = 1.0 (KCl).
[d]Reference 10.
[e]10% aqueous ethanol.

Table 2. Second-order rate constants for the aminolysis of some xanthic esters by free amines at 35°C.[a]

Ester	EDA	EA	BA
		pK_a(RNH_3^+)	
	7.27	9.21	10.27
		10^2 k_N (M^{-1} s^{-1})	
EXE	0.27	2.90	6.25
EXB	0.59	8.15	14.7
EXNB	1.03	8.40	12.0
CelXNB[b]	0.46	2.50	3.45
EXP	2.38	13.5	29.6
EXNP	4.02	20.6	32.3
EXDNP	10.8	38.7	138.7
CelXDNP	9.45	23.8	36.3

[a]In 20% v/v aqueous methanol; μ = 0.1 (KCl).
[b]Reference 9.

Table 3. Reaction of cellulose xanthate esters with polyalanine and lysozyme.

Ester	Polypeptide	C=O/mol	Area(C=O)	Area(C-1)	DS[d]
CelXDNP[a]	PolyAla[b]	70.4–14.1[c]	2.46	26.29	0.1–0.7[c]
CelXDNP[a]	Lysozyme[b]	129	16.95	23.64	0.6
CelXDNP[a]	Lysozyme[f]	129	22.8	43.4	0.4
CelXNB[e]	PolyAla[f]	70.4–14.1[c]	24.8	12.1	2.9–14.6[c]
CelXNB[e]	PolyAla[f,g]	70.4–14.1[c]	26.2	19.5	1.9–9.5[c]
CelXNB[e]	Lysozyme[f]	129	34.7	21.8	1.2
CelXNB[e]	Lysozyme[f,g]	129	21.3	20.5	0.8
CelXNB[h]	Lysozyme[i]	129	1.2	12.3	0.1

[a]DS = 7.9 (aminolysis); DS = 14.8 (NMR).
[b]In dried acetone, 48 h reaction.
[c]For molecular weight in the range of 5000 and 1000, respectively.
[d]Number of moles of polypeptide per 100 glucopyranoside units.
[e]DS = 15.2 (aminolysis); DS = 27.6–35.2 (NMR), DS = 29.1 (S).
[f]In aqueous saturated solution, 48 h reaction.
[g]After washing again exhaustively with water.
[h]DS = 6.76 (aminolysis); DS = 4.24 (NMR).
[i]In aqueous solution, 148 h reaction. A DS = 1.07 with lysozyme would duplicate the weight of the CelXR.

The plots of k_{obs} vs. N_T were all linear and can be represented by eq. [3],

$$[3] \qquad k_{obs} = k_o + k_N[N]$$

where k_o is the rate constant including all the terms of hydrolysis, and k_N and [N] are the second-order rate constant and the concentration of the free amine, respectively. Table 2 shows the values of k_N for the series of S-substituted *O*-ethylxanthates and some cellulose xanthate esters analogues.

The reaction of CelXNB and CelXDNP with polyalanine and lysozyme (Table 3) was followed by solid-state ^{13}C NMR, and the spectra did not change after extensive washing with water, ethanol, and diethyl ether, showing that the polypeptide was covalently bound to the cellulose matrix. The spectrum of each polypeptide was clearly superimposed on that of the cellulose. However, the signal of the expected thioncarbamate group at 190 ppm was not observed, and we are unable to come to any conclusion as to which reaction produced the bonding. The DS of the cellulose after reaction was calculated from the area of the signal of the carbonyl groups at about 177 ppm and the area of the signal due to C-1 of cellulose in the region of 90–110 ppm according to eq. [4]. In general, the DS was higher for CElXNB, probably

$$[4] \qquad DS = \frac{\text{Area(C=O)/number C=O per mol}}{\text{Area(C-1)}}$$

because the competitive hydrolysis is too fast for CelXDNP. It is important to note that a DS of about 1.0 would duplicate the weight of the cellulose ester in the reaction with lysozyme.

It is possible that the intensity of the signal of the carbon from the thiocarbonil group is too low to be detected. For the polyalanine, the ratio of the signal due to C=O per mol to one C=S should be in the range of 14–70, and for the lysozyme, this ratio is 129:1. It is also possible that the weak

© 1999 NRC Canada

Fig. 2. Brønsted-type plot of the spontaneous hydrolysis of S-substituted ethylxanthates (○) versus the pK_a of the leaving thiol, at 35°C in 20% v/v aqueous methanol, μ = 0.1 (KCl); □, sugar xanthates in 10% aqueous ethanol; ■, cellulose esters.

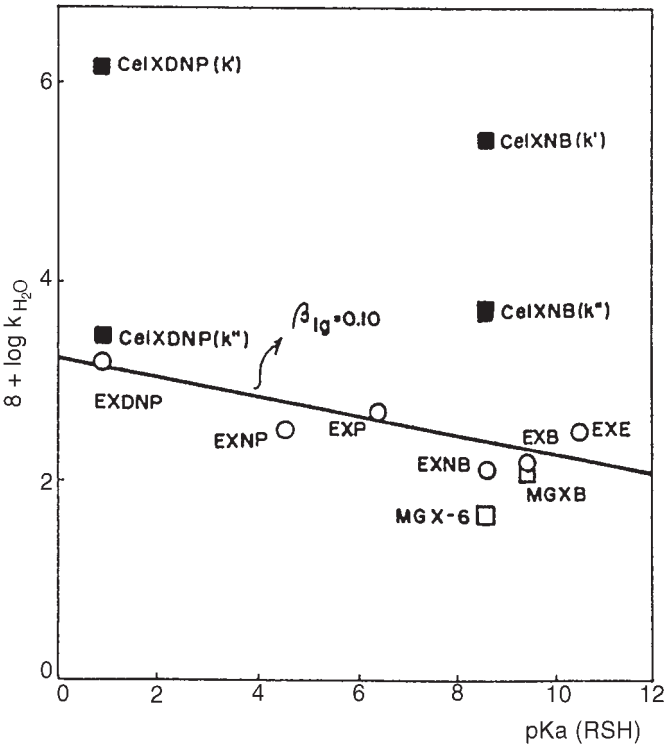

C=S signal was eliminated along with the side bands when using the TOSS technique.

Discussion

It is reasonable to assume that the reaction of xanthate esters with nucleophiles occurs, similar to the carboxylic esters, according to eq. [5] (19, 20) by an addition reaction that produces a tetrahedral intermediate followed by the elimination of the thiolate moiety.

[5] 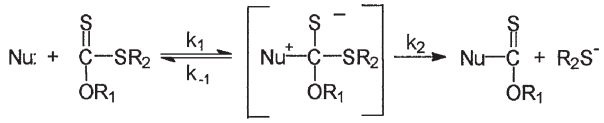

where

[6] $$k_{nu} = \frac{k_1}{1 + k_{-1}/k_2}$$

Brønsted plots of log k_{nu} against the pK_a of the nucleophile or the nucleofuge of the substrate, provide an insight into the rate-determining step of the reaction (21). Linear plots indicate no change in the rate-determining step, and β_{nu} and β_{lg} are related to the difference in charge between the initial and the corresponding transition state, that is, to the bond order of the Nu—C or C—S bonds.

Fig. 3. Brønsted-type plot of the hydroxide-catalyzed hydrolysis of S-substituted ethylxanthates (○) versus the pK_a of the leaving thiol, at 35°C in 20% v/v aqueous methanol, μ = 0.1 (KCl); □, sugar xanthates; ■, cellulose esters; μ = 1.0 (KCl): EXE, EXP, MGX-3, CelXNB, CelXDNP.

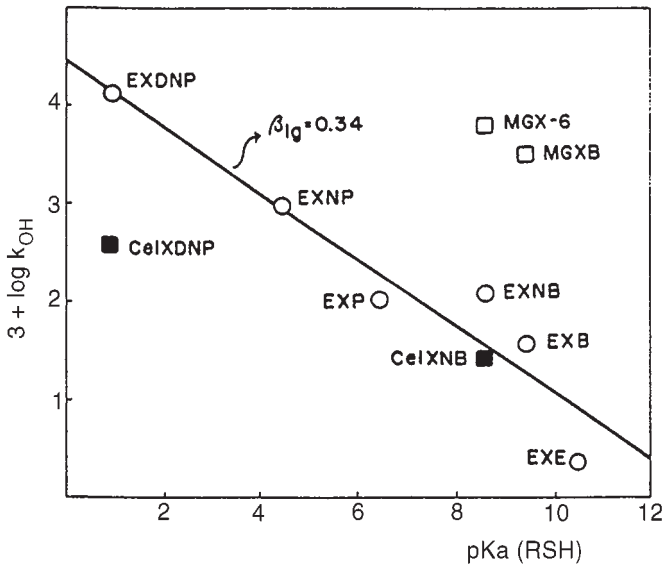

Hydrolyses

For the hydrolyses, Nu = H_2O, OH^-, the initial product is a thioncarbonate that decomposes rapidly to R_1OH and COS as shown in eq. [1]. The tetrahedral intermediate might be able to decompose through different pathways, but for EXE it was found that EtSH appears at the same rate of disappearance of the xanthic ester, and considering the difference of the pK_a values of ethanol and ethanethiol, the intermediate should decompose to product with C—SR_2 bond fission alone (22). This behavior should be similar when the pK_a of the nucleofuge thiol is lower.

The Brønsted-type plot of Fig. 2 for the spontaneous hydrolysis of the S-substituted *O*-ethylxanthate series is linear (the rate-determining step does not change), and β_{lg} = 0.10, suggesting that the virtual tetrahedral intermediate (23) presents a low perturbation of the C—S bond of an early transition state and that the rate-determining step must be the nucleophilic attack of the water molecule to form the intermediate. This conclusion supports the mechanism that has been postulated for cellulose xanthate esters, where a second water molecule acts as a general base catalyst for the deprotonation of the intermediate (8–10). In Fig. 2, it can be observed that small sugar xanthate molecules with hydrophilic R_1O moiety, such as MGXB and MGX-6, are somewhat less reactive than the ethyl analogue. However, the fast spontaneous hydrolysis of the cellulose esters CelXDNP and CelXNB, is 2 and 3 orders of magnitude faster than the *O*-ethylxanthate, and it has been proposed that this is a consequence of the supramolecular catalysis induced by the water molecules of the cybotactic region of the polysaccharide on the water molecule that acts as a nucleophile (9–10).

The Brønsted plot of Fig. 3 for the hydroxide-ion-catalyzed hydrolysis of the same *O*-ethylxanthate series is also linear, but β_{lg} = 0.34, indicating a later transition state

© 1999 NRC Canada

Table 4. Brønsted parameters for the reaction of S-substituted *O*-ethylxanthates in 20% v/v aqueous methanol at 35°C.[a]

Ester	pK_{lg}	H_2O	EDA	EA	BA	OH^-	β_{nu}[e]
				pK_{nu}			
		–1.74	7.27	9.21	10.27	15.74	
EXE	10.50					[bc]	0.48
EXB	9.43						0.46
EXNB	8.60						0.37
CelXNB[g]	8.60	[d]				[c]	0.33
EXP	6.43					[c]	0.36
EXNP	4.50					[c]	0.32
EXDNP	0.92					[c]	0.35
CelXDNP	0.92					[c]	0.20
				β_{lg}[f]			
		0.10	0.15	0.12	0.15	0.34	

[a] μ = 0.1 (KCl).
[b] 20% aqueous dioxane.
[c] μ = 1.0 (KCl).
[d] Fast hydrolysis (k'), in 10% aqueous ethanol.
[e] Calculated considering only aminolyses.
[f] Without considering the cellulose esters.
[g] Reference 9.

because of a higher activation barrier for the intermediate decomposition, and consequently, a change of rate-determining step: a fast intermediate formation is followed by a slower decomposition. These arguments will be supported by the discussion on the mechanism of aminolysis.

In this particular case, sugar xanthates are faster than the ethyl analogues, but a neighboring OH effect should be disregarded because the cellulose xanthate esters hydrolyze either at about the same rate (CelXNB) or much slower (CelXDNP) (Fig. 3). Considering the critical micelle concentration of MGXB, it is possible that the rate acceleration is due to micelle catalysis. With the present data, it is not possible to understand the slow basic hydrolysis of CelXDNP.

Aminolyses

When the nucleophile is an amine, the tetrahedral intermediate is a zwitterion that must deprotonate at a diffusion-controlled rate before forming the products (eq. [7]).

The second-order rate constants of the reaction of free amines with xanthic esters are presented in Table 2. The reaction allows the calculation of both β_{nu} and β_{lg} because the Brønsted plots are all linear. For the series of *O*-ethylxanthates, β_{nu} decreases from 0.48 for EXE to 0.35 for EXDNP (Table 4) because of the increasing electron-withdrawing effect of the nucleofuge that lowers the kinetic barrier and the transition state that occurs earlier in the reaction coordinate. On the other hand, the reaction of these amines with the xanthate series, produced low β_{lg} values. These results are consistent with a mechanism where the rate-determining step is the nucleophilic attack of the amine, and formation of the tetrahedral intermediate that disappears in a fast step because sulfur can expel the leaving group better than oxygen (19, 20). The situation is similar to that of the water-catalyzed reaction, while for the hydrolysis catalyzed by hydroxide ion the extent of the C—S bond breakage indicates that the intermediate is formed in a fast step, and the slower step is the second one. A change in the rate-determining step accompanies a significant change in the magnitude of β_{nu} and β_{lg} (19).

To compare a β-value with the calibrating equilibrium (24), the effective charge on the amine N or thiol S of the substrate has to be calculated. For primary alkyl amines, the effective charge on the N should be very close to zero, and the effective charge in the transition state should be essentially equal to β_{nu}. There is no information on the effective charge on the thiol S of xanthate esters. However, this value should be constant for the series of S-substituted esters, and $\Delta\beta_{lg}$ values for the different nucleophiles do not change, without consequences on the conclusions about the change of the rate-determining step.

Aminolyses of cellulose xanthate esters are slower than ethylxanthate analogues. Similar to the hydroxide ion-catalyzed hydrolyses, the aminolyses were strictly first-order, but the values of β_{nu} were lower than those for the *O*-ethylxanthates (Table 4). The slower attack by external nucleophiles can be interpreted as a consequence of the restricted diffusion through the tight cybotactic region. However, the lower β_{nu} values merit a more detailed study.

[7] 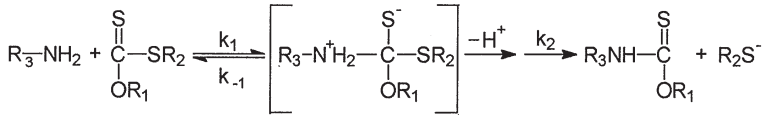

© 1999 NRC Canada

Acknowledgements

We thank the University College London for the solid-state NMR spectra that were obtained through the ULIRS Solid State NMR Service.

References

1. (*a*) H. Yoshida, T. Ogata, and S. Inokawa. Bull. Chem. Soc. Jpn. **44**, 3106 (1971); (*b*) S.M. Iqbal and L.N. Owen. J. Chem. Soc. 1030 (1960); (*c*) C. Overberger and A. Drucker. J. Org. Chem. **29**, 360 (1964); (*d*) S. Hashi, M. Furukawa, Y. Fujino, T. Nakao, and K. Nagato. Chem. Pharm. Bull. **19**, 1594 (1971); (*e*) K. Tomida and M. Nagano. Chem. Pharm. Bull. **17**, 2442 (1969); (*f*) Chem. Pharm. Bull. **20**, 2302 (1972).
2. T. Kawata, K. Harano, and T. Taguchi. Chem. Pharm. Bull. **21**, 604 (1973).
3. (*a*) E.S. Gould. Mechanism and structure in organic chemistry. Holt–Dryden Book, New York. 1959. Chap. 12; (*b*) T.H. Lowry and K.S. Richardson. Mechanism and theory in organic chemistry. Harper & Row, New York. 1976. Chap. 7.
4. (*a*) T. Taguchi, Y. Kiyoshima, O. Komori, and M. Mori. Tetrahedron Lett. **41**, 3631 (1969); (*b*) C. Djerassi, M. Gorman, F.X. Markley, and E.B. Oldenburg. J. Am. Chem. Soc. **77**, 568 (1955).
5. E.E. Reid. Organic chemistry of bivalent sulfur. Vol. 4. Chem. Publ. Co., New York. 1962.
6. (*a*) D. Trimnell, W.M. Doane, C.R. Russell, and C.E. Rist. Carbohydr. Res. **5**, 166 (1967); (*b*) J.J. Willard and E. Pacsu. J. Am. Chem. Soc. **82**, 4347 (1960).
7. A.V. Glemobtskii, L.Ya. Shubov, and A.K. Livshits. Tsvetn. Metal. **41**, 11 (1968).
8. E. Humeres, C.M.S. Oliveira, V.T. Osellame, and I. de Souza. J. Phys. Org. Chem. **4**, 573 (1991).
9. E. Humeres, L.F. Sequinel, M. Nunes, C.M.S. Oliveira, and P.J. Barrie. J. Phys. Org. Chem. **7**, 287 (1994).
10. E. Humeres, L.F. Sequinel, M. Nunes, C.M.S. Oliveira, and P.J. Barrie. Can. J. Chem. **76**, 960 (1998).
11. E. Humeres, M. Klug, and V. Soldi. Atual. Fis.-Quim. Org. 136 (1984).
12. A.I. Vogel. A textbook of practical organic chemistry. Longmans, London. 1971.
13. G. Bulmer and F.G. Mann. J. Chem. Soc. 666 (1945).
14. I.B. Douglas and T.B. Johnson. J. Am. Chem. Soc. **60**, 1486 (1938).
15. (*a*) B. Sturm and G.Z. Gattow. Anorg. Allg. Chem. **508**, 136 (1984); (*b*) D. Martin and W. Mucke. Chem. Ber. **98**, 2059 (1965); (*c*) N. Al-Awadi and R. Taylor. J. Chem. Soc. Perkin Trans. 2, 177 (1988).
16. J.R. Cox, Jr., C.L. Gladys, L. Field, and D.E. Pearson. J. Org. Chem. **25**, 1083 (1960).
17. (*a*) D.D. Perrin. Aust. J. Chem. **17**, 484 (1964); (*b*) E. Humeres, J. Quijano, and M.M. de S. Sierra. J. Braz. Chem. Soc. **1**, 99 (1990).
18. O. Scalco. M.Sc. dissertation. Universidade Federal de Santa Catarina, Florianópolis. 1980.
19. (*a*) A.C. Satterthwait and W.P. Jencks. J. Am. Chem. Soc. **96**, 7018 (1974); (*b*) D.J. Palling and W.P. Jencks. J. Am. Chem. Soc. **106**, 4869 (1984).
20. P. Campbell and B.A. Lapinskas. J. Am. Chem. Soc. **99**, 5378 (1977).
21. A. Williams. Acc. Chem. Res. **22**, 387 (1989).
22. J.R.B. Lobato. M.Sc. dissertation. Universidade Federal de Santa Catarina, Florianópolis. 1979.
23. R.L. Showen. *In* Transition states of biochemical processes. Part 1. *Edited by* R.D. Gandour and R.L. Schowen. Plenum Press, New York. 1978. Chap. 2.
24. A. Williams. Acc. Chem. Res. **17**, 425 (1984).

© 1999 NRC Canada

Cage peroxides having planar bridgehead nitrogen atoms

John T. Edward, Francis L. Chubb, Denis F.R. Gilson, Rosemary C. Hynes, Françoise Sauriol, and Alain Wiesenthal

Abstract: Three new cage peroxides, 1,6-diaza-3,4,8,9-tetraoxabicyclo[4.4.2]dodecane (**3a**),1,6-diaza-3,4,8,9-tetraoxa-11-methylbicyclo[4.4.2]dodecane (**3b**), and 1,6-diaza-3,4,8,9-tetraoxatricyclo[4.4.2.4^{11,12}]hexadecane (**4**), have been prepared by reaction of 1,2-diaminoethane, 1,2-diaminopropane, and *trans*-1,2-diaminocyclohexane, respectively, with formaldehyde and hydrogen peroxide in aqueous acidic solution. Their structures have been established by X-ray diffraction, and show the bridgehead nitrogen atoms to be predominantly sp^2 hybridized. The structures accord with ^{1}H and ^{13}C NMR spectra. Variable temperature NMR studies show that the diperoxide **3a** begins to undergo rapid inversion (on the NMR time scale) at about 303 K; up to 370 K the diperoxides **3b** and **4** show no conformational change.

Key words: cage compounds, formaldehyde, peroxides, amine nitrogen, hybridization.

Résumé : On a préparé trois nouveaux peroxydes en cage, les 1,6-diaza-3,4,8,9-tétraoxabicyclo[4.4.2]dodécane (**3a**), 1,6-diaza-3,4,8,9-tétraoxa-11-méthylbicyclo[4.4.2]dodécane (**3b**), et 1,6-diaza-3,4,8,9-tétraoxatricyclo[4.4.2.4^{11,12}]hexadécane (4) par réaction respectivement des 1,2-diaminoéthane, 1,2-diaminopropane et *trans*-1,2-diaminocyclohexane avec le formaldéhyde et le peroxyde d'hydrogène en solution aqueuse acide. On a identifié les structures par diffraction des rayons X et on a montré que les atomes d'azote en tête de pont sont hybridés principalement sous la forme sp^2. Les structures sont en accord avec les spectres RMN du ^{1}H et du ^{13}C. Des études de RMN à températures variables montrent que le diperoxyde **3a** commence à subir une inversion rapide (à l'échelle de temps de la RMN) à environ 303 K; à des températures allant jusqu'à 370 K, les composés **3b** et **4** ne présentent pas de changements conformationnels.

Mots clés : composés en cage, formaldéhyde, peroxydes, azote d'une amine, hybridation.

[Traduit par la Rédaction]

Introduction

Alder and his colleagues (1) prepared the cage compound **1** by a multistep synthesis, and the chemistry of this and other cage compounds having bridgehead nitrogen atoms has been reviewed (2). The formally similar cage triperoxide **2** (hexamethylene triperoxide diamine or HMTD), which also has bridgehead nitrogen atoms joined by three four-atom bridges, was prepared in 1900 by Baeyer and Villiger (3) in a one-pot synthesis (which must involve many steps) in which formaldehyde reacted with ammonium sulfate and hydrogen peroxide in aqueous solution.

At room temperature, Alder's cage diamine **1** exists in several conformations. In the conformation **1** represented above, the lone pairs of electrons of both tetrahedral nitrogen atoms point inwards (in–in) into the cage; in other conformations, the lone pairs are in–out and out–out. The tetrahedral nitrogen atoms of **1** are slightly flattened. In a typical tertiary amine, the nitrogen atom is 0.49 Å out of the plane of the three attached carbon atoms; in the diamine **1**, they are 0.31 Å out of this plane (4). This flattening probably takes place because of van der Waals repulsions between the two nitrogen atoms, which have van der Waals radii in the neighbourhood of 1.55 Å (5–8) and are only 2.806 Å apart in **1** (4).

1

2

On the other hand, in HMTD (2) the nitrogen atoms have been shown in crystallographic studies of Schaefer et al. (9) to be exactly planar with three-fold coordination, and with N—C distances of 1.42 Å, as compared with 1.47 Å for a

Received February 23, 1999.

This paper is dedicated to Jerry Kresge in recognition of his many achievements in chemistry.

J.T. Edward,[1] F.L. Chubb, D.F.R. Gilson,[1] R.C. Hynes,[1,2] F. Sauriol,[1,3] and A. Wiesenthal. Department of Chemistry, McGill University, 801 Sherbrooke St. W, Montreal, QC H3A 2K6, Canada.

[1]Authors to whom correspondence may be addressed.
[2]Present address: Department of Biochemistry, University of Toronto, Toronto, ON M5S 1A8, Canada.
[3]Present address: Department of Chemistry, Queen's University, Kingston, ON K7L 3N6, Canada.

© 1999 NRC Canada

typical tertiary amine. The molecule exists as a racemic mixture of two chiral helices having C-O-O-C torsional angles of ±129.3°, and not as the achiral cylinder **2** shown above (for ease of representation) with torsional angles of zero. Schaefer et al. have shown the nonbonded N···N distance in **2** to be 3.193 Å.

The cage compound **1** has two nitrogen atoms joined by three tetramethylene bridges, the cage **2** by three -CH_2-O-O-CH_2- bridges. Is a "mixed" cage possible, having the nitrogen atoms bridged by one tetramethylene and two -CH_2-O-O-CH_2- bridges? The attempt to prepare this compound failed, the reaction of 1,4-diaminobutane with formaldehyde and hydrogen peroxide in acidic solution yielding no insoluble product. However, the reactions of some 1,2-diaminoalkanes (1,2-diaminoethane, 1,2-diaminopropane, and *trans*-1,2-diaminocyclohexane) yielded peroxidic products. The structures of these three new peroxides have been established by X-ray crystallography and two-dimensional NMR, and proved to have some of the unusual features noted in the structure of HMTD (**2**).

Experimental

General

Melting points were recorded on a Gallenkamp apparatus and are uncorrected. Combustion analyses for C, H, and N were carried out by Galbraith Laboratories, Knoxville, Tenn. Proton magnetic resonance (^{1}H NMR) spectra were recorded on a Varian Unity-500 spectrometer operating at 499.843 MHz for protons and at 125.697 MHz for carbon-13. Chloroform-*d* was used as solvent unless otherwise noted.

Various 2D experiments were carried out to assign the structures: COSY, and the two-phase sensitive experiments: HMQC and NOESY. The phase in these 2D experiments was detected using the hypercomplex mode. For COSY, the acquisition was repeated for four transients, and 256 complex increments were acquired. The data were processed using a pseudo-echo-shaped function. The final data matrix having 1K by 1K points was symmetrized (zero filling was used only in the evolution domain). For NOESY, the data were obtained using a mixing time of 0.3 s and a relaxation delay of 1 s. The acquisition was repeated for 16 transients, and 256 complex increments were acquired. The data were processed using a Gaussian apodization function. The final data matrix had 2K by 1K points (zero filling was used only in the evolution domain).

The HMQC experiment was preceded by a BIRD nulling period. The recycling delay was set to 1 s, while the nulling period (following the BIRD pulse) was set to 0.3 s. The acquisition was repeated eight times and 256 fids were acquired. During acquisition of the proton spectra, ^{13}C broadband WALTZ decoupling was applied. The data were processed with Gaussian function, with zero filling in the evolution domain (^{13}C). The final matrix size was 2K by 1K. The spectral window in the carbon domain was about 100 ppm and in the proton domain about 7 ppm.

1,6-Diaza-3,4,8,9-tetraoxabicyclo[4.4.2]dodecane, ***3a***

Aqueous formaldehyde (37%, 22 mL) was added dropwise to a stirred solution of 1,2-diaminoethane (3.0 g) in acetic acid (12 mL), followed by hydrogen peroxide (30% w/w; 30 mL), the temperature being kept below 20°C by an ice bath. The diperoxide **3a** precipitated immediately and was removed by filtration, washed copiously with water to remove acidity, and dried under reduced pressure in a desiccator: yield 8.0 g (91%), mp 79–80°C, raised to 117°C by recrystallization from ethanol.

1,6-Diaza-3,4,8,9-tetraoxa-11-methylbicyclo[4.4.2]dodecane, ***3b***

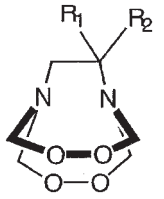

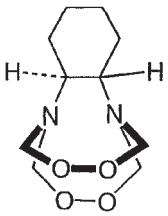

3a : $R_1 = R_2 = H$

3b : $R_1 = CH_3$, $R_2 = H$

3c : $R_1 = R_2 = CH_3$

4

Aqueous formaldehyde (37%, 22 mL) was added dropwise to stirred 1,2-diaminopropane (3.7 g), followed by acetic acid (12 mL), and then hydrogen peroxide (30% w/w; 30 mL), the temperature being kept below 20°C by an ice bath. The diperoxide **3b** precipated and was removed by filtration and washed with water: yield 6.2 g (72%), mp 80–81°C, decomp with frothing 90°C, unchanged by recrystallization from petroleum ether.

1,6-Diaza-3,4,8,9-tetraoxatricyclo[4.4.2.4^{11,12}]hexadecane, ***4***

Aqueous formaldehyde (38%; 11 mL) was added to *trans*-1,2-diaminocyclohexane (2.82 g) in glacial acetic acid (6 mL) – water (10 mL). The solution was cooled below 20°C, and hydrogen peroxide (30%; 30 mL) was added. The peroxide precipitated immediately and was removed by filtration, washed with water, and dried: yield 4.76 g (83%), mp 115–116°C, raised to 123°C by recrystallization from ethanol. Anal. calcd. for $C_{10}H_{18}N_2O_4$: C 52.16, H 7.88, N 12.17; found: C 52.03, H 7.94, N 12.02.

1,3,5,7-Tetraazapentacyclo[3.3.2.4^{9,10}.4^{11,12}]eicosane, ***5***

Aqueous formaldehyde (36% w/w; 3.33 g) was added to a solution of 2.28 g of *trans*-1,2-diaminocyclohexane in 10 mL of ethanol. The solution became warm. It was heated to boiling, and 10 mL of water was added. The solution,

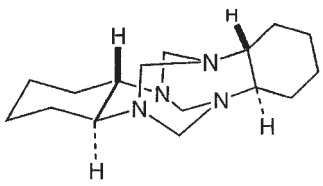

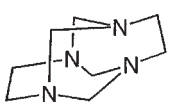

5 **6**

© 1999 NRC Canada

Table 1. Crystallographic data.

Compound	**3a**	**3b**	**4**
Formula	$C_6H_{12}N_2O_4$	$C_7H_{14}N_2O_4$	$C_{10}H_{18}N_2O_4$
Crystal size (mm^3)	0.3 × 0.3 × 0.27	0.5 × 0.45 × 0.35	0.4 × 0.25 × 0.15
Crystal system	Monoclinic	Monoclinic	Triclinic
Space group	*A*2/*a*	$P2_1/c$	*P*-1
Cell params: *A* (Å)	11.869(4)	11.1141(23)	6.9886(3)
B (Å)	5.8573(22)	6.408(3)	8.1717(17)
C (Å)	11.918(3)	13.1614(24)	11.202(3)
α (°)			73.836(18)
β (°)	109.99(2)	101.404(16)	76.15(3)
γ (°)			68.994(21)
Z	4	4	2
Density (g cm^{-1})	1.50	1.38	1.35
F(000)	376.21	408.22	248.12
μ (cm^{-1})	1.2	1.1	1.0
2θ max (°)	50.0	50.0	49.7
No. reflections	721	1275	2150
No. unique	683	1203	1974
No. refs >2.5σ*I*	497	911	1235
Decay of standards (%)	0.7	1.0	1.7
Merging *R* (%)	0.7	0.6	0.7
R_F (%)	3.3	4.0	4.6
R_W (%)	3.3	3.7	4.0
S	1.41	1.97	1.74
Highest peak in difference Fourier (e Å)	0.17	0.40	0.56

when cool, deposited crystals of the product **5** (1.22 g, 44%), mp 238–239°C, raised to 240°C by recrystallization from cyclohexane; ^{1}H NMR ($CDCl_3$): 1.37 (s, 8H, alicyclic CH_2), 1.83 (s, 8H, alicyclic CH_2), 2.67 (s, 4H, CH-N), 4.23 (m, 8H, N-CH_2-N). Anal. calcd. for $C_{16}H_{28}N_4$: C 69.52, H 10.71; found: C 69.24; H 10.33.

The monopicrate melted at 137–138°C. Anal. calcd. for $C_{22}H_{31}N_7O_7$: C 52.27, H 6.18; found: C 52.18, H 6.27.

Hydrolytic yields of formaldehyde

The di- or triperoxide (about 0.2 g) was hydrolyzed in 45% sulfuric acid (5 mL) for 1 h, and then a saturated solution of dimedone in methanol (30 mL) – water (450 mL) was added. The pH was adjusted to 4.6 by addition of sodium acetate, and the solution was left overnight. The precipitate was removed on a weighed sintered glass filter, washed with water, and dried for more than 24 h in a desiccator. Yields of the formal dimedone derivative were the following: from **2**, 94 and 87%; from **3a**, 93 and 96%; from **3b**, 95% of theoretical.

Analysis for peroxide content

The triperoxide **2** (80–100 mg) and potassium iodide (1 g) were added to 2 N sulfuric acid (5 mL), and after 20 min, the yellow solution was titrated with standard sodium thiosulfate solution using a starch indicator. Active oxygen: calcd. 23.1%; found 23.0, 22.9%.

For diperoxides **3a** and **3b**, the same procedure resulted in a black precipitate and erratic results, and a different titration procedure was devised. Sulfuric acid (2 N) was added dropwise to a suspension of diperoxide (80–90 mg) in a solution of potassium iodide (1 g) and starch indicator in water (5 mL), and after each drop, standard thiosulfate solution was added to decolourize the solution. After about 1.5 mL of acid had been added, no more colour was produced. For compound **3a**, active oxygen calcd. 18.2%; found 17.7, 17.9%; for **3b**, active oxygen calcd. 16.8%; found 16.6, 16.6%.

X-ray crystallography

Crystals of the cage diperoxides were obtained from solvents noted above, **3a** and **3b** as chunky prisms, **4** as rectangular plates. Details of crystal, data collection, and refinement parameters are given in Table 1. Data were collected on a Rigaku AFC6S diffractometer controlled by TEXRAY software.[4] Molybdenum K_α radiation (λ = 0.7093 Å) was used. The structures were solved using direct methods and refined by full-matrix least squares. Hydrogen atoms were located in a difference Fourier map and refined isotropically. All non-hydrogen atoms were refined anisotropically. Data processing, structure solution, and structure refinement were all carried out using the NRCVAX system of crystallographic software (10). In the structure of **3a**, the molecule lies across a crystallographic two-fold axis that bisects the ethylene carbon–carbon bond. Table 2 contains the atomic coordinates and B_{eq} for compounds **3a** and **3b**,and Table 3 the atomic coordinates and B_{eq} for compound

[4] Texray diffractometer control software. Molecular Structure Corp., Woodlands, Tex.

© 1999 NRC Canada

Table 2. Final atomic coordinates (fractional) and equivalent isotropic thermal parameters.[a]

Atom	*x*	*y*	*z*	B_{eq}[b]
		Compound **3a**		
O 1	0.878 26 (13)	0.0617 (3)	0.093 09 (13)	2.89 (8)
O 2	0.945 72 (13)	0.2322 (3)	0.051 90 (13)	2.81 (8)
N	0.730 63 (16)	0.3345 (3)	0.113 64 (15)	2.09 (8)
C 1	0.827 35 (22)	0.1855 (4)	0.168 82 (21)	2.73 (11)
C 2	0.888 78 (20)	0.2529 (5)	–0.075 05 (20)	2.55 (10)
C 3	0.753 54 (23)	0.5505 (4)	0.066 31 (20)	2.55 (11)
H 1A	0.8029 (19)	0.059 (4)	0.2100 (19)	2.7 (5)
H 1B	0.8954 (21)	0.275 (4)	0.2286 (21)	3.8 (6)
H 2A	0.8957 (21)	0.100 (5)	–0.1098 (21)	3.7 (6)
H 2B	0.9442 (18)	0.368 (4)	–0.0948 (17)	2.0 (4)
H 3A	0.8354 (22)	0.596 (4)	0.1176 (21)	3.4 (5)
H 3B	0.6967 (20)	0.662 (4)	0.0753 (20).	3.2 (5)
		Compound **3b**		
O 1	0.444 57 (19)	0.8234 (3)	0.091 02 (15)	5.00 (11)
O 2	0.470 61 (17)	0.6330 (4)	0.148 79 (15)	4.96 (11)
O 3	0.185 22 (24)	0.3197 (4)	0.0935 (3)	7.74 (17)
O 4	0.292 43 (23)	0.3059 (3)	0.046 74 (23)	6.81 (15)
N 1	0.271 94 (22)	0.6634 (4)	–0.019 51 (17)	3.86 (12)
N 2	0.270 24 (24)	0.6123 (4)	0.197 70 (18)	4.00 (12)
C 1	0.3836 (3)	0.7704 (6)	–0.011 39 (23)	4.46 (17)
C 2	0.3976 (3)	0.6469 (7)	0.229 14 (25)	5.00 (20)
C 3	0.2261 (5)	0.4078 (7)	0.1951 (4)	6.7 (3)
C 4	0.2666 (4)	0.4482 (6)	–0.0414 (3)	5.77 (22)
C 5	0.1750 (3)	0.7588 (6)	0.0229 (3)	4.65 (17)
C 6	0.1973 (3)	0.7787 (5)	0.1423 (3)	4.36 (17)
C 7	0.0761 (4)	0.8096 (10)	0.1775 (5)	6.7 (3)
H 1A	0.369 (3)	0.917 (5)	–0.0420 (22)	5.9 (8)
H 1B	0.444 (3)	0.692 (4)	–0.0464 (21)	5.4 (8)
H 2A	0.409 (3)	0.795 (6)	0.252 (3)	8.2 (12)
H 2B	0.433 (3)	0.541 (5)	0.2797 (21)	5.3 (8)
H 3A	0.294 (4)	0.321 (7)	0.235 (3)	10.4 (14)
H 3B	0.145 (4)	0.402 (6)	0.215 (3)	10.4 (13)
H 4A	0.328 (3)	0.410 (5)	–0.0794 (23)	6.5 (9)
H 4B	0.191 (3)	0.405 (5)	–0.0741 (24)	6.8 (10)
H 5A	0.104 (3)	0.681 (5)	0.0012 (22)	5.2 (8)
H 5B	0.165 (3)	0.899 (5)	–0.0014 (22)	5.2 (8)
H 6	0.2490 (24)	0.908 (4)	0.1603 (19)	4.4 (7)
H 7A	0.035 (4)	0.693 (6)	0.162 (3)	8.5 (14)
H 7B	0.039 (4)	0.928 (6)	0.144 (3)	8.8 (13)
H 7C	0.087 (3)	0.829 (6)	0.254 (3)	9.0 (12)

[a]esds refer to the last digit printed.

[b]B_{eq} is the mean of the principal axes of the thermal ellipsoid for atoms refined anisotropically (non-hydrogens). For hydrogens, $B_{eq} = B_{iso}$.

4. Anisotropic thermal parameters, torsion angles, and least-squares planes are included as supplementary material.[5]

Results and discussion

Properties of the cage triperoxide 2 and of the cage diperoxides 3a, 3b, and 4

By analogy with the reaction of ammonia with formaldehyde and hydrogen peroxide to give **2**, we assumed that reaction of 1,2-diaminoethane would give the diperoxide **3a**, of 1,2-diaminopropane would give **3b**, and of 1,2-diaminocyclohexane would give **4.** These assumptions proved to be true.

The triperoxide **2** is a powerful explosive (11) and should be handled with extreme caution. A small amount of it on a steel plate detonates with a loud report when hit with a hammer. The diperoxide **3a** proved to be more difficult to detonate, and the diperoxide **3** even more so, as expected from their progressively less favourable oxygen balances (12).

[5]Supplementary material mentioned in the text may be purchased from: The Depository of Unpublished Data, Document Delivery, CISTI, National Research Council Canada, Ottawa, Canada, K1A 0S2. This includes anisotropic thermal parameters, torsion angles, and least-squares planes, as well as stereo plots showing unit cell packing for all three structures.

© 1999 NRC Canada

Table 3. Final atom coordinates (fractional) and equivalent isotropic thermal parameters[a] for compound **4**.

Atom	*x*	*y*	*z*	B_{eq}[b]
O 1	0.1566 (4)	0.1551 (3)	0.010 54 (20)	4.41 (13)
O 2	0.2522 (4)	0.2910 (3)	–0.000 24 (21)	4.70 (13)
O 3	0.1744 (4)	0.1115 (3)	–0.313 73 (23)	5.31 (15)
O 4	0.3104 (4)	0.0022 (3)	–0.218 19 (22)	5.14 (14)
N 1	–0.0245 (4)	0.3144 (3)	–0.172 88 (22)	3.06 (12)
N 2	0.4214 (4)	0.2616 (3)	–0.212 87 (23)	3.43 (13)
C 1	–0.0392 (6)	0.2540 (5)	–0.0393 (3)	3.99 (18)
C 2	0.4434 (6)	0.2559 (5)	–0.0919 (3)	4.28 (19)
C 3	–0.0249 (6)	0.2002 (5)	–0.2470 (4)	4.33 (20)
C 4	0.4757 (6)	0.0829 (5)	–0.2457 (4)	4.54 (20)
C 5	0.0578 (4)	0.4648 (4)	–0.2308 (3)	2.75 (15)
C 6	0.2897 (5)	0.4099 (4)	–0.2883 (3)	3.03 (15)
C 7	0.3635 (5)	0.5741 (4)	–0.3203 (3)	3.66 (17)
C 8	0.2382 (6)	0.7245 (4)	–0.4144 (3)	4.14 (19)
C 9	0.0078 (6)	0.7725 (4)	–0.3661 (4)	4.33 (19)
C 10	–0.0683 (6)	0.6087 (4)	–0.3274 (3)	3.72 (18)
H 1A	–0.117 (4)	0.354 (3)	0.0019 (23)	2.8 (6)
H 1B	–0.119 (4)	0.170 (4)	–0.007 (3)	4.1 (7)
H 2A	0.469 (4)	0.360 (4)	–0.081 (3)	4.0 (7)
H 2B	0.548 (5)	0.140 (4)	–0.057 (3)	4.5 (7)
H 3A	–0.077 (4)	0.260 (3)	–0.329 (3)	3.5 (7)
H 3B	–0.091 (5)	0.107 (4)	–0193 (3)	6.4 (9)
H 4A	0.509 (5)	0.093 (4)	–0.338 (3)	4.1 (7)
H 4B	0.574 (5)	–0.001 (4)	–0.194 (3)	3.8 (7)
H 5	0.039 (3)	0.520 (3)	–0.1626 (20)	1.1 (5)
H 6	0.302 (4)	0.378 (3)	–0.3685 (25)	3.1 (6)
H 7A	0.505 (4)	0.547 (3)	–0.3530 (24)	3.0 (6)
H 7B	0.347 (4)	0.616 (4)	–0.240 (3)	4.1 (7)
H 8A	0.273 (5)	0.684 (4)	–0.499 (3)	5.5 (8)
H 8B	0.289 (4)	0.822 (4)	–0.433 (3)	4.2 (8)
H 9A	–0.068 (5)	0.855 (4)	–0.429 (3)	5.9 (9)
H 9B	–0.024 (4)	0.828 (4)	–0.289 (3)	4.1 (7)
H 10A	–0.206 (5)	0.639 (4)	–0.296 (3)	4.1 (8)
H 10B	–0.053 (4)	0.559 (3)	–0.407 (3)	4.0 (7)

[a]esds refer to the last digit printed.

[b]B_{eq} is the mean of the principal axes of the thermal ellipsoids for atoms refined anisotropically. For hydrogens, $B_{eq} = B_{iso}$.

The diperoxide **4** could not be detonated, and was submitted for combustion analysis in the usual way. The peroxides **3a** and **3b** were analyzed (along with **2** as a control) by decomposition of a small amount of the compound in a large excess of aqueous acid to yield formaldehyde (analyzed by formation of the derivative with dimedone (13, 14)) and hydrogen peroxide (titrated by an iodide–thiosulfate method (15)) in amounts close to theoretical. Treatment of the peroxides with aqueous picric acid did not give their picrate salts, but rather monopicrates of the diamines from which they had been made, and treatment of a very small amount of the solid peroxide with a drop of concentrated hydrochloric acid caused instantaneous decomposition to a sticky liquid. The reaction was particularly violent in the case of **2**. The solid compounds left standing on filter paper in the laboratory atmosphere eventually decomposed to a sticky mass. It seems likely that this decomposition was initiated by a trace of acid furnished by a dust or aerosol particle; the formaldehyde and hydrogen peroxide produced at the initial spot of decomposition would react to give formic acid, so that the decomposition would be autocatalytic.

Diffraction studies

The structures **3a**, **3b**, and **4** were established by X-ray diffraction.[5] ORTEP representations (16) are given in Figs. 1– 3, and in Table 4, the bond distances and angles of the three diperoxides are compared with corresponding bond distances and angles of the triperoxide **2**.

The torsional angles of the peroxide groups C-O-O-C in our three diperoxides lie between 113 and 116°, close to the equilibrium torsional angle of about 112° in hydrogen peroxide (17), while the corresponding torsional angle in HMTD is 129.3° (9). Schaefer et al. (9) point out that it takes little energy to open this angle from 112 to 129°, while closing this angle below 129° in HMTD would force nonbonded N···N atoms (3.193 Å apart) and O···O atoms (2.971 Å apart) to move closer together, with steep increases in van der Waals repulsions. Otherwise, most bond distances and an-

© 1999 NRC Canada

Fig. 1. ORTEP plot (16) of compound **3a**,showing numbering scheme. Ellipsoids are shown at 50% probability for non-hydrogen atoms.

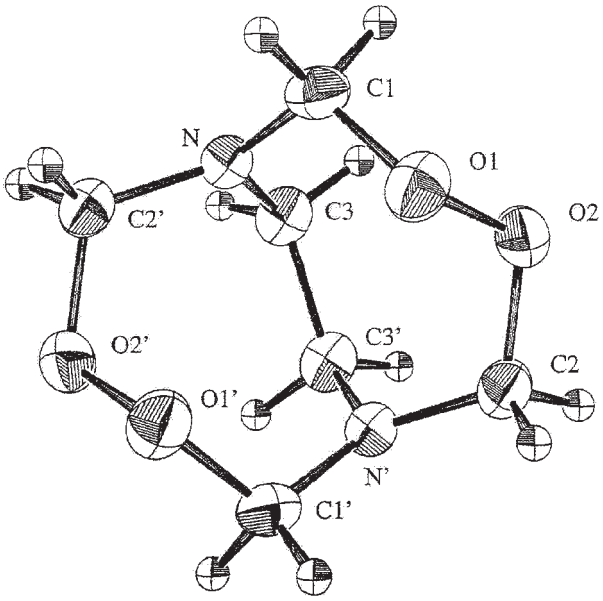

Fig. 2. ORTEP plot (16) of compound **3b**,showing numbering scheme. Ellipsoids are shown at 50% probability for non-hydrogen atoms.

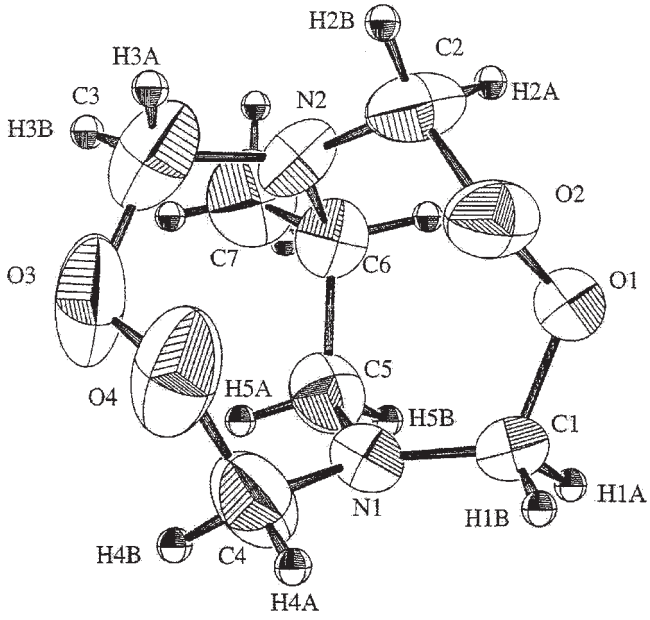

gles are fairly similar in all four compounds in Table 1. However, the bridgehead nitrogen atoms of the three new diperoxides are not completely planar, lying about 0.12–0.14 Å out of the plane of the three attached carbon atoms, while in **2** the nitrogen atoms lie exactly (within experimental limits) in this plane. Similarly, in the three new diperoxides all except one of the C-N-C angles are slightly less than 120°, whereas in **2** all are exactly 120°.

Schaefer et al. (9) suggested that the bridgehead nitrogen atoms of **2** are sp^2 hybridized because the electronegative peroxide groups withdraw electron density and lower the energy of the electron pair in the *p* orbital (the anomeric effect (19)). This hybridization explains the shortened N—C distances in **2**. Essentially, the same explanation is offered by Whittleton et al. (19) for N—C distances in the cage diperoxide formed by reaction of formaldehyde with hydrazine and hydrogen peroxide in acidic solution (20, 21). This effect would be expected to be greater in the triperoxide **2** than in the diperoxides **3a**, **3b**, and **4**, which might account for the less complete planarity of the bridgehead nitrogen atoms of the latter. Furthermore, the anomeric effect would explain why the N—C bonds of the peroxide bridges of **3a**, **3b**, and **4** are shortened, while the N—C bonds of the alkane bridges are not. It would also explain the nonbasic character of the tertiary amino groups, so that the compounds separate out of weakly acidic solutions as bases and not salts.

Fig. 3. ORTEP plot (16) of compound **4**, showing numbering scheme. Ellipsoids are shown at 50% probability for non-hydrogen atoms.

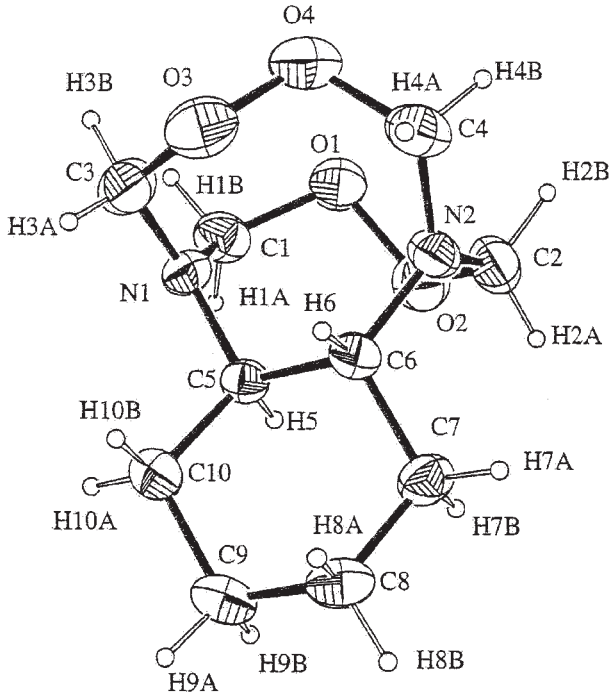

*PMR spectrum of HMTD **2***

The ^{1}H NMR spectrum of the highly symmetrical hexamethylenetetramine $(CH_2)_6N_4$ shows a sharp singlet at δ 4.64 ppm (22), and a similar spectrum would be expected for HMTD $(CH_2)_6N_2O_6$ if it had the symmetrical structure shown in **2** above, with dihedral angles of zero for the peroxide bridges CH_2-O-O-CH_2. However, the dihedral angles of ±129° of these bridges (9) result in HMTD existing as a racemic mixture of chiral helical conformers. The twist of the helix causes one hydrogen of each methylene group to point slightly inward toward the axis of the molecule, and the other slightly outward. The six methylene groups are all identical; each forms an AB system, so that the spectrum of HMTD in DMSO-d_6, shown in Fig. 4, has a pair of doublets (^2J 13.3 Hz) centered at δ 4.65 and 4.78 ppm. At higher temperatures, the helical conformers interconvert, as shown by the broadening of the NMR peaks, which eventually

© 1999 NRC Canada

Table 4. Bond distances (Å) and angles (°) in some cage peroxides.

	Compound			
Atoms	**2**[a]	**3a**	**3b**	**4**
	Distances			
N—C (peroxide bridge)	1.426 (8)	1.413 (3)	1.403 (4)	1.430 (4)
	1.416 (8)	1.415 (3)	1.412 (5)	1.413 (4)
			1.379 (5)	1.411 (5)
			1.408 (5)	1.421 (4)
N—C (ethylene bridge)	—	1.449 (3)	1.443 (5)	1.465 (3)
			1.447 (4)	1.464 (4)
O—O	1.456 (8)	1.466 (2)	1.437 (3)	1.469 (3)
			1.448 (4)	1.481 (3)
C—O	1.432 (8)	1.442 (3)	1.425 (4)	1.469 (4)
	1.410 (9)	1.436 (3)	1.457 (4)	1.453 (4)
			1.441 (6)	1.450 (5)
			1.459 (6)	1.458 (5)
C—C (ethylene)	—	1.554 (4)	1.547 (5)	1.543 (4)
		Angles		
OOC-N-COO	120.0 (5)	120.5 (2)	119.7 (3)	119.7 (3)
	120.0 (5)		118.8 (3)	119.1 (3)
OOC-N-CC	—	119.3 (2)	118.7 (3)	117.3 (3)
		118.0 (2)	119.3 (3)	119.9 (3)
			117.5 (3)	119.3 (3)
			121.3 (3)	118.5 (3)
N-C-O	116.6 (5)	117.9 (2)	115.9 (2)	116.7 (3)
	115.7 (5)	115.4 (2)	117.1 (3)	116.9 (3)
			116.6 (3)	116.4 (3)
			115.8 (3)	116.3 (3)
N-C-C	—	116.4 (2)	116.5 (3)	114.5 (2)
			114.3 (3)	114.6 (2)
C-O-O	107.3 (5)	105.1 (2)	107.8 (2)	105.4 (2)
	105.2 (5)	107.2 (2)	104.4 (2)	107.7 (2)
			106.5 (3)	107.2 (2)
			104.5 (3)	104 3 (2)
C-O-O-C	129.3 (5)	115.2 (2)	115.4 (3)	113.7 (2)
			115.5 (3)	115.8 (4)
N-C-C-N		25.7 (1)	32.5 (2)	40.7 (2)
		Nonbonded distances		
N···N	3.193 (7)	2.898 (3)	2.878 (4)	3.189 (4)

[a]From ref. 9.

collapse into a broad singlet at about 105°C, illustrated in Fig. 4.

Fig. 4. Effect of temperature on the PMR spectrum of HMTD (**2**).

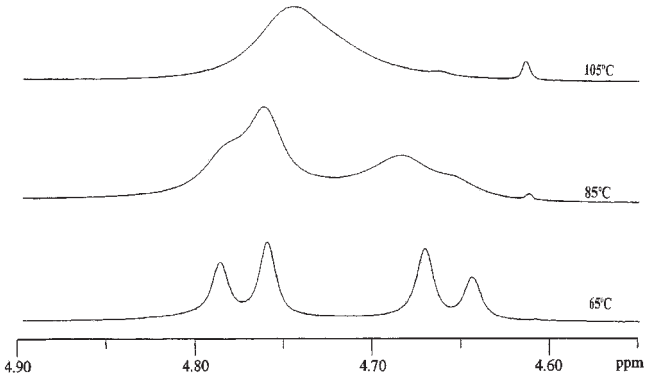

*NMR spectrum of compound **3a***

This compound, like **2**, is a racemic mixture of chiral conformers. The X-ray crystallographic studies (see Fig. 1) show that the dihedral angles of CH_2-O-O-CH_2 are not zero, as represented in **3a**, but ±115.2° (Table 4). Again, the hydrogen atoms of both N-CH_2-C and N-CH_2-O methylenes form an AB system. However, in $CDCl_3$ at 30°C, the ^{1}H NMR spectrum, shown in Fig. 5, is that of the symmetrical structure **3a**, having a doublet at δ 3.38 (4 H) for the protons of the ethylene bridge and a doublet at δ 4.83 (8 H) for the methylene protons of the peroxide bridges. The four-bond coupling is favoured by the W-configuration of the bonds between the protons of the two different types of methylenes.

Evidently, the interconversion of enantiomeric conformers of **3a**, which requires eclipsing of the bonds of two peroxide groups, takes place at a lower temperature than the interconversion of the enantiomeric conformers of **2**, which requires eclipsing of the bonds of three peroxide groups. The

© 1999 NRC Canada

Fig. 5. Effect of temperature on the PMR spectrum of **3a**.

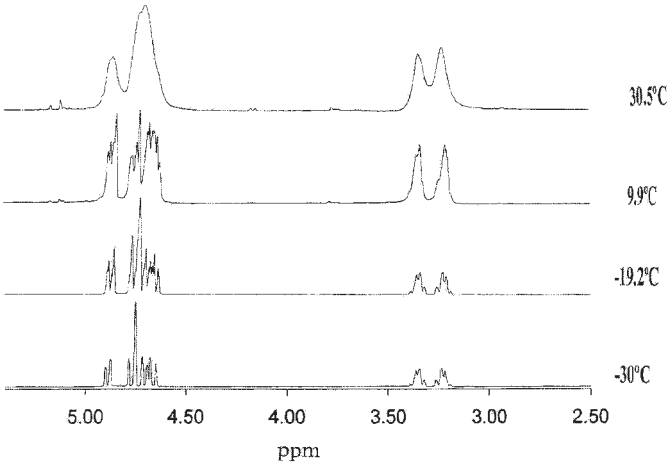

Fig. 6. The PMR spectrum of **3b**.

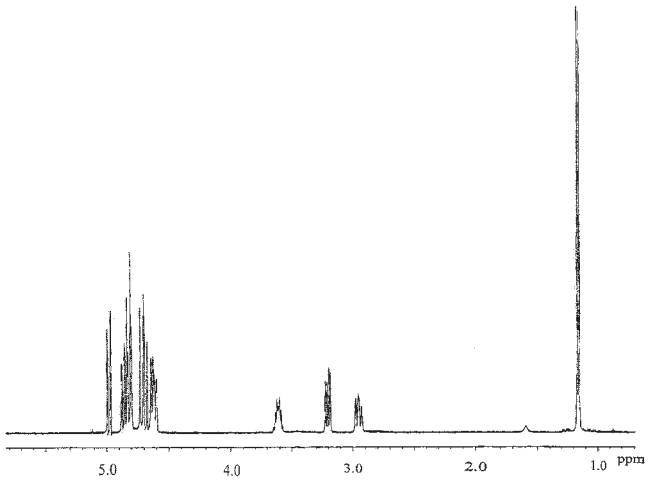

interconversion of **3a** requires also the eclipsing of the atoms of the ethylene bridge, but this is already more than half complete in the ground state of the molecule: the X-ray data (Table 4) show that the dihedral angle for N-CH_2-CH_2-N is not about 60°, as required for a staggered conformation, but 25.7° (Table 4).

At lower temperatures, the rate of interconversion drops, as evidenced by the changes in NMR spectra shown in Fig. 5. At –30°C, the ^{1}H peaks of N-CH_2-O (carbon atoms C1, C′1, C2, C′2) can be calculated as two AB quartets, one at δ = 4.66 and 4.88 ppm (^2J = 13.5 Hz), the other at δ = 4.70 and 4.77 ppm (^2J = 12.1 Hz). The high field doublet in each quartet shows a long-range splitting (^4J = 2 Hz) due to coupling to one of the ethylene protons. The spectrum for ethylene (C3 and C′3) shows symmetrical multiplets at δ = 3.347 and 3.227 ppm, and additional splitting from long-range coupling.

*NMR spectrum of compound **3b***

This compound does not show a rapid interconversion of conformers at 30°C, so that its ^{1}H NMR spectrum has a detailed structure not found in the spectrum of **3a** until the temperature of the latter has been reduced to about –20°C. The methyl group of **3b** is attached to the two-carbon bridge by a bond pointing outward; a conformational inversion would end with this bond pointing inward, into a region of steric congestion, and so is not possible. This steric effect also explains why 2-methyl-1,2-diaminopropane does not react with formaldehyde and hydrogen peroxide to form the cage diperoxide **3c**.

Table 5. NMR data for compound **3b** in $CDCl_3$.

Position	^{13}C δ (ppm)	^{1}H δ (ppm)	COSY
1	89.4	A 4.689 d of d	1A, 1B, 4B
		B 4.868 d of d	1B, 1A, 5A
2	91.5	A 4.633 d	2A, 2B, 3B, 6
		B 4.818 d	2B, 2A
3	84.3	A 4.720 d	3A, 3B
		B 4.984 d of d	3B, 3A, 2A, 6
4	91.8	A 4.824 d	4A, 4B, 5B
		B 4.616 d of d	4B, 4A, 1A
5	58.4	A 2.955 t	5A, 5B, 6, 1B
		B 3.239 m	5B, 5A, 6, 4A
6	56.3	–3.612 m	6, 5A, 5B, 7, 3A, 2A
7	15.6	–1.160 d	7, 6

The ^{1}H NMR spectrum of compound **3b** (Fig. 6; see also Table 5) corroborates the details of structure established by X-ray diffraction and shown in the ORTEP diagram of Fig 2. The signal for the three methyl protons (1.16 ppm) at position 7 is split by coupling (^3J 6.5 Hz) to the single proton at position 6 (m, 3.61 ppm). This proton in turn is coupled to the A (^3J 14 Hz) and B (^3J 7 Hz) protons at C5. The proximity of the C5 B proton to the C6 proton is shown by the NOESY spectrum.

The signals between δ 4.6 and 5.0 ppm in Fig. 6 are due to the protons at positions 1, 2, 3, and 4. The assignment of signals to positions 1–4 is possible because of their spin-coupling to the protons at positions 5, 6, and 7, as demonstrated by the COSY spectrum. The results are given in Table 5. The rigid cage structure of the molecule results in many pairs of protons being linked by four bonds in a W-configuration (see Table 5), and hence having measurable coupling constants.

The spectrum of **3b** in DMSO-d_6 has signals shifted very slightly to higher fields, but is essentially identical to the spectrum in $CDCl_3$.

NMR spectrum of compound 4

The *trans* fusion of a cyclohexane ring to the diperoxide ring of **4** results in a rigid compound incapable of any conformational change. Its ^{1}H and ^{13}C NMR (Table 6) and COSY and NOESY spectra are those expected from the structure (Fig. 3) established by X-ray diffraction, and require no comment.

Formaldehyde and cage compounds

The results reported above illustrate the proclivity of formaldehyde to form cage compounds (see also refs. 19, 20, 23–26). A further example is given by the reaction of formaldehyde with *trans*-1,2-diaminocyclohexane to give the compound **5**, analogous to cage compounds given by other 1,2-diamines (23, 24, 27). *cis*-1,2-Diaminocyclohexane does not react in this way, presumably for steric reasons. The reaction of formaldehyde with 1,2-diaminoethane gives

© 1999 NRC Canada

Table 6. NMR δ values (ppm) of compound **4**.

Position	^{13}C	^{1}H
1	91.4	4.62[a]
2	84.5	4.68[a]
3	84.5	4.78[a]
4	91.4	4.74[a]
5	65.2	3.08
6	65.2	3.08
7	30.4	1.65
8	25.8	1.29[b]
		1.74[c]
9	25.8	1.29[b]
		1.74[c]
10	30.4	1.65

[a] ^{2}J = 13.0 Hz, ^{4}J = 2.0 Hz.
[b] Axial hydrogen.
[c] Equatorial hydrogen.

the compound **6**, which may have the two methylenes of the ethylene bridge eclipsed (as represented in **6**) or staggered: the X-ray evidence is equivocal (28). However, the fused cyclohexane ring enforces staggering of the corresponding carbon atoms in **5**. Dreiding-type models show that only two enantiomeric forms of this compound are possible.

General conclusions

Small cycloalkane rings of 5 or 6 carbon atoms are more stable than medium-sized rings of 7–10 carbon atoms, because of steric and torsional effects. This is not true when the rings incorporate a peroxide group: medium-sized rings then become more stable than the five- or six-membered, because of the differing energies attendant on change of torsional angle for C-O-O-C and C-C-C-C chains. This fact has not often been recognized (cf. refs. 19–21, 27, 29). The structures **3a**, **3b**, and **4**, containing fused eight-membered rings, furnish further examples of this rule; alternative structures containing the peroxide groups in five-membered rings can be written for these compounds and for HMTD (20).

Acknowledgment

The financial support of the Natural Sciences and Engineering Research Council of Canada is gratefully acknowledged. We are also grateful to Prof. R.B. Lennox and his students for help and encouragement, to Bernadette Macdonald for analytical work, and to Dr. Anne-Marie Lebuis.

References

1. R.W. Alder, R.B. Sessions, A.J. Bennett, and R.E. Moss. J. Chem. Soc. Perkin Trans. 1, 603 (1982).
2. R.W. Alder. Acc. Chem. Res. **16**, 321 (1983).
3. A.v. Baeyer and A. Villiger. Ber. **33**, 2485 (1900).
4. R.W. Alder, A.G. Orpen, and R.W. Sessions. J. Chem. Soc. Chem. Commun. 999 (1983).
5. L. Pauling. The nature of the chemical bond. 2nd ed. Cornell University Press, Ithaca, N.Y. 1948. p. 189.
6. A. Bondi. J. Phys. Chem. **68**, 441 (1964).
7. A. Gavezzotti. J. Am. Chem. Soc. **105**, 5220 (1983).
8. A.I. Kitaigorodski. Molecular crystals and molecules. Academic Press, London. 1973. pp. 1–21.
9. W.P. Schaefer, J.T. Fourkas, and B.G. Tieman. J. Am. Chem. Soc. **107**, 2461 (1985).
10. E.J. Gabe, Y. LePage, J.P. Charland, F.I. Lee, and P.S. White. J. Appl. Cryst. **22**, 384 (1989).
11. C.A. Taylor and W.H. Rinkenbach. Army Ordnance, **5**, 463 (1924).
12. W.C. Lothrop and G.R. Hendrick. Chem. Rev. **44**, 419 (1949).
13. J.H. Yoe and L.C. Reid. Ind. Eng. Chem. **13**, 238 (1981).
14. D. Spencer and T. Henshall. J. Am. Chem. Soc. **77**, 1943 (1955).
15. E. Schmitz. Liebigs Ann. Chem. **635**, 73 (1960).
16. C.K. Johnson. ORTEP - a Fortran thermal ellipsoid plot program. Technical report ORNL-5138. Oak Ridge, Tenn. 1976.
17. R.M. Hunt, R.A. Leacock, C.W. Peters, and K.T. Hecht. J. Chem. Phys. **42**, 193 (1979).
18. A.J. Kirby. The anomeric effect and related stereoelectronic effects at oxygen. Springer Verlag, Berlin. 1983.
19. S.N. Whittleton, P. Seiler, and J.D. Dunitz. Helv. Chem. Acta, **64**, 2614 (1981).
20. C.v. Girsewald and H. Siegens. Ber. **54**, 492 (1921).
21. E. Schmitz. Liebigs Ann. Chem. **636**, 73 (1960).
22. C.J. Pouchert. The Aldrich library of NMR spectra. 2nd ed. Vol. 1. Aldrich Chemical Co., Milwaukee. 1983. p. 332d.
23. G. Volpp. Chem. Ber. **95**, 1493 (1962).
24. F.G. Riddell and P. Murray-Rust. Chem. Comm. 1075 (1970).
25. E. Schmitz and R. Ohme. Liebigs Ann. Chem. **635**, 82 (1960).
26. M.J.S. Dewar. A semiempirical life. A.C.S., Washington, D.C. 1992. p. 103.
27. C.A. Bischoff. Ber. **31**, 3248 (1898).
28. P. Murray-Rust. J. Chem. Soc. Perkin Trans. 2, 1136 (1974).
29. A.R. Katritzky, V.J. Baker, F.M.S. Brito-Palma, J.M. Sullivan, and R.B. Finzel. J. Chem. Soc. Perkin Trans. 2, 1133 (1979).

© 1999 NRC Canada

Spectroscopic studies on effects of triptycyl group on structures and reactivities of triplet arylcarbenes

Hideo Tomioka, Junichi Nakajima, Hidehiko Mizuno, Eiji Iiba, and Katsuyuki Hirai

Abstract: A series of triplet 9-triptycyl(aryl)carbenes, where aryl groups are phenyl, 1- and 2-naphthyl, and 9-anthryl, is generated by photolysis of the corresponding diazomethanes and observed directly by spectroscopic means. Their structures are characterized by electron spin resonance (ESR) spectroscopy in a 2-methyltetrahydrofuran matrix at 77 K, and the reactivities are investigated by laser flash photolysis in degassed benzene solution at room temperature. Comparison of the data with other arylcarbenes bearing a series of substituents, i.e., hydrogen, phenyl, naphthyl, and anthryl groups, revealed an interesting relationship between structures and reactivities of triplet arylcarbenes.

Key words: steric protection, stability of triplet carbenes, electron spin resonance, laser flash photolysis, structure–reactivity relationship.

Résumé : Utilisant la photolyse des diazométhanes correspondants, on a généré une série de 9-triptycyl(aryl)carbènes triplets dans lesquels les groupes aryles sont des groupes phényle, 1- et 2-naphtyle et 9-anthryle et on les a observés directement par des méthodes spectroscopiques. On a caractérisé leurs structures par spectroscopie RPE dans une matrice de 2-méthyltétrahydrofurane à 77 K et on a étudié leurs réactivités par photolyse éclair au laser dans une solution benzénique dégazé, à la température ambiante. Une comparaison de nos données avec celles d'arylcarbènes portant une série de substituants, comme l'hydrogène ou des groupes phényle, naphtyle et anthryle, met en évidence l'existence d'une relation intéressante entre les structures et les réactivités des arylcarbènes triplets.

Mots clés : protection stérique, stabilité des carbènes triplets, RPE, photolyse éclair au laser, relation structure–activité.

[Traduit par la Rédaction]

Introduction

Carbene chemistry has had a unique and interesting history (for a brief summary, see ref. 1). The pioneering work of Staundinger in the 1910s on the decomposition of diazo compounds and ketenes was recognized as the first independent generation of carbenes as a new reactive species. Since radicals were the intermediates "en vogue" in the following decades, they started by being generally regarded as diradicals. The subsequent work of Meerwein, Hine, and Doering contributed much to the recognition of this species as a new type of intermediate, giving characteristic reactions not encountered with radicals. Therefore, the modern history of carbene chemistry is usually considered to date from the 1950s, at a time when the chemistry of other important classes of intermediates, i.e., carbanions, carbocations, and radicals, was already relatively well classified (for reviews, see ref. 2). The complicated nature of carbene, not observed with other trivalent carbon intermediates, arises from the presence of two nonbonding electrons. Thus, carbenes can exist either as singlet or as triplet states, depending on the spins of the two nonbonding electrons. And so, probing the structural features that control the chemical properties of these intermediates always encounters the complicated issues of the relationship between reactivities, singlet–triplet energy gap (ΔG_{ST}), and structures (2, 3).

Product analysis methods have been extensively employed from the early stages of the research in this field and revealed perplexing aspects of reactions undergone by this exotic species (2). From the early 1960s, low-temperature spectroscopic techniques have enabled us to observe this ephemeral species and to understand its structural features, especially in the triplet manifolds (4). In the last two decades, laser flash photolysis has increasingly been applied to the study of carbene processes, and the dynamic properties of this highly reactive species have been investigated more quantitatively (5). Moreover, recent advances in computer technology, in both hardware and software, have dramatically increased the reliability and accuracy of computational chemistry in characterizing and predicting the reactivity–structure relationships of such computationally demanding species (for an excellent review on how to deal computationally with open-shell species, see ref. 6).

Received November 4, 1998.

This paper is dedicated to Jerry Kresge in recognition of his many achievements in chemistry.

H. Tomioka,[1] J. Nakajima, H. Mizuno, E. Iiba, and K. Hirai. Chemistry Department for Materials, Faculty of Engineering, Mie University, Tsu, Mie 514-8507, Japan.

[1]Author to whom correspondence may be addressed. Telephone: 81-59-231-9416. Fax: 81-59-231-9471. e-mail: tomioka@chem.mie-u.ac.jp

© 1999 NRC Canada

Scheme 1.

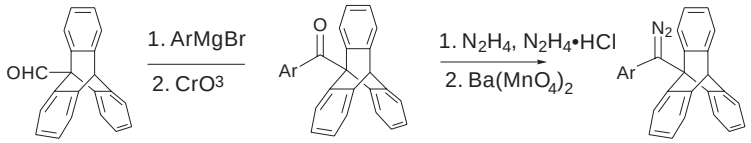

Ar = Ph, 1-Np, 2-Np

1a - c

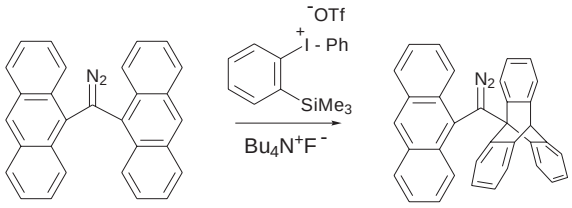

1d

Therefore, the entire picture of this challenging species, i.e., the fourth class of carbon-based reactive intermediates in organic chemistry, begins gradually to unfold from a combination of traditional product analysis coupled with modern spectroscopic methods and high-level theoretical calculations.

More importantly, recent advances in technology make it possible for even simple experimentalists to use these state-of-the-art techniques rather routinely with great ease. Even rather challenging issues can be tackled in sophisticated ways with precursor molecules designed to generate reactive species appropriate for studying a specific issue.

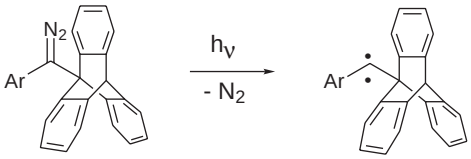

1 **2**

a; Ar = Ph, **b**; Ar = 1-Np, **c**; Ar = 2-Np, **d**; Ar = 9-An

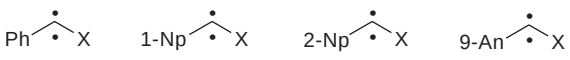

3 **4** **5** **6**

a; X = H, **b**; X = Ph, **c**; X = 1-Np, **d**; X = 2-Np, **e**; X = 9-An

The present study was undertaken in order to understand how the structure and reactivity of triplet carbenes are affected by electronic and steric effects (7). For this purpose, we designed and generated triptycyl(aryl)carbenes (**2**), where the triptycyl (Trp) group is expected to act as a kinetic protector, while aryl groups ranging from phenyl to anthryl will accept the unpaired electrons. We investigated the relationship between the structure and reactivities of **2** by ESR spectroscopy in matrices at low temperature and used time-resolved UV–vis spectroscopy in solution at room temperature. Data from these two complementary means were compared with those obtained in other arylcarbene systems, i.e., **3**–**6**, where π-conjugation effects are expected to play a more important role. The results revealed how these two factors affect the thermodynamic and kinetic stability of triplet carbenes. Preliminary reports of the present study have been published (8).

Results and discussion

Triptycyl(aryl)diazomethanes (**1**) employed in this study were prepared according to the reactions outlined in Scheme 1. When the aryl groups were phenyl (Ph) or 1- and 2-naphthyl (Np), the desired diazomethanes were obtained by the conventional hydrazonation of the corresponding ketones, followed by oxidation. This method could not be applied to the preparation of sterically more demanding diazomethane, i.e., **1d**, which was synthesized by the addition of benzyne to di(9-dianthryl)diazomethane under very mild conditions. Purification of the diazomethanes by repeated chromatography on a gel permeation column was carried out to obtain pure diazomethanes for spectroscopic studies.

ESR studies in rigid matrices at low temperatures

Irradiation of 9-triptycyl(phenyl)diazomethane (**1a**) in a 2-methyltetrahydrofuran (MTHF) glass at 77 K gave a fine-structured EPR spectrum. A lineshape characteristic of randomly oriented triplet molecules with a large *D* value attributable to a one-center $n\pi$ spin–spin interaction at the divalent carbon of arylcarbene **2a** was observed (Fig. 1*a*). The signals were analyzed in terms of *D* and *E* values and are reported in Table 1.

The *D* value is related to the separation between the unpaired electrons and the *E* value is a measure of the difference of the magnetic dipole interaction along the *x* and *y* axes. More plainly, the *D* value allows the determination of the amount of delocalization in carbenes with conjugated π-

© 1999 NRC Canada

Fig. 1. ESR spectra obtained by irradiation of 9-triptycyl(aryl)diazomethanes (**1**) in MTHF matrix at 77 K, where aryl groups are (*a*) Ph, (*b*) 1-Np, (*c*) 2-Np, and (*d*) 9-An.

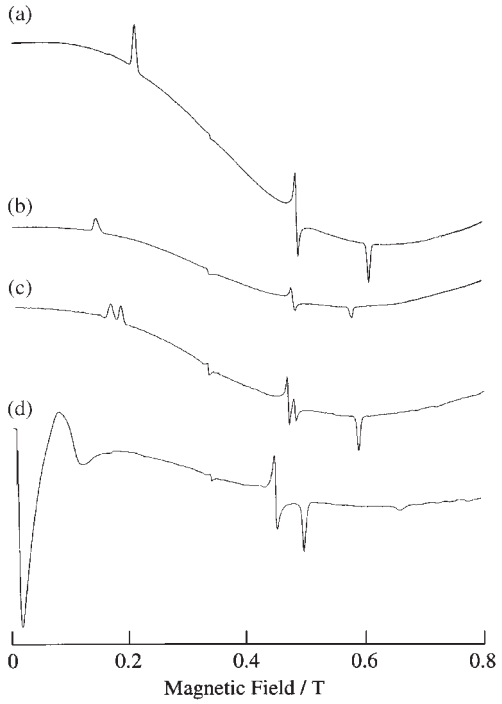

systems. The *D* value decreases with increasing delocalization of the unpaired electron, and the *E* value allows one to estimate the bond angles at the carbene center. For a linear carbene $E = 0$ is expected, while decreasing the bond angle leads to a larger value for *E*. The *E*/*D* ratio is frequently used to estimate the bond angle (4, 9).[2,3]

To obtain some insight into the effect of the Trp group on the structure of triplet carbene, it is useful to compare the zero-field splitting (ZFS) parameters observed for "parent" phenylcarbenes **3a** (10*a*). A very small difference in *D* values between the two is observed. This is not surprising, as little π interaction between the unpaired electrons and triptycyl phenyl rings is expected. However, a slight increase in *E* values on going from **3a** to **2a** is rather unexpected since one might expect a larger bond angle for **2a** than for **3a**, upon taking into account the large difference in steric bulkiness between H and Trp groups. A closer look at a molecular model soon reveals that steric interaction between the Ph and Trp groups in **2a** is negligible as the three phenyl rings on the tertiary carbon atom in the Trp group are held back tightly, allowing little steric interference with the phenyl ring on the carbenic carbon. In other words, the carbenic phenyl ring stays within the "spoke" region of the Trp group and hence its *ortho* hydrogens can only expand in the direction where the "peri" hydrogens on Trp cannot interact.

It is interesting to note here that a more significant decrease both in *D* and *E* values is observed on going from monophenylcarbene (**3a**) to diphenylcarbene (**3b**) than to phenyl(triptycyl)carbene (**2a**). The observation suggests that π-delocalization of the spin plays a more important role than the steric interaction in changing the structure of the triplet carbene.

Similar changes in ZFS parameters were observed for naphthylcarbene systems (Fig. 1, Table 1). The *D* and *E* values for "parent" naphthylcarbenes **4a** and **5a** decrease relative to phenylcarbene (**3a**), obviously due to extended π-delocalization (11). Again, very small changes in the *D* values and a rather slight increase in the *E* values are noted as one changes the substituent (X) from H to Trp not only in 2- but also in 1-naphthylcarbene systems. The observations suggest that the 1-Np group in **2b** is located in the cavity of triptycene moiety in order to avoid the interaction between the peri hydrogens, although the peri H on the 1-Np group can potentially interact with the peri H on the Trp group.

In the case of "parent" naphthylcarbenes, a mixture of two rotational isomers, namely s-*Z* and s-*E*, was usually found and these isomers could be readily distinguished by ESR spectroscopy (12). Assignment of ZFS parameters to a specific conformer is made possible by a point spin model as detailed by Roth and Hutton (12). Carbenes have noticeable secondary contributions to *D* due to the nearest carbons with π-electron spin densities. In the case of 2-naphthylcarbene, for instance, the π-electron density at the 1-position is twice that at the 3-position (13). This leads to a larger σ-electron–π-electron coupling for the *E* than for the *Z* isomer. Taking into account the fact that *r*, the distance between the divalent carbon and the C_1 carbon, is close to *z*, the *z* coordinate of C_1, this contribution to *D* is negative. Therefore, the *E* conformer would be expected to have the smaller *D* value.

The ESR spectrum of 9-triptycyl(2-naphthyl)carbene (**2c**) in MTHF at 77 K also consisted of two sets of triplet peaks of similar intensities, assignable to *Z* and *E* rotamers (Fig. 1*c*, Table 1). In marked contrast, only one set of triplet signals was observed in the ESR spectra of the corresponding 1-naphthylcarbene (**2b**) under the same conditions (Fig. 1*b*, Table 1). It may be that the difference in ZFS parameters between the two rotamers for **2b** is too small to be resolved by ESR under the present conditions. This is rather unlikely since the ZFS parameters between the two rotamers of parent 1-naphthylcarbene (**4a**) are well separated and no significant changes in the values are expected on going from 1-naphthylcarbene (**4a**) to triptycyl(1-naphthyl)carbene (**2b**), taking into account the small overall change in spin distribution in triplet **4a** when H is replaced with Trp.

The more likely explanation is ascribable to steric factors. It has been shown by a kinetic analysis that the *E* isomer of 1-naphthylcarbene (**4a**) is lower in energy than the *Z* isomer, probably because of steric interaction of the peri H with the hydrogen on the carbene carbon (14). In triptycyl(1-naphthyl)-carbene (**2b**), this hydrogen is replaced with the bridgehead tertiary carbon and hence steric repulsion with the peri H in

[2] A large number of triplet carbenes have been characterized by ESR spectroscopy since the pioneering work of Wasserman et al. (9).

[3] A referee has suggested that the ratio *E*/*D* is not always a reliable guide to the structure of triplet carbenes. Diphenylcarbene and fluorenylidene have very different geometries but almost exactly the same *D* and *E* values. We assume that comparison of the values observed for a series of carbenes with a similar structure would still provide some clues to the structural change of carbenes in a qualitative sense.

© 1999 NRC Canada

Table 1. ESR data ot triplet arylcarbenes (ArCX).[a]

	Carbenes			*D*/hc	*E*/hc		
	Ar	X		cm^{-1}		*E*/*D*	Reference
3a	Ph	H		0.515	0.0251	0.04873[b]	10*a*
2a		Trp		0.510	0.0288	0,0564	This work
3b		Ph		0.4055	0.0194	0.0478[c]	10*a*
4a	1-Np	H	*E*	0.4555	0.0202	0.0443[c]	11
			Z	0.4347	0.0208	0.0478[c]	
2b		Trp		0.455	0.0237	0.0522	This work
4b		Ph		0.353	0.016	0.0453	16*a*
4c		1-Np		0.3232	0.0105	0.0325	17
5a	2-Np	H	*E*	0.4711	0.0243	0.0516	11
			Z	0.4926	0.0209	0.0484	
			E	0.475	0.0289	0.0608	
2c		Trp	*Z*	0.491	0.0258	0.0524	This work
			E	0.3898	0.0195	0.0500	
5b		Ph	*Z*	0.4044	0.0168	0.0415	16*b*
			E	0.3832	0.0182	0.0475	
5d		2-Np	*Z*	0.3971	0.0158	0.0398	17
6a	9-An	H		0.3008	0.0132	0.0439[c]	11
2d		Trp		0.348	0.0075	0.0215	This work
6e		9-An		0.113	0.0011	0.0097[d]	19

[a]Measured in MTHF at 77 K unless otherwise noted.

[b]In *p*-dichlorobenzene.

[c]In benzophenone.

[d]In 9,9′-dianthrylketone.

the *Z* isomer is expected to be much more severe than the H–H interaction in *Z*-1-naphthylcarbene. Therefore the energy difference between the two isomers becomes large enough to form the more stable isomer almost exclusively.

It should be noted here that the internal rotation of the 9-substituent around the bridgehead C—C bond in 9-substituted triptycenes is known to be hindered even at room temperature, especially when the 9-substituent is bulky (15). Since triplet triptycyl(1-naphthyl)carbene (**2c**) still has a significantly bent structure as judged from the *E* value, it is not likely that ^{3}**2c** can undergo free rotation to convert the less stable *Z* isomer into the more stable *E* isomer in matrices at low temperature. It may be, then, that the precursor diazo compound also exists predominantly as one rotamer, generating the *E* isomer.

When Trp is replaced by phenyl and naphthyl groups, i.e., on going from **2b** to **4b** and **4c** (16, 17) and from **2c** to **5b** and **5d** (16, 18), respectively, a significant decrease both in the *D* and *E* values is again observed, obviously due to extended π-delocalization. The observation again suggests that π-delocalization of the spins has more influence on the structure of triplet carbenes than do steric factors.

The effects of the Trp group on 9-anthrylcarbene (19) were somewhat different from those observed with the former two carbenes. The most notable change in this case is a rather significant decrease in the *E* value (Fig. 1*d*, Table 1). This suggests that the central bond angle undergoes significant opening as one introduces the Trp group at the 9-position. This can be easily interpreted in terms of a steric interaction between the peri H and the bridgehead carbon, as advanced above. The anthryl group has peri hydrogens both at the 1- and 8-positions and therefore cannot avoid steric interaction with the bridgehead carbon. Thus triptycyl(9-anthryl)carbene (**2d**) exhibits the smallest *E*/*D* values among triplet triptycyl(aryl)carbenes (**2**) studied in this work.

Much more significant reduction in the ZFS parameters is observed for di(9-anthryl)carbene (**6e**), which is suggested to have an almost completely linear and perpendicular geometry in which extensive delocalization of the unpaired electrons into the anthryl portions is proposed (**2a**). Since the anthryl group is planar and considerably less bulky than the triptycyl group, the fact that di(9-anthryl)carbene has a more linear and perpendicular structure than triptycyl(9-anthryl)carbene (**2d**) clearly suggests again that π-delocalization of the unpaired electrons plays a more important role in determining the structure of carbenes than do steric effects.

Laser flash photolysis studies in solution at room temperature

Irradiation of 9-triptycyl(phenyl)diazomethane (**1a**) in MTHF matrix at 77 K was monitored by UV–vis spectroscopy, which revealed the rapid appearance of new absorption bands at the expense of the original absorption due to **1a**. As shown in Fig. 2*a*, the new spectrum consists of two identifiable features, a rather sharp UV band with maximum at 314 nm and a weak broad band with an apparent maximum around 400 nm. These features are usually present in the spectra of triplet arylcarbenes in organic glasses at 77 K (4, 20). The glassy solution did not exhibit any changes for several hours when kept at 77 K. However, when it was allowed to warm to room temperature and then cooled to 77 K, the characteristic bands disappeared. On the basis of these observations, coupled with the fact that EPR signals characteristic of triplet carbene were observed under identi-

© 1999 NRC Canada

Fig. 2. UV–vis spectra obtained before and after photolysis of 9-triptycyl(aryl)diazomethanes (**1**) in MTHF matrix at 77 K, where aryl groups are (*a*) Ph, (*b*) 1-Np, (*c*) 2-Np, and (*d*) 9-An.

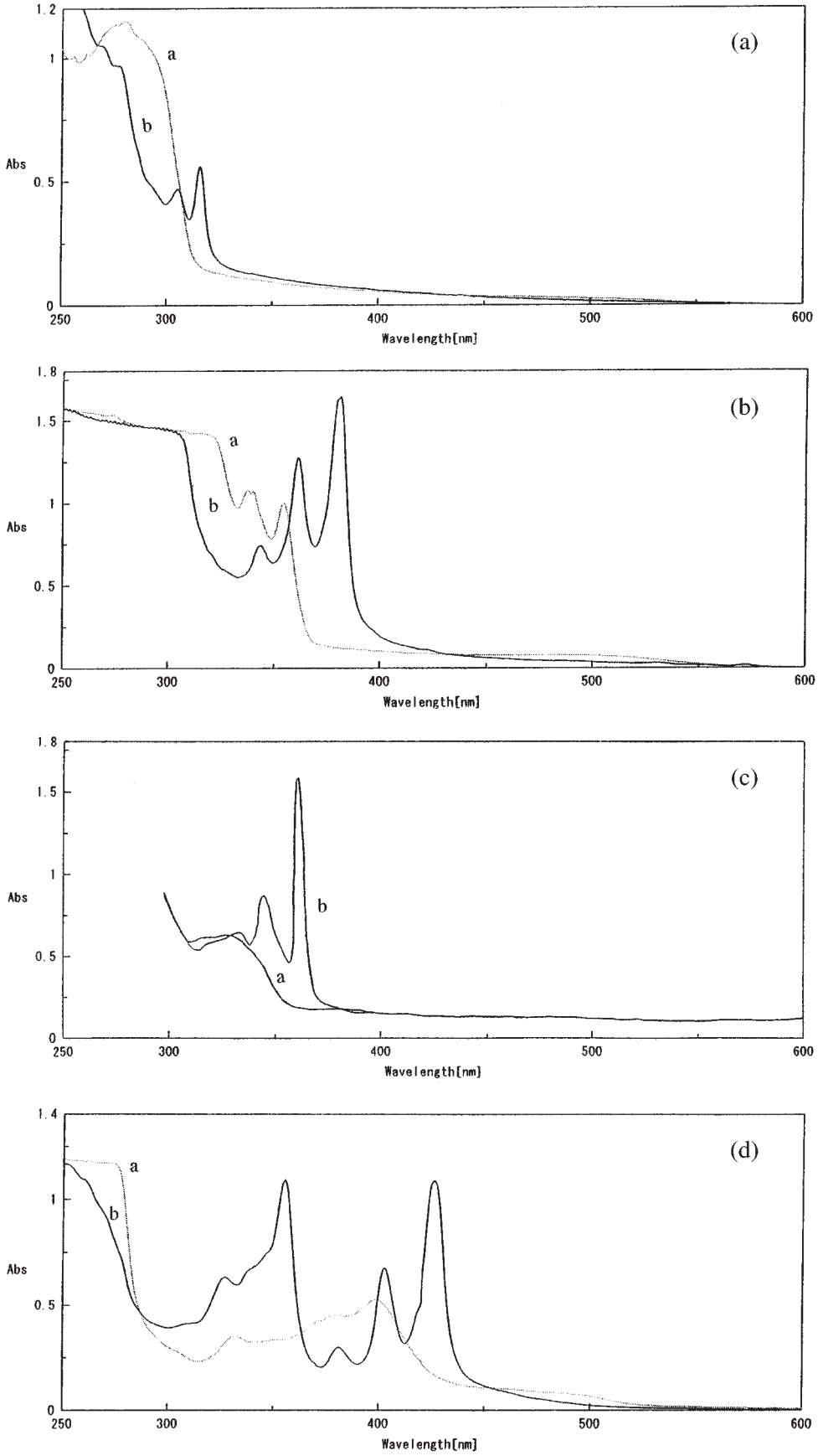

© 1999 NRC Canada

Table 2. Kinetics and spectroscopy of triplet arylcarbenes (ArCX).

	Carbenes		λ_{max}[a]		$t_{1/2}$ (or τ)[b, c]	
	Ar	X	(nm)	Decay kinetics[b]	(μs)	Reference
3a	Ph	H	—	$k = 1.9 \times 10^7$ M^{-1} s^{-1}	0.2 (in pyridine)	10*b*
2a		Trp	314	$k = 1.2 \times 10^3$ s^{-1}	(840)	This work
3b		Ph	300, 465		2	23
4a	1-Np	H	355	$k_H = 8.93 \times 10^5$ M^{-1} s^{-1}	0.3 (in CX)	25*b*
2b		Trp	347, 364	$k = 4.8 \times 10^5$ s^{-1}	(21 000)	This work
4b		Ph	262, 370	$2k/\varepsilon l = 1.8 \times 10^5$ M^{-1} s^{-1}	—	16*a*
4c		1-Np	330, 350, 362, 375, 412	$2k/\varepsilon l = 7.4 \times 10^4$ M^{-1} s^{-1}	70	17
5a	2-Np	H	362	$k = 1.64 \times 10^7$ M^{-1} s^{-1}	0.06	26
2c		Trp	358, 376	$k = 9.1 \times 10^2$ M^{-1} s^{-1}	(1100)	This work
5b		Ph		$k = 1.9 \times 10^5$ M^{-1} s^{-1}	5.2	16*b*
5d		2-Np	325, 360, 398	$k = 1.2 \times 10^6$ M^{-1} s^{-1}	(0.83)	17
6a	9-An	H	—	—	—	—
2d		Trp	355, 403, 426	$2k/\varepsilon l = 2.4 \times 10^4$ M^{-1} s^{-1}	280	This work
6e		9-An	355, 445	$k = 7 \times 10^9$ M^{-1} s^{-1}		30

[a]In 2-methyltetrahydrofurane at 77 K unless otherwise noted.

[b]In degassed benzene unless otherwise noted.

[c]Half-life ($t_{1/2}$) for carbene decaying in second order and lifetime (τ) for carbene decaying in first order.

cal conditions, the absorption spectrum is safely attributable to triplet carbene **2a**.

Laser flash photolysis (LFP) of **1a** in a degassed benzene solution at 20°C with a 10 ns, 70–90 mJ, 308 nm pulse from a XeCl excimer laser produced a transient species showing a strong absorption at 314 nm, which appeared coincident with the pulse. On the basis of the low-temperature spectrum, we assign the transient product to triplet **2a**. Support is lent to this assignment by trapping experiments using oxygen. Thus, LFP of **1a** in a non-degassed benzene solution resulted in a dramatic decrease in the lifetime of triplet **2a** and a concurrent appearance of a new absorption band at 410 nm. The rate of increase in the band at 410 nm is practically the same as that of the peak due to ^{3}**2a**, showing that triplet **2a** is quenched with oxygen to form a new species. Subsequent analysis of the spent solution showed the presence of a large amount of 9-triptycyl phenyl ketone. It is well documented that arylcarbenes with triplet ground states are readily trapped by oxygen to give the corresponding aryl ketone oxides, which usually show a rather broad band centered around 390–450 nm (21, 22). Thus, the observation can be interpreted as indicating that the triplet **2a** is trapped with oxygen to generate a carbonyl oxide, confirming that the transient absorption quenched by oxygen is due to ^{3}**2a**. A plot of the observed pseudo-first-order rate of carbonyl oxide formation versus oxygen concentration yields the quenching rate constant $k_{O2} = 1.6 \times 10^9$ M^{-1} s^{-1}.

The decay of the transient absorption due to ^{3}**2a** in the absence of oxygen was found to be first order ($k = 1.21 \times 10^3$ s^{-1}) and the lifetime is estimated to be 840 μs (Table 2). The lifetime of parent triplet phenylcarbene (**3a**) is estimated to be ~200 ns in pyridine (10*b*). Therefore, the lifetime increase of triplet phenylcarbene by addition of a Trp group is roughly estimated to be some 3 to 4 orders of magnitude. It should be noted here that this stabilization by Trp group originates mainly from kinetic factors, since no significant change in the structure of triplet carbenes is observed, at least in matrix at low temperature (vide supra). In this respect, it is very interesting to note that ^{3}**2a** is approximately 10^3 times longer lived than diphenylcarbene ^{3}**3b** (23), which must undergo significant thermodynamic stabilization as judged by considerable decrease in the ZFS parameters. Thus, kinetic stabilization is shown to play a dominant role in stabilizing triplet carbenes. Product analysis studies suggest that the Trp group is reluctant to undergo migration to the carbenic center. For instance, reactions in less reactive solvents such as benzene afforded rather complex mixtures, but no possible products arising from tribenzobicyclo[3.2.2]nonatetraene or -triene as a result of rearrangement in **2a** were detected to the limit of ^{1}H NMR detection. This is to be compared with other bicycloalkyl groups that undergo rather facile rearrangement to the carbenic center, leading to bridgehead alkenes (24). Taking into account that the [3.2.2]nonatetraene is not extremely strained, compared to other bridgehead olefins formed in the rearrangement of bicyclo(alkyl)carbenes, the slow migration of triptycyl group to the carbene center is rather puzzling. A possible explanation for the difference would appear to involve the difference in migratory aptitude between alkyl and phenyl in bicycloalkyl and triptycyl cases, respectively.

A remarkably thermal stability of triplet **2a** is also noted in monitoring the spectral changes as a function of temperature at low temperature. Thus, no appreciable changes were observed for the characteristic UV–vis spectrum of ^{3}**2a** in MTHF up to 115 K. Significant decomposition began only at 120 K. It should be noted that monophenylcarbene (^{3}**3a**) is not observable in MTHF even at 77 K since it is highly reactive under these conditions. EPR signals are observed at 77 K only when a more viscous and less reactive matrix, e.g., *p*-dichlorobenzene, is employed (see footnote 3). Moreover, diphenylcarbene (^{3}**3b**) can be observed in MTHF at 77 K but its absorption starts to disappear even below 90 K.[4]

[4]H. Tomioka and K. Hirai. Unpublished observations.

© 1999 NRC Canada

Fig. 3. Absorption spectra of the transient products formed during irradiation of 9-triptycyl(aryl)diazomethanes (**1**) in degassed benzene at room temperature, where aryl groups are (*a*) 1-Np, (*b*) 2-Np, and (*c*) 9-An. Inset in each figure shows oscillogram trace of the absorption.

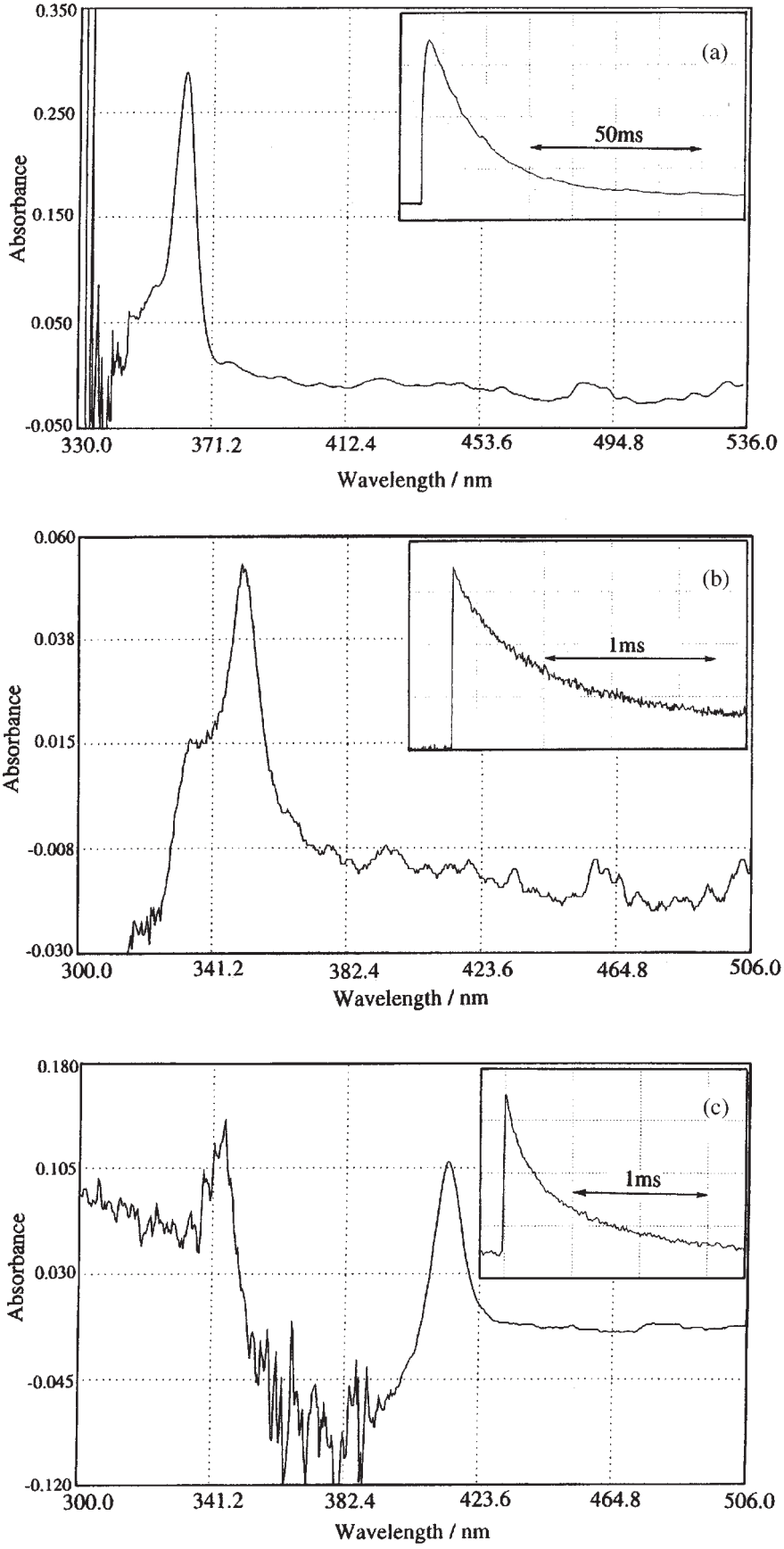

© 1999 NRC Canada

Similar trends were observed for the naphthylcarbene systems. Triptycyl(1-naphthyl)carbene (^{3}**2b**), for instance, also decayed in first-order fashion and has a lifetime of 21 ms (Fig. 3, Table 2), which is 10^5 times longer lived than the parent 1-naphthylcarbene (^{3}**4a**) (25, 26), and 10^3 times longer lived even than di(1-naphthyl)carbene (^{3}**4c**) (17), which must undergo significant thermodynamic stabilization by the two naphthyl groups in addition to kinetic stabilization resulting from steric repulsion between the two peri hydrogens. These observations again support the idea that kinetic stabilization plays a much more important role than thermodynamic factors in increasing the lifetime of triplet carbenes.

The effect of a Trp group on the reactivity of 2-naphthylcarbene (^{3}**5a**) is rather smaller than that of the 1-isomer (^{3}**4a**). The carbene center in ^{3}**5a** is essentially the same as that in phenylcarbene with respect to steric factors and therefore the effect of steric shielding by the Trp group would be expected to be similar between the two.

9-Anthrylcarbene (**6a**) is considered to be the most stable among the monoarylcarbenes studied since the carbenic center is shielded by the two peri hydrogens and the unpaired electrons are extensively delocalized into the anthryl ring, and hence **6a** is expected to be protected quite well once the Trp group is introduced at the 9-positions. ESR data in matrix at low temperature support these ideas.

Contrary to this expectation, the lifetime of triptycyl(9-anthryl)carbene (^{3}**2d**) was found to be shorter than most of its naphthyl analogues (^{3}**2b** and ^{3}**2c**), shorter even than the phenyl derivative (^{3}**2a**); transient absorption ascribable to ^{3}**2d** decayed in second order ($2k/\varepsilon l = 2.4 \times 10^4$ s^{-1}) and the half-life was estimated to be 280 μs (Fig. 3*c*, Table 2). A possible explanation for this rather unexpected decrease in lifetime may reside in an extensive delocalization of the unpaired electrons into the anthryl ring. Then, since the carbenic center in ^{3}**2d** is effectively shielded from external reagents by the two and three peri hydrogens on the aromatic and triptycyl rings, respectively, simple reaction at the carbenic center must suffer from severe steric hindrance. The carbene is then forced to react at the aromatic rings where the unpaired electrons are delocalized. It is well known that trityl radicals undergo either "head-to-tail" (methyl–*para*) or "tail-to-tail" (*para*–*para*) coupling depending on the substitution (27). Similar reactions on the aromatic rings are also suggested for the decay pathways of triplet diphenylcarbenes bearing steric protectors at the *ortho* positions. The decay rates of triplet 2,2′,6,6′-tetrabromodiphenylcarbenes, for instance, are highly sensitive to the *para* substituents and decrease as more bulky groups are introduced at the *para* positions (28). Such reactions are expected to become more facile as the numbers of fused aromatic rings are increased; the loss of the resonance energy as a result of such a reaction on the first aromatic ring is estimated to decrease from 36 to 25 to 11 kcal/mol on going from benzene to naphthalene to anthracene (29). It should be noted here that triplet di(9-anthryl)carbene (^{3}**6e**) decays significantly faster than triplet diphenylcarbene (^{3}**3b**) (30). Since ^{3}**6e** eventually produces a carbene trimer as a result of coupling at the 10,10′-positions, while the main decay pathway for ^{3}**3b** is simple dimerization at the carbenic carbon (31), the significant difference in stabilities between the two carbenes can be interpreted in terms of the difference in the facility of the reaction at the aromatic sites. Therefore, while the carbene center of ^{3}**2** is shielded more effectively on going from ^{3}**2a** to ^{3}**2d**, the extent of π-delocalization of the unpaired electrons and the facility of the reaction at the aromatic sites are increased in the same order. The steric and electronic factors are operating in opposite directions. The lifetime data observed for ^{3}**2** reflect the overall effects of these counteracting factors.

Summary

The relationship between structure and reactivity for triplet arylcarbenes has been investigated systematically for a series of 9-triptycyl(aryl)carbenes (**2**) by using matrix isolation techniques at low temperature and time-resolved spectroscopies in solution at room temperature.

It has been revealed that π-delocalization of the spin to aromatic rings is more influential than steric factors in causing triplet arylcarbenes to assume a thermodynamically more favorable structure with respect to the corresponding singlet state, but that extensive delocalization eventually tends to decrease the kinetic stability of triplet arylcarbenes as a result of spreading the reactive centers over the π framework of the molecules. Steric protectors, on the other hand, exhibit less significant effect on the structure of triplet carbenes than aromatic groups but increase the lifetime much more significantly, obviously as a result of kinetic stabilizations. Thus, a delicate balance between these two counteracting factors determines the overall reactivities of triplet arylcarbenes.

Experimental section

General methods

IR spectra were measured on a JASCO A-100 recording spectrometer and the mass spectra were recorded on a Shimadzu QP-1000 mass spectrometer (70 eV). ^{1}H and ^{13}C NMR spectra were determined with either JEOL JNM-EX 270 or JNM-500 spectrometers. UV–vis spectra were recorded on a Hitachi 220-S spectrometer. Thin-layer chromatography was done on Merck Kieselgel 60 PF 254. Column chromatography was carried out on silica gel (ICN for dry column chromatograph). HPLC and GPC measurements were undertaken with a JASCO 800 chromatograph equipped with a UVIDEC-100-II UV–vis detector using a Fine pack C18-T5 column (4.6 × 25 cm) and a Shodex GPC H-2001 (20 mm × 50 cm) column, respectively, and GLC was carried out with a Yanagimoto G-80 gas chromatograph using an OV-17 on a Diasolid L (5.0 mm × 50 cm) column.

Preparation of 9-triptycyl(phenyl)diazomethane (1a)

To a solution of PhLi, prepared by reacting PhBr (345 mg, 2.2 mmol) and Li (38 mg, 5.5 mmol) in anhydrous Et_2O (2 mL), was added 9-(formyl)triptycene (300 mg, 1.1 mmol) (32) in anhydrous PhH (3 mL) over a period of 30 min and the mixture was stirred until all of the aldehyde was consumed. The mixture was quenched with saturated aqueous NH_4Cl solution (15 mL) and extracted with three 10 mL portions of Et_2O. The organic layer was dried over Na_2SO_4 and the ether was evaporated to dryness. The crude product was purified by preparative TLC (SiO_2), eluting with

© 1999 NRC Canada

CH_2Cl_2–*n*-hexane (1:1), to give α-*(9-triptycyl)benzyl alcohol* as a white viscous oil in 86% yield; ^{1}H NMR ($CDCl_3$) δ: 1.62 (d, *J* = 7.6 Hz, 1 H), 5.42 (s, 1 H), 6.51 (s, 1 H), 6.89–7.04 (m, 3 H), 7.07–7.24 (m, 2 H), 7.30–7.40 (m, 5 H), 7.47–7.56 (m, 3 H), 7.72 (d, *J* = 7.59 Hz, 1 H), 7.91 (d, *J* = 7.59 Hz, 1 H). To a stirred solution of the benzyl alcohol (260 mg, 0.72 mmol) in acetone (10 mL) was added a mixture of CrO_3 (111 mg), concentrated H_2SO_4 (0.06 mL), and H_2O (0.72 mL) and the mixture was stirred under reflux until the alcohol was consumed. The mixture was poured into a 5% aqueous $NaHCO_3$ solution (100 mL) and extracted with three 15 mL portions of CH_2Cl_2. The organic layer was washed with H_2O and dried over Na_2SO_4, and CH_2Cl_2 was evaporated under reduced pressure. The crude product was purified by preparative TLC (SiO_2), eluting with CH_2Cl_2–*n*-C_6H_{14} (1:1), to give *9-triptycyl phenyl ketone* as a white viscous oil in 90% yield; ^{1}H NMR ($CDCl_3$) δ: 5.40 (s, 1 H), 6.89 (t, *J* = 7.26 Hz, 3 H), 7.00 (t, *J* = 7.59 Hz, 3 H), 7.32 (t, *J* = 7.76 Hz, 3 H), 7.42 (d, *J* = 7.26 Hz, 3 H), 7.52 (d, *J* = 7.58 Hz, 3 H), 7.81 (d, *J* = 6.93 Hz, 2 H). A mixture of the ketone (200 mg, 0.56 mmol), N_2H_4·HCl (200 mg, 1.9 mmol), anhydrous N_2H_4 (10 mL), and anhydrous EtOH (5 mL) was placed in a Pyrex heavy-walled, narrow-mouthed tube. The tube was sealed and placed in an oil bath heated at 100–110°C for 24 h, after which time it was chilled in an ice bath and opened. The contents were poured into ice-water and extracted with three 10 mL portions of CH_2Cl_2. The organic layer was washed with H_2O, dried over Na_2SO_4, and evaporated to dryness. The crude material was purified by preparative TLC, eluting with CH_2Cl_2–*n*-C_6H_{14} (1:1), to leave *9-triptycyl phenyl ketone hydrazone* as a gummy yellowish solid in 48% yield; ^{1}H NMR ($CDCl_3$) δ: 5.36 (s, 1 H), 5.92 (s, 2 H), 6.83–6.89 (m, 3 H), 6.92–6.97 (m, 3 H), 7.25 (d, *J* = 5.94 Hz, 3 H), 7.32–7.41 (m, 3 H), 7.46–7.53 (m, 3 H), 7.56–7.59 (m, 2 H). A mixture of the hydrazone (100 mg, 0.28 mmol) and $Ba(MnO_4)_2$ (193 mg, 0.56 mmol) in anhydrous Et_2O (10 mL) was stirred at room temperature in the dark for 5 h. The mixture was filtered and the filtrate was evaporated to dryness under reduced pressure at room temperature. The crude product was purified by chromatography on a gel permeation column with $CHCl_3$ to afford pure *9-triptycyl(phenyl)diazomethane* (**1a**) as a reddish semisolid in 61% yield; IR (KBr) ν_{max}: 2088 cm^{-1}; ^{1}H NMR ($CDCl_3$) δ: 5.44 (s, 1 H), 6.90–7.15 (m, 8 H), 7.25–7.34 (m, 6 H), 7.53 (d, *J* = 7.68, 3 H).

Preparation of 9-triptycyl(1-naphthyl)diazomethane (1b)

$SOCl_2$ (35.7 g, 0.4 mmol) was added to a solution of 9-triptycenecarboxylic acid (3.94 g, 13.2 mmol) (33) in anhydrous dioxan (25 mL) and the mixture was refluxed overnight. After evaporation of the solvent and unreacted $SOCl_2$ under reduced pressure, *9-triptycenecarboxylic chloride* was obtained as a yellowish crystal, which was used without further purification. To a solution of 1-naphthyl magnesium bromide, prepared by refluxing 1-bromonaphthalene (0.877 mg, 4.74 mmol) with Mg (113.7 mg, 4.74 mmol) in anhydrous THF (15 mL), was added the chloride (1.0 g, 3.16 mmol) in anhydrous THF (3 mL) and the mixture was stirred overnight. The mixture was quenched with saturated aqueous NH_4Cl solution and extracted with three 10 mL portions of CH_2Cl_2. After evaporation of the solvent, the crude mixture was purified by preparative TLC (SiO_2), eluting with CH_2Cl_2–*n*-C_6H_{14} (1:1), to give *9-triptycyl 1-naphthyl ketone* as a colorless solid in 30% yield; mp 112–114°C; ^{1}H NMR ($CDCl_3$) δ: 5.44 (s, 1 H), 6.90 (t, *J* = 7.59 Hz, 3 H), 7.01 (t, *J* = 7.43 Hz, 3 H), 7.20–7.26 (m, 1 H), 7.44 (d, *J* = 7.92 Hz, 6 H), 7.49–7.58 (m, 2 H), 7.62–7.68 (m, 1 H), 7.73–7.79 (m, 1 H), 7.98–8.03 (m, 1 H), 8.86 (d, *J* = 8.91 Hz, 1 H). A mixture of N_2H_4·HCl (300 mg, 2.85 mmol), anhydrous N_2H_4 (3 mL), and the ketone (200 mg, 0.49 mmol) in anhydrous PhH (1 mL) and EtOH (3 mL) was heated in a sealed tube at 100–110°C for a week. The usual work-up, followed by preparative TLC, gave *9-triptycyl 1-naphthyl ketone hydrazone* as a white semisolid in 53% yield; ^{1}H NMR ($CDCl_3$) δ: 5.38 (s, 1 H), 5.70 (s, 2 H), 6.67–6.73 (m, 3 H), 6.92–7.29 (m, 7 H), 7.34–7.48 (m, 3 H), 7.55–7.67 (m, 3 H), 7.92–8.03 (m, 2 H), 8.26–8.32 (m, 2 H). The hydrazone was oxidized and purified as described above to produce *9-triptycyl(1-naphthyl)diazomethane* (**1b**) as an orange solid in 65% yield; mp 183–184°C (dec.); IR (KBr) ν_{max}: 2040 cm^{-1}; ^{1}H NMR ($CDCl_3$) δ: 5.45 (s, 1 H), 6.83–7.25 (m, 6 H), 7.28–7.54 (m, 6 H), 7.59 (d, *J* = 8.25 Hz, 1 H), 7.61 (d, *J* = 8.25 Hz, 1 H), 7.69–7.82 (m, 2 H), 7.92–7.99 (m, 1 H), 8.50 (d, *J* = 8.58 Hz, 1 H).

Preparation of 9-triptycyl(2-naphthyl)diazomethane (1c)

This compound was prepared by essentially the same procedure as reported for **1b** by way of the following compounds. *9-Triptycyl 2-naphthyl ketone*: 90% yield; a white crystal; mp 185–186°C; ^{1}H NMR ($CDCl_3$) δ: 5.46 (s, 1 H), 6.87 (t, *J* = 7.59 Hz, 3 H), 7.02 (t, *J* = 7.92 Hz, 3 H), 7.44–7.70 (m, 10 H), 7.84 (t, *J* = 6.76 Hz, 2 H), 8.54 (s, 1 H). *9-Triptycyl 2-naphthyl ketone hydrazone*: 15% yield; a white solid; mp 134–141°C; ^{1}H NMR ($CDCl_3$) δ: 5.38 (s, 1 H), 5.95 (bs, 2 H), 6.81–6.97 (m, 6 H), 7.24–7.39 (m, 6 H), 7.49–7.63 (m, 3 H), 7.82–7.97 (m, 3 H), 8.09 (s, 1 H). *9-Triptycyl(2-naphthyl)diazomethane* (**1c**): 90% yield; a red solid; mp 178°C (dec.); IR (KBr) ν_{max}: 2045 cm^{-1}; ^{1}H NMR ($CDCl_3$) δ: 5.47 (s, 1 H), 6.85–7.06 (m, 6 H), 7.15 (d, *J* = 8.58 Hz, 1 H), 7.30–7.66 (m, 10 H), 7.70 (d, *J* = 8.58 Hz, 1 H), 7.75–7.80 (m, 2 H).

Preparation of 9-triptycyl(9-anthryl)diazomethane (1d)

To a stirred solution of di-(9-anthryl)diazomethane (150 mg, 0.38 mmol) (19) and phenyl[*o*-(trimethylsilyl)phenyl] iodonium triflate (1.3 g, 2.97 mmol) (34) in anhydrous THF (4 mL) at 0°C was slowly added a dry solution of tetrabutylammonium fluoride (1.5 g, 3.57 mmol) in anhydrous THF (2 mL), through a syringe in the dark. After stirring for 2 h, the mixture was poured into water and extracted with Et_2O. The usual work-up gave a crude mixture, which was purified by repeated chromatography on a gel permeation column with $CHCl_3$. The diazomethane (**1d**) was obtained as an orange solid in 18% yield; mp 69–70°C; IR (KBr) ν_{max}: 2038 cm^{-1}; ^{1}H NMR ($CDCl_3$) δ: 5.47 (s, 1 H), 6.20 (dd, *J* = 7.92, 7.59 Hz, 1 H), 6.75 (dd, *J* = 7.26, 7.26 Hz), 7.12–7.55 (m, 11 H), 8.12 (d, *J* = 7.59 Hz, 2 H), 8.58 (d, *J* = 7.59 Hz, 1 H), 8.64 (s, 1 H).

ESR measurements

The diazo compound was dissolved in 2-methyltetrahydrofuran (10^{-3} M) and the solution was degassed in a quartz

© 1999 NRC Canada

cell by three freeze–degas–thaw cycles. The sample was cooled in an optical transmission ESR cavity at 77 K and irradiated with a Wacom 500 W Xe lamp using a Pyrex filter. ESR spectra were measured on a JEOL JES TE 200 spectrometer (X-band microwave unit, 100 kHz field modulation). The signal positions were read by the use of a gauss meter.

Low-temperature UV–vis spectra

Low-temperature spectra at 77 K were obtained by using an Oxford variable-temperature liquid nitrogen cryostat (DN 1704) equipped with a quartz outer window and a sapphire inner window. The sample was dissolved in dry 2-MTHF, placed in a long-necked quartz cuvette of 1 mm path length, and degassed thoroughly by repeated freeze–degas–thaw cycles at a pressure near 10^{-5} Torr (1 Torr = 133.3 Pa). The cuvette was flame-sealed under reduced pressure, placed in the cryostat, and cooled to 77 K. The sample was irradiated for several minutes in the spectrometer with a Halos 300 W high-pressure mercury lamp using a Pyrex filter, and the spectral changes were recorded at appropriate time intervals. The spectral changes upon thawing were also monitored by carefully controlling the matrix temperature with an Oxford Instrument Intelligent Temperature Controller (ITC 4).

Flash photolysis

All flash measurements were made on a Unisoku TSP-601 flash spectrometer. Three excitation light sources were used depending on the precursor absorption bands and lifetime of the transient species. They were (*i*) a cylindrical 150 W Xe flash lamp (100 J/flash with 10 μs pulse duration), (*ii*) a Quanta-Ray GCR-11 Nd:YAG laser (355 nm pulses of up to 40 mJ/pulse and 5–6 ns duration; 266 nm pulses of up to 30 mJ/pulse and 4–5 ns duration), and (*iii*) a Lamda Physik LEXTRA XeCl excimer laser (308 nm pulses of up to 200 mJ/pulse and 17 ns duration). The beam shape and size were controlled by a focal length cylindrical lens.

A Hamamatsu 150 W xenon short-arc lamp (L 2195) was used as the probe source, and the monitoring beam, guided using an optical fiber scope, was arranged in an orientation perpendicular to the excitation source. The probe beam was monitored with a Hamamatsu R2949 photomultiplier tube through a Hamamatsu S3701-512Q MOS linear image sensor (512 photodiodes used). Timing of the excitation pulse, the probe beam, and the detection system was achieved through an Iwatsu model DS-8631 digital synchroscope that was interfaced to a NEC 9801 RX2 computer. This allowed for rapid processing and storage of the data and provided printed graphic capabilities. Each trace was also displayed on a NEC CRT N5913U monitor.

Samples were placed in a long-necked Pyrex tube that had a side arm connected to a quartz fluorescence cuvette and were degassed using a minimum of four freeze–degas–thaw cycles at a pressure near 10^{-5} Torr immediately prior to being flashed. The sample system was flame-sealed under reduced pressure, and the solution was transferred to the quartz cuvette, which was placed in the sample chamber of the flash spectrometer. A cell holder block of the sample chamber was equipped with a thermostat and allowed to come to thermal equilibrium. The concentration of the sample was adjusted so that it absorbed a significant portion of the excitation light.

Acknowledgment

The authors are grateful to the Ministry of Education, Science, and Culture of Japan for support of this work through a Grant-in-Aid for Scientific Research. We also wish to thank Professor T. Takui of Osaka City University for helpful discussions.

References

1. W. Kirmse. Carbene chemistry. Academic Press, New York. 1964. pp. 5–6.
2. (*a*) W. Kirmse. Carbene chemistry. 2nd ed. Academic Press, New York. 1971; (*b*) R.A. Moss and M. Jones, Jr. (*Editors*). Carbenes. Vols. 1 and 2. Wiley, New York. 1973 and 1975; (*c*) M. Regitz (*Editor*). Carbene(oide), carbine. Thieme, Stuttgart. 1989.
3. G.B. Schuster. Adv. Phys. Org. Chem. **22**, 311 (1986).
4. W. Sander, G. Bucher, and S. Wierlacher. Chem. Rev. **93**, 1583 (1993).
5. (*a*) R.A. Moss and N.J. Turro. *In* Kinetics and spectroscopy of carbenes and biradicals. *Edited by* M.S. Platz. Plenum Press, New York. 1990. pp. 213–238; (*b*) M.S. Platz and V.M. Maloney. *In* Kinetics and spectroscopy of carbenes and biradicals. *Edited by* M.S. Platz. Plenum Press, New York. 1990. pp. 239–352; (*c*) R.A. Moss. *In* Advances in carbene chemistry. *Edited by* U.H. Brinker. JAI Press, Greenwich, Conn. 1994. pp. 59–88; (*d*) J.E. Jackson and M.S. Platz. *In* Advances in carbene chemistry. *Edited by* U.H. Brinker. JAI Press, Greenwich, Conn. 1994. pp. 89–160.
6. T. Bally and W.T. Borden. *In* Reviews in computational chemistry. *Edited by* K.B. Lipowitz and D.B. Boyd. Wiley, New York. 1998.
7. (*a*) H. Tomioka. Acc. Chem. Res. **30**, 315 (1997); (*b*) *In* Advances in carbene chemistry. Vol. 2. *Edited by* U.H. Brinker. JAI Press, Greenwich, Conn. 1998. pp. 175–214.
8. H. Tomioka, J. Nakajima, H. Mizuno, T. Sone, and K. Hirai. J. Am. Chem. Soc. **117**, 11355 (1995).
9. E. Wasserman and R.S. Hutton. Acc. Chem. Res. **10**, 27 (1977); E. Wasserman, L.C. Snyder, and W.A. Yager. J. Chem. Phys. **41**, 1763 (1964).
10. (*a*) E. Wasserman, A.M. Trozzolo, and W.A. Yager. J. Chem. Phys. **40**, 2408 (1964); (*b*) A. Admasu, A.D. Gudmundsdóttir, and M.S. Platz. J. Phys. Chem. **101**, 3832 (1997).
11. A.M. Trozzolo, E. Wasserman, and W. Yager. J. Am. Chem. Soc. **87**, 129 (1965).
12. H.D. Roth and R.S. Hutton. J. Am. Chem. Soc. **104**, 7395 (1982).
13. M.J.S. Dewar and R.C. Dougherty. The PMO theory of organic chemistry. Plenum, New York. 1975.
14. V.P. Senthilnathan and M.S. Platz. J. Am. Chem. Soc. **103**, 5503 (1981).
15. M. Oki. Acc. Chem. Res. **23**, 351 (1990).
16. (*a*) Y. Fujiwara, M. Sasaki, Y. Tanimoto, and M. Itoh. Chem. Phys. Lett. **146**, 133 (1988); (*b*) V.M. Maloney and M.S. Platz. J. Phys. Org. Chem. **3**, 135 (1990); H.D. Roth and M.S. Platz. J. Phys. Org. Chem. **9**, 252 (1996); (*c*) A. Després, E. Migirdicyan, K. Haider, V.M. Maloney, and M.S. Platz. J. Phys. Chem. **94**, 6632 (1990); (*d*) B. Kozankiewicz, A.

© 1999 NRC Canada

Despres, V. Lejeune, E. Migirdicyan, D. Oslon, J. Michalak, and M.S. Platz. J. Phys. Chem. **98**, 10419 (1994).
17. H. Tomioka, T. Koshiyama, and K. Hirai. To be published.
18. H. Tukada, T. Sugawara, S. Murata, and H. Iwamura. Tetrahedron Lett. **27**, 235 (1986).
19. E. Wasserman, V.J. Kuck, W.A. Yager, R.S. Hutton, F.D. Greene, V.P. Abegg, and N.M. Weinshenker. J. Am. Chem. Soc. **93**, 6355 (1971).
20. (*a*) A.M. Trozzolo. Acc. Chem. Res. **1**, 329 (1968); (*b*) A M. Trozzolo and E. Wasserman. *In* Carbenes. *Edited by* R.A. Moss and M. Jones, Jr. Wiley, New York. 1975. pp. 185–206.
21. W. Sander. Angew. Chem. Int. Ed. Engl. **29**, 344 (1990).
22. J.C. Scaiano, W.G. McGimpsey, and H.L. Casal. J. Org. Chem. **54**, 1612 (1989).
23. (*a*) L.M. Hadel, V.M. Maloney, M.S. Platz, W.G. McGimpsey, and J.C. Scaiano. J. Phys. Chem. **90**, 2488 (1986).
24. M. Jones, Jr. *In* Advances in carbene chemistry. Vol. 2. *Edited by* U.H. Brinker. JAI Press, Greenwich, Conn. 1998. pp. 77–96.
25. (*a*) R.L. Barcus, L.M. Hadel, L.J. Johnston, M.S. Platz, T.G. Savino, and J.C. Scaiano. J. Am. Chem. Soc. **108**, 3928 (1986); (*b*) G.W. Griffin and K.A. Horn. J. Am. Chem. Soc. **109**, 4919 (1987); (*c*) L.M. Hadel, M.S. Platz, and J.C. Scaiano. Chem. Phys. Lett. **97**, 446 (1983).
26. K. Horn and J.E. Chateauneuf. Tetrahedron, **41**, 1465 (1985).
27. (*a*) V.D. Sholle and E.G. Rozantsev. Russ. Chem. Rev. **42**, 1011 (1973); (*b*) J.M. McBride. Tetrahedron, **30**, 2009 (1974).
28. (*a*) H. Tomioka, T. Watanabe, K. Hirai, K. Furukawa, T. Takui, and K. Itoh. J. Am. Chem. Soc. **117**, 6376 (1995); (*b*) H. Tomioka, M. Hattori, and K. Hirai. J. Am. Chem. Soc. **118**, 8723 (1996).
29. A.J. Gordon and R.A. Ford. *In* The chemists companion. Wiley, New York. 1972. p.131.
30. D.J. Astles, M. Girard, D. Griller, R.J. Kolt, and D.D.M. Wayner. J. Org. Chem. **53**, 6053 (1988).
31. H. Tomioka. To be published.
32. E.C. Kornfeld, P. Barney, J. Blankley, and W. Faul. J. Org. Chem. **8**, 342 (1965).
33. Y. Kawada and H. Iwamura. J. Am. Chem. Soc. **105**, 1449 (1983).
34. T. Kitamura, J. Matsuyuki, and H. Taniguchi. Synthesis, 147 (1994); T. Kitamura and M. Yamane. J. Chem. Soc. Chem. Commun. 983 (1995).

© 1999 NRC Canada

Spectral and cyclic voltammetric characterization of self-assembled monolayers on gold of pyrene end-labeled oligonucleotide duplexes

R. Scott Reese and Marye Anne Fox

Abstract: Self-assembled monolayers of sulfur-terminated oligonucleotide duplexes were formed on flat gold surfaces, either by exposure of a self-assembled monolayer bearing one oligonucleotide strand to the complementary strand or by preformation of a oligonucleotide duplex that was then deposited on a fresh gold surface. Virtually identical spectral behavior was observed whether the duplex was produced before deposition or by in situ complementary association. With a duplex bearing an appropriate pyrene end-label, the resulting thin film was photoresponsive. Surface emission measurements show no evidence for pyrene aggregation on the modified surfaces. The polarity of the photocurrent, reflecting photoinduced electron transfer initiated by photoexcitation of pyrene, is opposite that expected from the oligonucleotide-mediated reduction of the appended pyrene excited state.

Key words: oligonucleotide, self-assembled monolayer, duplex formation, photoelectrochemistry, surface emission.

Résumé : On a formé des monocouches autoassemblées de duplexes d'oligonucléotides se terminant avec des atomes de soufre; ces monocouches ont été formées sur des surfaces planes d'or par exposition d'une monocouche autoassemblée comportant un chaînon d'oligonucléotide vers le chaînon complémentaire ou par préformation d'un duplexe d'oligonucléotide qui est ensuite déposé sur une surface d'or fraîche. On a observé un comportement pratiquement identique quelle que soit la méthode de formation (préformation suivie d'un dépôt ou association in situ). Avec un duplexe comportant un marqueur pyrène approprié en bout de chaîne, le film mince qui en résulte est photosensible. Des mesures d'émission en surface ne fournissent aucune indication à l'effet qu'il se produirait une agrégation de pyrène sur les surfaces modifiées. La polarité du photocourant, qui est un reflet du transfert photoinduit d'électrons initié par la photoexcitation du pyrène, est de sens opposé à celui attendu sur la base d'une réduction, catalysée par l'oligonucléotide, de l'état excité du pyrène attaché.

Mots clés : oligonucléotide, monocouche autoassemblée, formation de duplexe, photoélectrochimie, émission de surface.

[Traduit par la Rédaction]

Introduction

Electron transfer in DNA and oligonucleotides has been studied intensely, in part because of an ongoing debate as to whether the aromatic base pairs can mediate long-range electron transfer via π-stacking interactions (1–4). Giese and co-workers (5) have recently indicated that the sequence of base pairs can strongly influence the rate and efficiency of electron migration in oligonucleotides, a conclusion supported by experiments within our own group in elaborating rates of photoinduced electron transfer in pyrene-labeled oligonucleotides (6). In that work, we showed that long-distance electron transfer may involve multiple short hops to and from guanines and that the distance dependence of the observed electron transfer rates is complicated because of a less efficient alternative quenching route by thymidine. If so, it may be possible to construct surface-anchored oligonucleotide thin films and (or) self-assembled monolayers through which directional electron flow can be achieved by controlling the sequence of component bases. Such control is important in building the framework for electronic interactions in molecular electronic devices (7–10).

There is, as well, a strong interest in developing DNA sequencing and gene mapping technologies by appending DNA or oligonucleotide segments to surfaces as thin films (11–15). A novel example (14) of this concept is demonstrated by a method in which noncomplementary oligonucleotides are bound to the surface of Au nanoparticles via a sulfur bond. Because the oligonucleotides on the particles are noncomplementary, they do not associate with each other and the particles remain dispersed in H_2O as a dark red suspension. When a solution of an oligonucleotide duplex with

Received January 6, 1999.

This paper is dedicated to Professor A.J. Kresge, with thanks and appreciation for his career-long dedication to physical organic chemistry and to the success of his many grateful students.

R.S. Reese and M.A. Fox.[1] Departments of Chemistry, North Carolina State University, Raleigh, NC 27695, U.S.A., and University of Texas at Austin, Austin, TX 78712, U.S.A.

[1]Author to whom correspondence may be addressed at North Carolina State University.

© 1999 NRC Canada

"sticky ends" that are complementary to the two surface-confined oligonucleotides is added to the solution, the nanoparticles aggregate.

For many technological applications, organic thin films (OTFs) are desirable. Because of the molecular-scale control offered by these methods, highly anisotropic films are often obtainable (8–10). This is particularly evident in self-assembled monolayers (SAMs), where surface-affinity and monolayer-packing interactions afford easy synthetic access to structurally well-defined arrays. Furthermore, if a conducting surface is used as a support for the film, the SAM may serve as an "antenna" with which to detect and harness the current generated by the electron transfer. The preparation and evaluation of such SAMs is also important from a fundamental scientific standpoint in that dimensionally controlled electron transfer is ubiquitous in the natural world and is vital in phenomena such as photosynthesis in plants and bacteria. Thus, an understanding of photoinduced electron transfer through a SAM will also play an important role in the development of systems to harness solar radiation as a source of clean, sustainable energy.

Combining our knowledge of photoinduced electron transfer in chromophore-labeled oligonucleotides with our expertise in the construction and characterization of SAMs may produce arrays that can increase our understanding of electron transfer in surface-confined architectures. In turn, this work may lead us closer to our goal of developing solid phase photosynthetic mimics, while contributing to the development of novel DNA probes based on photoactive monolayers. In this work, we describe the construction of photoactive monolayers using surface-confined oligonucleotides **1** and **2** associated with their pyrene end-labeled complements **3** and **4**. We then describe the observed photoresponsiveness of the resulting self-assembled monolayers.

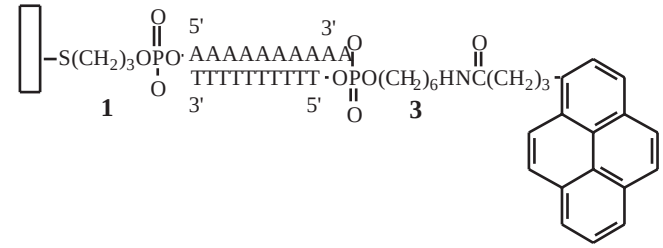

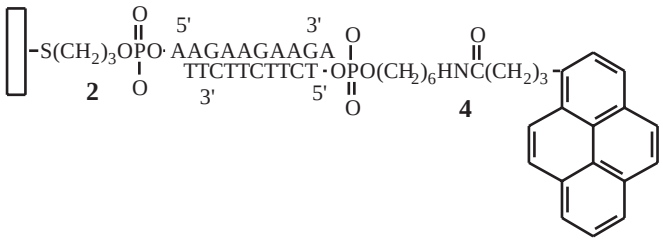

Experimental

General

Unless otherwise noted, all manipulations were carried out under air. Solvents were reagent grade and, like all reagents, were used as received. Oligonucleotides **1** and **2** modified with a free thiol terminus and their oligonucleotide complements as free amines were purchased from Integrated DNA Technology, Coralville, Iowa.

Absorption spectra were acquired on a Shimadzu UV-3101PC scanning instrument, grazing angle reflectance Fourier-transform infrared (GAR-FTIR) spectra on a Nicolet 550 FTIR, circular dichroism spectra (CD) on a Jasco-600, and fluorescence spectra on a SLM Aminco SPF 500 fluorometer.

Synthesis of 3 and 4

The functionalized oligonucleotides **3** and **4** were prepared by the method described by Zahavy and Fox (6). *N*-(3-Dimethylaminopropyl)-*N*′-ethylcarbodiimide HCl (EDC), and *N*-hydroxysulfosuccinimide sodium salt (SNHS) (16, 17) were used as coupling reagents in DMSO–water to append pyrenebutanoic acid to the oligonucleotides complementary to **1** and **2** (6). The modified oligonucleotides were characterized by electrospray mass spectroscopy. Calculated mass for **3:** 3528; found for the double charged ion: 1773.2(±0.4), which is 3546(±1) (M^{2+} + H_2O). Calculated mass for **4**: 3355; found for the double charged ion: 1724.2(±0.4), which is 3448(±1) (M^{2+} + PO_4). The number of the chromophores per strand was estimated by absorption spectrometry to be 0.7 pyrene per oligonucleotide for **3**, and 0.8 pyrene per oligonucleotide for **4**, with the oligonucleotide concentration calculated from its absorption at λ = 260 nm, $\varepsilon = 1 \times 10^5$ M^{-1} cm^{-1}, and the pyrene content calculated from its absorption at λ = 342 nm, $\varepsilon = 1.4 \times 10^4$ M^{-1} cm^{-1}.

Monolayer formation

Monolayers of **1** and **2** were formed by exposing fresh Au surfaces, prepared as previously described (18), to aqueous solutions of **1** and of **2** (400 μM in 10 mM NaCl) for 3–16 h at room temperature. The modified surfaces were rinsed with copious amounts of 10 mM NaCl prior to any measurements. Longer deposition times do not affect either the observed IR spectra of the SAMs or the cyclic voltammetry of a contacting solution redox probe observed on the modified Au electrodes.

Photoelectrochemical measurements

Photoelectrochemical measurements were conducted in aqueous methyl viologen (MV^{2+}, 1 mM in 0.1 M NaCl), which had been deaerated by bubbling with Ar. The experiments were carried out in an electrochemical cell equipped with a quartz optical flat window, with Ag/AgCl as a reference electrode, and a Pt coil as the auxiliary electrode. Photocurrents were obtained by sending the output of a 150 W high-pressure Xe arc lamp through an Oriel 77250 grating monochromator set to pass 346 nm light so that only pyrene-induced effects would be observed. The resulting steady-state photocurrent was recorded under a controlled potential bias. The electrodes were located at the focus of a condensing lens (illuminated area: 0.78 cm^2) held 25 cm from the monochromator. Short-circuit photocurrents and open-circuit photovoltages were measured according to previously described procedures (18).

© 1999 NRC Canada

Fig. 1. GAR-FTIR spectra of SAMs on Au of (*a*) **1** and (*b*) **2**.

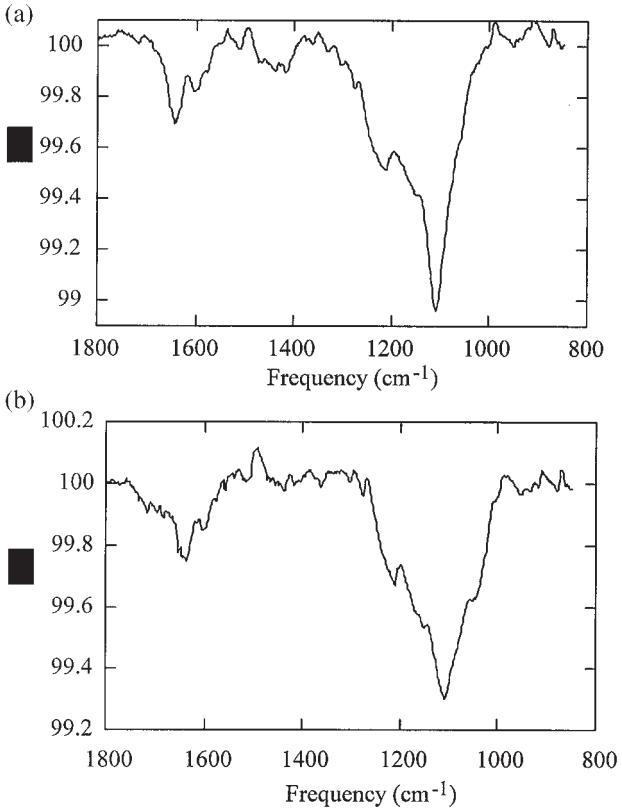

Fig. 2. Cyclic voltammetry of 0.1 M K_4 $Fe(CN)_6$ in deaerated 1 mM aqueous NaCl at bare gold (circles); Au modified with SAMs of **1** (solid line) and **1/3** (broken line). Scan rate: 100 mV/s.

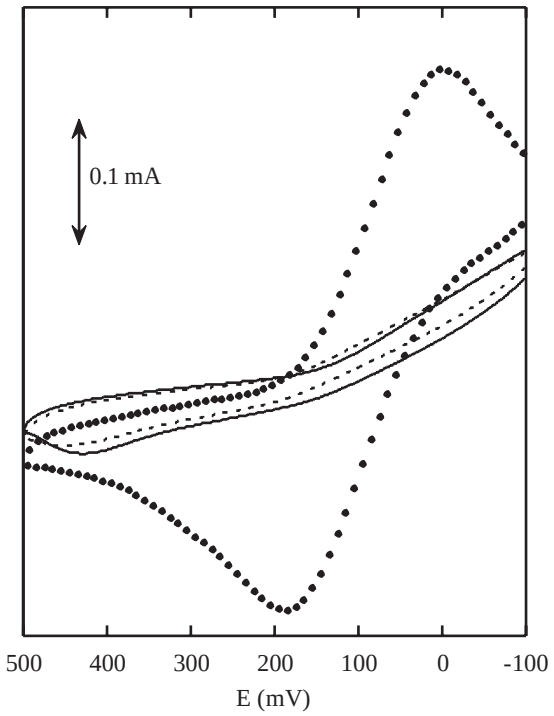

Results

SAMs of 1 and 2 on Au

GAR-FTIR spectra of the SAMs of **1** and **2** on Au exhibit absorptions characteristic of nucleotide oligomers (Fig. 1) (19–21). In the SAM of **1** on Au, a strong absorption assigned to the symmetric vibration of the phosphate group is observed at 1108 cm^{-1} and the asymmetric phosphate vibration occurs at 1213 cm^{-1}. The weak absorptions between 1380 and 1550 cm^{-1} are assigned to the in-plane ring vibrations of adenine and the stronger absorptions between 1550 and 1700 cm^{-1} to the double-bond in-plane vibrations of adenine. The spectrum of a SAM of **2** on Au closely resembles that of **1**, except that the weak absorptions between 1380 and 1550 cm^{-1} attributable to the in-plane ring vibrations of the aromatic bases are not observed.

To demonstrate oligonucleotide binding and to qualitatively evaluate packing of these films, cyclic voltammetry of a contacting 1 mM solution of $K_4Fe(CN)_6$ in 0.1 NaCl was performed at Au electrodes modified with SAMs of **1** and **2**. Although reversible curves are obtained upon repeated recycling of SAMS of either **1** or **2**, the current responses of the SAM-modified electrodes **1** and **1/3** are attenuated compared to the response at bare Au (Fig. 2). The shapes of the cyclic voltammograms are rendered less sigmoidal after exposure to the oligonucleotide, indicating that the electrodes are partially blocked by the films. The observed blocking behavior likely is dominated by electrostatic repulsion of the ferricyanide anion by the polyphosphate oligonucleotide (18).

The time course of the short-circuit current observed in an electrochemical cell employing as a working electrode an electrode modified with a SAM of **1** on Au equilibrated with an aqueous solution of MV^{2+} (1 mM in 0.1 M NaCl) at a potential of –100 mV is shown in Fig. 3. After a rapid initial drop-off of the charging current, the current approaches a limiting capacitative current. The inset is an enlarged plot of the time domain during which the electrode is alternately exposed to and shielded from illumination at 346 nm, with arrows showing when the shutter was open (on) and closed (off). No significant photoresponse beyond background can be observed. This is as expected since there is no absorptive chromophore at 346 nm in this SAM. Exactly analogous behavior was observed with an electrode modified with a SAM of **2** on Au.

SAMs of duplexes 1/3 and 2/4 on Au prepared by treatment of SAMs 1 and 2 with complements 3 and 4

Au surfaces modified with SAMs of **1** and **2** were subsequently exposed to their pyrene end-labeled complements **3** (520 μM in 10 mM NaCl) and **4** (540 μM in 10 mM NaCl), respectively, for 4–16 h. The resulting SAMs were then rinsed with 10 mM NaCl, providing GAR-FTIR spectra that are virtually identical before and after exposure to the complements, apart from weak absorptions assigned to pyrene ring C–C stretching at 1480 cm^{-1} and to C–H stretching at 2850–2975 cm^{-1} (22). The weakness of these additional bands likely reflects the small amounts of pyrene incorporated into the SAM and (or) an orientation of the appended

© 1999 NRC Canada

Fig. 3. Time course for the limiting current at a Au electrode modified with a SAM of **1** in a MV^{2+} solution (1 mM in 0.1 M NaCl) at an applied potential of –100 mV vs. Ag/AgCl. The inset shows the time domain in which the electrode is alternately exposed to, and shielded from, illumination at 346 nm, with arrows showing when the shutter was open (on) and closed (off).

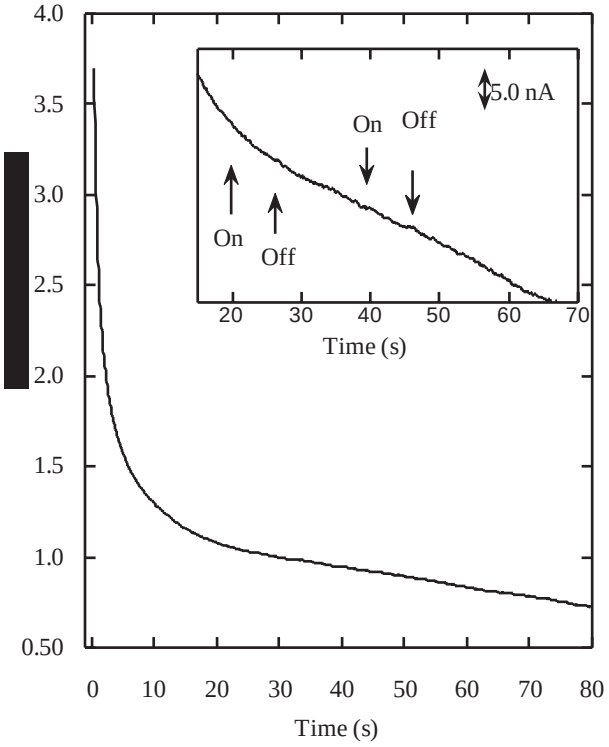

pyrene such that the IR absorptions are attenuated in the reflectance spectrum.

Figure 4 shows an emission spectrum of a film of **1** on Au before and after exposure to **3**. Although there is nearly no absorption in a SAM of **1** on Au in the region from 365 to 450 nm before exposure to the pyrene end-labeled complement, a new emission band is observed in the double-stranded complement with a maximum at 372 nm. This band is similar to the emission observed in micellar solutions incorporating very small concentrations of pyrene (23). Thus, **3** has been successfully incorporated into the **1**/**3** conjugate SAM. The absence of excimer emission at wavelengths longer than 410 nm indicates that the pyrene in this SAM does not form aggregates (23, 24) The emission from the **1**/**3** SAM is less structured than emission from **3** itself in a dilute deaerated 0.1 M KCl (OD = 0.07) solution. The emission from the film is weak and a poor signal-to-noise ratio makes complete subtraction of the scattered light from the Au background difficult. The relatively low intensity of the emission is probably caused by the low concentration of pyrene in the film but partial quenching of the pyrene emission by Au in disordered microdomains may also contribute to this effect (25). Exactly parallel emission effects are observed with a SAM of **2** on Au after exposure to **4**.

Cyclic voltammetry of a contacting 1 mM solution of $K_4Fe(CN)_6$ in 0.1 NaCl at a SAM of **2** before and after exposure to **4** is shown in Fig. 5. The magnitude of the current

Fig. 4. Emission spectra of **3** (OD = 0.7 AU) in deaerated aqueous 0.1 M KCl (broken line) and of SAMs of **1** (circles) and **1**/**3**(solid line) on contact with a deaerated 0.1 M KCl solution. Excitation at 342 nm. The emission spectra are roughly normalized to 375 nm.

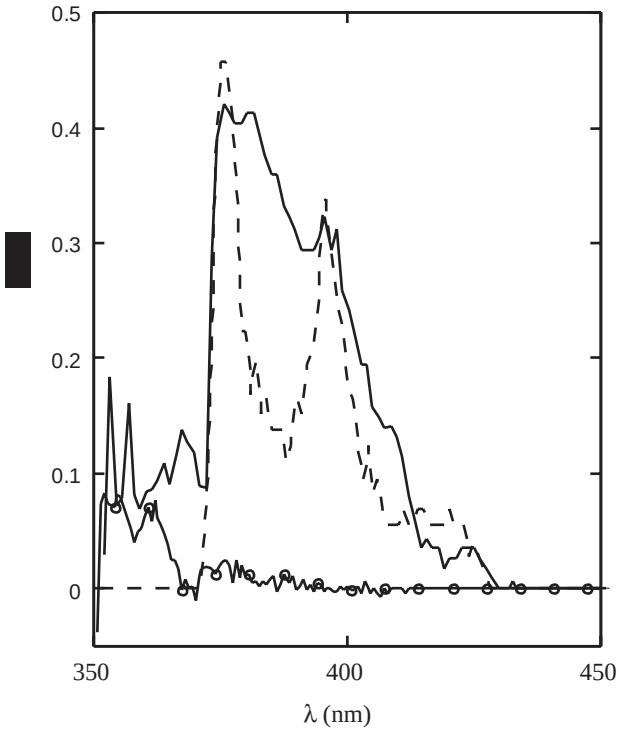

passed at the electrode modified with a SAM of **2** on Au decreases so that a small limiting dark current is observed at the modified electrode after it has been exposed to its complement. This indicates fewer pinholes or defect sites that permit access of the electroactive ferricyanide to the charged SAM surface after the film has been exposed to its complement (26). This is further evidence for incorporation of **4** into the **2**/**4** duplex SAM. Analogous behavior (not shown) is observed for a SAM of **1** on Au subsequent to exposure to **3**. In both cases, exposure to the complementary oligonucleotide induces essentially complete (largely electrostatic) shielding of the surface of the electrode from the contacting electroactive solution.

The time course of the current observed with an electrode modified with a SAM of duplex **2**/**4** on Au in contact with aqueous MV^{2+} and an external bias of –100 mV is shown in Fig. 6. It shows similar capacitative behavior as the SAM of **2** but the expanded view of the time domain between 20 and 26 s reveals an anodic current of about 4 nA upon illumination compared to the background dark current. Similar results are observed with a SAM of duplex **1**/**3**, which exhibits an anodic current of about 5 nA upon illumination compared to the background dark current.

Figures 7 and 8 show the time courses of the currents at SAMs of **2**/**4** on Au at potentials of 0 mV and +100 mV, respectively. The capacitative decay current is anodic. The current under illumination is still about 4 nA more anodic than the dark current. Neither the magnitude nor the polarity of the illumination current is affected by the applied poten-

© 1999 NRC Canada

Fig. 5. Cyclic voltammetry of a contacting solution of 1 mM $K_4Fe(CN)_6$ in deaerated 0.1 M NaCl of a SAM on gold of **2** (broken line) and **2**/**4** (solid line). Scan rate: 100 mV/s.

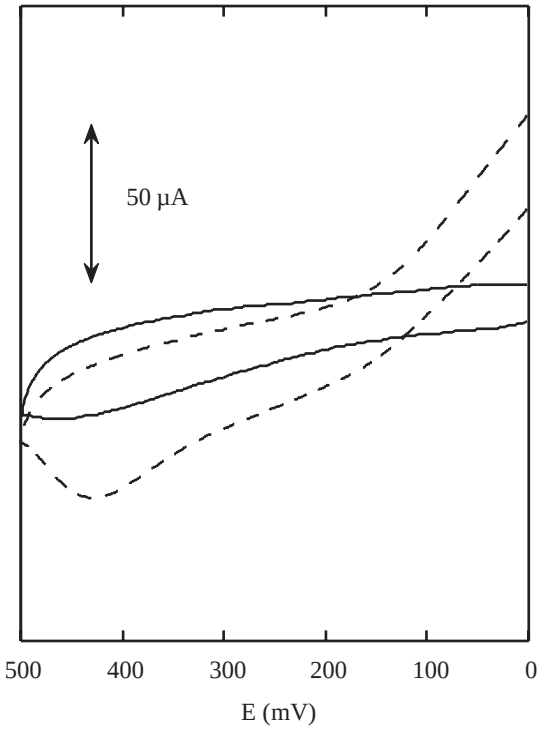

tial bias. Similar behavior is observed for SAMs of **1**/**3** on Au at these potentials.

Without MV^{2+} or when hydroquinone (HQ) is substituted for MV^{2+}(10 mM in 0.1 M NaCl) in the contacting solution, no photocurrent is observed at SAMs of **1**/**3** or **2**/**4** on Au.

SAMs prepared from duplexes 1/3 and 2/4 formed in solution and subsequently deposited on Au

An alternative synthesis of SAMs **1**/**3** and **2**/**4** was undertaken in which duplexes **1**/**3** and **2**/**4** were formed in solution and then allowed to assemble on the gold substrate. This synthesis was achieved by allowing **1** and **2**, respectively, to stir gently with equimolar amounts of their complements **3** and **4**, respectively, for 16 h in NaCl (0.01 M). α-Helix formation was established by a Cotton effect in the circular dichroism spectra of the duplexes (Fig. 9) (27). No Cotton effect was observed at wavelengths longer than 320 nm, thus indicating free rotation by the appended pyrene unit.

Solutions of these duplexes were subsequently exposed to clean Au surfaces for 6–20 h. Both the surface emission spectra and the GAR-FTIR spectra of the resulting thin films closely resemble the spectra of SAMs of the surface-formed duplexes **1**/**3** and **2**/**4** discussed above. Pyrene emission at 378 nm from the SAMs prepared from the preformed duplexes confirms the presence of pyrene and, as for the in situ duplex formation technique described above, the absence of excimer emission at longer wavelengths indicates that pyrene aggregates are not formed in the films. The emission spectra of the solution-formed duplexes are virtually identical to those observed for the corresponding surface-formed duplexes. As before, cyclic voltammetry of a contacting

Fig. 6. Time course for the limiting dark current at a Au electrode modified with a SAM of **2** in a MV^{2+} solution (1 mM in 0.1 M NaCl) at an applied potential of –100 mV vs. Ag/AgCl. The inset shows the time domain in which the electrode is alternately exposed to, and shielded from, illumination at 346 nm, with arrows showing when the shutter was open (on) and closed (off).

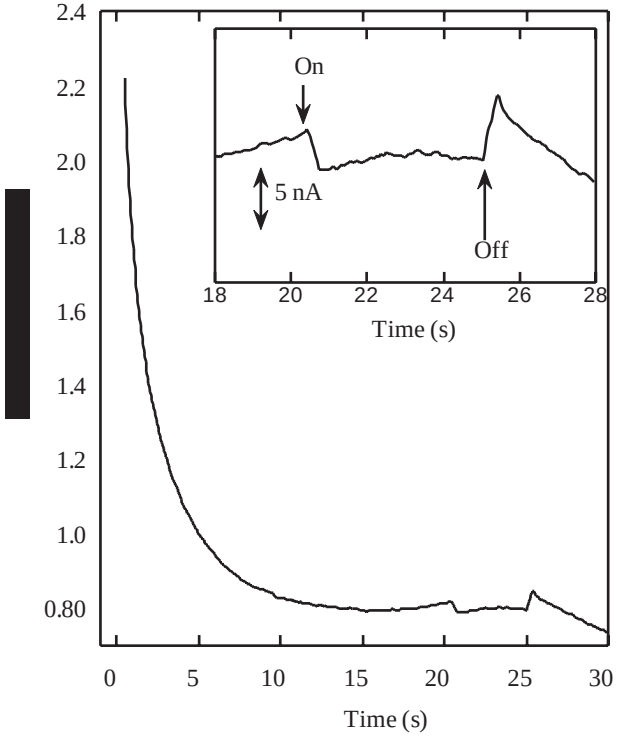

aqueous solution of $K_4Fe(CN)_6$ at electrodes modified with the solution-formed duplexes behave as microelectrode arrays, demonstrating that the Au surface is mostly blocked by the deposited thin film.

The time course of the currents observed at electrodes modified with films of the solution-formed duplexes **1**/**3** and **2**/**4** in MV^{2+} are completely parallel to those observed with the duplexes formed on the surface, as are the effects induced by the presence and absence of MV^{2+} or HQ.

Discussion

The origin of the photocurrent observed at the SAMs of duplexes **1**/**3** and **2**/**4** on Au in contact with aqueous solutions of MV^{2+} cannot be explained by a standard charge injection mechanism, Fig. 10. The observed wavelength dependence requires that photocurrent production follow from the photoexcitation of appended pyrene, producing a highly energetic electron at the ($pyr^{-\bullet}$/pyr = –2.09 V vs. SCE) (28) energetic level and a reactive hole at the ($pyr^{+\bullet}$/pyr = +1.32 V vs. SCE) (28) level, Fig. 10*a*. One possible route for photocurrent production takes place by excited pyrene ($pyr^{-\bullet}$/pyr = –2.09 V vs. SCE) (28) donating an electron to MV^{2+} ($MV^{+\bullet}/MV^{2+}$ = –0.46 V vs. SCE, ΔG = –1.63 eV) (29) present in the contacting solution. The resulting pyrene radical cation would subsequently be reduced by the poised electrode (28), producing cathodic current

© 1999 NRC Canada

Fig. 7. Time course for the limiting dark current at a Au electrode modified with a SAM of **2**/**4** in a MV^{2+} solution (1 mM in 0.1 M NaCl) at an applied potential of 0 mV vs. Ag/AgCl. The inset shows the time domain in which the electrode is alternately exposed to, and shielded from, illumination at 346 nm, with arrows showing when the shutter was open (on) and closed (off).

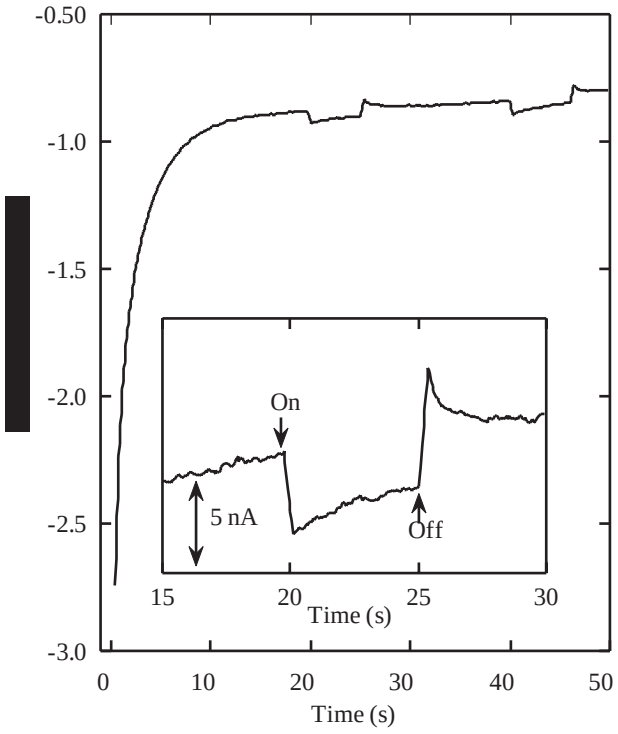

Fig. 8. Time course for the limiting current at a Au electrode modified with a SAM of **2**/**4** in a MV^{2+} solution (1 mM in 0.1 M Na Cl) at an applied potential of +100 mV vs. Ag/AgCl. The inset shows the time domain in which the electrode is alternately exposed to, and shielded from, illumination at 346 nm, with arrows showing when the shutter was open (on) and closed (off).

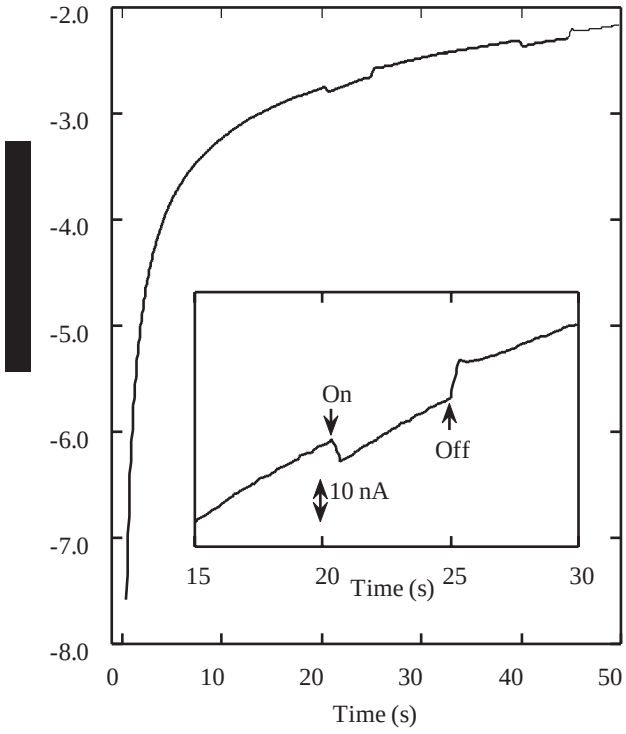

(Fig. 10*b*). In the case of duplex **2**/**4**, the intervening guanine bases ($G/G^{+\bullet}$ = +1.29 V vs. SCE) (30) may facilitate multiple electron hops between the electrode and pyrene (Fig. 10*c*). This would also result in cathodic current at the electrode under illumination. These predictions are opposite to the observed photocurrent on SAMs of **1**/**3** or **2**/**4** on Au, which are anodic.

Anodic photocurrent could be explained by direct injection of an electron from excited pyrene into the electrode. However, for a SAM of **1**/**3** or **2**/**4** on Au in contact with MV^{2+} in aqueous NaCl, there is no species present with the proper redox potential to reduce the resulting pyrene radical cation. Furthermore, when HQ ($HQ/HQ^{+\bullet}$ = +0.46 vs. SCE) (31) is substituted in the place of MV^{2+}, no photocurrent is observed. If electron injection from pyrene were responsible for the photocurrent, the response should be *enhanced*, not inhibited, by the presence of the electron donor HQ.

A conventional explanation for the sign of the observed photocurrent having been rejected, we surmise that another possible source of the observed photoeffects could be a change in the double-layer structure upon light absorption by the surface-bound pyrene. The potential at the electrode with respect to the bulk solution is known to be sensitive to double-layer structure, (32, 33) and changes in double-layer structure and capacitance have been shown to occur concomitant with a change in the redox state of surface-confined species (34, 35). In the case of the pyrene end-labeled polyphosphate duplexes **1**/**3** and **2**/**4** on Au in contact with aqueous MV^{2+}, strong electrostatic effects should produce a compact highly ordered double layer. The double-layer structure may also be affected by ground-state interactions between pyrene and MV^{2+}. Although there is no clear spectral evidence for such interactions in these thin films, ground-state complexes between MV^{2+} and pyrene have been shown to exist in aqueous solution (36) and in sodium dodecyl micelles (37). If such associations existed in the microheterogeneous environment of the thin film – electrolyte interface, they would be hard to detect directly because they would appear as small shifts in broad adsorption bands or as very low extinction charge transfer bands. The difficulty in obtaining electronic absorption spectra of SAMs on Au (by virtue of the very small amounts of absorptive chromophores present in a SAM) makes the detection of ground-state complexes in these particular experiments very difficult. If such complexes do exist and if they contribute to the equilibrium double-layer structure, such associations might be easily disrupted upon excitation of the appended pyrene. For example, charge transfer between the pyrene and MV^{2+} would result in repulsion between the pyrene radical cation and the $MV^{+\bullet}$ as well as a rearrangement of compensating ions and solvent molecules in the double-layer. Such a change in double-layer structure might be manifested as a difference in steady-state capacitative anodic current upon illumination. The possibility that changes in double-

© 1999 NRC Canada

Fig. 9. Circular dichroism spectra of **1**/**3** (13 μM, solid line) and **2**/**4** (9.5 μM, broken line) in 0.001 M phosphate buffer, pH = 7.5. Optical path is 1 cm.

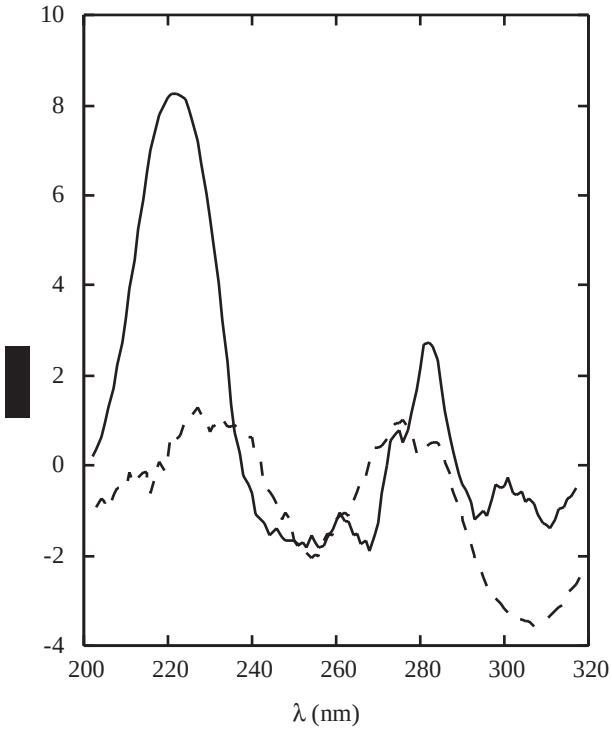

Fig. 10. Energetics of proposed electron transfer in monolayers of oligonucleotide duplexes **1**/**3** and **2**/**4**.

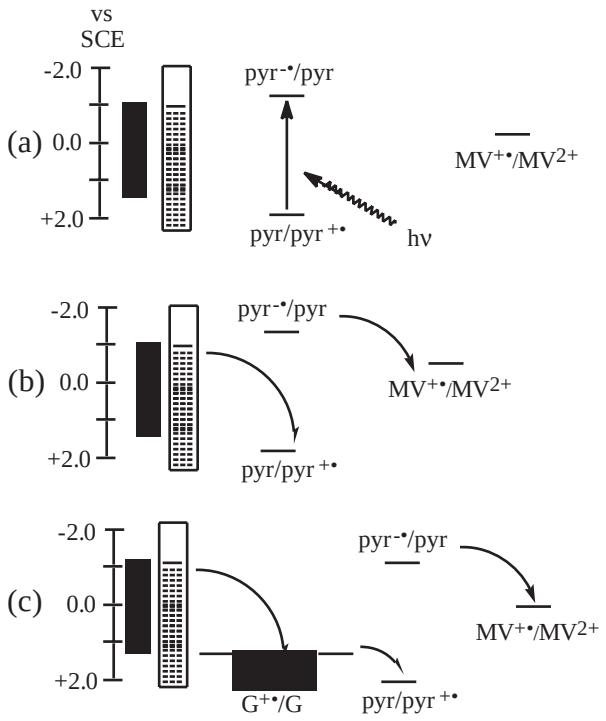

layer structure significantly contribute to photoelectrochemical effects observed at chemically modified eletrodes bears closer scrutiny and specific consideration in future studies.

Conclusions

Sulfur-terminated oligonucleotides **1** and **2** adsorb to flat Au surfaces as self-assembled monolayers. These films partially block the cyclic voltammetric response of $K_4Fe(CN)_6$ in a contacting electrolyte solution. When these SAMs are exposed to solutions of their pyrene end-labeled complements **3** and **4**, respectively, the complements are incorporated into the film and monomeric pyrene emission is observed upon excitation at 342 nm. No substantive change is observed in the GAR-FTIR spectra of SAMs of **1**/**3** or **2**/**4** on Au compared with SAMs of **1** or **2** on Au, but the composite films are more passivating to cyclic voltammetry of a contacting electrochemical couple than are the films of their monomeric counterparts. Virtually identical SAMs can also be prepared from duplexes **1**/**3** and **2**/**4** preformed in solution and subsequently deposited on Au surfaces. The GAR-FTIR and fluorescence spectra, as well as the passivating characteristics of the solution-formed films, are completely parallel to their surface-formed counterparts.

SAMS of **1** or **2** on gold are not photoelectrochemically active themselves, but anodic photocurrent is observed at SAMs of the duplexes **1**/**3** and **2**/**4** in the presence of aqueous MV^{2+} solution. This is consistent with a photocurrent produced by interaction with the appended excited pyrene moiety. The observed photocurrent does not derive from the conventional mechanism for photosensitization by an appended pyrenyl group, which would predict a cathodic, rather than the observed anodic, photoresponse.

Acknowledgements

This work was supported by the U.S. Department of Energy and by the Robert A. Welch Foundation.

References

1. F.D. Lewis, T. Wu, Y. Zhang, R.L. Letsinger, S.R. Greenfield, and M.R. Wasielewski. Science (Washington, D.C.), 673 (1997).
2. K. Fukui and K. Tanaka. Angew. Chem. Int. Ed. Engl. **37**, 158 (1998).
3. M.D. Purugganan, C.V. Kumar, N.J. Turro, and J.K. Barton. Science (Washington, D.C.), **241**, 1645 (1988).
4. M.R. Arkin, E.D.A. Stemp, R.E. Holmlin, J.K. Barton, A. Hörmann, E.J.C. Olson, and P.F. Barbara. Science (Washington, D.C.), **273**, 475 (1996).
5. B. Giese. J. Am. Chem. Soc. **120**, 12950 (1998).
6. E. Zahavy and M.A. Fox. J. Phys. Chem. (1999). Submitted.
7. M.A. Fox. Acc. Chem. Res. **25**, 569 (1992).
8. A. Ulman. An introduction to ultrathin organic films. Academic Press, San Diego. 1991.
9. A. Ulman. CHEMTECH, **25**, 22 (1995).
10. C.D. Bain and S.D. Evans. Chem. Br. **31**, 46 (1995).
11. J.J. Storhoff, R. Elghanian, R.C. Mucic, C.A. Mirkin, and R.L. Letsinger. J. Am. Chem. Soc. **120**, 1959 (1998).
12. T. Ihara, M. Nakayama, M. Murata, K. Nakano, and M. Maeda. Chem. Commun. 1609 (1997).
13. H. Korri-Youssoufi, F. Garnier, P. Srivastava, P. Godillot, and A. Yassar. J. Am. Chem. Soc. **119**, 7388 (1997).

© 1999 NRC Canada

14. C.A. Mirkin, R.L. Letsinger, R.C. Mucic, and J.J. Storhoff. Nature (London), **382**, 607 (1996).
15. T.M. Herne and M.J. Tarlov. J. Am. Chem. Soc. **119**, 8916 (1997).
16. G.H. Hermanson. Bioconjugate techniques. Academic Press, San Diego. 1996.
17. V.R. Shafirovich, S.H. Courtney, N. Ya, and N.E. Geacintov. J. Am. Chem. Soc. **117**, 4920 (1995).
18. R.S. Reese and M.A. Fox. J. Phys. Chem. **102**, 9820 (1999).
19. S. Pochet, T. Huynh-Dinh, J.-M. Neumann, S. Tran-Dinh, S. Adam, J. Tabouty, E. Taillandier, and J. Igolen. Nucleic Acids Res. **14**, 1107 (1986).
20. E. Taillandier, S. Adam, J.-P. Ridoux, and J. Liquier. Nucleic Acids Res. **16**, 5621 (1988).
21. E. Taillandier, J. Liquier, J. and A. Taboury. *In* Advances in infrared and Raman spectroscopy. Vol. 12. *Edited by* R.J.H. Clark and R.E. Hester. Wiley Heyden, London. 1985.
22. R.M. Silverstein, G.C. Bassler, and T.C. Morril. Spectrometric identification of organic compounds. Wiley, New York. 1991. Chap. 3.
23. A. Sivakumar and P. Somasundaran. Langmuir, **10**, 131 (1994).
24. A.K. Dutta, T.N. Misra, and A.J. Pal. Langmuir, **12**, 459 (1996).
25. R.R. Chance, A. Prock, and R. Silbey. Adv. Chem. Phys. **37**, 1 (1978).
26. C. Amatore, J.M. Savéant, and D.J. Tessier. Electroanal. Chem. **147**, 39 (1983).
27. W.C.J. Johnson. *In* Circular dichroism and the conformational analysis of biomolecules. *Edited by* G.D. Fasman. Plenum, New York. 1996. pp. 433–468.
28. V.Y. Shafirovich, P.P. Levin, V.A. Kuzmin, T.E. Thorgeirsson, D.S. Kliger, and N.E. Geacintov. J. Am. Chem. Soc. **116**, 63 (1994).
29. S.L. Murov, I. Carmichael, and G.L. Hug. Handbook of photochemistry. Marcel Dekker, New York. 1993.
30. S. Steenken and S.V. Jovanovic. J. Am. Chem. Soc. **119**, 617 (1997).
31. S. Steenken and P. Neta. J. Phys. Chem. **86**, 3661 (1982).
32. C.H. Hamann, A. Hamnett, and W. Vielstich. Electrochemistry. Wiley, New York. 1998.
33. A.J. Bard and L.R. Faulkner. Electrochemical methods. Fundamentals and applications. Wiley, New York. 1980. pp. 521–523.
34. D.D. Popenoe, R.S. Deinhammer, and M.D. Porter. Langmuir, **8**, 2521 (1992).
35. H.C. De Long and D.A. Butty. Langmuir, **6**, 1319 (1990).
36. Y. Kusomoto, S. Ihara, J. Kurawaki, and I. Satake. Chem. Lett. 1647 (1986).
37. M.H. Gehlen and F.C. DeSchryver. J. Phys. Chem. **97**, 11 242 (1993).

© 1999 NRC Canada

Proton and hydrogen atom tunnelling in hydrolytic and redox enzyme catalysis

A.M. Kuznetsov and Jens Ulstrup

Abstract: We discuss a broad theoretical frame for hydrogen transfer in chemical and biological systems. Hydrogen tunnelling, coupling between the tunnel modes and the environment, and fluctuational barrier preparation for hydrogen tunnelling are in focus and given precise analytical forms. Specific rate constants are provided for three limits, i.e., the fully diabatic, the partially adiabatic, and the fully adiabatic limits. These limits are all likely to represent real chemical or biological hydrogen transfer systems. The rate constants are referred particularly to the driving force and temperature dependence of the kinetic isotope effect (KIE). The origin of these correlations is different in the three limits. It is rooted in the tunnel factor and weak excitation of the heavier isotopes in the former two limits, giving a maximum for thermoneutral processes. A new observation is that the adiabatic limit also accords with a KIE maximum for thermoneutral processes but the KIE is here reflected solely in the activation Gibbs free energy differences, in this case rooted in the low-frequency environmental nuclear dynamics. Three systems of biological hydrogen tunnelling, viz. lipoxygenase, yeast alcohol dehydrogenase, and bovine serum amine oxygenase, offer unusual new cases for analysis and have been analysed using the theoretical frames. All the systems show large KIEs and strong indications of hydrogen tunnelling. They also represent different degrees of fluctuational barrier preparation, with lipoxygenase as the most rigid and bovine serum amine oxygenase as the softest system.

Key words: generalized Born–Oppenheimer scheme, kinetic isotope effect, gated proton transfer, partially adiabatic proton transfer, proton tunnelling in enzyme catalysis.

Résumé : On discute d'un cadre théorique général pour le transfert d'hydrogène dans des systèmes chimiques et biologiques. On s'est focalisé sur l'effet tunnel de l'hydrogène, le couplage entre les modes d'effet tunnel, l'environnement et la préparation de la barrière fluctuationnelle pour l'effet tunnel de l'hydrogène et on leur a donné des formes analytiques précises. On fournit des constantes de vitesse spécifique pour trois limites, à savoir les limites complètement diabatique, partiellement adiabatique et complètement adiabatique. Il est probable que ces limites représentent des systèmes réels de transfert de proton chimique ou biologique. Les constantes de vitesse sont reliées particulièrement à la force motrice et à la relation entre la température et l'effet isotopique cinétique (EIC). L'origine de ces corrélations est différente dans les trois limites. Dans les deux premières limites, elle est liée au facteur de l'effet tunnel et à la faible excitation des isotopes plus lourds et ceci conduit à un maximum pour les processus thermiquement neutres. Une nouvelle observation a été faite à l'effet que la limite adiabatique est aussi en accord avec un EIC maximal pour les processus thermiquement neutres; toutefois, dans ce cas, l'EIC n'est que le reflet des différences dans l'énergie libre d'activation de Gibbs qui, dans ce cas, tire son origine de la dynamique nucléaire environnementale de basse fréquence. Trois systèmes d'effet tunnel biologique de l'hydrogène, la lipoxygénase, la déshydrogénase d'alcool tirée de la levure et l'oxygénase d'amine tirée de sérum bovin, offrent des cas inusités pour l'analyse et on en a fait l'analyse dans un cadre théorique. Ils représentent aussi divers degrés de préparation de barrière fluctuationnelle alors que la lipoxygénase est la plus rigide et l'oxygénase d'amine tiré de sérum bovin est le système le plus souple.

Mots clés : schéma généralisé de Born–Oppenheimer, effet isotopique cinétique, transfert intermittent de proton, transfert de proton partiellement adiabatique, effet tunnel du proton, catalyse enzymatique.

[Traduit par la Rédaction]

1. Introduction

The ubiquity and importance of proton transfer (PT) as an "elementary" chemical and biological process is only equalled by electron transfer (ET) (1, 2). PT and ET show both mutual close physical resemblance and important differences. The most important common feature is that light particles, with conspicuous quantum mechanical character

Received December 9, 1998.

This paper is dedicated to Jerry Kresge in recognition of his many achievements in chemistry.

A.M. Kuznetsov. The A.N. Frumkin Institute of Electrochemistry of the Russian Academy of Sciences, Leninskij Prospect 31, 117071 Moscow, Russia.
J. Ulstrup.[1] Department of Chemistry, Technical University of Denmark, DK-2800 Lyngby, Denmark.

[1]Author to whom correspondence may be addressed. Telephone: +45 4525 2359. Fax: +45 4588 3136. e-mail: ju@kemi.dtu.dk

 © 1999 NRC Canada

(tunnelling), are transferred. Both particles are also strongly coupled to the environments. *Differences* are that protons are much more strongly localized than electrons. Proton tunnelling is thus only over a fraction of an angstrom while facile ET over tens of angstroms can occur. The notion of "long-range" *electron transfer* is thus well established (3–10), whereas *proton transfer* counterparts are of a quite different nature (1, 2). Proton tunnelling in chemical processes was recognised early (11–14). The view of chemical proton transfer as a quantum mechanical multiphonon electronic–vibrational transition was first introduced by Dogonadze, Kuznetsov, and Levich (15, 16). Most later achievements in quantum mechanical proton transfer theory rest in some way on the views in these reports (17–21). Condensed phase proton and hydrogen atom and hydride tunnelling are also abundantly documented experimentally (overviews in refs. 1 and 2). Along with ET, chemical PT thus offers cases for observation of room temperature nuclear tunnelling. In addition, kinetic deuterium and tritium isotope effects can be exploited, with unique prospects for characterization of proton barrier and environmental dynamics (1, 2).

Chemical proton, deuteron, and triton (overall hydron) tunnelling have been studied for several decades (22–26). Hydron tunnelling in *biological* systems is much less comprehensively characterized even though active-site structures as loci for PT in enzyme catalysis are known in detail. The reasons are associated with the multistep nature of enzyme processes, or rate-determining steps other than hydron transfer. Cases of well-characterized hydrogen atom tunnelling in enzyme processes, with large kinetic isotope effects, have, however, been reported recently, particularly by Klinman and co-workers (27–29). We shall presently address certain issues related to such new observations. In Sect. 2 we provide a formalism for hydrogen tunnelling viewed as a multiphonon quantum mechanical electronic–vibrational transition. New elements are disentanglement of *electronic* and *electron–proton* potential surfaces, kinetic isotope effects in strongly interacting proton donor–acceptor systems (the fully adiabatic limit), and ("gated") proton barrier preparation. In Sect. 3 the results are related to the Brønsted relation and kinetic isotope effects. Section 4 describes a convenient new approach to fluctuational barrier preparation ("gating") at all temperatures, important in the analysis of kinetic deuterium and tritium isotope effects. In Sect. 5 we discuss some of the recent cases of large kinetic deuterium and tritium isotope effects in redox enzyme processes, alluded to above, using the theoretical frames in Sects. 2–4. Concluding remarks are given in Sect. 6.

2. Proton tunnelling formalism in diabatic and adiabatic limits

2.1 Proton potentials and coupling to solvent and macromolecular environments

We note first two general issues (1, 2, 15, 16). One is that vibrational frequencies of C–H, N–H, and O–H stretching and bending modes, ≈3000 cm^{-1} and (or) ≈1500 cm^{-1}, respectively, are much higher than ≈200 cm^{-1}, corresponding to k_BT at room temperature. k_B is Boltzmann's constant and T the temperature. Proton dynamics in free molecules is therefore strongly quantized. This is illustrated by the harmonic potential along the proton coordinate R_p

$$[1] \qquad U_p(R_p) = \frac{1}{2} m_p \Omega_p^2 (R_p - R_{p0})^2$$

where m_p is the mass and Ω_p the vibrational frequency of the proton. R_{p0} is the equilibrium value of R_p. The full quantum mechanical bond length distribution function is given in eq. [2]:

$$[2] \qquad f_{qu}(R_p) = \left[\frac{\pi\hbar}{m_p\Omega_p \tanh(\hbar\Omega_p/2k_BT}\right]^{1/2} \times \exp\left[-\left(\frac{m_p\Omega_p}{\hbar}\right)(R_p - R_{p0})^2 \tanh\left(\frac{\hbar\Omega_p}{2k_BT}\right)\right]$$

where $2\pi\hbar$ represents Planck's constant. Equation [2] reduces to the classical Boltzmann distribution

$$[3] \qquad f_{cl}(R_p) = \left(\frac{2\pi k_BT}{m_p\Omega_p^2}\right)^{-1/2} \exp\left[-\frac{\frac{1}{2}m_p\Omega_p^2(R_p - R_{p0})^2}{k_BT}\right]$$

only when $\hbar\Omega_p << k_BT$. In the opposite limit $f_{qu}(R_p)$ is independent of T and takes the form

$$[4] \qquad f_{qu}(R_p) = \left[\frac{\pi\hbar}{m_p\Omega_p}\right]^{-1/2} \exp\left[-\left(\frac{m_p\Omega_p}{\hbar}\right)(R_p - R_{p0})^2\right]$$

Equation [4] coincides with the square of the ground state vibrational wave function, conspicuously reflecting proton tunnelling. This applies equally to other potentials such as the Morse potential (30–32). Reservations can be envisaged for strong donor–acceptor interactions (33), and for bond stretching towards dissociation, etc. (34) where barrier deformation and low frequencies may impose close to classical character. The second general observation is that proton dynamics is always strongly coupled to solvent or macromolecular environments, in the form

$$[5] \qquad V_{pol}^{prot} = -\int \vec{P}_{tot}(\vec{r})\vec{D}_s(\vec{r})(d\vec{r}); \quad S = R, P$$

$\vec{P}_{tot}(\vec{r})$ is the environmental polarization at the point $\vec{r}$ and $\vec{D}_s(\vec{r})$ the electrostatic induction induced by the proton in the state of the reactants (R) or products (P). As proton dynamics is much faster than most solvent motion, the $\vec{D}_s(\vec{r})$ monitored by the solvent is not determined by the proton coordinate but by the quantum mechanical proton probability density (Appendix).

2.2 Born–Oppenheimer schemes and the Franck Condon principle for proton and electron–proton transfer

A generalized Born–Oppenheimer (B–O) scheme and Franck Condon (FC) principle apply to PT and hydrogen atom transfer ("combined" electron and proton transfer, or ETPT). In a first step the "usual" B–O approximation is exploited to separate electronic motion from proton and slower solvent motion. This leads to the *electronic* wave functions

© 1999 NRC Canada

Fig. 1. Diabatic electronic–proton potential Gibbs free energy surfaces spanned by the classical environmental nuclear coordinate q, for different proton vibrational states in the reactants' and products' state.

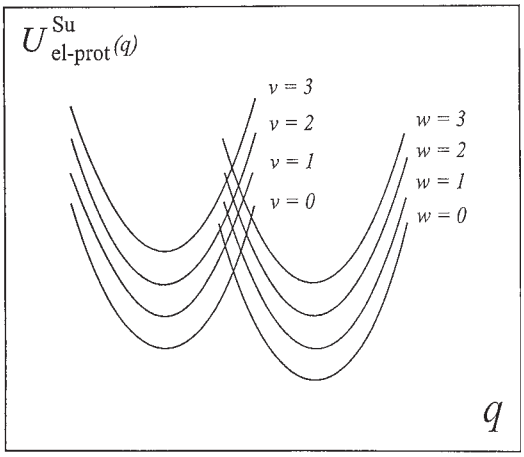

$\varphi^{el}_S(\vec{x}\,; R_p; \{q_k\})$ and *electronic* potential surfaces (S = R, P) $\varepsilon^{el}_S(R_p; \{q_k\})$. $\vec{x}$ represents the electronic coordinates. This step has an explicit perspective for hydrogen *atom* transfer (ETPT). In a *second* step the B–O approximation is used to separate the "fast" proton from the slower solvent or protein conformational motion. This step provides the *proton* wave functions, $\chi^p_{Su}(R_p; \{q_k\})$, and energies, $\varepsilon^p_{Su}(\{q_k\})$ (Sect. 2.3). Together with the pure solvent potential (Gibbs free) energy, these constitute the *electronic–proton* potential surfaces, spanned solely by the solvent/protein coordinates. The electronic potential surfaces are spanned by *all* the (fast and slow) nuclear coordinates, but the electronic–proton surfaces only by the (slow) environmental coordinates. The slower environmental, collective coordinates thus cannot depend on the much faster local, even quantum mechanical, coordinates, such as has sometimes been advanced (35).

The generalization of the B–O approximation carries over to the Franck Condon (FC) principle. The FC principle states that light particle transition only occurs near heavy nuclear configurations where the light particle energies match, i.e., at the transition configuration. The proton vibrational energies match only when environmental nuclear coordinate *fluctuations* have been taken to their transition configuration $\{q^*_k\}$, i.e., $\varepsilon^p_{Rv}(\{q^*_k\}) = \varepsilon^p_{Pw}(\{q^*_k\})$. The *proton* subsequently initiates sub-barrier tunnelling where the *electronic* levels are brought to match at the crossing along the *electronic* potential surfaces, $U^R_{el}(R^*_p; \{q^*_k\}) = U^P_{el}(R^*_p; \{q^*_k\})$, where electronic structure reorganization occurs. The proton subsequently relaxes in the products' potential $U^P_{el}(R_p; \{q_k\})$, followed by relaxation of the heavy nuclear system.

2.3 Electronic and electron–proton potential surfaces

A distinction between weakly and strongly interacting donor–acceptor systems is convenient. The former are framed by the diabatic approach (cf. above) where the reactants' and products' states constitute two different electronic states. The *electronic* potential surfaces are

$$[6] \qquad U^S_{el}(R_p; \{q_k\}) = V^S_{prot}(R_p) + \frac{1}{2}\sum_k \hbar\omega_k(q_k - q^S_{k0})^2 + U_{S0}$$

where $\{q_k\}$ and $\{\omega_k\}$ are collective solvent coordinates and vibrational frequencies, and $V^S_{prot}(R_p)$ electronically averaged bound proton potentials (= R, P). U_{S0} is the gas phase electronic energy in the equilibrium configuration and $\{q^S_{k0}\}$ the equilibrium values of $\{q_k\}$, in the states S. In the diabatic limit these quantities are averaged with respect to the electronic wave functions (Appendix). Excited proton vibrational states are, however, important and are reflected, for example, in the driving force dependence of the kinetic isotope effect. Instead of the *electronic* potential surfaces, *electron–proton* surfaces, spanned solely by the solvent coordinates, and corresponding to the vibrational proton energies ε^p_v and ε^p_w in the reactants' and products' state (v = 1, 2, ...; w = 1, 2, ...) are therefore also needed (Fig. 1). These are obtained by averaging eq. [6] with respect also to the *proton* vibrational wave functions,

$$[7] \quad U^S_{el-prot}(\{q_k\}) = \frac{1}{2}\sum_k \hbar\omega_k(q_k - q^S_{k0})^2 + \varepsilon^p_u + U_{S0}$$

S = R, P; $u = v,w$

Equations [6] and [7] are adequate in the fully *diabatic* limit. In the partially and fully *adiabatic* limits of stronger interactions, proton state averaging is no longer suitable as both the reactants' and products' states are now represented by a single adiabatic electronic state The explicit $\{q_k\}$ dependence of the proton potential is therefore left, giving the potential surface

$$[8] \qquad U^S_{pot}(R_p, \{q_k\}) = V^S_{prot}(R_p) + \frac{1}{2}\sum_k \hbar\omega_k q_k^2 - \sum_k q_k[g^S_k(R_p) + \nu^{prot}_k(R_p)]$$

S = gr, ex

These terms have been averaged with respect to the *adiabatic* electronic wave functions rather than the reactants' and products' state functions. The superscript "S" refers to the ground and first excited adiabatic electronic states. As the q_k dependence of the electronic wave functions may, further, not be negligible, the coupling factors g^S_k and $\nu^{prot}_k(R_p)$ could also depend on $\{q_k\}$, giving a nonlinear solvent coordinate dependence. Equations [6]–[8] are derived in the Appendix.

Equations [6]–[8] are the basis for most of the formalism to follow. They also apply broadly to the macromolecular protein environment where, however, the following features need attention:

(*i*) Protein environment is characterized by many local polar and charged residues. These strongly affect the transfer of localized charges such as the proton.

(*ii*) Conformational dynamics can be dominated by small configurational changes in many local groups. Motion along such collective coordinates can be equilibrated and regarded as friction free, or they can be diffusive. In either case the dynamics is not fundamentally different from other collective mode dynamics.

(*iii*) Conformational states separated by high local barriers lead to "gated" PT (Sect. 4).

© 1999 NRC Canada

Fig. 2. Electronic double-well Gibbs free energy surface spanned by the proton coordinate R_p at different values of the slow environmental coordinate q. Left: The reactants' equilibrium configuration (q_0^R). Middle: The transition configuration (q^*). Right: The products' equilibrium configuration (q_0^p).

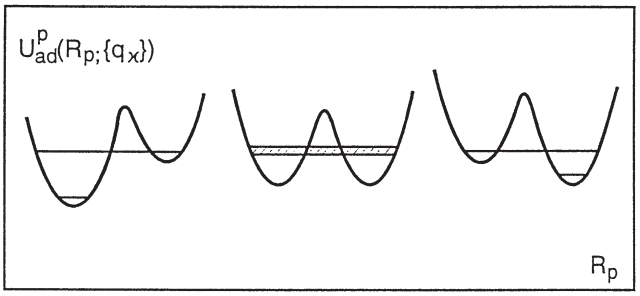

2.4 PT and ETPT between spatially fixed molecular fragments

We consider PT and ETPT along a linear path between two fixed molecular fragments. With a subsequent view on "gating," we introduce a general rate constant (1, 2):

$$W_{RP} = \int_{c-i\infty}^{c+i\infty} d\theta G(\theta)$$

$$G(\theta) = (\beta/i\hbar)(V_{RP}^{el})^2 \exp[-H(\theta) - \beta\theta\Delta G^0]$$

[9] $$H(\theta) = \beta\theta(1-\theta)E_R + \frac{2E_R^{prot}}{\hbar\Omega_p} \frac{\sinh\left[\frac{1}{2}\beta\hbar\Omega_p(1-\theta)\right]\sinh\frac{1}{2}\beta\hbar\Omega_p\theta}{\sinh(\frac{1}{2}\beta\hbar\Omega_p)}$$

$$\beta = (k_B T)^{-1}$$

V_{RP}^{el} is the electron exchange integral coupling the reactants' and products' states, E_R the environmental reorganization Gibbs free energy, and ΔG^0 the reaction Gibbs free energy (driving force). The contour in eq. [9] is along a line in θ-space parallel to the imaginary axis, with $0 < c < 1$. The origin and methods of treating eq. [9] are given elsewhere (1, 2, 36). As a particular note, eq. [9] also applies to the partially adiabatic limit (Sect. 2.4.2) where $\kappa(\alpha)$ is then replaced by K_{vw}^{ad}. Equation [9] gives the following other form using the saddle point method (37) in the θ-integration:

[10] $$W_{RP} = \kappa(\alpha)\frac{\omega_{eff}}{2\pi}\exp[\alpha H'(\alpha) - H(\alpha)]$$

$$\kappa(\alpha) = (V_{RP}^{el})^2\sqrt{\frac{4\pi}{H''(\alpha)\hbar\omega_{eff}^2}}$$

α is the saddle point, given by

[11] $$\Delta G^0 = -k_B T H'(\alpha)$$

$H'(\alpha)$ is the first and $H''(\alpha)$ the second derivative of $H(\alpha)$; $\kappa(\alpha)$ is the transmission coefficient, to be discussed below.

Equations [9]–[11] can be converted to the following form by available procedures (1, 2):

$$W_{RP} = Z_p^{-1}\sum_{v,w}\exp(-\varepsilon_{Rv}^p/k_B T)W_{RP}^{vw}$$

[12] $$W_{RP}^{vw} = \kappa_{vw}^p\frac{\omega_{eff}}{2\pi}\exp\left(-\frac{G_{vw}^{\neq}}{k_B T}\right)$$

$$Z_{Rp} = \sum_v \exp(-\varepsilon_{Rv}^p / K_B T)$$

This form incorporates proton mode anharmonicity, mode mixing, etc. In this sense it is more general than eqs. [9]–[11]. The quantities in eq. [12] have the following meaning:

(*a*) v and w, and ε_{Rv}^p and ε_{Pw}^p have been defined above. Z_{Rp} is the proton vibrational statistical sum in the reactants' state. In the harmonic approximation,

[13] $$\varepsilon_{Su}^p = \hbar\Omega_p^s(u + \tfrac{1}{2}); \quad S = R, P; \quad u = v, w$$

(*b*) The activation Gibbs free energy will be given the following form appropriate to a linearly responding solvent/protein environment and local harmonic modes:

[14] $$G_{vw}^{\neq} = (E_R + \Delta G^0 + \varepsilon_{Pw}^p - \varepsilon_{Rv}^p - \varepsilon_{Pw=0}^p + \varepsilon_{Rv=0}^p)^2/4E_R$$

ΔG^0 includes the zero point energy difference $\varepsilon_{Pw=0}^p - \varepsilon_{Rv=0}^p$ (cf. Sects. 3.2 and 5.1).

(*c*) The transmission coefficient κ_{vw}^p includes contributions from both "fast" systems, i.e., the *electrons* and the *proton*, and takes distinctive forms in different ranges of donor–acceptor interaction, cf. Sects. 2.4.1–2.4.3.

(*d*) ω_{eff} is the effective vibrational frequency of all modes classically reorganized (1, 2, 38).

We next introduce two computational schemes (39). The *diabatic* approach applies to weak interactions, and rests on two sets of electronic and proton wave functions corresponding to electron and proton localization on the donor and acceptor. In the *adiabatic* approach, appropriate to stronger interactions, the total proton donor–acceptor system is regarded as a supermolecule where the electron adiabatically follows proton and heavy nuclear dynamics but proton tunnelling may still control the transition, and the proton double-well potential depends parametrically on the environmental coordinates. The dependence extends to the spacing between the ground and first excited proton vibrational levels. The spacing is large at the reactant environmental *equilibrium* configuration where the proton potential is strongly asymmetric (Fig. 2). The ground vibrational level here corresponds to proton/electron trapping at the donor, the first excited state to localization at the acceptor. Heavy nuclear transfer to the transition configuration brings the proton potential to a symmetric form with minimum level spacing. PT or ETPT proceeds here, followed by environmental relaxation to the products' equilibrium, proton trapping in this state, and proton double-well potential conversion to a configuration opposite the reactants' state. Three limits are now appropriate.

2.4.1 The fully diabatic limit of PT and ETPT

This limit represents weak donor–acceptor interaction, with conspicuous tunnel features. Crucial theoretical concepts are most transparent here. These concepts carry over to the partially adiabatic limit, which then follows naturally from the diabatic limit. While not likely to be encountered

© 1999 NRC Canada

Fig. 3. Adiabatic potential surface spanned by the environmental coordinate *q*. The splitting at the transition configuration is given by eq. [22].

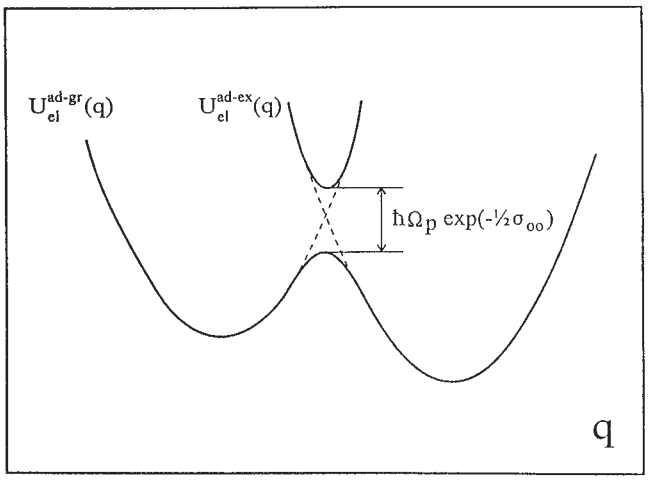

broadly in general acid–base catalysis and proton transfer in hydrolytic enzyme catalysis, the diabatic limit is, finally, appropriate in cases of hydrogen *atom* transfer (35) and at low temperatures. The donor and acceptor groups are here frozen at relatively long distances (40–42) with concomitant, unusually large, kinetic deuterium isotope effects (41). In the fully diabatic limit *proton* tunnelling is initiated at the crossing between $U_{el-prot}^{Rv}(\{q_k\})$ and $U_{el-prot}^{Pw}(\{q_k\})$, and followed by *electron* transfer at the crossing between $U_{el}^{R}(R_p, \{q_k\})$ and $U_{el}^{p}(R_p, \{q_k\})$, i.e., at R_p, $\{q_k\} \rightarrow R_p^*$, $\{q_k^*\}$, all in the given proton vibrational states *v* and *w*. The transmission coefficient is

$$[15] \quad \kappa_{vw}^{p} = (T_{RP}^{vw})^2 \sqrt{\frac{4\pi^3}{E_R k_B T \hbar^2 \omega_{eff}^2}} << 1$$

$$[16] \quad (T_{RP}^{vw})^2 = \left| \int \varphi_{el}^{R}(\vec{x}; R_p) \chi_{Rv}^{p}(R_p) V \chi_{Pw}^{p}(R_p)\, \varphi_{el}^{p}(\vec{x}; R_p) \right|^2 d\vec{x}\, dR_p \approx (V_{RP}^{el})^2\, S_{RP}^{vw}$$

$$[17] \quad V_{RP}^{el} = \int \varphi_{el}^{R}(\vec{x}; R_p) V \varphi_{el}^{p}(\vec{x}; R_p) d\vec{x}$$
$$S_{RP}^{vw} = \left| \int \chi_{Rv}^{p}(R_p) \chi_{Pw}^{p}(R_p)\, dR_p \right|^2$$

$\varphi_{el}^{S}(\vec{x}; R_p)$ (S = R, P) is the electronic wave function in the state S, depending parametrically on R_p. $\chi_{Su}^{p}(R_p)$ is the proton wave function in the vibrational state *u* (= *v*, *w*) and electronic state S. *V* is the physical donor–acceptor interaction. V_{RP}^{el} is thus the electron exchange integral, cf. eq. [9], and S_{RP}^{vw} is the proton Franck Condon overlap factor. Equations [15]–[17] combined with eqs. [12]–[14] apply formally, subject to eq. [15]. The totally diabatic limit, with respect to *both* the electronic and proton systems, requires the stronger conditions

$$[18] \quad (V_{RP}^{el})^2\, S_{RP}^{vw} << \hbar\omega_{eff} \sqrt{\frac{k_B T E_R}{4\pi^3}}\ ;\ (V_{RP}^{el})^2 << \frac{\hbar\Omega_p E_R^{prot}}{2\pi}$$

where $E_R^{prot} = \frac{1}{2} m_p \Omega_p^2 (R_{p0}^{P} - R_{p0}^{R})^2$ is the proton reorganization energy ($\Omega_p^R \approx \Omega_p^P$).

The Franck Condon overlap factors in eq. [17] are available for harmonic, Morse, and certain other potentials (31, 32). For displaced harmonic surfaces (2)

$$[19] \quad \begin{aligned} S_{RP}^{00} &= \exp(-\tfrac{1}{2}\Delta^2);\ \tfrac{1}{2}\Delta^2 = \tfrac{1}{2}\frac{m_p\Omega_p}{\hbar}(R_{p0}^{P} - R_{p0}^{R})^2 \\ S_{RP}^{v0} &= \exp(-\tfrac{1}{2}\Delta^2)(\tfrac{1}{2}\Delta^2)^v/v! \\ S_{RP}^{0w} &= \exp(-\tfrac{1}{2}\Delta^2)(\tfrac{1}{2}\Delta^2)^w/w! \\ S_{RP}^{vw} &= \exp(-\tfrac{1}{2}\Delta^2)(\tfrac{1}{2}\Delta^2)^{|v-w|}\frac{v!}{w!}\left[L_w^{|v-w|}(\tfrac{1}{2}\Delta^2)\right]^2 \end{aligned}$$

where $L_n^{\alpha}(x)$ is the associated Laguerre polynomial (43). Subject to broadly valid conditions the WKB approximation (44) also applies in the totally diabatic and partially adiabatic limits

$$[20] \quad \begin{aligned} S_{RP}^{vw} &\approx \exp(-\sigma_{vw})\ ; \\ \sigma_{vw} &\approx \frac{2}{\hbar}\int_{a_{vw}}^{R_p^*(v,w)} \left\{ 2m_p [U_{el}^{R}(R_p, \{q_k\}) - \varepsilon_{Rv}^{p}] \right\}^{1/2} dR_p \\ &\quad + \frac{2}{\hbar}\int_{R_p^*(v,w)}^{b_{vw}} \left\{ 2m_p [U_{el}^{p}(R_p, \{q_k\}) - \varepsilon_{Pw}^{p}] \right\}^{1/2} dR_p \end{aligned}$$

where a_{vw} and b_{vw} are the left and right turning points in the tunnelling region, and $R_p^*(v,w)$ the value of R_p at the $U_{el-prot}^{Rv}$ / $U_{el-prot}^{Pw}$ crossing. In this way the proton tunnel factor can be obtained for rather arbitrary potentials. Equations [12], [14], and [17]–[20] constitute the PT and ETPT frame in the *totally* diabatic limit. As noted, this limit is most representative of ETPT and low-temperature hydron transfer. Much of the formalism, however, carries over to the *partially* adiabatic limit more representative also of PT.

2.4.2 The partially adiabatic limit

This limit accords with stronger electronic interaction but PT or ETPT is still slow due to a significant proton tunnel barrier. The first part of eq. [18] therefore remains, whereas the inverse of the second part applies. The electronic potential surfaces are modified to the *adiabatic* set:

$$[21] \quad U_{el}^{adS}(R_p; \{q_k\}) = \tfrac{1}{2}[U_{el}^{R}(R_p, \{q_k\}) + U_{el}^{p}(R_p, \{q_k\})] \pm \sqrt{[U_{el}^{R}(R_p; \{q_k\}) - U_{el}^{p}(R_p, \{q_k\})]^2 + 4(V_{Rp}^{el})^2}$$

S = gr, ex

where "–" and "+" refer to the ground (gr) and excited (ex) states (Fig. 3). The activation Gibbs free energy, $G_{vw}^{\neq}$ is still primarily determined by the reactants' and products' *electronic–proton* forms, $U_{el-prot}^{Rv}(\{q_k\})$ and $U_{el-prot}^{Pw}(\{q_k\})$, because the total electronic–proton tunnel factor, $(V_{RP}^{el})^2\, S_{RP}^{vw}$, is small. The *proton* tunnelling barrier is, however, lowered significantly due to the (large) electronic resonance splitting The transmission coefficient κ_{vw}^{ad} is suitably recast in terms of the proton energy level splitting at the transition configuration $\{q_k^*\}$:

© 1999 NRC Canada

$$[22]\quad \kappa_{vw}^{ad} = (\tfrac{1}{2}\Delta\varepsilon_{vw}^{p})^2 \sqrt{\frac{4\pi^3}{E_R k_B T \hbar\omega_{eff}^2}}$$

$$\Delta\varepsilon_{vw}^{p} \approx \hbar\Omega_p \exp(-\tfrac{1}{2}\sigma_{vw})$$

where σ_{vw} can be given a form similar to that in eq. [20] and the symmetric barrier incorporates V_{RP}^{el}.

2.4.3 The totally adiabatic limit

The inverse of both inequalities in eq. [18] apply in this limit. Electronic motion follows the proton, which again follows the environmental motion. The rate constant is

$$[23]\quad W_{RP}^{tot\text{-}ad} = \frac{\omega_{eff}}{2\pi}\exp\left[-\frac{G_{tot\text{-}ad}^{\neq}}{k_B T}\right]$$

$$[24]\quad G_{tot\text{-}ad}^{\neq} = G_{00}^{\neq} - \Delta\varepsilon_{00}^{p}\sqrt{\alpha(1-\alpha)} \approx G_{00}^{\neq} - \tfrac{1}{2}\Delta\varepsilon_{00}^{p}$$

where the transfer coefficient α was introduced in eqs. [10] and [11]. Explicit forms of α are given in eqs. [25] and [26] below. Only the proton vibrational ground state is important. $G_{00}^{\neq}$ is given by eq. [14], $\Delta\varepsilon_{00}^{\neq}$ by eqs. [20]–[22]. The quantum mechanical feature is now solely reflected in the lower activation Gibbs free energy caused by proton level splitting, again determined by the (large) electron exchange factor. The quantum mechanical feature is, however, still important and transmitted, for example, to kinetic isotope effects.

3. The Brønsted relation and kinetic isotope effects

3.1 The Brønsted relation

The Brønsted relation between the rate constant and the reaction Gibbs free energy is framed by the formalism above. The driving force dependence is referred to *environmental* nuclear dynamics rather than to the proton. When the proton modes remain in their ground states the Brønsted coefficient is (eqs. [12] and [14])

$$[25]\quad \alpha = dG_{00}^{\neq}/d\Delta G^0 \approx \frac{1}{2} + \frac{\Delta G^0}{2E_R}$$

α varies between zero and unity over the ΔG^0 ranges $|\Delta G^0| \rightarrow E_R$. This pattern is encountered for many PT reactions (21–25).

Several features modify this view. *One* is that excited hydron modes are in fact important in the diabatic and partially adiabatic limits. Equation [22] is therefore generalized:

$$[26]\quad \alpha \approx -d\ln W_{RP}/d\Delta G^0$$

$$\approx \frac{1}{2} + \frac{\Delta G^0 + w^*(\Delta G^0)\hbar\Omega_p - v^*(\Delta G^0)\hbar\Omega_p}{2E_R}$$

where $v^*(\Delta G^0)$ and $w^*(\Delta G^0)$ are the dominating values of v and w in the rate constant. Finite v^* and w^* thus gain importance as $|\Delta G^0| \rightarrow E_R$. Further, from eqs. [25] and [26], $\alpha \rightarrow 0.5$ as $|\Delta G^0| \rightarrow 0$. A *second* observation is that α can in fact be larger or smaller than 0.5 for thermoneutral processes if local solvent or intramolecular motion is subject also to vibrational *frequency* changes. A *third* observation is that both local and proton mode deformations are much stronger in PT than in ET. Anharmonic potentials are therefore needed in more precise fits to experimental data. Anharmonicity also decreases the curvature in free energy relations, giving smaller level spacing and attenuating the quantum mechanical feature (31, 32). As pointed out by Kresge (25), a *final* observation is that, in contrast to weakly hydrogen bonding C—H donors, the transfer coefficient for O and N acids and bases is often shifted between the limiting values of zero and unity within a few p*K* units. This reflects major, driving-force-independent, environmental reorganization *prior* to PT, whereas the reorganization Gibbs free energy in this step, where the driving-force dependence is focused, itself is small.

3.2 The kinetic deuterium and tritium isotope effects

The kinetic deuterium and tritium isotope effects (KIE) hold unique perspectives both for room temperature nuclear tunnelling and for environmental dynamics. The latter transfers, interestingly, from thermal activation to *environmental* nuclear tunnelling at low (cryogenic) temperatures (41). The tunnel sensitivity to the PT *distance* also holds an intriguing implication. As deuteron and triton tunnelling is less facile than proton tunnelling, deuteron and triton transfer over *smaller* distances than proton transfer is favoured, at the expense of additional activation Gibbs free energy, along the intermolecular donor–acceptor mode. Fluctuational barrier preparation (Sect. 4) is therefore more important for PT than for ET. In experimental data analysis the rate constant, k_{rC} (s^{-1} or $M^{-1}\ s^{-1}$, C = H, D, T) must therefore be given the form

$$[27]\quad k_{rC} = \Phi(R_{pC}^*)\, W_{RP}(R_{pC}^*)$$

where $W_{RP}(R_{pC}^*)$ is the rate constant (eqs. [12–17] and [22]–[24]) at the most favourable transfer distance R_{pC}^*, and $\Phi(R_{pC})$ is the distribution function along the intermolecular donor–acceptor coordinate. R_{pC}^* is in general *different* for proton, deuteron, and triton transfer.

The kinetic *deuterium* isotope effect is

$$[28]\quad KIE = \frac{k_{rH}}{k_{rD}} = \frac{\Phi(R_{pH}^*)\, W_{RP}(R_{pH}^*)}{\Phi(R_{pD}^*)\, W_{RP}(R_{pD}^*)}$$

The classical Boltzmann distribution is presently an adequate representation of $\Phi(R_{pC})$:

$$[29]\quad \Phi(R_{pC}) \propto \exp\{-[w_R(R_{pC}) - w_R(R_{pC0})]/k_B T$$

where R_{pC0} is the equilibrium value of R_{pC} and $w_R(R_{pC})$ the donor–acceptor intermolecular potential, in the reactants' state. At low temperatures intermolecular donor–acceptor motion proceeds by nuclear tunnelling, and $\Phi(R_{pC})$ must be replaced by a quantum mechanical distribution function (cf. ref. 41). Quite similar considerations apply to k_{rH}/k_{rT} and k_{rD}/k_{rT} so that eqs. [28] and [29] also constitute a basis for quantum mechanical analogues of the Schaad–Swain relation (23, 45). The KIE is reflected in most of the kinetic quantities. In the activation Gibbs free energy there is KIE in the hydron vibrational frequencies; this is important when the frequencies are different in the reactants' and products' states. The dominating effect in the preexponential part is the more facile tunnelling of the lighter isotope(s). As tunnelling is from

© 1999 NRC Canada

Fig. 4. Distance dependence of the kinetic isotope effect (schematic). The declining branch for small ΔR_{p0} is representative of the totally adiabatic limit, the rising branch at larger ΔR_{p0} of the fully diabatic and partially adiabatic limits.

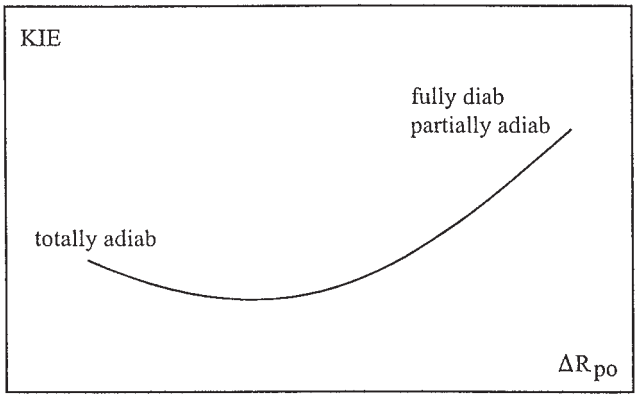

non-equilibrium donor–acceptor configurations, the KIE also reflects an interplay between donor–acceptor interaction and nuclear tunnelling. The effective frequency ω_{eff} could, finally, be isotope specific since ω_{eff} holds contributions from solvent librational modes.

The KIE appears rather differently in fully diabatic and partially adiabatic PT on the one hand, and in fully adiabatic PT on the other. In fully diabatic (ETPT) and partially adiabatic (PT or ETPT) processes the (deuterium) KIE is

$$[30]\qquad \frac{k_{rH}}{k_{rD}} \approx f(\Omega_{pH},\Omega_{pD}) \times \frac{\sum_{v_H,w_H} \exp\left(-\frac{v_H\hbar\Omega_{pH}}{k_BT}\right) S_{RP}^{v_H w_H} \exp\left(-\frac{G^{\neq}_{v_H,w_H}}{k_BT}\right)}{\sum_{v_D,w_D} \exp\left(-\frac{v_D\hbar\Omega_{pD}}{k_BT}\right) S_{RP}^{v_D w_D} \exp\left(-\frac{G^{\neq}_{v_D,w_D}}{k_BT}\right)}$$

$$[31]\qquad f(\Omega_{pH},\Omega_{pD}) = (\Omega_{pH}/\Omega_{pD})^2 \quad \text{in the partially adiabatic limit}$$

$$f(\Omega_{pH},\Omega_{pD}) = 1 \quad \text{in the diabatic limit}$$

with analogous equations for triton transfer. The KIE is reflected quite differently in the totally adiabatic limit, namely, in the isotope-dependent activation Gibbs free energy. This is rooted in the different electronic–proton potential surface splittings for proton, deuteron, and triton transfer. This offers an interesting parallel to classical views based on different zero point energies of the isotopes (22–24). In the present approach the origin of the activation Gibbs free energy difference is, however, quite different, and PT is also a tunnel process in the fully adiabatic limit. The kinetic deuterium isotope effect in the fully adiabatic limit is, thus, from eqs. [22]–[24] and disregarding isotope effects in ω_{eff}:

$$[32]\qquad \text{KIE} \approx \exp\{[G^{\neq}_{tot-ad}(\text{deuteron}) - G^{\neq}_{tot-ad}(\text{proton})]/k_BT\} \approx \exp\left[\{[\alpha(1-\alpha)]^{1/2}\hbar\Omega_{pH}\ \exp(-m_{pH}\Delta R_{p0}^2/4\hbar)\} \times \{1-\exp[(m_{pH}\Omega_{pH}\Delta R_{p0}^2/4\hbar)(1-\sqrt{2})/\sqrt{2})\right]/k_BT\}]$$

where $G^{\neq}_{tot-ad}$ is given by eq. [20] and ΔR_{p0} is the equilibrium hydron coordinate displacement (here taken as the same for all the isotopes). Analogous equations apply to triton KIEs.

Equations [28]–[32] hold some implications:

1. Large KIEs, for example, ≥2–3, have mostly been referred to the partially adiabatic limit (eqs. [30] and [31]) (31, 32). Significant KIEs, however, also accord with the fully adiabatic limit.

2. The KIE is *dominated* by the tunnel factor but KIE in other quantities were noted.

3. PT distances extracted from experimental data, using the partially adiabatic limit, are commonly small, i.e., 0.3–0.4 Å (see, for example, refs. 31 and 32), indicative of fluctuational effects prior to PT. This is not surprising in view of the distance sensitivity of proton tunnelling.

4. The KIE follows "normal" tunnelling distance behaviour in the totally diabatic and partially adiabatic limits in the sense of being larger the longer the PT distance. The *opposite* effect emerges in the fully adiabatic limit, i.e., the KIE is *smaller* the longer the PT distance. This is because the electronic–proton surface splitting is smaller the longer the PT distance. The *difference* between the proton and heavier isotope splittings is therefore also smaller, illustrated schematically in Fig. 4.

5. The driving-force dependence of the KIE has a maximum around thermoneutrality (2) but with different physical causes. ΔG^0-dependent slight vibrational deuteron and triton excitation is the cause in the totally diabatic and partially adiabatic limits. The maximum is shifted to finite $|\Delta G^0|$ for different reactants' and products' frequencies. In the fully adiabatic limit the ΔG^0 dependence follows the transfer coefficient, with a maximum also at $\alpha \approx 0.5$ but now dominated by low-frequency environmental dynamics.

6. The temperature dependence in the totally diabatic and partially adiabatic limits is small unless different hydron transfer distances and "soft" intermolecular donor–acceptor motion apply. Notably larger effects emerge in the fully adiabatic limit.

4. Fluctuational barrier preparation and gated proton transfer

4.1 Features of gating in proton transfer reactions

Intermolecular *donor–acceptor motion* is the basis for fluctuational tunnel barrier preparation where the proton donor and acceptor are preorganized *prior* to PT, attenuating the barrier and facilitating proton tunnelling (17–21). Proton barrier preparation accords with the notion of "gated" PT. PT is initially blocked by prohibitively long distances. Fluctuations, i.e., motion along the gating coordinate X_{gat}, opens the PT channel by lowering the PT distance, and subsequently returns to the *same* configuration as before PT.

© 1999 NRC Canada

"Gating" in this sense is a likely general feature of PT, ETPT, and hydride transfer. A specific case is proton relay in serine proteases (46) where a proton is transmitted from the donor to the acceptor via conformationally mobile His. Another example is the insertion step of olefin hydrogenation in coordination chemical catalysis where coordinated olefin is strongly shifted towards coordinated hydride and relaxed to its initial configuration subsequent to insertion (34).

In a broader sense, gating modes are also subject to reorganization. The proton or electron tunnelling factor would then compete intriguingly for the transition state configuration, which no longer coincides with the saddle point of the reactants' and product's potential surfaces.

4.2 A model for gated proton transfer

PT gating along the (dimensionless) gating coordinate X_{gat} is well illustrated by the following harmonic gating potential in the reactants' and products' state:

$$[33]\qquad U_R^{gat}(X_{gat}) = U_P^{gat}(X_{gat}) = \frac{1}{2}\hbar\omega_{gat}X_{gat}^2$$

The proton equilibrium coordinates and vibrational frequencies depend explicitly on X_{gat},

$$[34]\qquad R_{p0}^R = R_{p0}^R(X_{gat})\ ;\ R_{p0}^P = R_{p0}^P(X_{gat})\ ;\ \Omega_p = \Omega_p(X_{gat})$$

We assume that the X_{gat} dependence of Ω_p can be disregarded, and that the PT distance can be represented by the broadly appropriate linear form:

$$[35]\qquad R_{p0}^P(X_{gat}) - R_{p0}^R(X_{gat}) = \Delta R_{p0} - \gamma X_{gat}$$
$$\Delta R_{p0} = R_{p0}(X_{gat} = 0) - R_{p0}^R(X_{gat} = 0)$$

A final assumption is that relaxation along X_{gat} is fast compared to hydron tunnelling. Equilibrium along X_{gat} then prevails and the notion of a rate constant applies. Slow X_{gat} dynamics implies either that proton barrier preparation is a separate reaction step, or that PT occurs along the non-equilibrated gating coordinate. In either case composite time evolution emerges (1, 2, 47). Equations [9] and [10] are now modified to

$$[36]\qquad W_{RP} = \int_{c-i\infty}^{c+i\infty} d\theta G(\theta) S(\theta)$$

where $G(\theta)$ is given by the diabatic form in eq. [9] or [10], or the partially adiabatic form in eq. [12] combined with eq. [22], and $S(\theta)$ is the gating correction. $S(\theta)$ for the gating potential in eq. [33] is

$$[37]\qquad S(\theta) = \frac{1}{\sqrt{\pi}}\, g(\theta)\, \frac{\int dX_{gat}\, \exp[-g^2(\theta)X_{gat}^2]\exp\{-\frac{1}{2}(m_p\Omega_p/\hbar)[R_{p0}^P(X_{gat}) - R_{p0}^R(X_{gat})]^2\}}{\exp\{-\frac{1}{2}(m_p\Omega_p/\hbar)[R_{p0}^P(X_{gat} = 0) - R_{p0}^R(X_{gat} = 0)]^2\}}$$
$$g(\theta) = \frac{\sinh(\frac{1}{2}\beta\hbar\Omega_{gat})}{\{\cosh[\frac{1}{2}\beta\hbar\Omega_{gat}(1-\theta]\cosh(\frac{1}{2}\beta\hbar\Omega_{gat}\theta)\}}$$

valid at all temperatures, also when gating is by nuclear tunnelling along X_{gat}.

In the high-T limit eq. [37] takes the form

$$[38]\qquad S(\theta) = \left(\frac{\beta\hbar\Omega_{gat}}{2\pi}\right)^{1/2} \frac{\int dX_{gat}\, \exp(-\frac{1}{2}\beta\hbar\Omega_{gat}X^2{}_{gat})\, \exp\{-\frac{1}{2}(m_p\Omega_p/\hbar)[R_{p0}^R(X_{gat}) - R_{p0}^R(X_{gat})]\}}{\exp\{-\frac{1}{2}(m_p\Omega_p/\hbar[R_{p0}^R(X_{gat} = 0) - R_{p0}^R(X_{gat} = 0)]/\hbar\}}$$

Equation [38] shows that the correction involves activation energy from thermally activated motion along X_{gat} from $X_{gat} = 0$, and the *ratio* between the proton tunnel factor at the given value of X_{gat} and at equilibrium $X_{gat} = 0$. Integrating over X_{gat} in eq. [37] gives

$$[39]\qquad S(\theta) = \frac{g(\theta)}{\{[g(\theta)]^2 + (m_p\Omega_p/2\hbar)\gamma^2\}^{1/2}} \times \frac{\exp\left\{-\dfrac{[g(\theta)]^2(m_p\Omega_p/2\hbar)(\Delta R_{p0})^2}{[g(\theta)]^2 + (m_p\Omega_p/2\hbar)\gamma^2}\right\}}{\exp[-(m_p\Omega_p/2\hbar)(\Delta R_{p0})^2}$$

or, in the high-T limit

$$[40]\qquad S(\theta) = \frac{(\frac{1}{2}\beta\hbar\omega_{gat})^{1/2}}{[\frac{1}{2}\hbar\omega_{gat} + (m_p\Omega_p/2\hbar)\gamma^2]^{1/2}} \times \frac{\exp\left\{-\dfrac{\frac{1}{2}\beta\hbar\omega_{gat}(m_p\Omega_p/2\hbar)(\Delta R_{p0})^2}{\frac{1}{2}\beta\hbar\omega_{gat} + (m_p\Omega_p/2\hbar)\gamma^2}\right\}}{\exp[-(m_p\Omega_p/2\hbar)(\Delta R_{p0})^2}$$

These equations show that $S(\theta) > 1$ for finite γ while $S(\theta) \to 1$ for $\gamma \to 0$. Gating thus enhances hydron tunnelling by reducing the transfer distance.

Equation [40] can be used directly in combination with the rate constants in eqs. [12]–[15] and [22]–[24] whereas eq. [39] must be combined with the original form in eq. [9].

© 1999 NRC Canada

After insertion in eq. [36] θ-integration can be undertaken using the saddle point method (cf. Sect. 2.4).

5. Proton transfer in hydrolytic and redox enzyme catalysis

Absolute values, and the temperature and driving-force dependence of the KIE for general acid-based catalysed PT reactions, have been analysed using formalism related to the frames in Sects. 2 and 3 (1, 2, 31, 32), and the partially adiabatic limit. Maximum KIEs ≥10 only accord with the fully adiabatic limit for unphysically small PT distances. Some cases of hydrolytic enzyme processes (α-chymotrypsin (48), carboxypeptidase A (49)) have also been addressed. The smaller KIE here (1.3–2.5) can be brought in line with the fully adiabatic limit but these processes are entangled by stochastic solvent effects.

We consider here briefly some recent cases of hydrogen *atom* or *hydride* transfer in metalloenzyme kinetics, more specifically: hydroperoxidation of linoleic acid catalysed by lipoxygenase (50, 51); alcohol dehydrogenation catalysed by yeast alcohol dehydrogenase (27–29); and oxidative deamination of primary amines to aldehydes catalysed by amine oxidases (52, 53). Common denominators are the following: disentanglement of rate-determining hydrogen atom or hydride transfer; large kinetic isotope effects; temperature dependence of the KIE; and, in some cases, KIEs involving all three hydrogen isotopes. Details of the experimental investigations and mechanisms are given elsewhere (27–29, 50–55).

5.1 Lipoxygenases

Hydrogen atom transfer with radical formation is rate determining above 32°C. The kinetic deuterium isotope effect is unusually large, i.e., 56 (49, 50) while secondary isotope effects are small (<1.2). The apparent activation enthalpies are small and are almost the same for protium and deuterium transfer (5 and 7 kJ mol^{-1}, respectively).

The observed pattern accords broadly with the partially or even fully diabatic limit of hydrogen atom transfer (eqs. [12]–[17], [19], [20], and [22]), with the following notes:

1. The large isotope effects cannot be brought into accord with the fully *adiabatic* limit.

2. The insignificant KIE activation enthalpies are indicative of structurally rigid environments, i.e., similar transfer distances for the two isotopes.

3. The hydrogen transfer distance based on the data in ref. 49 can be calculated from eq. [30] combined with specific hydrogen potentials. In the harmonic approximation (eq. [19]), using $\Omega_p \approx 3000$ cm^{-1}, the transfer distance is calculated to be 0.45–0.50 Å. A Morse potential with the dissociation energy of ≈2 eV would give 0.6–0.7 Å. This is still notably smaller than common equilibrium transfer distances in hydrogen-bonded systems, indicative of fluctuational barrier preparation features for both isotopes.

4. The notion of the apparent activation enthalpy is elusive because secondary and tertiary macromolecular structures themselves depend on the temperature, implying that the kinetic parameters E_R and ΔG^0 (Sects. 2 and 3) also depend on the temperature. The small apparent activation enthalpies reflect such features, and not that the process should approach the activationless driving-force region.

5.2 Alcohol dehydrogenases

Large KIEs have been observed in both yeast and liver dehydrogenase (ADH) catalysed hydride transfer from alcohol substrates to NAD^+ (27–29). Hydride transfer is rate determining in yeast ADH action whereas liver ADH is partly controlled by product release (54). We consider briefly the former, but sophisticated investigations of liver ADH have illuminated the interplay between hydrogen transfer distance, the catalytic efficiency, and KIEs (55).

Experimental primary KIEs of yeast ADH are $k_{rH}/k_{rT} \approx 7.1$ and $k_{rD}/k_{rT} \approx 1.7$ (27, 28). The apparent activation enthalpy differences are $H_T^{\neq} - H_H^{\neq} \approx 5.1$ kJ and $H_T^{\neq} - H_D^{\neq} \approx 1.8$ kJ giving, by difference, $H_D^{\neq} - H_H^{\neq} \approx 3.3$ kJ (27). These values are significant. The detailed structural conversions are confused by coupling between primary and secondary hydrogens at the alcohol C-1 (27, 28), reflected also in the secondary isotope effects, and the overall patterns do not accord with a one-dimensional PT view. A one-dimensional frame does, however, illuminate the interplay between quantum mechanical hydride transfer and environmental dynamics. The frequency and amplitude values accord with other recent analyses of ADH and bovine serum amine oxidase based on notions quite different from the present analysis (56, 57).

According to the conditions for classical and quantum mechanical behaviour (Sect. 2.1) *all* the isotopes are dominated by quantum mechanical patterns. Approximate protium, deuterium, and tritium stretching vibrational frequencies would be ≈3000 cm^{-1}, 2100 cm^{-1}, and 1700 cm^{-1}, respectively, in accord with the condition $\hbar\Omega_p >> k_B T$. Reservations arise if the transfer mode contains conspicuous elements of hydrogen bending, or the motion is coupled to secondary hydrogen dynamics. The KIEs are large enough that the partially adiabatic limit is appropriate. Using eqs. [12]–[14] and [19], the two primary KIEs, i.e., k_{rH}/k_{rT} and k_{rD}/k_{rT}, would give the transfer distances 0.26–0.37 Å and 0.21–0.29 Å, respectively. The upper and lower limits correspond to stretching and bending. These values are small: 20–30% larger values emerge if Morse or Rosen–Morse potentials are used (31, 32) but the values are still likely to reflect an entangled hydride transfer trajectory. The two sets of values are also *different* but this could accord with different transfer distances for the isotopes and is supported by the apparent enthalpy differences. The latter then reflect motion along a "gating" coordinate up to varying reactive distances that are smaller the heavier the isotope. Distance differences of about 0.1 Å are formally needed and correspond to fluctuational gating frequencies in the appropriate range of 150–200 cm^{-1} for effective masses the size of individual residues. ADH therefore reveals a consistent pattern where hydrogen tunnelling, environmental dynamics, and fluctuational barrier preparation are all conspicuous. The present formalism, in principle, also frames these features but precise disentanglement requires a separate analysis.

5.3 Bovine serum amine oxidase

Amine oxidases catalyse the oxidation of amines to aldehydes by molecular dioxygen. Proton abstraction from the substrate to an active-site base residue is rate determining,

© 1999 NRC Canada

with little coupling to other modes. Bovine serum amine oxidase (BSAO) also shows some of the largest known KIEs in enzyme processes (27–29, 52, 53) and is therefore a very attractive target for investigations of hydrogen tunnelling in biological systems.

The KIEs for BSAO at 25°C are: $k_{rH}/k_{rT} = 35$ and $k_{rD}/k_{rT} = 3.0$ (27–29). The apparent activation enthalpies are large, i.e., 14 and 4.5 kJ, respectively, all strongly indicative of hydrogen tunnelling with significant and isotope-specific gating features. The tunnel distances calculated from the data at 25°C by eqs. [12]–[14] and [19] are 0.35–0.49 Å from k_{rH}/k_{rT} and 0.29–0.41 Å from k_{rD}/k_{rT}. The upper and lower limits are again based on hydrogen bending and stretching, respectively. If the large apparent activation enthalpies are associated solely with fluctuational barrier preparation, then the scenario is suggestive of different transfer distances for the three isotopes. The tunnel distances for protium, deuterium, and tritium transfer of ≈ 0.75 Å, ≈ 0.57 Å, and ≈ 0.5 Å, respectively, formally accord with both the absolute values and the apparent activation enthalpies of the KIEs.

6. Concluding remarks

Hydrogen transfers are basically quantum mechanical transitions. Classical hydrogen dynamics can be envisaged when the donor–acceptor interactions are strong and the hydrogen transfer barriers shallow, in which case environmental stochastic effects also become apparent (33). Chemical and biological hydron and hydride transfer are also strongly coupled to protein or solvent environments, imposing multiphonon character on the process. Hydrogen *atom* transfer (ETPT) does not arouse long-range electrostatic interactions but reorganization of short-range local group motion may still be important. The present formalism addresses both PT and ETPT as quantum mechanical (tunnel) transitions strongly coupled to the environment. Hydrogen dynamics is represented by high-frequency harmonic or anharmonic potentials. The environment is a linearly responding medium that can, however, be vibrationally or spatially dispersive (1, 2). Rate constants are derived for three limits of donor–acceptor interaction, viz. the fully diabatic, the partially adiabatic, and the totally adiabatic limits. The theory has been referred specifically to observable correlations such as the Brønsted relation and the kinetic isotope effects.

Some notions and results have been derived before (1, 2, 15–21, 31–33). A new result is, first, that the coupling features between the electronic, hydronic, and environmental systems have been precisely specified in *all* three limits (Appendix). The coupling, as appearing for example in the potential surfaces, has been recast in terms of quantum mechanical averaging with respect to either the electronic or both the electronic and hydrogen system parts, subject to choice of diabatic or adiabatic basis set. The second new result is that the rate constant has been combined with a new approach to conformational gating for hydrogen transfer. This formalism applies at all temperatures and extends to nuclear tunnelling along the gating mode. Particular attention has, further, been given to the totally adiabatic limit. The hydrogen tunnel feature is here reflected in the splitting of the adiabatic surfaces in the transition state with respect solely to the environmental nuclear coordinates. The splitting is isotope dependent and transmits to the driving-force and temperature dependence of the KIEs, with maximum at thermoneutrality. A third observation is, then, that the hydrogen transfer distance dependence of the KIE in this limit is opposite that of the fully diabatic and partially adiabatic limits.

The formalism has, finally, been used as a new frame for hydrogen transfer in three enzyme systems, all with large KIEs and strong indications of hydrogen tunnelling. One system, lipoxygenase, accords with the simplest view of H-transfer between "fixed" molecular fragments, in the sense of showing similar transfer distances for all the isotopes. Yeast ADH is indicative of conformational gating but is complicated by a composite hydrogen reaction coordinate reflected in the secondary isotope effect. BSAO finally shows straight H-transfer features but strong gating as revealed in the large apparent activation enthalpies of the KIE and the accompanying, rather different, transfer distances for the three isotopes.

Acknowledgements

Financial support from the Danish Technical Science Research Council and the EU programme INTAS is acknowledged.

References

1. A.M. Kuznetsov. Charge transfer in physics, chemistry, and biology. Gordon & Breach, Reading. 1995.
2. A.M. Kuznetsov and J. Ulstrup. Electron transfer in chemistry and biology. An introduction to the theory. Wiley, Chichester. 1999.
3. H.E.M. Christensen, L.S. Conrad, K.V. Mikkelsen, M.K. Nielsen, and J. Ulstrup. Inorg. Chem. **29**, 2808 (1990).
4. P. Siddarth and R.A. Marcus. J. Phys. Chem. **94**, 8430 (1990); A.A. Stuchebrukhov and R.A. Marcus. J. Phys. Chem. **99**, 7581 (1995).
5. C.C. Moser, J.M. Keske, K. Warncke, R.S. Farid, and P.L. Dutton. Nature (London), **355**, 796(1992).
6. J.M. Gruschus and A. Kuki. J. Phys. Chem. **97**, 5581 (1993).
7. J.R. Winkler and H.B. Gray. Chem. Rev. **92**, 369 (1992); H.B. Gray and J.R. Winkler. Annu. Rev. Biochem. **95**. 537 (1996).
8. R.A. Scott (*Editor*). Comments in: J. Biol. Inorg. Chem. **2**, 372 (1997); J.A. Cowan (*Editor*). Comments in: J. Biol. Inorg. Chem. **3**, 195 (1998).
9. D.S. Bendall (*Editor*). Protein electron transfer. BIOS Publishers, Oxford. 1996.
10. G. Iversen, Yu.I. Kharkats, A.M. Kuznetsov, and J. Ulstrup. Adv. Chem. Phys. **106**, 453 (1999).
11. D.G. Bourgin. Proc. Natl. Acad. Sci. U.S.A. **15**, 357 (1929).
12. E. Wigner. Z. Phys. Chem. Abt. B: **19**, 1903 (1932).
13. R.P. Bell. Proc. R. Soc. (London), Ser. A: **139**, 466 (1933).
14. F. Hund. Z. Phys. **43**, 805 (1927).
15. R.R. Dogonadze, A.M. Kuznetsov, and V.G. Levich. Elektrokhimiya, **3**, 739 (1967).
16. R.R. Dogonadze, A.M. Kuznetsov, and V.G. Levich. Electrochim. Acta, **13**, 1025 (1968).
17. D. Borgis and J.T. Hynes. J. Chem. Phys. **94**, 3619 (1991); Chem. Phys. **170**, 315 (1993).

© 1999 NRC Canada

18. D. Borgis, G. Tarjus, and H. Azzouz. J. Chem. Phys. **97**, 1390 (1992).
19. R.J. Cukier. J. Phys. Chem. **98**, 2377 (1994).
20. D. Borgis and J.T. Hynes. J. Phys. Chem. **100**, 1118 (1996), and refs. therein.
21. J.-Y. Fang and S. Hammes-Schiffer. J. Chem. Phys. **106**, 8442 (1997), and refs. therein.
22. R.P. Bell. The proton in chemistry. 2nd ed. Chapman and Hall, Oxford. 1973.
23. R.P. Bell. The tunnel effect in chemistry. Chapman and Hall, Oxford. 1980.
24 E.F. Caldin and V. Gold (*Editors*). Proton-transfer reactions. Chapman and Hall, London. 1975.
25. A.J. Kresge. Chem. Soc. Rev. **2**, 475 (1973).
26. A.J. Kresge. Acc. Chem. Res. **23**, 43 (1990).
27. Y. Cha, C.J. Murray, and J.P. Klinman. Science (Washington, D.C.), **243**, 1325 (1989).
28. B.J. Bahnson and J.P. Klinman. Meth. Enzymol. **249**, 373 (1995).
29. A. Kohen and J.P. Klinman. Acc. Chem. Res. **31**, 397 (1998).
30. P.M. Morse. Phys. Rev. **34**, 57 (1929).
31. E.D. German and A.M. Kuznetsov. J. Chem. Soc. Faraday Trans. 1, **77**, 397 (1981); J. Chem. Soc. Faraday Trans. 1, **77**, 2203 (1981).
32. N. Brüniche-Olsen and J. Ulstrup. J. Chem. Soc. Faraday Trans. 2, **74**, 1690 (1978); J. Chem. Soc. Faraday Trans. 1, **75**, 205 (1979).
33. A.M. Kuznetsov and J. Ulstrup. Chem. Phys.**188**, 131 (1994).
34. P. Søgaard Andersen and J. Ulstrup. Acta Chem. Scand. Ser. A: **A37**, 585 (1983).
35. R.I. Cukier. J. Phys. Chem. **100**, 15 428 (1996).
36. M.A. Vorotyntsev, R.R. Dogonadze, and A.M. Kuznetsov. Phys. Status Solidi B: **52**, 125(1972).
37. G. Arfken. Mathematical methods for physicists. 3rd ed. Academic Press, Orlando, Fla. 1985.
38. M.A. Vorotyntsev, R.R. Dogonadze, and A.M. Kuznetsov. Dokl. Akad. Nauk SSSR, Ser. Fiz. Khim. **195**, 1135 (1970).
39. M.A. Vorotyntsev, R.R. Dogonadze, and A.M. Kuznetsov. Dokl. Akad. Nauk SSSR, Ser. Fiz. Khim. **209**, 1135 (1973).
40. J.-T. Wang and F. Williams. J. Am. Chem. Soc. **94**, 2930 (1972); A. Campion and F. Williams. J. Am. Chem. Soc. **94**, 7633 (1972).
41. L.I. Trakhtenberg, V.L. Klochikin, and S.Ya. Pshezhetskij. Chem. Phys. **59**, 191 (1981).
42. W. Siebrand and T.A. Wildman. Acc. Chem. Res. **19**, 238 (1986).
43. M. Abramovitz and I.A. Stegun. Handbook of mathematical functions. Dover, New York. 1965.
44. L.D. Landau and E.M. Lifshitz. Quantum mechanics. 2nd ed. Pergamon, Oxford. 1965.
45. C.G. Swain, E.C. Stivers, J.F. Reuwer, and L.J. Schaad. J. Am. Chem. Soc. **80**, 5885 (1958).
46. H. Sumi and J. Ulstrup. Biochim. Biophys. Acta, **955**, 26 (1988).
47. H. Sumi and R.A. Marcus. J. Chem. Phys. **84**, 4894 (1986).
48. D.E. Khoshtariya and N.G. Goguadze. Bioorg. Khim. **11**, 1621 (1985); Biofizika, **31**, 220 (1986).
49. N.G. Goguadze, J.M. Hammerstad-Pedersen, D.I. Khoshtarya, and J. Ulstrup. Eur. J. Biochem. **200**, 423 (1991).
50. M. Glickman and J.P. Klinman. Biochemistry, **34**, 14 077 (1994).
51. T. Jonsson, M.H. Glickman, S. Sun, and J.P. Klinman. J. Am. Chem. Soc. **118**, 10 319 (1996). C. Hwang and C.B. Grisson. J. Am. Chem. Soc. **116**, 795 (1994).
52. K.L. Grant and J.P. Klinman. Biochemistry, **28**, 6597 (1989.
53. T. Jonsson, D.E. Edmonsson, and J.P. Klinman. Biochemistry, **33**, 14 871 (1994).
54. B.J. Bahnson, D. Park, K. Kim, B.V. Plapp, and J.P. Klinman. Biochemistry, **32**, 5503 (1993).
55. B.J. Bahnson, T.D. Colby, K.J. Chin, B.M. Goldstein, and J.P. Klinman. Proc. Natl. Acad. Sci. U.S.A. **94**, 12 797 (1997).
56. W.J. Bruno and W. Bialek. Biophys. J. **63**, 689 (1992).
57. D. Antoniou and S.S. Schwartz. Proc. Natl. Acad. Sci. U.S.A. **94**, 12 360 (1997).

Appendix

Derivation of eqs. [6]–[8]

The total system potential energy is

$$\begin{aligned}[A1]\quad \hat{U}_{pot}(\vec{x}, R_p, \{q_k\}) &= V^D_{elD}(\vec{x}) + V^D_{elA}(\vec{x}) + V^D_{elprot}(\vec{x}, R_p) + V^D_{elsolv}(\vec{x}, \{q_k\}) \\ &+ V^A_{elA}(\vec{x}) + V^A_{elD}(\vec{x}) + V^A_{elprot}(\vec{x}, R_p) + V^A_{elsolv}(\vec{x}, \{q_k\}) \\ &+ V_{protD}(R_p) + V_{protA}(R_p) + V_{protsolv}(R_p, \{q_k\}) + U^0_{solv}(\{q_k\})\end{aligned}$$

The terms in the second line denote the following: $V^D_{elD}(\vec{x})$ is the interaction between the transferring or relaxing electron(s) at the donor centre with the donor core, and $V^D_{elA}(\vec{x})$ the interaction with the acceptor core; $V^D_{elprot}(\vec{x}; R_p)$ is the electron–proton interaction when the proton is at the donor site, and $V^D_{elsolv}(\vec{x}, \{q_k\})$ the interaction between the electrons at the donor site and the solvent. The terms in the third line have an analogous meaning for the acceptor site. $V_{protD}(R_p)$ and $V_{protA}(R_p)$ are the proton potential energy at the donor and acceptor site, respectively, and $V_{prot,solv}(R_p,\{q_k\})$ the interaction between the proton and the solvent. $U^0_{solv}(\{q_k\})$ is the free solvent potential energy.

The total potential energy is suitably divided into reactants' or products' potential energies and donor–acceptor interaction terms. For the reactants' state

$$U^R = U^{0R}_{el}(\vec{x}) + V^D_{elprot}(\vec{x}, R_p) - \sum_k q_k v^{el}_k(\vec{x}) - \sum_k q_k v^{prot}_k(R_p) + U^{0R}_{prot}(R_p) + U^0_{solv}(\{q_k\})$$

$$\begin{aligned}[A2]\quad & U^{0R}_{prot}(\vec{x}) = V^D_{eD}(\vec{x}) + V^A_{eA}(\vec{x}); \\ & U^{0R}_{prot}(R_p) \rightarrow V_{protD}(R_p) \\ & -\sum_k q_k v^{el}_k(\vec{x}) = V^D_{elsolv}(\{q_k\}) + V^A_{elsolv}(\vec{x}, \{q_k\}) \\ & -\sum_k q_k v^{prot}_k(R_p) = V_{protsolv}(R_p\{q_k\})\end{aligned}$$

The terms

$$[A3]\quad V^D_{elA}(\vec{x}) + V^A_{elD}(\vec{x}) + V^A_{elprot}(\vec{x}, R_p) + V_{protA}(R_p)$$

have thus been omitted from the reactants' state potential energy in eq. [A2]. An equation equivalent to eq. [A2] applies to the products' state.

A distinction between the diabatic limit on the one hand, and the partially and fully adiabatic limits on the other hand, is now invoked. The concept of potential surfaces in the reactants' and products' states can be maintained in the diabatic limit and these are obtained by averaging eq. [A2]

© 1999 NRC Canada

or the equivalent equation for the products' state with respect to the *electronic* wave functions in the two states. For the reactants' state

$$[A4]\quad U^{R}_{pot}(R_p, \{q_k\}) = V^{R}_{pot}(R_p, \{q_k\}) - \sum_k q_k v^{prot}_k(R_p) + U^{0}_{solv}(\{q_k\})$$

where

$$[A5]\quad V^{R}_{pot}(R_p, \{q_k\}) = U^{0R}_{prot}(R_p) + \left\langle \varphi^{R}_{el}(\vec{x}; R_p, \{q_k\}) \middle| U^{0R}_{prot}(\vec{x}) + V^{R}_{prot}(\vec{x}; R_p) \right| \times \varphi^{R}_{elprot}(\vec{x}; R_p, \{q_k\}) \rangle - \sum_k q_k \left\langle \varphi^{R}_{el}(\vec{x}; R_p, \{q_k\}) \middle| v^{el}_k(\vec{x}) \middle| \varphi^{R}_{el}(\vec{x}; R_p, \{q_k\}) \right\rangle$$

Disregarding the weak dependence of the electronic wave functions $\varphi^{S}_{el}(\vec{x}; R_p, \{q_k\})$ (S = R, P) on the solvent coordinates $\{q_k\}$ (but not on the proton coordinate R_p) converts eq. [A5] to

$$[A6]\quad V^{S}_{pot}(R_p, \{q_k\}) = V^{S}_{prot}(R_p) - \sum_k q_k g^{S}_k(R_p); \qquad S = R,\ P$$

where

$$[A7]\quad V^{S}_{prot}(R_p) = U^{0S}_{prot}(R_p) + \left\langle \varphi^{S}_{el}(\vec{x}; R_p) \middle| U^{0R}_{el}(\vec{x}) + V^{S}_{elprot}(\vec{x}; R_p) \middle| \varphi^{S}_{el}(\vec{x}; R_p) \right\rangle$$
$$g^{S}_k(R_p) = \left\langle \varphi^{S}_{el}(\vec{x}; R_p) \middle| v^{el}_k(\vec{x}; R_p) \middle| \varphi^{S}_{el}(\vec{x}; R_p) \right\rangle$$

Altogether, from eqs. [A4] and [A6]

$$[A8]\quad U^{S}_{pot}(R_p, \{q_k\}) = V^{S}_{prot}(R_p) + U^{S}_{solv}(\{q_k\}) - \sum_k q_k [g^{S}_k(R_p) + V^{pot}_k(R_p)]$$

This equation coincides with eq. [8] if $U^{S}_{solv}(\{q_k\})$ is given the form $\frac{1}{2}\sum_k \hbar\omega_k q_k^2$. Averaging of the proton–solvent interaction term in eq. [A8] (the final term) with respect to the reactants' or products' (diabatic) *proton wave functions* gives the electronic potential surfaces in eq. [6]. The quantity q^{S}_{k0} is identified with

$$[A9]\quad q^{S}_{k0} = [< g^{S}_k >_s + < v^{prot}_k >_s]/\hbar\omega_k$$

$<\ldots>_S$ refers to averaging with respect to the diabatic *proton wave functions* in the states S (= R, P). The weak dependence of q^{S}_{k0} on the proton vibrational states has been disregarded.

All the steps leading to eq. [A8] also apply to the partially and fully adiabatic limits, with the following modifications:

1. The same terms as in eq. [A2] are included. The interactions in eq. [A3] are included in the V^{el}_{RP} term of eq. [18] when the partially or fully adiabatic potential surfaces are constructed.

2. Averaging with respect to the electronic states refers to the *adiabatic* electronic wave functions rather than the reactants' and products' wave functions. The Hamiltonian of the adiabatic wave functions corresponds to the full potential energy function in eq. [A1]. The superscript "S" in eqs. [A4]–[A8] then represents the ground and first excited adiabatic electronic states and not the reactants' and products' states.

3. Averaging with respect to the proton wave functions is not appropriate as the adiabatic proton wave functions do not represent proton localization solely in a given reactant's or products's well. Equations [6] and [7] therefore only apply in the *diabatic* limit whereas eq. [8] applies generally, subject to the choice of electronic basis set.

© 1999 NRC Canada

About environmental isomers and their existence in liquid water

Ernest Grunwald and Colin Steel

Abstract: Environmental isomers in a liquid are molecules of a single species that become distinguishable because they exist in distinct solvent cages. Concepts involved in environmental isomerism are defined and criteria for distinguishability derived, first by neglecting Brownian potential energy noise, then by including it. Two models are used in the simulations of a molecule jumping from a cage of one type to another. (*i*) On every Brownian "collision," the associated Schroedinger state wave is continuous, i.e., collisions and transits between cages are accompanied by zero phase change. (*ii*) On every collision and transit, there is a random phase change in the state wave. The properties of liquid water are reviewed in terms of a two-state model in which the states are environmental isomers. It is shown that (*i*) the difference in enthalpy and entropy between the isomers, (*ii*) the positions and width of their IR stretching frequencies, as well as (*iii*) dielectric constant, (*iv*) molar volume, and (*v*) O···O radial distribution data are in agreement with a model in which the more stable isomer is $H_2O\backslash 4w$ (a water molecule in a cage of four water molecules) and the less stable isomer is $H_2O\backslash 5w$. The widths of the IR bands indicate that the water–water interactions are through "linkage pairs" in which the motions of the individual molecules comprising a cage are essentially independent.

Key words: isomers, isomerism, water, liquid cages, Brownian noise, state broadening, exchange.

Résumé : Les isomères environnementaux dans un liquide sont des molécules d'une seule espèce que l'on peut différencier parce qu'elles existent dans des cages de solvant distinctes. Les concepts impliqués dans l'isomérie environnementale sont définis et on a mis au point les critères qui permettent de reconnaître les différences; ils impliquent, dans un premier temps, de négliger le bruit d'énergie du potentiel brownien et, dans un deuxième temps, de le réintroduire. On a fait appel à deux modèles de simulations pour le passage d'une molécule d'une cage à une autre. (*i*) À chaque collision brownienne, l'onde associée à l'état de Schroedinger est continue, c'est-à-dire les « collisions » et les transferts entre les cages sont accompagnés d'un changement de phase qui est égal à zéro. (*ii*) À chaque collision et transfert, il se produit un changement de phase aléatoire dans l'onde d'état. Les propriétés de l'eau liquide sont réexaminées en termes d'un modèle à deux états dans lequel les états sont des isomères environnementaux. On a montré que les données relatives à (*i*) la différence en enthalpie et en entropie entre les isomères, (*ii*) aux positions et aux largeurs de leurs fréquences d'élongation en IR, ainsi que celles relatives (*iii*) à la constante diélectrique, (*iv*) au volume molaire et (*v*) aux données de distribution radiale O···O sont toutes en accord avec un modèle dans lequel l'isomère le plus stable est $H_2O\backslash 4w$ (une molécule d'eau dans une cage de quatre molécules d'eau) et que le moins stable est l'isomère $H_2O\backslash 5w$. Les largeurs des bandes IR indiquent que les interactions eau–eau se font par des « paires de liaison » dans lesquelles les mouvements des molécules individuelles formant la cage sont essentiellement indépendants.

Mots clés : isomères, isomérie, eau cages liquides, bruit brownien, élargissement d'état, échange.

[Traduit par la Rédaction]

In a recent series of theoretical papers, we considered the conditions for distinguishability of molecular environments in liquids (1–3). In this essay, in honor of Jerry Kresge, we try to weave the strands together and amplify and develop the underlying concepts in particular as they relate to liquid water.

Some definitions

Environmental isomers are chemical species with the same molecular and structural formula that become distinguishable in a given solvent by virtue of their different solvent environments.

For a range of solvents, the phenomenon of solvent environment affecting molecular properties is familiar. For example, the fact that solvent can shift the position of the absorption spectrum of a molecule has been studied for many years (4–7). Even in a single solvent, there can be environmental effects. Thus, when a liquid phase absorption spectrum is broader than its gas-phase counterpart, we probably conclude that in the liquid, the absorbing molecules are

Received October 30, 1998.

This paper is dedicated to Jerry Kresge in recognition of his many achievements in chemistry.

E. Grunwald[1] and C. Steel.[1] Department of Chemistry, Brandeis University, Waltham, MA 02254, U.S.A.

[1]Authors to whom correspondence may be addressed. e-mail: steel@brandeis.edu; EEGRUN@AOL.COM

 © 1999 NRC Canada

Fig. 1. Cage potential for a central molecule, 1, with two molecules, 2, 3, in its solvent cage. The cage potential is given by $V_{cage} = V_{(2)}(r_{12}) + V_{(2)}(r_{13})$, where $V_{(2)}$ is a pair potential given by $V_{(2)} = 4\varepsilon[(\sigma/r)^{12} - (\sigma/r)^6]$ with $\sigma = 5.15$ Å and $\varepsilon = 4.63$ kJ/mol.

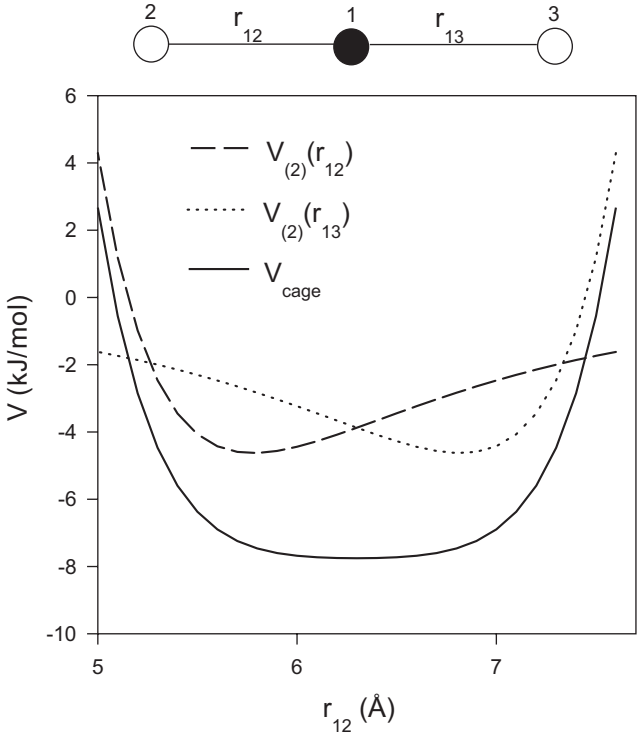

in a range of many environments, because of their ever-varying liquid cages.

A particularly interesting case arises when a small number of environments are sufficiently different, and occur with sufficient weight, so that distinguishable species result. It is in this last and more limited case that we shall employ the term *environmental isomers*.

Material and potential energy cages

A molecule resides in a "cage" when its freedom of translation and rotation are constrained by the molecular environment. There are two common models. The first emphasizes the material cage, the second the potential energy cage. In the model of a material cage, the molecule is imprisoned by the dense packing of neighbor molecules (8) — dense enough to restrict its translation and rotation. This model is often useful. For example, it provides a basis for the analysis of geminate recombination; that is, of the recombination of reactive fragments produced from a caged molecule in a free-radical or photochemical reaction (9, 10).

In the model of a potential-energy cage, the emphasis is placed on the potential well resulting from the sum of the pairwise interactions of the molecule with its surrounding molecules. A potential energy cage is also called a "cavity." In Fig. 1, we display the cage potential for a central molecule with two identical neighbors. The two pairwise potentials add up to produce steep walls on both sides of the central molecule; that is, the central molecule exists in a potential well. In more realistic models in which there are neighbors all around, the potential well becomes a three-dimensional cage.

The potential energy cage is useful in the discussion of environmental isomerism because potential energy is basic to the definition of a molecule. As the molecule moves in isolation, its potential energy remains constant; one might say that the potential energy accompanies the molecule. In a liquid, the motion of a molecule consists of a succession of jumps, from an initial material cage to a neighboring one. As the molecule diffuses through the liquid, it leaves behind a wake of material cages through which it has passed. By contrast, the potential energy cage is not left behind. The time scales of the microscopic events are such that the potential energy cage in effect accompanies the molecule, and thus may be regarded as a fundamental property of the molecule. Briefly, in diffusion there are three critical time constants. (*i*) The transit time taken by a molecule in crossing the barrier from one cage to the next (τ_{jump}), which is of order 10^{-13} s. (*ii*) After the jump, the time taken in the new cage for the nonequilibrium energy distribution of the molecular neighbors to relax to statistical equilibrium, the correlation time (τ_{corr}), which is of order 10^{-12} s. (*iii*) The time that a molecule spends in a cage (τ_{cage}) before it jumps to the next material cage, which is of order 10^{-10}–10^{-11} s.

Although these times (whose numerical values will be examined later) are only representative and depend on the diffusing entity and the solvent, the relative values inferred by them are typical. After a diffusive jump, the molecular surroundings reach statistical equilibrium in a time that is short compared to τ_{cage}. In effect, the diffusing molecule, on passing through a succession of material cages, interacts with the medium at statistical equilibrium, except for a relatively small fraction of the time. To a good approximation, therefore, the motion of the molecule in the liquid is correlated with that of its potential energy cage. The potential energy of the cage interaction may therefore be regarded as part of the potential energy of the molecular species.

Distinguishability and cage exchange

The next two sections will be theoretical. After that, we shall return to real phenomena. Theoretically, isomers are the populations of discrete minima on the potential surface for the interaction of the atoms in the molecule — minima that are linked by adiabatic motion. Note the requirement of "adiabatic." For example, in this definition ground state and triplet anthracene are not isomers because they cannot be interconverted on a single adiabatic surface. Note also that potential energy is here defined as in vibrational spectroscopy. That is, for an isolated molecule in its electronic/vibrational ground state, the potential energy V_o is equal to the state energy ε_o, minus the vibrational zero-point energy, $V_o = \varepsilon_o - \varepsilon_{vzp}$.

Suppose that the molecule is transferred to a liquid in which it can reside in alternate cages \a and \b. The substrate molecule in these two cages can then be represented by M\a and M\b. Let $V_{\backslash a}$ and $V_{\backslash b}$ denote the respective cage potentials for the molecule in cages \a and \b. Since the cage is part of the molecular entity in solution, the energies of a molecule in the cages are

$$[1a] \quad \varepsilon_{\backslash a} = V_o + \varepsilon_{vzp\backslash a} + V_{\backslash a}$$

© 1999 NRC Canada

Fig. 2. Partial wave trains when there is switching between two states \a and \b having different state frequencies or energies. In case 1, there is no phase shift accompanying the switch. In case 2, the phase shift is random.

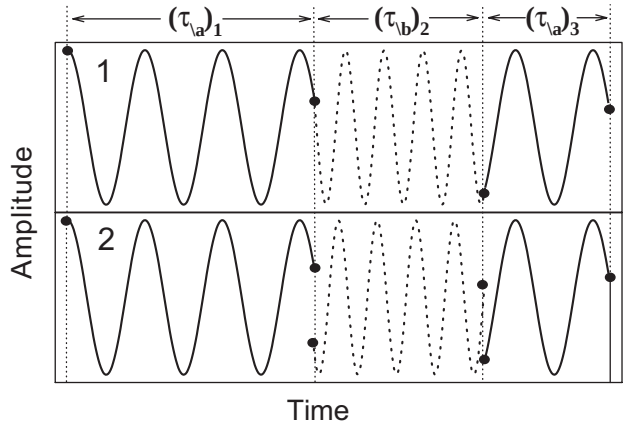

[1*b*] $\varepsilon_{\backslash b} = V_o + \varepsilon_{vzp\backslash b} + V_{\backslash b}$

The vibrational zero-point energies $\varepsilon_{vzp\backslash a}$ and $\varepsilon_{vzp\backslash b}$ are nearly equal to each other and to ε_{vzp} for the isolated molecule. Hence, in good approximation, the energy difference between M\a and M\b is equal to the difference in cage potentials:

[2] $\varepsilon_{\backslash a} - \varepsilon_{\backslash b} = V_{\backslash a} - V_{\backslash b}$

In both environments, the atoms of the caged molecule are the same, yet the two state energies are different, and the two states exist at alternate potential energy minima connected by an adiabatic path. Since the isomerism is generated by the difference in cage potentials in the given liquid, it is reasonable to call M\a and M\b *environmental isomers*.

Since we have so far discussed environmental isomerism in terms of different state energies, it is useful to examine this concept further and to look at problems that may arise from this simple definition. We first inquire about the size of the energy difference required for distinguishability. It turns out that there are two kinds of dynamic effects that may wipe out the required distinguishability: (*a*) cage exchange and (*b*) potential energy noise due to the Brownian motion of the liquid molecules.

Cage exchange may be represented by the simple kinetic scheme

[3] $\mathrm{M\backslash a} \underset{k_{\backslash b}}{\overset{k_{\backslash a}}{\rightleftharpoons}} \mathrm{M\backslash b}$

where $k_{\backslash a}$ and $k_{\backslash b}$ are the first-order rate constants for the processes $\mathrm{M\backslash a} \rightarrow \mathrm{M\backslash b}$ and $\mathrm{M\backslash b} \rightarrow \mathrm{M\backslash a}$, respectively. Also $\tau_{\backslash a}$ ($= 1/k_{\backslash a}$) is the mean lifetime of M in cage \a before jumping to cage \b, with a similar definition for $\tau_{\backslash b}$ ($= 1/k_{\backslash b}$).

We shall define the environments \a and \b so that at equilibrium, $[\mathrm{M\backslash a}] \geq [\mathrm{M\backslash b}]$. Because at dynamic equilbrium, $k_{\backslash a}[\mathrm{M\backslash a}] = k_{\backslash b}[\mathrm{M\backslash b}]$, it follows that $k_{\backslash a} \leq k_{\backslash b}$, and $\tau_{\backslash a} \geq \tau_{\backslash b}$. In exchange kinetics, it is useful to define an exchange time by

[4] $\tau_{exch} = 1/(k_{\backslash a} + k_{\backslash b})$
$= \tau_{\backslash a}\tau_{\backslash b}/(\tau_{\backslash a} + \tau_{\backslash b})$
$= \tau_{\backslash b}[\mathrm{M\backslash a}]/([\mathrm{M\backslash a}] + [\mathrm{M\backslash b}])$

In this work, $\tau_{\backslash b}$ (potentially the smaller of $\tau_{\backslash a}$ and $\tau_{\backslash b}$) will be approximated by the time for a solvent molecule to diffuse by a length equal to a cage radius, which is given by the familiar Einstein–Smoluchowski equation,

[5] $1/k_{\backslash b} = \tau_{\backslash b} = r_{cage}^2/6D$

where D is the coefficient for self diffusion of the solvent, and r_{cage} is the cage radius. This means that any energy barrier associated with $k_{\backslash b}$ is the same as that for diffusion.

The time of the Brownian motions is governed by the Brownian correlation time τ_{corr}. The latter is roughly 100 times shorter than $\tau_{\backslash b}$, so the Brownian noise is averaged fairly well during τ_{exch}. We shall therefore treat the two dynamic effects in series. We shall first treat cage exchange in the absence of Brownian noise; in the next section, we shall add the noise.

The time-dependent Schroedinger wave equation for a quantum system in a stationary state is given by eq. [6], where $\psi(x, t)$ is the total wave function and $\phi(x)$ is its spatial part.

[6] $\psi(x, t) = \phi(x) \exp[-2\pi i(\varepsilon/h)t]$

The time-dependent part — the exponential — describes a simple harmonic circularly polarized wave of frequency $\nu = \varepsilon/h$. In cage exchange, the molecule switches between two stationary wave functions, $\psi_{\backslash a}$ and $\psi_{\backslash b}$. The ψ values can be regarded as stationary because the transit time between cages (τ_{jump}), and the time the molecule takes to come to equilibrium in the new cage (τ_{corr}) is much shorter than the time the molecule spends in a cage ($\tau_{\backslash a}$ and $\tau_{\backslash b}$). Hence, the ψ values are given by eq. [7], with $\nu_{\backslash a} = \varepsilon_{\backslash a}/h$, and $\nu_{\backslash b} = \varepsilon_{\backslash b}/h$,

[7*a*] $\psi_{\backslash a}(x, t) = \phi_{\backslash a}(x) \exp(-2\pi i \nu_{\backslash a} t)$

[7*b*] $\psi_{\backslash b}(x, t) = \phi_{\backslash b}(x) \exp(-2\pi i \nu_{\backslash b} t)$

Switching between two state frequencies $\nu_{\backslash a}$ and $\nu_{\backslash b}$ is mathematically analogous to the switching of a nucleus between two chemical shifts (2, 11, 12). Borrowing from NMR concepts, we define a dimensionless *distinguishability index* (ξ) by

[8] $\xi = 2\pi|\nu_{\backslash a} - \nu_{\backslash b}|/(k_{\backslash a} + k_{\backslash b}) = 2\pi\,|\nu_{\backslash a} - \nu_{\backslash b}|\,\tau_{exch}$

In the case that $\varepsilon_{\backslash a} \neq \varepsilon_{\backslash b}$, the two frequencies will be different. As the caged molecule M jumps from environment \a to environment \b, the associated state wave switches from frequency $\nu_{\backslash a}$ to frequency $\nu_{\backslash b}$, and so on. This is displayed schematically in Fig. 2 for two cases. In the first, there is no phase change on switching. In the second, there is a random phase change on switching.

The fast Fourier transform (FFT) power spectra for long wave trains in these two situations are shown in Fig. 3. In each case, the individual lifetimes between switching, $(\tau_{\backslash a})_1$, $(\tau_{\backslash b})_2$, $(\tau_{\backslash a})_3$, $(\tau_{\backslash b})_4$, …., indicated in Fig. 2, are chosen stochastically to correspond to exponential lifetime distributions with mean values $\tau_{\backslash a}$ and $\tau_{\backslash b}$. In the case of zero phase change in Fig. 3, the reader will notice the similarity be-

© 1999 NRC Canada

Fig. 3. Fast Fourier transform spectra of wave trains with stochastic frequency switching between two states corresponding to two potential energy cages \a and \b. The lifetimes $\tau_{\backslash a}$ and $\tau_{\backslash b}$ are equal and have exponential distributions. In the left-hand panel, the wave train is continuous at switching (see Fig. 2, case 1). In the right-hand panel, the phase change is random (see Fig. 2, case 2).

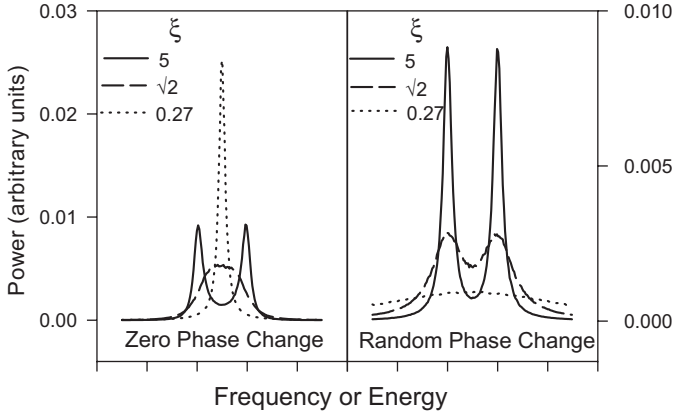

tween the state power spectrum and NMR line shapes for exchange between two chemical shifts (11, 12). The distinguishability index ξ in eq. [8] depends only on the frequency difference $|\nu_{\backslash a} - \nu_{\backslash b}|$. That is, for a given τ_{exch}, the spectrum is the same whether the waves have frequencies $\nu_{\backslash a}$ and $\nu_{\backslash b}$, or frequencies $(X + \nu_{\backslash a})$ and $(X + \nu_{\backslash b})$, where X is any constant. The relevant variable is the *beat frequency* $|\nu_{\backslash a} - \nu_{\backslash b}|$.

However, the magnitudes of X and of $|\nu_{\backslash a} - \nu_{\backslash b}|$ are quite different in NMR and in state spectra. In NMR, X is of order 10^8 s^{-1} and $|\nu_{\backslash a} - \nu_{\backslash b}|$ is of order 10^2 s^{-1}. On the other hand, when we deal with electronic state spectra, X is of order 10^{15} s^{-1}. The value of $|\nu_{\backslash a} - \nu_{\backslash b}|$ in this situation can be estimated as follows. We begin with an estimate of τ_{exch} via eqs. [4] and [5]. We shall use $D = 2.3 \times 10^{-5}$ cm^2 s^{-1} and $r_{cage} = 6.4 \times 10^{-8}$ cm to obtain $\tau_{\backslash b} = 3 \times 10^{-11}$ s and $\tau_{exch} = 1.5 \times 10^{-11}$ s. Assuming [M\a] = [M\b] and setting $\xi = 5$ (which we designate as the margin of distinguishability, see below), eq. [8] then yields $|\nu_{\backslash a} - \nu_{\backslash b}| = 5 \times 10^{10}$ s^{-1}.

We shall now compare the two sets of parameters. The transit time between states, τ_{jump}, is similar in both examples, ca. 10^{-13} s, since its equivalent frequency, $1/\tau_{jump}$, is of order kT/h as predicted by transition state theory. Thus, in NMR, $1/\tau_{jump}$ is much greater than both X and $|\nu_{\backslash a} - \nu_{\backslash b}|$, and it is easy to agree that the phase of the NMR wave will not change during the jump. On the other hand, for Schroedinger state waves near the margin of distinguishability, $X >> 1/\tau_{jump} >> |\nu_{\backslash a} - \nu_{\backslash b}|$. If X remains irrelevant, then the phase of the wave motion will not change during τ_{jump}. If not, there could be many oscillations of the wave during τ_{jump} so that the phase change on jumping is random. Figure 3 therefore shows simulations for continuous as well as randomly discontinuous phase behavior on state switching.

When $\xi = 5$, the state waves are well resolved *in both models*. When there is zero phase change on switching, the states coalesce at $\xi = \sqrt{2}$ and the coalesced line continues to narrow for lower values of ξ. When there is random phase change on switching, there is no coalescence. Instead, the lines simply broaden until they overlap so much that only one peak can be seen. When $\xi > 5$, the state spectrum in both models consists of two distinct "lines," showing that the two states, M\a and M\b, are distinct. We shall therefore propose for distinguishability that ξ should be >5. Again using 1.5×10^{-11} s for τ_{exch}, then for distinguishability $|\varepsilon_{\backslash a} - \varepsilon_{\backslash b}|$ need only be ≥20 J/mol. This requirement is so lenient that it is usually met when the number of molecules in the cage wall changes, or when a molecule of a different species replaces a molecule in the cage wall (13).

One might therefore imagine that environmental isomerism is common. But we have not yet taken the effect of the Brownian motion of the cage molecules into account.

Effect of Brownian motion

The widespread distinguishability of liquid cage environments inferred from eq. [8] is mostly cancelled by the effect of Brownian motion. We have published a semiquantitative theory of this phenomenon (3), but the development is intricate, and it will be described here only in outline. We shall also briefly amplify some aspects of the model.

Assume that the substrate molecule M is at rest in its cage, while the neighbors of M, which we shall call N, exist in cages of their own and librate with energies governed by Boltzmann distributions. When a neighbor moves towards or away from M, the pairwise interaction energy between M and N changes. Since there are several neighbors, and the pairwise interaction energies vary, the cage potential of M fluctuates. The standard deviation of these fluctuations can be calculated if the motions of the neighbors are independent, and if the neighbor number and the pairwise interaction function are known (13). We calculated that for a hypothetical liquid consisting of spherical molecules M with an average of 10 neighbors, and in which the pairwise interactions are given by Lennard–Jones potentials with parameters appropriate for benzene, the standard deviation (σ_{cage}) is 2.6 kJ/mol. Of course, this value is not that of real benzene, but it should be close to it, and it indicates the magnitude of the phenomenon in normal non-hydrogen bonding liquids. The 2.6 kJ noise is substantial enough to obscure environmental isomerism unless $|\varepsilon_{\backslash a} - \varepsilon_{\backslash b}|$ exceeds 7 or 8 kJ/mol (see below), which is orders of magnitude greater than the 20 J/mol estimated for frequency switching without Brownian noise. For a water-like liquid with four or five neighbors and steep cage walls, a similar calculation yields Brownian noise with a standard deviation of 1.1 kJ/mol (3, 13).

Noise in the cage potential induces a corresponding noise in the Schroedinger frequencies $\nu_{\backslash a}$ and $\nu_{\backslash b}$. Exchange now is no longer purely between $\nu_{\backslash a}$ and $\nu_{\backslash b}$ but between a noisy multitude of frequencies centered, respectively, on $\nu_{\backslash a}$ and $\nu_{\backslash b}$.

The time scale of the frequency fluctuations is governed by τ_{corr}, the Brownian correlation time. This parameter represents the time for which a system retains memory of some initial configuration as it relaxes towards equilibrium. The theory of Brownian motion (14) — with reasonable assumptions — lets us estimate its magnitude. For an ensemble of molecular oscillators librating in a harmonic potential well, the theory yields eq. [9] (13).

© 1999 NRC Canada

Fig. 4. Fast Fourier transform spectra of wave trains involving switching between two states. In contrast to Fig. 3, the potential energy cages now have Brownian induced noise with standard deviation σ_{cage} = 2.6 kJ/mol and correlation time (τ_{corr}) = 8×10^{-13} s, $\tau_{\backslash a} = \tau_{\backslash b} = 3 \times 10^{-11}$ s. These parameters correspond to a benzene-like liquid.

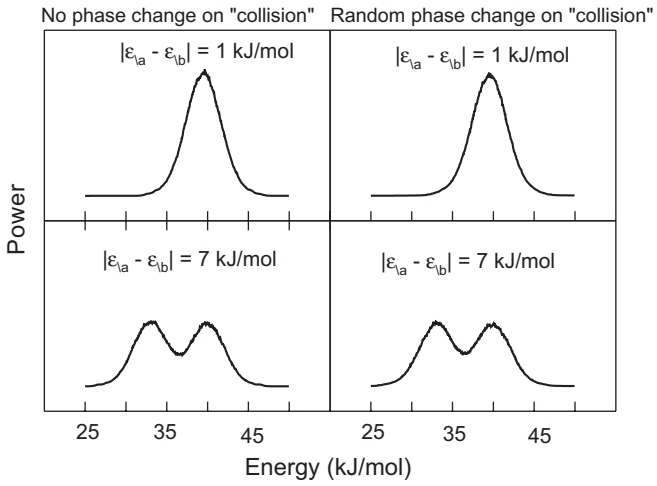

[9] $\tau_{corr} = q_{RT}^2 / 4D$

D is the macroscopic self-diffusion coefficient of the liquid, and q_{RT} is the displacement of the molecule from the cage center when the librational energy is RT. The actual cage potential is anharmonic, but for semiquantitative predictions, eq. [9] is good enough. In the following examples, D is 2.3×10^{-5} cm^2/s for benzene and 2.25×10^{-5} cm^2/s for water; q_{RT} is 8.8×10^{-9} cm for the benzene-like liquid and 2.5×10^{-9} cm for the water-like liquid. The values for τ_{corr} then are 8×10^{-13} s for the benzene-like liquid and 0.7×10^{-13} s for the water-like liquid. Notice that these correlation times are comparable to the collision times in an ideal gas at a pressure of about 1000 atm (1 atm = 101.3 kPa).

In the model (3), the potential energy is assumed to vary linearly with time until the next Brownian collision directs it towards a new value chosen at random from a Gaussian probability distribution, with standard deviation (σ_{cage}). The mean time between collisions is τ_{corr}, and the distribution of collision times about the mean is stochastic with first-order kinetics.

Figure 4 shows Fourier-transform power spectra of noisy Schroedinger wave trains for a benzene-like liquid. In the case of benzene, quantum-mechanical calculations indicate two pairwise potential minima with one 0.95 kJ/mol higher than the other (15). The simulations in Fig. 4 assume that there are two environmental isomers with [M\a] = [M\b] and with $|\varepsilon_{\backslash a} - \varepsilon_{\backslash b}|$ = 1 and 7 kJ/mol, respectively. The value of $\tau_{\backslash b}$ was estimated from eq. [5] as 3×10^{-11} s, using a cage radius of 6.4 Å, and since [M\a] = [M\b], $\tau_{\backslash a}$ was set equal to $\tau_{\backslash b}$. We considered two cases: (*i*) no phase change after a Brownian collision, (*ii*) random phase change after a collision. It is clear from Fig. 4 that $|\varepsilon_{\backslash a} - \varepsilon_{\backslash b}|$ would have to be about 7 kJ/mol or more in order for environmental isomers to be observed. Also, the difference between models (*i*) and (*ii*) is negligible. This is not surprising. In terms of the well-known gas phase spectral broadening induced by collisions

Fig. 5. Fast Fourier transform spectra of wave trains involving switching between two states. In this case, the parameters correspond to a water-like liquid with σ_{cage} = 1.05 kJ/mol, $\tau_{corr} = 0.72 \times 10^{-13}$ s, $\tau_{\backslash b} = 0.581 \times 10^{-11}$ s, $\tau_{\backslash a} = 1.36 \times 10^{-11}$ s.

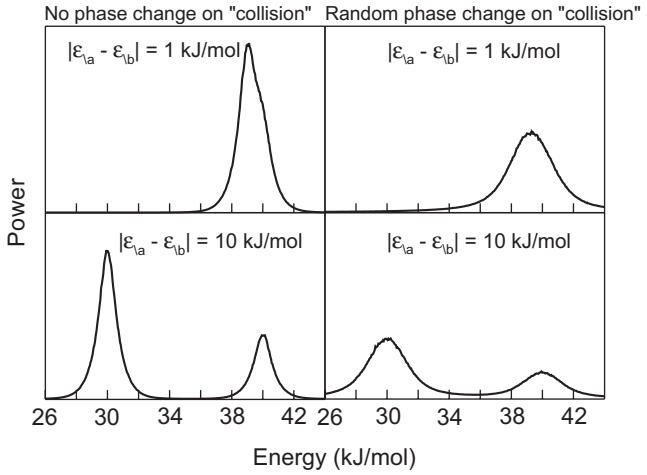

(16), the spectral line is broadened to an extent $\Delta\varepsilon = h\Delta\omega/2\pi = h/(\pi\tau_{coll})$ (17). In our case, the time between dephasing events is τ_{corr}, so dephasing should introduce a broadening of only 0.16 kJ/mol (= 13 cm^{-1}).

Figure 5 shows the results of a similar simulation for a liquid with water-like properties. The value used for [M\a]/[M\b] is 0.7/0.3 (see below). Equation [5] yields a value of 0.6×10^{-11} s for $\tau_{\backslash b}$, based on $D = 2.25 \times 10^{-5}$ cm^2/s and $r_{cage} = 2.8 \times 10^{-8}$ cm. The mean correlation time (τ_{corr}), according to eq. [9], is 0.7×10^{-13} s.

Figure 5 shows the results of two sets of simulations, one with zero phase change after a Brownian collision and one with a random phase change. Each set has two values of $|\varepsilon_{\backslash a} - \varepsilon_{\backslash b}|$. The value of 1 kJ/mol is simply representative and for comparison with Fig. 4; the 10 kJ/mol value corresponds to the difference in real water (see below). In the 1 kJ/mol simulation, the two states of water overlap and are not distinguishable, although the state bands do show some asymmetry. In the 10 kJ/mol simulations, the two bands are well resolved, so that distinguishability of the corresponding states is indicated. The state widths are greater in the random phase-change model. At 10 kJ/mol, the state half-width (FWHM) is 1.3 kJ/mol for the zero phase change model, and 3.0 kJ/mol for the random phase-change model. The extra broadening, associated with the short correlation time, will be discussed in the next section.

Experimental evidence for environmental isomerism in water

We believe that water molecules in liquid water form two environmental isomers. Water is often regarded as an anomalous liquid because its properties deviate from established norms. One way to rationalize the deviations is by a two-state model in which the water molecules exist in either of two unspecified "states" that are in 1:1 equilibrium. Although the fit of this model is not always quantitative, the experimental evidence in its support is strong. In particular, the two-state model accounts for the high heat capacity of

© 1999 NRC Canada

water (18). It fits quasi-elastic neutron scattering[2] ultrasonic relaxation (19), and entropies of solution of nonpolar solutes in water (20). In these fits, and in infrared and Raman spectra described below, the difference in enthalpy between the two states is consistently 10 ± 1 kJ/mol. The most accurate two-state parameters are based on the heat capacity, which gives $\Delta H_{\a\rightarrow\b}$ = 10.5 kJ/mol, and $\Delta S_{\a\rightarrow\b}$ = 28.2 J/mol K. At 25°C, the equilibrium ratio of H_2O\a to H_2O\b is then 0.7/0.3 = 2.33.

Perhaps the best experimental evidence for a two-state model comes from the existence of accurate isosbestic points in infrared and Raman OH- and OD-stretching spectra over a range of temperatures (21–23), which shows that the bulk of liquid water consists of two, and only two, significant species. If there were more than two species contributing to the spectra, it would be extremely unlikely that there would be several sharp isosbestic points.

Water is a single species in the gas phase, so if there are two water species in the liquid, they must arise in some way from water–water interactions. Benson and Siebert (24) assumed two hydrogen-bonded complexes, which they described as tetramers and octamers. The equilibrium then proceeds with 2:1 stoichiometry: $2(H_2O)_4 = (H_2O)_8$. However, the weight of the evidence is that the two-state equilibrium proceeds with 1:1 (rather than 2:1) stoichiometry. For example, when the 2:1 model is fitted to infrared OH-stretching data, the extinction coefficient for one of the states, regardless of its nature, becomes negative (13).

If the two states are environmental isomers, most difficulties disappear. The equilibrium between H_2O in two distinct solvent cages is comparable to the transfer of H_2O between two media, such as H_2O (dilute, in benzene) = H_2O (dilute in methanol), which is 1:1. Similarly, the process H_2O\a = H_2O\b is tantamount to the distribution of H_2O between two microscopic environments, and the equilibrium constant [H_2O\a]/[H_2O\b] is analogous to a 1:1 distribution ratio.

The polarity of the two cage environments can be determined by applying Kirkwood's theory of the dielectric constant (25, 26) and assuming that liquid water consists of two isomers (27). The Kirkwood correlation factor g is defined so that $(g - 1)\mu$ gives the component of the average dipole moment of the solvent cage (or cavity) along an axis parallel to the dipole vector μ of the central caged molecule. The contribution of the solvent cage to the polarization then is proportional to $(g - 1)\mu^2$. For a normal liquid, $(g - 1)$ is close to zero. For water, the two-state model fits the dielectric constant with the following values: (H_2O\a), $(g - 1)$ = 2.01 ± 0.12; (H_2O\b), $(g - 1)$ = 0.91 ± 0.18. The 2.01 value corresponds to a highly polar cage consisting of four tetrahedrally arranged water molecules that form flexible hydrogen bonds to the central molecule. This model is essentially that argued by Bernal and Fowler (28), and elaborated by Oster and Kirkwood (26). The 0.91 value corresponds to a solvent cage that is roughly half as polar as the one with four neighbors.

The mean nearest neighbor number in liquid water has been deduced from the area of the nearest-neighbor peak in the O···O radial distribution function. X-ray diffraction data interpreted in this way lead to an average of 4.4 neighbors at room temperature (29). If the predominant, more polar, state (H_2O\a = 0.7) has 4 neighbors, and the minor less polar state (H_2O\b = 0.3) has 5 neighbors, then the average number of neighbors is 0.3 × 5 + 0.7 × 4 = 4.3, in fair agreement with the X-ray data.

There is no consensus about the arrangement of the water dipoles in the less polar state. Certainly, there are differences of description, which may be partly semantic (27, 30). One of us believes that two of the neighbors occupy hydrogen-bonded tetrahedral sites (like those in the four-cage), while three remaining neighbors form less directional electrostatic bonds (27). Because these bonds are weaker and permit greater freedom of motion than regular hydrogen bonds, the five-cage should have the higher enthalpy and the higher entropy, as is observed. With only relatively minor disruption, a fifth molecule can slip into the open ice-like structure of a four-cage (30). This picture is consistent with the anomalous ratio of the density of ice to water, which is 0.92, the ratio expected from the model being ≈ 4/(4 × 0.7 + 5 × 0.3) = 0.93.

It is interesting to note in the infrared and Raman studies on H_2O and HDO, that in all cases the absorption due to the state favored at higher temperatures occurs at higher frequencies. For example, Walrafen et al. (22) assign peak positions of 3524 and 3370 cm^{-1} to the OH stretches in the two forms of water, which we would categorize as H_2O\5w (= H_2O\b) and H_2O\4w (= H_2O\a). The difference in the positions of the maxima is 154 cm^{-1}. It has long been recognized that A-H stretching frequencies shift to higher values as the (A—H···O) hydrogen bond becomes weaker. For example, Pimentel and McClennan (31) reported that a weakening of 11 kJ/mol in the H bond of phenol and alcohols to oxygen electron donors resulted in a 100 cm^{-1} shift in frequency. This is compatible with our model in which H_2O\b lies about 10.5 kJ/mol above H_2O\a.

Given that the interactions among the water molecules involve hydrogen bonds, why do we envision cages rather than molecular complexes? Adjacent molecules in liquids can be logically classified into three categories: encounter pairs, linkage pairs, and molecular complexes. In encounter pairs, the neighbors interact through regular van der Waals interactions, which depend only on separation distance and are basically nondirectional. Each molecule in the pair is a member of the cage wall of the other, but their motions are essentially independent. In linkage pairs, the neighbors interact more strongly and probably in preferred directions (possibly through forces that are electrostatic in origin), but their motions are still independent, and each is still a member of the cage wall of the other. Finally, in molecular complexes the interaction becomes so strong that the interacting molecules lose their motional independence and become a single kinetic unit, and we can no longer regard one as being a member of the cage wall of the other.

It is not clear whether hydrogen bonds in liquid water produce linkage pairs or molecular complexes. Some authors use the term hydrogen *bonds*; others use hydrogen bond *linkages*. The average strength of a hydrogen bond in liquid

[2] G.J. Safford. Cited in ref. 22.

© 1999 NRC Canada

water is about 20 kJ/mol. Is that strong enough to make molecular complexes more favorable, i.e., to have the lower Gibbs free energy, than linkage pairs?

The problem can be formulated in terms of statistical mechanics, but the required properties are known only crudely. An order-of-magnitude calculation (13) reaches the conclusion that molecular complexes become more stable than either encounter or linkage pairs when the magnitude of the interaction energy exceeds 20–30 kJ/mol. The strength of hydrogen bonds in liquid water is near that figure.

The linkage-pair cage model described in this paper also correctly predicts spectral line widths. If there is a random phase change in the Schroedinger state wave at each Brownian collision, the mean lifetime of a quantum state in a liquid is τ_{corr}. For a vibrational transition in a liquid, the energy uncertainty in the initial state indicates the probable width of the spectral line. If the FWHM ($\Delta\nu$) of the line is given in cm^{-1} then (17),

$$[10] \quad \Delta\nu = 1/(\pi c \tau_{corr})$$

This equation is exact if the line shape is Lorentzian and incurs an 18% error if the line shape is Gaussian.

For the benzene-like liquid, $\tau_{corr} = 8 \times 10^{-13}$ s. Correspondingly, as indicated above, $\Delta\nu = 13$ cm^{-1}, a typical line width for infrared spectra in nonpolar liquids. For the water-like liquid, $\tau_{corr} = 0.7 \times 10^{-13}$ s, and $\Delta\nu$ correspondingly is 150 cm^{-1}.

The predicted $\Delta\nu$ of 150 cm^{-1} is in agreement with experiment. Walrafen et al. (22) has deconvoluted the OH-stretching band in the Raman spectrum of water and obtains 160 cm^{-1} for $\Delta\nu$ for the band due to the more populous isomer \a, and 110 cm^{-1} for the less populous isomer \b. The latter is less accurate. In the region above 7060 cm^{-1}, in the first-overtone infrared stretching band of HOD in D_2O, absorption is due almost entirely to isomer \b (13). Based on that absorption, $\Delta\nu = 186$ cm^{-1} at 17°C and 194 cm^{-1} at 61°C.

The predictions based on eq. [10] depend critically on the assumption that the molecules are moving independently, as in the model of linkage pairs. This is true not only for the Brownian motion itself, but also for the calculation of τ_{corr}, which is sensitive to this issue. We regard the agreement of eq. [10] with observed OH-band widths in water as strong supporting evidence for the model of linkage pairs.

Concluding remarks

In the above, we have shown how environmental isomerism can account for the properties of water in a straightforward fashion. Examination of the structure of water gives us clues about the conditions for environmental isomerism in other liquids. In water, the optimum hydrogen-bonded arrangement produces cages whose walls have a low molecular density. In normal liquids, the optimum neighbor number is around 10, while the optimum hydrogen-bonded water cage has a neighbor number of only 4. This facilitates the formation of a second isomer, to fill some of the available space. The introduction of an additional water molecule distorts the optimum geometry and thereby weakens the hydrogen bonds. This causes the energy to rise significantly, but it introduces no serious steric crowding. The reduced pairwise interaction in turn reduces the frequencies of the librations, and thus raises the entropy. We believe that environmental isomers will occur also in other liquids under corresponding microscopic conditions. For example, in liquid methanol, the O-H stretching spectrum measured over a wide range of temperatures shows an accurate isosbestic point at 3410 cm^{-1} (32), reminiscent of that in liquid water.

The presence of environmental isomers can have important consequences in mixed solvents as well. For example, the plots of solute enthalpies and entropies versus solvent composition in *tert*-butanol–water mixtures show puzzling maxima and minima (33). At this time, there is no obvious explanation for these anomalies. However, the facts can be interpreted, at least in principle, on the basis that there are not only the water isomers already considered, but also environmental isomers in which particular water molecules in the cage walls are being replaced by *tert*-butanol molecules. This process will generate additional environmental isomers whose population increases with the fraction of *tert*-butanol. According to Grunwald (13), the formation of two such species in addition to the two water species is sufficient to produce maxima and minima like those that are observed.

References

1. E. Grunwald and C. Steel. Pure and Appl. Chem. **65**, 2543 (1993).
2. E. Grunwald and C. Steel. J. Phys. Chem. **97**, 13 326 (1993).
3. E. Grunwald and C. Steel. J. Phys. Org. Chem. **7**, 734 (1994).
4. E.G. McRae. J. Phys. Chem. **61**, 562 (1957).
5. H.C. Longuet-Higgins and J.A. Pople. J. Chem. Phys. **27**, 192 (1957).
6. J.P. Simons. Photochemistry and spectroscopy. Wiley–Interscience, New York. 1971. pp. 146–150.
7. M.J. Kamlet, J.L.M. Abboud, and R.W. Taft. Prog. Phys. Org. Chem. **13**, 485 (1981).
8. E. Rabinowitch and W.C. Wood. Trans. Faraday Soc. **32**, 1381 (1936).
9. L.M. Tolbert, X.-J. Sun, and E.C. Ashby. J. Am. Chem. Soc. **117**, 2681 (1995).
10. T. Koenig and H. Fischer. *In* Free radicals. Vol. 1. Wiley–Interscience, New York. 1973. Chap. 4.
11. H.M. McConnell. J. Chem. Phys. **28**, 430 (1958).
12. F.F. Knudsen and K.R. Naqvi. J. Phys. Chem. **99**, 6199 (1995).
13. E. Grunwald. Thermodynamics of molecular species. Wiley–Interscience, New York. 1997. Chaps. 8–10.
14. R.K. Pathria. Statistical mechanics. Sect. 13.5. Pergamon Press, Toronto. 1972. p. 462.
15. W.L. Jorgensen and D.L. Severance. J. Am. Chem. Soc. **112**, 4768 (1990).
16. A.E. Siegman. Introduction to lasers and masers. McGraw–Hill, New York. 1971. Chap. 3.
17. A. Carrington and A.D. McLachlan. Introduction to magnetic resonance. Harper and Row, New York. 1967. pp. 9–10.
18. S.W. Benson. J. Am. Chem. Soc. **100**, 5640 (1978).
19. C.M. Davis and T.A. Litovitz. J. Chem. Phys. **42**, 2563 (1965).
20. E. Grunwald. J. Am. Chem. Soc. **108**, 5762 (1986).
21. J.D. Worley and I.M. Klotz. J. Chem. Phys. **45**, 2868 (1966).
22. G.E. Walrafen, M.S. Hokmabadi, and W.-H. Wang. J. Chem. Phys. **85**, 6964 (1986); **85**, 6970 (1986).
23. G.E. Walrafen. J. Chem. Phys. **48**, 244 (1968).

© 1999 NRC Canada

24. S.W. Benson and E.D. Siebert. J. Am. Chem. Soc. **114**, 4269 (1992).
25. J.G. Kirkwood. Trans. Faraday Soc. **42A**, 7 (1946).
26. G. Oster and J.G. Kirkwood. J. Chem. Phys. **11**, 175 (1943).
27. E. Grunwald. J. Am. Chem. Soc. **108**, 5719 (1986).
28. S.D. Bernal and R.H. Fowler. J. Chem. Phys. **1**, 515 (1933).
29. A.H. Narten and H.A. Levy. J. Chem. Phys. **55**, 2263 (1971).
30. F. Sciortino, A. Geiger, and H.E. Stanley. J. Chem. Phys. **96**, 3857 (1992).
31. G.C. Pimentel and A.L. Mcclellan. Annu. Rev. Phys. Chem. **22**, 347 (1971).
32. W.A.P. Luck and M. Fritzsche. J. Mol. Liq. **52**, 215 (1992).
33. J.B.F.N. Engberts. *In* Water, a comprehensive treatise. Vol 6. *Edited by* F. Franks. Plenum Press, New York. 1979. Chap. 4.

© 1999 NRC Canada

A new silicon-mediated nitrogen to oxygen rearrangement

Stefano Talami and Charles J.M. Stirling

Abstract: Migration of silicon from nitrogen to oxygen has been quantified with respect to the distance between migration termini, substituents at silicon, and substitution on the chain linking oxygen to nitrogen.

Key words: silicon migration, nitrogen to oxygen, penta coordinate intermediate.

Résumé : On a quantité la migration du silicium de l'azote à l'oxygène par rapport à la distance entre les points de migration, les substituants sur le silicium et des substituants sur la chaîne reliant l'oxygène et l'azote.

Mots clés : migration du silicium, azote à oxygène, intermédiaire pentacoordiné.

[Traduit par la Rédaction]

Rearrangements involving migration of silicon from oxygen to oxygen are familiar (1, 2), and migration between nitrogen and oxygen in *N*-silyl carboxamides has been described (3). Migration between nitrogen and oxygen has not been otherwise studied except en passant in the example mentioned below.

In an earlier study (4), we had found that 1-aminopropane reacts ca. 200 times faster with *tert*-butyldimethylsilyl chloride to give the aminosilane **la** than does ethanol to give the silyl ether **2a**. When 2-aminoethanol was used, however, the rate constant was close to that for the reaction with 1-aminopropane but *the exclusive product was the aminosilyl ether* **2b.** These results clearly suggested that the initial product of the last reaction was **lb**, which then rapidly rearranged to **2b**.

In the present work, we have shown that the rearrangement is intra- and not intermolecular. The half life of the silylamine **lc** is about 2 weeks in methanol at 60°C (4) and TBDMS–amines are stable in ethanol–hexane mixtures (5). We have now studied a series of ω-hydroxyaminosilanes **1** obtained by the general route of Scheme 1,[2] a modification of that used by Overman and his collaborators (6) in which it was found that selective *O*-deprotection of **ld** gave the rearranged product **2c**, and intermediate formation of **le** was suggested. We find that conditions of *O*-deprotection are important to ensure that the silylamino function is not also

Received December 2, 1998.

This paper is dedicated to Jerry Kresge in recognition of his many achievements in chemistry.

S. Talami and C.J.M. Stirling.[1] Department of Chemistry, The University, Sheffield S3 7HF, U.K.

[1]Author to whom correspondence may be addressed. Telephone: 0114 222 9453. Fax: 273 8673.
e-mail: c.stirling@sheffield.ac.uk

[2]**Synthesis of *O*-trimethylsilyl-*N*-trialkylsilylamino alcohols**

Two methods were employed: (*i*) treatment of a stirred chloroform solution of amino alcohol (10 mmol) and triethylamine (80 mmol) in chloroform (100 mL) at 0°C with trimethylchlorosilane (10 mmol) gave the *O*-trimethylsilyl protected amino alcohol from which *N*-trialkylsilyl derivatives were obtained directly by addition of trialkylsilyl choride (11 mmol). Treatment of the chloroform solution with 10% aqueous NaOH or 1 M $NaHCO_3$ and subsequent distillation gave 90–99% crude yields. (*ii*) A two-step procedure was employed to obtain hindered *O*-trimethylsilyl derivatives of *N*-trialkylsilylamino alcohols or where high yields from trialkylsilylating agents were desirable. Treatment of a stirred solution of amino alcohol (12 mmol) and triethylamine (80 mmol) in THF (50 mL) at 0°C, with trimethylchlorosilane (10 mmol) and subsequent removal of the ammonium salt by filtration, gave the product which was purified by distillation under reduced pressure.

O-Trimethylsilyl-*N*-trialkylsilyl derivatives were obtained by addition of trialkylsilyl chloride (or triflate) (12 mmol) to *O*-trimethylsilylamino alcohol (10 mmol) and triethylamine (60 mmol) in THF (200 mL) at 0°C, followed by filtration and distillation.

N-tert-Butyldiphenylsilyl and *N-tert*-dibutylmethylsilyl derivatives of *O*-trimethylsilyl protected amino alcohol could be purified by flash chromatography using hexane containing 5–10% of triethylamine. In the absence of triethylamine, partial hydrolysis occurs during the chromatography. Yields 60–85% of pure product were obtained.

© 1999 NRC Canada

Scheme 1.

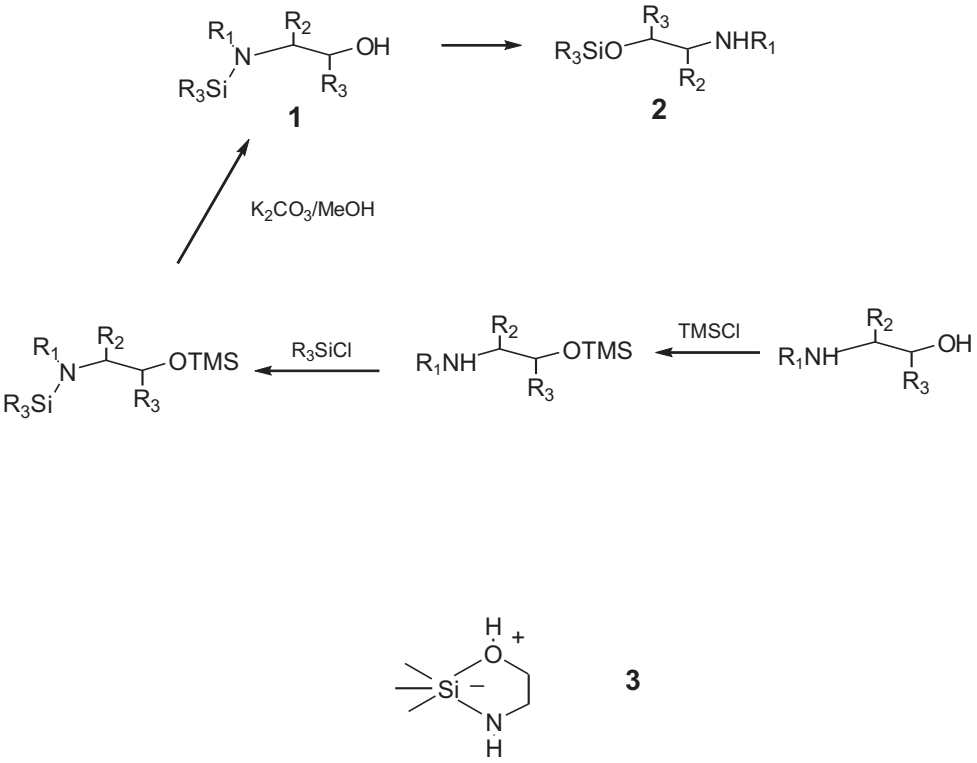

3

cleaved.[3] For each of the substrates we have studied, the pure hydroxyaminosilane in a perdeuterated solvent has been allowed to rearrange, and the progress of the rearrangement has been followed by changes in the ^{1}H and ^{13}C chemical shifts in alkyl groups on silicon and in the interconnecting chain. In addition, changes in the ^{29}Si chemical shifts have also been followed in some cases. All of the end products have been fully characterized; in some cases, deprotection of the hydroxyl group has been accompanied by partial hydrolysis of the aminosilanes, which are exceptionally sensitive to cleavage.

Silylamines, R_1NHR_2

1; **a**, R^1 = *t*-$BuMe_2Si$; R^2 = *n*-Pr
b, R^1 = *t*-$BuMe_2Si$; R^2 = CH_2CH_2OH
c, R^1 = *t*-$BuMe_2Si$; R^2 = $(CH_2)_5$
d, R^1 = *t*-$BuPh_2Si$; R^2 = $CH_2CHMe.OTMS$
e, R^1 = *t*-$BuPh_2Si$; R_2 = $CH_2CHMe.OH$
f, R^1 = *t*-$BuPh_2Si$; R^2 = CH_2CH_2OH
g, R^1 = *i*-Pr_3Si; R^2 = CH_2CH_2OH
h, R^1 = *t*-$BuPh_2Si$; R^2 = CH_2CH_2OH and NH = NMe
i, R^1 = *t*-$BuPh_2Si$; R^2 = $CHMe.CH_2OH$
j, R^1 = *t*-Bu_2MeSi; R^2 = CH_2CH_2OH

Silyl ethers, R^1OR^2

2; **a** R^1 = *t*-$BuMe_2Si$; R^2 = Et
b, R^1 = *t*-$BuMe_2Si$; R^2 = $CH_2CH_2NH_2$
c, R^1 = *t*-$BuPh_2Si$; R^2 = $CHMe.CH_2NH_2$
d, R^1 = *t*-$BuPh_2Si$; R^2 = $CH_2CH_2NH_2$

The intramolecularity of the reaction points to a cyclic transition state or intermediate, vide infra. We examined the effect of chain length (ring size) on the process. Rearrange-

[3] ***O*-Deprotection of *O*-trimethylsilyl-*N*-trialkylsilylamino alcohols**

Trimethylsilylethers can be solvolysed in anhydrous methanol (K_2CO_3 (0.1 equiv.), 0°C, 45 min, 100% yield) conditions in which *tert*-butyldiphenylsilylamines are stable.

In deprotecting *O*-trimethylsilyl-*N*-triisopropylsilyl-2-aminoethanol in these conditions, hydrolysis or methanolysis of triisopropylsilyl group was not detected, but a large amount of rearranged compound was obtained; better results were obtained performing the reaction at 0.1 M in methanol with 0.05 equiv. of K_2CO_3 for 10–12 min. at 0°C.

As the rearrangement is not temperature dependent but can be catalysed in methanol by K_2CO_3, *O*-deprotection of *O*-trimethylsilyl-*N*-*tert*-butyldiphenylsilyl derivatives was more effectively achieved using 0.01 equiv. of K_2CO_3 in methanol at room temperature under ultrasonication.

Acidic work-up is not advisable as the rearrangement is strongly acid catalysed. Dilution with pentane, filtration, and solvent distillation gave 99–100% recoveries.

Rearrangement of *N*-trialkylsilylamino alcohols

The *N*-silylamino alcohol was dissolved in the chosen deuterated solvent. The rearrangement was followed by ^{1}H and ^{13}C NMR. Similar rate constants were obtained using the integrals of C*H*O, C*H*N, and Si-alkyl signals. Trialkylsilylaminobutanes and trialkylsilyloxypropanes were used as reference standards.

Product identification was by comparison with ^{1}H or ^{13}C NMR spectra of pure compounds or by addition of solutions of pure *O*-alkylsilylamino alcohols.

© 1999 NRC Canada

Table 1. Catalysis of silicon migration: **1f** [a] to **2d**.

Catalyst	[Catalyst] (mM)	$pK_a^{H_2O}$	10^6k (s^{-1})	k_{rel}
None	—	~10	1.1	1[b]
$HOCH_2CH_2NH_2$	20	9.50	1.0	0.9
Et_3N	20	10.77	3.5	3.2
DMAP[c]	20	9.7	1.9	1.7
n-$BuNH_2$	20	10.7	4.0	3.6
$PhCO_2H$	0.5	4.19	1500	—[d]

[a]10 mM solutions in C_6D_6 at 28.2°C.
[b]$t_{1/2}$, 175 h.
[c]4-Dimethylaminopyridine.
[d]$t_{1/2}$, 480 s.

ment was observed only with two methylene groups between nitrogen and oxygen in the absence of catalysts; with 3, 4, or 5 methylene groups, i.e., with ring sizes of 6, 7, or 8 in the transition structure, the aminosilanes were inert even at 200°C. Catalysis was examined with a substrate **1f** which shows very feeble catalysis by bases (Table 1) either when these are strongly basic, e.g., Et_3N, or strongly nucleophilic, e.g., DMAP. Deprotonation of oxygen is clearly not a significant factor under these conditions and neither is external nucleophilic attack at silicon. By contrast, there is strong catalysis even by weak acids (Table 1), and enhancement of the nucleofugality of the leaving nitrogen atom is presumably involved (7).

Nucleophilic substitution at silicon is very sensitive to steric effects at silicon and in the nucleophile (4, 8). Such effects are also manifested in this rearrangement (Table 2). When the silyl group is DTBM, **1j**, rearrangement is not observable, and when it is TBDM, **1b**, the rearrangement is too fast to measure accurately. When the silyl group is TIP, **lg**, it occurs at one twentieth of the rate of TBDP, **lf**. This differential is highly sensitive to the solvent; **1g** is accelerated by a factor of 10^4 on transfer from benzene to methanol, whereas the factor for **lf** is only 7 for the same change. The reasons for this differential are not at present clear; the higher dielectric constant of methanol ($\varepsilon = 33$) over benzene ($\varepsilon = 2.3$) is not responsible, as the differential is not maintained in dimethyl sulfoxide ($\varepsilon = 47$) or in nitromethane ($\varepsilon = 36$) (Table 2). We tentatively suggest that change in a transition structure such as **3** for **1g** is less delocalized than for **lf** in which the silicon atom bears phenyl groups and that it is the hydrogen-bond donor capability of the solvent that produces greater stabilization in the transition state.

In relation to the foregoing, the effects of substituents on the chain linking oxygen and nitrogen would be expected to be considerable. When a methyl group is located α- to the hydroxyl group, as in **1e**, the reaction is inhibited (Table 2). This is consistent with the results of intermolecular reactions (4) in which propan-2-ol was found to be 154 times less reactive towards TBDMS–chloride than ethanol. Likewise, with a methyl group on the leaving nitrogen atom **1h**, rearrangement is very slow and not discernible even at 200°C, bearing in mind, however, that, vide infra, temperature coefficients in nucleophilic displacements at silicon are small

Table 2. Rearrangement of ω-hydroxysilylamines.

Silylamine	k^a (s^{-1})	k^b (s^{-1})
1b	[c]	—
1e	$4.5 \pm 0.9 \times 10^{-7}$	$6.8 \pm 1.4 \times 10^{-7}$
1f[d]	$1.1 \pm 0.1 \times 10^{-6}$	$8.2 \pm 0.7 \times 10^{-6}$
1g	$5.7 \pm 0.2 \times 10^{-8}$	$1.1 \pm 0.1 \times 10^{-4}$
1h	$<8.5 \times 10^{-8}$[e]	—
1i	$1.6 \pm 0.4 \times 10^{-5}$	—
1j	$<3.7 \times 10^{-9}$[f]	$<8.5 \times 10^{-8}$[e]

[a]10 mM in C_6D_6 at 28.2°C.
[b]10 mM in CD_3OD at 28.2°C.
[c]Too rapid for accurate determination.
[d]In CD_3NO_2, $k = 7.4 \times 10^{-7}$ in $(CD_3)_2SO$, $k = 1.5 \times 10^{-7}$.
[e]<5% reaction after 7 days.
[f]<5% reaction after 160 days.

(2, 4). Clearly, the *N*-methyl group obstructs access of the distal hydroxyl group to the silicon atom. In the cases where we have been able to measure the kinetics accurately, the temperature coefficient is very small, pointing to a highly negative entropy of activation. This in turn points to what appears to be a very tight transition structure, and presumably, access of the nucleophilic oxygen is easily hindered. By contrast, when a methyl group is situated α- to nitrogen as in **1i**, the reaction is accelerated by a factor of 15. It would be reasonable to ascribe this result to the Thorpe–Ingold effect (9). In this event, the modest inhibition by a methyl group α- to oxygen appears to be a compromise between steric inhibition and Thorpe–Ingold acceleration.

Acknowledgements

We thank the University of Sheffield for the support of this work, Dr. Brian Taylor for help with NMR spectral determinations, and Drs. Kevin Hughes and Francesco Lusardi for preliminary experiments.

References

1. S.S Jones and C.B. Reese. J. Chem. Soc. Perkin Trans. 1, 2762 (1979); K.K. Ogilvie and D.W. Entwistle. Carbohydr. Res. **89**, 203 (1981).
2. S. Patai and Z. Rappoport (*Editors*). The chemistry of organosilicon compounds. Wiley, Chichester. 1989.
3. J.C. Otter, L. Adamson, C.H. Yoder, and A.L. Rheingold. Organometallics, **9**, 1557 (1990).
4. K. Hughes. Ph.D. thesis. University of Sheffield, Sheffield. 1995.
5. T.P. Mawhinney and M.A. Madson. J. Org. Chem. **47**, 3336 (1982).
6. L.E. Overman, M.E Okazaki, and P.Mishra. Tetrahedron Lett. **27**, 4391 (1986).
7. A.R. Bassindale, C. Eaborn, and D.R.M. Walton. J. Organomet. Chem. **25**, 57 (1970).
8. N. Shimizu, N. Takesue, S. Yasuhara, and T. Inazu. Chem. Lett. 1807 (1993).
9. E.L. Eliel and S.H. Wilen. Stereochemistry of carbon compounds. Wiley, New York. 1994. p. 682ff.

© 1999 NRC Canada

The reversible enolization and hydration of pyruvate: possible roles of keto, enol, and hydrated pyruvate in lactate dehydrogenase catalysis

A. Esposito, A. Lukas, J.E. Meany, and Y. Pocker

Abstract: The reversible enolization and hydration of pyruvic acid and pyruvate anion were monitored using spectrophotometric methods at several temperatures. Widely varying values for the equilibrium constant for the enolization of pyruvic acid and pyruvate ion appear in the literature. To accurately determine the position of equilibrium for the enolization reaction, we have developed a method that gives consistent results in which purified samples of sodium pyruvate are first "titrated" with triiodide ion to remove any triiodide-scavenging impurities such as those resulting from aldol condensation reactions. After reequilibration to allow the regeneration of enol pyruvate, the addition of small quantities of triiodide result in an initial burst in the decrease of absorbance at 353 nm, followed by the much slower zero-order decrease due to the formation of new enol pyvuvate molecules. The absorbance change during the burst phase of the reaction is proportional to the enol concentration plus that of any triiodide-scavenging impurity which may be present in the original pyruvate solution. Thus, as the quantity of triiodide used in the pretreatment stage of the experiments is increased, these burst absorbance changes, ΔA, decrease until a constant value of ΔA is reached. Accordingly, this final ΔA value is proportional to enol pyruvate (or enol pyruvic acid) *in the absence of* triiodide-scavenging impurity, allowing the accurate and reproducible determinations of K_{enol}. The equilibrium constants for both pyruvate and pyruvic acid are relatively temperature insensitive and, typically, K_{enol} (pyruvate anion) = 2.6×10^{-5} and K_{enol} (pyruvic acid) = 7.8×10^{-5} at 25.0°C. The zero-order phase of the reaction of triiodide ion may be used to calculate rate constants for enolization. The hydration and dehydration of pyruvic acid were followed directly by following absorbance changes in the peak at 340 nm due to the keto group. The thermodynamic and kinetic results reported in this paper are used to help determine whether the observed "substrate" inhibition of the lactate dehydrogenase catalyzed reduction of pyruvate is actually caused by keto, hydrated, or enol pyruvate.

Key words: pyruvate, enolization, hydration, lactate dehydrogenase.

Résumé : Opérant à plusieurs températures et faisant appel à des méthodes spectrophotométriques, on a examiné l'énolisation réversible et l'hydratation de l'acide pyruvique et de l'anion pyruvate. Des valeurs très variables apparaissent dans la littérature pour la constante d'équilibre pour l'énolisation de l'acide pyruvique et de l'ion pyruvate. Dans le but de déterminer la position de l'équilibre pour la réaction d'énolisaton d'une façon précise, on a développé une méthode qui donne des résultats reproductibles; elle implique l'utilisation d'échantillons purifiés de pyruvate de sodium « prétitrés » avec l'ion triiodure pour enlever toutes les impuretés susceptibles de capter le triiodure, telles que celles résultant de réactions de condensation aldolique. Après une rééquilibration pour permettre une régénération de l'énol du pyruvate, l'addition de faibles quantités de triiodure provoque une diminution initiale rapide de l'absorbance à 353 nm, suivie d'une diminution beaucoup plus lente d'ordre zéro causée par la formation de nouvelles molécules d'énol du pyruvate. Le changement rapide d'absorbance dans la phase initiale de la réaction est proportionnel à la concentration d'énol plus celle de toute impureté susceptible de capter le triiodure qui peut encore être présente dans la solution originale de pyruvate. Donc, si l'on augmente la quantité de triiodure utilisée dans le stage de prétraitement des expériences, ces changements rapides d'absorbance, ΔA, diminuent jusqu'à l'atteinte d'une valeur de ΔA constante. Il en résulte que cette valeur finale de ΔA est proportionnelle à l'énol du pyruvate (ou à l'énol de l'acide pyruvique) *en l'absence* d'impureté susceptible de capter le triiodure et qu'elle permet d'obtenir des valeurs précises et reproductibles pour les déterminations de $K_{énol}$. Les constantes d'équilibre tant pour le pyruvate que pour l'acide pyruvique sont relativement peu sensibles à la température et les valeurs types de $K_{énol}$ (anion pyruvate) = $2{,}6 \times 10^{-5}$ et $K_{énol}$ (acide pyruvique) = $7{,}8 \times 10^{-5}$, à 25°C. On peut utiliser la phase d'ordre zéro de la réaction du

Received October 5, 1998.

This paper is dedicated to A. Jerry Kresge in recognition of his many contributions to physical organic chemistry.

A. Esposito, A. Lukas, and J.E. Meany.[1] Department of Chemistry, Seattle University, Seattle, WA 98122, U.S.A.
Y. Pocker.[1] Department of Chemistry, University of Washington, Seattle, WA 98195, U.S.A.

[1]Authors to whom correspondence may be addressed. J.E.M.: Telephone: (206) 296-5942; Y.P.: Telephone: (206) 543-1672.

 © 1999 NRC Canada

triiodure pour calculer les constantes de vitesse d'énolisation. Les réactions d'hydratation et de déshydratation de l'acide pyruvique sont suivies directement par les changements d'absorbance dans le pic à 340 nm dû au groupe cétonique. Les résultats thermodynamiques rapportés dans ce travail ont été utilisés pour déterminer si l'inhibition de « substrat » observé lors de la réduction du pyruvate catalysée par la déshydrogénase du lactate est de fait cause par le groupe cétonique, son hydrate ou l'énol du pyruvate.

Mots clés : pyruvate; énolisation; hydratation; déshydrogénase du lactate.

[Traduit par la Rédaction]

Introduction

Pyruvate is an important intermediate that is linked to many biochemical processes regulated by enzymes. In the glycolytic pathway, for example, the anaerobic regeneration of nicotinamide adenine dinucleotide (NAD^+) from its reduced form (NADH) is facilitated by the reduction of pyruvate to lactate in the presence of lactate dehydrogenase LDH (EC1.1.1.27). Under physiological conditions, pyruvate exists as an equilibrated mixture of enol, keto, and

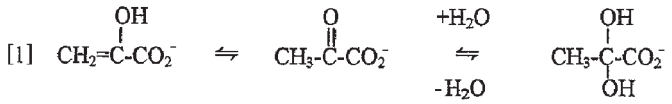

hydrated forms (1*a*–1*f*).

Equilibrium constants have been determined in previous work for the reversible hydrations of pyruvic acid and pyruvate anion using pmr (1*a*) and spectrophotometric methods (1*f*) and the various data obtained are in relatively good agreement when due consideration is taken of the fact that the stoichiometry of the hydration of pyruvic acid involves three water molecules (1*a*). Because of the electron-withdrawing effect of the carboxyl group, pyruvic acid is considerably more hydrated in aqueous solutions than is the pyruvate ion. The hydrations of pyruvic and pyruvate ion are both known to be exothermic (1*a*, 1*d*, 1*f*).

The results of kinetic studies demonstrate that the reversible hydration of pyruvate anion is a general-acid, general-base-catalyzed process, which includes a small catalytic term for general-base catalysis by the pyruvate anion itself (2*a*, 2*b*, 2*c*). The kinetic studies also suggest that the spontaneous hydration of pyruvate anion involves the contribution of a kinetic term representing an intramolecular general-base-catalyzed path involving the neighboring carboxylate group (2*b*).

Although there is little ambiguity associated with the determination of kinetic parameters for the enolization of pyruvate and pyruvic acid (2*b*, 3, 4*a*, 4*b*), reported equilibrium constants for these reversible processes vary (1*g*, 1*h*, 2*b*, 4*b*). In the Meyer method (5) the burst of triiodide uptake, presumably by enol pyruvate (or enol pyruvic acid), is spectrophotometrically measured at 353 nm. This method generally gives unreliable values of K_{enol} because solutions of pyruvic acid or pyruvate contain a triiodide-scavenging impurity. For this reason, the classic protocol for the Meyer method (5) often gives rise to inaccurate determinations of the enol content of carbonyl compounds in solution (6*a*, 6*b*). The existence of an impurity formed in samples of pyruvic acid was reported many years ago and identified as the aldol condensation product α-keto-γ-valerolactone-γ-carboxylic acid (6*c*). One may also envisage the bimolecular aldol condensation of pyruvic acid, followed by dehydration, to form an α,β-conjugated diacid. Accordingly, apparent K_{enol} values determined by the Meyer method (5) are typically larger than the actual value. In the present work, we have circumvented this problem by utilizing purified pyruvate solutions that have been pretreated with triiodide ion to "titrate" out the I_3^- scavenging impurity. After the reequilibration between enol and keto forms we utilize a modification of the Meyer (5) method to determine K_{enol}. On the other hand, because the burst of triiodide uptake is relatively rapid, the finite time required for the complete mixing of the reaction components renders it difficult to accurately extrapolate spectrophotometric absorbances back to the kinetic zero. And since the burst absorbance changes, ΔA, typically are relatively small, the uncertainty of the absorbance at the kinetic zero can result in large deviations of the apparent K_{enol} from the actual values. In this report, we describe our solution to this problem as well.

Investigators have also attempted to approximate K_{enol} by independently determining the rates of enolization of keto pyruvate and ketonization of enol pyruvate using the relationship $K_{enol} = k_{enol} / k_{keto}$ (1*g*, 1*h*, 2*b*). Again, using this method, uncertainties may arise because of differences in the experimental conditions under which the two reactions are independently carried out (7*a*–7*c*, 8*a*, 8*b*).

It has been demonstrated that keto pyruvate serves as the preferential substrate of LDH (9, 10). This enzyme is one of many oxidoreductase enzymes that is subject to "substrate" inhibition (11). Although substrate inhibition for LDH is more pronounced for the heart than for the muscle isoenzymes (12), the physiological importance of this mode of inhibition in warm-blooded animals is controversial (13*a*–13*d*). Somero (14), however, has shown that the substrate inhibition of the enzyme in certain fishes becomes increasingly more pronounced at lower temperatures and has suggested that this phenomenon serves an important role in biological adaptation.

An earlier report by Coulson and Rabin (15*a*) suggested that enol pyruvate is a potent inhibitor of LDH and is responsible for the observed substrate inhibition of the enzyme. That original report was quoted widely in biochemistry textbooks (15*b*) and other references (15*c*) for a number of years. Although the original suggestion (15*a*) was based on reasonable experimental results, an alternative interpretation of these results is indicated by more recent, detailed studies of the kinetics and thermodynamics of the various nonenzymatic reactions of pyruvic acid and pyruvate anion in aqueous solution. Indeed, studies have since been conducted to determine the possible role of hydrated pyruvate

© 1999 NRC Canada

as well as enol pyruvate in the observed substrate inhibition of the enzyme (16, 17).

It was first proposed by Fromm (18) that the substrate inhibition of the enzyme is the result of the formation of an abortive ternary complex with the stoichiometric composition of LDH, pyruvate, and NAD^+. Two modes of LDH inhibition by pyruvate have been proposed (17, 19) involving, respectively, (*i*) the rapidly reversible formation of a ternary complex ($LDH{\cdot}NAD^+{\cdot}$pyruvate), and (*ii*) the slowly reversible formation of a binary complex between LDH and a covalently bound adduct of NAD^+ and pyruvate resulting in the formation of $LDH{\cdot}NAD^+$–pyruvate. Both hydrated pyruvate and enol pyruvate have been reported to form ternary abortive complexes with LDH and NAD^+ (16, 17).

The kinetic and thermodynamic parameters associated with the reversible hydration and enolization of pyruvate may be used to assess the likelihood of each of the different forms of pyruvate serving as potential participants either as enzyme substrates or as enzyme inhibitors. Such data provide a basis to determine whether there exists a high enough concentration of a given form of pyruvate to explain a hypothetical kinetic scheme or whether a given form of pyruvate may be formed rapidly enough to be consistent with known kinetic parameters. Over the years, two of the present authors have carried out detailed investigations of the reversible hydration and enolization of pyruvic acid and pyruvate anion (1*a*, 2*a*–2*c*, 3*a*, 3*b*, 9, 16). In the present paper, we provide selected thermodynamic and kinetic data for these reactions and show how these data can help address two questions: (*i*) which chemical form of pyruvate (enol, keto, or hydrate) is involved in the substrate inhibition of LDH? (*ii*) is the substrate inhibition recognized by Somero at lower temperatures a property of the enzyme alone, or is it also dependent on variations in the position of equilibria between enol, keto, and hydrated pyruvate as a function of temperature?

Experimental section

Materials used to prepare buffer solutions, sodium pyruvate, pyruvic acid, and all other reagents were in their commercially available reagent-grade forms. Pyruvic acid was distilled through a Vigreux column in an atmosphere of nitrogen gas, and sodium pyruvate was recrystallized using methanol–water mixtures. All solutions were prepared from distilled, deionized water. Spectrophotometric measurements were made using either a Shimadzu UV-2101PC or a Varian Cary 210 spectrophotometer. Both instruments gave rise to essentially identical kinetic and thermodynamic parameters. The temperature of the cell compartments was regulated and maintained constant by a VWR 1160 thermostated bath and circulator.

The enolization of pyruvate anion was monitored by following its iodination at 353 nm as described in earlier work (2*b*, 3, 4). Typically, 0.10 M sodium pyruvate solutions were prepared directly prior to use in 0.04 M phosphate buffers in which the ionic strength was adjusted to 0.35 M by the addition of appropriate quantities of sodium chloride. Most of the reactions were initiated by the addition of 0.05 mL of 2.05×10^{-3} M I_2 in 1.0 M KI to the 3 mL reaction cuvettes containing the buffered solutions of pyruvate. For each temperature studied, we used the appropriate value of the association constant for the reaction $I_2 + I^- \rightleftharpoons I_3^-$, $K_{I_3^-} = [I_3^-]/[I_2][I^-]$ (20*a*, 20*b*). The initiation of all kinetic runs was accomplished with the rapid mixing of the final reaction components by means of a small stirring paddle attached to the needle tip of the Hamilton microlitre syringe (21).

These reactions are known to take place in two phases (2*b*, 3, 4): a rapid burst phase in which enol pyruvate (and any unsaturated impurities inherent in the original pyruvate sample) reacts directly with the added I_3^-, followed by the zero-order reaction of I_3^- with enol pyruvate as it is formed in the rate-determining step. In attempting to employ the Meyer method (5) in which the burst phase absorbance change, ΔA, is used to determine equilibrium concentrations of enol pyruvate, $[\text{enol}] = \Delta A/\varepsilon\{1 + 1/(K_{I_3^-}[I^-])\}$, it has been found by us (2*b*) and others (4*a*) that the values obtained are usually considerably larger than those determined through other methods, suggesting the existence of an I_3^- scavenging impurity in the pyruvate samples. Even using recrystallized sodium pyruvate, the method described above gives rise to an equilibrium constant for enolization, $K_{\text{enol}} = 1 \times 10^{-4}$, which is considerably larger than that reported previously (1*g*, 1*h*, 2*b*).

We found, however, that the Meyer method could be adapted to allow the determination of valid values of K_{enol} by removing or inactivating the I_3^- scavenging impurity. Accordingly, we pretreated the buffered pyruvate solutions with small quantities of I_3^- to react with and, therefore, remove the impurity. After the pyruvate in solution reacted completely with the added I_3^- (note the pyruvate concentration was always much larger than that of iodine) it was allowed to reequilibrate with its enol form. The time allowed for reequilibration was always greater than 10 half-lives for the known rate of reequilibration between keto and enol pyruvate (2*b*). After reequilibration had taken place, we injected 0.05 mL additional I_3^- to initiate the burst uptake of I_3^- by the *equilibrium concentration of enol pyruvate*. The burst was again followed by the zero-order production of new enol pyruvate. Thus, we were able to essentially titrate out the I_3^- scavenging impurity by varying the amount of triiodide used in pretreatment.

Because the time required for complete mixing of the reaction mixtures (ca. 3–5 s) interferes with monitoring the initial stages of the burst phase, it is not possible to accurately extrapolate absorbances of the burst phase back to the kinetic zero. Thus, the actual absorbance of the I_3^- solution used to initiate the run after pretreatment must be be determined independently, using experimental conditions that simulate those used in the actual iodination experiments. Even when using 0.1 M pyruvate, the absorbance differences, ΔA, used to calculate the equilibrium concentration of enol pyruvate are relatively small (typically from ca. 0.06 to 0.07), so that the precise determination of $A_{I_3^-}$ is crucial. In these determinations, account must be taken of the residual iodide ion left over from the original I_3^- pretreatment since the added I^- increases the concentration of I_3^-, thereby increasing the spectrophotometric absorbance. In Table 1, we exemplify the absorbancies observed from solutions at various initial concentrations of I^- and I_2 at 25°C. It will be noted that our values of $A_{I_3^-(\text{obsd})}$ in Table 1 are in excellent agreement with those calculated, $A_{I_3^-(\text{calcd})}$, on the basis of published values of $K_{I_3^-}$ (20*a*, 20*b*).

© 1999 NRC Canada

Table 1. Absorbance of I_3^- solutions at 353 nm and 25.0°C.

$[I^-]$ (M)	0.0082	0.0164	0.0263	0.0360	0.0455	0.0549	0.0639	0.0323[a]	0.0476[a]
$10^5[I_2]_0$ (M) [b]	1.68	3.36	3.36	3.36	3.36	3.36	3.36	3.30	3.29
$[I_3^-]$ (M) [c,d]	1.45	3.10	3.19	3.23	3.27	3.28	3.29	3.17	3.20
$A_{I_3^-}$(obsd) [e]	0.363	0.778	0.796	0.813	0.821	0.825	0.828	0.794	0.807
ε_{obsd} (M^{-1} cm^{-1})	25 030	25 100	24 960	25 170	25 110	25 150	25 170	25 020	25 220
$A_{I_3^-}$(calc) [f]	0.364	0.778	0.801	0.811	0.821	0.823	0.826	0.796	0.804

[a]The data in the last two columns refer to absorbances of I_3^- in the presence of 0.01 M pyruvate anion *prior* to enolization and in the *absence* of I_3^- scavenging impurity. See text for experimental protocol.
[b]Formal concentration.
[c]Assuming: $K_{I_3^-} = [I_3^-]/[I_2][I^-] = 774$ at 25.0°C. References 20*a* and 20*b* give comparable values of $K_{I_3^-}$ over two overlapping temperature ranges.
[d]$[I_3^-] = \{774(3.36 \times 10^{-5})[I^-]\}/(1 + 774[I^-])$.
[e]Each value represents the average of 10 determinations. The average standard deviation for these values was 0.0025 absorbance units.
[f]Using the average $\varepsilon = 25\ 100\ M^{-1}\ cm^{-1}$ calculated from the data in this table.

Our observed values of the absorbance of I_3^- in the absence of pyruvate, $A_{I_3^-(obsd)}$, were compared with the extrapolated linear portion of our iodination runs, $A_{0,extrap}$ to determine ΔA for the direct and rapid reaction of triiodide with enol pyruvate. According to Davies and Gwynne (20*a*), $K_{I_3^-}$ is independent of ionic strength up to 1 M, and our own observations are in agreement with this finding. Nonetheless, the question arises whether the value of $A_{I_3^-}$ in the *absence* of pyruvate is the same as that in the *presence* of the 0.098 M pyruvate solutions used in the iodination runs. To determine this, we performed a number of very simple experiments. We first added triiodide to the buffered solution of pyruvate and when the zero-order portion of the reaction was complete, we immediately injected 0.05 mL of the triiodide solution into the same reaction mixture. This latter injection gives rise to no burst reaction whatsoever, showing that the I_3^- scavenging impurity has been deactivated and that no new enol has yet had the time to form. The *linear* extrapolation of absorbance to the endpoint of the first reaction can be made with certainty and gives yet another means of determining $A_{I_3^-}$. It will be noted, then, that this value was determined in the presence of "pure" pyruvate, but in the *absence* of triiodide-scavenging material either in the form of impurity or as enol pyruvate. The last two columns of data in Table 1 exemplify values of $A_{I_3^-}$ determined in this way. These data demonstrate that $A_{I_3^-}$ is not only insensitive to ionic strength but also independent of the presence or absence of keto pyruvate anion.

For the determination of the kinetic data for the enolization of pyruvate anion and pyruvic acid, reaction velocities were calculated from the linear portions of the spectrophotometric traces at 353 nm, $v_{enol} = \Delta A/\varepsilon\Delta t\{1 + 1/(K_{I_3^-}[I^-])\}$ and the corresponding observed pseudo-zero-order rate constants, $k_{enol} = v_{enol}/[\text{keto pyruvate}]$. The reversible enolization of pyruvate is subject to general-base catalysis (2*b*, 2*c*) so that the observed rate constants are actually a sum of kinetic terms:

$$[2] \qquad k_{enol} = k_0 + k_B[B] + k_{OH^-}[OH^-]$$

where B is the basic buffer component and k_0 is the "spontaneous" rate usually taken to be $k_0 = k_{H_2O}[H_2O]$. Rate constants for the *equilibration* between enol and keto forms, $k_{equil,\ enol} = k_{enol} + k_{keto}$, were calculated using the equilibrium constant for the reaction, $K_{enol} = [\text{enol}]/[\text{keto}]$, and the half-lives for the equilibrations from $\tau_{1/2} = 0.693/k_{equil,enol}$.

In earlier papers, we (1*a*) and others (1*b*–1*h*) reported that aqueous solutions of pyruvic acid below pH 2.2 consist predominantly of the hydrated form, while at higher values of pH the pyruvate anion is hydrated to a much lesser extent. We also demonstrated from pmr experiments the third-power dependence of the ratio of 2,2-dihydroxypropionic to pyruvic acid on the water concentration (1*a*), [hydrate]/[keto] = $K_{eq}[H_2O]^3$ (3*a*), a finding that has not always been taken into consideration in reports from other laboratories. Our spectrophotometric determinations in the present work were carried out using 0.098 M pyruvic acid and the values of χ_{hyd} = [hydrate]/([hydrate] + [keto]) and K_{hyd} = [hydrate]/[keto] given in this paper were determined at that concentration.

The largely different fractions of hydration of pyruvic acid and pyruvate anion have been utilized in a kinetic method designed to follow the dehydration of 2,2-dihydroxypropionate in aqueous buffers (2*a*, *2b*). Rate constants reported in the present work were determined from kinetic runs that were initiated by the injection of an acidic solution of pyruvic acid (with a relatively high fraction of hydrated pyruvic acid) into a neutral buffered solution along with sufficient sodium hydroxide to immediately neutralize the added acid. The essentially instantaneous deprotonation of 2,2-dihydroxypropionic acid resulted in its dehydration to keto pyruvate, a reaction that was monitored directly by the increase in absorbance at 325nm (λ_{max} = 325 nm, ε = 20 M^{-1} cm^{-1}). Typically, 0.10 mL of an acidic solution of 0.23 M pyruvic acid (pH 1.45) was injected into 3.0 mL of the buffer solution. First-order rate constants, k_{dehyd}, were determined from the linear plots of $\ln(A_\infty - A_t)$ vs. t.

Since the dehydration of 2,2-dihydroxypropionate is sensitive to catalysis both by acids and bases (2*b*, 22)

$$[3] \qquad k_{dehyd} = k_0 + k_{H_3O^+}[H_3O^+] + k_{OH^-}[OH^-] + k_{HA}[HA] + k_{A^-}[A^-]$$

where HA and A^- refer, respectively, to the acid and conjugate base of the buffer system employed. At the approximately neutral pH's used in the present work, the kinetic term in hydronium ion is negligible (2*b*). The rate of equilibration between keto and enol forms, $k_{equil,hyd} = k_{hyd} + k_{dehyd}$, may be calculated from $k_{equil,hyd} = k_{dehyd}(1 + K_{hyd})$, where K_{hyd} is the equilibrium constant for hydration, K_{hyd} = [hydrate]/{keto].

© 1999 NRC Canada

Table 2. Half-lives, $t_{1/2}$, for the equilibration of the reversible enolization and hydration of pyruvate anion and pyruvic acid.

			Enolization[a,b]	Hydration[a,c]
T (°C)	Solution	pH	$\tau_{1/2}$ (s)	$\tau_{1/2}$ (s)
Pyruvate anion				
5	0.01 M Phosphate buffer	6.9	100[d]	120[d,e]
25	0.04 M Phosphate buffer	6.9	2.8[f]	22[f]
25	0.20 M Phosphate buffer	7.0	0.6[f]	8[f]
25	0.20 M Imidazole buffer	7.0	0.6[f]	15[f]
Pyruvic acid				
0	0.1 M HCl	1.15	570[g]	11[h]
11	0.1 M HCl	1.15	140[f]	
15	0.1 M HCl	1.15	110[g]	
20	0.1 M HCl	1.15	70[g]	
25	0.1 M HCl	1.15	40[g]	ca. 1[e]

[a] $k_{equil} = k_f + k_r$; $K_{eq} = k_f/k_r$, where K_{eq} values for enolization are taken from Table 2 of the present work and for hydration from ref. 1*a*.
[b] Where $t_{1/2} = 0.693/k_{obsd}$ and $k_{obsd} = k_0 + k_B[B]$.
[c] Where $t_{1/2} = 0.693/k_{obsd}$ and $k_{obsd} = k_0 + k_{H_3O^+}[H_3O^+] + k_{OH^-}[OH^-] + k_B[B] + k_{BH^+}[BH^+]$.
[d] Present work.
[e] This value is slightly dependent on pyruvate ion concentration (see ref. 2*b*) That reported here applies to 1×10^{-4} pyruvate so that it ccorresponds more closely to the concentration ranges used for its enzymatic reactions with LDH.
[f] Reference 2*b*.
[g] References 3*a*, 3*b*.
[h] Reference 2*a*.

Again, half-lives ($\tau_{1/2}$) were calculated from $\tau_{1/2} = 0.693/k_{equil,hyd}$.

Finally, the hydration of pyruvic acid in aqueous hydrochloric acid solutions (pH <2.2) was initiated by injecting 0.01 mL of neat pyruvic acid, or the equivalent amount diluted with acetonitrile, into 3 mL of hydrochloric acid solutions of varying concentrations. For the hydration of pyruvic acid (2*a*), $k_{hyd} = k_0 + k_{H_3O^+}[H_3O^+]$, $k_{equil,hyd} = k_{hyd}(1 + K_{hyd})/K_{hyd}$.

Results and discussion

In the present investigation, we observed that the magnitude of the "burst" region resulting from the intial reaction of triiodide in solutions of pyruvate and pyruvic acid sometimes increased markedly on standing, implying that a triiodide-scavenging impurity forms over time. The rate of formation of this impurity appears to depend on the pH of the solution. In neutral phosphate buffers, the initial triiodide uptake = $\Delta A/\varepsilon\{1 + 1/(K_{I_3^-}[I^-])\}$ remains constant for up to several days, while under more acidic conditions it increases much more rapidly. For example, at pH 1.3, triiodide uptake in pyruvic acid solutions (*unpretreated* with triiodide ion) varied as follows: 1.1×10^{-5} (1 h), 1.5×10^{-5} (2 h), 3.3×10^{-5} (4 h), 6.0×10^{-5} (8 h), 9.2×10^{-5} (24 h). Consequently, when using the Meyer method to make valid determinations of K_{enol}, one must be aware of a finite "window of opportunity" for the previously described pretreatment incubation studies using triiodide. Depending on the pH and temperature for a given series of such determinations, the limits of this "window" used in the present work were such that the experiments were always carried out *after* 10 half-lives for the reequilibration between keto and enol pyruvate, but *before* the time where a measurable quantity of I_3^- scavenging impurity was known to reform in the pyruvate solutions. Table 2 lists the half-lives for the equilibration of the enolization of pyruvate anion in selected buffer solutions and for the correspondinng equilibration for pyruvic acid in 0.1 M HCl.

In developing our experimental protocol for the Meyer method (5), we found that optimal conditions for determining accurate and reproducible values of K_{enol} utilized a concentration of pyruvate around 0.1 M (actually 0.098 M). The resultant equilibrium concentration of enol pyruvate allowed an easily measured burst of triiodide uptake, $\Delta A \approx 0.06$ absorbance units, while at the same time the background absorbance due to keto pyruvate at 353 nm was maintained low enough to allow the zeroing of the instrument. However, since the burst-phase absorbance change was relatively small, determination of the actual absorbance of triiodide at the kinetic zero for the enolization of pyruvic acid and pyruvate anion is crucial to the accurate determination of K_{enol}. Since it is not possible to directly *observe* the original absorbance due to triiodide anion, it must be determined as described in the Experimental section. The close comparison of the data in the last two columns of Table 1 with the rest of the data in the table demonstrates that $A_{I_3^-}$ in the *absence* of pyruvate is the same as that in the *presence* of 0.1 M sodium pyruvate. Not only is this an important finding that confirms the validity of the value of $A_{I_3^-}$ we have used in determining $K_{enol} = \Delta A/\varepsilon\{1 + 1/(K_{I_3^-}[I^-])\}$, but it also suggests the lack of formation of a complex from the reaction of hydrated pyruvate and I_3^- as proposed earlier by Albery and Bell (4*a*).

Figure 1 shows the results of experiments in which the magnitude of the burst phase, ΔA, was measured as a function of the amount of I_3^- used in the pretreatment of pyruvate solutions. The experiments were conducted as follows. Solutions (3 mL) of buffered pyruvate (0.098 M) were pretreated with various quantities of triiodide; this phase of the iodination was allowed to go to completion and then incubated for at least 10 half-lives to allow the reequilibration between enol and keto pyruvate. After that time, 0.05 mL of a solution of 2.05×10^{-3} M I_2 in 0.10 M KI was injected

© 1999 NRC Canada

Fig. 1. Burst as a function of the total iodine concentration used in pretreating solutions of pyruvate anion.

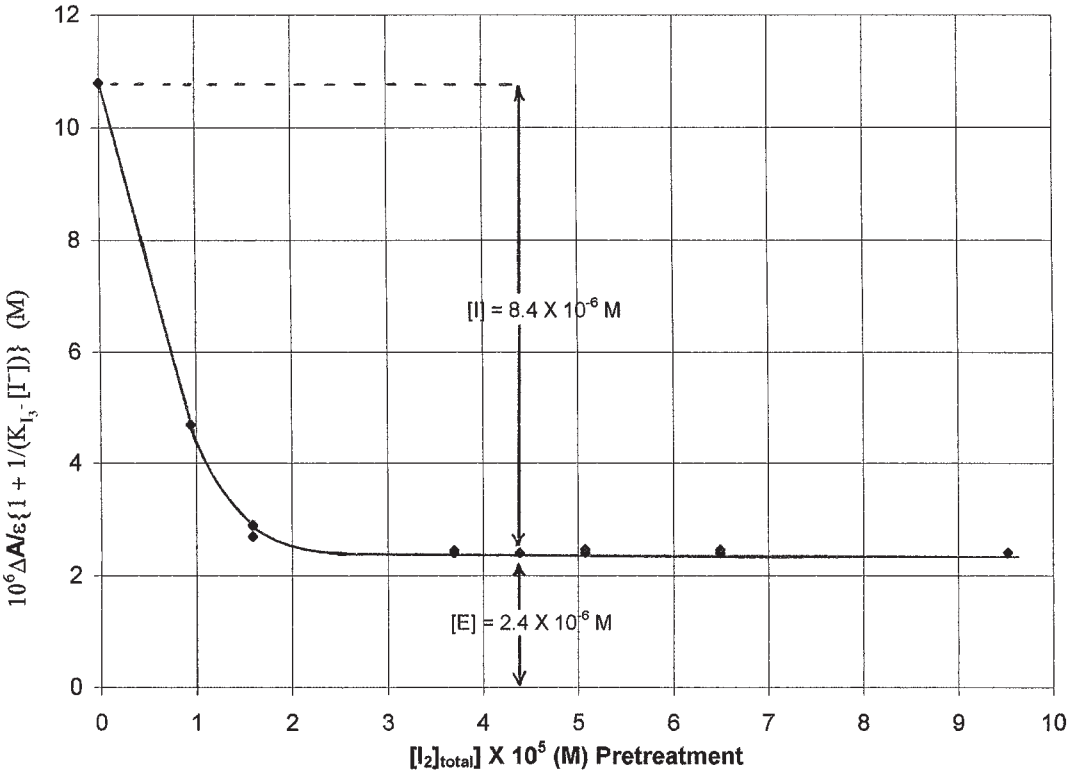

into the incubated mixture. The plot illustrated in the figure indicates that pretreatment of the buffered pyruvate solution with triiodide effectively removes the I_3^- scavenging impurity until, at approximately a total iodine concentration of 1.5×10^{-5} M, a constant value for the "burst" is reached.

Table 3 lists values of the fraction of enolization determined as described above for pyruvate and pyruvic acid at various temperatures. It is important to note from the data in the table that the calculated fractions of the enol forms, χ_{enol}, remain relatively constant in the temperature range 11–25°C both for pyruvate anion and for pyruvic acid and, for this reason, the evaluation and interpretation of thermodynamic parameters would not be meaningful. In fact, the corresponding values of $K_{enol} = \chi_{enol}/(1 - \chi_{hydration})$ are even more similar over the pH range studied. It will be noted that the *enolization* of pyruvate anion is apparently slightly endothermic in contrast to the exothermic *hydration* of keto pyruvate. While the variation in K_{enol} for pyruvic acid is within the limits of experimental error, the corresponding hydration of pyruvic acid is clearly exothermic.

For pyruvate anion, at 25°C, χ_{enol} = [enol]/([enol] + [keto]) = 2.5×10^{-5} (Table 3). It will be noted that this value is somewhat larger than that reported by other workers (1*g*, 1*h*) using the Meyer method. Actually, our attempts at estimating, via direct *extrapolation*, the absorbance of the burst phase at the kinetic zero gave a value which was very similar to that in the literature cited above (1*g*, 1*h*). However, we observed that the mixing time interrupted the spectrophotometric monitoring of the decrease in absorbance of triiodide to the extent that the *extrapolated* triiodide absorbance at the kinetic zero was impossible to measure accurately and was, in fact, consistently lower than the *actual* values of $A_{I_3^-}$ (obsd) given in Table 1.

We note that Meyer method determinations of K_{enol} reported earlier (1*g*, 1*h*) were made using approximately 1/10 the concentration of pyruvate used in the present work. Since no mention was made in those reports concerning the use of a longer pathlength reaction cell, we assume the pathlength was the standard 1 cm. Using the value of K_{enol} and the extinction coefficient $\varepsilon = 26\,000$ cm^{-1} M^{-1} used in those earlier calculations, the absorbance change resulting from the reaction of triiodide with the equilibrium concentration of enol pyruvate would be approximately 0.004 units, a value that would be difficult to measure reproducibly. Finally, we were surprised at the relatively low value of K_{enol} reported, given the fact that no precautions were apparently taken to rid the original pyruvate solution of triiodide-scavenging material.

Burgner and Ray (*4b*), on the other hand, reported the determination of $K_{enol} = 4.1 \times 10^{-6}$ for pyruvate anion using the Meyer method at a sodium pyruvate concentration of 1.0 M. We were unable to reproduce their experiments since, at 353 nm, a 1.0 M solution of pyruvate across a pathlength of 1 cm has an absorbance much greater than 10 units. Even using their reported pathlength of 0.4375 cm would result in an absorbance due to keto pyruvate of around 5 units, making it virtually impossible to obtain accurate values of ΔA using the instrumentation they reportedly used. Again, since the work was presumably carried out using unpurified keto pyruvate and was untreated with the necessary initial aliquot of I_3^- to rid the original pyruvate solution of triiodide-scavenging impurity, the reliability of these data must be questioned.

We found values of K_{enol} for pyruvic acid to be about 3 times larger than those for pyruvate anion, perhaps partially due to the electron-withdrawing inductive effect of the carboxyl group of pyruvic acid. We must note, however, that

© 1999 NRC Canada

Table 3. Equilibria for the enolization and hydration of pyruvate anion and pyruvic acid.

Pyruvate anion			
T (°C)	11	20	25
χ_{hyd}[a,b]	0.11	0.069	0.054
K_{hyd}[a,b]	0.12	0.074	0.057
χ_{enol}	$(1.6 \pm 0.2) \times 10^{-5}$	$(1.7 \pm 0.2) \times 10^{-5}$	$(2.5 \pm 0.2) \times 10^{-5}$
K_{enol}[b,c]	$(1.9 \pm 0.2) \times 10^{-5}$	$(2.0 \pm 0.2) \times 10^{-5}$	$(2.6 \pm 0.2) \times 10^{-5}$
Pyruvic acid			
T (°C)	11	15	25
χ_{hyd}[a,b]	0.68	0.65	0.58
K_{hyd}[a,b]	2.1	1.9	1.4
χ_{enol}	$(2.2 \pm 0.2) \times 10^{-5}$	$(2.4 \pm 0.2) \times 10^{-5}$	$(2.9 \pm 0.2) \times 10^{-5}$
K_{enol}[b,c]	$(6.9 \pm 0.5) \times 10^{-5}$	$(6.8 \pm 0.5) \times 10^{-5}$	$(6.9 \pm 0.5) \times 10^{-5}$

[a]These *apparent* values of χ_{hyd} and K_{hyd} for the hydration of pyruvic acid vary with the third power of the water concentration (see ref. 1*a*). The values of K_{hyd} and χ given in this table correspond to a total pyruvate or pyruvic acid concentration of 0.098 M.

[b]Portions of these data were taken from earlier work (see ref. 1*a*).

[c]Values take into consideration the fraction of hydration, so that K_{enol} = [enol pyruvate]/[keto pyruvate].

there is not always close correlation between inductive effects of groups attached to the carbonyl of ketones and the magnitude of their values of K_{enol}. For example, although the inductive effects exerted by $-CH_3$ and $-CO_2^-$ are similar, K_{enol} for acetone (4.7×10^{-9}) (23*a*, 23*b*) is almost four orders of magnitude lower than that for keto pyruvate (2.5×10^{-5}). It is conceivable that the enol form of the pyruvate anion is stabilized, to some extent, via intramolecular hydrogen bonding between the enol hydroxy and the negatively charged carboxylate oxygens. Thus any increase in K_{enol} for pyruvic acid in comparison to pyruvate anion, caused by the electron-withdrawing inductive effect of $-CO_2H$, may be partially offset by such a mode of stabilization of the enol pyruvate anion. Unfortunately, because of the small changes in values of K_{enol} as a function of temperature in the range studied, it is not possible to calculate reliable values for the entropies of the respective enolizations of pyruvate anion and pyruvic acid.

On the other hand, the data in Table 3 indicate a very large difference in the extent to which pyruvic acid and pyruvate anion undergo hydration. It will be noted that these acyl addition reactions involve bond making between the nucleophile and the electrophilic carbonyl carbon. Accordingly, one would expect that electronic inductive effects caused by groups directly attached to the carbonyl group would be of greater importance for hydration than for the corresponding enolization reaction. Indeed, α-halogen substituents are known to greatly increase fractions of hydration of carbonyls. For example, at 25°C, whereas the fraction of hydration for pyruvate anion is ca. 0.06, that for fluoropyruvate anion is about 0.85 (9), a value that is even greater than that for the neutral pyruvic acid molecule.

For pyruvic acid, a recent report (1*g*) gives the value $K_{enol} = 6.76 \times 10^{-4}$ using the Meyer method. This larger value, almost 10 times larger than the value determined in the present investigation (Table 3), may be due to the formation of the triiodide-scavenging impurity that we observed to occur in acidic solutions of pyruvic acid as described earlier.

The method of determining K_{enol} for carbonyl compounds from the ratio of rate constants for ketonization to the corresponding quantities for enolization obviates the difficulty associated with minute levels of triiodide-scavenging impurity in solutions of the carbonyl compound to be studied. However, in the case of the pyruvic acid – pyruvate anion system, there can exist uncertainties in the calculation of K_{enol} from the ratio of rates of enolization to ketonization. In our own analysis in earlier work (2*b*), for example, we approximated $K_{enol} = k_{enol}/k_{keto} = 8.6 \times 10^{-5}$ based on accurate and reproducible values for k_{enol} but, at the same time, using values for k_{keto} (7*a*) that necessitated approximation to compensate for the different experimental conditions (e.g., ionic strength, buffer composition, temperature) under which the two reactions were independently carried out. We are also concerned that, in general, the validity of k_{enol}/k_{keto} ratios may be weakened when the determination of values of k_{keto} require complex or ambiguous kinetic methods (1*g*, 1*h*, 7*a*, 7*b*, 8*a*, 8*b*) involving reaction intermediates. For example, when attempting to determine k_{keto} for pyruvic acid by introducing solutions rich in enol content into aqueous acidic solutions, the *ketonization* of pyruvic acid enol would be paralleled by the even more rapid *hydration* of keto pyruvic acid, thereby complicating the interpretation of the ensuing decreasing absorbances.

The comparison of catalytic ratios for the ketonization and enolization of the pyruvic acid – pyruvate anion system may present additional difficulties in which the analysis of data requires certain assumptions. For example, values of $K_{enol} = k_{OH^-,\,enol}/k_{OH^-,\,keto}$ and $K_{enol,\,pyruvic\ acid} = k_{H_3O^+,enol}/k_{H_3O^+,keto}$ were evaluated in earlier work (1*g*) It must first be noted that reported values (1*g*, 2*b*) of $k_{OH^-,enol}$ vary by as much as 60%. Furthermore, it was observed that k_{keto} is nonlinear for both pyruvate anion with increasing hydroxide concentration, and for pyruvic acid with increasing hydronium ion. Thus, although the kinetic experiments themselves may be carried out carefully, calculated values of $k_{OH^-,keto}$ and $k_{H_3O^+,keto}$ at higher concentrations of OH^- and H_3O^+, respec-

© 1999 NRC Canada

tively, depend on the appropriateness of the theoretical kinetic model used in its calculation. For these reasons, the use of spontaneous rate constants for ketonization and enolization may give less ambiguous values of $K_{enol} = k_{0,enol}/k_{0,keto}$, provided, of course, that valid determinations of the spontaneous rate constants are made under identical reaction conditions. For pyruvic acid, $k_{0,enol}$ values that are in close agreement (when corrected for fractions of hydration) have been reported at 25°C (3*a*, 3*b*, 4*a*), $k_{0,enol} = 1.2 \times 10^{-6}$ s, and when this average value is compared to $k_{0,keto}$ for pyruvic acid from the work of Chiang et al. (1*g*), $k_{0,keto} = 1.06 \times 10^{-2}$ s, it follows that $K_{enol} = k_{0,enol}/k_{0,keto} = 1.2 \times 10^{-6}$ s/1.06×10^{-2} s = 1.1×10^{-4}, which is in closer agreement with the value we report in Table 3 (6.9×10^{-5}, at 25°C), allowing for differences in experimental conditions.

The kinetic and thermodynamic parameters associated with the reversible hydration and enolization of pyruvate reported in this paper may be used to access the likelihood of the keto, hydrated, and enol forms of pyruvate to serve either as enzyme substrates or as enzyme inhibitors. Specifically, the availability of these data allow a closer look at the experimental data determined by Coulson and Rabin (15*a*).

In that report, it was concluded that the substrate inhibition observed in the LDH reduction of pyruvate by NADH was actually due to a substance that can be removed from pyruvate solutions by column chromatography. It was suggested that the enzyme-inhibiting substance was enol pyruvate and *not* 2,2-dihydroxypropionate (hydrated pyruvate) because, at that time, it was believed that hydrated pyruvate could not be observed at neutral values of pH. However, according to the thermodynamic data provided in Table 3 it is now known that there exists over 2000 times more hydrated pyruvate than enol pyruvate at neutral pH at room temperature.

It is also instructive to interpret other of Coulson and Rabin's results (15*a*) in light of the kinetic data presented in Table 2. Kinetic runs were carried out in the earlier study (15*a*) using chromatographically purified solutions of pyruvic acid to oxidize NADH in the presence of LDH at room temperature. Prior to the introduction of NADH and LDH to initiate the kinetic run, the pyruvate was incubated in 0.2 M buffer solutions for 2 min. It was noted that while substrate inhibition was not observed in 0.2 M imidazole buffer, rather strong inhibition was noted in 0.2 M phosphate buffer. Because of the lack of reliable kinetic data at that time, it was tentatively concluded that the purified pyruvate enolized rapidly in the phosphate buffer, thereby forming the actual substance that inhibited LDH. It was argued that the enolization was so slow in imidazole buffer that no such inhibition was observed. The data in Table 2, however, show that the half-life for the equilibration between keto and enol pyruvate is less than a second in either 0.2 M phosphate or 0.2 M imidazole buffer. Consequently, identical (equilibrium) concentrations of enol pyruvate would have prevailed under the experimental conditions in the article cited (15*a*). It was also stated in that article that purified pyruvic acid solutions were stable at pH 1.0 for several hours at 0°C. However, according to the results we now report at the beginning of this section, we find that measurable quantities of a triiodide-scavenging impurity begin to form after about 1 h in solutions of pyruvic acid at pH 1.3. Furthermore, the data in Table 2 demonstrate that at 0°C the half-life for enolization is around 10 min and, accordingly, after even 1 h the equilibrium between keto and enol pyruvate would have been virtually complete. Thus all of the enzyme assays carried out by Coulson and Rabin (15*a*) actually involved the same fraction of enolized pyruvate and, therefore, any variations in LDH inhibition in these experiments were unrelated to the content of enol pyruvate in solution. In fact, the thermodynamic data in Table 3 indicate that the pyruvic acid solutions at pH 1.0 at 0°C utilized in that study contained mostly hydrated pyruvate.

Buffer, ionic strength, and pH effects on the magnitude of inhibition constants have been observed for LDH (16) and for other enzymes (24*a*–24*f*). For example, whereas at neutral pH a solution of 1×10^{-3} M keto pyruvate results in 27% substrate inhibition in 0.1 M phosphate buffer, the same concentration of keto pyruvate causes only 9% substrate inhibition in 0.1 M diethylmalonate buffer(16). Schwert and Winer (25) have also observed greater substrate inhibition in phosphate buffers than in other buffers. Therefore we suggest that the differences Coulson observed in the degree of substrate inhibition arising from assays in 0.2 M imidazole and 0.2 M phosphate buffers were due to specific interactions between the buffer components and the enzymes.

Somero (14*a*, 14*b*) has demonstrated that the substrate inhibition observed for muscle LDH isolated from the fish *Gillichtghys mirabilis* is much stronger at colder temperatures than at warmer temperatures. He suggested that this phenomenon is a property of the enzyme itself. In a more recent article (26), it is reported that differences in enzyme–substrate binding and thermal stabilities of Sphyraena LDH-A from various barracuda species are actually due to amino acid residues outside the active site.

However, we have been able to show that for trout muscle LDH, the increased sensitivity of substrate inhibition with decreasing temperatures is due, at least in part, to the equilibrium shift that increases the fraction of hydrated pyruvate at lower temperatures (27*a*–27*c*). Similar results were obtained using purified beef muscle and beef heart isoenzymes of LDH (16, 27*a*–27*c*) in which substrate inhibition was observed to be more severe in the case of the latter. In a typical set of experiments with beef heart LDH (16), small quantities of preincubated solutions of pyruvate (pyruvic acid) were added to reaction mixtures containing NADH and LDH to initiate kinetic runs in phosphate buffer at neutral pH at 5.0°C. The preincubated solutions of pyruvate (pyruvic acid) were as follows: (*i*) prepared in phosphate buffer and preincubated at 41°C ($\chi_{hydrate} = 0.054$); (*ii*) prepared in phosphate buffer at 5.0°C ($\chi_{hydrate} = 0.136$); (*iii*) prepared in HCl, pH 4.5, at 41°C, yielding an aqueous pyruvic acid solution ($\chi_{hydrate} = 0.412$); (*iv*) prepared in HCl, pH 4.9, at 5.0°C, yielding an aqueous pyruvic acid solution ($\chi_{hydrate} = 0.801$). The data in Table 4 show that *increasing the initial fraction of hydrated pyruvate in the assay results in increased substrate inhibition in the enzymatic reactions*. Since the four experiments illustrated in Table 4 represent kinetic runs at 5.0°C, the kinetic differences cannot be a property of the enzyme alone but must, in fact, be related to the different initial compositions of the pyruvate solutions themselves (keto

© 1999 NRC Canada

Table 4. Lactate dehydrogenase catalysis reduction of pyruvate at various fractions of keto, hydrated, and enol pyruvate.[a]

T (°C)	pH	$\chi_{keto,initial}$	$\chi_{hydrate,initial}$	$\chi_{enol,initial}$	% "Substrate" inhibition at 5×10^{-4} M pyruvate
41	6.8	0.973	0.027	3×10^{-5}	15
5.0	6.8	0.864	0.136	1×10^{-5}	30
41	0.45	0.543	0.457	4×10^{-5}	80
5.0	0.49	0.137	0.863	2×10^{-5}	~100

[a]Runs initiated by injection of preincubated pyruvic acid solutions at various temperatures and values of pH. Kinetic runs in pH 6.8 phosphate buffers μ = 0.1 M (see ref. 16).

Fig. 2. Percent (%) inhibition of beef heart LDH as a function of initial fractions of hydration of pyruvate. All kinetic runs were carried out in phosphate buffer at 5.0°C.

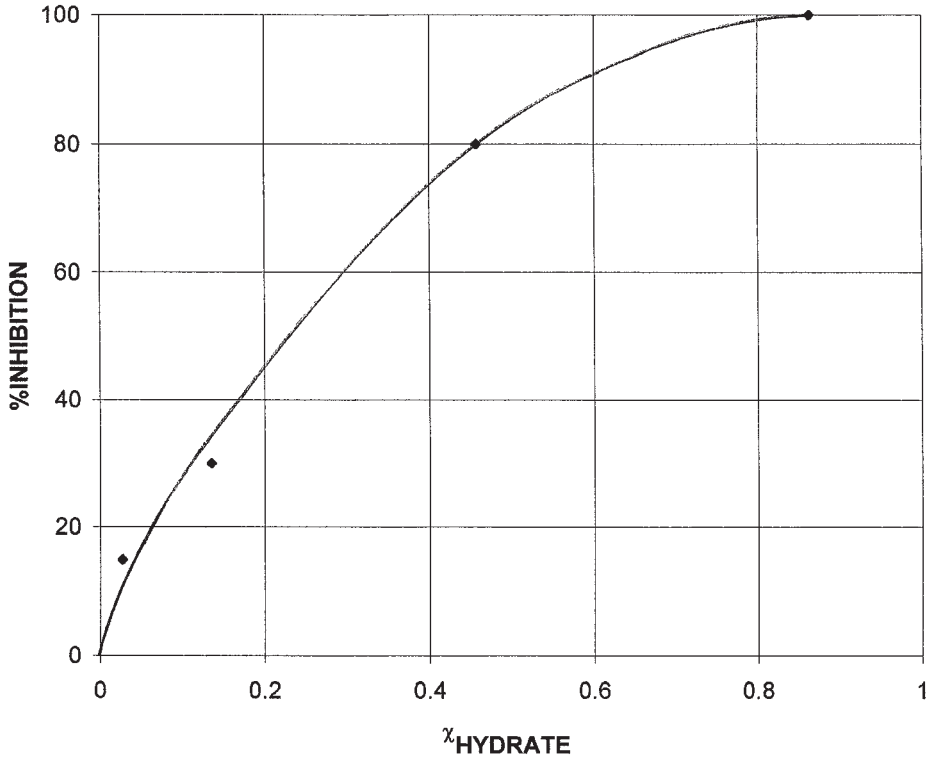

vs. hydrated). On the other hand, the entries in Table 4 demonstrate that there is no relationship between the fraction of available enol pyruvate and the degree of substrate inhibition. Figure 2 shows that the initial fraction of hydrated pyruvate during the enzymatic reaction is directly related to the severity of substrate inhibition. Finally, we note that the kinetic experiments illustrated in Table 4 were purposely conducted at 5.0°C, where the half-life for the hydration–dehydration reequilibration (Table 2) is 100 s. Since the "initial" velocities used to generate the data in Table 4 were taken 15 s following the kinetic zero, the reequilibration between ketopyruvate and hydrated pyruvate was less than 1/10 complete when the progress of the reactions were first recorded.

Pyruvate inhibition of LDH as observed from initial velocity studies such as those represented in Table 4 has been attributed to the reversible formation of a relatively loosely bound abortive ternary complex (17) composed of LDH, NAD^+, and some form of pyruvate, which we suggest is hydrated pyruvate. Given the similarity of the shapes and structures of 2,2-dihydroxypropanoate (hydrated pyruvate) and 2-hydroxypropanoate (lactate), one would expect that the enzyme·NAD^+ complex would, indeed, accommodate hydrated pyruvate. Related experiments, involving the incubation of LDH with pyruvate solutions containing varying fractions of hydrated pyruvate (16) also have suggested that a more stable inhibitory complex is formed, again with the same stoichiometry as the rapidly formed ternary complex. In light of the kinetic and thermodynamic analysis provided in the present paper, we again suggest that hydrated pyruvate is involved in the formation of the more stable ternary complex as well.

References

1. (*a*) Y. Pocker, J.E. Meany, B.J. Nist, and C. Zadorojny. J. Phys. Chem. **73**, 2879 (1969); (*b*) H. Strehlow. Z. Elektrochem. **66**, 392 (1962); (*c*) M. Eigen, K. Kustin, and H. Strehlow. Z. Phys. Chem. **31**, 140 (1962); (*d*) V. Gold, G. Socrates, and M.R. Crampton. J. Chem. Soc. 5888 (1964); (*e*) V.S. Griffiths and G. Socrates. Trans. Faraday Soc. 673 (1967);

© 1999 NRC Canada

(*f*) M. Becker. Ber. Bunsen-Ges. Phys. Chem. **68**, 669 (1964); (*g*) Y. Chiang, A.J. Kresge, and P. Pruszynski. J. Am. Chem. Soc. **114**, 3103 (1992); (*h*) A.J. Kresge. Pure Appl. Chem. **63**, 213 (1991).

2. (*a*) Y. Pocker and J.E. Meany. J. Phys. Chem. **74**, 1486 (1970); (*b*) J. Damitio, G. Smith, J.E. Meany, and Y. Pocker. J. Am. Chem. Soc. **114**, 3081 (1992); (*c*) T. Germay, J.E. Meany, and Y. Pocker. Joint 45th Northwest/Rocky Mountain Regional Meeting, American Chemical Society. 1990. Abstr. No. 255.
3. (*a*) J.E. Meany. J. Phys. Chem. **73**, 3421 (1969); (*b*) M. Hegazi and J.E. Meany. J. Phys. Chem. **76**, 3121 (1972).
4. (*a*) W.J. Albery and R.P. Bell. Trans. Faraday Soc. **61**, 1194 (1965); (*b*) J.W. Burgner II and W.J. Ray. Biochemistry, **13**, 4229 (1974).
5. K. Meyer. Justus Liebigs Ann. Chem. **380**, 212 (1911).
6. (*a*) Y. Chiang and A.J. Kresge. Science (Washington, D.C.), **253,** 395 (1991); (*b*) A.J. Kresge. Chem. Rev. 275 (1996); (*c*) L. Wolff. Ann. Chem. **317**, 8 (1901).
7. (*a*) D.J. Kuo, L. O'Connell, and I.A. Rose. J. Am. Chem. Soc. **101**, 5025 (1979); (*b*) M. Fisher and P. Warneck. Ber. Bunsen-Ges. Phys. Chem. **95**, 523 (1991); (*c*) J. Peliska and H. O'Leary. J. Am. Chem. Soc. **113**, 1841 (1991).
8. (*a*) B.A. Miller and D.L. Leussing. J. Am. Chem. Soc. **107**, 7146 (1985); (*b*) A. Schellenberger and G. Hubner. Chem. Ber. **98**, 1938 (1965).
9. R. Tienharra and J.E. Meany. Biochemistry, **12**, 2067 (1973).
10. B.J. Vennesland. J. Biol. Chem. **212**, 787 (1955).
11. I.H. Segel. Enzyme kinetics. Wiley, New York. 1975; (*b*) M. Dixon and E.C. Webb. Enzymes. 2nd ed. Academic Press, New York. 1964.
12. (*a*) P.G.W. Plagemann, K.F. Gregory, and F. Wrobiewski. Biochem. Z. **334**, 37 (1961); (*b*) R. Stambaugh and P. Post. J. Biol. Chem. **241**, 1462 (1966); (*c*) A. Pesce, T.P. Fondy, F.E. Stolzenbach, D. Castillo, and N.O. Kaplan. J. Biol. Chem. **242**, 2151 (1967).
13. (*a*) A.L. Latner, S.S. Siddiqui, and A.W. Skillen. Science (Washington, D.C.), **154**, 527 (1966); (*b*) R.D. Cahn, N.O. Kaplan, L. Levine, and E. Zwilling. Science (Washington, D.C.), **136**, 962 (1962); (*c*) D.M. Dawson, T.L. Goodfriend, and N.O. Kaplan. Science (Washington, D.C.), **143**, 929 (1964); (*d*) K.L. Manchester. Biochem. Educ. **22**, 9 (1994).
14. (*a*) G.N. Somero. Comp. Biochem. Physiol. B: Biochem. Mol. Biol. **44B**, 205 (1973); (*b*) P.W. Hochachka and G.N. Somero. Strategies of biochemical adaptation. W.B. Saunders Co., Philadelphia. 1973. p. 58.
15. (*a*) C.J. Coulson and B.R. Rabin. FEBS Lett. **3**, 333 (1969); (*b*) A.L. Lehniger. Biochemistry, 2nd ed. Worth Publishers, New York. 1975. p. 484; (*c*) M.G. Rossman and N.O. Kaplan. Structure function in lactate dehydrogenase. Proc. Natl. Acad. Sci. (U.S.A.), **70**, 1970 (1973).
16. M.D.Waddington and J.E. Meany. Arch. Biochem. Biophys. **211**, 447 (1981).
17. J.W. Burgner II and W.J. Ray. Biochemistry, **17**, 1654 (1978); J.W. Burgner, G.R. Ainslie, W.W. Cleland, and W.J. Ray. Biochemistry, **17**, 1646 (1978).
18. H.J. Fromm. Biochim. Biophys. Acta, **52**, 199 (1961).
19. W.E. Trommer, H. Huth, and H.R. Wenzel. Biochim. Biophys. Acta, **547**, 49 (1979).
20. (*a*) M. Davies and E. Gwynne. J. Am. Chem. Soc. **74**, 2748 (1952); (*b*) G. Jones and B. Kaplan. J. Am. Chem. Soc. **50**, 1845 (1928).
21. Y. Pocker, J.E. Meany, and R.C. Jones. J. Am. Chem. Soc. **104**, 4885 (1982).
22. G.T. Spyridis and J.E. Meany. J. Chem. Educ. **65**, 461 (1988).
23. (*a*) Y. Chiang, A.J. Kresge, and N.P. Schepp. J. Am. Chem. Soc. **111**, 3977 (1989); (*b*) J.E. Meany and J. Spaulding. Unpublished work.
24. (*a*) J.M. Wilson, Q. Tanko, M.M. Wenland, J.E. Meany, J.F. Nedved, and Y. Pocker. Physiol. Chem. Phys. Med. NMR, **30**, 149 (1998); (*b*) Y. Pocker and J.T. Stone. Biochemistry, **6,** 668 (1967); (*c*) Biochemistry, **7**, 2936 (1968); (*d*) Biochemistry, **7**, 3021 (1968); (*e*) Y. Pocker, N. Janjic, and C.H. Miao. *In* Zinc enzymes. *Edited by* I. Bertini, C. Luchinat, W. Maret, and M. Zeppezauer. Birkhauser, Boston. 1986. p. 341. (*f*) Y. Pocker and C.H. Miao. Biochemistry, **26**, 8481 (1987).
25. G.W. Schwert and A.D. Winer. Enzymes, **7**, 127 (1963).
26. L.Z. Holland, N.M. McFall, and G.N. Somero. Biochemistry, **36**, 3207 (1997).
27. (*a*) D.H. Robinson, J. Ju, and J.E.Meany. 40th Northwest Regional Meeting, American Chemical Society. 1985. Abstr. No. 255; (*b*) J. Ju and J.E. Meany. 41st Northwest Regional Meeting, American Chemical Society.1986. Abstr. No. 195. (*c*) 42nd Northwest Regional Meeting, American Chemical Society. 1987. Abstr. No. 101.

© 1999 NRC Canada

Correlation of the rates of solvolysis of phenyl chlorothionoformate and phenyl chlorodithioformate[1,2]

Dennis N. Kevill and Malcolm J. D'Souza

Abstract: The specific rates of solvolysis of phenyl chlorothionoformate (PhOCSCl) are remarkably similar to those previously reported for phenyl chlorothioformate (PhSCOCl). When analyzed using the extended Grunwald–Winstein equation over the usual range of solvent types, these solvolyses show essentially identical divisions into the solvents favoring the addition–elimination channel and those favoring the ionization channel. The introduction of one sulfur caused a partial shift away from the addition–elimination pathway, which was dominant over the full range of solvents for phenyl chloroformate (PhOCOCl). Consistent with these results, introduction of the second sulfur within phenyl chlorodithioformate (PhSCSCl) leads to a completion of this shift, such that an extended Grunwald–Winstein treatment of the specific rates of solvolysis now shows the ionization pathway to be dominant over the full range of solvents.

Key words: Grunwald–Winstein equation, solvent nucleophilicity, solvolysis, phenyl chlorothionoformate, phenyl chlorodithioformate.

Résumé : Il existe une similitude remarquable entre les vitesses spécifiques de solvolyse du chlorothionoformate de phényle (PhOCSCl) et celle rapportée antérieurement pour le chlorothioformate de phényle (PhSCOCl). Lorsqu'on les analyse en faisant appel à l'équation étendue de Grunwald–Winstein sur la plage habituelle des types de solvant, ces solvolyses présentent des divisions essentiellement identiques entre les solvants qui favorisent la voie de l'addition–élimination et ceux qui favorisent la voie de l'ionisation. L'introduction d'un atome de soufre provoque un déplacement partiel de la voie d'addition–élimination qui était dominante pour l'ensemble des solvants dans le cas du chloroformate de phényle (PhOCOCl). En accord avec ces résultats, l'introduction d'un deuxième atome de soufre dans le chlorodithioformate de phényle (PhSCSCl) conduit à un déplacement complet, tel que le traitement étendue de Grunwald–Winstein aux vitesses spécifiques de solvolyse indique maintenant que la voie de l'ionisation est devenue dominante pour l'ensemble des solvants.

Mots clés : équation de Grundwald–Winstein, caractère nucléophile d'un solvant, solvolyse, chlorothionoformate de phényle, chlorodithioformate de phényle.

[Traduit par la Rédaction]

Introduction

It has been established (1, 2) that the solvolysis of phenyl chloroformate (PhOCOCl, **1**) follows a bimolecular addition–elimination pathway over the full range of solvents commonly employed in studies of solvent effects using either the simple (3) or extended (4) forms of the Grunwald–Winstein equation (eqs. [1] and [2], respectively).

$$[1] \qquad \log (k/k_0) = mY + c$$

$$[2] \qquad \log (k/k_0) = lN + mY + c$$

In eqs. [1] and [2], k and k_0 are the specific rates of solvolysis in a given solvent and in 80% ethanol, respectively; l is the sensitivity to changes in solvent nucleophilicity (N); m is the sensitivity to changes in ionizing power (Y); and c is a constant (residual) term.

An extension to the solvolyses of phenyl chlorothioformate (PhSCOCl, **2**), led to a different pattern of behavior (5). The addition–elimination pathway was again dominant in ethanol, methanol, aqueous ethanol, aqueous methanol, and aqueous acetone. In aqueous fluoroalcohol solvents, however, this pathway was swamped out by an alternative one with a much lower l value and a much higher m value.

Received October 14, 1998.

This paper is dedicated to Professor A. Jerry Kresge in recognition of his many contributions to physical organic chemistry.

D.N. Kevill[3] and M.J. D'Souza.[4] Department of Chemistry and Biochemistry, Northern Illinois University, DeKalb, Illinois 60115-2862, U.S.A.

[1]Abstracted, in part, from the Ph.D. dissertation of M.J.D., Northern Illinois University, August 1992.
[2]Presented at the 14th International Conference on Physical Organic Chemistry, Florianópolis, Santa Catarina, Brazil, August 16–21, 1998; abstract P99.
[3]Author to whom correspondence may be addressed. Telephone: (815) 753-6882. Fax: (815) 753-4802.
[4]Current address: Department of Chemistry, University of Wisconsin–Waukesha, Waukesha, WI 53188-2799, U.S.A.

 © 1999 NRC Canada

For solvolyses in 100% H_2O, Queen (6) had previously proposed an addition–elimination pathway for solvolyses of **1** and an ionization pathway for solvolyses of **2**. The magnitudes of the *l* and *m* values for the solvolyses in aqueous fluoroalcohols were considered (5) to be consistent with an ionization pathway for **2**, incorporating an appreciable solvation of the developing acylium ion (hence, the *l* value of 0.62).

In the present paper, we report concerning studies of the solvolyses of analogs of **1** and **2** in which the carbonyl oxygen has been replaced by sulfur to give phenyl chlorothionoformate (**3**) and phenyl chlorodithioformate (**4**).

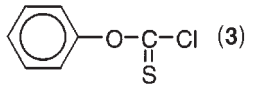

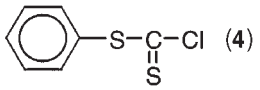

Previous studies of the solvolyses of **3** in H_2O and 65% acetone have indicated a difference in mechanism. McKinnon and Queen (7) studied the hydrolyses in 100% H_2O and found increases in rate as one went from **3** to the corresponding methyl and ethyl esters. This observation, taken together with a positive entropy of activation (+13.5 cal mol^{-1} K^{-1}) for the hydrolysis of the methyl ester, was rationalized in terms of an S_N1 mechanism. It was concluded (7) that replacement of either of the oxygens of **1** by sulfur, to give **2** or **3**, was sufficient to cause a shift in the mechanism for the hydrolysis in 100% water from bimolecular to unimolecular.

Csunderlik et al. (8) studied the hydrolysis of **3** and eight ring-substituted derivatives in 65% acetone. Under their conditions, they found, for each substrate, a very negative entropy of activation (–26 to –30 cal mol^{-1} K^{-1}). A Hammett treatment, using σ° values (1, 9) gave a good linear plot with a slope (ϱ value) of 1.26, somewhat less than the 1.59 observed for the identical solvolyses of a series of aryl chloroformates (9), but consistent with a bimolecular mechanism. Also indicating a bimolecular mechanism were the solvent deuterium isotope effects, which were essentially identical to those for the corresponding solvolyses in 65% acetone of identically substituted derivatives of **1** (9).

These studies of the solvolyses of **3** suggest a similarity with the solvolyses of **2**, which were also found (5) to be bimolecular in 65% acetone but dominantly unimolecular in 100% H_2O. It will be of considerable interest to see, from application of eq. [2], just how extensive is this similarity in behavior when comparisons are made over a wider range of solvent types.

In **4**, with *both* oxygen atoms of **1** replaced by sulfur, one would expect an even stronger tendency towards an ionization pathway. A low solubility did not allow a study in 100% water and the solvolyses of chlorodithioformate esters were studied (10, 11) in 70% acetone. The relative reactivities (phenyl <methyl <ethyl <isopropyl) suggested an ionization mechanism, an assignment supported by an only slightly negative entropy of activation for the solvolysis of the methyl ester. Powerful evidence for an S_N1 pathway involving product formation at the free ion stage was provided by the observation (10, 11) for the chlorodithioformate esters of a pronounced deceleration (common-ion rate depression) in the presence of added sodium chloride, coupled with a modest acceleration in the presence of added sodium perchlorate. Despite this strong evidence for a unimolecular solvolysis (12), enormous accelerations were observed upon addition of azide ion, presumably due to a superimposed bimolecular attack (10, 11). This observation requires consideration of the possibility of a bimolecular contribution to the solvolysis in solvents of relatively high nucleophilicity and (or) relatively low ionizing power. It will be of interest to see whether any evidence can be found for an addition–elimination pathway for the solvolysis of **4**.

Results

The specific rates of solvolysis of phenyl chlorothionoformate (**3**) and phenyl chlorodithioformate (**4**), at 25.0°C, were determined in methanol, ethanol, 2,2,2-trifluoroethanol (TFE) and in binary aqueous solvents, with the other component being ethanol, acetone, or TFE. Determinations were also made in TFE–ethanol mixtures and, for **3**, in aqueous 1,1,1,3,3,3-hexafluoro-2-propanol (HFIP) mixtures. The solvolyses of **4** in aqueous HFIP were too fast to measure by the sampling technique employed. A literature value (8) was available for **3** in 65% acetone. The specific rates of solvolysis of **3** in 19 solvents and of **4** in 14 solvents are presented in Table 1, together with the N_T (13) and Y_{Cl} (14) values used in the correlation analyses.

Discussion

Solvolyses of phenyl chlorothionoformate (3)

It has been shown previously (7, 8) that chlorothionoformate esters hydrolyze rapidly to give hydrochloric acid, carbonyl sulfide, and the alcohol (7) or phenol (8), as shown in eq. [3]. In particular, it was demonstrated (8) that the hydrolysis of ring-substituted derivatives of **3** did not involve any replacement of sulfur by oxygen, so as to then give products resulting from hydrolysis of the corresponding ring-substituted derivative of **1**.

[3] 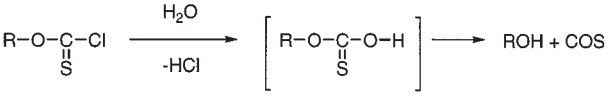

We have previously shown (5, 15) that the extended Grunwald–Winstein equation (eq. [2]) can be a powerful tool for the investigation of solvolysis reactions in which two reaction channels operate with appreciable differences in the sensitivities to both solvent nucleophilicity and solvent ionizing power. Previous claims for an ionization mechanism in 100% water (7) and a bimolecular mechanism in 65% acetone (8) for the solvolyses of **3** suggest that a duality of mechanism will be found similar to those previously observed for **2** (5), ethyl chloroformate (15), and ethyl chlorothioformate (15).

The specific rates of solvolysis of **3** closely parallel those for solvolysis of **2**. For 11 solvents (excluding the aqueous fluroroalcohols), the $k_{(3)}/k_{(2)}$ ratios are within the narrow range of 0.35–0.58. The corresponding ratios for six aqueous

© 1999 NRC Canada

Table 1. First-order rate coefficients[a] for the solvolyses of phenyl chlorothionoformate (PhOCSCl) and phenyl chlorodithioformate (PhSCSCl) at 25.0°C.

	$k/10^{-5}$ s^{-1}			
Solvent	PhOCSCl (**3**)	PhSCSCl (**4**)	N_T[b]	Y_{Cl}[b]
100% EtOH	3.15 ± 0.04	0.996 ± 0.022	+0.37	–2.52
90% EtOH	6.07 ± 0.11	8.01 ± 0.19	+0.16	–0.94
80% EtOH	6.78 ± 0.07	47.5 ± 1.1	0.00	0.00
70% EtOH	8.18 ± 0.08	182 ± 12	–0.20	0.78
60% EtOH	10.4 ± 0.5	689 ± 15	–0.38	1.38
100% MeOH	16.3 ± 0.4	18.8 ± 0.4	+0.17	–1.17
100% TFE	0.303 ± 0.003	66.6 ± 1.9[c]	–3.93	2.79
97% TFE	0.395 ± 0.014	324 ± 19[d]	–3.30	2.83
90% TFE	0.599 ± 0.016	511 ± 20	–2.55	2.85
70% TFE	2.25 ± 0.18		–1.98	2.96
50% TFE	6.02 ± 0.14		–1.73	3.16
80T-20E	0.134 ± 0.005	448 ± 18	–1.76	1.89
60T-40E	0.334 ± 0.009	75.0 ± 1.1	–0.94	0.63
97% HFIP	25.7 ± 0.5[e]		–5.26	5.08
90% HFIP	16.7 ± 0.3[f]		–3.84	4.31
70% HFIP	10.5 ± 0.3		–2.94	3.83
80% acetone	0.997 ± 0.012	3.12 ± 0.07	–0.37	–0.80
70% acetone		24.6 ± 1.5	–0.42	0.17
65% acetone	1.62 ± 0.01[g]		–0.48	0.60
60% acetone	3.03 ± 0.14	175 ± 3	–0.52	1.00

[a]Unless otherwise indicated, the average of all integrated rate coefficients from duplicate runs, with associated standard deviations.
[b]From listings in refs. 1, 5, and 13.
[c]Using the theoretical infinity titer and the extrapolated initial values (from four runs); experimental maximum titer of 58 ± 2% of the theoretical.
[d]Using theoretical infinity titer and the average of integrated rate coefficients in the first 55% of reaction; experimental maximum titer of 84 ± 1% of the theoretical.
[e]Initial value by extrapolation; integrated rate coefficient had fallen to 14.5 × 10^{-5} s^{-1} at 38% reaction.
[f]Initial value by extrapolation; integrated rate coefficient had fallen to 13.7 × 10^{-5} s^{-1} at 40% reaction.
[g]From ref. 8.

Fig. 1. Plot of log (k/k_0) for solvolyses of phenyl chlorothionoformate at 25.0°C against ($1.53N_T + 0.36Y_{Cl}$). The eight log (k/k_0) values for the TFE–H_2O and HFIP–H_2O solvents are not included in the correlation; they are added to show their considerable deviation from the correlation line.

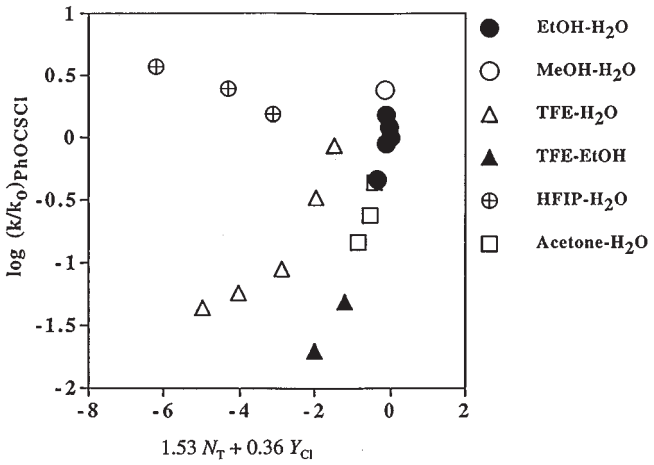

fluoroalcohol solvents, assigned to the ionization channel in the study (5) of the solvolyses of **2**, are within a similar range of 0.97–1.14. Consistent with these values, McKinnon and Queen (7) found that, for hydrolysis in 100% water at 5°C, the ratio had a value of 0.35. This suggests a rather remarkable similarity, not only in mechanism but also in rate, between the solvolyses of **2** and **3**. Indeed, the solvolyses of **3** can be treated, in exactly the same manner as **2**, by the dual application of eq. [2]. For 11 solvents (excluding aqueous fluoroalcohols), values are obtained of $l = 1.53 \pm 0.19$, $m = 0.36 \pm 0.08$, and $c = 0.11 \pm 0.22$, with a correlation coefficient of 0.953 and an *F*-test value of 39 (Fig. 1). The *m* value is at the lower end of the range observed for addition–elimination reactions at a trigonal carbon, and this could reflect a reduced demand for solvation when, at the transition state, the negative charge is developing on a sulfur atom rather than the oxygen atom of previously reported (1, 5, 15) examples.

For solvolyses of **3** in TFE, four aqueous-TFE mixtures, and three aqueous-HFIP mixtures, values are obtained of 0.43 ± 0.06 for *l*, 1.19 ± 0.08 for *m*, and –3.14 ± 0.12 for *c*, with a correlation coefficient of 0.9905 and an *F*-test value of 130 (Fig. 2). These values are in the range previously observed for ionization reactions at an acyl carbon. A large negative *c* value is observed because the experimental k_0 value is the one applying to the other reaction channel. Indeed, the value can be used to estimate a specific rate of solvolysis in 80% ethanol by the ionization channel of 4.9 × 10^{-8} s^{-1}, some 1400 times lower than the observed value for the addition–elimination pathway.

© 1999 NRC Canada

Fig. 2. Plot of log (k/k_0) for solvolyses of phenyl chlorothionoformate against ($0.43N_T + 1.19Y_{Cl}$).

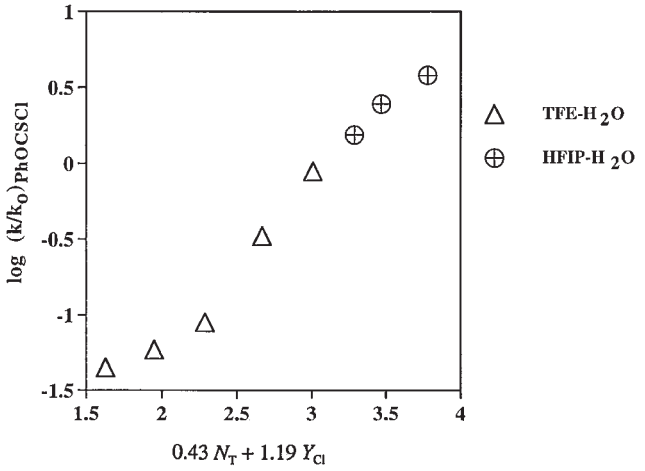

Fig. 3. Plot of log (k/k_0) for solvolyses of phenyl chlorodithioformate against ($0.55N_T + 0.84Y_{Cl}$).

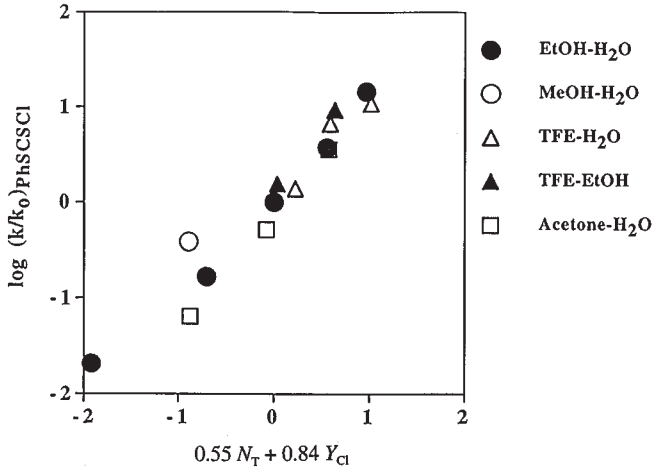

Solvolyses of phenyl chlorodithioformate (4)

McKinnon and Queen (7) found that a fairly concentrated solution of the methyl ester in 70% acetone gave dimethyl trithiocarbonate ($(MeS)_2C=S$) as the only organic product. It was postulated that the methanethiol formed initially reacted rapidly with remaining substrate (eq. [4]). In dilute solution, the ultraviolet spectrum of the product indicated an absence

[4]

of methyl trithiocarbonate, and the products were formed according to eq. [5]. Vapor phase chromatography gave no evidence for methanol formation, ruling out any reaction

[5] 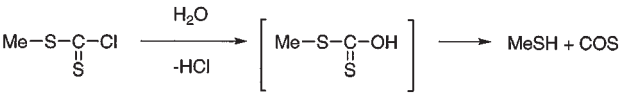

pathway involving methyl–sulfur bond fission. It is to be expected that the hydrolyses of **4** will follow a parallel pathway, but the scheme for the reaction with an alcohol (ROH) will terminate with the formation of PhSCSOR.

Since the introduction of one sulfur atom into **1** to give either **2** or **3** has been found to give an increased tendency towards ionization reaction, it is reasonable to expect that the introduction of two sulfur atoms, to give **4**, will lead to a further increase in this tendency. The observation of common-ion rate depression (11) during hydrolyses of **4** in 70% aqueous acetone (14), only a moderately ionizing solvent, indicates that this prediction is valid.

Values have been reported (11) for the solvolyses of **4** in 70% acetone at 4.94 and at 20.5°C. These values differ, however, by a factor of 25 for a 15.5°C difference in temperature and lead to an extrapolated specific rate at 25.0°C of 145×10^{-5} s^{-1}, about six times greater than our experimental value. Data simultaneously reported for the methyl ester lead to an extrapolated specific rate value at 20.5°C very close to that reported as being for **4**. One possibility is that the data at 20.5°C are for the methyl ester and not, as reported, for the phenyl ester.

The observation of one good linear extended Grunwald–Winstein plot over the full range of the 14 solvents with *l* and *m* values within the range one would expect (5, 15, 16) for the ionization mechanism suggests that this pathway now dominates over the full range of solvents. The observed sensitivity values are 0.55 ± 0.09 for *l* and 0.84 ± 0.08 for *m*; the *c* value is 0.07 ± 0.24, the correlation coefficient is 0.967, and the *F*-test value is 80 (Fig. 3). The solvent with the highest probability of an addition–elimination component is 100% ethanol, but we can calculate a value of –1.84 for log (k/k_0), in excellent agreement with the experimental value of –1.68. An analysis of the data accumulated for *tert*-butyl chloride solvolyses (17), using the identical set of solvents, leads to values for *l* of 0.37 ± 0.09 and for *m* of 0.83 ± 0.08 (correlation coefficient of 0.977), suggesting similar degrees of ionization at the transition state and with a slightly more pronounced nucleophilic solvation in the solvolyses of **4** than in those for *tert*-butyl chloride.

Conclusions

The solvolyses of **1** (PhOCOCl) and **4** (PhSCSCl) represent two extremes of solvolytic behavior. Both show a unity of mechanism over the full range of solvents commonly used in studies involving an application of the extended Grunwald–Winstein equation. The solvolyses of **1** follow an addition–elimination mechanism in which the rate-determining step involves nucleophilic addition. The solvolyses of **4** follow an ionization mechanism, with a considerable solvation of the developing carbocation. This solvation is indicated by the *l* values, from application of eq. [2], being slightly greater than for corresponding solvolyses of *tert*-butyl chloride.

In addition to being intermediate in structure, **2** (PhSCOCl) and **3** (PhOCSCl) are also intermediate in solvolytic behavior. Surprisingly, **2** and **3** behave very similarly, not only in the position of mechanistic change as the solvent is varied, but also as regards the measured specific rates of solvolysis. In ethanol, the specific rates fall when sulfur is introduced, but the fall-off from solvolysis of **2** or **3** to solvolysis of **4** is relatively small because of the change from an addition–elimination mechanism to an ionization

© 1999 NRC Canada

Table 2. Comparison of the specific rates of solvolysis, at 25.0°C, of **1**–**4** and correlations using the extended Grunwald–Winstein equation.

	Relative Rate					
Substrate	EtOH	97% TFE	n^a	l^b	m^b	R^c
1	1.00	1.00	21	1.68 ± 0.10	0.57 ± 0.06	0.973
2	0.026		16	1.74 ± 0.17	0.48 ± 0.07	0.946
2		5.9	6	0.62 ± 0.08	0.92 ± 0.11	0.983
3	0.012		11	1.53 ± 0.19	0.36 ± 0.08	0.953
3		6.9	8	0.43 ± 0.06	1.19 ± 0.08	0.991
4	0.0038	324	14	0.55 ± 0.09	0.84 ± 0.08	0.967

[a]Number of solvents.

[b]From eq. [2].

[c]Correlation coefficient.

mechanism. In 97% TFE, the opposite behavior is observed, with the initial rise from **1** to either **2** or **3** being relatively small because ionization is followed in this solvent for solvolyses of **2**–**4**, but the addition–elimination mechanism is dominant for **1**. These trends are summarized in Table 2.

The correlation analyses of the specific rates of solvolysis of **1**–**4** are also summarized in Table 2. The six entries divide into two groups of three. In one grouping, an *l* value of 1.53–1.74, coupled with an *m* value of 0.36–0.57, is considered to reflect the operation of an addition–elimination pathway. In the other grouping, *l* values of 0.43–0.62 and *m* values of 0.84–1.19 are considered as being a consequence of an ionization mechanism with appreciable nucleophilic solvation of the developing carbocation.

Experimental

Phenyl chlorothionoformate (Aldrich, 99%) and phenyl chlorodithioformate (Aldrich, 95%) were used without further purification. Solvents were purified and the kinetic runs carried out as previously described (18). The simple and multiple regression analyses were performed using the ABSTAT statistical package (Anderson–Bell, Arvada, Colorado).

Acknowledgment

D.N.K. thanks Professor H. Mayr (Universität München) for hospitality during the time that this manuscript was being prepared, and the Royal Society of Chemistry for a Journals Grant for International Authors.

References

1. D.N. Kevill and M.J. D'Souza. J. Chem. Soc. Perkin Trans. 2, 1721 (1997).
2. I.S. Koo, K. Yang, K. Kang, and I. Lee. Bull. Korean Chem. Soc. **19**, 968 (1998).
3. E. Grunwald and S. Winstein. J. Am. Chem. Soc. **70**, 846 (1948).
4. S. Winstein, E. Grunwald, and H.W. Jones. J. Am. Chem. Soc. **73**, 2700 (1951).
5. D.N. Kevill, M.W. Bond, and M.J. D'Souza. J. Org. Chem. **62**, 7869 (1997).
6. A. Queen. Can. J. Chem. **45**, 1619 (1967).
7. D.M. McKinnon and A. Queen. Can. J. Chem. **50**, 1401 (1972).
8. C. Csunderlik, R. Bacaloglu, and G. Ostrogovich. J. Prakt. Chem. **317**, 73 (1975).
9. G. Ostrogovich, C. Csunderlik, and R. Bacaloglu. J. Prakt. Chem. **317**, 62 (1975).
10. A. Queen and T.C. Matts. Tetrahedron Lett. 1303 (1975).
11. A. Queen, D.M. McKinnon, and A.W. Bell. Can. J. Chem. **54**, 1906 (1976).
12. C.K. Ingold. Structure and mechanism in organic chemistry. 2nd ed. Cornell University Press, Ithaca, New York. 1969. pp. 483–484.
13. D.N. Kevill. *In* Advances in quantitative structure-property relationships. Vol. 1. *Edited by* M. Charton. JAI Press, Greenwich, Conn. 1996. pp. 81–115.
14. T.W. Bentley and G. Llewellyn. Prog. Phys. Org. Chem. **17**, 121 (1990).
15. D.N. Kevill and M.J. D'Souza. J. Org. Chem. **63**, 2120 (1998).
16. D.N. Kevill, A.J. Casamassa, and M.J. D'Souza. J. Chem. Res. Synop. 472 (1996).
17. D.N. Kevill and M.J. D'Souza. J. Chem. Res. Synop. 174 (1993).
18. D.N. Kevill and S.W. Anderson. J. Org. Chem. **56**, 1845 (1991).

© 1999 NRC Canada

Picosecond radical kinetics. Rate constants for ring openings of 2-aryl-substituted cyclopropylcarbinyl radicals

Martin Newcomb, Seung-Yong Choi, and Patrick H. Toy

Abstract: The kinetics of ring openings of a series of eight (*trans*-2-arylcyclopropyl)methyl radicals (**1**) were studied by indirect kinetic methods using Barton's PTOC esters as radical precursors and reaction with PhSeH as the competition reaction. The substituents were CF_3, F, Me, and OMe located on both the *para* and *meta* positions of the aromatic ring. Syntheses of the radical precursors and the products of the radical reactions are described. Kinetics were determined between –43 and 25°C in four cases (CF_3 and OMe substituents) and at 0 and 25°C in the other four cases. The rate constants at 25°C ranged from 1.0×10^{11} s^{-1} (*p*-CH_3) to 4.1×10^{11} s^{-1} (*p*-CF_3). The relatively large acceleration of the *p*-CF_3 group, ca. 2.5 times as fast as the parent system with Ar = Ph, correlates well with Adam's ΔD substituent parameters but not with other radical substituent parameters. These calibrated radical rearrangements provide a new set of ultrafast reactions that can be applied in mechanistic probe studies.

Key words: cyclopropylcarbinyl radical, kinetics, PTOC esters, benzeneselenol.

Résumé : On a étudié la cinétique de l'ouverture de cycle d'une série de huit radicaux (*trans*-2-arylcyclopropyl)méthyles (**1**) à l'aide de méthodes cinétiques indirectes, en utilisant les esters PTOC de Barton comme précurseurs des radicaux et la réaction avec le PhSeH comme réaction en compétition. Des substituants CF_3, F, Me et OMe ont été placés dans les positions *ortho* ainsi que *méta* du noyau aromatique. On décrit les synthèses des précurseurs de radicaux ainsi que celles des produits des réactions radicalaires. Dans quatre cas (substituants CF_3 et OMe), on a déterminé les cinétiques à des températures entre –43 à +25°C et à 0 et 25°C dans les quatre autres cas. Les constantes de vitesse à 25°C vont de $1{,}0 \times 10^{11}$ s^{-1} (*p*-CH_3) à $4{,}1 \times 10^{11}$ s^{-1} (*p*-CF_3). L'accélération relativement importante observée avec le groupe *p*-CF_3, environ 2,5 fois plus rapide que le système parent dans lequel Ar = Ph, donne une bonne corrélation avec les paramètres de substituants ΔD de Adam, mais ce n'est pas le cas avec les autres paramètres de substituants radicalaires. Ces réarrangements radicalaires calibrés fournissent un nouvel ensemble de réactions ultrarapides qui peuvent être appliquées comme sonde dans des études mécanistiques.

Mots clés : radical cyclopropylcarbinyle, cinétique, esters PTOC, benzènesélénol.

[Traduit par la Rédaction]

Rearrangements of radicals have been employed qualitatively in mechanistic probes to implicate radical intermediates and quantitatively as clocks to time radical reactions (1, 2). 2-Aryl-substituted cyclopropylcarbinyl radicals fragment quite rapidly with transient lifetimes in the picosecond range at ambient temperature (3–5), and (*trans*-2-phenylcyclopropyl)methane and related species have been applied in studies of the mechanisms of enzyme-catalyzed hydroxylation reactions (6–14). The phenyl group provides acceleration of the radical reaction, but the aromatic ring is subject to oxidation by enzymes, resulting in phenolic by-products. In addition, because the skeletal reorganization of radical and cationic intermediates is the same, such probes do not permit an inherent distinction between these two types of intermediates. In an effort to provide a wide range of fast radical probes including species that are not oxidized to phenols and that might provide information permitting distinction between radicals and cations, we have calibrated a series of 2-aryl-substituted cyclopropylcarbinyl radical ring openings. The kinetics of the rearrangements are reported here.

Received December 2, 1998.

This paper is dedicated to Jerry Kresge in recognition of his many achievements in chemistry.

M. Newcomb,[1] S.-Y. Choi, and P.H. Toy. Department of Chemistry, Wayne State University, Detroit, MI 48202, U.S.A.

[1]Author to whom correspondence may be addressed. Telephone: (313) 577-2782. Fax: (313) 577-8822. e-mail: men@chem.wayne.edu

Precursors and products

The kinetics of ring openings for the series of radicals **1** were determined by an indirect method using Barton's PTOC esters (**2**) (15) as radical precursors and benzeneselenol trapping as the basis reaction (Scheme 1) (3, 16–18). The PTOC esters react in radical chain reactions to give acyloxyl radicals (**3**) that decarboxylate rapidly to give radicals **1**. Ring openings of radicals **1** give benzylic radicals **4** in competition with trapping by PhSeH that produces the cyclopropanes **5**. Benzylic radicals **4** also react with PhSeH

© 1999 NRC Canada

Scheme 1.

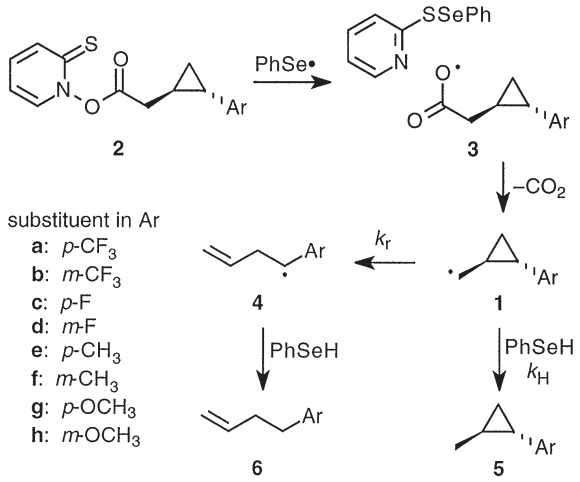

Scheme 2. (*a*) Ph_3P = CHC(O)NMeOMe, CH_2Cl_2; (*b*) $Me_3SO^+ I^-$, NaH, DMSO; (*c*) *t*-BuOK, H_2O, Et_2O; (*d*) i. $(COCl)_2$, DMF, C_6H_6, ii. CH_2N_2, Et_2O, iii. Ag_2O, $Na_2S_2O_3$, H_2O, reflux, iv. CH_2N_2, Et_2O; (*e*) LiOH, MeOH, H_2O; (*f*) Bu_3P, 2,2′-dipyridyl disulfide bis-*N*-oxide, CH_2Cl_2.

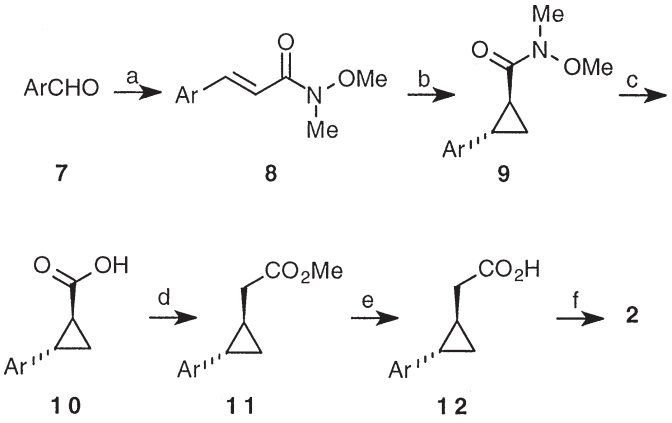

giving alkenes **6**, and the $PhSe^{\bullet}$ radical formed in these processes propagates the chain reaction.

PTOC esters are prepared from the corresponding carboxylic acids. For economy in synthesis, the sequence of reactions shown in Scheme 2 was employed. This sequence permits the preparation of the requisite carboxylic acids and the cyclic products of the radical reactions from advanced intermediates. The commercially available substituted benzaldehydes **7** were first converted to the corresponding Weinreb amides (19) **8** by Wittig olefination with *N*-methoxy-*N*-methyl-2-(triphenylphosphoranylidene)acetamide. The acrylamide derivatives **8** were cyclopropanated in reactions with the ylide from trimethylsulfoxonium iodide and sodium hydride according to the procedure developed by Rodriques (20) to afford the cyclopropylcarboxamides **9**. Hydrolysis of amides **9** by the anhydrous hydroxide procedure of Gassman et al. (21) gave acids **10,** which were homologated to the corresponding (2-arylcyclopropyl)acetic acids. For purification purposes, the homologated acids were converted to esters **11,** which were isolated and then

Scheme 3. (*a*) $LiAlH_4$, THF; (*b*) i. MsCl, Et_3N, THF, –30°C, ii. $LiBEt_3H$, THF, –78°C; (*c*) CH_2 = $CHCH_2MgCl$, Et_2O, reflux.

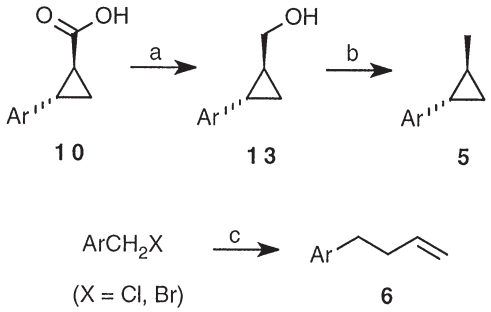

saponified to afford acids **12**. The requisite acids were converted to PTOC esters **2** by conventional methods.

Authentic samples of the trapped and rearranged products of the radical reactions were prepared (Scheme 3). The cyclopropanes **5** were prepared in two steps from acids **10**. Lithium aluminum hydride reduction of the acids gave alcohols **13** that were reduced to cyclopropanes **5** by conversion to the mesylate derivatives and reduction with lithium triethylborohydride (22). The acyclic products from radical ring opening (**6**) were prepared by reaction of the appropriate substituted benzylic halide with allylmagnesium chloride (23).

Kinetics

PTOC esters **2** were allowed to react in THF in the presence of PhSeH in indirect kinetic studies similar to those previously reported. Solutions were shielded from light during a thermal equilibration period. The solutions were then irradiated with visible light, which cleaves the PTOC esters and initiates the radical chain reactions. Following the radical chain reactions, the reaction mixtures were analyzed by GC. The yields of products were generally in the range of 60–80%, which is typical for this type of study. The *m*-CF_3-substituted system had yields of 40–50%. The PTOC esters are activated acyl derivatives that can react with PhSeH in polar reactions, and the intermediate acyloxyl radicals can be trapped by PhSeH in competition with decarboxylation; both side reactions reduce the overall yield but have no effect on the kinetics.

The indirect kinetic results are collected in Table 1. PhSeH is one of the fastest radical trapping agents available, but the ring-opening reactions are so fast that ring-opened products greatly predominated. Table 1 contains the ratios of rate constants for rearrangement and trapping (k_r/k_H) with errors at 1σ. For radicals **1a**,**1b**, **1g**, and **1h**, relative rate constants were determined between –43 and 25°C, and the relative Arrhenius functions for these radicals are shown graphically in Fig. 1. The log *A* terms in the relative Arrhenius functions are similar for these radicals, as expected for the case of remote substituents, giving a weighted average log *A* term of (2.4 ± 0.1) (error at 2σ).

The indirect kinetic method provides relative rate constants for rearrangement (k_r) and trapping by PhSeH (k_H). In the original calibration of the ring opening of the parent radical (**1**, Ar = Ph), the rate constants for reaction of PhSeH employed were determined by competition against ring

© 1999 NRC Canada

Table 1. Results of competition kinetic studies with radicals **1**.

Radical (subs)	Temp (°C)	Runs	k_r/k_H [a] (M)	Avg % yield
1a (*p*-CF_3)	25	4	327 ± 12	78
	0	4	305 ± 9	74
	–21	4	346 ± 40	79
	–42	4	297 ± 38	65
1b (*m*-CF_3)	25	3	96 ± 6	52
	0	3	84 ± 3	52
	–23	3	78 ± 5	46
	–43	3	73 ± 5	41
1g (*p*-OMe)	25	3	114 ± 10	72
	2	3	119 ± 11	84
	0	2	123 ± 14	84
	–23	3	98 ± 5	77
	–43	3	96 ± 2	65
1h (*m*-OMe)	25	3	160 ± 4	67
	0	3	128 ± 6	58
	–23	3	151 ± 16	63
	–42	4	135 ± 12	69
1e (*p*-CH_3)	25	3	83 ± 2	71
	0	3	80 ± 6	76
1f (*m*-CH_3)	25	3	207 ± 16	81
	0	3	141 ± 11	79
1c (*p*-F)	25	3	117 ± 4	86
	0	3	100 ± 2	85
1d (*m*-F)	25	3	159 ± 9	77
	0	3	159 ± 11	78

[a]Relative rate constants for ring opening and reaction with PhSeH; errors are 1σ.

Fig. 1. Relative rate constants for ring openings and PhSeH trapping of radicals **1a**, **1b**, **1g**, and **1h**. The lines are regression fits.

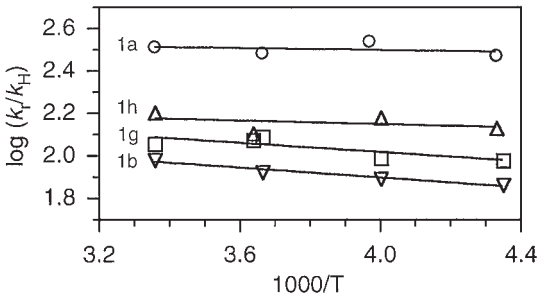

Table 2. Rate constants and estimated Arrhenius functions for ring openings of radicals **1**.

Radical (subs)	k_{25} (s^{-1}) [a]	Arrhenius function[b]
1 (Ar = Ph) [c]	1.6×10^{11}	13.1 – 2.58/θ
1a (*p*-CF_3)	4.1×10^{11}	13.1 – 2.02/θ
1b (*m*-CF_3)	1.2×10^{11}	13.1 – 2.75/θ
1c (*p*-F)	1.5×10^{11}	13.1 – 2.66/θ
1d (*m*-F)	2.0×10^{11}	13.1 – 2.45/θ
1e (*p*-Me)	1.0×10^{11}	13.1 – 2.86/θ
1f (*m*-Me)	2.6×10^{11}	13.1 – 2.29/θ
1g (*p*-OMe)	1.4×10^{11}	13.1 – 2.62/θ
1h (*m*-OMe)	2.0×10^{11}	13.1 – 2.45/θ

[a]Rate constant at 25°C.
[b]Equals (log k × s); θ = 2.3RT in kcal/mol. See text for assumptions.
[c]See ref. 18.

opening of the cyclopropylcarbinyl radical. However, a recent recalibration (18) of alkyl radical trapping by reactive H-atom donors indicated that the original rate constants for PhSeH were too large by about 30% due to an error in rate constants introduced early in the sequence of indirect kinetic studies. Accordingly, we suggested that the rate constants for reaction of PhSeH with cyclopropylcarbinyl radicals are likely to be quite similar to those for reaction of primary alkyl radicals (18).

We assume, therefore, that the rate constants for PhSeH trapping of radicals **1** are equal to those recently determined for reactions of PhSeH with a primary alkyl radical. The rate constants for PhSeH determined at ambient temperature are likely to be the most accurate, as previously discussed (18). In Table 2, we have used the rate constant for reaction of PhSeH with 1° alkyl radicals at 25°C (1.26×10^9 M^{-1} s^{-1}) (18) and the relative rate constants for ring openings and trapping of radicals **1** to calculate absolute rate constants for ring openings at 25°C. Radicals **1** are extremely short lived with lifetimes (τ = 1/k) at 25°C of only 2.4–10 ps.

In considering such reactive species, one might question whether or not the methods provide true statistical averaging. This appears to be the case for radicals **1**. In the recent study of PhSeH trapping kinetics, the radical clock used for calibration cyclized with a rate constant of 3.7×10^7 s^{-1} at 20°C and demonstrated excellent Arrhenius behavior in direct LFP kinetic studies (18). The relative rate constants and Arrhenius function for PhSeH trapping determined in that work should be quite reliable. Using the log A term for

© 1999 NRC Canada

Fig. 2. Correlations of relative rate constants for ring openings of radicals **1** at 25°C with Creary's σ(rad) scale (25), Arnold's σ_α scale (26), and Adam's Δ*D* scale (27). In each plot, the points for radicals **1a**, **1e**, and **1g** are labeled with the corresponding letters.

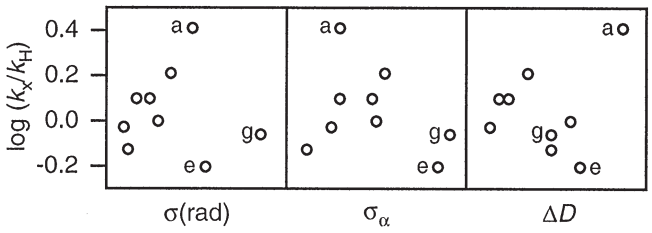

PhSeH trapping (log *A* = 10.73 ± 0.14) (18) and the weighted average relative log *A* term for ring opening and trapping of radicals **1** noted above, the calculated log *A* term for ring openings of radicals **1** is 13.1 ± 0.2. This value is in excellent agreement that those typically found for cyclopropylcarbinyl radical ring openings including those determined with high precision in direct LFP kinetic studies of a series of cyclopropylcarbinyl radicals containing UV-detectable reporter groups (24).

On the basis of the consistent Arrhenius entropic term and its agreement with previous results, one expects that good estimates of rate constants for ring openings of radicals **1** at varying temperatures can be calculated by employing the rate constants determined at 25°C, the most reliable values, and an Arrhenius log *A* term of 13.1. Table 2 contains temperature-dependent functions for rearrangements of radicals **1** thus calculated.

Remote substituent effects in radical reactions have been considered previously. These effects are generally small, and Hammett-type treatments have large relative errors. The rate constants for ring openings of radicals **1** correlate poorly with the substituent parameters σ(rad) of Creary et al. (25), σ_α of Wayner and Arnold (26), and Δ*D* of Adam et al.(27) (Fig. 2). The fit is especially poor for the *p*-CF_3 (**1a**), *p*-Me (**1e**), and *p*-OMe (**1g**) cases using the σ(rad) and σ_α parameters. It is interesting to note, however, that the large substituent value for *p*-CF_3 in the Δ*D* scale is in good agreement with the relatively large kinetic effect found in this work.

In summary, rate constants for ring openings of a variety of *trans*-2-arylcyclopropylcarbinyl radicals are now available. The ultrafast rearrangements permit quantitation of extremely short "radical" lifetimes including lifetimes in the transition states for insertion reactions. In addition, the corresponding (arylcyclopropyl)methanes containing the *p*-CF_3 and *p*-F substituents were found to be resistant to arene oxidation (i.e., phenol production) in reactions with cytochrome P450 enzymes (13) and methane monooxygenase hydroxylase enzyme (28).

Experimental section

General methods

Commercially available reagents were purchased from the Aldrich Chemical Company and were used as received. All moisture-sensitive reactions were carried out in flame-dried glassware under a nitrogen atmosphere. Tetrahydrofuran (THF) and diethyl ether were distilled under a nitrogen atmosphere over sodium and benzophenone ketyl. Methylene chloride was distilled under a nitrogen atmosphere over phosphorus pentoxide. Dimethyl sulfoxide (DMSO) was distilled in vacuo from calcium hydride.

^{1}H and ^{13}C NMR spectra of $CDCl_3$ solutions were obtained at 300 or 500 MHz and 75 or 125 MHz, respectively. Gas chromatographic analyses were performed using flame ionization detection on a Varian 3400 chromatograph (15 m × 0.54 mm bonded phase SE-30 and Carbowax columns, Alltech). High-resolution mass spectral analyses were performed by the Central Instrumentation Facility at Wayne State University (Detroit, Mich.). Melting points were determined using a Unimelt capillary melting point apparatus (Thomas Hoover) and are uncorrected. Radial chromatography was performed on a Chromatotron model 7294T (Harrison Research Corp.) using plates coated with TLC grade silica gel (Merck) with gypsum binder and fluorescent indicator.

trans-1-Methyl-2-(4-(trifluoromethyl)phenyl)cyclopropane (5a). Procedure G

A solution of **13a** (0.28 g, 1.31 mmol) in THF (8 mL) under a nitrogen atmosphere was cooled to –30°C. To this was added sequentially via syringe triethylamine (0.45 mL, 3.23 mmol) and methanesulfonyl chloride (0.11 mL, 1.42 mmol). The mixture was stirred at –30°C for 30 min and then cooled to –78°C. A solution of $LiBEt_3H$ (1.0 M in THF, 4.0 mL, 4.0 mmol) was added via syringe. The mixture was allowed to warm slowly to room temperature and was stirred for 13 h. The reaction mixture was quenched by the addition of 30% H_2O_2 (2 mL) and 15% aqueous NaOH (2 mL). The resulting mixture was heated at reflux for 1 h and then cooled to room temperature. The organic layer was separated, and the aqueous layer was extracted with ether (3 × 25 mL). The combined organic phase was washed with brine (50 mL), dried over $MgSO_4$, filtered, and concentrated in vacuo at 0°C. The crude product was purified by radial chromatography (pentane) to afford **5a** (0.21 g, 1.04 mmol, 79%) as a clear, colorless oil. ^{1}H NMR ($CDCl_3$) δ: 0.80–0.86 (1H, m), 0.94 (1H, dt, J_1 = 8.1 Hz, J_2 = 4.8 Hz), 1.06–1.16 (1H, m), 1.20 (3H, d, *J* = 5.7 Hz), 1.62 (1H, dt, J_1 = 8.7 Hz, J_2 = 4.5 Hz), 7.10 (2H, d, *J* = 8.4 Hz), 7.48 (2H, d, *J* = 8.4 Hz). ^{13}C NMR ($CDCl_3$) δ: 18.3, 18.9, 18.9, 24.2, 124.6 (q, J_{C-F} = 270.2 Hz), 125.1 (2C, q, J_{C-F} = 2.9 Hz), 125.6 (2C), 127.4 (q, J_{C-F} = 31.6 Hz), 148.6. HRMS calcd. for $C_{11}H_{11}F_3$: 200.0813; found: 200.0808.

***trans*-1-Methyl-2-(3-(trifluoromethyl)phenyl)cyclopropane (5b)** was prepared by procedure G, from **13b** (0.33 g, 1.53 mmol), triethylamine (0.45 mL, 3.23 mmol), methanesulfonyl chloride (0.14 mL, 1.83 mmol), and $LiBEt_3H$ (8.0 mL, 8.0 mmol), in 59% yield (0.18 g, 0.90 mmol). ^{1}H NMR ($CDCl_3$) δ: 0.83 (1H, dt, J_1 = 8.4 Hz, J_2 = 5.1 Hz), 0.94 (1H, dt, J_1 = 8.4 Hz, J_2 = 4.8 Hz), 1.05–1.17 (1H, m), 1.22 (3H, d, *J* = 5.7 Hz), 1.65 (1H, dt, J_1 = 8.7 Hz, J_2 = 4.5 Hz), 7.19–7.41 (4H, m). ^{13}C NMR ($CDCl_3$) δ: 17.8, 18.4, 18.9, 24.1, 121.9 (q, J_{C-F} = 3.3 Hz), 122.2 (q, J_{C-F} = 3.3 Hz), 124.3 (q, J_{C-F} = 270.2 Hz), 128.5, 128.8, 130.5 (q, J_{C-F} = 32.0 Hz), 145.1. HRMS calcd. for $C_{11}H_{11}F_3$: 200.0813; found: 200.0816.

© 1999 NRC Canada

***trans*-1-Methyl-2-(4-fluorophenyl)cyclopropane (5c)** was prepared by procedure G, from **13c** (0.83 g, 4.99 mmol), triethylamine (1.40 mL, 10.0 mmol), methanesulfonyl chloride (0.45 mL, 5.81 mmol), and $LiBEt_3H$ (20.0 mL, 20.0 mmol), in 53% yield (0.40 g, 2.66 mmol). ^1H NMR ($CDCl_3$) δ: 0.74 (1H, ddd, J_1 = 8.4 Hz, J_2 = 5.4 Hz, J_3 = 4.8 Hz), 0.85 (1H, dt, J_1 = 8.1 Hz, J_2 = 5.4 Hz), 0.96–1.08 (1H, m), 1.21 (3H, d, J = 5.7 Hz), 1.58 (1H, dt, J_1 = 9.0 Hz, J_2 = 4.8 Hz), 6.91–7.04 (4H, m). ^{13}C NMR ($CDCl_3$) δ: 17.3, 17.7, 19.0, 23.6, 114.9 (2C, d, J_{C-F} = 20.9 Hz), 126.8 (2C, d, J_{C-F} = 7.5 Hz), 139.5, 160.9 (d, J_{C-F} = 241.6 Hz). HRMS calcd. for $C_{10}H_{11}F$: 150.0845; found: 150.0842.

***trans*-1-Methyl-2-(3-fluorophenyl)cyclopropane (5d)** was prepared by procedure G, from **13d** (0.80 g, 4.81 mmol), triethylamine (1.40 mL, 10.0 mmol), methanesulfonyl chloride (0.45 mL, 5.81 mmol), and $LiBEt_3H$ (20.0 mL, 20.0 mmol), in 73% yield (0.53 g, 3.53 mmol). ^1H NMR ($CDCl_3$) δ: 0.81 (1H, ddd, J_1 = 8.4 Hz, J_2 = 5.4 Hz, J_3 = 4.5 Hz), 0.93 (1H, dt, J_1 = 8.7 Hz, J_2 = 4.8 Hz), 1.04–1.16 (1H, m), 1.23 (3H, d, J = 6.0 Hz), 1.61 (1H, dt, J_1 = 9.0 Hz, J_2 = 4.8 Hz), 6.72–6.89 (3H, m), 7.18–7.24 (1H, m). ^{13}C NMR ($CDCl_3$) δ: 17.9, 18.3, 18.9, 24.2, 111.9 (d, J_{C-F} = 7.1 Hz), 112.1 (d, J_{C-F} = 17.7 Hz), 121.3 (d, J_{C-F} = 2.3 Hz), 129.5 (d, J_{C-F} = 8.9 Hz), 147.0 (d, J_{C-F} = 6.7 Hz), 163.1 (d, J_{C-F} = 242.7 Hz). HRMS calcd. for $C_{10}H_{11}F$: 150.0845; found: 150.0851.

***trans*-1-Methyl-2-(4-methylphenyl)cyclopropane (5e)** was prepared by procedure G, from **13e** (0.86 g, 5.30 mmol), triethylamine (1.50 mL, 10.8 mmol), methanesulfonyl chloride (0.45 mL, 5.81 mmol), and $LiBEt_3H$ (25.0 mL, 25.0 mmol), in 45% yield (0.35 g, 2.39 mmol). ^1H NMR ($CDCl_3$) δ: 0.71–0.77 (1H, m), 0.85–0.91 (1H, m), 0.99–1.11 (1H, m), 1.21 (3H, d, J = 5.7 Hz), 1.64 (1H, dt, J_1 = 8.7 Hz, J_2 = 4.5 Hz), 2.42 (3H, s), 6.92–7.26 (4H, m). ^{13}C NMR ($CDCl_3$) δ: 17.3, 17.6, 19.1, 20.9, 24.0, 125.4 (2C), 128.9 (2C), 134.6, 140.9. HRMS calcd. for $C_{11}H_{14}$: 146.1096; found: 146.1099.

***trans*-1-Methyl-2-(3-methylphenyl)cyclopropane (5f)** was prepared by procedure G, from **13f** (0.76 g, 4.68 mmol), triethylamine (1.40 mL, 10.0 mmol), methanesulfonyl chloride (0.45 mL, 5.81 mmol), and $LiBEt_3H$ (20.0 mL, 20.0 mmol), in 76% yield (0.52 g, 3.56 mmol). ^1H NMR ($CDCl_3$) δ: 0.82 (1H, dt, J_1 = 8.7 Hz, J_2 = 4.5 Hz), 0.98 (1H, dt, J_1 = 8.1 Hz, J_2 = 4.8 Hz), 1.09–1.21 (1H, m), 1.22 (3H, d, J = 5.7 Hz), 1.58 (1H, dt, J_1 = 9.0 Hz, J_2 = 4.8 Hz), 2.34 (3H, s), 6.98 (2H, d, J = 8.1 Hz), 7.09 (2H, d, J = 8.1 Hz). ^{13}C NMR ($CDCl_3$) δ: 17.5, 17.9, 19.1, 21.5, 24.3, 122.5, 126.0, 126.4, 128.2, 137.8, 144.0. HRMS calcd. for $C_{11}H_{14}$: 146.1096; found: 146.1095.

***trans*-1-Methyl-2-(4-methoxyphenyl)cyclopropane (5g)** was prepared by procedure G, from **13g** (0.49 g, 2.75 mmol), triethylamine (0.80 mL, 5.74 mmol), methanesulfonyl chloride (0.25 mL, 3.23 mmol), and $LiBEt_3H$ (11.0 mL, 11.0 mmol), in 65% yield (0.29 g, 1.79 mmol). ^1H NMR ($CDCl_3$) δ: 0.67 (1H, dt, J_1 = 8.1 Hz, J_2 = 4.8 Hz), 0.80 (1H, dt, J_1 = 9.0 Hz, J_2 = 4.8 Hz), 0.91–1.03 (1H, m), 1.17 (3H, d, J = 6.3 Hz), 1.53 (1H, dt, J_1 = 8.7 Hz, J_2 = 4.5 Hz), 3.78 (3H, s), 6.80 (2H, dt, J_1 = 8.4 Hz, J_2 = 3.3 Hz), 6.97 (2H, dt, J_1 = 9.0 Hz, J_2 = 2.7 Hz). ^{13}C NMR ($CDCl_3$) δ: 17.0, 17.3, 19.1, 23.6, 55.3, 113.8 (2C), 126.6 (2C), 136.0, 157.5. HRMS calcd. for $C_{11}H_{14}O$: 162.1045; found: 162.1046.

***trans*-1-Methyl-2-(3-methoxyphenyl)cyclopropane (5h)** was prepared by procedure G, from **13h** (0.38 g, 2.13 mmol), triethylamine (0.60 mL, 4.30 mmol), methanesulfonyl chloride (0.20 mL, 2.58 mmol), and $LiBEt_3H$ (9.0 mL, 9.0 mmol), in 55% yield (0.19 g, 1.17 mmol). ^1H NMR ($CDCl_3$) δ: 0.86 (1H, dt, J_1 = 8.4 Hz, J_2 = 4.8 Hz), 1.02 (1H, dt, J_1 = 8.4 Hz, J_2 = 5.1 Hz), 1.13–1.25 (1H, m), 1.31 (3H, d, J = 5.7 Hz), 1.68 (1H, dt, J_1 = 9.0 Hz, J_2 = 5.1 Hz), 3.88 (3H, s), 6.73–6.82 (3H, m), 7.28 (1H, t, J = 7.8 Hz). ^{13}C NMR ($CDCl_3$) δ: 17.8, 18.1, 19.2, 24.5, 55.1, 110.5, 111.5, 118.0, 129.3, 145.9, 159.8. HRMS calcd. for $C_{11}H_{14}O$: 162.1045; found: 162.1047.

4-(4-(Trifluoromethyl)phenyl)but-1-ene (6a). Procedure H

A solution of 4-(trifluoromethyl)benzyl chloride (0.76 mL, 5.14 mmol) and allylmagnesium chloride (2.0 M in Et_2O, 5.0 mL, 10.0 mmol) in ether (20 mL) was refluxed under a nitrogen atmosphere for 16 h. This was cooled to room temperature and was quenched with saturated aqueous NH_4Cl (50 mL). The organic layer was separated, and the aqueous layer was extracted with additional ether (3 × 25 mL). The combined organic layer was washed with brine (50 mL), dried over $MgSO_4$, and concentrated in vacuo at 0°C. The crude product was purified by radial chromatography (pentane) to afford **6a** (0.90 g, 4.50 mmol, 88%) as a clear, colorless oil. ^1H NMR ($CDCl_3$) δ: 2.35–2.43 (2H, m), 2.77 (2H, t, J = 8.1 Hz), 4.97–5.08 (2H. m), 5.84 (1H, ddt, J_1 = 9.9 Hz, J_2 = 7.2 Hz, J_3 = 6.9 Hz), 7.29 (2H, d, J = 7.8 Hz), 7.53 (2H, d, J = 7.8 Hz). ^{13}C NMR ($CDCl_3$) δ: 35.0, 35.1, 115.4, 124.4 (q, J_{C-F} = 270.2 Hz), 125.2 (2C, J_{C-F} = 3.3 Hz), 128.2 (q, J_{C-F} = 32.0 Hz), 128.8 (2C), 147.7, 145.9. HRMS calcd. for $C_{11}H_{11}F_3$: 200.0813; found: 200.0810.

4-(3-(Trifluoromethyl)phenyl)but-1-ene (6b) was prepared by procedure H, from 3-(trifluoromethyl)benzyl chloride (0.80 mL, 5.16 mmol) and allylmagnesium chloride (5.0 mL, 10.0 mmol), in 85% yield (0.89 g, 4.40 mmol). ^1H NMR ($CDCl_3$) δ: 2.36–2.44 (2H, m), 2.78 (2H, dd, J_1 = 8.1 Hz, J_2 = 6.3 Hz), 4.99–5.09 (2H, m), 5.85 (1H, ddt, J_1 = 10.5 Hz, J_2 = 6.6 Hz, J_3 = 6.3 Hz), 7.35–7.47 (4H, m). ^{13}C NMR ($CDCl_3$) δ: 35.2, 35.2, 115.4, 122.7 (q, J_{C-F} = 3.3 Hz), 124.3 (q, J_{C-F} = 270.2 Hz), 125.2 (q, J_{C-F} = 3.3 Hz), 128.6, 130.5 (q, J_{C-F} = 32.0 Hz), 131.8, 137.3, 142.6. HRMS calcd. for $C_{11}H_{11}F_3$: 200.0813; found: 200.0808.

4-(4-Fluorophenyl)but-1-ene (6c) was prepared by procedure H, from 4-fluorobenzyl bromide (1 mL, 8.04 mmol) and allylmagnesium chloride (6.0 mL, 12.0 mmol), in 79% yield (0.96 g, 6.39 mmol). ^1H NMR ($CDCl_3$) δ: 2.34–2.42 (2H, m), 2.71 (2H, dd, J_1 = 8.1 Hz, J_2 = 7.5 Hz), 4.99–5.10 (2H, m), 5.87 (1H, ddt, J_1 = 10.5 Hz, J_2 = 6.6 Hz, J_3 = 6.3 Hz), 6.95–7.03 (2H, m), 7.13–7.19 (2H, m). ^{13}C NMR ($CDCl_3$) δ: 34.5, 35.6, 114.9 (2C, d, J_{C-F} = 20.2 Hz), 115.1, 129.8 (2C, d, J_{C-F} = 7.7 Hz), 137.4 (d, J_{C-F} = 2.3 Hz), 137.8, 161.3 (d, J_{C-F} = 241.6 Hz). HRMS calcd. for $C_{10}H_{11}F$: 150.0845; found: 150.0840.

© 1999 NRC Canada

4-(3-Fluorophenyl)but-1-ene (6d) was prepared by procedure H from 3-fluorobenzyl bromide (1 mL, 8.15 mmol) and allylmagnesium chloride (6.0 mL, 12.0 mmol), in 78% yield (0.95 g, 6.32 mmol). ^{1}H NMR ($CDCl_3$) δ: 2.39–2.47 (2H, m), 2.76 (2H, dd, J_1 = 8.1 Hz, J_2 = 6.3 Hz), 5.03–5.14 (2H, m), 5.90 (1H, ddt, J_1 = 9.9 Hz, J_2 = 6.9 Hz, J_3 = 6.6 Hz), 6.90–7.02 (3H, m), 7.24–7.32 (1H, m). ^{13}C NMR ($CDCl_3$) δ: 35.1, 35.2, 112.7 (d, J_{C-F} = 21.0 Hz), 115.2 (d, J_{C-F} = 20.9 Hz), 115.3, 124.1 (d, J_{C-F} = 2.3 Hz), 129.6 (d, J_{C-F} = 7.7 Hz), 137.6, 144.4 (d, J_{C-F} = 6.6 Hz), 162.9 (d, J_{C-F} = 243.8 Hz). HRMS calcd. for $C_{10}H_{11}F$: 150.0845; found: 150.0849.

4-(4-Methylphenyl)but-1-ene (6e) was prepared by procedure H, from 4-methylbenzyl bromide (1.10 g, 5.94 mmol) and allylmagnesium chloride (4.0 mL, 8.0 mmol), in 61% yield (0.53 g, 3.62 mmol). ^{1}H NMR ($CDCl_3$) δ: 2.50 (3H, s), 2.52–2.59 (2H, m), 2.85 (2H, dd, J_1 = 8.4 Hz, J_2 = 6.3 Hz), 5.15–5.27 (2H, m), 6.05 (1H, ddt, J_1 = 10.5 Hz, J_2 = 6.6 Hz, J_3 = 6.3 Hz), 7.27 (4H, s). ^{13}C NMR ($CDCl_3$) δ: 21.1, 35.1, 35.8, 114.9, 128.4 (2C), 129.1 (2C), 135.3, 138.3, 138.9. HRMS calcd. for $C_{11}H_{14}$: 146.1096; found: 146.1100.

4-(3-Methylphenyl)but-1-ene (6f) was prepared by procedure H, from 3-methylbenzyl bromide (1.10 g, 5.94 mmol) and allylmagnesium chloride (4.0 mL, 8.0 mmol), in 62% yield (0.54 g, 3.69 mmol). ^{1}H NMR ($CDCl_3$) δ: 2.41 (3H, s), 2.43–2.49 (2H, m), 2.75 (2H, dd, J_1 = 8.1 Hz, J_2 = 5.7 Hz), 5.04–5.17 (2H, m), 5.95 (1H, ddt, J_1 = 10.2, J_2 = 6.9 Hz, J_3 = 6.6 Hz), 7.07–7.28 (4H, m). ^{13}C NMR ($CDCl_3$) δ: 21.4, 35.4, 35.6, 114.8, 125.5, 126.6, 128.2, 129.3, 137.8, 138.2, 141.9. HRMS calcd. for $C_{11}H_{14}$: 146.1096; found: 146.1096.

4-(4-Methoxyphenyl)but-1-ene (6g) was prepared by procedure H, from 4-methoxybenzyl chloride (0.60 mL, 4.43 mmol) and allylmagnesium chloride (4.0 mL, 8.0 mmol), in 97% yield (0.70 g, 4.31 mmol). ^{1}H NMR ($CDCl_3$) δ: 2.31 (2H, m), 2.65 (2H, dd, J_1 = 8.1 Hz, J_2 = 6.0 Hz), 3.79 (3H, s), 4.95–5.08 (2H, m), 5.85 (1H, ddt, J_1 = 10.5, J_2 = 6.6 Hz, J_3 = 6.3 Hz), 6.83 (2H, dt, J_1 = 8.7 Hz, J_2 = 2.7 Hz), 7.10 (2H, dt, J_1 = 8.7 Hz, J_2 = 2.4 Hz). ^{13}C NMR ($CDCl_3$) δ: 34.6, 35.9, 55.2, 113.8 (2C), 114.9, 129.4 (2C), 134.0, 138.2, 157.9. HRMS calcd. for $C_{11}H_{14}O$: 162.1045; found: 162.1047.

4-(3-Methoxyphenyl)but-1-ene (6h) was prepared by procedure H, from 3-methoxybenzyl chloride (0.60 mL, 4.13 mmol) and allylmagnesium chloride (4.0 mL, 8.00 mmol), in 84% yield (0.56 g, 3.45 mmol). ^{1}H NMR ($CDCl_3$) δ: 2.34–2.42 (2H, m), 2.69 (2H, dd, J_1 = 8.1 Hz, J_2 = 6.0 Hz), 3.81 (3H, s), 4.96–5.09 (2H, m), 5.87 (1H, ddt, J_1 = 10.5, J_2 = 6.6 Hz, J_3 = 6.3 Hz), 6.73–6.81 (3H, s), 7.18–7.24 (1H, m). ^{13}C NMR ($CDCl_3$) δ: 35.4, 35.5, 55.1, 111.1, 114.3, 115.0, 120.9, 129.3, 138.1, 143.5, 159.7. HRMS calcd. for $C_{11}H_{14}O$: 162.1045; found: 162.1040.

N-Methoxy-*N*-methyl-*trans*-4-(trifluoromethyl)cinnamamide (8a). Procedure A

A solution of 4-(trifluoromethyl)benzaldehyde (10.0 g, 57.4 mmol) and *N*-methoxy-*N*-methyl-2-(triphenylphosphoranylidene)acetamide (23.1 g. 63.6 mmol) in CH_2Cl_2 (150 mL) was stirred at room temperature for 16 h. The solvent was then removed in vacuo, and the crude product was chromatographed on silica gel (40% ethyl acetate in hexanes) to afford **8a** (14.1 g, 54.3 mmol, 95%) as a white solid; mp 50–52°C. ^{1}H NMR ($CDCl_3$) δ: 3.32 (3H, s), 3.78 (3H, s), 7.10 (1H, d, J = 15.9 Hz), 7.65 (4H, dd, J_1 = 12.0 Hz, J_2 = 9.0 Hz), 7.74 (1H, d, J = 15.9 Hz). ^{13}C NMR ($CDCl_3$) δ: 32.5, 61.9, 118.4, 123.8 (q, J_{C-F} = 276.9 Hz), 125.6 (2C, q, J_{C-F} = 3.7 Hz), 128.1 (2C), 131.3 (q, J_{C-F} = 33.1 Hz), 138.6, 141.5, 166.2. HRMS calcd. for $C_{12}H_{12}F_3NO_2$: 259.0820; found: 259.0820.

***N*-Methoxy-*N*-methyl-*trans*-3-(trifluoromethyl)cinnamamide (8b)** was prepared by procedure A, using 3-(trifluoromethyl)benzaldehyde (3.20 mL, 23.9 mmol) and *N*-methoxy-*N*-methyl-2-(triphenylphosphoranylidene)acetamide (10.0 g. 27.5 mmol), in 99% yield (6.15 g, 23.7 mmol). ^{1}H NMR ($CDCl_3$) δ: 3.23 (3H, s), 3.70 (3H, s), 7.02 (1H, d, J = 15.9 Hz), 7.38–7.71 (4H, m), 7.65 (1H, d, J = 15.9 Hz). ^{13}C NMR ($CDCl_3$) δ: 32.3, 61.8, 117.7, 123.8 (q, J_{C-F} = 271.4 Hz), 124.2 (q, J_{C-F} = 3.3 Hz), 126.0 (q, J_{C-F} = 3.3 Hz), 129.3, 131.1, 131.1 (q, J_{C-F} = 32.0 Hz), 135.9, 141.5, 166.1. HRMS calcd. for $C_{12}H_{12}F_3NO_2$: 259.0820; found: 259.0825.

***N*-Methoxy-*N*-methyl-*trans*-4-fluorocinnamamide (8c)** was prepared by procedure A, using 4-fluorobenzaldehyde (4.40 mL, 42.0 mmol) and *N*-methoxy-*N*-methyl-2-(triphenylphosphoranylidene)acetamide (17.30 g. 47.6 mmol), in 99% yield (8.68 g, 41.5 mmol). ^{1}H NMR ($CDCl_3$) δ: 3.24 (3H, s), 3.70 (3H, s), 6.90 (1H, d, J = 15.9 Hz), 6.97–7.04 (2H, m), 7.46–7.51 (2H, m), 7.63 (1H, d, J = 15.9 Hz). ^{13}C NMR ($CDCl_3$) δ: 32.4, 61.8, 115.5, 115.7 (2C, d, J_{C-F} = 22.1 Hz), 129.7 (2C, d, J_{C-F} = 8.9 Hz), 131.3 (d, J_{C-F} = 3.3 Hz), 142.0, 163.5 (d, J_{C-F} = 249.2 Hz), 166.7. HRMS calcd. for $C_{11}H_{12}FNO_2$: 209.0852; found: 209.0855.

***N*-Methoxy-*N*-methyl-*trans*-3-fluorocinnamamide (8d)** was prepared by procedure A, using 3-fluorobenzaldehyde (1.80 mL, 17.4 mmol) and *N*-methoxy-*N*-methyl-2-(triphenylphosphoranylidene)acetamide (7.50 g. 20.6 mmol), in 98% yield (3.58 g, 17.1 mmol). ^{1}H NMR ($CDCl_3$) δ: 3.24 (3H, s), 3.70 (3H, s), 6.95–7.01 (1H, m), 6.97 (1H, d, J = 15.9 Hz), 7.17–7.31 (3H, m), 7.61 (1H, d, J = 15.9 Hz). ^{13}C NMR ($CDCl_3$) δ: 32.4, 61.8, 114.0 (d, J_{C-F} = 20.9 Hz), 116.6 (d, J_{C-F} = 21.0 Hz), 117.1, 124.1, 130.2 (d, J_{C-F} = 7.7 Hz), 137.3 (d, J_{C-F} = 7.7 Hz), 141.9 (d, J_{C-F} = 2.2 Hz), 162.9 (d, J_{C-F} = 244.8 Hz), 166.4. HRMS calcd. for $C_{11}H_{12}FNO_2$: 209.0852; found: 209.0855.

***N*-Methoxy-*N*-methyl-*trans*-4-methylcinnamamide (8e)** was prepared by procedure A, using 4-methylbenzaldehyde (3.0 mL, 25.5 mmol) and *N*-methoxy-*N*-methyl-2-(triphenylphosphoranylidene)acetamide (11.50 g. 31.6 mmol), in 100% yield (5.24 g, 25.5 mmol); mp 52–53°C. ^{1}H NMR ($CDCl_3$) δ: 2.37 (3H, s), 3.30 (3H, s), 3.76 (3H, s), 6.97 (1H, d, J = 15.9 Hz), 7.18 (2H, d, J = 8.1 Hz), 4.47 (2H, d, J = 8.1 Hz), 7.71 (1H, d, J = 15.9 Hz). ^{13}C NMR ($CDCl_3$) δ: 21.4, 32.5, 61.8, 114.7, 128.0 (2C), 129.5 (2C), 132.4, 140.1, 143.4, 167.2. HRMS calcd. for $C_{12}H_{15}NO_2$: 205.1103; found: 205.1109.

***N*-Methoxy-*N*-methyl-*trans*-3-methylcinnamamide (8f)** was prepared by procedure A, using 3-methylbenzaldehyde (3.0 mL, 25.5 mmol) and *N*-methoxy-*N*-methyl-2-

© 1999 NRC Canada

(triphenylphosphoranylidene)acetamide (11.5 g. 31.6 mmol), in 97% yield (5.06 g, 24.7 mmol). ^{1}H NMR ($CDCl_3$) δ: 2.35 (3H, s), 3.28 (3H, s), 3.74 (3H, s), 7.01 (1H, d, J = 15.9 Hz), 7.13–7.35 (4H, m), 7.69 (1H, d, J = 15.9 Hz). ^{13}C NMR ($CDCl_3$) δ: 21.3, 32.5, 61.8, 115.6, 125.2, 128.6, 128.7, 130.6, 135.1, 138.4, 143.5, 167.0. HRMS calcd. for $C_{12}H_{15}NO_2$: 205.1103; found: 205.1107.

***N*-Methoxy-*N*-methyl-*trans*-4-methoxycinnamamide (8g)** was prepared by procedure A, using 4-methoxybenzaldehyde (3.0 mL, 24.7 mmol) and *N*-methoxy-*N*-methyl-2-(triphenylphosphoranylidene)acetamide (10.0 g. 27.5 mmol), in 92% yield (5.03 g, 22.7 mmol). ^{1}H NMR ($CDCl_3$) δ: 3.27 (3H, s), 3.72 (3H, s), 3.79 (3H, s), 6.86 (2H, dt, J_1 = 8.7 Hz, J_2 = 1.8 Hz), 6.88 (1H, d, J = 15.9 Hz), 7.48 (2H, dt, J_1 = 9.0 Hz, J_2 = 2.4 Hz), 7.67 (1H, d, J = 15.9 Hz). ^{13}C NMR ($CDCl_3$) δ: 32.4, 55.3, 61.7, 113.3, 114.2 (2C), 127.8, 129.6 (2C), 143.0, 161.0, 167.2. HRMS calcd. for $C_{12}H_{15}NO_3$: 221.1052; found: 221.1052.

***N*-Methoxy-*N*-methyl-*trans*-3-methoxycinnamamide (8h)** was prepared by procedure A, using 3-methoxybenzaldehyde (4.0 mL, 32.9 mmol) and *N*-methoxy-*N*-methyl-2-(triphenylphosphoranylidene)acetamide (12.50 g. 34.4 mmol), in 98% yield (7.11 g, 32.1 mmol). ^{1}H NMR ($CDCl_3$) δ: 3.24 (3H, s), 3.69 (3H, s), 3.76 (3H, s), 6.83–7.26 (3H, m), 6.97 (1H, d, J = 15.9 Hz), 7.23 (1H, t, J = 7.8 Hz), 7.64 (1H, d, J = 15.9 Hz). ^{13}C NMR ($CDCl_3$) δ: 32.4, 55.2, 61.8, 113.3, 115.3, 116.1, 120.5, 129.7, 136.5, 143.2, 159.8, 166.7. HRMS calcd. for $C_{12}H_{15}NO_3$: 221.1052; found: 221.1058.

N-Methoxy-*N*-methyl-*trans*-2-(4-(trifluoromethyl)-phenyl)cyclopropanecarboxamide (9a). Procedure B

A solution of trimethylsulfoxonium iodide (24.1 g, 110 mmol) in DMSO (100 mL) under a nitrogen atmosphere was cooled with a room-temperature water bath, and NaH (2.6 g, 108 mmol) was added portionwise over 15 min. After the addition was complete, the suspension was allowed to stir for 1 h, during which time it became homogeneous. A solution of **8a** (14.1 g, 54.3 mmol) in DMSO (50 mL) was added via cannula, and the reaction mixture was stirred for 6 h. The reaction mixture was quenched by pouring it into saturated aqueous NH_4Cl solution (500 mL). The mixture was extracted with CH_2Cl_2 (3 × 250 mL). The combined organic layer was washed with brine (200 mL), dried over $MgSO_4$, filtered, and concentrated in vacuo. The crude material was chromatographed on silica gel (40% ethyl acetate in hexanes) to afford **9a** (12.8 g, 46.8 mmol, 86%) as a clear, colorless oil. ^{1}H NMR ($CDCl_3$) δ: 1.30 (1H, ddd, J_1 = 8.4 Hz, J_2 = 6.3 Hz, J_3 = 4.5 Hz), 1.65 (1H, ddd, J_1 = 9.0 Hz, J_2 = 5.4 Hz, J_3 = 4.2 Hz), 2.38–2.46 (1H, m), 2.50 (1H, ddd, J_1 = 9.3 Hz, J_2 = 6.6 Hz, J_3 = 4.2 Hz), 3.19 (3H, s), 3.65 (3H, s), 7.18 (2H, d, J = 9.0 Hz), 7.48 (2H, d, J = 9.0 Hz). ^{13}C NMR ($CDCl_3$) δ: 16.5, 21.8, 25.2, 32.4, 61.5, 124.1 (q, $J_{C–F}$ = 270.3 Hz), 125.2 (2C, q, $J_{C–F}$ = 3.3 Hz), 126.3 (2C), 128.3 (q, $J_{C–F}$ = 32.4 Hz), 145.0, 172.2. HRMS calcd. for $C_{13}H_{14}F_3NO_2$: 273.0977; found: 273.0974.

***N*-Methoxy-*N*-methyl-*trans*-2-(3-(trifluoromethyl)phenyl)-cyclopropanecarboxamide (9b)** was prepared by procedure B, using **8b** (6.15 g, 23.7 mmol), trimethylsulfoxonium iodide (10.50 g, 47.7 mmol), and NaH (1.15 g, 47.9 mmol), in 87% yield (5.55 g, 20.3 mmol). ^{1}H NMR ($CDCl_3$) δ: 1.26 (1H, ddd, J_1 = 8.7 Hz, J_2 = 6.6 Hz, J_3 = 4.8 Hz), 1.60 (1H, ddd, J_1 = 9.3 Hz, J_2 = 5.4 Hz, J_3 = 4.2 Hz), 2.34–2.44 (1H, m), 2.50 (1H, ddd, J_1 = 8.7 Hz, J_2 = 6.0 Hz, J_3 = 4.2 Hz), 3.16 (3H, s), 3.62 (3H, s), 7.22 - 7.37 (4H, m). ^{13}C NMR ($CDCl_3$) δ: 16.3, 21.6, 25.2, 32.4, 61.5, 122.9 (q, $J_{C–F}$ = 3.3 Hz), 123.0 (q, $J_{C–F}$ = 3.3 Hz), 124.1 (q, $J_{C–F}$ = 270.2 Hz), 128.8, 129.6, 130.6 (q, $J_{C–F}$ = 30.9 Hz), 141.9, 172.3. HRMS calcd. for $C_{13}H_{14}F_3NO_2$: 273.0977; found: 273.0983.

***N*-Methoxy-*N*-methyl-*trans*-2-(4-fluorophenyl)cyclopropanecarboxamide (9c)** was prepared by procedure B, using **8c** (8.50 g, 40.6 mmol), trimethylsulfoxonium iodide (17.90 g, 81.3 mmol), and NaH (1.95 g, 81.3 mmol), in 88% yield (7.95 g, 35.6 mmol). ^{1}H NMR ($CDCl_3$) δ: 1.21 (1H, ddd, J_1 = 8.4 Hz, J_2 = 6.3 Hz, J_3 = 4.2 Hz), 1.57 (1H, ddd, J_1 = 9.6 Hz, J_2 = 5.7 Hz, J_3 = 4.5 Hz), 2.26–2.36 (1H, m), 2.44 (1H, ddd, J_1 = 9.3 Hz, J_2 = 6.3 Hz, J_3 = 4.2 Hz), 3.19 (3H, s), 3.65 (3H, s), 6.87–6.95 (2H, m), 7.01–7.08 (2H, m). ^{13}C NMR ($CDCl_3$) δ: 16.2, 21.4, 25.0, 32.5, 61.6, 115.2 (d, $J_{C–F}$ = 20.9 Hz), 127.7 (d, $J_{C–F}$ = 7.7 Hz), 136.4 (d, $J_{C–F}$ = 3.3 Hz), 161.4 (d, $J_{C–F}$ = 242.6 Hz), 172.8. HRMS calcd. for $C_{12}H_{14}FNO_2$: 223.1009; found: 223.1013.

***N*-Methoxy-*N*-methyl-*trans*-2-(3-fluorophenyl)cyclopropanecarboxamide (9d)** was prepared by procedure B, using **8d** (3.19 g, 15.2 mmol), trimethylsulfoxonium iodide (6.70 g, 30.4 mmol), and NaH (0.73 g, 30.4 mmol), in 85% yield (2.87 g, 12.9 mmol). ^{1}H NMR ($CDCl_3$) δ: 1.26 (1H, ddd, J_1 = 8.4 Hz, J_2 = 6.3 Hz, J_3 = 4.5 Hz), 1.61 (1H, ddd, J_1 = 9.0 Hz, J_2 = 5.7 Hz, J_3 = 4.5 Hz), 2.35–2.42 (1H, m), 2.45 (1H, ddd, J_1 = 10.5 Hz, J_2 = 6.3 Hz, J_3 = 4.5 Hz), 3.20 (3H, s), 3.67 (3H, s), 6.75–6.91 (3H, m), 7.16–7.23 (1H, m). ^{13}C NMR ($CDCl_3$) δ: 16.5, 21.7, 25.4, 32.5, 61.6, 112.8 (d, $J_{C–F}$ = 20.8 Hz), 113.1 (d, $J_{C–F}$ = 20.8 Hz), 122.0 (d, $J_{C–F}$ = 2.2 Hz), 129.8 (d, $J_{C–F}$ = 7.7 Hz), 143.5 (d, $J_{C–F}$ = 7.7 Hz), 162.9 (d, $J_{C–F}$ = 243.8 Hz), 172.5. HRMS calcd. for $C_{12}H_{14}FNO_2$: 223.1009; found: 223.1015.

***N*-Methoxy-*N*-methyl-*trans*-2-(4-methylphenyl)cyclopropanecarboxamide (9e)** was prepared by procedure B, using **8e** (10.15 g, 49.4 mmol), trimethylsulfoxonium iodide (21.75 g, 98.8 mmol), and NaH (2.37 g, 98.8 mmol), in 78% yield (8.43 g, 38.4 mmol); mp 72–73°C. ^{1}H NMR ($CDCl_3$) δ: 1.28 (1H, ddd, J_1 = 8.1 Hz, J_2 = 6.0 Hz, J_3 = 4.2 Hz), 1.62 (1H, ddd, J_1 = 9.6 Hz, J_2 = 5.7 Hz, J_3 = 4.5 Hz), 2.32 (3H, s), 2.34–2.42 (1H, m), 2.48 (1H, ddd, J_1 = 8.7 Hz, J_2 = 6.0 Hz, J_3 = 3.9 Hz), 3.23 (3H, s), 3.68 (3H, s), 7.03 (2H, d, J = 8.4 Hz), 7.09 (2H, d, J = 8.4 Hz). ^{13}C NMR ($CDCl_3$) δ: 16.3, 21.0, 21.5, 25.7, 32.6, 61.6, 126.1 (2C), 129.1 (2C), 135.8, 137.7, 173.1. HRMS calcd. for $C_{13}H_{17}NO_2$: 219.1259; found: 219.1261.

***N*-Methoxy-*N*-methyl-*trans*-2-(3-methylphenyl)cyclopropanecarboxamide (9f)** was prepared by procedure B, using **8f** (10.12 g, 49.3 mmol), trimethylsulfoxonium iodide (21.70 g, 98.6 mmol), and NaH (2.30 g, 95.8 mmol), in 89% yield (9.65 g, 44.0 mmol). ^{1}H NMR ($CDCl_3$) δ: 1.30 (1H, ddd, J_1 = 8.4 Hz, J_2 = 6.3 Hz, J_3 = 4.2 Hz), 1.62 (1H, ddd, J_1 = 9.3 Hz, J_2 = 5.7 Hz, J_3 = 4.5 Hz), 2.33 (3H, s), 2.38–2.45 (1H, m), 2.48 (1H, ddd, J_1 = 9.0 Hz, J_2 = 6.3 Hz, J_3 =

© 1999 NRC Canada

4.2 Hz), 3.23 (3H, s), 3.69 (3H, s), 6.92–7.19 (4H, m). ^{13}C NMR ($CDCl_3$) δ: 16.4, 21.4, 21.5, 25.9, 32.6, 61.7, 123.2, 127.0, 127.1, 128.3, 138.0, 140.7, 173.0. HRMS calcd. for $C_{13}H_{17}NO_2$: 219.1259; found: 219.1261.

***N*-Methoxy-*N*-methyl-*trans*-2-(4-methoxyphenyl)cyclopropanecarboxamide (9g)** was prepared by procedure B, using **8g** (5.03 g, 23.7 mmol), trimethylsulfoxonium iodide (10.0 g, 45.4 mmol), and NaH (1.10 g, 45.8 mmol), in 86% yield (4.61 g, 19.6 mmol). ^{1}H NMR ($CDCl_3$) δ: 1.25 (1H, ddd, J_1 = 8.1 Hz, J_2 = 6.3 Hz, J_3 = 3.9 Hz), 1.58 (1H, ddd, J_1 = 9.3 Hz, J_2 = 5.4 Hz, J_3 = 4.2 Hz), 2.28–2.36 (1H, m), 2.46 (1H, ddd, J_1 = 9.0 Hz, J_2 = 6.6 Hz, J_3 = 4.2 Hz), 3.23 (3H, s), 3.69 (3H, s), 3.78 (3H, s), 6.82 (2H, dt, J_1 = 9.0 Hz, J_2 = 2.4 Hz), 7.07 (2H, dt, J_1 = 8.4 Hz, J_2 = 1.8 Hz). ^{13}C NMR ($CDCl_3$) δ: 16.0, 21.3, 25.3, 32.5, 55.2, 61.6, 113.8 (2C), 127.3 (2C), 132.6, 158.2, 173.1. HRMS calcd. for $C_{13}H_{17}NO_3$: 235.1208; found: 235.1205.

***N*-Methoxy-*N*-methyl-*trans*-2-(3-methoxyphenyl)cyclopropanecarboxamide (9h)** was prepared by procedure B, using **8h** (4.77 g, 21.6 mmol), trimethylsulfoxonium iodide (9.50 g, 43.0 mmol), and NaH (1.04 g, 43.3 mmol), in 92% yield (4.69 g, 19.9 mmol). ^{1}H NMR ($CDCl_3$) δ: 1.26 (1H, ddd, J_1 = 8.4 Hz, J_2 = 6.3 Hz, J_3 = 4.2 Hz), 1.58 (1H, ddd, J_1 = 9.3 Hz, J_2 = 5.4 Hz, J_3 = 4.2 Hz), 2.34–2.48 (2H, m), 3.19 (3H, s), 3.64 (3H, s), 3.74 (3H, s), 6.65–6.72 (3H, m), 7.15 (1H, t, J = 8.1 Hz). ^{13}C NMR ($CDCl_3$) δ: 16.4, 21.6, 25.9, 32.5, 55.1, 61.6, 111.4, 112.2, 118.4, 129.4, 142.4, 159.7, 172.9. HRMS calcd. for $C_{13}H_{17}NO_3$: 235.1208; found: 235.1205.

***trans*-2-(4-(Trifluoromethyl)phenyl)cyclopropanecarboxylic acid (10a). Procedure C**

A suspension of **9a** (7.71 g, 28.2 mmol) and potassium *tert*-butoxide (17.11 g, 152 mmol) in ether (200 mL) and water (1.0 mL, 55.6 mmol) was stirred at room temperature for 16 h. The mixture was acidified by the slow addition of concentrated HCl, and the aqueous mixture was extracted with CH_2Cl_2 (3 × 200 mL). The combined organic layer was washed with brine (200 mL), dried over Na_2SO_4, filtered, and concentrated in vacuo to afford **10a** (5.85 g, 25.4 mmol, 90%) as a white solid; mp 110–111°C. ^{1}H NMR ($CDCl_3$) δ: 1.45 (1H, ddd, J_1 = 8.4 Hz, J_2 = 6.6 Hz, J_3 = 4.8 Hz), 1.73 (1H, dt, J_1 = 9.3 Hz, J_2 = 5.1 Hz), 1.96 (1H, ddd, J_1 = 9.0 Hz, J_2 = 5.4 Hz, J_3 = 4.2 Hz), 2.65 (1H, ddd, J_1 = 9.3 Hz, J_2 = 6.6 Hz, J_3 = 3.9 Hz), 7.21 (2H, d, J = 8.4 Hz), 7.55 (2H, d, J = 8.4 Hz), 12.08 (1H, bs). ^{13}C NMR ($CDCl_3$) δ: 17.6, 24.2, 26.5, 124.1 (q, J_{C-F} = 270.2 Hz), 125.5 (2C, q, J_{C-F} = 3.3 Hz), 126.5 (2C), 129.0 (q, J_{C-F} = 33.1 Hz), 143.6, 179.4. HRMS calcd. for $C_{11}H_9F_3O_2$: 230.0555; found: 230.0560.

***trans*-2-(3-(Trifluoromethyl)phenyl)cyclopropanecarboxylic acid (10b)** was prepared by procedure C, using **9b** (2.42 g, 8.86 mmol), potassium *tert*-butoxide (5.97 g, 53.2 mmol), and water (0.34 mL, 18.9 mmol), in 95% yield (1.94 g, 8.42 mmol); mp 61–62°C. ^{1}H NMR ($CDCl_3$) δ: 1.45 (1H, ddd, J_1 = 8.1 Hz, J_2 = 6.3 Hz, J_3 = 4.5 Hz), 1.73 (1H, dt, J_1 = 9.3 Hz, J_2 = 5.1 Hz), 1.95 (1H, ddd, J_1 = 8.1 Hz, J_2 = 5.1 Hz, J_3 = 3.9 Hz), 2.67 (1H, ddd, J_1 = 9.0 Hz, J_2 = 6.3 Hz, J_3 = 3.9 Hz), 7.28–7.50 (4H, m), 12.35 (1H, bs). ^{13}C NMR ($CDCl_3$) δ: 17.4, 24.0, 26.6, 123.1 (q, J_{C-F} = 3.3 Hz), 123.5 (q, J_{C-F} = 3.3 Hz), 124.0 (q, J_{C-F} = 270.2 Hz), 129.0, 129.7, 130.9 (q, J_{C-F} = 32.0 Hz), 140.5, 179.6. HRMS calcd. for $C_{11}H_9F_3O_2$: 230.0555; found: 230.0560.

***trans*-2-(4-Fluorophenyl)cyclopropanecarboxylic acid (10c)** was prepared by procedure C, using **9c** (7.67 g, 34.4 mmol), potassium *tert*-butoxide (23.13 g, 206 mmol), and water (1.20 mL, 66.7 mmol), in 93% yield (5.77 g, 32.0 mmol); mp 107–108°C. ^{1}H NMR ($CDCl_3$) δ: 1.37 (1H, ddd, J_1 = 8.4 Hz, J_2 = 6.6 Hz, J_3 = 4.5 Hz), 1.66 (1H, dt, J_1 = 9.6 Hz, J_2 = 4.8 Hz), 1.85 (1H, ddd, J_1 = 8.4 Hz, J_2 = 5.4 Hz, J_3 = 4.2 Hz), 2.60 (1H, ddd, J_1 = 9.3 Hz, J_2 = 6.6 Hz, J_3 = 3.9 Hz), 6.94–7.01 (2H, m), 7.05–7.12 (2H, m) 11.53 (1H, bs). ^{13}C NMR ($CDCl_3$) δ: 17.3, 23.8, 26.4, 115.3 (2C, d, J_{C-F} = 22.1 Hz), 127.9 (2C, d, J_{C-F} = 7.7 Hz), 135.1 (d, J_{C-F} = 2.2 Hz), 161.7 (d, J_{C-F} = 243.8 Hz), 179.8. HRMS calcd. for $C_{10}H_9FO_2$: 180.0587; found: 180.0591.

***trans*-2-(3-Fluorophenyl)cyclopropanecarboxylic acid (10d)** was prepared by procedure C, using **9d** (2.87 g, 12.9 mmol), potassium *tert*-butoxide (8.00 g, 71.3 mmol), and water (0.40 mL, 22.2 mmol), in 98% yield (2.27 g, 12.6 mmol); mp 76–77°C. ^{1}H NMR ($CDCl_3$) δ: 1.39 (1H, ddd, J_1 = 8.7 Hz, J_2 = 6.9 Hz, J_3 = 5.1 Hz), 1.68 (1H, dt, J_1 = 9.3 Hz, J_2 = 5.4 Hz), 1.91 (1H, ddd, J_1 = 8.4 Hz, J_2 = 5.4 Hz, J_3 = 3.9 Hz), 2.60 (1H, ddd, J_1 = 9.3 Hz, J_2 = 6.6 Hz, J_3 = 4.2 Hz), 6.79 (1H, dt, J_1 = 9.9 Hz, J_2 = 2.1 Hz), 6.88–6.95 (2H, m) 7.25 (1H, dt, J_1 = 8.1 Hz, J_2 = 6.0 Hz), 10.31 (1H, bs). ^{13}C NMR ($CDCl_3$) δ: 17.5, 24.0, 26.6, 113.2 (d, J_{C-F} = 22.1 Hz), 113.6 (d, J_{C-F} = 22.1 Hz), 122.0 (d, J_{C-F} = 3.3 Hz), 129.9 (d, J_{C-F} = 7.7 Hz), 142.1 (d, J_{C-F} = 7.7 Hz), 161.6 (d, J_{C-F} = 243.8 Hz), 179.4. HRMS calcd. for $C_{10}H_9FO_2$: 180.0587; found: 180.0589.

***trans*-2-(4-Methylphenyl)cyclopropanecarboxylic acid (10e)** was prepared by procedure C, using **9e** (8.20g, 37.4 mmol), potassium *tert*-butoxide (25.18 g, 224 mmol), and water (1.35 mL, 75.0 mmol), in 98% yield (6.43 g, 36.5 mmol); mp 118–119°C. ^{1}H NMR ($CDCl_3$) δ: 1.39 (1H, ddd, J_1 = 8.4 Hz, J_2 = 6.9 Hz, J_3 = 4.5 Hz), 1.65 (1H, dt, J_1 = 9.3 Hz, J_2 = 5.1 Hz), 1.87 (1H, ddd, J_1 = 8.4 Hz, J_2 = 5.1 Hz, J_3 = 4.2 Hz), 2.33 (3H, s), 2.59 (1H, ddd, J_1 = 9.0 Hz, J_2 = 6.6 Hz, J_3 = 3.9 Hz), 7.02 (2H, d, J = 8.1 Hz), 7.10 (2H, d, J = 8.1 Hz), 10.62 (1H, bs). ^{13}C NMR ($CDCl_3$) δ: 17.4, 21.0, 23.9, 26.9, 126.2 (2C), 129.2 (2C), 136.3, 136.4, 180.0. HRMS calcd. for $C_{11}H_{12}O_2$: 176.0837; found: 176.0841.

***trans*-2-(3-Methylphenyl)cyclopropanecarboxylic acid (10f)** was prepared by procedure C, using **9f** (9.22 g, 42.0 mmol), potassium *tert*-butoxide (28.25 g, 252 mmol), and water (1.50 mL, 83.3 mmol), in 94% yield (6.96 g, 39.5 mmol); mp 87–88°C. ^{1}H NMR ($CDCl_3$) δ: 1.41 (1H, ddd, J_1 = 8.1 Hz, J_2 = 6.6 Hz, J_3 = 4.5 Hz), 1.66 (1H, dt, J_1 = 9.3 Hz, J_2 = 4.5 Hz), 1.91 (1H, ddd, J_1 = 8.7 Hz, J_2 = 5.1 Hz, J_3 = 4.2 Hz), 2.34 (3H, s), 2.58 (1H, ddd, J_1 = 9.3 Hz, J_2 = 6.6 Hz, J_3 = 4.2 Hz), 6.91–7.26 (4H, m), 10.44 (1H, bs). ^{13}C NMR ($CDCl_3$) δ: 17.4, 21.3, 23.9, 27.1, 123.3, 127.1, 127.5, 128.4, 138.2, 139.4, 179.9. HRMS calcd. for $C_{11}H_{12}O_2$: 176.0837; found: 176.0839.

© 1999 NRC Canada

***trans*-2-(4-Methoxyphenyl)cyclopropanecarboxylic acid (10g)** was prepared by procedure C, using **9g** (4.60 g, 19.6 mmol), potassium *tert*-butoxide (13.50 g, 120 mmol), and water (0.75 mL, 41.7 mmol), in 96% yield (3.62 g, 18.8 mmol); mp 112–113°C. ^{1}H NMR ($CDCl_3$) δ: 1.35 (1H, ddd, J_1 = 8.1 Hz, J_2 = 6.6 Hz, J_3 = 4.5 Hz), 1.62 (1H, dt, J_1 = 9.6 Hz, J_2 = 5.1 Hz), 1.82 (1H, ddd, J_1 = 8.1 Hz, J_2 = 4.8 Hz, J_3 = 3.9 Hz), 2.57 (1H, ddd, J_1 = 9.6 Hz, J_2 = 6.9 Hz, J_3 = 4.5 Hz), 3.79 (3H, s), 6.83 (2H, dt, J_1 = 9.0 Hz, J_2 = 2.4 Hz), 7.04 (2H, dt, J_1 = 8.7 Hz, J_2 = 2.1 Hz), 10.55 (1H, bs). ^{13}C NMR ($CDCl_3$) δ: 17.2, 23.7, 26.6, 55.3, 114.0 (2C), 127.5 (2C), 131.4, 158.5, 179.7. HRMS calcd. for $C_{11}H_{12}O_3$: 192.0786; found: 192.0782.

***trans*-2-(3-Methoxyphenyl)cyclopropanecarboxylic acid (10h)** was prepared by procedure C, using **9h** (3.79 g, 16.1 mmol), potassium *tert*-butoxide (10.85 g, 96.7 mmol), and water (0.60 mL, 33.3 mmol), in 97% yield (2.99 g, 15.6 mmol); mp 93–94°C. ^{1}H NMR ($CDCl_3$) δ: 1.40 (1H, ddd, J_1 = 8.4 Hz, J_2 = 6.6 Hz, J_3 = 4.8 Hz), 1.65 (1H, dt, J_1 = 9.6 Hz, J_2 = 5.1 Hz), 1.90 (1H, ddd, J_1 = 8.7 Hz, J_2 = 5.1 Hz, J_3 = 3.9 Hz), 2.58 (1H, ddd, J_1 = 9.9 Hz, J_2 = 6.6 Hz, J_3 = 4.2 Hz), 3.79 (3H, s), 6.45–6.78 (3H, m), 7.20 (1H, t, J = 8.1 Hz), acid O**H** not observed. ^{13}C NMR ($CDCl_3$) δ: 17.5, 24.0, 27.1, 55.2, 112.0, 112.2, 118.5, 129.6, 141.2, 159.7, 180.0. HRMS calcd. for $C_{11}H_{12}O_3$: 192.0786; found: 192.0783.

(*trans*-2-(4-(Trifluoromethyl)phenyl)cyclopropyl)methanol (13a). Procedure D

A solution of **10a** (2.00 g, 8.69 mmol) in THF (75 mL) under a nitrogen atmosphere was cooled to 0°C, and $LiAlH_4$ (0.70 g, 18.4 mmol) was added. The mixture was stirred for 2 h, after which time the reaction mixture was quenched by the sequential addition of water (0.7 mL), 15% NaOH (0.7 mL), and water (2.1 mL). After stirring for an additional 2 h, the suspension was filtered, and the filtrate was washed with additional THF (100 mL). The combined organic solution was concentrated in vacuo, and the resulting residue was chromatographed on silica gel (40% ethyl acetate in hexanes) to afford **13a** (1.77 g, 8.17 mmol, 94%) as a white solid; mp 61°C. ^{1}H NMR ($CDCl_3$) δ: 1.01–1.06 (2H, m), 1.41 (1H, bs), 1.46–1.57 (1H, m), 1.87–1.93 (1H, m), 3.66 (2H, d, J = 6.6 Hz), 7.17 (2H, d, J = 8.4 Hz), 7.52 (2H, d, J = 8.4 Hz). ^{13}C NMR ($CDCl_3$) δ: 14.3, 21.1, 25.9, 66.0, 124.3 (q, $J_{C–F}$ = 269.2 Hz), 125.2 (2C, q, $J_{C–F}$ = 3.5 Hz), 125.9 (2C), 127.8 (q, $J_{C–F}$ = 33.1 Hz), 146.9. HRMS calcd. for $C_{11}H_{11}F_3O$: 216.0762; found: 216.0759.

(*trans*-2-(3-(Trifluoromethyl)phenyl)cyclopropyl)methanol (13b) was prepared by procedure D, using **10b** (0.95 g, 4.13 mmol) and $LiAlH_4$ (0.30 g, 7.91 mmol), in 87% yield (0.78 g, 3.61 mmol). ^{1}H NMR ($CDCl_3$) δ: 0.96 (2H, dd, J_1 = 7.5 Hz, J_2 = 6.9 Hz), 1.37–1.48 (1H, m), 1.85 (1H, dt, J_1 = 6.9 Hz, J_2 = 4.2 Hz), 2.96 (1H, bs), 3.54 (1H, dd, J_1 = 11.4 Hz, J_2 = 6.3 Hz), 3.63 (1H, dd, J_1 = 11.4 Hz, J_2 = 6.3 Hz), 7.19–7.41 (4H, m). ^{13}C NMR ($CDCl_3$) δ: 13.9, 21.1, 25.4, 65.9, 122.3 (q, $J_{C–F}$ = 3.3 Hz), 122.2 (q, $J_{C–F}$ = 3.3 Hz), 124.2 (q, $J_{C–F}$ = 270.2 Hz), 128.7, 129.1, 130.5 (q, $J_{C–F}$ = 32.0 Hz), 143.7. HRMS calcd. for $C_{11}H_{11}F_3O$: 216.0762; found: 216.0766.

(*trans*-2-(4-Fluorophenyl)cyclopropyl)methanol (13c) was prepared by procedure D, using **10c** (1.95 g, 10.8 mmol) and $LiAlH_4$ (1.00 g, 26.4 mmol), in 91% yield (1.63 g, 9.81 mmol). ^{1}H NMR ($CDCl_3$) δ: 0.86–0.93 (2H, m), 1.30–1.41 (1H, m), 1.78 (1H, ddd, J_1 = 8.4 Hz, J_2 = 6.0 Hz, J_3 = 4.5 Hz) 2.45–2.51 (1H, m), 3.57 (2H, d, J = 6.9 Hz), 6.89–7.04 (4H, m). ^{13}C NMR ($CDCl_3$) δ: 13.5, 20.6, 25.0, 66.2, 115.0 (2C, d, $J_{C–F}$ = 20.9 Hz), 127.3 (2C, d, $J_{C–F}$ = 7.7 Hz), 138.0 (d, $J_{C–F}$ = 2.2 Hz), 161.1 (d, $J_{C–F}$ = 241.5 Hz). HRMS calcd. for $C_{10}H_{11}FO$: 166.0794; found: 166.0796.

(*trans*-2-(3-Fluorophenyl)cyclopropyl)methanol (13d) was prepared by procedure D, using **10d** (1.00 g, 5.55 mmol) and $LiAlH_4$ (0.50 g, 13.2 mmol), in 87% yield (0.80 g, 4.83 mmol). ^{1}H NMR ($CDCl_3$) δ: 0.92 (2H, t, J = 7.2 Hz), 1.34–1.44 (1H, m), 1.76–1.82 (1H, m), 3.30 (1H, s), 3.50–3.61 (2H, m), 6.75 (1H, dt, J_1 = 8.1 Hz, J_2 = 2.4 Hz), 6.80–6.87 (2H, m), 7.18 (1H, dt, J_1 = 8.4 Hz, J_2 = 6.0 Hz). ^{13}C NMR ($CDCl_3$) δ: 14.0, 21.1, 25.4, 65.8, 112.4 (d, $J_{C–F}$ = 20.9 Hz), 112.5 (d, $J_{C–F}$ = 20.9 Hz), 121.6 (d, $J_{C–F}$ = 2.3 Hz), 129.7 (d, $J_{C–F}$ = 8.8 Hz), 145.5 (d, $J_{C–F}$ = 7.7 Hz), 163.0 (d, $J_{C–F}$ = 243.8 Hz). HRMS calcd. for $C_{10}H_{11}FO$: 166.0794; found: 166.0796.

(*trans*-2-(4-Methylphenyl)cyclopropyl)methanol (13e) was prepared by procedure D, using **10e** (2.00 g, 11.3 mmol) and $LiAlH_4$ (1.00 g, 26.4 mmol), in 92% yield (1.68 g, 10.4 mmol). ^{1}H NMR ($CDCl_3$) δ: 0.88–0.97 (2H, m), 1.37–1.48 (1H, m), 1.80 (1H, dt, J_1 = 8.4 Hz, J_2 = 5.4 Hz), 2.12 (1H, s), 2.34 (3H, s), 3.55–3.66 (2H, m), 6.99 (2H, d, J = 7.8 Hz), 7.10 (2H, d, J = 7.8 Hz). ^{13}C NMR ($CDCl_3$) δ: 13.6, 21.0 (2C), 25.0, 66.5, 125.8 (2C), 129.0 (2C), 135.1, 139.4. HRMS calcd. for $C_{11}H_{14}O$: 162.1045; found: 162.1041.

(*trans*-2-(3-Methylphenyl)cyclopropyl)methanol (13f) was prepared by procedure D, using **10f** (2.00 g, 11.3 mmol) and $LiAlH_4$ (1.00 g, 26.4 mmol), in 97% yield (1.79 g, 11.0 mmol). ^{1}H NMR ($CDCl_3$) δ: 0.92–1.03 (2H, m), 1.42–1.53 (1H, m), 1.83 (1H, dt, J_1 = 9.0 Hz, J_2 = 5.1 Hz), 2.39 (3H, s), 2.82 (1H, s), 3.57–3.68 (2H, m), 6.92–7.24 (4H, m). ^{13}C NMR ($CDCl_3$) δ: 13.8, 21.3, 21.5, 25.1, 66.3, 122.9, 126.4, 126.7, 128.3., 137.9, 142.6. HRMS calcd. for $C_{11}H_{14}O$: 162.1045; found: 162.1042.

(*trans*-2-(4-Methoxyphenyl)cyclopropyl)methanol (13g) was prepared by procedure D, using **10g** (0.56 g, 2.88 mmol) and $LiAlH_4$ (0.25 g, 6.59 mmol), in 95% yield (0.49 g, 2.75 mmol). ^{1}H NMR ($CDCl_3$) δ: 0.84–0.93 (2H, m), 1.33–1.46 (1H, m), 1.44 (1H, s), 1.78 (1H, dt, J_1 = 8.4 Hz, J_2 = 4.8 Hz), 3.54–3.65 (2H, m), 3.78 (3H, s), 6.81 (2H, dt, J_1 = 8.4 Hz, J_2 = 2.1 Hz), 7.01 (2H, dt, J_1 = 8.7 Hz, J_2 = 2.4 Hz). ^{13}C NMR ($CDCl_3$) δ: 13.3, 20.6, 24.7, 55.3, 66.6, 113.8 (2C), 127.0 (2C), 134.4, 157.7. HRMS calcd. for $C_{11}H_{14}O_2$: 178.0994; found: 178.0990.

(*trans*-2-(3-Methoxyphenyl)cyclopropyl)methanol (13h) was prepared by procedure D, using **10h** (1.16 g, 6.34 mmol) and $LiAlH_4$ (0.50 g, 13.2 mmol), in 78% yield (0.88 g, 4.94 mmol). ^{1}H NMR ($CDCl_3$) δ: 0.90–1.00 (2H, m), 1.41–1.51 (1H, m). 1.43 (1H, s), 1.81 (1H, dt, J_1 = 9.0 Hz, J_2 = 4.8 Hz), 3.55–3.68 (2H, m), 3.79 (3H, s), 6.61–6.72 (3H, m), 7.18 (1H, t, J = 7.8 Hz). ^{13}C NMR ($CDCl_3$) δ: 13.9, 21.3,

© 1999 NRC Canada

25.3, 55.1, 66.2, 110.8, 111.8, 118.2, 129.3, 144.4, 160.0. HRMS calcd. for $C_{11}H_{14}O_2$: 178.0994; found: 178.1001.

Methyl (*trans*-2-(4-(trifluoromethyl)phenyl)cyclopropyl)-acetate (11a). Procedure E

A solution of **10a** (1.69 g, 7.34 mmol) and DMF (2 drops) in benzene (50 mL) under a nitrogen atmosphere was cooled with a water bath as oxalyl chloride (1.3 mL, 14.9 mmol) was added. The reaction mixture was stirred for 2 h, and volatiles were removed in vacuo. The crude carbonyl chloride was dissolved in CH_2Cl_2 (25 mL), and the resulting mixture was added slowly to a solution of CH_2N_2 in ether, prepared from Diazald® (10 g, 46.7 mmol). The reaction mixture was stirred at room temperature for 16 h and then concentrated in vacuo. The resulting diazoketone was chromatographed on silica gel (20% ethyl acetate in hexanes).

The diazoketone was dissolved in dioxane (30 mL), and the solution was added portionwise to a suspension of Ag_2O (3.00 g, 12.9 mmol) and $Na_2S_2O_3$ (2.04 g, 12.9 mmol) in water (100 mL) at 75°C. The resulting suspension was stirred for 2 h and then cooled to room temperature and filtered through Celite®. The filtrate was made basic (NaOH) and washed with ether (2 × 100 mL). The aqueous layer was acidified (concentrated HCl) and extracted with ether (2 × 100 mL). The combined organic layer was washed with brine (100 mL), dried over $MgSO_4$, filtered, and concentrated in vacuo.

The resulting acid was dissolved in CH_2Cl_2 (25 mL) and added slowly to a solution of CH_2N_2 in ether, prepared from Diazald® (10 g, 46.7 mmol). The mixture was stirred at room temperature for 16 h and then concentrated in vacuo. The crude product was purified by radial chromatography (10% ethyl acetate in hexanes) to afford **11a** (1.04 g, 4.04 mmol, 55% combined yield) as a clear, colorless oil. ^{1}H NMR ($CDCl_3$) δ: 0.94 (1H, dt, J_1 = 9.0 Hz, J_2 = 5.4 Hz), 1.05 (1H, dt, J_1 = 8.4 Hz, J_2 = 5.4 Hz), 1.37–1.48 (1H, m), 1.81 (1H, dt, J_1 = 9.0 Hz, J_2 = 4.8 Hz), 2.42 (2H, d, J = 7.2 Hz), 3.70 (3H, s), 7.17 (2H, d, J = 8.1 Hz), 7.49 (2H, d, J = 8.1 Hz). ^{13}C NMR ($CDCl_3$) δ: 15.8, 19.1, 22.8, 38.5, 51.6, 124.3 (q, $J_{C–F}$ = 270.3 Hz), 125.1 (2C, q, $J_{C–F}$ = 3.4 Hz), 126.1 (2C), 127.8 (q, $J_{C–F}$ = 33.1 Hz), 146.8, 172.8. HRMS calcd. for $C_{13}H_{13}F_3O_2$: 258.0868; found: 258.0871.

Methyl (*trans*-2-(3-(trifluoromethyl)phenyl)cyclopropyl)-acetate (11b) was prepared by procedure E, using **10b** (1.71 g, 7.43 mmol), oxalyl chloride (1.3 mL, 14.9 mmol), and Ag_2O (3.00 g, 12.9 mmol), in 51% yield (0.98 g, 3.79 mmol). ^{1}H NMR ($CDCl_3$) δ: 0.90 (1H, dt, J_1 = 8.7 Hz, J_2 = 5.1 Hz), 1.10 (1H, dt, J_1 = 8.7 Hz, J_2 = 5.1 Hz), 1.33–1.44 (1H, m), 1.79 (1H, dt, J_1 = 9.3 Hz, J_2 = 4.8 Hz), 2.39 (2H, d, J = 6.9 Hz), 3.67 (3H, s), 7.22–7.44 (4H, m). ^{13}C NMR ($CDCl_3$) δ: 15.3, 18.7, 22.6, 38.4, 51.5, 122.3 (q, $J_{C–F}$ = 3.3 Hz), 122.7 (q, $J_{C–F}$ = 3.3 Hz), 124.2 (q, $J_{C–F}$ = 270.8 Hz), 128.6, 129.4, 130.5 (q, $J_{C–F}$ = 32.0 Hz), 143.6, 172.7. HRMS calcd. for $C_{13}H_{13}F_3O_2$: 258.0868; found: 258.0868.

Methyl (*trans*-2-(4-fluorophenyl)cyclopropyl)acetate (11c) was prepared by procedure E, using **10c** (1.38 g, 7.66 mmol), oxalyl chloride (1.3 mL, 14.9 mmol), and Ag_2O (2.50 g, 10.8 mmol), in 40% yield (0.64 g, 3.07 mmol). ^{1}H NMR ($CDCl_3$) δ: 0.79–0.86 (1H, m), 0.90–0.97 (1H, m), 1.26–1.37 (1H, m), 1.70–1.76 (1H, m), 2.39 (2H, dd, J_1 = 6.9 Hz, J_2 = 2.4 Hz), 3.69 (3H, s), 6.85–7.10 (4H, m). ^{13}C NMR ($CDCl_3$) δ: 14.9, 18.1, 22.2, 38.6, 51.6, 114.9 (2C, d, $J_{C–F}$ = 21.0 Hz), 127.5 (2C, d, $J_{C–F}$ = 7.7 Hz), 138.1, 161.1 (d, $J_{C–F}$ = 242.7 Hz), 173.0. HRMS calcd. for $C_{12}H_{13}FO_2$: 208.0900; found: 208.0905.

Methyl (*trans*-2-(3-fluorophenyl)cyclopropyl)acetate (11d) was prepared by procedure E, using **10d** (1.33 g, 7.38 mmol), oxalyl chloride (1.3 mL, 14.9 mmol), and Ag_2O (2.50 g, 10.8 mmol), in 57% yield (0.87 g, 4.18 mmol). ^{1}H NMR ($CDCl_3$) δ: 0.87 (1H, dt, J_1 = 9.0 Hz, J_2 = 5.1 Hz), 0.98 (1H, dt, J_1 = 8.4 Hz, J_2 = 5.4 Hz), 1.30–1.41 (1H, m), 1.73 (1H, dt, J_1 = 9.3 Hz, J_2 = 5.1 Hz), 2.31–2.45 (2H, m), 3.67 (3H, s), 6.73–6.87 (3H, m), 7.17 (1H, dt, J_1 = 8.1 Hz, J_2 = 6.6 Hz). ^{13}C NMR ($CDCl_3$) δ: 15.5, 18.7, 22.6, 38.5, 51.6, 112.3 (d, J_{C-F} = 21.0 Hz), 112.8 (d, $J_{C–F}$ = 21.0 Hz), 121.7 (d, $J_{C–F}$ = 2.3 Hz), 129.6 (d, $J_{C–F}$ = 8.9 Hz), 145.3 (d, $J_{C–F}$ = 7.7 Hz), 162.9 (d, $J_{C–F}$ = 242.7 Hz), 172.8. HRMS calcd. for $C_{12}H_{13}FO_2$: 208.0900; found: 208.0896.

Methyl (*trans*-2-(4-methylphenyl)cyclopropyl)acetate (11e) was prepared by procedure E, using **10e** (1.34 g, 7.60 mmol), oxalyl chloride (1.3 mL, 14.9 mmol), and Ag_2O (2.50 g, 10.8 mmol), in 48% yield (0.75 g, 3.67 mmol). ^{1}H NMR ($CDCl_3$) δ: 0.87 (1H, dt, J_1 9.0 Hz, J_2 = 5.1 Hz), 1.02 (1H, dt, J_1 = 8.1 Hz, J_2 = 5.1 Hz), 1.34–1.45 (1H, m), 1.78 (1H, dt, J_1 = 9.3 Hz, J_2 = 4.8 Hz), 2.34–2.53 (2H, m), 2.35 (3H, s), 3.74 (3H, s), 7.03 (2H, d, J = 7.8 Hz), 7.11 (2H, d, J = 7.8 Hz). ^{13}C NMR ($CDCl_3$) δ: 15.1, 18.2, 21.0, 22.6, 38.8, 51.6, 126.0 (2C), 129.0 (2C), 135.1, 139.4, 172.1. HRMS calcd. for $C_{13}H_{16}O_2$: 204.1150; found: 204.1146.

Methyl (*trans*-2-(3-methylphenyl)cyclopropyl)acetate (11f) was prepared by procedure E, using **10f** (1.33 g, 7.55 mmol), oxalyl chloride (1.3 mL, 14.9 mmol), and Ag_2O (2.50 g, 10.8 mmol), in 46% yield (0.71 g, 3.48 mmol). ^{1}H NMR ($CDCl_3$) δ: 0.87 (1H, dt, J_1 = 8.7 Hz, J_2 = 5.1 Hz), 1.02 (1H, dt, J_1 = 8.4 Hz, J_2 = 5.4 Hz), 1.36–1.47 (1H, m), 1.75 (1H, dt, J_1 = 9.0 Hz, J_2 = 4.8 Hz), 2.32–2.53 (2H, m), 2.34 (3H, s), 3.72 (3H, s), 6.90–7.19 (4H, m). ^{13}C NMR ($CDCl_3$) δ: 15.4, 18.4, 21.4, 22.8, 38.8, 41.6, 123.0, 126.4, 126.7, 128.2, 137.8, 142.5, 172.1. HRMS calcd. for $C_{13}H_{16}O_2$: 204.1150; found: 204.1146.

Methyl (*trans*-2-(4-methoxyphenyl)cyclopropyl)acetate (11g) was prepared by procedure E, using **10g** (1.26 g, 6.56 mmol), oxalyl chloride (1.5 mL, 17.2 mmol), and Ag_2O (2.50 g, 10.8 mmol), in 42% yield (0.62 g, 2.82 mmol). ^{1}H NMR ($CDCl_3$) δ: 0.80 (1H, dt, J_1 = 8.7 Hz, J_2 = 5.1 Hz), 0.93 (1H, dt, J_1 = 8.1 Hz, J_2 = 5.1 Hz), 1.24–1.36 (1H, m), 1.72 (1H, dt, J_1 = 9.3 Hz, J_2 = 4.8 Hz), 2.32–2.47 (2H, m), 3.70 (3H, s), 3.77 (3H, s), 6.80 (2H, dt, J_1 = 8.7 Hz, J_2 = 3.3 Hz), 7.07 (2H, dt, J_1 = 8.7 Hz, J_2 = 3.3 Hz). ^{13}C NMR ($CDCl_3$) δ: 14.7, 17.8, 22.1, 38.8, 51.6, 55.3, 113.7 (2C), 127.2 (2C), 134.5, 157.7, 173.2. HRMS calcd. for $C_{13}H_{16}O_3$: 220.1099; found: 220.1105.

Methyl (*trans*-2-(3-methoxyphenyl)cyclopropyl)acetate (11h) was prepared by procedure E, using **10h** (1.25 g, 6.50 mmol), oxalyl chloride (1.5 mL, 17.2 mmol), and Ag_2O (2.50 g, 10.8 mmol), in 49% yield (0.70 g, 3.19 mmol). ^{1}H NMR ($CDCl_3$) δ: 0.87 (1H, dt, J_1 = 8.4 Hz, J_2 = 5.1 Hz),

© 1999 NRC Canada

1.01 (1H, dt, J_1 = 8.7 Hz, J_2 = 5.1 Hz), 1.35–1.45 (1H, m), 1.75 (1H, dt, J_1 = 9.0 Hz, J_2 = 4.8 Hz), 2.31–2.50 (2H, m), 3.70 (3H, s), 3.78 (3H, s), 6.65–6.73 (3H, m), 7.17 (1H, t, J = 7.5 Hz). ^{13}C NMR ($CDCl_3$) δ: 15.4, 18.5, 22.9, 38.7, 51.6, 55.0, 110.9, 111.8, 118.4, 129.2, 144.3, 159.7, 173.0. HRMS calcd. for $C_{13}H_{16}O_3$: 220.1099; found: 220.1104.

(*trans*-2-((4-Trifluoromethyl)phenyl)cyclopropyl)acetic acid (12a). Procedure F

A solution of **11a** (0.75 g, 2.90 mmol) and $LiOH·H_2O$ (0.90 g, 21.9 mmol) in methanol (35 mL) was stirred at room temperature for 6 h. This was concentrated in vacuo, and the residue was dissolved in water (75 mL). This was then acidified (concentrated HCl) and extracted with CH_2Cl_2 (3 × 30 mL). The combined organic layer was washed with brine (50 mL), dried over Na_2SO_4, filtered, and concentrated in vacuo to afford **12a** (0.69 g, 2.83 mmol, 98%) as a white solid; mp 79–80°C. ^{1}H NMR ($CDCl_3$) δ: 0.98 (1H, dt, J_1 = 10.8 Hz, J_2 = 5.4 Hz), 1.08 (1H, dt, J_1 = 10.8 Hz, J_2 = 5.4 Hz), 1.39–1.49 (1H, m), 1.84 (1H, dt, J_1 = 9.3 Hz, J_2 = 4.8 Hz), 2.48 (2H, d, J = 7.2 Hz), 7.18 (2H, d, J = 8.1 Hz), 7.51 (2H, d, J = 8.1 Hz), 11.21 (1H, bs). ^{13}C NMR ($CDCl_3$) δ: 15.7, 18.6, 22.8, 38.5, 124.3 (q, $J_{C–F}$ = 269.1 Hz), 125.2 (2C, q, $J_{C–F}$ = 3.3 Hz), 126.2 (2C), 128.0 (q, $J_{C–F}$ = 32.0 Hz), 146.6, 178.9. HRMS calcd. for $C_{12}H_{11}F_3O_2$: 244.0711; found: 244.0706.

(*trans*-2-((3-Trifluoromethyl)phenyl)cyclopropyl)acetic acid (12b) was prepared by procedure F, using **11b** (0.70 g, 2.71 mmol) and $LiOH·H_2O$ (0.90 g, 21.9 mmol), in 97% yield (0.64 g, 2.63 mmol). ^{1}H NMR ($CDCl_3$) δ: 0.97 (1H, dt, J_1 = 9.0 Hz, J_2 = 5.7 Hz), 1.08 (1H, dt, J_1 = 8.7 Hz, J_2 = 5.7 Hz), 1.39–1.50 (1H, m), 1.86 (1H, dt, J_1 = 9.3 Hz, J_2 = 5.1 Hz), 2.49 (2H, d, J = 7.2 Hz), 7.27–7.51 (4H, m), 11.88 (1H, bs). ^{13}C NMR ($CDCl_3$) δ: 15.4, 18.3, 22.7, 38.5, 122.5 (q, $J_{C–F}$ = 3.3 Hz), 122.8 (q, $J_{C–F}$ = 3.3 Hz), 124.2 (q, $J_{C–F}$ = 270.8 Hz), 128.7, 129.4, 130.6 (q, $J_{C–F}$ = 32.0 Hz), 143.3, 179.3. HRMS calcd. for $C_{12}H_{11}F_3O_2$: 244.0711; found: 244.0705.

(*trans*-2-(4-Fluorophenyl)cyclopropyl)acetic acid (12c) was prepared by procedure F, using **11c** (0.57 g, 2.74 mmol) and $LiOH·H_2O$ (0.80 g, 19.1 mmol), in 90% yield (0.48 g, 2.47 mmol); mp 62–63°C. ^{1}H NMR ($CDCl_3$) δ: 0.89 (1H, dt, J_1 = 9.0 Hz, J_2 = 5.1 Hz), 1.00 (1H, dt, J_1 = 8.4 Hz, J_2 = 5.1 Hz), 1.31–1.42 (1H, m), 1.80 (1H, dt, J_1 = 9.6 Hz, J_2 = 5.4 Hz), 2.47 (2H, d, J = 7.2 Hz), 6.93–7.01 (2H, m), 7.06–7.12 (2H, m), 11.98 (1H, s). ^{13}C NMR ($CDCl_3$) δ: 14.9, 17.8, 22.2, 38.7, 115.0 (2C, d, $J_{C–F}$ = 21.0 Hz), 127.7 (2C, d, $J_{C–F}$ = 7.7 Hz), 137.9 (d, $J_{C–F}$ = 2.2 Hz), 161.2 (d, $J_{C–F}$ = 241.6 Hz), 179.6. HRMS calcd. for $C_{11}H_{11}FO_2$: 194.0743; found: 194.0750.

(*trans*-2-(3-Fluorophenyl)cyclopropyl)acetic acid (12d) was prepared by procedure F, using **11d** (0.73 g, 3.51 mmol) and $LiOH·H_2O$ (0.70 g, 16.7 mmol), in 92% yield (0.63 g, 3.24 mmol). ^{1}H NMR ($CDCl_3$) δ: 0.96 (1H, dt, J_1 = 9.0 Hz, J_2 = 5.4 Hz), 1.06 (1H, dt, J_1 = 8.4 Hz, J_2 = 5.1 Hz), 1.39–1.50 (1H, m), 1.82 (1H, dt, J_1 = 9.0 Hz, J_2 = 4.8 Hz), 2.42–2.56 (2H, m), 6.82–6.94 (3H, m), 7.25 (1H, dt, J_1 = 7.8 Hz, J_2 = 6.0 Hz), 12.13 (1H, s). ^{13}C NMR ($CDCl_3$) δ: 15.5, 18.4, 22.7, 38.6, 112.5 (d, $J_{C–F}$ = 20.9 Hz), 112.8 (d, $J_{C–F}$ = 22.1 Hz), 121.8 (d, $J_{C–F}$ = 2.2 Hz), 129.7 (d, $J_{C–F}$ = 8.8 Hz), 145.2 (d, $J_{C–F}$ = 7.7 Hz), 163.0 (d, $J_{C–F}$ = 243.8 Hz), 179.6. HRMS calcd. for $C_{11}H_{11}FO_2$: 194.0743; found: 194.0736.

(*trans*-2-(4-Methylphenyl)cyclopropyl)acetic acid (12e) was prepared by procedure F, using **11e** (0.69 g, 3.38 mmol) and $LiOH·H_2O$ (0.70 g, 16.7 mmol), in 84% yield (0.54 g, 2.84 mmol); mp 62–63°C. ^{1}H NMR ($CDCl_3$) δ: 0.93 (1H, dt, J_1 = 9.0 Hz, J_2 = 5.1 Hz), 1.07 (1H, dt, J_1 = 8.7 Hz, J_2 = 5.1 Hz), 1.39–1.50 (1H, m), 1.83 (1H, dt, J_1 = 9.0 Hz, J_2 = 4.8 Hz), 2.39 (3H, s), 2.42–2.60 (2H, m), 7.08 (2H, d, J = 8.1 Hz), 7.15 (2H, d, J = 8.1 Hz), 12.00 (1H, s). ^{13}C NMR ($CDCl_3$) δ: 15.1, 17.9, 21.0, 22.6, 38.9, 126.0 (2C), 129.1 (2C), 135.2, 139.3, 179.7. HRMS calcd. for $C_{12}H_{14}O_2$: 190.0994; found: 190.0992.

(*trans*-2-(3-,Methylphenyl)cyclopropyl)acetic acid (12f) was prepared by procedure F, using **11f** (0.55 g, 2.69 mmol) and $LiOH·H_2O$ (0.60 g, 14.3 mmol), in 94% yield (0.48 g, 2.52 mmol). ^{1}H NMR ($CDCl_3$) δ: 1.00 (1H, dt, J_1 = 9.0 Hz, J_2 = 5.1 Hz), 1.16 (1H, dt, J_1 = 8.1 Hz, J_2 = 5.4 Hz), 1.49–1.60 (1H, m), 1.89 (1H, dt, J_1 = 9.3 Hz, J_2 = 5.1 Hz), 2.47 (3H, s), 2.47–2.67 (2H, m), 7.03–7.35 (4H, m), 12.17 (1H, s). ^{13}C NMR ($CDCl_3$) δ: 15.5, 18.1, 21.5, 22.9, 38.9, 123.2, 126.6, 126.9, 128.4, 137.9, 142.4, 179.8. HRMS calcd. for $C_{12}H_{14}O_2$: 190.0994; found: 190.0990.

(*trans*-2-(4-Methoxyphenyl)cyclopropyl)acetic acid (12g) was prepared by procedure F, using **11g** (0.50 g, 2.27 mmol) and $LiOH·H_2O$ (0.60 g, 14.3 mmol), in 98% yield (0.46 g, 2.22 mmol); mp 74–75°C. ^{1}H NMR ($CDCl_3$) δ: 0.82 (1H, dt, J_1 = 8.7 Hz, J_2 = 5.1 Hz), 0.95 (1H, dt, J_1 = 8.7 Hz, J_2 = 5.7 Hz), 1.27–1.37 (1H, m), 1.75 (1H, dt, J_1 = 9.0 Hz, J_2 = 4.8 Hz), 2.36–2.52 (2H, m), 3.78 (3H, s), 6.80 (2H, dt, J_1 = 8.7 Hz, J_2 = 3.0 Hz), 7.04 (2H, dt, J_1 = 8.7 Hz, J_2 = 3.0 Hz), 10.09 (1H, bs). ^{13}C NMR ($CDCl_3$) δ: 14.6, 17.5, 22.1, 38.7, 55.3, 113.8 (2C), 127.2 (2C), 134.3, 157.8, 179.3. HRMS calcd. for $C_{12}H_{14}O_3$: 206.0943; found: 206.0938.

(*trans*-2-(3-Methoxyphenyl)cyclopropyl)acetic acid (12h) was prepared by procedure F, using **11h** (0.52 g, 2.36 mmol) and $LiOH·H_2O$ (0.60 g, 14.3 mmol), in 98% yield (0.48 g, 2.31 mmol). ^{1}H NMR ($CDCl_3$) δ: 0.90 (1H, dt, J_1 = 9.0 Hz, J_2 = 5.7 Hz), 1.05 (1H, dt, J_1 = 8.4 Hz, J_2 = 5.1 Hz), 1.37–1.48 (1H, m), 1.79 (1H, dt, J_1 = 9.3 Hz, J_2 = 4.8 Hz), 2.37–2.56 (2H, m), 3.81 (3H, s), 6.67–6.75 (3H, m), 7.20 (1H, t, J = 7.8 Hz), 11.68 (1H, bs). ^{13}C NMR ($CDCl_3$) δ: 15.3, 18.1, 23.0, 38.7, 55.1, 111.1, 111.9, 118.4, 129.3, 144.1, 159.7, 179.4. HRMS calcd. for $C_{12}H_{14}O_3$: 206.0943; found: 206.0940.

1-[[[(*trans*-2-(4-(Trifluoromethyl)phenyl)cyclopropyl)-methyl]carbonyl]oxy]-2(1*H*)-pyridinethione (2a)

PTOC esters were generally prepared by either the standard method (15) or the mild method (29). To a solution of acid **12a** (0.50 g, 2.05 mmol) in dry benzene at 0°C under nitrogen was added dropwise oxalyl chloride (0.45 mL, 5.1 mmol) via syringe transfer followed by one drop of DMF. The reaction mixture was stirred for 3 h at room temperature until gas evolution ceased. The excess oxalyl chloride and benzene were removed under reduced pressure. The resulting acid chloride was dissolved in dry benzene (5 mL)

© 1999 NRC Canada

and transferred by cannula into a light-shielded flask in an ice bath containing a suspension of *N*-hydroxypyridine-2-thione sodium salt (0.37 g, 2.46 mmol) and a catalytic amount of DMAP (12.2 mg, 0.1 mmol) in 10 mL of benzene. The mixture was allowed to warm to room temperature with stirring and was maintained at room temperature for 3 h. The mixture was diluted with ether (10 mL) and washed with saturated $NaHCO_3$ solution (5 mL) and saturated NaCl solution (10 mL). The organic layer was dried over $MgSO_4$ and concentrated to give crude PTOC ester **2a**, which was purified by column chromatography on silica gel (hexanes–EtOAc = 1:1, v/v) to yield 0.56 g (1.59 mmol, 78%). ^{1}H NMR ($CDCl_3$) δ: 1.08 (1H, dt, J_1 = 9.0 Hz, J_2 = 6.0 Hz), 1.15 (1H, dt, J_1 = 8.5 Hz, J_2 = 5.5 Hz), 1.51–1.57 (1H, m), 1.99 (1H, dt, J_1 = 9.5 Hz, J_2 = 5.0 Hz), 2.76–2.92 (2H, m), 6.62 (1H, dt, J_1 = 7.5 Hz, J_2 = 2.0 Hz), 7.17–7.21 (3H, m), 7.47 (2H, d, J = 8.0 Hz), 7.57 (1H, d, J = 7.0 Hz), 7.66 (1H, dd, J_1 = 8.5 Hz, J_2 = 1.5 Hz). ^{13}C NMR ($CDCl_3$) δ: 15.6, 18.0, 22.8, 36.1, 112.7, 124.2 (q, $J_{C–F}$ = 270.5 Hz), 125.1 (2C, q, $J_{C–F}$ = 3.6 Hz), 126.2 (2C), 127.9 (q, $J_{C–F}$ = 32.3 Hz), 133.6, 137.2, 137.5, 146.1, 167.9, 175.5.

1-[[[(*trans*-2-(3-(Trifluoromethyl)phenyl)cyclopropyl)-methyl]carbonyl]oxy]-2(1*H*)-pyridinethione (2b)

To a solution of acid **12b** (146 mg, 0.60 mmol) and 2,2′-dipyridyl disulfide bis-*N*-oxide (1.1 equiv., 166 mg, 0.66 mmol) in dry CH_2Cl_2 (10 mL) in a flame-dried flask wrapped with aluminum foil was added Ph_3P (1.1 equiv., 172 mg, 0.66 mmol) at room temperature under nitrogen. The reaction mixture was stirred for 1 h and then treated with 5 mL of 10% aqueous Na_2CO_3 solution. The organic layer was separated, and the aqueous layer was extracted with 10 mL of CH_2Cl_2. The combined organic extracts were washed with saturated NaCl solution (10 mL), dried over $MgSO_4$, and concentrated under reduced pressure. Column chromatography of the residue on silica gel (hexanes–EtOAc = 1:1, v/v) under subdued light gave PTOC-ester **2b** (177 mg, 0.48 mmol, 80%).^{1}H NMR ($CDCl_3$) δ: 1.09 (1H, dt, J_1 = 9.0 Hz, J_2 = 5.5 Hz), 1.17 (1H, dt, J_1 = 8.5 Hz, J_2 = 5.5 Hz), 1.52–1.58 (1H, m), 2.01 (1H, dt, J_1 = 9.0 Hz, J_2 = 5.0 Hz), 2.80–2.92 (2H, m), 6.64 (1H, dt, J_1 = 6.5 Hz, J_2 = 1.5 Hz), 7.20–7.23 (1H, m), 7.31–7.42 (4H, m), 7.58 (1H, d, J = 7.0 Hz), 7.69 (1H, dd, J_1 = 9.0 Hz, J_2 = 1.5 Hz). ^{13}C NMR ($CDCl_3$) δ: 15.3, 17.6, 22.8, 36.2, 112.6, 122.6 (q, $J_{C–F}$ = 3.8 Hz), 122.9 (q, $J_{C–F}$ = 3.6 Hz), 124.1 (q, $J_{C–F}$ = 271.4 Hz), 128.8, 129.7, 130.6 (q, $J_{C–F}$ = 32.3 Hz), 133.6, 137.3, 137.5, 142.8, 168.0, 175.7.

1-[[[(*trans*-2-(4-Fluorophenyl)cyclopropyl)methyl]carbonyl]oxy]-2(1*H*)-pyridinethione (2c)

To a solution of acid **12c** (258 mg, 1.33 mmol) and 2,2′-dipyridyl disulfide bis-*N*-oxide (1.1 equiv., 369 mg, 1.46 mmol) in dry CH_2Cl_2 (10 mL) in a flame-dried flask wrapped with aluminum foil was added *n*-Bu_3P (1.1 equiv., 361 μL, 1.46 mmol) at 0°C under nitrogen. After 2 min, the ice bath was removed. The reaction mixture was stirred for 40 min before 10% aqueous Na_2CO_3 (10 mL) was added. The organic layer was separated and the aqueous layer was extracted with 10 mL of CH_2Cl_2. The combined organic extracts were washed with saturated NaCl solution (10 mL), dried over $MgSO_4$, and concentrated under reduced pressure. Column chromatography on silica gel (hexanes–EtOAc = 1:1, v/v) under subdued light gave PTOC-ester **2c** (225 mg, 0.74 mmol, 56%). ^{1}H NMR ($CDCl_3$) δ: 0.99 (1H, dt, J_1 = 8.4 Hz, J_2 = 5.4 Hz), 1.05 (1H, dt, J_1 = 8.4 Hz, J_2 = 5.4 Hz), 1.39–1.50 (1H, m), 1.91 (1H, dt, J_1 = 8.7 Hz, J_2 = 5.1 Hz), 2.72–2.90 (2H, m), 6.62 (1H, dt, J_1 = 7.2 Hz, J_2 = 1.8 Hz), 6.90–6.96 (2H, m), 7.05–7.11 (2H, m), 7.17–7.22 (1H, m), 7.57 (1H, dd, J_1 = 7.2 Hz, J_2 = 1.8 Hz), 7.67 (1H, dd, J_1 = 9.0 Hz, J_2 = 1.8 Hz). ^{13}C NMR ($CDCl_3$) δ: 14.7, 17.1, 22.3, 36.2, 112.5, 115.0 (2C, d, $J_{C–F}$ = 21.0 Hz), 127.7 (2C, d, $J_{C–F}$ = 7.7 Hz), 133.5, 137.3, 137.5 (d, $J_{C–F}$ = 2.2 Hz), 137.6, 161.2 (d, $J_{C–F}$ = 241.5 Hz), 168.2, 175.7.

1-[[[(*trans*-2-(3-Fluorophenyl)cyclopropyl)methyl]carbonyl]oxy]-2(1*H*)-pyridinethione (2d) was prepared by the procedure of **2c**, using acid **12d** (250 mg, 1.29 mmol), 2,2′-dipyridyl disulfide bis-*N*-oxide (358 mg, 1.42 mmol), and *n*-Bu_3P (350 μL, 1.42 mmol), in 70% yield (272 mg, 0.90 mmol). ^{1}H NMR ($CDCl_3$) δ: 1.03 (1H, dt, J_1 = 8.7 Hz, J_2 = 5.4 Hz), 1.11 (1H, dt, J_1 = 8.7 Hz, J_2 = 5.4 Hz), 1.45–1.56 (1H, m), 1.93 (1H, dt, J_1 = 8.4 Hz, J_2 = 5.1 Hz), 2.75–2.90 (2H, m), 6.63 (1H, dt, J_1 = 7.2 Hz, J_2 = 1.8 Hz), 6.70–6.92 (3H, m), 7.16–7.24 (2H, m), 7.57 (1H, dd, J_1 = 6.9 Hz, J_2 = 1.5 Hz), 7.68 (1H, dd, J_1 = 9.0 Hz, $J2$ = 1.8 Hz). ^{13}C NMR ($CDCl_3$) δ: 15.2, 17.5, 22.7, 36.0, 112.5 (d, $J_{C–F}$ = 21.0 Hz), 112.6, 112.8 (d, $J_{C–F}$ = 22.1 Hz), 121.8 (d, $J_{C–F}$ = 3.3 Hz), 129.6 (d, $J_{C–F}$ = 8.8 Hz), 133.5, 137.0, 137.5, 144.5 (d, $J_{C–F}$ = 6.6 Hz), 162.8 (d, $J_{C–F}$ = 243.8 Hz), 167.9, 175.4.

1-[[[(*trans*-2-(4-Methylphenyl)cyclopropyl)methyl]carbonyl]oxy]-2(1*H*)-pyridinethione (2e) was prepared by the procedure of **2c**, using acid **12e** (250 mg, 1.31 mmol), 2,2′-dipyridyl disulfide bis-*N*-oxide (364 mg, 1.45 mmol), and *n*-Bu_3P (358 μL, 1.45 mmol), in 76% yield (300 mg, 1.00 mmol). ^{1}H NMR ($CDCl_3$) δ: 0.98 (1H, dt, J_1 = 8.4 Hz, J_2 = 5.7 Hz), 1.07 (1H, dt, J_1 = 8.4 Hz, J_2 = 5.1 Hz), 1.42–1.51 (1H, m), 1.89 (1H, dt, J_1 = 8.7 Hz, J_2 = 5.1 Hz), 2.30 (3H, s), 2.81 (2H, d, J = 6.9 Hz), 6.60 (1H, dt, J_1 = 6.9 Hz, J_2 = 1.5 Hz), 7.00–7.08 (4H, m), 7.15–7.21 (1H, m), 7.57 (1H, dd, J_1 = 7.2 Hz, J_2 = 1.5 Hz), 7.66 (1H, dd, J_1 = 9.0 Hz, J_2 = 2.1 Hz). ^{13}C NMR ($CDCl_3$) δ: 14.9, 17.0, 20.8, 22.6, 36.3, 112.5, 126.0 (2C), 128.9 (2C), 133.4, 135.2, 137.1, 137.6, 138.6, 168.0, 175.6.

1-[[[(*trans*-2-(3-Methylphenyl)cyclopropyl)methyl]carbonyl]oxy]-2(1*H*)-pyridinethione (2f) was prepared by the procedure of **2c**, using acid **12f** (250 mg, 1.31 mmol), 2,2′-dipyridyl disulfide bis-*N*-oxide (364 mg, 1.45 mmol), and *n*-Bu_3P (358 μL, 1.45 mmol), in 82% yield (320 mg, 1.07 mmol). ^{1}H NMR ($CDCl_3$) δ: 0.99 (1H, dt, J_1 = 9.0 Hz, J_2 = 5.1 Hz), 1.10 (1H, dt, J_1 = 8.7 Hz, J_2 = 5.1 Hz), 1.47–1.55 (1H, m), 1.89 (1H, dt, J_1 = 8.7 Hz, J_2 = 5.1 Hz), 2.31 (3H, s), 2.74–2.90 (2H, m), 6.62 (1H, dt, J_1 = 7.2 Hz, J_2 = 1.8 Hz), 6.91–6.99 (3H, m), 7.12–7.22 (2H, m), 7.56 (1H, d, J = 7.2 Hz), 7.68 (1H, dd, J_1 = 9.0 Hz, J_2 = 1.5 Hz). ^{13}C NMR ($CDCl_3$) δ: 15.2, 17.2, 21.3, 22.9, 36.4, 112.5, 123.1, 126.6, 126.8, 128.2, 133.5, 137.3, 137.6, 137.9, 141.7, 168.1, 175.7.

1-[[[(*trans*-2-(4-Methoxyphenyl)cyclopropyl)methyl]carbonyl]oxy]-2(1*H*)-pyridinethione (2g) was prepared by the procedure of **2b**, using acid **12g** (200 mg, 0.97 mmol),

© 1999 NRC Canada

2,2′-dipyridyl disulfide bis-*N*-oxide (269 mg, 1.07 mmol), and Ph_3P (281 mg, 1.07 mmol), in 73% yield (222 mg, 0.705 mmol). ^{1}H NMR ($CDCl_3$) δ: 0.95 (1H, dt, J_1 = 9.0 Hz, J_2 = 5.5 Hz), 1.04 (1H, dt, J_1 = 8.5 Hz, J_2 = 5.5 Hz), 1.41–1.46 (1H, m), 1.89 (1H, dt, J_1 = 9.0 Hz, J_2 = 5.0 Hz), 2.77–2.86 (2H, m), 3.77 (3H, s), 6.63 (1H, dt, J_1 = 7.0 Hz, J_2 = 2.0 Hz), 6.80–6.81 (2H, m), 7.06–7.08 (2H, m), 7.19–7.22 (1H, m), 7.56 (1H, d, J = 7.0 Hz), 7.69 (1H, dd, J_1 = 9.0 Hz, J_2 = 1.5 Hz). ^{13}C NMR ($CDCl_3$) δ: 14.6, 16.8, 22.3, 36.4, 55.3, 112.6, 113.7 (2C), 127.4 (2C), 133.5, 133.7, 137.3, 137.6, 157.8, 168.2, 175.7.

1-[[[(*trans*-2-(3-Methoxyphenyl)cyclopropyl)methyl]carbonyl]oxy]-2(1*H*)-pyridinethione (2h) was prepared by the procedure of **2c**, using acid **12h** (400 mg, 1.94 mmol), 2,2′-dipyridyl disulfide bis-*N*-oxide (538 mg, 2.13 mmol), and *n*-Bu_3P (531 μL, 2.13 mmol), in 78% yield (477 mg, 1.51 mmol). ^{1}H NMR ($CDCl_3$) δ: 0.98 (1H, dt, J_1 = 8.4 Hz, J_2 = 5.1 Hz), 1.09 (1H, dt, J_1 = 8.4 Hz, J_2 = 5.4 Hz), 1.44–1.54 (1H, m), 1.89 (1H, dt, J_1 = 9.0 Hz, J_2 = 5.1 Hz), 2.80 (2H, d, J = 7.2 Hz), 3.76 (3H, s), 6.60 (1H, dt, J_1 = 6.6 Hz, J_2 = 1.8 Hz), 6.65–6.71 (3H, m), 7.13–7.20 (2H, m), 7.56 (1H, dd, J_1 = 7.2 Hz, J_2 = 1.5 Hz), 7.64 (1H, dd, J_1 = 7.2 Hz, J_2 = 1.5 Hz). ^{13}C NMR ($CDCl_3$) δ: 15.1, 17.3, 23.0, 36.2, 55.0, 111.1, 111.9, 112.4, 118.4, 129.2, 133.5, 137.0, 137.6, 143.4, 159.5, 167.9, 175.5.

Indirect kinetic studies

These studies followed the method of Newcomb et al. as previously described (4, 17). Benzeneselenol, prepared by the method of Foster (30), was distilled under subdued light. Samples were divided into 1 mL portions and sealed under vacuum in ampoules that were stored at ca. –70°C. The amount of diphenyl diselenide contaminant (typically < 4%) in each sample of PhSeH was determined by GC prior to use. In a flame-dried tube shielded from light containing a small stir bar, a mixture of radical precursors (0.04–0.05 M), PhSeH (0.5–2.0 M), and a hydrocarbon standard (octane or dodecane) in freshly distilled THF was sparged with nitrogen. The tubes were equilibrated in a temperature-regulated bath for several minutes. The shields were removed, and the stirring mixture was irradiated with a 150 W tungsten filament lamp placed 0.4 m from the tube. After 40 min, the tubes were cooled at –78°C, and the contents were analyzed by GC. All yields reported for indirect kinetic experiments were calculated from response factors determined with authentic samples.

Acknowledgments

We thank the National Science Foundation (CHE-9614968) and the National Institutes of Health (GM-48722) for financial support.

References

1. D. Griller and K.U. Ingold. Acc. Chem. Res. **13**, 317 (1980).
2. M. Newcomb. Tetrahedron, **49**, 1151 (1993).
3. M. Newcomb and M.B. Manek. J. Am. Chem. Soc. **112**, 9662 (1990).
4. M. Newcomb, C.C. Johnson, M.B. Manek, and T.R. Varick. J. Am. Chem. Soc. **114**, 10 915 (1992).
5. A.A. Martin-Esker, C.C. Johnson, J.H. Horner, and M. Newcomb. J. Am. Chem. Soc. **116**, 9174 (1994).
6. H. Fu, M. Newcomb, and C.-H. Wong. J. Am. Chem. Soc. **113**, 5878 (1991).
7. K.E. Liu, C.C. Johnson, M. Newcomb, and S.J. Lippard. J. Am. Chem. Soc. **115**, 939 (1993).
8. J.K. Atkinson and K.U. Ingold. Biochemistry, **32**, 9209 (1993).
9. J.K. Atkinson, P.F. Hollenberg, K.U. Ingold, C.C. Johnson, M.-H. Le Tadic, M. Newcomb, and D.A. Putt. Biochemistry, **33**, 10 630 (1994).
10. M. Newcomb, M.H. Le Tadic, D.A. Putt, and P.F. Hollenberg. J. Am. Chem. Soc. **117**, 3312 (1995).
11. M. Newcomb, M.H. Le Tadic-Biadatti, D.L. Chestney, E.S. Roberts, and P.F. Hollenberg. J. Am. Chem. Soc. **117**, 12 085 (1995).
12. A. Zaks and D.R. Dodds. J. Am. Chem. Soc. **117**, 10 419 (1995).
13. P.H. Toy, B. Dhanabalasingam, M. Newcomb, I.H. Hanna, and P.F. Hollenberg. J. Org. Chem. **62**, 9114 (1997).
14. P.H. Toy, M. Newcomb, and L.P. Hager. Chem. Res. Toxicol. **11**, 816 (1998).
15. D.H.R. Barton, D. Crich, and W.B. Motherwell. Tetrahedron, **41**, 3901 (1985).
16. M. Newcomb and A.G. Glenn. J. Am. Chem. Soc. **111**, 275 (1989).
17. M. Newcomb, T.R. Varick, C. Ha, M.B. Manek, and X. Yue. J. Am. Chem. Soc. **114**, 8158 (1992).
18. M. Newcomb, S.-Y. Choi, and J.H. Horner. J. Org. Chem. **64**, 1225 (1999).
19. S. Nahm and S.M. Weinreb. Tetrahedron Lett. **39**, 3815 (1981).
20. K.E. Rodriques. Tetrahedron Lett. **32**, 1275 (1991).
21. P.G. Gassman, P.K.G. Hodgson, and R.J. Balchunis. J. Am. Chem. Soc. **98**, 1275 (1976).
22. J.J. Gajewski and M.P. Squicciarini. J. Am. Chem. Soc. **111**, 6717 (1989).
23. M.M. Martin and G.J. Gleicher. J. Am. Chem. Soc. **86**, 233 (1964).
24. J.H. Horner, N. Tanaka, and M. Newcomb. J. Am. Chem. Soc. **120**, 10 379 (1998).
25. X. Creary, M.E. Mehrsheikh-Mohammadi, and S. McDonald. J. Org. Chem. **52**, 3254 (1987).
26. D.D.M. Wayner and D.R. Arnold. Can. J. Chem. **63**, 2378 (1985).
27. W. Adam, H.M. Harrer, F. Kita, H.G. Korth, and W.M. Nau. J. Org. Chem. **62**, 1419 (1997).
28. A.M. Valentine, M.-H. Le Tadic-Biadatti, P.H. Toy, M. Newcomb, and S.J. Lippard. J. Biol. Chem. **274**, 10771 (1999).
29. D.H.R. Barton, C. Chen, and G.M. Wall. Tetrahedron, **47**, 6127 (1991).
30. D.G. Foster. Org. Synth. Collect. Vol. III, 772 (1955).

© 1999 NRC Canada

Steady state and time-resolved spectroscopic studies of the photochemistry of 1-arylsilacyclobutanes and the chemistry of 1-arylsilenes

William J. Leigh, Rabah Boukherroub, Christine J. Bradaric, Christine C. Cserti, and Jennifer M. Schmeisser

Abstract: Direct photolysis of 1-phenylsilacyclobutane and 1-phenyl-, 1-(2-phenylethynyl)-, and 1-(4′-biphenylyl)-1-methylsilacyclobutane in hexane solution leads to the formation of ethylene and the corresponding 1-arylsilenes, which have been trapped by photolysis in the presence of methanol. Quantum yields for photolysis of the three methyl-substituted compounds have been determined to be 0.04, 0.26, and 0.29, respectively, using the photolysis of 1,1-diphenylsilacyclobutane (Φ_{silene} = 0.21) as the actinometer. The corresponding silenes have been detected by laser flash photolysis; they have lifetimes of several microseconds, exhibit UV absorption maxima ranging from 315 to 330 nm, and react with methanol with rate constants on the order of (2–5) × 10^9 M^{-1} s^{-1} in hexane. Absolute rate constants for reaction of 1-phenylsilene and 1-methyl-1-phenylsilene with water, methanol, *tert*-butanol, and acetic acid in acetonitrile solution have been determined, and are compared to those of 1,1-diphenylsilene under the same conditions. With the phenylethynyl- and biphenyl-substituted methylsilacyclobutanes, the triplet states can also be detected by laser flash photolysis, and are shown to not be involved in silene formation on the basis of triplet sensitization and (or) quenching experiments. Fluorescence emission spectra and singlet lifetimes have been determined for the three 1-aryl-1-methylsilacyclobutanes, 1,1-diphenylsilacyclobutane, and a series of acyclic arylmethylsilane model compounds. These data, along with the reaction quantum yields, allow estimates to be made of the rate constants for the excited singlet state reaction responsible for silene formation. 1-Methyl-1-phenylsilacyclobutane undergoes reaction from its lowest excited singlet state with a rate constant 10–80 times lower than those of the other three derivatives. The results are consistent with a stepwise mechanism for silene formation, involving a 1,4-biradicaloid intermediate that partitions between product and starting material.

Key words: silene, silacyclobutane, photochemistry, biradical.

Résumé : La photolyse directe du 1-phénylsilacyclobutane et des 1-phényl-, 1-(2-phényléthynyl)- et 1-(4′-biphénylyl)-1-méthylsilacyclobutane, en solution dans l'hexane, conduit à la formation d'éthylène et des 1-arylsilènes correspondants que l'on a piégés par photolyse en présence de méthanol. On a déterminé les rendements quantiques pour les photolyses des trois composés portant un groupe méthyle; si l'on utilise la photolyse du 1,1-diphénylcyclobutane ($\Phi_{silène}$ = 0,21) comme actinomètre, les valeurs sont respectivement 0,04, 0,26 et 0,29. On a détecté les silènes correspondants à l'aide de la photolyse éclair au laser; leurs temps de vie sont de plusieurs microsecondes, ils présentent des maxima d'absorption UV à des valeurs allant de 315 à 330 nm et ils réagissent avec le méthanol avec des constantes de vitesse de l'ordre de (2–5) × 10^9 M^{-1} s^{-1}, dans l'hexane. On a déterminé les constantes de vitesse absolue pour la réaction du 1-phénylsilène et du 1-méthyl-1-phénylsilène avec l'eau, le méthanol, l'alcool *tert*-butylique et l'acide acétique, en solution dans l'acétonitrile, et on les a comparées à celles du 1,1-diphénylsilène dans les mêmes conditions. Avec les méthylsilacyclobutanes substitués par des groupes phényléthynyle et biphényle, la photolyse éclair au laser permet aussi de détecter les états triplets et, en se basant sur des expériences de sensibilisation de triplets et/ou de désactivation, on a démontré qu'ils ne sont pas impliqués dans la formation du silène. On a déterminé les spectres d'émission de fluorescence et les temps de vie des singulets des trois 1-aryl-1-méthylsilacyclobutanes,du 1,1-diphénylsilacyclobutane et d'une série de composés arylméthylsilanes acycliques modèles. Ces données utilisées avec les rendements quantiques des réactions ont permis d'évaluer les constantes de vitesse de réaction de l'état singulet excité responsable de la formation du silène. La vitesse de réaction du 1-méthyl-1-phénylsilacyclobutane à partir de son

Received January 20, 1999.

This paper is dedicated to Jerry Kresge in recognition of his many achievements in chemistry.

W.J. Leigh,[1] R. Boukherroub, C.J. Bradaric, C.C. Cserti, and J.M. Schmeisser.[2] Department of Chemistry, McMaster University, 1280 Main Street West, Hamilton, ON L8S 4M1, Canada.

[1]Author to whom correspondence may be addressed. Fax: (905) 522-2509. e-mail: leigh@mcmaster.ca
[2]1998 Reactive Intermediate Student Exchange (RISE) Scholar.

 © 1999 NRC Canada

état singulet excité le plus bas est de 10 à 80 fois plus rapide que les vitesses des trois autres dérivés. Ces résultats sont en accord avec un mécanisme par lequel la formation du silène se ferait par étapes impliquant un intermédiaire 1,4-biradicaloïde qui se répartirait entre le produit de la réaction et le produit de départ.

Mots clés : silène, silacyclobutane, photochimie, biradical.

[Traduit par la Rédaction]

Introduction

Silacyclobutanes are well known to yield products consistent with the formation of silene-reactive intermediates upon photolysis in solution or the gas phase, or upon pyrolysis at high temperatures (1–8). These compounds have proven to be tremendously useful as photochemical precursors for transient silenes, in experiments aimed at detecting the silenes directly and studying the kinetics and mechanisms of their reactions with alcohols and other "silenophiles" (9–17). Photochemical silene formation proceeds with useful efficiencies from silacyclobutanes that bear alkyl, vinyl, ethynyl, silyl, and phenyl substituents at silicon, and possess UV absorption maxima between 190 and 250 nm (2, 4, 12, 13, 17–20). In contrast, alkoxy substitution either directly at silicon or on the aromatic rings of phenylated derivatives renders the silacyclobutane moiety inert to photocycloreversion (13, 17).

Several details of the mechanism for the photochemical cycloreversion of silacyclobutanes are known, at least for 1,1-dialkyl-substituted derivatives that absorb below ~230 nm. The reaction is initiated from the lowest (σ,σ^*) excited singlet state, by cleavage of one of the ring Si—C bonds to form a biradicaloid intermediate that cleaves to silene and alkene, recloses to starting material, and undergoes intramolecular disproportionation if an alkyl substituent is present at C2 (20). The presence of substituents at C2 of the silacyclobutane ring directs the regiochemistry of the initial cleavage toward the Si—C2 bond, leading to an intermediate whose lifetime is long enough to allow bond rotations that lead to partial scrambling of the stereochemistry at this carbon (20). This mechanism contrasts that of the thermal cleavage of silacyclobutanes, which has been shown to proceed by a stepwise mechanism involving initial C2—C3 bond cleavage (21–24).

The situation is less clear with 1-phenyl-substituted derivatives, in which the phenyl substituent is the primary chromophore. 1,1-Diphenylsilacyclobutane (**1**) affords 1,1-diphenylsilene (**2**; eq. [1]) with reasonable efficiency (Φ_2 = 0.21), and time-resolved experiments have shown that silene formation occurs on the nanosecond time scale and cannot be quenched by saturation of the solution with oxygen or other triplet quenchers (11). The reactive excited state is thus most likely the lowest excited singlet state, which in these cases is predominantly of benzenoid π,π^* character. For efficient cleavage to occur, however, the ring Si—C bonds in the reactive excited state must obviously be weakened compared to the situation in the ground state, so the lowest benzenoid excited singlet state is presumably mixed with σ,σ^*, σ,π^* or π,σ^* configurations that activate the ring toward cleavage. Whether the reaction occurs by a concerted or stepwise mechanism has not been conclusively established, although the question has in fact been addressed in two early papers on the photochemistry of 2-phenyl-substituted silacyclobutanes (4, 25).

[1] 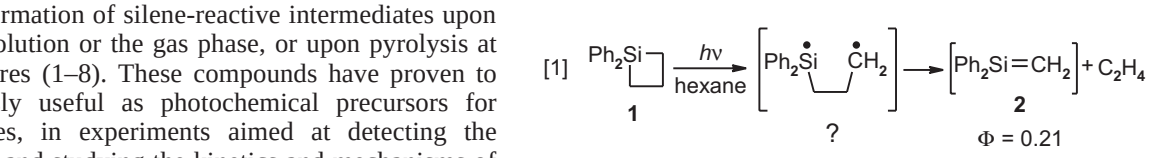

In this paper, we report the photochemistry of 1-phenylsilacyclobutane (**3**) and the series of 1-methyl-1-arylsilacyclobutane derivatives **4–6**, in which the aryl substituent is varied between phenyl, phenylethynyl, and biphenyl. The main goal of this work was to determine how the photophysical properties of the chromophore affect the rates and efficiencies of silene formation in arylsilacyclobutane photolysis, and hence to better define the scope and limitations of silacyclobutane photolysis as a source of reactive silenes. It seemed likely to us that the phenylacetylene and biphenyl chromophores in **5** and **6** would allow study of the photochemistry and photophysics of arylsilacyclobutanes in

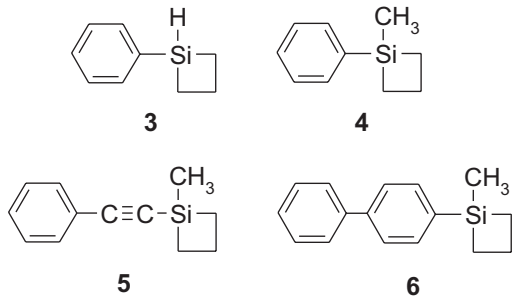

much greater detail than is convenient with simple phenyl derivatives, since these chromophores generally fluoresce strongly and promote efficient intersystem crossing to the lowest triplet states, which are usually detectable by laser flash photolysis. Thus, we have studied the photochemistry of the three 1-aryl-1-methylsilacyclobutanes (**4–6**) in detail, using steady state photolysis and time-resolved UV absorption and fluorescence emission spectroscopic techniques. Photolysis of all four compounds in hydrocarbon solvents yields the corresponding silenes (**7–10**), which have been detected directly by laser flash photolysis methods and characterized on the basis of their reactivity toward methanol and *tert*-butanol. Absolute rate constants for the reactions of **7** and **8** with the two alcohols, water, and acetic acid have been determined in acetonitrile solution, and are compared to those for 1,1-diphenylsilene (**2**) under similar conditions. Fluorescence spectra and lifetimes have also been determined for **1** and the acyclic arylsilanes **11–14**, to provide a more complete framework with which to understand the

© 1999 NRC Canada

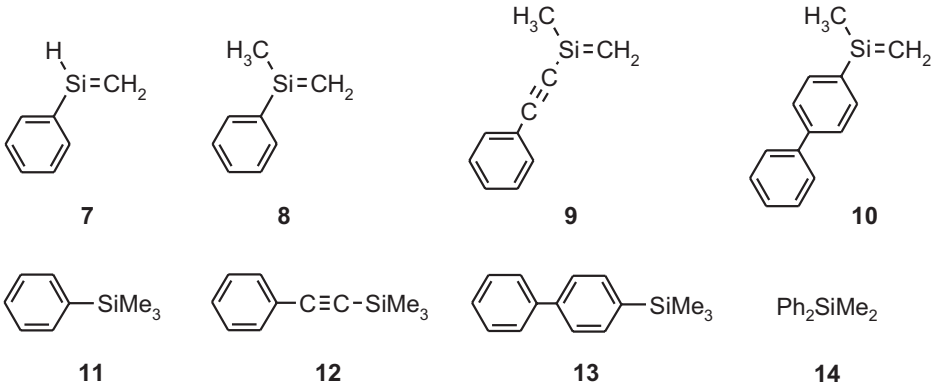

7 **8** **9** **10**

11 **12** **13** **14**

variations in photochemistry and photophysics of these arylsilacyclobutanes as a function of substituent.

Results

Silacyclobutanes **5** and **6** were prepared by reaction of 1-chloro-1-methylsilacyclobutane with phenylethynyllithium and 4-biphenylmagnesium bromide, respectively, using a procedure similar to those reported previously for the synthesis of **3** (26) and **4** (3). All four compounds were purified to >99% (GC) purity by vacuum distillation (**3–5**) or repeated recrystallization (**6**).

Photolysis (254 nm) of the four compounds as deoxygenated 0.04 M solutions in hexane containing methanol (0.05 M) led to the formation of ethylene and the methoxysilane **15** (eq. [2]). The methoxysilanes **15a–15c** were identified by GC–MS and GC coinjection with independently prepared authentic samples, while **15d** was isolated and identified on the basis of its ^{1}H NMR and mass spectra. No other products could be detected in the crude photolysates by GC analysis, up to ~20% conversion of the silacyclobutane, within the detection limits of our GC method.

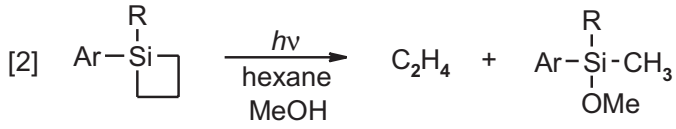

3-6 **15**

a. R = H; Ar = Ph
b. R = Me; Ar = Ph
c. R = Me; Ar = C≡C-Ph
d. R = Me; Ar = 4-C_6H_4-C_6H_5

Photolysis (350 nm) of a deoxygenated 0.05 M solution of benzophenone in hexane containing 0.01 M **6** and 0.1 M MeOH led to the slow formation of benzhydrol (identified by MS), but no destruction of the silacyclobutane. Methoxysilane **15d** could not be detected in the mixture, within the limits of our GC method.

Nanosecond laser flash photolysis (λ_{ex} = 248 nm) of continuously flowing, air-saturated solutions of **3** and **4** (~0.014 M) in hexane or acetonitrile leads to weak, but readily detectable, transient absorptions in the spectral region below ≈350 nm. The absorptions decay on the microsecond time scale with mixed first- and second-order kinetics to within 10% of the prepulse level, and exhibit lifetimes in the 2–3 μs range in scrupulously dried solvent. Time-resolved UV absorption spectra were recorded for air-saturated solutions of the two compounds, 0.1–0.4 μs after the laser pulse. The spectra recorded in hexane solution are shown in Fig. 1*a*, *b* along with typical decay traces, recorded at a monitoring wavelength of 315 nm. The lifetimes and intensities of the signals are unaffected by saturation of the solutions with either nitrogen or oxygen.

Addition of water, methanol, *tert*-butanol, or acetic acid ($(0.5–5) \times 10^{-3}$ M) results in a reduction in the lifetimes of both transients and a change in decay kinetics to pseudo first order. Plots of the rate constant for decay (k_{decay}) versus concentration of added quencher according to eq. [3] (where k_0 is the first-order rate constant for the decay of the transient in the absence of added quencher and k_{ROH} is the second-order quenching rate constant) were linear in all cases. Bimolecular rate constants for reaction of **3** and **4** with the four reagents in acetonitrile solution are listed in Table 1, while those for reaction with MeOH and *t*-BuOH in hexane are listed in Table 2. Similar experiments were carried out using MeOD, *t*-BuOD, and acetic acid-*d* in MeCN solution; the k_H/k_D values calculated from these rate constants and those for reaction of the corresponding protiated reagents are included in Table 1. Previously reported rate constants for reaction of **2** with these reagents in acetonitrile are included for comparison.

[3] $$k_{decay} = k_0 + k_{ROH}[Q]$$

Laser flash photolysis of deoxygenated hexane solutions of the phenylethynyl derivative **5** (2×10^{-5} M) led to complex behavior that could be shown to result from competing formation of the silacyclobutane triplet state and silene **9**, whose absorption spectra overlap almost exactly but differ considerably in intensity. Absorptions due to the triplet dominate the transient behavior in deoxygenated hexane solution. For example, flash photolysis of a deoxygenated solution of **5** gave rise to a long-lived ($\tau \sim 5$ μs), strongly absorbing, transient with λ_{max} = 315 nm. The lifetime of the transient was reduced substantially upon addition of oxygen or 1,3-octadiene, but was apparently unaffected upon addition of 0.005 M methanol. Monitoring at 260 nm, within the long-wavelength absorption band of the silacyclobutane, gave rise to a bleaching signal that recovered almost to the prepulse level with the same lifetime as that of the transient

© 1999 NRC Canada

Fig. 1. Time-resolved UV absorption spectra of silenes **7** (*a*), **8** (*b*), **9** (*c*), and **10** (*d*) in hexane solution at 23°C. The spectra of **9** and **10** were recorded in the presence of ~0.008 M 1,3-octadiene to shorten the lifetime of the corresponding silacyclobutane triplet to τ_T <20 ns.

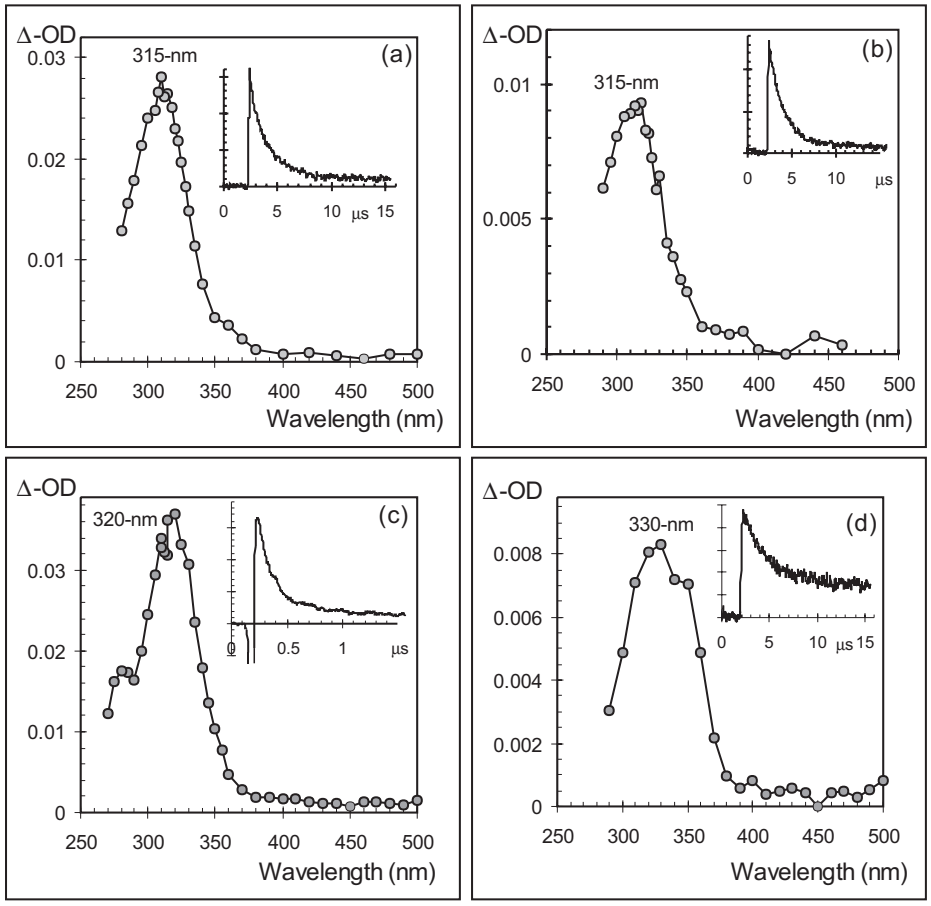

Table 1. Bimolecular rate constants for reaction of substituted 1-phenylsilenes **7**, **8**, and **2** with H_2O, MeOH(D), *t*-BuOH(D), and AcOH(D) in air-saturated acetonitrile solution at 23°C.[a]

Ph Si=CH$_2$ R	H_2O	MeOH		*t*-BuOH		HOAc	
R	k_q / 10^9 M^{-1} s^{-1}	k_q / 10^9 M^{-1} s^{-1}	k_H/k_D	k_q / 10^9 M^{-1} s^{-1}	k_H/k_D	k_q / 10^9 M^{-1} s^{-1}	k_H/k_D
H (**7**)	0.72 ± 0.01	1.63 ± 0.08	1.3 ± 0.1	0.67 ± 0.04	1.5 ± 0.1	1.85 ± 0.08	1.1 ± 0.1
Me (**8**)	0.56 ± 0.01	1.16 ± 0.02	1.6 ± 0.1	0.20 ± 0.09	1.4 ± 0.1	1.55 ± 0.04	1.0 ± 0.1
Ph (**2**)[b]	0.76 ± 0.09	1.2 ± 0.1	1.5 ± 0.2	0.22 ± 0.02	1.6 ± 0.1	1.23 ± 0.07	1.1 ± 0.1

[a]Errors are listed as twice the standard deviation from least-squares analysis of k_{decay} vs. concentration data according to eq. [3].

[b]Data from ref. 11.

Table 2. Time-resolved UV absorption spectra and bimolecular rate constants for reaction of substituted 1-phenylsilenes **7–10** and **2** with methanol and *tert*-butanol in hexane solution at 23°C.[a]

R Si=CH$_2$ Ar	Ar	R	λ_{max} (nm)	k_{MeOH} / 10^9 M^{-1} s^{-1}	$k_{t\text{-BuOH}}$ / 10^9 M^{-1} s^{-1}
7	Ph	H	315	3.1 ± 0.1	1.2 ± 0.1
8	Ph	Me	315	3.2 ± 0.2	1.2 ± 0.1
2[b]	Ph	Ph	325	1.9 ± 0.2	0.40 ± 0.07
9	PhC≡C	Me	320	5 ± 2	—
10	4-PhC_6H_4	Me	330	2.9 ± 0.3	—

[a]Measured by laser flash photolysis. Errors in the rate constants are listed as twice the standard deviation from least-squares analysis of k_{decay} vs. concentration data according to eq. [3].

[b]Data from ref. 11.

© 1999 NRC Canada

Fig. 2. Triplet–triplet absorption spectra for silacyclobutanes **5** (*a*) and **6** (*b*) in deoxygenated hexane solution containing 0.03 M methanol at 23°C.

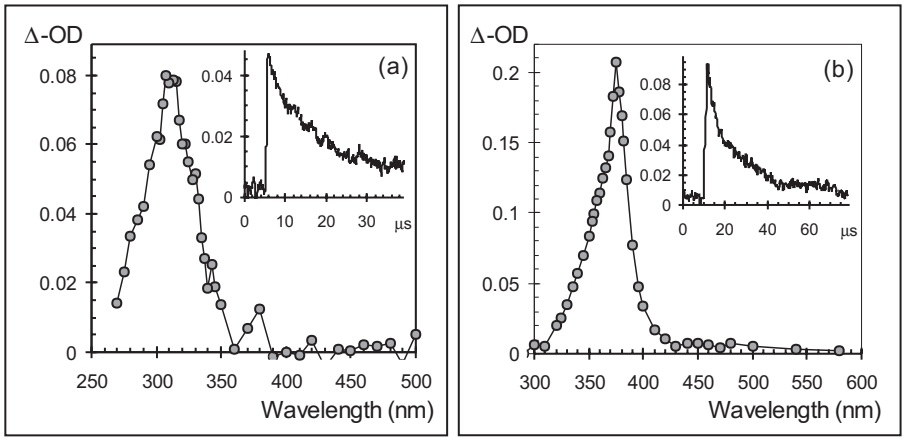

absorption at 315 nm. The lifetimes of the absorption and bleaching signals were also identical ($\tau \sim 500$ ns) in the presence of air, but differed in oxygen-saturated solution, where the 315 nm transient decay exhibited an average lifetime of $\tau \sim 240$ ns and the bleaching signal at 260 nm recovered with a clean pseudo-first-order lifetime $\tau \sim 100$ ns. Different behavior was noted upon addition of 0.0027 M 1,3-octadiene, where the bleaching signal was unresolvable from the laser pulse and the 315 nm transient decayed with a lifetime of $\tau \sim 600$ ns, was much weaker in intensity, and was superimposed on a strong fluorescence signal.

The kinetic behavior of the bleaching signal is consistent with the formation of a transient whose decay mainly regenerates the precursor, as would be expected for a triplet state. We thus assign the transient absorption spectrum recorded under deoxygenated conditions as consisting largely of the triplet–triplet absorption spectrum of silacyclobutane **5**, superimposed on a second, more weakly absorbing, transient (assigned to the silene **9**, vide infra) that is resolvable only under conditions where the triplet is strongly quenched. The spectrum of the triplet, recorded in deoxygenated hexane solution containing 0.03 M methanol to remove contributions from the silene (Fig. 2*a*), exhibits $\lambda_{max} = 315$ nm, in the range expected for a phenylacetylene triplet (27, 28). The rate constant for quenching of the triplet by 1,3-octadiene in hexane was found to be $(9.9 \pm 0.6) \times 10^9$ M^{-1} s^{-1}, which is also consistent with its assignment. A rate constant for triplet quenching by oxygen was estimated as $k_q \sim 6 \times 10^8$ M^{-1} s^{-1} from the rates of recovery of the precursor bleaching signal in air- and oxygen-saturated solution.

In hexane solution containing 0.001 M 1,3-octadiene or saturated with oxygen, the lifetime of the residual transient absorption at 315 nm is reduced upon addition of methanol. The spectrum of the transient observed under these conditions exhibits $\lambda_{max} = 320 \pm 2$ nm (Fig. 1*c*), and can thus be most reasonably assigned to 1-methyl-1-phenylethynylsilene (**9**). The transient is quenched efficiently by MeOH, though unfortunately we were able to obtain only a qualitative estimate of the rate constant ($k_{MeOH} = (5 \pm 2) \times 10^9$ M^{-1} s^{-1}), because of interference from the triplet absorptions and sample fluorescence at higher alcohol concentrations. Experiments with solutions containing higher concentrations of diene (e.g., 0.003 M) led to no improvement in accuracy because the silene signal was weaker due to screening of the excitation light by the diene. The fact that the silene is observable under conditions where the triplet lifetime is reduced to <25 ns indicates that the silene is formed from the lowest excited singlet state of the silacyclobutane, and not from the triplet.

Similar results were obtained in laser flash photolysis experiments with the 4′-biphenyl-substituted derivative **6**. Accordingly, flash photolysis of deoxygenated 6×10^{-5} M solutions of **6** in hexane containing 0.03 M MeOH gave rise to a long-lived ($\tau = 12.5$ μs) transient that decayed with pseudo-first-order kinetics at very low laser intensities, and exhibited $\lambda_{max} = 375$ nm (Fig. 2*b*). This transient is assigned to the triplet state of **6** on the basis of the similarity of its spectrum to that of the 4-trimethylsilyl-4′-biphenyl (**13**) triplet ($\lambda_{max} = 375$ nm under similar conditions) and the fact that it is quenched by 1,3-octadiene with a rate constant $k_q = (4.9 \pm 0.5) \times 10^9$ M^{-1} s^{-1}. Alternatively, flash photolysis of air-saturated solutions of **6** in hexane containing 0.008 M 1,3-octadiene gave rise to a transient that decayed with clean pseudo-first-order kinetics ($\tau = 2.1$ μs) and exhibited $\lambda_{max} = 330$ nm. The species proved to be sensitive to the presence of methanol; a plot of k_{decay} vs. [MeOH] according to eq. [2] was linear, and afforded a slope $k_{MeOH} = (2.9 \pm 0.3) \times 10^9$ M^{-1} s^{-1}. On the basis of these data, this transient is assigned to silene **10**.

The time-resolved UV absorption spectra of silenes **9** and **10** in air-saturated hexane solution containing 0.008 M 1,3-octadiene are shown in Figs. 2*c*,*d*. The bimolecular rate constants for their reaction with MeOH under the same conditions are summarized in Table 2, along with the corresponding data for **7**, **8** and 1,1-diphenylsilene (**2**) (11). Quenching by *t*-BuOH was not investigated in these two cases.

Quantum yields for disappearance of **4–6** were determined by 254 nm merry-go-round photolysis of deoxygenated 0.03–0.04 M solutions in hexane containing methanol (0.05 M), using 1,1-diphenylsilacyclobutane (**1**) as actinometer. Photolysis of **1** in methanolic hexane solution affords ethylene and diphenylmethoxymethylsilane (**16**) as the only detectable products (2, 4, 11) — the latter due to trapping of

© 1999 NRC Canada

Table 3. Reaction quantum yields (Φ_{sil}),[a] fluorescence emission maxima, and singlet lifetimes for 1-aryl-1-methylsilacyclobutanes **4–6**, 1,1-diphenylsilacyclobutane (**1**), and the corresponding model compounds **11–14**, determined in deoxygenated isooctane solution at 23°C. Estimates of excited state reaction rate constants and state efficiencies for formation and reaction of biradicaloid intermediates are also included.

Compound	Φ_{sil}	λ_F (nm)[b]	τ_S (ns)[b,c]	$k_{sil}/10^7$ s^{-1} [d]	$k_{BIR}/10^7$ s^{-1} [e]	ϕ_{BIR} [e]	ϕ_{sil} [f]
4	0.04 ± 0.02	284	30 ± 2	0.13 ± 0.07	0.7 ± 0.4	0.21	0.19
11 ($PhSiMe_3$)	—	284	38 ± 3	—	—		
5	0.26 ± 0.04	300	6.6 ± 0.2	3.9 ± 0.9	10.2 ± 0.8	0.67	0.38
12 ($PhCCSiMe_3$)	—	300	20.0 ± 0.1	—	—		
6	0.29 ± 0.03	310	7.0 ± 0.3	4.1 ± 0.5	6.7 ± 0.5	0.47	0.61
13 (4′-$BiphSiMe_3$)	—	310	13.2 ± 0.4	—	—		
1	0.21 ± 0.03	285	2.6 ± 0.1	8.1 ± 0.9	9.0 ± 0.9	0.23	0.90
14 (Ph_2SiMe_2)	—	285	3.4 ± 0.2	—	—		

[a]For disappearance of substrate, from photolysis of deoxygenated 0.03–0.04 M solutions of silacyclobutane in hexane containing 0.05 M MeOH, using **1** as actinometer. Errors are listed as the standard deviation from the mean of duplicate determinations.

[b]Recorded in deoxygenated isooctane solution, at concentrations of 10^{-5}–10^{-4} M.

[c]Determined by time-correlated single photon counting. Errors are listed as ±2σ.

[d]Calculated from Φ_{sil} and τ_S^{SCB} (see eq. [5]).

[e]Estimated from the fluorescence lifetimes of silacyclobutane and corresponding model compounds according to eqs. [8] and [9].

[f]Calculated from Φ_{sil} and ϕ_{BIR} according to eq. [7].

Fig. 3. Concentration vs. time plots for merry-go-round photolysis of deoxygenated 0.03–0.04 M solutions of silacyclobutanes **4** (□), **5** (◆), **6** (△), and **1** (●) in hexane containing methanol (0.05 M) at 25°C.

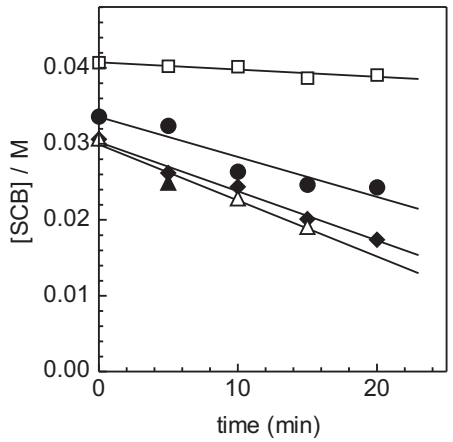

1,1-diphenylsilene (**2**) — and is characterized by a quantum yield of Φ_2 = 0.21 ± 0.03 (11). Quantum yields were calculated from the relative slopes of plots of concentration vs. photolysis time, which are shown in Fig. 3. The results of these experiments are collected in Table 3. Qualitative observations indicated the quantum yield for photolysis of **3** to be similar to that of **4** under similar conditions.

Steady state fluorescence emission spectra of **4–6** and **1** were recorded in deoxygenated isooctane solutions at concentrations in the 10^{-5}–10^{-4} M range. The fluorescence spectra of **4–6** were slightly weaker but otherwise indistinguishable from those of the corresponding model compounds **11–13** in each case. The fluorescence spectrum of dimethyldiphenylsilane (**14**) consisted of a prominent band centered at 285 nm along with a weaker shoulder centered at ~335 nm that is tentatively attributed to intramolecular excimer formation. A similar spectrum was observed for **1**, except the long-wavelength shoulder was much weaker than in the spectrum of **14**. The fluorescence excitation spectra of the eight compounds matched the static absorption spectra (in the region above ~240 nm) in each case. Fluorescence lifetimes were determined for all eight compounds at the emission maxima by time-correlated single photon counting, under the same conditions as those employed for the determination of the steady state fluorescence spectra. In all eight cases, the fluorescence decay profiles analysed either to single exponential kinetics or to two exponentials, which consisted of a prominent (>98%) short-lived decay superimposed on a very weak (<2%) long-lived decay whose origin was not investigated. Identical fluorescence lifetimes were obtained from solutions of ca. 2-fold higher concentration in substrate, within experimental error, indicating that, at these concentrations, self-quenching of fluorescence (due to *inter*molecular excimer formation, for example) is insignificant. The fluorescence emission maxima and singlet lifetimes obtained from these experiments are listed in Table 1, along with various kinetic parameters calculated from the reaction quantum yields and singlet lifetimes (vide infra).

Discussion

The steady state photochemistry and time-resolved spectroscopic behavior of all four of the silacyclobutanes **3–6** are consistent with the formation of ethylene and the corresponding arylsilenes **7–10** as the exclusive products of photolysis, within the limits of our (GC and ^{1}H NMR) detection limits. The four silenes exhibit the expected trends in lifetime (τ = 2–5 μs), λ_{max} (315–330 nm), and reactivity toward alcohols (k_{MeOH} = (2–5) × 10^9 M^{-1} s^{-1} in hexane at 23°C), considering our previously reported data for 1,1-diphenylsilene (**2**) (9, 11). The steady state results reported here for photolysis of **3** in the presence of methanol are analogous to those reported previously for the photolysis of this compound in the presence of other alcohols (26).

As we reported previously for **2** (11), the reactivities of silenes **7** and **8** are significantly lower in acetonitrile solution than in hexane, probably due to weak complexation by the nitrile solvent, and in all cases the rate constants follow

© 1999 NRC Canada

the trend $k_{HOAc} \sim k_{MeOH} > k_{H_2O} > k_{t\text{-}BuOH}$. The reactivities of the three phenylsilene derivatives with each reagent are remarkably similar to one another in this solvent, probably because the small differences in rate that are expected, based on the electronic effects of the substituents (17), are offset by opposing steric and solvation effects. The three compounds show a slightly greater spread in reactivity toward methanol in hexane solution than in acetonitrile, which might reflect differences in solvation throughout the series by the nitrile solvent. As we found previously for **2** (11), the rate constants for reaction with water and the alcohols are subject to small, but clearly primary, deuterium kinetic isotope effects. This is consistent with a reaction mechanism involving initial, reversible complexation followed by rate-controlling proton transfer from oxygen to carbon (eq. [4]) (10, 11, 13, 17, 29–33).

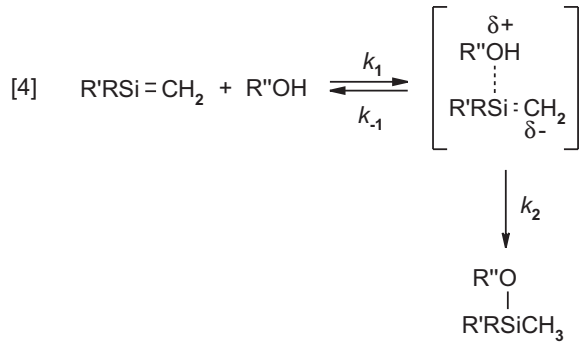

Laser flash photolysis studies of 1,1-diphenylsilacyclobutane (**1**) in nitrogen-saturated hexane solution have shown that 1,1-diphenylsilene (**2**) is formed within the duration of the excitation pulse from a KrF excimer laser (~15 ns) (11). This establishes an upper limit (of the same value) for the lifetime of the excited state responsible for the formation of the reactive intermediate. In this case, the identification of the reactive excited state (i.e., singlet or triplet) by conventional triplet sensitization or quenching experiments is not a trivial task, and we can rule out the triplet state as the precursor only providing that its lifetime is in excess of about 10 ns. We have been unsuccessful in our attempts to detect the triplet state of **1** directly by laser flash photolysis, but this is not unexpected for a benzene derivative bearing nonconjugative substituents (27).

The results reported here for **5** and **6** provide strong evidence that the lowest triplet states of 1-arylsilacyclobutanes are not involved in silene formation. In these two cases, the triplet states are easily detectable by laser flash photolysis because intersystem crossing is more efficient in phenylalkynes and biphenyls than in simple benzene derivatives, and the triplets absorb considerably more strongly (27, 28, 34). The triplet lifetimes of these two molecules were determined to be ~14 and 12 μs, respectively, in deoxygenated hexane solution at room temperature, which should be considered to be lower limits. Quenching of the triplets by oxygen or 1,3-octadiene proceeds rapidly in both cases, but has no discernible effect on the yield of silene (as measured by the initial ΔOD of the silene absorption in the presence of oxygen or diene). In fact, the presence of diene is necessary in order to detect the corresponding silenes (**9** and **10**) cleanly by laser flash photolysis, because their spectra overlap severely with those of the triplet states of the precursors. Similarly, benzophenone-sensitization experiments with **6**, at a concentration corresponding roughly to 90% efficient triplet sensitization, failed to produce detectable amounts of the methanol trapping product of silene **10**. These experiments conclusively demonstrate that the reactive excited state of arylsilacyclobutanes, with respect to [2 + 2] photocycloreversion to the corresponding silenes, is the lowest excited singlet state.

Comparison of the singlet lifetimes of the silacyclobutanes **1** and **4–6** with those of the corresponding model compounds (**11–14**), in which the silacyclobutane ring carbons are replaced by two methyl groups, provides additional evidence for the direct involvement of the lowest excited singlet state in silene formation. Compared to the corresponding silacyclobutanes, the latter four compounds are all essentially non-photoreactive, allowing the conclusion that their singlet lifetimes are controlled mainly by *nonproductive* decay processes such as fluorescence, intersystem crossing, and internal conversion. In fact, the singlet lifetimes of the three trimethylsilyl-substituted compounds **11–13** are similar to those of the corresponding methylarenes under similar conditions (toluene, 34 ns (35); 1-phenylpropyne, 15 ns;[3] 4′-methylbiphenyl, 15.2 ns (35)), indicating that trialkylsilyl substitution has little intrinsic effect on the photophysics of the arene chromophore in each of these compounds. In contrast, the singlet lifetime of dimethyldiphenylsilane (**14**; τ_S = 3.4 ns) is substantially shorter than that of diphenylmethane (τ_S = 25.3 ns (35)). We tentatively attribute this to intramolecular excimer formation on the basis of the long-wavelength shoulder in the static fluorescence emission spectrum of the diarylsilane. This weak emission band occurs at a position characteristic of inter- and intramolecular excimer emissions in substituted benzene derivatives (36). A similar band appears in the emission spectrum of **1**, though it is weaker than in that of **14**. Diphenylmethane does not form an intramolecular excimer (35, 36), and consequently its singlet lifetime is similar to that of toluene. In any event, the singlet lifetimes of the silacyclobutane derivatives are in each case significantly shorter than those of the corresponding model compounds, which is consistent with the presence of an additional mode of excited singlet state decay due to reaction involving the four-membered ring. The alternate possibility that the shorter singlet lifetimes of the cyclics are due to an enhancement in one or more of the nonproductive decay modes cannot, however, be rigorously ruled out. Fluorescence and intersystem crossing could be quantitatively evaluated through quantum yield measurements but, even then, possible differences in the rates of nonproductive internal conversion cannot be easily evaluated.

We were surprised to discover that the quantum yield for silene formation from 1-methyl-1-phenylsilacyclobutane (**4**) is ~5 times lower than that for 1,1-diphenylsilacyclobutane (**1**), and up to ~8 times lower than those for **5** and **6**, which have lower excited singlet state energies. This must be due to a substituent effect on the rate constants for reac-

[3] In deoxygenated isooctane at 25°C. We thank T.L. Morkin for this measurement.

© 1999 NRC Canada

Scheme 1.

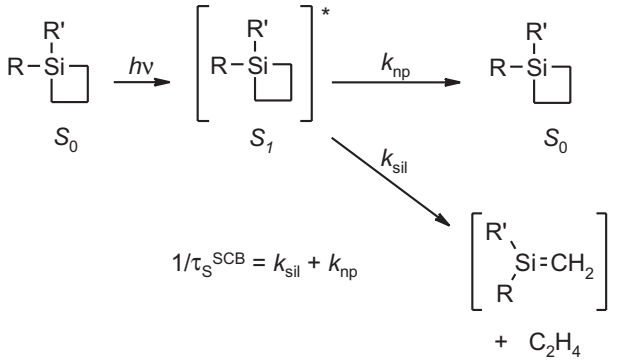

Scheme 2.

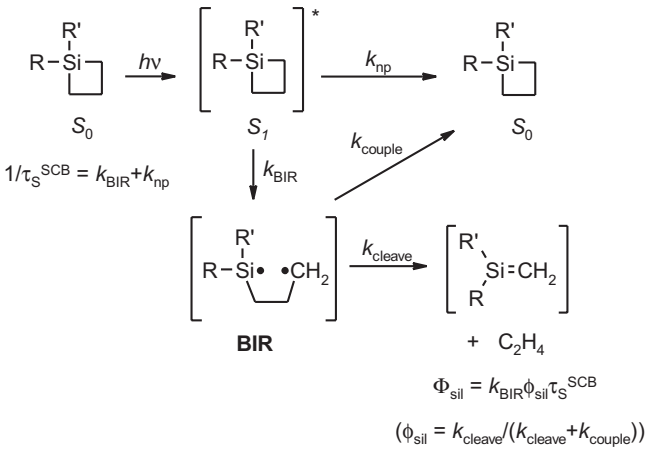

tive excited state decay and (or) (if silene formation is nonconcerted) the partitioning of the biradicaloid intermediate between silene and starting material. Scheme 1 depicts the simplest possible mechanism to account for excited state decay in these compounds, where silene formation occurs directly from the excited singlet state by concerted cycloreversion with rate constant k_{sil}, and k_{np} is the sum of the rate constants for all nonproductive pathways for excited state decay. The reaction rate constants can be calculated from the quantum yields and singlet lifetimes according to eq. [5], and are listed in Table 3. It should be noted that these are true elementary rate constants only if silene formation occurs directly from the lowest excited singlet state by a concerted mechanism.

$$[5] \qquad \Phi_{sil} = k_{sil}\,\tau_S^{SCB}$$

If silene formation occurs by a stepwise mechanism, then the k_{sil} values calculated above are a more complex function of the primary rate constant for excited state bond cleavage to form the biradicaloid intermediate (k_{BIR}) and an efficiency factor (ϕ_{sil}) that describes its partitioning between silene and the ground state of the silacyclobutane (Scheme 2 and eq. [6]). In other words, the overall quantum yield for reaction is given by the product of the state efficiencies for biradicaloid formation ($\phi_{BIR} = k_{BIR}\,\tau_S^{SCB}$) and for silene formation from the biradicaloid ($\phi_{sil} = k_{cleave}\,\tau_{BIR}$), as shown in eq. [7]. The rigorous determination of these parameters requires additional information, which could be obtained if the intermediate could be detected either directly or indirectly via chemical trapping. Unfortunately, no additional transient absorptions that might be assigned to such species have been observed on the nanosecond time scale, in these or any of the other arylsilacyclobutanes that we have studied.

$$[6] \qquad k_{sil} = k_{BIR} \cdot \phi_{sil}$$

$$[7] \qquad \Phi_{sil} = \phi_{BIR} \cdot \phi_{sil}$$

The best we can do at present is to approximate k_{BIR} values from the singlet lifetimes of the silacyclobutanes and their model compounds, making the admittedly crude assumption that the sum of the rates of the nonproductive decay processes in each of the silacyclobutanes is equal to the inverse singlet lifetime of its model compound. To the extent that this assumption is reasonable, k_{BIR} and ϕ_{BIR} can be estimated using eqs. [8] and [9], and ϕ_{sil} then follows from eq. [7]. These parameters are collected in Table 1.

$$[8] \qquad k_{BIR} \approx 1/\tau_S^{SCB} - 1/\tau_S^{mod}$$

$$[9] \qquad \phi_{BIR} = k_{BIR}\,\tau_S^{SCB} \approx 1 - (\tau_S^{SCB}/\tau_S^{mod})$$

The k_{sil} and k_{BIR} values summarized in Table 1 both indicate that the excited singlet state of 1-methyl-1-phenylsilacyclobutane (**4**) is significantly less reactive toward bond cleavage than those of **1**, **5**, and **6**. The most reasonable explanation for this is that the mixing of benzenoid π and (or) π* MOs with Si—C σ and (or) σ* MOs in the lowest excited singlet state, which is required in order to activate the silacyclobutane ring toward bond cleavage, is much less efficient in **4** than in the other three derivatives. Presumably, the more extended π-systems in **1**, **5,** and **6** assist in this mixing by perturbing the symmetries of the relevant π-type molecular orbitals.

The calculated ϕ_{BIR} and ϕ_{sil} values for the four silacyclobutanes also show some interesting trends. The data for **1** and **4** suggest that the difference in overall reaction quantum yield for these two compounds is primarily due to differences in the behavior of the biradicaloid intermediates, not to differences in the efficiencies of excited state Si—C bond cleavage. The approximately equal ϕ_{BIR} values for the two compounds result from the fact that substituent-induced perturbations that affect k_{BIR} also tend to affect the rates of the nonproductive decay processes: in spite of the fact that **4** is ~10 times less reactive than **1**, the intrinsic lifetime of its excited singlet state (as measured by τ_S^{mod}) is also ~10 times longer. In fact, the data indicate that ϕ_{BIR} varies relatively little throughout the entire series of compounds. On the other hand, ϕ_{sil} varies smoothly throughout the series, suggesting that the biradicaloid from **1** mainly cleaves ($k_{cleave} \sim 9k_{couple}$) while that from **4** mainly couples to regenerate starting material ($k_{couple} \sim 4k_{cleave}$).

Such a large variation in the relative rate constants for cleavage and coupling of the putative 1,4-biradicaloid intermediates is surprising. The two main factors that should affect the partitioning of such species between cleavage and coupling are the relative thermodynamic stabilities of the coupling and cleavage products and the conformational preferences of the 1,4-biradical as they are reflected in the relative transition state energies for cleavage and coupling (37–41). In the present cases, thermodynamics would clearly be expected to strongly favor coupling over cleavage in all

© 1999 NRC Canada

cases. Cleavage requires a colinear arrangement of the central C—C bond with the *p*-orbitals on the trivalent centers, but has little dependence on conformation about the central C—C bond. Coupling, on the other hand, can only occur from *gauche* conformers. While steric effects would clearly be predicted to lead to an increase in cleavage over coupling in the biradicaloid from **1** compared to that from **4**, it is difficult to rationalize the variation in ϕ_{sil} between **4**, **5**, and **6** on the basis of these simple arguments.

We stress again that our analysis of the data in terms of a stepwise reaction mechanism is based on the crude assumption that the singlet lifetimes of the model compounds **11–14** provide a reasonable estimate of the nonproductive contributions to the singlet lifetimes of the corresponding silacyclobutanes (i.e., $k_F + k_{IC} + k_{ISC}$). Further work will be required in order to address the validity of this assumption. To the extent that it is valid (and equally so in all cases), then the intermediacy of a 1,4-biradical en route to the corresponding silene is only really demanded for the monoaryl-substituted derivatives **4–6**, for which the k_{sil} and k_{BIR} values calculated from the lifetime data are significantly different. In the case of **1**, our data cannot rule out the possibility that silene formation occurs by a concerted $\sigma_{2s}+\sigma_{2s}$ cycloreversion mechanism.

Conclusions

The formation of 1-arylsilenes by formal $\sigma_{2s}+\sigma_{2s}$ photocycloreversion of 1-arylsilacyclobutanes is a reaction of the lowest excited singlet state, which is shown by the behavior of derivatives for which the arylsilacyclobutane triplet state can be detected directly by laser flash photolysis. Photocycloreversion proceeds with a quantum yield of only 0.04 in 1-methyl-1-phenylsilacyclobutane, which is 5 times lower than in 1,1-diphenylsilacyclobutane. The quantum yield is even higher in derivatives in which the phenyl group is replaced with 2-phenylethynyl or 4′-biphenyl substituents. The resulting silenes, 1-phenyl-, 1-methyl-1-phenyl-, 1-methyl-1-(2-phenylethynyl)-, and 1-(4′-biphenylyl)-1-methylsilene, react with aliphatic alcohols at rates on the order of (2–5) × 10^9 M^{-1} s^{-1} in hydrocarbon or acetonitrile solution at ambient temperature. Deuterium isotope and solvent effects on the rate constants are consistent with a mechanism involving reversible complexation of the silene with the alcohol, followed by rate-determining proton transfer from silicon to carbon.

Comparison of the singlet lifetimes of the three 1-aryl-1-methylsilacyclobutanes and the corresponding aryltrimethylsilane suggests that cycloreversion proceeds by cleavage of one of the ring Si—C bonds to yield a 1,4-biradicaloid that partitions between silene and starting material. A similar analysis for 1,1-diphenylsilacyclobutane is consistent with either concerted or stepwise mechanisms for silene formation. The lifetime data allow calculation of rate constants for the primary excited state ring cleavage process and state efficiencies for formation of the intermediate and its collapse to silene, assuming that the singlet lifetimes of the model compounds approximate the rates of the nonproductive contributions to excited state decay in the corresponding silacyclobutane. Variations in the rate constant for excited state cleavage throughout the series are tentatively attributed to the effects of substituents on the degree of mixing of the benzenoid π-type molecular orbitals of the chromophore with σ-type molecular orbitals localized in the silacyclobutane ring. Modest variations in excited singlet state energy have no discernible effect on the rate constant, within this limited series of compounds. The relative rates of cleavage and coupling in the putative 1,4-biradicaloid intermediate are very sensitive to substitution at the silicon center; coupling predominates in the biradical from 1-methyl-1-phenylsilacyclobutane, while cleavage predominates in that from 1,1-diphenylsilacyclobutane.

Future work in this area will be directed at developing a better understanding of the various factors that contribute to the efficient formation of reactive silenes from photolysis of arylsilacyclobutanes, and exploiting this reaction for potentially useful applications.

Experimental

Ultraviolet absorption spectra were recorded on a Perkin Elmer Lambda 9 spectrometer interfaced to a Pentium microcomputer. Fluorescence emission spectra and lifetimes were determined using a Photon Technologies Inc. LS-100 spectrofluorimeter, which also enables lifetime determinations by the time-correlated single-photon counting technique. Gas chromatographic (GC) analyses were carried out using a Hewlett–Packard 5890II + gas chromatograph equipped with a conventional heated injector, a flame ionization detector, a Hewlett–Packard 3396A integrator, and a DB1 megabore capillary column (15 m × 0.53 mm; Chromatographic Specialties, Inc.). Mass spectra and GC–MS analyses were recorded on a Hewlett–Packard 5890II gas chromatograph equipped with an HP-5971A mass selective detector and a DB5 fused silica capillary column (30 m × 0.25 mm; Chromatographic Specialties, Inc.). Semipreparative gas chromatographic separations were carried out using a Varian 3300 gas chromatograph equipped with a thermal conductivity detector and a 3.8% UCW982 on 80/100 Supelcoport (24 ft × 0.25 in.; Supelco, Inc.) stainless steel column. Elemental analyses were performed by Guelph Chemical Laboratories, Inc.

2,2,4-Trimethylpentane (isooctane) and hexane were BDH Omnisolv grade and were used as received from the supplier. Acetonitrile (BDH Omnisolv) was distilled from calcium hydride and then further dried by several passages through activated alumina. Methanol, methanol-*O*-*d*, *tert*-butanol, *tert*-butanol-*O*-*d*, glacial acetic acid, acetic acid-*d*, trimethylphenylsilane (**11**), and phenyl(trimethylsilyl)acetylene (**12**) were of the highest purity available, and were used as received from Aldrich Chemical Co. 4′-Trimethylsilylbiphenyl (**13**; mp 49–50°C) (42) and dimethyldiphenylsilane (**14**; bp 99°C (0.75 Torr; 1 Torr = 133.3 Pa) (43)) were prepared by the reported procedures, and purified by recrystallization or vacuum distillation to purities in excess of 99%, as estimated by capillary GC.

1-Phenylsilacyclobutane (**3**) was prepared by lithium aluminum hydride reduction of 1-phenyl-1-chloro-1-silacyclobutane as reported by Bertrand et al. (26). The compound was purified by vacuum distillation (bp 97–100°C/20 Torr (26)), and exhibited the following spectroscopic properties. IR: 2963.0 (m), 2924.0 (s), 2854.2 (s), 2122.6 (m), 1731.4

© 1999 NRC Canada

(m), 1625.5 (s) 1569.4 (s), 1510.1 (m), 1428.9 (m), 1119.5 (s), 699.4 (s), 499.2 (m); ^{1}H NMR, δ (ppm): 1.25 (m, 4H), 2.20 (m, 2H), 5.33–5.35 (m, 1H), 7.41 (m, 3H), 7.66 (m, 2H); ^{13}C NMR, δ (ppm): 12.7, 18.6, 19.7, 128.0, 128.2, 129.9, 134.4, 135.2, 135.8; MS, *m*/*z* (*I*): 148 (30), 120 (83), 105 (100), 79 (15), 67 (8), 53 (25), 43 (8).

1-Methyl-1-phenylsilacyclobutane (**4**) was prepared by the method of Auner and Grobe (3), and purified by column chromatography on silica gel using hexane as eluant. The compound was characterized on the basis of the following spectroscopic data. IR: 2963.8 (s), 2856.5 (m), 1428.2 (s), 1396.3 (s), 1249.9 (s), 1115.5 (s), 867.2 (s), 772.1 (s), 732.5 (s), 697.6 (s), 427.7 (s); ^{1}H NMR, δ (ppm): 0.55 (s, 3H), 1.26 (m, 4H), 2.19 (p, 2H), 7.40 (m, 3H), 7.64 (m, 2H); ^{13}C NMR, δ (ppm): –1.8, 14.3, 18.2, 127.9, 129.4, 133.5; MS, *m*/*z* (*I*): 162 (10), 134 (100), 119 (45), 105 (20), 93 (7), 79 (5), 53 (10), 43 (13).

1-Methyl-1-phenylethynylsilacyclobutane (5)

To a cooled (–78°C) solution of phenylacetylene (0.55 mL, 5.0 mmol) in anhydrous ether (20 mL) was added a 1.6 M hexane solution of *n*-butyllithium (3.1 mL, 5.0 mmol). The solution was allowed to warm to room temperature and stirred for an additional 2 h. The solution was recooled to –78°C, and a solution of 1-chloro-1-methylsilacyclobutane (0.48 g, 4 mmol) in dry diethyl ether (10 mL) was added dropwise over ~10 min with stirring. The solution was allowed to warm to room temperature over 12 h, and then hydrolyzed with water (20 mL). The aqueous layer was extracted with ether (3 × 10 mL). The ether extracts were combined and dried over anhydrous magnesium sulfate, filtered, and stripped of solvent to yield a colorless liquid that was purified by silica gel column chromatography using hexane as eluant. The product (0.63 g, 3.4 mmol, 85%) was obtained as a colorless liquid and identified as 1-methyl-1-phenylethynylsilacyclobutane (**3**) on the basis of the following data: IR (neat): 3096 (w), 2970 (m), 2928 (m), 2156 (s), 1488 (s), 1251 (m), 1220 (m), 1121 (s), 879 (s); UV, λ_{max}: 247-nm, $\varepsilon_{248\ nm}$: 78 990 ± 1200 M^{-1} cm^{-1}; ^{1}H NMR, δ: 0.5 (s, 3H), 1.12 (m, 2H), 1.28 (m, 2H), 2.15 (m, 2H), 7.32 (m, 3H), 7.48 (m, 2H); ^{13}C NMR, δ: –0.1, 15.4, 18.4, 92.4, 107.1, 122.8, 128.3, 128.8, 132.0; MS, *m*/*z*: 186 (20), 158 (67), 143 (100), 129 (20), 117 (11), 103 (10), 77 (8), 53 (15), 43 (25); HRMS, calcd. for $C_{12}H_{14}Si$: 186.08647; found: 186.08633.

1-(4′-Biphenylyl)-1-methylsilacyclobutane (6)

Magnesium turnings (6.0 g, 0.25 g-at.) were placed in a 250 mL 2-necked round-bottom flask fitted with a condenser, addition funnel, magnetic stirrer, and gas inlet, and covered with anhydrous ether. A solution of 4-bromobiphenyl (6.38 g, 0.027 mol) in anhydrous ether (100 mL) was then added dropwise, at a rate sufficient to sustain reflux of the reaction mixture (~1 mL/min). To the resulting dark gray reaction mixture was added, dropwise with stirring over 15 min, a solution of 1-chloro-1-methylsilacyclobutane (3.0 g, 0.025 mol) in anhydrous ether (20 mL). The mixture was stirred for a further 16 h at room temperature, the stirrer was removed, and the resulting grey-brown solution was decanted from the suspended magnesium salts into a 500 mL Erlenmeyer flask. Water (200 mL) was added; the mixture was stirred vigorously for 10 min and then placed in a separatory funnel to separate the aqueous and organic layers. The yellow ether solution was washed with water (3 × 25 mL) and dried over anhydrous magnesium sulfate. Evaporation of the solvent on the rotary evaporator afforded an oily yellow solid (5.1 g), whose ^{1}H NMR spectrum was consistent with the desired product **6**. The solid was recrystallized twice from 95% ethanol to yield the product as slightly yellow plates (2.5 g, 0.0105 mol, 42%). A portion of the material (0.2 g) was further purified by column chromatography on silica gel using hexane as the eluant. Three more recrystallizations from 95% ethanol afforded the product as colourless plates (mp 41–41.5°C), which were identified as 1-(4-biphenylyl)-1-methylsilacyclobutane (**6**) on the basis of the following data: IR (neat): 3068.7 (w), 3021.8 (w), 2960.8 (m), 2926.0 (m), 1382.8 (m), 1249.7 (m), 1116.1 (s), 863.2 (s), 757.4 (s), 723.2 (s), 695.9 (s), 653.5 (s); UV, λ_{max}: 257 nm, $\varepsilon_{248\ nm}$: 24 000 ± 2000 M^{-1} cm^{-1}; ^{1}H NMR, δ: 0.58 (s, 3H), 1.22 (m, 2H), 1.29 (m, 2H), 2.17 (m, 2H), 7.53 (m, 3H), 7.65 (m, 6H); ^{13}C NMR, δ: –1.81, 14.37, 18.25, 92.4, 126.58, 127.08, 127.37, 128.71, 133.94, 137.24, 140.93, 142.08; MS, *m*/*z*: 238 (17), 211 (22), 210 (100), 195 (49), 167 (18), 165 (22), 152 (10), 53 (25), 43 (67). Anal. calcd. for $C_{16}H_{18}Si$: C 80.63, H 7.62; found: C 80.60, H 7.80.

Methoxymethylphenylsilane (**15a**) and methoxydimethylphenylsilane (**15b**) were prepared by reaction of methylphenylchlorosilane and dimethylphenylchlorosilane, respectively, with methanol in ether in the presence of trimethylamine (43, 44).

Methoxydimethyl(phenylethynyl)silane (**15c**) was prepared by the method of Corriu et al. (45), and exhibited analytical and spectroscopic data similar to those reported. 4-Methoxydimethylsilyl-4′-biphenyl (**15d**) was identified after isolation from a semipreparative scale photolysis of a deoxygenated solution of **6** (0.24 g, 1 mmol) and methanol (0.4 mL, 10 mmol) in hexane (10 mL), in a quartz photolysis tube with 8 RPR-2537 low-pressure mercury vapor lamps. The photolysis was carried out to ca. 70% conversion of **6** (ca. 5 h). The resulting bright yellow photolysate was stripped of solvent to yield a yellow oil, which was chromatographed on a Florisil column using hexane–dichloromethane mixtures. The product, which was isolated in modest purity (ca. 95% by GC) as a light yellow oil (0.05 g, 0.2 mmol, 20%), exhibited ^{1}H NMR and mass spectral data consistent with its proposed structure: ^{1}H NMR, δ: 0.06 (s, 6H), 3.48 (s, 3H), 7.34–7.53 (m, 9H); MS, *m*/*z*: 243 (5), 242 (27), 228 (21), 227 (100), 197 (31), 181 (8), 167 (9), 165 (11), 152 (10), 59 (21).

Analytical-scale photolyses were carried out using a Rayonet reactor fitted with 4–8 RPR-2537 lamps and a merry-go-round apparatus. Aliquots of hexane or cyclohexane-d_{12} solutions containing **3–6** (0.03–0.04 M) and methanol (0.05 M) were placed in Suprasil quartz cuvettes (3 mm × 10 mm), sealed with rubber septums, and saturated with dry argon. Hexadecane (0.01 M) was included as an internal GC standard for the runs carried out in hexane. The only products detected in these photolyses were ethylene, the corresponding methoxysilane (**15a–15d**), and small amounts of products identified as the corresponding hydroxysilanes on the basis of GC–MS analysis, presumably due to the presence of small amounts of water. The alkoxysilanes were

© 1999 NRC Canada

identified by GC–MS and GC coinjection with the authentic samples. Quantum yield experiments were carried out in similar fashion, simultaneously irradiating solutions of **1** and **4–6** in hexane containing 0.05 M methanol.

Fluorescence emission spectra and lifetimes were recorded on argon-saturated isooctane solutions, whose concentrations were adjusted to yield an absorbance of 0.1–0.2 at the excitation wavelength (245–260 nm). In each case, the fluorescence excitation spectrum matched the UV absorption spectrum in the region above ~240 nm.

Nanosecond laser flash photolysis experiments employed the pulses (248 nm; ca.15–25 ns; 70–150 mJ) from Lumonics 510 or Lambda Physik Compex 120 excimer lasers filled with F_2–Kr mixtures in helium or neon, and a microcomputer-controlled detection system (46). The intensity of the beam was reduced to <10 mJ at the cell using a series of stainless steel wire meshes as neutral density filters. Solutions were prepared at concentrations such that the absorbance at the excitation wavelength was ca. 0.7 (~8×10^{-4} M), and were flowed continuously through a 3 × 7 mm Suprasil flow cell connected to a calibrated 100 mL reservoir. Nitrogen or oxygen was bubbled continuously through the reservoir throughout the experiments. Solution temperatures were controlled to within 0.1°C with a VWR 1166 constant temperature circulating bath plumbed to a brass sample holder, and measured with a Teflon-coated copper–constantan thermocouple which was inserted directly into the flow cell. Quenchers were added directly to the reservoir by microlitre syringe as aliquots of standard solutions. Rate constants were calculated by linear least-squares analysis of decay rate vs. concentration data (six or more points) that spanned at least one order of magnitude in the transient decay rate. Errors are quoted as twice the standard deviation obtained from the least-squares analysis in each case.

Acknowledgments

We wish to thank the McMaster Regional Centre for Mass Spectrometry for high-resolution mass spectra and exact mass determinations, Tracy Morkin and Nicholas Toltl for technical assistance, and the Natural Sciences and Engineering Research Council of Canada for financial support.

References

1. L.E. Gusel'nikov and M.C. Flowers. J. Chem. Soc. Chem. Commun. 864 (1967).
2. P. Boudjouk and L.H. Sommer. J. Chem. Soc. Chem. Commun. 54 (1973).
3. N. Auner and J. Grobe. J. Organomet. Chem. **197**, 147 (1980).
4. P. Jutzi and P. Langer. J. Organomet. Chem. **202**, 401 (1980).
5. L.E. Gusel'nikov, N.S. Nametkin, and V.M. Vdovin. Acc. Chem. Res. **8**, 18 (1975).
6. G. Raabe and J. Michl. Chem. Rev. **85**, 419 (1985).
7. A.G. Brook. *In* The chemistry of organic silicon compounds. *Edited by* S. Patai and Z. Rappoport. John Wiley & Sons, New York. 1989. p.965.
8. A.G. Brook and M.A. Brook. Adv. Organomet. Chem. **39**, 71 (1996).
9. W.J. Leigh, C.J. Bradaric, and G.W. Sluggett. J. Am. Chem. Soc. **115**, 5332 (1993).
10. C.J. Bradaric and W.J. Leigh. J. Am. Chem. Soc. **118**, 8971 (1996).
11. W.J. Leigh, C.J. Bradaric, C. Kerst, and J.H. Banisch. Organometallics, **15**, 2246 (1996).
12. R.K. Vatsa, A. Kumar, P.D. Naik, H.P. Upadhyaya, U.B. Pavanaja, R.D. Saini, J.P. Mittal, and J. Pola. Chem. Phys. Lett. **255**, 129 (1996).
13. C.J. Bradaric and W.J. Leigh. Can. J. Chem. **75**, 1393 (1997).
14. C. Kerst, R. Boukherroub, and W.J. Leigh. J. Photochem. Photobiol. A: **110**, 243 (1997).
15. C.J. Bradaric and W.J. Leigh. Organometallics, **17**, 645 (1998).
16. W.J. Leigh, C. Kerst, R. Boukherroub, T.L. Morkin, S.I. Jenkins, K. Sung, and T.T. Tidwell. J. Am. Chem. Soc. **121**, 4744 (1999).
17. W.J. Leigh, R. Boukherroub, and C. Kerst. J. Am. Chem. Soc. **120**, 9504 (1998).
18. G. Bertrand, G. Manuel, P. Mazerolles, and G. Trinquier. Tetrahedron, **37**, 2875 (1981).
19. T. Brix, N.L. Arthur, and P. Potzinger. J. Phys. Chem. **93**, 8193 (1989).
20. M.G. Steinmetz and H. Bai. Organometallics, **8**, 1112 (1989).
21. T.J. Barton, G. Marquardt, and J.A. Kilgour. J. Organomet. Chem. **85**, 317 (1975).
22. C.M. Golino, R.D. Bush, P. On, and L.H. Sommer. J. Am. Chem. Soc. **97**, 1957 (1975).
23. R.T. Conlin, M. Namavari, J.S. Chickos, and R. Walsh. Organometallics, **8**, 168 (1989).
24. M.S. Gordon, T.J. Barton, and H. Nakano. J. Am. Chem. Soc. **119**, 11 966 (1997).
25. P.B. Valkovich, T.I. Ito, and W.P. Weber. J. Org. Chem. **39**, 3543 (1974).
26. G. Bertrand, J. Dubac, P. Mazerolles, and J. Ancelle. Nouv. J. Chim. **6**, 381 (1982).
27. I. Carmichael and G.L. Hug. J. Phys. Chem. Ref. Data, **15**, 1 (1986).
28. C. Kerst, R. Ruffolo, and W.J. Leigh. Organometallics, **75**, 5804 (1997).
29. S. Nagase and T. Kudo. J. Chem. Soc. Chem. Commun. 363 (1983).
30. N. Wiberg. J. Organomet. Chem. **273**, 141 (1984).
31. M. Kira, T. Maruyama, and H. Sakurai. J. Am. Chem. Soc. **113**, 3986 (1991).
32. G.W. Sluggett and W.J. Leigh. J. Am. Chem. Soc. **114**, 1195 (1992).
33. W.J. Leigh and G.W. Sluggett. J. Am. Chem. Soc. **116**, 10 468 (1994).
34. I. Carmichael and G.L. Hug. *In* CRC handbook of organic photochemistry. Vol. I. *Edited by* J.C. Scaiano. CRC Press, Boca Raton, Fla. 1989. p. 369.
35. I.B. Berlman. Handbook of fluorescence spectra of aromatic molecules. Academic Press, London. 1965.
36. J.B. Birks. Organic molecular photophysics. Wiley–Interscience, New York. 1971.
37. F.D. Lewis and T.A. Hilliard. J. Am. Chem. Soc. **92**, 6672 (1970).
38. P.J. Wagner, P.A. Kelso, A.E. Kemppainen, J.M. McGrath, H.N. Schott, and R.G. Zepp. J. Am. Chem. Soc. **94**, 7506 (1972).
39. J.C. Scaiano, E.A. Lissi, and M.V. Encina. Rev. Chem. Intermed. **2**, 139 (1978).
40. S. Ariel, S.V. Evans, M.G. Garibay, B.R. Harkness, N. Omkaram, J.R. Scheffer, and J. Trotter. J. Am. Chem. Soc. **110**, 5591 (1988).
41. L.J. Johnston and J.C. Scaiano. Chem. Rev. **89**, 521 (1989).

© 1999 NRC Canada

42. H.A. Clark, A.F. Gordon, C.W. Young, and M.J. Hunter. J. Am. Chem. Soc. **73**, 3798 (1951).
43. R.M. Harrison, D.R.M. Walton, and T.M.J. Walton. Dictionary of organometallic compounds. 2nd ed. Chapman and Hall, London. 1995.
44. P.E. Rakita, J.P. Srebro, and L.S. Worsham. J. Organomet. Chem. **104**, 27 (1976).
45. R.J.P. Corriu, J.J.E. Moreau, and H. Praet. Organometallics, **9**, 2086 (1990).
46. W.J. Leigh, M.S. Workentin, and D. Andrew. J. Photochem. Photobiol. A: **57**, 97 (1991).

© 1999 NRC Canada

Formation and nucleophilic capture of *N*-nitrosiminium ions

Latifa Chahoua, Alain Vigroux, Yvonne Chiang, and James C. Fishbein

Abstract: A study of the solvolysis of a series of (*N*-nitrosomethylamino)arylmethyl esters and azides and the products of nucleophilic trapping of the corresponding *N*-nitrosiminium ion intermediates in aqueous media, 25°C, ionic strength 1 M is reported. Structure–reactivity data for the forward and reverse reactions have been obtained. In three cases, the rate constants for reactions of the cations with nucleophiles have been measured directly by laser flash photolysis. The data allow a comparison of the degree to which the *N*-methyl-*N*-nitroso functionality enhances cation stability from a thermodynamic and kinetic perspective. It has been possible to deduce that the carbon basicity of azide ion is less than 1 kcal/mol greater than that of acetate ion.

Key words: nitrosiminium ions, α-acetoxynitrosamines, carbocations, iminium ions, nucleophilicity.

Résumé : On a effectué une étude, en milieu aqueux, à 25°C et à une force ionique de 1 M, sur la solvolyse d'une série d'esters (*N*-nitrosométhylamino)arylméthyles et d'azotures apparentés et sur la nature des produits du piégeage nucléophile des ions intermédiaires *N*-nitrosiminium correspondants. On a obtenu des données relatives de structure–réactivité pour les réactions normales et inverses. Dans trois cas, faisant appel à la photolyse éclair au laser, on a pu mesurer directement les constantes de vitesse des réactions des cations avec les nucléophiles. Les données permettent de comparer à quel degré la fonction *N*-méthyl-*N*-nitroso accroît la stabilité du cation de points de vue tant thermodynamique que cinétique. On a pu déduire que la basicité du carbone de l'ion azoture n'est plus grande que celle de l'ion acétate que par moins de 1 kcal/mol.

Mots clés : ions nitrosiminium, α-acétoxynitrosamines, carbocations, ions iminium, nucléophilicité.

[Traduit par la Rédaction]

Introduction

α-Acetoxydialkylnitrosamines are important in understanding the mechanisms of mutagenesis and carcinogenesis of dialkylnitrosamines (1, 2). They serve as precursors to α-hydroxydialkynitrosmaines that are formed in the activation of dialkylnitrosamines by P-450 enzymes, as illustrated in eq. [1]. Evidence has been summarized that indicates that in the case of most α-acetoxydialkylnitrosamines, formation of the α-hydroxy intermediate occurs by formation of an *N*-nitrosiminium ion that is subsequently hydrated by solvent water, as in eq. [2] (3–6). Some characterization of the kinetic stability of certain of these intermediates has been reported (7), including the photochemical generation and direct determination of reactivity in one case (8). α-Substituted benzylic cations have been relatively well characterized with regard to the effects of substituents on cation stability and selectivity, and it is of interest to understand how the *N*-nitrosomethylamino group compares to others as a cation stabilizing substituent. The present study was undertaken to quantitatively elucidate this cation stabilizing ability in a

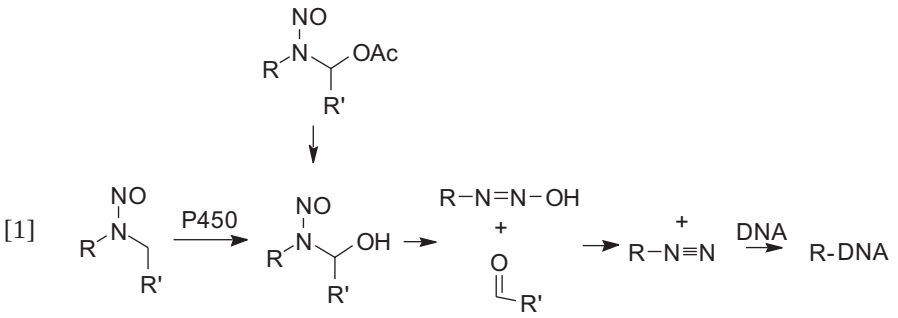

Received November 17, 1998.

This paper is dedicated to Jerry Kresge, an outstanding chemist, collaborator, and friend, in recognition of his many achievements in chemistry.

L. Chahoua, A. Vigroux, Y. Chiang, and J.C. Fishbein.[1] Dept. of Chemistry, Wake Forest University, Winston–Salem, NC 27109, U.S.A.

[1]Author to whom correspondence may be addressed. Telephone: (336) 758-5328. Fax: (336) 758-4656. e-mail: fishbein@wfu.edu

 © 1999 NRC Canada

[2] 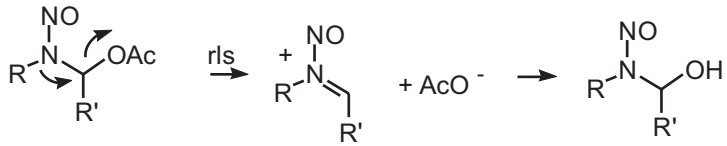

benzylic system. In summary, the *N*-nitrosomethylamino group stabilizes the adjacent benzyl cation both kinetically and thermodynamically to an extent that is similar to the stabilization that is provided by an α-azido group. In addition, it has been possible to compare the cation generating reactions involving the acetate and azide precursors and the cation capture reactions by acetate and azide ions, two nucleophiles of very similar proton basicity. An upper limit, of 1 kcal/mol, on the difference in carbon basicity of these two nucleophiles has been derived.

Experimental

Warning! Most α-acyloxynitrosamines are powerful direct acting carcinogens. Manipulations were carried out using frequently changed double pairs of disposable gloves and in the well-ventilated hood. Contaminated, and potentially contaminated, materials were treated with 50% aqueous sulfuric acid containing the commercially available oxidant "No Chromix" (Aldrich Chemical).

Materials

Organic solvents were dried and purified by distillation before use. Organic and inorganic chemicals for synthesis were ACS grade or better. Inorganic chemicals were used without further purification. Organic chemicals were typically purified prior to use in synthesis or kinetic experiments. Water was distilled in glass.

Methods

Kinetics

The kinetics of decomposition were observed using either a Hewlett Packard 8452A diode array spectrophotometer, or an Applied Photophysics DX 17MV stopped-flow spectrophotometer. For compounds **3k** and **4k**, rate constants for the addition of water and azide ion to the nitrosiminium ions generated by KrF laser flash photolysis were measured as described for the unsubstituted compound earlier (8). In all cases, temperature was maintained at 25°C by means of attached recirculating water baths.

The buffer solution in each reaction cell was made up by diluting a concentrated stock buffer solution. Ionic strength of reaction solutions was maintained at 1 M with $NaClO_4$. A stock solution of $NaClO_4$ was added to the cuvette to maintain the ionic strength of 1 M. The buffers that were used include phosphate, MOPS, MES, CHES, acetic acid, cyanoacetic acid, methoxyacetic acid, cacodylic acid, and morpholine.

The stock solution of the nitrosamine was made up in freshly distilled dry CH_3CN. Reactions performed in the stopped-flow spectrophotometer were carried out by mixing 25 parts of the aqueous buffer with 1 part of the nitrosoamine in CH_3CN solution using 2.5 and 0.1 mL syringes, respectively. Final concentration of the nitrosamine in the reactions was ~10^{-4} M.

The pH values were obtained after the kinetic run using an Orion model SA 720 pH meter equipped with a Corning combination electrode. Two point calibrations were done prior to recording pH values. Calibration of the meter was performed using commercially available standards or those prescribed by the *Merck Index* (9).

Product analysis

The products of decomposition under various conditions, vide infra, were quantitated after 10 halflives of reaction of the starting materials. Product quantitation involved either ^{1}H-NMR or HPLC. In the former case, the reactant concentrations were on the order of 0.01 M. In the latter case, concentrations were typically in the range of 10^{-4}–10^{-5} M and utilized a Waters chromatography system with Axxiom data system and Waters Wisp-Ultra autoinjector attached. Separations were carried out with 6:4 acetonitrile/water as eluent over a 15 cm waters C18 column. Quantitation of the products was accomplished using standard curves containing at least two points that were generated from products that were synthesized independently.

A series of experiments were carried out to examine the partitioning of the nitrosiminium ion intermediates between capture by water and alcohols. Reactions were carried out by dissolution of the starting ester in buffer solution that was, by volume, 1% ethanol, 9% other added alcohol, and 90% H_2O, ionic strength 1 M with $NaClO_4$.

Synthesis

Esters, azide ion adducts, and ethers, products of nitrosiminium ion trapping by alcohols, were synthesized and are listed and correspondingly numbered in Table 1.

The α-acyloxynitrosamines **1a**–**7a** and **1b**–**8b** were synthesized using previously published methods (3, 4). Physical data for **2a** and **2b** were reported previously (6). ^{1}H NMR ($CDCl_3$) δ (ppm): **1a**: (*E*) isomer (98%): 8.26 (1H, s), 7.32 (2H, s), 7.01 (2H, s), 3.83 (3H, s), 2.82 (3H, s), 2.24 (3H, s); (*Z*) isomer (2%): 3.57 (3H, s); 2.18 (3H, s); Anal. calcd.: C 55.46, H 5.88, N 11.76; found: C 56.96, H 5.82, N 10.86; **3a**:(*E*) isomer (86%): 8.28 (1H, s), 7.37 (4H, m), 2.8 (3H, s), 2.25 (3H, s); (*Z*) isomer (14%): 3.57 (3H, s), 2.18 (3H, s); **4a**: (*E*) isomer (96%): 8.28 (1H, s), 7.38 (4H, m), 2.80 (3H, s), 2.26 (3H,s); (*Z*) isomer (4%): 3.57 (3H, s), 2.2 (3H, s); **5a**: (*E*) isomer (96%): 8.34 (1H, s), 7.76 (2H, d), 7.53 (2H, d), 2.81 (3H, s), 2.28 (3H, s); **6a**: (*E*) isomer (96%): 8.38 (1H, s), 8.32 (2H, d), 7.61 (2H, d), 2.83 (3H, s), 2.30 (3H, s); (*Z*) isomer (4%): 3.60 (3H, s), 2.24 (3H, s). Anal. calcd.: C 47.43, H 4.35, N 16.60; found: C 47.50, H 4.35, N 16.52; **7a**: (*E*) isomer (96%): 8.38 (1H, s), 7.96 (1H, s), 7.86 (2H, s), 2.85 (3H, s), 2.31 (3H, s); (*Z*) isomer (4%): 3.62 (3H, s), 2.24 (3H, s); **1b**: (*E*) isomer (96%): 8.32 (1H, s), 7.34 (2H, d), 6.96 (2H, d), 4.21 (2H, s), 3.83 (3H, s), 2.83 (3H, s); **3b**: (*E*) isomer (96%): 8.35 (1H, s), 7.4 (5H, m), 4.22 (2H, d), 2.82 (3H, s); (*Z*) isomer (4%): 3.59 (3H, s). Anal. calcd.: C 43.32, H 3.61, N 10.11; found: C 43.47, H 3.65, N 10.09; **4b**: δ (*E*) isomer (94%): 8.35 (1H, s), 7.43 (5H, m), 4.24 (2H, d), 2.84 (3H, s); (*Z*) isomer

© 1999 NRC Canada

Table 1. α-Substituted nitrosamines studied in the present work.

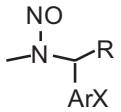

No.	X	R	No.	X	R	No.	X	R
1a	*p*-MeO	CH_3COO^-	**2c**	H	N_3^-	**3i**	*p*-Cl	$Cl_2CHCH_2O^-$
2a	H	CH_3COO^-	**3c**	*p*-Cl	N_3^-	**3j**	*p*-Cl	$F_3CCH_2O^-$
						3k	*p*-Cl	4-C*N*-PhO-
3a	*p*-Cl	CH_3COO^-	**4c**	*m*-Cl	N_3^-	**4d**	*m*-Cl	$CH_3CH_2O^-$
4a	*m*-Cl	CH_3COO^-	**5c**	*p*-CF_3	N_3^-	**4e**	*m*-Cl	CH_3O^-
5a	*p*-CN	CH_3COO^-	**2d**	H	$CH_3CH_2O^-$	**4f**	*m*-Cl	$CH_3OC_2H_4O^-$
6a	*p*-NO_2	CH_3COO^-	**2e**	H	CH_3O^-	**4g**	*m*-Cl	$ClCH_2CH_2O^-$
7a	3,5-$(CF_3)_2$	CH_3COO^-	**2f**	H	$CH_3OC_2H_4O^-$	**4h**	*m*-Cl	$NCCH_2CH_2O^-$
1b	*p*-MeO	$ClCH_2COO^-$	**2g**	H	$ClCH_2CH_2O^-$	**4i**	*m*-Cl	$Cl_2CHCH_2O^-$
2b	H	$ClCH_2COO^-$	**2h**	H	$NCCH_2CH_2O^-$	**4j**	*m*-Cl	$F_3CCH_2O^-$
						4k	*m*-Cl	4-C*N*-PhO-
3b	*p*-Cl	$ClCH_2COO^-$	**2i**	H	$Cl_2CHCH_2O^-$	**5d**	*p*-CF_3	$CH_3CH_2O^-$
4b	*m*-Cl	$ClCH_2COO^-$	**2j**	H	$F_3CCH_2O^-$	**5e**	*p*-CF_3	CH_3O^-
5b	*p*-CN	$ClCH_2COO^-$	**3d**	*p*-Cl	$CH_3CH_2O^-$	**5f**	*p*-CF_3	$CH_3OC_2H_4O^-$
6b	*p*-NO_2	$ClCH_2COO^-$	**3e**	*p*-Cl	CH_3O^-	**5g**	*p*-CF_3	$ClCH_2CH_2O^-$
7b	3,5-$(CF_3)_2$	$ClCH_2COO^-$	**3f**	*p*-Cl	$CH_3OC_2H_4O^-$	**5h**	*p*-CF_3	$NCCH_2CH_2O^-$
8b	*p*-CF_3	$ClCH_2COO^-$	**3g**	*p*-Cl	$ClCH_2CH_2O^-$	**5i**	*p*-CF_3	$Cl_2CHCH_2O^-$
1c	*p*-MeO	N_3^-	**3h**	*p*-Cl	$NCCH_2CH_2O^-$	**5j**	*p*-CF_3	$F_3CCH_2O^-$

(6%): 3.63 (3H, s). Anal. calcd.: C 43.32, H 3.61, N 10.11; found: C 43.60, H 3.85, N 9.84; **5b**: δ (*E*) isomer (96%): 8.45 (1H, s), 8.35 (2H, d), 7.65 (2H, d), 4.28 (2H, s), 2.84 (3H, s); (*Z*) isomer (4%): 3.62 (3H, s); **6b**: (*E*) isomer (96%): 8.45 (1H, s), 8.35 (2H, d), 7.65 (2H, d), 4.28 (32H, s), 2.84 (3H, s); (*Z*) isomer (4%): 3.62 (3H, s); **8b**: (*E*) isomer (94%): 8.41 (1H, s), 7.8 (2H, d), 7.6 (2H, d), 4.25 (2H, d), 2.84 (3H, s); (*Z*) isomer (6%): 3.63 (3H, s).

*(*N-*Methyl*-N-*nitroso)arylmethyl azides **1c**–**3c***

α-Chloroacetoxy-*N*-nitrosamine ester (2.4 mmol) was dissolved in a solution (35 mL H_2O/25 mL methanol) containing 1.0 M NaN_3. The solution was stirred at room temperature overnight (for **3c**, we stirred at –10°C for 2 h). A large amount of water was added to precipitate the product. The product was extracted with methylene chloride. The organic layer was dried over $MgSO_4$ and was filtered. Methylene chloride was then evaporated off using a flow of Argon and a warm water bath. Compound **1c** was purified by preparative TLC using 1:7 ether:pentane as the eluting solvent. The crude material of **2c** was washed with pentane to get rid of aldehyde. The purification of **3c** was hampered by the presence of aldehyde, the mixture of crude material was treated with bisulfite in methanol and subsequently purified by preparative TLC using 1:9 ethyl acetate/pentane. ^{1}H NMR ($CDCl_3$) δ (ppm): **1c**: (*E*) isomer (100%): 7.42 (1H, s), 7.33 (2H, d), 6.93 (2H, d), 3.83 (3H, s), 2.82 (3H, s). Anal. calcd.: C 48.84, H 5.01, N 31.7; found: C 49.1, H 5.05, N 31.43; **2c**: (*E*) isomer (94%): 7.44 (1H, s), 7.42 (5H, s), 2.82 (3H, s); (*Z*) isomer (6%): 3.51 (3H, s); **3c**: (*E*) isomer (93%): 7.4 (1H, s), 7.37 (5H, 2d), 2.8 (3H, s); (*Z*) isomer (7%): 3.5 (3H, s). Anal. calcd.: C 42.58, H 3.57, N 31.04; found: C 42.64, H 3.60, N 30.92.

The synthesis of **4c** and **5c** was accomplish using Wiessler's procedure (10), since the method above was not successful. The imines (11) (6.5 mmol) were dissolved in 10 mL of dry methylene chloride and added slowly to NOCl (6.5 mmol) in 20 mL of dry methylene chloride at –30°C. Sodium azide (6.5 mmol), dissolved in 5 mL of DMSO, was added dropwise to the previous mixture. After 5 min, the product was washed with water and extracted with methylene chloride. The organic layer was dried over $MgSO_4$ and was filtered. The methylenechloride was then evaporated off using a flow of Argon. The product was purified by preparative TLC using 0.5:9.5 ether/pentane.^{1}H NMR ($CDCl_3$) δ (ppm): **4c**: (*E*) isomer (91%): 7.4 (5H, m), 7.27 (1H, s), 2.82 (3H, s); (*Z*) isomer (9%): 3.53 (3H, s); **5c**: (*E*) isomer (87%): 7.63 (5H, 2d), 7.5 (1H, s), 2.82 (3H, s); (*Z*) isomer (13%): 3.53 (3H, s). ^{13}C NMR ($CDCl_3$) δ **4c**: 135.5–124.6 (6 pics, Ar), 79.0 (*C*H-N), 27.18 (*C*H_3-N).

The ethers were synthesized by decomposition of an ester in the neat alcohol. Thus, in a typical procedure, the acetoxy or chloroacetoxy compound (1.0 mmol) was dissolved in dry alcohol (4 mL) and allowed to reflux for 16 h. A large amount of water was then added, the product was extracted with methylene chloride, the organic layer was dried over $MgSO_4$, and the solvent was removed under a stream of argon. The crude material was purified by preparative TLC using 1:20 ether/petroleum ether. ^{1}H NMR ($CDCl_3$) δ (ppm): **2d**: (*E*) isomer (96%): 7.34 (5H, m), 6.78 (1H, s), 3.57 (2H, m), 2.68 (3H, s), 1.25 (3H, t); (*Z*) isomer (4%): 3.4 (3H, s). Anal. calcd.: C 61.85, H 7.2, N 14.4; found: C 61.95, H 7.26, N 14.31; **2e**: (*E*) isomer (98%): 7.41 (5H, s), 6.75 (1H, s), 3.47 (3H, s), 2.75 (3H, s); (*Z*) isomer (2%): 3.38 (3H, s). Anal. calcd.: C 60.00, H 6.67, N 15.55; found: C 60.21, H 6.75, N 15.52; **2f**: 7.41 (5H, s), 6.91 (1H, s), 3.71

© 1999 NRC Canada

(4H, m), 3.4 (3H, s), 2.76 (3H, s); **2g**: (*E*) isomer (94%): 7.42 (5H, s), 6.93 (1H, s), 3.84 (4H, m), 2.78 (3H, s); (*Z*) isomer (6%): 3.5 (3H, s). Anal. calcd.: C 52.52, H 5.69, N 12.25; found: C 52.26, H 5.61, N 11.97: **2h**: (*E*) isomer (97%): 7.43 (5H, s), 6.95 (1H, s), 3.8 (2H, m), 2.78 (3H, s), 2.74 (2H, m); (*Z*) isomer (3%): 3.41 (3H, s). Anal. calcd.: C 60.26, H 5.98, N 19.16; found: C 59.84, H 6.91, N 18.48; **2i**: (*E*) isomer (93.3%): 7.58 (5H, s), 7.16 (1H, s), 6.00 (1H, t), 4.19 (2H, m), 2.92 (3H, s); (*Z*) isomer (6.7%): 3.61 (3H, s). Anal. calcd.: C 45.65, H 4.6, N 10.65; found: C 46.08, H 4.63, N 9.3; **2j**: (*E*) isomer (98%): 7.43 (5H, s), 7.00 (1H, s), 4.00 (2H, m), 2.77 (3H, s); (*Z*) isomer (2%): 3.49 (3H, s). Anal. calcd.: C 48.4, H 4.44, N 11.29; found: C 48.56, H 4.41, N 11.09; **3d**: 7.38 (4H, s), 6.83 (1H, s), 3.63 (2H, m), 2.73 (3H, s), 1.33 (3H, t). Anal. calcd.: C 52.52, H 5.73, N 12.25; found: C 53.74, H 5.92, N 11.66; **3e**: 7.38 (4H, s), 6.73 (1H, s), 3.47 (3H, s), 2.73 (3H, s). Anal. calcd.: C 50.36, H 5.16, N 13.05; found: C 50.45, H 5.19, N 12.96; **3f**: 7.38 (4H, s), 6.89 (1H, s), 3.69 (4H, m), 3.39 (3H, s), 2.74 (3H, s); **3g**: (*E*) isomer (94%): 7.4 (4H, s), 6.9 (1H, s), 3.81 (4H, m), 2.76 (3H, s); (*Z*) isomer (6%): 3.5 (3H, s). Anal. calcd.: C 45.65, H 4.6, N 10.65; found: C 45.6, H 4.59, N 10.48; **3h**: (*E*) isomer (98%): 7.4 (4H, s), 6.92 (1H, s), 3.82 (2H, m), 2.77 (3H, s), 2.76 (2H, m); (*Z*) isomer (2%): 3.51 (3H, s). Anal. calcd.: C 52.08, H 4.77, N 16.56; found: C 51.94, H 4.81, N 16.37; **3i**: (*E*) isomer (98%): 7.4 (4H, s), 7.00 (1H, s), 5.87 (1H, t), 4.00 (2H, m), 2.77 (3H, s); (*Z*) isomer (2%): 3.5 (3H, s). Anal. calcd.: C 40.36, H 3.73, N 9.41; found: C 40.16, H 3.67, N 9.28; **3j**: (*E*) isomer (98%): 7.41 (4H, s), 6.99 (1H, s), 4.00 (2H, m), 2.75 (3H, s); (*Z*) isomer (2%): 3.49 (3H, s). Anal. calcd.: C 42.49, H 3.56, N 9.91; found: C 42.63, H 3.57, N 9.97; **4d**: (*E*) isomer (97.5%): 7.5 (1H, s), 7.33 (3H, m), 6.83 (1H, s), 3.64 (2H, m), 2.75 (3H, s), 1.33 (3H, t); (*Z*) isomer (2.5%): 3.47 (3H, s). Anal. calcd.: C 52.52, H 5.73, N 12.25; found: C 52.66, H 5.71, N 12.21; **4e**: (*E*) isomer (98%): 7.49(1H, s), 7.32 (3H, m), 6.73 (1H, s), 3.47 (3H, s), 2.75 (3H, s); (*Z*) isomer (2%): 3.38 (3H, s). Anal. calcd.: C 50.36, H 5.16, N 13.05; found: C 50.47, H 5.17, N 12.97; **4f**: 7.51 (1H, s), 7.33 (3H, m), 6.89 (1H, s), 3.71 (4H, m), 3.4 (3H, s), 2.76 (3H, s). Anal. calcd.: C 51.07, H 5.84, N 10.84; found: C 51.19, H 5.83, N 10.69; **4g**: (*E*) isomer (98%): 7.52 (1H, s), 7.44 (3H, m), 7.02 (1H, s), 4.06 (4H, m), 2.9 (3H, s); (*Z*) isomer (3%): 3.41 (3H, s). Anal. calcd.: C 45.65, H 4.6, N 10.65; found: C 45.39, H 4.58, N 10.4; **4h**: (*E*) isomer (97%): 7.47 (1H, s), 7.34 (3H, m), 6.92 (1H, s), 3.8 (2H, m), 2.78 (5H, m); (*Z*) isomer (2%): 3.5 (3H, s); **4i**: (*E*) isomer (97%): 7.49 (1H, s), 7.33 (3H, m), 6.99 (1H, s), 5.87 (1H, t), 4.00 (2H, m), 2.78 (3H, s); (*Z*) isomer (3%): 3.55 (3H, s). Anal. calcd.: C 40.36, H 3.73, N 9.41; found: C 40.21, H 3.71, N 9.48; **4j**: (*E*) isomer (95.6%): 7.47 (1H, s), 7.34 (3H, m), 6.98 (1H, s), 4.00 (2H, m), 2.77 (3H, s); (*Z*) isomer (4.4%): 3.49 (3H, s). Anal. calcd.: C 42.49, H 3.57, N 9.91; found: C 43.68, H 3.66, N 9.68; **5d**: (*E*) isomer (97%): 7.62(4H, 2d), 6.91 (1H, s), 3.66 (2H, m), 2.74 (3H, s), 1.34 (3H, t); (*Z*) isomer (3%): 3.45 (3H, s); **5e**: (*E*) isomer (98%): 7.62 (4H, 2d), 6.80 (1H, s), 3.50 (3H, s), 2.74 (3H, s); (*Z*) isomer (2%): 3.39 (3H, s); **5f**: 7.64 (4H, 2d), 6.981 (1H, s), 3.8 (4H, m), 3.41 (3H, s), 2.79 (3H, s); **5g**: (*E*) isomer (93%): 7.65 (4H, 2d), 6.99 (1H, s), 3.90 (4H, m), 2.77 (3H, s); (*Z*) isomer (7%): 3.5 (3H, s); **5h**: (*E*) isomer (98%): 7.65 (4H, 2d), 7.00 (1H, s), 3.85 (2H, m), 2.78 (5H, s); (*Z*) isomer (2%): 3.51 (3H, s); **5i**: (*E*) isomer (97%): 7.66 (4H, 2d), 7.09 (1H, s), 5.9 (1H, t), 4.00 (2H, m), 2.78 (3H, s); (*Z*) isomer (3%): 3.61 (3H, s); **5j**: (*E*) isomer (97%): 7.65 (5H, s), 7.07 (1H, s), 4.03 (2H, m), 2.76 (3H, s); (*Z*) isomer (3%): 3.5 (3H, s).

*(*N-*Methyl*-N-*nitroso)arylmethyl* p-*cyanophenyl ethers **3k**, **4k***

These were made by the method reported for the unsubstituted compound. ^{1}H NMR ($CDCl_3$) δ (ppm): **3k**: (*E*) isomer (95%): 7.88 (1H, s), 7.62 (2H, m), 7.44 (4H, s), 7.20 (2H, m), 2.77 (3H, s); (*Z*) isomer (5%): 3.51 (3H, s); **4k**: (*E*) isomer (96%): 7.78 (1H, s), 7.62 (3H, m), 7.40 (2H, m), 7.22 (3H, m), 2.79 (3H, s); (*Z*) isomer (4%): 3.63 (3H, s). ^{13}C NMR ($CDCl_3$) δ: **3k**: 158.61, 135.82, 134.27, 132.47, 129.37, 127.40, 118.37, 117.25, 106.78, 88.70, 26.78; **4k**: 158.58, 136.04, 135.33, 134.33, 130.49, 129.99, 126.29, 124.17, 118.39, 117.28, 106.91, 88.52, 26.87.

Results

The decay of (*N*-methyl-*N*-nitroso)arylmethyl acetates, chloroacetates, and azides exhibited good first-order kinetics of absorbance decay in the range of conditions studied for 4–6 halflives of reaction. In the case of the azides, the reactions were carried out only in acidic solutions containing 0.01–0.1 M $HClO_4$ in order to prevent nonsimple kinetics of decay due to the formation of azide ion product that could inhibit decay of the starting material due to common ion inhibition. The rate constants k_{obsd} in these cases were independent of the acid concentration, agreeing within experimental error for at least two different acid concentrations that differed by at least a factor of two. In the cases of the esters, the values of k_{obsd} were determined typically at three buffer concentrations for a given buffer ratio and a concentration range between 0.05 and 0.3 M. The values of k_{obsd} in all cases increased less than 10% from low to high buffer concentration, and extrapolation of the plot of k_{obsd} against buffer concentration to the *y*-axis yielded to value of k_1, the buffer-independent, pH-independent rate constant. Determinations of k_1 were carried out in a minimum of two different buffers, typically acetic and cacodylic acids, and the values generally agreed within 10%. The mean values of k_1 for all compounds are reported in Table 2.

For a number of α-acetoxydialkylnitrosamines, the effect on k_{obsd} of increasing acetate ion concentration, while maintaining constant ionic strength (1 M) with $NaClO_4$, was determined. A plot illustrating the effect for a number of compounds is indicated in Fig. 1. The value of k_{obsd} decreases, in all cases measured, to less than 25% the value of k_{obsd} in the absence of added acetate ion. Specific salt effects, due to replacement of sodium perchlorate by sodium trifluoroacetate, have been shown to decrease the value of k_{obsd} by less than 10% at comparable concentrations (6).

To clarify the nature of the reaction that appeared to be acetate independent at very high acetate ion concentrations, a single experiment was run with compound **2a** in which the effect of acetate concentrations up to 1.35 M was determined at an ionic strength of 3 M ($NaClO_4$) in D_2O. The data are plotted in Fig. 2. Product analysis by ^{1}H-NMR of a reaction at completion that originally contained 1.35 M ace-

© 1999 NRC Canada

Table 2. Rate constants for the solvolysis of α-substituted (*N*-nitrosomethylamino)arylmethylamines in cacodylic acid buffer, ionic strength μ = 1 ($NaClO_4$) at 25°C.[a]

	Leaving group		
	Acetate	Chloroacetate	Azide
	$10^3 \times k_1$ (s^{-1})	k_1 (s^{-1})	$10^3 \times k_1$ (s^{-1})
Ring substituent	<1% CH_3CN	<1% CH_3CN	<1% CH_3CN
4-CH_3O	6.9	0.60	1.17
4-F		0.057[b]	
H	0.49	0.053	0.049
4-CL	0.23	0.027[b]	0.022
3-CL	0.059[c]	0.0095	0.002[d]
4-CF_3		0.0053	
4-CN	0.023	0.0037	
4-NO_2	0.0128	0.0022	
3,5-$(CF_3)_2$	0.0083	0.00107	

[a]Average of at least two values of intecepts of plots of k_{obsd} against buffer concentration containing 3–4 points, typically 0.05–0.3 M. Standard error of < ±5% except where otherwise indicated.

[b]Standard error < ±20%.

[c]From a single value of the intecept of a plot of k_{obsd} against buffer concentration containing 4 points, typically 0.05–0.2 M.

[d]Standard error < ±10%.

Fig. 1. Plot of k_{obsd} against acetate ion concentration for the solvolysis of acetates **2a** (circles), **3a** (squares), and **4a** (diamonds) at 25°C, ionic stength 1 M ($NaClO_4$).

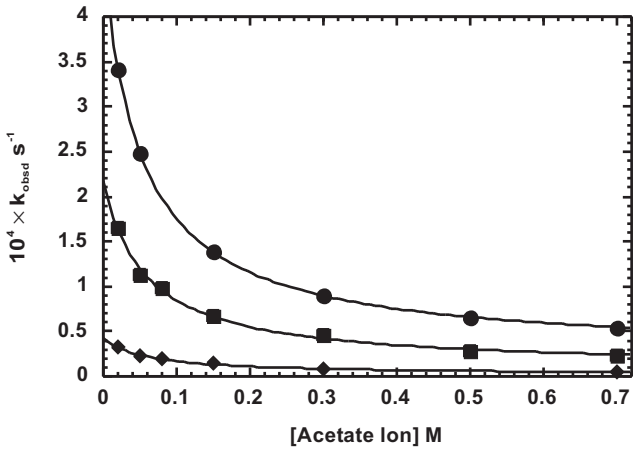

Fig. 2. Plot of k_{obsd} against acetate ion concentration for the solvolysis of acetate **2a** at 25°C, ionic strength 3 M ($NaClO_4$).

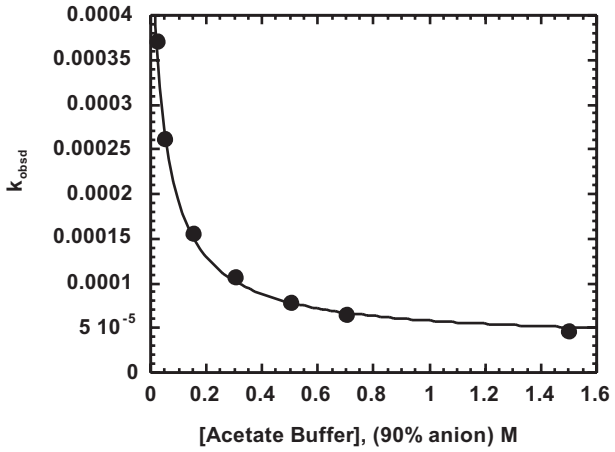

tate ion in D_2O showed a 12% yield of methylammonium ion. The analysis of these experiments are discussed in more detail later.

The rate constants for reactions of two *N*-nitrosiminium ions with water and azide ion were measured by laser flash photolysis using the *p*-cyanophenyl ethers, as described earlier (8). The decay of absorbance of the cations exhibited clean first-order kinetics for five halflives of decay. Rate constants for decay of the cation were measured in 0.01 and 0.02 M cacodylic acid buffer (50% anion), and the two values of k_{obsd} agreed within 5%. The rate constant for decay of **3k** in aqueous media containing 0.01 M cacodylic acid buffer (50% anion) and 10% by volume trifluoroethanol was identical with that in buffered water within experimental error. The second-order rate constants for reaction of azide ion were taken as the slopes of plots of k_{obsd} against azide ion concentration that contained three points. The rate constants for addition of water to the cations derived from **3k** and **4k** are 1.15 (± 0.1) × 10^6 s^{-1} and 1.35 (± 0.1) × 10^6 s^{-1}, respectively. The rate constants for the addition of azide ion are 2.4 (± 0.2) × 10^9 M^{-1} s^{-1} and 2.8 (± 0.2) × 10^9 M^{-1} s^{-1}, respectively.

Characterization of products and yields were initally performed under various conditions to check the generality of what has previously been reported — these are summarized in Table 3. Decay of the esters gives quantitative yields of the aryl moiety. Analysis by ^{1}H-NMR gives less than quantitative yields of the methyl fragment, likely due to proton exchange of the methyl diazonium ion intermediate that gives rise to the alcohol product (12). An experiment was carried out to quantitate the extent of acetate ion stimulated denitrosation of a nitrosiminium ion; this is discussed later.

A series of experiments was carried out to determine the partitioning of the nitrosiminium ions, derived from chloroacetate esters, between capture by water, ethanol, and a second alcohol, as indicated in eq. [3]. The observed product ratios were corrected for the differences in nucleophile

© 1999 NRC Canada

Table 3. Product yields for the decomposition of *N*-methyl-*N*-nitroso-*N*-arylmethyl acetates at 25°C, ionic strength 1 M, $NaClO_4$.

Compound	Conditions	Product	Yield %	Technique
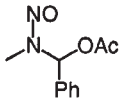	10% EtOH pH 6.55	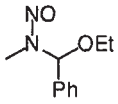	19.1	HPLC
		HC(O)Ph	81.5	
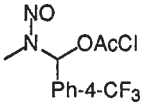	H_2O pH 6.50	HC(O)Ph-4-CF_3	98	HPLC
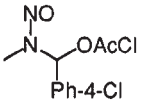	D_2O pH 6.50	HC(O)Ph-4-Cl	102	^{1}H-NMR
		^{1}H-CL_3OD	75	
		^{1}H-$CL_3ND_3^+$	7	
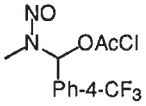	D_2O pH 6.50	HC(O)Ph-4-CF_3	102	^{1}H-NMR
		^{1}H-CL_3OD	64	
		^{1}H-$CL_3ND_3^+$	7	

[3] 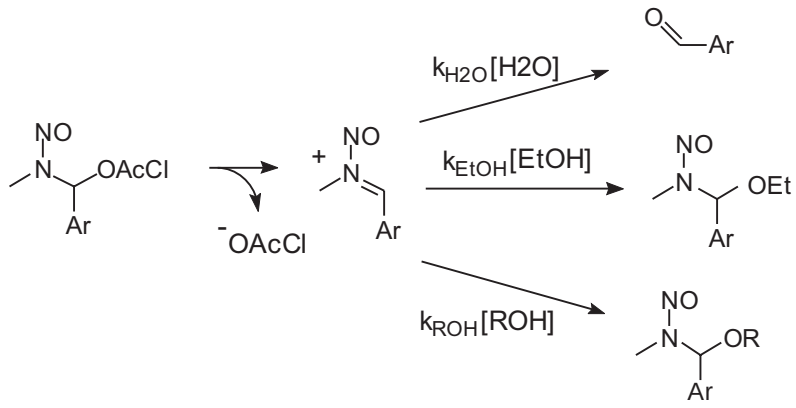

concentrations to give ratios of second-order rate constants, and these are summarized in Table 4.

Studies were carried out to trap the similarly generated nitrosiminium ions by azide ion. A plot of the fraction of azide ion adduct as a function of azide ion concentration is illustrated in Fig. 3. Control experiments establish that there is no measurable effect on the rate constant, k_{obsd}, for the decay of the esters with increasing concentrations of azide ion up to 0.01 M. Plots of k_{obsd} against azide ion concentration containing 4–5 azide ion concentrations between 0.001 and 0.01 M indicate that the value of k_{obsd} at 0.01 M azide ion is less than 10% larger than the intercept extrapolated to 0 M azide ion.

Discussion

Cation formation

Rate constants for the pH independent solvolysis of α-acetoxy, α-chloracetoxy, and α-azido (*N*-nitrosomethylamino)arylmethane amines were measured at 25°C, in aqueous media of ionic strength 1 M ($NaClO_4$) that contained 4%

© 1999 NRC Canada

Table 4. Ratios of second-order rate constants for the capture of *N*-nitrosiminium ions formed in the decay of (*N*-nitrosomethylamino)arylmethyl chloroacetates in 0.05 M morpholino ethane sulfonic acid (MES) buffer (pH = 6.5), ionic strength 1 M ($NaClO_4$), in 90:1:9 H_2O:EtOH:ROH (v:v) at 25 C.[a]

Alcohol	Substituent			
	H	*p*-Cl	*m*-Cl	*p*-CF_3
		k_{ROH}/k_{H2O}		
CH_3-OH	7.9	7.8	5.6	6.5
	(0.1)	(0.1)	(0.2)	(0.6)
CH_3-CH_2-OH	7.1	6.1	3.9	5.2
	(0.2)	(0.1)	(0.1)	(0.3)
CH_3O-$(CH_2)_2$OH	2.4	2.11	1.63	1.54
	(0.05)	(0.08)	(0.02)	(0.02)
$ClCH_2$-CH_2-OH	1.09	0.85	0.61	
	(0.01)	(0.03)	(0.03)	
$CNCH_2$-CH_2-OH	0.58	0.45	0.49	0.41
	(0.04)	(0.01)	(0.01)	(0.02)
Cl_2CH_2-CH_2-OH	0.15	0.21	0.18	0.14
	(0.01)	(0.01)	(0.01)	(0.02)
CF_3-CH_2OH	0.075	0.040	0.078	0.037
	(0.04)	(0.003)	(0.005)	(0.001)

[a]Rate constants as in eq. [3].

Fig. 3. Plot of the fractional yield of azide ion adduct against azide ion concentration for the reaction of **1b** (squares), **2b** (triangles), **3b** (diamonds), **4b** (circles), and **8b** (inverted triangles) at 25°C, ionic strength 1 M ($NaClO_4$).

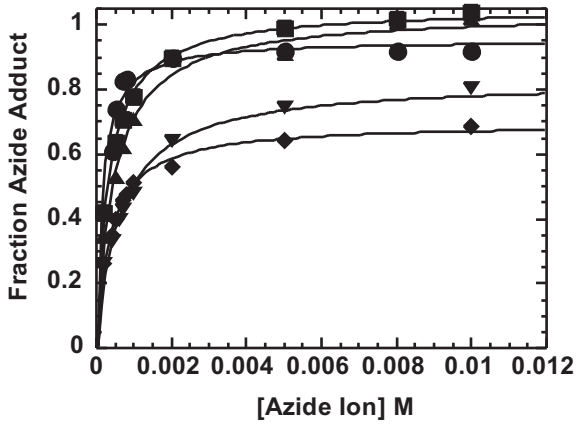

Fig. 4. Plot of log k_1 against σ^+ for the solvolysis of acetates, chloroacetates, and azides at 25°C, ionic strength 1 M ($NaClO_4$).

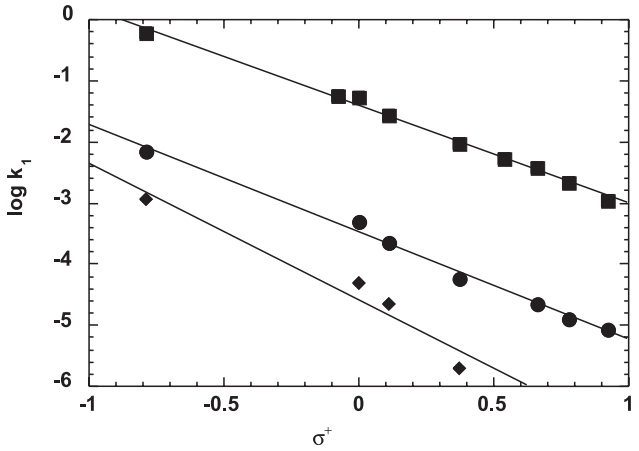

by volume acetonitrile. Figure 4 is a plot of the log k_1 against σ^+. The slopes of the plots are –2.23 (r^2 = 0.949), –1.76 (r^2 = 0.993), and –1.61 (r^2 = 0.994) for the azides, acetates, and chloroacetates, respectively. The uncertainty in the value for the azides is greatest due to the fewer data points, but the slope is likely greater than for the other systems. Inspection of the plot shows that the deviations of the four points in the azide correlation are similar in the esters. A plot of the log k_1 values for the azide (*y*-axis) against those for the same substituents in the acetate series (*x*-axis) is linear with a slope of 1.31 (r^2 = 0.998). Plots of log k_1 against σ give slightly larger slopes of –3.53 (r^2 = 0.834), –1.98 (r^2 = 0.978), and –1.90 (r^2 = 0.988) for the azides, acetates, and chloroacetates, respectively, when the point for the *para*-methoxy substituent is excluded. This point deviates positively from all three such correlations, by 0.3, 0.56, and 0.46 log units for the azides, acetates, and chloroacetates, respectively.

The negative values of the slopes are consistent with positive charge buildup in the transition state for formation of nitrosiminium ion intermediates, as in eq. [2]. These values are considerably smaller than the values of ρ^+ ~–5 for the solvolysis of simple benzylic and phenethyl substrates (13). This is expected due to the substantial resonance stabilizing effect of the *N*-nitrosomethylamino substituent that can donate electrons to the developing electron deficient center in the transition state. Similar smaller values of ρ and ρ^+ have been reported for systems in which there are additional substituents in the α-position that are capable of stablization by resonance electron donation (14).

Cation capture

There have been numerous reports indicating that the dominant reaction of nitrosiminium ions with alcohol, carboxylic acid, and water solvents involves carbon–oxygen bond formation to give α-oxy substituted nitrosamines (3–8, 15–17). That this is the dominant reaction here, at neutral

© 1999 NRC Canada

pH, is confirmed by the data in Table 3. It was recently reported that nitrosiminium ions can undergo denitrosation (7), in particular in the presence of azide ion and a thiolate ion. The last two experiments in Table 3 were carried out as a check on the extent of this reaction with solvent water and dilute (0.05 M) buffer. The yields of methylammonium ion of 7% confirm that there is denitrosation of the nitrosiminium ion in weakly buffered solvent, although it is clearly a minor pathway. The dominant pathway involves the production of methanol by formation of the α-hydroxynitrosamine, which decomposes to the methanediazonium ion that yields methanol. The less than quantitative yield is almost certainly accounted for by proton exchange involving the diazonium ion that occurs to an appreciable extent at this pH in the presence of low buffer concentrations (12). It must be noted that the literature does contain a single report of what appears to extensive denitrosation of a nitrosiminium ion intermediate by solvent (18). Decomposition of the cyclic α-acetoxynitrosamine, eq. [4], in aqueous media gives a 54% yield of myosmine that presumably arises by denitrosation that is competitive with α-carbon–oxygen bond formation.

[4] 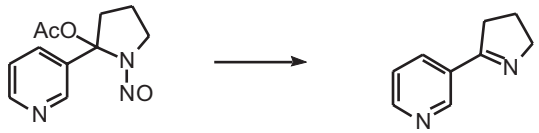

myosmine

The common ion rate depression illustrated in Fig. 1 indicates that acetate ion acts predominantly as a nucleophile at the α-carbon to yield the starting α-acetoxynitrosamine. The effect of acetate appears to diminish at high acetate concentrations such that there is remnant of reaction that is not further inhibited by the addition of acetate ion. This has been reported previously (6) and was analyzed according to the mechanism of eq. [5] in which acetate can react to either

[5] 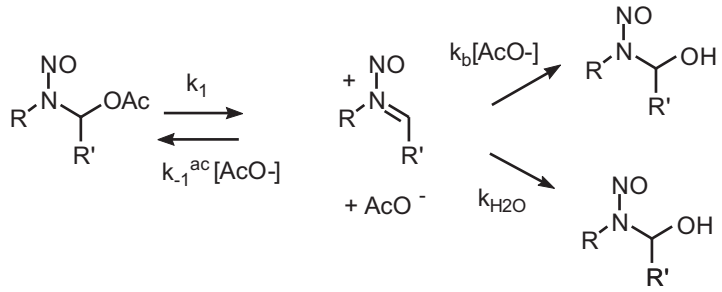

regenerate starting material, by k_{-1}^{ac}, or assist formation of the α-hydroxynitrosamine by general base catalyzed addition of water, k_b. An alternative to this scheme would be either nucleophilic attack, or general base catalyzed attack of water, by acetate ion, on the nitrogen of the nitrosiminium ion to yield the imine which subsequently hydrolyzes. This is illustrated in the mechanism of eq. [6].

[6] 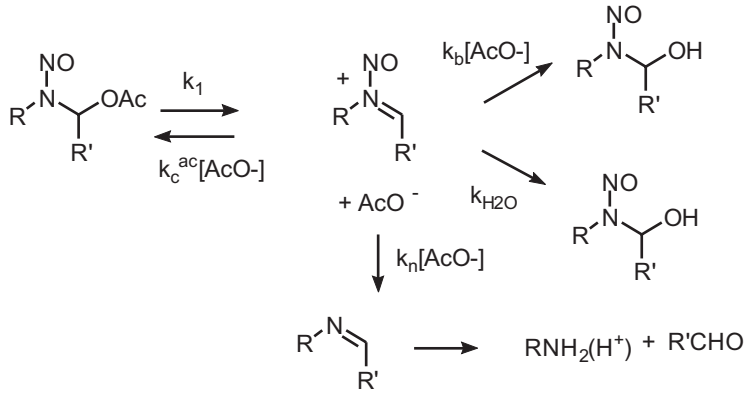

An experiment comparing common ion rate depression in D_2O with the yield of methylammonium ion at high acetate ion concentration indicates that denitrosation of the nitrosiminium ion is a minor pathway. The common ion rate depression of **2a** in D_2O was determined at 3 M ionic strength ($NaClO_4$) at acetate concentrations up to 1.35 M, the data are shown in Fig. 2. The most general mechanism, eq. [6], includes both general base catalyzed addition of water attack at carbon, k_b, and

© 1999 NRC Canada

Table 5. Partioning rate constant ratios for the reactions of (*N*-nitrosomethylamino)arylmethyl acetates in aqueous acetate buffer at 25°C (μ = 1, $NaClO_4$).

Ring substituent	k_{-1}^{ac}/k_{H2O}[a] (M^{-1})	k_b/k_{H2O}[a] (M^{-1})	k_{ACO-}/k_{H2O}[b] (M^{-1})
p-MeO	27.48 (0.57)	0.71 (0.06)	28.19
H	17.97 (0.34)	0.99 (0.05)	19.08
p-Cl	16.79 (2.94)	0.71 (0.48)	17.49
m-Cl	16.06 (2.23)	0.68 (0.42)	16.68

[a]Values determined from common ion inhibition experiments, constants defined in eq. [5]. Standard errors in parentheses.
[b]$k_{ACO-}/k_{H2O} = k_{-1}^{ac}/k_{H2O} + k_b/k_{H2O}$.

denitrosation via k_n, by whatever mechanism. The rate equation for this mechanism is shown in eq. [7]. The best fit of the data to this equation is shown as the solid line in Fig. 2 for which the following values are used for the given parameters:

$$[7] \qquad k_{obsd} = \frac{k_1}{\left[\dfrac{1}{\dfrac{k_{H_2O}}{k_c[AcO^-]} + \dfrac{k_n + k_b}{k_c}}\right] + 1}$$

k_1 = 0.00051 (± 0.00002), k_{H2O}/k_c = 0.054 (± 0.006), and $(k_n + k_b)/k_{-1}$ = 0.077 (± 0.008). At 1.35 M acetate ion, based on these parameters, 68% of the remaining reaction entails acetate assisted product formation, by $k_b + k_n$. The yield of methylammonium ion at 1.35 M acetate ion was determined by ^{1}H-NMR to be 12%. This represents an upper limit of the part of the acetate ion assisted product formation that involves denitrosation. This 12% is an upper limit because it is assumed that no methylammonium ion is formed in the remaining 38% of the reaction that involves product formation through pathways that are not assisted by acetate ion. Based on this analysis then, less than 18% (= 100 × 12%/68%) of the acetate assisted product formation involves denitrosation, and the remaining 82% must involve general base catalyzed attack of water on the cation, consistent with our original notion eq. [6].

The data on common ion inhibition at 1 M ionic strength in Fig. 1, and that not shown for compound **4a**, were treated according to the mechanism of eq. [6], which ignores the minor denitrosation pathway. The appropriate expression for k_{obsd} is indicated in eq. [8] and best fits to the data in Fig. 1, solid lines were drawn using the values for the parameters indicated in Table 5.

$$[8] \qquad k_{obsd} = \frac{k_1}{\left[\dfrac{1}{\dfrac{k_{H_2O}}{k_c[AcO^-]} + \dfrac{k_b}{k_c}}\right] + 1}$$

The reactivity of azide ion with several cations was also investigated. One method involved the azide ion trapping studies, for which the data are included in Fig. 3. Azide ion proves to be quite effective, with limiting amounts of the azide ion product being reached in the millimolar concentration range. Figure 3 indicates that in two cases the upper limit of the trappable fraction of cation falls well below 1.0. This has been observed previously and ascribed to azide ion stimulated denitrosation that competes with N—C bond formation, as illustrated in the mechanism of eq. [9] (7). There is no clear correlation of substituents with the

[9]

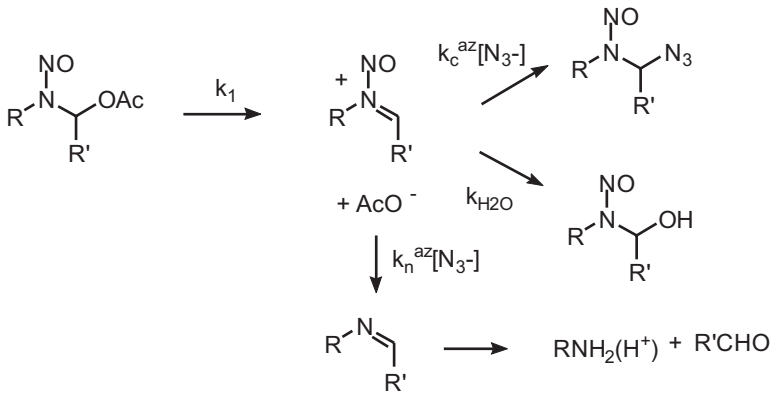

© 1999 NRC Canada

Table 6. Partioning rate constant ratios for the reactions of *N*-(nitrosomethylamino)arylmethyl chloroacetate with azide ion in cacodylic acid buffer at 25°C, ionic strength 1 M ($NaClO_4$).[a]

	p-MeO	H	*p*-Cl	*m*-Cl	*p*-CF_3
k_{N3}/k_{H2O}[b]	6300	3000	2700	2100	1600
	(200)	(300)	(100)	(100)	(100)
k_n^{az}/k_c^{az}	0.047	0.055	0.44	0.058	0.21
	(0.027)	(0.005)	(0.02)	(0.011)	(0.04)

[a]Rate constants defined in eq. [9], standard errors in parentheses.

[b]$k_{N3}/k_{H2O} = (k_n^{az} + k_c^{az})/k_{H2O}$.

Table 7. Rate and equilibrium constants for reactions of esters, azides, and *N*-nitrosiminium ions.[a]

	p-MeO^-	H	*p*-Cl	*m*-Cl
$10^9 k_c^{az}$ (M^{-1} s^{-1})	0.83[b]	1.8[c]	1.9[c]	2.6[c]
$10^6 k_{H2O}$ (s^{-1})	0.14[d]	0.76[e]	1.15[e]	1.35[e]
$10^7 k_{-1}^{ac}$ (M^{-1} s^{-1}) [f]	0.38	1.4	1.9	2.2
$10^{11} K_1^{ac}$ (M)[g]	180	3.5	1.2	0.27
$10^{14} K_1^{az}$ (M)[h]	140	2.7	1.1	0.077

[a]Rate and equilibrium constants are for processes defined in eqs. [10] and [11].

[b]Calculated by extrapolation of the plot of log k_c^{az} against σ^+ determined from the data for the three other compounds for which the values were directly determined (log $k_c^{az} = 0.416\sigma^+ + 9.25$, $R^2 = 0.989$).

[c]Directly measured values of k_{az} combined with k_n^{az}/k_c^{az} from the trapping studied, Fig. 2 and Table 2.

[d]Calculated from k_c^{az}/k_{H2O} based on the measured values of k_{N3}/k_{H2O} and k_n^{az}/k_c^{az} and the calculated value of k_c^{az}.

[e]Determined by laser flash photolysis in the present report and as previously published (8).

[f]Calculated from k_{-1}^{ac}/k_{H2O} (Table 5) and the determined or calculated value of k_{H2O}.

[g]From the values of k_1 (Table 2) and k_{-1}^{ac}.

[h]From the values of k_1 (Table 2) and k_{-1}^{az}.

limiting fraction of azide adduct. The two substituents with the smallest limiting fractions, the *p*-Cl and *p*-CF_3, are electron withdrawing, but the *m*-Cl substituent of intermediate character between the two gives azide adduct in excess of 90%. The appropriate expression for the fraction of azide adduct (F_{az}) as a function of azide ion concentration is given in eq. [10]. Best fits to the data are indicated by the solid

$$[10] \qquad F_{az} = \frac{1}{1 + \dfrac{k_n^{az}}{k_c^{az}} + \dfrac{k_{H_2O}}{k_c^{az}[N_{3^-}]}}$$

lines in Fig. 3 using values for the parameters that are included in Table 6. The data for k_{N3}/k_{H2O} ($= (k_n^{az} + k_c^{az})/k_{H2O}$) are in reasonable agreement with the ratios obtained from the rate constants that were directly measured for three of the compounds using laser flash photolysis (see Results). The values of k_{N3}/k_{H2O} show a small decrease with increasing electron-withdrawing character of the substituent, the plot of log k_{N3}/k_{H2O} against σ^+ has a slope of –0.44 (r^2 = 0.961, maximum deviation in y = 0.1 log unit).

Based on the quantitative relationships established in Tables 5 and 6 and the directly measured rate constants for reactions of azide and water with the cations, microscopic constants can be calculated that allow a clearer view of the cation stabilizing characteristics of the *N*-methyl-*N*-nitroso moiety. The equilibria of interest appear in eqs. [11] and [12]. A summary of the relevant rate and equilibrium constants appears in Table 7. Rate constants, k_c^{az}, for reaction of azide ion at the α-carbon of the cations with H, *p*-Cl, and *m*-Cl substituents were determined from the rate constants for disappearance of the cations measured by laser flash

[11] 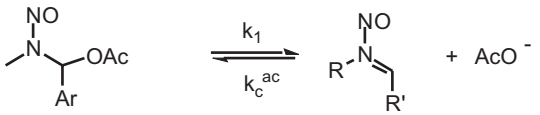

[12] 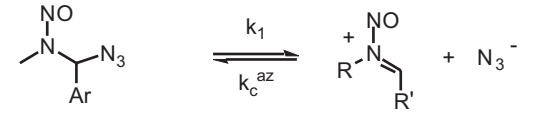

photolysis and the ratio k_n^{az}/k_c^{az} in Table 6 that were determined from the azide ion trapping analysis. No correction for the reaction of water at nitrogen was made, as this appears to be minimal (vide supra). For the *p*-methoxyphenyl cation, the value for k_c^{az} was calculated from linear extrapolation of the plot of log k_c^{az} against σ^+ for the unsubstituted, *p*-Cl and *m*-Cl compounds. The value of k_{H2O} was calculated from the value k_c^{az} and the appropriate combination of ratios in Table 6. Values for the reaction at carbon by acetate ion, k_c^{ac}, were then determined from the values of k_{H2O} and the values of k_c^{ac}/k_{H2O} in Table 5. The values of k_c^{az} and k_c^{ac} can then be combined with values of k_1 (Table 2) for the decomposition of the azide and acetate adducts, respectively, to give the equilibrium constants for cation formation.

The equilibrium constants for cation formation from the acetates exceed those for formation from the azide, for a given substituent, by a factor of ~1000.

Comparison of some of the values in Table 7 with some previously reported similar numbers for other α-substituted arylmethyl cations is instructive relative to the cation stabilizing ability of the *N*-methyl-*N*-nitroso group. Scheme 1 illustrates the relevant cations and their equilibrium and rate constants for reaction with solvent water (19). As can be

© 1999 NRC Canada

Scheme 1.

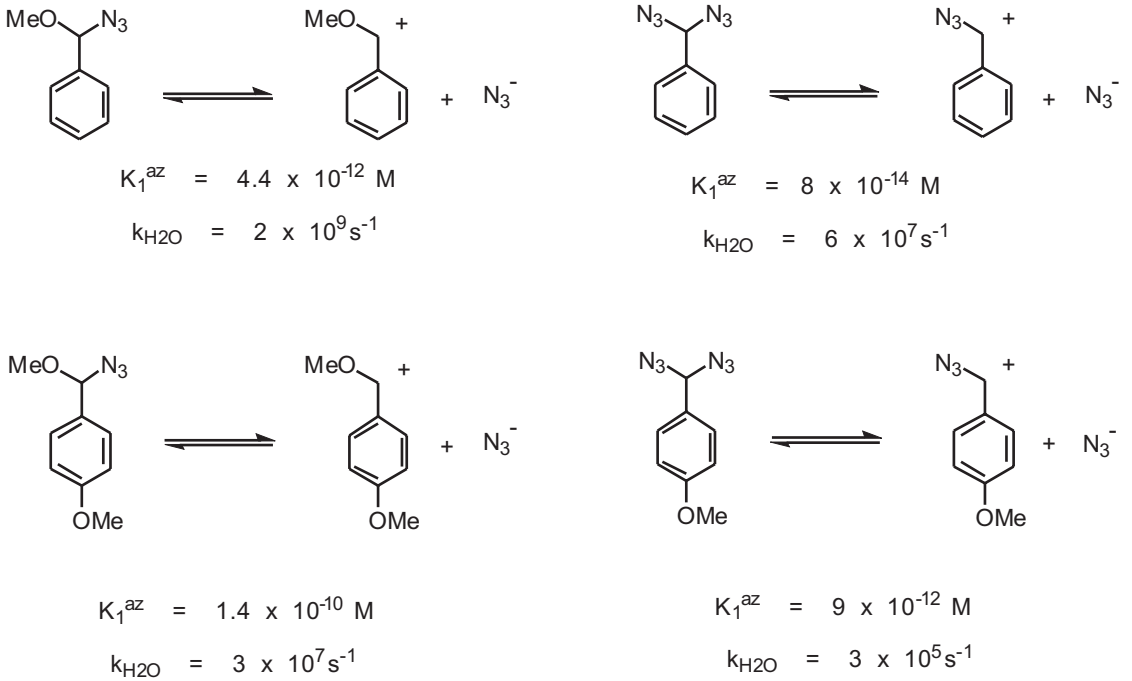

seen for both the benzylic and *p*-methoxybenzyl systems, the equilibrium constants for formation of the α-nitrosomethylamino cations are slightly smaller than those for formation of the analogous α-azido cations, right pair in Scheme 1, by less than 1.1 kcal/mol. The equilibrium constants for α-nitrosomethylamino cations are smaller by 3 and 2.7 kcal/mol than the corresponding α-methoxy-benzyl and *p*-methoxybenzyl cations, respectively. Thus, regarding equilibrium stablization, the α-nitrosomethylamino group is the least effective. In contrast, the α-nitrosomethylamino cations are the most kinetically stable of the cations. They react with water with rate constants that are a factor of 80 and 2 slower than the corresponding α-azido-benzyl and *p*-methoxybenzyl cations, respectively; and factors of 10^3 and 40 slower than the corresponding α-methoxybenzyl and *p*-methoxybenzyl cations, respectively.

Amyes and Richard (19) rationalized the contrasting kinetic and thermodynamic effects in Scheme 1 — the smaller rate constants for cation capture of the thermodynamically less stable α-azido cations — as being due to a larger intrinsic barrier for cation capture in the case of the α-azido cations due to loss of more extensive resonance delocalization compared to the α-methoxy cations. The more extensive loss of resonance contributes to a larger intrinsic barrier (20*a*). This explanation appears applicable to the present case. Resonance in the α-nitrosomethylamino cations is similarly more extensive than in the case of the α-methoxy cations, and so, the intrisic barrier for capture may be larger despite the lesser thermodynamic stability of the former cations. It should be noted that not only is there a more extensive loss of resonance stablization in the case of the α-azido and α-nitrosmethylamino compared to α-methoxy cations, but additionally, there is likely the contribution of *re-establishment of resonance delocalization* in the product cation-hydrates that may contribute to the larger intrinsic barriers for capture of the α-azido and α-nitrosomethylamino cations. There is no resonance delocalization involving the α-methoxy group *in the product* of water attack on the α-methoxy cation.

It is surprising that despite the slightly greater stability of the α-azido cations compared to the α-nitrosomethylamino cations, the $\rho_{eq} = -3.8$ for formation of the α-azido cations is more negative than $\rho_{eq} = -2.7$ for the α-nitrosomethylamino cations.[2] These values suggest greater delocalization into the benzene ring in the case of the α-azido system than for the α-nitrosomethylamino system. It is possible that some of the carbocation stabilization in the case of the α-azido cations may arise from the relatively strong N≡N triple bond in the imino-diazonium ion character of one of the resonance forms.[3]

It is notable that the values of k_{H2O} are similar for the comparable α-azido and α-nitroamino cations, given the differences in the functionalities involved. A range of Lewis structures that need to be considered is illustrated in Scheme 2 and highlights important uncertainties suggested by the present results. It is the shift, in going from the cation to the transition state, in the dominance of the various Lewis forms, and the consequent changes in bond lengths and angles, that contributes to the larger intrinsic barrier for capture of the α-azido and α-nitrosmethylamino cations compared to the α-methoxy cations. The structure of the transition state is a weighted average of reactant and product, and probably other, structures. The larger values of k_{H2O} for the α-azido cations than for the α-nitrosmethylamino cations may be due to less resonance delocalization in the α-

[2] We had not initially noted this but it was kindly pointed out by a referee (see ref. 20*b*).
[3] Prof. J. Richard (SUNY, Buffalo) suggested this possibility.

© 1999 NRC Canada

Scheme 2.

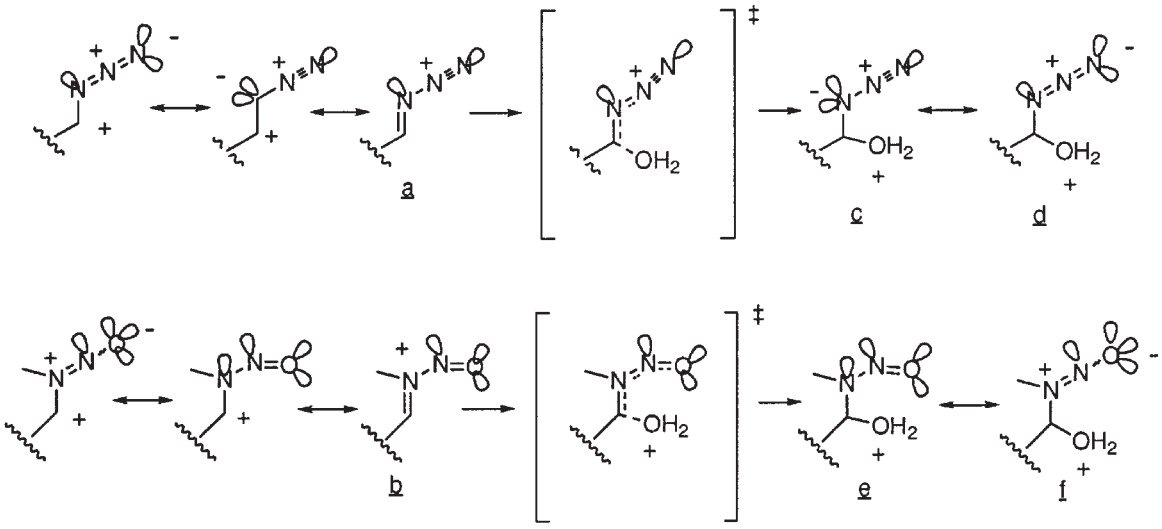

azido cation than in the α-nitsosomethylamino cation. This would be consistent with what is expected on the basis of the electron-withdrawing abilities of the diazonium ion and nitroso groups. The value of σ^- is σ^- = 1.46 for the nitroso group, while σ^- = 3–3.4 for the diazonium ion (21). Thus, structure **a** (Scheme 2) should be relatively less important to the total structure of the α-azido cation than structure **b** is to the nitrosomethylamino cation. The smaller resonance stabilization by the α-azido group should give rise to a smaller intrinsic barrier — consistent with the larger rate constants k_{H2O} for capture of these cations by water.

Of the product structures, the contribution of **d** to the total structure of α-azido compound is likely significantly greater than that of **c**; and this difference is likely larger than the difference in contribution of **f** compared to **e** in the α-nitrosamino compound. This deduction is based on the relatively energetically unfavorable unpaired electrons on the anionic nitrogen in **c** compared to those on the amino nitrogen in **e** and on the differences in σ^-, mentioned above. All things being equal, this would suggest more bond length and angle reorganization in going to the transition state for capture of the α-azido cation. This would lead to the expectation of larger barriers for capture of the α-azido cations — opposite the experimental observation. But Scheme 2 shows that the comparison is not simple: the relevant resonance forms have different bond multiplicities and orbital structures in the α-azido compared to the α-nitrosaminomethyl system, and these differences likely impact on the extent of structural reorganization in ground and transition states and in the degree to which this is manifest in the intrinsic barriers. An alternative explanation is that there is relatively little contribution to the transition state of the product-like resonance forms, but this seems unlikely. It is the change from the dominant resonance forms of the cations to the different dominant product-like resonance forms in the transition state that contributes to the larger intrinsic barrier for capture of the α-azido cations compared to the α-methoxycarbocations.

The equilibrium constants for cation formation show only small changes as a function of the substituent on the benzene ring. The values of ρ^+ are –2.41 (r^2 = 0.993) and 2.67 (r^2 = 0.948) for the acetates and azides, respectively. This is considerably smaller than the value of ρ^+ = –9 for the equilibrium formation of 1-phenethyl cations from the chlorides (13, 22). The smaller values of ρ^+ are consistent with considerable resonance donation by the nitrosomethylamino group in the cation that lessens the demand for stabilization of the cation by substituents in the benzene ring. Similar smaller values of ρ^+ are seen in the acid catalyzed formation of oxocarbocations from substituted benzaldehyde diethyl acetals for which ρ^+ = –3.3 (14).

Comparison of the equilibrium constants for the azide and acetate adducts with identical substituents yields information on the differences in carbon basicity between acetate and azide ions. This is because the reaction of azide ion, as well as acetate, with the unsubstituted nitrosomethylamino benzyl cation appears to be significantly activation limited, not simply diffusion controlled. The rate constant for the azide ion reaction was measured directly by laser flash photolysis (8) and the increase in the rate constant for azide ion capture of the *m*-chloro compound shows that the reaction with the unsubstituted compound cannot be diffusion limited. In addition, it was shown (8) that a thiolate nucleophile reacts with the nitrosomethylamino benzyl cation with a rate constant of 2.8×10^9 M^{-1} s^{-1} that is larger than that for azide ion. Further, the rate constant for reaction with azide ion is significantly smaller than the values of $5–7 \times 10^9$ M^{-1} s^{-1} that have been directly measured for the reaction of azide ion with diaryl- and triarylmethyl cations that do not appear to be appreciably less hindered than the nitrosiminium ions studied here (23). The smaller rate constant for the reaction of acetate ion is also smaller than the value of $\sim 5 \times 10^8$ s^{-1}, which represents the upper limit for encounter-controlled capture of cations by acetate ion (24). Thus, the differences, between the acetate and azide adducts, in the equilibrium constants for cation formation reflect the balance of differences in intrinsic carbon basicity and (or) other properties between the two nucleophiles.

The observed differences in equilibrium constants can almost entirely be accounted for by differences in solvation of the acetate and azide anions. This indicates, surprisingly,

© 1999 NRC Canada

that there is little difference between the carbon basicity of acetate and azide ions. This is most easily understood by combination of the two equilibria for cation formation to give eq. [13] below.

[13] 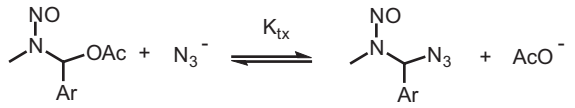

Appropriate combination of the two equilibrium constants gives the value of K_{tx} = 1300 for transfer of the carbon fragment between the two nucleophiles, 4.3 kcal/mol in favor of the azide adduct. This preference is a combination of the differences in intrinsic carbon affinity of the two nucleophiles as well as the differences in the strength of solvation of the two anions, and the two neutral species as well. The free energy of transfer from the gas phase to water is larger for acetate ion than azide ion by 6.6 kcal/mol (25). The free energy of transfer from the gas phase to water is larger for acetic acid than hydrazoic acid by 3.3 kcal/mol (25). If is is assumed that there is a similar difference for the acetate adduct compared to the azide adduct in eq. [13], then 3.3 (= 6.6 – 3.3) kcal/mol of the 4.3 kcal/mol for the equilibrium in eq. [13] is due to the stronger solvation of acetate ion than azide ion. This means that the difference between azide ion and acetate ion in intrinsic carbon basicity is on the order of 1 kcal/mol in favor of azide ion. The assumption that the difference in solvation of the neutral species is the same as that for the corresponding neutral acids may be incorrect if some of the difference in the case of the acids is due to stronger hydrogen bond donation by acetic acid than by HN_3. This would make the difference in free energy of transfer of the neutral species in eq. [13] less than 3.3 kcal/mol, which would indicate that a larger fraction of the observed 4.3 kcal/mol for the equilibrium in eq. [13] would be accounted for simply by differences in the solvation of the anions. This makes the calculated difference of 1 kcal/mol between the carbon basicities of azide and acetate ions an upper limit.

The recognition of the important contribution of solvation to the equilibrium in eq. [13] may also account for the unexpected observation that the difference, between acetate and azide ion, in the rate constants for the highly exoergic capture of the cations is larger than the difference, between azide and acetate adducts, in the rate constants for the highly endoergic formation of the cations. Table 7 shows that the ratio, k_c^{az}/k_c^{ac}, is a factor of ~100, whereas Table 2 indicates that the values of k_1 for the azides is only a factor of 10 smaller than the acetates. The requirement for extensive desolvation prior to the small amount of bond formation that likely exists in the transition state for the highly exothermic cation capture reaction could explain the larger difference in reactivity between the two nucleophiles, given the stronger solvation of the acetate ion that exists (vide supra). More facile desolvation of azide ion has been invoked previously to account for the larger limiting rate constants for reaction of azide ion compared to carboxylate ions and amines with carbocations (24, 26).

The reactivities of a series of alcohols with four of the cations was determined in 90% H_2O/1% EtOH/9% ROH solutions, ionic strength 1 M ($NaClO_4$), and show that there is little change in selectivity as a function of the aryl group substituent. This is illustrated in Fig. 5, which plots the alcohol water selectivity as a function of alcohol pK_a. For the *p*-H, *p*-Cl, and *p*-CF_3 substituents, the slopes of the least-squares correlations are 0.62 (r^2 = 0.983), 0.66 (r^2 = 0.989), 0.60 (r^2 = 0.989), respectively. The *m*-Cl substituent, of intermediate electron-withdrawing power, gives the smallest slope, β = 0.52 (r^2 = 0.989). The reason for this apparent anomaly is not understood. The intermediate values of β suggest there is considerable charge buildup on the attacking alcohol, and significant bond formation in the transition state for cation capture by these weak nucleophiles.

Fig. 5. Plot of log (ROH/H_2O) against pK_a ROH for the alcohol–water selectivity of cations from chloroacetates **2b** (circles, C = 1.5), **3b** (triangles, C = 1), **4b** (diamonds, C = 0.5), **8b** (triangles, C=0) at 25°C, ionic strength 1 M ($NaClO_4$), solvent H_2O/EtOH/ROH = 90/1/9.

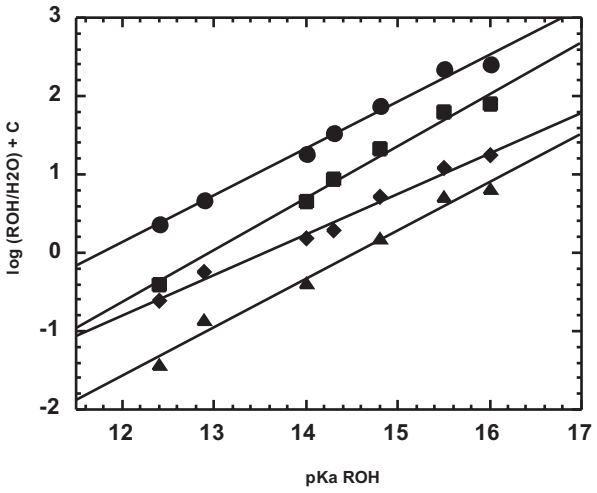

Notably, Fig. 5 indicates that trifluoroethanol (pK_a = 12.4) behaves as a normal nucleophile for its pK_a, and this contrasts with previous reports. In the capture of 1-phenylethyl cations (24) and oxocarbocations (27), trifluoroethanol is a significantly poorer nucleophile than expected for its pK_a. The reason for the different, "normal" behavior in comparison with other alcohols in the present case is unclear.

Acknowledgements

We are grateful to Prof. J. Bartmess (Tennessee) for providing the information on free energies of transfer from the gas phase to water. This work was supported by grants RO1-CA 52881 and KO4-CA 62124 from the U.S. National Institutes of Health (NCI).

References

1. P.D. Lawley. *In* Chemical carcinogens. ACS monograph 182. *Edited by* C.D. Searle. American Chemical Society, Washington, D.C. 1984.
2. W. Lijinsky. Chemistry and biology of *N*-nitroso compounds. Cambridge University Press, Cambridge. 1992.
3. J.E. Baldwin, A. Scott, S.E. Branz, S.R. Tannenbaum, and L. Green. J. Org. Chem. **43**, 2427 (1978).

© 1999 NRC Canada

4. C. Revis, M. Rajamaki, and J.C. Fishbein. J. Org. Chem. **6**0 7733 (1995).
5. L. Chahoua, M. Mesic', A. Vigroux, and J.C. Fishbein. J. Org. Chem. **62**, 2500 (1997);H. Cai and J.C. Fishbein. Tetrahedron, 10 671 (1997).
6. H. Cai and J.C. Fishbein. J. Am. Chem. Soc. In press.
7. M. Rajamaki, A. Vigroux, L. Chahoua, and J.C. Fishbein. J. Org. Chem. **60**, 2324 (1995).
8. A. Vigroux, A.J. Kresge, and J.C. Fishbein. J. Am. Chem. Soc. **117**, 4433 (1995).
9. P.G. Stecher (*Editor*). The Merck index. 8th ed. Merck & Co., Rahway, N.J. 1968.
10. M. Wiessler. Angew. Chem. Int. Ed. **13**, 743 (1974).
11. J. Graymore. J. Chem. Soc. 1353 (1932).
12. J. Hovinen. J.I. Finneman, S.N. Satapathy, J. Ho, and J.C. Fishbein. J. Am. Chem. Soc. **114**, 10 321 (1992), and refs. within.
13. J.P. Richard, M.E. Rothenberg, and W.P. Jencks. J. Am. Chem. Soc. **106**, 1361 (1984).
14. R.B. Dunlap, G.A. Ghanim, and E.H. Cordes. J. Phys. Chem. **73**, 1898 (1970); P.R. Young and W.P. Jencks. J. Am. Chem. Soc. **99**, 8238 (1977).
15. M. Wiessler, G. Rossnagel, and B. Rugewitz-Blackholm. *N*-Nitroso compounds: occurrence, biological effects and relevence to human cancer. Vol. 52. *Edited by* I.K. O'Neill, R.C. von Borstel, R.C. Miller, J. Long, and H. Bartsch. IARC Sci. Pub., Lyon. 1977. p. 465; N. Frank and M. Wiessler. Carcinogen, **7**, 365 (1986).
16. M. Mochizuki, T. Anjo, N. Sekiguchi, A. Ikarashi, A. Suzuki, Y. Wakabayashi, and M. Okada. Chem. Pharm. Bull. **34**, 3956 (1986).
17. M. Wiessler. *N*-Nitrosamines. *Edited by* J.-P. Anselme. ACS, Washington, D.C. 1979. p. 57.
18. S.S. Hecht and C.B. Chen. J. Org. Chem. **44**,1563 (1979).
19. T.L. Amyes and J.P. Richard. J. Am. Chem. Soc. **113**, 1867 (1991).
20. (*a*) C.F. Bernaconi. Tetrahedron, **41**, 3219 (1985); J.P. Richard. Tetrahedron, **51**, 1535 (1995); (*b*) J.P. Richard, T.L. Amyes, V. Jagannadham, Y.G. Lee, and D.J. Rice. J. Am. Chem. Soc. **117**, 5198 (1995)
21. O. Exner. *In* Correlation analysis in chemistry, recent advances. *Edited by* N.B. Chapman and J. Shorter. Plenum, New York. 1978.
22. N.C. Deno and W.L. Evans. J. Am. Chem. Soc. **79**, 5804 (1957).
23. R.A. McClelland, V.M. Kanagasabapathy, N.S. Banait, and S. Steenken. J. Am. Chem. Soc. **113**, 1009 (1991).
24. J.P. Richard and W.P. Jencks. J. Am. Chem. Soc. **106**, 1373 (1984).
25. B. Wilson and J.E. Bartmess. J. Am. Chem. Soc. **113**, 1762 (1991).
26. R.A. McClelland, V.M. Kanagsabapathy, N.S. Banait, and S. Steenken. J. Am. Chem. Soc. **114**, 1816 (1992).
27. M.L. Sinnott and W.P. Jencks. J. Am. Chem. Soc. **102**, 2026 (1980).

© 1999 NRC Canada

1998 Alcan Award Lecture
Surface electrochemistry — surface science with a joy stick[1]

Jacek Lipkowski

Abstract: This lecture gives a review of thermodynamic, spectroscopic, STM and AFM imaging, and X-ray diffraction studies of molecular and ionic adsorption at Au(111) electrodes. In the first part, thermodynamics of adsorption of simple ions such as sulfate, chloride, bromide, and iodide will be discussed. At high coverages, anions adsorbed at a single crystal surface form ordered 2D adlayers. We show that the structure of these adlayers can be studied by STM and surface X-ray diffraction techniques. Next, the information concerning adsorption of simple ions is used to describe mixed adlayers formed by coadsorption of anions and metal adatoms. We demonstrate how to combine electrochemical experiments with in situ polarization-dependent Cu K-edge X-ray absorption spectroscopy to determine the composition and the structure of mixed films formed by deposition of Cu on Au(111) in the presence of SO_4^{2-}. In the last part we review our efforts to describe coordination of organic molecules to gold electrodes. First, we will discuss adsorption of benzonitrile at the Au(111) electrode surface. We combine electrochemical methods with in situ infrared spectroscopy to describe (*i*) the energetics of molecular adsorption at the gold electrode surface, (*ii*) the character of the interaction of the adsorbed molecule with the metal substrate, and (*iii*) the influence of the electric field on the orientation of the adsorbed molecule. In the last section we describe surface aggregation phenomena. We apply AFM and STM to determine the structure of hemimicelles formed at the Au(111) electrode surface by adsorbed molecules of sodium dodecyl sulfate and we discuss the potential-controlled transformation of these hemimicelles into a condensed monolayer.

Key words: surface electrochemistry, electrosorption, surface aggregation, gold electrodes, molecular adsorption, ionic adsorption.

Résumé : Ce travail passe en revue les données thermodynamiques, spectroscopiques, d'imagerie « STM » et « AFM » ainsi que les études de diffraction des rayons X relatives à l'adsorption moléculaire et ionique sur des électrodes d'Au(111). Dans la première partie de ce travail, on discute de la thermodynamique d'adsorption d'ions simples, tels les ions sulfate, chlorure, bromure et iodure. À des couvertures élevées, les anions adsorbés sur une seule surface cristalline forment des couches d'adsorption 2D bien ordonnées. On démontre que la structure de ces couches d'adsorption peut être étudiée par les techniques d'imagerie STM et par diffraction des rayons X par la surface. Ensuite, on utilise l'information relative à l'adsorption d'ions simples pour décrire des couches d'adsorption mixtes formées par coadsorption d'anions et d'atomes métalliques adsorbés. On montre comment on peut combiner des expériences électrochimiques avec la spectroscopie in situ d'adsorption des rayons X Cu à la limite du K dépendante de la polarisation pour déterminer la composition et la structure de films mixtes formés par le dépôt de Cu sur Au(111), en présence de SO_4^{2-}. Dans la dernière partie, on passe en revue les efforts que nous avons faits pour décrire la coordination de molécules organiques sur les électrodes d'or. Nous discuterons en premier lieu de l'adsorption du benzonitrile sur la surface de l'électrode Au(111). On combine les méthodes électrochimiques avec la spectroscopie infrarouge in situ pour décrire : (*i*) les énergies impliquées dans l'adsorption moléculaire au niveau de la surface d'une électrode d'or; (*ii*) le caractère de l'interaction de la molécule adsorbée avec le substrat métallique et (*iii*) l'influence du champ électrique sur l'orientation de la molécule adsorbée. Dans la dernière section, on décrit le phénomène d'agrégation à la surface. On applique les méthodes AFM et STM pour déterminer la structure des hémimicelles qui se forment au niveau de la surface de l'électrode d'Au(111) par les molécules de dodécylsulfate de sodium adsorbées et on discute de la transformation, à potentiel contrôlé, de ces hémimicelles en une monocouche condensée.

Mots clés : électrochimie de surface, électroabsorption, agrégation en surface, électrodes d'or, adsorption moléculaire, adsorption ionique.

[Traduit par la Rédaction]

Received March 5, 1999.

J. Lipkowski.[2] Department of Chemistry and Biochemistry, University of Guelph, Guelph, ON N1G 2W1, Canada.

[1]The 1998 Alcan Award Lecture was presented by Professor Lipkowski at the 81st Conference of the Canadian Society for Chemistry, Whistler, British Columbia, June 1998.

[2]e-mail: lipkowski@chembio.uoguelph.ca

© 1999 NRC Canada

1. Introduction

In classical surface science one works in ultra high vacuum (UHV) where the residual pressure is on the order of 10^{-10} Torr (1 Torr = 133.3 Pa). Under that condition, a plethora of photon and electron spectroscopies, electron diffraction, and atom and ion scattering techniques may be employed to study the coordination of atoms and molecules to solid surfaces. The character of adsorbate–substrate and adsorbate–adsorbate interaction can then be investigated in great detail. The two-dimensional ordering in adlayers of adsorbed atoms and molecules may also be interrogated with the help of these techniques. However, systems investigated in UHV conditions are out of equilibrium and the adsorbates have to interact very strongly with the solid surface or the experiments have to be performed at very low temperatures to prevent their desorption into vacuum.

Surface electrochemistry describes phenomena at the electrified solid–liquid interface. The presence of the solvent restricts the number of techniques that may be employed to study surface coordination at electrode surfaces. For years these processes were investigated chiefly with the use of traditional electrochemical methods that measured only macroscopic quantities such as charge, surface concentrations, or surface energies. Surface electrochemistry has gone through a period of scientific and technological revolution in the last decade. New spectroscopic techniques were developed and applied to study interfacial phenomena at the molecular level. Thus infrared reflection spectroscopy may be employed today to study the attachment of ions and molecules to electrode surfaces (1–4). Synchrotron-based X-ray diffraction and X-ray absorption techniques are used to determine long-range and short-range order at the interface (5–8). Electroreflectance (9), second harmonic generation (10, 11), and sum frequency generation (12) spectroscopies are applied to probe the electronic structure of the electrode surface and the molecular dynamics of interfacial phenomena. Finally, last but not least, scanning probe microscopies such as atomic force and scanning tunneling microscopy provide real-time and real-space images of the interface with atomic resolution (13–16). In electrochemistry, these spectroscopic, diffraction, and surface imaging methods are frequently referred to as nontraditional. Today, by a careful combination of traditional and nontraditional methods, one can provide an atomistic picture of interfacial phenomena that does not differ in detail from the picture of surface processes observed in the UHV environment. In contrast to vacuum, surface electrochemistry may be employed to study processes at equilibrium and under ambient conditions. The knowledge gained from these studies is relevant to many other disciplines such as energy storage and conversion, corrosion protection, electroplating and electrolytic production of metals, and biomimetic research, to give a few examples.

In an electrochemical experiment one applies a potential to the electrode and measures the charge flowing to the electrode surface. This charge generates a field on the order of 10^7–10^8 V/m that drives ions and dipolar molecules. By turning a dial on a control instrument one can manipulate the ions and molecules present at the interface. Therefore, electrochemistry provides surface science with a "joy stick" that can be used to force ions and molecules to adsorb or desorb, to form ordered or disordered adlayers, change their surface orientation, spread them into a uniform film, or group them together into surface aggregates.

This review describes our efforts to determine the structure of the electrified solid–solution interface by a combination of electrochemical, spectroscopic, diffraction, and surface imaging techniques. We will present results acquired chiefly with the Au(111) electrode. At the interface with an electrolyte solution, this gold single-crystal plane behaves as a nearly ideal capacitor over a range of potentials exceeding 1 V and the adsorption processes may be investigated over a range of charge densities that spans almost 100 μC cm^{-2}. For other metals, the metal dissolution and hydrogen adsorption/evolution processes restrict this range of potentials and charges significantly. That range of potentials and charges constitutes a tremendous force to control the interfacial phenomena. We will show how to use the "joy stick" to study adsorption of ions, coordination of small aromatic molecules, and surface aggregation of long-chain surfactant molecules. The objective of this review is to show a cross section of our research. Therefore, we will present our own results without giving exhaustive coverage of the literature. This paper is based on a plenary lecture and is addressed to a general reader; a specialist should look to the original literature for technical details.

2. Ionic adsorption and coadsorption at electrode surfaces

2.1 Energetics

We will begin by describing the energetics of ionic adsorption with the help of electrochemical techniques. We have developed an original method based on the measurement of charge at the solid electrode surface (capacitive chronocoulometry) to determine thermodynamic data such as surface concentrations (Gibbs excesses) and Gibbs energies of adsorption. Capacitive chronocoulometry has been applied to study ionic adsorption and coadsorption at gold electrode surfaces. Details of these investigations are described in three recent review articles (17–19). Figure 1 shows representative results of these studies. As an example, the adsorption of sulfate and halides illustrates how the surface concentration of an anion, its Gibbs energy of adsorption, and the charge on the metal vary as a function of applied potential.

The top panel shows changes in the surface concentration of the four anions. The middle panel shows the corresponding changes in the charge density at the metal surface. The data in the middle panel may be used to correlate changes in the surface concentration of anion to the charge density on the metal. The adsorption of anions starts at a negatively charged surface. When the metal surface is negatively charged, the surface concentration of the anion changes slowly with potential so that a long "foot" is seen on the Γ versus E plot. When the charge on the metal approaches zero, the surface concentration of the anion rises steeply. At more positive charge densities changes in the surface concentration of the anion are slow again. We will refer to this section as the quasi-plateau. For halides, the maximum surface concentrations observed at the most positive potentials

© 1999 NRC Canada

Fig. 1. Comparison of SO_4^{2-}, Cl^-, Br^-, and I^- adsorption at the Au(111) electrode surface from 0.1 M $HClO_4$ + 10^{-3} M K_2SO_4 and 0.1 M $KClO_4$ + 10^{-3} M KCl, KBr, and KI solutions. Top panel, surface concentration versus potential plots. Middle panel, charge density curves. Bottom panel, Gibbs enegry of adsorption. Standard state is an "ideal" Γ = 1 ion cm^{-2} for the surface species and an "ideal" c = 1 mol dm^{-3} for the bulk species (taken from ref. 19).

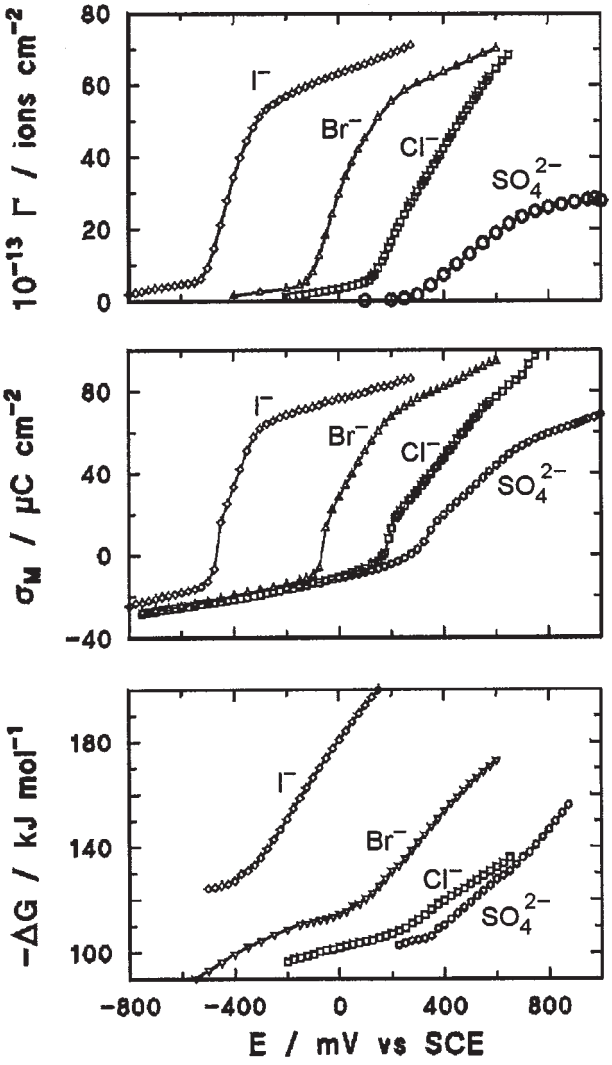

agree within a few percent with the packing densities, estimated from the van der Waals radii to be 6.3 × 10^{14} ions/cm^2 for iodide, 8 × 10^{14} ions/cm^2 for bromide, 9 × 10^{14} ions/cm^2 for chloride. In contrast to the halides, the maximum measured concentration of sulfate is only about one third of the maximum packing density, estimated on the basis of crystallographic data, to be 6.6 × 10^{14} ions/cm^2. This result indicates that adsorption of sulfate and halide ions has somewhat different character. Within the plateau region, the surface concentrations of anion vary smoothly and do not display discontinuities, indicating that close to saturation the monolayer of adsorbed anion is compressible. We will show later that anions form ordered adlayers at surface concentrations close to saturation. The bottom panel in Fig. 1 shows the Gibbs energy plots. These data demonstrate that the

Fig. 2. Plots of the surface dipole moment of adsorbed anion at the Au(111) surface for (○) SO_4^{2-}; Cl^- (□); Br^- (Δ) (taken from ref. 17).

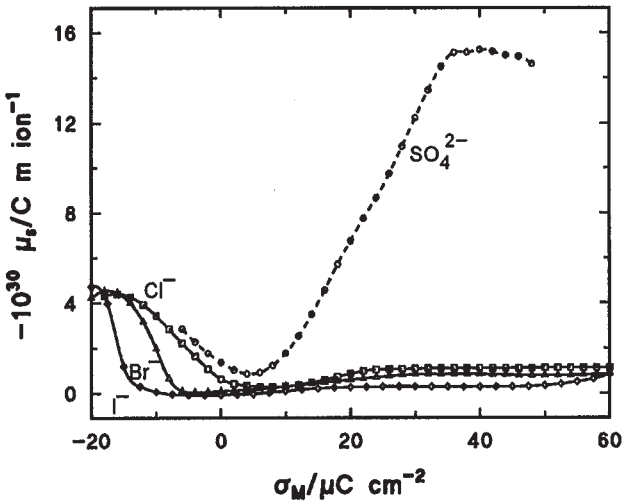

strength of ionic adsorption increases by moving from sulfate to iodide. The Gibbs energy plots are nonlinear and this nonlinearity suggests that ionic adsorption has a multiple state character and that the nature of the surface coordination changes with potential or with the charge on the metal.

Electrochemical data may be used to calculate the surface dipole (μ_s), which represents a dipole formed by an adsorbed anion and its image charge in the metal. The surface dipole is a good measure of the polarity of the chemisorption bond (20). The dipole moments calculated for sulfate, chloride, and bromide at the Au(111) surface are plotted against the charge on the metal in Fig. 2. The dipole moments for adsorbed anions have negative sign; however, in the following we will discuss their absolute values only. Overall, the values of the dipole moment increase in the order $Br^- < Cl^- < SO_4^{2-}$, indicating that the polarity of the chemisorption bond increases by moving from Br^- to SO_4^{2-}. Apparently, the polarity of the electrosorption bond is a strong function of the charge on the metal. For adsorbed Br^- and Cl^-, the polarity is large at the negatively charged surface, but decreases significantly at positive charges. The very small dipole moment for halides may be a result of charge redistribution due to the mixing of electronic states of the adsorbed anion with electronic states of the metal. In contrast, for adsorbed SO_4^{2-} the polarity of the bond becomes quite large at positive charges. These results confirm that there are significant differences between the adsorption behavior of simple halide ions and this polyatomic oxy-anion.

The electrochemical measurements described in this section provide fundamental knowledge concerning the surface concentration of adsorbed anions, its dependence on charge and potential, the energetics of ionic adsorption, and the polarity of the chemisorption bond. These macroscopic data have to be acquired before imaging, diffraction, or spectroscopic experiments are performed to probe the structure of the interface at the molecular level. Numerous examples in the literature show that without the availability of such macroscopic data the interpretation of experiments performed

© 1999 NRC Canada

Fig. 3. STM images of the Au(111) electrode surface: top image, the reconstructed surface at negative charge densities; bottom image, (1 × 1) unreconstructed surface at positive charge densities.

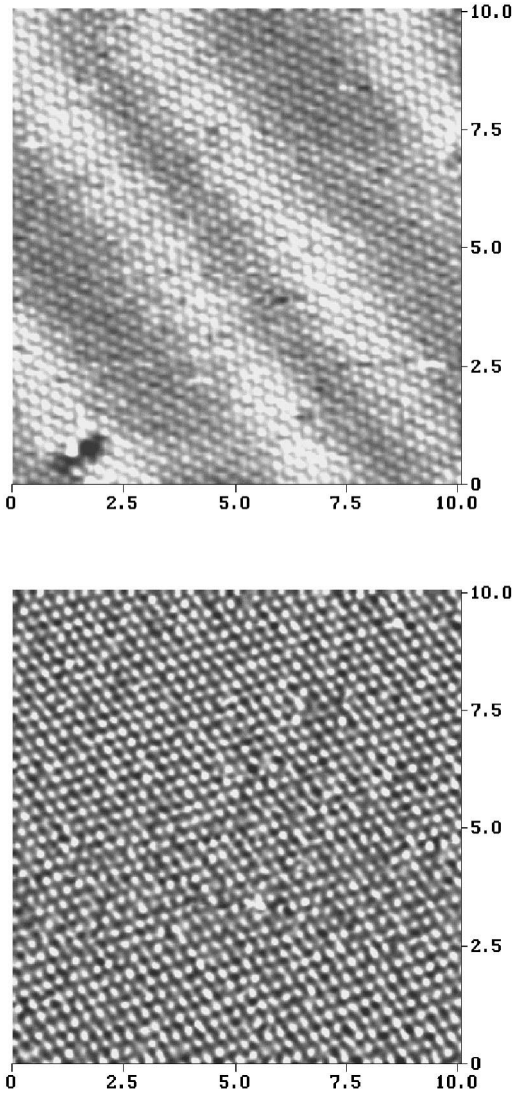

with these advanced techniques may be erroneous, as emphasized by Weaver and co-workers in ref. 21.

2.2 Surface reconstruction phenomena

We will now present structural data to complement the thermodynamic description of ionic adsorption given in the preceding section. Adsorbed anions have a significant impact on the crystallography of the Au(111) electrode surface. The Au(111) electrode surface is known to be reconstructed if it is negatively charged, and the reconstruction is lifted when the metal is charged positively (22, 23). The reconstructed surface has a 4% higher atom density than the unreconstructed surface. The gold atoms in the top reconstructed layer of gold are driven out of registry with respect to the position of atoms in the bulk of the crystal. As a result, the reconstructed surface has a characteristic stripe-like appearance shown in the STM image in the top panel of Fig. 3. When the surface is positively charged, the reconstruction is lifted and the gold atoms relax back into the positions on the

Fig. 4. Potential dependence of: (top panel) integrated scattered X-ray intensity in the vicinity of (–0.044, 1.022, 0.2); (middle panel) charge density at the metal surface; (bottom panel) surface concentration of adsorbed Br^- for Au(111) electrode in 0.1 M $KClO_4$ + 0.01 M KBr (adapted from ref. 24).

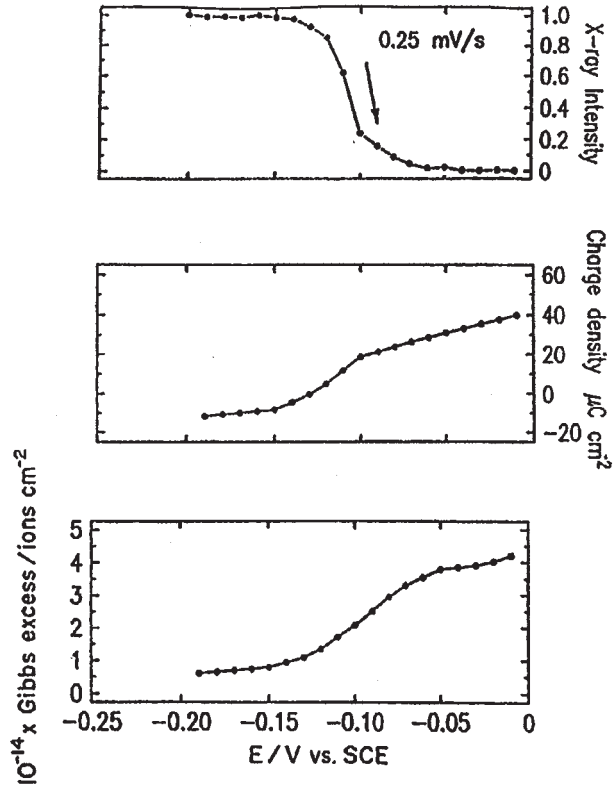

truncated 3D lattice, to form a hexagonal structure as shown in the bottom panel of Fig. 3.

The impact of ionic adsorption on the surface reconstruction phenomenon may be conveniently studied with the use of the surface X-ray scattering technique (SXS). In this technique, the gold electrode is pressed against a thin polypropylene foil so that a thin layer of electrolyte (a few micrometers thick) is trapped between the film and the electrode surface. An intense X-ray beam from a synchrotron penetrates the foil and the electrolyte and the X-ray photons diffracted from the surface are detected (6, 19). To determine the charge densities and the surface concentrations of the adsorbed anion at which the reconstruction is lifted, one has to combine the results of SXS experiments with the knowledge of surface charges and coverages determined by electrochemical techniques. This point is illustrated with an example from a collaborative work between groups at Guelph and Brookhaven (24) in which surface X-ray scattering and chronocoulometric techniques were applied to study the lifting of the reconstruction of the Au(111) electrode in the presence of adsorbed Br^- ions.

Figure 4 summarizes the main results of these experiments. The three panels show the potential dependence of (*i*) the integrated intensity of the X ray scattered by the reconstructed surface (top panel), (*ii*) the charge density at the metal (middle panel), and (*iii*) the surface concentration of adsorbed Br (bottom panel). The intensity of the X-ray scattered from the reconstructed surface is a good measure of

© 1999 NRC Canada

Fig. 5. STM images of the ordered adlayer formed by sulfate adsorbed at the Au(111) electrode surface. Top picture: top view; bottom picture: side view. The image was acquired by recording the bottom part at potential E = 0.9 V vs. SCE, where the ($\sqrt{3} \times \sqrt{7}$) structure is formed, and the top part at potential E = 0.3 V vs. SCE, where sulfate is desorbed and the Au(111) surface is seen. The potential was stepped from E = 0.9 V to E = 0.3 V vs. SCE during the acquisition of the image. 0.5 M H_2SO_4 solution.

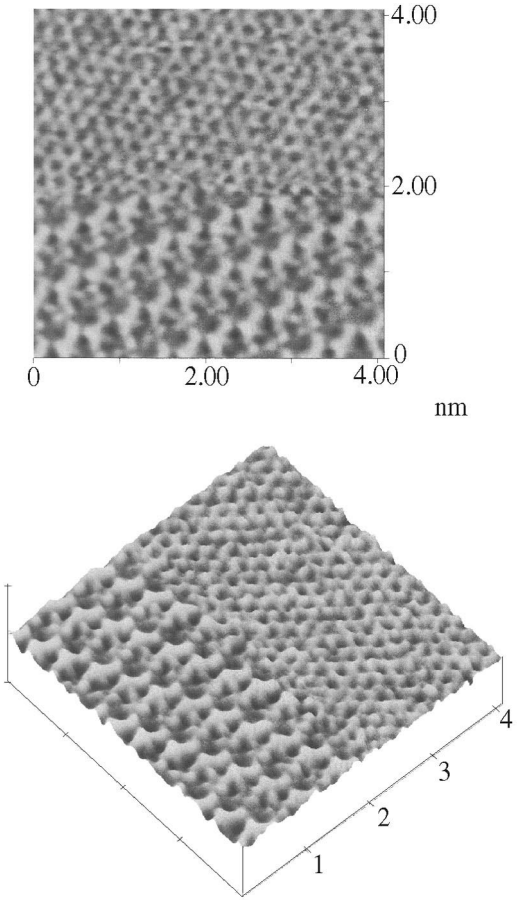

the extent of the reconstruction. Below E = –0.15 V the surface is reconstructed and the intensity has a maximum value. This region corresponds to charge densities lower than –8 μC/cm^2 and a surface concentration of Br^- lower than 8 × 10^{13} ions/cm^2. This latter value corresponds to about 10% of the saturated bromide surface concentration of 8 × 10^{14} ions/cm^2. At E = –0.15 V the X-ray intensity begins to drop and by E = –0.095 V it has only 20% of its original value. In this range, the charge density has increased to +20 μC/cm^2 and the surface concentration has risen to 2 × 10^{14} ions/cm^2. This latter value corresponds to one quarter of the saturated bromide surface concentration. Apparently, the lifting of the reconstruction spans a potential range of about 60 mV, where the surface charge changes from –10 to 20 μC/cm^2 and bromide coverage increases from 10 to 25% of its saturation value. Since the changes of charge are paralleled by a significant increase in the surface coverage by adsorbed bromide, it is difficult to establish whether the reconstruction is lifted by surface charge or by bromide adsorption.

The above studies demonstrate that the structure of the Au(111) surface changes with potential, charge, and coverage. At negative charge densities and low surface coverages, ions are adsorbed at the reconstructed surface, while at positive charges and high coverages the data represent adsorption at the unreconstructed (1 × 1) substrate. The structural transformation takes place around the potential of zero charge (pzc) at the metal. The pzc is located at the fast rising section of the surface coverage versus potential plot shown in Fig. 1. This behavior is representative for all anions. In general, the adsorption of anions (particularly halides) assists in lifting the reconstruction of the Au(111) surface.

2.3 Structure of the ordered adlayers

It is now well established that adlayers of adsorbed anions are disordered (mobile) up to coverages of about 94% of the saturated value (25). At higher coverages, the formation of ordered two-dimensional structures is observed. These ordered adlayers are formed at the unreconstructed (1 × 1) gold surface. All three halides form uniaxial-incommensurate $c(p \times \sqrt{3})$ structures, which in the case of iodide is transformed into the rotated-hexagonal structure at higher coverages (25). These structures are electrocompressible and the spacing between the adsorbed species decreases continuously with the electrode potential. The electrocompressibility of these adlayers is responsible for the linear variation of the coverage with potential, seen earlier in Fig. 1, in the upper portion of the surface–concentration plots. The incommensurate character of the overlayer structure indicates that the halide–gold bond does not have a well-defined directionality and can not be described in terms of singular values of bond length, bond angle, and coordination number.

An interesting case that has been debated extensively in the literature is the structure of the ordered adlayer formed by adsorbed sulfate ions. Figure 5 shows an STM image of the ordered sulfate ions adsorbed at the Au(111) surface at the positive end of potentials, near the onset of gold oxidation. The top image shows the top view while the bottom image shows the side view of the superstructure. Similar structures were observed at Pt(111) (26, 27), Ru(111) (28), and Cu(111) (29) electrodes. The model of this structure and the interpretation of the STM images evolved with time. The first STM images for the ordered sulfate adlayer, reported by Magnussen et al. (30), were interpreted as images of hydrogen-bound bisulfate corresponding to a total coverage of 0.4 ML (where 1 ML coverage (ML = monolayer) corresponds to the surface concentration of gold atoms at an ideal Au(111) surface, 1.39 × 10^{15} atoms/cm^2). However, chronocoulometric measurements performed at Guelph and radiochemical experiments at Urbana, Ill. (31), subsequently demonstrated that the adsorbed species is sulfate, not bisulfate, and that the limiting sulfate coverage amounts to only 0.2 ML. Weaver and co-workers (32) performed additional STM and FTIR studies of this system and, to reconcile the results of the chronocoulometric and STM measurements, proposed a model in which hydronium ions are incorporated into the ($\sqrt{3} \times \sqrt{7}$) network. This model was further developed by Itaya and co-workers (28), who incorporated hydrogen-bonded water chains into the ($\sqrt{3} \times \sqrt{7}$) network of adsorbed sulfate. The Itaya model was recently refined by Ataka and Osawa (33) with the help of additional information extracted from IR spectroscopic experiments. This is therefore a case where the availability of precise

© 1999 NRC Canada

Fig. 6. Surface concentration of copper and sulfate at the Au(111) electrode surface from 0.1 M $KClO_4$ + 10^{-3} M $Cu(ClO_4)_2$ + 10^{-3} M K_2SO_4 + 10^{-3} M $HClO_4$ solution. Open points: surface concentration of copper; solid points: surface concentration of sulfate. The cartoons show schematically the structure of Cu adlayer (taken from ref. 34).

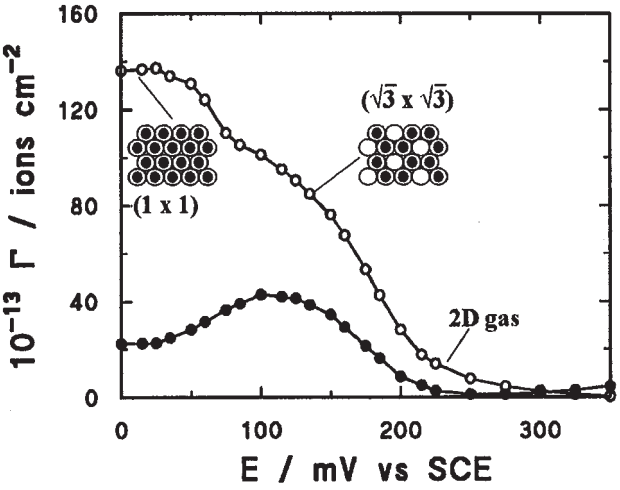

electrochemical data forced the reinterpretation of structural information obtained by STM. It elegantly illustrates the point that a modern description of the solid–solution interface requires concerted use of both electrochemical and nonelectrochemical (imaging, diffraction, spectroscopic) techniques.

2.4 Mixed adlayers form by anions coadsorbed with copper adatoms

Anions are known to form mixed overlayers with copper adatoms, electrodeposited from a solution onto a surface of a foreign substrate. The two-dimensional ordering of copper adatoms is significantly affected by the presence of coadsorbed anions. Our major contribution to this field has been to develop a method of measuring the surface composition of these mixed adlayers (34–36). Knowing the surface concentrations of copper and anion, we were able to give a new interpretation to the STM data published in the literature. We will illustrate this point with the example of coadsorption of sulfate and copper at the Au(111) electrode surface. This system has been investigated by so many surface-specific techniques that it may be considered as the touchstone of surface electrochemistry.

The surface composition of this mixed adlayer is shown in Fig 6. In the presence of SO_4^{2-}, the copper deposition starts at potentials where the initial surface concentration of the anion is very small. The surface concentration of sulfate increases quickly with the copper coverage until a maximum is reached at a potential where the copper coverage is 2/3 ML. The maximum sulfate concentration corresponds to 1/3 ML. At that point the sum of the surface concentrations of copper and sulfate is equal to 1 ML. When the copper coverage increases above 2/3 ML the surface concentration of sulfate decreases to reach a limiting value of 1/6 ML at a copper coverage of 1 ML. At the same time the surface concentration of adsorbed copper becomes equal to the surface concentration of gold atoms. It is now well established that this adlayer consists of an epitaxial (1 × 1) monoalyer of Cu atoms and that the sulfate ions are adsorbed on top of the copper layer (37).

The structure corresponding to the surface concentration of copper 2/3ML and sulfate concentration 1/3 ML has been the subject of a major controversy. The STM image of the long-range structure of this adlayer is shown in Fig. 7. Similar STM images of this structure have been published before (37–42). Anions were believed to be invisible to STM and hence the images were interpreted as showing copper adatoms. This interpretation implies that copper coverage is 1/3 ML. In contrast, surface concentrations determined by electrochemical techniques and shown in Fig. 6 gave the copper coverage 2/3ML. To explain these discrepancies, we proposed (34) that, in agreement with the statistical model by Hackaby and Blum (43), the structure of the mixed overlayer corresponds to a honeycomb ($\sqrt{3} \times \sqrt{3}$)R30° lattice of Cu atoms, as shown schematically in Fig 6. We have also suggested that the STM/AFM images are images of sulfate rather than copper atoms.

To determine the location of the sulfate ions in the mixed adlayers we performed complementary X-ray absorption experiments at the Cornell High Energy Synchrotron Source (CHESS) (18, 44, 45). This was a collaborative work with T. Tyliszczak and A. Hitchcock from McMaster University. For the X-ray absorption spectrum of the mixed 2/3ML copper and 1/3ML sulfate adlayer, we performed FEFF 6.01 multiple scattering calculations using different models of the mixed adlayers. The calculations were carried out assuming a constant framework of Cu adatoms arranged in a ($\sqrt{3} \times \sqrt{3}$)R30° lattice and various positions of the sulfate ions. The spectra were calculated for sulfate ions turned either with one oxygen atom toward the centers of the honeycombs and the three other oxygens toward the solution or with three oxygens toward the honeycombs and one oxygen toward the solution. The calculations were carried out by positioning the sulfate ion in front of the honeycomb center and moving it in and out of the plane of copper atoms, in the direction normal to the surface. The experimental and calculated extended X-ray absorption fine structures (EXAFS) of these spectra are compared in Fig. 8. Here, the EXAFS spectra plot the normalized modulation of the absorption coefficient for copper atoms on the surface versus the wave vector defined as $k = \sqrt{[2m(h\nu - E_0)]}/h$, where $h\nu$ is the photon energy, E_0 is the energy of the absorption edge, and m is the electron mass. The characteristic oscillations of the normalized modulation of the absorption coefficient are caused by the scattering of photoelectrons emitted by the absorber (copper atom) from atoms present in its coordination shell. A good match between the measured and simulated spectra was observed only when (*i*) the three oxygens of the sulfate ion were directed towards the empty center of the honeycomb; (*ii*) the sulfate ion was moved above the plane of copper adatoms so that the bond angle between the oxygen and copper atoms is equal to 45°; (*iii*) each of the three oxygen atoms of the sulfate ion were coordinated to two copper atoms of the honeycomb. This model is presented in Fig. 9 (18, 44). Independently, the IBM group (46) proposed an essentially identical model on the basis of surface X-ray scattering experiments. Therefore, the XAS and SXS studies confirmed that STM and AFM images determined for this system are images of sulfate ions rather than copper atoms.

© 1999 NRC Canada

Fig. 7. STM images of the mixed adlayer formed by copper atoms (2/3 ML) coadsorbed with sulfate (1/3 ML) at the Au(111) electrode surface. The top image was acquired by recording the bottom part at potential E = 0.1 V vs. SCE, where the ($\sqrt{3} \times \sqrt{3}$)R30° structure is formed, and the top part at potential E = 0.3 V vs. SCE where copper and sulfate are desorbed from the electrode surface. That section of the image reveals the hexagonal structure of the unreconstructed Au(111) surface. The potential was stepped from E = 0.3 V to E = 0.1 V vs. SCE during the acquisition of the image. 0.1 M $KClO_4$ + 10^{-3} M $HClO_4$ + 10^{-3} M K_2SO_4 + 10^{-3} M $Cu(ClO_4)_2$ solution. The bottom image shows a long-range order for the ($\sqrt{3} \times \sqrt{3}$)R30° structure formed at E = 0.1 V vs. SCE.

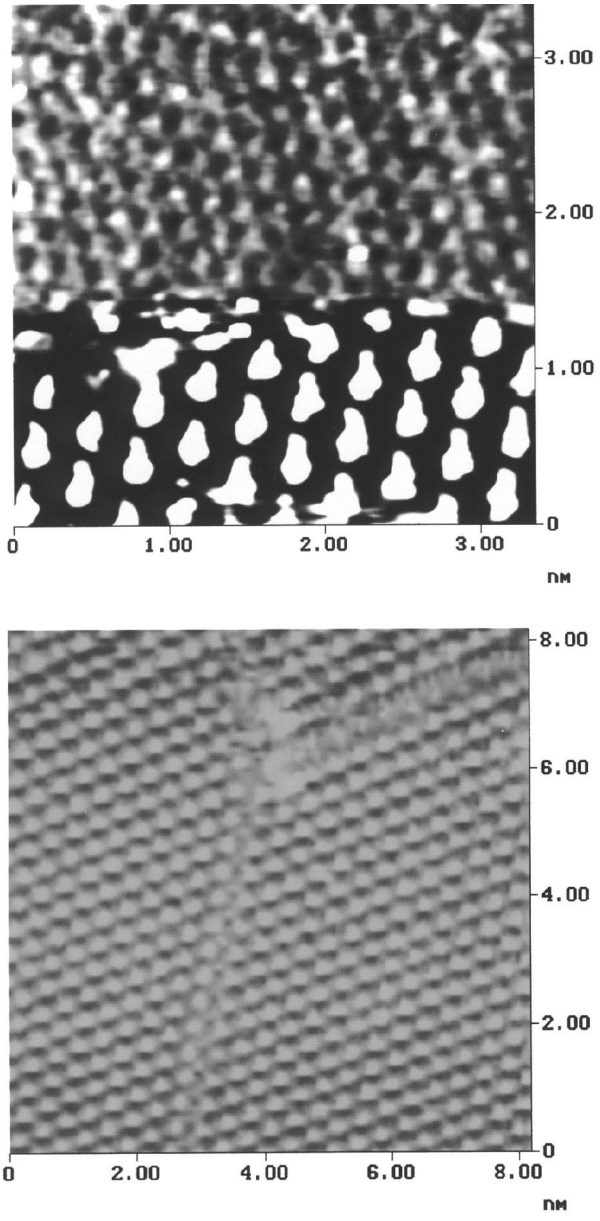

3. Surface coordination of organic molecules

A significant fraction of our efforts has been directed to the study of the coordination of organic molecules to metal electrode surfaces. Similar to the case of ionic adsorption, our strategy involved a concerted use of electrochemical methods to provide a macroscopic description of organic molecules at metal surfaces in terms of surface concentrations and Gibbs energies of adsorption, in addition to the use of spectroscopic and diffraction techniques to probe the nature of the surface coordination bond and the effect of adsorbed molecules on the electronic and crystallographic structure of the metal. Our research has focused chiefly on adsorption at gold electrodes. The results of the thermodynamic studies were described in two reviews (47, 48). Investigations of the effect of molecular adsorption on the electronic and crystallographic structure of gold single crystal electrodes by second harmonics generation are published in refs. 49–51, and by UV–visible electroreflectance are described in refs. 52 and 53. Recent surface X-ray scattering studies of the impact of organic molecules on the reconstruction of the Au(111) surface are presented therein (54, 55). Finally, we employed external reflection Fourier transform infrared (FTIR) spectroscopy to study the orientation of organic molecules at the Au(111) electrode surface (56, 57).

Fig. 8. Comparison of the experimental k weighted EXAFS $k\chi(k)$ (dotted line) with the calculated EXAFS (solid line), for the honeycomb ($\sqrt{3} \times \sqrt{3}$)R30° structure of copper and sulfate coadsorbed on the Au(111) surface (taken from ref. 18).

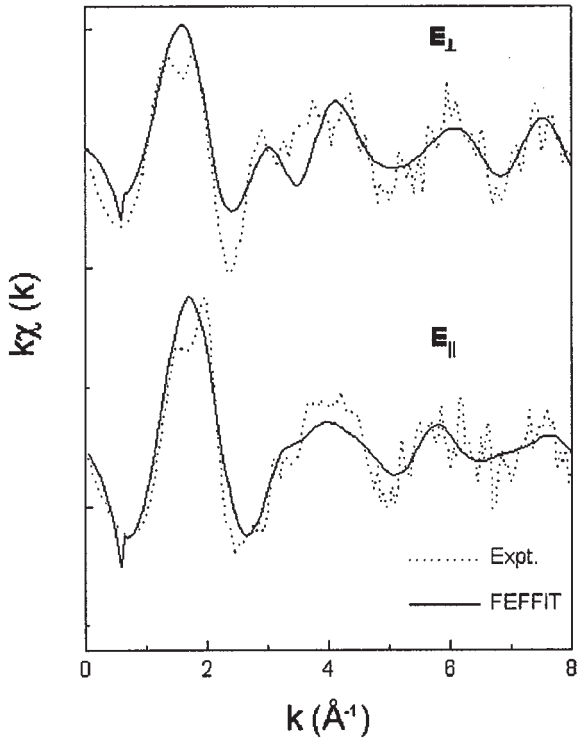

We have learned that FTIR spectroscopy is perhaps the most useful non-electrochemical method for studying the coordination of organic molecules to the surface of a metal electrode. The adsorption of organic molecules frequently has a dissociative character. The dissociation of the molecule at the electrode surface may be assisted either by the formation of the surface coordination bond or by the high electric field present at the interface. The dissociative or non-dissociative character of molecular adsorption can easily be determined with the help of the FTIR technique. We would

© 1999 NRC Canada

Fig. 9. Model for the honeycomb ($\sqrt{3} \times \sqrt{3}$)R30° structure of copper and sulfate coadsorbed on the Au(111) surface: (*a*) top view, (*b*) side view(taken from ref. 44).

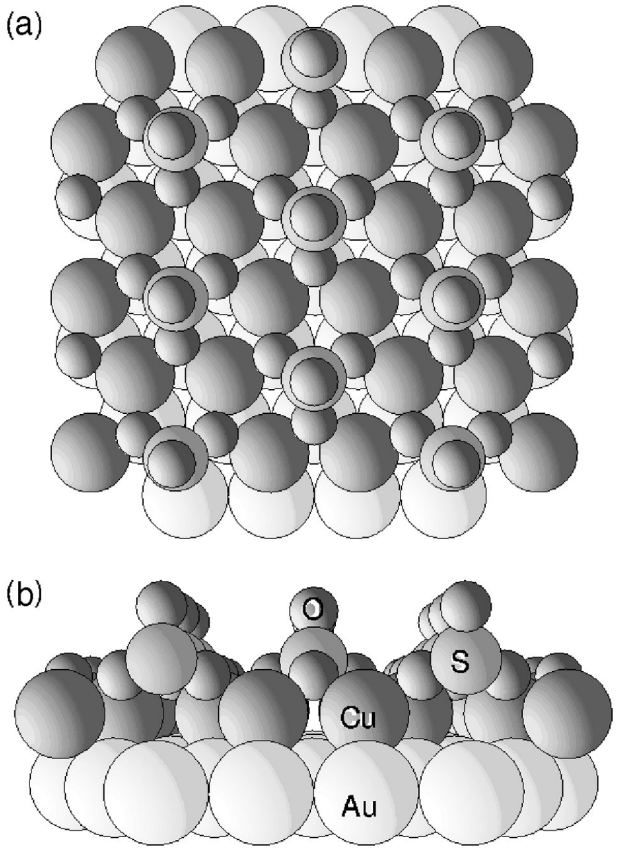

like to illustrate this point with the example of benzonitrile (BN) adsorption at the Au(111) surface. In the preceding sections, we have presented a few cases where the availability of quantitative thermodynamic data caused a reinterpretation of the results of spectroscopic or surface imaging experiments. The adsorption of BN at gold is an opposite example. FTIR studies of this system changed the interpretation of the thermodynamic data (57).

Figure 10 shows the surface concentration of BN at the Au(111) electrode surface plotted as a function of electrode potential and bulk BN concentration in 3D coordinates. The black points overlaid on these plots show the position of the pzc over the range of BN concentration studied. The adsorption isotherm displays a well-defined plateau at potentials around the pzc. The surface concentration corresponding to the plateau region is very close to the maximum packing density for adsorbed flat (π-bonded) molecules estimated to be 0.35 nmol cm^{-2}. At potentials higher than the pzc and bulk BN concentrations higher than 10^{-3} M the surface concentration increases above the plateau value. We initially interpreted this increase of the surface concentration as a potential-induced reorientation of adsorbed BN molecules from the π-bonded to the vertical N-bonded surface coordination (58).

More recently, we employed external reflection FTIR spectroscopy to verify this interpretation (57). Figure 11 compares the transmission spectrum of pure BN with the reflection spectrum recorded for the bulk BN concentration

Fig. 10. Three-dimensional plot representing the adsorption isotherms determined as a function of the electrode potential for BN adsorbed on the Au(111) electrode surface. The dots shown on the plots correspond to the position of the potential of zero charge (taken from ref. 58).

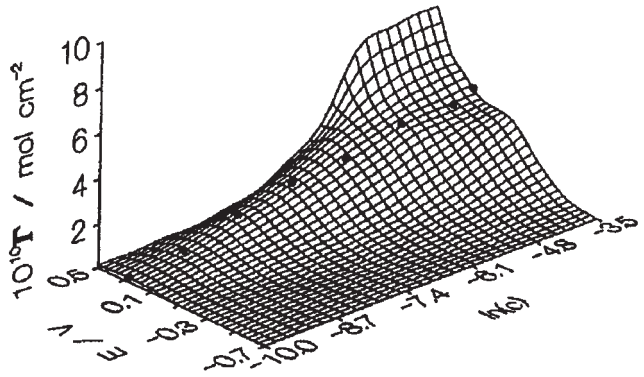

and the electrode potential corresponding to the far right corner of the isotherm in Fig 10. In reflection FTIR spectroscopy one measures electrode reflectivity at the potential at which the molecules are adsorbed at the electrode surface (E_2) and at the potential at which the molecules are desorbed from the electrode surface into the thin-layer cavity (E_1). The spectrum that is plotted is then the normalized difference between the reflectivities at E_2 and E_1. This technique is known as subtractively normalized interfacial Fourier transform infrared spectroscopy (SNIFTIRS). The SNFTIRS shows the difference between the IR spectra for molecules in solution and at the electrode surface. For these reasons the SNIFTIRS spectrum in Fig. 11 displays bipolar features. The bands that are directed below the background line (negative bands) correspond to IR absorption by adsorbed molecules, and the bands that are directed above the background (positive bands) correspond to IR absorption by molecules desorbed into the thin-layer cavity. Apparently, the bands in the SNIFTIRS do not match the bands in the transmission spectrum of pure BN. That behavior suggests that adsorption of BN has a dissociative character at positive potentials. It is well known that nitriles may be easily hydrolyzed to amides according to the reaction scheme shown at the bottom of Fig. 11. It is therefore likely that at positive potentials BN molecules are converted into benzamide (BA) as a result of a surface-catalyzed reaction.

To test this hypothesis, Fig. 12 compares transmission spectrum for pure BA with the SNIFTIR spectra for 0.03 M solutions of BA and BN, respectively. This time the fingerprint of the SNFTIR spectrum for BA matches the transmission spectrum for pure benzamide. Significantly, the shape of the SNIFTIR spectrum for benzonitrile resembles the spectrum for benzamide. This result confirms that at positive potentials and higher bulk concentrations, the adsorption of benzonitrile at the Au(111) electrode surface has a dissociative character. By careful analysis of the evolution of the SNIFTIR spectra with the electrode potential we were able to demonstrate that, at the negatively charged surface, BN adsorption has a nondissociative character. At negative charge densities, the adsorbed molecules are adsorbed flat, π-bonded to the metal. When the potential and charge are moved in the positive direction (the potential approaches the

© 1999 NRC Canada

Fig. 11. Top portion, comparison of (*a*) the transmission spectrum of liquid BN and (*b*) SNIFTIR spectrum for 0.03 M BN + 0.1 M $KClO_4$ solution acquired for the adsorption potential E_2 = +0.35 V. Bottom portion, schematic mechanism describing hydrolysis of BN (adapted from ref. 57).

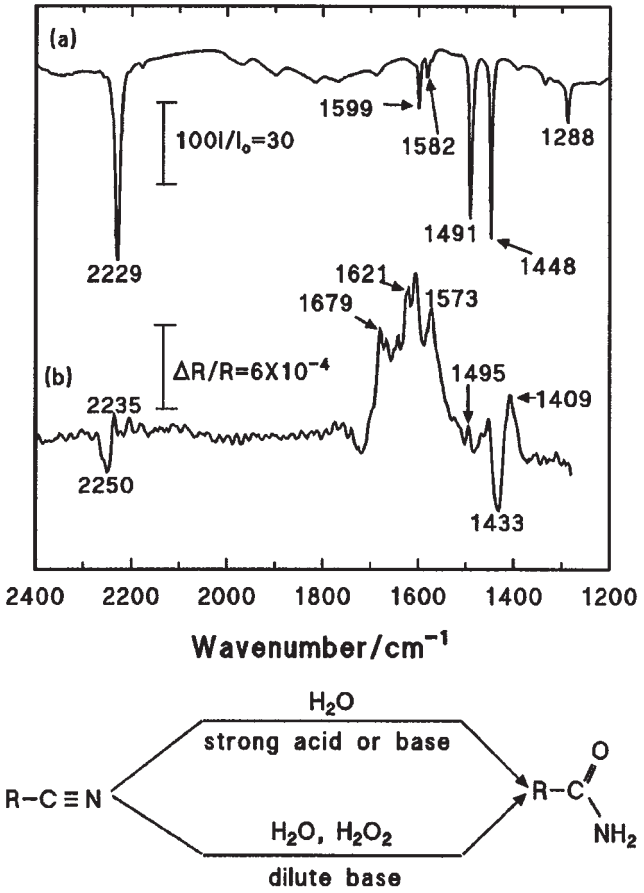

Fig. 12. Comparison of the spectra of benzamide (BA) and BN. (*a*) Transmission spectrum of BA, (*b*) and (*c*) SNIFTIR spectra obtained at E_1 = –0.75 and E_2 = +0.45 V *p*-polarized infraredbeams. (*b*) from 0.1 M $KClO_4$ + 0 03 M BA solution, and (*c*) from 0.1 M $KClO_4$ + 0.03 M BN solution (adapted from ref. 57).

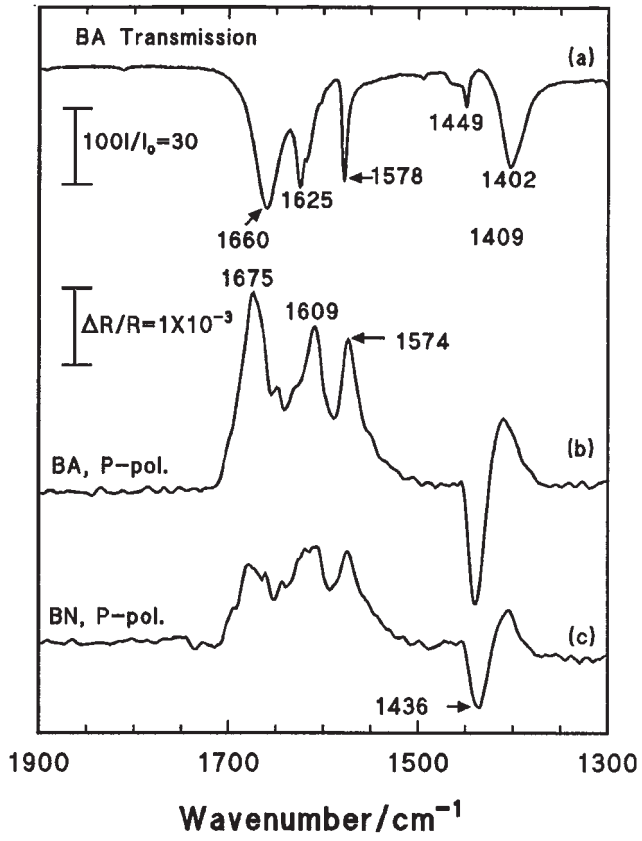

pzc) the BN molecules progressively reorient to assume a tilted N-bonded coordination and the tilt angle increases. At the positively charged surface the hydrolysis of benzonitrile begins and benzamide is formed. In this case, by a combination of thermodynamic and spectroscopic techniques, we were able to determine not only the composition of the interface but also the changes in the character of surface coordination of BN caused by a change of the electrode potential.

4. Surface aggregation phenomena

Investigations of the adsorption of amphiphilic and ionic surfactants at electrode surfaces constitute another important direction of our research. Surfactants are ubiquitous in our daily activities and find use in a host of technologies. Knowledge of the forces that control the assembly of surfactant molecules at the solid–liquid interface is vital for such traditional fields as detergency, flotation, oil recovery, and tribology (59). Thin organic films deposited at solid surfaces also find application in the fabrication of optoelectronic devices, sensors, biosensors, and chemically modified electrodes (60). Monolayers and bilayers of phospholipids deposited at solid supports are used as models of biological membranes in biomimetic research (61, 62).

Electrochemistry provides a unique opportunity to study the assembly of amphiphilic and ionic surfactants at electrode surfaces and to investigate the influence on surface aggregation phenomena of the charge at the metal. We have extensively studied the mechanism by which the long-chain surfactant molecules that are spread at the gas–solution (GS) interface in a Langmuir trough can be transferred onto the solid–solution interface of a metal electrode (metal–solution interface (MS)). We have developed an original technique in which a Wilhelmy plate (WP) is used to measure the film pressure of surfactant spread at the GS interface while the film pressure at the MS interface is simultaneously determined using in situ electrochemical methods (63–65). Using this technique, we have demonstrated that the transfer of the insoluble monolayer from the GS onto the MS interface can be investigated quantitatively. We have also employed elastic light scattering experiments and UV-visible and fluorescence spectroscopies to study how the film of surfactant molecules behaves over a wide range of potentials and charge densities applied to the metal side of the interface (66–69).

Figure 13 summarizes the main results of our research on the adsorption of 4-pentadecyl-pyridine (C_{15}-4-Py) at the Au(111) electrode surface. The metal–electrolyte interface behaves as a capacitor. Adsorption of an organic molecule

© 1999 NRC Canada

Fig. 13. A schematic of the proposed mechanism for the adsorption/desorption of a flm of insoluble surfactants from/to the Au electrode (taken from ref. 68).

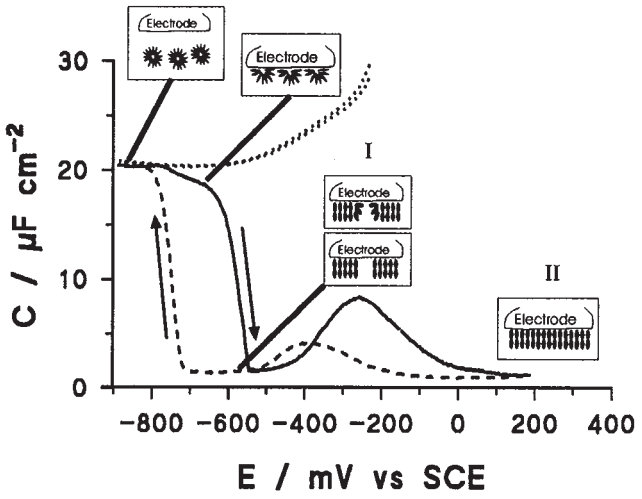

decreases the interfacial capacity. In Fig. 13, the change in the differential capacity is used to show how the structure of the film changes with the electrode potential. The cartoons depict the various states of the surfactant molecules. The dotted line represents the differential capacity of the film-free electrode. At potentials near the pzc (E = 270 mV), the surfactant spreads to form a condensed film. This could be seen as a significant decrease of the capacity. When the potential becomes more negative the capacity increases somewhat. Here, the film becomes less ordered and the organic layer is either porated or surface aggregates are formed, a prelude to desorption that occurs at the most negative potential. When the organic molecules desorb from the surface, the capacity of the electrode initially covered by the film becomes equal to the capacity of the film-free interface. Light scattering and fluorescence quenching experiments demonstrated that, at this potential, the surfactant exists as an organized structure (micelles) near the electrode surface. Interestingly, these organizations do not diffuse away from the interface and are easily readsorbed when the potential is made less negative.

When the direction of the change of potential is reversed, re-spreading of the aggregates occurs. Initially, the micelles adhere to the metal surface and form hemimicelles. The shape of the hemimicelles is controlled by the magnitude of the contact angle. The contact angle changes from 90° to 0° as the electrode potential becomes more positive and the film pressure increases. This progressive change in the contact angle explains a progressive quenching of light scattering and fluorescence within the potential range in which hemimicelles are formed (66–68). When the contact angle is large, the hemimicelle-covered electrode surface is rough and scatters electromagnetic radiation. In addition, a significant fraction of the surfactant molecules contained in a hemimicelle is sufficiently far from the metal surface so that their fluorescence is not quenched. When the contact angle decreases, the surface becomes smoother and the surfactant molecules come closer to the electrode surface. The light scattering decreases and the fluorescence is quenched. At potentials close to the pzc, the hemimicelles spread onto the metal surface to form initially a loose, and later a more ordered, film. The desorption/spreading of surfactants has similarities to the potential-dependent spreading of oil droplets onto the Hg electrode surface described recently by Zutic and co-workers (70–72). In addition, it has also been demonstrated that the so-called reductive desorption of self-assembled monolayers of thiols involves formation of micelles in the subsurface region (73, 74). It appears that all these phenomena may be described by a common model.

We provided a very convincing argument in support of the above mechanism when we succeeded in imaging hemimicelles of sodium dodecyl sulfate (SDS) and in spreading these hemimicelles into a condensed film with the help of AFM and STM microscopies (75). The adsorption of SDS at solid surfaces has long attracted the attention of the surface science community. Direct atomic force microscopy images of surface aggregates of SDS at graphite (76–79) and gold (80) surfaces have recently been published. These images were acquired without any potential control. The coupling of electrochemistry with AFM and STM imaging was accomplished in our laboratory and we have succeeded in providing the first direct visualization of the potential-controlled transformation of hemimicellar aggregates of SDS into a condensed film at the Au(111) electrode surface. Figure 14 shows an STM image of the SDS covered gold surface at a potential close to the pzc of the Au(111) electrode surface. The image shows a characteristic pattern of stripes arranged in domains rotated by 60° or 120°. The stripes have a periodicity of 4.5 ± 0.5 nm, which is close to the dimensions of a micelle of SDS in the bulk of the solution. The image shows that the gold surface is covered by a number of gold islands of monoatomic height. The adsorbed SDS molecules form the stripe-like aggregates on the top of these islands as well. They are not visible in the black and white image shown in Fig. 14, but they can be seen in color images available in the electronic version of ref. 75.

Figure 14*b* shows a high-resolution image of the stripes. This image reveals an ordered array of individual SDS molecules at the edge of the stripes and a frizzy interior of the stripes. Apparently, the surfactant molecules are immobilized at the edge of the stripe while they are relatively mobile in the stripe interior. The molecules belonging to the edges of two neighboring stripes are apparently correlated so that the border between the two stripes has a characteristic zipper-like appearance. The distance between the spots on the rim of a stripe amounts to 5 ± 0.5 Å and the distance between spots belonging to the nearest rims of the zipper amounts to 7 ± 0.5 Å. These dimensions correspond well to the size of the so called ($\sqrt{3} \times \sqrt{7}$) structure formed by sulfate adsorbed at the Au(111) electrode surface and shown earlier in Fig. 5. In fact, one can easily see that the positions of SDS molecules belonging to different zippers are also correlated to the extent that the adsorbed molecules form a long-range two-dimensional lattice. A unit cell of this lattice consists of two vectors that are 4.4 and 0.5 nm long and are oriented at an angle of 70°. We used this lattice to build a model of the hemimicelle, shown in Fig. 15. In each unit cell, we placed two flat-lying SDS molecules that are stretched out along the longer axis of the cell and are directed with the hydrocarbon tails towards the interior of the cell. In this packing the sulfate groups from four adjacent

© 1999 NRC Canada

Fig. 14. STM images of hemicylindrical SDS aggregates formed at the Au(111) electrode surface at E = 300 mV (SCE) from 16 mM SDS solution. The images were acquired with a constant tunneling current 0.2 nA and the tip voltage –200 mV; (*a*) image of a 100 × 100 nm section of the electrode area; (*b*) unfiltered high-resolution image showing individual SDS molecules at the edge of hemicylindrical aggregates (taken from ref. 75).

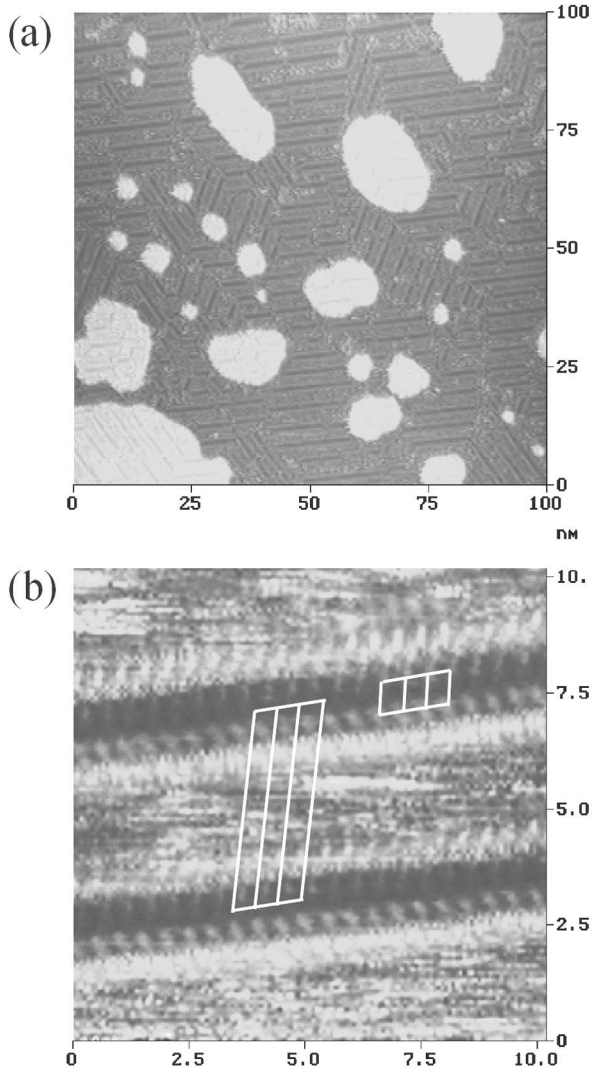

cells are arranged into the characteristic (√3 × √7) structure. We demonstrated earlier that adsorbed sulfate ions form the (√3 × √7) ordered adlayers at (111) surfaces of many metals and that this particular structure is stabilized by water molecules bridging neighboring sulfate ions through hydrogen bonding. We propose that the same interaction stabilizes the sulfate groups of the flat adsorbed SDS molecules. We also propose that the characteristic pattern of long stripe-like surface aggregates of SDS results from the interaction between the sulfate groups from adjacent hemicelles. The sulfate groups are ordered in an array of (√3 × √7) cells forming a "zipper" that cements the large unit cells of the SDS aggregates. The remaining molecules in the hemimicelle aggregate on the top of the flat adsorbed molecules to form a hemicylindrical shape as proposed by Manne (77) and Wanless and Ducker (78). The cross section of the hemimicelle along the direction of the longer vector of the unit cell is schematically shown in Fig. 14*b*. Following Wanless and Ducker (78), we have assumed that seven SDS molecules may be accommodated in the hemimicelle. The resolution of STM images is much better than the resolution of images acquired by AFM. Consequently, STM images provide details of the molecular structure of the hemimicellar aggregates formed by SDS unknown to the previous AFM studies of this system.

We have also investigated the effect of the electrode potential (charge) on the structure of the SDS aggregates (75). We have provided the first direct visualization of the potential-controlled transformation of hemimicellar aggregates of SDS into a condensed film, most likely a monolayer. Our data show that the hemimicellar aggregates are formed at small or moderate absolute charge densities and that the condensed film is formed when the amount of positive charge on the metal is either equal or superequivalent with respect to the charge of the adsorbed surfactant. These results demonstrate a tremendous potential of electrochemistry to study the influence of the charge on the solid upon the surface aggregation of surfactants. Electrochemistry provides a unique opportunity to study continuously the different stages involved in the interaction of surfactants with solid surfaces, such as adsorption of micelles, formation of hemimicelles, and spreading of hemimicelles into a condensed monolayer.

5. Summary and outlook

We have attempted to demonstrate the benefits of a concerted use of traditional (electrochemical) and nontraditional (spectroscopic, diffraction, imaging) techniques in studying the structure and composition of the solid–solution interface. The traditional methods provide fundamental information concerning the composition of the interface. They allow the measurement of the charge density at the solid surface and the characterization of the energetics of the interfacial phenomena in terms of Gibbs energies. In addition, if temperature-dependent experiments are performed, the enthalpies and entropies of the systems can be obtained (81, 82). However, if electrochemical methods are to contribute to surface science, they have to be applied to perform quantitative measurements that can be rigorously processed using the Gibbs–Duhem (electrocapillary) equation of the interface (83). Too often, however, electrochemical measurements are restricted to recording a cyclic voltammogram. The information provided by such measurements is then of a qualitative nature and attempts to estimate surface coverages from these data are based on extra-thermodynamic assumptions that are frequently erroneous.

Today, surface electrochemistry is equipped with almost all the tools that are needed for both macroscopic and microscopic description of interfacial phenomena. Many issues that were unresolved in the past may be addressed again today. The revival of electrocatalysis is perhaps the best example (84). The methodological progress has spawned new disciplines such as electrochemical nano-technology (16). Surface electrochemistry is making significant inroads into other disciplines such as materials science (85) and it is my personal opinion that, in the near future, surface electrochemistry will play a significant role in biomimetic research. Electron and ion transfer are fundamental processes in the

© 1999 NRC Canada

Fig. 15. Model of the structure of SDS aggregates built around the ($\sqrt{3} \times \sqrt{7}$) lattice: (*a*) long-range stracture; (*b*) packing of SDS molecules around the ($\sqrt{3} \times \sqrt{7}$) lattice formed by sulfate head groups hydrogen bonded through water; (*c*) side view of the hemimicellar structure(taken from ref. 75).

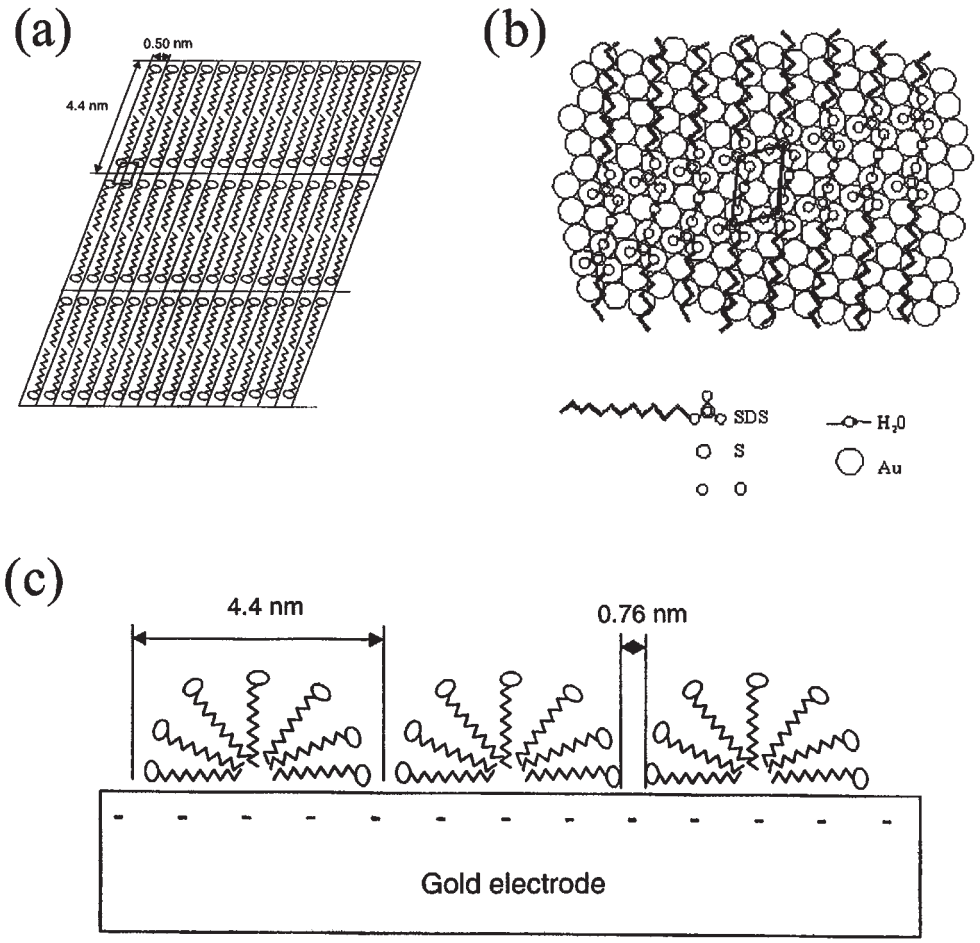

activity of biological membranes. These processes also play a central role in electrochemical science. Fortunately, electrochemistry is well equipped to study these reactions. It is already known that phospholipid bilayers may be deposited onto nonconductive solids and we have just learned that they may also be coated onto a metal electrode surface (61, 62). The macroscopic and microscopic techniques of surface electrochemistry may therefore be employed to study membrane processes. This will certainly constitute an important thrust in our research.

Acknowledgements

I would like to acknowledge the work of my students. The studies of ionic adsorption were carried out by Z. Shi, S. Wu, A. Chen, W. Savich, X. Cai, and N. Li. The coordination of organic molecules was investigated by J. Richer, L. Stolberg, A. Iannelli, S. Morin, A. Chen, and H.-Q. Li. The work on Langmuir–Blodgett films was the effort of D. Bizzotto, J. Noel, V. Zamlynny, H. -Q. Li, and J. Rubinstein. The surface aggregation phenomena were investigated by I. Burgess, C. Jeffrey, and X. Cai. The help of Dr. G. Szymanski was invaluable for many of these projects. Our work involved many national and international collaborations. X-ray absorption experiments were carried out in collaboration with A. Hitchcock and T. Tyliszczak from McMaster University. Surface X-ray scattering involved collaboration with B.M. Ocko, O.M. Magnussen, and Th. Wandlowski from Brookhaven National Laboratory. I would like also to acknowledge many years of collaboration with D.M. Kolb of the University of Ulm, B. Pettinger of the Fritz Haber Institute in Berlin, Z. Galus of the University of Warsaw, S.-G. Sun of Xiamen University, D.E. Irish of the University of Waterloo, and S. Roscoe of Acadia University. This research was supported by grants from the Natural Sciences and Engineering Research Council of Canada.

References

1. B. Beden and C. Lamy. *In* Spectroelectrochemistry: theory and practice. *Edited by* R.J. Gale. Plenum Press, New York. 1988. pp. 189–261.
2. S.M. Stole, D.D. Popenoe, and M.D. Porter. *In* Electrochemical interfaces. Techiques for in situ interface characterization. *Edited by* H.D. Abruna. VCH, New York. 1992. pp. 341–412.
3. R.J. Nichols. *In* Adsorption of molecules at metal electrodes. *Edited by* J. Lipkowski and P.N. Ross. VCH, New York. 1992. pp. 347–389.

© 1999 NRC Canada

4. S.-G. Sun. *In* Electrocatalysis. *Edited by* J. Lipkowski and P.N. Ross. VCH–Wiley, New York. 1998. pp. 243–290.
5. H.D. Abruna (*Editor*). Electrochemical interfaces. Techiques for in situ interface characterization. VCH, New York. 1992.
6. M.F. Toney and O.R. Melroy. *In* Electrochemical interfaces. Techiques for in situ interface characterization. *Edited by* H.D. Abruna. VCH, New York. 1992. pp. 57–129.
7. C.A. Melandres and A. Tadjeddine (*Editors*). Synchrotron techniques in interfacial electrochemistry. Kluwer Academic Publishers, Dordrecht. 1994.
8. H.-H. Strehblow (*Editor*). Synchrotron Radiat. News (special issue on electrochemistry), **11**, no. 3 (1998).
9. D.M. Kolb. *In* Spectroelectrochemistry theory and practice. *Edited by* R.J. Gale. Plenum Press, New York. 1988. pp. 87–188.
10. G.L. Richmond. *In* Electrochemical interfaces. Techiques for in situ interface characterization. *Edited by* H.D. Abruna. VCH, New York. 1992. pp. 267–337.
11. B. Pettinger, C. Bilger, J. Lipkowski, and W. Schmickler. *In* Interfacial electrochemistry, theory, experiment and applications. *Edited by* A. Wieckowski. Marcel Dekker, New York. 1999. In press.
12. W. Schmickler. Chem. Rev. **96**, 3177 (1996).
13. J. Lipkowski and P.N. Ross (*Editors*). Structure of electrified interfaces. VCH, New York. 1993.
14. A. Gewirth and A. Sigenthaler (*Editors*). Nanoscale probes of the solid/liquid interface. Kluwer Academic Publishers, Dordrecht. 1995.
15. J. Lipkowski and P.N. Ross (*Editors*). Imaging of surfaces and interfaces. Wiley–VCH, New York. 1999.
16. W.J. Lorenz and W. Plieth (*Editors*). Electrochemical nanotechnology. Wiley–VCH, New York. 1998.
17. J. Lipkowski, Z. Shi, A. Chen, B. Pettinger, and C. Bilger. Electrochim. Acta, **43**, 2875 (1998).
18. T. Tyliszczak, A. Hitchcock, S. Wu, A. Chen, G. Szymanski, and J. Lipkowski. Synchrotron Radiat. News, **11**, 31 (1998).
19. J. Lipkowski, X. Cai, A. Chen, Z. Shi, G. Szymanski, T. Tyliszczak, and A. P. Hitchcock. NATO ASI Ser. Metal–ligand interaction in chemistry, physics and biology. *Edited by* N. Rousso and D. Salahub. Kluwer Academic Publishers, Dordrecht. 1999.
20. W. Schmickler. J. Electroanal. Chem. **249**, 25 (1988).
21. X. Gao, G.J. Edens, and M.J. Weaver. J. Electroanal. Chem. **376**, 21 (1994).
22. D.M. Kolb. Prog. Surf. Sci. **51**, 109 (1996).
23. J. Wang, B.M. Ocko, A.J. Devenport, and H.S. Isaacs. Phys. Rev. B: Condens. Matter, **34**, 10 321 (1992).
24. B.M. Ocko, O.M. Magnussen, J. Wang, R.R. Adzic, Z. Shi, and J. Lipkowski. J. Electroanal. Chem. **376**, 35 (1994).
25. B.M. Ocko and Th. Wandlowski. *In* Electrochemical synthesis and modification of materials. *Edited by* E.P. Andicacos, J.-P. Deplancke, S. Corcoran, and T. Moffat. Mater. Res. Soc. Symp. Proc. **455**, 55 (1997).
26. A.M. Funtikov, U. Linke, U. Stimming, and R. Vogel. Surf. Sci. **324**, L343 (1995).
27. A.M. Funtikov, U. Stimming, and R. Vogel. J. Electroanal. Chem. **428**, 147 (1997).
28. L.-J. Wan, S.-L. Yau, and K. Itaya. J. Phys. Chem. **99**, 9507 (1995).
29. W.H. Li and R.J. Nichols. J. Electroanal. Chem. **459**, 153 (1998).
30. O.M. Magnussen, J. Hageboeck, J. Hotlos, and R.J. Behm. Faraday Discuss. Chem. Soc. **94**, 329 (1992).
31. Z. Shi, J. Lipkowski, M. Gamboa, P. Zelenay, and A. Wieckowski. J. Electroanal. Chem. **366**, 317 (1994).
32. G.J. Eden, X. Gao, and M.J. Weaver. J. Electroanal. Chem. **375**, 357 (1994).
33. K. Ataka and M. Osawa. Langmuir, **14**, 951 (1998).
34. Z. Shi and J. Lipkowski. J. Electroanal. Chem. **365**, 303 (1994).
35. Z. Shi and J. Lipkowski. J. Electroanal. Chem. **364**, 289 (1994).
36. Z. Shi, S. Wu, and J. Lipkowski. Electrochim. Acta, **40**, 9 (1995).
37. D.M. Kolb. The initial stages of metal deposition: an atomistic view. Schering Lecture. Schering Lecture's Publications, Vol. 1. Berlin. 1991.
38. O.M. Magnussen, J. Hotlos, R.J. Nichols, D.M. Kolb, and R.J. Behm. Phys. Rev. Lett. **64**, 2929 (1990).
39. J. Hotlos, O.M. Magnussen, and R.J. Behm. Surf. Sci. **335**, 129 (1995).
40. W. Haiss, D. Lackey, J.K. Sass, H. Meyer, and R.J. Nichols. Chem. Phys. Lett. **200**, 343 (1994).
41. T. Hachiya, T. Honobo, and K. Itaya. J. Electroanal. Chem. **315**, 275 (1991).
42. S. Manne, P.K. Hansma, J. Massie, B.V. Elings, and A.A. Gewirth. Science (Washington, D.C.), **251**, 183 (1991).
43. D.A. Huckaby and L. Blum. J. Electroanal. Chem. **315**, 255 (1991).
44. S. Wu, J. Lipkowski, T. Tyliszczak, and H.P. Hitchcock. Prog. Surf. Sci. **50**, 227 (1995).
45. S. Wu, J. Lipkowski, T. Tyliszczak, and H. P. Hitchcock. J. Phys. Chem. **101**, 10 310 (1997).
46. M.F. Toney, J.N. Howard, J. Richer, D. Yee, and L.B. Sorensen. Phys. Rev. Lett. **75**, 4472 (1995).
47. J. Lipkowski and L. Stolberg. *In* Adsorption of molecules at metal electrodes. *Edited by* J. Lipkowski and P.N. Ross. VCH Publishers, New York. 1992. pp. 171–238.
48. J. Lipkowski, L. Stolberg, D.-F. Yang, B. Pettinger, S. Mirwald, F. Henglein, and D.M. Kolb. Electrochim. Acta, **39**, 1057 (1994).
49. B. Pettinger, S. Mirwald, and J. Lipkowski. Ber. Bunsen-Ges. Phys. Chem. **97**, 395 (1993).
50. D.F. Yang, D. Bizzotto, J. Lipkowski, B. Pettinger, and S. Mirwald. J. Phys. Chem. **98**, 7083 (1994).
51. B. Pettinger, J. Lipkowski, and S. Mirwald. Electrochim. Acta, **40**, 133 (1994).
52. F. Henglein, D.M. Kolb, and J. Lipkowski. J. Electroanal. Chem. **303**, 245 (1991).
53. F. Henglein, D.M. Kolb, L. Stolberg, and J. Lipkowski. Surf. Sci. **291**, 325 (1993).
54. Th. Wandlowski, B. Ocko, O.M. Magnussen, S. Wu, and J. Lipkowski. J. Electroanal. Chem. **409**, 155 (1996).
55. S. Wu, J. Lipkowski, O.M. Magnussen, B.M. Ocko, and Th. Wandlowski. J. Electroanal. Chem. **446**, 67 (1998).
56. A. Chen, S.-G. Sun, D.-F. Yang, B. Pettiner, and J. Lipkowski. Can. J. Chem. **74**, 2321 (1996).
57. A. Chen, J. Richer, S.G. Roscoe, and J. Lipkowski. Langmuir, **13**, 4737 (1997).
58. J. Richer, A. Iannelli, and J. Lipkowski. J. Electroanal. Chem. **324**, 339 (1992).
59. A.W. Adamson. Physical chemistry of surfaces. 5th ed. John Wiley and Sons, New York. 1990.
60. J. Swalen, D. Allara, D. Andrade, E.A. Chandross, S. Garoff, J. Israelachivili, T.J. McCarthy, R. Murray, R.F. Pease, J.F. Rabolt, K.J. Wynne, and H. Yu. Langmuir, **3**, 932 (1987).
61. E. Sackmann. Science (Washington, D.C.), **271**, 43 (1996).
62. M. Stelze, W. Weissmuller, and E. Sackmann. J. Phys. Chem. **97**, 2974 (1993).

© 1999 NRC Canada

63. J. Noël, D. Bizzotto, and J. Lipkowski. J. Electroanal. Chem. **344**, 343 (1993).
64. D. Bizzotto, J. Noël, and J. Lipkowski. Thin Solid Films, **248**, 69 (1993).
65. D. Bizzotto, J. Noël, and J. Lipkowski. J. Electroanal. Chem. **369**, 259 (1994).
66. D. Bizzotto and J. Lipkowski. J. Electroanal. Chem. **409**,33(1996)
67. D. Bizzotto and J. Lipkowski. J. Prog. Colloid Polym. Sci. **103**, 201 (1997).
68. T. Sagara, V. Zamlynny, D. Bizzotto, A. McAlees, R. McCrindle, and J. Lipkowski. Isr. J. Chem. **37**, 197 (1997).
69. D. Bizzotto, V. Zamlynny, I. Burgess, C.A. Jeffey, H.-Q. Li, J. Rubinstein, Z. Galus, A. Nelson, B. Pettinger, A.R. Merill, and J. Lipkowski. *In* Interfacial electrochemistry, theory, experiment and applications. *Edited by* A.Wieckowski. Marcel Dekker, New York. 1999.
70. V. Zutic, S. Kovac, J. Tomaic, and V. Sveltlicic. J. Electroanal. Chem. **349**, 173 (1993).
71. N. Ivosevic, J. Tomaic, and V. Zutic. Langmuir, **10**, 2415 (1994).
72. N. Ivosevic and V. Zutic. Langmuir, **14**, 231 (1998).
73. D.F. Yang, C.P. Wilde, and M. Morin. Langmuir, **13**, 243 (1997).
74. C.J. Zhong, J. Zak, and M.D. Porter. J. Electroanal. Chem. **421**, 9 (1997).
75. I. Burgess, C.A. Jeffrey, X. Cai, G. Szymanski, Z. Galus, and J. Lipkowski. Langmuir, **15,** 2607 (1999).
76. S. Manne and H.E. Gaub. Science (Washington, D.C.), **270**, 1480 (1995).
77. S. Manne. Prog. Colloid Polym. Sci. **103**, 226 (1997).
78. E.J. Wanless and W.A. Ducker. Langmuir, **12**, 5915 (1996).
79. E.J. Wanless, T.W. Davey, and W.A. Ducker. Langmuir, **13**, 4223 (1997).
80. M. Jaschke, H.-J. Butt, H.E. Gaub, and S. Manne. Langmuir, **13**, 1381 (1997).
81. G. Jerkiewicz and A. Zolfaghari. J. Electrochem. Soc. **143**, 1240 (1996).
82. G. Jerkiewicz and A. Zolfaghari. J. Phys. Chem. **100**, 8454 (1996).
83. J. Lipkowski, W. Schmickler, D.M. Kolb, and R. Parsons. **452**, 193 (1998).
84. J. Lipkowski and P.N. Ross (*Editors*). Electrocatalysis. Wiley–VCH, New York. 1998.
85. J. Lipkowski and P.N. Ross (*Editors*). Electrochemistry of novel materials. Wiley–VCH, New York. 1994.

© 1999 NRC Canada

Étude expérimentale et modélisation des réactions d'oxydation du néopentane et de l'isopentane

S. Taconnet, Y. Simon, G. Scacchi et F. Baronnet

Résumé : Les phénomènes responsables de la différence de comportement des hydrocarbures vis à vis de l'autoinflammation sont encore, à ce jour, très mal connus. Nous avons donc tenté de déterminer les processus qui sont à l'origine du phénomène de cliquetis dans les moteurs à allumage commandé à partir de l'étude des mécanismes réactionnels d'hydrocarbures d'indice d'octane différents : le néopentane et l'isopentane. Cette étude a été réalisée à 873 K, en utilisant un réacteur continu auto-agité par jets gazeux. Les résultats expérimentaux ont été modélisés à l'aide du logiciel de simulation de mécanismes réactionnels CHEMKIN. Ces mécanismes ont alors été comparés à ceux du *n*-pentane, du cyclopentane, du *n*-heptane et de l'isooctane déterminés, dans des conditions expérimentales identiques, lors d'études que nous avons effectuées antérieurement. Cette comparaison montre que l'on peut expliquer, au moins en partie, la sensibilité d'un hydrocarbure à l'autoinflammation par la présence, dans le milieu réactionnel, de radicaux stabilisés par résonance.

Mots clés : oxydation, néopentane, isopentane, autoinflammation, modélisation.

Abstract: The different behaviour of hydrocarbons with respect to autoignition phenomena is, at present, not yet fully explained. We have therefore investigated the oxidation of two alkanes that have different octane numbers: neopentane (85.5) and isopentane (92.3), to obtain a better understanding of their reaction mechanisms, in particular, those reactions that are responsible for the onset of knock in spark ignition engines. The experimental study was performed at 873 K in a jet-stirred flow reaction vessel. The oxidation mechanisms were simplified by using the CHEMKIN programme of simulation of reaction mechanisms. These mechanisms were compared to those accounting for the oxidation of *n*-pentane, cyclopentane, *n*-heptane, and isooctane that we have previously studied. This comparison shows that the different behaviour of these hydrocarbons can be explained, at least in part, by the presence, in the reaction medium, of resonance-stabilized radicals.

Key words: oxidation, neopentane, isopentane, autoignition, modelling.

Introduction

Dès 1921, T. Midgley et T.A. Boyd, chercheurs des laboratoires de la société « General Motors », découvrirent que l'on pouvait limiter les phénomènes de cliquetis en ajoutant aux essences de petites quantités d'organométalliques. Parmi ces additifs, permettant l'utilisation de taux de compression élevés dans les moteurs, les plus efficaces sont les alkyles de plomb. Le plomb tétraéthyle puis le plomb tétraméthyle furent utilisés comme additifs antidétonants pendant plus de 50 ans, jusqu'à ce que de nouvelles normes antipollution apparaissent aux États Unis dans les années 70 puis en Europe dans les années 80 et imposent la suppression de ces dérivés du plomb dans les essences, incompatibles avec l'utilisation de pots catalytiques.

Le développement de l'essence sans plomb a relancé, ces dernières années, l'intérêt pour les recherches sur les mécanismes d'oxydation des hydrocarbures (1–4). En effet, l'abandon des additifs et la recherche de carburants d'indice d'octane élevé nécessitent une meilleure compréhension du mécanisme de combustion.

Dans cette optique, nous avons tenté d'élucider les mécanismes d'oxydation de deux hydrocarbures (5) : l'isopentane (méthyl-2 butane) d'indice d'octane recherche (RON) : 92,3 et le néopentane (diméthyl-2,2 propane) d'indice d'octane recherche : 85,5.

Ces recherches entrent dans le cadre d'une étude générale sur la compréhension des mécanismes chimiques à l'origine des phénomènes d'autoinflammation et font suite aux recherches déjà effectuées sur les mécanismes d'oxydation du *n*-pentane, du cyclopentane (6), du *n*-heptane et de l'isooctane (7). En particulier, cette étude permettra d'examiner l'influence de la structure sur le comportement de quatre hydrocarbures saturés en C5.

Dans cet article nous présentons une étude expérimentale des réactions d'oxydation de l'isopentane et du néopentane

Reçu le 12 mai 1998.[1]

S. Taconnet, Y. Simon,[2] G. Scacchi et F. Baronnet. Département de chimie physique des réactions, UMR n° 7630 du Centre national de la recherche scientifique, Institut national polytechnique de Lorraine, École nationale supérieure des industries chimiques, 1, rue Grandville, BP 451, 54001 Nancy Cedex, France.

1. Révision reçue le 8 février 1999.
2. Auteur à qui adresser toute correspondance. Tél : 33 (0)3 83 17 51 22. Téléc : 33 (0)3 83 37 81 20. Mél : dcpr@ensic.u-nancy.fr

 © 1999 CNRC Canada

Fig. 1. Schéma de l'appareillage expérimental. VP : vanne pointeau. V_1, V_2 : vannes électromagnétiques. A_1, A_2 : ampoules chromatographiques. C_1, C_2 : capteurs de pression. D_1, D_2 : débitmètres massiques. S : volume tampon.

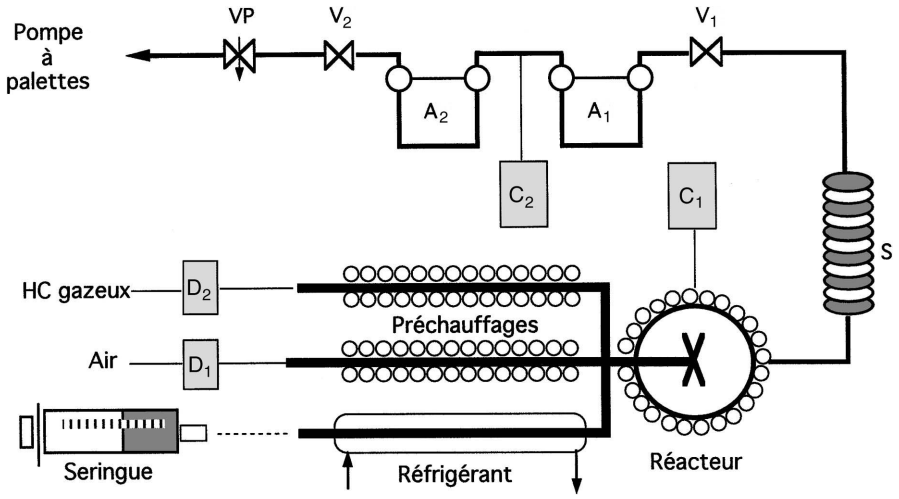

mises en oeuvre dans un réacteur continu auto-agité par jets gazeux. Ces résultats expérimentaux ont permis, grâce à une simulation, de présenter les mécanismes réactionnels simplifiés de l'oxydation de ces deux hydrocarbures.

Technique expérimentale

L'étude expérimentale de l'oxydation de l'isopentane et du néopentane est réalisée à 873 K en utilisant un réacteur continu auto-agité par jets gazeux dont le chauffage est assuré par des résistances électriques isolées de marque Thermocoax.

L'alimentation du réacteur se fait grâce à trois voies d'alimentation en réactifs (fig. 1) : (*i*) une voie d'introduction des hydrocarbures gazeux (néopentane), préchauffée à 723 K; (*ii*) une voie d'introduction des hydrocarbures liquides (isopentane); et (*iii*) une voie d'alimentation en air, préchauffée à 823 K.

Les débits d'air et d'hydrocarbure gazeux sont régulés et mesurés par les débitmètres massiques (RDM 280 de la société Air Liquide) D_1 et D_2.

Le débit d'hydrocarbure liquide est régulé, quant à lui, grâce à un pousse-seringue (Precidor 5003).

La prise d'échantillon s'effectue à l'aide de deux ampoules de chromatographie A_1 et A_2 montées en série et encadrées par deux vannes électromagnétiques qui se ferment successivement (V_2 puis V_1) pour isoler le flux gazeux sortant du réacteur. La pression totale dans les ampoules est mesurée par un capteur de pression C_2. Les produits de réaction sont analysés par chromatographie en phase gazeuse.

Enfin, le circuit se termine par une vanne pointeau VP qui permet de régler le débit total des gaz sortant du réacteur et ainsi modifier le temps de passage tout en gardant une pression totale constante dans le réacteur (mesurée par le capteur C_1). La circulation des gaz est assurée par une pompe à palettes.

Afin d'éviter des problèmes de vaporisation de l'isopentane liquide au niveau du système d'injection, la pression totale au sein du réacteur a été fixée à 630 torr (1 torr = 133,3 Pa), valeur supérieure à la pression de vapeur saturante de ce composé. Les pressions partielles d'oxygène et d'hydrocarbure ont été choisies de façon à obtenir un rapport hydrocarbure/O_2 de 1/4 (richesse 2). Des conditions expérimentales identiques ont été utilisées lors de l'étude de l'oxydation du néopentane.

Résultats expérimentaux

Les réactions d'oxydation de l'isopentane et du néopentane ont été étudiées pour des temps de passage, dans le réacteur, variant entre 0,4 et 1,2 s. Les réactifs et produits de réaction ont été dosés par chromatographie en phase gazeuse. La majorité des produits (hydrocarbures) a été analysée sur un chromatographe Shimadzu Mini 3 équipé d'un détecteur à ionisation de flamme. La colonne utilisée a une longueur de 5 m et un diamètre de 1/4 de pouce; elle est remplie de squalane et est maintenue à une température constante de 60°C. Les bilans effectués sur les éléments C, H et O (proches de 100 % pour les temps de passage les plus faibles) montrent qu'aucun produit primaire[3] important n'a été omis.

Oxydation du néopentane

L'étude a été menée pour des avancements de réaction, par rapport au néopentane, variant entre 10 % (pour un temps de passage : τ = 0,4 s) et 17 % (τ = 1,2 s). La consommation en O_2 est de seulement 2 % pour un temps de passage, dans le réacteur, de 1,2 s.

Dans le cas de l'oxydation du néopentane, les produits identifiés et dosés sont les suivants : hydrogène, méthane, éthylène, éthane, propène, isobutène, dioxyde de carbone et eau. Les courbes de formation de ces composés sont représentées sur les figures 2, 3 et 4. On peut noter l'allure inhabituelle de la courbe de formation de l'hydrogène dont nous reparlerons par la suite.

[3] Un produit de réaction est dit « primaire » lorsqu'il est formé à partir des réactifs ou des radicaux libres uniquement. Il est dit « secondaire » lorsqu'il est formé à partir des produits primaires. Un produit primaire se caractérise par une vitesse de formation initiale non nulle, alors qu'un produit secondaire possède une vitesse de formation initiale nulle.

© 1999 CNRC Canada

Fig. 2. Oxydation du néopentane à 873 K. Courbes de formation de CH_4 et $isoC_4H_8$.

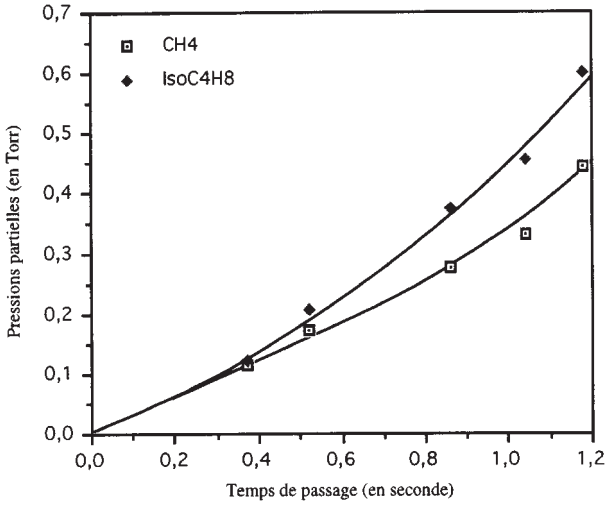

Fig. 3. Oxydation du néopentane à 873 K. Courbes de formation de C_2H_4, C_2H_6 et C_3H_6.

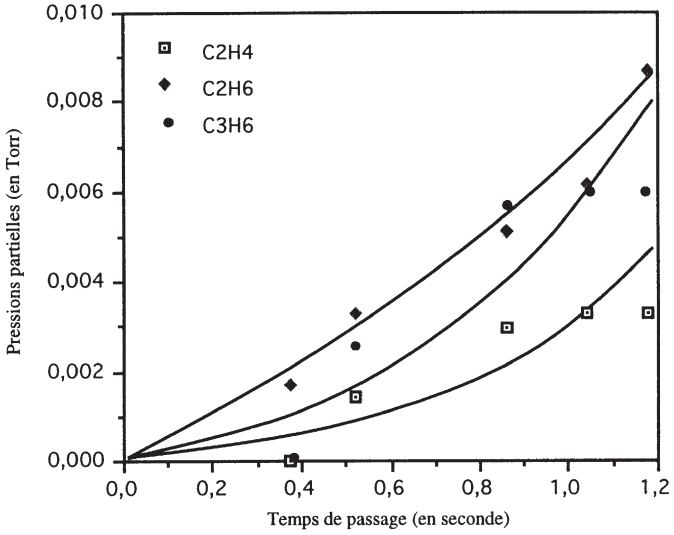

Le caractère primaire ou secondaire des produits de réaction a été déterminé en traçant les diagrammes « horizontaux » correspondants (figs. 5, 6 et 7). Ces diagrammes sont tracés en portant le pourcentage molaire du produit considéré par rapport à l'ensemble des produits dosés (réactifs non compris) en fonction du temps de passage. Sur ces diagrammes, le caractère primaire d'un composé est caractérisé par une courbe ne passant pas par l'origine, alors que, au contraire, le caractère secondaire se distingue par une courbe passant par l'origine. En effet, un produit secondaire (vitesse initiale nulle) est absent du milieu réactionnel pour des avancements très faibles; la limite du pourcentage molaire de ce composé par rapport à l'ensemble des produits formés tend vers 0 quand le temps de passage tend vers 0. Par contre, un produit primaire (vitesse initiale non nulle) est déjà présent dès les premiers instants de la réaction, le pourcentage considéré plus haut aura donc une limite différente de 0 quand le temps de passage tend vers 0. Les diagrammes « horizontaux » (figs. 5, 6 et 7) montrent que l'isobutène, le

Fig. 4. Oxydation du néopentane à 873 K. Courbes de formation de H_2, CO_2 et H_2O.

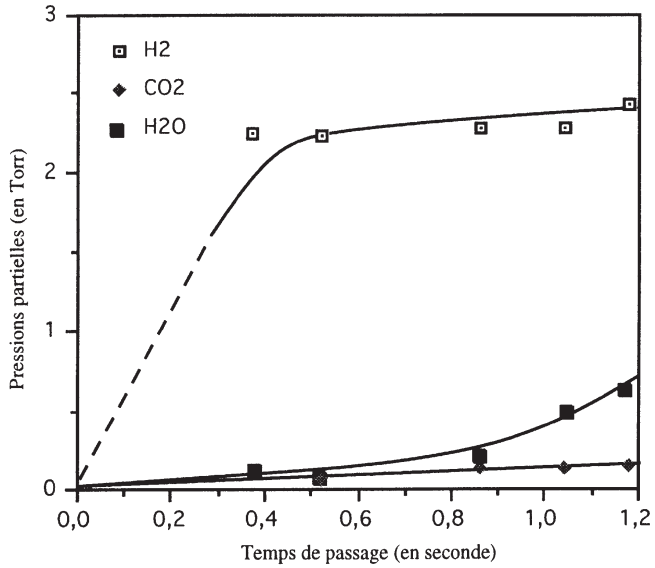

Fig. 5. Oxydation du néopentane à 873 K. Répartition des produits de la réaction en fonction du temps de passage pour CH_4 et $isoC_4H_8$.

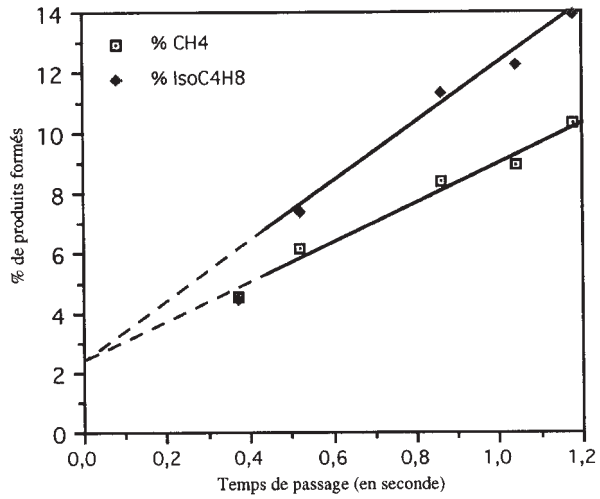

méthane et l'hydrogène sont des produits primaires, alors que l'éthylène, le propène et le dioxyde de carbone sont secondaires. Il subsiste cependant un doute quant au caractère primaire ou secondaire de l'eau et de l'éthane.

Oxydation de l'isopentane

La réaction d'oxydation de l'isopentane a été étudiée pour des avancements, par rapport à l'hydrocarbure, variant de quelques % (non mesurables) à 0,4 s jusqu'à 37 % à 1,2 s. La consommation d'oxygène atteint, quant à elle, 7 % pour le temps de passage le plus élevé.

Cette étude a permis d'identifier 15 produits d'oxydation différents : hydrogène, méthane, éthylène, propène, allène, butène-1, isobutène, butadiène-1,3, butènes-2 *cis* et *trans*, méthyl-3 butène-1, méthyl-2 butène-1, méthyl-2 butène-2, dioxyde de carbone et eau.

L'allène a été identifié mais est présent en quantité trop faible pour pouvoir être dosé. Les courbes de formation des

© 1999 CNRC Canada

Fig. 6. Oxydation du néopentane à 873 K. Répartition des produits de la réaction en fonction du temps de passage pour C_2H_4, C_2H_6 et C_3H_6.

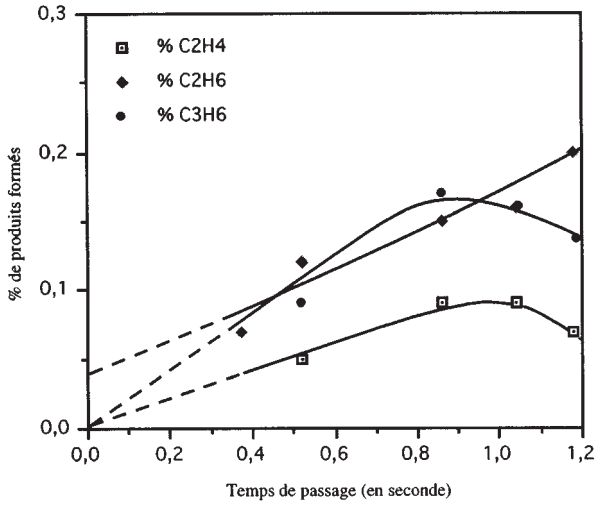

Fig. 7. Oxydation du néopentane à 873 K Répartition des produits de la réaction en fonction du temps de passage pour H_2, CO_2 et H_2O.

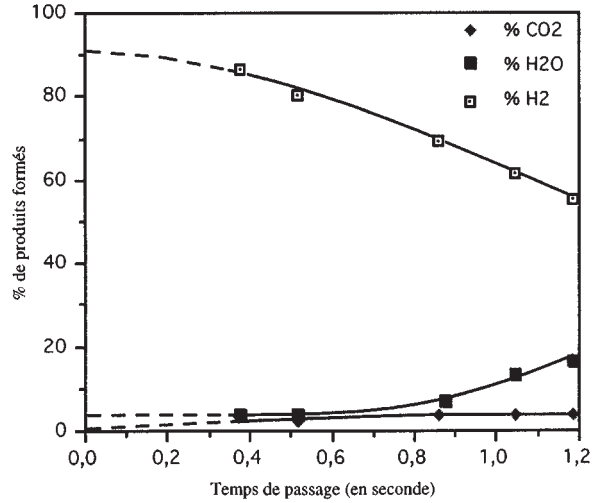

produits de réaction sont représentées sur les figures 8, 9 et 10.

L'analyse des diagrammes « horizontaux » (figs. 11, 12 et 13) montre que tous les produits dosés sont primaires, sauf le butadiène-1,3 et peut-être le méthyl-3 butène-1. Dans le cas de CO_2 et H_2O, la dispersion des points expérimentaux est telle que l'on ne peut déterminer si la courbe passe ou non par l'origine. Comme dans le cas du néopentane, l'allure de la courbe de formation de l'hydrogène sera discutée par la suite.

Interprétation des résultats expérimentaux

Les réactions d'oxydation des hydrocarbures peuvent évoluer suivant deux voies très différentes en fonction du domaine de température exploré. Cette caractéristique provient

Fig. 8. Oxydation de l'isopentane à 873 K. Courbes de formation de CH_4, C_2H_4, C_3H_6, 1-C_4H_8, 2-C_4H_8, isoC_4H_8 et 1,3-C_4H_6.

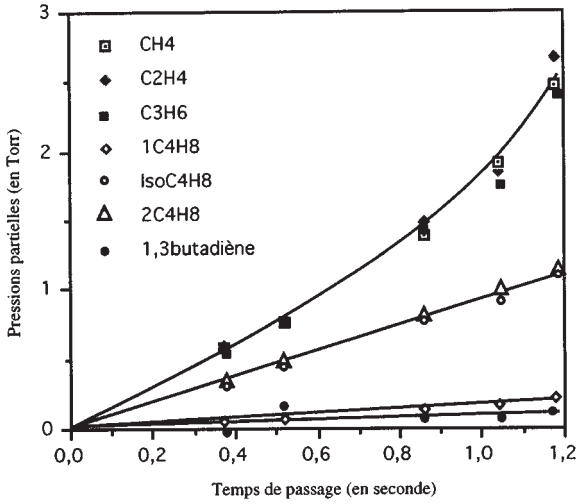

Fig. 9. Oxydation de l'isopentane à 873 K. Courbes de formation de méthyl-2 butène-1, méthyl-2 butène-2 et méthyl-3 butène-1.

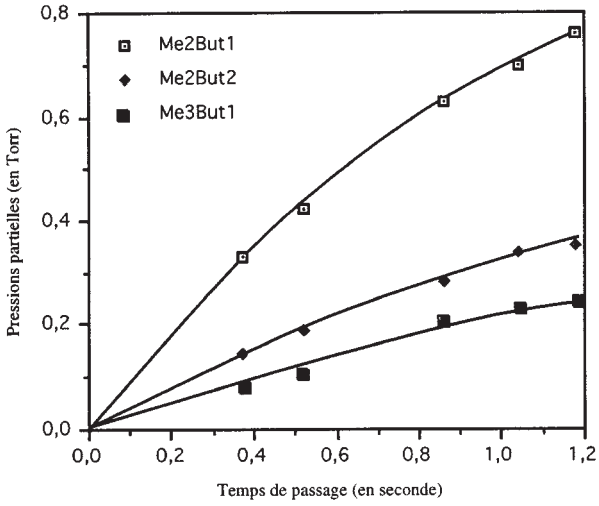

Fig. 10. Oxydation de l'isopentane à 873 K. Courbes de formation de H_2, CO_2 et H_2O.

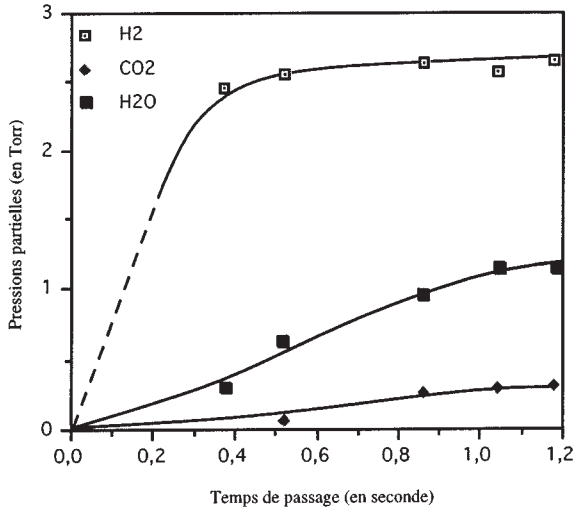

© 1999 CNRC Canada

Fig. 11. Oxydation de l'isopentane à 873 K. Répartition des produits de la réaction en fonction du temps de passage pour CH_4, C_2H_4, C_3H_6, 1-C_4H_8, isoC_4H_8 et 1,3-C_4H_6.

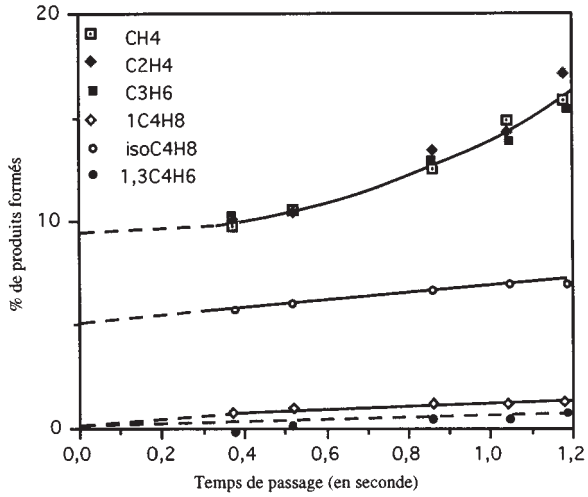

Fig. 12. Oxydation de l'isopentane à 873 K Répartition des produits de la réaction en fonction du temps de passage pour 2-C_4H_8, méthyl-3 butène-1, méthyl-2 butène-1 et méthyl-2 butène-2.

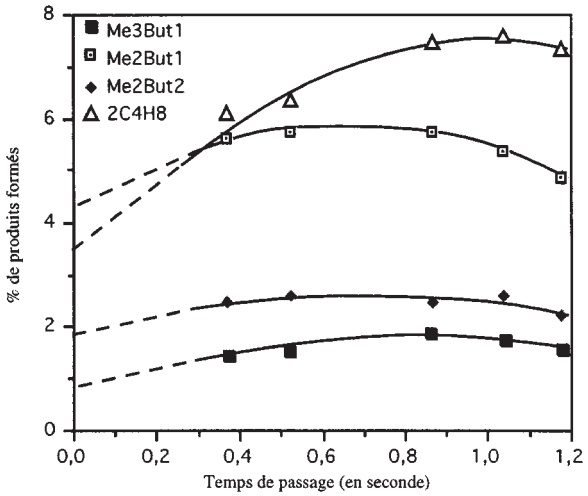

Schéma 1. Mécanisme « basse température » de l'oxydation du néopentane.

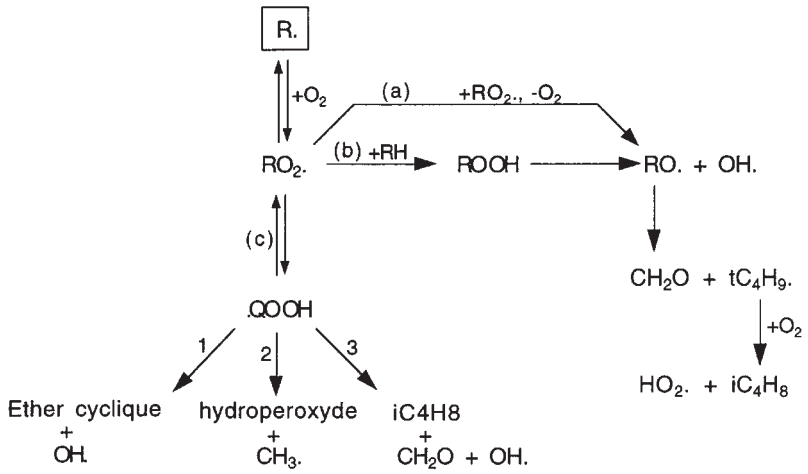

de la réversibilité de la réaction d'addition d'une molécule d'oxygène sur le radical alcoyle R$^\bullet$ formé par l'amorçage :

$$R^\bullet + O_2 \underset{2}{\overset{1}{\rightleftharpoons}} RO_2^\bullet$$

Pour des températures modérées (inférieures à 800 K), cette réaction est fortement déplacée dans le sens 1 de la formation du radical peroxyalcoyle $RO_2^\bullet$ qui s'isomérise en radical hydroperoxyalcoyle $^\bullet$QOOH et conduit, finalement, à des composés oxygénés (éthers cycliques, aldéhydes, cétones, alcools). Ce mécanisme est appelé mécanisme de « basse température » (8–13).

Pour des températures plus élevées (supérieures à 1000 K), la réaction précédente est déplacée dans le sens 2. Les radicaux R$^\bullet$ ne s'oxydent plus mais se décomposent par rupture de liaisons C—C en petits radicaux ($CH_3^\bullet$, $C_2H_5^\bullet$) qui seuls s'oxydent. C'est alors un mécanisme dit de « haute température » (14–27).

Le radical alcoyle R$^\bullet$ peut également réagir avec O_2 pour former l'alcène conjugué correspondant :

$$R^\bullet + O_2 \rightarrow \text{alcène conjugué} + HO_2^\bullet$$

Cette réaction est effectivement importante à une température que l'on peut qualifier d'intermédiaire, entre 800 et 1000 K (28).

Oxydation du néopentane

L'amorçage de la réaction d'oxydation du néopentane conduit à la formation d'un seul radical alcoyle R$^\bullet$, le radical : $(CH_3)_3CCH_2^\bullet$. Le mécanisme général de l'oxydation du néopentane à « basse température » peut être schématisé de la façon suivante (voir Schéma 1).

La voie réactionnelle (b) conduit à la formation d'isobutène secondaire, par décomposition d'une molécule d'hydroperoxyde ROOH. Expérimentalement, nous avons montré que l'isobutène formé par l'oxydation du néopentane est primaire (fig. 5) et ne peut donc pas être formé de façon prépondérante par la voie (b).

La voie réactionnelle (c) correspond à l'isomérisation du radical $RO_2^\bullet$ [$(CH_3)_3CCH_2OO^\bullet$] en radical $^\bullet$QOOH [$(CH_3)_2(CH_2OOH)CCH_2^\bullet$] qui se décompose pour former de l'isobutène ou des composés oxygénés (éthers cycliques ou hydroperoxydes insaturés). Les constantes de vitesse des processus 1 et 3 sont respectivement : $k_1 = 10^7$ s^{-1}, et k_3 =

© 1999 CNRC Canada

Fig. 13. Oxydation de l'isopentane à 873 K. Répartition des produits de la réaction en fonction du temps de passage pour H_2, CO_2 et H_2O.

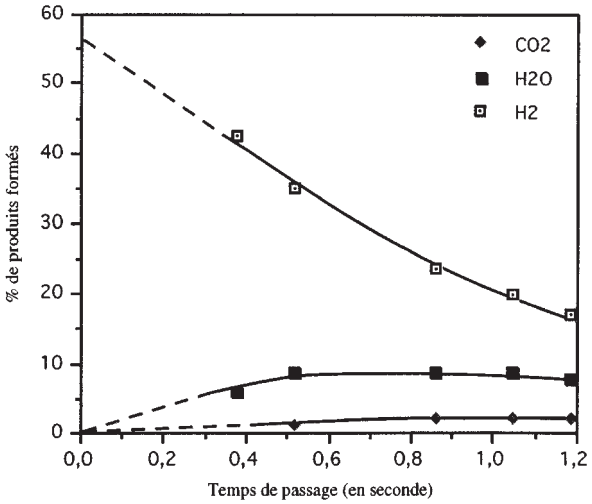

$8{,}4 \times 10^5\ s^{-1}$ (29). Les éthers formés par cette séquence réactionnelle devraient donc être présents en quantité au moins égale voire plus importante que l'isobutène, ce qui n'est pas le cas puisque ces composés oxygénés n'ont même pas été détectés. Cette voie réactionnelle (c) est donc probablement négligeable dans le mécanisme d'oxydation du néopentane.

La voie réactionnelle (a) conduit, quant à elle, à la formation d'isobutène primaire et les résultats expérimentaux ne permettent pas d'évaluer son importance relative dans le mécanisme général car l'isobutène peut provenir du mécanisme de « haute température ».

La décomposition du radical alcoyle $R^{\bullet}$ suivant le mécanisme de « haute température » conduit à la formation du radical $CH_3^{\bullet}$ et de l'isobutène :

$$R^{\bullet} \rightarrow CH_3^{\bullet} + \text{isobutène}$$

Le radical $CH_3^{\bullet}$ peut ensuite réagir de la façon suivante (voir Schéma 2) :

Schéma 2. Mécanisme « haute température » de l'oxydation du néopentane.

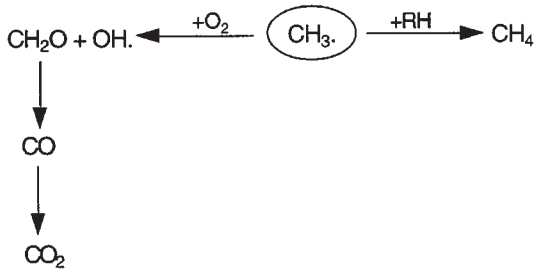

Ce mécanisme concorde avec le fait que l'isobutène est formé en quantité plus importante que le méthane et plus particulièrement avec la relation entre les concentrations : (isobutène) ≈ (CH_4) + (CO_2) que l'on observe expérimentalement.

En conclusion, le mécanisme d'oxydation du néopentane à 873 K est probablement, presque exclusivement, un mécanisme de « haute température ». La modélisation, présentée dans le paragraphe suivant, nous permettra de vérifier cette hypothèse.

Revenons sur le mécanisme de formation de l'hydrogène. La figure 4 montre que la quantité d'hydrogène formée à faible temps de passage est anormalement élevée. Nous avons, de plus, observé à faible temps de passage, la formation d'un dépôt de produits lourds à la sortie du réacteur. Ces produits n'ont pas été dosés puisqu'ils se condensent dans l'appareillage expérimental.

Des réactions de combinaisons, de déshydrogénations et de condensations pourraient expliquer ces deux observations, mais leur importance à faible temps de passage, alors que seules des réactions primaires devraient se produire, ne peut s'expliquer que par un mauvais fonctionnement hydrodynamique du réacteur pour les forts débits.

Il pourrait se former, dans le réacteur, des zones de faible agitation et donc de fort temps de passage où se produiraient ces réactions de polymérisation; puis on retrouverait, en diminuant le débit, une agitation correcte et donc une formation normale d'hydrogène dans ces conditions, ceci bien que le réacteur soit, en théorie, agité à partir d'un temps de passage de 0,05 s.

Oxydation de l'isopentane

Contrairement à l'oxydation du néopentane, l'amorçage de la réaction d'oxydation de l'isopentane conduit à quatre radicaux alcoyles différents : CH_3-CH_2-$CH(CH_3)(CH_2^{\bullet})$; CH_3-CH_2-$C^{\bullet}(CH_3)_2$; CH_3-$CH^{\bullet}$-$CH(CH_3)_2$; $CH_2^{\bullet}$-CH_2-$CH(CH_3)_2$.

Le mécanisme d'oxydation de l'isopentane à « basse température » étant beaucoup plus complexe que celui du néopentane, il est très difficile de conclure quant à l'importance relative des différentes voies réactionnelles à partir des seuls résultats expérimentaux.

Dans ce mécanisme, la seule voie négligeable est la décomposition de l'hydroperoxyde ROOH:

$$RO_2^{\bullet} \rightleftarrows ROOH \rightarrow OH^{\bullet} + RO^{\bullet}$$

$$\rightarrow \text{aldéhyde ou cétone} + \text{radical alcoyle}$$

$$\xrightarrow{+O_2} \text{alcène} + HO_2^{\bullet}$$

En effet, cette séquence réactionnelle conduit à la formation d'alcènes secondaires, alors que tous les alcènes dosés dans l'oxydation de l'isopentane sont primaires (figs. 11 et 12).

Pour le mécanisme de « haute température », la décomposition des quatre radicaux isopentyle formés par l'amorçage conduit à la formation d'alcènes : éthylène, propène, butènes 1 et 2, isobutène (Schéma 3) :

Schéma 3. Mécanisme « haute température » de l'oxydation de l'isopentane.

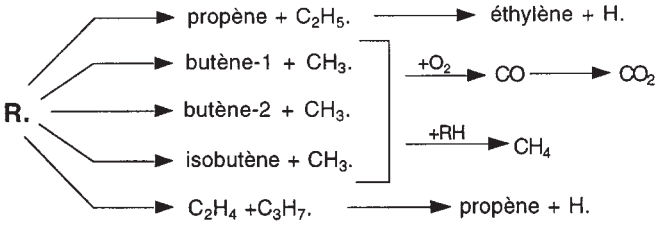

© 1999 CNRC Canada

Si le mécanisme « haute température » est prépondérant dans la formation des alcènes, les concentrations de ces composés doivent être compatibles, à l'instant initial, avec les relations :

$$(C_3H_6) = (C_2H_4)$$

et

$$(1\text{-}C_4H_8) + (2\text{-}C_4H_8) + (iC_4H_8) = (CH_4) + (CO) + (CO_2)$$

Or, expérimentalement, on trouve à l'instant initial :

$(C_3H_6)_0$	= 9,5 %	$(iC_4H_8)_0$	= 5 %
$(C_2H_4)_0$	= 9,5 %	$(CH_4)_0$	= 9,5 %
$(1\text{-}C_4H_8)_0$	= 0,5 %	$(CO)_0$	= 0
$(2\text{-}C_4H_8)_0$	= 4 %	$(CO_2)_0$	= 0

Les relations précédentes sont tout à fait vérifiées à très faible avancement. Il semblerait, finalement, que le mécanisme de « haute température » soit majoritaire dans la formation des alcènes non conjugués (autres que les méthylbutènes). Les seuls composés formés, essentiellement, par le mécanisme de « basse température » sont les méthylbutènes et les aldéhydes ou cétones (non dosés) qui sont vraisemblablement formés par les processus :

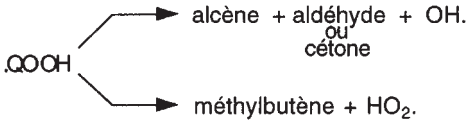

Modélisation des réactions d'oxydation du néopentane et de l'isopentane

Les mécanismes réactionnels utilisés pour la simulation des réactions d'oxydation du néopentane et de l'isopentane ont été générés par le logiciel EXGAS, mis au point au laboratoire, qui permet une écriture systématique des mécanismes réactionnels en phase gazeuse (30, 31).

Ce logiciel est composé de trois parties :

(*i*) une base de données C_0–C_2 comprenant tous les processus uni et bimoléculaires mettant en jeu des réactifs et des produits qui contiennent au plus deux atomes de carbone (32). Les grandeurs cinétiques utilisées pour les réactions de cette base (781 processus) sont principalement extraites de la littérature (réfs. 33 et 34);

(*ii*) un générateur de mécanisme primaire pour lequel les seules espèces moléculaires pouvant réagir sont l'hydrocarbure et l'oxygène;

(*iii*) un générateur de mécanisme secondaire qui permet de faire réagir les produits issus du mécanisme primaire.

Pour garder un fichier de taille raisonnable, la génération du mécanisme secondaire ne se fait pas de la même façon que celle du mécanisme primaire. Dans le but de faciliter la génération du mécanisme secondaire, toutes les espèces moléculaires contenant plus de deux atomes de carbone, ayant la même formule brute et le même groupement fonctionnel, sont regroupées sous le même nom sans distinction des différents isomères. Une telle opération est appelée le « lumping » des molécules.

Les paramètres cinétiques relatifs aux processus issus des mécanismes générés sont calculés par le logiciel KINGAS (31, 35) à partir de grandeurs thermodynamiques fournies par le logiciel THERGAS (36). Ces deux logiciels ont été développés au DCPR, à partir des méthodes de Benson (37).

Finalement, le mécanisme réactionnel servant à la simulation est constitué de la base C_0–C_2 à laquelle est ajouté le mécanisme issu du générateur en respectant les règles suivantes :

(*i*) aucune des réactions écrites dans la base n'est réécrite dans le mécanisme généré;

(ii) doivent être générées : les métathèses impliquant des radicaux de la base, les réactions de terminaison entre radicaux de la base et ceux issus du générateur, les réactions impliquant des réactifs de la base mais conduisant à des produits contenant plus de deux atomes de carbone.

Les réactions d'oxydation du néopentane et de l'isopentane sont alors simulées en utilisant le logiciel CHEMKIN développé par Sandia National Laboratories (Livermore, Calif., U.S.A.).

Simulation de l'oxydation du néopentane

La réaction d'oxydation du néopentane a été simulée en utilisant un mécanisme généré suivant les règles exposées précédemment. Les tentatives de simulation utilisant un mécanisme « primaire + secondaire » n'ayant pas abouti pour des raisons numériques (divergence), le mécanisme de départ est donc un mécanisme primaire qui comprend 106 espèces et 888 réactions.

Les constantes de vitesse des réactions de ce mécanisme ont été modifiées de façon à obtenir des courbes de formation des produits de réaction aussi proches que possible des courbes expérimentales. Cette modification ne porte que sur le facteur préexponentiel *A* et ceci dans des limites raisonnables compte tenu de l'incertitude que nous avons sur ces paramètres (au maximum un facteur 10).

Afin d'améliorer cet ajustement entre courbes théoriques et expérimentales, nous avons ajouté au mécanisme primaire précédent des réactions secondaires de l'isobutène (Tableau 1 : réactions 27 et 29) qui est le produit primaire majoritaire dans cette réaction d'oxydation (hormis H_2 non simulé). On a tenu compte également de la réaction de branchement : $C_5H_{10}(OOH)OO^{\bullet} \rightarrow CH_3^{\bullet} + 2\ OH^{\bullet} + 2\ CH_2O + C_2H_2$ (Tableau 1 : réaction 26) qui accélère très fortement la production d'eau, ainsi que des réactions de métathèse et de terminaison utilisant des radicaux secondaires (Tableau 1 : réactions 28 et 30).

Enfin, nous avons effectué une analyse de sensibilité des différentes réactions de ce mécanisme, dont le but est de déterminer les réactions négligeables. Ces réactions peuvent être éliminées du mécanisme sans que cela modifie les courbes de formation des produits de la réaction d'oxydation.

Ces simplifications conduisent à un mécanisme final qui ne comporte plus que 53 espèces et 243 réactions (Tableau 1 + base C_0–C_2 non représentée). Les résultats de ces simulations sont représentés, pour les produits les plus importants, sur les figures 14–17.

© 1999 CNRC Canada

Tableau 1. Mécanisme final de l'oxydation du néopentane.[a]

Réactions	*A*	*b*	*E*
(1) $C_5H_{12} \rightarrow CH_3^{\bullet} + C_4H_9^{\bullet}$	$8{,}3 \times 10^{17}$	0	82 894
(2) $C_5H_{12} + O_2 \rightarrow HO_2^{\bullet} + C_5H_{11}^{\bullet}$	$5{,}0 \times 10^{13}$	0	49 000
(3) $C_5H_{11}^{\bullet} + O_2 \rightarrow C_5H_{11}OO^{\bullet}$	$4{,}0 \times 10^{12}$	0	0
(4) $^{\bullet}C_5H_{10}OOH + O_2 \rightarrow C_5H_{10}(OOH)OO^{\bullet}$	$4{,}0 \times 10^{12}$	0	0
(5) $C_5H_{11}OO^{\bullet} \rightarrow {}^{\bullet}C_5H_{10}(OOH)$	$1{,}8 \times 10^{12}$	0	28 500
(6) $C_5H_{11}^{\bullet} \rightarrow CH_3^{\bullet} + C_4H_8$	$2{,}0 \times 10^{13}$	0	31 000
(7) $C_4H_9^{\bullet} + O_2 \rightarrow C_4H_8 + HO_2^{\bullet}$	$8{,}1 \times 10^{10}$	0	3000
(8) $C_5H_{12} + O^{\bullet\bullet} \rightarrow OH^{\bullet} + C_5H_{11}^{\bullet}$	$2{,}0 \times 10^{14}$	0	7850
(9) $C_5H_{12} + H^{\bullet} \rightarrow H_2 + C_5H_{11}^{\bullet}$	$1{,}1 \times 10^{8}$	2	7700
(10) $C_5H_{12} + OH^{\bullet} \rightarrow H_2O + C_5H_{11}^{\bullet}$	$1{,}7 \times 10^{10}$	1	1810
(11) $C_5H_{12} + HO_2^{\bullet} \rightarrow H_2O_2 + C_5H_{11}^{\bullet}$	$2{,}4 \times 10^{12}$	0	17 000
(12) $C_5H_{12} + CH_3^{\bullet} \rightarrow CH_4 + C_5H_{11}^{\bullet}$	$1{,}2 \times 10^{0}$	4	8200
(13) $C_5H_{12} + CH_3O^{\bullet} \rightarrow CH_3OH + C_5H_{11}^{\bullet}$	$6{,}5 \times 10^{11}$	0	7300
(14) $C_5H_{12} + CH_3OO^{\bullet} \rightarrow CH_3OOH + C_5H_{11}^{\bullet}$	$2{,}4 \times 10^{13}$	0	20 000
(15) $C_5H_{12} + C_2H_5^{\bullet} \rightarrow C_2H_6 + C_5H_{11}^{\bullet}$	$1{,}2 \times 10^{12}$	0	13 500
(16) $C_5H_{12} + C_4H_9^{\bullet} \rightarrow C_4H_{10} + C_5H_{11}^{\bullet}$	$1{,}2 \times 10^{12}$	0	15 000
(17) $OH^{\bullet} + C_4H_9^{\bullet} \rightarrow C_4H_9OH$	$6{,}2 \times 10^{12}$	0	0
(18) $CH_3^{\bullet} + C_2H_5^{\bullet} \rightarrow C_3H_8$	$1{,}8 \times 10^{13}$	0	0
(19) $CH_3^{\bullet} + C_4H_9^{\bullet} \rightarrow C_5H_{12}$	$1{,}7 \times 10^{13}$	0	0
(20) $CH_3O^{\bullet} + C_2H_5^{\bullet} \rightarrow C_3H_8O$	$5{,}8 \times 10^{12}$	0	0
(21) $CH_3O^{\bullet} + C_4H_9^{\bullet} \rightarrow C_5H_{12}O$	$5{,}0 \times 10^{12}$	0	0
(22) $C_2H_5^{\bullet} + C_2H_5^{\bullet} \rightarrow C_4H_{10}$	$3{,}0 \times 10^{12}$	0	0
(23) $C_2H_5^{\bullet} + C_4H_9. \rightarrow C_6H_{14}$	$5{,}3 \times 10^{12}$	0	0
(24) $C_4H_9. + C_4H_9^{\bullet} \rightarrow C_8H_{18}$	$2{,}2 \times 10^{13}$	0	0
(25) $C_5H_{11}OO^{\bullet} + HO_2^{\bullet} \rightarrow C_5H_{11}(OOH) + O_2$	$1{,}0 \times 10^{11}$	0	–2600
(26) $C_5H_{10}(OOH)OO^{\bullet} \rightarrow CH_3^{\bullet} + 2OH^{\bullet} + 2HCHO + C_2H_2$	$7{,}0 \times 10^{16}$	0	42 000
(27) $C_4H_8 \rightarrow CH_3^{\bullet} + C_3H_5^{\bullet}$	$5{,}5 \times 10^{18}$	0	83 080
(28) $C_5H_{12} + C_3H_5^{\bullet} \rightarrow C_3H_6 + C_5H_{11}^{\bullet}$	$1{,}1 \times 10^{8}$	2	7700
(29) $C_4H_8 + CH_3^{\bullet} \rightarrow C_4H_7^{\bullet} + CH_4$	$2{,}2 \times 10^{-2}$	3,5	5775
(30) $C_4H_7^{\bullet} + CH_3^{\bullet} \rightarrow C_5H_{10}$	$1{,}0 \times 10^{12}$	0	0

[a] *A* en $cm^3\ mol^{-1}\ s^{-1}$; *E* en cal mol^{-1}; $k = AT^b \exp(-E/RT)$.

Fig. 14. Oxydation du néopentane à 873 K. Courbes de formation simulées de CH_4 et $isoC_4H_8$.

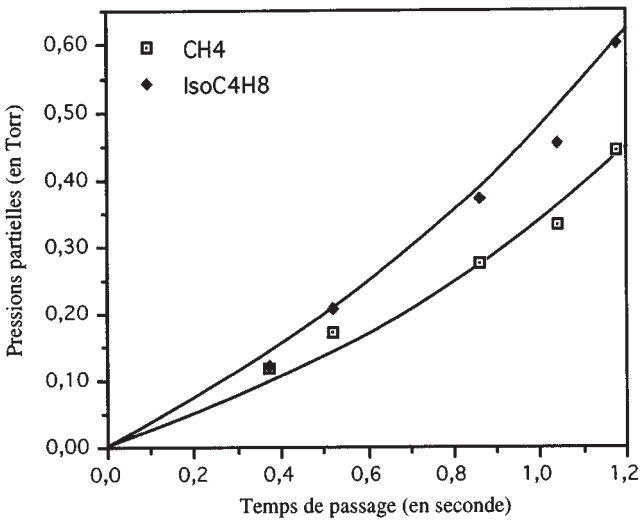

Fig. 15. Oxydation du néopentane à 873 K. Courbes de formation simulées de C_2H_4 et C_2H_6.

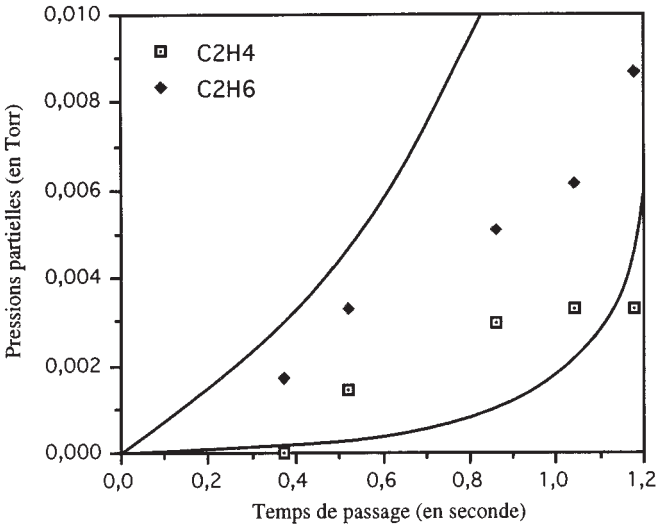

L'ajustement entre courbes théoriques et expérimentales obtenu est très bon pour les hydrocarbures principaux (CH_4 et iC_4H_8) et convenable pour les autres (C_2H_4, C_2H_6 et C_3H_6). Cependant, les points expérimentaux concernant les deux alcènes montrent que ces espèces sont consommées. Comme les réactions correspondantes n'ont pas été écrites dans notre mécanisme, il est normal que les courbes simulées s'écartent des points expérimentaux lorsque le temps de passage augmente. De plus, ces alcènes sont présents en petites quantités et la mesure de faibles pressions partielles est

© 1999 CNRC Canada

Fig. 16. Oxydation du néopentane à 873 K. Courbe de formation simulée de C_3H_6.

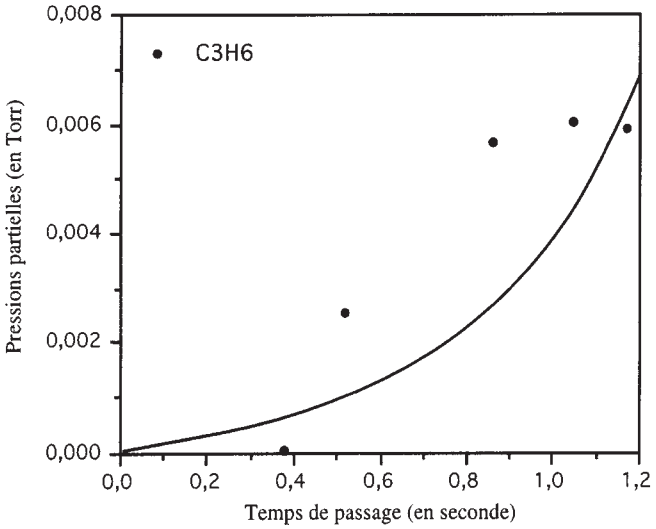

Fig. 17. Oxydation du néopentane à 873 K. Courbe de formation simulée de H_2O.

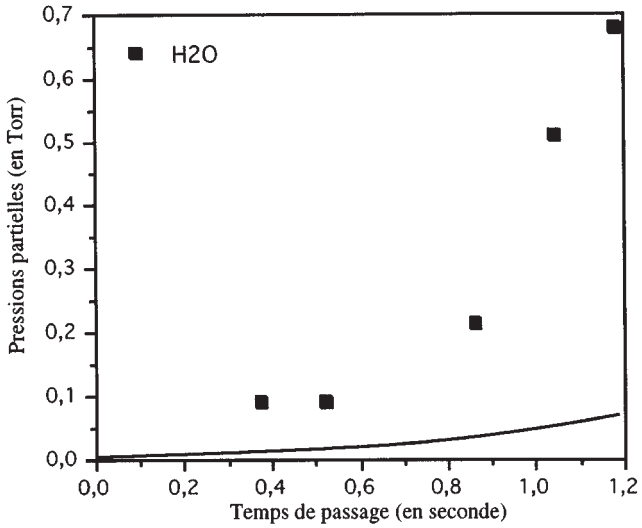

Schéma 4. Mécanisme final de l'oxydation du néopentane.

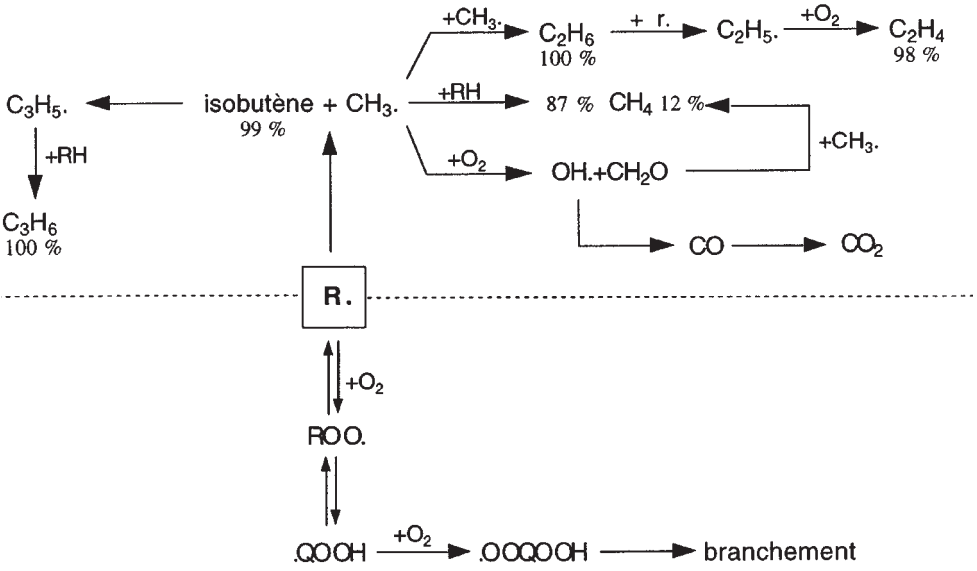

très délicate. On peut estimer la précision de ces mesures à ±0,001 torr, ce qui inclut la reproductibilité, les erreurs d'échantillonnage et les erreurs d'analyse. Par contre il n'a pas été possible de simuler quantitativement la formation des produits oxygénés H_2O et CO_2. En effet, la production de CO_2 et H_2O est contrôlée, principalement, par la réaction de branchement à partir du radical HOOQOO•, mais nous n'avons pas pu augmenter la constante de vitesse de cette réaction plus que nous ne l'avons fait sans faire diverger le système. La production de H_2 n'a pas été simulée pour les raisons évoquées précédemment.

Finalement, le mécanisme d'oxydation du néopentane peut être schématisé (voir Schéma 4) où R• représente le radical néopentyle (les % correspondent au pourcentage de formation du produit par la voie indiquée).

Le mécanisme d'oxydation du néopentane est donc essentiellement un mécanisme de « haute température », c'est à dire un mécanisme dans lequel le radical alcoyle R• se décompose jusqu'à l'obtention de petits radicaux (CH_3•, C_2H_5•) qui seuls s'oxydent. L'accélération de la réaction par rapport à une réaction de pyrolyse s'explique par la présence, dans le mécanisme d'oxydation, de réactions de branchement.

Simulation de l'oxydation de l'isopentane

Comme dans le cas de l'oxydation du néopentane, le mécanisme de départ ayant servi à la simulation de l'oxydation de l'isopentane est constitué de la base C_0–C_2 et du mécanisme primaire généré par le système. Ce mécanisme comprend 365 espèces et 1498 réactions. Afin d'améliorer l'ajustement entre courbes expérimentales et théoriques, nous avons rajouté à ce mécanisme des réactions secondaires de métathèse des pentènes (Tableau 2 : réactions 56–66) et des réactions de terminaisons des radicaux secondaires (Tableau 2 : réactions 67–69). Les pentènes sont regroupés

© 1999 CNRC Canada

Tableau 2. Mécanisme final « haute température » de l'oxydation de l'isopentane.[a]

Réactions	*A*	*b*	*E*
(1) $RH^{\bullet} \rightarrow CH_3^{\bullet} + 2\text{-}C_4H_9^{\bullet}$	$1{,}6 \times 10^{17}$	0	87 875
(2) $R2^{\bullet} \rightarrow R4^{\bullet}$	$7{,}5 \times 10^{11}$	0	19 800
(3) $R4^{\bullet} \rightarrow R2^{\bullet}$	$1{,}5 \times 10^{12}$	0	19800
(4) $R1^{\bullet} \rightarrow CH_3^{\bullet} + i\ C_4H_8$	$2{,}0 \times 10^{13}$	0	31 000
(5) $2\text{-}C_4H_9^{\bullet} \rightarrow CH_3^{\bullet} + C_3H_6$	$2{,}0 \times 10^{13}$	0	31 000
(6) $R2^{\bullet} \rightarrow CH_3^{\bullet} + 1\text{-}C_4H_8$	$2{,}0 \times 10^{13}$	0	31 000
(7) $R2^{\bullet} \rightarrow C_2H_5^{\bullet} + C_3H6$	$2{,}0 \times 10^{13}$	0	28 700
(8) $R3^{\bullet} \rightarrow CH_3^{\bullet} + 2\text{-}C_4H_8$	$2{,}0 \times 10^{13}$	0	31 000
(9) $R4^{\bullet} \rightarrow 2\text{-}C_3H_7^{\bullet} + C_2H_4$	$2{,}0 \times 10^{13}$	0	28 700
(11) $R1^{\bullet} + O_2 \rightarrow$ méthyl-2 butène 1 $+ HO_2^{\bullet}$	$5{,}4 \times 10^{10}$	0	5000
(12) $R1^{\bullet} + O_2 \rightarrow$ méthyl-2 butène 2 $+ HO_2^{\bullet}$	$1{,}1 \times 10^{10}$	0	5000
(13) $R3^{\bullet} + O_2 \rightarrow$ méthyl-3 butène 1 $+ HO_2^{\bullet}$	$2{,}7 \times 10^{10}$	0	5000
(14) $2\text{-}C_3H_7^{\bullet} + O_2 \rightarrow C_3H_6 + HO_2$.	$5{,}4 \times 10^{10}$	0	5000
(15) $RH + O^{\bullet\bullet} \rightarrow OH^{\bullet} + R1^{\bullet}$	$1{,}0 \times 10^{13}$	0	3280
(16) $RH + O^{\bullet\bullet} \rightarrow OH^{\bullet} + R2^{\bullet}$	$1{,}0 \times 10^{14}$	0	7850
(17) $RH + O^{\bullet\bullet} \rightarrow OH^{\bullet} + R3^{\bullet}$	$2{,}6 \times 10^{13}$	0	5200
(18) $RH + O^{\bullet\bullet} \rightarrow OH^{\bullet} + R4^{\bullet}$	$5{,}1 \times 10^{13}$	0	7850
(19) $RH + H^{\bullet} \rightarrow H_2 + R1^{\bullet}$	$4{,}2 \times 10^{6}$	2	2400
(20) $RH + H^{\bullet} \rightarrow H_2 + R2^{\bullet}$	$5{,}6 \times 10^{7}$	2	7700
(21) $RH + H^{\bullet} \rightarrow H_2 + R3^{\bullet}$	$9{,}0 \times 10^{6}$	2	5000
(22) $RH + H^{\bullet} \rightarrow H_2 + R4^{\bullet}$	$2{,}8 \times 10^{7}$	2	7700
(23) $RH + OH^{\bullet} \rightarrow H_2O + R1^{\bullet}$	$4{,}0 \times 10^{12}$	0	443
(24) $RH + OH^{\bullet} \rightarrow H_2O + R2^{\bullet}$	$8{,}4 \times 10^{9}$	1	1810
(25) $RH + OH^{\bullet} \rightarrow H_2O + R3^{\bullet}$	$1{,}3 \times 10^{9}$	1,3	702
(26) $RH + OH^{\bullet} \rightarrow H_2O + R4^{\bullet}$	$4{,}1 \times 10^{9}$	1	1810
(27) $RH + HO_2^{\bullet} \rightarrow H_2O_2 + R1^{\bullet}$	$1{,}0 \times 10^{12}$	0	14 000
(28) $RH + HO_2^{\bullet} \rightarrow H_2O_2 + R2^{\bullet}$	$1{,}2 \times 10^{12}$	0	17 000
(29) $RH + HO_2^{\bullet} \rightarrow H_2O_2 + R3^{\bullet}$	$4{,}0 \times 10^{11}$	0	15 500
(30) $RH + HO_2^{\bullet} \rightarrow H_2O_2 + R4^{\bullet}$	$6{,}0 \times 10^{11}$	0	7900
(31) $RH + CH_3^{\bullet} \rightarrow CH_4 + R1^{\bullet}$	$1{,}0 \times 10^{11}$	0	7900
(32) $RH + CH_3^{\bullet} \rightarrow CH_4 + R2^{\bullet}$	$6{,}0 \times 10^{-1}$	4	8200
(33) $RH + CH_3^{\bullet} \rightarrow CH_4 + R3^{\bullet}$	$2{,}0 \times 10^{11}$	0	9600
(34) $RH + CH_3^{\bullet} \rightarrow CH_4 + R4^{\bullet}$	$3{,}0 \times 10^{-1}$	4	8200
(35) $RH + CH_3O^{\bullet} \rightarrow CH_3OH + R1^{\bullet}$	$2{,}3 \times 10^{10}$	0	2900
(36) $RH + CH_3O^{\bullet} \rightarrow CH_3OH + R2^{\bullet}$	$3{,}2 \times 10^{11}$	0	7300
(37) $RH + CH_3O^{\bullet} \rightarrow CH_3OH + R3^{\bullet}$	$1{,}5 \times 10^{11}$	0	4500
(38) $RH + CH_3O^{\bullet} \rightarrow CH_3OH + R4^{\bullet}$	$1{,}6 \times 10^{11}$	0	7300
(39) $RH + CH_3OO^{\bullet} \rightarrow CH_3OOH + R1^{\bullet}$	$1{,}5 \times 10^{12}$	0	15 000
(40) $RH + CH_3OO^{\bullet} \rightarrow CH_3OOH + R2^{\bullet}$	$1{,}2 \times 10^{13}$	0	20 000
(41) $RH + CH_3OO^{\bullet} \rightarrow CH_3OOH + R3^{\bullet}$	$3{,}0 \times 10^{12}$	0	17 500
(42) $RH + CH_3OO^{\bullet} \rightarrow CH_3OOH + R4^{\bullet}$	$6{,}0 \times 10^{12}$	0	20 000
(43) $RH + 2\text{-}C_3H_7^{\bullet} \rightarrow C_3H_8 + R1^{\bullet}$	$1{,}4 \times 10^{-3}$	4,2	6000
(44) $RH + 2\text{-}C_3H_7^{\bullet} \rightarrow C_3H_8 + R1^{\bullet}$	$8{,}4 \times 10^{-3}$	4,2	8700
(45) $RH + 2\text{-}C_3H_7^{\bullet} \rightarrow C_3H_8 + R1^{\bullet}$	$2{,}8 \times 10^{-3}$	4,2	8000
(46) $RH + 2\text{-}C_3H_7^{\bullet} \rightarrow C_3H_8 + R1^{\bullet}$	$4{,}2 \times 10^{-3}$	4,2	8700
(47) $2\text{-}C_3H_7^{\bullet} + OH^{\bullet} \rightarrow C_3H_7OH$	$5{,}6 \times 10^{12}$	0	0
(48) $2\text{-}C_3H_7^{\bullet} + CH_3^{\bullet} \rightarrow i\ C_4H_{10}$	$1{,}4 \times 10^{13}$	0	0
(49) $CHO^{\bullet} + C_2H_5^{\bullet} \rightarrow C_2H_5CHO$	$5{,}3 \times 10^{12}$	0	0
(50) $CHO^{\bullet} + 2\text{-}C_3H_7^{\bullet} \rightarrow C_3H_7CHO$	$4{,}9 \times 10^{12}$	0	0
(51) $CH_2OH^{\bullet} + C_2H_5^{\bullet} \rightarrow C_3H_7OH$	$5{,}2 \times 10^{12}$	0	0
(52) $CH_2OH^{\bullet} + C_3H_7^{\bullet} \rightarrow C_4H_9OH$	$5{,}2 \times 10^{12}$	0	0
(53) $CH_3O^{\bullet} + C_2H5^{\bullet} \rightarrow C_3H_8O$	5×10^{12}	0	0
(54) $CH_3O^{\bullet} + C_3H_7^{\bullet} \rightarrow C_4H_{10}O$	$4{,}6 \times 10^{12}$	0	0
(55) $C_2H_5^{\bullet} + C_2H_5^{\bullet} \rightarrow C_4H_{10}$	$2{,}7 \times 10^{12}$	0	0
(56) Méthyl-2 butène 1 $+ OH^{\bullet} \rightarrow C_5H_9^{\bullet} + H_2O$	$3{,}1 \times 10^{6}$	2	–300
(57) Méthyl-2 butène 1 $+ HO_2^{\bullet} \rightarrow C_5H_9^{\bullet} + H_2O_2$	$9{,}6 \times 10^{3}$	2,6	13 900
(58) Méthyl-2 butène 1+ $CH_3^{\bullet} \rightarrow C_5H_9^{\bullet} + CH_4$	$2{,}2 \times 10^{0}$	3,5	5775
(59) Méthyl-2 butène 2 $+ H^{\bullet} \rightarrow C_5H_9^{\bullet} + H_2$	$8{,}5 \times 10^{5}$	2,6	2490

© 1999 CNRC Canada

Tableau 2. (*fin*).

Réactions	*A*	*b*	*E*
(60) Méthyl-2 butène 2 + $OH^{\bullet} \rightarrow C_5H_9^{\bullet} + H_2O$	$1{,}5 \times 10^7$	2	–300
(61) Méthyl-2 butène 2 + $HO_2^{\bullet} \rightarrow C_5H_9^{\bullet} + H_2O_2$	$4{,}8 \times 10^4$	2,6	13 900
(62) Méthyl-2 butène 2 + $CH_3^{\bullet} \rightarrow C_5H_9^{\bullet} + CH_4$	$1{,}1 \times 10^1$	3,5	5775
(63) Méthyl-3 butène 1 + $H^{\bullet} \rightarrow C_5H_9^{\bullet} + H_2$	$8{,}5 \times 10^5$	2,6	2490
(64) Méthyl-3 butène 1 + $OH^{\bullet} \rightarrow C_5H_9^{\bullet} + H_2O$	$1{,}5 \times 10^7$	2,0	–300
(65) Méthyl-3 butène 1 + $HO_2^{\bullet} \rightarrow C_5H_9^{\bullet} + H_2O_2$	$4{,}8 \times 10^4$	2,6	13 900
(66) Méthyl-3 butène 1 + $CH_3^{\bullet} \rightarrow C_5H_9^{\bullet} + CH_4$	$1{,}1 \times 10^1$	3,5	5775
(67) $C_5H_9^{\bullet} + OH^{\bullet} \rightarrow C_5H_9OH$	$1{,}0 \times 10^{12}$	0	0
(68) $C_5H_9^{\bullet} + HO_2^{\bullet} \rightarrow C_5H_9OOH$	$1{,}0 \times 10^{12}$	0	0
(69) $C_5H_9^{\bullet} + CH_3^{\bullet} \rightarrow C_6H_{12}$	$1{,}0 \times 10^{12}$	0	0

[a] *A* en $cm^3\ mol^{-1}\ s^{-1}$; *E* en cal mol^{-1}; $k = AT^b \exp(-E/RT)$.
Nota : RH représente la molécule d'isopentane. R1$^{\bullet}$, R2$^{\bullet}$, R3$^{\bullet}$ et R4$^{\bullet}$ sont respectivement les radicaux : $(CH_3)_2C^{\bullet}CH_2CH_3$, $(CH_3)(CH_2^{\bullet})CHCH_2CH_3$, $(CH_3)_2CHCH^{\bullet}CH_3$ et $(CH_3)_2CHCH_2CH_2^{\bullet}$.

Tableau 2bis. Mécanisme final « basse température » de l'oxydation de l'isopentane.[a]

Réactions	*A*	*b*	*E*
(1) $R^{\bullet} + O_2 \rightarrow RO_2^{\bullet}$	$4{,}0 \times 10^{12}$	0	0
(2) $RO_2^{\bullet} \rightarrow R^{\bullet} + O_2$	$1{,}0 \times 10^{15}$	0	30 000
(3) $RO_2^{\bullet} \rightarrow {}^{\bullet}QOOH$	$2{,}5 \times 10^{12}$	0	33 500
(4) ${}^{\bullet}QOOH + O_2 \rightarrow Q(OOH)OO^{\bullet}$	$4{,}0 \times 10^{12}$	0	0
(5) $Q(OOH)OO^{\bullet} \rightarrow {}^{\bullet}Q(OOH)_2$	$2{,}5 \times 10^{12}$	0	33 500
(6) ${}^{\bullet}QOOH \rightarrow r^{\bullet}$ + peroxyde	$2{,}0 \times 10^{13}$	0	31 000
(7) ${}^{\bullet}QOOH \rightarrow HO_2^{\bullet}$ + alcène	$5{,}0 \times 10^{13}$	0	23 000
(8) ${}^{\bullet}QOOH \rightarrow {}^{\bullet}rOOH$ + alcène	$2{,}0 \times 10^{13}$	0	28 700
(9) ${}^{\bullet}QOOH \rightarrow OH^{\bullet}$ + aldéhyde	$1{,}0 \times 10^9$	0	7500
(10) ${}^{\bullet}QOOH \rightarrow OH^{\bullet}$ + éther cyclique	$2{,}0 \times 10^{11}$	0	17 700
(11) ${}^{\bullet}Q(OOH)_2 \rightarrow {}^{\bullet}rOOH$ + peroxyde	$1{,}0 \times 10^9$	0	7500
(12) ${}^{\bullet}Q(OOH)_2 \rightarrow HO_2^{\bullet}$ + peroxyde	$5{,}0 \times 10^{13}$	0	23 000
(13) ${}^{\bullet}Q(OOH)_2 \rightarrow r^{\bullet}$ + dihydroperoxyde	$2{,}0 \times 10^{13}$	0	31 000
(14) ${}^{\bullet}Q(OOH)_2 \rightarrow OH^{\bullet}$ + QO(OOH)	$1{,}0 \times 10^9$	0	7500
(15) ${}^{\bullet}Q(OOH)_2 \rightarrow OH^{\bullet}$ + éther peroxydique cyclique	$2{,}0 \times 10^{11}$	0	15 200
(16) ${}^{\bullet}QOOH + O_2 \rightarrow HO_2^{\bullet}$ + peroxyde	$2{,}0 \times 10^{10}$	0	5000
(17) ${}^{\bullet}Q(OOH)_2 + O_2 \rightarrow HO_2^{\bullet}$ + dihydroperoxyde	$2{,}0 \times 10^{10}$	0	5000

[a] *A* en $cm^3\ mol^{-1}\ s^{-1}$; *E* en cal mol^{-1}; $k = AT^b \exp(-E/RT)$.
Nota : Ce tableau présente les paramètres cinétiques moyens des différents types de processus du mécanisme de « basse température ». La simulation a, quant à elle, été effectuée en différenciant les isomères possibles; ceci engendre un nombre très important de processus (405) que nous ne pouvons présenter ici.

(sans distinction d'isomères) car la simulation s'effectue, pour les réactions secondaires, en utilisant la technique du « lumping ».

Les modifications apportées aux constantes de vitesse portent uniquement sur le facteur préexponentiel *A* qui n'a pas été modifié de plus d'un facteur 10.

L'analyse de sensibilité effectuée sur ce mécanisme a permis de le simplifier en portant le nombre de réactions à 606 (base C_0–C_2 comprise mais non représentée) et le nombre d'espèces à 299 (Tableaux 2 et 2bis). La comparaison entre les courbes de formation des produits de réaction simulées et expérimentales est représentée sur les figures 18–22. Les courbes simulées sont en accord avec les résultats expérimentaux. L'ajustement est très bon dans le cas des hydrocarbures et un peu moins en ce qui concerne CO_2 et H_2O. Comme dans le cas du néopentane, l'hydrogène n'a pas été simulé.

Finalement, le mécanisme d'oxydation de l'isopentane peut être schématisé de la façon suivante (Schéma 5) :

Fig. 18. Oxydation de l'isopentane à 873 K. Courbes de formation simulées de CH_4, $isoC_4H_8$ et méthyl-2 butène-2.

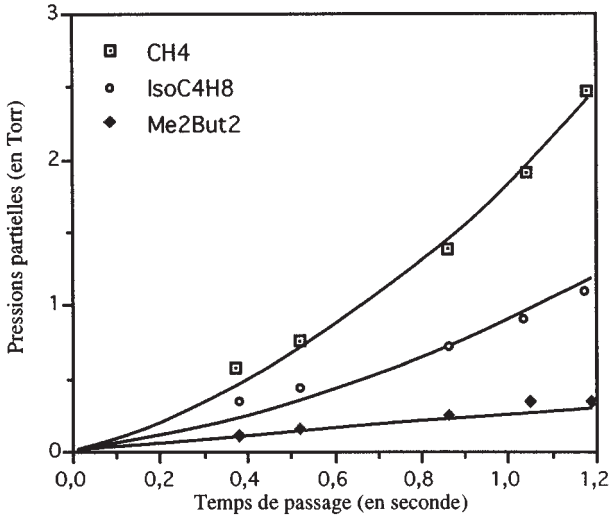

© 1999 CNRC Canada

Schéma 5. Mécanisme final de l'oxydation de l'isopentane.

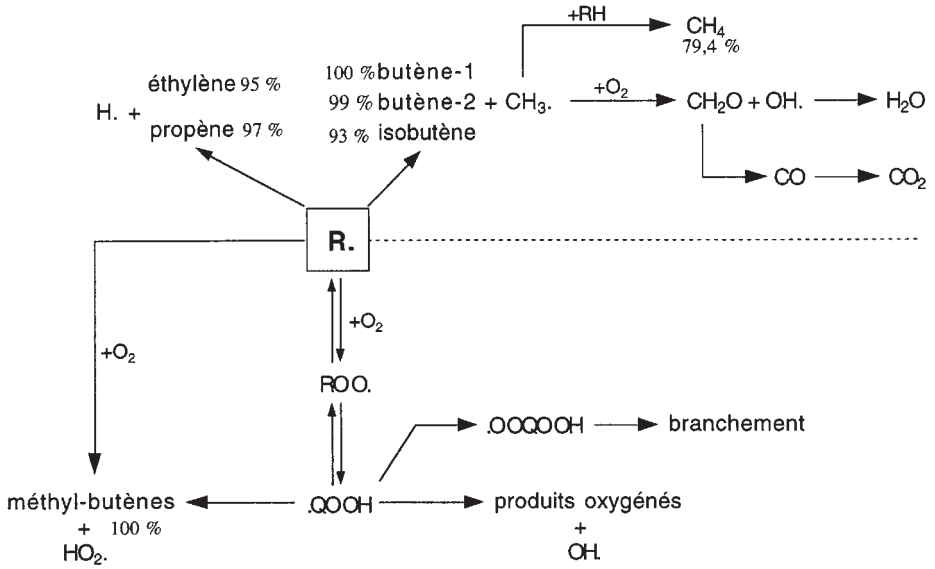

Fig. 19. Oxydation de l'isopentane à 873 K. Courbes de formation simulées de C_3H_6 et méthyl-2 butène-1.

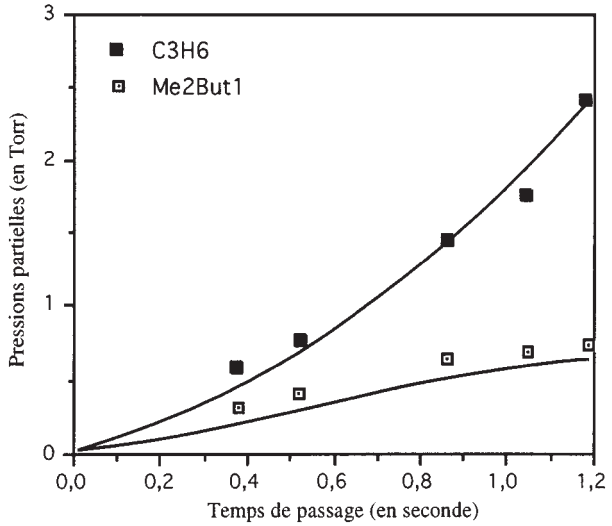

Fig. 20. Oxydation de l'isopentane à 873 K. Courbes de formation simulées de C_2H_4 et méthyl-3 butène-1.

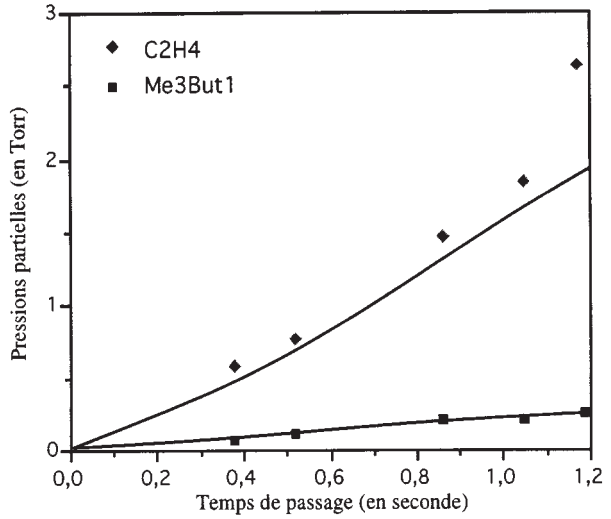

Discussion et conclusion

La comparaison des mécanismes d'oxydation du néopentane et de l'isopentane montre que ces deux réactions évoluent de façon assez différente. En effet, l'oxydation de l'isopentane est partagée entre les deux mécanismes de « haute et basse températures », alors que l'oxydation du néopentane évolue uniquement suivant la voie de « haute température ».

Cette différence peut s'expliquer en considérant les deux voies possibles de formation de l'alcène conjugué et du radical $HO_2^{\bullet}$:

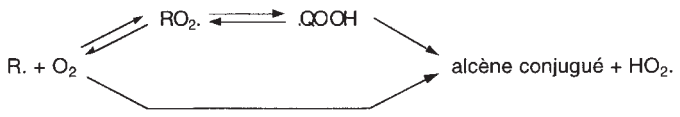

Dans le cas de l'isopentane, l'alcène conjugué existe (méthylbutènes) et le radical associé $HO_2^{\bullet}$ participe à la réaction de terminaison la plus rapide : $2\ HO_2^{\bullet} \rightarrow H_2O_2 + O_2$ conduisant à l'agent de branchement dégénéré H_2O_2 qui se décompose ensuite en deux radicaux $OH^{\bullet}$ très réactifs. Cette terminaison principale n'est, en réalité, pas une « vraie » terminaison puisqu'elle revient à remplacer des radicaux peu réactifs $HO_2^{\bullet}$ par des radicaux $OH^{\bullet}$ très réactifs.

En revanche, dans le cas du néopentane, l'alcène conjugué n'existe pas et il ne se forme donc pas de radicaux $HO_2^{\bullet}$ par les deux voies ci-dessus. La terminaison principale est : $2\ CH_3^{\bullet} \rightarrow C_2H_6$ qui ne conduit pas à un agent de branchement dégénéré.

La molécule de néopentane aurait donc tendance à s'oxyder plus difficilement que celle de l'isopentane, comme l'a confirmé l'étude expérimentale dans laquelle nous avons pu noter un avancement de réaction, par rapport à l'hydrocarbure, beaucoup plus élevé pour l'oxydation de l'isopentane que pour l'oxydation du néopentane (les expériences étant réalisées dans les mêmes conditions).

© 1999 CNRC Canada

Fig. 21. Oxydation de l'isopentane à 873 K. Courbes de formation simulées de 1-C_4H_8 et 2-C_4H_8.

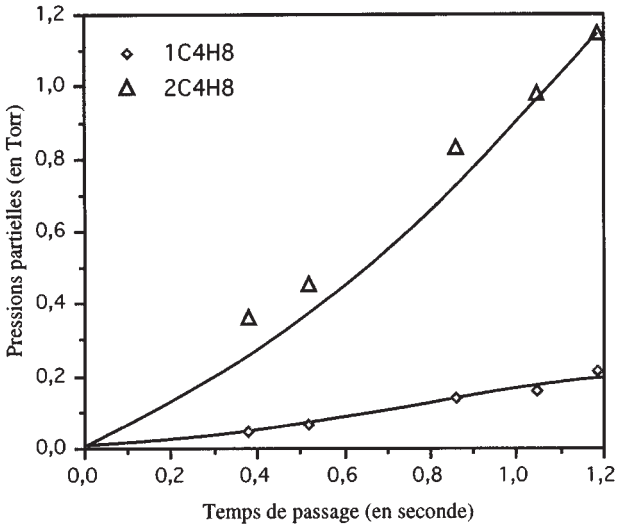

Fig. 22. Oxydation de l'isopentane à 873 K. Courbes de formation simulées de CO_2 et H_2O.

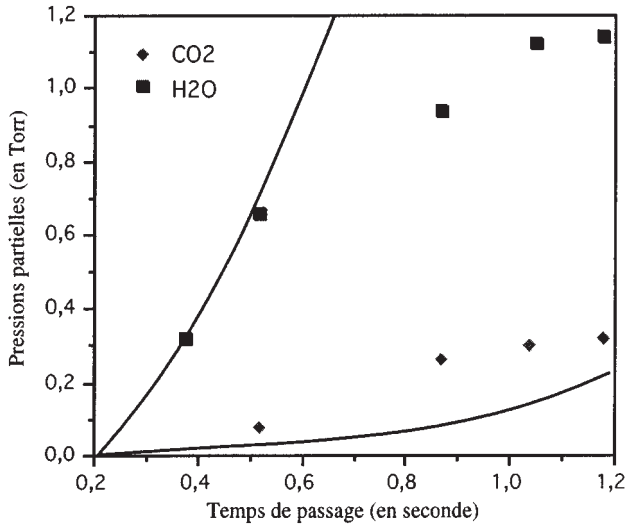

Tableau 3. Répartition (en %) des alcènes précurseurs de radicaux stabilisés par résonance, à 20 % d'avancement, dans l'oxydation de 6 hydrocarbures saturés.

	Hydrocarbure (RON)					
Alcène (BRON)	nC_7H_{16} (0)	nC_5H_{12} (61,7)	**neoC_5H12 (85,8)**	**isoC_5H_{12} (92,3)**	isoC_8H_{18} (100)	cyC_5H_{10} (102)
C_3H_6 (–)	9	7,5	—	**13**	7,5	—
1-C_4H_8 (144)	—	3,5	—	**1**	—	—
Met2-But1 (146)	—	—	—	**5,5**	—	—
2-C_4H_8 (155)	—	—	—	**7**	—	—
isoC_4H_8 (170)	—	—	**14**	**6,5**	26	—
cyC_5H_8 (171)	—	—	—	—	—	33
Met2-But2 (176)	—	—	—	**2,5**	—	—
cyC_5H_6 (218)	—	—	—	—	—	2,5
Total %	9	11	**14**	**35,5**	33,5	35,5

Cependant, cette constatation est en contradiction avec les valeurs d'indice d'octane recherche de ces deux composés. En effet, l'indice d'octane de l'isopentane (92,3) est plus élevé que celui du néopentane (85,5).

Les mécanismes primaires d'oxydation ne permettent donc pas d'interpréter la différence d'indice d'octane existant entre ces deux hydrocarbures et il semble donc nécessaire de faire intervenir un mécanisme secondaire plus complet de la réaction.

Considérons la nature et la répartition des produits primaires formés par ces deux réactions d'oxydation et plus particulièrement celle des alcènes. Les alcènes formés (sauf C_2H_4) sont en majorité des composés précurseurs de radicaux allyliques stabilisés par résonance. Ces radicaux, très peu réactifs, peuvent inhiber la réaction d'oxydation en participant à de nouvelles terminaisons. Ceci pourrait expliquer l'indice d'octane élevé de ces deux hydrocarbures.

D'autre part, la comparaison des quantités d'alcènes formés par ces réactions (Tableau 3) pour un avancement identique de 20 % montre que le pourcentage d'alcènes précurseurs de radicaux stabilisés par résonance est plus important dans le cas de l'isopentane que dans le cas du néopentane, ce qui expliquerait que l'indice d'octane du néopentane soit inférieur à celui de l'isopentane.

Cette constatation a, par ailleurs, déjà été faite lors de l'étude des réactions d'oxydation du *n*-heptane et de l'isooctane (7), ainsi que celles du *n*-pentane et du cyclopentane (6) pour lesquels la différence d'indice d'octane avait pu être interprétée par la présence ou l'absence de radicaux stabilisés par résonance.

Le tableau 3 résume la répartition des alcènes précurseurs de radicaux stabilisés par résonance formés lors des réactions d'oxydation des six hydrocarbures étudiés, pour un avancement de réaction identique de 20 %. L'analyse de ce tableau montre que la quantité totale d'alcènes formés augmente avec l'indice d'octane de l'hydrocarbure. La différence d'indice d'octane existant entre ces différents hydrocarbures pourrait donc s'expliquer par la présence plus ou moins importante d'alcènes d'indice d'octane de mélange élevé (BRON, Blending Research Octane Number) (38) qui réagiraient suivant un mécanisme secondaire pour former des radicaux stabilisés par résonance. Cette corrélation qualitative entre la quantité d'alcènes formés et l'indice d'octane de l'hydrocarbure n'est cependant qu'une première approche qui pourrait être affinée en tenant compte de

© 1999 CNRC Canada

l'efficacité de chacun des alcènes formés en tant que précurseur de radicaux stabilisés.

Références

1. S.W. Benson. J. Phys. Chem. **92**, 1531 (1988).
2. P.G. Lignola et E. Reverchon. Oxid. Commun. **14**, 81 (1991).
3. C. Chevalier, W.J. Pitz, J. Warnatz, C.K. Westbrook et H. Melenk. Int. Symp. Combustion, 24th, The Combustion Institute, Pittsburgh, Pa. 1992. p. 93.
4. H.J. Curran, W.J. Pitz, C.K. Westbrook, M.W.M. Hisham et R.W. Walker. Int. Symp. Combustion, 26th, The Combustion Institute, Pittsburgh, Pa. 1996.
5. S. Taconnet. Thèse de Doctorat INPL, Nancy. 1996.
6. V. Simon, Y. Simon, G. Scacchi et F. Baronnet. Can. J. Chem. **75**, 575 (1997).
7. Y. Simon, G. Scacchi et F. Baronnet. Can. J. Chem. **74**, 1391 (1996).
8. W S. Affleck et A. Fish. Combust. Flame, **12**, 243 (1968).
9. A. Fish. Proc. R. Soc. London, Ser. A: **293**, 378 (1966).
10. A. Fish. Proc. R. Soc. London, Ser. A: **298**, 204 (1967).
11. A. Fish. Angew. Chem. **7**, 45 (1968).
12. M.P. Halstead, L.J. Kirsch, A. Prothero et C.P. Quinn. Proc. R. Soc. London, Ser. A: **346**, 515 (1975).
13. R.A. Cox et J.A. Cole. Combust. Flame, **60**, 109 (1985).
14. C.K. Westbrook et F.L. Dryer. Int. Symp. Combustion, 18th, The Combustion Institute, Pittsburgh, Pa. 1981. p. 749.
15. C.K. Westbrook et W.J. Pitz. Combust. Flame, **63**, 113 (1986).
16. C.K. Westbrook, W.J. Pitz et M.M. Thornton. Combust. Flame, **72**, 45 (1988).
17. N.P. Cernansky, R.M. Green, W.J. Pitz et C.K. Westbrook. Combust. Sci. Technol, **50**, 3 (1986).
18. C.K. Westbrook. AIAA Aerosp. Sci. Meet. 24th, Reno, Nev. 1986.
19. W.J. Pitz, C.K. Westbrook, W.M. Proscia et F.L. Dryer. Int. Symp. Combustion, 20th, The Combustion Institute, Pittsburgh, Pa. 1984. p. 831.
20. C.K. Westbrook et W.J. Pitz. SAE Tech. Pap. Ser. 872 107 (1987).
21. C.K. Westbrook et W.J. Pitz. 2nd Workshop Modelling of Chemical Reaction Systems, Heidelberg, Germany. 1986. Proc. 2nd Workshop. *Édité par* J. Warnatz et W. Jager. Springer-Verlag, Heidelberg. 1987. p. 39.
22. E.I. Axelsson, K. Brezinsky, F.L. Dryer, W.J. Pitz et C.K. Westbrook. Int. Symp. Combustion, 21st, The Combustion Institute, Pittsburgh, Pa. 1986. p. 783.
23. C.K. Westbrook et W.J. Pitz. Commun. ACS Natl. Meet., 189th, Division of Petroleum Chemistry Inc., Miami Beach, Fla. Preprints. 1985. p. 321.
24. J. Warnatz. Int. Symp. Combustion, 20th, The Combustion Institute, Pittsburgh, Pa. 1984. p. 845.
25. J. Warnatz. Communication à la Réunion de Sophia Antipolis, Nice. 1985.
26. C. Esser, U. Maas et J. Warnatz. Int. Colloq.Gas Dynamics of Explosions and Reactive Systems (ICODERS), 10th, Berkeley, Calif. 1985.
27. J. Warnatz. Ber. Bunsen-ges. Phys. Chem. **87**, 1008 (1983).
28. S.W. Benson et P.S. Nangia. Acc. Chem. Res. **12**, 223 (1979).
29. C. Morley. Joint Meet. British and German Sections Combustion Institute, Cambridge, U.K. 1993.
30. G.M. Côme, V. Warth, P.A. Glaude, R. Fournet, F. Battin-Leclerc et G. Scacchi. Int. Symp. Combustion, 26th, The Combustion Institute, Pittsburgh, Pa. 1996. p. 755.
31. V. Warth, N. Stef, P.A. Glaude, F. Battin-Leclerc, G. Scacchi et G.M. Côme. Combust. Flame, **114**, 81 (1998).
32. P. Barbe, F. Battin-Leclerc et G.M. Côme. J. Chim. Phys. **92,** 1666 (1995).
33. D.L. Baulch, C.J. Cobos, R.A. Cox, P. Franck, G.D. Hayman, T.H. Just, J.A. Kerr, T.P. Murrells, M.J. Pilling, J. Troe, R.W. Walker et J. Warnatz. Combust. Flame, **98**, 59 (1994).
34. W. Tsang et R.F. Hampson. J. Phys. Chem. Ref. Data, **15**, 1087 (1986).
35. V. Bloch-Michel. Thèse de doctorat INPL, Nancy. 1995.
36. C. Muller, V. Michel, G. Scacchi et G.M. Côme. J. Chim. Phys. **92**, 1154 (1995).
37. S.W. Benson. Thermochemical kinetics. 2^{e} éd. John Wiley, New York. 1976.
38. Knocking characteristics of pure hydrocarbons. API Research Project 45. ASTM Spec. Tech. Publ. 225 (1958).

© 1999 CNRC Canada

Hypervalent iodine oxidation of α-substituted 2,4-dihydroxyacetophenones: synthesis of novel *o*-iodophenoxy ethers via rearrangement of iodonium ylides

Om Prakash, Vijay Sharma, and Madan P. Tanwar

Abstract: α-Substituted 2,4-dihydroxyacetophenones (**1a–1i**) have been oxidized with phenyliodonium diacetate (PIDA) under three conditions (*i*) PIDA–KOH–MeOH (basic) at 0°C, (*ii*) PIDA–MeOH (neutral) at reflux temperature, and (*iii*) PIDA–AcOH (acidic) at reflux temperature, to afford novel *o*-iodophenoxy ethers (**4a–4i**) via rearrangement of respective iodonium ylides (**5a–5i**).

Key words: hypervalent iodine reagents, phenyliodonium diacetate, α-substituted 2,4-dihydroxyacetophenones, α-substituted 2-hydroxy-3-iodo-4-phenoxyacetophenones, iodonium ylides rearrangement.

Résumé : On a oxydé des 2,4-dihydroxyacétophénones α-substituées (**1a–1i**) à l'aide du diacétate de phényliodonium (« PIDA ») dans trois conditions : (*i*) PIDA–KOH–MeOH (basique), à 0°C; (*ii*) PIDA–MeOH (neutre), à la température de reflux et (*iii*) PIDA–AcOH (acide), à la température de reflux; ces oxydations conduisent à de nouveaux éthers *o*-iodophénoy (**4a–4i**) par le biais d'un réarrangement des ylures d'iodonium respectifs (**5a–5i**).

Mots clés : réactifs hypervalents de l'iode, diacétate de phényliodonium, 2,4-dihydroxyacétophénones α-substituées, 2-hydroxy-3-iodo-4-phénoxyacétophénones α-substituées, réarrangement d'ylures d'iodonium.

[Traduit par la Rédaction]

Introduction

A surge of interest in the use of hypervalent iodine reagents in organic synthesis has been witnessed by its explosive growth during few last decades (1–5). Major areas of interest are hypervalent iodine oxidation of carbonyl compounds (4), phenolic oxidations (2*a*, 5), oxidative rearrangements (1*e*), etc. These studies have provided a large number of new and convenient methods for the synthesis of a wide variety of organic compounds, including various heterocyclic compounds and bridgehead compounds (3, 6).

A notable hypervalent iodine oxidation of enolizable ketones with PIDA and potassium hydroxide in methanol leads to the formation of α-dimethylacetals (7, 8) (eq. [1]). However, the presence of a phenolic group at the *ortho* position of ketones such as acetophenone, etc. affords coumaran-3-ones by intramolecular participation in this oxidation (9, 10) (eq. [2]). On the other hand, hypervalent iodine oxidation of various phenols has provided attractive routes for the synthesis of valuable *p*-quinones, *o*-quinones, quinone acetals, etc., which are otherwise difficult to obtain (eq. [3]) (11, 12).

[1] 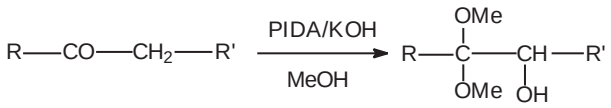

[2] 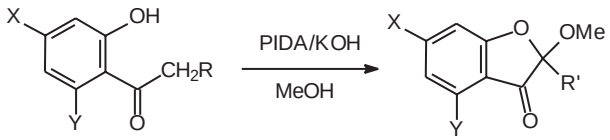

[3] 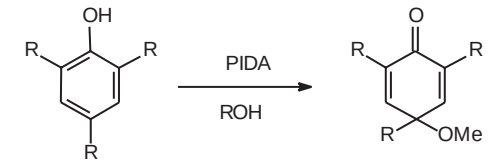

Results and discussion

Based upon these observations, we became interested in oxidizing those compounds containing *ortho* and *para* phenolic groups and an enolizable ketonic moiety, for example, 5-acetyl-2,4-dihydroxyacetophenone (**1a**), with phenyliodonium diacetate (PIDA) and KOH in MeOH. The attempted reaction yielded a yellow crystalline solid (mp 143–145°C; yield 75%), which separated out during the stirring of the reaction mixture. Instead of obtaining bis-coumaranones **2** (via a route analogous to eq. [2]) or compound **3** (via a route analogous to eq. [3]), interestingly, a novel formation of 5-

Received April 7, 1998.[1]

O. Prakash,[2] V. Sharma, and M.P. Tanwar. Department of Chemistry, Kurukshetra University, Kurukshetra, 136 119, Haryana, India.

[1]Revision received March 7, 1999.
[2]Author to whom correspondence may be addressed.
e-mail: kuru@doe.ernet.in

© 1999 NRC Canada

Table 1. Physical data for **4a–4i**, **5c**, and **5g**.

Compound no.	X	R	Melting point (°C)	Yield (%)[a]		
				(i)[b]	(ii)[b]	(iii)[b]
4a	$COCH_3$	H	143–145	75	40	64
4b	H	H	116–118	20	10	15
4c	NO_2	H	190–191	77	40	60
4d	Br	H	160–161	35	10	25
4e	H	CH_3	136–138	68	40	55
4f	COC_2H_5	CH_3	119–120	75	40	60
4g	NO_2	CH_3	190–192	48	27	41
4h	Br	CH_3	146–147	38	10	20
4i	H	C_6H_5	129–130	65	52	58
5c	NO_2	H	>200	82	—	—
5g	NO_2	CH_3	196–198	56	—	—

[a]Yields are based upon the pure products.

[b]Reaction conditions: (i) PIDA – KOH in MeOH; (ii) PIDA–MeOH; (iii) PIDA–AcOH.

Scheme 1.

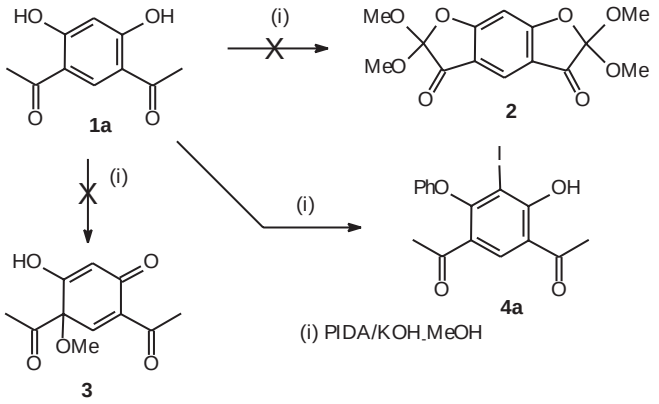

Scheme 2.

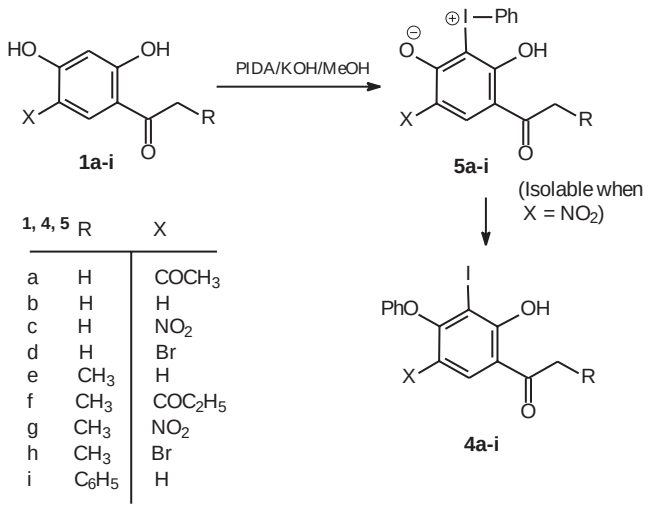

acetyl-2-hydroxy-3-iodo-4-phenoxyacetophenone (**4a**) was observed (Scheme 1).

A preliminary account of this study was reported earlier (13). This observation, coupled with the fact that the rearranged products from this reaction i.e., *o*-iodo ethers, are potential precursors for the synthesis of a variety of interesting compounds such as dibenzofurans, which are associated with diverse physiological activities (14), prompted us to study the scope of this novel route.

In the present study, a full account of our detailed investigations on the oxidation of α-substituted 2,4-dihydroxyacetophenones (**4a–4i**) with phenyliodonium diacetate under different conditions is described.

Accordingly, we first carried out oxidation of 2,4-dihydroxyacetophenones (**1b–1d**) with PIDA – KOH in MeOH, to afford the corresponding rearranged *o*-iodo ethers (**4b–4d**). This rearrangement occurred via the intermediacy of iodonium ylides of the type **5b–5d** as evidenced by the isolation of ylide **5c** as a high-melting yellow solid, from the oxidation of ketone **1c**. Acidification of **5c** with hydrochloric acid, followed by refluxing the methanolic solution of the resultant solid (mp 153–154°C), afforded a rearranged product **4c** (mp 190–191°C; yield 77%). However, our attempt to isolate similar intermediates **5a**, **5b**, **5d** in other cases ended up with no success, as only the rearranged products **4a**, **4b**, **4d** were obtained from these reactions. The physical data for the products **4a–4d** are listed in Table 1.

Similarly, oxidation of 2,4-dihydroxy-5-nitropropiophenone (**1g**) with PIDA with KOH in MeOH at 0°C (condition (i)) afforded iodonium ylide **5g** as a yellow crystalline solid (based on ^{1}H NMR and mp). This ylide, on acidification with hydrochloric acid followed by refluxing, gave 2-hydroxy-3-iodo-4-phenoxy-5-nitroacetophenone (**4g**) in 48% yield.

2,4-dihydroxypropiophenone (**1e**), 2,4-dihydroxy-5-propionylpropiophenone (**1f**), 5-bromo-2,4-dihydroxypropiophenone (**1h**), and 2,4-dihydroxydeoxybenzoin (**1i**) also underwent smooth transformation to 2-hydroxy-3-iodo-4-phenoxypropiophenone (**4e**) 2-hydroxy-3-iodo-4-phenoxy-5-propionylpropiophenone (**4f**), 5-bromo-2-hydroxy-3-iodo-4-phenoxypropiophenone (**4h**), and 2-hydroxy-3-iodo-4-phenoxydeoxybenzoin (**4i**), respectively. The intermediates, iodonium ylides **5e**, **5f**, **5h**, and **5i**, could not be isolated.

In view of the marked effect of conditions on the course of various hypervalent iodine-mediated transformations, it was considered worthwhile to investigate the role of other reaction conditions on the oxidation of compounds **1a–1i**.

© 1999 NRC Canada

Scheme 3.

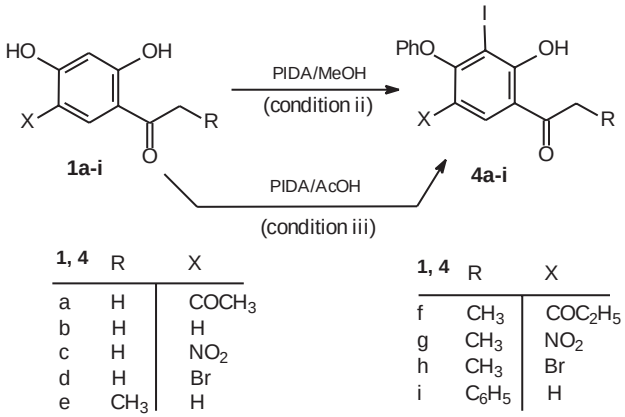

1, 4	R	X
a	H	$COCH_3$
b	H	H
c	H	NO_2
d	H	Br
e	CH_3	H

1, 4	R	X
f	CH_3	COC_2H_5
g	CH_3	NO_2
h	CH_3	Br
i	C_6H_5	H

Thus substrate **1a** was also oxidized with PIDA under condition (ii), viz. PIDA in methanol (neutral) at reflux temperature, and under condition (iii), PIDA in acetic acid (acidic) at reflux temperature (Scheme 3). The product, obtained after the usual work-up under these conditions, was characterized as **4a,** which was found to be identical to that prepared under reaction condition (i). However, yields of the products were found to be lower in conditions (ii) and (iii) than in condition (i).

Similarly, applying conditions (ii) and (iii), other phenolic ketones **1b–1i** were oxidatively rearranged to the corresponding *o*-iodophenoxy ethers **4b**–**4i**. The physical data for the products (% yields and melting points under different conditions) are given in Table 1.

A plausible mechanistic pathway for **1**→**4** via rearrangement of iodonium ylide (15, 16) of type **5** is outlined in Scheme 4. Under strong basic conditions (KOH in MeOH) PIDA is converted into dimethoxyiodobenzene (17), ($PhI(OMe)_2$), while substrate **1** changes in situ into the corresponding potassium phenolate **6**. Dimethoxyiodobenzene attacks at position 3 of phenolate **6** to form intermediate **7**, which loses methanol to produce iodonium ylide **5**. The iodonium ylide **5** finally rearranges to product **4**. It is to be noted that under conditions (ii) and (iii) the electrophilic attack of PIDA itself takes place, on substrate **1** (in place of dimethoxyiodobenzene), to afford the final product via intermediates of type **5** and **7**. Since PIDA in acetic acid gives the products in lower yields (5–18%), basic conditions presumably assist the removal of a proton from intermediate **7**. Thus $PhI(OMe)_2$ may not be an obligatory reagent for the products **4** and **5**.

It is relevant to mention that while our detailed investigation of this rearrangement was in progress and a preliminary communication had also appeared (13), Mallik and Mallik reported the oxidation of 2,4-dihydroxyacetophenone and other phenolic ketones with PIDA–MeOH at reflux temperature to afford *o*-iodophenoxy ethers (18). Although these reaction conditions also afforded the same *o*-iodo ethers **4**, PIDA – KOH in MeOH (our condition i) gave better results in terms of yields and isolation of products.

Finally, the formation and rearrangement of phenolic iodonium ylides containing an enolizable ketone moiety offers a novel route for the synthesis of new *o*-iodophenoxy ethers that are otherwise difficult to prepare using conventional methods. The most striking feature of this approach is that the enolizable ketonic group present in compounds **1a–1i** remains unaffected under these reaction conditions, which normally oxidize the α-position of the enolizable ketones (7, 8). Another noteworthy feature of this oxidative rearrangement is that phenolic ketones having electron-withdrawing substituents ($COCH_2R$ and NO_2) at the 5-position yield better results. The products obtained from this study are potential precursors of various organic compounds, especially heterocyclic compounds. For example, *o*-iododiaryl ethers are useful intermediates for dibenzofuran synthesis as they could be readily cyclized either photochemically (15) or chemically through the use of Ph(II) salts(16), *n*-Bu_3SnH–AIBN (19), etc.

Scheme 4.

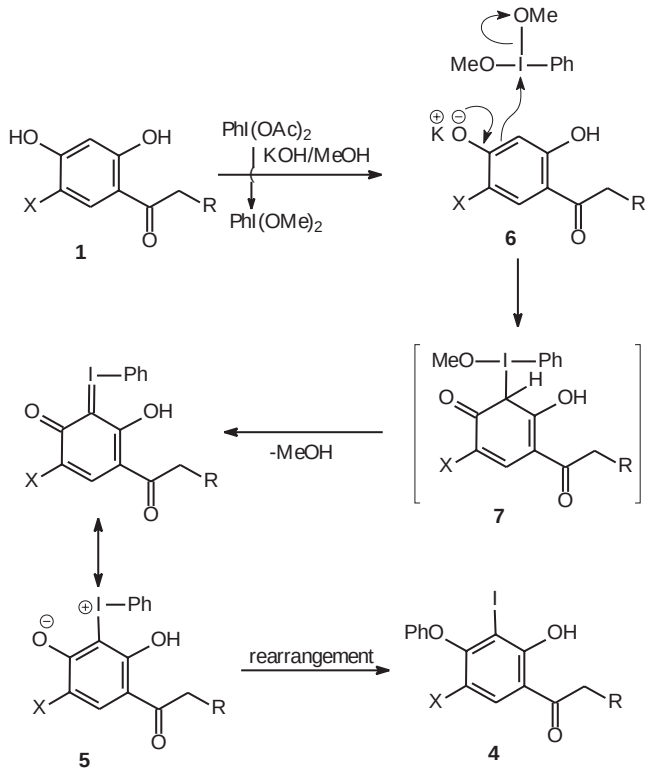

Experimental

Melting points were measured in open capillaries in a sulfuric acid bath and are uncorrected. IR spectra were recorded on a Beckmann IR-20 spectrophotometer. ^1H NMR spectra were taken on a Perkin Elmer (90 MHz) instrument. EI mass spectra were recorded on a mass spectrophotometer operating at 70 eV. 2,4-Dihydroxyacetophenone (**1b**) (20) and its analogues (5-bromo-2,4-dihydroxyacetophenone (**1d**) (21), 2,4-dihydroxy-5-nitroacetophenone (**1c**) (22), 5-acetyl-2,4-dihydroxyacetophenone (**1a**) (20, 21)), 2,4-dihydroxypropiophenone (**1e**) (20) and its analogues 5-bromo-2,4-dihydroxypropiophenone (**1h**) (23), 2,4-dihydroxy-5-nitropropiophenone (**1g**) (22*a*), 5-propionyl-2,4-dihydroxypropiophenone) (**1f**) (21), and 2,4-dihydroxydeoxybenzoin (**1i**) (24) were prepared according to literature procedure.

© 1999 NRC Canada

Oxidation of 5-substituted 2,4-dihydroxyacetophenones (1a–1d), 5-substituted 2,4-dihydroxypropiophenones (1e–1h), and 2,4-dihydroxydeoxybenzoin (1i) with phenyliodonium diacetate – potassium hydroxide in methanol (condition i). General procedure

To a stirred solution of potassium hydroxide (0.03 mol) in methanol (20 mL) at 0°C in a conical flask placed in an ice bath was added 5-substituted 2,4-dihydroxyacetophenone, 5-substituted 2,4-dihydroxypropiophenone, or 2,4-dihydroxydeoxybenzoin (**1**) (0.01 mol). PIDA (0.011 mol) was slowly added to the resulting solution and the stirring was continued overnight. Water was added to the resulting reaction mixture followed by dilute HCl. Subsequently, the mixture was extracted with dichloromethane (3 × 50 mL). The combined organic phases were washed with water and dried over anhydrous sodium sulphate. The solvent was distilled off at reduced pressure. The crude product, so obtained, was purified by passing through a column using silica gel (60–120 mesh size) and ethyl acetate – petroleum ether (1:10) as eluent to afford pure product **4**.

The yields and melting points of products **4a**–**4i** are given in Table 1.

*Isolation of iodonium ylides **5c** and **5g***

To a stirred solution of potassium hydroxide (1.680 g, 0.03 mol) in methanol (20 mL) at 0°C in a conical flask placed in an ice bath was added 2,4-dihydroxy-5-nitroacetophenone (**1c**, 1.970 g, 0.01 mol) or 2,4-dihydroxy-5-nitropropiophenone (**1g**, 2.110 g, 0.01 mol). The reaction mixture was stirred for 10 min. PIDA (3.542 g, 0.011 mol) was added slowly to the resulting solution and the stirring was continued for half an hour. A yellow crystalline solid (separated out of the solution) was isolated by filtration, followed by washing with methanol. **5c**: yield, 3.272 g, 82%, mp >200°C. **5g**: yield 2.312 g, 56%, mp 196–198°C; ^{1}H NMR (DMSO) δ 1.2 (t, 3H, C_1-$COCH_2C\mathbf{H}_3$), 2.97(q, 2H, C_1-$COC\mathbf{H}_2CH_3$), 6.70–7.25(m, 5H, C_4-I-$C_6\mathbf{H}_5$), 8.6(s, 1H, C_6-**H**).

Oxidation of 5-substituted 2,4-dihydroxyacetophenones (1a–1d), 5-substituted 2,4-dihydroxypropiophenones (1e–1h), and 2,4-dihydroxydeoxybenzoin (1i) with phenyliodonium diacetate in methanol (condition ii). General procedure

PIDA (0.01 mol) was added to a solution of 5-substituted 2,4-dihydroxyacetophenone, 5-substituted 2,4-dihydroxypropiophenone, or 2,4-dihydroxydeoxybenzoin **1** (0.01 mol) in methanol (20 mL) and the reaction mixture was refluxed. The progress of the reaction was monitored by TLC. After about 12 h the solvent was removed in vacuo To the resulting mixture was added water, followed by extraction with dichloromethane (3 × 50 mL). The combined organic phases were washed with water and dried over anhydrous sodium sulphate. The solvent was distilled at reduced pressure to obtain the crude product, which was purified by passing through a column using silica gel (60–120 mesh size) and petroleum ether – ethyl acetate (10:1) as an eluent to afford pure product **4.**

The physical data of the pure products are listed in Table 1.

Oxidation of 5-substituted 2,4-dihydroxyacetophenones (1a–1d), 5-substituted 2,4-dihydroxypropiophenones (1e–1h), and 2,4-dihydroxydeoxybenzoin (1i) with phenyliodonium diacetate in acetic acid (condition iii). General procedure

PIDA (0.01 mol) was added to a solution of 5-substituted 2,4-dihydroxyacetophenone, 5-substituted 2,4-dihydroxypropiophenone, or 2,4-dihydroxydeoxybenzoin **1** (0.01 mol) in acetic acid (20 mL) and the reaction mixture was refluxed. The progress of the reaction was monitored by TLC. After about 8 h the solvent was removed in vacuo. To the resulting mixture was added water, followed by extraction with dichloromethane (3 × 50 mL). The combined organic extracts were washed with water and dried over anhydrous sodium sulphate. The solvent was distilled at reduced pressure to obtain the crude product, which was purified by passing through a column using silica gel (60–120 mesh size) and petroleum ether – ethyl acetate (10:1) as an eluent to afford pure product **4**.

The physical data of the pure products are listed in Table 1.

Spectral and analytical data of products 4a–4i

*5-Acetyl-2-hydroxy-3-iodo-4-phenoxyacetophenone (**4a**)*: IR (Nujol, cm^{-1}): 1630, 1670 (C=O). ^{1}H NMR ($CDCl_3$) δ: 2.47 (s, 3H, C_1-$COC\mathbf{H}_3$), 2.72 (s, 3H, C_5-$COC\mathbf{H}_3$), 6.80–7.42 (m, 5H, C_4-$OC_6\mathbf{H}_5$), 8.45 (s, 1H, C_6-**H**). MS (70 eV) *m*/*z*: 396 (M^+, 34), 305 (26), 303 (100), 287 (9). Anal. calcd. for $C_{16}H_{13}IO_4$: C 48.48, H 3.28; found: C 48.34, H 3.35.

*2-Hydroxy-3-iodo-4-phenoxyacetophenone (**4b**)*: IR (Nujol, cm^{-1}): 1625 (C=O). ^{1}H NMR ($CDCl_3$) δ: 2.60 (s, 3H, C_1-$COC\mathbf{H}_3$), 6.25 (d, 1H, C_5-**H**, J = 8.9 Hz), 7.00–7.50 (m, 5H, C_4-$OC_6\mathbf{H}_5$), 7.63 (d, 1H, C_6-**H**). Anal. calcd. for $C_{14}H_{11}IO_3$: C 47.45, H 3.10; found: C 47.14, H 2.80.

*2-Hydroxy-3-iodo-5-nitro-4-phenoxyacetophenone (**4c**)*: IR (Nujol, cm^{-1}): 1645 (C=O). ^{1}H NMR ($CDCl_3$) δ: 2.70 (s, 3H, C_1-$COC\mathbf{H}_3$), 6.80–7.32 (m, 5H, C_4-$OC_6\mathbf{H}_5$), 8.50 (s, 1H, C_6-**H**), 13.30 (bs, 1H, C_2-O**H**). Anal. calcd. for $C_{14}H_{10}NIO_5$: C 42.10, H 2.50; found: C 41.39, H 2.45.

*5-Bromo-2-hydroxy-3-iodo-4-phenoxyacetophenone (**4d**)*: IR (Nujol, cm^{-1}): 1630 (C=O). ^{1}H NMR ($CDCl_3$) δ: 2.20 (s, 3H, C_1-$COC\mathbf{H}_3$), 6.50–7.30 (m, 5H, C_4-$OC_6\mathbf{H}_5$), 7.86 (s, 1H, C_6-**H**), 13.40 (bs, 1H, C_2-O**H**). MS (70 eV) *m*/*z*: 434 (M^+, 8.9), 434 (M^+, 7.7), 433 (49), 431 (48), 342 (15), 340 (100), 338 (92), 291 (12). Anal. calcd. for $C_{14}H_{10}BrIO_3$: C 38.80, H 2.31; found: C 38.70, H 2.40.

*2-Hydroxy-3-iodo-4-phenoxypropiophenone (**4e**)*: IR (Nujol, cm^{-1}): 1635 (C=O). ^{1}H NMR ($CDCl_3$) δ: 0.80–0.96 (t, 3H, C_1-$COCH_2$-$C\mathbf{H}_3$), 2.50–3.00 (q, 2H, C_1-$COC\mathbf{H}_2CH_3$), 6.50–7.90 (m, 7H, C_4-$OC_6\mathbf{H}_5$, C_5-**H** and C_6-**H**). Anal. calcd. for $C_{15}H_{13}IO_3$: C 48.91, H 3.53; found: C 48.71, H 3.36.

*2-Hydroxy-3-iodo-5-propionyl-4-phenoxypropiophenone (**4f**)*: IR (Nujol, cm^{-1}): 1630 (C=O). ^{1}H NMR ($CDCl_3$) δ: 0.70–1.30 (t, 6H, C_1- and C_5-$COCH_2$-$C\mathbf{H}_3$), 2.50–3.20 (q, 4H, C_1- and C_5-$COC\mathbf{H}_2CH_3$), 6.45–7.30 (m, 5H, C_4-$OC_6\mathbf{H}_5$), 8.25 (s,

© 1999 NRC Canada

1H, C_6-**H**), 9.55 (bs, 1H, C_2-O**H**). Anal. calcd. for $C_{18}H_{17}IO_4$: C 50.94, H 4.00; found: C 50.86, H 3.86.

*2-Hydroxy-3-iodo-5-nitro-4-phenoxypropiophenone (**4g**)*: IR (Nujol, cm^{-1}): 3300 (OH), 1645 (C=O). ^{1}H NMR ($CDCl_3$) δ: 1.17 (t, 3H, C_1-$COCH_2$-C**H**$_3$), 2.95 (q, 2H, C_1-COC**H**$_2CH_3$), 6.54–7.30 (m, 5H, C_4-OC_6**H**$_5$), 8.60 (s, IH, C_6-Ar-**H**). Exact Mass (70 eV) *m*/*z* calcd. for $C_{15}H_{12}INO_5$: 413.00; found: 412.98. MS *m*/*z*: 412.98 (77.7), 383.94 (53.8), 336.94 (27.8), 319.97 (47.9), 286.7 (39.6), 215.97 (26.0), 193.04 (100.0), 152.4 (23.0), 94.04 (68.2), 77.04 (32.6).

*5-Bromo-2-hydroxy-3-iodo-4-phenoxypropiophenone (**4h**)*: IR (Nujol, cm^{-1}): 3300 (OH), 1640 (C=O). ^{1}H NMR ($CDCl_3$) δ: 0.95 (t, 3H, C_1-$COCH_2$C**H**$_3$), 2.75 (q, 2H, C_1-COC**H**$_2CH_3$), 6.60–7.40 (m, 5H, C_4-OC_6**H**$_5$), 7.98 (s, IH, C_6-Ar-**H**). Exact Mass (70 eV) *m*/*z* calcd. for $C_{15}H_{12}BrIO_3$: 448.00; found: 447.90. MS *m*/*z*: 447.90 (74.6), 445.90 (77.1), 418.86 (99.9), 416.87 (100.0), 354.86 (52.3), 352.87 (54.8), 342.83 (25.9), 340.83 (25.6), 296.85(34.6), 294.86 (70.3), 292.85 (35.0), 291.97 (25.5), 290.97 (27.4), 289.97 (24.6), 243.98 (22.6), 216.93 (73.6), 214.94 (75.6), 77.03 (34.0).

*2-Hydroxy-3-iodo-4-phenoxydeoxybenzoin (**4i**)*: IR (Nujol, cm^{-1}): 3300 (OH), 1645 (C=O). ^{1}H NMR ($CDCl_3$) δ: 4.14 (s, 2H, C_1-COC**H**$_2C_6H_5$), 6.15 (d, 1H, C_5-Ar-**H**), 6.90–7.70 (m, 11H, C_1-$COCH_2C_6$**H**$_5$, C_4-OC_6**H**$_5$, C_6-Ar-**H**). Exact Mass (70 eV) *m*/*z* calcd.: 430.00; found: 431.00. MS *m*/*z*: 431 (4.44), 430 (19.61), 341 (5.10), 340 (37.98), 339 (100.0), 302 (0.9), 263 (5.83), 234 (2.05), 211 (16.31), 184 (16.64), 128 (14.74), 102 (3.33), 101 (1.19).

Acknowledgment

We are grateful to the Council of Scientific and Industrial Research (New Delhi) for financial assistance and to the Mass Spectrometry Facility, Department of Pharmaceutical Chemistry, San Francisco, California, for the scanning high-resolution mass spectra.

References

1. (*a*) D.F. Banks. Chem. Rev. **66**, 243 (1966); (*b*) A. Varvoglis. Chem. Soc. Rev. **10**, 377 (1981); (*c*) E.B. Merkushev. Russ. Chem. Rev. **56**, 826 (1987); (*d*) R.M. Moriarty, R.K. Vaid, and G.F. Koser. Synlett, 365 (1990); (*e*) O. Prakash. Aldrichimica Acta, **28**, 63 (1995); (*f*) P.J. Stang and V.V. Zhdankin. Chem. Rev. **96**, 1123 (1996).
2. (*a*) A. Varvoglis. The organic chemistry of polycoordinated iodine. VCH Publishers, New York. 1992; (*b*) G.F. Koser. *In* The chemistry of halides, pseudo-halides, and azides. Suppl D2. *Edited by* S. Patai and Z. Rapport. Wiley–Interscience, Chichester. 1995. Chap. 21. p. 1173; (*c*) A. Varvoglis. Hypervalent iodine in organic synthesis. Academic Press, New York. 1997.
3. R.M. Moriarty and O. Prakash. Adv. Heterocycl. Chem **69**, 1 (1998).
4. R.M. Moriarty and O. Prakash. Org. React. **54**, 273 (1999).
5. R.M. Moriarty and O. Prakash. Org. React. In press.
6. O. Prakash and S.P. Singh. Aldrichimica Acta, **27**, 15 (1994).
7. R.M. Moriarty and O. Prakash. Acc. Chem. Res. **19**, 244 (1988).
8. O. Prakash, S. Goyal, S.P. Singh, and R.M. Moriarty. Indian J. Chem. Sect. B: Org. Chem. Incl. Med. Chem. **27B**, 929 (1988).
9. R.M. Moriarty, O. Prakash, I. Prakash, and H.A. Musallam. J. Chem. Soc. Chem. Commun. 1342 (1984).
10. O. Prakash, S. Goyal, S. Pahuja, and S.P. Singh. Synth. Commun. **20**, 1409 (1990).
11. A. Pelter and S.A. Elegendy. J. Chem. Soc. Perkin Trans. 1, 1891 (1993).
12. N. Lewis and P. Wallbank. Synthesis, 1103 (1987).
13. O.Prakash, M.P. Tanwar, S. Goyal, and S. Pahuja. Tetrahedron Lett. **33**, 6519 (1992).
14. (*a*) A.R. Katritzky and C.W. Ress. Comprehensive heterocyclic chemistry. Vol. 4. Pergamon Press, Oxford. 1984. p. 708; (*b*) R.S. Burden, M.S. Kemp, C.W. Whiltshire, and J.D Owen. J. Chem. Soc. Perkin Trans. 1, 1445 (1984).
15. (*a*) T. Kappe, G. Korbuly, and W. Stadlbauer. Chem. Ber. **111**, 3857 (1978); (*b*) M.V. Sargent and P.O. Stransky. J. Chem. Soc. Perkin Trans. 1, 1605 (1982).
16. (*a*) R. Laschober and T. Kappe. Synthesis, 387 (1990); (*b*) D.E. Ames and A. Opalko. Synthesis, 234 (1983).
17. B.C. Schardt and C.L. Hill. Inorg. Chem. **22**, 1563 (1983).
18. U.K. Mallik and A.K. Mallik. Indian J. Chem. Sect. B: Org. Chem. Incl. Med. Chem. **31B**, 696 (1992); S. Spyroudis and P. Tarantili. Tetrahedron, **50**, 11541 (1994).
19. N.S. Narasimhan, I.S. Aidhen, and N.M Sunder. J. Indian Chem. Soc. **66**, 703 (1989).
20. S.R. Cooper. Org. Synth. Collect. Vol. III, 761 (1953).
21. M.P. Tanwar. Ph.D. Thesis, Kurukshetra University, Kurukshetra, India. 1994. pp. 66–73.
22. (*a*) R.E. Omer and C.S. Hamilton. J. Am Chem. Soc. 642 (1937); (*b*) A. Bobik, G.M. Holder, and A.J. Ryan. J. Med. Chem. 1194 (1977).
23. V.J. Dalvi and G.V. Jadhav. J. Indian Chem. Soc. **33**, 440 (1956).
24. G.G. Bedcock, G.W.K. Cavill, A. Robertson, and W.B. Whalley. J. Chem. Soc. 2961 (1950).

© 1999 NRC Canada

Reactions of aminoboron compounds with palladium and platinum complexes

Christopher M. Vogels, Heather L. Wellwood, Kumar Biradha, Michael J. Zaworotko, and Stephen A. Westcott

Abstract: Reactions of 3-$NH_2C_6H_4B(OH)_2$ (**1**, APBA) with $[MCl_4]^{2-}$ (M = Pd, Pt) give the boronic acid-containing complexes, $MCl_2(APBA)_2$ (M = Pd, **2**; M = Pt, **3**). Addition of **1** to $[PdCl_2(COE)]_2$ (COE = η^2-C_8H_{14}) ultimately led to $PdCl_2(APBA)_2$ (**2**). The pinacol derivative $PdCl_2(APBpin)_2$ (**5,** pin = $O_2C_2Me_4$) was characterized by an X-ray diffraction study. Crystals of **5** were monoclinic, a = 13.836(5), b = 14.937(5), c = 11.287(5) Å, β = 99.042(9)°, Z = 2, with space group $P2_1/c$. Monoalkene complexes $PtCl_2(COE)(APBA)$ (**8**) and $PtCl_2(COE)(APBpin)$ (**9**) were generated from the addition of APBA and APBpin, respectively, to $[PtCl_2(COE)]_2$. Reactions of 2-$NMe_2CH_2C_6H_4B(OH)_2$ (**10**) with palladium complex $[PdCl_2(COE)]_2$ proceed via selective B—C bond cleavage to give the cyclopalladated dimer $[PdCl(2\text{-}NMe_2CH_2C_6H_4)]_2$ as the major amine-containing product. Likewise, reactions with borinic esters $H_2NCH_2CH_2OBR_2$ (R = Bu, **14**; R = Ph, **15**) give products derived from cleavage of the B—O bond. The unique palladium complex $PdCl_2[3\text{-}NC_5H_4B(OH)_2]_2$ (**19**) was prepared by addition of $(3\text{-}NC_5H_4BEt_2)_4$ (**18**) to $[PdCl_2(COE)]_2$ in wet methylene chloride, where adventitious water was used to convert the organoborane product into the corresponding boronic acid moiety.

Key words: aminoboronic acids, platinum, palladium, cyclometallation.

Résumé : Le 3-$NH_2C_6H_4B(OH)_2$ (**1**, APBA) réagit avec les ions $[MCl_4]^{2-}$ (M = Pd, Pt) pour donner des complexes contenant de l'acide boronique, $MCl_2(APBA)_2$ (M = Pd, **2**; M = Pt, **3**). L'addition de **1** au $[PdCl_2(COE)]_2$ (COE = η^2-C_8H_{14}) conduit finalement au $PdCl_2(APBA)_2$ (**2**). Le dérivé du pinacol, $PdCl_2(APBpin)_2$ (**5**, pin = $O_2C_2Me_4$) a été caractérisé par une étude de diffraction des rayons X. Les cristaux du produit **5** sont monocliniques, groupe d'espace $P2_1/c$, avec a = 13,836(5), b = 14,937(5) et c = 11,287(5) Å, β = 99,042(9)° et Z = 2. On a généré des complexes monoalcéniques, $PtCl_2(COE)(APBA)$ (8) et $PtCl_2(COE)(APBpin)$ (**9**), par addition respectivement de APBA et de APBpin sur le $[PtCl_2(COE)]_2$. Les réactions du 2-$NMe_2CH_2C_6H_4B(OH)_2$ (**1**0) avec le complexe de palladium $[PdCl_2(COE)]_2$ se font avec un clivage sélectif de la liaison B—C et la formation du dimère cyclopalladié $[PdCl(2\text{-}NMe_2CH_2C_6H_4)]_2$ comme principal produit contenant de l'amine. De la même manière, les réactions avec des esters de l'acide boronique, $H_2NCH_2CH_2OBR_2$ (R = Bu, **14**; R = Ph, **15**), conduisent à la formation de produits dérivés du clivage de la liaison B—O. On a préparé le complexe de palladium unique, $PdCl_2[3\text{-}NC_5H_4B(OH)_2]_2$ (**19**) par addition de $(3\text{-}NC_5H_4BEt_2)_4$ (**18**) sur du $[PdCl_2(COE)]_2$ dans du chlorure de méthylène humide dont l'eau accidentelle est utilisée sert à transformer le produit organoborane en portion acide boronique correspondante.

Mots clés : acides aminoboroniques, platine, palladium, cyclométallation.

[Traduit par la Rédaction]

Introduction

The bioinorganic chemistry of compounds containing boronic acid groups, $B(OH)_2$, is an area of growing interest and has recently expanded to include boron-containing purine nucleosides (1), psuedocryptands (2) (which mimic the naturally occurring antibiotics boromycin and aplasmomycin), steroids (3), calixarenes (4), carbohydrates (5), fatty acids (6), porphyrins (7), and amino acids (8). Interestingly, boronic acids have been found to facilitate the transport of various ribonucleosides in and out of liposomes (9). Recent interest in compounds containing boronic acid groups arises from the ability of the boron atom to coordinate (via an empty *p*-orbital) with certain atoms, such as nitrogen and oxygen, of biomolecules. As a result, compounds containing boronic acids are able to act as selective targets for specific

Received October 28, 1998.

C.M. Vogels, H.L. Wellwood, and S.A. Westcott.[1] Department of Chemistry, Mount Allison University, Sackville, NB E4L 1G8, Canada.
K. Biradha and M.J. Zaworotko.[2] Department of Chemistry, St. Mary's University, Halifax, NS B3H 3C3, Canada.

[1]Author to whom correspondence may be addressed. Telephone: (506) 364-2372. Fax: (506) 364-2313. e-mail: swestcott@mta.ca
[2]Current address: Department of Chemistry, University of Winnipeg, Winnipeg, MB R3B 2E9, Canada.

 © 1999 NRC Canada

binding sites. For example, aromatic boronic acids have been shown to inhibit the serine proteases chymotrypsin and subtilisin (10). Serine proteases are a diverse group of proteolytic enzymes whose physiological functions include digestion of proteins, blood clotting, and cell lysis in the immune response. The crystal structure of subtilisin complexed with either phenylboronic acid or phenylethaneboronic acid (11) shows that the boron moiety exists as a tetrahedral adduct with the active hydroxyl site of the serine protease.

Work by Matteson et al. (12*d*) has shown that (*R*)-acetamido-2-phenylethaneboronic acid, a boron analogue of *N*-acetyl-phenylalanine, also acts as an effective and reversible inhibitor of serine proteases. Indeed, this compound is several orders of magnitude more effective than the corresponding aromatic boronic acids for the inhibition of chymotrypsin even in the micromolar concentration range. Since this discovery, much effort has focused on the synthesis of related boron-containing amino acid and peptide derivatives for possible applications as enzyme inhibitors (12, 13).

The observed biochemical activities and ability of boronic acids to facilitate the transport of molecules intracellularly prompted us to investigate the use of aminoboron compounds as ligands for biologically active transition metals. For instance, while both *cis* and *trans* amine complexes of platinum display anticancer properties, the overall efficacy of these chemotherapeutic compounds is limited by their numerous toxicities and poor cellular-uptake rates (arising from low solubility in water). As a result, a great deal of research has focused on improving aminoplatinum-based drugs for use in cancer therapy (14). With this in mind, we have begun to examine the possibility of generating new complexes of platinum and palladium containing aminoboron appendages. The results of our initial investigations are described herein.

Experimental

General procedures

Reagents and solvents used were obtained from Aldrich Chemicals. Palladium chloride and potassium tetrachloroplatinate were obtained from Strem. NMR spectra were recorded on a JEOL JNM-GSX270 FT NMR spectrometer. ^{1}H NMR chemical shifts are reported in ppm and referenced to residual protons in deuterated solvent at 270.05 MHz. ^{11}B{^{1}H} NMR chemical shifts are referenced to external $F_3B{\cdot}OEt_2$ at 86.55 MHz. ^{13}C{^{1}H} NMR chemical shifts are referenced to solvent carbon resonances as internal standards at 67.80 MHz. Multiplicities are reported as (s) singlet, (d) doublet, (t) triplet, (q) quartet, (quint) quintet, (m) multiplet, (br) broad, and (ov) overlapping. Infrared spectra were obtained using a Mattson Polaris FT-IR spectrometer and reported in cm^{-1}. Melting points were measured uncorrected with a Mel-Temp apparatus. Microanalyses for C, H, and N were carried out at Desert Analytics (Tucson, Ariz.).

μ-[Dichloro(*cis*-cyclooctene)palladium(II)]

μ-[Dichloro(*cis*-cyclooctene)palladium(II)], $[PdCl_2(COE)]_2$, was prepared by modification of a known synthesis (15*a*). Sodium chloride (363 mg, 6.21 mmol) was added as a solid to an isopropanol–water suspension (11:16 mL ratio by volume) of palladium chloride (500 mg, 2.82 mmol). After 1 h of stirring, cyclooctene (3 mL, 23.03 mmol) and a catalytic amount of tin(II) chloride (27 mg, 0.14 mmol) were added. After 20 h, solvent was removed under vacuum to afford a dark orange solid. $[PdCl_2(COE)]_2$ was extracted with methylene chloride, filtered to remove impurities, and collected following the removal of methylene chloride under vacuum. Yield: 620 mg (77%) of an orange solid; mp 164°C (decomposition). NMR spectroscopic data (in $CDCl_3$): ^{1}H δ: 6.20 (m, 4H, =C*H*R), 2.33 (s, 8H), 1.67 (s, 8H), 1.40 (s, 8H); ^{13}C{^{1}H} δ: 109.5 (br, =*C*HR), 29.1, 28.8, 26.3.

$PdCl_2(APBA)_2$ (2)

Method A

Sodium chloride (36 mg, 0.62 mmol) was added in small portions as a solid to a 25 mL methanol suspension of palladium chloride (50 mg, 0.28 mmol) to generate the methanol soluble species, sodium tetrachloropalladate. After 1 h of stirring, a 5 mL methanol solution of 3-aminophenylboronic acid (87 mg, 0.56 mmol) was added dropwise to the clear amber solution. Within 2 h, an isomeric mixture of *cis* and *trans* **2** precipitated and was collected by filtration and washed with methanol (3 × 5 mL) and methylene chloride (3 × 5 mL). Yield: 110 mg (81%) of a yellow solid.

Method B

In another reaction, 3-aminophenylboronic acid (91 mg, 0.58 mmol) was added in small portions as a solid to a stirred 25 mL methylene chloride solution of $[PdCl_2(COE)]_2$ (75 mg, 0.13 mmol). After 20 h, the reaction was filtered and a yellow solid was collected. The solid was washed three times with 10 mL portions of hexane and methylene chloride. Complex **2** was crystallized from a tetrahydrofuran–hexane solution. Yield: 50 mg (39%) of a yellow solid; mp 276°C (decomposition). IR (nujol): 3233 (m), 3125 (m), 2946 (s), 1582 (m), 1462 (m), 1377 (m). NMR spectroscopic data (in DMSO-d_6): ^{1}H δ: 8.14 (s, 4H, B(O*H*)$_2$), 7.63 (s, 2H), 7.33 (ov, 4H), 6.86 (s, 2H), 6.07 (s, 4H, N*H*$_2$); ^{11}B{^{1}H} δ 35.1 (br); ^{13}C{^{1}H} δ 147.6, 135.2 (br, *C*-B), 130.6, 125.0, 122.4, 120.4. Anal. calcd. for $PdCl_2C_{12}H_{16}N_2B_2O_4$: C 31.94, H 3.58, N 6.21; found: C 32.04, H 3.66, N 5.90.

$PtCl_2(APBA)_2$ (3)

A 25 mL aqueous solution of 3-aminophenylboronic acid (224 mg, 1.45 mmol) was added dropwise to a 25 mL water solution of potassium tetrachloroplatinate (300 mg, 0.72 mmol). Within 4 h, the solution became yellow, and a fine brown–yellow precipitate was collected by filtration and discarded. The clear yellow filtrate was chilled to 0°C, and after 24 h, **3** precipitated and was collected by filtration. Yield: 230 mg (55%) of a yellow solid; mp 267°C (decomposition). IR (nujol): 3266 (w), 3186 (w), 2885 (s), 1582 (m), 1461 (s), 1377 (s). NMR spectroscopic data (in acetone-d_6): ^{1}H δ: 7.88 (s, 2H), 7.72 (d, J_{H-H} = 5 Hz, 2H), 7.45 (m, 2H), 7.24 (t, J_{H-H} = 5 Hz, 2H), 6.74 (s, 4H, N*H*$_2$); ^{11}B{^{1}H} δ 30.9 (br); ^{13}C{^{1}H} δ: 141.5, 136.3 (br, *C*-B), 132.6, 129.5, 129.4, 124.0. Anal. calcd. for

© 1999 NRC Canada

$PtCl_2C_{12}H_{16}N_2B_2O_4$: C 26.69, H 2.99; found: C 26.34, H 2.92.

APBpin (4)

3-Aminophenylboronic acid (250 mg, 1.61 mmol) and 10 g of activated molecular sieves (BDH 4A) were added to a 25 mL methylene chloride solution of pinacol (190 mg, 1.61 mmol). After 5 days, the sieves were removed by filtration, and methylene chloride was removed under vacuum to give **4**. Yield: 350 mg (95%) of a light yellow solid; mp 93°C. IR (nujol): 3465 (w), 3375 (w), 3125 (s), 1628 (m), 1578 (m), 1452 (s), 1376 (s), 1145 (m). NMR spectroscopic data (in $CDCl_3$): ^{1}H δ: 7.20 (m, 2H), 7.14 (s, 1H), 6.80 (m, 1H), 3.63 (s, 2H, N*H*$_2$), 1.31 (s, 12H, BO_2C_2*Me*$_4$); ^{11}B{^{1}H} δ 31.8 (br); ^{13}C{^{1}H} δ: 145.9, 129.2 (br, *C*-B), 128.4, 124.9, 121.2, 118.1, 83.7 (BO_2*C*$_2$Me$_4$), 24.9 (BO_2C_2*Me*$_4$). Anal. calcd. for $C_{12}H_{18}NBO_2$: C 65.78, H 8.30, N 6.39; found: C 65.87, H 8.39, N 6.33.

$PdCl_2$(APBpin)$_2$ (5)

Method A

Complex **2** (250 mg, 0.51 mmol) was added slowly as a solid to a tetrahydrofuran solution of pinacol (140 mg, 1.20 mmol) and 10 g of activated molecular sieves (BDH 4A). After 3 days, the sieves and unreacted **2** were removed by filtration, and the filtrate was collected. Complex **5** was collected following the removal of tetrahydrofuran under vacuum. Yield: 50 mg (16%) of an orange solid.

Method B

To a 50 mL methylene chloride solution of $[PdCl_2(COE)]_2$ (200 mg, 0.35 mmol), a 15 mL methylene chloride solution of **4** (305 mg, 1.39 mmol) was added dropwise. The reaction was allowed to proceed for 2 h before the solvent was removed under vacuum. Complex **5** was crystallized from a tetrahydrofuran–hexane solution. Yield: 300 mg (70%) of an orange solid; mp 152°C (decomposition). IR (nujol): 3187 (w), 3121 (w), 2968 (s), 2891 (s), 1583 (w), 1461 (s), 1377 (s), 1148 (m), 722 (w). NMR spectroscopic data (in $CDCl_3$): ^{1}H δ 7.67 (s, 4H), 7.57 (s, 2H), 7.32 (s, 2H), 5.06 (br s, 4H, N*H*$_2$), 1.33 (s, 24H, BO_2C_2*Me*$_4$); ^{11}B{^{1}H} δ: 31.5 (br); ^{13}C{^{1}H} δ: 139.3, 132.7, 130.8 (br, *C*-B), 129.0, 127.7, 125.5, 84.2 (BO_2*C*$_2$Me$_4$), 25.1 (BO_2C_2*Me*$_4$). Anal. calcd. for $PdCl_2C_{24}H_{36}N_2B_2O_4$: C 46.82, H 5.91, N 4.55; found: C 46.46, H 5.89, N 4.48.

$PtCl_2$(APBpin)$_2$ (6)

Complex **3** (360 mg, 0.63 mmol) and 10 g of activated molecular sieves (BDH 4A) were added to a tetrahydrofuran solution of pinacol (163 mg, 1.34 mmol). The mixture was allowed to stand for 3 days before the sieves and unreacted **3** were removed by filtration. Complex **6** was isolated following removal of solvent under vacuum. Yield: 40 mg (9%) of a yellow solid; mp 224°C. IR (nujol): 1591 (m), 1400 (m), 1359 (m), 1332 (w), 1145 (m), 853 (w). NMR spectroscopic data (in DMSO-d_6): ^{1}H δ: 7.63 (s, 2H), 7.49 (m, 4H), 7.30 (m, 4H), 1.36 (s, 24H), ^{11}B{^{1}H} δ: 32.6 (br); ^{13}C{^{1}H} δ: 148.0, 141 (br, *C*-B), 128.3, 121.8, 120.1, 116.8, 67.0, 21.7. Anal. calcd. for $PtCl_2C_{24}H_{36}N_2B_2O_4$: C 40.93, H 5.16, N 3.98; found: C 40.63, H 5.31, N 4.02.

Reaction of $[PdCl_2(COE)]_2$ and 4

A 20 mL methylene chloride solution of **4** (114 mg, 0.52 mmol) was added dropwise to a stirred 50 mL methylene chloride solution of $[PdCl_2(COE)]_2$ (150 mg, 0.26 mmol). After 30 min, the clear orange solution became clear red, at which point methylene chloride was removed under vacuum to afford complex **7**, which was washed with hexane (3 × 5 mL). Yield: 120 mg (91%) of a red–orange solid; mp 138°C (decomposition). IR (nujol): 3194 (m), 3123 (m), 2973 (s), 2885 (s), 2842 (s), 1583 (m), 1461 (s), 1364 (s), 1146 (m), 695 (m). NMR spectroscopic data of **7** (in $CDCl_3$): ^{1}H δ: 7.65 (s, 2H), 7.56 (s, 1H), 7.29 (s, 1H), 6.03 (m, 2H, =CHR), 5.24 (s, 2H, N*H*$_2$), 2.31 (br s, 4H), 1.60 (br s, 4H), 1.45 (br s, 4H), 1.34 (s, 12H, BO_2C_2*Me*$_4$); ^{11}B{^{1}H} δ: 32.1 (br); ^{13}C{^{1}H} δ 139.0, 132.8, 131.0 (br, *C*-B), 129.1, 127.7, 125.5, 117.3 (br, =*C*HR), 84.2 (BO_2*C*$_2$Me$_4$), 29.3, 27.8, 26.3, 25.1 (BO_2C_2*Me*$_4$). Reactions gave minor amounts of the diamine complex, which complicated elemental analyses.

Reaction of 7 and PPh_3

Complex **7** (44 mg, 0.09 mmol) was dissolved in 10 mL of methylene chloride, and a 10 mL methylene chloride solution of triphenylphosphine (25 mg, 0.09 mmol) was added dropwise to the clear red solution. Within 1 h, a yellow precipitate formed and was collected by filtration. Yield: 25 mg of a yellow solid. Selected NMR data (in $CDCl_3$): ^{1}H δ: 7.70 (m, *Ar*, 2H), 7.41 (m, *Ar*, 3H); $PdCl_2(PPh_3)_2$.

$PtCl_2$(COE)(APBA) (8)

To a stirred 50 mL methylene chloride solution of $[PtCl_2(COE)]_2$ (100 mg, 0.13 mmol), 3-aminophenylboronic acid (41 mg, 0.26 mmol) was added in small portions as a solid. The cloudy, yellow mixture was filtered after 2 days, and the clear yellow filtrate was stored under dinitrogen at 0°C. Within 48 h, **8** precipitated and was collected by filtration. The yellow solid was washed with ether (3 × 10 mL), hexane (3 × 10 mL), and cold methylene chloride (1 × 2 mL). Yield: 80 mg (29%) of a yellow solid; mp 169°C. IR (nujol): 3186 (w), 3116 (w), 2965 (s), 2890 (s), 1584 (m), 1462 (s), 1377 (s), 723 (m). NMR spectroscopic data (in acetone-d_6): ^{1}H δ: 7.95 (s, 1H), 7.77 (s, 1H), 7.54 (m, 2H), 5.95 (s, J_{H-Pt} = 27 Hz, 2H, =C*H*R), 2.46 (s, 4H), 2.14 (s, 4H), 1.81 (s, 4H); ^{11}B{^{1}H} δ 29.6 (br); ^{13}C{^{1}H} δ: 146.9, 136.4 (br, *C*-B), 133.6, 129.3, 128.9, 126.4, 93.3 (s, J_{C-Pt} = 80 Hz, =*C*HR), 28.4, 26.8, 26.1.

$PtCl_2$(COE)(APBpin) (9)

To a 50 mL methylene chloride solution of $[PtCl_2(COE)]_2$ (145 mg, 0.19 mmol), a 10 mL methylene chloride solution of **4** (89 mg, 0.41 mmol) was added dropwise. After 5 h, methylene chloride was removed under vacuum to afford a yellow solid. Complex **9** was crystallized from a methylene chloride – hexane solution. Yield: 150 mg (66%) of a yellow powder; mp 236°C (decomposition). IR (nujol): 3116 (w), 2935 (s), 1578 (w), 1461 (s), 1377 (s), 1145 (m), 726 (m). NMR spectroscopic data (in $CDCl_3$): ^{1}H δ: 7.70 (s, 2H), 7.61 (s, 1H), 7.36 (s, 1H), 5.91 (br s, 2H, =C*H*R), 5.35 (s, J_{H-Pt} = 32 Hz, 2H, N*H*$_2$), 2.36 (br s, 2H), 2.25 (br s, 2H), 1.74 (br s, 2H), 1.41 (br s, 6H), 1.34 (s, 12H, BO_2*Me*$_4$); ^{11}B{^{1}H} δ 32.2 (br); ^{13}C{^{1}H} δ: 139.4, 131.7, 131.0 (br, *C*-B), 129.2, 126.7,

© 1999 NRC Canada

124.1, 93.1 (J_{C-Pt} = 164 Hz, =*C*HR), 84.3 ($BO_2C_2Me_4$), 29.3, 28.2, 26.3, 25.1 ($BO_2C_2Me_4$). Anal. calcd. for $PtCl_2C_{20}H_{32}NBO_2$: C 40.35, H 5.43, N 2.35; found: C 41.08, H 5.68, N 2.46.

2-$NMe_2CH_2C_6H_4B(OH)_2$ (10)

Compound **10** was prepared by modification of a known procedure (16). To a 20 mL ether solution of *N*,*N*-dimethylbenzylamine (10.0 g, 74 mmol), a 10.0 M solution of *n*-butyllithium in hexanes (8.2 mL, 82 mmol) was added dropwise under an atmosphere of dinitrogen. The lithiation of *N*,*N*-dimethylbenzylamine was allowed to proceed at room temperature for 18 h. Trimethylborate (10.0 mL, 88 mmol) was added at 0 °C, and the reaction mixture was allowed to warm to room temperature. After 4 h, 10 mL of water was added and the aqueous phase separated. The addition of 20 mL of isopropanol and subsequent cooling of the mixture to 0 °C resulted in the precipitation of lithium borate, which was removed by filtration. Complex **10** was isolated upon removal of water under vacuum. Yield: 3.25 g (25%) of an off-white powder. NMR spectroscopic data (in D_2O): ^{1}H δ: 7.41 (m, 1H), 7.20 (m, 2H), 7.08 (m, 1H), 3.81 (s, 2H, Ar-CH_2-N), 2.34 (s, 6H, NMe_2); ^{11}B{^{1}H} δ: 8.9 (br); ^{13}C{^{1}H} δ: 150 (br, *C*-B), 145.5, 135.0, 132.9, 132.4, 128.6, 69.6 (Ar-*C*H_2-N), 49.4 (NMe_2).

Reaction of Na_2PdCl_4 + 10

A fresh solution of sodium tetrachloropalladate was prepared by the addition of sodium chloride (36 mg, 0.62 mmol) to a 30 mL methanol suspension of palladium chloride (50 mg, 0.28 mmol). After 1 h of stirring, a 10 mL methanol solution of **10** (111 mg, 0.62 mmol) was added dropwise. The yellow precipitate that formed over 1 h was collected by filtration and washed with water (3 × 5 mL). Selected NMR data (in $CDCl_3$): ^{1}H δ: 7.16 (m, 2H), 6.97 (m, 2H), 6.87 (m, 4H), 3.93 (s, 4H, Ar-CH_2-N), 2.86 (s, 12H, NMe_2); $[PdCl(2\text{-}NMe_2CH_2C_6H_4)]_2$.

Reaction of $[PtCl_2(COE)]_2$ + 10

To a stirred 35 mL methylene chloride solution of $[PtCl_2(COE)]_2$ (150 mg, 0.20 mmol), compound **10** (75 mg, 0.42 mmol) was added in small portions as a solid. After 20 h, the reaction was filtered and methylene chloride removed under vacuum. Complex **13** was extracted from the resulting brown–orange solid with hexane (10 × 10 mL). Attempts at isolating compound **13** were complicated by the ubiquitous presence of a minor amount of an unidentified compound. IR (nujol): 3060 (w), 3001 (w), 2927 (s), 2854 (s), 1586 (w), 1471 (m), 717 (s), 651 (s). Selected NMR data (crude) for **13** (in $CDCl_3$): ^{1}H δ: 7.03 (m, 3H), 6.57 (s, J_{H-Pt} = 43 Hz, 1H), 4.84 (s, J_{H-Pt} = 68 Hz, 2H, =C*H*R), 4.05 (s, J_{H-Pt} = 38 Hz, 2H, Ar-CH_2-N), 2.99 (s, J_{H-Pt} = 32 Hz, 6H, NMe_2), 2.73 (br s, 4H), 2.28 (br s, 4H), 1.81 (br s, 4H); ^{13}C{^{1}H} δ: 147.3, 133.1, 127.4 (J_{C-Pt} = 43 Hz, *C*-Pt), 126.2, 124.9, 122.1, 87.7 (s, J_{C-Pt} = 191 Hz, =*C*HR), 74.8 (s, J_{C-Pt} = 44 Hz, Ar-*C*H_2-N), 51.8 (NMe_2), 30.0, 28.5, 26.5.

2-$NMe_2CH_2C_6H_4Bpin$ (11)

A 10 mL methylene chloride solution of pinacol (330 mg, 2.79 mmol) was added dropwise to a 35 mL methylene chloride suspension of **10** (600 mg, 3.35 mmol). Ten grams of activated molecular sieves (BDH 4A) were added to the mixture to facilitate the formation of **11**. The reaction was allowed to stand for 5 days at which point the sieves and unreacted **10** were removed by filtration. Compound **11** was isolated following removal of methylene chloride under vacuum. Yield: 0.52 g (72%) of an off-white solid; mp 75°C. IR (nujol): 3150 (s), 1476 (w), 1348 (m), 1151 (s), 1107 (s), 1043 (s), 748 (m). NMR spectroscopic data (in $CDCl_3$): ^{1}H δ: 7.55 (d, J_{H-H} = 5 Hz, 1H), 7.19 (app. quint, J_{H-H} = 8 Hz, 2H), 7.01 (d, J_{H-H} = 8 Hz, 1H), 3.86 (s, 2H, Ar-CH_2-N), 2.57 (s, 6H, NMe_2), 1.31 (s, 12 H, $BO_2C_2Me_4$); ^{11}B{^{1}H} δ: 15.3 (br); ^{13}C{^{1}H} δ: 143.9 (br, *C*-B), 139.8, 131.6, 127.6, 127.5, 123.1, 80.5 ($BO_2C_2Me_4$), 65.6 (Ar-*C*H_2-N), 45.9 (NMe_2), 26.8 ($BO_2C_2Me_4$). Anal. calcd. for $C_{15}H_{24}NBO_2$: C 68.97, H 9.28, N 5.36; found: C 68.80, H 9.60, N 5.38.

Reaction of Na_2PdCl_4 + 11

A fresh solution of sodium tetrachloropalladate was generated by the addition of sodium chloride (22 mg, 0.37 mmol) to a stirred 15 mL methanol suspension of palladium chloride (30 mg, 0.17 mmol). After 1 h of stirring, a 10 mL methanol solution of **11** (88 mg, 0.338 mmol) was added dropwise. After 3 h, a yellow precipitate had formed and was collected by filtration. Yield: 35 mg (75%) of a yellow solid. NMR spectroscopic data (in $CDCl_3$): ^{1}H δ: 7.16 (m, 1H), 6.97 (m, 2H), 6.87 (m, 4H), 3.93 (s, 4H, CH_2N(Me)$_2$), 2.86 (s, 12H, $CH_2N(Me)_2$), $[PdCl(2\text{-}NMe_2CH_2C_6H_4)]_2$.

Reaction of $[PdCl_2(COE)]_2$ + 11

A 10 mL methylene chloride solution of **11** (182 mg, 0.70 mmol) was added dropwise to a stirred 25 mL methylene chloride solution of $[PdCl_2(COE)]_2$ (100 mg, 0.17 mmol). After 6 h, solvent was removed under vacuum to yield an orange–brown oil. Selected NMR data (in $CDCl_3$): ^{1}H δ: 7.16 (m, 2H), 6.97 (m, 2H), 6.87 (m, 4H), 3.93 (s, 4H, CH_2N(Me)$_2$), 2.86 (s, 12H, $CH_2N(Me)_2$) $[PdCl(2\text{-}NMe_2CH_2C_6H_4)]_2$; 9.19 (br), 8.06 (m), 7.92 (m), 7.60 (m), 7.42 (m), 4.72 (m), 2.98 (s) [2-$HNMe_2CH_2C_6H_4Bpin]_2[PdCl_4]$; 1.38 (s) $(Bpin)_2O$. ^{11}B{^{1}H} δ: 31.9 (br, $[2\text{-}HNMe_2CH_2C_6H_4Bpin]_2[PdCl_4]$), 23.1 (br, $(Bpin)_2O$).

$PtCl_2(COE)(2\text{-}Me_2NCH_2C_6H_4Bpin)$ (12)

The addition of a 0.5 mL deuterated chloroform solution of **11** (24 mg, 0.09 mmol) to a 0.5 mL deuterated chloroform solution of $[PtCl_2(COE)]_2$ (35 mg, 0.05 mmol) was performed under an atmosphere of dinitrogen. The reaction was allowed to proceed for 4 h before characterization by NMR spectroscopy was performed. IR ($CHCl_3$): 2981 (m), 2929 (s), 2854 (m), 1600 (w), 1471 (m), 1346 (s), 1145 (m), 906 (s), 745 (s), 651 (s). NMR spectroscopic data (in $CDCl_3$): ^{1}H δ: 8.87 (s, 1H), 7.89 (s, 1H), 7.58 (s, 1H), 7.39 (s, 1H), 5.35 (ov m, J_{H-Pt} = 78 Hz, 2H, =C*H*R), 4.68 (s, 2H, Ar-CH_2-N), 2.80 (s, 6H, NMe_2), 2.53 (br, 2H), 2.23 (br, 2H), 1.81 (br, 2H), 1.40 (br, 6H), 1.35 (s, 12H, $BO_2C_2Me_4$); ^{11}B{^{1}H} δ: 35.1 (br); ^{13}C{^{1}H} δ: 139.9, 136.6, 133.0, 131.0, 129.0 (br, *C*-B), 128.1, 91.4 (s, J_{C-Pt} = 161 Hz, =*C*HR), 84.1 ($BO_2C_2Me_4$), 64.8 (Ar-*C*H_2-N), 52.1 (NMe_2), 29.2, 28.1, 26.3, 25.1 ($BO_2C_2Me_4$).

© 1999 NRC Canada

Reaction of Na_2PdCl_4 + 14

Sodium chloride (18 mg, 0.31 mmol) was added to a stirred 15 mL methanol suspension of palladium chloride (25 mg, 0.14 mmol) to produce sodium tetrachloropalladate. A 5 mL methanol solution of dibutylborinic acid, ethanolamine ester (57 mg, 0.31 mmol) was added dropwise to the solution, and the reaction was allowed to proceed for 45 h. The product was obtained upon removal of methanol under vacuum. NMR spectroscopic data (in D_2O): ^1H δ: 3.76 (m, 4H), 3.44 (br, 4H, N*H*$_2$), 2.68 (m, 4H); $PdCl_2(NH_2CH_2CH_2OH)_2$.

Reaction of K_2PtCl_4 + 14

Dibutylborinic acid, ethanolamine ester (29 mg, 0.16 mmol) was added as a solid to a stirred 20 mL aqueous solution of potassium tetrachloroplatinate (30 mg, 0.07 mmol). The reaction was allowed to proceed for 18 h. A yellow solid was isolated following the removal of water under vacuum. Selected NMR data (in D_2O): ^1H δ: 3.79 (m, 4H), 3.08 (m, 4H), 2.82 (br, 4H, N*H*$_2$), $PtCl_2(NH_2CH_2CH_2OH)_2$; $^{11}B\{^1H\}$ δ: 19.9 (s, $B(OH)_3$).

Reaction of Na_2PdCl_4 + 15

Sodium chloride (22 mg, 0.38 mmol) was added as a solid to a stirred 15 mL methanol suspension of palladium chloride (30 mg, 0.17 mmol) to produce the methanol soluble species, sodium tetrachloropalladate. After 1 h of stirring, a 10 mL methanol solution of diphenylborinic acid, ethanolamine ester (80 mg, 0.36 mmol) was added dropwise, and the clear amber solution became black immediately. Methanol was removed under vacuum, and the aqueous and organic soluble species were characterized by NMR spectroscopy. For the water soluble phase, NMR data (in D_2O): ^1H δ: 3.76 (m, 4H), 3.44 (m, 4H), 2.68 (m, 4H); $PdCl_2(NH_2CH_2CH_2OH)_2$. $^{11}B\{^1H\}$ δ: 19.9 (s, $B(OH)_3$). For the organic soluble phase, NMR data (in $CDCl_3$): ^1H δ: 8.22 (m), 7.57 (m), 7.45 (ov); $^{11}B\{^1H\}$ δ: 29.6 (br, $PhB(OH)_2$).

Reaction of K_2PtCl_4 + 15

Diphenylborinic acid, ethanolamine ester (29 mg, 0.13 mmol) was added in small portions as a solid to a stirred 20 mL aqueous solution of potassium tetrachloroplatinate (25 mg, 0.06 mmol). Water was removed under vacuum after 10 h, and the aqueous and organic soluble products were characterized by NMR spectroscopy. NMR data (in D_2O): ^1H δ: 3.79 (m, 4H), 3.08 (m, 4H), 2.82 (m, 4H); $PtCl_2(NH_2CH_2CH_2OH)_2$. $^{11}B\{^1H\}$ δ: 19.9 (s, $B(OH)_3$). For the organic soluble phase, NMR data (in $CDCl_3$): ^1H δ: 8.22 (m), 7.57 (ov) 7.45 (ov); $^{11}B\{^1H\}$ δ: 29.6 (br, $PhB(OH)_2$).

Reaction of $[PdCl_2(COE)]_2$ + 14

Under an atmosphere of dinitrogen using an MBraun glovebox, a 2 mL THF solution of dibutylborinic acid, ethanolamine ester (39 mg, 0.21 mmol) was added dropwise to a stirred 5 mL THF solution of $[PdCl_2(COE)]_2$ (30 mg, 0.05 mmol). The reaction was allowed to proceed for 1.5 h before solvent was removed under vacuum. The resulting yellow solid was washed with hexane (2 × 3 mL) to remove cyclooctene. The solid was dried under vacuum, and the product was extracted with 1 mL of deuterated chloroform. Selected NMR data (in $CDCl_3$): ^1H δ 4.12, (s), 3.24 (br), 2.84 (s), 1.31 (s), 0.89 (s); $^{11}B\{^1H\}$ δ 60.5 (br). The product decomposed (1 h) in solution to give palladium metal.

Reaction of $[PtCl_2(COE)]_2$ + 14

Under an atmosphere of dinitrogen using an MBraun glovebox, a 0.5 mL deuterated chloroform solution of dibutylborinic acid, ethanolamine ester (12 mg, 0.07 mmol) was added dropwise to a 0.5 mL deuterated chloroform solution of $[PtCl_2(COE)]_2$ (25 mg, 0.03 mmol). The reaction was allowed to proceed for 3 h before the product was characterized by IR and NMR spectroscopy. IR ($CHCl_3$): 3319 (w), 2930 (m), 1571 (w), 1468 (w), 1330 (w), 901 (s), 726 (s), 651 (s). Selected NMR data for $PtCl_2(COE)(NH_2CH_2CH_2OBBu_2)$ **16** (in $CDCl_3$): ^1H δ: 5.61 (br, 2H, C=C*H*R), 5.29 (br, J_{H-Pt} = 68 Hz, 2H, N*H*$_2$), 4.10, (br), 3.22 (br), 2.38 (br), 2.27 (br) 2.12, (br) 1.78, (br) 1.47 (br), 1.30 (br), 0.87 (br); $^{11}B\{^1H\}$ δ: 56.1 (br). The product decomposed (1 h) in solution to give platinum metal.

Reaction of $[PtCl_2(COE)]_2$ + 15

Under an atmosphere of dinitrogen using an MBraun glovebox, a 0.5 mL deuterated chloroform solution of diphenylborinic acid, ethanolamine ester (15 mg, 0.07 mmol) was added dropwise to a 0.5 mL deuterated chloroform solution of $[PtCl_2(COE)]_2$ (25 mg, 0.03 mmol). The reaction was allowed to proceed for 3 h before the clear yellow solution was characterized by NMR and IR spectroscopy. NMR data for $PtCl_2(COE)(NH_2CH_2CH_2OBPh_2)$ (**17**) (in $CDCl_3$): ^1H δ: 7.63 (m, 4H), 7.43 (m, 6H), 5.62 (br s, 2H, C=C*H*R), 5.30 (br s, J_{H-Pt} = 62 Hz, 2H, N*H*$_2$), 4.17 (s, 2H), 3.33 (s, 2H), 2.36 (br, 4H), 2.14 (br, 4H), 1.76 (br s, 4H); $^{11}B\{^1H\}$ δ: 47.8 (br); $^{13}C\{^1H\}$ δ 136.6 (br, *C*-B), 134.4, 131.7, 130.5, 130.1, 127.7, 93.7 (s, J_{C-Pt} = 165 Hz, *C*=*C*HR), 63.5, 46.6, 29.4, 28.0, 26.3. IR ($CHCl_3$): 2929 (w), 2853 (w), 1576 (w), 1470 (w), 1438 (w), 1322 (w), 905 (s), 727 (s), 851 (s).

$PdCl_2(3\text{-}NC_5H_4B(OH)_2)_2$ (19)

A 10 mL methylene chloride solution of 3-(diethylboryl)pyridine (102 mg, 0.69 mmol) was added dropwise to a stirred 30 mL methylene chloride solution of $[PdCl_2(COE)]_2$ (100 mg, 0.17 mmol). After 48 h, an orange precipitate was collected by filtration and washed with methylene chloride (3 × 5 mL). Yield: 60 mg (42%) of an orange solid; mp 234°C. IR (nujol): 3197 (w), 2923 (s), 2856 (s), 1576 (w), 1462 (m), 1377 (m). Selected NMR data (in acetone-d_6): ^1H δ: 9.24 (s, 4H, B(O*H*)$_2$), 8.94 (m, 2H), 8.41 (m, 4H), 7.61 (m, 2H); $^{11}B\{^1H\}$ δ: 29.2 (br). Solubility problems precluded $^{13}C\{^1H\}$ NMR data collection.

$PdCl_2(3\text{-}NC_5H_4Bpin)_2$ (20)

To a 40 mL methylene chloride suspension of **19** (134 mg, 0.32 mmol), pinacol (45 mg, 0.38 mmol) and 10 g of activated molecular sieves (BDH 4A) were added. The mixture was allowed to stand for 7 days before the sieves and unreacted **19** were removed by filtration. The filtrate was collected, and methylene chloride removed under vacuum to afford a yellow solid, which was washed with hexane (3 × 10 mL) to remove excess pinacol. The product was crystallized from a CH_2Cl_2–hexane solution. Yield: 160 mg (86%)

© 1999 NRC Canada

Table 1. Crystallographic data collection parameters for *trans*-$PdCl_2(APBpin)_2$ (**5**).

Complex	**5**
Formula	$C_{24}H_{36}B_2Cl_2N_2O_4Pd \cdot 4C_4H_8O$
fw	903.88
Crystal system	Monoclinic
Space group	$P2_1/c$
a, Å	13.836(5)
b, Å	14.937(5)
c, Å	11.287(5)
β, deg	99.042(9)
V, Å^3	2304(2)
Z	2
ρ_{calcd}, g cm^{-3}	1.303
Crystal size, mm	0.25 × 0.20 × 0.20
Temperature, K	203(2)
Radiation	MoKα (λ = 0.71073)
μ, mm^{-1}	0.567
Max 2θ, deg	25
Data collection method	ω
Total unique reflections	4023
Total observed reflections[a]	3893
No. of variables	258
Max. res. density/hole, e Å^{-3}	0.464/–0.532
R^b	0.0449
R_w	0.1161
GoF[c]	1.071

[a] $I_o > 3\sigma(I_o)$.
[b] $R = \Sigma||F_o| - |F_c||/\Sigma|F_o|$; $Rw = [\Sigma(w(|F_o| - |F_c|)^2/\Sigma(w|F_o|)^2]^{1/2}$.
[c] $[\Sigma(w(|F_o| - |F_c|)^2/(NO - NV)]^{1/2}$.

of a yellow solid, mp 276°C. IR (nujol): 2949 (s), 2859 (s), 1603 (w), 1461 (m), 1376 (m). NMR spectroscopic data (in $CDCl_3$): ^{1}H δ: 9.13 (s, 2H), 8.85 (d, J_{H-H} = 5 Hz, 2H), 8.12 (d, J_{H-H} = 8 Hz, 2H), 7.33 (t, J_{H-H} = 8 Hz, 2H), 1.35 (s, 24H, BO_2Me_4); ^{11}B{^{1}H} δ: 31.0 (br); ^{13}C{^{1}H} δ 158.7, 154.7, 144.5, 126.5 (br, *C*-B), 124.5, 84.9 ($BO_2C_2Me_4$), 24.9 ($BO_2C_2Me_4$). Anal. calcd. for $PdCl_2C_{22}H_{32}N_2B_2O_4 \cdot H_2O$: C 43.63, H 5.65, N 4.62; found: C 43.61, H 5.39, N 4.89.

X-ray crystallographic data for 5

Crystals of **5** suitable for X-ray diffraction studies were obtained by recrystallization from a THF–hexane mixture at 5°C. A summary of the crystal data and parameters for data collection is given in Table 1. Data were collected at 203 K on a Siemens SMART/CCD diffractometer equipped with an LT-II low-temperature device. Diffracted data were corrected for absorption using the SADABS[3] program. SHELXTL was used for structure solution, and refinement was based on F^2.[4] All non-hydrogen atoms were refined anisotropically. Hydrogen atoms were fixed at calculated positions. Selected bond distances and angles are given in Table 2 and final atomic coordinates in Table 3. Complete tables of bond distances and angles, final atomic coordinates, and anisotropic displacement parameters have been deposited as supporting material.[5]

Results and discussion

1. Reactions with 3-aminophenylboronic acid

The synthesis of amines containing boronic acid groups is often a complicated procedure requiring several complex organic transformations (12*d*). As a result, the range of compounds containing both an amine and a boronic acid functionality is surprisingly small. Indeed, the use of aminoboronic acids as ligands for transition metals has not yet been explored. As part of our initial investigation into this area, we set out to prepare palladium and platinum complexes containing commercially available 3-aminophenylboronic acid (3-$NH_2C_6H_4B(OH)_2$, APBA, **1**). We have found that addition of **1** to aqueous solutions of $[MCl_4]^{2-}$ (M = Pd, Pt) gives the corresponding boronic acid-containing complexes $MCl_2(APBA)_2$ (M = Pd, **2**; M = Pt, **3**). These complexes are insoluble in most common organic solvents, and attempts to dissolve them in coordinating solvents such as DMSO led to decomposition where the solvent was clearly displacing the weakly bound aminoboron group. Although aniline derivatives are known to coordinate to palladium and platinum (17), the addition of an electron-withdrawing boronic acid group to the phenyl moiety, not surprisingly, severely reduces the nucleophilicity of the already weak aniline group (pK_a = 4.6 for conjugate acid, anilinium ion). Attempts to generate diaqua complexes $[M(OH_2)_2(APBA)_2](NO_3)_2$ by addition of $AgNO_3$ to **2** and **3** in water gave rapid degradation to the corresponding metals along with the formation of boric acid.

Compounds containing boronic acids are extremely difficult to characterize in terms of elemental composition, owing to the ease with which they partially dehydrate to the corresponding trimeric or oligomeric anhydrides (12*a*). To alleviate this complication, as well as to increase solubilities in organic solvents, we replaced the hydroxyl groups on **1** with the more electron donating pinacol-derived group (pin = $O_2C_2Me_4$) (18) to give 3-$NH_2C_6H_4$Bpin (**4**, APBpin). Unfortunately, substitution reactions in water involving **4** and the tetrachloro salts suffered from competing cleavage of the pinacol groups to give complicated mixtures of products. However, transesterification of the boronic acid derivatives **2** and **3** with pinacol ultimately generated the corresponding complexes $MCl_2(APBpin)_2$ (M = Pd, **5**; M = Pt, **6**) in low yields (9–16%).

The molecular structure of diamine complex **5**, which crystallizes with four molecules of tetrahydrofuran per complex, is shown in Fig. 1, and selected bond distances and angles provided in Table 2. The aminoboron ligands lie in a *trans* configuration with Pd—N bond distances of 2.047(3) Å being similar to that observed for the analogous

[3] G.M. Sheldrick. SADABS Univ. Gottingen. 1996.
[4] G.M. Sheldrick. SHELXTL Release 5.03. Siemens Analytical X-ray Instruments Inc., Madison, Wis. 1994.
[5] A complete set of data may be purchased from: The Depository of Unpublished Data, Document Delivery, CISTI, National Research Council Canada, Ottawa, Canada, K1A 0S2. Tables of coordinates, bond distances and angles, and alternative views of **5** have also been deposited with the Cambridge Crystallographic Data Centre and can be obtained on request from: The Director, Cambridge Crystallographic Data Centre, University Chemical Laboratory, 12 Union Road, Cambridge, CB2 1EZ, U.K.

© 1999 NRC Canada

Table 2. Selected bond distances (Å) and angles (deg) for *trans*-$PdCl_2(3\text{-}NH_2C_6H_4Bpin)_2$ (**5**).

Pd(1)—N(1)	2.047(3)
Pd(1)—N(1)#1	2.047(3)
Pd(1)—Cl(1)#1	2.3028(11)
Pd(1)—Cl(1)	2.3028(11)
O(1)—B(1)	1.354(5)
O(1)—C(7)	1.481(4)
O(2)—B(1)	1.372(5)
O(2)—C(8)	1.464(4)
N(1)—C(1)	1.438(4)
B(1)—C(3)	1.555(5)
C(1)—C(6)	1.382(5)
C(1)—C(2)	1.394(4)
C(2)—C(3)	1.402(5)
C(3)—C(4)	1.390(5)
C(4)—C(5)	1.390(5)
C(5)—C(6)	1.380(5)
C(7)—C(11)	1.512(5)
C(7)—C(12)	1.514(5)
C(7)—C(8)	1.559(5)
C(8)—C(10)	1.518(5)
C(8)—C(9)	1.527(6)
O(1A)—C(1A)	1.361(6)
O(1A)—C(4A)	1.424(5)
C(1A)—C(2A)	1.453(7)
C(2A)—C(3A)	1.470(7)
C(3A)—C(4A)	1.493(6)
O(1B)—C(4B)	1.409(5)
O(1B)—C(1B)	1.427(5)
C(1B)—C(2B)	1.417(7)
C(2B)—C(3B)	1.458(7)
C(3B)—C(4B)	1.453(7)
N(1)-Pd(1)-N(1)#1	180.0
N(1)-Pd(1)-Cl(1)#1	90.14(11)
N(1)#1-Pd(1)-Cl(1)#1	89.86(11)
N(1)-Pd(1)-Cl(1)	89.86(11)
N(1)#1-Pd(1)-Cl(1)	90.14(11)
Cl(1)#1-Pd(1)-Cl(1)	180.0
B(1)-O(1)-C(7)	107.1(3)
B(1)-O(2)-C(8)	107.0(3)
C(1)-N(1)-Pd(1)	114.1(2)
O(1)-B(1)-O(2)	113.8(3)
O(1)-B(1)-C(3)	124.1(3)
O(2)-B(1)-C(3)	122.1(4)
C(6)-C(1)-C(2)	120.0(3)
C(6)-C(1)-N(1)	120.0(3)
C(2)-C(1)-N(1)	120.1(3)
C(1)-C(2)-C(3)	121.0(3)
C(4)-C(3)-C(2)	117.9(3)
C(4)-C(3)-B(1)	121.7(3)
C(2)-C(3)-B(1)	120.4(3)
C(3)-C(4)-C(5)	120.8(4)
C(6)-C(5)-C(4)	120.7(4)
C(5)-C(6)-C(1)	119.5(3)
O(1)-C(7)-C(11)	108.5(3)
O(1)-C(7)-C(12)	106.1(3)
C(11)-C(7)-C(12)	110.7(3)
O(1)-C(7)-C(8)	102.0(3)
C(11)-C(7)-C(8)	114.4(3)
C(12)-C(7)-C(8)	114.2(3)
O(2)-C(8)-C(10)	108.8(3)
O(2)-C(8)-C(9)	107.0(3)
C(10)-C(8)-C(9)	109.8(3)
O(2)-C(8)-C(7)	102.5(3)
C(10)-C(8)-C(7)	115.1(3)
C(9)-C(8)-C(7)	113.0(3)
C(1A)-O(1A)-C(4A)	105.6(3)
O(1A)-C(1A)-C(2A)	108.4(5)
C(1A)-C(2A)-C(3A)	105.5(5)
C(2A)-C(3A)-C(4A)	103.9(4)
O(1A)-C(4A)-C(3A)	105.4(4)
C(4B)-O(1B)-C(1B)	108.4(4)
C(2B)-C(1B)-O(1B)	106.6(4)
C(1B)-C(2B)-C(3B)	105.7(5)
C(4B)-C(3B)-C(2B)	105.7(5)
O(1B)-C(4B)-C(3B)	107.2(4)

Table 2 (*concluded*).

bonds in *trans*-$PdCl_2(NH_2CH_2Ph)_2$ (19). The boronate ester functionality (BO_2R_2) lies in the plane of the arene ring and has two short B—O bonds (1.354(5) and 1.372(5) Å). These results indicate that "dative" bonding is significant for both the aromatic ring π-electrons and oxygen atoms with boron. The slight difference in the two B—O bond lengths has been observed previously in chelate complexes of phenylboronic acid (20). To the best of our knowledge, this is the first structurally characterized example of an aminoboronate–metal complex.

To avoid problems arising from reactions carried out in aqueous solutions, we decided to examine the reactivities of both APBA and APBpin with $PtCl_2(COD)$ (COD = 1,5-cyclooctadiene) in organic solvents. Unfortunately, no reaction, or decomposition, was observed when this platinum complex was treated with either aminoboron species at room or elevated temperatures. We then decided to prepare the analogous *trans* amine complexes from the monoalkene metal compounds $[MCl_2(COE)]_2$ (M = Pd, Pt; COE = η^2-C_8H_{14}) (Scheme 1), as both *cis* and *trans* platinum amine complexes are known to be biologically active (14). The starting organometallic dimers, which are soluble in common organic solvents, were prepared by the addition of *cis*-cyclooctene to aqueous solutions of the corresponding metal tetrachloride salts (15). Diamine complex $PdCl_2(APBA)_2$ (**2**) was obtained in moderate yields (39%) from reactions of boronic acid **1** with $[PdCl_2(COE)]_2$. Interestingly, dropwise addition of 1 equiv. of pinacol derivative **4** to the palladium dimer gave rapid formation of the novel air-stable organometallic complex $PdCl_2(COE)(APBpin)$ (**7**). Attempts to generate the corresponding boronic acid derivative via this route afforded equal amounts of disubstituted amine **2** along with starting alkene complex $[PdCl_2(COE)]_2$. The difficulty in generating the boronic acid analogue of **7** presumably arises from the insoluble nature of the amine starting material in organic solvents. In an attempt to generate a mixed phosphine-amine complex, we have found that addition of 1 equiv. of PPh_3 to **7**, however, afforded $PdCl_2(PPh_3)_2$ where the phosphines have displaced both the weakly bound cyclooctene and aminoboron ligands. Interestingly, subsequent addition of a second equivalent of

© 1999 NRC Canada

Table 3. Atomic coordinates ($\times 10^4$) and equivalent isotropic displacement coefficients for *trans*-$PdCl_2(3\text{-}NH_2C_6H_4Bpin)_2$ (**5**).

	x	*y*	*z*	*U*(eq)
Pd(1)	5000	0	5000	32(1)
Cl(1)	3525(1)	79(1)	3735(1)	47(1)
O(1)	724(2)	872(2)	6450(2)	43(1)
O(2)	663(2)	162(2)	8228(2)	47(1)
N(1)	4503(3)	910(2)	6120(3)	38(1)
B(1)	1228(3)	429(3)	7397(4)	38(1)
C(1)	3934(2)	523(2)	6951(3)	34(1)
C(2)	2919(2)	617(2)	6762(3)	35(1)
C(3)	2351(3)	259(2)	7572(3)	35(1)
C(4)	2827(3)	–228(3)	8540(3)	44(1)
C(5)	3838(3)	–333(3)	8715(4)	54(1)
C(6)	4392(3)	44(2)	7929(3)	43(1)
C(7)	–271(3)	1039(3)	6730(3)	44(1)
C(8)	–359(3)	308(3)	7693(4)	44(1)
C(9)	–749(3)	–581(3)	7148(4)	66(1)
C(10)	–934(3)	585(3)	8673(4)	63(1)
C(11)	–998(3)	941(3)	5588(4)	63(1)
C(12)	–266(3)	1989(3)	7197(4)	67(1)
O(1A)	3468(2)	2556(2)	9912(3)	69(1)
C(1A)	3648(4)	1812(4)	10 608(7)	113(2)
C(2A)	2751(5)	1562(5)	11 042(5)	112(2)
C(3A)	1960(3)	2019(4)	10 246(5)	81(2)
C(4A)	2475(4)	2482(3)	9352(4)	73(1)
O(1B)	5777(2)	2266(2)	7460(3)	80(1)
C(1B)	6819(3)	2229(4)	7730(5)	88(2)
C(2B)	7062(5)	2299(6)	8994(5)	136(3)
C(3B)	6252(5)	2780(5)	9387(5)	124(3)
C(4B)	5419(4)	2653(4)	8444(5)	86(2)

Fig 1. Molecular structure of $PdCl_2(APBpin)_2$ (**5**, pin = $O_2C_2Me_4$) with hydrogen atoms and molecules of THF omitted for clarity.

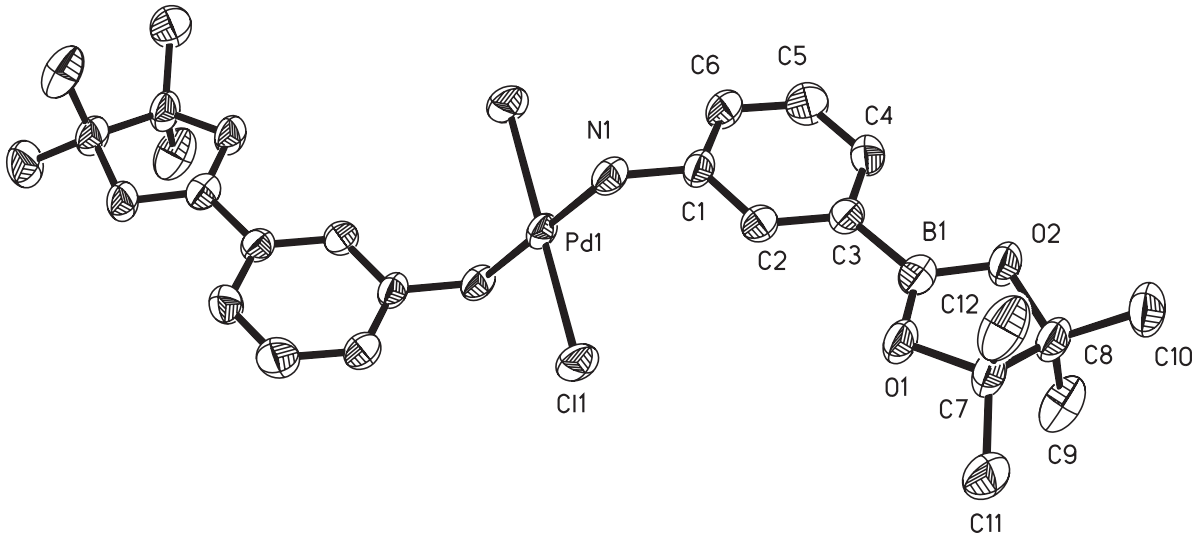

aminoboronic ester to **7** resulted in facile loss of the labile cyclooctene ligand with concomitant formation of $PdCl_2(APBpin)_2$ (**5**). Similar studies on the addition of pyridines to palladium monoalkene complexes have been reported previously (21).

Unlike reactions with palladium, only monoalkene complexes $PtCl_2(COE)(APBA)$ (**8**) and $PtCl_2(COE)(APBpin)$ (**9**) were generated from the addition of the corresponding aminoboron derivatives to $[PtCl_2(COE)]_2$. Attempts to displace the alkene proved unsuccessful, even with addition of

© 1999 NRC Canada

Scheme 1.

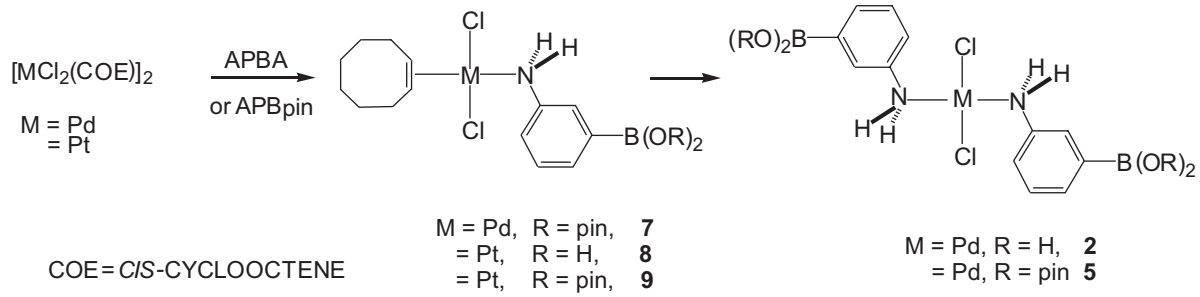

excess aminoboron ligand at elevated temperatures.[6] This observation is consistent with the known ability of platinum to form stronger M–alkene bonds than palladium, owing to an increase in the amount of π-backbonding (22). Spectroscopic and X-ray diffraction studies of similar *trans*-$PtCl_2(\eta^2$-alkene)(L) (L = nitrogen-containing ligand) complexes have been reported previously (23).

2. Reactions with *N*,*N*-dimethylbenzylamineboronic acid

Boron derivatives of *N*,*N*-dimethylbenzylamine, 2-$NMe_2CH_2C_6H_4B(OH)_2$ (**10**) and 2-$NMe_2CH_2C_6H_4$Bpin (**11**), were prepared by established procedures (16). Significant intramolecular interaction exists between the nitrogen atom and the boron atom in solution as evidenced by $^{11}B\{^1H\}$ NMR spectroscopy (24). Peaks at δ 8.9 and 15.3 ppm observed for **10** and **11**, respectively, are shifted considerably upfield from phenylboronic acid (δ 29.6 ppm), indicating that the boron atom is four coordinate. Not surprisingly, a distinct solvent effect is observed on the rates of N—B bond dissociation in these systems, as shown previously using NMR spectroscopy (25).

Reactions of **10** or **11** with Na_2PdCl_4 in water or methanol gave the known cyclopalladated dimer $[PdCl(2\text{-}NMe_2CH_2C_6H_4)]_2$ (26) as the major amine-containing product (identified using ^1H NMR spectroscopy and mp) along with formation of boric acid; this latter species presumably arising from the addition of water to liberated "Cl-$B(OH)_2$". The cyclopalladated compound has been prepared previously from the addition of *N*,*N*-dimethylbenzylamine to Na_2PdCl_4, along with concomitant formation of HCl, where the *ortho* C(sp^2)—H bond of the phenyl group is broken as a new C(sp^2)—Pd bond forms (26). Our observation is intriguing in that it shows a preference for activation of the C(sp^2)—B bond over the conventional C(sp^2)—H bond. This selectivity suggests that intramolecular coordination of the nitrogen atom to boron severely weakens the corresponding C—B bond. A strong base (typically NaOH or TlOH) is usually required to facilitate cleavage of the C—B in the Suzuki–Muyari cross-coupling reactions of organic halides with organoboronic acids (27). No reaction was observed in analogous reactions with the platinum salt, K_2PtCl_4, and either **10** or **11**.

The cyclometallated dimer $[PdCl(2\text{-}NMe_2CH_2C_6H_4)]_2$ was also obtained from reactions of alkene complex $[PdCl_2(COE)]_2$ with **10** in reactions carried out in wet CH_2Cl_2. This reaction probably proceeds via initial coordination of the aminoboron ligand followed by loss of cyclooctene to provide a 14-electron intermediate "$PdCl_2L$" (where L = aminoboron ligand) (28). Addition of water or an extra equivalent of amine may coordinate putatively to the boron atom and facilitate rapid B—C bond cleavage to give the desired cyclopalladated fragment, which will subsequently dimerize to give $[PdCl(2\text{-}NMe_2CH_2C_6H_4)]_2$. No reaction was observed when $[PdCl_2(COE)]_2$ was treated with **10** in dry solvent under an inert atmosphere. Reactions of $[PdCl_2(COE)]_2$ with 2-$NMe_2CH_2C_6H_4$Bpin **11** in wet methylene chloride also generated the cyclopalladated dimer $[PdCl(2\text{-}NMe_2CH_2C_6H_4)]_2$ along with pinB-O-Bpin and the ammonium salt $[2\text{-}HNMe_2CH_2C_6H_4Bpin]_2[PdCl_4]$, where an extra equivalent of the aminoboron ligand has been used to mop up the liberated Cl-Bpin. Addition of Cl-Bpin to **11** would result in initial formation of $[2\text{-}pinBNMe_2CH_2C_6H_4Bpin]^+Cl^-$, which would rapidly degrade with addition of adventitious water to the protonated ammonium salt along with "HO-Bpin," the latter of which will further degrade to give pinB-O-Bpin (similar nucleophilic degradation reactions have been reported previously for catechol derivatives, see ref. 29).

Consistent with this proposed pathway, the pinacol derivative **11** reacts initially with $[PtCl_2(COE)]_2$ to give an air-sensitive species, which we have tentatively assigned as the coordination complex $PtCl_2(COE)(\eta^1\text{-}2\text{-}NMe_2CH_2C_6H_4Bpin)$ (**12**). The proton NMR spectrum of **12** indicates that one C(sp^2)-H is significantly deshielded (δ 8.87 ppm) with respect to starting aminoboron compound (δ 7.55 ppm), which we postulate may lie over the metal square plane, as noted previously for the bisamine adduct $PdCl_2$(1-tetralone oxime)$_2$ (30). Attempts to grow crystals of this coordination complex suitable for X-ray diffraction studies were unsuccessful, as compound **12** decomposes to give a number of unidentified products (by NMR spectroscopy) along with the cycloplatinated monomer $PtCl(COE)(2\text{-}NMe_2CH_2C_6H_4)$ (**13**) (Scheme 2).

Initial loss of cyclooctene followed by oxidative addition of the B—C bond with subsequent reductive elimination of the Cl-Bpin fragment and recoordination of the alkene moiety would give the cycloplatinated product (28, 31). Formation of this cycloplatinated species was also observed in analogous reactions with the boronic acid **10**. Interestingly, no reaction was observed between alkene complex

[6] A minor amount (<5%) of the diamine complex *trans*-$PtCl_2(APBpin)_2$ was generated upon heating for prolonged periods (days). An X-ray diffraction study on this compound was carried out, and the platinum analogue proved to be isostructural with complex **5**. Complete details of this study are provided in the supplementary data.

© 1999 NRC Canada

Scheme 2.

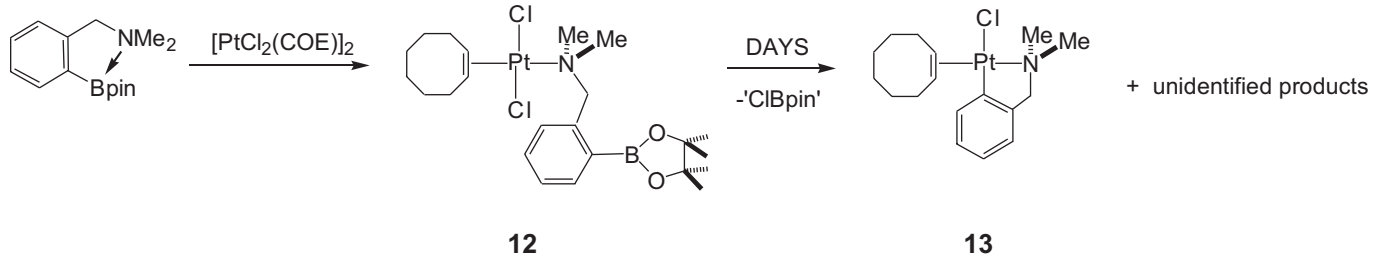

12 **13**

Scheme 3.

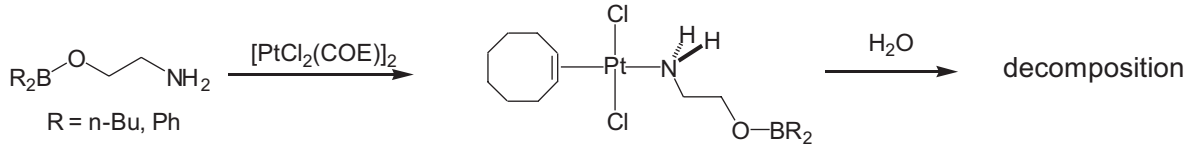

R = n-Bu, **16**
R = Ph, **17**

Scheme 4.

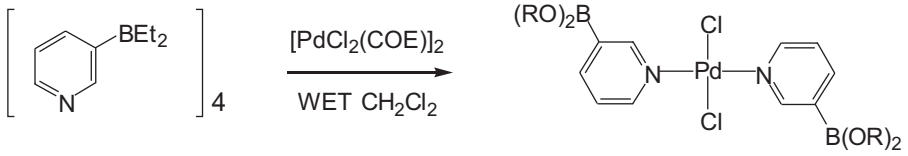

R = H, **19**
R = pin, **20**

$[PtCl_2(COE)]_2$ and *N*,*N*-dimethylbenzylamine even at elevated temperatures.

3. Reactions with borinic esters

Reactions of dibutylborinic acid, ethanolamine ester, $H_2NCH_2CH_2OBBu_2$ (**14**), or diphenylborinic acid, ethanolamine ester, $H_2NCH_2CH_2OBPh_2$ (**15**), with the tetrachloro salts, $[MCl_4]^{2-}$, in aqueous solvents proceed via cleavage of the B—O bond to give a mixture of metal–ethanolamine complexes (32). Formation of these degradation products was confirmed by independently adding commercially available ethanolamine to the corresponding metal salts. Reactions with **14** gave boric acid, and presumably butane, while phenylboronic acid, $PhB(OH)_2$, was generated as the major boron-containing product in reactions using **15**. Although the boron atom is initially stabilized by intramolecular coordination of the amine nitrogen atom in the free ligand, nucleophilic degradation of the borinic group appears to be rapid once the B←N bond is broken and the amine coordinates to the metal centre. Cleavage of the B—O bond in these ligands has been observed previously (33). Likewise, similar degradation products were observed with reactions of **14** and **15** with $[PdCl_2(COE)]_2$. Reactions with $[PtCl_2(COE)]_2$, however, gave the corresponding monoamine complexes $PtCl_2(COE)(NH_2CH_2CH_2OBBu_2)$ (**16**) (^{11}B NMR δ 56.1 ppm) and $PtCl_2(COE)(NH_2CH_2CH_2OBPh_2)$ (**17**) (^{11}B NMR δ 47.8 ppm), respectively, both of which rapidly decompose in air to give a number of unidentified ethanolamine-derived products (Scheme 3).

4. Reactions with 3-(diethylboryl)pyridine

3-(Diethylboryl)pyridine (**18**) was originally prepared in 1983 (34) and its use in coupling reactions is well established (35). The remarkable stability of this compound under ambient conditions is due to its cyclic-tetrameric nature in the solid state and in solution. Four molecules of **18** are bound together through intermolecular nitrogen–boron bonds (36). We hypothesized that reactions of **18** with either $[MCl_4]^{2-}$ or $[MCl_2(COE)]_2$ (M = Pd, Pt) would result in the formation of metal–pyridine complexes by breaking the N→B bonds. Nucleophilic attack by water on the boron atom should therefore result in breaking the B—C_{Et} bonds and concomitantly generating the corresponding pyridine – boronic acid metal complexes. Interestingly, although no product formation was observed using the metal chloride salts, reactions with $[PdCl_2(COE)]_2$ in wet methylene chloride gave modest yields (42%) of the desired boronic acid complex $PdCl_2[NC_5H_4B(OH)_2]_2$ (**19**) (Scheme 4). This result implies that coupling reactions carried out in an aqueous or basic environment may initially transform tetrameric **18** to the corresponding boronic acid analogue in the presence of a palladium catalyst (35). We are presently investigating coupling reactions using aminoboronic acid derivatives and

© 1999 NRC Canada

will report our findings in due course. Complex $PdCl_2(NC_5H_4Bpin)_2$ (**20**) was prepared by transesterification of **19** with pinacol. Not surprisingly, no reaction was observed using the less reactive platinum complex $[PtCl_2(COE)]_2$.

Conclusions

We have investigated the reactivity of several aminoboron compounds with $[MCl_4]^{2-}$ salts and monoalkene dimers $[MCl_2(COE)]_2$ (M = Pd, Pt). Addition of 3-aminophenylboronic acid (APBA) to $[MCl_4]^{2-}$ (M = Pd, Pt) gave the corresponding metal derivatives $MCl_2(APBA)_2$. Diamine complexes were also generated by addition of APBA and APBpin (pin = $O_2C_2Me_4$) to the palladium alkene dimer $[PdCl_2(COE)]_2$. The aminoboron ligands were ineffective in displacing the coordinated cyclooctene group in analogous reactions with the platinum dimer. Interestingly, cleavage of the B—C and B—O bonds dominated reactions involving aminoboron ligands, $2\text{-}NMe_2CH_2C_6H_4B(OR)_2$ and $H_2NCH_2CH_2OBR_2$, respectively. Although 3-(diethylboryl)pyridine is stabilized by intramolecular N→B interactions, the novel boronic acid-containing complex $PdCl_2[NC_5H_4B(OH)_2]_2$ was prepared by addition of this aminoboron ligand to the palladium alkene dimer. We are presently investigating the biological activities of several of these new platinum derivatives, the results of which will be published in due course.

Acknowledgements

Thanks are gratefully extended to the Natural Sciences and Engineering Research Council of Canada, Mount Allison University, St. Mary's University for financial support, as well as Johnson Matthey Ltd. for the generous supplies of platinum salts. We also thank Dan Durant, Roger and Marilyn Smith, and John Marcone (DuPont) for their expert technical assistance, Dr. H. Jenkins (S.M.U.) for assistance with the X-ray data, and anonymous reviewers for helpful comments.

References

1. M.P. Groziak, A.D. Ganguly, and P.D. Robinson. J. Am. Chem. Soc. **116**, 7597 (1994).
2. (*a*) E. Graf, M.W. Hosseini, R. Ruppert, N. Kyritaskas, A. De Cian, J. Fischer, C. Estournes, and F. Taulelle. Angew. Chem. Int. Ed. Engl. **34**, 1115 (1995); (*b*) E. Graf, M.W. Hosseini, R. Ruppert, A. De Cain, and J. Fischer. J. Chem. Soc. Chem. Commun. 1505 (1995).
3. D. Roy and D.M. Birney. Synlett. 798 (1994).
4. P. Linnane, T.D. James, and S. Shinkai. J. Chem. Soc. Chem. Commun. 1997 (1995).
5. V. Vill and H-W. Tunger. J. Chem. Soc. Chem. Commun. 1047 (1995).
6. V. Martichonok and J.B. Jones. J. Chem. Soc. Perkin Trans. 1, 2927 (1995).
7. (*a*) T. Imada, H. Murakami, and S. Shinkai. J. Chem. Soc. Chem. Commun. 1557 (1994); (*b*) I. Hamachi, O. Kimura, H. Takeshita, and S. Shinkai. Chem. Lett. 529 (1995).
8. H. Nemoto, J. Cai, and N. Asao. J. Med. Chem. **38**, 1673 (1995).
9. (*a*) P.R. Westmark and B.D. Smith. J. Pharm. Sci. **85**, 266 (1996); (*b*) J. Am. Chem. Soc. **116**, 9343 (1994); (*c*) G.T. Morin, M-F. Paugam, M.P. Hughes, and B.D. Smith. J. Org. Chem. **59**, 2724 (1994).
10. (*a*) K.A. Koehler and G.E. Lienhard. Biochemistry, **10**, 2477 (1971); (*b*) R.N. Lindquist and G. Terry. Arch. Biochem. Biophys. **160**, 135 (1974); (*c*) C.A. Kettner and A.B. Shenvi. J. Biol. Chem. **259**, 15 106 (1984).
11. D.A. Matthews, R.A. Alden, J.J. Birktoft, S.T. Freer, and J. Kraut. J. Biol. Chem. **250**, 7120 (1975).
12. (*a*) V. Martichonok and J.B. Jones. J. Am. Chem. Soc. **118**, 950 (1996); (*b*) T. Lee, R. Sakowicz, V. Martichonok, J.K. Hogan, M. Gold, and J.B. Jones. Acta. Chem. Scandinavica, **50**, 697 (1996); (*c*) S.J. Coutts, T.A. Kelly, R.J. Snow, C.A. Kennedy, R.W. Barton, J. Adams, D.A. Krolikowski, D.M. Freeman, S.J. Campbell, J.F. Ksiazek, and W.W. Bachovchin. J. Med. Chem. **39**, 2087 (1996); (*d*) D.S. Matteson, K.M. Sadhu, and G.E. Lienhard. J. Am. Chem. Soc. **103**, 5241 (1981).
13. (*a*) C. Gao, B.J. Lavey, C-H.L. Lo, A. Datta, P. Wentworth, Jr., and K.D. Janda. J. Am. Chem. Soc. **120**, 2211 (1998); (*b*) E. Skordalakes, R. Tyrell, S. Elgendy, C.A. Goodwin, D. Green, G. Dodson, M.F. Scully, J-M.H. Freyssinet, V.V. Kakkar, and J.J. Deadman. J. Am. Chem. Soc. **119**, 9935 (1997); (*c*) T.A. Kelly, V.U. Fuchs, C.W. Perry, and R.J. Snow. Tetrahedron, **49**, 1009 (1993); (*d*) S. Zhong, F. Jordan, C. Kettner, and L. Polgar. J. Am. Chem. Soc. **113**, 9429 (1991); (*e*) A.B. Shenvi. Biochemistry, **25**, 1286 (1986); (*f*) D.H. Kinder and J.A. Katzenellenbogen. J. Med. Chem. **28**, 1917 (1985).
14. (*a*) H. Rauter, R.D. Domencio, E. Menta, A. Oliva, Y. Qu, and N. Farrell. Inorg. Chem. **36**, 3919 (1997); (*b*) S.U. Dunham and S.J. Lippard. J. Am. Chem. Soc. **117**, 10 702 (1995), and refs. therein.
15. (*a*) E. Kuljian and H. Frye. Z. Natursforsch. **20b**, 204 (1965); (*b*) M.S. Karasch, R.C. Seyler, and F.R. Mayo. J. Am. Chem. Soc. **60**, 882 (1938).
16. (*a*) M. Lauer, H. Böhnke, R. Grotstollen, M. Salehnia, and G. Wulff. Chem. Ber. **118**, 246 (1985); (*b*) M. Lauer and G. Wulff. J. Organomet. Chem. **256**, 1 (1983).
17. (*a*) N.I. Pavlenko, and A.I. Rubailo. Koord. Khim. **14**, 1042 (1988); (*b*) P.C. Kong and F.D. Rochon. Inorg. Chim. Acta, **61**, 269 (1982); (*c*) T.P.E. Auf der Heyde, G.A. Foulds, D.A. Thornton, and G.M. Watkins. J. Mol. Struct. **77**, 19 (1981).
18. H.C. Brown, N.G. Bhat, and V. Somayaji. Organometallics, **2**, 1311 (1983).
19. G.L. Pisegna, S.A. Westcott, and A. Decken. Acta. Cryst. C. In press.
20. (*a*) W. Kliegel, J. Metge, S.J. Rettig, and J. Trotter. Can. J. Chem. **75**, 1203 (1997); (*b*) F.M.G. de Rege, W.M. Davis, and S.L. Buchwald. Organometallics, **14**, 4799 (1995)
21. W. Partenheimer and B. Durham. J. Am. Chem. Soc. **96**, 3800 (1974), and refs. therein.
22. F.R. Hartley. Chem. Rev. **73**, 163 (1973).
23. (*a*) M.A.M. Meester, D.J. Stufkens, and K. Vrieze. Inorg. Chim. Acta, **21**, 251 (1977), and refs. therein; (*b*) W. Partenheimer. J. Am. Chem. Soc. **98**, 2779 (1976); (*c*) P. Schmidt and M. Orchin. Inorg. Chem. **6**, 1260 (1967); (*d*) A. Panunzi and G. Paiaro. J. Am. Chem. Soc. **88**, 4843 (1966).
24. (*a*) S. Toyota, T. Futawaka, M. Asakura, H. Ikeda, and M. Ōki. Organometallics, **17**, 4155 (1998); (*b*) S. Toyota and M. Ōki. Bull. Chem. Soc. Jpn. **63**, 1168 (1990).
25. S. Toyota and M. Ōki. Bull. Chem. Soc. Jpn. **64**, 1554 (1991).
26. A.C. Cope and E.C. Friedrich. J. Am. Chem. Soc. **90**, 909 (1968).
27. K. Matos and J.A. Soderquist. J. Org. Chem. **63**, 461 (1998).

© 1999 NRC Canada

28. A.D. Ryabov. Chem. Rev. **90**, 403 (1990).
29. S.A. Westcott, H.P. Blom, T.B. Marder, and R.T. Baker. Inorg. Chem. **32**, 2175 (1993).
30. A.J. Nielson. J. Chem. Soc. Dalton Trans. 205 (1981).
31. (*a*) D.C. Griffiths and G.B. Young. Organometallics, **8**, 875 (1989); (*b*) R.H. Reamey and G.M. Whitesides. J. Am. Chem. Soc. **106**, 81 (1984), and refs. therein; (*c*) G. Longoni, P. Fantucci, P. Chini, and F. Canziani. J. Organomet. Chem. **39**, 413 (1972).
32. G.M. Kapteijn, P.J. Baesjou, P.L. Alsters, D.M. Groove, W.J.J. Smeets, H. Kooijman, A.L. Spek, and G. van Koten. Chem. Ber. **130**, 35 (1997), and refs. therein.
33. W. Kliegel, U. Riebe, S.J. Rettig, and J. Trotter. Can. J. Chem. **73**, 835 (1995).
34. M. Terashima, H. Kakimi, M. Ishikura, and M. Kamada. Chem. Pharm. Bull. **31**, 4573 (1983).
35. M. Ishikura, M. Kamada, T. Ohta, and M. Terashima. Heterocycles, **22**, 2475 (1984).
36. Y. Sugihara, K. Takakura, T. Murafuji, R. Miyatake, K. Nakasuji, M. Kato, and S. Yano. J. Org. Chem. **61**, 6829 (1996).

© 1999 NRC Canada

Surface tension studies of lauryl sulfobetaine – β-cyclodextrin and dodecyltrimethylammonium bromide – β-cyclodextrin inclusion complexes in aqueous solution

S. Göktürk, M. Mahramanlıoğlu, and M. Tunçay

Abstract: β-Cyclodextrin (β-CD) is a cyclic oligosaccaride with an apolar cavity that shows a certain degree of selectivity in binding organic and inorganic compounds. Lauryl sulfobetaine (LSB) and dodecyltrimethylammonium bromide (DTAB), having the same hydrophobic and different polar groups are used in order to compare the influence of the polar group on complex formation with β-CD. The surface tension increased as β-CD is added to premicellar region of amphoteric (LSB) and cationic surfactant (DTAB) solutions. The relation between the surface tension and surfactant concentration can be expressed by the Szyszkowski equation, which combines the Langmuir adsorption model and the Gibbs equation. Binding constants were determined from the effect of added β-CD on the surface tension vs. concentration curves for LSB and DTAB aqueous solutions.

Key words: β-cyclodextrin, surfactant, surface tension method, complex formation, binding constant.

Résumé : La β-cyclodextrine (β-CD) est un oligosaccharide cyclique comportant une cavité apolaire qui présente une certaine sélectivité pour fixer des composés organiques et inorganiques. Dans le but de comparer l'influence du groupe polaire sur la formation d'un complexe avec une β-CD, on a utilisé la sulfobétaïne de lauryle (SBL) et le bromure de dodécyltriméthylammonium (BDTA) qui ont le même caractère hydrophobe et des groupes polaires différents. La tension superficielle augmente lorsqu'on ajoute de la β-CD à la région prémicellaire des solutions des agents de surface amphothère (SBL) et cationique (BDTA). La relation entre la tension superficielle et la concentration d'agent de surface peut être exprimée par l'équation de Szyskowski qui combine le modèle d'adsorption de Langmuir et l'équation de Gibbs. On a déterminé les constantes de fixation à partir de l'effet produit par l'addition de la β-CD sur la tension superficielle en fonction des courbes de concentration de solutions aqueuses de SBL et de BDTA.

Mots clés : β-cyclodextrine, agent de surface, méthode de la tension superficielle, formation de complexe, constante de fixation.

[Traduit par la Rédaction]

1. Introduction

The host–guest chemistry of inclusion complexes of the α- and β-cyclodextrins has been widely studied in relation to the general problem of understanding structural and ligand binding effects (1–5). Cyclodextrins (CDs) are shaped like a truncated cone with relatively hydrophobic hollow cylindrical cavities, and show a certain degree of selectivity in binding organic and inorganic compounds (6). β-Cyclodextrin (β-CD) shows amphiphilic character due to an apolar cavity and a hydrophilic annulus consisting of a number of hydroxyl groups. Surfactants that contain both hydrophobic and hydrophilic moieties are ideal guests for studying complexation with cyclodextrins. It is known that there are several types of inclusion complexes of β-CD in solutions. Inclusion complexes with a 1:1 host–guest ratio are commonly known (2). In some cases, when the hydrophobicity of the guest molecules increases, it may complex with two β-CD molecules to form a 2:1 inclusion compounds (7).

The ability of a cyclodextrin molecule to form an inclusion complex with a solute is dependent on (among other things) the diameter of the cyclodextrin cavity, the size, and geometry of the solute (3).

The difference among the cyclodextrins is in the number of glucopyranose units: six in α-CD, seven in β-CD, and eight in γ-CD, and also in the size of the cavity: α-CD (internal diameter = 5 Å), β-CD (internal diameter = 6.9 Å), γ-CD (internal diameter = 8.5 Å). The cavity of β-CD is of a hydrophobic character and has a diameter of 6.9 Å, which is ideally suited to accommodate the hydrophobic, i.e.,

Received September 1, 1998.

S. Göktürk,[1] M. Mahramanlıoğlu, and M. Tunçay. Istanbul University Faculty of Engineering Department of Chemistry, Avcılar 34850, Istanbul, Turkey.

[1]Author to whom correspondence may be addressed. Telephone: (90) 212 591 19 98. Fax: (90) 212 591 19 97. e-mail: gokturk@istanbul.edu.tr

© 1999 NRC Canada

Fig. 1. Surface tension results for 5 mM (■) and 8 mM DTAB (+) solutions as a function of the concentration of added β-CD. The symbols represent experimental data, and the solid lines represent the best fit.

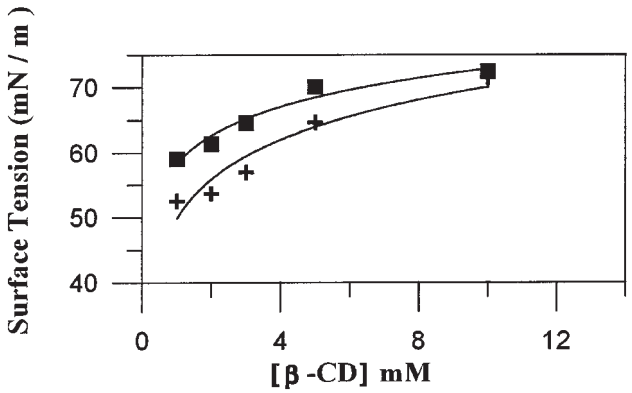

Fig. 2. Surface tension results for 1 mM (◆), 2 mM (✳), and 4 mM (●) LSB solutions as a function of the concentration of added β-CD. The symbols represent experimental data, and the solid lines represent the best fit.

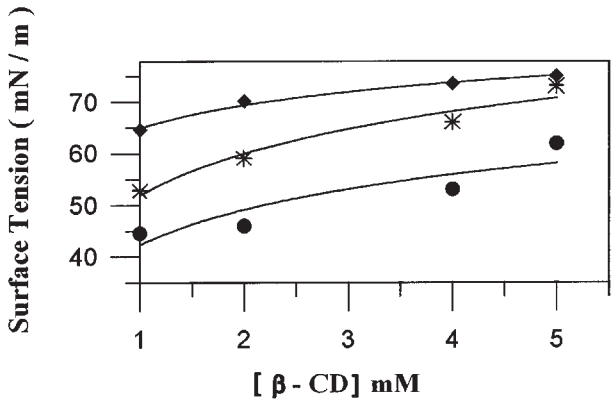

aliphatic part of the chosen surfactant that has a diameter of about 5 Å. Since the interior wall of the CD cavity is hydrophobic in nature, a hydrophobic alkyl group of the aliphatic part of surfactant molecules enters the cavity. Moreover, the rims of the CD cavity are lined with OH groups, which can form hydrogen bonds with the hydrophilic part of the surfactant molecule and thus add to the stability of the complexes formed (8).

Association constants for such complexes have been determined using various physical methods (9), including UV and visible spectroscopy (10, 11), calorimetry (12, 13), conductivity (14), NMR spectroscopy (15, 16), vapor pressure (17), and surface tension measurement (18). Each method has advantages and disadvantages, as well as limitations. Of the methods mentioned for studying complexation of CD with aqueous solutes, surface tension experiments appear to be the most suitable for inferring accurate values of binding constants between surfactants and β-CD (18). This method is based on the use of surface tension measurements to infer changes in the thermodynamic activity of the surfactant. The technique requires measuring the change in surface tension by addition of a solute to aqueous solutions of the surfactants, but it is necessary to ensure that both the solute and the complex are nonsurface active.

Binding constants of β-CD with surface active agents (S) were determined from the change of surface tension of solutions of the surface active agents in the presence of β-CD. The effect of β-CD on the surface tension and on the critical micelle concentration (CMC) of the different surfactants studied here can be explained by the formation of inclusion complexes. The correlation of surface activities with surface tension values in the β-CD–S solutions were made using the Szyszkowski equation, which combines the Langmuir adsorption model and the Gibbs equation.

In this work, the binding between β-CD and two surfactants having the same alkyl chain but different polar head group, i.e., lauryl sulfobetaine (LSB) and dodecyltrimethylammonium bromide (DTAB) was studied to gain further insight into the relative roles of the hydrophobic effect vs. interactions between the annular hydroxyl groups of β-CD and the surfactant head group in the complexes.

2. Experimental

a. Materials

The surfactants used in this study were DTAB, obtained from Aldrich Chemical Co., and LSB, obtained from Sigma Chemical Co. The β-CD was obtained from Aldrich Chemical Co., and all of these compounds were used as received. The water was distilled twice and deionized.

b. Surface tension method

The surface tension of the aqueous solutions was determined by stalagmometry in bidistilled water. The weight of 30 drops of the respective solution was determined, and the mean weight of 1 drop calculated (19).

The surface tension was then computed according to the equation

$$\gamma = \frac{m_{sol}}{m_{H_2O}} \gamma_{H_2O}$$

where γ = surface tension of respective solution, m_{sol} = mean weight of one drop of the solution, m_{H_2O} = mean weight of one drop of water, γ_{H_2O} = surface tension of water at 20°C (72, 77 mN m^{-1}). About 6–8 measurements were made for each solution, and the standard deviation of the surface tension from the mean value was found to be less than ±0.2 mN m^{-1}. All surface tension measurements were made at 20 (±0.2)°C. Surface tension versus concentration measurements were made for DTAB and LSB. All experiments were repeated under the same conditions in the presence of fixed β-CD concentrations.

3. Results and discussion

The surface tension of the system DTAB and LSB, with and without various amounts of added β-CD, were measured at 20°C as a function of surfactant concentration.

Preliminary surface tension measurements indicated that both β-CD–LSB and β-CD–DTAB complexes are nonsurface active. Surface tension values of the surfactant solutions approached the surface tension of pure water when sufficient β-CD was present to complex virtually all of the LSB and DTAB. Figures 1 and 2 show the influence of added β-CD

© 1999 NRC Canada

Fig. 3. Surface tension versus the logarithm of the molar concentration of DTAB in aqueous solution at 20°C in the absence (+) and presence of 2 mM (▲), 5 mM (■), and 10 mM (●) β-CD.

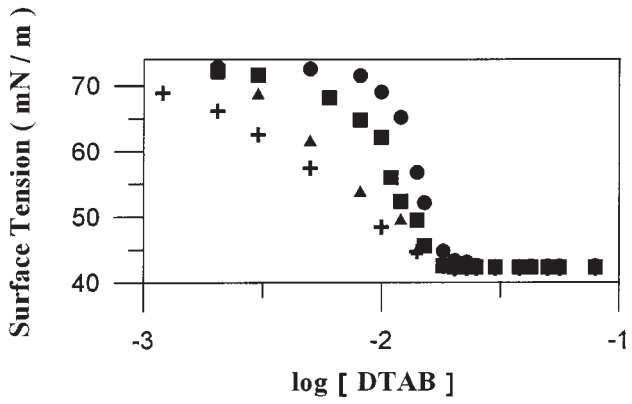

Fig. 4. Surface tension versus the logarithm of the molar concentration of LSB in aqueous solution at 20°C in the absence (+) and presence of 2 mM (◆), 5 mM (✳) β-CD.

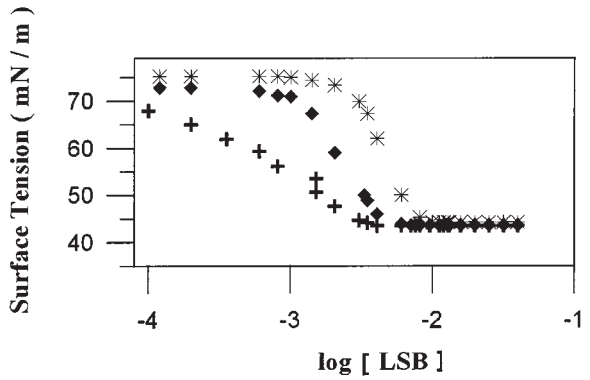

on the surface tension of the solutions containing fixed concentrations of DTAB (5 and 8 mM) and LSB (1, 2, and 4 mM), respectively. A mean least-squares computer fitting program was applied to experimental surface tension data in order to find the best fit. The curves drawn in Figs. 1 and 2 represent the surface tension values predicted by curve fitting.

The surface tension values obtained were plotted versus the logarithms of the surfactant concentration to derive the CMC of DTAB and LSB in the presence and absence of β-CD (Figs. 3 and 4). For both surfactants, the addition of β-CD shifted the CMC to higher concentrations. As seen in Figs. 3 and 4, addition of β-CD invariably increases the concentration of both DTAB and LSB required to attain a given degree of surface tension lowering and to reach the critical micelle concentration (CMC), reflecting the fact that the thermodynamic activity of the surfactants is decreased by the formation of inclusion complexes with β-CD. The increase in the CMC values was found to be proportional to the β-CD concentration. The dependence of the CMC of DTAB and LSB on the β-CD concentration are shown in Figs. 5 and 6, respectively. The experimental data for premicellar solutions of DTAB and LSB, with and without

Fig. 5. Dependence of the critical micelle concentration of aqueous solutions of DTAB on the concentration of β-CD at 20°C.

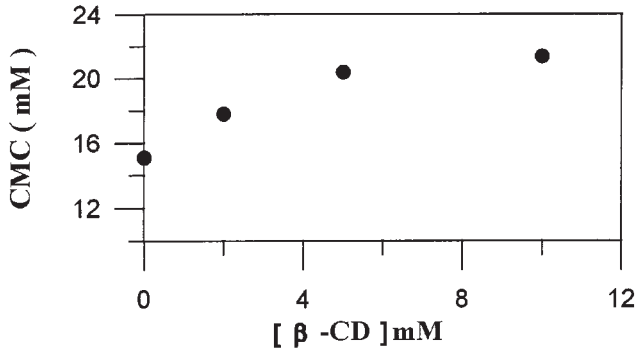

Fig. 6. Dependence of the critical micelle concentration of aqueous solutions of LSB on the concentration of β-CD at 20°C.

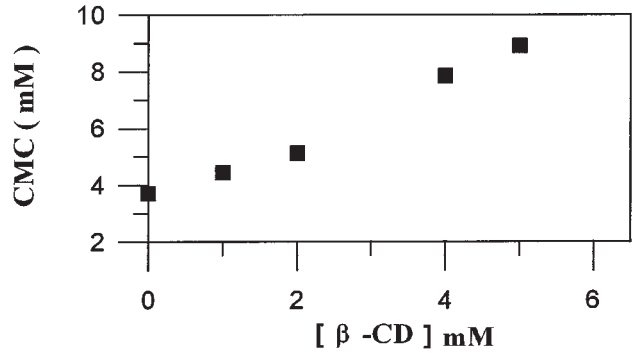

the presence of a fixed β-CD concentration, are shown in Figs. 7*a–c* and 8*a*, *b*, respectively.

By analyzing all of the surface tension vs. concentration data for systems below and above the CMC, for solutions with and without added β-CD, it was possible to infer the best values of the β-CD–S association constant as well as some of the parameters in the mass action model for micelle formation (20–22). The solid curves in Figs. 7*a–c* and 8*a*, *b* correspond to regions in which the surface tension of surfactant solutions (in the absence of β-CD) varies nearly linearly with the logarithm of the surfactant concentration; the condition of semi-log linearity seems to apply to most of the surface tension results obtained between about 45 and 65 mN m^{-1}. Equations for the lines were calculated by fitting surface tension vs. log [DTAB] and log [LSB] data using least-squares analysis.

To interpret the surface tension data, two binding reactions were considered:

$$S + CD \overset{K_1}{\rightleftharpoons} S(CD)$$

$$S + CD + CD \overset{K_2}{\rightleftharpoons} S(CD)_2$$

The surface tension data are modelled by assuming that the total concentration of β-CD and surfactant are given by

$$[S]_{total} = C_s + K_1 C_{\beta\text{-}CD} C_s + K_1 K_2 C^2_{\beta\text{-}CD} C_s$$

$$[\beta\text{-}CD]_{total} = C_{\beta\text{-}CD} + K_1 C_{\beta\text{-}CD} C_s + 2K_1 K_2 C^2_{\beta\text{-}CD} C_s$$

© 1999 NRC Canada

Fig. 7. Surface tension results for DTAB in the absence (+) and presence of (*a*) 2 mM (▲) (*b*) 5 mM (■), and (*c*) 10 mM (●) β-CD. Symbols represent the experimental data, and the lines conform to the model.

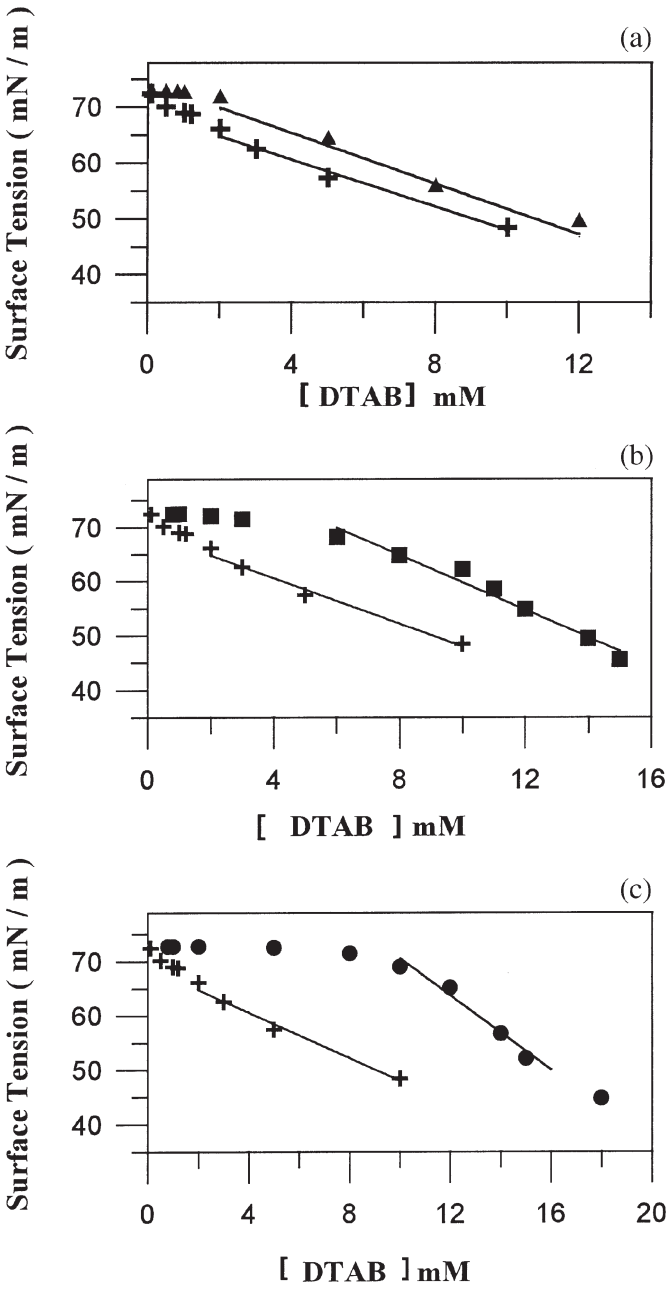

Fig. 8. Surface tension results for LSB in the absence (+) and presence of (*a*) 2 mM (◆) β-CD and (*b*) 5 mM (✳) β-CD. Symbols represent the experimental data, and the lines conform to the model.

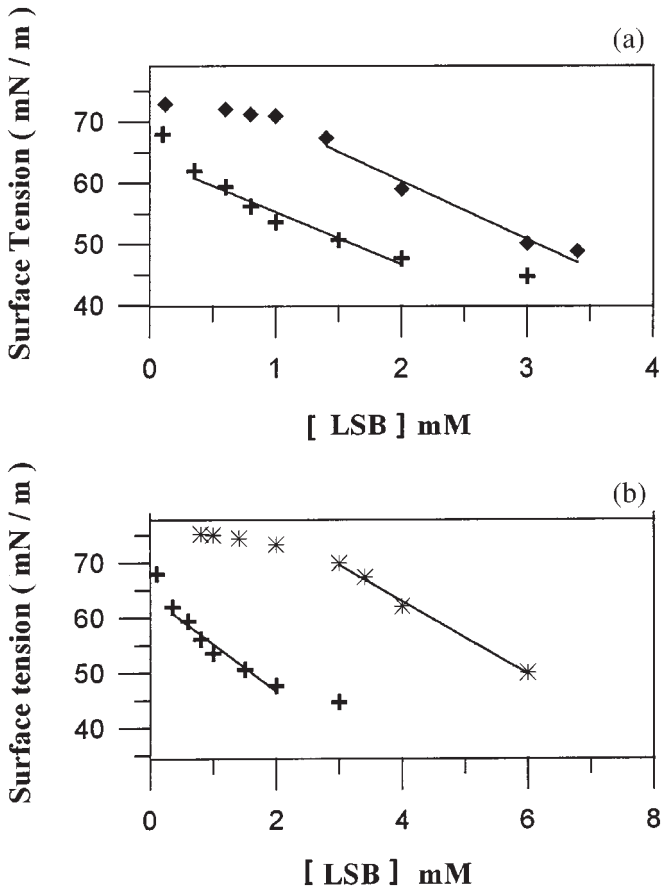

where K_1 represents the binding constants for the 1:1 β-CD surfactant complex, and K_2 is the equilibrium constant for binding an additional β-CD molecule to the 1:1 complex. C_s and $C_{\beta\text{-CD}}$ are the concentrations of free surfactant and β-CD, respectively.

The effect of DTAB and LSB on the surface tension curves was used to infer values of binding constant for 1:1 and 1:2 complexes for each of the five systems, utilizing the data analysis method described previously (23). It was tested whether the complexation between DTAB, LSB, and β-CD only result in a 1:1 complex. Results indicated that only 1:1 complexes and not 2:1 complexes formed for both surfactants at least in the concentration range studied. This suggests that in the case of β-CD–DTAB and β-CD–LSB, steric and dipolar repulsive forces dominate to an extent that 2:1 complex is unfavourable. Nonexistence of a 2:1 complex between both DTAB, LSB, and β-CD agree with the conclusion obtained previously for dimethyldodecylammonium oxide (DDAO) (18) and (DTAB) (24).

The Γ*RT* values inferred from the Gibbs equation (where Γ is the Gibbs surface excess quantity) were calculated from the slopes of the semi-log curves presented in Figs. 7*a–c* and 8*a*, *b*. Surface tension data presented in Figs. 7*a–c* and 8*a*, *b* were also fitted to the Szyszkowski equation, which combines the Langmuir adsorption model for surface adsorption and the Gibbs equation.

$$\gamma = \gamma_0 - t_d \ln (1 + BC_s)$$

where $t_d = \Gamma^{\infty}RT$, Γ^{∞} is the value of the surface excess of the surfactant when a complete monolayer is present, and B is related to the equilibrium constant in the Langmuir equation for adsorption of the surfactant at the liquid–gas interface.

The least-squares analysis of data for two surfactants in the absence of β-CD indicated that a good correlation can be obtained by using the Szyszkowski equation. In fitting the surface tension data for solutions containing β-CD in the

© 1999 NRC Canada

Table 1. Szyszkowski parameters and 1:1 binding constant obtained by least-squares regression analysis.

	DTAB	LSB
B (M^{-2})	1650 ± 200	281 ± 50
t_D (mN m^{-1})	6 ± 0.8	22 ± 0.7
K_1 (mol^{-1} dm^3)	1900 ± 400	2900 ± 350

premicellar region, a good correlation was obtained for the inclusion of 1:1 complex in the model.

The derived K_1 values for DTAB–β-CD systems are somewhat smaller than those inferred from other methods (K_1 = 18 100 mol^{-1} dm^3) (24). It was previously found that the surface tension method yields lower value of the binding constant than those of other methods (18, 23).

4. Conclusions

For both DTAB and LSB, the addition of β-CD shifts the CMC to higher concentrations and also shifts the surface tension to higher values.

The effects of β-CD on the surface tension and on the CMC of the DTAB and LSB can be explained by the formation of inclusion complexes. It is known that inclusion complexation makes surfactant molecules more hydrophilic and causes transport from the micelles or from the surface into the bulk.

For the addition of the same concentration of β-CD, the change in surface tension is less for DTAB than for LSB. For 2 mM LSB and 8 mM DTAB, the addition of 5 mM β-CD shifts the surface tension from 47.6 to 72 mN m^{-1} and from 51.6 to 64.6 mN m^{-1}, respectively. The addition of 5 mM β-CD also shifts the CMC of DTAB from 1.51×10^{-2} to 2.04×10^{-2} mol dm^{-3} and the CMC of LSB from 3.71×10^{-3} to 8.91×10^{-3} mol dm^{-3}.

The ΓRT values inferred from the Gibbs equation are not constant for both surfactants; this can be explained by the change of ionic strength with concentration, since the activity of the surfactant does not vary in direct proportion to its molar concentration. As seen in Table 1, the influence of ionic strength on ΓRT is more pronounced for LSB.

The results suggest that the complex-forming ability of the β-CD is greater for LSB than for DTAB. The 1:1 binding model applied here to fit surface tension results for both DTAB–β-CD and LSB–β-CD solutions provides a good correlation of data obtained throughout a relatively large range of concentrations of both surfactants.

The 1:2 binding constants are calculated as zero, which is reasonable, since the C_{12} hydrocarbon chain is not long enough to accommodate more than one β-CD molecule. Also, steric and dipolar repulsive forces are dominant to an extent that 2:1 complex formation is unfavourable in case of DTAB and LSB.

The values determined here for the 1:1 binding constant are lower than those reported in literature for most compounds containing a C_{12} group. Previous work shows that the binding constant depends on the nature of the surfactant head group and its ability to interact with water and with β-CD in the 1:1 complex. The value of K_1 (1900 ± 400 mol^{-1} dm^3) obtained for DTAB is found to be in quite good agreement with the K_1 constant previously obtained for the cationic form of DDAO (1800 ± 300 mol^{-1} dm^3) (18).

Comparison of the binding constants indicate that the β-CD cavity has a preferential affinity for the amphoteric form of $C_{12}H_{25}$, that is, LSB is more strongly bound than DTAB. This result is not surprising, since binding tendency is expected to vary with the nature of the head group (25). Additional head groups (SO_3) may change the degree of polar–apolar and apolar–apolar interaction that results in changes in the value of binding constant. Therefore, higher value of K_1 obtained for LSB can be explained by the formation of hydrogen bonds between the SO_3 group of this molecule and hydroxyl groups on the rims of the β-CD cavity. We have to infer that the complex formation between LSB and β-CD is of a more complicated nature than that of inclusion complexes. Consequently, in addition to the inclusion complex, an interfacial complex may also be formed between the annular hydroxyl group and the SO_3 group.

Acknowledgments

This work was supported by The Research Fund of The University of Istanbul. Project number Ö-III/49/280598.

References

1. J. Szetli (*Editor*). Proc. 1st Int. Symp. Cyclodextrins. Budapest, Hungary. 1981. D. Reidel Publishing Co. Dordrecht (Holland) Boston, London. 1982.
2. W. Saenger. Angew. Chem. Int. Ed. Engl. **19**, 344 (1980).
3. M.L. Bender and M.Komiyama. Cyclodextrine chemistry. Springer–Verlag, Berlin. 1978.
4. L. Mandelcorn. Non-stoichiometric compounds. Academic Press, New York. 1964.
5. F. Cramer. Einschlussverbindungen. Springer-Verlag, Heidelberg. 1954.
6. S. Hamai. J. Phys. Chem. **94**, 2595 (1990).
7. H. Kondo, H. Nakatani, and K. Hiromi. J. Biochem. **79**, 393 (1976).
8. W. Saenger and A.M. Fahrnow. Angew. Chem. Int. Ed. Engl. **27**, 393 (1988).
9. J. Szejtli. Cyclodextrin technology. Kluwer Academic Pub., Norwell. 1988.
10. K.J. Sasaki, S.D. Christian, and E.E. Tucker. Fluid Phase Equlib. **49**, 281 (1989).
11. K.J. Sasaki, S.D. Christian, and E.E. Tucker. J. Colloid Interface Sci. **134**, 412 (1990).
12. E.A. Lewis and L.D. Hansen. J. Chem. Soc. Perkin Trans. 2, 2081 (1973).
13. (*a*) W.C. Cromwell, K. Byström, and M.R. Eftink. J. Phys. Chem. **89**, 326 (1985); (*b*) A. Cooper and D.D. MacNicol. J. Chem. Soc. Perkin Trans. 2, 760 (1978).
14. T. Okubo, H. Kitano, and N. Ise. J. Phys. Chem. **80**, 2661 (1976).
15. A. Wishnia and S.J. Lappi. J. Mol. Biol. **82**, 77 (1974).
16. W. Guo, B.M. Fung, and S.D. Christian. Langmuir, **8**, 446 (1992).
17. E.E. Tucker and S.D. Christian. J. Am. Chem. Soc. **106**, 1942 (1984).
18. M. Tunçay and S.D. Christian. J. Colloid Interface Sci. **167**, 181 (1994).
19. K.Kralova and L. Mitterhauszerova. Tenside Surfactants Deterg. **25**, 3 (1988).
20. P.H. Elworthy and K.J. Mysels. J. Colloid Interface Sci. **21**, 331 (1966).

© 1999 NRC Canada

21. E.E. Tucker and S.D. Christian. J. Colloid Interface Sci. **104**, 562 (1985).
22. S.D. Christian, E.E. Tucker, and E.H. Lane. J. Colloid Interface Sci. **84**, 423 (1981).
23. U.R. Dharmawardana, S.D. Christian, E.E. Tucker, W.R. Taylor, and J.F. Scamehorn. Langmuir, **9**, 2258 (1993).
24. W.M.Z. Wan Yunus, J. Taylor, D.M. Bloor, D.G. Hall, and E. Wyn-Jones. J. Phys. Chem. **96**, 8979 (1992).
25. L.D. Wilson and R.E. Verral. J. Phys. Chem. B, **101**, 9270 (1997).

© 1999 NRC Canada

Solubility of diphenyl sulfone in organic nonelectrolyte solvents. Comparison of observed versus predicted values based upon the general solvation model

Kristin A. Fletcher, Carmen E. Hernández, Lindsay E. Roy, Karen S. Coym, and William E. Acree, Jr.

Abstract: Experimental solubilities are reported for diphenyl sulfone dissolved in 8 alkane, 10 alcohol, and in aqueous solvent media at 25°C. Results of these measurements are used to test the predictive ability of the general solvation model

$$\log C^{sat}_{A,org}/C^{sat}_{A,aq} = c + rR_2 + s\pi^H_2 + a\sum\alpha^H_2 + b\sum\beta^H_2 + vV_x$$

where $C^{sat}_{A,org}$ and $C^{sat}_{A,aq}$ refer to the solute solubility in the organic solvent and in water, respectively, R_2 is the solute's excess molar refraction, V_x is the McGowan characteristic volume of the solute, π^H_2 denotes the solute's dipolarity/polarizability, and $\Sigma\alpha^H_2$ and $\Sigma\beta^H_2$ are the overall hydrogen-bond acidity and basicity descriptors for the solute. The remaining symbols in the above expression are known solvent coefficients, which have been determined previously through regressional analysis of published organic solvent – water partition coefficient and vapor–liquid equilibrium data. Computations show that the general solvation model predicts the solubility behavior of diphenyl sulfone in the 11 organic solvents for which predictions could be made to within an overall average absolute deviation of about ±20%.

Key words: diphenyl sulfone solubilities, organic solvents, solubility predictions, general solvation model.

Résumé : On a déterminé les solubilités expérimentales de la diphénylsulfone dans 8 alcanes, 10 alcools et dans un milieu aqueux à 25°C. Les résultats de ces mesures ont été utilisés pour vérifier les capacités de prédiction du modèle général de solvatation

$$\log C^{sat}_{A,org}/C^{sat}_{A,aq} = c + rR_2 + s\pi^H_2 + a\sum\alpha^H_2 + b\sum\beta^H_2 + vV_x$$

dans lequel $C^{sat}_{A,org}$ et $C^{sat}_{A,aq}$ se réfèrent à la solubilité du soluté dans le solvant organique et dans l'eau, respectivement, R_2 est la réfraction molaire en excès du soluté, V_x est le volume caractéristique de McGowan du soluté, π^H_2 spécifie le caractère dipolaire et la polarisabilité du soluté alors que $\Sigma\alpha^H_2$ et $\Sigma\beta^H_2$ sont les descripteurs d'acidité et de basicité globale du pont hydrogène du soluté. Les symboles résiduels de l'équation sont des coefficients de solvant connus qui ont été déterminés antérieurement par le biais dune analyse régressionnelle de coefficients de partage eau – solvant organique et de données d'équilibre vapeur–liquide publiés. Les calculs montrent que le modèle général de solvatation permet de prédire le comportement de la solubilité de la diphénylsulfone dans les 11 solvants organiques pour lesquels on a pu faire des prédictions à l'intérieur dune déviation absolue moyenne globale d'environ ±20%.

Mots clés : solubilités de la diphénylsulfone, solvants organiques, prédictions de la solubilité, modèle général de solvatation.

[Traduit par la Rédaction]

Introduction

Solid–liquid equilibrium data of organic nonelectrolyte systems are becoming increasingly important in the petroleum industry, particularly in light of present trends towards heavier feedstocks and known carcinogenicity/mutagenicity of many of the larger polycyclic aromatic compounds. Solubility data for a number of polycyclic aromatic hydrocarbons (e.g., anthracene and pyrene) and hetero-atom polynuclear aromatics (e.g., carbazole, dibenzothiophene, and xanthene) have been published in the recent chemical literature (for listing of references see Acree (1–3)). Despite efforts by experimentalists and scientific organizations, both in terms of new experimental measurements and critically evaluated

Received August 17, 1998.

K.A. Fletcher, C.E. Hernández, L.E. Roy, K.S. Coym, and W.E. Acree, Jr.[1] Department of Chemistry, University of North Texas, Denton, TX 76203-5070, U.S.A.

[1]Author to whom correspondence may be addressed. e-mail: Acree@unt.edu

 © 1999 NRC Canada

Table 1. Comparison between experimental diphenyl sulfone molar solubilities and organic solvent – water. Partition coefficients and predicted values based upon eq. [2].

	Experimental values		Predicted values		
Solvent	C_A^{sat}	log P^a	C_A^{sat}	log P	% dev.^{b}
Hexane	0.00398	1.244	0.00358	1.198	–10.1
Heptane	0.00402	1.248	0.00191	0.924	–52.4
Octane	0.00411	1.258	0.00579	1.407	40.9
Nonane	0.00414	1.261	0.00431	1.278	4.1
Decane	0.00418	1.265	0.00321	1.150	–23.2
Hexadecane	0.00480	1.325	0.00525	1.364	9.4
Cyclohexane	0.00801	1.547	0.0116	1.710	44.8
2,2,4-Trimethylpentane	0.00299	1.119	0.00301	1.122	0.7
Methanol	0.1189	2.719	0.0947	2.620	20.4
Ethanol	0.0903	2.599	0.0789	2.541	–12.6
1-Propanol	0.0697	2.487			
2-Propanol	0.0452	2.299			
1-Butanol	0.0571	2.400			
2-Butanol	0.0470	2.316			
1-Pentanol	0.0489	2.333			
1-Hexanol	0.0421	2.268			
1-Heptanol	0.0351	2.189			
1-Octanol	0.0306	2.130	0.0305	2.128	–0.3
Water	0.0002271				
					Average absolute deviation 19.9

[a]Calculated as log $[C_{A,org}^{sat}/C_{A,aq}^{sat}]$, where $C_{A,org}^{sat}$ and $C_{A,aq}^{sat}$ refer to the molar solubility of the solute in the organic solvent and in water, respectively.
[b]% dev. = $100[(C_{A,org}^{sat})^{pred} - (C_{A,org}^{sat})^{exp}]/(C_{A,org}^{sat})^{exp}$.

data compilations, there still exist numerous systems for which solubility data are not readily available.

To address this problem, researchers have turned to group contribution methods and semiempirical expressions to predict desired quantities. Group contribution methods have proved fairly successful in estimating solid solubility in pure and binary solvent mixtures from structural information (4–11). Practical application, though, is limited to systems for which all group interaction parameters are known. Interaction parameters can be evaluated from liquid–vapor, liquid–liquid, and solid–liquid equilibria data. It is important that the database contain as many different functional groups as possible, preferably with adequate representation from both mono- and multifunctional solute/solvent molecules to permit evaluation of potential synergistic effects. The database should contain sufficient experimental values near infinite dilution in the event that one wishes to determine separate interaction parameters for finite concentration and infinite dilution activity coefficient predictions. For this reason, we have measured diphenyl sulfone solubilities in both water and in 18 different organic solvents. These measurements will be used to further test the applications and limitations of correlational expressions derived from the general solvation model.

Materials and methods

Diphenyl sulfone (Aldrich, 97%) was recrystallized several times from methanol. *n*-Hexane (Aldrich, 99%), *n*-heptane (Aldrich, HPLC), *n*-octane (Aldrich, 99+%, anhydrous), *n*-nonane (TCI, 99+%), *n*-decane (TCI, 99+%), *n*-hexadecane (Aldrich, 99%), cyclohexane (Aldrich, HPLC), 2,2,4-trimethylpentane (Aldrich, HPLC), methanol (Aldrich, 99.9+%), ethanol (Aaper Alcohol and Chemical Co., absolute), 1-propanol (Aldrich, 99+%, anhydrous), 2-propanol (Aldrich, 99+%, anhydrous), 1-butanol (Aldrich HPLC, 99.8+%), 2-butanol (Aldrich, 99+%, anhydrous), 1-pentanol (Aldrich, 99+%), 1-hexanol (Alfa Aesar, 99+%), 1-heptanol (Alfa Aesar, 99+%), and 1-octanol (Aldrich, 99+%, anhydrous) were stored over molecular sieves before use. Gas chromatographic analysis showed the organic solvent purities to be 99.7 mol% or better. Water (Aldrich HPLC grade) was used as received.

Excess solute and solvent were placed in amber glass bottles and allowed to equilibrate in a constant temperature water bath at 25.0 ± 0.1°C for at least 3 days (often longer). Attainment of equilibrium was verified both by repetitive measurements after several additional days and by approaching equilibrium from supersaturation by pre-equilibrating the solutions at a higher temperature. Aliquots of saturated diphenyl sulfone solutions were transferred through a coarse filter into a tared volumetric flask to determine the amount of sample and diluted quantitatively with methanol for spectrophotometric analysis at 267 nm on a Bausch and Lomb Spectronic 2000. Concentrations of the dilute solutions were determined from a Beer–Lambert law absorbance versus concentration working curve for nine standard solutions. The concentration of diphenyl sulfone in the standard solutions varied from 2.08×10^{-4} to 9.35×10^{-4} M. The calculated molar absorptivity of the standard solutions varied slightly over the concentration range, from $\varepsilon \approx 1850$ L mol^{-1} cm^{-1} (2.08×10^{-4} M) to $\varepsilon \approx 1750$ L mol^{-1} cm^{-1} (9.35×10^{-4} M).

© 1999 NRC Canada

Table 2. Regressional coefficients for calculating log *P* values from eq. [2] of the general solvation model.

Solvent	*c*	*r*	*s*	*a*	*b*	*v*
Hexane	0.361	0.579	–1.723	–3.599	–4.764	4.344
Heptane	0.325	0.670	–2.061	–3.317	–4.733	4.543
Octane	0.223	0.642	–1.647	–3.480	–5.067	4.526
Nonane	0.240	0.619	–1.713	–3.532	–4.921	4.482
Decane	0.160	0.585	–1.734	–3.435	–5.078	4.582
Hexadecane	0.087	0.667	–1.617	–3.587	–4.869	4.433
Cyclohexane	0.127	0.816	–1.731	–3.778	–4.905	4.646
2,2,4-Trimethylpentane	0.288	0.382	–1.668	–3.639	–5.000	4.561
Methanol	0.329	0.299	–0.671	0.080	–3.389	3.512
Ethanol (dry)	0.208	0.409	–0.959	0.186	–3.645	3.928
Octanol (dry)	0.013	0.550	–1.205	–0.020	–4.262	4.253

Identical molar absorptivities were obtained for select diphenyl sulfone solutions that contained up to 5 vol.% of the neat organic solvents. All solvents studied were optically transparent at the analysis wavelength of 267 nm.

Experimental molar solubilities of diphenyl sulfone, C_A^{sat}, in water and in the 18 organic solvents studied are listed in the second column of Table 1. Numerical values represent the average of between four and eight independent determinations, with the measurements being reproducible to ±1.5%. We were unable to find any experimental diphenyl sulfone solubility data in the published chemical literature for these solvent systems to compare our measured values against.

Results and discussion

Solvents studied include both noncomplexing alkanes and self-associating alcohols. Of the many solution models proposed in recent years, Mobile Order theory (12–19) and the general solvation model (20, 21) are perhaps the only ones that are capable of describing solute behavior in such a wide range of solvent mixtures. Lack of enthalpy of fusion data for diphenyl sulfone eliminates Mobile Order theory from consideration. The enthalpy of fusion is required in Mobile Order theory predictions to calculate the fluidization term that describes the breaking of solute–solute interactions in the crystalline lattice.

The general solvation model, on the other hand, correlates gas/solvent partition coefficients (as log *L*)

$$[1] \qquad \log L = c + rR_2 + s\pi_2^H + a\sum\alpha_2^H + b\sum\beta_2^H + d \log L^{16}$$

and water/solvent partition coefficients (as log *P*)

$$[2] \qquad \log P = c + rR_2 + s\pi_2^H + a\sum\alpha_2^H + b\sum\beta_2^H + vV_x$$

where R_2 and V_x refer to the molar refraction and McGowan volume of the solute, respectively, π_2^H is the solute dipolarity/polarizability descriptor, and $\Sigma\alpha_2^H$ and $\Sigma\beta_2^H$ are measures of the solute's hydrogen-bond acidity and hydrogen-bond basicity. For any given solvent, numerical values of the six curve-fit coefficients (*c*, *r*, *s*, *a*, *d*, *b*, and *v*) are deduced by regressing experimental partition coefficient data in accordance with eqs. [1] and [2]. Neither equation requires knowledge of the solute's enthalpy of fusion.

Previous papers have documented the ability of eq. [1] to describe processes that occur in condensed phases. Processes that have been successfully described include water – organic solvent partitions (22), water–micelle partitions (23), water–skin permeation (24), blood–brain distribution (25), and high-performance liquid chromatographic retention behavior (26). The alternative eq. [2] is generally used for systems that involve both a gas and a condensed phase, examples of which would include the solubility of gases (21, 27, 28), and retention times for gas–liquid and gas–solid chromatography (29, 30). Abraham et al. (31) recently proposed a computational method for determining the numerical values of the three solute descriptors (π_2^H, $\Sigma\alpha_2^H$, and $\Sigma\beta_2^H$) from measured saturation solubilities of the solute in different solvents as the prime experimental observation. The partition coefficient *P* was calculated as the molar solubility ratio for the solute dissolved in the organic solvent and in water, i.e., $P = C_{A,org}^{sat}/C_{A,aq}^{sat}$. In closing, the authors noted that by reversing the computational procedure, one could use the general solvation model to predict the solubility behavior of a solute dissolved in different organic solvents. Such predictions would require knowledge of the solute's aqueous solubility, numerical values of all five solute descriptors, and the regression coefficients for the solvents under consideration.

Three specific conditions must be met in order to use eqs. [1] and [2] to predict the solubility of a crystalline solute. First, the same solid phase must be in equilibrium with the saturated solutions in the organic solvent and in water. This requires that there should be no solvate or hydrate formation. Second, the secondary activity coefficient of the solute in the saturated solutions must be unity (or near unity). This particular condition may restrict the general solvation model to solids having only limited solubility in water and nonaqueous solvents. Finally, for solutes that ionize in aqueous solution, C_A^{sat} is the molar solubility of the molecular form.

Table 1 summarizes the predictive ability of eq. [2] for the 11 different organic solvents for which regressional coefficients could be found (31). For convenience, we have listed the regressional coefficients in Table 2. As a point of information, the coefficients refer to "dry" solvents not in actual contact with water. Abraham et al. (20) have reported numerical values for several additional alcohol solvents, but unfortunately their regressional analyses used experimentally determined partition coefficients. Water is fairly soluble

© 1999 NRC Canada

in alcohols such as 1-butanol through 1-octanol. Dissolved water alters the solvent's polarizability and hydrogen-bonding character, which is reflected in the numerical values of the regressional coefficients. Predictions were thus limited to the eight saturated hydrocarbons, methanol, ethanol, and 1-octanol. Numerical values of the solute descriptors (R_2 = 1.570; π_2^H = 2.15; $\Sigma\alpha_2^H$ = 0; $\Sigma\beta_2^H$ = 0.70 and V_x = 1.605) were taken from a published compilation (22) containing over 700 different solutes.

Examination of the numerical entries in Table 1 reveals that eq. [2] does provide fairly reasonable (though by no means perfect) estimates for the solubility behavior of diphenyl sulfone in both alkane and alcohol solvents. The average absolute deviation between the predicted and observed partition coefficients is 0.094 log units, which is comparable in magnitude to the standard deviations associated with the regressional analysis for *c*, *r*, *s*, *a*, *b*, and *v* coefficients for the individual solvent systems. A deviation of 0.094 log units in the water – organic solvent partition coefficient corresponds to approximately a ± 20% error in the predicted molar solubility. Readers are reminded that in evaluating the predictive applicability of the general solvation model that several of these systems are highly nonideal, and that the molar solubility covers up to 35-fold range. Our past experience in using solution models has been that the better models will generally give predicted values that fall within ±40% or so of the observed solute solubility. For example, this was the case in using Mobile Order theory to predict the solubility behavior of *trans*-stilbene (32), benzil (33), pyrene (34), fluoranthene (35), anthracene (36), and thioxanthen-9-one (37) in a wide range of organic nonelectrolyte solvents. The computations performed in the present study suggest that expressions derived from the general solvation model can be used to predict solute solubilities. The general solvation model is limited in application at the present time, however, to the 25 or so organic solvents for which regressional coefficients have been evaluated.

Acknowledgements

Carmen Hernández thanks the University of North Texas and the U.S. Department of Education for support provided under the Ronald E. McNair Postbaccalaureate Achievement Program.

References

1. W.E. Acree, Jr. Polycyclic aromatic hydrocarbons in pure and binary solvents. IUPAC solubility data series. Vol. 54. Oxford University Press, Oxford. 1994.
2. W.E. Acree, Jr. Polycyclic aromatic hydrocarbons: binary nonaqueous systems: part 1 (solutes A–E). IUPAC solubility data series. Vol. 58. Oxford University Press, Oxford. 1995.
3. W.E. Acree, Jr. Polycyclic aromatic hydrocarbons: binary nonaqueous systems: part 2 (solutes F–Z). IUPAC solubility data series. Vol. 59. Oxford University Press, Oxford. 1995.
4. W.E. Acree, Jr. Int. J. Pharm. **18**, 47 (1984).
5. U. Domanska and T. Hofman. J. Solution Chem. **14**, 531 (1985).
6. U. Domanska. Fluid Phase Equilibr. **35**, 217 (1985).
7. R.S. Basu, H. Pham, and D.P. Wilson. Int. J. Pharm. **7**, 319 (1986).
8. A.B. Ochsner and T.D. Sokoloski. J. Pharm. Sci. **74**, 634 (1985).
9. R. Carta and S. Dernini. J. Chem. Eng. Data, **28**, 328 (1983).
10. W.E. Acree, Jr. and J.H. Rytting. Int. J. Pharm. **13**, 197 (1983).
11. A. Martin, P.L. Wu, A. Adjei, A. Beerbower, and J.M. Prausnitz. J. Pharm. Sci. **70**, 1260 (1981).
12. P.L. Huyskens and G.G. Siegel. Bull. Soc. Chim. Belg. **97**, 821 (1988).
13. G.G. Siegel, P.L. Huyskens, and G. Vanderheyden. Ber. Bunsenges. Phys. **94**, 549 (1990).
14. P.L. Huyskens. J. Mol. Struct. **274**, 223 (1992).
15. P. Ruelle, C. Rey-Mermet, M. Buchmann, H. Nam-Tran, U.W. Kesselring, and P.L. Huyskens. Pharm. Res. **8**, 840 (1991).
16. P. Ruelle, M. Buchmann, H. Nam-Tran, and U.W. Kesselring. Int. J. Pharm. **87**, 47 (1992).
17. P. Ruelle, M. Buchmann, and U.W. Kesselring. J. Pharm. Sci. **83**, 396 (1994).
18. P. Ruelle, E. Sarraf, and U.W. Kesselring. Int. J. Pharm. **104**, 125 (1994).
19. P. Ruelle, E. Sarraf, L. Van den Berge, K. Seghers, M. Buchmann, and U.W. Kesselring. Pharm. Acta Helv. **68**, 49 (1993).
20. M.H. Abraham, H.S. Chadha, J.P. Dixon, and A.J. Leo. J. Phys. Org. Chem. **7**, 712 (1994).
21. M.H. Abraham, J. Andonian-Haftvan, J.P. Osei-Owasu, P. Sakellariou, J.S. Urieta, M.C. Lopez, and R. Fuchs. J. Chem. Soc. Perkin Trans. 2, 299 (1993).
22. M.H. Abraham, H.S. Chadha, G.S. Whiting, and R.C. Mitchell. J. Pharm. Sci. **83**, 1085 (1994).
23. M.H. Abraham, H.S. Chadha, J.P. Dixon, C. Rafols, and C. Treiner. J. Chem. Soc. Perkin Trans. 2, 887 (1995).
24. M.H. Abraham, H.S. Chadha, and R.C. Mitchell. J. Pharm. Pharmacol. **47**, 8 (1995).
25. M.H. Abraham, H.S. Chadha, and R.C. Mitchell. J. Pharm. Sci. **83**, 1257 (1994).
26. M.H. Abraham and M. Roses. J. Phys. Org. Chem. **7**, 672 (1994).
27. M.H. Abraham, J. Andonian-Haftvan, G.S. Whiting, A. Leo, and R.W. Taft. J. Chem. Soc. Perkin Trans. 2, 1777 (1994).
28. M.H. Abraham and P.K. Weathersby. J. Pharm. Sci. **83**, 1450 (1994).
29. M.H. Abraham and C. Rafols. J. Chem. Soc. Perkin Trans. 2, 1843 (1995).
30. M.H. Abraham, G.S. Whiting, R.M. Doherty, and W.J. Shuely. J. Chromatogr. **587**, 213 (1991).
31. M.H. Abraham, C.E. Green, W.E. Acree, Jr., C.E. Hernández, and L.E. Roy. J. Chem. Soc. Perkin Trans. 2, 2677 (1998).
32. K.A. Fletcher, M.E.R. McHale, K.S. Coym, and W.E. Acree, Jr. Can. J. Chem. **75**, 258 (1997).
33. K.A. Fletcher, S. Pandey, M.E.R. McHale, and W.E. Acree, Jr. Phys. Chem. Liq. **33**, 181 (1996).
34. J.R. Powell, D. Voisinet, A. Salazar, and W.E. Acree, Jr. Phys. Chem. Liq. **28**, 269 (1994).
35. C.E. Hernández and W.E. Acree, Jr. Can. J. Chem. **76**, 1312 (1998).
36. L.E. Roy, C.E. Hernández, and W.E. Acree, Jr. Polycyclic Aromat. Compds. **13**, 105 (1999).
37. K.A. Fletcher, K.S. Coym, L.E. Roy, C.E. Hernández, M.E.R. McHale, and W.E. Acree, Jr. Phys. Chem. Liq. **35**, 243 (1998).

© 1999 NRC Canada

Chiral recognition in solution. Interactions of α-amino acids in concentrated aqueous solutions of urea or ethanol

Giuseppina Castronuovo, Vittorio Elia, Anna Pierro, and Filomena Velleca

Abstract: Enthalpies of dilution of the L and D forms of glutamine, citrulline, and phenylalanine in concentrated aqueous solutions of urea or ethanol were measured calorimetrically at 298 K. Glycine, urea, formamide, and phenol were also studied under the same experimental conditions, to get information about the behaviour of the zwitterion and of the functional group in the side chain of the cited amino acids when the concentration of the cosolvent changes. The derived pairwise enthalpic interaction coefficients for the three amino acids were rationalized according to the preferential configuration model. Indications are that, in concentrated urea, the coefficients for citrulline and glutamine are determined mainly by the interactions between the cosolvent and the hydrophilic groups in the molecule of the amino acids. For phenylalanine, coefficients are less positive than in water, because the presence of urea, which solvates preferentially the zwitterions, attenuates hydrophobic interactions between the benzene rings. In ethanol, coefficients for the three amino acid become negative or more negative than in water, because in this medium hydrophilic interactions are enhanced. Chiral recognition, namely the difference in the values of homo- and heterochiral interaction coefficients, was detected only for phenylalanine in urea. Hence, the nature of the cosolvent, influencing differently hydrophilic and hydrophobic interactions, can lead to the detection of chiral recognition also for those systems that, as phenylalanine, do not present this effect in pure water.

Key words: α-amino acids, excess functions, molecular interactions, preferential configuration.

Résumé : Faisant appel à la calorimétrie et opérant à 298 K, on a mesuré les enthalpies de dilution des formes D et L de la glutamine, de la citrulline et de la phénylalanine dans des solutions concentrées aqueuses d'urée ou d'éthanol. Utilisant les mêmes conditions, on a aussi étudié la glycine, l'urée, le formamide et le phénol pour tirer des informations concernant le comportement du zwitterion et du groupe fonctionnel de la chaîne latérale des acides aminés cités lorsqu'on modifie les concentrations de cosolvant. Les coefficients d'interaction enthalpiques par paires qu'on en a dérivé pour les trois acides aminés sont rationalisés en fonction du modèle configurationnel préférentiel. On a recueilli des indications à l'effet que, dans l'urée concentrée, les coefficients de la citrulline et de la glutamine sont déterminés principalement par les interactions entre le cosolvant et les groupes hydrophiles des molécules d'acides aminés. Pour la phénylalanine, les coefficients sont moins positifs que dans l'eau à cause de la présence de l'urée qui solvate les zwitterions de façon préférentielle et qui atténue les interactions hydrophobes entre les noyaux benzéniques. Dans l'éthanol, les coefficients des trois acides aminés deviennent négatifs (ou plus négatifs) que dans l'eau parce que, dans ce milieu, il y a augmentation des interactions hydrophiles. On n'a détecté de reconnaissance chirale, à savoir, une différence dans les valeurs des coefficients d'interaction homo- et hétérochirales, que pour la phénylalanine dans l'urée. En conséquence, la nature du cosolvant, qui influence de façons différentes les interactions hydrophile et hydrophobe, peut aussi conduire à la détection d'une reconnaissance chirale pour des systèmes qui, comme la phénylalanine, ne donnent pas lieu à cet effet dans l'eau pure.

Mots clés : acides α-aminés, fonctions d'excès, interactions moléculaires, configuration préférentielle.

[Traduit par la Rédaction]

Introduction

Nonbonding interactions in aqueous solutions of nonelectrolytes have reached a good qualitative understanding from the analysis of the excess thermodynamic properties using a group additivity approach (1). The results of this approach for the excess Gibbs free energies have shown that interactions between domains having the same effect on water structure (hydrophilic–hydrophilic or hydrophobic–hydrophobic) are favourable, while interactions between domains having contrasting effects (hydrophilic–hydrophobic) are unfavourable (2). On these bases, calorimetric and spectroscopic data col-

Received March 5, 1998.

G. Castronuovo,[1] V. Elia, A. Pierro, and F. Velleca. Department of Chemistry, University Federico II of Naples, via Mezzocannone, 4-80134 Naples, Italy.

[1]Author to whom correspondence may be addressed. Telephone: (081) 5476517. Fax: (081) 5527771. e-mail: castronuovo@chemna.dichi.unina.it

 © 1999 NRC Canada

lected in our laboratory in the last years have been rationalized through a qualitative model that hypothesizes the occurrence of more probable configurations in solution. Two hydrated, interacting molecules bearing hydrophilic and hydrophobic domains interact through a preferential configuration which maximizes favorable interactions between similar domains (i.e., hydrophilic–hydrophilic or hydrophobic–hydrophobic or in general like–like domains), while minimizing unfavorable interactions between unlike domains (i.e., hydrophilic–hydrophobic or like–unlike domains) (3, 4).

The "preferential configuration" model was successfully employed to explain chiral recognition occurring in aqueous solutions of α-amino acids (5–9). Coulombic forces acting in the aqueous solutions of free α-amino acids, where dipolar ions predominate, were long thought to screen the subtle differences in the interactions between molecules of the same or different chirality (10, 11). For these reasons, attention was mainly focused on nonionic α-amino acid derivatives, obtaining encouraging results (12–14). To the contrary, systematic studies from this laboratory, concerning the investigation of the homologous series of α-amino acids bearing unsubstituted alkyl chains, have shown that the presence of dipolar ions is the main factor that determines chiral recogniton, namely, the difference in the energetics of homo- and heterochiral interactions (5, 6). In fact, electrostatic interactions between the opposite charges of the zwitterions determine two different preferential configurations, depending on the chirality of the molecules (5, 6, 8, 9). When chirality is the same, the two interacting molecules have the side chains in the same half-space determined by the imaginary plane containing the charged groups. In contrast, for molecules of different chirality, the alkyl groups lie in two different half-spaces. These two different configurations, enhancing the steric differences of the two interacting solutes, lead to rather large differences in the interactions between the side chains, thus making chiral recognition to be detected. The preferential configuration sustained by the interactions between the four charges of zwitterions must be regarded as one of the possible configurations of two interacting molecules, but it is the only one able to differentiate interactions between the alkyl chains. Other configurations exist in solution: among them, the most important is the side-by-side juxtaposing only two of the oppositely charged groups of zwitterions (15). This configuration maximizes the juxtaposition of hydrophilic and hydrophobic domains, but is inactive toward chiral recognition. Hence, the absence of this last effect in 1 M HCl, where dipolar ions disappear (16), is probably due to a side-by-side prevailing configuration, determined by the simultaneous juxtaposition of the alkyl and carboxyl groups, with the charged amino groups occupying remote positions.

To gain a further understanding of the interaction mechanism in the aqueous solutions of α-amino acids, we are carrying out a research program on the physical chemical properties of these solutes in mixed solvents. The second coefficient of the virial expansion of the excess enthalpy as a function of molalities is the quantity considered, because it has revealed particularly useful to get information about the interaction mechanism. Here, we examine the enthalpies of dilution of the L and D forms of citrulline, phenylalanine, and glutamine in concentrated aqueous solutions of urea or ethanol, two solutes often employed as denaturing agents for polypeptides, proteins, and other biopolymers. The delicate balance of intra- and intermolecular interactions responsible for the only biologically active conformation of proteins in water is greatly modified at high urea or ethanol concentrations, provoking denaturation. In such situations, the mixed solvent has properties quite different from those of pure water. For the α-amino acids here reported, the presence of urea or ethanol causes variations in the relative intensities of the interactions between different domains. That could change the prevailing mechanism of interaction acting in pure water. That allows to gain information about the factors responsible of this interaction mechanism and of the presence or absence of chiral recognition in water. To that, glutamine and citrulline were chosen because they behave as prevailingly hydrophilic solutes in water, being negative the enthalpic interaction coefficient characterizing their binary solutions. Phenylalanine, instead, is a prevailingly hydrophobic solute, being positive its enthalpic coefficient in water. Glycine, urea, formamide and phenol have also been studied in the same experimental conditions, in that they mimic the behaviour of the functional groups of the investigated α-amino acids when the structure of the medium changes. Hence, through the analysis of homo- and heterochiral enthalpic interaction coefficients, we aim to ascertain whether the hypothesis of preferential configurations holds in these systems, and what are the various contributions acting in the interaction.

Experimental

Solutes employed were Sigma–Aldrich products. Their purity was assessed by the company to be greater than 98–99%. They were used without further purification. Measurements of the heats of dilution were carried out using an LKB flow microcalorimeter and a thermal activity monitor from Thermometric. Calorimeters were equipped with a GP 10 gradient programmer, a 500 μL mixing chamber, a PSV 50 electrovalve, and a P3 peristaltic pump (all from Pharmacia) for the automatic preparation and the pumping of solutions into the cells of the calorimeters. The method has been tested through known systems. Enthalpies of dilution in water of urea and hexane-1,2-diol have been determined, and the evaluated pairwise enthalpic interaction coefficients (h_{xx} = –331 ± 3 J kg mol^{-2} for urea and h_{xx} = 2999 ± 46 J kg mol^{-2} for hexane-1,2-diol) were in good agreement with the literature value (h_{xx} = –350 ± 13 J kg mol^{-2} for urea (1) and h_{xx} = 2955 ± 55J kg mol^{-2} for hexane-1,2-diol (3)). The values of the dilution enthalpies, ΔH_{dil}, were obtained from

$$\Delta H_{dil}(m_x^{i} \rightarrow m_x^{f}) = -(dQ/dt)/P_S$$

where (dQ/dt) is the heat evolved per unit time, P_S is the total mass flow rate of mixed solvent for unit time, and m_x^{i} and m_x^{f} are the initial and final molalities, respectively. ΔH_{dil} is given in J kg^{-1} of solvent in the final solution.

Results

An excess function is defined as the difference between the values of that function referred to a real and an ideal solution. Then, the excess enthalpy is obtained by

© 1999 NRC Canada

$$[1] \qquad H^E = H(m) - H^{id} = H(m) - (H^\circ_S - \Sigma m_x \bar{H}^\circ_x)$$

where $H(m)$ and H^E, the absolute and the excess enthalpy, respectively, both refer to 1 kg of solvent and m_x moles of each solute; H^{id} is the enthalpy of the ideal solution; $\bar{H}^\circ_s$ is the enthalpy of 1 kg of solvent, and $\bar{H}^\circ_x$ is the limiting partial molal enthalpy of each solute. According to the treatment of solution properties originally proposed by McMillan and Mayer (17) and specifically applied to those of aqueous solutions of nonelectrolytes by Kauzmann and co-workers (18) and other authors (19, 21), an excess thermodynamic property, of a solution containing n solutes, J^E, can be expressed as a virial expansion of molalities of pair and higher order interaction coefficients, j, as follows

$$[2] \qquad J^E = \sum_{i=1}^{n} \sum_{k=1}^{n} j_{ik} m_i m_k + \text{higher terms}$$

For ternary solutions containing the solutes x and y, virial coefficients of the power series of the excess enthalpies, h_{xy}, as a function of molalities can be derived from the enthalpies of dilution, ΔH_{dil}, as follows

$$[3] \qquad \Delta H_{dil}(m_x^i, m_y^i \rightarrow m_x^f, m_y^f)$$
$$= H^E(m_x^f, m_y^f) - m_x^f/m_x^i \, H^E(m_x^i, m_y^i)$$
$$= h_{xx} m_x^f (m_x^f - m_x^i) + h_{yy} m_y^f (m_y^f - m_y^i)$$
$$+ 2h_{xy} m_x^f (m_y^f - m_y^i) + \text{higher terms}$$

where m_x^i, m_y^i, m_x^f, m_y^f are the molalities of the x and y solutes before and after the dilution process, respectively. According to the Mc Millan–Mayer approach (17), the h coefficients appearing in eq. [3] represent the enthalpic contributions to the Gibbs free energy coefficients characterizing the interaction between pairs, triplets, or higher order interactions. They implicitly account also for all variations of solvent–solvent and solute–solvent interactions. Considering as solvent the mixture of ethanol–water or urea–water, a solution of the solute x can be regarded as a binary one and then eq. [3] reduces to

$$[4] \qquad \Delta H_{dil}(m_x^i \rightarrow m_x^f)$$
$$= h_{xx} \, m_x^f \, (m_x^f - m_x^i) + \text{higher terms}$$

where ΔH_{dil} is expressed in J kg^{-1} of mixed solvent, and the molalities are calculated as moles per kg of mixed solvent.

Two-solute solutions, as the D and L forms of an amino acid, are, instead, ternary solutions which are characterized by cross-coefficients evaluated by means of an auxiliary function ΔH^{**}:

$$[5] \qquad \Delta H^{**} = \Delta H_{dil}(m_D^i, m_L^i \rightarrow m_D^f, m_L^f)$$
$$- \Delta H_{dil}(m_D^i \rightarrow m_D^f) - \Delta H_{dil}(m_L^i \rightarrow m_L^f)$$
$$= 2h_{DL} m_D^f (m_L^f - m_L^i) + \text{higher terms}$$
$$= 2h_{DL} m_L^f (m_D^f - m_D^i) + \text{higher terms}$$

where $h_{DD} \equiv h_{LL}$ and h_{DL} are the homochiral and heterochiral pairwise enthalpic interaction coefficients, respectively, in the mixed solvent used. The values of the coefficients of the excess enthalpies were obtained by fitting ΔH_{dil} or ΔH^{**} by a least-squares method. The fitting was tried with polynomials of increasing degree, choosing finally the one of the highest degree for which all the coefficients are significant with respect to their own 95% confidence limits. For most of the examined systems, the concentration ranges studied are limited, so that only the second homochiral or heterochiral coefficients, h_{LL} and h_{DL}, are to be determined.

To examine the role of urea or ethanol in affecting like solute – like solute interactions, the present data could be treated differently to evaluate the triplet term h_{xxy}, where y is urea or ethanol. In this case, we refer to a process through which a ternary solution of the x and y solutes in water is diluted by a binary solution containing the cosolute y at the same concentration (m_y) as that in the ternary solution. It can be demonstrated that in this case h_{xy} and h_{xyy} cannot be evaluated, and the dilution enthalpy, expressed in J kg^{-1} of water, is

$$[6] \qquad \Delta H_{dil} = (h_{xx}^w + 3h_{xxy}^w m_y) m_x^f (m_x^f - m_x^i)$$
$$+ \text{higher terms}$$

where w stands for water. Fitting ΔH_{dil} as a function of the abscissa m_x^f $(m_x^f - m_x^i)$ and knowing h_{xx}^w, it is possible to derive h_{xxy}^w.

However, the parameter we will employ in the following is h_{xx} determined in the mixed solvent: two reasons urge us to do that. Firstly, like solute – unlike solute interactions are certainly significant in a denaturation process, which actually requires high concentrations of the cosolute: the properties of this mixed solvent are different from those of water and modify like solute – like solute interactions. We want to explore just how this mixed solvent acts on the pair interactions in the same experimental conditions as those acting in the denaturation process. Besides, using such high concentrations of urea or ethanol is not suitable to evaluate the triplet term: coefficient for like solute – unlike solute interactions in water are better obtained using comparable concentrations of both solutes. Calculations performed for glycine in concentrated urea prove that. The derived triplet coefficient does not remain constant at increasing urea concentration, an indication that, in such conditions, water changes its properties depending on cosolute concentration.

Enthalpic pair interaction coefficients for glycine, urea, formamide, and phenol in concentrated aqueous solutions of urea or ethanol are reported in Tables 1–3. For urea in solutions of urea as cosolvent, the coefficients increase toward less negative values at increasing cosolvent concentration; for glycine and formamide, they even change sign, passing from negative to positive. In ethanol as cosolvent, glycine exhibits a very pronounced variation towards large negative values, while urea and formamide show a flat minimum. For phenol, the decrease towards negative values is very steep.

In Tables 4–6, homo- and heterochiral pairwise enthalpic interaction coefficients are summarized for the aqueous solutions of citrulline, glutamine, and phenylalanine containing urea or ethanol. Glutamine and citrulline present a behaviour very similar to that of glycine, formamide, and urea in urea or ethanol: their homo- and heterochiral coefficients go toward positive or less negative values at increasing urea concentration, and toward highly negative values at increasing ethanol concentrations. Chiral recognition is detected for both amino acids only at the highest ethanol concentration.

© 1999 NRC Canada

Table 1. Enthalpic interaction coefficients for aqueous solutions of glycine (x) and urea (y), at various concentrations of urea, m_U, at 25°C.

m_U[a]	h_{xx}[b]	h_{yy}[b]	h_{yyy}[c]	n[d]	c.r.[e]
0	–404 ± 9[f]	–350 ± 13[g]	22[g]		
1.00	–298 ± 6[f]	–293 ± 5	—[h]	27	0.48–0.28
3.00	–140 ± 5[f]	–262 ± 18	65 ± 30	28	0.46–0.26
5.00	–15 ± 5[f]	–206 ± 16	51 ± 26	28	0.51–0.29
7.00	53 ± 8[f]	–165 ± 11	41 ± 16	28	0.55–0.31

[a]mol/kg.
[b]J kg mol^{-2}. Errors reported are the 95% confidence limits.
[c]J kg^2 mol^{-3}.
[d]Number of experimental data.
[e]Concentration range, mol/kg.
[f]Reference 24. That reference reports also a value at 9.0 m urea, namely 109 ± 3 J kg mol^{-2}.
[g]Reference 1.
[h]Only the second coefficient was needed to best fit the experimental data. The enthalpic coefficient for formamide in water is –115 ± 1 J kg mol^{-2} (ref. 25), and it is 32 ± 4 J kg mol^{-2} in 8 m urea (ref. 21).

For phenylalanine in urea, coefficients are positive and become smaller at increasing concentration of the cosolvent. Chiral recognition is not detected for this amino acid in water, but it is very large in urea, disappearing only at the highest concentration of the cosolvent. In ethanol solutions, a very rapid decrease from positive to negative values is exhibited by both homochiral and heterochiral coefficients, repeating the behaviour of phenol. A small chiral recognition is detected only at the highest ethanol concentration.

Discussion

The results presented in this work aim to give an indirect contribution to the understanding of the phenomenon occurring upon the denaturation of proteins by high concentrations of urea or ethanol. Comparison between the properties of solutes in water and in water–cosolvent mixtures is useful for obtaining a deeper insight into the factors promoting the unfolding of biopolymers in such solutions (21). It must be underlined that the conclusions which will be drawn about the systems presently investigated, containing concentrated urea or ethanol, are based only on enthalpic data; however, Gibbs energy data would be necessary for a more satisfactory interpretation.

The enthalpic interaction coefficients for citrulline and glutamine in water are negative, thus indicating a typical behaviour of prevailingly hydrophilic solutes. Probably, hydrophobic interactions are shielded, attenuated by the bulky hydrophilic groups. In concentrated urea, coefficients become positive for citrulline and less negative for glutamine (see Tables 4 and 5). That reproduces the behaviour shown by glycine, formamide, and urea, prevailingly hydrophilic solutes, whose pair enthalpic interaction coefficients become positive or less negative at increasing urea, as reported in Table 1. The transition to a thermochemically unfavourable behaviour at increasing concentration of cosolvent can probably be ascribed to the increased dielectric constant of the medium; that reduces polar hydrophilic interactions. In addition, given that hydrophilic–hydrophilic interactions are favoured for a negative contribution to the excess free energy, it seems reasonable to hypothesize that the cosolvent urea interacts mainly with the hydrophilic groups, whose increased hindrance contributes to the attenuation of the interactions. To that, it is useful to remember that also other authors report that energetically favourable interactions exist between the polar peptide groups and zwitterionic groups (22), or that urea molecules preferentially adsorb onto charged hydrophilic residues on the surface of globular proteins (23). Phenylalanine, instead, shows coefficients becoming less positive at increasing urea for the attenuated ability of the zwitterions to force interactions between the benzene rings. The behaviour shown by phenylalanine is similar to that found in a preceding study on α-amino acids bearing unsubstituted alkyl chains in concentrated aqueous solutions of urea. There, evidence was given that, at increasing urea concentration, the contribution of the zwitterionic group to the pairwise enthalpic interaction coefficient varies from a negative to an almost null value, underlining a transition towards a thermochemically unfavorable behavior (24). At the same time, hydrophobic contributions decrease linearly at increasing urea concentration: the coupled effects should lessen the value of the coefficients. On the other hand, being the final state (bulk) less structured than pure water for the presence of urea, water released to the bulk should undergo a larger enthalpic and entropic change, making larger the value of the coefficient. The attenuation of hydrophobic interactions in urea, as respect to water, is found to be the prevailing effect, as in the case of alkan-1-ols (27), alkan-*m*,*n*-diols (28), *N*-acetylamides of α-amino acids in 7 M (29) or

Table 2. Enthalpic interaction coefficients for aqueous solutions of glycine at various concentrations of ethanol, m_{EtOH}, at 25°C.[a]

m_{EtOH}[b]	h_{xx}[c]	h_{xxx}[d]
0[f]	–404 ± 9	—
1.00	–339 ± 10	—
2.00	–746 ± 18	—
3.00	–1055 ± 50	378 ± 78
5.00	–1148 ± 42	737 ± 70
7.00	–1299 ± 20	—
9.00	–1693 ± 20	—
11.0	–2324 ± 52	1254 ± 138

[a]Data from ref. 26.
[b]mol kg^{-1}.
[c]J kg mol^{-2}. Errors reported are the 95% confidence limits.
[d]J kg^2 mol^{-3}. A dash means that only the second coefficient was needed to best fit the experimental data.

© 1999 NRC Canada

Table 3. Enthalpic pair interaction coefficients for aqueous solutions of urea (x), formamide (y), and phenol (z), at various concentrations of ethanol, at 25°C.

m_{EtOH}[a]	h_{xx}[b]	n[c]	c.r.[d]	h_{yy}[b]	n[c]	c.r.[d]	h_{zz}[b]	n[c]	c.r.[d]
0	–350 ± 13[e]	—	—	–115 ± 1[f]	—	—	816 ± 8	19	0.10–0.050
1.00	—	—	—	–176 ± 3	20	0.1–0.05	1069 ± 15	12	0.10–0.050
2.00	–511 ± 30	12	0.12–0.10	—	—	—	961 ± 13	12	0.10–0.050
3.00	–535 ± 30	12	0.20–0.11	—	—	—	222 ± 4	20	0.10–0.050
5.00	–615 ± 38	12	0.20–0.10	–424 ± 5	20	0.12–0.06	–639 ± 4	12	0.10–0.050
7.00	–569 ± 40	12	0.20–0.11	–408 ± 5	20	0.13–0.07	–2389 ± 22	15	0.10–0.050
9.00	–501 ± 22	12	0.19–0.10	–358 ± 12	17	0.12–0.06	–3921 ± 98	12	0.10–0.050

[a]mol/kg.
[b]J kg mol^{-2}. Errors reported are the 95% confidence limits.
[c]Number of experimental data.
[d]Concentration range, mol/kg.
[e]Reference 1.
[f]Reference 25.

Table 4. Homo- and heterochiral enthalpic pair interaction coefficients for aqueous solutions of citrulline at different concentrations of urea and ethanol, m_U and m_{EtOH}, respectively, at 25°C.

Conc.[a]	h_{LL}[b]	n[c]	c.r.[d]	h_{DL}[b]	n[c]	c.r.[d]
m_U						
0[e]	–847 ± 9	11	0.090–0.025	–890 ± 30	12	0.09–0.020
1.00	–564 ± 14	59	0.19–0.10	–513 ± 30	28	0.080–0.040
2.00	–408 ± 12	23	0.15–0.09	–535 ± 34	28	0.070–0.037
3.00	–308 ± 16	16	0.15–0.10	–332 ± 30	14	0.080–0.050
4.00	–71 ± 3	18	0.30–0.16	–105 ± 9	20	0.15–0.080
5.00	–129 ± 20	24	0.16–0.09	–142 ± 34	20	0.070–0.040
7.00	64 ± 5	12	0.17–0.09	37 ± 22	8	0.070–0.050
m_{EtOH}						
1.00	–1208 ± 18	20	0.060–0.030	–1218 ± 30	20	0.060–0.030
3.00	–1941 ± 44	12	0.060–0.030	–1908 ± 76	20	0.060–0.030
5.00	–2373 ± 30	11	0.060–0.030	–2572 ± 62	20	0.060–0.030
7.00	–2728 ± 56	12	0.050–0.025	–2779 ± 142	20	0.050–0.025
9.00	–3259 ± 88	24	0.050–0.025	–3598 ± 122	20	0.050–0.025
11.0	–3271 ± 62	20	0.050–0.025	–3522 ± 176	20	0.050–0.025

[a]mol/kg.
[b]J kg mol^{-2}. Errors reported are the 95% confidence limits.
[c]Number of experimental data.
[d]Concentration range, mol/kg.
[e]From ref. 7.

8 M urea (30), and amides in 6 M guanidinium chloride (31).

The preferential configuration model accounts for the enhanced cooperativity of hydrophobic interactions when sustained by hydrophilic interactions. The presence of a hydrophilic domain on the side chain of an α-amino acid determines an enthalpic, favorable contribution to the interaction between the hydrophobic domains in the homochiral configuration. Sometimes, the failure of this interaction in the heterochiral configuration is the origin of chiral recognition, larger than that detected in the presence of unsubstituted side chains (7, 9). Citrulline and glutamine do not exhibit chiral recognition in pure water, or for the shortness of the side chain or, alternatively, because the two different preferential configurations cannot exist. Probably, the comparable strength of the interactions between the residues in the alkyl chain and between zwitterions can impose a unique, side-by-side configuration for both homo- and heterochiral systems. Urea, formamide, and glycine, whose residues represent the functional groups of the two amino acids, are characterized by similar enthalpic coefficients in water. The hypothesis that the two functional groups concur in imposing a side-by-side configuration in water is supported by the negative values of the coefficients for citrulline and glutamine, which are clearly determined by the hydrophilic functional groups. At increasing urea concentration, glycine, urea, and formamide transit to a thermochemically unfavourable behaviour, losing rapidly their capability to explicate the interaction responsible for chiral recognition in α-amino acids. Then, citrulline and glutamine do not exhibit this last effect, nor in water, nor varying urea concentration (Table 4 and 5).

Phenylalanine does not exhibit chiral recognition in water, too. Coefficients, however, are positive, probably because

© 1999 NRC Canada

Table 5. Homo- and heterochiral enthalpic pair interaction coefficients for aqueous solutions of glutamine at different concentrations of urea and ethanol, m_U and m_{EtOH}, respectivley, at 25°C.

Conc.[a]	h_{LL}[b]	n[c]	c.r.[d]	h_{DL}[b]	n[c]	c.r.[d]
m_U						
0	–876 ± 11[e]	41	0.14–0.040	–914 ± 24[e]	42	0.12–0.040
1.00	–490 ± 18	20	0.14–0.070	–773 ± 140	12	0.14–0.070
3.00	–357 ± 18	11	0.15–0.080	–326 ± 14	20	0.060–0.030
5.00	–373 ± 38	76	0.16–0.025	–378 ± 226	40	0.16–0.050
7.00	–410 ± 48	92	0.26–0.025	–346 ± 98	60	0.050–0.025
m_{EtOH}						
0.500	–1096 ± 22	12	0.080–0.040	–1116 ± 64	20	0.090–0.045
1.00	–1248 ± 15	19	0.10–0.050	–1250 ± 56	20	0.10–0.050
3.00	–1737 ± 40	12	0.070–0.035	–1806 ± 76	20	0.080–0.040
7.00	–2528 ± 60	12	0.060–0.030	–2840 ± 156	20	0.050–0.025

[a]mol/kg.
[b]J kg mol^{-2}. Errors reported are the 95% confidence limits.
[c]Number of experimental data.
[d]Concentration range, mol/kg.
[e]Coefficients in water, already reported in ref. 9, have been redetermined in the course of the present work.

Table 6. Homo- and heterochiral enthalpic pair interaction coefficients for aqueous solutions of phenylalanine at different concentrations of urea and ethanol at 25°C.

Conc.[a]	h_{LL}[b]	n[c]	c.r.[d]	h_{DL}[b]	n[c]	c.r.[d]
m_U						
0	1140 ± 30[e]	22	0.020–0.070	1104 ± 83[e]	12	0.10–0.030
1.00	672 ± 52	12	0.070–0.040	1200 ± 24	15	0.030–0.020
3.00	597 ± 48	20	0.060–0.040	1179 ± 19	20	0.030–0.020
7.00	504 ± 44	32	0.070–0.040	1252 ± 9	20	0.030–0.020
9.00	772 ± 18	12	0.070–0.040	760 ± 36	15	0.030–0.020
m_{EtOH}						
1.00	1069 ± 12	20	0.090–0.045	1088 ± 16	19	0.060–0.030
2.00	981 ± 14	16	0.060–0.030	756 ± 24	20	0.060–0.030
3.00	652 ± 4	19	0.070–0.035	549 ± 15	20	0.040–0.020
5.00	–599 ± 36	16	0.040–0.020	–676 ± 66	20	0.030–0.015
7.00	–1841 ± 42	20	0.040–0.020	–1868 ± 126	20	0.040–0.020
9.00	–2750 ± 62	20	0.040–0.020	–3091 ± 146	20	0.040–0.020

[a]mol/kg.
[b]J kg mol^{-2}. Errors are the 95% confidence limits.
[c]Number of experimental data.
[d]Concentration range, mol/kg.
[e]From ref. 7.

they are determined by the presence of a preferential configuration imposed by the interaction between the two rings and sustained by the hydrophobic interaction between the methylene groups (7). The very high and negative value of the volume pairwise coefficient in water for this amino acid, $v_{LL} = -8 \pm 4$ cm^3 kg mol^{-2}, is an important indication of the hydrophobic structure-maker nature of benzene rings (32). The interaction between these hydrophobic domains could concur with the one between zwitterions, imposing a unique, side-by-side configuration in the homo- and heterochiral systems that does not allow chiral recognition to be observed in water. In concentrated urea, instead, phenylalanine exhibits a large chiral recognition (Table 6). In fact, while the homochiral coefficient presents a sudden decrease between 0 and 1 m urea, varying slightly thereafter, the heterochiral coefficient maintains almost the same value as in water up to 7 m urea. The presence of urea influences differently hydrophobic and hydrophilic interactions. Therefore, the almost invariant value of the heterochiral coefficient means that the induced variations balance, leaving the coefficients to the same value as in water. The rapid decrease of the homochiral coefficient indicates that the prevailing effect is the attenuation of hydrophobic interactions. At 9 m urea, the decreased interactions between zwitterions implies the impossibility of determining the configuration leading to chiral recognition and, consequently, the disappearance of the last effect. It must be underlined that while zwitterions become "inactive," hydrophobic interactions are still effective, thus determining identical and positive values for both homo- and heterochiral coefficients. This behaviour

© 1999 NRC Canada

resembles that shown by another prevailingly hydrophobic amino acid, namely norleucine, in concentrated urea (24).

In aqueous solutions containing ethanol as cosolvent, the behaviour of the substances employed is evidence that the nature of the medium greatly influences the strength of nonbonding interactions. Urea, glycine, formamide, and phenol are characterized by enthalpic interaction coefficients which, independently of their sign in water, go toward negative values in ethanol. That is in agreement with the decrease of the dielectric constant of the medium, favouring hydrophilic interactions. The coefficients for urea and formamide approach slowly more negative values, while those for glycine and phenol change rapidly toward highly negative values (Tables 2 and 3). Then, glycine and phenol, more markedly than urea and formamide, show an increased ability in imposing preferential configurations for thermochemically favourable contributions. At increasing ethanol concentration, citrulline and glutamine behave similarly to glycine, urea, and formamide with a rapid decrease toward highly negative values of both homo- and heterochiral coefficients. For both amino acids, a small chiral recognition is detected only at the highest cosolvent concentrations, where interactions between zwitterions become highly predominant, allowing preferential configurations, responsible of chiral recognition, to be present. Phenylalanine shows a monotonous and similar trend for both homo- and heterochiral coefficients, which invert sign at about 5 m ethanol. Then, they attain a large negative value (about –3000 J kg mol^{-2}) at 9 m ethanol, similar to that found for phenol. The change in the structure of the solvent and the decrease of the dielectric constant determine two opposite effects. Hydrophilic interactions are improved, and consequently, the cooperativity of hydrophobic interactions between the side chains increases. On the other hand, the presence of ethanol as cosolvent improves the number of hydrogen bonds in the bulk solution, thus lowering its energetic level. At increasing concentrations of ethanol, that leads both coefficients to be smaller than those obtained in water, and determines the inversion of their sign at m_{EtOH} >3 (see Table 6). Only at the highest ethanol concentration a small chiral recognition is detected, whose origin is probably the same as that found for citrulline and glutamine.

To conclude, the presence of urea or ethanol influences differently the very complex and delicate balance of hydrophilic and hydrophobic interactions. Because of that, chiral recognition can be detected also for those amino acids that do not present this effect in water. However, that occurs only when the side-by-side configuration prevailing in water is stabilized simultaneously by hydrophobic and hydrophilic interactions, as in the case of phenylalanine. On the contrary, when the side-by-side in water is stabilized prevailingly by hydrophilic interactions, as for citrulline and glutamine, chiral recognition cannot be detected. Then, the study in mixed solvents confirms the validity of the preferential configuration model used to explain the results obtained in water.

Acknowledgements

This work was financially supported by the Ministry of University and Scientific Research, Rome, Cofin. MURST 97 CFSIB.

References

1. J.J. Savage and R.H. Wood.J. Solution Chem. **5**, 733 (1976).
2. B.Y. Okamoto, R.H. Wood, and P.T. Thompson. J. Chem. Soc. Faraday Trans. 1, **74**, 1990 (1978).
3. C. Cascella, G. Castronuovo, V. Elia, R. Sartorio, and S. Wurzburger. J. Chem. Soc. Faraday Trans. 1, **86**, 85 (1990).
4. C. Cascella, V. Elia, R. Sartorio, and S. Wurzburger. J. Chem. Soc. Faraday Trans. **86**, 3891 (1990).
5. G. Barone, G. Castronuovo, P. Del Vecchio, V. Elia, and S. Puzziello. J. Solution Chem. **18**, 1105 (1989).
6. G. Castronuovo, V. Elia, and M. Magliulo. Can. J. Chem. **69**, 794 (1991).
7. G. Castronuovo, V. Elia, and F. Velleca. J. Solution Chem. **24**, 1209 (1995)
8. G. Castronuovo, V. Elia, and F. Velleca. J. Solution Chem. **25**, 51 (1996).
9. S. Andini, G. Castronuovo, V. Elia, and F. Velleca. J. Solution Chem. **24**, 485 (1995).
10. M.K. Kumaran, G.R. Hedwig, and I.D. Watson. J. Chem. Thermodyn. **14**, 93 (1985).
11. E.J. Cohn and T.J. Edsall. Proteins, aminoacids and peptides. Reinhold, New York. 1943.
12. G.M. Blackburn, T.H. Lilley, and P.J. Milburn. J. Chem. Soc. Chem. Commun. 299, (1985).
13. G. Barone, G. Castronuovo, V. Elia, and C. Giancola. J. Therm. Anal. **30**, 1367 (1985).
14. G. Barone, G. Castronuovo, P. Del Vecchio, V. Elia, and C. Giancola. Thermochim. Acta, **122**, 105 (1987).
15. M.A. Gallardo, T.H. Lilley, H. Linsdell, and S. Otin. Thermochim. Acta, **223**, 41 (1993).
16. G. Castronuovo, V. Elia, C. Giancola, and S. Puzziello. J. Solution Chem. **19**, 855 (1990).
17. W.G. McMillan, Jr. and J.E. Mayer. J. Chem. Phys. **13**, 276 (1945).
18. J.J. Kozak, W.S. Knight, and W. Kauzman. J. Chem. Phys. **48**, 675 (1968).
19. H.L. Friedmann and C.V. Krishnann.J. Solution Chem. **2**, 2460 (1973).
20. F. Franks, M. Pedley, and S. Reid. J. Chem. Soc. Faraday Trans. 1, **72**, 359 (1976).
21. T.H. Lilley. *In* Biochemical thermodynamics. *Edited by* M.N. Jones. Elsevier, Amsterdam. 2nd ed. 1988. pp. 1–52.
22. J. Fernandez and T.H. Lilley. J. Chem. Soc. Faraday Trans. **88**, 2503 (1992).
23. A. Vallqvist and D.G. Covell. J. Am. Chem. Soc. **120**, 427 (1998).
24. S. Andini, G. Castronuovo, V. Elia, A. Pignone, and F. Velleca. J. Solution Chem. **25**, 837 (1996).
25. I.R. Tasker and R.H. Wood. J. Solution Chem. **11**, 295 (1982).
26. G. Castronuovo, V. Elia, C. Postiglione, and F. Velleca. Thermochim. Acta. In press.
27. M. Abbate, G. Barone, G. Borghesani, G. Cirillo, C. Giancola, and M. Remelli. J. Solution Chem. **22**, 695(1993).
28. G. Castronuovo, G. d'Isanto, V. Elia, and F. Velleca.J. Chem. Soc. Faraday Trans. **92**, 3087 (1996).
29. G. Barone and C. Giancola. Pure Appl. Chem. **62**, 57 (1990).
30. A.H. Sijpkes, G. Somsen, and T.H. Lilley. J. Chem. Soc. Faraday Trans. **86**, 2943 (1990).
31. G.R. Hedwig, T.H. Lilley, and H. Linsdell. J. Chem. Soc. Faraday Trans. **87**, 2975 (1991).
32. A.K. Mishra and J.C. Ahluwalia. J. Phys. Chem. **88**, 86 (1984).

© 1999 NRC Canada

Electrocatalytic hydrogenation of 4-phenoxyphenol on active powders highly dispersed in a reticulated vitreous carbon electrode

Pierre Dabo, André Cyr, Jean Lessard, Louis Brossard, and Hugues Ménard

Abstract: Electrodes consisting of particles of a transition metal entrapped and dispersed in a reticulated vitreous carbon (RVC) matrix were prepared in situ by stirring the particles in the presence of an RVC cathode. Such electrodes were used for the electrocatalytic hydrogenolysis (ECHsis) of 4-phenoxyphenol, a compound representative of the 4-O-5 type linkage in lignins. The electrolyses were carried out under galvanostatic control in aqueous 1 M NaOH. Raney nickel, nickel boride, and transition metals supported on activated charcoal or alumina were used as catalytic powders. The extent and efficiency of the ECHsis of 4-phenoxyphenol was found to depend on the catalyst and on the temperature.

Key words: electrocatalytic hydrogenation, electrocatalytic hydrogenolysis, 4-phenoxyphenol, Raney nickel, palladium on charcoal, palladium on alumina.

Résumé : Des électrodes constituées de particules d'un métal de transition incorporées et dispersées dans une matrice de carbone vitreux réticulé ont été préparées in situ en agitant les particules en présence d'une cathode de carbone vitreux. Ces électrodes se sont avérées actives pour l'hydrogénolyse électrocatalytique du 4-phénoxyphénol, un composé représentatif des liaisons de type 4-O-5 des lignines. Les électrolyses ont été effectuées à courant constant en milieu aqueux NaOH 1 M. Les poudres catalytiques étudiées et évaluées sont le nickel de Raney, le borure de nickel et des métaux de transition déposés sur charbon activé ou sur alumine. Les résultats montrent que l'efficacité de l'électrohydrogénolyse dépend de la nature de la poudre catalytique et de la température.

Mots clés : hydrogénation électrocatalytique, hydrogénolyse électrocatalytique, 4-phénoxyphénol, nickel de Raney, palladium sur charbon, palladium sur alumine.

Introduction

It is now recognized that the electrocatalytic hydrogenation (ECH) of organic compounds (1, 2), a process in which chemisorbed hydrogen is first generated at the electrode surface by electrolysis of water and then reacts with the adsorbed organic substrate, offers several advantages over both catalytic hydrogenation and direct electrochemical reduction. One of the main advantages over catalytic hydrogenation is the lower temperature and pressure needed. With respect to direct electrochemical reduction, ECH usually requires less energy (a less negative potential) and, furthermore, secondary reactions involving radical anions (and (or) radicals) are avoided. Among the parameters affecting the ECH efficiency, the nature of the electrode material and the electrode surface, the latter related to the technique of electrode preparation, are of prime importance (1, 3, 4). Most of the electrodes used so far for ECH consist of a coating of a catalytic material such as Raney nickel (R-Ni) or a transition metal (Pt, Pd, Rh) on a metal support (5), the coating being formed by electrodeposition, plasma spraying, sputtering, thermal decomposition, etc. Such electrodes usually have a relatively large surface area. Alternatively, in the case of R-Ni, the particles, which are characterized by a large surface area, have been used directly as the electrocatalyst, either by depositing them on a horizontal metallic plate (6–9), by using them in a flow-through packed bed reactor (10, 11), or by stirring the powder in the presence of a gold cathode (gold having a high hydrogen overvoltage), in which case the particles are charged with chemisorbed hydrogen when in contact with the cathode (12). Agglomeration of the R-Ni particles leading to a loss of activity (10–12) represents a possible drawback for the use of R-Ni powders in ECH.

Depolymerization of renewable biomass compounds such as coal, peat, or lignin is arousing much interest today. For example, many studies have been devoted to coal liquefac-

Received August 17, 1998.

P. Dabo, A. Cyr, J. Lessard,[1] and H. Ménard.[1] Centre de recherche en électrochimie et électrocatalyse, Département de chimie, Université de Sherbrooke, Sherbrooke, QC J1K 2R1, Canada.
L. Brossard. Institut de Recherche d'Hydro-Québec (IREQ), 1800 boul. Lionel Boulet, Varennes, QC J3X 1S1, Canada.

[1]Authors to whom correspondence may be addressed. (JL) Telephone: (819) 821-7091. Fax: (819) 821-8017. e-mail: jlessard@courrier.usherb.ca; (HM) Telephone: (819) 821-7084. Fax: (819) 821-8017. e-mail: hmenard@courrier.usherb.ca

 © 1999 NRC Canada

tion (13) or to the degradation of lignin into valuable products (14). Ether linkage cleavage appears to be of prime importance for the success of these degradations (15) and various diaryl model compounds containing C—O bonds have been extensively investigated (16–18). Recently it has been shown that the C—O bond of α and β aryl ethers, model dimers representative of the α-O-4 and β-O-4 bonds of lignin (19), can be successfully cleaved by electrocatalytic hydrogenolysis (ECHsis) (20). However, little attention has been paid to diphenyl ethers, dimers that model the 4-O-5 bonds of lignin (19). This type of C—O bond is stronger than the α-O-4 and even the β-O-4 bonds, and thermal cracking or catalytic hydrogenation of diphenyl ethers usually gives low conversion rates (13, 21). Thus, the ECHsis of a diphenyl ether constitutes a stringent test for the effectiveness of ECH as a method for the hydrogenolysis of C—O bonds of aryl ethers and for the activity of various electrocatalysts.

This paper reports the results of an investigation of the ECH of 4-phenoxyphenol on an in situ built-up electrode consisting of a transition metal powder embedded in the open-pore structure of a piece of reticulated vitreous carbon (RVC). Upon stirring the catholyte, the catalyst powder is forced inside the pores by convection and remains in the pores throughout the electrolysis. Such a technique has the advantage of allowing any type of catalyst to be easily tested in a powdery form. Thus, catalysts commonly used for catalytic hydrogenation of organic compounds such as R-Ni, nickel boride (Ni_2B), transition metals dispersed on activated charcoal (M/C) and on alumina (M/Al_2O_3), and other catalysts such as fractal nickel (Ni) and palladium deposited on nickel particles (Pd/Ni) were tested for the ECH of 4-phenoxyphenol. ECH efficiency was also investigated with special attention paid to the effect of temperature and the type of carbon onto which the metal is dispersed.

Experimental

Electrolyses

The electrolyses were carried out at constant current using an Electrosynthesis Company (ESC) 410 potentiostat connected to an ECS 640 digital coulometer and an ECS 2830 digital multimeter. A two-compartment jacketed glass H-cell (volume of each compartment: 50 mL) having a Nafion-324 (E.I. duPont de Nemours & Co.) membrane (1.8 cm^2) as separator and equipped with a condenser, was connected to a constant-temperature circulating bath (Haake 1). The cathode was a piece of reticulated vitreous carbon (from ECS, $2.5 \times 2 \times 0.6$ cm^3, 100 ppi) to which a nickel stripe for electrical contact was fixed and into which the catalyst powder was embedded in the following way: (*i*) the powder was introduced into the cathodic compartment containing the solvent and supporting electrolyte (30 mL); (*ii*) the anodic compartment was filled with a 1 M NaOH solution (30 mL); and (*iii*) the catholyte was stirred (magnetic bar) prior to the application of a constant current. The counter electrode was a graphite rod. After less than 30 min of polarization, almost all the particles were entrapped in the RVC matrix and 4-phenoxyphenol (140 mg, 2.5×10^{-4} mol, 8.3×10^{-3} M solution) was then added to the catholyte.

Electrocatalysts

For each of the following electrocatalysts, the amount of powder added to the catholyte for the entrapment of the particles was adjusted to optimize the rate of ECH. (*i*) Fractal nickel (Ni): 0.5 g (Inco 255) used without any further treatment. (*ii*) Crystalline nickel boride (Ni_2B): 0.5 g (Aldrich) used without further treatment. (*iii*) Amorphous Ni_2B: 0.5 g, prepared according to the procedure described by Brown (22). (*iv*) Raney nickel (R-Ni): 1.0 g of Raney alloy (Ni/Al 50/50 w/w, Fluka) was treated with 10% aqueous NaOH at 50°C for 1 h. After decanting the solution, the powder was stirred for 2 h in an aqueous solution of cinnamic acid (500 mg in 50 mL) in order to remove the chemisorbed H resulting from the leaching of aluminum. Cinnamic acid was chosen because it has an activated double bond that is easily hydrogenated over R-Ni. The solution was decanted and the resulting R-Ni powder was thoroughly rinsed with 1 M aqueous NaOH and immediately transferred into the cathodic compartment. (*v*) Activated charcoal (C) and metals deposited on activated charcoal (M/C): 0.2 g of C, of Pd/C (5 and 10% w/w), of Ru/C (5% w/w), and of Pt/C (5% w/w) purchased from Aldrich; 0.2 g of Rh/C (5% w/w; Fluka). (*vi*) Metals deposited on alumina (M/Al_2O_3): 0.2 g of Pd/Al_2O_3 (5% w/w) and Rh/Al_2O_3 (5% w/w) used without further treatment. (*vii*) Palladium deposited on fractal nickel (Pd/Ni): 0.5 g prepared according to a procedure previously described (23).

Products analysis

After the electrolysis, the reticulated vitreous carbon electrode was thoroughly rinsed successively with 1 M NaOH and distilled ethanol. The solution was filtered, saturated with NaCl, acidified to pH ≈ 1 with 5 M HCl, and extracted with ethyl acetate. The products were analyzed by gas–liquid chromatography (GLC) and (or) high-pressure liquid chromatography (HPLC) and identified by comparing their retention times with those of authentic samples. The progress of the electrolysis was followed by GLC and (or) HPLC from aliquots (0.5 mL) treated as above. The GLC analyses were carried out on a Hewlett Packard (HP) 5790a chromatograph equipped with a FID detector using a 30 m long DB-5 fused silica column, and the HPLC analyses were carried out on a system composed of a C_{18} column packing, Beckmann 100A pumps, a Beckmann 420 controller, a Hitachi 100-40 spectrometer at $\lambda = 272$ nm, and a HP3390A integrator.

General considerations

The ECHsis of the carbon–oxygen bond of 4-phenoxyphenol was studied in a 1 M aqueous NaOH solution (the phenol, $pK_a \approx 10$, is converted to the phenolate salt, which is soluble in water) under constant current conditions. The charge passed corresponded to six electrons per molecule of phenoxyphenol (6 F/mol), which is three times the charge required for complete hydrogenolysis of a C—O bond. Phenol was the main product. In some cases, cyclohexanone and cyclohexanol were also formed in small amounts. The formation of phenol, cyclohexanone, and cyclohexanol is readily explained by the classical ECH mechanism, i.e., by reactions [1]–[6]. First, chemisorbed hy-

© 1999 NRC Canada

Table 1. Electrolyses of 4-phenoxyphenol at various active powders.[a]

Entry	Type of catalytic material powder	4-Phenoxyphenol %	Phenol %	Catalyst activity
1	None[b]	97	0	Nil
2	Ni	92	0	Nil
3	Ni_2B (crystalline)	100	0	Nil
4	Ni_2B (amorphous)	70	30	Fair
5	R-Ni[c]	39	49	Fair
6	R-Ni[d]	0	83	Very good
7	R-Ni[c,e]	0	90	Very good
8	C	83	0	Nil
9	Rh(5%)/C	82	0	Nil
10	Pt(5%)/C	80	7	Poor
11	Ru(5%)/C	71	4	Poor
12	Pd(5%)/C	33	38	Fair
13	Pd(10%)/C	13	55	Good
14	Pd(5%)/Al_2O_3	27	62	Good
15	Rh(5%)/Al_2O_3	84	8	Poor
16	Pd(5%)/$BaSO_4$	85	7	Poor
17	Pd(5%)/Ni	93	3	Poor

[a]Electrolysis conditions: 0.75 mmol of substrate, 1 M NaOH, I = 5 mA, Q = 6 F/mol, T = 50°C.

[b]Electrolysis performed on the reticulated vitreous carbon matrix without active powder.

[c]Electrolysis performed on R-Ni treated with cinnamic acid (see text).

[d]Electrolysis performed on R-Ni not treated in an aqueous cinnamic solution. Cyclohexanol (15%) was formed.

[e]No potential was applied. Cyclohexanol (5%) was formed.

drogen is formed at the surface of the cathode by reduction of water (reaction [1])

[1] $$2H_2O + 2M \xrightarrow{2e^-} 2M(H) + 2OH^-$$

where M is the metallic surface and (H)M chemisorbed hydrogen. Hydrogenolysis of the C—O bond then proceeds as in catalytic hydrogenation, i.e., by reaction of the adsorbed substrate (adsorption step shown in reaction [2]) with chemisorbed hydrogen (reaction [3]) followed by desorption of the product (reaction [4]).

[2] 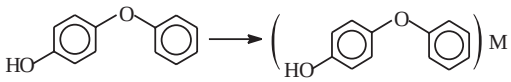

[3] 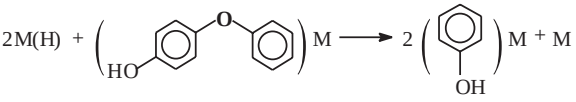

[4] 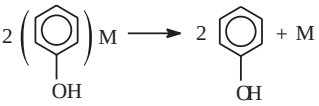

Phenol may then be hydrogenated further to cyclohexanone and cyclohexanol (reactions [5] and [6]).

It is important to point out that the efficiency of the ECH of a given organic compound depends on the relative rates of the hydrogenation step [3] (i.e., hydrogenolysis) and of hydrogen desorption (reactions [7] and (or) [8]) (1, 3). If reaction [3] is too slow with respect to reactions [7] or [8], only hydrogen evolution occurs and no formation of hydrogenation products (through reactions [2]–[4], then [5] and [6]) is observed.

[5] 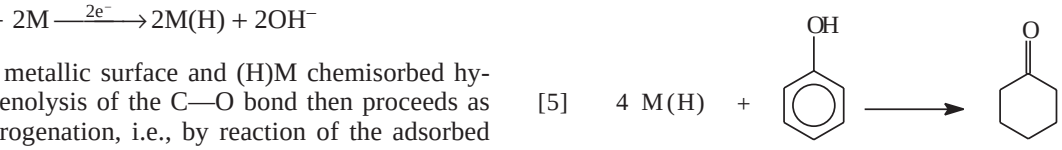

[6] 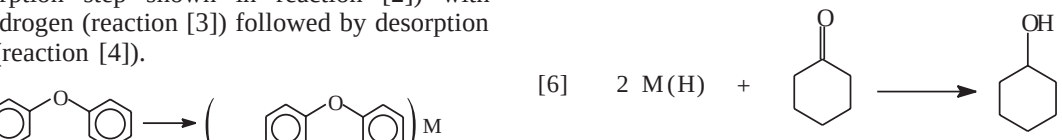

[7] $$M(H) + H_2O + e^- \rightarrow H_2 + OH^- + M$$

[8] $$2M(H) \rightarrow H_2 + 2M$$

Results and discussion

The data on the effect of the electrocatalyst and temperature upon the efficiency of the ECHsis of 4-phenoxyphenol in 1 M aqueous NaOH as measured by the yield of phenol formed (determined by HPLC) are summarized in Tables 1 and 2. Cyclohexanone and cyclohexanol were formed in small amounts only in the case of high conversion of the substrate, i.e., with the most active catalysts (see Table 1, entries 6 and 7, and Table 2, entry 3). Thus the hydrogenation of phenol is slower than the hydrogenolysis of the C—O bond. It is noteworthy that hydroquinone (1,4-dihydroxybenzene) and benzene were not detected, which shows that the C—O bond attached to the 4-hydroxyphenyl ring is cleaved with a high selectivity and must be weaker than the other C—O bond. Also, no aromatic ring hydrogenation prior to the cleavage of the C—O bond was observed. As well, no aromatic ring hydrogenation prior to the C—O

© 1999 NRC Canada

Table 2. Effect of the temperature on the electrolysis of 4-phenoxyphenol at Pd(5%)/C and Pd(5%)/Al_2O_3.[a]

Entry	Catalyst	Temperature °C	Phenol %	4-Phenoxyphenol %	ECHsis efficiency
1	Pd(5%)/C	25	14	64	Poor
2	Pd(5%)/C	50	38	33	Fair
3	Pd(5%)/C[b]	75	51	14	Good
4	Pd(5%)/Al_2O_3	50	27	62	Good
5	Pd(5%)/Al_2O_3	75	32	57	Good

[a]Electrolysis conditions: 0.75 mmol of substrate; 1 M NaOH: I = 5 mA; Q = 6 F/mol.

[b]Cyclohexanone (4%) and cyclohexanol (4%) were formed.

bond cleavage was observed despite the fact that the C—O bonds of phenoxyphenol are expected to be stronger than those of the previous model compounds studied (20).

Effect of the electrocatalyst

The electrocatalysts considered in Table 1 can be arbitrarily divided into four classes: nickel-type catalysts (entries 2–7), which are known to be efficient for the ECH of organic molecules (24); transition metals supported on active carbon (M/C) (entries 9–13); transition metals supported on alumina (M/Al_2O_3) (entries 14 and 15); and palladium supported on various substrates (entries 16 and 17). To the authors' knowledge, this is the first time that transition metals supported on alumina are reported to be employed as electrocatalysts for ECH, despite the fact that they are extensively used as catalysts for the catalytic hydrogenation of organic compounds (25).

The high hydrogen overvoltage on vitreous carbon (26) contributes to rendering the vitreous carbon an inert cathode material (i.e., no chemisorption or weak chemisorption of hydrogen) in the presence of a transition metal catalyst, as in the case of a gold cathode in the presence of R-Ni (12). As anticipated from the fact that there is little or no chemisorption of hydrogen on vitreous carbon, only hydrogen evolution occurred at the RVC electrode in the absence of a catalyst (see entry 1).

For fractal nickel (Ni, entry 2) and crystalline Ni_2B (entry 3), the rate of desorption of chemisorbed hydrogen (reactions [7] and (or) [8]) is much faster than the rate of C—O bond hydrogenolysis (reaction [3]) as evidenced by the absence of phenol and by the nearly quantitative recovery of the starting phenoxyphenol after the electrolysis. The two latter electrocatalysts are inactive for the ECHsis of an aryl–O–aryl bond. However, amorphous Ni_2B is active, as seen in entry 4 where 30% of phenoxyphenol was hydrogenolysed to phenol (mass balance of 100%). For the catalytic hydrogenation of olefins, it has been observed before that crystalline Ni_2B is a less active catalyst than amorphous Ni_2B (27). The factors responsible for this difference have not yet been clearly identified: they might consist of electronic effects and (or) surface effects.

Based on entries 4 and 5, it can be seen that R-Ni (49% of phenol, entry 5) is a more efficient electrocatalyst than amorphous Ni_2B (30% of phenol, entry 4). For the ECH of phenanthrene, it has been reported that the two latter catalysts have the same intrinsic activity (3). They have also approximately the same activity in catalytic hydrogenation of unsaturated hydrocarbons (22, 28). Thus, the relative activity of R-Ni and Ni_2B as catalytic hydrogenation catalysts depends on the type of bond hydrogenated, such as polar C—O σ-bonds compared to nonpolar π-bonds. In the electrolysis of entry 5, the hydrogen present on the R-Ni catalyst after leaching of the alloy was removed by stirring the particles in an aqueous solution of cinnamic acid, the double bond of which is easily hydrogenated by catalytic hydrogenation. When the electrolysis was carried out with freshly leached R-Ni not treated with cinnamic acid (entry 6), phenoxyphenol was completely hydrogenolysed to phenol, about 15% of which was hydrogenated further to cyclohexanol (mass balance of 98%: 83% of phenol and 15% of cyclohexanol). Similar results were obtained under open circuit conditions (entry 7), after the same time as that used for the electrolysis of entry 6: complete conversion of phenoxyphenol with a 95% mass balance (90% of phenol and 5% of cyclohexanol). The experiments of entries 6 and 7 show that (*i*) with the relative quantities of substrate and R-Ni used, there was enough chemisorbed hydrogen on the R-Ni particles after leaching to completely hydrogenolyse 4-phenoxyphenol; (*ii*) most of the current passed in the electrolysis of entry 6 was used to generate molecular hydrogen (hydrogen evolution), and (*iii*) the R-Ni catalyst treated with cinnamic acid appears less active than the freshly prepared R-Ni catalyst that has retained the chemisorbed hydrogen formed in the leaching process.

Data for entries 9–13 are related to noble metals dispersed on activated charcoal (M/C catalysts). Activated charcoal is inactive for the electrohydrogenolysis of 4-phenoxyphenol (entry 8) as anticipated from the fact that there is little or no hydrogen chemisorption on carbon, as already pointed out. The mass balances of 68–83% for entries 8–13 are due to the loss of phenol and phenoxyphenol remaining strongly adsorbed on the charcoal particles. It should be noted that even after a 24 h reflux in ethanol, it was not possible to desorb the products (phenol and 4-phenoxyphenol) from the active powder. Indeed, the weight ratio of charcoal powder to phenoxyphenol was about 1.7 and activated charcoal is well known to strongly adsorb organic compounds. This is why only small quantities of activated charcoal are used to remove colored impurities from organic solutions. The results of entries 9–12 indicate that the nature of the noble metal dispersed onto the active carbon has a determining effect on the efficiency of the electrohydrogenolysis of 4-phenoxyphenol. On the one hand, with the Rh/C, Pt/C, and Ru/C catalysts (entries 9–11), the rate of hydrogen desorption (reaction [7] and (or) [8]) is much faster than that for hydrogenolysis of 4-phenoxyphenol, which results in a very poor efficiency of electrohydrogenolysis (0–7%) for the three catalysts. On the other hand, for the Pd/C catalysts, hydrogenolysis and hydrogen desorption have comparable rates, resulting in fair to good electrogenolysis efficiencies (38–55%, entries 12 and 13). The concentration of dispersed palladium on the active carbon is a key parameter since 38%

© 1999 NRC Canada

of phenol is generated with Pd(5%)/C compared to 55% for Pd(10%)/C, the other experimental parameters being the same. It should be added that a twofold increase of the amount of Pd(5%)/C catalyst did not lead to a higher conversion rate. It is relevant to note that for catalytic hydrogenolysis of C—O bonds, Pd/C powder is a commonly used catalyst (24), Rh/C and Pt/C catalysts being also efficient, and Ru/C being totally inefficient (29).

The electrohydrogenolysis of 4-phenoxyphenol is efficient when alumina is used as support for palladium (entry 14: 62% yield of phenol). A great advantage of alumina over activated charcoal as support material is that phenol and phenoxyphenol are not retained on the alumina particles after rinsing the electrode, leading to a higher mass balance (89% in entry 14) than when activated charcoal is the support (71% in entry 12). The use of Rh for the electrohydrogenolysis of 4-phenoxyphenol remains deceptive even with alumina as a support material, as illustrated by the data of entry 15.

Based on entries 14, 12, 16, and 17, it is shown that 62, 38, 7, and 3% of phenol is formed when Pd is supported on alumina, active carbon, barium sulfate, and fractal nickel, respectively. The higher conversion rate obtained with Pd/C and Pd/Al $_2O_3$ may tentatively be ascribed to the higher adsorption capacity of active carbon and alumina towards organic compounds compared to nickel, as the mechanism of ECH involves the adsorption of the organic compound (reaction [2]). Further, it must be stressed that, when dealing with dispersed catalysts, the crystallite size effect and the interaction of the metal support play a very important role (30).

Effect of temperature

The data related to the electrolysis of 4-phenoxyphenol at 25°C, 50°C, and 75 °C with Pd(5%)/C and Pd(5%)/Al_2O_3 as catalysts are given in Table 2. As far as Pd(5%)/C electrocatalyst is concerned, the higher the temperature, the higher the amount of phenol. In addition, small amounts of both cyclohexanone and cyclohexanol were detected at 75°C (entry 3). By contrast, with Pd(5%)/Al_2O_3, an increase of the temperature had little effect on the extent of electrohydrogenolysis (compare entries 4 and 5).

Conclusions

A new device, with which a powdered catalyst active for catalytic hydrogenation of organic compounds can be used as electrode material, has been designed and tested for the ECHsis of 4-phenoxyphenol. High efficiencies (50–60%) of electrohydrogenolysis to phenol have been obtained with Pd/Al_2O_3, Pd/C, and R-Ni catalysts and the efficiency was found to decrease in the following order: Pd/Al_2O_3 ≥ Pd/C ≥ R-Ni >Ni_2B (amorphous) >> (Rh/Al_2O_3 ≈ Pt/C ≈ Pd/$BaSO_4$) > (Ru/C ≈ Pd/Ni) > (Rh/C ≈ Ni ≈ Ni_2B (crystalline)). The cleavage of a diphenyl ether bond is very promising for the recovery of biomass compounds, as these types of bonds are often found in Kraft lignin.

Acknowledgments

The financial support of Hydro-Québec is gratefully acknowledged.

References

1. D. Robin, M. Comtois, A. Martel, A.K. Cheong, G. Belot, and J. Lessard. Can. J. Chem. **68**, 1218 (1990).
2. J.M. Chapuzet, A. Lasia, and J. Lessard. *In* Electrocatalysis (Frontiers of electrochemistry series). *Edited by* J. Lipkowski and P.N. Ross. VCH Publishers Inc., New York. 1998. pp. 155–196.
3. B. Mahdavi, P. Chambrion, J. Binette, E. Martel, and J. Lessard. Can. J. Chem. **73**, 846 (1995).
4. P. Dabo, B. Mahdavi, H. Ménard, and J. Lessard. Electrochim. Acta, **42**, 1457 (1997).
5. A.M. Couper, D. Pletcher, and F.C. Walsh. Chem. Rev. **90**, 837 (1990).
6. T. Chiba, M. Okimoto, H. Nagai, and Y. Takata. Bull. Chem. Soc. Jpn. **56**, 719 (1983).
7. M. Fujihara, A. Yokozawa, H. Kinoshita, and T. Osa. Chem. Lett. 1089 (1982).
8. T. Yamada, T. Osa, and T. Matsue. Chem. Lett. 995 (1987).
9. Y. Senda, M. Tatekoa, H. Itoh, and J.Ishiyama. Bull. Chem. Soc. Jpn. **64**, 3302 (1991).
10. K. Park, P.N. Pintauro, M.M. Baizer, and K. Nobe. J. Electrochem. Soc. **132**, 1850 (1985).
11. G. Yusem, P.N. Pintauro, P.C. Cheng, and W. An. J. Appl. Electrochem. **26**, 989 (1996).
12. V. Anantharaman and P.N. Pintauro. J. Electrochem. Soc. **141**, 2729 (1994).
13. L. Artok, O. Erbatur, and H.H. Schobert. Fuel Proc. Technol. **47,** 153 (1996).
14. P. Bersier and J. Bersier. Electrochemistry and lignin: the state of the art. 2nd International forum on markets for sulfur-free lignin. Schwarzsee, Fribourg, Switzerland. March, 1992.
15. Y. Takegame, S. Kajiyama, and C. Yokokawa. Fuel, **42,** 291 (1963).
16. V.Y. Korobkov, E.N. Grigorieva, O.V. Senko, and I.V. Klochits. Fuel Proc. Technol. **19**, 243 (1988).
17. A.I. Afifi, J.P. Hindermann, E. Chornet, and R.P. Overend. Fuel, **68**, 498 (1989).
18. D. Meyer, P. Oviawe, D. Nicole, J.C. Lauer, and J. Clement. Fuel, **69**, 1309 (1990).
19. W.G. Glasser, C.A. Barnett, P.C. Muller, and K.V. Sarkanen. J. Agric. Food Chem. **31**, 921 (1983).
20. B. Mahdavi, A. Lafrance, A. Martel, J. Lessard, L. Brossard, and H. Ménard. J. Appl. Electrochem. **27**, 605 (1997).
21. Y. Kamiya, E. Ogata, K. Goto, and T. Nomi. Fuel, **65**, 586 (1986).
22. C.A. Brown. J. Org. Chem. **35**, 1900 (1970).
23. H. Dumont, P. Los, L. Brossard, A. Lasia, and H. Ménard. J. Electrochem. Soc. **139**, 2143 (1992).
24. R.L. Augustine. *In* Catalytic hydrogenation. Marcel Dekker, New York. 1965. p. 36.
25. P.N. Rylander. *In* Catalytic hydrogenation over platinum metals. Academic Press, New York. 1967. p. 3.
26. K. Kinoshita. *In* Carbon: electrochemical and physicochemical properties. John Wiley, New York. 1988.
27. S. Yoshida, H. Yamashita, T. Funabiki, and T. Yonezawa. J. Chem. Soc. Chem. Commun. 964 (1982).
28. R. Paul, P. Buisson, and N. Joseph. Ind. Eng. Chem. **44**, 1006 (1952).
29. R.L. Augustine. *In* Catalytic hydrogenation. Marcel Dekker, New York. 1965. p. 72.
30. K. Kinoshita and P. Stonehart. *In* Modern aspects of electrochemistry. Vol. 12. *Edited by* J'O.M. Bockris and B.E. Conway. Plenum Press, New York. 1977. p. 183.

© 1999 NRC Canada

Normal acid/base behaviour in proton transfer reactions to alkoxy substituted carbenes: estimates for intrinsic barriers to reaction and pK_a values

John Paul Pezacki

Abstract: Theoretical Eigen curves can be drawn through Brønsted data for dimethoxycarbene (**1**), phenyltrimethylsiloxycarbene (**3a**), 4-methylphenyl(trimethylsiloxy)carbene (**3b**), 4-methoxyphenyl(trimethylsiloxy)carbene (**3c**), and β-naphthyl(trimethylsiloxy)carbene (**3d**). The Brønsted plots for these data are clearly curved with α values near 1 when proton transfer is thermodynamically unfavourable and α values near 0 when proton transfer is thermodynamically favourable, suggesting that these carbenes behave as "normal" Brønsted bases. Estimates of the intrinsic barriers ($\Delta G_0^{\ddagger}$) for proton transfer reactions and of the pK_a values for the conjugate acids of the carbenes, extracted from these theoretical curves, have been made. The magnitudes of the intrinsic barriers ($\Delta G_0^{\ddagger}$) for these proton transfer reactions determined by Eigen and Marcus theories are all 1–5 kcal mol^{-1}, suggesting that these reactions are intrinsically fast. Small intrinsic barriers also imply "normal" acid/base behaviour. Extrapolated pK_a values are also the first estimates for the pK_a values of the conjugate acids of carbenes **1** and **3a–3d**.

Key words: carbenes, proton transfer reactions, carbocations, Marcus theory, Brønsted plots.

Résumé : On peut tracer des courbes théoriques de Eigen à partir de données de Brønsted pour les diméthoxycarbène (**1**), phényltriméthylsiloxycarbène (**3a**), 4-méthylphényl(triméthylsiloxy)carbène (**3b**), 4-méthoxyphényl(triméthylsiloxy)-carbène (**3c**) et β-naphtyl(triméthylsiloxy)carbène (**3d**). Les courbes de Brønsted pour ces données sont vraiment incurvées, avec des valeurs de α près de 1 quand le transfert de proton est thermodynamiquement défavorisé et des valeurs de α près de 0 quand le transfert de proton est thermodynamiquement favorisé; ceci suggère que ces carbènes se comportent comme des bases de Brønsted « normales ». On a évalué les barrières intrinsèques ($\Delta G_0^{\ddagger}$) pour les réactions de transfert de proton et les valeurs de pK_a pour les acides conjugués des carbènes à partir de ces courbes théoriques. Les amplitudes des barrières intrinsèques ($\Delta G_0^{\ddagger}$) pour les réactions de transfert de proton déterminées par les théories de Eigen et Marcus sont toutes de l'ordre de 1 à 5 kcal mol^{-1}, ce qui suggère que ces réactions sont intrinsèquement rapides. Des barrières intrinsèques faibles impliquent aussi un comportement acide/base « normal ». Les valeurs de pK_a extrapolées correspondent aussi aux premières estimations de valeurs de pK_a d'acides conjugués des carbènes **1** et **3a–3d**.

Mots clés : carbènes, réactions de transfert de proton, carbocations, théorie de Marcus, courbes de Brønsted.

[Traduit par la Rédaction]

Introduction

Proton transfer reactions to and from carbon atoms are usually quite different from those to and from heteroatoms (commonly referred to as "normal" Brønsted acids and bases) (for some reviews, see ref. 1). Carbon-centered acids and bases usually undergo proton transfer reactions more slowly than do their heteroatom counterparts and are believed to do so directly rather than through a solvent molecule in aqueous solvents. Normal Brønsted acids and bases are thought to donate or accept a proton through one or more water molecules, according to the Swain–Grunwald mechanism (2, 3), as well as directly from acid to base. Furthermore, Brønsted plots for proton transfer reactions between normal acids and bases follow *Eigen curves* with slopes (α) equal to zero when proton transfer is thermodynamically favourable, with rate constants for proton transfer being at or near the diffusion-controlled limit. When proton transfer is thermodynamically unfavourable, diffusion-controlled separation of the products is rate limiting (4) and the slopes (α)

Received February 10, 1998.[1]

This paper is dedicated to the memory of Dr. Edmund Cary West, Jr. (1936–1998; University of Toronto; Stanford, B.Sc.; Wisconsin, Ph.D. (Physics)) for many years of guidance, support, and inspiration in scientific and other pursuits.

J.P. Pezacki.[2] Department of Chemistry, McMaster University, Hamilton, ON L8S 4M1, Canada.

[1]Revision received February 7, 1999.
[2]Current address: Department of Chemistry, University of Toronto, Toronto, ON M5S 3H6. Telephone: (416) 978-8186.
e-mail: jpezacki@chem.utoronto.ca

 © 1999 NRC Canada

Scheme 1.

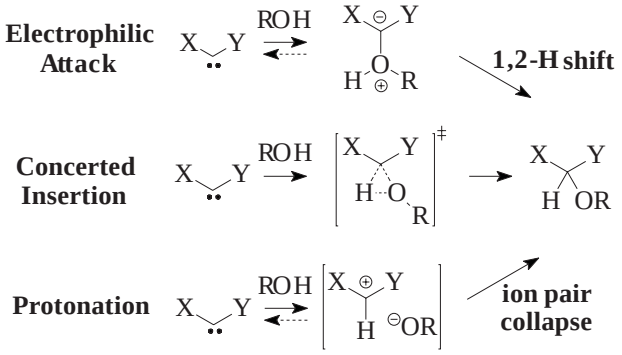

equal one. There is only a small region near $\Delta pK = 0$ where proton transfer is partially rate limiting and deuterium isotope effects are observed. Carbon-centered acids and bases generally give Brønsted plots that, by comparison, are not as sharply curved, if they show curvature at all. This lack of curvature in Brønsted plots for carbon acids and bases is presumably the result of changes in hybridization, changes in heavy-atom bond lengths and angles, desolvation in the rate-limiting transition state, differences in hydrogen-bonding ability, and changes in delocalization of charge. Any or all of these effects are believed to result in higher activation barriers, even when proton transfer is thermodynamically favourable (i.e., higher intrinsic barriers), and therefore smaller changes in transition state position (and in slope α) as a function of ΔpK for the reaction (1). However, nearly all of the studies related to the acid/base chemistry at carbon atoms have been restricted to carbanions and their conjugate acids; by comparison, the acid/base chemistry of divalent carbon atoms, carbenes, and their conjugate acids is not well established.

The formal insertions of carbene intermediates into O—H bonds are well-known processes and can occur by different mechanisms depending on the nature of the carbene intermediate (5). Carbenes may insert into O—H bonds from the singlet spin state by a concerted mechanism, or by initial formation of an oxonium ylide intermediate followed by a 1,2-hydrogen shift, or by proton transfer (Scheme 1).

The proton transfer mechanism leads to the formation of a carbocation – alkoxy anion pair, which can collapse to form formal O—H insertion products. The observation of carbocationic intermediates after the photochemical generation of carbenes in solutions containing hydroxylic reactants, in laser flash photolysis (LFP) experiments, has shown that several carbenes of different structure undergo O—H insertion into alcohols via this mechanism. For example, diphenyl and diarylcarbenes have been shown to insert into the OH bonds of alcohols by a proton transfer mechanism, by direct observation of the resulting carbocationic intermediates by LFP, eq. [1] (6).

[1] 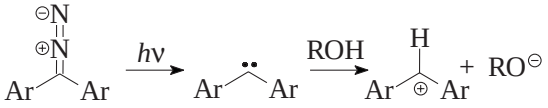

In other cases, proton transfers to carbenes have been implied, based on product distributions. An example is the trapping of cycloheptatrienylidene with deuterated alcohols, which leads to mixtures of products with deuterium and the alkoxy substituent located at different positions in the cycloheptatriene products (eq. [2]) (7). Deuterium scrambling implicates a mechanism involving initial proton transfer to the carbene center, which leads to the formation of the aromatic tropylium cation and an alkoxide ion. Ion pair collapse occurs at any of the ring carbons of the tropylium ion, which results in a mixture of products. Benzotropylium cations have also been implicated in reactions of benzoannelated cycloheptatrienylidenes with alcohols (7*b*).

[2] 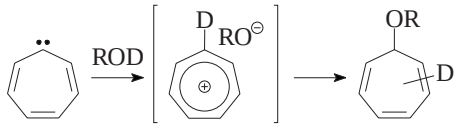

In general, the stepwise mechanism for O—H insertion of carbenes into hydroxyl groups involving initial proton transfer to the carbene carbon is favoured when the conjugate acid of the carbene is a relatively stable and persistent carbocationic intermediate. Even highly electrophilic carbenes can undergo OH insertions via a proton transfer mechanism. For example, tight ion pairs have been implicated in OH insertion reactions by highly electrophilic 2-bicyclo[2.1.1]hexylidene, suggesting a proton transfer mechanism (8). For carbenes whose conjugate acids are highly unstable species, a concerted mechanism is *enforced* by the lack of a significant lifetime of the resulting carbocation – alkoxy anion pair in solution. However, predicting which mechanistic pathway in Scheme 1 will dominate for a given carbene is difficult since more *electrophilic* carbenes may also attack at oxygen, even when proton transfer leads to the formation of stable carbocationic intermediates.

The proton transfer mechanism has been implicated in several systems based on direct observations of resulting carbocations, or on product distributions, or on slopes of Brønsted plots. Non-zero slopes in Brønsted plots suggest that the reactions depend on the acidity of the O—H containing substrate with the rate constants for O—H insertion (assuming that proton transfer is rate limiting) and are proportional to the pK_a's of the protonating acid. Often overlooked is the fact that such rate constants will also depend on the thermodynamics of the overall reaction, according to the Hammond postulate, and the pK_a's of the conjugate acids of carbene intermediates are also important in determining how fast a given proton transfer event will occur. Unfortunately, for most carbenes such thermodynamic parameters are unknown and virtually impossible to measure directly with present-day equipment. However, in some cases, when the conjugate acids of carbenes are stable and unreactive, it is possible to gain information about their pK_a values.

Many nucleophilic nitrogen-substituted carbenes have been generated by deprotonation of conjugate acid iminium ions. Examples include the C-2 deprotonation of imidazolinium salts (9*a*) (eq. [3]) and of thiazolium salts (10) including

© 1999 NRC Canada

[3] 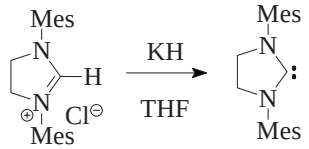

[4] 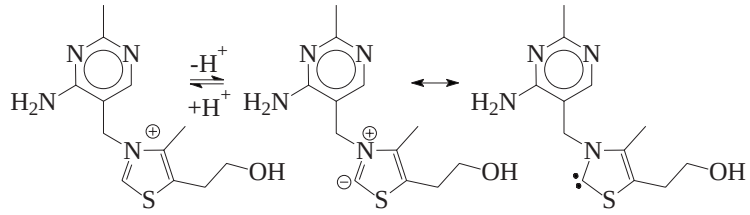

thiamin **C_2-ylide of thiamin** **C_2-ylidene of thiamin**

thiamin[3] (11) (eq. [4]. A pK_a value of ca. 16 has been estimated for thiamin (eq. [4]) (12), and those for thiazolium ions fall between ca. 16 and 22 (13). Also, "normal" acid/base behaviour has been implicated in proton transfer reactions of thiazolium ions including thiamin (12–14). More recently, a pK_a of 24 for the conjugate acid of the stable carbene 1,3-diisopropyl-4,5-dimethylimidazol-2-ylidene (eq. [5]) has been measured by ^{1}H NMR in DMSO solvent by monitoring hydrocarbon acids (such as 2,3-benzofluorene, eq. [5]) and their conjugate bases (15). Alder et al. also noted that while the carbon acids and their conjugate bases were distinguishable by ^{1}H NMR, suggesting that proton transfer is slow compared to the NMR time scale, proton transfer between 1,3-diisopropyl-4,5-dimethylimidazol-2-ylidene and its conjugate acid is fast as evidenced by the fact that the carbene and its conjugate acid appear as an averaged spectrum in the presence of base (15).

[5] 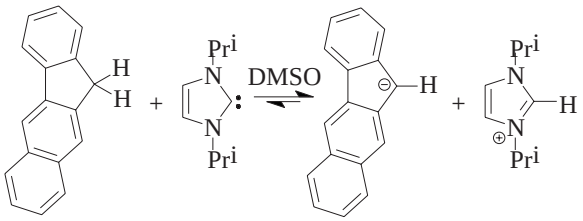

The reported acid/base reactivity of diamino and aminothiocarbenes suggests that other π-donor-substituted carbenes may also behave as normal Brønsted bases and that equilibria between carbenes and their conjugate acids may be established in solution. The evaluation of the acid/base chemistry of dimethoxycarbene and four aryltrimethylsiloxycarbenes, as well as the first estimates of the pK_a values for their conjugate acids, is presented here.

1. Brønsted relations and Eigen curves

1.a Proton transfer to dimethoxycarbene

Like diamino and aminothiocarbenes, dimethoxycarbene (**1**) is considered to be a *nucleophilic* carbene due to conjugative stabilization through donation by the lone pairs on the oxygen atoms of the methoxy substituents to the formally vacant virtual *p*-orbital at the carbene carbon (16, 17). Conjugative donation to the carbene carbon gives dimethoxycarbene (**1**) dipolar character and also strongly stabilizes the singlet state. The singlet–triplet energy gap ($\Delta\epsilon_{ST}$) of **1** has been calculated to be ~ 76 kcal mol^{-1} (17). The inductively electron-withdrawing methoxy substituents also interact with the filled sp^2 orbital (the lone pair on the carbene carbon), which results in extra stabilization of **1**.

[6] 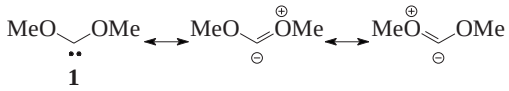

1

Dimethoxycarbene (**1**) has been generated from 7,7-dimethoxynorbornadienes (18), an oxadiazoline (19), dimethoxydiazirine (20), and hexamethoxycyclopropane (21), and its preference for reaction with electron-deficient olefins, for reaction with carbonyl groups at carbon (19), and for displacing leaving groups (chlorine) via S_N2 type reactions in solutions of benzene (22) supports the premise that carbene **1** is *nucleophilic* in character.

It is thought that dimethoxycarbene behaves as a nucleophile because of its dipolar character and because of the resonance stabilization of positive charge at the carbene carbon in the transition states and intermediates of reactions involving attack of the carbene carbon lone pair onto its reaction partner (23). Resonance stabilization in the ground state of **1**, in the transition states and in carbocationic intermediates, makes proton transfer to dimethoxycarbene (**l**) the most likely mechanism for formal OH insertion reactions. Such a proton transfer mechanism is supported by observed kinetic isotope effects (20*e*).

In a previous investigation (20*c*), rate constants for the reactions of dimethoxycarbene with a series of oxygen-centered acids were measured by LFP in acetonitrile, and a Brønsted plot, based on the linear free energy relationship in eq. [7] or its differential form in eq. [8], was constructed based on the data for **1** in Table 1.

[3] Although some C-2 anions of thiazolium and imidazolium ions are considered to be more ylide-like than carbene-like, recent crystal structures of stable compounds have shown that the carbon heteroatom bonds are more like single bonds than double bonds and that the carbene carbons in these structures are very nearly neutral in charge, suggesting that they are better represented as carbenes rather than ylides (9*a*, 9*b*) although these views have been challenged (9*c*).

© 1999 NRC Canada

Table 1. Observed proton transfer rate constants (k_a) for the protonation of dimethoxycarbene[a] and aryl(siloxy)carbenes[b] by oxygen acids in acetonitrile at 20°C.

		k_a, M^{-1} s^{-1} [b]				
Acid	pK_a [c]	**1**	**3a**	**3b**	**3c**	**3d**
H_2O	15.7		9.3×10^7[e]	9.2×10^7[e]	1.0×10^8[e]	1.2×10^8[e]
CH_3OH	15.5	8.8×10^4	3.0×10^8[e]	2.7×10^8[e]	3.8×10^8[e]	2.2×10^8[e]
CH_3CH_2OH	15.9	3.2×10^4	—	—	2.0×10^8[e]	—
$HOCH_2CH_2OH$	15.1		9.1×10^8[e]	1.5×10^9[e]	3.0×10^9[e]	—
$CH_3OCH_2CH_2OH$	14.8		1.6×10^8[e]	2.6×10^8[e]	6.3×10^8[e]	—
$ClCH_2CH_2OH$	14.3	9.1×10^5[d]	1.1×10^9	—	2×10^9[e]	—
FCH_2CH_2OH	14.2	2.3×10^6[d]	—	—	—	—
Cl_2CHCH_2OH	12.9		2.0×10^9	—	2.1×10^9[e]	—
F_3CCH_2OH (TFE)	12.8	6.3×10^7[d]	1.5×10^9	1.8×10^9	1.5×10^9	1.5×10^9
Cl_3CCH_2OH	12.2		1.6×10^9	—	2.0×10^9[e]	—
$(CF_3)_2CHOH$ (HFIP)	9.3	6.7×10^8	1.2×10^9	1.0×10^9	1.2×10^9	9.6×10^8
CH_3CO_2H	4.76	2.4×10^9	1.1×10^9	1.2×10^9	1.0×10^9	9.9×10^8
4-$O_2NC_6H_4OH$	7.15		$\sim 3 \times 10^9$	—	—	—

[a]Reference 20*c*.
[b]Rate constants from ref. 35*b*.
[c]pK_a values in water (24).
[d]Quenching plots for dimethoxycarbene by $ClCH_2CH_2OH$, FCH_2CH_2OH, and 2,2,2-trifluoroethanol (TFE) were found to be concave upward due to the contribution of oligomeric alcohol to the rate constants for the decay of this carbene. The rate constants for these acidic species therefore represent upper limits for the rate constants for reaction with the monomeric form.
[e]k_a values are approximations based on low concentration ranges of curved quenching plots where the plots are approximately linear.

A slope of $\alpha \sim 0.66$ was determined by Du et al. (20*c*). The pK_a values used by Du et al. (20*c*) and for all Brønsted correlations reported here are those determined in water (24) (see Table 1) as a result of a lack of appropriate thermodynamic data for these acids in acetonitrile solvent (the pK_a values of various acids in acetonitrile have been compiled by K. Izutsu, see ref. 25). Therefore correlations of the data should be considered to be *semi-quantitative*, although the pK_a values for phenols and carboxylic acids in acetonitrile and in water may be approximated by eq. [9] (1*a*), which is assumed to be valid for the acidic species in Table 1. Knowledge of the pK_a's in acetonitrile would make the interpretation of these data quantitative.

$$[7] \quad \log(k_a) = \alpha \cdot \log(K_a) + \text{constant}$$

$$[8] \quad \delta \log(k_a) = \alpha \cdot \delta \log(K_a)$$

$$[9] \quad pK_a^{MeCN} - pK_a^{H_2O} \approx 14.0$$

Slopes of Brønsted plots (α) are considered to be a measure of the extent of proton transfer at the transition state for the reaction, with $\alpha = 0$ representing the structure of the reactants and $\alpha = 1$ representing that of the products, respectively. An α value of 0.66 suggests that the transition state for proton transfer to dimethoxycarbene is more product-like than reactant-like over the pK_a range studied. However, the structure of the transition state may change with pK_a, following the thermodynamics of the reaction, according to the Hammond postulate (26). Reactions that are exothermic have transition states that are more reactant-like and those that are endothermic have transition states that are more product-like. Such changes in transition state structure lead to curvature in Brønsted plots. Curvature in Brønsted plots can be evaluated with Marcus rate theory (27)[4] and such evaluations follow.

When proton transfer reactions are fast, as in those to and from electronegative atoms ("normal" Brønsted acids and bases), then diffusion becomes a limiting factor except for small values of ΔpK when proton transfer is, at least, partially rate determining. Curvature in Brønsted plots for proton transfers to and from normal Brønsted acids and bases then arises from changes in the rate-determining step. When proton transfer is thermodynamically unfavourable, diffusional separation of the products is rate limiting (α approaches 1), and when proton transfer is thermodynamically favourable then diffusional encounter becomes rate limiting (α approaches 0). In such cases, the rate-determining proton transfer step can itself be divided into three steps as described by Eigen (4).

The reactions of dimethoxycarbene (**1**) with oxygen-centered acids (the forward reaction in eq. [10]) appear to be at least partially diffusion controlled when proton transfer is thermodynamically favourable, given that the observed rate constants for proton transfer to these carbenes reach a maximum at values greater than 10^9 M^{-1} s^{-1}. If dimethoxycarbene behaves as a normal Brønsted base, then it should be possible to draw an Eigen curve (4) through the data points in the Brønsted plot, based on the three-step mechanism for proton transfer in eq. [10], where k_d is the rate constant for diffusion together of the reactants, k_{-d} is the rate constant for diffusional separation of the products, and k_p and k_{-p} are the rate constants for proton transfer within the encounter complex.

The steady-state solution to eq. [10], where k_a (eq. [11]) is the observed bimolecular rate constant for proton transfer to

[4]For examples of the use of quadratic Brønsted correlations to solve for Marcus theory parameters, see ref. 28.

© 1999 NRC Canada

[10] 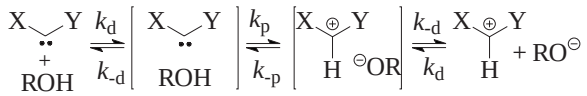

1 by the oxygen-centered acids, is given in eq. [12]. The values for k_p and k_{-p} are defined in eqs. [13] and [14], respectively (13, 29).

[11] 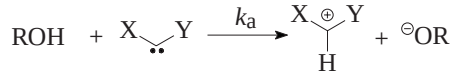

$$[12] \quad k_a = \frac{k_d k_p k_{-d}}{k_p k_{-d} + k_{-d} k_{-d} + k_{-d} k_{-p}}$$

$$[13] \quad k_p = k_{p\,(\Delta pK=0)} \cdot 10^{0.5(\Delta pK)}$$

$$[14] \quad k_{-p} = k_{p\,(\Delta pK=0)} / 10^{0.5(\Delta pK)}$$

The values for ΔpK are defined by the relation in eq. [15], where pK_a^{AH} are the pK_a's of the oxygen acids, pK_a^{CH+} is the pK_a for the conjugate acid of the carbene, and α for the proton transfer step is assumed to be 0.5 at $\Delta pK = 0$.

$$[15] \quad \Delta pK = pK_a^{AH} - pK_a^{CH+}$$

[16] 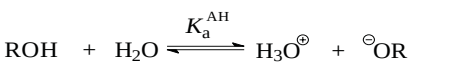

[17] 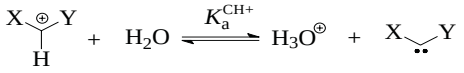

After statistical correction for the number of equivalent acidic sites on the protonating species (p), and substituting values of $k_d = 3.2 \times 10^9$ M^{-1} s^{-1} and $k_{-d} = 1 \times 10^{10}$ s^{-1}, least-squares fitting of the expression in eq. [18] to the data for **1** in Table 1 yielded a smooth Eigen curve (middle curve in Fig. 1) with coefficients of $pK_a^{CH+} = 11.0 \pm 0.1$ (water, ~25 in MeCN) and $\log k_{p\,(\Delta pK\,=\,0)} = 8.92 \pm 0.23$ M^{-1} s^{-1}.

$$[18] \quad \log k_a = \log \left(\frac{k_d \cdot k_p \cdot k_{-d}}{k_p \cdot k_{-d} + k_{-d} k_{-d} + k_{-d} \cdot k_{-p}} \right)$$

where

$$k_p + k_{p(\Delta pK=0)} \cdot 10^{0.5(pK_a^{AH} - pK_a^{CH+})}$$

and

$$k_{-p} = \frac{k_{p\Delta pK=0}}{10^{0.5(pK_a^{AH} - pK_a^{CH+})}}$$

Similar least-squares fitting of the expression in eq. [18] to the data for **1** in Table 1, with $k_{-d} = 1 \times 10^{10}$ s^{-1} and k_d determined by the fit, yielded a different Eigen curve (lower curve in Fig. 1) with computed values of $pK_a^{CH+} = 11.2 \pm 0.2$ (water, ~25 in MeCN), $\log k_d = 9.27 \pm 0.16$ M^{-1} s^{-1}, and $\log k_{p\,(\Delta pK\,=\,0)} = 9.18 \pm 0.31$ M^{-1} s^{-1} from the fit. Analogous least-squares fitting (upper curve in Fig. 1), with $k_d = 5 \times 10^9$ M^{-1} s^{-1}, $k_{-d} = 1 \times 10^{11}$ s^{-1}, and $k_{p\,(\Delta pK\,=\,0)} = 10^{12}$ M^{-1} s^{-1} (essentially no intrinsic barrier) defined, yielded a value for pK_a^{CH+} of 10.6 ± 0.2 (water, ~25 in MeCN) with a much poorer fit through the data. Since the actual rate constants for diffusional encounter of carbenes with alcohols and diffusional separation of conjugate acids – alkoxide ion pairs are not known, a variety of different values were chosen in a series of fits. A summary of these results obtained from all the least-squares fits is presented in Table 2. Interestingly, all least-squares fits yielded similar pK_a values for the conjugate acid of dimethoxycarbene (1) despite widely different values for k_d and k_{-d}.

Fig. 1. Brønsted plot for the protonation of dimethoxycarbene in acetonitrile at 20°C. Arrows indicate that the corresponding data points are upper limits for the log k_a values (see text). The solid lines are theoretical Eigen curves (see text), the dotted lines are extrapolated from the portions of the middle Eigen curve where $\alpha_{obs} = 0$ and $\alpha_{obs} = 1$. These dotted lines cross at $pK_a^{AH} = pK_a^{CH+}$ ($\Delta pK = 0$) (4). The broken line is the Marcus curve through the data.

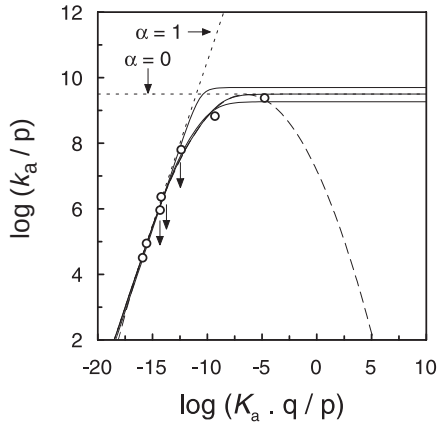

Kirmse et al. (35*b*) have suggested that proton transfers to aryltriphenylsiloxycarbenes occur via a preassociation mechanism. Such proton transfers would obey the relation in eq. [19], where K_{ass} is the association constant.[5]

$$[19] \quad k_a = \left(\frac{K_{ass} k_d k_p k_{-d}}{k_p k_{-d} + k_{-d} k_{-d} + k_{-d} k_{-p}} \right)$$

The least-squares fitting of the logarithmic form of the expression in eq. [19] to the data for **1** in Table 1, assuming $k_d = 4 \times 10^{10}$ M^{-1} s^{-1} and $k_{-d} = 4 \times 10^{10}$ s^{-1}, yielded a smooth Eigen curve through the data with coefficients yielding values of $pK_a^{CH+} = 11.2 \pm 0.2$ (water, ~25 in MeCN), $\log k_{p\,(\Delta pK\,=\,0)} = 9.78 \pm 0.32$ M^{-1} s^{-1}, and $K_{ass} = 4.6 \times 10^{-2}$.

In all cases, least-squares fitting of the data, using the Eigen model with reasonable assumptions regarding rate constants for diffusional encounter and separation (29), yields reasonable curves through the data and computed values of

[5] For eq. [19] to hold, K_{ass} must be dimensionless. K_{ass} will be dimensionless when ROH (the proton donor) is in large excess and when [ROH] remains constant over the course of the reaction.

© 1999 NRC Canada

Table 2. Parameters derived from curve fitting of the data for proton transfer to oxygen-substituted carbenes to eq. [18].

Carbene	log k_d	log k_{-d}[b]	log $k_{p\ (at\ \Delta pK = 0)}$	K_{ass}	pK_a^{CH+} in water (in MeCN)
1	9.27 ± 0.26	8.0	7.19 ± 0.31[a]	—	11.2 ± 0.2 (~25)
	9.27 ± 0.16	9.0	8.18 ± 0.31[a]	—	11.2 ± 0.2 (~25)
	9.5[b]	10.0	8.92 ± 0.23	—	11.0 ± 0.1 (~25)
	9.27 ± 0.16	10.0	9.18 ± 0.31[a]	—	11.2 ± 0.2 (~25)
	9.27 ± 0.16	11.0	10.2 ± 0.32[a]	—	11.2 ± 0.2 (~25)
	9.5[b]	10.0	9.19 ± 0.32	$(5.8 \pm 2.2) \times 10^{-1}$	11.2 ± 0.2 (~25)
	10.6[b]	10.6	9.78 ± 0.32	$(4.6 \pm 1.7) \times 10^{-2}$	11.2 ± 0.2 (~25)
	9.5[b]	10.0	8.0[b]	—	11.6 ± 0.3(~26)
	9.5[b]	10.0	9.0[b]	—	11.0 ± 0.1(~25)
	9.5[b]	10.0	10.0[b]	—	10.9 ± 0.1(~25)
	9.5[b]	10.0	11.0[b]	—	10.9 ± 0.1(~25)
	9.5[b]	10.0	12.0[b]	—	10.9 ± 0.1(~25)
	9.7[b]	11.0	12.0[b]	—	10.6 ± 0.2 (~25)[c]
	10.6[b]	10.6	12.0[b]	—	9.7 ± 0.4(~24)[c]
3a	9.25[b]	10.0	9.69 ± 0.72	—	14.8 ± 0.6 (~29)
	10.2 ± 2.5	10.0	9.45 ± 0.10	—	14.9 ± 0.6 (~29)
	9.5[b]	10.0	9.45 ± 1.1	$(6.8 \pm 4.0) \times 10^{-1}$	14.9 ± 0.9 (~29)
	10.6[b]	10.6	10.1 ± 1.1	$(5.4 \pm 3.6) \times 10^{-2}$	14.9 ± 0.9 (~29)
3b	9.25[b]	10.0	9.8 ± 1.8	—	14.8 ± 0.7 (~29)
	9.10 ± 0.16	10.0	10.3 ± 2.5	—	14.9 ± 0.9 (~29)
	9.5[b]	10	10.3 ± 2.5	$(4.0 \pm 1.5) \times 10^{-1}$	14.9 ± 0.6 (~29)
	10.6[b]	10.6	10.9 ± 2.5	$(3.2 \pm 1.2) \times 10^{-2}$	14.9 ± 0.6 (~29)
3c	9.25[b]	10.0	10.7 ± 2.7	—	14.7 ± 2.6 (~29)
	9.33 ± 0.12	10.0	10.3 ± 2.2	—	14.9 ± 0.23 (~29)
	10.6[b]	10.6	10.9	$(5.4 \pm 1.5) \times 10^{-2}$	14.9 ± 0.22 (~29)
3d	9.25[b]	10.0	~8.9	—	~16 (~30)
	9.10[b]	10.0	~9.1	—	~16 (~30)

[a]These Eigen curves are identical graphically. See ref. 30 for discussions on the coupling of diffusion and apparent intrinsic barriers to reaction.
[b]These values were defined and are not results from curve fitting of the data.
[c]These curves clearly do not go through the data points.

~11 (water, ~25 in MeCN) for the pK_a of the conjugate acid of dimethoxycarbene, and computed intrinsic barriers[6] (the barrier to reaction at $\Delta pK = 0$) of 2.4–3.7 kcal mol^{-1}. The small variation within each theoretical model then depends on what values of k_d and k_{-d} are used (30). The magnitude of the "apparent" intrinsic barrier (larger than 1 kcal mol^{-1}) suggests that the proton transfer step (k_b) may be coupled with other molecular events that contribute to this barrier and that are not accounted for by this model (4). The fact that reasonable Eigen curves can be drawn through the Brønsted data suggests that dimethoxycarbene is a "normal" Brønsted base and that the pK_a of its conjugate acid lies between those of 2,2,2-trifluoroethanol (TFE) and 1,1,1,3,3,3-hexafluoroisopropanol (HFIP) in acetonitrile. Thiazolium ions and thiamin (which itself is a thiazolium cation) have pK_a'*s* of ~14–20 in aqueous solution (12–14). As well, the pK_a of a conjugate acid of a diaminocarbene has been measured to be 24 in DMSO (15). Since the conjugate bases of these cations may be written as carbenes, they are good model systems for comparison. The cations are stable species and the carbene–ylide conjugate bases would be more stable/less reactive than oxygen-substituted carbenes. The computed pK_a of the conjugate acid of **1** suggests that it is more acidic than thiazolium ions, which is expected as a result of the increased electronegativity of oxygen as compared with nitrogen and sulfur. Oxazolium ions are known to be more acidic than their imidazolium and thiazolium ion counterparts (31). Interestingly, the pK_a's of the electron-deficient 4-biphenylnitrenium ion and 4-aminobiphenyl dication in 20% aqueous acetonitrile have been estimated as 16 and 0.1 (32), respectively, suggesting that the conjugate acid of 4-biphenylnitrenium ion is much more acidic than the conjugate acid of **1.**[7]

Curvature in Brønsted plots can also be evaluated with Marcus rate theory (27, 28) by taking advantage of the relation in eq. [20], where w^r is the work required to bring the reactants into a reaction complex, $\Delta G_0^{\ddagger}$ is the intrinsic reaction barrier, $\Delta G^{\ddagger}$ is the overall free energy of activation, and ΔG^0 is the difference in free energy between the reactants and the products (28). The slope parameter α is defined by the differential in eq. [8], and differentiation of $\Delta G^{\ddagger}$ with respect to ΔG^0 in eq. [20] gives an alternative mathematical representation for α in eq. [21]. The second derivative in eq. [22] reflects the change in α as a function of the intrinsic

[6]There are many potential factors that may influence the magnitudes of apparent intrinsic barriers to reaction (1, 3, 30) so that interpretation of the computed values for the intrinsic barriers should be made with caution.
[7]Nitrenium ions are isoelectronic with carbenes.

© 1999 NRC Canada

barrier for reaction ($\Delta G_0^{\ddagger}$), implying that intrinsically fast reactions will show more distinct curvature in Brønsted plots than will those with large intrinsic barriers.

$$[20] \quad \Delta G^{\ddagger} = w^{r} + \left(1 + \frac{\Delta G^0}{4\Delta G_0^{\ddagger}}\right)^2 \Delta G_0^{\ddagger}$$

$$[21] \quad \alpha = \frac{\partial \Delta G^{\ddagger}}{\partial \Delta G^0} = \left(1 + \frac{\Delta G^0}{4\Delta G_0^{\ddagger}}\right) / 2$$

$$[22] \quad \frac{\partial \alpha}{\partial \Delta G^0} = \frac{1}{8\Delta G_0^{\ddagger}}$$

After statistical correction for the number of equivalent acidic sites on the protonating species (q), least-squares fitting of the quadratic expression in eq. [23], which is a form of eq. [20] (28), to the data for **1** in Table 1 yielded a smooth curve (Fig. 1) with the following coefficients: a = 7.17, b = –0.715, c = –0.0552. The correlation coefficient (R) is 0.996, which is statistically a better fit than that to a straight line (R = 0.929).

$$[23] \quad \log(k_a/p) = a + b\,\log(K_a q/p) + c\,\log(K_a q/p)^2$$

After substitution and rearrangement in eqs. [20] and [23], coefficients a, b, and c yielded values of the Marcus theory parameters (27, 28) for the work required to bring the reactants into a reaction complex, $w^r \approx 4.5$ kcal mol^{-1}, and for the intrinsic reaction barrier, $\Delta G_0^{\ddagger} \approx 1.5$ kcal mol^{-1}. The calculated value for the intrinsic barrier to proton transfer to dimethoxycarbene, although semiquantitative due to the lack of thermodynamic data for the protonating acids in acetonitrile solutions, indicates that proton transfer to the carbene carbon is an intrinsically fast reaction akin to those of normal acids/bases. The value of the intrinsic barrier computed here may in fact be too low as the influence of diffusion may not be accounted for properly in the Marcus model (30). In fact, proton transfer may never be completely rate determining. When this is the case then the Eigen model is preferred.

One can determine the tangents to the curve in the Brønsted plot in Fig. 1 by determining the first derivative of the quadratic expression in eq. [23] (eq. [24]). Coefficients b and c come from the least-squares fitting of the data to eq. [23], and substituting those values and values for log ($K_a q/p$) into eq. [24] yields values for α (the slope of the tangent at a point on the graph). Likewise, one may substitute values for b, c, and α into eq. [24] and determine which point on the curve corresponds to a particular value of α.

$$[24] \quad \alpha = \frac{\partial[\log(k_a/p)]}{\partial[\log(K_a q/p)]} = b + 2c[\log(K_a q/p)]$$

In this manner log ($K_a q/p$) values where α equals 0, 0.5, and 1 were computed using the quadratic expression (eq. [23]) for the Brønsted curve for the protonation of dimethoxycarbene. These values of α are the slopes of the tangent lines to the curve at points (log K_a, log k_a) = (–6.48, 9.49), (–11.0, 8.34), and (–15.5, 4.99), respectively. Since α can be considered to be a measure of transition state structure, a reasonable approximation for the point on the Brønsted curve where the acid/base reaction is thermoneutral (i.e., $\Delta G^0 = 0$) is the point where the transition state lies exactly halfway between reactants and products (α = 0.5).[8] If the proton transfer reaction between an oxygen-centered Brønsted acid and dimethoxycarbene reaction is to be considered thermoneutral then $K_{C:}$ in eq. [25] must equal unity, and K_a^{AH} (eq. [16]) must equal the acid dissociation constant for the conjugate acid of dimethoxycarbene, K_a^{CH+} (eq. [17]). The tangent to the curve with slope of α = 0.5 at the point (–11.0, 8.34) therefore suggests that the log K_a^{CH+} for the conjugate acid of dimethoxycarbene is approximately –11.0 (water) and that the pK_a for dimethoxymethyl cation is ~ 11.0 (water, ~ 25 in acetonitrile). In fact, substituting the calculated values for the intrinsic barrier and work term for proton transfer to dimethoxycarbene into eq. [20], with $\Delta G^0 = 0$, gives a value of ~ 6 kcal mol^{-1} for the free energy of activation ($\Delta G^{\ddagger}$) when the reaction is thermoneutral. This value corresponds to a bimolecular rate constant of $k_a \approx 2.0 \times 10^8$ M^{-1} s^{-1} (log k_a = 8.30), which corresponds to the point (–11.1, 8.30) on the Brønsted curve (by solving the quadratic expression in eq. [23]) indicating that the interpretations here are, at least, self-consistent. Although the Eigen model more accurately accounts for the contributions of diffusional rate constants to the overall reactions when the transfer step is not fully rate determining, both the Eigen and the Marcus models predict similar pK_a values for the conjugate acid of dimethoxycarbene.

[25] 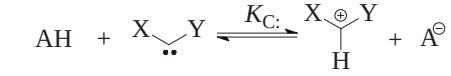

$$[26] \quad K_{C:} = \frac{K_a^{AH}}{K_a^{CH+}}$$

1.b Proton transfer to aryltrimethylsiloxycarbenes

Aryltrimethylsiloxycarbenes (**3**) have been generated from the corresponding acylsilanes (**2**) both thermally and photochemically (for a review of α-siloxy carbenes generated from acylsilanes see ref. 34). Rate constants for the protonation of **3a–3d** by hydroxylic acids in organic media have been measured by LFP (35). The direct observation of carbocationic intermediates **4a–4d** unambiguously proves that proton transfer to arylsiloxycarbenes **3a–3d** is the initial step in formal OH insertion reactions of these carbenes.

[27] 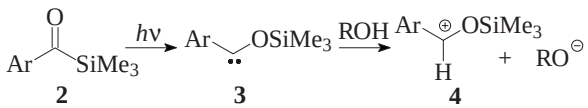

2 **3** **4**

2a: Ar = Ph;
2b: Ar = 4-methylphenyl;
2c: Ar = 4-methoxyphenyl;
2d: Ar = β-Naphthyl.

[8] It has been shown that the slope of a Brønsted plot can be influenced by pre-equilibrium desolvation. Thus, the magnitude of the obtained coefficient alone may not exactly reflect the thermodynamics of the reaction. See Murray et al. (33).

© 1999 NRC Canada

Arylsiloxycarbenes are expected to be *nucleophilic* in character. Evidence for this comes from addition reactions with carbonyl compounds (presumably at carbon) (36). Conjugative stabilization occurs in carbenes **3a–3d** through donation from the aryl substituents and by the lone pairs on the oxygen atoms of the trimethylsiloxy substituents to the formally vacant *p*-orbital at the carbene carbon. Additional stabilization of carbenes **3a–3d** and cations **4a–4d** results from hyperconjugation of the trimethylsilyl group, with resulting positive charge on silicon and negative charge at the carbene carbon.

[28]

The analysis of the kinetic data for proton transfer to aryltrimethylsiloxycarbenes **3a**–**3d**, obtained by Kirmse et al. (35*b*), according to Eigen theory and to Marcus theory (27, 28) are presented here. The relevant kinetic data may be found in Table 1.[9]

From the data in Table 1, Brønsted plots for the proton transfer reactions to aryltrimethylsiloxycarbenes **3a**–**3d** by oxygen acids were constructed by plotting log (k_a/p) vs. log ($K_a^{AH}q/p$) (Fig. 2) for each carbene, where q and p are statistical factors for the number of equivalent basic sites on the carbene (always 1) and the number of equivalent acidic sites on the protonating acid. Linear least-squares fitting of these data to eqs. [18] and [19] was performed in a fashion analogous to that for the data for dimethoxycarbene protonation. The results are summarized in Table 2.

Although Kirmse, Guth, and Steenken (35*b*) have suggested that the proton transfer reactions to carbenes **3a**–**3d** are probably not diffusion controlled because the largest rate constants measured are at least an order of magnitude lower than that of diffusion in acetonitrile ((2–4) × 10^{10} M^{-1} s^{-1}), according to the Eigen model, these proton transfers can be diffusion controlled even when the rate constants are far below the diffusion-controlled limit provided that the reactions are reversible. In fact, the actual proton transfer step may never be fully rate determining, even at small values of ΔpK, provided that the reactions are intrinsically fast. Normal acid/base behaviour in these carbenes and their conjugate acids also explains the lack of significant isotope effects.[10]

For carbenes **3a–3d**, the computed intrinsic barriers were 1–3.7 kcal mol^{-1}. The pre-equilibrium model predicted lower values for the intrinsic barriers to proton transfer (1–2.4 kcal mol^{-1}) as compared to those predicted by the three-step model. Within experimental error, the pK_a's for the conjugate acids of carbenes **3a**–**3d** were all ~15 (water, ~ 29 in acetonitrile), regardless of which values of k_d and k_{-d} were used, suggesting that there is not a significant substituent effect on the acid dissociation constant for phenyl(trimethylsiloxy)carbenium ion (the conjugate acid of phenyltrimethylsiloxycarbene). This is not surprising since π-donor substituents interact favourably with both the empty *p*-orbital of the carbene and the conjugate acid carbenium

Fig. 2. Brønsted plot for the protonation of (*a*) Ph(Me_3SiO)C: (●); (*b*) 4-MeC_6H_4(Me_3SiO)C: (□); (*c*) 4-$MeOC_6H_4$(Me_3SiO)C: (■); (*d*) β-$C_{10}H_7$(Me_3SiO)C: (▲), all in acetonitrile at 20°C. The upper solid lines are theoretical Eigen curves (see text) where k_d = 3.2 × 10^9 M^{-1} s^{-1} and k_{-d} = 1 × 10^{10} s^{-1} (see Table 2); the lower solid lines are theoretical Eigen curves where k_d values were defined by least-squares fits and k_{-d} = 1 × 10^{10} M^{-1} s^{-1} (see Table 2), and the broken line is the Marcus curve through the data.

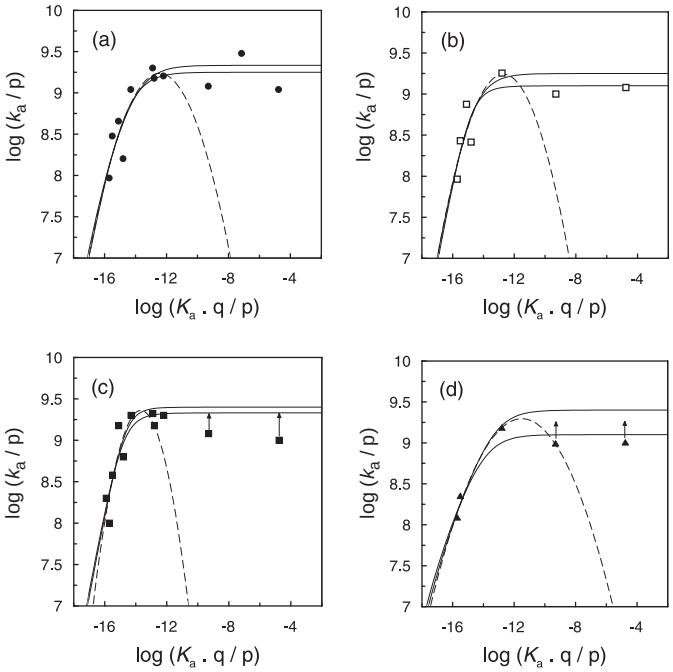

[9] Many of the plots of k_{obs} vs. [ROH] obtained by Kirmse et al. (35*b*) were curved; however, the rate constants in Table 2 are all bimolecular. Those that are approximations of bimolecular rate constants, obtained at low [ROH], are marked as such. Curved plots of k_{obs} vs. [ROH] are the consequence of a second competing (faster) reaction of carbene with ROH that is second order with respect to [ROH] at higher [ROH]: $k_{obs} = k_o + k_a[ROH] + k_a'[ROH]^2$. The rate constants associated with the higher order term in the quadratic expression of k_{obs} (k_a') in these instances can be considered as "pseudo bimolecular" because [ROH] is high and essentially constant over the course of the reaction. The higher order term starts to dominate k_{obs} when the [ROH] is sufficiently large to allow for a preassociation step prior to proton transfer (or in self-association of ROH when the carbene reacts with ROH dimers).

[10] Kirmse et al. (35*b*) measured rate constants for the protonation of α- and β-naphtholate anions by $HClO_4$ in acetonitrile (k_{H+} ~ 4 × 10^{10} M^{-1} s^{-1}). Larger intrinsic barriers for proton transfers to carbenes **3a–3d**, compared with those for the protonation of α- and β-naphtholate anions, combined with preassociation mechanisms for carbenes **3a–3d** would explain the apparent discrepancy. The preassociation mechanism proposed by Kirmse et al. involves proton transfer through a second molecule of alcohol. This type of mechanism is analogous to the Swain–Grunwald mechanism for "normal" acids/bases in water (2, 3). Such mechanisms do not display detectable kinetic isotope effects. However, at low concentrations of alcohol, the preassociation mechanism probably does not occur in favour of a direct mechanism since the carbenes have a finite lifetime (~100–200 ns) in solution. A preassociation mechanism, where the acid is not bulk solvent, requires two molecules of acid and two diffusional steps prior to proton transfer.

© 1999 NRC Canada

ion, resulting in ground state stabilization of both the reactant and the product and a small change in $\Delta\Delta G^{o}$. Conversely, π-acceptor substituents should cause ground state destabilization of both carbene and conjugate acid carbenium ion. In both cases the bond order between the carbene carbon and the attached group (aryl in this case) bearing the substituent does not change dramatically after proton transfer. The situation is quite different from that of the acid dissociation constants for benzoic acids or phenols where the stabilities of the protonated forms are not dramatically affected by the presence of substituents. Since the carbenes (**1**, **3a–3d**) have finite lifetimes in solution, the reactions may not be reversible (i.e., no internal return). For such cases Marcus theory can be used to explain curvature in Brønsted plots.

[29] 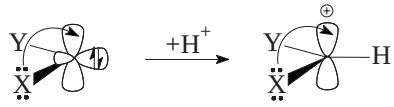

Marcus rate theory (27, 28) was also applied to the data in Table 1 for **3a–3d** in a fashion analogous to that applied to the data for dimethoxycarbene protonation. In each case, the rate constants for proton transfer by acids with pK_a's of 12 and higher (in water) were essentially the same; this is the portion of the Brønsted plots where $\alpha \approx 0$ and diffusion is at least partially rate determining. Therefore, data for only those acids with p$K_a \leq 12$ were fitted to the quadratic expression in eq. [24]. Least-squares fitting of the data to the quadratic expression in eq. [24] gave coefficients *a*, *b*, and *c* that yielded values of the Marcus theory parameters of 0.8, 0.7, 0.3, and 1 kcal mol^{-1} for the intrinsic reaction barriers ($\Delta G_0^{\ddagger}$), and 4.9, 4.8, 4.7, and 7 kcal mol^{-1} for the work terms (w^r), for phenyltrimethylsiloxycarbene (**3a**), 4-methylphenyl-(trimethylsiloxy)-carbene (**3b**), 4-methoxyphenyl(trimethylsiloxy)carbene (**3c**), and β-naphthyl(trimethylsiloxy)carbene (**3d**), respectively. Again, the pK_a values for the conjugate acids (pK_a^{CH+}) of carbenes **3a–3d** computed from Marcus parabolas were very similar to those predicted by Eigen theory.

1.c Variation in transition state structure

Substitution of the intrinsic barriers determined for dimethoxycarbene and aryltrimethylsiloxycarbenes **3a–3d**, from the coefficients of quadratic Brønsted correlations, into the partial derivative in eq. [22] allows for the evaluation of the change in α as a function of the change in ΔG^{o} for proton transfer reactions to these carbenes. For dimethoxycarbene, α is predicted to change from a value of 1 to a value of 0 over a $\Delta\Delta G^{o}$ range (12 kcal mol^{-1}) that corresponds to a range of ~9 pK_a units for the protonating acids. This change in α corresponds to a change in transition state structure, from very product-like (α = 1) to essentially reactant-like (α = 0). Similarly, α values for arylsiloxycarbenes **3a–3d** are predicted to change from $\alpha \approx 1$ to $\alpha \approx 0$ over pK_a ranges of ~5, ~4, ~2, and ~6, respectively. Such dramatic changes in the slope parameter α and in transition state structure are typical for "normal" acids and bases where α changes from near 0 to near 1 over a $\Delta\Delta G^{o}$ range that corresponds to ~4 pK_a units (4), but are rarely observed in carbon acids and bases.

2. "Normal" acid/base behaviour

The fact that the Brønsted plots for carbenes **1** and **3a–3d** are all curved and that theoretical Eigen curves or Marcus parabolas can be drawn through these data provides strong evidence that these π-donor-substituted carbenes behave as "normal" Brønsted bases. The dramatic change in the slope parameter α (and in transition state structure) over a narrow range of Δp*K* of the protonating acids for these carbenes is also consistent with normal acid/base behaviour. Brønsted plots for the protonation of normal bases typically change slope from unity to zero over a ΔpK_a range of ~4 units (1, 4).

Small intrinsic barriers to proton transfer are also common for "normal" acids and bases and intrinsic barriers of 1–5 kcal mol^{-1}, computed for carbenes **1** and **3a–3d**, are consistent with their normal acid/base behaviour. Examples of other carbon bases, which have small intrinsic barriers to proton transfer reactions and show some "normal" acid/base behaviour, include cyanide (29*c*, 37), acetylide (38), C-2 thiazolium ions (12–14), the C-2 ylide of thiamin (14), and C-2α anions of covalent intermediates of thiamin (39). The small intrinsic barriers determined here for dimethoxycarbene and carbenes **3a–3d** support the idea that electron delocalization, rehybridization (carbenes do not undergo a change in hybridization either during or after proton transfer), changes in bond lengths and angles of heavy atoms, and changes in solvation do not significantly affect the barriers to proton transfer to these π-donor-substituted carbon bases as is the case for other carbon acids and bases with larger intrinsic barriers to proton transfer. Presumably the most stable ground state conformations of these carbenes are those where the π-donor substituents (methoxy and aryl) are already aligned with, and are already donating electron density to, the vacant *p*-orbital at the carbene carbon so that bond angles, lengths,[11] and electron delocalization do not change dramatically at the transition state for proton transfer.

Other criteria for evaluating "normal" acid/base behaviour such as acid inhibition cannot be evaluated in acetonitrile solvent because of the increased rate constants for reaction by oligomeric acids at higher concentrations of acid, and clearly the Swain–Grunwald mechanism does not apply in this solvent system although the participation of a second molecule of acid in a reaction complex has been proposed previously (35*b*). It is evident that oxygen-substituted carbenes behave very much like "normal" Brønsted bases.

3. Conclusions

Brønsted plots for proton transfer data for dimethoxycarbene and for aryltrimethylsiloxycarbenes **3a–3d** show distinct Eigen curvature that is characteristic of reactions between "normal" acids and bases. Values of α that are near 1 when proton transfer is thermodynamically unfavourable and near 0 when proton transfer is thermodynamically

[11]Professor Denk et al. have found only small differences (~0.3 Å) in C—N bond lengths in stable diaminocarbenes compared with those in their conjugate acids from X-ray crystallographic data (M.K. Denk, S. Gupta, and A.J. Lough, personal communication).

© 1999 NRC Canada

favourable, combined with rate constants of ~10^9 M^{-1} s^{-1} for thermodynamically favourable proton transfer reactions, support the notion that these carbenes behave as "normal" Brønsted bases. Values for intrinsic barriers ($\Delta G_0^{\ddagger}$) calculated from Eigen curves and using the Marcus theory formalism indicate that these reactions are intrinsically fast, which provides further support for normal acid/base behaviour. A consequence of normal acid/base behaviour is that proton transfer in the thermodynamically favourable direction proceeds with maximum rate constants of ~10^9 M^{-1} s^{-1}, and that proton transfer may be reversible depending on the lifetimes of the carbenes and their conjugate acids (carbocations) in solution. Ultimately, curvature in the Brønsted plots for dimethoxycarbene and for aryltrimethylsiloxycarbenes **3a**–**3d** can be explained by changes in the rate-determining step for proton transfer as a function of the pK_a for the protonating acid and (or) by variation in transition state structure, near pK = 0, according to the Hammond postulate. These observations bring to light the fact that caution must be taken in making mechanistic claims (i.e., ruling out proton transfer mechanisms) for reactions of carbenes with normal Brønsted acids based solely on negligible (or 0) Brønsted slopes. *For carbenes that behave as "normal" Brønsted bases, near-zero Brønsted slopes may simply reflect the fact that proton transfer is thermodynamically favourable over the p*K_a *range of acids that is studied and that diffusion is at least partly rate limiting.* Estimates for pK_a values of the conjugate acids of carbenes **1** and **3a**–**3d** have been computed directly from Eigen curves and from tangents to Marcus parabolas (α values at individual points on the curves). The pK_a values computed by both methods are roughly the same for each carbene. These pK_a values are ~11 (water, ~25 MeCN) for dimethoxymethyl cation and ~15 (water, ~29 in MeCN) for aryltrimethylsiloxymethyl cations **4a**–**4d**. These pK_a values should be viewed as very rough "ballpark" first estimates because the analyses that yielded them are *semi-quantitative or qualitative*.

Acknowledgments

J.P.P. would like to thank the Natural Sciences and Engineering Research Council of Canada for continued financial support in the form of a post-graduate scholarship, and Professor Wolfgang Kirmse (Ruhr – Universität Bochum) for useful discussions and advice.

References

1. (*a*) R.P. Bell. The proton in chemistry. 2nd ed. Cornell University Press, Ithaca, N.Y. 1973; (*b*) A.J. Kresge. Chem. Soc. Rev. **4**, 475 (1973); (*c*) *In* Proton transfer reactions. *Edited by* E.F. Caldin and V. Gold. Chapman and Hall, London. 1975. Chap. 7; (*d*) W.P. Jencks. Acc. Chem. Res. **9**, 425 (1976); (*e*) A.J. Kresge. Acc. Chem. Res. **8**, 354 (1975); (*e*) J. Hine. Adv. Phys. Org. Chem. **15**, 1 (1977); (*f*) C.F. Bernasconi. Acc. Chem. Res. **25**, 9 (1992); (*g*) Adv. Phys. Org. Chem. **27**, 119 (1991); (*h*) Acc. Chem. Res. **20**, 301 (1987).
2. (*a*) M.T. Emerson, E. Grunwald, M.L. Kaplan, and R.A. Kromhout. J. Am. Chem. Soc. **82**, 6307 (1960); (*b*) E. Grunwald. J. Phys. Chem. **67**, 2211 (1963); (*c*) E. Grunwald and E.K. Ralph. Acc. Chem. Res. **4**, 107 (1971); (*d*) E. Grunwald and D. Eustace. *In* Proton transfer reactions. *Edited by* E.F. Caldin and V. Gold. Chapman and Hall, London. 1975. pp. 103–120.
3. J.P. Guthrie. J. Am. Chem. Soc. **118**, 12886 (1996), and refs. therein.
4. M. Eigen. Angew. Chem. Int. Ed. Engl. **3**, 1 (1964).
5. W. Kirmse. *In* Advances in carbene chemistry. *Edited by* U. Brinker. JAI Press Inc., London. 1994. pp. 1–57, and refs. therein.
6. (*a*) S.T. Belt, C. Bohne, G. Charette, S.E. Sugamori, and J.C. Scaiano. J. Am. Chem. Soc. **115**, 2200 (1993); (*b*) E.J. Dix and J.L. Goodman. J. Phys. Chem. **98,** 12609 (1994); (*c*) W. Kirmse, B. Krzossa, and S. Steenken. J. Am. Chem. Soc. **118**, 7473 (1996); (*d*) J.E. Chateauneuf. J. Chem. Soc. Chem. Commun. 1437 (1991); (*e*) W. Kirmse, J. Kilian, and S. Steenken. J. Am. Chem. Soc. **112**, 6399 (1990).
7. (*a*) W. Kirmse, K. Loosen, and H.-D. Sluma. J. Am. Chem. Soc. **103**, 5935 (1981); (*b*) W. Kirmse and H.-D. Sluma. J. Org. Chem. **53**, 763 (1988).
8. W. Kirmse, T. Meinert, D.A. Modarelli, and M.S. Platz. J. Am. Chem. Soc. **115**, 8918 (1993).
9. (*a*) A.J. Arduengo III, J.R. Goerlich, and W.J. Marshall. J. Am. Chem. Soc. **117**, 11027 (1995); (*b*) G. Boche, C. Hilf, K. Harms, M. Marsch, and J.C.W. Lohrenz. Angew. Chem. Int. Ed. Engl. **34**, 487 (1995); (*c*) M.K. Denk, A. Thadani, K. Hatano, and A.J. Lough. Angew. Chem. Int. Ed. Engl. **36**, 2607 (1997).
10. (*a*) R.W. Hoffmann, B. Hagenbruch, and D.M. Smith. Chem. Ber. **110**, 23 (1977); (*b*) H.A. Staab, H. Irngartinger, A. Mannschreck, and M.-T. Wu. Justus Liebigs Ann. Chem. 55 (1966); (*c*) G. Scherowsky, K. Dünnbier, and G. Höfle. Tetrahedron Lett. 2095 (1977); (*d*) R.A. Olofson and J.M. Landesberg. J. Am. Chem. Soc. **88**, 4263 (1966); (*e*) R.A. Olofson, J.M. Landesberg, K.N. Houk, and J.S. Michelman. J. Am. Chem. Soc. **88**, 4265 (1966); (*f*) G. Scherowsky. Chem. Ber. **107**, 1092 (1974); (*g*) A.J. Arduengo III, J.R. Goerlich, and W.J. Marshall. Liebigs Ann. Chem. 365 (1997).
11. (*a*) R. Breslow. J. Am. Chem. Soc. **79**, 1762 (1957); (*b*) R. Kluger. Chem. Rev. **87**, 863 (1987).
12. F.G. Bordwell and A.V. Satish. J. Am. Chem. Soc. **113**, 985 (1991).
13. M.W. Washabaugh and W.P. Jencks. J. Am. Chem. Soc. **111**, 674 (1989); **111**, 683 (1989).
14. M.W. Washabaugh and W.P. Jencks. Biochemistry, **27**, 5044 (1988).
15. R.W. Alder, P.R. Allen, and S.J. Williams. J. Chem. Soc. Chem. Commun. 1267 (1995).
16. N.G. Rondan, K.N. Houk, and R.A. Moss. J. Am. Chem. Soc. **102**, 1770 (1980).
17. R.A. Moss, M. Wostowski, S. Shen, K. Krogh-Jespersen, and A. Matro. J. Am. Chem. Soc. **110**, 4443 (1988).
18. (*a*) R.W. Hoffmann. Acc. Chem. Res. **18**, 248 (1985); (*b*) R.W. Hoffmann, B. Hagenbruch, and D.M. Smith. Chem. Ber. **110**, 23 (1977); (*c*) W. Lilienblum and R.W. Hoffmann. Chem. Ber. **110**, 3405 (1977); (*d*) R.W. Hoffmann and M. Reiffen. Chem. Ber. **109**, 2565 (1976); (*e*) R.A. Moss and J.K. Huselton. J. Chem. Soc. Chem. Commun. 950 (1976); (*f*) R.W. Hoffmann, K. Steinbach, and W. Lilienblum. Chem. Ber. **109,** 1759 (1976); (*g*) R.W. Hoffmann, W. Lilienblum, and B. Dittrich. Chem. Ber. **107**, 3395 (1974); (*h*) R.W. Hoffmann, K. Steinbach, and B. Dittrich. Chem. Ber. **106,** 2174 (1973); (*i*) R.W. Hoffmann. Angew. Chem. Int. Ed. Engl. **10**, 529 (1971); (*j*) R.W. Hoffmann and C. Wunsche. Chem. Ber. **100**, 943 (1967); (*k*) D.M. Lemal, E.P. Gosselink, and S.D. McGregor. J. Am. Chem. Soc. **88**, 582 (1966); (*l*) D.M. Lemal, R.W. Lovald, and R.W. Harrington. Tetrahedron Lett. 2779 (1965); (*m*) R.W. Hoffmann and H. Hauser. Tetrahedron**, 21**,

© 1999 NRC Canada

891 (1965); (*n*) Tetrahedron Lett. 197 (1964); (*o*) D.M. Lemal, E.P. Gosselink, and A. Ault. Tetrahedron Lett. 579 (1964).
19. (*a*) M. El-Saidi, K. Kassam, D.L. Pole, T. Tadey, and J. Warkentin. J. Am. Chem. Soc. **114**, 8751 (1992); (*b*) K. Kassam, D.L. Pole, M. El-Saidi, and J. Warkentin. J. Am. Chem. Soc. **116**, 1161 (1994); (*c*) W.W. Win, M. Kao, M. Eiermann, J.J. McNamara, F. Wudl, D.L. Pole, K. Kassam, and J. Warkentin. J. Org. Chem. **59**, 5871 (1994); (*d*) J.D. Colomvakos, I. Egle, J. Ma, D.L. Pole, T.T. Tidwell, and J. Warkentin. J. Org. Chem. **61**, 9522 (1996); (*e*) A. de Meijere, S.I. Kozhushkov, D.S. Yufit, R. Boese, T. Haumann, D.L. Pole, P.K. Sharma, and J. Warkentin. Liebigs Ann. Chem. 601 (1996); (*f*) D. L. Pole and J. Warkentin. Liebigs Ann. 1907 (1995); (*g*) J. Org. Chem. **62**, 4065 (1997); (*h*) P. Couture, D.L. Pole, and J. Warkentin. J. Chem. Soc. Perkin Trans. 2, 1565 (1997).
20. (*a*) C.-S. Ge, E.A. Jefferson, and R.A. Moss. Tetrahedron Lett. **34**, 7549 (1993); (*b*) R.A. Moss, M. Wostowski, J. Terpinski, G. Kmiecik-Lawrynowicz, and K. Krogh-Jespersen. J. Am. Chem. Soc. **109**, 3811 (1987); (*c*) X.-M. Du, H. Fan, J.L. Goodman, M.A. Kesselmayer, K. Krogh-Jespersen, J.A. LaVilla, R.A. Moss, S. Shen, and R.S. Sheridan. J. Am. Chem. Soc. **112**, 1920 (1990); (*d*) R.A. Moss, M. Wostowski, S. Shen, K. Krogh-Jespersen, and A. Matro. J. Am. Chem. Soc. **110**, 4443 (1988); (*e*) R.A. Moss, S. Shen, and M. Wostowski. Tetrahedron Lett. **29**, 6417 (1988).
21. R.A. Moss and D. P. Cox. Tetrahedron Lett. **26**, 1931 (1985).
22. J.A. Dunn, J.P. Pezacki, M.J. McGlinchey, and J. Warkentin. J. Org. Chem. **64**, 4344 (1999).
23. J. Warkentin. *In* Advances in carbene chemistry. *Edited by* U. Brinker. JAI Press Inc., Greenwich, Conn. 1998. pp. 245–295.
24. (*a*) P. Ballinger and F.A. Long. J. Am. Chem. Soc. **82**, 795 (1960); (*b*) B.L. Dyatkin, E.P. Mochalina, and I.L. Knunyants. Tetrahedron, **21**, 2991 (1965); (*c*) S. Takahashi, L.A. Cohen, H.K. Miller, and E.G. Peake. J. Org. Chem. **36**, 1205 (1971).
25. The IUPAC Chemical Data Series. No. 35, 1990 (compiled by K. Izutsu).
26. G.S. Hammond. J. Am. Chem. Soc. **77**, 334 (1955).
27. R.A. Marcus. J. Phys. Chem. **72**, 891 (1968).
28. (*a*) J.P. Pezacki, B.D. Wagner, C.S.Q. Lew, J. Warkentin, and J. Lusztyk. J. Am. Chem. Soc.**119**, 1789 (1997); (*b*) Y. Chiang, A.S. Grant, A.J. Kresge, and S.W. Paine. J. Am. Chem. Soc. **118**, 4366 (1996); (*c*) W.J. Albery, A.J. Campbell-Crawford, and J.S. Curran. J. Chem. Soc. Perkin Trans. 2, 2206 (1972); (*d*) A.J. Kresge. Chem. Soc. Rev. **4**, 475 (1973).
29. (*a*) H. Fischer, F.X. DeCandis, S.D. Ogden, and W.P. Jencks. J. Am. Chem. Soc. **102**, 1340 (1980); (*b*) H.F. Gilbert and W.P. Jencks. J. Am. Chem. Soc. **99**, 7931 (1977); (*c*) R.A. Bednar and W.P. Jencks. J. Am. Chem. Soc. **107**, 7117 (1985).
30. J.R. Murdoch. J. Am. Chem. Soc. **102**, 71 (1980).
31. (*a*) J.A. Elvidge, J.R. Jones, C. O'Brien, E.A. Evans, and H.C. Sheppard. Adv. Heterocycl. Chem. **16**, 1 (1974); (*b*) J.H. Ridd. Phys. Methods Heterocycl. Chem. **4**, 55 (1971).
32. R.A. McClelland, M.J. Kahley, P.A. Davidse, and G. Hadzialic. J. Am. Chem. Soc. **118**, 4794 (1996).
33. C.J. Murray and W.P. Jencks. J. Am. Chem. Soc. **112**, 1880 (1990).
34. A.G. Brook. *In* The chemistry of organic silicon compounds. *Edited by* S. Patai and Z. Rappoport. Wiley, New York. 1989. Chap. 15, and refs. therein.
35. (*a*) H.M. Perrin, W.R. White, and M.S. Platz. Tetrahedron Lett. **32**, 4443 (1991); (*b*) W. Kirmse, M. Guth, and S. Steenken. J. Am. Chem. Soc.**118**, 10838 (1996).
36. (*a*) A.G. Brook, R. Kiviskk, and G.E. Legrow. Can. J. Chem. **43**, 1175 (1965); (*b*) A.G. Brook and J.B. Pierce. J. Org. Chem. **30**, 2566 (1965).
37. J.W. Larson and T.B. McMahon. J. Am. Chem. Soc. **109**, 6230 (1987).
38. A.J. Kresge and M.F. Powell. J. Org. Chem. **51**, 819 (1986); **51**, 822 (1986).
39. (*a*) J.T. Stivers and M.W. Washabaugh. Bioorg. Chem.**19**, 369 (1991); (*b*) R. Kluger, J.F. Lam, J.P. Pezacki, and C.-M. Yang. J. Am. Chem. Soc. **117**, 11383 (1995).

© 1999 NRC Canada

A 2-D NMR investigation of the micellar solubilization site in ionic micellar solutions

Brent E. Hawrylak and D. Gerrard Marangoni

Abstract: Two-dimensional NOE spectroscopy (NOESY) experiments have been used to examine the dissolution of two typical solubilizates (1-butanol and benzene) in anionic sodium dodecyl sulfate (SDS) micelles and of benzene in cationic dodecyltrimethyammonium (DTAB) micelles. In all cases, significant, positive NOESY cross peaks were obtained that appeared to correlate well with the expected locus of solubilization of these solubilizates in these surfactant systems. The NOESY technique, which is a noninvasive experiment, is found to provide significant insight in terms of the solubilization of these molecules in the interior of ionic micelles.

Key words: solubilization, surfactants, NMR spectroscopy, 2-D NOESY experiments.

Résumé : On a fait appel à des expériences de spectroscopie EON bidimensionnelle (« NOESY ») pour étudier la dissolution de solubilisats typiques de butan-1-ol + benzène dans des micelles anioniques de dodécylsulfate de sodium et de benzène dans des micelles cationiques de dodécyltriméthylammonium. Dans tous les cas, on a obtenu des pics NOESY croisés qui semblaient donnés une bonne corrélation avec le locus de solubilisation attendu pour des solubilisats dans ces systèmes d'agents de surface. On a observé que la technique de NOESY, qui n'est pas invasive, fournit des informations significatives en termes de solubilisation de ces molécules à l'intérieur de ces micelles ioniques.

Mots clés : solubilisation, agents de surface, spectroscopie RMN, expériences de spectroscopie EON bidimensionnelle.

[Traduit par la Rédaction]

Introduction

The solubilization of substances inside micelles and bilayers that are otherwise insoluble in an aqueous medium has received considerable academic and industrial attention. Much of the literature has focused on the determination of the partition constant (the *p*-values) of the solubilizates in micelles. There have been, by comparison, relatively few investigations of the location of solubilizates inside micelles (1).

In water – nonaqueous solvent systems, a significant factor in the determination of the micellar properties (i.e., cmc values, aggregation numbers, degrees of counterion binding) is the degree to which the nonelectrolyte penetrates into the micellar phase (1–4). The mole fraction of solubilizate in the micellar phase, *p*, is defined as

$$[1] \qquad p = \frac{c_{s,mic}}{c_{s,t}}$$

Here, $c_{s,mic}$ is the concentration of solubilizate in the micellar phase and $c_{s,t}$ is the total concentration of solubilizate. The *p*-values of solubilizates have been measured by a number of different techniques (1). NMR determinations of the *p*-values of solubilizates are accomplished by the application of the Fourier transform pulsed-gradient spin echo (FT-PGSE) experiment as described by Stilbs (5–7), or by the NMR – paramagnetic relaxation enhancement experiment (the NMR–PRE) (8–11). This method is based on the changes in the relaxation rate of the solubilizate in surfactant and surfactant-free solutions, in the presence of paramagnetic ions, and has been successfully applied in a number of surfactant–solubilizate systems (8–12).

In recent years, however, there has been a significant amount of interest in the location of solubilizates in the micellar interior. One of the most widely used experiments for examining the location of a solubilizate in the micellar phase has been to determine the aromatic ring current induced shifts of aromatic solubilizates on surfactant chain protons (13–15). Paramagnetic relaxation enhancement experiments have also been used to determine the average location of the solubilizate in the micellar interior (16–18). Fluorescence probing experiments have yielded significant information on the location of certain molecules in the micellar interior (19). However, the NMR aromatic solute induced shift experiments (ASIS experiments) and the fluorescence probing experiments are limited to specific classes of molecules. The NMR paramagnetic relaxation enhancement experiments are more general in their implementation; however, these experiments rely on the presence of a small amount of a paramagnetic probe on the surface of the micelles. Although extreme care is taken to insure that the ratio of paramagnetic probe to surfactant is kept small, perturbations of the micellar structure are unavoidable.

Two-dimensional nuclear Overhauser enhancement experiments (NOESY) have been shown to provide significant information on the intra- and intermolecular proximity of

Received September 30, 1998.

B.E. Hawrylak and D.G. Marangoni.[1] Department of Chemistry, St. Francis Xavier University, P.O. Box 5000, Antigonish, NS B2G 2W5, Canada.

[1]Author to whom correspondence may be addressed. Telephone: (902) 867-2324. Fax: (902) 867-2414. e-mail: gmarango@stfx.ca

© 1999 NRC Canada

protons (20). In the case of macromolecules such as proteins, the 2-D NOESY experiment has been shown to provide valuable information in the determination of the conformation and dynamics of these large molecules (21). If the motions of the respective protons undergoing cross-relaxation are in the extreme narrowing region, then the cross peaks of the 2-D NOESY spectrum will be of opposite sign to those of the diagonal (a small-molecule NOESY results). In the case of large molecules like proteins, the motions of these molecules are outside of the extreme narrowing limit; hence, the nOe is negative and the cross peaks of these large molecules in the NOESY spectrum are of the same sign as the diagonal peaks (i.e., a large-molecule NOESY results). For a micellar solution, it is well known that there are two motions that are fairly well separated in time (22). Firstly, a slow motion that is ascribed to the translation diffusion of the surfactant molecule across the micellar surface, or to the rotational tumbling of the whole micelle, occurs in the nanosecond range (out of the extreme narrowing region). However, the reorientational motions of the chains inside the micellar interior are in the picosecond range, i.e., well inside the extreme narrowing limit. Hence, for a surfactant–solubilizate system, the motions of the molecules inside the micelles are in the extreme narrowing region (22), and a small-molecule NOESY may be expected.

There are a few papers in the literature dealing with the application of the 2-D NOESY technique to probe micellar solubilization (23, 24). However, a detailed study on well-characterized mixed micellar systems is lacking. In this paper, we report our results on the determination of the NOESY contour plots for two typical solubilizates (1-butanol and benzene) in a micellar solution of SDS and for benzene in a micellar solution of DTAB. In all cases, we observe positive cross peaks between the solubilizate and the surfactant protons in the NOESY contour plots. These cross peaks appear to be consistent with the known locus of solubilization of these molecules in the micellar interior. It is demonstrated that the NOESY technique may provide a relatively straightforward and noninvasive way of determining the solubilization site of a number of different molecules in various micellar systems.

Experimental

Sodium dodecyl sulfate (SDS) was purchased from BDH (specially pure). Repeated recrystallizations from methanol and Soxhlet extraction from diethyl ether were used to purify the surfactant. Dodecyltrimethylammonium bromide (DTAB) was obtained from the Sigma Chemical Company, and it was purified by at least three recrystallizations from an acetone–ethanol mixture. The solubilizates (1-butanol and benzene) were all high-purity reagent from the Aldrich Chemical Company and were used as received. D_2O (99.8%) was purchased from Aldrich or CDN Isotopes.

The 1-D NMR spectra (^1H) for the surfactant–solubilizate systems were obtained on a Bruker AC-200 at St. Francis Xavier University operating at 200.13 MHz for protons and on a Bruker AC-250 at the Atlantic Region Magnetic Resonance Centre (ARMRC) at Dalhousie University. A typical ^1H spectrum for the SDS–1-butanol system is given in Fig. 1. D_2O was used as solvent for all the NMR experiments. The ^1H spectra were referenced to the HOD peak, which was assigned a value of $\delta = 4.810$ ppm. 2-D NOESY experiments were performed on the Bruker AC-250 NMR spectrometer at the ARMRC. The mixing times and the delay times for the NOESY experiments were estimated from the spin-lattice relaxation times of the surfactant–solubilizate systems. In all cases, we used an acquisition delay of $\approx 3 \times T_1$ and a mixing time of $\approx 1 \times T_1$ to obtain the NOESY spectra. This corresponded to a mixing time of 1.0 s for the SDS–1-butanol system and ≈ 3.5 s for both the SDS–benzene and the DTAB–benzene surfactant–solubilizate systems. Solutions of 70 mg/mL of SDS (243 mM) or 50 mg/mL of DTAB (0.162 M) were prepared directly in small sample vials. The appropriate quantity of the SDS or DTAB stock solution was transferred to an NMR tube and 8–10 μL of the solubilizate was added directly to the NMR tube with a Hamilton syringe.

Fig. 1. Proton NMR spectrum for the system SDS–1-butanol.

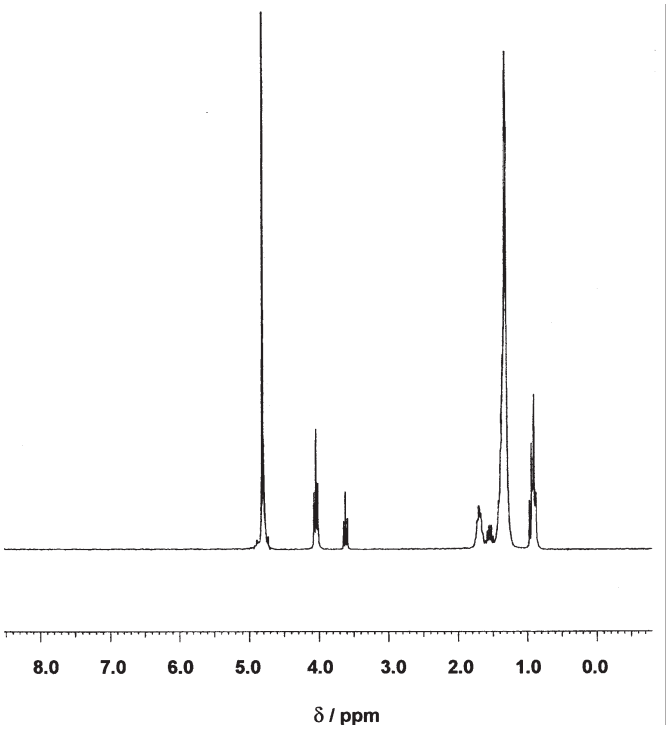

Results and discussion

The NOESY contour plots for each of the solubilizate–surfactant systems are given in Figs. 2–4. In all cases, it is clear that significant cross peaks occur in the NOESY experiments that would indicate the proximity of the protons between the solubilizate and the surfactants. For each of the surfactant–solubilizate systems, we observed positive cross peaks in the NOESY experiments between the protons on the solubilizates and the surfactant protons, indicating that the motions of the protons on both the surfactants and solubilizates are in the extreme narrowing range. It is clear then from Figs. 2–4 that despite the dynamic nature of the surfactant–solubilizate systems (i.e., a wide range of motions well separated in time), the nOe's have not been reduced in magnitude to near-zero values. The presence of

© 1999 NRC Canada

Fig. 2. Contour plots for the 2-D NOESY experiment on the system SDS–1-butanol at 293 K.

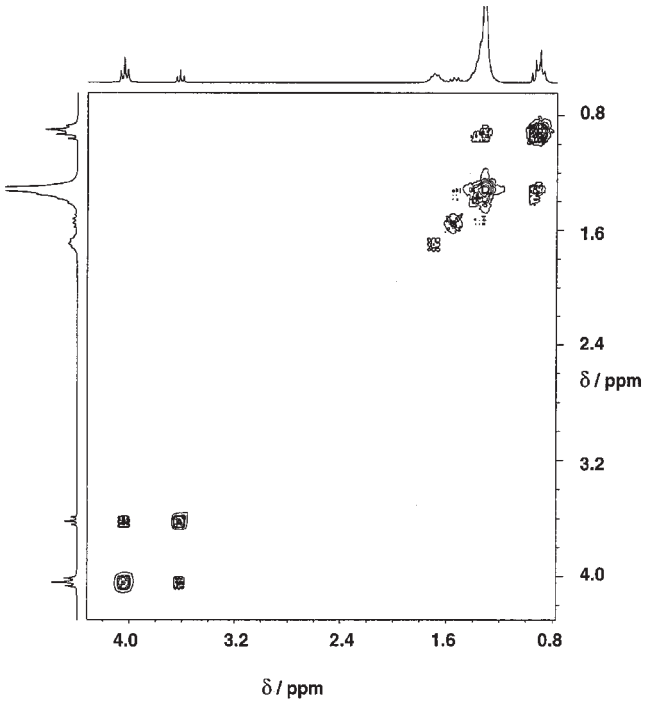

Fig. 3. Contour plots for the 2-D NOESY experiment on the system SDS–Bz at 293 K.

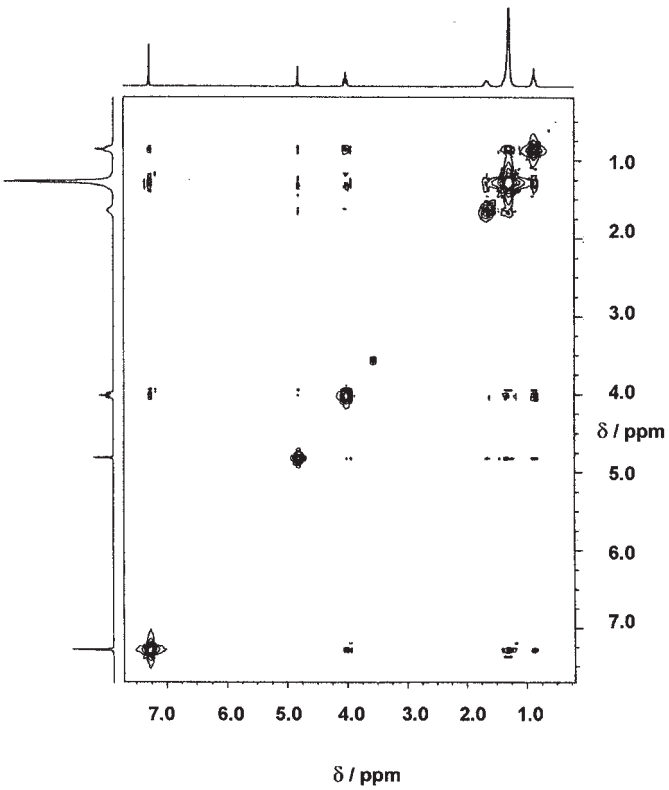

these cross peaks must then indicate the presence of significant intermolecular dipolar interactions between the surfactant and the solubilizate (i.e., generally representing a spatial proximity of <0.50 nm).

The NOESY spectrum for the system SDS–1-butanol is given in Fig. 2. From the spectrum, we observe strong correlations between the α-protons of the SDS (δ ≈ 4.0 ppm) and the 1-butanol (δ ≈ 3.8 ppm). We also observe a strong correlation between the methyl protons of the butanol (δ ≈ 0.9 ppm) and the SDS chain protons (δ ≈ 1.4 ppm). A number of other correlations exist in the region around 1 ppm that are likely cross peaks between the -CH_3 peak and the C-11 protons of the SDS, as well as cross peaks between the methyl protons and the C-3 protons of 1-butanol. These cross peaks may be due to the folding of the carbon chains of SDS and 1-butanol occurring in the micellar interior. This is consistent with the literature explanation for the location of the solubilizate in the SDS micelles, i.e., the alcohol is located in the micelle with its headgroup in intimate contact with the SDS micellar headgroups, while the hydrocarbon chain is pointed inwards towards the centre of the micelle.

While the NOESY spectrum for 1-butanol in the SDS micellar system indicates that the alcohol molecules are confined primarily to the headgroup region of the SDS micelles, the NOESY contour plot for the SDS–benzene system (Fig. 3) is significantly different. In this case, we observe positive cross peaks between the benzene protons (δ ≈ 7.2 ppm) and all the SDS surfactant protons. This is consistent with the benzene molecules being able to sample the entire micellar interior, with no particular region of the micelle being a favoured locus of solubilization for benzene. This is in excellent agreement with the NMR paramagnetic relaxation experiments and ASIS experiments of Wasylishen et al. for benzene in SDS micelles (16). These authors concluded that benzene molecules are distributed rather uniformly throughout the interior of the SDS micelles. In our NOESY experiments, since we observe no particular difference in the magnitude of the benzene cross peaks, we can conclude that the benzene molecules have no real preference for one part of the micellar interior over another.

The NOESY spectrum for the system DTAB/benzene is given in Fig. 4. It is clear from Fig. 4 that this NOESY spectrum is remarkably different than the SDS–benzene NOESY contour plot (Fig. 3). In this spectrum, the correlations between the benzene protons (δ ≈ 7.2 ppm) and the DTAB headgroup protons (3.0–3.2 ppm) are strong, while somewhat weaker correlations exist between benzene protons and the chain protons of the DTAB molecules inside the micelles. The presence of the large cross peak between the benzene and the headgroup protons indicates a preferential interaction between the benzene molecule and the headgroup region of the micelle. This is in excellent agreement with the well-known locus of solubilization of benzene in DTAB micelles (16). This localization of the benzene molecules in the DTAB headgroup region may be due to the hydrophobic nature of the DTAB headgroup (three methyl groups attached to the quatenary nitrogen), which may lead to significant hydration differences in the headgroup of the positively charged surfactant micelle. It may also be that the presence of the aromatic π-electrons will electrostatically attract the benzene molecules towards the headgroup region of the cationic micelles.

© 1999 NRC Canada

Fig. 4. Contour plots for the 2-D NOESY experiment on the system DTAB–Bz at 293 K.

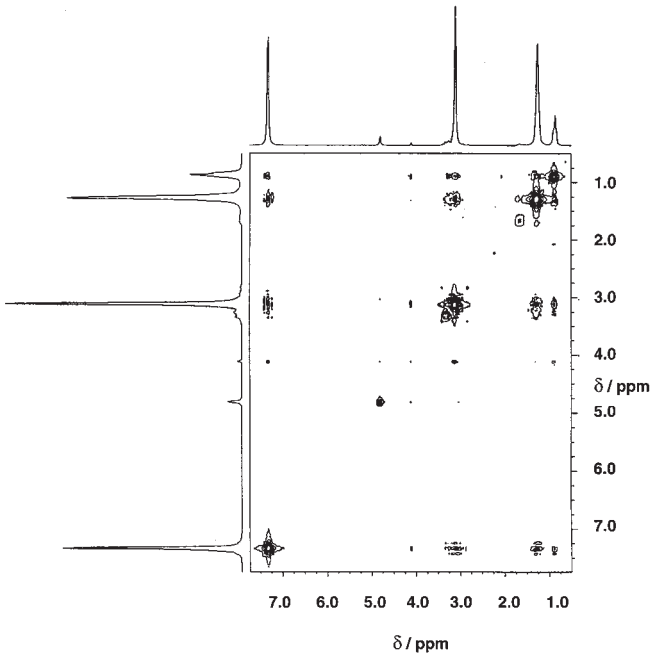

Summary and conclusions

The NOESY spectra for 1-butanol–SDS, benzene–SDS, and benzene–DTAB indicate that the locus of solubilization of these typical solubilizates can be reliably determined by analysing the cross peaks in the NOESY spectrum of the surfactant–solubilizate system. In the case of the 1-butanol–SDS system, the NOESY spectrum indicates that the alcohol is solubilized with the alcohol headgroups in intimate contact with the surfactant headgroups. In addition, the manner in which the alcohol chain is buried in the micelle can be obtained from the NOESY spectra. For benzene, the NOESY spectra indicate a rather even distribution of benzene molecules throughout the SDS micellar interior, whereas for the DTAB–benzene system, the NOESY spectra indicate the preference of benzene molecules for the micellar headgroup region. It should be noted that when we examine the 2-D COSY experiments for these systems, there is a complete lack of any cross peaks in the regions where we observe dipolar correlations in the NOESY contour plots.

The main advantage of the 2-D NOESY experiment lies in the noninvasive nature of the technique; the locus of solubilization is determined without the need of solubilized aromatic molecules or added paramagnetic agents, which can perturb the micellar structure. We are currently examining the locus of solubilization via the NOESY technique for a wide variety of surfactant–solubilizate combinations. These will be the subjects of future publications.

Acknowledgements

The financial support of the Natural Sciences and Engineering Research Council of Canada (NSERC) (research grant, D.G.M.) and of St. Francis Xavier University (B.E.H.) is greatly appreciated. B.E.H. also acknowledges the grant of an NSERC Undergraduate Summer Research Award. We are grateful to Don Hooper, Mike Lumsden, and Rod Wasylishen for stimulating discussions.

References

1. S.A. Christian and J.F. Scamehorn. *In* Surfactant science series: solubilization. *Edited by* S.A. Christian and J.F. Scamehorn. Marcel Dekker, New York. 1995. Chap. 1.
2. M. Almgren and S. Swarup. J. Colloid Interface Sci. **91**, 256 (1983).
3. D.G. Marangoni and J.C.T. Kwak. Langmuir, **7**, 2083 (1991).
4. R. Zana, S. Yiv, C. Straizelle, and P. Lianos. J. Colloid Interface Sci. **80**, 208(1981).
5. P. Stilbs. Prog. Nucl. Magn. Reson. Spectrosc. **19**, 1 (1987).
6. P. Stilbs. J. Colloid Interface Sci. **87**, 385 (1982).
7. P. Stilbs. J. Colloid Interface Sci. **89**, 547 (1982).
8. Z. Gao, R.E. Wasylishen, and J.C.T. Kwak. J. Phys. Chem. **93**, 2190 (1989).
9. Z. Gao, D.G. Marangoni, R. Labonté, R.E. Wasylishen, and J.C.T. Kwak. Colloids Surf. **45**, 269 (1990).
10. Z. Gao, R.E. Wasylishen, and J.C.T. Kwak. J. Phys. Chem. **95**, 462 (1991).
11. A.P. Rodenhiser, J.M. Thomas, D.G. Marangoni, and J.C.T. Kwak. ACS Symp. Ser. **501**, 194 (1992).
12. A. Yoshino, K. Murate, T. Yoshida, H. Okabayashi, P.R. Krishna, H. Kamaya, and I. Ueda. J. Colloid Interface Sci. **166**, 375 (1994).
13. J.C. Eriksson and G. Gillberg. Acta Chem. Scand. **20**, 2019 (1966).
14. C.A. Bunton and C.P. Cowell. J. Colloid Interface Sci. **122**, 154 (1988).
15. J. Ulmius, B. Lindman, G. Lindblom, and T. Drakenberg. J. Colloid Interface Sci. **65**, 88 (1978).
16. R.E. Wasylishen, J.C.T. Kwak, Z. Gao, E. Verpoorte, J.B. MacDonald, and R.M. Dickson. Can. J. Chem. **69**, 822 (1991).
17. K.K. Fox, I.D. Robb, and R. Smith. J. Chem. Soc. Faraday Trans. 1, **68**, 445 (1972).
18. N.R. Jagannathan, K. Venkateswaran, F.G. Herring, G.N. Patey, and D.C. Walker. J. Phys. Chem. **91**, 4553 (1987).
19. M. Almgren, F. Grieser, and J.K. Thomas. J. Am. Chem. Soc. **101**, 279 (1979).
20. S. Macura and R.R. Ernst. Mol. Phys. **41**, 95 (1980).
21. K. Wüthrich. NMR of proteins and nucleic acids. Wiley, New York. 1986.
22. H. Wennerström, B. Lindman, O. Söderman, T. Drakenberg, and J.B. Rosenholm. J. Am. Chem. Soc. **101**, 6860 (1979).
23. M.I. Gjerde, W. Nerdal, and H. Høiland. J. Colloid Interface Sci. **183**, 285 (1996).
24. E. Kolehmainen. Magn. Reson. Chem. **26**, 760 (1988).

© 1999 NRC Canada

Photocycloelimination of α,α-dichlorocyclobutanones

Jailall Ramnauth and Edward Lee-Ruff

Abstract: Direct irradiation of a series of α,α-dichlorocyclobutanones in benzene solutions results in photocycloelimination to give 1,1-dichloroalkenes in yields ranging from 30–65%. The α,α-dichlorocyclobutanones were formed in good yields from the [2+2] cycloaddition of the terminal olefins with dichloroketene. This two-step sequence formally represents a "metathesis" of two olefinic functions and provides an easy access to functionalized 1,1-dichloroalkenes. Irradiation of the dichlorocyclobutanones in the solid state led to poor yields of 1,1-dichloroalkenes and polymeric mixtures, however, photoreactions performed in zeolites gave similar yields as those run in benzene solutions.

Key words: dichlorocyclobutanones, dichloroalkenes, olefin metathesis, photocycloelimination.

Résumé : L'irradiation directe d'une série de α,α-dichlorocyclobutanones, en solutions benzéniques, provoque une photocycloélémination qui conduit à la formation de 1,1-dichloroalcènes, avec des rendements allant de 30 à 65%. Les α,α-dichlorocyclobutanones se formes avec de bons rendements par la cycloaddition [2+2] d'oléfines thermiques avec le dichlorocétène. Cette séquence en deux étapes correspond à une "métathèse" de deux fonctions oléfiniques et elle fournit une voie d'accès facile aux 1,1-dichloroalcènes fonctionnalisés. L'irradiation des dichlorocyclobutanones à l'état solide conduit, avec de mauvais rendements, aux 1,1-dichloroalcènes avec des mélanges de polymères; toutefois, les photoréactions effectuées dans des zéolites donnent des rendements semblables à ceux obtenus en solution dans le benzène.

Mots clés : dichlorocyclobutanones, dichloroalcènes, métathèse d'oléfine, photocycloélimination.

[Traduit par la Rédaction]

Introduction

Photocycloelimination is one of three principal reaction channels from electronically excited cyclobutanones, which also include decarbonylation and ring expansion (1). If the photocycloelimination process occurs in an orthogonal fashion with respect to the ketene–olefin cycloaddition to form cyclobutanones, such a two-step sequence formally represents a metathesis of two olefinic groups (2). Furthermore, since a large number of functionalized terminal olefins are commercially available and dichloroketene adds easily to terminal olefins (3), such a scheme would constitute a convenient route to substituted 1,1-dichloroalkenes.

1,1-Dichloroalkenes are important synthetic intermediates, especially for the synthesis of arylacetic acids (4) and various alkynes (5). The commonly used methods for the preparation of 1,1-dichloroalkenes include the dichloromethylenation of carbon–oxygen double bond of carbonyl compounds with Wittig-type reagents obtained from organophosphines and carbon tetrachloride, and Horner–Emmons reagent generated from cathodic reduction of diethyl trichloromethyl phosphonate (6).

Received June 24, 1998.

J. Ramnauth and E. Lee-Ruff.[1] Department of Chemistry, York University, Toronto, ON M3J 1P3, Canada.

[1]Author to whom correspondence may be addressed. Telephone: (416) 736-5443. Fax: (416) 736-5936. e-mail: leeruff@yorku.ca

Previously, we reported the photocycloelimination of bicyclic cyclobutanones in nonpolar aprotic solvents containing a minimal amount of an alcohol to quench the intermediate ketene produced, generating substituted terminally functionalized carboxylic esters (7). Although the yields are excellent, the complete elimination of the ring expansion pathway could not be achieved in some cases. Also, the [2+2] cycloaddition with ketenes requires activated olefins such as enol ethers and conjugated dienes.

Herein, we report the direct irradiation of a series of α,α-dichlorocyclobutanones generated from the [2+2] cycloaddition of dichloroketene to the corresponding terminal olefins, giving 1,1-dichloroalkenes. Such a reaction can be formally represented by Scheme 1 in which terminal chlorination of a terminal alkene is the net conversion. Such direct chlorination reactions cannot be effectively performed on terminal alkenes.

Scheme 1.

Results and discussion

The dichlorocyclobutanone derivatives **2**(a) and **2**(b) were prepared according to literature methods (8, 9) from the commercially available alkenes **1**(a) and (b), respectively. Irradiation of a 6×10^{-3} M solutions of **2**(a) and **2**(b) in

© 1999 NRC Canada

Scheme 2.

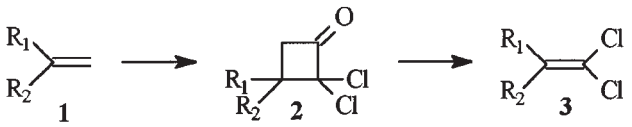

1(a) R_1=H, R_2=Ph	**2**(a)	**3**(a)
1(b) R_1=Ph, R_2=Ph	**2**(b)	**3**(b)
1(c) R_1=H, R_2=CH_2OBz	**2**(c)	**3**(c)
1(d) R_1=H, R_2=CH_2CH_2OBz	**2**(d)	**3**(d)
1(e) R_1=CH_3, R_2=CH_2OBz	**2**(e)	**3**(e)
1(f) R_1=CH_3, R_2=CH_2CH_2OBz	**2**(f)	**3**(f)

benzene for 2 h using a medium pressure mercury lamp with a pyrex filter went to ca. 70% conversion to give the known compounds **3**(a) (10) and **3**(b) (11) in 30 and 40% isolated yields, respectively, with trace amounts (<1%) of starting olefins **1**(*a*) and **1**(b) (see Scheme 2). The structures of **3**(a) and **3**(b) were based on ^{1}H-NMR spectra and comparison with literature data. Compound **3**(a) exhibited a single proton singlet at δ 6.86 ppm assigned to the vinylic proton, while **3**(b) showed only aromatic signals. It was somewhat surprising to detect the presence of trace amounts of starting olefins **1**(*a*) and (b), indicating that the photocyclo eliminations also occurred on the less substituted side, however, only to a minor extent. The low yields of these derivatives could be attributed to some polymerization of the 1,1-dichloroalkenes.

The dichloroketene adducts **2**(c)–**2**(f) were prepared from the cycloaddition of dichloroketene (generated in situ from trichloroacetyl chloride and activated zinc) to the corresponding olefins **1**(c)–**1**(f) in the presence of 1,2-dimethoxyethane (DME) (12) as cosolvent in yields ranging from 74 to 85% after purification. The structures of these compounds were fully characterized by spectral and analytical data. The olefins **1**(c)–**1**(f) were prepared from the benzoylation of the commercially available alcohols in excellent yields (90–96%). The dichlorocyclobutanones **2**(c)–**2**(f) were irradiated as before (ca. 80% conversions) to give exclusively the dichloroalkenes **3**(c)–**3**(f) in yields ranging form 54 to 65% after chromatography. The structures of these alkenes were confirmed by spectral data. The ^{1}H-NMR data of **3**(c) exhibited a one proton triplet (J = 6.7 Hz) at δ 6.21 ppm assigned to the vinylic proton. This proton appeared at δ 5.9 ppm in the original olefin. The ^{13}C-NMR spectrum showed the eight unique carbon signals. For compound **3**(d),the ^{1}H-NMR spectrum showed a single triplet (J = 7.1 Hz) at 6.00 ppm associated with the vinylic proton, and the ^{13}C-NMR spectrum revealed the nine signals one would expect for this compound. The ^{13}C-NMR spectrum revealed the nine unique carbons of compound **3**(e), and the ^{1}H-NMR spectrum showed sharp singlets at δ 5.01 and δ 2.00 corresponding to the methylene and methyl protons, respectively. Olefin **3**(f) showed two triplets at δ 4.45 (J = 6.6 Hz) and δ 2.77 (J = 6.4 Hz) associated with a substituted ethyl group and a sharp methyl singlet at δ 2.10 in its ^{1}H-NMR spectrum. The ^{13}C-NMR spectrum showed 10 signals in accordance with the assigned structure for **3**(f).

In the continuation of our work on the triplet photosensitized reaction of cyclobutanones to form cyclopropanes (13), we were interested in the possibility of preparing dichlorocyclopropanes via the photodecarbonylation of dichlorocyclobutanones. Some dichlorocyclopropanes have been shown to exhibit insecticidal properties (14). Under triplet sensitized conditions, using acetone as both the sensitizer and solvent, the dichlorocyclobutanone **2**(c) and **2**(d) gave olefins **3**(c) and **3**(d), respectively, as the major nonpolar products. These results were somewhat surprising and contrary to the behaviour of alkyl substituted cyclobutanones. To rationalize these results, one must consider the mechanism of cyclobutanone photochemistry. It has been shown that cycloelimination can occur form a vibrationally excited ground state of cyclobutanone formed from internal conversion (15). This is based on observations of cycloeliminations occurring in the thermal reactions of cyclobutanones (16). The triplet state of cyclobutanone has been implicated in the decarbonylation process (17). The fact that decarbonylation does not occur in these α,α-dichlorocyclobutanones can be explained by a simple but very reasonable model proposed by Moule (18). The triplet state may be too short-lived due to efficient intersystem crossing to $S°$ in the presence of a heavy atom (19). This deactivation process would compete with decarbonylation and form a hot ground state resulting in cycloelimination.

Another rationalization for the lack of decarbonylation in these systems is the increase of the triplet state energy level brought about by an electron-withdrawing substituent. Ketones possessing an electron-withdrawing α-substituent such as oxygen and chlorine show a hypsochromic shift of the $n\rightarrow\pi^*$ absorption band (20). This electronic effect would also be expected to increase the triplet energy level, which may result in inefficient triplet sensitization by acetone (E_T = 78 kcal), resulting in an endothermic process. Thus, direct excitation of cyclobutanone might be expected to give only cycloelimination products.

Radicals and diradicals that are produced in solution suffer a different fate from those produced in the solid state. To explore the possibility that the 1,4-acyl-alkyl diradical might undergo decarbonylation in the solid state, we explored the photochemistry of **2** in the crystal lattice.

© 1999 NRC Canada

Solid state photolysis often differs from solution photochemistry due to the rigidity associated with the crystal lattice and has received a great deal of attention recently (21). The solid state photolyses of **2**(a)–**2**(c) and **2**(e) were done according to a modified literature procedure (22). After the usual work-up and chromatography, poor yields of the 1,1-dichloroalkenes were obtained but no cyclopropanes were detected. The photolysate consisted primarily of intractable polymeric materials. This problem did not occur to any great extent in the solution state photolyses due to the dilute conditions under which these reactions were conducted.

To minimize the extent of polymerization due to radical processes, we explored these photochemical reactions in zeolites (23). For this work, incorporation of the dichlorocyclobutanones within the supercages was accomplished by stirring hexane solutions in the presence of anhydrous Na-Y zeolite, followed by thorough washings with hexane. Analysis of the hexane washings revealed no residual starting materials, indicating complete incorporation of the substrate within the zeolite cages. The vacuum-dried complexes were photolyzed as hexane slurries for 2 h with stirring. After work-up, which involved extraction with ether and then chromatography, the yields were about the same as those in the solution phase. However, the conversions were on average 10% lower than those in the solution phase.

It has been shown that the photocycloelimination of α,α-dichlorocyclobutanones can provide an easy route to 1,1-dichloroalkenes. This method formally represents a metathesis of two olefinic groups. With the limited number of methods available for the synthesis of these derivatives, this method provides an easy two-step alternative. What is attractive is the generality in terms of the wide range of functionalized terminal olefins that can add to dichloroketene.

Experimental

Melting points (mp) were determined on a Reichert melting point apparatus and are uncorrected. NMR spectra were recorded on a Bruker ARX 400 spectrometer in $CDCl_3$ containing 1% TMS or unless otherwise noted. Fourier Transform Infrared (FT-IR) spectra were recorded on a Pye Unicam SP3-200 spectrometer as thin films or as KBr pellets. Photolyses were carried out using a Hanovia 450W medium-pressure mercury arc lamp in a water-cooled quartz immersion well. Pyrex tubes containing the samples were strapped around this well and the assembly immersed in an ice-water bath. The samples were degassed for 30 min prior to irradiation. All solvents used in these reactions were dried and distilled. Analytical thin layer chromatography (TLC) was done using commercially prepared silica gel 60F 254 plastic sheets (E. Merck & Co.). Preparative TLC was carried out with Aldrich silica gel 60F 254 precoated glass plates. Elemental analyses were performed by Guelph Chemical Laboratories Limited. All reactions were performed under inert atmosphere conditions. All precursor chemicals were purchased from the Aldrich chemical company. Olefins **1**(c)–**1**(f) were prepared from benzoylation of the corresponding alcohol using benzoyl chloride in pyridine. The cyclobutanones **2**(a) and **2**(b) were prepared according to literature methods (8, 9).

General photolysis procedures

A solution of dichlorocyclobutanones **2**(a)–**2**(e) (0.4 mmol) in 70 mL of benzene was degassed with argon for 30 min and then irradiated for 2 h. The solvent was removed under reduced pressure, and the residue was chromatographed on TLC plates (hexane:ethyl acetate, 90:10). The conversions were ca. 70–80%. The yields reported are the isolated yields based on starting materials. Solid-phase photolyses were done by sandwiching the solids between two pyrex microscope slides. The slides were secured with tape and placed in a quartz tube. After the irradiation, the slides were rinsed with CH_2Cl_2, the solvent removed under reduced pressure, and the residue was chromatographed as before. For the zeolite work, 1 g of Na-Y zeolite was added to the dichlorocyclobutanone (0.4 mmol) in 50 mL hexane. This suspension was stirred overnight at room temperature. After this time, the suspension was filtered, and the solid washed with 4 × 100 mL hexane. Evaporation of the hexane washings revealed no starting materials. The vacuum dried solids were suspended in 70 mL of hexane and photolyzed for 2 h with constant stirring. After this time, the solid was filtered and subjected to a soxhlet extraction overnight. Conversions were ca. 60–70%.

General procedure for the preparation of dichlorocyclobutanones 2(c)–2(e)

A two-neck round-bottom flask, equipped with a magnetic stirrer, dropping funnel, and argon inlet was charged with activated zinc (9) (4 equiv.) and the olefin (1 equiv.) in anhydrous ether (2 mL/mmol of olefin). To this vigorously stirred suspension was added dropwise a mixture of trichloroacetyl chloride (2 equiv.), 1,2-dimethoxyethane (DME) (2 equiv.), and anhydrous ether (1 mL/mmol) over a period of about 30 min. This mixture was stirred at room temperature overnight. After this time, hexane was added (~50 mL) and the suspension stirred for 5 min to precipitate the zinc salts. The solution was then decanted and treated sequentially with 100 mL H_2O, 3 × 100 mL saturated $NaHCO_3$, 100 mL saturated NaCl and then dried over Na_2SO_4.

*3-(Benzoyloxy)methyl-2,2-dichlorocyclobutanone (**2**(c))*: Prepared in 85% yield from olefin **1**(c). The crude product was recrystallized from hexane to give a white solid; mp 71–72°C; ^{1}H-NMR δ: 8.04–7.26 (m, 5H), 4.71–4.64 (m, 2H), 3.57–3.50 (dd, 1H, J = 9.9, 7.7 Hz), 3.44–3.41 (m, 1H), 3.27–3.21 (dd, 1H, J = 7.7, 9.8 Hz); FT-IR (KBr): 1809, 1713, 1599 cm^{-1}; ^{13}C-NMR δ: 191.1, 166.0, 133.5, 129.7, 129.4, 128.6, 87.4, 63.3, 45.2, 44.3. Anal. calcd. for $C_{12}H_{10}O_3Cl_2$: C 52.77, H 3.69; found: C 52.69, H 3.64.

*3-[2-(Benzoyloxy)ethyl]-2,2-dichlorocyclobutanone (**2**(d))*: Prepared in 80% yield from olefin **1**(d). The crude product was passed through a short plug of silica gel to give a colourless oil. ^{1}H-NMR δ: 8.06–7.44 (m, 5H), 4.51–4.46 (m, 2H), 3.47–3.39 (m, 1H), 3.17–3.06 (m, 2H), 2.47–2.38 (m, 1H), 2.16–2.04 (m, 1H); FT-IR(neat): 1812, 1718 cm^{-1}; ^{13}C-NMR δ: 192.4, 166.4, 133.2, 129.8, 129.6, 128.5, 88.8, 62.5, 48.0, 43.5, 30.4. Anal. calcd. for $C_{13}H_{12}O_3Cl_2$: C 54.38, H 4.21; found: C 54.33, H 4.30.

© 1999 NRC Canada

*3-(Benzoyloxy)methyl-2,2-dichloro-3-methylcyclobutanone (**2**(e))*: Prepared in 84% yield from the olefin **1**(e). The crude product was chromatographed through a short plug of silica gel to give a viscous oil, which solidified on standing at –10°C overnight; mp 48–49°C. ^{1}H-NMR δ: 8.02–7.46 (m, 5H), 4.59 (s, 2H), 3.34–3.39 (d, 1H, *J* = 17.0 Hz), 3.16–3.11 (d, 1H, *J* = 17.6 Hz); FT-IR (KBr): 1811, 1732 cm^{-1}; ^{13}C-NMR δ: 191.4, 165.9, 133.5, 129.7, 129.3, 128.6, 91.0, 68.1, 51.6. 44.9, 20.6. Anal. calcd. for $C_{13}H_{12}O_3Cl_2$: C 54.38, H 4.21; found: C 54.37, H 4.07.

*3-[2-(Benzoyloxy)ethyl]-2,2-dichloro-3-methylcyclobutanone (**2**(d))*: Prepared in 75% yield from olefin **1**(f). The crude product was passed through a short plug of silica gel to give a colourless oil. ^{1}H-NMR δ: 8.05–7.44 (m, 5H), 4.55–4.50 (m, 2H), 3.41–3.36 (d, 1H, *J* = 16.8 Hz), 2.93–2.89 (d, 1H, *J* = 15.8 Hz), 2.41–2.30 (m, 2H), 1.48 (s, 3H); FT-IR (KBr): 1811, 1732 cm^{-1}; ^{13}C-NMR δ: 192.5, 166.3, 133.2, 129.9, 129.6, 128.5 92.7, 61.5, 54.7. 43.8, 35.3, 22.7. Anal. calcd. for $C_{14}H_{14}O_3Cl_2$: C 55.83, H 4.69; found: C 55.48, H 4.41.

*1,1-Dichloro-2-phenylethene (**3**(a)) (10)*: Yield: 30%; ^{1}H-NMR δ: 7.54–7.31 (m, 5H), 6.26 (s, 1H).

*1,1-Dichloro-2,2-diphenylethene (**3**(b)) (11)*: Yield: 40%; ^{1}H-NMR δ: 7.33–7.29 (m).

*3-Benzoyloxy-1,1-dichloro-1-propene (**3**(c))*: Yield: 65%; ^{1}H-NMR δ: 8.06–7.43 (m, 5H), 6.21–6.18 (t, 1H, *J* = 6.7 Hz), 4.93–4.91 (d, 2H, *J* = 6.8 Hz); ^{13}C-NMR (acetone-d_6) δ: 166.4, 134.2, 130.6, 130.3, 129.5, 126.3, 125.1, 61.9. Anal. calcd. for $C_{10}H_8O_2Cl_2$: C 51.89, H 3.49; found: C 51.12, H 3.53.

*4-Benzoyloxy-1,1-dichloro-1-butene (**3**(d))*: Yield: 58%; ^{1}H-NMR δ: 8.05–7.43 (m, 5H), 6.00–5.96 (t, 1H, *J* = 7.1 Hz), 4.39–4.36 (t, 2H, *J* = 6.2 Hz), 2.69–2.64 (m, 2H); ^{13}C-NMR (acetone-d_6) δ: 166.6, 133.9, 131.1, 130.2, 129.4, 127.9, 121.9, 63.2, 30.2. Anal. calcd. for $C_{11}H_{10}O_2Cl_2$: C 53.90, H 4.11; found: C 53.77, H 3.90.

*3-Benzoyloxy-1,1-dichloro-2-methyl-1-propene (**3**(e))*: Yield: 54%; ^{1}H-NMR δ: 8.06–7.44 (m, 5H), 5.01 (s, 2H), 2.00 (s, 3H); ^{13}C-NMR (acetone-d_6) δ: 166.4, 133.9, 132.3, 130.5, 130.3, 129.5, 119.2, 65.5, 18.1. Anal. calcd. for $C_{11}H_{10}O_2Cl_2$: C 53.90, H 4.11; found: C 55.14, H 4.60.

*4-Benzoyloxy-1,1-dichloro-2-methyl-1-butene (**3**(e))*: Yield: 60%; ^{1}H-NMR δ: 8.05–7.44 (m, 5H), 4.45–4.42 (t, 2H, *J* = 6.6 Hz), 2.77–2.74 (t, 2H, *J* = 6.4 Hz), 1.98 (s, 3H); ^{13}C-NMR δ: 166.5, 133.1, 131.4, 130.0, 129.6, 128.4, 116.9, 61.9, 34.7, 20.3.

Acknowledgements

We would like to thank the Natural Sciences and Engineering Research Council (NSERC) for financial support.

References

1. D.R. Morton and N.J. Turro. Adv. Photochem. **9**, 197 (1974).
2. K.J. Ivin. *In* Olefin metathesis. Academic Press, New York. 1983.
3. L. Ghosez, R. Montaigne, A. Roussel, H. Vanlierde, and P. Mollet. Tetrahedron, **27**, 615 (1971).
4. T. Shono. Chem. Abstr. **97**, 215 767u (1982).
5. J. Villieras, P. Perriot, and J.F. Normant. Synthesis, 458 (1975).
6. P. Savignac, J. Petrova, M. Dreux, and P. Coutrot. Synthesis, 535 (1975).
7. E. Lee-Ruff, H. Kazarians-Moghaddam, and A.C. Hopkinson. Tetrahedron Lett. **24**, 2067 (1983).
8. L.R. Krepski and A. Hassner. J. Org. Chem. **43**, 2879 (1978).
9. A. Maercker and W. Berkulin. Chem. Ber. **123**, 185 (1990).
10. P. Jubault, C. Feasson, and N. Collignon. Bull. Soc. Chim. Fr. **131**, 1001 (1994).
11. S. Braverman and Y. Zafrani. Tetrahedron, **54**, 1901 (1998).
12. B.D. Johnston, E. Czyzewska, and A.C. Oehlschlager. J. Org. Chem. **52**, 3693 (1987).
13. J. Ramnauth and E. Lee-Ruff. Can. J. Chem. **75**, 518 (1997).
14. M. Elliot and N.F. James. Chem. Soc. Rev. **7**, 473 (1978).
15. N.E. Lee and E.K.C. Lee. J. Chem. Phys. **50**, 2094 (1969).
16. H.A.J. Carless and E.K.C. Lee. J. Am. Chem. Soc. **92**, 4482 (1970).
17. H.O. Denschlag and E.K.C. Lee. J. Am. Chem. Soc. **90**, 3628 (1968).
18. D.C. Moule. Can. J. Phys. **47**, 1235 (1969).
19. I.V. Khudyakov, Y.A. Serebrennikov, and N.J. Turro. Chem. Rev. **93**, 537 (1993).
20. D.L. Pavia, G.M. Lampman, and G.S. Kriz. *In* Introduction to spectroscopy. 2nd ed. Saunders College Publishing. 1996. p. 283.
21. Y. Ito. Synthesis, 1 (1998).
22. A.D. Gudmundsdottir, J.R. Scheffer, and J. Trotter. Tetrahedron Lett. **35**, 1397 (1994).
23. D.W. Breck. *In* Zeolite molecular sieves: structure, chemistry, and use. Wiley, New York. 1974.

© 1999 NRC Canada

Synthesis, characterization, and biological relevance of hydroxypyrone and hydroxypyridinone complexes of molybdenum

Sarah J. Lord, Noah A. Epstein, Robert L. Paddock, Christopher M. Vogels, Tracy L. Hennigar, Michael J. Zaworotko, Nicholas J. Taylor, William R. Driedzic, Tom L. Broderick, and Stephen A. Westcott

Abstract: We have prepared a number of complexes of the type *cis*-MoO_2L_2 where L represents a hydroxypyronato or hydroxypyridinonato ligand. Both the maltol (3-hydroxy-2-methyl-4-pyrone, Hma) and kojic acid (5-hydroxy-2-hydroxymethyl-4-pyrone, Hka) complexes, *cis*-$MoO_2(ma)_2$ (**1**) and *cis*-$MoO_2(ka)_2$ (**2**), have been characterized by X-ray diffraction studies. The pyrone ligands are bound to molybdenum in a *cis* bidentate fashion via the deprotonated hydroxyl groups and the ketone moieties. Crystals of **1** are orthorhombic, a = 12.107 (1), b = 8.6169 (8), c = 16.472 (1) Å, Z = 4, space group $Pca2_1$, and those of **2** are monoclinic, a = 8.4591 (5), b = 16.3453 (10), c = 10.2954 (7) Å, β = 103.0320 (10)°, Z = 4, space group $P2_1/c$. Hydroxypyridinone molybdenum complexes have been prepared for both maltol and kojic acid derivatives with the substituents Me, *n*-Pr, CH_2Ph, Ph at the ring nitrogen. Crystals of the 3-hydroxy-2-methyl-1-phenyl-4-pyridinone (Hppp) derivative, $MoO_2(ppp)_2$ (**9**), are monoclinic, a = 10.9476 (6), b = 13.5353 (9), c = 17.4877 (10) Å, β = 93.465 (4)°, Z = 4, space group $P2_1/n$. Initial investigations into the effects molybdenum compounds have on diabetic hearts are presented. Both Na_2MoO_4 (used as a control) and **1** were effective in lowering blood glucose and free fatty acid levels. Diabetic rats treated with molybdate showed significant improvements in postischemic cardiac function.

Key words: molybdenum, hydroxypyrones, hydroxypyridinones, heart function.

Résumé : On a préparé un certain nombre de complexes du type *cis*-MoO_2L_2 dans lesquels L est un ligand hydroxypyronato ou hydroxypyridinonato. On a caractérisé ces complexes avec le maltol (3-hydroxy-2-méthyl-4-pyrone, Hma) et l'acide kojique (5-hydroxy-2-hydroxyméthyl-4-pyrone, Hka), *cis*-$Mo(ma)_2L_2$ (**1**) et *cis*-$MoO_2(ka)_2$ (**2**) par diffraction des rayons X. Les ligands pyrone sont liés au molybdène d'une façon bidentate *cis* par le biais des groupes hydroxyméthyles déprotonés et des portions cétoniques. Les cristaux de **1** sont orthorhombiques, groupe d'espace $Pca2_1$, avec a = 12,107 (1), b = 8,6159 (8) et c = 16,472 (1) Å et Z = 4 alors que ceux de **2** sont monocliniques, groupe d'espace $P2_1/c$, avec a = 8,4591 (5), b = 16,3453 (10) et c = 10,2954 (7) Å, β = 103,0320 (10)° et Z = 4. Les complexes du molybdène et de l'hydroxypyrone ont été préparés avec des dérivés du maltol et de l'acide kojique portant des substituants Me, Pr, CH_2Ph et Ph sur l'azote du cycle. Les cristaux du dérivé 3-hydroxy-2-méthyl-1-phényl-4-pyridone (Hppp), $MoO_2(ppp)_2$ (**9**), sont monocliniques, groupe d'espace $P2_1/n$, avec a = 10,9476 (6), b = 13,5353 (9) et c = 17,4877 (10) Å, β = 93,465 (4)° et Z = 4. On présente les résultats d'études préliminaires relatives à l'effet des composés du molybdène sur des coeurs diabétiques. Le Na_2MoO_4 (utilisé comme contrôle) ainsi que le composé **1** sont tous les deux efficaces pour diminuer les niveaux de glucose et des acides gras libres dans le sang. Des rats diabétiques traités au molybdate ont montré des améliorations significatives dans la fonction cardiaque postischémique.

Mots clés : molybdène, hydroxypyrones, hydroxypyridinones, fonction cardiaque.

[Traduit par la Rédaction]

Received November 16, 1998.

S.J. Lord, N.A. Epstein, R.L. Paddock, C.M. Vogels, and S.A. Westcott.[1] Department of Chemistry, Mount Allison University, Sackville, NB E4L 1G8, Canada.
W.R. Driedzic and T.L. Broderick.[2] Department of Biology and Biochemistry, Mount Allison University, Sackville, NB E4L 1G7, Canada.
N.J. Taylor. Department of Chemistry, University of Waterloo, Waterloo, ON N2L 3G1, Canada.
T.L. Hennigar and M.J. Zaworotko.[3] Department of Chemistry, St. Mary's University, Halifax, NS B3H 3C3, Canada.

[1]Author to whom correspondence may be addressed. Telephone: (506) 364-2372. Fax: (506) 364-2313. e-mail: swestcott@mta.ca
[2]Author to whom correspondence regarding biological studies may be addressed. Current address: Department of Physiology, Midwestern University, Glendale, AZ 85308, U.S.A. Telephone: (602) 572-3664. Fax: (602) 572-3226. e-mail: tbrode@arizona.midwestern.edu
[3]Current address: Department of Chemistry, University of Winnipeg, Winnipeg, MB R3B 2E9, Canada.

 © 1999 NRC Canada

Introduction

Maltol (3-hydroxy-2-methyl-4-pyrone, Hma) and kojic acid (5-hydroxy-2-hydroxymethyl-4-pyrone, Hka) are naturally occurring nontoxic compounds that have found recent applications in bioinorganic chemistry (1). Interest in maltol and kojic acid arises from their ability to deprotonate readily (pK_a for Hma = 8.38, pK_a for Hka = 7.72) and act as anionic chelating, bidentate O,O′ ligands towards a number of biologically active metals. For instance, iron–maltol complexes have found some potential in the treatment of iron-deficiency anaemia (2) and maltol has been examined as a possible chelating agent for lowering aluminum levels in the body (3).

Although metal complexes containing maltol (4) and kojic acid (5) groups are well known, the most significant and well-studied example is the vanadium complex, $VO(ma)_2$ (BMOV) (4*h*). This remarkable compound displays potent insulinomimetic properties and has been the subject of numerous chemical and physiological studies (6). Indeed, Orvig, McNeill and co-workers have shown that BMOV is effective in lowering blood glucose levels in diabetic rats and is relatively nontoxic over a six month administration period (6*b*). BMOV also facilitates the prevention of long-term diabetes-induced pathology and attenuation of hyperinsulinemia and hypertension in genetically hypertensive rats (6*a*). Prevention of cardiac dysfunction in diabetic rats treated with BMOV is of singular importance as Type I (Insulin-Dependent Diabetes Mellitus – IDDM) diabetics are particularly susceptible to heart failure (7). With the advent of insulin therapy, deaths arising from cardiovascular complications associated with diabetes mellitus have risen from 20% to 80% (7). Attempts to develop new compounds for the oral treatment of diabetes should, therefore, have potent insulinomimetic properties as well as show improvement in cardiac pump function over conventional insulin therapy.

Much effort has focused on generating new vanadium compounds to meet these requirements (8). Vanadium complexes containing 3-hydroxy-2-methyl-pyridinone ligands, derived from the addition of primary amines to maltol, have been reported (8*c*, 8*d*). Variation of the amine substituent allows for fine tuning of the hydrophilic/lipophilic balance of the ligands and, therefore, of the corresponding metal complexes (2*b*). The ability to tailor the physical properties of pyridinone ligands has also been utilized to transport metal ions across biological membranes (9).

Recent studies have shown that other transition metals also display certain insulinomimetic properties (10). For example, insulin-like effects on blood lipids have been reported recently in diabetic rats treated with sodium molybdate, Na_2MoO_4 (10*b*). With this in mind, we postulated that oxomolybdenum complexes containing organic ligands may also prove effective for the oral treatment of diabetes. As part of our initial investigation, we have prepared a number of hydroxypyrone and hydroxypyridinone molybdenum complexes and report herein on the amelioration of heart function defects in diabetic rats treated with Na_2MoO_4 and the molybdenum analogue of BMOV, *cis*-bis(maltolato)dioxomolybdenum(VI) (**1**).

Experimental

Materials and methods

Chemicals used were of reagent grade. Maltol, kojic acid, amines, and 3-hydroxy-1,2-dimethyl-4-pyridinone were obtained from Aldrich Chemicals and molybdic acid was purchased from Strem. NMR spectra were recorded on a JEOL JNM-GSX270 FT-NMR spectrometer. ^1H NMR chemical shifts are reported in ppm and referenced to residual protons in $CDCl_3$, D_2O, and DMSO-d_6 at 270.05 MHz. $^{13}C\{^1H\}$ NMR chemical shifts are referenced to internal solvent peaks at 67.80 MHz. Multiplicities are reported as (s) singlet, (d) doublet, (t) triplet, (q) quartet, (m) multiplet, (br) broad, and (ov) overlapping. Infrared spectra were obtained with Nujol on KBr/NaCl plates using a Perkin–Elmer 710B and a Mattson Polaris spectrometer and are reported in cm^{-1}. Melting points were measured uncorrected with a Mel-Temp apparatus. Microanalyses for C, N, and H were carried out at Desert Analytics (Tucson, Ariz.).

Complex **1** (4*a*) and complex **3** (11*g*) were prepared by established methods using molybdic acid. Compounds Hhmp (5*d*), Hhnp (5*d*), Hbpp (5*d*), Hnpp (9*a*), and Hppp (12*b*) were all prepared by previously reported methods with slight modifications. Selected spectroscopic data for these ligands are reported as follows.

3-Hydroxy-6-hydroxymethyl-1-methyl-4-pyridinone, (Hhmp): mp 204°C (dec.); IR (Nujol): 870 (m), 1079 (w), 1129 (m), 1225 (w), 1268 (w), 1310 (m), 1454 (s), 1480 (m), 1552 (s), 1627 (m), 2964 (s), 3310 (br); $^{13}C\{^1H\}$ (in D_2O), δ: 43.2, 62.1, 116.5, 131.3, 148.4, 150.6, 173.3.

3-Hydroxy-6-hydroxymethyl-1-propyl-4-pyridinone, (Hhnp): mp 186°C (dec.); IR (Nujol): 722 (m), 859 (s), 972 (s), 1083 (s), 1131 (s), 1217 (s), 1270 (m), 1454 (s), 1463 (m), 1564 (m), 1643 (m), 2722 (m), 3178 (br); $^{13}C\{^1H\}$ (in D_2O), δ: 12.5, 26.3, 57.3, 62.0, 116.9, 130.1, 148.5, 150.1, 173.3.

Benzyl-3-hydroxy-2-methyl-4-pyridinone, (Hbpp): mp 204°C (dec.); IR (KBr): 855 (m), 1455 (m), 1500 (m), 1570 (s), 1620 (s), 3152 (m); $^{13}C\{^1H\}$ (in $CDCl_3$), δ: 12.2, 57.4, 111.3, 126.0, 128.5, 128.6, 129.5, 135.4, 137.8, 146.6, 170.0; ^1H δ: 2.27 (s, 3H), 4.72 (br s, 1H), 5.09 (s, 2H), 6.45 (d, J = 7 Hz, 1H), 7.01 (br d, J = 7 Hz, 2H), 7.31 (m, 4H).

3-Hydroxy-2-methyl-1-propyl-4-pyridinone, (Hnpp): mp 161°C (dec.); IR (Nujol): 844 (s), 1033 (m), 1223 (s), 1349 (m), 1462 (s), 1504 (m), 1571 (s), 1625 (s), 2971 (s), 3145 (br); $^{13}C\{^1H\}$ (in D_2O), δ: 12.5, 14.0, 25.9, 58.6, 114.8, 137.1, 141.0, 147.3, 171.1.

3-Hydroxy-2-methyl-1-phenyl-4-pyridinone, (Hppp): $^{13}C\{^1H\}$ (in $CDCl_3$), δ: 13.8, 111.2, 126.9, 128.9, 129.7, 130.1, 137.5, 141.9, 145.9, 170.4.

Preparation of *cis*-bis(5-hydroxy-2-hydroxymethyl-4-pyronato)dioxomolybdenum(VI), $MoO_2(ka)_2$, 2

To a stirred suspension of molybdic acid (0.25 g, 0.74 mmol) in 10 mL of water, a 10 mL aqueous solution of kojic acid (0.42 g, 2.96 mmol) was added dropwise. The addition of isopropanol to the solution resulted in the crystallization of white starting material. The yellow product was crystallized following further addition of isopropanol and was collected by suction filtration. The product was washed with ether (2 × 50 mL) and dried under vacuum. Yield: 0.22 g (36%) of a light yellow powder; mp 170°C (dec.). IR

© 1999 NRC Canada

(Nujol): 701 (s), 876 (m), 919 (m), 1154 (m), 1405 (s), 1520 (s), 1574 (m), 1647 (s), 3112 (m). NMR spectroscopic data (in DMSO-d_6): ^{1}H δ: 4.56 (s, 4H), 5.98 (s, 2H), 6.93 (s, 2H), 8.67 (s, 2H); ^{13}C{^{1}H} δ: 59.8, 106.9, 142.4, 154.1, 173.8, 179.3.

Preparation of *cis*-bis(3-hydroxy-6-hydroxymethyl-1-methyl-4-pyridinonato)dioxomolybdenum(VI), $MoO_2(hmp)_2$, 4

3-Hydroxy-6-hydroxymethyl-1-methyl-4-pyridinone (0.38 g, 2.45 mmol) was added as a solid to a 35 mL aqueous solution of molybdic acid (0.20 g, 0.59 mmol). After 24 h, the resulting yellow precipitate was collected by suction filtration and washed with water (3 × 10 mL) and methanol (2 × 10 mL). Yield 0.34 g (66%) of a yellow solid; mp 295°C (dec.). IR (KBr): 900 (s), 935 (s), 1100 (m), 1135 (m), 1255 (m), 1305 (s), 1380 (m), 1470 (s), 1515 (s), 1560 (s), 1620 (m), 3070 (w), 3390 (br). NMR spectroscopic data (in DMSO-d_6): ^{1}H δ: 3.77 (s, 6H), 4.48 (s, 4H), 5.82 (s, 2H), 6.53 (s, 2H), 7.67 (s, 2H); ^{13}C{^{1}H} δ: 41.2, 59.4, 108.9, 126.7, 149.4, 155.7, 172.0. Anal. calcd. for $MoO_8C_{14}H_{16}N_2$: C 38.55, H 3.70, N 6.42; found: C 38.42, H 3.90, N 6.29.

Preparation of *cis*-bis(3-hydroxy-2-methyl-1-propyl-4-pyridinonato)dioxomolybdenum(VI), $MoO_2(npp)_2$, 5

A 10 mL water solution of molybdic acid (0.16 g, 0.47 mmol) was cooled to 0°C in an ice–water bath. To this chilled solution, Hnpp (0.35 g, 2.10 mmol) was added in small portions as a solid. After 18 h of stirring, the solution was allowed to return to room temperature and the yellow precipitate collected by vacuum filtration. Complex **5** was recrystallized from a methylene chloride – hexane solution and collected by suction filtration. Yield: 0.33 g (76%) of a yellow solid; mp 283°C (dec.). IR (Nujol): 721 (w), 818 (w), 890 (w), 1268 (m), 1377 (m), 1462 (s), 1496 (m), 1551 (m), 1612 (w), 2940 (s). NMR spectroscopic data (in DMSO-d_6): ^{1}H δ: 0.89 (t, $J_{H–H}$ = 5 Hz, 6H), 1.73 (m, $J_{H–H}$ = 5 Hz, 4H), 2.50 (s, 6H), 4.08 (t, $J_{H–H}$ = 5 Hz, 4H), 6.47 (d, $J_{H–H}$ = 5 Hz, 2H), 7.87 (d, $J_{H–H}$ = 5 Hz, 2H); ^{13}C{^{1}H} δ: 10.4, 11.6, 23.3, 54.8, 108.3, 133.0, 137.7, 154.4, 169.6. Anal. calcd. for $MoO_6C_{18}H_{24}N_2$: C 46.95, H 5.25, N 6.09; found: C 46.60, H 5.35, N 5.95.

Preparation of *cis*-bis(3-hydroxy-6-hydroxymethyl-1-propyl-4-pyridinonato)dioxomolybdenum(VI), $MoO_2(hnp)_2$, 6

Solid Hhnp (0.12 g, 0.65 mmol) was added in small portions to a stirred 15 mL aqueous solution of molybdic acid (0.05 g, 0.15 mmol). After 18 h, a yellow precipitate was collected by vacuum filtration and washed with water (3 × 10 mL) and diethyl ether (3 × 10 mL). Yield: 0.07 g (47%) of a yellow solid; mp 238°C (dec.). IR (Nujol): 722 (s), 863 (m), 927 (m), 1106 (s), 1244 (s), 1290 (m), 1454 (s), 1537 (m), 1620 (m), 2883 (s). NMR spectroscopic data (in DMSO-d_6): ^{1}H δ: 0.92 (t, $J_{H–H}$ = 8 Hz, 6H), 1.77 (d, $J_{H–H}$ = 5 Hz, 4H), 4.02 (s, 4H), 4.50 (s, 4H), 5.76 (br s, 2H), 6.54 (s, 2H), 7.75 (s, 2H); ^{13}C{^{1}H} δ: 10.7, 23.9, 54.4, 59.2, 109.3, 125.3, 148.5, 155.8, 171.9. Anal. calcd. for $MoO_8C_{18}H_{24}N_2 \cdot 3H_2O$: C 39.56, H 5.53, N 5.13; found: C 40.04, H 5.63, N 5.19.

Preparation of *cis*-bis(1-benzyl-3-hydroxy-2-methyl-4-pyridinonato)dioxomolybdenum(VI), $MoO_2(bpp)_2$, 7

To a 25 mL aqueous solution of molybdic acid (0.14 g, 0.41 mmol), 1-benzyl-3-hydroxy-2-methyl-4-pyridinone (0.39 g, 1.81 mmol) was added as a solid in small portions. After 24 h, a yellow precipitate was collected by vacuum filtration and washed with water (2 × 10 mL) and methanol (3 × 10 mL). Yield: 0.38 g (83%) of a yellow solid; mp 295°C (dec.). IR (KBr): 830 (w), 895 (s), 930 (m), 1270 (s), 1360 (m), 1490 (s), 1550 (s), 1615 (m), 3170 (w). NMR spectroscopic data (in DMSO-d_6): ^{1}H δ: 2.27 (s, 6H), 5.46 (s, 4H), 6.58 (d, $J_{H–H}$ = 8 Hz, 2H), 7.12–7.44 (ov m, 10H), 8.06 (d, $J_{H–H}$ = 8 Hz, 2H). ^{13}C{^{1}H} δ: 12.2, 57.4, 108.9, 126.6, 128.2, 129.2, 133.6, 135.9, 139.0, 154.9, 170.3. Anal. calcd. for $MoO_6C_{26}H_{24}N_2$: C 56.12, H 4.35, N 5.03; found: C 56.06, H 4.40, N 5.00.

Synthesis of 1-benzyl-3-hydroxy-6-hydroxymethyl- 4-pyridinone, (Hhbp)

1-Benzyl-3-hydroxy-6-hydroxymethyl-4-pyridinone was prepared by modification of a known procedure (5*d*). Kojic acid (1.40 g, 9.85 mmol) was dissolved in a 3:1 mixture of water:ethanol (40 mL) whereupon benzylamine (1.50 g, 14.00 mmol) was added dropwise. The reaction mixture was heated to reflux under an atmosphere of dinitrogen for 12 h and then cooled to 5°C. After 3 h, a dark brown precipitate was collected by vacuum filtration and washed with water (2 × 10 mL) and methanol (3 × 10 mL). Yield: 0.24 g (11%) of light brown crystals; mp 258°C. IR (Nujol): 879 (m), 1124 (m), 1245 (m), 1377 (m), 1462 (s), 1518 (w), 1563 (m), 1643 (m), 2930 (s), 3196 (br). NMR spectroscopic data (in DMSO-d_6): ^{1}H δ: 4.28 (s, 2H), 5.19 (s, 2H), 6.29 (s, 1H), 7.13 (d, $J_{H–H}$ = 5 Hz, 2H), 7.35 (m, 3H), 7.48 (s, 1H); ^{13}C{^{1}H} δ: 54.2, 59.2, 112.2, 123.9, 126.3, 127.6, 128.8, 136.9, 146.8, 147.6, 170.8.

Preparation of *cis*-bis(1-benzyl-3-hydroxy-6-hydroxymethyl-4-pyridinonato)dioxomolybdenum(VI), $MoO_2(hbp)_2$, 8

1-Benzyl-3-hydroxy-6-hydroxymethyl-4-pyridinone (0.40 g, 1.73 mmol) was added in small portions to a stirred 15 mL aqueous solution of molybdic acid (0.13 g, 0.38 mmol). After 24 h, complex **8** had precipitated from solution and was collected by filtration and washed with water (3 × 10 mL) and methanol (2 × 15 mL). Yield: 0.40 g (89%) of a yellow solid; mp 240°C (dec.). IR (KBr): 895 (m), 924 (m), 1172 (m), 1248 (s), 1313 (m), 1468 (s), 1522 (s), 1563 (s), 1614 (s), 1642 (m), 3219 (br). NMR spectroscopic data (in DMSO-d_6): ^{1}H δ: 4.44 (t, $J_{H–H}$ = 16 Hz, 4H), 5.41 (s, 4H), 5.84 (br s, 2H), 6.66 (s, 2H), 7.18–7.42 (m, 10H), 7.85 (s, 2H); ^{13}C{^{1}H} δ: 55.7, 58.9, 109.9, 125.9, 126.6, 128.0, 128.7, 135.6, 149.2, 155.6, 172.2. Anal. calcd. for $MoO_8C_{26}H_{24}N_2 \cdot H_2O$: C 51.49, H 4.32, N 4.62; found: C 51.73, H 4.26, N 4.67.

Preparation of *cis*-bis(3-hydroxy-2-methyl-1-phenyl-4-pyridinonato)dioxomolybdenum(VI), $MoO_2(ppp)_2$, 9

To a stirred 30 mL aqueous solution of molybdic acid (0.20 g, 0.59 mmol), 3-hydroxy-2-methyl-1-phenyl-4-pyridinone (0.59 g, 2.93 mmol) was added in small portions as a solid. After 18 h, **9** precipitated from solution and was

© 1999 NRC Canada

collected by vacuum filtration. The resulting solid was washed with water (5 × 25 mL) and methanol (3 × 5 mL). Yield: 0.51 g (82%) of a yellow powder; mp 272°C. IR (Nujol): 895 (s), 1298 (s), 1365 (s), 1480 (s), 1515 (w), 1543 (s), 1610 (m), 2925 (s), 3058 (br). NMR spectroscopic data (in DMSO-d_6): ^{1}H δ: 2.09 (s, 6H), 6.64 (s, 2H), 7.61 (m, 10H), 7.90 (s, 2H); ^{13}C{^{1}H} δ: 13.8, 108.6, 126.7, 129.9, 133.3, 138.6, 141.2, 154.1, 170.9. Anal. calcd. for $MoO_6C_{24}H_{20}N_2$: C 54.55, H 3.82, N 5.30; found: C 54.11, H 4.02, N 5.21.

Synthesis of 3-hydroxy-6-hydroxymethyl-1-phenyl-4-pyridinone, (Hhpp)

Aniline was added dropwise (1.38 g, 14.82 mmol) to a 25 mL aqueous solution of kojic acid (1.00 g, 7.04 mmol). The reaction was heated to reflux for 96 h and was filtered hot to remove a black oil. After the mixture was allowed to stand for 18 h at 0°C a dark precipitate was collected and dissolved in 5 mL of methanol. Following the addition of 25 mL of water, a brown solid precipitated and was discarded. The filtrate was collected and solvent removed under vacuum to afford a red oil and dark solid. This mixture was dissolved in a minimum of hot methanol and cooled to 2°C. Within 18 h, Hhpp precipitated and was collected by suction filtration. Yield: 0.11 g (7%) of a light brown solid; mp 224°C. IR (Nujol): 703 (m), 854(m), 1152 (m), 1314 (m), 1488 (m), 1515 (m), 1573 (s), 1644 (s), 3057 (br), 3219 (br). NMR spectroscopic data (in DMSO-d_6): ^{1}H δ: 4.02 (s, 2H), 5.91 (br s, 1H), 6.47 (s, 1H), 7.32 (s, 1H), 7.48 (s, 2H), 7.53 (s, 3H); ^{13}C{^{1}H} δ: 59.2, 111.1, 123.6, 126.9, 129.3, 129.7, 140.7, 146.3, 148.2, 171.4. Isolation of Hhpp was problematic. This is presumably due to a significant amount of hydrogen bonding between aniline and the resulting pyridinone compound. Indeed, a pyridinone–aniline adduct (Hhpp·H_2NPh) could be isolated in certain instances from solutions of hot methanol. IR (Nujol): 700 (m), 745 (m), 863 (m), 1210 (m), 1307 (m), 1487 (m), 1515 (m), 1573 (s), 1640 (m), 3068 (br). NMR spectroscopic data (in DMSO-d_6): ^{1}H δ: 3.87 (d, J_{H-H} = 5 Hz, 2H), 6.25 (s, 1H), 6.34 (s, 1H), 6.52 (d, J_{H-H} = 8 Hz, 2H), 6.62 (t, J_{H-H} = 8 Hz, 1H), 7.12 (t, J_{H-H} = 8 Hz, 2H), 7.41 (s, 1H), 7.65 (s, 5H); ^{13}C{^{1}H} δ: 43.7, 111.0, 112.1, 116.5, 123.7, 127.0, 129.0, 129.4, 130.0, 140.8, 146.0, 146.3, 147.5, 171.0.

Preparation of *cis*-bis(3-hydroxy-6-hydroxymethyl-1-phenyl-4-pyridinonato)dioxomolybdenum(VI), $MoO_2(hpp)_2$, 10

To a stirred 10 mL aqueous solution of molybdic acid (0.02 g, 0.06 mmol), 3-hydroxy-6-hydroxymethyl-1-phenyl-4-pyridinone (0.06 g, 0.28 mmol) was added in small portions as a solid. After 18 h, **10** precipitated from solution and was collected by vacuum filtration. The solid was washed with water (5 × 25 mL) and methanol (3 × 5 mL). Yield: 0.03 g (45%) of a yellow solid; mp 261°C. IR (Nujol): 771 (m), 853 (m), 902 (m), 935 (m), 1163 (m), 1305 (s), 1523 (s), 1552 (s), 1590 (m), 1611 (m), 3205 (w). NMR spectroscopic data (in DMSO-d_6): ^{1}H δ: 4.09 (s, 4H), 5.68 (s, 2H), 6.73 (s, 2H), 7.60 (s, 8H), 7.72 (s, 2H); ^{13}C{^{1}H} δ: 59.2, 108.0, 125.7, 126.6, 129.8, 130.0, 140.2, 150.0, 155.1, 173.1. Anal. calcd. for $MoO_8C_{24}H_{20}N_2$: C 51.44, H 3.60, N 5.00; found: C 51.24, H 3.51, N 4.80.

X-ray crystallography

Crystal data for complexes **1**, **2**, and **9** are provided in Table 1. Data for **1** and **9** were collected on a Nicolet LT2 equipped Siemens P4 diffractometer using the ω method ($4° \leq 2\theta \leq 60°$). Data for **2** were collected on a Siemens SMART/CCD diffractometer equipped with an LT-II low-temperature device. The data were corrected for absorption by a faced-indexed analytical method. Three standard reflections every 100 showed no significant decay. The structures were solved by Patterson and Fourier methods, and refined by full-matrix least squares (SHELXTL IRIS). For complex **1**, the alternate polarity cell gave R and wR values of 0.0221 and 0.0251. A weighting scheme of $w^{-1} = \sigma^2(F)$ was used in the last cycles of refinement. All non-hydrogen atoms were refined anisotropically. Hydrogen atoms were located and refined using a riding model. Atomic coordinates, thermal parameters, bond lengths and angles, and alternate views of the complexes have been deposited as supplementary material.[4]

Animal model and induction of diabetes

Male Sprague–Dawley rats with an initial body weight of 200 g were used in this study. Diabetes was induced in ether-anesthetized rats by an intravenous injection of 60 mg/kg of streptozotocin freshly dissolved in 50 mM sodium citrate buffer, pH 4.5. Control animals received citrate buffer only. After 48 h, the induction of diabetes was confirmed by glucose testing in the urine using Keto-diastix (Ames). Animals were caged in groups of two and provided with food and water ad libitum until the time of experimentation. Animals used in this study were cared for according to the recommendations in the Canadian Council on Animal Care's Guide to the Care and Use of Experimental Animals.

Treatment protocol

After confirmation of diabetes, treatment was initiated by adding $MoO_2(ma)_2$ and sodium molybdate to the drinking water. Intake of compounds was determined on a molar basis adjusted for body weight over a 24 h period. During the 6 week treatment period, the average daily intake of $MoO_2(ma)_2$ by diabetic animals was 0.15 mmol/kg per 24 h and that of molybdate-treated diabetic animals was 0.13 mmol/kg per 24 h. Analytically pure $MoO_2(ma)_2$ was used in this study (Anal. calcd. for $MoO_8C_{12}H_{10}$: C 38.12, H 2.67; found: C 38.08, H 2.66). The pH of the drinking water was adjusted to 7.4 with sodium hydroxide. Under these conditions complex **1** formed a salt that could be recovered by titration with HCl (as ascertained by ^{1}H NMR spectroscopy). Treatment was initiated immediately following the

[4] A complete set of data may be purchased from: The Depository of Unpublished Data, Document Delivery, CISTI, National Research Council of Canada, Ottawa, ON K1A 0S2, Canada. Tables of atomic coordinates, bond distances and angles, and alternative views of the complexes have also been deposited with the Cambridge Crystallographic Data Centre, University Chemical Laboratory, 12 Union Road, Cambridge, CB2 1EZ, U.K.

© 1999 NRC Canada

Table 1. Crystallographic data for **1, 2,** and **9**.

Complex	**1**	**2**	**9**
Formula	$C_{12}H_{10}MoO_8 \cdot CH_2Cl_2$	$C_{12}H_{10}MoO_{10}$	$C_{24}H_{20}MoN_2O_6 \cdot (CH_3)_2CO$
Crystal system	Orthorhombic	Monoclinic	Monoclinic
fw	463.1	410.14	586.4
Space group	$Pca2_1$	$P2_1/c$	$P2_1/n$
a, Å	12.107(1)	8.4591(5)	10.9476(6)
b, Å	8.6169(8)	16.3453(10)	13.5353(9)
c, Å	16.472(1)	10.2954(7)	17.4877(10)
β		103.0320(10)	93.465(4)
V, Å^3	1718.4(3)	1386.8(2)	2586.6(3)
Z	4	4	4
D_{calcd} g cm^{-3}	1.790	1.964	1.506
Size, mm	0.58{100} × 0.60{010} × 0.42{001}	0.04 × 0.4 × 0.4	0.21(1$\bar{1}$0)($\bar{1}$10) × .36{101} × 0.38{10$\bar{1}$} × 0.40{001}
Temperature, K	160	293	180
μ, cm^{-1}	11.11	10.01	5.56
Max 2θ, deg	60	27.90	56.0
Reflections:			
Measured	2580	8458	6540
Observed[a]	2466	3214	4747
Parameters	229	216	390
Data collection method	ω	ω	ω
Max. res. density/hole, e Å^{-3}	0.45/–0.41	0.555/–0.762	0.35/–0.36
R[b]	0.0210	0.0288	0.0255
R_w	0.0237	0.0862	0.0290
GoF	2.69	0.713	1.93

[a] $F_o > 6\sigma(F_o)$.

[b] $R = \Sigma||F_o| - |F_c||/\Sigma|F_o|$; $Rw = [\Sigma(w(|F_o| - |F_c|)^2/\Sigma(w|F_o|)^2]^{1/2}$.

confirmation of diabetes for a 6 week period. Control animals received water only.

Heart perfusions

Following treatment, hearts from sodium pentobarbital-anesthetized rats were quickly excised, placed in ice-cold buffer and immediately perfused retrogradely via the aorta with Krebs–Henseleit buffer containing 11 mM glucose and 1.75 mM Ca^{2+} (pH 7.4, gassed with 95% O_2 – 5% CO_2). During this perfusion, the hearts were trimmed of excess tissue, the pulmonary arteries were cut, and the openings of the left atria were cannulated. Hearts were then switched to the working mode and perfused at a 15 cm H_2O left atrial filling pressure and 100 cm H_2O hydrostatic aortic afterload in a recirculating buffer system containing 11 mM glucose and 1.2 mM palmitate prebound to 3% bovine serum albumin. Hearts were initially perfused under aerobic conditions for a 15 min period. Global ischemia was induced by clamping off both aortic and preload lines for a period of 25 min. Following ischemia, flow was restored and hearts were allowed to recover for a further 30 min period. Throughout the perfusion, heart rate and aortic pressure development were recorded using a Biotronix pressure recorder (model BL630) interfaced with a Biotronix chart recording system (model BL882). Aortic flow was measured by timed collections. At the end of the reperfusion period, hearts were rapidly frozen with clamps cooled to the temperature of liquid nitrogen, and stored at –80°C.

Fig. 1. Synthesis of molybdenum hydroxypyrone and hydroxypyridinone complexes.

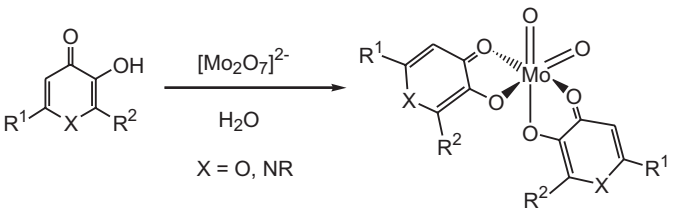

Statistical analysis

A one-way analysis of variance, followed by the Newman–Keuls test, was used to determine statistical significance for comparisons between group means. A value of $p < 0.05$ was considered significant. All data are reported as mean ± S.E.M.

Results and discussion

Hydroxypyrone complexes

$MoO_2(ma)_2$ (**1**, ma = maltolato) is readily prepared in high yield (87%) from addition of maltol to molybdic acid, $(NH_4)_2Mo_2O_7$, in aqueous solutions at neutral pH (Fig. 1, ref. 4*a*). IR and NMR spectroscopic data are consistent with a *cis*-dioxo complex containing two chelating maltolato ligands. Analogous reactions with kojic acid afford the corresponding complex, $MoO_2(ka)_2$ (**2**), in much lower yields (36%). Both **1** and **2** are yellow crystalline complexes, stable indefinitely in the solid state and relatively soluble in water.

© 1999 NRC Canada

Table 2. Atomic coordinates ($\times 10^4$) and equivalent isotropic displacement parameters ($Å^2 \times 10^3$) for **1** and **2**. U(eq) is defined as one third of the trace of the orthogonalized U_{ij} tensor.

	x	*y*	*z*	*U*(eq)
Compound 1				
Mo(1)	3148.9(2)	2171.0(2)	2500	181.2(5)
O(1)	1935(1)	1167(2)	2499(2)	251(5)
O(2)	3812(2)	1581 (3)	1646(1)	259(6)
O(3)	4370(2)	4037(2)	2690(1)	248(6)
O(4)	2382(2)	4096(2)	2130(1)	230(5)
O(5)	2744(2)	3009(2)	3754(1)	249(6)
O(6)	4128(2)	948(2)	3225(1)	225(5)
O(7)	3218(2)	8048(3)	1788(2)	419(9)
O(8)	4391(2)	401(4)	5374(2)	435(9)
C(1)	4054(2)	5345(3)	2419(2)	234(7)
C(2)	2963(2)	5420(3)	2094(2)	236(8)
C(3)	2562(3)	6761(4)	1786(2)	342(9)
C(4)	4235(3)	8004(4)	2088(3)	438(12)
C(5)	4690(2)	6720(3)	2401(3)	329(10)
C(6)	1465(3)	7015(5)	1416(3)	547(15)
C(7)	3241(2)	2238(3)	4295(2)	220(8)
C(8)	4007(2)	1085(3)	4029(2)	201(7)
C(9)	4570(3)	198(4)	4566(2)	289(8)
C(10)	3676(3)	1452(6)	5635(2)	480(13)
C(11)	3098(3)	2410(5)	5143(2)	362(10)
C(12)	5377(3)	–1044(5)	4380(2)	405(12)
C(13)	1430(3)	6237(4)	3993(2)	405(11)
Cl(1)	902(1)	5817(2)	4961(1)	666(4)
Cl(2)	2352(1)	7804(2)	4016(1)	773(5)
Compound 2				
Mo(1)	3747(1)	1260(1)	7138(1)	36(1)
O(1)	3327(3)	398(1)	8388(2)	41(1)
O(2)	2139(2)	1870(1)	8370(2)	35(1)
O(3)	1692(3)	325(1)	11315(2)	45(1)
O(4)	–440(3)	1964(1)	12480(2)	47(1)
O(5)	4266(2)	2405(1)	6757(2)	38(1)
O(6)	5504(2)	1668(1)	8986(2)	38(1)
O(7)	6711(3)	4018(1)	8548(2)	44(1)
O(8)	8818(4)	3891(2)	11944(3)	71(1)
O(9)	5217(3)	701(1)	6675(3)	57(1)
O(10)	2140(3)	1216(2)	5817(2)	58(1)
C(1)	2584(3)	598(2)	9360(3)	35(1)
C(2)	2440(4)	89(2)	10340(3)	43(1)
C(3)	1055(3)	1080(2)	11302(3)	36(1)
C(4)	1122(3)	1629(2)	10333(3)	34(1)
C(5)	1917(3)	1412(2)	9312(3)	32(1)
C(6)	327(4)	1211(2)	12489(3)	47(1)
C(7)	5270(3)	2833(2)	7700(3)	33(1)
C(8)	5709(4)	3618(2)	7547(3)	43(1)
C(9)	7314(3)	3646(2)	9716(3)	36(1)
C(10)	6965(3)	2856(2)	9942(3)	35(1)
C(11)	5925(3)	2416(2)	8928(3)	31(1)
C(12)	8359(4)	4218(2)	10682(3)	50(1)

Increased solubility observed for **2** in aqueous solutions presumably arises due to the pendant CH_2OH group on the pyrone ring. Unlike the maltol derivative, however, **2** decomposes in water at elevated temperatures to give a mixture of molybdates.

As with **1** (4*a*), the IR spectrum for **2** shows that the strong band at 1660 cm^{-1}, assigned as mainly ν(C=O) in kojic acid, decreases in intensity and shifts to a lower wavenumber (1647 cm^{-1}) upon coordination to the d^0 metal centre. Likewise, the bands at 1611 cm^{-1} (strong) and 1578 cm^{-1} (medium), belonging to the strongly mixed ν(C=C) and ν(C=O) modes in pyrones (3*a*, 4*a*), also shift to lower energies upon complexation and are observed at 1574 cm^{-1} and 1520 cm^{-1}, respectively. The band at

© 1999 NRC Canada

Table 3. Selected bond lengths (Å) and angles (°) for **1**.

Bond lengths			
Mo(1)—O(1)	1.705(2)	Mo(1)—O(2)	1.697(2)
Mo(1)—O(3)	2.207(2)	Mo(1)—O(4)	1.997(2)
Mo(1)—O(5)	2.242(2)	Mo(1)—O6)	1.986(2)
O(3)—C(1)	1.207(3)	O(4)—C(2)	1.341(3)
O(5)—C(7)	1.265(4)	O(6)—C(8)	1.336(4)
O(7)—C(3)	1.364(4)	O(7)—C(4)	1.327(5)
O(8)—C(9)	1.360(4)	O(8)—C(10)	1.325(5)
C(1)—C(2)	1.427(4)	C(1)—C(5)	1.413(4)
C(2)—C(3)	1.353(4)	C(3)—C(6)	1.477(6)
C(4)—C(5)	1.339(5)	C(7)—C(8)	1.428(4)
C(7)—C(11)	1.414(5)	C(8)—C(9)	1.353(4)
C(9)—C(12)	1.481(5)	C(10)—C(11)	1.353(6)
Bond angles			
O(1)-Mo(1)-O(2)	104.8(1)	O(1)-Mo(1)-O(3)	161.3(1)
O(2)-Mo(1)-O(3)	91.1(1)	O(1)-Mo(1)-O(4)	91.2(1)
O(2)-Mo(1)-O(4)	102.5(1)	O(3)-Mo(1)-O(4)	75.5(1)
O(1)-Mo(1)-O(5)	88.6(1)	O(2)-Mo(1)-O(5)	164.4(1)
O(3)-Mo(1)-O(5)	77.4(1)	O(4)-Mo(1)-O(5)	85.0(1)
O(1)-Mo(1)-O(6)	104.2(1)	O(2)-Mo(1)-O(6)	93.3(1)
O(3)-Mo(1)-O(6)	84.3(1)	O(4)-Mo(1)-O(6)	154.5(1)
O(5)-Mo(1)-O(6)	75.4(1)	Mo(1)-O(3)-C(1)	113.3(2)
Mo(1)-O(4)-C(2)	118.4(2)	Mo(1)–O(5)-C(7)	112.1(2)
Mo(1)-O(6)-C(8)	118.9(2)		

Fig. 2. The molecular structure of $MoO_2(ma)_2$, **1**.

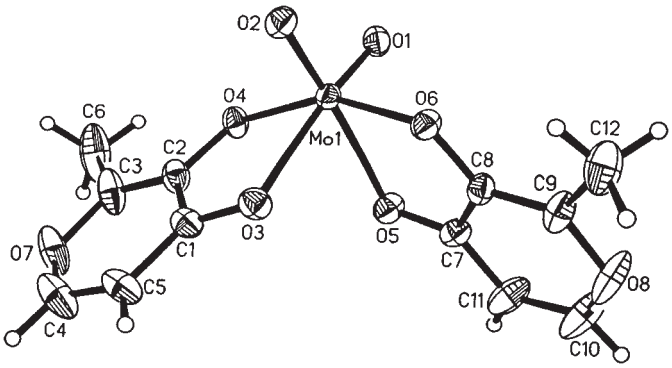

Fig. 3. The molecular structure of $MoO_2(ka)_2$, **2**.

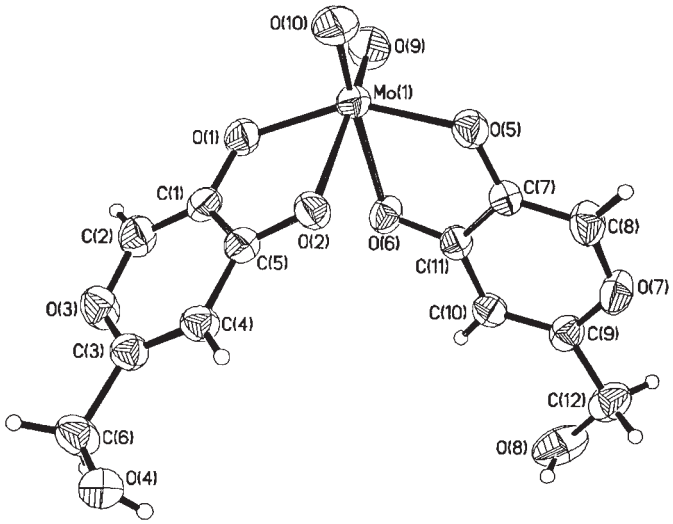

3168 cm^{-1} for the OH stretches of kojic acid is observed at 3122 cm^{-1} for **2**. The two strong IR bands present at 919 and 890 cm^{-1} assigned to ν_s (Mo=O) and ν_{as}(Mo=O) are similar to those reported previously for **1** and for the tropolone complex, *cis*-$MoO_2(trop)_2$ (12). The wavenumbers observed in kojic acid and its metal derivatives are lower than those for the maltol derivatives, presumably because of the electron-withdrawing nature of the hydroxymethyl group as opposed to the electron-donating ability of the methyl group in maltol (5*b*).

The proton NMR spectra of **2** in D_2O indicates a pair of broad singlets at δ 6.67 and 7.87 due to the ring CH protons. The singlet at 6.67 ppm is shifted downfield by 0.23 ppm in comparison with kojic acid while the other ring proton is shifted upfield by 0.06 ppm. The exocyclic methylene protons of the hydroxymethyl group appear as a singlet at δ 4.42 in **2** while the chemical shift of the analogous protons in starting pyrone appear at δ 4.73.

Single crystals of **1** were grown from a wet methylene chloride solution cooled to 5°C and those for **2** grown from a H_2O–i-PrOH mixture. An X-ray diffraction study of **1** was carried out to determine unequivocally the nature of the compound about to undergo biological testing. The molecular structures of $MoO_2(ma)_2$ and $MoO_2(ka)_2$ are depicted in Figs. 2 and 3, respectively, and crystallographic data for both compounds are given in Table 1. Atomic coordinates and displacement parameters for **1** and **2** are given in Table 2. Selected bond distances and angles for **1** and **2** are provided in Tables 3 and 4, respectively. The coordination sphere about the molybdenum atoms in both cases consists of six oxygen atoms arranged in a distorted octahedral geometry. The molecular structures confirm a *cis* arrangement of dioxo

© 1999 NRC Canada

Table 4. Selected bond lengths (Å) and angles (°) for **2**.

Bond lengths			
Mo(1)—O(10)	1.694(2)	Mo(1)—O(9)	1.695(2)
Mo(1)—O(5)	1.981(2)	Mo(1)—O(1)	1.994(2)
Mo(1)—O(6)	2.236(2)	Mo(1)—O(2)	2.286(2)
O(1)—C(1)	1.337(3)	O(2)—C(5)	1.272(3)
O(3)—C(3)	1.346(3)	O(3)—C(2)	1.357(4)
O(4)—C(6)	1.390(4)	O(5)—C(7)	1.335(3)
O(6)—C(11)	1.278(3)	O(7)—C(9)	1.342(3)
O(7)—C(8)	1.346(4)	O(8)—C(12)	1.378(5)
C(1)—C(2)	1.334(4)	C(1)—C(5)	1.442(3)
C(3)—C(4)	1.352(4)	C(3)—C(6)	1.503(4)
C(4)—C(5)	1.416(4)	C(7)—C(8)	1.355(4)
C(7)—C(11)	1.433(4)	C(9)—C(10)	1.355(4)
C(9)—C(12)	1.499(4)	C(10)—C(11)	1.403(4)
Bond angles			
O(10)-Mo(1)-O(9)	104.95(13)	O(10)-Mo(1)-O(5)	93.15(10)
O(9)-Mo(1)-O(5)	104.13(10)	O(10)-Mo(1)-O(1)	105.10(10)
O(9)-Mo(1)-O(1)	92.82(10)	O(5)-Mo(1)-O(1)	151.05(8)
O(10)-Mo(1)-O(6)	162.77(10)	O(9)-Mo(1)-O(6)	90.64(10)
O(5)-Mo(1)-O(6)	75.65(7)	O(1)-Mo(1)-O(6)	80.94(8)
O(10)-Mo(1)-O(2)	89.64(10)	O(9)-Mo(1)-O(2)	162.99(10)
O(5)-Mo(1)-O(2)	83.36(7)	O(1)-Mo(1)-O(2)	74.64(7)
O(6)-Mo(1-O(2)	76.26(7)	C(1)–O(1)-Mo(1)	119.5(2)
C(5)-O(2)-Mo(1)	112.0(2)	C(3)–O(3)-C(2)	120.3(2)
C(7)-O(5)-Mo(1)	119.0(2)	C(11)–O(6)-Mo(1)	112.6(2)
C(9)-O(7)-C(8)	120.8(2)	C(2)-C(1)-O(1)	123.6(2)
C(2)-C(1)-C(5)	119.9(3)	O(1)-C(1)-C(5)	116.5(2)
C(1)-C(2)–O(3)	121.4(3)	O(3)-C(3)-C(4)	122.2(2)
O(3)-C(3)-C(6)	111.0(2)	C(4)-C(3)-C(6)	126.8(3)

Fig. 4. Hydroxypyrone and hydroxypyridinone ligands and metal complexes.

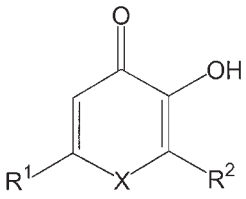

				Molybdenum Complex	
Pyrones					
R^1 = H	R^2 = CH_3	X = O	(Hma)	$MoO_2(ma)_2$	(**1**)
R^1 = CH_2OH	R^2 = H	X = O	(Hka)	$MoO_2(ka)_2$	(**2**)
Pyridinones					
R^1 = H	R^2 = CH_3	X = NMe	(Hdpp)	$MoO_2(dpp)_2$	(**3**)
R^1 = CH_2OH	R^2 = H	X = NMe	(Hhmp)	$MoO_2(hmp)_2$	(**4**)
R^1 = H	R^2 = CH_3	X = N-*n*-C_3H_7	(Hnpp)	$MoO_2(npp)_2$	(**5**)
R^1 = CH_2OH	R^2 = H	X = N-*n*-C_3H_7	(Hhnp)	$MoO_2(hnp)_2$	(**6**)
R^1 = H	R^2 = CH_3	X = NCH_2Ph	(Hbpp)	$MoO_2(bpp)_2$	(**7**)
R^1 = CH_2OH	R^2 = H	X = NCH_2Ph	(Hhbp)	$MoO_2(hbp)_2$	(**8**)
R^1 = H	R^2 = CH_3	X = NPh	(Hppp)	$MoO_2(ppp)_2$	(**9**)
R^1 = CH_2OH	R^2 = H	X = NPh	(Hhpp)	$MoO_2(hpp)_2$	(**10**)

ligands as predicted by extended spectroscopic data and Hückel calculations (13). The Mo=O bond lengths (avg. = 1.701 (2) Å, **1**; avg. = 1.695 (2) Å, **2**) are comparable to those found in other oxomolybdenum(VI) complexes (14). The two ketonic oxygen atoms of the pyrone moieties are *trans* to the oxo ligands and the stronger field hydroxyl oxygens are *trans* to one another. Similar coordination environments have been observed previously in analogous vanadium–maltol (15) and iron – kojic acid complexes (5*d*).

As expected, a slight lengthening of the ketone C=O bond is observed upon complexation, with a mean distance of 1.268 (4) Å in **1** and 1.275 (3) Å in **2** compared with 1.244 Å found in free kojic acid (16). The molybdenum–oxygen (ketone) bond in this case is somewhat longer (avg. = 2.225 (2) Å, **1**; avg. = 2.261 (2) Å, **2**) than the Mo – deprotonated oxygen distance, the average being only 1.992 (2) Å in **1** and 1.989 (2) Å in **2**. This observation provides a distinction between Lewis acid–base versus covalent bonding for these two types of oxygen atoms. It is interesting to note that the ketone oxygen–molybdenum bond length is slightly longer in **2** than in **1**, indicating weaker bonding interaction for this hydroxypyrone. Low metal-binding constants have been reported previously for kojic acid derivatives (5*c*). Interestingly, average C(6)—O(4) bond lengths of 1.384 (5) Å observed for the hydroxymethyl groups in **2** are somewhat shorter than those seen in kojic acid (1.406 Å), presumably due to a slight reduction in the degree of intermolecular hydrogen bonding for the molybdenum complex. Indeed, O–H···O interactions in **2** occur at 2.887 and 3.069 Å, while distances of 1.87 and 2.08 Å are reported for kojic acid.

Hydroxypyridinone complexes

A series of *N*-substituted 3-hydroxy-4-pyridinones were readily prepared (Fig. 4) from the addition of primary amine ($MeNH_2$, *n*-$PrNH_2$, $PhCH_2NH_2$, and $PhNH_2$) and either maltol (9) or kojic acid (5*d*). Functionalization of the ring

© 1999 NRC Canada

Table 5. Atomic coordinates (× 10^4) and equivalent isotropic displacement parameters (Å^2 × 10^3) for **9**. *U*(eq) is defined as one third of the trace of the orthogonalized U_{ij} tensor.

	x	*y*	*z*	*U*(eq)
Mo(1)	5232.4(2)	733.9(1)	2715.4(1)	21.49(5)
O(1)	6479(1)	829(1)	3344.8(9)	30.4(5)
O(2)	4160(2)	150(1)	3224.1(9)	30.6(5)
O(3)	4011(1)	442(1)	1676.1(9)	24.6(5)
O(4)	6079(1)	–326(1)	2153.2(9)	23.0(5)
O(5)	6050(1)	1697(1)	1869.4(9)	24.5(5)
O(6)	4444(1)	2058(1)	2850.2(9)	24.8(5)
C(1)	4415(2)	–238(2)	1243(1)	21.6(6)
C(2)	5560(2)	–672(2)	1491(1)	21.2(6)
C(3)	6093(2)	–1398(2)	1081(1)	23.0(6)
N(4)	5471(2)	–1731(1)	422(1)	24.9(6)
C(5)	4376(2)	–1336(2)	165(1)	28.6(7)
C(6)	3842(2)	–594(2)	557(1)	26.6(7)
C(7)	5954(2)	–2573(2)	17(1)	26.2(7)
C(8)	5827(3)	–3505(2)	323(2)	40.4(9)
C(9)	6335(3)	4303(2)	–28(2)	48(1)
C(10)	6975(2)	4168(2)	–679(1)	38.2(8)
C(11)	7066(2)	–3240(2)	–988(1)	34.8(8)
C(12)	6551(2)	–2428(2)	–641(1)	29.4(8)
C(13)	7323(2)	–1812(2)	1316(1)	33.4(8)
C(14)	5812(2)	2619(2)	1967(1)	20.0(6)
C(15)	6343(2)	3410(2)	1591 (1)	23.0(7)
C(16)	6054(2)	4349(2)	1787(1)	25.0(7)
N(17)	5219(2)	4550(1)	2316(1)	21.5(5)
C(18)	4638(2)	3802(2)	2690(1)	21.3(7)
C(19)	4939(2)	2846(2)	2517(1)	20.4(6)
C(20)	4965(2)	5587(2)	2462(1)	23.3(7)
C(21)	3808(2)	5965(2)	2283(1)	29.8(7)
C(22)	3598(2)	6965(2)	2385(2)	35.2(8)
C(23)	4537(3)	7570(2)	2658(2)	38.0(9)
C(24)	5685(3)	7185(2)	2834(2)	40.7(9)
C(25)	5911(2)	6183(2)	2742(1)	31.1(8)
C(26)	3736(2)	4049(2)	3273(1)	31.8(8)
50:50 disordered acetone of solvation				
O(7A)	3184(8)	2746(7)	5291(5)	87(3)
O(7B)	2927(9)	2101(10)	5049(7)	154(7)
C(27A)	4131 (22)	2515(18)	5189(10)	98(8)
C(27B)	4009(20)	1931(17)	5064(10)	85(7)
C(28A)	4695(22)	1537(15)	5070(10)	148(11)
C(28B)	4394(17)	884(8)	5180(8)	93(5)
C(29A)	5096(10)	3322(11)	5277(6)	112(6)
C(29B)	5017(14)	2573(12)	4912(8)	101(5)

nitrogen in the hydroxypyridinones allows for fine tuning of physical properties such as water solubility, hydrolytic stability, and lipophilicity without compromising thermodynamic binding constants (9*b*). Indeed, the corresponding pyridinone complexes are somewhat less water soluble and slightly more lipophilic than the pyrone complexes **1** and **2**. For instance, although the N–Me complex $MoO_2(dpp)_2$ **3** is only sparingly soluble in dimethyl sulfoxide, the kojic acid – aniline derivative **10** is readily soluble in methylene chloride. While metal complexes containing *N*-substituted 3-hydroxy-4-pyridinones are well known (2*b*, 8*c*–8*d*, 9, 11), the only molybdenum complex reported containing these biologically relevant ligands is the 3-hydroxy-1,2-dimethyl- 4-pyridinone (Hdpp) derivative, $MoO_2(dpp)_2$ **3** (11*g*).

Upon complexation with molybdenum, the four-band infrared spectral pattern between 1400 and 1610 cm^{-1}, characteristic of pyrone and pyridinone ligands (4*a*, 17), is also observed, along with an expected bathochromatic shift. These four bands are assigned collectively as ν(C=C) and ν(C=O). Of the four possible isomers for complexes of the type *cis*-MoO_2L_2 (18), the most likely isomer is the one in which both ketone oxygens of the pyridinone ligands are *trans* to the molybdenum oxo groups (13). A single-crystal X-ray diffraction study was carried out on the 3-hydroxy- 2-methyl-1-phenyl-pyridinone derivative **9** to confirm this assignment.

The molecular structure of **9** is shown in Fig. 5, atomic coordinates and displacement parameters in Table 5, and

© 1999 NRC Canada

Table 6. Selected bond lengths (Å) and angles (°) for **9**.

Bond lengths			
Mo(1)—O(1)	1.705(2)	Mo(1)—O(2)	1.709(2)
Mo(1)—O(3)	2.226(2)	Mo(1)—O(4)	1.999(2)
Mo(1)—O(5)	2.202(2)	Mo(1)—O(6)	2.009(1)
O(3)—C(1)	1.287(3)	O(4)—C(2)	1.343(3)
O(5)—C(14)	1.288(3)	O(6)—C(19)	1.345(3)
C(1)—C(2)	1.427(3)	C(1)—C(6)	1.406(3)
C(2)—C(3)	1.369(3)	C(3)—N(4)	1.379(3)
C(3)—C(13)	1.493(3)	N(4)—C(5)	1.364(3)
N(4)—C(7)	1.458(3)	C(5)—C(6)	1.367(3)
C(7)—C(8)	1.380(3)	C(7)—C(12)	1.372(3)
C(8)—C(9)	1.376(4)	C(9)—C(10)	1.386(4)
C(10)—C(11)	1.373(4)	C(11)—C(12)	1.391(4)
C(14)—C(15)	1.401(3)	C(14)—C(19)	1.430(3)
C(15)—C(16)	1.359(3)	C(16)—N(17)	1.366(3)
N(17)—C(18)	1.380(3)	N(17)—C(20)	1.457(3)
C(18)—C(19)	1.373(3)	C(18)—C(26)	1.500(3)
C(20)—C(21)	1.385(3)	C(20)—C(25)	1.379(3)
C(21)—C(22)	1.386(3)	C(22)—C(23)	1.377(4)
C(23)—C(24)	1.378(4)	C(24)—C(25)	1.390(4)
Bond angles			
O(1)-Mo(1)-O(2)	104.3(1)	O(1)-Mo(1)-O(3)	163.4(1)
O(2)-Mo(1)-O(3)	86.9(1)	O(1)-Mo(1)-O(4)	89.7(1)
O(2)-Mo(1)-O(4)	106.1(1)	O(3)-Mo(1)-O(4)	75.2(1)
O(1)-Mo(1)-O(5)	92.7(1)	O(2)-Mo(1)-O(5)	160.6(1)
O(3)-Mo(1)-O(5)	78.7(1)	O(4)-Mo(1)-O(5)	82.8(1)
O(1)-Mo(1)-O(6)	100.9(1)	O(2)-Mo(1)-O(6)	92.2(1)
O(3)-Mo(1)-O(6)	90.7(1)	O(4)-Mo(1)-O(6)	156.0(1)
O(5)-Mo(1)-O(6)	75.3(1)	Mo(1)-O(3)-C(1)	113.3(1)
Mo(1)-O(4)-C(2)	119.3(1)	Mo(1)-O(5)-C(14)	113.0(1)
Mo(1)-O(6)-C(19)	118.0(1)	O(3)-C(1)-C(2)	116.3(2)
O(3)-C(1)-C(6)	126.6(2)	C(2)-C(1)-C(6)	117.1(2)
O(4)-C(2)-C(1)	115.9(2)	O(4)-C(2)-C(3)	122.0(2)
C(1)-C(2)-C(3)	122.1(2)	C(2)-C(3)-N(4)	117.9(2)
C(2)-C(3)-C(13)	122.1(2)	N(4)-C(3)-C(13)	120.0(2)
C(3)-N(4)-C(5)	121.8(2)	C(3)-N(4)-C(7)	119.1(2)
C(5)-N(4)-C(7)	119.0(2)	N(4)-C(5)-C(6)	121.1(2)
C(1)-C(6)-C(5)	119.9(2)	N(4)-C(7)-C(8)	118.6(2)
N(4)-C(7)-C(12)	120.0(2)	C(8)-C(7)-C(12)	121.4(2)
C(7)-C(8)-C(9)	119.4(3)	C(8)-C(9)-C(10)	120.1(3)

Fig. 5. The molecular structure of $MoO_2(ppp)_2$, **9**.

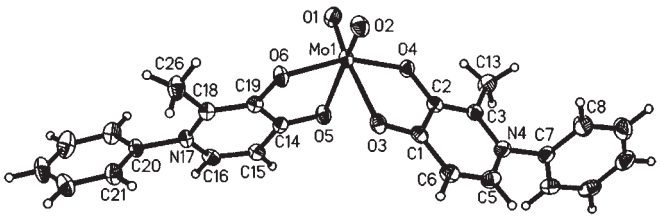

bond distances and angles are provided in Table 6. Similar Mo—O bond distances are observed in **9** and the parent pyrone complex **1**. The bond distances within the pyridinone ring also display trends similar to those described for **1** and other metal–pyridinone complexes (11). A pronounced localization of the formal double bonds in the ring, albeit to a lesser extent than that observed for the pyrone systems, is clearly indicated by the short C(2)—C(3), C(5)—C(6), and ketone C(1)—O(3) bonds. Resonance forms for pyridinone ligands have been described in detail elsewhere (11, 19). A N(4)—C(7) bond distance of 1.458 (3) Å, however, is slightly shorter than that reported for the free ligands 3-hydroxy-1-*p*-methoxyphenyl-2-methyl-4-pyridinone (cf. 1.474 (1) Å) (19) and 3-hydroxy-1,2-dimethyl-4-pyridinone (cf. 1.482 (4) Å) (20). Average C-N-C angles of 120.0° are similar to those reported earlier (11, 19, 20).

Biological relevance

We have begun our investigation into the effect of molybdenum complexes on heart function in diabetic rats and report our findings herein. Initial work was conducted using **1**, the molybdenum analogue of BMOV, because of the efficacy of this latter compound as an insulin mimic, along with the control (10) sodium molybdate, Na_2MoO_4. Confirming the diabetic state, plasma glucose and free fatty acid levels

© 1999 NRC Canada

Table 7. Physical characteristics and blood profile of control and diabetic rats.

Group	Glucose (mM)	Free fatty acids (mM)	Body weight (g)	Fluid intake (mL/kg per 24 h)
Control	6.1 ± 0.1	0.37 ± 0.04	492 ± 8	43 ± 2
Diabetic	23.2 + 1.5[a,c]	0.51 + 0.09[a,c]	291 + 19[a]	163 + 22[a,c]
+ molybdate	13.2 + 1.4[a,b]	0.17 + 0.02[a,b]	286 + 12[a]	90 + 12[a,b]
+ $MoO_2(ma)_2$	16.3 + 1.3[a,b]	0.13 + 0.02[a,b]	328 + 17[a]	115 + 13[a,b]

Values are presented as mean ± S.E.M. for six to eight animals in each group. Average daily intake of $MoO_2(ma)_2$ by diabetic animals was 0.15 mmol/kg per 24 h, whereas that of molybdate was 0.13 mmol/kg per 24 h.

[a]Significant vs. control.

[b]Significant vs. diabetic.

[c]Significant vs. diabetic treated with molybdate.

Table 8. Effects of $MoO_2(ma)_2$ and sodium molybdate treatment on heart function.

Perfusion condition	HR (beats/min)	PSP (mmHg)	RPP (beats mmHg $min^{-1)}$	DP (mmHg)	AF (mL/min)
Aerobic perfusion					
Control	250 ± 8	92 ± 5	23 ± 1	59 ± 2	42 ± 4
Diabetic	200 ± 13[a]	94 ± 4	19 ± 1[a]	63 ± 2	20 ± 3[a]
+ molybdate	243 ± 20	97 ± 3	23 ± 2	62 ± 3	36 ± 4[b]
+$MoO_2(ma)_2$	214 ± 12	87 ± 5	18 ± 1	63 ± 4	17 ± 3[a,c]
Reperfusion following ischemia					
Control	190 ± 21	87 ± 9	16 ± 2	57 ± 5	16 ± 6
Diabetic	164 ± 25	74 ± 11	14 ± 2	61 ± 9	6 ± 2[a]
+ molybdate	235 ± 11	94 ± 3	22 ± 1	64 ± 2	25 ± 3[b]
+ $MoO_2(ma)_2$	114 ± 14[c]	45 ± 16[c]	9 ± 3[c]	35 ± 12	3 ± 2[ac]

Values are presented as mean ± S.E.M. for six to eight animals in each group. HR, heart rate; PSP, peak systolic pressure; RPP, heart rate pressure product; DP, diastolic pressure; AF, aortic flow. Hearts were perfused under aerobic conditions for 15 min, then subjected to 25 min of global ischemia followed by 30 min of aerobic reperfusion. Reperfusion data obtained at the end of the 30 min.

[a]Significant vs. control.

[b]Significant vs. diabetic.

[c]Significant vs. diabetic treated with molybdate.

were markedly elevated in the diabetic rats (Table 7). Body weight, as expected, was lower in diabetic rats than in the controls. Food and fluid intake was maintained during the 6 week period. Treatment of diabetic animals with either sodium molybdate or $MoO_2(ma)_2$ (**1**) significantly reduced levels of plasma glucose but proved to have weaker insulin-like effects when compared to BMOV (4*h*, 5, 6). It is interesting to observe that treatment with $MoO_2(ma)_2$ and sodium molybdate also reduced plasma glucose and free fatty acid levels in diabetic rats. Rats treated with both molybdenum complexes suffered from initial weight loss although those given complex **1** gained weight at the end of the treatment. No animals suffered from diarrhea and all survived treatment with these molybdenum complexes.

The 6 week period of diabetes was selected because alterations in heart function occur within this period (21–23). As shown in Table 8, if hearts from diabetic rats are perfused under aerobic conditions, significant differences in function are noted. Diabetic rat hearts show a significant depression in rate–pressure product as a result of a decrease in heart rate. Aortic flow in these rats is also depressed compared to that in control hearts. Treatment of diabetic rats with sodium molybdate, however, prevented this depression in aortic flow from occurring, an effect not observed in diabetic rats treated with $MoO_2(ma)_2$. During reperfusion of previously ischemic hearts, the benefits of sodium molybdate on mechanical function of diabetic rat hearts are also clearly observed. These are associated with significant and dramatic increases in aortic flow. No benefits of $MoO_2(ma)_2$ treatment on reperfusion recovery of diabetic hearts were seen.

Preventing the diabetes-induced depressions in heart function can be accomplished with agents that decrease circulating levels of lipids and glucose (21–24), which could possibly explain the benefits of molybdate on reperfusion on recovery of diabetic hearts. Diabetic hearts exposed to low levels of fatty acids can oxidize glucose as an additional substrate (24) since the poorly controlled state is characterized by energy requirements met primarily from the oxidation of fatty acids (25). Although conjectural, the possibility exists that molybdate-treated diabetic hearts oxidized more glucose during reperfusion, allowing them to be less sensitive to ischemia (26).

Conclusions

A series of hydroxypyrone and hydroxypyridinone complexes of molybdenum have been prepared and were characterized by a number of physical methods including X-ray diffraction studies. Initial biological data demonstrate that treatment of diabetic animals with sodium molybdate not only reduces plasma levels of glucose and fatty acids, but also prevents the depression in cardiac function from occur-

© 1999 NRC Canada

ring in diabetic hearts. The maltolato complex, $MoO_2(ma)_2$, also showed some improvement in blood glucose and free fatty acid levels but had no effect on heart function. We are currently investigating the physical properties necessary to generate a more active molybdenum complex for the treatment of cardiac dysfunction associated with diabetes.

Acknowledgements

Thanks are gratefully extended to the Heart and Stroke Foundation of New Brunswick (S.A.W.), the Medical Research Fund of New Brunswick (T.L.B.), the University of Waterloo, St. Mary's University, and Mount Allison University for financial support. We also thank Dan Durant, Roger and Marilyn Smith, and Jacqueline Jacob for their expert technical assistance, as well as Dr. John Bailey for many helpful discussions.

References

1. (*a*) L.F. Cavalieri. Chem. Rev. **41**, 525 (1947); (*b*) Š. Baláz, E. Šturdík, R. Ujheyová, D. Valigura, M. Uher, M. Veverka, V. Konečný, J. Adamcová, P. Michalík, and J. Brtko. Collect. Czech. Chem. Commun. **58**, 693 (1993); (*c*) G.R. Hanson, Y. Sun, and C. Orvig. Inorg. Chem. **35**, 6507 (1996), and refs. therein.
2. (*a*) M.T. Ahmet, C.S. Frampton, and J. Silver. J. Chem. Soc. Dalton Trans. 1159 (1988); (*b*) R.C. Hider and A.D. Hall. Prog. Med. Chem. **28**, 41 (1991).
3. (*a*) M.M. Finnegan, S.J. Rettig, and C. Orvig. J. Am. Chem. Soc. **108**, 5033 (1986); (*b*) M.M. Finnegan, T.G. Lutz, W.O. Nelson, A. Smith, and C. Orvig. Inorg. Chem. **26**, 2171 (1987); (*c*) C.D. Hewitt, M.M. Herman, M.B.S. Lopes, J. Savory, and R.W. Wills. Neuropathol. Appl. Neurobiol. **17**, 47 (1991); (*d*) E. Beatty, J. Burgess, and M.S. Patel. Can. J. Chem. **72**, 1370 (1994).
4. (*a*) S.J. Greaves and W.P. Griffith. Polyhedron, **7**, 1973 (1988); (*b*) T.A. Annan, C. Peppe, and D.G. Tuck. Can. J. Chem. **68**, 1598 (1990); (*c*) C.M. Archer, J.D. Dilworth, P. Jobanputra, M.E. Harman, M.B. Hursthouse, and A. Karaulov. Polyhedron, **10**, 1539 (1991); (*d*) H. Luo, S.J. Rettig, and C. Orvig. Inorg. Chem. **32**, 4491 (1993); (*e*) S. Bhattacharya, N. Seth, V.D. Gupta, H. Nöth, K. Polborn, M. Thomann, and H. Schwenk. Chem. Ber. **127**, 1895 (1994); (*f*) D. Fregona, G. Faraglia, R. Graziani, U. Casellato, and S. Sitran. Gazz. Chim. Ital. **124**, 153 (1994), and refs. therein; (*g*) S.S. Marwaha, J. Kaur, and G.S. Sodhi. J. Inorg. Biochem. **54**, 67 (1994); (*h*) P. Caravan, L. Gelmini, N. Glover, F.G. Herring, H. Li, J.H. McNeill, S.J. Rettig, I.A. Setawati, E. Shuter, Y. Sun, A.S. Tracey, V.G. Yuen, and C. Orvig. J. Am. Chem. Soc. **117**, 12 759 (1995), and refs. therein; (*i*) M.D. Fryzuk, M.J. Jonker, and S.J. Rettig. J. Chem. Soc. Chem. Commun. 377 (1997).
5. (*a*) C.A. Matsuba, W.O. Nelson, S.J. Rettig, and C. Orvig. Inorg. Chem. **27**, 3935 (1988); (*b*) Z. Zhang, T.L.T. Hui, and C. Orvig. Can. J. Chem. **67**, 1708 (1989); (*c*) S. Katoh, J. Toyama, I. Kodama, K. Kamiya, T. Akita, and T. Abe. Eur. Surg. Res. **24**, 349 (1992); (*d*) J.J. Molenda, M.A. Basinger, T.P. Hanusa, and M.M. Jones. J. Inorg. Biochem. **55**, 131 (1994).
6. (*a*) V.G. Yuen, C. Orvig, K.H. Thompson, and J.H. McNeill. Can. J. Physiol. Pharmacol. **71**, 270 (1993); (*b*) S. Bhanot, M. Bryer-Ash, A. Cheung, and J.H. McNeill. Diabetes, **43**, 857 (1994); (*c*) G.L. Schieven, A.F. Wahl, S. Myrdal, L. Grosmaire, and J.A. Ledbetter. J. Biol. Chem. **270**, 20 824 (1995); (*d*) V.G. Yuen, C. Orvig, and J.H. McNeill. Can. J. Physiol. Pharmacol. **73**, 55 (1995); (*e*) J.H. McNeill, V.G. Yuen, S. Dai, and C. Orvig. Mol. Cell. Biochem. **153**, 175 (1995); (*f*) V.G. Yuen, R.A. Pederson, S. Dai, C. Orvig, and J.H. McNeill. Can. J. Physiol. Pharmacol. **74**, 1001 (1996); (*g*) K. Elvingson, A. González Baró, and L. Pettersson. Inorg. Chem. **35**, 3388 (1996); (*h*) V.G. Yuen, P. Caravan, L. Gelmini, N. Glover, J.H. McNeill, I.A. Setyawati, Y. Zhou, and C. Orvig. J. Inorg. Biochem. **68**, 109 (1997); (*i*) V.G. Yuen, C. Orvig, and J.H. McNeill. Am. J. Physiol. **272**, E30 (1997).
7. N.S. Dhalla, G.N. Pierce, I.R. Innes, and R.E. Beamish. Can. J. Cardiol. **1**, 263 (1985).
8. (*a*) B.I. Posner, R. Faure, J.W. Burgess, A.P. Bevan, D. Lachance, G. Zhang-Sun, I.G. Fantus, J.B. Ng, D.A. Hall, B.S. Lum, and A. Shaver. J. Biol. Chem. **269**, 4596 (1994); (*b*) A. Shaver, J.B. Ng, D.A. Hall, and B.I. Posner. Mol. Cell. Biochem. **153**, 5 (1995); (*c*) P.D. Taylor. Chem. Commun. 405, (1996); (*d*) J. Burgess, B. De Castro, C. Oliveira, M. Rangel, and W. Schlindwein. Polyhedron, **16**, 798 (1997); (*e*) D.C. Crans, A.D. Keramidas, H. Hoover-Litty, O.P. Anderson, M.M. Miller, L.M. Lemoine, S. Pleasic-Williams, M. Vandenberg, A.J. Rossomando, and L.J. Sweet. J. Am. Chem. Soc. **119**, 5447 (1997), and refs. therein.
9. (*a*) G.J. Kontoghiorghes. Inorg. Chim. Acta, **135**, 145 (1987); (*b*) D.J. Clevette, D.M. Lyster, W.O. Nelson, T. Rihela, G.A. Webb, and C. Orvig. Inorg. Chem. **29**, 667 (1990), and refs. therein; (*c*) M.-H. Feng, L. van der Does, and A. Bantjes. J. Med. Chem. **36**, 2822 (1993); (*d*) R. Ma, J.J. Reibenspies, and A.E. Martell. Inorg. Chim. Acta, **223**, 21 (1994); (*e*) Y. Shi, E.M. Eyring, R. van Eldik, G. Liu, F.W. Bruenger, and S.C. Miller. J. Biol. Inorg. Chem. **2**, 728 (1997).
10. (*a*) Y. Goto, K. Kida, M. Ikeuchi, Y. Kaino, and H. Matsuda. Biochem. Pharmacol. **44**, 177 (1992); (*b*) C. Fillat, J.E. Rodríguez-Gil, and J.J. Guinovart. Biochem. J. **282**, 659 (1992); (*c*) A. Barberà, J.E. Rodríguez-Gil, and J.J. Guinovart. J. Biol. Chem. **269**, 20 047 (1994); (*d*) B. Rodrigues, M.C. Cam, and J.H. McNeill. J. Mol. Cell. Cardiol. **27**, 169 (1995); (*e*) A.T. Özcelikay, D.J. Becker, L.N. Ongemba, A.-M. Pottier, J.-C. Henquin, and S.M. Brichard. Am. J. Physiol. **270**, E344 (1996).
11. (*a*) H. Stünzi, R.L.N. Harris, D.D. Perrin, and T. Teitei. Aust. J. Chem. **33**, 2207 (1980); (*b*) J. Charalambous, A. Dodd, M. McPartlin, S.O.C. Matondo, N.D. Pathirana, and H.R. Powell. Polyhedron, **7**, 2235 (1988); (*c*) D.J. Clevette, W.O. Nelson, A. Nordin, C. Orvig, and S. Sjöberg. Inorg. Chem. **28**, 2079 (1989); (*d*) L. Simpson, S.J. Rettig, J. Trotter, and C. Orvig. Can. J. Chem. **69**, 893 (1991); (*e*) G. Xiao, D. van der Helm, R.C. Hider, and P.S. Dobbin. J. Chem. Soc. Dalton Trans. 3265 (1992); (*f*) E.T. Clarke and A.E. Martell. Inorg. Chim. Acta, **191**, 57 (1992); (*g*) W.P. Griffith and S.I. Mostafa. Polyhedron, **11**, 2997 (1992); (*h*) G. Liu, F.W. Bruenger, A.M. Barrios, and S.C. Miller. Nucleosides Nucleotides, **14,** 1901 (1995).
12. W.P. Griffith, C.A. Pumphrey, and A.C. Skapski. Polyhedron, **6**, 891 (1987).
13. (*a*) K. Tatsumi and R. Hoffmann. Inorg. Chem. **19**, 2656 (1980); (*b*) G. Barea, A. Lledos, F. Maseras, and Y. Jean. Inorg. Chem. **37**, 3321 (1998).
14. M.T. Pope. Prog. Inorg. Chem. **39**, 181 (1991).
15. (*a*) Y. Sun, B.R. James, S.J. Rettig, and C. Orvig. Inorg. Chem. **35**, 1667 (1996); (*b*) Y. Sun, M. Melchior, D.A. Summers, R.C. Thompson, S.J. Rettig, and C. Orvig. Inorg. Chem. **37**, 3119 (1998).
16. J. Lokaj, J. Kožíšek, B. Koreň, M. Uher, and V. Vrábel. Acta Crystallogr. Sect. C: Cryst. Struct. Commun. **C47**, 193 (1991).
17. A.R. Katritzky and R.A. Jones. J. Chem. Soc. 2947 (1960).

© 1999 NRC Canada

18. (*a*) K. Jakopčić, B. Tamhina, F. Zorko, and M.J. Herak. J. Inorg. Nucl. Chem. **39**, 1201 (1977); (*b*) Z. Zhang, S.J. Rettig, and C. Orvig. Inorg. Chem. **30**, 509 (1991).
19. Z. Zhang, S.J. Rettig, and C. Orvig. Can. J. Chem. **70**, 763 (1992).
20. W.O. Nelson, T.B. Karpishin, S.J. Rettig, and C. Orvig. Can. J. Chem. **66**, 123 (1988).
21. B. Rodrigues, R.K. Goyal, and J.H. McNeill. J. Pharmacol. Exp. Ther. **237**, 292 (1986).
22. T.A. Nicholl, G.D. Lopaschuk, and J.H. McNeill. Am. J. Physiol. **266**, H1053 (1991).
23. A.J. Liedtke, S.H. Nellis, and O.D. Mjos. Am. J. Physiol. **247**, H387 (1983).
24. S.R. Wall and G.D. Lopaschuk. Biochem. Biophys. Acta, **1006**, 97 (1989).
25. J.R. Neely and H.E.Morgan. Annu. Rev. Physiol. **36**, 413 (1974).
26. T.L. Broderick, A.H. Quinney, and G.D. Lopaschik. Cardiovasc. Res. **29**, 373 (1995).

© 1999 NRC Canada

Dimethyltellurium(IV) derivatives with mixed 1,1-dithio ligands. Crystal structures of $Me_2Te[S_2CNMe_2][S_2COEt]$ and $Me_2Te[S_2CNEt_2][S_2COMe]$

John E. Drake, Layla N. Khasrou, Anil G. Mislankar, and Raju Ratnani

Abstract: Mixed ligand derivatives of $Me_2TeLL'_2$, where L = *N*,*N*-dialkyl dithiocarbamate or *O*,*O*-alkylene dithiophosphate and L′ = *O*-alkyl dithiocarbonate, have been synthesized and characterized by elemental analysis, ^1H, ^{13}C, ^{31}P, and ^{125}Te NMR spectroscopy and infrared and Raman spectroscopy, and X-ray crystallography. $Me_2Te[S_2CNMe_2][S_2COEt]$, **8**: $P\bar{1}$ (no. 2), with cell parameters a = 10.073(3) Å, b = 10.139(2) Å, c = 9.108(2) Å, α = 92.36(2)°, β = 115.55(2)°, γ = 111.19(2)°, V = 760.7(4) Å^3, Z = 2, R = 0.0343, R_w = 0.0296. $Me_2Te[S_2CNEt_2][S_2COMe]$, **9**: $P2_1/c$ (no. 14) with cell parameters a = 9.881(4) Å, b = 17.671(3) Å, c = 10.149(4) Å, β = 113.65(3)°, V = 1623.3(10) Å^3, Z = 4, R = 0.0567, R_w = 0.0514. The immediate environment about tellurium in both molecules is essentially that of a saw-horse structure in which the lone pair is apparently stereochemically active and occupying an equatorial position in a distorted trigonal bipyramid. The S-Te-S angles in the two molecules are 166.87(6)° and 162.0(1)° for **8** and **9**, respectively. In both molecules, the Te—S bonds to the dithiocarbamate groups are slightly shorter than those to dithiocarbonates. The dithiocarbamate groups are oriented to give secondary interactions involving the apparently terminal sulfur atoms resulting in Te—S distances of 3.205(2) and 3.277(4) Å, respectively, in **8** and **9**. However, only in **9** is there a similar Te—S distance of 3.346(5) Å involving the S_2COMe group because in **8**, the OEt group of S_2COEt, rather than the terminal S atom, is oriented toward Te.

Key words: structure, tellurium, methyl, dithiocarbamates, dithiocarbonates, dithiophosphates.

Résumé : On a synthétisé des dérivés à ligands mixtes du $Me_2TeLL'_2$ dans lesquels L = dithiocarbamate de *N*,*N*-dialkyle ou dithiophosphate de *O*,*O*-alkylène et L′ = dithiocarbonate de *O*-alkyle et on les a caractérisés par analyse élémentaire, spectroscopie RMN du ^1H, ^{13}C, ^{31}P et ^{125}Te, spectroscopie infrarouge et Raman et par diffraction des rayons X. $Me_2Te[S_2CNMe_2][S_2COEt]$, **8**, $P\bar{1}$ (no. 2), avec a = 10,073(3), b = 10,139(2) et c = 9,108(2) Å, α = 92,36(2), β = 115,55(2) et γ = 111,19(2)°, V = 760,7(4) Å^3, Z = 2, R = 0,0343, R_w = 0,0296. $Me_2Te[S_2CNEt_2][S_2COMe]$, **9**, $P2_1/c$ (no. 14), avec a = 9,881(4), b = 17,671(3) et c = 10,149(4) Å, β = 113,65(3)°, V = 1623,3(10) Å^3, Z = 4, R = 0,0567, R_w = 0,0514. Dans les deux molécules, l'environnement immédiat autour du tellure est essentiellement celui d'une structure cavalière dans laquelle la paire d'électrons libres est apparemment stéréochimiquement active et elle occupe une position équatoriale dans une bipyramide trigonale déformée. Dans les deux molécules, les angles S-Te-S sont de 166,87(6) et 162,0(1)° pour les molécules **8** et **9** respectivement. Dans chacune des molécules, les liaisons Te—S vers les groupes dithiocarbamates sont légèrement plus courtes que celles dans les dithiocarbonates. Les groupes dithiocarbonates sont orientés de façon à donner des interactions secondaires impliquant les atomes de soufre apparemment terminaux; il en résulte des distances Te—S de 3,205(2) et 3,277(4) Å pour les composés **8** et **9** respectivement. Toutefois, seul le composé **9** donne lieu à une distance Te—S semblable, 3,346(5) Å, impliquant le groupe S_2COMe; cette situation résulte du fait que, dans le composé **8**, c'est le groupe OEt du S_2COEt qui est orienté vers le Te et non l'atome S terminal.

Mots clés : structure, tellure, méthyle, dithiocarbamates, dithiocarbamates, dithiophosphonates.

[Traduit par la Rédaction]

Introduction

Several reports have appeared on organotellurium(IV) compounds with a variety of 1,1-dithio ligands including *O*-alkyl dithiocarbonates (1–6), *N*,*N*-dialkyl dithiocarbamates (5–14), and *O*,*O*-dialkyl (alkylene) dithiophosphates (4–6, 13–20), but relatively few refer to the formation of mixed ligand moieties, such as those of the general type

Received February 3, 1999.

J.E. Drake[1] and L.N. Khasrou. Chemistry and Biochemistry, University of Windsor, Windsor, ON N9B 3P4, Canada.
A.G. Mislankar. Information Technology, Celestica Inc., 844 Don Mills Road, Toronto, ON M3C 1V7, Canada.
R. Ratnani. Department of Applied Chemistry and Chemical Technology, M.D.S. University, Ajmer, India.

[1]Author to whom correspondence may be addressed. Telephone: (519) 253-4232. Fax: (519) 973-7098. e-mail: ak4@uwindsor.ca

 © 1999 NRC Canada

$RTeL_2L'$ (14) or R_2TeLL' (21). We report on the synthesis of nine dimethyltellurium(IV) compounds with mixed 1,1-dithio ligands along with their characterization by ^1H, ^{13}C, ^{31}P, and ^{125}Te NMR spectroscopy, infrared and Raman spectroscopy, and elemental analysis. X-ray crystal structures of $Me_2Te[S_2CNMe_2][S_2COEt]$, **8**, and $Me_2Te[S_2CNEt_2][S_2COMe]$, **9**, confirm that these are mixed ligand species and not 1:1 mixtures of the bis derivatives.

Experimental

Materials

$TeCl_4$, Me_4Sn, NaS_2CNMe_2, and NaS_2CNEt_2 were obtained from Aldrich, and the latter two were dried in vacuo for 4–5 days prior to use. Me_2TeCl_2 was prepared by the reaction of $TeCl_4$ and Me_4Sn in toluene at 60°C under reflux for 4 h by adaptation of the method used for the preparation of Ph_2TeCl_2 (22). $Me_2TeCl[S_2CNMe_2]$ and $Me_2TeCl[S_2CNEt_2]$ were prepared as described in the literature (12) as were the sodium and ammonium salts of *O,O*-alkylene dithiophosphatic acids and the potassium salts of *O*-alkyl dithiocarbonic acids (23, 24). All solvents were dried and distilled prior to use, and all reactions carried out under anhydrous conditions.

Preparation of dimethyl(*N,N*-alkyl dithiocarbamato)(*O,O*-alkylene dithiophosphato)tellurium(IV) compounds

Typically, $NaS_2POCMe_2CMe_2O$ (ca. 1.4 mmol) was added to a solution of an equimolar amount of Me_2TeCl_2 in dried dichloromethane (20 mL). The mixture was stirred for 2 h and then filtered to remove NaCl and unreacted dithiophosphate salt. The solvent was reduced to 5 mL under vacuum, *n*-hexane (5 mL) was added, and the solution left overnight in the refrigerator at –6°C. The resulting crystals were washed with *n*-hexane and dried in vacuum to give $Me_2TeCl[S_2POCMe_2CMe_2O]$ as white crystals. $Me_2TeCl[S_2POCMe_2CMe_2O]$ (0.470 g, 1.16 mmol) was then dissolved in dichloromethane (20 mL), NaS_2CNMe_2 (0.168 g, 1.17 mmol) added with constant stirring, and the colorless solution turned yellow. The mixture was stirred for 2 h at ambient temperature and then filtered to remove NaCl or any unreacted dithiocarbamate salt. The volume of the solvent was reduced to 5 mL, *n*-hexane (5 mL) was added, and the solution was left overnight in the refrigerator at –6°C. The solvent was decanted off the crystals, which were then pumped on to dryness on the vacuum line to give $Me_2Te[S_2CNMe_2][S_2POCMe_2CMe_2O]$, **1**, as yellow crystals (0.459 g, yield 81%; mp 129°C). Anal. calcd. for $C_{11}H_{24}NO_2PS_4Te$: C 27.01, H 4.95; found: C 26.85, H 4.75. Similarly, using NaS_2CNEt_2 was formed $Me_2Te[S_2CNEt_2][S_2POCMe_2CMe_2O]$, **2**, as yellow crystals (yield 86%, mp 127–128°C). Anal. calcd. for $C_{13}H_{28}NO_2PS_4Te$: C 30.20, H 5.46; found: C 29.74, H 5.28. Similarly, starting with $Me_2TeCl[S_2POCH_2CMe_2CH_2O]$ was formed $Me_2Te[S_2CNMe_2][S_2POCH_2CMe_2CH_2O]$, **3**, as yellow crystals (yield 83%, mp 114–115°C). Anal. calcd. for $C_{10}H_{22}NO_2PS_4Te$: C 25.28, H 4.67; found: C 25.58, H 4.54. $Me_2Te[S_2CNEt_2][S_2POCH_2CMe_2CH_2O]$, **4**, as yellow crystals (yield 87%, mp 88–89°C). Anal. calcd. for $C_{12}H_{26}NO_2PS_4Te$: C 28.64, H 5.21; found: C 28.43, H 5.27. Unfortunately, no crystals suitable for X-ray diffraction studies were obtained for compounds **1**–**4** despite extensive efforts at recrystallization.

Preparation of dimethyl(*O*-alkyl dithiocarbonato)(*O,O*-alkylene dithiophosphato)tellurium(IV) compounds

In a manner essentially the same as described above, the reaction of $Me_2TeCl[S_2POCMe_2CMe_2O]$ (0.234 g, 0.58 mmol) in dichloromethane (20 mL) with KS_2COMe (0.087 g, 0.59 mmol) gave $Me_2Te[S_2COMe][S_2POCMe_2CMe_2O]$, **5**, as pale-yellow crystalline material: 0.223 g, yield 81%, mp 87–88°C. Anal. calcd. for $C_{10}H_{21}O_3PS_4Te$: C 25.23, H 4.45; found: C 25.30, H 4.85. Similarly, using KS_2COEt was formed $Me_2Te[S_2COEt][S_2POCMe_2CMe_2O]$, **6**, as pale-yellow crystals: yield 83%, mp 72°C. Anal. calcd. for $C_{11}H_{23}O_3PS_4Te$: C 26.96, H 4.73; found: C 27.07, H 4.83. Unfortunately, attempts to grow X-ray quality crystals of **5** and **6** were not successful.

Preparation of dimethyl(*N,N*-dialkyl dithiocarbamato)(*O*-alkyl dithiocarbonato)tellurium(IV) compounds

Typically, KS_2COMe (0.154 g, 1.05 mmol) was added, with constant stirring, to a solution of $Me_2TeCl[S_2CNMe_2]$ (0.324 g. 1.03 mmol) in dichloromethane (20 mL). The colorless reaction mixture changed to yellow after a few minutes. The stirring was continued for 1 h after which KCl and unreacted dithiocarbonate salt were filtered off before the solvent was pumped off under vacuum to yield a yellow powder. The crude product was recrystallized from dichloromethane–*n*-hexane to give $Me_2Te[S_2CNMe_2][S_2COMe]$, **7**, as yellow crystals: 0.176 g, yield 88%, mp 95–97°C. Anal. calcd. for $C_7H_{15}NOS_4Te$: C 21.84, H 3.93; found: C 22.22, H 3.85. Similarly were obtained $Me_2Te[S_2CNMe_2][S_2COEt]$, **8**, as yellow crystals: yield 88%, mp 106–108°C. Anal. calcd. for $C_8H_{17}NOS_4Te$: C 24.08, H 4.29; found: C 24.15, H 4.18. $Me_2Te[S_2CNEt_2][S_2COMe]$, **9**, as yellow crystals: yield 89%, mp 75–77°C. Anal. calcd. for $C_9H_{19}NOS_4Te$: C 26.17, H 4.62; found: C 25.56, H 4.71. X-ray quality crystals were obtained for compounds **8** and **9**, but not for **7** despite extensive attempts at recrystallization.

Alternative synthesis of $Me_2Te[S_2CNMe_2][S_2POCMe_2CMe_2O]$, 1, and compounds 2–6

In essentially the same manner as described above, $NH_4S_2POCMe_2CMe_2O$ (0.124 g, 0.54 mmol) was added, with constant stirring, to a solution of $Me_2TeCl[S_2CNMe_2]$ (0.165 g, 0.53 mmol) in dichloromethane (20 mL). The colorless reaction mixture immediately changed to yellow. The reaction mixture was stirred for 2 h, filtered to remove NH_4Cl or any unreacted dithiophosphate salt, and then *n*-hexane (approximately 5 mL) was added after the solvent had been reduced to 5 mL by pumping. Crystals were formed when the solution was left overnight in the refrigerator at –6°C. The solvent was decanted and the crystals pumped to dryness to give $Me_2Te[S_2CNMe_2][S_2POCMe_2CMe_2O]$, **1**, as yellow crystals: 0.218 g, yield 85%, mp 129°C. Similarly were formed compounds **2**–**6**.

Alternative in situ preparation of $Me_2Te[S_2CNMe_2][S_2COMe]$, 7

Typically, NaS_2CNMe_2 (0.147 g, 1 mmol) was added to a solution of Me_2TeCl_2 (0.228 g, 1 mmol) in dried carbon

© 1999 NRC Canada

Table 1. Summary of crystal data, intensity collection, and structural refinement for $Me_2Te[S_2CNMe_2][S_2COEt]$, **8**, and $Me_2Te[S_2CNEt_2][S_2COMe]$, **9**.

Parameter	**8**	**9**
a, Å	10.073 (3)	9.881 (4)
b, Å	10.139 (2)	17.671 (3)
c, Å	9.108 (2)	10.149 (4)
α, deg	92.36 (2)	90.00
β, deg	115.55 (2)	113.65 (3)
γ, deg	111.19 (2)	90.00
V, Å^3	760.7 (4)	1623.3 (10)
Crystal system	Triclinic	Monoclinic
Space group	$P\bar{1}$ (no. 2)	$P2_1/c$ (no. 14)
Mol. wt., g mol^{-1}	399.07	413.10
Z	2	4
Crystal dimensions, mm	0.31 × 0.19 × 0.12	0.28 × 0.23 × 0.15
ρ (calcd.), g cm^{-1}	1.742	1.690
μ, cm^{-1}	24.66	23.3
Transmission factors	0.67–1.00	0.62–1.00
Temperature, °C	23	23
Radiation, Å	MoKα 0.71069	MoKα 0.71069
Monochromator	Highly oriented graphite	Highly oriented graphite
Scan method	ω-2θ	ω-2θ
Scan speed, °/min	16.0	16.0
Max. 2θ	50	50
Total reflections measured	2850	6052
No. of unique data	2682	2207
No. of obsd. data ($I > 3.00\sigma(I)$)	1824	1339
No. of parameters (NP)	136	145
$R = \Sigma\|\|F_o\| - \|F_c\|\|/\Sigma\|F_o\|$	0.0343	0.0567
$R_w = [(\Sigma w(\|F_o\| - \|F_c\|)^2/\Sigma wF_o^2)]^{1/2}$	0.0296	0.0514
Goodness of fit	1.29	2.33
Largest shift/esd, final cycle	0.001	0.001
Largest residual electron density, e Å^{-3}	0.51	0.72
Atom associated with residual density	Te	Te

disulfide or dichloromethane (20 mL). The reaction mixture was stirred for 2 h, and then KS_2COMe (0.146 g, 1 mmol) was added before the mixture was stirred for a further 2 h. The resulting mixture was filtered to remove NaCl, KCl, and unreacted materials, and the solvent reduced to 5 mL under vacuum before *n*-hexane (5 mL) was added. A yellow powder resulted, which was dried under vacuum after the solvent was decanted. The compound was recrystallized from dichoromethane–*n*-hexane to give $Me_2Te[S_2CNMe_2][S_2COMe]$, **7**, as yellow crystals: 0.280 g, yield 72%, mp 95–97°C. All of the compounds **1**–**9** were also prepared in this manner.

Physical measurements

Elemental analyses were performed at Guelph Chemical Laboratories, Guelph, Ontario. The ^{1}H and ^{13}C NMR spectra were recorded on a Bruker 300 FT/NMR spectrometer in $CDCl_3$ using Me_4Si as internal standard. The ^{31}P and ^{125}Te NMR spectra were recorded on a Bruker 200 FT/NMR spectrometer in $CDCl_3$ using 85% H_3PO_4 andMe_2Te, respectively, as external standard. The infrared spectra were recorded on a Nicolet 5DX FT spectrometer as KBr pellets and far infrared spectra on a Bomem IR spectrometer between polyethylene films as Nujol mulls. Raman spectra were recorded using samples in sealed capillary tubes on a Spectra-Physics 164 spectrometer using the 5145 Å exciting line of an argon ion laser. The melting points were determined on a Fisher–Johns apparatus.

X-ray crystallographic analysis

Pale yellow block-shaped crystals of $Me_2Te[S_2CNMe_2][S_2COEt]$, **8**, and $Me_2Te[S_2CNEt_2][S_2COMe]$, **9**, were sealed in thin-walled glass capillaries and mounted on a Rigaku AFC6S diffractometer, with graphite-monochromated MoKα radiation.

Cell constants corresponded to triclinic and monoclinic cell for **8** and **9**, respectively, whose dimensions are given in Table 1, along with other experimental parameters. Based on the appropriate systematic absences for **9**, statistical analyses of intensity distributions, and the successful solution and refinement of the structures, the space groups were determined to be $P\bar{1}$ (no. 2) for **8** and $P2_1/c$ (no. 14) for **9**. The data were corrected for Lorentz and polarization effects, and an empirical absorption correction was applied.

The structures were solved by direct methods (25), and all calculations were performed using the TEXSAN (26) crystallographic software package of Molecular Structure Corp.[2]

[2] Least-squares function minimized: $\Sigma w(|F_o| - |F_c|)^2$, where $w = 4F_o^2(F_o^2)$, $\sigma^2(F_o^2) = [S^2(C + R^2B) + (pF_o^2)^2]/(\mathrm{Lp})^2$, S = scan rate, C = total integrated peak count, R = ratio of scan time to background counting time, Lp = Lorentz-polarization factor, and p = p factor.

© 1999 NRC Canada

The non-hydrogen atoms were refined anisotropically, and the hydrogen atoms were included in their idealized positions with C—H set at 0.95 Å and with isotropic thermal parameters set at 1.2 times that of the carbon atom to which they were attached.

The weighted and unweighted agreement factors and standard deviation of an observation of unit weight[3] are given in Table 1. Plots of $\Sigma w(|F_o| - |F_c|)^2$ versus $|F_o|$, reflection order in data collection, sin θ/λ, and various classes of indices showed no unusual trends. Interatomic distances and bond angles are given in Table 2, and the molecular structures of the two compounds are displayed as ORTEP diagrams in Figs. 1–4. The final atomic coordinates and equivalent isotropic thermal parameters for the non-hydrogen atoms, anisotropic thermal parameters for non-hydrogen atoms, and final fractional coordinates and thermal parameters for hydrogen atoms, have been deposited.[4]

Calculation of Pauling partial bond order

The formula proposed by Pauling (27) for calculating the bond orders of partial bonds is given by $d_n - d = -0.60 \log n$, where d_n is the bond length for bond number, n, and d is the length of the single bond of the same type. Based on the C—C single bond of 1.54 Å, Pauling's formula gives bond lengths of 1.36 Å for $n = 2$; 1.72 Å for $n = 0.5$; and 1.90 Å for $n = 0.25$. These give percentage increases in bond length for the partial bonds of approximately 12 and 23%, respectively, for $n = 0.5$ and 0.25. It is reasonable to assume that similar relationships relating bond order to interatomic distances for the much longer secondary interactions or partial bonds involving Te and S should utilize percentage differences "normalized" to 1.54 as follows rather than absolute differences.

Pauling's relationship, which can be written as $n = 10^X$, where $X = (d - d_n)/0.6$, can be modified to allow for percentage differences normalized to 1.54 to give $X = [1.54(d - d_n)/d]/0.6$ or $X = 2.5(d - d_n)/d$. Based on a Te—S single bond length of 2.63 Å, typical calculated values of the lengths of partial bonds for various values of n are as follows: 1.0, 2.63; 0.75, 2.76; 0.50, 2.95; 0.25, 3.26; 0.10, 3.68; n, bond length (Å). This scale appears to be compatible with the sum of the van der Waals radii of 3.86 Å for Te and S (28).

Results and discussion

The preparation of a variety of dimethyltellurium(IV) compounds with two different 1,1 dithio ligands is achieved in 80–90% yield by the action of approximately equimolar amounts of the sodium or potassium salt of a dithiocarbamic or dithiocarbonic acid with an *O,O*-alkylene dithiophosphate or *N,N*-dialkyl dithiocarbamate derivative of chlorodimethyltellurium(IV) such as $Me_2TeCl[S_2POCMe_2CMe_2O]$, $Me_2TeCl[S_2POCH_2CMe_2CH_2O]$, or $Me_2TeCl[S_2CNMe_2]$ in dichloromethane, in accord with the eqs. [1]–[3]:

[1] $Me_2TeCl[S_2\overline{POGO}] + NaS_2CNR_2 \rightarrow Me_2Te[S_2CNR_2][S_2\overline{POGO}]$

[2] $Me_2TeCl[S_2\overline{POCMe_2CMe_2O}] + KS_2COR' \rightarrow Me_2Te[S_2COR'][S_2\overline{POCMe_2CMe_2O}]$

[3] $Me_2TeCl[S_2CNR_2] + KS_2COR' \rightarrow Me_2Te[S_2CNR_2][S_2COR']$

(G = -CMe_2CMe_2-, -$CH_2CMe_2CH_2$-; R = Me, Et; R′ = Me, Et)

These mixed ligand dimethyltellurium(IV) compounds can also be formed in similar yields by the addition of the ammonium salt of the dithiophosphoric acid to chlorodimethyl (*N,N*-dialkyl dithiocarbamato)tellurium(IV) as exemplified by eq. [4]:

[4] $Me_2TeCl[S_2CNMe_2] + NH_4S_2\overline{POCMe_2CMe_2O} \rightarrow Me_2Te[S_2CNMe_2][S_2\overline{POCMe_2CMe_2O}]$

The Me_2TeClL species can also be prepared in situ in which case the reaction involves the complete addition of an equimolar amount of the salt of one 1,1-dithio acid to dimethyltellurium dichloride, the removal of insoluble salts, and the addition of an equimolar amount of the salt of a different 1,1-dithio acid, as exemplified by eqs. [5] and [6]. The overall yield based on Me_2TeCl_2 is close to 70%

[5] $Me_2TeCl_2 + KS_2COR' \rightarrow Me_2TeCl[S_2COR'] + KCl$

[6] $Me_2TeCl[S_2COR'] + NaS_2CNR_2 \rightarrow Me_2Te[S_2CNR_2][S_2COR'] + NaCl$

Solid samples of compounds **1**–**9** are stable over extended periods, particularly when stored in the refrigerator, as can be confirmed by the fact that NMR spectra recorded after several months show no changes from the spectra recorded immediately after the formation of the compounds. All of the compounds are soluble in common organic solvents such as benzene, toluene, carbon disulfide, dichloromethane, and chloroform, the later being used as the solvent for spectroscopic studies. The vibrational spectra as well as the NMR spectra of the freshly prepared samples provide definitive evidence that these compounds are indeed the mixed ligand species, Me_2TeLL', and not 1:1 mixtures of the bis species Me_2TeL_2 and $Me_2TeL'_2$. This is of course further confirmed by the X-ray structures of **8** and **9**. The NMR spectra recorded over time also indicate that eventually all derivatives, Me_2TeLL', slowly disproportionate to the two bis derivatives, Me_2TeL_2 and $Me_2TeL'_2$. The three species appear to be in equilibrium because the addition of more Me_2TeL_2 to a solution brings about the expected changes in the relative

[3] Standard deviation of an observation of unit weight: $\Sigma w(|F_o| - |F_c|)^2/(N_o - N_v)^{1/2}$, where N_o = number of observations and N_v = number of variables.

[4] Copies of material deposited may be purchased from: The Depository of Unpublished Data, Document Delivery, CISTI, National Research Council Canada, Ottawa, Canada, K1A 0S2. Tables of atomic coordinates have also been deposited with the Cambridge Crystallographic Data Centre and can be obtained on request from: The Director, Cambridge Crystallographic Data Centre, University Chemical Laboratory, 12 Union Road, Cambridge, CB2 1EZ, U.K. Structure factor amplitudes are no longer being deposited and may be obtained directly from the author.

© 1999 NRC Canada

Table 2. Interatomic distances (Å) and angles (deg) for $Me_2Te[S_2CNMe_2][S_2COEt]$, **8**, and $Me_2Te[S_2CNEt_2][S_2COMe]$, **9**.[a]

$Me_2Te[S_2CNMe_2][S_2COEt]$, **8**		$Me_2Te[S_2CNEt_2][S_2COMe]$, **9**	
Te(1)—S(1)	2.620(2)	Te(1)—S(1)	2.608(5)
Te(1)—S(3)	2.650(2)	Te(1)—S(3)	2.620(5)
Te(1)—C(1)	2.128(6)	Te(1)—C(1)	2.11(1)
Te(1)—C(2)	2.132(7)	Te(1)—C(2)	2.10(2)
S(1)—C(3)	1.762(7)	S(1)—C(3)	1.75(1)
S(2)—C(3)	1.682(7)	S(2)—C(3)	1.67(2)
N(1)—C(3)	1.311(8)	N(1)—C(3)	1.38(2)
N(1)—C(4)	1.435(9)	N(1)—C(4)	1.46(2)
N(1)—C(5)	1.445(9)	N(1)—C(6)	1.46(2)
S(3)—C(6)	1.729(7)	S(3)—C(8)	1.74(2)
S(4)—C(6)	1.633(7)	S(4)—C(8)	1.66(2)
O(1)—C(6)	1.343(8)	O(1)—C(8)	1.32(2)
O(1)—C(7)	1.451(9)	O(1)—C(9)	1.43(2)
C(7)—C(8)	1.46(1)	C(4)—C(5)	1.51(2)
		C(6)—C(7)	1.52(2)
S(1)—S(2)	2.994(3)	S(1)—S(2)	2.987(6)
S(3)—S(4)	2.956(3)	S(3)—S(4)	3.007(7)
Te(1)—S(2)	3.205(2)	Te(1)—S(2)	3.277(4)
Te(1)—S(4)	5.085(2)	Te(1)—S(4)	3.346(5)
Te(1)—O(1)	3.145(5)	Te(1)—O(1)	4.64(1)
Te(1)—S(2)′	3.567(2)	Te(1)—S(2)″	3.585(5)
Te(1)—Te(1)′	4.0251(9)	Te(1)—Te(1)″	4.072(2)
S(1)-Te(1)-S(3)	166.87(6)	S(1)-Te(1)-S(3)	162.0(2)
S(1)-Te(1)-C(1)	88.5(2)	S(1)-Te(1)-C(1)	87.1(5)
S(1)-Te(1)-C(2)	83.4(2)	S(1)-Te(1)-C(2)	81.3(5)
S(3)-Te(1)-C(1)	87.8(2)	S(3)-Te(1)-C(1)	88.2(5)
S(3)-Te(1)-C(2)	84.4(2)	S(3)-Te(1)-C(2)	82.0(4)
C(1)-Te(1)-C(2)	95.3(3)	C(1)-Te(1)-C(2)	96.4(7)
Te(1)-S(1)-C(3)	98.1(2)	Te(1)-S(1)-C(3)	99.3(6)
S(1)-C(3)-S(2)	120.8(4)	S(1)-C(3)-S(2)	122(1)
S(1)-C(3)-N(1)	117.0(5)	S(1)-C(3)-N(1)	114(1)
S(2)-C(3)-N(1)	122.2(6)	S(2)-C(3)-N(1)	124(1)
C(3)-N(1)-C(4)	124.9(7)	C(3)-N(1)-C(4)	124(1)
C(3)-N(1)-C(5)	121.5(7)	C(3)-N(1)-C(6)	120(1)
C(4)-N(1)-C(5)	113.6(6)	C(4)-N(1)-C(6)	116(1)
		N(1)-C(4)-C(5)	115(1)
		N(1)-C(6)-C(7)	114(1)
Te(1)-S(3)-C(6)	103.0(3)	Te(1)-S(3)-C(8)	99.6(6)
S(3)-C(6)-S(4)	123.1(5)	S(3)-C(8)-S(4)	124(1)
S(3)-C(6)-O(1)	111.9(5)	S(3)-C(8)-O(1)	110(1)
S(4)-C(6)-O(1)	125.0(5)	S(4)-C(8)-O(1)	126(1)
C(6)-O(1)-C(7)	118.9(6)	C(8)-O(1)-C(9)	119(1)
O(1)-C(7)-C(8)	107.7(7)		
S(1)-Te(1)--S(2)	60.89(5)	S(1)-Te(1)--S(2)	59.7(1)
S(3)-Te(1)--O(1)	51.5(1)	S(3)-Te(1)--S(4)	59.1(1)
S(3)-Te(1)--S(2)	130.83(5)	S(3)-Te(1)--S(2)	136.7(1)
S(1)-Te(1)--O(1)	139.7(1)	S(1)-Te(1)--S(4)	136.3(1)
S(2)--Te(1)--O(1)	79.4(1)	S(2)--Te(1)--S(4)	77.7(1)
C(1)-Te(1)--S(2)	82.1(2)	C(1)-Te(1)--S(2)	83.2(5)
C(2)-Te(1)--S(2)	144.1(2)	C(2)-Te(1)--S(2)	141.0(5)
C(1)-Te(1)--O(1)	79.5(2)	C(1)-Te(1)--S(4)	78.3(5)
C(2)-Te(1)--O(1)	135.6(2)	C(2)-Te(1)--S(4)	140.7(4)
C(1)-Te(1)--S(2)′	170.5(2)	C(1)-Te(1)--S(2)″	169.2(5)
S(2)-Te(1)--S(2)′	107.28(4)	S(2)-Te(1)--S(2)″	107.37(9)
Te(1)-S(2)--Te(1)′	72.72(4)	Te(1)-S(2)--Te(1)″	72.63(9)

[a]Symmetry equivalent position (1 – *x*, –*y*, –*z*) and (–*x*, –*y*, –*z*) by a double prime.

© 1999 NRC Canada

Fig. 1. ORTEP plots of the molecules (*a*) $Me_2Te[S_2CNMe_2][S_2COEt]$, **8**, and (*b*) $Me_2Te[S_2CNEt_2][S_2COMe]$, **9**. Atoms are drawn with 30% probability ellipsoids and spheres with hydrogen atoms omitted for clarity.

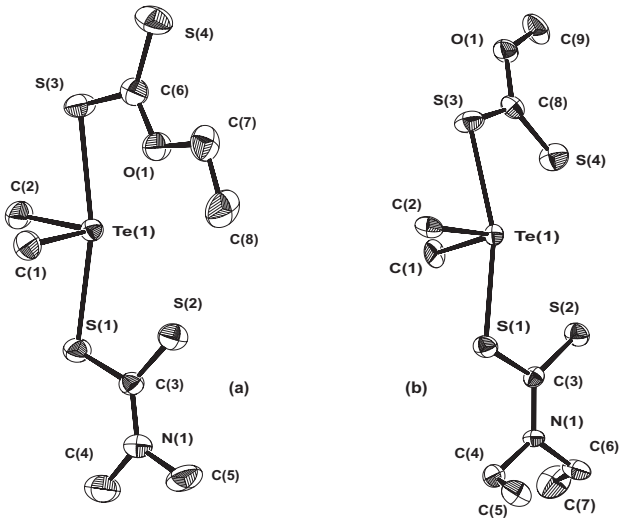

amounts of Me_2TeLL' and $Me_2TeL'_2$. However, all three species, simultaneously also undergo reductive elimination to Me_2Te and the diligands, so that the spectra become very complicated. Qualitatively, the reductive elimination does not appear to be a reversible process so eventually the solution becomes depleted of tellurium(IV) species. Qualitatively, the disproportionation and reductive elimination appear to be most evident for derivatives containing dithiocarbonate ligands and least evident for those containing the cyclic dithiophosphate ligands.

Crystal structures of $Me_2Te[S_2CNMe_2][S_2COEt]$, 8, and $Me_2Te[S_2CNEt_2][S_2COMe]$, 9

$Me_2Te[S_2CNMe_2][S_2COEt]$, **8**, crystallizes in the space group $P\bar{1}$ and $Me_2Te[S_2CNEt_2][S_2COMe]$, **9**, in $P2_1/c$. The ORTEP diagrams in Fig. 1*a* and 1*b* illustrate that in both compounds the immediate environment about tellurium is that of the sawhorse structure typical of tellurium(IV) compounds in which the lone pair is assumed to be active stereochemically and occupying an equatorial position in a distorted trigonal bipyramid, approximately in the position of the Te(1) label. The two methyl groups occupy the other two equatorial positions; the C-Te-C bond angles of 95.3(3)° and 96.4(7)° in **8** and **9**, respectively, being close to the value of 96(1)° in $Me_2Te[S_2CN(CH_2)_3CH_2][S_2CN(CH_2)_4CH_2]$ (21), and similar to those of 93.9(2)°, 96.6(2)°, and 96.2(2)° in related bis derivatives, $Me_2Te[S_2CNMe_2]_2$ (12), $Me_2Te[S_2COMe]_2$ (1),and $Me_2Te[S_2COEt]_2$ (2), respectively. The average Te—C bond length of 2.12(1) Å in **8** and **9** is essentially the same as that in $Me_2Te[S_2NCMe_2]_2$ and the two $Me_2Te[S_2COR]_2$ species. The S-Te-S bond angle of 166.87(6)° for the axial sulfur atoms in **8** is close to that in the mixed species, $Me_2Te[S_2CN(CH_2)_3CH_2][S_2CN(CH_2)_4CH_2]$ (166.1(2)°), as well as in $Me_2Te[S_2NCMe_2]_2$ and $Me_2Te[S_2COR]_2$ (167.58(7)° and166.2(2)° avg., respectively). By contrast, the value of 162.0(1)° in **9** is the same as in $Me_2Te[S_2CN(CH_2)_3CH_2]_2$ (21), so it is difficult to detect an obvious pattern or trend. The two Te—S bonds in the

Fig. 2. ORTEP plots of the molecules (*a*) $Me_2Te[S_2CNMe_2][S_2COEt]$, **8**, and (*b*) $Me_2Te[S_2CNEt_2][S_2COMe]$, **9**, showing the stereochemistry about tellurium when the intramolecular interactions leading to unsymmetrical ligands are included. The atoms are drawn with 30% probability ellipsoids and spheres. Hydrogen atoms are omitted for clarity.

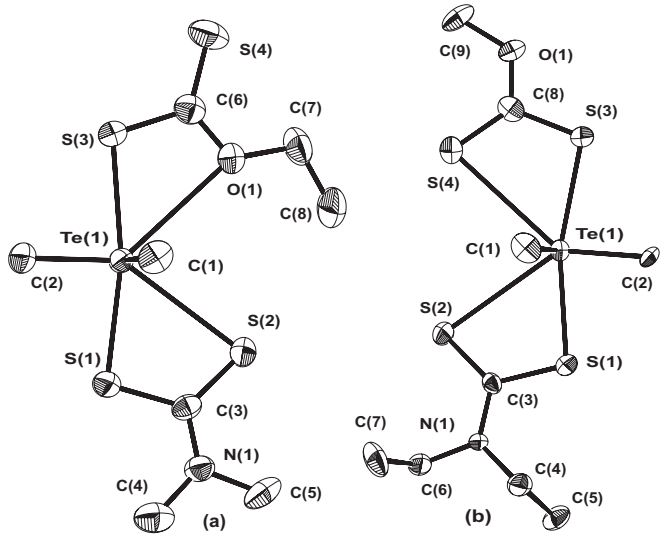

bis species $Me_2Te[S_2NCMe_2]_2$, $Me_2Te[S_2COMe]_2$, and $Me_2Te[S_2COEt]_2$ have an average value of 2.63(1) Å, even though in all three cases the two Te—S bonds have quite different lengths ranging from 2.566(1) to 2.680(1) Å. In **8** and **9**, the Te—S bonds to the S_2CNR_2 groups, 2.620(2) in **8** and 2.608(5) Å in **9**, are shorter than those to the S_2COR groups, 2.650(2) in **8** and 2.620(5) Å in **9**. In the absence of any Te--S associations involving the bonded S atom at contact distances less than the sum of the van der Waals radii of 3.86 Å (28), bonding to dithiocarbamates is apparently slightly favored.

The pendant sulfur atoms in the dithiocarbamate groups are oriented toward the tellurium center to give Te—S anisobonds of 3.205(1) in **8** and 3.277(4) Å in **9** (see Fig. 2*a* and 2*b*). These values are typical for analogous dithiocarbamates and correspond to normalized Pauling partial bond orders of about 0.25, which is compatible with their being part of the coordination sphere. Similar Te—S anisobonds, varying from 3.274(2) to 3.521(1) Å, occur in $Me_2Te[S_2COMe]_2$ and $Me_2Te[S_2COEt]_2$ (2) as well as in the two independent molecules of $Me_2TeCl[S_2COEt]$ with values of 3.210(3) and 3.292(3) Å (29). Similarly, in $Me_2Te[S_2CNEt_2][S_2COMe]$, **9**, there is an anisobond between Te(1)—S(4) of 3.346(5) Å involving the S_2COMe group (see Fig. 2*b*). Surprisingly, the orientation of the S_2COEt group in $Me_2Te[S_2CNMe_2][S_2COEt]$, **8**, is such that the second sulfur atom is turned away from tellurium so that Te(1)—S(4) is 5.085(2) Å and so clearly not bonded (see Fig. 2*a*). The intramolecular association now involves the oxygen of the OEt group with a Te(1)—O(1) distance of 3.145(5) Å. In a study of analogous monothiocarbonates (30), the terminal oxygen atom is oriented toward the tellurium center in $Me_2Te[SCO_2(i\text{-}Pr)]_2$ and $Me_2TeCl[SCO_2Me]$, with Te—O (terminal) distances averaging 3.05(8) Å in the former and 2.948(8) Å in the latter. However, in $Ph_2Te[SCO_2(i\text{-}Pr)]_2$, one of the $SCO_2(i\text{-}Pr)$ groups has a Te—O

© 1999 NRC Canada

Fig. 3. Plot of the molecule $Me_2Te[S_2CNMe_2][S_2COEt]$, **8**, showing the intermolecular interactions involving the anisobonded sulfur atoms leading to a dimer. Hydrogen atoms and the carbon atoms of the phenyl rings other than those attached to phosphorus are omitted for clarity.

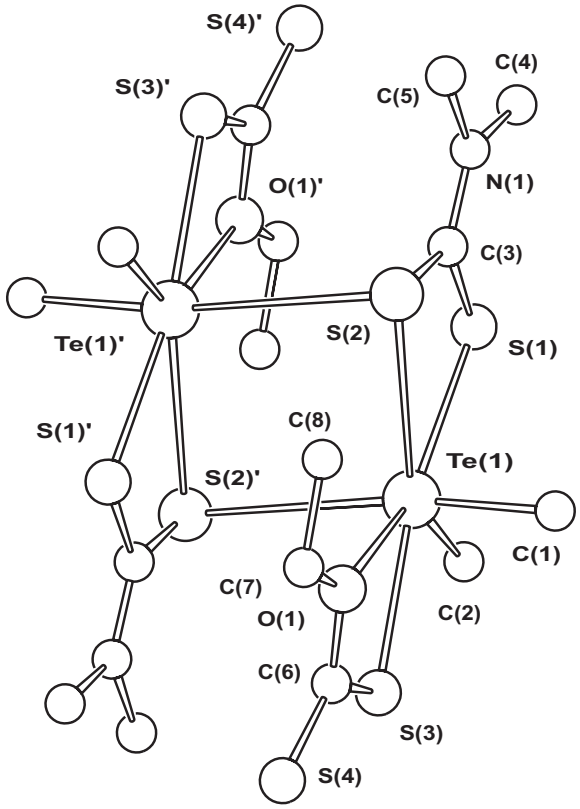

Fig. 4. Plot of the molecule $Me_2Te[S_2CNEt_2][S_2COMe]$, **9**, showing the intermolecular interactions involving the anisobonded sulfur atoms leading to a dimer. Hydrogen atoms and the carbon atoms of the phenyl rings other than those attached to phosphorus are omitted for clarity.

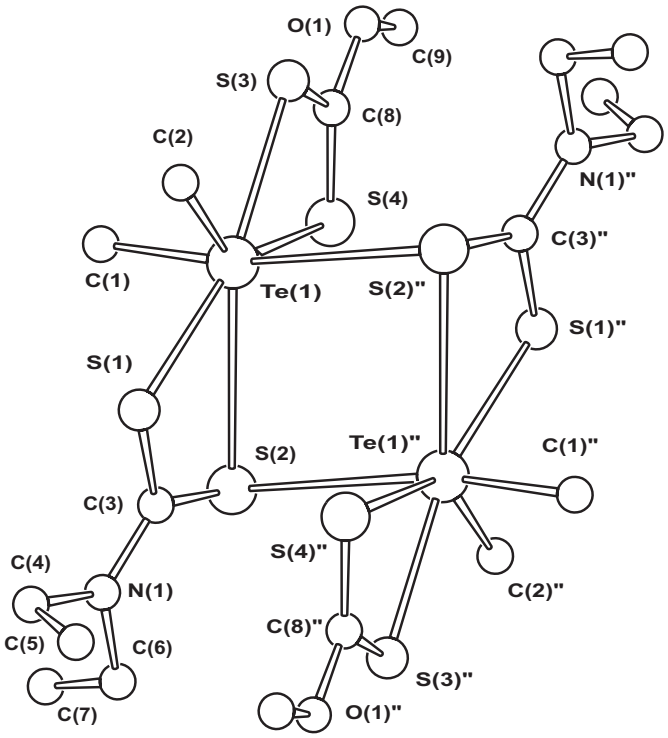

(terminal) distance of 3.050(5) Å, but the other is oriented so that the Te—O(i-Pr) distance is 3.150(5) Å. This orientation is repeated in $Me_2TeBr[SCO_2(i\text{-}Pr)]$ where the Te—O(i-Pr) distance is 2.930(6) Å. Thus, again it is difficult to detect a consistent trend.

In $Me_2Te[S_2CNEt_2][S_2COMe]$, **9**, the orientations of the dithiocarbamate and dithiocarbonate groups result in the five atoms, S(1), S(2), S(3), S(4), and C(2), as well as Te(1) forming an approximate plane (mean deviation from plane of 0.1164 Å) with C(1) above the plane (2.06(1) Å) to give an approximate pentagonal pyramidal arrangement about Te(1) or a pentagonal bipyramidal arrangement if the lone pair is assumed to be occupying the axial position *trans* to C(1) (see Fig. 2*b*). The two planar S_2CN and S_2CO cores of the dithio groups have a dihedral angle of 10.4(1)°. By contrast, in $Me_2Te[S_2CN(CH_2)_3CH_2][S_2CN(CH_2)_4CH_2]$, the dihedral angle between the two different dithiocarbamate groups is only 1.4(1)°. Despite the fact that the oxygen atom of the OEt group is turned toward tellurium in $Me_2Te[S_2CNMe_2][S_2COEt]$, **8**, rather than the terminal sulfur atom as can be seen from Fig. 2*a*, there is still an approximate plane (mean deviation from plane of 0.0946 Å) around tellurium with the five atoms, S(1), S(2), S(3), C(2), and now O(1) as well as Te(1) forming the plane with C(1) above the plane (2.08(1) Å). The two planar S_2CN and S_2CO cores of the dithio groups have a dihedral angle of only 3.9(1)°. Similar pentagonal planes appear to be a common feature for dimethyltellurium derivatives with sulfur ligands having been reported for $Me_2Te[S_2COR]_2$ (1, 2), $Me_2Te[SCO_2R]_2$ (30), $Me_2Te[SCONR_2]_2$ (31), and $Me_2Te[S_2CN(CH_2)_3CH_2]_2$ (21), where the two dithio groups have small dihedral angles. However, by contrast, in $Me_2Te[S_2CN(CH_2)_4CH_2]_2$, the orientation of the two dithiocarbamates results in a dihedral angle between the two planar S_2CN cores being 69.6(2)° so that the arrangement about tellurium is better described as a distorted octahedral with the lone pair apparently inactive (21). A similar arrangement is found in $Ph_2Te[S_2COEt]_2$ so again it is difficult to identify factors that determine these orientations.

An examination of possible intermolecular associations reveals that both **8** and **9** have similar Te--S′ interactions involving only the anisobonded sulfur atoms of the dithiocarbamate groups as is illustrated by Figs. 3 and 4. The Te(1)—S(2)′ distances are 3.567(2) and 3.585(5) Å for **8** and **9**, respectively, which correspond to bond orders close to 0.15, leading to pseudo-dimers. Thus, despite the different orientations of the dithiocarbonate groups in **8** and **9**, neither of which show any intermolecular distances indicative of associations, similar dimeric units are formed in **8** and **9** by bridges in which the Te(1)-S(2)--Te′(1) and S(2)-Te(1)--S′(2) angles are 72.72(4)° and 107.28(4)°, respectively, for **8** (see Fig. 3) and 72.63(9)° and 107.37(9)°, respectively, for **9** (see Fig. 4). A similar bridging system is found in $Me_2TeI[S_2CN(CH_2)_3CH_2]$, where, in contrast with the $Me_2TeX[S_2CN(CH_2)_4CH_2]$ analogues which all have the halogen atoms acting as bridges, a rectangular bridge again

© 1999 NRC Canada

leads to pseudo-dimers with Te(1)-S(2)--Te′(1) and S(2)-Te(1)--S′(2) angles of 76.19(9)° and 103.8(1)°, respectively (21). Surprisingly, there are no comparable Te--S--Te bridges in the bis-$Me_2Te[S_2CN(CH_2)_nCH_2]_2$ species. In general, dithiocarbonates apparently do not tend to form intermolecular interactions through the sulfur atoms.

As with other dithiocarbamates, the (Te)S-C-N angles are all less than 120°, at 117.0(5)° and 114(1)° for **8** and **9**, respectively, whereas the (Te)S-C-S and S-C-N angles are all over 120°, averaging 122(1)°, which is consistent with the π-bond delocalization within the S_2CN planar moiety being of greater importance in the S_2C—N and TeS(N)C—S bonds. The (Te)S—C bonds (1.756(9) Å avg.) are typical of an S—C bond attached to the stronger Te—S bond in anisobidentate di- and monothiocarbamate derivatives (31) and also shorter than the sum of the covalent radii of C and S of 1.81 Å, suggesting a small degree of participation in the delocalized π-bonding. The C—S bond involving the anisobonded sulfur atom is shorter, with an average length of 1.676(9) Å. This is still considerably longer than a C=S bond (ca. 1.56 Å in CS_2, COS, or CSTe (32)) but similar to that observed in species such as $(NH_2)_2CS$ and thus consistent with a considerable degree of partial π-bond character as well as an anisobidentate link. Not only are the dithiocarbonate groups planar in terms of the sulfur and oxygen atoms about the central carbon, with a mean deviation of 0.003 Å in **8** and 0.004 Å in **9**, but so to a first approximation are the ethyl and methyl groups; C(7) and C(8) being out of plane by only 0.050 and 0.068 Å, respectively, in **8** and C(9) only 0.018 Å out of the plane in **9**. The terminal C=S bond in **8** (1.633(7) Å) is apparently shorter than the anisobonded C=S(--Te) bond in **9** (1.66(2) Å), and conversely, the C—STe bond in **8** (1.74(2) Å) is longer than in **9** (1.729(7) Å). The bond lengths and angles within the S_2CO moiety are in the same range as those reported for $Me_2Te[S_2COEt]_2$ (2), $Me_2Te[S_2COMe]_2$ (1), and $Me_2TeCl[S_2COEt]_2$ (29), which emphasizes the rigidity of the ligand regardless of its orientation about tellurium or whether it is in a mixed ligand species, bis compound, or haloderivative.

The S(1)-Te(1)-S(2) bite angles of the two dithiocarbamate groups are 60.89(2)° and 59.7(1)° with "bites" of 2.994(3) and 2.987(6) Å in **8** and **9**, respectively, which are typical of anisobidentate dithiocarbamates. Similarly, the S(3)--S(4) bite angle in **9** of 59.1(1)° in the dithiocarbonate is close to the average of the two angles in $Me_2Te[S_2COEt]_2$ (2). In view of the rigidity of the planar groups, not surprisingly, the S(3)—S(4) distances in **8** and **9** are similar.

Infrared and Raman spectra

Selected features in the infrared and Raman spectra and their assignments are given in Table 3. In considering these mixed species, it is useful to establish those features among the plethora of peaks, especially those associated with the presence of the CH_3 and CH_2 groups, that most clearly identify the presence of the particular dithiocarbamate, dithiocarbonate, or alkylene dithiophosphate group. In tellurium dithiocarbamate species, a distinctive peak in the infrared spectrum between 1484 and 1508 cm^{-1} corresponds to the ν(C-NR_2) stretching vibration, and one generally of medium intensity in both effects between 963 and 985 cm^{-1} corresponds to the ν(C-S) stretch of the terminal or aniso sulfur atom (7, 8, 12). In tellurium dithiocarbonates, three strong features define the presence of stretching modes involving the stretching of the CO and CS bonds within the moiety S_2COC. As was confirmed by normal coordinates analyses, there is considerable mixing amongst these modes that are seen at ca. 1200, 1120, and 1040 cm^{-1}, and hence, they are assigned as $\nu(S_2COC)_a$, $\nu(S_2COC)_b$, and $\nu(S_2COC)_c$, respectively (29). Strong bands in the infrared spectra in the region 995–900 cm^{-1} provide characteristic features indicative of the presence of the alkylene dithiophosphate group in $Me_2Te[S_2POCMe_2CMe_2O]_2$ and $Me_2Te[S_2POCH_2CMe_2CH_2O]_2$, which are attributable to ring vibrations that are probably coupled with C-C stretching vibrations (20, 30, 31). In compounds **1**–**9**, the above features are seen for the appropriate groups at similar, but not identical positions, to the corresponding bis compounds. Thus, for example, for $Me_2Te[S_2CNMe_2][S_2POCH_2CMe_2CH_2O]$ (**3**), ν(C-NR_2) and ν(C-S) are seen at 1517 and 968 cm^{-1}, respectively, in the infrared and Raman spectra, compared to 1491 and 973 cm^{-1} in $Me_2Te[S_2CNMe_2]_2$ (12), and the most distinct ring vibration in $Me_2Te[S_2POCH_2CMe_2CH_2O]_2$ at 994 cm^{-1} is seen at 985 cm^{-1} in **3**. All of this data is indicative of the presence of a mixed species rather than a mixture of two bis compounds.

The characteristic peaks corresponding to the Te-C asymmetric and symmetric stretches are prominent in all of the Raman spectra of **1**–**9**, in general having values for ν(Te-C)asym (531–541 cm^{-1}) that are closer to those found in $Me_2Te[S_2COR]_2$ or $Me_2TeCl[S_2COR]$ (533–544 cm^{-1}) than to $Me_2Te[S_2POCMe_2CMe_2O]_2$ and $Me_2Te[S_2POCH_2CMe_2CH_2O]_2$ (ca. 529 cm^{-1}) (20). In $Me_2Te[S_2CNMe_2][S_2COEt]$, **8**, whose structure has been described above, the two Te-S stretches are assigned to 359 and 317 cm^{-1}, compared to the asymmetric and symmetric stretches in $Me_2Te[S_2CNMe_2]_2$ (362 and 349 cm^{-1}) and $Me_2Te[S_2COEt]_2$ (382 and 301 cm^{-1}), which is of course consistent with the mixed compound rather than a mixture, as can be illustrated for all nine compounds. While the mixing between the two Te-S modes is going to still be significant in **1**–**9**, the groups are not equivalent as in bis compounds. The Te—S bond to the dithiocarbamate is slightly shorter, so the band at 359 cm^{-1} probably has a greater contribution from Te-S(CNR_2) and that at 317 cm^{-1} a corresponding contribution from Te-S(COR). Both bands are seen at slightly higher wave number in $Me_2Te[S_2CNEt_2][S_2COMe]$, **9**, at 369 and 328 cm^{-1}, which is at least consistent with both bonds being slightly shorter in **9** than in **8**. For the compounds containing a dithiophosphate group, **1**–**6**, it is reasonable to assign the band at higher wave number as having more contribution from Te-S(CNR_2) or Te-S(COR), because in the bis compounds, $Me_2Te[S_2POCMe_2CMe_2O]_2$ and $Me_2Te[S_2POCH_2CMe_2CH_2O]_2$, the Te-S stretches were assigned at lower wave number than in the bis dithiocarbamates and -carbonates (20).

NMR spectra

The $^{13}C\{^1H\}$ NMR spectral data for compounds **1**–**9** are presented in Table 4. Although the peaks corresponding to the S_2CN and S_2CO carbon atom are the weakest in every spectrum, they provide definitive evidence for the formation

© 1999 NRC Canada

Table 3. Selected features (cm^{-1}) and their assignments in the vibrational spectra of $Me_2Te[S_2CNMe_2][S_2POCMe_2CMe_2O]$, **1**, $Me_2Te[S_2CNEt_2][S_2POCMe_2CMe_2O]$, **2**, $Me_2Te[S_2CNMe_2][S_2POCH_2CMe_2CH_2O]$, **3**, $Me_2Te[S_2CNEt_2][S_2POCH_2CMe_2CH_2O]$, **4**, $Me_2Te[S_2COMe][S_2POCMe_2CMe_2O]$, **5**, $Me_2Te[S_2COEt][S_2POCMe_2CMe_2O]$, **6**, $Me_2Te[S_2CNMe_2][S_2COMe]$, **7**, $Me_2Te[S_2CNMe_2][S_2COEt]$, **8**, $Me_2Te[S_2CNEt_2][S_2COMe]$, **9**.[a,b,c]

1	**2**	**3**	**4**	**5**	**6**	**7**	**8**	**9**	Assignment
1504 ms	*1490 s*	*1517 s*	*1483 s*			*1496 ms*	*1501 s*	*1483 vs*	ν (C-NR_2)
				1205 vs	*1200 vs*	*1195 ms*	*1187 s*	*1201 vs*	ν (S_2COC)[a]
				1145 vs	*1140 vs*	*1130 s*	*1110 s*	*1139 vs*	ν (S_2COC)[b]
				1048 vs	*1042 vs*	*1045 vs*	*1031 vs*	*1050 vs*	ν (S_2COC)[c]
1009 mw	1007 m	*1046 vs*	*1045 s*	*1013 sh*	*1010 sh*				ν (PO-C)
		985 vs, br 980 [5]	*992 vs*, br 995 [5]						Ring
961 s 966 [35]	*989 m* 985 [15]	*965 sh* 968 [30]	983 [20]			*971 s* 969 [20]	*968 s* 968 [10]	*984 ms* 982 [15]	ν (S=$CSNR_2$)
911 vs 915 [5]	*917 s* 911 [10]	*910 m*	*909 ms* 914 [15]	*908 vs*	*910 vs*				Ring
818 mw 820 [10]	*815 ms* 820 [5]	*806 m* 814 [5]	*805 s* 810 [10]	*821 mw* 820 [15]	*815 mw* 820 [15]				ν (PO_2)sym
537 [40]	537 [40]	539 [40]	537 [60]	532 [30]	533 [30]	531 [20]	541 [30]	534 [100]	ν (Te-C)asym
515 [90]	512 [80]	517 [90]	523 [100]	525 [50]	525 [50]	515 [40]	527 [40]	520 [60]	ν (Te-C)sym
373 m 372 [100]	*377 s* 378 [100]	*373 ms* 372 [100]	*374 ms* 373 [90]	*352 m* 361 [30]	*361 mw* 361 [20]	*370 ms* 368 [100]	*356 ms* 359 [70]	*358 ms* 369 [80]	ν (Te-S)asym
296 mw 293 [30]	*330 ms* 333 [25]	*298 mw* 303 [5]	*333 ms* 335 [20]	309 mw 313 [100]	310 ms 313 [100]	*351 s* 350 [10]	316 ms 317 [100]	*326 m* 328 [10]	ν (Te-S)sym

[a]IR assignments in italic with s = strong, m = medium, w = weak, sh = shoulder, br = broad, and v = very.

[b]Square brackets denote relative intensities in the Raman effect.

[c]IR spectra run between KBr plates down to 400 cm^{-1} and between polyethylene below 400 cm^{-1}.

[d]Raman spectra run neat in sealed tubes.

Table 4. ^{13}C, ^{31}P, and ^{125}Te NMR chemical shifts for the mixed ligand dimethyltellurium derivatives **1**–**9**.[a,b,c]

Compounds **1**–**9**	$TeCH_3$	POC	POCC	NC	NCC	OC	OCC	NCS_2	OCS_2	^{31}P	^{125}Te
$Me_2Te[S_2CNMe_2][S_2POCMe_2CMe_2O]$, **1**[d]	17.32	89.25	24.40 d [17.6]	44.35					196.0	109.5	525
$Me_2Te[S_2CNEt_2][S_2POCMe_2CMe_2O]$, **2**	17.29	89.09	24.4	49.01	12.14				194.8	110.0	525
$Me_2Te[S_2CNMe_2][S_2POCH_2CMe_2CH_2O]$, **3**[d]	17.40	75.98 d [29.4]	32.67	44.59					196	97.6	522
$Me_2Te[S_2CNEt_2][S_2POCH_2CMe_2CH_2O]$, **4**[d]	17.55	75.81 d [29.4]	32.70 d [18.0]	49.22	12.69				194.2	98.1	519
$Me_2Te[S_2COMe][S_2POCMe_2CMe_2O]$, **5**	16.89	89.70	24.32 d [19.4]			61.22			222.9	107.5	539
$Me_2Te[S_2COEt][S_2POCMe_2CMe_2O]$, **6**	16.85	89.89	24.30			71.24	13.95		222.3	107.7	536
$Me_2Te[S_2CNMe_2][S_2COMe]$, **7**	16.19			44.34		60.62		198.9	222.2		491
$Me_2Te[S_2CNMe_2][S_2COEt]$, **8**	16.17			44.25		70.42	14.16	199.1	221.2		488
$Me_2Te[S_2CNEt_2][S_2COMe]$, **9**	16.34			48.88	12.59	60.29		197.2	222.0		474

[a]The spectra were recorded in $CDCl_3$ and reported in ppm from Me_4Si for ^{13}C, from H_3PO_4 for ^{31}P, and from Me_2Te for ^{125}Te.

[b]All peaks are singlets, the doublets arising from *J*(PC) coupling are marked with a d.

[c]Coupling constants in Hz shown in square brackets.

[d]POCC*C* for **3** and **4**, 21.93 and 21.95 ppm, respectively.

© 1999 NRC Canada

Table 5. ^{1}H NMR chemical shifts for the mixed ligand dimethyltellurium derivatives **1**–**9**.[a,b,c]

Compounds **1**–**9**	Te-CH_3	POC_nCH_3	PO-CH_2	N-CH_3/CH_2	NCH_2-CH_3	O-CH_3/CH_2	OC-CH_3
$Me_2Te[S_2CNMe_2][S_2POCMe_2CMe_2O]$, **1**	2.54 (6 H, s)	1.43 (12 H, s)		3.43 (6 H, s)			
$Me_2Te[S_2CNEt_2][S_2POCMe_2CMe_2O]$, **2**	2.54 (6 H, s)	1.43 (12 H, s)		3.83 (4 H, q) [*J*(HH) 7.0]	1.25 (6 H, t) [*J*(HH) 7.0]		
$Me_2Te[S_2CNMe_2][S_2POCH_2CMe_2CH_2O]$, **3**[d]	2.59 (6 H, s)	1.04 (6 H, s)	4.02 (4 H, d) [*J*(PH) 15.5]	3.43 (6 H, s)			
$Me_2Te[S_2CNEt_2][S_2POCH_2CMe_2CH_2O]$, **4**[d]	2.59 (6 H, s)	1.03 (6 H, s)	4.02 (4 H,d) [*J*(PH) 15.5]	3.82 (4 H, q) [*J*(HH) 7.1]	1.26 (6 H, t) [*J*(HH) 7.1]		
$Me_2Te[S_2COMe][S_2POCMe_2CMe_2O]$, **5**	2.61 (6 H, s)	1.43 (12 H, s)				4.12 (3 H, s)	
$Me_2Te[S_2COEt][S_2POCMe_2CMe_2O]$, **6**	2.58 (6 H, s)	1.41 (12 H, s)				4.55 (2 H, q) [*J*(HH) 7.1]	1.39 (3 H, t)[e]
$Me_2Te[S_2CNMe_2][S_2COMe]$, **7**	2.47 (6 H, s)			3.42 (6 H, s)		4.07 (3 H, s)	
$Me_2Te[S_2CNMe_2][S_2COEt]$, **8**	2.49 (6 H, s)			3.44 (6 H, s)		4.55 (2 H, q) [*J*(HH) 7.1]	1.39 (3 H, t) [*J*(HH) 7.1]
$Me_2Te[S_2CNEt_2][S_2COMe]$, **9**	2.45 (6 H, s)			3.85 (4 H, q) [*J*(HH) 7.1]	1.26 (6 H, t) [*J*(HH) 7.1]	4.05 (3 H, s)	

[a]The spectra were recorded in $CDCl_3$ and reported in ppm from Me_4Si.

[b]Number of protons and multiplicities are in parentheses (s = singlet; t = triplet; d = doublet; q = quartet).

[c]Coupling constants in Hz shown in square brackets.

[d]PO-CH_2 for **3** and **4** are both 4.02 (4 H, d) (*J*(PH) = 15.5) ppm.

[e]Partially masked by the large singlet at 1.41 ppm.

© 1999 NRC Canada

of the mixed ligand Me_2TeLL' species. Thus, for example, in the spectrum of $Me_2Te[S_2CNMe_2][S_2COMe]$, **9**, for which we have the solid state structure, two peaks are seen at 198.9 and 222.2 ppm which correspond to the S_2CN and S_2CO peaks, respectively. These are shifted slightly but definitively from those of the corresponding bis species, $Me_2Te[S_2CNMe_2]_2$ at 200.0 and $Me_2Te[S_2COMe]_2$ at 220.9 ppm (12, 2). When the spectra are rerecorded after 24 h, two additional peaks corresponding to the two bis species are present. Identical features are seen in the spectra of compounds **7** and **8**. In compounds **1**–**4**, which contain a cyclic dithiophosphate instead of a dithiocarbonate, the shift of the S_2CN carbon is more marked.

The peak attributed to the $TeCH_3$ carbon is at 17.32 ppm in $Me_2Te[S_2CNMe_2][S_2POCMe_2CMe_2O]$, **1**, which is slightly less than the average value of the chemical shift for their bis analogues $Me_2Te[S_2POCMe_2CMe_2O]_2$ and $Me_2Te[S_2CNMe_2]_2$, which are at 19.2 and 16.6 ppm, respectively (12, 20). The chemical shifts in **2**–**4** range from 17.29 to 17.55 ppm but in compounds **5** and **6** are at ca. 16.9 ppm, which is closer to the value of ca. 15.6 ppm found in the bis dithiocarbonates (2). In the mixed ligand compounds that contain dithiocarbamate and -carbonate, **7**–**9**, the $TeCH_3$ shifts are essentially the average of the bis species, so the contributions appear to be additive. All of the carbon atoms in the ligands have very similar, though not identical, chemical shifts to those observed in the analogous bis compounds (2, 12, 20). The doublets arising from P-C coupling and the values of the J^{PC} coupling constants are as observed for the bis compounds and (or) related cyclic dithiophosphate derivatives (20, 33).

The $^{31}P\{H\}$ NMR spectra of fresh samples show single peaks (see Table 4) in the region 107.5–110.0 ppm for compounds **1**, **2**, **5**, and **6**, relative to a peak at 105.0 ppm in $Me_2Te[S_2POCMe_2CMe_2O]_2$, and at 97.6 and 98.1 ppm for compounds **3** and **4**, respectively, relative to 92.0 ppm in $Me_2Te[S_2POCH_2CMe_2CH_2O]_2$ (20). These constitute downfield shifts relative to the free cyclic dithiophosphoric acids of the order of 15.1–17.6 ppm when a dithiocarbamate is present with the dithiophosphate and of the order of 20.5–21.0 ppm when a dithiocarbonate is present. These shifts appear to favor the concept that the dithiophosphates are essentially bidentate in solution (34), presumably through rapid exchange. When the spectra were recorded again after the solutions had been left standing, peaks at 105 or 92 ppm were observed arising from the formation of $Me_2Te[S_2POCMe_2CMe_2O]_2$ or $Me_2Te[S_2POCH_2CMe_2CH_2O]_2$, respectively, as the result of disproportionation and grew over several days to be approximately equal in height with that of the Me_2TeLL' species.

The ^{125}Te NMR spectra of freshly prepared solutions (Table 4) show a single peak whose chemical shift is reasonably close to the average value for the related bis compounds and hence in the range 519–528 ppm for compounds **1**–**4**, 539 and 536 ppm for **5** and **6**, and 474–491 ppm for **7**–**9**. The spectra of compounds **7**–**9** show evidence of the presence of the bis species, indicating that disproportionation is already significant in the time taken to run a ^{125}Te NMR spectrum in species that do not contain a cyclic dithiophosphate. Over a period of approximately three days, the relative peak heights of the bis species increase, although all are decreasing in intensity. The peak due to $Me_2Te[S_2COR]_2$ dies away more rapidly, presumably reflecting the fact that the dithiocarbonate derivatives more readily undergo reductive elimination to Me_2Te and diligand.

The ^1H NMR spectral data for compounds **1**–**9** are summarized in Table 5. The splitting patterns and intensities of peaks in the ^1H NMR spectra of all of these compounds are found to be consistent with the structures of **7** and **8**, and by extension to all of the other derivatives. All compounds, **1**–**9**, show a sharp singlet assignable to the CH_3 groups attached to tellurium in the range 2.45–2.54 ppm. The CH_3Te chemical shifts are close to but not quite additive for compounds **1**–**6** and essentially additive for **7**–**9** in that they all lie close to the average value of the two analogous bis derivatives. As was the case for the ^{13}C NMR spectra, the chemical shifts of protons within the ligands are close to but not identical to those of the bis ligand species. In all derivatives containing a dithiocarbamate group, compounds **1**–**4** and **7**–**9**, the two CH_3 or CH_3CH_2 groups show no signs of nonequivalence despite the fact that the nitrogen atom is clearly planar in the solid state structures of **8** and **9**. There is still no sign of coalescence in low-temperature runs. Similarly, in the compounds containing the dithiophosphate groups, **1**–**6**, only single peaks are seen for the CH_3 protons of the dithiophosphate groups even though they have the potential to be in nonequivalent positions. This is the same as was observed for the corresponding bis species, where nonequivalent positions were seen in solid state structures (20). Compounds **3** and **4** have hydrogen atoms attached to the α-carbon atom of the glycoxy groups, which display geminal coupling with phosphorus with $^J(PH)$ values of 15.5 Hz that are the same as in the bis species and appear to be more typical of bidentate than monodentate linkages.

Concluding comments

The study demonstrates that, despite the well-known propensity of Me_2TeL_2 species, where L is a dithio ligand, to undergo exchange and reductive elimination, mixed ligand species of the type Me_2TeLL', are formed in both stepwise and in situ reactions and are not just fortuitous 1:1 mixtures of Me_2TeL_2 and $Me_2TeL'_2$ derivatives. Surprisingly, the orientations of the dithiocarbonate groups differ in $Me_2Te[S_2CNMe_2][S_2COEt]$, **8**, and $Me_2Te[S_2CNEt_2][S_2COMe]$, **9**; having the pendant sulfur atom turned toward tellurium in **9** as has been found for the corresponding bis dithiocarbonate species, $Me_2Te[S_2COEt]_2$ and $Me_2Te[S_2COMe]_2$, but away from tellurium in **8**. This suggests that the difference in energy when aniso bonds are formed between OR groups or terminal S atoms, must be very small and easily overridden by other effects. Despite the difference in the intramolecular associations in **8** and **9**, the intermolecular association to make pseudo dimers is identical in both resulting in Te–S–Te–S rectangular bridges involving the pendant sulfur atom of the dithiocarbamate groups.

Acknowledgement

We wish to thank the Natural Sciences and Engineering Research Council of Canada and Imperial Oil Canada for financial support. One of us (R.R.) thanks Dayanand College,

© 1999 NRC Canada

Ajmer, India for granting a leave of absence, and one of us (L.N.K.) thanks the former for an NSERC Research Reorientation Associateship.

References

1. M.Wieber, E. Schmidt, and C. Burschka. Z. Anorg. Allg. Chem. **525**, 127 (1985).
2. J.H.E. Bailey, J.E. Drake, L.N. Khasrou, and J. Yang. Inorg. Chem. **34**, 124 (1995).
3. A.K. Singh, J.K. Basumatary, T.P. Singh, and B. Padmanabhan. J. Organomet. Chem. **424**, 33 (1993).
4. S. Husebye, K. Maartmann-Moe, and O. Mikalsen. Acta Chem. Scand. **44**, 464 (1990).
5. D. Dakternieks, R. Di Giacomo, R.W. Gable, and B.F. Hoskins. J. Am. Chem. Soc. **110**, 6753 (1988).
6. A.K. Singh and J.K. Basumatary. J. Organomet. Chem. **364**, 73 (1989).
7. J.H.E. Bailey, J.E. Drake, A.B. Sarkar, and M.L.Y. Wong. Can. J. Chem. **67**, 1735 (1989).
8. J.H.E. Bailey, J.E. Drake, and M.L.Y. Wong. Can. J. Chem. **69**, 1948 (1991).
9. J.E. Drake and M.L.Y. Wong. J. Organomet. Chem. **377**, 43 (1989).
10. S. Husebye, K. Maartmann-Moe, and W. Steffenson. Acta Chem. Scand. **44**, 139 (1990).
11. S. Husebye, K. Maartmann-Moe, and W. Steffenson. Acta Chem. Scand. **44**, 579 (1990).
12. J.H.E. Bailey and J.E. Drake. Can. J. Chem. **71**, 42 (1993).
13. D. Dakternieks, R. Di Giacomo, R.W. Gable, and B.F. Hoskins. J. Organomet. Chem. **349**, 305 (1988).
14. D. Dakternieks, R. Di Giacomo, R.W. Gable, and B.F. Hoskins. J. Am. Chem. Soc. **110**, 6762 (1988).
15. R.K. Chadha, J.E. Drake, N.T. McManus, B.A. Quinlan, A.B. Sarkar. Organometallics, **6**, 813 (1987).
16. D. Dakternieks, R. Di Giacomo, R.W. Gable, and B.F. Hoskins. J. Am. Chem. Soc. **110**, 6541 (1988).
17. S. Husebye, K. Maartmann-Moe, and O. Mikalsen. Acta Chem. Scand. **43**, 863 (1989).
18. T.N. Srivastava, J.D. Singh, and S.K. Srivastava. Synth. React. Inorg. Metal. Org. Chem. **20**, 503 (1990).
19. T.N. Srivastava, J.D. Singh, and S.K. Srivastava. Phosphorus Sulfur Silicon Relat. Elem. **55**, 117 (1991).
20. J.E. Drake, L.N. Khasrou, A.G. Mislankar, and R. Ratnani. Can. J. Chem. **72**, 1328 (1994).
21. J.E. Drake and J. Yang. Inorg. Chem. **36**, 1890 (1997).
22. R.C. Paul, K.K. Bhasin, and R.K. Chadha. J. Inorg. Nucl. Chem. **37**, 2337 (1975).
23. H.P.S. Chauhan, C.P. Bhasin, G. Srivastava, and R.C. Mehrotra, Phosphorus Sulfur, **15**, 99 (1983).
24. A.I. Vogel. Practical organic chemistry. Longmans, New York. 499 (1956).
25. G.M. Sheldrick. Acta Crystallogr. **A46**, 467 (1990).
26. TEXSAN-TEXRAY structure analysis package. Molecular Structure Corp., Woodlands, Tex. 1985.
27. L. Pauling. J. Am. Chem. Soc. **69**, 542 (1947); The nature of the chemical bond. 3rd ed. Cornell University Press, Ithaca, New York. 1960. p. 255.
28. A. Bondi. J. Phys. Chem. **68**, 441 (1964); L. Pauling. The nature of the chemical bond. 3rd ed. Cornell University Press, Ithaca, New York. 1960. p. 260.
29. J.E. Drake, R.J. Drake, L.N. Khasrou, and R. Ratnani. Inorg. Chem. **35**, 2831 (1996).
30. J.E. Drake, R.J. Drake, L.N. Khasrou, A.G. Mislankar, R. Ratnani, and J. Yang. Can. J. Chem. **74**, 1968 (1996).
31. J.E. Drake, R.J. Drake, L.N. Khasrou, and R. Ratnani. Inorg. Chem. **33**, 6154 (1994).
32. A.F. Wells. Structural inorganic chemistry. 4th ed. Clarendon Press, Oxford. 1975. p. 739.
33. S. Pandey, G. Srivastava, and R.C. Mehrotra, Transition Met. Chem. **16**, 252 (1991); R. Ratnani, G. Srivastava, and R.C. Mehrotra. Transition Met. Chem. **16**, 204 (1991); Inorg. Chim. Acta, **161**, 253 (1989); R.J. Rao, G. Srivastava, R.C. Mehrotra, B.S. Saraswat, and J. Mason. Polyhedron, **3**, 485 (1984).
34. C. Glidewell. Inorg. Chim. Acta, **25**, 159 (1977).

© 1999 NRC Canada

Stereospecific thionation of 2-ethoxy-1,2-oxaphosphorinane 2-oxide and its derivatives with Lawesson's reagent

Alexandre M. Polozov, Sheldon E. Cremer, and Phillip E. Fanwick

Abstract: The parent phostone, 2-ethoxy-1,2-oxaphosphorinane 2-oxide **1**, and derivatives with substituents at the 3-position (methyl, phenyl, and benzyl; compounds **2**–**4**) were converted with Lawesson's reagent to provide the corresponding sulfide analogues **5**–**8** in moderate yields. The conversion of **2**–**4** occurred with retention of configuration at the phosphorus center. This was implied from the relative R_f values and ^{13}C and ^{31}P NMR chemical shifts of the individual isomers and confirmed for the transformation of **3b** to **7b** by X-ray structures of each of these. Oxidation of **7b**, **8a**, and **8b** with *m*-chloroperoxybenzoic acid alone led to the corresponding oxides **3b**, **4a**, and **4b** with retention. The presence of trifluoroacetic acid during this oxidation process led to varying degrees of epimerization about phosphorus and was dependent on the relative molar equivalents of this acid.

Key words: 2-ethoxy-1,2-oxaphosphorinane 2-oxide, 2-ethoxy-1,2-oxaphosphorinane 2-sulfide, phostone, thiophostone, Lawesson's reagent, stereoselective synthesis, X-ray diffraction.

Résumé : Utilisant le réactif de Lawesson, on a transformé la phostone fondamentale, la 2-oxyde de 2-éthoxy-1,2-oxaphophorinane (**1**), et ses dérivés portant des substituants en position 3 (méthyle, phényle et benzyle, composés **2**–**4**) en analogues sulfurés correspondants (**5**–**8**) avec des rendements modérés. La conversion des composés **2**–**4** se fait avec rétention de configuration au niveau du centre phosphoré. On a déduit cette conclusion sur la base des les valeurs relatives des R_f et des déplacements chimiques en RMN du ^{13}C et du ^{31}P des isomères individuels et elle est confirmée, pour la conversion de **3b** en **7b**, par les structures de chacun telles que déterminées par diffraction des rayons X. L'oxydation des composés **7b**, **8a** et **8b** à l'aide de l'acide *m*-chloroperbenzoïque seul conduit aux oxydes correspondants **3b**, **4a** et **4b** avec rétention de configuration. Lors de ces oxydations, l'addition d'acide trifluoroacétique au milieu réactionnel conduit à divers degrés d'épimérisation autour du phosphore et celui-ci dépend des quantités molaires relatives de cet acide.

Mots clés : 2-oxyde de 2-éthoxy-1,2-oxaphophorinane, 2-sulfure de 2-éthoxy-1,2-oxaphophorinane, phostone, réactif de Lawesson, synthèse stéréosélective, diffraction des rayons X.

[Traduit par la Rédaction]

Introduction

The thionation of the phosphoryl group (P=O) is a fundamental reaction in organophosphorus chemistry. In recent years, Lawesson's Reagent (LR) has become a reagent of choice for this transformation due to improved yields of thiophosphoryl products and milder reaction conditions (1–7) compared to the conventional use of P_2S_5 (8–10). Another advantage of LR over P_2S_5 was its stereochemical predictability. Whereas chiral phosphorus compounds led to predominant retention of configuration (1, 5, 6) with this reagent, reports using P_2S_5 were sometimes variable (predominant retention (8–10) or racemization (9, 10)). In the present study, a careful investigation of the stereochemistry of thionation of 2-ethoxy-1,2-oxaphosphorinane 2-oxides (phostones) with LR was undertaken, including an analysis of the reaction products and correlation of their stereochemical configuration with the starting materials.

Stereochemical research in organophosphorus chemistry is often based on phosphorinane systems (11), because of their relevance to biologically important substances. For example, 1,2-oxaphosphorinane derivatives were recently studied as analogs of natural carbohydrates with emphasis on a potential medical application (12–17). Thus, we selected the phostone series **1**–**4** (Scheme 1) for thionation, since these materials were previously studied in our laboratory (18–22).

To our knowledge, no attempts have been made to prepare the thio analogs **5**–**8**. Herein, we describe the stereochemical results of the reactions of 2-ethoxy-3-alkyl-1,2-oxaphosphorinane 2-oxides **2** and **4** as well as the 3-phenyl derivative **3** with LR. The stereospecific course for **3b** to **7b** was confirmed by X-ray crystal structure studies; the relative R_f values and relative nmr spectral data enabled tentative isomer assignments for compounds **2**, **4**, **6**, and **8**.

Received December 17, 1998.

A.M. Polozov. A.M.Butlerov Research Chemical Institute, Kazan State University, Kazan 18, 420008, Russia.
S.E. Cremer.[1] Department of Chemistry, Marquette University, Box 1881, Milwaukee, WI 53201-1881, U.S.A.
P.E. Fanwick. Purdue University, Department of Chemistry, 1393 Brown Building, West Lafayette, IN 47907-1393, U.S.A.

[1]Author to whom correspondence may be addressed. Telephone: 414-2887191. Fax: 414-2887066. e-mail: 6278cremers@vms.csd.mu.edu

© 1999 NRC Canada

Scheme 1.

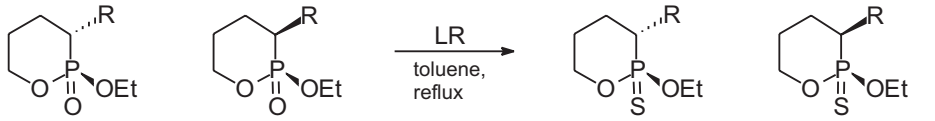

1 R=H
2a R=Me **2b** R=Me
3a R=Ph **3b** R=Ph
4a R=CH_2Ph **4b** R=CH_2Ph

5 R=H
6a R=Me **6b** R=Me
7a R=Ph **7b** R=Ph
8a R=CH_2Ph **8b** R=CH_2Ph

Table 1. Thionation reactions of 2-ethoxy-1,2-oxaphosphorinanes **1**–**4**.

Substrate	Product[a]	Yield, %	R_f (solvent)[g]	^{31}P NMR (ppm)
1	**5**	64	0.30 (1:9)	91.0
2a/2b[b] = 1.3	**6a/6b** = 1.2	36/23[c]	0.33/0.13[c] (15:85)	103.6/95.8[c]
3b (99%)[d]	**7b** (98%)[e]	54		
3a/3b = 3.2	**7a/7b** = 3.2	20/17[f]	0.53/0.33[f] (15:85)	98.8/89.8[f]
4a (97%)[d]	**8a** (95%)[e]	68	0.38 (7:93)	101.9
4b (96%)[d]	**8b** (96%)[e]	44	0.21 (7:93)	94.3

[a]Isomer ratios were determined from the ^{31}P NMR spectra.
[b]These isomers have not been separated.
[c]**6a**/**6b**.
[d]Stereoisomer purity.
[e]Stereoisomer purity in the mixture prior to reaction work-up.
[f]**7a**/**7b**.
[g]EtOAc/hexane in parentheses.

Results and discussion

1. Optimization of the reaction conditions of the thionation reaction

Thionation of phosphoryl compounds has been carried out in benzene or toluene solutions up to reflux temperatures and with 1/0.5 ratio of reactant/reagent (1–3). Similar reaction conditions were employed in subsequent papers (4–7). The distillation or chromatography of the resultant reaction mixture with or without water work-up gave products in moderate yields.

Heating the parent oxaphosphorinane **1** at reflux temperatures with 0.55 equiv. of LR in toluene for 1.5 h and subsequent distillation resulted in a 52% yield of the 1,2-oxaphosphorinane 2-sulfide **5**. The yield was lower upon water work-up followed by silica gel chromatography (47%). Utilization of other solvents at reflux (benzene for 22 h; acetonitrile for 27 h) gave only 31 and 29% yields, respectively. The yield of **5** was improved through multiple extraction of the original reaction mixture (nonaqueous work-up) with EtOAc/hexane (15:85) under ultrasound irradiation followed by distillation (64%). GC–MS spectra of the extract showed less impurities than the original reaction mixture; impurities made the purification of the product by any method more difficult.

2. Synthesis of thionophosphorinates 6–8. Sterochemistry of the thionation reaction

Synthesis of starting materials and separation of the individual isomers followed previous methods (20–22). Furthermore, isomer **3b** was separated from the isomeric mixture **3a**,**b** by fractional recrystallization to provide a single crystal for X-ray structural analysis.

The optimized reaction conditions found during the synthesis of **5** were applied to the thionation of isomeric compounds **2**–**4**. Moreover, a 1:0.75 equivalent ratio of **2**–**4** to LR was used to accelerate the slower reactions; in addition, the reactions were allowed to proceed for a longer time. The slower reactions were possibly due to greater steric demands in **2**–**4** than in the unsubstituted oxaphosphorinane **1**.

The reactions were conducted with highly enriched isomers of **3b**, **4a**, and **4b** and on isomer mixtures of **2a**,**b** and **3a**,**b**; in all cases, the isomers were racemic mixtures. The reactions products were then analyzed by GS–MS and ^{31}P nmr spectroscopy. Separation and purification was readily achieved by flash chromatography of the individual isomers (large R_f difference). Although the yields were only moderate, each reaction occurred in a stereospecific fashion. (Table 1).

The reaction rates of the *cis* versus the *trans* isomers of **2**–**4** with LR were very similar. This was determined by monitoring their ratio in the GC as the reaction progressed. The ratio was constant throughout the reaction. Since the rates of reaction with LR were reported to increase with an increase in the nucleophilicity of phosphoryl oxygen (3, 4), the nucleophility of the P=O in the individual isomers of **2**–**4** is concluded to be comparable.

A single crystal X-ray study of both **3b** and the 2-ethoxy-1,2-oxaphosphorinane 2-sulfide **7b** revealed these to be *cis* isomers (vide infra). This established that this reaction proceeded with retention of configuration about phosphorus. A relative comparison of R_f values, GC retention times, and ^{31}P nmr chemical shift data of *cis*-**7b**, enabled the isomers **6b**, **7b**, and **8b** to be assigned to the *cis* configuration. The *cis* isomers (**6b**, **7b**, and **8b**) had smaller R_f values (more polar) on silica gel TLC plates and longer GC retention times. Likewise, the corresponding ^{31}P NMR shifts of the *cis* iso-

© 1999 NRC Canada

Table 2. ^{13}C NMR data for 2-ethoxy-1,2-oxaphosphorinane 2-sulfide and derivatives (**5**–**8**).[a]

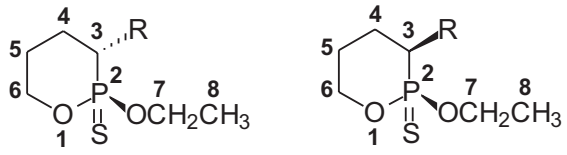

a : *trans* **b** : *cis*

5–**8**[b]	C-3 ($^1J_{CP}$)	C-4 ($^2J_{CP}$)	C-5 ($^3J_{CP}$)	C-6 ($^2J_{CP}$)	C-7 ($^2J_{CP}$)	C-8 ($^3J_{CP}$)	Exocyclic R group
5	31.64 (99.0)	21.11 (9.8)	25.60 (6.7)	68.99 (8.9)	61.28 (7.3)	15.88 (7.3)	
6a	35.17 (97.6)	25.34 (4.7)	29.62 (3.2)	68.57 (6.3)	62.20 (8.3)	16.15 (5.0)	14.74 (2.5)
6b	37.51 (100.6)	26.76 (5.2)	29.82 (7.1)	69.09 (8.9)	61.55 (7.1)	16.06 (5.9)	14.62 (2.5)
7a	48.81 (93.4)	28.33 (2.4)	27.06 (1.8)	68.51 (6.8)	63.18 (7.7)	16.09 (5.7)	136.08 ($^2J_{CP}$ 6.2), 128.52 ($^3J_{CP}$ 5.9), 128.01 ($^4J_{CP}$ 2.5), 127.13 ($^5J_{CP}$ 3.6)
7b	49.76 (93.1)	28.22 (7.6)	26.96 (4.2)	68.97 (6.8)	62.28 (7.5)	15.81 (4.9)	135.52 ($^2J_{CP}$ 6.2), 128.78 ($^3J_{CP}$ 6.3), 127.99 ($^4J_{CP}$ 2.4), 127.55 ($^5J_{CP}$ 3.6)
8a	42.73 (97.5)	26.92 (4.2)	25.80 (5.5)	68.59 (6.0)	62.51 (6.1)	16.10 (6.9)	35.74, 138.55 ($^3J_{CP}$ 14.8), 129.18, 128.30, 126.33
8b	44.26 (97.5)	26.55 (4.7)	26.17 (7.5)	69.11 (10.3)	61.70 (7.2)	16.12 (6.6)	34.71, 138.64 ($^3J_{CP}$ 19.6), 129.12, 128.44, 126.40

[a]The ^{13}C assignments were supported by analysis of cosy and hetcor (^{13}C-^1H) spectra.

[b]**5** (R = H); **6** (R = Me); **7** (R = Ph); **8** (R = $PhCH_2$).

Scheme 2.

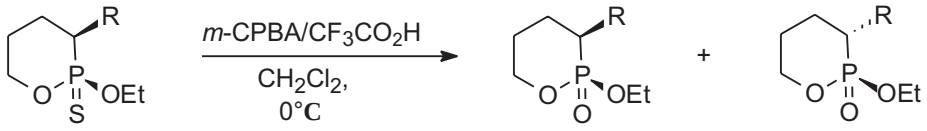

7b **3b** **3a**

mers were upfield from the *trans* isomers. These assignments were supported by the relative consistency of their ^{13}C NMR spectra (Table 2). The chemical shifts of endocyclic C-3 and C-6 of the *cis* isomers (**b**) are downfield, and the ^{31}P-$^{13}C(5)$ coupling constants are somewhat larger than those in the *trans* isomers (**a**); moreover, C-7 for the *cis* isomers are slightly upfield from the *trans* isomers.

3. Stereochemistry of the oxidation reactions

The *m*-chloroperoxybenzoic acid (MCPB) oxidation of menthyl phenylphosphinothiolates compounds is known to proceed with predominant retention of configuration at phosphorus (23). However, the addition of trifluoroacetic acid (CF_3CO_2H) resulted in partial to predominant inversion of configuration at the phosphorus centre, and depended upon the molar equivalents of added acid (23).

The pure isomers **7b**, **8a**, and **8b** were stereospecifically oxidized to **3b**, **4a**, and **4b** respectively with *m*-CPBA in CH_2Cl_2 at 0°C. When 1 and 5 equiv. of CF_3CO_2H were added to the oxidation of **7b**, the resultant ratio of **3a**/**3b** was 1:24 and 1:1.4, respectively (Scheme 2). However, no isomerization was observed when single isomers **7b** or **3b** were subjected to CF_3CO_2H alone under the same reaction conditions (concentrations and temperature). Thus, the mechanism of the oxidation itself must be altered by the presence of CF_3CO_2H.

Structural study

Upon evaporation from CH_2Cl_2–cyclohexane solutions, single crystals of **3b** and **7b** suitable for X-ray studies were prepared. Figures 1 and 2 display the ORTEP structures along with a list of selected geometrical parameters.[2]

The X-ray crystal study of the racemic molecules **3b** and **7b** revealed no unusual features of the molecular structures. The molecules adopted chair conformations, with both the phosphoryl (thiophosphoryl) and phenyl groups in equatorial positions. The structural parameters (bond length and angles) in **3b** were close to those measured in **7b**. In both molecules, the phosphorus end of the molecule is flatter than the hydrocarbon end of the ring. The flattening around the phosphorus site in **3b** is greater than in **7b**, which is evident from the smaller torsional angles of 50.15(0.19)° for C(4)-P(1)-O(1)-C(1) and –47.23(0.17)° for O(1)-P(1)-C(4)-C(3) in **3b** compared to the analogous torsional angles of –53.08(0.31)°

[2]Tables of crystallographic data, structure solution and refinement, positional parameters, bond distances and angles, torsion angles, and anisotropic temperature factors have been deposited as supplementary material and may be purchased from: The Depository of Unpublished Data, Document Delivery, CISTI, National Research Council Canada, Ottawa, Canada, K1A 0S2. With the exception of bond and torsion angles and anisotropic temperature factors, these have also been deposited with the Cambridge Crystallographic Data Centre and can be obtained on request from: The Director, Cambridge Crystallographic Data Centre, University Chemical Laboratory, 12 Union Road, Cambridge, CB2 1EZ, U.K.

© 1999 NRC Canada

Fig. 1. ORTEP representation from the X-ray crystal structure of **3b**.

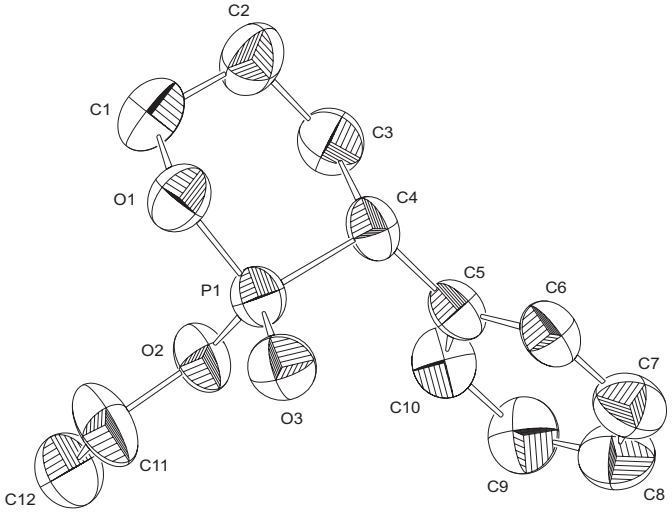

Fig. 2. ORTEP representation from the X-ray crystal structure of **7b**.

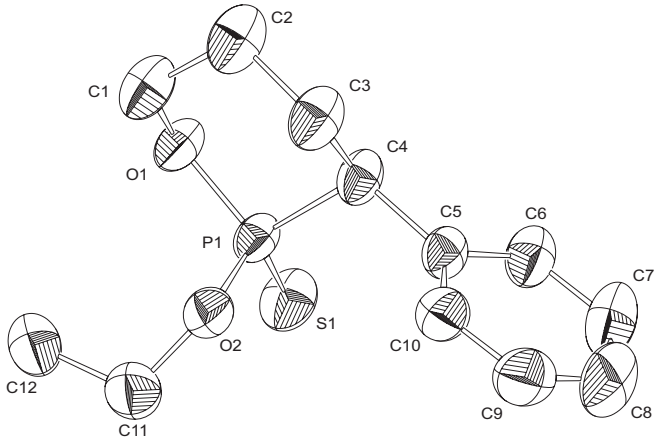

for C(4)-P(1)-O(1)-C(1) and 49.84(0.31)° for O(1)-P(1)-C(4)-C(3) in **7b.** The phenyl ring in both molecules is close to perpendicular to the plane of the phosphorinane ring plane as defined by the dihedral angle formed from the two planes in **3b**: C(10)C(5)C(6)/C(2)O(1)C(4) of –76.30°; and the two planes in **7b**: C(10)C(5)C(6)/ C(2)O(1)C(4) of –71.63°.

Additional selected geometrical bond lengths (Å), bond angles, and torsional angles for **3b** are the following: P(1)—O(3) 1.4576(15), P(1)—O(2) 1.5769(14), P(1)—O(1) 1.5828(15), P(1)—C(4) 1.798(2); O(1)-P(1)-C(4) 104.27(9)°, O(3)-P(1)-O(1) 110.44(8)°; C(1)-C(2)-C(3)-C(4) –60.99(0.28)°, O(1)-C(1)-C(2)-C(3) 59.09(0.28)°. Likewise selected geometrical parameters for **7b** are the following: P(1)—S(1) 1.9208(13), P(1)—O(2) 1.583(2), P(1)—O(1) 1.587(2), P(1)—C(4) 1.818(3); O(1)-P(1)-C(4) 102.24(14)°, S(1)-P(1)-O(1) 110.71(10)°; C(4)-C(3)-C(2)-C(1) 60.78(0.51)°, C(3)-C(2)-C(1)-O(1) –58.70(0.51)°.

Experimental

General

All reactions with LR were carried out in flame-dried glassware under a nitrogen atmosphere. NMR spectra were recorded on a GE OMEGA 300 NMR spectrometer (300 MHz). $CDCl_3$ was used as the solvent in all cases unless stated otherwise. Chemical shifts for ^1H, ^{13}C (75 MHz), and ^{31}P (121 MHz) NMR were reported in ppm relative to TMS, $CHCl_3$, and 85% H_3PO_4, respectively. Coupling constants, *J*, are given in Hz. GC–MS data were obtained on a Hewlett–Packard 5890A Gas Chromatograph-5970 series mass selective detector: capillary column DB-1, 0.25 mm id × 30 m; inj. temp. 260°C; det. temp. 265°C; init. temp. 70°C for 5 min then 10°C min^{-1}; final temp. 250°C. Elemental analyses were performed by Quantitative Technologies Inc., N.J.. HRMS were performed at the Washington University Resource for Biomedical and Bio-organic Mass Spectrometry in St. Louis, Mo. Melting points were determined with Thomas–Hoover capillary melting point apparatus and are uncorrected. TLC (Aldrich) plates were developed by iodine. All chemicals were purchased from the Aldrich Chemical Co. and used without further purification. Preparative flash chromatography was performed with Acros silica gel (0.035–0.075 mm).

X-ray diffraction

The crystals were mounted on a glass fiber in a random orientation in an Enraf–Nonius CAD-4 computer controlled κ axis diffractometer equipped with a graphite crystal, incident beam monochromator, using Mo K_α radiation (λ = 0.71073 Å). Cell constants and an orientation matrix for data collection were obtained from least-squares refinement, using the setting angles of 25 reflections in the range $20 < \theta < 23°$. The data were collected at a temperature of 296 ± 1 K using the ω-2θ scan technique. For **3b**, a total of 3344 reflections were collected of which 2986 were unique; for **7b**, a total of 2061 reflections were collected of which 1973 were unique. Lorentz and polarization corrections were applied to the data. No absorption correction was made. The structures were solved by direct methods using SIR92 (24). The remaining atoms were located in succeeding difference Fourier syntheses. Hydrogen atoms were included in the refinement but restrained to ride on the atom to which they are bonded. Refinement was performed on an AlphaServer 2100 using SHELX-93 (25). Final R = 0.043 (**3b**), 0.043 (**7b**); R_w = 0.125 (**3b**), 0.123(**7b**). Crystallographic drawings were constructed using programs ORTEP (26).

Crystal data

3b: $C_{12}H_{17}O_3P$, M = 240.24, a = 10.1773(11) Å, b = 9.3449(9) Å, c = 13.4417(10) Å, β = 99.361 (8)°, V = 1261.4(4) $Å^3$, space group $P2_1/c$ (no. 14), Z = 4, D_c = 1.264 g cm^{-3}. Colorless crystals were obtained by slow evaporation from CH_2Cl_2–cyclohexane solution; crystal dimensions 0.70 × 0.70 × 0.70 mm; μ(Mo-K_α) = 2.0 cm^{-1}.

7b: $C_{12}H_{17}O_2PS$, M = 256.31, a = 12.4075(8) Å, b = 8.0847(13) Å, c = 14.2526(12) Å, β = 114.744 (6)°, V = 1298.4(5) $Å^3$, space group $P2_1/n$ (no. 14), Z = 4, D_c = 1.310 g cm^{-3}. Colorless crystals were obtained by slow

© 1999 NRC Canada

evaporation from CH_2Cl_2–cyclohexane solution; crystal dimensions 0.50 × 0.35 × 0.10 mm; μ(Mo-K_α) = 3.4 cm^{-1}.

Isolation of crystalline *cis*-2-ethoxy-3-phenyl-1,2-oxaphosphorinane 2-oxide 3b

A solution of a mixture of isomers **3a**,**b** (3.2 g, **3a**:**3b** ratio 1.3:1) in CH_2Cl_2–cyclohexane (1:1) was allowed to slowly evaporate at room temperature. A single isomer **3b** (0.70 g, mp 79–81°C) was filtered out as colorless crystals: R_f 0.43 (EtOAc); ^{1}H NMR δ: 7.39–7.22 (m, 5H), 4.42–4.18 (m, 2H), 4.06–3.82 (m, 2H), 3.26–3.13 (m, 1H), 2.39–2.12 (m, 2H), 2.07–1.83 (m, 2H), 1.17 (dt, 3H, $^3J_{HH}$ = 7.0 Hz); *m*/*z*: 240 (M^+, 24%), 184 (11), 130 (100), 115 (20), 104 (40), 91 (45), and 77 (17). ^{13}C NMR δ: 135.62 ($^2J_{CP}$ = 8.5), 128.47, 128.42, 127.18 (d, $^3J_{CP}$ = 2.4), 69.99 (d, $^2J_{CP}$ = 7.4), 62.01 (d, $^2J_{CP}$ = 7.3), 42.96 ($^1J_{CP}$ = 124.5), 28.85 ($^3J_{CP}$ = 6.1), 27.19 ($^2J_{CP}$ = 4.9), 16.26 ($^3J_{CP}$ = 6.1 Hz); ^{31}P NMR δ: 22.4 ppm. HREI–MS calcd. for $C_{12}H_{17}O_3P$: 240.0915; found: 240.0919; R_f 0.33 (EtOAc); *m*/*z*: 240 (M^+, 26%), 184 (21), 130 (100), 115 (23), 104 (53), 91 (47), and 77 (19). By comparison, the *trans* isomer **3a** had an R_f value of 0.33 (EtOAc) and a ^{31}P NMR shift at 26.5 ppm.

2-Ethoxy-1,2-oxaphosphorinane 2-sulfide 5

The preparation and properties of compound **1** have been reported (21, 22, 27–32). A solution of **1** (0.5 g, 3 mmol) and LR (0.68 g, 1.7 mmol) in toluene (3 mL) was stirred and heated at reflux for 1.5 h. Three variants of the work-up were used:

(*i*) The reaction mixture was washed by water (3 mL) and extracted with toluene (3 × 3 mL). The combined extracts were dried over anhydrous $MgSO_4$, filtered, the solvent was removed in vacuum, and the residue was purified by flash column chromatography on SiO_2 (EtOAc/hexane, 1:9) to give **5** (0.26 g, 47% yield) as a colorless liquid.

(*ii*) The reaction mixture was distilled in vacuum (bp 79–81°C/0.45 mmHg) (1 mmHg = 133.3 Pa) to give **5** (0.29 g, 52% yield).

(*iii*) The toluene was removed in vacuum, and the oily residue was extracted with EtOAc/hexane, 15:85 (4 × 10 mL) under ultrasound radiation (5 min for each extraction). Then, the solvent was removed in vacuum, and the residue was distilled in vacuum (bp 79–81°C/0.45 mmHg) to give **5** (0.35 g, 64% yield).

^{1}H NMR δ: 4.34–4.09 (m, 4H), 2.21–2.06 (m, 4H), 1.86–1.63 (m, 2H), 1.35 (t, 3H, $^3J_{HH}$ = 9.0 Hz); *m*/*z*: 180 (M^+, 60%), 136 (39), 119 (19), 103 (18), 93 (17), 65 (22), 55 (100), and 41(26). Anal. calcd. for $C_6H_{13}O_2PS$: C 40.00, H 7.27; found: C 39.71, H 7.06.

2-Ethoxy-3-methyl-1,2-oxaphosphorinane 2-sulfide 6

A solution of **2** (0.67 g, 3.76 mmol; **2a**:**2b**, 1.3:1) and LR(1.14 g, 2.11 mmol) in toluene (4 mL) was stirred and heated at reflux for 3.0 h. A mixture of **6a**:**6b** (1.2:1) was obtained. The toluene was removed in vacuum, and the oily residue was extracted with EtOAc/hexane, 15:85 (3 × 25 mL) under ultrasonic radiation. The solvent was removed in vacuum, and the residue was purified by flash column chromatography on SiO_2 (60 g, EtOAc/hexane, 5:95, then 7:93) to give **6a** (0.26 g, 36% yield) and **6b** (0.17g, 23% yield) as clear oils. HREI–MS calcd. for $C_7H_{15}O_2PS$ (mixture of isomers): 194.0530, found: 194.0524. This compound, prepared by a different method, has been reported previously (33).

***trans*-2-Ethoxy-3-methyl-1,2-oxaphosphorinane 2-sulfide 6a**

^{1}H NMR δ: 4.33–4.08 (m, 4H), 2.10–1.61 (m, 5H), 1.30 (t, 3H, $^3J_{HH}$ = 7.1 Hz), 1.13 (dd, 3H, $^3J_{HH}$ = 6.5, $^3J_{HP}$ = 21.7 Hz); *m*/*z*: 194 (M^+, 42%), 166 (4), 150 (18), 133 (10), 93 (18), 69 (77), and 41 (100).

***cis*-2-Ethoxy-3-methyl-1,2-oxaphosphorinane 2-sulfide 6b**

^{1}H NMR δ: 4.29–4.05 (m, 4H), 2.10–1.61 (m, 5H), 1.33 (t, 3H, $^3J_{HH}$ = 7.1 Hz), 1.20 (dd, 3H, $^3J_{HH}$ = 6.8, $^3J_{HP}$ = 20.5 Hz); *m*/*z*: 194 (M^+, 50%), 166(5), 150(24), 133 (14), 93(13), 69(84), and 41(100).

2-Ethoxy-3-phenyl-1,2-oxaphosphorinane 2-sulfide 7

A solution of **3** (0.9 g, 3.75 mmol; **3a**:**3b**, 3.2:1) and LR (1.14 g, 2.8 mmol) in toluene (4 mL) was stirred and heated at reflux for 3.0 h. A mixture of **7a**:**7b** (3.2:1) was obtained. The toluene was removed in vacuum, and the oily residue was extracted with EtOAc/hexane, 15:85 (3 × 30 mL) under ultrasonic radiation. The solvent was removed in vacuum, and the residue was purified by flash column chromatography on SiO_2 (EtOAc/hexane, 5:95, then 15:85) to give **7a** (0.19 g, 20%) as a clear oil and **7b** (0.17 g, 17% yield) as colorless crystals; mp 84–86°C (CH_2Cl_2–cyclohexane).

A similar protocol was applied to the pure isomer **3b** (0.14 g, 5.83 mmol). After work-up and flash chromatography, pure **7b** (0.07 g, 47%) was isolated.

***trans*-2-Ethoxy-3-phenyl-1,2-oxaphosphorinane 2-sulfide 7a**

^{1}H NMR δ: 7.32–7.26 (m, 5H), 4.55–4.00 (m, 4H), 3.38–3.25 (m, 1H), 2.61–2.42 (1 H), 2.24–1.78 (m, 3H), 1.21 (dt, 3H, $^3J_{HH}$ = 7.2, $^2J_{HP}$ = 1.1 Hz); *m*/*z*: 256 (M^+, 74%), 131 (100), 115 (15), 104 (38), 91 (53), 77 (16), and 63 (11). Anal. calcd. for $C_{12}H_{17}O_2PS$ (%): C 56.24, H 6.69; found: C 56.12, H 6.69.

***cis*-2-Ethoxy-3-phenyl-1,2-oxaphosphorinane 2-sulfide 7b**

^{1}H NMR δ: 7.37–7.26 (m, 5H), 4.37–4.23 (m, 2H), 4.14–3.95 (m, 2H), 3.30–3.19 (m, 1H), 2.54–2.37 (m, 1H), 2.27–1.87 (m, 3H), 1.24 (dt, 3H, $^3J_{HH}$ = 7.1, $^2J_{HP}$ 0.9 Hz); *m*/*z* 256 (M^+, 77%), 131 (100), 115 (19), 104 (38), 91 (61), 78 (18), and 63 (13). Anal. calcd. for $C_{12}H_{17}O_2PS$ (%): C 56.24, H 6.69; found: C 56.04, H 6.65.

***trans*-2-Ethoxy-3-benzyl-1,2-oxaphosphorinane 2-sulfide 8a**

A solution of **4a** (0.064 g, 0.025 mmol; 97% isomer purity) and LR (0.077 g, 0.19 mmol) in toluene (1 mL) was stirred and heated at reflux for 3.0 h. The toluene was removed in vacuum, and the oily residue was extracted with EtOAc/hexane, 15:85 (3 × 3 mL) under ultrasonic radiation. The solvent was removed in vacuum, and the residue was purified by flash column chromatography on SiO_2 (EtOAc/hexane, 7:93) to give 95% pure **8a** (0.046 g, 68%

© 1999 NRC Canada

yield) as a clear oil. ^{1}H NMR δ: 7.32–7.19 (m, 5H), 4.39–3.95 (m, 4H), 3.08–3.03 (ddd, 1H, $^2J_{HH}$ = 14.0, $^3J_{HH}$ = 6.1 Hz, $^3J_{HP}$ = 11.0 Hz), 2.62 (ddd, 1H, $^2J_{HH}$ = 14.0, $^3J_{HH}$ = 9.2 Hz, $^3J_{HP}$ = 18.2 Hz), 2.30–2.14 (m, 1H), 1.88–1.64 (m, 4H), 1.20 (t, 3H, $^3J_{HH}$ = 7.0 Hz); *m*/*z*: 270 (M^+, 100%), 195 (10), 179 (18), 144 (62), 129 (45), 115 (25), 91 (77), 65 (30), and 41 (24). Anal. calcd. for $C_{13}H_{19}O_2PS$ (mixture of 95% **8a** and 5% **8b**) (%): C 57.76, H 7.08; found: C 57.89, H 7.17.

cis-2-Ethoxy-3-benzyl-1,2-oxaphosphorinane 2-sulfide 8b

A solution of **4b** (0.039 g, 0.015 mmol; 96% isomer purity) and LR (0.046 g, 0.012 mmol) in toluene (0.5 mL) was stirred and heated at reflux for 3.0 h. Toluene was removed in vacuum, and the oily residue was extracted with EtOAc/hexane, 15:85 (3 × 3 mL) under ultrasonic radiation. Solvent was removed in vacuum, and the residue was purified by flash column chromatography on SiO_2 (EtOAc/hexane, 10:90) to give **8b** (0.018 g, 44% yield; 96% isomer purity) as a clear oil.

^{1}H NMR δ: 7.33–7.17 (m, 5H), 4.35–4.01 (m, 4H), 3.36 (ddd, 1H, $^2J_{HH}$ = 13.6, $^3J_{HH}$ = 0.8, $^3J_{HP}$ = 2.3 Hz), 2.41 (ddd, 1H, $^2J_{HH}$ = 13.6, $^3J_{HH}$ = 5.5, $^3J_{HP}$ 11.5 Hz), 2.23 –2.02 (m, 1H), 1.79–1.61 (m, 4H), 1.37 (t, 3H, $^3J_{HH}$ = 7.1 Hz); *m*/*z*: 270 (M^+, 100%), 195 (9), 179 (17), 151 (15), 144 (72), 129 (45), 115 (26), 91 (85), 65 (33), and 41(25).

Oxidation of _cis_-2-ethoxy-3-phenyl-1,2-oxaphosphorinane 2-sulfide 7b with _m_-CPBA

A solution of *m*-CPBA (26 mg; 0.086 mmol, based on 57% content) in CH_2Cl_2 (0.5 mL) was added over 1 min to a stirred solution of **7b** (20 mg, 0.078 mmol, 100% isomeric purity) in CH_2Cl_2 (4 mL) at 0°C. Stirring was continued for 5 min and then the mixture was treated with aq. Na_2CO_3 sat. (3 mL) and extracted by CH_2Cl_2 (3 × 3 mL). The combined extracts were dried over anhydrous $MgSO_4$, filtered, and analyzed by GC–MS and ^{31}P NMR. Only **3b** was detected. Evaporation of solvent gave **3b** (17 mg, 91%).

Oxidation of _cis_-2-ethoxy-3-phenyl-1,2-oxaphosphorinane 2 sulfide 7b with _m_-CPBA in the presence of CF_3CO_2H

A solution of *m*-CPBA (26 mg; 0.086 mmol, based on 57% content) in CH_2Cl_2 (0.5 mL) was added over 1 min to a stirred solution of **7b** (20 mg, 0.078 mmol, 100% isomeric purity) and 1 equiv. of CF_3CO_2H (8.9 mg, 0.78 mmol) in CH_2Cl_2 (4 mL) at 0°C. Stirring was continued for 5 min, and the mixture was then treated with aq. Na_2CO_3 sat. (3 mL) and extracted with CH_2Cl_2 (3 × 3 mL). The combined extracts were dried over anhydrous $MgSO_4$, filtered, and analyzed by GC–MS and ^{31}P NMR. A mixture of **3b** (96%) and **3a** (4%) was detected by ^{31}P NMR and GC–MS.

The identical procedure using 5 equiv. of CF_3CO_2H (45 mg, 3.9 mmol) gave a mixture of **3b** (42%) and **3a** (58%).

Oxidation of _cis_-2-ethoxy-3-benzyl-1,2-oxaphosphorinane 2-sulfide 8b with _m_-CPBA

A solution of *m*-CPBA (27 mg; 0.089 mmol, based on 57% content) in CH_2Cl_2 (0.5 mL) was added over 1 min to a stirred solution of **8b** (22 mg, 0.081 mmol, 100% isomeric purity) in CH_2Cl_2 (4 mL) at 0°C. Stirring was continued for 5 min and then the reaction worked up as before (see oxidation of **7b**). Only **4b** was detected by ^{31}P NMR and GC–MS. Evaporation of the solvent gave **4b** (18 mg, 86%). ^{31}P NMR δ: 26.8 ppm; R_f 0.34 (EtOAc); *m*/*z*: 254 (M^+, 44%), 163 (72), 144 (29), 135 (65), 129 (49), 117 (42), 91 (100), and 65 (39).

Oxidation of _trans_-2-ethoxy-3-benzyl-1,2-oxaphosphorinane 2-sulfide 8a with _m_-CPBA

A solution of *m*-CPBA (27 mg; 0.089 mmol, based on 57% content) in CH_2Cl_2 (0.5 mL) was added over 1 min to a stirred solution of **8a** (22 mg, 0.081 mmol, 100% isomeric purity) in CH_2Cl_2 (4 mL) at 0°C and then stirred for an additional 5 min and worked up as before (supra infra). Only **4a** was detected in the ^{31}P NMR spectrum and by GC–MS. Evaporation of the solvent gave **4a** (19 mg, 93%). ^{31}P NMR δ: 29.6 ppm; R_f 0.26 (EtOAc); *m*/*z*: 254 (M^+, 75%), 163 (14), 144 (45), 135 (28), 129 (66), 117 (53), 91 (100), and 65 (43).

Acknowledgments

We thank the Marquette University Committee on Research and S.C. Johnson and Son for their financial support. High-resolution mass spectra were provided by the Washington University Mass Spectrometry Resource, an NIH Research Resource (grant no. P41RR0954). We thank Dr. Maciej Tasz (S.C. Johnson) for discussions and assistance with the ORTEP drawings.

References

1. H. Hoffman and G. Schuhmacher. Tetrahedron Lett. 2963 (1967).
2. C.C. Santini, J. Fischer, F. Mathey, and A. Mitschler. J. Am. Chem. Soc. **102**, 5809 (1980).
3. L. Horner and H. Lindel. Phosphorus Sulfur, **12**, 259 (1982).
4. R.A. Cherkasov, G.A. Kutyrev, and A.N. Pudovik. Tetrahedron, **42**, 2567 (1985).
5. N.G. Zabirov, R.A. Cherkasov, I.S. Khalilov, and A.N. Pudovik. Zh. Obshch. Khim. **59**, 1493 (1989).
6. T. Kawashima, S. Kojima, and N. Inamoto. Chem. Lett. 849 (1989).
7. H-J. Zhou, Y-Q. Zhang, and Y-G. Li. Phosphorus Sulfur, **102**, 185 (1995).
8. L.J. Szafraniec, L.P. Reiff, and H.S. Aaron. J. Am. Chem. Soc. **92**, 6391 (1970).
9. L.P. Reiff, L.J. Szafraniec, and H.S. Aaron. Chem. Comm. 366 (1971).
10. J. Omelańczuk and M. Mikołajczyk. Tetrahedron, **27**, 5587 (1971).
11. B.E. Maryanoff, R.O. Hutchins, and C. Maryanoff. Top. Stereochem. **11**, 187 (1979).
12. T.C. Harvey, C. Simiand, L. Weiler, and S.G. Withers. J. Org. Chem. **62**, 6722 (1997).
13. J.W. Darrow and D.G. Drueckhammer. Bioorg. Med. Chem. **4**, 1341 (1996).
14. D.G. Drueckhammer and J.W. Darrow. J. Org. Chem. **59**, 2976 (1994).
15. S. Hanessian, N. Galeotti, P. Rosen, G. Oliva, and S. Babu. Bioorg. Med. Chem. Lett. **4**, 2763 (1994).
16. A.E. Wroblewski. Phosphorus Sulfur, **61**, 97 (1991).

© 1999 NRC Canada

17. J. Thiem and M. Guenther. Phosphorus Sulfur, **20**, 67 (1984).
18. M.K. Tasz, O.P. Rodriguez, S.E. Cremer, M.S. Hussain, and Mazhar-ul-Haque. J. Chem. Soc. Perkin Trans. 2, 2221 (1996).
19. T.M. Lane, O.P. Rodriguez, S.E. Cremer, and D.W. Bennett. Phosphorus Sulfur, **103**, 63 (1995).
20. S.E. Cremer, A.G. Sommese, and O.P. Rodriguez. Phosphorus Sulfur Silicon Relat. Elem. **75**, 107 (1993).
21. O.P. Rodriguez. Ph.D. thesis. Marquette University, Milwaukee. 1995; Diss. Abstr. Int. B, **56**, 4891 (1996).
22. S.M. Levsen. Ph.D. thesis. Marquette University, Milwaukee. 1996; Diss. Abstr. Int. B, **58**, 5400 (1998).
23. A.W. Herriott. J. Am. Chem. Soc. **93**, 3304 (1971).
24. A. Altomare, G. Cascarano, C. Giacovazzo, M. Co Burla, G. Polidori, and M. Camalli. J. Appl. Cryst. **27**, 435, (1994).
25. G.M. Sheldrick. SHELXS93, A program for crystal structure refinement. University of Gottingen, Germany. 1993.
26. C.K. Johnson. ORTEPII Report ORNL-5138. Oak Ridge National Laboratory, Tennessee. 1976.
27. K. Bergesen. Acta Chem. Scand. **21**, 578 (1967).
28. K. Bergesen. Acta. Chem. Scand. **26**, 1794 (1972).
29. J. Songstad. Acta. Chem. Scand. **21**, 1681 (1967).
30. B.A. Arbuzov and D. Yarmukhanetova. Izv. Akad. Nauk. SSSR Ser. Khim. 1767 (1960).
31. A.Y. Garner. Chem. Abstr. **55**, 5346 (1961); U.S. Patent 2,953,591 (Sept. 1960).
32. G. Aksnes and K. Bergesen. Acta Chem. Scand. **20**, 2508 (1966).
33. K. Bergesen and T. Vilkane. Acta. Chem. Scand. **25**, 1147 (1971).

© 1999 NRC Canada

Electrochemical reduction and oxidation of DDT

Simona G. Merica, Wojceich Jędral, Susan Lait, Peter Keech, and Nigel J. Bunce

Abstract: Electrolysis has been studied as a possible method to treat DDT wastes. In methanol, the major process was dehydrochlorination to DDE followed by further reduction. In an aqueous emulsion containing 1% heptane and 0.1% Triton SP-175®, DDT was reduced at a deposited lead electrode with sodium sulphate as the supporting electrolyte by sequential hydrodechlorination of the aliphatic chlorine atoms. An excellent material balance was achieved, but the current efficiency was poor, even at low current densities. Electrooxidation of DDT was also investigated; in aqueous solutions or emulsion, little oxidation occurred because of competing oxidation of water at the highly positive potentials needed to oxidize DDT. In acetonitrile, electrooxidation occurred with high current efficiency by way of "electrochemical combustion" of DDT and its intermediate oxidation products to CO_2. We conclude that development of an electrolytic technology for destroying DDT wastes is unlikely.

Key words: electroreduction, electrooxidation, voltammetry, surfactant media.

Résumé : On a évalué l'utilité potentielle de l'électrolyse comme méthode de se débarrasser de résidus de DDT. Dans le méthanol, le processus majeur est une déhydrochloruration en DDE qui est suivie d'une réduction ultérieure. Dans une émulsion aqueuse contenant 1% d'heptane et 0,1% de Triton SP-175®, en présence de sulfate de sodium comme électrolyte de support, le DDT peut être réduit au niveau d'une électrode de plomb, par hydrodéchlorurations successives des atomes de chlore aliphatiques. On a pu établir une excellente balance des produits, mais l'efficacité de courant est mauvaise, même à de faibles densités de courant. On a aussi étudié l'électrooxydation du DDT; en solution aqueuse ou à l'état d'émulsion, il se produit peu d'oxydation à cause d'une oxydation compétitive de l'eau aux potentiels hautement positifs requis pour oxyder le DDT. Dans l'acétonitrile, l'électrooxydation se produit avec de très bonnes efficacités de courant par le biais d'une "combustion électrochimique" du DDT et de son produit d'oxydation intermédiaire en CO_2. On conclut que le développement d'une technologie électrolytique d'élimination des résidus du DDT est peu probable.

Mots clés : électroréduction, électrooxydation, voltampérométrie, milieu d'agents de surface.

[Traduit par la Rédaction]

Introduction

Although the use of DDT (1,1-bis(*p*-chlorophenyl)-2,2,2-trichloroethane) was discontinued in North America in the early 1970s, it remains a significant environmental problem, both because of leaching from abandoned waste dumps and because it is still used for mosquito control elsewhere. DDT is persistent in the environment due to its resistance to biodegradation (1). Along with previous authors, we have been studying electrolysis as a possible method for converting DDT to more biodegradable compounds. Figure 1 shows the structures and common abbreviations of DDT and its derivatives.

Fukami and Nakajima in 1953 (2) electrolysed DDT at a dropping mercury electrode at –1.6 V vs. a saturated calomel electrode (SCE) and obtained DDD in 80% yield together with a small amount of yellow resinous substance (this may have been DDMS, which is a pale yellow oil). Reddy and Reddy (3) showed the reduction of DDT to DDD to be an irreversible two-electron reaction. They proposed, following the work of Lambert and Ingall (4), that two electrons were added to DDT, to produce Cl^- + DDD^- which then protonated. (Unlike aryl chlorides (5), the electroreduction of alkyl chlorides does not afford radical anions as discrete intermediates).

Rosenthal and Lacoste (6) observed three two-electron reductions in 90% ethanol:10% 1.0 M aqueous methyltributylammonium chloride. These were attributed to successive hydrodechlorination of DDT's three aliphatic chlorines, on the evidence that DDD showed reduction waves at the same potentials as the second and third reduction waves for DDT. Tandon et al. (7), who worked in 4% DMF:50% ethanol:46% aqueous tetramethylammonium bromide, noted three well-defined reduction waves at –0.370 to –0.430 V, –0.795 to –0.955 V, and –1.110 to –1.225 V vs. SCE, and observed the three stepwise reductions, ultimately to DDO,

Received January 7, 1999.

S.G. Merica, W. Jędral, S. Lait, P. Keech, and N.J. Bunce.[1] Department of Chemistry and Biochemistry, University of Guelph, Guelph, ON N1G 2W1, Canada.

[1]Author to whom correspondence may be addressed. Telephone: (519) 824-4120, ext. 3962. Fax: (519) 766-1499. e-mail: bunce@chembio.uoguelph.ca

 © 1999 NRC Canada

Fig. 1. Names and structures of DDT and derivatives.

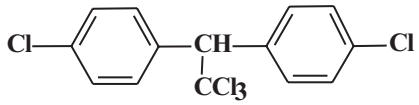

1,1'-(2,2,2-trichloroethylidene)bis(4-chlorobenzene) ("DichloroDiphenylTrichloroethane" = DDT)

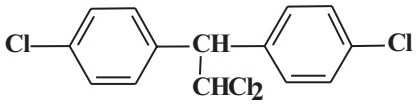

1,1'-(2,2-dichloroethylidene)bis(4-chlorobenzene) ("DichloroDiphenylDichloroethane" = DDD)

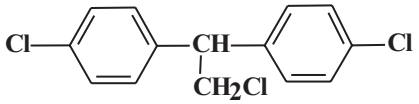

1,1'-(2-chloroethylidene)bis(4-chlorobenzene) ("DichloroDiphenylMonochloroethane, Saturated" = DDMS)

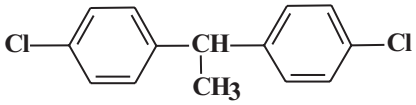

1,1'-ethylidenebis(4-chlorobenzene) ("DichloroDiphenylethane, 0 aliphatic chlorines" = DDO)

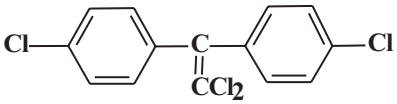

1,1'-(2,2-dichloroethenylidene)bis(4-chlorobenzene) ("DichloroDiphenyldichloroEtylene" = DDE)

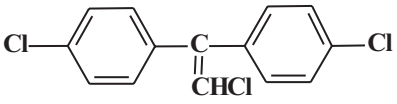

1,1'-(2-chloroethenylidene)bis(4-chlorobenzene) ("DichloroDiphenylMonochloroethylene, Unsaturated" = DDMU)

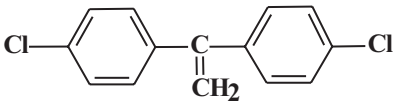

1,1'-(ethenylidene)bis(4-chlorobenzene) ("DichloroDiphenylethylene, No aliphatic chlorines, Unsaturated" = DDNU)

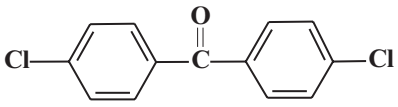

4,4'-dichlorobenzophenone (DBP)

at these respective potentials. They proposed a mechanism in which each dechlorination step involves a fast electron transfer and proton addition to give the alkyl radical, followed by a second, rate-limiting, electron transfer and proton addition to complete the replacement of -Cl by -H. This mechanism is consistent with the localization of 98% of the electron density in the LUMO of DDT in aliphatic C-Cl σ^* antibonding orbitals (8). Four irreversible reduction steps were also observed by cyclic voltammetry in carefully dried acetonitrile (ACN) and DMF using tetraethylammonium phosphate as the supporting electrolyte (9), also suggesting consecutive ECE mechanisms (10).

Electrochemical oxidation of DDT has been studied less extensively than reduction. Keenan and Stuart (11) oxidized DDT at +2.10 V vs. SCE in 5% aq 0.1 M tetraethylammonium perchlorate:95% ACN solution at a Pt anode, and obtained 4,4′-dichlorobenzophenone (DBP), 1,1,1-trichloro-2-(4-chlorophenyl)-2-(4-chloro-2,5-benzoquinone)ethane and a small amount of 2,2,2-trichloro-1,1-bis-(4-chlorophenyl) ethanol (Kelthane). The low yield of Kelthane was not surprising given that its oxidation peak is only 0.02 V more positive than that of DDT. Cyclic voltammetry indicated that all of the oxidation steps were irreversible; the peak potentials for DDT were at +2.3 and +2.6 V vs. SCE.

The ability to remove all three aliphatic chlorines from DDT by electrolysis suggested that it might be possible to develop a technology in which DDT could be transformed electrochemically into less toxic, more biodegradable products, provided that the reaction could be achieved with high chemical and electrical efficiency under "environmentally friendly" conditions. An ideal situation would be a sequence in which "side chain" reduction of DDT to DDO at the cathode would be followed by anodic oxidation of DDO to products that might be compatible with a subsequent biological treatment.

Experimental

DDT, DDD, DDE, 4,4′-dichlorobenzophenone (DBP), and tetraethylammonium chloride (TEACl) were obtained from

© 1999 NRC Canada

Aldrich; a standard solution of DDMU in methanol was obtained from AccuStandard. DDNU, DDO, and DDMS were synthesized as described below. All compounds were assayed by HPLC and (or) GC–MS. Sodium sulfate supporting electrolyte and HPLC grade solvents were obtained from Fisher. Triton SP-175® was generously supplied by Union Carbide Canada.

DDNU

The method employed was part of a longer synthesis by Grummitt et al. (12). 2,2,2-Trichloro-1,1-bis-(4-chlorophenyl) ethanol (1.0474 g, 3.92 mmol) was heated under reflux in an oil bath at 210–220°C for 15 min. After cooling to 80°C and addition of 1.0 mL of 20% aq H_2SO_4, the mixture was stirred at reflux at 140–150°C for 1 h. Cooling and two recrystallizations from ethanol (10 mL) gave pale yellow needles of DDNU (0.4884 g, 1.96 mmol, 50.0%, mp 83–84°C, lit. (12) 84–86°C); ^{1}H NMR ($CDCl_3$) δ (ppm): 5.45 (s), 7.3 (m).

DDO

DDNU (0.3639 g, 1.461 mmol), $AlCl_3$ (10 mg), 5% Pd–C (77.1 mg), and cyclohexene (4.0 mL) were stirred for 5 days under dry argon. Filtration and removal of solvent gave a yellow oil, which was chromatographed over silica gel (60–200 mesh, 22 g) and eluted with hexane (5 mL fractions). Fractions were checked for composition by TLC, and the presence of DDO was verified by GC–MS. The DDO-rich fractions were pooled, evaporated, and crystallized from 95% ethanol (1 mL) to give white fluffy needles of DDO (40.6 mg, 0.162 mmol, 11.1%, mp 44–45°C); ^{1}H NMR ($CDCl_3$) δ (ppm): 1.6 (d), 4.1 (q), 7.3 (m). The literature melting point for DDO is 54–55°C (4); however, GC–MS and HPLC analysis showed contamination by traces of DDNU even after purification.

DDMS

2,2-Bis-(4-chlorophenyl)ethanol (201.6 mg, 0.755 mmol) and $SOCl_2$ (0.500 mL, 7.15 mmol) were refluxed for 2 h with stirring under dry air. The reflux condenser was removed, allowing most of the $SOCl_2$ to evaporate while the solution boiled for a further 15 min, then the residue was stirred for 1 h and the remaining $SOCl_2$ allowed to evaporate overnight. The gummy yellow product (121.4 mg, 0.425 mmol, 56.3%) was dissolved in hexane (1 mL), chromatographed over silica gel (60–200 mesh, 20 g), and eluted with hexane (10 mL fractions). The composition of fractions was checked by TLC and GC–MS. The fractions containing DDMS with no significant contaminants were pooled to give a very pale yellow oil, DDMS (27.4 mg, 0.0959 mmol, 12.7%); ^{1}H NMR ($CDCl_3$) δ (ppm): 4.0 (d), 4.3 (t), 7.3 (m).

HPLC

The system comprised a Waters U6K injector, Waters 600E system controller, and Model 486 tuneable absorbance detector set to λ = 240 nm (electroreduction) and 227 nm (electrooxidation). The system was connected to a PC controlled by Millennium 2010 chromatographic software. Analytical separations were performed on a Waters μBondapack C_{18}, 3.9 × 300 mm column. The column was eluted with 55/45 ACN/water at 2.5 mL/min, for electroreduction experiments, while for electrooxidation a 90/10 MeOH/water mixture at 2 mL/min was employed. All solvents were HPLC grade and filtered using 0.45 μm Nylon 66 membranes.

GC–MS

The instrument was a Hewlett Packard 5971 Series mass selective detector interfaced to a Hewlett Packard 5890 Series II gas chromatograph equipped with a J&W DB5 capillary column (0.25 mm i.d. × 30 m, 0.25 μm thick film) using helium as the carrier gas. The temperature program used for identification of electroreduction products was 100°C (3 min); 100–180°C at 12°/min; 180–300°C at 7°/min, 300°C (5 min). In the case of electrooxidation, the following program was employed: 70°C (3 min); 70–200°C at 20°/min; 200–300°C at 15°/min.

Electrolyses

The solvents used in exhaustive electrolyses were HPLC grade methanol, HPLC grade acetonitrile, reagent grade *t*-BuOH (which was purified by successive recrystallization), and Triton SP-175 emulsion (surfactant:heptane:water = 0.1:1:98.9 v/v). The latter contained 0.05 M Na_2SO_4 as supporting electrolyte; it was prepared by sonication and was indefinitely stable at neutral pH.

Continuous flow electroreductions

These experiments were performed using a sandwich-type flow-through cell previously described (13). Current-controlled electroreduction at a Hg pool cathode (A = 6 cm^2) was performed using a Ti/IrO_2 anode (A = 20 cm^2) and saturated Ag/AgCl reference electrode. Prior to electrolysis, the catholyte was purged with argon for 20 min, and a slow argon flow was maintained throughout the experiment. A 25.0 mL sample of 1 mM, DDT 0.05 M TEACl in methanol was circulated through the cathodic compartment at 2.5 mL/min using a peristaltic pump, and 25 mL of TEACl–methanol was pumped through the anodic compartment. Samples (0.1 mL) were taken at intervals during the electrolysis. Extraction of the electrolyzed solution with CH_2Cl_2 allowed for product analysis by GC–MS.

Current-controlled electroreductions were also performed using a cathode of deposited lead (A = 40 cm^2) and an anode of Ti/IrO_2 (A = 20 cm^2). Deposition on a lead wire frame was accomplished by circulating 50 mL of 10 mM $Pb(NO_3)_2$ + 125 mM disodium citrate through the cathodic compartment while applying a current of 20 mA for 45 min. A 25.0 mL sample of 0.1 mM, DDT in Triton SP-175 emulsion was circulated through the cathodic compartment at 5 mL/min, and 25 mL emulsion was circulated through the anodic compartment. The reservoir of the cathodic emulsion was stirred magnetically, and heptane was added periodically to maintain the emulsion. Samples (0.5 mL) taken at intervals during electrolysis were treated with 5 M H_2SO_4 (50 μL) and heptane (0.25 mL) to destroy the emulsion and to extract DDT and reduction products. Reaction rates were corrected for the consequent change in the volume of the solution.

Current-controlled electroreductions were also performed using a cathode of deposited nickel (from a 1:1 $NiSO_4$:$NiCl_2$ solution, A = 40 cm^2) on a nickel wire frame. Experimental conditions were comparable as for current-controlled electroreduction on deposited lead.

© 1999 NRC Canada

Single-flow electroreductions

A peristaltic pump passed 0.1 mM DDT in emulsion from a 500 mL container through the cathodic compartment at 0.4 mL/min and circulated 25 mL emulsion through the anodic compartment. Unlike the continuous flow electrolyses, the output from the cathodic compartment was directed to waste. Samples were taken from the cathodic compartment output and treated with H_2SO_4 and heptane as in continuous flow experiments. To achieve a steady state, current was applied for 30 min before sampling.

Anodic voltammetry

The electrochemical cell was a glass container with a Teflon lid which had four openings for electrodes and an argon purging tube. The anode was a Pt wire (0.20 cm^2); an external reference Ag/AgCl electrode was used, with a bridge filled with two solutions. The part that was in contact with the Ag/AgCl electrode contained saturated aqueous KCl solution, while the part that was in contact with the analyzed solution was filled with 0.1 M $LiClO_4$ – acetonitrile. The counter electrode was a Pt foil with area of 5 cm^2. The solutions were deaerated prior to electrolysis. The cell was controlled by a EG&G, model 273, potentiostat–galvanostat interfaced with a PC and operated by M270 electrochemical software. The following parameters were used: pulse height, 100 mV; pulse width, 50 ms; scan rate, 2 mV s^{-1}. The solutions were purged with argon for 15 min before taking measurements. All potential data were reported using SHE as common point of reference, and the anodic current was reported as positive.

Electrooxidations

These experiments used the same type of cells as used for electroreductions. For the electrolyses performed in acetonitrile and in 1:1 *t*-BuOH:H_2O, the cell was made of high-density polypropylene, while for the experiments performed in emulsion, the cell was made of Plexiglas. Care was taken to select appropriate solvent-resistant tubing for the peristaltic pump. The working electrode had an area of 25 cm^2 and was either a Pt foil or a Ti/IrO_2 plate. The counter electrode was a glassy carbon electrode. The cell was controlled amperostatically by means of a EG&G, model 173, potentiostat–galvanostat. In continuous flow experiments, a 25.0 mL sample of DDT solution (1 mM DDT – 0.1 M $LiClO_4$ – acetonitrile; 0.2 mM DDT in 50/50 *t*-BuOH/H_2O – 0.05 M Na_2SO_4; or 0.1 mM DDT – emulsion – 0.05 M Na_2SO_4) was continuously recirculated through the anodic compartment using a peristaltic pump (flow rate = 5 mL min^{-1}), and 25.0 mL of electrolyte was pumped through the cathodic compartment. The electrolysis was monitored by HPLC by removing samples from the bulk solution; for product identification, the electrolyzed solution was extracted in dichloromethane and analyzed by GC–MS. In single-flow experiments, a solution of 0.1 mM DDT in 0.1 M $LiClO_4$ – acetonitrile was pumped from a 0.25 L container through the anodic compartment at 1 mL/min, and the output from the anode was directed to waste. Approximately 25 mL of electrolyte solution was recirculated through the cathodic compartment, as in continuous flow experiments. Both solutions were purged with argon for ~30 min before electrolysis to remove dissolved CO_2. After current was applied, an equilibration time of 10 min was allowed before samples were collected.

Carbon dioxide was quantitated using the single-flow procedure, by directing the output from the cell to a closed container connected to a methanol trap (3 mL) followed by a $Ba(OH)_2$ trap (25 mL of 3 mM). During the sample collection period (10 min), Ar was flushed through the sample. The $Ba(OH)_2$ solution was allowed to stand for few hours to clear, and the residual hydroxide ion was then titrated against 10 mM HNO_3.

Results and discussion

Electroreductions

We first performed continuous flow electrolysis of 1 mM DDT in methanol with TEACl as the supporting electrolyte using an Hg pool cathode, to allow product identification corresponding to the reduction waves observed polarographically. Methanol was chosen because it is inexpensive, miscible with water, and not toxic to microorganisms. Although TEACl is too expensive an electrolyte for use on an industrial scale, tetraalkylammonium salts have been used in most of the published voltammetric studies involving DDT (1, 5–7, 10, 13).

After 20 min of amperostatic electrolysis at 2 mA cm^{-2}, most of the DDT had reacted. DDE was the major product; DDD, DDMU, and a small amount of DDMS were minor products. After 60 min, DDE was still the major product; the concentration of DDT was not greatly altered, but the relative amounts of DDMU and DDMS had increased, and DDNU and DDO became detectable. Similar products were obtained by Schweizer et al. (1) who electrolyzed 10 mM DDT in a bicontinuous emulsion of dodecane, didodecyldimethylammonium bromide (DDAB), and water. They observed two reduction waves at –1.4 and –2.0 V vs. Ag/AgBr. Potentiostatic electrolysis at –1.4 V under deoxygenated conditions gave DDE (31%) and DDD (10%) at 51% conversion of DDT, with minor amounts of DDO, DDMU, and DDMS. Electrolysis at –2.0 V to 100% conversion gave more extensive reduction to DDO (55%), DDMS (27%), and traces of 1,1-diphenylethane. Under aerated conditions, the yield of 1,1-diphenylethane increased to 34%, and 1-(4-chlorophenyl)-1-phenylethane (22%) and DDO (37%) were also formed.

The formation of DDE and its further reduction products DDMU and DDNU is not compatible with DDT → DDD → DDMS → DDO as the proposed pathway for electroreduction (2, 6, 7, 10). One possible mechanism is an initial reduction to $DDT^{\cdot -}$ and loss of Cl^-, giving $Ar_2CH\text{-}CCl_2^{\cdot}$ radicals, which can disproportionate into DDD and DDE. Another is base-catalyzed elimination of HCl from DDT, in which the base is formed in situ at the cathode as the by-product of reduction of other DDT molecules.

$$DDT + 2e^- + MeOH \rightarrow DDD + Cl^- + MeO^-$$

Experimental evidence in favour of the second option was obtained by allowing DDT (10^{-3} mol L^{-1} in methanol) to react with different concentrations of methanolic sodium methoxide for time periods up to 140 min. After 50 min, for example, the fraction of DDT converted to DDE was 0.0022 (10^{-4} mol L^{-1} NaOMe), 0.015 (10^{-3} mol L^{-1} NaOMe), and

© 1999 NRC Canada

Table 1. Pseudo-first-order rate constants for electrochemical reduction of 0.1 mM DDT in Triton SP-175 emulsion – 0.05 M Na_2SO_4 at deposited Pb and Ni cathodes.

Cathode	Current density/mA cm^{-2}	$(k \pm SE) \times 10^{-5}/s^{-1}$
Pb	0.5	1.7 ± 0.3
	1	8.5 ± 0.3
	3	7.3 ± 0.8
	5	14 ± 0.7
	10	18 ± 0.5
Ni	0.5	2.2 ± 0.5
	3	5.8 ± 0.5
	5	5.5 ± 0.7

Fig. 2. Electroreduction of 0.1 mM DDT in 0.5 M Na_2SO_4 – emulsion at a Pb cathode (A = 40 cm^2, i = 5 mA cm^{-2}, continuous flow, F = 5 mL min^{-1}).

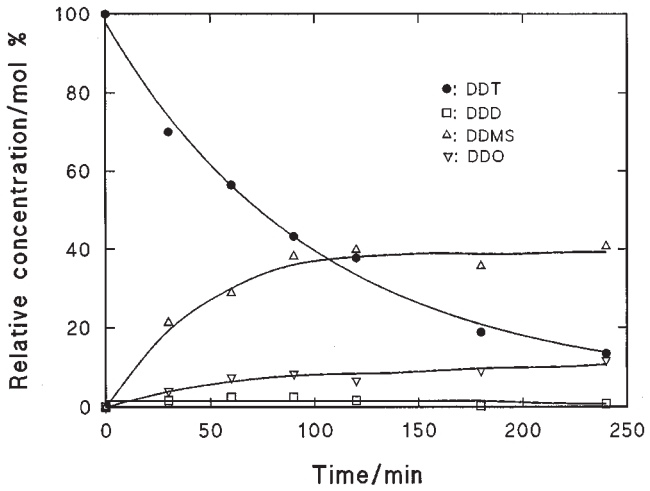

0.14 (10^{-2} mol L^{-1} NaOMe). Detectable amounts of DDE were even obtained at time zero (immediate quench of the solution). Direct comparison with the electrolytic experiments is not possible because the local concentration of MeO^- in the vicinity of the cathode is unknown.

The bicontinuous emulsion used by Schweizer et al. (1) employs large volumes of surfactant and organic solvent and is only 22% water. We showed previously (14) that aqueous emulsions of 1% heptane, 0.1% Triton SP-175 were stable for hours of electrolysis when stirred. We therefore investigated the use of this medium for the electroreduction of 0.1 mM DDT. Lead was selected as a cathode based on our previous work (14), and nickel was selected based on the work of Liu et al. (15) involving electroreduction of carbon tetrachloride. Both metals were freshly deposited prior to electrolysis of DDT. Small amounts of heptane had to be added periodically when the current density was greater than 3 mA cm^{-2} to replace heptane lost through ohmic heating of the solution and through entrainment by the H_2 evolved. Sodium sulphate was selected as an inexpensive, nontoxic electrolyte. The electrolyses were performed in the same way as those in methanol except that a two-electrode system was used. The loss of DDT followed first-order kinetics in all cases: see Table 1.

In the Triton SP-175 emulsion, the products were consistent with the pathway DDT → DDD → DDMS → DDO.

Fig. 3. Electroreduction of 0.1 mM DDT in 0.5 M Na_2SO_4 – emulsion at a Pb cathode (A = 40 cm^2, single flow, F = 0.4 mL min^{-1}).

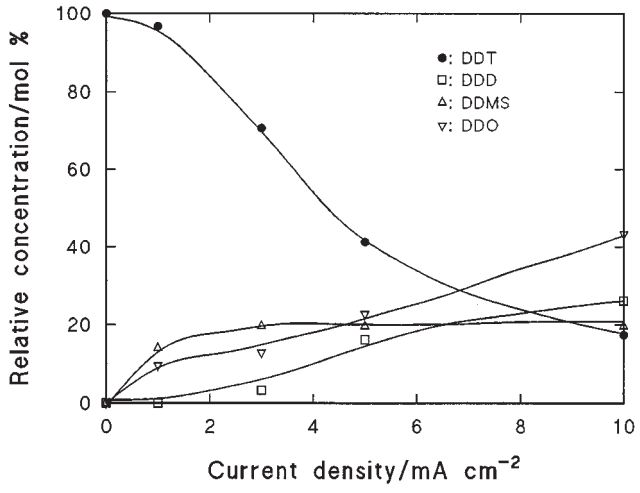

DDE was not formed, consistent with the concentration of base (OH^- in this case) being low in the emulsion phase. Figure 2 shows the progress of the reaction at Pb using a current density of 5 mA cm^{-2}. No more than traces of DDD were present at any stage of the reaction, indicating that this intermediate was immediately reduced to DDMS before reentering the bulk solution. Mass balances at the Pb cathode were at least 97% at current densities ≤3 mA cm^{-2}; at higher current densities, loss of heptane caused by H_2 evolution led to deposition of products from the solution.

The electroreductions at Ni also followed pseudo-first-order kinetics, but gave poorer mass balances (typically ~80% after 3 h electrolysis). HPLC analysis showed an unidentified peak with a retention time more than twice as long (less polar) than any of the standard DDT derivatives. The identified reduction products were also counter-intuitive. At 0.5 mA cm^{-2}, the major product was DDO, corresponding to complete dechlorination of the side chain; DDMS was the major product at 3 mA cm^{-2} and was formed exclusively at 5 mA cm^{-2}. We anticipated that increasing the current density, and hence the polarization of the cathode, would increase the extent of dechlorination, not the reverse. A possible explanation is competing reduction by chemisorbed H_2, given that nickel is well known as a hydrogenation catalyst.

Single-flow electrolyses (i = 0.1–10 mA cm^{-2}) were performed at Pb in order to determine the current efficiency in the emulsion medium. There was no significant disappearance of DDT at current densities <1 mA cm^{-2}; at these low current densities, the polarization of the cathode was insufficient for efficient electron transfer. The yield of DDMS was nearly constant at $i \geq 1$ mA cm^{-2}, while the yields of DDD and DDO increased with current (Fig. 3). At 10 mA cm^{-2}, 84% of the DDT was reduced to DDD (24%), DDMS (19%), and DDO (41%). The current efficiency was greatest at i = 1 mA cm^{-2} but, even so, was only 0.2%.

Schweizer et al. (1) also studied "mediated" (16) electrochemical reduction in the bicontinuous emulsions, using $Co(bipy)_3^{2+}$ as a mediator. Significant electrolysis occurred at the relatively positive potential of –1.0 V, consistent with $Co(bipy)_3^{+}$, formed by reduction of $Co(bipy)_3^{2+}$, acting as

© 1999 NRC Canada

Table 2. Electrooxidation of 0.1 mM DDT – 0.1 M $LiClO_4$ at Pt and Ti/IrO_2 anodes.

Electrode	Pt				IrO_2/Ti			
i/mA cm^{-2}	0.5	1	3	5	0.5	1	3	5
DDT left/%	58.4	42	21.4	7.8	81.6	66.8	14	9.4
DBP/%	—	8.8	5.4	2	1.9	6.2	24.5	14.2
CO_2/%	37.9	42.9	65.7	85.7	14.3	21.4	57.1	71.4
Mass balance	96	93	92	95	97	94	94	94
Current efficiency/%	31.7	18.2	9.2	7.2	12.1	9.2	8.2	6.1

Fig. 4. Differential pulse voltammograms of 1 mM DDT, DBP, and HQ in 0.1 M $LiClO_4$ – acetonitrile at a Pt anode.

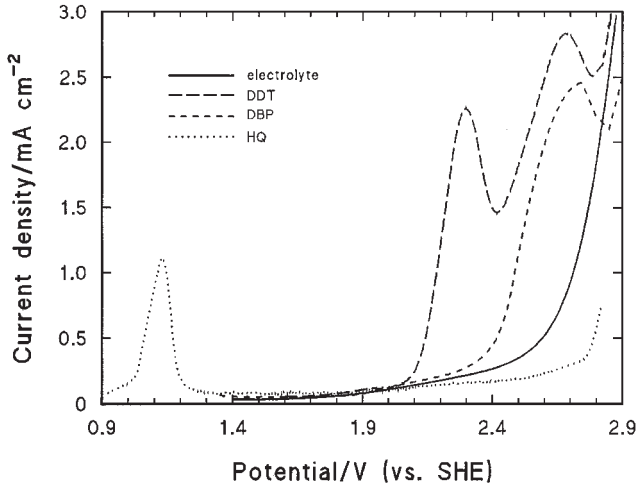

Fig. 5. Electrooxidation of 1 mM DDT in 0.1 M $LiClO_4$ – acetonitrile at Pt and IrO_2/Ti anodes (i = 5 mA cm^{-2}).

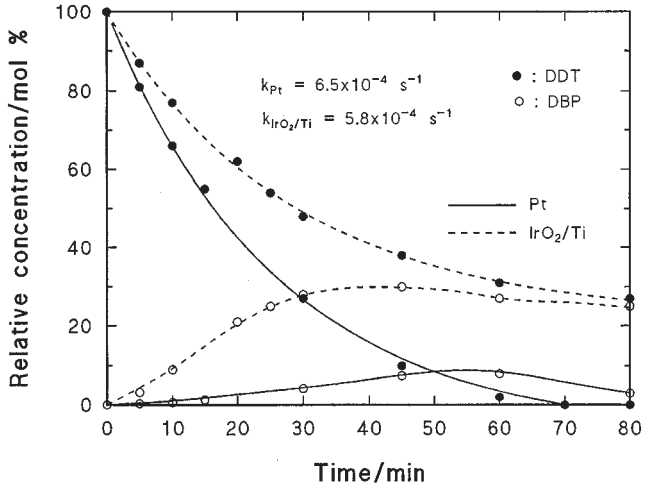

the reducing agent for DDT. After 3 h, the major products were DDE (24%), DDMU (17%), DDD (17%), DDMS (12%) and DDO (24%). Further electrolysis increased the yield of DDMU at the expense of DDD and DDMS.

Electrooxidations

Voltammetry of DDT at a Pt anode in ACN – 0.1 M $LiClO_4$ revealed half-wave potentials at +2.29 and +2.58 V vs. SHE (cf. ref. 11). Oxidation at +2.29 V involves conversion of DDT to 4,4′-dichlorobenzophenone (DBP), demonstrated by showing that the second oxidation corresponded to the oxidation potential of DBP. Differential pulse voltammograms of 1 mM DDT, DBP, and hydroquinone (HQ, which is known to undergo a 2e$^-$ oxidation (17)) in 0.1 M $LiClO_4$ – ACN at a Pt anode (Fig. 4) were obtained. The relative heights of these voltammetric peaks show that both DDT and DBP undergo 4e$^-$ oxidations.

Continuous flow electrolyses were performed in various solvents: 0.1 M $LiClO_4$ – acetonitrile, 0.05 M Na_2SO_4 in 50/50 t-BuOH/H_2O, and 0.05 M Na_2SO_4 – Triton SP-175 emulsion. The disappearance of starting material and appearance of products were monitored by removing samples from bulk solution and analyzing them by HPLC. Pt and Ti/IrO_2 were used as anodes; Ti/IrO_2 is an example of a "dimensionally stable anode," the mechanism of action of which has been proposed to involve surface-generated hydroxyl radicals as the reactive oxidant. This type of anode was of interest in that the hydroxyl radicals might be able to attack DDT (or its reduction products) at potentials less positive than those needed for direct oxidation of the substrate. This is an important consideration for substances like DDT that are resistant to oxidation, because it is impossible to avoid concurrent, parasitic oxidation of water.

Using Triton SP-175 emulsion as the reaction medium, no loss of DDT was observed at either Pt or Ti/IrO_2, using various current densities 0.2–20 mA cm^{-2}. In both acetonitrile and 50/50 t-BuOH/H_2O, the starting material was observed to disappear but the mass balance of organic products was very poor. Using a Pt anode and current density i = 5 mA cm^{-2}, DDT disappeared more than 10 times faster in 0.1 M $LiClO_4$ – ACN ($k = 6.5 \times 10^{-4}$ s^{-1}) than in 50/50 t-BuOH/H_2O ($k = 5.3 \times 10^{-5}$ s^{-1}). In the former case, the only product detected was DBP (Fig. 5), but in t-BuOH/H_2O, DBP was accompanied by traces of 2,2,2-trichloro-1-(4-chlorophenyl)ethanone. In 0.1 M $LiClO_4$ – acetonitrile, the rate of disappearance of DDT at a Ti/IrO_2 anode (i = 5 mA cm^{-2}) was slower ($k = 5.8 \times 10^{-4}$ s^{-1}) than at Pt; DBP was again the major organic product, along with traces of chlorophenol and 2,2,2-trichloro-1-(4-chlorophenyl)ethanone. A rationalization of these products involves proton loss from $DDT^{\cdot+}$ to give $Ar_2C^{\cdot}$-CCl_3, followed by either attack of O_2 (from the atmosphere) at the radical centre or a second oxidation to Ar_2C^+-CCl_3 and nucleophilic attack by water.

We considered that the poor mass balance of organic products might result from "electrochemical combustion" (18) of DDT and intermediate products at the anode. We therefore modified the apparatus to trap any CO_2 formed during electrooxidation in ACN – 0.1 M $LiClO_4$ in $Ba(OH)_2$ solution. The residual amount of HO^- was determined by titration. Experiments were performed at both Pt and Ti/IrO_2 using various current densities. Once CO_2 was included,

© 1999 NRC Canada

mass balances improved to ≥92%; current efficiencies ranged up to >30% (Table 2), with the highest current efficiencies being achieved by operating at the smallest practical current densities. The first step in the oxidation yields DBP; however, at the potential required to oxidize DDT, DBP is further oxidized at the electrode surface.

Conclusions

At a Pb cathode, DDT is sequentially reduced to less chlorinated derivatives, particularly DDMS and DDO. No loss of chlorine is observed from the phenyl rings, consistent with our earlier experiments with polychlorinated benzenes (13, 14). Reduction takes place in an almost entirely aqueous medium, based on the new surfactant Triton SP-175, using sodium sulfate as an environmentally friendly supporting electrolyte. Mass balances are excellent at all stages of the reaction, but the current efficiency of the process (0.2%) is completely unacceptable for any practical technology to be contemplated.

Conversely, in the case of electrooxidations, high current efficiencies (>30%) were obtained, but only in a nonaqueous solvent; this time, it is the solvent that is technologically impractical. The potential required to oxidize DDT is sufficiently positive that neither an aqueous cosolvent (*t*-BuOH) nor an aqueous surfactant allowed oxidation of DDT to compete successfully with oxidation of water. In acetonitrile, the highly positive potential required to oxidize DDT leads to concurrent oxidation of all reaction intermediates, and "electrochemical combustion" gives CO_2 as a major product.

Acknowledgements

We thank the Natural Sciences and Engineering Research Council of Canada for financial support, Union Carbide for providing Triton SP-175 surfactant, and a referee for suggesting base-catalyzed elimination from DDT.

References

1. S. Schweizer, J.F. Rusling, and Q. Huang. Chemosphere, **28**, 961 (1994).
2. H. Fukami and M. Nakajima. Botyu-Kagaku, **18**, 6 (1953), through Chem. Abstr. **47**, 5815g (1953).
3. A.S. Reddy and S.J. Reddy. Indian J. Chem. **23A**, 619 (1984).
4. F.L. Lambert and G.B. Ingall. Tetrahedron Lett. 3231 (1974).
5. N.J. Bunce, S.G. Merica, and J. Lipkowski. Chemosphere, **35**, 2719 (1997).
6. I. Rosenthal and R.J. Lacoste. J. Am. Chem. Soc. **81**, 3268 (1959).
7. R. Tandon, I. Bala, and M. Singh. Z. Phys. Chem. Leipzig, **267**, 340 (1986).
8. F.A. Beland, S.O. Farwell, P.R. Callis, and R.D. Geer. J. Electroanal. Chem. **78**, 145 (1997).
9. G.I. Udovich. An electrochemical investigation of the reduction of DDT in ethanol, acetonitrile and *N*,*N*-dimethylformamide and the development of a method for the differential pulse polarographic determination of DDT. Ph.D. thesis. University of Wyoming, Wyoming. 1979.
10. R.S. Nicholson and I. Shain. Anal. Chem. **37**, 178 (1965).
11. R.R. Keenan and J.D. Stuart. J. Electrochem. Soc. **123**, 1637 (1976).
12. O. Grummitt, A.C. Buck, and E.I. Becker. J. Am. Chem. Soc. **67**, 2265 (1945).
13. S.G. Merica, N.J. Bunce, W. Jedral, and J. Lipkowski. J. Appl. Electrochem. **28**, 645 (1998).
14. S.G. Merica, C.E. Banceu, W. Jedral, J. Lipkowski, and N.J. Bunce. Environ. Sci. Technol. **32**, 1509 (1998).
15. Z. Liu, R.G. Arnold, and E.A. Betterton. *In* Physical, chemical, and thermal technologies remediation of chlorinated and recalcitrant compounds. *Edited by* G.B. Wickramanayake and R.E. Hinchee. Battelle Press, Columbus. 1998. p. 473.
16. J.W. Sease and R.C. Reed. Tetrahedron Lett. 393 (1975).
17. M. Gattrell and D.W. Kirk. J. Electrochem. Soc. **140**, 1534 (1993).
18. C. Comninellis and C. Pulgarin. J. Appl. Electrochem. **21**, 703 (1991).

© 1999 NRC Canada

Apparent molar volume of some ω-amino acids in aqueous electrolyte systems

D. Kumar

Abstract: Apparent molar volumes (V_ϕ) of some ω-amino acids have been determined in aqueous guanidine hydrochloride (6 *m* GuHCl) and sodium sulphate (2 *m* Na_2SO_4) solutions at 288.15 and 298.15 K using a vibrating tube digital densimeter. The transfer volumes of amino acids from water to aqueous electrolyte systems have been reported. The transfer properties are interpreted in terms of strong interactions, based on a cosphere overlap model of guanidine hydrochloride/sodium sulphate molecules with the charged centers of the zwitterions (amino acid molecules), as compared to ion – nonpolar group interactions.

Key words: amino acids, denaturation, guanidine hydrochloride, sodium sulphate, apparent molar volume, zwitterions, limiting apparent molar volume.

Résumé : Faisant appel à un densimètre digital à tube vibrant et opérant à 288,15 et 298,15 K, en solutions aqueuses de chlorhydrate de guanidine (6 *m* GuHCl) et de sulfate de sodium (2 *m* Na_2SO_4), on a déterminé les volumes molaires apparents (V_ϕ) de quelques acides ω-aminés. On a calculé les volumes de transfert des acides aminés de l'eau aux systèmes aqueux d'électrolyte. On interprète les propriétés de transfert en fonction de fortes interactions, découlant d'un modèle de recouvrement de cosphères des molécules de chlorhydrate de guanidine/sulfate de sodium avec les centres chargés des zwitterions (molécules d'acides aminés) par opposition aux interactions ion – groupe non polaire.

Mots clés : acides aminés, dénaturation, chlorhydrate de guanidine, sulfate de sodium, volumes molaires apparents, zwitterions, volume molaire apparent limite.

[Traduit par la Rédaction]

Introduction

Investigations on the volumetric properties of model compounds such as amino acids provide valuable information that ultimately leads to a better understanding of the behavior of biological macromolecules or proteins. A small change in water structure can greatly inhibit the physiological reactions in tissues or cells, which are made up of biological macromolecules. The change in water structure can be brought about by the presence of electrolytes. Sometimes, these changes are helpful in controlling undesired physiological reactions (1–4) occurring in living organisms. In view of the above, the study of the effect of electrolytes on model compounds of biological macromolecules is of fundamental importance.

Volumetric studies on amino acids in aqueous electrolyte systems reflect the combined effect of various hydrophilic and hydrophobic interactions in these systems. It was observed that concentrated salt solutions have large effects on the structure and properties of proteins, including solubility, denaturation, and the activity of enzymes. Nandi and Robinson (5) studied the *salting in* or *salting out* effects of several salts on macromolecules or proteins, and suggested that the salts interact directly with the peptide group. Denaturation of proteins in the presence of urea and guanidine hydrochloride has been studied extensively (6, 7).

In this paper, the limiting apparent molar volumes of five ω-amino acids in aqueous guanidine hydrochloride and sodium sulphate solutions over the concentration range 0.05–0.70 mol kg^{-1} have been presented, with the aim of deducing possible correlations between structural interactions of amino acids in aqueous salt solutions and the effects of salt on proteins.

Materials and methods

Five ω-amino acids chosen for the study were glycine (**Gly**), β-alanine (**β-Ala**), γ-aminobutyric acid (**γ-Aba**), δ-aminovaleric acid (**δ-Amv**), and ε-aminocaproic acid (**ε-Ahx**). All amino acids and guanidine hydrochloride were procured from Sigma Chemical Company, St. Louis, Mo., U.S.A. Anhydrous sodium sulphate (G.R.) was obtained from Sarabhai M. Chemicals, India. Guanidine hydrochloride, sodium sulphate, and all the amino acids except δ-aminovaleric acid were used after drying at 373.15 K for 10 h in a vacuum oven and were stored in a desiccator over P_2O_5. δ-Aminovaleric acid was dried in vacuo over P_2O_5 at 277.15 K before use. Doubly distilled water was deionized by passing it through two Cole–Parmer mixed-bed ion-exchange columns and degassed by boiling it before use in preparation of solutions. Solutions were prepared by mass using a Mettler AE-163 electronic balance. All density measurements were carried out only on freshly prepared solutions.

An Anton Paar high-precision vibrating tube digital densimeter (model DMA 60/601) with precision of $\pm 3 \times 10^{-3}$ kg m^{-3}

Received December 19, 1997.[1]

D. Kumar. Department of Applied Chemistry, Delhi College of Engineering, University of Delhi, Delhi-110006, India.

[1]Revision received January 15, 1999.

© 1999 NRC Canada

Fig. 1. Plot of $1000(\rho - \rho_0)$ versus molality of NaCl. Present work (○); ref. 10 (□).

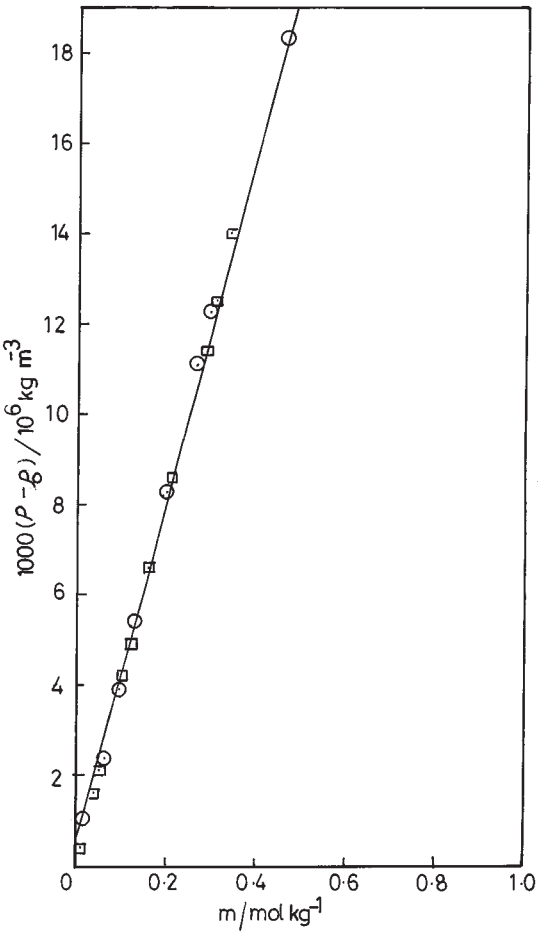

was used for the density measurements of the solutions. The temperature in the measuring cell was controlled to ±0.01 K and monitored with a Paar model DT-100-20 digital thermometer. The densimeter was calibrated using the literature data for densities of dry air (8) and pure water (9) at 288.15 and 298.15 K. The densities of pure water at 288.15 and 298.15 K are 0.999 098 and 0.997 048 (10^3 kg m^{-3}) and of air at the same two temperatures are taken as 0.001 161 and 0.001 122 (10^3 kg m^{-3}), respectively. The density and apparent molar volume data of aqueous sodium chloride from this study are compared (Appendix A) with the literature values (10). The data were plotted as $1000(\rho - \rho_0)$ against molality of sodium chloride (Fig. 1). The apparent molar volume at infinite dilution from the present study (16.50 cm^3 mol^{-1}) has been compared with the literature value (16.62 cm^3 mol^{-1}), which is in fairly good agreement.

Results and discussion

The results of density measurements on aqueous solutions of guanidine hydrochloride, sodium sulphate, and solutions of ω-amino acids in 6 *m* guanidine hydrochloride and 2 *m* sodium sulphate at 288.15 and 298.15 K were used to determine the apparent molar volumes (Appendix B). The apparent molar volumes (V_ϕ) of amino acids in 6 *m* GuHCl and 2 *m* Na_2SO_4 solutions at two temperatures were calculated using the relation

Fig. 2. Plot of V_ϕ^0 versus N_{CH_2}. GuHCl at 288.15 K (○); GuHCl at 298.15 K (●); Na_2SO_4 at 288.15 K (□); Na_2SO_4 at 298.15 K (■).

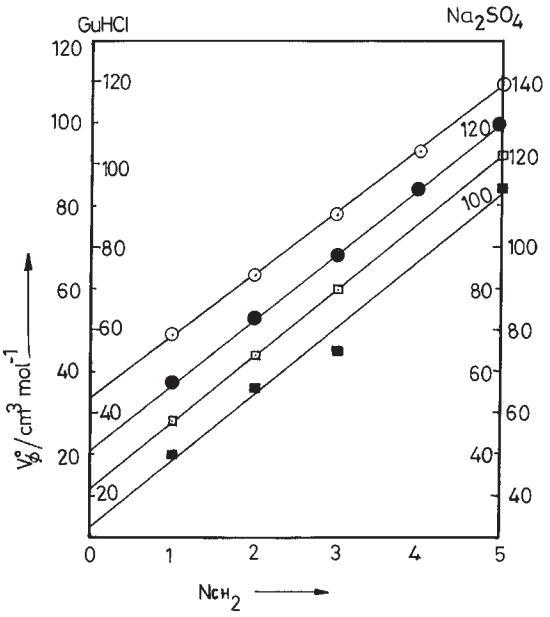

$$[1] \qquad V_\phi = 1000(\rho_0 - \rho)/\ m\ \rho\ \rho_0 + M/\rho$$

where *m* is the molality, *M* is the molar mass of the solute, ρ is the measured density of solution, and ρ_0 the density of the 6 *m* GuHCl / 2 *m* Na_2SO_4 solution at 288.15 and 298.15 K. Since the apparent molar volumes (V_ϕ) were found to vary linearly with molality, the limiting apparent molar volumes have been calculated by using the equation

$$[2] \qquad V_\phi = V_\phi^0 + b_V\ m$$

where V_ϕ^0 is the limiting apparent molar volume and b_V is an experimental slope. The values of apparent molar volumes at infinite dilution (V_ϕ^0) and experimental slope (b_V) are presented in Table 1.

The limiting apparent molar volumes of the amino acids in aqueous guanidine hydrochloride and sodium sulphate at each temperature are larger than the corresponding values in water (7). It is also noted that the limiting apparent molar volumes of the amino acids in aqueous guanidine hydrochloride at 298.15 K are larger than at 288.15 K, except for glycine. However, for aqueous sodium sulphate, V_ϕ^0 shows an increase with temperature, except in the case of γ-Aba. The V_ϕ^0 values plotted against N_{CH_2}, the number of CH_2 groups (Fig. 2) in the backbone chain, yielded straight lines at 288.15 and 298.15 K. The V_ϕ^0 vs. N_{CH_2} data could, therefore, be regressed by

$$[3] \qquad V_\phi^0 = V_\phi^0\ (NH_3^+,\ COO^-) + \sum_{n=1}^{N_{CH_2}} n\ V_\phi^0\ (CH_2)$$

© 1999 NRC Canada

Table 1. Tabulation of V_ϕ^0 and b_V values for amino acids in 6 *m* GuHCl and 2 *m* Na_2SO_4 at 288.15 and 298.15 K.[a]

		288.15 K		298.15 K	
Amino acid	Solvent	V_ϕ^0 (cm^3 mol^{-1})	b_V (cm^3 kg mol^{-2})	V_ϕ^0 (cm^3 mol^{-1})	b_V (cm^3 kg mol^{-2})
Glycine	6 *m* GuHCl	48.72	–1.75	46.83	0.83
		(0.16)	(0.37)	(0.11)	(0.28)
	2 *m* Na_2SO_4	47.61	3.25	50.10	0.97
		(0.33)	(1.48)	(0.18)	(1.55)
β-Alanine	6 *m* GuHCl	62.78	–0.10	63.52	–2.06
		(0.04)	(0.10)	(0.24)	(0.88)
	2 *m* Na_2SO_4	64.27	–0.12	66.35	–6.83
		(0.34)	(1.80)	(0.43)	(1.68)
γ-Aminobutyric	6 *m* GuHCl	77.63	0.27	77.74	0.69
		(0.05)	(0.14)	(0.09)	(0.30)
	2 *m* Na_2SO_4	79.93	–0.86	75.06	10.06
		(0.27)	(1.52)	(0.50)	(2.88)
δ-Aminovaleric	6 *m* GuHCl	92.84	0.48	93.68	–1.26
		(0.12)	(0.33)	(0.14)	(0.77)
ε-Aminocaproic	6 *m* GuHCl	109.25	0.44	109.94	–0.54
		(0.10)	(0.29)	(0.17)	(0.79)
	2 *m* Na_2SO_4	111.57	–2.38	112.91	–3.23
		(0.31)	(1.40)	(0.21)	(1.22)

[a]The values in parentheses are standard errors.

Fig. 3. Plot of V_ϕ^0 versus molar mass of amino acids. GuHCl at 288.15 K (○); GuHCl at 298.15 K (●); Na_2SO_4 at 288.15 K (□); Na_2SO_4 at 298.15 K (■).

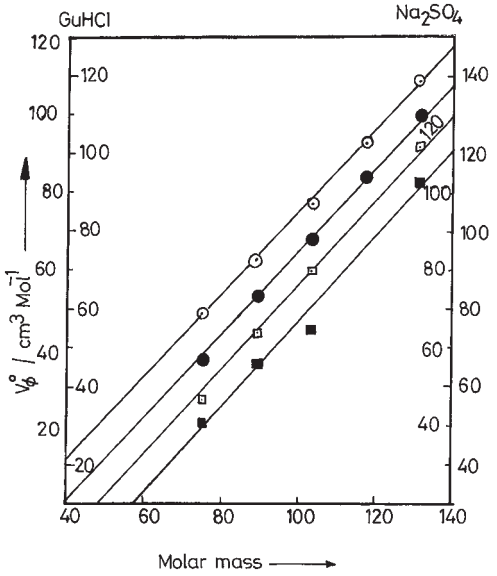

where V_ϕ^0 (CH_2) is the volume contribution of the CH_2 group in appropriate units and V_ϕ^0 (NH_3^+, COO^-) is identified as the contribution due to polar end groups, NH_3^+ and COO^-. The average values of V_ϕ^0 (CH_2) in aqueous guanidine hydrochloride solutions are found to be 15.15 and 15.78 cm^3 mol^{-1}, while in aqueous sodium sulphate solutions the values are 16.04 and 16.25 cm^3 mol^{-1} at 288.15 and 298.15 K, respectively. These calculated values are compared with literature values (11), 15.3–15.8 cm^3 mol^{-1} in aqueous KSCN solutions at the two temperatures, and this value approaches 15.8–16.0 cm^3 mol^{-1} as the KSCN concentration increases at 298.15 K.

It has been found that the apparent molar volume, in general, increases with the increasing molar mass and size of the amino acids (Fig. 3). These results indicate that the volume contribution of the hydrocarbon portion of the amino acid is proportional to the molecular weight (similar to other organic solutes) and the volume contribution due to $^+H_3N(CH_2)_nCOO^-$ ($1 \le n \le 5$) is not strongly affected by the hydrocarbon groups. The trend of the limiting apparent molar volume V_ϕ^0 is found to be Gly < β-Ala < γ-Aba < δ-Amv < ε-Ahx.

The limiting apparent molar volumes of transfer were calculated by subtracting the limiting apparent molar volumes of amino acids in water from the limiting apparent molar volumes in aqueous electrolyte solutions. The limiting apparent molar volume of transfer, ΔV_{tr}^0, for amino acids studied in going from water to aqueous electrolyte systems, is calculated using the relation

$$[4] \qquad \Delta V_{tr}^0 = V_\phi^0 \text{ (aq. electrolyte)} - V_\phi^0 \text{ (water)}$$

where the limiting apparent molar volumes for ω-amino acids in water are taken from the author's work reported elsewhere (7).

The limiting apparent molar volumes of transfer, ΔV_{tr}^0, for transfer of amino acids from water to aqueous guanidine hydrochloride and sodium sulphate systems are presented in Table 2. An examination of the ΔV_{tr}^0 values indicates that the ΔV_{tr}^0 is highest for γ-Aba at 288.15 K and for ε-Ahx at 298.15 K. The ΔV_{tr}^0 for Gly is lower than that for β-Ala at 288.15 and 298.15 K for both GuHCl and Na_2SO_4 (except 6 *m* GuHCl at 288.15 K). However, the variation of ΔV_{tr}^0 in GuHCl and Na_2SO_4 with the number of carbon atoms N_{CH_2} in the backbone chain is not so regular for ω-amino acids at 288.15 and 298.15 K. The fact is that, with the increase in N_{CH_2}, the charge separation increases and hence the NH_3^+ and COO^- cosphere overlap decreases, leading to an in-

© 1999 NRC Canada

Table 2. Tabulation of ΔV_{tr}^0 of amino acids in 6 *m* GuHCl and 2 *m* Na_2SO_4 at 288.15 and 298.15 K.

	ΔV_{tr}^0 (cm^3 mol^{-1})	
Amino acid	288.15 K	298.15 K
	6 *m* GuHCl	
Glycine	6.37	3.63
β-Alanine	5.30	4.81
γ-Aminobutyric	6.38	4.39
δ-Aminovaleric	5.46	5.67
ε-Aminocaproic	6.23	5.74
	2 *m* Na_2SO_4	
Glycine	5.26	6.90
β-Alanine	6.79	7.64
γ-Aminobutyric	8.68	1.71
ε-Aminocaproic	8.55	8.71

crease in salt – polar group interactions. Thus, the decrease in the number of electrostricted water molecules results in an increase in volume (12). Also, when cosolute, i.e., GuHCl/Na_2SO_4 molecules, interact with the charged centers of amino acids, some of the previously electrostricted water molecules around these centers return to their normal structure due to the hydration cosphere overlap effect, causing a net decrease in electrostriction that ultimately gives rise to an increase in transfer volume. The variation of ΔV_{tr}^0 with the number of CH_2 groups for ω-amino acids gives volume contributions for different groups. The intercepts give the volume contributions of the charged end or head groups (NH_3^+, COO^-), while the slopes give the volume contribution of the methylene (-CH_2) groups.

As the hydrophobic hydration of the -CH_2 groups in ω-amino acids is suppressed by overlap of the hydration cospheres of the polar end groups and in the presence of electrolyte, strong polar–polar group (=NH_2^+--COO^- and Cl^---NH_3^+ or Na^+--COO^- and SO_4^{2-}--NH_3^+) interactions enhance the hydrophobic hydration, thereby resulting in the positive transfer volume contribution of the -CH_2 groups. The resulting positive transfer volumes, ΔV_{tr}^0, for the transfer of amino acids from water to aqueous guanidine hydrochloride and sodium sulphate can be explained by assuming a decreased electrostriction of the solvent around the charged groups on the amino acid due to strong interactions between these groups and the $(H_2N)_2C{=}NH_2^+$ and Cl^- ions. The reduced structure-breaking tendency of $(H_2N)_2C{=}NH_2^+$ and Cl^- ions, due to their interactions with the amino acid, also contributes to the positive transfer volumes. However, Belibagli and Ayranci (13) proposed that the positive transfer volume ΔV_{tr}^0 is due to the solute–cosolute–solvent interactions. The discrepancy between their result with the present work on glycine is explained on the basis of the difference in the instrument used for density measurements. Belibagli and Ayranci conducted the density measurements using the buoyancy balance method, which is not capable of the high precision offered by the Anton Paar high-precision vibrating tube digital densimeter. The present work also supports a similar variation of ΔV_{tr}^0 with the number of CH_2 groups observed in water + KSCN + amino acid and water + NH_4Cl + amino acid systems (11, 14).

Conclusions

The present work, which is confined to volumetric studies of ω-amino acids in aqueous electrolyte systems, reflects the combined effect of various hydrophilic and hydrophobic interactions in these systems. It is concluded that the limiting apparent molar volume increases with increase in temperature as well as with a -CH_2 group increment in the backbone of the amino acids. Positive transfer volumes, ΔV_{tr}^0, for the transfer of amino acids from water to aqueous GuHCl and Na_2SO_4 systems, have been observed. The results reveal that guanidine hydrochloride is a water-structure breaker and interacts with charged end groups of the zwitterionic amino acids, causing a net decrease in electrostriction of the solvent, while sodium sulphate is a water-structure maker.

References

1. M. Joly. A physicochemical approach to the denaturation of proteins. Academic, London. 1965.
2. T.H. Lilley. *In* Chemistry and biochemistry of amino acids. *Edited by* G.C. Barrett. Chapman and Hall, London. 1985.
3. J.C. Ahluwalia. J. Indian Chem. Soc. **63**, 727 (1986).
4. A.W. Hakin, A.K. Copeland, J.L. Liu, R.A. Marriott, and K.E. Preuss. J. Chem. Eng. Data, **42**, 84 (1997); S. Milito, M.S. Bakshi, R. Crisantino, and De Lisir. J. Solution Chem. **24**, 103 (1995).
5. P.K. Nandi and D.R. Robinson. J. Am. Chem. Soc. **94**, 1299 (1972); **94**, 1308 (1972).
6. J.C. Lee and S.N. Timasheff. Arch. Biochem. Biophys. **165**, 268 (1974); Methods Enzymol. **61**, 49 (1979); Biochemistry, **13**, 257 (1974).
7. D. Kumar. J. Indian Chem. Soc. **74**, 610 (1997); M. Phil. Dissertation, University of Delhi, Delhi. 1991.
8. R.C. Weast. Handbook of chemistry and physics.CRC Press, Cleveland, Ohio. 1969.
9. G.S. Kell. J. Chem. Eng. Data, **20**, 97 (1975).
10. F.J. Millero. J. Phys. Chem. **74**, 356 (1970).
11. R.K. Wadi and R.K. Goyal. J. Solution Chem. **21**, 163 (1992).
12. J.C. Ahluwalia, C. Ostiguy, G. Perron, and J.E. Desnoyers. Can. J. Chem. **55**, 3364 (1977); G.R. Hedwig and J.F. Reading. J. Chem. Soc. Faraday Trans. 1, **87**, 1751 (1991).
13. K. Belibagli and E. Agranci. J. Solution Chem. **19**, 867 (1990).
14. M. Natarajan, R.K. Wadi, and H.C. Gaur. J. Chem. Eng. Data, **35**, 87 (1990).

© 1999 NRC Canada

Appendix A

Table A1. Comparison of densities of aqueous sodium chloride at 298.15 K obtained in present work with literature values.

m^a (mol kg^{-1})	ρ^a (10^3 kg m^{-3})	$1000(\rho - \rho_0)^a$ (10^6 kg m^{-3})	m^b (mol kg^{-1})	$1000(\rho - \rho_0)^b$ (10^6 kg m^{-3})
0	0.997 048			
0.0221	0.997 969	0.9210	0.010 021	0.4167
0.0561	0.999 364	2.3160	0.039 766	1.6417
0.0963	1.000 997	3.9490	0.052 243	2.1589
0.1309	1.002 415	5.3670	0.103 490	4.2519
0.2028	1.005 320	8.2720	0.120 759	4.9440
0.2046	1.005 393	8.3450	0.162 253	6.6329
0.2727	1.008 110	11.0620	0.201 720	8.2289
0.3027	1.009 316	12.2680	0.212 622	8.6609
0.4557	1.015 339	18.2910	0.280 763	11.3876
			0.309 342	12.5349
			0.347 819	14.0509

[a]Present work.

[b]Reference 10.

Appendix B

Table B1. Densities and apparent molar volumes of solutions of ω-amino acids in aqueous guanidine hydrochloride and sodium sulphate as a function of molality of the amino acid at 288.15 and 298.15 K.

m (mol kg^{-1})	ρ (10^3 kg m^{-3})	V_ϕ (cm^3 mol^{-1})	m (mol kg^{-1})	ρ (10^3 kg m^{-3})	V_ϕ (cm^3 mol^{-1})
	6 *m* GuHCl at 288.15 K			6 *m* GuHCl at 298.15 K	
	Glycine			Glycine	
0	1.105 278		0	1.100 756	
0.1982	1.109 953	48.40	0.0988	1.103 286	46.96
0.2504	1.111 188	48.34	0.1398	1.104 368	46.73
0.3493	1.113 499	48.29	0.1770	1.105 252	47.05
0.3968	1.114 830	47.80	0.2481	1.107 017	47.11
0.5019	1.117 360	47.69	0.2799	1.107 805	47.11
0.6021	1.119 743	47.63	0.3001	1.108 322	47.07
0.6980	1.121 946	47.65	0.3499	1.109 464	47.29
			0.4007	1.110 804	47.07
			0.4481	1.111 926	47.15
			0.4989	1.113 111	47.23
	β-Alanine			β-Alanine	
0	1.105 283		0	1.100 747	
0.2002	1.109 582	62.79	0.0994	1.102 812	63.67
0.2496	1.110 631	62.77	0.1255	1.103 422	63.20
0.2996	1.111 696	62.73	0.1994	1.105 062	62.84
0.3496	1.112 697	62.83	0.2452	1.106 037	62.83
0.4460	1.114 688	62.82	0.2881	1.106 934	62.87
0.5004	1.115 857	62.71	0.3506	1.108 263	62.82
0.5976	1.117 796	62.76	0.3985	1.109 221	62.91
0.6988	1.119 788	62.80			
	γ-Aminobutyric acid			γ-Aminobutyric acid	
0	1.105 293		0	1.100 728	
0.2005	1.109 051	77.67	0.0992	1.102 606	77.91
0.2497	1.109 948	77.69	0.1230	1.103 089	77.66
0.3485	1.111 710	77.76	0.1647	1.103 832	77.87
0.3981	1.112 576	77.79	0.2514	1.105 403	77.98
0.4970	1.114 365	77.80	0.3000	1.106 295	77.95

© 1999 NRC Canada

Table B1 (*continued*).

m (mol kg^{-1})	ρ (10^3 kg m^{-3})	V_ϕ (cm^3 mol^{-1})	m (mol kg^{-1})	ρ (10^3 kg m^{-3})	V_ϕ (cm^3 mol^{-1})
0.6020	1.116 109	77.81	0.3532	1.107 279	77.89
			0.3861	1.107 803	78.04
			0.3909	1.107 894	78.03
	δ-Aminovaleric acid			δ-Aminovaleric acid	
0	1.105 279		0	1.100 733	
0.2002	1.108 394	93.04	0.0989	1.102 248	93.70
0.2498	1.109 158	93.00	0.1500	1.103 064	93.45
0.2980	1.109 912	92.92	0.1958	1.103 801	93.28
0.3997	1.111 477	92.82	0.2295	1.104 301	93.34
0.4492	1.112 098	93.04	0.2731	1.104 993	93.24
0.4980	1.112 762	93.11	0.2781	1.105 037	93.33
0.6004	1.114 133	93.22	0.2993	1.105 295	93.50
	ε-Aminocaproic acid			ε-Aminocaproic acid	
0	1.105 289		0	1.100 749	
0.1982	1.107 542	109.18	0.0599	1.101 404	110.11
0.2482	1.107 998	109.50	0.0999	1.101 893	109.63
0.2995	1.108 556	109.45	0.1397	1.102 318	109.76
0.3497	1.109 092	109.42	0.1719	1.102 626	109.99
0.3893	1.109 503	109.42	0.2198	1.103 172	109.85
0.4475	1.110 129	109.37	0.2791	1.103 852	109.71
0.4909	1.110 476	109.54	0.3000	1.104 030	109.84
0.6034	1.111 625	109.48			
	2 *m* Na_2SO_4 at 288.15 K			2 *m* Na_2SO_4 at 298.15 K	
	Glycine			Glycine	
0	1.216 405		0	1.211 810	
0.0498	1.217 420	47.90	0.1482	1.214 356	50.15
0.1000	1.218 420	48.01	0.2191	1.215 522	50.26
0.1200	1.218 886	47.64	0.2380	1.215 736	50.55
0.1734	1.219 739	48.59	0.2449	1.215 892	50.43
0.2005	1.220 320	48.36	0.2793	1.216 445	50.46
0.2196	1.220 836	47.91	0.2979	1.216 877	50.15
0.2500	1.221 331	48.20			
0.2994	1.221 997	48.87			
	β-Alanine			β-Alanine	
0	1.216 462		0	1.211 478	
0.1000	1.217 846	63.82	0.0536	1.212 032	66.47
0.1199	1.217 973	64.65	0.1465	1.213 341	64.78
0.1796	1.218 724	64.61	0.1805	1.213 712	64.99
0.1995	1.219106	64.15	0.2169	1.214 307	64.51
0.2134	1.219 342	63.97	0.2556	1.214 689	64.81
0.2488	1.219 613	64.52	0.2864	1.215 056	64.84
0.2791	1.220 190	64.02	0.3186	1.215 911	63.83
0.3000	1.220 361	64.26	0.3465	1.216 100	64.21
	γ-Aminobutyric acid			γ-Aminobutyric acid	
0	1.216 458		0	1.210 748	
0.0995	1.217 162	79.93	0.0996	1.212 013	76.41
0.1198	1.217 390	79.43	0.1199	1.212 385	75.74
0.1501	1.217 697	79.10	0.1500	1.212 542	76.88
0.1801	1.217 890	79.29	0.2501	1.213 609	77.17
0.1999	1.217 994	79.46	0.2992	1.213 646	78.36
0.2216	1.218 073	79.72			
0.2503	1.218 412	79.35			
0.3000	1.218 761	79.42			
	ε-Aminocaproic acid			ε-Aminocaproic acid	
0	1.216 266		0	1.211 381	
0.0500	1.215 974	111.85	0.0497	1.211 054	112.82

© 1999 NRC Canada

Table B1 (*concluded*).

m (mol kg^{-1})	ρ (10^3 kg m^{-3})	V_ϕ (cm^3 mol^{-1})	m (mol kg^{-1})	ρ (10^3 kg m^{-3})	V_ϕ (cm^3 mol^{-1})
0.1013	1.215 809	110.96	0.1493	1.210 514	112.34
0.1201	1.215 657	111.36	0.1799	1.210 322	112.41
0.1801	1.215 539	110.67	0.1962	1.210 275	112.25
0.1996	1.215 306	111.21	0.2399	1.210 178	111.83
0.2199	1.215 264	111.04	0.2731	1.209 841	112.29
0.2503	1.215 121	111.07			
0.2998	1.214929	111.01			

© 1999 NRC Canada

The structure and some molecular properties of acetone-picrylhydrazone

K.C. Brown, B.R. Nelson, J.W. Quail, B.E. Robertson, J.A. Weil, and Z. Zimpel

Abstract: Various physical measurements and quantum-mechanical computations to characterize molecular 2-propanone(2,4,6-trinitrophenyl)hydrazone, alias acetone-picrylhydrazine (AH), are reported, including an X-ray diffraction structural determination, an ^{1}H and ^{13}C NMR study of its internal hindered reorientation, and a theoretical (SCF-MO) interpretation of these observations. The structure of AH was determined by X-ray crystallography. The space group is $P\bar{1}$, with a = 10.1768(9) Å, b = 7.7968(18) Å, c = 8.0018(5) Å, α = 92.102(6)°, β = 99.919(7)°, γ = 105.926(6)°, Z = 2, $wR2(F^2)$ = 0.1995 based on all 2748 unique reflections. The (picryl) proton NMR thermal work yielded a Gibbs activation energy $\Delta G^{\ddagger}$ = 46.9 ± 0.4 kJ mol^{-1} in acetone-d_6 and 48.1 ± 0.2 kJ mol^{-1} in chloroform-d, whereas ^{13}C NMR (two pairs in the picryl ring) yielded 46.6 ± 1.0 and 46.4 ± 1.0 kJ mol^{-1} in acetone-d_6. The SCF-MO computations yielded a detailed model of the conformerization path. Various model conformations and tautomers of AH have been considered, as has removal of H^+ or of H^0 from its hydrazinic linkage.

Key words: dynamic NMR, picrylhydrazone, hindered rotation, activation parameters, SCF-MO model.

Résumé : On a caractérisé 2,4,6-trinitrophénylhydrazone de la propan-2-one (AH, obtenue à partir de l'acétone et de la picrylhydrazine) par des mesures physiques et des calculs de mécanique quantique, comportant une détermination de structure par diffraction des rayons X, une étude de la réorientation interne empêchée par examen des spectres RMN du ^{1}H et du ^{13}C et une interprétation théorique (SCF-MO) de ces observations. On a déterminé la structure de AH par diffraction des rayons X: groupe d'espace $P\bar{1}$, avec a = 10,1768(9), b = 7,7968(18) et c = 8,0018(5) Å, α = 92,102(6)°, β = 99,919(7)° et γ = 105,926(6)°, Z = 2, $wR2(F^2)$ = 0,1995 sur la base des 2748 réflexions uniques. Le travail thermique en RMN du proton (picryle) permet de tirer une énergie d'activation de Gibbs de $\Delta G^{\ddagger}$ = 46,9 ± 0,4 kJ mol^{-1} dans l'acétone-d_6 et de 48,1 ± 0,2 kJ mol^{-1} dans le chloroforme-d; par ailleurs, la RMN du ^{13}C (deux paires dans le noyau picryle) conduit à des valeurs de 46,6 ± 1,0 et de 46,4 ± 1,0 kJ mol^{-1} dans l'acétone-d_6. Les calculs SCF-MO ont permis de tirer un modèle détaillé de la voie conformationnelle. On a considéré divers modèles de conformations et de tautomères pour AH et pour ses dérivés obtenus par enlèvement de H^+ ou de H^0 de sa liaison hydrazinique.

Mots clés : RMN dynamique, 2,4,6-trinitrophénylhydrazone de l'acétone, rotation empêchée, paramètres d'activation, modèle SCF-MO.

[Traduit par la Rédaction]

Introduction

The present paper presents our recent study of 2-propanone(2,4,6-trinitrophenyl)hydrazone (alias: acetone-picrylhydrazine ≡ AH), a molecule that presents much of interest for structural studies (Fig. 1). We include an X-ray diffraction single-crystal determination of the molecular structure, a detailed nuclear magnetic resonance (NMR) study of internal molecular motions, and a molecular-orbital (self-consistent-field Hartree–Fock) examination of its energetics and geometric configuration. Certain aspects of its acidity and oxidizability will also be discussed. With regard to the former, our interest in AH stems in part from its ability to form stable alkali salts (1) and its reaction to form picryl-ring addition compounds with the enolate of acetone (2).

General reviews dealing with hydrazones are available (3, 4). However, relatively little information dealing specifically with AH is to be found, but the recent literature does contain a preparative recipe (5), slightly modified herein, and also describes some polarographic reduction work (6).

Preparation and characterization of AH

A solution containing 10 g of 2,4,6-trinitrophenylhydrazine[2] in 300 mL of acetone, after adding one drop of 6 M aqueous HCl, was refluxed for 30 min. The solvent was then

Received January 21, 1998.

K.C. Brown, B.R. Nelson, J.W. Quail, J.A. Weil,[1] and Z. Zimpel. Department of Chemistry, University of Saskatchewan, 110 Science Place, Saskatoon, SK S7N 5C9, Canada.
B.E. Robertson. Department of Physics, University of Regina, Regina, SK S4S 0A2, Canada.

[1]Author to whom correspondence may be addressed. Telephone: (306) 966-4658. Fax: (306) 966-4730. e-mail: john.weil@usask.ca

[2]This compound, picrylhydrazine, was prepared by reaction of picrylchloride (10 g in 160 mL methanol) with hydrazine hydrochloride (8.5 g in 20 mL water), followed by treatment with aqueous Na_2CO_3 (8.5 g in 40 mL water, added in batches). Addition of aqueous HCl (60 mL of 2 M acid) then yielded the solid yellow product.

 © 1999 NRC Canada

Fig. 1. Projection diagrams of the two primary conformers of AH as obtained from the X-ray diffraction results, including the atom numbering scheme. The two chiral species are related by an inversion point (or, equivalently, a reflection plane) located midway between them.

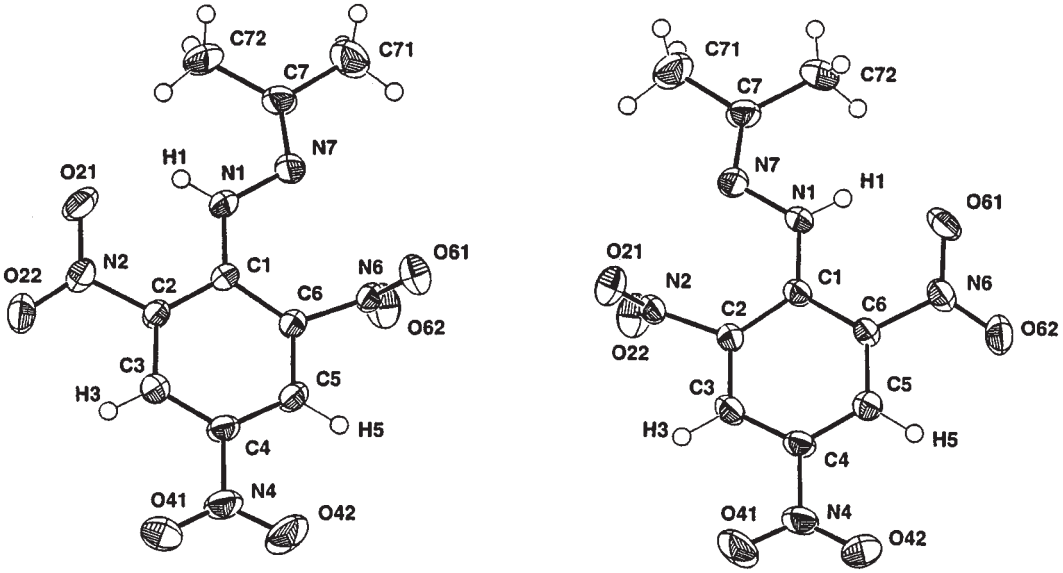

removed by rotary evaporation. The impure hydrazone was crystallized from 95% EtOH to give bright yellow crystals: mp 129.5–130.5°C. FT IR (cm^{-1}): 3280 (N–H), 3108–3075 (C–H, ar), 2944–2918 (C–H, al). ^{1}H NMR δ (300.13 MHz, 280 K, acetone-d_6) (ppm): 11.06 (1 H, s), 8.98 (2 H, s), 2.14 (3 H, s), 2.04 (3 H, s). ^{1}H NMR δ (300.13 MHz, 290 K, chloroform-*d*) (ppm): 11.12 (1 H, s), 8.91 (2 H, s), 2.08 (6 H, s). See Fig. 2. ^{13}C NMR δ (75.47 MHz, 330 K, acetone-d_6) (ppm): 159.33 (C7), 138.15 (C1), 136.56 (C2, C6), 136.04 (C4), 125.82 (C3, C5), 24.01 and 16.50 (C71 and C72). See Fig. 3. Anal. calcd. for $C_9H_9N_5O_6$: C 38.17, H 3.20, N 24.73; found: C 38.62, H 3.24, N 24.88.

X-ray diffraction structural study of AH

A yellow plate-shaped crystal was mounted on a glass fibre on a Picker FACS-1 diffractometer, equipped with graphite-monochromated Mo-K_α radiation (λ = 0.71073 Å). Data collection and initial data processing were carried out using the NRCC diffractometer control system (7). Data processing and structure solution used XTAL3.4 (8). SHELXL-97 (9) was used for refinement of the structure. Cell constants and orientation matrices were obtained from least-squares refinement, using 32 reflections and their Friedel mates in the range $45° < 2\theta < 55°$. Details of the structure determination results are given in Table 1. The intensities of three representative reflections were measured after data for sets of 47 reflections had been obtained. Over the course of data collection, the standards decreased by 3.5%, and a linear correction factor was applied to the data. No correction was made for absorption. Lorentz and polarization corrections were applied to the data. The structure was solved by direct methods in space group *P*1 and then converted into space group $P\bar{1}$. The non-hydrogen atoms were refined anisotropically; hydrogen atoms were located on Δ*F* maps and then adjusted to ideal positions and not refined. The final cycle of full-matrix least-squares refinement was based on all 2748 reflections and 181 parameters, refining the parameter $wR2 = [\Sigma\, w(F_o^2 - F_c^2)^2 / \Sigma\, w\, F_o^4]^{1/2}$. The refinement converged to a value of $wR2(F^2) = 0.1995$ on all data. A final Fourier difference map calculation showed no peaks of chemical significance. The atomic coordinates are given in Table 2, and various interatomic distances and angles of interest are set out in Table 3. Tables of thermal parameters, anisotropic thermal parameters, atomic coordinates and bond lengths involving hydrogen atoms, torsion angles, and contact distances are available as supplementary data.[3]

When positional restraints on H1 were removed, followed by eight cycles of refinement, the H1 position was found to be consistent with sp^2 hybridization of N1 and within 3σ of the idealized position.

The standard unit cell contains two conformeric molecules (Fig. 1) related by a center of inversion. There is no crystal mirror plane, but in fact the two isomers are nonsuperposable mirror-image conformers (enantiomers). They differ primarily in the relative orientations of the nitro groups *ortho* to the hydrazine linkage at carbon C1.

NMR experimental

The solvents used were acetone-d_6 and chloroform-*d*, in order to be able to reach down to ca. 200 K and also because they differ appreciably in H-bonding capability (10). Tetramethylsilane was used as the line-position standard. The ^{1}H and ^{13}C NMR experiments were performed on a Bruker AMX-300 spectrometer at 300.13 and 75.47 MHz,

[3] These data can be purchased from: The Depository of Unpublished Data, Document Delivery, CISTI, National Research Council of Canada, Ottawa, ON K1A 0S2, Canada. Tables of hydrogen atom coordinates and of bond lengths involving hydrogen atoms have also been deposited with the Cambridge Crystallographic Data Centre, and can be obtained on request from the Director, Cambridge Crystallographic Data Centre, University Chemical Laboratory, 12 Union Road, Cambridge, CB2 1EZ, England.

© 1999 NRC Canada

Table 1. Summary of crystal and intensity data for 2-propanone(2,4,6-trinitrophenyl)hydrazone (AH).

Chemical formula	$C_9H_9N_5O_6$
M, g mol^{-1}	283.21
Crystal system	Triclinic
Crystal dimensions, mm	0.67 × 0.66 × 0.08
Space group	$P\bar{1}$
a, Å	10.1768(9)
b, Å	7.7968(18)
c, Å	8.0018(5)
α, deg	92.102(6)
β, deg	99.919(7)
γ, deg	105.926(6)
V, Å^3	599.05(15)
T, K	293(2)
Z	2
ρ_{calc}, g cm^{-3}	1.570
F(000)	292
Absorption coefficient μ, cm^{-1}	1.34
λ, Å	0.71073
$2\theta_{max}$, deg	55.0
Unique data used (all reflections)	2748
Data collected	$+h, \pm k, \pm l$
Reflection intensities > 3σ(I)	2286
Refinement	F^2
No. of parameters	181
$R[F^2 > 2\sigma(F^2)]$ [a]	0.0676
$wR2(F^2)$ (all data)	0.1995
S (goodness of fit on F^2)	1.045
Maximum shift/error in final cycle	0.001
Maximum, minimum peaks in final difference map (|e| Å^{-3})	+0.493, –0.488

[a] Weighting scheme (ref. 9): $[\sigma^2 F_o^2 + (0.1298P)^2 + 0.2926P]^{-1}$ where $P = (F_o^2 + 2F_c^2)/3$.

Table 2. Atomic coordinates (× 10^4) and equivalent isotropic displacement parameters U(eq) (Å^2 × 10^3) for acetone-picrylhydrazone. See Fig. 1, left model.

	x	y	z	U(eq) [a]
C1	18(2)	2514(2)	480(2)	25(1)
C2	–1215(2)	1566(2)	1057(2)	26(1)
C3	–2374(2)	455(2)	–5(2)	29(1)
C4	–2347(2)	209(3)	–1708(2)	31(1)
C5	–1201(2)	1099(3)	–2382(2)	31(1)
C6	–75(2)	2238(2)	–1312(2)	26(1)
C7	3262(2)	5540(3)	2169(3)	36(1)
C71	4563(3)	6570(4)	1625(4)	58(1)
C72	3179(3)	5724(4)	4013(3)	51(1)
N1	1128(2)	3552(2)	1562(2)	31(1)
N2	–1312(2)	1673(2)	2857(2)	32(1)
N4	–3533(2)	–1045(3)	–2819(2)	43(1)
N6	1055(2)	3184(2)	–2182(2)	28(1)
N7	2300(2)	4528(2)	1000(2)	36(1)
O21	–216(2)	2173(2)	3932(2)	46(1)
O22	–2451(2)	1233(2)	3233(3)	45(1)
O41	–4573(2)	–1702(3)	–2240(3)	65(1)
O42	–3402(2)	–1424(3)	–4273(2)	73(1)
O61	1844(2)	2369(2)	–2529(2)	42(1)
O62	1060(2)	4666(2)	–2597(2)	46(1)

[a] U(eq) is defined as one third of the trace of the orthogonalized U^{ij} tensor.

respectively. Temperature control on the AMX-300 was provided by a B-VT-1000 variable-temperature unit. Temperature calibration was performed using the chemical shift difference between the methyl and hydroxy peaks of neat methanol, at and below room temperature.

Nuclear magnetic resonance spectroscopic study of AH

The proton spectrum of AH (Fig. 2) is well suited to a study of the internal dynamics of the molecule. In the past, we have performed similar studies on 2,2-diphenyl-1-picrylhydrazine (≡ DH) (10, 11).

The picryl protons are convenient probes of the interchange process, which transforms one conformer into the other (Fig. 1). These protons experience different magnetic environments primarily because the two *ortho*-nitro groups, on carbons 2 and 6 of the picryl ring, are at different orientations relative to the ring, largely due to hydrogen bonding to the hydrazinic hydrogen in AH. In this compound the picryl protons therefore have a non-zero chemical shift difference Δ_{H3-H5} (61.6 Hz in acetone-d_6 (T = 210 K), and 209.5 Hz in chloroform-d (T = 210 K; Fig. 2, lower)). Also, an electron-coupled scalar interaction (J) between them is observed in the very slow exchange spectrum as a small line splitting, e.g., 2.7 Hz at 183 ± 1 K in acetone-d_6 and 2.5 Hz at 210 ± 1 K in chloroform-d.

© 1999 NRC Canada

Table 3. Comparison of X-ray diffraction results for AH at 300 K with the computational results (Fig. 1, left model). The distances are given in Å, and the angles are in degrees. Estimated ± error values are set in parentheses. Double dashes between atom labels denote non-bond distances. Note that torsion angles $\Omega + 180°$ and $\Omega - 180°$ are of course equivalent.

Parameter definition	Measured value	Calculated value (ground state)
C1—C2	1.431 (2)	1.423
C1—C6	1.425 (2)	1.418
C1—N1	1.339 (2)	1.327
C2—C3	1.380 (2)	1.376
C2—N2	1.461 (2)	1.435
C3—C4	1.375 (3)	1.365
C4—C5	1.390 (3)	1.381
C4—N4	1.457 (2)	1.447
C5—C6	1.373 (2)	1.362
C6—N6	1.483 (2)	1.430
C7—C71	1.492 (3)	1.505
C7—C72	1.497 (3)	1.511
C7—N7	1.290 (2)	1.266
N1—N7	1.384 (2)	1.417
N2—O21	1.242 (2)	1.263
N2—O22	1.209 (2)	1.237
N4—O41	1.219 (3)	1.245
N4—O42	1.228 (3)	1.245
N6—O61	1.212 (2)	1.236
N6—O62	1.213 (2)	1.247
N7--O61	3.130 (2)	2.646
N7--O62	2.956 (2)	3.546
C3—H3	0.930 [a]	1.066
C5—H5	0.931 [a]	1.066
N1—H1	0.860 [a]	1.003
O21—H1	1.976 [a]	1.804
O22--H1	3.715 [a]	3.705
O61--H1	4.441 [a]	3.834
O62--H1	4.289 [a]	5.009
C2-C1-C6	113.6 (2)	114.7
C2-C1-N1	121.5 (2)	121.9
C6-C1-N1	124.9 (2)	123.4
C1-C2-C3	123.6 (2)	122.0
C1-C2-N2	121.5 (2)	122.0
C3-C2-N2	114.9 (2)	116.1
C2-C3-C4	118.8 (2)	120.3
C3-C4-C5	121.5 (2)	120.0
C3-C4-N4	119.1 (2)	120.0
C5-C4-N4	119.4 (2)	119.9
C4-C5-C6	118.8 (2)	120.3
C1-C6-C5	123.7 (2)	122.3
C1-C6-N6	122.2 (2)	122.3
C5-C6-N6	114.1 (2)	114.9
C71-C7-C72	118.3 (2)	117.6
C71-C7-N7	116.7 (2)	117.3
C72-C7-N7	125.0 (2)	125.1
C1-N1-N7	121.6 (2)	119.1
C2-N2-O21	118.4 (2)	119.1
C2-N2-O22	118.6 (2)	117.9
O21-N2-O22	123.0 (2)	123.0
C4-N4-O41	118.5 (2)	117.3
C4-N4-O42	117.6 (2)	117.1
O41-N4-O42	123.9 (2)	125.6
C6-N6-O61	117.4 (2)	117.7
C6-N6-O62	117.5 (2)	116.4
O61-N6-O62	124.9 (2)	125.7
C7-N7-N1	115.0 (2)	116.6
C1-N1-H1	119.2 [a]	117.2
N7-N1-H1	119.2 [a]	121.9
C1-C2-C3-C4	1.3 (3)	0.5
N2-C2-C3-C1 [b]	–178.2 (3)	177.8
C1-C2-N2-O21	–19.7 (3)	–4.9
C1-C2-N2-O22	162.0 (2)	175.7
C2-C3-C4-N4	176.3 (2)	–178.7
C3-C4-N4-O41	7.4 (3)	0.3
C3-C4-N4-O42	–170.1 (2)	–179.8
C1-C5-C6-N6 [b]	–179.7 (3)	174.5
C1-C6-N6-O61	100.0 (2)	41.5
C1-C6-N6-O62	–85.0 (2)	–144.7
N1-C1-C2-C3	–178.8 (2)	172.0
N1-C1-C6-C5	176.8 (2)	–169.8
C2-C1-N1-N7	–177.3 (2)	–156.8
C6-C1-N1-N7	2.4 (3)	20.4
C1-N1-N7-C7	176.6 (2)	–172.4
C2-C1-N1-H1	2.6 [a]	8.2
C6-C1-N1-H1	–177.6 [a]	–174.6
C71-C7-N7-N1	178.1 (2)	–178.1
C72-C7-N7-N1	–0.7 (3)	2.1

[a]The proton position was fixed by the geometric configuration of the neighbor atoms.

[b]Not a bond torsion angle.

The ^{13}C nuclei also can be used to give information about the internal dynamics. At low temperature (210 K) there are nine distinct peaks in the ^{13}C NMR spectrum, six of which correspond to nonequivalent carbons in the picryl ring Here $\Delta_{C2–C6}$ = 491.5 Hz and $\Delta_{C3–C5}$ = 127.1 Hz (Fig. 3, lower). As the temperature is raised, these pairs of peaks coalesce and there are only seven peaks observed at 330 K (Fig. 3, upper). One can use the peaks due to carbons 2 and 6 (which are interchanging) and carbons 3 and 5 (which are interchanging) for lineshape analysis. In practice, however, there is a large difference in the signal strengths for these pairs of carbons, the latter pair having the larger signal-to-noise ratio. This presumably is due to the nuclear Overhauser effect on carbons 3 and 5 resulting from the decoupling radiation applied to the protons attached to these carbons. Sufficient acquisition time, especially near the peak-coalescence temperature, overcame this problem. Thus carbons 2 and 6 as well as carbons 3 and 5 were used for the rate study. To our knowledge, this is the first case in which two sets of peaks in the same NMR spectrum have been used to investigate the same conformational interchange phenomenon. The assignment of resonances in the ^{13}C spectrum for carbons 3 and 5 was verified using a *J*-modulation experiment (12).

It was thought at first that the two methyl groups might potentially be useful as another probe into the reorientation

© 1999 NRC Canada

Fig. 2. The ^{1}H NMR spectrum of AH taken at 300.13 MHz in chloroform-*d* at 210 K (lower) and 310 K (upper).

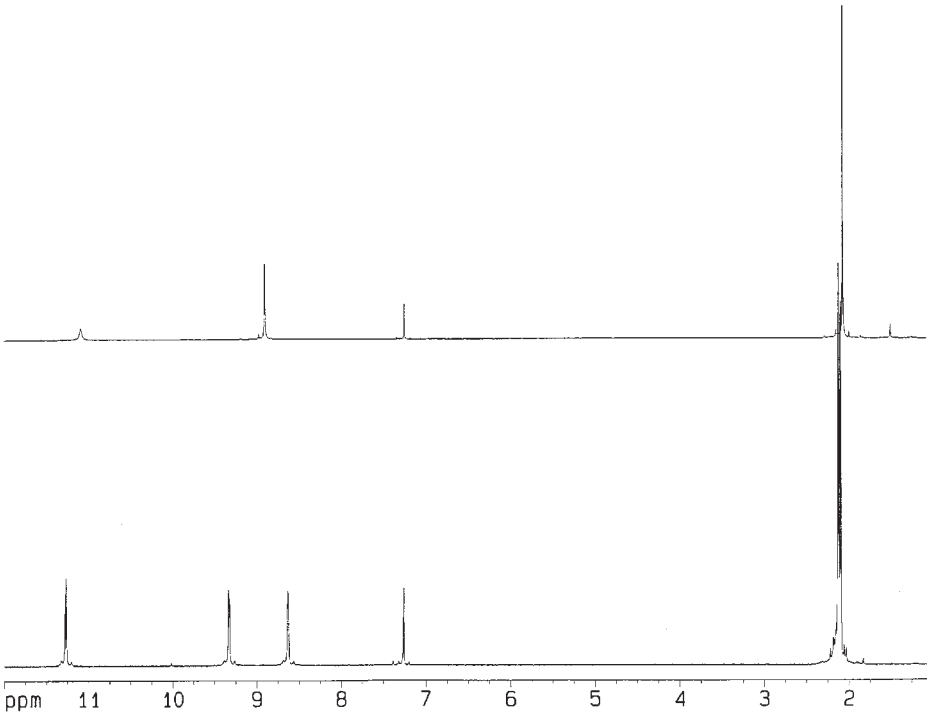

Fig. 3. The ^{13}C NMR spectrum of AH taken at 75.47 MHz in acetone-d_6 at 210 K (lower) and 330 K (upper).

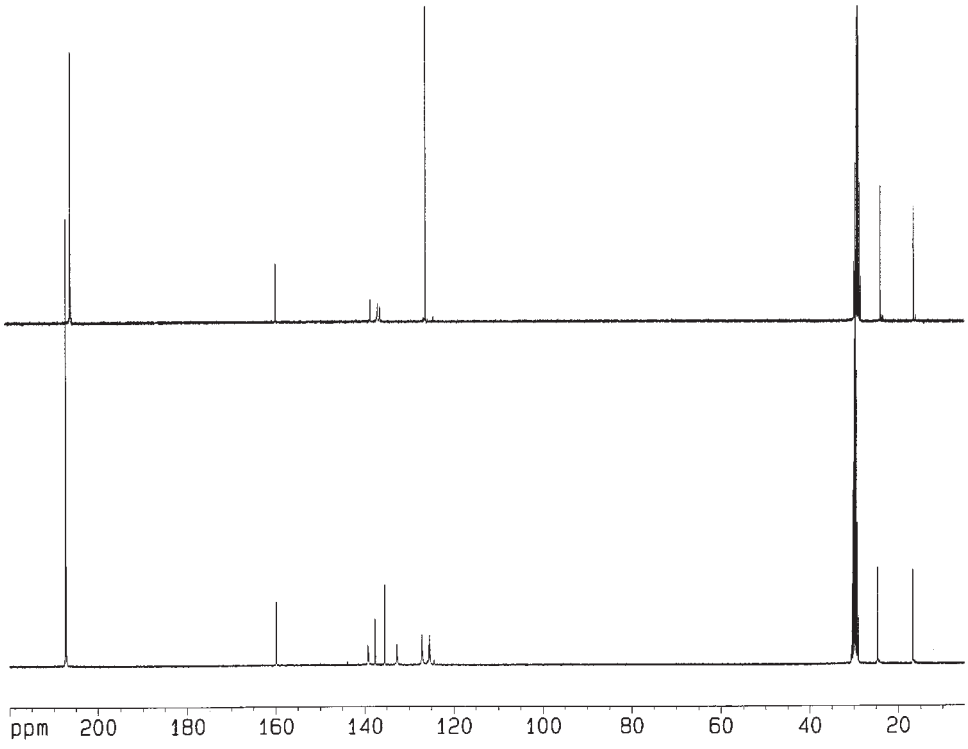

process. At low temperature (210 K), two distinct ^{1}H NMR peaks are observed, since the protons in each methyl group act as equivalent; the peaks are separated by 30.8 Hz in acetone-d_6 and by 8.1 Hz in chloroform-*d*. However, there is little or no change in either peak shape or separation as the temperature is raised. On heating from 183 to 240 K in acetone-d_6, the methyl ^{1}H peak separation increases slightly. It then decreases slowly on going to higher temperatures. In

© 1999 NRC Canada

Table 4. Activation energy E_a, natural logarithm of the frequency factor k_∞, the standard molar activation enthalpy change $\Delta H^\ddagger$, entropy change $\Delta S^\ddagger$, and Gibbs free-energy change $\Delta G^\ddagger$, all at 298.15 K, as a function of the nuclide and the solvent. The number n_T of temperatures at which lineshapes were measured, respectively, was 13, 9, 10, 14. The observed low-temperature relaxation times T_2 used to give the basic line widths for the fittings were (in Hz) 0.20, 0.159, 0.076, 0.21 taken at temperatures 183 K for the first value, 190 K for the middle pair, and 210 K for the fourth. Estimated errors (in parentheses) were calculated according to the procedure given in Sandström (ref. 14, Chap. 7).

Nuclide	Solvent	E_a (kJ mol^{-1})	ln k_∞ (k_∞ in s^{-1})	$\Delta H^\ddagger$ (kJ mol^{-1})	$\Delta S^\ddagger$ (J mol^{-1} K^{-1})	$\Delta G^\ddagger$ (kJ mol^{-1})
^{1}H3,5	Acetone-d_6	40.1 (4)	26.7 (4)	37.6 (4)	–31.2 (2)	46.9 (4)
^{13}C2,6	Acetone-d_6	44.1 (8)	28.5 (4)	41.7 (8)	–16.4 (3)	46.6 (1.0)
^{13}C3,5	Acetone-d_6	44.6 (8)	28.7 (4)	42.1 (8)	–14.5 (3)	46.4 (1.0)
^{1}H3,5	Chloroform-*d*	55.3 (5)	32.4 (4)	52.9 (5)	15.9 (9)	48.1 (2)

the same solvent, the ^{13}C peak separation decreases slowly from 183 to 330 K at a rate of –0.2 Hz K^{-1}. In $CDCl_3$, the ^{1}H peak separation of the methyl peaks decreases at a rate of approximately –0.06 Hz K^{-1}. Here, on heating, the peaks merge at approximately 300 K and then reappear at 320 K. In summary, kinetic broadening and coalescence of the methyl doublets was not observed.

For the ^{1}H NMR (acetone-d_6) experiments, spectra at n_T = 13 different temperatures between 183 and 280 K were obtained, at approximately 10 K intervals. The NMR samples were allowed to equilibrate at each new temperature for 20 min. With chloroform-*d*, n_T was 14, for temperatures between 210 and 340 K. For the ^{13}C NMR work (C2,6 and C3,5 in the acetone), n_T was 9, within the range 210–330 K.

The temperature dependences of the chemical shift differences at the lower temperatures (183–240 K) below onset of conformerization effects were investigated. The slopes with increasing temperature were estimated to be (Hz K^{-1}) 1.89 (H3,5), 0.44 (C2,6), and 0.00 (C3,5) in acetone-d_6 and 0.15 (H3,5) for chloroform-*d*. These data were used to extrapolate the appropriate chemical shift differences for the lineshape fitting. It proved to be important for accuracy to use line widths (i.e., T_2 values; see Table 4) obtained at the lowest temperatures attainable.

Spectral analyses were performed using the Maple symbolic computation program (13). Input consisted of the chemical shifts of the resonances, line-width parameter, rate parameter, and the lineshape equations (14). It was assumed that the lineshapes are Lorentzian, that the reorientation time is small compared to the mean lifetime of the two configurations (Fig. 1) of the AH molecules in solution, and that the reorientation process is mutual.

The Arrhenius model (15)

$$[1] \qquad \ln(k_T) = \ln(k_\infty) - E_a/(RT)$$

for an isothermal process was used to determine the molar activation energy E_a, where R is the ideal gas constant and T is the temperature in degrees kelvin. The pseudo-thermodynamic activation parameters (see ref. 14) were calculated via the equations

$$[2] \qquad \Delta H^\ddagger = E_a - RT$$

$$[3] \qquad \Delta S^\ddagger = R[\ln(k_\infty hN_A/(eRT))]$$

$$[4a] \qquad \Delta G^\ddagger = \Delta H^\ddagger - T\Delta S^\ddagger$$

$$[4b] \qquad = RT\,[\ln(RT/(k_T hN_A))]$$

where h is Planck's constant, N_A is Avogadro's number, and e is the base of the natural logarithm.

Lineshape analysis of the picryl ^{1}H and ^{13}C NMR spectra gave a set of synthesized shapes corresponding nicely to the experimental shapes, yielding values of the rate constant k_T, in s^{-1}, for each temperature T. The Arrhenius plots obtained from the k_T versus T data yielded values of E_a as presented in Table 4. Application of eqs. [2]–[4] then yielded the molar pseudo-thermodynamic parameters $\Delta H^\ddagger$, $\Delta S^\ddagger$, and $\Delta G^\ddagger$ at 298.15 K, also given in Table 4. Of these, $\Delta G^\ddagger$ is thought to yield the most reliable numbers, due to statistical cancellation of certain errors (10, 14). It is evident then from the NMR data that there is a mechanism (hindered reorientation of the nitro groups at C2 and C6, and of H1) via which the hydrogen bond can be temporarily broken.

We have also investigated the oxidizability of AH, in part using ^{1}H NMR spectroscopy. For comparison, acetone (and also chloroform) solutions of 2,2-diphenyl-1-picrylhydrazine (DH) were run in tandem with these. The oxidants PbO_2(s) and $KMnO_4$(s) were used, both of which are well known (16) to rapidly generate the stable free radical 2,2-diphenyl-1-picrylhydrazyl (≡ D, alias DPPH) from DH at room temperature, with resulting purple color and immediate EPR signal.[4] No color change or EPR signal was detected on such treatment of AH. The room-temperature 300 MHz ^{1}H NMR spectrum of AH showed virtually no change after 4 h of exposure to oxidant, but did show some new peaks, both in the methyl and phenyl regions, after 24 contact hours. The NMR line widths continued to be narrow, and were unshifted. By contrast, the ^{1}H spectrum of DH after contact with oxidant immediately yielded much broadened lines of DH, and no new lines developed. We conclude that AH is much more inert to oxidation than is DH, despite their various structural similarities.

Molecular orbital study of AH

Ab initio restricted Hartree–Fock calculations for the isolated AH model molecule were performed using Gaussian 92 with an Alpha DEC 5000 computer. Several optimum nu-

[4] One condition for stability of a hydrazyl free radical has been stated (17) to be equality of the electron spin population on the two hydrazinic nitrogens, as is the case with radical D (DPPH) derived from DH.

© 1999 NRC Canada

clear configurations (minima on the potential energy surface) of the AH molecule were found using the split-valence 3-21G basis set of atomic orbitals. The use of an even higher basis set was made impossible by the size of our molecule (29 atoms, 146 electrons); such a project would require prohibitively more computer time to finalize the calculations. On the other hand, the set 3-21G of atomic orbitals is relatively inexpensive but works well with hydrogen, carbon, nitrogen, and oxygen atoms (18).

The set of optimized variables (set I) found for the electronic ground state of AH is to be compared with the crystallographic data.[5] One can see that, with a few interesting exceptions, our computational results agree well with the X-ray diffraction data (Table 3). The carbon–hydrogen and nitrogen–hydrogen bond lengths always tend to be overestimated by the relatively low level (small basis set of atomic orbitals, Hartree–Fock approximation) of our ab initio computations. Therefore such consistent differences between these pairs of bond lengths should not raise major concerns. The lengths of bonds C1—N1, N1—N7, and N7—C7 demonstrate the double-bond character of the N7—C7 bond and the mixed character of the C1—N1 bond, which is in agreement with how we represent this molecule using resonance structure formulas. This is also in agreement with the carbon–carbon distances in the picryl ring: the bonds C1—C2 and C1—C6 (of length ca. 1.43 Å) are appreciably longer than the other ring C—C bonds (of length close to 1.37 Å).

The picryl ring, as revealed both by the experiment and by theory, is almost perfectly planar. The six ring carbons have a root-mean-square deviation of 0.013 Å from such an ideal plane, with maximal displacements (Å) between +0.018(2) (C6) and –0.015(3) (C4) from the plane.

The computational results are consistent with the existence of a hydrogen bond between H1 and O21: the O21—H1 distance of 1.8 Å (Table 3) is typical for the hydrogen bond, and the atoms N1, H1, O21, and N2 are in the picryl-ring plane. The intramolecular hydrogen-bond energy is difficult to define, since the breaking of such a hydrogen bond involves a change of the nuclear configuration in the molecule. We note that there is a tautomer of our model molecule, with "H1" attached to N7 (see below). In this configuration there is no intramolecular hydrogen bond. The energy difference between these two tautomers is about 53 kJ mol^{-1}, which is within the energy range of typical hydrogen bonds.

One way to quantify the nonequivalence of the two methyl groups in the isolated ground-state molecule is to calculate the electron density at each of these. We find that the Mulliken charge numbers are –0.6233 and –0.6827 at the carbon atoms, for C71 and C72, and 0.1029 and 0.0660 when the hydrogens are included. This suggests that methyl C71 is less screened than C72, with its ^{1}H and ^{13}C NMR peaks thus occurring further from the TMS signal.

There are two appreciable differences between the computational results and the X-ray diffraction measurements:

1. The X-ray data revealed a torsion angle C2-C1-N1-N7 of –177.3° (Table 3) while the calculation of this angle gave –156.8°. Thus in the crystal, utilizing the values of two other torsion angles, C1-N1-N7-C7 and C71-C7-N7-N1 or C72-C7-N7-N1 (Table 3), one finds that the plane defined by atoms N1, N7, and C7 is nearly identical with the picryl ring, yielding an extended π-electron system. However, in our optimized structure these two planes form an angle of ca. 20°. We ascribe this difference (which is not energetically very sensitive) to the influence of neighbouring molecules. The trend towards planarity of the molecules influenes the manner in which they stack within the crystal.

2. The second difference is in the rotational position (e.g., see torsion angle C1-C6-N6-O62 in Table 3) of the nitro group at carbon C6: –85.1° (measured) versus –144.7° (calculated). Thus, while in the crystal the plane of the NO_2 group is almost perpendicular to the picryl ring, the computations show that in the model it is rotated by only ca. 35° with respect to this ring. We think that here, too, the most probable reason for this difference is that there are intermolecular interactions in the crystal that favor the observed configuration. Moreover, the distortion discussed in paragraph 1 above can contribute to this effect: the electrons on nitrogen atom N7 (having an atomic charge number of –0.36) can interfere with the electrons on oxygen O61. This conclusion is also supported by the fact that nitrogen N6 of the rotated nitro group does not lie exactly in the picryl-ring plane, as is demonstrated by the C1-C5-C6-N6 angle of 174.5° (Table 3).

In addition to the minima in the total (Born–Oppenheimer) electronic energy discussed above for the two equivalent conformers (Fig. 1), we have found several other unconstrained minima. The configuration of the model molecule in a second (and higher) minimum in the energy, with parameters referred to as set II of nuclear coordinates, is characterized by a C1-N1-N7-C7 torsion angle of 79.2°. This is saying that the plane containing the atoms N1, N7, and C7 is almost perpendicular to the plane defined by atoms C1, N1, and N7, which are close to coplanar with the picryl-ring plane. The rotational position of the nitro group attached to C6, as measured by the torsion angle C1-C6-N6-O62, is ca. –126.1°. The nitro group attached to C2 and H1 remain in the plane, with the H-bond intact.

There also are two other "tautomers", with the hydrogen atom "H1" at N7 (set III) and at C7 (set IV). The energies of the four stable configurations II, III, and IV relative to the energy of set I were found to be 36.2, 53.3, and 149.1 kJ mol^{-1}. Clearly these energies are very large relative to the thermal energy (ca. 2.5 kJ mol^{-1}) of AH molecules at room temperature, so that the thermal populations of the conformational states defined by sets II, III, and IV are expected to be very small compared to the population of the lowest-energy conformation (set I).

Calculations were also performed to investigate the intermediate states for conformerization of AH to depict the journey of H1 from its location in one ground-state (GS) conformer to that in the other. For this, it was convenient to study a series of model molecules with the (only) constraint imposed that the torsion angle $\Omega_2 \equiv$ C2-C1-N1-H1 be equal to selected angles ranging from 0° to 180°; the range 0° to –180° is obtained by symmetry. The choice of angle Ω_2

[5] There is a second such state, with equal energy, featuring the opposite sign of all torsion angles. The chiral nature of our molecule thus leads to existence of pairs of conformers.

© 1999 NRC Canada

Fig. 4. Plot of the SCF-MO model of molecule AH: (*a*) minimized energy, (*b*) bond length C1—N1, and (*c*) torsion angle C2-C1-N1-N7, all versus the constraining torsion angle Ω_2 = C2-C1-N1-H1.

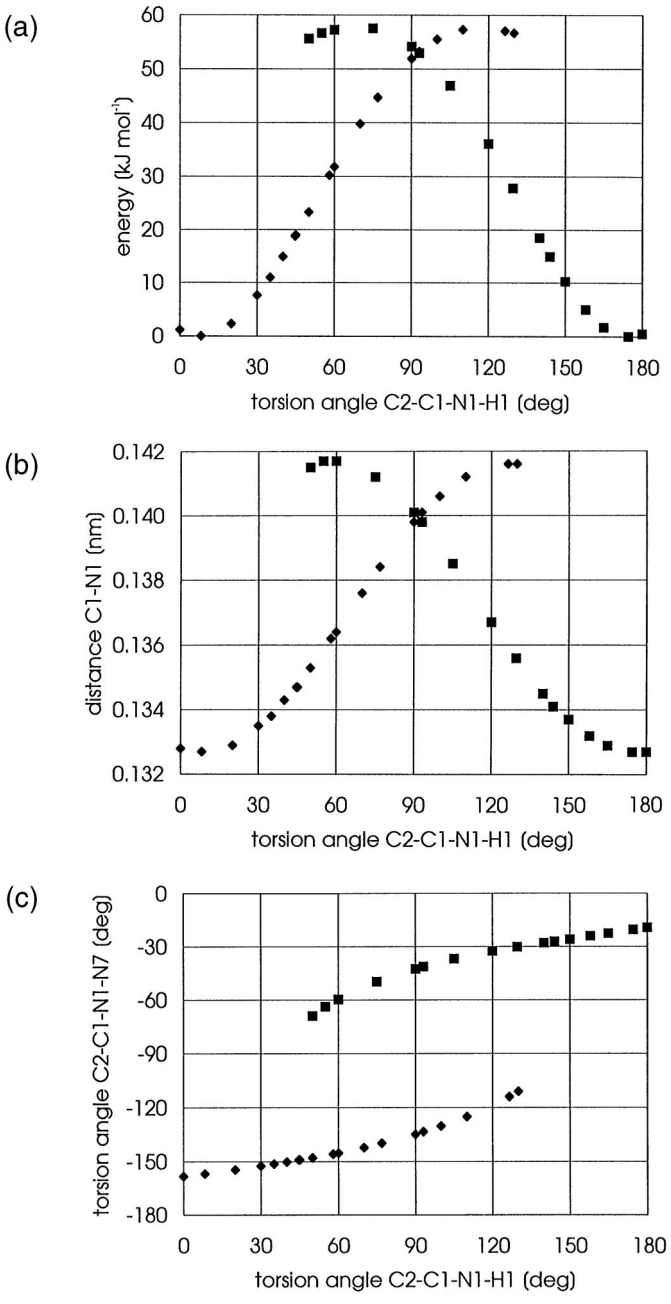

rather than $\Omega_6 \equiv$ C6-C1-N1-H1 is arbitrary. We note that the relationship between Ω_2 and Ω_6 is not a simple analytical one; Ω_2 is equal to $\Omega_6 - 180°$ only when atoms C1, C2, C6, and N1 all occur in one plane.

The conformations at Ω_2 = 8.2° and at 174.6° (Fig. 4*a*), attained without imposing any constraint, correspond to the minimum energy (ground state GS, as shown in Fig. 1 left model and right model, and discussed above; also see Table 3). These angles correspond to Ω_6 = –174.6° and –8.2°, respectively. The curves of the electronic energy, of the distance C1—N1, and of torsion angle C2-C1-N1-N7 in the model molecule in the optimized configurations are plotted as functions of Ω_2 in Figs. 4*a*–4*c*, respectively. It is evident from Fig. 4*a* that two values of the energy are obtainable from our calculation, within an extensive Ω_2 region (ca. 50°–130°). It was not possible for us to obtain energy-minima solutions beyond the ones plotted in the upper regions, i.e., outside the angle range indicated. It may well be that here we have a relatively rare example of a mathematical "catastrophe" event (unstable critical point) occurring within a single molecule, as discussed (with focus on charge density) in a review by Bader et al. (19). As such, it may be worthy of a detailed analysis not appropriate herein. A description of the two states encountered within the ca. 80° range of Ω_2 where duplicity occurs will be furnished below.

Further discussion and summary

We now examine some details of the internal electronic structure and bonding in ground-state AH. The bond angle C1-N1-N7 is 121.6(2)° (expt.) and 119.1° (theor.), as seen in Table 3. This suggests that, to good approximation, the electron hybridization at N1 for the three bonds is sp^2, and that there is a well-defined lone pair in a pure *z* orbital (oriented normal to the picryl ring). This is very similar to the situation in 2,2-diphenyl-1-picrylhydrazine (≡ DH), where the angle is ca. 121° (20). The bond lengths at N1 are C1—N1 = 1.339(2) Å (1.355 in DH) and N1—N7 = 1.384(2) Å (1.381 in DH).

In AH, the lone-pair orbitals in the hydrazinic nitrogens are literally orthogonal to each other. The one on N1 is a pure *p* orbital while the other (on N7) is a member of an sp^2 hybrid set. By contrast, in DH they are both pure *p* orbitals, close to parallel, as well as normal to the picryl ring, so as to form an extended π system; the π-electron orbitals of the two phenyl rings in DH are tilted away from this.

It is clear that $\Delta G^{\ddagger}$ is smaller (ca. 47 as compared to ca. 63 kJ mol^{-1}, in acetone-d_6) for AH than for DH. One may question whether bond C1—N1 might have less π character in the former; the bond lengths observed (in the solid) are inconsistent with this notion. Perhaps the smaller bulk and mass (~3×) of the dimethylmethanimino (DMMI) group in AH is easier to reorient than the diphenylamino (DPA) group in DH. More particularly, one needs to consider the impedance (e.g., hydrogen bonding) created by the solvent surroundings. Thus the N7-DMMI group in AH may be easier to reorient than the picryl ring, whereas in DH the latter may be easier to rotate than the DPA group.

The differences found with the two solvents show the same trends for AH (Table 4) and for DH (Table 9 of ref. 10). Thus the values of $\Delta G^{\ddagger}$ are slightly higher in chloroform than in acetone, correlatable with the trend in the solvent hydrogen-bonding characteristics (Taft β parameter). The values of $\Delta S^{\ddagger}$ are of opposite sign for the two solvents, for both AH and DH. Perhaps, in the future, this phenomenon can be linked to the reorganization of the solvent molecules during the reorientation process.

We turn now to further discussion of the modeled conformerization process and to detailed consideration of

© 1999 NRC Canada

Figs. 4*a*–4c. We shall consider the path from the ground-state $\Omega_2 = 8.2°$ with increase in Ω_2, but could equivalently have started at $\Omega_2 = 174.6°$ with decrease in Ω_2.

Use of the Cahn–Ingold–Prelog chirality rule yields that the computed configuration at atom N1 for the $\Omega_2 = 8.2°$ ground state is *S*, that the three atoms bonded to N1 then go through a planar configuration at ca. 25°, and thereafter have the *R* configuration as Ω_2 increases, with the N1 moiety becoming more and more tetrahedral. The opposite chirality event occurs for the other curve, departing from the 174.6° ground state (chirality *R*) towards smaller Ω_2. In the duplicity range, transfer from one state to the other (at fixed Ω_2) implies a change in chirality.

We see that the energies of the two configurations become equal at $\Omega_2 \sim 92.5°$. We call this the crossing angle Ω_2^x. One major effect in going from 8.2° (GS) towards Ω_2^x (and beyond) is that C1—N1 becomes substantially longer, going from 1.327 to 1.416 Å at $\Omega_2 = 130°$, as seen in the plot of this bond distance versus Ω_2 (Fig. 4*b*). We note that the angle C1-N1-N7 is 119.1° at GS, going to 110.9° at Ω_2^x (almost tetrahedral) and on to 106.9° at 130° (upper-energy state). These results indicate that a major aspect of this excitation is the loss of the double-bond character of C1—N1. Simultaneously the hydrogen bonding involving H1 disappears on going from $\Omega_2 = 8.2°$ towards Ω_2^x. The N7-DMMI group, which remains basically intact, rotates about C1—N1, with torsion angle C2-C1-N1-N7 (Fig. 4*c*) moving from –156.8° at $\Omega_2 = 8.2°$ to –133.7° at Ω_2^x, and to –111.1° at 130° (upper-energy state). Note the dramatic jump in this angle when switching configurations, maximal at Ω_2^x.

The picryl ring, in the Ω_2 range 50°–130°, is close to having a reflection plane $\sigma_\perp$ through C1 and C4, perpendicular to the ring. For instance, at Ω_2^x, the nitro groups at C2 and C6 occur rotated by similar torsional angles (the NO_2 planes lie at about 33° from the picryl plane). Hence there is no hydrogen bond between H1 and O21 (or O61), as is also evident from the large H1—O21 distances (2.781 and 2.618 Å), in the two Ω_2^x configurations. It is worth pointing out that the complete molecule is far from having $\sigma_\perp$ as a symmetry plane, anywhere in the Ω_2 range, due to the two methyl groups. These are inequivalent (at Ω_2^x, the Mulliken charge numbers are –0.6213 for C71 and –0.6751 for C72, when excluding the hydrogens). We note that they do not appear to interchange surroundings during the conformerization.

What now can one deduce about the transition process, going from the minimum at $\Omega_2 = 8.2°$ to the other minimum at $\Omega_2 = 174.6°$? If molecule AH follows the lower-energy curve from the ground state upward to Ω_2^x, there is an energy requirement of 53 kJ mol^{-1}.[6] This compares very satisfactorily with the measured values of E_a given in Table 4, especially so since all solvent molecules had to be ignored in our modeling. At Ω_2^x, C1—N1 = 1.400 Å and C1-N1-N7 = 110.9° for both states. One must note, however, that switching configurations at this point is not isoenergetic, in that rotating the DMMI group appropriately might well require substantially more energy. One low-energy mechanism that comes to mind for switching configurations is intra-atomic transfer of proton H1 from its bond to the lone-pair orbital on N1, which has almost tetrahedral (*R*) configuration at Ω_2^x. This would leave the molecule with an effective Ω_2 of ca. 210° and an *S* configuration at N1, and its energy could then readily descend from there to that at the $\Omega_2 = 174.6°$ minimum. There then would be no need to rotate the DMMI group, which is consistent with the absence of a major solvent effect. More detailed study of this type of internal proton-transfer process is called for. Note that, conceivably, proton H1 at (near) Ω_2^x could also transfer temporarily to either of the *ortho* NO_2 groups. Finally, we note that, of course, transition between the two curves (Fig. 4*a*) could take place anywhere within a wide range of Ω_2; it is relevant that the upper energy is almost constant from 50° to 130°.

One can now turn briefly to some chemical comparisons of AH and DH. The hydrazinic proton is acidic in both. The alkali salts of both seem quite similar (21)[7]. On the other hand, as seen above, AH and DH differ greatly in oxidizability.

One might rationalize the difficulty in oxidizing AH as compared to DH by invoking the need of the MnO_4^- ion (or PbO_2) to react at a linkage with appreciable double-bond character (C1—N1 in the present case), i.e., initial complexation might be needed, as seems to be the case with oxidation of carbon–carbon double bonds by chromyl chloride (22). Perhaps attachment to double bond C7—N7 present in AH prevents such attack at C1—N1. In general, the mechanisms for the transition-ion/oxide-mediated reaction with double bonds are still in need of clarification (e.g., the oxidation of such bonds by OsO_4 (23)).

Furthermore, of course, radical A may well be quite unstable relative to D (DPPH) due to relatively attenuated unpaired-electron delocalization in the former, and considerable difference in hybridization at N7. More work on this question is planned. UHF/3-21 calculations on the unreported radical A suggest that its energy is higher than that of the molecule AH in its ground state: the sum of the energies of A and the free hydrogen atom H (derived with the 3-21 basis of atomic orbitals) is 6.3 kJ mol^{-1} higher than the ground-state energy (UHF/3-21) of AH. The model radical has an almost planar picryl ring, with approximately a mirror symmetry plane $\sigma_\perp$ through C1 and C4, perpendicular to the ring. The two *ortho* nitro groups are rotated by about 30° about their C—N bonds, away from the picryl-ring plane. The computed central bond lengths are C1—N1, 1.357; N1—N7, 1.396; C7—N7, 1.300 Å; the hydrazine bond angles are: C1-N1-N7 116.5°, N1-N7-C7 114.0°. The DMMI group in A is much like the one in AH.

Acknowledgments

This work was performed under the auspices of the Natural Sciences and Engineering Research Council of Canada. One coauthor (Z.Z.) was the beneficiary of an International Fellowship grant from NSERC. We are grateful to J.R. Barton for participation in early phases of the X-ray diffrac-

[6] For comparison, we note that constraining model AH to mirror symmetry (group C_s) yields a minimum energy of 98.4 kJ mol^{-1} above that of GS, and occurs with the methyl carbons in the plane $\sigma_\perp$.

[7] Also, K.C. Brown, Y. Upadrashta, and J.A. Weil. Work in progress (1999).

© 1999 NRC Canada

tion work. We thank Mr. J. Donnen and Prof. M. Singh for their help in preparing pure picrylhydrazine, and Ms. R. Duke and Dr. J.-L. Du for their word-processing assistance.

References

1. J.A. Weil and G.A. Janusonis. J. Org. Chem. **27**, 1248 (1962).
2. B.R. Nelson. Doctoral Dissertation, University of Saskatchewan, Saskatoon. 1994.
3. N.V. Sidgwick. The organic chemistry of nitrogen. 3rd ed. *Edited by* I.T. Millar and H.D. Springall. Clarendon Press, Oxford, England. 1966. Chap. 15.
4. P.A.S. Smith. Derivatives of hydrazine and other hydronitrogens having N—N bonds. Benjamin Cummings, Reading, Mass., U.S.A. 1983. Chap. 2.
5. T.C. Morrill and A.R. Bayley. Org. Prep. Proced. Int. **7**, 67 (1975).
6. Yu.P. Kitaev and I.M. Skrebkova. J. Gen. Chem. USSR (Engl. Transl.) **37**, 1142 (1967).
7. E.J. Gabe, A.C. Larson, F.L. Lee, and Y. Wang. The NRC PDP-8a crystal structure system. National Research Council of Canada, Ottawa, Ont. 1979.
8. S.R. Hall, G.S.D. King, and J.M. Stewart. The XTAL system. University of Western Australia, Perth, Australia. 1995.
9. G.M. Sheldrick. SHELXL97. Program for the refinement of crystal structures. University of Göttingen, Germany. 1997.
10. R.L. Tyson and J.A. Weil. J. Phys. Chem. **94**, 3951 (1990).
11. J. Heidberg, J.A. Weil, G.A. Janusonis, and J.K. Anderson. J. Chem. Phys. **41**, 1033 (1964). Also see: K.C. Brown, R.L. Tyson, and J.A. Weil. J. Chem. Educ. **75**, 1632 (1998).
12. J.K.M. Sanders and B.K. Hunter. Modern NMR spectroscopy. 2nd ed. Oxford University Press, Oxford, U.K. 1993. pp. 71 ff.
13. MAPLE V, Release 3. Waterloo Maple Inc., Waterloo, Ont. 1993.
14. J. Sandström. Dynamic NMR spectroscopy. Academic Press, Toronto, Ont. 1982.
15. S. Arrhenius. Z. Phys. Chem. **4**, 226 (1889).
16. K.C. Brown and J.A. Weil. Can. J. Chem. **64**, 1836 (1986).
17. A.T. Balaban, M. Marculescu, I. Pascaru, M. Rotaru, A. Valeriu, and M. Weiner. Z. Phys. Chem. **219**, 285 (1962).
18. J.B. Foresman and A. Frisch. Exploring chemistry with electronic structure methods: a guide to using Gaussian. Gaussian Inc., Pittsburgh, Pa., U.S.A. 1993.
19. R.F.W. Bader, T.T. Nguyen-Dang, and Y. Tal. Rep. Prog. Phys. **44**, 893 (1981).
20. H. Wang, R.J. Barton, B.E. Robertson, and J.A. Weil. J. Inclusion Phenom. Mol. Recognit. Chem. **10**, 203 (1991).
21. R. Gopal, B.E. Robertson, and J.A. Weil. Can. J. Chem. **61**, 2735 (1983).
22. K.B. Sharpless, A.Y. Teranishi, and J.-E. Bäckvall. J. Am. Chem. Soc. **99**, 3120 (1977).
23. A.M. Rouhi. Chem. Eng. News, **75**(44), 23 (1997).

© 1999 NRC Canada

Thermodynamics of substituted pyrazolone. V: Potentiometric and conductometric studies of complexes of some transition metals with 4-(4-acetophenyl)hydrazono-3-methyl-2-pyrazolin-5-one

Ashraf A. El-Bindary, Adel Z. El-Sonbati, and Hanan M. Kera

Abstract: Proton-ligand dissociation constants of 4-(4-acetophenyl)hydrazono-3-methyl-2-pyrazolin-5-one (AHMP) and metal-ligand stability constants of its complexes with some transition metal ions were calculated potentiometrically in 0.1 M KCl and 50% (v/v) ethanol–water mixture. The order of stability constants was found to be $Th^{4+} > UO_2^{2+} > Ce^{3+} > La^{3+} > Mn^{2+} < Co^{2+} < Ni^{2+} < Cu^{2+} > Zn^{2+}$. The dissociation constant, pK_1^H, of AHMP and the stability constants, log *K*, of their complexes were determined at different temperatures (298, 308, and 318 K). The corresponding thermodynamic parameters (ΔG, ΔH, and ΔS) were derived and discussed. The dissociation process is nonspontaneous, endothermic, and entropically unfavourable. The formation of the metal complexes has been found to be spontaneous, exothermic, or endothermic (depending the metal), and entropically favourable. The stoichiometries of these complexes were determined conductometrically and indicated the formation of 1:1 and 1:2 (metal:ligand) complexes.

Key words: 4-(4-acetophenyl)hydrazono-3-methyl-2-pyrazolin-5-one, dissociation and stability constants, thermodynamic parameters, stoichiometries.

Résumé : Faisant appel à une méthode potentiométrique et opérant dans des solutions 0,1 M de KCl dans un mélange à 50% (v/v) d'éthanol–eau, on a déterminé les constantes de dissociation proton-ligand de la 4-(4-acétophényl)hydrazono-3-méthyl-2-pyrazolin-5-one (AHMP) et les constantes de stabilité métal-ligand de ses complexes avec des ions de quelques métaux de transition. On a trouvé que l'ordre de stabilité est $Th^{4+} > UO_2^{2+} > Ce^{3+} > La^{3+} > Mn^{2+} > Co^{2+} > Ni^{2+} > Cu^{2+} > Zn^{2+}$. La constante de dissociation, pK_1^H, de l'AHMP et les constantes de stabilité des complexes ont été déterminées à diverses températures (298, 308 et 318 K). On en a tiré les paramètres thermodynamiques correspondants (ΔG, ΔH et ΔS) et on en discute. Le processus de dissociation non pas spontané, il est endothermique et défavorisé d'un point de vue entropique. On a trouvé que la formation de complexes métalliques est spontanée, exothermique ou endothermique (suivant le métal) et favorisée d'un point de vue entropique. On a déterminé les stoechiométries de ces complexes par conductimétrie et elles indiquent qu'il y a formation de complexes 1:1 et 1:2 (métal:ligand).

Mots clés : 4-(4-acétophényl)hydrazono-3-méthyl-2-pyrazolin-5-one, constantes de dissociation et de stabilité, paramètres thermodynamiques, stoechiométries.

[Traduit par la Rédaction]

Introduction

In recent years, there has been considerable interest in the coordination chemistry of the azo pyrazolone donor. In part, this interest has arisen because of the biological importance of this donor system (1). A number of metal complexes containing azo pyrazolone donors have been characterized (2–4). In continuation of our earlier work (5–8) on metal complexes, we report herein the dissociation constant of AHMP, and the stability constants for its compelexes with Mn^{2+}, Co^{2+}, Ni^{2+}, Cu^{2+}, Zn^{2+}, La^{3+}, Ce^{3+}, UO_2^{2+}, and Th^{4+} at different temperatures, determined potentiometrically. The corresponding thermodynamic parameters are derived and discussed. Moreover, the stoichiometeries of these complexes are determined conductometrically at 298 K.

Received May 4, 1998.

A.A. El-Bindary,[1] A.Z. El-Sonbati, and H.M. Kera. Chemistry Department, Faculty of Science (Demiatta), Mansoura University, Demiatta, Egypt.

[1]Author to whom correspondence may be addressed. Fax: +057325803.

Experimental

Preparation of the ligand

AHMP (Fig. 1) was prepared by gradual addition of an aqueous solution of 0.01 mol (0.69 g) of sodium nitrite to a concentrated hydrochloric acid solution of 0.01 mol (1.35 g) of *p*-aminoacetophenone with stirring and kept for about

 © 1999 NRC Canada

Table 1. Thermodynamic functions for the dissociation of AHMP in 50% (v/v) ethanol–water mixture and 0.1 M KCl at different temperatures.

Temp. (K)	Dissociation constant[a] pK_1^H	Free energy change (kJ mol^{-1}) ΔG_1	Enthalpy change (kJ mol^{-1}) ΔH_1	Entropy change (J mol^{-1} K^{-1}) $-\Delta S_1$
298	9.56 (0.08)	54.55		138.09
308	9.42 (0.09)	55.55	13.4	136.85
318	9.28 (0.11)	56.32		134.97

[a]Standard deviations are given in parentheses.

Fig. 1.

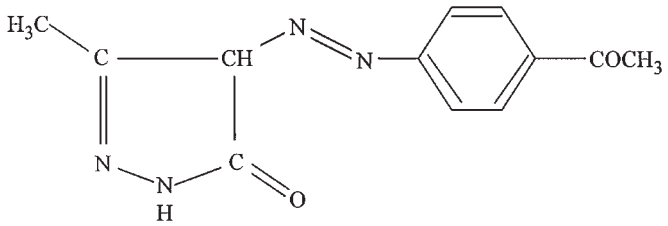

Fig. 2.

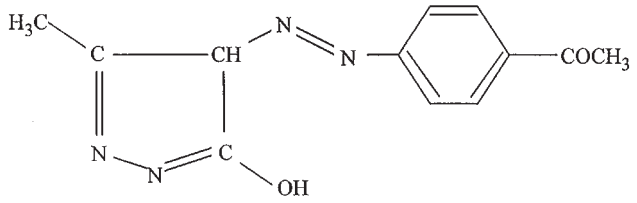

20 min in the ice bath. The formed diazonium chloride solution was added gradually with stirring to a 0.01 mol (0.98 g) cold solution of pyrazolinone in 50 mL ethyl alcohol containing 5 g sodium acetate. After diluation, the azo pyrazolone compound formed was filtered off and was washed with ethyl alcohol. The crude material was recrystallized from ethyl alcohol and then dried in a vacuum desiccator over anhydrous calcium chloride. The purity (mp 138°C) was checked by elemental analysis (found: C 59.20, H 5.00, N 23.01; calcd.: C 59.01, H 4.95, N 22.93).

The IR spectrum of AHMP was recorded on a Perkin–Elmer 883 spectrophotometer using KBr discs (4000–400 cm^{-1}). The IR spectrum show a strong band at 3276 cm^{-1} assigned to the ν(NH) of the pyrazolone ring. The strong band at 1670 and a medium one at 1600 cm^{-1} are both assigned to the carbonyl oxygen of the side chain and pyrazolone ring, respectively. The bands corresponding to the ν(N=N) symmetric stretching vibration appears at 1570 and 1500 cm^{-1}.

The ^{1}H NMR spectrum of AHMP was recorded on a EM-390 MHz spectrophotometer using d_6-DMSO as solvent with TMS as the internal standard. The ^{1}H NMR spectrum exhibited a signal at 5.2 ppm, assigned to the NH proton of pyrazolone ring (9). The δ CH_3 signal appeared at 2.6 ppm (10). The protons of the aromatic ring resonate downfield in the δ 7.2–8.5 ppm range (11).

Reagents and materials

Metal ion solutions (0.001 M) were prepared from AnalaR metal salt samples (BDH) in doubly distilled water and standardized with EDTA (12). The ligand solution (0.01 M) was prepared by dissolving the accurate weight of the solid in ethanol (AnalaR). Solutions of 0.005 M HCl and 1 M KCl were also prepared in doubly distilled water. A carbonate-free sodium hydroxide solution in 50% (v/v) ethanol–water mixture was used as titrant and standardized against AnalaR oxalic acid.

Potentiometric measurements

The apparatus, general conditions, and methods of calculation were the same as in the previous work (13, 14). The following mixtures were prepared and titrated potentiometrically at 298 K against standard 0.02 M NaOH in 50% (v/v) ethanol–water mixture:

(*i*) 5 mL 0.005 M HCl + 5 mL 1 M KCl + 25 mL ethanol;
(*ii*) 5 mL 0.005 M HCl + 5 mL 1 M KCl + 20 mL ethanol + 5 mL 0.01 M ligand;
(*iii*) 5 mL 0.005 M HCl + 5 mL 1 M KCl + 20 mL ethanol + 5 mL 0.01 M ligand + 10 mL 0.001 M metal salt.

For each mixture, the volume was made up to 50 mL with doubly distilled water before the titration. These titrations were repeated for temperatures of 308 and 318 K. A constant temperature was maintained to ±0.05 K by using an ultrathermostat (Gallenkamp thermo stirrer 85). The pH-meter readings in 50% (v/v) ethanol–water mixture are corrected according to the Van Uitert and Hass relation (15).

Conductometeric measurements

Solutions of 10^{-4} M of metal ions were titrated with 10^{-3} M of AHMP. These titrations were performed using a YSI model 32 conductance meter and carried out at 298 K.

Results and discussion

Potentiometric studies

Proton-ligand stability constants

The average number of protons associated with the AHMP at different pH values, $\bar{n}_A$, was calculated from the titration curves of the acid in the absence and presence of AHMP. Thus, the formation curves ($\bar{n}_A$ vs. pH) for the proton-ligand systems were constructed and found to extend between 0 and 1 in the $\bar{n}_A$ scale. This means that AHMP has one ionizable proton (the enolized hydrogen ion of the carbonyl oxygen in the pyrazolone moiety). Different computational methods (16) were applied to evaluate the dissociation constant. The number of replicates is five, and the average values obtained are listed in Table 1.

The AHMP has a lower acidic character (higher pK_1^H value than 4-(4-acetophenyl)hydrazono-1-phenyl-3-methyl-2-pyrazolin-5-one).[2] This is quite reasonable because the presence of the NH group (pyrazolone moiety) will enhance the amidic form, whereby a stronger O—H bond is formed. Therefore, the amidic nature of the molecule retards the re-

© 1999 NRC Canada

Table 2. Stepwise stability constants for ML and ML_2 complexes of AHMP in 50% (v/v) ethanol–water mixture and 0.1 M KCl at different temperatures.

	298 K				308 K				318 K			
M	log K_1	log K_2	log K_β	log K_1/ log K_2	log K_1	log K_2	log K_β	log K_1/ log K_2	log K_1	log K_2	log K_β	log K_1/ log K_2
Mn^{2+}	5.95	5.24	11.19	1.14	5.7	5	10.70	1.14	5.45	4.76	10.21	1.14
	–0.1	–0.11			–0.1	–0.13			–0.1	–0.1		
Co^{2+}	6.15	5.25	11.40	1.17	6.4	5.75	12.15	1.11	6.47	6.25	12.72	1.04
	–0.1	–0.13			–0.1	–0.1			–0.1	–0.1		
Ni^{2+}	6.2	5.75	11.95	1.08	6.46	6.05	12.51	1.70	6.55	6.45	13.00	1.02
	–0.1	–0.1			–0.1	–0.11			–0.1	–0.11		
Cu^{2+}	6.85	6.63	13.48	1.03	6.77	6.6	13.37	1.03	6.68	6.57	13.25	1.02
	–0.1	–0.1			–0.1	–0.15			–0.1	–0.13		
Zn^{2+}	6.4	6.12	12.52	1.05	6.5	6.35	12.95	1.01	6.6	6.55	13.10	1.02
	–0.1	–0.15			–0.1	–0.1			–0.11	–0.15		
La^{3+}	6.63	6.48	13.11	1.02	6.2	6.05	12.25	1.03	5.71	5.55	11.26	1.03
	–0.1	–0.15			–0.1	–0.14			–0.1	–0.12		
Ce^{3+}	6.72	6.6	13.32	1.02	6.22	6.1	12.32	1.02	5.8	5.71	11.51	1.02
	–0.11	–0.14			–0.1	–0.15			–0.1	–0.16		
UO_2^{2+}	6.99	6.68	13.67	1.05	6.6	6.35	12.95	1.04	6.24	5.99	12.23	1.04
	–0.1	–0.12			–0.11	–0.16			–0.1	–0.14		
Th^{4+}	7.62	7.26	14.88	1.05	7.25	6.8	14.05	1.07	6.88	6.32	13.20	1.09
	–0.1	–0.16			–0.1	–0.12			–0.1	–0.15		

moval of the ligand proton and hence increases the basicity of the ligand (Fig. 2).

Metal-ligand stability constants

The formation curves for the metal complexes were obtained by plotting the average number of ligands attached per metal ion ($\bar{n}$) versus the free ligand exponent (pL), according to Irving and Rossotti (17). These curves were analyzed, and the successive stability constants were determined using different computational methods (18, 19). The values of the stability constants (log K_1, log K_2, and log β), as well as the ratio log K_1/log K_2, are given in Table 2. The following general remarks can be made:

(*i*) The maximum $\bar{n}$ values in all cases were found to be ≅2, revealing that both ML and ML_2 types of complexes are formed in solution.

(*ii*) No precipitate was observed in the titration vessel, indicating that the possibility of formation of metal hydroxide can be excluded.

(*iii*) For all complexes, the tendency of a metal ion to coordinate with ligand is proportional to the number of vacant sites. The ratio between consecutive stability constants, is to certain extent, statistically determined (20).

(*iv*) The order of stability constants of the metal complexes of AHMP was found to be

$$Th^{4+} > UO_2^{2+} > Ce^{3+} > La^{3+} > Mn^{2+} < Co^{2+} < Ni^{2+} < Cu^{2+} > Zn^{2+}$$

The sequence of stability ($Mn^{2+} < Co^{2+} < Ni^{2+} < Cu^{2+} > Zn^{2+}$) of the complexes of AHMP reflects the changes in the heat of complex formation across the series and arises from a combination of the influence of both polarizing ability of the metal ion (21) and crystal-field stabilization energies (22). The greater stability of Cu^{2+} complexes is produced by the well-known Jahn–Teller effect. The stability constant of the divalent oxygenated cation complex (UO_2^{2+}) has a higher value than the other divalent cation complexes (Table 2). This may be attributed to the bonded oxygen atoms, which may increase the electrostatic attraction between the metal ion and the coordinated ligands and overcome any steric hindrance offered by the oxygen of the oxygenated cation (23). The higher values of the stability constants of the Th^{4+} complexes compared to that of the other divalent metal complexes is expected on the basis of the charge and ionization potential of Th^{4+} ion.

Effect of temperature

The dissociation constant (pK_1^H) for AHMP, as well as the stability constants of its complexes with Mn^{2+}, Co^{2+}, Ni^{2+}, Cu^{2+}, Zn^{2+}, La^{3+}, Ce^{3+}, UO_2^{2+}, and Th^{4+}, have been evaluated at 298, 308, and 318 K, and are given in Tables 1 and 2. The slope of the plot (pK_1^H or log K vs. 1/T) was utilized to evaluate the enthalpy change (ΔH) for the dissociation or complexation process, respectively. From the free energy change (ΔG) and (ΔH) values, one can deduce the entropy change (ΔS), using the well-known relationships [1] and [2]:

$$[1] \qquad \Delta G = -2.303RT \log K = 2.303RT\ pK$$

$$[2] \qquad \Delta S = (\Delta H - \Delta G)/T$$

All thermodynamic parameters of the dissociation process of AHMP are recorded in Table 1. Inspection of these values reveals that

(*i*) The pK_1^H value decreases with increasing temperature, revealing that its acidity increases with increasing temperature.

(*ii*) A positive value of ΔH indicates that its dissociation is accompanied by adsorption of heat and the process is endothermic.

(*iii*) A large positive value of ΔG indicates that the dissociation process is not spontaneous.

© 1999 NRC Canada

Table 3. Thermodynamic functions for ML and ML_2 complexes of AHMP in 50% (v/v) ethanol–water mixture and 0.1 M KCl.

		Free energy change (kJ mol^{-1})			Enthalpy change (kJ mol^{-1})			Entropy change (J mol^{-1} K^{-1})		
M	Temp. (K)	$-\Delta G_1$	$-\Delta G_2$	$-\Delta G_\beta$	ΔH_1	ΔH_2	ΔH_β	ΔS_1	ΔS_2	ΔS_β
Mn^{2+}	298	33.95	29.9	63.85				33.62	20.03	53.65
	308	33.61	29.49	63.1	–23.93	–22.98	–46.91	31.43	18.05	49.48
	318	33.18	28.98	62.16				29.09	15.88	44.97
Co^{2+}	298	35.09	29.95	65.04				169.16	261.14	430.30
	308	37.74	33.91	71.65	+15.32	+47.87	+63.19	172.27	265.52	437.79
	318	39.39	38.05	77.44				172.04	270.19	442.23
Ni^{2+}	298	35.38	32.81	68.19				175.27	230.87	406.14
	308	38.1	35.68	73.78	+16.85	+35.99	+52.84	178.41	232.70	411.11
	318	39.88	39.27	79.15				178.40	236.67	415.07
Cu^{2+}	298	39.09	37.83	76.92				103.56	117.45	221.01
	308	39.92	38.92	78.84	–8.23	–2.87	–11.10	102.89	117.05	219.94
	318	40.67	40	80.67				102.01	116.76	218.77
Zn^{2+}	298	36.52	34.92	71.44				154.66	181.44	336.10
	308	38.33	38.04	76.37	+9.57	+19.15	+28.72	155.58	185.68	341.36
	318	40.19	39.88	79.77				156.48	185.63	342.11
La^{3+}	298	37.83	36.97	74.8				–6.50	–9.60	–16.10
	308	36.56	35.68	72.24	–39.77	–39.83	–79.60	–10.42	–13.47	–23.89
	318	34.77	33.79	68.56				–15.72	–18.99	–34.74
Ce^{3+}	298	38.34	37.66	76				–12.05	–11.11	–23.16
	308	36.68	35.97	72.65	–41.93	–40.97	–82.90	–17.05	–15.23	–32.28
	318	35.31	34.77	70.08				–20.82	–19.50	–40.32
UO_2^{2+}	298	39.88	40.67	80.55				10.47	21.48	31.95
	308	38.92	37.45	76.37	–36.76	–34.27	–71.03	7.01	10.33	17.34
	318	37.99	36.47	74.46				3.87	6.92	10.79
Th^{4+}	298	43.48	41.42	84.9				44.40	21.54	65.94
	308	42.76	40.1	82.86	–30.25	–35.00	–65.25	40.62	16.56	57.14
	318	41.89	38.48	80.37				36.60	10.94	47.54

(*iv*) A negative value of ΔS is obtained, due to extensive solvation of metal chelates in ethanol–water mixture.

All the thermodynamic parameters of the stepwise stability constants of AHMP complexes are recorded in Table 3. It is known that the divalent metal ions exist in solution as octahedrally hydrated species, and the obtained values of ΔH and ΔS can then be considered as the sum of two contributions: (*i*) release of H_2O molecules, and (*ii*) metal-ligand bond formation.

It was suggested (24) that the ions in aqueous solution order the water molecules around them and, during complex formation between oppositely charged ions (ligand L^- and M^{n+}), will lead to the breakdown of the metal–water arrangement, resulting in positive entropy and enthalpy changes. Examination of these values shows that

(*i*) The stepwise stability constants (log K_1 and log K_2) for AHMP complexes decreases with increasing temperature in the case of Mn^{2+}, Cu^{2+}, La^{3+}, Ce^{3+}, UO_2^{2+}, and Th^{4+}, whereas in the case of Co^{2+}, Ni^{2+}, and Zn^{2+}, the reverse happens, i.e., the stability constants increase with increasing temperature.

(*ii*) The negative values of ΔG for the complexation process of Mn^{2+}, Co^{2+}, Ni^{2+}, Cu^{2+}, Zn^{2+}, La^{3+}, Ce^{3+}, UO_2^{2+}, and Th^{4+} with AHMP suggest a spontaneous nature of this process.

(*iii*) The ΔH values are positive in the case of Co^{2+}, Ni^{2+}, and Zn^{2+}, whereas in the case of Mn^{2+}, Cu^{2+}, La^{3+}, Ce^{3+}, UO_2^{2+}, and Th^{4+}, these are negative. This means that these processes are endothermic and favourable at higher temperatures for Co^{2+}, Ni^{2+}, and Zn^{2+} complexes, while in the case of Mn^{2+}, Cu^{2+}, La^{3+}, Ce^{3+}, UO_2^{2+}, and Th^{4+} complexes, the process are exothermic and favourable at lower temperature.

(*iv*) The positive values of ΔS for the complexation process of AHMP with Mn^{2+}, Cu^{2+}, Zn^{2+}, Co^{2+}, Ni^{2+}, UO_2^{2+}, and Th^{4+} confirm that complex formation is entropically favourable. In contrast, the La^{3+} and Ce^{3+} complexes have negative ΔS values (8). Such negative entropy changes can be attributed to the extensive solvation of metal chelates in the aqueous–ethanol medium. This may be due to the exposure of the polar oxygen, nitrogen, and metal ion of the chelate to the solvent molecules (25).

Conductometric studies

Stoichiometries

Stoichiometries of the complexes of AHMP with Mn^{2+}, Co^{2+}, Ni^{2+}, Cu^{2+}, Zn^{2+}, La^{3+}, Ce^{3+}, UO_2^{2+}, and Th^{4+} are obtained from the conductometric measurements. These studies were carried out to investigate the stoichiometries of the formed complexes by breaks in the titration curves denoting the formation of 1:1 and 1:2 (metal:ligand) complexes. Therefore, the reaction between the metal ions and AHMP occurs via the formation of a covalent linkage with the oxygen of the OH group (pyrazolone moiety) and the nitrogen

© 1999 NRC Canada

of the azo group. The increase in conductance upon titrating metal ions by AHMP is probably due to the liberation of the hydrogen ions from the OH during the complex formation (5). The decrease of the conductance value occurs due to (*i*) the increase of the volume of the metal ion chelate formation, which is accompanied by a decrease in the value of the diffusion coefficient of the particle, and (*ii*) the lowering of the charge on the metal ion through covalent bond formation with AHMP.

References

1. B. Foth. Cancer Res. **32**, 804 (1972).
2. S.B. El-Maraghy, B. El-Shetary, K.A.R. Salib, M.S. El-Moez, and S.L. Stefan. Orient. J. Chem. **2**, 72 (1986).
3. B. El-Shetary, S.L. Stefan, F. Zidan, and M.S. Moez. J. Chin. Chem. Soc. **33**, 41 (1986).
4. S.L. Stefan. J. Therm. Anal. **42**, 1299 (1994).
5. A.A. El-Bindary. Spectrosc. Lett. **32**(3), 383 (1999).
6. A.A. El-Bindary. Transition Met. Chem. **22**, 381 (1997).
7. A.A. El-Bindary and A.Z. El-Sonbati. Gazz. Chim. Ital. **127**, 597 (1997).
8. A.A. El-Bindary, M.M. Ghoneim, A.Z. El-Sonbati, and S.A. Barakat. Monatsh. Chem. **129**, 1259 (1998).
9. K.U. Sadek, M.A. Selim, and M.A. El-Nagdy. J. Am. Chem. Soc. **30**, 514 (1985).
10. F.A. Snavely and C.H. Yoder. J. Org. Chem. **33**, 513 (1968).
11. K.M. Ibrahim, A.M. Shallaby, A.A. El-Bindary, and M.M. Mostafa. Polyhedron, **5**, 1105 (1986).
12. G.H. Jeffery, J. Bassett, J. Mendham, and R.C. Denney. Vogel's textbook of quantitative chemical analysis. Vol. 5. Longman, London. 1989.
13. A.Z. El-Sonbati and A.A. El-Bindary. New Polym. Mater. **5**, 51 (1996).
14. M.M. Ghoneim, A.A. El-Bindary, A.Z. El-Sonbati, and S.A. Barakat. Spectrosc. Lett. **32** (1) (1999). In press.
15. L.G. Van Uitert and C.G. Hass. J. Am. Chem. Soc. **75**, 451 (1953).
16. H. Irving and H.S. Rossotti. J. Chem. Soc. 2904 (1954).
17. H. Irving and H.S. Rossotti. J. Chem. Soc. 3397 (1953).
18. F.I.C. Rossotti and H.S. Rossotti. Acta Chem. Scand. **9**, 1166 (1955).
19. M.T. Beck and I. Nagybal. Chemistry of complex equilibria. Wiley, New York. 1990.
20. J. Bjerrum. Metal amine formation in aqueous solution. Haase, Copenhagen. 1941.
21. F.R. Harlly, R.M. Burgess, and R.M. Alcock. Solution equilibria. Ellis Harwood, Chichester. 1980. p. 257.
22. C.S.G. Phillips and R.J.P. Williams. Inorganic chemistry. Vol. 2. Oxford, Oxford. 1966. p. 268.
23. M. Abdel-Moez, H. Sleem, and B. El-Shetary. Thermochim. Acta, **149**, 317 (1989).
24. H. Frank and L. Evans. J. Phys. Chem. **13**, 507 (1945).
25. W.D. Johnston and H. Frieser. Anal. Chem. Acta, **11**, 201 (1954).

© 1999 NRC Canada

Additions and corrections: Modeling complex solution equilibria. II. Systems involving ligand substitutions and uncertainties in equilibrium constants derived from formation constants

Pierre G. Potvin

Ref.: Can. J. Chem. **68**, 2208 (1990)

Some equations in this paper contain minor errors, with no consequence to the arguments, calculations, or conclusions. The correct forms are given here.

$$\begin{bmatrix} \log[H^+] \\ \log[Cu(en)_2^{2+}] \\ \log[en] \\ \log[C_2O_4^{2-}] \\ \log[OH^-] \\ \log[enH^+] \\ \log[enH_2^{2+}] \\ \log[Cu(en)C_2O_4] \\ \log[Cu(C_2O_4)_2^{2-}] \end{bmatrix} = \begin{bmatrix} & & & & & & & & \\ 1 & 0 & 0 & 0 & 0 & 0 & 0 & 0 & 0 \\ 0 & 1 & 0 & 0 & 0 & 0 & 0 & 0 & 0 \\ 0 & 0 & 1 & 0 & 0 & 0 & 0 & 0 & 0 \\ 0 & 0 & 0 & 1 & 0 & 0 & 0 & 0 & 0 \\ -1 & 0 & 0 & 0 & 1 & 0 & 0 & 0 & 0 \\ 1 & 0 & 1 & 0 & 0 & 1 & 0 & 0 & 0 \\ 2 & 0 & 1 & 0 & 0 & 1 & 1 & 0 & 0 \\ 0 & 1 & -1 & 1 & 0 & 0 & 0 & 1 & 0 \\ 0 & 1 & -2 & 2 & 0 & 0 & 0 & 1 & 1 \end{bmatrix} \begin{bmatrix} \log[H^+] \\ \log[Cu(en)_2^{2+}] \\ \log[en] \\ \log[C_2O_4^{2-}] \\ \log K_w \\ \log K_{a1} \\ \log K_{a2} \\ \log K_{s1} \\ \log K_{s2} \end{bmatrix}$$

$$\begin{aligned} c_{K_iK_j} &= (H_K)_{i,j}/\{(H_K)_{i,i}(H_K)_{j,j}\}^{1/2} \\ &= (\sigma_0^2/\sigma_{K_i}\sigma_{K_j})\sum_{k=1}^{n_e} q_{i,n_r+k} \sum_{l=1}^{n_e} q_{j,n_r+l}(H_\psi)_{k,l} \\ &= (\sigma_0^2/\sigma_{K_i}\sigma_{K_j})\sum_{k=1}^{n_e} q_{i,n_r+k} \sum_{l=1}^{n_e} q_{j,n_r+l}\, c_{\psi_k\psi_l}(H_\psi)_{k,k}^{1/2}(H_\psi)_{l,l}^{1/2} \\ &= (1/\sigma_{K_i}\sigma_{K_j})\sum_{k=1}^{n_e} q_{i,n_r+k} \sum_{l=1}^{n_e} q_{j,n_r+l}\, c_{\psi_k\psi_l}\sigma_{\psi_k}\sigma_{\psi_l} \end{aligned}$$

$$\begin{bmatrix} \log\beta_{011} \\ \log\beta_{-111} \\ \log\beta_{111} \end{bmatrix} = \begin{bmatrix} \log[LZn^{2+}] \\ \log[LZnOH^+] \\ \log[LZnH^{3+}] \end{bmatrix} - \begin{bmatrix} 0 & 1 & 1 \\ -1 & 1 & 1 \\ 1 & 1 & 1 \end{bmatrix} \begin{bmatrix} \log[H^+] \\ \log[L] \\ \log[Zn^{2+}] \end{bmatrix}$$

© 1999 NRC Canada

1998 E.W.R. Steacie Award Lecture Asymmetric amphiphilic block copolymers in solution: a morphological wonderland[1]

Neil S. Cameron, Muriel K. Corbierre, and Adi Eisenberg

Abstract: Asymmetric amphiphilic diblock copolymers self-assemble in selective solvents. Since 1995, when we first reported the systematic preparation of a sequence of various "crew-cut" aggregate morphologies from this class of copolymer in solution (1), we have identified a vast array of structures and have begun a detailed investigation of the thermodynamic and kinetic parameters that induce morphogenesis. Not only spheres, rods, bilayer and bicontinuous architectures, as well as inverted structures are observed, but also a selection of mixed, combined and much more complex aggregates is documented. All of these aggregates have a phase-separated insoluble core and a crew-cut soluble corona. Thus, all parameters that permit selective modification of the component of either phase or of the interface provide a window for morphological control. By carefully adjusting the polymer chain environment, it has been possible to develop a systematic understanding of morphogenic parameters, which include, among others, polymer composition, common solvent, initial concentration, temperature, type and concentration of added ions, method of preparation, and added homopolymer. To date, more than 30 publications have appeared in the literature from our group alone on this subject. One of the problems inherent with such a complicated system is the taxonomy or classification: which morphologies correspond to equilibrium positions and which are intermediate or trapped? An attempt at a logical presentation of the observed aggregates is given, preceded by a qualitative discussion of the thermodynamic framework for this system. Where possible, the transitions between morphologies are explained in the context of the thermodynamic parameters. Finally, parallels are drawn between the copolymer aggregates and biological architectures.

Key words: crew-cut, morphology, block copolymer, self-assembly, amphiphile.

Résumé : Les copolymères amphiphiles à blocs asymmétriques s'auto-assemblent en présence de solvants sélectifs. Depuis 1995, lorsque nous avons rapporté pour la première fois la préparation systématique d'une séquence de plusieurs morphologies « coupées en brosse » à partir de cette classe de polymères en solution (1), nous avons identifié une grande variété d'aggrégats et avons commencé une étude détaillée des paramètres thermodynamiques et cinétiques responsables de la morphogénèse. Nous avons observé non seulement des sphères, des batonnets, des bicouches et des structures bicontinues ainsi que des structures inversées, mais aussi une sélection de morphologies mélangées, combinées et bien plus complexes. Tous les aggrégats possèdent deux phases distinctes, un coeur insoluble et une couronne coupée en brosse soluble. Par conséquent, tous les paramètres permettant la modification sélective d'un composant d'une des phases ou de l'interface fournissent un moyen de bien contrôler les morphologies. En ajustant avec précaution l'environnement des chaînes de polymère, il a été possible de développer une compréhension systématique des paramètres morphogéniques incluant la composition du polymère, le solvant commun aux deux blocs, la concentration initiale, la température, le type et la concentration d'ions ajoutés, la méthode de préparation et l'ajout d'homopolymère. A ce jour, plus de 30 publications par notre groupe sont apparues dans la littérature sur ce sujet. La classification des divers aggrégats présente un problème inhérent à un système aussi compliqué: quelles morphologies correspondent à des positions d'équilibre, et quelles morphologies sont intermédiaires ou piégées? Suite à une dicussion qualitative sur le cadre thermodynamique de ce système, nous tentons de présenter de manière logique les aggrégats observés. Les transitions entre les morphologies sont expliquées en fonction des paramètres thermodynamiques lorsque cela est possible. Finalement, les similarités entre les aggrégats de copolymères et les architectures biologiques sont présentées.

Mots clés : coupé en brosse (crew-cut), morphologie, copolymère à bloc, auto-assemblage, amphiphile.

Received April 14, 1999.

N.S. Cameron, M.K. Corbierre, and A. Eisenberg.[2] Department of Chemistry, McGill University, 801 Sherbrooke Street West, Montréal, QC H3A 2K6, Canada.

[1]This review follows the E.W.R. Steacie Award address given by A.E. at the 81st Annual Conference of the Canadian Society for Chemistry, Whistler, British Columbia, June 1998.

[2]Author to whom correspondence may be addressed. e-mail: eisenber@chemistry.mcgill.ca

 © 1999 NRC Canada

1.0. Introduction

Self-assembly of highly asymmetric amphiphilic block copolymers in selective solvents has been of paramount interest in our laboratories since 1994 (2) but morphologies of amphiphilic species, such as small molecule surfactants, have attracted a great deal of interest for many decades (3). The underlying principle is that two fundamentally different sub-units of the amphiphile are driven to phase separate like oil and water, with the limiting condition that they are covalently attached to each other. Molecules, and in our case, *macro*molecules, are therefore thermodynamically driven to self-assemble in order to minimize the contact between the immiscible components (the solvent and the insoluble block). Block copolymer self-assembly in solution has been a topic of active research for more than 30 years (see for example ref. 4). A convenient term for the most commonly observed morphology is the star-micelle. "Star" refers to the fundamental core–corona structure where the core is small and the corona large; micelle reflects the dynamic equilibrium conditions under which these aggregates frequently form. Star micelles can be further divided into two types: regular and reverse. Regular micelles are formed in polar solvents such as water and alcohols; thus, the corona has hydrophilic character. Micelles formed in apolar solvents such as toluene have a hydrophobic corona and are referred to as "reverse." Recently, we have devoted most of our attention to highly asymmetric block copolymers that form aggregates characterized by a large core and a thin coronal shell of the soluble block: the crew-cut systems (1, 2, 5–28).

1.1. Small molecule amphiphiles

Self-assembly of molecules is a rich field for scientific investigation, and a great deal of groundwork has already been completed in the study of small molecule surfactants. Biologically, one of the most important surfactants is the phospholipid that makes up all cell walls. Without highly controlled self-assembly, our living cells could not exist. A typical small molecule surfactant such as sodium dodecyl sulfate (SDS) aggregates at concentrations in excess of 8 mM, the critical micelle concentration (cmc). The free energy of micellization in aqueous media has three components: a favourable hydrophobic component due to the association of the hydrocarbon tails, a surface term that takes into account the opposing requirements to both fully shield the hydrocarbon tails from the polar environment and the electrostatic repulsion inherent for the charged head groups, and also a packing term that determines the morphology (3). Aggregation of surfactants has been described as a start–stop mechanism in that self-assembly occurs until all surfactant molecules are directly involved in the equilibrium morphology whereupon only dynamic chain exchange occurs. Addition of further surfactant molecules induces further self-assembly of aggregates similar to the pre-existing ones.

Many morphologies have been observed for these small molecule amphiphilic systems including simple micelles, rods, planar bilayers, inverted micelles, bicontinuous structures, and vesicles. With increasing surfactant concentration, the morphology spectrum runs from micelles (L_1), through a cubic array of micelles (I_1), hexagonally packed rods (H_1), cubic bicontinuous spheres (V_1), to lamellae (L_3) where phase inversion takes place, and the inverted morphologies develop: Cubic (V_2), Reversed Hexagonal (H_2), Cubic (I_2), and Reversed Micelle (L_2) (29, 30). Furthermore, for systems such as didodecylammonium bromide in oil, micro-emulsions characterized by interconnected tubes are observed (3). The addition of water causes tube dilation until the increased curvature induces droplet formation. Further water addition causes the droplets to grow until the system is no longer able to maintain curvature, and phase separation occurs. Thus, the self-assembly of small molecule surfactants is characterized by relatively high cmc's, three contributions to the free energy of micellization, and dynamic morphology changes.

1.2. Diblock copolymers in the bulk

Diblock copolymers in the bulk also exhibit a spectrum of morphologies analogous to the series observed for small molecule surfactants. Much of the experimental work in this regard has been carried out on polystyrene-*b*-poly(isoprene) (PS-*b*-PI) and polystyrene-*b*-polybutadiene (PS-*b*-PBD). With these systems, it has been possible to study phase separation in the strong segregation limit where $\chi N > 10$.[3] As an example, with increasing volume fraction of PI, the morphological transitions go from body centered cubic (BCC) spheres of PI in a PS matrix through hexagonally packed cylinders of PI in PS, gyroid (G), metastable hexagonally perforated layers (HPL) (31), and finally lamellae (LAM) form when the volume fractions of the two blocks approach equality. As the PI volume fraction increases further, phase inversion occurs, and HPL, G, HEX, and finally BCC morphologies are observed where PI forms the continuous phase. The full spectrum of morphologies is not observed for all polymers, as not only the volume fraction of each block but also the total degree of polymerization plays a role (32).

1.3. Diblock copolymers at the air–water interface

Various morphologies are also observed in two dimensions for block copolymers at the air–water interface. Systems investigated include polystyrene-*b*-poly(4-vinyl pyridine.alkyl iodide) (PS-*b*-P4VP.RI) (33, 34) and the structures identified with changing relative block composition progressed from circles ("starfish") to ribbons and lamellae. Inverted circles (two-dimensional nanofoams) were also observed for polystyrene-*b*-poly(sodium acrylate) (PS(90)-*b*-PANa(32)). The diblock copolymer is dissolved in an organic solvent that is then spread on a water surface in a Langmuir trough. Upon evaporation of the solvent, aggregation occurs. The 2D "films" have been studied by X-ray and neutron scattering (SAXS, SANS) (35), as well as atomic force microscopy (AFM) and transmission electron microscopy (TEM) (36).

1.4. Diblock copolymers in solution

Self-assembly of amphiphilic block copolymers in selective low molecular weight solvents has been studied now for many years. The principle of aggregation of the amphiphilic block copolymers is similar to that undergone by small mol-

[3] The product of the Flory–Huggins segment–segment interaction parameter, χ, and the degree of polymerization, N, is much greater than 10.

© 1999 NRC Canada

ecule amphiphiles in solution; however, the critical micelle concentration (cmc) is usually much lower in the case of block copolymers (6). The dynamics of the chain exchange between the micelles are also different for block copolymers and small molecule surfactants. Indeed, at equilibrium, the micelles exchange chains with one another, and this exchange is fast in the case of small molecules. However, the chain exchange in block copolymer systems is generally much slower, due to a number of factors including the high molecular weight, the low cmc, and the possible entanglement and low mobility of the chains in the core (14). For example, when the glass transition temperature (T_g) of the core-forming chains is very high (T_g of PS ca. 100°C) and no plasticizer is present, the micelles are considered to be "frozen," since the mobility of the core-forming chains is extremely low.

Depending on the relative block lengths, either star or crew-cut micelles are formed. A small core surrounded by a long corona characterizes star micelles, whereas crew-cut micelles consist of a large core and a thin corona. The term crew-cut was originally proposed by Halperin et al. (37). Two features enhance the difference between crew-cut and star micelles: the process of the formation of the micelles and the morphologies of the aggregates. Star micelles can often be prepared by direct dissolution of the block copolymer in a solvent selective for the long block. Thus, the insoluble short blocks associate and form the core, and the soluble long blocks form the corona of the micelles. This process is usually impossible to apply to the formation of crew-cut micelles, since the insoluble blocks represent a very high fraction of the block copolymer. Instead of the direct dissolution process, the diblock copolymers are first dissolved in a solvent good for both blocks, and then a precipitant for the long block is added, resulting in the aggregation of these long blocks. The preparation of crew-cut micelles therefore involves a more delicate process, and the resulting aggregates present a more complicated system than star-like micelles, since they involve solvent mixtures of variable composition. Star micelles are essentially spherical aggregates. Aggregates in the star regime other than small solid spheres have only rarely been observed and have not been studied as extensively (38–45). Very recently, the groups of Winnik and Manners (46) have developed a novel organometallic block copolymer of ferrocenyldimethylsilane and dimethyl siloxane (PFS-*b*-PDMS). This copolymer self-assembles in hot hexane to form wormlike micelles with an iron-rich core.

Starting in 1995 (1), a wide range of different crew-cut morphologies has been observed among aggregates prepared from asymmetric amphiphilic block copolymer systems. The aggregation behaviour shadows small molecule surfactants, where a long hydrophobic tail and a small polar head group generate a wide variety of morphologies in solution. For asymmetric amphiphilic diblock copolymers, the observed morphologies include, but are by no means limited to, spheres, rods, bicontinuous structures, vesicles, lamellae, large compound micelles, large compound vesicles, tubules, "eggshells," baroclinic tubules, porous spheres, and multilamellar vesicles. Overall, we have identified on the order of 30 morphologies (1, 5–28), but their taxonomy presents problems. Some of the morphologies are thermodynamically induced in which case equilibrium trends are observed from simple spheres to inverted micelles; others are kinetically controlled, and their classification is more difficult. Where the mode of aggregation is primarily under thermodynamic control, we observe a spectrum of morphologies (as is also seen both in the bulk and in small molecule surfactant systems) from spheres through rods, bicontinuous rods, bilayers (lamellae and vesicles) to inverse rods and spheres as well as mixtures. Polystyrene-*b*-poly(acrylic acid) (PS-*b*-PAA), polystyrene-*b*-poly-(ethylene oxide) (PS-*b*-PEO), and polystyrene-*b*-poly(4-vinyl pyridine) (PS-*b*-P4VP) are the diblock copolymers that have received the most attention in our studies.

1.5. Others working in the field

More recently, other groups have also studied crew-cut morphologies of copolymers other than simple spheres, including the group of Liu (47), who investigate, among others, polyisoprene-*b*-poly(2-cinnamoylethyl methacrylate) (PI-*b*-PCEMA) in THF with the addition of hexanes, a selective precipitant for PCEMA. They also prepare spherical micelles from polystyrene-*b*-poly(2-cinnamoylethyl methacrylate) (PS-*b*-PCEMA) in THF–cyclohexane or chloroform–cyclohexane mixtures (48). PCEMA-*b*-PAA has also been shown to give various morphologies, including nanofibres (49) and hollow nanospheres, among others (50). One particularly interesting characteristic of PCEMA is that it can be cross-linked, thereby adding stability to the aggregates. The group of Nose (51) has also published examples of crew-cut aggregates.

1.6. Statement of purpose

In this review, the intent is to present and interpret the conditions leading to the formation of aggregates of the various morphologies of highly asymmetric amphiphilic diblock copolymers. The thermodynamic framework as well as parallels to small molecule systems are considered. A detailed review of the various morphogenic parameters including block length, additives, temperature, solvent, and block composition will be presented as a foundation for a survey of the solution morphologies we have observed. Parallels will be drawn between these aggregates and biological subcellular architectures.

2.0. Thermodynamic and experimental parameters

2.1. Three components of the free energy of aggregation

The morphology of self-assembled block copolymer aggregates is governed primarily by three components of the free energy of aggregation: (*i*) core–chain stretching, (*ii*) interfacial energy, and (*iii*) intercoronal chain interactions (21, 37). The effects of these parameters can be more easily understood using the following two examples: in one case, only the hydrophilic block length is varied; in the other, a polymer of constant composition is used in a binary solvent mixture of DMF and water, but we increase the water concentration.

Using a block copolymer with a constant polystyrene block length and starting with a relatively long PAA block, spherical micelles are observed initially. As we decrease the

© 1999 NRC Canada

Fig. 1. Schematic plot of relative free energies and degree of core–chain stretching to indicate morphological boundaries as a function of morphogenic parameters.

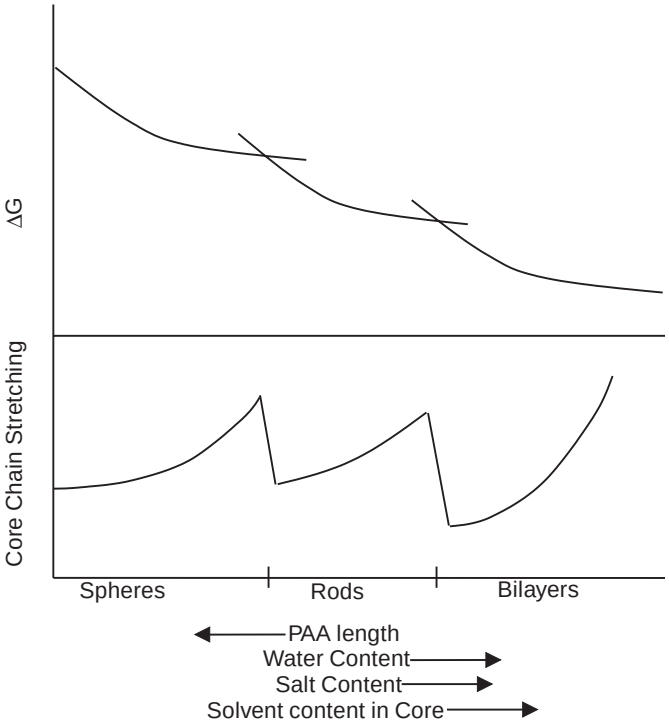

PAA length, the repulsive interactions between coronal block chains decrease, thus more chains can aggregate, leading to larger spheres. Some of the polystyrene blocks, however, must reach from the centre of the core to the core–corona interface, and in general, the larger the PS core, the greater the average degree of core–chain stretching. When the aggregates become very large, the entropic penalty of core–block stretching renders simple spheres unfavourable as a low energy morphology, and rods are formed with a decreased core diameter. Reducing the PAA block to an even greater degree leads to an increase in the rod diameter as the aggregation number increases due to reduced coronal block repulsion. Ultimately, in the same manner as for the simple sphere–rod transitions, the core–block stretching term will dictate a further morphological transition to the bilayer structures.

On the other hand, starting with a diblock copolymer of a particular composition in pure common solvent, as we increase the water concentration, we get self-assembly of spheres at some critical concentration (cwc). As the water content increases, the total interfacial energy increases, so the drive is to minimize the total interface surface area. In the limit, a single styrene sphere would minimize the interfacial energy, but the finite styrene block length precludes this option. As soon as the chain stretching and coronal terms exceed the interfacial energy term, a new rod-like morphology with a smaller radius becomes favourable. If the PAA block length is too long, however, then the spherical micelles formed are thermodynamically "stuck" and do not undergo the transition. In this case, the net surface area decrease does not compensate for the electrostatic repulsion implied by the long acrylic acid block. Where the PAA block is short enough, the rod to bilayer morphology change can be induced by more water addition.

If any of these free energy parameters is stressed, for example, by further water addition or reduction of the hydrophilic block length, morphological transition to inverted structures is possible. The PS stretching term and corona–chain repulsion term are balanced by the interfacial term to give a comparatively smooth series of transitions in the total free energy of aggregation[4] (see Fig. 1).

2.2. Preparation of the aggregates

Small molecule surfactants can usually be dissolved directly in a solvent that is good for either the hydrophobic or the hydrophilic component, and due to rapid molecule exchange, equilibrium morphologies are rapidly established (cf. start–stop mechanism). This approach does not work easily for aqueous systems involving amphiphilic PS-*b*-PAA because of the extreme insolubility of polystyrene in water. As mentioned earlier, in an effort to achieve equilibrium conditions, dilute polymer solutions (1% w/w) in dimethyl formamide (DMF) are prepared and then deionized water is slowly added, thereby approaching the critical water concentration (cwc) where self-assembly begins. As the water concentration increases from the cwc, the kinetics of chain exchange slow, and it is possible to trap the then present morphologies. When the water content reaches 25% (w/w), the sample is dialyzed against distilled water to remove DMF. The cwc is usually around 5% H_2O, and at about 10% H_2O, the three-dimensional architectures are considered to be "frozen."

2.3. Environmental parameters

Having detailed the contributing factors to the free energy of aggregation, any parameter that perturbs the core stretching, coronal repulsion, or interfacial energy terms provides a window to morphological control. While the stability of the aggregates, once formed, is very high, the self-assembly of crew-cut PS-*b*-PAA is, in fact, extremely sensitive to the preparative conditions. We have therefore been able to probe the effects of parameter modification that directly affect one or more of the three contributions to the free energy of aggregation: precipitant addition, initial polymer concentration, additives (salt, acid, base and homopolymer), block composition, temperature, and common solvent.

2.3.1. Water addition

Two methods of aggregate preparation are exploited for the DMF–water system. In the vast majority of our samples, aggregation is induced by the water addition method (WA) as described above (Sect. 2.2). The direct dissolution method (DD) in DMF–water mixtures has also been exploited where, for example, the PS-*b*-PAA is dissolved in a solvent mixture containing between 5.5 and 9.5 wt.% water. Table 1 demonstrates the effect of WA from 0 to 7.5% as compared with direct dissolution into a binary solvent mixture at 7.5% water on the aggregate morphology (26).

[4] H. Shen and A. Eisenberg. Phase Diagram I. Manuscript submitted to J. Phys. Chem.

© 1999 NRC Canada

Table 1. Major morphologies vs. water content as a function of preparative method and initial polymer concentration for PS(190)-*b*-PAA(20) (26).

	7.5% water content in DMF (w/w)	
Pol. wt.%	DD	WA
1.0	Long rods	Spheres
1.5	Long and interconnected rods	Spheres
2.5	Bilayers	Spheres
3.5	Bilayers	Rods, vesicles, and spheres

Table 2. Summary of the effect of salt or acid addition on the dominant morphology for PS(410)-*b*-PAA(25) (8, 12).

	[Acid or salt] (mM)	R^a	Dominant morphology
NaCl			
	<2.1	<0.40	Spheres
	3.2–5.3	0.60–1.0	Rods
	5.3–16	1.0–3.0	Vesicles
	21	4.0	LCVs
$CaCl_2$			
	<0.12	<0.023	Spheres
	0.14–0.20	0.026–0.038	Vesicles
	0.24–0.48	0.045–0.09	LCVs
HCl			
	0.19	0.035	Spheres
	0.21	0.040	Rods
	0.24	0.045	Vesicles
	0.27	0.050	LCVs
NaOH[b]			
	0	0	Vesicles
	0.028	0.005	Spheres

[a] R = molar ratio (salt:acrylic acid groups).
[b] PS(410)-*b*-PAA(13).

These methods of sample preparation provide further insight to the thermodynamic and kinetic parameters of morphogenesis. At low water concentrations, the kinetics of exchange are rapid, and therefore, it is the thermodynamically most stable morphology that will dominate. At higher water concentrations, the speed at which aggregation occurs or morphologies change controls the prevalent morphology to a much larger extent. The WA method certainly optimizes chain exchange, since during the onset of aggregation the nonsolvent concentration is low, whereas the DD method is limited by the kinetics of chain exchange at a specific precipitant content. In both cases, the thermodynamics of aggregation appreciably control morphology at low water contents; however, due to the initially high water concentration for DD, rods are possible, for example, in a system that forms simple spheres using the WA method. On the whole, the aggregates formed via DD exhibit more complicated morphologies, whereas the morphologies observed via WA reflect the faster kinetics of chain exchange and the morphologies formed at lower water concentrations, which freeze when the rate of water addition exceeds the dynamics of morphological transition. A possible mechanism for these method-dependent differences depends on the initial state of the polymer. For WA, the polymer is in a molecularly disperse solution of DMF, and aggregation is induced at a low water concentration. At higher water concentration, chain exchange is very slow, and thus, despite the same final water concentration (e.g., 7.5% in Table 1), the exhibited morphology is often the simple sphere. For DD, polymer is added as a solid to a binary solvent mixture, and swelling followed by fission can lead to more complex morphologies that may better reflect thermodynamic equilibrium. In the limit of very slow water addition or very long storage times for direct dissolution, the observed morphologies converge.

2.3.2. Initial polymer concentration

Table 1 not only highlights the effect of water concentration and the preparation method, but also indicates the strong dependence of morphology on the initial polymer concentration. As with most of the trends, which we observe by progressively modifying the aggregation conditions, the morphological progression is from spheres to rods to vesicles and on to inverted and more complicated architectures with various intermediates. Thus, at low initial polymer concentration, simple spheres dominate; however, at higher polymer concentrations, more complicated morphologies become possible (26).

2.3.3. Additives

Water is not the only additive that can have a profound impact on morphology. Any reagent that affects the coil dimensions, inter and intra coronal block interactions, or solvent quality, can be induced to have an effect on aggregation morphology. The results from experiments involving acid, base, and various salts as well as homopolymer are described below. For the ionic additives, the absolute concentration of additive, though important, is not as interesting as the molar ratio, *R*, which relates the number of ions added to the number of coronal repeat units (in our case AA, 4VP, etc.) present. The morphogenic effect of added ions has been investigated over a molar ratio range up to 4.0 (see Table 2) (8, 12). The morphogenic effect of salt has also been studied at millimolar ratios (m*R*) for PS(310)-*b*-P4VP(58). More extraordinary is that *micro*molar ratios (μR) of acid and base induce morphological transitions for this system (24).

2.3.3.1. Salt: The addition of salts induces electrostatic shielding along the partially ionized corona-forming block (for the polyelectrolytes). As the charges along the chain become shielded from one another, the coil dimension decreases thereby reducing steric and electrostatic repulsion among the chains. It is no great surprise then that for a given polymer (e.g., PS(410)-*b*-PAA(25)) the progressive addition of NaCl to a final *R* value of 4.0, while the system is dynamic, can be used to induce the formation of rods, vesicles, or large compound vesicles from a suspension of spheres

© 1999 NRC Canada

Table 3. Effect of homo-PS addition on aggregation (7).

PS-*b*-PAA (units)	Homo-PS units	Weight ratio PS-PAA:PS	Morphology	Diameter or wall thickness (nm)
500-*b*-58	—	100:0	Sphere	30
500-*b*-58	180	90:10	Sphere	31
500-*b*-58	180	80:20	Sphere	36
500-*b*-58	180	70:30	Sphere	37
180-*b*-14	—	100:0	Rod	23
180-*b*-14	38	95:5	Sphere	27
200-*b*-8	—	100:0	Vesicle	18
200-*b*-8	38	95:5	Sphere	33

(see Table 2) (8, 12). By adding a divalent cation ($CaCl_2$), bridging becomes possible, and morphological transitions occur at even lower concentrations and *R* values (Table 2). PS(310)-*b*-P4VP(58) follows the same trend from spheres to bilayers on addition of simple electrolytes (24).

2.3.3.2. Acid: The addition of a protic acid is also a potent morphogenic device, since protonation of any anionic acrylate pendant groups will be assured. Thus, protonation provides a valid mechanism for morphological transitions (see Table 2). At a molar ratio (*R*) less than 0.035 HCl per acrylic acid unit for PS(410)-*b*-PAA(25 or 13), only spheres are observed. By raising the molar ratio progressively to 0.050, rods, vesicles, and LCVs are obtained (8, 12). Amphiprotic PS(310)-*b*-P4VP(58) undergoes a sphere–rod transition on the μR addition of HCl. Further addition induces a rod–sphere transition due to increased charge density, and continued addition reverses the trend direction again due to electrostatic shielding (24).

2.3.3.3. Base: The effect of the addition of a strong base is simply to enhance the charge density of the coronal block for PS-*b*-PAA due to deprotonation of the pendant acrylic acid. As charge density increases, coronal repulsion also increases, thus aggregation number and core diameter decrease, and the morphological trend is reversed (Table 2) (8, 12). For the PS(310)-*b*-P4VP(58) system, the situation is more complicated. The micromolar ratio addition of NaOH causes a transition from spheres to rods, but the progressive addition increases charge density due to the abstraction of the α backbone hydrogen so the anticipated sequence of rods to spheres is observed. Still, more NaOH leads to shielding, and the trend is again reversed in the direction of spheres to bilayers (24).

2.3.3.4. Homopolymer (7, 25): The addition of homopolymer to a molecularly disperse solution of PS-*b*-PAA can be used to induce minor variations in diameter within the spherical morphology regime or regime transitions from rods or vesicles to spheres (see Table 3) (7). The effect of added homopolystyrene is to decrease the cwc due to the higher overall content of hydrophobic polymer, but the onset of rod formation is delayed, since the additional homopolymer can volume-fill the core, thereby relieving the core–chain stretch. Experimentally, the block copolymer was dissolved in DMF along with homo-PS, and then water was added in the standard way. It was necessary to use homo-PS samples that were shorter than the PS block of the copolymer in order to avoid premature precipitation of the homopolymer. As long as the copolymer and homopolymer self-assemble before the homo-PS precipitates, then the DMF swollen nascent cores solubilize the homo-PS chains, and therefore, within the spherical regime, the core diameters increase. The addition of homo-PS to samples that form aggregates other than solid spheres may induce spherical morphologies, since it is primarily the inability of the PS block to stretch and completely fill a sphere that leads to nonsphericity in the "native" state (see Table 3).

Table 4. Diblock composition and morphology (7).

PS-*b*-PAA (units)	PAA (mol %)	Morphology
170-*b*-33	16.3	Sphere
180-*b*-28	13.5	Sphere
180-*b*-14	7.2	Rod
410-*b*-20	4.7	Vesicle
410-*b*-16	3.8	Lamella
200-*b*-4	2.0	LCM

2.3.4. Block length (scaling relations)

As discussed within the context of the section on the three components of the force-balance, the block length of each block affects the morphology. Scaling relations have been determined that relate core radius (R_{core}), as well as the related surface area per chain (A_c), and the degree of PS stretching (S_c) within the core for crew-cut primary spheres (7). For example, eq. [1] shows that the radius increases with PS length due to the increased volume of PS in the core.

$$[1] \qquad R_{core} \propto N_{PS}^{0.4} N_{PAA}^{-0.15}$$

With increasing PAA length, however, increasing coronal chain repulsion decreases the aggregation number, therefore, the aggregate size decreases. By varying just the PAA content of the polymer, many of the equilibrium-type morphologies can be induced (see Table 4) (7).

2.3.5. Temperature

The single solvent preparation of aggregates from highly asymmetric diblock copolymers is very desirable not only from the perspective of potential industrial applications but also as a means of simplifying the system in order to control it better. A nontoxic single solvent would be even more desirable if the applications were to have pharmacological

© 1999 NRC Canada

Table 5. Solvent and polymer parameters (52).

Material	Solubility parameter δ	Dielectric constant ε
DMF	24.8	38.2
Dioxane	20.5	2.2
THF	18.6	7.5
Water	47.9	80.1
Styrene	19.0	
Acrylic acid	24.6	

leanings. For PS-*b*-PAA, where the PS block is very much longer than the PAA block, direct preparation in water, even at 200°C and elevated pressure, has proven impossible. However, in less polar low alkanols (methanol, ethanol, *sec*-propanol, and *n*-butanol), elevated temperatures are sufficient to permit at least chain transfer from the bulk to nano and mesoscopic aggregates including spheres, vesicles, tubules, and interconnected vesicles. Given the monodisperse spheres of diameter ~25 nm observed for PS(386)-*b*-PAA(79) formed on cooling in *n*-butanol (0.07 wt.%, 170°C), we infer that while at 170°C, the complete dissolution of the polymer may have been achieved in this solvent, or at least that the kinetics were fast enough for morphogenesis (23). Essentially, this method mimics the effect of water addition to a copolymer solution in a common solvent, since solubility decreases both as the water content increases for binary solvent mixtures and as the temperature decreases for our polymers in single solvent systems.

2.3.6. Common solvent

The role of solvent is crucial to all aspects of the free energy of aggregation. Polymer–solvent interactions determine the coil dimension for each block of a diblock copolymer, which, in turn, has a profound impact on the aggregate dimensions and modes of assembly.

Dissolution of polymers is optimal where the δ values for polymer and solvent are similar (see Table 5) (52). As these values diverge, the polymer chain dimensions decrease. High dielectric constant (ε) values improve the solubility of the corona block. The choice of common solvent therefore permits a qualitative exploration of the principal terms of the free energy of aggregation, since the common solvent directly affects both the core and corona chain dimensions, and the dielectric constant of the nonsolvent affects the coronal chain dimension as well as the interfacial energy.

Solvents common for both blocks in the PS-*b*-PAA system other than DMF and low alkanols have also been investigated. The core dimension of a nascent aggregate during the early stages of water addition is highly dependent on the polymer–solvent interaction parameters. Where the common solvent is better for the core-forming block, during the addition of water, the partition of organic solvent will dictate that the core be more swollen than is the case for DMF. Due to the swelling, more complex morphologies are possible. Some examples of the available morphologies from PS-*b*-PAA copolymers using DMF, dioxane, or THF as a common solvent are given in Table 6. Using just one polymer that exhibits different morphologies in different solvents, any of the intermediate morphologies is made accessible through solvent mixtures (18).

Table 6. Morphology of PS-*b*-PAA from different common solvents (18).

Polymer	PAA content (mol%)	Common solvent		
		DMF	Dioxane	THF
PS(168)-*b*-PAA(59)	26.0	Sphere	Sphere	Sphere
PS(490)-*b*-PAA(87)	15.1	Sphere	Rod	Sphere
PS(500)-*b*-PAA(58)	10.4	Sphere	Vesicle	Vesicle
PS(420)-*b*-PAA(26)	5.8	Sphere	Vesicle	LCM

Table 7. Morphologies observed to date for our various crew-cut systems (1, 5–28).

System	Observed morphologies[a]
PS-*b*-PAA	S, R, V, L, LCM, LCV, T, other
PS-*b*-PEO	S, R, V, L, LCM, LCV, other
PS-*b*-PVP.MeI	S, R, V, L, LCM
PS-PMMA-PAA	S, R, V
PBD-*b*-PAA	S,[b] R, V, other
PCL-*b*-PEO	Large aggregates d ~ 0.5 μm.

[a]Key: S, sphere; R, rod; V, vesicle; L, lamellae; LCM, large compound micelle; LCV, large compound vesicle; T, tubule; other, more complex structures.

[b]Near sphere.

2.3.7. Other block copolymers

Most of the variable parameters discussed above have been presented in the context of PS-*b*-PAA; however, other asymmetric diblock copolymer systems have also been investigated in our laboratories albeit less extensively (see Table 7). The hydrophilic block characteristics change significantly for the different samples; nevertheless, the underlying principles for the self-assembly of asymmetric amphiphilic diblock copolymers are universal. Due to narrow morphological boundaries in their respective phase diagrams, as seen for the polymer bulk morphologies described earlier, it may be that some morphologies are not observable for practical reasons. Some morphologies may not be stable at all for some systems under the conditions of the experiment.

The PS-based systems have a glassy styrene phase at room temperature in water. The other core-forming blocks, poly(caprolactone) (PCL), and poly(butadiene) (PBD), have T_g values of about –65°C (53) and –90 to –8°C (14), respectively. Polyelectrolytic coronae can be formed for PAA and derivatives of poly(4-vinyl pyridine) (P4VP). Uncharged coronae arise from PEO systems. The PS–PMMA–PAA triblock system (20) permitted a preliminary investigation of the effect of a second hydrophobic block on the cwc and subsequent morphologies. Despite the incomplete investigation to date for some of the systems described in Table 7, it is clear that all of these highly asymmetric amphiphilic diblock copolymers follow the same rules. By varying the parameters discussed in some detail above, each system has been induced to form a range of morphologies, and each adds to our understanding of micro-phase separation and aggregation for this particularly rich class of macromolecule.

© 1999 NRC Canada

2.4. Phase diagram and kinetics studies

Summarizing multidimensional phase behaviour is a complicated undertaking; however, we have begun the construction of a ternary phase diagram as a function of water, dioxane, and the polymer PS(310)-*b*-PAA(52).[4] Given the detailed information on the necessary conditions for the formation of the various equilibrium and near-equilibrium morphologies presented in Sect. 3 that can be presented in phase diagrams, it becomes feasible to design systems for desired properties.

A further consideration is the speed at which aggregates can be formed. Early studies started with two populations of solid spheres formed from two different PS-*b*-PAA samples and followed the time scale over which they formed a single population when mixed (13, 54). More recently, attention has been devoted to the formation of complex inverted structures (HHH and TWV, discussed below) from vesicles (17, 22, 27) and bilayers from rods.[5]

3.0. Equilibrium and near-equilibrium morphologies

As a consequence of the kinetics and thermodynamics studies, most aggregates can now be sorted into equilibrium, near-equilibrium, and metastable morphologies. Equilibrium studies have positively identified spheres, rods, and vesicles as well as wide boundary regions between each morphology where, for example, spheres and rods coexist at equilibrium.[4] Furthermore, in a similar fashion to small molecule surfactants and also diblock copolymers in the bulk, a phase inversion occurs in the spectrum of morphologies. In a limited sense to be discussed further, the inverted equilibrium morphologies include hexagonally packed hollow hoops (HHHs) and large compound micelles (LCMs). As observed under the electron microscope, these aggregates represent morphologies at or near equilibrium that were quenched and isolated. Equilibrium and near-equilibrium morphologies (Figs. 2–5) are described below. A discussion of nonequilibrium morphologies (Fig. 6) follow in Sect. 4.0. Some morphologies presented are paradigms from the polymer literature, and some are novel for polymers (e.g., tubules; see below). Still others are novel in their own right, and to our knowledge are without precedent in the self-assembly literature (e.g., pincushions; see below).

3.1. Equilibrium

Simple *spheres*, shown schematically in Fig. 3, of PS-*b*-PAA block copolymer formed in an aqueous environment, consist of a PS core surrounded by PAA coronal chains (1, 2). Usually, PS-*b*-PAA block copolymers with a relatively high PAA content (>10%) form simple spheres. The polydispersity of such micelles is low ($2\sigma_r/d < 5\%$),[6] and the size of the spheres is affected by a number of factors, such as the block lengths, addition of salts (HCl, NaCl, $CaCl_2$) or homopolystyrene to the solution. An obvious restriction for simple spheres is that the total hydrophobic block length in its planar zigzag configuration must not exceed the radius of the core. The entropic penalty of chain stretching dictates, however, that well before the chains become fully extended, a morphological transition is induced. The simple sphere is the parent morphology for all crew-cut aggregates, since under our classical preparative conditions, it is usually the first aggregate to form. We take this morphology as the most basic example of the effect of the force balance equation. The subsequent morphologies are explained as a function of their deviation from this standard where the core–chain stretching, core–corona interfacial energy, and the coronal chain repulsive forces are optimized with respect to the lowest accessible free energy of aggregation available (cf. Fig. 1). Figure 2*A* demonstrates the typically low polydispersity of spherical crew-cut micelles formed, for example, from PS(200)-*b*-PAA(21).

Rods (1, 7, 21) as sketched in Fig. 3, need little description. They are characterized by diameters of the same order of magnitude as those of primary micelles (ca. 30 nm) but can be of widely variable length that can exceed 10 μm (Fig. 2*B*). It should be noted that the energetic contributions to the free energy of aggregation still include core–chain stretching which, at the transition, is decreased slightly relative to the simple sphere, but generally is comparable since the diameters are comparable, and also corona–chain repulsion, which experiences a net decrease due to a decrease in the chain length or due to the addition of simple electrolytes. While the radii of spheres and rods are comparable, the greater length of the rods means that the total aggregate volume increases, thereby reducing the net interfacial energy per chain between the core and the solvent. A further contribution is the end-capping energy arising from the high curvature of the hemispherical caps at rod ends. Under a wide range of conditions, this term is not especially significant although hooped rods ("doughnuts") have been observed. For example, in the case of some of the more complex aggregates presented later, the end-capping energy penalty is sufficiently large that hoops are formed despite the extra curvature energy.

The *bicontinuous rod* morphology (Fig. 2*C*) consists of networks of interconnected branched rods in three dimensions. The diameters of the rods are monodisperse, and the origin of the branch points is the same as for the bicontinuous morphology in the bulk. Disordered bicontinuous rods are schematically represented in Fig. 3. We have observed not only disordered bicontinuous morphologies (25), but also highly ordered examples (28). It is not especially surprising that we find a range of morphologies for asymmetric diblock copolymers in solution. Detailed equilibrium studies have confirmed the status of the simpler solution morphologies; however, due to the fact that this morphology is not seen for all samples, and furthermore, where it is seen, it is only over a very narrow range of parameters, we are unable to categorically assign equilibrium status. It is likely that the highly ordered bicontinuous samples better represent equilibrium.

Bilayers (Figs. 2*D–F*) represent the next step in the arrangement of diblock copolymers as block or environmental parameters change. As shown schematically in Fig. 3, *lamellae* (Figs. 2*D*, 2*E*) and *vesicles* (Fig. 2*F*) are character-

[5] L. Chen, H. Shen, and A. Eisenberg. Kinetics. Manuscript submitted to J. Phys. Chem.

[6] σ_r, radial standard deviation; *d*, diameter of the sphere.

© 1999 NRC Canada

Fig. 2. "Pure" morphologies: the degree of polymerization for each block is given in parentheses.

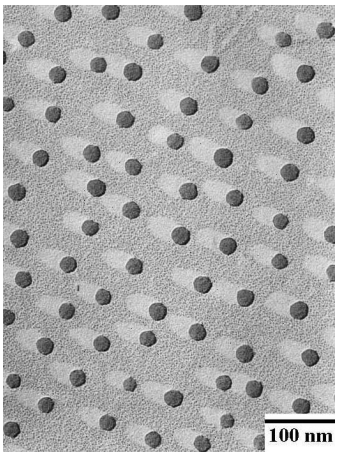

A: Spherical micelles
PS(200)-*b*-PAA(21)

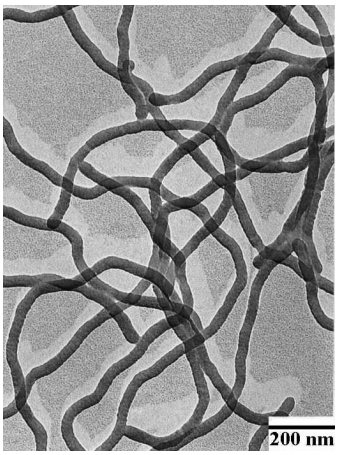

B: Rods
PS(190)-*b*-PAA(20)

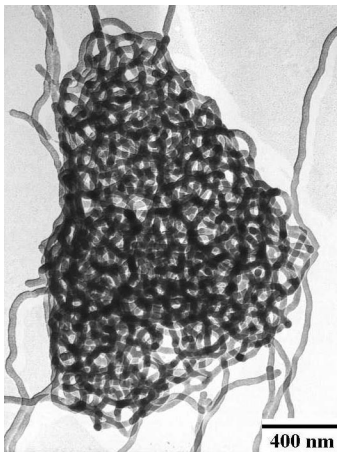

C: Bicontinuous rods
PS(190)-*b*-PAA(20)

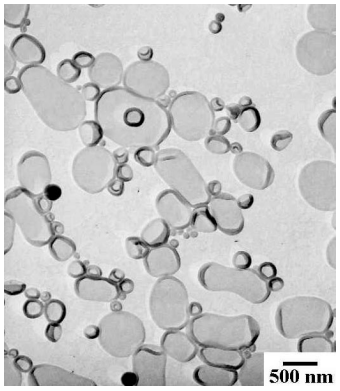

D: Lamellae
PS(132)-*b*-PAA(20)

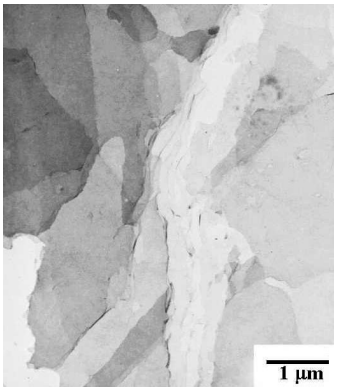

E: Lamellae
PS(49)-*b*-PAA(10)

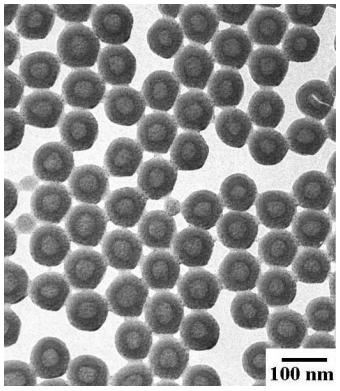

F: Vesicles
PS(410)-*b*-PAA(13)

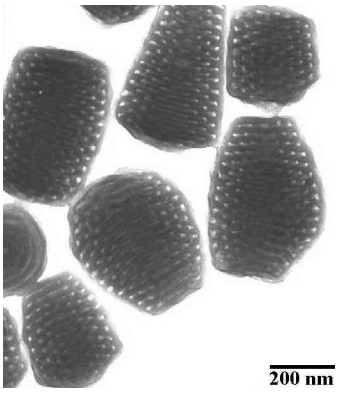

G: HHH
PS(410)-*b*-PAA(13)

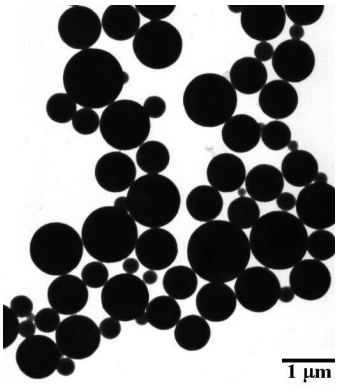

H: LCM
PS(200)-*b*-PAA(4)

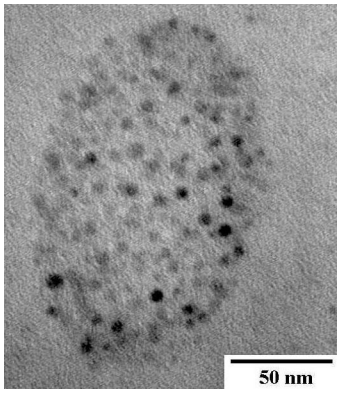

I: LCM
Internal structure

ized by flat or curved bilayer "walls" of polymer. It should be noted that under some preparative conditions, lamellae appear in vesicular suspensions, but under other conditions, pure lamellae can be prepared.[5] Figure 2*D* demonstrates isolated lamellae, whereas Fig. 2*E* shows the superposition of much larger lamellae, in which the different shades of grey represent different numbers of lamellar layers. Vesicles are a particularly versatile morphology, as they can be prepared from many polymers. While small, nearly monodisperse vesicles are often formed, larger, more polydisperse aggregates can also be obtained.

It is highly possible that the *inverse bicontinuous rod* morphology exists under certain equilibrium conditions. To date, we have had only indications of its existence in our studies of the transition from vesicles to the HHH morphology; however, we have not been able to identify it posi-

© 1999 NRC Canada

Fig. 3. Schematic drawings of equilibrium morphologies. Where convenient, coronal chains are indicated; core-forming chains are symbolically represented for the sphere. The surface for HHH represents the interface between hydrophilic and hydrophophic domains. Thus, for PS-*b*-PAA, these hoops contain water swollen PAA, and the whole structure is embedded in a PS matrix.

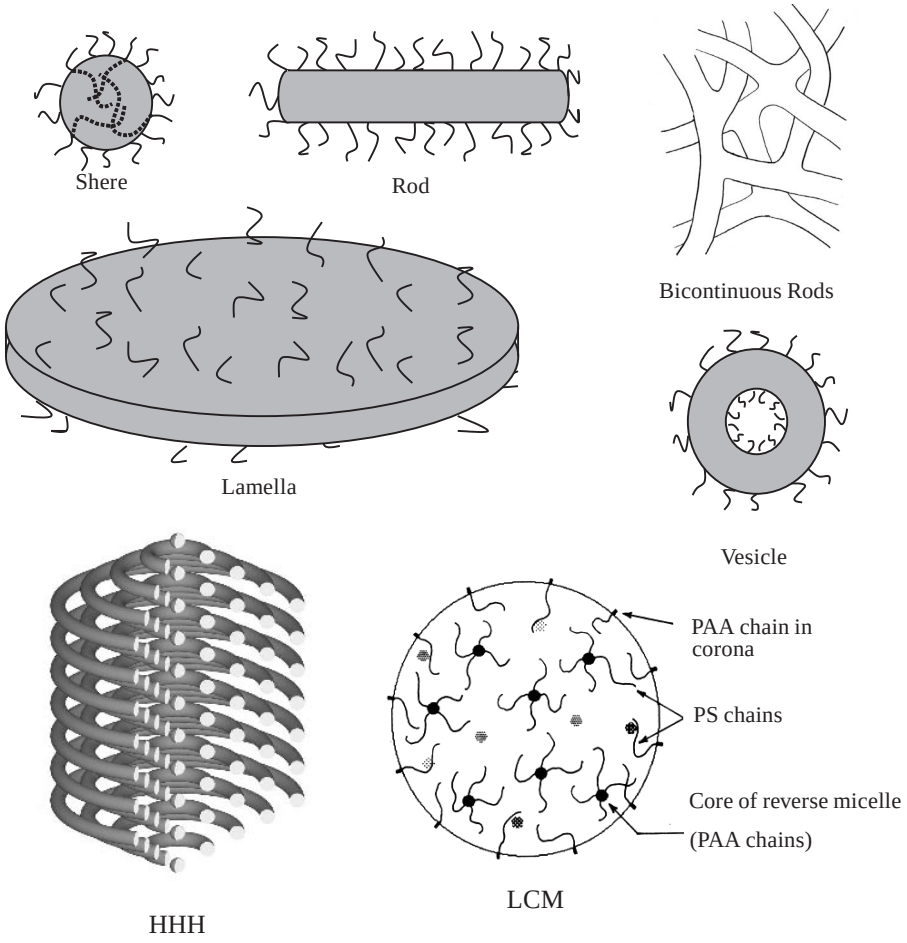

Fig. 4. Primary spheres induced to rearrange into necklaces (one-dimensional), sheets (two-dimensional); and even mesoscopic, birefringent needles (three-dimensional).

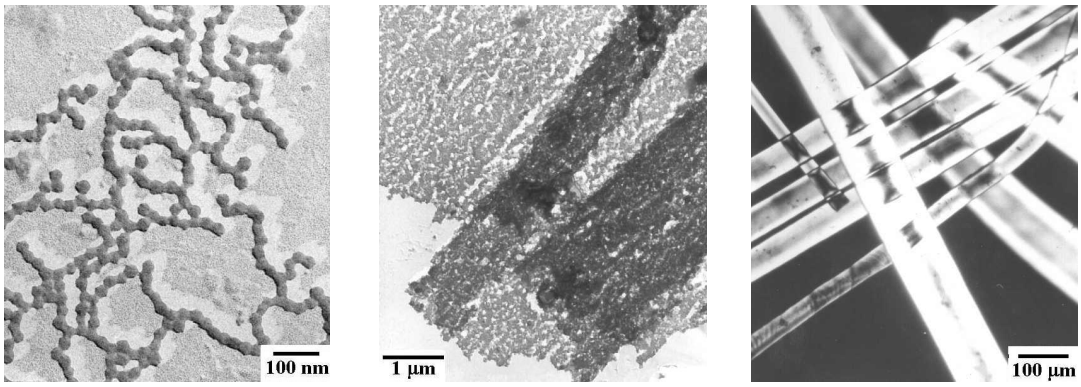

A: Pearl necklace
PS(500)-*b*-PAA(60)

B: Micelle Sheets
PS(240)-*b*-PEO(80)

C: Needles
PS(180)-*b*-PAA(28)

tively. This morphology is the phase-inverted counterpart of the bicontinuous rod described above (17).

The preparation of *hexagonally packed hollow hoop* structures (*HHH*) (Fig. 2*G*) involves first the formation of small vesicles of PS-*b*-PAA by addition of water; subsequent addition of NaCl ions to the solution of vesicles leads to the assembly and rearrangement of the vesicles into HHH aggregates (17). The HHH structure of the aggregates is depicted in a computer visualization (Fig. 3), and consists of an arrangement of multiple "hollow" concentric rings in a hexag-

© 1999 NRC Canada

Fig. 5. Near-equilibrium morphologies of asymmetric block copolymers in solution.

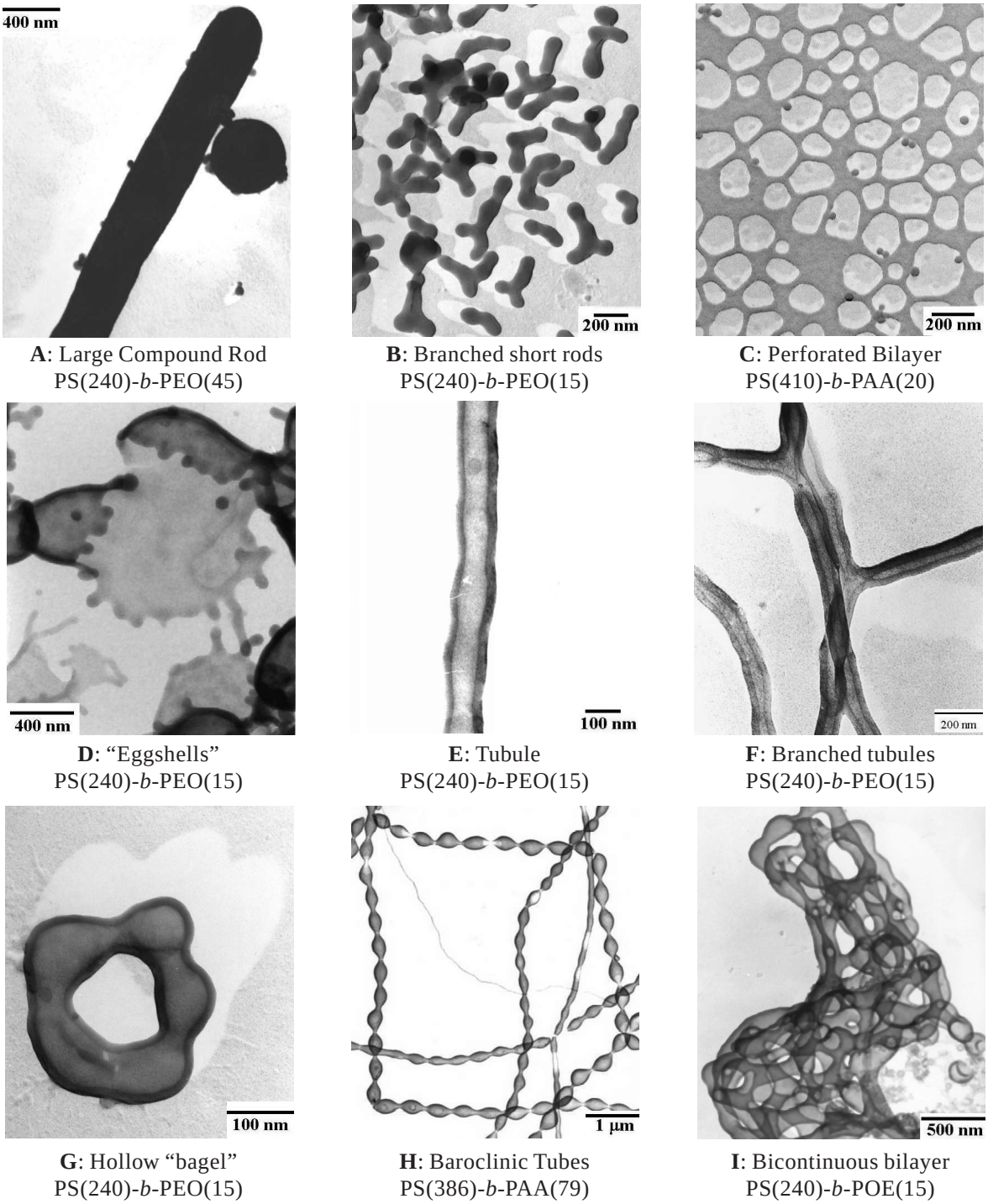

A: Large Compound Rod
PS(240)-*b*-PEO(45)

B: Branched short rods
PS(240)-*b*-PEO(15)

C: Perforated Bilayer
PS(410)-*b*-PAA(20)

D: "Eggshells"
PS(240)-*b*-PEO(15)

E: Tubule
PS(240)-*b*-PEO(15)

F: Branched tubules
PS(240)-*b*-PEO(15)

G: Hollow "bagel"
PS(240)-*b*-PEO(15)

H: Baroclinic Tubes
PS(386)-*b*-PAA(79)

I: Bicontinuous bilayer
PS(240)-*b*-POE(15)

onal pattern. The external surface of the aggregates, as well as the internal surface of the hollow hoops, consists of short PAA chains. The hoops are embedded in a PS matrix.

The addition of NaCl to the single vesicles allows for the decrease of the repulsion between them, since NaCl increases the electrostatic screening among the PAA chains, thus reducing the electrostatic repulsion. The vesicles, therefore, come into contact and form large compound vesicles (LCVs). Minimization of the surface free energy and that of chain stretching lead to the formation of HHH aggregates. The end-capping energy of a rod is replaced by a mesoscopic curvature energy on this size scale (i.e., several hundreds of nanometers), imposing the hoop morphology. Indeed, there are two ways of packing rods in a cylindrical space: one consists of a hexagonal packing of straight rods parallel to the direction of the principal axis in which case there is an end-capping energy penalty, resulting from the formation of hemispherical caps at the end of the rods. The other way avoids the end-capping energy penalty by forming hoops, but involves a curvature energy penalty. In the pres-

© 1999 NRC Canada

Fig. 6. Nonequilibrium trapped morphologies.

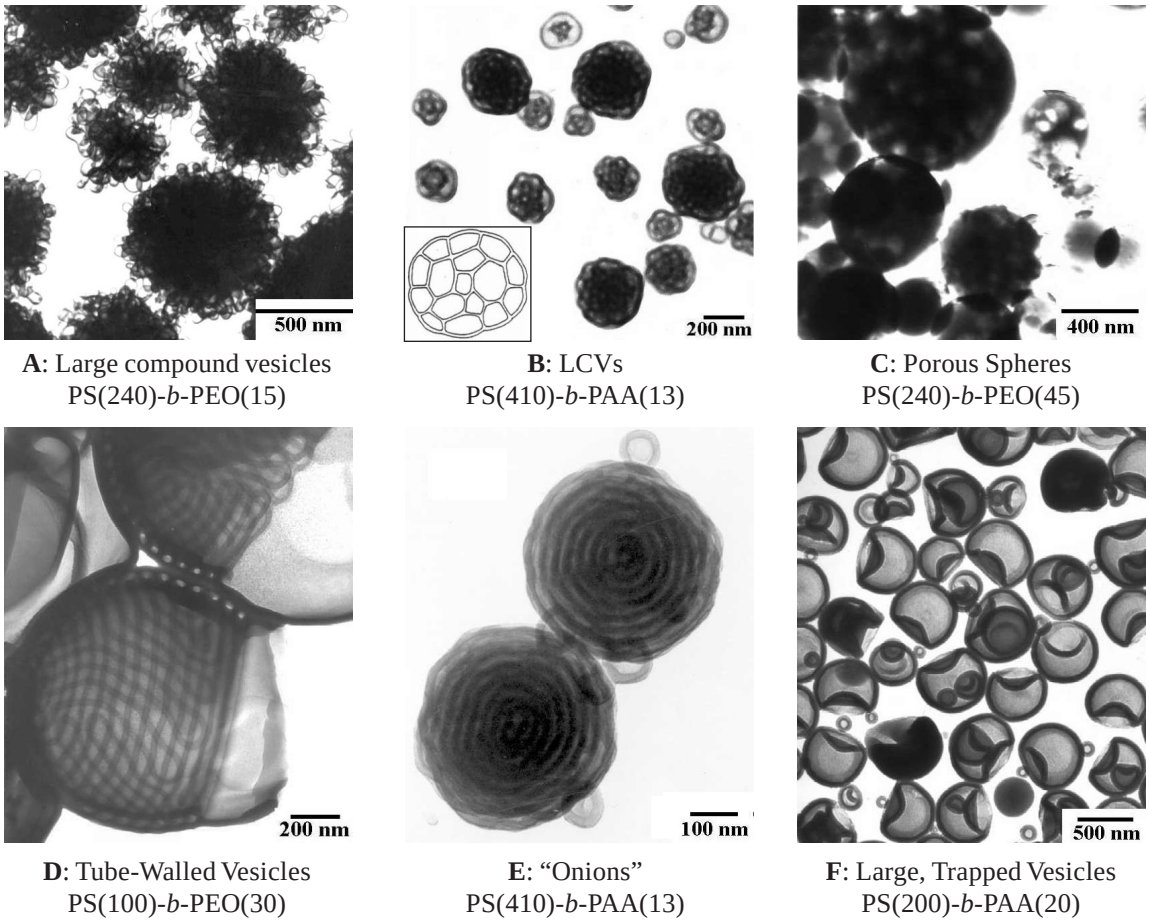

A: Large compound vesicles
PS(240)-*b*-PEO(15)

B: LCVs
PS(410)-*b*-PAA(13)

C: Porous Spheres
PS(240)-*b*-PEO(45)

D: Tube-Walled Vesicles
PS(100)-*b*-PEO(30)

E: "Onions"
PS(410)-*b*-PAA(13)

F: Large, Trapped Vesicles
PS(200)-*b*-PAA(20)

ent case, for particle sizes less than 1 μm, the end-capping energy is more important than the curvature energy, and hollow hoops are formed in a hexagonal pattern. This morphology may represent equilibrium as long as the particle is isolated, in analogy to the thermodynamic aspects of the vapor pressure of a small drop. Near a large surface, a small drop is unstable due to its higher vapor pressure, however, an isolated small drop can be considered to be at equilibrium.

Secondary copolymer aggregates present a further solution to the problem of how to arrange a large, insoluble block where the solubilizing block is very short. *Large compound micelles* (*LCMs*), illustrated in Fig. 3, bear a strong resemblance to bulk reverse micelles. For LCMs, islands of PAA chains are found in a continuous phase of core-forming polymer (PS) all of which is surrounded by the solvent-soluble PAA corona (1).

It should be noted that LCMs are highly polydisperse (Fig. 2*H*) and that they tend to settle due to gravity because of their large size. Figure 2*I* represents the internal morphology of an LCM obtained by microtoming a sample embedded in epoxy resin. The 60 nm sections were stained with CsOH(aq) and rinsed with deionized water to remove the excess CsOH. Staining increases the contrast between the PAA and PS regions. The elongated shape of the spheres is most likely due to the strong shear force when microtoming (7).

3.2. Aggregates of spheres

HHH is an excellent example of the end result of a morphological rearrangement in that vesicles are induced to form inverse rods on addition of salt. Another type of rearrangement involves coronal and core–chain interactions for simple spheres that, on addition of acid, yields predominantly one-dimensional "*pearl necklaces*" (Fig. 4*A*) in transition from spheres to rods (8). Drying conditions can yield *2D sheets of micelles* (Fig. 4*B* includes sheet folding), which might conceivably be precursors to lamellae[7]; when drying is performed at elevated temperatures (60–80°C), crack patterns develop, which give very large three-dimensional *birefringent needles* (Fig. 4*C*) that resuspend in water to give simple spheres if the PAA block is sufficiently long (1).

3.3. Near equilibrium

We have identified several other discrete morphologies that structurally resemble pure equilibrium morphologies. We are unable to unequivocally classify them; however, it seems clear that the aggregates are at least near equilibrium.

Large rod-shaped compound micelles (*LRCMs*) have been observed (Fig. 5*A*); we believe their internal structure to be identical to that of large compound micelles. Their lengths can reach several micrometers, and their diameters, several hundreds of nanometers (11).

[7] K. Yu. Unpublished data.

© 1999 NRC Canada

Branched short rods (Fig. 5*B*) may be the result of a situation in which the branching energy is comparable to the end-capping energy. Short branched rods may represent an intermediate structure between rods and bicontinuous rods (11).

The hexagonally perforated bilayer morphology obtained in the case of small molecule amphiphiles, where the pores are hexagonally arranged throughout a bilayer of molecules, has not yet been observed for asymmetric diblock copolymers in solution. However, we commonly isolated *disordered perforated bilayers* (Fig. 5*C*) (26).

The *eggshell* morphology (Fig. 5*D*) consists of a bent lamella, and therefore could possibly be an intermediate structure between a lamella and a vesicle (19).

Tubules (Fig. 5*E*) were rarely isolated with PS-*b*-PAA block copolymers except in low polarity solvents (18, 23), but were observed very often with nonionizable PS-*b*-PEO block copolymers (19). The wall thickness of the tubules is typically ca. 20 nm, and their outside diameter is ca. 100 nm. The length of the tubules can reach many micrometers. The difference between rods and tubules is that the latter are hollow. Tubules therefore belong to the family of bilayers; however, it is not yet clear whether they are true equilibrium morphologies.

Branched tubules (Fig. 5*F*) most probably occur when the free energy of the branching points is energetically comparable to the linear midsections. The diameters of branched tubules are similar to the diameters of the single tubules (19).

The "*bagel*" structure (Fig. 5*G*) is an example of many three-dimensional bilayer oddities (19). It can be described as a tubule in which the two ends are connected. This structure was occasionally observed among other bilayer structures for PS-*b*-PEO block copolymers, including structures with several holes that can be considered hollow "pretzels."

Baroclinic tubes (Fig. 5*H*) can be considered to be strings of attached vesicles, and are possibly an intermediary state between tubules and vesicles. This morphology was isolated for several polymers under radically different conditions (19, 23).

Bicontinuous bilayers (called "plumber's nightmare" in small molecule systems) are three-dimensional arrangements of bicontinuous tubes (11, 19). As in Fig. 5*I*, they are observed along with vesicles, which may be the building units for such complicated structures.

3.3.1. Structural parallels

There are many parallels to be drawn between the "solid" and bilayer structures. The theme of morphological transition seems universal among small molecule amphiphiles, copolymers in the bulk, copolymers at the air–water interface, and copolymers in solution. Similarly, there is an obvious parallel to be drawn between the sequence of spheres, pearl necklace, rods, doughnuts, and bicontinuous rods, and the sequence of vesicles, baroclinic tubules, tubules, hollow doughnuts (or "bagels"), and bicontinuous bilayers within the family of copolymers in solution. The formal similarity of the block copolymer bicontinuous architectures to small molecule amphiphilic bicontinuous cubic phases (3) is also noteworthy.

4.0. Nonequilibrium

The equilibrium and near-equilibrium morphologies previously discussed and demonstrated both schematically and in TEM images represent only a fraction of the aggregates we observe. We also observe kinetically trapped morphologies, metastable morphologies, and also various combinations of otherwise stable morphologies. The classification of some of the observed structures into one of these groups is by no means trivial. Furthermore, the definition of each distinct morphology is, in some cases, quite arbitrary, and these morphologies remain open to interpretation and further investigation.

Large compound vesicles, *LCVs*, (8, 12) some of which resemble compartmented spheres or aggregated soap bubbles (Figs. 6*A*, 6*B*) are perhaps among the best examples of a metastable morphology where clear classification is difficult. The inset in Fig. 6*B* is a schematic representation of the internal bilayer structure. Despite the fact that we can choose a polymer and conditions to create a suspension solely of LCVs, the polydispersity remains quite high, and the substructure is highly irregular. Essentially spherical LCVs as well as LCVs with clearly protruding vesicular structures have been observed. It is tempting to conclude that this morphology is in transition. PS(410)-*b*-PAA(13) at 1% initial concentration (w/w) in DMF forms spacious LCVs on the addition of water and very dilute HCl (225 μM). By increasing the HCl concentration to 253 μM, the LCVs formed are much more dense with smaller cavities. As the cavities get smaller, the aggregate begins to resemble more and more the inverse bicontinuous rod or even HHH morphology.

Porous spheres (Fig. 6*C*) are morphologically between LCMs and LCVs, though where exactly they fit in the continuum remains to be seen. The continuous phase is hydrophobic, and there are large cavities within each aggregate, which suggests a "Swiss cheese" analogy. These aggregates form not only from PS-*b*-PEO (11), but also from PS-*b*-PAA with additional homo-PS (25).

Tube-Walled Vesicles (*TWVs*), seen in Fig. 6*D*, are an interesting hybrid of bilayers and inverse rods (22, 27). Although vesicular, the walls are also constructed of hollow tubes. We have many examples of aggregates that follow this motif and believe these aggregates are formed in transition from vesicles to HHH, where for steric reasons the vesicles do not fuse but rather the wall thickens and hollow tubes develop.

"*Onions*"[8] and *entrapped large vesicles* (19) (Figs. 6*E*, 6*F*) are variations on a theme. Multilamellar vesicles have been observed in at least two of our polymer systems and are likely possible in the rest. TEM shadowing experiments confirm the sphericity of the onions that for PS(410)-*b*-PAA(13) are formed from a suspension of vesicles in DMF with 5% water on the addition of salt. Onions have also been observed from PS(260)-*b*-P(4VP.DecI) prepared from a dilute solution in THF by simply adding water dropwise to 50% (w/w) followed by dialysis. Interestingly, there is a precedent for diblock copolymer onions where symmetric diblock copolymers in the bulk have been shown to form

[8] H. Shen, L. Zhang, and A. Eisenberg. To be published.

© 1999 NRC Canada

Fig. 7. Mixed and combined morphologies.

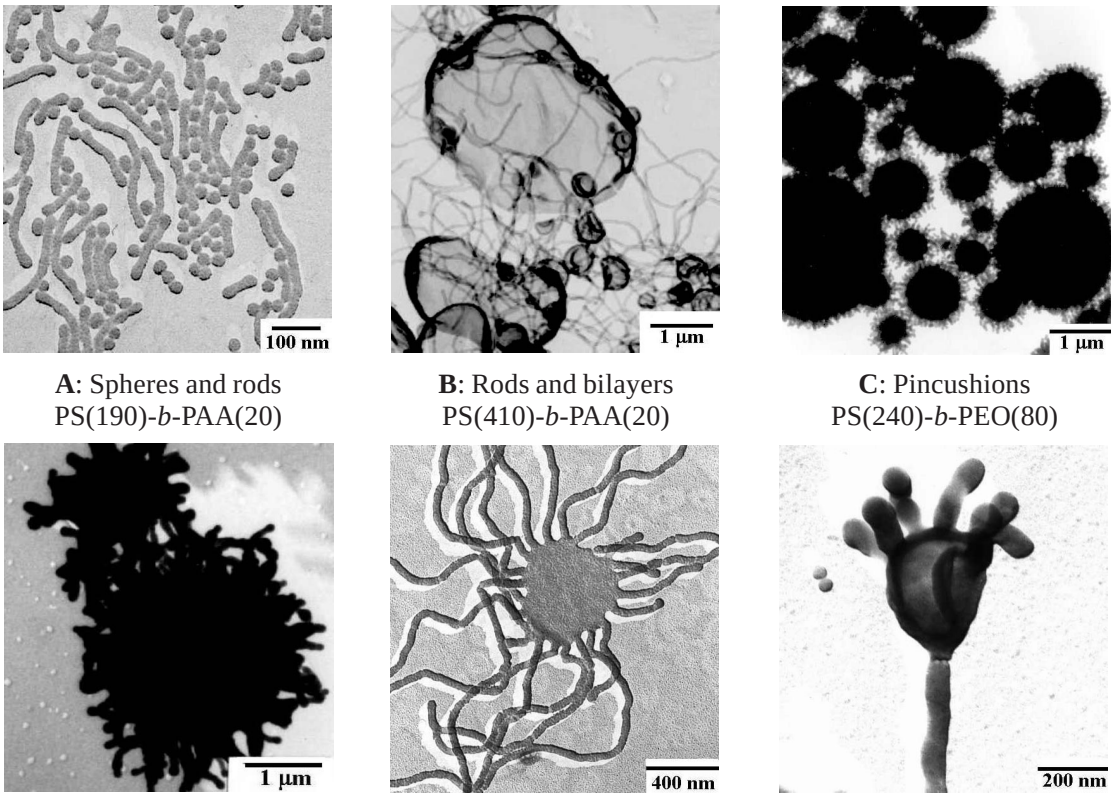

A: Spheres and rods
PS(190)-*b*-PAA(20)

B: Rods and bilayers
PS(410)-*b*-PAA(20)

C: Pincushions
PS(240)-*b*-PEO(80)

D: Long-pin pincushions
PS(240)-*b*-PEO(80)

E: Rods & Lamella
PS(190)-*b*-PAA(20)

F: Vesicle & attached rods
PS(240)-*b*-PEO(45)

multilamellar spheres when a polymer solution is sprayed, giving small drops that are subsequently dried (55).

An important feature of the large and trapped ("pregnant") vesicles is their size. While nearly monodisperse small vesicles (Fig. 2*F*) are often possible for asymmetrical diblock copolymers, under other conditions, we also observe very much larger vesicles that are usually quite polydisperse. Each large vesicle appears to have an indentation; however, this is an artifact of sample preparation, since each TEM grid is subjected to and released from high vacuum in shadowing, and there is plenty of opportunity for an imbalance of internal and external pressure.

Some samples under certain preparative conditions give *mixed morphologies*. Careful phase diagram work[9] demonstrates appreciably wide equilibrium coexistence regions between the pure sphere and pure rod as well as between the pure rod and pure bilayer regimes. Figures 7*A* and 7*B* are representative examples of such mixed morphologies.

Combined morphologies should be distinguished from the transitional morphologies such as TWVs in that for true combination, simple morphologies are fused. The structural elements of LCMs and rods combine to give a variety of "pincushions" (Figs. 7*C* and 7*D*) where the "pins" can be long or short (11). Rods and lamellae fuse to give "many-armed starfish" (Fig. 7*E*), and vesicles and rods are also occasionally joined (Fig. 7*F*).

4.1. Structurally biomimetic morphologies

It is interesting to note that many of these architectures and their combinations superficially resemble much more complicated biological and cellular systems. Consider the following pairs: lamellae and cell walls, tubules and cellular microtubules, rods and biological filaments, nucleoli and short branched rods or small pincushions, the smooth endoplasmic reticulum and the bicontinuous rod, and finally, microvilli vs. the pincushion. As with lipid-based biosystems, we observe budding transitions at the fusion points for combined morphologies of copolymer aggregates (19). A further point of similarity is the extreme versatility of both biolipids and asymmetric amphiphilic diblock copolymers. In summary, although the biomimetic analogy cannot be taken very far, what remains true is that nature chooses low-energy biological structures, and we observe low-energy architectures that, with small changes in environment, are subject to morphogenesis.

5.0. Conclusions

A morphological wonderland is made possible by asymmetric copolymers that mimic, on a macromolecular level, highly asymmetric small molecule amphiphiles. The critical components of the free energy of aggregation are the core–chain stretching, the coronal chain repulsion, and the interfacial energy. Any parameter that can be induced to modify

[9] H. Shen and A. Eisenberg. Phase Diagram II. Manuscript submitted to Macromolecules.

© 1999 NRC Canada

these terms has a morphogenic effect, and due to the slow kinetics of macromolecules, we have enormous control over their ultimate aggregated morphology. Furthermore, slow kinetics lend themselves to detailed study of morphological transitions better than the kinetics of small molecules, which are fast. The range of equilibrium morphologies is broad and follows, in a sense, the same sort of sequence as observed for small molecule systems as well as diblock copolymers in the bulk. The many near-equilibrium, nonequilibrium, and combined morphologies make unequivocal classification difficult, and furthermore, the definitions of the nonequilibrium morphologies are sometimes arbitrary.

What is a taxonomical nightmare, however, is an engineer's dream as the various morphologies formed by asymmetric diblock copolymers in solution have many potential applications. We are actively pursuing the use of our systems as drug-delivery vehicles (56), but other useful roles include nanoconductors (46) and insulators, nano-filters, timed and chemically induced release capsules (50) as well as nano-reactors (57, 58) for this rich morphological field.

Acknowledgements

N.S.C. and M.K.C. would like to thank Lifeng Zhang and Hongwei Shen for useful discussions during the preparation of this manuscript. A.E. is indebted to the Canadian Society for Chemistry for giving him the EWR Steacie Award for Chemistry, to Sciex Inc. for sponsoring the award, and to the Natural Sciences and Engineering Reseach Council of Canada (NSERC) for funding most of the research, with more recent contributions from the PRF. Most importantly, A.E. deeply is indebted to his current and former graduate students and postdoctoral co-workers, an outstanding group of scientists with whom he has had the good fortune to interact and who have enriched his life both academically and personally for nearly 40 years. For this most recent work, special thanks are due to Zhisheng Gao, Lifeng Zhang, Kui Yu, Yisong Yu, and Hongwei Shen for their seminal contributions.

References

1. L. Zhang and A. Eisenberg. Science (Washington, D.C.), **268**, 1728 (1995).
2. Z. Gao, S.K. Varshney, S. Wong, and A. Eisenberg. Macromolecules, **27**, 7923 (1994).
3. D.F. Evans and H. Wennerström. The colloidal domain: where physics, chemistry, biology and technology meet. VCH Publishers, New York. 1994.
4. (*a*) Z. Tuzar and P. Kratochvil. *In* Surface and colloid science. Vol. 15. *Edited by* E. Matijevic. Plenum Press, New York. 1993. pp. 1–83; (*b*) C. Price. *In* Developments in block copolymers. Vol 1. *Edited by* I. Goodman. Elsevier Applied Science, London. 1982. pp. 39–80; (*c*) J. Selb and Y. Gallot. *In* Developments in block copolymers. Vol 2. *Edited by* I. Goodman. Elsevier Applied Science, London. 1985. pp. 27–96.
5. L. Zhang, R. J. Barlow, and A. Eisenberg. Macromolecules, **28**, 6055 (1995).
6. M. Moffitt, K. Khougaz, and A. Eisenberg. Acc. Chem. Res. **29**, 95 (1996).
7. L. Zhang and A. Eisenberg. J. Am. Chem. Soc. **118**, 3168 (1996).
8. L. Zhang, K. Yu, and A. Eisenberg. Science (Washington, D.C.), **272**, 1777 (1996).
9. K. Yu and A. Eisenberg. Macromolecules, **29**, 6359 (1996).
10. M. Moffitt, L. Zhang, K. Khougaz, and A. Eisenberg. *In* Solvents and self-organization of polymers. *Edited by* S.E. Webber, P. Munk, and Z. Tuzar. Kluwer, Dordrecht. 1996. pp. 53–72.
11. K. Yu, L. Zhang, and A. Eisenberg. Langmuir, **12**, 5980 (1996).
12. L. Zhang and A. Eisenberg. Macromolecules, **29**, 8805 (1996).
13. L. Zhang, H. Shen, and A. Eisenberg. Macromolecules, **30**, 1001 (1997).
14. Y. Yu, L. Zhang, and A. Eisenberg. Langmuir, **13**, 2578 (1997).
15. H. Shen, L. Zhang, and A. Eisenberg. J. Phys. Chem. B, **161**, 4697 (1997).
16. Y. Yu and A. Eisenberg. J. Am. Chem. Soc. **119**, 8383 (1997).
17. L. Zhang, C. Bartels, Y. Yu, H. Shen, and A. Eisenberg. Phys. Rev. Lett. **79**, 5034 (1997).
18. Y. Yu, L. Zhang, and A. Eisenberg. Macromolecules, **31**, 1144 (1998).
19. K. Yu and A. Eisenberg. Macromolecules, **31**, 3509 (1998).
20. G. E. Yu and A. Eisenberg. Macromolecules, **31**, 5546 (1998).
21. L. Zhang and A. Eisenberg. Polym. Adv. Technol. **9**, 677 (1998).
22. K. Yu, C. Bartels, and A. Eisenberg. Macromolecules, **31**, 9399 (1998).
23. L. Desbaumes and A. Eisenberg. Langmuir, **15**, 36 (1999).
24. H. Shen, L. Zhang, and A. Eisenberg. J. Am. Chem. Soc. **121**, 2728 (1999).
25. L. Zhang and A. Eisenberg. J. Polym. Sci. B: Polym. Phys. **37**, 1469 (1999).
26. L. Zhang and A. Eisenberg. Macromolecules. **32**, 2239 (1999).
27. K. Yu, C. Bartels, and A. Eisenberg. Langmuir. In press.
28. L. Desbaumes and A. Eisenberg. Presented at the 73rd ACS Collord Surf. Sci. Symp. 1999. Full manuscript in preparation.
29. D.J. Mitchell, G.J.T. Tiddy, L. Waring, T. Bostock, and M.P. MacDonald. Chem. Soc. Faraday Trans. 1, **79**, 975 (1983).
30. M.J. Lawrence. Chem. Soc. Rev. 417 (1994).
31. M.W. Matsen and F.S. Bates. Macromolecules, **29**, 7641 (1996).
32. A.K. Khandpur, S. Förster, F.S. Bates, I.W. Hamley, A.J. Ryan, W. Bras, K. Almdhal, and K. Mortensen. Macromolecules, **28**, 8796 (1995).
33. J. Zhu, A. Eisenberg, and R.B. Lennox. J. Am.Chem. Soc. **113**, 5583 (1991); J. Zhu, R.B. Lennox, and A. Eisenberg. J. Phys. Chem. **96**, 4727 (1992).
34. M. Meszaros, A. Eisenberg, and R.B. Lennox. Faraday Disc. **98**, 283 (1994).
35. Y. Liu, J. Quinn, M. H. Rafailovich, J. Sokoloff, X. Zhong, and A. Eisenberg. Macromolecules, **28**, 6347 (1995); D. Nguyen, C.J. Clarke, A. Eisenberg, M.H. Rafailovich, J. Sokolov, and G.S. Smith. J. Appl. Cryst. **30**, 680 (1997).
36. J. Zhu, S. Hanley, A. Eisenberg, and R.B. Lennox. Die makromolecularle chemie, macromolecular symposia, 53, 211 (1992); S. Li, S. Hanley, I. Khan, S.K. Varshney, A. Eisenberg, and R.B. Lennox. Langmuir, **9**, 2243 (1993).
37. A. Halperin, M. Tirrell, and T.P. Lodge. Adv. Polym. Sci. **100**, 31 (1992).
38. P. Canham, T. Lally, C. Price, and R.B. Stubbersfield, J. Chem. Soc. Faraday Trans. 1, **76**, 1857 (1980); C. Price. Pure Appl. Chem. **55**, 1563 (1983); C. Price, E.K.M. Chan, A.L. Hudd, and R.B. Stubbersfield. Polym. Commun. **27**, 196 (1986).
39. Z. Zhou and B. Chu. Macromolecules, **21**, 2548 (1988); R. Hilfiker, D.Q. Wu, and B. Chu. J. Colloid Interface Sci. **135**, 573 (1990).
40. A.P. Gast, P.K. Vinson, and K.A. Cogan-Farinas. Macromolecules, **26**, 1774 (1993).
41. M. Antonietti, S. Heinz, M. Schmidt, and C. Rosenauer. Macromolecules, **27**, 3276 (1994).

© 1999 NRC Canada

42. K. Schillen, W. Brown, and R. M. Johnsen. Macromolecules, **27**, 4825 (1994); O. Glatter, G. Scherf, K. Schillen, and W. Brown. Macromolecules, **27**, 6046 (1994).
43. J.Q. Zhao, E.M. Pearce, T.K. Kwei, H.S. Jeon, P.K. Kesani, and N.P. Balsara. Macromolecules, **28**, 1972 (1995).
44. J.P. Spatz, S. Sheiko, and M. Möller. Macromolecules, **29**, 3220 (1996); J.P. Spatz, S. Mößmer, and M. Möller. Angew. Chem. Int. Ed. Engl. **35**, 1510 (1996).
45. A.V. Kabanov, T.K. Bronich, V.A. Kabanov, K. Yu, and A. Eisenberg. J. Am. Chem. Soc. **120**, 9941 (1998).
46. J. Massey, K.N. Power, I. Manners, and M.A. Winnik. J. Am. Chem. Soc. **120**, 9533 (1998).
47. J. Ding and G. Liu. Macromolecules, **30**, 655 (1997); G. Liu. Adv. Mater. **9**, 437 (1997).
48. A. Guo, G. Liu, and J. Tao. Macromolecules, **29**, 2487 (1996).
49. G. Liu, L. Qiao, and A. Guo. Macromolecules, **29**, 5508 (1996).
50. J. Ding and G. Liu. Chem. Mater. 10, 537, (1998); J. Phys. Chem. B, **102**, 6107 (1998).
51. C. Honda, K. Sakaki, and T. Nose. Polymer, **35**, 5309 (1994); K. Iyama and T. Nose. Macromolecules, **31**, 7356 (1998).
52. J. Brandrup and E. H. Immergut. *In* Polymer handbook. Vol. VII. 3rd ed. Wiley–Interscience, New York. 1989. pp. 38, 526; D.R. Lide. *In* CRC handbook of chemistry and physics. 78th ed. CRC Press, New York. 1997–1998. pp. 6–139.
53. A. Sodergard. J. Polym. Sci. A: Polym. Chem. **36**, 1805 (1998).
54. M. Tian, A. Qin, C. Ramireddy, S.E. Webber, P. Munk, Z. Tuzar, and K. Prochazka. Langmuir, **9**, 1741 (1993).
55. E.L. Thomas, J.R. Reffner, and J. Bellare. J. Colloq. Phys. **51**, C7, 363 (1990).
56. C. Allen, Y. Yu, D. Maysinger, and A. Eisenberg. Biconjugate Chem. **9**, 564 (1998).
57. M. Moffitt, H. Vali, and A. Eisenberg. Chem. Mater. **10**, 1021 (1998).
58. M. Moffitt and A. Eisenberg. Macromolecules, **30**, 4363 (1997).

© 1999 NRC Canada

Dicarbonylcyclopentadienyliridium, $(\eta\text{-}C_5H_5)Ir(CO)_2$, as a ligand

Faming Jiang, Kumar Biradha, Weng Kee Leong, Roland K. Pomeroy, and Michael J. Zaworotko

Abstract: The following complexes, in which $CpIr(CO)_2$ acts as a 2e donor ligand, have been prepared: $Cp(OC)_2IrW(CO)_5$ (**1**), $Cp(OC)_2IrRu(CO)_3(SiCl_3)_2$, $Cp(OC)_2IrOs(CO)_3(GeCl_3)(Cl)$ (**2**), $Cp(OC)_2IrOs(CO)_3(X)_2$ (X = Cl, Br (**3**), I). The characterization of the complexes included the crystal structures of **1**, **2**, and **3,** which reveal that all contain an unbridged metal–metal bond. The carbonyl ligands of **1** in solution undergo exchange on the NMR time scale above –40°C. With the exception of **2,** all the complexes dissociate in solution at room temperature, some rapidly so. Only in the case of **3** is an equilibrium with the dissociation products established. The results indicate that $CpIr(CO)_2$ is a weak ligand.

Key words: tungsten, osmium, iridium, binuclear.

Résumé : On a préparé les complexes suivants dans lesquels le $CpIr(CO)_2$ agit comme ligand donneur de $2e^-$: $Cp(OC)_2IrW(CO)_5$ (**1**), $Cp(OC)_2IrRu(CO)_3(SiCl_3)_2$, $Cp(OC)_2IrOs(CO)_3(GeCl_3)(Cl)$ (**2**), $Cp(OC)_2IrOs(CO)_3(X)_2$ (X = Cl, Br (**3**), I). La caractérisation des complexes inclus la détermination des structures cristallines des composés **1**, **2** et **3** qui révèlent la présence dans chacun d'une liaison métal–métal non pontée. En solution, au-dessus de –40°C, les ligands carbonyles du composé **1** subissent un échange à l'échelle de temps de la RMN. À l'exception du produit **2**, tous les complexes se dissocient en solution, à la température ambiante; dans certains cas, la dissociation est rapide. On n'a pu établir l'existence d'un équilibre avec les produits de dissociation que dans le cas du composé **3**. Les résultats indiquent que le $CpIr(CO)_2$ est un ligand faible.

Mots clés : tungstène, osmium, iridium, binucléaire.

[Traduit par la Rédaction]

Introduction

Work from this laboratory over the past 15 years has described complexes in which an 18-electron organometallic compound acts as a 2-electron donor ligand to a 16-electron organometallic fragment in much the same way as a conventional ligand such as PPh_3. Typical examples of molecules of this type are $(OC)_5OsOs(CO)_3(GeCl_3)(Cl)$ (1), $(L)(OC)_4OsM'(CO)_5$ (M′ = Cr, Mo, W; L = PR_3 (2), $CNBu^t$ (3)) and $(R_3P)(OC)_4MRu(CO)_3(SiCl_3)_2$ (M = Ru, Os, but not Fe) (4). These complexes contain an unbridged dative bond between two transition metal atoms, which are rare. Only two complexes in this class that are relevant to this study have been reported by others; these are $(\eta^5\text{-}C_5Me_5)[(Pr^iO)_3P](OC)IrRh(CO)[P(OPr^i)_3](Cl)$ (5*a*) and $(\eta\text{-}C_5H_5)(OC)_2RhPt(CO)(C_6F_5)_2$ (5*b*). Complexes with dative metal–metal bonds supported by bridging ligands are more common. Some recent examples are $[RhIr(\mu\text{-dppm})_2(Me)(CO)_3][CF_3SO_3]$ (dppm = $Ph_2PCH_2PPh_2$), $[Pt_2\{Rh(Cl)(CNXyl)\}(\mu\text{-dpmp})_2(CNXyl)][PF_6]_2$ (dpmp = $Ph_2PCH_2P(Ph)CH_2PPh_2$), $(OC)_3(XylNC)Fe(\mu\text{-dppm})Re(CO)_3(Br)$, $Ni(\mu\text{-}S_2fc)(PMe_2Ph)$ (S_2fc = -$(\eta\text{-}SC_5H_4)_2Fe$), and $Mo_2Pd_2(\mu_3\text{-pyphos})_4$ (pyphos = 6-diphenylphosphino-2-pyridonate) (6).

One of the first complexes of this type that we reported was $Cp^*(OC)_2IrW(CO)_5$ (Cp^* = $\eta^5\text{-}C_5Me_5$), which was of marginal stability (7). No attempt was made to prepare the analogous complex in which $(\eta\text{-}C_5H_5)Ir(CO)_2$ acted as a ligand. It was expected that this molecule would be a much weaker donor than its $\eta^5\text{-}C_5Me_5$ analogue. It was known that $Os(CO)_4(PR_3)$ (R = Me, OMe, Ph etc.) were far superior ligands than $Os(CO)_5$ (2). It is presumed that replacing a carbonyl ligand in $Os(CO)_5$ with a stronger σ donor PR_3 ligand increases the electron density on the Os atom and hence increases the dative metal–metal bond strength. More recent studies have, however, revealed that $Os(CO)_3(PR_3)_2$ compounds are weaker ligands than the monosubstituted compounds. For example, although it was possible to isolate $(Me_3P)_2(OC)_3OsW(CO)_5$, the chromium compound could not be prepared (8), whereas $(Me_3P)(OC)_4OsCr(CO)_5$ is an air-stable crystalline solid (2).

The failure to prepare $(Me_3P)_2(OC)_3OsCr(CO)_5$ was attributed to excessive steric interactions between the PMe_3 ligand, which would necessarily be *cis* to the OsCr bond and the radial carbonyls on the Cr atom. This suggested that

Received October 15, 1998.

F. Jiang and R.K. Pomeroy.[1] Department of Chemistry, Simon Fraser University, Burnaby, BC V5A 1S6, Canada.
K. Biradha and M.J. Zaworotko. Department of Chemistry, Saint Mary's University, Halifax, NS B3H 3C3, Canada.
W.K. Leong. Department of Chemistry, National University of Singapore, Lower Kent Ridge Rd., Singapore 119260, Republic of Singapore.

[1]Author to whom correspondence may be addressed. Telephone: (604) 291-3347. Fax: (604) 291-3765. e-mail: pomeroy@sfu.ca

© 1999 NRC Canada

Table 1. Analytical and infrared data[a] for the $CpIr(CO)_2$ derivatives.

Compound (L = $CpIr(CO)_2$)	%C (calcd.)	%H (calcd.)	(CO) cm^{-1}
(L)$W(CO)_5$ (**1**)	22.88(22.62)	0.94(0.79)	2077.5(m), 2047.5(m), 2014.5(m), 1931.0 (s), 1924.0(s), 1911.0(m)
(L)$Os(CO)_3(GeCl_3)(Cl)$ (**2**)	15.10(14.98)	0.67(0.63)	2122.0(w), 2113.0(vw, sh), 2080.5(m), 2055.5(s), 2047.0(vw, sh) 1999.5(m)
(L)$Ru(CO)_3(SiCl_3)_2$	15.76(15.65)	0.72(0.66)	2138.0(w), 2106.0(m), 2064.5(s), 2055.5(w, sh), 2031.0(vs)[b,c]
(L)$Os(CO)_3(Cl)_2$	18.13(18.24)	0.77(0.77)	2112.0(s), 2090.5(s), 2077.0(vw, sh), 2048.5(s), 2037.5 (vw, sh), 2021.5(m), 1999.0(m)
(L)$Os(CO)_3(Br)_2$ (**3**)	16.21(16.07)	0.69(0.67)	2109.0(s), 2088.5(s), 2076.5(vw, sh), 2047.5(vs), 2037.5 (vw, sh), 2021.0(m), 1998.5(m)
(L)$Os(CO)_3(I)_2$	[c]	—	2101.5(s), 2084.0(s) 2073.0(vw, sh) 2045.5 (vs), 2017(m) 1996.5(m)[c]

[a]In CH_2Cl_2.
[b]Cold solution.
[c]Unstable.

Table 2. NMR data for complexes of the $(Cp)Ir(CO)_2$ derivatives.

Compound	^1H NMR[a]	^{13}C NMR[b]	
(L = $CpIr(CO)_2$)		CO	Cp
(L)$W(CO)_5$ (**1**)	5.84	202.6(1C), 199.3(4C)[c] 167.4(2C)[d]	87.9
(L)$Os(CO)_3(GeCl_3)(Cl)$ (**2**)	6.10	180.1(2C), 172.4(1C), 165.0(2C)[e]	91.6
(L)$Os(CO)_3(Cl)_2$	5.98	Not determined	
(L)$Os(CO)_3(Br)_2$ (**3**)	6.00	172.1(2C), 165.9(1C), 164.6(2C)[d]	92.1

[a]In CD_2Cl_2.
[b]In CH_2Cl_2/CD_2Cl_2 (4:1).
[c]J_{WC} = 127.4Hz.
[d]Sample ^{13}CO enriched.
[e]C-13 in natural abundance.

complexes with the sterically undemanding $(\eta\text{-}C_5H_5)Ir(CO)_2$ molecule acting as a ligand might be more stable than originally thought. Herein, we report the results of an investigation into this possibility that shows that $CpIr(CO)_2$ can indeed act as ligand, but only with strong acceptor fragments can the resulting complexes be isolated.

Experimental section

Unless otherwise stated, manipulations of starting materials and products were carried out under a nitrogen atmosphere with the use of standard Schlenk techniques. Solvents were thoroughly dried before use. The iridium precursory complex, $(\eta\text{-}C_5H_5)Ir(CO)_2$, was prepared by the reaction of $[Ir(CO)_3(Cl)]_n$ with Tl[Cp] in thf, a minor modification of the original preparation (9). The $W(CO)_5$(thf) (2), *cis*-$Ru(CO)_4(SiCl_3)_2$ (10), $Os(CO)_5$ (11), and *cis*-$Os(CO)_4(I)_2$ (12) were synthesized by literature procedures. The preparations of *cis*-$Os(CO)_4(X)_2$ (X = Cl, Br) (13) and *cis*-$Os(CO)_4(GeCl_3)(Cl)$ (14) are modifications of literature procedures and are given below for completeness.

Infrared spectra were recorded on a Bomen MB100 spectrometer; nuclear magnetic resonance spectra were recorded on a Bruker WM400 or Bruker SY-100 spectrometer; microanalyses were determined by M.K. Yang of the Microanalytical Laboratory of Simon Fraser University. Infrared data and elemental analyses for the new compounds are given in Table 1; ^1H and $^{13}C\{^1H\}$ NMR data are given in Table 2. Because they are unstable, no attempt was made to obtain mass spectra of the new derivatives.

Preparation of *cis*-$Os(CO)_4(GeCl_3)(Cl)$

An autoclave (Parr Instrument Co.; 200 mL) was charged with a solution of $Os(CO)_5$ (~350 mg, ~0.94 mmol) and $GeCl_4$ (2.00 mL, 3.75 g, 17.5 mmol) in hexane (75 mL) and sealed. The autoclave was flushed three times with CO and then pressurized with CO (ultrapure grade; 90 atm (1 atm = 101.3 kPa)). It was then heated at 90°C for 24 h. The bomb was cooled and the gases vented; the pale yellow solution was removed from a white crystalline precipitate, which was washed with hexane and dried under a stream of nitrogen. The resulting solid *cis*-$Os(CO)_4(GeCl_3)(Cl)$ (0.53 g, ~95%) was pure by infrared spectroscopy. (The mother solution yielded 31 mg of yellow crystals that were impure product.) Infrared (warm hexane) ν_{CO}: 2173.5(w), 2106.0(vs), 2083.0(vw), 2061.0(s) cm^{-1}; (CH_2Cl_2) ν_{CO}: 2179.5(m), 2118.5(w,sh), 2110.0(vs), 2069.5(s) cm^{-1}.

Preparation of *cis*-$Os(CO)_4(Cl)_2$

A solution of $Os(CO)_4(H)_2$ in hexane (80 mL) was prepared by the reaction of OsO_4 (1.0 g, 3.9 mmol) in hexane

© 1999 NRC Canada

with CO–H_2 (3:1; total pressure 180 atm) at 170°C overnight (13). After slowly cooling the reaction vessel to room temperature and venting the gases, the solution was transferred to a Schlenk flask. The flask was cooled to 0°C and chlorine gently bubbled through the solution until no more precipitate formed. The solvent was removed from the white precipitate, which was washed with hexane and dried on the vacuum line to give *cis*-$Os(CO)_4(Cl)_2$ in essentially quantitative yield. Infrared (CH_2Cl_2) ν_{CO}: 2189.5(w), 2121.5(vs), 2099.5(ms), 2059.5(s) cm^{-1}. The bromo analogue, *cis*-$Os(CO)_4(Br)_2$, was synthesized in a similar manner. Infrared (warm hexane) ν_{CO}: 2177.0(vw), 2112.0(vs), 2089.0(ms), 2050.5(s) cm^{-1}; (CH_2Cl_2) ν_{CO}: 2182.5, 2115.5, 2098.0, 2059.5 cm^{-1}. The spectra of both derivatives are in excellent agreement with those reported in the literature (13).

Preparation of $Cp(OC)_2IrW(CO)_5$ (1)

A sample of $W(CO)_5$(thf) was prepared from $W(CO)_6$ (40 mg, 0.11 mmol) and the solvent reduced to ~0.5 mL on the vacuum line. A solution of $CpIr(CO)_2$ (~15 mg, ~0.045 mmol) in cold hexane (8 mL) was immediately added to the cold $W(CO)_5$(thf)–thf mixture and the resulting solution stored without stirring at –25°C for 19 h. The solvent was decanted from the solid that had formed, which was dried on the vacuum line. Unreacted $W(CO)_6$ was removed from the solid by sublimation under high vacuum at room temperature to a cold finger. The residue was dissolved in a minimum amount of CH_2Cl_2 at –20°C and quickly filtered through a short column of Florisil (2 × 1 cm) and the solvent was removed on the vacuum line at –20°C. As such, **1** was obtained in low yield as a yellow microcrystalline solid that was analytically pure. In a second preparation the Schlenk flask containing the reagents was kept at –25°C for 6.5 d, whereupon yellow crystals of **1** were obtained that were handpicked from black decomposition material to afford the sample used in the X-ray analysis.

Preparation of $Cp(OC)_2IrOs(CO)_3(GeCl_3)(Cl)$ (2)

A round-bottom flask (~100 mL; fitted with a Teflon valve) was charged with $CpIr(CO)_2$ (~55 mg; 0.18 mmol), *cis*-$Os(CO)_4(GeCl_3)(Cl)$ (100 mg, 0.194 mmol), and hexane (30 mL). The flask and contents were cooled to –196°C and the flask was evacuated; the solution was degassed with three freeze–pump–thaw cycles. The flask was allowed to warm to room temperature and then heated at 60°C for 3 h. The flask was cooled to room temperature and the solvent and excess reagents removed from an off-yellow precipitate. The precipitate was recrystallized from CH_2Cl_2–hexane to yield **2** (83 mg, 59%) as fawn-yellow crystals that appeared stable in air.

Preparation of $Cp(OC)_2IrRu(CO)_3(SiCl_3)_2$

A Schlenk tube with *cis*-$Ru(CO)_3(SiCl_3)_2$ (31 mg, 0.064 mmol) and $CpIr(CO)_2$ (15 mg; 0.048 mmol) in hexane (8.0 mL) was stored at –15°C for 6 d. After this period pale yellow crystals had formed along with gray decomposition material. The solvent and excess reagents were removed and the solids washed with a small volume of hexane and dried on the vacuum line. A sample of the yellow crystals of $Cp(OC)_2IrRu(CO)_3(SiCl_3)_2$ were immediately hand picked for chemical analysis and an infrared spectrum. The compound decomposes both in solution (in a period of minutes) and in the solid state (after several hours) under nitrogen at room temperature.

Preparation of $Cp(OC)_2IrOs(CO)_3(Br)_2$ (3)

A round-bottom flask with $CpIr(CO)_2$ (~40 mg; 0.13 mmol), *cis*-$Os(CO)_4(Br)_2$ (35 mg, 0.076 mmol), and hexane (20 mL) was evacuated and the solution degassed as described above. The reaction vessel was heated at 55–60°C for ~40 h. The flask was cooled and the solvent removed from a pale yellow precipitate. An IR spectrum of the precipitate indicated that it consisted mainly of **3**, but also of a small amount of $[Os(\mu\text{-}Br)(CO)_3(Br)]_2$. The precipitate was therefore subjected to chromatography on silica (12 × 1 cm) with CH_2Cl_2 as the eluant. The pale yellow fraction was collected, concentrated, and stored at –25°C to afford **3** (41 mg; 72%) as pale yellow crystals. The chloro analogue was prepared in a similar manner. Attempts to prepare the iodo compound gave a red-brown precipitate, an infrared spectrum of which (Table 1) indicated that it contained mainly $Cp(OC)_2IrOs(CO)_3(I)_2$, but the compound rapidly decomposed in solution to give $CpIr(CO)_2$ and $[Os(\mu\text{-}I)(CO)_3(I)]_2$ and could therefore not be further purified.

X-ray structure determination of 1, 2, and 3

The X-ray diffraction data for **1**–**3** were collected on Siemens SMART/CCD diffractometers. Data for **2** were collected with the sample at 20°C, the data for **1** and **3** were collected at –70°C with an LT-II low-temperature device. The diffraction data were corrected for absorption with the SADABS program. The program SHELXTL was used for the structure solution and the refinement was based on F^2 (15). The non hydrogen atoms in the structures were refined anisotropically. Hydrogen atoms were fixed in calculated positions and refined isotropically on the basis of the corresponding C atoms (U(H) = 1.2 U_{eq}(C)). Pertinent crystallographic data are given in Table 3; selected bond lengths and angles for **1**, **2**, and **3** are given in Tables 4–6. Supplementary tables of crystal structure and refinement data, atomic coordinates, thermal parameters, and bond lengths and angles for compounds **1, 2** and **3** have been deposited.[2]

Results and discussion

$Cp(OC)_2IrW(CO)_5$ (1)

Compound **1** was prepared in low yield by the addition of $CpIr(CO)_2$ to $W(CO)_5$(thf) in hexane at low temperature (eq. [1]).

[2] Copies of the supplementary material may be purchased from: The Depository of Unpublished Data, Document Delivery, CISTI, National Research Council of Canada, Ottawa, On K1A 0S2, Canada. Tables of crystal structure and refinement data, atomic coordinates, and bond lengths and angles have also been deposited with the Cambridge Crystallographic Data Centre and can be obtained on request from: The Director, Cambridge Crystallographic Data Centre, University Chemical Laboratory, 12 Union Road, Cambridge, CB2 1EZ, U.K.

© 1999 NRC Canada

Table 3. Crystal data and experimental details for compounds **1**, **2**, and **3**.

	1	**2**	**3**
Compound	$C_{12}H_5IrO_7W$	$C_{10}H_5Cl_4GeIrO_5Os$	$C_{10}H_5Br_2IrO_5Os$
Formula weight	637.21	801.93	747.36
Crystal system	Monoclinic	Monoclinic	Monoclinic
Space group	$P2_1/n^a$	$P2_1/n^a$	$P2_1/n^a$
Temperature (°C)	–70 ± 3	20 ± 2	–70 ± 3
a, Å	9.5131(6)	7.9666(1)	8.0754(5)
b, Å	12.5714(8)	13.7214(1)	13.6114(9)
c, Å	12.1197(8)	17.6252(3)	13.7135(9)
β, deg	99.4060(10)	102.6760(10)	102.7510(10)
Cell volume (Å^3)	1429.9(2)	1879.70(4)	1470.2(2)
z	4	4	4
Density, Mg m^{-3} calcd.	2.960	2.834	3.377
Abs. coeff. (mm^{-1})	17.363	15.975	23.121
Unique data ($I \geq 2\sigma$)	3332	4728	3410
Parameters	190	199	172
R^b	0.0338	0.0474	0.0506
$R_w{}^c$	0.0562	0.0960	0.1114

[a]Nonstandard setting of $P2_1/c$.

[b]$R_F = S(||F_o| - |F_c||)/S|F_o|$.

[c]$R_{wF} = [S(w(|F_o| - |F_c|)^2)/S(wF_o^2)]^{1/2} \cdot w = [s^2(F_o)^2 + kF_o^2]^{-1}$.

Table 4. Selected bond lengths and angles for **1**.

Bond lengths (Å)			
W—Ir	3.0418(4)	Ir—C(8)	2.242(7)
W—C(1)	2.038(8)	Ir—C(9)	2.236(7)
W—C(2)	2.034(8)	Ir—C(10)	2.258(7)
W—C(3)	2.044(8)	Ir—C(11)	2.233(7)
W—C(4)	2.041(8)	Ir—C(12)	2.271(7)
W—C(5)	1.945(7)		
Ir—C(6)	1.852(9)	C—O (range)	1.141(9)–1.162(8)
Ir—C(7)	1.857(8)	C—C (range)	1.40(1)–1.42(1)
Bond angles (deg)			
Ir-W-C(5)	169.6(2)	W-C-O (range)	175.9(7)–178.1(7)
Ir-W-C(1)	97.3(2)	C(5)-W-C (range)	85.6(3)–90.3(3)
Ir-W-C(2)	98.5(2)	*cis*-C-W-C (range)	86.9(3)–92.0(3)
Ir-W-C(3)	85.8(2)	C(6)-Ir-C(7)	91.3(4)
Ir-W-C(4)	85.8(2)	Ir-C(6)-O(6)	175.0(7)
C(6)-Ir-W	79.9(2)	Ir-C(7)-O(7)	175.7(7)
C(7)-Ir-W	80.9(2)	C-C-C(Cp) (range)	107.2(7)–109.2(7)
C(6)-Ir-C(7)	91.3(4)		

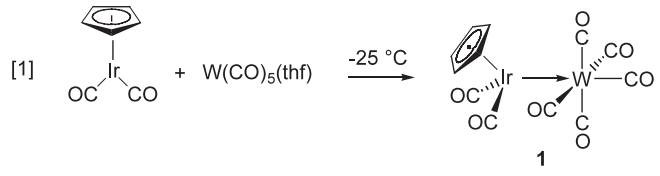

It is a yellow crystalline solid that can be handled for short periods in air, but turns black upon prolonged exposure. In hexane at room temperature **1** decomposed within 20 min to $CpIr(CO)_2$, $W(CO)_6$, and, presumably, tungsten metal. In this respect it is somewhat less stable than $Cp^*(OC)_2IrW(CO)_5$ (**1***) (7). Attempts to prepare $Cp(OC)_2IrCr(CO)_5$ were unsuccessful.

A view of the structure of **1** as determined by X-ray crystallography is shown in Fig. 1; selected bond length and angle data are given in Table 4. As can be seen from the figure, the $CpIr(CO)_2$ molecule is bound to the $W(CO)_5$ unit via an unbridged IrW bond. Given the 18 and 16 electron counts of the respective Ir and W moieties, the bond is considered a dative interaction (Ir →W). The length of the IrW bond in **1** (3.0418(4) Å) is only marginally shorter than that in **1*** (3.054(1) Å) and, as discussed previously for **1*** (7), this is almost 0.2 Å longer than IrW lengths found in cluster compounds of these elements. As in other complexes with dative metal–metal bonds (2–4) and the other structures described here, the carbonyls on the donor metal atom lean toward the acceptor atom. In **1** the appropriate W-Ir-C(CO) angles are 79.9(2)° and 80.9(2)°. (If the Ir moiety had a typical 3-legged piano stool geometry these angles would be ~90°.) Another interesting feature of the geometry adopted by **1** is that the carbonyls on the Ir atom are eclipsed with

© 1999 NRC Canada

Table 5. Selected bond lengths and angles for **2**.

Bond lengths (Å)			
Os—Ir	2.8702(5)	Ir—C(4)	1.87(2)
Os—Ge	2.421(1)	Ir—C(5)	1.84(2)
Os—Cl(1)	2.430(2)	Ir—C(6)	2.21(1)
Ge—Cl(2)	2.133(4)	Ir—C(7)	2.22(2)
Ge—Cl(3)	2.149(5)	Ir—C(8)	2.22(1)
Ge—Cl(4)	2.151(4)	Ir—C(9)	2.21(1)
Os—C(1)	1.95(1)	Ir—C(10)	2.26(1)
Os—C(2)	1.85(1)		
Os—C(3)	1.94(1)	C—O (range)	1.12(1)–1.16(1)
		C—C (range)	1.32(2)–1.42(2)
Bond angles (deg)			
Ir-Os-Ge	173.85(4)	C(4)-Ir-C(5)	92.3(9)
Ir-Os-Cl(1)	89.91(6)	Os-Ge-Cl (range)	116.2(1)–117.8(2)
Ir-Os-C(1)	87.6(4)	Cl-Ge-Cl (range)	100.5(2)–101.3(3)
Ir-Os-C(2)	93.7(4)	Os-C-O (range)	176(1)–178(1)
Ir-Os-C(3)	91.2(4)	Ir-C(4)-O(4)	174(1)
Os-Ir-C(4)	82.0(4)	Ir-C(5)-O(5)	176(2)
Os-Ir- C(5)	85.8(4)	C-C-C(Cp) (range)	105(2)–109(2)

Table 6. Selected bond lengths and angles for **3**.

Bond lengths (Å)			
Os—Ir	2.8540(7)	Ir—C(6)	2.25(2)
Os—Br(1)	2.585(2)	Ir—C(7)	2.27(2)
Os—Br(2)	2.574(2)	Ir—C(8)	2.24(1)
Os—C(1)	1.87(1)	Ir—C(9)	2.29(1)
Os—C(2)	1.91(2)	Ir—C(10)	2.23(2)
Os—C(3)	1.92(2)		
Ir—C(4)	1.87(1)	C—O (range)	1.12(2)–1.17(2)
Ir—C(5)	1.83(2)	C—C (range)	1.39(2)–1.41(2)
Bond angles (deg)			
Ir-Os-C(3)	176.1(4)	C(3)-Os-Br(1)	85.0(4)
Ir-Os-Br(1)	92.45(4)	C(3)-Os-Br(2)	87.9(5)
Ir-Os-Br(2)	89.33(4)	C(1)-Os-C(2)	94.0(6)
Ir-Os-C(1)	89.4(4)	C(1)-Os-C(3)	93.3(5)
Ir-Os-C(2)	91.3(4)	C(2)-Os-C(3)	91.4(6)
C(4)-Ir-Os	83.2(5)	Os-C-O (range)	176(1)–178(1)
C(5)-Ir-Os	83.9(4)	Ir-C(4)-O(4)	172(1)
C(4)-Ir-C(5)	90.8(6)	Ir-C(5)-O(5)	175(1)
Br(1)-Os-Br(2)	92.22(5)	C-C-C(Cp) (range)	107(1)–108(1)

Fig. 1. Molecular structure of $Cp(OC)_2IrW(CO)_5$ (**1**).

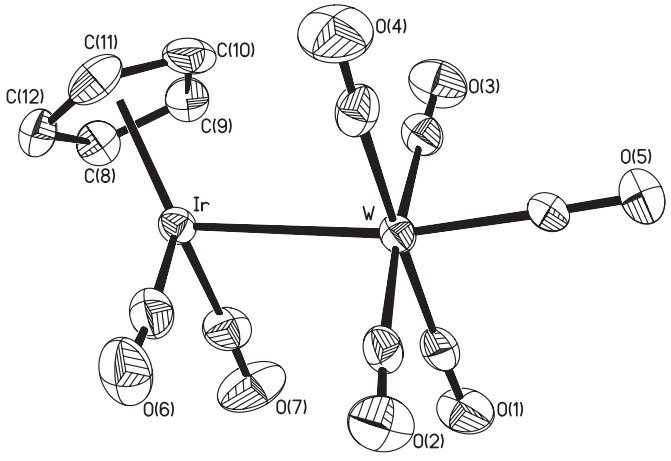

two CO ligands on the W atom. The torsion angles between C(1)—W and Ir—C(7), and between C(2)—W and Ir—C(6), are 1.1° and 6.1°, respectively. This is also observed in **1*** but not in other complexes with dative metal–metal bonds (e.g., the structures of **2** and **3** described below).

Shown in Fig. 2 are variable temperature $^{13}C\{^1H\}$ NMR spectra (carbonyl region) of **1** in CD_2Cl_2/CH_2Cl_2. The spectrum at –40°C indicates that the solution structure of **1** is the same as that in the solid state provided there is rapid rotation about the IrW bond. The sample was prepared from ^{13}CO-enriched $W(CO)_5$(thf) (2) and it is apparent that CO exchange has occurred so that the ^{13}CO label is scrambled over all carbonyl sites in the molecule. On warming the solution above –40°C, the carbonyl signals broaden and collapse to the base line (Fig. 2), consistent with the carbonyl exchange taking place on the NMR time scale. This exchange also oc-

© 1999 NRC Canada

Fig. 2. Variable temperature $^{13}C\{^1H\}$ NMR spectra (CO region) of **1** in CH_2Cl_2/CD_2Cl_2 (4:1). The peak marked with an asterisk is due to $W(CO)_6$.

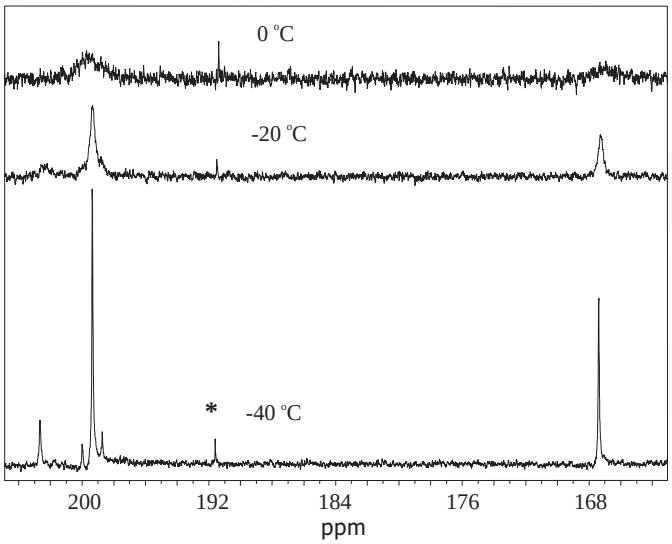

curs in **1*** such that the carbonyl resonances are virtually collapsed to the base line in the corresponding ^{13}C NMR spectrum at –40°C (7). In other words, the barrier to carbonyl exchange in **1*** is much lower than that in **1**. A similar difference in the barriers to carbonyl exchange is observed in $(\eta^5\text{-}C_5R_5)IrOs_2(CO)_9$ (R = H, Me) (16). For the latter molecules, it was proposed that the pentamethylcyclopentadienyl ligand increases the electron density at the Ir atom, which expands the Ir 5*d* orbitals due to the increased screening of the nuclear charge; this in turn results in better overlap with the empty π^* orbitals on the carbonyl ligands on the adjacent osmium atoms and hence lowers the energy needed to form the presumed intermediate with bridging carbonyls. The same arguments can be used to rationalize the difference in the barriers to CO exchange in **1** and **1***.

$Cp(OC)_2IrOs(CO)_3(GeCl_3)(Cl)$ (2)

Compound **2** was isolated in moderate yield by the route depicted in eq. [2]. The yellow-fawn crystals of **2** showed no visible sign of decomposition after 2 d of exposure to air.

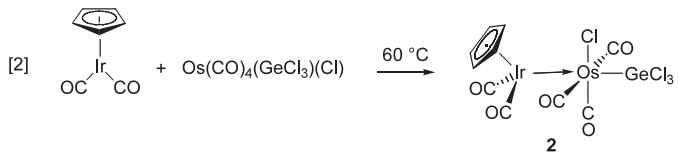

Similarly, using infrared and NMR spectroscopy, **2** showed no decomposition in CH_2Cl_2 solution (under nitrogen) after 24 h. We had previously found that the $Os(CO)_3(GeCl_3)(Cl)$ fragment is a superior acceptor to the $W(CO)_5$ unit for $Os(CO)_4(L)$ (L = CO, $CNBu^t$) ligands. For example, whereas $(OC)_5OsOs(CO)_3(GeCl_3)(Cl)$ is an air-stable crystalline solid that is stable in solution to at least 60°C (1), we have been unable to prepare $(OC)_5OsW(CO)_5$ (2).

Fig. 3. Molecular structure of $Cp(OC)_2IrOs(CO)_3(GeCl_3)(Cl)$ (**2**).

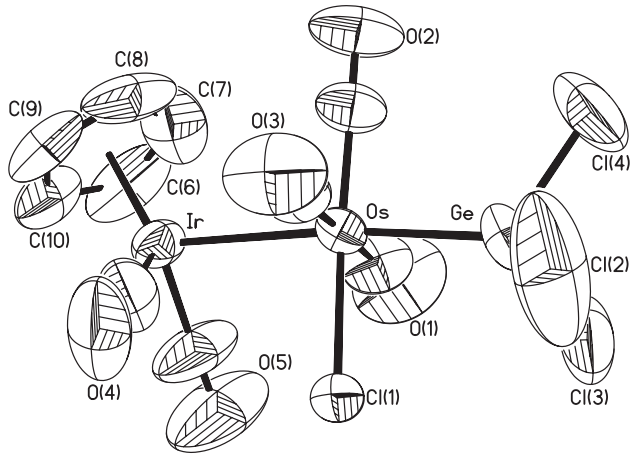

The infrared spectrum of **2** in CH_2Cl_2 in the carbonyl stretching region exhibits shoulders on the main peaks (Table 1). We attribute this to the presence of two conformers of **2**, one with the Cp ligand in a *cis* orientation to the Cl ligand, the other with a *trans* configuration of these ligands. The $^{13}C\{^1H\}$ NMR spectrum of **2** in CH_2Cl_2/CD_2Cl_2 after an overnight accumulation of spectral data revealed no other species present (Table 2). The ^1H NMR spectrum of **2** in CD_2Cl_2 at –90°C exhibited a singlet for the Cp ligand that was only slightly broadened from that at ambient temperature. Barring accidental degeneracy, the spectra indicate that at –90°C there is still rapid rotation on the NMR time scale about the IrOs bond in **2**.

A view of the structure of **2** is shown in Fig. 3; the structure was determined at 20°C and consequently the thermal ellipsoids are much larger than those for **1** and **3** (see below), which were determined at –70°C. The length of the (unbridged) IrOs bond in **2** is 2.8702(2) Å. We have found that unbridged dative metal–metal bonds are comparable in length to corresponding nondative bonds in dinuclear complexes, but longer than corresponding bonds in cluster compounds (2–4, 17). There does not appear to be any report of a dinuclear complex with an unbridged nondative OsIr bond length to compare with that in **2** and, as expected, the length is significantly longer than those in osmium–iridium carbonyl cluster compounds. For example, in $(\eta^5\text{-}C_5Me_5)(OC)IrOs_2(CO)_8$ the OsIr distances are 2.7902(5) and 2.8124(5) Å (16).

We have previously argued that because of the repulsive $d\pi - d\pi$ interactions between the two transition metal atoms, complexes with dative metal–metal bonds will be more stable, with strong acceptor ligands in both sites *trans* to the bond if steric interactions allow (4). In compound **2** we believe that the $GeCl_3$ unit has excellent acceptor ability, as proposed for the $SiCl_3$ ligand in $(R_3P)(OC)_4MRu(CO)_3(SiCl_3)_2$ complexes mentioned in the Introduction (4). The structural parameters found for the $Os(CO)_3(GeCl_3)(Cl)$ grouping are not significantly different from those in $(OC)_5OsOs(CO)_3(GeCl_3)(Cl)$ (1).

We have found that $Ru(CO)_3(SiCl_3)_2$ is also superior to $W(CO)_5$ as an acceptor fragment (4, 18). Addition of $CpIr(CO)_2$ to *cis*-$Ru(CO)_4(SiCl_3)_2$ in hexane at –15°C produced yellow crystals along with decomposition products. The handpicked crystals gave a satisfactory chemical analy-

© 1999 NRC Canada

Fig. 4. The $^{13}C\{^1H\}$ NMR spectrum (CO region) of $Cp(OC)_2IrOs(CO)_3(Br)_2$ (^{13}CO in natural abundance) in CH_2Cl_2/CD_2Cl_2 (4:1) after an overnight accumulation of spectral data. The peaks marked with an asterisk are due to dissociation products (see eq. [4] and text).

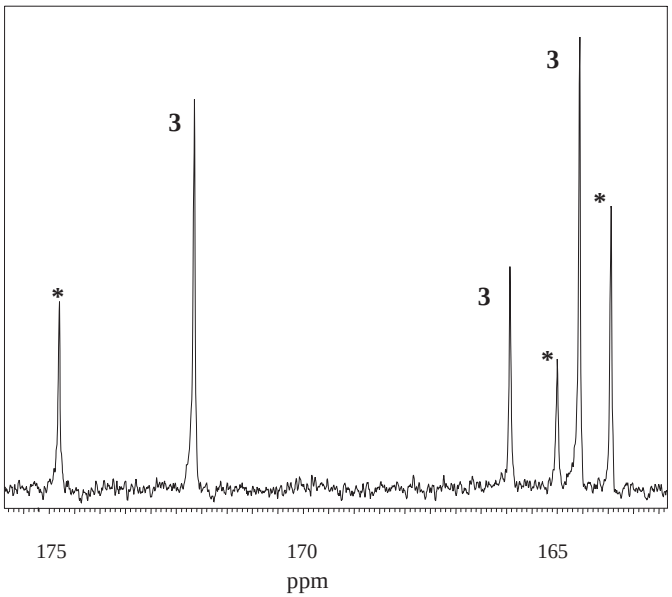

sis and an infrared spectrum (Table 1) expected for $Cp(OC)_2IrRu(CO)_3(SiCl_3)_2$, but the compound was too unstable in the solid or in solution (under nitrogen) to characterize further. Because of the smaller covalent radius of Ir compared to Os, dative metal–metal bonds involving iridium are shorter than similar bonds where the donor atom is Os. For example, whereas the IrOs distance in **2** is 2.870 Å, the OsOs lengths in the independent molecules of $(OC)_5OsOs(CO)_3(GeCl_3)(Cl)$ are in the range 2.916(2)–2.931(1) Å (1); in $(Me_3P)(OC)_4OsRu(CO)_3(SiCl_3)_2$ the OsRu lengths are 2.984(1) and 3.014(1) Å (4). For this reason, it may be that the hydrogen atoms of the cyclopentadienyl ligand in $Cp(OC)_2IrRu(CO)_3(SiCl_3)_2$ make close contact with the $SiCl_3$ ligand, which is by necessity *cis* to the IrOs bond and leads to destabilization of the complex.

$Cp(OC)_2IrOs(CO)_3(X)_2$ (X = Cl, Br: 3, I)

The chloro and bromo (**3**, eq. [3]) derivatives were prepared in good yield by using a procedure similar to that for synthesizing **2**. The compounds were isolated as pale yellow

[3] 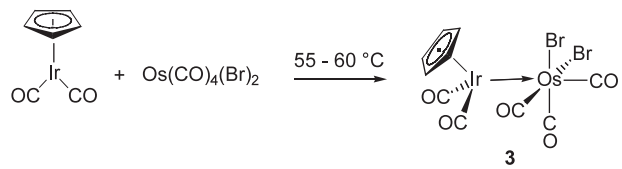

Fig. 5. Molecular structure of **3**.

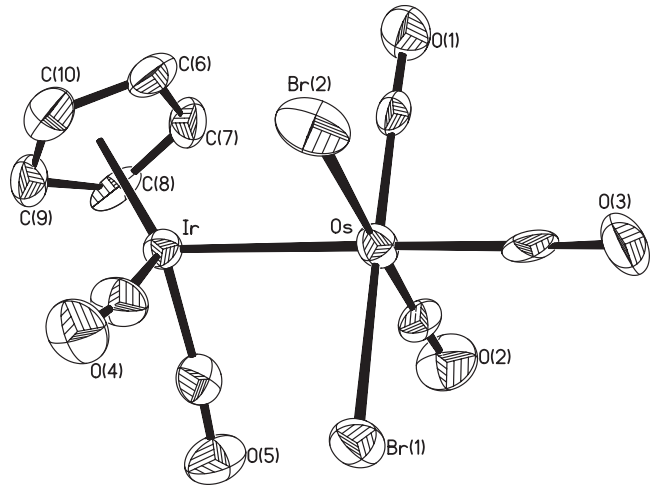

crystals that appeared stable in air. In these reactions the product precipitates from the (nonpolar) hexane solution, which prevents the dissociation described below. In the corresponding reaction of $CpIr(CO)_2$ with *cis*-$Os(CO)_4(I)_2$ a precipitate also formed that gave an infrared spectrum containing bands (Table 1) consistent with the presence of $Cp(OC)_2IrOs(CO)_3(I)_2$, but also bands due to $[Os(\mu\text{-}I)(CO)_3(I)]_2$, identified by analogy to the chloro (19, 20) and ruthenium analogues (20, 21).[3] When the solution was allowed to stand at room temperature there was essentially complete decomposition to $CpIr(CO)_2$ and $[Os(\mu\text{-}I)(CO)_3(I)]_2$ after 1 h.

When **3** was stirred in CH_2Cl_2 (or CD_2Cl_2) there was conversion over 24 h to an apparent equilibrium mixture containing **3** and $CpIr(CO)_2$ and $[Os(\mu\text{-}Br)(CO)_3(Br)]_2$ (eq. [4]), in an approximate 1:1 ratio, by ^1H NMR spectroscopy.

[4] 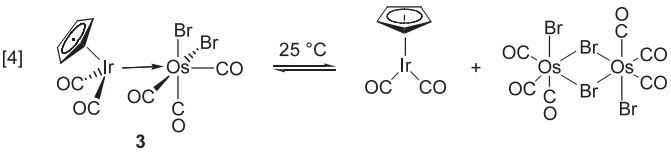

(The bromo dimer was similarly identified by comparison of its infrared spectrum[3] with those of the chloro and ruthenium analogues (19–21).) The ratio was unchanged, by infrared spectroscopy, after standing for a further 24 h. The ^{13}C NMR spectrum of **3** (^{13}C in natural abundance) in CH_2Cl_2/CD_2Cl_2 after an overnight accumulation of spectral data at room temperature showed additional peaks besides those due to **3** at 175.0 and 85.8 assigned to $CpIr(CO)_2$ (22) and signals at 165.0 and 163.9 (in a 1:2 ratio) assigned to $[Os(\mu\text{-}Br)(CO)_3(Br)]_2$ (Fig. 4). The signals due to the dissociation products were barely visible in the corresponding spectrum of **3** (^{13}CO enriched)[4] after ~1 h of data accumula-

[3] Infrared for $[Os(\mu\text{-}X)(CO)_3(X)]_2$, ($CH_2Cl_2$) ν_{CO} (X = Cl): 2135(s), 2061(s, br) (20); (X = Br): 2130.5(m), 2057.5(s, br); (X = I): 2119.5(s), 20045.0(s, br) cm^{-1}.

[4] The sample of **3** enriched with ^{13}CO was prepared from ^{13}CO-enriched $Os(CO)_4(Br)_2$, which was in turn synthesized by heating a hexane solution of unenriched $Os(CO)_4(Br)_2$ under ^{13}CO (99%; 2 atm) overnight. The ^{13}C NMR spectrum indicated all carbonyl sites in **3** were equally enriched, consistent with CO exchange on the synthetic time scale.

© 1999 NRC Canada

tion. The equilibrium depicted in eq. [4] is similar to the equilibrium that we have observed for $(OC)_5OsRu(CO)_3(SiCl_3)(Br)$ (18).

The chloro analogue of **3**, $Cp(OC)_2IrOs(CO)_3(Cl)_2$, similarly dissociated in CH_2Cl_2 at room temperature at approximately the same rate as **3**, but there was apparently also decomposition of $[Os(\mu\text{-}Cl)(CO)_3(Cl)]_2$ so that after 24 h an infrared spectrum of the reaction solution showed bands due to $CpIr(CO)_2$, trace amounts of $Cp(OC)_2IrOs(CO)_3(Cl)_2$, and $[Os(\mu\text{-}Cl)(CO)_3(Cl)]_2$, plus unidentified products.

These preliminary results indicate that $Os(CO)_3(Br)_2$ is a better acceptor than the iodo analogue, as might be expected from the electronegativities of the two halogens. That the acceptor abilities of the $Os(CO)_3(X)_2$ (X = Cl, Br) fragments toward $CpIr(CO)_2$ are similar may be rationalized by invoking more $p\pi$ donation from the halogen atoms to the $d\pi$ orbitals of osmium for the chloro fragment compared to the bromo analogue. This would decrease the Lewis acidity of $Os(CO)_3(Cl)_2$ and offset the superior electron-withdrawing ability of the Cl atoms. This is of course similar to the arguments that have been used to explain why BF_3 is a weaker Lewis acid than BCl_3 or BBr_3 (23). Consistent with the view that Cl $p\pi$ donation to Os $d\pi$ orbitals is significant is that the Os—CO length *trans* to the Cl atom in **2** (1.85(1) Å) is considerably shorter than the Os—C distances (1.94(1), 1.95(1) Å) to the carbonyl ligands that are in a mutually *trans* configuration (Table 5).

The structure of **3** reveals (Fig. 5), once again, an unbridged metal–metal bond. The length of the IrOs bond in **3** is 2.8540(7) Å, which is 0.016 Å shorter than the corresponding length in **2**. From a ground state viewpoint, therefore, the IrOs bonds in **2** and **3** are of comparable strength. It has been proposed, however, that transition state stabilization effects are important in determining the lability of dative metal–metal bonds (4, 24). Besides the bond lengths mentioned above, the IrOs distance in **3** may be compared to the OsOs distance of 2.9104(6) Å in the related $(OC)_5OsOs(CO)_3(Cl)_2$ recently prepared in this laboratory. An interesting feature of the structure of **3** is that both the Br atoms are *cis* to the IrOs bond rather than one Br atom *trans* to the bond. Because the Br ligand is a π donor, the electronically preferred position is expected to be *cis* to the dative bond (see above). An alternative view is that the *fac* arrangement of ligands on the acceptor moiety allows each carbonyl ligand to be *trans* to a poor π acceptor ligand and avoids two CO groups competing for the same electron density on the central Os atom. The Os—Br distances in **3** (2.574(2), 2.585(2)Å) are essentially the same as the Os—Br lengths of 2.592(3) Å in $Os_3(CO)_{10}[P(OMe_3)_3]_2(Br)_2$ (25).

Conclusions

The results of this study indicate that $CpIr(CO)_2$ is a weak ligand and only with 16e organometallic fragments that are strong acceptors can complexes be isolated. Except for $Cp(OC)_2IrOs(CO)_3(GeCl_3)(Cl)$, the complexes dissociate in solution, which results in most cases in decomposition. The ligating ability of $CpIr(CO)_2$ therefore appears comparable to that of $Os(CO)_5$ (1, 2). Since $Os(CO)_4(PR_3)$ compounds are better ligands than $Os(CO)_5$ (2*a*, 18), molecules of the type $CpIr(CO)(PR_3)$ with small P ligands will probably act as better donor ligands than the parent $CpIr(CO)_2$. It should also be pointed out that the acceptor fragments employed in this investigation were neutral five-coordinate fragments and it may be that complexes of $CpIr(CO)_2$ with fragments positively charged or of lower coordination numbers (with fewer steric interactions) might be more stable. The stable $(\eta^5\text{-}C_5Me_5)[(Pr^iO)_3P](OC)IrRh(CO)[P(OPr^i)_3](Cl)$ (5*a*) and $(\eta\text{-}C_5H_5)(OC)_2RhPt(CO)(C_6F_5)_2$ (5*b*) complexes mentioned in the Introduction are consistent with the latter suggestion.

Acknowledgments

We thank the Natural Sciences and Engineering Research Council of Canada, the National University of Singapore, and St. Mary's University for financial support.

References

1. F.W.B Einstein, R.K Pomeroy, P. Rushman, and A.C. Willis. J. Chem. Soc. Chem. Commun. 854 (1983).
2. H.B. Davis, F.W.B. Einstein, P.G. Glavina, T. Jones, R.K. Pomeroy, and P. Rushman. Organometallics, **8**, 1030 (1989).
3. J.A. Shipley, R.J. Batchelor, F.W.B. Einstein, and R.K. Pomeroy. Organometallics, **10**, 3620 (1991).
4. F. Jiang, J.L. Male, K. Biradha, W.K. Leong, R.K. Pomeroy, and M.J. Zaworotko. Organometallics, **17**, 5810 (1998).
5. (*a*) A.A. Del Paggio, E.L. Muetterties, D.M. Heinekey, V.W. Day, and C.S. Day. Organometallics,**5**, 575 (1986); (*b*) R. Usón, J. Forniés, P. Espinet, C. Fortuño, M. Tomas, and A.J. Welch. J. Chem. Soc. Dalton Trans. 3005 (1988).
6. (*a*) F.H. Antwi-Nsiah, O. Oke, and M. Cowie. Organometallics, **15**, 1042 (1996); (*b*) T. Tanase, H. Toda, K. Kobayashi, and Y. Yamamoto. Organometallics, **15**, 5272 (1996); (*c*) M. Knorr, P. Braunstein, A. Tiripicchio, and F. Ugozzoli. J. Organomet. Chem. **526,** 105 (1996); (*d*) S. Takemoto, S. Kuwata, Y. Nishibayashi, and M. Hidai. Inorg. Chem. **37**, 6428 (1998); (*e*) K. Mashima, A. Fukumoto, H. Nakano, Y. Kaneda, K. Tani, and A. Nakamura. J. Am. Chem. Soc. **120**, 12 151 (1998).
7. F.W.B. Einstein, R.K. Pomeroy, P. Rushman, and A.C. Willis. Organometallics, **4**, 250 (1985).
8. F. Jiang, H.B. Davis, K. Biradha, R.K. Pomeroy, and M.J. Zaworotko. Organometallics. Submitted.
9. (*a*) E.O. Fischer and K.S. Brenner. Z. Naturforsch. Teil B, **17**, 774 (1962); (*b*) S.A. Garder, P.S. Andrews, and M.R. Rausch. Inorg. Chem. **12**,2396 (1973); (*c*) J.K. Hoyano and W.A.G. Graham. Personal communication.
10. R.K. Pomeroy and K.S. Wijesekera. Inorg. Chem. **19**, 3729 (1980).
11. P. Rushman, G.N. van Buuren, M. Shiralian, and R.K. Pomeroy. Organometallics, **2**, 693 (1983).
12. L. Vancea and W.A.G. Graham. J. Organomet. Chem. **134**, 219 (1977).
13. F. L'Eplattenier and F. Calderazzo. Inorg. Chem. **6**, 2092 (1967).
14. J. L. Male. Ph.D. Thesis, Simon Fraser University. 1996.
15. G.M. Sheldrick. SHELXTL, Siemens, Madison, Wis. 1995.
16. A. Riesen, F.W.B. Einstein, A.K. Ma, R.K. Pomeroy, and J.A. Shipley. Organometallics, **10**, 3629 (1991).
17. F.W.B. Einstein, M.C. Jennings, R. Krentz, R.K. Pomeroy, P. Rushman, and A.C Willis. Inorg. Chem. **26**, 1341 (1987).
18. M.M. Fleming, R. K. Pomeroy, and P. Rushman. J. Organomet. Chem. **278**, C33 (1984).

© 1999 NRC Canada

19. (*a*) R. Psaro and C. Dossi. Inorg. Chim. Acta, **77**, L255 (1983); (*b*) M.J. Cleare and W.P. Griffith. J. Chem. Soc. A, 372 (1969); (*c*) M.I. Bruce, M. Cooke, M. Green, and D.J. Westlake. J. Chem. Soc. A, 987 (1969).
20. R.K. Pomeroy. Ph.D. Thesis, University of Alberta. 1971.
21. (*a*) E. Benedetti, G. Braca, S. Sbrana, F. Salvetti, and B. Grassi. J. Organomet. Chem. **37**, 361 (1972); (*b*) B.F.G. Johnson, R.D. Johnston, and J. Lewis. J. Chem. Soc. A, 792 (1969).
22. B.E. Mann and B.F. Taylor. ^{13}C NMR data for organometallic compounds. Academic Press, London. 1981. p. 180.
23. N.N. Greenwood and A. Earnshaw. Chemistry of the elements. Butterworth–Heinemann, Oxford. 1997. p. 196.
24. H. Nakatsuji, M. Hada, and A. Kawashima. Inorg. Chem. **31**, 1740 (1992).
25. Y.-S. Chen, S.-L. Wang, R.A. Jacobson, and R.J. Angelici. Inorg. Chem. **25**, 1118 (1986).

© 1999 NRC Canada

Butenolide annelation using a manganese(III) oxidation. A synthesis of chromolaenin (Laevigatin)

Ayhan S. Demir, Zuhal Gercek, Nese Duygu, A. Cigdem Igdir, and Omer Reis

Abstract: A procedure was developed for the annelation of a butenolide to an aromatic ketone that highlighted a manganese(III) oxidation of an aromatic ketone. The merit of this procedure was illustrated in a synthesis of Chromolaenin (Laevigatin) (**1**) from 4,7-dimethyl-1-tetralone (**2c**). Oxidation of tetralone and indanone with manganese(III) acetate in the presence of chloro- or bromopropionic acid or their Mn(II) salts furnished a α-haloesters **3a**–**d**. An Arbuzov reaction of haloesters with triethylphosphite and an intramolecular Horner–Watsworth–Emmons cyclization of the resulting phosphonate gave butenolide **5a**, **b** in 77–79% yield. This methodology was also applied to 4,7-dimethyl-1-tetralone (**2c**), and the corresponding butenolide **6** is synthesized in 85% yield, which was then converted to Chromolaenin (**1**) using DIBAL-H.

Key words: chromolaenin (Laevigatin), manganese(III) acetate oxidation, aromatic ketones, butenolide annelation, lactone, Horner–Watsworth–Emmons cyclization, Arbuzov reaction.

Résumé : On a développé une nouvelle méthode pour l'annélation d'un buténolide à une cétone aromatique qui souligne l'utilité du manganèse(III) pour l'oxydation d'une cétone aromatique. L'intérêt de cette méthode est illustré par une synthèse de la chromolaénine (laevigatine) (**1**) à partir de la 4,7-diméthyl-1-tétralone (**2c**). L'oxydation de la tétralone et de l'indanone par l'acétate de manganèse(III) en présence d'acide chloro- ou bromopropanoïque ou de leurs sels de Mn(II) conduit aux α-halogénoesters **3a**–**d**. Une réaction d'Arbuzov des halogénoesters avec le phosphite de triéthyle et une cyclisation intramoléculaire d'Horner–Watsworth–Emmons sur le phosphonate qui en résulte fournit les buténolides **5a**, **b** avec un rendement de 77–79%. Cette méthodologie a aussi été appliquée à la 4,7-diméthyl-1-tétralone pour conduire au buténolide **6** correspondant (avec un rendement de 85%) qui a été transformé en chromolaenine (**1**) à l'aide de DIBAL-H.

Mots clés : chromolaenine (laevigatine), oxydation à l'aide d'acétate de manganèse(III), cétones aromatiques, annélation en buténolide, lactone, cyclisation de Horner–Watsworth–Emmons, réaction d'Arbuzov.

[Traduit par la Rédaction]

Chromolaenin (Laevigatin) **1** was first isolated in an optically active form of unknown absolute configuration from *Chromolaena laevigata* (Lam.) by King and Robinson (1). Few examples are published for the synthesis of this natural product. Kano et al. (2) started from 4,7-dimethyl-1-tetralone and converted it to 3-alkylideneazetidin-2-one. Isomerization of double bond, epoxidation followed by the reaction with methanesulfonic acid afforded butenolides, which were then converted to a furane ring using DIBAL-H. Juo and Herz (3) synthesized chromolaenin in six steps via photooxygenation of a naphthalene derivative. Racemic and chiral synthesis was established from Chavan et al. (4) starting from racemic and optically pure 4,7-dimethyl-1-tetralone via formation of β,γ-unsaturated ester. Osmylation and oxidative conversion of β,γ-unsaturated acid gave a butenolide, which was reduced to chromolaenin.

In our previous work, we developed a procedure for the acyloxylation of enones in α′-position using manganese(III) acetate in combination either with manganese(II) carboxylate or carboxylic acids, and a general procedure was developed for the annelation of a butenolide to an enone that highlighted a manganese(III) oxidation of enone (5). Using manganese(III) oxidation, we report in this work the simple butenolide anellation on indanone and tetralone as a model system and application of this to an efficient synthesis of chromoleanin.

In an initial study shown in Scheme 1, the oxidation of indanone **(2a)** with 4 equiv. of manganese(III) acetate in combination with 6 equiv. of manganese(II) 2-bromopropanoate, prepared according to the literature procedure (6), or 12 equiv. of 2-bromopropanoic acid furnished the desired 2-(2-bromopropanoyloxy) ketone **3a** in 71–78% yield. Using chloropropanoic acid instead of bromopropanoic acid afforded chloropropanoyloxy derivative **3b** in 68–77% yield. A negligible amount of α-acetoxylated ketone was also obtained in this reaction (5–7% according to GLPC), but separation of the 2-acetoxy and 2-(2-bromo- and chloropropanoyloxy) ketones **3a**, **b** was readily accomplished by column chromato-

Received November 4, 1998.

A.S. Demir,[1] Z. Gercek, N. Duygu, A.C. Igdir, and O. Reis. Department of Chemistry, Middle East Technical University, 06531 Ankara, Turkey.

[1]Author to whom correspondence may be addressed. Telephone: 90-312 2103242. Fax: 90-312 210 1280. e-mail: asdemir@metu.edu.tr

© 1999 NRC Canada

Scheme 1. (*a*) $Mn(OAc)_3$ and $CH_3CHBrCOOH$ or $Mn(CH_3CHBrCOO)_2$, benzene, reflux; (*b*) $P(OC_2H_5)_3$, heat; (*c*) NaH, THF; (*d*) DIBAL-H, THF.

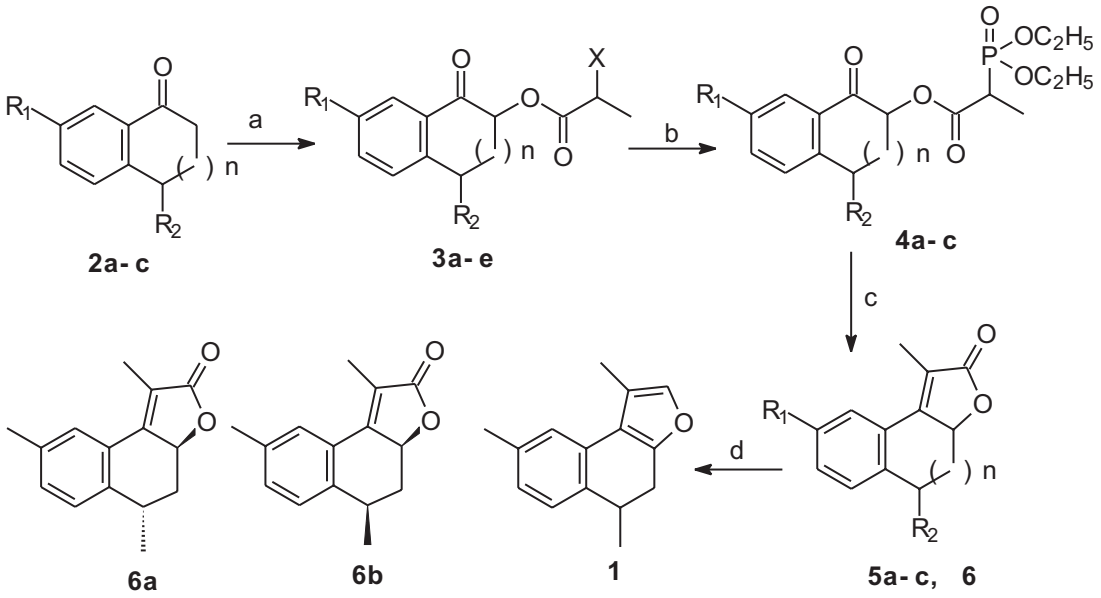

Table 1. The synthesis of butenolides.

Ketone	Acyloxy ketone **3**						Phosphonate **4**	Furanone **5**
2	*n*	R_1	R_2	X	Mn(II) salt Yield (%)	Free acid Yield (%)	Yield (%)	Yield (%)
a	0	H	H	Br	71	78	79	77
					a		**a**	**a**
a	0	H	H	Cl	68	77	67	
					b		**a**	
b	1	H	H	Br	74	81	81	79
					c		**b**	**b**
b	1	H	H	Cl	67	78	77	
					d		**b**	
c	1	CH_3	CH_3	Br	73	82	83	85
					e		**c**	**c**

graphy. Using the same reaction, starting with tetralone, the corresponding 2-(2-bromopropanoyloxy) derivatives **3c**, **d** are synthesized in good yield (Table 1). The chloro- and bromopropanoyloxy ketones are mainly semisolids and show multiplets of X-CH between δ 4.0 and 4.5.

The highest yield for haloacyloxylation of the ketones was obtained with 12 equiv. of halo acid or 6 equiv. of its Mn(II) salt. Using the free acid gives higher yield than the corresponding Mn(II) salt. Decreasing the bromoacetic acid component increases the yield of acetoxy ketones.

In connection with ongoing research (5), we found that the source of manganese(III) acetate is very important for the yield of the reactions. The anhydrous manganese(III) acetate used in this oxidation was prepared from manganese(II) nitrate and acetic anhydride and dried using phosphorus pentoxide under vacuum prior to use (5*k*, *l*).

The Arbuzov reaction of **3a** with an excess of triethylphosphite proceeded in 79% yield to give the phosphonate **4a**. An intramolecular Horner–Wadsworth–Emmons cyclization of **4a** with sodium hydride in THF gave the desired 3-methyl-8,8a-dihydro-1-oxa-cyclopenta[*a*]inden-2-one (**5a**) in 77% yield. The spectroscopic and physical properties of **5a** are identical in all respects with the reported values (mp 135–137°C, lit. (7) 136–137°C). Using the same reaction sequence starting with tetralone (**2b**), the corresponding 1-methyl-4,5-dihdro-3a*H*-naphtho[2,1-*b*]furan-2-one (**5b**) is synthesized via bromo- and chloroacetoxy ketone **3c**, **3d** and phosphonate **4b** (Scheme 1). The spectroscopic and physical properties of **5b** are identical in all respects with the reported values (mp 152–154°C, lit. (4, 8) 153–154.5°C). With the successful completion of this study, attention was focused on the synthesis of chromolaenin using the same procedure. As shown in Scheme 1, the manganese(III) oxidation of 4,7-dimethyltetralone (**2c**) using manganese(III) acetate in combination with 2-bromopropanoic acid led regioselectively to the bromopropanoyloxy ketone **3e** in 82% yield as a diastereomeric mixture. The use of manganese(II) salt furnished **3e** in 73% yield. The ^1H NMR spectrum of **3e** shows complex splitting from the α-hydrogen at δ 5.16. Completion of the synthesis of chromolaenin involved

© 1999 NRC Canada

an Arbuzov reaction of 2-bromopropanoyloxyketone **3e** with an excess triethylphosphite to give the corresponding phosphonate **4c** in 83% yield. The CH-P proton shows complex splitting around 3.1 ppm. The cyclization of **4c** with sodium hydride in THF furnished the corresponding butenolide **6** as a mixture of diastereomers **6a** and **6b** in 85% yield in a 4:3 ratio, as determined by NMR (9). The ^{1}H NMR spectra of the two diastereomers exhibited signals for α-CH, and CH_3 at different fields. α-CH appears as a ddq at δ 4.91 (J = 12.6, 4.5, 1.7 Hz, **6b**) and δ 5.21 (J = 12.2, 4.1, 1.5 Hz, **6a**). CH_3 protons appear at δ 1.46 (**6b**) and 1.42 (**6a**) (d, J = 7.2 Hz). Since the stereochemistry at the newly created centers was of no consequence as far the synthesis of Chromolaenin is concerned, as they would be destroyed in the subsequent steps, no attempt was made to separate the isomers.

Reduction of butenolide **6** with DIBAL-H (10) in THF at –40°C provided chromolaenin **1** in 83% yield. The spectroscopic and physical properties of chromolaenin thus obtained were found to be identical in all respects with the reported values for **1**, obtained from natural sources (mp 65–67°C, lit. (1) 65–66°C).

As we suggest earlier (5), by the acyloxylation of aromatic ketones, the initial reaction between the manganese(III) acetate and bromopropanoic acid or its manganese(II) salt lead to a mixed manganese(III) complex, which has both acetate and bromopropanoyloxy ligands. This mixed manganese(III) complex may interact with the ketone to form a metal enolate analogous to the enol-lead triacetate intermediate proposed by Corey and Schaefer (11) for the α-acetoxylation reaction of ketones. In accordance with the works of Willams and Hunter (12) and Snider et al. (13), the oxidation of an enolate by Mn(III) yields a α-keto radical (14), which is trapped oxidatively with carboxylate to yield the product.

This work has demonstrated the novel application of manganese(III) oxidation for the synthesis of butenolide from aromatic ketones to the synthesis of chromolaenin. The reactions provide a quick, easy, and mild approach to functionalized butenolide and furane ring systems. This method gives an entry for the chiral synthesis of **1**, starting from known optically pure ketone **2c**.

Experimental

All reagents were of commercial quality, and reagent quality solvents were used without further purification. IR spectra were determined on a Philips model PU9700 spectrometer. ^{1}H NMR spectra were determined on a Bruker AC 80 MHz FT and Varian 200 MHz spectrometers. GC analyses were made on a HP 5890 gas chromatography.

General procedure (representative example) for 2-[(2-chloropropanoyl)oxy] ketone

A mixture of manganese(III) acetate (2.12 g, 10 mmol) and 2-chloropropanoic acid (3.24 g, 30 mmol) or manganese(II) 2-chloropropionate (60 mmol) in benzene (40 mL) was refluxed for 1 h in a Dean–Stark trap. The mixture was cooled, and ketone (2.5 mmol) was added. The mixture was refluxed for 6–12 h, and the reaction was monitored by TLC on silica-gel (EtOAc/hexane 1:3), then cooled to 25°C, diluted with EtOAc, washed with 1 M aqueous HCl, saturated aqueous $NaHCO_3$, and brine, and dried over anhydrous $MgSO_4$. The crude product was purified on preparative thick-layer chromatography silica-gel F-254 plates or by flash column chromatography (15) (EtOAc/hexane 1:3).

General procedure for Arbuzov reaction

A mixture of 2-[(2-chloropropanoyl)oxy] ketone (2.5 mmol) and triethyl phosphite (1.3 g, 8 mmol) was refluxed under argon for 3 h. The reaction was monitored by TLC on silica-gel (EtOAc/hexane 1:1). During this time, an additional triethyl phosphite (1.3 g, 8 mmol) was added at 1 h intervals. The excess triethyl phosphite was removed by distillation under vacuum, and the residue was chromatographed on preparative thick-layer chromatography silica-gel F-254 plates (EtOAc/hexane 1:1) to afford the phosphonate.

General procedure for annulation

To a suspension of NaH (0.096 g, 4 mmol) (washed with pentane) in anhydrous THF (25 mL) at 25°C under argon was added phosphonate (2.5 mmol) dropwise. The mixture was refluxed for 1h and then quenched with H_2O and extracted with EtOAc. The organic layer was washed with brine and dried over anhydrous $MgSO_4$. The residue was chromatographed on preparative thick-layer chromatography silica-gel F-254 plates (EtOAc/hexane 1:5) to afford the butenolide.

*2-[(2-Bromopropanoyl)oxy]indanone (**3a**)*: Semisolid. IR (film): 1770, 1750, 1610 cm^{-1}. ^{1}H NMR (200 MHz, $CDCl_3$) δ: 1.66 (m, CH_3, 3H), 3.14–3.50 (m, 2H, CH_2), 4.03 (m, 1H, CH), 5.41 (m, 1H, CH), 7.41–7.39 (m, 2H), and 7.66–7.75 (m, 2H, Ar-H). Anal. calcd. for $C_{12}H_{11}BrO_3$ (283.12): C 50.91, H 3.92; found: C 51.23, H 4.12.

*2-[(2-Chloropropanoyl)oxy]indanone (**3b**)*: Yellowish semisolid. IR (film): 1770, 1740, 1610 cm^{-1}. ^{1}H NMR (200 MHz, $CDCl_3$) δ: 1.72 (m, 3H,CH_3), 3.03–3.58 (m, 2H, CH_2), 4.51 (m, 1H, CH), 5.51 (m, 1H, CH), 7.42–7.47 (m, 2H), and 7.64–7.75 (m, 2H, Ar-H). Anal. calcd. for $C_{12}H_{11}ClO_3$ (238.67): C 60.38, H 4.64; found: C 60.11, H 4.61.

*2-[(2-Bromopropanoyl)oxy]tetralone (**3c**)*: Semisolid. IR (KBr): 1760, 1680, 1625 cm^{-1}. ^{1}H NMR (200 MHz, $CDCl_3$) δ: 1.71 (m, 3H, CH_3), 2.16–2.48 (m, 2H, CH_2), 3.01–3.24 (m, 2H, CH_2), 4.11 (m, 1H, CH), 5.41 (m, 1H, CH), 6.65–6.96 and 7.06–7.78 (m, 4H, Ar-H). Anal. calcd. for $C_{13}H_{13}BrO_3$ (297.15): C 52.55, H 4.41; found: C 52.88, H 4.27.

*2-[(2-Chloropropanoyl)oxy]tetralone (**3d**)*: Yellowish solid; mp 112–114°C. IR (KBr): 1765, 1680, 1620 cm^{-1}. ^{1}H NMR (200 MHz, $CDCl_3$) δ: 1.73 (m, 3H, CH_3), 2.15–2.48 (m, 2H, CH_2), 3.01–3.25 (m, 2H, CH_2), 4.52 (m, 1H, CH), 5.38 (m, 1H, CH), 6.65–6.96 and 7.08–8.01 (m, 4H, Ar-H). Anal. calcd. for $C_{13}H_{13}ClO_3$ (252.69): C 61.79, H 5.18; found: C 61.76, H 5.34.

© 1999 NRC Canada

*2-[(2-Bromopropanoyl)oxy]-4,7-dimethyltetralone (**3e**)*: Colorless semisolid. IR (film): 1760, 1660, 1610 cm^{-1}. ^1H NMR (200 MHz, $CDCl_3$) δ: 1.31 (m, 3H, CH_3), 1.62 (m, 3H, CH_3), 2.12–2.44 (m, 2H, CH_2), 2.30 (s, 3H, CH_3), 3.30 (m, 1H, CH), 4.02 (m, 1H, CH), 5.16 (m, 1H, CH), 7.12–7.49 (m, 3H, Ar-H). Anal. calcd. for $C_{15}H_{17}BrO_3$(325.20): C 55.40, H 5.27; found: C 55.78, H 5.11.

*2-(2-(Diethoxyphosphinoxyl)propanoyloxy)indanone (**4a**)*: Colorless semisolid. IR (film): 1740, 1635, 1610 cm^{-1}. ^1H NMR (200 MHz, $CDCl_3$) δ: 1.12–1.40 (m, 6H, OCH_2CH_3, $2CH_3$), 1.92 (m, 3H, CH_3), 2.85–3.25 and 3.32–3.78 (m, 2H, CH_2), 3.80–4.29 (m, 5H, OCH_2, $2CH_2$, CH), 5.52 (m, 1H, CH), 7.42–7.48 (m, 2H), and 7.64–7.75 (m, 2H, Ar-H). HRMS calcd. for $C_{16}H_{21}O_6P$: 340.1076; found: 340.1074.

*2-(2-(Diethoxyphosphinoxyl)propanoyloxy)tetralone (**4b**)*: Colorless semisolid. IR (film): 1730, 1630, 1610 cm^{-1}. ^1H NMR (200 MHz, $CDCl_3$) δ: 1.14–1.38 (m, 6H, OCH_2CH_3, $2CH_3$), 1.96 (m, 3H, CH_3), 2.17–2.51 (m, 2H, CH_2), 3.03–3.30 (m, 2H, CH_2), 3.85–4.36 (m, 5H, OCH_2, $2CH_2$, CH), 5.41 (m, 1H, CH), 6.71–6.96 and 7.08–7.93 (m, 4H, Ar-H). HRMS calcd. for $C_{17}H_{23}O_6P$: 354.1232; found: 354.1230.

*2-(2-(Diethoxyphosphinoxyl)propanoyloxy)-4,7-dimethyltetralone (**4c**)*: Colorless semisolid. IR (film): 1720, 1640, 1610 cm^{-1}. ^1H NMR (200 MHz, $CDCl_3$) δ: 1.12–1.33 (m, 9H, OCH_2CH_3, 3 CH_3), 1.92 (m, 3H, CH_3), 2.10–2.38 (m, 2H, CH_2), 2.30 (broad s, 3H, CH_3), 3.30 (m, 1H, CH), 3.86–4.43 (m, 5H, OCH_2, $2CH_2$, CH), 5.42 (m, 1H, CH), 7.03–7.51 (m, 3H, Ar-H). HRMS calcd. for $C_{19}H_{27}O_6P$: 382.1545; found: 382.1540.

*3-Methyl-8,8a-dihydro-1-oxa-cyclopenta[a]inden-2-one (**5a**)* (ref. 7): Colorless crystals: mp 135–137°C (lit. (7) 136–137°C). IR (KBr): 1750, 1690 cm^{-1}. ^1H NMR δ: 2.07 (d, J = 2.0 Hz, 3H, CH_3), 2.81 (dd, J = 15.0, 7.4 Hz, 1H, CH), 3.40 (dd, J = 15.0, 7.4 Hz, 1H, CH), 5.40 (m, 1H, CH), 7.35–7.45 (m, 3H, ArH), 7.62 (m, 1H, ArH). ^{13}C NMR ($CDCl_3$) δ: 9.8, 36.3, 83.2, 118.4, 124.3, 126.9, 128.2, 132.1, 132.4, 145.1, 165.3, 176.6.

*1-Methyl-4,5-dihdro-3aH-naphtho[2,1-b]furan-2-one (**5b**)* (ref. 8): mp 152–154°C (lit. (8) 153–154.5°C). ^1H NMR ($CDCl_3$) δ: 2.17–2.51 (m, 2H, CH_2), 2.30 (s, 3H, CH_3), 3.03–3.30 (m, 2H, CH_2), 5.16 (m, 1H, CH), 7.08–7.61 (m, 4H, ArH).

*1,5,8-Trimethyl-4,5-dihydro-3aH-naphtho[2,1-b]furan-2-one (**6**)* (ref. 4) (mixture of diastereomers): mp 112–114°C. ^1H NMR ($CDCl_3$) δ: 1.42 and 1.46 (2d, J = 7.2 Hz, 3H, CH_3), 2.12–2.42 (m, 2H, CH_2), 2.28 (s, 3H, CH_3), 2.33 (s, 3H, CH_3), 3.30 (m, 1H, CH), 4.91 (ddq, J = 12.6, 4.5, 1.7 Hz), 5.21 (ddq, J = 12.2, 4.1, 1.5 Hz, 1H, CH), 7.09–7.60 (m, 4H, Ar-H).

Chromolaenin (Laevigatin) (1) (ref. 1): ^1H NMR ($CDCl_3$) δ: 1.36 (d, J = 7.5 Hz, 3H, CH_3), 2.28 (s, 3H, CH_3), 2.32 (s, 3H, CH_3), 2.71 (m, 1H, CH), 3.08 (m, 2H, CH_2), 6.98–7.48 (m, 3H, Ar-H).

Acknowledgments

This work was supported by Middle East Technical University AFP-1997 and Turkish State Planning Organization (DPT 1998 for 400 MHz NMR).

References

1. (*a*) F. Bohlmann and C. Zdero. Chem. Ber. **110**, 4687 (1997); (*b*) B. Filho, C.T.M.L. Bacha, L. Bauer, G.A.A.B. de Silva, and N.C.S. Sequira. Tetrahedron Lett. **19**, 2653 (1978).
2. S. Kano, J. Ebata, and S. Shibuya. Heterocycles, **14**, 43 (1980).
3. R.R. Juo and W. Herz. J. Org. Chem. **50**, 700 (1985).
4. (*a*) S.P. Chavan, P.K. Zubaidha, and N.R. Ayyangar. Tetrahedron Lett. **33**, 4605 (1992); (*b*) S.P. Chavan, Y.T.S. Rao, C.A. Govande, P.K. Zubaidha, and V.D. Dhonge. Tetrahedron Lett. **38**, 7633 (1997); (*c*) S.P. Chavan, V.D. Dhondge, S.P. Sachindra, Y.T.S. Rao, and C.A. Govande. Tetrahedron: Asymmetry, **8**, 2517, (1997); (*d*) S.P. Chavan, P.K. Zubaidha, C.A. Govande, and Y.T.S. Rao. J. Chem. Soc. Chem. Commun. 1101 (1994).
5. (*a*) A.S.Demir and A. Jeganathan. Synthesis, 235 (1992); (*b*) A.S. Demir and A. Saatcioglu. Synth. Commun. **23**(5), 571 (1993); (*c*) A.S. Demir, N. Çamkerten, H. Akgün, C. Tanyeli, A.S. Mahasneh, and D.S. Watt. Synth. Commun. **20**(15), 2279 (1990); (*d*) A.S. Demir, T. Sayraç, and D.S. Watt. Synthesis, 1119 (1990); (*e*) A.S. Demir, H. Akgün, C. Tanyeli, and D.S. Watt. Synthesis, 719 (1991); (*f*) A.S. Demir, C. Tanyeli, H. Akgün, Z. Çaliskan, and E. Özgül. Bull. Chem. Soc. Fr. **132**, 423 (1995); (*g*) A.S. Demir, C. Tanyeli, V. Gülbeyaz, and H. Akgün. Turkish J. Chem. **20**, 244 (1996); (*h*) A. Chretien and G. Varga. Bull. Soc. Chim. Fr. **3**, 2385 (1936); (*i*) A.S. Demir, H. Hamamci, C. Tanyeli, I.M. Akhmedov, and F. Doganel. Tetrahedron: Asymmetry, **9**, 1673 (1998); (*k*) A.S. Demir, Z. Gercek, O. Reis, N. Duygu, and E. Arikan. Tetrahedron, **55**, 2441 (1999); (*l*) G. Bauer. Handbuch der praeparativen anorganischen chemie. Enke, Stuttgart, 1962. p. 1283; (*m*) G.I. Nikishin, M.G. Vinogradov, and S.P. Verenchikov. Izv. Akad. Nauk SSSR Ser. Khim. 1835 (1969); Bull. Acad. Sci. U.S.S.R. Div. Chem. Sci. 1698 (1969).
6. W.G. Espersen and R.B. Martin. J. Phys. Chem. **80**, 161 (1976).
7. Y.Ishii, C. Gao, W-X. Xu, M. Ivasaki, and M. Hidai. J. Org. Chem. **58**, 6818 (1993).
8. R.A. Clement and T-C. Shieh. J. Org. Chem. **25**, 1850 (1960).
9. (*a*) D. Plusquellec and M. Kerfanto. Tetrahedron Lett. **16**, 1495 (1974); (*b*) P.K. Subaitha, S.P. Chavan, and U.S. Racheria. Tetrahedron, **47**, 5759 (1991).
10. I. Kitagava, S. Tsujii, F. Nishikava, and H. Shibuya. Chem. Pharm. Bull. **31**, 2639 (1983).
11. E.J. Corey and J.P. Schaefer. J. Am. Chem Soc. **82**, 918 (1960).
12. G.J. Williams and N.R. Hunter. Can. J. Chem. **54**, 3830 (1976).
13. (*a*) B.B. Snider, L. Han, and C. Xie. J. Org. Chem. **62**, 6978 (1997); (*b*) B.B. Snider. Chem. Rev. **96**, 339 (1996); (*c*) B.B. Snider and A.Y. Kiselhof. Tetrahedron Lett. **52**, 6073 (1996).
14. D. Arndt. Manganese compounds as oxidizing agents in organic chemistry. Open Court Publishing Co., La Salle. 1981. Chap. 1.
15. C.F. Poole and S.A. Schuette. Contemporary practice of chromatography. Elsevier, Amsterdam. 1984. Chap. 6.

© 1999 NRC Canada

A reinterpretation of the substituent effect on the amide barrier. An experimental and theoretical study

Alex. D. Bain, P. Hazendonk, and P. Couture

Abstract: Recent theoretical work on amide systems has brought into question the application of the concept of resonance. In particular, the role of the oxygen atom was questioned, since the calculations showed little change in its properties when the amide bond was rotated. This paper investigates, both experimentally and computationally, the effect of a substituent on the carbonyl carbon on the amide barrier, in order to test this view. The barriers to the amide rotation in seven spiro-fused oxazolidines were measured by NMR, to within 1 kJ mol^{-1}. A subset of three of them was modelled to the 6-31G** level. For all three substituents the computed and measured barriers corresponded to within 7 kJ mol^{-1}. The electron densities were analyzed using the Atoms in Molecules (AIM) theory. The AIM analysis revealed that the oxazolidines behaved similarly to formamide. The substituent effect was described in terms of the atomic populations and energies of the amide C, O, and N. A substituent on the carbonyl carbon caused electron redistributions between N and C, changing their basin attractive energies. Neither the population nor the energy of oxygen changed significantly. When interactions outside the basin of interest were considered, the energy of C was seen to be more sensitive to changing the substituent than the energy of N. However, the atomic parameters from the AIM analysis did not fully reflect the substituent effects observed. For these molecules, the barrier includes contributions from several sources — there is no single, dominant contribution.

Key words: amides, barrier, substituent, nuclear magnetic resonance spectroscopy, chemical exchange, atoms in molecules, slow exchange, NMR lineshape analysis.

Résumé : Un travail théorique récent a remis en question l'application du concept de résonance. En particulier, le rôle de l'atome d'oxygène est remis en question puisque les calculs ont montré qu'il y a peu de changements dans ses propriétés lorsqu'on soumet une liaison amide à une rotation. Dans le but de vérifier cette position, des travaux tant expérimentaux que théoriques ont été effectués pour déterminer l'effet d'un substituant au niveau du carbone du carbonyle sur la barrière à la rotation de l'amide. Faisant appel à la RMN, on a mesuré les barrières à la rotation de l'amide dans sept oxazolidines à fusion spiro avec une précision inférieure à 1 kJ mol^{-1}. On a fait des calculs au niveau 6-31G** sur un sous-ensemble de trois de ces produits. Pour chacun des trois substituants, les barrières calculées et mesurées concordent dans des limites de 7 kJ mol^{-1}. On a analysé les densités d'électron à l'aide de la théorie des atomes dans les molécules (ADM). L'analyse ADM révèle que les oxazolidines se comportent comme le formamide. On décrit l'effet de substituant en fonction de populations atomiques et d'énergies des C, O et N de l'amide. Un substituant sur le carbone du carbonyle provoque une redistribution des électrons entre N et C, ce qui provoque un changement dans leur basin d'énergies d'attraction. Il n'y a pratiquement aucun changement dans la population ni dans l'énergie de l'oxygène. Quand on considère les interactions provenant de l'extérieur du basin d'énergie, on observe que l'énergie de C est plus susceptible au changement de substituant que l'énergie de N. Toutefois, les paramètres atomiques tirés de l'analyse ADM ne reflètent pas complètement les effets de substituant observés. Pour ces molécules, la barrière comprend des contributions de plusieurs sources, sans qu'on puisse discerner de contribution dominante.

Mots clés : amides, barrière, substituant, spectroscopie de résonance magnétique nucléaire, échange chimique, atomes dans les molécules, analyse de la forme des bandes de RMN.

[Traduit par la Rédaction]

Received April 20, 1998.[1]

A.D. Bain,[2] P. Hazendonk, and P. Couture. Department of Chemistry, McMaster University, 1280 Main St. W., Hamilton, ON L8S 4M1, Canada.

[1]Revision received April 28, 1999.
[2]Author to whom correspondence may be addressed. Telephone: (905) 525-9140. Fax: (905) 522-2509. e-mail: bain@mcmaster.ca

 © 1999 NRC Canada

Fig. 1. Resonance structures of an amide including interactions with a substituent on the carbon.

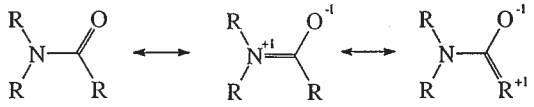

Introduction

Barriers to internal rotational in amides are commonly explained as resulting from resonance between the oxygen and nitrogen (1–13). One of the resonance structures has a double bond between the carbon and the nitrogen, and a negative charge on oxygen, as in Fig. 1. Recent theoretical studies have proposed that this may not be appropriate (8, 9, 14, 15). Instead, they suggest that the barrier is dominated by energy differences in the carbon and nitrogen, and that oxygen is hardly involved. However, this view is still controversial (16–18). One way to test this hypothesis is to look at substituent effects on the barrier and see if they fit into this interpretation. What aspects of the substituent are important to the amide barrier?

Resonance theory predicts that in the planar form of amides there is interaction between the carbonyl π bond and the lone pair on the amide nitrogen (1). This increases the C—N bond order, leading to a net stabilization. In the transition state this interaction is lost, since the orbitals are orthogonal. Substituents on the carbon capable of resonance interactions should reduce the interaction between oxygen and nitrogen (see Fig. 1). As a result, the net stabilization in the planar form is reduced, and the barrier decreases. Recently, the application of the resonance model to formamide has been brought into question (8). These studies employ Atoms in Molecules (AIM) (19) analysis on electron density functions of formamide as the C—N bond is rotated. As the NH_2 group is rotated out of the plane, the main electron transfer is calculated to occur from the nitrogen to the carbon. The calculated atomic population of oxygen is virtually unchanged throughout this process. This disagrees with the resonance model, which requires significant participation of oxygen. As the molecule departs from the planar form, the calculations suggest that the nitrogen pyramidalizes and the C—N bond lengthens. The C=O bond increases only marginally. The calculated energies of the nitrogen and carbon atoms in the molecule dominate the energy changes of the whole system. The energy of oxygen changes insignificantly. Because of the central role of nitrogen, it is perhaps better to view this system as a particular case of an amine rather than a hindered rotation (8, 20).

The AIM theory suggests that in amines, nitrogen is most stable in a planar form (20). However, in this geometry the N—R bonds are shorter than in the pyramidal form, which increases the repulsive energies between the substituents. Furthermore, planar nitrogen is more electronegative, due to higher s character in the N—R bonds. Consequently nitrogen requires a net transfer of charge from the substituents, destabilizing them further. Any consequent stabilization of N in the planar form is overwhelmed by the loss of stability in the substituents, leaving the pyramidal form as most stable (20). Thus the origin of the inversion barrier in amines depends on two factors: (*i*) the stability of nitrogen, and its electronegativity; and (*ii*) the stability of the substituents, especially with regard to changes in repulsive and attractive energies.

Scheme 1. Spiro-fused oxazolidine derivatives and their dimethylaminocarbonyl analogs. R = H, CH_3, OCH_3, $C(CH_3)=CH_2$, Ph, *p*-OCH_3Ph, *p*-NO_2Ph.

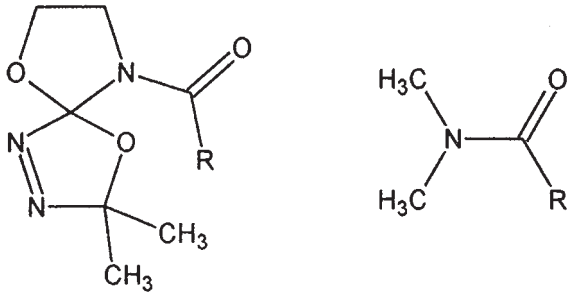

In this picture, amides are treated as amines — the carbonyl is just another substituent on the nitrogen. In the planar geometry, nitrogen stabilizes more than the substituents destabilize. In the transition state, nitrogen is predicted to be somewhat pyramidal, where it is least stable. The analysis of the substituent effect on amide barriers should therefore attempt to answer the following questions:

1. Does the substituent alter the charge distribution between C and N, altering their atomic energies?
2. Does the substituent stability drive the changes in the barrier?

In this study, barriers of a series of spiro-fused oxazolidines (see Scheme 1) were measured using a suite of nuclear magnetic resonance (NMR) spectroscopic techniques. The barriers of selected amides were computed and the electron densities were subjected to AIM analysis. The effect of substitution on the amide carbon was assessed by looking for changes in the atomic charges and energy contributions of the nitrogen, carbon, and oxygen.

Methodology

NMR methods

Accurate activation parameters determined by NMR techniques require rate measurements over a wide temperature range (21–23). Several methods can be employed to measure rates, each being optimal in different rate regimes (21, 22, 24–28). Using selective inversion experiments during slow exchange (0.1–10 s^{-1}) (27, 29–31) and lineshape fitting during medium and fast exchange (2, 13, 24, 25, 32–36), it is possible to obtain $\Delta H^{\ddagger}$ and $\Delta S^{\ddagger}$ values to within 1 kJ mol^{-1} and 10 J mol^{-1} K^{-1} (22), respectively.

The selective inversion experiments are best applied when the conformer lifetime is of the same order of magnitude as the spin-lattice relaxation time (27, 28, 30). The line corresponding to one site, often the major site, is inverted selectively, and the relaxation of both lines is observed. The exchange rate is extracted by fitting the data to a set of differential equations that describe the relaxation and exchange behaviour.

Lineshape methods are employed most effectively when the rates are comparable with the difference in the Larmor

© 1999 NRC Canada

Scheme 2. Synthesis of spiro-fused oxazolidine derivatives.

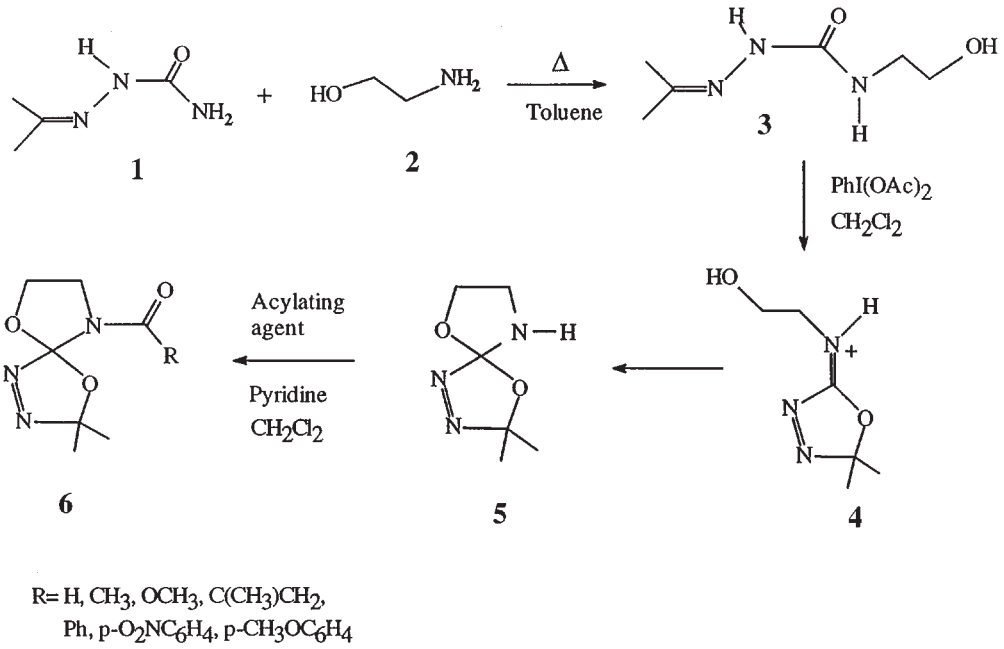

frequency between the two sites (13, 21, 30). Experimental spectra are compared visually with sample spectra computed with varying exchange rates.

Theoretical methods

Initially, the electron densities (ρ) of selected amides are obtained from the wave functions (Ψ) as in eq. [1].

$$[1] \qquad \rho = N \int \Psi^{*}\Psi \, d\tau$$

Using methods prescribed by the Atoms in Molecules theory (19, 37–39), these densities were analyzed for their topological properties, such as bond critical points (bcp) and bond paths. A critical point occurs where the gradient of ρ vanishes. These critical points are characterized by the properties of eigenvalues of the Hessian matrix at that location. The number of non-zero eigenvalues is its rank, and the sum of their signs is its signature. A bond critical point is a (3,–1) critical point, and nuclear positions are (3,–3) critical points. The path of maximum density connecting two (3,–3) critical points and which passes through the BCP is known as the bond path.

Several properties of ρ at a bcp are commonly used in the analysis of ρ. The density at the bcp is related to the bond order, and the Laplacian at the bcp, $\nabla^2\rho$, indicates whether charge is locally concentrated or depleted (37). A negative Laplacian indicates that charge is locally concentrated, while a positive value suggests that charge is locally depleted.

The next stage of analysis involves searching ρ for interatomic surfaces. These surfaces partition the molecule into atomic domains (Ω), which are used as integration boundaries to calculate atomic properties. Atomic populations, $N(\Omega)$, are calculated by integrating the electron density up to these boundaries (eq. [2]).

$$[2] \qquad N(\Omega) = \int_{\Omega} \rho(r) \, d\tau$$

The atomic energies are computed by invoking an atomic virial theorem (37), as in eq. [3]. For an equilibrium geometry, the total energy of subsystem, $E(\Omega)$, is given in eq. [3].

$$[3] \qquad E(\Omega) = -T(\Omega) = T(\Omega) + V(\Omega)$$

$T(\Omega)$ and $V(\Omega)$ are the kinetic and potential energies, respectively. Thus $E(\Omega)$ and $T(\Omega)$ can be computed by integrating the potential energy within the relevant interatomic surface.

The potential energy of a system can be divided into contributions from repulsive (V_{rp}) and attractive terms in the Hamiltonian. The attractive contribution, $V_{ne}(\Omega)$ (eq. [4]), is the integral of the electron–nuclear potential, with all the nuclei of the system, over the atomic basin.

$$[4] \qquad < V_{ne} > = \sum_{\alpha} Z_{\alpha} e^2 \int_{\Omega} \frac{1}{r} \rho(r) \, d\tau$$

If only the nucleus within the basin is considered, V_{neo} is the basin attractive potential energy, as in eq. [5].

$$[5] \qquad < V_{neo} > = Z_{\Omega} e^2 \int_{\Omega} \frac{1}{r} \rho(r) \, d\tau$$

The contributions from repulsive interactions are computed by integrating the electron–electron potential between electrons within the same basin, $V_{ee}(\Omega,\Omega)$, or a given basin (Ω) and remainder of the electron density (Ω′), $V_{ee}(\Omega,\Omega')$. The repulsion energy is given in eq. [6].

$$[6] \qquad V_{rp} = V_{ee}(\Omega,\Omega) + \frac{1}{2} V_{ee}(\Omega,\Omega')$$

Experimental

Sample preparation

Oxazolidines were prepared by the procedure shown in Scheme 2 (40–42). The semicarbazone of acetone (**1**), prepared by standard methods, was refluxed with 2-

© 1999 NRC Canada

Fig. 2. Eyring plot for the H, $C(CH_3)=CH_2$, C_6H_5, *p*-$NO_2C_6H_4$, and *p*-$OCH_3C_6H_4$ derivatives in acetone using rate data obtained from NMR chemical exchange measurements.

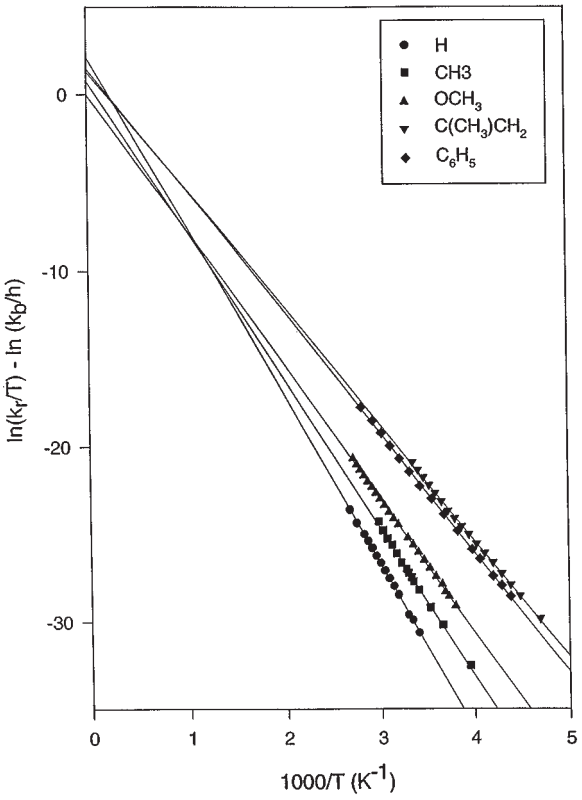

Fig. 3. Eyring plot for the H, CH_3, OCH_3, $C(CH_3)=CH_2$, and C_6H_5 derivatives in toluene using rate data obtained from NMR chemical exchange measurements.

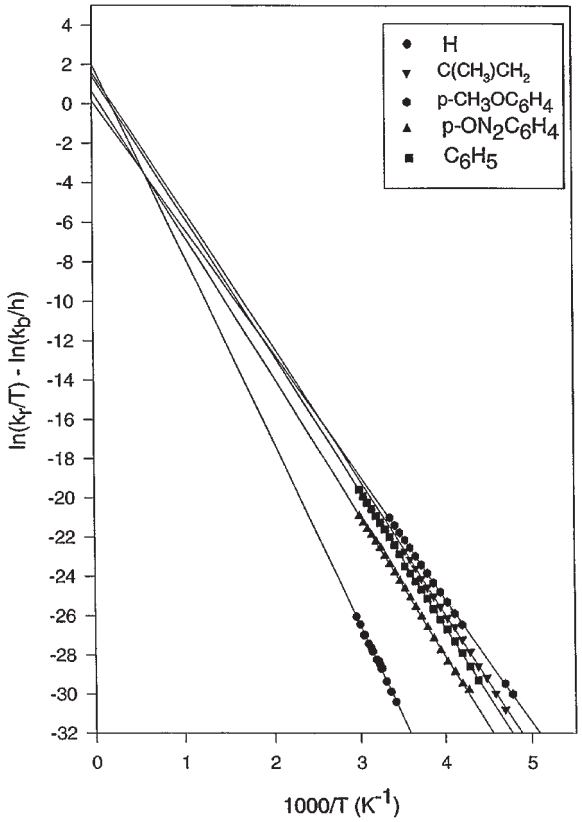

aminoethanol (**2**) in toluene for 7–15 h, to give the substituted semicarbazone (**3**). This compound was oxidized with $PhI(OAc)_2$ in dichloromethane to afford oxazolidines (**4**), which were acetylated or benzoylated by standard methods to afford **6**. A total of seven derivatives were made with the following substituents (R): H, CH_3, OCH_3, $C(CH_3)=CH_2$, phenyl, *p*-nitrophenyl, and *p*-methoxyphenyl. Samples, of approximately 5 mg, were prepared in toluene-d_8 and acetone-d_6, depending on solubility. Tetramethylsilane was used as an internal chemical shift and line-width reference.

NMR measurements

All ^1H NMR measurements were performed on a Bruker AC-300 spectrometer using a 5 mm four-nucleus probe. Temperature control was maintained to within ±0.5°C using a BVT 2000 temperature controller, and was monitored periodically by inserting a copper–constantan thermocouple in a 5 mm NMR tube into the probe. The two readings always agreed to within 0.5°C, and the BVT 2000 reading was used.

The selective inversion experiments were carried out employing the RD–π/2–τ–π/2–VD–π/2–Acq. pulse sequence. The carrier frequency was set to the line to be inverted, typically corresponding to the major site. The delay, τ, was set to $1/(2\Delta\nu_{cis-trans})$, where $\Delta\nu_{cis-trans}$ is the frequency difference (in Hz) between the *cis* and *trans* signals, which varied with substituent from 100 to 489 Hz. The variable delays, VD, were chosen from a range of 10 ms to 5 s, and the relaxation delay (RD) was typically 30 s. Data were transferred over a parallel interface to an SGI INDY workstation for processing. Line intensity measurements of these data were obtained via the XWINNMR package, and were analyzed with CIFIT (28).

Lineshape analysis was performed with the MEX program (24, 25). MEX simulates lineshapes of exchanging systems without scalar coupling. The simulated spectra are directly imported into the Bruker XWINNMR program on a Silicon Graphics Indy computer and compared with experiment using the dual display mode.

Molecular orbital calculations and atoms in molecules analysis

Restricted Hartree–Fock calculations were performed using Gaussian 94 (43) with an IBM RS 6000 470 series computer. Calculations were performed only on the five-membered ring including the amide group and substituents, the second five-membered ring was not included (see Fig. 2). Optimum geometries of both the *cis* and *trans* conformers (see Fig. 3) were calculated with the 6-31G** basis set. Only the H, CH_3, OCH_3, and $C(CH_3)=CH_2$ derivatives were investigated, due to restricted cpu time. The transition state calculations were performed on the H, CH_3, and $C(CH_3)=CH_2$ derivatives using the QST3 method of searching for saddle points in the energy surface, available in Gaussian 94. For the OCH_3 derivative, all attempts at finding the transition state failed.

Topological features of the electron densities were analyzed with EXTREME, which is a program developed in Dr

© 1999 NRC Canada

Fig. 4. Experimental and simulated spectrum of the ring protons in the methyl derivative. Simulation was done with XSIM.

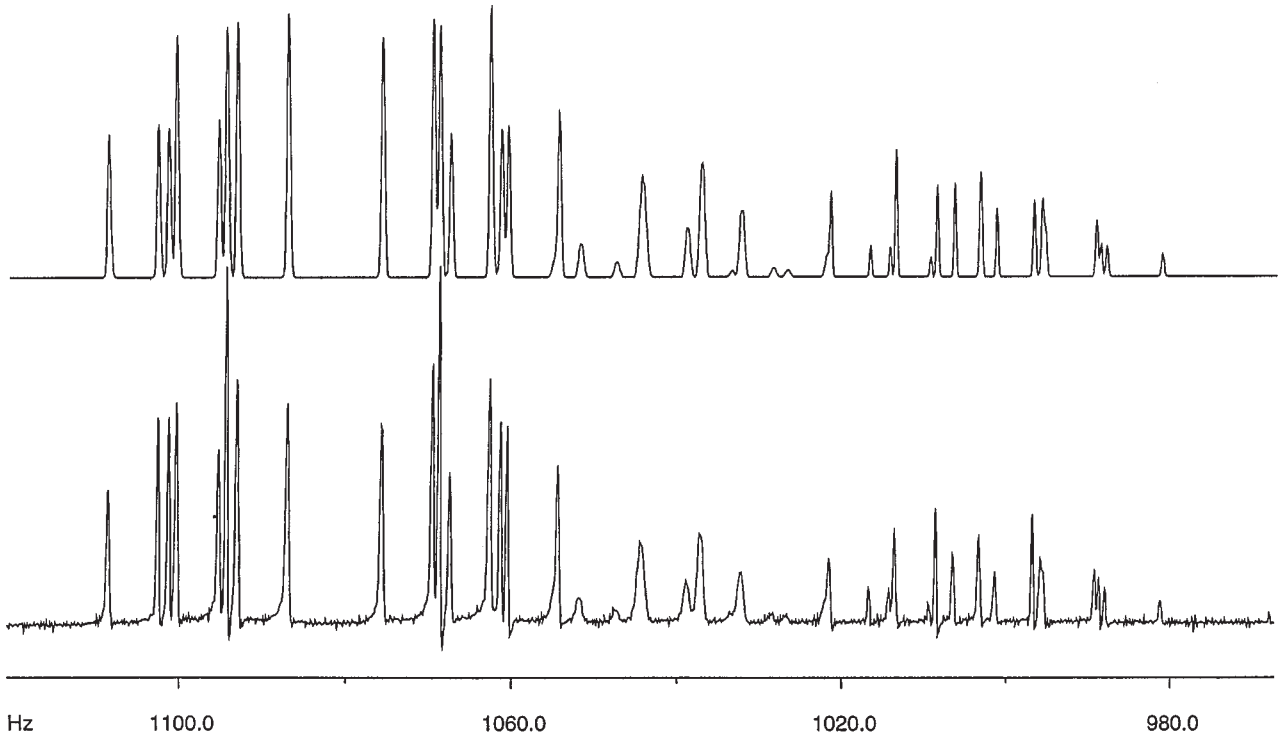

Table 1. Gibbs' free energies of spiro-fused oxazolidine derivatives and *N,N′*-dimethylaminocarbonyl analogs.[a]

	$\Delta G^{\ddagger}$			ΔG^{0}	
R	Toluene	Acetone	Analog	Toluene	Acetone
H	75	74	87	6	4
CH_3	68		72	2	
OCH_3	64		74	1	
$C(CH_3)=CH_2$	52	53	59	1	3
Ph	54	55	65	2	4
p-OCH_3Ph		52	61		7
p-NO_2Ph		59	69		4

[a]All values in kJ mol^{-1} with errors of approximately ±1 kJ mol^{-1}. Data for the analogs are taken from ref. 59. Gas-phase data for the analogs can be obtained from ref. 56.

R.F.W. Bader's laboratory. The parameters $\rho(r)$ and $\nabla^2\rho(r)$ were determined at the bond critical points. The atomic populations and energies were computed using PROAIMV (23), developed by the same group. This software package finds the interatomic surfaces, and uses them for integration boundaries. All integrations were carried out to $L < 0.001$ a.u. Atomic energies were also divided into their contributions from repulsive and attractive potential energy terms.

Results

The Eyring plots of the H, CH_3, OCH_3, $C(CH_3)=CH_2$, and phenyl derivatives in toluene are shown in Fig. 2. Those of H, $C(CH_3)=CH_2$, phenyl, *p*-methoxyphenyl, and *p*-nitrophenyl compounds in acetone are shown in Fig. 3. Note that the graphs include the intercept at $1/T = 0$, to aid in judging the error in the entropy of activation. The equilibrium constants for unequally populated systems were measured at low temperature by integrating the methyl resonances of the major and minor conformers. Due to the large chemical shift differences, it was possible to obtain equilibrium constants at several temperatures, which in turn allowed prediction at high temperature by extrapolation using the van't Hoff isochore. Rate measurements were made over a wide temperature range, ca. 100°C. The activation parameters are shown in Tables 1–3. Uncertainties in $\Delta H^{\ddagger}$ and $\Delta S^{\ddagger}$ are estimated to be in the range of 1–10 J mol^{-1} K^{-1}, respectively.

To determine whether the ring changes geometry between the *cis* and *trans* forms, the vicinal coupling constants between the methylene protons of the ring were measured for the methyl derivative. This was achieved with XSIM (available from K. Marat, University of Manitoba), a program that simulates static NMR spectra. The iterated spectral parameters are given in Table 4. The simulated spectrum is seen in Fig. 4.

© 1999 NRC Canada

Table 2. Enthalpies of the barrier and the equilibrium constant in spiro-fused oxazolidine derivatives.[a]

	$\Delta H^{\ddagger}$			ΔH^{0}		
R group	Toluene	Acetone	Calculated	Toluene	Acetone	Calculated
H	80	79	77.1	5.3	3.8	2.9
CH_3	70		66.1	2.3		2.4
OCH_3	63			2.4		
$C(CH_3)=CH_2$	55	57	48.0	1.4	5.2	0.1
Ph	57	58		3.5	7.0	
p-OCH_3 Ph		54			2.9	
p-NO_2 Ph		60			7.4	

[a]All values in kJ mol^{-1} with errors of approximately ±2kJ mol^{-1}.

Table 3. Entropies of the barrier and the equilibrium constant in spiro-fused oxazolidine derivatives.[a]

	$\Delta S^{\ddagger}$		ΔS^{0}	
R	Toluene	Acetone	Toluene	Acetone
H	18	4	0	0
CH_3	4		0	
OCH_3	0		4	
$C(CH_3)=CH_2$	11	5	0	8
Ph	12	7	4	12
p-OCH_3Ph		3		–13
p-NO_2Ph		7		10

[a]All values in J K^{-1} mol^{-1} have statistical errors of approximately ±10 J K^{-1} $mol^{-1.}$

The barriers of the H, CH_3, and $C(CH_3)=CH_2$ derivatives, from MO calculations at the HF/6-31G** level, are shown in Table 1. These are to be compared with the measured enthalpies of activation, $\Delta H^{\ddagger}$. Throughout this analysis, the lowest-energy transition states were used where the carbonyl group was *gauche* to both ring carbons. The electron density and the Laplacian are shown in Tables 5 and 6 (Δ denotes the change in value going from *cis* to the transition state). Table 7 contains atomic populations, and the atomic energies of N, C, and O. These energies are divided into V_{ne}, V_{neo}, and V_{rp}. The values in parentheses represent changes when going to the transition state.

Discussion

Rotational barriers of amides have been studied extensively using NMR methods (2–4, 10–13, 21, 44–51). The effects of substituent (10, 13, 47, 48, 50) and solvent (5, 44, 47, 52–54) have received considerable attention. However, many barrier determinations were performed with few rate measurements. These often covered a narrow temperature range and employed only one experimental technique. As a result most barriers were reported as free energies, without a separation of enthalpy and entropy. Using a combination of selective inversion and lineshape methods, rate measurements can be made over a large temperature range, allowing the enthalpies of the barriers to be reported, since the enthalpies are more compatible with calculations.

In this work, the effects of the substituents on the carbonyl carbon corresponded to previous investigations (6, 10, 13, 44, 47, 48, 54, 55). Replacing H with CH_3 caused the activation enthalpy to decrease by 10 kJ mol^{-1}, which is in line with values between 10 and 13.5 kJ mol^{-1} in the literature

Table 4. ^{1}H NMR spectral parameters for the methyl derivative in toluene at 240 K at 300.13 MHz.[a]

	Major	Minor		Major	Minor
ν_A(C7)	1097.2	1011.3	$^2J_{A,B}$	–8.25	–8.26
	(3.656)	(3.370)	$^3J_{A,C}$	7.34	5.41
ν_B(C7)	1065.5	993.9	$^3J_{A,D}$	5.96	7.46
	(3.550)	(3.312)	$^3J_{B,C}$	6.14	6.96
ν_C(C8)	822.7	1034.3	$^3J_{B,D}$	6.95	7.07
	(2.741)	(3.446)	$^2J_{C,D}$	–8.67	–10.70
ν_D(C8)	786.1	1047.1	$^5J_{C,CH3}$	0.12	0.28
	(2.619)	(3.489)	$^5J_{D,CH3}$	0.14	0.28

[a]All chemical shift and coupling constants are given in Hz, at a spectrometer frequency of 300.13 MHz. Chemical shifts in parentheses are in ppm with respect to TMS.

Fig. 5. Some geometrical changes in the H derivative during the rotational process predicted by MO calculations.

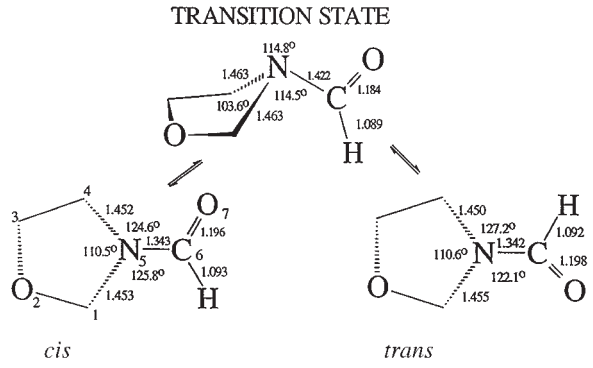

(6, 13, 44, 56). The barriers were typically lower than in dimethylaminocarbonyl analogs (Table 1 and Scheme 2), which can be attributed to ring strain forcing the nitrogen to take on greater sp^3 character in the low-energy geometries. This is consistent with studies done by Pinto et al. (48), who observed significant variation in amide barriers with changes in ring size. In this study the activation enthalpy for the OCH_3 substituent was 16 kJ mol^{-1} smaller than that of the H derivative, which is quite different from the literature (13). Rather than this molecule being considered as a methoxyl derivative of an amide, it can be regarded as a carbamate ester. Carbamates are known to be similar to amides (57, 58), but they do not behave identically. The $C(CH_3)=CH_2$ substituent lowered the barrier by 24 kJ mol^{-1}, similar to values for analogous systems (59). The phenyl substituents

© 1999 NRC Canada

Table 5. Electron density at bond critical points of interest in the amide portion of the molecules.[a]

	H		CH_3		OCH_3		$C(CH_3)=CH_2$	
ρ	*cis*	Δ	*cis*	Δ	*cis*	Δ	*cis*	Δ
N_5-C_6	0.335	–0.024	0.329	–0.025	0.345	N/A	0.329	–0.023
N_5-C_4	0.266	0.001	0.268	–0.002	0.266	N/A	0.265	0.004
C_6-O_7	0.430	0.004	0.426	0.007	0.437	N/A	0.426	0.003
C_6-R_8	0.299	0.004	0.271	0.005	0.316	N/A	0.277	0.006

[a] Values are reported for the *cis* conformers along with their change when going to the transition state. Attempts to find the transition state for the methoxyl derivative failed. The columns are ordered according to the measured barrier to rotation. All values are in atomic units.

Table 6. The Laplacian of the electron density at bond critical points of interest in the amide portion of the molecules.[a]

	H		CH_3		OCH_3		$C(CH_3)=CH_2$	
$\nabla^2\rho$	*cis*	Δ	*cis*	Δ	*cis*	Δ	*cis*	Δ
N_5-C_6	–0.726	–0.503	–0.750	–0.415	–1.005	N/A	–0.847	–0.342
N_5-C_4	–0.666	–0.165	–0.713	–0.129	–0.627	N/A	–0.699	–0.142
C_6-O_7	0.368	0.421	0.297	0.400	0.180	N/A	0.319	0.334
C_6-R_8	–1.196	–0.043	–0.779	–0.026	–0.218	N/A	–0.815	–0.023

[a] The values in the *cis* conformer are reported along with its corresponding change when going to the transition state. The columns are ordered according to the measured barrier to rotation. All values for the Laplacian are given in atomic units.

Table 7. The atomic populations (*N*) and energy contributions of N_5, C_6, and O_7 for the *cis* conformers of the H, CH_3, OCH_3, and $C(CH_3)=CH_2$ derivatives.

	H	CH_3	OCH_3	$C(CH_3)=CH_2$
Nitrogen				
N	8.63 (–0.26)	8.63 (–0.27)	8.64	8.60 (–0.23)
E^a	–55.48 (0.27)	–55.46 (0.30)	–55.50	–55.40 (0.22)
$V_{neo}{}^b$	–136.56 (1.17)	–136.52 (1.24)	–136.63	–136.34 (0.97)
$V_{ne}{}^c$	–252.79 (6.78)	–266.48 (8.33)	–278.79	–283.35 (6.34)
$V_{rp}{}^d$	141.79 (–6.21)	155.52 (–7.73)	167.77	172.50 (–5.89)
Carbon				
N	4.04 (0.20)	4.15 (0.21)	3.38	4.16 (0.21)
E	–36.55 (–0.16)	–36.61 (–0.17)	–36.09	–36.63 (–0.15)
V_{neo}	–81.61 (–0.93)	–82.07 (–0.96)	–78.84	–82.15 (–0.92)
V_{ne}	–130.24 (–3.21)	–142.02 (–5.29)	–136.00	–153.94 (–4.32)
V_{rp}	57.13 (2.89)	68.77 (4.94)	63.8	80.66 (4.02)
Oxygen				
N	9.39 (–0.05)	9.41 (–0.04)	9.44	9.40 (–0.08)
E	–75.60 (–0.02)	–75.60 (–0.02)	–75.66	–75.60 (–0.01)
V_{neo}	–185.59 (0.25)	–185.67 (0.18)	–185.90	–185.63 (0.19)
V_{ne}	–272.41 (–2.07)	–289.02 (–7.11)	–305.27	–310.38 (–1.69)
V_{rp}	121.17 (2.04)	137.780(7.06)	153.91	159.15 (1.67)

[a] *E* is the total energy of the basin (in a.u.).

[b] V_{neo} is the basin attractive energy (in a.u.), to its own nucleus only, as given in eq. [5].

[c] V_{no} is the total attractive energy (in a.u.) of the basin as in eq. [4].

[d] V_{rp} is the total basin repulsion energy (in a.u.). The values in parentheses indicate the change in the respective value upon going to the transition state.

decreased the barrier by as much as 25 kJ mol^{-1}, where the effect of the substituents in the *para* position of the ring were as expected. The *p*-nitrophenyl substituent had a barrier 4 kJ mol^{-1} larger than the phenyl substituent and the *p*-methoxyphenyl was 3 kJ mol^{-1} smaller.

The computed barriers correspond reasonably well to experiment, in both trend and absolute value (Table 2). The computed barriers are consistently smaller, by as much as 7 kJ mol^{-1} for the $C(CH_3)=CH_2$ derivative. This may be due to the fact that solvation almost always increases barriers, relative to gas-phase values (55).

The methyl groups in the major conformer are all deshielded with respect to those in the minor site, which suggests that the *trans* form predominates. This was confirmed by one- and two-dimensional NOE experiments, which showed interactions between the N-methyl of the ma-

© 1999 NRC Canada

jor conformer and the two low-frequency ring protons at 2.62 and 2.74 ppm. Changes in the vicinal couplings in the ring between the major and minor conformers indicate small changes in the average conformation of the ring between amide conformations (Table 4). All four vicinal couplings fall within 5–7.5 Hz, which are typical values for five-membered rings (60). These are larger than normal *gauche* couplings and smaller than regular *trans* couplings suggested by Karplus-type relationships (61–64), which implies that the torsional angles are closer to 30° for a *gauche*-like and to 150° for *trans*-like couplings. In both these ranges of dihedral angles, vicinal couplings are similar, thus it is not possible to quantify the change in the ring pucker.

The computed behaviour of the amide portion of the oxazolidines was similar to that of formamide. MO calculations suggest that the nitrogen is planar in the *cis* geometry and pyramidal in the transition state. The C—N bond length increases much more than the C—O bond decreases when going to the transition state from the *cis* form. X-ray crystallographic data of a series of 3,4-dihydro-2-oxo-1,4-propanoquinolines (7, 65, 66), which contain severely distorted amide fragments, indicated similar behaviour.

Further similarities between formamide and these oxazolidines are seen in the electron density at the bond critical point, ρ(bcp), and the Laplacian, $\nabla^2\rho$(bcp). Values of these are given in Tables 5 and 6 for the C—N and C—O bonds. Table 7 gives values of the calculated atomic properties, $E(\Omega)$, $N(\Omega)$, $V_{neo}(\Omega)$, $V_{ne}(\Omega)$, and $V_{rp}(\Omega)$ of C, N, and O in the amide group. The electron density at the bcp of the C—N bond diminishes by about 7% in the transition state with respect to the *cis* form for all derivatives (Table 5). The electron density at the bcp of the C—O bond is left virtually unchanged. The Laplacian at the C—N bcp (Table 6) is nearly identical to that of formamide in both the *cis* and transition forms. In all three derivatives, when going to the transition states there is a net transfer of charge from N to C of ca. 0.2 a.u., and the charge on O changes much less. Nitrogen is destabilized by the loss of charge, which is seen as an increase in V_{neo}(N). Carbon, on the other hand, is stabilized by the gain in charge, thus V_{neo}(C) decreases. As in formamide, the increase in attractive energies on going to the transition state, ΔV_{ne}, is greater than the corresponding decrease in the repulsive energies, ΔV_{rp}. In carbon, the attractive energies decrease more than the repulsive energies increase, causing the carbon to be greatly stabilized.

The Laplacian seems to be the most sensitive to changes in substituent. In the C—N bond of the *cis* conformer, it decreases in the order H, CH_3, $C(CH_3)=CH_2$, but OCH_3 is anomalous (Table 6). The absolute value of the change in the Laplacian from *cis* to the saddle-point geometry decreases in the same order. Unfortunately, the search for the saddle point for the OCH_3 derivative failed, so data are not available for it. In all three derivatives available, the Laplacian in the transition state approaches the same value (ca. –1.2 a.u.).

Similarly, the trends in the atomic properties (Table 7) follow the barriers, but the methoxyl derivative is the exception. In general, there is no single dominant atomic contribution to the energy. The carbon and the nitrogen give the major contribution, but the combination of their energies does not duplicate the trend in the experimental barriers. This may be due to inaccuracies in the atomic integrations, which are good to roughly one part in 1000. For a relatively large system such as this, the energies are determined by a balancing of the energies of all the atoms.

Conclusions

The main goal of this study was to look into the effect of substituents on amide rotational barriers, in order to test recent models. The experimental results on the spiro-fused oxazolidines follow the trends in simpler substituted amides. Calculations on the system, combined with an Atoms in Molecules (AIM) analysis, show similarities to calculations on formamide. However, the trends with substituent are not accurately reflected in the calculated results. For molecules of this size, the AIM analysis is helpful in interpreting the data, but it does not improve on the more traditional resonance model of the barrier.

Acknowledgements

We would like to extend our gratitude to Dr. T. Schaefer in lending us his computational facilities over an extended period, Dr. K. Marat and G. Bernard for assistance with our computations, Dr. Bader for the AIM software, C. Kozak for assisting with the spectrometer work, and the Natural Sciences and Engineering Research Council of Canada (NSERC) for providing financial assistance.

References

1. A. Streitweiser, C.H. Heathcock, and E. M. Kosower. Introduction to organic chemistry. MacMillan, New York. 1992.
2. H.S. Gutowsky and C.H. Holm. J. Chem. Phys. **25,** 1228 (1956).
3. K.-I. Dahlqvist and S. Forsen. J. Phys. Chem. **73**, 4124 (1969).
4. M.T. Rogers and J.C. Woodbrey. J. Phys. Chem. **66**, 540 (1962).
5. R.J. Gillespie and T. Birchall. Can. J. Chem. **41**, 148 (1963).
6. L.L. Graham and R.E. Diel. J. Phys. Chem. **73**, 2696 (1969).
7. A.J. Bennet, Q.P. Wang, H. Slebocka-Tilk, V. Somayaji, R.S. Brown, and B.D. Santarsiero. J. Am. Chem. Soc. **112**, 6383 (1990).
8. K.E. Laidig and L.M. Cameron. Can. J. Chem. **71**, 872 (1993).
9. K.E. Laidig and L.M. Cameron. J. Am. Chem. Soc. **118**, 1737 (1996).
10. W.E. Stewart and T.H. Siddall. Chem. Rev. **70**, 517 (1970).
11. K.G. Orrell, V. Sik, and D. Stephenson. Prog. Nucl. Magn. Reson. Spectrosc. **22**, 141 (1990).
12. I.O. Sutherland. Annu. Rep. NMR Spectrosc. **4**, 71 (1971).
13. H. Kessler. Angew. Chem. Int. Ed. Engl. **9**, 219 (1970).
14. K.B. Wiberg and C. Breneman. J. Am. Chem. Soc. **114**, 831 (1992).
15. K.B. Wiberg and K.E. Laidig. J. Am. Chem. Soc. **109**, 5935 (1987).
16. C.L. Perrin. J. Am. Chem. Soc. **113**, 2865 (1991).
17. D. Lauvergnat and P.C. Hiberty. J. Am. Chem. Soc. **119**, 9478 (1997).
18. G. Fogarasi and P.G. Szalay. J. Phys. Chem. A, **101**, 1400 (1997).
19. R.F.W. Bader. Atoms in molecules: a quantum theory. Clarendon Press, Oxford. 1994.
20. R.F.W. Bader, J.R. Cheeseman, K.E. Laidig, K.B. Wiberg, and C. Breneman. J. Am. Chem. Soc. **112**, 6530 (1990).

© 1999 NRC Canada

21. A.D. Bain, G.J. Duns, S. Ternieden, J. Ma, and N.H. Werstiuk. J. Phys. Chem. **98,** 7458 (1994).
22. A.D. Bain, G.J. Duns, F. Rathgeb, and J. Vanderkloet. J. Phys. Chem. **99**, 17 338 (1995).
23. F.W. Biegler-Konig, R.F.W. Bader, and T. Tang. J. Comput. Chem. **3**, 317 (1982).
24. A.D. Bain and G.J. Duns. Can. J. Chem. **74**, 819 (1996).
25. A.D. Bain and G.J. Duns. J. Magn. Reson. Ser. A, **112**, 258 (1995).
26. A.D. Bain and G.J. Duns. J. Magn. Reson. Ser. A, **109**, 56 (1994).
27. A.D. Bain and J.A. Cramer. J. Phys. Chem. **97**, 2884 (1993).
28. A.D. Bain and J.A. Cramer. J. Magn. Reson. Ser. A, **103**, 217 (1993).
29. A.D. Bain and G.J. Duns. Bull. Magn. Reson. **15**, 64 (1993).
30. S. Forsen and R.A. Hoffman. J. Chem. Phys. **39**, 2892 (1963).
31. R.E. Hoffman and S. Forsen. Prog. Nucl. Magn. Reson. Spectrosc. **1**, 15 (1966).
32. S. Szymanski, M. Witanowski, and A.M. Gryff-Keller. Annu. Rep. NMR Spectrosc. **8**, 227 (1978).
33. L.H. Piette and W.A. Anderson. J. Chem. Phys. **30**, 899 (1959).
34. K.G. Orrell and V. Sik. Annu. Rep. NMR Spectrosc. **19**, 79 (1987).
35. G. Binsch. J. Am. Chem. Soc. **91**, 1304 (1969).
36. P.T. Inglefield, E. Krakower, L.W. Reeves, and R. Stewart. Mol. Phys. **15**, 65 (1968).
37. R.F.W. Bader. Acc. Chem. Res. **18**, 9 (1985).
38. R.F.W. Bader. Int. J. Quantum Chem. **49**, 299 (1994).
39. R.F.W. Bader. Chem. Rev. **91**, 893 (1991).
40. P. Couture, J.K. Terlouw, and J. Warkentin. J. Am. Chem. Soc. **118**, 4214 (1996).
41. P. Couture and J. Warkentin. Can. J. Chem. **75**, 1264 (1997).
42. P. Couture and J. Warkentin. Can. J. Chem. **75**, 1281 (1997).
43. M.J. Frisch, G.W. Truck, H.B. Schlegel, P.M.W. Gill, B.G. Johnson, M.A. Robb, J.R. Cheeseman, T.A. Keith, G. Petersen, J.A. Montgomery, K. Raghavachari, M.A. Al-Laham, V.G. Zakrzewski, J.V. Ortiz, J.B. Forseman, J. Cioslowski, B. Stefanov, A. Nanayakkara, M. Challacombe, C.Y. Peng, P.Y. Ayala, W. Chen, M.W. Wong, J.L. Andres, E.S. Replogle, R. Gomperts, R.L. Martin, D.J. Fox, J.S. Binkley, D.J. Defrees, J. Baker, J.P. Stewart, M.W. Head-Gordon, C. Gonzalez, and J.A. Pople. Gaussian 94. Gaussian Inc., Pittsburgh, Pa. (1995).
44. T.H. Siddall, W.E. Stewart, and F.D. Knight. J. Phys. Chem. **74**, 3580 (1970).
45. R.C. Neuman and V. Jonas. J. Am. Chem. Soc. **90**, 1970 (1968).
46. T. Drakenberg and S. Forsen. J. Phys. Chem. **74**, 1 (1970).
47. M.M. Turnbull, D.J. Nelson, W. Lekouses, M.L. Sarnov, K.A. Tartarini, and T. Huang. Tetrahedron, **46**, 6613 (1990).
48. B.M. Pinto, T.B. Grindley, and W.A. Szarek. Magn. Reson. Chem. **24**, 323 (1986).
49. K.A. Haushalter, J. Lau, and J.D. Roberts. J. Am. Chem. Soc. **118**, 8891 (1996).
50. H.G. Bonacorso, M.S.B. Caro, N. Zanatta, and M.A.P. Martins. Magn. Reson. Chem. **31**, 451 (1993).
51. M.W. Wong, K.B. Wiberg, and M.J. Frisch. J. Am. Chem. Soc. **114**, 1645 (1992).
52. M.C. Ou and S.Y. Chu. J. Phys. Chem. **99**, 556 (1995).
53. H.L. Maia, K.G. Orrell, and H.N. Rydon. J. Chem. Soc. Chem. Commun.1209 (1971).
54. K.B. Wiberg, P.R. Rablen, D.J. Rush, and T.A. Keith. J. Am. Chem. Soc. **117**, 4261 (1995).
55. C.B. LeMaster. Prog. Nucl. Magn. Reson. Spectrosc. **31**, 119 (1997).
56. C.L. Mayne, D.W. Alderman, and D.M. Grant. J. Chem. Phys. **63**, 2514 (1975).
57. M.L. Martin, F. Mabon, and M. Trierweiler. J. Phys. Chem. **85**, 76 (1981).
58. M. Remko and S. Scheiner. J. Mol. Struct. (Theochem.), **180**, 175 (1988).
59. L.M. Jackman. *In* Dynamic nuclear magnetic resonance spectroscopy. *Edited by* L.M. Jackman and F.A. Cotton. Academic Press, New York. 1975. pp. 203–252.
60. R.M. Silverstein, G.C. Bassler, and T.C. Morril. Spectrometric identification of organic compounds. John Wiley & Sons, Inc., Toronto. 1991. pp. 165–225.
61. M. Karplus. J. Chem. Phys. **30**, 11 (1959).
62. C.A.G. Haasnoot, F.A.A.M. De Leeuw, and C. Altona. Tetrahedron, **36**, 2783 (1980).
63. K. Imai and E. Osawa. Magn. Reson. Chem. **28**, 668 (1990).
64. E. Osawa, K. Imai, T. Fuijiyoshi-Yonda, C. Jaime, P. Ma, and S. Masamune. Tetrahedron, **47**, 4579 (1991).
65. Q.P. Wang, A.J. Bennet, and R.S. Brown. Can. J. Chem. **68**, 1732 (1990).
66. Q.P. Wang, A.J. Bennet, R.S. Brown, and B.D. Santarsiero. J. Am. Chem. Soc. **113**, 5757 (1991).

© 1999 NRC Canada

Électrosynthèse de films de polyparaphénylène déposés sur carbones

S. Sadki, J.F. Fauvarque, M.T. Descarsin et P. Simon

Résumé : Des dépôts réguliers et reproductibles de polyparaphénylène (PPP) sur des supports carbonés (tissus et charbons actifs) ont été obtenus par électrosynthèse catalysée et examinés au microscope électronique à balayage. Les propriétés électrochimiques du PPP ainsi préparé, déposé sur des carbones conducteurs, ont été étudiées dans le milieu sulfolane – tétrafluoroborate de tétrabutylammonium. Le dépôt de PPP sur carbone présente bonne une cyclabilité et des densités de courant apparentes (2 mA/cm^2) élevées.

Mots clés : polymères conducteurs, polyparaphénylène, électrodéposition.

Abstract: This present work deals with the formation of polyparaphenylene (PPP) electrodes in which the polymer is associated with conductive carbons. Regular and reproducible coatings of PPP on different types of carbon electrodes were obtained by catalytic electrosynthesis (Fauvarque method) and were examined by electron microscopy. Electrochemical properties of PPP, coated on conductive carbons, were studied in sulfolane–NBu_4BF_4 electrolyte. Coatings on carbon lead to a good cyclability and a high apparent current density (as high as 2 mA/cm^2).

Key words : conductive polymers, polyparaphenylene, electrolytic coating.

1. Introduction

Depuis le début des années 1970, les polymères conducteurs électroniques (1–4) suscitent un intérêt considérable et sont à ce titre l'objet de recherches théoriques et expérimentales interdisciplinaires. Les applications potentielles de ces polymères électroactifs sont liées aux propriétés originales de ces matériaux dans les domaines électrique, électronique, optique ou électrochimique. De nombreuses applications sont envisagées, telles que le blindage électromagnétique (5), les accumulateurs (6, 7), l'affichage électrochrome (8, 9), les composants électroniques (10, 11), les détecteurs à gaz (12)⋯. Cependant, la production de ces matériaux à l'échelle industrielle est peu développée.

Du point de vue fondamental, la connaissance des mécanismes qui confèrent aux polymères électroactifs leurs étonnantes propriétés reste encore succincte (13). Parmi ces matériaux, le polyparaphénylène (PPP) présente à l'état non dopé des propriétés semi conductrices et optiques remarquables et constitue un matériau de choix pour l'industrie électronique (14).

Le PPP peut être aisément obtenu par synthèse chimique (15–19). Il est également synthétisable soit par électro-oxydation (dopage *p*) (20–31), soit par électro-réduction (dopage *n*) (32, 33). Pour réaliser l'électropolymérisation du PPP, nous avons utilisé la réaction électrochimique proposée par Fauvarque et al. (34). Le principe consiste à réaliser la réduction électrochimique d'aryles paradihalogénés catalysés par des complexes de Ni(0) électrogénérés in situ. La réaction globale d'électro-réduction catalytique s'écrit :

[1] 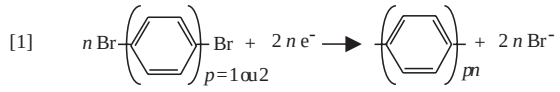

Cette méthode permet d'obtenir du polyparaphénylène soit sous forme de poudre (34) en utilisant comme électrode de travail une nappe de mercure de grande surface, soit sous forme de films sur des supports métalliques (35, 36) ou de carbone.

Les précédents travaux recensés dans la littérature, réalisés par Aboulkassim et Chevrot (37), ne décrivant les dépôts de polyparaphénylène que sur carbone vitreux, nous nous proposons d'étudier l'électropolymérisation du PPP pour la réalisation de films sur des supports de carbone. Le but de ce travail est la réalisation de dépôts de polymères épais sur des carbones et des graphites de surfaces spécifiques élevées, présentant une bonne conduction électronique, pour une application comme matériau d'électrode dans les supercondensateurs (38, 39). Les matériaux une fois synthétisés seront étudiés par voltampérométrie cyclique et en charge galvanostatique dans un electrolyte sulfolane – tétrafluoroborate de tétrabutylammonium (NBu_4BF_4).

2. Partie expérimentale

Le monomère utilisé au cours de l'électrosynthèse est le 4,4′-dibromobiphényle à la concentration de 0,05 M. Le catalyseur (chlorure de (1.2 (diphénylphosphino)éthane)nickel(II))

Reçu 20 avril 1998.

S. Sadki,[1] J.F. Fauvarque, M.T. Descarsin et P. Simon. Laboratoire d' Électrochimie Industrielle du Conservatoire National des Arts et Métiers, 2 rue Conté, 75003 Paris, France.

1.Auteur à qui adresser toute correspondance. Adresse actuelle : Équipe Réactivités aux Interfaces, EA 2528, L.R.P.M.E., Université de Cergy Pontoise, 5 Mail Gay Lussac, Neuville sur Oise, 95031 Cergy Pontoise Cedex. Tél. : 01. 34. 25. 70. 57. Téléc. : 01. 34. 25. 70. 71. Mél. : sadki@u-cergy.fr

© 1999 CNRC Canada

de masse molaire 528,05 g/mol est utilisé à la concentration de 0,0025 M. Le solvant est soit du diméthylacétamide seul (DMA), soit un mélange diméthoxyéthane (DME) – hexaméthylphosphorotriamide (HMPT) (70 : 30). Pour les caractérisations électrochimiques des matériaux, le choix s'est porté sur le sulfolane. Ce solvant possède une constante diélectrique assez élevée (40). Le perchlorate de lithium et le tétrafluoroborate de tétrabutylammonium (NBu_4BF_4) sont utilisés comme sel de fond. Les solvants et les sels sont séchés suivant la procédure décrite dans la référence 34.

La pseudo-électrode de référence est une électrode Ag/AgCl plongeant dans une solution de chlorure de potassium saturée dans de l'acide acétique anhydre. La contre électrode est un barreau de magnésium de 12 mm de diamètre et de 40 mm de hauteur.

Différentes types d'électrodes de travail ont été successivement testées pour la réalisation de dépôts de polyparaphénylène : (*i*) des tissus de Carbone–Lorraine® TCM 128. Ces tissus ont une épaisseur de 0,35 mm et de masse 25 mg. Leur surface spécifique est comprise entre 58 et 78 m^2/g; (*ii*) des feuilles poreuses constituées par des grains de carbone de grande surface (Norit®) agglomérés par du polytétrafluoroéthylène (PTFE 20 %) et contenant 10 % en masse de graphite. Le Norit® est un charbon actif constitué de grains de carbone dont la surface spécifique est de 1200 m^2/g (la masse de carbone est de 10 mg).

Pour la réalisation des dépôts de polymères, les électrodes de travail sont découpées en disques de 1 cm de diamètre puis encapsulées dans des grilles en déployé de nickel ou nickel doré. Les électrodes sont séchées pendant 24 h dans une étuve sous vide.

La cellule électrochimique se compose de deux compartiments séparés par un poreux (porosité de 4 Å). La solution est dégazée avec de l'argon U (pureté 99,995 %, impurétés en ppmv : O_2 = 5, N_2 = 20, H_2 = 10, CH_4 = 5, H_2O (5 bar) = 5) avant chaque manipulation (1 bar = 100 kPa).

Mode opératoire

Une pré-électrolyse de 1 h est réalisée sur l'électrode de travail ET à un potentiel de –3 V par rapport à l'électrode de référence, pour réduire l'eau et les impuretés résiduelles. Le catalyseur est ajouté dans le compartiment cathodique à la concentration de 0,0025 M, puis dissout par agitation. La solution est de nouveau dégazée par barbotage de gaz argon. La cathode est portée au potentiel d'électrolyse de –2,5 V. Dès la polarisation de la cathode à ce potentiel, il se forme un dépôt de polyparaphénylène. Simultanément, le courant chute brutalement en fonction du temps de polarisation. Le composite polymère–carbone obtenu est lavé à l'acétone, à l'eau, à l'acide chlorhydrique 5 M, de nouveau à l'eau, puis séché à 50°C pendant 12 h. Une fois séchée, la masse de polymère déposée est déduite par différence avec la masse du support de carbone préalablement pesé.

3. Résultats et discussion

3.1. Dépôts de film de polyparaphénylène sur supports de carbone

3.1.a. Influence du potentiel d'électrolyse

Fig. 1. Masse de PPP déposée sur un tissu de carbone TCM 128 en fonction de la quantité d'électricité mise en ouvre.

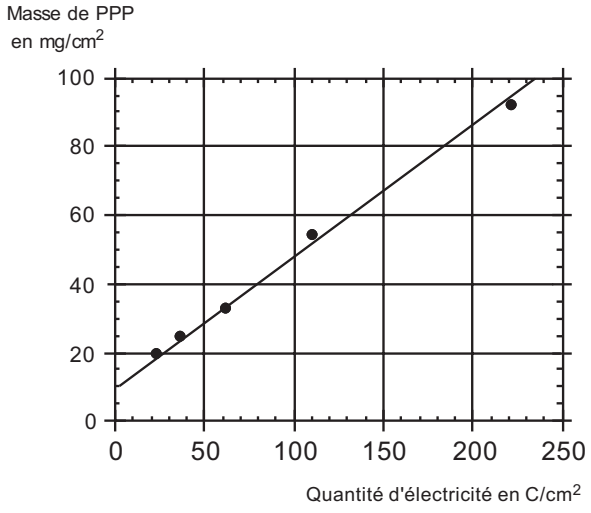

L'électrolyse est réalisée à potentiel constant. Le potentiel d'électrolyse conditionnant les propriétés du film de polyparaphénylène déposé, il est indispensable d'en optimiser la valeur en fonction des propriétés recherchées.

La plage de potentiel de formation du polymère est relativement restreinte. Le potentiel optimum trouvé lors de l'électropolymérisation est de –2,5 V. Cette valeur correspond à la réduction du complexe d'insertion Br-$(j)_2$–Ni(dppe)–Br. Dans ces conditions, les films de polymère déposés possèdent de bonnes propriétés d'adhérence vis-à-vis du substrat en carbone. Cette valeur du potentiel est également celle utilisée pour la formation de poudres de polymères.

Pour des valeurs de potentiel comprises entre –2,4 et –2,6 V (autre que –2,5 V) il y a formation de polymère à la surface du carbone mais l'aspect du polymère est granuleux et surtout peu adhérent. Dans cette plage de potentiel, le film est obtenu à l'état neutre isolant de couleur jaune, ce qui peut expliquer les difficultés rencontrées pour la réalisation de films épais.

Pour des potentiels supérieurs à –2,4 V, il n'y a pas de formation de film de PPP sur la surface du carbone du fait de l'absence de régénération de l'espèce électrocatalytique Ni(0).

La synthèse de polymères dopés a également été étudiée en travaillant à des potentiels plus négatifs ($-3\ V < E < -2,6\ V$). Dans ces conditions, le polymère est déposé en subissant de surcroît une réduction électrochimique et un dopage *n* par le cation Li^+. Pour ces valeurs de potentiel, du PPP de coloration bleu, caractéristique du polymère à l'état dopé, se dépose sur le carbone. Le film obtenu est très mince et le rendement de la réaction très faible.

3.1.b. Dépôts sur tissus de carbone

Ces tissus présentent une bonne résistance à la réduction électrochimique (7) quelque soit l'électrolyte organique utilisé (DMA–$LiClO_4$,DME/HMPT–$LiClO_4$, DME/HMPT–NBu_4BF_4).

Les dépôts de polyparaphénylène sont facilement réalisés à la surface du tissu de carbone au potentiel de –2,5 V. La figure 1 représente la masse de PPP déposée en fonction de la quantité d'électricité fournie. Cette figure met en évidence

© 1999 CNRC Canada

l'existence d'une relation linéaire entre la quantité d'électricité Q fournie et la masse de PPP déposée, dans le domaine étudié ($Q < 200$ C). La quantité de PPP introduite dans le composite est donc facilement contrôlable.

La pente de la droite est de 0,5 mg de polymère par coulomb (dans ces expériences, la masse des supports utilisés en carbone est de 50 mg). Lorsque la quantité d'électricité est inférieure ou égale à 3,2 C/cm^2 de surface apparente d'électrode, le PPP se dépose alors. Les photographies des dépôts (fig. 2), réalisées au microscope électronique à balayage (MEB), montrent la présence de points de germination sur les fibres constituant le tissu de carbone (photographies n° 1 et 2).

Pour des quantités d'électricité comprises entre 2,5 C/cm^2 et 50 C/cm^2, les dépôts de PPP sont bien adhérents. La coloration jaune caractéristique du PPP à l'état neutre apparaît.

La photographie MEB n° 3 montre la croissance d'amas de polymère le long des fibres du tissu. Lorsque la masse du polymère déposé est supérieure à 50 mg, les dépôts présentent une structure granuleuse et s'effritent facilement. Mais dans tous les cas, l'encapsulage des électrodes améliore l'homogénéité des dépôts (l'absence de dépôts sur la grille de nickel a été vérifiée au préalable).

3.1.c. Dépôts sur carbones de grandes surfaces

La figure 3 représente la voltampérométrie cyclique d'une électrode en charbon actif de type Norit®, mélangé à du graphite pour améliorer la conductivité électronique. Les courants capacitifs sont élevés. Les capacités obtenues pour le carbone Norit® et le mélange Norit®–graphite sont de l'ordre de 80 F/g de carbone (fig. 3). Il sera donc nécessaire, lors de l'étude du composite polymère – charbon actif, d'utiliser des vitesses de balayage plus faibles pour mettre en évidence les réactions faradiques du polymère.

Les courants d'électrolyse au cours de l'électropolymérisation sont très élevés, de l'ordre de 10 mA/cm^2 de surface apparente d'électrode. La plus grande surface spécifique de ces électrodes, comparativement au tissu, permet d'expliquer ce résultat. La masse de PPP déposée étant toujours proportionnelle à la quantité d'électricité fournie au cours de l'électrolyse, la quantité de polymère déposée sur cette électrode est donc plus importante que celle déposée sur l'électrode en tissu de carbone. Les photographies 4 et 5 montrent que les dépôts de PPP sont compactes et peu visibles sur ces supports (en comparaison à ceux obtenus sur les tissus de Carbone–Lorraine).

En résumé, des dépôts homogènes de polyparaphénylène ont été réalisés sur différents supports de carbone (tissus, et charbons actifs), après optimisation du potentiel de polymérisation. Les quantités de polymères déposées sont facilement contrôlables. Tant que la masse du polymère déposé est inférieure à celle du support, les dépôts présentent une bonne tenue mécanique.

Une caractérisation par voltammétrie cyclique à balayage devrait permettre d'obtenir la contribution faradique du polymère déposé par unité de surface apparente d'électrode. Il sera alors possible entre autre de comparer l'électroactivité des polymères déposés sur chaque type de support. C'est l'objet de la seconde partie de ce travail.

3.2. Propriétés électrochimiques et cyclabilité du polyparaphénylène

Les dépôts de PPP sur supports de carbone obtenus précédemment vont être étudiés en réduction (dopage *n*) puis en oxydation (dopage *p*) électrochimique dans différents électrolytes.

3.2.a. Tissus de Carbone–Lorraine

3.2.a.1. Dopage n. *Voltampérogramme du film* : Les courbes de voltampérométrie cyclique à différentes vitesses de balayage d'un film de polyparaphénylène déposé sur un support en tissu de carbone sont présentées sur la figure 4. Le potentiel de repos est de –0,249 V.

La réaction de dopage–dédopage *n* peut s'écrire de la manière suivante :

$$[2] \qquad (C_6H_4)_x + xy\ NBu_4^+ + xy\ e^- \Leftrightarrow ((C_6H_4)^{-y}(NBu_4^+)_y)_x$$

couleur jaune — couleur bleue

Pour une vitesse de balayage de 10 mV/s, le pic de réduction du PPP situé à –2,2 V, correspondant à la réaction de dopage *n*, est peu visible car masqué par le courant de réduction de l'électrolyte (sulfolane – NBu_4BF_4 0,1 M). Pour cette même vitesse, en balayage retour, le pic apparaissant vers –2 V est lié à la réaction de dédopage.

Le tracé des voltammogrammes à diverses vitesses de balayage (fig. 4) montre un accroissement de la hauteur du pic en fonction de la vitesse de balayage. L'évolution du courant I_p du pic d'oxydation du dépôt de PPP sur tissu de Carbone–Lorraine en fonction de la racine carrée de la vitesse de balayage, visible sur la figure 5, présente un comportement linéaire caractéristique d'un processus diffusionnel. Ce processus est lié à la réaction de dédopage (désinsertion) du cation NBu_4^+ de la matrice polymère (13*a*). Calandra et al. (13*b*) expliquent ce processus par une variation due à un contrôle ohmique compte tenu du fait que la réoxydation a lieu dans une zone où le film redevient isolant. L'explication de la limitation diffusionnel nous semble plus appropriée pour ce processus.

Les intensités mesurées sur le voltammogramme pour la réaction de dopage *n* (pic de ré-oxydation vers –2 V) sont de l'ordre de 100 mA/cm^2 de surface apparente d'électrode. Cette valeur est comparable à celle obtenue précédemment par Aboulkassim et al. (37) lors de l'étude d'un film de PPP déposé sur une électrode en carbone vitreux.

3.2.a.2. Dopage p : La figure 6 représente la voltampérométrie cyclique en dopage *p* d'un film de PPP déposé sur un tissu de Carbone–Lorraine. L'électrode de polyparaphénylène est étudiée en oxydation.

La réaction de dopage–dédopage *p* peut s'écrire de la manière suivante :

$$[3] \qquad (C_6H_4)_x + xy\ BF_4^- \Leftrightarrow ((C_6H_4)^{+y}(BF_4^-)_y)_x + xy\ e^-$$

couleur jaune — couleur rouge

Le pic caractéristique de la réaction de dopage *p* n'est pas visible du fait de l'oxydation du solvant dans la gamme de

© 1999 CNRC Canada

Fig. 2. Photographie MEB d'un dépôt de PPP sur tissu de carbone et sur plaque de carbone Norit à différents quantités d'electricité. (1) MEB d'un tissu de Carbone–Lorraine TCM 129; (2) MEB d'un dépôt de PPP sur tissu de Carbone–Lorraine Q = 3,2 C/cm^2; (3) MEB d'un dépôt de PPP sur tissu de Carbone–Lorraine Q = 31,8 C/cm^2; (4) MEB sur une plaque de carbone Norit; (5) MEB d'un dépôt de PPP sur tissu de carbone Norit Q = 3,2 C/cm^2.

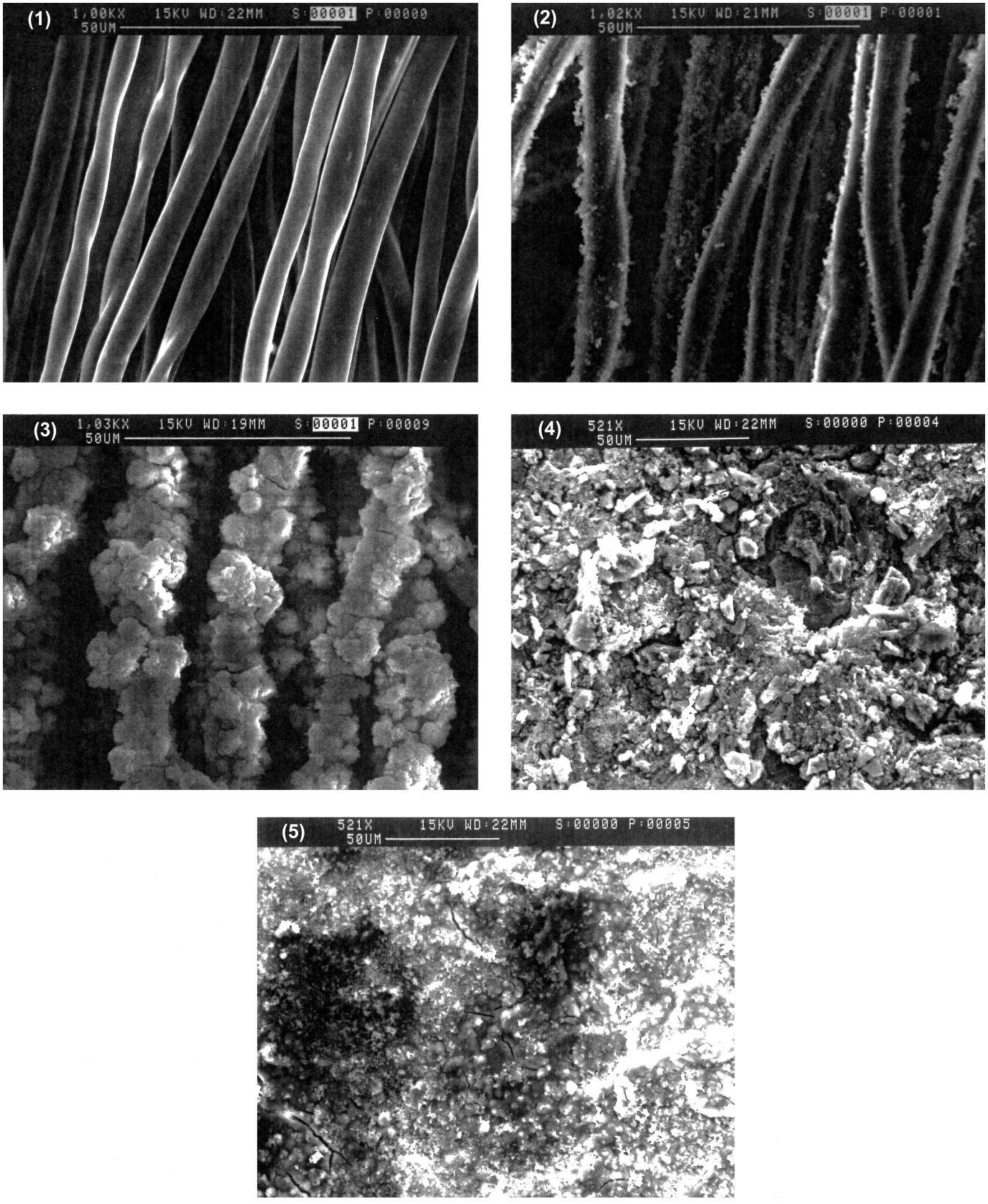

© 1999 CNRC Canada

Fig. 3. Voltampérométrie cyclique à 10 mV/s d'une électrode en charbon actif – graphite (Norit® 31 %, graphite 15 %, PTFE 54 %), milieu sulfolane – NBu_4BF_4 0,1M.

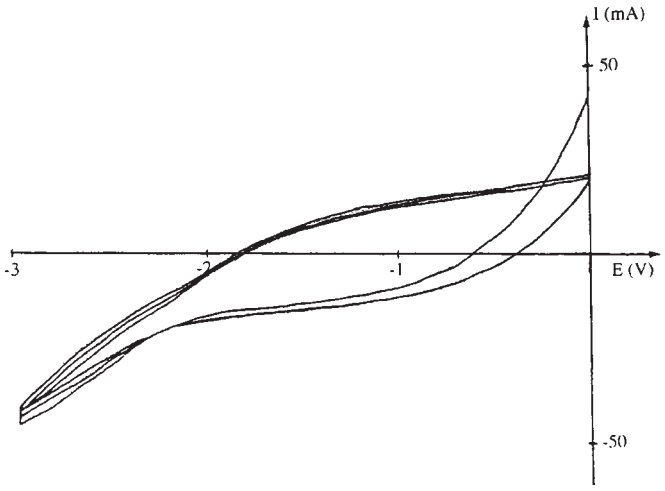

Fig. 4. Voltampérométrie cyclique d'un film de PPP déposé sur un tissu de Carbone–Lorraine®. Influence de la vitesse de balayage en milieu sulfolane – NBu_4BF_4 0,1M, à T = 22°C.

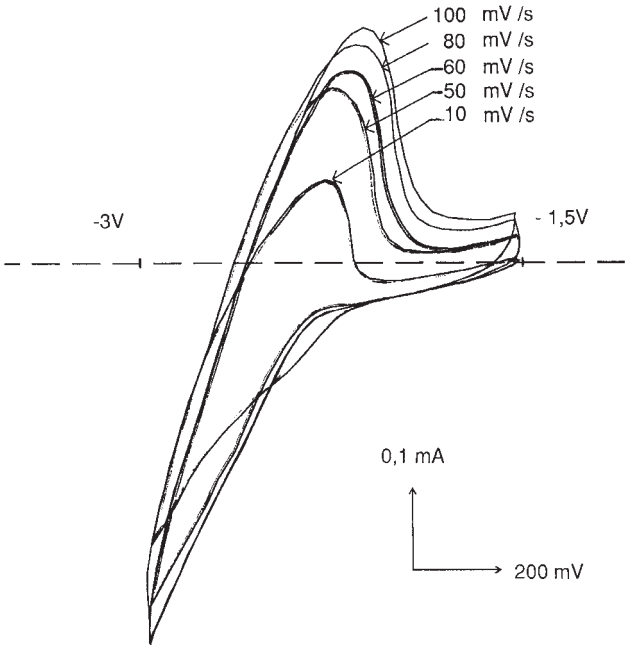

Fig. 5. Étude de l'évolution du courant I_p du pic d'oxydation du dépôt de PPP sur tissu de Carbone–Lorraine® en fonction de la vitesse de balayage en milieu sulfolane – NBu_4BF_4 0,1M, à T = 22°C.

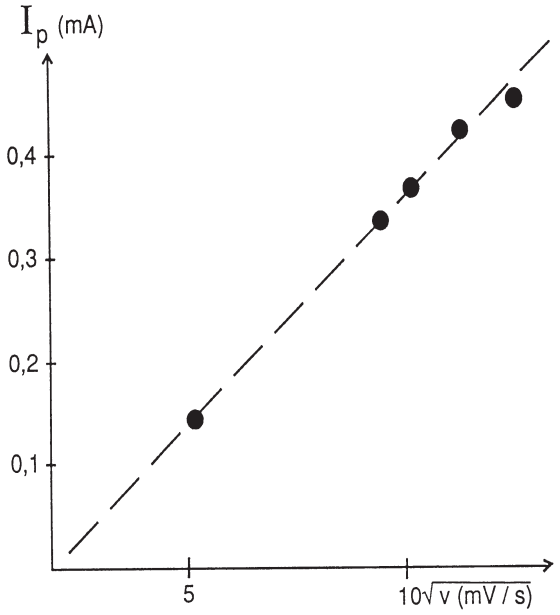

Fig. 6. Voltampérométrie cyclique en dopage *p* d'un film sur tissu de Carbone–Lorraine; v = 18 mV/s; sulfolane – NBu_4BF_4 0,1 M, 22°C.

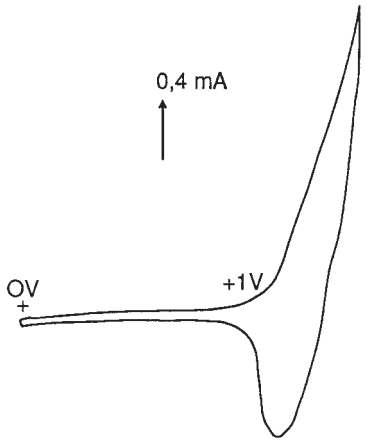

potentiel étudié. Lors du balayage retour, le pic correspondant à la réaction de dédopage apparaît à +1,2 V.

3.2.b. Carbones de grandes surfaces

La figure 7 représente la voltampérométrie cyclique en dopage *n* d'un film sur une électrode charbon actif Norit® 70 % – graphite 10 % – PTFE 20 %.

Le pic de réduction correspondant au dopage n'est visible que vers –2,3 V. Le potentiel de ce pic est donc décalé vers les valeurs négatives, comparativement au composite PPP – tissu de carbone. Pour cette raison, le pic d'oxydation n'est pas visible sur le voltammogramme, étant lui aussi décalé vers les valeurs négatives des potentiels.

La valeur de l'intensité mesurée au sommet du pic de dédopage est de 10 mA, ce qui correspond à une densité de courant de 3 mA/cm^2 de surface apparente d'électrode, compte tenu de la contribution du support seul dans le domaine de potentiel étudié (fig. 3). Pour le tissu de carbone, l'extrapolation du courant du pic de dédopage pour une vitesse de 5 mV/s (fig. 5) donne une valeur de 15 mA/cm^2 de surface apparente d'électrode. Il existe donc un facteur 200 entre les densités de courant mesurées sur les deux électrodes. Dans la première partie de cette étude, il apparaissait que les densités de courant utilisées pour le dépôt de PPP étaient très élevés pour l'électrode en charbon actif, c'est à dire que la masse de polymère déposée sur ce support est su-

© 1999 CNRC Canada

Fig. 7. Voltampérométrie cyclique en dopage *n* d'un film de polymère déposé sur une électrode charbon actif Norit® 70 % – graphite 10 % – PTFE 20 %; *v* = 18 mV/s ; milieu DME/HMPT (70/30) – NBu_4BF_4 0,1 M; *T* = 22°C.

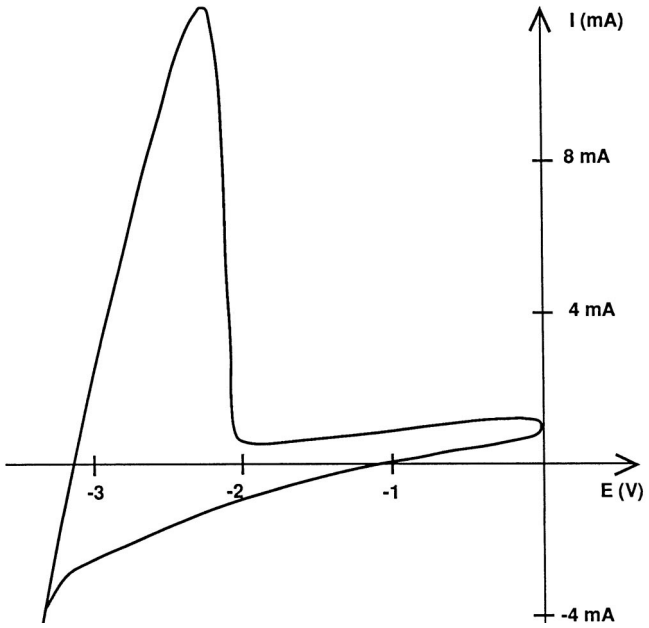

périeure à la masse de polymère déposée sur tissu. L'analyse des voltammogrammes confirme que le polymère déposé est bien électroactif.

Ce dernier résultat semble être intéressant dans l'objectif de la réalisation de supercondensateurs : l'utilisation de composites PPP – charbons actifs pourraient permettre d'augmenter la densité de puissance, du fait de la densité de courant de cyclage, et également l'énergie volumique disponible. Pour ce faire, il reste encore à améliorer les qualités de l'électrolyte en réduction, de façon à pouvoir mettre en évidence le pic de dopage *n*. Des travaux sont actuellement en cours au laboratoire.

4. Conclusions

Des dépôts de PPP sont réalisés de manière quantitative sur des supports en tissu de carbone et sur des charbons actifs agglomérés par du PTFE. Il existe dans chaque cas une relation linéaire entre la quantité d'électricité mise en oeuvre et la masse de PPP déposée, ce qui permet de contrôler la quantité de polymère déposée. La présence de PPP est observable par microscopie à balayage. Un dépôt homogène est obtenu sur toute la surface de l'électrode de carbone. Des films de PPP bien adhérents sont réalisés lorsque la masse du dépôt de PPP est inférieure à celle du support de carbone.

Dans le cas de dépôts sur tissu de carbone, les densités de courant de pic mesurées sur le voltammogramme correspondant au dédopage *n* sont de l'ordre de 100 mA/cm^2 de surface apparente d'électrode, valeurs comparables à celles déjà décrites dans la littérature (37).

Dans le cas de dépôts sur des électrodes en charbon actif, les densités de courant d'électrolyse obtenues sont égales à 10 mA/cm^2 de surface apparente d'électrode, et les densités de courant pic de dédopage *n* sont de l'ordre de 3 mA/cm^2. Il y a donc un facteur 200 entre les densités de courant mesurées sur les deux types de composites. Ces résultats semblent prometteurs quant à l'utilisation de composites polyparaphénylène – charbon actif comme matière active dans une application de type supercondensateurs.

Remerciements

Les auteurs tiennent à remercier les Laboratoires d'Alcatel Alsthom Recherche pour leur contribution financière.

Bibliographie

1. H.S. Nalwa. Handbook of organic conductive molecules and polymers. J. Wiley and Sons, New York. 1997.
2. A.F. Diaz, K.K. Kanazawa et G.P. Gardini. J. Chem. Soc. Chem. Commun. **111**, 635(1980).
3. A.F. Diaz et J. A. Logan. J. Electroanal. Chem. **111**, 111 (1980).
4. R.J. Waltman, J. Bargon et A. F. Diaz. J. Phys. Chem. **8**7 1459 (1983).
5. D.M. Bigg et E.J. Bradbury. *Dans* Conductive polymers. *Edité par* R.B. Seymour. Plenum, New York. 1981. pp. 22–38.
6. D. Naegele et R. Bitthin. Solid State Ionics, **28**–**30**, 983 (1988).
7. S. Sadki. Thèse Université Pierre et Marie Curie, Paris VI. 1992.
8. O. Brihaye, C. Legrand, A. Chapoton, C. Chevrot et A. Siove. Synth. Met. **55**, 2 (1993).
9. M. Mastragostino. *Dans* Applications of electroactive polymers. *Edité par* B. Scrosati. Chapman & Hall, U.K. 1993. pp. 223–249.
10. G. Horowitz, W. Peng, D. Fichou et F. Garnier. Synth. Met. **51**, 419 (1992).
11. O. Brihaye, C. Legrand, A. Chapoton, C. Chevrot et A. Siove. Synth. Met. **55**, 2 (1993).
12. T. Hanawa et H. Yoneyama. Synth. Met. **30**, 341 (1989).
13. (*a*) M.E.G. Lyons. Electroactive polymer electrochemistry, Part 1 : Fundamentals. Plenum Press, New York. 1994; (*b*) A.J. Calandra, N.R. De Tacconi, R. Pereiro et A.J. Arvia. Electrochim. Acta, **19**, 901 (1974).
14. (*a*) P. Kovacic et M.B. Jones. Chem. Rev. **87**, 357(1987); (*b*) M. Dubois et D. Billaud. J. Solid State Chem. **132**, 434 (1997); (*c*) M. Endo, C. Kim et M.S. Dresslhaus. Carbon, **36**, 1403 (1998).
15. (*a*) P. Kovacic et A. Kyriakis. J. Am. Chem. Soc. **85**, 454 (1963); (*b*) G. Leising, T. Vernon, G. Louarn et S. Lefrant. Synth. Met. **41–43**, 279(1991).
16. P. Kovacic et J. Oziomek. J. Org. Chem. **29**, 100 (1964).
17. F. Maurice, G. Froyer, M. Minier et M. Gauneau. J. Phys. Lett. **42**, L. 425 (1981).
18. M.B. Jones, P. Kovacic et D. Lanska. J. Polym. Sci. **19**, 89 (1981).
19. T. Yamamoto, Y. Hayaski et A. Yamamoto. Bull Chem. Soc. Jpn. **51**, 2091 (1978).
20. A.F. Sheppard et B.F. Dannels. J. Polym. Sci. Polym. Chem. Ed. **4**, 511 (1966).
21. I. Rubinstein. J. Electrochem. Soc. **130**, 7, 1507 (1983).
22. I. Rubinstein. J. Polym. Sci. Polym. Chem. Ed. **21**, 3035 (1983).

© 1999 CNRC Canada

23. (*a*) G. Brilmyer et R. Jasinski. J. Electrochem. Soc. **129**, 9 (1982); **129**, 1950 (1982); (*b*) E.Y. Pisarevskaya et M.D. Levi. Soviet Electrochem. **27**, 449 (1991).
24. (*a*) M. Delamar, P.C. Lacaze, J.Y. Dumousseau et J.E. Dubois. Electrochim. Acta, **27**, 66 (1982); (*b*) S. Hara, S. Aeiyach et P.C. Lacaze. J. Electroanal. Chem. **370**, 197 (1994).
25. K. Kaeriyama, M. Sato, K. Someno et S. Tanaka. J. Chem. Soc. Chem. Commun. 1199 (1984).
26. M. Satoh, M. Tabata, K. Kaneto et K. Yoshino. J. Electroanal. Chem. **195**, 203 (1985).
27. M. Satoh, M. Tabata, K. Kaneto et K. Yoshino. J. Chem. Soc. Chem. Commun. 1929 (1985).
28. M. Satoh, M. Tabata, K. Kaneto et K. Yoshino. Polym. Commun. **26**, 356 (1985).
29. T. Ohsawa, T. Inoue, S. Takada, K. Kaneto et K. Yoshino. Polym. Commun. **27**, 246 (1986).
30. K. Asley, D.B. Parry, J.M. Harris, S. Pons, D.N. Bennion, R. LaFollette, J. Jones et E.J. King. Electrochim. Acta, **34**, 599 (1989).
31. (*a*) M. Satoh, M. Tabata, K. Kaneto et K. Yoshino. Jpn. J. Appl. Phys. **25**, L. 73 (1986); (*b*) C. Kvarnström et A. Ivaska. Synth. Met. **41–43**, 2917 (1991).
32. (*a*) G. Shiavon, G. Zotti et G. Bontempelli. J. Electroanal. Chem. **186**, 1961 (1985); (*b*) C. Hérold et D. Billaud. Solid State Ionics, **40/41**, 985 (1990).
33. G. Shiavon, G. Zotti et G. Bontempelli. J. Electroanal. Chem. **161**, 323 (1984).
34. J.F. Fauvarque, M. Petit, F. Pfluger, A. Jutant, C. Chevrot et M. Troupel. Makromol. Chem. Rapid. Commun. **4**, 455 (1983).
35. J.F. Fauvarque, M.A. Petit, A. Digua et G. Froyer. Makromol. Chem. **188**, 1833 (1987).
36. G. Froyer, F. Maurice, M.A. Petit, J.F. Fauvarque, et Y. Pelous. Brevet Français, 85, 18666 (1985).
37. A. Aboulkassim et C. Chevrot. Polymer, **34**, 401 (1993).
38. R.L. McCreery. Electroanal. Chem. **18**, 221 (1991).
39. (*a*) K. Kinoshita. Carbon: electrochemical and physico-chemical properties. Wiley, New-York. 1988; (*b*) S.Z. Shi, J. Davey, X. Ren et S. Gottesfeld. 8th Int. Semin. on Double Layer Capacitors and Similar Energy Storage Devices. Florida Educational Seminars. 1998; (*c*) T. Morimoto, K. Hiratsuka, Y. Sanada et K. Kurihara. J. Power Sources, **60**, 239 (1996); (*d*) D. Qu et H. Shi. J. Power Sources, **74**, 99 (1998).
40. M.M. Baizer. Organic electrochemistry. Marcel Dekker, New-York. 1973. p. 224.

© 1999 CNRC Canada

Effect of cyclodextrin complexation on the photochemistry of the lignin model α-guaiacoxyacetoveratrone

L.T. Okano, R. Ovans, V. Zunic, J.N. Moorthy, and C. Bohne

Abstract: The photodecomposition of α-guaiacoxyacetoveratrone (GAV) in homogeneous solvents and in aqueous cyclodextrin solutions was studied by following the fluorescence emission of the photoproducts formed. The same qualitative behavior as previously observed for the photodegradation quantum yield measurements was reproduced in the fluorescence studies in dry or wet methanol and acetonitrile. The yield for GAV photodegradation in water is smaller than in the organic solvents. Complexation of GAV to β- and γ-cyclodextrins leads to an increase in the photodecomposition yield, especially during the early part of the photodecomposition kinetics. The transients formed in the photolysis of GAV in water are similar to those observed in acetonitrile, and the lifetime of triplet GAV in water is 130 ns. In addition, solvated electrons were formed when GAV was photolyzed in water. Complexation of GAV to cyclodextrins leads to an increase in the triplet yield compared to the radical yield and a moderate shortening of the triplet lifetime.

Key words: α-guaiacoxyacetoveratrone, cyclodextrin, excited singlet states, excited triplet states, radicals.

Résumé : Utilisant l'émission de fluorescence des photoproduits formés, on a étudié la photodécomposition de l'α-guaïacoxyacétovératrone (GAV) dans des solvants homogènes et dans des solutions aqueuses de cyclodextrine. Dans les études de fluorescence dans le méthanol sec ou aqueux ainsi que dans l'acétonitrile, on a reproduit le même comportement qualitatif que celui observé antérieurement lors de mesures de rendements quantiques pour la photodégradation. Le rendement pour la photodégradation de la GAV dans l'eau est inférieur à celui observé dans les solvants organiques. La complexation de la GAV par les β- et γ-cyclodextrines provoque une augmentation du rendement de photodécomposition, particulièrement au début de la cinétique de photodécomposition. Les espèces transitoires qui se forment lors de la photolyse de la GAV dans l'eau sont semblables à celles observées dans l'acétonitrile et le temps de vie de l'état triplet de la GAV dans l'eau est de 130 ns. De plus, il se forme des électrons solvatés lors de la photolyse de la GAV dans l'eau. La complexation de la GAV par les cyclodextrines provoque une augmentation du rendement de l'état triplet par rapport au rendement en radical ainsi qu'à une diminution modérée du temps de vie du triplet.

Mots clés : α-guaïacoxyacétovératrone, cyclodextrine, états singulets excités, états triplets excités, radicaux.

[Traduit par la Rédaction]

Introduction

The photodecomposition of lignin is responsible for the yellowing observed in paper manufactured from mechanical pulp. In recent years, a significant effort has been made to find efficient inhibition strategies to eliminate or considerably slow down the yellowing of lignin-containing paper. The mechanisms for lignin photodegradation are complex involving several reactive intermediates (1, 2). Most mechanistic studies have been performed in solution employing model compounds because lignin is a high molecular weight polymer that is difficult to handle in solution. Solution studies were important to determine the decomposition pathways, the multiplicity of the excited states involved, and to characterize spectroscopically the reactive intermediates involved (3–13). α-Guaiacoxyacetoveratrone (GAV) has frequently been used as a model compound (8, 9, 13, 14), because it contains key features of lignin. In contrast to other aryl ketones, it was shown that α-phenoxyacetophenones, such as GAV, react from their excited singlet state (8, 11–14) to form the corresponding phenacyl and phenoxy radicals (Scheme 1). This reactivity suggests that the β-cleavage process from the excited singlet state readily competes with intersystem crossing, leading to quantum yields for the latter process that are significantly smaller than unity (13). Compared to α-phenoxyacetophenone (15), the triplet reactivity of GAV is diminished because its lowest triplet state has a π,π^* configuration (9). The triplet lifetime is determined by the efficiency for intramolecular deactivation through β-phenyl quenching, as was observed for β-arylpropiophenone and α-(aryloxy)acetophenones (15–21), and the rate constant for β-cleavage (14). The photodecomposition quantum yields and triplet lifetimes of GAV vary significantly in different solvents (8, 14). This complex behavior is

Received March 9, 1999.

L.T. Okano, R. Ovans, V. Zunic, J.N. Moorthy, and C. Bohne.[1] Department of Chemistry, University of Victoria, P.O. Box 3065, Victoria, BC V8W 3V6, Canada.

[1]Author to whom correspondence may be addressed. Telephone: (250) 721-7151. Fax: (250) 721-7147. e-mail: bohne@uvic.ca

© 1999 NRC Canada

Scheme 1.

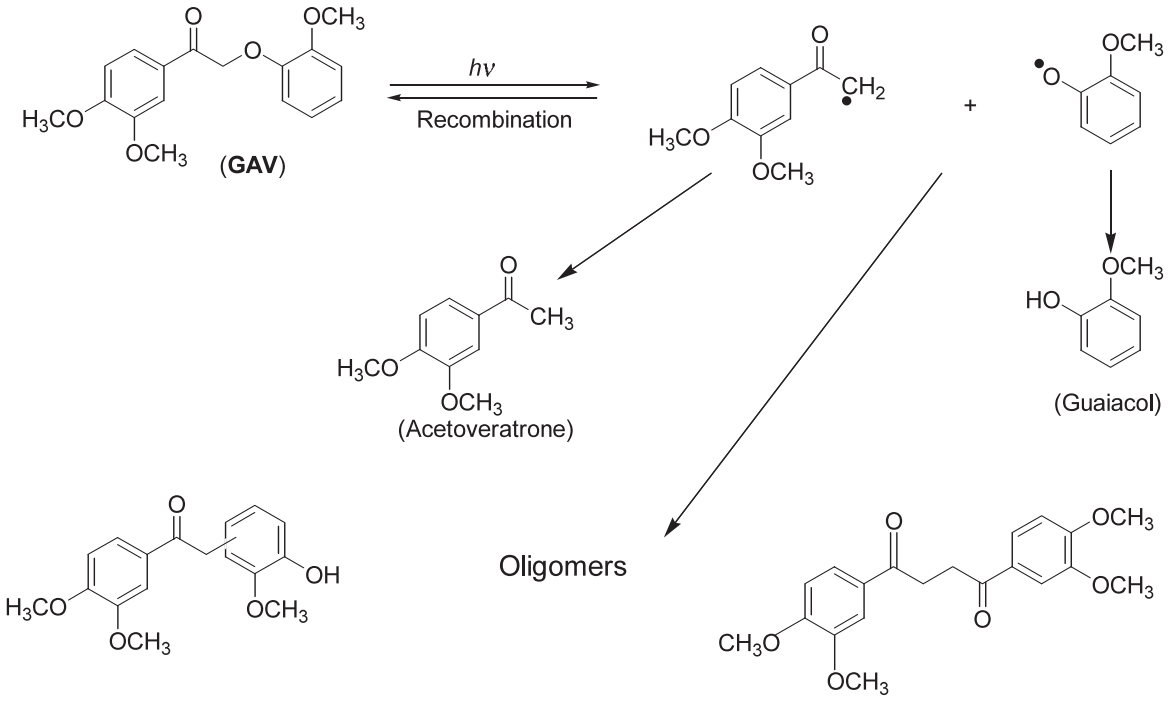

related to the reactivity from the GAV singlet excited state and a solvent effect on the intramolecular quenching in the triplet state.

Lignin is located in a constrained environment in the cell wall of wood fibers that influences to a different extent the deactivation pathways of the excited singlet and triplet states when compared to these processes in solution. There are a limited number of studies on the photoreactivity of lignin model compounds in constrained environments or on solid supports. The photodegradation of GAV has been shown to decrease when this compound is adsorbed on paper fibers (9). In addition, GAV is stable in the crystalline state, a fact that was attributed to the formation of excimer-like arrangements in the solid state (6). The photochemistry of α-(aryloxy)acetoveratrones was studied on solid silica gel, Na-X zeolites, and cellulose (4). In the case of cellulose, an inefficient photodecomposition and an enhanced triplet lifetime were observed. These experiments show that the confinement of lignin in the fibers of paper can alter the lignin photoreactivity. Furthermore, the mobility of oxygen through the paper fiber may also be important, since yellow products are only formed in the presence of oxygen (2). In this respect, it has been shown that the quenching of reactive intermediates on cellulose or paper by oxygen is very inefficient (3, 4, 22–24), suggesting that the reaction of reactive intermediates with oxygen may be the rate-limiting step in the photoyellowing process.

The objective of this work is to establish how constrained environments can affect the photochemistry of GAV and the mobility of the radicals formed in its photodecomposition. Since the work on solids has proven to be difficult, we decided to investigate the effect of a constrained environment on the photochemistry of GAV in solution. Cyclodextrins (CDs) were chosen, since they provide a chemical environment similar to cellulose, and the effect of CD inclusion on the photochemistry of β-phenylpropiophenone (25, 26) and α-phenoxyacetophenone (27) have been previously reported. In addition, we chose to work in water, since paper has some moisture (5–10% water), and lignin is probably exposed to a hydroxylic environment.

Experimental

The β- (lot F6080–191) and γ-CDs (lot E 8056) were a kind gift from Cerestar and were used as received. Guaiacol (98%, Aldrich) and 3,4-dimethoxyacetophenone (acetoveratrone) (98%, Aldrich) were distilled under reduced pressure, methanol (ACP, spectrograde) was distilled from CaH_2, and acetonitrile (ACP, HPLC grade) was distilled under N_2 from $LiAlH_4$. Deionized water (SYBRON, Barnstead deionizing system) was used for all aqueous samples. Whatman filter papers (number 1001 125) were used as received.

The α-guaiacoxyacetoveratrone (3′,4′-dimethoxy-α-(2-methoxyphenoxy)acetophenone, GAV) was synthesized by the method previously reported (28). The required synthesis of 3,4-dimethoxy-α-bromoacetophenone was modified from that previously reported in that dimethoxyacetophenone was reacted with pyridinium bromide perbromide in chloroform and under nitrogen (29–33). GAV was purified by repeated recrystallization from ethanol (95%), and its purity was checked by mp (77–80°C) and ^1H NMR measurements.

UV-vis absorption spectra were measured on Cary 1 or Cary 5 spectrometers from Varian. Induced circular dichroism spectra were measured on a Jasco J-720 spectropolarimeter. Fluorescence was measured with a PTI QM-2 fluorimeter at 20.0 ± 0.5°C. Most samples were excited at 280 nm, however, when necessary the excitation wavelength was shortened to avoid the Raman emission from the solvents. Emission spectra were collected before and after the photodecomposition kinetics to monitor prod-

© 1999 NRC Canada

uct formation. Narrow slits (bandwidth 1–2 nm) were employed to measure the emission spectra to minimize the photodecomposition of GAV. The photodecomposition kinetics of GAV was monitored simultaneously by the product emission at 310 and 350 nm. The rate of decomposition was dependent on the excitation intensity and bandwidth (5 or 7 nm) employed for the excitation slits. Solutions were contained in 10 × 10 mm quartz cells and were purged with N_2 or O_2 for 30 min before the fluorescence measurements were performed. Solid samples were either mounted on a triangular metal support or were suspended within the sample holder. In both cases, the excitation beam and detector were in a 90° arrangement, and for the solid samples, the surface of the paper was placed at a 45° angle with respect to the excitation beam.

The laser flash photolysis system used for the transient studies has been previously described (34). Samples at 20 ± 2°C were excited either with a Lumonics excimer laser at 308 nm (<30 mJ/pulse, 5 ns pulse width) or a Spectra Physics Nd:YAG laser at 266 nm (<20 mJ/pulse, 6 ns pulse width). A program written with Labview 4.0™ (National Instruments) was used to control the laser flash photolysis systems, acquire the data, and for initial analysis of the decay curves. A flow cell (7 × 7 mm Suprasil) was employed for solutions purged with N_2 and O_2 (30–40 min) so that a fresh portion of the solution was irradiated at each laser pulse. The solution in the reservoir before entering the flow cell was covered with aluminum foil to avoid photodecomposition by ambient light. A 7 × 7 mm Suprasil cell stoppered with a rubber septum was used for N_2O purged (20 min) solutions. The photodecomposition in the static samples was followed by UV-vis absorption, and the sample was subjected to a small number of laser shots so that only limited decomposition of GAV occurred.

Solutions of GAV in all solvents except water were prepared by dissolving the solid in the respective solvent. Aqueous solutions were prepared by the injection of a small amount (<1%) of the methanolic GAV solution into water. In all cases, the concentration of GAV was 15.8 μM. The CD solutions were prepared by dissolving, in the aqueous GAV solution, the appropriate amounts of β- and γ-CD to reach final concentrations of 10 and 30 mM, respectively. These solutions were warmed in hot water for 5 min and were left stirring for at least 12 h. Some insoluble material was removed by filtering the solutions through 40 μm Millipore filters. For this reason, it is likely that the GAV and CD concentrations quoted are somewhat lower than stated. During preparation and storage, all solutions were shielded as much as possible from ambient light.

Filter paper samples (5 × 1.1 cm) containing GAV were prepared by using either the drop or immersion methods (35). For the drop method, 0.15–0.5 mL of a methanolic or methanol–water solution of GAV (≤0.01 M) was slowly dropped with a microsyringe on samples mounted in Delrin frames. Two samples were always prepared from the same GAV solutions. After application of GAV, the samples were protected from light and were dried for at least 12 h. In the case of the immersion method, two samples were simultaneously placed for 20 min in Petri dishes containing GAV solutions (≤0.01 M). After the immersion period, the paper samples were mounted on Delrin frames and were dried as described above. The immersion method leads to a more homogeneous distribution of additives in paper (35). The amount of GAV added was established by comparing the weight of each paper sample before and after the application of GAV. Filter papers without any treatment were employed as a reference. The samples were irradiated for 1 h in front of a 75W Xe lamp (PTI).

Fig. 1. Induced circular dichroism of 15.8 μM GAV in the presence of 5 mM β-CD (*a*, 1) and 10 mM γ-CD (*b*, 1). The spectra for CDs (2) are also shown.

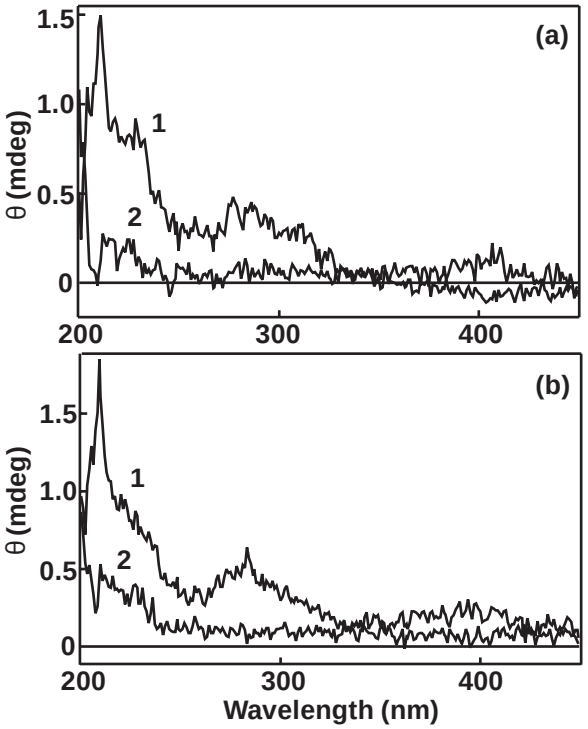

Results

Several spectroscopic techniques can be employed to establish the complexation of guest molecules with CDs. The primary consideration in choosing a technique is that a change of a spectroscopic property has to be observed for the free and complexed guest molecule. The formation of the GAV–CD complexes was observed by circular dichroism spectroscopy. GAV in water does not show a circular dichroism signal because it is achiral. In the presence of β- or γ-CD, induced circular dichroism signals were observed in the spectral region where GAV absorbs (Fig. 1). These experiments clearly show that GAV is incorporated to some extent into both CD cavities. Unfortunately, circular dichroism could not be employed to determine the equilibrium constants values and the complexation stoichiometries due to the poor signal-to-noise ratio observed and the fact that some photodestruction (<10%) occurs upon irradiation in the spectrometer. Likewise, ^1H NMR could not be employed to determine the complexation efficiency because of the low solubility of GAV in water (<20 μM).

Fluorescence is, in principle, an ideal technique to establish the complexation of guest molecules with CDs, because fluorescence properties, such as the emission quantum yields

© 1999 NRC Canada

Fig. 2. Emission spectra before (2) and after (1) irradiation of 15.8 μM GAV for 1 h at 280 nm in (*a*) water, (*b*) methanol, and (*c*) acetonitrile.

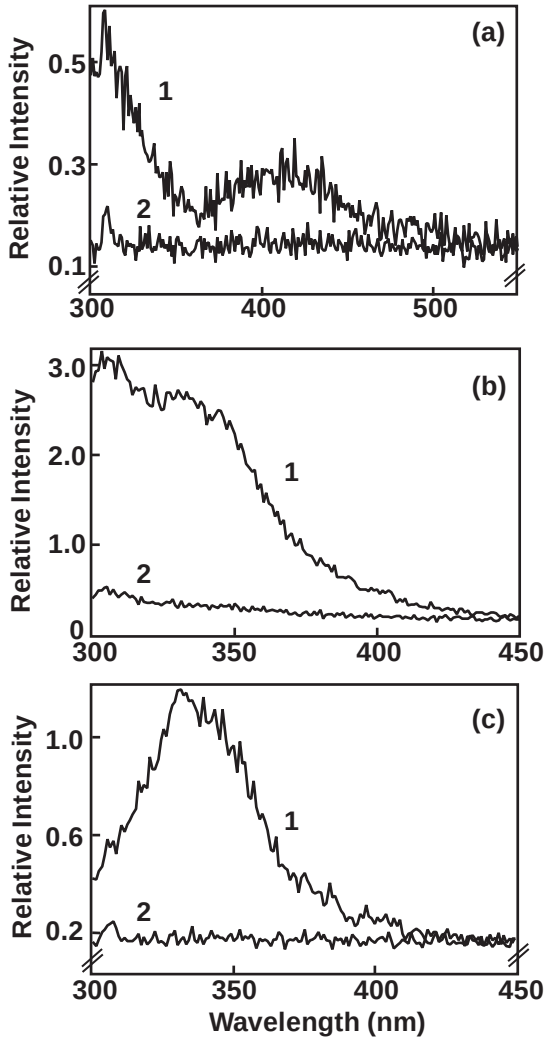

and lifetimes, can be very sensitive to the environment around the fluorophore. The first approach tried to establish the complexation of GAV to β and γ-CD was fluorimetry, since an emission assigned to the fluorescence of GAV in methanol had been previously reported (6). Unfortunately, we established that GAV does not fluoresce when the samples are shielded from the exposure to ambient light (Fig. 2). Appreciable fluorescence is only observed after the samples are exposed to the excitation beam in the fluorimeter (Fig. 2). This emission was assigned to the fluorescence of photoproducts. The spectral distribution of the emission is solvent dependent. The emission observed in water and methanol between 310 and 320 nm, after exposure of the sample to the excitation beam, is not due to Raman emission of the solvent because the spectra are the same at different excitation wavelengths.

Guaiacol and acetoveratrone are likely products in the photolysis of GAV (Scheme 1). For this reason, their fluorescence spectra in various solvents was measured (Fig. 3). Guaiacol has a higher fluorescence quantum yield by about one order of magnitude than acetoveratrone. In addition, the

Fig. 3. Fluorescence spectra of 15.8 μM acetoveratrone (*a*, λ_{ex} = 280 nm) and guaiacol (*b*, λ_{ex} = 240 nm) in water (1), methanol (2), and acetonitrile (3). The sharp peak at 260 nm (*b*) corresponds to the Raman emission of the solvent.

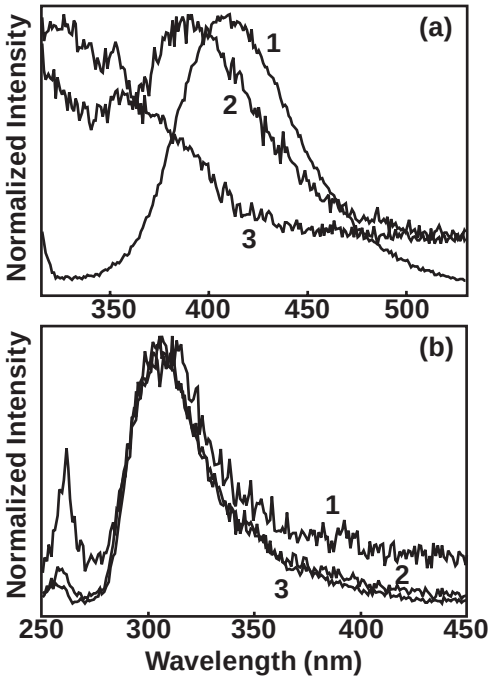

fluorescence spectra for guaiacol were the same for all three solvents, and its emission efficiency in acetonitrile and methanol was somewhat higher (ca. 2) than in water. In contrast, the acetoveratrone emission is very solvent dependent with emission maxima at 420, 390, and ca. 330 nm, respectively, in water, methanol, and acetonitrile, and the emission quantum yield is higher in water than in the organic solvents.

The decomposition quantum yields of GAV in homogeneous solution are very dependent on the nature of the solvent and the presence of water (8). For this reason, we used the appearance of the photoproduct emission to measure relative photodecomposition yields of GAV in different solvents. The kinetic traces for the appearance of photoproducts were measured at 310 and 350 nm (Fig. 4). The rate of appearance was faster in methanol than in acetonitrile. At 310 nm, the photoproduct formation rate follows a fairly linear relationship, whereas at 350 nm, a considerable slowdown is observed as the photodecomposition of GAV proceeds. Most kinetic traces showed initially a fast increase in the fluorescence intensity. This burst kinetics appears as an initial jump in the traces shown in Fig. 4. The initial jump also incorporates any product formed when spectra were collected with narrow slits before the kinetic run and any product formed due to exposure to ambient light during sample preparation and handling.

Relative yields for the formation of products were estimated from the initial slopes of the photodecomposition kinetics after the burst phase (Table 1). In the absence of oxygen, the rate for appearance of photoproduct emission at 310 nm is highest in methanol and comparable in acetonitrile and water. At 350 nm, the photodecomposition

© 1999 NRC Canada

Table 1. Relative rates for the appearance of the photoproduct emission at 310 or 350 nm, estimated from the initial slopes and normalized to the rate at 310 nm in water in the presence of nitrogen.

	Relative rates			
Solvent	310 nm/N_2	310 nm/O_2	350 nm/N_2	350 nm/O_2
H_2O	1	1	0.3	0.5
CH_3OH	8	1	22	3
CH_3OH/H_2O (60/40)	9	3	2	1
CH_3OH/H_2O (40/60)	2	2	12	6
CH_3CN	1	0.2	3	1
CH_3CN/H_2O (60/40)	3	2	5	3
CH_3CN/H_2O (40/60)	4	4	11	2

Fig. 4. Kinetics for the appearance of photoproduct emission for the photolysis (λ_{ex} = 280 nm) of 15.8 μM GAV monitored at 310 (*a*) and 350 (*b*) nm in methanol (1), acetonitrile (2), and water (3). The opening of the shutter leads to the initial jump in the emission intensities.

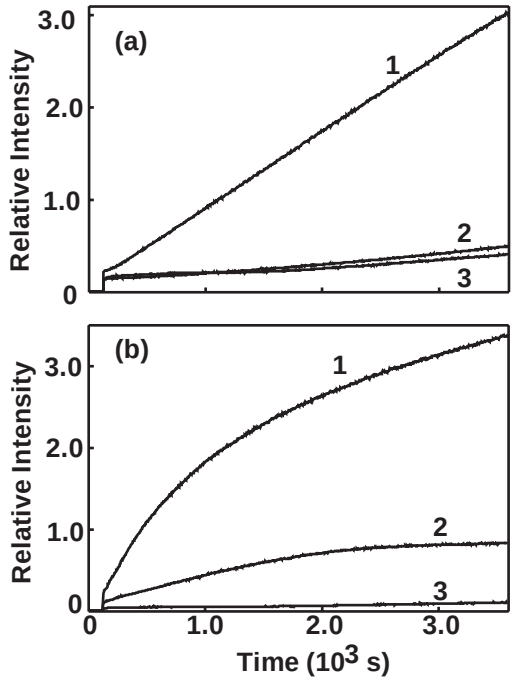

Fig. 5. Kinetics for the appearance of photoproduct emission for the photolysis (λ_{ex} = 280 nm) of 15.8 μM GAV monitored at 310 (*a*) and 345 (*b*) nm in the presence of 10 mM β-CD (1), 30 mM γ-CD (2), 10 mM γ-CD (3), 5 mM β-CD (4), and in water (5). The traces in (*a*) show the kinetics after the initial jump, while the experiments in (*b*) show the burst kinetics at short times.

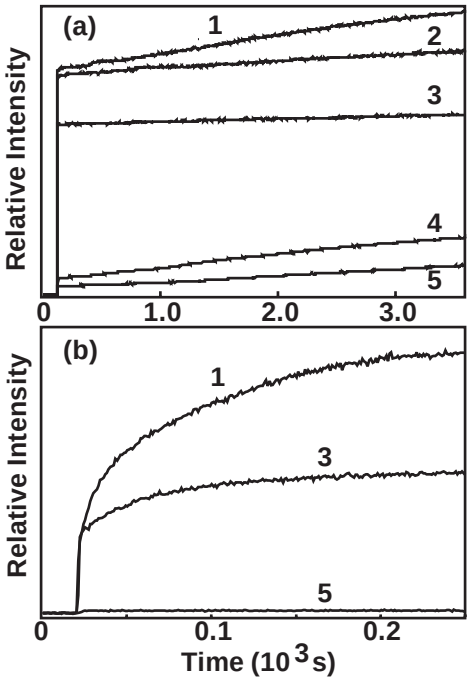

rate is highest in methanol and lowest in water (Fig. 4). The presence of oxygen has only a small effect on the rate of product appearance in water, due to the low solubility of oxygen in this solvent (1.4 mM) (36). In methanol and acetonitrile, the presence of oxygen led to a marked decrease in the rate of emission of the photoproducts, suggesting that oxygen efficiently quenched the excited state responsible for product formation.

The presence of water in methanol was shown to decrease the degradation quantum yield of GAV, whereas the opposite effect was reported for the photolysis in acetonitrile (8). The relative rates for photoproduct emission showed a similar trend. The emission rate at 310 nm in methanol was only decreased at a high water content (60%), whereas a more significant decrease of the rate was measured at 350 nm (Table 1). In the case of GAV photolysis in acetonitrile, an increase of the photoproduct formation was observed in the presence of water (Table 1).

The emission spectrum of GAV in the presence of β- and γ-CD is similar to that observed for GAV in water. However, the contribution of the emission at 450 nm is higher in the presence of CDs. The complexation of GAV to β- and γ-CD led to a slight increase in the rate of appearance of the photoproduct emission when monitored at 310 and 350 nm (Fig. 5, Table 2). Some of this enhancement is quenched in the presence of oxygen. A more significant effect of the CD complexation is observed on the initial jump corresponding to the burst phase (Table 3). The enhancement of the initial jump increases when the β-CD concentration is raised, and this enhancement is not sensitive to the presence of oxygen. In contrast, the enhancement in the presence of γ-CD is sensitive to the presence of oxygen (Table 3).

© 1999 NRC Canada

Table 2. Relative rate ratio for the estimated appearance of the GAV photoproduct emission in the presence of β- and γ-CD with respect to the appearance rate in water.

	Relative rate ratio (CD/H_2O)	
CDs	310 nm/N_2	350 nm/N_2
5 mM β-	3	2
10 mM β-	4	6
10 mM γ-	1	2
30 mM γ-	3	4

Table 3. Ratios for the intensities of the initial jump in the presence of β- and γ-CD with respect to the intensity in water.

	Relative rate ratio (CD/H_2O)			
CDs	310 nm/N_2	310 nm/O_2	350 nm/N_2	350 nm/O_2
5 mM β-	2	2	3	2
10 mM β-	29	24	15	13
10 mM γ-	22	5	13	5
30 mM γ-	28	6	20	14

The emission of filter paper with and without GAV was measured to determine whether fluorescence spectroscopy could be employed to monitor the photodecomposition of GAV absorbed into the paper matrix. The filter paper without GAV showed some background emission. In the presence of GAV (≤3% w/w), the same emission spectra were observed when the sample was excited at 270, 280, or 310 nm. The emission spectra were also measured after the reference and paper sample containing GAV were irradiated for 1 h. The emission intensities measured for the reference and GAV samples were nonreproducible. In some cases, an increase of the emission intensity was observed, whereas for duplicate samples prepared from the same GAV solution a decrease of the intensity was measured. The same pattern was observed for samples prepared either by the drop or the immersion methods. Although the contradictory results on the emission intensity are difficult to explain at this point, it was observed that the magnitude of the enhancement or the decrease is dependent on the amount of GAV adsorbed into the paper and the duration of the irradiation of the sample.

Laser flash photolysis was employed to study the transient species formed in the photolysis of GAV. All transient studies, with the exception of those in the presence of N_2O, were performed using flow cells. When static cells were employed, a higher yield of radicals compared to the triplet yield was observed. This is particularly noticeable when GAV is excited in the presence of CDs. The higher yield of radicals is probably due to the accumulation of long-lived radicals after subsequent laser shots.

The transient phenomena observed after excitation at 308 nm of GAV in acetonitrile were similar to those previously reported (5, 7, 8, 13). The short-lived triplet (τ = 254 ns) was observed around 400 nm, and the weak transient absorption in the 400–500 nm region of the phenacyl radical was also present. Both these transients were efficiently quenched by oxygen. The remaining transient absorption in the 300–400 nm region in the presence of oxygen is due to the guaiacoxy radical.

Fig. 6. Transient absorption spectra of 15.8 μM GAV/N_2 after excitation at 308 nm in water (*a*, (■) 90 and (○) 570 ns delays), in the presence of 10 mM β-CD (*b*, (■) 70 and (○) 360 ns delays), and in the presence of 10 mM γ-CD (*c*, (■) 80 and (○) 640 ns delays).

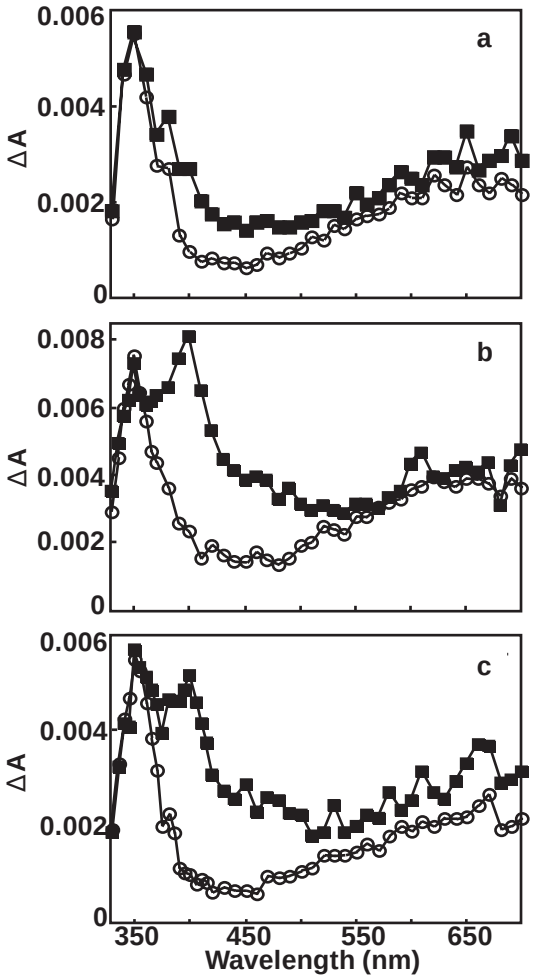

The transient phenomena of GAV in water have not been previously described. The same transients as observed in acetonitrile were also present in water (Fig. 6*a*). In addition, in water we observed the formation of solvated electrons that absorb above 600 nm. The solvated electrons are probably formed in a two-photon process leading to the photoionization of GAV. The presence of solvated electrons was established by the disappearance, in the presence of N_2O, of the short-lived absorption measured at 640 nm. The triplet lifetime of GAV in water was (130 ± 10) ns, and it is shortened to (76 ± 3) ns in oxygen saturated solutions. This result is consistent with a diffusional quenching rate constant by oxygen, taking into account the oxygen solubility in water (1.4 mM).

Complexation of GAV to 10 mM β- or γ-CD leads to a larger yield of triplets when compared to the radical yield measured for the photolysis of GAV in water (Fig. 6). The triplet GAV lifetime in the presence of β-CD is (110 ± 3) ns and (104 ± 4) ns in the absence and presence of oxygen, whereas in the presence of γ-CD the respective triplet lifetimes are (97 ± 5) and (88 ± 7) ns. The residual absorption

© 1999 NRC Canada

Table 4. Average ratios for the solvated electron yield formed in the photolysis at 308 nm of GAV in the presence of CDs and in water. The number in parentheses corresponds to the number of experiments averaged.

CD	Solvated electron ratio (CD/H_2O)
10 mM β-	1.4 ± 0.2 (5)
10 mM γ-	1.2 ± 0.1 (5)
30 mM γ-	1.3 ± 0.2 (2)

observed after the decay of the triplet corresponds to the guaiacoxy radical, which is very long lived (>100 μs).

In the presence of CDs, an increase was observed for the yield of solvated electrons. The amount of solvated electrons formed was estimated by subtracting the ΔA values at 640 nm in the presence of N_2O, where all solvated electrons are quenched, from the value determined in the presence of N_2. Since the photoionization of GAV is likely to be a two-photon process, the absolute yield for solvated electron formation is very dependent on the laser energy that excites the sample. For this reason, the yields for solvated electron formation have to be compared for measurements performed for the same experimental conditions. Although the absolute values for these yields changed between experiments performed on different days, it was always observed that the yields in the presence of β- and γ-CD were higher than those measured in water (Table 4). Experiments performed by exciting GAV at 266 nm in the presence of 10 mM of both CDs led to the same ratios for solvated electron formation as observed for the excitation at 308 nm.

Discussion

The photodecomposition of GAV in homogeneous solution leads to the formation several products (Scheme 1) (8, 13, 14). Some of these photoproducts fluoresce, and since fluorescence spectroscopy is a very sensitive technique, a small amount of product formation can be detected before any decomposition is visible by other spectroscopic techniques, such as UV-vis absorption and NMR. The spectral distribution for the photoproduct emission following the photolysis of GAV is very dependent on the nature of the solvent. This difference could be due to changes in the product distribution or different emission quantum yields for each product in the different solvents. Since the emission quantum yields of guaiacol or acetoveratrone were shown not to vary by more than a factor of 2, we explain the different spectra observed to be due to different product distributions.

The products from the photolysis of GAV will have different fluorescence spectra as exemplified for guaiacol and acetoveratrone. The coupling products shown in Scheme 1 are expected to have a fluorescence emission that is similar to that of acetoveratrone, since the chromophore of the latter is present in these compounds. The emission between 300 and 320 nm observed for the photoproduct formation of GAV in methanol and water is assigned to the formation of guaiacol. This spectral feature is absent for the photolysis of GAV in acetonitrile, suggesting that guaiacol is not formed in this solvent. The lack of detection of guaiacol is not due to a sensitivity problem, since the guaiacol emission quantum yield is about one order of magnitude higher than that for acetoveratrone. The emission observed at 420 nm in water and between 320 and 340 nm in methanol and acetonitrile is assigned to products with the acetoveratrone moiety. This blue shift of the emission maxima was also observed when the fluorescence of acetoveratrone was measured in these organic solvents. The larger blue shift observed for the photoproduct emission of GAV could be due to a more significant solvent effect on the emission spectra of the coupling products when compared to the shift for acetoveratrone.

A brief comment on the fact that acetoveratrone fluoresces is justified because it has implications on why GAV is reactive from the excited singlet state. The fluorescence of some methoxy substituted aryl ketones in water has been previously reported (37), but in most cases, ketones do not fluoresce because their intersystem crossing quantum yield is close to unity (38). The intersystem crossing efficiency depends on the configurations and the energy difference between the singlet and triplet states involved in the transition. The configuration of the excited states of ketones can be influenced by the presence of electron-donating substituents that stabilize π,π^* states compared to n,π^* states (39). In the case of acetoveratrone, the presence of two methoxy substituents will stabilize the π,π^* states in the singlet and triplet manifold, leading to a decrease of the intersystem crossing rate constant by either switching the configuration of S_1 to a π,π^* one or by influencing the S_1–T_n energy gap involved in the intersystem crossing process. This decrease of the intersystem crossing quantum yield leads to lengthening of the excited singlet lifetime and the observation of fluorescence. This stabilization in the case of GAV leads to a less reactive triplet state when compared to ketones with n,π^* triplets (13). Furthermore, the GAV photophysics will primarily be determined by the acetoveratrone moiety. This ensures that the rate constant for intersystem crossing of GAV is lower than for other ketones (13) and that the GAV excited singlet state can undergo a β-cleavage reaction. In contrast to acetoveratrone, GAV does not fluoresce in solution, suggesting that the rate constant for β-cleavage is larger than the radiative rate constant responsible for fluorescence. The emission of the photoproducts of GAV in methanol was previously assigned incorrectly to the fluorescence of GAV (6), and based on this assignment, the authors explained the crystalline GAV emission with a maximum at 450 nm to be due to an excimer formed from two adjacent acetoveratrone moieties. The emission observed in the solid state may be due to the emission of GAV, since this emission occurs in the spectral region where acetoveratrone fluoresces in water. However, other evidence previously reported (6) supports this emission to be due to excimer formation. A definite assignment of this emission is problematic, since the emission spectra of acetoveratrone was shown to depend on the solvent polarity, and a similar effect is expected to be observed for GAV.

The objective of the kinetic studies for photoproduct appearance was to investigate if the relative rates observed in the fluorescence measurements can be correlated to the reported photodegradation quantum yields (8). It is important to take into account that the fluorescence intensity is directly proportional to the emission quantum yield of the excited

© 1999 NRC Canada

fluorophores. For this reason, the presence in solution of any substance that quenches the emission of the fluorophore will lead to a decrease of the measured fluorescence intensity. For example, if during the photolysis of GAV one of the products is an efficient quencher of the fluorescence from a second product, the emission intensity of the latter will be decreased. Due to this possible quenching effect, any analysis of the shape of the kinetic trace (i.e., linear at 310 nm and curved at 350 nm) was not attempted. Furthermore, the photolysis of GAV leads to a mixture of products that can fluoresce. At each wavelength, the intensity measured is a function of the concentration of each product, its absorption coefficient at the excitation wavelength, and its emission quantum yield at the wavelength where the kinetics is being monitored; we did not expect to observe the same relative rates when the photoproduct formation was monitored at 310 and 350 nm. Clearly, no quantitative information is available from the kinetic studies performed. However, the relative ordering of the photodegradation yields in methanol and acetonitrile as well as the effect of water addition to these solvents were reproduced. This adequate qualitative correspondence of the photodegradation quantum yield with the relative fluorescence rates shows that fluorescence can be used as a first screening technique to determine the photodecomposition yields of lignin model compounds. The advantage of using fluorescence for preliminary studies is that the experiments are much quicker to perform than the determination of quantum yields, and fluorescence can be employed for the screening of different experimental conditions before performing quantum yield measurements.

The fluorescence experiments were employed to estimate the GAV photodecomposition quantum yield in water, since this value has not been previously reported. The quantum yield in water is much smaller than in methanol and is probably also smaller than in acetonitrile. The emission spectra for the photoproducts indicate that the product distribution observed in water is closer to that in methanol than the product distribution observed in acetonitrile. These experiments show that the photodecomposition pattern of GAV in water, and probably other lignin model molecules, cannot be extrapolated from studies in organic solvents. This is an important point when trying to understand the photodegradation of lignin because the paper matrix contains some water.

We tried preliminary experiments to explore the fluorescence of product formation for the decomposition of GAV when incorporated into paper. These experiments were inconclusive, suggesting that the decomposition rate and (or) the emission properties of the photodecomposition products are affected by the incorporation in the paper matrix. Moreover, these experiments show the complexity of the behavior of fluorophores in paper and that degradation of lignin may have a quenching effect when fluorescent brightners are employed to counteract the yellowing of paper made from mechanical pulp.

The complexation of GAV to β- and γ-CD was established by the appearance of an induced circular dichroism signal when GAV was solubilized in the presence of CD. The direction and strengths of the induced circular dichroism signals of an achiral guest in the CD cavity can be related to the position of the guest within the CD cavity (40–42). The fact that the same direction was observed for the induced circular dichroism signals of GAV in β- and γ-CD suggests that the guest is incorporated in a similar environment in both cavities. No detailed information on the complexation environment could be obtained because the signal-to-noise ratio of the spectra is too poor to warrant any further analysis. The complexation of α-phenoxyacetophenone with β-CD has been previously reported (27), and a 1:1 complex in which the benzoyl moiety is encapsulated was proposed. GAV is too large to completely fit within the β-CD cavity, and for 1:1 complexes, part of the molecule will be exposed to the aqueous phase. However, the possibility exists that at higher β-CD concentrations, a 1:2 (GAV:CD) complex is formed that protects the guest from the aqueous environment. In the case of the larger γ-CD, the benzoyl and phenoxy moieties could be included in the same cavity as was previously proposed for the inclusion of β-phenyl-*p*-methoxypropiophenone (25).

In principle, the complexation of GAV to CDs could lead to either a decrease or increase of the photodegradation rate. In the case of a 1:2 (GAV:CD) complex, we would expect a decrease of the photodegradation rate, since separation of the radicals would be inhibited, leading to an increase in the probability for GAV regeneration. Since such an increase was not observed, it is likely that 1:2 complexes are not present to an appreciable amount. In contrast, the entrapment of one of the radical moieties within the CD cavity and efficient release of the second radical could lead to an enhancement of the GAV photodecomposition quantum yield. Surprisingly, most of the enhancement effect is observed on the initial jump and not on the relative rates at longer times. The relative rates are increased moderately (2–6) by the presence of CDs, indicating that complexation of the radicals to the CD cavity does not affect significantly the rate of product formation after the burst phase (initial jump). In the laser flash photolysis studies, we established that at least the phenoxy radicals are very long lived (>100 μs). Since the exit rate constants of guests from CD cavities are of the order of 10^5–10^6 s^{-1} (43, 44), the long radical lifetimes ensure that radicals formed from the GAV photoreaction can exit and enter CD cavities for many times before they are involved in recombination reactions. Consequently, the entrapment of the radicals does not lead to a significant alteration of the rate for product formation.

The most pronounced effect of CD complexation on the GAV photodecomposition was observed on the enhancement of the amount of product formed during the burst phase. The magnitude of this effect depends on the CD concentration, indicating that this enhancement is due to the complexation of GAV to CDs. This increase is not due to an inhibition of the recombination probability of the phenacyl and guaiacoxy radicals to regenerate GAV, since this inhibition would mean that the exit of one of the radicals from the CD cavity is faster than the separation of the radicals in the solvent cage formed in water. This is an unlikely scenario because it was shown that polar molecules such as triplet xanthone, which are not completely included in the CD cavity (45), have an exit constant of 8.4×10^6 s^{-1} (46), which is much slower than the separation of encounter complexes of neutral molecules in aqueous solution. For this reason, it is likely that the phenacyl and guaiacoxy radicals remain in close contact within the CD cavity for a longer period of time than an en-

© 1999 NRC Canada

counter complex in the aqueous phase. In this case, the enhanced emission intensity is due to a larger yield of coupling product formation in the CD cavities when compared to the reaction in the bulk phase.

An increase of the intersystem crossing quantum yield of GAV when this molecule is complexed to the CDs could also be responsible for the increase of products formed during the burst phase. The laser flash photolysis data suggest that the intersystem crossing quantum yield increased, since a higher triplet to radical concentration is observed for GAV in the presence of CDs than in water. The triplet lifetimes of GAV in β- (110 ns) and γ-CD (97 ns) are short enough that some β-cleavage will occur within the CD cavity. The radical pair formed from the cleavage of a triplet excited state has triplet multiplicity, and an intersystem crossing process has to occur before these radicals can react. For this reason, it is likely that one of the radicals will have to escape the CD cavity before any of the recombination or coupling reactions can occur. In this respect, the increased intersystem crossing for GAV leads to a decrease of the probability for the recombination of GAV and an enhancement of the product formation.

A puzzling effect was observed when oxygen was added to the solutions containing GAV and CDs. The initial jump for the fluorescence experiments decreased when GAV was complexed to γ-CD, but no effect was observed in the presence of β-CD or for GAV solubilized in the aqueous phase. Since the excited triplet state of GAV is quenched in the aqueous phase, the lack of oxygen quenching in the homogeneous solution suggests that the products formed in the initial burst are mainly due to the reactivity from the excited singlet GAV. The same explanation can be employed for the results with β-CD. In the case of γ-CD, the quenching by oxygen indicates that some of the products formed during the burst phase involve a long-lived transient that can react with oxygen. The triplet lifetime of GAV when complexed to γ-CD is decreased by a factor of 1.1 when oxygen is present in solution. This decrease is much smaller than observed for the quenching of triplet GAV in water, and it suggests that the triplet GAV complexed to γ-CD is mainly protected from the interaction with oxygen. This eliminates the triplet as the candidate for the transient being intercepted by oxygen. The phenacyl radical is the other transient in the GAV photolysis that reacts readily with oxygen (7). Thus, the oxygen effect in the presence of γ-CD could be explained by the trapping of this radical when it exits the CD cavity. Although we cannot fully explain the oxygen result, it is worth noting that the GAV complexes with β- and γ-CD must have sufficiently different geometries to lead to the photochemical behavior observed.

The transients formed in the photolysis of GAV in water were studied by laser flash photolysis. As already emphasized above, the comparison of the photochemistry of GAV in water to the previously reported reactions in organic solvents is relevant, since lignin will be exposed to an aqueous like environment in paper. The same transients, i.e., excited triplet state, and phenacyl and guaiacoxy radicals as observed in acetonitrile were also detected in water. The triplet lifetime of GAV in water is shorter than observed in the organic solvents (8). This result explains why the GAV triplet lifetimes in alcohols containing water are shorter than in the pure alcohols leading to a decrease of the photodecomposition quantum yield of GAV (8). The triplet lifetime of GAV in water is also shorter than in pure acetonitrile. In contrast to the results in alcohols, a slight increase (ca. 1.25) (8) was observed for the triplet lifetime in acetonitrile containing 40% water, which is accompanied with a significant increase (2.6) of the photodecomposition quantum yield (14). Our qualitative fluorescence results indicate that the photodegradation rate is smaller in water than in acetonitrile, which is in line with the shorter triplet lifetimes. The fluorescence results also show the same trend as previously reported (8) for the GAV degradation in acetonitrile–water mixtures. These results show that it is not easy to predict the photochemistry of GAV in mixed solvents.

In addition to the formation of the excited triplet states and radicals, we also observed that GAV in water is photoionized, leading to the observation of solvated electrons in the laser flash photolysis experiments. This photoionization reaction is common for ketones in aqueous solution and is augmented when the ketone is complexed to supramolecular structures, such as SDS micelles and bile salt aggregates (47). The same effect was observed for GAV when complexed to both CDs, suggesting that incorporation of GAV into the CD cavity leads to a more efficient separation of the solvated electron and the GAV radical cation. No transient signals were observed for the GAV radical cation probably because its decomposition is very fast. A similar effect has been reported for other ketones (47). Since the photoionization process involves the sequential absorption of two photons, this process can only contribute to the yellowing of paper made from mechanical pulp when very high irradiation intensities are employed. In most applications this reaction will not be relevant.

In summary, complexation of GAV to β- and γ-CD leads to an increase of the initial product formation but has only a small effect on the rate following the burst kinetics. This result indicates that the constrained environment around lignin within the paper matrix could determine the ratio between coupling of the radicals at different positions of the phenol ring and recombination to reform GAV, which will influence the degree of photoyellowing of the paper. The small effect observed for the relative rates after the initial burst are a consequence of the fast entry and exit dynamics of the radicals compared to the time domain for the radical–radical reactions. A more viscous environment will have to be employed to study how the decrease of the mobility of radicals by encapsulation into constrained environments affects the photochemistry of GAV. Finally, we report that GAV does not fluoresce in homogeneous solution, but the fluorescence of the products of GAV photolysis can be employed to gain qualitative information on the photodegradation kinetics.

Acknowledgments

The Natural Sciences and Engineering Research Council of Canada (NSERC) is thanked for the financial support under the Industrially Oriented Research Grant with Ciba Additives Canada. In addition, the authors thanks Dr. J. Ausio (Dep. Biochem. Microbiol.) for the use of the circular

© 1999 NRC Canada

dichroism spectrometer, Dr. W.S. Patterson for the synthesis of GAV, Cerestar for the kind gift of the cyclodextrins samples, and Dr. L. Netter for software support.

References

1. C. Heitner and J.C. Scaiano. Photochemistry of lignocellulosic materials. ACS Symp. Ser. **531** (1993).
2. G.J. Leary. J. Pulp Paper Sci. **20**, J514 (1994).
3. D. Shukla, N.P. Schepp, N. Mathivanan, and L.J. Johnston. Can. J. Chem. **75**, 1820 (1997).
4. L. Hurrell, L.J. Johnston, N. Mathivanan, and D. Vong. Can. J. Chem. **71**, 1340 (1993).
5. S.V. Jovanovic, J. Renaud, A.B. Berinstain, and J.C. Scaiano. Can. J. Chem. **73**, 223 (1995).
6. J.C. Scaiano, A.B. Berinstain, M.K. Whittlesey, P.R.L. Malenfant, and C. Bensimon. Chem. Mater. **5**, 700 (1993).
7. J.C. Scaiano, M.K. Whittlesey, A.B. Berinstain, P.R.L. Malenfant, and R.H. Schuler. Chem. Mater. **6**, 836 (1994).
8. J.A. Schmidt, A.B. Berinstain, F. de Rege, C. Heitner, L.J. Johnston, and J.C. Scaiano. Can. J. Chem. **69**, 104 (1991).
9. C. Vanucci, P. Fornier de Violet, H. Bouas-Laurent and A. Castellan. J. Photochem. Photobiol. A: Chem. **41**, 251 (1988).
10. A. Castellan, N. Colombo, C. Vanucci, P.F. de Violet, and H. Bouas-Laurent. J. Photochem. Photobiol. A: Chem. **51**, 451 (1990).
11. W.U. Palm and H. Dreeskamp. J. Photochem. Photobiol. A: Chem. **52**, 439 (1990).
12. W.-U. Palm, H. Dreeskamp, H. Bouas-Laurent, and A. Castellan. Ber. Bunsenges. Phys. Chem. **96**, 50 (1992).
13. A.B. Berinstain, M.K. Whittlesey, and J.C. Scaiano. *In* Photochemistry of lignocellulosic materials. *Edited by* C. Heitner and J.C. Scaiano. American Chemical Society, Washington. 1993. p. 111.
14. J.A. Schmidt, E. Goldsmidt, C. Heitner, J.C. Scaiano, A.B. Berinstain, and L.J. Johnston. *In* Photochemistry of lignocellulosic materials. *Edited by* C. Heitner and J.C. Scaiano. American Chemical Society, Washington. 1993. p. 122.
15. J.C. Netto-Ferreira, I.G.J. Avellar, and J.C. Scaiano. J. Org. Chem. **55**, 89 (1990).
16. F.R. Stermitz, D.E. Nicodem, V.P. Muralidhadran, and C.M. O'Donnell. Mol. Photochem. **2**, 87 (1970).
17. P.J. Wagner, P.A. Kelso, A.E. Kemppainen, A. Haug, and D.R. Graber. Mol. Photochem. **2**, 81 (1970).
18. D.G. Whitten and W.E. Punch. Mol. Photochem. **2**, 77 (1970).
19. T. Wismontski-Knittel and T. Kilp. J. Phys. Chem. **88**, 110 (1984).
20. J.C. Netto-Ferreira, W.J. Leigh, and J.C. Scaiano. J. Am. Chem. Soc. **107**, 2617 (1985).
21. W.J. Leigh, J.H. Banisch, and M.S. Workentin. J. Chem. Soc. Chem. Commun. 988 (1993).
22. F. Wilkinson, P.A. Leicester, L.F.V. Ferreira, and V.M.M.R. Freire. Photochem. Photobiol. **54**, 599 (1991).
23. L.F. Vieira Ferreira, A.R. Garcia, M.R. Freixo, and S.M.B. Costa. J. Chem. Soc. Faraday Trans. **89**, 1937 (1993).
24. P.P. Levin, L.F. Vieira Ferreira, and S.M.B. Costa. Chem. Phys. Lett. **173**, 277 (1990).
25. J.C. Netto-Ferreira and J.C. Scaiano. J. Photochem. Photobiol. A: Chem. **45**, 109 (1988).
26. C. Bohne, M. Barra, R. Boch, E.B. Abuin, and J.C. Scaiano. J. Photochem. Photobiol. A: Chem. **65**, 249 (1992).
27. N.C. de Lucas and J.C. Netto-Ferreira. J. Photochem. Photobiol. A: Chem. **103**, 137 (1997).
28. E. Adler, B.O. Lindgren, and U. Saedén. Svensk Papperstidning. **55**, 245 (1952).
29. A. Arrieta, I. Ganboa, and C. Palomo. Synth. Commun. **14**, 939 (1984).
30. R.M. Cowper and L.H. Davidson. Org. Synth. Coll. vol. II, 480 (1943).
31. C. Djerassi and C.R. Scholz. J. Am. Chem. Soc. **70**, 417 (1948).
32. L.L. Landucci, S.A. Geddes, and T.K. Kirk. Holzforschung, **35**, 66 (1981).
33. K. Itoh, S. Tachibana, and M. Sumimoto. Mok. Gakk. **38**, 579 (1992).
34. Y. Liao and C. Bohne. J. Phys. Chem. **100**, 734 (1996).
35. M.P. Fernandez, T.C. Barros, and C. Bohne. J. Photochem. Photobiol. A: Chem. **116**, 171 (1998).
36. S.L. Murov, I. Carmichael, and G. L. Hug. Handbook of photochemistry. Marcel Dekker, Inc., New York. 1993.
37. K. Lundquist, B. Josefsson, and G. Nyquist. Holzforschung, **32**, 27 (1978).
38. J. Michl and V. Bonacic-Koutecky. Electronic aspects of organic photochemistry. John Wiley & Sons Inc., New York. 1990.
39. N.J. Turro. Modern molecular photochemistry. Benjamin/Cummings Publishing Co., Menlo Park. 1978.
40. M. Kodaka. J. Am. Chem. Soc. **115**, 3702 (1993).
41. G. Marconi and B. Mayer. Pure Appl. Chem. **69**, 779 (1997).
42. B. Mayer, G. Marconi, C. Klein, G. Köhler, and P. Wolschann. J. Incl. Phenom. Molec. Recog. Chem. **29**, 79 (1997).
43. M.H. Kleinman and C. Bohne. *In* Molecular and supramolecular photochemistry. *Edited by* V. Ramamurthy and K.S. Schanze. Marcel Dekker Inc., New York. 1997. p. 391.
44. T.C. Barros, K. Stefaniak, J.F. Holzwarth, and C. Bohne. J. Phys. Chem. A, **102**, 5639 (1998).
45. R.S. Murphy, T.C. Barros, J. Barnes, B. Mayer, G. Marconi, and C. Bohne. J. Phys. Chem. A, **103**, 137 (1999).
46. Y. Liao, J. Frank, J.F. Holzwarth, and C. Bohne. J. Chem. Soc. Chem. Commun. 199 (1995).
47. R. Boch, M.K. Whittlesey, and J.C. Scaiano. J. Phys. Chem. **98**, 7854 (1994).

© 1999 NRC Canada

Successive photocyanation of highly chlorinated aromatic compounds

Alexandre D. Konstantinov, Andrea N. Johnston, and Nigel J. Bunce

Abstract: Successive photocyanation was found to be a general reaction when chlorinated aromatic compounds were photolyzed with sodium cyanide. The products were polycyanated hydroxychloro compounds with various degrees of chlorine replacement. Although the products from some substrates could be isolated, identified, and characterized, most reactions proceeded with low regioselectivity, which limits their synthetic potential. Quantum yields of substrate disappearance increased with the number of chlorine substituents on a substrate, and followed the expected relationship $\phi^{-1} \propto [CN^-]^{-1}$. In some cases, ϕ depended also on the concentration of the chloro compound, indicating the involvement of excimers, although the major reaction channel appears to be S_N2Ar^*. Sensitization and quenching experiments established the triplet excited state to be reactive for all substrates tested.

Key words: photocyanation, chlorinated aromatic compounds.

Résumé : On a trouvé que la photocyanuration successive est une réaction générale lorsqu'on soumet des composés aromatiques chlorés à une photolyse avec du cyanure de sodium. Les produits obtenus sont les composés hydroxylés, chlorés et polycyanurés ayant donné lieu à des degrés divers de remplacement du chlore. Même s'il a été possible d'isoler, d'identifier et de caractériser les produits obtenus à partir de certains substrats, les réactions se font généralement avec des faibles régiosélectivités et cette caractéristique limite leur potentiel en synthèse. Les rendements quantiques pour la disparition du substrat augmentent avec le nombre d'atomes de chlore substituant un substrat et ils peuvent être décrits par la relation attendue: $\phi^{-1} \propto [CN^-]^{-1}$. Dans un certain nombre de cas, ϕ dépend aussi de la concentration du composé chloré; ceci indique une implication des excimères, même si la voie de réaction principale semble être S_N2Ar^*. Des expériences de sensibilisation et de désactivation ont permis de démontrer que l'état triplet excité est réactif pour chacun des substrats étudiés.

Mots clés : photocyanuration, composés organiques chlorés.

[Traduit par la Rédaction]

Introduction

Recently (1), we reported a novel nucleophilic polysubstitution reaction of hexachlorobenzene (HCB) with cyanide ion in acetonitrile–water. Successive photocyanations of HCB occurred with high quantum yield ($\phi_{diss} \rightarrow 0.18$) without the need for an electron acceptor, giving polycyano(chloro)phenols as products. The phenol functional group is introduced by competing hydrolysis of the polycyanochlorinated benzenes. Sensitization and quenching experiments indicated a triplet reactive excited state. Variation of $[CN^-]$ at constant [HCB] followed the expected relationship $\phi_{diss}^{-1} \propto [CN^-]^{-1}$, but variation of [HCB] at constant $[CN^-]$ showed that the reaction becomes less efficient with increasing [HCB], consistent with the formation of an unproductive excimer.

The objectives of the present research were to examine the scope of the new reaction for various classes of highly chlorinated aromatic compounds, to investigate its reaction mechanism further, and to evaluate its possible synthetic potential.

Experimental

Chemicals

Chlorinated benzenes, 1,2-dicyanobenzene, 1,2,4,5-tetracyanobenzene, and hexafluorobenzene were purchased from Aldrich; polychlorobiphenyls, octachloronaphthalene, and octachlorodibenzo-*p*-dioxin from AccuStandard. HPLC grade acetonitrile, methanol, and ethyl acetate were obtained from Fisher. All solvents were used as received. 2,3,4,5,6-Pentachlorobenzonitrile[2] was obtained by cyanation of pentachloroiodobenzene[3], which was synthesized by iododeamination of 4-chloroaniline (4) followed by polychlorination of 1-iodo-4-chlorobenzene[4] (5).

Received February 9, 1999.

A.D. Konstantinov, A.N. Johnston, and N.J. Bunce.[1] Department of Chemistry and Biochemistry, University of Guelph, Guelph, ON N1G 2W1, Canada.

[1]Author to whom correspondence may be addressed. Telephone: (519) 824-4120, ext. 3962. Fax: (519) 766-1499. e-mail: bunce@chembio.uoguelph.ca

[2]Yield 110 mg (54%), 95% pure by GC–MS, pale-yellow crystals, mp 209°C (lit. mp 210°C, ref. 2). Mass spectrum (EI), *m*/*z* (%): 279 (21), 277 (67), 275(100), 273 (43), 240 (18), 238 (15), 205 (8), 203 (8) 168 (7), 133 (20), 118 (10), 109 (11).

[3]Yield 0.63 g (40%) of pale-yellow crystals, mp 53°C (lit. 53–54°C, ref. 3), purity 98% (GC–MS).

[4]Yield 5.02 g (97%), mp 53°C (lit. 55°C, ref. 5), purity 98% (GC–MS).

© 1999 NRC Canada

Table 1. Products[a] of photocyanation of chlorinated benzenes.

	Product			
Reactant	$C_6H_2(CN)_3O^-$	$C_6H(CN_4)O^-$	$C_6(CN)_5O^-$	$C_6Cl(CN)_4O^-$
1,2-Dichlorobenzene	11	25	65	—
1,3-Dichlorobenzene	15	10	75	—
1,4-Dichlorobenzene	13	10	78	—
1,2,3-Trichlorobenzene	—	12	88	—
1,2,3,4-Tetrachlorobenzene	—	19	73	8
1,2,4,5-Tetrachlorobenzene	—	29	60	11
Pentachlorobenzene	—	13	36	51

[a]Relative product yields (%) based on intensities of molecular ions by ES–MS.

Irradiations

Solutions were photolyzed in 8 mm o.d. Pyrex® test tubes in a Rayonet RPR photochemical reactor equipped with 16 RPR-3000 low-pressure mercury lamps that emit a band at 300 nm with a bandwidth of 25 nm at a half-intensity. When necessary, samples were degassed and sealed on a vacuum manifold using four freeze–pump–thaw cycles (last two cycles using an oil-diffusion pump, $P < 0.01$ Torr (1 Torr = 133.3 Pa)). Preparative photocyanations were done using up to four 30 mm o.d. Pyrex® test tubes sealed with rubber septa and placed in a Rayonet merry-go-round photoreactor (Table 1).

Analytical methods

Reactions were monitored by HPLC equipped with Waters U6K injector, Waters 600E system controller, and Waters 486 tunable absorbance detector, and Waters μ-Bondapack C_{18} 3.9 × 300 mm column, using acetonitrile/water (9/1) as the mobile phase. Calibration curves for analytes ($r^2 = 0.99$) were built using Millennium II software. Absorption spectra of analytes and transmittance spectra of optical filters were acquired on a double-beam Shimadzu UV-vis recording spectrophotometer (Model UV-160A). Carbon Nuclear Magnetic Resonance (^{13}C NMR) and Hydrogen Nuclear Magnetic Resonance (^1H-NMR) spectra were recorded at 100.6 MHz and 400 Hz, respectively, on Avance400 Bruker spectrometer, using acetonitrile-d_3 as a solvent.

Electrospray mass spectral analyses of the photoproducts (negative ionization) were obtained using a VG Quattro II (Fisons U.K. Ltd.) triple quadrupole mass spectrometer equipped with an atmospheric pressure ion source, and MassLynx™ software package. The sample solutions were introduced into the mass spectrometer via a 10 μL Rheodyne™ 7010 injection valve. The mobile phase (50/50 v/v NANOpure water (Barnstead) and acetonitrile (Caledon)) was delivered using a Hewlett Packard 1090 Series II/L binary LC pump at 15 μL/min. The mass spectra were acquired and averaged over at least 8 scans in multi channel analysis (MCA) data acquisition mode by scanning the first quadrupole in 0.1 u increments from m/z 100 to 800 in 1.2 s.

Measurement of quantum yields

Quantum yields of substrate disappearance were determined by potassium ferrioxalate actinometry (6) using solutions of potassium chromate and nickel sulphate (7) as an optical filter. The actinometer in water and the test solution in acetonitrile, containing 5% water, were placed in 8 mm o.d. test Pyrex® tubes that were positioned coaxially in 25 mm o.d. Pyrex® test tubes filled with optical filter. The filter transmitted in the 285–335 nm region, with maximum transmittance of approximately 20% at 313 nm. The actinometer and test solutions were irradiated simultaneously in the photoreactor using the merry-go-round to assure equal light intensity incident on all solutions. All the light was absorbed by the actinometer, and the photon intensity absorbed by the actinometer ($I_o = 7.09 \times 10^{-7} \pm 7.55 \times 10^{-8}$ mol min^{-1}) was calculated based on $\phi_{313} = 1.24$ for potassium ferrioxalate (8). The light flux absorbed by the test solution I_{abs} was calculated using the following equation:

$$I_{abs}\ (\text{mol}) = I_o\ (\text{mol min}^{-1}) \times \text{time (min)} \times (1 - 10^{-A})$$

Solutions of substrates (1.00×10^{-5} to 4.00×10^{-4} mol L^{-1}) and NaCN (0.18–0.25 mol L^{-1}) in acetonitrile–water (5% H_2O) were irradiated for time intervals ranging from 10 min to 2 h. After irradiation, substrate disappearance was determined by HPLC analysis (averaged results of triplicate experiments are presented in supplementary materials)[5]. The apparent quantum yields were calculated and plotted against time.

Sensitization of photocyanation by acetone and acetophenone and oxygen removal

Concentrations of acetone and acetophenone were chosen such that most of the incident light was absorbed by the sensitizers. In a typical experiment, eight substrate solutions in acetonitrile–water (5% H_2O) containing NaCN were prepared, with two having acetone (0.125 mol L^{-1}, $A_{300} = 0.78$) and the other two having acetophenone (1.12×10^{-2} mol L^{-1}, $A_{300} = 0.57$) added. The samples, except two of those without sensitizers, were degassed by four freeze–pump–thaw cycles, sealed under vacuum, and irradiated at 300 nm for 7–20 min in the merry-go-round photoreactor. The results of HPLC analysis of duplicate samples are presented in supplementary materials.

Quenching of photocyanation by ferrocene

In a typical experiment, eight sample tubes, each containing 1.0 mL aliquots with various concentrations of ferrocene and fixed concentrations of substrate and sodium cyanide,

[5]Supplementary material may be purchased from: The Depository of Unpublished Data, Document Delivery, CISTI, National Research Council Canada, Ottawa, Canada, K1A 0S2.

© 1999 NRC Canada

Fig. 1. Photocyanation of 1,4-dicyano- and 1,2,4,5-tetracyanobenzenes; *, possible structures; products not isolated.

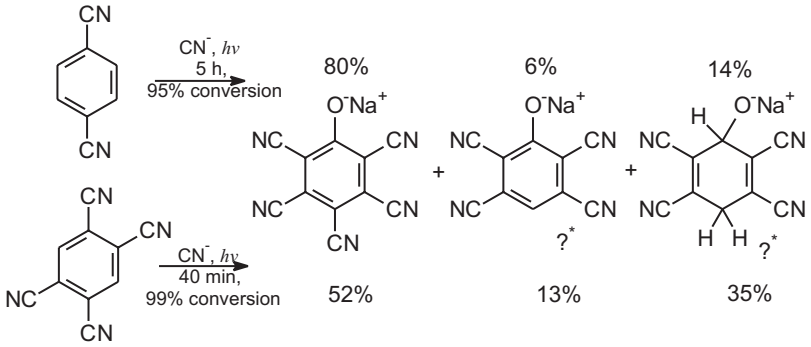

were irradiated for 4–30 min in a merry-go-round photoreactor and analyzed by HPLC. The concentrations of ferrocene were selected to maintain the absorbance of ferrocene <0.1 at 300 nm.

Preparative photocyanation of 2,3,4,5,6-pentachlorobiphenyl

Forty-one milligrams (1.25×10^{-4} mol) of 2,3,4,5,6-pentachlorobiphenyl and 0.5 g (10 mmol) of NaCN were dissolved in 50.0 mL of acetonitrile – 5% water. The solution was placed in two 30 mm Pyrex® tubes, sealed with rubber septa, and irradiated at 300 nm for 24 h. The resultant yellow liquid was treated with 3.2 g Dowex® 50W and extracted with 3 × 20 mL hexane. Approximately 30 mg of starting material, which was recovered from hexane, was redissolved in 50 mL of acetonitrile – 5% water with 0.5 g of NaCN and irradiated for additional 48 h. After treatment with Dowex® 50W and hexane extraction, 18 mg of the starting pentachlorobiphenyl was recovered. The product, a tetracyanochlorohydroxybiphenyl, was isolated by flash chromatography (ethyl acetate: acetonitrile = 4:1). Yield: 12.5 mg, 4.12×10^{-5} mol (59% based on reacted material). ^{1}H NMR (δ, CD_3CN): 7.41, dd, J = 7.4 Hz, ^4J = 2 Hz, 1H (H3′); 7.49, ddd, J = 7.4 Hz, J = 7.6 Hz, ^4J = 1.4 Hz, 1H (H4′); 7.52, ddd, J = 7.6 Hz, J = 8.0 Hz, ^4J = 2 Hz, 1H (H5′); 7.60, dd, J = 8 Hz, ^4J = 2 Hz, 1H (H6′). ^{13}C NMR (partial spectrum) (δ, CD_3CN): 125.7 (C2′), 128.6 (C4′), 131.1(C6′), 131.4 (C3′), 132.6 (C5′), 151.3 (C1′). Mass spectrum, *m*/*z* (%): 303 (M – H) (100), 266 (10.5), 241(9.5) 224 (5.9); MS/MS, daughters of *m*/*z* 303, *m*/*z* (%): 293 (142), 213(29), 201(14) 188 (26), 163 (10.5), 35 (56).

Results and discussion

Scope of the reaction

Chlorinated benzenes

Our previous work showed that irradiation of HCB with excess NaCN at 300 nm in aqueous acetonitrile results in rapid disappearance of the title compound and the formation of pentacyanophenol **1** (14%), 4-chloro-2,3,5,6-tetracyanophenol **2** (54%), and a tricyanodichlorophenol **3** (29%) as highly polar sodium salts. Similar irradiations of penta and less-chlorinated benzenes with NaCN resulted in the disappearance of the starting materials and formation of polar products, visually similar (yellow–greenish solutions) to those formed in photocyanation of HCB. ES–MS analysis of the products of photocyanation revealed that pentacyanophenol was the major product for all congeners, except pentachlorobenzene for which 4-chloro-2,3,5,6-tetracyanophenol predominated. The rate of the reaction decreased in parallel with the number of chlorine substituents; 20 h were required to reach 95% conversion of dichlorobenzene, compared with 2 h for pentachlorobenzene and 1 h for HCB. In penta and less-chlorinated benzenes, both hydrogen and chloro substituents were replaced by cyanide (reactions take place in air, which acts as an oxidant for the H^- that is formally replaced (9–11)).

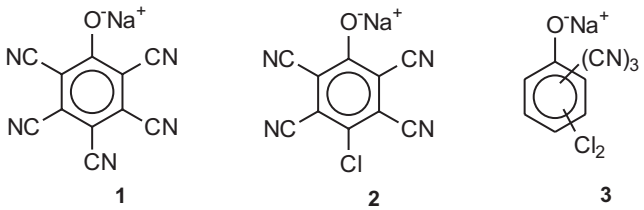

1 **2** **3**

Polycyanobenzenes

Irradiation of 1,4-dicyanobenzene in the presence of NaCN gave pentacyanophenoxide **1** as a major product (Fig. 1). ES–MS analysis of the reaction products at 95% conversion also revealed the presence of small amounts of products with *m*/*z* 193 and 195 in the ratio of 1:2.5. These products correspond to a tetracyanophenoxide ($C_6H(CN)_4O^-$) and a dihydrotetracyanophenoxide ($C_6H_3(CN)_4O^-$). The formation of a dihydro product is often observed when hydrogen is replaced by CN in the absence of oxidants (10, 12). Photocyanation of 1,2,4,5-tetracyanobenzene gave similar products, except that more dihydro product was formed (Fig. 1).

Although CN^- did not react with 1,4-dicyanobenzene in the dark, a dark reaction was observed upon addition of 0.1 mol L^{-1} solution of NaCN in 9:1 acetonitrile:water to 1,2,4,5-tetracyanobenzene in acetonitrile. The starting material disappeared rapidly (50 min) with development of a deep purple colour. ES–MS analysis of the reaction mixture showed peaks at *m*/*z* 384 (71%), 406 (26%), and 455 (3%) of which *m*/*z* 384 corresponds to the molecular mass of octacyanodiphenoquinone.

Polychlorinated biphenyls

Photolysis of decachlorobiphenyl (DCB) with NaCN in aqueous acetonitrile gave a complex mixture of hydroxybiphenyls bearing from one to eight cyano groups according

© 1999 NRC Canada

Table 2. Products of photocyanation of decachlorobiphenyl.

Molecular formula	$C_{13}Cl_8NO^-$	$C_{14}Cl_7N_2O^-$	$C_{15}Cl_6N_3O^-$	$C_{16}Cl_5N_4O^-$	$C_{17}Cl_4N_5O^-$	$C_{18}Cl_3N_6O^-$	$C_{19}Cl_2N_7O^-$	$C_{20}ClN_8O^-$
m/*z*	466	457	448	439	430	421	412	403
Relative abundance, %	7	12	20	24	16	8	7	6

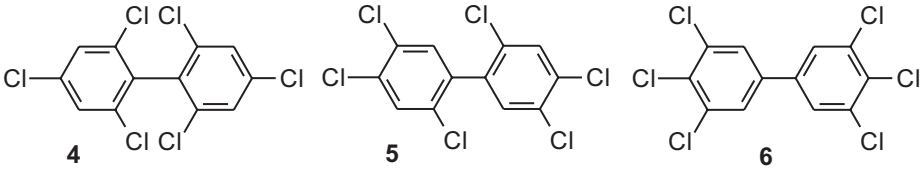

to ES–MS (Table 2). No attempt was made to isolate products, but we can draw the following conclusions:

(*i*) Introduction of an hydroxy group can occur at early stages of reaction, when just one or two chlorines have been substituted by CN^-, possibly inhibiting further cyanation.

(*ii*) Cyano substitution can occur on both rings of decachlorobiphenyl, since biphenyls bearing >5 CN substituents were formed.

(*iii*) Simultaneous hydroxylation of both aromatic rings of highly cyanated biphenyls is unlikely, since no dihydroxy products were found.[6]

Although the symmetrically substituted biphenyls **4**, **5**, and **6** also gave complex mixtures, photocyanation of 2,3,4,5,6-pentachlorobiphenyl, which has one ring fully chlorinated and the other unsubstituted, gave 80% (ES–MS) of a single substance with *m*/*z* 303 and a one-chlorine pattern corresponding to $C_{12}H_4Cl(CN)_4O^-$ (**7**). The minor products included *m*/*z* 337 (a two-chlorine pattern, $C_{12}H_3Cl_2(CN)_4O^-$) and *m*/*z* 294 (no chlorines, $C_{12}H_4(CN)_5O^-$). Continuous irradiation of the product mixture for 48 h resulted in the decrease of relative intensity of the ion *m*/*z* 303, with formation of single-ring products (*m*/*z*: 218, 193, and 195). These were tentatively identified as **1**, a tetracyanophenoxide ($C_6H(CN)_4O^-$), and a dihydrotetacyanophenoxide ($C_6H_3(CN)_4O^-$), respectively.

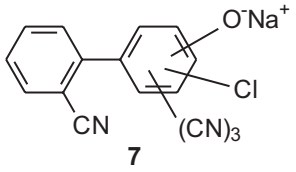

Compound **7** was isolated in 59% yield as the sodium salt from a large-scale photocyanation of 2,3,4,5,6-pentachlorobiphenyl. Attempts to protonate this salt by treatment with 20% hydrochloric acid resulted in decomposition, while less concentrated acid failed to cause protonation (based on the UV spectrum of the product); attempts to crystallize this salt for X-ray analysis were also unsuccessful.

The partial structure of **7** was deduced from ES–MS, ES–MS–MS. and 2D NMR. The molecular formula of **7** indicates that during the photocyanation of 2,3,4,5,6-pentachlorobiphenyl, one hydrogen was substituted by CN^- ($C_{12}H_5Cl_5$ has five substituents, $C_{12}H_4Cl(CN)_4O^-$ has six). The MS–MS spectrum showed a fragment with *m*/*z* 201 corresponding to $C_6(CN)_3ClO^{\cdot -}$ in which the biphenyl bond of **7** has cleaved. Proton NMR (400 MHz) for $C_{12}H_4Cl(CN)_4O^-$ exhibited a complex coupling pattern that could be interpreted as an ABCD pattern with the aid of COSY and HSQC experiments ($J_{A–B} \approx J_{B–C} \approx J_{C–D} \approx 7.4–7.6$ Hz, $J_{A–C} \approx J_{B–D} \approx 1.4–2$ Hz). COSY data were compatible only with a 3,4,5,6 pattern of C—H bonds, hence the CN group had been incorporated at the 2 position.

Heteronuclear connectivity was established from HSQC NMR (supplementary material). With the aid of a long-range proton to carbon coupling experiment (HMBC, supplementary material) chemical shifts for carbon 1′ (δ = 151.3 ppm, downfield due to the phenoxide substituent) and carbon 2′ (δ = 125.7.3 ppm, upfield due to the CN substituent) were determined. Cross signals between H_A and C1′, and between H_D and C6′ indicate that H_A is on the position 3′, and H_D is on the position 6′ of the biphenyl ring. One-dimensional ^{13}C NMR data could not determine the placement of the substituents in the second aromatic ring, and 2D ^{13}C experiments like DQF_PS COSY or INADEQUATE were infeasible due to insufficient quantity of **7**.

Octachloronaphthalene and octachlorodibenzo-p-*dioxin*

Photolysis of octachloronaphthalene (OCN) and octachlorodibenzo-*p*-dioxin (OCDD) with NaCN both gave highly complex product mixtures, and no attempts to isolate the cyanated products were made. According to ES–MS, a tetrachlorotricyanonaphthol (*m*/*z* 354) and a pentachlorodicyanonaphthalene (*m*/*z* 363) predominated in the product mixture from OCN; only traces of higher cyanated naphthalenes were found. Knowing the strong preference of naphthalene derivatives for α rather than β substitution (13), we speculate that the low reactivity of β-chlorines may inhibit further photocyanation.

Hexafluorobenzene

Fluorine is considered the best leaving group among halogens in photochemical nucleophilic substitution (10). At 300 nm, where C_6F_6 is transparent, photolysis was slow

[6] Under the conditions of negative ionization, the possible dihydroxy products would form dianions with *m*/*z* corresponding (FW-2)/2. Careful examination of the ES–MS spectra revealed the absence of peaks near *m*/*z* 220, which would correspond to polychloro-polycyano-dihydroxybiphenyls.

© 1999 NRC Canada

Fig. 2. Pseudo-first-order kinetics in photocyanation of HCB and pentachlorobenzonitrile.

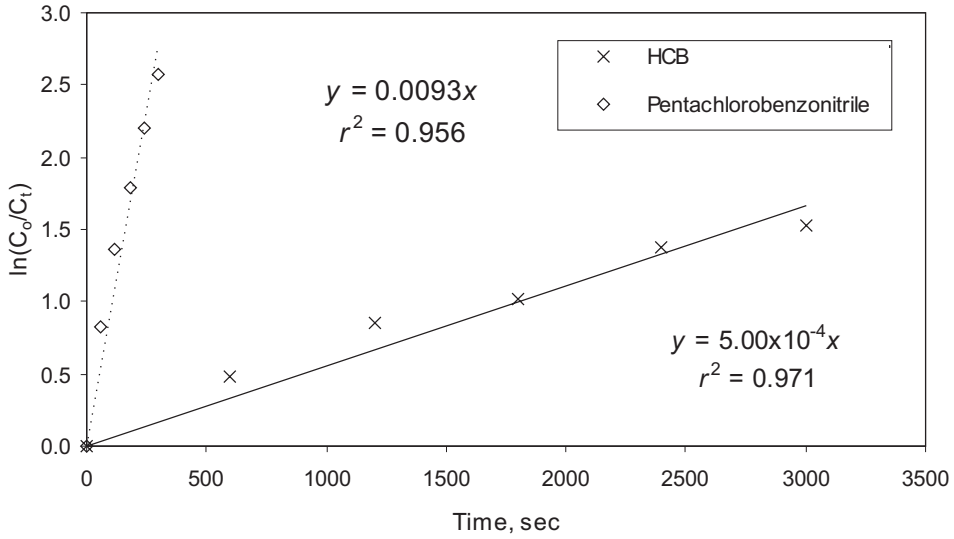

(55% conversion in 47 h). Irradiation of an 8.75×10^{-4} mol L^{-1} solution of C_6F_6 in the presence of 0.05 mol L^{-1} NaCN at 254 nm ($A_{C_6F_6} = 0.136$) resulted in rapid disappearance of the starting material. Analysis of the reaction mixture by ES–MS revealed a product mixture rather analogous to that that obtained from hexachlorobenzene, principally a difluorotetracyanobenzene (*m*/*z* 214), with trace amounts of **1** (*m*/*z* 218), a difluorotricyanophenoxide (*m*/*z* 204), a tetrafluorocyanophenoxide (*m*/*z* 190), and pentafluorophenoxide (*m*/*z* 183).

Reaction kinetics and quantum yields

Photocyanation was pseudo-first order in substrate (under conditions of low absorbance $I_{abs} = I_0(1 - 10^{-A}) \sim 2.303 I_0 A$) for all compounds studied, with rate constants ranging from 1.1×10^{-3} s^{-1} to 6.7×10^{-5} s^{-1}. The only exception was hexafluorobenzene at 254 nm for which the reaction did not follow pseudo-first order kinetics, and 85% conversion was reached within 5 min of irradiation.

As observed previously for HCB (1), the apparent quantum yields of substrate disappearance declined with conversion. Extrapolation to zero conversion gave the limiting value $\phi_{diss} = 0.26$ for decachlorobiphenyl ($\phi = \phi_0 - 0.013$ min^{-1} × time).[7] The quantum yield is higher than that of HCB (0.14). The quantum yields of disappearance of OCN and OCDD were rather small, 2×10^{-4} and 0.001, respectively.

For all the above compounds, reductive dechlorination competed with photocyanation, and significant amounts of reductive dechlorination products were found by GC–MS. The relative rate constants for substrate disappearance in the absence and the presence of 0.25 mol L^{-1} NaCN indicated that ~15% each of DCB and OCN was consumed by reductive dechlorination, but for OCDD photocyanation and dechlorination occurred at almost equal rates.

Photolysis of DCB at a range of concentrations of NaCN gave the relationship $1/\phi_{diss} \propto 1/[NaCN]$; the limiting (low conversion) ϕ_{diss} ranged from 0.29 to 0.07 as [NaCN] changed from 0.285 to 0.020 mol L^{-1}. Thus, photocyanation is first order in both excited DCB and sodium cyanide, and is even more efficient photochemically than the reaction with HCB (1).

Increasing the water content of the solvent decreased ϕ_{diss} for DCB, but the effect was less profound than for HCB, where increasing $[H_2O]$ from 1.4 to 14% caused a threefold drop in ϕ_{diss} (1). The plot of ϕ_{diss} vs. $[H_2O]$ was linear (r^2 = 0.973), and from the intercept at $[H_2O] \rightarrow 0$, $\phi_{diss} = 0.27$ at $[NaCN] = 2.55 \times 10^{-2}$ mol L^{-1}, and $[DCB]^\circ = 2.63 \times 10^{-5}$ mol L^{-1} (supplementary material). ϕ_{diss} for OCDD and OCN also decreased with increasing water content in the solvent.

Photocyanation steps beyond replacing the first chlorine must proceed with successively higher quantum yield, because no mono- or dicyano products were detected in any of the product mixtures. We determined the quantum yield for the secondary cyanation of HCB by comparing the rates of disappearance of HCB and pentachlorobenzonitrile at constant substrate concentration, nucleophile concentration, and solvent composition (Fig. 2). The quantum yield of disappearance of pentachlorobenzonitrile ϕ_s was calculated to be 0.51 from eq. [1], using ϕ_{diss} for HCB = 0.14, and the absorbances of HCB ($A_{313} = 0.054$) and pentachlorobenzonitrile ($A_{313} = 0.278$). This is an example of a photochemical autoacceleration reaction in which each consecutive step occurs with the higher quantum efficiency. Therefore, the total photon efficiency of photocyanation of HCB is very high.

$$[1] \qquad \phi_s = \phi_{HCB} \frac{\left\{(c_0 - c_t) - \frac{1}{\varepsilon l} \ln\left[\frac{(1 - e^{-2.303\varepsilon c_t l})}{(1 - e^{-2.303\varepsilon c_0 l})}\right]\right\}^s}{\left\{(c_0 - c_t) - \frac{1}{\varepsilon l} \ln\left[\frac{(1 - e^{-2.303\varepsilon c_t l})}{(1 - e^{-2.303\varepsilon c_0 l})}\right]\right\}^{HCB}}$$

The photoefficiency of photocyanation of chlorinated benzenes depends directly on the number of electron-withdrawing chlorine substituents. HCB, pentachlorobenzene, and 1,2,3,4-tetrachlorobenzene were irradiated with NaCN at equal substrate absorbances, so that the pseudo-

[7] $\phi_0 = 0.259$; time in minutes; $r^2 = 0.955$.

© 1999 NRC Canada

Fig. 3. Measurement of pseudo-first-order rate constants for photocyanation of HCB, pentachlorobenzene, and 1,2,3,4-tetrachlorobenzene in solutions with equal absorbancies.

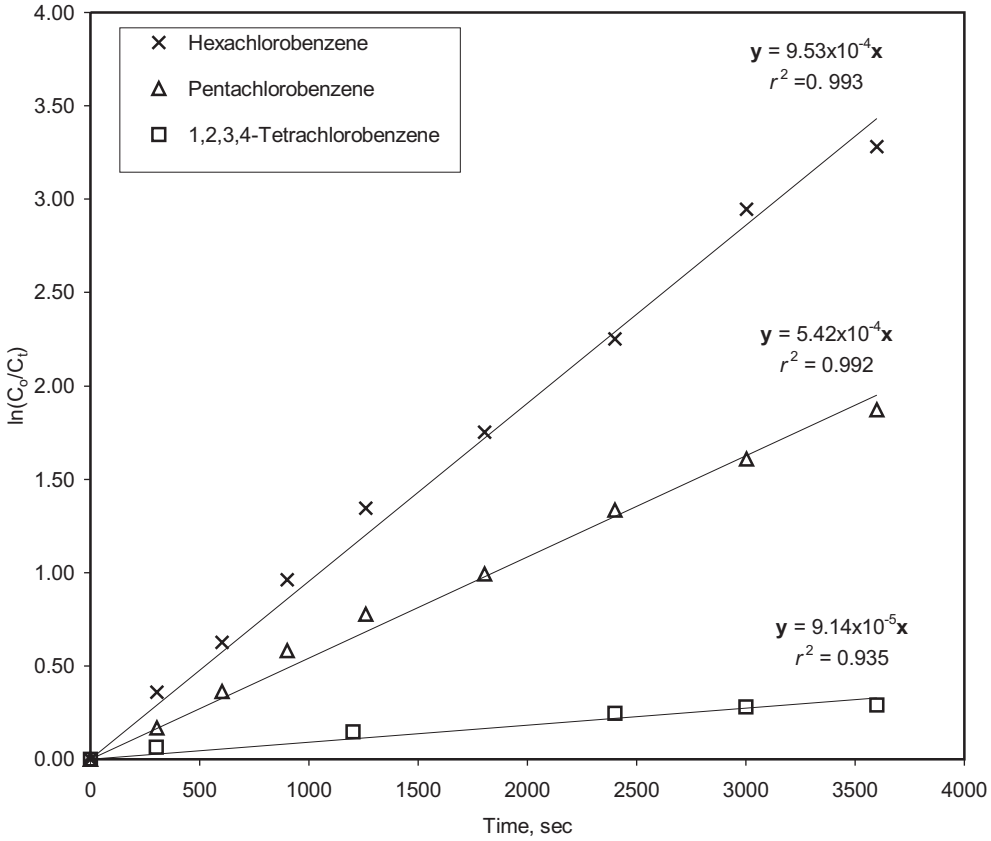

first-order rate constants for substrate disappearance (Fig. 3) would be proportional to ϕ_{diss}. HCB, pentachlorobenzene, and 1,2,3,4-tetrachlorobenzene had ϕ_{diss} under these conditions 0.14, 0.07, and 1.4×10^{-2}, respectively.

Chlorinated biphenyls show a strong *ortho* effect in reductive dechlorination, because steric interference between the substituents raises the energy of the (planar) excited state (14). The *ortho* effect is also observed in photocyanation, as shown by studying the hexachlorobiphenyls **4**, **5**, and **6**, which have four, two, and no *ortho* chlorines, respectively. Rates of homolysis were an order of magnitude smaller than those for photocyanation of all three hexachlorobiphenyls and at equal substrate concentrations, ϕ_{diss} values calculated using eq. [1] were in the ratio 1:0.45:0.05 for **4**, **5**, and **6**.

Reactive excited state

Sensitization and quenching experiments provided evidence that photocyanation of DCB, like that of HCB, is a triplet state process. The ϕ_{diss} value increased in the presence of acetone and acetophenone, and when oxygen was removed by freeze–pump–thaw. A Stern–Volmer plot of the quenching of decachlorobiphenyl photocyanation by ferrocene had a positive slope of 784 mol^{-1} L with r^2 = 0.975. From the slope, the triplet lifetime of DCB is 80 ns, assuming that the quenching of the DCB photocyanation is diffusion-controlled. Sensitization experiments with acetophenone and acetone suggest that photocyanations of OCN and OCDD are also triplet state reactions, but attempts to quench these photolyses by ferrocene failed; increasing the concentration of ferrocene resulted in the enhancement of the reaction in both cases. Examination of the half-wave reduction potentials for OCN ($E_{1/2}$ = 1.29 V, ref. 15) and ferrocene ($E_{1/2}$ = 1.33 V, ref. 16) revealed that the electron transfer from ferrocene to excited OCN is possible. Although the half-wave reduction potential for OCDD is not reported in the literature, electron transfer is likely to occur, since the addition of electron donors significantly enhances photolysis of OCDD in hydrocarbon solvents (17). Electron transfer from ferrocene to DCB is less favourable (for DCB $E_{1/2}$ = 1.76 V, ref. 15). All substrates examined to date therefore appear to exhibit triplet state reactivity.

Reaction mechanism

The candidate mechanisms for photocyanation reactions are S_N2Ar^*, photoionization, excimer-mediated, and electron-acceptor assisted (18).

S_N2Ar^*

$ArX^* + CN^- \rightarrow ArXCN$ (σ-complex)

$ArXCN \rightarrow ArCN + X^-$

Photoionization

$ArX^* \rightarrow ArX^{\cdot+} + e^-_{diss}$

$ArX^{\cdot+} + CN^- \rightarrow ArXCN^{\cdot}$

$ArXCN^{\cdot} \rightarrow ArCN + X^{\cdot}$

© 1999 NRC Canada

Excimer

$ArX^* + ArX \rightarrow \{ArX^{\cdot+}\ ArX^{\cdot-}\}^*$

$ArX^{\cdot+} + CN^- \rightarrow ArXCN^{\cdot}$

$ArXCN^{\cdot} \rightarrow ArCN + X^{\cdot}$

When X = H: $2ArHCN^{\cdot} \rightarrow ArCN + \text{“Ar”}H_2CN$ (a dihydro product)

$S_{ET}Ar^*$, or exciplex

$ArH- \xrightarrow{hv} {}^1ArH^*$

$^1ArH^* + 1,4\text{-DCB} \rightarrow ArH^{+\cdot} + 1,4\text{-DCB}^{-\cdot}$

$Ar^{+\cdot} + CN^- \rightarrow ArH\text{-}CN^{\cdot}$

$2\ ArH\text{-}CN^{\cdot} \rightarrow H\text{-}ArH\text{-}CN + ArCN$

$ArH\text{-}CN^{\cdot} + DCB^{-\cdot} \rightarrow ArH\text{-}CN^- + DCB$

$ArH\text{-}CN^- + H^+ \rightarrow H\text{-}ArH\text{-}CN$

$ArH\text{-}CN^{\cdot} + Ox \rightarrow ArCN + OxH^{\cdot}$

1,4-DCB is 1,4-dicyanobenzene (an array of other e^- donors can be used)

Photoionization can be ruled out based on the observation that in the benzene series, ϕ_{diss} increases with the number of Cl substituents. We showed previously that the excimer of HCB, though formed, appears to be unproductive (1). By contrast, increasing the initial concentration of OCN results in higher ϕ_{diss}, (Fig. 4), suggesting that photocyanation of OCN may proceed in part via the intermediacy of an excimer. Low solubility in acetonitrile precluded a test of the dependence of ϕ_{diss} on the concentration of DCB; however, an excimer involvement in the photocyanation mechanism in this case is unlikely due to low initial concentration of the reactant (2.5×10^{-5} mol L^{-1}). Assuming a μs lifetime for the excited state, even a diffusion-controlled encounter between the excited and ground state molecules could not compete significantly with first-order decay of the excited state.

Regarding the initial step of photocyanation, the S_N2Ar^* mechanism is most probable. At this stage, there are no available electron-accepting substances available in the reaction mixture to promote the $S_{ET}2Ar^*$ mechanism (11); this is not true once photocyanation is under way, and cyanoaromatic compounds, which are well known electron acceptors, are present in solution. Autoacceleration of the disappearance of the original substrate due to the involvement of electron-accepting products has been observed previously in the photocyanation of naphthalene (19).

The $S_{ET}2Ar^*$ mechanism also accounts for the replacement of -H by -CN in the photocyanation of penta and less-chlorinated benzenes, since replacement of -H by -CN usually occurs by this mechanism (11). After accepting an electron, the cyano compound undergoes parasitic reactions leading to loss of material balance (20) except, as in our system, when an oxidant (O_2) is present to reoxidize $ArCN^{\cdot-}$ to ArCN. Indirect evidence for this proposal is observation of dihydro by-products, typical for $S_{ET}2Ar^*$ during photolysis of 1,4-dicyanobenzene and 1,2,4,5-tetracyanobenzene on the presence of CN^- (Fig. 1).

Conclusions

Successive photocyanation can be achieved for a wide variety of polyhaloaromatic compounds, including polychlorinated benzenes, biphenyls, naphthalenes, and dioxins, and probably also their polyfluorinated analogs. Unfortunately, the synthetic potential of the successive photocyanation is low. Most substrates undergo the reaction with low regioselectivity, giving complex mixtures of products, and even when some selectivity exists, the photocyanation products can only be isolated as their conjugate bases because of the high acidity of polycyanophenols.

All compounds studied undergo photocyanation from the triplet excited state. The initial replacement of -Cl by -CN can generally be rationalized by the S_N2Ar^* mechanism, but subsequent steps involving substitution of -CN for -H are more likely $S_{ET}2Ar^*$ reactions. In either case, autoacceleration of the reaction is observed because increasing the number of -CN substituents makes the molecule more susceptible to nucleophilic attack.

Fig. 4. A double reciprocal relationship of the quantum yield of disappearance of OCN and the initial concentration of OCN.

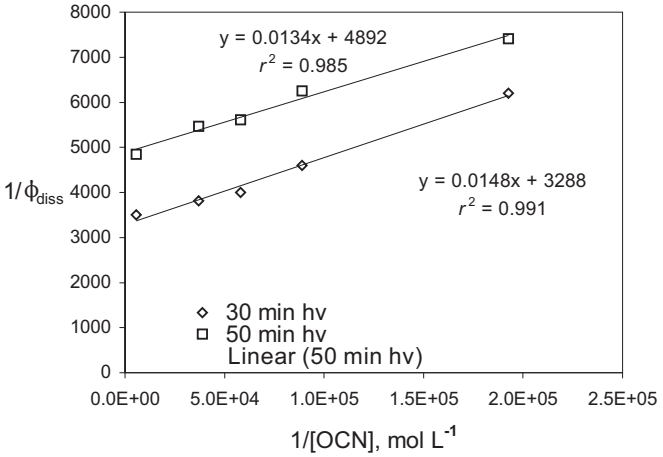

Acknowledgements

We thank the Natural Sciences and Engineering Research Council for financial support.

References

1. A. Konstantinov, C.A. Kingsmill, G. Ferguson, and N.J. Bunce. J. Am. Chem. Soc. **120**, 5464 (1998).
2. Catalog handbook of fine chemicals. Aldrich Chemical Co., Milwaukee, Wis. 1984. p. 344.
3. W. Merz. Ber. **20**, 1627 (1888).
4. I. Vogel. Practical organic chemistry. 2nd ed. Longmans, Green and Co., Toronto. 1951, p. 574.
5. R.G.W. Cramlyn and J. Gronjc. Phosphorus sulfur, **6**, 494 (1979).
6. C.G. Hatchard and C.A. Parker. Proc. Roy. Soc. A, **236**, 518 (1956).
7. I.R. Gould. *In* Handbook of organic photochemistry. Vol. 1. *Edited by* J.C. Scaiano. CRC Press, Boca Raton. 1989. p. 47.
8. S.L. Murov, I. Carmichael, and G.L. Hug. Handbook of photochemistry. 2nd ed. Marcel Dekker, Inc. New York. 1993. p. 299.
9. J. Cornelisse and E. Havinga. Chem. Rev. **75**, 353 (1975).
10. J. Den Heijer, O.B. Shadid, J. Cornelisse, and E. Havinga. Tetrahedron, **33**, 779 (1977).
11. A. Zuilhof, F.A. van Gelderen, J. Cornelisse, and G. Lodder. J. Phys. Chem. **102**, 5456 (1998).
12. H.J. Lemmetyinen. J. Chem. Soc. Perkin Trans. 2, 1269 (1983).

© 1999 NRC Canada

13. J.A.J. Vink, C.M. Lok, J. Cornelisse, and E. Havinga. Chem. Commun. 710 (1972).
14. N.J. Bunce, Y. Kumar, L. Ravanal, and S. Safe. J. Chem. Soc. Perkin Trans. 2, 880 (1978).
15. J.R. Wiley, E.C.M. Chen, E.S.D. Chen, R. Richardson, W.R. Reed, and W.E. Wentworth. J. Electroanal. Chem. **307**, 169 (1991).
16. S. Shadev and D.H. Evans. J. Am. Chem. Soc. **111**, 2667 (1989).
17. A. Konstantinov and N.J. Bunce. J. Photochem. Photobiol. A, **94**, 27 (1996).
18. A. Konstantinov and N.J. Bunce. J. Photochem. Photobiol. A. In press.
19. N.J. Bunce, J.P. Bergsma, and J.L. Schmidt. J. Chem. Soc. Perkin Trans. 2, 713 (1981).
20. J. Niiranen, K. Nieminen, and H. Lemmetyinen. J. Photochem. Photobiol. A, **56**, 43 (1991).

© 1999 NRC Canada

A novel photorearrangement of 1,3-diketonatoborinate: a photoinduced intramolecular alkylation on a conjugated carbonyl system

Jun-ichi Ishiyama and Yuan L. Chow

Abstract: Irradiation of borinates derived from 9-borabicyclo[3,3,1]nonane and 1,3-diketones at their π–π* transition band caused a rearrangement from their triplet excited state to give boronate intermediates that could be hydrolyzed to the corresponding aldols. The primary photolysis involves the scission of one of the B—C bonds followed by a 1,3- or 1,5-migration and the formation of a more stable B—O bond by radical pathways. The triplet state reaction was established by quenching and heavy atom effect experiments. The overall reaction pattern is an irreversible 1,2- or 1,4-addition of an alkyl-boron group to an α,β-conjugated ketone system by radical processes. Evidence showed that the non-isolated boronates also underwent secondary photoreactions followed by hydrolysis to afford enones corresponding to dehydration products of aldols; mechanisms are suggested for these secondary steps. The photoreaction was more facile in nonpolar solvents than in polar solvents; different solvents also gave different product compositions. In the presence of dilute acetic acid, the photolysis gave a high yield of aldols, suggesting a rapid acetolysis of the B—C bond in boronates to acetylborates. Under oxygen, the photolysis was complicated by radical oxidation to give totally different products.

Key words: borinate photochemistry, charge transfer absorption, alkylborane addition, boronate intermediates, B—C bond homolytic scission.

Résumé : L'irradiation de borinates dérivés du 9-borabicyclo[3.3.1]nonane et des 1,3-dicétones au niveau de leur bande de transition π–π* provoque un réarrangement à partir de leur état excité triplet pour conduire à des boronates intermédiaires que l'on peut hydrolyser en aldols correspondants. La photolyse primaire implique la scission de l'une des liaisons B—C, suivie d'une migration 1,3 ou 1,5 et la formation d'une liaison B—O plus stable par le biais de voies radicalaires. On a établi l'implication d'une réaction de l'état triplet à l'aide d'expériences de désactivation et d'effets isotopiques. Le schéma de la réaction globale est une addition, 1,2 ou 1,4 irréversible, d'un groupe alkyl-bore sur un système cétonique α,β-insaturé par des processus radicalaires. Les données montrent que les boronates qui n'ont pas été isolés subissent aussi des photoréactions secondaires qui, suivies d'une hydrolyse, fournissent les énones qui correspondent aux produits de déshydratation des aldols; on suggère des mécanismes pour ces étapes secondaires. La photoréaction est plus facile dans les solvants non polaires; les divers solvants donnent aussi des compositions de produits différentes. En présence d'acide acétique dilué, la photolyse fournit un rendement élevé d'aldols; ceci suggère que, dans les boronates, il se produit une acétolyse rapide de la liaison B—C pour donner des acétylboronates. En présence d'oxygène, la photolyse est compliquée par une oxydation radicalaire qui conduit à des produits totalement différents.

Mots clés : photochimie du borinate, absorption du transfert de charge, addition d'alkylborane, intermédiaires boronates, scission homolytique de la liaison B—C.

[Traduit par la Rédaction]

Introduction

We observed some 10 years ago that dialkylborinates derived from simple 1,3-diketones (such as **5–7** in Scheme 1, see below) underwent photolysis to give rearranged products. The work has been left dormant since we noted that two short communications on the photoreaction of allied borinates (where the bicyclononane ring in **5–7** is replaced by di-*n*-butyl or dicyclohexyl groups) had already been published in 1986 (1). These works were a study based on suggestions derived from an earlier communication by another group (2). While an additional related communication was

Received February 17, 1999.

J. Ishiyama[1] and Y.L. Chow.[2] Department of Chemistry, Simon Fraser University, Burnaby, BC V5A 1S6, Canada.

[1]Visiting Professor from Fukushima National College of Technology, Taira, Fukushima, Japan; Overseas Research Fellow (1997) supported by the Ministry of Education, Science, Sports and Culture, Government of Japan.
[2]Author to whom correspondence may be addressed. Telephone: (604) 291-3352. Fax: (604) 291-3765. e-mail: ychow@sfu.ca

 © 1999 NRC Canada

Scheme 1.

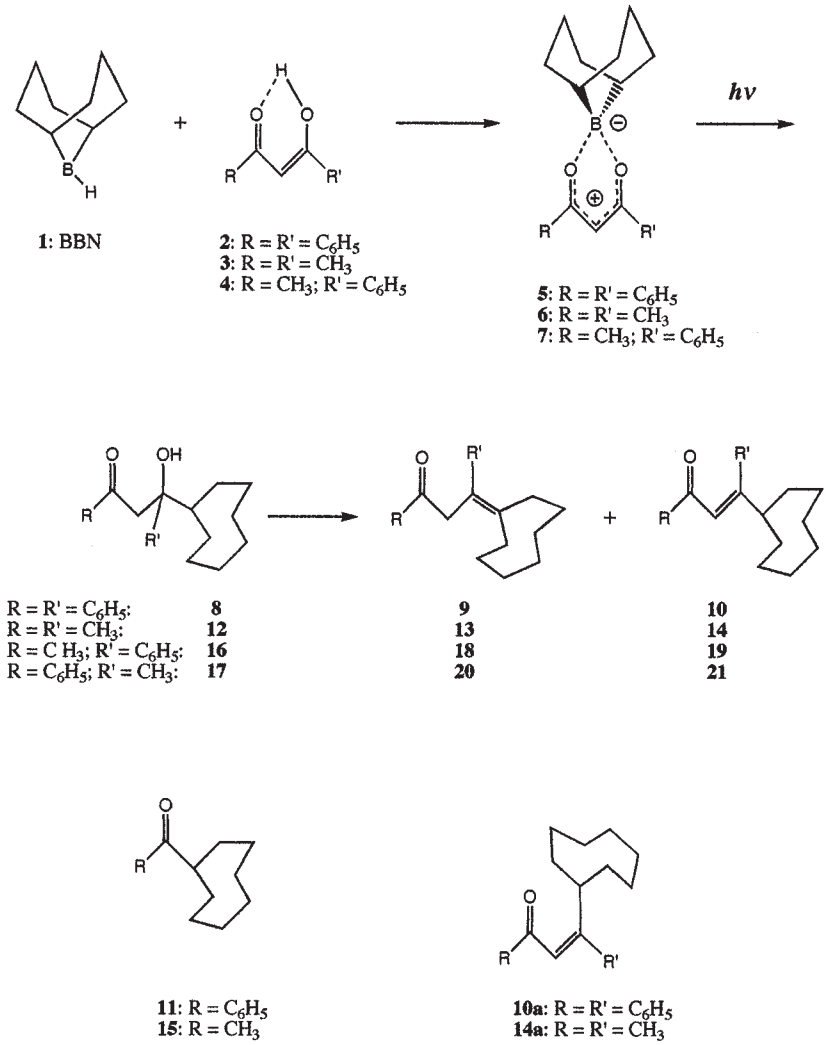

published later (3), the detailed photochemical reaction of allied borinates has not, to our knowledge, been described. In the meantime, the photochemistry and photophysics of boron compounds continue to attract investigations, and interesting results have been published in relation to photoinduced electron transfer (4), photo-cycloadditions (5), exciplex formations (5), and unusual emission patterns (6, 7). We were attracted by the abnormally deep-colored appearance of these borinates, and were puzzled by what appeared to be an unusually strong CT band in their UV–visible spectra. More recently, we undertook an in-depth investigation of borinates **5–7**, and discovered that our results were not in total agreement with the earlier communications (1). The chemical and physical behavior of these borinates is interesting and promises to stimulate new studies of allied boron compounds, particularly in relation to their excited states and radical reactions. We wish to describe the results from our group.

Results

The reaction of 9-borabicyclo[3,3,1]nonane (BBN, **1**) with a 1,3-diketone (**2–4**) in THF readily gave the corresponding *B*-diketonato-9-borabicyclo[3,3,1]nonane, **5–7**, in high yields (8); these borinates were abbreviated as AABBN (for *B*-acetylacetonato-, **6**) (8*b*), BABBN (for *B*-benzoylacetonato-, **7**) and DBMBBN (for *B*-dibenzoylmethanato-, **5**). They were prepared equally easily from 9-methoxy-BBN (**1**, H = OCH_3) and 9-(2-aminoethanolato)-BBN (**1**, H = $NH_2CH_2CH_2O$) in comparable yields. These colored (from yellow to orange) crystalline dialkylborinates **5–7** prominently showed strong UV absorption that is slightly blue-shifted from that of the parent diketone (6); this UV band was red-shifted in more polar solvents and must arise from a π–π* transition. They also showed a broad and weaker but well-defined band that was assigned as a CT transition (Fig. 1). Since the intensity of these absorption bands obeyed the Beer–Lambert law in cyclohexane and methylene chloride, it was concluded that these borinates existed as monomers up to 0.1 M. The borinates showed a strong IR absorption band for the B—O bond at 1376–1378 cm^{-1} and a ^{13}C NMR signal for the C-B carbon at about 23 ppm, which was slightly broadened owing to the boron quadrupole couplings. It should be noted that whereas the chemical shift of olefinic hydrogen moved downfield in the order **6–7–5**, the ^{13}C chemical shift of the corresponding

© 1999 NRC Canada

Fig. 1. The absorption spectra of (*a*) **6** at 1.05×10^{-4} M, (*b*) **7** at 3.69×10^{-5} M, and (*c*) **5** at 3.48×10^{-5} M in cyclohexane.

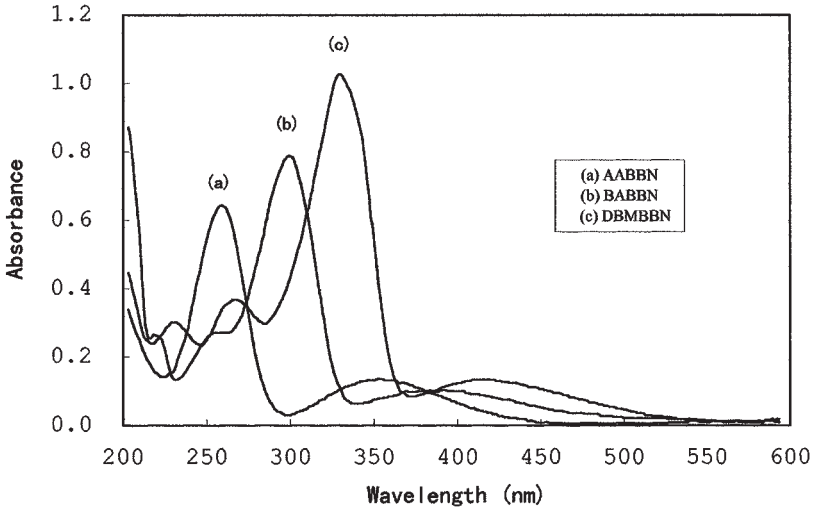

Table 1. Relative peak % of the photolysis of **6** from GC analysis.

	R_T(min)[a]								
	1.23	1.82	3.89	4.25	4.87	5.23	6.09	8.73	13.44
300 nm	1.9	13.0	1.8	3.3	1.4	5.8	41.0	24.0	4.3
254 nm[e]	7.7	11.0	0.6	14.0	1.8	1.7	31.0	25.0	3.8
Products	[b]	**15**	**14a**	**13**	[c]	**14**	**12**	**6**	[d]

[a]There are more peaks in the vicinity of solvent that were identified as acetylacetone, cyclooctane, and bicyclo[3,3,0]octane by the coinjection of an authentic sample or by its mass spectral pattern.

[b]Cyclooctanone by coinjection.

[c]1,1′-Bicyclooctyl by the MS pattern.

[d]Unknown.

[e]There are more peaks of small areas over the whole range in this than in the photolysis with the 300 nm source.

olefinic carbon moved upfield in the same order. The reversed order of chemical shifts could be related to the ring current generated by resonance involving the borinate ring.

DBMBBN **5** gave a broad (380–500 nm) fluorescence band with λ_{max} 415 nm in methylene chloride on excitation at the π–π^* transition at 330 nm, but no emission on excitation at the CT band. AABBN **6** in cyclohexane (and methylene chloride) showed a narrow fluorescence peak at 280 nm on excitation at 259 nm, and at 393 on excitation of the CT band at 353 nm. In both spectra weak emission humps at longer wavelengths (e.g., those at 320 and 370 nm in the former and at 432 and 507 nm in the latter) were assumed to arise from decomposed intermediates. While these fluorescence spectra were stable in cyclohexane, those in acetonitrile showed complex shapes and changed with time lapses. Their study remains to be continued later.

Irradiation of DBMBBN **5** in methylene chloride at 350 nm gave unconjugated enone **9** and a mixture of isomeric enones **10** in addition to a smaller amount of aldol **8**; the amount of all enones increased at the expense of **8** during isolation. Injection of this sample into GC showed that **9** and **10** were present in 14 and 30%, respectively, but **8** was thermally decomposed to give a new peak showing M^+ = 217 by a CI mode. By the EI mode, this GC peak showed the major *m*/*e* fragment at 216 (M^+), 133 ($C_6H_5COCH_2CH_2$), 105 (C_6H_5CO, 100%), and 77 (C_6H_5); this MS pattern is compatible with the structure of **11**,which could be easily formed from the retro-aldol reaction of **8** on injection into GC. Similar photolysis of **5** in a solution containing 0.2% of acetic acid (by volume) afforded aldol **8**, in a 41% isolated yield, but no enones **9** and **10**; the yields of the latter two were small as shown by GC analysis. However, in the presence of methanol (<1%) or acetic anhydride, analogous photolysis caused marginal effects. On the other hand, similar photolysis of **5** in a mixture of methylene chloride and acetonitrile (1:4) gave only enones **9** and **10** in 38 and 36% yield, respectively. While enone **9** could be isolated by chromatography, enone **10** decomposed during the operation.

In the initial stage, AABBN **6** was photolyzed in a mixture of cyclohexane and methylene chloride (9:1) under a blanket of dry nitrogen with 300 nm light in order to obtain a higher yield of aldol **12** at a reasonable rate. Irradiation with 254 nm light was faster by a factor of two than that with 300 nm light, but irradiation with 350 nm light (i.e., excitation of the CT band), on the contrary, caused no significant decomposition in 24 h. Photolysates were chromatographed to give aldol **12** and enones **13** and **14** in yields of 54, 7 and 1%, respectively, by 254 nm irradiation, and 54, <1, and 14%, respectively, by 300 nm irradiation. The GC spectrum of the crude product showed these and other product peaks, including those of acetylcyclooctane (**15**) and the geometric isomer **14a**; both of them were too small to be isolated (see Table 1). As is typical of a radical reaction, there were also several small by-product peaks that

© 1999 NRC Canada

Table 2. Relative product % from photolysis [a] of **6**.

	R_T (min)				
	3.66[b]	6.43	6.97	8.20	9.38
Product	**15**	**14a**	**13**	**14**	**12**
Tube	2	2	3	4	2
Tube 2[c]	9	2	3	4	28
Tube 3[d]	4	12	57	22	5
Tube 4[d]	2	11	37	24	3
Tube 7[e]	2	9	22	20	5
Tube 8[e]	2	8	38	18	6
Tube 9[e]	2	10	51	13	8

[a]See text for details of the solutions; the irradiation time was 4 h for tubes 1–4 and 2.5 h for tubes 7 and 8; the corresponding factor for products to the internal standard (hexadecane) was arbitrarily set at 10:1.
[b]This peak is derived from **12** upon injection of photolysates.
[c]Tube 3 contains 0.167 M acetic acid.
[d]Tubes 3 and 4 contain phenyl bromide, 0.0082 and 0.0041 M, respectively.
[e]Tubes 7–9 contain 1,2-dibromoethane, 0.02, 0.04, and 0.08 M, respectively.

were more visible in the 254 nm irradiation. GC–MS and (or) the coinjection of authentic samples identified these minor GC peaks as those of cyclooctane, cyclooctene, 1,1′-bicyclooctyl, and cyclooctanone. In the presence of <1% acetic acid, a similar 300 nm photolysis of AABBN **6** gave predominantly aldol **12** and only trace amounts of enones **13–14**, though the rate of AABBN conversion was scarcely affected (Table 2); indeed **12** was prepared in good yield by this procedure. Aldol **12** was partially decomposed on GC injection to give the peaks of itself and **15** in a 6:4 ratio; GC–MS by the CI mode showed two peaks to have M^+ at 213 and 155. The latter GC peak exhibited the *m*/*e* at 154 (M^+), 139, 111, 69 (100%), and 43, which supported the structure of **15**. Aldol **12** also slowly decomposed to **15** either in solution or neat; decomposition was more rapid on heating, during which enones **13** and **14** were also formed in small amounts as shown by GC and NMR monitors. In dilute acidic (HCl) methanol, **12** decomposed slowly to **14** and **15** at room temperature, but rapidly and mainly to enone **13** on refluxing. The enone distribution suggested that unconjugated enone **13** is thermally more stable than the conjugated **14**, probably because of steric crowding.

BABBN **7** in methylene chloride was irradiated with 300 nm light to give low yields of four enones that could be derived from aldols **16** and **17**; these aldols continued to decompose during separation. With difficulty, enones **20–21** were finally isolated only in semi-pure states by preparative TLC. The same solution containing 1% of acetic acid was irradiated under similar conditions to give aldol **16** (46%) and a small amount of a mixture containing the alternative aldol **17**. Aldol **16** when injected into the GC gave only one peak, which showed the MS pattern corresponding to **11** both by EI and CI modes. The fact that both aldols **8** and **16** decomposed to give the common ketone **11** provided a rationale for the structural correlation among them. The GC injection of the impure fraction of **17** under the same conditions gave the major peak corresponding to **15** as shown by the R_T and MS pattern. A crude product obtained from terminating a 60% photoreaction of **7** at 300 nm irradiation was subjected to GC analysis conditions as above to record the ketone peaks of **11** and **15** in a 27%/15% ratio in the absence, and in a 56%/20% ratio in the presence, of acetic acid. Similar photoreaction at 350 nm irradiation either in the presence or absence of acetic acid recorded the ketone peaks in a ratio of 12:10 by GC analysis. As the ratio of **11:15** virtually represents the ratio of **16:17** in the crude product, the latter must be coalescing to the 1:1 ratio.

AABBN **6** was used as a model to study the excited state reaction of these borinates. Photolysis of **6** with 300 nm light in various solvents showed the decreasing efficiency order of cyclohexane >> THF ~ benzene > acetonitrile > methylene chloride in the ratio of 1.00:0.74:0.71:0.60:0.49. When the photolysis was carried out in the presence of a trace amount of water (i.e., using purging nitrogen directly from a cylinder without drying), it was noteworthy that this ratio was nearly leveled, although cyclohexane and benzene were still the better solvents. GC examinations showed that the major product was aldol **12** for the reaction in methylene chloride and enone **14** for those in cyclohexane and benzene. Sensitized photodecomposition of **6** with benzophenone by 350 nm irradiation was an ideal setup since the sensitizer absorbed strongly in the 350 nm region where **6** showed no photoreactivity; this irradiation caused much more efficient decomposition than that by direct irradiation at 300 nm, and resulted in enormously accelerated disappearance of **6** as well as the efficient formation of enones **13** and **14a** in addition to a few unknown GC peaks. The reaction was complicated by the sensitizer itself being consumed, but the occurrence of triplet energy transfer was indicated by the absence of benzopinacol in the crude product; this implied that triplet excited benzophenone had been quenched (9). While the interpretation was not unambiguous, this observation, coupled with the efficient product yields, supported that efficient sensitization must have occurred. Under the oxygen blanket, the photolysis of **6** was not totally quenched but instead slightly accelerated, and gave oxidation products obviously due to the participation of O_2 in the product formation as is often observed in free radical reactions (10). While the result was inconclusive, in view of the smallness in the rate increase, oxygen quenching had probably occurred but was masked by the enhanced radical reactions.

The photoreaction of **6** was quenched efficiently by 1,3-pentadiene at the 3.5 mM level, and also by vinyl ethyl ether and furan (at 5 mM). The former diene is a typical triplet quencher, but the latter ethers do quenching by some other mechanisms, most likely intercepting the singlet state by electron transfer (9). No new compound was formed from these quenching experiments. Further, the consumption of **6** was accelerated by more than an order of magnitude in the presence of bromobenzene (4 mM) and 1,2-dibromoethane (5 mM). In both cases, both enones **13** and **14**, particularly the former unconjugated one, were produced in significantly increased amounts with increasing bromide concentrations, while the yield of aldol **12** was affected little, as shown in Table 2. The fluorescence peak of AABBN **6** in cyclohexane at 280 nm by excitation at λ_{ex} 259 nm was quenched by the presence of increasing concentrations of 1,2-dibromoethane. The Stern–Volmer plot was a straight line with the slope (K_{sv}) of 20.0. This demonstrated that singlet excited **6** interacted with the bromide and mutated rapidly to the triplet state by heavy atom effects (11). Similar spectroscopic ex-

© 1999 NRC Canada

Scheme 2.

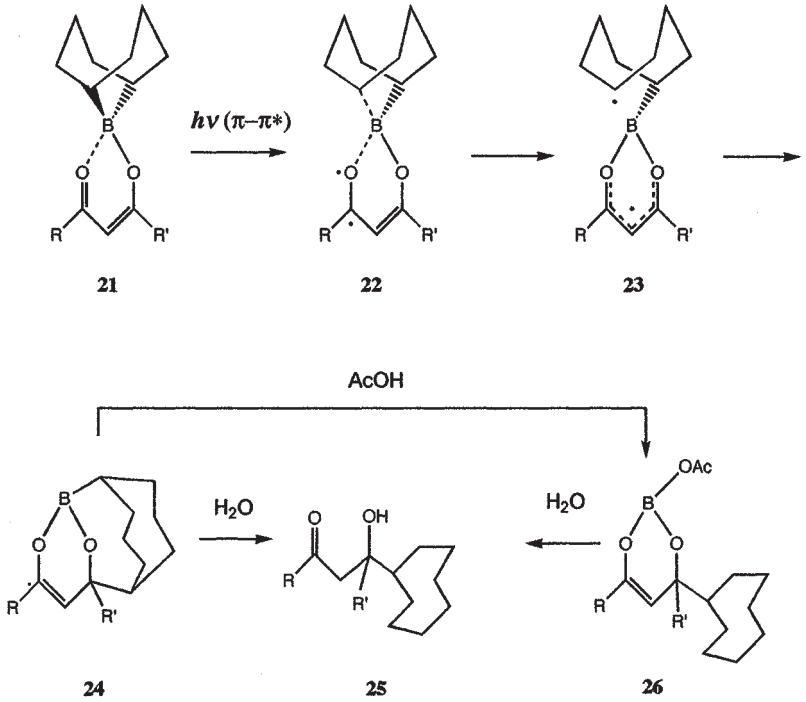

periments with bromobenzene and 1,3-pentadiene could not be carried out owing to the overlap of the absorption in the 260 nm region.

The structure of the products was primarily determined from NMR spectral evidence, in some cases with partially pure samples. The primary photoproducts were obviously aldols **8**, **12**, **16**, and **17**, which served as the source for the observed products, enones and acylcyclooctanes, derived from the secondary reactions as shown in Scheme 1. The isolated aldols showed, among other required signals, the following key NMR signals to define the structure unambiguously. Firstly, they showed a pair of AB quartets due to the diastereotopic proton of -CO-CH_2-, with the chemical shifts progressively moved downfield as a CH_3 group was replaced by a C_6H_5 group. Secondly, they had the carbonyl ^{13}C signal at 211 ppm for the acetyl and at 202 ppm for the benzoyl group. Finally, the monosubstituted cyclooctyl group showed eight ^{13}C signals indicating that the eight carbons are nonequivalent, that is, in each pair the corresponding -CH_2- groups were diastereotopic to one another due to the vicinal chiral centers. The unconjugated enones **9**, **13**, and **20** showed (*i*) a two-proton singlet in the 3.0–4.0 ppm region and a carbonyl ^{13}C signal at 199–208 ppm for the CH_2-CO, and (*ii*) eight ^{13}C signals (including one olefinic at about 137 ppm) for the cyclooctylidene group. Among the conjugated enones, only **14**, **14a**, and **21** were isolated, the last two as mixtures. Both **14** and **21** were always formed as the major isomer and assigned to the configuration shown for steric reasons. Both enones **10** and **19** (and (or) their isomers) could be detected with GC–MS but could not be isolated because of decomposition during column chromatography. The isomeric enone pair **14** and **14a** showed nearly identical spectral patterns not only in MS but also in the ^{13}C and ^{1}H NMR spectra, which gave little evidence to assign the *cis–trans* isomerism. These two conjugated enones and **21** exhibited (*i*) an olefinic proton singlet at 6.05, 6.05, and 6.72 ppm, (*ii*) a set of pertinent ^{13}C signals for an α,β-unsaturated carbonyl system, and (*iii*) five ^{13}C signals for the cyclooctyl group due to its rapid rotation. In addition, the NMR spectra of these enones also showed the required signals with appropriate chemical shifts.

Discussion

The overall reaction resembles the well-known classic 1,2- or 1,4-addition of an alkylborane onto α,β-unsaturated carbonyl compounds (12), except that the present reaction is promoted by light and occurs intramolecularly through free radical mechanisms. Thus, electronic excitation provides an alternative pathway to promote this alkylborane addition. The failure for excitation in the CT band to promote the reaction must imply that this excited state is rapidly deactivated to the ground state, i.e., that is the only channel available. These borinates **5–7** undergo a deep-seated rearrangement upon excitation of the π–π* transition band in a wide range of solvents; the photolytic efficiency is better in nonpolar than in polar media and the product patterns vary widely depending on reaction conditions. The overall result indicates that the products are formed in consecutive multistep processes involving intermediates that are sensitive to the photolysis conditions. The overall reaction is approximated as the primary photoinduced rearrangement to give the precursors of aldols **8**, **12**, **16**, and **17**, followed by secondary decomposition of the precursors under the photolysis conditions.

The experimental probes described provide good qualitative evidence that the primary photoreaction is derived from the triplet excited state of these borinates **5–7**. Two of these probes are unambiguous; that is, efficient triplet quenching (9) by 1,3-pentadiene, and a heavy atom effect to enhance

© 1999 NRC Canada

Scheme 3.

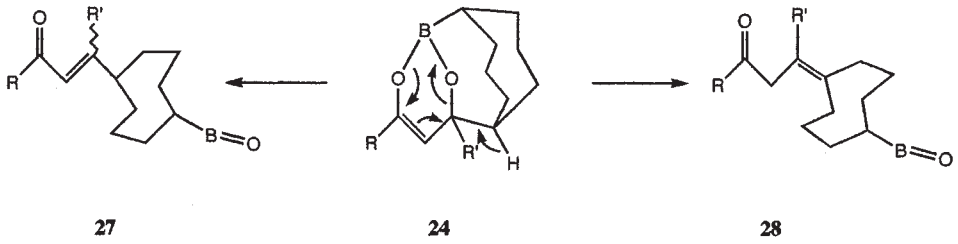

27 **24** **28**

the population of the triplet state induced by bromine-containing compounds (11). The other two, the benzophenone sensitization and oxygen quenching, are complicated by the participation of the reagents in the reactions; the former, which cannot be analyzed quantitatively owing to the change in the product pattern, also supports triplet state energy transfer on the basis of the detailed observations.

In the previous communications (1), the authors stated that the photoreaction of some similar dialkylborinates could not be quenched by either oxygen or 1,3-pentadiene, which led them to suggest a singlet state reaction. Though the present dialkylborinates **5–7** are not exactly the same as theirs, the corresponding results for these two quenchers are just the opposite to, and more complicated than, those stated in their reports. It is interesting to compare details of the two experimental descriptions.

The reaction mechanism is proposed in Scheme 2, in which the carbonyl triplet excited state **22**, as represented by the diradical model (9), is the species initiating the radical pathway. The step **22** to **23** is analogous to the homolytic substitution of a borane by an alkoxy radical, the driving force of which is derived from a bond energy gain of about 30–40 kcal/mol in the conversion of a B—C bond to a B—O bond (13). Triplet excited state biacetyl has been shown to interact with borane either directly or through the acetyl radical (14). The intramolecular attack in **22–23** should be more facile than any intermolecular attacks. The subsequent recombination of the radical pair **23** can occur at the carbon of either O—C bond; the direction is controlled by the nature of the R groups to give boronate **24**. The migration can be highly regiospecific if the R and R′ groups possess a large electronic gradient (1). Thus, the primary photolysis is assumed to terminate on the formation of **24**. Its simple hydrolysis should give aldols **25**, the process of which appears to be relatively sluggish under the photolysis conditions; thus GC analysis at times shows poor reproducibility depending upon sampling times. As will be discussed below, the conversion of **24–25** can also involve an excitation step. However, the work-up does not require highly nucleophilic hydrogen peroxide anion (1) to hydrolyze borate esters. While the efficiency of the borinate photodecomposition does not correlate strictly with solvent polarity, its rate is generally faster in hydrocarbons than in polar solvents. It is noteworthy that water, even in a trace amount, can retard the efficiency; the retardation is more significant in cyclohexane. The mechanism may be related to the coordination process at the boron center and remains to be elucidated. Efforts to isolate boronate **24** for an intermediate identification under anhydrous conditions have not been successful in providing a workable sample.

The mechanistic studies have been encumbered by unpredictable variations of the product pattern on changing the photolysis conditions; their effects have been traced to the secondary reactions and the reactivity of accompanying intermediates. The probable concurrence of thermal as well as photolytic pathways for intermediates adds further complexity that poses a formidable problem in portraying the mechanism(s). Nevertheless, certain observations can be explained with obvious and straightforward rationales. First of all, about 1% acetic acid does not affect the rate of photolysis, as shown in Table 2, but may rapidly attack boronate **24** by a pre-rate-determining nucleophilic coordination (15, 16) to form acetyl-borate **26**, which should be more easily hydrolyzed than **24** to afford **25.** Unless absorbing excitation light, both **25** and **26** are not photolabile and can afford good yields of aldols such as is the case for **8** and **12**, which are obtained clean even after prolonged irradiation under the given conditions. In contrast, the photolysis of borinate **7** generates borate **26** with R = C_6H_5 and R′ = CH_3 (corresponding to aldol **17**), which possesses the α-boratoxystyryl chromophore and must be labile to 300 nm irradiation, but not to 350 nm irradiation. Indeed, two observations support this argument; they are the formation of much less **17** than **16** (as measured by the GC peak of **15** and **11**) under the former (300 nm) irradiation and that of as much **17** as **16** under the latter (350 nm) irradiation. The high yield of aldol **8** in the photolysis of **5** under 350 nm irradiation must have a similar cause. Likewise, if aldols **25** with R = C_6H_5 are formed by adventitious water, they will be sensitive to 300 nm light and may cause a further complication to product patterns. To avoid these uncertainties, photolysis should be carried out under dry conditions. Further, there is no doubt that ketones **11** and **15** are formed by thermal and (or) acid-catalyzed retro-reactions from the aldols, slowly during isolation and more rapidly on injection in the GC port; when the port is cleaned the decomposition of **12** is drastically reduced.

Explanations of other observations are less straightforward and must rely on indirect rationales. In view of the sluggish acid-catalyzed dehydration of **12** at a room temperature (16), enone formation through simple thermal reactions cannot make a substantial contribution to high yields of enones such as those shown in Table 1. On the basis of the following evidence, we propose, as the cause of the enone formation, that boronate **24** undergoes photo-rearrangement followed by hydrolysis (Scheme 3). Firstly, the photoreaction of borinates **5–7** affords lower yields of aldols in the absence of acetic acid than in the presence, suggesting that exposure of **24** to light causes photoreactions to give enones (e.g., see Table 2). The borinate photoreactions car-

© 1999 NRC Canada

ried to a high conversion always furnish more enones. Secondly, the photolysis of **7** with 300 nm irradiation always gives much less **17** than 1**6**, particularly in the absence of acetic acid. This is a good indication that the intermediate **24** (R = C_6H_5, R′ = CH_3), corresponding to **17**, having an α-boronatostyryl chromophore, can absorb more light energy from 300 nm irradiation and undergo photolysis more extensively. The corroborating evidence is the formation of nearly the same amount of **16** and **17** in 350 nm irradiation, in which both corresponding intermediates **24** are scarcely irradiated. Thirdly, the dominance of either **13** or **14**, depending on the wavelength of excitation (see Table 1), supports the participation of an excited state of **24,** which is the intermediate in the absence of acetic acid. Finally, in the presence of benzophenone as a sensitizer or a bromide as a triplet enhancer, enones **13** and **14** are disproportionately increased in comparison to aldol. We speculate that the excited state of either promoter interacts with intermediates, through exciplexes or otherwise, which may increase either conjugated **14** (e.g., in the presence of bromobenzene) or unconjugated enone **13** (e.g., in the presence of 1,2-dibromoethane) **12,** as shown in Table 2.

While **24** is not available for study at this stage, the bond reorganization as shown in Scheme 3 is suggested to account for the photochemical transformations to give the enone precursors **27** and **28**. The former, **27,** can be arrived at by a retro-Diels–Alder reaction; the latter, **28**, by a 1,3-hydrogen shift from **24**. The alkyl B=O bond may be regarded as an analogue of an acyl carbonium ion, and is expected to react with water vigorously to give the observed enones. The proposed boronate intermediates in Scheme 3 involve much unexplored chemistry of their ground and excited states, which promises to open up a new area of investigation. In this regard, the origin of the broad CT absorption band must be related to the electronic structure of borinates **5–7** and will be studied.

Experimental section

Materials and instrumentation

Commercial 1,3-diketones (Aldrich) were recrystallized or distilled, but 9-borabicyclo[3.3.1]nonane (9-BBN, 0.5 M solution in THF) was used as received. For preparative photolysis, reagent grade solvents were distilled with proper dehydrating agents. Solvents of spectroscopic grade (BDH) were used for optical spectra. Benzophenone, 1,3-pentadiene, bromobenzene, and 1,2-dibromoethane were purified as described in earlier publications (5, 10, 11). The sample of 1,3-pentadiene was a mixture of *trans/cis* 55:45 by GC.

Melting points were determined on a Fisher–Johns block and not corrected. Infrared spectra were recorded with a Perkin–Elmer model FT1605 spectrometer, ultraviolet and visible spectra with a Varian–Cary 210 spectrophotometer, fluorescence spectra with either a PTI LS-1 or Perkin–Elmer MPF-44B, and GC–MS with a Hewlett–Packard 5985B. NMR spectra were taken with Bruker AMX-400 or AMX-600 using TMS as the internal standard. Gas chromatography was carried out at the injection port temperature of 150–250° C with a Hewlett–Packard 5790 equipped with a 15 m × 0.2 mm BB-1 or OV-1 capillary column and HP 3390A integrator.

Irradiation was carried out in a Rayonet Photochemical Reactor in quartz (for 254 and 300 nm irradiation) or Pyrex (for 350 nm irradiation) test tubes (12 × 100 mm) placed in a "merry-go-round." A bottom fan circulated the air to maintain a constant temperature of 30–34°C. For analytical and sensitized photolysis, solutions were added with a known concentration of hexadecane or eicosane as the internal standard before irradiation. The corresponding factor of AABBN to hexadecane was determined for each column to calculate percent conversions.

Preparation of borinates 5–7

To a solution of a 1,3-diketone in THF, a calculated amount of 9-BBN was added by syringe under a nitrogen blanket at room temperature while the solution was stirred magnetically. The precipitate in nearly a quantitative yield was filtered and recrystallized under nitrogen purging. 9-Methoxy-9-borabicyclo[3,3,1]nonane (1.0 M solution in hexane) or 9-(2-aminoethyleneoxy)-9-BBN was also used to give nearly quantitative yields.

DBMBBN (5)

The precipitate was recrystallized in CH_2Cl_2 and hexane (2:1) or THF and hexane (2:1) and cooled to –20°C to give deep red crystals, mp 266–267°C; IR (Nujol): B–O stretching at 1376.5 cm^{-1}; ^1H NMR ($CDCl_3$) δ: 1.00 (2H, br s), 1.55–1.65 (2H, m), 1.70–1.80 (4H, m), 1.90–2.10 (6H, m), 6.90 (1H, s), 7.50 (4H, t), 7.60 (2H, t), 8.10 (4H, d); ^{13}C NMR ($CDCl_3$) δ: 23.0 (br), 24.91, 31.41, 92.67, 128.24, 128.86, 133.73, 134.14, 183.11; MS (EI) *m*/*e* (relative intensity): 344 (16, M^+), 287 (18), 261 (28), 248 (43), 235 (17), 105 (100). Anal. calcd. for $C_{23}H_{25}BO_2$: C 80.23, H 7.27; found: C 80.32, H 7.35. This compound is soluble in THF and methylene chloride but much less soluble in benzene and acetonitrile.

BABBN (7)

The precipitate was recrystallized in THF and diethyl ether (1:1) by cooling to –20°C to give brilliant red crystals, mp 196–197°C; IR (Nujol): B–O stretching at 1377.7 cm^{-1}; ^1H NMR ($CDCl_3$) δ: 0.90 (2H, br s), 1.50–1.60 (2H, m), 1.60–1.70 (4H, m), 1.80–2.00 (6H, m), 2.25 (3H, s), 6.30 (1H, s), 7.45 (2H, t), 7.60 (1H, t), 7.95 (2H, d); ^{13}C NMR ($CDCl_3$) δ: 23.0 (br), 24.79, 24.83, 24.98, 31.14, 31.36, 96.42, 128.15, 128.78, 133.53, 133.63, 181.79, 191.84; MS (EI) *m*/*e* (relative intensity): 282 (22, M^+), 239 (13), 225 (35), 199 (55), 186 (100), 173 (40). Anal. calcd. for $C_{18}H_{23}BO_2$: C 76.61, H 8.21; found: C 76.75, H 8.45.

AABBN (6)

The precipitate was recrystallized in degassed hexane to give bright yellow crystals, mp 121–122° C; IR(Nujol): B–O stretching at 1376.6 cm^{-1}; ^1H NMR ($CDCl_3$) δ: 0.80 (2H, br s), 1.40–1.50 (2H, m), 1.58–1.66 (4H, m), 1.70–1.90 (6H, m), 2.10 (6H, s), 5.55 (1H, s); ^{13}C NMR ($CDCl_3$) δ: 23.0 (br), 24.29, 24.73, 31.07, 100.63, 190.44; MS (EI) *m*/*e* (relative intensity): 220 (25, M^+), 177 (12), 163 (50), 137 (80), 124 (100), 111 (31). Anal. calcd. for $C_{13}H_{21}BO_2$: C 70.91, H 9.55; found: C 70.68, H 9.45. **6** is soluble in cyclo-

© 1999 NRC Canada

hexane and benzene but less soluble in methylene chloride and acetonitrile.

Preparative photolysis of borinates

DBMBBN

A solution of **5** (0.10 g, 0.29 mmol) in anhydrous THF (50 mL) was distributed in 12 Pyrex tubes, sealed with septa, and purged with dry nitrogen for 5 min. The tubes were rotated in a merry-go-round under irradiation with RPR 3500 A lamps (24 W × 16) for 24 h. The photolysate gave two major GC peaks, at R_T 3.60 and 4.20. The crude product was chromatographed on a short column of silica gel 60 (20 cm^3) to afford an impure fraction of the former peak that was rechromatographed to give **9**; ^{1}H NMR ($CDCl_3$) δ: 1.50–1.80 (10H, m), 2.11 (2H, br t), 2.30 (2H, br t), 4.10 (2H, s), 7.20–7.60 (8H, m), 7.81 (2H, m); MS (EI) *m*/*e*: 318 (5, M^+), 213 (11), 105 (100), 91 (15), 77 (25); MS (CI) *m*/*e*: 319 (100, M^++1). Anal. calcd. for $C_{23}H_{26}O$: C 86.75, H 8.23; found: C 86.95, H 8.64.

When the photolysis was carried out in a mixture of methylene chloride and acetonitrile (1:1), the GC spectra showed both peaks in 38 and 36% yields. The fraction of R_T 4.20 (**10**) decreased rapidly on chromatography; one of its impure fractions showed ^{1}H NMR ($CDCl_3$) δ: 0.90 (2H, m), 1.50–2.00 (12H, m), 2.72 (1H, m), 6.60 (1H, s), 7.11 (2H, m), 7.22 (3H, m), 7.30 (2H, m), 7.70 (2H, m), 8.01 (H, m); MS (EI) *m*/*e* (relative intensity): 318 (60, M^+), 207 (5), 192 (5), 105 (100), 91 (11), 77 (31); MS (CI) *m*/*e*: 319 (100, M^++1).

In a separate photolysis, DBMBBN (0.17 g) in methylene chloride (50 mL) containing acetic acid (0.5 mL) was irradiated in a similar way to afford a 65% conversion. Repeated chromatography on a long silica gel column (40 cm^3) gave **8** as colorless crystals; ^{1}H NMR ($CDCl_3$) δ: 1.20–1.80 (14H, m), 1.96 (1H, q), 3.25 and 3.95 (AB quartet, diastereotopic -CH_2-, J = 16.3 Hz), 4.88 (1H, br s), 7.12 (1H, t), 7.23 (2H, t), 7.40 (2H, d), 7.43 (2H, t), 7.55 (1H, t), 7.84 (2H, d); ^{13}C NMR ($CDCl_3$) δ: 26.31, 26.40, 26.70, 26.93, 27.08, 27.76, 28.03, 44.13, 47.49, 79.43, 125.75, 126.34, 127.79, 127.98, 128.59, 133.49, 137.35, 146.19, 202.56. Anal. calcd. for $C_{23}H_{28}O_2$: C 82.10, H 8.39; found: C 82.45, H8.12. This compound on injection to GC–MS gave a single peak for **11**, at an early R_T of 1.77 min, which showed M^++1 = 217 by the CI mode, and *m*/*e*: 216 (M^+, 10%), 133 (12), 120 (12), 105 (100), and 77 (35) by the EI mode.

BABBN

A solution of **7** in methylene chloride was irradiated for 24 h with RPR 3000A lamps, and the crude product was chromatographed to give four fractions, each containing a major component, that showed the R_T of the major component at 7.6, 8.5, 8.8, and 9.7 min and M^++1 = 257 of the major peak by the CI mode. Fraction one contained mostly **20** (R_T 8.8); ^{1}H NMR ($CDCl_3$) δ: 1.50–1.68 (10H, m), 1.69 (3H, s), 2.20 (2H, br t), 2.31 (2H, br t), 3.75 (2H, s), 7.40 (2H, m), 7.51 (1H, t), 7.95 (2H, m); ^{13}C NMR ($CDCl_3$) δ: 19.30, 16.19, 26.22, 26.67, 26.99, 27.56, 31.41, 32.11, 44.38, 121.92, 128.09, 128.52, 132.70, 132.76, 137.63, 198.96; MS (EI) *m*/*e*: 256 (15, M^+), 241 (3), 105 (100), 95 (21), 77 (31); MS (CI) *m*/*e*: 257 (M^++1). Fraction two contained **21** (R_T 9.7) as the major component; ^{1}H NMR ($CDCl_3$) δ: 1.50–1.80 (14H, m), 2.18 (3H, s), 2.35 (1H, tt), 6.71 (1H, br s), 7.45 (2H, m), 7.51 (1H, m), 7.90 (2H, m); ^{13}C NMR ($CDCl_3$) δ: 18.09, 26.08, 26.43, 26.70, 31.78, 41.19, 118.73, 123.38, 128.14, 139.09, 139.76, 166.44, 192.22; MS (EI) *m*/*e*: 256 (5, M^+), 241 (6), 171 (12), 145 (71), 105 (100), 77 (41); MS (CI) *m*/*e*: 257 (M^++1). Fraction three contained **18** (R_T 7.6); ^{1}H NMR ($CDCl_3$) δ: 1.50–1.70 (10H, m), 2.05 (3H, s), 2.10 (2H, br t), 2.35 (2H, br t), 3.45 (2H, s), 7.05 (2H, m), 7.20 (3H, m); MS (EI) *m*/*e*: 256 (60, M^+), 241 (100), 238 (26), 213 (45), 198 (25), 143 (51), 131 (80), 117 (75), 91 (90); MS (CI) *m*/*e*: 257 (100, M^++1), 239 (25), 199 (81). Fraction four contained **19** (R_T 8.5); ^{1}H NMR ($CDCl_3$) δ: 1.40–1.60 (10H, m), 1.61 (2H, m), 1.70 (3H, s), 1.81 (2H, m), 2.60 (1H, m), 6.05 (1H, s), 7.10 (2H, m), 7.30 (3H, m); MS (EI) *m*/*e*: 256 (15, M^+), 241 (3), 105 (100), 95 (22), 77 (32); MS (CI) *m*/*e*: 257 (M^++1).

In a similar experiment, **7** (0.142 g, 0.51 mmol) in a solution of methylene chloride (50 mL) and acetic acid (0.5 mL) was irradiated for 23 h, and the photolysate was neutralized with K_2CO_3. The crude product was chromatographed twice on a silica gel column to give a small fraction containing **17** and a fraction of **16** (0.026 g). ^{1}H NMR ($CDCl_3$) δ: 1.20–1.90 (15H, m), 1.98 (3H, s), 2.87 and 3.22 (AB quartet, diastereotopic -CH_2-, J = 16.3 Hz), 4.45 (1H, br), 7.19 (1H, m), 7.28 (2H, m), 7.36 (2H, m); ^{13}C NMR ($CDCl_3$) δ 26.20, 26.35, 26.72, 26.85, 27.04, 27.20, 27.46, 27.79, 32.22, 46.99, 49.88, 79.06, 125.61, 126.43, 127.65, 145.94, 211.72. The injection of **16** to GC gave a single peak at R_T 1.77 min, and the fragmentation pattern of **11**. The former fraction containing **17** was contaminated by benzoylacetone, and showed, on GC–MS determination, a peak at R_T 1.45 and the fragmentation pattern of **15** (vide infra).

A solution of **7** (0.023 g, 0.081 mmol) and eicosane (0.02 g, 0.071 mmol) in methylene chloride (10 mL) was divided in two quartz tubes; acetic acid (10) was added to the second one. These tubes, sealed with septa and purged with dry nitrogen, were irradiated with RPR 3000A for 19 h to give 70% conversions. The GC analysis of the photolysates (injection temperature 250°C) gave two peaks at 1.40 min (for **15**) and 1.59 min (for **11**) with a yield of 27%/15% for the first and 56%/20% for the second tube (with acetic acid).

Separately, two tubes of methylene chloride solution containing **7** (0.0078 M) and eicosane (0.0071 M), one with the presence (10 μL) and the other with the absence of acetic acid, were irradiated under similar conditions except for using RPR 3500A lamps for 24 h to cause a 40% conversion. The GC analysis gave a yield for **15**/**11** of 12%/10%, within experimental error, for both photolysates.

AABBN

A solution of AABBN **6** (0.048 g, 0.22 mmol) in a mixture of cyclohexane and methylene chloride (9:1, 20 mL) was distributed in four quartz tubes and sealed under nitrogen. The solution was irradiated with RPR 2540A lamps for 8 h to cause about 80% conversion. A separate solution prepared from 0.04 g of **6** was irradiated with RPR 3000A lamps under the same conditions for 18 h to cause a 75% conversion. Both solutions were examined by GC–MS analysis to afford the major peaks shown in Table 1. A similar experiment was carried out with RPR 3500A lamps for 24 h

© 1999 NRC Canada

to give a 15% conversion of **6**. The crude product from 254 nm irradiation was chromatographed on silica gel columns with *n*-hexane elution to give unreacted **6**. With increasing amounts of methylene chloride in *n*-hexane, **13** (7.8 mg), **14** (trace amount), and **12** (18 mg, 54%) were isolated. The physical data of **12**: IR (Nujol): 3488 (O–H stretching), 1699.7 (C=O stretching), 1171.8 (*tert*-C–O stretching) cm^{-1}. ^1H NMR ($CDCl_3$) δ: 1.12 (3H, s), 1.15–1.25 (2H, m), 1.35–1.83 (13H, m), 2.19 (3H, s), 2.55 and 2.66 (diastereotopic -CH_2-, J = 16.3 Hz); ^{13}C NMR ($CDCl_3$) δ 23.36, 26.40, 26.53, 26.98, 27.14, 27.75, 29.01, 32.10, 46.60, 50.04, 75.09, 211.52. Anal. calcd. for $C_{13}H_{24}O_2$: C 73.54, H 11.39; found: C 73.82, H 11.48. The injection of **12** into GC at 250°C gave two peaks at R_T 1.85 and 6.04 min in the ratio of 6:4. The former peak arising from **15** showed M^++1 at 155 by theCI mode, and *m*/*e* at 154 (1), 139 (1), 111 (10), 97 (14), 69 (100%), 43 (60) by the EI mode. The latter peak was due to **12** itself and showed *m*/*e* by the CI mode at 213 (M^++1, 2), 195 (31), 155 (100) and by the EI mode at 197 (1), 111 (10), 101 (100), 69 (21), 43 (61). The physical data of **13**: ^1H NMR ($CDCl_3$) δ: 1.40–1.55 (6H, m), 1.15–1.72 (4H, m), 1.68 (3H, s), 2.10 (3H, s), 2.14–2.20 (2H, m), 2.20–2.26 (2H, m), 3.13 (2H, s); ^{13}C NMR ($CDCl_3$) δ: 19.18, 26.07, 26.22, 26.70, 26.90, 27.59, 29.15, 31.29, 32.02, 49.80, 121.58, 138.15, 207.56; MS (EI) *m*/*e*: 194 (15, M^+), 179 (16), 151 (10), 136 (12), 109 (26), 95 (100), 81 (35), 69 (42). Anal. calcd. for $C_{13}H_{22}O$: C 80.35, H 11.41; found: C 80.11, H 11.58.

The crude product from 300 nm photolysis was worked up similarly to give **13** (trace amount), **14** (4.3 mg), and **12** (14.3 mg, 54%). **14** showed the following physical constants: ^1H NMR ($CDCl_3$) δ: 1.40–1.78 (14H, m), 2.09 (3H, d, J = 1.5 Hz), 2.16 (1H, br s), 2.18 (3H, s), 6.05 (1H, q, J = 1.5 Hz); ^{13}C NMR ($CDCl_3$) δ: 17.47, 26.02, 26.39, 26.59, 31.65, 48.84, 121.60, 166.11, 199.32; MS (EI) *m*/*e*: 194 (10, M^+), 179 (41), 151 (10), 136 (15), 111 (41), 109 (55), 98 (30), 95 (81), 81 (45), 69 (75), 43 (100). Anal. calcd. for $C_{13}H_{22}O$: C 80.35, H 11.41; found: C 80.28, H 11.21.

Sensitized photolysis of AABBN 6

AABBN (0.101 g, 0.46 mmol), hexadecane (0.05 mmol), and benzophenone (0.042 g, 0.23 mmol) in a mixture of cyclohexane and methylene chloride (9:1, 50 mL) were irradiated with RPR 3000A as above for 6 h to cause a 76% conversion of **6**. GC analysis of the photolysate showed the peak % of **15**, **14a**, **13**, **14**, and **12** to be 4.3, 11, 16, 3.1, and 4.2%. Separately, a cyclohexane solution of **6** (0.0052 M), hexadecane (0.00033 M), and benzophenone (0.0032 M) was irradiated with RPR 3500A for 2.6 h to give a 60% conversion; the control experiment without benzophenone gave a <2% conversion. The GC analysis gave the peak % for **15**, **14a**, **13**, **14**, and **12** of 0.5, 3.5, 6.1, 3.2, and 0.5%. In both GC analyses the benzophenone peak decreased and several minor peaks were observed in R_T >10 min. Examination of the crude products with HPLC gave no benzopinacol peak by coinjection.

The former solution was worked up in the usual way to give **13** (5.4 mg, 8%), **14** (10.0 mg, 15%), **12** (30.3 mg, 42%), and a mixture of **14a** and benzophenone. This mixture showed ^1H NMR ($CDCl_3$) δ: 1.40–1.80 (14H, m), 2.08 (3H, d, J = 1.2 Hz), 2.15 (3H, s), 6.05 (1H, br s); ^{13}C NMR δ: 17.42, 26.34, 26.54, 25.97, 31.60, 31.82, 48.80, 121.56, 165.09, 199.31. This sample showed a GC peak at R_T 3.7 in contrast to that of 5.4 for **14**; the GC–MS of the former peak showed MS (EI) *m*/*e*: 194 (40, M^+), 179 (42), 151 (10), 136 (12), 123 (25), 109 (71), 95 (100), 81 (50), 69 (40), 43 (98).

Quantitative analysis of the photoreaction of AABBN 6

A solution of **6** (7.2 mg, 0.0364 mmol) in cyclohexane (25 mL) was divided between five test tubes (5 mL each); tubes 3 and 4 also contained acetic acid (2 μL). Tubes 1–4 were sealed under dry nitrogen and kept in a dark place. Tube 5 was sealed under dry oxygen. After 5 days, GC analysis showed a peak at R_T 1.23 min, in trace amounts, for tubes 1 and 5, and 2% for tube 3; after 8 days the intensity was 2–3% for all tubes.

Solutions of **6** (0.054–0.056 M) in cyclohexane, benzene, THF, methylene chloride, and acetonitrile were prepared to contain fixed concentrations of hexadecane (0.0131–0.0121 M). These solutions, placed in quartz tubes and sealed under nitrogen dried over solid $CaCl_2$ and NaOH pellets, were irradiated with RPR 3000A lamps for 21 h. The photolysates were analyzed by GC, and the % conversion of **6** was determined to give >96, 71, 74, 52, and 61% with respect to the internal standard. A set of similar experiments purged with nitrogen directly from a tank without drying gave the % conversion of 60, 64, no data, 41, and 56%.

Four tubes of a solution of **6** (0.007 M) in cyclohexane containing hexadecane as the internal standard and 1,3-pentadiene (45:55 mixture of *cis/trans*) at 0.014, 0.007, 0.0035, and 0.0 M were prepared and sealed under nitrogen. A solution containing the same substrate concentrations in a mixture of cyclohexane and methylene chloride was also prepared and distributed in four tubes to make the second set. They were irradiated for 5 h, and analyzed by GC for the % conversion of **6** to give 21, 22, 23, and 60% for the first set in cyclohexane, and 16, 19, 20, and 64% for the second set in the mixture. No new reaction product with the dienes was detected.

Five tubes of solution in a mixture of cyclohexane and methylene chloride (9:1) containing **6** (0.0082 M) and hexadecane (0.0046 M) were prepared. Tube 1 served as the control run. Acetic acid (0.167 M) was added to tube 2, and phenyl bromide (0.0082 and 0.0041 M) to tubes 3 and 4, respectively. These tubes were sealed under dry nitrogen except for tube 5, which was bubbled with a slow stream of dry oxygen while all of them were irradiated with RPR 3000 lamps. GC analysis of the photolysates showed the remaining % of **6** in each tube to be 100, 100, 85, 88, and 90%, respectively, at 1 h irradiation, and 88, 84, 44, 46, and 52%, respectively, at 4 h irradiation. The details of GC analysis of photolysates 1–4 after 4 h irradiation are given in Table 2. The photolysate of **6** under oxygen contained completely different products of highly oxidized materials with R_T 2–5 min; column chromatography failed to give pure products.

Four tubes of similar solutions containing **6** (0.0088 M) and hexadecane (0.0034 M) were prepared as tubes 6–9, to which were added 1,2-dibromoethane at 0.0, 0.02, 0.04, and 0.081 M, respectively. These tubes were irradiated as above. GC analysis of the photolysates gave % of remaining **6** to be 100, 67, 63, and 52%, respectively, after 1 h irradiation, and 98, 47, 46, 29%, respectively, after 2.5 h irradiation. The de-

© 1999 NRC Canada

tailed product analyses of the 2.5 h photolysate by GC for tubes 7–9 are given in Table 2, but those for the control run (tube 6) were too small and are assumed to be similar to that shown for tube 1.

Acknowledgments

The authors wish to thank the Natural Sciences and Engineering Research Council of Canada for generous support of this project. J.I. gratefully acknowledges the award of an Overseas Research Fellowship from the Japanese Government through the Ministry of Education, Science, Sports, and Culture.

References

1. (*a*) K. Okada, Y. Hosoda, and M. Oda. J. Am. Chem. Soc. **108**, 321 (1986); (*b*) Tetrahedron Lett. **27**, 6213 (1986).
2. K. Utimoto, T. Tanaka, and H. Nozaki. Tetrahedron Lett. 1167 (1972).
3. K. Okada, H. Inokawa, and M. Oda. Tetrahedron Lett. **30**, 4395 (1989).
4. (*a*) S. Chatterjee, P.D. Davis, P. Gottschalk, M.E. Kurz, B. Sauerwein, X. Yang, and G.B. Schuster. J. Am. Chem. Soc. **112**, 6329 (1990); (*b*) J.D. Wilkey and G.B. Schuster. J. Am. Chem. Soc. **113**, 2149 (1991).
5. (*a*) Y.L. Chow and X.-E. Cheng. Can. J. Chem. **69**, 1331 (1991); **69**, 1575 (1991); (*b*) Y.L. Chow, S.S. Wang, C.I. Johansson, and Z.-L. Liu. J. Am. Chem. Soc. **118**, 11 725 (1996).
6. (*a*) Y.L. Chow, Y.-H. Zhang, M.X. Zhang, and A. Rassat. Chem. Phys. Lett. **272**, 471 (1997); (*b*) H.-D. Ilge, E. Birckner, D. Fassler, D. Kozmenko, M.D. Kuz'min, and H. Hartmann. J. Photochem. **32**, 177 (1986).
7. J. Yoon and A.W. Czarnik. J. Am. Chem. Soc. **114**, 3874 (1992).
8. (*a*) M.F. Hawthorne and M. Reintjes. J. Org. Chem. **30**, 3851 (1965); (*b*) R. Koster and G.W. Rotermund. Liebigs Ann. Chem. **689**, 40 (1965); (*c*) L.H. Toporcer, R.E.Dessy, and S.I.E. Green. Inorg. Chem. **4**, 1649 (1965); (*d*) R. Boese, R. Koster, and M. Yalpani. Chem. Ber. **118**, 670 (1985).
9. (*a*) N.J. Turro. Modern molecular photochemistry. Benjamin–Cummings, Menlo Park, Calif. 1978; (*b*) J. Gersdorf, J. Mattay, and H. Gorner. J. Am. Chem. Soc. **109**, 1203 (1987); (*c*) Y.L. Chow, M. Vanossi, and S.-S. Wang. J. Photochem. Photobiol. A: **88**, 125 (1995).
10. K.L. Pillay, K. Hanaya, and Y.L. Chow. Can. J. Chem. **53**, 3022 (1975).
11. Y.L. Chow and X. Liu. Can. J. Chem. **69**, 1261 (1991).
12. (*a*) K. Negishi and H.C. Brown. J. Am. Chem. Soc. **95**, 6757 (1973); (*b*) P. Jacob III. J. Organomet. Chem. **156**, 101 (1978).
13. K.U. Ingold and B.P. Roberts. Free-radical substitution reactions. John Wiley & Sons, New York. 1971. pp. 46–62.
14. (*a*) J. Grotewold and E.A. Lissi. Chem. Commun. 1367 (1968); (*b*) J. Chem. Soc. (B), 264 (1968).
15. L.H. Toporcer, D.E. Dessy, and S.I.E. Green. J. Am. Chem. Soc. **87**, 1236 (1965).
16. (*a*) W. Gerrard, M.F. Lappert, and R. Shafferman. J. Chem. Soc. 3648 (1958); (*b*) E.W. Abel, W. Gerrard, and M.F. Lappert. J. Chem. Soc. 5051 (1957); 1451 (1958).

© 1999 NRC Canada

Étude du système U-Sr-O par diffraction X à haute température

André Pialoux et Bernard Touzelin

Résumé : La diffractométrie de rayons X à chaud ($293 \leq T(K) \leq 1773$) est utilisée pour étudier la réaction entre monoxyde de strontium et dioxyde d'uranium sous atmosphère contrôlée ($10^5 \geq P_{O_2}(Pa) \geq 10^{-24}$), avec mesure des paramètres cristallins et évaluation de la composition des divers uranates formés. C'est ainsi qu'avec un échantillon de rapport Sr/U = 1, prennent naissance les phases successives : (*a*) α-« $SrUO_4$ » orthorhombique dont la réduction ($3{,}67 \geq O/U \geq 3{,}62$) se traduit par l'observation d'un volume de maille constant ($V = 0{,}367$ nm^3) entre 1173 et 1373 K; (*b*) β-« $SrUO_4$ » rhomboédrique qui manifeste une forte variation de composition entre la forme oxydée (β-$SrUO_{3,60}$) métastable en dessous de 1108 K et la forme réduite (β′-« $SrUO_{3,11}$ ») stable à toute température; (*c*) « $SrUO_3$ » de composition constante ($O/U \approx 3$) entre 293 et 1533 K puis variable ($O/U < 3$) au-dessus de 1533 K, avec pour cette pérovskite déformée une probable transition du second ordre (α-*Pnma*, β-*Imma*) au voisinage de 1073 K; (*d*) $U_{1-\delta}Sr_\delta O_{2-\delta}$ de structure fluorine et dont la teneur maximale en SrO ($\delta \approx 0{,}25$) provoque à 1673 K un accroissement du paramètre de 0,5 % par rapport à celui de l'$UO_{2,00}$. Un diagramme de phases est proposé pour le système pseudo-binaire « $SrUO_3$ » – « $SrUO_4$ ». Avec un échantillon de rapport Sr/U = 3, la pérovskite « Sr_3UO_6 » monoclinique se montre stable sous $P_{O_2} \approx 10^5$ Pa jusqu'à 1373 K. Par contre, en milieu réducteur ($P_{O_2} \leq 10^{-19}$ Pa), elle cède la place à la phase « Sr_3UO_5 » orthorhombique de paramètres beaucoup plus grands quelle que soit la température.

Mots clés : diffraction X à haute température, réactivité des oxydes métalliques, système U-Sr-O, combustibles nucléaires.

Abstract : High-temperature X-ray diffraction ($293 \leq T(K) \leq 1773$) is used to investigate the reaction between strontium monoxide and uranium dioxide under controlled atmosphere ($10^5 \geq P_{O_2}(Pa) \geq 10^{-24}$), with lattice parameter measurements and composition estimates of the different uranates obtained. Thus, with a Sr/U = 1 sample, we successively observe the phases: (*a*) orthorhombic α-"$SrUO_4$", whose reduction ($3.67 \geq O/U \geq 3.62$) is shown by a constant volume of the cell ($V = 0.367$ nm^3) between 1173 et 1373 K; (*b*) rhombohedral β-"$SrUO_4$", which shows a large composition variation between the metastable oxidized form (β-$SrUO_{3.60}$) below 1108 K and the stable conjugate reduced form (β′-$SrUO_{3.11}$) at whatever temperature; (*c*) "$SrUO_3$" of constant composition ($O/U \approx 3$) between 293 and 1533 K, then variable ($O/U < 3$) above 1533 K, with a probable second-order transformation (α-*Pnma*, β-*Imma*) for this distorted perovskite near 1073 K; (*d*) fluorite type $U_{1-\delta}Sr_\delta O_{2-\delta}$ solid solution for which a maximal account in SrO ($\delta \approx 0.25$) induces a 0.5 % thermal expansion parameter in comparison with $UO_{2.00}$. A pseudo-binary "$SrUO_3$"–"$SrUO_4$" phase diagram is propounded. With a sample compound of Sr/U = 3, the monoclinic "Sr_3UO_6" perovskite is stable under $P_{O_2} \approx 10^5$ Pa up to 1373 K. On the other hand, in reducing atmosphere ($P_{O_2} \leq 10^{-19}$ Pa), it becomes orthorhombic "Sr_3UO_5" with much greater lattice constants at every temperature.

Key words: high-temperature X-ray diffraction, reactivity in metallic oxides, U-Sr-O system, nuclear fuels.

Introduction

Il est bien connu que les propriétés physicochimiques et cristallographiques des composés du strontium sont intermédiaires entre celles des composés homologues du calcium et du baryum. Pour illustrer ce fait, il suffit par exemple de comparer la stabilité des trois monoxydes alcalino-terreux (de structure type NaCl), que l'on se réfère aux valeurs des enthalpies libres de formation standard à 298 K ($\Delta_f G^0$ (CaO) = –646,5 kJ mol^{-1}, $\Delta_f G^0$ (SrO) = –608,9 kJ mol^{-1} et $\Delta_f G^0$ (BaO) = –574,8 kJ mol^{-1} (1)) ou à celles des paramètres cristallins (*a* (CaO) = 0,4811 nm, *a* (SrO) = 0,5160 nm et *a* (BaO) = 0,5523 nm (2)). Une évolution similaire est donc prévisible chez les divers oxydes mixtes susceptibles de se former au-dessus de 1273 K et sous des pressions d'oxygène variables par réaction des phases CaO, SrO et BaO sur le dioxyde d'uranium. C'est bien à ce genre de conclusion qu'ont abouti les études de Lang et al. (3) (pour les phases $Me(U,Me)O_x$ ou « $BaUO_3$ » et $U_{1-\delta}Me_\delta O_{2-\delta}$ respectivement de structures types pérovskite et fluorine), Rietvield (4)

Reçu le 4 décembre 1998.

A. Pialoux[1] et B. Touzelin. Laboratoire de chimie générale, Bâtiment 462, Université de Paris-Sud, Centre d'Orsay, 91405 Orsay Cédex, France.

1. Auteur à qui adresser toute correspondance. Tél. : 33 (0)1 69 15 63 83 et 74 28. Téléc. : 33 (0)1 69 15 48 19.

© 1999 CNRC Canada

(pour la perovskite « Me_3UO_6 »), Loopstra et Rietveld (5) (pour l'oxyde α-« $MeUO_4$ » orthorhombique), Cordfunke et Loopstra (6), Tagawa et al. (7–9) puis Takahashi et al. (10) (pour les phases α-« $MeUO_4$ » et β-« $SrUO_4$ » rhomboédrique,[2] ainsi que Voronov et Sofronova (11–13) (pour l'ensemble des phases stables au-dessus de 1673 K). Mais si les études en question se montrent en règle générale complémentaires, voire en bon accord sur le plan cristallographique, l'emploi exclusif de produits trempés fait qu'elles sont émaillées de fréquentes contradictions tant sur les conditions de formation que sur la composition des phases examinées. Il arrive même, comme c'est le cas pour l'étude cristallographique de Zachariasen (14) sur les oxydes β-« $CaUO_4$ » et β-« $SrUO_4$ », qu'aucune indication ne soit fournie quant à la différence de stabilité, pourtant très grande, qui existe entre ces deux composés. On peut en outre regretter que les recherches approfondies de Brisi et de son équipe sur les systèmes U-Sr-O (15, 16) et U-Ca-O (17) n'aient pas été étendues au système U-Ba-O. Aussi nous est-il paru intéressant d'appliquer notre technique de diffractométrie de rayons X à haute température à l'étude des oxydes mixtes d'uranium et de strontium, ainsi que nous l'avions fait précédemment pour leurs homologues à base de baryum (18) et de calcium (19). Une telle étude in situ, inédite sur le système U-Sr-O, était d'autant plus souhaitable qu'elle devrait permettre de préciser les caractéristiques structurales et la composition des diverses phases coexistant dans ce système au-dessus de 1273 K, en vue de compléter les précédents résultats obtenus à 293 K (3–17) et ainsi faciliter une comparaison ultérieure avec le système U-Ba-O (18) notamment. L'importance technologique de ces deux systèmes mérite en effet d'être soulignée, du fait que les éléments Sr et Ba sont les produits majeurs de fission du dioxyde d'uranium utilisé comme combustible nucléaire (20, 21).

Conditions expérimentales

Comme précédemment (18, 19), nous employons deux ensembles diffractométriques complémentaires, chacun d'entre eux étant pourvu de son propre four pour rayons X. Le premier de ces fours, de marque Rigaku–Denki (R.D.) possède une résistance de platine rhodié assurant son fonctionnement jusqu'au voisinage de 1423 K dans un courant gazeux oxydo-réducteur de 24 $dm^3\ h^{-1}$ et sous une pression partielle d'oxygène contrôlée ($10^{-19} \le P_{O_2}$(Pa) $\le 10^5$). Le second est un four dont la résistance de graphite permet de travailler entre 293 et 2273 K dans un milieu fortement réducteur ($10^{-1} \le P_{CO}$(Pa) $\le 10^5$, $P_{O_2} \le 10^{-19}$ Pa), que l'on opère sous vide entretenu ($10^{-4} \le P$ (Pa) $\le 10^{-1}$) ou sous pression atmosphérique d'azote avec un lent débit gazeux ($V_{N_2} \approx 0{,}5\ dm^3\ h^{-1}$).

Les échantillons polycristallins utilisés au cours de cette étude sont confectionnés à partir de dioxyde d'uranium Koch–Light à 99,97 % et de carbonate de strontium Johnson–Matthey de qualité « Specpure ». Ils se distinguent par leurs compositions globales et leurs modes de préparation comme suit :

(*i*) Échantillons de compositions $1UO_2 + 1SrCO_3$ et $1UO_2 + 3SrCO_3$ obtenus par broyage puis compression uniaxiale (pastilles cylindriques de diamètre 8 mm et de hauteur 3 mm) en vue d'examens exclusivement effectués dans le four à graphite.

(*ii*) Échantillons de compositions approximatives $SrUO_{3,7}$ (phase α-« $SrUO_4$ » orthorhombique (5, 6, 10, 13, 16, 22, 23) pure) et $Sr_3UO_{5,7}$ (mélange de l'uranate « Sr_3UO_6 » monoclinique (4) avec moins de 5 % des oxydes α-« $SrUO_4$ » et « Sr_2UO_5 » monoclinique (24)) préparés dans un four annexe à partir des mélanges $1UO_2 + 1SrCO_3$ et $1UO_2 + 3SrCO_3$ chauffés pendant 48 h à 1273 K sous courant d'oxygène.

(*iii*) Échantillons constitués par la phase β-« $SrUO_4$ » (de rapport $3{,}30 \le O/U \le 3{,}70$ (6, 16)) et obtenus, toujours dans le four annexe, après 2 h de réduction à 1273 K de l'α-« $SrUO_4$ » par un mélange gazeux $H_2 + N_2$ à 10 % d'hydrogène.

Chaque essai consiste à contrôler aux rayons X l'évolution structurale que provoque, à la surface de l'échantillon, soit une modification de la température ($293 \le T$(K) ≤ 1773) dans un potentiel d'oxygène constant au cours de paliers successifs espacés d'une cinquantaine de K toutes les 2 h environ, soit un maintien à température constante (avec un éventuel changement de P_{O_2}) aussi longtemps qu'on le juge utile. L'échantillon est alors progressivement refroidi jusqu'à 293 K (four R.D.) ou trempé, examiné à l'ambiante et conservé sous vide, dans l'attente de recuits ultérieurs (jusqu'à 6 recuits dans le four à graphite).

Résultats et discussion

Le premier traitement sous vide d'un comprimé $1UO_2 + 1SrCO_3$ dans le four à graphite nous a permis d'observer successivement :

(*i*) La dissociation totale du carbonate orthorhombique en monoxyde de strontium dès 1073 K et la formation progressive, à partir de 1173 K, des uranates β-« $SrUO_4$ » et « $SrUO_3$ ».

(*ii*) La coexistence des quatre oxydes UO_2, SrO, β-« $SrUO_4$ » et « $SrUO_3$ » entre 1173 et 1513 K.

(*iii*) La disparition des phases β-« $SrUO_4$ », SrO et « $SrUO_3$ » aux températures respectives de 1513, 1588 et 1663 K au profit de la seule solution solide $U_{1-\delta}Sr_\delta O_{2-\delta}$ dont le paramètre cristallin à 1663 K (a = 0,5570 nm) est plus grand que celui de l'oxyde $UO_{2,00}$ (a = 0,5547 nm).

Les températures de formation obtenues dans ces conditions extrêmes ($P_{O_2} \le 10^{-19}$ Pa) pour les oxydes SrO, β-« $SrUO_4$ », « $SrUO_3$ » et $U_{1-\delta}Sr_\delta O_{2-\delta}$, de même que celles précédemment signalées pour les composés homologues du Ba (18) et du Ca (19), ainsi que pour l'α-« $BaUO_4$ » (18), ont été indiquées dans le tableau 1. On pourra notamment constater que la réactivité du dioxyde d'uranium avec chacun des trois monoxydes CaO, SrO et BaO est d'autant plus importante que l'élément alcalino-terreux considéré est lourd. À noter l'absence des phases α-« $CaUO_4$ », β-« $BaUO_4$ » et $U_{1-\delta}Ba_\delta O_{2-\delta}$, alors qu'au contraire la présence des deux oxydes α- et β-« $SrUO_4$ » souligne le caractère intermédiaire du système U-Sr-O par rapport aux systèmes U-Ba-O et U-Ca-O. Il est vrai qu'en raison de son instabilité

[2] Conformément aux usages et à l'inverse des auteurs japonais (7–10), nous utilisons la lettre β pour distinguer la phase « $MeUO_4$ » la plus réduite (et aussi la plus ancienne (14)) de la plus riche en oxygène (α-« $MeUO_4$ »), en principe la moins stable à haute température.

© 1999 CNRC Canada

Tableau 1. Températures de formation des divers oxydes observés dans le four à graphite ($P_{O_2} \leq 10^{-19}$ Pa).

	Températures de formation (K)				
	MeO	α-« $MeUO_4$ »	β-« $MeUO_4$ »	« $MeUO_3$ »	$U_{1-\delta}Me_\delta O_{2-\delta}$
Me = Ca (19)	1093	—	1373	1473	1663
Me = Sr présente étude	1073	≤1073 [a]	1173	1173	1663
Me = Ba (18)	1053	1143	—	1073	1723 [b]

[a] Estimation effectuée dans le four annexe sous $P_{O_2} \approx 10^5$ Pa.

[b] Formation de l'oxyde UO_{2-x}.

Fig. 1. Variations des paramètres cristallins de la phase α-« $SrUO_4$ » en fonction de la température. □, α sous oxygène pur; ■, α dans l'air (four R.D.).

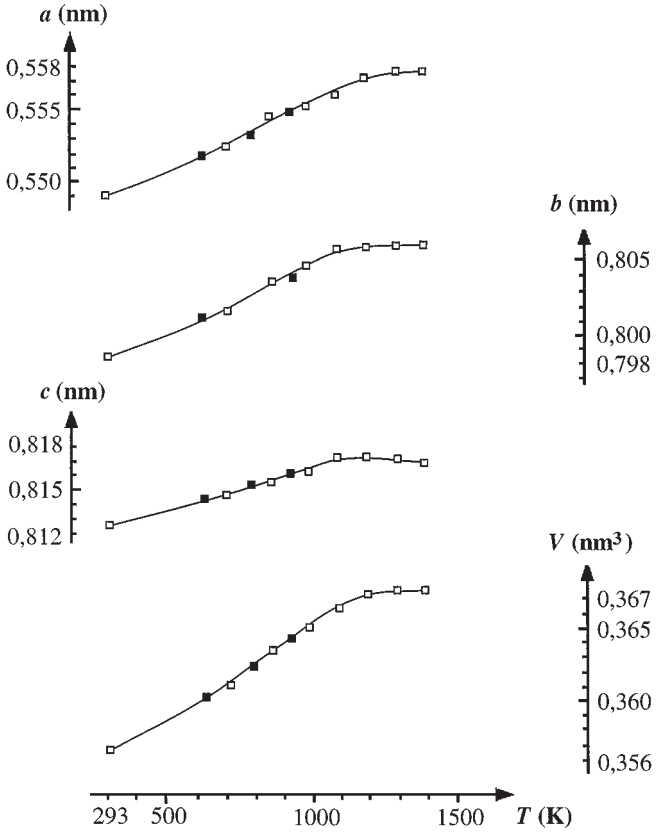

dans le four à graphite, l'oxyde α-« $SrUO_4$ » fait l'objet d'une mention spéciale au tableau 1. Aussi commencerons-nous par préciser le comportement de cet oxyde en fonction de la température (fig. 1), avant d'étudier celui des uranates β-« $SrUO_4$ » (fig. 2), « $SrUO_3$ » (fig. 3) et $U_{1-\delta}Sr_\delta O_{2-\delta}$ (fig. 4), les mesures de paramètres cristallins relatives aux deux phases « Sr_3UO_6 » et « Sr_3UO_5 » ayant été jointes à celles de « $SrUO_3$ » (fig. 3), afin de faciliter la comparaison entre ces trois pérovskites.

Étude des oxydes « $SrUO_4$ »

La phase α-« $SrUO_4$ » dite basse température

Stable dans l'oxygène pur, la phase α-« $SrUO_4$ » orthorhombique (groupe spatial *Pbcm*, 4 groupements formulaires par maille (5, 23)) est de couleur jaune, comme le sont aussi les phases α-« $BaUO_4$ » et β-« $CaUO_4$ » formées dans les mêmes conditions ($P_{O_2} \approx 10^5$ Pa à 1273 K). À température ambiante, les paramètres cristallins de ce monouranate (a = 0,5491 nm, b = 0,7980 nm et c = 0,8126 nm) sont en parfait accord avec ceux qui ont été proposés par de nombreux auteurs (5, 6, 10, 13, 16, 22, 23).

Comme le montre la fig. 1, les trois constantes réticulaires, ainsi que le volume de la maille orthorhombique, augmentent de façon continue jusqu'au voisinage de 1123 K, avec de faibles écarts positifs par rapport à la linéarité pour chacune des quatre courbes d'expansion obtenues. Après quoi, celles-ci demeurent horizontales dans l'intervalle de température compris entre 1123 et 1373 K. Un tel comportement, en tout point comparable à ceux que manifestent les phases α-« $BaUO_4$ » (18) et β-« $CaUO_4$ » (19), s'interprète par un changement de composition de l'oxyde examiné. Contrairement à ce qui se produit avec l'α-« $BaUO_4$ », tout risque d'évaporation doit toutefois être écarté pour l'α-« $SrUO_4$ », la tension de vapeur de l'oxyde BaO étant environ 10^3 fois plus élevée que celle de l'oxyde SrO (1). Si bien qu'il convient d'envisager, par analogie avec l'oxyde « U_3O_8 » (25), et ainsi que nous l'avons déjà fait pour la phase β-« $CaUO_4$ » (19), un départ d'oxygène avec création simultanée de lacunes plus ou moins ionisées au sein du cristal orthorhombique de α-« $SrUO_4$ ». La composition de cet uranate ne devrait donc pas varier entre 293 et 1123 K, avec un rapport O/U ≈ 3,67, égal à celui de « U_3O_8 » (O/U = 2,67 (25)) augmenté de celui de la chaux (O/Ca = 1,00). Par contre, elle devrait évoluer entre $SrUO_{3,67}$ à 1123 K et $SrUO_{3,62}$ à 1373 K (25). Dès lors, nous sommes conduits à admettre a posteriori que la constance des paramètres cristallins de l'α-« $BaUO_4$ » est indépendante de la vaporisation et doit être associée à la même diminution du rapport O/U (3,67 ≥ O/U ≥ 3,62) que celle de l'α-« $SrUO_4$ ». Cette conclusion est en totale contradiction avec les affirmations des précédents auteurs (5, 6, 8–10, 13, 16, 22, 23) d'après lesquelles ces oxydes ne s'écartent pratiquement pas de la composition stœchiométrique (O/U ≈ 4).

Signalons qu'une toute autre interprétation que la nôtre a été proposée pour justifier l'existence de « plateaux naturels d'expansion » et de dilatations négatives qui caractérisent d'autres oxydes, à des températures beaucoup moins élevées que les précédentes toutefois. De récentes études de diffraction de neutrons entre 10 et 450 K (26, 27) ont permis notamment d'attribuer la dilatation négative des composés $Sc_2(WO_4)_3$ et $Lu_2(WO_4)_3$ à un déplacement thermique des atomes d'oxygène dans les liaisons Me-O-W. Ces déplacements semblent être reliés à des mouvements oscillatoires que subissent les polyèdres présents dans l'édifice cristallin, à condition que ceux-ci puissent se déformer.

© 1999 CNRC Canada

Tableau 2. Paramètres cristallins de la maille hexagonale et indices d'oxygène proposés pour la forme oxydée de l'uranate β-« $SrUO_4$ » à 293 K.

	Études antérieures						La présente étude dans le four R.D. (sous azote, $P_{O_2} < 1$ Pa)
	Cordfunke et Loopstra (6)	Fujino et al. (7)	Takahashi et al. (10)	Voronov et al. (13)	Zachariasen (14)	Brisi et al. (16)	
a (nm)	0,3995	0,3920	0,3922	0,3910	0,3993	0,3920	0,3920
c (nm)	1,849	1,863	1,845	1,834	1,837	1,836	1,843
c/*a*	4,628	4,753	4,703	4,691	4,601	4,684	4,702
V (nm^3)	0,2555	0,2479	0,2457	0,2428	0,2536	0,2443	0,2453
O/U	3,75	3,948	3,978	3,95	4,00	3,70	3,60

La phase « β-$SrUO_4$ » dite haute température

Formée par réduction de l'α-« $SrUO_4$ » au voisinage de 1273 K, la phase β-« $SrUO_4$ » rhomboédrique ($R\bar{3}m$, $z = 1$ (14)) existe elle-même sous deux formes distinctes :

(*i*) La forme oxydée β identifiée exclusivement dans le four R.D. sous courant d'azote pur ($10^{-1} \leq P_{O_2}$(Pa) ≤ 1);

(*ii*) La forme réduite β′ observée aussi bien dans le four R.D. sous atmosphère d'hydrogène dilué à 10 % dans l'azote que dans le four à graphite fonctionnant sous vide ($P_{O_2} \leq 10^{-19}$ Pa).

Quelle que soit la forme de l'oxyde examiné, nous considèrerons la maille hexagonale correspondante (constituée de 3 groupements formulaires $SrUO_4$), afin de faciliter la comparaison entre nos mesures pour $293 \leq T$(K) ≤ 1718 (fig. 2) et celles que les précédents auteurs (7, 10, 13, 14, 16) ont effectuées à 293 K (tableaux 2 et 3).

(a) La forme oxydée β-« $SrUO_4$ » : Le tableau 2 permet de constater la dispersion considérable qui se manifeste sur les valeurs des paramètres cristallins proposés pour cet oxyde à 293 K par les différents auteurs et par nous-mêmes (écarts entre les valeurs extrêmes de *c*, *a*, *c*/*a* et *V* atteignant respectivement 0,8, 2,2, 3,3 et 5,2 %). Une telle dispersion est d'autant plus surprenante qu'elle est pratiquement inexistante pour la forme oxydée de β-« $CaUO_4$ » (19) isomorphe de β-« $SrUO_4$ » mais stable dans l'oxygène pur (écarts sur les paramètres ne dépassant pas 0,13 % à 293 K). Les valeurs que nous avons attribuées à ces paramètres à chaud (fig. 2, symboles ■ et ▲) se montrent d'ailleurs tout autant dispersées entre 293 et 1108 K que les précédentes à 293 K, une atténuation de ce phénomène se produisant toutefois au-dessus de 1108 K. C'est ainsi que les plus faibles valeurs du rapport *c*/*a* (symboles ■, ▲ et □) obéissent à une loi de variation en fonction de *T* qui est totalement déconcertante : obtention de la courbe (1) tour à tour croissante entre 293 et 758 K, décroissante pour $758 \leq T$(K) ≤ 1108, puis de nouveau croissante de 1108 à 1343 K. Indépendamment de l'anisotropie qui caractérise cette structure (19), il n'est pas douteux qu'une telle courbe $c/a = f(T)$ doive être associée à de fortes variations de composition de l'oxyde examiné. Comme celles-ci se montrent en outre imprévisibles, incontrôlables et difficilement reproductibles, on doit admettre que la forme oxydée β-« $SrUO_4$ » est métastable entre 293 et 1108 K. Cette métastabilité est de plus étayée par l'obtention simultanée des deux formes β oxydée et β′ réduite de « $SrUO_4$ » à l'ambiante (à la suite d'une trempe de la forme oxydée sous azote depuis 1363 K), puis entre 293 et 498 K lors de recuits ultérieurs. Ajoutons que, contrairement à toute attente, ces recuits ont eu pour effet de provoquer une homogénéisation de l'oxyde rhomboédrique dans sa forme réduite β′ pour $498 \leq T$(K) ≤ 593 en présence d'azote (symbole ■) et pour $478 \leq T$(K) ≤ 783 dans l'air (symbole ▲). Après quoi, les diminutions observées sur le rapport *c*/*a* entre 593 et 1108 K dans l'azote (symbole ■) et de 783 à 1073 K dans l'air (symbole ▲) n'ont fait que traduire une réoxydation progressive de l'échantillon jusqu'à l'obtention de la forme oxydée β-« $SrUO_4$ » dans le premier cas et de l'α-« $SrUO_4$ » dans le second.

Fig. 2. Variations des paramètres cristallins et du volume de la maille hexagonale des phases β et β′-« $SrUO_4$ » en fonction de la température. Dans le four R.D. : ■, β seule sous N_2 pur; ▲, β seule par oxydation sous air de β′; □, β′ seule sous H_2. Dans le four à graphite : ●, β′ + UO_2 + SrO + $SrUO_3$; ○, β′ + $SrUO_3$; △, β′ + UO_2; ▽, β′ + UO_2 + $SrUO_3$.

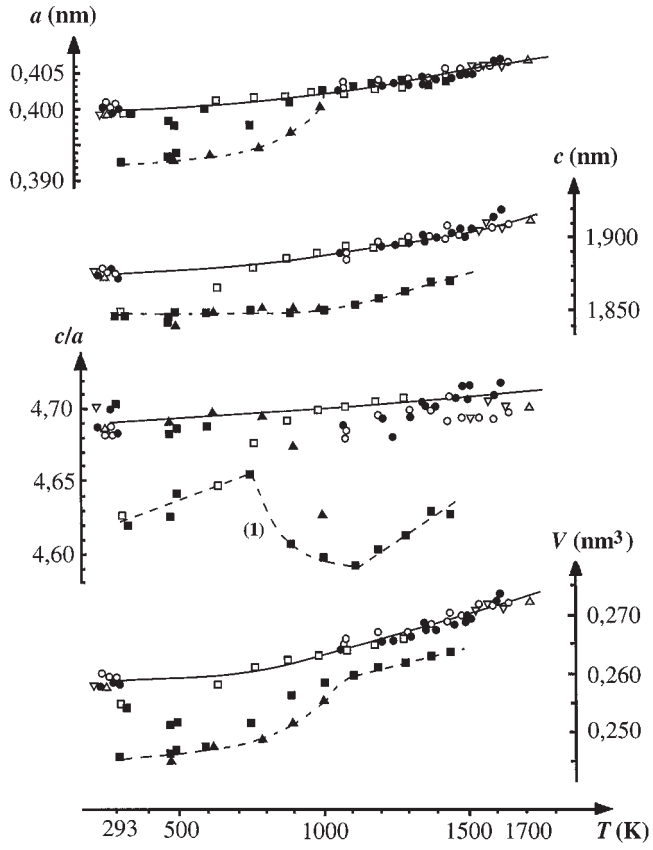

© 1999 CNRC Canada

Tableau 3. Paramètres cristallins de la maille hexagonale et indices d'oxygène proposés pour la forme réduite β′ de l'uranate β-« $SrUO_4$ » à 293 K.

	Études antérieures							La présente étude	
	Cordfunke et Loopstra (6)	Fujino et al. (7)		Takahashi et al. (10)		Voronov et al. (13)	Brisi et al. (16)	Four R.D.	Four à graphite
a (nm)	0,3993	0,3993	0,3994	0,3994	0,3995	0,4000	0,3993	0,3992	0,3992
c (nm)	1,868	1,836	1,851	1,837	1,851	1,834	1,837	1,847	1,871
c/*a*	4,678	4,599	4,634	4,599	4,634	4,585	4,601	4,627	4,687
V (nm^3)	0,2580	0,2535	0,2556	0,2537	0,2558	0,2541	0,2537	0,2549	0,2582
O/U	3,30	3,777	3,597	3,777	3,597	<3,95	<3,70	≈ 3,30	3,11

Quant à l'accroissement linéaire que subit le rapport *c*/*a* entre 1108 et 1343 K, il s'interprète, ainsi que nous l'avons fait pour β-« $CaUO_4$ » (19), par un début de réduction de la forme oxydée β-« $SrUO_4$ », le changement du nombre d'oxydation de quelques atomes d'uranium (passage U^{VI}/U^{V}, voire U^{VI}/U^{IV}) devenant prépondérant devant la création de lacunes d'oxygène.

C'est donc à partir de 1108 K que cette forme oxydée β devrait se manifester à l'état thermodynamiquement stable, avec une composition qui ne devrait pas trop s'éloigner de $SrUO_{3,60}$ entre 1108 et 1343 K, si l'on se réfère aux compositions limites adoptées pour l'α-« $SrUO_4$ » dans un intervalle de température voisin.

Signalons qu'à trois reprises, de précédents auteurs (7, 8, 13) ont envisagé la phase β-« $SrUO_4$ » comme étant métastable en dessous d'une température limite comprise entre 973 et 1073 K et, par conséquent, peu éloignée de la nôtre (T = 1108 K). D'autres auteurs ont en outre observé les deux formes β et β′ coexister à 293 K, à la suite de trempes qui avaient été effectuées respectivement depuis 1173 K sous H_2 (Corfunke et Loopstra (6)) et 1673 K dans l'air (Brisi et al. (16)). En revanche, selon Takahashi et al. (10), il existe une solution solide continue β rhomboédrique à toute température (3,978 ≥ O/U ≥ 3,597), les phases limites s'étant vues attribuer pour $\Delta_f H^0(298)$ des valeurs comprises entre –1890 et –1990 kJ mol^{-1} et pour paramètres cristallins des valeurs proches des nôtres (tableaux 2 et 3).

(b) La forme réduite β′-« *$SrUO_4$* » : Les valeurs des paramètres cristallins obtenues pour cet oxyde sont moins dispersées que les précédentes, tant à l'ambiante (tableau 3) qu'entre 293 et 1713 K (fig. 2, symboles □, ●, ○, △, et ▽). D'une manière générale, elles se montrent les plus fortes à toute température, exception faite des valeurs anormalement faibles du paramètre *c* et du rapport *c*/*a* dont l'obtention pour 293 ≤ T(K) ≤ 873 (symbole □) doit être attribuée à la réduction progressive des échantillons partiellement oxydés lors de leur transfert du four annexe au four R.D. en début d'essai. On peut notamment constater que le rapport *c*/*a* s'accroît peu avec la température (4,69 ≤ *c*/*a* ≤ 4,71 pour 293 ≤ T(K) ≤ 1713) mais que, pour une température donnée, l'augmentation que subit ce rapport entre les deux formes β et β′de « $SrUO_4$ » est considérable. Ainsi, pour T = 1108 K, le rapport passe de 4,59 ± 0,01 à 4,70 ± 0,01, soit une variation relative de 2,2 % encore plus élevée que celle de 1,8 % précédemment obtenue pour l'oxyde β-« $CaUO_4$ » à 1373 K (19). Si donc l'on admet que ces valeurs sont consécutives à la même diminution du rapport O/U (soit Δ(O/U) = 0,49 (19)), ainsi que la composition $SrUO_{3,60}$ pour la forme oxydée β-« $SrUO_4$ », la réduction de celle-ci devrait se traduire par l'obtention du composé β′-$SrUO_{3,11}$ dès 1108 K. Cette composition ne devrait d'ailleurs guère évoluer entre 1108 et 1713 K, compte tenu de la faible variation du rapport *c*/*a*, et cela que la forme réduite β′ soit seule (symbole □) ou coexiste avec les diverses phases UO_2, SrO et $SrUO_3$ (symboles ●, ○, △ et ▽). En tout état de cause, le rapport O/U = 3,11 est de loin le plus faible qui ait été proposé (tableau 3) pour la forme réduite β′-« $SrUO_4$ », celui qui s'en rapproche le plus (O/U = 3,30) étant dû à Cordfunke et Loopstra (6). Du fait que la phase β′-$SrUO_{3,11}$ subit parfaitement l'effet de trempe (symboles ●, ○, △ et ▽) et prend systématiquement naissance aux dépens de l'oxyde β-$SrUO_{3,60}$ entre 293 et 783 K, nous estimons qu'elle est thermodynamiquement stable à toute température. Bien que non confirmée par nos mesures, l'existence d'une solution solide β rhomboédrique entre les deux composés limites n'est possible qu'au-dessus de 1108 K et non pas dès 293 K comme l'ont prétendu Takahashi et al. (10). Une toute autre interprétation de nos résultats sera toutefois suggérée dans le dernier chapitre de cette discussion.

La transition (α,β) entre les oxydes « $SrUO_4$ »

À notre connaissance, il n'existe pas de relation cristallographique entre les deux structures α orthorhombique et β rhomboédrique de l'oxyde « $SrUO_4$ » (28). Comme en outre, l'une et l'autre se manifestent dans un grand intervalle de température (293 ≤ T(K) ≤ 1373), mais jamais simultanément, nous préférons considérer les oxydes α et β « $SrUO_4$ » comme étant des phases distinctes plutôt que des variétés polymorphes. De ce point de vue, il existe une certaine analogie entre le comportement de ces oxydes (1,83 ≥ Δ(O/U+Sr) ≥ 1,55) et celui des sesquinitrures α et β « U_2N_3 » (1,75 ≥ Δ(N/U) ≥ 1,45) (29, 30). De précédents auteurs (8, 13, 17) ont néanmoins admis l'existence de la transition polymorphique α-« $SrUO_4$ » ⇄ β-« $SrUO_4$ » comme se produisant dans l'air ($P_{O_2} \approx 2 \times 10^4$ Pa) à la température de 1523 ± 30 K, données que nous n'avons pu vérifier en raison du fonctionnement limité du four R.D. Cependant, la constance des paramètres cristallins de l'α-« $SrUO_4$ » observée dans l'oxygène pur ($P_{O_2} \approx 10^5$ Pa) entre 1173 et 1373 K (fig. 1) s'interprète, nous l'avons vu, comme un début de réduction de cet oxyde et constitue, somme toute, un signe prémonitoire de la transition annoncée. De plus, nous avons observé les deux transformations β → α et α → β s'amorcer à

© 1999 CNRC Canada

Fig. 3. Variations des paramètres cristallins des phases « $SrUO_3$ », « Sr_3UO_5 » et « Sr_3UO_6 » en fonction de la température. Dans le four à graphite : phase « $SrUO_3$ » en présence de : ●, UO_2 + SrO + β′-« $SrUO_4$ »; ◑, UO_2 + SrO; ○, UO_2; □, β′-« $SrUO_4$ »; ◪, UO_2 + β′-« $SrUO_4$ »; phase « Sr_3UO_5 » en présence de : ▼, SrO + β′-« $SrUO_4$ »; △, UO_2 + SrO + β′-« $SrUO_4$ »; ◆, UO_2 + SrO; ▲, seule à 1633 K; ▽, seule à 293 K. Dans le four R.D. : +, phase « Sr_3UO_6 » seule sous O_2.

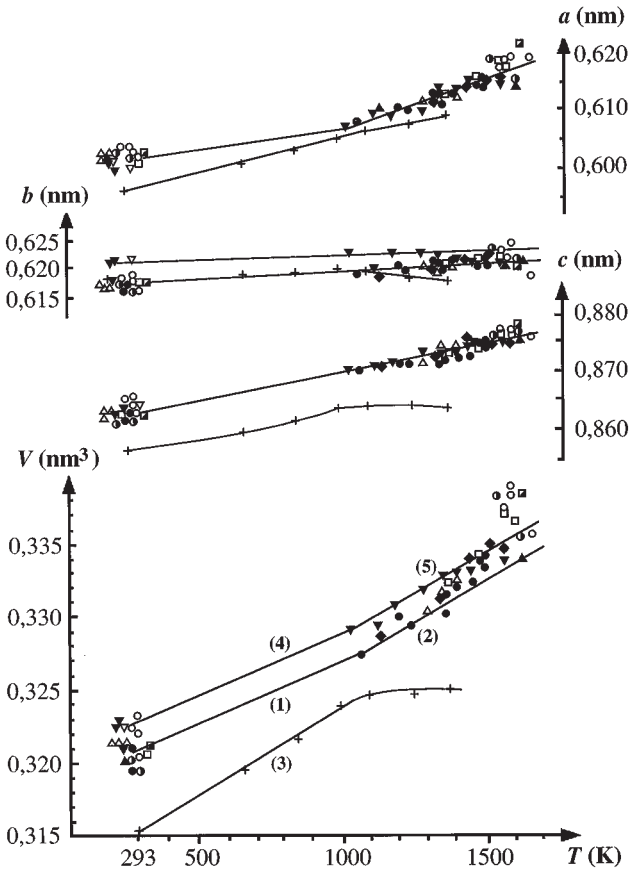

la même température de 1363 K respectivement sous courant d'air et sous courant d'azote ($P_{O_2} \leq 1$ Pa). On peut donc admettre que la transition (α,β) devient réversible à 1523 K dans l'air, les uranates concernés ayant des compositions voisines ($3{,}62 \geq O/U \geq 3{,}60$).

Étude des pérovskites mixtes d'uranium et de strontium

La phase « $SrUO_3$ »

Apparue dès 1173 K et formée progressivement sous $P_{O_2} \leq 10^{-19}$ Pa aux dépens des oxydes « UO_2 », SrO et β′-« $SrUO_4$ » jusqu'à 1663 K, la phase « $SrUO_3$ » orthorhombique (*Pnma*, $z = 4$ (15)) n'a jamais pu être préparée isolément, et cela quelle que soit la composition de départ ($1UO_2 + 1SrCO_3$ ou $SrUO_{3,7}$). Comme néanmoins les proportions en oxydes résiduels « UO_2 » et SrO se confondaient le plus souvent, on peut estimer avec Brisi (15) que la pérovskite « $SrUO_3$ » ne s'écarte guère de la composition stœchiométrique, ce qui est d'ailleurs aussi le cas de ses isomorphes à base de baryum au-dessus de 1423 K (18) ou de calcium entre 293 et 1723 K (19).

Les paramètres cristallins que nous attribuons à la maille élémentaire de « $SrUO_3$ » à 293 K (sur la base d'une moyenne de 10 déterminations) sont respectivement : a = 0,6030 nm, b = 0,6175 nm, c = 0,8630 nm et V = 0,321 nm^3. Ils sont en parfait accord avec ceux (a = 0,603 nm, b = 0,618 nm, c = 0,862 nm et V = 0,321 nm^3) de Brisi (15), eux-mêmes légèrement plus grands que les paramètres (a = 0,601 nm, b = 0,617 nm, c = 0,860 nm et V = 0,319 nm^3) initialement proposés par Lang et al. (3) pour le composé $Sr(U,Sr)O_x$.

Pour ce qui concerne les mesures effectuées à chaud, la fig. 3 permet de constater (symboles ●, ◑, ○, □ et ◪), outre leur dispersion caractéristique de l'anisotropie de cette structure (19), que le paramètre a est celui qui augmente le plus entre 293 et 1553 K ($\Delta a/a \approx 3{,}3$ %) par rapport aux paramètres c et b ($\Delta c/c \approx 1{,}7$ % et $\Delta b/b \approx 0{,}8$ %). Quant aux valeurs du volume entre 293 et 1553 K, elles permettent de définir deux droites (**1**) et (**2**) s'interceptant à 1073 K puis, pour $1553 \leq T(K) \leq 1663$, elles se distribuent nettement au-dessus de la droite (**2**). Les droites (**1**) et (**2**) conduisent respectivement aux coefficients moyens de dilatation volumique $\overline{\alpha}_1 = 28 \times 10^{-6}$ K^{-1} et $\overline{\alpha}_2 = 43 \times 10^{-6}$ K^{-1}. Ces coefficients se montrent voisins de ceux ($\overline{\alpha}_1' = 33 \times 10^{-6}$ K^{-1} et $\overline{\alpha}_2' = 45 \times 10^{-6}$ K^{-1}) précédemment déterminés (19) pour la phase « $CaUO_3$ » monoclinique dont l'angle β subit une brutale diminution de 90,1° à 90,0° précisément au voisinage de 1073 K, sans que pour autant cette pérovskite ne devienne orthorhombique (transition α-orthorhombique, β-monoclinique observée à 1773 K (19)). Or la cassure de pente qui se manifeste dans le cas de « $SrUO_3$ » (fig. 3) s'accompagne soit de la disparition au-dessus de 1073 K du pic indexé (111) dans le système orthorhombique (15), soit de sa réapparition systématique à l'ambiante après une trempe. Ce pic (111) de faible intensité ($I/I_0 \approx 10$ selon Brisi (15) et ≤ 5 d'après nos mesures) est le seul pic (*hkl*) dont la somme des indices de Miller soit impaire et qui soit bien séparé (angle ≈ 23° 2θ de Bragg) des autres pics enregistrés dans nos diffractogrammes. Il implique l'appartenance de l'oxyde au réseau orthorhombique primitif (mode *P*). La disparition de ce pic, conforme à la règle de sélection ($h + k + l = 2n$ (31), équivaut donc à l'obtention d'un réseau centré (mode *I*), avec changement simultané de groupe spatial au sein du même groupe ponctuel 2/*m*2/*m*2/*m*. La cassure de pente observée à 1073 K ne fait donc que traduire l'existence d'une discrète transition du second ordre qui pourrait s'écrire (31) :

[1] α-« $SrUO_3$ » (*Pnma*) ⇌ β-« $SrUO_3$ » (*Imma*)

À noter encore que la proximité des valeurs prises par les paramètres cristallins a et b de la phase orthorhombique (a = 0,618 ± 0,004 nm et b = 0,623 ± 0,003 nm) aux températures les plus élevées de nos essais ($1553 \leq T(K) \leq 1663$) annonce l'existence d'une seconde transition (β-orthorhombique, γ-quadratique) de la pérovskite « $SrUO_3$ ». Aucune vérification de cette transition n'a cependant pu être effectuée, nos examens ayant dû se limiter à la température de 1663 K, du fait que la solution solide $U_{1-\delta}Sr_\delta O_{2-\delta}$ se formait alors en grande quantité. En tout état de cause,

© 1999 CNRC Canada

l'augmentation constatée sur le volume de la maille au-dessus de 1553 K (symboles ○, ◐, □ et ◪) est significative d'un début de réduction de l'oxyde « $SrUO_3$ », selon un processus similaire à celui que nous avons proposé pour les phases UO_{2-x}, ThO_{2-x} et $CaUO_3$ (19), le départ d'oxygène étant probablement compensé par la substitution de quelques ions U^{4+} (r_i = 0,100 nm) par des ions U^{3+} légèrement plus gros (r_i = 0,106 nm) (31) et répartis au hasard dans le réseau centré de cette pérovskite orthorhombique.

La phase « Sr_3UO_6 »

Après avoir été préparée sous $P_{O_2} \approx 10^5$ Pa dans le four annexe fonctionnant à 1273 K, la phase « Sr_3UO_6 » monoclinique ($P2_1$, z = 2 (4)) est transférée dans le four R.D. puis examinée sous le même potentiel d'oxygène entre 293 et 1373 K. C'est ainsi que nous proposons, pour la maille monoclinique à 293 K, des paramètres cristallins (a = 0,596 nm, b = 0,618 nm, c = 0,856 nm, β = 90,1° et V = 0,315 nm^3) qui sont très proches de ceux (a = 0,5959 nm, b = 0,6179 nm, c = 0,8553 nm, β = 90,19° et V = 0,3149 nm^3) précédemment indiqués par Rietveld (4). La qualité de nos enregistrements est toutefois insuffisante pour préciser à mieux de ±0,1° près la valeur de l'angle β. Comme cet angle a toute chance de diminuer encore avec l'accroissement de T (19), nous considèrerons la phase « Sr_3UO_6 » comme étant pseudo-orthorhombique à toute température. Dans ces conditions, la fig. 3 permet de constater que les paramètres ainsi obtenus (symbole +) sont les plus faibles de tous, avec cependant un volume de maille augmentant plus vite entre 293 et 1073 K pour « Sr_3UO_6 » (droite (**3**), $\bar{\alpha}_3 = 33 \times 10^{-6}$ K^{-1}) que pour « $SrUO_3$ » (droite (**1**), $\bar{\alpha}_1 = 28 \times 10^{-6}$ K^{-1}), puis se montrant constant au-dessus de 1073 K. Ces différences de paramètres et de coefficients de dilatation sont dues au changement du nombre d'oxydation des atomes d'uranium (de U^{VI} à U^{IV}) présents dans ces deux pérovskites. Quant à la constance du volume observée entre 1073 et 1373 K, elle s'explique, de la même manière que nous l'avons fait pour l'α-« $SrUO_4$ », par une réduction progressive de la phase « Sr_3UO_6 » se traduisant par une légère variation de composition ($5{,}67 \geq O/U \geq 5{,}62$), avec formation simultanée de lacunes d'oxygène ionisées et sans diminution du degré d'oxydation des atomes d'uranium.

La phase « Sr_3UO_5 »

Il était intéressant de connaître le comportement de la pérovskite « Sr_3UO_6 » dans l'atmosphère réductrice ($P_{O_2} \leq 10^{-19}$ Pa) du four à graphite. À notre vive surprise, et contrairement à ce que nous avions réalisé avec la phase isomorphe « Ca_3UO_6 » (19), aucune mesure n'a cependant été possible sur l'oxyde « Sr_3UO_6 », sa pression d'oxygène étant selon toute vraisemblance trop élevée. On peut en effet constater sur la fig. 3 que les valeurs des paramètres cristallins obtenues dans ces conditions, notamment celles du volume (symboles ▽ et ▼), se distribuent toutes au-dessus non seulement de la courbe (**3**) caractéristique de « Sr_3UO_6 » (symbole +), mais aussi des droites (**1**) et (**2**) caractéristiques de « $SrUO_3$ » (symboles ●, ◑, ○, ◪ et □). Par la suite, ces résultats ont été confirmés par l'examen des phases formées à la surface d'un échantillon $1UO_2 + 3SrCO_3$ progressivement réduit sous vide entretenu entre 293 et 1633 K, les mesures effectuées lors de cet essai (symboles △, ◆et ▲), ainsi que les précédentes (symboles ▽et ▼) ayant permis de tracer les nouvelles droites (**4**) et (**5**) sensiblement parallèles aux droites (**1**) et (**2**).

Précisons que cet essai est le seul nous ayant permis de préparer une pérovskite de strontium à l'état pur, les oxydes « UO_2 » et SrO avec lesquels elle coexistait depuis 1183 K ayant fini par disparaitre simultanément à la température de 1633 K. Cette pérovskite répond donc bien à la composition Sr_3UO_5, conformément aux observations antérieures que Charvillat et al. (32) ont réalisées à 293 K sur des produits trempés depuis une température maximale de 1173 K.

Comme nos propres observations permettent en outre de constater (fig. 3) l'existence d'une cassure de pente entre les droites (**4**) et (**5**) se produisant au voisinage de 1073 K, ainsi que l'absence du pic (111) de la structure orthorhombique au-dessus de 1073 K, il y a tout lieu d'admettre que les deux phases Sr_3UO_5 et « $SrUO_3$ » sont isomorphes et manifestent la même transition (α,β) du second ordre. La diminution du nombre d'oxydation de l'uranium (de U^{VI} à U^{IV}), ainsi que la substitution d'un ion U^{4+} (r_i = 0,100 nm) sur deux par un ion Sr^{2+} (r_i = 0,116 nm) dans le sous-réseau cationique de la pérovskite simple, conditionnent les passages respectifs « Sr_3UO_6 » → Sr_3UO_5 et « $SrUO_3$ » → Sr_3UO_5 (ou $Sr_2(Sr,U)O_5$). Elles sont responsables de l'accroissement des dimensions réticulaires et des variations d'intensité relative que l'on observe entre ces trois composés.

Le domaine monophasé de type pérovskite ainsi délimité se distingue de ceux précédemment mis en évidence pour les systèmes U-Ba-O (18) et U-Ca-O (19) par le fait que, des trois phases Sr_3UO_5, « Ba_3UO_5 » et « Ca_3UO_5 », seule la première est identifiable à 293 K, la seconde ne subissant pas l'effet de trempe et la troisième demeurant un composé hypothétique du fait qu'elle est indiscernable de l'oxyde « $CaUO_3$ » monoclinique par notre technique.

Le rôle intermédiaire de l'ion Sr^{2+} (r_i = 0,116 nm) par rapport à ceux des ions Ba^{2+} (r_i = 0,136 nm) et Ca^{2+} (r_i = 0,100 nm) (31) est particulièrement mis en lumière par l'évolution structurale des trois types de pérovskites doubles examinées :

(*i*) La symétrie monoclinique, commune aux oxydes de calcium, ne subsiste qu'avec « Sr_3UO_6 » pour faire place à la symétrie orthorhombique de Sr_3UO_5, « $SrUO_3$ » et « $BaUO_3$ » (33), puis à la symétrie quadratique, voire cubique pour $T \geq 1063$ K, de « Ba_3UO_5 » et « Ba_3UO_6 » (18, 32, 34).

(*ii*) Au composé « Me_3UO_5 » correspond toujours la plus grande maille pérovskite, mais alors que le volume de la maille diminue dans l'ordre « Me_3UO_5 », « $MeUO_3$ », « Me_3UO_6 » pour Me = Ca et Sr, il y a permutation de « $MeUO_3$ » et « Me_3UO_6 » dans le cas du baryum.

Étude de la solution solide $U_{1-\delta}Sr_\delta O_{2-\delta}$

À notre connaissance, seuls les travaux de Lang et al. (3) et de Voronov et Sofrana (11) font état de l'existence de la phase $U_{1-\delta}Sr_\delta O_{2-\delta}$ désordonnée ($Fm3m$, z = 4) résultant de la miscibilité partielle des oxydes UO_2 et SrO à une température au moins égale à 1273 K. Mais alors que les auteurs américains (3) proposent une teneur maximale en monoxyde de strontium de 25 % au voisinage de 2073 K, d'après l'équipe soviétique (11), cette teneur dépendrait de la tempé-

© 1999 CNRC Canada

Fig. 4. Variation du paramètre cristallin de la solution solide $U_{1-\delta}Sr_\delta O_{2-\delta}$ en fonction de la température. Étude dans le four à graphite : +, UO_2 + $SrCO_3$ à 293 K; ● $(s.s.)_1$ + éventuelle $(s.s.)_2$ + SrO + $SrUO_3$ + β′-« $SrUO_4$ »; ○, $(s.s.)_1$ + éventuelle $(s.s.)_2$ + SrO + $SrUO_3$; □, $(s.s.)_1$ + éventuelle $(s.s.)_2$ + $SrUO_3$; ■, $(s.s.)_1$ + β′-« $SrUO_4$ »; ▽, $(s.s.)_1$ + $SrUO_3$ + β′-«,$SrUO_4$ »; ×, $(s.s.)_1$ + $(s.s.)_2$ + $(s.s.)_3$. Précédente étude (35) : ▲, $UO_{2,00}$ (droite **1**) et UO_{2-x} (droite **2**) en présence de C, α-« UC_2 » et CO.

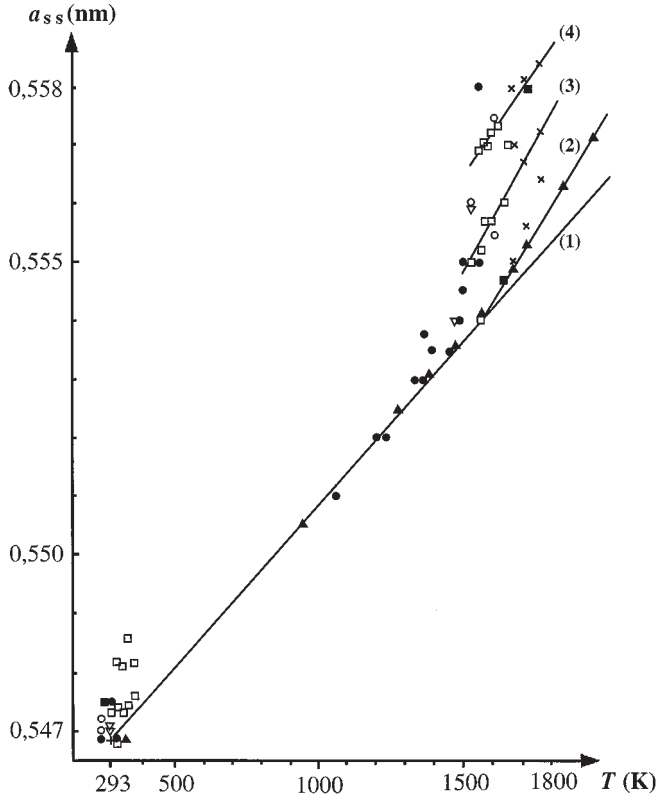

rature ($9 \leq SrO(\%) \leq 20$ pour $1273 \leq T(K) \leq 1773$) et s'accompagnerait d'une légère diminution du paramètre cristallin ($0{,}5465 \geq a(nm) \geq 0{,}5460$).

Cette dernière conclusion s'avère en totale contradiction avec nos résultats expérimentaux. La fig. 4 permet en effet de constater qu'aussi bien à l'ambiante qu'à température élevée ($1373 \leq T(K) \leq 1773$), le paramètre de la phase « UO_2 » en la présence éventuelle des oxydes SrO, β′-« $SrUO_4$ » et « $SrUO_3$ » (symboles ●, ○, □, ■, ▽ et ×) se montre systématiquement plus grand que celui de l'$UO_{2,00}$ (droite (**1**)) et supérieur ou égal à celui de l'UO_{2-x} (courbe (**2**), symbole ▲) qui coexiste avec les phases C, CO et α-« UC_2 » (35). Un examen minutieux des diagrammes de diffraction aux grands angles permet en outre de constater la coexistence fréquente de deux phases de type fluorine (courbes (**3**) et (**4**), symboles ●, ○ et □) en présence des autres oxydes, voire de trois de ces phases c.f.c. (courbes (**2**), (**3**) et (**4**), symbole ×) en l'absence de toute autre phase. Ces observations, au demeurant plus aisées à chaud qu'à 293 K, soulignent la difficulté de maintenir la structure cubique désordonnée dans un état bien cristallisé après trempe. Elles s'interprètent, de même que nous l'avons fait pour la phase $U_{1-\delta'}Ca_{\delta'}O_{2-\delta'}$ (19), par l'existence d'un domaine homogène de solution solide $U_{1-\delta}Sr_\delta O_{2-\delta}$ encadré par les domaines

Fig. 5. Diagramme de phases du système pseudo-binaire « $SrUO_3$ » – « $SrUO_4$ ».

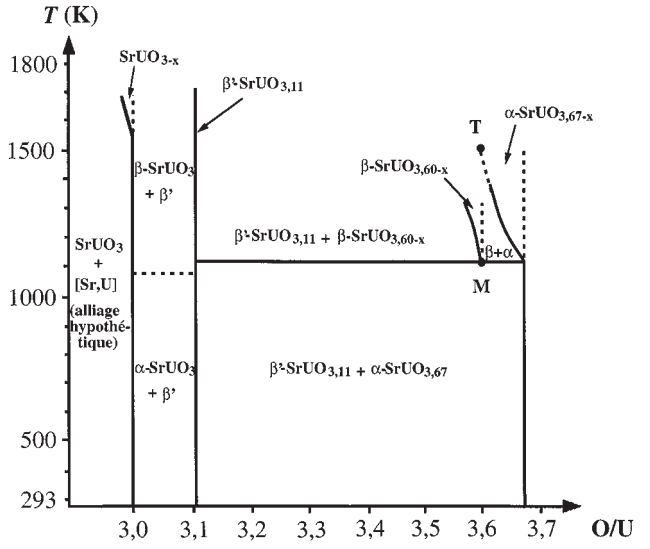

diphasés | s.s.(courbe (**3**)) + UO_{2-x} (courbe (**2**)) | et | s.s.(courbe (**4**)) + « $SrUO_3$ » |. La résolution des différentes composantes entrant dans la constitution des pics diffractés par la phase $U_{1-\delta}Sr_\delta O_{2-\delta}$ est toutefois plus délicate à réaliser en raison d'une moindre dissolution de SrO et d'une diminution concomitante de l'angle de Bragg, au lieu d'un accroissement de cet angle dans le cas de $U_{1-\delta'}Ca_{\delta'}O_{2-\delta'}$.

Il n'est pas douteux que les variations opposées que manifestent les paramètres cristallins des solutions solides $U_{1-\delta}Sr_\delta O_{2-\delta}$ et $U_{1-\delta'}Ca_{\delta'}O_{2-\delta'}$ soient dues à la différence de rayon entre les ions Sr^{2+} et Ca^{2+} lorsque ceux-ci se substituent progressivement aux ions U^{4+}, la substitution U^{4+}/Sr^{2+} apparaissant de ce fait plus limitée que la substitution U^{4+}/Ca^{2+}, alors que la substitution U^{4+}/Ba^{2+} est pratiquement interdite par la taille excessive de l'ion Ba^{2+} ($\delta < 0{,}01$ d'après Kleykamp (20)).

Afin d'évaluer l'indice de substitution δ de la phase $U_{1-\delta}Sr_\delta O_{2-\delta}$, nous avons adopté comme référence un indice δ′ connu (19) pour la phase $U_{1-\delta'}Ca_{\delta'}O_{2-\delta'}$. Après quoi, nous avons admis que ces indices étaient dans le même rapport que celui des variations relatives de paramètres auxquelles ils donnaient lieu, et cela indépendamment du sens de ces variations. C'est ainsi que ces calculs approximatifs ont été effectués à deux reprises pour chacune des limites de phases à 1673 K (fig. 4) correspondant aux courbes (**3**) ($\Delta a/a$ = 0,23 %) et (**4**) ($\Delta a/a$ = 0,51 %), sur la base d'un indice δ′ prenant les valeurs successives 0,25 ($\Delta a/a$ = 0,54 %) et 0,45 ($\Delta a/a$ = 0,90 %) (19). Ils conduisent aux teneurs limites en monoxyde SrO respectivement égales à 11,0 ± 0,5 % (courbe (**3**)) et 25 ± 1 % (courbe (**4**)), en bon accord avec les teneurs limites en chaux qui ont été proposées pour la solution solide $U_{1-\delta'}Ca_{\delta'}O_{2-\delta'}$ en dessous de 1523 K (19). Aucune réaction de type péritectoïde n'a toutefois pu être observée entre les composés $U_{1-\delta}Sr_\delta O_{2-\delta}$, « $SrUO_3$ » et SrO.

Le diagramme de phases du système pseudo-binaire « $SrUO_3$ » – « $SrUO_4$ »

Compte tenu de nos résultats expérimentaux et de quelques hypothèses simplificatrices, nous suggérons le dia-

© 1999 CNRC Canada

gramme représenté sur la fig. 5. Il permet de préciser et éventuellement de corriger un certain nombre de données bibliographiques (3, 6, 8–13, 15, 16) sur les points suivants.

Il n'existe que trois uranates thermodynamiquement stables à 293 K : ce sont les composés α-$SrUO_{3,67}$ orthorhombique, β′-$SrUO_{3,11}$ rhomboédrique et $SrUO_{3,00}$ de structure pérovskite.

L'uranate intermédiaire β-$SrUO_{3,60}$, isomorphe de β′-$SrUO_{3,11}$, ne se montre stable qu'au-dessus de 1108 K. Sa formation (point M sur la fig. 5) correspond donc à une réaction de type monotectoïde que l'on peut écrire :

[2] $\beta'\text{-}SrUO_{3,11} + \alpha\text{-}SrUO_{3,67} \rightleftharpoons \beta\text{-}SrUO_{3,60}$

Si la décomposition monotectoïde de β-$SrUO_{3,60}$ ne provoque jamais l'apparition de l'α-$SrUO_{3,67}$ à 293 K, ce sont probablement des contraintes qui en sont responsables. Un tel comportement a d'ailleurs été signalé sur d'autres systèmes tels que le système U–C, avec la réaction eutectoïde :

[3] U_2C_3 (c.c.) + C $\rightleftharpoons$ α-UC_2 (quadratique)

dont la réversibilité à 1793 K par précipitation du sesquicarbure d'uranium est impossible à vérifier par diffraction X à chaud quelle que soit la durée des recuits (36, 37).

Le diagramme proposé montre en outre que, des quatre oxydes examinés, seul l'oxyde β′-$SrUO_{3,11}$ ne subit pas de variation de composition entre 293 et 1713 K et, qu'à ce titre, il doit être considéré comme un véritable composé défini.

À gauche, il coexiste avec l'oxyde « $SrUO_3$ », le diagramme rappelant que cette pérovskite est le siège d'une transition du second ordre à 1073 K (représentée en pointillés dans le domaine diphasé $SrUO_3$ + β′-$SrUO_{3,11}$) et devient légèrement sous-stœchiométrique ($3{,}00 \geq O/U \geq 2{,}97$) entre 1553 et 1663 K.

À droite, le composé β′-$SrUO_{3,11}$ est en équilibre soit avec l'oxyde α-$SrUO_{3,67}$ entre 293 et 1108 K, soit avec son isomorphe β-$SrUO_{3,60-x}$ dont l'accroissement du rapport *c*/*a* atteste d'une légère diminution de la teneur en oxygène entre 1108 et 1343 K. Une limite droite verticale ($O/U \approx 3{,}60$) est, par contre, admise pour la phase monotectoïde qui coexiste avec l'oxyde α-« $SrUO_4$ » de composition variable ($3{,}67 \geq O/U \geq 3{,}62$) entre 1108 et 1373 K.

On voit que l'existence de la solution solide rhomboédrique ($3{,}98 \geq O/U \geq 3{,}60$) que Takahashi et al. (10) ont annoncée sur la base de leur étude de produits trempés est en totale contradiction avec le présent diagramme de phases. D'après celui-ci, une telle solution solide n'est guère concevable avant 1523 K, température pour laquelle se produirait la transformation (α,β) de la phase « $SrUO_4$ » (point T sur la fig. 5), peut-être à la suite d'une réaction de type péritectoïde.

Conclusions

Le présent travail de diffraction X à haute température a permis d'étudier les diverses phases solides qui prennent naissance au-dessus de 1073 K lorsque l'on fait réagir en proportions variables et sous pression d'oxygène contrôlée le dioxyde d'uranium et le monoxyde de strontium.

Pour chacune de ces phases (α-« $SrUO_4$ » orthorhombique, β et β′-« $SrUO_4$ » rhomboédriques, « $SrUO_3$ », « Sr_3UO_6 » et Sr_3UO_5 de structure pérovskite, ainsi que $U_{1-\delta}Sr_\delta O_{2-\delta}$ cubique), nous avons déterminé les paramètres cristallins et évalué les variations de composition dans l'intervalle de température compris entre 293 et 1713 K.

Compte tenu de ces évaluations, nous pouvons proposer les diagrammes de phases qui correspondent respectivement aux systèmes pseudo-binaires UO_2–SrO et « $SrUO_3$ » – « $SrUO_4$ ». Le premier de ces diagrammes se déduit immédiatement de celui précédemment attribué au système UO_2–CaO (19), à la différence près que la teneur minimale en oxygène de la solution solide $U_{1-\delta}Sr_\delta O_{2-\delta}$ est constante à toute température ($2 - \delta \approx 1{,}75$ au lieu de $1{,}75 \geq 2 - \delta \geq 1{,}45$ pour $U_{1-\delta'}Ca_{\delta'}O_{2-\delta'}$), et que la transformation péritectoïde de $CaUO_3$ à 1663 K disparait dans le cas de $SrUO_3$. Quant au second diagramme (fig. 5), il est pour l'essentiel basé sur l'existence de la phase monotectoïde β-« $SrUO_4$ » à 1108 K, la solution solide rhomboédrique précédemment annoncée (10) étant par conséquent métastable à 293 K.

Postface

Avec ce troisième mémoire consacré aux oxydes mixtes d'uranium et de métaux alcalino-terreux s'achève un long travail, commencé 35 ans plus tôt sur les oxydes d'uranium eux-mêmes (38), puis poursuivi sur de nombreux composés (oxydes, carbures, nitrures...) aussi bien de l'uranium et du thorium que d'autres métaux de transition. Tout au long de nos publications, nous avons tenté de faire partager au lecteur l'intérêt exceptionnel qu'offre, au triple point de vue structural, thermodynamique et cinétique, l'étude de l'état solide par diffraction X à haute température sous atmosphère conditionnée. Il y a en effet quelque chose de fascinant dans le fait que de petites modifications provoquées tant sur la température que sur une pression partielle gazeuse suffisent pour faire défiler les structures dans le temps et de manière réversible, ce qui donne à la matière cristallisée une véritable apparence de vie. Souhaitons que les recherches en ce domaine se perpétuent pour la plus grande satisfaction de leurs auteurs.

Bibliographie

1. O. Kubaschewski et C.B. Alcock. Metallurgical thermochemistry. 5e éd. Pergamon, London. 1979.
2. R.W.G. Wyckoff. Crystal structures. Vol. 1. 2e éd. Interscience, New York. 1965.
3. S.M. Lang, F.P. Knudsen, C.L. Fillmore et R.S. Roth. Natl. Bur. Stand. (U.S.A.), Circ. 568 (1956).
4. H.M. Rietveld. Acta Crystallogr. **20**, 508 (1966).
5. B.O. Loopstra et H.M. Rietveld. Acta Crystallogr. Sect. B: Struct. Crystallogr. Cryst. Chem. **B25**, 787 (1969).
6. E.H.P. Cordfunke et B.O. Loopstra. J. Inorg. Nucl. Chem. **29**, 51 (1967).
7. T. Fujino, N. Masaki et H. Tagawa. Z. Kristallogr. **145**, 299 (1977).
8. H. Tagawa et T. Fujino. J. Inorg. Nucl. Chem. **40**, 2033 (1978).
9. H. Tagawa, T. Fujino et T. Yamashita. J. Inorg. Nucl. Chem. **41**, 1729 (1979).

© 1999 CNRC Canada

10. K. Takahashi, T. Fujino et L.R. Morss. J. Solid State Chem. **105**, 234 (1993).
11. N.M. Voronov et R.M. Sofronova. *Dans* Physical chemistry of alloys and refractory compounds of thorium and uranium. *Edité par* O.S. Ivanov. Israël Program for Scientific Translation, Jerusalem. 1972. p. 204.
12. N.M. Voronov et R.M. Sofronova. *Dans* Physical chemistry of alloys and refractory compounds of thorium and uranium. *Edité par* O.S. Ivanov. Israël Program for Scientific Translation, Jerusalem. 1972. p. 215.
13. N.M. Voronov, R.M. Sofronova et E.A. Voitekhova. *Dans* Physical chemistry of alloys and refractory compounds of thorium and uranium. *Edité par* O.S. Ivanov. Israël Program for Scientific Translation, Jerusalem. 1972. p. 222.
14. W.H. Zachariasen. Acta Crystallogr. **1**, 281 (1948).
15. C. Brisi. Ric. Sci. **12**, 2376 (1960).
16. C. Brisi, M.Montorsi et G. Acquarone Burlando. Rev. Int. Hautes Temp. Réfract. **8**, 37 (1971).
17. C. Brisi et M.Montorsi Appendino. Ann. Chim. Rome, **59**, 400 (1969).
18. B. Touzelin et A. Pialoux. J. Nucl. Mater. **217**, 233 (1994).
19. A. Pialoux et B. Touzelin. J. Nucl. Mater. **255**, 14 (1998).
20. H. Kleykamp. J. Nucl. Mater. **131**, 221 (1985).
21. E.H.P. Cordfunke et R.J.M. Konings. J. Nucl. Mater. **201**, 57 (1993).
22. W. Rüdorff et F. Pfitzer. Z. Naturforsch. B: Anorg. Chem. Org. Chem. Biochem. Biophys. Biol. **9B**, 568 (1954).
23. J.O. Sawyer. J. Inorg. Nucl. Chem. **34**, 3268 (1972).
24. J.O. Sawyer. J. Inorg. Nucl. Chem. **25**, 899 (1963).
25. A. Kotlar, P. Gerdanian et M. Dodé. J. Chim. Phys. **64**, 1135 (1967).
26. J.S.O. Evans, T.A. Mary et A.W. Sleight. J. Solid State Chem. **137**, 148 (1998).
27. P.M. Forster, A. Yokochi et A.W. Sleight. J. Solid State Chem. **140**, 157 (1998).
28. P.C. Burns, R.C. Ewing et F.C. Hawthorne. Can. Minearalog. **35**, 1551 (1997).
29. H. Tagawa. J. Nucl. Mater. **51**, 78 (1974).
30. A. Pialoux. J. Nucl. Mater. **74**, 328 (1978).
31. F.D. Bloss. Crystallography and crystal chemistry, an introduction. Holt, Rinehart and Winston, New York. 1971.
32. J.P. Charvillat, G. Baud et J.P. Besse. Mater. Res. Bull. **5**, 933 (1970).
33. S.A. Barrett, A.J. Jacobson, B.C. Tofield et B.E.F. Fender. Acta Crystallogr. Sect. B: Struct. Crystallogr. Cryst. Chem. **B38**, 2775 (1982).
34. T. Nakamura. Chem. Lett. 429 (1974).
35. A.Pialoux et M. Dodé. Rev. Int. Hautes Temp. Réfract. **8**, 155 (1971).
36. J. Laugier et P.L. Blum. J. Nucl. Mater. **39**, 245 (1971).
37. A.Pialoux. Rev. Int. Hautes Temp. Réfract. **11**, 147 (1974).
38. A.Pialoux et M. Dodé. Rev. Hautes Temp. Réfract. **2**, 319 (1965).

© 1999 CNRC Canada

NMR conformational analysis on cyclic decapeptide template molecule

Zhenghong Peng

Abstract: We report the synthesis and conformational analysis of a series of cyclic and bicyclic decapeptide templates for combinatorial chemistry. The peptides were synthesized via solid phase synthesis and followed by solution cyclization. The conformation of the peptides was studied by proton NMR spectroscopy in DMSO and in TFE–water. The structure of the peptide template was calculated with the program DIANA and followed by SA from the NMR experimental constraints. The peptide adopts a fold comprising two β-strands and two type II β-turns. The design of such a restained cyclic decapeptide template will be discussed along with Template Assembled Synthetic Proteins (TASP).

Key words: solid phase peptide synthesis, cyclic decapeptide, NMR, conformational analysis, β-sheet.

Résumé : On a réalisé la synthèse d'une série de gabarits décapeptidiques cycliques et bicycliques pour la chimie combinatoire et on en a fait l'analyse conformationnelle. On a synthétisé les peptides par synthèse en phase solide et on a réalisé leur cyclisation en solution. On a étudié la conformation des peptides par spectroscopie RMN du proton en solution dans le DMSO ou dans des mélanges de TFE–eau. On a calculé la structure du gabarit peptidique à l'aide des programmes « DIANA », puis « SA », à partir des contraintes RMN expérimentales. Le peptide se replie avec deux brins β et deux plis β de type II. On discute de la conception d'un tel gabarit décapeptidique cyclique contraint ainsi que des protéines de synthèse assemblées à l'aide d'un gabarit (« TASP »).

Mots clés : synthèse peptidique en phase solide, décapeptide cyclique, RMN, analyse conformationnelle, feuillet-β.

[Traduit par la Rédaction]

Introduction

Topological templates that contain well defined functional groups are well known for protein de novo design and combinatorial chemistry (1–6). One approach of peptide library assembly, rather than being linked via a linear polypeptide fashion, the secondary structure forming peptide building blocks is assembled by covalent attachment to a template molecule (7–11). The template plays a determining role with the respect to the interaction of building blocks, the topological packing of the TASP, and predetermining the number, type, and spatial arrangement of its functional groups.

We report solid phase synthesis and conformational analysis for a series of decapeptide template molecules (Fig. 1). The model of the template is cyclic KXKPGKXKPG (X is any amino acid), where the orthogonal protecting groups of lysine side chain can be used to assemble secondary peptides as well as application to combinatorial chemistry. The templates were anticipated to provide conformationally well-defined structure based on two linked type II beta turns, by analogy with systems like the naturally occurring cyclic decapeptide antibiotic, gramicidin S4 (12). The templates have also been studied extensively in Mutter's group (3, 13, 14). However, they find out that the conformations of these molecules were initially inferred from considerations of their amino acid sequence, and several families of favored conformations were found, some of which had the lysine side chains pointing to both sides of the template in a random fashion. The template molecule is difficult to study partially because it contains four lysyl residues, and the highly symmetric molecule leads to considerable loss of information for NMR conformational analysis. Therefore, we assembled peptides with the sequence XXXPGXXXPG (X is any amino acid) or XXXPGXXXFP where XXX is designed to mimic the structure of KXK and to examine the conformations of these molecules from different amino acid sequences. We use XPGX sequence to adopt a type I or type II β-turn, which is also present in the GPGR sequence, a tight turn for the central conservative loop region of HIV-1 (15, 16). On the other hand, we use the XFPX sequence to adopt likely a type VI β-turn, which is present in the VFPA sequence of *RS-AFP*1, an antifungal protein isolated from radish seeds (17, 18). To define a more rigid structure, we further model the template by disulfide bond formation in the center of the template (Fig. 1).

Received November 5, 1998.

Z. Peng.[1] Institute of Biosciences and Technology, Texas A&M University, 2121 West Holcombe Boulevard, Houston, TX 77030, U.S.A.

[1]Telephone: (713) 677-7662. Fax: (713) 677-7689. e-mail: zpeng@ibt.tamu.edu.

Materials and methods

Peptide synthesis and purification

The linear peptides (NH2-XCXPGXCXPG-COOH) were prepared from solid phase synthesis according to the Fmoc strategy. Highly acid-labile resin (HALH or 2-Cl-Trt resin) was employed, thus allowing the completed linear peptides

© 1999 NRC Canada

Fig. 1. Schematic representation of the investigated decapeptides.

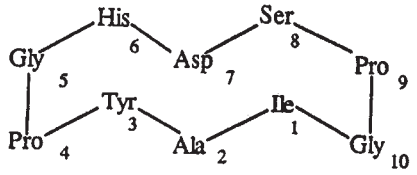

No. 1m

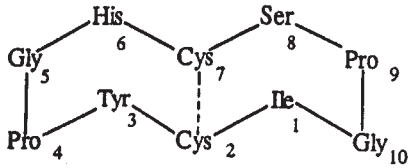

No. 1b

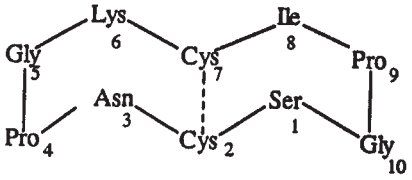

No. 2b

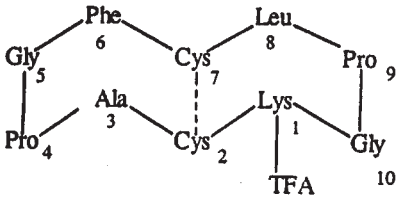

No. 3b

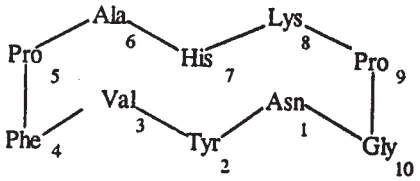

No. 4m

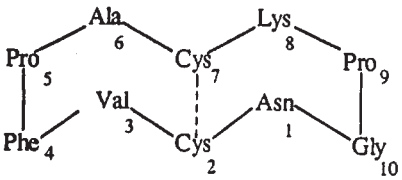

No. 4b

to be detached from the solid phase resin under very mild conditions, with 1% TFA in DCM for HALH resin and 10% acetic acid for 2-Cl-Trt resin. Mild conditions both in peptide assembly and cleavage gave the degree of flexibility needed to incorporate various protecting groups of the peptide side chain (Boc, *t*-Bu, Acm, Trt). The protecting groups are intact after cleavage from the solid support, and the linear peptide was subsequently cyclized in high dilution with HBTU–DIPEA. The disulfide bond was formed via air oxidation or iodine oxidation (19–21).

Synthesis details

A complete synthesis strategy of the bicyclo-[KCIPGSCNPG] decapeptide (No. 2b) is shown in Fig. 2. The first residue Fmoc-Gly-OH 0.2 g (0.3 mmol) was dissolved in 5 mL dry DCM (a few drops of DMF was added just enough to dissolve Fmoc-Gly-OH), then the solution together with DIPEA (0.21 mL, 1.2 mmol) was added to 0.5 g 2-Cl-Trt resin (1.05 mmol/g substitution, 0.53 mmol total). The mixture was shaking mechanically for 25 min, the resin was filtered, and end capped with three times 10 mL of DCM/MeOH/DIPEA (17:2:1 vol.), followed by wash steps with 10 mL of 3 × DCM, 2 × DMF, 2 × DCM, and 2 × MeOH. Finally, the solvent was removed under suction, and the resin was dried by vacuum. A substitution of 0.56 mmol/g resin was obtained according to the UV detection of the deprotection of the Fmoc group. The Fmoc-Pro-OH, Fmoc-Asn(Trt)-OH, Fmoc-Cys(Acm)-OH, Fmoc-Ser(*t*-Bu)-OH, Fmoc-Gly-OH, Fmoc-Pro-OH, Fmoc-Ile-OH, Fmoc-Cys(Acm)-OH, Fmoc-Lys(Boc)-OH were sequentially assembled onto the Fmoc-Gly-Trt resin, employing the peptide synthesizer. Freshly distilled DMF was the unique solvent; 2.5 equiv. of Fmoc – amino acid, 2.5 equiv. of HBTU, 5 equiv. of DIPEA relative to the resin were preactivated in 5 mL DMF for 2 min, added to the reaction column, magnetic stirring intermittently for 30 min. The integration of the Fmoc deprotection peak was used to examine the completeness of the coupling reaction. The Fmoc group was removed with 3 mL of 20% piperidine in DMF for 3 min, repeated five times, after the peptide chain was assembled on the resin, the *N*-terminal Fmoc group was removed, the resin-bound side chain protected peptide was treated with 20 mL of acetic acid/TFE/DCM (1:1:8 by vol.) at room temperature for 30 min, the filtrate was concentrated under reduced pressure (300 mg, >90% pure by RP HPLC).

The linear protected peptide NH_2-Lys(Boc)-Cys(Acm)-Ile-Pro-Gly-Ser(*t*-Bu)-Cys(Acm)-Asn(Trt)-Pro-Gly-OH, 150 mg (0.1 mmol), was dissolved in 4 mL of DMF and added

© 1999 NRC Canada

Fig. 2. The synthesis strategy of the decapeptide No. 2b.

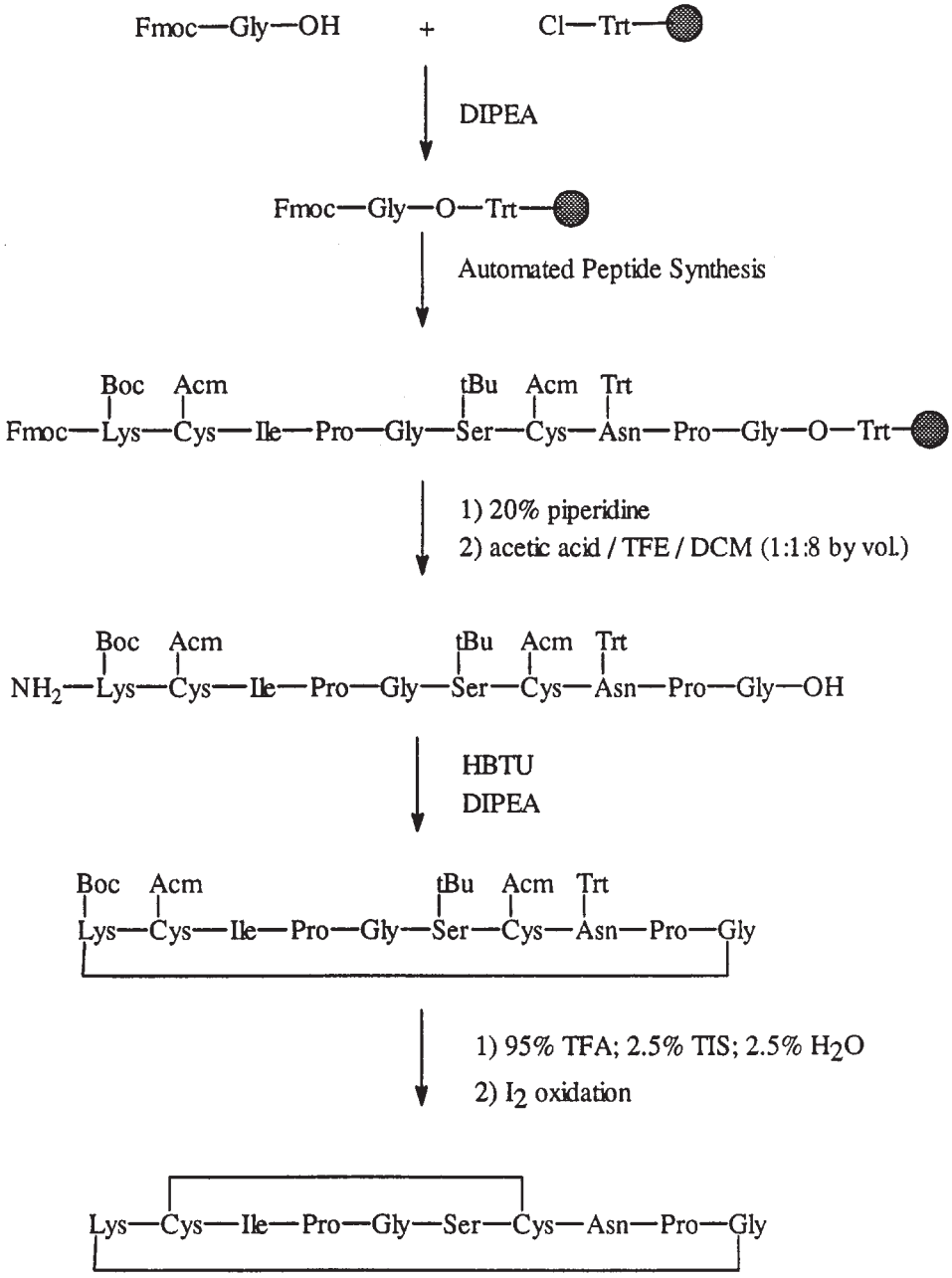

through a capillary by siphonage to a solution of HBTU (152 mg, 0.4 mmol) and of DIPEA (70 μL, 0.4 mmol) in DMF (100 mL) at room temperature over 30 min. The cyclization was complete after an additional 30 min, as determined from the analytical RP HPLC (22, 23). The solution was concentrated under reduced pressure. The Boc and *t*-Bu protecting groups were removed with a mixture of 20 mL of 95% TFA, 2.5% TIS, 2.5% water for 2 h, and the reaction was monitored by analytical RP HPLC (24). The solvent was evaporated, and the peptide was then dissolved in 75% aqueous methanol (250 mL), 35 mg iodine in 75 mL methanol was added dropwise into the peptide solution over 60 min, and the reaction proceeded overnight. The crude product was separated by RP HPLC with pharmacia C18 0.95 × 50 cm column, linear gradient A: 0.1 TFA in water, B CH_3CN from 10~50%, over 25 min, flowrate 4 mL/min; 16 mg of peptide No. 2b was obtained.

The peptides Nos. 3b, 4m, and 4b were prepared under similar conditions, the chemical structure of the peptides was further identified by the complete assignments of the ^{1}D NMR spectra.

The peptide No. 1b was prepared on hyper-acid labile (HALH) resin. The preparation of the HALH resin is shown in Fig. 3 (25).

4-Hydroxymethyl-3-methoxyphenoxybutyric amino – methyl copolystyrene – divinyl benzene was prepared as amino methylated resin. First, the resin (Nova Biochem, substitution: 0.81 mmol/g) 5 g (4.05 mmol), was swollen in DMF–

© 1999 NRC Canada

Fig. 3. The preparation of the Fmoc-Gly-HALH resin.

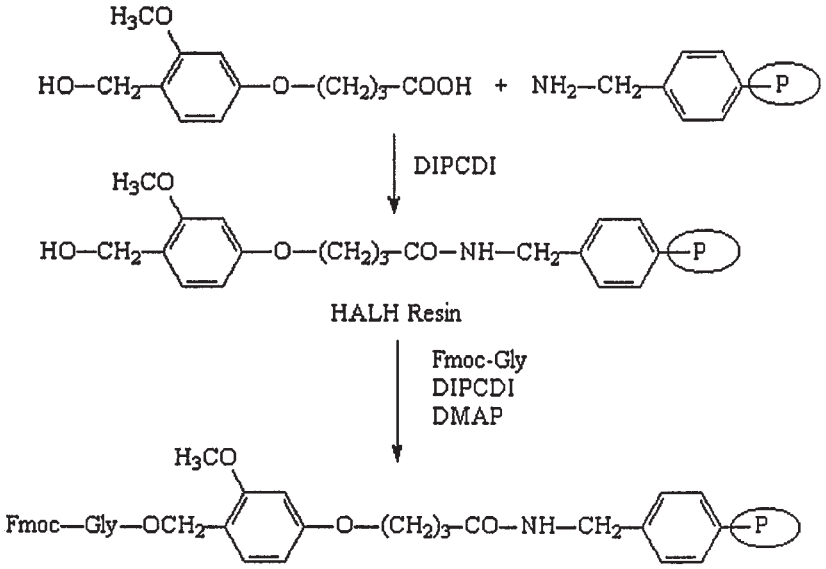

CH_2Cl_2 washed successively with 10 mL of DMF, 3 × 1 min, 20% piperidine in DMF, 1 × 3 min, 1 × 7 min, DMF, 3 × 1 min, CH_2Cl_2, 3 × 1 min. To the swollen resin was added a mixture of 2.9 g (12.15 mmol) of 4-(4-hydroxymethyl-3-methoxyphenoxyl)butyric acid and 0.2 mL (1.2 mmol) of diisopropylcarbodiimide (DIPCDI). The reaction mixture was swirled at room temperature for 1 h, then the resin was collected, washed with DMF, CH_2Cl_2, and ethyl ether each three times, dried in a vacuum desiccator over P_2O_5 overnight; weighed 5.873 g, substitution based on the weight increase was 0.78 mmol/g.

The first load of Fmoc-Gly onto HALH the resin

Fmoc-Gly, 2.4 g (8.1 mmol), was dissolved in CH_2Cl_2/DMF (1:1), with stirring. DIPCDI, 0.63 mL (4.05 mmol), was added to the solution. After 10 min, the above prepared dry resin, 2 g (1.62 mmol), was added, followed by addition of 100 mg (0.8 mmol) of DMAP. After swirling at room temperature for 1 h, the resin was drained, washed successively with DMF, CH_2Cl_2, CH_3OH, diethyl ether; dried resin weighed 2.424 g, substitution: 0.76 mmol/g.

The solid phase synthesis of the linear peptide was proceeded with similar conditions described above. After the peptide chain was assembled on the resin, the *N*-terminal Fmoc group was removed, followed by thorough washes with DMF, DCM, MeOH, and ethyl ether, dried in a vacuum desiccator over P_2O_5, weighed 1.008 g, weight increase 500.8 mg (0.2 mmol).

The resin-bound protected peptide was treated with 25 mL of 1.0% TFA in DCM at room temperature for 40 min, the filtrate was collected into 1.5 mL of prechilled DMF, the coloured resin was washed with 10 mL of MeOH, the combined filtrate was concentrated to ca. 2 mL by evaporation in vacuum, and directly separated on a RP-phase HPLC; column: pharmacia C18 10u 0.98 × 50 cm; linear gradient: A: 0.1% TFA in water, B: CH_3CN, B from 40 to 95% over 25 min; flow rate: 4 mL/min UV dual monitoring at 214 and 254 nm. The main peak, which was eluted at 21 min, was pooled, lyophilized to give a white powder, weighed 300 mg.

The following reaction of head-to-tail cyclization and deprotection from the side chain and disulfide bridge formation was prepared under similar conditions described in the synthesis of peptide No. 2b. Peptide No. 1m was also synthesized via HALH resin and purified using RP HPLC and proved by ES – mass spectroscopy and NMR.

NMR measurements

All the degassed samples had a final peptide concentration of 15 mM in DMSO-d_6,

The NMR spectra were recorded on a Bruker AM-500 spectrometer at 315 K. DQF-COSY (26, 27), TOCSY (28, 29), NOESY (30), and ROESY (31–33) spectra, with a spectral width of 6024.10 Hz, were recorded using standard pulse sequences. Phase-sensitive acquisition in t_1 was achieved by TPPI (34). The digital resolution in t_2 was 5.8 Hz/point and in t_1 was 11.6 Hz/point. Two-dimensional spectra were obtained with 2048 real data points and 512 t_2-increments (64–128 scans and 4 dummy scans per experiment). The spin lock in the TOCSY spectrum with field strength of 8.4 kHz was achieved with a MLEV-17 sequence preceded by a 1.5 ms trim pulse (28). In the ROESY spectra, continuous irradiation with field strength of 3.8 kHz was used for spin lock during 150 ms.

The data were processed on a X32 workstation with the UXNMR program. A $\pi/2$ shifted squared sine window function in the F2 dimension and a $\pi/2$ shifted sine window function in the F1 dimension was used. A polynomial baseline correction was performed in both dimensions.

The temperature coefficients of the amide proton resonance were extracted from a series of 1D spectra taken at several temperatures within the range of 295–325 K. Approximate hydrogen–deuterium exchange rates of the amide protons were measured from a series of 1D 16K spectra (96 scans and 4 dummy scans) with a spectral width of 6024.10 Hz after addition of two drops D_2O into the DMSO-d_6 solution. An E.COSY spectrum of the D_2O/DMSO-d_6 sample was recorded with a spectral width of 3496.50 Hz

© 1999 NRC Canada

under similar conditions as above. $^3J_{HN\alpha}$ interproton coupling constants were measured from 1D spectrum after a Lorentz to Gauss multiplication (GB = 0.15, LB = –3) and from the DQF-COSY spectrum at 315 K. $^3J_{\alpha\beta}$ interproton coupling constants were extracted from the 1D and E.COSY spectra. The NOESY buildup curve was sampled at the mixing times of 80, 120, 160, 200, 250, and 300 ms and was still linear up to 160 ms, therefore, the NOE cross-peak volumes were extracted from the NOESY spectra with the mixing time of 160 ms. Based on the two-spin approximation and the NOE contacts between the geminal C_α-protons of glycine (with a fixed distance of 1.78 Å), the NOE cross-peak intensities were calibrated versus distances (35). The upper limits of the distances $d_{N\alpha}$ (i, i), $d_{\alpha N}$ (i, i + 1), and d_{NN} (i, i + 1) were smaller than 3.0, 3.6, and 4.5 Å, respectively. For the lower limit, the VDW radius of 1.8 Å was used. The calculated distances were multiplied by a factor of 1.1 in order to achieve upper limits and to correct for possible experimental errors. Pseudoatom corrections were applied for the methyl groups and not the stereospecific assigned prochiral groups (36). A total of 76 distance constraints comprising 42 intraresidual, 19 sequential, and 16 transannular were used in the structure calculation. In addition, two constraints for the disulfide $2.0 < S_i^\gamma - S_j^\gamma < 2.2$ Å, $2.8 < C^\beta_i - S_j^\gamma < 3.3$ Å and one constraint for head-to-tail cyclization (1.23 < N1-C10 < 1.50 Å) were included.

The 10% TFE–water (by vol.) sample has a peptide concentration of 12.6 mM at pH 4.2. DSS was added as an internal chemical shift reference. The 20 and 30% (by vol.) TFE–water solutions are obtained by adding appropriate amounts of TFE to the 10% TFE–water sample. Two TOCSY spectra were recorded in 10% TFE and 30% TFE, respectively, under similar conditions as above.

Structure calculations

Stereospecific assignments for the prochiral β-methylene groups were obtained with the program Habas based on 31 distance constraints and 19 vicinal interproton coupling constants (37). These, together with the allowed ranges for the ϕ, φ, and χ^1 dihedral angles and the distance constraints, were used in all structure calculations, which are performed with the program DIANA version 2.1 (38). Additional stereospecific assignments were obtained with the program GLOMSA (38), using the 20 conformers with the lowest target function from the first DIANA calculation. The new assignments together with the other data were subjected to a new DIANA calculation. A subset of the 30 conformers with the lowest target function was further optimized by simulated annealing (SA protocol) in the AMBER force field (39). All distance constraints and dihedral angles were enforced through the usual harmonic "pseudo" energy terms with force constants of 32 kcal mol^{-1} $Å^{-2}$ (40) and 100 kcal mol^{-1} rad^{-2} respectively (41). A Lennard–Jones potential and a distance dependent dielectric constant in the coulombic energy term were used throughout. The structures were first energy minimized in 150 iterations by steepest descent and 500 iterations by conjugate gradients followed by heating of the molecule to 1000 K in 2 ps and kept there during 18 ps. The time steps were always 1 fs. In eight steps, the molecule was cooled to 300 K (850, 750, 675, 600, 525, 425, and 375 K) and finally energy minimized by 500 iteration of steepest descent and 5000 iterations of conjugate gradients. The cutoff was always 13 Å except for the two last steps (15 Å). The SA protocol was executed with in InsightII/Discover (Insight II and Discover User Guide, version 3.0, Biosym Technologies, San Diego, 1995, and NMRchitect 95.0).

Results

Conformation of the peptides

The proton resonance signals for the synthetic decapeptides were assigned from a combination of DQF-COSY, TOCSY, ROESY, and NOESY spectra following the standard assignment procedure of Wüthrich (42). The individual spin system connectivities were traced in the DQF-COSY and TOCSY spectra, and the sequence specific assignments of the spin systems were obtained from NOESY and ROESY spectra.

In the case of cyclo-[IAYPGHDSPG] peptide No. 1m (Fig. 1), two isomers are present, more precisely, a *cis* and *trans* conformation of the peptide bond Ser8–Pro9 with a ratio of 30/70. The *trans* conformation is evidenced by the presence of the strong $d_{\alpha\delta}$ (Ser8, Pro9) contact and the absence of the $d_{\alpha\alpha}$ (Ser8, Pro9) contact, while *cis* conformation is supported by the strong $d_{\alpha\alpha}$ (Ser8, Pro9) contact and the absence of $d_{\alpha\delta}$ (Ser8, Pro9) contacts. The peptide bond Tyr3–Pro4 adopts exclusively a *trans* conformation. For both isomers, all the resonance signals were assigned and are on the NMR time scales in slow exchange with each other as established from the ROESY spectrum.

Since peptide No. 1m adopts two conformations, the bicyclic form of bicyclo-[ICYPGHCSPG] peptide No. 1b was tested (Fig. 1). The NMR results reveal a single structure with a (*trans*, *trans*) conformation of the Ser8–Pro9 and Tyr3–Pro4 peptide bond as evidenced by the strong sequential NOE contacts $d_{\alpha\delta}$ (Tyr3, Pro4) and $d_{\alpha\delta}$ (Ser8, Pro9). No other isomers are observed. Strong sequential $d_{\alpha N}$ NOE contacts reveal the extended structure of the template and the strong interstrand NOE contacts d_{NN} (Ile1, Ser8), $d_{N\alpha}$ (Ile1, Pro9), $d_{\alpha N}$ (Pro4, His6), and d_{NN} (Tyr3, His6) confirm the antiparallel β-sheet orientation (42–44). The close contact between the phenyl ring of Tyr3 and methyl group of Ile1 shows that the side chains are oriented to the same side of the template. The chemical shift temperature coefficient patterns for the interproton of peptide No.1b, No. 2b, and No. 3b are shown in Fig. 4. In the case of peptide No. 2b, the slightly positive temperature coefficient of Ser1 (1.26 ppb/K) and Lys6 (1.1 ppb/K) prove the existence of the hydrogen bonds between the amide protons and the carbonyl group of, respectively, Ser1-NH and Ile8-CO, Lys6-NH and Asn3-CO, which is a common feature in β-turns. The value of Asn3 (–4.01 ppb/K) and Ile8 (–4.2 ppb/K) indicates weak hydrogen bonds between the Asn3-NH and Lys6-CO, Ile8-NH and Ser1-CO. The data shows that the four NH protons were hydrogen bonded in the β-sheet. Similar hydrogen bonding patterns were observed in peptide No. 1b and No. 3b. Thus, in contrast to the result of Floegel and Mutter (13), we obtained a well-defined conformer despite their different amino acids constitution of the bicyclic template molecule.

The results of bicyclic templates (Nos. 1b–3b) reveal a single structure and that the Xxx-Pro-Gly-Xxx β-turn adopts exclusively *trans* conformation when the disulfide bridge is

© 1999 NRC Canada

Fig. 4. Amide proton chemical shift temperature coefficients in DMSO-d_6 (top: peptide No. 1b; middle: peptide No. 2b; bottom: peptide No. 3b).

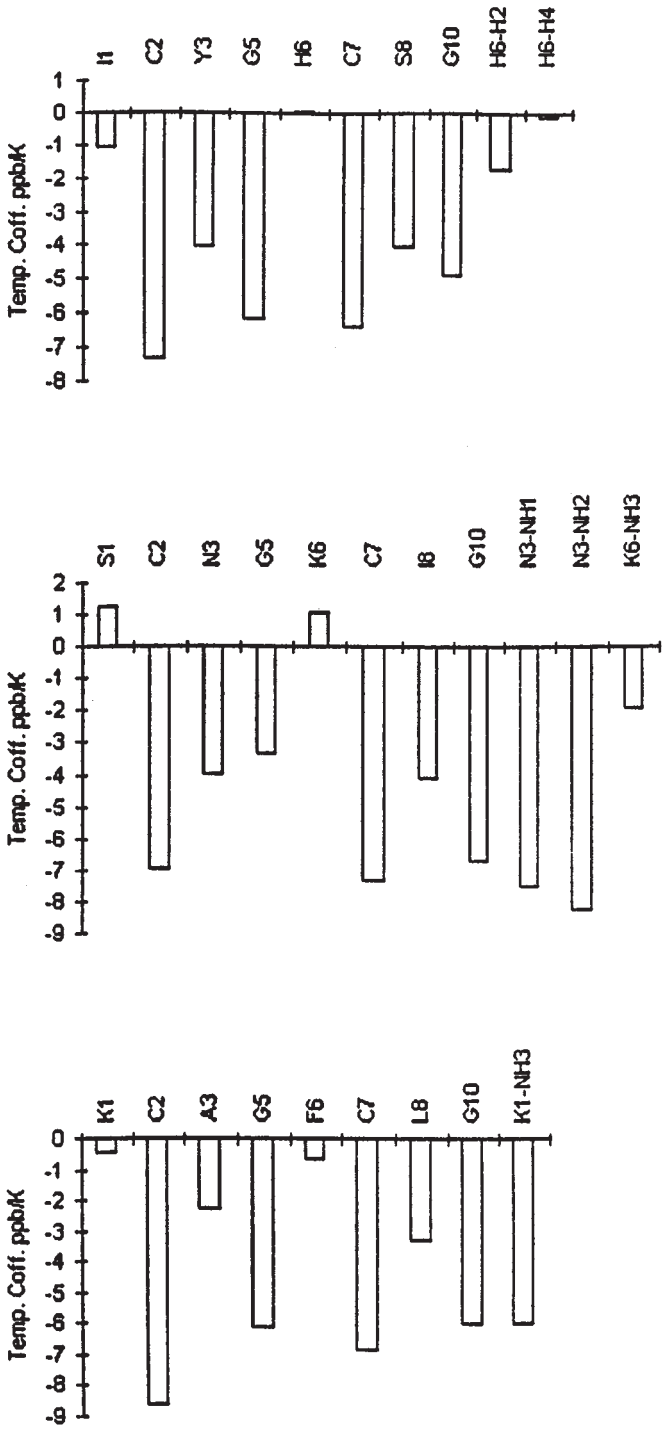

presented. We further test the Val-Phe-Pro-Ala β-turn where the Phe–Pro peptide bond adopts *cis* conformation, as the type VI β-turn observed in *RS-AFP*1 (17). More than two conformers can be identified from 1D NMR spectra for the cyclo-[NYVFPAHKPG] peptide No. 4m. Two isomers can be identified from bicyclo-[NCVFPACKPG] peptide No. 4b. The peptide bond Phe4–Pro5 adopts both a *cis* and *trans* conformation, while the peptide bond Lys8–Pro9 adopts only a *trans* conformation. The ratio of the *cis* and *trans* conformation is about 50:50, as measured from the integration of the methyl groups of Val3 and Ala6 from both isomers in the 1D spectrum. The $d_{\alpha\alpha}$ (Phe4, Pro5) contact proves the presence of the *cis* conformation. The typical strong upfield shifts of the chemical shifts of Pro5 protons are consistent with a nearby aromatic ring of the side chain of Phe4, which stabilizes a type VI β-turn by hydrophobic interactions with Pro5 (14, 44–46). In contrast, for the *trans* isomer, the $d_{\alpha\delta}$ (Phe4, Pro5) contact is observed, and the upfield shift of 0.5 ppm for the methyl protons of Val3 indicates the aromatic ring current contact of Phe4, which is not observed for Pro5.

In conclusion, the Val-Phe-Pro-Ala β-turn adopts both conformations, even though the disulfide bridge is presented in peptide No. 4b, while the Xxx-Pro-Gly-Xxx β-turn adopts only a *trans* conformation when the disulfide bridge is presented. Since only peptides Nos. 1b, 2b, and 3b are presented as a single isomer and have also similar structural properties, further structure determination will be focused on peptide No. 2b.

Chemical shifts and $^3J_{HN\alpha}$ coupling constants for peptide No. 2b are shown in Table 1. The chemical shifts of the amide protons show a good dispersion, over a range of 1.8 ppm in DMSO and 1.3 ppm in TFE–water. No line broading effect was observed at different temperatures, indicative of the absence of conformational exchange on the NMR time scale. The prochiral C_α protons of Gly10 and Gly5 have a $\Delta\delta$ value of 0.7 and 0.3 ppm, indicating that the protons are not in the same environment. The relatively large $^3J_{HN\alpha}$ coupling constants of Cys2, Asn3, Cys7, and Ile8 indicate the β sheet conformation (Table 1). The $^3J_{HN\alpha}$ coupling constants of Ser1 and Lys6 have averaged values indicative for possible flexibility in the segments Asn3-Pro4-Gly5-Lys6 and Ile8-Pro9-Gly10-Ser1 where Ser1 and Lys6 are located at the end of the type II β-turn structure.

The α-proton Wishart Chemical Shift Index (CSI) is a fast and simple method for the preliminary assignment of protein secondary structure by NMR spectroscopy (47). The results of the α-proton chemical shift difference between the observed value and the typical random coil value are shown for different solvents in Fig. 5. The large downfield shifts of the α-protons of Cys2, Asn3, Cys7, and Ile8 are in agreement with a β-strand conformation. In comparison with the different solvents (DMSO, 10, 20, 30% TFE–water), the Wishard CSI does not change significantly, which proves that the conformation of the peptide is preserved in different solvents.

In conclusion, the NOE contacts, the $^3J_{HN\alpha}$ coupling constants, the hydrogen bonding pattern, and the chemical shifts of α-protons at different solvents proves that the synthesized decapeptide adopts a β-sheet conformation and two type II β-turns.

Solution structure of the peptide No. 2b

Using the program DIANA, 250 starting conformers were calculated with the following structural constraints: 71 interproton distances extracted from the NOE crosspeaks, 23 torsion angles from 19 vicinal coupling constants, and 5 distance constraints from disulfide bridge and ring closure. From the 150 structures with a final target function value

© 1999 NRC Canada

Table 1. Chemical shift and $^3J_{HN\alpha}$ coupling constant for peptide No. 2b bicyclo-[SCNPGKCIPG] in DMSO-d_6, T = 302 K.

		Chemical shift (ppm)			
Residue	$^3J_{HN\alpha}$ (Hz)	NH	αH	βH	Others
Ser1	7.0	7.69	4.38	3.48, 3.34	
Cys2	9.2	9.11	5.35	3.10, 2.67	
Asn3	8.8	8.43	4.94	2.80, 2.67	
Pro4			4.12	2.20, 1.69	γCH_2 1.96, 1.86; δCH_2 3.76, 3.48
Gly5	12.5	8.53	3.84 3.50		
Lys6	6.4	7.29	4.28	1.72, 1.58	γCH_2 1.18; δCH_2 1.54; ϵCH_2 2.69; ζNH_3 7.65
Cys7	8.9	9.17	5.41	3.10, 2.80	
Ile8	10.7	8.33	4.70	2.00	γCH_2 1.32, 1.18; γCH_3 0.88; $\delta CH_3$0.80
Pro9			4.12	1.99, 1.88	γCH_2 2.08, 1.87; δCH_2 3.76, 3.46
Gly10	12.4	8.83	4.01 3.31		

Fig. 5. Chemical shift difference between the observed value and the random coil value for the C_α protons in different solvents (DMSO-d_6, 10, 20, and 30% TFE–water).

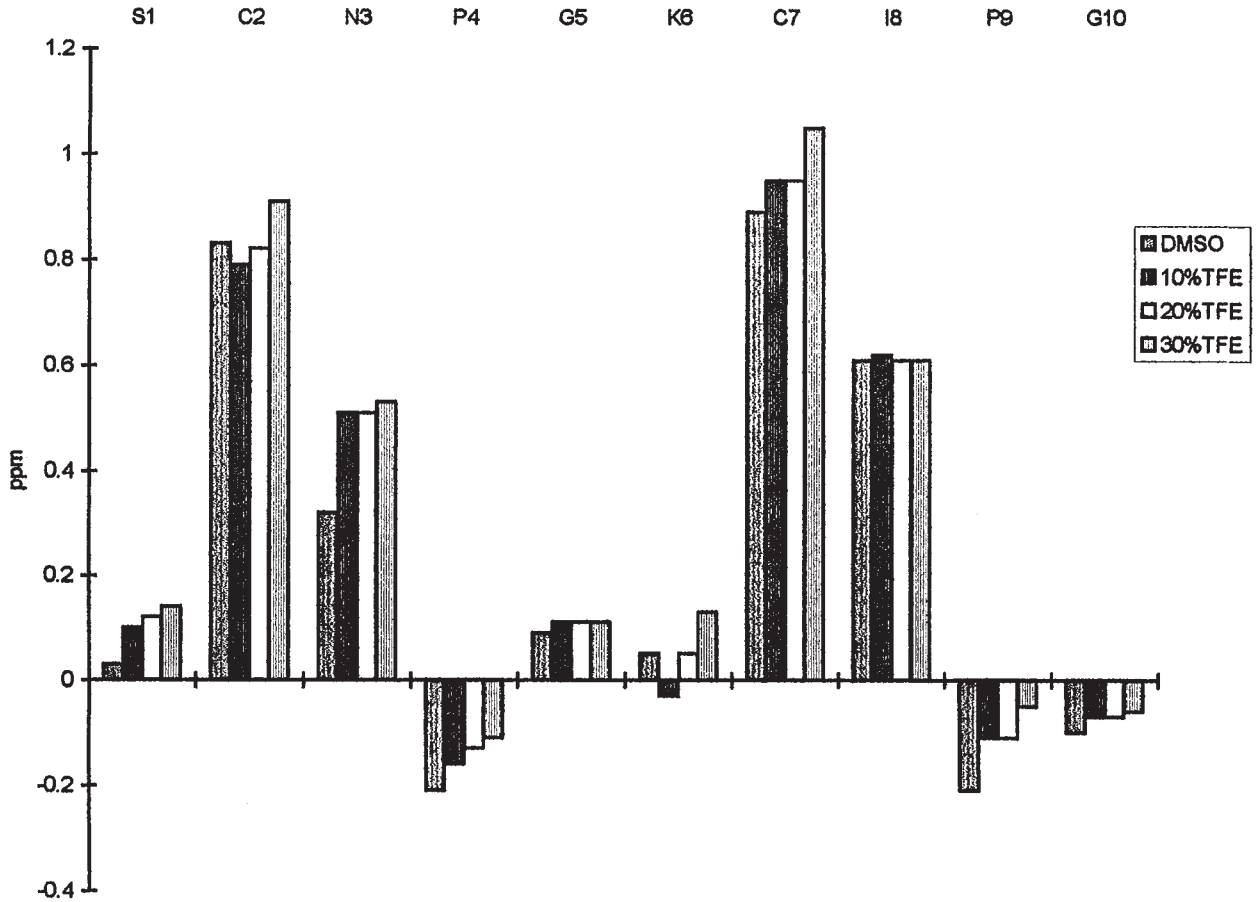

© 1999 NRC Canada

Fig. 6. Stereoview of the heavy atoms of peptide No. 2b in the 20 SA structures. Conformers 2–20 are superimposed for minimum pairwise rmsd of the backbone atoms with conformer 1.

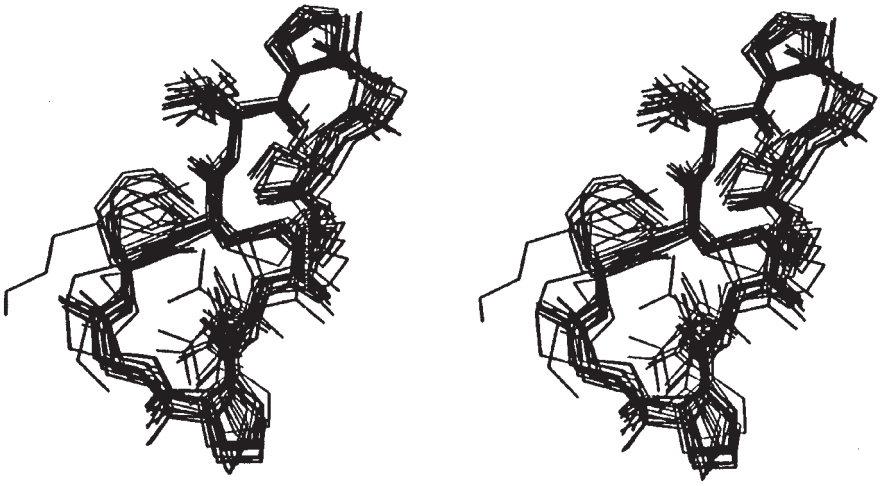

Table 2. Target function, residual violations on the constraints, energies and rmsd values for the 30 best DIANA structures and the 20 best structures after simulated annealing for peptide No. 2b.

Parameter	DIANA[a,b]	DIANA-SA[b,c]
Target function (Å^2)	(3.26 ± 2.90) × 10^{-5}	— [d]
Upper limit violations		
Number >0.2 Å	0	0
Number >0.1 Å	0.03 ± 0.18	0.60 ± 0.68
Sum of violations (Å)	0.12 ± 0.07	0.40 ± 0.07
Maximum violation (Å)	0.06 ± 0.03	0.10 ± 0.01
Lower limit violation	0	0
Dihedral angle violations		
Number >5°	0	0
Sum of violations (°)	0.20 ± 0.64	2.18 ± 0.88
Maximum violation (°)	0.20 ± 0.64	0.99 ± 0.43
AMBER energy (kcal mol^{-1})		
Bond energy	78.57 ± 4.17	2.29 ± 0.21
Valence angle energy	30.08 ± 5.50	16.86 ± 1.53
Improper energy	57.70 ± 7.33	19.08 ± 1.42
van der Waals energy	23.67 ± 5.57	–8.60 ± 1.08
Electrostatic energy	–55.59 ± 4.34	–96.41 ± 4.61
Total energy	133.66 ± 16.83	–69.85 ± 4.52
rmsd value (Å)		
Backbone atoms	0.34 ± 0.10	0.51 ± 0.16
All atoms	1.40 ± 0.36	1.46 ± 0.53

[a]The structures after the final DIANA calculation.

[b]The given numbers are the mean ± standard deviation. The rmsd values are the average pairwise rmsd taken over all structure pairs.

[c]The structures after simulated annealing.

[d]The target function is not defined for the simulated annealing structures, since they do not have the standard ECEPP geometry any more.

smaller than 0.1 Å^2, only 30 best structures were selected. None of these structures exhibited violation of experimental distance constraints by more than 0.2 Å, and for torsional angle constraints, more than 5°. The good convergence of the structures was clear from the small rmsd value, (0.34 ± 0.10 Å) for the backbone atoms and (1.40 ± 0.36 Å) for all atoms. After the energy optimization by SA, none of the structures exhibited large violation of the experimental data (distance constraints by more than 0.2 Å and torsional angle constraints more than 5°). The selection of the 20 solution SA structures (Fig. 6) is based on the values of the total energies. From the statistical analysis of the DIANA and DIANA/SA final structures (Table 2), it is clear that the SA structures gave substantial improvement of the van der Waals energy, which on average drops by 33.27 kcal mol^{-1}, and more important, is going from a positive to a negative value. Also, the electrostatic contribution to the energy decreases by 40.82 kcal mol^{-1}, showing that the distribution of

© 1999 NRC Canada

Table 3. Hydrogen bonds, chemical shift temperature coefficients $\Delta\delta_{NH}/\Delta T$ (ppb/K), and slow exchange constant k_m ($\times 10^{-3}$ min^{-1}) for the amide protons in peptide No. 2b.

Donor	Acceptor	Number[a]	$\Delta\delta_{NH}/\Delta T$ (ppb/K)	k_m ($\times 10^{-3}$ min^{-1})
Ser^1NH	Ile^8 O	20	1.26	8.7
Asn^3NH	Lys^6 O	18	–4.01	3.2
Lys^6NH	Asn^3O	13	1.10	9.15
Ile^8NH	Ser^1O	10	–4.17	0.9
Ser^1H^{γ}	$Gly^{10}O$	13	—[b]	>27
$Lys^6H^{\zeta 1}$	Lys^6 O	6	–1.98	>27
$Lys^6H^{\zeta 3}$	$Asn^3O^{\delta 1}$	4	–1.98	>27

[a]This column lists how many of the 20 simulated annealing structures contain the corresponding hydrogen bond according to the criteria $d_{DHA} \leq 2.5$ Å and $\theta_{DHA} > 155°$.

[b]Not observable.

Fig. 7. Ramachandran plot of the 20 SA structures of peptide No. 2b. (■) Gly5 and Gly10; (▲) Pro4 and Por9; (◆) Ser1, Cys2, Asn3, Lys6, Cys7, and Ile8.

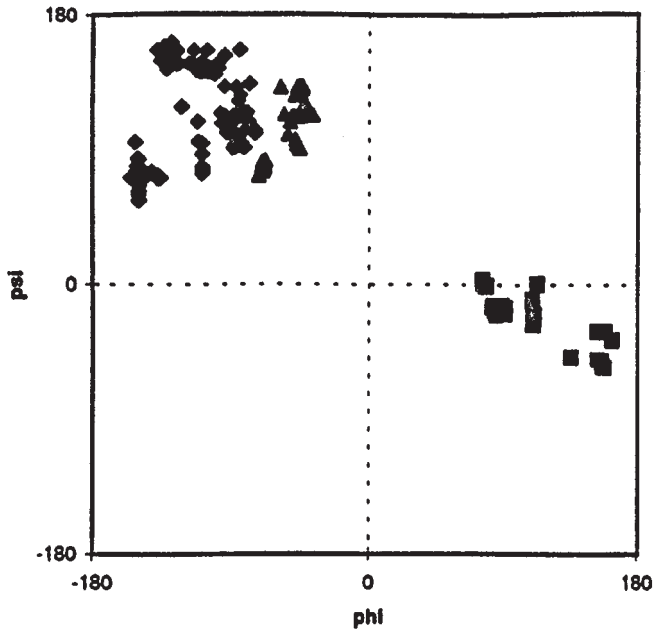

Fig. 8. Average rmsd deviations for each residue over the 20 SA structures to the average structure. (◆) backbone atoms; (■) all atoms.

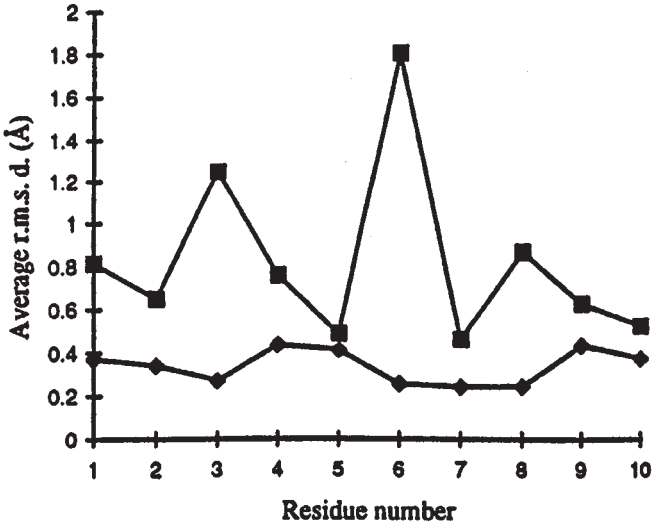

the charges in the conformer is significantly improved. The decrease of the bond energies, valence angle energy, and improper energy were achieved without a significant increase of the residual violations of the experimental constraints as compared with the DIANA conformers. More remarkably, the geometry of most hydrogen bonds in the individual structures was improved as a result of the electrostatic term in the force field. Finally, the narrow range of the rmsd values (0.51 ± 0.16 Å for the backbone atoms and 1.46 ± 0.53 Å for all atoms) implies that the obtained solution structures are identical so as to be in a single family.

The Ramanchandran plot for all the residues in the 20 refined conformers (Fig. 7) (48) clearly indicates the overall quality, and gives an impression of the main structural elements presented in the peptide. These are an antiparallel β-sheet conformation with β-strand I: Ser1-Cys2-Asn3 and β-strand II: Lys6-Cys7-Ile8, two β-turns centered around residues Pro4-Gly5 and Pro9-Gly10. This is clearly dictated by the central Cys2–Cys7 disulfide bridge.

The ϕ, φ values of Ser1, Cys2, Asn3, Lys6, Cys7, Ile8 clearly falls into the antiparallel β-sheet region with 53% in the most favored regions and 47% in the additional allowed regions (the Ramanchandran plot, data not shown) (48). Hydrogen bonds between Ser1-NH and Ile8-CO, Asn3-NH and Lys6-CO, Lys6-NH and Asn3-CO, Ile8-NH and Ser1-CO were identified in the solution structures using the criteria that the distance between the donor hydrogen and the acceptor oxygen must be less that 2.5 Å and that the angle between the donor–proton, donor atom, and the acceptor atom must be larger than 155°. These hydrogen bonds are in agreement with the small chemical shift temperature coefficient and the reduced amide exchange rates and confirm the interstrand hydrogen bonds of antiparallel β-sheet conformation (Table 3). The ϕ, φ values of the prolyl residues are in the region of (–70, –40) for ϕ angles and (70, 130) for φ angles; and the ϕ, φ values of the glycyl residues are in the region of (60, 175) for ϕ angles and (–50, 0) for φ angles. These values are characteristic for type-II β-turn. Hydrogen bonds between Ser1-NH and Ile8-CO, Asn3-NH and Lys6-CO are characteristic features of 1← 4 hydrogen bonding in the β-turn.

© 1999 NRC Canada

Fig. 9. Stereoview of the average of the 20 SA structures (heavy atoms). The ribbon is generated with MolMol (49).

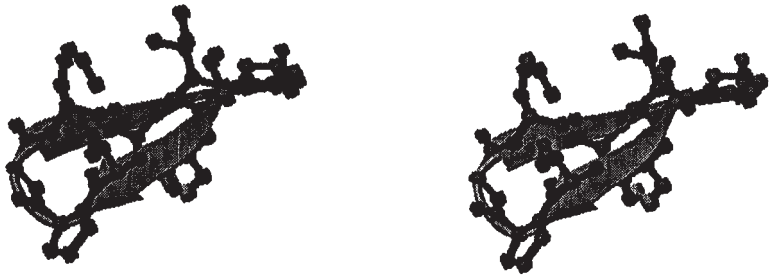

The average rmsd value for each residue in the 20 SA structures is shown in Fig. 8. It is clear that the backbone from Ser1 to Asn3 and from Lys6 to Ile8, which is a β-sheet region, is better defined than the segment of Pro4-Gly5 and Pro9-Gly10, which are the central residues of the β-turn. The large rmsd value for all atoms of Ser1, Asn3, Lys6, and Ile8 indicate the side chain of these residues are ill defined, and they are all solvent exposed.

In conclusion, the solution structure of the decapeptide bicyclo-[SCNPGKCIPG] consists of an antiparallel β-sheet with dimensions of ~13 Å for the extension of the β-strands and ~4 Å for the interstrand distance. Strand I extends from Ser1 to Asn3 and is followed by the type II β-turn around Pro4 and Gly5. Strand II runs from Lys6 to Ile8 and is followed by the other type II β-turn around Pro9 and Gly10 to make the ring closure of the peptide. The stereoview of the average of the final best 20 SA-refined structures is shown in Fig. 9. It is clearly that the side chain of Ser1, Asn3, Lys6, and Ile8 extends one side of the template, while the disulfide bridge is formed from the other side. The conformation of this bicyclic template molecule is devoid of different amino acids constitutions and reserves a rigid core central scaffold. The orientation of the side chain functional groups has been rigorously determined. The solution structure of these decapeptides presents an excellent model for orthogonal protected template bicyclo-[KCKPGKCKPG]. Cyclic peptide templates containing four orthogonal protecting groups have been already used as scaffolds for preparation of chemical libraries with a positional scanning format (9). In the area of de novo protein design, the different peptides building blocks can be attached and oriented to the template and give rise to different types of TASP molecule (3). Ongoing efforts in the group are focused to the solution synthesis of the template molecule and anchor it to the solid phase for the application of protein de novo design and combinatorial chemistry.

Acknowledgements

The author thanks Prof. Dr. Frans Borremans and Dr. Franky Fant at the University of Gent for their help and support in obtaining NMR spectrum and calculations.

References

1. G.D. Fasman (*Editor*). *In* Prediction of protein structure and the principles of protein conformation. Plenum Press, New York. 1989.
2. J.S. Richardson. Adv. Protein Chem. **34**, 167 (1981).
3. M. Mutter and S. Vuillemier. Angew. Chem. Int. Ed. Engl. **28**, 535 (1989).
4. J.S. Richardson and D.C. Richardson. Trends Biochem. Sci. **14**, 304 (1989).
5. K.W. Hahn, A.K. Wieslaw, and J.M. Stewart. Science (Washington, D.C.), **248**, 1544 (1990).
6. J.W. Taylor and E.T. Kaiser. Pharmacol. Rev. **38**, 291 (1986).
7. C.P. Hill, D.H. Anderson, L. Wesson, W.F. Degrado, and D. Eisenberg. Science (Washington, D.C.), **249**, 543 (1990).
8. J. Eichler, A.W. Lucka, and R.A. Houghten. Peptide Res. **7**, 300 (1994).
9. J.M. Ostresh, G.M. Husar, S.E. Blondelle, B. Doerner, P.A. Weber, and R.A. Houghten. Proc. Natl. Acad. Sci. U.S.A. **91**, 11 138 (1994).
10. M. Liebermann and T. Sasaki. J. Am. Chem. Soc. **113**, 1470 (1991).
11. C.T. Choma, J.D. Lear, M.J. Nelson, P.L. Dutton, D.E. Robertson, and W.F. DeGrado. J. Am. Chem. Soc. **116**, 856 (1994).
12. P. DeSantis and A.M. Liquori. Biopolymers, **10**, 699 (1971).
13. R. Floegel and M. Mutter. Biopolymers, **32**, 1283 (1992).
14. U. Sila and M. Mutter. J. Mol. Recognit. **8**, 29 (1995).
15. W.F. Vranken, M. Budešinsky, J.C. Martins, F. Fant, K. Boulez, H. Gras-Mass, and F.A.M. Borremans. Eur. J. Biochem. **236**, 100 (1996).
16. W.F. Vranken, M. Budešinsky, F. Fant, K. Boulez, and F.A.M. Borremans. FEBS Lett. **374**, 117 (1995).
17. F. Fant. Ph.D. dissertation. University of Gent, Belgium. 1997.
18. F. Fant, W.F. Vranken, J.C. Martins, and F.A.M. Borremans. Bull. Soc. Belg. **106**, 51 (1997).
19. J.M. Stewart and J.D. Young. *In* Solid phase peptide synthesis. W.H. Freeman, San Francisco. 1969.
20. M. Bodanszky and A. Bodanszky. *In* The practice of peptide synthesis. *Edited by* B.M. Trost. Springer-Verlag, New York. 1994.
21. E. Atherton and R.C. Sheppard. *In* Solid phase peptide synthesis. A practical approach. *Edited by* D. Rickwook and B.D.Hames. Oxford University Press, New York. 1989.
22. J.X. He, W.L. Cody, and A.M. Doherty. Lett. Pept. Sci. **1**, 25 (1994).
23. N. Izumiya, T. Kato, and M. Waki. Biopolymers, **20**, 1785 (1981).
24. D.A. Pearson. Tetrahedron Lett. **30**, 2739 (1989).
25. A. Flörsheimer and B. Riniker. Peptides, 131 (1990).
26. M. Rance, G. Bodenhausen, G. Wager, R.R. Ernst, and K. Wüthrich. Biochem. Biophys. Res. Commun. **117**, 479 (1984).
27. D. Neuhaus, G. Wagner, M. Vašak, J.H.R. Kagi, and K. Wüthrich. Eur. J. Biochem. **151**, 257 (1985).
28. L. Braunschweiler and R.R. Ernst. J. Magn. Reson. **53**, 521 (1983).
29. A. Bax and D.G. Davis. J. Magn. Reson. **65**, 355 (1985).
30. A. Kumar, G. Wagner, R.R. Ernst, and K. Wüthrich. Biochem. Biophys. Res. Commun. **96**, 1156 (1980).

© 1999 NRC Canada

31. A.A. Bothner-By, R.L. Stephens, J.T. Lee, C.D. Warren, and R.W. Jeanloz. J. Am. Chem. Soc. **106**, 811 (1984).
32. A. Bax and D.G. Davis. J. Magn. Reson. **63**, 207 (1985).
33. H. Kessler, C. Griesinger, R. Kerssebaum, K. Wagner, and R.R. Ernst. J. Am. Chem. Soc. **109**, 607 (1987).
34. D. Marion and K. Wüthrich. Biochem. Biophys. Res. Commun. **113**, 967 (1983).
35. J.L. Smith, M.J. Sutcliffe, C. Redfield, and M.C. Dobson. Biochemistry, **30**, 986 (1991).
36. K. Wüthrich, M. Billeter, and W. Braun. J. Mol. Biol. **169**, 941 (1983).
37. P. Güntert, W. Braun, M. Billeter, and K. Wüthrich. J. Am. Chem. Soc. **111**, 3997 (1989).
38. P. Güntert, W. Braun, and K. Wüthrich. J. Mol. Biol. **217**, 517 (1991).
39. S.J. Weiner, P.A. Kollman, D.A. Case, C. Singh, C. Ghio, G. Alagona, S. Profeta, and P. Weiner. J. Am. Chem. Soc. **106**, 765 (1984).
40. J.M. Moore, C.A. Lepre, G.P. Gippert, W.J. Chazin, D.A. Case, and P.A. Wright. J. Mol. Biol. **221**, 533 (1991).
41. J.C. Martins, F.J.M. Van de Ven, and F.A.M. Borremans. J. Mol. Biol. **253**, 590. (1995).
42. K. Wüthrich. *In* NMR of proteins and nucleic acids. John Wiley, New York. 1986.
43. G. Boussard and M. Marraud. J. Am. Chem. Soc. **107**, 1825 (1985).
44. G. Müller, M. Gurrath, M. Kurz, and H. Kessler. Proteins: Struct. Funct. Genet. **15**, 235 (1993).
45. J. Yao, R. Brüschweiler, H.J. Dyson, and P.E. Wright. J. Am. Chem. Soc. **116**, 12 051 (1994).
46. J. Yao, V.A. Heher, B.F. Espejo, M.T. Reymond, P.E. Wright, and H.J. Dyson. J. Mol. Biol. **243**, 736 (1994).
47. D.S. Wishart, B.D. Sykes, and F.M. Richards. J. Mol. Biol. **222**, 311 (1991).
48. R.A. Laskowski, J.A.C. Rullmann, M.W. MacArthur, R. Kaptein, and J.M. Thornton. J. Biomol. NMR, **8**, 477 (1996).
49. R. Koradi, M. Billeter, and K. Wüthrich. J. Mol. Graphics, **14**, 51 (1996).

Abbreviations

TASP	Template Assembled Synthetic Proteins
*RS-AFP*1	raphanus sativus antifungal protein 1
DCM	dichloromethane
DIPEA	diisopropylethylamine
DMF	*N*,*N*′-dimethylformamide
DMSO	dimethylsulfoxide
TFA	trifluoroacetic acid
TFE	trifluoroethanol
Fmoc	9-fluorenylmethoxylcarbonyl
HALH	hyper acid labile handle
HBTU	2-(1*H*-benzotriazole-1-yl)-1,1,3,3-tetramethyluronim hexafluorophosphate
Boc	*tert*-butoxylcarbonyl
DSS	2,2-dimethyl-2-silapentane–5-sulfonate, sodium salt
Trt	trityl
t-Bu	*tert*-butyl
2-Cl-Trt resin	2-chlorotrityl chloride resin
ACM	acetamidomethyl
2D	two-dimensional
DQF-COSY	double quantum filtered correlated spectroscopy
E.COSY	exclusive two-dimensional correlated spectroscopy
ROESY	rotating frame nuclear overhauser and exchange spectroscopy
TOCSY	total correlation spectroscopy
DMAP	4-(dimethylamino)pyridine

© 1999 NRC Canada

Determination of trace silicon in zirconium matrices and steels by inductively coupled plasma – atomic emission spectrometry

Kwang-Soon Choi, Kih-Soo Joe, Steven L. Mitchell, Candace J. Everall, and Keith R. Betty

Abstract: The determination of trace silicon by inductively coupled plasma – atomic emission spectrometry in samples containing HF is inhibited by the high blank caused by attack of the quartz torch. Use of a proprietary commercial amine to neutralize the HF and increase the pH to between 7 and 7.5 allows the simultaneous determination of silicon and other impurities in zirconium or zircaloy samples. The determination of silicon in steels requires the addition of an auxiliary complexing agent to the amine solution to prevent precipitation of iron(III). The analytical results obtained for several Standard Reference Materials (SRMs) with and without the amine reagent agree well with one another, and also with the certified values.

Key words: silicon, zirconium, zirconium alloys, steel, amine neutralization.

Résumé : La détermination de traces de silicium, par spectrométrie d'émission à plasma atomique couplé de façon inductive, dans des échantillons contenant du HF est inhibée par la valeur élevée du blanc causée par l'attaque de la torche de quartz. L'utilisation d'une amine commerciale de formule déposée permet de neutraliser le HF, d'augmenter le pH à des valeurs variant de 7,0 à 7,5 et de déterminer de façon simultanée le silicium et les autres impuretés contenues dans le zirconium ou dans des échantillons de zircaloy. La détermination du silicium dans les aciers nécessite l'addition d'un agent complexant auxiliaire à la solution d'amine afin de prévenir la précipitation du fer(III). Les résultats analytiques obtenus pour plusieurs matériaux de référence standard (MRS), avec et sans amine, sont en bon accord les uns avec les autres ainsi qu'avec les valeurs certifiées.

Mots clés : silicium, zirconium, alliages de zirconium, acier, amine, neutralisation.

Silicon is a minor or trace constituent of many alloys, and its determination is often necessary to ensure that the alloy specifications are met. Zirconium metal and zircaloy (an alloy of zirconium and tin) are used in the nuclear industry for fuel cladding, and in the CANDU®[2] reactors, a Zr – 2.5% Nb alloy is used for pressure tubes. The levels of trace impurities in Zr metal and its alloys are closely controlled to ensure they meet the specification values. The analysis of zirconium metals and alloys is often performed by Inductively Coupled Plasma – Atomic Emission spectrometry (ICP–AES) (1, 2). These alloys must be dissolved with the aid of HF, which has been reported to cause high and irreproducible silicon blanks and memory effects (3) when ICP–AES is used for silicon determinations, even when an "HF-resistant" torch, nebulizer, and spray chamber are used. We also were not able to obtain acceptable results for silicon with a commercial "HF-resistant" torch, but these blanks can be reduced by neutralizing the solution with tertiary amines (3) or with the addition of ammonia and an auxiliary complexing agent (4) prior to analysis. Although the determination of silicon in zirconium can also be performed colorimetrically with molybdenum blue (5), the procedure is very technique dependent. We have also encountered a low bias in the determination of silicon in steels with aqua regia dissolution using the procedure of Ward and Marciello (6) unless HF is added to the solutions. We have investigated the use of a new commercial amine neutralization reagent for the determination of silicon and other impurities in zirconium and zirconium alloys, and for the determination of trace silicon in stainless steel.

Experimental

Apparatus

Measurements were performed on an ARL 3520B ICP spectrometer using the operating conditions given in Table 1. A mass flow controller (Model FC-2805, Tylan General) was used to control nebulizer gas flow rate. A two-head

Received December 3, 1998.

K.-S. Choi and K.-S. Joe. Nuclear Chemistry Laboratory, Korea Atomic Energy Research Institute, P.O. Box 105, Yusong, Taejon 305-600, Korea.
S.L. Mitchell, C.J. Everall, and K.R. Betty.[1] AECL, Chalk River Laboratories, Chalk River, ON KOJ 1J0, Canada.

[1]Author to whom correspondence may be addressed. Telephone: (613) 584-3311. Fax: (613) 584-1220.
[2]CANDU® is a registered trademark of Atomic Energy of Canada.

 © 1999 NRC Canada

Table 1. Operating conditions for the ARL 3520B spectrometer.

System	Sequential type
Focal length	1 m
Mounting	Paschen–Runge
Grating	1080 grooves mm^{-1}
Light path	Vacuum
Slits	Entrance slit 20 μm
	Exit slit 20 μm
Torch	Fassel type
Nebulizer	Perkin–Elmer conespray
Spray chamber	Quartz, Scott type
Outer gas flow	12 L min^{-1}
Intermediate gas flow	0.8 L min^{-1}
Injector gas flow	1 L min^{-1}
Sample uptake rate	2 mL min^{-1}
Incident power	1200 W
Integration time	3 × 5 s
Observation height	15 mm above load coil

peristaltic pump (Gilson Minipuls 2) was used both for sample uptake and to pump the spray chamber drain. Plastic laboratory ware was used to avoid silicon contamination from glassware.

Reagents

All the reagents were of analytical reagent grade and were used without further purification. Nitric acid, hydrofluoric acid, and ammonium hydroxide were obtained from J.T. Baker (Phillipsburg, N.J., U.S.A.). A proprietary mixture of water-soluble amines ("amine reagent," Unisolve UNS-100, Inorganic Ventures, Lakewood, N.J., U.S.A.) was used to neutralize the HF. Zirconium oxychloride octahydrate, $ZrOCl_2 \cdot 8H_2O$, was obtained from Teledyne Wah Chang Albany (Albany, Oreg., U.S.A.) for use in matrix-matched zirconium standards. Tartaric acid was obtained from Aldrich (Milwaukee, Wisc.), citric and oxalic acids from Anachemia (Montreal, Canada), and EDTA (disodium salt of ethylenediamine tetraacetic acid) was obtained from Sigma (St. Louis, Mo.). Standard 1000 mg/L stock solutions were obtained from Spex (Edison, N.J.), Plasmachem (Farmingdale, N.J.), Inorganic Ventures (Lakewood, N.J.) and High Purity Standards (Charleston, S.C.). Zirconium and zircaloy Standard Reference Materials (SRMs) 360a, 360b, and 1234–1239, and steel SRMs 8j, 36a, and 101f were obtained from the National Institute of Standards and Technology (Gaithersburg, Md., U.S.A.). Zircaloy Certified Reference Materials Z11, Z12, Z21, Z22, and Z23 were obtained from the Japan Atomic Energy Research Institute (JAERI, Tokai-mura, Ibaraki-ken, Japan).

Sample dissolution

Zirconium and zircaloy

Place a known amount of sample (0.5 g) into a PTFE beaker. Add 10 mL of distilled deionized water (DDW) and 2 mL of concentrated nitric acid. Carefully add 0.5 mL of 48% hydrofluoric acid. Swirl gently to mix and cover with a PTFE watch glass. After cooling add three additional increments of 0.5 mL of 48% hydrofluoric acid at 30 min intervals, swirling after each addition. Quantitatively transfer the sample into a 50 mL plastic volumetric flask and add 0.25 mL of 1000 ppm of scandium stock solution as an internal standard (preliminary experiments showed that Sc gave better results as an internal standard than did Zr). Add 12.5 mL of Unisolve UNS-100 UHC amine reagent and swirl to mix. Let cool to room temperature and dilute to the mark with DDW. Mix and let cool.

Steel

Place a known amount of sample (0.2 g) into a PTFE beaker. Add 9.5 mL of 24% (v/v) aqua regia and wait for the reaction to subside. Cover with a PTFE watch glass. Place on a hot plate and boil for 20–30 min. Let cool to room temperature. Add 0.5 mL of 48% HF and let stand overnight. Quantitatively transfer the sample into a 200 mL plastic volumetric flask. Add 4 mL of 1 M tartaric, citric, or oxalic acid, or 40 mL of 0.1 M EDTA. Add 40 mL of 25% v/v UNS-100 UHC amine reagent and swirl to mix. Let cool to room temperature and dilute to the mark with DDW. Mix and let cool.

Standard preparation

Zirconium

Matrix matching of standards is desirable during analysis of zirconium to compensate for spectral interferences and background shifts (1, 2). Zirconium standard solutions were matrix-matched at a final concentration of 10 g/L Zr. Although zirconium samples containing 1–2% Sn were stable in solution for several weeks, it was found that Sn in the standards was not stable in the presence of HF for more than a few days. Since the nominal concentrations of HF are identical in the samples and standards, it is believed that HF is sparged from the samples by the copious amounts of hydrogen released during their dissolution. To eliminate this problem of instability of the standards, two different stock solutions were made as follows: (*i*) To matrix-match the standards for the determination of all elements except Sn, to a 1000 mL plastic volumetric flask add 70.74 g of $ZrOCl_2 \cdot 8H_2O$, 40 mL of concentrated HNO_3 and 75 mL of 48% HF. Make to volume with DDW and mix. (*ii*) For matrix-matching the Sn standards, to a 100 mL volumetric flask add 7.074 g of $ZrOCl_2 \cdot 8H_2O$ and 17.5 mL of concentrated HNO_3. Make to volume with DDW and mix.

Standards were prepared by adding the appropriate amount of 1000 ppm stock solution, 25 mL of matrix-matching solution, 0.25 mL of 1000 mg/L Sc, and 12.5 mL of amine to a 50 mL plastic volumetric flask. The amount of nitric acid added to the standards was reduced from that added to the samples to account for the acid consumed during sample dissolution.

Steel

Silicon standards for steel analysis were matrix-matched to contain the same amount of amine and complexing agent as the samples. The pH was adjusted to between 7 and 7.5 with NH_4OH.

Line selection

The complex spectrum of zirconium causes considerable difficulties in selecting emission lines for the determination of impurities (1). Additional problems were encountered in

© 1999 NRC Canada

Table 2. Selected lines and background correction positions.

Element	Wavelength, nm	Background position, nm	MDL, µg/g solids basis	
			No amine[a]	Amine[b]
Al	308.215	+0.058	2.7	6.1
Co	230.786	+0.033	3.6	5.9
Cr	205.552	+0.033	NT[c]	2.9[d]
Cu	324.754	+0.050	NT	0.7
Fe	239.562	+0.050	NT	0.9[d]
Hf	264.141	+0.050	2.7	11.5
Mg	280.27	–0.060	2.4	0.3
Mn	257.61	+0.050	NT	0.5
Mo	204.598	+0.030	2.4	11
Na	589.592	–0.050	2.1	57
Nb	316.34	–0.070	2.4	4
Ni	231.604	–0.040	1.8	5
P	177.5	+0.022	2.7	27
Sc	363.075	+0.050	NT	NT
Si (zirconium)	251.611	+0.046	NT	5
Si (steel)	288.158	+0.050	NT	5 (citric) 8 (tartaric)
Sn	242.949	+0.050	NT	18[d]
Ta	268.517	–0.070	5	6
Ti	334.941	+0.050	NT	0.4
V	309.311	+0.035	0.6	0.9

[a] $n = 10$.
[b] $n = 13$.
[c] NT = not tested.
[d] $n = 18$.

this work because of band spectra produced by the amine, which inhibit line selection at wavelengths below 200 nm. The wavelengths found to be free of interferences or problems and thus used in these analyses are listed in Table 2.

Results and discussion

Zirconium

Although Steffan and Vujicic (1) used a zirconium concentration of 20 g/L for zirconium analysis, we found that this zirconium level clogs the torch injector tube after several hours of operation. We therefore adopted a zirconium concentration of 10 g/L for this work. A rinse solution of 0.1% NH_4OH was found to give a lower silicon blank than did a DDW rinse. Method Detection Limits (MDLs) in µg/g solids basis with and without amine reagent are given in Table 2. For elements other than Cr, Fe, and Sn, the MDLs were calculated as three times the standard deviation determined from the dissolution and measurement of 13 SRM 360b samples. The MDLs for Cr, Fe, and Sn, which are present in significant quantities in SRM 360b, were calculated as three times the standard deviation determined from the measurement of 18 processed reagent blank solutions containing 10 g/L Zr and 25% v/v of amine reagent. This procedure for estimating MDLs may underestimate the detection limits that can be achieved in practice, but is in accord with common practice. The addition of amine causes a loss in sensitivity of approximately 40%, resulting in generally higher detection limits. The presence of Na in the amine substantially raises its detection limit. The detection limit for P is raised by spectral interference from the amine.

The results must be corrected for residual impurities in the zirconium used for matrix matching the standards. The only significant known impurity, based on the certificate obtained from the manufacturer, is hafnium. The hafnium content of the $ZrOCl_2 \cdot 8H_2O$ as determined by ICP–AES was calculated to be the difference between the measured ICP–AES values and the certified hafnium values for SRMs 1234–1239 and CRMs Z11 and Z12. The hafnium result for SRM 360b was not included as part of this calculation because of a higher uncertainty in its certified hafnium concentration. The hafnium values for the other SRMs and CRMs are shown in Table 3, and agree well with values obtained by neutron activation analysis (NAA) and inductively coupled plasma – mass spectrometry (ICP–MS) determinations.

The results of analysis of SRMs and CRMs are given in Tables 4 and 5. The relative standard deviation (RSD) of Ni in JAERI-Z21 and JAERI-Z23 is high because the value is very close to the MDL. For the determination of all other elements certified in the SRMs and CRMs, the RSDs vary from 0.4% for Fe in the SRM 360a to 13% for Hf in the JAERI-Z22. The RSD depends on the concentrations and elements. The analytical results obtained with and without the amine reagent agree well with one another, and also with the certified values.

Steel

Use of the amine reagent for neutralizing steel samples prior to the determination of silicon results in the precipitation of iron(III) hydroxide. Four auxiliary complexing agents

© 1999 NRC Canada

Table 3. Hafnium content of $ZrOCl_2 \cdot 8H_2O$.

Method	SRM	Hf Content of $ZrOCl_2 \cdot 8H_2O$, μg/g Zr[a]	*n*
ICP–AES	SRM 1234	29 ± 5	4
(see text)	SRM 1235	30 ± 5	4
	SRM 1236	30 ± 5	4
	SRM 1237	30 ± 5	4
	SRM 1238	34 ± 7	4
	SRM 1239	32 ± 5	4
	CRM Z11	31 ± 5	3
	CRM Z12	33 ± 5	3
	Mean	31 ± 2	8
NAA	$ZrOCl_2 \cdot 8H_2O$	34 ± 2	2
ICP–MS	$ZrOCl_2 \cdot 8H_2O$	32.2 ± 0.7	3

[a]The uncertainties are 1 s.

Table 4. Comparison of analytical results for Zircaloy SRMs with and without amine reagent.

	SRM 360a, μg/g			SRM 360b, μg/g		
		Found			Found	
Element	Certified	No amine[b]	Amine[c]	Certified[a]	No amine[d]	Amine[e]
Al	—	28 ± 4	29.4 ± 1.4	40	62.9 ± 0.9	63.6 ± 2.0
Cr	1060	1023 ± 12	1034 ± 35	1000	1027 ± 8	1045 ± 27
Cu	140	147 ± 7	147 ± 6	20	11.2 ± 0.6	10.8 ± 0.2
Fe	1441	1418 ± 25	1490 ± 6	2100	2024 ± 19	2152 ± 29
Hf	—	86 ± 4	82.8 ± 2.6	80	76.8 ± 0.9	78 ± 4
Mn	3	1.8 ± 0.2	2.1 ± 0.2	10	8.1 ± 0.4	8.0 ± 0.15
Ni	554	539 ± 4	573 ± 8	25	26.4 ± 0.6	27.3 ± 1.7
P	—	—	—	(10)	4.9 ± 0.9	—
Si	51	—	51.2 ± 1.7	(60)	—	73.3 ± 1.5
Sn (%)	1.42	1.42 ± 0.08	1.47 ± 0.01	1.55	1.58 ± 0.009	1.58 ± 0.03
Ti	27	23.6 ± 0.3	23.3 ± 0.3	20	9.8 ± 0.2	9.2 ± 0.13

[a]Values in parentheses are informational.
[b]$n = 4$.
[c]$n = 7$.
[d]$n = 10$.
[e]$n = 13$.

Table 5. Analytical results for elements in Zircaloy CRMs.

Element	JAERI-Z21, μg/g		JAERI-Z22, μg/g		JAERI-Z23, μg/g	
	Certified	Found[a]	Certified	Found[a]	Certified	Found[a]
Al	22	21.7 ± 0.8	40	39.0 ± 1.6	42	42.4 ± 2.4
Cr	130	146 ± 4	960	968 ± 16	1120	1142 ± 38
Cu	2	2.1 ± 0.1	8	8.1 ± 0.4	8	7.6 ± 0.05
Fe	1020	999 ± 9	1440	1434 ± 14	2260	2290 ± 20
Hf	82	81.9 ± 2.8	35	31 ± 4	73	69 ± 7
Mn	11	11 ± 0.4	6	5.5 ± 0.3	17	16.8 ± 0.4
Ni	(5)	4.8 ± 1.5	500	507 ± 6	(10)	9.5 ± 2.1
Si	18	17 ± 0.5	90	89.7 ± 1.9	23	19.5 ± 1.6
Sn (%)	300[b]	304 ± 13[b]	1.43	1.49 ± 0.02	1.52	1.54 ± 0.05
Ti	9	8.4 ± 0.08	3	2.0 ± 0.1	6	5.9 ± 0.3

[a]$n = 7$.
[b]μg/g.

for masking this precipitation were tested. Oxalic acid did not inhibit the precipitation reaction. Although tartaric acid, citric acid, and EDTA all inhibit precipitation, the lower solubility of the EDTA and the slow rate of formation of the iron–EDTA complex make its use inferior. The MDLs were determined as three times the standard deviation of a set of seven processed reagent blank solutions, and are included in Table 2. Results of silicon determinations in steel SRMs

© 1999 NRC Canada

Table 6. Analytical results for Si in stainless steels.

Standard	Certified Si, µg/g	Found Si, µg/g[a]	
		Citric acid	Tartaric acid
SRM 8j	580	581 ± 5	585 ± 6
SRM 36a	3560	3535 ± 18	3564 ± 4
SRM 101f	8760	8747 ± 46	8663 ± 30

[a] $n = 5$.

with amine neutralization and with tartaric or citric acid masking are shown in Table 6. The results are in excellent agreement with each other and with the certified values.

Conclusions

The use of a commercial high-capacity amine reagent to raise the pH allows the determination of silicon in zirconium and zircaloy standards by ICP–AES with a quartz spray chamber and torch, thus allowing replacement of the time consuming colorimetric procedure. Several other impurities can also be determined with no significant bias observed between the results with and without the amine procedure. However, the presence of sodium in the amine substantially raises the detection limit for Na, and spectral interference from the amine significantly raises the detection limits for phosphorous. Use of the amine reagent prior to the determination of silicon in stainless steels by ICP–AES requires an auxiliary complexing agent. Either tartaric or citric acid was found suitable.

Acknowledgments

The assistance of M.M. Totland, P.A. Robinson, and R. Ryan for NAA and ICP–MS determinations, and of K. Watanabe of JAERI in supplying CRMs Z21, Z22, and Z23, is gratefully acknowledged.

References

1. I. Steffan and G. Vujicic. J. Anal. At. Spectrom. **9**, 785 (1994).
2. J. Vinot. 25th Colloq. Metall. 299 (1982).
3. A.P. Krushevska and R. Barnes. J. Anal. At. Spectrom. **9**, 981 (1994).
4. A.P.M. de Win. J. Anal. At. Spectrom. **13**, 315 (1998).
5. A.B. Carlson and C.V. Banks. Anal. Chem. **24**, 472 (1952).
6. A.F. Ward and L.F. Marciello. Anal. Chem. **51**, 2264 (1979).

© 1999 NRC Canada

A versatile approach to the synthesis of oligonucleotide analogs containing neutral 5′-thioformacetal internucleoside linkages

Yves Ducharme and Kimberly A. Harrison

Abstract: Activation of nucleoside donors **5** by sulfuryl chloride followed by the addition of 5′-thionucleoside acceptors **3** yields 5′-thioformacetal dinucleotide analogs **6** with in situ trapping of liberated methanesulfenyl chloride with cyclohexene. Purine as well as pyrimidine derivatives can be part of a coupling reaction as nucleoside donors or acceptors. The dimethoxytrityl protecting group is compatible with the present coupling methodology allowing differential 3′,5′-end protection. The synthesis of longer oligonucleotides is also possible as shown by the preparation of trinucleotide analog **23**.

Key words: oligonucleotides, 5′-thioformacetal.

Résumé : L'activation de donneurs nucléosides (**5**) à l'aide de chlorure de sulfuryle, suivie d'une addition d'accepteurs 5′-thionucléosides (**3**), conduit aux analogues dinucléotide 5′-thioformacétal (**6**) avec piégeage in situ du chlorure de méthanesulfényle libéré à l'aide de cyclohexène. Les dérivés de la purine aussi bien que ceux de la pyrimidine peuvent faire partie d'une réaction de couplage comme nucléosides donneurs ou accepteurs. Le groupe protecteur diméthoxytrityle est compatible avec la présente méthodologie de couplage ce qui permet une protection différentielle des extrémités 3′ et 5′. La synthèse d'oligonucléotides plus longs est aussi possible comme on l'a démontré par la préparation de l'analogue trinucléotide **23**.

Mots clés : oligonucléotide, 5′-thioformacétal.

[Traduit par la Rédaction]

Introduction

In view of their potential use as antisense agents (1), numerous efforts have recently been devoted to the synthesis of oligonucleotide analogs with modified backbones (2). In the course of our study on the molecular recognition properties of oligonucleotide analogs, we required access to a variety of dinucleotide derivatives **1** containing a neutral 5′-thioformacetal internucleoside linkage, acid labile protecting groups P_1 and P_2, and where the nucleic bases B_1 and B_2 would be indiscriminately thymine, cytosine, guanine, or adenine.

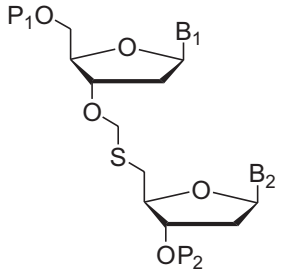

1

The only previous synthesis of a 5′-thioformacetal dinucleotide analog was reported by Matteucci et al. (3*a*) who have prepared dimer **4** by activating nucleoside donor **2** with molecular bromine followed by the addition of nucleoside acceptor **3t** (Scheme 1). While this method is very useful for the coupling of nucleoside derivatives bearing pyrimidine bases, it is inefficient for the preparation of dinucleotide analogs containing purine bases. We now report an efficient and versatile method for the synthesis of 5′-thioformacetal oligonucleotide analogs containing purine as well as pyrimidine nucleic bases (part of this work was published as a communication: see ref. 3*b*).

Results and discussion

The methylthiomethyl ether function found in nucleoside donor **2** is known to be transformed into a α-chloromethyl ether upon treatment with sulfuryl chloride (4). A previous report (5) on the use of this reaction in the context of nucleic acid chemistry suggested to us its potential utility for the synthesis of 5′-thioformacetal dinucleotide analogs. In a preliminary experiment, the coupling of nucleoside donor **5a**, a purine derivative, with nucleoside acceptor **3t** by sulfuryl chloride activation was attempted (Scheme 2). Thus, treatment of 2′-deoxyadenosine derivative **5a** with sulfuryl chloride (1.1 equiv.) in the presence of *N*,*N*-diisopropylethylamine (1.1 equiv.) for 10 min followed by the ad-

Received February 26, 1999.

Y. Ducharme[1] and K.A. Harrison.[2] Merck Frosst Centre for Therapeutic Research, P.O. Box 1005, Pointe Claire-Dorval, QC H9R 4P8, Canada.

[1]Author to whom correspondence may be addressed. Telephone: (514) 428-8621. Fax: (514) 428-4900.
[2]Undergraduate co-op student, University of Waterloo.

© 1999 NRC Canada

Scheme 1.

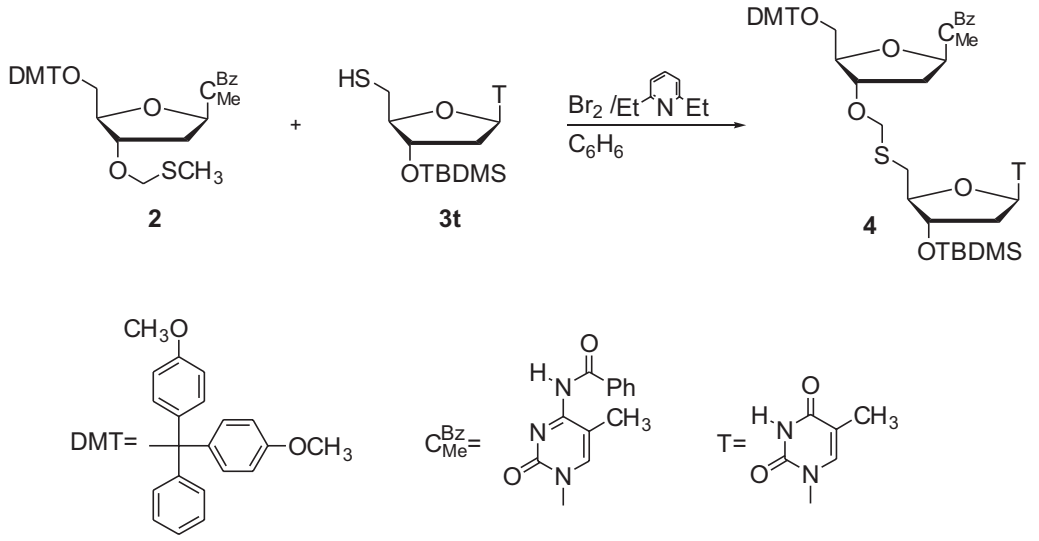

Scheme 2.

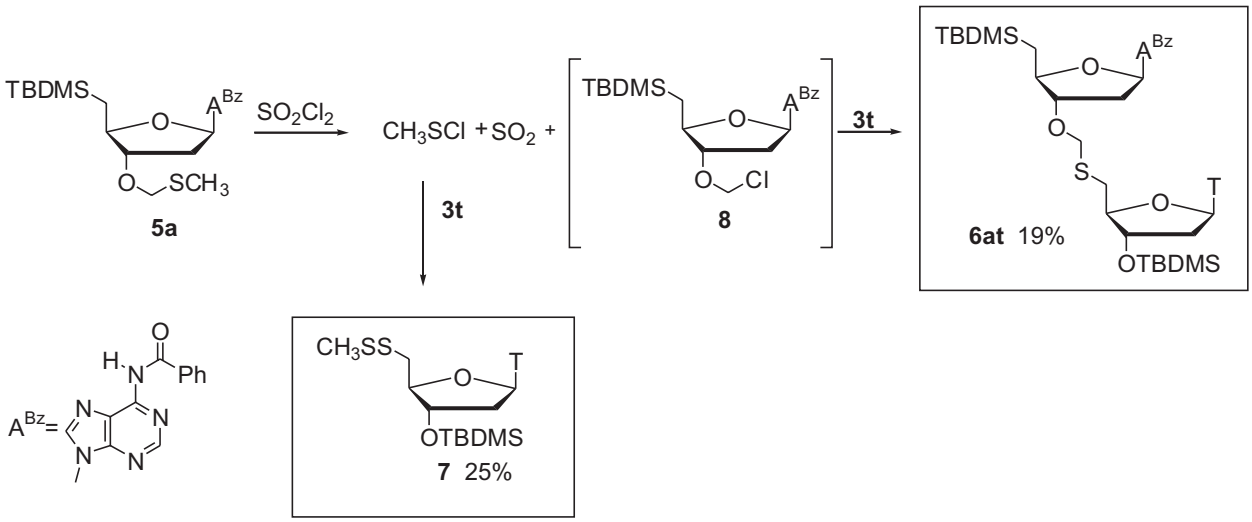

dition of 5′-thiothymidine (**3t**) (1.0 equiv.) and *N*,*N*-diisopropylethylamine (1.1 equiv.) afforded the desired dinucleotide analog **6at** albeit in a low 19% yield. A careful analysis of the reaction mixture revealed the presence of asymmetric methyl disulfide **7** (25%). The formation of this unwanted disulfide results from the liberation of highly electrophilic methanesulfenyl chloride upon reaction of methylthiomethyl ether **5a** with sulfuryl chloride. Reaction of mercaptan **3t** with methanesulfenyl chloride forms disulfide **7**. The yield of desired dinucleotide analog **6at** is greatly improved by trapping the liberated methanesulfenyl chloride with cyclohexene (4*a*) prior to the addition of nucleoside acceptor **3t**. In a typical reaction, sulfuryl chloride (1.3 equiv.) is added dropwise to a 0°C mixture of nucleoside donor **5a** (1 equiv.), *N*,*N*-diisopropylethylamine (1.4 equiv.), and 3 Å molecular sieves in dichloromethane. After 2 min, cyclohexene (2 equiv.) is added, and the reaction mixture is allowed to reach room temperature. Ten minutes later, a solution of nucleoside acceptor **3t** (1.3 equiv.) and *N*,*N*-diisopropylethylamine (1.4 equiv.) in dichloromethane is added, and the reaction mixture is stirred under nitrogen for 3 h. After an aqueous work-up and a purification by flash chromatography, the desired dinucleotide analog **6at** is obtained in 68% yield. The versatility of the method is demonstrated by the results presented in Table 1. Purine as well as pyrimidine derivatives can be part of a coupling reaction as nucleoside donors **5** or acceptors **3**. 5′-Thioformacetal dinucleotide analogs containing two purines such as **6aa** and **6ag** are easily obtained.

The required nucleoside donors and acceptors were prepared in the following ways. A Pummerer reaction (6) on N^6-benzoyl-5′-*O*-*tert*-butyldimethylsilyl-2′-deoxyadenosine (**9**) (7) gave access to donor **5a** (Scheme 3). Nucleoside donor **5t** was prepared by the alkylation of 5′-*O*-*tert*-butyldimethylsilylthymidine (**10**) (7) with chloromethyl methyl sulfide. The four nucleoside acceptors **3a**, **3c**, **3g**, and **3t** were prepared by the method of Kawai et al. (8) (Table 2). Mitsunobu coupling of suitably base-protected deoxynucleosides **11** (9) with thiolacetic acid afforded the 5′-*S*-acetyl nucleoside derivatives **12**. Silylation of the sec-

© 1999 NRC Canada

Table 1. Preparation of 5′-thioformacetal dinucleotide analogs **6**.

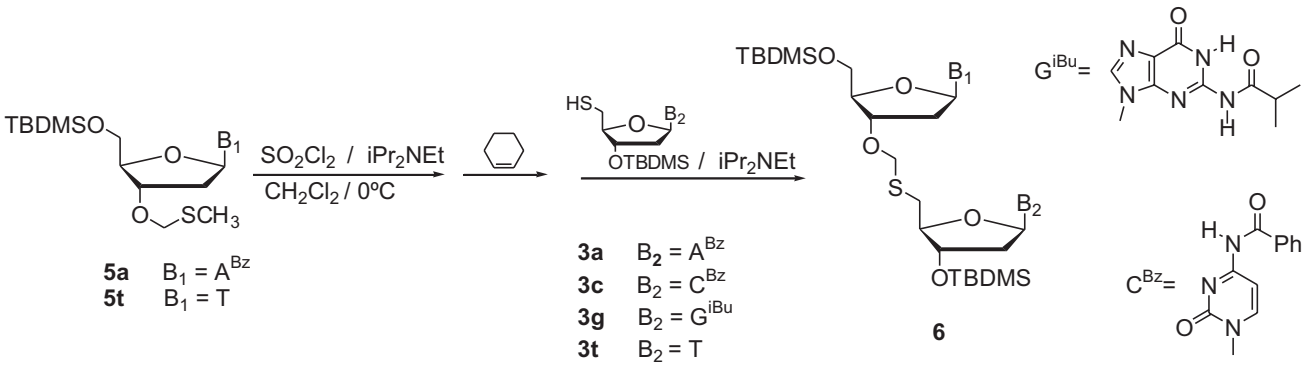

Nucleoside donor	Nucleoside acceptor	Dinucleotide analog	B_1	B_2	Yield (%)
5a	**3a**	**6aa**	A^{Bz}	A^{Bz}	64
5a	**3c**	**6ac**	A^{Bz}	C^{Bz}	58
5a	**3g**	**6ag**	A^{Bz}	G^{iBu}	49
5a	**3t**	**6at**	A^{Bz}	T	68
5t	**3a**	**6ta**	T	A^{Bz}	51
5t	**3c**	**6tc**	T	C^{Bz}	58
5t	**3g**	**6tg**	T	G^{iBu}	30
5t	**3t**	**6tt**	T	T	60

Table 2. Preparation of nucleoside acceptors **3**.

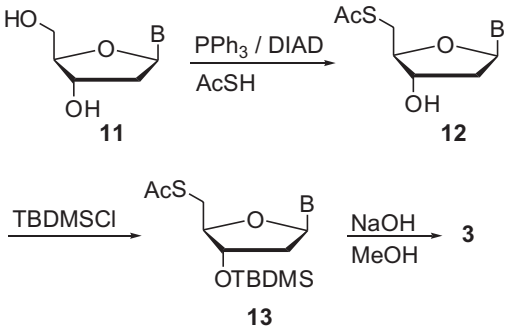

		Yields (%)		
Entry	B	**12**	**13**	**3**
a	A^{Bz}	76	91	52
c	C^{Bz}	41	92	56
g	G^{iBu}	94	78	64
t	T	42	98	82

ondary alcohols with *tert*-butyldimethylsilyl chloride gave fully protected nucleosides **13**. Methanolysis of the thioesters finally provided the desired nucleoside acceptors **3**.

The dimethoxytrityl protecting group is compatible with the present coupling methodology as shown by the coupling of donor **14** (10) with acceptor **3t** to afford 3′,5′ differentially protected dinucleotide analog **15** in 58% yield (Scheme 4).

The synthesis of longer oligonucleotides is also possible as shown by the preparation of trinucleotide analog **23**

Scheme 3.

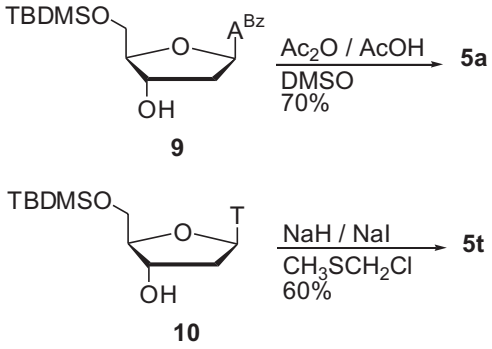

Scheme 4.

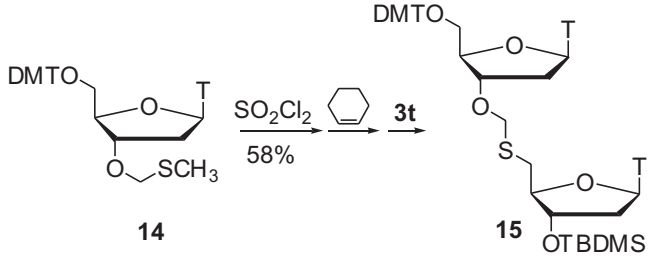

(Scheme 5). The 5′-dimethoxytrityl protecting group of thymidine derivative **14** (10) was selectively removed by treatment with *p*-toluenesulfonic acid in 85% yield. Mitsunobu coupling of the resulting primary alcohol **16** with thiolacetic acid gave thioester **17** (96% yield). This nucleoside donor was activated by sulfuryl chloride to be coupled with acceptor **3a** and thus provided dinucleotide an-

© 1999 NRC Canada

Scheme 5.

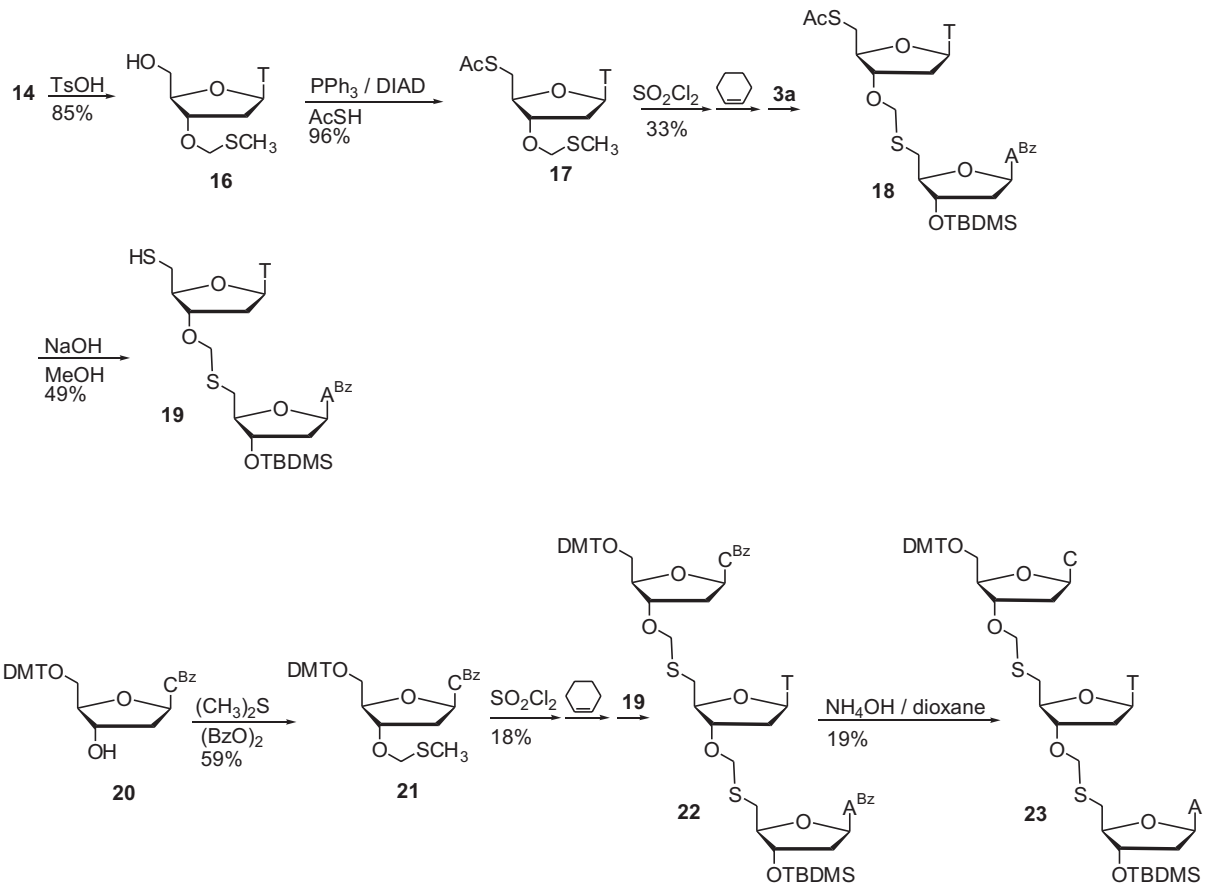

alog **18** in 33% yield. Methanolysis of the 5′-thioacetate group (50% yield) provided dinucleotide acceptor **19**. The 5′-dimethoxytrityl protected cytidine donor **21** was prepared by the treatment of secondary alcohol **20** (9) with dimethyl sulfide and benzoyl peroxide (11) in 59% yield. Sulfuryl chloride promoted coupling of donor **21** with dinucleotide acceptor **19**, then afforded trinucleotide analog **22** in 18% yield. Since the 3′ and 5′ terminus of trimer **22** are conveniently protected with acid labile *tert*-butyldimethylsilyl and dimethoxytrityl groups, it was possible to selectively liberate the benzoylated nucleic bases with aqueous ammonia to afford 5′-thioformacetal trinucleotide **23** in 19% yield.

Conclusions

A versatile methodology for the synthesis of oligonucleotide analogs containing 5′-thioformacetal internucleoside linkages has been developed. The 5′-thioformacetal link is formed by the activation of nucleoside donors bearing a 3′-methylthiomethyl ether moiety by sulfuryl chloride followed by the addition of 5′-thionucleoside acceptors with in situ trapping of liberated methanesulfenyl chloride by cyclohexene. Using this methodology, purine as well as pyrimidine derivatives can be part of a coupling reaction as nucleoside donors and acceptors. The dimethoxytrityl protecting group is compatible with the present methodology, allowing differential 3′,5′-end protection. The synthesis of longer oligonucleotides is possible as shown by the preparation of trinucleotide analog **23**.

Experimental section

General

Proton NMR spectra were recorded on Varian Gemini 200, Bruker AMX 300, or Bruker ARX 400 spectrometers, and proton chemical shifts are relative to tetramethylsilane as internal standard. Carbon NMR spectra were recorded on a Bruker AMX 400 spectrometer, and chemical shifts are relative to residual solvent signals. Low-resolution mass spectra were recorded by Oneida Research Services, Whitesboro, N.Y. High-resolution mass spectra were recorded by the Biomedical Mass Spectrometry Unit of McGill University, Montreal.[3]

[3] Copies of ^{1}H NMR spectra of compounds **3**, **5**, **6**, **12**, **13**, **15**–**19** and **21**–**23** (27 pages) have been deposited as supplementary material and may be purchased from: The Depository of Unpublished Data, Document Delivery, CISTI, National Research Council Canada, Ottawa, Canada, K1A 0S2.

© 1999 NRC Canada

Preparation of nucleoside acceptors 3

Step 1

5′-S-*Acetyl*-N^6-*benzoyl-2′,5′-dideoxy-5′-thioadenosine* ***(12a)***: Diisopropyl azodicarboxylate (7.4 mL, 37.6 mmol) was added to a 0°C solution of triphenylphosphine (9.85 g, 37.6 mmol) in THF (70 mL). The mixture was stirred for 30 min at 0°C. *N*^{6}-Benzoyl-2′-deoxyadenosine (9) (**11a**) (7.0 g, 19.7 mmol), THF (40 mL), and thiolacetic acid (2.7 mL, 37.8 mmol) were consecutively added, and the reaction mixture was stirred for 30 min at 0°C and 90 min at room temperature. The volatiles were then evaporated, and flash chromatography of the residue (silica gel; dichloromethane/methanol (90/10)) afforded thioester **12a** (6.2 g, 76%) as a colorless gum: ^{1}H NMR (400 MHz, $CDCl_3$) δ: 2.35 (s, 3H), 2.60 (m, 1H), 2.95 (m, 1H), 3.30 (m, 2H), 4.15 (m, 1H), 4.50 (m, 1H), 6.45 (t, 1H), 7.50 (m, 2H), 7.60 (m, 1H), 8.05 (m, 2H), 8.20 (s, 1H), 8.80 (s, 1H), 9.15 (s, 1H); MS (CI): 414 (MH^+), 240.

5′-S-*Acetyl*-N^4*-benzoyl-2′,5′-dideoxy-5′-thiocytidine* ***(12c)***: The procedure used to prepare thioester **12a** applied to *N*^{4}-benzoyl-2′-deoxycytidine (**11c**) (9) gave thioester **12c** (41%) as a white solid: ^{1}H NMR (200 MHz, CD_3OD) δ: 2.25 (m, 1H), 2.40 (s, 3H), 2.55 (m, 1H), 3.30 (m, 2H), 4.10 (m, 1H), 4.25 (m, 1H), 6.20 (t, 1H), 7.60 (m, 6H), 8.00 (d, 1H), 8.30 (d, 1H).

5′-S-*Acetyl*-N^2*-isobutyryl-2′,5′-dideoxy-5′-thioguanosine* ***(12g)***: The procedure used to prepare thioester **12a** applied to *N*^{2}-isobutyryl-2′-deoxyguanosine (9) (**11g**) gave thioester **12g** (94%) as a white solid: ^{1}H NMR (200 MHz, $CDCl_3$) δ: 1.25 (d, 6H), 2.35 (s, 3H), 2.50 (m, 1H), 2.85 (m, 2H), 3.10 (m, 1H), 3.50 (m, 1H), 4.10 (m, 1H), 4.30 (bs, 1H), 4.65 (m, 1H), 6.20 (t, 1H), 7.85 (s, 1H).

5′-S-*Acetyl-5′-deoxy-5′-thiothymidine* ***(12t)*** *(8)*: The procedure used to prepare thioester **12a** applied to thymidine (**11t**) gave thioester **12t** (8) (42%) as a white solid. This compound showed spectroscopic properties identical to those published in the literature (8).

Step 2

5′-S-*Acetyl*-N^6*-benzoyl-3′*-O-tert-*butyldimethylsilyl-2′,5′-dideoxy-5′-thioadenosine* ***(13a)***: A solution of alcohol **12a** (5.80 g, 14.0 mmol), imidazole (4.03 g, 59.2 mmol), and *tert*-butyldimethylsilyl chloride (6.09 g, 40.4 mmol) in DMF (80 mL) was stirred at room temperature for 20 h before EtOAc (1000 mL) was added. The organic phase was washed with water (3 × 500 mL) and brine, dried ($MgSO_4$), and evaporated. Flash chromatography of the residue (silica gel; hexane/EtOAc (50:50)) afforded compound **13a** (6.68 g, 91%) as a white solid: ^{1}H NMR (400 MHz, $CDCl_3$) δ: 0.15 (d, 6H), 0.95 (s, 9H), 2.35 (s, 3H), 2.45 (m, 1H), 3.00 (m, 1H), 3.25 (dd, 1H), 3.35 (dd, 1H), 4.10 (m, 1H), 4.50 (m, 1H), 6.45 (t, 1H), 7.55 (m, 2H), 7.60 (m, 1H), 8.05 (d, 2H), 8.20 (s, 1H), 8.80 (s, 1H), 9.20 (s, 1H); MS (CI): 528 (MH^+), 289, 240.

5′-S-*Acetyl*-N^4*-benzoyl-3′*-O-tert-*butyldimethylsilyl-2′,5′-dideoxy-5′-thiocytidine* ***(13c)***: The procedure used to prepare compound **13a** applied to thioester **12c** gave compound **13c** (92%) as a white solid: ^{1}H NMR (200 MHz, $CDCl_3$) δ: 0.10 (s, 6H), 0.90 (s, 9H), 2.15 (m, 1H), 2.40 (s, 3H), 2.60 (m, 1H), 3.25 (d, 2H), 4.10 (m, 2H), 6.20 (t, 1H), 7.55 (m, 4H), 7.90 (d, 2H), 8.10 (d, 1H), 8.65 (bs, 1H).

5′-S-*Acetyl*-N^2*-isobutyryl-3′*-O-tert-*butyldimethylsilyl-2′,5′-dideoxy-5′-thioguanosine* ***(13g)***: The procedure used to prepare compound **13a** applied to thioester **12g** gave compound **13g** (78%) as a white solid: ^{1}H NMR (200 MHz, $CDCl_3$) δ: 0.10 (s, 6H), 0.90 (s, 9H), 1.30 (t, 6H), 2.30 (m, 1H), 2.40 (s, 3H), 2.70 (m, 1H), 3.05 (m, 2H), 3.90 (m, 1H), 4.10 (m, 1H), 4.50 (m, 1H), 6.20 (t, 1H), 7.75 (s, 1H), 9.05 (bs, 1H); MS (CI): 510 (MH^+), 279.

5′-S-*Acetyl-3′*-O-tert-*butyldimethylsilyl-5′-deoxy-5′-thiothymidine* ***(13t)*** *(8)*: The procedure used to prepare compound **13a** applied to thioester **12t** gave compound **13t** (8) (98%) as a colorless oil. This compound showed spectroscopic properties identical to those published in the literature (8).

Step 3

N^6*-Benzoyl-3′*-O-tert-*butyldimethylsilyl-2′,5′-dideoxy-5′-thioadenosine* ***(3a)***: A methanolic sodium hydroxide solution (0.5 N; 49 mL, 24.5 mmol) was added to a deoxygenated solution of thioester **13a** (6.68 g, 12.7 mmol) in methanol (120 mL). The reaction mixture was stirred at 0°C for 1 h before it was neutralized by the addition of acidic Amberlyst 15 resin. The resin was filtered and washed thoroughly with methanol, and the filtrate was evaporated. Flash chromatography of the residue (silica gel; hexane/EtOAc (50:50)) afforded thiol **3a** (3.18 g, 52%) as a white solid: ^{1}H NMR (400 MHz, $CDCl_3$) δ: 0.14 (s, 3H), 0.15 (s, 3H), 0.94 (s, 9H), 1.56 (t, 1H), 2.46 (m, 1H), 2.77–3.02 (m, 3H), 4.12 (m, 1H), 4.65 (m, 1H), 6.44 (t, 1H), 7.53 (m, 2H), 7.61 (m, 1H), 8.02 (m, 2H), 8.22 (s, 1H), 8.80 (s, 1H), 8.95 (s, 1H); MS (CI): 486 (MH^+), 382, 240.

N^4*-Benzoyl-3′*-O-tert-*butyldimethylsilyl-2′,5′-dideoxy-5′-thiocytidine* ***(3c)***: The procedure used to prepare compound **3a** applied to thioester **13c** gave thiol **3c** (56%) as a white solid: ^{1}H NMR (400 MHz, $CDCl_3$) δ: 0.10 (s, 6H), 0.90 (s, 9H), 1.55 (t, 1H), 2.15 (m, 1H), 2.60 (m, 1H), 2.85 (m, 2H), 4.10 (m, 1H), 4.30 (m, 1H), 6.25 (t, 1H), 7.55 (m, 3H), 7.60 (m, 1H), 7.90 (d, 2H), 8.20 (d, 1H), 8.80 (bs, 1H).

N^2*-Isobutyryl-3′*-O-tert-*butyldimethylsilyl-2′,5′-dideoxy-5′-thioguanosine* ***(3g)***: The procedure used to prepare compound **3a** applied to thioester **13g** gave thiol **3g** (64%) as a white solid: ^{1}H NMR (200 MHz, $CDCl_3$) δ: 0.15 (s, 6H), 0.95 (s, 9H), 1.30 (dd, 6H), 1.55 (t, 1H), 2.40 (m, 1H), 2.65 (m, 2H), 2.80 (m, 2H), 4.05 (m, 1H), 4.50 (m, 1H), 6.20 (t, 1H), 7.85 (s, 1H), 8.50 (bs, 1H); MS (CI): 468 (MH^+), 279, 222.

3′-O-tert-*Butyldimethylsilyl-5′-deoxy-5′-thio-thymidine* ***(3t)*** *(8)*: The procedure used to prepare compound **3a** applied to thioester **13t** gave thiol **3t** (8) (82%) as a white solid. This compound showed spectroscopic properties identical to those published in the literature (8).

© 1999 NRC Canada

Preparation of nucleoside donors 5

N^6-*Benzoyl-5′*-O-tert-*butyldimethylsilyl-3′*-O-*methylthiomethyl-2′-deoxyadenosine (**5a**)*: A solution of *N*^{6}-benzoyl-5′-*O-tert*-butyldimethylsilyl-2′-deoxyadenosine (7) (**9**) (9.51 g, 20.2 mmol), acetic acid (20 mL), and acetic anhydride (66 mL) in DMSO (100 mL) was stirred at room temperature for 17 h before it was slowly poured in a 0°C solution of potassium carbonate (100 g) in water (1 L). The aqueous phase was extracted with chloroform (3 × 200 mL), and the combined organic phases were washed with water and brine, dried ($MgSO_4$), and evaporated. Flash chromatography of the residue (silica gel; hexane/EtOAc (30:70)) afforded methylthiomethyl ether **5a** (7.52 g, 70%) as a white solid: ^{1}H NMR (300 MHz, $CDCl_3$) δ: 0.11 (s, 6H), 0.92 (s, 9H), 2.18 (s, 3H), 2.68 (m, 2H), 3.86 (m, 2H), 4.21 (m, 1H), 4.66 (m, 1H), 4.70 (ABq, 2H), 6.52 (t, 1H), 7.52 (m, 2H), 7.60 (m, 1H), 8.03 (d, 2H), 8.34 (s, 1H), 8.80 (s, 1H), 9.12 (bs, 1H); MS (CI): 530 (MH^+), 240.

5′-O-tert-*Butyldimethylsilyl-3′*-O-*methylthiomethylthymidine (**5t**)*: Sodium hydride (97%; 0.78 g, 31.4 mmol) was added to a 0°C solution of 5′-*O-tert*-butyldimethylsilylthymidine (7) (**10**) (2.00 g, 5.6 mmol) in THF (66 mL). The mixture was stirred for 20 min at 0°C. Sodium iodide (0.92 g, 6.1 mmol), HMPA (5.6 mL), and chloromethyl methyl sulfide (0.52 mL, 6.2 mmol) were then consecutively added, and the reaction mixture was stirred at room temperature for 1.5 h before water was added slowly. EtOAc was added, and the organic phase was washed successively with saturated aqueous NH_4Cl, aqueous 5% $NaHCO_3$, water, and brine. The organic phase was then dried ($MgSO_4$) and evaporated. Flash chromatography of the residue (silica gel; hexane/EtOAc (50:50)) afforded methylthiomethyl ether **5t** (1.40 g, 60%) as a colorless gum: ^{1}H NMR (200 MHz, $CDCl_3$) δ: 0.15 (s, 6H), 0.90 (s, 9H), 1.95 (s, 3H), 2.00 (m, 1H), 2.15 (s, 3H), 2.40 (m, 1H), 3.85 (m, 2H), 4.10 (m, 1H), 4.50 (m, 1H), 4.65 (AB q, 2H), 6.30 (dd, 1H), 7.50 (s, 1H), 8.35 (bs, 1H); MS (CI) *m*/*e*: 417 MH^+, 291.

Preparation of 5′-thioformacetal dinucleotide analogs 6 and 15

5′-O-tert-*Butyldimethylsilyl-3′*-O-*methylenethymidylyl-(3′→5′)-3′*-O-tert-*butyldimethylsilyl-5′-deoxy-5′-thiothymidine (**6tt**)*: To a mixture of 5′-*O-tert*-butyldimethylsilyl-3′-O-methylthiomethylthymidine (**5t**) (83 mg, 0.20 mmol), *N*,*N*-diisopropylethylamine (49 μL, 0.28 mmol), and 3 Å molecular sieves (100 mg) in dichloromethane (1.5 mL) stirred at 0°C was added sulfuryl chloride (21 μL, 0.26 mmol). After 2 min, cyclohexene (41 μL, 0.40 mmol) was added, and the cold bath was removed. After 10 min at room temperature, a solution of 3′-*O-tert*-butyldimethylsilyl-5′-deoxy-5′-thiothymidine (**3t**) (97 mg, 0.26 mmol) and *N*,*N*-diisopropylethylamine (49 μL, 0.28 mmol) in dichloromethane (1.0 mL) was added to the reaction mixture. After 3.5 h, aqueous 5% $NaHCO_3$ was added, and the aqueous phase was extracted twice with dichloromethane. The combined organic phases were washed with water and brine and then dried ($MgSO_4$). Evaporation and flash chromatography of the residue (silica gel; hexane/EtOAc (25:75)) afforded dinucleotide analog **6tt** (89 mg, 60%) as a pale yellow solid: ^{1}H NMR (400 MHz, $CDCl_3$) δ: 0.10 (s, 6H), 0.12 (s, 6H), 0.90 (s, 9H), 0.93 (s, 9H), 1.92 (d, *J* = 0.9 Hz, 3H), 1.94 (s, 3H), 1.95 (m, 1H), 2.15 (m, 1H), 2.25 (m, 1H), 2.43 (dd, *J* = 12.2, 5.5 Hz, 1H), 2.85 (dd, *J* = 13.8, 5.9 Hz, 1H), 2.96 (dd, *J* = 13.8, 4.9 Hz, 1H), 3.78 (dd, *J* = 11.2, 2.5 Hz, 1H), 3.87 (dd, *J* = 11.2, 3.0 Hz, 1H), 4.02 (m, 1H), 4.10 (bs, 1H), 4.29 (m, 1H), 4.45 (d, 1H), 4.72 (s, 2H), 6.20 (m, 1H), 6.27 (dd, *J* = 8.6, 5.5 Hz, 1H), 7.27 (s, 1H), 7.46 (s, 1H), 9.08 (bs, 2H); ^{13}C NMR (100 MHz, $CDCl_3$) δ: 12.48, 12.60, 17.85, 18.28, 25.64, 25.86, 32.23, 37.84, 40.35, 63.44, 72.24, 73.62, 84.86, 84.96, 85.59, 110.97, 111.16, 135.07, 135.53, 150.26, 150.44, 163.83, 163.92; HRFABMS *m*/*e* calcd. for $C_{33}H_{57}N_4O_9SSi_2$ (MH^+): 741.3385; found: 741.3382.

N^6-*Benzoyl-5′*-O-tert-*butyldimethylsilyl-3′*-O-*methylene-2′-deoxyadenosynyl-(3′→5′)*-N^6-*benzoyl-3′*-O-tert-*butyldimethylsilyl-2′,5′-dideoxy-5′-thioadenosine (**6aa**)*: The procedure used to prepare 5′-thioformacetal dinucleotide analog **6tt** applied to nucleoside donor **5a** and to nucleoside acceptor **3a** gave 5′-thioformacetal dinucleotide analog **6aa** (64%) as a pale yellow solid: ^{1}H NMR (400 MHz, $CDCl_3$) δ: 0.08 (s, 3H), 0.09 (s, 3H), 0.14 (s, 3H), 0.15 (s, 3H), 0.90 (s, 9H), 0.94 (s, 9H), 2.49 (m, 1H), 2.59 (m, 1H), 2.71 (m, 1H), 2.98 (m, 3H), 3.77 (dd, *J* = 11.0, 3.4 Hz, 1H), 3.85 (dd, *J* = 11.0, 4.8 Hz, 1H), 4.15 (m, 1H), 4.20 (m, 1H), 4.62 (m, 2H), 4.70 (ABq, *J* = 11.6 Hz, 2H), 6.46 (m, 2H), 7.52 (m, 4H), 7.60 (m, 2H), 8.02 (m, 4H), 8.23 (s, 1H), 8.30 (s, 1H), 8.76 (s, 1H), 8.79 (s, 1H), 9.01 (bs, 1H), 9.07 (bs, 1H); ^{13}C NMR (100 MHz, $CDCl_3$) δ: 166.72, 164.93, 152.32, 151.29, 149.64, 149.46, 141.85, 141.31, 133.61, 133.45, 132.60, 132.05, 128.92, 128.66, 127.89, 123.70, 123.20, 86.85, 85.24, 84.76, 74.17, 72.08, 63.11, 39.82, 38.12, 32.29, 25.84, 25.65, 18.23, 17.87; HRFABMS *m*/*e* calcd. for $C_{47}H_{63}N_{10}O_7SSi_2$ (MH^+): 967.4140; found: 967.4137.

N^6-*Benzoyl-5′*-O-tert-*butyldimethylsilyl-3′*-O-*methylene-2′-deoxyadenosynyl-(3′→5′)*-N^4-*benzoyl-3′*-O-tert-*butyldimethylsilyl-2′,5′-dideoxy-5′-thiocytidine (**6ac**)*: The procedure used to prepare 5′-thioformacetal dinucleotide analog **6tt** applied to nucleoside donor **5a** and to nucleoside acceptor **3c** gave 5′-thioformacetal dinucleotide analog **6ac** (58%) as a yellow solid: ^{1}H NMR (400 MHz, $CDCl_3$) δ: 0.10 (s, 6H), 0.11 (s, 6H), 0.90 (s, 9H), 0.92 (s, 9H), 2.16 (m, 1H), 2.63 (m, 1H), 2.82 (m, 1H), 2.91 (dd, *J* = 13.8, 6.2 Hz, 1H), 2.99 (dd, *J* = 13.8, 4.8 Hz, 1H), 3.82 (dd, *J* = 11.0, 3.5 Hz, 1H), 3.89 (dd, *J* = 10.9, 4.9 Hz, 1H), 4.17 (dd, *J* = 10.8, 4.8 Hz, 1H), 4.24 (m, 3H), 4.68 (m, 1H), 4.82 (ABq, *J* = 11.6 Hz, 2H), 6.23 (t, 1H), 6.52 (dd, *J* = 7.7, 5.9 Hz, 1H), 7.53 (m, 5H), 7.61 (m, 2H), 7.88 (m, 2H), 8.02 (m, 2H), 8.14 (m, 1H), 8.32 (s, 1H), 8.66 (bs, 1H), 8.79 (s, 1H), 8.96 (bs, 1H); ^{13}C NMR (100 MHz, $CDCl_3$) δ: 162.22, 154.42, 152.33, 151.36, 149.50, 143.97, 141.32, 133.61, 133.06, 132.85, 132.54, 128.83, 128.62, 127.86, 127.60, 123.43, 96.51, 87.05, 86.26, 85.20, 84.84, 77.31, 77.00, 76.68, 73.38, 72.12, 63.10, 41.40, 38.01, 32.29, 25.82, 25.58, 18.21, 17.79; HRFABMS *m*/*e* calcd. for $C_{46}H_{63}N_8O_8SSi_2$ (MH^+): 943.4028; found: 943.4029.

N^6-*Benzoyl-5′*-O-tert-*butyldimethylsilyl-3′*-O-*methylene-2′-deoxyadenosynyl-(3′→5′)*-N^2-*isobutyryl-3′*-O-tert-*butyldimethylsilyl-2′,5′-dideoxy-5′-thioguanosine (**6ag**)*: The procedure used to prepare 5′-thioformacetal dinucleotide an-

© 1999 NRC Canada

alog **6tt** applied to nucleoside donor **5a** and to nucleoside acceptor **3g** gave 5′-thioformacetal dinucleotide analog **6ag** (49%) as a pale yellow solid: ^{1}H NMR (400 MHz, $CDCl_3$) δ: 0.08 (s, 6H), 0.12 (s, 3H), 0.13 (s, 3H), 0.89 (s, 9H), 0.92 (s, 9H), 1.24 (s, 3H), 1.26 (s, 3H), 2.40 (m, 1H), 2.60–2.75 (m, 4H), 2.87 (dd, *J* = 14.0, 6.0 Hz, 1H), 2.96 (dd, *J* = 14.0, 5.3 Hz, 1H), 3.78 (dd, *J* = 10.9, 3.5 Hz, 1H), 3.84 (dd, *J* = 10.9, 4.8 Hz, 1H), 4.15 (m, 2H), 4.48 (dd, *J* = 10.5, 4.5 Hz, 1H), 4.60 (m, 1H), 4.71 (ABq, *J* = 11.6 Hz, 2H), 6.20 (t, 1H), 6.46 (dd, *J* = 7.6, 6.1 Hz, 1H), 7.51 (m, 2H), 7.60 (m, 1H), 7.87 (s, 1H), 8.01 (m, 2H), 8.30 (s, 1H), 8.72 (bs, 1H), 8.79 (s, 1H), 9.07 (bs, 1H); HRFABMS *m*/*e* calcd. for $C_{44}H_{64}N_{10}NaO_8SSi_2$ (MNa^+): 971.4066; found: 971.4061.

N^6-*Benzoyl-5′*-O-tert-*butyldimethylsilyl-3′*-O-*methylene-2′-deoxyadenosynyl-(3′→5′)-3′*-O-tert-*butyldimethylsilyl-5′-deoxy-5′-thiothymidine* ***(6at)***: The procedure used to prepare 5′-thioformacetal dinucleotide analog **6tt** applied to nucleoside donor **5a** and to nucleoside acceptor **3t** gave 5′-thioformacetal dinucleotide analog **6at** (68%) as a pale yellow solid: ^{1}H NMR (400 MHz, $CDCl_3$) δ: 0.10 (s, 6H), 0.11 (s, 6H), 0.90 (s, 9H), 0.91 (s, 9H), 1.94 (d, *J* = 0.7 Hz, 3H), 2.18 (m, 1H), 2.30 (m, 1H), 2.64 (m, 1H), 2.74 (m, 1H), 2.88 (dd, *J* = 13.9, 5.8 Hz, 1H), 2.99 (dd, *J* = 13.9, 5.0 Hz, 1H), 3.81 (dd, *J* = 11.0, 3.4 Hz, 1H), 3.87 (dd, *J* = 10.9, 4.8 Hz, 1H), 4.05 (dd, *J* = 10.0, 5.2 Hz, 1H), 4.21 (bs, 1H), 4.31 (m, 1H), 4.65 (m, 1H), 4.78 (ABq, *J* = 11.5 Hz, 2H), 6.20 (t, 1H), 6.49 (dd, *J* = 7.6, 5.8 Hz, 1H), 7.27 (d, *J* = 0.9 Hz, 1H), 7.53 (m, 2H), 7.61 (m, 1H), 8.03 (m, 2H), 8.31 (s, 1H), 8.35 (bs, 1H), 8.81 (s, 1H), 9.03 (bs, 1H); ^{13}C NMR (100 MHz, $CDCl_3$) δ: 12.53, 17.82, 18.23, 25.61, 25.84, 32.22, 38.00, 40.33, 63.10, 72.23, 73.54, 77.17, 84.77, 84.81, 85.27, 85.55, 111.16, 123.56, 128.21, 128.46, 132.50, 133.54, 135.34, 141.32, 149.76, 150.40, 151.60, 152.31, 163.94, 165.14; HRFABMS *m*/*e* calcd. for $C_{40}H_{60}N_7O_8SSi_2$ (MH^+): 854.3763; found: 854.3760.

5′-O-tert-*Butyldimethylsilyl-3′*-O-*methylenethymidylyl-(3′→5′)-N^6-benzoyl-3′*-O-tert-*butyldimethylsilyl-2′,5′-dideoxy-5′-thioadenosine* ***(6ta)***: The procedure used to prepare 5′-thioformacetal dinucleotide analog **6tt** applied to nucleoside donor **5t** and to nucleoside acceptor **3a** gave 5′-thioformacetal dinucleotide analog **6ta** (51%) as a pale yellow solid: ^{1}H NMR (400 MHz, $CDCl_3$) δ: 0.10 (s, 6H), 0.14 (s, 3H), 0.15 (s, 3H), 0.91 (s, 9H), 0.93 (s, 9H), 1.88 (d, *J* = 1.0 Hz, 3H), 1.95 (m, 1H), 2.47 (m, 1H), 2.89–3.08 (m, 4H), 3.74 (dd, *J* = 11.3, 2.5 Hz, 1H), 3.83 (dd, *J* = 11.3, 3.0 Hz, 1H), 4.03 (m, 1H), 4.18 (m, 1H), 4.38 (d, *J* = 6.0 Hz, 1H), 4.62–4.69 (m, 3H), 6.22 (dd, *J* = 8.6, 5.5 Hz, 1H), 6.45 (t, 1H), 7.44 (d, *J* = 1.2 Hz, 1H), 7.49 (m, 2H), 7.56 (m, 1H), 8.05 (m, 2H), 8.29 (s, 1H), 8.81 (s, 1H), 9.63 (bs, 1H); ^{13}C NMR (100 MHz, $CDCl_3$) δ: 12.40, 17.91, 18.27, 25.70, 25.87, 32.44, 37.90, 39.81, 63.43, 74.23, 74.57, 76.47, 84.73, 84.82, 84.93, 86.75, 110.92, 123.89, 128.06, 128.21, 128.56, 128.61, 128.90, 132.58, 133.36, 135.19, 142.14, 148.59, 150.48, 152.42, 163.83, 164.03; HRFABMS *m*/*e* calcd. for $C_{40}H_{59}N_7NaO_8SSi_2$ (MNa^+): 876.3582; found: 876.3580.

5′-O-tert-Butyldimethylsilyl-3′-O-methylenethymidylyl-(3′→5′)-N^4-benzoyl-3′-O-tert-butyldimethylsilyl-2′,5′-dideoxy-5′-thiocytidine ***(6tc)***: The procedure used to prepare 5′-thioformacetal dinucleotide analog **6tt** applied to nucleoside donor **5t** and to nucleoside acceptor **3c** gave 5′-thioformacetal dinucleotide analog **6tc** (58%) as a pale yellow solid: ^{1}H NMR (400 MHz, $CDCl_3$) δ: 0.09 (s, 6H), 0.13 (s, 6H), 0.90 (s, 9H), 0.93 (s, 9H), 1.92 (d, *J* = 1.1 Hz, 3H), 2.04 (m, 1H), 2.15 (m, 1H), 2.43 (m, 1H), 2.61 (m, 1H), 2.88 (dd, *J* = 13.7, 6.1 Hz, 1H), 2.97 (dd, *J* = 13.7, 4.9 Hz, 1H), 3.80 (dd, *J* = 11.3, 2.6 Hz, 1H), 3.88 (dd, *J* = 11.3, 3.1 Hz, 1H), 4.14 (m, 2H), 4.24 (m, 1H), 4.44 (d, 1H), 4.75 (ABq, *J* = 11.6 Hz, 2H), 6.22 (t, 1H), 6.28 (dd, *J* = 8.6, 5.5 Hz, 1H), 7.46 (d, *J* = 1.2 Hz, 1H), 7.52 (m, 2H), 7.62 (m, 2H), 7.91 (m, 2H), 8.12 (d, *J* = 7.3 Hz, 1H), 8.35 (b, 1H), 8.90 (b, 1H); ^{13}C NMR (100 MHz, $CDCl_3$) δ: 12.44, 17.85, 18.27, 25.63, 25.86, 32.41, 37.85, 41.47, 63.46, 72.15, 73.45, 84.78, 85.02, 86.21, 87.21, 96.58, 110.89, 127.84, 128.86, 132.79, 133.17, 135.09, 144.42, 150.28, 162.15, 163.80; HRFABMS *m*/*e* calcd. for $C_{39}H_{60}N_5O_9SSi_2$ (MH^+): 830.3650; found: 830.3654.

5′-O-tert-*Butyldimethylsilyl-3′*-O-*methylenethymidylyl-(3′→5′)*-N^2-*isobutyryl-3′*-O-tert-*butyldimethylsilyl-2′,5′-dideoxy-5′-thioguanosine* ***(6tg)***: The procedure used to prepare 5′-thioformacetal dinucleotide analog **6tt** applied to nucleoside donor **5t** and to nucleoside acceptor **3g** gave 5′-thioformacetal dinucleotide analog **6tg** (30%) as a pale yellow solid: ^{1}H NMR (400 MHz, $CDCl_3$) δ: 0.11 (s, 6H), 0.12 (s, 6H), 0.90 (s, 9H), 0.92 (s, 9H), 1.25 (d, 3H), 1.26 (d, 3H), 1.92 (s, 3H), 1.97 (m, 1H), 2.39 (m, 2H), 2.68 (m, 2H), 2.83 (dd, *J* = 14.1, 5.9 Hz, 1H), 2.94 (dd, *J* = 14.0, 5.2 Hz, 1H), 3.76 (dd, *J* = 11.2, 2.2 Hz, 1H), 3.84 (dd, *J* = 11.2, 2.6 Hz, 1H), 4.07 (m, 1H), 4.10 (m, 1H), 4.35 (m, 1H), 4.46 (dd, *J* = 9.9, 4.6 Hz, 1H), 4.62 (s, 2H), 6.24 (m, 2H), 7.48 (s, 1H), 7.87 (s, 1H), 9.10 (bs, 2H); HRFABMS *m*/*e* calcd. for $C_{37}H_{62}N_7O_9SSi_2$ (MH^+): 836.3868; found: 836.3871.

5′-O-*Dimethoxytrityl-3′*-O-*methylenethymidylyl-(3′→5′)-3′*-O-tert-*butyldimethylsilyl-5′-deoxy-5′-thiothymidine* ***(15)***: The procedure used to prepare 5′-thioformacetal dinucleotide analog **6tt** applied to nucleoside donor **14** (10) and to nucleoside acceptor **3t** gave 5′-thioformacetal dinucleotide analog **15** (58%) as a pale yellow solid: ^{1}H NMR (400 MHz, $CDCl_3$) δ: 0.11 (s, 6H), 0.12 (s, 6H), 0.90 (s, 9H), 0.92 (s, 9H), 1.25 (d, 3H), 1.26 (d, 3H), 1.92 (s, 3H), 1.97 (m, 1H), 2.39 (m, 2H), 2.68 (m, 2H), 2.83 (dd, *J* = 14.1, 5.9 Hz, 1H), 2.94 (dd, *J* = 14.0, 5.2 Hz, 1H), 3.76 (dd, *J* = 11.2, 2.2 Hz, 1H), 3.84 (dd, *J* = 11.2, 2.6 Hz, 1H), 4.07 (m, 1H), 4.10 (m, 1H), 4.35 (m, 1H), 4.46 (dd, *J* = 9.9, 4.6 Hz, 1H), 4.62 (s, 2H), 6.24 (m, 2H), 7.48 (s, 1H), 7.87 (s, 1H), 9.10 (bs, 2H); HRFABMS *m*/*e* calcd. for $C_{37}H_{62}N_7O_9SSi_2$ (MH^+): 836.3868; found: 836.3871.

Preparation of 5′-thioformacetal trinucleotide analog 23

3′-O-*Methylthiomethylthymidine* ***(16)***: *p*-Toluenesulfonic acid monohydrate (444 mg, 2.33 mmol) was added to a 0°C solution of 5′-*O*-dimethoxytrityl-3′-*O*-methylthiomethylthymidine **14** (10) (596 mg, 0.99 mmol) in dichloromethane (7 mL) and methanol (3 mL). After being stirred at 0°C for 15 min, the reaction mixture was treated with saturated aqueous sodium bicarbonate and extracted with dichloromethane. The organic layer was dried ($MgSO_4$) and evaporated. Flash chromatography of the residue (silica gel; hexane/EtOAc (10:90)) afforded primary alcohol **16** (252 mg, 85%) as a

© 1999 NRC Canada

white solid: ^{1}H NMR (400 MHz, $CDCl_3$) δ: 1.90 (s, 3H), 2.16 (s, 3H), 2.35 (m, 2H), 3.01 (bs, 1H), 3.81 (m, 1H), 3.92 (m, 1H), 4.10 (m, 1H), 4.54 (m, 1H), 4.66 (ABq, *J* = 11.7 Hz, 2H), 6.18 (t, 1H), 7.45 (s, 1H), 9.35 (bs, 1H).

5′-S-*Acetyl-3′*-O-*methylthiomethyl-5′-deoxy-5′-thiothymidine (**17**)*: Diisopropyl azodicarboxylate (0.33 mL, 1.6 mmol) was added to a 0°C solution of triphenylphosphine (434 mg, 1.6 mmol) in THF (4 mL). The mixture was stirred for 30 min at 0°C. A solution of 3′-*O*-methylthiomethylthymidine (**16**) (200 mg, 0.66 mmol) and thiolacetic acid (0.12 mL, 1.6 mmol) in THF (2 mL) was added, and the reaction mixture was stirred for 30 min at 0°C and 80 min at room temperature. The volatiles were then evaporated, and flash chromatography of the residue (silica gel; hexane/EtOAc (40/60)) afforded thioester **17** (228 mg, 96%) as a colorless gum: ^{1}H NMR (400 MHz, $CDCl_3$) δ: 1.96 (s, 3H), 2.00 (m, 1H), 2.16 (s, 3H), 2.41 (s, 3H), 2.45 (m, 1H), 3.25 (d, 2H), 4.12 (m, 1H), 4.25 (m, 1H), 4.64 (ABq, *J* = 11.7 Hz, 2H), 6.20 (t, 1H), 7.24 (s, 1H), 9.40 (bs, 1H); MS (CI): 361 (MH^+), 235.

5′-S-*Acetyl-3′*-O-*methylene-5′-deoxy-5′-thiothymidylyl-(3′→5′)*-N^6-*benzoyl-3′*-O-tert-*butyldimethylsilyl-2′,5′-dideoxy-5′-thioadenosine (**18**)*: The procedure used to prepare 5′-thioformacetal dinucleotide analog **6tt** applied to nucleoside donor **17** and to nucleoside acceptor **3a** gave 5′-thioformacetal dinucleotide analog **18** (33%) as a beige solid: ^{1}H NMR (400 MHz, $CDCl_3$) δ: 0.14 (s, 3H), 0.15 (s, 3H), 0.93 (s, 9H), 1.91 (d, *J* = 1.1 Hz, 3H), 2.05 (m, 1H), 2.35 (m, 1H), 2.37 (s, 3H), 2.48 (m, 1H), 2.91–3.02 (m, 3H), 3.18 (m, 2H), 4.03 (m, 1H), 4.17 (m, 2H), 4.64 (m, 3H), 6.10 (dd, *J* = 8.0, 5.9 Hz, 1H), 6.45 (t, 1H), 7.18 (d, *J* = 1.2 Hz, 1H), 7.49 (m, 2H), 7.56 (m, 1H), 8.05 (m, 2H), 8.31 (s, 1H), 8.81 (s, 1H), 9.63 (bs, 1H); ^{13}C NMR (100 MHz, $CDCl_3$) δ: 12.43, 17.86, 25.65, 31.19, 31.46, 32.44, 37.05, 39.78, 72.55, 74.13, 74.57, 77.97, 82.36, 84.62, 85.08, 86.60, 111.21, 123.75, 128.33, 128.41, 132.51, 133.44, 135.09, 142.23, 149.88, 150.39, 151.54, 152.17, 163.95, 165.40, 194.42; HRFABMS *m/e* calcd. for $C_{36}H_{48}N_7O_8S_2Si$ (MH^+): 798.2775; found: 798.2778.

3′-O-*Methylene-5′-deoxy-5′-thiothymidylyl-(3′→5′)*-N^6-*benzoyl-3′*-O-tert-*butyldimethylsilyl-2′,5′-dideoxy-5′-thioadenosine (**19**)*: An aqueous sodium hydroxide solution (1.0 N; 0.94 mL, 0.94 mmol) was added to a solution of thioester **18** (237 mg, 0.30 mmol) in methanol/THF (50/50) (5 mL). The reaction mixture was stirred at 0°C for 1 h before EtOAc was added. The organic phase was washed with 5% aqueous $NaHCO_3$, water, and brine and then dried ($MgSO_4$). Evaporation and flash chromatography of the residue (silica gel; chloroform/acetone (60:40)) afforded thiol **19** (112 mg, 49%) as a pale beige solid: ^{1}H NMR (400 MHz, $CDCl_3$) δ: 0.14 (s, 3H), 0.15 (s, 3H), 0.94 (s, 9H), 1.54 (t, 1H), 1.88 (s, 3H), 1.90 (m, 1H), 2.08 (m, 1H), 2.35 (m, 1H), 2.48 (m, 1H), 2.77 (m, 1H), 2.90–3.04 (m, 3H), 4.00 (m, 1H), 4.17 (m, 1H), 4.32 (m, 1H), 4.67 (m, 3H), 6.13 (t, 1H), 6.44 (t, 1H), 7.28 (d, 1H), 7.49 (m, 2H), 7.58 (m, 1H), 8.05 (m, 2H), 8.29 (s, 1H), 8.82 (s, 1H), 9.61 (bs, 1H), 9.96 (bs, 1H); HRFABMS *m/e* calcd. for $C_{34}H_{46}N_7O_7S_2Si$ (MH^+): 756.2669; found: 756.2666.

N^4-*Benzoyl-5′*-O-*dimethoxytrityl-3′*-O-*methylthiomethyl-2′-deoxycytidine (**21**)*: A mixture of N^4-benzoyl-5′-O-dimethoxytrityl-2′-deoxycytidine (9) (**20**) (5.84 g, 9.2 mmol), 2,6-lutidine (3.5 mL, 30 mmol), dimethyl sulfide (18.4 mL, 250 mmol) and benzoyl peroxide (24.2 g, 100 mmol) in acetonitrile (130 mL) and dichloromethane (130 mL) was stirred at room temperature for 5 h. Ethyl acetate was then added, and the reaction mixture was washed with water, saturated aqueous ammonium chloride, and brine. The organic layer was dried ($MgSO_4$) and evaporated. Flash chromatography of the residue (silica gel; hexane/EtOAc (25:75)) afforded methylthiomethyl ether **21** (3.77 g, 59%) as a white solid: ^{1}H NMR (400 MHz, $CDCl_3$) δ: 2.05 (s, 3H), 2.28 (m, 1H), 2.73 (m, 1H), 3.41 (dd, 1H), 3.53 (dd, 1H), 3.80 (s, 6H), 4.21 (m, 1H), 4.59 (ABq, 2H), 4.63 (m, 1H), 6.25 (t, 1H), 6.87 (m, 4H), 7.29 (m, 8H), 7.41 (m, 2H), 7.52 (m, 2H), 7.61 (m, 1H), 7.98 (d, 2H), 8.36 (d, 1H).

N^4-*Benzoyl-5′*-O-*dimethoxytrityl-3′*-O-*methylene-2′-deoxycytidylyl-(3′→5′)-3′*-O-*methylene-5′-deoxy-5′-thiothymidylyl-(3′→5′)*-N^6-*benzoyl-3′*-O-tert-*butyldimethylsilyl-2′,5′-dideoxy-5′-thioadenosine (**22**)*: The procedure used to prepare 5′-thioformacetal dinucleotide analog **6tt** applied to nucleoside donor **21** and to dinucleotide acceptor **19** gave 5′-thioformacetal trinucleotide analog **22** (18%) as a beige solid. This compound was purified by flash chromatography (silica gel; dichloromethane/acetone/triethylamine (60:38:2)) followed by preparative thin layer chromatography (silica gel; dichloromethane/acetone/triethylamine (60:38:2)): ^{1}H NMR (400 MHz, $CDCl_3$) δ: 0.13 (s, 6H), 0.92 (s, 9H), 1.87 (s, 3H), 2.09 (m, 1H), 2.22 (m, 1H), 2.35 (m, 1H), 2.50 (m, 1H), 2.77 (m, 3H), 2.97 (m, 3H), 3.39 (m, 1H), 3.47 (m, 1H), 3.78 (s, 6H), 4.08 (m, 1H), 4.16 (m, 1H), 4.19 (m, 1H), 4.24 (m, 1H), 4.51 (m, 1H), 4.64 (m, 5H), 6.09 (t, 1H), 6.21 (t, 1H), 6.43 (t, 1H), 6.85 (d, 4H), 7.20–7.60 (m, 19H), 7.88 (m, 2H), 8.05 (m, 2H), 8.22 (d, 1H), 8.28 (s, 1H), 8.70 (bs, 1H), 8.78 (s, 1H), 9.29 (bs, 1H), 9.45 (bs, 1H); ^{13}C NMR (100 MHz, $CDCl_3$) δ: 12.46, 18.42, 26.09, 32.14, 33.37, 36.82, 39.43, 39.80, 55.43, 72.79, 73.16, 75.49, 75.52, 76.91, 79.43, 84.22, 84.86, 85.21, 85.74, 86.03, 87.49, 87.73, 96.94, 111.07, 113.93, 126.11, 127.64, 128.62, 128.92, 128.97, 129.14, 129.19, 129.29, 130.84, 130.87, 133.02, 133.43, 136.28, 136.35, 136.51, 143.73, 144.97, 145.47, 151.21, 152.47, 152.75, 154.85, 163.51, 164.19, 164.26,165.93; HRFABMS *m/e* calcd. for $C_{72}H_{80}CsN_{10}O_{14}S_2Si$ (MCs^+): 1533, 4121; found: 1533.4118.

5′-O-*Dimethoxytrityl-3′*-O-*methylene-2′-deoxycytidylyl-(3′→5′)-3′*-O-*methylene-5′-deoxy-5′-thiothymidylyl-(3′→5′)-3′*-O-tert-*butyldimethylsilyl-2′,5′-dideoxy-5′-thioadenosine (**23**)*: A solution of trinucleotide analog **22** (42.3 mg, 30 μmol) in dioxane (2 mL) and concentrated aqueous ammonium hydroxide (1 mL) was stirred at room temperature for 2 days. The volatiles were then evaporated, and water was added. The resulting suspension was extracted twice with 2-butanol, and the combined organic phases were washed successively with water and brine and evaporated. The residue thus obtained was triturated in acetone and filtered. Evaporation of the filtrate and purification of the residue by preparative thin layer chromatography (silica gel; dichloromethane/methanol (92:8)) afforded base-deprotected

© 1999 NRC Canada

trinucleotide analog **23** (6.9 mg, 19%) as a white solid: ^{1}H NMR (400 MHz, acetone-d_6) δ: 0.17 (s, 3H), 0.18 (s, 3H), 0.94 (s, 9H), 1.80 (s, 3H), 2.21 (m, 1H), 2.32 (m, 1H), 2.42 (m, 1H), 2.54 (m, 1H), 2.90 (m, 3H), 3.02 (m, 2H), 3.12 (m, 1H), 3.39 (m, 2H), 3.77 (s, 6H), 4.11 (m, 3H), 4.41 (m, 1H), 4.64 (m, 1H), 4.78 (m, 5H), 5.70 (d, 1H), 6.21 (t, 1H), 6.27 (t, 1H), 6.44 (t, 1H), 6.79 (bs, 3H), 6.88 (d, 4H), 7.22 (m, 1H), 7.33 (m, 7H), 7.47 (m, 3H), 7.81 (d, 1H), 8.21 (s, 1H), 8.23 (s, 1H), 10.40 (bs, 1H); HRFABMS *m*/*e* calcd. for $C_{58}H_{72}CsN_{10}O_{12}S_2Si$ (MCs^+): 1325.3596; found: 1325.3602.

References

1. (*a*) E. Uhlmann and A. Peyman. Chem. Rev. **90**, 543 (1990); (*b*) J.F. Milligan, M.D. Matteucci, and J.C. Martin. J. Med. Chem. **36**, 1923 (1993).
2. R.S. Varma. Synlett, 621 (1993).
3. (*a*) M.D. Matteucci, K.-Y. Lin, S. Butcher, and C. Moulds. J. Am. Chem. Soc. **113**, 7767 (1991); (*b*) Y. Ducharme and K.A. Harrison. Tetrahedron Lett. **36**, 6643 (1995).
4. (*a*) T. Benneche and K. Undheim. Acta Chem. Scand. B, **37**, 93 (1983); (*b*) T. Benneche, P. Strande, and K. Undheim. Synthesis, 762 (1983).
5. S. Zavgorodny, M. Polianski, E. Besidsky, V. Kriukov, A. Sanin, M. Pokrovskaya, G. Gurskay, H. Lönnberg, and A. Azhayev. Tetrahedron Lett. **32**, 7593 (1991).
6. P.M. Pojer and S.J. Angyal. Tetrahedron Lett. **17**, 3067 (1976).
7. K.K. Ogilvie. Can. J. Chem. **51**, 3799 (1973).
8. S.H. Kawai, D. Wang, and G. Just. Can. J. Chem. **70**, 1573 (1992).
9. G.S. Ti, B.L. Gaffney, and R.A. Jones. J. Am. Chem. Soc. **104**, 1316 (1982).
10. M. Matteucci. Tetrahedron Lett. 31, 2385 (1990).
11. J.C. Medina, M. Salomon, and K.S. Kyler. Tetrahedron Lett. **29**, 3773 (1988).

© 1999 NRC Canada

Mechanism of silylene extrusion reaction in cyclic polysilane via triplet energy surface: a direct MO dynamics study

Hiroto Tachikawa, Yoshihisa Yamada, and Tetsuji Iyama

Abstract: Dynamics of photoreaction of permethylcycloheptasilane $(Me_2Si)_7$ on the triplet state surface, $(Me_2Si)_7$ (T_1) $\rightarrow$ $(Me_2Si)_6$ + Me_2Si (T_1), has been investigated by means of the direct MO dynamics method in order to elucidate mechanism of silylene extrusion from the Si-ring following the triplet energy transfer from a carbonyl compound. Full dimensional potential energy surface calculated at the PM3 method was employed in the dynamics calculation: the total energy and energy gradient on each atom were calculated at each time step during the reaction. The calculations showed that the seven-membered Si-ring is spontaneously changed to the six-membered ring without activation barrier on T_1 surface. The photoreaction of $(Me_2Si)_7$ is significantly fast (reaction is completed within 1.0 ps), although heavy molecule (silylene radical) is dissociated. This is due to the fact that the T_1 surface is strongly repulsive for the coordinate between the silylene and the Si-ring. The mechanism of the silylene extraction from the Si-ring was discussed on the basis of theoretical results.

Key words: direct MO dynamics, polysilane, photoreaction, permethylcycloheptasilane, silylene.

Résumé : Faisant appel de la méthode de la dynamique d'OM directe, on a étudié la dynamique de la photoréaction du perméthylcycloheptasilane $(Me_2Si)_7$ sur la surface de l'état triplet, $(Me_2Si)_7$ (T_1) $\rightarrow$ $(Me_2Si)_6$ + Me_2Si (T_1) dans le but d'élucider le mécanisme de l'extrusion du silylène du cycle de silicium à la suite d'un transfert d'énergie triplet à partir d'un composé carbonylé. Pour les calculs dynamiques, on a utilisé une surface d'énergie potentielle à pleine dimension calculée par la méthode PM3: l'énergie totale et le gradient d'énergie de chaque atome ont été évaluées pour chaque étape temporelle de la réaction. Les calculs ont montré que, sur la surface T_1, le cycle à sept chaînons de silicium se transforme spontanément en un cycle à six chaînons, sans barrière d'activation. La photoréaction du $(Me_2Si)_7$ est assez rapide (la réaction est complète en dedans de 1,0 ps), même s'il se produit une dissociation d'une molécule lourde (radical silylène). Ceci est dû au fait que la surface T_1 est fortement répulsive pour la coordination entre le silylène et le cycle de silicium. On discute du mécanisme d'extraction du silylène du cycle de silicium sur la base des résultats théoriques.

Mots clés : dynamique d'OM directe, polysilane, photoréaction, perméthylcyclopentasilane, silylène.

[Traduit par la Rédaction]

1. Introduction

Polysilanes are σ-conjugated polymers composed of Si-Si backbone and organic side groups. Photochemical property and electronic structure of polysilanes have received much attention from both experimental and theoretical points of view, because they play an important role in photoresists, one-dimensional conductors, high-density optical data storage materials (1). Current interest has been focused on the localization and delocalization mechanism of electron (hole) in polymer chain (2–4) and on the photoreaction of polysilanes. (5).

Cyclic polysilane $(R_2Si)_n$ (where R is alkyl-group) is one of the photosensitive polysilanes in which silylene extrusion occurs in the excited electronic state. Also, it is known that $(R_2Si)_n$ is an intermediate in synthesis of the oligosilanes. Studying of the reaction of the cyclosilanes in the excited electronic state provides detailed information on the photochemistry of polysilane.

Permethylcyclohexasilane $(Me_2Si)_6$ is one of the cyclic polysilanes, and the photoreaction causes a silylene extrusion reaction expressed by

$$(Me_2Si)_6 \xrightarrow{h\nu} (Me_2Si)_5 + Me_2Si$$

Drahnak et al. (5) reported that the silylene extrusion reaction is occurred in 3-methylpentane/methylcyclohexane matrices at 77 K. They detected the products (Me_2Si and $(Me_2Si)_5$) by means of UV-visible and infrared spectroscopes. The reaction was also observed in argon matrix at 77 K. It has been considered from the experiment that this reaction mainly proceeds via singlet state (5). This originates only from the experiment that silylene radical Me_2Si has a singlet electronic state. However, a recent experiment (6) showed that a cyclic polysilane $(Me_2Si)_6$ quenches effi-

Received October 28, 1998.

H. Tachikawa,[1] Y. Yamada, and T. Iyama. Division of Molecular Chemistry, Graduate School of Engineering, Hokkaido University, Sapporo 060-8628, Japan.

[1]Author to whom correspondence may be addressed. Fax: +81 11706-7897. e-mail: hiroto@eng.hokudai.ac.jp

© 1999 NRC Canada

ciently the triplet excited states of carbonyl compound $^3(R_2C{=}O)$ in benzene. The triplet energy transfer can be expressed by

$$(Me_2Si)_6 + {}^3(R_2C{=}O) \rightarrow (Me_2Si)_6\ (T_1) + {}^1(R_2C{=}O)$$

where $^3(R_2C{=}O)$ and $^1(R_2C{=}O)$ are carbonyl compounds at the triplet and singlet states, respectively. As a course of reaction of $(Me_2Si)_6$ (T_1), the silylene extrusion reaction,

$$(Me_2Si)_6\ (T_1) \rightarrow (Me_2Si)_5 + Me_2Si$$

may consequently take place on the triplet state surface as well as on singlet state. It is experimentally known that the silylene radical is also generated from photoirradiation of other number of rings, namely, the photoirradiation of the cyclosilanes $(Me_2Si)_n$ (n = 5 and 7) gives the smaller sized ring $(Me_2Si)_{n-1}$ and Me_2Si.

In previous papers, we investigated the photoreactions of $(Me_2Si)_n$ (n = 5 and 6) at triplet state by means of direct MO dynamics method (7, 8). The calculations show that the extrusion reaction spontaneously occurred on the T_1 state and is completed within 1.0 ps, which is much faster in spite of the heavy atom (silylene radical Me_2Si) extrusion processes. This is due to the fact that the bonding nature of Si—Si bond is strongly changed to a repulsive surface in the excited electronic state. Also, we showed that the reaction via S_1 state has an activation barrier.

In the present study, in order to obtain the general feature of the photoreactions of cyclic polysilanes in the excited electronic state, we extend direct MO dynamics calculation to the similar photochemical reaction of $(Me_2Si)_7$, which possesses a less steric energy than for reactions with n = 5 and 6. The reaction is expressed by

$$[1] \qquad (Me_2Si)_7\ (T_1) \rightarrow (Me_2Si)_6 + Me_2Si$$

For this reaction system, Ishikawa and Kumada (9) reported that the photochemical reaction of $(Me_2Si)_7$ was observed in cyclohexane solution at 318 K as well as in $(Me_2Si)_6$. Studying reaction [1] would provide more detailed information on photochemistry of cyclic polysilanes.

2. Method of the calculations

Usually, the classical trajectory (10) is performed on an analytically fitted potential energy surface as previously carried out by us (11). However, it is not appropriate to predetermine the reaction surface of reaction [1] due to the large number of degrees of freedom ($3N - 6 = 57$ where N is number of atoms in the reaction system). Therefore, in the present study, we applied the direct trajectory calculation with all degrees of freedom (12). The energy gradients on all atoms were calculated at the PM3-MO level at each time step.

In the trajectory calculation, we used optimized geometry of $(Me_2Si)_7$ as an initial structure. At a starting point of the trajectory calculation, atomic velocities for all atoms were adjusted to give a temperature of 300 K. The potential energy (total energy) and energy gradients at each time step was calculated at the PM3-MO level (8). The program code to calculate the trajectory and the program for the dynamics calculation were created by our group (12).

In the calculation of the classical trajectory, we assumed that each atom moves as a classical particle on the PM3 multidimensional potential energy surfaces. The equations of motion for n atoms in a molecule are given by

$$m_i\, dv_{\mu i}/dt = F_{\mu i}$$

$$dx_{\mu i}/dt = v_{\mu i}$$

where $x_{\mu i}$ (μ = 1, 2, 3) are the three Cartesian coordinates of the ith atom with mass m_i, $F_{\mu i}$ values are the three components of the force acting on the ith atom. These equations were numerically solved by the Runge–Kutta method. No symmetry restriction was applied in the calculation of the gradients in the Runge–Kutta method. The time step size chosen was 0.2 fs. The drift of the total energy was confirmed to be less than 0.1% for an entire trajectory. It was also confirmed that the momentum of the center of mass and the angular momentum around the center of mass retained their initial value of zero. The present reaction system has a large degree of freedom ($3N - 6 = 57$), so that a backflow from the kinetic energy to the potential energy was not observed.

3. Results

A. Structures of $(Me_2Si)_7$ for the ground and excited electronic states

The structure of $(Me_2Si)_7$ in the ground state (S_0) is determined by the energy gradient method under no-symmetry restriction. Fully optimized structure is illustrated in Fig. 1. The distance of Si—Si atoms is calculated to be 2.4280 Å for all Si—Si bonds, while the angle of Si-Si-Si is 108.7°. These are normal angle and distance in cyclic silane. It should be noted that the interatomic distance between Si_2 and Si_3 atoms is calculated to be 3.9443 Å.

The structure for the excited electronic state (T_1 state) is fully optimized by the same manner. The result is illustrated in Fig. 1. The optimized structure for the triplet (T_1) state is much different from that of S_0 state. The interatomic distance between Si_2 and Si_3 atoms is calculated to be 2.4887 Å, which is significantly shorter than that of S_0 state (3.9443 Å). Furthermore, the angle of Si_2-Si_1-Si_3 at T_1 state is strikingly smaller than that at S_0 state (58.2° vs. 108.7°). These results suggest that the silylene radical (Me_2Si radical) can be dissociated from $(Me_2Si)_7$ and smaller Si ring $(Me_2Si)_6$ is formed at T_1 state. However, the silylene radical is not completely dissociated from $(Me_2Si)_6$, because the radical is weakly bound to $(Me_2Si)_6$ and forms an intermediate complex $(Me_2Si)_6...Me_2Si$.

B. Dynamics of reaction [1]

As described in the previous section, the PM3 calculations showed that the structure of $(Me_2Si)_7$ is strongly deformed at T_1 state. Also, it is expected that silylene radical is extruded from the ring. In this section, in order to elucidate the dynamics of the silylene extrusion reaction, the direct MO dynamics calculation is carried out for the triplet state surface. The initial geometry used in the dynamics calculation is chosen by the optimized structure of $(Me_2Si)_7$ obtained at S_0 state.

The results of the dynamics calculation are given in Fig. 2. Potential energy (PE) of the system calculated as a function of reaction time is plotted in Fig. 2*A*. PE is sud-

© 1999 NRC Canada

Fig. 1. Optimized structures of $(Me_2Si)_7$ in the ground state (S_0), and triplet state (T_1) calculated by PM3-CI method. Bond lengths and angles are in angstroms and degrees, respectively. Open and closed circles mean silicon and carbon atoms, respectively. Hydrogens in methyl group are omitted.

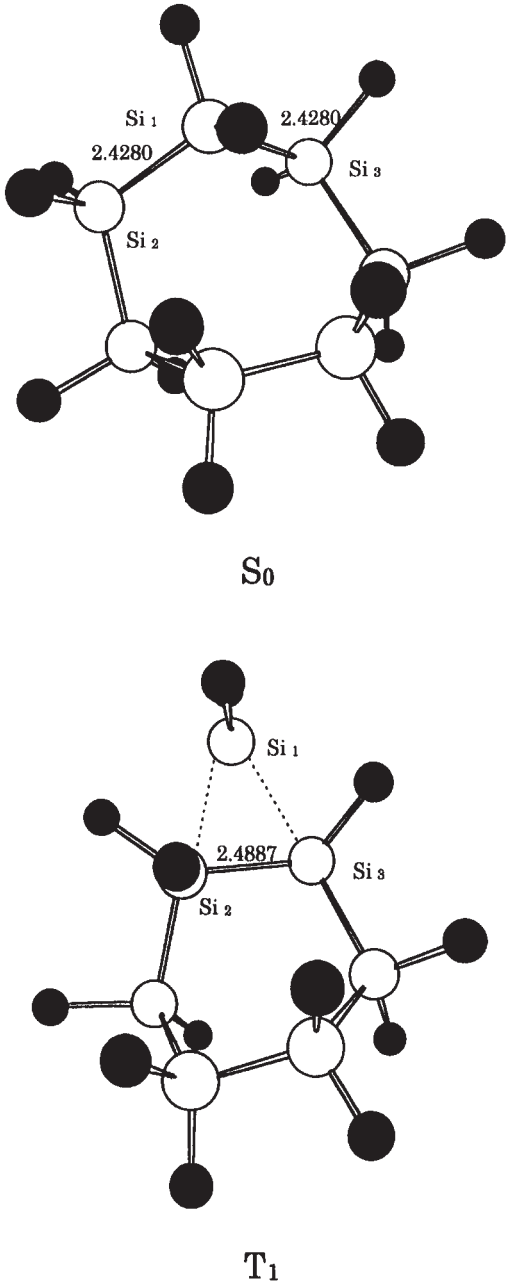

denly down in short time region (0.0–0.2 ps). The lowest energy is –17.3 kcal/mol with respect to the initial point at time zero. At the middle time region (0.2–1.0 ps), PE is gradually and slightly lowered. The interatomic distances calculated as a function of time are plotted in Fig. 2*B*. The distance between Si_1 and Si_2 is almost constant throughout, while a normal vibration of Si-Si stretching mode is observed around 2.50 Å. On the other hand, the interatomic distance between Si_2 and Si_3 is significantly changed: the distance is shortened from 3.90 to 2.50 Å. In addition, the

Fig. 2. Sample trajectory calculated by the direct PM3-MO dynamics method with T_1 potential energy surface. (*A*) Potential energy, (*B*) interatomic distances, and (*C*) angle of Si_2-Si_1-Si_3 versus reaction time.

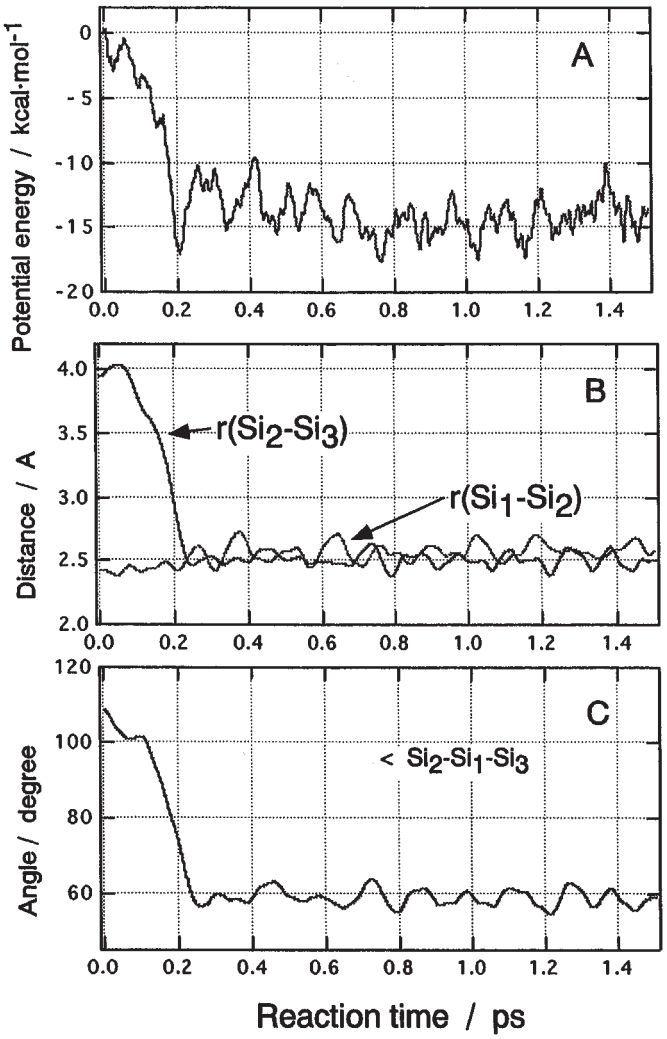

angle of Si_2-Si_1-Si_3 is largely changed from 108.0° to 60.0°. These results indicate strongly that seven-membered ring is spontaneously changed to six-membered ring on T_1 surface. As shown in Fig. 2, the silylene radical was not completely dissociated from the six-membered ring. Instead, the intermediate complex $(Me_2Si)_6$...Me_2Si is formed. This complex is precursor in reaction [1].

C. Bond alternation as a function of reaction time

A simple Mulliken population analysis is useful to describe the bonding nature in molecules. Therefore, Mulliken populations for all Si—Si bonds are monitored as a function of reaction time. The results are summarized in Table 1. A normal value of population between Si—Si bond in the ground state (S_0) is calculated to be 0.349, which is comparable to that of $(Me_2Si)_6$. The value for the Si_2—Si_3 bond is –0.040, which is close to zero, suggesting that there is no interaction between Si_2 and Si_3 atoms at S_0 state.

In contrast, the population of Si_1—Si_3 bond is a negative sign (–0.941) at T_1 state, meaning that the bond of Si_1—Si_3

© 1999 NRC Canada

Fig. 3. Snapshots of the structures of the system and spin orbitals in $(Me_2Si)_7$ on the triplet state surface.

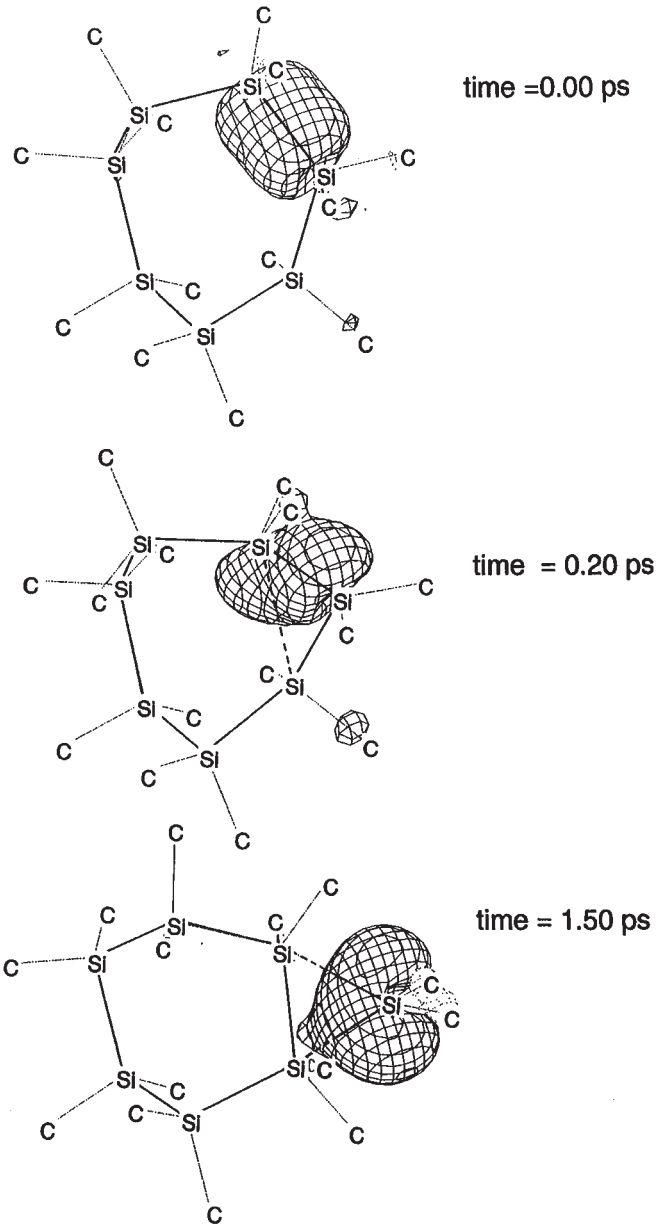

is strongly repulsive. This may cause the bond breaking for Si_1—Si_3 bond. The population of Si_1—Si_2 bond is calculated to be 0.254, which is close to the normal value of Si—Si bond (0.349). It should be emphasized that the bond population between Si_2 and Si_3 is not zero, but a positive value (0.036) in spite of the long separation (3.95 Å). After 1.50 ps (final stage of the reaction), the populations of Si_1—Si_2 and Si_1—Si_3 bonds are –0.436 and –0.253, respectively, meaning that Me_2Si can be dissociated from the ring. Thus, the population analysis also indicates that the silylene extrusion is spontaneously occurred on T_1 surface.

D. Spin orbitals

Snapshots of the structures and spin orbitals are illustrated in Fig. 3. At time zero, the spin orbital is localized on one of the Si—Si bonds as clearly seen in Fig. 3 (time = 0.0 ps). At time of 0.20 ps, the orbital is slightly expanded by the deformation of Si-skeleton. At time of 1.00 ps (figure is not given), the spin orbital concentrates to one of silylene groups so that unpaired electron is localized mainly on the Si atom. As seen in Fig. 3 (time = 1.50 ps), the spin orbital is composed of π-orbital of silylene radical, and the unpaired electron is fully localized on silylene group. The reaction is terminated at this point.

Table 1. Bond populations calculated as a function of reaction time.[a]

		Bond population		
State	Time/ps	Si_2—Si_3	Si_1—Si_2	Si_1—Si_3
S_0	0.0	–0.040	0.349	0.349
T_1	0.0	0.036	0.254	–0.941
	0.10	0.038	0.251	–0.826
	0.20	–0.090	0.261	–0.653
	0.50	0.244	–0.570	–0.106
	1.00	0.362	–0.433	–0.297
	1.50	0.366	–0.436	–0.253

[a]Dissociating silylere is composed of Si_1 atom.

4. Discussion

In previous papers (7, 8), we proposed reaction model on the photoinduced silylene extrusion reaction in $(Me_2Si)_6$ (T_1) following the triplet energy transfer from carbonyl compound on the basis of direct MO dynamics calculation. The potential energy surface for T_1 state calculated by us is favored for the silylene extrusion to occur: T_1 surface is strongly repulsive for interaction between Me_2Si and $(Me_2Si)_5$. Hence, the silylene extrusion proceeds efficiently on T_1 surface. In the present study, we have extended the direct dynamics calculation to a larger cyclic silane compound $(Me_2Si)_7$. The present results are essentially similar to that obtained for $(Me_2Si)_6$ system (7). This means that the model presented by us may be general in photoreaction of cyclic polysilane compounds.

Here, let us discuss the photoreaction mechanism of $(Me_2Si)_7$ following the triplet energy transfer in terms of the orbital interaction. Schematic representation of the orbital interaction on the Si_2-Si_1-Si_3 moiety during the photoreaction process is illustrated in Fig. 4. In the ground state (S_0), the highest occupied molecular orbital (HOMO) shows that all Si—Si bonds have a bonding nature, suggesting that the regular cyclic structure is most stable. When the triplet energy transfer from $^3(R_2C{=}O)$ to the polysilane takes place, the electronic state of $(Me_2Si)_7$ is suddenly changed from S_0 to T_1 state. At the T_1 state, the orbital interaction of Si—Si bonds is composed of anti-bonding type, and the unpaired electrons are localized on one of Si—Si bonds. After that, the silylene extrusion occurs on this state. The interaction between Si_1 and Si_j (j = 2 or 3) is composed of strong anti-bonding interaction. Magnitude of the anti-bonding interaction may be enough for the elongation of Si_1—Si_j bond to occur. Accompanying the slight elongation of Si_1—Si_j bond, the Si_2—Si_3 bond is newly formed because of the same orbital phase. After more elongation of the Si_1—Si_j bonds, the

© 1999 NRC Canada

Fig. 4. Schematic representation of orbital interactions of the Si atoms in the T_1 excited electronic state. $^3(R_2C{=}O)$ means a carbonyl compound at the triplet state (T_1).

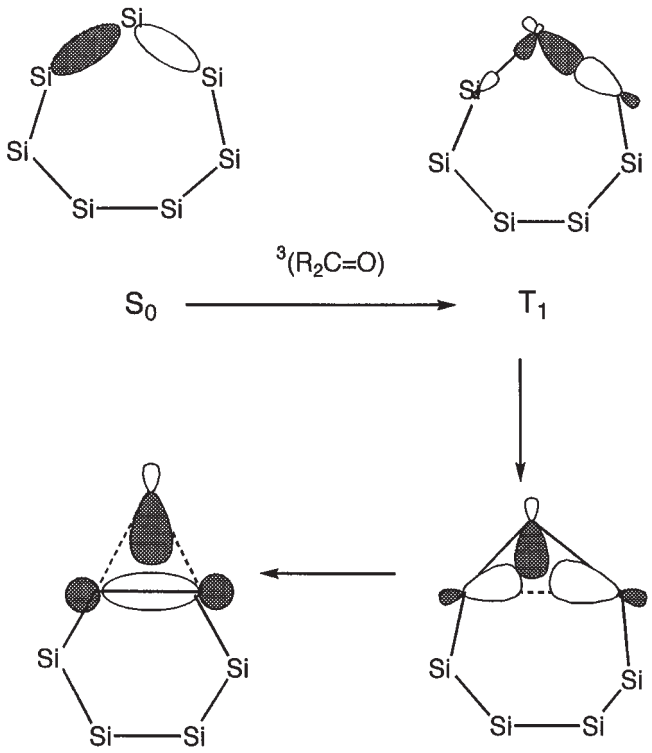

Si_2—Si_3 bond is completely formed, and silylene radical is dissociated from seven-membered ring. This mechanism is in reasonable agreement with our previous model for the photoreaction mechanism proposed for $(Me_2Si)_n$ (T_1) $\rightarrow$ $(Me_2Si)_{n-1}$ + Me_2Si (T_1) (where n = 5 and 6) (7, 8). The present calculation indicates that the silylene radical is also extruded from the seven-membered ring $(Me_2Si)_7$ at the T_1 state, and this reaction proceeds in terms of the same mechanism as that of $(Me_2Si)_6$.

From the basis of Woodward–Hoffmann selection rule, Ramsey suggested that both singlet and triplet excited states, denoted respectively by $^1(\sigma\sigma^*)$ and $^3(\sigma\sigma^*)$, correlate to silylene radical dissociation channel (14). This is consistent with the present model.

Several approximations to calculate the potential energy surface and to treat the reaction dynamics were introduced in the present study. Firstly, we assumed that $(Me_2Si)_7$ (T_1) has no excess energy at the initial point of the trajectory calculation (time = 0.0 ps). This may cause a slight change of lifetime for $(Me_2Si)_6$...Me_2Si intermediate in which the silylene radical weakly interacts with $(Me_2Si)_6$. Hence, the present calculation shows that the trajectory was trapped in the intermediate region, while the silylene radical did not escape from $(Me_2Si)_6$. The dissociation of Me_2Si may occur in the case of higher excess energy. This effect was not considered in the present calculations. It should be noted therefore that the present model is limited in the case of no excess energy. Furthermore, we did not consider the solvent effect in the dynamics calculation, although almost all experiments for reaction [1] have been carried out in condensed phase. The solvent effects may play an important role in the dissociation of Me_2Si from $(Me_2Si)_7$.

Secondary, we assumed PM3 multidimensional potential energy surface in the trajectory calculations throughout. A more accurate wave function may provide deeper insight in the dynamics. Despite several assumptions introduced here, the results enable us to obtain valuable information on the photoreaction process in $(Me_2Si)_7$.

Acknowledgment

The authors are indebted to the Computer Center at the Institute for Molecular Science (IMS) for the use of the computing facilities. This work was supported in part by a Grant-in-Aid for Research from the Ministry of Education, Science, Sports, and Culture of Japan.

References

1. R.D. Miller and J. Michl. Chem. Rev. **89**, 1359 (1989).
2. (*a*) H. Tachikawa. Chem. Phys. Lett. **265**, 455 (1997); (*b*) Chem. Phys. Lett. **281**, 221 (1997).
3. H. Tachikawa. J. Phys. Chem. A, **103**, 2501 (1999).
4. (*a*) S. Irie and M. Irie. Macromolecules, **30**, 7906 (1997); (*b*) J. Kumagai, H. Tachikawa, H. Yoshida, and T. Ichikawa. J. Phys. Chem. **100**, 16 777 (1996).
5. T.J. Drahnak, J. Michl, and R. West. J. Am. Chem. Soc. **101**, 5427 (1979).
6. L. Heisler, J.M. Hossenlopp, Y.P. Niu, M.G. Steinmets, and Y. Zhang. J. Photochem. Photobiol. A, **107**, 125 (1997).
7. H. Tachikawa. J. Organomet. Chem. **555**, 161 (1998).
8. Y. Yamada and H. Tachikawa. J. Photochem. Photobiol. A, **122**, 145 (1999).
9. M. Ishikawa and M. Kumada. J. Organometal. Chem. **42**, 325 (1972).
10. M. Karplus, R.N. Porter, and R.D. Sharma. J. Chem. Phys. **43**, 3259 (1965).
11. (*a*) H. Tachikawa. J. Chem. Phys. **108**, 3966 (1998); (*b*) Chem. Phys. **211**, 305 (1996); (*c*) J. Phys. Chem. **99**, 255 (1995).
12. (*a*) H. Tachikawa and M. Igarashi. J. Phys. Chem. A, **102**, 8648 (1998); (*b*) H. Tachikawa. J. Phys. Chem. A, **102**, 7065 (1998); (*c*) J. Phys. Chem. A, **101**, 7454 (1997).
13. (*a*) J.J.P. Stewart. J. Comput. Chem. **10**, 209 (1989); (*b*) J. Comput. Chem. **10**, 221 (1989); (*c*) M.J. Frisch, G.W. Trucks, M. Head-Gordon, P.M.W. Gill, M.W.Wong, J.B. Foresman, B.G. Johnson, H.B. Schlegel, M.A. Robb, E.S. Replogle, R. Gomperts, J.L. Andres, K. Raghavachari, J.S. Binkley, C. Gonzalez, R.L. Martin, D.J. Fox, D.J. Defrees, J. Baker, J.J.P. Stewart, and J.A. Pople. An ab-initio molecular orbital calculation program; Gaussian 92, Revision F.3. Gaussian, Inc., Pittsburgh, Pa. 1992.
14. B.G. Ramsey. J. Organomet. Chem. **67**, C67 (1974).

© 1999 NRC Canada

Polynuclear Co(II) and Cu(II) complexes of tetraacetylethane: $Cu^{II}_2(dpa)_2(tae)(O_2CCF_3)_2$, $\{[Cu^{II}_2(dpa)_2(tae)(4,4'\text{-bipy})](O_2CCF_3)_2\}_n$, and $[Co^{II}_2(dpa)_4(tae)](O_2CCH_3)_2(H_2O)_2$, dpa = 2,2′-dipyridylamine, tae = tetraacetylethane dianion

Yousheng Zhang, Steven R. Breeze, Suning Wang, John E. Greedan, N.P. Raju, and Lijuan Li

Abstract: The syntheses and structures of copper(II) and cobalt(II) complexes employing tetraacetylethane as the bridging ligand have been investigated. The reaction of $Cu(O_2CCF_3)_2$ with tetraacetylethane (tae) and 2,2′-dipyridylamine (dpa) yielded a dinuclear complex $Cu^{II}_2(dpa)_2(tae)(O_2CCF_3)_2$ (**1**), which has an extended hydrogen-bonded chain structure in the solid state. The reaction of 4,4′-dipyridyl (4,4′-bipy) with compound **1** resulted in the formation of a polymeric compound $\{[Cu^{II}_2(dpa)_2(tae)(4,4'\text{-bipy})](O_2CCF_3)_2\}_n$ (**2**), where the dinuclear unit is cross-linked by the 4,4′-dipyridyl ligand. The reaction of $Co(O_2CCH_3)_2$ with tetraacetylethane and 2,2′-dipyridylamine yielded a helical dinuclear complex $[Co^{II}_2(dpa)_4(tae)](O_2CCH_3)_2(H_2O)_2$ (**3**), which forms a hydrogen-bonded band architecture in the solid state. The three-dimensional structure of **3** has molecular sieve-like channels that host methanol molecules reversibly. While only either negligible or weak magnetic exchanges appear to be present in compounds **1** and **2**, there appears to be a significant ferromagnetic exchange in **3**, which is likely caused by orbital orthogonality of the Co(II) ions, as supported by the crystal structure and EHMO calculations.

Key words: cobalt, copper, polynuclear, tetraacetylethane complex, magnetism.

Résumé : On a réalisé la synthèse et on a examiné les structures des complexes de cuivre(II) et de cobalt(III) impliquant le tétraacétyléthane comme ligand de pont. La réaction du $Cu(O_2CCF_3)$ avec le tétraacétyléthane (tae) et la 2,2′-dipyridylamide (dpa) conduit à un complexe dinucléaire, $Cu(II)_2(dpa)_2(tae)(O_2CCF_3)_2$ (**1**), qui, à l'état solide, comporte une structure en chaîne avec liaison hydrogène étendue. La réaction du 4,4′-dipyridyle (4,4′-bipy) avec le composé **1** conduit à la formation d'un composé polymérique, $\{[Cu(II)_2(dpa)_2(tae)(4,4'\text{-bypy})](O_2CCF_3)_2\}_n$ (**2**), dans lequel l'unité dinucléaire est réticulée par le ligand 4,4′-dipyridyle. La réaction du $Co(O_2CCH_3)_2$ avec le tétraacétyléthane et la 2,2′-dipyridylamine fournit un complexe dinucléaire hélicoïdal, $[Co(II)_2(dpa)_4(tae)](O_2CCH_3)_2(H_2O)_2$ (**3**), qui, à l'état solide, donne lieu à une architecture en bande avec liaisons hydrogènes. La structure tridimensionnelle du composé **3** comporte des canaux semblables à ceux des tamis moléculaires qui permettent d'accueillir des molécules de méthanol de façon réversible. Même si on ne peut détecter que des échanges magnétiques faibles ou négligeables dans les composés **1** et **2**, il semble exister un échange ferromagnétique important dans le composé **3**; celui-ci découle vraisemblablement de l'orthogonalité de l'orbitale des ions Co(II) qui serait supportée par la structure cristalline et les calculs d'OM.

Mots clés : cobalt, cuivre, polynucléaire, complexe tétraacétyléthane, magnétisme.

[Traduit par la Rédaction]

Introduction

Polynuclear metal complexes containing paramagnetic metal ions are an important class of molecules because they not only provide the opportunity for the study of magnetic exchange mechanisms involving several metal ions, but also provide the fundamentals for the systematic assembly of extended structures that may have a long-range magnetic ordering (1). Previously, we studied the assembly of polynuclear copper(II) complexes by using amino alcohols or hydroxypyridines as the bridging ligands. We have found that antiferromagnetic exchanges are dominant in most of the amino alcohol or hydroxypyridine complexes (2). Recently, we explored the synthesis of polynuclear metal com-

Received November 4, 1998.

Y. Zhang, S.R. Breeze, and S. Wang.[1] Department of Chemistry, Queen's University, Kingston, ON K7L 3N6, Canada.
J.E. Greedan, N.P. Raju, and L. Li. Department of Chemistry, McMaster University, Hamilton, ON L8S 4M1, Canada.

[1]Author to whom correspondence may be addressed. Fax: (613) 545-6669. e-mail: wangs@chem.queensu.ca

 © 1999 NRC Canada

Fig. 1. The tae ligand.

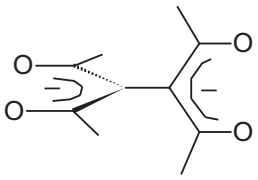

plexes by using the doubly deprotonated tetraacetylethane ligand (tae, Fig. 1). As demonstrated by previously reported Ni(II) and Cu(II) dinuclear complexes (3) that contain the tae ligand, steric constraint forces the two diketone portions of the tae ligand to be non-coplanar but about 90° to each other, which, when bonded to two metal ions, may promote ferromagnetic exchange via orthogonal orbitals (1*e*, 4). In addition, the ~90° twisting of the ligand could also promote the formation of dinuclear helical structures when bonded by two octahedral metal ions, which is also an area of much interest (5). In our studies we have obtained new copper(II) and cobalt(II) compounds containing the tae ligand with structures ranging from dimers, one-dimensional polymers, to chiral molecular squares (6). The common feature of these new compounds is that they all have extended structures in the solid state via either hydrogen bonds or covalent bonds, in contrast to the discrete dinuclear Ni(II) and Cu(II) molecules reported previously (3). We report herein the syntheses, structures, and properties of three new Co(II) and Cu(II) complexes containing the tae ligand.

Experimental section

All reactions were carried out by using standard Schlenk vacuum line techniques under nitrogen atmosphere. Tetraacetylethane was synthesized according to published procedures (7). All other chemicals were purchased from Aldrich Chemical Co. Elemental analyses were performed at Canadian Microanalytical Service. Ltd, Delta, B.C. The EPR spectra were recorded at 100 K on a Bruker 420 spectrometer. Magnetic susceptibility data were collected at 1 kG on a SQUID instrument from Quantum Design in the temperature range 2–300 K. Thermogravimetric analyses were performed on a Perkin–Elmer TGA-7 analyzer.

Synthesis of $Cu_2(tae)(dpa)_2(CF_3CO_2)_2$ (1)

$Cu(CF_3CO_2)_2$ (200 mg, 0.69 mmol) was dissolved in 15 mL of methanol. With stirring, tetracetylethane (68 mg, 0.35 mmol) was added to the flask. A green solution was obtained immediately. After the addition was complete, the mixture was stirred for 2 h, and 2,2′-dipyridylamine (118 mg, 0.69 mmol) was added to the solution. The solution immediately turned dark green. After being stirred for an additional 4 h, the solution was filtered and concentrated in vacuo to about 5 mL. Dark green thin plate crystals were harvested after the solution was kept standing at room temperature for 1 week. Yield 262 mg (84%); mp 215–220°C. Anal. calcd. for vacuum-dried sample, $C_{34}H_{30}N_6O_8F_6Cu_2$: C 45.60, H 3.62, N 9.39; found: C 45.30, H 3.61, N 9.48%.

Synthesis of $[Cu_2(tae)\ (dpa)_2(4,4'\text{-bipy})](CF_3CO_2)_2$ (2)

Method A

$Cu(CF_3CO_2)_2$ (200 mg, 0.69 mmol) was dissolved in 15 mL methanol.Tetraacetylethane (68 mg, 0.35 mmol) was added to the solution with stirring. The color of the solution immediately changed to green. After 2 h, 2,2′-dipyridylamine (118 mg, 0.69 mmol) was added to the solution. The color changed to dark green. After stirring for another 4 h, 4,4′-dipyridyl (54 mg, 0.34 mmol) was added without further color change. The mixture was stirred for 24 h, and then concentrated to 5 mL. Diethyl ether (2 mL) was added. Upon standing at room temperature for 1 week, dark green block crystals were obtained (249 mg, yield, 69%).

Method B

$Cu_2(tae)(dpa)_2(CF_3CO_2)_2$ (1) (200 mg, 0.22 mmol) was dissolved in 15 mL methanol. 4,4′-Dipyridyl (35 mg, 0.22 mmol) was added. No obvious color change of the solution was observed. The mixture was stirred for ~24 h, and then concentrated to 5 mL. Ether (2 mL) was added and the solution was kept standing at room temperature. After 1 week, dark green block crystals of compound **2** were harvested (207 mg, yield, 90%), mp 195°C. Anal. calcd.: C 50.34, H 3.84, N 10.67; found: C 50.12, H 3.67, N 10.56%.

Synthesis of $[Co_2(tae)(dpa)_4](CH_3CO_2)_2(H_2O)_2/CH_3OH$ (3)

$Co(OAc)_2{\cdot}4H_2O$ (200 mg, 0.80 mmol) was dissolved in 15 mL of methanol. With stirring, tetraacetylethane (79 mg, 0.40 mmol) was added to the flask. The solution immediately turned red. After the addition was complete, the mixture was stirred for 1 h, and 2,2′-dipyridylamine (275 mg, 1.61 mmol) was added to the solution. The solution immediately turned dark red. After being stirred for an additional 2 h, the solution was filtered and concentrated invacuo to about 5 mL. After adding 2 mL diethyl ether to the solution, the solution was kept standing at room temperature for 2 days. Red thin plate crystals of compound **3** were obtained. Yield 392 mg (vacuum-dried sample, 87%), mp 198–200°C. Anal. calcd. for the vacuum-dried sample, $C_{54}H_{58}N_{12}O_{10}Co_2$: C 56.26, H 5.04, N 14.59; found: C 56.38, H 4.80, N 14.28%.

X-ray diffraction analysis

The crystal of **2** was mounted on glass fibers with epoxy glue while the crystals of **1** and **3** were sealed inside glass capillaries with the saturated methanol solution. Data were collected over the ranges $2° < 2\theta < 45°$ for **1** and **3** and $2° < 2\theta < 50°$ for **2** on a Siemens P4 single-crystal X-ray diffractometer with graphite-monochromated Mo Kα radiation (λ = 0.71073 Å) operated at 50 kV and 40 mA at 23°C. No significant decay was observed for all crystals. Data were processed on a Pentium PC using Siemens SHELXTL (version 5.0) software package.[2] An empirical absorption correction based on azimuthal scans of several reflections was applied for all crystals. The data were corrected for Lorentz polar-

[2] SHELXTL, Version 5, Siemens Industrial Automation, Inc., Madison, Wis.

© 1999 NRC Canada

Table 1. Crystallographic data.

Compound	**1**	**2**	**3**
Formula	$C_{34}H_{30}N_6O_8F_6Cu_2$ /CH_3OH	$C_{44}H_{38}Cu_2F_6N_8O_8$	$C_{54}H_{58}N_{12}O_{10}Co_2$/$CH_3OH$
fw	890.75	1047.9	1152.0
Space group	*C*2/*c*	$P2_1/c$	*C*2/*c*
a/Å	15.718(1)	11.454(4)	32.493(7)
b/Å	10.245(1)	22.598(5)	7.982(2)
c/Å	24.113(2)	17.805(7)	28.035(6)
β/°	91.27(1)	100.28(3)	107.87(3)
V/Å^3	3883.3(3)	4535(3)	6920(2)
Z	4	4	4
D_c, g cm^{-3}	1.58	1.53	1.14
T (°C)	23	23	23
Radiation, λ, Å	Mo Kα, 0.71073	Mo Kα, 0.71073	Mo Kα, 0.71073
μ, cm^{-1}	11.8	11.0	5.37
R ($I > 2\sigma(I)$)	$R1^a$ = 0.0631	$R1^a$ = 0.0745	R1 =0.0849
	$wR2^b$ = 0.1463	$wR2^b$ = 0.1610	*wR*2 = 0.1995
Goodness-of-fit on F^2	1.05	1.05	1.10
Largest electron-density peak, e Å^{-3}	0.690	0.709	0.895

$^aR1 = \Sigma||F_o| - |F_c|| / \Sigma |F_o|$.

$^bwR2 = [\Sigma w [(F_o^2 - F_c^2)^2] / \Sigma[w(F_o^2)^2]]^{1/2}$.

$w = 1/ [\sigma^2(F_o^2) + (0.075P)^2]$, where $P = [\text{Max } (F_o^2, 0) + 2F_c^2]/3$.

ization effects. Neutral atom scattering factors were taken from Cromer and Waber (8). The crystal of **2** belongs to the monoclinic space group $P2_1/c$, uniquely determined by systematic absences ($0k0$, $k = 2n + 1$, $h0l$, $l = 2n + 1$). The systematic absences for compounds **1** and **3** agree with both *Cc* and *C*2/*c* space groups. The structural solution and refinement confirmed that *C*2/*c* is the correct choice for both compounds. All structures were solved by direct methods. Full-matrix least-squares refinements minimizing the function $\Sigma w(F_o^2 - F_c^2)^2$ were applied to all compounds. Both compounds **1** and **3** contain a disordered methanol solvent molecule in the crystal lattice (one methanol per dimer), which could not be fully modeled. The fluorine atoms of one of the $CF_3CO_2^-$ groups in compound **2** showed a twofold rotational disorder. The carbon atoms and oxygen atoms on this trifluoroacetate group also showed some degree of disorder that could not be modeled. The positions of hydrogen atoms except those of water and methanol molecules were calculated and their contribution was included in structural factor calculations. The data of crystallographic analysis are given in Table 1.

Results and discussion

Synthesis and structure of $Cu_2(tae)(dpa)_2(CF_3CO_2)_2$ (1)

Compound **1** was obtained in good yield from the reaction of $Cu(O_2CCF_3)_2$ with 2,2′-dipyridylamine and tetraacetylethane in a 2:2:1 ratio in methanol. The neutral tetraacetylethane molecule became the dianion, tae, in the product. The driving force for the formation of the tae dianion could be attributed to the chelating effect of the tae ligand. Complexes of tae involving Ni(II) and Cu(II) have previously been reported by Fukuda et al. (3*a*). Recently the structure of a dinuclear copper(II) compound, $[Cu_2(tae)(tmed)_2](NO_3)_2$, was also reported (3*c*). Single-crystal X-ray diffraction and elemental analyses established the composition and structure of compound **1**. A diagram showing the molecular structure of **1** is given in Fig. 2. Selected bond lengths and angles are listed in Table 2.

Compound **1** has C_2 symmetry where the two Cu(II) units are related by a twofold rotation axis with the Cu(1) and Cu(1A) separation distance being 7.968 Å. The tae ligand acts as a bridging ligand to the two copper(II) centers. As observed previously in Ni(II) and Cu(II) compounds, the tae ligand in compound **1** is not planar. The twisting angle of the two diketone portions of the tae ligand is 81.5°, smaller than that (84.6°) of $[Cu_2(tae)(tmed)_2](NO_3)_2$ (3*c*). The Cu—O (tae) bond lengths are comparable to those of previously reported acetylacetonato copper(II) compounds (9). The dpa ligand is chelated to the copper(II) center through the two pyridyl groups with normal Cu—N bond lengths. The fifth position of the copper center is occupied by a trifluoroacetate ligand with a long Cu—O bond (Cu(1)—O(3) = 2.331(9) Å). While the O(2)-Cu(1)-N(3) angle is nearly linear (173.0(3)°), the O(1)-Cu(1)-N(1) angle of 145.3(3)° deviates significantly from linearity. The geometry of the Cu(II) ion can therefore be best described as a distorted square pyramid. The amino N(2) atom is coplanar with the two pyridyl rings (the dihedral angle between the N(2)C(6)N(3) and N(2)C(5)N(1) planes is 1.3°) and the N(2)—C(5) and N(2)—C(6) bond lengths (1.378(12), 1.365(12) Å) are close to that of N—C double bonds, indicative of the N(2) conjugation with the two pyridyl rings. The structure of the dinuclear unit of **1** resembles that of $[Cu_2(tae)(tmed)_2](NO_3)_2$ (3*b*).

The amino N(2) group plays an important role in the extended solid state structure of **1**. The proton on N(2) forms a hydrogen bond with the noncoordinating O(4) atom of the acetate from the neighboring dimer, as evident by the N(2)···O(4A) distance of 2.81(2) Å. The two dpa ligands and the two trifluoroacetate ligands form a hydrogen-bonded box as shown in Fig. 2. As a consequence of the hydrogen bonds, compound **1** forms an extended one-dimensional chain struc-

© 1999 NRC Canada

Fig. 2. Top: a diagram showing the structure of **1** with 50% thermal ellipsoids and labeling scheme. Bottom: A diagram showing the hydrogen bonds between the dinuclear units of **1**.

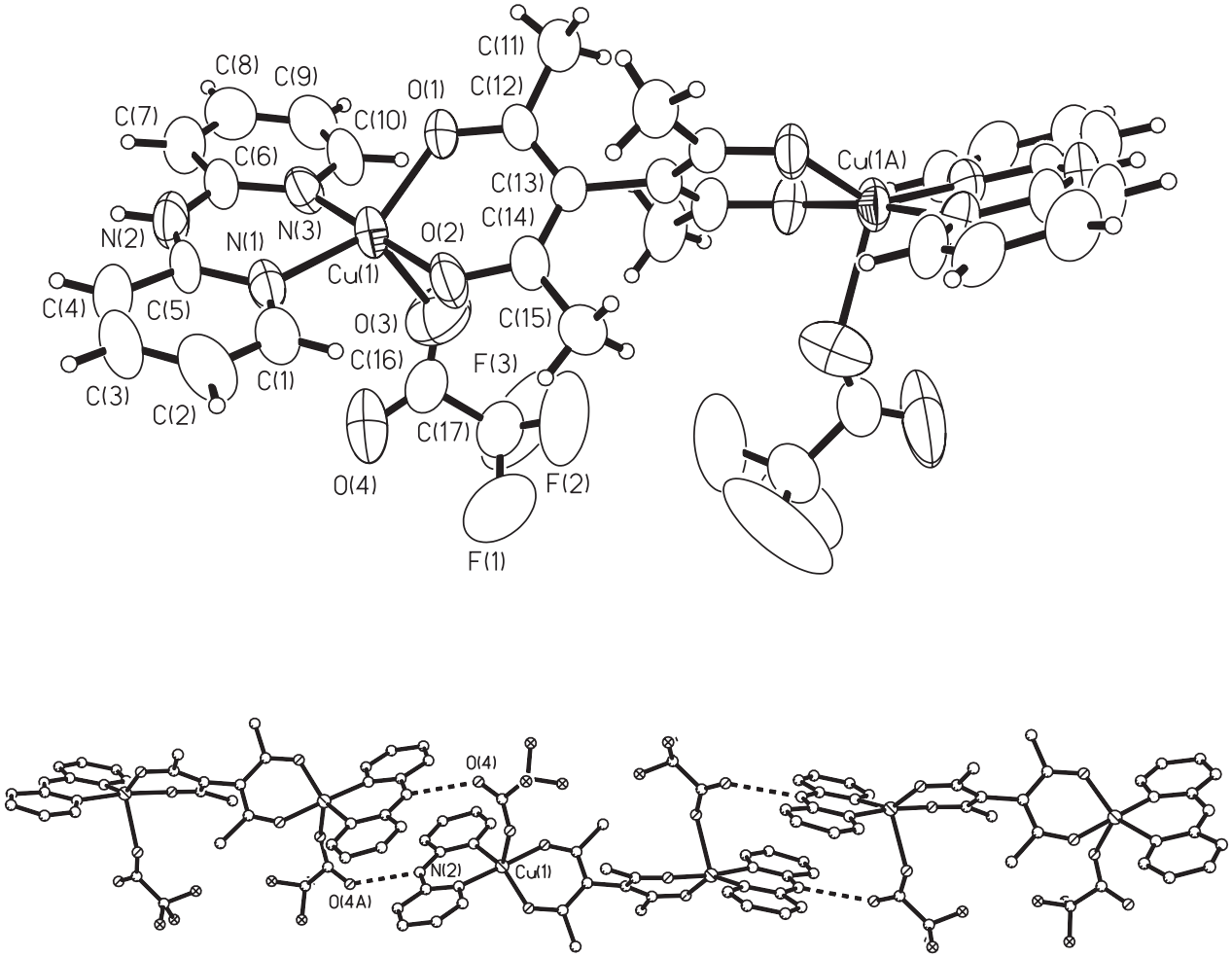

ture in the solid state (Fig. 2, bottom). Hydrogen-bonded extended structures involving copper(II) ions have been observed frequently (10). The geometry of the dpa ligand allows it to function as a chelating ligand and a proton donor as well, making it an ideal candidate for the building of complexes with extended hydrogen-bonded structures.

Synthesis and structure of $[Cu_2(tae)(dpa)_2(4,4\text{-bipy})](CF_3CO_2)_2$ (2)

The copper(II) ion in compound **1** is five-coordinate. Since a Cu(II) ion can also have a six-coordinate pseudo-octahedral geometry, we anticipated that it may be possible to link the dinuclear unit together through covalent bonds by introducing a cross-linking ligand at the unoccupied axial position. The ligand we chose is 4,4′-dipyridyl. Indeed, the reaction of compound **1** with 1 equiv. of 4,4′-dipyridyl produced a polymeric compound **2**, $[Cu_2(tae)(dpa)_2(4,4'\text{-bipy})](CF_3CO_2)_2$,in good yield. Compound **2** can also be obtained directly from the reaction of $Cu(O_2CCF_3)_2$, di-2-pyridylamine, tetraacetylethane, and 4,4′-bipy in a 2:2:1:1 ratio. The crystal structure of **2** was determined by single-crystal X-ray diffraction analysis. A diagram showing the structure of the dinuclear unit of **2** is given in Fig. 3. Selected bond lengths and angles are given in Table 2.

As shown in Fig. 3 (top), the structure of the dinuclear unit of **2** has some resemblance to that of **1**. Each copper(II) center is coordinated by a chelating dpa ligand and linked to the other copper(II) center by the bridging tae ligand. The twisting angle between the two diketone planes is 89.7°, much larger than that in compound **1**. As a consequence, the two planar Cu(II) units are essentially orthogonal to each other (the dihedral angle between the Cu(1)O(1)O(2)N(1)N(3) and Cu(2)O(3)O(4)N(4)N(6) planes is 94.4°). In contrast to compound **1** where the trifluoroacetate ligand occupies the axial position, the two trifluoroacetates in **2** are not bound to the copper centers but form hydrogen bonds with the amino hydrogen atoms (N(2), N(5)) of the dpa ligands as indicated by the N(2)···O(5) (2.74 Å) and N(5)···O(8) (2.76 Å) distances. As anticipated, the 4,4′-bipy ligand occupies the axial position of the copper center (Cu(1)—N(7) = 2.278(6) Å, Cu(2)—N(8A) = 2.274(6) Å), thus linking the dinuclear units together to form a one-dimensional polymer (Fig. 3, bottom). The deviation of Cu(1) from the O(1)O(2)N(1)N(3) plane is 0.085 Å while the deviation of Cu(2) from the O(3)O(4)N(4)N(6) plane is 0.137 Å. The geometry of each copper(II) center is therefore square pyramidal. Due to the orthogonality of the Cu(1) and Cu(2) planar units, the two neighbouring 4,4′-dipyridyl bridging ligands are also at ap-

© 1999 NRC Canada

Table 2. Selected bond lengths (Å) and angles (deg).

Compound 1	
Cu(1)—O(2)	1.892(6)
Cu(1)—O(1)	1.931(6)
Cu(1)—N(3)	1.961(7)
Cu(1)—N(1)	2.022(7)
Cu(1)—O(3)	2.331(9)
N(1)—C(1)	1.344(12)
N(1)—C(5)	1.349(11)
O(1)—C(12)	1.289(9)
O(2)—C(14)	1.286(10)
N(2)—C(6)	1.365(12)
N(2)—C(5)	1.378(12)
N(3)—C(6)	1.354(10)
N(3)—C(10)	1.360(11)
O(3)—C(16)	1.206(13)
O(4)—C(16)	1.176(14)
C(11)—C(12)	1.508(12)
C(12)—C(13)	1.398(12)
C(13)—C(14)	1.413(13)
C(13)—C(13A)	1.50(2)
C(14)—C(15)	1.492(13)
C(16)—C(17)	1.49(2)
O(2)-Cu(1)-O(1)	89.6(2)
O(2)-Cu(1)-N(3)	173.0(3)
O(1)-Cu(1)-N(3)	89.5(3)
O(2)-Cu(1)-N(1)	93.1(3)
O(1)-Cu(1)-N(1)	145.3(3)
N(3)-Cu(1)-N(1)	91.5(3)
O(2)-Cu(1)-O(3)	85.0(3)
O(1)-Cu(1)-O(3)	99.5(3)
N(3)-Cu(1)-O(3)	88.4(3)
N(1)-Cu(1)-O(3)	115.2(4)
C(1)-N(1)-C(5)	117.4(8)
C(1)-N(1)-Cu(1)	117.7(6)
C(5)-N(1)-Cu(1)	124.3(7)
C(12)-O(1)-Cu(1)	126.9(6)
N(1)-C(1)-C(2)	123.8(10)
C(14)-O(2)-Cu(1)	127.1(6)
C(6)-N(2)-C(5)	134.2(8)
C(6)-N(3)-C(10)	114.5(8)
C(6)-N(3)-Cu(1)	128.3(7)
C(10)-N(3)-Cu(1)	116.8(6)
C(16)-O(3)-Cu(1)	127.7(9)
C(4)-C(3)-C(2)	119.8(10)
C(3)-C(4)-C(5)	120.7(10)
N(1)-C(5)-N(2)	121.1(8)
N(1)-C(5)-C(4)	121.3(10)
N(2)-C(5)-C(4)	117.6(9)
N(3)-C(6)-N(2)	118.5(9)
N(3)-C(6)-C(7)	123.3(10)
N(2)-C(6)-C(7)	118.2(9)
C(9)-C(10)-N(3)	125.7(9)
O(1)-C(12)-C(13)	125.5(8)
O(1)-C(12)-C(11)	114.6(8)
C(13)-C(12)-C(11)	119.9(7)
C(12)-C(13)-C(14)	120.4(7)
C(12)-C(13)-C(13A)	121.2(8)
C(14)-C(13)-C(13A)	118.4(8)
O(2)-C(14)-C(13)	125.1(8)
O(2)-C(14)-C(15)	114.5(9)
C(13)-C(14)-C(15)	120.4(8)
O(4)-C(16)-O(3)	131.6(13)
O(4)-C(16)-C(17)	114.8(13)
O(3)-C(16)-C(17)	113.5(12)
Symmetry transformations used to generate equivalent atoms:	
#1 $-x - ½, -y + 3/2, -z + 1$	#2 $-x, y, -z + ½$
Compound 2	
Cu(1)—O(1)	1.921(5)
Cu(1)—O(2)	1.927(6)
Cu(1)—N(1)	1.997(7)
Cu(1)—N(3)	2.001(7)
Cu(1)—N(7)	2.280(6)
O(1)—C(24)	1.287(9)
N(1)—C(1)	1.345(10)
N(1)—C(5)	1.346(10)
C(1)—N(2)	1.380(11)
Cu(2)—O(4)	1.921(6)
Cu(2)—O(3)	1.953(5)
Cu(2)—N(4)	2.013(6)
Cu(2)—N(6)	2.020(6)
Cu(2)—N(8A)	2.274(6)
O(2)—C(22)	1.262(8)
N(2)—C(10)	1.347(11)
O(3)—C(27)	1.294(8)
N(3)—C(10)	1.332(10)
N(3)—C(6)	1.351(11)
O(4)—C(29)	1.280(9)
N(4)—C(15)	1.336(10)
N(4)—C(11)	1.340(10)
N(5)—C(16)	1.357(11)
N(5)—C(15)	1.372(11)
N(6)—C(16)	1.318(10)
N(6)—C(20)	1.345(11)
N(7)—C(35)	1.305(10)
N(7)—C(31)	1.319(10)
N(8)—C(36)	1.312(10)
N(8)—C(40)	1.326(10)
C(21)—C(22)	1.508(12)
C(22)—C(23)	1.415(10)
C(23)—C(24)	1.394(10)
C(23)—C(28)	1.513(9)
C(24)—C(25)	1.504(10)
C(26)—C(27)	1.501(10)
C(27)—C(28)	1.382(10)
C(28)—C(29)	1.398(10)
C(29)—C(30)	1.490(11)
O(1)-Cu(1)-O(2)	89.5(2)
O(1)-Cu(1)-N(1)	91.5(2)
O(2)-Cu(1)-N(1)	176.4(3)
O(1)-Cu(1)-N(3)	170.7(3)
O(2)-Cu(1)-N(3)	88.9(3)
N(1)-Cu(1)-N(3)	89.6(3)
O(1)-Cu(1)-N(7)	92.8(2)
O(2)-Cu(1)-N(7)	91.1(3)
N(1)-Cu(1)-N(7)	92.3(3)

© 1999 NRC Canada

Table 2 (*continued*).

N(3)-Cu(1)-N(7)	96.4(3)
C(24)-O(1)-Cu(1)	126.2(5)
O(4)-Cu(2)-N(4)	171.0(3)
O(3)-Cu(2)-N(4)	91.3(2)
O(4)-Cu(2)-N(6)	88.6(3)
O(3)-Cu(2)-N(6)	172.0(2)
N(4)-Cu(2)-N(6)	91.9(3)
O(4)-Cu(2)-N(8A)	95.9(2)
O(3)-Cu(2)-N(8A)	91.9(2)
N(4)-Cu(2)-N(8A)	93.0(3)
N(6)-Cu(2)-N(8A)	95.2(2)
C(10)-N(2)-C(1)	130.5(8)
C(16)-N(5)-C(15)	134.4(7)
O(2)-C(22)-C(23)	124.9(8)
O(2)-C(22)-C(21)	113.8(7)
C(23)-C(22)-C(21)	121.2(7)
C(24)-C(23)-C(22)	121.6(7)
C(24)-C(23)-C(28)	118.4(7)
C(22)-C(23)-C(28)	119.9(7)
O(1)-C(24)-C(23)	124.8(7)
O(1)-C(24)-C(25)	114.7(7)
C(23)-C(24)-C(25)	120.5(7)
O(3)-C(27)-C(28)	125.4(7)
O(3)-C(27)-C(26)	113.0(7)
C(28)-C(27)-C(26)	121.6(7)
C(27)-C(28)-C(29)	120.9(7)
C(27)-C(28)-C(23)	120.2(7)
C(29)-C(28)-C(23)	118.7(7)
O(4)-C(29)-C(28)	124.5(7)
O(4)-C(29)-C(30)	113.4(7)
C(28)-C(29)-C(30)	122.0(7)
O(5)-C(41)-O(6)	110(2)
O(8)-C(43)-O(7)	119(2)

Symmetry transformations used to generate equivalent atoms:
#1 $x, -y + ½, z + ½$ #2 $x, -y + ½, z - ½$

Compound 3

Co(1)—O(1)	2.026(6)
Co(1)—O(2)	2.026(7)
Co(1)—N(1)	2.125(8)
Co(1)—N(6)	2.131(7)
Co(1)—N(3)	2.141(8)
Co(1)—N(4)	2.143(8)
O(1)—C(22)	1.284(10)
N(1)—C(1)	1.335(12)
N(1)—C(5)	1.346(13)
C(1)—N(2)	1.376(12)
O(2)—C(24)	1.280(11)
N(2)—C(6)	1.393(13)
N(3)—C(6)	1.335(12)
N(3)—C(10)	1.359(13)
O(3)—C(26)	1.22(2)
N(4)—C(15)	1.335(12)
N(4)—C(11)	1.359(12)
O(4)—C(26)	1.16(2)
N(5)—C(15)	1.372(13)
N(5)—C(16)	1.379(12)
N(6)—C(20)	1.335(12)

Table 2 (*concluded*).

N(6)—C(16)	1.345(11)
C(21)—C(22)	1.536(13)
C(22)—C(23)	1.395(13)
C(23)—C(24)	1.398(13)
C(23)—C(23A)	1.50(2)
C(24)—C(25)	1.531(14)
C(26)—C(27)	1.36(3)
O(1)-Co(1)-O(2)	88.1(3)
O(1)-Co(1)-N(1)	173.3(3)
O(2)-Co(1)-N(1)	87.5(3)
O(1)-Co(1)-N(6)	88.4(3)
O(2)-Co(1)-N(6)	173.7(3)
N(1)-Co(1)-N(6)	96.5(3)
O(1)-Co(1)-N(3)	91.0(3)
O(2)-Co(1)-N(3)	89.3(3)
N(1)-Co(1)-N(3)	83.9(3)
N(6)-Co(1)-N(3)	96.0(3)
O(1)-Co(1)-N(4)	89.0(3)
O(2)-Co(1)-N(4)	91.1(3)
N(1)-Co(1)-N(4)	96.1(3)
N(6)-Co(1)-N(4)	83.5(3)
N(3)-Co(1)-N(4)	179.5(3)
C(6)-N(3)-C(10)	117.3(9)
C(15)-N(5)-C(16)	128.7(9)
O(1)-C(22)-C(23)	126.6(9)
O(1)-C(22)-C(21)	113.5(9)
C(23)-C(22)-C(21)	119.9(8)
C(22)-C(23)-C(24)	122.6(8)
C(22)-C(23)-C(23A)	118.6(8)
C(24)-C(23)-C(23A)	118.7(8)
O(2)-C(24)-C(23)	127.2(9)
O(2)-C(24)-C(25)	112.9(9)
C(23)-C(24)-C(25)	119.8(9)
O(4)-C(26)-O(3)	119(2)
O(4)-C(26)-C(27)	122(2)
O(3)-C(26)-C(27)	119(2)

Symmetry transformations used to generate equivalent atoms:
#1 $-x, -y + 1, -z + 1$ #2 $-x, y, -z + ½$

proximately right angles with respect to one another. The Cu(1)—Cu(2) distance in the dinuclear unit is 8.027 Å, comparable to that in **1**, while the Cu(1)—Cu(2A) distance between the dimer is 11.618 Å. The hydrogen-bound trifluoroacetate molecules are situated in the cavities between the polymer chains. 4,4′-Dipyridyl bridged polynuclear copper(II) complexes have been reported previously (11*a*). The most notable utility of 4,4′-dipyridyl is as a spacer in tetranuclear compounds with square or extended ladder structures (11*b*–11*e*). In order for 4,4′-dipyridyl to link compound **1** to form a square or rectangular structure, the two copper(II) units in **1** have to be coplanar. The orthogonal arrangement of the two copper(II) units in **1** appar-

© 1999 NRC Canada

Fig. 3. Top: a diagram showing the dinuclear structure of **2** with 50% thermal ellipsoids and labeling scheme. For clarity, the fluorine atoms are omitted. Bottom: a diagram showing the polymeric structure of **2**. Trifluoroacetate groups are omitted for clarity.

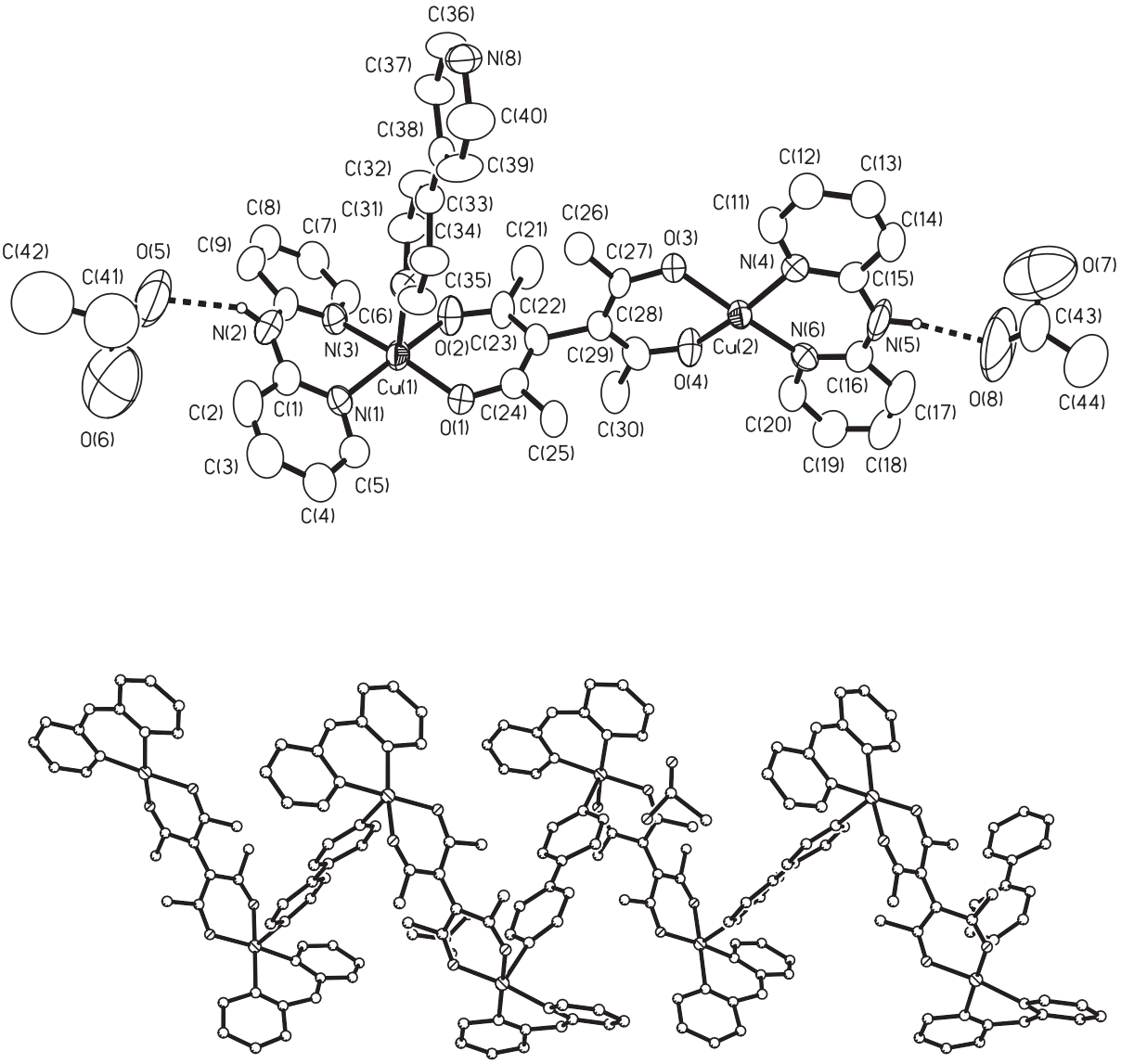

ently precludes the formation of such a structure but favors the formation of the polymer structure in **2**.

Synthesis and structure of $[Co_2(tae)(dpa)_4](CH_3CO_2)_2(H_2O)_2$ (3)

The dinuclear cobalt(II) compound was obtained in good yield from the reaction of $Co(O_2CCH_3)_2(H_2O)_4$ with 2,2′-dipyridylamine and tetraacetylethane in a 2:4:1 ratio in methanol. The crystal structure of **3** was determined by a single-crystal X-ray diffraction analysis. Selected bond lengths and angles are given in Table 2.

As shown in Fig. 4, the tae ligand bridges two cobalt(II) ions in the same manner as observed in **1** and **2**. The Co(1) and Co(1A) separation distance (8.286 Å) is, however, longer than those in **1** and **2**, attributable to the relatively long Co–ligand bond lengths, in comparison to those of the Cu–ligand bonds. The molecule of **3** has a C_2 symmetry. The Co—O(tae) bond lengths are similar to the previously reported Co(II)—O bonds (12). The twisting angle (88.9°) between the two diketone portions of the tae ligand is much larger than that in **1**, but similar to that in **2**, which results in a 85.6° dihedral angle between the Co(1)O(1)O(2)N(1)N(6) and Co(1A)O(1A)O(2A)N(1A)N(6A) planes. Unlike compounds **1** and **2**, where the copper(II) centers are chelated by one dpa ligand, in compound **3** the cobalt(II) ion is coordinated by two chelating dpa ligands with typical Co—N bond lengths. The geometry around the cobalt center is almost an ideal octahedron, as indicated by the bond angles of O(2)-Co(1)-N(6) = 173.3(3)°, O(1)-Co(1)-N(1) = 173.7(3)°, and N(3)-Co(1)-N(4) = 179.5(3)°. In contrast to compounds **1** and **2**, where the dpa ligands are essentially planar, the dpa ligands in compound **3** are buckled. The dihedral angle between the two pyridyl rings is 17.3° for the N(2) dpa ligand

© 1999 NRC Canada

Fig. 4. A diagram showing the molecular structure of **3** with 50% thermal ellipsoids and labeling scheme. All carbon atoms are shown as ideal spheres for clarity.

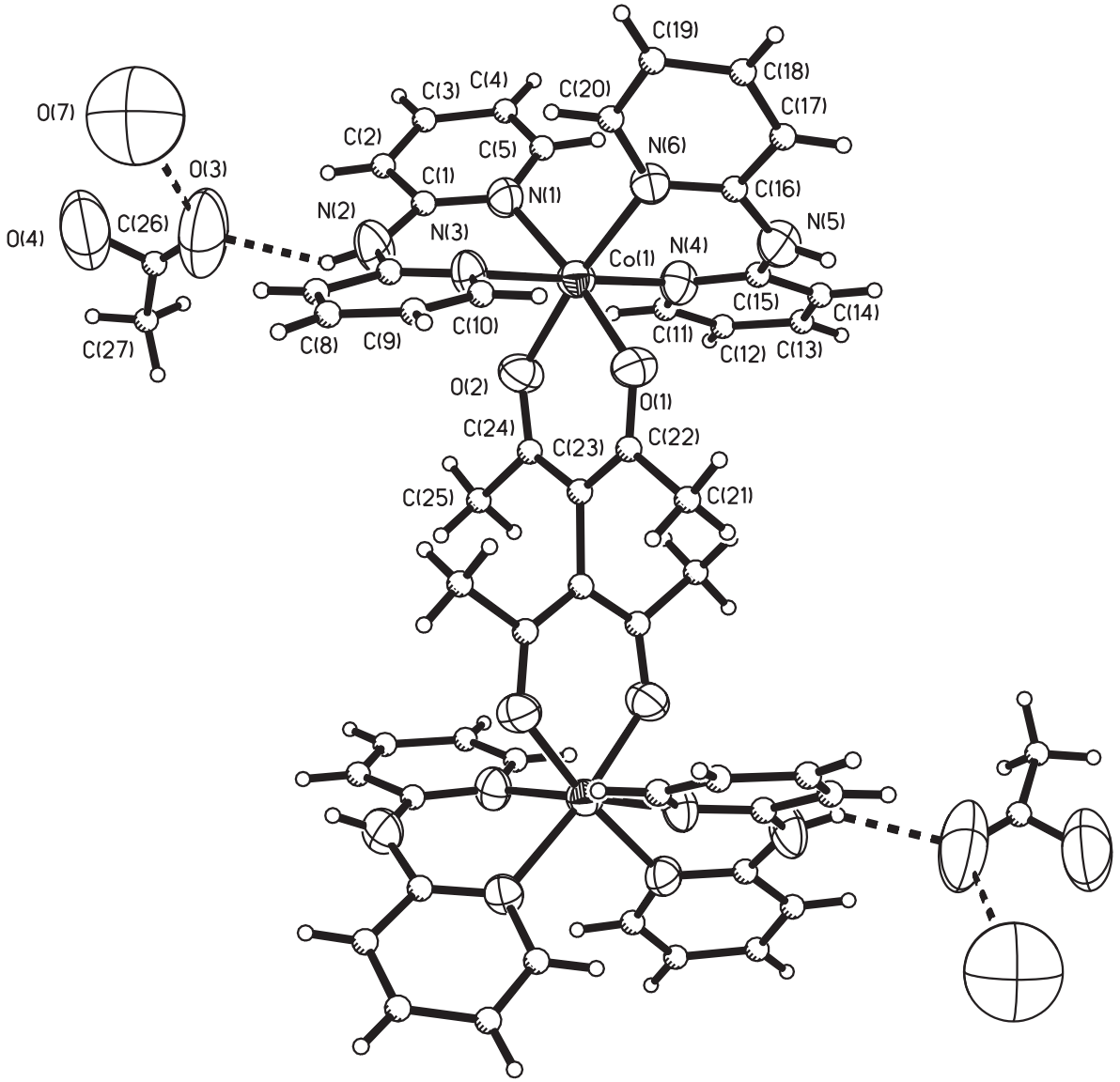

and 22.0° for the N(5) dpa ligand. The buckling of the dpa ligand in **3** can be attributed to the increased crowdedness of the cobalt ion, in comparison to the copper ions in **1** and **2**, and the relatively long Co—N bonds.

As observed in compound **2**, the dinuclear portion of compound **3** is a dication. The two acetate ligands are not coordinated to the metal centers. One interesting feature of the dication is that it has a helical chiral structure as shown by the space-filling diagram of Fig. 5. The two Co(II) units linked by the tae ligand have the same chirality, i.e., (Λ, Λ) or (Δ, Δ). Both enantiomers co-crystallize in the solid state. We have not been able to isolate any of the (Λ, Δ) diastereomer from the same reaction. The helical structure of **3** is apparently promoted by the nonplanarity of the tae ligand. The fact that the (Λ, Λ) and (Δ, Δ) isomers were obtained in >80% yield suggested to us that these isomers must be thermodynamically more favorable than the (Λ, Δ) isomer. Coordination compounds with helical structures have been reported previously (5). The simplicity of the tae ligand makes it very attractive for the synthesis of helical coordination compounds involving octahedral metal ions.

Another interesting feature of **3** is the formation of an extended hydrogen-bonded architecture. The acetate forms two hydrogen bonds with two amino groups from two dications, as indicated by the bond distances of N(2)···O(3) = 2.821 Å and N(5A)···O(4) = 2.726 Å. Unlike compound **1**, where the dimers are linked via hydrogen bonds in a head-to-tail fashion, the (Λ, Λ) dication in **3** is linked via hydrogen bonds to the (Δ, Δ) dication via two acetate ligands in a parallel head-to-head and tail-to-tail fashion to form a one-dimensional band (Fig. 6). In the cavity between two hydrogen-bonded bands are water molecules that are hydrogen bonded to the acetate (O(6)···O(3) = 2.948 Å). The box formed by the two acetates and two dianions is about 8 Å × 11 Å in two dimen-

© 1999 NRC Canada

Fig. 5. A space-filling diagram showing the helical structure of the (Δ,Δ) enantiomer of **3**. The acetate groups are omitted for clarity.

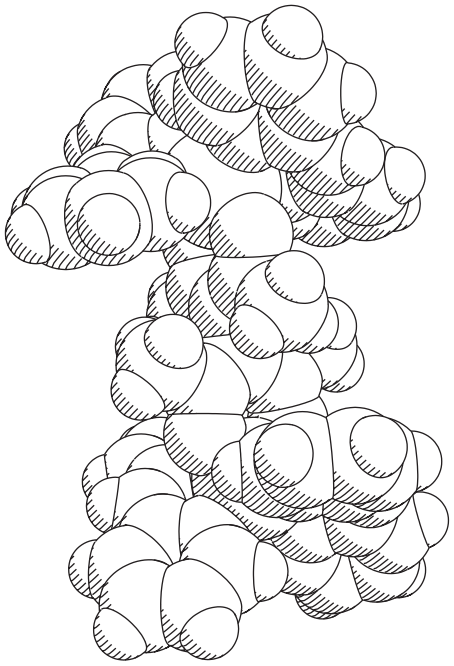

sions and extends along the third dimension to form a one-dimensional channel. Disordered methanol solvent molecules are located in these channels (Fig. 6).

The molecular sieve-like behavior of 3

Most interestingly, the methanol guest molecules in the lattice of **3** go in and out of the channel reversibly, as established by TGA experiments. The freshly prepared compound **3** loses 2.7% weight in the temperature range 20–38°C, consistent with the loss of methanol solvent molecule (2.7%, one methanol per compound **3**). Compound **3** also readily loses the methanol solvent molecule, without loss of crystallinity, when subjected to vacuum. The vacuum-dried sample has no significant weight loss in the temperature range 20–60°C. However, after being exposed to the methanol vapor, the vacuum-dried sample shows a similar TGA curve to that of the freshly prepared sample, indicative of the reabsorption of the methanol guest molecule. Examples of inorganic complexes that host organic solvent molecules in the crystal lattice are abundant (11). However, most crystal lattices of these complexes collapse when the guest molecules leave the lattice, resulting in an irreversible loss of the guest molecule. In fact, inorganic complexes that absorb organic molecules in the lattice in a reversible fashion are still a rare occurrence. The behavior of compound **3** resembles that of molecular sieves (1*k*, 13), which prompted us to examine the utility of the crystals of compound **3** in hosting small organic molecules other than methanol, such as ace-

Fig. 6. A packing diagram showing the three-dimensional hydrogen-bonded extended structure of **3**. The disordered methanol solvent molecules are in the large channels (shown in the middle of the diagram).

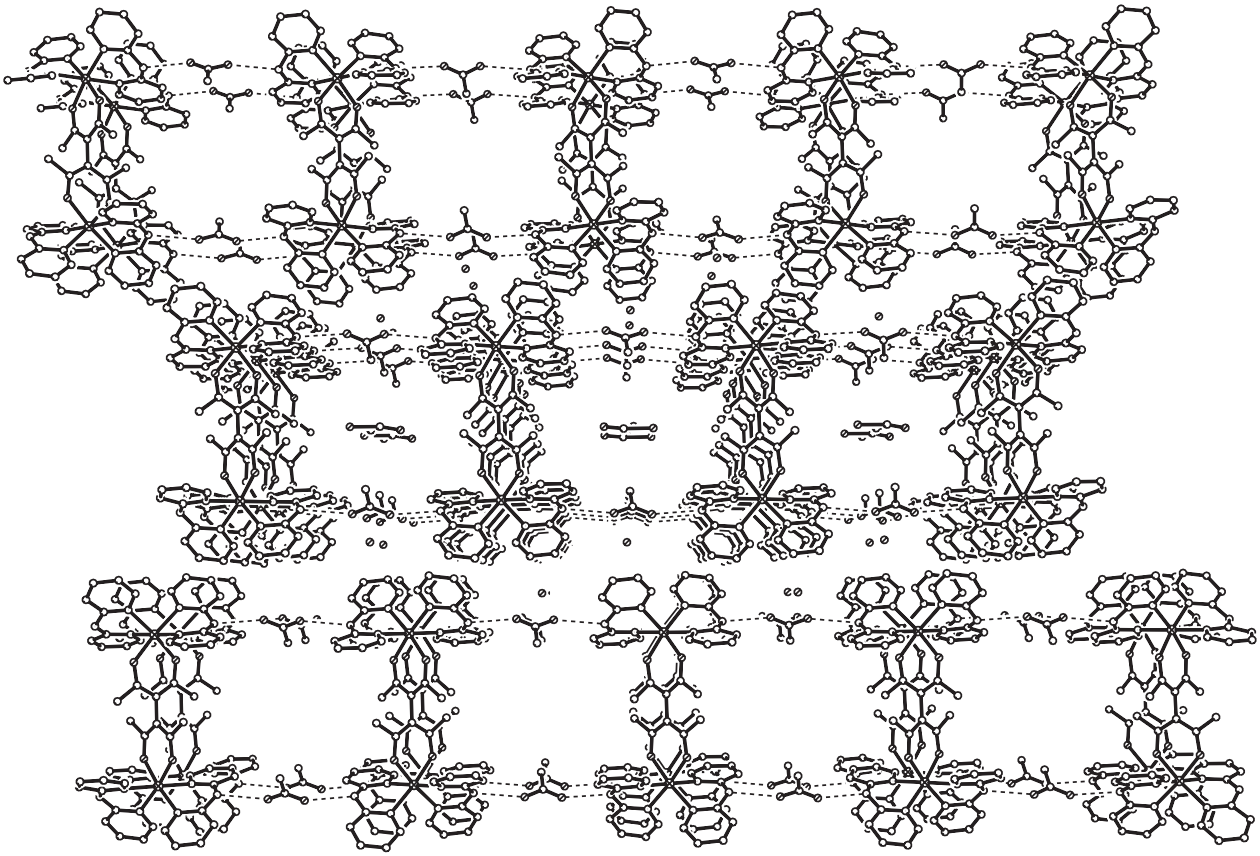

© 1999 NRC Canada

tonitrile. However, at present, methanol is the only known guest molecule that can be reversibly hosted by the crystals of compound **3**.

Magnetic properties of compounds 1–3

The paramagnetic metal ions in the dinuclear units of compounds **1–3** are about 8 Å away from each other. It is therefore of interest to see if there is any magnetic exchange between the two metal ions. In addition, the tae ligand links the two mononuclear units together in an approximately orthogonal fashion, which could result in either weak ferromagnetic exchange or no exchange at all (1, 3, 14). Previous studies on dinuclear copper(II) tae complexes by Lim et al. (3*c*) indicated that antiferromagnetic exchanges dominate in their compounds. The difference between our copper(II) compounds and Lim's copper(II) compounds lies in the fact that our compounds have either a hydrogen-bonded or covalently bonded extended structure in the solid state while Lim's compounds are discrete dinuclear molecules. To determine the presence and nature of possible magnetic exchange in **1–3**, magnetic susceptibility data of compounds **1**–**3** were measured over the temperature range 2–300 K. The data were corrected for diamagnetism by using Pascal constants.

As shown in Fig. 7 (top), compound **1** is a nearly ideal paramagnet in the temperature range 20–300 K. The drop of magnetic moment at temperatures below 20 K is likely caused by intermolecular antiferromagnetic exchange. The behavior of compound **1** contradicts that of Lim's compound where significant intramolecular antiferromagnetic exchange appears to be present. The cause for this discrepancy has not been understood. The magnetic moment vs. temperature plot (Fig. 7, middle) for compound **2** clearly indicates that antiferromagnetic exchanges dominate. The plot of moment vs. *T* (Fig. 7, bottom) for compound **3** shows a gradual increase of moment with decrease in temperature, indicative of the presence of weak ferromagnetic exchanges.

EHMO calculations

To further understand the magnetic exchange in compound **3**, we performed molecular orbital calculations by using the extended Hückel molecular orbital methods (EHMO) (15). The molecular geometry was established by using the crystallographic coordinates of compound **3**. The result of the EHMO calculations showed that the HOMO (**1b**) and LUMO (**1a**) levels consist mostly of the two $d(x^2 - y^2)$ atomic orbitals from the two Co(II) ions. There are also considerable contributions from the coordinating atoms to these two molecular orbitals. The energy difference between the HOMO and the LUMO level (–10.180 eV vs. –10.179 eV) is negligible. Thus, the HOMO and LUMO can be considered as one doubly quasi-degenerate molecular orbital, consistent with a ferromagnetic exchange ground state. As shown in Fig. 8, the $d(x^2 - y^2)$ orbitals of the two Co(II) ions at the HOMO level are orthogonal with a dihedral angle of 85.6°. The ferromagnetic exchange in compound **3** could be therefore attributed to the orbital orthogonality of the two Co(II) ions, imposed by the tae ligand. Other mechanisms such as spin-orbital couplings may also be responsible for the magnetic behavior of **3**, which requires further theoretical investigations.

Fig. 7. Diagrams showing χ_M vs. *T*(K) and μ_{eff} vs. *T* plots of **1–3**.

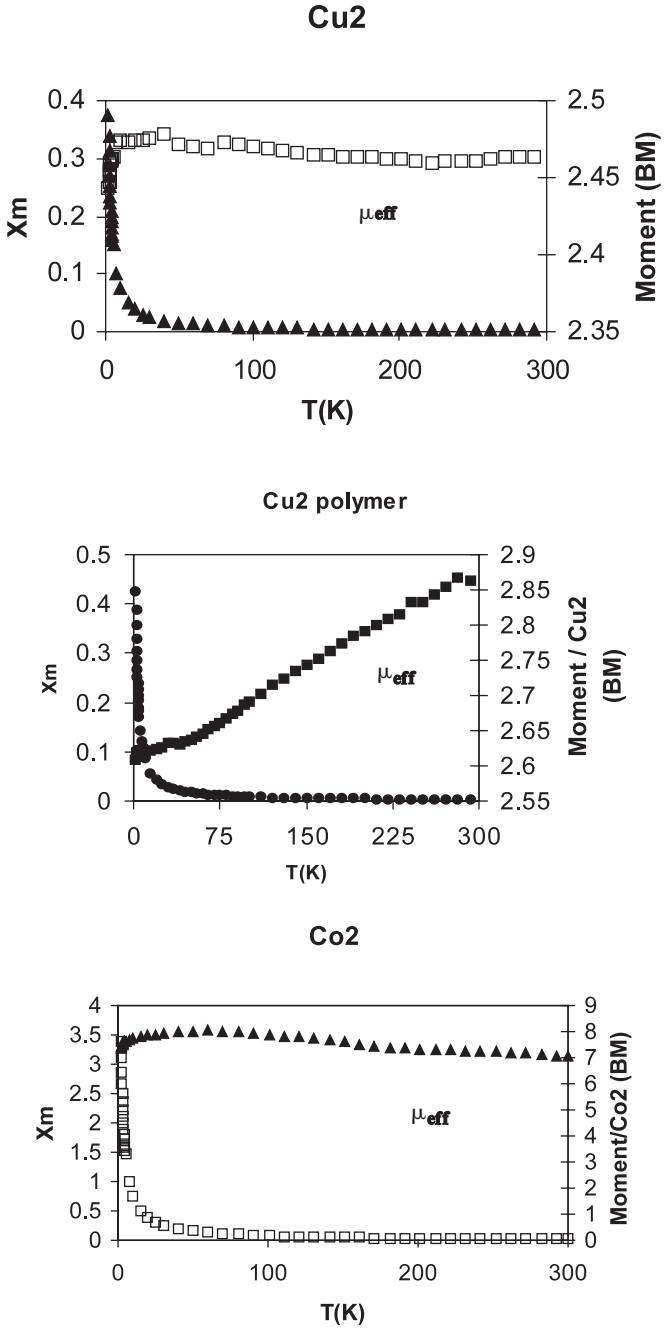

Conclusion

The nonplanarity of the tae ligand appears to promote helical structures of complexes containing octahedral metal ions and ferromagnetic exchange in the dinuclear Co(II) complex as well. The dpa ligand is a good bifuctional ligand and promotes the formation of extended hydrogen-bonded structures in the solid state by interacting with proton acceptors such as acetate via the noncoordinating amino site. Compound **3** is one of the rare examples of hydrogen-bound extended structures that hosts methanol solvent molecules reversibly.

© 1999 NRC Canada

Fig. 8. The two degenerate molecular orbitals of compound **3** at the HOMO level.

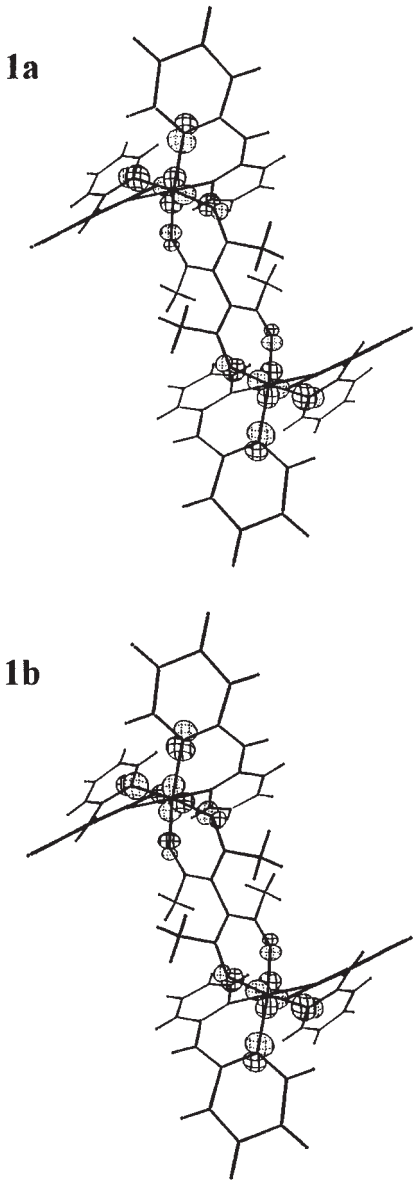

Acknowledgment

We thank the Natural Sciences and Engineering Research Council of Canada for financial support.

References

1. (*a*) D. Gatteschi. Adv. Mater. **6**, 635 (1994); (*b*) M. Kinoshita. Jpn. J. Appl. Phys. **33**, 5718 (1994); (*c*) H.O. Stumpf, L. Ouahab, Y. Pei, D. Grandjean, and O. Kahn. Science (Washington, D.C.), **261**, 447 (1993); (*d*) J.S. Miller and A.J. Epstein. Angew. Chem. Int. Ed. Engl. **33**, 385 (1994); (*e*) O. Kahn. Molecular magnetism. VCH Publishers, Inc., New York. 1993; (*f*) K. Inoue and H. Iwamura. J. Am. Chem. Soc. **116**, 3174 (1994); (*g*) Y. Pei, O. Kahn, K. Nakatani, E. Codjovi, C. Mathonière, and J. Sletten. J. Am. Chem. Soc. **113**, 6558 (1991); (*h*) S. Decurtins, H.W. Schmalle, P. Schneuwly, J. Ensling, and P. Gütlich. J. Am. Chem. Soc. **116**, 9521 (1994); (*i*) H.O. Stumpf, Y. Pei, O. Kahn, J. Sletten, and J.P. Renard. J. Am. Chem. Soc. **115**, 6738 (1993); (*j*) H. Tamaki, Z.J. Zhong, N. Matsumoto, S. Kida, M. Koikawa, N. Achiwa, Y. Hashimoto, and H. Okawa. J. Am. Chem. Soc. **114**, 6974 (1992); (*k*) D.W. Bruce and D. O'Hare. Inorg. Mater. John Wiley & Sons, New York, 1995; (*l*) C. Benelli, D. Gatteschi, D.W. Carnegie, Jr., and R.L. Carlin. J. Am. Chem. Soc. **107**, 2560 (1985).
2. (*a*) S. Wang and J. Cluster. Science (Washington, D.C.), 463 (1996); (*b*) S.R. Breeze and S.Wang. J. Chem. Soc. Dalton Trans. 134 (1996); (*c*) S. Wang, Z. Pang, J.C. Zheng, and M.J. Wagner. Inorg. Chem. **32**, 5975 (1993); (*d*) S. Wang, S.J. Trepanier, J.C. Zheng, and Z. Pang. Inorg. Chem. **31**, 2118 (1992).
3. (*a*) Y. Fukuda, A. Seino, K. Mafune, H. Nakagawa, and W. Linert. J. Coord. Chem. **33**, 123 (1994); (*b*) Y. Fukuda and K. Mafune. Chem. Lett. 697 (1988); (*c*) Y.Y. Lim, W. Chen, L.L. Tan, X.Z. You, and T.M. Yao. Polyhedron, 13, 2861 (1994).
4. R.L. Carlin. Magnetochemistry. Springer-Verlag, Berlin. 1986.
5. (*a*) J.-M. Lehn, A. Rigault, J. Siegel, J. Harrowfiled, B. Chevrier, and D. Moras. Proc. Natl. Acad. Sci. U.S.A. **84**, 2565 (1987); (*b*) J.-M. Lehn, J.P. Sauvage, R. Ziessel, C. Piccinni-Leopardi, G. Germain, J.P. Declerq, and M. Van Meerssche. Nouv. J. Chim. **7**, 413 (1983); (*c*) T.M. Garrett, U. Koert, J.-M. Lehn, A. Rigault, D. Meyer, and J. Fisher. J. Chem. Soc. Chem. Commun. 557 (1990); (*d*) U. Koert, M.M. Harding, and J.-M. Lehn. Nature (London), **346**, 339 (1990); (*e*) E.C. Constable, S.M. Elder, J.A. Healy, M.D. Ward, and D.A. Tocher. J. Am. Chem. Soc. **112**, 4590 (1990); (*f*) E.C. Constable and J.V. Walker. J. Chem. Soc. Chem. Commun. 884 (1992); (*g*) K.T. Potts, M. Keshavarz-K, F.S. Tham, K.A.G. Raiford, C. Arana, and H.D. Abruna. Inorg. Chem. **32**, 5447 (1993); (*h*) C. Piquet, A.F. Williams, G. Bernardinelli, and J.C.G. Bunzli. Inorg. Chem. **32**, 4139 (1993).
6. Y.S. Zhang, S. Wang, G. Enright, and S.R. Breeze. J. Am. Chem. Soc. **120**, 9398 (1998).
7. Org. Synth. Collect. Vol. **4**, 869 (1963).
8. D.T. Cromer and J.T. Waber. International tables for X-ray crystallography. Vol. 4. Kynoch Press, Birmingham. 1974. Table 2–2A.
9. (*a*) S. Wang, J.C. Zheng, and J.R. Hall. Polyhedron, **13**, 1039 (1994); (*b*) H.E. LeMay, Jr., D.J. Hodgson, P. Pruettiangkura, and L.J. Theriot. J. Chem. Soc. Dalton Trans. 781 (1979); (*c*) J.E. Andrew and A.B. Blake. J. Chem. Soc. Dalton Trans. 1102 (1973); (*d*) J.A. Bertrand and R.I. Kaplan. Inorg. Chem. **4**, 1657 (1965).
10. (*a*) S.R. Breeze and S. Wang. Inorg. Chem. **32**, 5981 (1993); (*b*) A. Hassan and S. Wang. J. Chem. Soc. Dalton Trans. 2009 (1997); (*c*) M. Zaworotko. Chem. Soc. Rev. 283 (1994); (*d*) L. Fabbrizzi and A. Poggi (*Editors*). Transition metals in supramolecular chemistry. Kluwer Academic, Dordrecht. 1994.
11. (*a*) M. Julve, M. Verdaguer, J. Faus, F. Tinti, J. Moratal, A. Monge, and E. Gutiérrez-Puebla. Inorg. Chem. **26**, 3520 (1987); (*b*) M. Fujita, J. Yazaki, and K. Ogura. J. Am. Chem. Soc. **112**, 5645 (1990); (*c*) M. Fujita, O. Sasaki, T. Mitsuhashi, T. Fujita, J. Yazaki, and K. Yamaguchi. J. Chem. Soc. Chem. Commun. 1535 (1996); (*d*) P. Losier and M.J. Zaworotko. Angew. Chem. Int. Ed. Engl. **35,** 2779 (1996); (*e*) P.J. Stang and D.H. Cao. J. Am. Chem. Soc. **116,** 4981 (1994).
12. D.A. Buckinghum and C.R. Clark. *In* Comprehensive coordination chemistry. Vol. 4. *Edited by* G. Wilkinson, R.D. Gillard, and J.A. McCleverty. Pergamon Press, Oxford. 1987. Chap. 47.

© 1999 NRC Canada

13. A. Dyer. An introduction to zeolite molecular sieves. John Wiley & Sons, New York. 1988.
14. W.E. Hatfield. *In* Magneto-structural correlations in exchange coupled systems. *Edited by* R.D. Willett, D. Gatteschi, and O. Kahn. NATO ASI. Reidel, Dordrecht. 1985. p. 555.
15. (*a*) C. Mealli and D.M. Proserpio. J. Chem. Educ. **67**, 399 (1990); (*b*) J.H. Ammeter, H.-B. Bürgi, J.L. Thibeault, and R. Hoffmann. J. Am. Chem. Soc. **100**, 3686 (1978); (*c*) P.J. Hay, J.C. Thibeault, and R. Hoffmann. J. Am. Chem. Soc. **97**, 4884 (1975).

© 1999 NRC Canada

Crystal structures of dihydroquercetin 3-acetate and dihydroquercetin 3,3′,4′,7-tetraacetate: hydrogen bonding in 5-hydroxyflavanones

Eberhard Kiehlmann, Kumar Biradha, Konstantin V. Domasevitch, and Michael J. Zaworotko

Abstract: The molecular structures of dihydroquercetin 3-acetate **3** and dihydroquercetin 3,3′,4′,7-tetraacetate **4** were determined by single crystal X-ray analysis. Comparison of their crystal data with those of 16 known 5-hydroxyflavanones shows intramolecular O(5)-H···O(4)=C hydrogen bonding, preference for nearly perpendicular orientation of the two aromatic rings and preferred sofa conformation of the heterocyclic ring. The major stabilizing force in the crystal packing pattern of **3** is intermolecular hydrogen bonding.

Key words: crystal structure, dihydroquercetin, flavanones, hydrogen bonding.

Résumé : On a déterminé les structures moléculaires du 3-acétate de dihydroquercétine (3) et du 3,3′,4′,7-tétraacétate de dihydroquercétine (4) par diffraction des rayons X sur des cristaux uniques. Une comparaison de leurs structures cristallines avec celles de seize autres 5-hydroxyflavones connues démontre l'existence d'une liaison hydrogène intramoléculaire O(5)-H···O(4)=C, d'une préférence pour une orientation pratiquement perpendiculaire des deux noyaux aromatiques et d'une préférence pour la conformation sofa du cycle hétérocyclique. La liaison hydrogène intramoléculaire est la principale force stabilisante dans le patron d'empilement cristallin du composé **3**.

Mots clés : structure cristalline, dihydroquercétine, flavones, liaison hydrogène.

[Traduit par la Rédaction]

Introduction

Dihydroflavonols (2-aryl-3-hydroxy-2,3-dihydrobenzopyran-4-ones) are widely distributed in the plant kingdom and exhibit a large variety of physiological effects (1). Dihydroquercetin (3,3′,4′,5,7-pentahydroxyflavanone, **1**) (dhq), the most common member of this group of flavonoids, occurs in Douglas fir bark and has been found in *O*-methylated, *O*-acetylated, and glycosidic forms in many other plants. The close similarity in the chemical and spectral properties of various partially derivatized dhq isomers has led to inconsistent and erroneous structural (2) and spectral assignments (3) in the past. Following the synthesis of 22 of the 31 possible dhq acetates (4), we now report the crystal parameters of dhq 3-acetate **3** and dhq 3,3′,4′,7-tetraacetate **4**, the only two that yielded single crystals of sufficient size for X-ray diffraction studies, and compare them to those of 16 known 5-hydroxyflavanones.

Discussion

(2*R*,3*R*)-Dihydroquercetin 3-acetate **3**, the sweet principle of several subtropical plants (3, 5–7), was prepared by exhaustive acetylation of (+)-dihydroquercetin with excess acetic anhydride and pyridine (8, 9) and subsequent deacetylation of the pentaacetate **2** with sodium sulfite in aqueous methanol (4) (Scheme 1). Integration of its ^{1}H NMR spectrum showed the product to be a monoacetate, with the following characteristic proton chemical shifts (in Me_2CO-d_6) indicating the presence of an aliphatic rather than an aromatic ester: δ 1.96 (3-O*Ac*, vs. 2.26 and 2.28 for ArO*Ac* of **2** and **4**), 5.82 (H-3, vs. 4.4–4.8 for 3-C*H*OH of **1**), and 11.57 ppm (5-O*H*, H-bonded to >C=O). The absolute configurations of **3** and **4** follow from their optical activity, the proven stereochemistry of the (+)-dhq (10) used as starting material, and the known retention of configuration at the chiral centers during mild base-catalyzed *O*-acetylation (11) and *O*-deacetylation (12) of flavonoids.

The 3,3′,4′,7-tetraacetate **4** is obtained as major acetylation product of dhq when only catalytic amounts of pyridine are used as base catalyst (4, 8). It can be readily separated from the pentaacetate **2** formed as byproduct by crystallization from methanol. Contrary to a previous literature report (2), acid-catalyzed deacetylation of **2** yields the isomeric 3,3′,4′,5-tetraacetate. The structure with the free hydroxyl

Received February 15, 1999.

E. Kiehlmann.[1] Department of Chemistry, Simon Fraser University, Burnaby, BC V5A 1S6, Canada.
K. Biradha. Department of Chemistry, Saint Mary's University, Halifax, NS B3H 3C3, Canada.
K.V. Domasevitch and M. Zaworotko. Department of Chemistry, University of Winnipeg, 515 Portage Avenue, Winnipeg, MB R3B 2E9, Canada.

[1]Author to whom correspondence may be addressed. Telephone: (604) 291-4880. Fax: (604) 291-3765. e-mail: ekie@sfu.ca

 © 1999 NRC Canada

Scheme 1.

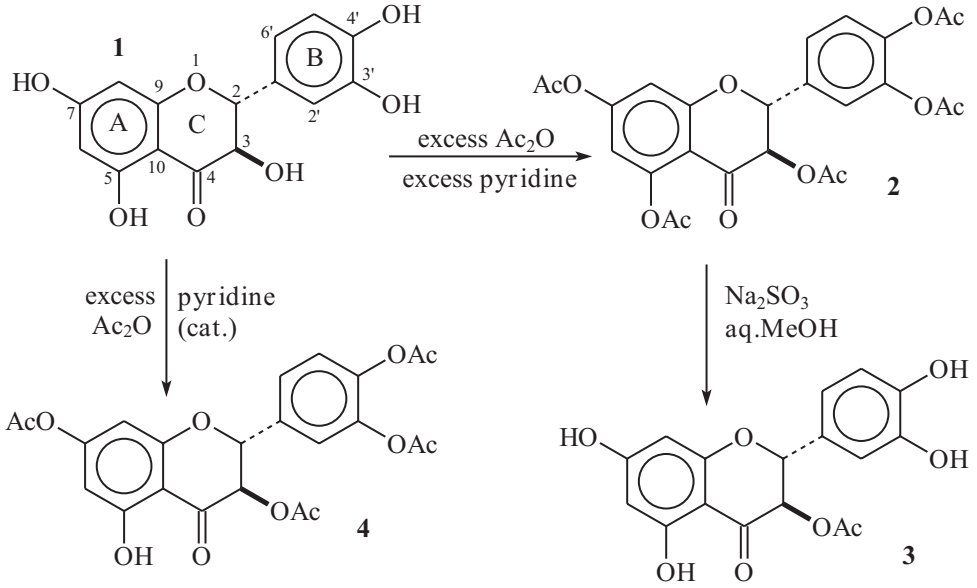

group at C-5 (**4**, systematic name: (2*R*,3*R*)-3,7-bis(acetyloxy)-2-[3,4-bis(acetyloxy)phenyl]-2,3-dihydro-5-hydroxy-4*H*-1-benzopyran-4-one) was first proposed by Aft (8, 13) on the basis of IR- and UV-spectral evidence and is consistent with the results of our NMR and X-ray crystallographic studies.

Comparison of the chemical shifts of its aromatic protons and C-13 nuclei with those of **2** and other flavanone acetates (4, 14) shows that the A-ring is monoacetylated, and the downfield position and sharpness of the OH peak (11.35 ppm in Me_2CO-d_6, 11.28 ppm in $CDCl_3$) in the ^1H NMR spectrum are typical of a strongly hydrogen-bonded proton. Since this proton exchanges slowly, it broadens the signals of adjacent C-13 nuclei, a feature which has been previously exploited for the unambiguous assignment of tertiary and quaternary carbons in the ^{13}C NMR spectra of 5-hydroxyflavanones (15, 16) and 5-hydroxyisoflavones (17). Thus, in the proton-coupled ^{13}C NMR spectrum of **4**, the broad singlet at 163.8 ppm must be assigned to the hydroxyl-substituted C-5, the sharp triplet at 160.1 ppm to the acetoxy-substituted C-7 (coupled to H-6 and H-8) and the broad triplet at 105.8 ppm to C-4a. Likewise, the broadened double doublet at 104.5 ppm (^1J = 166 Hz, $^3J_{H8}$ = 3.8 Hz) is due to C-6 and can be readily distinguished from the sharp C-8 double doublet at 102.9 ppm.

Single-crystal X-ray diffraction analysis confirmed the structure of **3** as *trans*-2-(3,4-dihydroxyphenyl)-2,3-dihydro-3-acetoxy-5,7-dihydroxy-4*H*-1-benzopyran-4-one, with one organic molecule and two molecules of water comprising the asymmetric unit (Fig. 1). The 3-acetoxy group and the B-ring are linked to the pyranone ring equatorially (angle C1′-C2-C3-OAc 64°), placing H-2 and H-3 into *trans*-diaxial position, in good agreement with the large ^1H NMR coupling constant (J_{23} = 12.0 Hz) observed in solution. The heterocyclic ring adopts a sofa conformation, with C-2 as the only atom deviating significantly (by 0.61 Å; C-3 deviates by 0.04 Å) from the mean plane defined by O-1, the six carbon atoms of the A-ring and C-4. The plane of the pendant catechol ring (B) forms a torsional angle of 73° with the A-ring. This appears to be energetically more favorable than a parallel alignment because it minimizes repulsive steric interactions between the *ortho* hydrogens (H-2′ and H-6′) and the bulky 3-acetoxy substituent. The 5-OH proton is displaced by 0.18 Å from the O5-CCC-O4 mean plane, and the large C5-O5-H bond angle of 136(5)° places it into a relatively unfavorable position for efficient intramolecular hydrogen bonding to the carbonyl oxygen (O4) via a puckered six-membered ring. Intermolecular hydrogen bonding forces, on the other hand, are strong (O···H distances <2.0 Å) and account for the stability of the crystal. They involve the 3′-, 4′-, and 7-OH groups as donors, 4′-OH, 5-OH, and the ester carbonyl as acceptors, and the water of hydration. Each water molecule is tetrahedrally connected to two others and two phenolic OH groups: one links OH-4′ and OH-7, the other OH-3′ and OH-5 of adjacent organic moieties (Fig. 2). In addition, a hydrogen bond between OH-4′ and the carbonyl oxygen of the acetoxy group links molecules related by the screw axis. The H-bonding parameters are summarized in Tables 1 and 2.

The tetraacetate **4** crystallizes in the triclinic *P*1 space group and exhibits three-center bifurcated hydrogen bonding. Its asymmetric unit comprises two residues (Fig. 3). In the crystal lattice, each hydroxyl proton is hydrogen-bonded to two pyranone carbonyl oxygen atoms (one intra-, the other intermolecularly), and each of the carbonyl oxygens in turn is surrounded by two hydroxyl protons. Although the hydrogen atoms are positioned slightly above the O5-CCC-O4 plane (as in **3**), the smaller C5-O-H angles of 116(4)° and 98(4)° (vs. 136° for **3**) indicate that in this case intramolecular attractive forces predominate. The heterocyclic ring adopts a half-chair conformation with C-2 above (0.46, 0.47 Å) and C-3 below (–0.25, –0.41 Å) the mean plane defined by the A-ring, O-1 and C-4. As in **3**, ring B is nearly orthogonal (75°, 73°) to ring A, and the two hydrogens of ring C are again *trans*-diaxial. Large Ar-OCO (63°–90°) and small ArO-CO torsional angles (2°–10°), as found in most aryl acetate crystal structures (18), suggest that the lone electron pairs of the three acetylated phenolic oxygens are delocalized mainly into the carbonyl groups. Crystal data,

© 1999 NRC Canada

Fig. 1. ORTEP diagram of **3** with atomic numbering scheme.

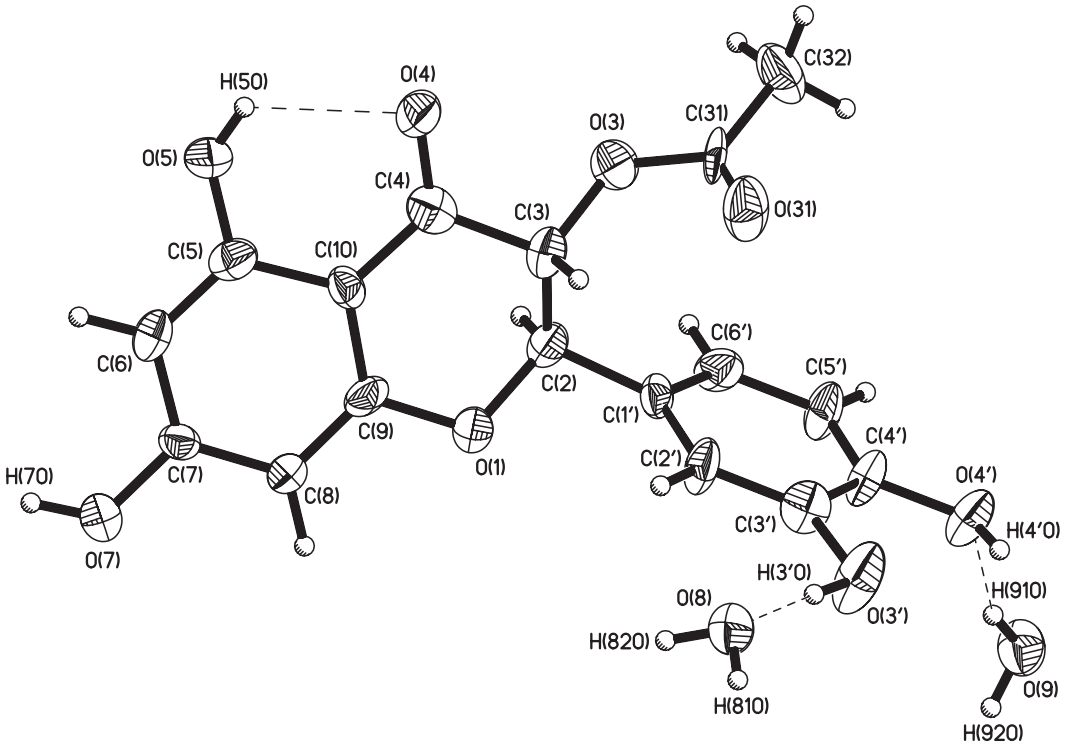

Fig. 2. Packing diagram of **3** (projection on the *bc* plane).Hydrogen bonds are represented by broken lines. Not shown (for clarity of presentation) are additional hydrogen bonds from O(8) to H(3′O), O(4′) to H(9O), and O(31) to H(4′O). The water molecules form an infinite network, with bulky flavanones attached as pendants.

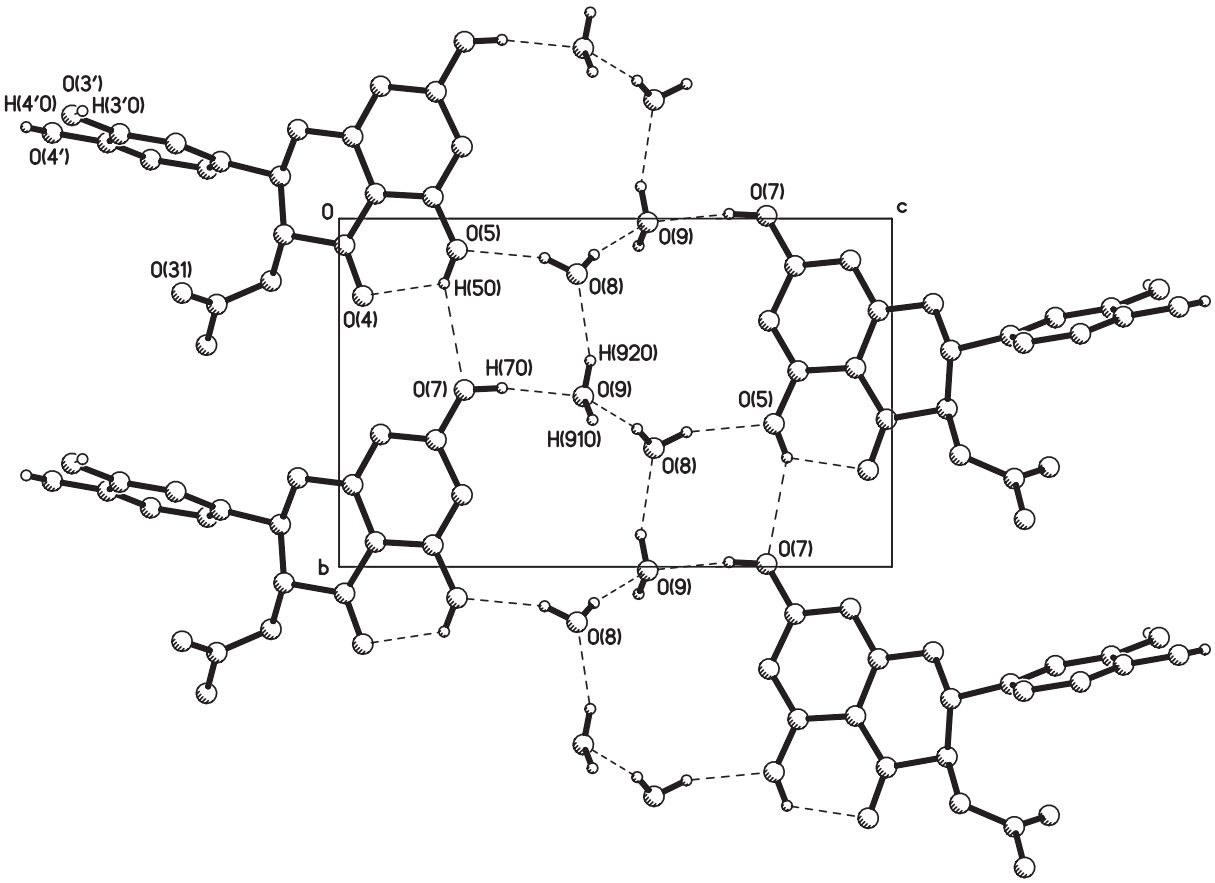

© 1999 NRC Canada

Table 1. Intermolecular hydrogen-bonding in dhq acetates **3** and **4**.[a]

Compd.	Donor, D	Hydrogen atom, H	Acceptor, A	Distances (Å)			Angle (°)
				D—H	D---A	H---A	D-H---A
3	O(5)	H(5O)	O(7) (*x*, 1+*y*, *z*)	0.83(9)	3.187(8)	2.20(8)	150(7)
	O(7)	H(7O)	O(9) (1+*x*, *y*, 1+*z*)	0.90(8)	2.705(8)	1.84(8)	163(8)
	O(3′)	H(3′O)	O(8)	0.81(6)	2.747(9)	1.95(7)	165(6)
	O(4′)	H(4′O)	O(31) (1–*x*, –0.5+*y*, 1–*z*)	0.76(5)	2.670(7)	1.94(5)	159(6)
	O(8)	H(82O)	O(5) (2–*x*, –0.5+*y*, 2–*z*)	0.83(7)	2.870(10)	2.09(8)	159(7)
	O(8)	H(81O)	O(9) (1+*x*, *y*, *z*)	0.77(6)	2.791(9)	2.05(8)	167(8)
	O(9)	H(91O)	O(4′)	1.02(14)	2.733(9)	1.73(13)	160(11)
	O(9)	H(92O)	O(8) (1–*x*, –0.5+*y*, 1–*z*)	0.83(8)	2.790(10)	1.99(8)	161(7)
4	O(5A)	H(5OA)	O(4B) (–1+*x*, *y*, –1+*z*)	0.89(8)	2.934(8)	2.48(8)	112(6)
	O(5B)	H(5OB)	O(4A) (1+*x*, *y*, 1+*z*)	1.02(9)	2.875(8)	2.08(8)	133(6)

[a]Intramolecular hydrogen bonds are listed in Table 2.

Fig. 3. ORTEP diagram of **4** with atomic numbering scheme. Perspective projection of the dimeric moiety, with 40% probability thermal ellipsoids. The acetyl groups attached to atoms O(3′A), O(4′A), O(3′B), and O(4′B) are omitted for clarity.

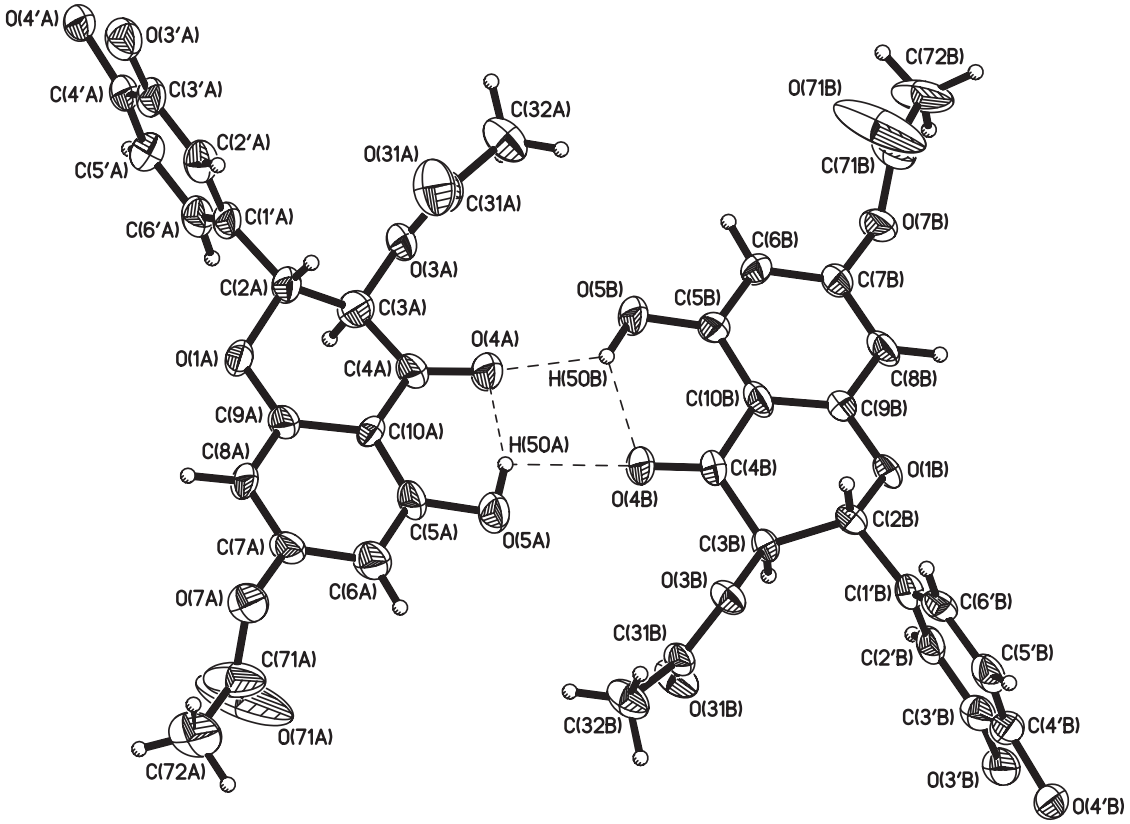

structure refinement parameters, and selected bond lengths and angles of **3** and **4** are listed in Tables 3 and 4, the refined atomic coordinates in Tables 5–7.

The Cambridge Crystallographic Database[2] contains 16 5-hydroxy-flavanones: 10 (**5***a–j*, Scheme 2) (19) with and 6 (16, 20) without hydrogen coordinates. Comparison of their crystal parameters with those of **3** and **4** (Table 2) permits the following generalizations about the conformational preferences that are common to this class of compounds and applicable to both the solid and solution state.

The pyranone ring prefers the sofa over the half-chair conformation in all compounds except **4**, **5b**, and **5e**. In silybin (**5k**, R_3 = OH, $R_{3'}$-$R_{4'}$ = O-CH(CH_2OH)-CHAr-O, ref. 20*a*) and uvarinol (**5l**, R_8 = 2-hydroxybenzyl, R_6 = 2-hydroxy-5-(2-hydroxybenzyl)-benzyl, ref. 20*b*), one residue of the asymmetric unit is a slightly distorted sofa, the other a half-chair, demonstrating the flexible response of the

[2]Cambridge Crystallographic Data Centre (CCDC), http://www.ccdc.cam.ac.uk (see footnote 4 for address).

© 1999 NRC Canada

Table 2. Crystal parameters of 5-hydroxyflavanones.

Compd.	Additional substituents	Torsional angles		(Å) from plane O(1)-A ring-C(4)		C ring conformation	Intramol. H bonding (Å)		Intermolecular H bonds (H···O < 2.2 Å)	Ref.
		A/B planes	C(4a)-C(5)-O-H	C-2	C-3		O(5)···O(4)	OH(5)···O(4) [angle at H]		
3	3-OAc-3′,4′,7-OH·2H_2O	73°	–17°	–0.61	0.04	Sofa	2.619(8)	2.20(8) [112(6)°]	See Table 1	
4	3,3′,4′,7-OAc	105°	9°	0.46	–0.25	1/2-chair	2.650(8)	1.81(7) [157(6)°]	See Table 1	
		108°	9°	0.47	-0.41	1/2-chair	2.688(8)	1.91(8) [130(7)°]		
5a	3,7,3′,4′-OH-8,2′,6′-prenyl	106°	6°	0.58	–0.22	Distorted Sofa	2.58	1.74 [143°]	O(5)···O(7), O(3)···O(4)	16*a*
5b	3-OAc-6-Me-7-OH	87°	–7°	0.53	–0.34	1/2-chair	2.61	1.73 [139°]	O(7)···O=C-Me	16*b*
5c	3′,7-OH-4′-OMe·H_2O	1°	–1°	0.57	–0.07	Sofa	2.55	1.67 [136°]	H_2O···O(3)···O(5), H_2O···O(7)	16*c*
5d	4′,7-OH	86°	–10°	0.49	–0.11	Sofa	2.65	1.88 [147°]	O(4)···O(4)···O(7)	16*d*
5e	4′-OH-7-Oglyc	11°	1°	0.13	–0.13		2.60	1.76 [142°]	(4′-*OH* not located)	16*e*
5f	4′-OH-7-OMe	86°	2°	–0.68	0.02	Sofa	2.63	1.82 [149°]	O(4)···O(4)	16*f*
5g	4′,7-OMe	71°	8°	0.34	–0.03	Sofa	2.58	1.43 [147°]	None	16*g*
5h	7-OMe	113°	–5°	–0.55	0.16	Dist. sofa	2.57	1.60 [174°]	None	16*h*
5i	6,8-Me-7-OH	83°	–12°	–0.37	0.05	Sofa	2.57	1.84 [128°]	O(4)···O(7)	16*i*
5j	6,7-OMe	78°	–3°	0.58	–0.08	Sofa	2.59	1.77 [156°]	None	16*j*

heterocyclic ring to packing forces. In all cases, H-2 and H-3 are *trans*-diaxial, and except for hesperetin hydrate (**5c**) and naringin hydrate (**5e**), the plane of the equatorial B-ring is oriented nearly perpendicular (71–113°) to that of the A-ring.

Strong intramolecular hydrogen bonding with planar six-membered ring geometry (21) is characteristic of all 5-hydroxyflavanones. The OH(5)···O(4) distances are short (1.43–1.92 Å), the bond angles at the hydrogen atom have a mean value of 143° (esd 9°), and the Ar-OH torsional angles are close to zero (1°–12°). In addition, all molecules with extra phenolic hydroxyl groups form intermolecular hydrogen bonds. The carbonyl oxygen of each of the nine anhydrous compounds accepts two OH protons in bifurcated fashion, while in the three hydrated structures **3**, **5c**, and **5e**, water serves as acceptor, and the 5-OH proton is engaged in three-center hydrogen bonding. Thus, in the presence of water, inter- rather than intramolecular hydrogen bonding appears to determine the crystal geometry. Hesperetin hydrate **5c** is the only structure that may also be stabilized by aromatic ring stacking: its two benzene rings lie in the same plane, and successive molecular layers are approximately 3.6 Å apart.

Experimental

Acetylation of (+)-dhq, extracted from Douglas fir bark as described previously (22), with excess acetic anhydride in the presence of a catalytic amount of pyridine (4) gave the 3,3′,4′,7-tetraacetate **4** in 50% yield, mp 144–6° (MeOH). Proton-coupled ^{13}C NMR (Bruker AMX-400, chemical shifts relative to Me_2CO-d_6 at 29.80) δ (ppm): 169.4 (3-OAc), 168.7–168.4 (ArOAc), 163.8 (br, C-5), 162.6 (d, ^2J = 4 Hz, C-8a), 160.1 (t, ^2J = 4 Hz, C-7), 144.2/143.4 (C-3′/4′), 134.9 (br d, ^2J = 9 Hz, C-1′), 126.4/124.7/124.0 (^1J = 164 Hz, ^3J = 4/8 Hz, H-2′/5′/6′), 105.8 (br t, ^3J = 5 Hz, C-4a), 104.5 (br dd, ^1J = 166 Hz, ^3J = 4 Hz, C-6), 102.9 (dd, ^1J = 169 Hz, ^3J = 4.6 Hz, C-8), 81.1 (m, ^1J = 151 Hz, C-2), 73.3 (dd, ^1J = 147 Hz, ^2J = 2.3 Hz, C-3), 21.0 (q, J = 130 Hz, 7-OAc), 20.5 (q, J = 130 Hz, 3′/4′-OAc), and 20.1 (q, J = 130 Hz, 3-OAc). MS (HP-5985 quadrupole instrument) *m*/*z* (% intensity): 472 (0.7, M), 412 (1.3, M – HOAc), 388 (1.7, M – 2 ketene), 370 (3.1, M – ketene – HOAc), 346 (3.5, M – 3 ketene), 328 (14.4, M – 2 ketene – HOAc), 286 (24.3, M – HOAc – 3 ketene), 250 (4.5, M – ring B – CHO), 237 (3.0), 236 (3.6, RDA fragment with ring B – ketene), 223 (3.8), 208 (7.8), 195 (25.1), 194 (20.3, RDA fragment with ring A), 192 (15.1), 153 (100), 152 (73.8, RDA fragment with ring A – ketene), 150 (54.1, $(HO)_2C_6H_3CH{=}CO^{+\cdot}$), 123 (20.9, $(HO)_2C_6H_3CH_2^+$). $[\alpha]_D^{22}$ +41° (Autopol II polarimeter, c 1.07, Me_2CO) (lit. (8) +18.6°, c 1.07). (2*R*,3*R*)-Dihydroquercetin 3-acetate **3** was obtained in 70% yield by deacetylation of the pentaacetate **2** with sodium sulfite in aqueous methanol (41 h/25°) as described previously (4), pale yellow needles, mp 125–7° (aq. MeOH).

Crystal structure determination

The X-ray diffraction data for **3** and **4** were collected on a Siemens SMART/CCD diffractometer equipped with an LT-II low-temperature device, using monochromatic Mo K_α radiation (λ = 0.710 73 Å). Diffracted data were corrected

© 1999 NRC Canada

Table 3. Crystal data and structure refinement parameters for **3** and **4**.

	3	**4**
Empirical formula	$C_{17}H_{18}O_{10}$ ($C_{17}H_{14}O_8 \cdot 2H_2O$)	$C_{23}H_{20}O_{11}$
Formula weight	382.32	472.41
Temperature (°C)	–70 ± 2	–60 ± 2
Crystal system	Monoclinic	Triclinic
Space group	$P2_1$	$P1$
Unit cell: a (Å)	9.1036(14)	5.5715(6)
b, c (Å)	7.8843(11), 12.705(2)	13.1685(13), 15.428(2)
α, β, γ (deg)	90, 99.888(3), 90	85.599(2), 89.629(2), 80.368(2)
Cell volume (Å^3)	898.4(2)	1112.7(2)
Density (calculated) (g cm^{-3})	1.413 (Z = 2)	1.410 (Z = 2)
Absorption coefficient (mm^{-1})	0.118	0.114
F(000)	400	492
Crystal size (mm)	0.20 × 0.15 × 0.15	0.25 × 0.20 × 0.20
θ range for data collection (°)	1.63–25.00	1.31–27.94
Reflections collected	3690	6244
Independent reflections	2784 (R(int) = 0.0413)	5296 (R(int) = 0.0300)
Observed reflections ($I > 2\sigma(I)$)	1618	3073
Data/restraints/parameters	2784/1/276	5296/3/621
Goodness-of-fit on F^2	0.971	0.965
Final R^a indices (obs.)	$R1$ = 0.0772, $wR2^b$ = 0.1397	$R1$ = 0.0705, $wR2^b$ = 0.1628
R^a indices (all data)	$R1$ = 0.1471, $wR2^b$ = 0.1679	$R1$ = 0.1267, $wR2^b$ = 0.1927
Largest diff. peak and hole (e Å^{-3})	0.231 and –0.224	0.271 and –0.233

[a] $R = \Sigma||F_o| - |F_c||/\Sigma|F_o|$.

[b] $1/w = [\sigma^2(F_o^2) + (aP)^2 + bP]$ where $3P = (F_o^2 + 2F_c^2)$; a and b are constants adjusted by the program.

Table 4. Selected bond distances (Å) and angles (deg) (X = H or Ac).

Distance	**3**	**4A**	**4B**	Angle	**3**	**4A**	**4B**
O(1)—C(9)	1.388(7)	1.359(9)	1.367(8)	C(9)-O(1)-C(2)	115.9(6)	115.3(5)	116.1(5)
O(1)—C(2)	1.452(8)	1.446(8)	1.451(8)	O(1)-C(2)-C(3)	108.9(5)	109.4(6)	107.0(5)
O(3)—C(3)	1.450(8)	1.429(8)	1.446(7)	O(3)-C(3)-C(4)	109.6(6)	111.5(6)	108.1(5)
O(4)—C(4)	1.229(8)	1.226(9)	1.221(8)	C(2)-C(3)-C(4)	112.6(6)	110.3(6)	107.6(5)
O(5)—C(5)	1.331(9)	1.351(9)	1.338(9)	O(4)-C(4)-C(10)	124.5(7)	124.2(7)	124.8(7)
O(7)—C(7)	1.343(9)	1.417(9)	1.397(9)	O(4)-C(4)-C(3)	120.1(7)	120.7(7)	122.2(6)
O(7)—X	0.90(8)	1.320(10)	1.323(10)	C(10)-C(4)-C(3)	115.4(7)	114.8(7)	112.8(6)
O(3′)—X	0.81(6)	1.326(11)	1.365(9)	C(9)-C(10)-C(4)	122.1(7)	119.8(7)	121.3(7)
O(4′)— X	0.76(5)	1.380(10)	1.358(9)	C(9)-C(10)-C(5)	116.2(7)	118.2(6)	118.4(6)
C(2)—C(1′)	1.488(9)	1.516(10)	1.520(10)	C(4)-C(10)-C(5)	121.6(7)	122.0(7)	119.9(7)
C(2)—C(3)	1.501(10)	1.493(10)	1.518(9)	O(5)-C(5)-C(6)	120.5(7)	115.7(8)	119.3(7)
C(3)—C(4)	1.518(10)	1.514(11)	1.515(9)	O(5)-C(5)-C(10)	119.2(8)	121.7(7)	122.4(6)
C(4)—C(10)	1.419(10)	1.431(10)	1.467(9)	C(5)-O(5)-H	136(5)	98(4)	116(4)
C(10)—C(5)	1.446(10)	1.396(10)	1.440(10)	C(7)-O(7)-X	125(6)	118.1(7)	120.8(7)
C(9)—C(10)	1.409(10)	1.435(10)	1.381(10)	O(1)-C(9)-C(10)	119.7(7)	121.7(6)	120.8(6)

for absorption using the SADABS program, SHELXTL was used for the structure solution,[3] and full-matrix least-squares refinement was based on F^2. All the non-hydrogen atoms were refined anisotropically. Hydrogen atoms attached to carbon were fixed at calculated positions and refined isotropically on the basis of corresponding C-atoms (U(H) = 1.2 Ueq (C)); those of O-H groups were located and refined isotropically. Pertinent crystallographic details are given in Tables 3–6. Supplementary tables of crystal structure and refinement, atomic coordinates, bond lengths and angles, anisotropic thermal parameters, and hydrogen coordinates have been deposited.[4]

[3] G.M. Sheldrick. SADABS. Univ. Göttingen, 1996; SHELXTL, Release 5.03. Siemens Analytical X-ray Instruments Inc., Madison, Wis. 1994.

[4] Supplementary material may be purchased from: The Depository of Unpublished Data, Document Delivery, CISTI, National Research Council Canada, Ottawa, Canada, K1A 0S2. With the exception of tables of displacement parameters, these have also been deposited with the Cambridge Crystallographic Data Centre and can be obtained on request from: The Director, Cambridge Crystallographic Data Centre, University Chemical Laboratory, 12 Union Road, Cambridge, CB2 1EZ, U.K.

© 1999 NRC Canada

Table 5. Atomic coordinates (× 10^4) and equivalent isotropic displacement parameters (Å^2 × 10^3) for refined atoms of **3**. *U*(eq) is defined as one third of the trace of the orthogonalized U^{ij} tensor.

	x	*y*	*z*	*U*(eq)
O(1)	7206(5)	7446(6)	9254(3)	38(1)
O(31)	6461(5)	12137(7)	7158(4)	49(2)
O(3)	5826(5)	11793(6)	8768(4)	36(1)
O(4)	8110(6)	12219(6)	10429(4)	45(1)
O(5)	9736(7)	10892(8)	12132(5)	41(2)
O(7)	9996(6)	4919(7)	12267(5)	37(1)
O(3′)	5904(5)	7034(9)	5167(4)	56(2)
O(4′)	2947(5)	7535(7)	4812(4)	39(1)
O(8)	8929(7)	6591(8)	5696(5)	42(2)
O(9)	784(6)	5105(10)	4418(4)	42(2)
C(2)	6128(8)	8787(9)	8934(5)	31(2)
C(3)	6928(8)	10457(9)	9005(5)	34(2)
C(4)	7864(8)	10763(11)	10098(6)	34(2)
C(10)	8426(8)	9283(9)	10659(5)	26(2)
C(5)	9377(8)	9376(11)	11696(6)	33(2)
C(6)	9888(7)	7932(11)	12224(5)	34(2)
C(7)	9513(7)	6355(10)	11753(6)	25(2)
C(8)	8634(8)	6198(9)	10751(5)	30(2)
C(9)	8105(7)	7643(10)	10244(5)	31(2)
C(1′)	5297(7)	8363(9)	7854(5)	26(2)
C(2′)	6049(7)	7841(10)	7044(5)	38(2)
C(3′)	5291(7)	7566(11)	6030(5)	37(2)
C(4′)	3757(7)	7814(11)	5812(5)	33(2)
C(5′)	3000(7)	8304(10)	6590(5)	36(2)
C(6′)	3751(7)	8569(9)	7617(5)	34(2)
C(31)	5655(8)	12466(10)	7787(5)	37(2)
C(32)	4362(8)	13632(11)	7601(6)	52(2)
H(5O)	9700(80)	11860(110)	11900(60)	50(30)
H(7O)	10390(80)	4870(110)	12950(60)	60(30)
H(3′O)	6760(70)	6830(80)	5400(50)	18(18)
H(4′O)	3340(60)	7370(70)	4340(40)	6(17)
H(81O)	9410(70)	6040(90)	5390(50)	20(30)
H(82O)	9210(80)	6130(90)	6280(60)	40(30)
H(91O)	1760(140)	5780(180)	4580(100)	170(60)
H(92O)	950(80)	4080(100)	4540(60)	40(30)

Table 6. Atomic coordinates (× 10^4) and equivalent isotropic displacement parameters (Å^2 × 10^3) for refined atoms of molecule **4A**. *U*(eq) is defined as one third of the trace of the orthogonalized U^{ij} tensor.

	x	*y*	*z*	*U*(eq)
O(1A)	6675(9)	3344(3)	5253(3)	43(1)
O(31A)	3340(11)	6091(5)	3908(4)	74(2)
O(3A)	977(10)	5145(4)	4656(3)	51(1)
O(4A)	1746(10)	4020(4)	3257(4)	53(1)
O(5A)	4262(11)	2506(4)	2425(3)	55(2)
O(7A)	11472(9)	722(4)	3759(4)	53(2)
O(3′A)	8065(10)	6731(4)	6936(4)	56(2)
O(4′A)	4527(10)	6515(4)	8178(3)	51(1)
O(3′1)	5877(20)	7926(6)	6079(8)	163(5)
O(4′1)	8149(11)	5718(4)	8708(3)	54(1)
O(71A)	9491(16)	–568(6)	4012(10)	181(6)
C(2A)	5159(14)	4349(6)	5122(5)	49(2)
C(3A)	2795(14)	4237(6)	4720(5)	52(2)
C(4A)	3226(15)	3776(5)	3852(5)	45(2)
C(10A)	5318(14)	2984(5)	3825(4)	35(2)
C(5A)	5763(15)	2371(6)	3124(5)	46(2)
C(6A)	7714(15)	1580(6)	3104(6)	53(2)
C(7A)	9289(14)	1440(5)	3817(5)	46(2)
C(8A)	9008(13)	2025(5)	4508(5)	42(2)
C(9A)	7019(14)	2799(5)	4537(5)	41(2)
C(1′A)	4978(14)	4843(6)	5981(5)	43(2)
C(2′A)	6540(15)	5525(6)	6093(5)	50(2)
C(3′A)	6440(14)	6063(6)	6822(5)	44(2)
C(4′A)	4781(15)	5892(6)	7473(5)	48(2)
C(5′A)	3261(15)	5201(6)	7386(5)	46(2)
C(6′A)	3378(16)	4662(6)	6648(5)	54(2)
C(3′1)	7637(22)	7660(8)	6514(8)	87(3)
C(3′2)	9632(21)	8258(8)	6642(9)	106(4)
C(4′1)	6455(17)	6380(6)	8756(5)	50(2)
C(4′2)	6009(18)	7170(6)	9401(5)	60(2)
C(31A)	1369(16)	5976(6)	4156(5)	50(2)
C(32A)	–935(17)	6736(6)	3989(6)	67(3)
C(71A)	11326(19)	–271(7)	3808(9)	83(3)
C(72A)	13770(16)	–963(7)	3697(8)	82(3)
H(5OA)	3334(147)	3086(55)	2558(44)	47(22)

Scheme 2.

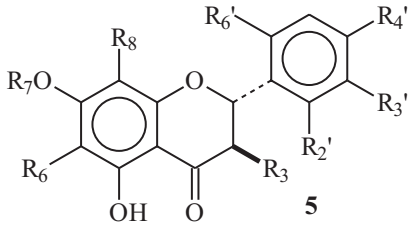

5

All R=H except as listed
(with CCDC RefCode)

a) $R_3 = R_3' = R_4' = OH$, $R_2' = R_6' = R_8 =$ prenyl (PIJCIU)
b) $R_3 = OAc$, $R_6 = Me$ (JEDVAP)
c) $R_3' = OH$, $R_4' = OMe$ (FOYTOC)
d) $R_4' = OH$ (DOLRIF)
e) $R_4' = OH$, $R_7 =$ glyc (TAFBEH)
f) $R_4' = OH$, $R_7 = Me$ (JESGET)
g) $R_4' = OMe$, $R_7 = Me$ (SATDAS)
h) $R_7 = Me$ (KEDDAY)
i) $R_6 = R_8 = Me$ (FUNWUG)
j) $R_6 = OMe$, $R_7 = Me$ (RAVMIK)

© 1999 NRC Canada

Table 7. Atomic coordinates (× 10^4) and equivalent isotropic displacement parameters (Å^2 × 10^3) for refined atoms of molecule **4B**. *U*(eq) is defined as one third of the trace of the orthogonalized U^{ij} tensor.

	x	*y*	*z*	*U*(eq)
O(1B)	4538(9)	4229(3)	9737(3)	43(1)
O(31B)	8453(11)	1005(4)	11090(4)	60(2)
O(3B)	9924(9)	2302(3)	10342(3)	41(1)
O(4B)	9474(10)	3457(4)	11710(3)	53(2)
O(5B)	7228(11)	5095(4)	12510(4)	56(2)
O(7B)	–127(10)	6870(4)	11207(4)	52(2)
O(3′B)	3160(9)	1118(4)	8119(4)	55(2)
O(4′B)	6587(11)	1127(4)	6794(3)	53(2)
O(3′3)	5737(13)	–215(5)	8750(7)	117(3)
O(4′3)	3118(10)	2041(4)	6204(3)	50(1)
O(71B)	1796(15)	8177(5)	10998(9)	161(5)
C(2B)	6930(13)	3628(5)	9611(4)	40(2)
C(3B)	7604(11)	2959(5)	10447(4)	33(2)
C(4B)	7889(14)	3672(5)	11152(5)	38(2)
C(10B)	5983(14)	4590(5)	11117(5)	43(2)
C(5B)	5673(14)	5233(5)	11837(5)	39(2)
C(6B)	3645(15)	6006(5)	11837(5)	43(2)
C(7B)	2004(13)	6144(5)	11181(5)	39(2)
C(8B)	2275(14)	5553(5)	10455(5)	44(2)
C(9B)	4287(13)	4792(5)	10451(4)	34(2)
C(1′B)	6754(14)	3012(5)	8826(5)	40(2)
C(2′B)	5002(14)	2365(5)	8819(5)	42(2)
C(3′B)	4958(14)	1762(5)	8143(5)	44(2)
C(4′B)	6515(14)	1807(6)	7466(5)	44(2)
C(5′B)	8212(15)	2476(6)	7455(5)	49(2)
C(6′B)	8285(14)	3069(5)	8145(5)	39(2)
C(3′3)	3770(16)	122(6)	8464(7)	65(3)
C(3′4)	1541(23)	–392(8)	8479(10)	122(6)
C(4′3)	4721(16)	1317(6)	6211(5)	45(2)
C(4′4)	4999(19)	492(7)	5585(7)	73(3)
C(31B)	10126(14)	1347(5)	10765(5)	39(2)
C(32B)	12676(14)	785(6)	10803(6)	55(2)
C(71B)	–43(16)	7872(7)	11152(7)	62(2)
C(72B)	–2350(17)	8491(6)	11355(8)	91(4)
H(5OB)	8799(159)	4581(61)	12442(48)	63(24)

Acknowledgements

We thank the Natural Sciences and Engineering Research Council of Canada and St. Mary's University for financial support.

References

1. B.A. Bohm. *In* The flavonoids: advances in research since 1986. *Edited by* J.B. Harborne. Chapman & Hall, London. 1994. Chap. 9.
2. V. Brewerton and R.C. Cambie. New Zealand J. Sci. **2**, 95 (1959).
3. F. Bohlmann, C. Zdero, M. Grenz, A.K. Dhar, H. Robinson, and R.M. King. Phytochemistry, **20**, 281 (1981).
4. E. Kiehlmann. Org. Prep. Proced. Int. **31**, 87 (1999).
5. (*a*) N.P.D. Nanayakkara, R.A. Hussain, J.M. Pezzuto, D.D. Soejarto, and A.D. Kinghorn. J. Med. Chem. **31**, 1250 (1988); (*b*) F. Gao, H. Wang, T.J. Mabry, and A.D. Kinghorn. Phytochemistry, **29**, 2865 (1990).
6. M. Grande, F. Piera, A. Cuenca, P. Torres, and I.S. Bellido. Planta Med. 414 (1985).
7. S. Öksüz and G. Topçu. Phytochemistry, **31**, 195 (1992).
8. H. Aft. J. Org. Chem. **26**, 1958 (1961).
9. K. Weinges, R. Kolb, and P. Kloss. Phytochemistry, **10**, 829 (1971).
10. J.W. Clark-Lewis and W. Korytnyk. J. Chem. Soc. 2367 (1958).
11. M. Urano, H. Kagawa, Y. Harigaya, S. Li, and M. Onda. J. Heterocycl. Chem. **28**, 1845 (1991).
12. K. Freudenberg, O. Böhme, and L. Purrmann. Chem. Berichte, **55**, 1734 (1922).
13. H. Aft. J. Org. Chem. **30**, 897 (1965).
14. H. Kolodziej. J. Chem. Soc. Perkin Trans. 1, **1988**, 219.
15. J.H. Jung and J.L. McLaughlin. Phytochemistry, **29**, 1271 (1990).
16. L.T. Byrne, J.R. Cannon, D.H. Gawad, B.S. Joshi, B.W. Skelton, R.F. Toia, and A.H. White. Aust. J. Chem. **35**, 1851 (1982).
17. A.P. Mazurek, L. Kozerski, J. Sadlej, R. Kawecki, E. Bednarek, J. Sitkowski, J.C. Dobrowolski, J.K. Maurin, K. Biniecki, J. Witowska, P. Fiedor, and J. Pachecka. J. Chem. Soc. Perkin Trans. 2, 1223 (1998).
18. E. Kiehlmann, N. Lehto, and D. Cherniwchan. Can. J. Chem. **66**, 2431 (1988).
19. (*a*) C.D. Hufford, Y. Jia, E.M. Croom, Jr., I. Muhammed, A.L.Okunade, A.M. Clark, and R.D. Rogers. J. Nat. Prod. **56**, 1878 (1993); (*b*) M.C. Cheng, Y.S. Cheng, C.F. Chang, and Y. Wang. Acta Crystallogr. Sect. C: Cryst. Struct. Commun. **46**, 719 (1990); (*c*) W. Shin, S. Kim, and K.S. Chun. **43**,Acta Crystallogr. Sect. C: Cryst. Struct. Commun.1946 (1987); (*d*) W. Shin and M.S. Lah. Acta Crystallogr. Sect. C: Cryst. Struct. Commun. **42**, 626 (1986); (*e*) G.-Z. Jin, S. Fujii, and K.-i. Tomita, Acta Crystallogr. Sect. C: Cryst. Struct. Commun. **46**, 1866 (1990); (*f*) M. Shoja. Acta Crystallogr. Sect. C: Cryst. Struct. Commun. **46**, 1969 (1990); (*g*) C.O. Miles, L. Main, and B.K. Nicholson. Acta Crystallogr. Sect. C: Cryst. Struct. Commun. **45**, 681 (1989); (*h*) M. Shoja. Z. Kristallogr. **189**, 89 (1989); (*i*) N. Tanrisever, F.R. Fronczek, N.H. Fischer, and G.B. Williamson. Phytochemistry, **26**, 175 (1987); (*j*) K. Chantrapromma, V. Seechamnan-Turakit, C. Ponglimanont, C. Pakawatchai, H.-K. Fun, and K. Sivakumar. Acta Crystallogr. Sect. C: Cryst. Struct. Commun. **53**, 734 (1997).
20. (*a*) H. Lotter and H. Wagner. Z. Naturforsch. C: Biosci. **38**, 339 (1983); (*b*) C.D. Hufford, W.L. Lasswell, Jr., K. Hirotsu, and J. Clardy. J. Org. Chem. **44**, 4709 (1979); (*c*) K. Chantrapromma, C. Pakawatchai, B.W. Skelton, A.H. White, and S. Worapatamasri. Aust. J. Chem. **42**, 2289 (1989); (*d*) P. Narayanan, K. Zechmeister, M. Rohrl, and W. Hoppe. Acta Crystallogr. Sect. B: Struct. Sci. **27**, 718 (1971); (*e*) S. Fujii, Y. Yamagata, G.-Z. Jin, and K. Tomita. Chem. Pharm. Bull. **42**, 1143 (1994).
21. M.C. Etter. Acc. Chem. Res. **23**, 120 (1990).
22. E. Kiehlmann and E.P.M. Li. J. Nat. Prod. **58**, 450 (1995).

© 1999 NRC Canada

Dendritic aryl imides containing the tetrahydro[5]helicene unit: synthesis, characterization, electrochemical behavior, and comparison with a linear oligoimide analogue

Timothy P. Bender, Yu Qi, Pierre Desjardins, and Zhi Yuan Wang

Abstract: Herein, we describe the synthesis, characterization, and electrochemical behavior of dendritic aryl imides derived from a core compound 3,12-dinitro-5,6,9,10-tetrahydro[5]helicene-7,8-dicarboxylic anhydride (**3**). Compound **3** is an AX_2 type system (where X is a masked or protected group), possesses a well-defined spatial orientation, is conformationally rigid, and contains a conjugated *o*-terphenyl moiety as part of its molecular structure. This compound is used as a building block in the construction of dendritic aryl imides using a divergent synthetic approach. Dendrons from generations one through three were synthesized, and their identities were confirmed. A comparison of the properties of the dendrons, several model compounds, and a linear oligoimide, all containing either the tetrahydro[5]helicene or *o*-terphenyl units, has been made. There are differences in their hydrodynamic volume, glass transition temperature, and electrochemical behaviour. All dendrons are electrochemically active and exhibit well-defined and reversible redox cycles. Furthermore, all dendrons are fluorescent, and the intensity of the fluorescent emission is dependent on the generation of the dendron.

Key words: dendrimer, dendron, electrochemistry, helicene, tetrahydro[5]helicene.

Résumé : On décrit la synthèse, la caractérisation et le comportement électrochimique d'aryl imides dendritriques dérivés d'un composé commun, l'anhydride de l'acide 3,12-dinitro-5,6,9,10-tétrahydro[5]hélicène-7,8-dicarboxylique (**3**). Le composé **3** est un système du type AX_2 (dans lequel X est un groupe caché ou protégé), il possède une orientation spatiale bien définie, il est conformationnellement rigide et sa structure moléculaire comporte une partie *o*-terphényle. Ce composé est utilisé comme bloc dans la construction d'aryl imides dendritiques par une approche synthétique divergente. On a synthétisé des « dendrons » des générations un à trois et on a confirmé leurs identités. On a fait une comparaison des propriétés des dendrons avec celles de plusieurs composés modèles et un oligoimide linéaire qui contenaient tous des unités tétrahydro[5]hélicène ou *o*-terphényle. On a noté des différences dans leur volume hydrodynamique, leur température de transition vitreuse et leur comportement électrochimique. Tous les dendrons sont électrochimiquement actifs et ils présentent tous des cycles redox réversibles bien définis. De plus, tous les dendrons sont fluorescents et l'intensité de l'émission fluorescente dépend de la génération du dendron.

Mots clés : dendrimère, dendron, électrochimie, hélicène, tétrahydro[5]hélicène.

[Traduit par la Rédaction]

Introduction

The incorporation of functionalized [5]helicene derivatives into macromolecular systems has been a focus of our research group for some time now. More specifically, we have found that the tetrahydro[5]helicene moiety, a known precursor to [5]helicene (1, 2), provides a unique and versatile building block for several compounds, all suitable for incorporation into a variety of macromolecular systems (3). All of the compounds we have investigated thus far can be derived from a single core molecule, 5,6,9,10-tetrahydro[5]helicene-7,8-dicarboxylic anhydride (**1**, Scheme 1). This C_2 symmetric molecule has a rigid polycyclic aromatic structure and contains a helical *o*-terphenyl moiety as part of its molecular structure. We have previously shown that compound **1** (Scheme 1) can be selectively derivatized to give an AB-type amino anhydride (**10**, Scheme 2) as well as AA-type diamine and difluoride monomers. Subsequent polymerization of these monomers gave high molecular weight polyimides and poly(ether sulfone)s, respectively (3). In these

Received March 12, 1999.

Dedicated to Dr. Allan S. Hay on the occasion of his 70th birthday.

T.P. Bender, Y. Qi, P. Desjardins, and Z.Y. Wang.[1] Department of Chemistry, Carleton University, 1125 Colonel By Drive, Ottawa, ON K1S 5B6, Canada.

[1]Author to whom correspondence may be addressed. Telephone: (613) 520-2600, ext. 2713. Fax: (613) 520-2316. e-mail: wangw@ccs.carleton.ca

 © 1999 NRC Canada

Scheme 1. Synthesis of key building blocks of the dendrons. (*i*) HNO_3, H_2SO_4, acetic acid, $CHCl_3$, rt, 3–4 days. (*ii*) 1. Ethanolamine, C_6H_5Cl, DMF. 2. Fe, HCl. (*iii*) Ethanolamine, DMF. (*iv*) 1,3,5-Benzenetricarbonyl trichloride, DMAP, CH_2Cl_2, rt, overnight.

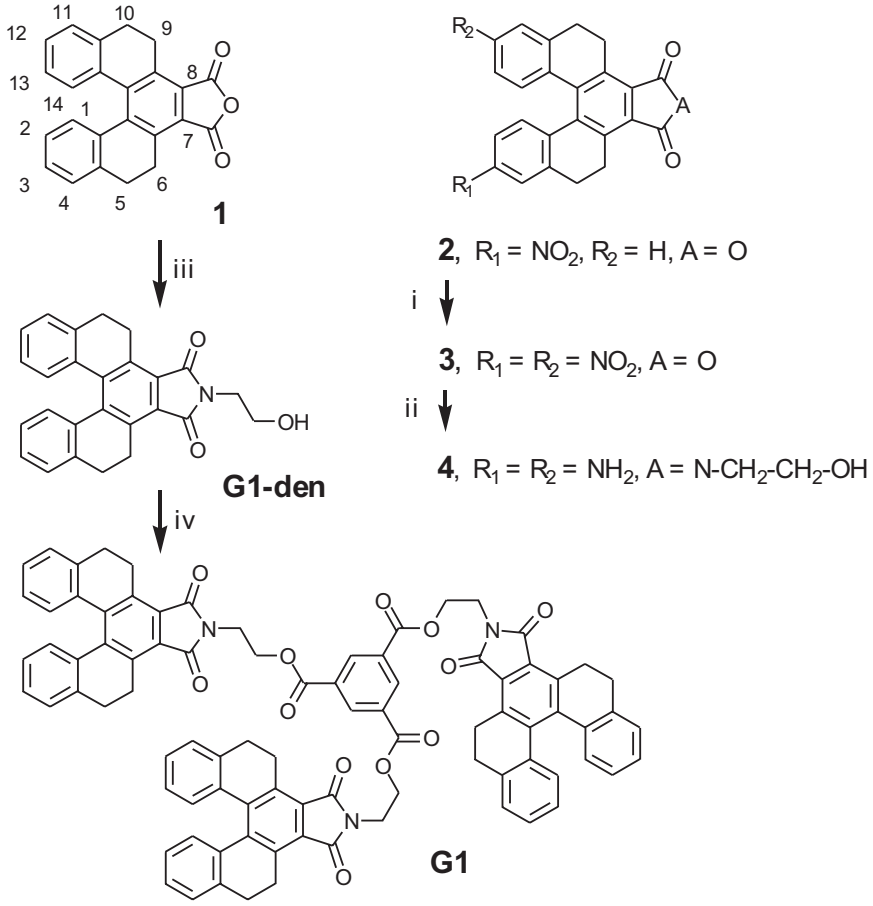

Scheme 2. Synthesis of oligoimide **11** (*n* = 4–10). (*i*) *m*-Cresol, 200°C, time controlled, fractionated from $CHCl_3$–MeOH.

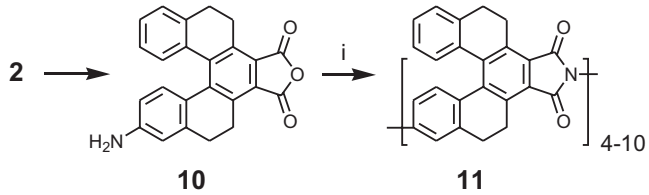

studies, a markable increase in the solubility of the polyimides containing the tetrahydro[5]helicene unit, as compared to the same containing a [5]helicene unit, was observed. Furthermore, the tetrahydro[5]helicene unit was shown to increase the glass transition temperature, proportionally to its content, in a series of random copoly(ether sulfone)s (3*d*). Wide angle X-ray diffraction (WAXD) experiments performed on the polyimide derived from the AB-type amino anhydride monomer **10** showed it to be completely amorphous.[2]

High molecular weight polymers containing the [5]helicene moiety were readily obtained from precursor polyimides containing the tetrahydro[5]helicene unit by post polymer transformation using elemental bromine or atmospheric oxygen (3*a*, *b*); whereas we were unable to obtain high molecular weight polyimides that contained the [5]helicene moiety by direct solution polymerization of the corresponding monomer, presumably due to its rigidity and low solubility in the polymerization medium. Through the use of molecular modeling, it is speculated that although both the tetrahydro[5]helicene and [5]helicene moieties occupy the same molecular level spacial volume, the tetrahydro[5]helicene unit is more flexible within that volume and therefore imparts greater solubility to the macromolecules for which it is a part (3*c*). Additionally, due to the bridging carbons at positions 5, 6, 9, and 10 (see numbering Scheme 1) the *o*-terphenyl moiety within the tetrahydro[5]helicene unit remains conformationally locked so as to allow a state of conjugation between these benzene rings.

Having explored the properties and characteristics of linear macromolecules containing the tetrahydro[5]helicene unit, it would now be of interest to study the properties of the same unit within a macromolecule having dendritic architecture (for a general reference on dendrimers and dendrimer synthesis, see ref. 4). The synthesis of regular dendritic aryl imides would allow not only for the study of such molecules, but gives a direct avenue for the comparison of such dendritic molecules with their linear analogues, which we have previously synthesized and studied (3*a*). For example, the dendrimer should also possess a relatively lower glass

[2] Z.Y. Wang. Unpublished results.

© 1999 NRC Canada

Scheme 3. Synthesis of higher generation dendrons. (*i*) **1**, *m*-cresol, 200°C. (*ii*) 1. **3**, *m*-cresol, 200°C. 2. Fe, HCl. (*iii*) **1**, *m*-cresol, 200°C.

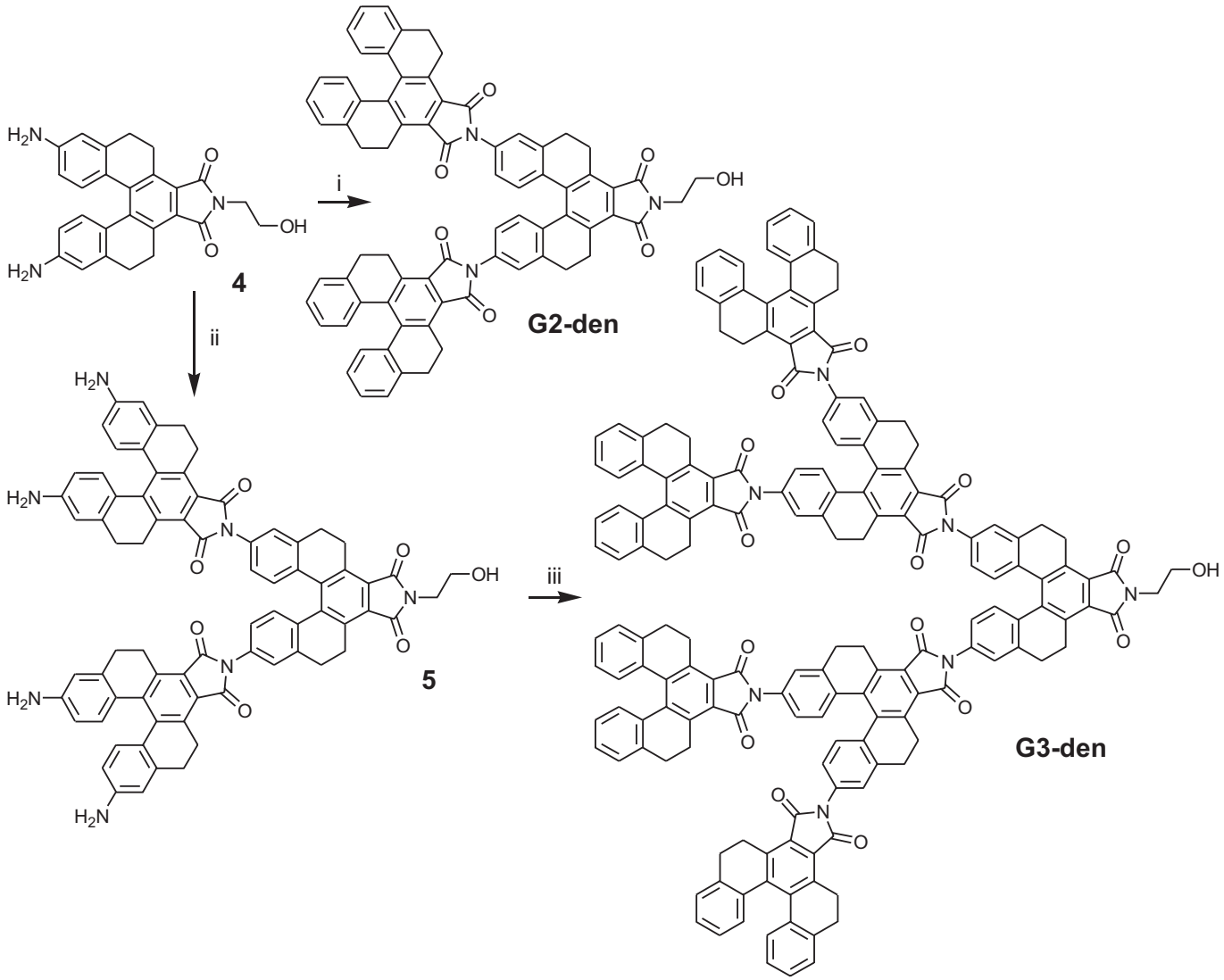

transition temperature (T_g) as compared to its linear analogue. Disc-shaped dendritic poly(aryl ether)s have been previously used to modify the properties of poly(*p*-phenylene) (5). Furthermore, given the dendrimer's extended array of *o*-terphenyl moieties, one may expect these dendritic macromolecules to possess some unique and interesting electrochemical properties as compared to their monomeric and oligomeric counterparts. Therefore, we have set out to construct dendritic aryl imides containing the tetrahydro[5]helicene unit using a divergent synthetic sequence, as presented herein.

Experimental section

Nomenclature

G1-den (Scheme 1), **G2-den** (Scheme 3), and **G3-den** (Scheme 3) refer to the first, second, and third generation dendrons, respectively. **G1** and **G2** refer to the first and second generation dendrimers, respectively.

Materials

The synthesis and characterization of compounds **1**, **2**, **6**, and **10** were previously reported (3*a*). Compound **7** was made according to our established synthesis for compound **1** (3*a*). Compounds **8** (6) and **9** (7) are known. Oligoimide **11** was synthesized using the published method except that the polycondensation was time-controlled so as to produce low molecular weight polyimide (3*a*). Fractionation of the produced oligoimide, to give material containing 4–10 repeat units, was accomplished from chloroform solution with methanol. Chlorobenzene and *N*,*N*-dimethylformamide (DMF) were reagent grade (Aldrich) and dried over 4 Å molecular sieves prior to use. Ethanolamine, iron powder, *m*-cresol, isoquinoline, 1,3,5- benzenetricarbonyl trichloride, *N*,*N*-dimethyl-4-aminopyridine (DMAP), and toluene were reagent grade (Aldrich) and used as received. Spectrophotometric grade DMF (Aldrich), NMP (1-methyl-2-pyrrolidinone, Aldrich), and Bu_4NPF_6 (Sigma) were used as received. Purification of dendrons and dendrimers was done using a gravity fed preparative size exclusion chromatogra-

© 1999 NRC Canada

phy (SEC) column packed with Bio-Beads SX-3 (purchased from Bio-Rad). Flash chromatography was performed using standard grade silica gel (Merck).

Characterization

^{1}H and ^{13}C NMR spectra were recorded on either a Varian Gemini-200 or a Bruker-400 instrument using tetramethylsilane as an internal reference. Infrared measurements were performed on a Bomen Michelson 120 FTIR spectrometer. Low- (EI) and high-resolution mass spectra were obtained on VG 7070E and Kratos Concept IIH spectrometers, respectively. Melting points were obtained with a Fisher–Johns apparatus and are uncorrected. Gel permeation chromatography (GPC) was performed using chloroform at ambient temperature at a flow rate of 1.0 mL per min; a UV detector set at 254 nm wavelength was used for detection. The glass transition temperatures were determined on a Seiko 220C DSC at a heating rate of 10°C/min under nitrogen flow (200 mL/min). MALDI-TOF mass spectra were obtained on a Kratos Kompact MALDI 3 time-of-flight mass spectrometer, using a dithranol/lithium bromide (20:1 by weight) or dithranol/silver trifluoroacetate (20:1 by weight) matrix. Electrochemical measurements were performed on a custom-made electrochemical workstation using a silver wire pseudo-reference, BAS MF2013 platinum disc working electrode, and platinum wire counter electrode. Measurements were made in DMF or NMP solution containing 0.1 M Bu_4NPF_6. The solutions were deoxygenated with argon for at least 15 min prior to measurements. All electrochemical potentials were corrected versus SCE using the position of the $Fe(cp)_2^{+/0}$ couple determined in DMF solution, by relation to the position of the $Co(cp)_2^{+/0}$ couple (8). Molecular modeling was performed on a personal computer using HyperChem version 5.01. Models were optimized using the MM+ molecular mechanics method.

3,12-Dinitro-5,6,9,10-tetrahydro[5]helicene-7,8-dicarboxylic anhydride (3)

Compound **2** (30.0 g) was dissolved in 1.0 L of chloroform to which was added 300 mL of acetic acid. The nitrating agent (275 mL of 70% nitric acid and 250 mL of concentrated sulfuric acid in 450 mL of acetic acid) was added dropwise with vigourous stirring at room temperature (22°C) over a 0.5 h period. The reaction continued for 3 days until TLC showed no more starting material. Stirring was stopped, and the organic phase (top) was separated from the acid phase (bottom). Extraction of the acid phase with chloroform gave no product. The organic phase was washed with water (6 × 250 mL, until the washings were pH 5 to litmus) and 10% $KHCO_3$ solution (2 × 250 mL) and dried over $MgSO_4$. After removal of the solvent, the residual solid was dissolved in hot CH_2Cl_2 (450 mL), which upon slow recrystallization gave compound **3** as yellow crystals: 14.0 g (43% yield); mp > 300°C; IR (KBr, C=O): 1762, 1835 cm^{-1}; ^{1}H NMR (400 MHz, $CDCl_3$) δ 8.19 (d, 1H, ^4J = 2.3 Hz), 7.75 (dd, 1H, ^3J = 8.6 Hz, ^4J = 2.3 Hz), 7.13 (d, 1H, ^3J = 8.6 Hz), 4.0 (d, 1H, ^2J = 15.5 Hz), 3.1 (d, 1H, ^2J = 12.1 Hz), 2.9 (td, 1H, ^2J = 12.1 Hz, ^3J = 3.3 Hz), 2.6 (t, 1H, ^2J = 15.5 Hz) ppm; ^{13}C NMR (100 MHz, $CDCl_3$) δ 163.2, 148.6, 141.9, 141.7, 140.5, 139.19, 132.0, 128.1, 124.5, 122.4, 29.1, 24.8 ppm; MS (EI, *m*/*e*, relative intensity %) 442 ($M^{\cdot+}$, 100); HRMS calcd. for $C_{24}H_{14}N_2O_7$: 442.0801; found: 442.0808.

G1-den

To a suspension of compound **1** (6.0 g, 15.0 mmol) in DMF (60 mL) was added ethanolamine (2.0 mL, 30 mmol). After stirring at room temperature for 1 h, the solution was clear and homogeneous at which point it was set to reflux overnight. The solution was cooled to room temperature and added dropwise with vigourous stirring to an HCl aqueous solution (10%, 300 mL). The resulting yellow precipitate was filtered, washed with water (until the washings were neutral to litmus). and dried in vacuo overnight (80°C, 5 mmHg (1 mmHg = 133.3 Pa)) to give **G1-den**: 5.8 g (97% yield); mp > 300°C; IR (KBr): 3536 (OH), 1757, 1706 (C=O) cm^{-1}; ^{1}H NMR (400 MHz, $CDCl_3$) δ 7.33 (d, 2H), 7.15–7.25 (m, 4H), 6.95 (t, 2H), 4.1 (b, 2H), 3.9 (m, 2H), 2.9 (m, 4H), 2.5 (b, 2H) ppm; ^{13}C NMR (100 MHz, $CDCl_3$) δ 176.6, 170.1, 139.8, 139.51, 134.18, 130.9, 129.09, 128.44, 126.5, 119.3, 62.2, 41.3, 29.2, 24.9 ppm; MS (EI, *m*/*e*, relative intensity %): 395 ($M^{\cdot+}$, 100); HRMS calcd. for $C_{26}H_{21}NO_3$: 395.1521; found: 395.1512.

G1

A solution of **G1-den** (2.7415 g, 6.94 mmol), 1,3,5-benzenetricarbonyl chloride (0.6142 g, 2.27 mmol), and DMAP (1.3866 g, 11.40 mmol) in dichloromethane (50 mL) was set to stir under argon atmosphere overnight. The dichloromethane solution was washed with HCl (1 M, 2 × 50 mL) and water (2 × 50 mL). The insoluble materials were filtered, and the filtrate was dried and concentrated to give **G1** as a yellow glass: 2.54 g (65% yield); IR (KBr): 1759, 1732, 1704 (C=O) cm^{-1}; ^{1}H NMR (400 MHz, $CDCl_3$) δ 8.67 (s, 1H), 7.22 (d, 2H), 7.03–7.12 (m, 4H), 6.82 (t, 1H), 4.41–4.50 (m, 2H), 3.92–3.97 (m, 4H), 2.78–2.87 (m, 4H), 2.3–2.5 (m, 2H) ppm; ^{13}C NMR (100 MHz, $CDCl_3$) δ 170.1, 169.2, 139.8, 139.6, 139.4, 135.7, 134.2, 131.6, 130.9, 129.1, 128.4, 126.7, 126.4, 63.5, 37.1, 29.2, 24.9 ppm; MS (MALDI-TOF-MS, dithranol/LiBr matrix, *m*/*e*, relative intensity %) calcd. for $C_{87}H_{63}N_3O_{12}$: 1341.4; found: 1348.0 (M + Li^+, 100).

G2-den

To a solution of compound **3** (2.00 g, 4.52 mmol) in chlorobenzene (25 mL) in a round-bottomed flask fitted with a Dean–Stark trap was added ethanolamine (0.41 g, 1.5 equiv, 6.80 mmol) in DMF (0.3 mL). The solution was stirred at room temperature for 1 h and then set to reflux overnight. The chlorobenzene solution was concentrated, then precipitated into *n*-pentane, and the resulting yellow solid was filtered (2.06 g, 95%). IR, ^{1}H and ^{13}C NMR, and MS confirmed the identity of the product. This imide product (4.70 g, 9.5 mmol) was placed in a mixture of THF (80 mL), ethanol (40 mL), water (20 mL), and conc. HCl (1 mL). To this was added iron powder (18 g), and the mixture was sonicated at 60°C (water bath) for 1 h. The iron–oxide powders were filtered and then washed with boiling ethyl acetate (150 mL). The combined solutions were partitioned, and the aqueous layer was extracted with ethyl acetate (2 × 50 mL). The combined organic phases were dried over $MgSO_4$ and concentrated to give a red solid that was

© 1999 NRC Canada

further purified by flash column chromatography (60/40 v/v ethyl acetate/hexane then ethyl acetate) to give compound **4** (1.57 g, 39%). IR, ^{1}H and ^{13}C NMR, and MS confirmed the identity of the product. Compounds **4** (1.06 g, 2.5 mmol) and **1** (1.98 g, 5.6 mmol, 2.2 equiv.) were dissolved in *m*-cresol (15 mL) with isoquinoline (0.5 mL) and heated at 200°C under argon flow overnight. The reaction mixture was precipitated into methanol (50 mL), and the resulting yellow precipitate was filtered. The yellow compound was further purified by preparative SEC (toluene). Removal of the solvent and drying overnight (80°C, 5 mmHg) gave **G2-den**: 1.79 g (65% yield); IR (KBr): 3439 (OH), 1756, 1710 (C=O) cm^{-1}; ^{13}C NMR (50 MHz, $CDCl_3$) δ 169.3, 167.7, 140.1, 139.4, 139.2, 138.9, 138.6, 133.5, 132.7, 131,8, 130.8, 130.4, 130.3, 128.5, 127.8, 126.4, 126.1, 125.9, 125.8, 125.7, 125.6, 124.1, 28.7, 28.6, 24.2, 24.1 ppm; MS (MALDI-TOF-MS, dithranol/LiBr matrix, *m*/*e*, relative intensity %) calcd. for $C_{74}H_{51}N_3O_7$: 1093.3; found: 1093.1 (M^+, 100).

G2

A solution of **G2-den** (0.602 g, 0.55 mmol), 1,3,5-benzenetricarbonyl chloride (50.1 mg, 0.18 mmol), and DMAP (0.1284 g, 1.00 mmol) in dichloromethane (20 mL) was stirred at room temperature for 3 days under argon atmosphere. The dichloromethane solution was washed with aqueous HCl solution (1 M, 2 × 50 mL), water (2 × 50 mL), dried over $MgSO_4$, and concentrated to give a yellow–orange glassy compound. The compound was further purified by preparative SEC (toluene). Removal of the solvent and drying overnight gave **G2** as a yellow–orange glass: 0.428 g (68% yield); IR (KBr): 1760, 1734, 1706 (C=O) cm^{-1}; MS (MALDI-TOF-MS, dithranol/LiBr matrix, *m*/*e*, relative intensity %) calcd. for $C_{231}H_{153}N_9O_{24}$: 3436.1; found: 3445.0 ($M + 1 + Li^+$, 100).

G3-den

As described for the synthesis of **G2-den**, compound **3** was imidized with **4** in *m*-cresol at 200°C, followed by reduction with iron powder to give compound **5**. Subsequent imidization of **1** with **5** afforded **G3-den** in 70% yield after purification by SEC (toluene). IR (KBr): 3442 (OH), 1763, 1711 (C=O) cm^{-1}; MS (MALDI-TOF-MS, dithranol/LiBr matrix, *m*/*e*, relative intensity %) calcd. for $C_{170}H_{111}N_7O_{15}$: 2489.8; found: 2496.1 ($M + Li^+$, 100); T_g = 346°C.

Results and discussion

Synthesis

We have previously reported the synthesis of **2** from compound **1** (Scheme 1) (3). Nitration of this product under mild conditions gave the dinitrated product **3** and a structural isomer of which **3** could be isolated in moderate yield (43%) after recrystallization from dichloromethane. Direct dinitration of **1** gave a mixture of nitrated compounds, which were difficult to separate by recrystallization and other common means. The first generation dendron (**G1-den**, Scheme 1) could be made by reaction of compound **1** with ethanolamine in refluxing DMF. Assembly of this dendron around the trimesic acid (1,3,5-benzenetricarboxylic acid) core was accomplished by reaction with 1,3,5-benzenetricarbonyl trichloride in dichloromethane using DMAP as a base. After purification, the first generation dendrimer **G1** was obtained as a yellow glassy solid in good yield (65%).

Imidization of dinitro compound **3** with ethanolamine in chlorobenzene and DMF followed by reduction with iron powder gave compound **4** in moderate yield (Scheme 1). It was found that the anhydride group of compound **1** (as well as compound **3**) either remains unreactive towards alcohols or the ester–acid derivative reverts back to the free alcohol and anhydride during work-up or under the reaction conditions. Therefore, imidization of compound **4** with compound **1** in *m*-cresol at 200°C (Scheme 3) afforded the second generation dendron (**G2-den**) in good yield after purification by SEC. Assembly of **G2** was accomplished by reaction of **G2-den** with 1,3,5-benzenetricarbonyl trichloride for 3 days in dichloromethane.

Synthesis of the third generation dendron (**G3-den**) began with imidization of compound **4** with compound **3**, followed by reduction with iron powder to give compound **5** (Scheme 3). Imidization of compound **1** with compound **5** in *m*-cresol at 200°C gave the third generation dendron (**G3-den**, Fig. 1) in good yield (70%) after purification by SEC. However, this dendron could not be assembled around the trimesic acid core, even after the coupling reaction was carried out for 28 days, under similar conditions used for the assembly of the second generation dendrimer. The highest molecular weight compound, isolated from the reaction mixture by SEC, had a mass corresponding to a trimesic acid core having only two dendrons assembled around it (*m*/*e* = 5289, MALDI-TOF-MS, dithranol/silver trifluoroacetate matrix). It is postulated that due to steric crowding, **G3-den** cannot get close enough in space to the trimesic acid core to couple.

Structural characterization

Gel permeation chromatography (GPC) was performed on each dendron from generation one (**G1-den**, Scheme 1) to three (**G3-den**, Fig. 1), which showed an increase in apparent molecular weight for increasing generation and the expected monodispersity. However, comparing these molecular weight profiles against polystyrene standards provided no useful information regarding molecular weight. This is not unexpected, given the obvious difference in molecular conformation between polystyrene and these rigid aryl dendrites. Figure 1 illustrates both stick and space-filled molecular models of **G3-den**. From this model, the conformation of each of the tetrahydro[5]helicene units as well as the shape and conformation of the dendron itself is illustrated.

The identity of each dendron and dendrimer was confirmed using IR spectroscopy, and its mass was confirmed using MALDI-TOF mass spectrometry. In each case, the mass spectrum was used as the primary means for structural determination, since for every dendron and dendrimer higher than generation one, the ^{1}H NMR spectra were cluttered and not easily interpretable. A single peak was observed in the MALDI-TOF mass spectrum, corresponding to the mass of the parent molecular species plus Li^+ (from the matrix) except for **G2-den**, which had only its parent molecular ion.

© 1999 NRC Canada

Fig. 1. Stick (left) and space-filled (right) molecular models of the third generation dendron (**G3-den**).

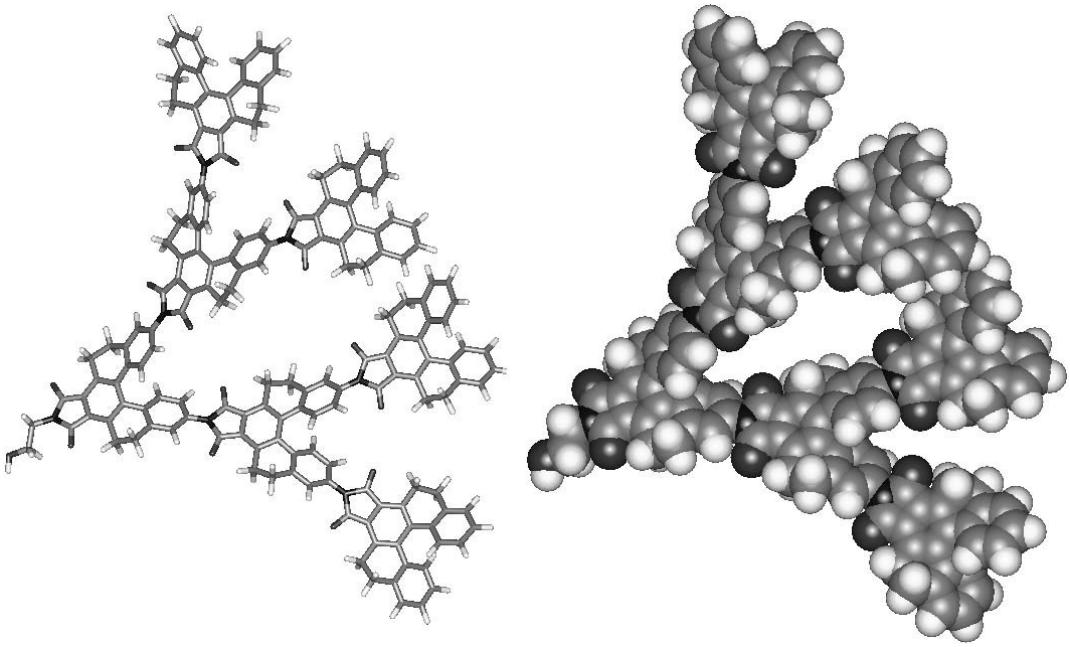

Fig. 2. MALDI-TOF mass spectra (dithranol/silver trifluoroacetate matrix) of oligoimide **11**. Peaks indicated are M + Ag^+ for a given number (*n*).

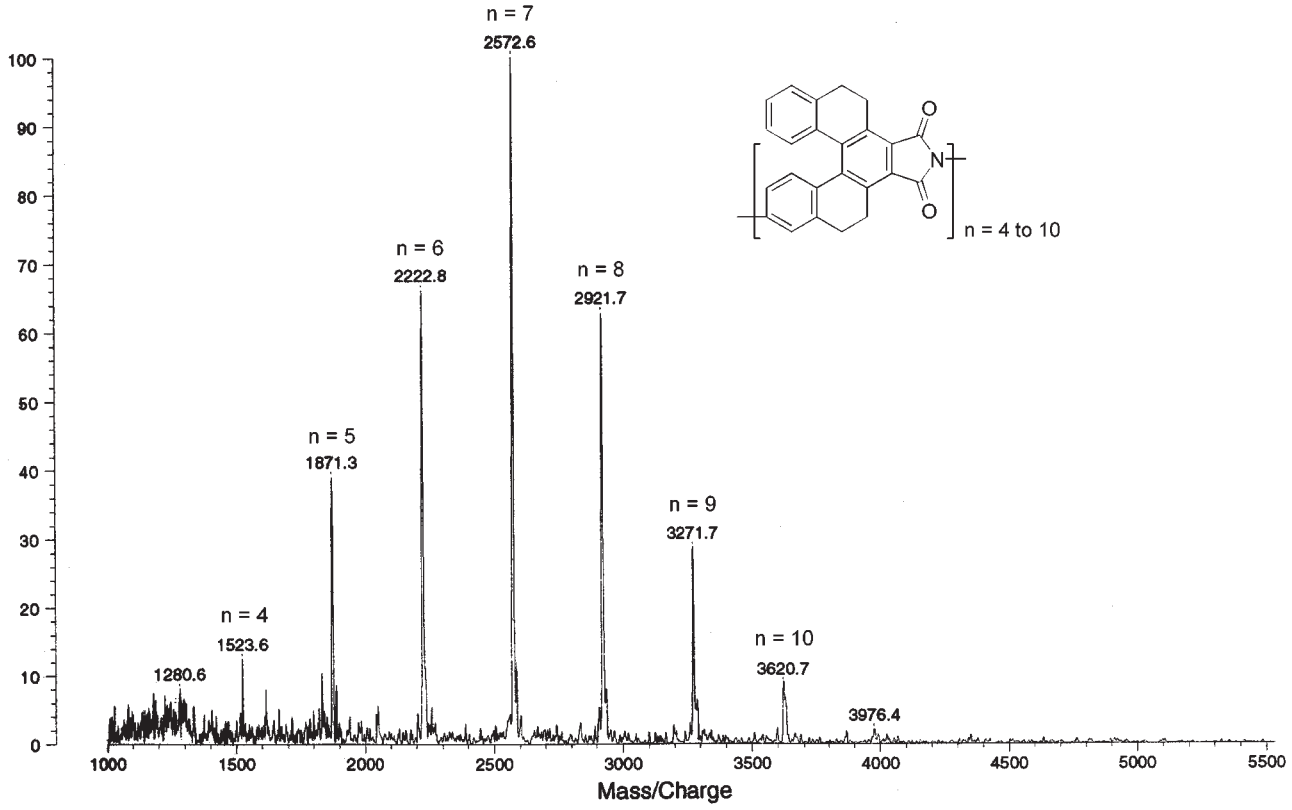

Physical properties

To compare the physical properties of these dendritic aryl imides with analogous linear imides, oligoimides were needed of approximately the same molecular weight that contained only the tetrahydro[5]helicene unit. Consequently, the synthesis of oligoimide **11** was accomplished using our published method, except the polymerization reaction was time controlled so as to produce the oligoimides (3*a*). The produced oligoimides were fractionated using chloroform (good solvent) and methanol (poor solvent). A fraction was obtained that had a distribution of oligomers corresponding to oligoimide **11** with 4–10 repeat units, which was confirmed by its MALDI-TOF mass spectrum (Fig. 2). The distribution of molecular weights for oligoimide **11** was

© 1999 NRC Canada

Fig. 3. GPC traces of **G3-den** and oligoimide **11**.

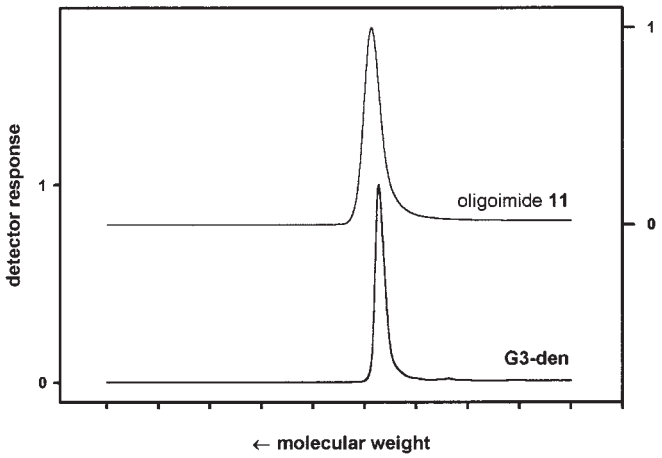

Fig. 4. Normalized absorption (*a*) and emission (*b*) spectra of **G1-den**, **G2-den**, **G3-den**, and oligoimide **11** as taken in dichloromethane solution (3×10^{-5} M).

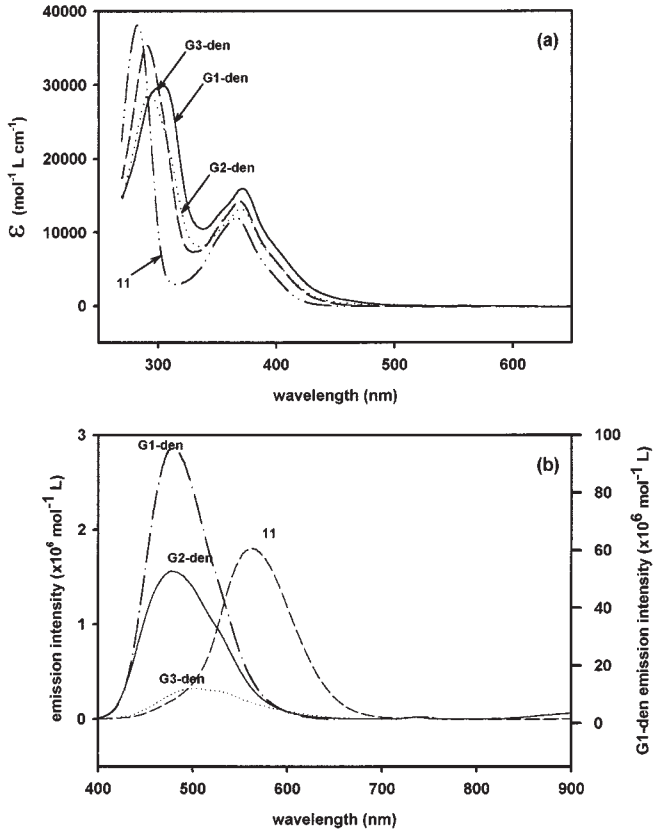

centered around $n = 7$ and a mass of $m/e = 2461$, which were close to that of **G3-den** ($n = 7$, $m/e = 2489$).

Figure 3 illustrates GPC traces of oligoimide **11** and **G3-den**. Both compounds have similar absolute molecular weights by MALDI-TOF. However, oligoimide **11** showed a higher apparent molecular weight, which can be attributed to its rigid-rod conformation and consequently larger hydrodynamic volume. This difference in hydrodynamic volume is a direct indication that the presented dendritic aryl imides would have a lower solution and melt viscosity when compared with their linear counterparts. These observations further confirm a widely held opinion for which there has only recently been direct evidence (9). DSC measurements showed that **G3-den** possessed a detectable glass transition (T_g) at 346°C, whereas oligoimide **11** did not show a glass transition up to 450°C. The measured lower T_g suggests that the dendritic aryl imide is more flexible than the linear aromatic oligoimide. Both of these properties suggest that dendritic aryl imides could be used to modify the properties of traditional linear polyimides.

Fluorescence study

Figure 4*a* illustrates the UV-vis absorption spectra of the dendrons **G1-den**, **G2-den**, and **G3-den** as well as oligoimide **11**, taken in dichloromethane solution at a concentration of 3×10^{-5} M.[3] Each compound exhibits two maximum absorptions at about 290 and 370 nm. The repeat unit equivalent molar extinction coefficients for each dendron at each $\lambda_{max,abs}$ are approximately equal. However, when the same series of compounds are irradiated at either wavelength, they fluoresce, and both the wavelength and intensity of the fluorescent emission vary widely among the compounds (Fig. 4*b*). For example, the emission intensity of **G1-den** ($\lambda_{max,em}$ = 480 nm) is over 30 times greater than the emission intensity of **G2-den** ($\lambda_{max,em}$ = 477 nm), which is itself 5 times larger than that of **G3-den** ($\lambda_{max,em}$ = 501 nm). The shift of the fluorescent emission of **G3-den** compared to **G2-den** indicates a loss of radiant energy by some pathway. Furthermore, there is a progressive decrease in the emission intensity with increasing dendron generation. Additionally, the linear oligoimide **11** exhibits larger emission intensity (although shifted to longer wavelength) than **G3-den**. Coupling these observations leads to the conclusion that within the higher generation dendrons intermolecular quenching of the emitted radiation takes place. One may expect these observations, given the dendritic structure and conformation of **G3-den**. It would be more likely to undergo intramolecular quenching, as compared to its linear rod-like analogue, given that any intermolecular quenching would have to be a result of the *o*-terphenyl moieties overlapping and interacting in solution.

Electrochemical behavior

Given the indication that the tetrahydro[5]helicene units of the higher generation dendrons are capable of interacting in solution, it would be of interest to see whether or not there exists a redox activity, not observed in isolated *o*-terphenyl moieties, tetrahydro[5]helicene units, or imide functionalities, that does exist within the higher generation dendrons (**G2-den** and **G3-den**). Thus, cyclic voltammetry was performed in DMF solution, using tetrabutylammonium hexafluorophosphate (Bu_4NPF_6) as the supporting electrolyte, in order to examine the electrochemical behaviour of the dendritic aryl imides (**G1-den**, **G2-den**, and **G3-den**).

[3] The absorptions and emissions have been corrected by a factor equal to the repeat unit equivalent molar concentration for each compound.

© 1999 NRC Canada

Fig. 5. Cyclic voltammograms of **G3-den** (*a*) and oligoimide **11** (*b*).

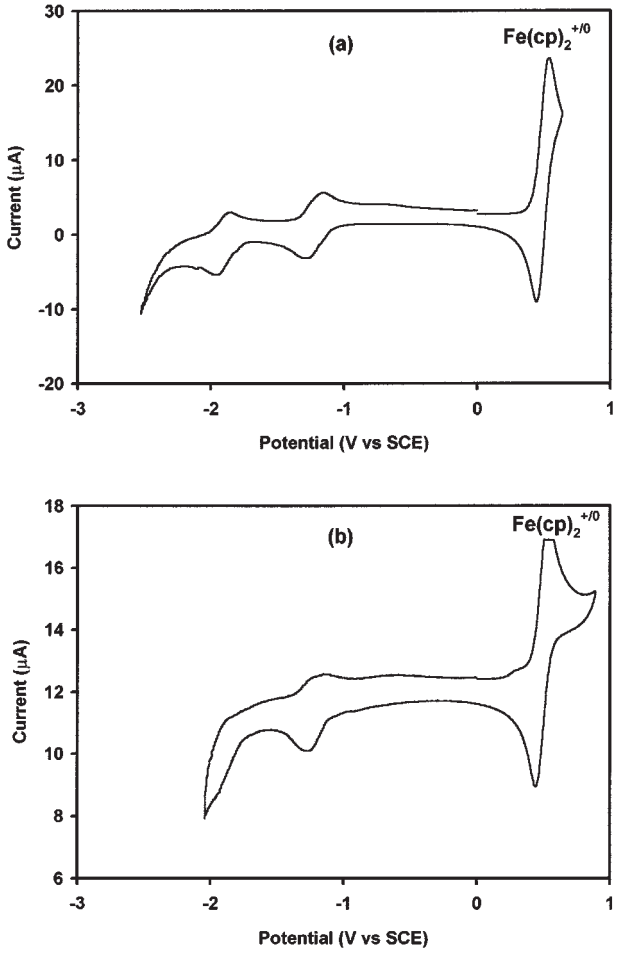

All the three dendrons exhibited electrochemical activity, although only one reversible[4] redox couple was observed for **G1-den** (at –1.28 V), whereas two were observed for **G2-den** and **G3-den** (Fig. 5, Table 1). The first reversible redox couple at approximately –1.28 V was consistently present for all the dendrons. If **G1-den** was submitted to potentials more negative than –1.3 V, a second redox couple was observed. However, under these conditions, neither the first nor the second redox couples were reversible, indicating that chemical degradation occurred at the more negative potentials.

To explain these observations and the nature of this electrochemical behaviour, cyclic voltammograms for a series of compounds (Fig. 6) containing both *o*-terphenyl and anhydride moieties were obtained. Within compound **1**, the *o*-terphenyl moiety is bridged and held in place by the ethylene unit (at positions 5–6 and 9–10). The twist angle of the *o*-terphenyl moiety within compound **1** is approximately 32° as shown by X-ray diffraction analysis of a single crystal.[5] Compounds **7**– **9** differ in the degree of conjugation within the *o*-terphenyl moiety, brought about by the difference in the number of bridging carbon atoms as compared with

Table 1. Electrochemical data for **G1-den**, **G2-den**, **G3-den**, **1**, and **6**–**9**.

	$E_{1/2}$ reduction (V vs. SCE)	
Compound	1st	2nd
G1-den	–1.28	
G2-den	–1.24	–1.93
G3-den	–1.24	–1.92
11	–1.23[a]	
1	–1.10	
6	–0.78	–1.55
7	–1.09	–1.18
8	–1.20	
9	–1.25	
o-Terphenyl	—[b]	

[a]Measured in NMP solution.
[b]Not observed.

Fig. 6. Analogs of compound **1**, containing both *o*-terphenyl and anhydride moieties.

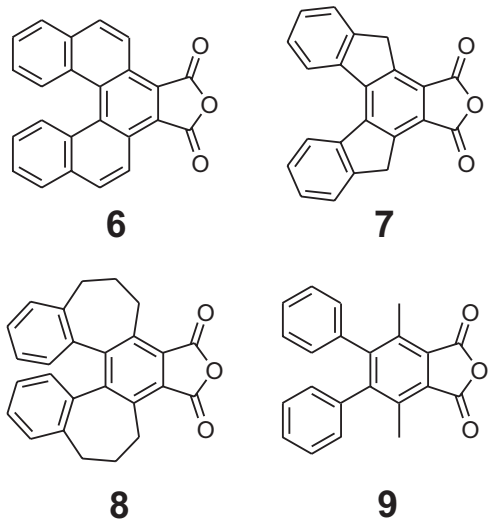

compound **1**. The *o*-terphenyl moiety within compound **9** is not bridged at all and therefore is least conjugated within this series. Whereas, compound **6** ([5]helicene-7,8-dicarboxylic anhydride) contains an *o*-terphenyl moiety, which is bridged by a vinylene group and is therefore the most conjugated within the series. Therefore, this series of compounds can be thought to undergo a shift in the degree of conjugation of the *o*-terphenyl moiety as follows: **6** ≥ **7** > **1** > **8** > **9** ≈ *o*-terphenyl.

All the compounds illustrated in Fig. 6, except for *o*-terphenyl itself, exhibited electrochemical activity, with redox couples in the range of –0.70 to –2.00 V vs. SCE (Table 1). For compounds **1**, **8**, and **9**, only one reversible redox couple was observed. Compounds **6** and **7** exhibited two reversible redox couples, with the second couple at more negative potential. The first redox couple is shifted to more positive potentials as the degree of conjugation increases, in

[4]Reversible couple is defined in this work as the ability of the molecule to undergo identical redox couples (i.e., superimposable CV waves) over 12 consecutive scans within the applied potential range.
[5]T.P. Bender and Z.Y. Unpublished results.

© 1999 NRC Canada

the order **6** > **7** > **1** > **8** > **9**. Furthermore, when compound **1** was submitted to higher negative potentials, it underwent an additional reductive process at approximately –1.9 V. However, this reduction was not reversible and resulted in the degeneration of the measured current over consecutive scans and a shift of the reduction potential for both the first and second redox couples, behaviour similar to that observed for **G1-den**.

Based on these observations and by analogy to compounds **1** and **6**–**9**, the electrochemical behaviour of the tetrahydro[5]helicene containing dendrons (**G1-den**, **G2-den**, and **G3-den**) can be partially explained. The presence and approximate position of the first redox couple is consistent within the dendrons (**G1-den**, **G2-den**, and **G3-den**) and the model compounds (**1**, **6**–**9**). The potential of the first redox couple is invariant with generation. Therefore, the first redox couple must be attributed to a redox process occurring at the anhydride–imide functionality. This is consistent with the reported findings from the electrochemical study of soluble linear polyimides (10). Since the first redox couple moves to more negative potential on the series **6** > **7** > **1** > **8** > **9**, its position is directly proportional to the degree of conjugation present within the *o*-terphenyl moiety (which is attached to the anhydride–imide functionality). The lower the degree of conjugation within the aromatic ring system, the more difficult the reduction of the anhydride carbonyl group becomes. For compounds **6** and **7**, a second reversible redox couple at more negative potential was also observed. These two compounds possess the highest degree of conjugation within the series of model compounds. Thus, this second redox couple must originate within the *o*-terphenyl moiety and is stabilized within these compounds due to their increased degree of π-conjugation.

Two reversible reductive processes were observed for the higher generation dendrons (**G2-den** and **G3-den**, Fig. 5). Although within these dendrons, there is an extended array of tetrahydro[5]helicene units (and consequently the *o*-terphenyl moieties), they cannot be in a state of extended conjugation because of the imide functionality. Given the presence of a nonreversible reductive process at approximately –1.90 V for compound **1** and **G1-den**, the second reduction of the higher dendrons at –1.93 and –1.92 V, for **G2-den** and **G3-den**, respectively, must originate within the *o*-terphenyl moiety. Furthermore, due to its reversibility, the intermediate of the second reduction must be stabilized by interaction with other *o*-terphenyl moieties within the dendritic structure itself. This is consistent with the observations made using fluorescence spectroscopy, which indicated an interaction between tetrahydro[5]helicene units of the higher generation dendrons in solution. Further to this, linear oligoimide **11**, which on average has the same number of repeat units as **G3-den**, exhibits only one, all be it broad, redox couple at –1.23 V when measured in NMP solution (Table 1, Fig. 5). The presence of only one redox couple for linear oligomer **11** further implies that the second redox couple observed for **G3-den** is attributed to the dendritic structure of the molecule. Further spectroelectrochemical investigation of the higher dendrons may help determine the exact nature of the second redox couple.

Conclusions

In conclusion, we have shown that a new tetrahydro[5]helicene derivative, compound **3** containing a conformationally locked *o*-terphenyl moiety, can be used in the synthesis of dendritic aryl imides by a divergent synthetic approach. First and second generation dendrons could be assembled around a trimesic acid core to give first and second generation dendrimers, **G1** and **G2**, respectively. In each case, MALDI-TOF-MS and spectroscopic methods were used to confirm the identity of each dendron and dendrimer. Each of the dendrons underwent either one or two electrochemical reductions on the range –1.2 to –2.1 V vs. SCE. When a dendritic aryl imide was compared with its linear analog, differences were found in the hydrodynamic volumes, glass transition temperatures, and fluorescence and electrochemical behaviour.

Acknowledgments

The authors would like to thank Dr. A.S. Hay's group (McGill University, Montreal) for performing the MALDI-TOF-MS analysis, Dr. Chuncai Yang for the synthesis of the oligoimide (**11**), and Dr. Wen Lu for the useful discussions on electrochemistry. This work was financially supported by the Natural Sciences and Engineering Research Council (NSERC) of Canada. T.P.B. would like to acknowledge the financial support of NSERC through a PGS-A.

References

1. (*a*) W.H. Laarhoven and W.J.C. Prinsen. Top. Curr. Chem.: Stereochem. **125**, 63 (1984); (*b*) K.P. Meuer and F. Vögtle. Top. Curr. Chem.: Org. Chem. **127**, 32 (1985).
2. (*a*) H.A. Weidlich. Chem. Ber. **71**, 1203 (1938); (*b*) F. Bergmann, H.E. Eschinazi, and M. Neeman. J. Org. Chem. **8**, 179 (1943).
3. (*a*) Z.Y. Wang, Y. Qi, T.P. Bender, and J.P. Gao. Macromolecules, **30**, 764 (1997); (*b*) T.P. Bender, Y. Qi, J.P. Gao, and Z.Y. Wang. Macromolecules, **30**, 6001 (1997); (*c*) T.P. Bender and Z.Y. Wang. J. Polym. Sci. Part. A: Polym. Chem. **36**, 1349 (1998); (*d*) S.M. MacKinnon and Z.Y. Wang. Macromolecules, **31**, 7970 (1998).
4. G.R. Newkome, C.N. Moorefield, and F. Vogtle. Dendritic molecules: concepts, syntheses, perspectives, VCH Weinheim (1996).
5. B. Karakaya, W. Claussen, K. Gessler, W. Saenger, and A.D. Schlüter. J. Am. Chem. Soc. **119**, 3296 (1997).
6. (*a*) E.B. Barnett and C.A. Lawrence. J. Chem. Soc. 1104 (1935); (*b*) Y. Altman, and D. Grunsburg. J. Chem. Soc. 1498 (1961).
7. (*a*) C.F.H. Allen and J. Van Allan. J. Am. Chem. Soc. **64**, 1260 (1942); (*b*) Synthesis adapted from: F.W. Gray. J. Chem. Soc. 2131 (1909); and O. Grummit. Org. Synth. Coll. Vol. 3, 807.
8. T. Gennett, D.F. Milner, and M.W. Weaver. J. Phys. Chem. **89**, 2787 (1985).
9. C.J. Hawker, E.E. Malmström, C.W. Frank, and J.P. Kampf. J. Am. Chem. Soc. **119**, 9903 (1997); and refs. cited therein.
10. H.Y. Wang, J. Chou, H. Zhao, Y.S. Li, H.Q. Hou, W. Xing, M.X. Ding, and T.H. Lu. Chem. J. Chin. Univer. **19**, 48 (1998).

© 1999 NRC Canada

1998 J.C. Polanyi Award Lecture Fullerene ions in the gas phase: chemistry as a function of charge state[1]

Diethard K. Böhme

Abstract: Results of recent measurements in the Ion Chemistry Laboratory at York University using the Selected-Ion Flow Tube (SIFT) technique are surveyed for reactions of singly, doubly, and triply charged buckminsterfullerene C_{60}^{n+} cations proceeding at room temperature in helium buffer gas at 0.35 Torr (1 Torr = 133.3 Pa). Measured rate coefficients and observed product channels for reactions with a variety of inorganic and organic molecules depend strongly on the charge state of the reactant ion. The measured rate coefficients span more than four orders of magnitude. Primary product channels observed include attachment, dissociative attachment, dissociative attachment with charge separation, single-electron transfer, dissociative single-electron transfer, and two-electron transfer. A qualitative description of the potential-energy profiles associated with these reaction channels is provided. The observed higher order chemistry of derivatized C_{60}^{n+} cations and of atomic exohedral adduct ions is also described. This chemistry includes cation-transfer reactions, surface derivatization, and "ball-and-chain" polymerization. Finally, results are presented that provide insight into the influence of surface strain on the reactivities of fullerene ions.

Key words: fullerenes, ions, electron transfer, charge separation, surface derivatization.

Résumé : On présente une revue des résultats de mesures récentes effectuées dans le « Ion Chemistry Laboratory at York University », utilisant la technique du tube à écoulement d'ions choisis (« SIFT »), pour des réactions des cations buckminsterfullerènes portant une, deux ou trois charges, C_{60}^{n+}, se produisant à la température ambiante, dans de l'hélium à 0,35 Torr agissant comme gaz tampon. Les coefficients de vitesse mesurés et les voies observées pour les produits de réactions avec une grande variété de molécules inorganiques et organiques dépendent fortement de la charge de l'ion qui réagit. Les coefficients de vitesse observés s'étalent sur quatre ordres de grandeur. Les principales voies observées pour les produits comprennent la fixation, la fixation dissociative, la fixation dissociative avec séparation de charge, le transfert d'un seul électron, le transfert dissociatif d'un seul électron et le transfert de deux électrons. On fournit une description qualitative des profils d'énergie potentielle reliées à ces voies réactionnelles. On décrit aussi la chimie d'ordre élevée observée pour les cations C_{60}^{n+} dérivatisés et pour les ions adduits exoédriques atomiques. Cette chimie inclut des réactions de transfert de cation, de dérivatisation en surface et de polymérisation en collier de perle avec bâtonnets. Enfin, on présente des résultats qui permettent de comprendre l'influence de la tension de surface sur les réactivités des ions fullerènes.

Mots clés : fullerènes, ions, transfert d'électron, séparation de charge, dérivatisation en surface.

[Traduit par la Rédaction]

1. Introduction

One of the many remarkable features of the isolated buckminsterfullerene molecule, C_{60}, is its stability as a multiply charged cation against Coulomb explosion. Tilmann Märk and his group at the University of Innsbruck have been able to produce and identify mass-spectrometrically C_{60} with up to 7 electrons removed from the ocean of 240 valence electrons that surround its hollow cage of 60 carbon atoms in this molecule (1). This has been achieved in a dedicated ion source that delivers high electron currents at high electron energies. In the Ion Chemistry Laboratory at York University we have found that it is straightforward to remove up to three electrons from C_{60} in the conventional electron-impact ion source that delivers ions into our selected-ion flow tube (SIFT) apparatus (2). The SIFT apparatus is a flow reactor designed to measure reaction-rate coefficients and product-ion distributions for reactions between gas-

Received March 26, 1999.

D.K. Böhme.[2] Department of Chemistry, York University, Toronto, ON M3J 1P3, Canada.

[1]This is an invited paper based on the 1998 J.C. Polanyi Award Lecture presented by Professor Böhme at the 81st Annual Conference of the Canadian Society for Chemistry in Whistler, British Columbia, June 1998.

[2]Telephone: (416) 736-2100, ext. 66188. Fax: (416) 736-5936. e-mail: dkbohme@yorku.ca

© 1999 NRC Canada

Fig. 1. Energy-level diagram for various charge states of C_{60}, a selection of singly charged atomic ions, and several rare-gas metastable atoms.

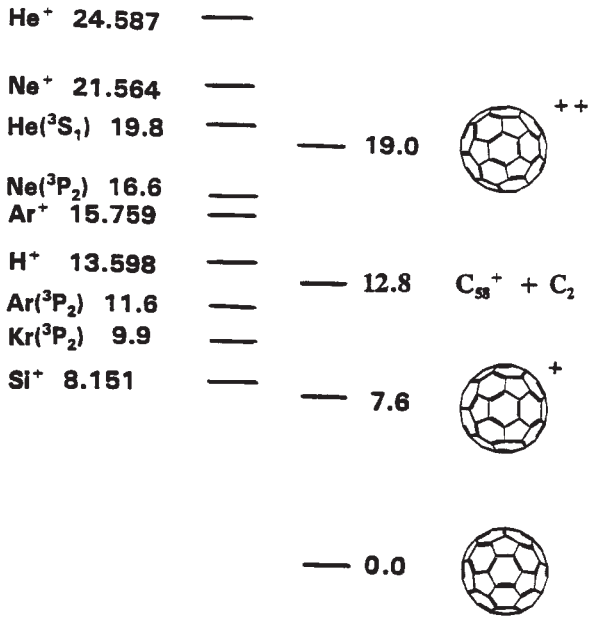

phase ions and neutral molecules. The ease of production of the first three ionized states of C_{60} has prompted us to explore systematically the uncharted chemistry of C_{60}^{n+} as a function of charge state from n = +1 to +3. Investigations of reactivity as a function of charge state are unprecedented in the greater world of gas-phase ion chemistry, in part because many molecular ions explode by intramolecular Coulombic repulsion already in the second charge state. We shall see in this overview that C_{60}^{n+} carbocations are extensively reactive in the gas phase at room temperature and more so as the charge state increases. New reaction pathways become accessible at higher degrees of ionization as, in a sense, physics increasingly preempts the occurrence of chemistry.

This overview is restricted to the research on the chemistry of fullerene ions performed in the author's own laboratory since 1991. No attempt has been made to review the larger body of gas-phase fullerene ion chemistry nor the gas-phase chemistry and physics of multiply charged ions generally that has been reported in the literature.

2. Electron transfer and chemi-ionization of C_{60}

Before embarking on measurements of the chemistry of C_{60}^{n+} ions, we first attempted the gas-phase ionization of C_{60} with methods other than electron-impact ionization. These early experiments showed that metastable atoms of He, Ne, Ar, and Kr induce the loss of electrons from C_{60} in the gas phase *at room temperature* in chemi-ionization (or Penning ionization) reactions of type [1] (3).

[1] $X^* + C_{60} \rightarrow C_{60}^+ + X + e$

Fig. 2. Schematic view of the Selected-Ion Flow Tube (SIFT) apparatus.

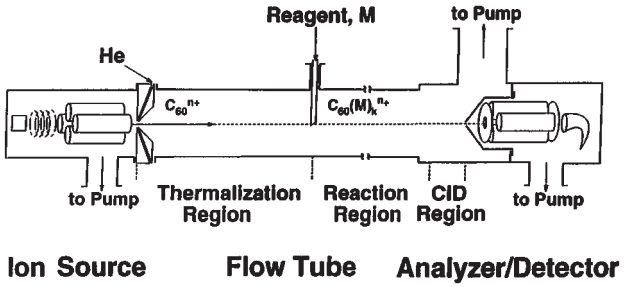

As shown in Fig. 1, these metastable atoms all have energies that lie above the first ionization energy of C_{60}, IE(C_{60}) = 7.61 ± 0.02 eV (4). The mechanism of reaction (1) can be understood in terms of the formation of an excited quasi-molecule $(XC_{60})^*$ that undergoes autoionization (3). We also found that C_{60} is readily ionized at room temperature in electron-transfer reactions of type [2] with ions that have a recombination energy (RE) larger than IE(C_{60}).

[2] $X^+ + C_{60} \rightarrow C_{60}^+ + X$

Such reactions have been observed in our laboratory with the atomic ions listed in Fig. 1 (5). While exothermic dissociative electron transfer leading to the rupture of C_{60}^+ through loss of C_2 was not observed to compete under our experimental operating conditions, we did see novel electron transfer/electron emission reactions of type [3] with X^+ = He^+ and Ne^+.

[3] $X^+ + C_{60} \rightarrow C_{60}^{2+} + X + e$

The mechanism of this novel reaction is not known. It has been suggested[3] that it proceeds by the initial transfer of a deeply embedded electron in C_{60} followed by an Auger emission of a second electron in a manner analogous to that which is known to occur when metals are exposed to slow beams of He^+ ions (6). The occurrence of reaction [3] may therefore be a manifestation of the metallic character of C_{60} due to the ocean of electrons that surround its hollow cage of 60 carbon nuclei.

3. The Selected-Ion Flow Tube (SIFT) apparatus

Our SIFT apparatus shown in Fig. 2 is essentially a tandem-quadrupole mass spectrometer in which the two quadrupoles are separated by a flow tube (2). Fullerene cations are generated in a conventional "open" electron-impact source at electron-impact energies from 60 to 100 eV, depending on the desired charge state: C_{60}^+ at ca. 50 eV, C_{60}^{2+} at ca. 80 eV, and C_{60}^{3+} at ca. 100 eV. The cations are selected upstream with the first quadrupole mass filter, injected through an aspirator-type inlet into He carrier gas at 0.35 Torr, allowed to thermalize to room temperature with ca. 10^5 collisions with He bath gas atoms, and then reacted with a desired reagent added into the flow tube. A large variety of stable gases and vapors of volatile liquids were added

[3] C.E. Klots. Private communication. 1993.

© 1999 NRC Canada

Fig. 3. Experimental data for the chemistry initiated by the reaction of $C_{60}^{\cdot 3+}$ with deuterated chloroform. $C_{60}^{\cdot 3+}$ was produced in a low-pressure ion source by electron impact at 100 eV with C_{60} vapour derived from a fullerene powder. The lines represent fits to the experimental data with solutions of the systems of differential equations appropriate for the observed reactions.

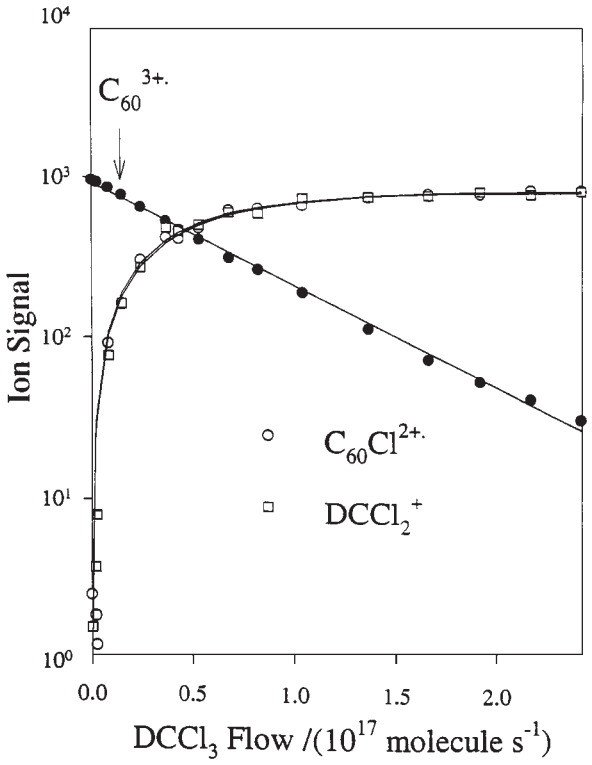

as reagents. Also, reagent hydrogen atoms were generated by the action of a microwave discharge upon a mixture of (5%) hydrogen and helium. The reacting mixture communicates with a second quadrupole mass spectrometer downstream and an electron multiplier, which monitor the reagent and product ions as a function of the flow of the neutral reagent. The reaction time is fixed at a few milliseconds by the buffer-gas flow velocity and the positions of the inlet and sampling ports.

Reaction profiles are obtained by monitoring reactant and product ions as a function of the flow of the neutral reagent. These profiles can be analyzed to provide rate coefficients for primary and secondary (or higher order) reactions as well as ion-product distributions. Representative reaction profiles for the chemistry initiated by C_{60}^{3+} in deuterated chloroform (7) are shown in Fig. 3. Bond connectivities in the product ions can be investigated in multicollision induced dissociation (CID) experiments by raising the sampling nose–cone voltage from 0 to –80 V while concomitantly varying the potentials of front and rear quadrupole focussing lenses so as not to introduce mass discrimination (8). The latter voltages are predetermined manually and then delivered with a programmable power supply.

Fig. 4. An overview of derivatization reactions of C_{60}^+ observed at a room temperature of 294 ± 2 K and a helium pressure of 0.35 ± 0.01 Torr. The assigned structures are speculative.

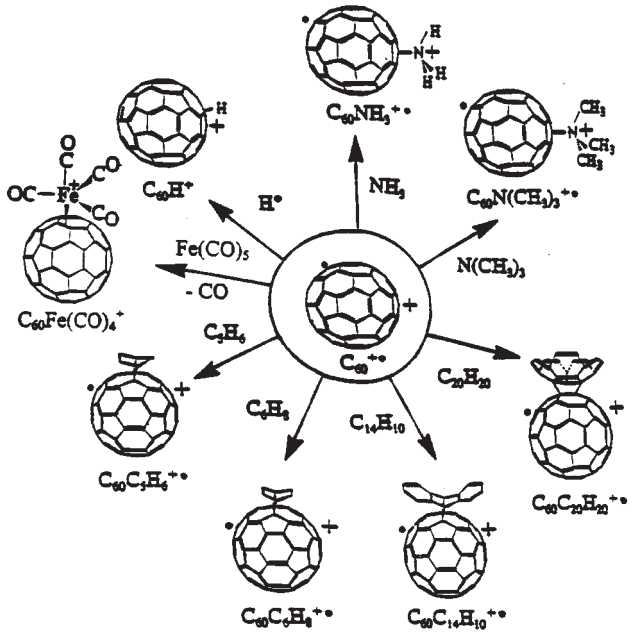

4. The chemistry of C_{60}^{n+} cations

A. Reactions of C_{60}^+

C_{60}^+ is generally quite nonreactive under SIFT conditions: we have found C_{60}^+ to be nonreactive towards more than 50 nonpolar, but also polar, inorganic and organic molecules. Electron transfer is rare because of the low electron-recombination energy of C_{60}^+ (7.6 eV (4)). The few chemical reactions of C_{60}^+ that we have observed so far under SIFT conditions are largely *termolecular* addition reactions that lead to chemical-bond formation with the carbonaceous surface of C_{60}^+. These are summarized in Fig. 4. We have found that C_{60}^+ can be derivatized with H atoms (9, 10), strong nucleophiles such as ammonia and aliphatic amines (11), and with molecules capable of Diels–Alder additions such as 1,3-cyclopentadiene, 1,3-cyclohexadiene, anthracene, and corannulene (12). A reaction of C_{60}^+ with iron pentacarbonyl produces $C_{60}Fe(CO)_4^+$ (13) and is the only example of a *bimolecular* derivatization reaction with C_{60}^+ that we have observed to date.

A remarkable trend is observed for the reactions of C_{60}^+ with amines: ammonia adds only slowly, but the rate of addition approaches the collision rate with increasing alkyl substitution. This behaviour is consistent with a trend in inductive electron donation (the Lewis basicity of the amine) and a trend in the number of degrees of freedom in the intermediate adduct ion effective in energy dispersal (11).

Here is how we envisage the progress of chemical reactions with singly charged C_{60}^+ (14). At long range the charge on the *isolated* cation, initially delocalized over the entire C_{60} surface, will become localized due to electrostatic interaction with the induced and (or) permanent dipole of the incoming molecule. Chemical attack at short separations should occur at the carbon site of a localized charge. For re-

© 1999 NRC Canada

Fig. 5. Schematic view of the increasing well depth of the potential-energy well leading to adduct formation, and of the barrier to covalent-bond formation in the double-well model, with increasing charge state.

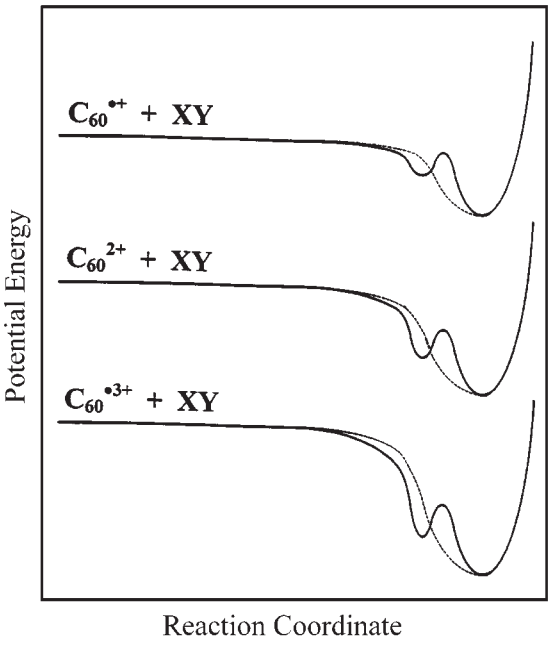

action to take place, a transition is required from largely sp^2 to largely sp^3 hybridization at the C-atom which becomes bonded. This requires surface deformation and so will involve an activation barrier that we estimate to be ca. 15 kcal mol^{-1}. Although this barrier can be overcome by electrostatic interaction with an incoming molecule, its presence can account for the relatively low reactivity of C_{60}^{+} at room temperature. The barrier is presumably located between the initial electrostatically bound complex and the ultimate chemically bound adduct, and should be easier to overcome if the electrostatic interaction is larger (see Fig. 5).

B. Reactions of C_{60}^{2+}

C_{60}^{2+} is much more reactive than C_{60}^{+} in both electron transfer and chemical bonding. We have attributed this enhanced reactivity to the higher recombination energy of C_{60}^{2+}, RE = 11.36 ± 0.05 eV (15), and to the stronger electrostatic interaction between molecules and C_{60}^{2+} that may serve to overcome the energy barrier associated with the change in hybridization required at the site of bonding (14), respectively. Figure 6 summarizes derivatization reactions observed with C_{60}^{2+}. The chemistry of C_{60}^{2+} has been explored with H atoms (9, 10), ammonia, and aliphatic amines (11), nitriles (16), water, alcohols, and ethers (17), aldehydes, ketones, carboxylic acids, and esters (18), cyclic aliphatic oxides (19), and unsaturated hydrocarbons (20–23). Electron transfer is an important competitive channel for

Fig. 6. An overview of derivatization reactions of C_{60}^{2+} observed at a room temperature of 294 ± 2 K and a helium pressure of 0.35 ± 0.01 Torr. The assigned structures are speculative.

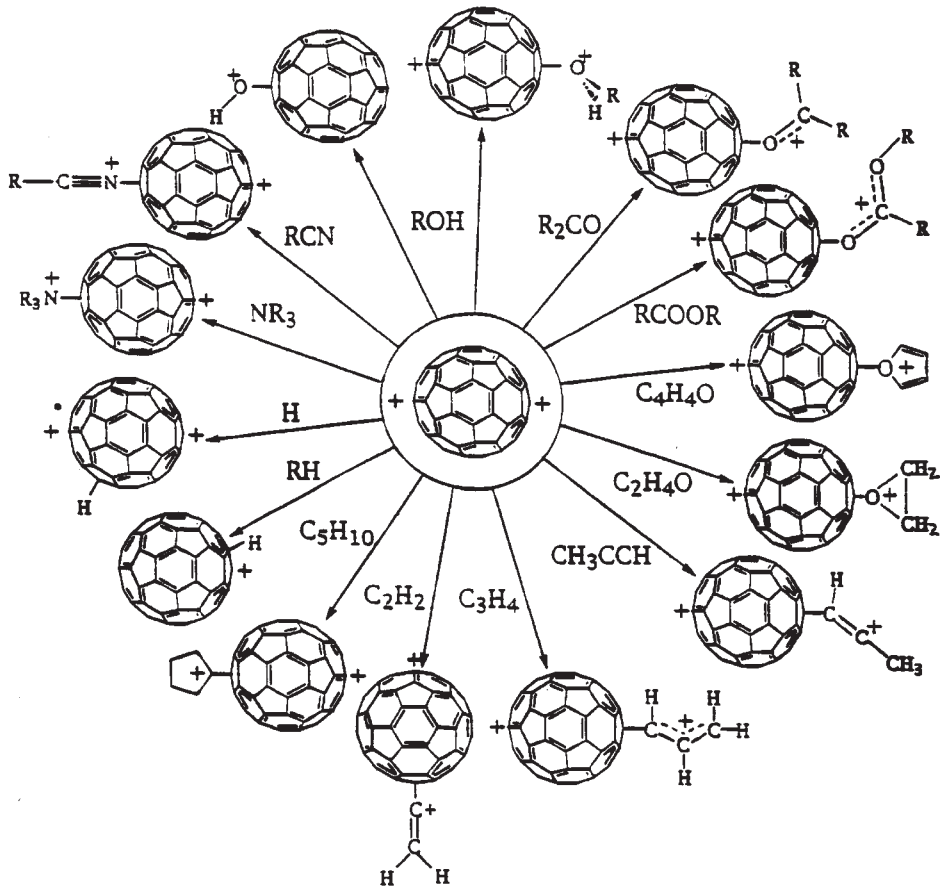

© 1999 NRC Canada

Fig. 7. Competition between electron transfer (broken line) and adduct formation (solid line) observed for reactions of C_{60}^{2+} with ammonia and amines at room temperature 294 ± 2 K and a helium pressure of 0.35 ± 0.01 Torr.

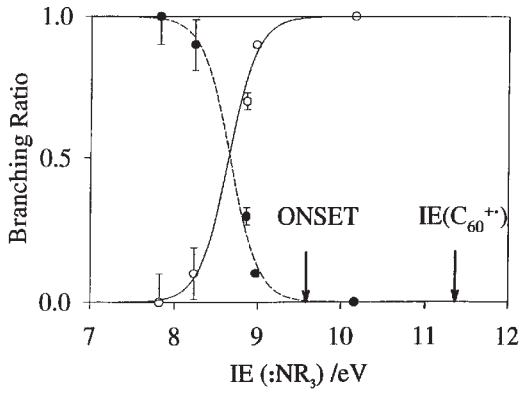

some of the observed derivatization reactions and, for molecules with sufficiently low ionization energies, becomes the only reaction channel. However, electron transfer with C_{60}^{2+} occurs in the presence of an activation barrier that arises from Coulomb repulsion between the charged product ions (24, 25). This is evident in Fig. 7 that shows a delayed onset for competing electron transfer at about 9.6 eV, which is well below the recombination energy of C_{60}^{2+} (11.36 ± 0.05 eV). Electron transfer must be exothermic by at least 1.8 eV in order to compete effectively.

C. Reactions of C_{60}^{3+}

Derivatization reactions also have been observed with C_{60}^{3+}, but electron transfer is even more competitive than with C_{60}^{2+}. For example, although we have observed ammonia to add to C_{60}^{3+}, only electron transfer has been seen with amines (11). The ionization-energy threshold for electron transfer to C_{60}^{3+} lies 4.4 eV below the thermodynamic threshold of RE (C_{60}^{3+}) = 15.6 eV (15). This threshold is higher in energy than observed for electron transfer to C_{60}^{2+} and again can be rationalized in terms of an energy barrier arising from Coulombic repulsion between the product ions (24, 25). We have also observed C_{60}^{3+} cations to abstract *two* electrons from corannulene and the PAH molecules anthracene, pyrene, and benzo[*rst*]pentaphene in reactions of type [4] (26).

$$[4] \qquad C_{60}^{3+} + M \rightarrow M^{2+} + C_{60}^{+}$$

All of these PAH molecules have sufficiently low first and second ionization energies to make double-electron transfer thermodynamically and kinetically favourable. The mechanism of the two-electron transfer reaction [4], whether electron transfer is concomitant or sequential, is not known. Reaction [4] occurs in competition with single-electron transfer. It was observed as a minor channel (<5%) with anthracene, corannulene, and pyrene and occurs in almost equal amounts with benzo[*rst*]pentaphene, which requires the lowest energy for double ionization of these four PAH molecules. The single and two-electron transfer observed with corannulene is illustrated in eq. [5]. (The structure of corannulene is assumed not to change upon ionization.)

[5]

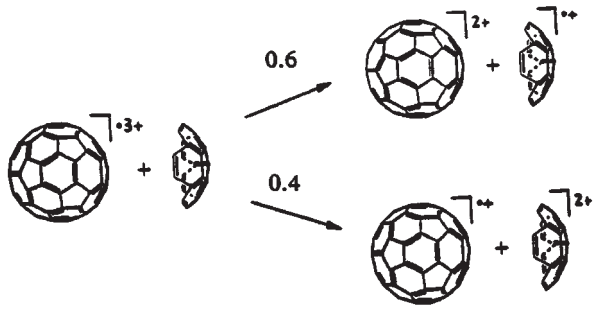

Reactions of C_{60}^{3+} have been investigated with H atoms (9, 10), nitriles (16), water, alcohols, and ethers (17), aldehydes, ketones, carboxylic acids, and esters (18), cyclic aliphatic oxides (19), and unsaturated hydrocarbons (20–23). Figure 8 provides a summary of addition reactions observed. New, charge separation, channels appear for some of the reactions with C_{60}^{3+}. For example, dissociative electron transfer to produce $C_{60}^{2+}/CH_2NH_2^+$ and C_{60}^{2+}/CH_3^+ is the dominant reaction channel with ethylamine [12]. Also, dissociative addition reactions such as hydride and hydroxide transfer, become more effective. This is the case with water, some alcohols, and some alkanes. Halide transfer from HCl and HBr also has been observed. HCl reacts both by Cl^- transfer to produce, remarkably, a free proton as the second ion product (88%) and by hydride transfer (12%) according to reaction [6]. HBr also reacts by halide transfer, but the competing channel in this case is dissociative electron transfer (27).

$$[6a] \qquad C_{60}^{3+} + HCl \rightarrow C_{60}Cl^{2+} + H^+$$

$$[6b] \qquad \rightarrow C_{60}H^{2+} + Cl^+$$

5. Trends with charge state

Reactions [7*a*]–[7*f*] summarize the various types of reactive encounters we have observed between the first three charge states of C_{60}^{n+} and some 30 different reactive molecules that we have surveyed. These include addition [7*a*], dissociative addition [7*b*], dissociative addition with charge separation [7*c*], single-electron transfer [7*d*], dissociative single-electron transfer [7*e*], and two-electron transfer [7*f*].

$$[7a] \qquad C_{60}^{n+} + XY \rightarrow C_{60}XY^{n+}$$

$$[7b] \qquad \rightarrow C_{60}X^{n+} + Y$$

$$[7c] \qquad \rightarrow C_{60}X^{(n-1)+} + Y^+$$

$$[7d] \qquad \rightarrow C_{60}^{(n-1)+} + XY^+$$

$$[7e] \qquad \rightarrow C_{60}^{(n-1)+} + X^+ + Y$$

$$[7f] \qquad \rightarrow C_{60}^{(n-2)+} + XY^{2+}$$

Both the nature of the product channel and the rate of reaction were observed to be a function of the charge state of C_{60}^{n+}. This is indicated qualitatively in Fig. 9. A unified model for these reactive encounters in terms of schematic potential-energy profiles is given in Fig. 10 (28). An analogous model was originally introduced by Herman (29) to account for the observed reactivities of other, smaller doubly

© 1999 NRC Canada

Fig. 8. An overview of derivatization reactions of C_{60}^{3+} observed at a room temperature of 294 ± 2 K and a helium pressure of 0.35 ± 0.01 Torr. The assigned structures are speculative.

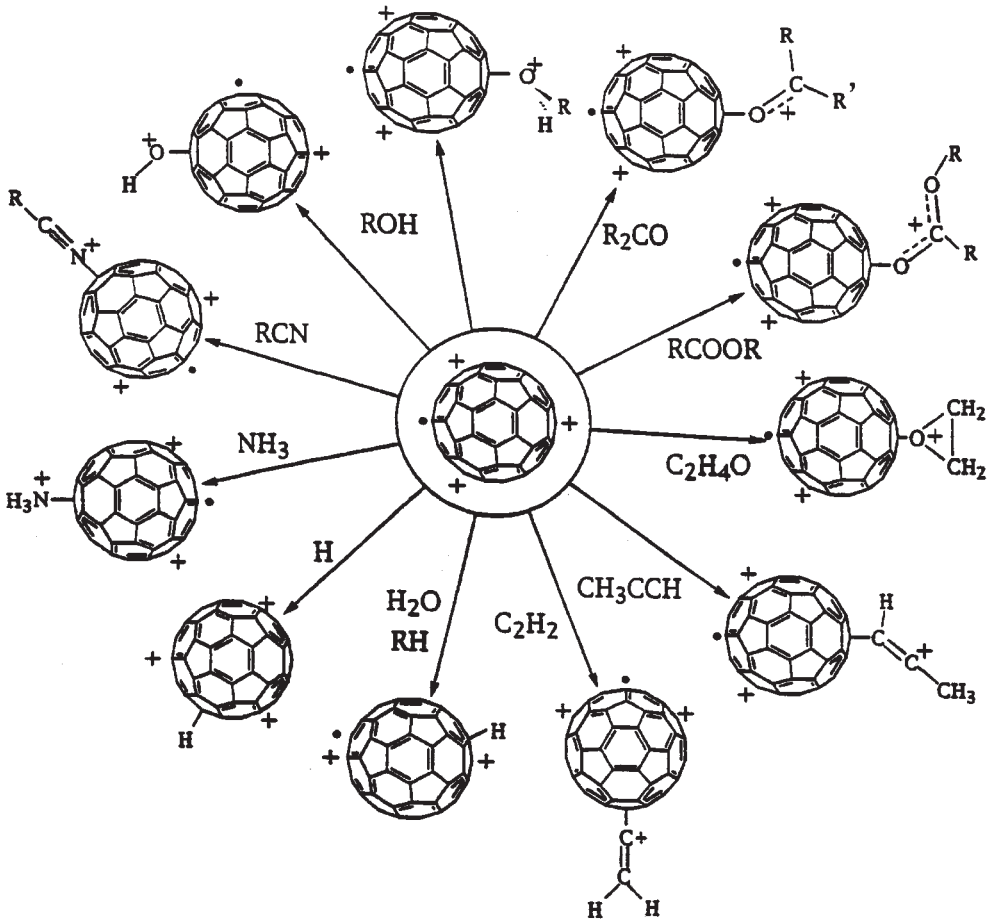

Fig. 9. Qualitative overview of the trend in the reactivity of C_{60}^{n+} cations with charge state. The predominant reaction channels that were observed are indicated in the order of general importance. RE is the recombination energy.

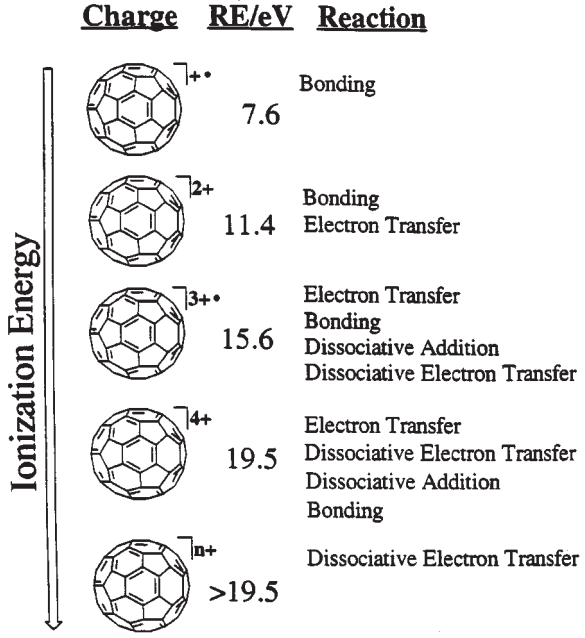

charged ions. As reactants approach each other within this model, a multiply charged fullerene cation encounters single, double, and dissociative electron-transfer potential-energy curve crossings first whereupon a nonadiabatic transition may occur leading to the transfer of an electron. Those C_{60}^{n+}-M pairs that survive the electron-transfer crossings may undergo inelastic collisions with He buffer-gas atoms to produce stable adduct ions $C_{60}M^{n+}$. Failing that, bond redisposition may occur by dissociative addition with or without charge separation. The opportunity for electron transfer increases with increasing charge state. In a sense, chemistry is increasingly preempted by physics with increasing charge state.

6. Higher order chemistry

We have shown that C_{60}^{n+} cations may be derivatized in primary addition or dissociative addition reactions of types [7*a*], [7*b*], and [7*c*]. Now we explore the higher order chemistry of these derivatized ions. Figure 11 provides an overview of this chemistry.

A. Cation-transfer reactions

A number of secondary reactions have been observed with derivatized fullerene cations that involve the transfer of a

© 1999 NRC Canada

Fig. 10. Summary of plausible potential-energy profiles for reactions [6*a*]–[6*f*] as a function of charge state. The minima in these profiles represent bound adducts $C_{60}M^{n+}$. The repulsive curves on the left represent charge separation channels corresponding to single, double, and dissociative electron transfer. Those on the right represent bond formation by dissociative addition with or without charge separation.

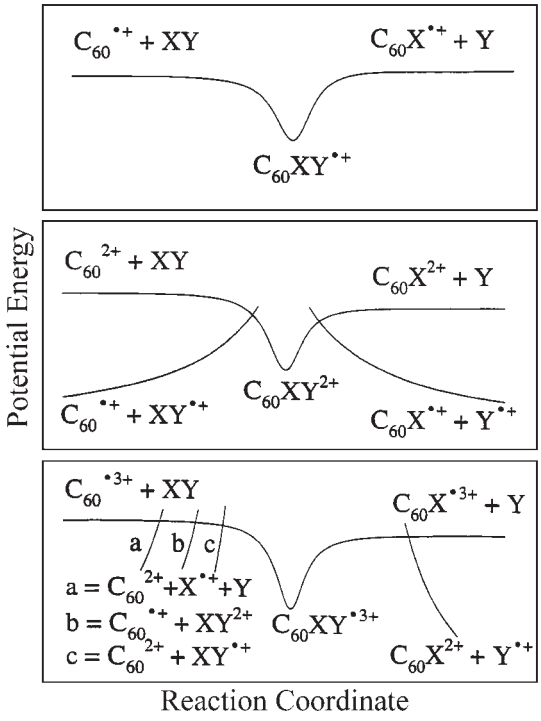

proton, a methyl cation, or the entire ionized substituent. When the substituent contains a hydrogen atom, $C_{60}XH^{n+}$ may undergo partial or complete proton transfer with a suitable proton acceptor. Thus, secondary reactions of singly charged $C_{60}XH^{+}$ ions produce proton-bound adducts of the type $C_{60}X\cdots H^{+}\cdots XH$ with XH = NH_3, CH_3NH_2, $C_2H_5NH_2$, and $(CH_3)_2NH$ (13). Doubly charged derivatized $C_{60}(XH)_m^{2+}$ (m = 1, 2) cations have been observed to undergo rapid proton-transfer reactions of type [8] with XH = ammonia, amines, alcohols, carboxylic acids, ketones, and cyanides (30).

[8] $C_{60}(XH)_m^{2+} + XH \rightarrow C_{60}(XH)_{m-1}X^{+} + XH_2^{+}$

Reaction [9] provides one example of such a proton transfer for XH = NH_3 and m = 1.

[9]

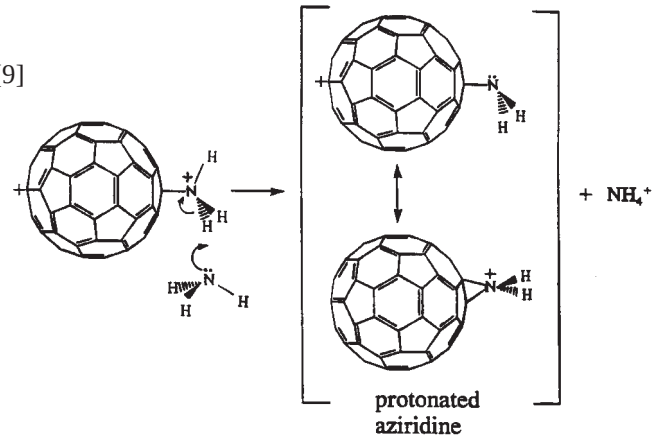

We have assessed this proton-transfer reactivity in terms of an apparent gas-phase acidity of the dicationic species $C_{60}(XH)_m^{2+}$ and have taken the first steps towards establishing a gas-phase acidity ladder for derivatized fullerene cations (30). Also, we have established the gas-phase acidity of $C_{60}H^{2+}$ from the occurrence and nonoccurrence of proton-transfer reactions with this cation (31).

Reactions with methyl formate and methyl acetate involve the transfer of a methyl cation according to eq. [10] proceeding in competition with adduct formation and proton transfer (18).

[10] $C_{60}(XCH_3)^{3+} + XCH_3 \rightarrow C_{60}(X)^{2+} + X(CH_3)_2^{+}$

Fig. 11. Overview of the higher order chemistry of C_{60} adduct ions, designated as $C_{60}AB^{n+}$, with molecules M.

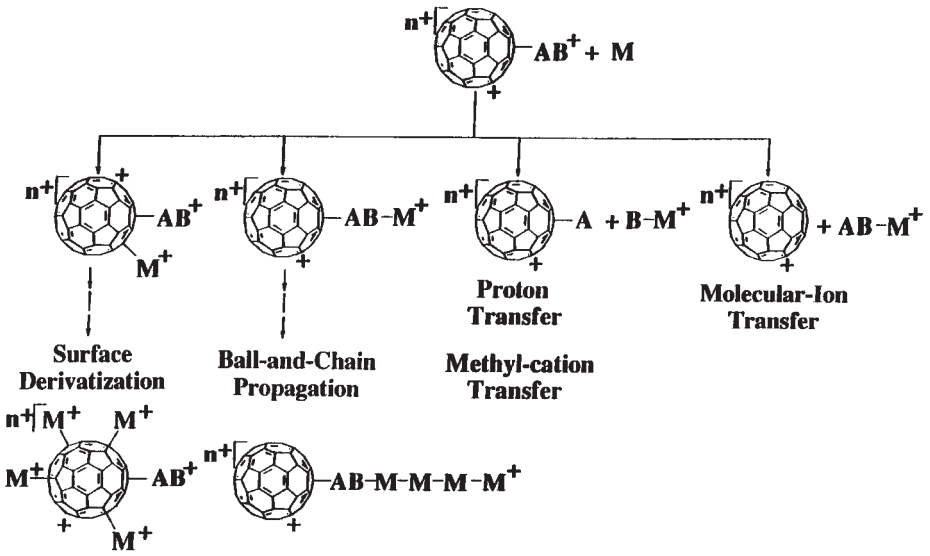

© 1999 NRC Canada

Fig. 12. Variation in the rate coefficient measured for the sequential methoxylation reaction of C_{60}^{2+} with methyl nitrite at room temperature in helium buffer gas at 0.35 Torr.

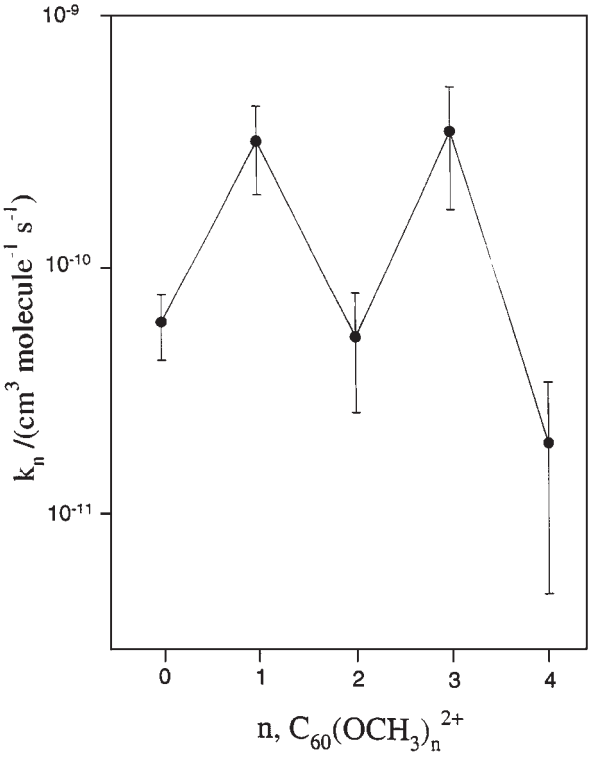

Also, we have observed several reactions of derivatized fullerene cations that involve the complete transfer of the ionized substituent according to eq. [11] with R = CN, C_2H_3, C_3H_3, and CH_2CN (16).

[11] $C_{60}(NCR)^{3+} + RCN \rightarrow C_{60}^{2+} + (RCN)_2^+$

Presumably such reactions are driven by the stability of the product dimer cation.

B. Surface derivatization

A number of higher order reactions have been observed in our laboratory that result in the sequential derivatization of the *surface* of the fullerene cation to produce what have been called "fuzzy ball" structures. H atoms were seen to add sequentially to the first three charge states of C_{60}^{n+} to produce $C_{60}H_m^{n+}$ according to reaction [12], with *m* up to 9 and constrained only by the number density of H atoms that we were able to generate in the flow tube experimentally (8, 9).

[12] $C_{60}H_m^{n+} + H \rightarrow C_{60}H_{m+1}^{n+}$

Several aliphatic nitriles have been observed to add rapidly to C_{60}^{n+} in numbers equal to the number of charges on C_{60}^{n+} to produce adducts according to reaction [13], with *n* up to 4 (16).

[13] $C_{60}(NCR)_m^{n+} + RCN \rightarrow C_{60}(NCR)_{m+1}^{n+}$

These adducts have the following plausible structures (16).

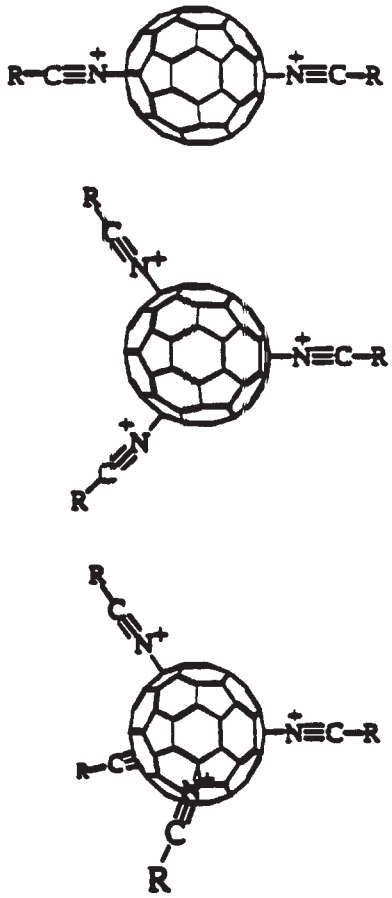

Also, C_{60}^{2+} has been observed to react with methyl nitrite in sequential bimolecular reactions leading to the sequential transfer of at least 15 methoxy groups according to reaction [14] (31).

[14] $C_{60}(CH_3O)_m^{2+} + CH_3ONO \rightarrow C_{60}(CH_3O)_{m+1}^{2+} + NO$

The addition kinetics exhibits periodicities of 2 and 4 that have been attributed to periodicities in the stabilities of the resulting surface-derivatized cations of which the following structure is representative.

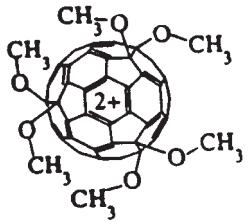

The occurrence of surface derivatization was deduced from observations of the collision-induced dissociation of the $C_{60}(CH_3O)_{m+1}^{2+}$ product ions that indicated loss of a single CH_3O group for all values of *m*. The periodicity in reaction rate is shown in Fig. 12. The higher reactivities of the odd-numbered $C_{60}(CH_3O)_m^{2+}$ adduct ions have been attributed to their radical nature. The lower reactivities of the 4th and 8th adducts have been ascribed to an aromatic character for these cations as they contain $(4n + 2)$ π electrons (32).

© 1999 NRC Canada

Fig. 13. Data for the sequential addition of allene to C_{60}^{2+} observed at a room temperature of 294 ± 2 K and a helium pressure of 0.35 ± 0.01 Torr.

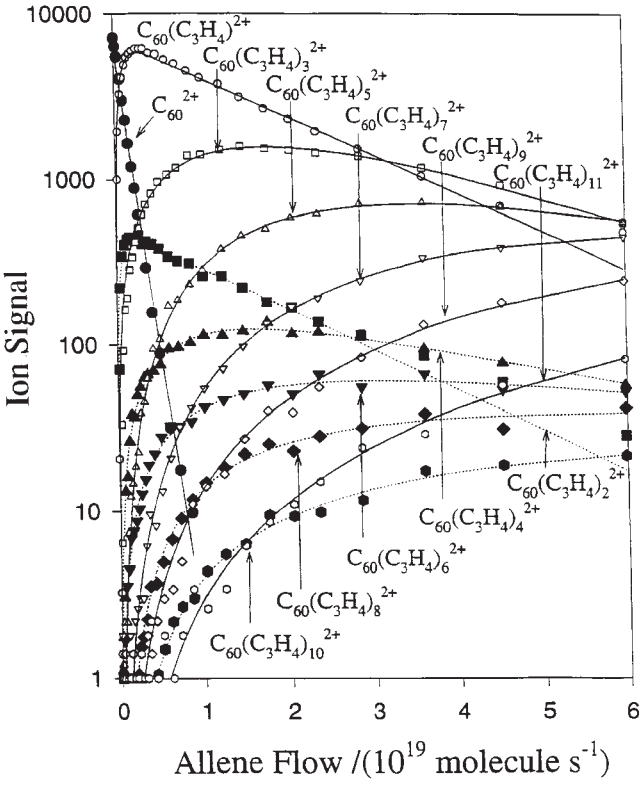

Fig. 14. Measured profiles for the multicollision-induced dissociation of $C_{60}(allene)^{2+}$ at an allene flow of 4.5×10^{19} molecules s^{-1} in 10% argon–helium at a total pressure of 0.30 ± 0.01 Torr and 294 ± 2 K.

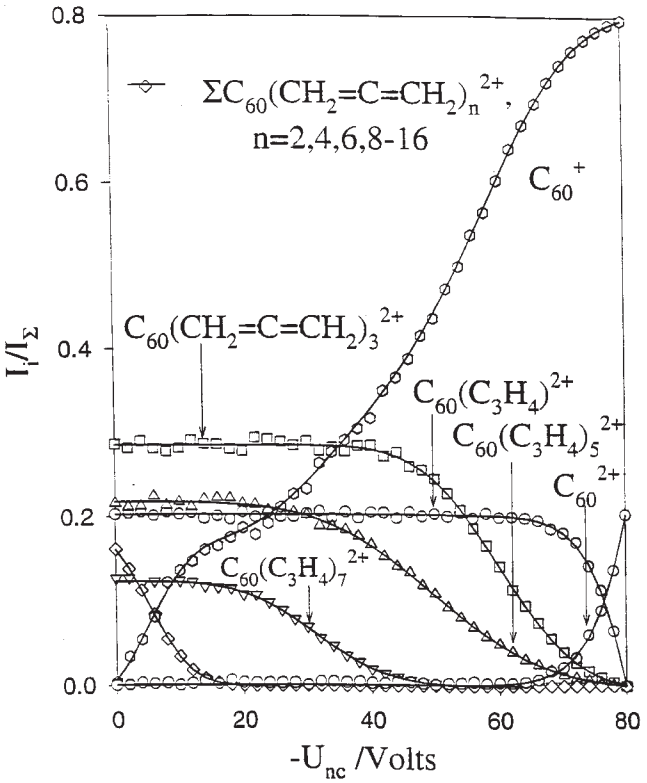

C. Ball-and-chain propagation

With some molecules we have observed multiple derivatization that we suggest leads to chain propagation or ball-and-chain formation in the manner indicated by reaction [15].

[15] 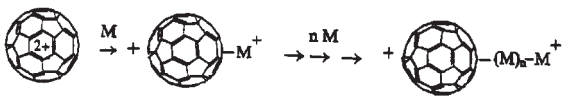

We have proposed such reactions for C_{60}^{2+} reacting sequentially with ethylene (33), propene, allene (33), 1,3-butadiene (21), *cis*, and *trans*–1,3-pentadiene, acetylene (33), methyl acetylene (34), diacetylene, cyanoacetylene, ethylene oxide (19), and propylene oxide. Many of these molecules are well known as monomers in traditional polymer chemistry. Indeed, reaction [15] may be regarded as an ion-induced polymerization reaction. A noteworthy feature of reaction [15] is the concomitant intramolecular charge separation. We have postulated that one of the charges is propagated along the substituent driven by Coulombic repulsion, which directs chain growth away from the C_{60} surface (21).

The chemistry of C_{60}^{2+} and allene is of particularly interest, since the sequential addition exhibits a striking periodicity in reactivity, with the *even*-numbered adducts reacting about 10 times faster than the *odd*-numbered adducts (see Fig. 13). We have managed to probe the bond connectivity in these adducts using multicollision induced dissociation. Figure 14 shows that the first allene molecule comes off intact by *heterolytic* dissociation to regenerate the C_{60}^{2+} dication. Higher adducts appear to completely eliminate polymers of allene in one step by *homolytic* dissociation, leading to charge separation and formation of singly charged C_{60}^{+}. Also, Fig. 14 shows that the odd adducts have a higher stability than the even adducts, which exhibit a much lower threshold for dissociation. Taken together, the kinetic and collision-induced dissociation results have led us to propose a mechanism involving the alternating formation of *charge-localized even-numbered acyclic allyl cations*,which can be expected to be more reactive, and the formation of *charge-delocalized cyclic odd-numbered allyl cations*, which would be less reactive. The following semi-empirical MP3 structure calculated for $C_{60}(allene)_7^{2+}$ is representative of an odd-numbered allyl cation.

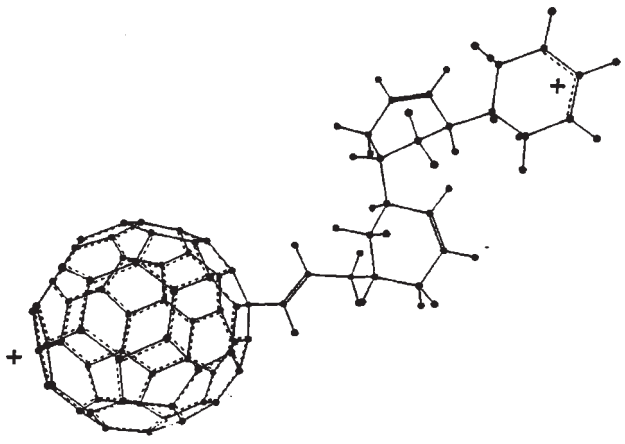

© 1999 NRC Canada

Fig. 15. Experimental data for the reaction of $C_{60}Fe^+$ with CO in helium buffer gas at a total pressure of 0.30 ± 0.01 Torr and 294 ± 2 K. The fifth adduct, $C_{60}Fe(CO)_5^+$ could not be detected.

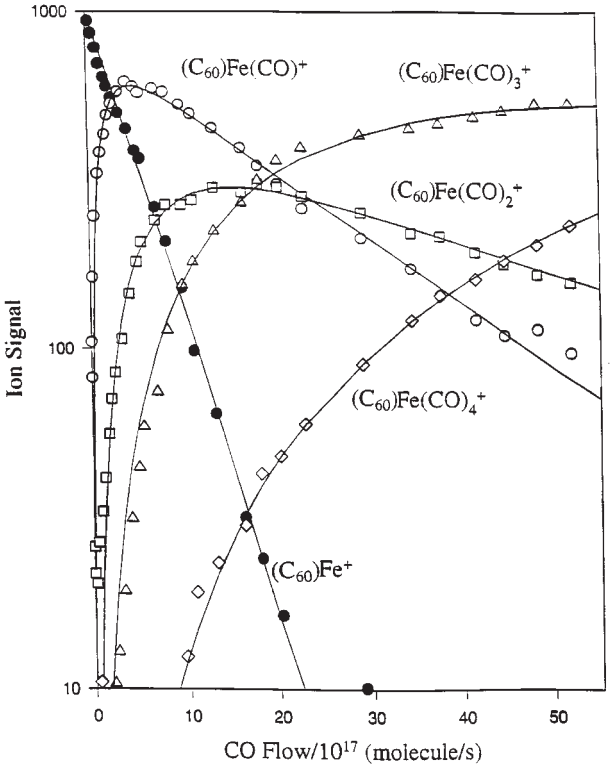

7. Reactions of atomic exohedral adduct ions

Recently we have become interested in elucidating the influence of C_{60} as a ligand on the reactivity of metal ions. Atomic ions readily can be attached to C_{60} upstream in the flow tube of our SIFT apparatus by attachment reactions of type [16], and the chemistry of the adduct ion then can be followed downstream.

[16] $A^+ + C_{60} + He \rightarrow C_{60}A^+ + He$

For example, we have already observed the attachment of Si^+, Fe^+, and Mg^+ to C_{60} under SIFT conditions. Questions arise regarding the nature of the bonding in $C_{60}A^+$ and the location of A^+ on the C_{60} surface. Possible sites for the location of Fe^+ on the C_{60} surface are illustrated below.

We hypothesized that a comparative study of the chemical reactivity of Fe^+ ligated to C_2H_4, *c*-C_5H_5, C_6H_6, and C_{60} would provide insight into the mode of bonding in $C_{60}Fe^+$. Indeed, reactivity measurements with CO and N_2O indicated a match between $(C_2H_4)Fe^+$ and $C_{60}Fe^+$ that suggests that the $(\eta^2\text{-}C_{60})Fe^+$ structures are preferred for $C_{60}Fe^+$ generated under SIFT conditions (35).

A comparison of the reactivities of $C_{60}Fe^+$ and the unligated Fe^+ ion provides a measure of the influence of the C_{60} ligand on chemical reactivity. Thus the addition reaction of CO with Fe^+, which does not occur measurably for the isolated cation ($k < 10^{-14}$ cm^3 molecule^{-1} s^{-1}), proceeds rapidly in the presence of C_{60} ($k = 1.3 \times 10^{-10}$ cm^3 molecule^{-1} s^{-1}). Three more molecules add sequentially (see Fig. 15), presumably to the Fe center according to reaction [17].

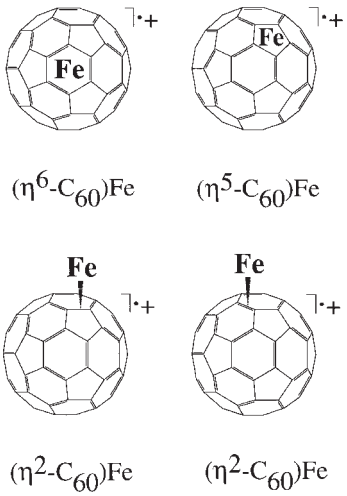

[17]

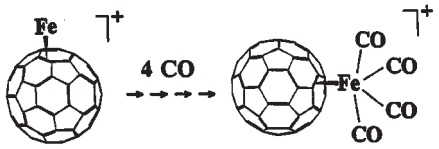

Also, the rate of the bimolecular O-atom transfer reaction of nitrous oxide with Fe^+ ($k = 3.1 \times 10^{-11}$ cm^3 molecule^{-1} s^{-1}) is enhanced by a factor of more than three in the presence of C_{60} ($k = 1.0 \times 10^{-10}$ cm^3 molecule^{-1} s^{-1}). Again, the O-atom transfer presumably occurs at the Fe site as shown in reaction [18].

[18]

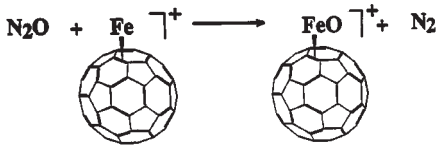

8. On the influence of surface strain on the reactivities of fullerene ions

Fullerene molecules, and presumably also their ions, provide a range of reactive C sites with different degrees of hybridization and strain (36). We have made some progress in investigating the influence of such surface features on the chemical reactivity of fullerene cations. Our early investigations of addition reactions of fullerene cations C_{56}^+, C_{58}^+, and C_{60}^+ with NH_3, of addition reactions of C_{56}^{2+}, C_{58}^{2+}, and C_{60}^{2+} with C_2H_4 and CH_3CN, and of hydride-transfer reactions of C_{56}^{2+}, C_{58}^{2+}, and C_{60}^{2+} with *n*-C_4H_{10}, revealed an enhanced reactivity for the adjacent-pentagon fullerene ions of C_{56} and C_{58} relative to those of C_{60} (37). Adjacent pentagons enhance the curvature of the carbon surface and the sp^3 character of selected C sites (37). More recent systematic studies of addition reactions of C_{56}^+, C_{58}^+, C_{60}^+, C_{70}^+, corannulene$^+$, and coronene$^+$ with cyclopentadiene and 1,3-cyclohexadiene indicated that the efficiency of bond forma-

© 1999 NRC Canada

Fig. 16. Semi-logarithmic plot for the dependence of reaction efficiency on the square of the POAV angle and the strain energy for reactions with cyclopentadiene in helium buffer gas at 0.35 Torr and 294 ± 2 K. k_{obs} is the measured rate coefficient and k_c is the collision rate coefficient, which is estimated to be 10^{-9} cm^3 molecule^{-1} s^{-1}. The horizontal bars represent the range in strain energy presented by the various cations, which could not be resolved, since the exact C site(s) being bonded could not be determined.

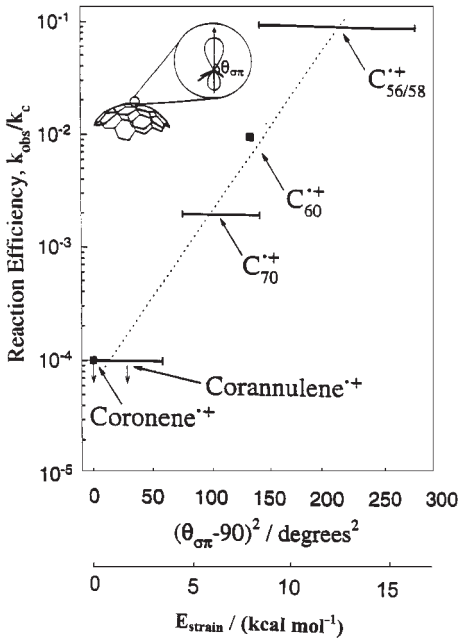

Table 1. POAV angles for various sites on selected carbonaceous molecules.

POAV angle, θ_x (deg)	C_{60}	C_{70}	Corannulene	Coronene
θ_1	11.6[a]	12.0[a]	7.7[b] (8.2)[c]	0
θ_2	—	11.9[a]	3.0[b] (3.8)[c]	0
θ_3	—	11.5[a]	0	0
θ_4	—	10.0[a]	—	—
θ_5	—	8.9[a]	—	—

[a]Reference 39.
[b]Reference 40.
[c]Reference 41.

tion with these two molecules also depends strongly on the curvature of the carbonaceous surface of the reacting cation (38).

On a carbonaceous surface the strain energy will depend upon the π orbital axis vector (POAV) angle, θ (36): the angle between the π-orbital at the bonding C site and one of the σ bonds on the adjacent carbonaceous surface minus 90° (see Fig. 16). For a planar sp^2 carbon atom this angle is 0°, and for a tetrahedral sp^3 carbon atom it is 19.47°. The POAV angles for the different sites in C_{60} and C_{70} and the related corannulene and coronene molecules shown below are given in Table 1. C_{70} has five different types of C sites with different surface strain, while C_{60} has only one such site. There is no strain in the flat PAH coronene whereas the bowl-shaped corannulene molecule has three types of C sites including one without strain.

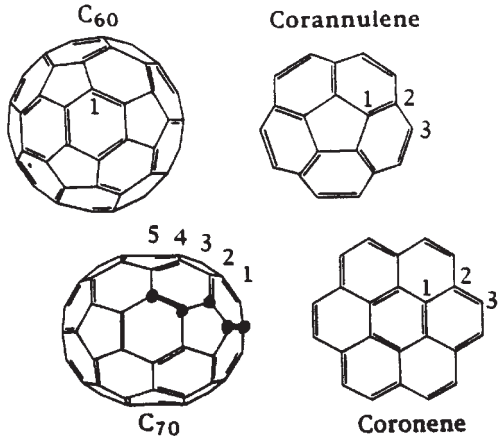

Figure 16 shows that the Diels–Alder addition with cyclopentadiene is faster with the smaller, more strained fullerenes and that the efficiencies of addition to the less-strained corannulene cation and the flat coronene cation are immeasurably small. Apparently the addition is driven by the relief of strain energy. The correlation presented in Fig. 16 leads to the following approximate dependence of the rate coefficient for addition on strain energy *E*, in kcal mol^{-1}, over the range in POAV angle explored.

[19] $k = 6.0 \times 10^{-14}\ e^{0.595E}$

These results also suggest a preference in reactivity for C sites with the highest strain energy (or the site with the highest local curvature) in those cations with more than one site of different strain as is the case, for example, with C_{70}^+ and corannulene$^+$. Such regioselectivity has been identified in earlier solution studies of the osmylation of C_{70} (42).

Conclusions

I have surveyed here much of the remarkable chemistry of buckminsterfullerene cations that has been revealed by our laboratory measurements using the SIFT technique since we began our studies in 1991. The charge state of C_{60}^{n+} has been shown to be decisive in determining the nature of this chemistry. Multiple derivatization, both of the C_{60} surface and in a ball-and-chain fashion, is an important feature of the higher order chemistry, particularly in the chemistry initiated by C_{60}^{2+} and C_{60}^{3+}. But, as the electron recombination energy of C_{60}^{n+} increases with increasing ionization, the transfer of one or more electrons from a reacting molecule eventually dominates.

Singly charged fullerene ions are known to be produced naturally in certain hydrocarbon flames where they have been shown to add hydrogen atoms (43). We have proposed elsewhere that mechanisms exist for the production of singly and doubly charged fullerenes from neutral fullerenes thought to be present in interstellar clouds and circumstellar atmospheres (44). The chemistry of these fullerene ions may have important consequences in these environments. For example, additions of hydrogen atoms to ionized fullerenes

© 1999 NRC Canada

that we have observed under SIFT conditions are expected to be efficient and may lead to the production of *fulleranes* (hydrogenated fullerenes) upon neutralization or even to the formation of molecular hydrogen by hydrogen-atom recombination on the fullerene-ion surface. Furthermore, additions of a variety of other known interstellar and circumstellar atoms and molecules to ionized fullerenes, particularly to doubly charged fullerenes, as well as additions of ions to neutral fullerenes are also likely. Finally, our results in the gas phase for the chemistry of C_{60}^{n+} should serve as a useful benchmark for the chemistries of fullerene cations in solution. These chemistries have not yet been elucidated, although persistent singly and multiply charged cations of C_{60} and other fullerenes have been observed in solution (45–47).

Acknowledgements

A number of graduate students and postdoctoral fellows have participated in the fullerene-ion research over the years, and I am grateful for their contributions. Special thanks go to Dr. Simon Petrie, Dr. Reza Javahery, and Dr. Vladimir Baranov for their inspiring collaboration. Also, I wish to thank the Natural Sciences and Engineering Research Council of Canada for ongoing financial support and the Canada Council for a Killam Research Fellowship during the formative part of this research.

References

1. P. Scheier, B. Dünser, R. Wörgötter, S. Matt, D. Muigg, G. Senn, and T.D. Märk. Int. Rev. Phys. Chem. **15**, 93 (1996).
2. G.I. Mackay, G.D. Vlachos, D.K. Böhme, and H.I. Schiff. Int. J. Mass Spectrom. Ion Phys. **36**, 259 (1980).
3. G. Javahery, S. Petrie, J. Wang, X. Wang, and D.K. Böhme. Int. J. Mass Spectrom. Ion Processes **125**, R13 (1992).
4. D.L. Lichtenburger, M.E. Rempe, and S.B. Gogosha. Chem. Phys. Lett. **198**, 454 (1992).
5. G. Javahery, S. Petrie, J. Wang, and D.K. Böhme. Chem. Phys. Lett. **195**, 76 (1992).
6. H.D. Hagstrum. Phys. Rev. **96**, 336 (1954).
7. Y. Ling, G.K. Koyanagi, D. Caraiman, V. Baranov, and D.K. Böhme. Int. J. Mass Spectrom. **192**, 215 (1999).
8. V. Baranov and D.K. Böhme. Int. J. Mass Spectrom. Ion Processes, **154**, 71 (1996).
9. S. Petrie, G. Javahery, J. Wang, and D.K. Böhme. J. Am. Chem. Soc. **114**, 6268 (1992).
10. S. Petrie, H. Becker, V.I. Baranov, and D.K. Böhme. Int. J. Mass Spectrom. Ion Processes, **145**, 79 (1995).
11. G. Javahery, S. Petrie, H. Wincel, J. Wang, and D.K. Böhme. J. Am. Chem. Soc. **115**, 5716 (1993).
12. H. Becker, G. Javahery, S. Petrie, and D.K. Böhme. J. Phys. Chem. **98**, 5591 (1994).
13. V. Baranov and D.K. Böhme. Int. J. Mass Spectrom. Ion Processes, **165**/**166**, 249 (1997).
14. S. Petrie and D.K. Böhme. Can. J. Chem. **72**, 577 (1994).
15. D.K. Böhme. Int. Rev. Phys. Chem. **13**, 163 (1994).
16. G. Javahery, S. Petrie, J. Wang, H. Wincel, and D.K. Böhme. J. Am. Chem. Soc. **115**, 9701 (1993).
17. G. Javahery, S. Petrie, H. Wincel, J. Wang, and D.K. Böhme. J. Am. Chem. Soc. **115**, 6295 (1993).
18. S. Petrie, G. Javahery, H. Wincel, J. Wang, and D.K. Böhme, Int. J. Mass Spectrom. Ion Processes, **138**, 187 (1994).
19. J. Wang, G. Javahery, S. Petrie, A.C. Hopkinson, and D.K. Böhme. Angew. Chem. Int. Ed. Engl. **33**, 206 (1994).
20. J. Wang, G. Javahery, S. Petrie, and D.K. Böhme. J. Am. Chem. Soc. **114**, 9665 (1992).
21. J. Wang, V. Baranov, and D.K. Böhme. J. Am. Soc. Mass Spectrom. **7**, 261 (1996).
22. J. Wang, G. Javahery, V. Baranov, and D.K. Böhme. Tetrahedron, **52**, 5191 (1996).
23. V. Baranov, J.Wang, A.C. Hopkinson, and D.K. Böhme. J. Am. Chem. Soc. **119**, 2040 (1997).
24. S. Petrie, J. Javahery, J. Wang, and D.K. Böhme. J. Phys. Chem. **96**, 6121 (1992).
25. S. Petrie, G. Javahery, J. Wang, and D.K. Böhme. J. Am. Chem. Soc. **114**, 6268 (1992).
26. G. Javahery, H. Becker, S. Petrie, P.C. Cheng, H. Schwarz, L.T. Scott, and D.K. Böhme. Org. Mass Spectrom. **20**, 1005 (1993).
27. V. Baranov and D.K. Böhme. Chem. Phys. Lett. **258**, 203 (1996).
28. D.K. Böhme. *In* Recent advances in the chemistry and physics of fullerenes and related materials.. Electrochem. Soc. Proc. Vol. 97-14. *Edited by* R.S. Ruoff and K.M. Kadish. Electrochemical Society, Inc., Pennington, N.J. 1997. p. 763.
29. Z. Herman. Int. Rev. Phys. Chem. **15**, 299 (1996).
30. S. Petrie, G. Javahery, and D.K. Böhme. Int. J. Mass Spectrom. Ion Processes, **124**, 145 (1993).
31. S. Petrie, G. Javahery, H. Wincel, and D.K. Böhme. J. Am. Chem. Soc. **113**, 6290 (1993).
32. V. Baranov, A.C. Hopkinson, and D.K. Böhme. J. Am. Chem. Soc. **119**, 7055 (1997).
33. J. Wang, G. Javahery, V. Baranov, and D.K. Böhme. Tetrahedron, **52**, 5191 (1996).
34. V. Baranov, J. Wang, A.C. Hopkinson, and D.K. Böhme. J. Am. Chem. Soc. **119**, 2040 (1997).
35. V. Baranov and D.K. Böhme. Int. J. Mass Spectrom. Ion Processes, **149**/**150**, 543 (1995).
36. R.C. Haddon. Science (Washington, D.C.), **261**, 1545 (1993).
37. S. Petrie and D.K. Böhme. Nature (London), **365**, 426 (1993).
38. H. Becker, L.T. Scott, and D.K. Böhme. Int. J. Mass Spectrom. Ion Processes, **167**/**168**, 519 (1997).
39. K. Raghavachari and C.M. Rohlfing. J. Phys. Chem. **95**, 5768 (1991).
40. D. Bakowski and W. Thiel. J. Am. Chem. Soc. **113**, 3704 (1991).
41. J.C. Hanson and C.E. Nordman. Acta Crystallogr. Sect. B: Struct. Crystallogr. Cryst. Chem. **32**, 1147 (1976).
42. J.M. Hawkins, A. Meyer, and M.A.J. Solow. J. Am. Chem. Soc. **115**, 7499 (1994).
43. J. Ahrens, M. Bachmann, Th. Baum, J. Griesheimer, R. Kovacs, P. Weilmünster, and K.-H. Homann. Int. J. Mass Spectrom. Ion Processes, **138**, 133 (1994).
44. S. Petrie, G. Javahery, and D.K. Böhme. Astron. Astrophys. **271**, 662 (1993).
45. S.G. Kukolich and D.R. Huffman. Chem. Phys. Lett. **182**, 263 (1991).
46. H. Thomann, M. Bernardo, and G.P. Miller. J. Am. Chem. Soc. **114**, 6593 (1992).
47. R.D. Bolskar, R.S. Mathur, and C.A. Reed. J. Am. Chem. Soc. **118**, 13093 (1996).

© 1999 NRC Canada

Solubility of phenanthrene in organic nonelectrolyte solvents. Comparison of observed versus predicted values based upon Mobile Order theory

Carmen E. Hernández, Karina M. De Fina, Lindsay E. Roy, Tina L. Sharp, and William E. Acree, Jr.

Abstract: Experimental solubilities are reported at 25.0°C for phenanthrene dissolved in 41 different organic nonelectrolyte solvents containing ether, carbonyl, hydroxy, chloro, amino, ester, methyl and *tert*-butyl functional groups. Results of these measurements are used to test the applications and limitations of expressions derived from Mobile Order theory. For the 31 solvents for which predictions could be made, computations show that Mobile Order theory does provide fairly reasonable estimates of the saturation mole fraction solubilities. Average absolute deviation between predicted and observed values is 41.3% (excluding acetonitrile). In comparison, the average absolute deviation is 1610% when ideal solution behavior is assumed. Also reported are experimental solubilities at 26°C for pyrene dissolved in 1-hexanol, 1-heptanol, ethylbenzene, aniline, and 2-butanone.

Key words: phenanthrene solubilities, organic nonelectrolyte solvents, solubility predictions.

Résumé : Opérant à 25°C, on a déterminé les solubilités expérimentales du phénanthrène en solution dans 41 solvants organiques non électrolytiques différents comportant les substituants et groupes fonctionnels suivants : éther, carbonyle, hydroxyle, bromo, amino, ester, méthyle et *tert*-butyle. On a utilisé les résultats de ces mesures pour évaluer les applications et les limitations d'expressions dérivées de la théorie de l'ordre mobile. Les 31 solvants pour lesquels il est possible de faire des prédictions par calculs permettent de démontrer que la théorie de l'ordre mobile fournit des évaluations assez raisonnables des solubilités en fraction molaire de saturation. La déviation absolue moyenne entre les valeurs observées et calculées est de 41,3% (en excluant l'acétonitrile). Par comparaison, la déviation absolue moyenne est de 1610% lorsqu'on assume un comportement de solution idéale. On rapporte aussi les solubilités expérimentales, à 26°C, du pyrène en solution dans l'hexan-1-ol, l'heptan-1-ol, l'éthylbenzène, l'aniline et la butan-2-one.

Mots clés : solubilités du phénanthrène, solvants organiques non électrolytiques, prédictions de la solubilité.

[Traduit par la Rédaction]

Introduction

Solid–liquid equilibrium data of organic nonelectrolyte systems are becoming increasingly important in the petroleum industry, particularly in light of present trends towards heavier feedstocks and known carcinogenicity/mutagenicity of many of the larger polycyclic aromatic compounds. Solubility data for a number of polycyclic aromatic hydrocarbons (e.g., anthracene and pyrene) and hetero-atom polynuclear aromatics (e.g., carbazole, dibenzothiophene, and xanthene) have been published in the recent chemical literature (for listing of references see Acree (1–3)). Despite efforts by experimentalists and scientific organizations, both in terms of new experimental measurements and critically evaluated data compilations, there still exist numerous systems for which solubility data are not readily available.

To address this problem, researchers have turned to group contribution methods and semiempirical expressions to predict desired quantities. Group contribution methods have proved fairly successful in estimating solid solubility in pure and binary solvent mixtures from structural information (4–11). Practical application, however, is limited to systems for which all group interaction parameters are known. Interaction parameters can be evaluated from liquid–vapor, liquid–liquid, and solid–liquid equilibria data. It is important that the data base contain as many different functional groups as possible, preferably with adequate representation from both mono- and multi-functional solute/solvent molecules to permit evaluation of potential synergistic effects. The data base should contain sufficient experimental values near infinite dilution in the event that one wishes to determine separate interaction parameters for finite concentration and infinite dilution activity coefficient predictions.

Abraham et al. (12, 13) recently developed a general solvation equation that can be used in the correlation and understanding of physicochemical and biochemical phenomena.

Received December 4, 1998.

C.E. Hernández, K.M. De Fina, L.E. Roy, T.L. Sharp, and W.E. Acree, Jr.[1] Department of Chemistry, University of North Texas, Denton, TX 76203-5070, U.S.A.

[1]Author to whom correspondence may be addressed. e-mail: Acree@unt.edu

© 1999 NRC Canada

Physical properties that have been correlated include gas–solvent partition coefficients (as log L):

$$[1] \quad \log L = c + rR_2 + s\pi_2^H + a\sum\alpha_2^H + b\sum\beta_2^H + d\log L^{16}$$

and water–solvent partition coefficients (as log P):

$$[2] \quad \log P = c + rR_2 + s\pi_2^H + a\sum\alpha_2^H + b\sum\beta_2^H + vV_x$$

where R_2 and V_x refer to the molar refraction and McGowan volume of the solute, respectively, π_2^H is the solute dipolarity/polarizability descriptor, L^{16} is the solute's gas–liquid partition coefficient on hexadecane, and $\sum\alpha_2^H$ and $\sum\beta_2^H$ are measures of the solute's hydrogen-bond acidity and hydrogen-bond basicity. For any given solvent, numerical values of the seven curve-fit coefficients (c, r, s, a, b, d, and v) are deduced by regressing experimental partition coefficient data in accordance with eqs. [1] and [2]. The input partition coefficients were sometimes calculated as the ratio of the solute molar solubilities in the organic solvent and water, $P = C_A^{org}/C_A^{aq}$, and as the ratio of the solute molar solubility in the organic solvent and vapor concentration, $L = C_A^{org}/C_A^{gas}$. Published papers have reported curve-fit coefficients for water (12, 13) and a few select organic solvents (13).

To increase the solubility database available for developing group contribution methods and general solvation correlations, we are in the process of measuring solubility data for polycyclic aromatic hydrocarbons (PAHs) and polycyclic aromatic nitrogen hetero-atoms (PANHs). In the present communication, we report phenanthrene solubilities in 41 different organic solvents at 25°C and pyrene solubilities in 1-hexanol, 1-heptanol, ethylbenzene, aniline, and 2-butanone at 26°C. Results of the phenanthraene measurements are used to further test the applications and limitations of predictive expressions derived from Mobile Order theory. Subsequent studies will use the experimental phenanthrene and pyrene solubilities in developing gas–liquid partition and water – organic solvent partition correlations based upon eqs. [1] and [2].

Materials and methods

Phenanthrene (Aldrich, 98%) and pyrene (Aldrich, 99+%) were recrystallized several times from methanol. *n*-Hexane (Aldrich, 99%), *n*-heptane (Aldrich, HPLC), *n*-octane (Aldrich, 99+%, anhydrous), *n*-nonane (TCI, 99+%), *n*-decane (TCI, 99+%), *n*-hexadecane (Aldrich, 99%), cyclohexane (Aldrich, HPLC), methylcyclohexane (Aldrich, 99+%, anhydrous), cyclooctane (Aldrich, 99+%), 2,2,4-trimethylpentane (Aldrich, HPLC), *tert*-butylcyclohexane (Aldrich, 99+%), dibutyl ether (Aldrich, 99%), methanol (Aldrich, 99.9+%), ethanol (Aaper Alcohol and Chemical Company, absolute), 1-propanol (Aldrich, 99+%, anhydrous), 2-propanol (Aldrich, 99+%, anhydrous), 1-butanol (Aldrich HPLC, 99.8+%), 2-butanol (Aldrich, 99+%, anhydrous), 1-pentanol (Aldrich, 99+%), 2-pentanol (Acros 99+%), 1-hexanol (Alfa Aesar, 99+%), 1-heptanol (Alfa Aesar, 99+%), 2-methyl-2-butanol (Acros, 99+%), 2-methyl-1-propanol (Aldrich, 99+%, anhydrous), 3-methyl-1-butanol (Aldrich, 99+%, anhydrous), 1-octanol (Aldrich, 99+%, anhydrous), 4-methyl-2-pentanol (Acros, 99+%), 2-ethyl-1-hexanol (Aldrich, 99+%), 2-methyl-1-pentanol (Aldrich, 99%), cyclopentanol (Aldrich, 99%), ethylene glycol (Aldrich, 99.8%, anhydrous), acetonitrile (Aldrich HPLC, 99.93+%), 1,4-dioxane (Aldrich, 99.8%, anhydrous), tetrahydrofuran (Aldrich, 99.9%, anhydrous), carbon tetrachloride (Aldrich HPLC, 99.9+%), 2-butanone (Aldrich HPLC, 99.5+%), ethylbenzene (Aldrich, 99.8%, anhydrous), aniline (Aldrich, ACS Reagent, 99.5+%), cyclohexanone (Aldrich, 99.8%), ethyl acetate (Aldrich HPLC, 99.9%), butyl acetate (Aldrich HPLC, 99.8%), and 2,2,2-trifluoroethanol (Aldrich, 99+%) were stored over molecular sieves before use. Gas chromatographic analysis showed solvent purities to be 99.7 mol% or better.

Excess solute and solvent were placed in amber glass bottles and allowed to equilibrate in a constant temperature water bath at 25.0 ± 0.1°C for at least 3 days (often longer). Attainment of equilibrium was verified both by repetitive measurements after several additional days and by approaching equilibrium from supersaturation by pre-equilibrating the solutions at a higher temperature. Aliquots of saturated phenanthrene solutions were transferred through a coarse filter into a tared volumetric flask to determine the amount of sample and diluted quantitatively with 2-propanol for spectrophotometric analysis at 347 nm on a Bausch and Lomb Spectronic 2000. Concentrations of the dilute solutions were determined from a Beer–Lambert Law absorbance versus concentration working curve for nine standard solutions. The concentration of phenanthrene in the standard solutions varied from 2.29×10^{-3} to 7.64×10^{-3} M. The calculated molar absorptivity of the standard solutions varied slightly over the concentration range, from $\varepsilon \approx 212$ L mol^{-1} cm^{-1} (2.29×10^{-3} M) to $\varepsilon \approx 191$ L mol^{-1} cm^{-1} (7.64×10^{-3} M).

Experimental molar concentrations were converted to (mass/mass) solubility fractions by multiplying by the molar mass of phenanthrene, volume(s) of volumetric flask(s) used, and any dilutions required to place the measured absorbances on the Beer–Lambert Law absorbance versus concentration working curve, and then dividing by the mass of the saturated solution analyzed. Mole fraction solubilities were computed from (mass/mass) solubility fractions using the molar masses of the solute and solvent. Experimental phenanthrene solubilities, X_A^{sat}, in 41 organic solvents studied are listed in Table 1. Numerical values represent the average of between four and eight independent determinations, with the measurements being reproducible to ±1.5%. Also measured were the solubilities of pyrene at 26°C in 1-hexanol (X_A^{sat} = 0.012 73), 1-heptanol (X_A^{sat} = 0.016 94), ethylbenzene (X_A^{sat} = 0.064 24), aniline (X_A^{sat} = 0.033 98), and 2-butanone (X_A^{sat} = 0.067 52). Pyrene solubilities were measured spectrophotometrically at 372 nm.

Results and discussion

Solubility data for phenanthrene are available in the chemical literature for 8 of the 41 solvents listed in Table 1. Doane and Drickamer (14) previously reported the solubility

© 1999 NRC Canada

Table 1. Comparison between experimental phenanthrene mole fraction solubilities and predicted values based upon Mobile Order theory.

Organic solvent	$(X_A^{sat})^{exp,\,a}$	$(X_A^{sat})^{calc}$	% Dev[b]
n-Hexane	0.031 89	0.035 29	10.7
n-Heptane	0.038 88	0.037 16	–4.4
n-Octane	0.044 43	0.042 32	–4.7
n-Nonane	0.047 85	0.049 30	3.0
n-Decane	0.055 31	0.051 54	7.3
n-Hexadecane	0.079 72	0.071 94	–9.8
Cyclohexane	0.036 48	0.047 24	29.5
Methylcyclohexane	0.045 72	0.050 46	10.4
Cyclooctane	0.060 02	0.066 38	10.6
2,2,4-Trimethylpentane	0.024 86	0.027 21	9.5
tert-Butylcyclohexane	0.051 24	0.066 84	30.4
Dibutyl ether	0.094 54	0.1748	84.9
Tetrahydrofuran	0.2884	0.2662	–7.7
1,4-Dioxane	0.2165	0.2705	24.9
Methanol	0.005 89	0.012 44	111.2
Ethanol	0.011 14	0.019 19	72.3
1-Propanol	0.013 55	0.023 96	76.8
2-Propanol	0.009 77	0.028 11	187.7
1-Butanol	0.017 71	0.030 40	71.7
2-Butanol	0.011 78	0.023 46	99.2
2-Methyl-1-propanol	0.010 20	0.018 37	80.0
1-Pentanol	0.024 91	0.032 59	30.8
2-Pentanol	0.017 64		
3-Methyl-1-butanol	0.016 06		
2-Methyl-2-butanol	0.019 26		
1-Hexanol	0.030 28	0.030 56	0.9
2-Methyl-1-pentanol	0.018 01		
4-Methyl-2-pentanol	0.017 54		
1-Heptanol	0.039 37	0.034 70	–11.9
1-Octanol	0.054 18	0.038 44	–29.1
2-Ethyl-1-hexanol	0.028 76		
Cyclopentanol	0.030 70		
Ethylene glycol	0.001 134	0.001 457	28.5
2,2,2-Trifluoroethanol	0.001 826		
2-Butanone	0.2090	0.2686	28.5
Aniline	0.1101		
Cyclohexanone	0.2716		
Ethyl acetate	0.1499	0.2661	77.5
Butyl acetate	0.1812	0.2555	41.0
Acetonitrile	0.032 67	0.2569	686.3
Carbon tetrachloride	0.1262	0.1807	43.2

[a]Numerical values represent the average of between four and eight independent determinations with the measurements being reproducible to ±1.5%.

[b]Deviations (%) = 100 $[(X_A^{sat})^{calc} - (X_A^{sat})^{exp}]/(X_A^{sat})^{exp}$.

of phenanthrene in several saturated hydrocarbon solvents as a function of pressure. At a pressure of P = 1 atm (= 101.3 kPa), the measured mole fraction solubilities were X_A^{sat} = 0.0326, X_A^{sat} = 0.0401, and X_A^{sat} = 0.0464 for hexane, heptane, and octane, respectively. Our experimental values listed in Table 1 differ from the published values by less than ±5%. Differences in chemical purities and experimental methodologies (static versus dynamic methods) can lead to differences of a few percent between values determined by two different research groups.

Speyers (15) measured the solubility of phenanthrene in ethanol as a function of temperature. The five temperatures studied by the author ranged from 273.2 K to 343.4 K, and did not include 298.15 K. The mole fraction solubility at 298.15 K can be obtained by curve-fitting the experimental data to

$$[3] \qquad \ln X_A^{sat} = 50.276 - 30{,}302/T + 4\,167\,980/T^2$$

a 1/T polynomial. Three terms were needed to accurately describe the experimental values. Using the above mathematical representation, we calculate a mole fraction solubility of X_A^{sat} = 0.011 44 at 298.15 K, which is in excellent agreement with our measured value of X_A^{sat} = 0.011 14.

Three experimental values were found for the solubility of phenanthrene in cyclohexane. McLaughlin and Zainal (16), Choi et al. (17), and Gordon and Scott (18) determined the solubility of phenanthrene as a function of temperature. Temperatures for the first two studies ranged from 300 K to 340 K. The latter study covered a slightly larger temperature range of 286 K to 340 K. Least-squares analysis of the three sets of experimental data gave the following three polynomials:

$$[4] \qquad \ln X_A^{sat} = 15.405 - 5{,}611.0/T$$

$$[5] \qquad \ln X_A^{sat} = 13.666 - 5{,}071.0/T$$

$$[6] \qquad \ln X_A^{sat} = 62.745 - 35{,}818/T + 4\,803\,930/T^2$$

from which we calculate extrapolated/interpolated mole fraction solubilities of X_A^{sat} = 0.032 89, X_A^{sat} = 0.035 37, and X_A^{sat} = 0.035 17 at T = 298.15 K. Our experimental value of X_A^{sat} = 0.036 48 is only slightly larger than the values reported by both Choi et al. and Gordon and Scott.

McLaughlin and Zainal (19) also studied the solubility behavior of phenanthrene in carbon tetrachloride at five temperatures from T = 305.6 K to T = 319.2 K. Least-squares analysis of the published solubility data yielded the following correlation:

$$[7] \qquad \ln X_A^{sat} = 9.9251 - 3{,}562.8/T$$

from which we calculate an extrapolated mole fraction solubility of X_A^{sat} = 0.1246 at T = 298.15 K. Our experimental value of X_A^{sat} = 0.1262 is again in good agreement with the published literature data.

Niimi (20) reported the millimolar solubility of phenanthrene in 1-octanol at 277.15 K, 285.15 K, and 293.15 K. From a plot of log molar solubility versus 1/T we extrapolate the published solubility data to T = 298.15 K, obtaining a numerical value of C_A^{sat} = 0.3226 M. There is some uncertainty in this extrapolation because three experimental data points did not fall on a straight line. A slightly larger value of C_A^{sat} = 0.3579 M is obtained if the value at T = 277.15 K is excluded from the least-squares analysis. Molar solubilities can be converted to mole fractions using $V_{octanol}$ = 158.30 cm^3 mol^{-1} and V_{phenan} = 155.8 cm^3 mol^{-1} (21), and by assuming that the excess volume is negligible. Performing this computation, mole fraction solubilities of X_A^{sat} = 0.051 02 and X_A^{sat} = 0.056 60 were calculated for phenanthrene dissolved in 1-octanol. Our experimental solubility of X_A^{sat} = 0.054 18 falls in between the two extrapo-

© 1999 NRC Canada

lated values. Finally, Li et al. (22) reported activity coefficients and mole fraction solubilities of six aromatic hydrocarbons in acetonitrile at 298.15 K. No details were given regarding the chemical purities and experimental methodology. Our measured value of $X_A^{sat} = 0.032\,67$ is slightly less than the published literature value of $X_A^{sat} = 0.035$.

Solvents listed in Table 1 include both noncomplexing alkanes and self-associating alcohols. Of the many solution models proposed in recent years, Mobile Order theory is perhaps the only one that is capable of describing solute behavior in such a wide range of solvent mixtures. The basic model (23–30) assumes that all molecular groups perpetually move, and that neighbors of a given kind of external atom in a molecule constantly change identity. All molecules of a given kind dispose of the same volume, equal to the total volume V of the liquid divided by the number N_A of molecules of the same kind, i.e., Dom A = V/N_A. The center of this domain perpetually moves. The highest mobile disorder is achieved whenever groups visit all parts of their domain without preference. Preferential contacts lead to deviations with respect to this "random" visiting. This is especially true in the case of hydrogen bonding, as specific interactions result in a specific orientation of the "donor" molecule with respect to an adjacent "acceptor" molecule.

In the case of an inert crystalline solute dissolved in a self-associating solvent, Mobile Order theory expresses the volume fraction saturation solubility, ϕ_A^{sat}, as (26–30)

$$[8]\quad \ln \phi_A^{sat} = \ln a_A^{solid} - 0.5\,(1 - V_A/V_{solvent})\,\phi_{solvent} + 0.5 \ln [\phi_A^{sat} + \phi_{solvent}(V_A/V_{solvent})] - \phi^2_{solvent}\, V_A(\delta'_A - \delta'_{solvent})^2\,(RT)^{-1} - r_{solvent}\,(V_A/V_{solvent})\,\phi_{solvent}$$

where the $r_{solvent}\,(V_A/V_{solvent})\,\phi_{solvent}$ term represents the contributions resulting from hydrogen-bond formation between the solvent molecules. For most of the published applications, $r_{solvent}$ was assumed to be unity for strongly associated solvents with single hydrogen-bonded chains such as monofunctional alcohols, to be two for water or diols, and to equal zero for nonassociated solvents such as saturated hydrocarbons. A more exact value for alcoholic solvents can be calculated (25) based upon

$$[9]\quad r_{solvent} = \frac{K_{solvent}\,\phi_{solvent}/V_{solvent}}{1 + K_{solvent}\,\phi_{solvent}/V_{solvent}}$$

with a numerical value of $K_{solvent} = 5000$ cm^3 mol^{-1} assumed for all monofunctional alcohols.

If complexation does occur between the crystalline solute and solvent (26–30):

$$[10]\quad \ln \phi_A^{sat} = \ln a_A^{solid} - 0.5\,(1 - V_A/V_{solvent})\,\phi_{solvent} + 0.5 \ln [\phi_A^{sat} + \phi_{solvent}(V_A/V_{solvent})] - \phi^2_{solvent}\, V_A(\delta'_A - \delta'_{solvent})^2\,(RT)^{-1} + \ln [1 + \phi_{solvent}(K_{ASolvent}/V_{solvent})]$$

then an additional term involving the solute–solvent equilibrium constant, $K_{ASolvent}$, must be introduced to describe the solubility enhancement that arises as a result of specific interactions. A slightly more complex expression applies in the case of solute complexation with a self-associating solvent. The symbols δ'_A and $\delta'_{solvent}$ denote the modified solubility parameters of the solute and solvent, respectively, V_i is the molar volume, and a_A^{solid} is the activity of the solid solute. This latter quantity is defined as the ratio of the fugacity of the solid to the fugacity of the pure hypothetical supercooled liquid. The numerical value of a_A^{solid}

$$[11]\quad \ln a_A^{solid} = -\Delta H_A^{fus}\,(T_{mp} - T)/(RTT_{mp}) + (\Delta C_{p,A}/RT)(T_{mp} - T) - (\Delta C_{p,A}/T) \ln (T_{mp}/T) - (\Delta S_A^{trans}/RT)(T_{trans} - T)$$

can be computed (17, 31, 32) from the solute's molar enthalpy of fusion, ΔH_A^{fus}, and heat capacity difference, $\Delta C_{p,A}$, at the normal melting point temperature, T_{mp}. The last term in eq. [11] accounts for the additional first-order phase transition that occurs at $T_{trans} \approx 339.2$ K. Contributions from nonspecific interaction are incorporated into Mobile Order theory through the $\phi^2_{solvent}\, V_A(\delta'_A - \delta'_{solvent})^2\,(RT)^{-1}$ term. Ruelle et al. (26–30) have presented an impressive set of comparisons between experimental and predicted values for anthracene, naphthalene, pyrene, biphenyl, carbazole, benzil, *p*-benzoquinone, tricosane, octacosane, 10-nonadecanone, 11-heneicosanone, and 12-tricosanone solubilities in a wide range of both noncomplexing and complexing solvents to document the predictive ability of Mobile Order theory.

Predictive application of eqs. [8] and [10] is relatively straightforward. First, an average numerical value of $\delta'_{phenan} = 20.45$ MPa$^{1/2}$ is computed by requiring that each equation (with $r_{solvent} = 0$ and (or) $K_{ASolvent} = 0$) perfectly describes phenanthrene mole fraction solubility data in *n*-hexane ($\delta'_{phenan} = 20.57$ MPa$^{1/2}$), *n*-heptane ($\delta'_{phenan} = 20.39$ MPa$^{1/2}$), and *n*-octane ($\delta'_{phenan} = 20.39$ MPa$^{1/2}$). The numerical value of $a_A^{solid} = 0.2596$ is calculated using eq. [11] with $\Delta H_A^{fus} = 16\,474$ J mol^{-1}, $\Delta C_{p,A} = 12.586$ J mol^{-1} K^{-1}, $T_{mp} = 372.4$ K, $\Delta S_A^{trans} = 3.853$ J mol^{-1} K^{-1}, and $T_{trans} = 339.2$ K (32). A numerical value of $V_{phenan} = 155.8$ cm^3 mol^{-1} was used for the molar volume of the hypothetical subcooled liquid solute. The numerical value of $V_{phenan} = 155.8$ cm^3 mol^{-1} corresponds to the experimentally determined partial molar volume of phenanthrene in carbon tetrachloride (21).

Table 1 summarizes the predictive ability of Mobile Order theory for the 31 different organic solvents for which both phenanthrene solubility data and modified solubility parameters could be found. Solvent molar volumes and modified solubility parameters are listed in Table 2. The modified solubility parameters account for only nonspecific interactions, and in the case of the alcoholic solvents the hydrogen-bonding contributions have been removed. Numerical values of $\delta'_{solvent}$ were obtained from published compilations (26, 27, 29, 30), and were either deduced by regressing actual solubility data of solid *n*-alkanes in organic solvents in accordance with the configurational entropic model of Huyskens and Haulait-Pirson (33) or estimated using known values for similar organic solvents. Examination of the entries in Table 1 reveals that Mobile Order theory does pro-

© 1999 NRC Canada

Table 2. Solvent and solute properties used in Mobile Order predictions.

Component (i)	V_i /(cm^3 mol^{-1})	δ'_i/(MPa$^{1/2}$)[a]
n-Hexane	131.51	14.56
n-Heptane	147.48	14.66
n-Octane	163.46	14.85
n-Nonane	179.87	15.07
n-Decane	195.88	15.14
n-Hexadecane	294.12	15.61
Cyclohexane	108.76	14.82
Methylcyclohexane	128.32	15.00
2,2,4-Trimethylpentane	166.09	14.30
Cyclooctane	134.9	15.40
tert-Butylcyclohexane	173.9	15.50
Dibutyl ether	170.3	17.45
Tetrahydrofuran	81.4	19.30
1,4-Dioxane	85.8	20.89
Methanol	40.7	19.25
Ethanol	58.7	17.81
1-Propanol	75.10	17.29
2-Propanol	76.90	17.60
1-Butanol	92.00	17.16
2-Butanol	92.4	16.60
2-Methyl-1-propanol	92.8	16.14
1-Pentanol	108.6	16.85
1-Hexanol	125.2	16.40
1-Heptanol	141.9	16.39
1-Octanol	158.3	16.38
Ethylene glycol	56.0	19.90
Acetonitrile	52.9	23.62
Carbon tetrachloride	97.8	17.04
2-Butanone	90.2	20.90
Ethyl acetate	98.5	20.79
Butyl acetate	132.5	19.66
Phenanthrene[b]	155.8[c]	20.45[d]

[a]Tabulated values are taken from a compilation given in Ruelle et al. (26, 27, 29, 30).

[b]The numerical value of a_A^{solid} = 0.2596 was calculated from eq. [11] using ΔH_A^{fus} = 16,474 J mol^{-1}, $\Delta C_{p,A}$ = 12.586 J mol^{-1} K^{-1}, T_{mp} = 372.4 K, ΔS_A^{trans} = 3.853 J mol^{-1} K^{-1}, and T_{trans} = 339.2 K (32).

[c]Numerical value of V_{phenan} = 155.8 cm^3 mol^{-1} corresponds to the experimentally determined partial molar volume of phenanthrene in carbon tetrachloride (21).

[d]Numerical value was calculated using the measured phenanthrene mole fraction solubilities in *n*-hexane, *n*-heptane, and *n*-octane, in accordance with eqs. [8] and [10]; with $r_{solvent}$ = 0 and (or) $K_{ASolvent}$ = 0.

vide fairly reasonable estimates of the solubility behavior of phenanthrene in a wide range of organic solvents. Average absolute deviation between predicted and observed values is 62.2%.

The next to last entry in Table 1 shows that Mobile Order theory grossly overpredicts the solubility of phenanthrene in acetonitrile. Similar failures were noted previously in the case of anthracene (34), fluoranthene (35), and pyrene (35). We suspect that the overprediction results from either failure of the Scatchard–Hildebrand solubility parameter theory to describe the nonspecific interactions between acetonitrile and these four polycyclic aromatic hydrocarbon solutes, or perhaps from an incorrect value for this solvent's modified solubility parameter. If acetonitrile is excluded from the comparison, the average absolute deviation is reduced to 41.3%. This results in a significant improvement in the predictive ability. Readers are reminded that in evaluating the applicability of Mobile Order theory one must realize that many of these particular systems are highly non-ideal, and that the experimental solubility data cover over a 250-fold range in mole fraction. Had an ideal solution been assumed, then the predicted mole fraction solubility would be $X_A^{sat} = a_A^{solid}$ = 0.2596 for each solvent. The ideal solution approximation corresponds to a considerably larger average absolute deviation of 1610% between predicted and observed values.

Acknowledgments

Carmen Hernández and Tina Sharp thank the University of North Texas and the U. S. Department of Education for support provided under the Ronald E. McNair Postbaccalaureate Achievement Program.

References

1. W.E. Acree, Jr. Polycyclic aromatic hydrocarbons in pure and binary solvents. IUPAC solubility data series. Vol. 54. Oxford University Press, Oxford, U. K. 1994.
2. W.E. Acree, Jr. Polycyclic aromatic hydrocarbons: binary nonaqueous systems: Part 1 (Solutes A–E). IUPAC solubility data series. Vol. 58. Oxford University Press, Oxford, U. K. 1995.
3. W.E. Acree, Jr. Polycyclic aromatic hydrocarbons: binary nonaqueous systems: Part 2 (Solutes F–Z). IUPAC solubility data series. Vol. 59. Oxford University Press, Oxford, U. K. 1995.
4. W.E. Acree, Jr. Int. J. Pharm. **18**, 47 (1984).
5. U. Domanska and T. Hofman. J. Solution Chem. **14**, 531 (1985).
6. U. Domanska. Fluid Phase Equilibr. **35**, 217 (1985).
7. R.S. Basu, H. Pham, and D.P. Wilson. Int. J. Pharm. **7**, 319 (1986).
8. A.B. Ochsner and T.D. Sokoloski, J. Pharm. Sci. **74**, 634 (1985).
9. R. Carta and S. Dernini. J. Chem. Eng. Data, **28**, 328 (1983).
10. W.E. Acree, Jr. and J.H. Rytting. Int. J. Pharm. **13**, 197 (1983).
11. A. Martin, P.L. Wu, A. Adjei, A. Beerbower, and J.M. Prausnitz. J. Pharm. Sci. **70**, 1260 (1981).
12. M.H. Abraham, H.S. Chadha, J.P. Dixon, and A.J. Leo. J. Phys. Org. Chem. **7**, 712 (1994).
13. M.H. Abraham, J. Andonian-Haftvan, J.P. Osei-Owasu, P. Sakellariou, J.S. Urieta, M.C. Lopez, and R. Fuchs. J. Chem. Soc. Perkin Trans. 2, 299 (1993).
14. E.P. Doane and H.G. Drickamer. J. Phys. Chem. **59**, 454 (1955).
15. C.L. Speyers. Am. J. Sci. **14**, 293 (1902).
16. E. McLaughlin and H.A. Zainal. J. Chem. Soc. 3854 (1960).
17. P.B. Choi, C.P. Williams, K.G. Buehring, and E. McLaughlin. J. Chem. Eng. Data, **30**, 403 (1985).
18. L.J. Gordon and R.L. Scott. J. Am. Chem. Soc. **74**, 4138 (1952).
19. E. McLaughlin and H.A. Zainal. J. Chem. Soc. 2485 (1960).
20. A.J. Niimi. Water Res. **12**, 1515 (1991).
21. F. Shahidi, P.G. Farrell, J.T. Edward, and P.J. Canonne. J. Org. Chem. **44**, 950 (1979).

© 1999 NRC Canada

22. I.F. Li, L.V. Semenov, A.A. Gaile, and M.N. Pul'stin. Russ. J. Phys. Chem. **58**, 1481 (1984).
23. P.L. Huyskens and G.G. Siegel. Bull. Soc. Chim. Belg. **97**, 821 (1988).
24. G.G. Siegel, P.L. Huyskens, and G. Vanderheyden. Ber. Bunsen-Ges. Phys. **94**, 549 (1990).
25. P.L. Huyskens and K. Seghers. J. Mol. Struct. **332**, 75 (1994).
26. P. Ruelle, C. Rey-Mermet, M. Buchmann, H. Nam-Tran, U.W. Kesselring, and P.L. Huyskens. Pharm. Res. **8**, 840 (1991).
27. P. Ruelle, M. Buchmann, H. Nam-Tran, and U.W. Kesselring. Int. J. Pharm. **87**, 47 (1992).
28. P. Ruelle, M. Buchmann, and U.W. Kesselring. J. Pharm. Sci. **83**, 396 (1994).
29. P. Ruelle, E. Sarraf, and U.W. Kesselring. Int. J. Pharm. **104**, 125 (1994).
30. P. Ruelle, E. Sarraf, L. Van den Berge, K. Seghers, M. Buchmann, and U.W. Kesselring. Pharm. Acta Helv. **68**, 49 (1993).
31. R.F. Weimer and J.M. Prausnitz. J. Chem. Phys. **42**, 3643 (1965).
32. H.L. Finke, J.F. Messerly, S.H. Lee, A.G. Osborn, and D.R. Douslin. J. Chem. Thermodyn. **9**, 937 (1977).
33. P.L. Huyskens and M.C. Haulait-Pirson. J. Mol. Liq. **31**, 135 (1985).
34. L.E. Roy, C.E. Hernández, and W.E. Acree, Jr. Polycyclic Aromat. Compd. **13**, 105 (1999).
35. L.E. Roy, C.E. Hernández, and W.E. Acree, Jr. Polycyclic Aromat. Compd. In press.

© 1999 NRC Canada

Kinetic and equilibrium studies of the acid dissociation of the cobalt(II) complexes of *N,N′*-dialkyl-1,10-phenanthroline-2,9-dimathanamine ligands

Hongwei Sun, Zhifen Zhou, Huakuan Lin, Guanghua Zhao, Shourong Zhu, Xuncheng Su, and Yunti Chen

Abstract: The complexation property and the acid dissociation kinetics of four *N,N′*-dialkyl-1,10-phenanthroline-2,9-dimathanamine complexes with cobalt(II) were studied using a pH meter and a stopped-flow spectrophotometer. In 6.6×10^{-3}~0.5 mol dm^{-3} HCl (I = 0.5 mol dm^{-3} HCl + NaCl), the dissociation rate follows the law $k_{obs} = kK_2[H^+]/(1 + K_2[H^+])$. The acid dissociation can be rationalized in terms of a four-step kinetic process involving two rapid pre-equilibrium protonations and rate-determining cleavage of the Co(II)—N(phenanthroline) bond. The temperature dependence of the rate was determined, and the appropriate thermodynamic parameters were obtained. The linear relationship between $\Delta H^{\neq}$ and $\Delta S^{\neq}$ suggests that an isokinetic temperature, T_{iso} of 282 ± 2 K exists.

Key words: *N,N′*-dialkyl-1,10-phenanthroline-2,9-dimathanamine, complexation property, acid dissociation kinetics, mechanism, cobalt(II) complex.

Résumé : Faisant appel à un pH-mètre et un spectrophotomètre à écoulement interrompu, on a mesuré les propriétés de complexation et la cinétique de dissociation acide de quatre complexes *N,N′*-dialkyl-1,10-phénanthroline-2,9-dimathamine avec le cobalt(II). Dans le domaine de concentration de $6{,}6 \times 10^{-3}$ à 0,5 mol dm^{-3} de HCl (I = 0,5 mol dm^{-3} HCl + NaCl), la vitesse de dissociation obéit à la loi: $k_{obs} = kK_2[H^+]/(1 + K_2[H^+])$. On peut rationaliser la dissociation acide en termes d'un processus cinétique en quatre étapes impliquant deux protonations rapides de prééquilibre et un clivage cinétiquement limitant de la liaison Co(II)—N(phénanthroline). On a déterminé la relation entre la température et la vitesse de la réaction et on en a tiré les paramètres thermodynamiques appropriés. La relation linéaire entre le ΔH et le ΔS suggère l'existence d'une température isocinétique, T_{iso} = 282 ± 2 K.

Mots clés : *N,N′*-dialkyl-1,10-phénanthroline-2,9-dimathanamine, propriété de complexation, cinétique de la dissociation acide, mécanisme, complexe du Co(II).

[Traduit par la Rédaction]

Introduction

Acid-assisted dissociation kinetics of open-chain and macrocyclic polyamine complexes hav been extensively studied (1–7), and many of these works have been reviewed (8, 9). Recently, there has been renewed interest in this field. Many experiment results were studied and the possible mechanisms for the reactions, the factors influencing the rates, and the factors affecting the relative importance of each of the possible pathways were discussed (10–16). Nearly all such studies support the general mechanism proposed by Read and Margerum (9). We mentioned that almost all the systems studied are linear or macrocyclic aliphatic polyamines, which are excellent electron donors, and the coordinated nitrogens are of similar basicity. The corresponding kinetics of acid-assisted dissociation of linear and microcyclic ligands with different type of nitrogens have received little attention (17).

1,10-Phenanthroline have been extensively used as ligands in both analytical and preparative coordination chemistry (18). The π-electron deficiency makes phenanthroline excellent π acceptors. If amine was assembled on the 1,10-phenanthroline, the ligands would contain both soft and hard sites. Recently, we have prepared a series of *N,N′*-dialkyl-1,10-phenanthroline-2,9-dimathanamine ligands (Fig. 1) with two electron deficient nitrogens (phenanthroline) and two electron donor nitrogens (alphatic amine) (19). It was of interest to learn the effects of different coordinated nitrogens on the dissociation kinetics of the cobalt(II) complexes. In this paper, we report the results of our systematic studies on the complexation property and the acid dissociation reaction of cobalt(II) complexes of our novel *N,N′*-dialkyl-1,10-

Received March 11, 1999.

H. Sun, Z. Zhou, H. Lin,[1] G. Zhao, S. Zhu, X. Su, and Y. Chen. Department of Chemistry, Nankai University, Tianjin 300071, P.R. China.

[1]Author to whom correspondence may be addressed. Fax: +86 22 23502458. e-mail: chemczl@sun.nankai.edu.cn

 © 1999 NRC Canada

Fig. 1. Structure of the ligands.

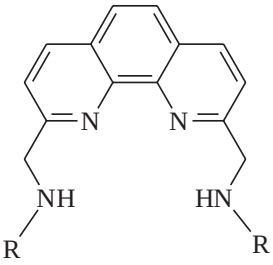

L^1:R=CH_3; L^2:R=CH_2CH_3; L^3:R=$CH(CH_3)_2$; L^4:R=$C(CH_3)_3$

phenanthroline-2,9-dimathanamine ligands in order to determine the effect of different coordinated nitrogens and some important kinetic parameters to gain an insight into the reaction mechanism.

Experimental

Reagents

The *N,N′*-dialkyl-1,10-phenanthroline-2,9-dimathanamine ligands were prepared according to our novel synthesis methods (19). All other chemicals used in this work were of GR grade. NaCl was recrystallized before use. Redistilled water was used for all solutions.

Instruments

Electronic spectra were recorded on a Shimadzu UV-240 spectrophotometer. Protonation constants of *N,N′*-dialkyl-1,10-phenanthroline-2,9-dimathanamines and complex formation constants of cobalt(II) complexes were determined by potentiometric pH titration using a Beckman Φ71 pH meter. The kinetics of the acid-catalyzed dissociation of the cobalt complexes were studied with a Union Giken RA-401 stopped-flow spectrophotometer equipped with a Union-415 rapid-scan attachment.

Potentiometric measurements

Potentiometric titrations of the ligands in the absence and presence of cobalt(II) (as nitrate salt) were carried out with a Beckman pH meter Model Φ71. The apparatus and procedure have been described before (20). Computation of equilibrium constants was made using the SCMAR (21) program. Species–distribution curves were calculated and plotted with DP (21) program. For each system at least two titration were performed, each titration contained about 50 experimental points.

Kinetic measurements

Pseudo-first-order conditions were maintained by using at least a 20-fold excess of acid in each run. Complex conc. = 1.0×10^{-4} mol dm^{-3} (I = 0.5 mol dm^{-3} NaCl), conc. acid = 6.6×10^{-3}~0.5 mol dm^{-3} HCl (I = 0.5 mol dm^{-3} HCl + NaCl). Good first-order kinetics were observed in all cases. The reaction has excellent reproducibility. Complex solutions were prepared by mixing equimolar quantities of the ligand and standard $CoCl_2$, followed by adjustment of pH to 8.0 with NaOH at which point the complex is fully formed in the form CoL (Fig. 2*b*). Absorbance vs. time data were collected at 295 nm and temperature maintained at 10 ± 0.1, 20 ± 0.1, 30 ± 0.1, and 40 ± 0.1°C under a N_2 atmosphere. Reaction time ranges from 50 to 2000 ms. Each kinetic run has been repeated at least six times.

Fig. 2. Distribution curves for the protonated L^1 species (*a*) and Co(II)–L^1 system (*b*) as a function of pH in 0.1 mol dm^{-3} $NaNO_3$ solution at 298.15 K.

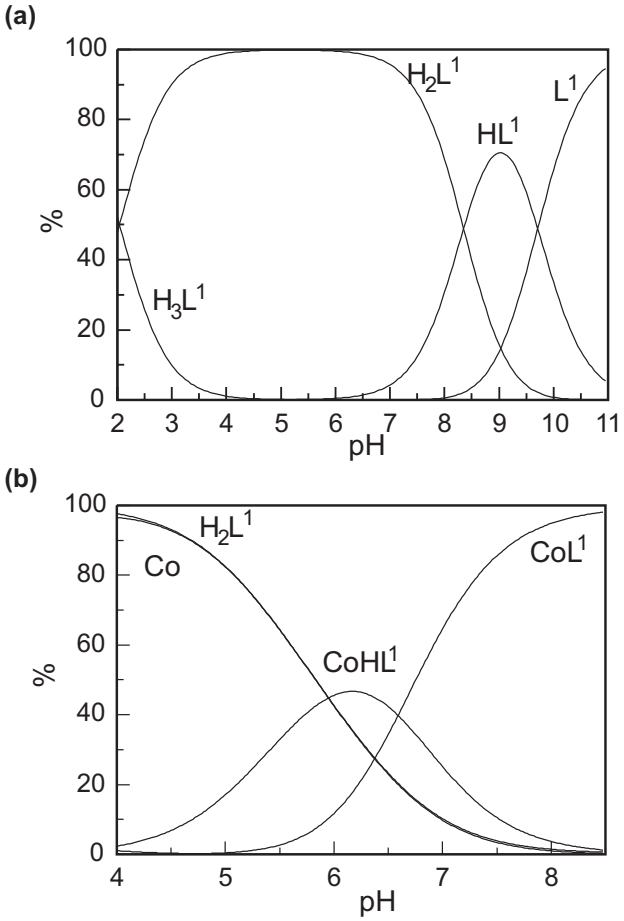

Results and discussion

Protonation and cobalt(II) complex equilibria

The protonation constants of L^1 to L^4 were determined by potentiometric pH titration at I = 0.1 ($NaNO_3$) and 25°C. Table 1 summarizes the protonation constants as logarithmic values. In the pH range investigated (2.5~11), equilibria involve three protonation steps related to the phenanthroline nitrogen and two amino nitrogens (defined in eqs. [1]–[3]). K_1 and K_2 are the protonation constants of the amino nitrogens. The second amine protonation step of the ligands involves a decrease of the log K value (1.3~1.4) due to electrostatic repulsive effects. For the same reason, log K_3 values that corresponded to the protonation of 1,10-phenanthroline are smaller than that of 1,10-phenanthroline (log K = 4.748 (ref. 22)). The basicity of two amines is mainly determined by inductive effects of N-substituted alkyls. The order is $L^1 < L^2 < L^3 < L^4$.

[1] $H^+ + L \rightleftharpoons HL^+, \qquad K_1 = [HL^+]/[H^+][L]$

© 1999 NRC Canada

Table 1. Protonation constants and Co(II) complex formation constants for *N*,*N*′-dialkyl-1,10-phenanthroline-2,9-dimathanamines at 25 ± 0.1°C and I = 0.1 mol dm^{-3} $NaNO_3$.

	L^1	L^2	L^3	L^4
log K_1	9.71 ± 0.01	9.84 ± 0.02	9.90 ± 0.01	10.08 ± 0.01
log K_2	8.35 ± 0.02	8.50 ± 0.04	8.51 ± 0.02	8.77 ± 0.01
log K_3	2.04 ± 0.07	2.09 ± 0.04	2.17 ± 0.07	2.31 ± 0.02
log β_{110}	8.87 ± 0.02	8.52 ± 0.02	7.33 ± 0.02	6.62 ± 0.01
log β_{111}	15.47 ± 0.02	15.16 ± 0.03	14.35 ± 0.04	14.05 ± 0.02
log K	6.60	6.64	7.02	7.43

Fig. 3. Plot of k_{obs} vs. [H^+] for the dissociation of $[CoL^1]^{2+}$ at 10, 20, 30, and 40°C. The solid lines are calculated from eq. [14].

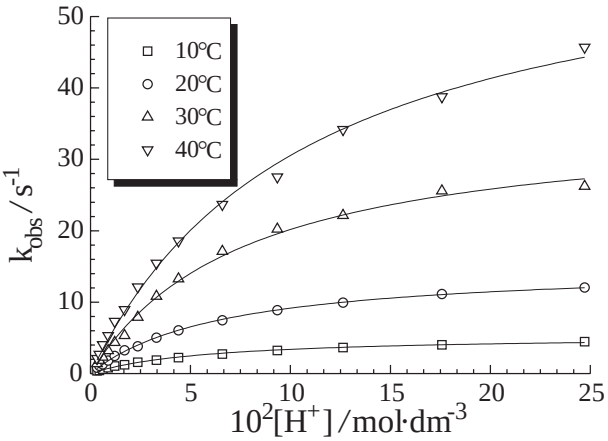

Fig. 4. Plot of k_{obs}. vs. [H^+] for the dissociation of $[CoL^4]^{2+}$ at 10, 20, 30, and 40°C. The solid lines are calculated from eq. [15].

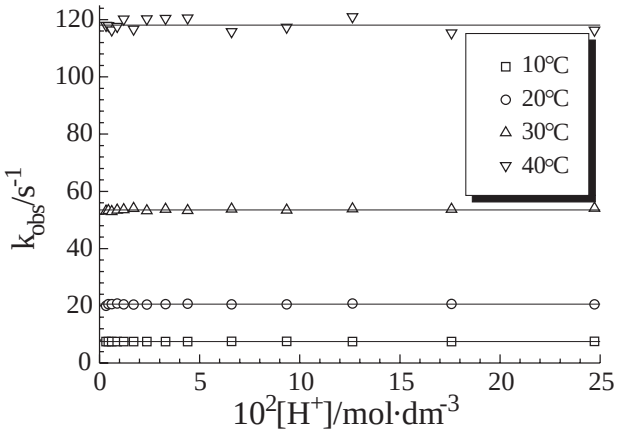

[2] $H^+ + HL \rightleftharpoons H_2L^{2+}, \quad K_2 = [H_2L^{2+}]/[H^+][HL^+]$

[3] $H^+ + H_2L^{2+} \rightleftharpoons H_3L^{3+}, \quad K_3 = [H_3L^{3+}]/[H^+][H_3L^{2+}]$

The incorporation of Co^{2+} by the ligands in aqueous solution was studied to identify the species formed and to evaluate the complexation constants of these compounds. The following reactions were found to take place:

[4] $Co^{2+} + L \rightleftharpoons CoL^{2+}, \quad \log\beta_{110} = [CoL^{2+}]/[Co^{2+}][L]$

[5] $Co^{2+} + L + H^+ \rightleftharpoons CoHL^{3+}, \quad \log\beta_{111} = [CoHL^{3+}]/[Co^{2+}][L][H^+]$

As shown in Table 1, for CoL^{2+} and $CoHL^{3+}$ species, complexes of Co^{2+} with L, shown the stability order $L^1 > L^2 > L^3 > L^4$, indicated that steric effects play a more important role than electron inductive effects.

Kinetic measurements

At 295 nm where the dissociation reactions of the complexes were monitored, perchlorate and nitrate have absorption, so sodium chloride was used to maintain the ionic strength, and hydrochloric acid to change the pH.

Under the experimental conditions of constant hydrogen concentration, the dissociation reaction of these complexes was found to proceed to completion and to occur by a single stage. A first-order reaction with respect to the concentration of complex was observed. The rate equation can be expressed by eq. [6].

[6] $-d[CoL^{2+}]/dt = k_{obs}[CoL^{2+}]$

Figure 3 shows the dependence of the rate constants k_{obs} on the concentration of hydrogen ion at different temperature for CoL^1 complex. As shown in Fig. 3, the observed rate constants k_{obs} increases with the increase of [H^+] and tends to attain limiting values at high acidities. Same phenomenon appears for CoL^2 and CoL^3 complex. From a mathematical view, the tendency coincides with the hyperbolical function (eq. [7]) where a and b are constants.

[7] $k_{obs} = a[H^+]/(1 + b[H^+])$

As shown in Fig. 4, the observed rate constants k_{obs} for CoL^4 keeps invariable with the increase of [H^+]. From a mathematical view, the tendency also coincides with eq. [7] under the condition of $b[H^+] >> 1$.

The phenomenon of complexes we studied is quite different from that of copper(II) complexes with linear aliphatic tetraamine. For linear tetramine copper(II) complexes, the plot of k_{obs} vs. [H^+] gives a straight line; the rate-determining step for the dissociation reactions is the breakage of the first copper–nitrogen bond according to Chao and Chun (15). The ligands we studied show a different behaviour compared to linear tetraamine. For linear tetraamine cobalt(II) complexes, the four coordinated amino nitrogens are of similar property. For the complexes we studied, the basicity of two nitrogens of phenanthroline is significantly weaker than that of two amino nitrogens, and the π backdonor

© 1999 NRC Canada

Table 2. Rate constants k at different temperatures (I = 0.5 mol dm^{-3} NaCl + HCl).

	k (s^{-1})				$\Delta H^{\neq}$	$\Delta S^{\neq}$
	10°C	20°C	30°C	40°C	(kJ mol^{-1})	(J mol^{-1} K^{-1})
L[1]	5.48	15.1	34.8	65.9	58.8 ± 3.1	–22.0 ± 10.5
L[2]	5.69	16.1	42.1	101	68.4 ± 0.4	11.5 ± 1.3
L[3]	6.37	16.9	43.0	128	70.7 ± 3.1	20.0 ± 10.3
L[4]	7.52	20.5	53.5	118	65.6 ± 1.3	3.94 ± 4.22

Table 3. Pre-equilibrium constant $1/K_2 \times 10^2$ at different temperatures (I = 0.5 mol dm^{-3} NaCl + HCl).

	$1/K_2 \times 10^2$ (mol dm^{-3})				ΔH°	ΔS°
	10°C	20°C	30°C	40°C	(kJ mol^{-1})	(J mol^{-1} K^{-1})
L[1]	5.51	6.79	8.21	10.2	–15.0 ± 0.5	–28.9 ± 1.6
L[2]	1.28	2.12	3.16	4.70	–31.7 ± 0.8	–75.8 ± 2.7
L[3]	3.62	4.66	5.98	7.37	–17.6 ± 0.2	–15.3 ± 0.8

bond exists between cobalt(II) and two phenanthroline nitrogens (23). The first protonation process of complex CoL must be the protonation of amino nitrogen. As shown in Table 1, the intermediates $CoLH^{3+}$ can exist stably in the solution. The equilibrium constants log K of the following reaction (eq. [8]) range from 6.6 to 7.4 for the complexes with the four ligands studied (Table 1).

$$[8] \qquad CoL^{2+} + H^+ \overset{K}{\rightleftharpoons} CoLH^{3+}$$

In strongly acidic, aqueous media, the two amino nitrogens are easier protonated than that of phenanthroline; the protonation rates are very fast, therefore, the first two protonation processes of amino nitrogens are pre-equilibrium processes. Being the most difficult, the third step, the breakage of the cobalt–nitrogens (phenanthroline) bond, is the rate-determining step. After three steps, the products are solvated cobalt(II) ion and partly protonated ligand. Finally, the ligand is quickly fully protonated in the acid solution. We proposed the following acid-dissociation mechanism (eqs. [9]–[12]):

According to the mechanism, we obtained

$$[13] \qquad k_{obs} = \frac{kK_1K_2[H^+]^2}{1 + K_1[H^+] + K_1K_2[H^+]^2}$$

From Table 1 we can see that even at the lowest concentration of acid used ($[H^+] = 3.3 \times 10^{-3}$ mol dm^{-3}), the product of K and $[H^+]$, $K[H^+] \approx 1.3 \times 10^4 >> 1$. Considering that the eq. [8] is the same as eq. [9], we assumed that $1/(K_1[H^+]) << 1$. Consequently, under the conditions used in this study the limiting rate law that operates is

$$[14] \qquad k_{obs} = \frac{kK_2[H^+]}{1 + K_2[H^+]} = \frac{k[H^+]}{1/K_2 + [H^+]}$$

The eq. [14] is exactly the same as the experimental rate law (eq. [7]). Therefore, the mechanism proposed by us is reasonable. For CoL[4], when we assume $1/K_2 << [H^+]$, we can obtain

$$[15] \qquad k_{obs} = k$$

which coincides with the phenomenon in Fig. 4.

The rate constant k and the pre-equilibrium constant K_2 can be calculated from eqs. [14] and [15], the results have been listed in Tables 2 and 3. From Figs. 3 and 4, we can see

[9] 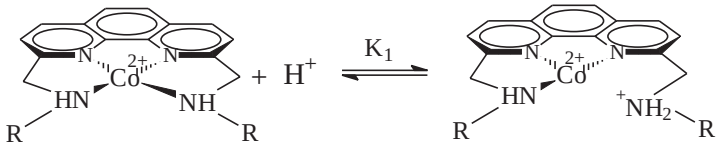

[10] 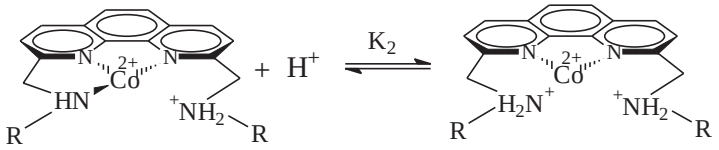

[11] 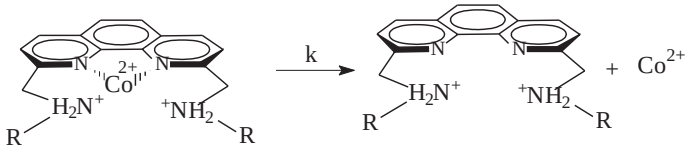

[12] 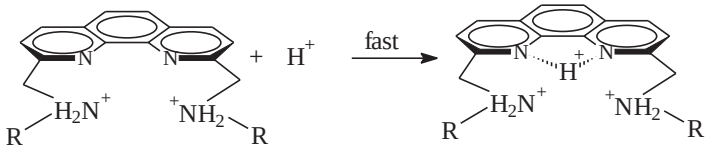

© 1999 NRC Canada

Fig. 5. The isokinetic relationship of reaction [11].

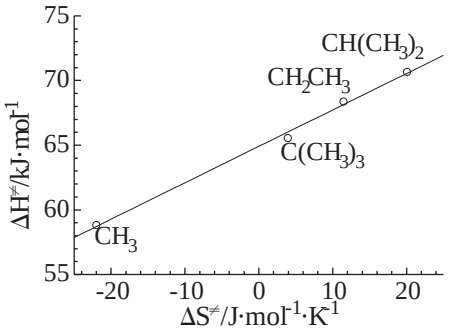

that the experimental points are coincident with those of calculations from eqs. [14] and [15].

From Eyring's equation

$$\ln (k/T) = -\Delta H^{\neq}/RT + \Delta S^{\neq}/R + \ln (R/N_A h)$$

Regression of ln (k/T) vs. 1/T, activation parameters $\Delta H^{\neq}$ and $\Delta S^{\neq}$ of the rate-determining step can be obtained. The values of $\Delta H^{\neq}$ and $\Delta S^{\neq}$ are summarized in Table 2. Regressing of ln K_2 vs. 1/T, the values of ΔH° and ΔS° were obtained; they are listed in Table 3.

From Tables 1 and 3, we can find that, due to electrostatic repulsive effects, the second protonation constants of the metal complexes are about 12~50 for ligands L^1~L^3, about 3.0×10^3 for ligand L^4 (estimated from the assumption of $1/K_2 << [H^+]$), much smaller than that of the first protonation ($4.0 \times 10^6 \sim 2.7 \times 10^7$). From Table 1, we can find that, due to steric effects of N-substituted alkyl, the coordination ability of amino nitrogens decreases obviously with the increase of alkyl cubage; this can be see from the increase of the first protonation constants of the complexes (log K increase from 6.6 to 7.4). It is apparent that the second protonation K_2 of the complex L^4 is larger than that of L^1~L^3, since the substituted alkyl-tetrabutyl appears obviously to have greater steric effects than in L^1~L^3.

We find that for different *N*-alkyl substituents, the activation enthalpies and entropies appear to have a linear relationship. The plot of $\Delta H^{\neq}$ verus $\Delta S^{\neq}$ for reaction of eq. [11] with four different complexes studied was shown to be clearly linear (R^2 = 0.996) with an apparent isokinetic temperature (24, 25), T_{iso}(app), of 282 ± 10 K (Fig. 5). The Krug–Greiger (26) method confirms the existence of an isokinetic relationship (IKR), but only if the data for the complex of L^4 are omitted, when T_{iso} = 282 ± 2 K and R^2 = 0.990 (Fig. 6). The fact that the complex of L^4 appears abnormal presumably arises due to the effect of steric of *tert*-butyl.

Fig. 6. Modified Krug–Grieger plot of $\Delta H^{\neq}$ vs. $\Delta G^{\neq}$ (at 313 K) for reactions. (Data for the complex of L^4 (△) not included in least-squares analysis).

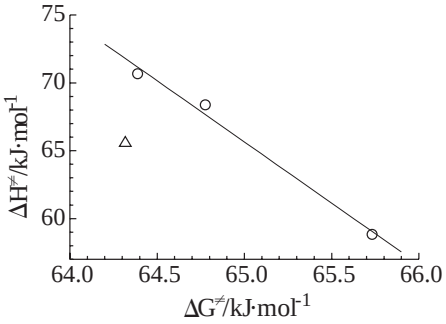

Acknowledgments

This project 29671020 was supported by the National Natural Science Foundation of P.R. China, the Nature Science Foundation of Tianjin, and the National Key Laboratory of the Coordination Chemistry, Nanjing University.

References

1. G.A. Melson and R.G. Wilkins. J. Chem. Soc. 4208 (1962).
2. R.G. Wilkins. J. Chem. Soc. 4475 (1962).
3. D.W. Margerum, D.B. Rorabacher, and J.F.G. Clarke. Jr. Inorg. Chem. **2**, 667 (1963).
4. G.B. Kolski and D.W. Margerum. Inorg. Chem. **8**, 1125 (1969).
5. R.F. Childers and R.A.D. Wentworth. Inorg. Chem. **8**, 2118 (1969).
6. D.B. Rorabacher and C.A. Melendez-Cepeda. J. Am. Chem. Soc. **93**, 6071 (1971).
7. T.S. Turan and D.B. Rorabacher. Inorg. Chem. **11**, 288 (1972).
8. D.W. Margerum, G.R. Cayley, D.C. Weatherburn, and G.K. Pagenkopf. ACS Monogr. **174**, 1 (1978).
9. R.A. Read and D.W. Margerum. Inorg. Chem. **20**, 3143 (1980).
10. B. Liang and C. Chun. Inorg. Chem. **22**, 1017 (1983).
11. B. Liang and C. Chun. Inorg. Chem. **20**, 2152 (1981).
12. J. Chen, D. Wu, and C. Chun. Inorg. Chem. **25**, 1940 (1986).
13. L. Chen and C. Chun. Inorg. Chem. **27**, 1880 (1988).
14. L. Chen and C. Chun. Inorg. Chem. **28**, 1402 (1989).
15. M. Chao and C. Chun. Inorg. Chem. **26**, 3600 (1987).
16. W. Lan and C. Chun. J. Chem. Soc. Dalton Trans. 192 (1994).
17. R.W. Hay and M.M. Hassan. Trans. Met. Chem. **19**, 559 (1994).
18. J. Reedijk. *In* Comprehensive coordination chemistry. Vol. 2. *Edited by* G. Wilkinson, R.D. Gillard, and J.A. McCleaverty. Pergamon, Oxford. U.K. 1987.
19. G. Zhao, H. Sun, H. Lin, S. Zhu, X. Su, and R. Chen. J. Bioinorg. Chem. **72**, 173 (1998).
20. H. Sun, H. Lin, S. Zhu, G. Zhao, X. Su, and R. Chen. Trans. Met. Chem. **24**, 362 (1999).
21. H. Sun, Ph.D. thesis. Department of Chemistry, Nankai University. 1998.
22. H. Lin, H. Xia, J. Xian, and R. Chen. Acta Chim. Sin. **52**, 1182 (1994).
23. F.A. Walker, H. Sigel, and D.B. McCormick. Inorg. Chem. **11**, 2756 (1972).
24. W. Kinert and R.F. Jameson. Chem. Soc. Rev. **18**, 477 (1989).
25. J. Hao and A.J. Poe. Trans. Met. Chem. **23**, 739 (1998).
26. R.R. Krug, W.G. Hunter, and R.A. Grieger. J. Phys. Chem. **80**, 2335 (1976); **80**, 2341 (1976).

© 1999 NRC Canada

Mechanisms for the formation of epoxide and chlorine-containing products in the oxidation of ethylene by chromyl chloride: a density functional study

Maricel Torrent, Liqun Deng, Miquel Duran, Miquel Solà, and Tom Ziegler

Abstract: The reaction between CrO_2Cl_2 and ethylene leading to the formation of epoxide and chlorohydrin precursors or directly to 1,2-dichloroethane has been studied by density functional theory. The formation of the epoxide precursor ($Cl_2(O)Cr\text{-}OC_2H_4$) was found to take place via a [3+2] addition of ethylene to two Cr=O bonds followed by rearrangement of the five-membered diol to the epoxide product. The alternative mechanisms involving a direct addition of oxygen to ethylene or the [2+2] addition of the olefin to a Cr=O bond were found to have much higher activation energies. The formation of the chlorohydrin precursor ($Cl(O)Cr\text{-}OCH_2{=}CHCl$) was found to take place via a [3+2] addition to one Cr—Cl and one Cr=O bond. Pathways involving initial [2+2] addition to a Cr—Cl or Cr=O bond had much higher activation barriers. The generation of 1,2-dichloroethane is highly unfavorable with an endothermicity of 44.7 kcal/mol and an even higher activation barrier. It is suggested that the formation of epoxide and chlorohydrin from the respective precursors requires the addition of H_2O.

Key words: reaction mechanisms, epoxide, oxidation of ethylene, chromyl chloride, DFT.

Résumé : Faisant appel à la théorie de la densité fonctionnelle, on a étudié la réaction du CrO_2Cl_2 avec l'éthylène qui conduit à la formation de précurseurs époxyde et chlorohydrine ou directement de 1,2-dichloroéthane. On a trouvé que la formation du précurseur époxyde [$Cl_2(O)Cr\text{-}OC_2H_4$] se produit par le biais d'une addition [3+2] de l'éthylène sur deux liaisons Cr=O, suivie d'un réarrangement du diol à cinq chaînons en produit époxyde. On a trouvé que les autres mécanismes possibles, addition directe d'oxygène à l'éthylène ou l'addition [2+2] de l'oléfine sur une liaison Cr=O, comportent des énergies d'activation beaucoup plus élevées. On a trouvé que la formation du précurseur chlorhydrine [$Cl(O)Cr\text{-}OCH_2{=}CHCl$] se fait par le biais d'une addition [3+2] sur une liaison Cr—Cl et une sur une liaison Cr=O. Les voies réactionnelles impliquant une addition [2+2] initiale à une liaison Cr—Cl ou Cr=O comportent des barrières d'activation beaucoup plus élevées. La formation de 1,2-dichloroéthane est très défavorisée par son grand caractère endothermique (44,7 kcal/mol) et sa barrière d'activation encore plus élevée. Il est suggéré qu'une addition d'eau est nécessaire pour la formation de l'époxyde et de la chlorohydrine à partir de leurs précurseurs respectifs.

Mots clés : mécanismes réactionnels, époxyde, oxydation de l'éthylène, chlorure de chromyle, « DFT ».

[Traduit par la Rédaction]

I. Introduction

The oxygen-transfer reaction from CrO_2Cl_2 to olefins is an old (1) and now well-established process (2). Unlike other oxo transition metal compounds, CrO_2Cl_2 reacts with alkenes to form predominantly an epoxide product, whereas $KMnO_4$ and OsO_4 form diols without significant epoxide formation (3). Some time ago it was found that, in fact, the three primary products in the oxidation of alkenes with CrO_2Cl_2 are epoxide, chlorohydrin, and, in some cases, vicinal dichloride (4, 5). The full mechanism by which these products are formed still remains unsolved despite having been the subject of extensive studies (6–9).

To explain the formation of the abovementioned products, Sharpless et al. (5) originally proposed a mechanism involving organometallic intermediates with Cr—C σ bonds. In particular, the key feature in the formation of epoxide was claimed to be the involvement of a chromaoxetane, i.e., a four-membered cyclic compound formed via a [2+2] interaction between the olefin and an oxo group on the chromium (5). This mechanism was very much contrary to the previously suggested mechanisms for this reaction in which a di-

Received December 15, 1998.

M. Torrent, M. Duran, and M. Solà. Department of Chemistry, and Institute of Computational Chemistry, University of Girona, Girona E-17071, Catalonia, Spain.
L. Deng and T. Ziegler.[1] Department of Chemistry, University of Calgary, Calgary, AB T2N 1N4, Canada.

[1]Author to whom correspondence may be addressed. Telephone: (403) 220-5368. Fax: (403) 289-9488. e-mail: ziegler@zinc.chem.ucalgary.ca

 © 1999 NRC Canada

rect interaction between the alkene and the oxo groups of CrO_2Cl_2 had been postulated (1, 6).

Although the new idea was suggested as an alternative path based only on the observed products of the reaction (no evidence for a chromaoxetane intermediate was established), it was quickly adapted within a few years in the discussion of many types of oxygen-transfer reactions involving high-valent oxochromium compounds (10) and other oxo transition metal species (11).The advantage of the novel proposal was that experimental observations concerning *cis* addition (5) could now be more easily accommodated. Sharpless et al. (5), however, introduced their hypothesis with reserve because some mechanisms involving direct interaction with the ligands were able to account for experimental facts as well. Particularly, neither a direct addition of the olefin to one oxygen atom nor a [3+2] addition of the olefin to two heteroatom ligands could be excluded at that time as operative routes for the mechanism of epoxidation. Some years later, Samsel et al. (7) argued for a direct interaction between the alkene and the oxygen in OCr(V)–salen complexes in the epoxidation of alkenes, rather than a chromaoxetane. Some interesting results that cast doubt on the metallaoxetane reaction path were also reported by Barrett et al. (12), and later on by Groves and Nemo (13). To date, experimental input has not been sufficient to rule out either of the mechanistic channels.

To obtain further insight into the sequence of this reaction, some theoretical contributions have appeared. The most notable earlier computational study is that of Rappé et al. (8, 9) where a thermodynamic analysis by means of the generalized valence bond method was performed, with attention being devoted to the energies of the intermediates in the oxidation of ethylene with CrO_2Cl_2 and MoO_2Cl_2. Unfortunately, due to limitations in methodology and computational facilities at that time, these authors were not able to fully optimize the geometrical structures of the different species involved. Their results favored a [2+2] cycloaddition path involving a four-centered intermediate, and confirmed the proposal that the metallaoxetane is a likely common precursor for all of the observed oxygen-containing products (8).

Further theoretical support for a chromaoxetane was provided (14) later by an ab initio study of the addition of ethylene to $Cr{=}O^{n+}$ (n = 1–3). Several gas-phase investigations have also supported the chromaoxetane as an intermediate in the reaction of oxochromium species with alkenes (15). In fact, the metallaoxetane intermediate derived from a [2+2] cycloaddition has been proposed in many other studies of oxygen-transfer reactions from oxomanganese and oxoiron porphyrins to alkenes (11), but often without detailed mechanistic investigations or without any direct experimental evidence to support it (16). A few isolated metallaoxetanes are known for Rh (17), Ir (18), Pd (19), and Pt (20). However, none of these species were synthesized by direct addition of olefin to a M=O bond. Also to date no chromaoxetane has been isolated.

It appears that at least three different reaction modes have been used to explain the formation of epoxide (Scheme 1): (1) a direct addition of ethylene to one oxygen atom, (2) a [2+2] addition of ethylene to one Cr=O linkage, and (3) a [3+2] addition to two Cr=O bonds. However, what appears to have been forgotten, at least in some of the proposed mechanisms, is that the reaction $CrCl_2O_2 + C_2H_4 \rightarrow CrCl_2O + C_2H_4O$ is endothermic with an experimental heat of reaction (21) given by 24.8 kcal/mol. Thus, the intermediates formed in the three mechanisms will not spontaneously decompose to epoxide. In fact, experimentally, epoxide is only isolated after the original reaction mixture in an organic solvent (such as CH_2Cl_2) is extracted into aqueous solution. Thus, it is likely that epoxide is formed from the reaction of water with one or more of the precursors in Scheme 1. Regarding the formation of the chlorine-containing products (Scheme 2), both a [2+2] and (or) a [3+2] cycloaddition pathway can account in principle for the mechanisms leading to a chlorohydrin (left) precursor and dichloride (right). However, again for the chlorohydrin (left) precursor a hydrogen containing agent such as water is needed to release $CH_2(OH)CH_2Cl$.

In the present paper, the pathways outlined in Schemes 1 and 2 are explored in terms of reaction energies and activation barriers. The objective of our study is (*i*) to examine the energetics and kinetics of the mechanism leading to the epoxide precursors of Scheme 1 when ethylene is oxidized by CrO_2Cl_2, (*ii*) to provide an interpretation for the formation of chlorohydrin precursor of Scheme 2 as one of the main products in the reaction of CrO_2Cl_2 with ethylene, and (*iii*) to rationalize why only in some cases dichloride is observed among the products. Finally, we shall briefly discuss the thermochemistry of the reaction between H_2O and the precursors in Schemes 1 and 2. To the best of our knowledge, this is the first time that mechanistic insight is given into the formation of epoxide, chlorohydrin, and dichloride using optimization procedures, and transition state search schemes.

II. Computational details

The reported calculations were carried out using the Amsterdam Density Functional (ADF) package developed by Baerends et al. (22*a*). and vectorized by Ravenek (22*b*). The adopted numerical integration procedure was due to te Velde et al. (23). A set of auxiliary s, *p*, *d*, *f*, and *g* STO functions, centered on all nuclei, were introduced in order to fit the molecular density and Coulomb potential accurately in each SCF cycle (24). An uncontracted STO basis set was employed for the valence orbitals of the chromium atom (double-ζ 3*s* and 3*p*, triple-ζ 3*d* and 4*s*, and a single- ζ 4*p* orbital). For carbon (2*s*, 2*p*), oxygen (2*s*, 2*p*), chlorine (3*s*, 3*p*), and hydrogen (1*s*), use was made of a double-ζ basis set augmented by an extra polarization function (25). The fully occupied inner shells of chlorine and chromium (1*s*2*s*2*p*), as well as carbon and oxygen (1*s*) were assigned to the cores and treated by the frozen-core approximation (26). All the geometries and frequencies were calculated at the local density approximation (LDA) level(27) with the parametrization of Vosko et al. (28). The relative energies were evaluated by including Becke's nonlocal exchange (29) and Perdew's nonlocal correlation corrections (30) as perturbations based on the LDA density. This approach is denoted NL-P, and its validity to treat CrO_2X_2 (X = halogen) complexes (31) and similar systems (32) has been demonstrated elsewhere. The

© 1999 NRC Canada

Scheme 1. Mechanisms for the CrO_2Cl_2-mediated formation of epoxide.

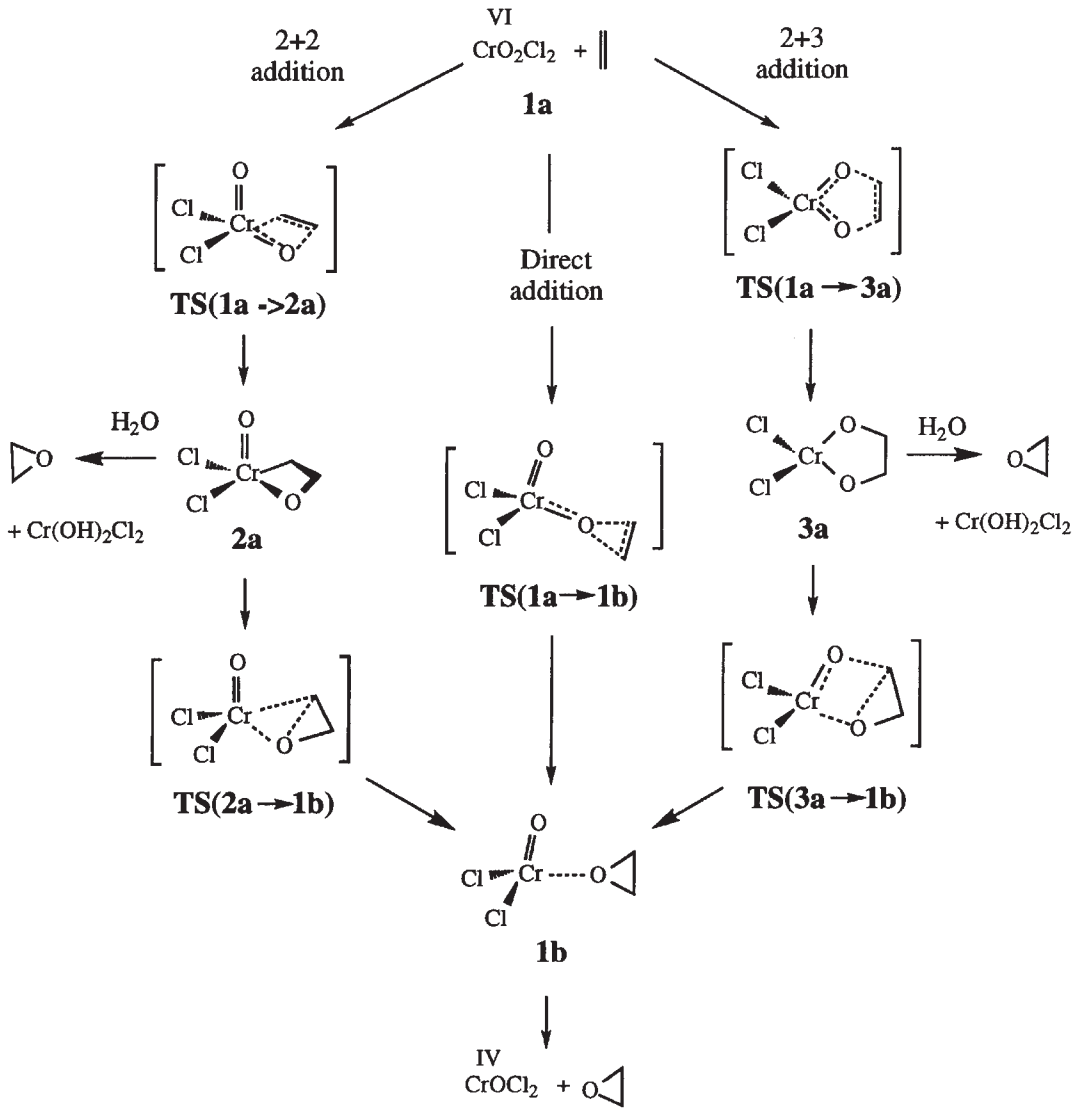

geometry optimization procedure was based on an analytical gradient scheme developed by Ziegler and co-workers (33). The harmonic vibrational frequencies were computed from the force constants obtained by numerical differentiation of the energy gradients (34). The transition state (TS) structures were located by a series of constraint geometry optimizations in which the bonds formed and broken were fixed at various lengths while the remaining internal coordinates were optimized. The approximate TSs located from such a procedure were then fully optimized using the standard TS optimization procedure with an algorithm due to Banerjee et al. (35) and Baker (36) in the ADF implementation due to Fan and Ziegler (37). All first-order saddle points were shown to have a Hessian matrix with a single negative eigenvalue. The reaction pathways were traced by the intrinsic reaction coordinate (IRC) method due to Fukui (38) based on a search scheme by González and Schlegel (39), and incorporated into the ADF program by Deng and Ziegler (40). Zero-point energy contributions were not included because energy differences for a related system have been reported not to change significantly when such contributions are taken into account (41*a*).

Previous validations (32*b*, 41*b–d*) have shown that the present DFT method affords metal–ligand bond energies with an accuracy of ±5 kcal/mol. Table 1 affords calculated and experimental heats of reaction for the oxidation of ethylene and norbornene by, respectively, $CrCl_2O_2$, CrF_2O_2, and Cp^*ReO_3. The comparison indicates that a similar accuracy of ±5 kcal/mol can be expected for the type of systems under investigation here. It is further clear from Table 1 that epoxidation of olefin by CrX_2O_2 (X = F, Cl) and Cp^*ReO_3 in all cases is endothermic.

Also shown in Table 1 are the heats of reaction obtained by an extended basis. An increase in the basis changes the heats of reaction by 2–3 kcal/mol. This change is within the error limits of the employed BP86 functional. To further assess the quality of the employed basis, we compare in Table 2 our calculated results with those reported by Rappé

© 1999 NRC Canada

Scheme 2. Mechanisms for the formation of chlorohydrin (left) and dichloride (right).

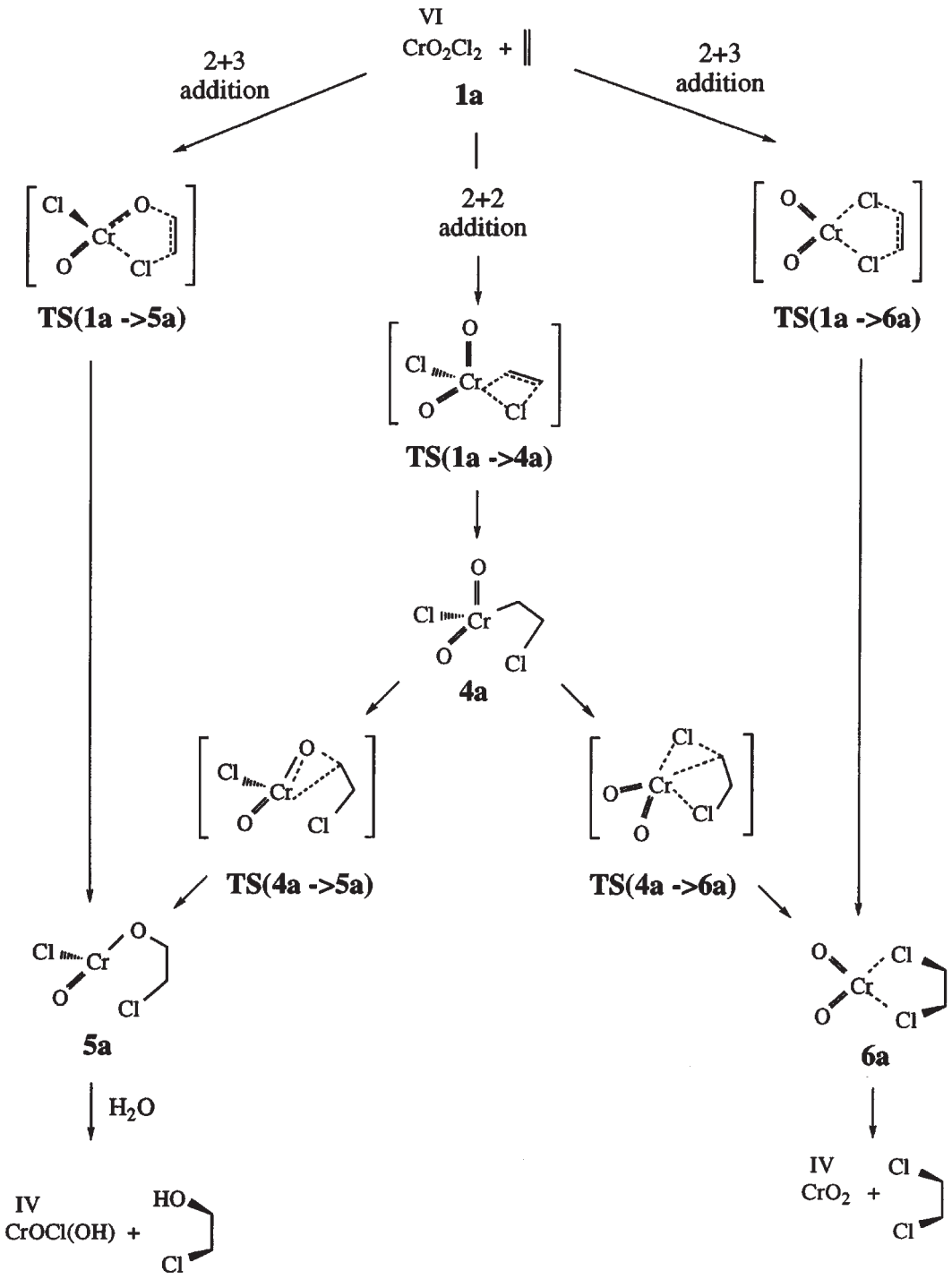

and co-workers (51) in a study that employed an extended basis set and the B3LYP functionals to calculated reaction enthalpies for oxidation of ethylene by a series of Re–oxo complexes. It can be deduced from Table 2 that the root mean square difference between Rappé estimates and our corresponding values is 1.8 kcal/mol with a maximum discrepancy of 2.9 kcal/mol. Again, this comparison indicates that the basis set we used can produce reliable relative energies for the systems under investigation.

III. Results and discussion

The first part of this section is dedicated to thoroughly analyze three different mechanistic proposals for the formation of epoxide precursor in terms of reaction energies and activation barriers. This is, in fact, the main goal of the present paper. The second part is devoted to the elucidation of the reaction steps leading to the formation of chlorohydrin precursor, together with the characterization of the main inter-

© 1999 NRC Canada

Table 1. Comparison of the DFT values with the experimental data for the reaction enthalpies of the oxidation of olefin.

	Energy (kcal/mol)	
Reaction[a]	BP86[b]	Expt.
$CrO_2Cl_2 + C_2H_4 \rightarrow CrOCl_2$ + epoxide	26.7 (29.2[c])	24.8[d]
$CrO_2Cl_2 + C_2H_4 \rightarrow CrOCl_2$ + acetaldehyde	1.7 (3.7[c])	–3[e]
$CrO_2F_2 + C_2H_4 \rightarrow CrOF_2$ + epoxide	28.0	23.2[d]
$Cp^*ReO_3 + C_2H_4 \rightarrow Cp^*ReO(OCH_2CH_2O)$	–2.8	–5 ± 3[f]
$Cp^*ReO_3 + C_2H_4 \rightarrow Cp^*ReO_2$ + epoxide	32.6	
Cp^*ReO_3 + norbornene → Cp*Re(O)(1,2-norbornanediolate)	–8.0	–10.9 ± 0.9[f]
Cp^*ReO_3 + norbornene → Cp^*ReO_2 + norbornene epoxide	28.0	

[a]$CrOCl_2$ and $CrOF_2$ have triplet ground state, all the rest species have singlet ground state.

[b]Unless otherwise specified, all ADF calculations were carried out with double-ζ plus polarization basis set for nonmetals (the standard ADF basis set III), and triple-ζ for Cr and Re atoms (the standard ADF basis set IV).

[c]ADF calculations were performed with triple-ζ plus 3*d* and 4*f* polarization functions for C and Cl atoms, triple-ζ plus 2*p* and 3*d* polarization functions for H, and triple-ζ plus two 4*f* functions for Cr; the basis set for the nonmetals was taken from standard ADF basis set V, and the basis set IVB of ref. 49 was used for Cr atom.

[d]Reference 21*a*.

[e]Reference 21*b*.

[f]Reference 50.

Table 2. Comparison of calculated reaction enthalpies by the BP86 and B3LYP functionals for the reactions $LReO_3 + C_2H_4 \rightarrow LRe(OCH_2CH_2O)$[a].

	Energy (kcal/mol)	
Reaction[a]	BP86[b]	B3LYP[c]
$Cp^*ReO_3 + C_2H_4 \rightarrow Cp^*ReO(OCH_2CH_2O)$	–2.8	–4
$CpReO_3 + C_2H_4 \rightarrow CpReO(OCH_2CH_2O)$	–5.7	–8
$ClReO_3 + C_2H_4 \rightarrow ClReO(OCH_2CH_2O)$	17.4	16
$(OH)ReO_3 + C_2H_4 \rightarrow (OH)ReO(OCH_2CH_2O)$	19.5	19
$(OCH_3)ReO_3 + C_2H_4 \rightarrow (OCH_3O)ReO(OCH_2CH_2O)$	19.9	17
$CH_3ReO_3 + C_2H_4 \rightarrow CH_3ReO(OCH_2CH_2O)$	30.6	31
$(O)ReO_3^- + C_2H_4 \rightarrow (O)ReO(OCH_2CH_2O)^-$	30.9	33

[a]The BP86 calculations show that (*i*) all species have singlet ground sate, and (*ii*) the singlet and triplet states of the diolate $ClReO(OCH_2CH_2O)$ are nearly degenerated.

[b]This work, BP86 calculations were carried out with double-ζ plus polarization basis set (ADF standard basis set III/H, C.1*s*, O.1*s*, Cl.2*p*) for nonmetal atoms, and triple-ζ basis set (ADF standard basis set IV/Re.4*f*) for Re atom, geometries were optimized by the quansirelativistic method (ref. 52).

[c]Reference 51, the B3LYP results were based on the geometries optimization with 6-31G* basis set for nonmetals, and the modified LANL2DZ basis with a single *f* function for Re, and the relative energies were determined by single-point calculations at the minima using an extended basis in which the metal *f* function was replaced by two, and the nonmetal basis set expanded to 6-31+G*.

mediates and TS structures involved in the potential energy surface (PES) of the two suggested paths. Finally, the formation of dichloride is also discussed.

III.1. Formation of the epoxide precursor

The CrO_2Cl_2-mediated transformation of ethylene to epoxide can be viewed as a one-oxygen atom transfer reaction. As seen from Scheme 1, it involves formally a reduction of the metal center from Cr(VI) d^0 in the reactants, **1a**, to Cr(IV) d^2 in the products. Regardless of the path leading to epoxide, a common direct precursor in all suggested mechanisms has been species **1b** (Fig. 1).This species was already postulated by Sharpless et al. (5) as the immediate precursor of epoxide, and more recently (21*b*), also as the oxirane adduct intermediate leading to acetaldehyde. The two forming C—O bond distances are certainly close to the ones in the final epoxide (1.416 Å), and the C—C bond is no longer the double bond in ethylene (1.323 Å). We find that **1b** has a d^2 configuration with a triplet ground state. We shall in the following discuss the energetics and kinetics for the suggested mechanisms leading to **1b**.

Figure 2 summarizes the energy profiles for the three mechanisms we are going to describe in the following paragraphs. Energetic aspects will be discussed in connection to the molecular structures obtained for each path (Figs. 3–6) following the sequence: direct addition, [2+2] cycloaddition, and [3+2] cycloaddition.

Starting from **1a**, the possible routes leading to **1b** can be classified according to the number of steps required in the transformation. Either the [2+2] or the [3+2] cycloaddition turns out to be two-step processes. A possible alternative to these routes is the apparently more simple direct addition of ethylene to one of the oxygen atoms in a single step. Since the ground-state structures of **1a** and **1b** lie on different PESs (singlet and triplet, respectively), a crossing point is expected to be found somewhere along the reaction path.

Figure 3 displays the optimized geometries of the two possible transition states connecting **1a** and **1b**:

© 1999 NRC Canada

Fig. 1. Optimized geometrical parameters of reactants **1a** and intermediate **1b**. Distances in Å, and angles in degrees.

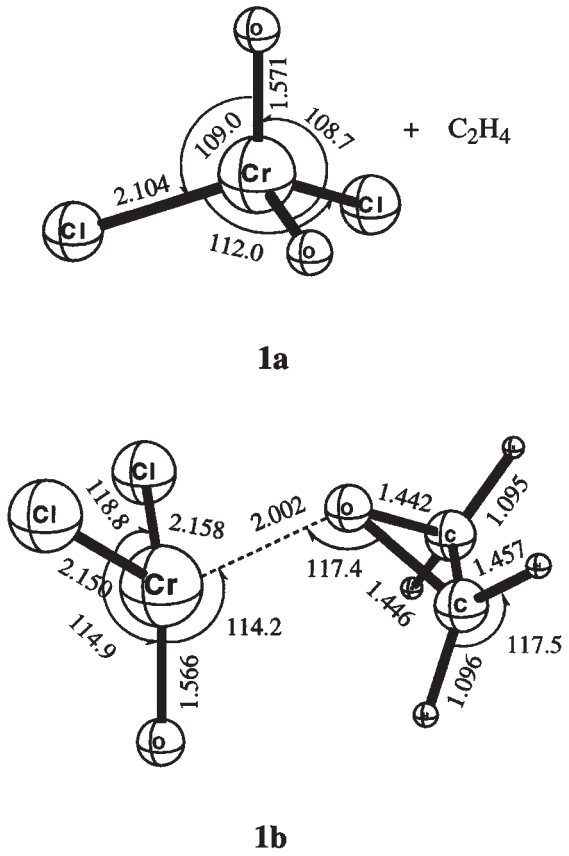

TS(1a→1b)/s (s = singlet) and **TS(1a→1b)/t** (t = triplet). Geometrical analysis reveals that the former TS resembles species **1b** (elongation of the Cr—O bond and stretching of the C—C bond to similar extents) whereas, in the latter, both the olefin and the metal fragment mainly retain the original character they have in the separated reactant species. Thus, **TS(1a→1b)/s** can be considered a product-like TS and **TS(1a→1b)/t** a reactant-like.

Table 3 gathers the energies of first-order saddle points involved in the three suggested mechanisms for the formation of epoxide. **TS(1a→1b)/t** is found to be only 4.8 kcal/mol less stable than **TS(1a→1b)/s**, and 34.8 kcal/mol above the reactants species. Further exploration of the PES shows that the crossing point might be located on the reactant side of the reaction path. Under these circumstances, the real TS for the reaction **1a→1b** cannot be directly taken as either **TS(1a→1b)/s** or **TS(1a→1b)/t**. Thus, it is only possible to estimate an upper bound to the energy of the actual TS from the crossing point where the two PESs merge. To locate this crossing point, IRC calculations have been performed (*i*) from **TS(1a→1b)/t** to the products, and (*ii*) from **TS(1a→1b)/s** to the reactants, Fig. 4.

The crossing point was located on the singlet PES immediately before **TS(1a→1b)/s** is reached from the reactant side. In the region where the two PESs intersect, the molecular geometries from the two reaction paths are very similar. It means that the activation barrier for the reaction **1a→1b** corresponds closely to the amount of energy required to surmount **TS(1a→1b)/s** (+30.0 kcal/mol, Fig. 2). Since it is the singlet TS that governs the reaction path from the reactant side, the oxygen-transfer process is not concerted: the two

Fig. 2. Reaction profile of the three suggested mechanisms for the formation of epoxide precursor from the addition of CrO_2Cl_2 to ethylene. Energies (in kcal/mol) are relative to singlet **1a**.

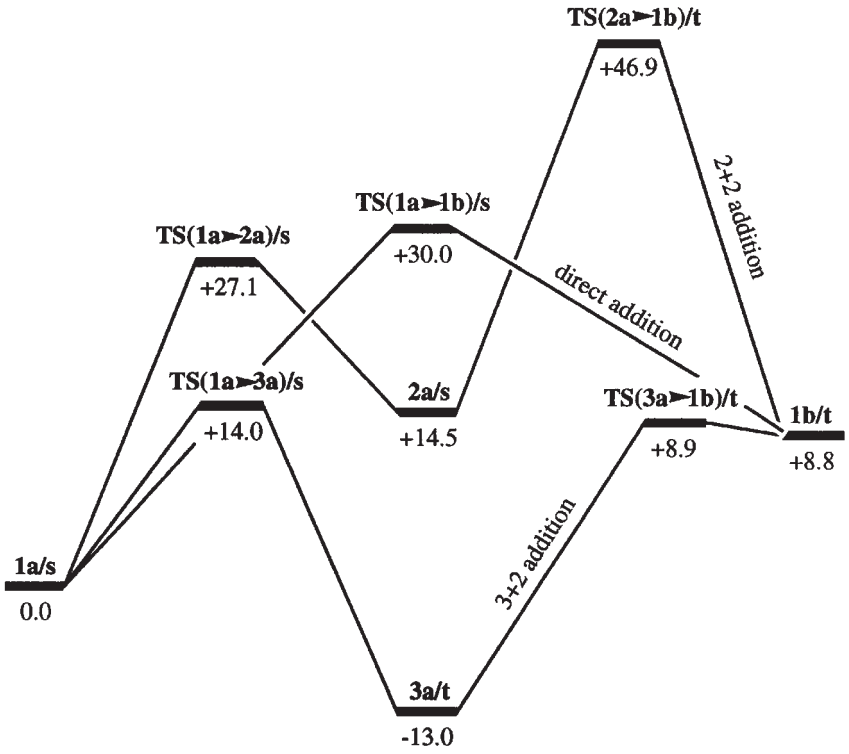

© 1999 NRC Canada

Fig. 3. Optimized geometrical parameters of the two possible transition state structures involved in the mechanism of direct addition for the formation of epoxide precursor. Distances in Å, and angles in degrees.

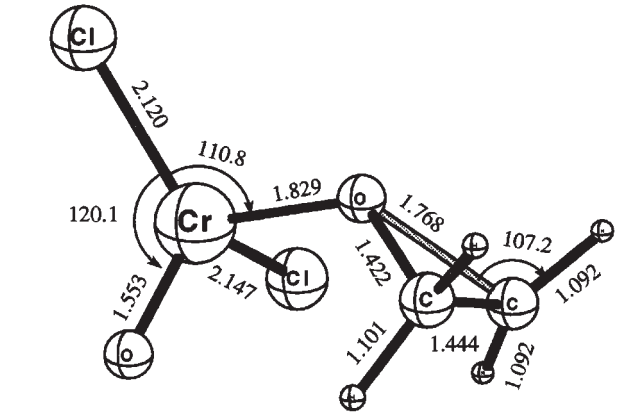

TS(1a→1b)/s

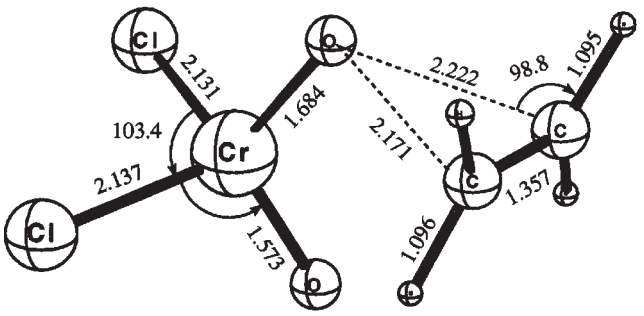

TS(1a→1b)/t

emerging C—O bonds are quite dissimilar (1.422 and 1.768 Å) in **TS(1a→1b)/s** (Fig. 3). Once the maximum has been reached on the singlet PES, the reaction can proceed along the triplet PES while the energy keeps decreasing until species **1b** is formed. The crossing from the singlet to the triplet PESs can be facilitated under the adiabatic assumption (42) by spin-orbit coupling.

Let us turn now our attention to the mechanism by postulated Sharpless et al. (5) involving a [2+2] interaction. The initial step was suggested to be the formation of a chromyl chloride olefin π complex. Despite looking for such a complex, we have not been able to localize any minimum on the PES close to the reactants region. This notwithstanding, its existence cannot be definitively ruled out, keeping in mind the well-known difficulties for DFT methods to describe weak interactions (43).

From that hypothetical complex, a four-centered intermediate **2a** was postulated to be formed via a [2+2] interaction between the olefin and an oxo group on the chromium (5). Indirect support for this process was provided by means of similar reported examples involving block-*p* elements (44).

Table 3. Energies[a] (in kcal/mol) and imaginary frequencies (in cm^{-1}) of all first-order saddle points involved in the three suggested mechanisms for the formation of the epoxide precursor (s = singlet, t = triplet).

TS	$\nu^{\neq}$	Energy
TS(1a→1b)/s	385.6*i*	30.0
TS(1a→1b)/t	229.5*i*	34.8
TS(1a→2a)/s	394.6*i*	27.1
TS(2a→1b)/s	555.0*i*	46.9
TS(2a→1b)/t	406.6*i*	31.4
TS(1a→3a)/s	363.8*i*	14.0
TS(1a→3a)/t	220.3*i*	21.7
TS(3a→1b)/t	27.4*i*	8.9

[a]Energies relative to free CrO_2Cl_2 + C_2H_4.

The optimized geometry of intermediate **2a**, together with the corresponding TSs of the whole [2+2] path are sketched in Fig. 5.

No change of the PES occurs in the reaction step **1a→2a**, since both reactants and product have singlet ground states. In contrast, the crossing takes place in the step **2a→1b**. The first step, **1a→2a**, turns out to be endothermic by 14.5 kcal/mol, and has an activation barrier of 27.1 kcal/mol (Fig. 2). The high energy required to reach **TS(1a→2a)** mainly arises from the Cr—O and C=C bond-breaking processes, which are slightly ahead of the bond-making ones (Fig. 5). This value is close to the 24.6 kcal/mol energy barrier found for the [2σ+2π] attack between CrO_2Cl_2 and CH_3OH (32*c*). Remarkably, the corresponding [2+2] addition involving OsO_4 has been found to have an even higher energy barrier of 39.7 kcal/mol (45*a*).

Regarding the second step, it is found to be slightly exothermic (–5.7 kcal/mol), with an activation barrier as high as 46.9 kcal/mol (Fig. 2). By inspection of Fig. 5, such an energy-demanding barrier can be mainly ascribed to the strain around the oxygen atom in the four-center kite-shaped **TS(2a→1b)**. Also the loss of the Cr-C σ interaction is a destabilizing factor.

We have tentatively (Fig. 2) assigned **TS(2a→1b)/t** as the transition state for the second rearrangement step, since it lies 15.5 kcal/mol below **TS(2a→1b)/s**. According to Fig. 5, **TS(2a→1b)/s** is ahead of **TS(2a→1b)/t** along the reaction coordinate from **2a/s** to **1b/t**. It means that there are two different possibilities for the crossover to occur: (*i*) at the early stages of the reaction, prior to any of the two TSs, or (*ii*) still in the reactant-side of the reaction, but between the two TSs. Only in the former case the true TS governing the reaction step is **TS(2a→1b)/t** (as depicted in Fig. 2). If the crossover took place between the two TSs, then the highest point in energy in the step **2a→1b** would not correspond to **TS(2a→1b)/t** but to the crossing point of the two surfaces, and the barrier would be somewhat lower than the reported 46.9 kcal/mol. This second possibility cannot be discarded. However, it is clear from Fig. 2 that the structures of the two TSs are similar enough to ensure that the crossing point would not be far away in energy from **TS(2a→1b)/t**.

Up to this point, none of the two presented mechanisms seems to afford a low-energy path to the epoxide precursor **1b**. A third alternative for the reaction to proceed is via a [3+2] cycloaddition. Figure 6 shows the optimized geome-

© 1999 NRC Canada

Fig. 4. Energy profile for the reaction involving direct addition of CrO_2Cl_2 to ethylene along the IRC path in the region where the crossing between the two PESs occurs. The TS in the singlet surface is at $s = 0.0$, and the TS in the triplet surface at $s = -2.6$. Energies (in kcal/mol) are relative to singlet **1a**.

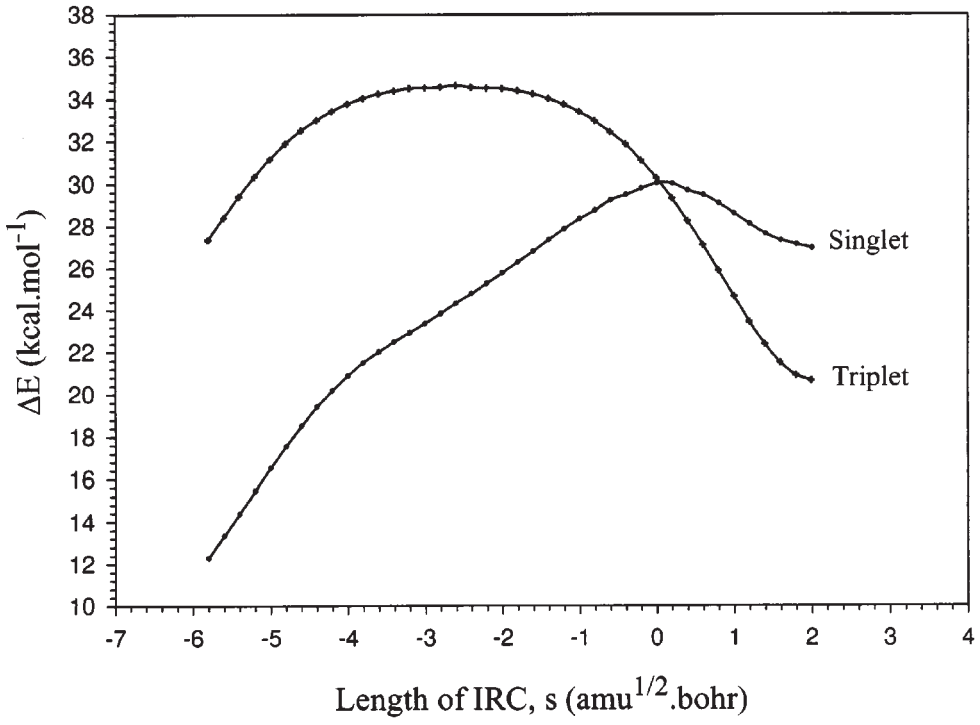

tries of the main stationary points corresponding to the [3+2] mechanism. The activation barriers for the two-step process involving a [3+2] interaction are +14.0 kcal/mol for the **1a**→**3a** reaction step (for the same OsO_4-catalyzed process (45), the energy barrier is 1.8 kcal/mol), and 21.9 kcal/mol for the **3a**→**1b** reaction step. The former step involves a crossover from the singlet surface in **1a** to the triplet surface in **3a** (Table 2). Such a crossover has been analyzed in detail in a previous study by means of IRC calculations (46). It has been found that the crossing point is located in the product side of the reaction path, the corresponding **TS(1a→3a)** lying on the singlet surface. Should this crossing be made possible by spin-orbit coupling (42), nothing seems to prevent the **1a**→**3a** reaction step from being kinetically feasible. From a thermodynamic viewpoint, this process is found to be exothermic (–13.0 kcal/mol), and therefore also very favorable.

As seen from Fig. 6, the TS for the second reaction step, **3a**→**1b**, resembles very much intermediate **1b**. For instance, the geometry of the $O(CH_2)_2$ skeleton in this product-like TS is very close to the geometrical arrangement found in the precursor of the epoxide (Fig. 1). This is consistent with the fact that **TS(3a→1b)** is only 0.1 kcal/mol above **1b** (Fig. 2). Also notice the low value of the unique imaginary frequency for this TS (Table 2), which is indicative of a flat region.

It follows from the previous discussion that the most suitable path leading to the epoxide precursor **1b** is through [3+2] cycloaddition. The [3+2] addition of ethylene to CrO_2Cl_2 has a relatively low activation barrier of 14.0 kcal/mol, as the occupied π-orbital of ethylene can interact, stabilizing with the CrO_2Cl_2 LUMO throughout the reaction (46). Further, the resulting five-membered ring, **3a**/**t**, is sufficiently flexible to allow for a facile rearrangement route to the epoxide product **1b**/**t** with the transition state being only 8.9 kcal/mol above the separated reactants. We note that the recent photochemical matrix isolation study by Limberg and Köppe (53) found complexed epoxides to be formed by CrO_2Cl_2 whereas they found no evidence for the formation of a dioxylate. This, however, does not contradict our theoretical result that, on the ground-state potential energy surface, complexed epoxide can easily rearrange to the dioxylate with a barrier of 0.1 kcal/mol. As the authors pointed out, "the PES investigated in the matrix experiments under photolytic conditions is probably different from the one the system moves on when the reactions are induced thermally. Light of the wavelength 411 nm is far below the Cr=O dissociation threshold so that CrO_2Cl_2, which shows a visible absorption band nearby, takes up energy via this transition to reach an excited state capable of reacting with olefins under matrix conditions. Consequently the first transition states and intermediate geometries which have to be passed will be different from the thermal ones" (53).

In contrast to the [3+2] path, the [2+2] addition has a sizable barrier of 27.1 kcal/mol due to (46) the poor overlap between the occupied π-orbital of ethylene and the LUMO of CrO_2Cl_2. It is as a consequence not likely to be the first step in the epoxidation process. Also, the further rearrangement of chromaoxetane, **2a**/**s**, leads to a strained transition state, **TS(2a→1b)/t** with a large estimated barrier of 31.4 kcal/mol. Finally, the direct [1+2] addition is also hampered by poor initial interaction between ethylene and CrO_2Cl_2, leading to a prohibitive barrier of 30.0 kcal/mol.

© 1999 NRC Canada

Fig. 5. Optimized geometrical parameters of the main stationary points (minima and first-order saddle points) for the mechanism involving a [2+2] cycloaddition between CrO_2Cl_2 and ethylene for the formation of epoxide precursor. Distances in Å, and angles in degrees.

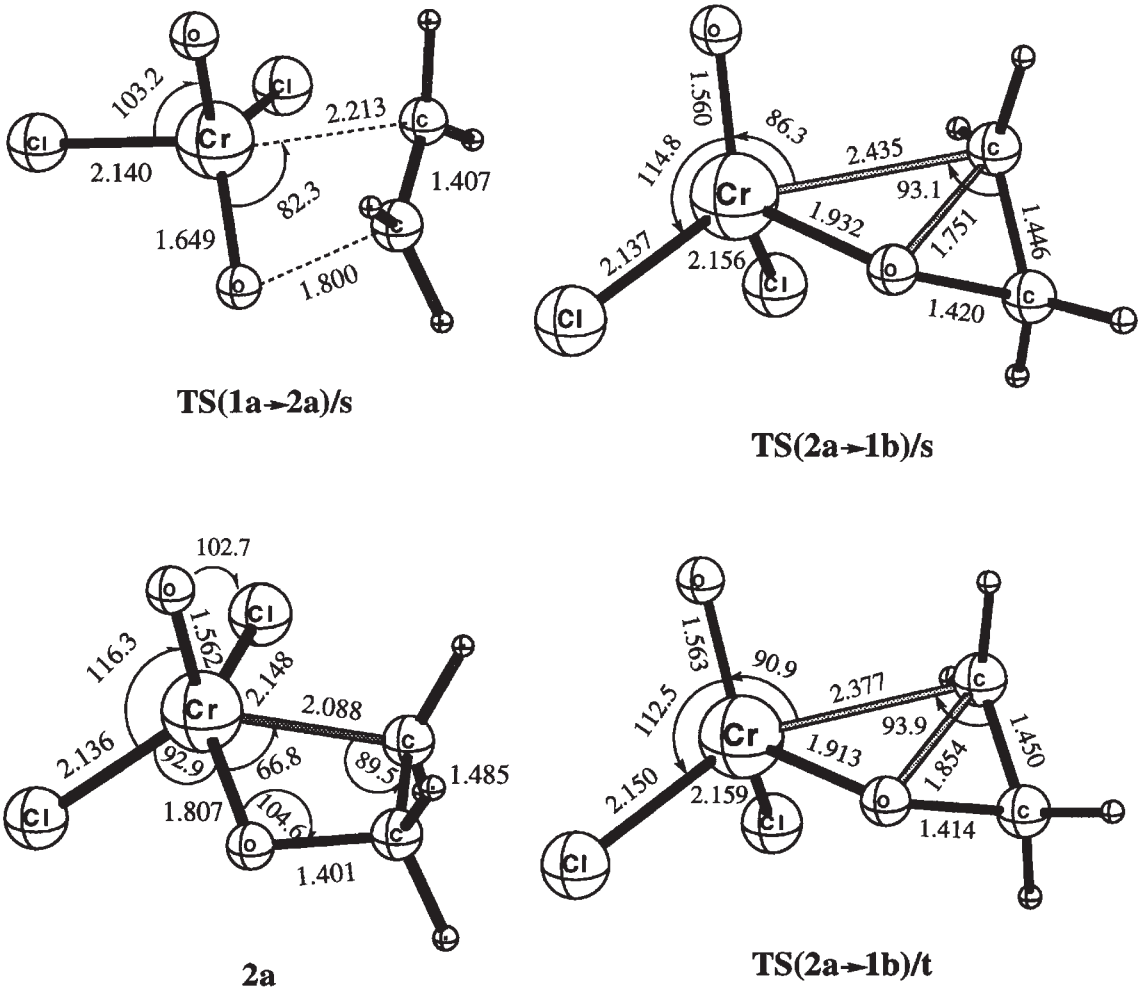

Similar conclusions have been drawn recently with regard to the relative feasibility of [2+2] and [3+2] addition for the osmium-catalyzed hydroxylation of olefins (41, 45, 47, 48). Our results contradict previous findings by Rappé et al. (8). In that work, the [3+2] path was ruled out because it was found to be strongly endothermic (+56 kcal/mol), whereas the [2+2] path was concluded to be exothermic (–14 kcal/mol) and actually the only one capable of yielding epoxide. However, that work was hampered by the lack of fully optimized structures. Also, Rappé et al. (8) find the reaction $CrCl_2O_2 + C_2H_4 \rightarrow CrCl_2O + C_2H_4O$ to be exothermic by –35 kcal/mol whereas our DFT method and experiment find it to be endothermic by 26.7 kcal/mol and 24.8 kcal/mol, respectively.

The assumed epoxide precursor **1b/t** does not readily decompose into epoxide. In fact, we calculate the reaction **1b/t** $\rightarrow CrCl_2O + C_2H_4O$ to be endothermic by 16.9 kcal/mol, in keeping with the fact that the overall reaction $CrCl_2O_2 + C_2H_4 \rightarrow CrCl_2O + C_2H_4O$ is calculated to be endothermic by 26.7 kcal/mol. Thus, the many mechanisms invoking **1b/t** (and an implied exothermicity for the overall reaction $CrCl_2O_2 + C_2H_4 \rightarrow CrCl_2O + C_2H_4O$) might not be valid. We speculate that H_2O instead is involved in the formation of epoxide as the reaction mixture of Scheme 1 is extracted from an organic solvent (such as CH_2Cl_2) into aqueous solution. This possibility will be the subject of an upcoming investigation (45*a*).

It is worthwhile pointing out that dioxylate complexes of Re and Os are both known and well characterized. Unlike the Cr system, these complexes are known to hydrolyze to *cis* diols rather than epoxides. This can be understood because both the Re and Os system contain only oxygen ligands whereas the Cr system involves both oxygen and chlorine ligands.

III.2. Formation of the chlorohydrin precursor

The conversion of olefins into chlorohydrins was originally suggested to result from highly stereoselective *cis* addition of the elements of HOCl across the olefinic linkage (5). Chlorohydrins resulting from *trans* addition were concluded to be secondary products derived by opening of the epoxide (5). According to Scheme 2, *cis*-oxychlorination can be accounted for by two different mechanistic routes: inter-

© 1999 NRC Canada

Fig. 6. Optimized geometrical parameters of the main stationary points (minima and first-order saddle points) for the mechanism involving a [3+2] cycloaddition between CrO_2Cl_2 and ethylene for the formation of epoxide precursor. Distances in Å, and angles in degrees.

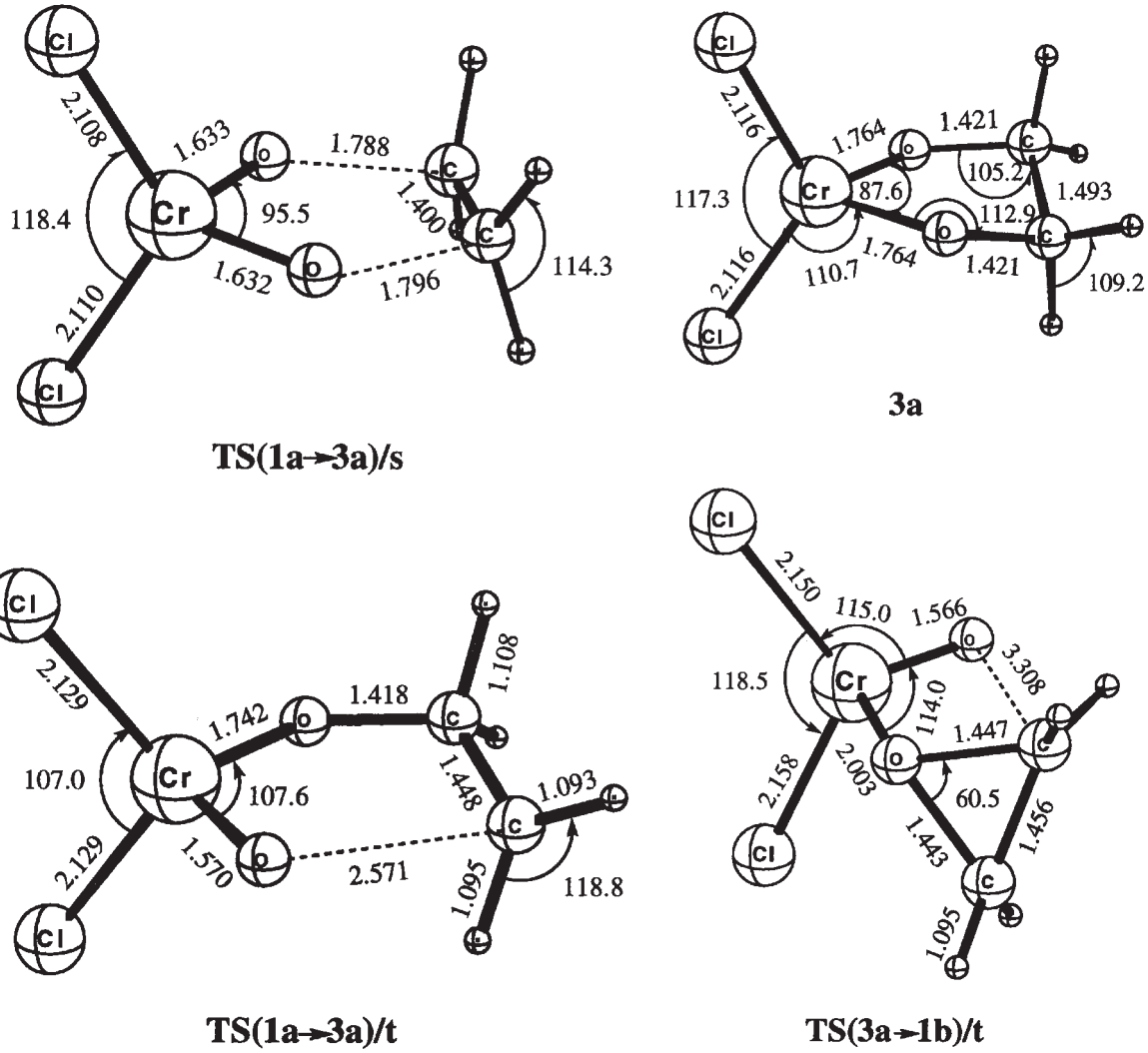

Table 4. Energies[a] (in kcal/mol) of all minima involved in the suggested mechanisms for the formation of chlorohydrin and dichloride precursors (s = singlet, t = triplet).

Minima	Ground state	Energy
4a	s	7.6
5a	t	3.8
6a	t	44.7

[a]Energies relative to free CrO_2Cl_2 + C_2H_4.

mediate **5a** (the immediate precursor of 1,2-chlorohydrin) can be thought to derive from either a [2+2] addition (center) or a [3+2] addition (left).

In the mechanism involving a [2+2] cycloaddition, the formal transfer of O and Cl from CrO_2Cl_2 to ethylene occurs in two separated steps, whereas in the [3+2] mechanism the two heteroatoms are transferred in the same reaction step. As far as the [2+2] route is concerned, there are even two different possibilities for the reaction to proceed, depending on the relative order by which the heteroatoms are inserted: (*i*) insertion of Cl in the first step, then O, or (*ii*) first O, then Cl. Only the former possibility has been depicted in Scheme 2. The latter possibility would mean that, instead of intermediate **4a**, the product obtained after the first reaction step would be the highly energetic chromaoxetane **2a**, whose endothermic formation has been already discussed in the previous section; afterwards, the second step would be a bond migration between **2a** and **5a**. We will come to this point later on.

Tables 4 and 5 gather relevant information concerning all the stationary points involved in the mechanisms for the CrO_2Cl_2-mediated formation of chlorine-containing products from ethylene. Notice that the immediate precursor of 1,2-chlorohydrin, **5a**, lies on the triplet surface in its ground state, whereas **4a** is more stable on the singlet surface. To ensure that these conformations (Fig. 7) are the more stable ones, we also examined three other conformers in which the ligands that do not participate in the ring adopt different orientations. All the isomers were found to be very close in energy to **4a** and **5a** (higher by only 0.1–0.9 kcal/mol). The

© 1999 NRC Canada

Table 5. Energies[a] (in kcal/mol) and imaginary frequencies (in cm^{-1}) of all first-order saddle points involved in the suggested mechanisms for the formation of chlorohydrin and dichloride precursors (s = singlet, t = triplet).

TS	ν–	Energy
TS(1a→4a)/s	52.0*i*	9.1
TS(1a→5a)/s	131.3*i*	15.7
TS(1a→5a)/t	69.4*i*	37.3
TS(4a→5a)/s	532.7*i*	49.8
TS(4a→5a)/t	121.7*i*	50.5

[a]Energies relative to free CrO_2Cl_2 + C_2H_4.

differences are so small that those species must be thought to coexist and easily interconvert between each other during the reaction.

The relative energies and activation barriers for the two pathways leading to chlorohydrin are summarized in Fig. 8. Figures 9 and 10 display the molecular structures of the TSs corresponding to the [2+2] and [3+2] mechanisms, respectively. The [2+2] attack of ethylene on the Cr—Cl bond (Fig. 8) has an energy barrier (9.1 kcal/mol), which is only one third of the barrier corresponding to the same attack on the Cr=O bond (Fig. 2).

However, as can be seen from Fig. 8, the whole [2+2] pathway cannot compete in energy with the [3+2] path. In particular, the main bottleneck for the former route happens to take place in the second step. The conversion of **4a** to **5a**, despite being formally exothermic (ΔE = –3.8 kcal/mol), is kinetically prevented ($\Delta E^{\#}$ = +49.8 kcal/mol). Indeed, the TS connecting **4a** and **5a** (either singlet or triplet) suffers from substantial constraint due to the tight three-membered ring formed during the transfer of the second heteroatom (one O atom in this case) to the organic skeleton. It can be inferred that, if the second heteroatom to be transferred was Cl instead of O (as it would occur in the bond migration **2a→5a**), similar constraints would be also responsible for the strain and, therefore, for the large amount of energy required for this process to take place.

Complex **5a/t** (ground state) is computed to lie 10.2 kcal/mol below **5a/s** (first excited state). According to our calculations, the alternative [3+2] cycloaddition reaction should proceed from **1a** to **5a/t** in a single step involving a change of the PES. Notice from Fig. 10 that **TS(1a→5a)/s** is slightly ahead of **TS(1a→5a)/t**. The crossing point is expected to be found somewhere between the two TSs, and much closer to **TS(1a→5a)/s** than to **TS(1a→5a)/t**, since the latter lies 21.6 kcal/mol above the former. In principle, one could make a rough approximation and assume that the crossover occurs at **TS(1a→5a)/s** (as aforeseen for the **1a→1b** step). In this way, the barrier assigned to the **1a→5a** step (+15.7 kcal/mol) should be better considered as an upper bound to the real activation barrier. Strictly speaking, the crossing point might not coincide with the singlet TS. The closer the two points, the more valid the approximation. However, even in the case that the crossing point happened to occur much earlier than **TS(1a→5a)/s**, the global result would not be significantly affected because the trend is in the direction of making the barrier even smaller.

Taking into account such an assumption, notice from Fig. 10 that **TS(1a→5a)/s** does not suffer from much distortion. The most remarkable point is the closing of the ClCrO bond angle (89.2°) in order to better assist the olefin attack, which proceeds coplanar to the Cl-Cr-O plane (dihedral angle Cl-C-C-O = 2.2°). Once in the product side, the reaction is predicted to proceed smoothly along the triplet PES.

Fig. 7. Optimized geometrical parameters of intermediate **4a** and ester **5a** derived, respectively, from a [2+2] addition of ethylene to one Cr—Cl bond, and from a [3+2] addition of ethylene to one Cr—Cl bond and one Cr=O bond in CrO_2Cl_2. Distances in Å, and angles in degrees.

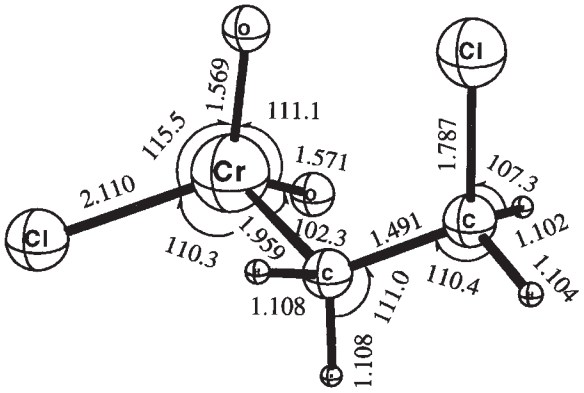

4a

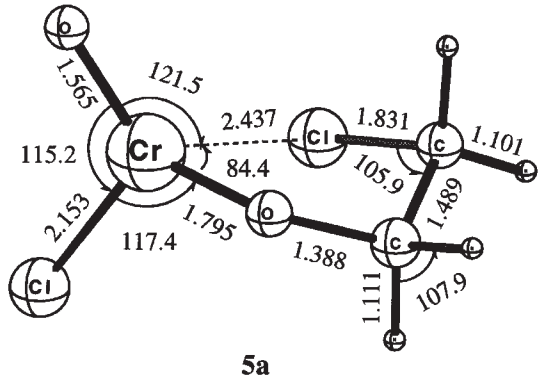

5a

Weighing up both mechanisms, the [2+2] cycloaddition proves less beneficial to the energetics of *cis*-oxychlorination than the [3+2], regardless of the relative order by which the two heteroatoms are inserted. Consequently, it can be concluded that the mechanism that actually operates in the formation of the chlorohydrin precursor (**5a/t**) from the addition of ethylene to CrO_2Cl_2 is the one involving the direct formation of the five-membered intermediate **5a/t** from a [3+2] addition.

We have previously shown (45*a*) that the [3+2] addition of ethylene to two Cr=O bonds has a low barrier due to stabilizing interactions between the LUMO of CrO_2Cl_2 and the occupied ethylene π-orbital. Quite similar interactions are operative for the [3+2] addition of ethylene to, respectively, a Cr=O and Cr—Cl bond. It is thus not surprising that the two types of [3+2] addition have nearly the same activation energies.

The final formation of chlorohydrin from **5a/t** requires a hydrogen agent. We speculate again that H_2O is involved as

© 1999 NRC Canada

Fig. 8. Reaction profile of the two possible mechanisms for the formation of 1,2-chlorohydrin precursor from the addition of CrO_2Cl_2 to ethylene. Energies (in kcal/mol) are relative to **1a**.

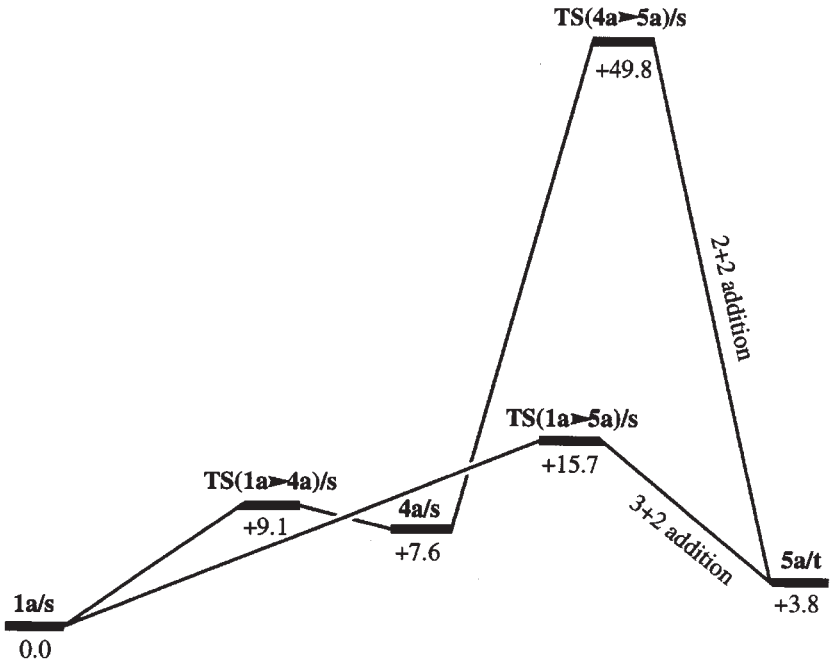

the reaction mixture of Scheme 2 is extracted from an organic solvent (such as CH_2Cl_2) into aqueous solution. Thus, the reaction of H_2O with **5a/t** to produce Cr(OH)OCl/t + chlorohydrin is calculated to have a modest endothermicity of 2.4 kcal/mol. We shall examine this step in an upcoming investigation.[2]

III.3. Dichloride formation

Chromyl chloride oxidations of olefins are known to produce complex mixtures of products (1). However, it was found that when these reactions are performed at low temperature the epoxide and the chlorohydrin become the major products. Only in a few cases does *cis*-dichlorination really occur (5). According to Scheme 2, formation of dichloride may proceed through two different reaction pathways. Again, either a [2+2] (center) or a [3+2] addition path (right) seem conceivable modes of reaction. In the former case, ethylene may insert into a chlorine–chromium bond (*cis*-chlorometalation) to produce the alkylchromium intermediate **4a**. Such a process has been already analyzed in the previous section. This species could then lead to the precursor of dichloride, **6a**, by reductive elimination in the second step. The first step, however, has to occur with retention of configuration at the carbon center bound to the chromium in **4a** in order to result in overall *cis* addition. Alternatively, the two chlorine atoms may be transferred in a one-step process.

Figure 11 shows the optimized geometry of the immediate precursor of dichloride, **6a**. This can be considered a five-membered species such as **3a** and **5a**. However, notice that, unlike in **3a** and **5a**, the five atoms of the ring in intermediate **6a** are not coplanar. This conformation ensures the optimal interaction between ethylene π-orbital and the LUMO of CrO_2Cl_2. The energetics of the reaction leading to dichloride is summarized in Fig. 12. The most remarkable point here is the high endothermicity of the net reaction (+44.7 kcal/mol), which prevents dichloride formation from being favored at low temperatures. Since already the thermodynamics makes dichloride formation prohibitive under normal condition, the TSs involved in the path from **1a** to **6a** have not been investigated.

To sum up, comparison of Figs. 2, 8, and 12 allows us to conclude that the formation of dichloride, regardless of the mechanistic path being followed, cannot compete energetically with the formation of either epoxide or chlorohydrin. Our calculations reveal that, thermodynamically, *cis*-dichlorination is more unlikely to occur than any other of the processes leading to the observed products.

III.4. Dependence of the reaction mechanism on the organic substrates

We shall finally briefly discuss changes of relative energies and possibly the reaction mechanism when considering olefins other than ethylene. Table 6 compares the reaction enthalpies for the formation of diolate and epoxide complexes as well as the fully separated epoxides from reaction between $CrCl_2O_2$ and the two olefins cyclohexene and tetramethyl ethylene. It follows from Table 6 that, although the relative energies change to a certain extent when the organic substrates changes, the main conclusions drawn from the discussion for oxidation of ethylene remain the same. That is, (*i*) diolate is the most stable complex in all cases; (*ii*) difference in relative energies between the diolate and epoxide complexes are substantial; and (*iii*) oxidation of olefin to the separated epoxide is highly endothermic. We

[2] M. Torrent, L. Deng, M. Solà, and T. Ziegler. Work in progress.

© 1999 NRC Canada

Fig. 9. Optimized geometrical parameters of the transition state structures involved in the [2+2] cycloaddition between CrO_2Cl_2 and ethylene leading to the formation of chlorine-containing products. Distances in Å, and angles in degrees.

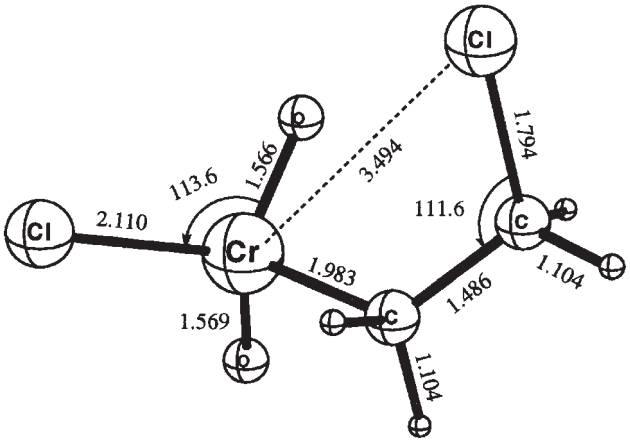

TS(1a→4a)/s

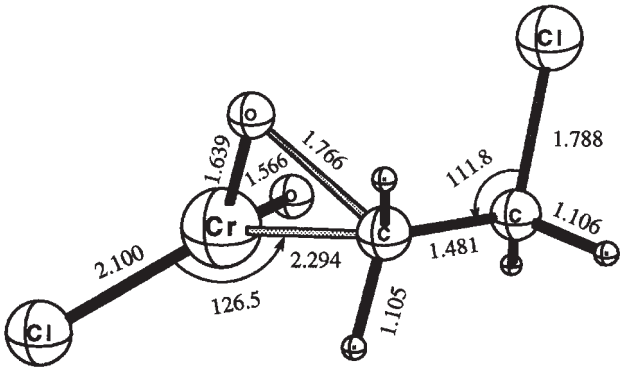

TS(4a→5a)/s

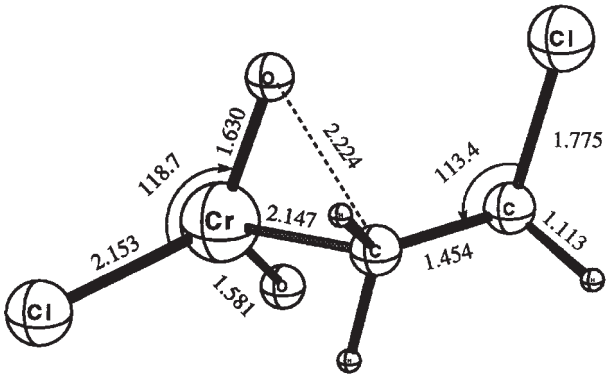

TS(4a→5a)/t

Fig. 10. Optimized geometrical parameters of the transition state structures involved in the [3+2] cycloaddition between CrO_2Cl_2 and ethylene leading to the formation of 1,2-chlorohydrin precursor. Distances in Å, and angles in degrees.

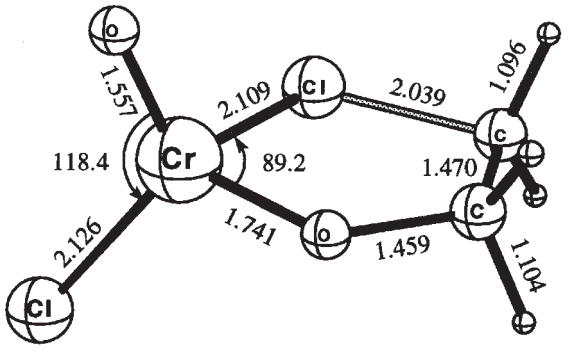

TS(1a→5a)/s

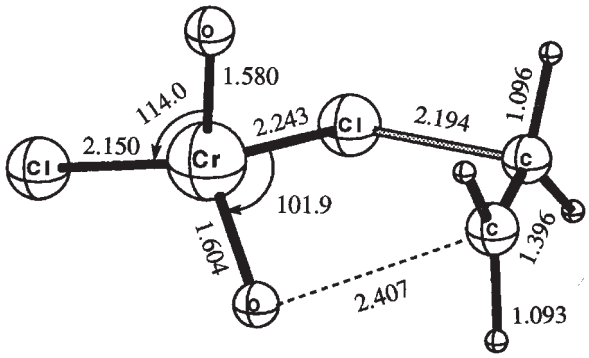

TS(1a→5a)/t

Fig. 11. Optimized geometrical parameters of the immediate precursor of 1,2-dichloride. Distances in Å, and angles in degrees.

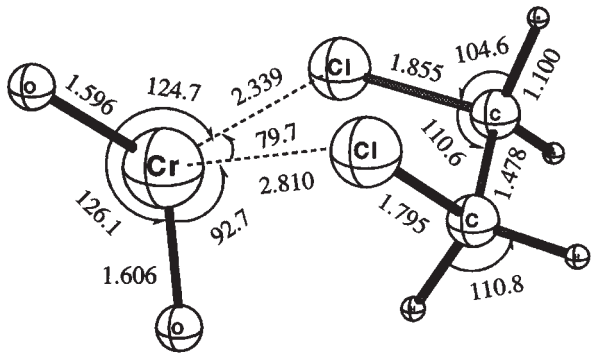

6a

© 1999 NRC Canada

Fig. 12. Reaction profile for the formation of 1,2-dichloride precursor from the addition of ethylene to CrO_2Cl_2. Energies (in kcal/mol) are relative to **1a**.

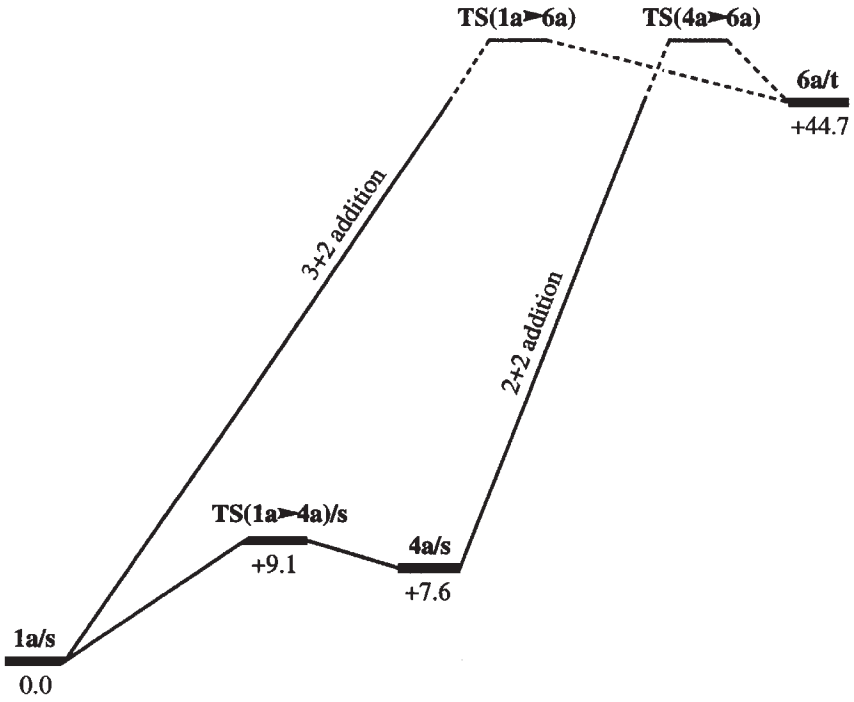

Table 6. Comparison of reaction enthalpies of the oxidation of olefin by CrO_2Cl_2 to chromyl diolate and epoxide complexes for different olefins.

Reaction[a]	Energy[b] (kcal/mol)	ΔE[c] (kcal/mol)
$CrO_2Cl_2 + C_2H_4 \rightarrow CrCl_2(OCH_2CH_2O)$	–13.0 (–10.6[d])	0
$CrO_2Cl_2 + C_2H_4 \rightarrow CrCl_2(O)(OCH_2CH_2)$	8.6	21.6
$CrO_2Cl_2 + C_2H_4 \rightarrow CrOCl_2$ + epoxide	26.7	39.7
$CrO_2Cl_2 + C_2Me_4 \rightarrow CrCl_2(OCMe_2CMe_2O)$	–19.5	0.0
$CrO_2Cl_2 + C_2Me_4 \rightarrow CrCl_2(O)(OCMe_2CMe_2)$	–4.8	14.7
$CrO_2Cl_2 + C_2Me_4 \rightarrow CrOCl_2$ + tetramethylethylene epoxide	3.7	23.2
CrO_2Cl_2 + cyclohexene → Cr(O)(1,2-cyclohexanediolate)	–12.4	0.0
CrO_2Cl_2 + cyclohexene → Cr(O)(1,2-cyclohexene epoxide)	5.9	18.3
CrO_2Cl_2 + cyclohexene → $CrOCl_2$ + cyclohexene epoxide	30.0	42.4

[a]The BP86 calculations show that all the reactants have singlet ground state and all the products have triplet ground state.

[b]Unless otherwise specified, the BP86 calculations were carried out with double-ζ basis set plus polarization (the standard ADF basis set III/H, C.1*s*, O.1*s*, Cl.2*p*) for nonmetal atoms, and triple-ζ basis set (the standard ADF basis set IV/Cr.2*p*) for Cr atom.

[c]Energy difference relative to the diolate complexes for each different organic substrates, respectively.

[d]The ADF calculations were performed with triple-ζ plus 3*d* and 4*f* polarization functions for C and Cl atoms, triple-ζ plus 2*p* and 3*d* polarization functions for H, and triple-ζ plus two 4*f* functions for Cr; the basis set for the nonmetals was taken from standard ADF basis set V, and the basis set IVB of ref. 49 was used for Cr atom.

therefore conclude that the mechanistic picture drawn from ethylene is not likely to change qualitatively with other olefins.

IV. Conclusions

We have shown that the formation of the reputed epoxide intermediate **1b/t** from the reaction between CrO_2Cl_2 and ethylene is unlikely to involve a chromaoxetane intermediate derived from a [2+2] cycloaddition as previously assumed (5). Our calculations reveal that the [3+2] addition of ethylene to chromium–oxygen bonds in CrO_2Cl_2 is favored over the [2+2] addition to a Cr=O linkage, and also over the direct addition of ethylene to one oxygen atom. It is concluded that epoxides originate from an ester intermediate, which in turn is formed via a [3+2] cycloaddition.

We also suggest that chlorohydrin, the other major product observed in the oxidation of olefins by CrO_2Cl_2, should arise from a [3+2] cycloaddition as well, in particular from the addition of ethylene to two different heteroatoms in the chromium reagent. Our theoretical results do not support an alternative two-step mechanism involving a [2+2] addition followed by a bond migration. Such a process is found to be too demanding in terms of energy, especially as far as the

© 1999 NRC Canada

activation barrier for the second step is concerned. In addition, the present investigation justifies why only in some cases dichloride is found among the observed products. Dichlorination is computed to be thermodynamically far less favorable than either epoxidation or oxychlorination as a product.

The decomposition of the reputed epoxide precursor **1b/t** into the final product (**1b/t** $\rightarrow CrCl_2O + C_2H_4O$) was found to be endothermic by 16.9 kcal/mol, in keeping with the fact that the overall reaction $CrCl_2O_2 + C_2H_4 \rightarrow CrCl_2O + C_2H_4O$ is calculated to be endothermic by 26.7 kcal/mol. Thus, the many mechanisms invoking **1b/t** (and an implied exothermicity for the overall reaction $CrCl_2O_2 + C_2H_4 \rightarrow CrCl_2O + C_2H_4O$) might not be valid. We plan in an upcoming investigation[2] to study the role of H_2O (or H^+/OH^-)for the formation of epoxide as the reaction mixture of Scheme 1 is extracted from an organic solvent (such as CH_2Cl_2) into aqueous solution. This investigation should also explain why diols are absent as products in the reaction between $CrCl_2O_2$ and olefins whereas the corresponding reaction between OsO_4 and olefins generates exclusively diols with little epoxide as a product.

Acknowledgments

This investigation was supported by the Natural Sciences and Engineering Research Council of Canada (NSERC), and by the Donors of the Petroleum Research Fund, administered by the American Chemical Society (ACS-PRF No 31205-AC3), as well as by the Spanish DGICYT Project No. PB95-0762. We also acknowledge access to the computer facilities at the universities of Calgary and Girona. One of us (M.T.) thanks the Direcció General de Recerca de la Generalitat de Catalunya for financial help through a FI Fellowship.

References

1. (*a*) S.J. Cristol and K.R. Eilar. J. Am. Chem. Soc **72**, 4353 (1950); (*b*) R.A. Stairs, D.G.M. Diaper, and A.L. Gatzke. Can. J. Chem **41**, 1059 (1963); (*c*) F. Freeman. Rev. React. Species Chem. React **1**, 37 (1973); (*d*) A. Wahhab. Ph.D. thesis. University of Calgary, Calgary. 1987. (*d*) F.W. Bachelor and U.O. Cheriyan. Can. J. Chem. **50**, 4022 (1972).
2. (*a*) F.A. Carey and R.J. Sundberg. Advanced organic chemistry. Plenum, New York. 359 1977; (*b*) W.A. Nugent and J.M. Mayer. Metal-ligand multiple bonds. Wiley, New York. 248 1988.
3. (*a*) K.B. Wiberg (*Editor*). Oxidation in organic chemistry. Part A. Academic Press, New York. 1965. pp. 1–68; (*b*) M. Schröder. Chem. Rev **80**, 187 (1980).
4. (*a*) R.A. Walton. Prog. Inorg. Chem **16**, 1 (1972); (*b*) J. San Filippo, Jr., and C. Chern. J. Org. Chem **42**, 2182 (1977); (*c*) F. Freeman, C.R. Armstead, M.G. Essig, E.L. Karchefski, C.J. Kojima, V.C. Manopoli, and A.H. Wickman. J. Chem. Soc. Chem. Commun **65** (1980).
5. K.B. Sharpless, A.Y. Teranishi, and J.-E. Bäckvall. J. Am. Chem. Soc. **99**, 3120 (1977).
6. F. Freeman. Chem. Rev. **75**, 439 (1975).
7. E.G. Samsel, K. Srinivasan, and J.K. Kochi. J. Am. Chem. Soc. **107**, 7606 (1985).
8. (*a*) A.K. Rappé and W.A. Goddard. J. Am. Chem. Soc **102**, 5114 (1980); (*b*) J. Am. Chem. Soc **104**, 3287 (1982); (*c*) T.H. Upton and A.K. Rappé. J. Am. Chem. Soc. **107**, 1206 (1985).
9. A.K. Rappé and W.A. Goddard. Nature (London), **285**, 311 (1980).
10. (*a*) J.-E. Bäckvall, M.W. Young, and K.B. Sharpless. Tetrahedron Lett. **40**, 3523 (1977); (*b*) M.F. Schlecht and H.-J. Kim. Tetrahedron Lett. **27**, 4889 (1986); (*c*) M.F. Schlecht and H.-J. Kim. J. Org. Chem **54**, 583 (1989).
11. (*a*) D. Mansuy, J. Leclaire, M. Fontecave, and P. Dausette. Tetrahedron, **40**, 2847 (1984); (*b*) J.P. Collman, J.I. Brauman, B. Meunier, S.A. Raybuck, and T. Kodadek. Proc. Natl. Acad. Sci. U.S.A. **81**, 3245 (1984); (*c*) P.R. Ortiz de Montellano and E.A. Komives. J. Biol. Chem. **260**, 3330 (1985); (*d*) J.P. Collman, J.I. Brauman, B. Meunier, T. Hayashi, T. Kodadek, and S.A. Raybuck. J. Am. Chem. Soc. **107**, 2000 (1985); (*e*) J.T. Groves and Y. Watanabe. J. Am. Chem. Soc. **108**, 507 (1986); (*f*) E.A. Komives and Ortiz de P.R. Montellano. J. Biol. Chem. **262**, 9793 (1987).
12. A.G.M. Barrett, D.H.R. Barton, and T. Tsushima. J. Chem. Soc. Perkin Trans. 1, 639 (1980).
13. J.T. Groves and T.E. Nemo. J. Am. Chem. Soc. **105**, 5786 (1983).
14. K. Yamaguchi, Y. Tekahara, and T. Fueno. *In* Applied quantum chemistry. *Edited by* V.H. Smith, H.F. Schaefer, and K. Morokuma. D. Reidel, Dordrecht. 155 (1986).
15. (*a*) D.M. Walba, C.H. DePuy, J.J. Grabowski, and V.M. Bierbaum. Organometallics, **3**, 498 (1984); (*b*) H. Kang and J.L. Beauchamp. J. Am. Chem. Soc. **101**, 6449 (1979).
16. K.A. Jørgensen and B. Schiøtt. Chem. Rev **90**, 1483 (1990).
17. (*a*) M.J. Calhorda, A.M. Galvão, C. Ünaleroglu, A.A. Zlota, F. Frolow, and D. Milstein. Organometallics, **12**, 3316 (1993); (*b*) J. Bakos, Á. Orosz, S. Cserépi, I. Tóth, and D. Sinou. J. Mol. Catal.A, **116**, 85 (1997); (*c*) B. Bruin, M.J. Boerakker, J.J.J.M. Donners, B.E.C. Christiaans, P.P.J. Schlebos, R. Gelder, J.M.M. Smits, A.L. Spek, and A.W. Gal. Angew. Chem. Int. Ed. Engl **36**, 2064 (1997); Angew. Chem. **109**, 2153 (1997).
18. V.W. Day, W.G. Klemperer, S.P. Lockledge, and D.J. Main. J. Am. Chem. Soc. **112**, 2031 (1990).
19. S. Baba, T. Ogura, and S. Kawaguchi. J. Chem. Soc. Chem. Commun. 910 (1972).
20. M. Lenarda, N.B. Pahor, M. Calligaris, M. Graziani, and L. Randaccio. J. Chem. Soc. Dalton Trans. 279 (1978).
21. (*a*) B.B. Ebbinghaus. Combust. Flame, **101**, 311 (1995); (*b*) C. Limberg, R. Köppe, and H. Schnöckel. Angew. Chem. **110**, 512 (1998).
22. (*a*) E.J. Baerends, D.E. Ellis, and P. Ros. Chem. Phys. **2**, 41 (1973); (*b*) W. Ravenek. *In* Algorithms and applications on vector and parallel computers. *Edited by* H.J.J. te Riele, T.J. Dekker, and H.A. van de Vorst. Elsevier, Amsterdam. 1987.
23. (*a*) P.M. Borrigter, G. te Velde, and E.J. Baerends. Int. J. Quantum Chem. **33**, 87 (1987); (*b*) G. te Velde and E.J. Baerends. J. Comput. Phys **99**, 84 (1992).
24. J. Krijn and E.J. Baerends. Fit functions in the HFS-methods; internal report. Free University of Amsterdam, Amsterdam. 1984.
25. (*a*) G.J. Snijders, E.J. Baerends, and P. Vernooijs. At. Nucl. Data Tables, **26**, 483 (1982); (*b*) P. Vernoois, G.J. Snijders, and E.J. Baerends. Slater type basis functions for the whole periodic system; internal report. Free University of Amsterdam, The Netherlands. 1981.
26. (*a*) G.J. Snijders, E.J. Baerends, and P. Ros. Mol. Phys. **36**, 1789 (1978); (*b*) Mol. Phys. **38**, 1909 (1979).

© 1999 NRC Canada

27. O. Gunnarson and I. Lundquist. Phys. Rev **B10**, 1319 (1974).
28. S.H. Vosko, L. Wilk, and M. Nusair. Can. J. Phys **58**, 1200 (1980).
29. A.D. Becke. Phys. Rev. A, **38**, 2398 (1988).
30. (*a*) J.P. Perdew. Phys. Rev. Lett **55**, 1655 (1985); (*b*) Phys. Rev. B: Condens. Matter, **33**, 8822 (1986); (*c*) J.P. Perdew and Y. Wang. Phys. Rev. B: Condens. Matter, **33**, 8800 (1986).
31. M. Torrent, P. Gili, M. Duran, and M. Solà. J. Chem. Phys. **104**, 9499 (1996).
32. (*a*) L. Deng and T. Ziegler. Organometallics, **15**, 3011 (1996); (*b*) T. Ziegler and J. Li. Organometallics, **14**, 214 (1995); (*c*) L. Deng and T. Ziegler. Organometallics, **16**, 716 (1997).
33. (*a*) L. Versluis and T. Ziegler. J. Chem. Phys **88**, 322 (1988); (*b*) L. Fan and T. Ziegler. J. Chem. Phys **95**, 7401 (1991); (*c*) G. Schreckenbach, J. Li, and T. Ziegler. Int. J. Quantum Chem. **56**, 477 (1995).
34. L. Fan, L. Versluis, T. Ziegler, E.J. Baerends, and W. Ravenek. Int. J. Quantum Chem. Symp. **22**, 173 (1988).
35. A. Banerjee, N. Adams, J. Simons, and R. Shephard. J. Phys. Chem **89**, 52. (1985).
36. J. Baker. J. Comput. Chem **7**, 385 (1986).
37. L. Fan and T. Ziegler. J. Chem. Phys. **92**, 46 (1990).
38. K. Fukui. Acc. Chem. Res. **14**, 363 (1981).
39. C. González and H.B. Schlegel. J. Phys. Chem **94**, 5523 (1990).
40. L. Deng and T. Ziegler. Int. J. Quantum Chem. **52**, 731 (1994).
41. (*a*) U. Pidun, C. Boehme, and G. Frenking. Angew. Chem. Int. Ed. Engl. **35**, 2817 (1996); (*b*) O. Gonzalez-Blanco, V. Branchadell, K. Monteyne, and T. Ziegler. Inorg. Chem. **37**, 1744 (1998); (*c*) J. Li, G. Schreckenbach, and T. Ziegler. J. Am. Chem. Soc. **117**, 486 (1995); (*d*) E. Folga and T. Ziegler. J. Am. Chem. Soc. **115**, 5150 (1993).
42. R. Poli. Chem. Rev. **96**, 2135 (1996).
43. (*a*) S. Kristyán and P. Pulay. Chem. Phys. Lett. **229**, 175 (1994); (*b*) T.C. Wright. J. Chem. Phys. **105**, 7579 (1996); (*c*) J.M. Pérez-Jordà and A.D. Becke. Chem. Phys. Lett. **233**, 134 (1995); (*d*) E. Ruiz, D.R. Salahub, and A. Vela. J. Phys. Chem. **100**, 12 265 (1996); (*e*) A. García, E.M. Cruz, C. Sarasola, and J.M. Ugalde. J. Phys. Chem. A, **101**, 3021 (1997).
44. (*a*) E. Vedejs and K.A.J. Snoble. J. Am. Chem. Soc **95**, 5778 (1973); (*b*) M. Nagayama, O. Okumura, S. Noda, and A. Mori. J. Chem. Soc. Chem. Commun. 841 (1973).
45. M. Torrent, L. Deng, M. Duran, M. Solà, and T. Ziegler. Organometallics, **16**, 13 (1997);
46. M. Torrent, L. Deng, and T. Ziegler. Inorg. Chem. **37**, 1307 (1998).
47. S. Dapprich, G. Ujaque, F. Maseras, A. Lledós, D.G. Musaev, and K. Morokuma. J. Am. Chem. Soc. **118**, 11 660 (1996).
48. A.J. DelMonte, J. Haller, K.N. Houk, K.B. Sharpless, D.A. Singleton, T. Strassner, and A.A. Thomas. J. Am. Chem. Soc **119**, 9907 (1997).
49. A. Rosa, A.W. Ehlers, E.J. Baerends, J.G. Snijders, and G. te Velde. J. Phys. Chem. **100**, 5690 (1996).
50. (*a*) K.P. Gable and T.N. Phan. J. Am. Chem. Soc. **115**, 3036 (1993); (*b*) J. Am. Chem. Soc. **116**, 833 (1994).
51. M.A. Pietsch, T.V. Russo, R.B. Murphy, R.L. Martin, and A.K. Rappé. Organometallics, **17**, 2716 (1998).
52. (*a*) T. Ziegler, J.G. Snijders, and E.J. Baerends. J. Chem. Phys. **74**, 1271 (1981); (*b*) G. Schreckenbach, J. Li, and T. Ziegler. Int. J. Quantum Chem. **56**, 477 (1995).
53. C. Limberg and R. Köppe. Inorg. Chem. **38**, 2106 (1999).

© 1999 NRC Canada

3-Deoxy-D-erythro-hexos-2-ulose bis(thiosemicarbazone) copper(II) chelate. Studies in solution and in the solid state

Sandra Signorella, Claudia Palopoli, Alejandro Frutos, Graciela Escandar, Tomoaki Tanase, and Luis F. Sala

Abstract: The 3-deoxy-D-erythro-hexos-2-ulose bis(thiosemicarbazone) (LH_2) acts as a tetradentate ligand with S_2N_2 donor sites to form a copper(II) chelate (Cu(II)L). The Cu K-edge X-ray absorption spectra analysis of a powdered sample revealed a square-planar S_2N_2 local coordination geometry with average Cu—N and Cu—S distances of 1.92 and 2.33 Å. The EXAFS and XANES spectra and the structural parameters of a DMF solution sample indicate the retention of the square-planar local structure of the Cu(II)S_2N_2 chromophore upon dissolution. Semiempirical PM3 calculations indicate that the structure of Cu(II)L with the copper(II) ion bound to the S_2N_2 donor set disposed in a square-planar geometry is the most favorable one (with the highest $|\Delta H_f|$). The formation constant (log K_f = 20.65 ± 0.06) of the neutral [CuL] species was calculated in 30% v/v dioxane–water and the protonation and deprotonation constants determined.

Key words: bis(thiosemicarbazone), copper(II), chelate, structure, stability constant.

Résumé : La bis(thiosemicarbazone) du 3-désoxy-D-érythro-hexos-2-ulose (LH_2) agit comme ligand tétradentate avec les sites donneurs S_2N_2 pour former un chélate du cuivre(II) [Cu(II)L]. Une analyse du spectre d'absorption des rayons X du Cu sur l'arête K d'un échantillon en poudre démontre que la géométrie de la coordination locale du S_2N_2 est de type plan carré avec des distances moyennes Cu—N et Cu—S de 1,92 et 2,33 Å. Les spectres « EXAFS » (de structure fine d'absorption étendue des rayons X) et XANES et les paramètres structuraux d'un échantillon en solution dans le DMF indiquent que le chromophore Cu(II)S_2N_2 conserve sa structure locale plan carré lors de sa dissolution. Des calculs semi-empiriques au niveau PM3 indiquent que la structure la plus favorable (avec la valeur la plus élevée du $|\Delta H_f|$) est celle du Cu(II)L lié au donneur S_2N_2 dans une disposition géométrique plan carré. On a calculé la constante de formation (log K_f = 20,65 ± 0,06) de l'espèce neutre [CuL] dans un mélange dioxane–eau à 30% v/v et on a déterminé les constantes de protonation et de déprotonation.

Mots clés : bis(thiosemicarbazone), cuivre(II), chélate, structure, constante de stabilité.

[Traduit par la Rédaction]

Introduction

We are interested in the coordination chemistry of sugar derivatives with the first row transition metal ions (1–7). The sugar derivative of specific concern here is a bis(thiosemicarbazone) derived from glucose and its copper(II) chelate. Transition metal complexes of thiosemicarbazones have been extensively studied (8, 9). Thiosemicarbazones exhibit a range of types of biological activity, and transition metal complexes of thiosemicarbazones, in some instances, have enhanced or modified activity in comparison to the uncomplexed ligands (8, 10). Compounds such as 3-deoxyaldos-2-uloses themselves may be involved in preparation having

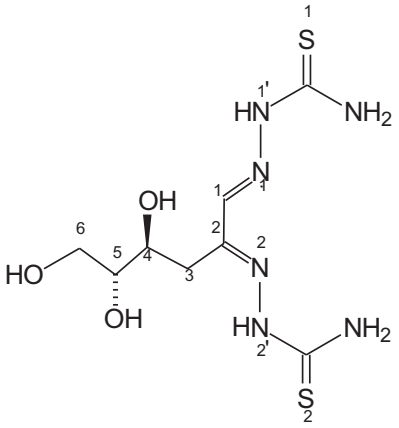

LH_2

Received March 8, 1999.

S. Signorella, C. Palopoli, A. Frutos, and L.F. Sala.[1] Departamento de Química Física, Facultad de Ciencias Bioquímicas y Farmacéuticas, Universidad Nacional de Rosario, Suipacha 531 (2000) Rosario, Argentina.
G. Escandar. Departamento de Química Analítica, Facultad de Ciencias Bioquímicas y Farmacéuticas, Universidad Nacional de Rosario, Suipacha 531 (2000) Rosario, Argentina.
T. Tanase. Faculty of Sciences, Nara Women's University, Nara 630, Japan.

[1]Author to whom correspondence may be addressed. Fax: 54-41-4350214. e-mail: inquibir@satlink.com

© 1999 NRC Canada

Table 1. Structural parameters derived from EXAFS analysis.

		N[b]		r, Å[c]		σ, Å		R, %	
Shell	A–B[a]	Powder	DMF	Powder	DMF	Powder	DMF	Powder	DMF
1st	Cu–N	1.3	2.1	1.92	1.96	0.068	0.079	6.91	3.23
	Cu–S	1.3	1.8	2.33	2.3	0.05	0.065		
2nd	Cu–C	6	5.3	2.97	3	0.078	0.073		

[a]A is absorber and B is back-scatter.

[b]Estimated errors are within ±1.

[c]Estimated errors are within ±0.03 Å for the 1st shell and ±0.04 Å for the 2nd shell.

carcinostatic activity (11), and Cu(II)–thiosemicarbazone complexes are among the most potent antiviral, antitumor, and antiinflammatory agents (8, 9).

Preliminary studies performed on the copper(II) chelate of 3-deoxy-D-erythro-hexos-2-ulose bis(thiosemicarbazone) (LH_2) have shown that it possesses in vivo antitumor activity in the murine L-1210 assay (12). The Cu(II)L chelate has been characterized in solution by spectroscopic methods (^{13}C NMR, EPR, UV-vis), but the reported spectroscopic data on the structure of this complex in the solid state are not conclusive (13). Besides, since the biological potential of this kind of complex might be related to the water solubility enhancement due to the presence of the monosaccharide moiety, the behavior of the complex in solution merits to be studied. We report here the structure of this copper(II) chelate in the solid state and the quantitative equilibrium data for the complex in solution.

Experimental section

Physical measurements

X-ray absorption measurements around Cu K-edge (8300–10 300 eV with 800 steps) were carried out at the Photon Factory of the National Laboratory for High Energy Physics on beam line 10B using synchrotron radiation (2.5 GeV, ~350 mA). The experiments were done at room temperature in transmission mode on a BN pellet of the sample by using Si(311) monochromator, details being already reported elsewhere (14).

The extended X-ray absorption spectrum (EXAFS) is derived from the absorption spectrum above the Cu K-edge (E_0 = 8983.39 eV) and is extracted by cubic spline method and Victreen's fit to give the raw EXAFS wave, $k^3\chi(k)$, where k is the photoelectron wave vector defined as $k = [(2m/\hbar^2)(E - E_0)]^{1/2}$. The $k^3\chi(k)$ oscillation (k = 4.50–16.15 Å^{-1}) is Fourier transformed into r-space to clear the contributions of back-scattering atoms, and the r-space ranging from 0.8 to 4.5 Å was back Fourier transformed to produce a Fourier filtered EXAFS oscillation, $k^3\chi(k)_{obsd}$, which was subject to the curve-fitting analysis by a three-terms model, $k^3\chi(k)_{calcd} = k^3\chi_N(k) + k^3\chi_S(k) + k^3\chi_C(k)$, on the basis of a single scattering theory (15). The back-scattering amplitude and the phase shift functions used were the theoretical parameters tabulated by MacKale et al. (16). Parameters, interatomic distance r_i, coordination number N_i, and the Debye–Waller factor σ_i, for each atom were varied in the nonlinear least-squares refined curve fitting. The least-squares fitting was converged at $R = [\Sigma (k^3\chi(k)_{obsd} - k^3\chi(k)_{calcd})^2 / \Sigma (k^3\chi(k)_{obsd})^2]^{1/2}$ = 0.069 (and 0.032 in dimethylformamide (DMF)) to give the structural parameters listed in Table 1. All calculations were performed with the systematic program REX (Rigaku Co. Ltd.) on a IBM PC Master P120.

Geometry optimizations were carried out with HYPERCHEM modeling software using a personal computer.[2] The geometry of the copper(II) complex was obtained from PM3 calculations.

Reagents and solvents used in quantitative determinations

A 0.0100 mol dm^{-3} stock solution of copper(II) ion was prepared from $Cu(NO_3)_2 \cdot 3H_2O$ (Riedel – de Haën) and its exact concentration was determined by titration with ethylenediaminetetraacetic acid using murexide as indicator (17). Solutions of NaOH in 30% dioxane – 70% water (v/v) were standardized with the use of Gran's plots (18). 1,4–Dioxane (p.a.) was obtained from Merck and was purified according standard methods. Deionized water was employed and doubly distilled under potassium permanganate.

Synthesis of the Cu(II)L complex

The complex was synthesized as previously described (12). Anal. calcd. for $CuC_8H_{14}N_6O_3S_2$: Cu 17.18, C 25.98, H 3.82, S 17.33, N 22.72; found: Cu 18.0 (determined by complexiometric titration), C 25.76, H 3.78, S 17.31, N 22.58.

Equilibrium constant determinations

Since the ligand and the cupric complex were not soluble in water, the determinations were carried out in mixtures of water with dioxane. A minimum value of 30% v/v dioxane–water was found to be adequate for those proposes. Both the deprotonation constants of the ligand and the complex deprotonation constants were evaluated through potentiometric techniques. Due to the fact that the complex found in acid media was fully formed below the lower limit at which the pH can be accurately determined in potentiometric titrations (ca. pH 2), its formation constant was spectrophotometrically determined in a separate experiment (19). All measurements were made at 20.0°C, I = 0.10 mol dm^{-3} ($NaNO_3$), and under nitrogen atmosphere.

The pH values were obtained with a Metrohm 713 pH meter fitted with a glass and reference electrodes. The electrode calibration was made with buffer solutions at 0.10 mol dm^{-3} ionic strength. The ligand was dissolved in the solvent medium both in the absence and presence of metal

[2]Hyperchem 5.02 for Windows. Hypercube Inc. 1997.

© 1999 NRC Canada

ion in order to obtain concentrations of 1×10^{-3} mol dm^{-3} in both metal ion and ligand. The potentiometric titrations were carried out by addition of NaOH prepared in 30% v/v dioxane–water, so that 40 or more experimental points were provided for each run. The pH range studied was 2–12. The effect of the solvent composition in the pH measurements was taken into account by correcting each meter reading with a conversion factor (20). This factor was obtained, prior to each experiment, by titration of 30% v/v dioxane–water solutions with standard NaOH solution in the same solvent mixture, at 20°C and I = 0.10 mol dm^{-3}. The water hydrolysis constant was found to be $10^{-14.6}$ for 30% v/v dioxane–water. There was no need of invoking cupric hydrolytic species in the present study. The potentiometric data were converted into equilibrium constant with the use of the program BEST (21*a*). All refinements showed a σ_{fit} <<0.02 (21*b*).

The absorption spectra were read on a Beckman DU640 spectrophotometer in 1.00 cm quartz microcells. Conformity to Beer's law in the concentration range used was verified prior to the determinations. The initial concentrations of LH_2 and Cu(II) ion in the 1:1 metal–ligand experimental solutions were 2×10^{-5} mol dm^{-3}. A typical spectrophotometric titration was previously described in the literature (22). Briefly, profiles of absorbances (at a selected wavelength) vs. pH were obtained according to the following procedure: small increments of a 30% v/v dioxane–water NaOH solution were added to the solution containing LH_2 and Cu(II) ion in the same solvent system. For each pH point (in the range 1.3–4) a known aliquot of solution was extracted, and the absorption spectrum was measured. The data processing for the computation of the equilibrium constants and the species distribution diagram were performed by use the EPSILON program (23).

Both potentiometric and spectrophotometric titrations were run in triplicate.

Results and discussion

To obtain direct structural parameters relevant to the copper centre, X-ray absorption spectroscopic analysis was performed on a powdered sample of the Cu(II)L complex. The XANES spectrum of the complex (Fig. 1) shows a characteristic feature of a square-planar coordinated copper(II) ion (24–27). The isotropic K-edge XANES spectra of many copper(II) complexes have a shoulder or partially resolved peak on the rising edge at ~8986 eV in addition to the $3d \leftarrow 1s$ pre-edge transition at ~8979 eV (28). Although it is not easy to assign all the peaks of the present spectrum in detail, the main peak can be assigned to the $4p \leftarrow 1s$ transition, and specially the partially resolved peak on the absorption edge at 8986 eV can be assigned to the $1s \rightarrow 4p_\pi$ transition accompanied by a shakedown process through ligand to metal copper (3*d* hole) charge transfer (l.m.c.t.), which enhances the screening of the core hole, resulting in lower transition energy (26, 29).

The radial structure function describing the local coordination about the copper ion is shown in Fig. 2. The Fourier transform of the raw EXAFS oscillation shows two intense peaks at about 1.6 and 2 Å and a moderate peak around 2.5 Å (before the phase-shift correction), which was back

Fig. 1. X-ray absorption near edge spectrum (XANES) (*A*) powder; (*B*) DMF solution.

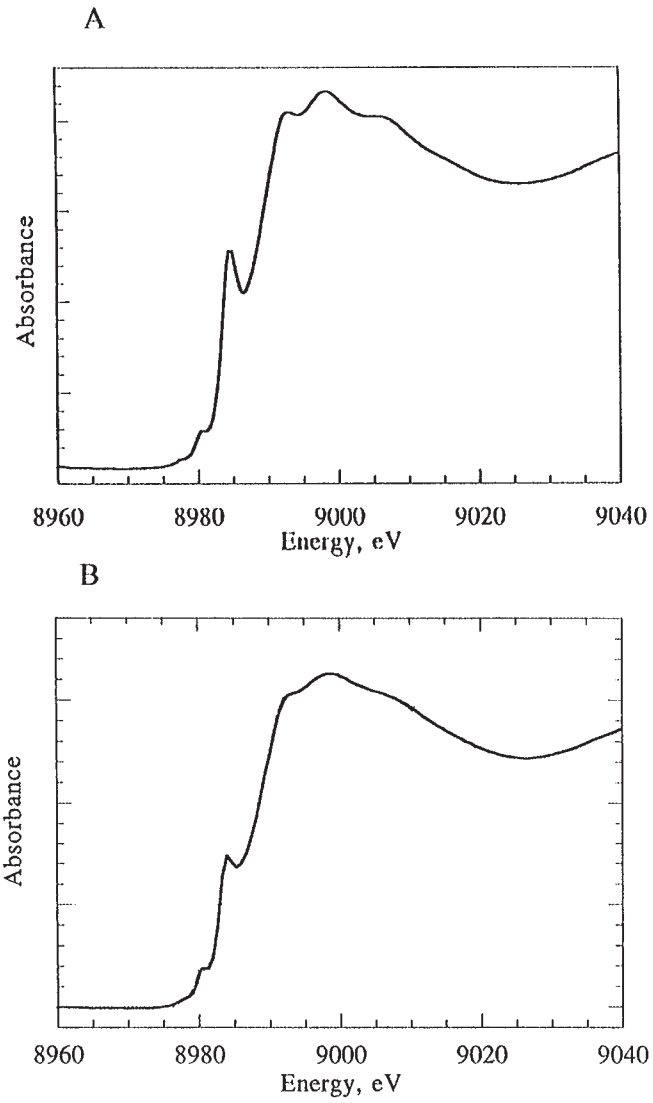

Fourier transformed by the use of an appropriate window to produce abstracted EXAFS oscillation subject to curve-fitting analysis (Fig. 3). The structural parameters from the three-terms curve-fitting technique (summarized in Table 1) indicate that the two large peaks attributable to nitrogen and sulfur atoms directly coordinate to the copper, and the third peak to the contribution of the carbon/nitrogen atoms in the chelation rings. These results support that the donor system (first coordination sphere) consists of N_2S_2 with average Cu—N and Cu—S distances of 1.92 and 2.33 Å, respectively, which is consistent with the feature of the XANES spectrum previously discussed and are similar to those observed by X-ray diffraction for S_2N_2 square-planar copper(II) complexes (30–33).

To verify if the square-planar geometry of the Cu(II)-S_2N_2 chromophore is retained upon dissolution, the X-ray absorption spectrum of a 0.1 M Cu(II)L DMF solution was measured (path length 5 mm) and analyzed by using the single scattering theory (Figs. 1–3 and Table 1). The EXAFS and

© 1999 NRC Canada

Fig. 2. Fourier transform of the raw EXAFS oscillation, $k^3\chi(k)$ (*A*) powder; (*B*) DMF solution.

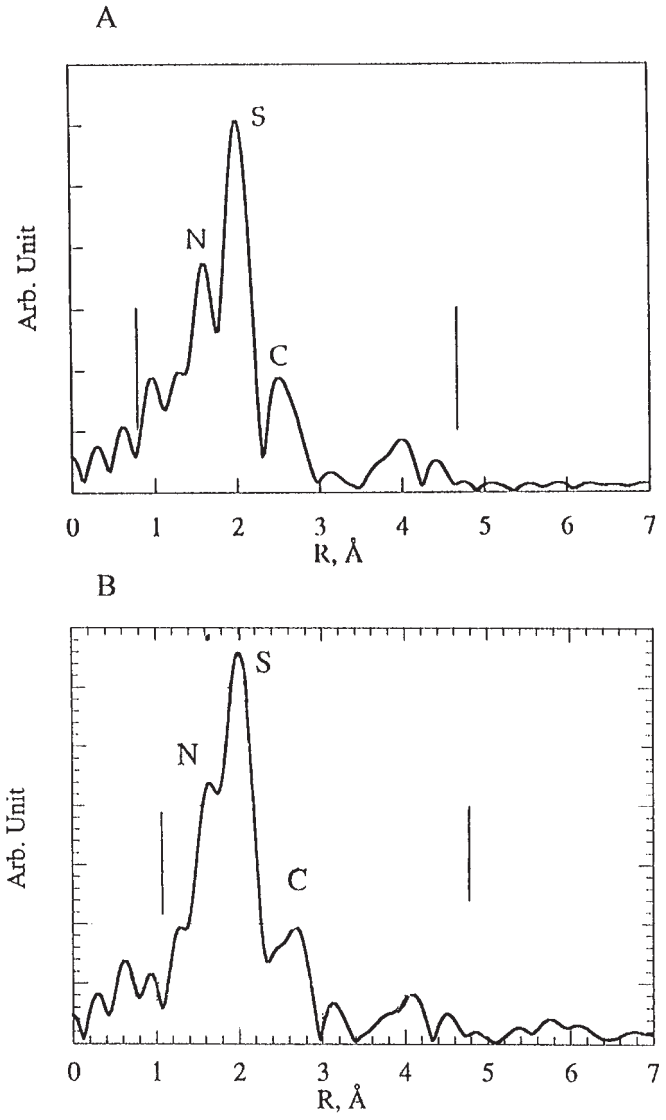

Fig. 3. Curve fitted data, $k^3\chi(k)_{calcd}$ (---), over the range of k = 4.5–16 Å^{-1}, to the Fourier filtered data, $k^3\chi(k)_{obsd}$ (—) (*A*) powder; (*B*) DMF solution.

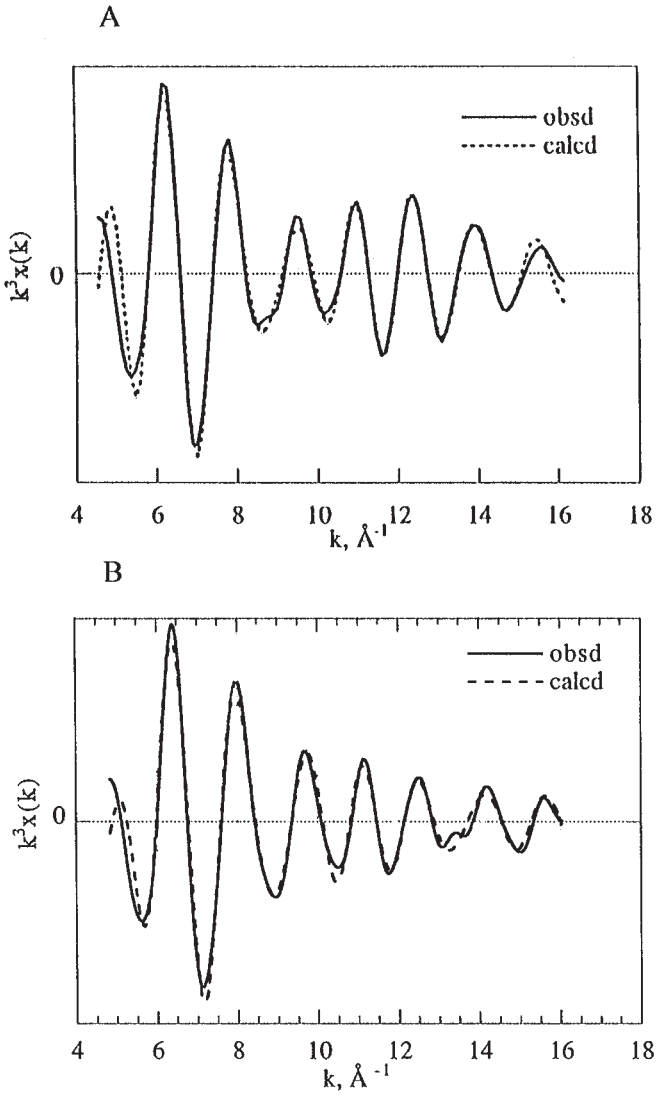

XANES spectra and the structural parameters of the solution sample are closely similar to those of the powdered sample, which strongly indicates that the Cu(II) centre retains the square-planar local structure in solution.

These results are in agreement with the energy minimization calculations for the complex. PM3 calculations were performed for several probable Cu(II)L linkage isomers, and the results indicate that **I** (Fig. 4) is the most favorable structure. The optimized geometry of **I** has a global minimum of –686.51 kJ mol^{-1} on the potential energy surface, and it corresponds to the isomer with the copper(II) ion bound to the S_2N_2 donor set disposed in a square-planar array, a structure stabilized through the formation of the three five-membered chelate rings. The calculated Cu—N and Cu—S distances are 1.88 and 2.12 Å, respectively, and the N^1CuN^2, S^1CuN^1, S^2CuN^2, S^1CuS^2 angles are around 86°, 88º, 88°, and 98°, respectively.

Fig. 4. Optimized geometry of Cu(II)L.

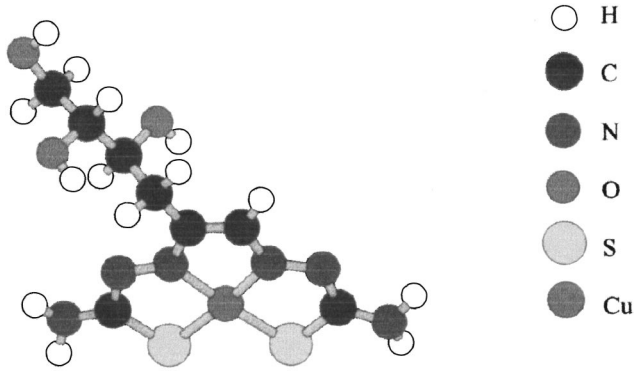

I

$\Delta H°_f$ = -686.51 kJ/mol

© 1999 NRC Canada

Fig. 5. Experimental pH values vs. a (where a = mol of base added per mol of ligand) for (*A*) LH_2 alone ($C_L = 1 \times 10^{-3}$ mol dm^{-3}); (*B*) Cu(II)–LH_2 system ($C_L = C_M = 1 \times 10^{-3}$ mol dm^{-3}). In both cases, solvent: 30% v/v dioxane–water, I = 0.10 mol dm^{-3}, t = 20.0°C.

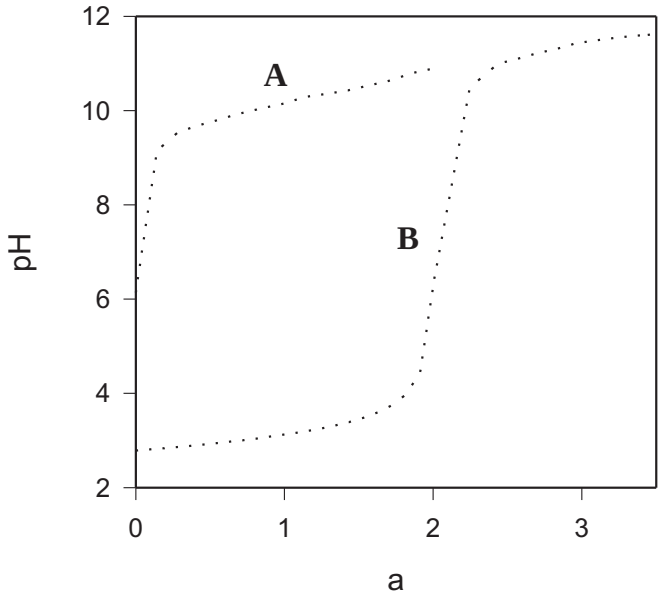

Table 2. Deprotonation constants of LH_2 and its cupric complex equilibrium constants in 30% v/v dioxane–water, I = 0.10 mol dm^{-3} ($NaNO_3$), t = 20.0°C.[a]

	log K	
Quotient	Potentiometry	Spectrophotometry
$[H][LH]/[LH_2]$	–10.11 ± 0.02	
$[H][L]/[LH]$	–10.23 ± 0.01	
$[CuL]/[Cu][L]$		20.65 ± 0.06
$[CuL][H]/[CuLH]$	–2.59 ± 0.02	
$[CuLH_{-1}][H]/[CuL]$	–11.85 ± 0.01	

[a]Charges are omitted. Standard deviations for the reported constants refer only to random errors and were calculated according to ref. 34.

Solution studies

Potentiometric measurements

Figure 5 shows the potentiometric curve of LH_2 in 30% v/v dioxane–water solution. The deprotonation constant values obtained from this curve are shown in Table 2.

Preliminary studies of the potentiometric profile for the Cu(II)– LH_2 system in purely aqueous solution showed the formation of a red precipitate in the pH range 2–11, which dissolved in highly alkaline media. In principle, the solid phase was attributed to a neutral complex formation, which dissolved at high pH to give a more deprotonated species. The potentiometric curve for the Cu(II)–LH_2 system in 30% v/v dioxane–water (Fig. 5) did not show any precipitation and was satisfactorily fitted by considering the species $[CuLH]^+$, [CuL], and $[CuLH_{-1}]^-$, in agreement with the observations in the exploratory experiments in aqueous solution. In the latter formulas, L represents the ligand in its deprotonated form, and H_{-n} indicates the protons released in the complex formation in addition to the two lost ligand protons. Since the free concentrations of the interacting species at the beginning of the titration are very low, only deprotonation complex constants could be determined from this experiment. Table 2 displays these constant values.

Fig. 6. Absorbance at different pH values of Cu(II)–LH_2 system in 30% v/v dioxane–water, initial $C_L = 2 \times 10^{-5}$ mol dm^{-3}, initial $C_M = 2 \times 10^{-5}$ mol dm^{-3}, I = 0.10 mol dm^{-3}, t = 20.0°C.

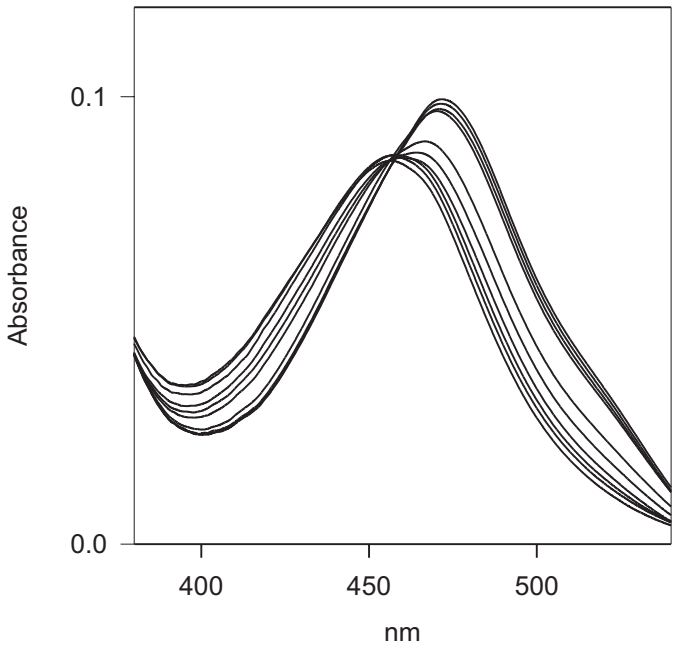

Spectrophotometric determinations

With the purpose of determining the formation constants for the cupric complexes, a more diluted Cu(II)–LH_2 system was spectrophotometrically evaluated at acid pH. Figure 6 displays the absorption spectra for the Cu(II)–LH_2 system at different pH values. As the pH is increased, the absorption maximum at 456 nm was slightly red-shifted with a concomitant increase in the absorption intensity. An isosbestic point was observed around 456 nm. All these facts were understood as indicative of a complex formation. Figure 7 shows the absorbance profile at λ = 470 nm vs. pH for the system under study. The best fit for this curve involved the formation of only the [CuL] species, and its equilibrium constant value is listed in Table 2.

Concluding remarks

Our X-ray absorption studies reveal that the Cu(II)L complex presents a square-planar S_2N_2 local coordination geometry in the solid state with retention of the metal centre geometry upon dissolution. The high stability of the neutral Cu(II)L complex in solution is revealed by the high formation constant measured spectrophotometrically in a 30% v/v dioxane–water mixture. The hydrophilicity conferred by the sugar moiety is not enough to avoid the precipitation of the complex in water in the 2–11 pH range, at least for the concentrations used in the potentiometric measurements.

© 1999 NRC Canada

Fig. 7. Experimental (●) and calculated (---) absorbance values at 470 nm vs. pH in the Cu(II)–LH_2 system in 30% v/v dioxane–water, initial $C_L = 2 \times 10^{-5}$ mol dm^{-3}, initial $C_M = 2 \times 10^{-5}$ mol dm^{-3}, $I = 0.10$ mol dm^{-3}, $t = 20.0$°C.

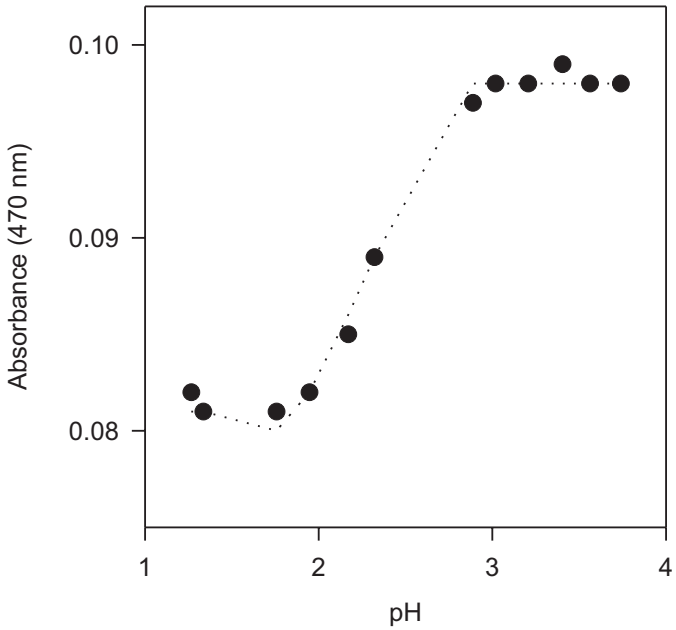

Acknowledgments

We thank the National Research Council of Argentina (CONICET), The Third World Academy of Sciences (TWAS), the National University of Rosario, Antorchas Foundation, and The International Foundation for Sciences (IFS) for financial support.

References

1. G.M. Escandar and L.F Sala. Can. J. Chem. **69**, 1994 (1991).
2. G.M. Escandar and L.F. Sala. Can. J. Chem. **70**, 2053 (1992).
3. G.M. Escandar, L.F. Sala, and M. González-Sierra. Polyhedron, **13**, 143 (1994).
4. G.M. Escandar, M. González-Sierra, J.M. Salas Peregrin, G. Labadié, M. Santoro, A. Frutos, and L.F. Sala. Polyhedron, **13**, 909 (1994).
5. G.M. Escandar, A.C. Olivieri, M. González-Sierra, and L.F. Sala. J. Chem. Soc. Dalton Trans. 1189 (1994).
6. G.M. Escandar, J.M. Salas Peregrin, M. González-Sierra, D. Martino, M. Santoro, A. Frutos, S.I. García, G. Labadié, and L.F. Sala. Polyhedron, **15**, 2251 (1994).
7. A. Frutos, G.M. Escandar, J.M. Salas Peregrin, M. González-Sierra, and L.F. Sala. Can. J. Chem. **75**, 405 (1997).
8. D.X. West, S.B. Padhye, and P.B. Sonawane. Structure and bonding 76. Springer Verlag, Heidelberg. 1991. p. 1.
9. D.X. West, A.E. Liberta, S.B. Padhye, R.C. Chikate, P.B. Sonawane, A.S. Kumbhar, and R.G. Yerande. Coord. Chem. Rev. **123**, 49 (1993).
10. G. Kanagaraj and G.N. Rao. Polyhedron, **12**, 383 (1993).
11. A. Szent-Gyorgyl, L. Egyud, and J. McLaughlin. Science (Washington, D.C.), **155**, 539 (1967).
12. D. Horton, R.G. Nickol, O. Varela. Carbohydr. Res. **168**, 295 (1987).
13. A. Diaz, I. García, R. Cao, H. Beraldo, M.M. Salberg, D.X. West, L. González, and E. Ochoa. Polyhedron, **16**, 3549 (1997).
14. Photon factory activity report. No. 3. National Laboratory for High Energy Physics, Ibaraki, Japan. 1986.
15. D.E. Sayers, E.A. Stern, and F.W. Lytle. Phys. Rev. Lett. **27**, 1204 (1971).
16. A.G. MacKale, B.W. Veal, A.P. Paulikas, S.K. Chan, and G.S. Knapp. J. Am. Chem. Soc. **110**, 3763 (1988).
17. G. Schwarzenbach. Complexometric titrations. Interscience, New York. 1960. p. 82.
18. F.J.C. Rossotti and H.J. Rossotti. J. Chem. Educ. **42**, 375 (1965).
19. E.T. Clarke and A.E. Martell. Inorg. Chim. Acta, **196**, 185 (1992).
20. L.G. Van Uitert and C.G. Haas. J. Am. Chem. Soc. **75**, 451 (1953).
21. (*a*) A.E. Martell and R.J. Motekaitis. The determination and use of stability constants. 2nd ed. VCH, New York. 1992. p. 143; (*b*) The determination and use of stability constants. 2nd ed. VCH, New York. 1992. p. 25.
22. G.A. Ibañez, A.C. Olivieri, and G.M. Escandar. J. Chem. Soc. Faraday Trans. **93**, 545 (1997).
23. C.L. Araujo, G.A. Ibañez, G.N. Ledesma, G.M. Escandar, and A.C. Olivieri. Comput. Chem. **22**, 161 (1998).
24. T.A. Smith, J.P. Penner-Hahn, M.A. Berding, S. Doniach, and K.O. Hodgson. J. Am. Chem Soc. **107**, 5945 (1985).
25. W. Wakita, T. Yamaguchi, N. Yoshida, and M. Fujiwara. Jpn. J. Appl. Phys. Suppl. **2 32**, 836 (1993).
26. J. Choy, D. Kim, S. Hwang, and J. Park. J. Am. Chem. Soc. **117**, 7556 (1995).
27. L. Kau, D. Spira-Solomon, J. Penner-Hahn, K. Hodgson, and E. Solomon. J. Am. Chem. Soc. **109**, 6433 (1987).
28. J.E. Hahn, R.A. Scott, K.O. Hodgson, S. Doniach, S.R. Desjardins, and E.I. Solomon. Chem. Phys. Lett. **88**, 595 (1982).
29. T. Yokoyama, N. Kosugi, and H. Kuroda. Chem. Phys. **103**, 101 (1986).
30. S.B. Padhye and G.B. Kauffman. Coord. Chem. Rev. **1**, 127 (1985).
31. G.W. Bushnell and A.Y.M. Tasang. Can. J. Chem. **57**, 603 (1979).
32. E.K. John, P.E. Fanwick, A.T. McKenzie, J.G. Stowell, and M.A. Green. Nucl. Med. Biol. **16**, 791 (1989).
33. A. Castineiras, E. Bermejo, D.X. West, A.K. El-Sawaf, and J.K. Swearingen. Polyhedron, **17**, 2751 (1998).
34. A.C. Olivieri and G.M. Escandar. Anal. Lett. **30**, 1967 (1997).

© 1999 NRC Canada

Electron self-exchange, oxidation, and reduction reactions of bis(2,9-dimethyl-4,7-diphenyl-1,10-phenanthroline)copper(II/I) and bis(6,6′-dimethyl-2,2′-bipyridine)copper(II/I) couples in acetonitrile: gated ET for the reduction, oxidation, and self-exchange processes

Nobuyoshi Koshino, Yoshio Kuchiyama, Shigenobu Funahashi, and Hideo D. Takagi

Abstract: The electron self-exchange rate constant for the $Cu(dmbp)_2^{2+/+}$ couple (dmbp = 6,6′-dimethyl-2,2′-bipyridine) was measured in acetonitrile by the NMR method (k_{ex} = 5.5 × 10^3 kg mol^{-1} s^{-1}, ΔH^* = 35.0 ± 0.3 kJ mol^{-1} and ΔS^* = –56 ± 1 J mol^{-1} K^{-1}). Reduction reactions of $Cu(bcp)_2^{2+}$ (bcp = 2,9-dimethyl-4,7-diphenyl-1,10-phenanthroline) and $Cu(dmbp)_2^{2+}$ with $Co(bipy)_3^{2+}$ (bipy = 2,2′-bipyridine) and ferrocene ($Fe(Cp)_2$ = bis(cyclopentadienyl)iron(II)), and oxidation reactions of $Cu(bcp)_2^{+}$ and $Cu(dmbp)_2^{+}$ by $Ni(tacn)_2^{3+}$ (tacn = 1,4,7-triazacyclononane) and $Mn(bipyO_2)_3^{3+}$ ($bipyO_2$ = *N*,*N*′-dioxo-2,2′-bipyridine) were also studied in acetonitrile. The electron self-exchange rate constants, k_{ex}, estimated for the $Cu(bcp)_2^{2+/+}$ and $Cu(dmbp)_2^{2+/+}$ couples from the oxidation reactions of $Cu(bcp)_2^{+}$ and $Cu(dmbp)_2^{+}$ by $Ni(tacn)_2^{3+}$ and $Mn(bipyO_2)_3^{3+}$ were consistent with the directly measured values by NMR, while k_{ex} estimated from the reduction reactions of $Cu(bcp)_2^{2+}$ and $Cu(dmbp)_2^{2+}$ by $Co(bipy)_3^{2+}$ ($[Cu(bcp)_2^{2+}]_0$, $[Cu(dmbp)_2^{2+}]_0$ >> $[Co(bipy)_3^{2+}]_0$) were 10^3 times smaller than those directly measured by the NMR method. The pseudo-first-order rate constant for the reduction reaction of $Cu(bcp)_2^{2+}$ and $Cu(dmbp)_2^{2+}$ by $Fe(Cp)_2$ was not linear against the concentration of excess amounts of $Fe(Cp)_2$. Analyses of the reactions revealed that the reductions of $Cu(bcp)_2^{2+}$ and $Cu(dmbp)_2^{2+}$ involve slow paths related to the deformation of $Cu(II)N_4$ center from tetragonal to tetrahedral coordination. The energetic preference for the deformation of Cu(II) species rather than that of Cu(I) was discussed on the basis of the ligand field activation energy (LFAE).

Key words: electron transfer, copper(II) and copper(I) complexes, gated behavior.

Résumé : Opérant dans l'acétonitrile et faisant appel à la RMN, on a mesuré la constante de vitesse d'auto-échange électronique du couple $Cu(dmbp)_2^{2+/+}$ (dmbp = 6,6′-diméthyl-2,2′-bipyridine) (k_{ex} = 5,5 × 10^3 kg mol^{-1} s^{-1}, ΔH^* = 35,0 ± 0,3 kJ mol^{-1} et. ΔS^* = –56 ± 1 J mol^{-1} K^{-1}). Opérant dans l'acétonitrile, on a aussi étudié les réactions de réduction du $Cu(bcp)_2^{2+}$ (bcp = 2,9-diméthyl-4,7-diphényl-1,10-phénanthroline) et du $Cu(dmbp)_2^{2+}$ par le $Co(bipy)_3^{2+}$ (bipy = 2,2′-bipyridine) et le ferrocène ($Fe(Cp)_2$ = bis(cyclopentadiényl)fer(II)) et les réactions d'oxydation du $Cu(bpc)_2^{+}$ et du $Cu(dmbp)_2^{+}$ par le $Ni(tacn)_2^{3+}$ (tacn = 1,4,7-triazacyclononane) et le $Mn(bipyO_2)_3^{3+}$ ($bipyO_2$ = *N*,*N*′-dioxo-2,2′-bipyridine). Les constantes de vitesse d'auto-échange électronique, k_{ex}, évaluées pour les couples $Cu(bcp)_2^{2+/+}$ et $Cu(dmbp)_2^{2+/+}$ à partir des réactions d'oxydation du $Cu(bcp)_2^{+}$ et du $Cu(dmbp)_2^{+}$ par $Ni(tacn)_2^{3+}$ et $Mn(bipyO_2)_3^{3+}$, sont en accord avec les valeurs mesurées directement par RMN; par ailleurs, les valeurs de k_{ex} évaluées à partir des réactions de réduction du $Cu(bcp)_2^{2+}$ et du $Cu(dmbp)_2^{2+}$ par le $Co(bipy)_3^{2+}$ ($[Cu(bipy)_2^{2+}]_0$, $[Cu(dmbp)_2^{2+}]_0$ >> $[Co(bipy)_3^{2+}]_0$) sont 10^3 fois plus faibles que celles mesurées directement par la méthode de RMN. La constante de vitesse de pseudo-ordre un pour la réaction de réduction du $Cu(bcp)_2^{2+}$ et du $Cu(dmbp)_2^{2+}$ par le $Fe(Cp)_2$ n'est pas linéaire par rapports à la concentration de quantités excédentaires de $Fe(Cp)_2$. L'analyse des réactions révèle que les réductions du $Cu(bcp)_2^{2+}$ et du $Cu(dmbp)_2^{2+}$ impliquent des voies lentes reliées à la déformation du centre $Cu(II)N_4$ d'une coordination tétragonale à tétraédrique. On fait appel à l'énergie d'activation du champ de ligand pour discuter de la préférence énergétique pour la déformation de l'espèce Cu(II) par rapport à celle de l'espèce Cu(I).

Received March 23, 1999.

N. Koshino,[1] Y. Kuchiyama, S. Funahashi, and H.D. Takagi.[1] Inorganic and Analytical Chemistry Division, Department of Chemistry and Physics, Graduate School of Sciences, Nagoya University, Furocho, Chikusa, Nagoya 464-8602, Japan.

[1]Authors to whom correspondence may be addressed. Telephone and fax: +81-52-789-5473. e-mail: NK: nkoshino@chem4.chem.nagoya-u.ac.jp; HDT: htakagi@chem4.chem.nagoya-u.ac.jp

© 1999 NRC Canada

Mots clés : transfert d'électron, complexes du cuivre(II) et cuivre(I), comportement intermittent.

[Traduit par la Rédaction]

Introduction

For ordinary outer-sphere electron transfer reactions, concerted inner- and outer-sphere reorganizations are assumed (1, 2). Therefore, the electron transfer reaction is slow for the reactions involving a large coordination geometry change during the course of the electron transfer process. Recent theoretical investigations by Hoffman and Ratner (3) and Brunschwig and Sutin (4) indicate that the "gated *intramolecular* process" with high-energy intermediates never competes with the direct outer-sphere process in the *normal* region. This indication, however, does not exclude the "gated electron transfer" phenomena postulated by Rorabacher et al. (5–9) in which large stereochemical changes take place *prior to* the ordinary outer-sphere electron transfer processes. Although such gated reactions cannot be treated as a simple outer-sphere process (i.e., the Ratner type cross relation has the possibility of failing to predict proper electron self-exchange rate constants for such reactions), the outer-sphere electron transfer reactions between the deformed species and the outer-sphere redox reagents may follow the norm of the Ratner type cross relation (10). Therefore, the classical "entatic state view," saying that the rate of the electron transfer is slow for the redox couple with large coordination geometry changes, seems still valid irrespective of the condition whether the reaction is gated or not (11, 12).

Results of the early works on the reactions of $Cu(bpy)_2^{2+/+}$, $Cu(phen)_2^{2+/+}$, and its derivative $Cu(dmp)_2^{2+/+}$ (13–15) indicated the gated ET, as the self-exchange rate constants for these redox couples estimated by the Marcus cross relation from the *forward* and *backward* reactions were inconsistent with each other. In 1983, Lee and Anson (16) pointed out that steric interconversion may have an important role in the electron transfer processes of the $Cu(bpy)_2^{2+/+}$ and $Cu(phen)_2^{2+/+}$ couples. The studies of electron transfer reactions for $Cu(dmp)_2^{2+/+}$ with various reaction partners in aqueous solution were also reported (17–22). However, ambiguities in the coordination structures of these ions as well as the low solubility of these ions in water made it difficult to analyze the reactions more precisely. The studies of the reduction of water-soluble $Cu(dpsmp)_2^{2-}$ (dpsmp = 2,9-dimethyl-4,7-bis((sulfonyloxy)phenyl)-1,10-phenanthroline) by Sykes and co-workers (23, 24) and Lappin and co-workers (25) indicated the involvement of such steric interconversion. There are some cases where electron exchange is extremely slow even for the near tetrahedral Cu(II/I) couples (26–28). Most recently, Stanbury and co-workers (29) reported a very slow electron exchange reaction of $Cu(bib)_2^{2+/+}$ (bib = 2,2′-bis(2-imidazoly)biphenyl). The estimated self-exchange rate constant of $Cu(bib)_2^{2+/+}$ is merely 0.16 kg mol^{-1} s^{-1}. Takagi and Swaddle (30, 31) have been studying Cu(II/I) electron self-exchange reactions by NMR where the coordination geometry of Cu(I) and Cu(II) are constrained to be similar, in which the kinetic behavior *was* expected to follow the context of the moderately fast electron transfer case, and no significant change in coordination number or coordination geometry *had been* expected in the electron transfer processes.

In the case of the gated ET reactions, a *slow* equilibrium corresponding to the deformation of one of the reactants precedes the outer-sphere ET process. For copper(II/I) couples, a tetragonal four or five coordination (D_{2d} symmetry) is expected for Cu(II), while tetrahedral geometry is expected for copper(I). When cyclic polythiaethers were used as ligands, Rorabacher et al. (5–9) showed that the oxidation reaction of Cu(I) is gated, which implies that the deformation of Cu(I) from tetrahedral to tetragonal conformation takes place prior to the ET process. In such a case, the principle of the microscopic reversibility requires that the deformation of Cu(II) is energetically less favored compared to that of Cu(I).

In this article, we examined electron transfer reactions of two $Cu(II/I)(N_2)_2$ couples and found that the electron transfer reactions for $Cu(bcp)_2^{2+/+}$ and $Cu(dmbp)_2^{2+/+}$ are gated. When the normal coordination geometry (slightly twisted structure from the ordinary tetragonal 4 or 5 coordination preferred by the Cu(II) species) is in equilibrium with the deformed tetrahedral state, the electron transfer processes involving the deformed tetrahedral Cu(II) may be much faster than those involving the ground state Cu(II). The energetic origin of the gated ET is discussed on the basis of the ligand field activation energies (LFAE) corresponding to the Cu(II) deformation. A possibility of the mixing of the *gated* and *direct* ET was also examined for the electron self-exchange processes of $Cu(bcp)_2^{2+/+}$ and $Cu(dmbp)_2^{2+/+}$ couples.[2]

Experimental section

Chemicals

Acetonitrile was obtained from Wako Pure Chemicals Inc. and purified by distillation from phosphorus pentoxide. The content of the residual water in thus purified acetonitrile was examined by a Mitsubishi Kasei CA01 Karl–Fisher apparatus by which the amount of residual water was determined to be less than 5 mmol kg^{-1}. Ferrocene (Wako) was purified by sublimation at ambient pressure. All other chemicals from Wako, Aldrich, and Fluka were used without further purification. Bis(2,9-dimethyl-4,7-diphenyl-1,10-phenanthroline)-copper(II) and -(I) perchlorate were synthesized by the reported method (32, 33). Anal. calcd. for $CuC_{52}H_{40}N_4Cl_2O_8$: C 63.5, N 5.70, H 4.10; found: C 63.8, N 5.62, H 4.18. Anal. calcd. for $CuC_{52}H_{40}N_4ClO_4$: C 70.7, N 6.34, H 4.56; found: C 71.0, N 6.42, H 4.52. Bis(6,6′-dimethyl-2,2′-bipyridine)-copper(II) and -(I) perchlorate were synthesized by the reported method (32, 33). Anal. calcd. for $CuC_{24}H_{24}N_4Cl_2O_8$: C 45.7, N 8.88; found: C 44.7, N 8.72. Anal. calcd. for $CuC_{24}H_{24}N_4ClO_4$: C 54.2, N 10.5, H 4.55; found: C 54.4, N 9.98, H 4.60.

$[Co(bipy)_3](ClO_4)_2$, $[Ni(tacn)_2](ClO_4)_3$, and $[Mn(bipyO_2)_3](ClO_4)_2$ were synthesized by the literature method (34–36). Anal. calcd. for $CoC_{30}H_{24}N_6Cl_2O_8$: C 49.6, H 3.33, N 11.6; found:

[2] Tables of rate constants (Tables SI to SV) have been deposited as supplementary material and may be purchased from: The Depository of Unpublished Data, Document Delivery, CISTI, National Research Council Canada, Ottawa, Canada, K1A 0S2.

© 1999 NRC Canada

Table 1. Electron self-exchange rate constants and activation parameters for the reactions of $Cu(bcp)_2^{2+/+}$ and $Cu(dmbp)_2^{2+/+}$ at 298 K in acetonitrile.[a]

Reaction	k_{12}/kg mol^{-1} s^{-1}	$k_{CuL_2^{2+/+}}$[b]/kg mol^{-1} s^{-1}	ΔH^*/kJ mol^{-1}	ΔS^*/J mol^{-1} K^{-1}
$Cu(bcp)_2^{2+}$ + $Cu(bcp)_2^{+}$	—	1.4×10^3	38.1 ± 2.4	–57 ± 8
$Cu(bcp)_2^{+}$ + $Ni(tacn)_2^{3+}$	5.20×10^5	2.0×10^3	21.9 ± 0.2	–61.9 ± 0.8
$Cu(bcp)_2^{2+}$ + $Co(bipy)_3^{2+}$	5.71×10^2	1.2	33 ± 2	–158 ± 0.6
$Cu(dmbp)_2^{2+}$ + $Cu(dmbp)_2^{+}$	—	5.5×10^3	35.0 ± 0.3	–56 ± 1
$Cu(dmbp)_2^{+}$ + $Ni(tacn)_2^{3+}$	9.3×10^4	6.7×10^2	24.9 ± 0.5	–66 ± 2
$Cu(dmbp)_2^{+}$ + $Mn(bipyO_2)_3^{3+}$	2.14×10^3	1.9×10^3	32 ± 1	–75 ± 4
$Cu(dmbp)_2^{2+}$ + $Co(bipy)_3^{2+}$	1.92×10^3	1.4	21.0 ± 0.4	–112 ± 1

[a]Ionic strength of the solutions was adjusted to 0.1 mol kg^{-1} by (n-Bu_4N)ClO_4 or (Et_4N)BF_4.
[b]Calculated by the redox potential (V vs. $Fc^{+/0}$), self-exchange rate constant (kg mol^{-1} s^{-1}), and ionic radii (pm): 0.275, 1.40×10^3[c], 760 for $Cu(bcp)_2^{2+/+}$; 0.346, 5.5×10^3, 650 for $Cu(dmbp)_2^{2+/+}$; 0.555, 6.0×10^3[d], 380 for $Ni(tacn)_2^{3+/2+}$; 0.435, 80[e], 400 for $Mn(bipyO_2)_3^{3+/2+}$; –0.081, 0.645[f], 700 for $Co(bipy)_3^{3+/2+}$.
[c]Reference 33.
[d]Reference 56.
[e]Reference 57.
[f]Reference 58.

Fig. 1. Dependence of k_{obs} on the concentration of $Cu(dmbp)_2^{2+}$ for the electron self-exchange reaction of $Cu(dmbp)_2^{2+/+}$. [$Cu(dmbp)_2^{+}$] = 7.90×10^{-2} mol kg^{-1}, I = 0.1 mol kg^{-1} (TBAP). The symbols represent the data obtained at 319.1 (◆), 313.1 (○), 308.5 (●), 302.9 (□), and 297.8 (■) K.

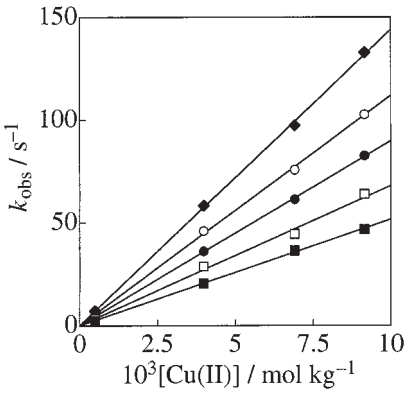

C 50.0, H 3.23, N 11.6. Anal. calcd. for $NiC_{12}H_{30}N_6Cl_3O_{12}$: C 23.42, H 4.91, N 13.66; found: C 23.42, H 4.96, N 13.55. Anal. calcd. for $MnC_{30}H_{24}N_6O_{14}Cl_2$: C 44.0, H 2.96, N 10.3; found: C 43.2, H 2.87, N 9.87. (*Caution: Perchlorate salts of metal complexes with organic ligands are potentially explosive.*)

General

All manipulations were carried out in an atmosphere of dry nitrogen to avoid any possible contamination by water and oxygen from the environment. Unisoku stopped-flow apparatus was used for the kinetic measurements at various temperatures controlled by a Hetofrig circulation bath. The reservoirs for the reactant solutions were kept under nitrogen atmosphere during the experiments. At least 10 kinetic traces were collected for each run, and the results were analyzed by an NEC personal computer fitted with an interface for the stopped-flow apparatus. Unisoku software was used for the data analyses. Under the conditions of [Cu(II)] << [L] (L = dmbp or bcp), no electroactive species other than $Cu(bcp)_2^{2+}$ or $Cu(dmbp)_2^{2+}$ was observed within the redox window of acetonitrile (–2 ~ +2 V) by cyclic voltammetry, which indicates that either $Cu(bcp)^{2+}$, $Cu(dmbp)^{2+}$, or Cu^{2+} produced by the decomposition of $Cu(bcp)_2^{2+}$ or $Cu(dmbp)_2^{2+}$ in solution does not oxidize ferrocene and $Co(bipy)_3^{2+}$ used in this study. The absorbance changes at 470 and 454 nm, corresponding to the absorption maxima of $Cu(bcp)_2^{+}$ and $Cu(dmbp)_2^{+}$, respectively, were monitored for the kinetic measurements.

Electrochemical measurements were carried out by a BAS 100BW electrochemical analyzer with a 1.5 mm ϕ platinum disk or glassy carbon disk as the working electrode, and a 0.5 mm ϕ platinum wire as the counter electrode. A silver/silver nitrate electrode with 0.1 mol kg^{-1} tetrabutylammonium perchlorate (TBAP) in acetonitrile was used as a reference electrode. A solution of $Mn(bipyO_2)_3^{3+}$ was prepared electrochemically in acetonitrile, containing 0.10 mol kg^{-1} TBAP at carbon electrode (Hokuto Denko HX-201). The NMR measurements were carried out by a Bruker AMX-400WB spectrometer.

Results

Electron self-exchange rate constant for $Cu(dmbp)_2^{2+/+}$

$$[1] \quad Cu(dmbp)_2^{2+} + {}^*Cu(dmbp)_2^{+} \xrightarrow{k_{ex}} Cu(dmbp)_2^{+} + {}^*Cu(dmbp)_2^{2+}$$

The electron self-exchange rate constant, k_{ex}, of the $Cu(dmbp)_2^{2+/+}$ couple was measured by monitoring the broadening of the methyl proton signal on diamagnetic $Cu(dmbp)_2^{+}$ by the addition of $Cu(dmbp)_2^{2+}$.

$$[2] \quad k_{obs} = \pi(\nu_{obs} - \nu_0) = k_{ex}[Cu(dmbp)_2^{2+}]$$

where ν_{obs} is the line width of the methyl proton signal at the half signal height in the presence of $Cu(dmbp)_2^{2+}$, while ν_0 is the line width at the half signal height in the absence of $Cu(dmbp)_2^{2+}$. The dependence of k_{obs} on the concentration of added $Cu(dmbp)_2^{2+}$ at constant ionic strength (0.10 mol kg^{-1} by TBAP) is shown in Fig. 1 at various temperatures. The estimated electron self-exchange rate constant at 298 K and the activation parameters are listed in Table 1.

© 1999 NRC Canada

Fig. 2. Dependence of k_{obs} on the concentration of $Ni(tacn)_2^{3+}$ for the oxidation reaction of $Cu(bcp)_2^{+}$. $[Cu(bcp)_2^{+}] = 1.50 \times 10^{-5}$ mol kg^{-1}, $I = 0.1$ mol kg^{-1} (TBAP). The symbols represent the data obtained at 303.0 (◆), 298.0 (○), 293.2 (●), 288.4 (□), and 283.2 (■) K.

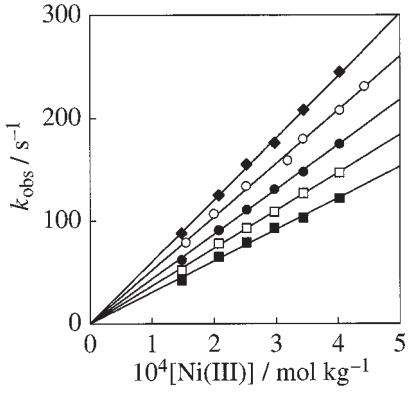

Fig. 3. Dependence of k_{obs} on the concentration of $Fe(Cp)_2$ for the reduction reaction of $Cu(bcp)_2^{2+}$. $[Cu(bcp)_2^{2+}] = 8.47 \times 10^{-6}$ mol kg^{-1}, $[bcp]_{free} = 1.01 \times 10^{-4}$ mol kg^{-1}, $I = 0.1$ mol kg^{-1} (TBAP). The symbols represent the data obtained at 308.2 (◇), 303.2 (◆), 298.2 (○), 293.2 (●), and 288.2 (□) K.

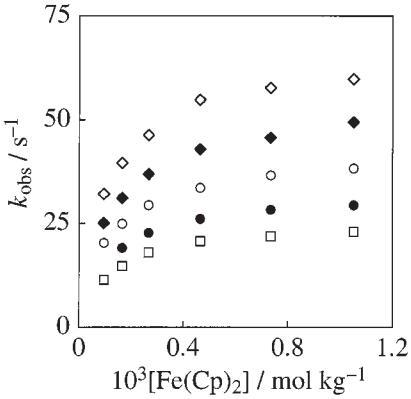

Oxidation reactions of $Cu(bcp)_2^{+}$ and $Cu(dmbp)_2^{+}$ by $Ni(tacn)_2^{3+}$ and $Mn(bipyO)_3^{3+}$

The reaction of $Cu(bcp)_2^{+}$ with $Ni(tacn)_2^{3+}$ in acetonitrile was first order for up to three half-lives and was described by eq. [3] under the pseudo-first-order conditions of $[Cu(bcp)_2^{+}]_0 << [Ni(tacn)_2^{3+}]_0$.

$$[3] \quad Cu(bcp)_2^{+} + Ni(tacn)_2^{3+} \xrightarrow{k_{12}} Cu(bcp)_2^{2+} + Ni(tacn)_2^{2+}$$

$$[4] \quad k_{obs} = k_{12}[Ni(tacn)_2^{3+}]_0$$

The dependence of k_{obs} on the concentration of $Ni(tacn)_2^{3+}$ at various temperatures is shown in Fig. 2 for the reaction of $Cu(bcp)_2^{+}$. The second-order rate constants thus estimated at 298 K, $I = 0.1$ mol kg^{-1} are listed in Table 1 for the reactions of $Cu(bcp)_2^{+}$ and $Cu(dmbp)_2^{+}$, together with the activation parameters of the reactions. The estimated electron self-exchange rate constants for the $Cu(bcp)_2^{2+/+}$ and $Cu(dmbp)_2^{2+/+}$ couples by the Marcus cross relation were 2.0×10^3 and 6.7×10^2 kg mol^{-1} s^{-1}, respectively, both of which were in fair agreement with the values (1.4×10^3 and 5.5×10^3 kg mol^{-1} s^{-1}, respectively) obtained from the NMR measurements (33) in view of the uncertainties inherent in the Marcus cross relation (37).

The oxidation reaction of $Cu(dmbp)_2^{+}$ by $Mn(bipyO)_3^{3+}$ was also carried out under the conditions of $[Cu(dmbp)_2^{+}]_0 >> [Mn(bipyO)_3^{3+}]_0$. The second-order rate constants as well as the activation parameters are also listed in Table 1. The electron self-exchange rate constants for $Cu(dmbp)_2^{2+/+}$ was estimated as 1.9×10^3 kg mol^{-1} s^{-1} by the Marcus cross relation.

Reduction reactions of $Cu(bcp)_2^{2+}$ and $Cu(dmbp)_2^{2+}$ by $Co(bipy)_3^{2+}$

The reactions were observed under the conditions of $[Cu(bcp)_2^{2+}]_0$, $[Cu(dmbp)_2^{2+}]_0 >> [Co(bipy)_3^{2+}]_0$. The kinetic traces were first order for up to three half lives. The dependence of the pseudo-first-order rate constant on the concentration of $Cu(bcp)_2^{2+}$ or $Cu(dmbp)_2^{2+}$ was linear at various temperatures. The second-order rate constants at 298 K and the corresponding activation parameters for these reactions are listed in Table 1. The application of the Marcus cross relation to these reactions yielded 1.2 and 1.4 kg mol^{-1} s^{-1}, respectively, as the electron self-exchange rate constant, which are some 10^3 times smaller than those directly estimated by the NMR method.

Reduction reaction of $Cu(bcp)_2^{2+}$ and $Cu(dmbp)_2^{2+}$ by $Fe(Cp)_2$

The kinetic traces were excellently first-order for Cu(II) up to three half lives.

$$[5] \quad -\frac{d[Cu(II)]}{dt} = k_{obs}[Cu(II)] \qquad [Fe(Cp)_2]_0 >> [Cu(II)]_0$$

However, the dependence of the pseudo-first-order rate constants on the concentration of $Fe(Cp)_2$ was not linear as shown in Fig. 3. The curvature in Fig. 3 may be explained by the following two-step mechanism involving a conformational change of Cu(II) *prior to* the fast electron transfer reaction (Path B in Scheme 1 proposed by Rorabacher et al. (5–9)).

$$[6] \quad Cu(II) \underset{k_{QO}}{\overset{k_{OQ}}{\rightleftharpoons}} Cu(II)^* \qquad Cu(II)^* + A_{Red} \xrightarrow{k_{B2}} Cu(I) + A_{Ox}$$

where Cu(II), Cu(II)*, A_{Red}, and A_{Ox} represent $Cu(bcp)_2^{2+}$ or $Cu(dmbp)_2^{2+}$ in the ground state, deformed $Cu(bcp)_2^{2+}$ or $Cu(dmbp)_2^{2+}$, $Fe(Cp)_2$ and $Fe(Cp)_2^{+}$, respectively. When the conformational change (k_{OQ}) is slower than the electron transfer process (k_{B2}), the pseudo-first-order rate constant is expressed by eq. [7] by using the terms in Scheme 1.

$$[7] \quad Rate = \frac{k_{B2}k_{OQ}}{k_{B2}[A_{Red}] + k_{QO}} [A_{Red}][Cu^{II}L]$$

© 1999 NRC Canada

Scheme 1.

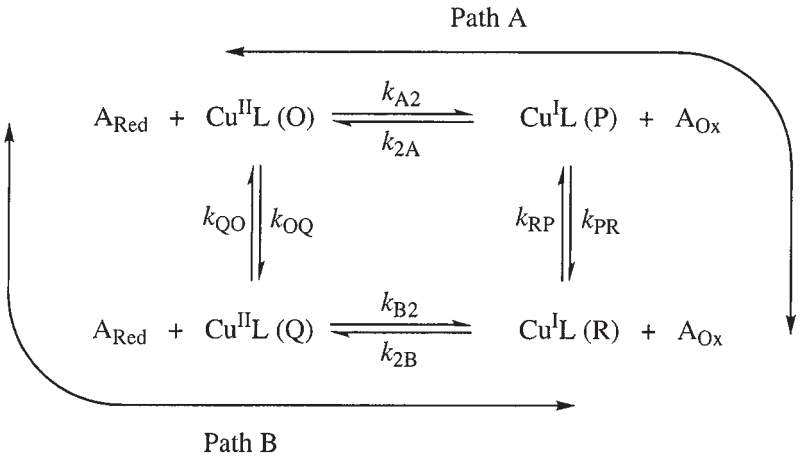

Table 2. Estimated rate constants for the reactions of $Cu(bcp)_2^{2+}$ and $Cu(dmbp)_2^{2+}$ at 298 K.[a]

Reaction			ΔH^{*b}	ΔS^{*c}
$Cu(bcp)_2^{2+}$ + $Fe(Cp)_2$	k_{OQ}	40 s^{-1}	32.0 ± 0.3	–107 ± 1
	k_{QO}	6.5×10^6 s^{-1}		
	$k_{OQ}/k_{QO} = K_{OQ}$	6.2×10^{-6}		
	k_{B2}[d]	6.6×10^{10} kg mol^{-1} s^{-1}		
$Cu(dmbp)_2^{2+}$ + $Fe(Cp)_2$	k_{OQ}	50 s^{-1}	30.5 ± 1.3	–110 ± 4
	k_{QO}	1.7×10^7 s^{-1}		
	$k_{OQ}/k_{QO} = K_{OQ}$	3.0×10^{-6}		
	k_{B2}[d]	9.1×10^{10} kg mol^{-1} s^{-1}		

[a]Ionic strength of the solutions was adjusted to 0.1 mol kg^{-1} by $(n\text{-}Bu_4N)ClO_4$.
[b]kJ mol^{-1}.
[c]J mol^{-1} K^{-1}.
[d]Using the estimated values of the electron self-exchange rate constant for $Cu(bcp)_2^{2+*/+}$ (3.8×10^{10} kg mol^{-1} s^{-1}) or $Cu(dmbp)_2^{2+*/+}$ (1.3×10^{10} kg mol^{-1} s^{-1}) and the self-exchange rate constant for $Fe(Cp)_2^{+/0}$ (9×10^6 dm^3 mol^{-1} s^{-1}). Ionic radii for $Fe(Cp)_2^{+/0}$ = 600 pm.

$$[8] \qquad k_{obs} = \frac{k_{OQ}k_{B2}}{k_{B2}[A_{Red}] + k_{QO}} \quad [A_{Red}]\,([A_{Red}] >> [Cu^{II}L])$$

Therefore, the plots of the reciprocal value of k_{obs} against $[A_{Red}]^{-1}$ should be linear with an intercept when $[A_{Red}]_0 >> [Cu^{II}L]_0$. Such plots are shown in Fig. 4.

$$[9] \qquad \frac{1}{k_{obs}} = \frac{k_{QO}}{k_{OQ}k_{B2}[A_{Red}]} + \frac{1}{k_{OQ}}$$

The values of the rate constant, k_{OQ}, and the corresponding activation parameters are also listed in Table 2. It is clear that the estimation of k_{QO} and K_{OQ} is possible once the k_{B2} value is known.

Fig. 4. Plots of k_{obs}^{-1} vs. $[Fe(Cp)_2]^{-1}$ for the reduction reaction of $Cu(bcp)_2^{2+}$ by $Fe(Cp)_2$. The symbols are the same in Fig. 3.

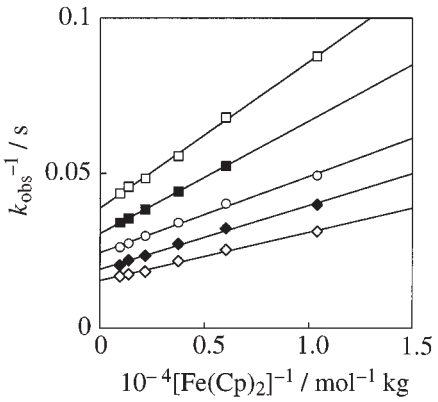

Discussion

General

Rorabacher et al. (5–9) explained the "gated" electron transfer for copper – cyclic thioether ions using the mechanism described by Scheme 1. The reactions proceeded mostly through Path A for the copper–thioether complexes by comparing the electron self-exchange rate constants estimated from both the reduction and oxidation cross reactions.

In this study, the electron self-exchange rate constants for the $Cu(bcp)_2^{2+/+}$ and $Cu(dmbp)_2^{2+/+}$ couples were estimated from both the oxidation and reduction reactions by using the Marcus cross relation, which were then compared with the values measured directly by the NMR method. The estimated self-exchange rate constants from the cross reactions were 2.0×10^3 and $(0.67–1.9) \times 10^3$ kg mol^{-1} s^{-1} from the oxidation reactions of $Cu(bcp)_2^{+}$ and $Cu(dmbp)_2^{+}$, respectively, while the estimated self-exchange rate constants from the reduction cross reactions were merely 1.2 and 1.4 kg mol^{-1} s^{-1}. As the electron self-exchange rate constants mea-

© 1999 NRC Canada

Table 3. Absorption band maxima for $Cu(bcp)_2(ClO_4)_2$ and $Cu(dmbp)_2(ClO_4)_2$ observed by the diffuse reflectance spectrophotometry.[a]

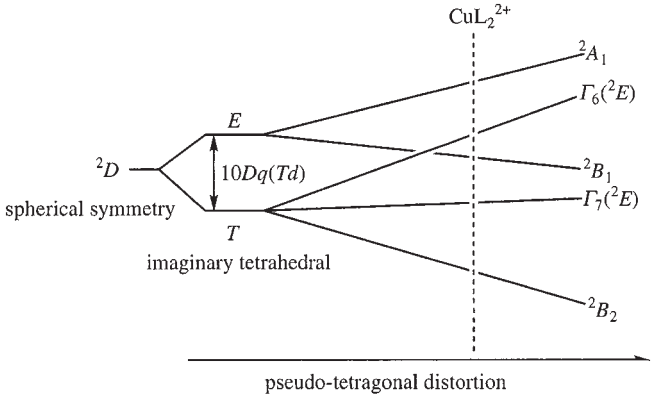

Assignment	$Cu(bcp)_2(ClO_4)_2$[b]	$Cu(dmbp)_2(ClO_4)_2$[b]
Charge transfer	23697	27027
$^2B_2 \rightarrow {}^2A_1$	14064	13698
$^2B_2 \rightarrow \Gamma_6(^2E)$	9891 (broad)	9900 (broad)
$^2B_2 \rightarrow {}^2B_1$	8658 (shoulder)	8620 (shoulder)
$^2B_2 \rightarrow \Gamma_7(^2E)$	5984	6042

[a]The 10*Dq* value for the imaginary tetrahedral field was estimated as 6.4×10^3 cm^{-1} for $Cu(bcp)_2^{2+}$ and 6.2×10^3 cm^{-1} for $Cu(dmbp)_2^{2+}$ from the difference between the average value of the $^2B_2 \rightarrow {}^2B_1$ and $^2B_2 \rightarrow {}^2A_1$ transition and the average value of the energy levels of $^2B_2$, $\Gamma_7(^2E)$, and $\Gamma_6(^2E)$ (see text).

[b]Band maximum/cm^{-1}.

sured by the NMR method are 1.4×10^3 and 5.5×10^3 kg mol^{-1} s^{-1} for the $Cu(bcp)_2^{2+/+}$ and $Cu(dmbp)_2^{2+/+}$ couples, respectively, the reactions involving the $Cu(bcp)_2^{2+/+}$ and $Cu(dmbp)_2^{2+/+}$ couples may also be gated, and the preferred pathway for the redox reactions of these couples seems Path B in Scheme 1, rather than Path A observed for the reactions of copper – macrocyclic thioether complexes.

According to Scheme 1, Rorabacher and co-workers (5, 6) derived rate laws for oxidation and reduction reactions corresponding to Path A and Path B as follows, by assuming steady state for the concentrations of the intermediates, $Cu^{II}L(Q)$ and $Cu^{I}L(P)$.

Reduction reaction:

$$[10] \quad -\frac{d[Cu^{II}L]}{dt} = \left(\frac{k_{A2}k_{PR}}{k_{2A}[A_{Ox}] + k_{PR}} + \frac{k_{B2}k_{OQ}}{k_{B2}[A_{Red}] + k_{QO}} \right) [Cu^{II}L(O)][A_{Red}]$$

Oxidation reaction:

$$[11] \quad -\frac{d[Cu^{I}L]}{dt} = \left(\frac{k_{2A}k_{RP}}{k_{2A}[A_{Ox}] + k_{PR}} + \frac{k_{2B}k_{QO}}{k_{B2}[A_{Red}] + k_{QO}} \right) [Cu^{I}L(R)][A_{Ox}]$$

$Cu^{II}L(O)$ and $Cu^{I}L(R)$ represent the Cu(II) and Cu(I) species in the ground state: i.e., $Cu^{II}L(O) = Cu(bcp)_2^{2+}$ or $Cu(dmbp)_2^{2+}$ in the D_{2d} symmetry, and $Cu^{I}L(R) = Cu(bcp)_2^{+}$ or $Cu(dmbp)_2^{+}$ in the T_d symmetry. As the reduction reactions of $Cu(bcp)_2^{2+}$ and $Cu(dmbp)_2^{2+}$ take place through Path B, the rate law is expressed by eq. [7]. When $k_{B2}[A_{Red}] << k_{QO}$, eq. [7] is reduced to eq. [12], and the dependence of the pseudo-first-order rate constant on the concentration of $Cu^{II}L$ becomes linear as seen for the reduction reactions of $Cu(bcp)_2^{2+}$ or $Cu(dmbp)_2^{2+}$ by $Co(bipy)_3^{2+}$.

$$[12] \quad k_{obs} = \frac{k_{OQ}k_{B2}}{k_{QO}}[Cu^{II}L] \qquad ([A_{Red}]_0 << [Cu^{II}L]_0)$$

On the other hand, when $[A_{Red}] >> [Cu^{II}L]$, the dependence of k_{obs} on $[A_{Red}]_0$ deviates from a straight line as seen in Fig. 3. The slopes of the plots in Fig. 4 are given by $k_{QO}/k_{B2}k_{OQ}$ $(= 1/K_{OQ}k_{B2})$.

As the theoretical investigation for intramolecular ET reactions by Brunschwig and Sutin (4) suggests that no reaction path with high-λ intermediate compete with the direct electron transfer in the *normal* region, the kinetic results obtained in this study strongly indicate the *intermolecular* gated electron transfer after a conformational change.

With a d^9 configuration, Cu(II) ion prefers tetragonal structure in general. In the case of $Cu(bcp)_2^{2+}$, it has been reported that the ground state structure is already largely distorted from the normal tetragonal structure, and the dihedral angle between the two phenanthroline planes is close to 60° (33), while the dihedral angle for $Cu(dmbp)_2^{2+}$ is merely 35° from the ESR measurements (33).[3] However, the similar values of the electron self-exchange rate constants for the $Cu(bcp)_2^{2+/+}$ and $Cu(dmbp)_2^{2+/+}$ couples indicate that either the coordination geometry or the ligand field in $Cu(bcp)_2^{2+}$ and $Cu(dmbp)_2^{2+}$ is similar to each other. The similarity of the absorption spectra of these ions (Table 3) also indicates that the ligand fields by the bcp and dmbp ligands are similar to each other. From the crystal structures, these Cu(II) species may be the five coordination in solution (39, 40). However, the water exchange rate constant of five coordinated Cu(II)-2,2′,2″-triaminotriethylamine complex is 2×10^5 s^{-1} (41), which is much larger than the conformational change process, k_{OQ}. Therefore, such a fast solvent exchange for the fifth coordinated solvent molecule on Cu(II) may not affect the very slow conformational change from $Cu^{II}L(O)$ to $Cu^{II}L(Q)$.

The crystal structures of the Cu(I) species have been reported: the dihedral angles between the two ligands for $Cu(bcp)_2^{+}$ and $Cu(dmbp)_2^{+}$ are 87.5° and 80.9°, respectively (32, 42). By considering the flexibility along the C—C bond

[3]ESR parameters, $g_{//}$ and $A_{//}$, were estimated for $Cu(dmbp)_2^{2+}$ as 2.22 and 127 G, respectively, in glassy methanol at 77 K in this study. According to the relation of the dihedral angle and $g_{//}$ postulated by Yokoi and Addison (38), an apparent dihedral angle was estimated as 35°. However, the flexible bipyridine ligands such as dmbp may not follow the norm postulated by Yokoi and Addison.

© 1999 NRC Canada

of the dmbp ligand, the coordination structures of Cu(I) species examined in this study may be considered to be close to T_d in solution, as the strong preference of the tetrahedral structure by Cu(I) is well established (43).

It is possible to estimate the energy difference (LFAE) between the tetragonal $Cu^{II}L(O)$ ground state and the hypothetical tetrahedral $Cu^{II}L(Q)$ state, by calculating the 10*Dq* value corresponding to the hypothetical tetrahedral conformation of $Cu^{II}L(Q)$ ($4\Delta_o/9$) from the diffuse reflectance spectra of $Cu(bcp)_2(ClO_4)_2$ and $Cu(dmbp)_2(ClO_4)_2$ species (44). The absorption band maxima were observed as shown in Table 3. As the distortion from the ordinary tetragonal structure lifts the degeneracy of all *d* orbitals (45, 46), four major absorptions corresponding to $^2B_2 \rightarrow {}^2\Gamma_7(^2E)$, $^2B_2 \rightarrow {}^2B_1$, $^2B_2 \rightarrow {}^2\Gamma_6(^2E)$, $^2B_2 \rightarrow {}^2A_1$ should appear in the visible and near IR regions (the notation for the D_{2d} symmetry is used). The observed band maxima were assigned to these transitions. Following the method of Gouge et al. (45), the 10*Dq* values for the hypothetically tetrahedral $Cu(bcp)_2^{2+*}$ and $Cu(dmbp)_2^{2+*}$ (= $Cu^{II}L(Q)$) were estimated as shown in Table 3. It is assumed that the original energy level for the spherically symmetrical CuN_4 geometry lies close to the difference in the weighted mean energy levels of *T* and *E* terms.[4] By using the 10*Dq* values of hypothetical $Cu^{II}L(Q)$, the ligand field stabilization energies (LFSE) for the imaginary tetrahedral geometry and the ground state geometry of d^9 $Cu(bcp)_2^{2+}$ were calculated as –2560 and –7720 cm^{-1} relative to the energy of the spherically symmetric CuN_4^{2+} (–2500 and –7650 cm^{-1} were calculated for $Cu(dmbp)_2^{2+}$). The largely distorted tetragonal structures of $Cu(bcp)_2^{2+}$ and $Cu(dmbp)_2^{2+}$ in the ground state are, therefore, still ca. 62 kJ mol^{-1} more stabilized compared with perfectly tetrahedral geometry for both of the bcp and dmbp complexes, and this value may be taken as the upper limit of the free energy difference between $Cu(bcp)_2^{2+}$ or $Cu(dmbp)_2^{2+}$ (= $Cu^{II}L(O)$) in the ground state and hypothetical $Cu(bcp)_2^{2+*}$ or $Cu(dmbp)_2^{2+*}$ (= $Cu^{II}L(Q)$) in the tetrahedral configuration. It should be noted that the LFAE calculation above does not include the entropic contribution to the free energy.

As it is clear that the reduction reactions of $Cu^{II}L(O)$ (= $Cu(bcp)_2^{2+}$ and $Cu(dmbp)_2^{2+}$ complexes) take place through Path B in Scheme 1, microscopic reversibility requires that the oxidation reaction of $Cu^{I}L(R)$ should also take place through Path B. Therefore, $Cu^{I}L(P)$ is necessarily less stable than $Cu^{II}L(Q)$. Cu(I) with d^{10} electronic configuration is well known to be stabilized as its tetrahedral form. The less stability of $Cu^{I}L(P)$ (distorted tetragonal form) may, therefore, be attributed to the nature of Cu(I) with a strong thermodynamic preference to form the tetrahedral geometry. Such tendency is explained by the possible hybridization of the 3*d*, 4*s*, and 4*p* orbitals and by the covalent character of the bonding. The tetrahedral $Cu(I)(N_2)_2$ is some 100 kJ mol^{-1} more stable than the hydrated Cu(I) ions, from the stability constant of Cu(I) species.[5] Therefore, the deformation of Cu(II) species seems preferred compared with the deformation of Cu(I) for the cases of $Cu(N_2)_2^{2+/+}$ couples. The preference of Path A in the case of Cu – macrocyclic thioether complexes (5–9) may be attributed to the less stable structures of $Cu^{I}L(R)$ species in solution: water or solvent coordination to the fourth position of Cu(I) is suggested for the [12]aneS$_4$, [13]aneS$_4$, [14]aneS$_4$ complexes, while corresponding Cu(II) complexes hold relatively planar coordination geometry suitable for the stabilization of $Cu^{II}L(O)$.

Estimation of K_{OQ} and k_{B2}

The value of the k_{B2} process depends on the nature of the reaction partner, as this process includes the effect of the inner-sphere free energy change and the redox potential of the reductant. However, k_{B2} may be very fast: the deformation of $Cu(bcp)_2^{2+}$ to $Cu(bcp)_2^{2+*}$ raises the redox potential of the $Cu(bcp)_2^{2+*}/Cu(bcp)_2^{+}$ couple as much as the structural deformation of $Cu(bcp)_2^{2+}$ to $Cu(bcp)_2^{2+*}$ before the electron transfer process, and the electron transfer (k_{B2}) with minimal internal rearrangement for Cu(II) species must be very fast. The rise of the redox potential, which is equivalent to the LFAE, is estimated by using the Nernst equation.

$$[13] \quad E^\circ_{Cu^{2+*/+}} = E^\circ_{Cu^{2+/+}} - \frac{RT}{F} \ln K_{OQ}$$

where $E^\circ_{Cu^{2+*/+}}$, $E^\circ_{Cu^{2+/+}}$, and *F* are the standard redox potentials of the $Cu(bcp)_2^{2+*/+}$ and $Cu(bcp)_2^{2+/+}$ couples and the Faraday constant, respectively. In this study, we obtained 0.275 V as $E^\circ_{Cu^{2+/+}}$ with reference to ferricinium/ferrocene couple. As the value of K_{OQ} (= k_{OQ}/k_{QO}) is expected to be small (no significant spectral change corresponding to the existence of such intermediate was observed throughout the study), $E^\circ_{Cu^{2+*/+}}$ may be large.

To the outer-sphere electron transfer reaction corresponding to the k_{B2} process, the Marcus cross relation is applicable. Coulombic work terms may be ignored for the reactions of $Cu(bcp)_2^{2+*}$ with ferrocene (29, 37).

$$[14] \quad k_{B2} = \sqrt{k_{Cu^{2+*/+}} k_{Fe^{+/0}} K_{Cu^{2+*}/Fe} f W}$$

$$[15] \quad \ln f = \frac{[\ln K_{Cu^{2+*}/Fe} + (w_{Cu^{2+*}/Fe} - w_{Cu^{+}/Fe^{+}})/RT]^2}{4[\ln (k_{Cu^{2+*/+}} k_{Fe^{+/0}} / Z^2) + (w_{Cu^{2+*/+}} + w_{Fe^{+/0}})/RT]}$$

$$[16] \quad W = \exp\left(\frac{-(w_{Cu^{2+*}/Fe} + w_{Cu^{+}/Fe^{+}} - w_{Cu^{2+*/+}} - w_{Fe^{+/0}})}{2RT}\right)$$

$$[17] \quad w_{ij} = \frac{37.9 z_i z_j}{a(1 + 0.481 a\sqrt{\mu})} \quad (\text{kJ mol}^{-1})$$

where *a*, *z*, and μ are the interatomic distances (Å) between the reacting species, charge on complex ions, and the ionic

[4] The octahedral 10*Dq* value for $Cu(en)_3^{2+}$ was reported as 1.64×10^4 cm^{-1} by Orgel (47). The 4/9 of this value, 7.2×10^3 cm^{-1}, may be taken as the 10*Dq* for the tetrahedral coordination. Therefore, the values of 6.4×10^3 and 6.2×10^3 cm^{-1} obtained here seem reasonable as hypothetical 10*Dq* for the bcp and dmbp complexes.

[5] The stability constant for $Cu(dmp)_2^{+}$ (dmp = 2,9-dimethyl-1,10-phenanthroline) is reported as $10^{19.1}$ in water (48). With a naive assumption that the chemical potential of the distorted tetragonal form of Cu(I) is close to that for solvated Cu(I), the free energy difference between the solvated Cu_{aq}^{+} and $Cu(dmp)_2^{+}$ in water is estimated as 109 kJ mol^{-1} at 298 K. This value may be regarded as the upper limit for the energy difference between $Cu^{I}L(R)$ and $Cu^{I}L(P)$.

© 1999 NRC Canada

Scheme 2.

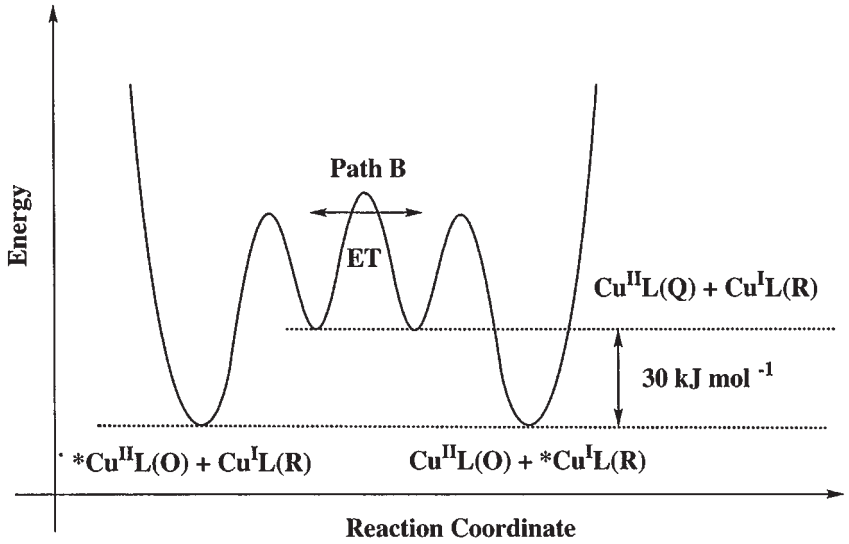

strength of the solution, respectively. By using the slope of the plot in Fig. 4, eq. [14] is rearranged to eq. [18].

$$[18] \quad k_{B2} = 4.6\times10^4\, k_{Cu^{2+*/+}} k_{Fe^{+/0}}\, Sf$$

where S denotes the slope obtained from the plot in Fig. 4, and 4.6×10^4 represents the equilibrium constant for the overall reaction of $Cu(bcp)_2^{2+}$ with ferrocene ($\Delta E° = 0.275$ V).

The value of $k_{Cu^{2+*/+}}$ may be estimated as the limiting electron transfer rate constant by using Marcus theory (1), assuming this process is essentially controlled by the outer-sphere reorganization free energy and the electrostatic terms: 12 kJ mol^{-1} for ΔG^*_{os} and 0.5 kJ mol^{-1} for $\Delta G^*_{coul} + \Delta G^*_{DH}$, respectively, by setting the ionic radii of both $Cu(bcp)_2^{2+/+}$ to 760 pm in acetonitrile at 298 K (33). Using the value of ΔG^*_{os}, $k_{Cu^{2+*/+}}$ can be calculated as 3.8×10^{10} kg mol^{-1} s^{-1}. This result was obtained under the assumption that the reactions (each self-exchange reaction and the cross reaction) are adiabatic with the transmission coefficient, κ, is unity. As the driving force of the cross reaction is very large, the f factor in the Marcus cross relation becomes significantly smaller than 1. As a result, the calculated self-exchange rate constant for the $Cu^{2+*/+}$ couple becomes very large. Therefore, the value of 3.8×10^{10} kg mol^{-1} s^{-1} estimated here indicates that the electron self-exchange rate constant for the $Cu^{2+*/+}$ couple is taken to be close to the diffusion limit in acetonitrile. A similar explanation is possible for the value of k_{B2} estimated below. With 3.8×10^{10} kg mol^{-1} s^{-1} thus estimated for $k_{Cu^{2+*/+}}$, a value of 6.6×10^{10} kg mol^{-1} s^{-1} was obtained for k_{B2} by using the reported value of $k_{Fe^{+/0}}$, the electron self-exchange rate constant for the ferricinium/ferrocene couple (49). Therefore, $K_{OQ} = 6.2 \times 10^{-6}$, and $k_{QO} = 6.5 \times 10^6$ s^{-1}. The free energy difference between $Cu(bcp)_2^{2+}$ and $Cu(bcp)_2^{2+*}$ is ca. 31 kJ mol^{-1}, which is rather small compared with the estimated value, 62 kJ mol^{-1} from the LFAE calculation. These results indicate that the structure of $Cu^{II}L(Q)$ is either not perfectly tetrahedral as assumed for the above LFAE calculation, or the contribution of the entropy or the steric repulsion between four methyl groups on the ligands to the free energy is close to 31 kJ mol^{-1}. Similar results were obtained for the reaction of $Cu(dmbp)_2^{2+}$ with ferrocene. The kinetic parameters estimated for the reactions of $Cu(bcp)_2^{2+}$ and $Cu(dmbp)_2^{2+}$ are summarized in Table 2. The large negative activation entropies for the k_{OQ} process may be explained by the similar effect observed for several racemization reactions through the "twist" mechanism (50). The estimated pre-equilibrium constant for Path A (K_{RP}) by Villeneuve et al. (51) is in the order of 1×10^{-3} to 1×10^{-6} for Cu^+ – macrocyclic polythiaether complex. The value for K_{OQ} estimated in this study for CuN_4^{2+} ($\approx 10^{-6}$) is close to the lowest limit of the estimated value for Cu^+ – macrocyclic polythiaether complexes, which indicates that the deformation in the Cu(I)-S species is the more preferable to that in the Cu(II)-S species (intermediate P is the more stable compared with Q).

Apparent electron self-exchange rate constant directly measured by NMR for the gated reactions

It is possible that Path B is also the more preferred for the electron self-exchange reactions of the $Cu(bcp)_2^{2+/+}$ and $Cu(dmbp)_2^{2+/+}$ couples. As the free energy profile for the electron self-exchange reaction is symmetric along the reaction coordinate (Scheme 2), the rate law of the electron self-exchange reaction is described by eq. [19], assuming steady state for $Cu^{II}L(Q)$.

$$Cu^{II}L(O) \underset{k_{QO}}{\overset{k_{OQ}}{\rightleftharpoons}} Cu^{II}L(Q)$$

$$Cu^{II}L(Q) + *Cu^{I}L(R) \xrightarrow{k_{ET}} Cu^{I}L(R) + *Cu^{II}L(Q)$$

$$[19] \quad \text{Rate} = \frac{k_{ET}k_{OQ}/k_{QO}}{1 + k_{OQ}/k_{QO}}\,[Cu(I)]_T[Cu(II)]_T$$

$$[20] \quad \tau_{ex}^{-1} = k_{ex}[Cu(II)]_T$$

$$[21] \quad k_{ex} = \frac{k_{ET}k_{OQ}/k_{QO}}{1 + k_{OQ}/k_{QO}}$$

© 1999 NRC Canada

where $[Cu(I)]_T$ and $[Cu(II)]_T$ denote the total concentrations of Cu(I) and Cu(II) species, respectively. When k_{OQ} is small compared with k_{QO}

$$[22] \quad k_{ex} = k_{ET}k_{OQ}/k_{QO}$$

The values of k_{QO} and k_{OQ} are 6.5×10^6 s^{-1} and 40 s^{-1} for the deformation of $Cu(bcp)_2^{2+}$ while k_{ET} (ET rate constant for the $Cu^{II}L(Q)/Cu^{I}L(R)$ couple without structural change, $k_{Cu^{2+*/+}}$) is 3.8×10^{10} kg mol^{-1} s^{-1} as estimated above. Therefore, k_{ex} for the $Cu(bcp)_2^{2+/+}$ couple is calculated as 2.4×10^5 kg mol^{-1} s^{-1}, which may be compared with the directly measured value by NMR (1.4×10^3 kg mol^{-1} s^{-1}). For the electron self-exchange of $Cu(dmbp)_2^{2+/+}$, a value of 3.9×10^4 kg mol^{-1} s^{-1} was calculated from eq. [22], while k_{ex} estimated by the NMR method was 5.5×10^3 kg mol^{-1} s^{-1}. Such differences may be attributed to the error introduced by the rough nature of the estimation of $k_{Cu^{2+*/+}}$. The activation free energy for the *gated* exchange reaction is, therefore, close to 50 ± 10 kJ mol^{-1}.

Direct (concerted) ET and Gated ET

The activation free energies obtained for the cross reactions examined in this study may be compared with those expected for the *direct* (concerted) electron transfer processes. The reorganization parameter for the cross reaction, λ_{rp}^{cross}, is generally described by eq. [23] (1, 2, 4).

$$[23] \quad \lambda_{rp}^{cross} = \frac{\lambda_{rp}^{Cu} + \lambda_{rp}^{Fe}}{2}$$

where λ_{rp}^{Cu} and λ_{rp}^{Fe} represent the reorganization parameters of the imaginary *direct* self-exchange reactions for $Cu(dmbp)_2^{2+/+}$ and $Fe(Cp)_2^{+/0}$. The experimental results indicate that the reduction reaction of $Cu(dmbp)_2^{2+}$ by ferrocene is gated. As the free energy difference for the reaction of $Cu(dmbp)_2^{2+}$ with ferrocene, $\Delta G°$, is 32 kJ mol^{-1}, the following relation should be satisfied to achieve the observed *gated* ET

$$[24] \quad \frac{(\lambda_{rp}^{cross} - \Delta G°)^2}{4\lambda_{rp}^{cross}} >> \Delta G_{gated}^{*}$$

where ΔG_{gated}^{*} is the activation free energy observed for the cross reaction of $Cu(dmbp)_2^{2+}$ and ferrocene, ca. 50 kJ mol^{-1} ($k_{12} = K_{OQ}k_{B2}$). Therefore, λ_{rp}^{Cu} >> 388 kJ mol^{-1} by solving inequality [24] as $\lambda_{rp}^{Fe}/4$ is 33 kJ mol^{-1} ($k_{Fe^{+/0}} = 9 \times 10^6$ dm^3 mol^{-1} s^{-1}). A similar result was obtained for the reactions of $Cu(bcp)_2^{2+/+}$. The expected activation free energy, ΔG^*, for the direct exchange reaction of the $Cu(L)_2^{2+/+}$ couple (L = bcp or dmbp) should then be larger than 100 kJ mol^{-1}. The reorganization parameter for an electron self-exchange reaction is defined as the sum of the free energy of the products at the equilibrium nuclear configuration of the product's state (1, 4). The estimated very large reorganization parameter, >>400 kJ mol^{-1}, for the direct self-exchange reaction of $Cu(L)_2^{2+/+}$ indicates that the inner-sphere and outer-sphere contribution to the reorganization parameter is significantly larger than the sum of the estimated values: 31 kJ mol^{-1} for the deformation of $Cu^{II}L(O)$ to $Cu^{II}L(Q)$ and 100 kJ mol^{-1} for the deformation of $Cu^{I}L(R)$ to $Cu^{I}L(P)$. Therefore, either (*i*) the free energy change for the deformation of $Cu^{I}L(R)$ to $Cu^{I}L(P)$ may be underestimated; or (*ii*) the relation of eq. [23] is not applicable to the cross reactions with very large reorganization parameters (1, 2), probably through the anharmonic nature of the potential surface; or (*iii*) the direct ET is nonadiabatic. In either case, the self-exchange, oxidation, and reduction cross reactions involving $Cu(bcp)_2^{2+/+}$ and $Cu(dmbp)_2^{2+/+}$ are all *gated*, as the gated process is energetically preferred. It is known that anharmonicity of the potential surface increases the value of transition probability (52), and quantum mechanical correction also increases the ET rate (53). Moreover, it is not probable that the reorganization energy required for the structural change from $Cu^{I}L(R)$ to $Cu^{I}L(P)$ is as large as 350 kJ mol^{-1}. Therefore, it may be concluded that the very slow *direct* (concerted) electron exchange between $Cu^{II}L(O)$ and $Cu^{I}L(R)$ is attributed to the nonadiabaticity of the reaction: a poor electronic coupling between $Cu^{I}L(R)$ and $Cu^{II}L(O)$ may originate from the ion pairing, the extensive solvation of these species in acetonitrile, and (or) the delocalization of the metal *d* electrons on the central Cu(II)/(I) ions because of the weak orbital interactions between Cu(II)/(I) and ligands in the deformed geometry (49, 54, 55). Nonadiabaticity of the direct ET process was also suggested for a certain *directional* (or intramolecular gated) reaction by Brunschwig and Sutin [4].

Conclusions

Reduction and oxidation reactions of the $Cu(bcp)_2^{2+/+}$ and $Cu(dmbp)_2^{2+/+}$ couples were examined in acetonitrile. It was found that the reduction reactions of $Cu(bcp)_2^{2+}$ and $Cu(dmbp)_2^{2+}$ were regulated by the slow conformational change, and the reactions proceeded through Path B in Scheme 1. The conformational change in Cu(II) species was attributed to the large LFAE from tetragonal $Cu^{II}L(O)$ to the pseudo-tetrahedral $Cu^{II}L(Q)$.

The apparent self-electron exchange rate constants for the $Cu(bcp)_2^{2+/+}$ and $Cu(dmbp)_2^{2+/+}$ couples were examined on the basis of the gated mechanism through Path B, and the calculated electron self-exchange rate constants using k_{OQ} and k_{QO} estimated from the results of the cross reactions were in fair agreement with the directly measured k_{ex} by the NMR method. Theoretical calculations of the activation free energies for the *direct* exchange reaction indicate that all the reactions, including the self-exchange reactions, examined in this study are *gated* through Path B in Scheme 1. Nonadiabaticity was suggested for the explanation of the very large free energy barrier of the *direct* exchange between $Cu^{II}L(O)$ and $Cu^{I}L(R)$.

Acknowledgments

This research was supported by the Grant-in-Aid for Scientific Research (grant no. 10440193) from the Ministry of Education, Science, Sports and Culture of Japan. N. Koshino held a scholarship from Sasagawa Foundation for Young Scientists.

References

1. N. Sutin. Prog. Inorg. Chem. **30**, 441 (1983).

© 1999 NRC Canada

2. R.D. Cannon. Electron transfer reactions. Butterworth, London. 1980.
3. B.M. Hoffman and M.A. Ratner. J. Am. Chem. Soc. **109**, 6237 (1987).
4. B.S. Brunschwig and N. Sutin. J. Am. Chem. Soc. **111**, 7457 (1989).
5. M.J. Martin, J.F. Endicott, L.A. Ochrymowycz, and D.B. Rorabacher. Inorg. Chem. **26**, 3012 (1987).
6. N.E. Meagher, K.L. Juntunen, C.A. Salhi, L.A. Ochrymowycz, and D.B. Rorabacher. J. Am. Chem. Soc. **114**, 10 411 (1992).
7. D.B. Rorabacher, N.E. Meagher, K.L. Juntunen, P.V. Robandt, G.H. Leggett, C.A. Salhi, B.C. Dunn, R.R. Schroeder, and L.A. Ochrymowycz. Pure Appl. Chem. **65**, 573 (1993).
8. N.E. Meagher, K.L. Juntunen, M.J. Heeg, C.A. Salhi, B.C. Dunn, L.A. Ochrymowycz, and D.B. Rorabacher. Inorg. Chem. **33**, 670 (1994).
9. C.A. Salhi, Q. Yu, M.J. Heeg, N.M. Villeneuve, K.L. Juntunen, R.R. Schroeder, L.A. Ochrymowycz, and D.B. Rorabacher. Inorg. Chem. **34**, 6053 (1995).
10. M.A. Ratner and R.D. Levine. J. Am. Chem. Soc. **102**, 4898 (1980).
11. R.J.P. Williams. Eur. J. Biochem. **234**, 363 (1995).
12. W. Kaim and B. Schwederski. Bioinorganic chemistry: inorganic elements in the chemistry of life. Wiley, Chichester. U.K. 1994.
13. G.S. Yoneda, G.L. Blackmer, and R.A. Holwerda. Inorg. Chem. **16**, 3376 (1977).
14. M.A. Augustin and J.K. Yandell. J. Chem. Soc. Chem. Commun. 370 (1978).
15. J.K. Yandell. *In* Biochemical and inorganic perspectives: copper coordination chemistry. Adenine Press, Guilderland, New York. 1983. p. 157, and refs. therein.
16. C.-W. Lee and F.C. Anson. J. Phys. Chem. **87**, 3360 (1983).
17. M.A. Augustin and J.K. Yandell. Inorg. Chem. **18**, 577 (1979).
18. J.D. Clemmer, G.K. Hogaboom, and R.A. Holwerda. Inorg. Chem. **18**, 2567 (1979).
19. R.A. Holwerda. Inorg. Chem. **21**, 2107 (1982).
20. K.M. Davies. Inorg. Chem. **22**, 615 (1983)..
21. K.M. Davies and B. Byers. Inorg. Chem. **26**, 3823 (1987).
22. A.G. Lappin, M.P. Youngblood, and D.W. Margerum. Inorg. Chem. **19**, 407 (1980).
23. N. Al-Shatti, A.G. Lappin, and A.G. Sykes. Inorg. Chem. **20**, 1466 (1981).
24. P. Leupin, N. Al-Shatti, and A.G. Sykes. J. Chem. Soc. Dalton Trans. 927 (1982).
25. A.E. Allan, A.G. Lappin, and M.C.M. Laranjeira. Inorg. Chem. **23**, 477 (1984).
26. A.G. Lappin and R.D. Peacock. Inorg. Chim. Acta, **46**, L71 (1980).
27. S. Knapp, T.P. Keenan, X. Zhang, R. Fikar, J.A. Potenza, and H.J. Schugar. J. Am. Chem. Soc. **112**, 3452 (1990).
28. S. Flanagan, J. Dong, K. Haller, S. Wang, W.R. Scheidt, R.A. Scott, T.R. Webb, D.M. Stanbury, and L.J. Wilson. J. Am. Chem. Soc. **119**, 8857 (1997).
29. B. Xie, T. Elder, L.J. Wilson, and D.M. Stanbury. Inorg. Chem. **38**, 12 (1999).
30. H. Doine (Takagi), Y. Yano, and T.W. Swaddle. Inorg. Chem. **28**, 2319 (1989).
31. P.D. Metelski, A.S. Hinman, H.D. Takagi, and T.W. Swaddle. Can. J. Chem. **73**, 61 (1995).
32. F.K. Klemens, P.E. Fanwick, J.K. Bibler, and D.R. McMillin. Inorg. Chem. **28**, 3076 (1989).
33. Y. Kuchiyama, N. Kobayashi, and H.D. Takagi. Inorg. Chim. Acta, **277**, 31 (1998).
34. F.H. Burstall and R.S. Nyholm. J. Chem. Soc. 3570 (1952).
35. A. McAuley, P.R. Norman, and O. Olubuyide. Inorg. Chem. **23**, 1938 (1984).
36. P.G. Simpson, A. Vinciguerra, and J.V. Quagliano. Inorg. Chem. **2**, 283 (1963).
37. R.B. Jordan. Reaction mechanisms of inorganic and organometallic systems. Oxford University Press, New York. 1991.
38. H. Yokoi and A.W. Addison. Inorg. Chem. **16**, 1341 (1977).
39. M. van Meerssche, G. Germain, and J.P. Declercq. Cryst. Struct. Commun. **10**, 47 (1981).
40. P.J. Burke, K. Henrick, and D.R. McMillin. Inorg. Chem. **21**, 1881 (1982).
41. D.H. Powell, A.E. Merbach, I. Fábián, S. Schindler, and R. van Eldik. Inorg. Chem. **33**, 4468 (1994), and refs. therein.
42. P.J. Burke, D.R. McMillin, and W.R. Robinson. Inorg. Chem. **19**, 1211 (1980).
43. R.J. Gillespie and I. Hargittai. The VSEPR model of molecular geometry. Allyn and Bacon, Boston, Mass. 1991.
44. B.N. Figgis. Introduction to ligand fields. John Wiley and Sons, Inc., New York. 1966.
45. E.M. Gouge, J.F. Geldard, and E. Sinn. Inorg. Chem. **19**, 3356 (1980).
46. E.M. Gouge and J.F. Geldard. Inorg. Chem. **17**, 270 (1978).
47. L.E. Orgel. An introduction to transition-metal chemistry. Methuen, London. 1960
48. L.G. Sillen and L.E. Martell. Stability constants of metal-ion complexes. Alden Press, Oxford. 1971.
49. G.E. McManis, R.M. Neilson, A. Gochev, and M.J. Weaver. J. Am. Chem. Soc. **111**, 5533 (1989), and refs. therein.
50. G.A. Lawrance and D.R. Stranks. Inorg. Chem. **16**, 929 (1977).
51. N.M. Villeneuve, R.R. Schroeder, L.A. Ochrymowycz, and D.B. Rorabacher. Inorg. Chem. **36**, 4475 (1997).
52. J. Ulstrup and J. Jortner. J. Chem. Phys. **63**, 4358 (1975).
53. P. Siders and R.A. Marcus. J. Am. Chem. Soc. **103**, 741 (1981).
54. M.D. Newton. J. Phys. Chem. **90**, 3734 (1986).
55. M.D. Newton. J. Phys. Chem. **92**, 3049 (1988).
56. D.H. Macartney. Inorg. Chim. Acta, **127**, 9 (1987).
57. D.H. Macartney and D.W. Thompson. J. Chem. Res. Synop. 344 (1992).
58. B.C. Dunn, L.A. Ochrymowycz, and D.B. Rorabacher. Inorg. Chem. **34**, 1954 (1995).

© 1999 NRC Canada

Étude thermodynamique des acides phtalique, isophtalique et téréphtalique

Raphaël Sabbah et Laurence Perez

Résumé : Dans le présent travail a été réalisée l'étude thermodynamique des acides phtalique, isophtalique et téréphtalique de formule générale $C_8H_6O_4$ par calorimétrie de sublimation et par analyse thermique différentielle. En empruntant à la littérature les valeurs des enthalpies de combustion, nous avons pu calculer les enthalpies de formation à l'état gazeux et à 298,15 K de ces acides ainsi que leurs énergies de conjugaison. À partir de ces valeurs, nous avons effectué une étude sur la stabilité relative de ces composés, d'une part, et de divers dérivés du benzène disubstitué, d'autre part. À partir de l'enthalpie de sublimation, nous avons pu déterminer la part énergétique des différentes forces intermoléculaires dans les cristaux de ces trois acides.

Mots clés : thermodynamique, calorimétrie, analyse thermique différentielle, acides phtalique, isophtalique, téréphtalique, enthalpie de fusion, de sublimation, de formation, de liaisons intermoléculaires, énergie de conjugaison, température du point triple.

Abstract: A thermodynamic study of phthalic, isophthalic, and terephthalic acids (general formula: $C_8H_6O_4$) was carried out by sublimation calorimetry and differential thermal analysis. With values of combustion enthalpy taken from the literature, it was possible to determine their enthalpies of formation in the gaseous state and at 298.15 K and their resonance energy. The results enabled us to do a comparative study of the relative stability of the three acids, on the one hand, and of different benzene disubstituted derivatives, on the other hand. From the enthalpy of sublimation, it was possible to determine the energetic contribution of the different intermolecular forces in the crystals of the three acids.

Key words: thermodynamic, calorimetry, differential thermal analysis, phthalic, isophthalic, terephthalic acids, enthalpy of fusion, of sublimation, of formation, of intermolecular bonds, resonance energy, triple point temperature.

1. Introduction

Cette étude s'inscrit dans la continuité de celles qui ont été entreprises au laboratoire depuis quelques années sur les dérivés disubstitués du benzène (1–6). Les résultats obtenus, ajoutés à ceux qui ont été précédemment obtenus au laboratoire, nous ont permis de réaliser, dans ce mémoire, une étude comparative sur la stabilité des isomères d'une même série et sur celle des dérivés de séries différentes. Toutes ces études s'inscrivent dans le cadre de notre thème de recherche « Énergétique des liaisons inter- et intramoléculaires » visant la mise en évidence du lien existant entre grandeurs énergétiques et structure.

Les données thermodynamiques de la littérature relatives à la combustion des acides phtalique, isophtalique et téréphtalique sont très cohérentes (7). Aussi, n'avons-nous pas jugé utile de refaire des mesures de l'enthalpie de combustion. En revanche, on ne trouve que quelques rares résultats divergeants relatifs à l'enthalpie de sublimation des acides isophtalique (8) et téréphtalique (8–10) obtenus par méthodes indirectes à partir de mesure de pression de vapeur en fonction de la température. En conséquence, nous avons étudié ces trois acides par calorimétrie de sublimation. Ce travail a été complété par une analyse thermique différentielle de ces acides qui nous a permis de déterminer leurs enthalpies de fusion et la température de leur point triple. Comme il sera précisé plus loin dans le texte, nous avons rencontré avec cette technique des difficultés expérimentales lors de l'étude de l'acide téréphtalique. Par ailleurs, nous n'avons trouvé aucune donnée dans la littérature concernant les enthalpies de fusion de ces acides.

Notons que les travaux sur leur structure cristalline sont peu nombreux et concernent les trois isomères (11–13).

Du point de vue pratique, signalons, au passage, que l'acide téréphtalique est un important intermédiaire chimique dans la synthèse de polymères.

Reçu le 26 mars 1999.

R. Sabbah[1] et L. Perez. Centre de thermodynamique et de microcalorimétrie du Centre national de la recherche scientifique, 26, rue du 141ème RIA, 13331 - Marseille, Cedex 03, France.

1. Auteur auquel la correspondance doit être adressée. Tél. : 33 4 91 28 20 62. Téléc. : 33 4 91 50 38 29. Mél. : raphael.sabbah@ctm.cnrs-mrs.fr

2. Partie expérimentale

2.1. Produits utilisés

Les acides phtalique et isophtalique sont des produits Aldrich de pureté 99,5 % et 99 %, l'acide téréphtalique est un produit Fluka de pureté >99 %. Ce dernier, se décomposant à la fusion avec bris d'ampoule, n'a pu être étudié par analyse thermique différentielle. Par ailleurs, le degré de pureté du produit commercial nous a paru suffisamment élevé pour l'utiliser tel quel. L'analyse thermique différentielle de

© 1999 CNRC Canada

l'acide isophtalique commercial ayant révélé un degré de pureté jugé suffisant, nous n'avons pas procédé à sa purification. Par contre, nous avons repurifié l'acide phtalique par sublimation à 373 K et sous une pression résiduelle de 1,3 Pa. Les résultats de l'analyse thermique sont consignés dans le tableau 1.

2.2. Appareillages, techniques et modes opératoires

2.2.1. Analyse thermique différentielle

Nous avons utilisé la version moyenne température de l'analyseur thermique différentiel du laboratoire et les cellules en verre décrites dans la référence 14.

Dans toutes nos expériences : (*i*) la vitesse de montée en température du four a été de 0,2 K min^{-1}; (*ii*) la masse de substance utilisée a été d'environ 100 mg, déterminée par double pesée à l'aide d'une balance Mettler, type M5, sensible au μg et dont l'exactitude des pesées est de ±2 μg; (*iii*) la préparation des échantillons et leur mise en container ont été conduites de la façon décrite dans la référence 14.

La mesure des températures a été faite à l'aide de deux thermocouples (thermocoax, type 2ABI 15); l'un est solidaire de l'échantillon, l'autre de la référence (alumine-α). La différence entre les f.e.m délivrées par ces deux thermocouples est amplifiée par un microvoltmètre AOIP, type EVA, sensibilité 100 μV pleine échelle. Le signal ainsi amplifié est envoyé simultanément sur un enregistreur Sefram, type Gépérac, pour le visualiser et sur un multimètre Keithley, modèle 175, pour le numériser. Un autre multimètre Keithley, modèle 196, sensibilité 300 mV (résolution 100 nV) est utilisé pour mesurer la f.e.m. correspondant à la température de l'échantillon. Les données issues de ces deux multimètres sont envoyées vers un ordinateur en vue de leur traitement à l'aide d'un programme écrit et mis au point au laboratoire. En appliquant l'équation de Clausius–Clapeyron et la loi de Raoult, ce programme permet de déterminer la pureté de l'échantillon, son enthalpie de fusion ainsi que la température de son point triple.

Comme indiqué dans la référence 14, l'étalonnage en température de notre analyseur thermique a été réalisé à partir d'échantillons rigoureusement purs de naphtalène, de fluorène, d'acides benzoïque, diphénylacétique et anisique, de carbazole et d'anthraquinone, dont la température de leur point triple est bien connue dans la littérature. Quant à son étalonnage en énergie, il a été fait à partir d'échantillons rigoureusement purs de naphtalène, de fluorène, d'acides benzoïque et diphénylacétique, dont l'enthalpie de fusion est bien connue dans la littérature.

2.2.2. Calorimétrie de sublimation

Nous avons utilisé un calorimètre Tian–Calvet (sensibilité 0,0149 V W^{-1} à 415 K et 0,0628 V W^{-1} à 437,2 K) associé à un montage différentiel doté de cellules d'effusion de Knudsen pour déterminer les enthalpies de sublimation de nos composés. L'étalonnage de notre système calorimétrique a été réalisé par effet Joule avant et après chaque série d'expériences. Le mode opératoire a été décrit dans la référence 15. Précisons que :

(*i*) le signal issu du calorimètre est amplifié par un nanovoltmètre Keithley modèle 147, sensibilité 30 ou 100 μV pleine échelle suivant le cas, puis numérisé par un multimètre numérique Keithley modèle 175 et enregistré sur un enregistreur potentiométrique Sefram, modèle Servotrace.

(*ii*) L'isomère *ortho* a été étudié à 415,0 K alors que les deux autres isomères l'ont été à 437,2 K en raison de leur faible pression de vapeur saturante P_s (cf. tableau 2). Compte tenu de ces faibles valeurs, nous avons admis l'identité $\Delta_{sub}H_m(T) \equiv \Delta_{sub}H°_m(T)$.

(*iii*) D'après les résultats de la littérature, l'acide téréphtalique existerait sous deux formes cristallines (13, 16) dont la température de transition serait située à 423 K (16). En conséquence, nos expériences ont été vraisemblablement réalisées avec la forme dite « haute température » de cet acide.

(*iv*) Le diamètre des trous d'effusion pratiqués dans des joints métalliques de 0,1 mm d'épaisseur est de 0,7, 0,7 et 3 mm respectivement dans le cas des acides phtalique, isophtalique et téréphtalique.

(*v*) Toutes les pesées ont été effectuées à l'aide d'une balance « Mettler », type UM3 équipée d'un jeu de poids étalonnés par le NIST (sensibilité 0,1 μg, exactitude ±0,2 μg sur une pesée de quelques milligrammes, portée 3 g).

L'acquisition et le traitement des données ont été réalisés à l'aide de l'ordinateur et d'un programme conçu et mis au point au laboratoire. Il permet, entre autres, de déterminer la pression de vapeur saturante, l'aire des thermogrammes et, à partir du coefficient d'étalonnage, l'enthalpie molaire de sublimation de nos composés à la température de l'expérience $\Delta_{sub}H°_m(T)$.

2.2.3. Mesure des capacités calorifiques

Pour calculer $\Delta_{sub}H°_m$ (298,15 K) à partir de $\Delta_{sub}H°_m(T)$, il est nécessaire de connaître :

(*i*) le comportement thermique de nos substances entre 298,15 K et *T*. Nous nous sommes donc assurés qu'elles ne présentaient aucun changement de phase dans cet intervalle;

(*ii*) la capacité calorifique à pression constante des phases condensée et gazeuse des substances étudiées à 298,15 K et *T* de façon à pouvoir appliquer la relation suivante :

$$\Delta_{sub}H°_m(298,\ 15\ K) = \Delta_{sub}H°_m(T) + \int_T^{298,15\,K} [C°_{p,m}(g) - C°_{p,m}(cr)]dT$$

La différence enthalpique $H°_m(T) - H°_m(298,15\ K)$ à l'état solide a été calculée par la méthode de chute à l'aide d'un calorimètre Tian–Calvet et d'un four maintenus respectivement à 298,15 K et *T*. Le calorimètre a été préalablement étalonné en utilisant des échantillons d'alumine-α (6*d*).

Quant aux valeurs des capacités calorifiques à l'état gazeux $C°_{p,m}(g)$ et aux températures 298,15 K et *T*, elles ont été déterminées à partir d'une méthode incrémentale en utilisant, à chacune de ces deux températures, les capacités calorifiques à l'état gazeux des molécules de benzène et d'acide benzoïque (17), ce qui nous a permis, dans un premier temps et à chacune de ces deux températures, de déterminer la part du chaînon COOH puis de calculer une valeur moyenne de $C°_{p,m}$ pour les trois acides étudiés en ajoutant cette quantité au $C°_{p,m}$ de l'acide benzoïque.

© 1999 CNRC Canada

Tableau 1. Analyse thermique différentielle des acides phtalique et isophtalique.

Isomère	Pureté (mol %)	T_{pt} [a] (K)	$\Delta_{fus}H_m$ (kJ mol^{-1})
ortho	99,87±0,02	463,45±0,01	36,5±1,2
méta	99,96±0,01	617,41±0,04	43,2±1,2

[a]Températures du point triple définies par rapport à l'EIT-90.

Tableau 2. Sublimation des acides étudiés.

Isomère	T (K)	m (mg)	$\Delta_{sub}\overline{H}_m(T)$ (kJ mol^{-1})	$\Delta_{sub}H_m(T)$ (kJ mol^{-1})	$\int_{298,15K}^{T} C^\circ_{p,m}(g)dT$ (kJ mol^{-1})	$\int_{298,15K}^{T} C^\circ_{p,m}(cr)dT$ (kJ mol^{-1})	$\Delta_{sub}H^\circ_m(298,15\ K)$ (kJ mol^{-1})	$P_s(T)$ (Pa)
		7,3909	117,47					
		10,4831	120,13					
		9,9502	119,06					
ortho	415,0	9,8570	121,63	119,06±0,58	17,32±0,15	28,05±0,03	129,79±0,60	0,54
		10,9237	116,41					
		10,7016	118,76					
		10,6619	120,33					
		11,5716	118,70					
		9,0287	128,50					
		16,2983	128,36					
		16,6923	126,74					
méta	437,2	12,0605	129,48	129,23±0,70	21,17±0,15	33,95±0,09	142,01±0,72	0,56
		16,8728	131,72					
		15,6264	131,62					
		13,8197	128,20					
		10,3810	134,08					
		9,8084	136,13					
para	437,2	9,1905	135,14	134,81±0,47	21,17±0,15	32,94±0,05	146,58±0,50	0,023
		9,9593	133,03					
		9,4610	133,63					
		10,3788	135,39					
		12,5141	136,29					

Les différents calorimètres et analyseur thermique, leurs périphériques ainsi que les balances, sont placés dans des salles thermorégulées à (19,0 ± 0,2)°C.

3. Résultats

3.1. Analyse thermique différentielle

Les résultats obtenus sont consignés dans le tableau 1. Les isomères *ortho* et *méta* se décomposent à la fusion (8, 18) en prenant une légère coloration brune. Quant à l'isomère *para*, comme signalé dans le paragraphe 2.1, il n'a pu être étudié car sa décomposition à la fusion s'accompagne du bris de la cellule.

Le manque de données de la littérature relatives à l'enthalpie de fusion ne nous a pas permis d'en faire une comparaison avec nos résultats expérimentaux.

Quant aux températures de leur point triple, la référence 18 indique les valeurs suivantes : acide phtalique : 464 K en tube scellé; acide isophtalique : 621 K (614–616 K d'après le catalogue Aldrich); acide téréphtalique : >573 K (698 K en tube scellé d'après la référence 16).

Comme nous pouvons le constater, nos résultats expérimentaux sont tout à fait compatibles avec ces données.

3.2. Calorimétrie de sublimation

L'ensemble des résultats est consigné dans le tableau 2. La littérature mentionne quelques valeurs de l'enthalpie de sublimation des isomères *méta* et *para* obtenues par méthode indirecte à partir de mesures de pression de vapeur en fonction de la température :

Isomère *méta* : 106,7 kJ mol^{-1} à 523 K (8), valeur consignée dans la compilation de Pedley et al. (7).

Isomère *para* : 98,2 kJ mol^{-1} à $392 \leq T/K \leq 425$ (9), valeur consignée dans la compilation de Pedley et al. (7); 131 kJ mol^{-1} à 573 K (8); 139,3 kJ mol^{-1} à $568 \leq T/K \leq 675$ (10).

Signalons que la masse molaire des trois acides phtalique, isophtalique et téréphtalique a été calculée à partir des masses atomiques de 1993 (19); elle est égale à 166,1332 g mol^{-1}.

Dans le présent travail, l'incertitude qui accompagne les résultats expérimentaux représente l'écart moyen, $\sigma_m = \pm \{\sum (x - x_0)^2 / n(n-1)\}^{1/2}$, x étant chacune des n valeurs entrant dans le calcul de la moyenne x_0. Lorsque la valeur expérimentale est fonction de plusieurs variables, l'incertitude

© 1999 CNRC Canada

Tableau 3. Grandeurs thermodynamiques des acides étudiés à 298,15 K.

Isomère	$-\Delta_c H°_m$(cr, 298,15 K)[a] (kJ mol^{-1})	$\Delta_{sub} H°_m$(298,15 K) (kJ mol^{-1})	$-\Delta_c H°_m$(g, 298,15 K) (kJ mol^{-1})	$-\Delta_f H°_m$(cr, 298,15 K)[b] (kJ mol^{-1})	$-\Delta_f H°_m$(g, 298,15 K) (kJ mol^{-1})
ortho	3223,63±0,93	129,79±0,60	3353,42±1,11	782,0±0,9	652,2±1,1
méta	3202,60±0,75	142,01±0,72	3344,61±1,04	803,0±0,8	661,0±1,1
para	3189,45±0,60	146,58±0,50	3336,03±0,78	816,1±0,7	669,5±0,9

[a]Moyenne des résultats consignés dans la référence 7.

[b]Valeurs consignées dans la référence 7.

Tableau 4. Enthalpies de formation à l'état gazeux et à 298,15 K de divers dérivés du benzène disubstitué.

Dérivé	$\Delta_f H°_m$(g, 298,15 K) (kJ mol^{-1})		
φ (A,B)	*ortho*	*méta*	*para*
A=B=COOH	–652,2 ± 1,1	–661,0 ± 1,1	–669,5 ± 0,9
A=B=OH[a]	–274,8 ± 1,2	–284,7 ± 1,2	–277,0 ± 1,4
A=B=NH_2[b]	92,0 ± 1,3	84,0 ± 1,4	88,7 ± 1,4

[a]Les valeurs numériques sont consignées dans la référence 2.

[b]Les valeurs numériques sont consignées dans la référence 3.

Tableau 5. Energie de conjugaison à 298,15 K de divers dérivés du benzène disubstitué.

Dérivé	E_{conj}(298,15 K) (kJ mol^{-1})		
φ (A,B)	*ortho*	*méta*	*para*
A=B=COOH	293,4	299,2	307,8
A=B=OH[a]	177,5	184,4	176,7
A=B=NH_2[b]	165,1	170,1	165,4

[a]Les valeurs numériques sont consignées dans la référence 2.

[b]Les valeurs numériques sont consignées dans la référence 3.

calculée tient compte de l'erreur sur chacune de ces variables.

4. Discussion

Les principales fonctions thermodynamiques des trois acides étudiés dans ce mémoire sont rassemblées dans le tableau 3.

4.1. Enthalpie de formation à l'état gazeux

Nous avons voulu comparer entre elles les valeurs de l'enthalpie de formation à l'état gazeux et à 298,15 K des trois isomères de divers dérivés du benzène disubstitué se différenciant par la nature du substituant. Ces différentes valeurs sont rassemblées dans le tableau 4. Cette comparaison nous permet de faire les constatations suivantes :

1. Les substances étudiées dans ce travail sont les plus stables. En effet, les valeurs de leur $\Delta_f H°_m$(g, 298,15 K) sont négatives et élevées (en valeur absolue). La stabilité semble décroître dans l'ordre suivant : benzènediacides carboxyliques, dihydroxybenzènes et benzènediamines.

2. Quelle que soit la famille considérée, l'isomère *ortho* paraît être le moins stable. Ceci peut s'expliquer par l'effet stérique provoqué par les deux substituants adjacents.

4.2. Energie de conjugaison

L'énergie de conjugaison est la différence entre l'énergie réelle de la molécule et celle qu'elle aurait si les divers systèmes insaturés qu'elle comporte étaient indépendants. Sur le plan pratique, pour la déterminer, il suffit d'utiliser les enthalpies standard de combustion à l'état gazeux de la molécule réelle et de la molécule fictive non conjuguée à 298,15 K. La première de ces grandeurs s'obtient expérimentalement et la seconde nécessite le recours aux systématiques. En ce qui nous concerne, nous avons utilisé celle de Klages qui est consignée dans la référence 20.

Les valeurs de l'énergie de conjugaison des acides phtalique, isophtalique et téréphtalique sont consignées dans le tableau 5 avec celles de divers dérivés du benzène disubstitué. Ce tableau nous permet de constater que :

(*i*) Les benzènediacides carboxyliques sont les dérivés les plus conjugués. Ceci est vraisemblablement dû au fait que les groupements (COOH), donneurs d'électrons, consolident la conjugaison du cycle.

(*ii*) Comme dans le cas de l'enthalpie de formation à l'état gazeux et pour la même raison, quelle que soit la famille considérée, l'isomère *ortho* paraît être le moins stable.

4.3. Liaisons intermoléculaires dans les acides phtalique, isophtalique et téréphtalique

4.3.1. Liaisons hydrogène intermoléculaires

L'enthalpie de sublimation d'une substance organique est liée aux interactions intermoléculaires comprenant la part énergétique due aux forces de van der Waals (de dispersion et dipolaires) et, le cas échéant, celle qui est relative aux liaisons hydrogène.

Un procédé de calcul, plusieurs fois utilisé avec succès au laboratoire (2, 3, 5, 21–25) nous a permis de déterminer la contribution énergétique des liaisons hydrogène intermoléculaires dans les cristaux d'acides phtalique, isophtalique et téréphtalique. Il consiste, dans notre cas, à comparer l'enthalpie de sublimation des molécules de ces acides à celle d'une molécule isoélectronique (ici la molécule de 1,4-dinitrobenzène) possédant les mêmes forces de dispersion et d'interactions dipolaires. Malheureusement, nous n'avons pas trouvé dans la littérature la valeur de l'enthalpie de sublimation de cette molécule.

L'expérience acquise au laboratoire nous ayant montré que la différence entre les valeurs de l'enthalpie de sublimation des isomères *méta* et *para* d'une même série n'est que de quelques kJ mol^{-1}, nous avons utilisé dans nos calculs la valeur de l'enthalpie de sublimation de la molécule de 1,3-dinitrobenzène empruntée à la référence 7 ($\Delta_{sub} H°_m$(298,15 K) = (81,2 ± 1,7) kJ mol^{-1}). Cette dernière valeur correspond, en première approximation, à la part des forces de dis-

© 1999 CNRC Canada

persion et dipolaires dans les cristaux des trois acides étudiés dans ce mémoire. Malheureusement, il ne nous a pas été possible de départager ces deux types d'interaction. En effet, la littérature ne propose aucune valeur de l'enthalpie de sublimation de la molécule d'hydrocarbure isoélectronique

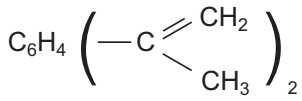

qui nous aurait permis de déterminer la part énergétique due aux forces de dispersion dans les cristaux d'acides phtalique, isophtalique et téréphtalique. Il s'ensuit que la contribution des liaisons hydrogène intermoléculaires dans les isomères *ortho*, *méta* et *para* est respectivement égale à 48,6 kJ mol^{-1}, 60,8 kJ mol^{-1} et 65,4 kJ mol^{-1}.

Si l'on considère la molécule d'isomère *para*, qui est dépourvue de tout effet stérique dû aux substituants et dans laquelle il ne peut y avoir que des liaisons hydrogène intermoléculaires et compte tenu qu'il ne peut se former que deux liaisons de ce type par molécule, il s'ensuit que l'enthalpie d'une liaison hydrogène intermoléculaire est environ égale à 32,7 kJ mol^{-1}. Cette valeur est tout à fait compatible avec celle que donnent Saska et Myerson (26) dans le cas des cristaux de cet acide (26,2 kJ mol^{-1}) et celles qui sont proposées dans celui des acides carboxyliques par Pimentel et Clellan (27).

Quant à la différence observée entre les valeurs de l'enthalpie de sublimation des isomères *ortho* et *para*, on pourrait, à première vue, penser, comme c'est le cas pour d'autres isomères de dérivés disubstitués du benzène (acides hydroxybenzoïques (4) et aminobenzoïques (1)) que cette différence est due à une chélation entre les deux groupements fonctionnels dans l'isomère *ortho* avec formation de liaison hydrogène intramoléculaire. En réalité, il n'en est rien compte tenu de la structure cristalline de l'acide phtalique proposée par Küppers (11) dans laquelle les deux groupements fonctionnels sont perpendiculaires. En conséquence, la valeur la plus basse de l'enthalpie de sublimation observée pour cet isomère est vraisemblablement due à un manque de liaison hydrogène dans ses cristaux en raison de l'effet stérique provoqué par les deux groupements fonctionnels adjacents.

4.3.2. Calcul de l'enthalpie moyenne de sublimation des trois acides par voie incrémentale

La valeur moyenne de l'enthalpie de sublimation des trois acides étudiés dans ce mémoire est égale à 139,46 à 298,15 K kJ mol^{-1}. Nous avons tenté de retrouver cette valeur par voie incrémentale. Pour cela, nous avons déterminé la contribution du chaînon (COOH) en retranchant à la valeur de $\Delta_{sub}H°_m$(298,15 K) de la molécule d'acide benzoïque (89,74 kJ mol^{-1}) (28) celle de la molécule de benzène. Cette dernière est, en première approximation, calculée à partir de la relation :

$$\Delta_{sub}H°_m(298{,}15\ \text{K}) = \Delta_{fus}H_m(298{,}15\ \text{K}) + \Delta_{vap}H°_m(298{,}15\ \text{K})$$

où $\Delta_{fus}H$(298,15 K) est obtenue à l'aide de la règle de Sidgwick (29) :

$$\Delta_{fus}H_m(298{,}15\ \text{K}) = \Delta_{fus}H_m(T_{fus}) - 0{,}055\ (T_{fus} - 298{,}15)$$

Les valeurs relatives à la molécule de benzène sont empruntées aux références 30 et 31. Après calcul, nous trouvons $\Delta_{sub}H°_m$(298,15 K) = 44,88 kJ mol^{-1} pour cette molécule. La part du chaînon (COOH) est donc estimée à 44,88 kJ mol^{-1}.

Il s'ensuit que l'enthalpie moyenne de sublimation des trois acides à 298,15 K, calculée en ajoutant à l'enthalpie de sublimation du benzène deux fois la contribution énergétique du chaînon (COOH) à cette température, est égale à 134,62 kJ mol^{-1}. Elle diffère d'environ 3,5 % de la valeur moyenne expérimentale.

Bibliographie

1. M. Nabavian, R. Sabbah, R. Chastel et M. Laffitte. J. Chim. Phys. **74**, 115 (1977).
2. R. Sabbah et E.N.L.E. Buluku. Can. J. Chem. **69**, 481 (1991).
3. R. Sabbah et L. Perez. Can. J. Chem. **75**, 357 (1997).
4. R. Sabbah et T.H.D. Le. Can. J. Chem. **71**, 1378 (1993).
5. (*a*) R. Sabbah et M. Gouali. Aust. J. Chem. **47**, 1651 (1994); (*b*) Can. J. Chem. **74**, 500 (1996).
6. (*a*) R. Sabbah et H. Hirtz. Bull. Soc. Chim. Fr. **128**, 26 (1991); (*b*) R. Sabbah et A. Rojas Aguilar. Can. J. Chem. **73**, 1538 (1995); (*c*) Z.C. Tan et R. Sabbah. Sci. China, Ser. B: **37**, 641 (1994); (*d*) Z.C. Tan et R. Sabbah. Thermochim. Acta, **231**, 109 (1994); (*e*) R. Sabbah et A. Rojas Aguilar. Struct. Chem. **7**, 383 (1996).
7. J.B. Pedley, R.D. Naylor et P. Kirby. Thermodynamic data of organic compounds. 2ème éd. Chapman et Hall, New York. 1986.
8. M. Kraus, L. Beranek, K. Kochloeff et V. Bazant. Chem. Prum. **12**, 649 (1962).
9. H. Hirsbrunner. Helv. Chim. Acta, **17**, 477 (1934).
10. C.A. Lucchesi et W.T. Lewis. J. Chem. Eng. Data, **13**, 389 (1968).
11. H. Küppers. Cryst. Struct. Commun. **10**, 989 (1981).
12. R. Alcala et S. Martinez-Carrera. Acta Crystallogr. Sect. B: Struct. Crystallogr. Cryst. Chem. **B28**, 1671 (1972).
13. M. Bailey et C. J. Brown. Acta Crystallogr. **22**, 387 (1967).
14. (*a*) R. Sabbah et L. El Watik. J. Therm. Anal. **36**, 2291 (1990); (*b*) R. Sabbah et I. Antipine. J. Therm. Anal. **32**, 1929 (1987).
15. R. Sabbah, I. Antipine, M. Coten et L. Davy. Thermochim. Acta, **115**, 153 (1987).
16. V.P. Gerasimov, N.K. Zharikov, V.S. Korobkov, I.V. Ovchinnikov et L.V. Rud. Zh. Prikl. Spektrosk. **34**, 308 (1981).
17. D.R. Stull, E.F. Westrum, Jr. et G.C. Sinke. The chemical thermodynamics of organic compounds. Wiley, New York. 1969.
18. D.R. Lide. Handbook of chemistry and physics. 71 éd. CRC Press, Boca Raton, Fla. 1990–1991.
19. Atomic weights of the elements 1993. Pure Appl. Chem. **66**, 2423 (1994).
20. G.W. Wheland. Resonance in organic chemistry. Wiley, New York. 1955. Chap. 3.
21. R. Sabbah et M.E.S. Eusébio. Can. J. Chem. **76**, 18 (1998).
22. R. Sabbah et O. Pemenzi. C.R. Acad. Sci. Paris, **317**, 575 (1993).
23. P. Knauth et R. Sabbah. Can. J. Chem. **68**, 731 (1990).
24. P. Knauth et R. Sabbah. Bull. Soc. Chim. Fr. **5**, 834 (1988).
25. S. Skoulika et R. Sabbah. Thermochim. Acta, **61**, 203 (1983).
26. M. Saska et A.S. Myerson. Cryst. Res. Technol. **20**, 201 (1985).

© 1999 CNRC Canada

27. G. Pimentel et A.L. McClellan. The hydrogen bond. Freeman, San Francisco. 1960.
28. R. Chastel, F. Steckel et H. Tachoire. Proc. 1st Int. Conf. Calorimetry Thermodynamics, Warsaw 1969. Polish Scientific Publishers, Warsaw. 1969. p. 115.
29. T.L. Cottrell. The strengths of chemical bonds. 2ème éd. Butterworths, London. 1958.
30. G.D. Oliver, M. Eaton et H.M. Huffman. J. Am.Chem. Soc. **70**, 1502 (1948).
31. V. Majer, V. Svoboda et H.V. Kehiaian. Enthalpies of vaporization of organic compounds: a critical review and data compilation. I.U.P.A.C. Chemical Data Series N° 32. Blackwell, Oxford. 1985.

© 1999 CNRC Canada

Annotinine revisited. A new pentacyclo[7.3.3.0^{1,13}.0^{2,12}.0^{5,13}]pentadecane ester and other products derived from annotinine

William A. Ayer, Monika Wichlacz, and Latchezar S. Trifonov

Abstract: Several annotinine derivatives were prepared and their conformations were determined on the basis of 1D NMR and 2D NMR spectra (GCOSY, HMQC, HMBC, TROESY). One of these compounds has new unique 5-ring skeleton.

Key words: alkaloids, chemical tranformations, structure elucidation, conformation.

Résumé : On a préparé plusieurs dérivés de l'annotinine et on a déterminé leurs conformations en se basant sur les spectres de RMN 1D et 2D (« GCOSY », « HMQC », « HMBC », « TROESY »). L'un de ces composés comporte un squelette pentacyclique unique.

Mots clés : alcaloïdes, transformations chimiques, élucidation de structure, conformation.

[Traduit par la Rédaction]

Introduction

Annotinine (**1**, Fig. 1) is a major alkaloid of the club mosses *Lycopodium annotinum* and *L. annotinum* var. *acrifolium*, and a minor alkaloid of *L. flabelliforme* and *L. obscurum* (1). The unique structure of this compound was solved in 1957 by Wiesner et al. as a result of extensive degradative studies (2) culminating later with the total synthesis of the optically active enantiomer (3). The structure was verified by X-ray analysis (4).

The large quantities of annotinine available permitted the performance of a variety of reactions. In 1957 Martin-Smith et al. reported that methyl epiannotinate (**2**) was the only product isolated in 75% yield when annotinine was treated with KOMe–MeOH at room temperature (r.t.) (5). In our laboratory in the late 50s the same reaction afforded several minor products (**2**, **3**, **4**) in addition to a major product with interesting properties, designated "ester M," whose structure was suggested to be **5**. However, this was not supported by solid spectroscopic data (6). Even a simple ^{1}H NMR spectrum was not available at that time due to the exceptionally low solubility of **5** in conventional NMR solvents. The routine use of powerful 2D NMR techniques in recent years and a simple solution to the solubility problem prompted us to reinvestigate the above reaction of annotinine. In this study we report the structure determination of ester M and of the minor reaction products, as well as complete assignments of all NMR signals.

Received December 7, 1998.

W.A. Ayer,[1] M. Wichlacz, and L.S. Trifonov. Department of Chemistry, University of Alberta, Edmonton, AB T6G 2G2, Canada.

[1]Author to whom correspondence may be addressed. Telephone: (780) 492-5476. Fax: (780) 492-8231. e-mail: bill.ayer@ualberta.ca

Results and discussion

The epimeric methyl epiannotinate (**2**) and methyl annotinate (**3**) have molecular formula $C_{17}H_{25}NO_4$ as determined by HRMS spectra. In both compounds the epoxide ring is preserved and a CH(OH) group and a CH-COOCH$_3$ group replace the lactone functionality of annotinine. Although in both isomers H1 appears as a doublet of doublets with one large and one small coupling constant (Table 1), the large coupling in **2** (12.3 Hz) is due to coupling to H2α, while in **3** (14.6 Hz) it is due to coupling to H2β. This pattern of couplings is only attainable if the C1–C6 ring adopts a chair conformation in **2** and a boat conformation in **3**. The TROESY spectra (7) further support this conformational assignment (Fig. 2). Thus, in compound **2** H1 shows a cross peak with H15, while in compound **3** H1 shows a cross peak with H7. In both isomers H15 is correlated to H2β, but not to H2α, and the correlations H15–H13b and H14–H13a, and H2β–H13b as well, allow us to assign the signals for H13a and H13b. The correlation H4–H9α (both axial) is crucial for the assignment of H9α and H9β in **2** and **3**. The correlations H10β–H13a, H12α–H3, H12β–H13b, and 9α–11α as well as H10β–H12β (axial–axial) and H10α–H11α allow us to assign H10, H11, and H12.

Interestingly, H10α is correlated to H9β but not to H9α, and also H12α is correlated to H3 but not to H4, which is in agreement with the proximities shown in molecular model studies.

The complete assignment of all ^{1}H and ^{13}C signals shown in Tables 1–3 is based on ^{1}H–^{1}H COSY, HMQC, HMBC, and TROESY spectra (Figs. 2 and 3).

© 1999 NRC Canada

Fig. 1.

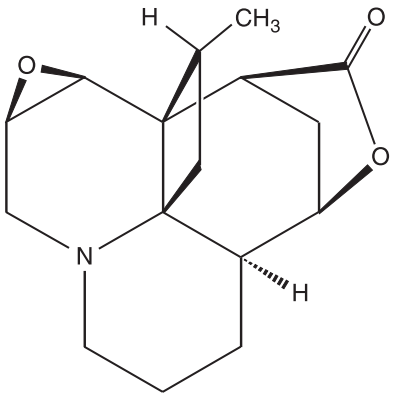

Annotinine (**1**)

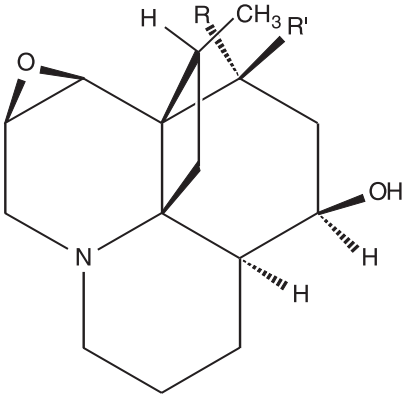

2 R = $COOCH_3$, R' = H
3 R = H, R' = $COOCH_3$

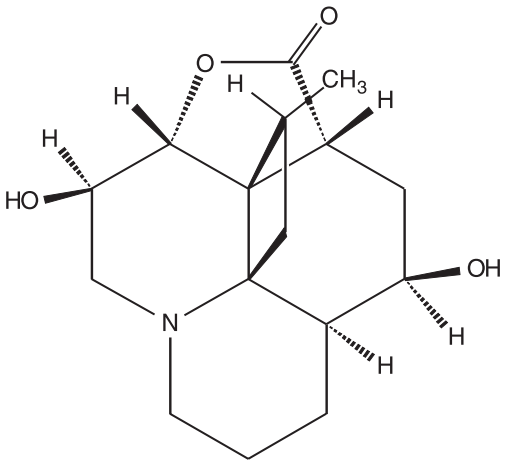

Annotinine hydrate (**4**)

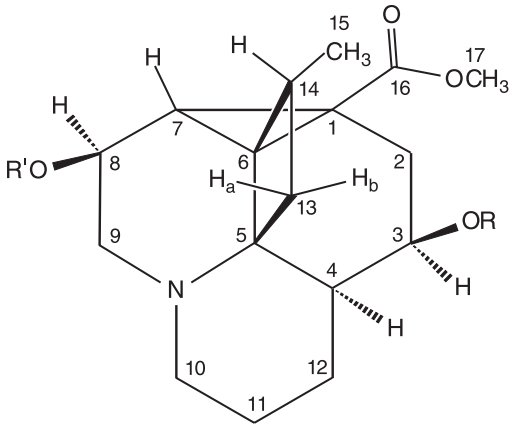

5 R = R' = H
6 R = Ac, R' = H
7 R = H, R' = Ac
8 R = R' = Ac

The structure of annotinine hydrate (**4**), proposed in the 50s, was also corroborated by extensive 2D NMR studies. The presence of a lactone ring is reflected in the signals for C7 and a CO-O group (at 80.7 and 180.0 ppm, respectively, Table 3). The two CH-OH groups are at C3 and C8 as indicated by the coupling patterns in the ^{1}H NMR spectrum (Table 1), as well as by the HMBC correlations (Fig. 4).

The stereochemistry at C1 and C7 was deduced from the TROESY spectrum. Thus, H1 showed correlation to H15, while H7 was correlated to H14, a pattern consistent only with α orientation of the lactone ring, which forces the C1–C6 ring to adopt a boat conformation. Consequently, the coupling constants of H1 (6.4 and 2.8 Hz) are significantly different from those of H1 in **3** (14.6 and 3.5 Hz), also having the C1–C6 ring with a boat conformation, but axial H1 (Table 1).

Additional TROESY correlations of annotinine hydrate (**4**) are shown in Fig. 3, and complete ^{1}H and ^{13}C assignments in Tables 1–3.

Ester M was obtained as a colorless solid having very low solubility in the conventional NMR solvents. Its hydrochloride, however, was quite soluble in methanol. Consequently, all NMR studies were conducted with the hydrochloride in CD_3OD.

The molecular formula $C_{17}H_{25}NO_4$ of ester M was obtained from the HREIMS spectrum. Thus ester M is isomeric to methyl epiannotinate (**2**) and methyl annotinate (**3**). The presence of a $COOCH_3$ group in ester M was deduced from the ^{1}H and ^{13}C NMR spectra (Tables 2 and 3, respectively). Since there is no evidence for the presence of double bonds or other carbonyl groups, ester M must be penta-

© 1999 NRC Canada

Fig. 2. TROESY correlations of **2** and **3**.

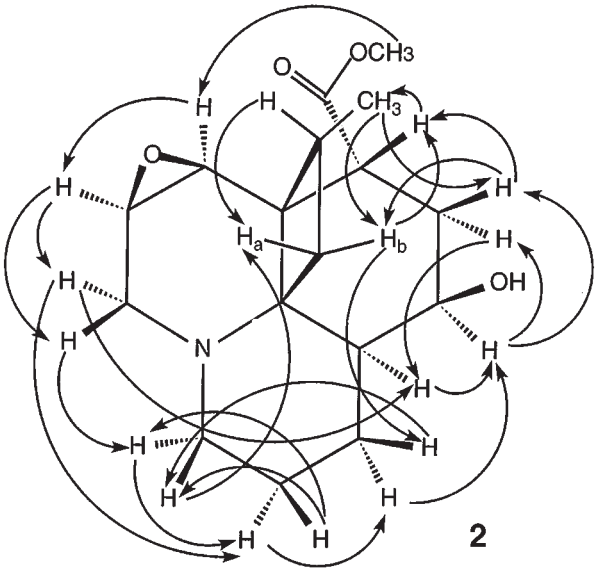

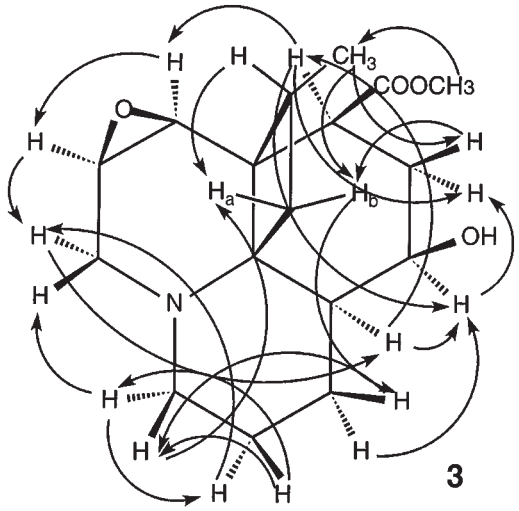

Fig. 3. TROESY correlations of **4** and **8**.

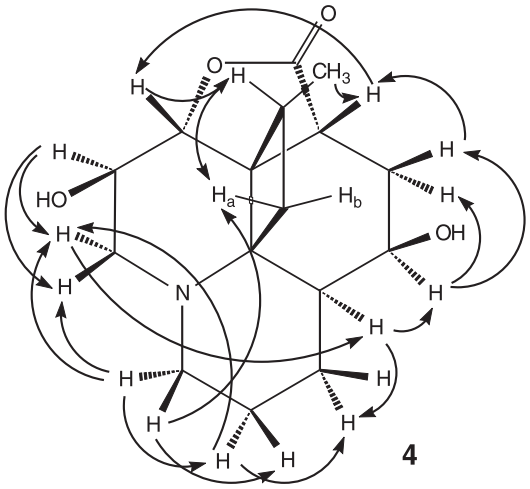

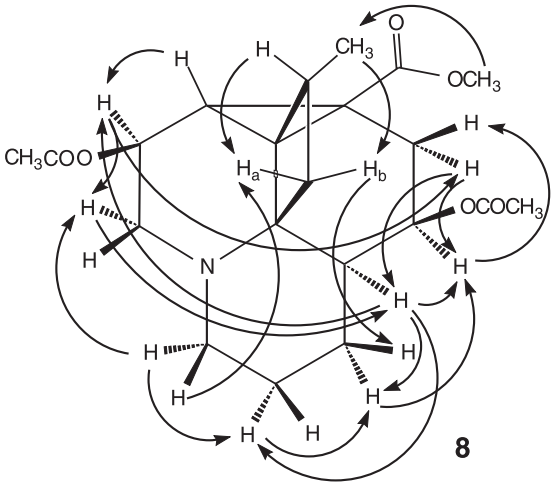

cyclic. The presence of two CH-OH groups is indicated by the ^{1}H NMR (a broad singlet at δ 3.88 and a ddd at δ 3.87) and by the ^{13}C NMR (doublets at δ 68.9 and δ 59.5) spectra. A comparison with the NMR data of annotinine (8) reveals that ester M does not have an epoxide ring. Another difference between annotinine and ester M is the presence of three quaternary carbon atoms in ester M, two of which had to be assigned to C5 (at δ 63.4) and C6 (at δ 38.5), not significantly different from the corresponding signals of annotinine (8). The third signal, at δ 29.2, is attributed to C1 in order to explain the HMBC correlation to H2α, H2β, H3, H8, and H14 (Fig. 4). The correlation C1–H8 necessitates a direct bond between C1 and C7 leading to the formation of a cyclopropane ring. The only proton attached to this ring, at C7, is coupled only to H8 (J = 4.0 Hz). All the above information is in agreement with the unprecedented 9-azapentacyclo[7.3.3.$0^{1,13}$.$0^{2,12}$.$0^{5,13}$]pentadecane structure **5** for ester M.

Complete assignment of all ^{1}H and ^{13}C NMR signals of **5** was further facilitated by the HMQC spectrum and especially by the TROESY spectrum. The cross peaks in the TROESY spectrum between H15 and H13b, and between H14 and H13a, allow us to assign the two signals for the H13 methylene group. The cross peaks H9α-H4, H9α-H8, and H4-H2α allow assignment of the α orientation to all these protons since the α orientation of H4 is known (2, 4). All other correlations shown in Fig. 3 are in agreement with the remaining assignments included in Tables 2 and 3.

The overlapping of the signals of H-3 and H-8 under the above conditions, however, did not allow complete assignment of all HMBC correlations of compound **5**. Consequently, we undertook acetylation with Ac_2O–Py, which afforded a mixture of a monoacetate and a diacetate. Interestingly, a

© 1999 NRC Canada

Table 1. ^{1}H NMR data[a] of **2**, **3**, and **4**.

Assignment	**2**	**3**	**4**
H1	3.49 (dd, 12.3,3.7)	2.48 (dd, 14.6,3.5)	2.91(dd, 6.4,2.8)
H2α	1.70–1.76 (m)	2.70 (ddd, 14.6,9.7,3.5)	2.69 (ddd, 15.3,9.5,2.8)
H2β	2.08 (dt, 14.3,4.0)	2.09 (dt, 14.6,8.0)	1.84 (dt, 15.3,6.3)
H3	3.96 (br q, 3.7)	4.09 (ddd, 9.7,8.0,7.0)	3.99 (dt, 9.3,6.2)
H4	1.62 (dt, 11.7,3.5)	1.71 (ddd, 12.2,7.0,4.0)	1.61 (dd, 15.9,6.2)
H7	2.94 (d, 4.2)	3.64 (d, 4.5)	4.08 (d, 2.4)
H8	3.15 (d, 4.2)	3.22 (dd, 4.5,2.4)	3.92 (dt, 3.3,2.4)
H9α	3.27 (d, 13.9)	3.24 (d, 13.8)	3.14 (dd, 13.0,2.2)
H9β	3.01 (dd, 13.9,1.5)	2.97 (dd, 13.8,2.2)	2.51 (dd, 13.0,3.3)
H10α	2.53 (ddt, 14.5,4.5,1.5)	2.58 (ddt, 14.3,3.7,1.8)	2.62 (ddt, 13.7,3.3,1.7)
H10β	3.22 (dt, 12.9,3.5)	2.99–3.06 (m)	3.03 (td, 13.7,3.0)
H11α	1.71 (tt, 13.2,4.5)	1.67 (tt, 13.2,4.0)	1.68 (m)
H11β	1.30 (br d, 13.4)	1.28 (dquint, 13.2,2.8)	1.34 (dquint, 13.2,2.8)
H12α	1.41–1.46 (m)	1.52 (dddd, 12.0,4.0,2.3,1.8)	1.47–1.51 (m)
H12β	1.40 (dq, 12.3,3.7)	1.48 (dq, 12.5,4.0)	1.47 (dq, 12.5,3.7)
H13a	2.02 (dd, 11.0,8.6)	2.03 (dd, 11.5,10.4)	2.03 (dd, 11.7,9.5)
H13b	1.99 (t, 11.0)	1.92 (t, 11.5)	1.95 (dd, 11.7,10.0)
H14	2.89–2.96 (m)	2.99–3.06 (m)	2.86 (tq, 9.7,7.1)
H15	1.09 (d, 7.2)	1.08 (d, 7.5)	1.09 (d, 7.1)
H17	3.68 (s)	3.68 (s)	

[a]600 MHz. $CDCl_3$.

Table 2. ^{1}H NMR data of **5**·HCl (CD_3OD, 600 MHz), **6**, **7**, and **8** ($CDCl_3$, 600 MHz).

Assignment	**5**·HCl	**6**	**7**
H2α	1.48 (dd, 15.9,2.3)	1.30 (dd, 16.1,2.4)	1.49 (dd, 16.0,2.4)
H2β	3.12 (dd, 15.9,3.0)	3.21 (ddd, 16.1, 3.3, 0.8)	2.96 (dd, 16.0,2.5)
H3	3.88 (br s)	4.83 (dd, 4.9,2.5)	3.86 (br s)
H4	1.03 (br d, 11.5)	0.93 (br d, 11.5)	0.85 (br d, 11.5)
H7	2.32 (d, 4.0)	2.23 (d, 3.6)	2.19 (d, 3.9)
H8	3.87 (ddd, 8.2,7.9,4.0)	3.74 (dt, 7.6,3.5)	4.73 (dt, 7.7,3.9)
H9α	3.40 (dd, 13.0,7.9)	3.00 (dd, 12.1,7.7)	2.95 (dd, 11.8,7.7)
H9β	3.01 (dd, 13.0,8.2)	2.86 (dd, 12.1,7.5)	2.78 (dd, 11.8,7.7)
H10α	3.16–3.22 (m)	2.63 (dt, 14.0,3.5)	2.58 (dt, 13.0,3.6)
H10β	3.58 (ddd, 13.5,12.5,4.2)	3.19–3.24 (m)	3.20 (dt, 13.9,3.6)
H11α	1.93 (ddddd, 14.8,12.5,11.0,5.2,5.0)	1.64–1.73 (m)	1.68 (dddd, 13.2,11.3,10.5,5.0)
H11β	1.82 (dquint, 14.8,3.5)	1.38–1.46 (m)	1.36–1.42 (m)
H12α	1.58 (dquint, 12.4,2.5)	1.48–1.54 (m)	1.59 (dddd, 11.5,11.5,10.5,4.5)
H12β	1.65 (dddd, 12.4,11.6,11.0,4.6)	1.38–1.46 (m)	1.47–1.52 (m)
H13a	2.40 (dd, 12.8,8.6)	2.21 (dd, 11.3,8.7)	2.11–2.17 (m)
H13b	2.64 (dd, 12.8,8.8)	1.99 (dd, 11.3,8.7)	2.11–2.17 (m)
H14	3.16–3.22 (m)	3.06 (tq, 8.7,6.8)	2.94–3.02 (m)
H15	1.00 (d, 6.8)	0.92 (d, 6.8)	0.90 (d, 6.8)
H17	3.67 (s)	3.61 (s)	3.63 (s)
$COCH_3$		2.05 (s)	2.06 (s)

partial hydrolysis occurred during chromatographic purification of the diacetate, providing a monoacetate different from the monoacetate produced by direct acetylation. A detailed analysis of all spectroscopic data revealed that monoacetylation occurs at the less sterically hindered hydroxyl group at C-8, leading to derivative **7**, while the partial hydrolysis of the diacetate **8** leads to monoacetate **6**, having an acetoxy group at C-3. The complete assignment of all ^{1}H and ^{13}C signals of the acetates **6**, **7**, and **8** are given in Tables 2 and 3 and are based on ^{1}H NMR, ^{1}H–^{1}H COSY, HMQC, HMBC, and TROESY spectra.

Several cases of base-induced cyclization of carbonyl compounds leading to the formation of a cyclopropane ring have been documented in the literature. A close analogy involving a carbanion attack on an epoxide ring is described in ref. 9.

Experimental

General methods

Melting points are uncorrected. The HREIMS spectra were recorded on a AEI-50 mass spectrometer. ^{1}H NMR, ^{1}H–^{1}H COSY, HMQC, HMBC, and TROESY spectra were re-

© 1999 NRC Canada

Table 3. ^{13}C NMR data of compounds **2**–**8**.

C [a]	**2** [b]	**3** [b]	**4** [b]	**5**·HCl [c]	**6** [b]	**7** [b]	**8** [b]
C1	37.8	40.7	40.8	29.2	28.2	27.7	28.0
C2	32.5	32.3	30.5	29.3	26.3	30.3	26.2
C3	69.4	67.1	66.2	68.9	71.0	69.2	71.1
C4	34.1	32.0	35.8	38.8	38.8	39.7	38.8
C5	58.1	58.0	59.1	63.4	56.0	55.2	55.2
C6	41.6	41.5	46.8	38.5	38.8	38.9	39.0
C7	51.8	53.8	80.7	33.9	32.7	29.2	29.3
C8	51.6	51.5	67.1	59.5	61.5	64.4	64.2
C9	43.8	44.2	48.5	50.9	51.6	48.4	48.3
C10	47.6	48.1	50.4	49.4	46.5	46.8	46.5
C11	21.2	19.9	22.3	21.4	22.0	22.2	22.0
C12	24.9	22.9	24.9	21.9	22.7	23.0	22.9
C13	34.5	35.2	33.8	35.3	35.4	36.1	35.8
C14	33.2	31.3	30.9	29.9	28.6	28.9	28.6
C15	16.2	16.6	14.7	17.3	16.9	16.9	16.7
C16	175.0	173.7	180.0	173.7	173.0	173.9	172.9
C17	51.7	51.8		52.8	52.0	52.1	52.0
$COCH_3$					170.4, 21.2	170.5, 21.1	170.4, 170.5, 21.0, 21.2

[a]The assignments were verified by HMQC and APT spectra.
[b]In $CDCl_3$.
[c]In CD_3OD.

corded on a Varian Inova 600 spectrometer, and routine ^1H NMR spectra on a Varian Inova 300. ^{13}C NMR and APT spectra were recorded on a Bruker AM-400 spectrometer. Chemical shifts are reported in ppm downfield of TMS, and carbon multiplicities were measured with the APT and HMQC sequence. UV spectra were recorded on a Hewlett–Packard diode array UV–VIS spectrometer (ICP) with a cell path of 1 mm, and IR spectra on a Nicolet 7199 FTIR spectrometer in solution or under a NIC-PLAN microscope (USCOPE). The optical rotation was measured on a Perkin–Elmer 241 polarimeter with a cell path of 10 cm, and CD spectra were measured on a Jasco ORD-CD spectrometer with a cell path of 1 mm.

Preparation of ester M (5)

Potassium (540 mg, 13.8 mmol) was dissolved in 30 mL of anhydrous methanol and, after cooling to room temperature, annotinine (514 mg, 1.87 mmol) was added. After 3 days at r.t. the reaction mixture was evaporated to dryness in vacuo, treated with 20 mL of distilled cold water, filtered, and dried in vacuo to afford ester M (**5**) as colorless crystals (291 mg, 51%). The aqueous residue was extracted with EtOAc (5 × 20 mL). The extract was dried over $MgSO_4$, filtered, evaporated in vacuo to 1 mL, and kept overnight at r.t. to provide annotinine hydrate (**4**, 79 mg, 15% yield). The mother liquor was evaporated to dryness and subjected to flash chromatography on neutral alumina. Elution with hexane:EtOAc 1:1 provided methyl epiannotinate (**2**, 12.7 mg).

Preparation of 2, 3, and 4

Potassium hydroxide (229 mg, 4.08 mmol) was dissolved in anhydrous methanol (20 mL) and annotinine (450 mg, 1.63 mmol) was added. After standing for 3 days at r.t. the reaction mixture was evaporated to dryness in vacuo, treated with 20 mL of distilled water, and extracted with CH_2Cl_2 (5 × 20 mL). The organic extract was dried over $MgSO_4$, filtered, and evaporated in vacuo to dryness. The crude extract (440 mg) was subjected to flash chromatography on silica gel. Elution with CH_2Cl_2:MeOH 95:5 provided annotinine hydrate (**4**, 87.3 mg), methyl epiannotinate (**2**, 286.5 mg), and, with CH_2Cl_2:MeOH 1:1, methyl annotinate (**3**, 59.6 mg). Ester M was not obtained under these conditions.

Preparation of hydrochloride of ester M

To a solution of ester M (3.8 mg) in MeOH (200 μL) was added 5% HCl (15 μL). Toluene (500 μL) was added and the solvent was removed in vacuo. The residue was crystallized from methanol to provide the hydrochloride of ester M (**5**·HCl, 4.1 mg) as colorless prisms.

Acetylation of ester M

Ester M (10 mg) was dissolved in 0.5 mL of hot acetic anhydride. After cooling to room temperature 0.5 mL of pyridine was added. The reaction mixture was evaporated to dryness in vacuo, then dissolved in CH_2Cl_2 and washed with 1% aqueous ammonia. The organic layer was dried with $MgSO_4$, filtered, and evaporated in vacuo. The crude mixture was separated by flash chromatography on neutral alumina using hexane:EtOAc 7:3 to provide the diacetate of ester M (**8**), and hexane:EtOAc 1:1 to elute the monoacetate of ester M (**7**). The reaction was monitored using TLC and ^1H NMR. Immediately after dissolving ester M in hot acetic anhydride a mixture (10 mg) of **7** and **8** in 5:1 ratio was obtained; after 4 h 2:1, 20 h 1:1, after 4 days 1:2, and after 7 days 0:1.

Hydrolysis of the diacetate of ester M (8)

Distilled water (300 μL) and 36% HCl (100 μL) were added to a solution of diacetate **8** (8.5 mg) in MeOH (100 μL). The solution was left at r.t. for 17 h. Methylene chloride (10 mL) was added and the mixture was washed

© 1999 NRC Canada

Fig. 4. Pertinent HMBC correlations of **2**, **4**, and **8**.

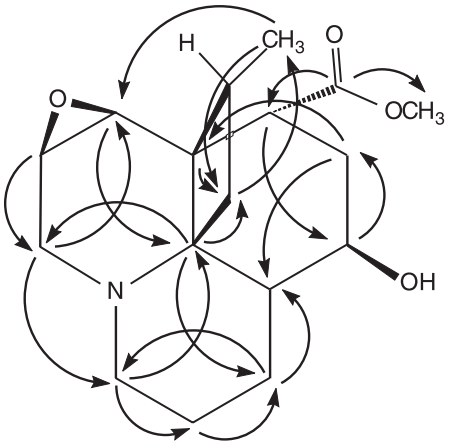

2

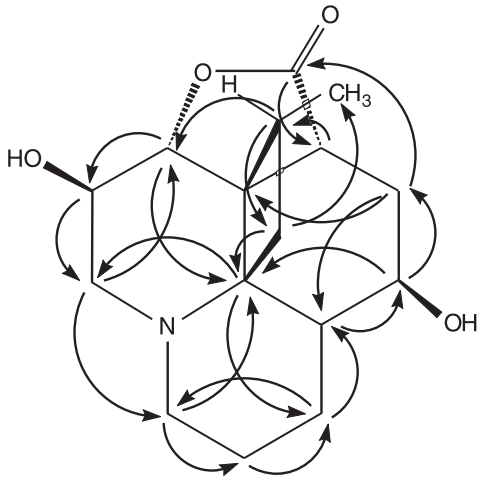

4

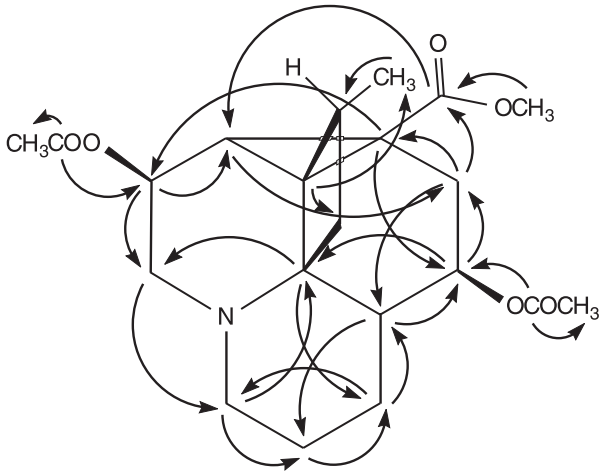

8

with 10 mL of 1% aqueous ammonia. The organic layer was dried with $MgSO_4$ and the solvent was reduced in vacuo to 1 mL and kept overnight at r.t. to provide the monoacetate **6** (4.1 mg) as colorless crystals.

*Methyl epiannotinate (**2**)*: colorless amorphous solid; $[\alpha]_D$ +12.6 (MeOH, *c* 0.23); UV λ_{max}^{MeOH} nm (log ε): 340 (2.52); CD: $\Delta\varepsilon_{223}$ –0.32, $\Delta\varepsilon_{297}$ +0.46, $\Delta\varepsilon_{337}$ –0.40 (MeOH, *c* 0.23); IR ($CHCl_3$) ν_{max}: 3416 (OH), 2929, 2862, 1727 (C=O), 1446, 1300, 1230, 1190, 1132, 1113, 1088, 1031, 1013, 840, 752, 405 cm^{-1}; ^1H NMR, Table 1; ^{13}C NMR, Table 3; HREIMS *m/z* (rel. int.): 307.1803 $[M]^+$ (2.4%, calcd. for $C_{17}H_{25}NO_4$: 307.1783), 273 (2) $[M - OCH_3]^+$.

*Methyl annotinate (**3**)*: colorless amorphous solid; $[\alpha]_D$ –40.4 (MeOH, *c* 0.23); UV λ_{max}^{MeOH} nm (log ε): 338 (1.94); CD: $\Delta\varepsilon_{219}$ –1.11, $\Delta\varepsilon_{249}$ +0.12, $\Delta\varepsilon_{337}$ –0.08 (MeOH, *c* 0.23); IR ($CHCl_3$) ν_{max}: 3439, 2932, 2862, 1726, 1436, 1356, 1316, 1261, 1225, 1204, 1174, 1114, 1089, 1054, 1030, 1014, 991, 974, 962, 899, 882, 843, 824, 778, 733, 699, 622, 583, 497, 439 cm^{-1}; ^1H NMR, Table 1; ^{13}C NMR, Table 3; HREIMS *m/z* (rel. int.): 307.1776 $[M]^+$ (6.9%, calcd. for $C_{17}H_{25}NO_4$: 307.1783), 276 (7) $[M - OCH_3]^+$.

*Annotinine hydrate (**4**)*: colorless prisms, mp 211–213°C; $[\alpha]_D$ –26.5 (MeOH, *c* 0.20); CD: $\Delta\varepsilon_{225}$ –2.09 (MeOH, *c* 0.2); IR (USCOPE) ν_{max}: 3503 (OH), 2981, 2956, 2932,

© 1999 NRC Canada

2861, 2592, 1762 (lactone), 1462, 1446, 1408, 1378, 1361, 1334, 1321, 1309, 1294, 1269, 1242, 1219, 1205, 1195, 1181, 1170, 1155, 1130, 1109, 1090, 1075, 1047, 1008, 989, 966, 956, 928, 887, 875, 855, 841, 809, 776, 742, 715, 683, 630, 593, 577 cm^{-1}; ^1H NMR, Table 1; ^{13}C NMR, Table 3; HREIMS *m/z* (rel. int.): 293.1609 $[M]^+$ (2.5%, calcd. for $C_{16}H_{23}NO_4$: 293.1627).

*Ester M (**5**)*: colorless prisms, mp 250–251°C; $[\alpha]_D$ –31.4 (DMSO, *c* 0.10); CD: $\Delta\varepsilon_{245}$ –0.98 (DMSO, *c* 0.10); IR (USCOPE) ν_{max}: 3376 (OH), 2977, 2950, 2907, 2865, 1718 (C=O), 1462, 1433, 1276, 1236, 1185,1130, 1115, 1092, 1082, 1059, 1016; HREIMS *m/z* (rel. int.): 307.1781 $[M]^+$ (33.9%, calcd. for $C_{17}H_{25}NO_4$: 307.1783), 292 (12) $[M - CH_3]^+$, 278 (7) $[M - CH_3 - H_2O]^+$, 260 (4) $[M - CH_3 - H_2O - H_2O]^+$.

*Ester M hydrochloride (**5**·HCl)*: colorless prisms, mp 253–254°C; $[\alpha]_D$ –51.0 (MeOH, *c* 0.20); CD: $\Delta\varepsilon_{215}$ –1.93 (MeOH, *c* 0.20); IR (USCOPE) ν_{max}: 3376 (OH), 2977, 2950, 2865, 2349, 2302, 1717 (C=O), 1462, 1433, 1364, 1349, 1314, 1276, 1254, 1236, 1206, 1185, 1169, 1149, 1130, 1115, 1092, 1081, 1059, 1034, 1015, 994, 975, 932, 919, 902, 859, 801, 773, 738, 709, 672, 630, 593 cm^{-1}; ^1H NMR, Table 2; ^{13}C NMR, Table 3; HREIMS *m/z* (rel. int.): 307.1780 $[M]^+$ (23.1%, calcd. for $C_{17}H_{25}NO_4$: 307.1783), 292 (10) $[M - CH_3]^+$, 278 (7) $[M - CH_3 - H_2O]^+$, 260 (4) $[M - CH_3 - H_2O - H_2O]^+$.

*Monoacetate **6***: colorless needles mp 155–157°C; $[\alpha]_D$ –35.6 (MeOH, *c* 0.18); CD: $\Delta\varepsilon_{220}$ –1.35 (MeOH, *c* 0.18); IR ($CHCl_3$) ν_{max}: 3320 (OH), 2949, 2868, 1739 (C=O), 1723 (C=O), 1435, 1376, 1284, 1241, 1196, 1169, 1113, 1024, 955, 932, 755, 667 cm^{-1}; ^1H NMR, Table 2; ^{13}C NMR, Table 3; HREIMS *m/z* (rel. int.): 349.1890 $[M]^+$ (54.2%, calcd. for $C_{19}H_{27}NO_5$: 349.1889), 334 (18) $[M - CH_3]^+$, 320 (12) $[M - CH_3 - H_2O]^+$.

*Monoacetate **7***: colorless amorphous solid; $[\alpha]_D$ –20.2 (MeOH, *c* 0.42); CD: $\Delta\varepsilon_{218}$ –1.94 (MeOH, *c* 0.24); IR ($CHCl_3$) ν_{max}: 3516 (OH), 2946, 2865, 1720 (br, C=O), 1435, 1369, 1280, 1240, 1205, 1168, 1143, 1116, 1099, 1083, 1031, 1017, 988, 945, 755, 506 cm^{-1}; ^1H NMR, Table 2; ^{13}C NMR, Table 3; HREIMS *m/z* (rel. int.): 349.1884 $[M]^+$ (1.6%, calcd. for $C_{19}H_{27}NO_5$: 349.1889), 334 (2) $[M - CH_3]^+$.

*Diacetate **8***: colorless amorphous solid; $[\alpha]_D$ –35.2 (MeOH, *c* 0.27); CD: $\Delta\varepsilon_{236}$ –2.50 (MeOH, *c* 0.14); IR ($CHCl_3$) ν_{max}: 2948, 2864, 1740 (C=O), 1720 (C=O), 1435, 1372, 1282, 1240, 1169, 1145, 1110, 1083, 1023, 988, 955, 756 cm^{-1}; ^1H NMR, Table 2; ^{13}C NMR, Table 3; HREIMS *m/z* (rel. int.): 391.1994 $[M]^+$ (39.8%, calcd. for $C_{21}H_{29}NO_6$: 391.1995), 376 (8) $[M - CH_3]^+$, 360 (9) $[M - OCH_3]^+$.

Acknowledgements

The financial support of the Natural Sciences and Engineering Research Council of Canada is gratefully acknowledged. We also thank Glen Bigam of the High-Resolution NMR Laboratory for technical assistance.

References

1. D.B. MacLean. *In* The alkaloids. Vol. 10. *Edited by* R.H.F. Manske. Academic Press, New York. 1968. p. 306.
2. K. Wiesner, W.A. Ayer, L.R. Fowler, and Z. Valenta. Chem. Ind. (London), 564 (1957).
3. K. Wiesner, L. Poon, I. Jirkovsky, and M. Fishman. Can. J. Chem. **47**, 433 (1969).
4. M. Przybylska and L. Marion. Can. J. Chem. **35**, 1075 (1957).
5. M. Martin-Smith, R. Greenhalgh, and L. Marion. Can. J. Chem. **35**, 409 (1957).
6. P.W. Braithwaite. M.S.Thesis. University of Alberta, Canada. 1960.
7. T.L. Hwang and A.J. Shaka. J. Magn. Reson. Ser. B **102**, 155 (1993).
8. D.W. Hughes, R.V. Gerard, and D.B. MacLean. Can. J. Chem. **67**, 1765 (1989).
9. G. Büchi and W.S. Saari. J. Am. Chem. Soc. **79**, 3519 (1957).

© 1999 NRC Canada

New aspects on the reactivity of $MoO_2(S_2CNEt_2)_2$ with Me_3SiX. A peculiar *trans* effect control

H. Teruel and A. Sierraalta

Abstract: The reaction of $MoO_2(S_2CNEt_2)_2$ with Me_3SiI and Me_3SiNCS yielded $MoOI_2(S_2CNEt_2)_2$ and $MoO(NCS)_2(S_2CNEt_2)_2$, respectively, similar to results reported for Me_3SiCl and Me_3SiBr. On the contrary, $MoO(OSiMe_3)CN(S_2CNEt_2)_2$ was the only compound isolated from the reaction of $MoO_2(S_2CNEt_2)_2$ with Me_3SiCN. To study the effects of ligands on the reactivity of siloxy compounds, ab initio calculations were undertaken for $Mo(OSiH_3)L(S_2CNH_2)_2$ molecules, for L = Cl, Br, I, NCS, and CN. The electronic density, $\rho(\boldsymbol{r})$, was analysed by means of the topological theory of Atoms in Molecules (AIM). The analysis of $-\nabla^2\rho(\boldsymbol{r})$ critical points (CPs) at the molybdenum valence shell showed, only in the case of L = CN, a local charge concentration region (N-type CPs) susceptible to electrophilic attacks. However, for L = Cl, Br, I, and NCS, local charge depletion sites (E-type CPs) were found in a bond-free region. The absence of any accessible E-type CPs and the presence of an N-type CP in the same region, opposite to the Mo=O group, justified the stability of $Mo(OSiMe_3)L(S_2CNEt_2)_2$ for L = CN, and the formation of $MoOL_2(S_2CNEt_2)_2$ for L = Cl, Br, I, and NCS by further reaction with the corresponding Me_3SiL.

Key words: ab initio calculation, electronic density, Mo-siloxy compound, reactivity, theoretical.

Résumé : Les réactions du $MoO_2(S_2CNEt_2)_2$ avec le Me_3SiI et le Me_3SiNCS conduisent respectivement au $MoOI_2(S_2CNEt_2)_2$ et $MoO(NCS)_2(S_2CNEt_2)_2$; ces résultats sont semblables à ceux obtenus avec le Me_3SiCl et Me_3SiBr. Par ailleurs, lors de la réaction du $MoO_2(S_2CNEt_2)_2$ avec le Me_3SiCN, le seul produit isolé est le $MoO(OSiMe_3)CN(S_2CNEt_2)_2$. Afin d'étudier les effets des ligands sur la réactivité des composés siloxy, on a effectué des calculs ab initio sur les molécules $Mo(OSiMe_3)L(S_2CNEt_2)_2$ dans lesquelles L = Cl, Br, I, NCS et CN. On a analysé la densité électronique, $\rho(\boldsymbol{r})$, à l'aide de la théorie topologique des atomes dans les molécules. L'analyse des points critiques (PC) du $-\nabla^2\rho(\boldsymbol{r})$ au niveau de la couche de valence du molybdène a montré que le cas où L = CN est le seul à comporter une région de concentration locale de charge (PC de type N) susceptible de subir des attaques électrophiles. Au contraire, dans les cas où L = Cl, Br, I et NCS, on a observé l'existence de sites dépourvus de charge locale (PC de type E) dans une région sans liaison. L'absence de tout PC de type E accessible et la présence d'un PC de type N dans la même région, à l'opposé du groupe Mo=O, explique la stabilité du $Mo(OSiMe_3)L(S_2CNEt_2)_2$ dans le cas où L = CN ainsi que la formation, dans les cas où L = Cl, Br, I et NCS, de $MoOL_2(S_2CNEt_2)_2$ qui résulte d'une réaction additionnelle avec le Me_3SiL correspondant.

Mots clés : calculs ab initio, densité électronique, composé Mo-siloxy, réactivité, théorique.

[Traduit par la Rédaction]

Introduction

Metallosiloxanes have been found to be structurally similar to modified silica surfaces (1). This structural resemblance has proved useful in interpreting reaction mechanisms for different catalytic transformations. In view of the latter, there have been many attempts to develop suitable homogeneous compounds as models for heterogeneous catalysts. The reactions of CrO_3 (2), Me_3ReO_3 (3), $(\eta^5\text{-}C_5Me_5)ReO_3$ (3), $(\eta^5\text{-}C_5Me_5)_2WO$ (4), $AgTcO_4$ (5), $AgReO_4$ (5), and $[(\eta^5\text{-}C_5Me_5)WO_3][NEt_4]$ (6) with R_3SiCl are some examples of these studies. However, in nearly all cases it has been reported that the expected metalsiloxy compound is rarely isolated, a dihalogenated compound being obtained instead.

It has been proposed (7) that the reaction of oxocompounds and halosilanes takes places in two steps, both involving a 1,2-addition (Scheme 1).

The initial adduct containing the silyl fragment is not isolated, as it reacts, very quickly, with a second mole of the R_3SiX compound. Nevertheless, it is not clear what determines the isolation of the siloxy or disubstituted compound. For instance, the preparation of $MoO(OSiMe_3)CN(S_2CNEt_2)_2$ has been reported from the reaction of $MoO_2(S_2CNEt_2)_2$ with Me_3SiCN (8) while $MoOCl_2(S_2CNEt_2)_2$ is the sole product isolated from the analogous reaction with Me_3SiCl (7).

A better understanding of this reactivity can be obtained from an analysis of the quantum electronic properties of the siloxy compounds, as this provides a better insight into the electronic factors that may control the silylation of oxocompounds. In the quantum-mechanical theory "Atoms

Received November 13, 1998.

H. Teruel.[1] Universidad Simón Bolivar, Baruta 89000, Caracas1081, Venezuela.
A. Sierraalta.[1] Instituto Venezolano de Investigaciones Científicas, Centro de Química, Apartado 21827, Caracas, Venezuela.

[1]Authors to whom correspondence may be addressed. HT: e-mail: hteruel@usb.ve; AS: e-mail: asierral@quimica.ivic.ve

© 1999 NRC Canada

Scheme 1.

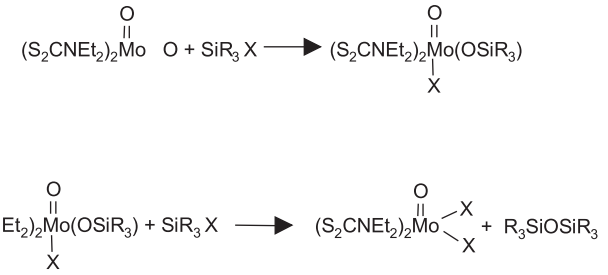

in molecules" (AIM) (9–11), the chemical bonds, electronic structure, and molecular reactivity are interpreted in terms of the total molecular electronic density, $\rho(\boldsymbol{r})$, and its corresponding Laplacian, $\nabla^2\rho(\boldsymbol{r})$. The $\rho(\boldsymbol{r})$, which is an observable parameter, allows the categorization of the atomic interactions in a molecule. The atomic and bond properties are settled in terms of well-defined parameters providing a rigorous interpretation of quantum-chemical calculations. Therefore, the AIM theory allows a more precise description of the chemical phenomena than the use of atomic or localized orbitals. A topological analysis of $-\nabla^2\rho(\boldsymbol{r})$, that is, the spatial array and absolute values of $-\nabla^2\rho(\boldsymbol{r})$, maximal and saddle points, provides useful information concerning the localization and characterization of the nucleophilic and electrophilic sites in a molecule.

In this work, a systematic theoretical study based on the quantum-mechanical theory "Atoms in molecules" (AIM) for $MoO(OSiH_3)L(S_2CNH_2)_2$ compounds, L = Cl, Br, I, NCS, and CN, was made. Experimentally, the reactions of $MoO_2(S_2CNEt_2)_2$ with Me_3SiI and with $Me_3Si(NCS)$ were carried out and the new compounds, $MoO(NCS)_2(S_2CNEt_2)_2$ and $MoOI_2(S_2CNEt_2)_2$, were prepared.

Experimental section

Manipulations involving air-sensitive reagents were performed under nitrogen with the aid of Schlenk techniques. Solvents were purified as follows: dichloromethane and acetonitrile were distilled using P_2O_5; diethyl ether was thoroughly degassed prior to use by repeated evacuation followed by admission of dry and oxygen-free nitrogen. $MoO_2(S_2CNEt_2)$ (12) and $MoO(OSiMe_3)CN(S_2CNEt_2)_2$ (8) were prepared by previously reported methods. All other reagents were purchased from commercial sources and used without prior purification. Infrared spectra were recorded on a Brucker IFS 55 FT-IR spectrometer. ^1H and ^{13}C NMR were recorded on a Brucker MX300 spectrometer. Chemical shifts were obtained by residual solvent protons. Elemental analyses were performed on a Perkin–Elmer 2400 microanalyzer.

Reaction of $MoO_2(S_2CNEt_2)_2$ with $(CH_3)_3Si(NCS)$

$(CH_3)_3Si(NCS)$ (0.05 mL; 0.557 mmol) was added at 25°C, while stirring, to a CH_2Cl_2 solution (20 cm^3) containing $MoO_2(S_2CNEt_2)_2$ (0.200 g; 0.472 mmol). An immediate colour change from the original light yellow to red was observed. After 3 h, the volume of the solution was reduced to 5 cm^3 under reduced pressure. Diethyl ether (5 cm^3) was then added. The red microcrystalline solid formed was filtered, washed with cold diethyl ether (3 × 5 cm^3), and dried under vacuum. Yield (based on $MoO_2(S_2CNEt_2)_2$) was 0.215 g, 87%. The main IR bands were (KBr/cm^{-1}) 2050 (s, sh), 2018 (vs) (N-C); 951 m (Mo=O); 2987 w, 2940 w, 176, 1545 s, 1462 m, 1445 m, 1386 w, 1353 m, 1290 s, 1203 m, 1077 w, 1009, 850 w, 577 w (S_2CNEt_2). Anal. calcd. for $MoC_{12}H_{20}N_4S_6O$: C 27.38, H 3.83, N 10.65, S 36.48; found: C 27.78, H 3.76, N 10.13, S 35.88.

Reaction of $MoO_2(S_2CNEt_2)_2$ with $(CH_3)_3SiI$

$(CH_3)_3SiI$ (0.05 mL; 0.354 mmol), was added at 25°C, while stirring, to a CH_2Cl_2 solution (20 cm^3) containing $MoO_2(S_2CNEt_2)_2$ (0.100 g; 0.236 mmol). An immediate darkening from light yellow to red occurred. After 3 h, the volume of the solution was reduced to 5 cm^3 under reduced pressure and diethyl ether (5 cm^3) was added. The red microcrystalline solid formed was filtered, washed with cold diethyl ether (3 × 5 cm^3), and dried under vacuum. Yield (based on $MoO_2(S_2CNEt_2)_2$) was 0.103 g, 66%). ^1H NMR (300 MHz, $CDCl_3$, ppm): 1.46 (12H, t, CH_3), 3.97 (8H, m, CH_2). The main IR bands were (KBr/cm^{-1}) 937 m (Mo=O); 2975 w, 2929 w, 176, 1541 s, 1515 s, 1456 m, 1437 m, 1351 m, 1298 m, 1276 m, 1204 m, 1151 m, 1070 m, 848 m, (S_2CNEt_2). Anal. calcd. for $MoC_{10}H_{20}N_2S_4OI$: C 18.08, H 3.04, N 4.22; found: C 18.45, H 3.22, N 4.06.

Theoretical section

Theoretical background

According to the AIM theory $\nabla^2\rho(\boldsymbol{r})$ provides information concerning electronic charge: $\nabla^2\rho(\boldsymbol{r}) > 0$ (or $-\nabla^2\rho(\boldsymbol{r}) < 0$) implies locally depleted charge while $\nabla^2\rho(\boldsymbol{r}) < 0$ (or $-\nabla^2\rho(\boldsymbol{r}) > 0$) signifies locally concentrated charge (13–16). There are two important types of $-\nabla^2\rho(\boldsymbol{r})$ CPs at the atoms: maximum and saddle points, or electronic holes. The former are classified as (3, –3) CPs or N-type CPs since they possess local concentrations of electronic charge and represent nucleophilic sites susceptible to attack by electrophiles. The saddle points are (3, +1) or E-type CPs and represent local charge depletion, or electronic holes, that are associated with electrophilic sites susceptible to nucleophile attack. Thus, the AIM theory explains the Lewis model for acid–base reactions by the alignment of local charge concentrations, N-type CPs, at the base, with charge depletions, and E-type CPs, at the acid centre. This proposed scheme is quite general and, for instance, it has been shown that in hydrogen abstraction from CH_4, by MgO or LiO, the oxide active sites correspond to the $-\nabla^2\rho(\boldsymbol{r})$ N-type CPs (17).

Computational details

All calculations and geometry optimizations were carried out using the Gaussian 94 program (18) at the HF-SCF level. The basis sets and the ab initio relativistic effective potentials proposed by Christiansen and co-workers (19) were used for Si, S, Cl, Br, and I atoms. The 3*d* and 4*d* electrons were included in the valence space of the Br and I, respectively. The basis sets for these atoms were augmented with diffuse *p* functions ($\xi_p(Cl) = 0.049$, $\xi_p(Br) = 0.044$) and *d* polarization functions ($\xi_d(Cl) = 0.50$, $\xi_d(Br) = 0.36$) (20). For Si and S atoms only *d* polarization functions ($\xi_d(Si) = 0.45$, $\xi_d(S) = 0.65$) were added. These changes result in the following contraction schemes: Si(31/31/1), S(31/31/1), Cl(31/311/1), Br(21/211/311), I(21/211/311). The all-

© 1999 NRC Canada

Fig. 1. Calculated geometry for $MoOL_2(S_2CNH_2)_2$, where L = Cl or Br.

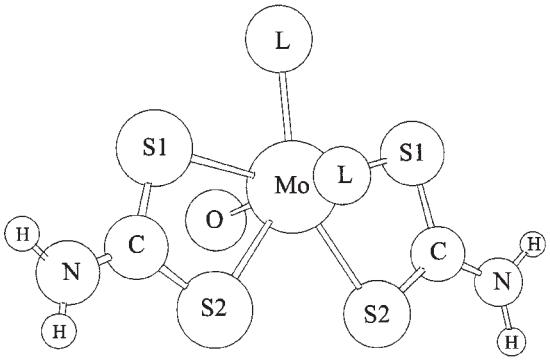

Table 1. Comparison of the bond distances (Å) and bond angles (degrees) for compounds $MoOL_2(S_2CNH_2)_2$, where L = Cl or Br.

Bond distances and angles	$MoOL_2(S_2CNH_2)_2$			
	Cl [a]	Cl [b]	Br [a]	Br [b]
Mo—O	1.701	1.636	1.648	1.633
Mo—L1	2.417	2.435	2.550	2.592
Mo—L2	2.504	2.508	2.729	2.707
Mo—S1	2.481	2.543	2.490	2.543
Mo—S2	2.519	2.583	2.498	2.576
Mo—S3	2.515	2.583	2.481	2.543
O1-Mo-L1	95.4	96.0	94.4	95.2
O1-Mo-L2	175.9	173.2	178.1	174.3
O1-Mo-S2	96.7	95.5	93.3	91.2
O1-Mo-S3	92.2	90.5	95.4	95.7
O1-Mo-S4	92.5	90.5	96.2	91.2
L1-Mo-S1	96.4	95.5	94.2	95.7
L1-Mo-L2	88.6	90.8	87.1	90.5

[a]Reported for $MoOL_2(S_2CNEt_2)_2$, where L = Cl or Br (19).
[b]This work.

electron 6-31G* basis sets from the Gaussian library were employed for the H, C, N, and O atoms. The basis set and the relativistic compact effective potentials proposed by Stevens et al. (21) were used, without any modification, for the Mo atom.

The topological properties of $\rho(\boldsymbol{r})$ and $-\nabla^2\rho(\boldsymbol{r})$ were calculated with a locally modified version of the EXTREM program.[2] In the calculations of $\rho(\boldsymbol{r})$ the wfn file was generated using the HF-SCF geometry with the Gaussian 94 program at the MP2 level.

Calculated geometry for $MoO_2(S_2CNH_2)_2$ and $MoOL_2(S_2CNH)_2$

Due to the lack of X-ray structural information available for compounds $MoO(SiMe_3)L(S_2CNEt_2)_2$ where L = Cl, Br, I, or NCS, we performed quantum chemical calculations to determine their optimal geometry. Thus, to test the accuracy of the geometry optimization procedure the structures of $MoOCl_2(S_2CNH_2)_2$ and $MoOBr_2(S_2CNH_2)_2$ were calculated (Fig. 1). These results were compared with those reported by X-ray diffraction for $MoOCl_2(S_2CNEt_2)_2$ and $MoOBr_2(S_2CNEt_2)_2$, respectively (23). Selected calculated and experimental bond lengths and angles are given in Table 1, showing good agreement in all cases.

Fig. 2. Calculated geometry for $MoO_2(S_2CNH_2)_2$.

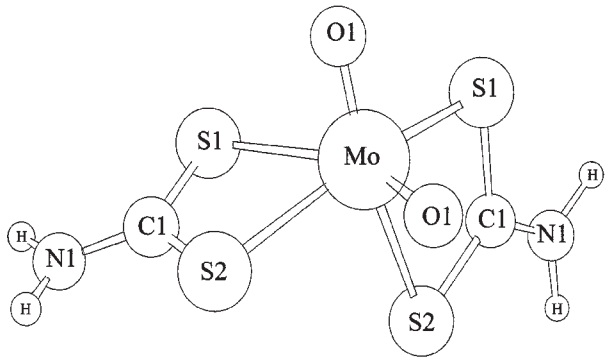

Table 2. Comparison of some important bond distances (Å) and angles (degrees) between $MoO_2(S_2CNEt_2)_2$ (13) and $MoO_2(S_2CNH_2)_2$.

Bond distances and angles	Experimental	Calculated
Mo—O1	1.703	1.661
Mo—S1	2.450	2.512
Mo—S2	2.639	2.793
S1—C1	1.738	1.728
S2—C2	1.700	1.683
C1—N1	1.315	1.315
O1-Mo-O1	105.3	105.3
S1-Mo-S1	148.5	148.6
S1-Mo-S2	68.8	66.7
S1-Mo-S2′	87.0	93.2
S1-Mo-O1	110.3	105.8
S2-Mo-S2′	80.1	80.5
S2-Mo-O1	91.0	90.0
S2-Mo-O1′	155.6	157.7

As an additional test, the optimal geometry of $MoO_2(S_2CNH_2)_2$, **1**, was calculated (Fig. 2). The results were compared with the crystallographic structure reported for $MoO_2(S_2CNEt_2)_2$ (12). Some relevant calculated and experimental bond lengths and angles are compared in Table 2. The deviation observed between both geometries can be attributed mainly to the theoretical level used in this work.

In a similar way, the structures for $MoO(OSiH_3)L(S_2CNH_2)_2$, where L = NCS **2**, Cl **3**, Br **4**, I **5**, and CN **6**, were calculated (Fig. 3). Selected bond lengths (Å) and angles (deg) along with structural data reported for $MoO(OSiMe_3)CN(S_2CNEt_2)_2$ (8) are shown in Table 3. The calculated Mo—O1, Mo—O2, Mo—S1, Mo—S2, and Mo—L bond lengths match rather well the X-ray structure values reported for $MoO(OSiMe_3)CN(S_2CNEt_2)_2$.

Results and discussion

$MoO(NCS)_2(S_2CNEt_2)$ and $MoOI_2(S_2CNEt_2)_2$ preparation

The reaction of $MoO_2(S_2CNEt_2)_2$ with a twofold excess of Me_3SiI or $Me_3Si(NCS)$ produces $MoOI_2(S_2CNEt_2)_2$ and

[2]Y. Aray. Personal communication (1992). See also ref. 22.

© 1999 NRC Canada

Table 3. Relevant bond distances (Å) and bond angles (degrees) for compounds **2–6**.

Bond distances and angles	$MoO(OSiH_3)L(S_2CNH_2)_2$					
	CN[a]	CN[b]	NCS[b]	Cl[b]	Br[b]	I[b]
Mo—O1	1.684	1.653	1.652	1.650	1.650	1.651
Mo—O2	1.945	1.987	1.982	1.984	1.985	1.989
Mo—S1	2.507	2.556	2.557	2.556	2.561	2589
Mo—S2	2.520	2.589	2.608	2.600	2.597	2.568
Mo—L	2.158	2.151	2.056	2.435	2.598	2.837
O1-Mo-O2	177.4	176.6	170.0	171.7	173.1	176.2
O1-Mo-L	93.7	94.6	97.9	96.6	95.6	93.7
L-Mo-O2	88.9	88.8	92.1	91.7	91.2	90.2
S1-Mo-L	73.1	75.9	73.4	75.7	75.6	75.0
S1-Mo-S2	68.6	67.6	66.9	66.9	67.0	67.1
O1-Mo-S2	92.2	91.7	88.3	89.3	89.9	93.9

[a]Experimental values for $MoO(OSiMe_3)CN(S_2CNEt_2)_2$ (8).
[b]This work.

Fig. 3. Calculated geometry for $MoO(OSiH_3)L(S_2CNH_2)_2$, where L = NCS, Cl, Br, I or CN.

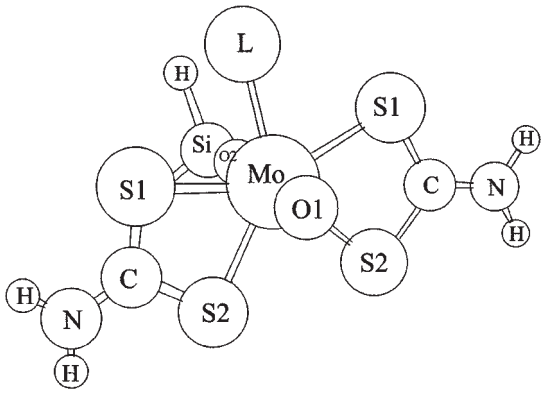

$MoO(NCS)_2(S_2CNEt_2)_2$, respectively. This product distribution is similar to that reported for the same reaction with Me_3SiCl and with Me_3SiBr, where the only products were the dihalogenated compounds $MoOCl_2(S_2CNEt_2)_2$ and $MoOBr_2(S_2CNEt_2)_2$, respectively (7). Under the same experimental conditions $MoO(OSiMe_3)(CN)(S_2CNEt_2)_2$ can be prepared in good yields when M_3SiCN is used (8). The fact that no changes in the stoichiometry were observed when this compound was tested with $(CH_3)_3SiCl$ indicates that the presence of the CN ligand inhibits further reaction with either Me_3SiCN or Me_3SiCl.

Theoretical part

N-type CPs or nucleophilic sites

The values of $-\nabla^2\rho(\boldsymbol{r})$ at the N-type CPs, and the distance from the molybdenum to the CPs $R_{\text{Mo-N,}}$ for compounds **2–6** are reported in Table 4. In all cases, the molybdenum valence shell shows three different local charge concentration groups, N1, N2, and N3. The first of these groups, N1, is composed of an N-type CP positioned opposite the double-bonded oxygen atom, O1, in the Mo—O2 bond direction (Figs. 4 and 5). The $-\nabla^2\rho(\boldsymbol{r}_{N1})$ value for the Mo—O1 bond shows that the O1 atom induces a large charge concentration on the metallic atom at the N1 critical point position. In fact, as a consequence of the electronic repulsion between the

Fig. 4. Distribution of the N-type critical points calculated in $MoO(OSiH_3)L(S_2CNH_2)_2$. The hydrogen atoms are omitted.

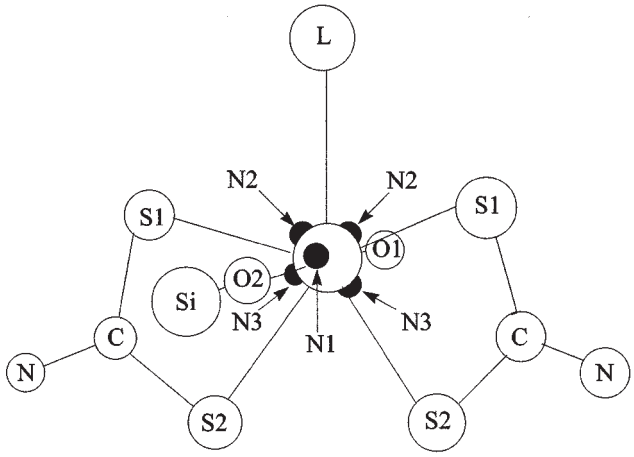

Fig. 5. Distribution of the N-type critical points calculated in $MoO(OSiH_3)CN(S_2CNH_2)_2$. The hydrogen atoms are omitted.

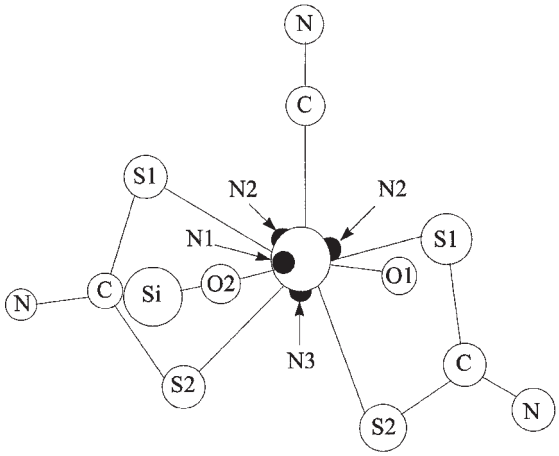

Mo—O2 single bond and the local charge concentration at the N1 position, an O1-Mo-O2 bending angle in **2** is observed when compared to **6**, as shown in Table 3. These results coincide with previous reports, where it has been

© 1999 NRC Canada

Table 4. Values of $-\nabla^2\rho(\boldsymbol{r})$ at the N-type critical points and the distance from the molybdenum to the CPs, $R_{\text{Mo-N,}}$ for the molybdenum valence shell in $MoO(OSiH_3)L(S_2CNH_2)_2$ molecules, **2**–**6**.

	N1			N2			N3		
Compounds	Number of CPs	$R_{\text{Mo-E1}}{}^b$	$-\nabla^2\rho(\boldsymbol{r})^a$	Number of CPs	$R_{\text{Mo-E2}}{}^b$	$-\nabla^2\rho(\boldsymbol{r})^a$	Number of CPs	$R_{\text{Mo-E3}}{}^b$	$-\nabla^2\rho(\boldsymbol{r})^a$
2	1	0.455	10.458	2	0.455	9.861	2	0.455	9.809
3	1	0.455	10.451	2	0.455	9.757	2	0.455	9.753
4	1	0.455	10.445	2	0.455	9.731	2	0.455	9.734
5	1	0.455	10.451	2	0.455	9.761	2	0.455	9.782
6	1	0.455	10.467	2	0.455	9.800	1	0.455	9.902

[a]Values in atomic units.
[b]Distance from the molybdenum to the critical point in angstrom.

Table 5. Values of $-\nabla^2\rho(\boldsymbol{r})$ and $R_{\text{Mo-E,}}$ obtained at the E-type critical points at the molybdenum valence shell in the $MoO(OSiH_3)L(S_2CNH_2)_2$ molecules, **2**–**6**.

	E1			E2			E3			E4		
Compound	Number of CPs	$R_{\text{Mo-E1}}{}^a$	$-\nabla^2\rho(\boldsymbol{r})^b$	Number of CPs	$R_{\text{Mo-E2}}{}^a$	$-\nabla^2\rho(\boldsymbol{r})^b$	Number of CPs	$R_{\text{Mo-E3}}{}^a$	$-\nabla^2\rho(\boldsymbol{r})^b$	Number of CPs	$R_{\text{Mo-E4}}{}^a$	$-\nabla^2\rho(\boldsymbol{r})^b$
2	2	0.457	8.968	1	0.458	9.093	1	0.455	8.563	1	0.456	9.283
3	2	0.457	9.042	1	0.457	9.137	1	0.455	8.610	1	0.457	9.184
4	2	0.457	9.056	1	0.457	9.120	1	0.455	8.620	1	0.457	9.133
5	2	0.457	9.054	1	0.457	9.065	1	0.455	8.639	1	0.457	9.056
6	2	0.457	9.064	1	0.456	9.052	1	0.455	8.598	0	—	—

[a]Values in atomic units.
[b]Distance from molybdenum to the critical point in angstrom.

shown that, in oxocompounds, double-bonded oxygen atoms produce charge concentration at the metal valence shell in the direction opposite to the oxygen atom (24–26).

The second group of N-type CPs, or N2, is composed of two components located in the plane comprising the S1-Mo-S1 moiety, in the region of the Mo—L bond (Figs. 4 and 5). For **2**–**5**, two points facing the latter N2 CP, i.e., around the Mo—S2 bonds (Fig. 4), constitute N3, the last of these CP groups. The values of $-\nabla^2\rho(\boldsymbol{r})$ at the N2 and N3 points, $-\nabla^2\rho(\boldsymbol{r}_{N2})$ and $-\nabla^2\rho(\boldsymbol{r}_{N3})$, respectively, are quite similar (Table 4). Similar to double-bond oxygen atoms (vide supra), sulphur atoms induce charge concentrations at the positions opposite to metal–S bonds (26). This charge concentration phenomenon, generated by the sulphur atoms, either S1 or S2, or the double-bonded O atom (O1), can be rationalized in terms of an electronic *trans* effect. That is, the strong σ and π charge donation from S1, S2, or O1 to the Mo atom generates a local charge concentration, or nucleophilic site, at the position *trans* to these atoms. Thus the O1 atom produces the N1 site, while S1 and S2 generate N3 and N2, respectively.

In the case of, **6**, there is only one N3-type CP located in the S2-Mo-S2 angle, facing the CN ligand, instead of the two N3 obtained for **2**–**5** (Fig. 5). Furthermore, considering that the CN group is a stronger *trans* director than sulphur atoms, such as S1, a combined electronic *trans* effect would explain the difference in N-type CPs for compounds **2–5** and **6**. In the latter, the combined electron donation by the S1 and CN ligands produces the coalescence of the two N3 CPs present in **2**–**5**. Thus it is this unique N3 critical point in complex **6** that is responsible for the S2-Mo-S2 angle opening to 77.3°, compared to that in **2**, 74.0°. This geometry modification by charge concentration has been observed and explained before in inorganic compounds (24, 25).

The spatial distribution of the $-\nabla^2\rho(\boldsymbol{r})$ N-type CPs discussed above has clear chemical implications for the reactivity of compounds **2**–**6** towards electrophiles. For complexes **2**–**5**, the proximity of Mo—O2, Mo—S1, and Mo—S2 bonds to N1, N2, and N3 groups, respectively, blocks or sterically hinders any electrophilic attack, unless there is a simultaneous scission of the bond involved. On the contrary, in **6** the nucleophilic site N3 is located in a bond-free region and an electrophilic attack can take place without bond rupture. Therefore, it is expected that **6** would react with electrophiles while **2**–**5** would remain unaltered.

E-type CPs, or electrophilic sites

An analysis of the $-\nabla^2\rho(\boldsymbol{r})$ E-type CPs, or electronic charge holes, obtained for compounds **2**–**5** yielded four different groups or electrophilic sites: E1, E2, E3, and E4 (Table 5). The E1 group is formed by two CPs located at the middle of the S1-Mo-S2 angle, while the E2 and E3 CP groups are situated in the Mo—L and Mo—O1 bonding regions, respectively (Fig. 6). Previous reports have established that this CP distribution is related to certain types of ligands, such as oxo groups, with a preference for face-charge depletion sites (24, 26). The remaining E-type CP, the E4 group, is located at the S2-Mo-S2 angle, while in **6** there are only E1, E2, and E3 groups (Fig. 7).

Thus, due to the spatial distribution of the different electrophilic sites for compounds **2**–**6,** where the E1, E2, and E3 groups are sterically hindered, a nucleophilic attack cannot occur at these points without simultaneous bond breaking. However, for **2**–**5,** because E4 is located in a bond-free

© 1999 NRC Canada

Fig. 6. Distribution of the E-type critical points calculated in $MoO(OSiH_3)L(S_2CNH_2)_2$. The hydrogen atoms are omitted.

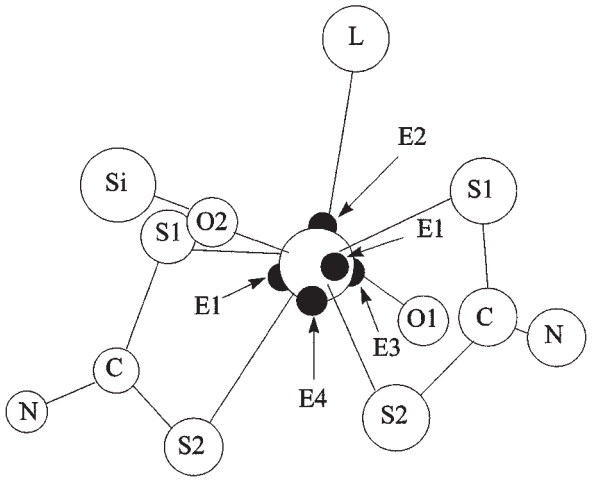

Fig. 7. Distribution of the E-type critical points calculated in $MoO(OSiH_3)CN(S_2CNH_2)_2$. The hydrogen atoms are omitted.

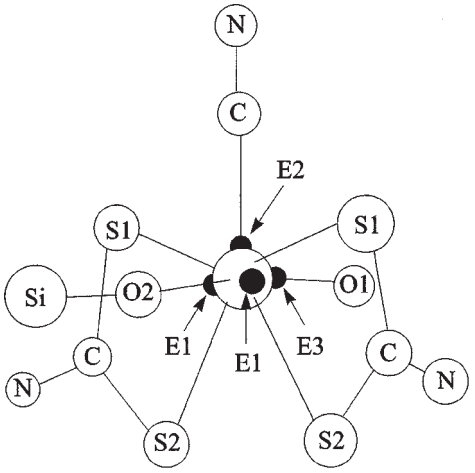

region, an electrophilic attack is possible and energetically favoured at this site. On the contrary, compound **6** will show a lack of reactivity towards nucleophiles due to the absence of any accessible electrophilic site (Fig. 7).

So, for compounds **2**–**5** further reaction with H_3SiL takes place with $MoOL_2(S_2CNH_2)_2$ formation while **6** will never yield $MoO(CN)_2(S_2CNH_2)_2$. In fact, this relation between reactive site accessibility and reactivity is observed experimentally. In the reaction of $MoO(OSiMe_3)CN(S_2CNEt_2)_2$ with a large excess of Me_3SiCl, the starting material was completely recovered after 3 days, while the only product obtained for the reaction of $MoO_2(S_2CNEt_2)_2$ and Me_3SiL was $MoOL_2(S_2CNEt_2)_2$ for L = Cl, Br, I, and NCS. Furthermore, the isolation of an oxosiloxy compound, $MoO(OSiMe_2{}^tBu)Cl(S_2CNEt_2)_2$, from the reaction of $MoO_2(S_2CNEt_2)_2$ and $(Me_2{}^tBu)SiCl$ (7), can also be explained by the accessibility of the E-type CPs. As discussed for $MoOCl(OSiH_3)(S_2CNH_2)_2$, four E-type groups should be present but, in this case, the E4 point, located at the S2-Mo-S2 angle, Fig. 6, should become quite hindered by the bulkiest $(Me_2{}^tBu)Si$ ligand compared to H_3Si.

On the other hand, it has been reported that the magnitude of $-\nabla^2\rho(\boldsymbol{r})$ at the E-type CPs can be related to the site reactivity towards nucleophilic additions, i.e., the higher the $-\nabla^2\rho(\boldsymbol{r})$ value the more reactive the site (13, 15). For the $MoO(OSiH_3)L(S_2CNH_2)_2$ compounds **2**–**5**, the values obtained for $-\nabla^2\rho(\boldsymbol{r})$ at the E4 point, Table 6, indicate the following reactivity order for nucleophilic additions: **2** > **3** > **4** > **5**, or L = NCS > Cl > Br > I. Unfortunately, this reactivity order was difficult to confirm experimentally as the reaction of $MoO_2(S_2CNEt_2)_2$ with Me_3SiL to produce $MoOL_2(S_2CNEt_2)_2$ turned out to be so fast that the formation of $MoO(OSiMe_3)L(S_2CNEt_2)_2$ was never observed even when the reaction was followed by ^{29}Si NMR at low temperature.

In addition, a rather different situation is expected for the reactivity of **2**–**6** towards electrophiles. Despite the fact that reactive nucleophilic sites (N-type CPs) are inaccessible in **2**–**5**, compound **6** exhibits an N4 CP at a sterically unhindered region and this situation should permit an electrophilic attack. The reactivity of $MoO(OSiMe_3)CN(S_2CNEt_2)_2$ with electrophiles has not yet been reported but, according to this study, this reaction could lead to an interesting new family of compounds.

Conclusions

According to this study, if the reaction of $MoO_2(S_2CNEt_2)_2$ with R_3SiX proceeds through a 1,2-addition at the Mo=O bond (7), compounds like $MoO(OSiMe_3)L(S_2CNEt_2)_2$ should be isolated only in those cases where further nucleophilic attacks on the molybdenum atom, by X, are obstructed. Thus, unlike the compound $MoOL_2(S_2CNEt_2)_2$, isolated from the reaction of $MoO_2(S_2CNEt_2)_2$ with R_3SiX, when X = NCS, Cl, Br, and I, $MoO(OSiMe_3)CN(S_2CNEt_2)$ does not react further, due to the absence of any suitable electrophilic site.

In addition, in the case of σ and π donating ligands, stronger than dithiocarbamates, S_2CNEt_2, the only compound obtained should be $MoO(OSiMe_3)X(S_2CNEt_2)$ instead of $MoOX_2(S_2CNEt_2)$.

Acknowledgements

The authors are grateful to Mr. B. Perillo and Miss Y. Moret for their help in the preparation of $MoO(NCS)_2(S_2CNEt_2)_2$ and $MoOI_2(S_2CNEt_2)_2$. This work was supported by the Decanato de Investigación y Desarrollo de la Universidad Simón Bolívar (Grant S1-CB116–97) and by CONICIT (Grant S1-96001399).

References

1. H.W. Roesky. Chem. Rev. **96**, 2205 (1996).
2. P. Stavropoulos, N. Bryson, M. Youlnov, and J.A. Osborn. Inorg. Chem. **29**, 1807 (1990).
3. W.A. Herrman. Angew. Chem. Int. Ed. Engl. **27**, 1297 (1988).
4. G. Parkin and J.E. Bercaw. J. Am. Chem. Soc. **111**, 391 (1989).
5. C.W. De Kock and M. Huang. Inorg. Chem. **32**, 2287 (1993).
6. M.S. Rau, C.M. Kretz, G.L. Geoffroy, and A.L. Rheingold. Organometallics, **12**, 3447 (1993).
7. H. Arzoumanian, H. Krentzien, C. Corao, R. López, and G. Agrifoglio. Polyhedron, **14**, 2887 (1995); H. Teruel, B. Perillo, and Y. Moret. Polyhedron, **18**, 419 (1998).
8. H. Arzoumanian, C. Corao, H. Krentzien, R. López, and H.Teruel. J. Chem. Soc. Chem. Commun. **11**, 856 (1992).

© 1999 NRC Canada

9. R.F.W. Bader. Chem. Rev. **91**, 893 (1991).
10. R.F.W. Bader and H. Essen. J. Chem. Phys. **80**, 1943 (1984).
11. R.F.W. Bader. *In* Atoms in molecules: a quantum theory. *Edited by* J. Halpern and M.L.H. Green. Clarendon Press, Oxford. (1990).
12. J. Dirand, L. Ricard, and R. Weiss. J. Chem. Soc. Dalton. Trans. 278 (1976).
13. R.F.W. Bader, P.J. MacDougall, and C.D.H. Lau. J. Am. Chem. Soc. **106**, 1594 (1984).
14. R.F.W. Bader and P.J. MacDougall. J. Am. Chem. Soc. **107**, 6788 (1985).
15. M.T. Carrol, J.R. Cheeseman, R. Osman, and H. Weinstein. J. Phys. Chem. **93**, 5120 (1989).
16. R.F.W. Bader, P.L.A. Popelier, and C. Chang. J. Mol. Struct. (Theochem), **255**, 145 (1992).
17. Y. Aray, J. Rodriguez, J. Murgich, and F. Ruette. J. Phys. Chem. **97**, 8389 (1993).
18. Gaussian 94. Revision D.4. M.J. Frish, G.W. Trucks, H.B. Schlegel, P.M.W. Gill, B.G. Johnson, M.A. Robb, J.R. Cheeseman, T. Keith, G.A. Petersson, J.A. Montgomery, K. Raghavachari, M.A. Al-Laham, V.G. Zakrzewski, J.V. Ortiz, J.B. Foresman, J. Cioslowski, B.B. Stefanov, A. Nanayakkara, M. Challacombe, C.Y. Peny, P.Y. Ayala, W. Chen, M.W. Wong, J.L. Andres, E.S. Replogle, R. Gomperts, R.L. Martin, D.J. Fox, J.S. Binkey, D.J. Defrees, J. Baker, P.J. Stewart, M. Head-Gordon, C. Gonzales, and J.A. Pople. Gaussian, Inc., Pittsburgh, Pa. (1995).
19. L.F. Pacios and P.A. Christiansen. J. Chem. Phys. **82**, 2664 (1985); M.M. Hurley, L.F. Pacios, P.A. Christiansen, R.B. Ross, and W.C. Ermler. J. Chem. Phys. **84**, 6840 (1986); L.A. LaJohn, P.A. Christiansen, R.B. Ross, T. Atashroo, and W.C. Ermler. J. Chem. Phys. **87**, 2812 (1987).
20. W.R. Wadt and P.J. Hay. J. Chem. Phys. **82**, 284 (1985).
21. W.J.Stevens, M. Krauss, H. Basch, and P.G. Jasien. Can. J. Chem. **70**, 612 (1992).
22. F.W. Biegler-Konig, R.F.W. Bader, and T.H. Tang. J. Comput. Chem. **3**, 317 (1982).
23. F.W. Moore and M.L. Larson. Inorg. Chem. **6**, 998 (1967).
24. R.J. Gillespie, I. Bytheway, R.S. DeWitte, and R.F.W. Bader. Inorg. Chem. **33**, 2115 (1994).
25. R.J. Gillespie, I. Bytheway, T.-H. Tang, and R.F.W. Bader. Inorg. Chem. **35**, 3954 (1996).
26. A. Sierraalta and F. Ruette. J. Comput. Chem. **15**, 313 (1994).

© 1999 NRC Canada

Carboxylic acid amide enols: keto–enol/enolate interconversion of *N*-methylindoline-2-one and its 2-thione and 2-selone analogs in aqueous solution

A. Jerry Kresge and Qingshui Meng

Abstract: Carbon-acid ionization constants, Q_a^K (concentration quotient at ionic strength = 0.10 M), were determined by spectrophotometric titration in aqueous solution for *N*-methylindoline-2-one, pQ_a^K = 15.70, *N*-methylindoline-2-thione, pQ_a^K = 8.93, and *N*-methylindoline-2-selone, pQ_a^K = 7.25. Rate profiles were also constructed for the thione and selone. These were interpreted, with support from the form of acid–base catalysis as well as solvent and substrate isotope effects, as representing keto – enol/enolate ion interconversion. That led to the enol acidity constant pQ_a^E = 4.05 and the keto–enol equilibrium constant pK_E = 4.88 for the thione and estimates of the limits on these quantities, $pQ_a^E < 3$ and $pK_E > 4$, for the selone.

Key words: lactam, thiolactam, selenolactam, keto–enol equilibria, carbon-acid ionization constants.

Résumé : Opérant en solution aqueuse et faisant appel à des titrages spectrophotométriques, on a mesuré les constantes d'ionisation d'acide carboné, Q_a^K (quotient des concentrations à une force ionique = 0,10 M), de la *N*-méthylindoline-2-one, pQ_a^K = 15,70, de la *N*-méthylindoline-2-thione, pQ_a^K = 8,93 et de la *N*-méthylindoline-2-sélénone, pQ_a^K = 7,25. On a aussi élaboré les profils de vitesse de la thione et de la sélénone. En se basant sur la forme de la catalyse acide–base ainsi que sur les effets isotopiques du solvant et du substrat, on peut interpréter ces résultats sur la base d'une interconversion cétoénolique/ion énolate. Sur cette base, la constante d'acidité énolique, pQ_a^E = 4,05, et la constante d'équilibre cétoénolique, pK_E = 4,88, pour la thione alors que les évaluations des limites de ces grandeurs pour la sélénone sont $pQ_a^E < 3$ et $pK_E > 4$.

Mots clés : lactame, thiolactame, sélénolactame, équilibre cétoénolique, constantes d'ionisation d'acide carboné.

[Traduit par la Rédaction]

Enol isomers of simple carboxyic acids and their functional derivatives, such as esters and amides, are very labile and thermodynamically unstable substances, and their lifetimes in aqueous solution are expected to be exceedingly short. For example, the keto–enol equilibrium constant for acetic acid in aqueous solution, though not yet determined experimentally, has been reliably estimated as pK_E = 20 (1), and the hydronium-ion catalytic coefficient for conversion of acetic acid enol to its keto form, also not yet measured experimentally, is believed to lie in the range $k_{H^+} = 10^8$–10^9 M^{-1} s^{-1} (2). Recent high-level calculations (3) suggest that keto–enol equilibrium constants for esters and amides will be not very different from those for carboxylic acids, and this is borne out by the estimate pK_E = 19 for ethyl acetate (4), similar to pK_E = 20 for acetic acid.

Daunting realities such as this have driven the study of enols of carboxylic acids and their derivatives to systems where the enol is stabilized by some special structural features. Bulky groups in the β-position of enols can accomplish this by blocking access to the enol double bond (5), through whose protonation ketonization must take place (6), and this strategy has recently been used to make stable enols of bis(2,4,6-triisopropylphenyl)acetic acid amides (7).

In the present study of amide enols, we have used a somewhat different approach: we have examined systems in which the enol or enolate ion is stabilized by formation of a new aromatic ring, eq. [1], and also by replacement of the carbonyl oxygen atom with sulfur or selenium. Replacement of oxygen by sulfur has recently been shown to increase enol content by a large factor (8), and it seemed likely that selenium would have a similar effect.

We have found that the enol isomers (**2a**, **b**, and **c**) and enolate ions (**3a**, **b**, and **c**) of *N*-methylindoline-2-one (**1a**), *N*-methylindoline-2-thione (**1b**), and *N*-methylindoline-2-

[1]

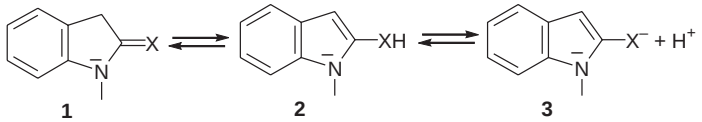

1 **2** **3**

(**a**: X = O, **b**: X = S, **c**: X = Se)

Received June 25, 1999.

A.J. Kresge[1] and Q. Meng. Department of Chemistry, University of Toronto, Toronto, ON M5S 3H6, Canada.

[1]Author to whom correspondence may be addressed. Telephone: (416) 978-7259. Fax: (416) 978-7259. e-mail: akresge@chem.utoronto.ca

© 1999 NRC Canada

selone (**1c**) are stable enough to exist in aqueous solution. This has allowed us to determine acidity constants for these substances ionizing as carbon acids in that medium. We have also found that rates of keto–enol/enolate interconversion in the thione and selone systems can be measured by stopped flow methods, and this has enabled us to determine keto–enol and enol acidity constants for the thione system and to set limits on these quantities for the selone system.

Experimental section

Materials

N-*Methylindoline-2-one* was prepared by methylating oxindole (Aldrich) using a published procedure (9).

N-*Methylindoline-2-thione* was prepared by treating *N*-methylindole-2-one (1.00 g) with Lawesson's reagent (10) (1.64 g) in dry toluene at 100°C for 2 h under an argon atmosphere. The solvent was removed, and the residue was purified by flash chromatography on silica gel with 20% ethyl acetate in pentane as the eluent. Recrystallization from ethyl acetate:pentane gave a solid, mp 109–110°C (lit. (9) 106.5–108°C) whose NMR spectra were consistent with literature values (9, 11).

N-*Methylindoline-2-selone* was prepared by adapting a method used to synthesize the parent *N*–methyl-2-pyrroline-2-selone (12). To a solution of 2.0 g *N*-methylindole in 30 mL tetrahydrofuran maintained at 0°C in an argon atmosphere, 8.5 mL of 1.8 M phenyllithium dissolved in 70:30 cyclohexane:ether was added. When the addition was complete, the temperature was raised to 40°C, and the reaction mixture was stirred for 2 h. It was then cooled to 0°C, 1.2 g of selenium was added, and stirring was continued for another hour. The resulting reaction mixture was quenched with cold aqueous acetic acid, was extracted with chloroform, and the extract was washed with water and brine and was dried over magnesium sulfate. The residue obtained upon evaporation of the solvent was purified by flash chromatography on silica gel using 5% ethyl acetate in hexane as the eluent. Repeated recrystallization from chloroform:hexane gave 100 mg (3% yield) of a yellow solid; mp: 131–133°C; ^{1}H NMR ($CDCl_3$), δ/ppm: 7.02–7.36 (m, 4 H), 3.81 (s, 2 H), 3.70 (s, 3 H); ^{13}C NMR ($CDCl_3$), δ/ppm: 203.25, 146.79, 131.17, 128.08, 124.72, 124.03, 110.01, 53.63, 34.03; HRMS, *m*/*e*: 210.9895 (calc.), 210.9900 (obs.). Only part of the starting material had reacted, suggesting that a higher yield would have been obtained if a stronger base, such as butyllithium, had been used.

All other materials were best available commercial grades.

Acidity constants

Carbon-acid ionization constants of *N*-methylindoline-2-one, -thione, and -selone were determined by monitoring the reversible UV spectral changes that these substances undergo upon ionization. Absorbance (*A*) measurements were made at λ = 310 nm for *N*-methylindoline-2-one, at λ = 240 nm for *N*-methylindoline-2-thione, and at λ = 330 nm for *N*-methylindoline-2-selone, using a Cary Model 2200 spectrometer whose cell compartment was thermostatted at 25.0 ± 0.05°C. Constant stoichiometric substrate concentrations (2×10^{-5} M) were used, and the data were analyzed by nonlinear least-squares fitting of the titration curve expression shown as eq. [2], where Q_a^K is the carbon-acid ionization constant of the substrate, and A_{HA} and A_B are the limiting absorbances of its acidic and basic forms, respectively.

$$[2] \qquad A = (A_B Q_a^K + A_{HA}[H^+])/(Q_a^K + [H^+])$$

Kinetics

Rates of approach to keto–enol/enolate equilibrium in the *N*-methylindoline-2-thione and -selone systems were determined using a Hi-Tech Scientific Model SF-S1 stopped-flow spectrometer operating at 25.0 ± 0.1°C. For studies on solutions more basic than the carbon-acid dissociation constant of the substrate, Q_a^K, kinetic runs were initiated by mixing a solution of substrate in water contained in one syringe with a solution of sodium hydroxide or buffer contained in the other syringe, and for studies in solutions more acidic than Q_a^K, runs were initiated by mixing a solution of initially deprotonated substrate in 0.0002 M sodium hydroxide solution in one syringe with a solution of perchloric acid or buffer in the other syringe. Reactions were monitored by following changes in enol and enolate absorbance at λ = 240 nm or keto form absorbance at λ = 310 nm for *N*-methylindoline-2-thione and changes in keto form absorbance at λ = 330 nm for *N*-methylindoline-2-selone. Substrate concentrations in the final reaction mixtures were 5×10^{-6} M. The rate data conformed to the first-order rate law well, and observed first-order rate constants were obtained by least-squares fitting of an exponential function.

Results

Carbon-acid ionization constants

For *N*-methylindoline-2-thione and -selone, reversible UV spectral changes characteristic of carbon-acid ionization took place in aqueous solution in the pH range, and measurements could consequently be made in dilute sodium hydroxide and buffer solutions. For *N*-methylindoline-2-one, on the other hand, these spectral changes occurred only in more basic solutions, and measurements for this substrate were therefore made in concentrated aqueous potassium hydroxide solution.

For the thione and selone, HCO_3^-, NH_4^+, $(CH_2OH)_3CNH_3^+$, $H_2PO_4^-$, and CH_3CO_2H buffers were used. Two to four different buffer ratios were employed for each buffer system, and several different sodium hydroxide concentrations were used as well; triplicate absorbance measurements were made with each solution. The ionic strength of all solutions was maintained at 0.10 M using $NaClO_4$ as required. Hydrogen ion concentrations were obtained by calculation using literature pK_a values and activity coefficients recommended by Bates (13). These data are summarized in Table S1.[2]

As Fig. 1 illustrates, the data so obtained conformed to the expected titration curve expression of eq. [2] quite well. Least-squares fitting gave $Q_a^K = (1.18 \pm 0.04) \times 10^{-9}$ M,

[2] Tables of equilibrium and rate data (Tables S1–S8) have been deposited and may be purchased from: The Depository of Unpublished Data, Document Delivery, CISTI, National Research Council Canada, Ottawa, Canada, K1A 0S2.

© 1999 NRC Canada

Fig. 1. Spectrophotometric titration curve for *N*-methylindoline-2-thione in aqueous solution at 25°C.

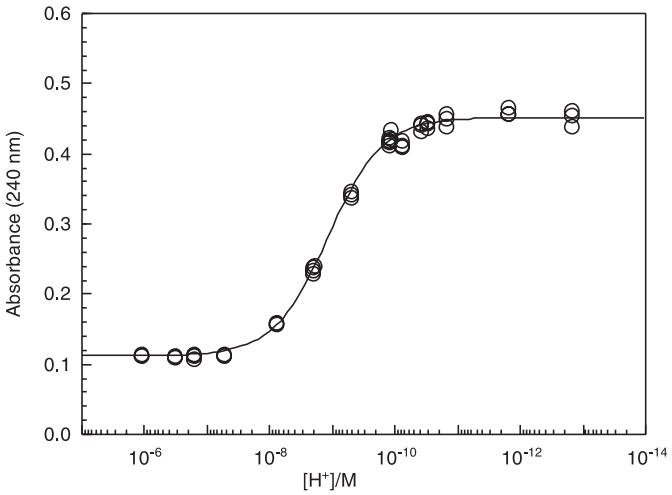

pQ_a^K = 8.93 ± 0.02 (see footnote 3) for *N*-methylindoline-2-thione, and Q_a^K = (5.66 ± 0.29) × 10^{-8} M, pQ_a^K = 7.25 ± 0.02 (see footnote 3) for *N*-methylindoline-2-selone.

Absorbance measurements for *N*-methylindoline-2-one were made in KOH solutions over the concentration range 0.1–11 M. The data so obtained, summarized in Table S2,[2] were transformed into values of log *I* (= [enolate ion]/[keto form]), and the fit of log *I* to different basicity functions was examined. Three functions were tried: an H_- scale based on neutral indole indicators (14), an $H_=$ scale based on indoles bearing carboxylate groups (14), and an $H_=$ scale based on aromatic amines bearing carboxylate and sulfonate groups (15). The H_- scale was found to be the most appropriate: it gave a plot of log *I* vs. H_- whose slope was near unity (0.95 ± 0.02), whereas the other basicity functions produced slopes significantly farther from unity (0.77 ± 0.01 and 0.78 ± 0.01). The data were therefore analyzed using the H_- scale, i.e., were fitted using the titration curve expression of eq. [2] with 10^{-H_-} replacing [H^+]. This gave K_a^K = (1.40 ± 0.08) × 10^{-16} M, pK_a^K = 15.86 ± 0.03.

Since basicity functions are referenced to an infinitely dilute standard state whose ionic strength is zero, this value is a thermodynamic ionization constant, expressed in terms of activities, unlike the concentration constants determined above for *N*-methylindoline-2-thione and -selone. This thermodynamic value may be converted into a concentration ionization constant by applying appropriate activity coefficients. The result for ionic strength = 0.10 M, obtained using the activity coefficient for the hydrogen ion recommended by Bates (13) and that for picrate ion (16) as a surrogate for the unavailable activity coefficient of the present enolate ion, is pQ_a^K = 15.70 ± 0.03.

Carbon-acid ionization constants for two of the substrates studied here, *N*-methylindoline-2-one and *N*-methylindoline-2-thione, have been measured in DMSO solution (9). The results obtained, pK_a = 18.5 and 10.0, respectively, show these substances to be stronger acids in H_2O than in DMSO by relatively small amounts, as expected for acids whose ionization produces highly delocalized anions (17).

Fig. 2. Rate profile for keto–enol/enolate interconversion in the *N*-methylindoline-2-thione system in aqueous solution at 25°C; circles and solid line: rate of approach to equilibrium, dashed line: rate of enolization, dotted line: rate of ketonization.

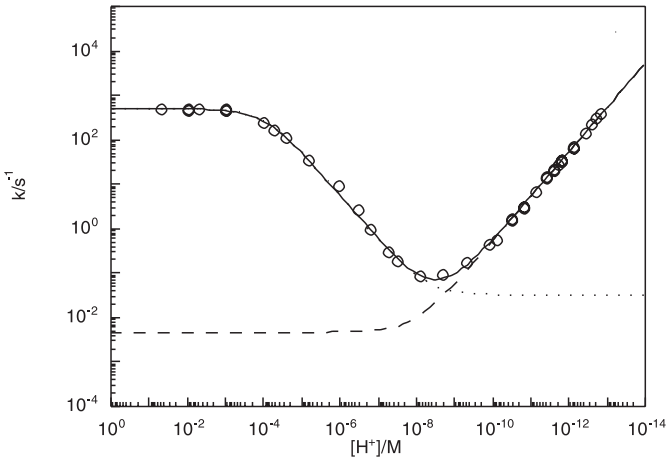

Kinetics: *N*-methylindoline-2-thione

Rates of approach to keto–enol/enolate ion equilibrium for *N*-methylindoline-2-thione were measured in aqueous perchloric acid solutions over the concentration range 0.001–0.05 M, and in aqueous sodium hydroxide solutions over the concentration range 0.0004–0.1 M. The ionic strength of these solutions was maintained at 0.10 M using $NaClO_4$ as required. These data are summarized in Tables S3 and S4.[2]

Rate measurements for this substrate were also made in aqueous CH_3CO_2H, $H_2PO_4^-$, $(CH_2OH)_3CNH_3^+$, and NH_4^+ buffer solutions, using series of buffer solutions of different total buffer concentration but constant buffer ratio and constant ionic strength (0.10 M). For the $H_2PO_4^-$ and $(CH_2OH)_3CNH_3^+$ buffers, this served to hold [H^+] constant along a given buffer series, but in some of the CH_3CO_2H and NH_4^+ buffers "buffer failure" (18) occurred; i.e., [H^+] changed systematically somewhat as the buffer was made more dilute. In these cases, observed rate constants were adjusted to values they would have had had [H^+] been constant; these adjustments were made using required rate and equilibrium constants obtained from the rate profile (vide infra). Such adjustments were minor — never more than a few percent. The data are summarized in Table S5.[2]

Buffer catalysis was strong, with rate constants increasing with increasing buffer concentration in a linear fashion. The data were therefore analyzed by least-squares fitting of eq. [3] in which k_{exp} represents either observed or adjusted rates of approach to equilibrium.

$$[3] \qquad k_{exp} = k_o + k_{Buff}[\text{Buffer}]$$

Values of k_o obtained in this way, together with the rate constants measured in perchloric acid and sodium hydroxide solutions, were used to construct the rate profile shown in Fig. 2. This profile describes the rate of approach to keto–enol/enolate equilibrium by reaction through solvent-related species. It can be analyzed as the sum of rate constants for enolization occurring through rate-determining proton

[3] This is a concentration ionization constant, applicable at the ionic strength of its determination.

© 1999 NRC Canada

removal from the keto isomer by either hydroxide ion or a water molecule to give an equilibrium mixture of enol and enolate, eq. [4], plus rate constants for ketonization occurring through rate-determining carbon protonation of enolate ion, in equilibrium with enol, by either hydronium ion or a water molecule, eq. [5].

[4] 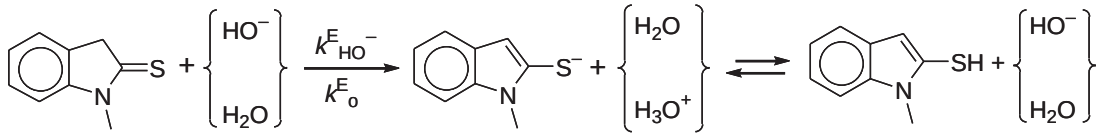

[5] 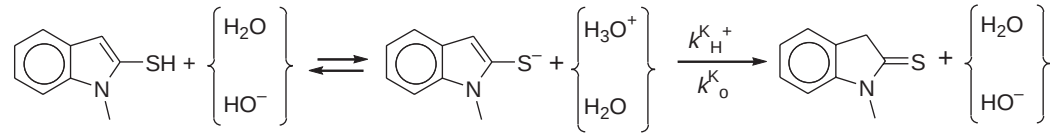

This interpretation is consistent with the established reaction mechanisms for enolization and ketonization (6), and it is supported in the present instance by isotope effects and the form of acid–base catalysis by buffer species (vide infra).

The rate law for this reaction scheme is given in eq. [6], whose rate constants are defined by eqs. [4] and [5], and Q_a^E

$$[6] \quad k_{exp} = k^E{}_o + k^E{}_{HO^-}[HO^-] + (k^K{}_o + k^K{}_{H^+}[H^+])\{Q_a^E/(Q_a^E + [H^+])\}$$

is the acidity constant of the enol ionizing as an oxygen acid. Least-squares fitting of this expression as it stands could not be effected, because the fraction modifying $k^K{}_o$, $Q_a^E/(Q_a^E + [H^+])$, is essentially unity in the region where this rate constant makes a significant contribution: $[H^+] = 10^{-8}$–10^{-9} M ($Q_a^E \cong 10^{-4}$ M, vide infra). That makes the relationship between this rate constant and solvent acidity effectively the same as that of $k^E{}_o$; these two rates are therefore strongly correlated and cannot be evaluated separately by analysis of the rate profile. They are consequently combined as $k^E{}_o + k^K{}_o = k_{uc}$, giving eq. [7]. Least-squares fitting of this

$$[7] \quad k_{exp} = k^E{}_{HO^-}[HO^-] + k_{uc} + k^K{}_{H^+}[H^+]\{Q_a^E/(Q_a^E + [H^+])\}$$

expression produced $k^E{}_{HO^-} = (3.42 \pm 0.06) \times 10^3$ M^{-1} s^{-1}, $k_{uc} = (3.75 \pm 0.65) \times 10^{-2}$ s^{-1}, $k^K{}_{H^+} = (5.62 \pm 0.27) \times 10^6$ M^{-1} s^{-1}, and $Q_a^E = (8.85 \pm 0.54) \times 10^{-5}$ M, $pQ_a^E = 4.05 \pm 0.03$.[3] Combination of the latter constant with Q_a^K according to the relationship $Q_a^K/Q_a^E = K_E$ then gave the keto–enol equilibrium constant $K_E = (1.33 \pm 0.10) \times 10^{-5}$, $pK_E = 4.88 \pm 0.03$.

Although only the sum of the rate constants $k^E{}_o$ and $k^K{}_o$ can be evaluated from the rate profile, individual values may be obtained by combining this sum with the ratio $k^E{}_o/k^K{}_o$ derived in the following way. The equilibrium constant for the process shown in eq. [8], $Q^K{}_a$, is also equal to the ratio of forward to reverse rate constants for this reaction: $Q_a^K = k^E{}_o/k^K{}_{H^+}$; this leads to the expression $k^E{}_o = Q_a^K k^K{}_{H^+}$. An

[8] 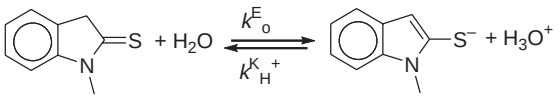

analogous expression for $k^K{}_o$ may be derived using the process shown in eq. [9] whose equilibrium constant, the

[9] 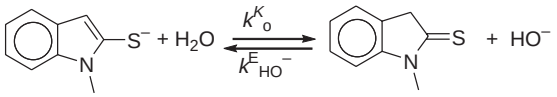

ionization constant of water Q_w divided by Q_a^K, is also equal to the rate constant ratio $k^K{}_o/k^E{}_{HO^-}$; this leads to $k^K{}_o = Q_w k^E{}_{HO^-}/Q_a^K$. Combination of these expressions then gives the relationship shown in eq. [10]. Since all the quantities on

$$[10] \quad k^E{}_o/k^K{}_o = k^K{}_{H^+}(Q_a^K)^2/\ k^E{}_{HO^-}Q_w$$

the right side of eq. [10] are known, the ratio $k^E{}_o/k^K{}_o$ can be evaluated, and combination of that with the sum $k^E{}_o + k^K{}_o$ obtained from the rate profile produces the results $k^E{}_o = (4.72 \pm 0.87) \times 10^{-3}$ s^{-1} and $k^K{}_o = (3.27 \pm 0.65) \times 10^{-2}$ s^{-1}.

These results, coupled with values of $k^E{}_{HO^-}$ and $k^K{}_{H^+}$ obtained from the rate profile, provide complete rate laws for the enolization and ketonization reactions effected by solvent-related species over the range of acidity studied. This allows separation of observed rates of equilibration into rates of enolization and rates of ketonization, as illustrated in Fig. 2. Such dissection shows that ketonization dominates observed rates of equilibration in acidic solutions down to about $[H^+] = 10^{-8}$ M and that enolization dominates in basic solutions beginning at about $[H^+] = 10^{-9}$ M.

These dominances are consistent with the nature of buffer catalysis in the buffer solutions examined. The buffer catalytic coefficients of eq. [3] may be separated into general acid, k_{HA}, and general base, k_B, contributions with the aid of eq. [11], in which f_A is the fraction of buffer present in the

$$[11] \quad k_{Buff} = k_B + (k_{HA} - k_B)f_A$$

acid form. The data obtained obeyed this relationship well; an example is shown in Fig. 3. Least-squares analysis gave the results listed in Table 1.[4] This analysis showed that only general acid catalysis was significant in CH_3CO_2H and $H_2PO_4^-$ buffers, which is consistent with the fact that these buffers gave solutions in the region $[H^+] = 1 \times 10^{-4}$ to 6×10^{-8} M where ketonization dominates; ketonization, being a reaction involving rate-determining proton transfer from acid catalyst to substrate, can be expected to show only gen-

[4] Data obtained in acetic acid buffers were adjusted to allow for the fact that the enolate ion exists in equilibrium with significant amounts of enol in these solutions.

© 1999 NRC Canada

Table 1. General-acid and general-base catalytic coefficients for enolization and ketonization in the *N*-methylindoline-2-thione and -selone systems in aqueous solution at 25°C.[a]

Catalyst		Thione		Selone	
Acid	Base	$k_{HA}/10^2$ M^{-1} s^{-1}	$k_B/10^2$ M^{-1} s^{-1}	$k_{HA}/10^2$ M^{-1} s^{-1}	$k_B/10^2$ M^{-1} s^{-1}
CH_3CO_2H	$CH_3CO_2^-$	327.	—	44.6	—
$H_2PO_4^-$	$HPO_4^=$	16.0	—	2.21	0.551
$(CH_2OH)_3CNH_3^+$	$(CH_3OH)_2CCNH_2$	3.06	0.460	0.335	2.31
NH_4^+	NH_3	0.114	0.247	—	1.38

[a]Ionic strength = 0.10 M.

eral acid catalysis. The data for $(CH_2OH)_3CNH_3^+$ and NH_4^+ buffers, on the other hand, gave significant general base as well as general acid catalysis, which is consistent with the fact that these buffers gave solutions in the region $[H^+] = 3 \times 10^{-8}$ to 1×10^{-10} M where both enolization and ketonization make important contributions to observed rates; enolization, being a reaction that involves rate-determining proton removal from the substrate by a basic catalyst will show general base catalysis.

The numerical values of the general acid and general base catalytic coefficients obtained by this analysis offer further support for the interpretation made. The equilibrium constant for keto–enolate interconversion catalyzed by a general acid–base pair, shown in eq. [12], has the value Q_a^K/Q_a^{HA}, in

[12]

which Q_a^{HA} is the acidity constant of the catalyzing acid. This equilibrium constant is also equal to the rate constant ratio k^E_B/k^K_{HA}, and equating these two values leads to eq. [13], which shows that an estimate of Q_a^K may be obtained from the rate constant pair and Q_a^{HA}. Data for $(CH_2OH)_3CNH_3^+$

[13] $$Q_a^K = Q_a^{HA} k^E_B / k^K_{HA}$$

buffers give $pQ_a^K = 8.91 \pm 0.12$, and data for NH_4^+ buffers give $pQ_a^K = 8.95 \pm 0.04$; both of these results are in very good agreement with $pQ_a^K = 8.93 \pm 0.02$ obtained by spectrophotometric titration of this substrate.

Additional support for the interpretation made may be had from estimates of K_E based on keto–enol interconversion by the two routes of eqs. [14] and [15]. The route of eq. [14] gives $K_E = k^E_o/k^K_{H^+} Q_a^E$, and the route of eq. [15] gives $K_E = k^E_{HO^-} Q_w/k^K_o Q_a^E$. Insertion of the quantities required into the first of these expressions produces $pK_E = 5.02 \pm 0.09$ and into the second, $pK_E = 4.73 \pm 0.09$; both of these results agree well with $pK_E = 4.88 \pm 0.03$ obtained by combining Q_a^K determined by the spectrophtometric titration with Q_a^E based upon the rate profile.

Fig. 3. Relationship between buffer catalytic coefficients and fraction of buffer present in the acid form for keto–enol/enolate interconversion of the *N*-methylindoline-2-thione system in aqueous $H_2PO_4^-/HPO_4^=$ buffer solutions at 25°C.

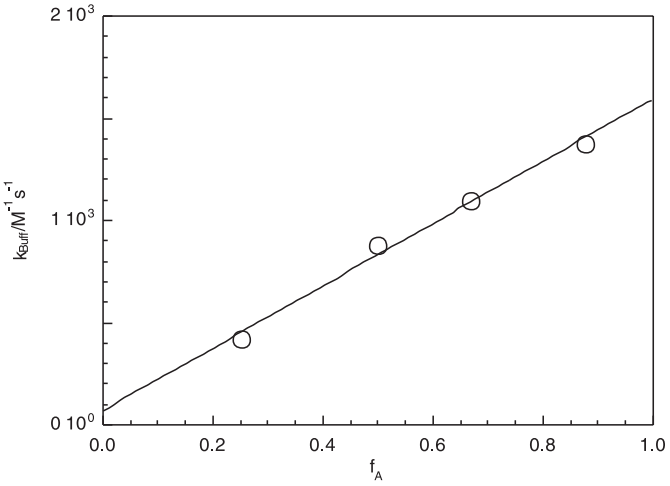

Further support for the interpretation made comes from isotope effects. These are provided by rate measurements performed in D_2O solutions of $DClO_4$, summarized in Table S3,[2] and in CH_3CO_2D buffers, summarized in Table S5.[2] The measurements in buffers were done in series of solutions of constant buffer ratio and ionic strength, just like the measurements in H_2O solutions of CH_3CO_2H, and the data were treated in an analogous fashion. Only general acid catalysis was found, again just like in H_2O, and combination of the general acid catalytic coefficient determined, $k_{DA} = (3.27 \pm 0.11) \times 10^3$ M^{-1} s^{-1}, with its H_2O counterpart gives the isotope effect $k_{HA}/k_{DA} = 9.98 \pm 0.65$. This is a large kinetic isotope effect, fully consistent with the dominance of ketonization in this region of acidity and the expectation that ketonization occurs by rate-determining hydron transfer from acetic acid to the enolate substrate.

The intercepts of the D_2O buffer dilution plots (k_o, eq. [3]), together with the rate constants measured in $DClO_4$ solutions, are compared with their H_2O counterparts in Fig. 4. It

[14] 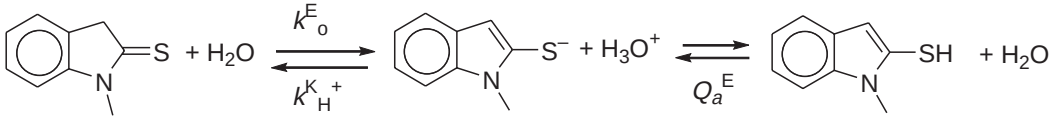

[15] 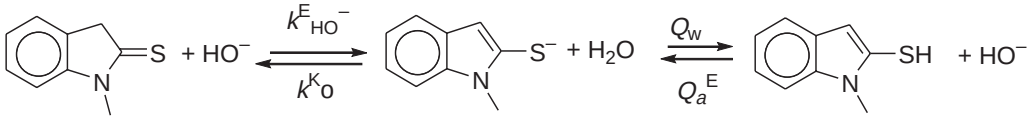

© 1999 NRC Canada

Fig. 4. Comparison of rates of ketonization of *N*-methylindoline-2-thione enol/enolate in acidic H_2O (○) and D_2O (△) solutions at 25°C.

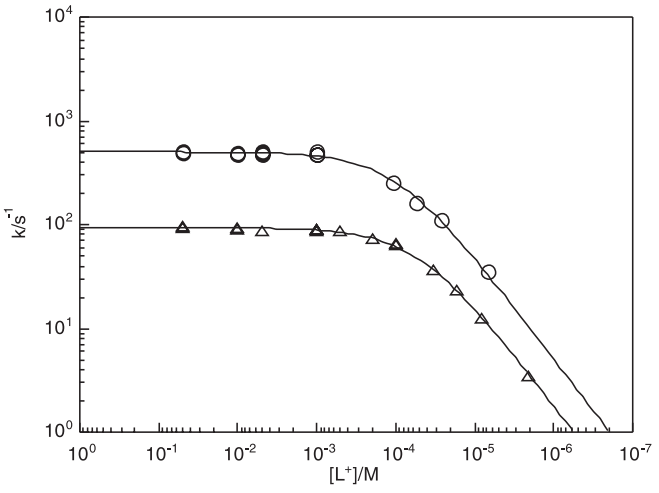

Fig. 5. Rate profile for keto–enol/enolate interconversion in the *N*-methylindoline-2-selone system in aqueous solutions at 25°C; circles and solid line: rate of approach to equilibrium, dashed line: rate of enolization, dotted line: rate of ketonization.

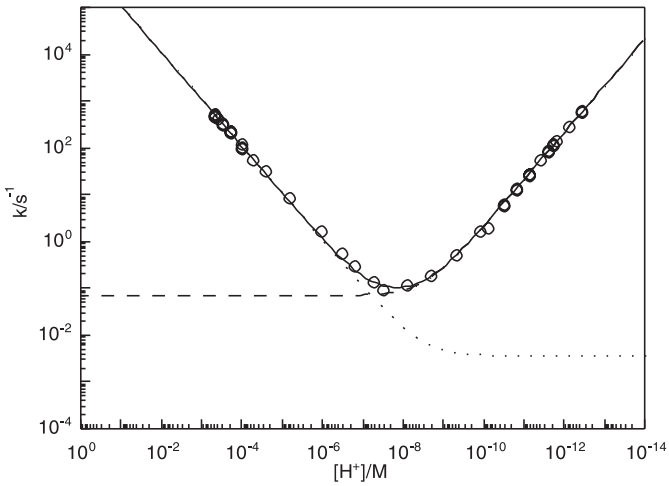

[16]

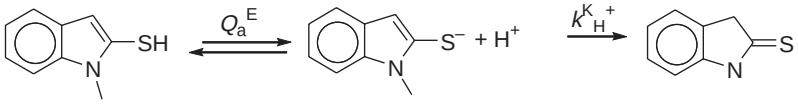

may be seen that reactions in H_2O are faster than those in D_2O throughout the range of acidity examined, as expected for ketonization occurring by rate-determining hydron transfer to carbon. The difference between rates in H_2O and those in D_2O, however, is greater in the horizontal plateau region at higher acidity than it is in the diagonal region at lower acidity. This again is consistent with the general ketonization mechanism assigned in eq. [5], shown in the specific form that applies here as eq. [16]. Enolate ions are known to be orders of magnitude more reactive to protonation on carbon than are the corresponding unionized enols (19), and ketonization consequently occurs by rate-determining reaction of the enolate ion throughout the region of acidity examined here. In the more acidic solutions, however, the process starts with unionized enol as the initial state, and this species must first undergo equilibrium ionization to provide the more reactive enolate. In this region, therefore, the isotope effect is on the enol equilibrium ionization constant as well as on the rate-determining rate constant. In the region of lower acidity where enolate ion is the initial state, on the other hand, the isotope effect is on the rate constant alone.

Analysis of the D_2O data by least-squares fitting of the acidic portion of the rate law of eq. [7] gave the results $(Q_a^E)_{D_2O} = (5.16 \pm 0.12) \times 10^{-5}$ M, $p(Q_a^E)_{D_2O} = 4.29 \pm 0.01$ (see footnote 3), and $k^K{}_{D^+} = (1.81 \pm 0.03) \times 10^{-6}$ M^{-1} s^{-1}, and combination of these with their H_2O counterparts gives $(Q_a^E)_{H_2O}/(Q_a^E)_{D_2O} = 1.90 \pm 0.09$ and $k^K{}_{H^+}/k^K{}_{D^+} = 2.83 \pm 0.11$. Both of these isotope effects are entirely consistent with expectation. The equilibrium constant Q_a^E refers to the ionization of a thiol acid, and solvent isotope effects on the ionization of a number of thiols have been found to be $K_{H_2O}/K_{D_2O} \cong 2$ (20). The rate constant $k^K{}_{H^+}$ refers to hydron transfer from the hydronium ion to substrate, a process whose solvent isotope effect includes an inverse ($k_H/k_D < 1$) secondary component in addition to a normal ($k_H/k_D > 1$) primary component (21); the result obtained here, in fact, is a near-maximum value (22), consistent with the large isotope effect found for ketonization of this substrate catalyzed by acetic acid (vide supra).

A substrate isotope effect was also determined by allowing *N*-methylindoline-2-thione to undergo deuteration at the 3-position in 0.001 M $DClO_4$–D_2O for 30 min and then adding enough NaOD to give $[OD^-] = 0.01$ M and measuring the rate of the subsequent enolization reaction. The data so obtained are summarized in Table S4[2]; when combined with rates of reaction of the undeuterated substrate in H_2O solutions of NaOH, they give the isotope effect $k_H/k_D = 4.35 \pm 0.07$. This isotope effect contains, in addition to its primary component, an inverse secondary component on the consumption of hydroxide ion (21). It consequently is a strong effect, as expected for enolization effected by rate-determining removal of a hydron from the substrate by hydroxide ion. This reinforces the conclusion that the basic portion of the rate profile corresponds to an enolization process.

Kinetics: *N*-methylindoline-2-selone

Rates of approach to keto–enol/enolate equilibrium for this substrate were measured, as for *N*-methylindoline-2-thione, in aqueous perchloric acid and sodium hydroxide solutions and in CH_3CO_2H, $H_2PO_4^-$, $(CH_2OH)_3CNH_3^+$, and NH_4^+ buffers. These data are summarized in Tables S6–S8.[2]

The results obtained in buffer solution were analyzed in a manner similar to that applied to buffer data for the thione (vide supra). The zero buffer concentration intercepts obtained in this way were then used, together with the rate constants determined in perchloric acid and sodium hydroxide solutions, to construct the rate profile shown in Fig. 5. It may be seen that this rate profile differs from that for the thione system (Fig. 2) in that it lacks a bend in acid solution.

© 1999 NRC Canada

Table 2. Summary of rate and equilibrium constants for the *N*-methylindoline-2-thione and -selone systems at 25°C.[a]

Process		X = S	X = Se
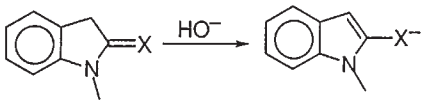	$k^{E}_{HO^-}/10^3\ M^{-1}\ s^{-1}$:	3.42	13.3
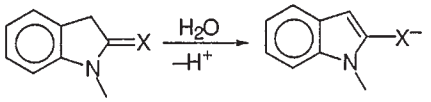	$k^{E}_{o}/10^{-3}\ s^{-1}$:	4.72	70.1
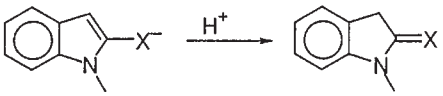	$k^{K}_{H^+}/10^6\ M^{-1}\ s^{-1}$:	5.62	1.08
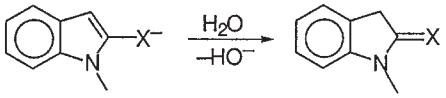	$k^{K}_{o}/10^{-2}\ s^{-1}$:	3.27	0.428
	$K_E/10^{-5}$:	1.33	<10
	pK_E:	4.88	>4
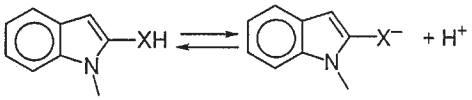	$Q_a^{E}/10^{-5}$ M:	8.85	>100
	pQ_a^{E}:	4.05	<3
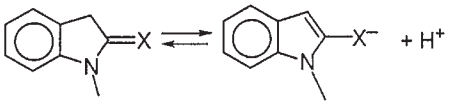	$Q_a^{K}/10^{-9}$ M:	1.18	56.6
	pQ_a^{K}:	8.93	7.25

[a]Aqueous solution; ionic strength = 0.10 M; acidity constants are concentration quotients applicable at ionic strength = 0.10 M.

Such bends are produced by acid ionization of the enol, and absence of this bend here means that ionization of the selone enol occurs at acidities that produce rates beyond the capability of our stopped-flow method (upper limit: $k \cong 500\ s^{-1}$). We were therefore unable to determine this acidity constant for the selone enol. We could, however, set a lower limit of $Q^{E}_{a} > 5 \times 10^{-4}$ M, $pQ^{E}_{a} < 3.3$, based upon the highest acidity we were able to use, $[H^+] = 5 \times 10^{-4}$ M.

Once again, the rate constants for uncatalyzed enolization, k^{E}_{o}, and ketonization, k^{K}_{o}, could not be separated, and the rate–profile data were analyzed by least-squares fitting of a version, eq. [17], of the general rate law of eq. [6] that combines these rate constants as k_{uc}; this rate law is also without

$$[17] \quad k_{obs} = k^{E}_{HO^-}[HO^-] + k_{uc} + k^{K}_{H^+}[H^+]$$

Q_a^{E} because $Q_a^{E} > [H^+]$ throughout the region examined. The results obtained are $k^{E}_{HO^-} = (1.33 \pm 0.03) \times 10^4\ M^{-1}\ s^{-1}$, $k_{uc} = (7.44 \pm 0.72) \times 10^{-2}\ s^{-1}$, and $k^{K}_{H^+} = (1.08 \pm 0.02) \times 10^6\ M^{-1}\ s^{-1}$.

Resolution of k_{uc} into its components with the aid of eq. [10] gave $k^{E}_{o} = (7.01 \pm 0.68) \times 10^{-2}\ s^{-1}$ and $k^{K}_{o} = (4.28 \pm 0.54) \times 10^{-3}\ s^{-1}$. This result, coupled with values of $k^{E}_{HO^-}$ and $k^{K}_{H^+}$, then provides complete rate laws for enolization and ketonization promoted by solvent-related species, and that in turn allows separation of observed rates of equilibration into rates of enolization and ketonization, as shown in Fig. 5. It may be seen that the two rates become equal at about $[H^+] = 10^{-7}$ M, and that ketonization dominates at acidities greater than this while enolization dominates at acidities lower than this.

The nature of buffer catalysis was once again consistent with these dominances: CH_3CO_2H buffers gave only general acid catalysis, and NH_4^+ buffers gave only general base catalysis, whereas $H_2PO_4^-$ and $(CH_2OH)_3NH_3^+$ buffers showed both general acid and general base catalysis. These catalytic coefficients are summarized in Table 1. Combination of the results with Q_a^{HA} according to eq. [13] gave $pQ_a^{K} = 7.38 \pm 0.06$ for $H_2PO_4^-$ buffers and $pQ_a^{K} = 7.25 \pm 0.04$ for

© 1999 NRC Canada

$(CH_2OH)_3NH_3^+$ buffers, consistent with $pQ_a^K = 7.25 \pm 0.02$ obtained by spectrophotometric titration.

Rate measurements in the *N*-methylindoline-2-selone system were also made in D_2O solutions of $DClO_4$ and of NaOD, the latter using deuterated substrates generated as described above for the thione system. These data are summarized in Tables S6 and S7.[2] When combined with the appropriate H_2O data they give the isotope effect $k^K_{H^+}/k^K_{D^+} = 2.61 \pm 0.10$, as expected for the ketonization reaction that dominates in acid solutions, and $k^E_{HO^-}/k^E_{DO^-} = 4.12 \pm 0.03$, again as expected for the enolization that dominates in basic solution.

N-Methylindoline-2-one

Measurement of rates of keto–enol/enolate interconversion by the methods used in the present study require the keto form to be a sufficiently strong carbon acid to allow significant amounts of enolate ion to be present at equilibrium in dilute aqueous solution. This is necessary, both for direct observation of enolate formation from the keto form, and also for preparation of enolate in dilute base for quenching into acid to generate greater than equilibrium amounts of enol. Since the carbon-acid ionization of *N*-methylindoline-2-one occurs only in concentrated base solution (pQ^K_a = 15.86), this requirement is not met, and rate measurements could not be made with this substrate. We hope, however, to be able to make these measurements by another technique at some future time.

Discussion

Keto–enol equilibria

The keto–enol equilibrium constant determined here for *N*-methylindoline-2-thione, $pK_E = 4.88$, is remarkably large for a carboxylic acid amide: it is nearly as great as that for 2-indanone, **4**, ($pK_E = 3.84$) (23), a structurally similar simple ketone. On the assumption that the keto–enol equilibrium constants for carboxylic acid amides are similar to those of carboxylic acid esters (3), and using the value $pK_E = 19$ for ethyl acetate (4), the present result makes the enol content of *N*-methylindoline-2-thione some 14 orders of magnitude greater than that of a simple acyclic carboxylic acid amide such as acetamide, **5**.

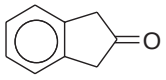

4

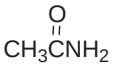

5

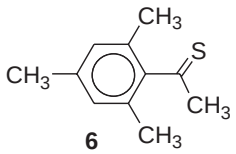

6

A good portion of this large difference may be attributed to replacement of carbonyl oxygen by sulfur in going from acetamide to *N*-methylindoline-2-thione. Thioketones are well known to have considerably greater enol contents than oxygen ketones, a phenomenon generally attributed to the relative weakness of the sulfur–carbon π-bond (24), and a recent comparison of keto–enol equilibrium constants for 2,4,6-trimethylthioacetophenone, **6**, with that of its oxygen analog puts this effect at six orders of magnitude (8). That leaves eight orders of magnitude for other effects, the strongest of which is likely to be formation of a new aromatic ring upon enolization of *N*-methylindoline-2-thione, as illustrated in eq. [1]. Formation of such a new aromatic ring has been shown to have a strong influence upon the ionization of indoline-2-ones and related substances in DMSO solution (9). It is likely, however, that reduced conjugation between the carbonyl group and amide nitrogen in *N*-methylindoline-2-thione will play a role as well. It is conjugative stabilization of the keto form that makes enol contents of simple oxygen amides so low, and in thioamides this conjugation will be weaker than in oxygen amides because of mismatch of orbital size. In an aromatic amide such as *N*-methylindoline-2-thione, moreover, conjugation of carbonyl and nitrogen will be reduced further by offsetting conjugation of nitrogen with the aromatic ring.

Fig. 6. Comparison of rate profiles for keto–enol/enolate interconversion in the *N*-methylindoline-2-thione (○) and *N*-methylindoline-2-selone (△) systems in aqueous solution at 25°C.

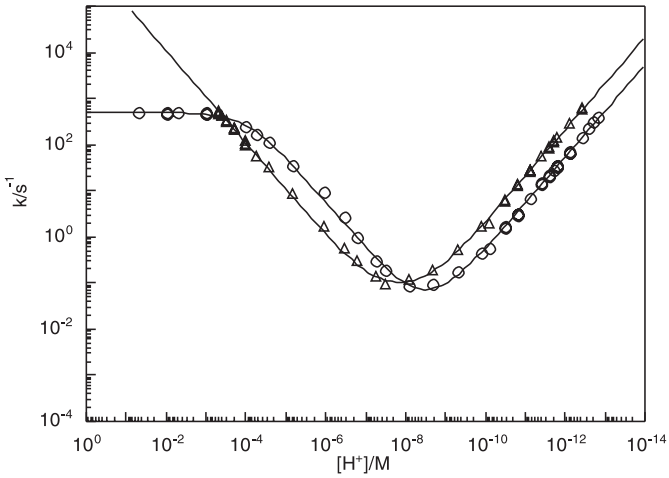

Determination of a keto–enol equilibrium constant by the method employed here requires knowledge of the acidity constant of the enol, Q_a^E, which in turn is evaluated from a bend in the rate profile for ketonization in acidic solution. Unfortunately, rate constants in the *N*-methylindoline-2-selone system became too fast to measure before this bend could be reached (see Fig. 5), and we consequently could not determine a keto–enol equilibrium constant for this substrate. We were, however, able to set the limit $pQ_a^E < 3.3$, and use of this in the relationship $pK_E = pQ_a^K - pQ_a^E$, coupled with $pQ_a^K = 7.25$, then gives the lower limit $pK_E > 4.0$.

This limit is consistent with an estimate that can be made based on the fact that selenols are generally more acidic than the corresponding thiols by a roughly constant 3p*K* units (25). Application of this difference to $pQ_a^E = 4.05$ for the enol of *N*-methylindoline-2-thione then gives $pQ_a^E = 1$ for the selone, and that leads to $pK_E = 6$ for the selone system.

This result is not very different from $pK_E = 4.88$ for *N*-methylindoline-2-thione, and that suggests that, whereas replacing carbonyl oxygen by sulfur produces a marked increase in enol content, further replacement of sulfur by selenium has little effect.

Reaction rates

The comparison of rate profiles provided by Fig. 6 shows that ketonization of the enol of *N*-methylindoline-2-thione in

© 1999 NRC Canada

acid solution is more rapid than that of *N*-methylindoline-2-selone, whereas for enolization in basic solution this order is reversed. The greater rate of ketonization of the thione enol is consistent with the fact that aryl vinyl sulfides undergo acid-catalyzed hydrolysis faster than the corresponding aryl vinyl selenides (26); both of the hydrolyses are cation-forming reactions that occur by rate-determining hydron transfer to carbon, just like enol ketonization, and the difference in reactivity indicates that sulfur is better able to stabilize an adjacent positive charge than is selenium. Enolization, on the other hand, is an anion-generating reaction, and the superiority of the selone here indicates that selenium is better than sulfur at stabilizing negative charge; this is consistent with the greater C-H acidity of *N*-methylindoline-2-selone (pQ^K_a = 7.25) over *N*-methylindoline-2-thione (pQ^K_a = 8.93) as well as the greater acid strength of selenols over thiols (25).

Acknowledgments

We are grateful to the Natural Sciences and Engineering Research Council of Canada for financial support of this work.

References

1. J.P. Guthrie. Can. J. Chem. **71**, 2123 (1993); J.P. Guthrie and Z. Liu. Can. J. Chem. **73**, 1395 (1995).
2. A.J. Kresge. Chem. Soc. Rev. **25**, 275 (1996).
3. S. Sklenak, Y. Apeloig, and Z. Rappoport. J. Am. Chem. Soc. **120**, 10 359 (1998).
4. T.L. Amyes and J.P. Richard. J. Am. Chem. Soc. **118**, 3129 (1996).
5. H. Hart, Z. Rappoport, and S.E. Biali. *In* The chemistry of enols. *Edited by* Z. Rappoport. Wiley, New York. 1990. Chap. 8.
6. J.R. Keeffe and A.J. Kresge. *In* The chemistry of enols. *Edited by* Z. Rappoport. Wiley, New York. 1990. Chap. 7.
7. J. Frey and Z. Rappoport. J. Am. Chem. Soc. **118**, 3994 (1996); Z. Rappoport, J. Frey, M. Sigalov, and E. Rochlin. Pure Appl. Chem. **69**, 1933 (1997).
8. A.J. Kresge and Q. Meng. J. Am. Chem. Soc. **120**, 11 830 (1998).
9. F.G. Bordwell and H.E. Fried. J. Org. Chem. **56**, 4218 (1991).
10. B.S. Pedersen, S. Scheibye, N.H. Nilsson, and S.-O. Lawesson. Bull. Soc. Chim. Belg. **87**, 223 (1978); M.P. Cava and M.I. Levinson. Tetrahedron, **41**, 5061 (1985).
11. J.-B. Baudin, M. Bekhazi, S.A. Julia, O. Ruel, R.L.P. de Jong, and L. Brandsma. Synthesis, 956 (1985).
12. V.Y. Vvedensky, L. Brandsma, E.D. Sheftan, and B.A. Trofimov. Tetrahedron, **53**, 16 783 (1997).
13. R.G. Bates. Determination of pH theory and practice. John Wiley & Sons, New York. 1973. p. 49.
14. G. Yagil..J. Phys. Chem. **71**, 1034 (1967).
15. J.-C. Halle, F. Terrier, and R. Schall. Bull. Soc. Chim. Fr. 4569 (1969).
16. J. Kielland. J. Am. Chem. Soc. **59**, 1675 (1937).
17. F.G. Bordwell. Acc. Chem. Res. **21**, 456 (1988).
18. J.R. Keeffe and A.J. Kresge. *In* Techniques of chemistry. Vol. VI. Investigation of rates and mechanisms of reactions. Part 1. *Edited by* C.F. Bernasconi. John Wiley & Sons, New York. 1986. p. 776.
19. P. Pruszynski, Y. Chiang, A.J. Kresge, N.P. Schepp, and P.A. Walsh. J. Phys. Chem. **90**, 3760 (1986); Y. Chiang, A.J. Kresge, J.A. Santabella, and J. Wirz. J. Am. Chem. Soc. **110**, 5506 (1988).
20. W.P. Jencks and K. Salvesen. J. Am. Chem. Soc. **93**, 4433 (1971).
21. A.J. Kresge, R.A. More O'Ferrall, and M.F. Powell. *In* Isotopes in organic chemistry. *Edited by* E. Buncel and C.C. Lee. Elsevier, New York. 1987. Chap. 4.
22. A.J. Kresge, D.S. Sagatys, and H.L. Chen. J. Am. Chem. Soc. **99**, 7228 (1977).
23. J.R. Keeffe, A.J. Kresge, and Y. Yin. J. Am. Chem. Soc. **110**, 8201 (1988).
24. T. Selzer and Z. Rappoport. J. Org. Chem. **61**, 5462 (1996).
25. F. Fringuellim and A. Taticchi. *In* The chemistry of organic selenium and tellurium compounds. Vol. 1. *Edited by* S. Patai and Z. Rappoport. John Wiley & Sons, New York. 1986. p. 600.
26. R.A. McClelland and M. Leung. J. Org. Chem. **45**, 187 (1980).

© 1999 NRC Canada

Solubility of acenaphthene in organic nonelectrolyte solvents. Comparison of observed versus predicted values based upon Mobile Order theory

Karina M. De Fina, Tina L. Sharp, and William E. Acree, Jr.

Abstract: Experimental solubilities are reported at 25.0°C for acenaphthene dissolved in 36 different organic nonelectrolyte solvents containing ether-, carbonyl-, hydroxy-, ester, methyl-, and *tert*-butyl functional groups. Results of these measurements are used to test the applications and limitations of expressions derived from Mobile Order theory. For the 29 solvents for which predictions could be made computations show that Mobile Order theory does provide fairly reasonable estimates of the saturation mole fraction solubilities. Average absolute deviation between predicted and observed values is 37.8%. In comparison, the average absolute deviation is 1080% when ideal solution behavior is assumed.

Key words: acenaphthene solubilities, organic nonelectrolyte solvents, solubility predictions.

Résumé : Opérant à 25.0°C, on a mesuré les solubilités expérimentales de l'acénaphtène dissous dans 36 solvants organiques non électrolytiques différents contenant des groupes fonctionnels éther, carbonyle, hydroxyle, ester, méthyle et *tert*-butyle. Les résultats de ces mesures sont utilisés pour évaluer les applications et les limitations d'expressions dérivées de la théorie de l'ordre mobile. Pour les 29 solvants pour lesquels il était possible de faire de prédictions, les calculs montrent que la théorie de l'ordre fonctionnel conduit à des évaluations assez raisonnables des solubilités exprimées en fraction molaire de saturation. La déviation absolue moyenne entre les valeurs prévues et observées est de 37,8%. En comparaison, la déviation absolue moyenne est de 1080% quand on fait l'hypothèse que le comportement de la solution est idéal.

Mots clés : solubilités de l'acénaphtène, solvants organiques non électrolytiques, prédictions des solubilités.

[Traduit par la Rédaction]

Introduction

Solid–liquid equilibrium data of organic nonelectrolyte systems are becoming increasingly important in the petroleum industry, particularly in light of present trends towards heavier feedstocks and known carcinogenicity/mutagenicity of many of the larger polycyclic aromatic compounds. Solubility data for a number of polycyclic aromatic hydrocarbons (e.g., anthracene and pyrene) and hetero-atom polynuclear aromatics (e.g., carbazole, dibenzothiophene, and xanthene) have been published in the recent chemical literature (for listing of references see Acree (1–3)). Despite efforts by experimentalists and scientific organizations, both in terms of new experimental measurements and critically evaluated data compilations, there still exist numerous systems for which solubility data are not readily available.

To address this problem, researchers have turned to group contribution methods and semi-empirical expressions to predict desired quantities. Group contribution methods have proved fairly successful in estimating solid solubility in pure and binary solvent mixtures from structural information (4–11). Practical application, though, is limited to systems for which all group interaction parameters are known. Interaction parameters can be evaluated from liquid–vapor, liquid–liquid, and solid–liquid equilibria data. It is important that the database contain as many different functional groups as possible, preferably with adequate representation from both mono- and multi-functional solute/solvent molecules to permit evaluation of potential synergistic effects. The database should contain sufficient experimental values near infinite dilution in the event that one wishes to determine separate interaction parameters for finite concentration and infinite dilution activity coefficient predictions.

Abraham et al. (12, 13) recently developed a general solvation equation that can be used in the correlation and understanding of physico-chemical and biochemical phenomena. Physical properties that have been correlated include gas/solvent partition coefficients (as log L)

$$[1] \qquad \log L = c + rR_2 + s\pi_2^H + a\sum \alpha_2^H + b\sum \beta_2^H + d \log L^{16}$$

and water/solvent partition coefficients (as log P)

Received April 6, 1999.

K.M. De Fina, T.L. Sharp, and W.E. Acree, Jr.[1]
Department of Chemistry, University of North Texas, Denton, TX 76203-5070, U.S.A.

[1]Author to whom correspondence may be addressed.
e-mail: acree@unt.edu

© 1999 NRC Canada

[2] $$\log P = c + rR_2 + s\pi_2^H + a\sum \alpha_2^H + b\sum \beta_2^H + vV_x$$

where R_2 and V_x refer to the excess molar refraction and McGowan volume of the solute, respectively, π_2^H is the solute dipolarity/polarizability descriptor, and $\sum\alpha_2^H$ and $\sum\beta_2^H$ are measures of the hydrogen-bond acidity and hydrogen-bond basicity of the solute. For any given solvent, numerical values of the seven curve-fit coefficients (*c*, *r*, *s*, *a*, *b*, *d*, and *v*) are deduced by regressing experimental partition coefficient data in accordance with eqs. [1] and [2]. The input partition coefficients were sometimes calculated as the ratio of the solute molar solubilities in the organic solvent and water, $P = C_A^{org}/C_A^{aq}$, and as the ratio of the solute molar solubility in the organic solvent and vapor concentration, $L = C_A^{org}/C_A^{gas}$. Published papers have reported curve-fit coefficients for water (12, 13) and a few select organic solvents (13).

To increase the solubility database available for developing group contribution methods and general solvation correlations, we are in the process of measuring solubility data for polycyclic aromatic hydrocarbons (PAHs) and polycyclic aromatic nitrogen hetero-atoms (PANHs). In the present communication, we report acenaphthene solubilities in 36 different organic solvents at 25°C. Results of the measurements are used to further test the applications and limitations of predictive expressions derived from Mobile Order theory. Subsequent studies will use the experimental acenaphthene solubilities in developing gas/liquid partition and water/organic solvent partition correlations based upon eqs. [1] and [2].

Materials and methods

Acenaphthene (Aldrich, 98%) was recrystallized several times from methanol. *n*-Hexane (Aldrich, 99%), *n*-heptane (Aldrich, HPLC), *n*-octane (Aldrich, 99+%, anhydrous), *n*-nonane (TCI, 99+%), *n*-decane (TCI, 99+%), *n*-hexadecane (Aldrich, 99%), cyclohexane (Aldrich, HPLC), methylcyclohexane (Aldrich, 99+%, anhydrous), cyclooctane (Aldrich, 99+%), 2,2,4-trimethylpentane (Aldrich, HPLC), *tert*-butylcyclohexane (Aldrich, 99+%), dibutyl ether (Aldrich, 99 %), methanol (Aldrich, 99.9+%), ethanol (Aaper Alcohol and Chemical Co., absolute), 1-propanol (Aldrich, 99+%, anhydrous), 2-propanol (Aldrich, 99+%, anhydrous), 1-butanol (Aldrich HPLC, 99.8+%), 2-butanol (Aldrich, 99+%, anhydrous), 1-pentanol (Aldrich, 99+%), 2-pentanol (Acros, 99+%), 1-hexanol (Alfa Aesar, 99+%), 1-heptanol (Alfa Aesar, 99+%), 2-methyl-2-butanol (Acros, 99+%), 2-methyl-1-propanol (Aldrich, 99+%, anhydrous), 3-methyl-1-butanol (Aldrich, 99+%, anhydrous), 1-octanol (Aldrich, 99+%, anhydrous), 4-methyl-2-pentanol (Acros, 99+%), 2-ethyl-1-hexanol (Aldrich, 99+%), 2-methyl-1-pentanol (Aldrich, 99%), ethylene glycol (Aldrich, 99.8%, anhydrous), 1,4-dioxane (Aldrich, 99.8%, anhydrous), tetrahydrofuran (Aldrich, 99.9%, anhydrous), 2-butanone (Aldrich HPLC, 99.5+%), ethyl acetate (Aldrich, HPLC, 99.9%), 2-methyl-2-propanol (Arco Chemical Company, 99+%), and butyl acetate (Aldrich HPLC, 99.7%) were stored over molecular sieves before use. Gas chromatographic analysis showed solvent purities to be 99.7 mol% or better.

Excess solute and solvent were placed in amber glass bottles and allowed to equilibrate in a constant temperature water bath at 25.0 ± 0.1°C for at least 3 days (often longer). Attainment of equilibrium was verified both by repetitive measurements after several additional days and by approaching equilibrium from supersaturation by pre-equilibrating the solutions at a higher temperature. Aliquots of saturated acenaphthene solutions were transferred through a coarse filter into a tared volumetric flask to determine the amount of sample and diluted quantitatively with 2-propanol for spectrophotometric analysis at 289 nm on a Bausch and Lomb Spectronic 2000. Concentrations of the dilute solutions were determined from a Beer–Lambert law absorbance versus concentration working curve for nine standard solutions. The concentration of acenaphthene in the standard solutions varied from 5.34×10^{-5} M to 2.67×10^{-4} M. The calculated molar absorptivity of the standard solutions varied slightly over the concentration range, from $\varepsilon \approx 6430$ L mol^{-1} cm^{-1} (5.34×10^{-5} M) to $\varepsilon \approx 6200$ L mol^{-1} cm^{-1} (2.67×10^{-4} M). 2-Butanone did absorb at the analysis wavelength. Acenaphthene was sufficiently soluble in this solvent that by the time the saturated solution was appropriately diluted for the measured absorbance to fall on the Beer–Lambert Law curve the solvent background absorbance was negligible.

Experimental molar concentrations were converted to (mass/mass) solubility fractions by multiplying by the molar mass of acenaphthene, volume(s) of volumetric flask(s) used, and any dilutions required to place the measured absorbances on the Beer–Lambert law absorbance versus concentration working curve, and then dividing by the mass of the saturated solution analyzed. Mole fraction solubilities were computed from (mass/mass) solubility fractions using the molar masses of the solute and solvent. Experimental acenaphthene solubilities, X_A^{sat}, in 36 organic solvents studied are listed in Table 1. Numerical values represent the average of between four and eight independent determinations, with the measurements being reproducible to ±1.5%.

Results and discussion

Solvents listed in Table 1 include both noncomplexing alkanes and self-associating alcohols. Of the many solution models proposed in recent years, Mobile Order theory is perhaps the only one that is capable of describing solute behavior in such a wide range of solvent mixtures. The basic model (14–21) assumes that all molecular groups perpetually move, and that neighbors of a given kind of external atom in a molecule constantly change identity. All molecules of a given kind dispose of the same volume, equal to the total volume *V* of the liquid divided by the number N_A of molecules of the same kind, i.e., Dom A = V/N_A. The center of this domain perpetually moves. The highest mobile disorder is achieved whenever groups visit all parts of their domain without preference. Preferential contacts lead to deviations with respect to this "random" visiting. This is especially true in the case of hydrogen bonding as specific interactions result in a specific orientation of the "donor" molecule with respect to an adjacent "acceptor" molecule.

© 1999 NRC Canada

Table 1. Comparison between experimental acenaphthene mole fraction solubilities and predicted values based upon Mobile Order theory.

Organic solvent	$(X_A^{sat})^{exp}$ [a]	$(X_A^{sat})^{calc}$	% dev[b]
n-Hexane	0.05192	0.05670	9.2
n-Heptane	0.06075	0.05899	–2.9
n-Octane	0.06826	0.06496	–4.8
n-Nonane	0.07210	0.07268	0.8
n-Decane	0.07852	0.07535	–4.0
n-Hexadecane	0.1065	0.0980	–8.0
Cyclohexane	0.07043	0.06935	–1.5
Methylcyclohexane	0.08093	0.07278	–10.1
Cyclooctane	0.09739	0.08769	–10.0
2,2,4-Trimethylpentane	0.04668	0.04718	–1.1
tert-Butylcyclohexane	0.07763	0.08940	15.2
Dibutyl ether	0.1116	0.1645	47.4
Tetrahydrofuran	0.1973	0.2061	4.5
1,4-Dioxane	0.1415	0.1955	38.2
Methanol	0.00544	0.01333	145.0
Ethanol	0.01068	0.02285	114.0
1-Propanol	0.01686	0.02959	75.5
2-Propanol	0.01336	0.03296	146.7
1-Butanol	0.02373	0.03727	57.1
2-Butanol	0.01877	0.03156	68.2
2-Methyl-1-propanol	0.01691	0.02679	58.4
2-Methyl-2-propanol	0.01705		
1-Pentanol	0.03176	0.04126	29.9
2-Pentanol	0.02443		
3-Methyl-1-butanol	0.02347		
2-Methyl-2-butanol	0.02867		
1-Hexanol	0.03922	0.04124	5.2
2-Methyl-1-pentanol	0.02904		
4-Methyl-2-pentanol	0.02551		
1-Heptanol	0.04617	0.04642	0.5
1-Octanol	0.05089	0.05110	0.4
2-Ethyl-1-hexanol	0.04402		
Ethylene glycol	0.001157	0.001941	67.8
2-Butanone	0.1307	0.1936	48.1
Butyl acetate	0.1370	0.1977	44.3
Ethyl acetate	0.1086	0.1927	77.4

[a]Numerical values represent the average of between four and eight independent determinations, with the measurements being reproducible to ±1.5%.

[b]Deviations (%) = $100[(X_A^{sat})^{calc} - (X_A^{sat})^{exp}]/(X_A^{sat})^{exp}$.

In the case of an inert crystalline solute dissolved in a self-associating solvent, Mobile Order theory expresses the volume fraction saturation solubility, ϕ_A^{sat}, as

$$[3]\quad \ln \phi_A^{sat} = \ln a_A^{solid} - 0.5(1 - V_A/V_{solvent})\phi_{solvent} + 0.5 \ln [\phi_A^{sat} + \phi_{solvent}(V_A/V_{solvent})] - \phi_{solvent}^2 V_A(\delta_A' - \delta_{solvent}')^2(RT)^{-1} - r_{solvent}(V_A/V_{solvent})\phi_{solvent}$$

where the $r_{solvent}(V_A/V_{solvent})\,\phi_{solvent}$ term represents the contributions resulting from hydrogen-bond formation between the solvent molecules. For most of the published applications, $r_{solvent}$ was assumed to be unity for strongly associated solvents with single hydrogen-bonded chains such as monofunctional alcohols, to be 2 for water or diols, and to equal 0 for nonassociated solvents such as saturated hydrocarbons. A more exact value for alcoholic solvents can be calculated based upon

$$[4]\quad r_{solvent} = (K_{solvent}\,\phi_{solvent}/V_{solvent})/(1 + K_{solvent}\,\phi_{solvent}/V_{solvent})$$

with a numerical value of $K_{solvent}$ = 5000 cm^3 mol^{-1} assumed for all mono-functional alcohols.

If complexation does occur between the crystalline solute and solvent

$$[5]\quad \ln \phi_A^{sat} = \ln a_A^{solid} - 0.5(1 - V_A/V_{solvent})\phi_{solvent} + 0.5 \ln [\phi_A^{sat} + \phi_{solvent}(V_A/V_{solvent})] - \phi_{solvent}^2 V_A(\delta_A' - \delta_{solvent}')^2(RT)^{-1} + \ln [1 + \phi_{solvent}(K_{ASolvent}/V_{solvent})]$$

then an additional term involving the solute–solvent equilibrium constant, $K_{ASolvent}$, must be introduced to describe the solubility enhancement that arises as a result of specific interactions. A slightly more complex expression applies in the case of solute complexation with a self-associating solvent. The symbols δ_A' and $\delta_{solvent}'$ denote the modified solubility parameters of the solute and solvent, respectively, V_i is the molar volume, and a_A^{solid} is the activity of the solid solute. This latter quantity is defined as the ratio of the fugacity of the solid to the fugacity of the pure hypothetical supercooled liquid. The numerical value of a_A^{solid} can be computed from

$$[6]\quad \ln a_A^{solid} = -\Delta H_A^{fus}(T_{mp} - T)/(RTT_{mp}) + (\Delta C_{p,A}/RT)(T_{mp} - T) - (\Delta C_{p,A}/T) \ln (T_{mp}/T)$$

the solute's molar enthalpy of fusion, ΔH_A^{fus}, and heat capacity difference, $\Delta C_{p,A}$, at the normal melting point temperature, T_{mp}. Contributions from nonspecific interaction are incorporated into Mobile Order theory through the $\phi_{solvent}^2 V_A(\delta_A' - \delta_{solvent}')^2(RT)^{-1}$ term. Ruelle et al. (17–21) have presented an impressive set of comparisons between experimental and predicted values for anthracene, naphthalene, pyrene, biphenyl, carbazole, benzil, *p*-benzoquinone, tricosane, octacosane, 10-nonadecanone, 11-heneicosanone, and 12-tricosanone solubilities in a wide range of both noncomplexing and complexing solvents to document the predictive ability of Mobile Order theory.

Predictive application of eqs. [3] and [5] is relatively straightforward. First, an average numerical value of $\delta_{acenaph}'$ = 19.60 MPa$^{1/2}$ is computed by requiring that each equation (with $r_{solvent}$ = 0 and (or) $K_{ASolvent}$ = 0) perfectly describes acenaphthene mole fraction solubility data in *n*-hexane ($\delta_{acenaph}'$ = 19.75 MPa$^{1/2}$), *n*-heptane ($\delta_{acenaph}'$ = 19.54 MPa$^{1/2}$), and *n*-octane ($\delta_{acenaph}'$ = 19.51 MPa$^{1/2}$). The numerical value of a_A^{solid} = 0.1976 is calculated using eq. [6] with ΔH_A^{fus} = 21 540 J mol^{-1} and T_{mp} = 366.56 K (22). The two heat capacity terms in eq. [6] were set equal to zero, as we were unable to find heat capacity data for the subcooled liquid solute. A numerical value of $V_{acenaph}$ = 137.77 cm^3 mol^{-1} was used for the molar volume of the hypothetical

© 1999 NRC Canada

Table 2. Solvent and solute properties used in Mobile Order predictions.

Component (*i*)	V_i/(cm^3 mol^{-1})	δ'_i/(MPa$^{1/2}$)[a]
n-Hexane	131.51	14.56
n-Heptane	147.48	14.66
n-Octane	163.46	14.85
n-Nonane	179.87	15.07
n-Decane	195.88	15.14
n-Hexadecane	294.12	15.61
Cyclohexane	108.76	14.82
Methylcyclohexane	128.32	15.00
2,2,4-Trimethylpentane	166.09	14.30
Cyclooctane	134.9	15.40
tert-Butylcyclohexane	173.9	15.50
Dibutyl ether	170.3	17.45
Tetrahydrofuran	81.4	19.30
1,4-Dioxane	85.8	20.89
Methanol	40.7	19.25
Ethanol	58.7	17.81
1-Propanol	75.10	17.29
2-Propanol	76.90	17.60
1-Butanol	92.00	17.16
2-Butanol	92.4	16.60
2-Methyl-1-propanol	92.8	16.14
1-Pentanol	108.6	16.85
1-Hexanol	125.2	16.40
1-Heptanol	141.9	16.39
1-Octanol	158.3	16.38
Ethylene glycol	56.0	19.90
Butyl acetate	132.5	19.66
Ethyl acetate	98.5	20.79
2-Butanone	90.2	20.90
Acenaphthene[b]	137.77[c]	19.60[d]

[a]Tabulated values are taken from a compilation given in Ruelle et al. (17, 18, 20, 21).

[b]The numerical value of a_A^{solid} = 0.1976 was calculated from eq. [6] using ΔH_A^{fus} = 21 540 J mol^{-1} and T_{mp} = 366.56 K (22).

[c]Numerical value of $V_{acenaph}$ = 137.77 cm^3 mol^{-1} was estimated using the group contribution method of Shahidi et al. (23).

[d]Numerical value was calculated using the measured acenaphthene mole fraction solubilities in *n*-hexane, *n*-heptane, and *n*-octane, in accordance with eqs. [3] and [5]; with $r_{solvent}$ = 0 and (or) $K_{ASolvent}$ = 0.

subcooled liquid solute. The molar volume of the solute was estimated using the group contribution method of Shahidi et al. (23) for partial molar volumes of aromatic hydrocarbons dissolved in carbon tetrachloride.

Table 1 summarizes the predictive ability of Mobile Order theory for the 29 different organic solvents for which both acenaphthene solubility data and modified solubility parameters could be found. Solvent molar volumes and modified solubility parameters are listed in Table 2. The modified solubility parameters account for only nonspecific interactions, and in the case of the alcoholic solvents the hydrogen-bonding contributions have been removed. Numerical values of $\delta'_{solvent}$ were obtained from published compilations (17, 18, 20, 21), and were either deduced by regressing actual solubility data of solid *n*-alkanes in organic solvents in accordance with the configurational entropic model of Huyskens and Haulait-Pirson (24) or estimated using known values for similar organic solvents. Examination of the entries in Table 1 reveals that Mobile Order theory does provide fairly reasonable estimates of the solubility behavior of acenaphthene in a wide range of organic solvents. Average absolute deviation between predicted and observed values is 37.8%. Expressed on a natural logarithmic mole fraction scale, Mobile Order theory predicts the acenaphthene solubilities to within ±0.281 ln units. Readers are reminded that in evaluating the applicability of Mobile Order theory one must realize that many of these particular systems are highly nonideal, and that the experimental solubility data covers over a 165-fold range in mole fraction. Had an ideal solution been assumed, then the predicted mole fraction solubility would be $X_A^{sat} = a_A^{solid} = 0.1976$ for each solvent. The ideal solution approximation corresponds to a considerably larger average absolute deviation of 1080% between predicted and observed values.

Acknowledgements

Tina Sharp thanks the University of North Texas and the U.S. Department of Education for support provided under the Ronald E. McNair Postbaccalaureate Achievement Program.

References

1. W.E. Acree, Jr. Polycyclic aromatic hydrocarbons in pure and binary solvents. IUPAC solubility data series. Vol. 54. Oxford University Press, Oxford, U.K. 1994.
2. W.E. Acree, Jr. Polycyclic aromatic hydrocarbons: binary nonaqueous systems: part 1 (solutes A–E). IUPAC Solubility data series. Vol. 58. Oxford University Press, Oxford, U.K. 1995.
3. W.E. Acree, Jr. Polycyclic aromatic hydrocarbons: binary nonaqueous systems: part 2 (solutes F–Z). IUPAC Solubility data series. Vol. 59. Oxford University Press, Oxford, U.K. 1995.
4. W.E. Acree, Jr. Int. J. Pharm. **18**, 47 (1984).
5. U. Domanska and T. Hofman. J. Solution Chem. **14**, 531 (1985).
6. U. Domanska. Fluid Phase Equilibr. **35**, 217 (1985).
7. R.S. Basu, H. Pham, and D.P. Wilson. Int. J. Pharm. **7**, 319 (1986).
8. A.B. Ochsner and T.D. Sokoloski. J. Pharm. Sci. **74**, 634 (1985).
9. R. Carta and S. Dernini. J. Chem. Eng. Data, **28**, 328 (1983).
10. W.E. Acree, Jr. and J.H. Rytting. Int. J. Pharm. **13**, 197 (1983).
11. A. Martin, P.L. Wu, A. Adjei, A. Beerbower, and J.M. Prausnitz. J. Pharm. Sci. **70**, 1260 (1981).
12. M.H. Abraham, H.S. Chadha, J.P. Dixon, and A.J. Leo. J. Phys. Org. Chem. **7**, 712 (1994).
13. M.H. Abraham, J. Andonian-Haftvan, J.P. Osei-Owasu, P. Sakellariou, J.S. Urieta, M.C. Lopez, and R. Fuchs. J. Chem. Soc. Perkin Trans. 2, 299 (1993).
14. P.L. Huyskens and G.G. Siegel. Bull. Soc. Chim. Belg. **97**, 821 (1988).
15. G.G. Siegel, P.L. Huyskens, and G. Vanderheyden. Ber. Bunsenges. Phys. **94**, 549 (1990).
16. P.L. Huyskens. J. Mol. Struct. **274**, 223 (1992).
17. P. Ruelle, C. Rey-Mermet, M. Buchmann, H. Nam-Tran, U.W. Kesselring, and P.L. Huyskens. Pharm. Res. **8**, 840 (1991).
18. P. Ruelle, M. Buchmann, H. Nam-Tran, and U.W. Kesselring. Int. J. Pharm. **87**, 47 (1992).

© 1999 NRC Canada

19. P. Ruelle, M. Buchmann, and U.W. Kesselring. J. Pharm. Sci. **83**, 396 (1994).
20. P. Ruelle, E. Sarraf, and U.W. Kesselring. Int. J. Pharm. **104**, 125 (1994).
21. P. Ruelle, E. Sarraf, L. Van den Berge, K. Seghers, M. Buchmann, and U.W. Kesselring. Pharm. Acta Helv. **68**, 49 (1993).
22. S.C. Mraw and D.F. O'Rourke. J. Chem. Thermodyn. **13**, 199 (1981).
23. F. Shahidi, P.G. Farrell, J.T. Edward, and P.J. Cannone. J. Org. Chem. **44**, 950 (1979).
24. P.L. Huyskens and M.C. Haulait-Pirson. J. Mol. Liq. **31**, 135 (1985).

© 1999 NRC Canada

La radiolyse de l'eau et des solutions aqueuses : historique et actualité

Christiane Ferradini et Jean-Paul Jay-Gerin

Résumé : Les premières expériences montrant la décomposition de l'eau par action des rayonnements ionisants datent d'un siècle. À l'occasion de cet anniversaire, nous avons tenté de réaliser une synthèse des travaux concernant ce sujet depuis son origine, en insistant plus particulièrement sur les diverses étapes physicochimiques ayant conduit à l'état actuel de cette science. Dans ce but, nous décrivons l'influence sur la radiolyse de l'eau des paramètres intervenant, tels que la concentration du soluté, le pH, le débit de dose, la nature et l'énergie du rayonnement, la présence d'oxygène, la température, la nature de la phase et la pression. Bien qu'elle soit incomplète, une bonne description des phénomènes a pu être obtenue. Elle conduit à diverses perspectives concernant, d'une part, le développement de cette science et, d'autre part, ses possibilités d'applications et de retombées.

Mots clés : chimie radicalaire, courbe de dilution, eau, électron hydraté, radicaux hydroxyle et superoxyde, radicaux libres, radiolyse, réactions en chaîne, rendements radicalaires et moléculaires, survie cellulaire, transfert d'énergie linéique.

Abstract : Experiments showing that water is decomposed by the action of high-energy radiations date back to the first days of the discovery of radioactivity, a century ago. On the occasion of this anniversary, we have attempted to give a comprehensive account of the radiation chemistry of water and its solutions since its origin, with special emphasis on the various physical and chemical stages that led to the present state of this science. To this aim, we describe the effect of different intervening factors on the molecular and radical yields, including dissolved solute concentration, pH, radiation intensity (or dose rate), type and energy of the radiation, presence of oxygen, temperature, phase, and pressure. We also discuss briefly the chemical behavior of the free radicals produced in radiolyzed aqueous solutions. A good, albeit incomplete, description of the phenomena is obtained that leads to various perspectives concerning, on the one hand, the development of this science and, on the other hand, its potential for applications.

Key words : radical chemistry, dilution curve, water, hydrated electron, hydroxyl and superoxide radicals, free radicals, radiolysis, chain reactions, molecular and radical yields, cell survival, linear energy transfer.

Table des matières

I. Introduction
II. De la découverte de la radioactivité à celle de l'électron hydraté (e^-_{aq})
A. Premières expériences concernant la radiolyse de l'eau
B. Premières expériences concernant les solutions aqueuses diluées 1544
C. Avènement de la radiolyse pulsée 1545
D. Nature des intermédiaires réactionnels 1545
E. Écriture de la réaction fondamentale 1546
III. De la découverte de l'électron hydraté jusqu'à la fin du XX^{ème} siècle 1547
A. Détermination expérimentale des rendements radicalaires et moléculaires (RRM) : cas des rayons γ et X et des milieux neutres 1547
B. Élaboration de modèles diffusionnels 1549
C. Influence de divers paramètres sur les RRM 1550
1. Influence de la concentration du soluté 1550
(a) Exceptions aux courbes de dilution 1550
(b) Utilisations des courbes de dilution 1551
(c) Effet direct 1551
(d) Cas des macromolécules biologiques 1552
2. Influence du pH 1552
3. Influence du débit de dose 1553
4. Influence de la nature et de l'énergie du rayonnement 1555
5. Influence de la présence d'oxygène 1557
(a) Introduction 1557
(b) Actions de l'oxygène sur la radiolyse de solutions diluées 1557
(c) Réactions gouvernant la radiolyse des solutions aérées 1557

Reçu le 25 novembre 1998.

C. Ferradini. Laboratoire de chimie-physique, Unité mixte de recherche n° 8601 au Centre national de la recherche scientifique, Université René Descartes, 45, Rue des Saints-Pères, 75270 Paris Cedex 06, France.
J.-P. Jay-Gerin.[1] Département de médecine nucléaire et de radiobiologie, Faculté de médecine, Université de Sherbrooke, Sherbrooke, QC J1H 5N4, Canada.

1. Auteur à qui adresser toute correspondance. Tél. : (819) 346-1110, poste : 14682. Téléc. : (819) 564-5442. Mél. : jaygerin@courrier.usherb.ca

 © 1999 CNRC Canada

(d) Action à l'échelle cellulaire 1558
6. Influence de la température 1559
(a) Variation des RRM en fonction de la température 1559
(b) Spectre d'absorption de e^-_{aq} en fonction de la température 1560
(c) Influence de la température sur diverses constantes de vitesse de réaction 1560
7. Influence de la nature de la phase 1561
8. Influence de la pression 1562
IV. Conclusion : la radiolyse de l'eau à l'orée du XXI^{ème} siècle 1563
A. État actuel des connaissances 1563
B. Applications 1565
C. Retombées 1566
1. Apport à l'étude des interactions matière – rayonnements ionisants 1566
2. Chimie radicalaire 1566
3. Chimie bioradicalaire 1567
Bibliographie 1567

I. Introduction

La plus grande partie des premiers travaux de radiolyse a concerné l'irradiation de l'eau. Ceci est dû à différentes raisons. D'une part, les méthodes utilisées dès l'abord consistaient principalement à analyser un faisceau de données expérimentales impliquant des solutés variés : par rapport à d'autres solvants, l'eau offre à ce point de vue une chimie plus riche et mieux établie. D'autre part, les études de radiolyse des solutions aqueuses ne perdaient pas de vue les apports éventuels vers les applications radiobiologiques qui se développaient parallèlement; or l'eau est un constituant majeur de la matière vivante, au moins pondéralement.

Un grand nombre de résultats expérimentaux et théoriques concerne donc la radiolyse de l'eau et de ses solutions et a permis de développer les connaissances à ce sujet. Toutefois, l'évolution de celles-ci se poursuit rapidement et il n'y a pas actuellement de mises au point récentes facilitant l'accès à ce domaine. Cette constatation nous a conduits à envisager et à décrire, sous un jour actuel, le passé et le présent des recherches portant sur l'action des rayonnements ionisants sur l'eau et les solutions aqueuses.

Après un rappel de l'historique de la radiolyse de l'eau, nous décrirons comment ont été identifiés les intermédiaires réactionnels alors impliqués et leurs devenirs. La notion de « rendements radicalaires et moléculaires » a ainsi pu être introduite; elle donne un certain nombre de renseignements sur les événements se produisant pour des temps pouvant aller jusqu'à ~10^{-7} s après l'absorption du rayonnement ionisant. L'influence de divers paramètres sera ensuite développée et justifiée, et finalement un certain nombre d'applications sera évoqué.

II. De la découverte de la radioactivité à celle de l'électron hydraté (e^-_{aq})

A. Premières expériences concernant la radiolyse de l'eau

On sait que, quelques mois seulement après la découverte des rayons X par Wilhelm C. Röntgen, la radioactivité fut à son tour découverte en février–mai 1896 par Henri Becquerel à Paris et que le polonium (1) et le radium (2) furent mis en évidence en 1898 par Pierre et Marie Curie. C'est en 1902 que fut observée pour la première fois, par Giesel (3), la décomposition de l'eau sous l'influence d'un sel de radium dissous. Il constata que de telles solutions donnaient lieu à un dégagement permanent d'hydrogène et d'oxygène, phénomène comparable, d'après Marie Curie (4), à une *« électrolyse sans électrodes »*. Ces résultats furent confirmés l'année suivante par Ramsay et Soddy (5) qui trouvèrent, de plus, que de faibles quantités d'hélium étaient présentes dans ce dégagement. Peu après, Debierne (6) souligne qu'il est admis *« que cet hélium résulte de la désagrégation de l'atome de radium »*. Il étudie quantitativement les dégagements gazeux provenant de solutions de bromure de radium ou de chlorure d'actinium et conclut que *« le gaz hélium résulte bien de la présence des corps radioactifs »*. Rappelons que l'expérience magistrale de Rutherford et Royds (7) montrant directement que les particules α sont des atomes d'hélium ionisés date de 1909. Divers autres travaux concernant les dégagements gazeux provenant de l'action du radon sur l'eau ont été ensuite développés par Ramsay et Cameron (8, 9) et par Usher (10).

La question alors posée concernait l'origine de cette décomposition de l'eau; elle pouvait être attribuée, soit à une action chimique du radioélément mis en solution, de ses dérivés ou de leurs produits de transformation, soit à l'effet des divers rayonnements intervenants. Debierne (11, 12) a établi que l'action sur l'eau pouvait être observée même lorsque la source et la solution n'étaient pas en contact direct, ce qui l'a conduit à écrire : *« l'énergie nécessaire à la décomposition ne peut être empruntée qu'au rayonnement absorbé par l'eau »*. Ces résultats furent confirmés très rapidement par Kernbaum (13). À titre d'exemple, la filiation principale des radioéléments impliqués dans le cas observé est indiquée figure 1, selon les données actuelles. On voit que le passage de ^{226}Ra à ^{206}Pb (stable) met en jeu cinq émissions α successives et quatre émissions β^-. Diverses transitions γ sont également incluses dans ces décroissances, permettant le retour à l'état fondamental des noyaux excités. L'eau est donc généralement soumise à trois types de rayonnements : α, β^- et γ provenant du radium et de ses descendants (voir fig. 1). D'après les différents auteurs, les durées d'irradiation étaient bien supérieures aux temps nécessaires aux radioéléments précédents pour atteindre l'équilibre radioactif. Dans ces expériences, les rayons α sont totalement absorbés dans l'eau, alors que les rayons β^- et γ ne le sont que partiellement ou très partiellement. Toutefois, les doses relatives cédées à l'eau pour les trois types de rayonnements varient dans ces travaux avec les conditions expérimentales (géométrie du récipient, volume mort au-dessus de la solution irradiée, etc.). Les auteurs précédemment cités (8–10) ont montré, de plus, que ce sont les particules α qui sont responsables de la très grande partie des effets chimiques observés. Par ailleurs, Kernbaum (13) a mis en évidence le fait que les rayons X ne donnent pas, dans ces conditions, de dégagement gazeux observable. Des remarques analogues ont été faites ultérieurement par Risse (15) et par Fricke et Brownscombe (16). On sait en effet, maintenant, que les rayons α conduisent à une radiolyse de l'eau en produits stables mesurables, tandis que dans le cas des rayons γ ou X la radiolyse en l'absence d'air

© 1999 CNRC Canada

Fig. 1. Famille radioactive du radium 226 : séquence principale (voir, par exemple, réf. 14). Soulignons que diverses transitions γ, traduisant le retour à l'état fondamental des noyaux excités, doivent également être incluses dans ces décroissances. À titre d'exemple, dans la transition de ^{226}Ra à ^{222}Rn, environ 6 % du bilan énergétique emprunte la voie impliquant l'émission d'un rayon α de 4,676 MeV et d'un rayon γ de 0,187 MeV, la fraction restante ne mettant en jeu qu'un seul rayon α (4,863 MeV) par désintégration.

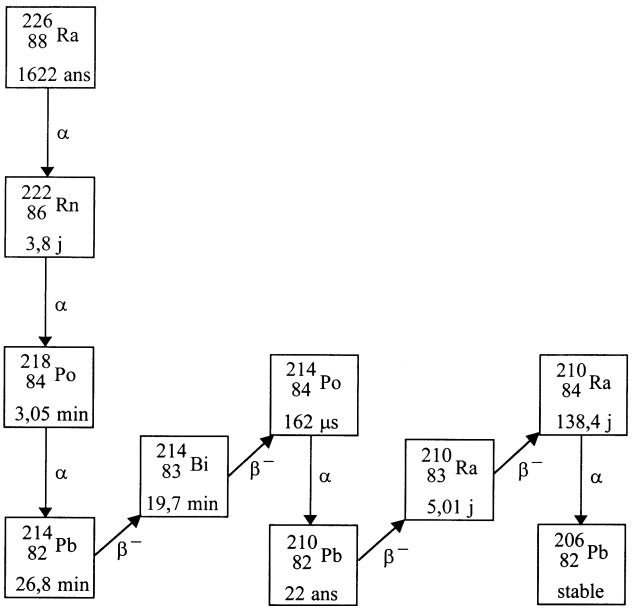

est très faible par suite de réactions inverses importantes et rapides.

En 1911, Usher (10) a conclu de ses résultats qu'un atome d'*« émanation »* (c'est-à-dire de ^{222}Rn) peut décomposer 154 000 molécules d'eau. Pour le rayonnement β^-, la quantité de gaz dégagé est bien inférieure à celle observée dans le cas des rayons α.

Il est apparu, d'après les mesures de gaz, que le bilan en hydrogène et en oxygène n'était pas vérifié (3, 8, 11–13, 17 (cité par F. Giesel, réf. 3), 18). Kernbaum (13), le premier, a montré que le déficit en oxygène est compensé par une formation parallèle d'eau oxygénée (ou peroxyde d'hydrogène) H_2O_2.

Une première tentative d'interprétation de la radiolyse de l'eau pure remonte à 1914, date à laquelle Debierne (12) a émis l'hypothèse de la dissociation de l'eau en atomes H• et en radicaux •OH sous l'influence des rayonnements. Il écrit (12) : *« On peut supposer que chaque molécule d'eau est décomposée en un atome H et un radical hydroxyl OH, deux atomes d'hydrogène se soudant pour faire une molécule d'hydrogène, et deux radicaux hydroxyls donnant lieu à la production d'une molécule d'eau oxygénée »*. Les espèces H• et •OH seraient formées à partir des ions primaires de l'eau. Une telle interprétation, reposant en grande partie sur des bases justes, a été ignorée pendant de nombreuses années jusqu'à ce qu'elle soit énoncée, indépendamment, par Risse (19), par le groupe de Burton et Franck (voir, par exemple, réf. 20) et par Weiss (21).

On voit que des résultats intéressants ont été obtenus avec des moyens simples dès les premières années suivant la découverte de la radioactivité. Toutefois, long a été ensuite le chemin conduisant à la compréhension actuelle de la radiolyse de l'eau. Une étape particulièrement importante dans cette voie a été l'étude de l'influence de l'oxygène dissous. En effet, en irradiant, par des rayons γ ou X, de l'eau contenant de l'oxygène, on observe, dans ce cas, la formation d'eau oxygénée (15, 22, 23), un dégagement d'hydrogène (24, 25) et une consommation d'oxygène.

On le sait, pour l'eau pure, donc désaérée, aucun produit stable ne peut être mesuré dans les conditions précédentes d'irradiation. L'eau aérée contient, à température ambiante, seulement ~4×10^{-6} molécule d'oxygène pour une molécule d'eau, et cela suffit pourtant à modifier profondément sa radiolyse. Ce rôle important joué par un soluté a incité de nombreux chercheurs à étudier la radiolyse de solutions de composés minéraux et organiques. Comme nous allons le voir, l'étude de l'action des rayonnements ionisants sur les solutions aqueuses diluées a contribué grandement à la compréhension des mécanismes intervenant lors de la radiolyse de l'eau. De plus, un intérêt croissant pour l'étude des effets chimiques des rayonnements était suscité, ainsi qu'il a été mentionné, par la nécessité de comprendre les processus mis en jeu en radiobiologie (voir, par exemple, réf. 26).

B. Premières expériences concernant les solutions aqueuses diluées

Dès 1911, Kailan a irradié un certain nombre de solutions aqueuses avec les rayonnements associés au radium.[2] Mais, à partir des années 1930, on a pu disposer de sources de rayons X équivalentes à plusieurs milliers de curies, alors que les expériences utilisant le radium impliquaient des activités inférieures au curie.[3] Mieux encore, à partir de 1950, le développement des réacteurs nucléaires a permis d'obtenir des quantités de plus en plus importantes de radioéléments, et en particulier de cobalt 60 émetteur de rayons γ d'énergies 1,17 et 1,33 MeV, de période 5,27 ans et dont l'activité pouvait dépasser 10^4 curies.

Les irradiations de solutions aqueuses se développèrent rapidement et on peut aujourd'hui évaluer à plusieurs centaines le nombre de systèmes minéraux ou organiques ainsi étudiés. Pour rendre ces études quantitatives, on a défini le rendement G reliant la transformation chimique induite à l'énergie cédée au milieu par le rayonnement.[4] G s'exprime en molécules pour 100 eV absorbés (que nous écrirons, dans

[2] Pour une description d'ensemble des travaux d'Anton Kailan, voir, par exemple, réf. 27.

[3] On sait que l'activité de 1,025 g de radium correspond à 1 curie (Ci), le curie étant l'ancienne unité de radioactivité et représentant la quantité d'un élément radioactif dans lequel le nombre de désintégrations par seconde est égal à $3{,}700 \times 10^{10}$. L'unité SI, on le sait, est le becquerel (Bq) qui correspond à une désintégration par seconde.

[4] Plus précisément, le rendement $G(P)$ est défini comme la dérivée de la concentration [P] de l'espèce « P », formée ou détruite, par rapport à la dose absorbée D : $G(P) = (1/\rho)(d[P]/dD)$, où ρ est la masse volumique du système irradié. Du point de vue pratique, on retient généralement le *rendement initial*, calculé à partir de la pente de la tangente à l'origine de la courbe expérimentale représentant [P] en fonction de D. Puisque $D = It$, où I et t sont respectivement l'intensité ou débit de dose et le temps d'irradiation, on a : $G(P) = (1/\rho I)(d[P]/dt)$.

© 1999 CNRC Canada

ce travail, moléc./100 eV) ou, dans le système SI, en mol/J.[5] Nous évoquerons ici seulement le comportement de trois solutés : les ions ferreux, les ions cérium IV et l'acide formique, qui ont été choisis principalement par suite de leur intérêt historique.

Les ions ferreux, en solution acide (H_2SO_4 0,4 M) aérée et irradiée avec les rayons γ de ^{60}Co ou les rayons X de même énergie, sont oxydés en ions ferriques avec un rendement $G(Fe^{3+})$ = 15,6 moléc./100 eV (voir, par exemple, réfs. 28–30).[6] Il a été montré expérimentalement (31, 32) que la quantité d'ions ferreux oxydés croît linéairement en fonction de la dose absorbée et que le facteur de proportionnalité est, dans ce cas, indépendant du débit de dose dans une large gamme,[7] ainsi que de la concentration initiale en ions ferreux entre ~5×10^{-5} et 10^{-1} M. Le choix initial de l'acide sulfurique a été dicté par sa relative inertie vis-à-vis du rayonnement et au fait qu'à la concentration 0,4 M la solution a un pouvoir d'arrêt équivalent à celui de l'air (34). Les caractéristiques précédentes, associées aux facilités de dosage de Fe^{3+} par spectrophotométrie, montrent que ce système, appelé « dosimètre de Fricke »,[8] a toutes les qualités nécessaires pour jouer un tel rôle.

Pour certains solutés, à l'inverse des ions ferreux, on peut parfois observer une réduction. Tel est le cas des ions cérium IV, étudiés tout d'abord par Clark et Coe (36). Le rendement de réduction pour ce système a été trouvé égal à une valeur voisine de 2,45 moléc./100 eV, en milieu H_2SO_4 0,4 M, pour les rayons γ de ^{60}Co (voir, par exemple, réfs. 28, 30, 37 et 38).[6] Cette facilité de réduction de l'ion cérium IV doit être rapprochée de la valeur relativement élevée du potentiel de réduction du couple Ce^{IV}/Ce^{III} (1,44 V), celui du couple Fe^{3+}/Fe^{2+} étant égal à 0,77 V. Le rendement de disparition des ions Ce^{IV} est le même en la présence ou en l'absence d'air. À cela s'ajoutent des dégagements d'hydrogène et d'oxygène avec des rendements respectivement de 0,40 et 0,84 moléc./100 eV (38).

Une des premières études concernant les solutés organiques porte sur l'acide formique (HCOOH) en solution aqueuse diluée (39, 40). Ce système a l'avantage sur les précédents de pouvoir être étudié pour une large gamme de pH. Les principaux produits formés en radiolyse γ ou X et en la présence d'air ou d'oxygène sont l'hydrogène, l'eau oxygénée et le dioxyde de carbone. Lors d'irradiations avec les rayons γ de ^{60}Co, les rendements correspondants, d'après Hart (40), seraient environ respectivement 0,44, 3,42 et 2,62 moléc./100 eV, pour une concentration initiale de 10^{-3} M en acide formique.

C. Avènement de la radiolyse pulsée

En 1952, des essais consistant à irradier la cible de façon discontinue (procédé dit du « secteur tournant »; voir, par exemple, réf. 41) ont été développés pour étudier quantitativement les réactions en chaîne[9] produites lors de la radiolyse γ de solutions aqueuses (42, 43). Par la suite, les progrès de l'électronique rapide ont permis l'avènement de la radiolyse pulsée proprement dite, dont la mise en oeuvre, à l'échelle de la microseconde, date du début des années 1960 (44–47). Cette méthode a ensuite pris rapidement un essor considérable grâce au développement d'accélérateurs d'électrons produisant des impulsions intenses et de plus en plus brèves (voir, par exemple, réfs. 48–51). Le principe de celle-ci est basé sur l'emploi d'un montage optoélectronique approprié permettant de suivre, le plus fréquemment en spectrophotométrie ultra-rapide, l'évolution des radicaux libres formés ou des produits transitoires de leurs réactions, ceci pour des échelles de temps allant jusqu'à quelques nanosecondes (voir, par exemple, réfs. 49 et 50) et même quelques picosecondes (52–54). L'utilisation de la radiolyse pulsée s'est avérée, nous le verrons, des plus utiles et fructueuses au cours des études développées dans le cadre de la radiolyse de l'eau et des solutions aqueuses.

Fig. 2. Allure typique d'une « courbe de dilution » pour un soluté S.

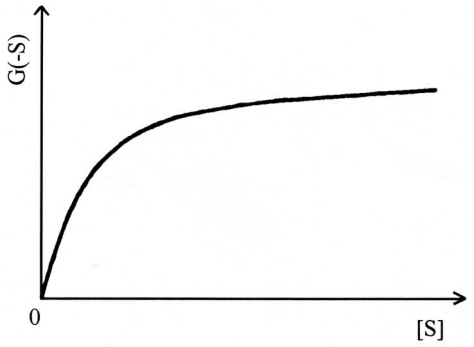

D. Nature des intermédiaires réactionnels

On pouvait se demander, dans le cas des solutions diluées, si les rendements mesurés résultaient de l'absorption du rayonnement par l'eau (« effet indirect ») ou de l'absorption par le soluté (« effet direct »). Il est apparu que, dans la plupart des cas, les courbes donnant le rendement de disparition du soluté en fonction de sa concentration aboutissaient à un palier (fig. 2). Cet *effet de dilution* a été mis en évidence pour la première fois par Dale (55) dans ses travaux sur la désactivation « radiochimique » d'enzymes en solution aqueuse. Ce fait prouvait péremptoirement que c'était la fraction d'énergie absorbée par l'eau, de beaucoup la plus importante, qui entraînait la modification du soluté par « effet indirect » (21, 55, 56). Il fallait donc invoquer l'intervention d'intermédiaires provenant de la radiolyse de l'eau elle-même et agissant sur le soluté. Le palier observé dans l'effet de dilution correspond alors à la capture totale des intermédiaires transitoires. À la lumière des hypothèses de Debierne (12), Risse (19), Burton et Franck (20) et Weiss (21) précédemment citées, ces intermédiaires semblaient devoir être les radicaux $H^{\bullet}$ et $^{\bullet}OH$. Effectivement, les réac-

[5] 1 moléc./100 eV = $1{,}0364 \times 10^{-7}$ mol/J.
[6] Pour une compilation antérieure à 1961 et concernant en particulier les rendements radiolytiques des ions ferreux et cériques, voir réf. 30.
[7] Dans le cas de la radiolyse pulsée (voir sect. II-C), pour lequel le débit de dose est parfois très important, l'influence de celui-ci peut se faire sentir, le rendement de disparition des ions ferreux commençant à baisser à partir d'environ 10^{25} eV L^{-1} s^{-1}, soit ~10^6 Gy/s (réf. 33; voir aussi sect. III-C.3). Le gray (Gy) est l'unité SI de dose absorbée : 1 Gy = 1 J/kg.
[8] Pour le mode d'emploi de ce dosimètre, voir, par exemple, réfs. 33 et 35.
[9] Pour les caractéristiques d'une réaction en chaîne, voir sect. III-C.1.a.

© 1999 CNRC Canada

tions d'oxydation étaient comparables à celles du radical $^{\bullet}OH$. Au contraire, des difficultés se sont présentées pour l'atome $H^{\bullet}$. En effet, on trouvait, pour cette espèce, des résultats différents en milieu acide et en milieu neutre. C'est ainsi, par exemple, que les « atomes H » réagissaient avec des vitesses différentes sur H_2O_2 selon l'acidité du milieu (57). De même, le mécanisme de leur réaction vis-à-vis de l'acide monochloracétique variait avec le pH. Cela a conduit à penser que l'entité réductrice existait sous deux formes distinctes selon l'acidité de la solution, formes qui furent dénommées H et H′ (58). L'identification de ces espèces est restée douteuse pendant un certain temps. Ainsi, on a assimilé H et H′ soit au couple $H^{\bullet}$ et $H_2^{\bullet+}$ (59), soit à $H_2O^{\bullet-}$ et $H^{\bullet}$ ou encore à l'électron hydraté (e^-_{aq}) et $H^{\bullet}$. Cette dernière hypothèse a été suggérée en 1959 par Barr et Allen (60) en étudiant la réaction en chaîne[9] de décomposition de H_2 et H_2O_2 et en comparant le comportement cinétique de H et H′ vis-à-vis de O_2 et H_2O_2. Ce n'est cependant qu'à partir de la fin 1961 qu'il a été montré que l'entité réductrice en milieu neutre avait une charge négative (61, 62). Ce résultat favorisait l'hypothèse de l'existence de l'électron hydraté en milieu neutre. Soulignons que l'intervention d'une telle entité avait déjà été invoquée théoriquement par Stein (63) dès 1952, par Platzman (64) en 1953 et par Weiss (65) en 1953 et 1960.

D'autre part, en 1960 (66), l'avènement de la radiolyse pulsée a permis à Keene (44, 67) d'observer l'existence d'une forte absorption transitoire dans la partie visible du spectre de l'eau irradiée, à l'échelle de la microseconde, avec des électrons de 4 MeV. Matheson (68) a suggéré en ces termes que cette absorption pouvait être due à l'électron hydraté : *« Could the short-lived absorption observed by Keene at about 6000 Å in deaerated water be related to* e^-_{aq}*? »*. Durant l'été 1962 (69), Hart et Boag (45, 70) ont observé une espèce transitoire absorbant dans l'eau irradiée. Ces auteurs ont indiqué que le spectre d'absorption correspondant présentait un maximum vers 700 nm. De plus, ce spectre pouvait être inhibé par l'oxygène et par diverses molécules avides d'électrons, telles que CO_2 et N_2O. Ils ont conclu que l'espèce considérée était l'électron hydraté. De nombreux travaux ont rapidement confirmé cette identification et ont déterminé les propriétés cinétiques et thermodynamiques de cette espèce radicalaire : *« As a matter of fact, the hydrated electron fascinated radiation chemists so much when it was discovered that they diverted attention to measure its reactivity with everything they could think of. The specific reaction rates of* e^-_{aq} *with 3000 substances are known »* (71). Divers modèles théoriques ont parallèlement été proposés dans le but de décrire ces caractéristiques (pour une revue d'ensemble récente, voir, par exemple, réf. 72).

À partir de la mise en évidence de l'électron hydraté, la radiolyse pulsée a donné lieu à de fructueux développements et a conduit en particulier à l'identification de nombreuses espèces transitoires jusqu'alors inconnues.

Il semblerait que, désormais, le mécanisme de radiolyse de l'eau et des solutions aqueuses puisse être principalement décrit en termes de la chimie des radicaux formés, à savoir : e^-_{aq}, $H^{\bullet}$ et $^{\bullet}OH$. En milieu acide, l'entité réductrice est entièrement sous la forme $H^{\bullet}$, tandis qu'en milieu neutre, la plus grande partie de celle-ci se trouve sous forme d'électrons hydratés. Toutefois, pour ce dernier milieu, il a été mesuré en plus un rendement relativement faible en atomes $H^{\bullet}$ (73).

E. Écriture de la réaction fondamentale

Un autre ensemble de résultats a posé de nouveaux problèmes. On s'est en effet aperçu que de l'hydrogène et de l'eau oxygénée pouvaient très souvent être formés lors de l'irradiation de solutions aqueuses diluées, en quantités variant avec la nature du rayonnement. Il a été admis que ces deux espèces proviennent de la combinaison des entités radicalaires : $^{\bullet}OH + {}^{\bullet}OH \rightarrow H_2O_2$, $H^{\bullet} + H^{\bullet} \rightarrow H_2$ ou plutôt $e^-_{aq} + e^-_{aq} \rightarrow H_2 + 2\ OH^-$. Ces rendements se sont avérés être indépendants, dans certaines limites, de la concentration du soluté, de sa nature et du débit de dose. On s'attendait pourtant à ce que les variations de ces paramètres déplacent les compétitions portant sur les réactions précédentes, et par conséquent agissent sur les rendements d'hydrogène et d'eau oxygénée. L'interprétation de ces résultats ne pouvait donc être faite sur des bases de cinétique homogène (74). Allen (75) a décrit qualitativement, dès 1948, un processus hétérogène[10] de la radiolyse des solutions aqueuses : *« ...the source of these products* (H_2 et H_2O_2) *is probably the small regions of high ionization density... which lie at the end of each electron track... Radicals formed in these little regions will react with one another to produce a certain yield of reaction products before they have a chance to get out into the solution and suffer reaction with the* (solutes) *»*.

Ainsi, selon ce modèle, les *« ...produits, soit radicalaires (OH et H), soit moléculaires (*H_2O_2 *et* H_2*), sont formés dans des sites privilégiés autour des grappes d'ionisations primaires et l'approximation d'Allen consiste à dire que ces sites sont suffisamment petits pour qu'en général, le soluté n'intervienne sensiblement pas dans cette formation, du moins pour un domaine de concentration assez large. Les vitesses d'apparition dans le milieu des espèces radicalaires et moléculaires seraient alors indépendantes du soluté... Après cette apparition les réactions secondaires avec le soluté auraient lieu dans l'ensemble de la solution d'une manière homogène et il serait possible de leur appliquer les règles classiques de calcul cinétique, notamment les équations d'état stationnaire pour les produits intermédiaires »* (77). Dans les années qui suivirent, l'interprétation d'Allen, comme nous le verrons, s'affirma quantitativement, tant par l'analyse de nouveaux résultats expérimentaux que par la description analytique de modèles théoriques.

On est donc amené à considérer que la radiolyse de l'eau ne conduit pas seulement à l'électron hydraté et au radical $^{\bullet}OH$, mais implique de plus une formation de H_2 et H_2O_2. Elle pourrait, dans ce cas, être représentée par la *réaction chimique* suivante (78, 79) :

$$[1] \qquad G_{-H_2O}\ H_2O \overset{100\ eV}{\rightsquigarrow} G_{H^{\bullet}}\ H^{\bullet} + G_{e^-_{aq}}\ e^-_{aq} + G_{H^+}\ H^+ + G_{^{\bullet}OH}\ {}^{\bullet}OH + G_{H_2}\ H_2 + G_{H_2O_2}\ H_2O_2$$

dans laquelle la notation G_S représente les rendements, dits *« rendements radicalaires et moléculaires »* (RRM), concernant la disparition ou la formation des espèces S considérées

[10]Mentionnons ici que certains auteurs (voir, par exemple, réf. 76) utilisent parfois, à ce propos, « nonhomogeneous » ou « inhomogeneous » comme traductions anglaises de *hétérogène*. Nous avons employé ici seulement le terme « hétérogène » pour ces deux vocables.

© 1999 CNRC Canada

Tableau 1. La radiolyse de l'eau, de 1902 à 1962.

Dates	Principales sources de rayonnements utilisées et événements marquants
1895 (décembre)	Découverte des rayons X (W.C. Röntgen)
1896 (février–mai)	Découverte de la radioactivité (H. Becquerel)
1898 (juillet)	Découverte du polonium (P. Curie et M^{me} S. Curie)
1898 (décembre)	Découverte du radium (P. Curie, M^{me} P. Curie et G. Bémont)
1902	Premières irradiations d'eau pure (F. Giesel) par les rayons α de radioéléments naturels
1914	Hypothèse radicalaire concernant la décomposition de l'eau (A. Debierne)
1930	Disponibilité de sources intenses de rayons X
1940	Mise en évidence de l'« effet indirect » (W.M. Dale)
1944	Théorie radicalaire concernant la décomposition de l'eau (J. Weiss)
1948	Modèle des zones d'hétérogénéité des espèces radiolytiques (A.O. Allen)
1950	Disponibilité de sources de haute activité de rayons γ (^{60}Co)
	Début des études intensives de systèmes minéraux et organiques en solutions aqueuses
1960	Début de la radiolyse pulsée permettant l'étude des espèces intermédiaires
1962	Mise en évidence de l'électron hydraté (E.J. Hart et J.W. Boag).

pour 100 eV absorbés dans la solution.[11] Bien entendu, ce n'est qu'à partir de 1962 que l'électron hydraté fut impliqué dans cette écriture. Les coefficients G_S sont reliés par les deux relations stœchiométriques suivantes, traduisant le bilan de charge et de masse de la réaction globale [1] :

$$[2] \qquad G_{e^-_{aq}} = G_{H^+}$$

$$[3] \qquad G_{e^-_{aq}} + G_{H^\bullet} + 2\,G_{H_2} = G_{^\bullet OH} + 2\,G_{H_2O_2} = G_{-H_2O}$$

Ils peuvent être calculés d'après les données expérimentales et apporter ainsi d'utiles indications sur la distribution spatio-temporelle des zones hétérogènes intervenant alors.[12]

L'ensemble des faits expérimentaux et théoriques que nous venons de décrire sont résumés dans le tableau 1.[13]

III. De la découverte de l'électron hydraté jusqu'à la fin du XX^{ème} siècle

La réaction [1] résume les conséquences de la radiolyse de l'eau à un stade considéré alors comme primaire. Dans la mesure où les hypothèses ayant conduit à cette réaction apparaissaient comme valables, les recherches se sont développées selon plusieurs directions que nous allons successivement envisager :

(*a*) Tout d'abord, la détermination des RRM a pu être réalisée vers la fin des années cinquante en utilisant les résultats expérimentaux disponibles à ce moment-là, et en particulier ceux concernant la radiolyse γ ou X de solutions diluées en milieu neutre.

(*b*) Il était évident que l'influence de la concentration du soluté réclamait d'être examinée en détail tant au point de vue théorique qu'expérimental, puisque l'interprétation d'une partie des phénomènes était basée, comme nous l'avons vu précédemment, sur l'intervention de processus cinétiques hétérogènes.

(*c*) La mise au point de modèles quantitatifs fut entreprise parallèlement afin de justifier théoriquement les valeurs précédentes.

(*d*) Les modèles établis pour la radiolyse γ ou X de l'eau et de ses solutions ont été étendus à des conditions expérimentales différentes : grands débits de dose, solutions acides et surtout rayonnements d'autre nature. En effet, nous avons vu que les toutes premières expériences de radiolyse utilisaient les rayons α. Depuis lors, les rayonnements à grande densité d'ionisation n'ont pas cessé d'être étudiés, d'autant plus que la construction d'accélérateurs a permis un grand développement de la gamme utilisable des pouvoirs d'arrêt. Ces recherches ont conduit à diverses ouvertures. En particulier, de tels rayonnements se sont avérés, dans certains cas, intéressants à utiliser en radiothérapie (voir, par exemple, réf. 81).

Nous allons examiner comment le développement des différents points qui viennent d'être évoqués a conduit à de nouveaux aspects de la radiolyse.

A. Détermination expérimentale des rendements radicalaires et moléculaires (RRM) : cas des rayons γ et X et des milieux neutres

Pour rendre quantitative et utilisable la réaction chimique [1], il faut déterminer les valeurs des coefficients impliqués, à savoir, trois rendements radicalaires et quatre moléculaires. Ces valeurs vérifiant les relations [2] et [3], il reste à établir entre elles quatre relations indépendantes.

Pour ce faire, parmi tous les résultats expérimentaux existants, nous pouvons utiliser, à titre d'exemple, les irradiations γ de solutions aqueuses d'ions formiate en milieu neutre et en la présence d'air dont il a déjà été question plus haut (voir sect. II-B). Les produits stables mesurés sont CO_2,

[11] La notation G_S est employée pour représenter le rendement « primaire » de l'espèce S, écrite en indice, c'est-à-dire le rendement qui est normalement mesuré après réactions complètes dans les zones hétérogènes et avant que cette espèce n'ait eu une opportunité de réagir en dehors de ces zones. Rappelons que l'écriture *G*(P) correspond, quant à elle, au rendement final mesuré du produit P (voir note 4 de bas de page). Le symbole ⇝ est utilisé pour signaler les réactions attribuées à l'absorption de radiations ionisantes.

[12] Une zone d'hétérogénéité radiolytique est un site privilégié pour lequel la concentration en diverses espèces (produits radicalaires et moléculaires et éventuellement solutés) est relativement élevée, de sorte que la probabilité que certaines d'entre elles réagissent les unes avec les autres est supérieure à cette même probabilité dans l'ensemble de la solution irradiée (voir, par exemple, réf. 76).

[13] Leur déroulement dans différents pays est raconté de façon détaillée dans la réf. 80.

© 1999 CNRC Canada

H_2O_2 et H_2. Leurs rendements expérimentaux sont représentés sous la forme $G(CO_2)$, $G(H_2O_2)$ et $G(H_2)$, notation évitant toute confusion avec les coefficients de la réaction [1].[11] Pour interpréter les résultats concernant la radiolyse de l'ion formiate en solution aqueuse diluée, le schéma de réaction suivant a été adopté (40) :

Les radicaux $^{\bullet}OH$ sont oxydants et forment le radical formyle $COO^{\bullet-}$:

$$HCOO^- + {}^{\bullet}OH \rightarrow COO^{\bullet-} + H_2O$$

Les atomes $H^{\bullet}$, l'électron hydraté et le radical $COO^{\bullet-}$ sont oxydés par l'oxygène O_2 en donnant le radical anion superoxyde $O_2^{\bullet-}$, forme basique du radical $HO_2^{\bullet}$:

$$H^{\bullet} + O_2 \rightarrow HO_2^{\bullet}$$

$$e^-_{aq} + O_2 \rightarrow O_2^{\bullet-}$$

$$COO^{\bullet-} + O_2 \rightarrow CO_2 + O_2^{\bullet-}$$

$$HO_2^{\bullet} \rightleftarrows H^+ + O_2^{\bullet-},\ pK_a = 4{,}8$$

Le radical $O_2^{\bullet-}$ disparaît par dismutation selon (82) :

$$O_2^{\bullet-} + HO_2^{\bullet} \xrightarrow{H^+} H_2O_2 + O_2$$

On sait que les radicaux libres réagissent en général très rapidement et ne s'accumulent pas. Ils sont à l'état quasi stationnaire, hypothèse émise très tôt puis vérifiée quantitativement lorsque l'aspect cinétique a été maîtrisé.

Le schéma ci-dessus conduit aux équations suivantes si on prend les valeurs expérimentales déterminées en 1954 par Hart (40) et données plus haut (voir sect. II-B), concernant des solutions 10^{-3} M en acide formique :[14]

$$G(H_2O_2) = G_{H_2O_2} + (\tfrac{1}{2})(G_{e^-_{aq}} + G_{{}^{\bullet}OH} + G_{H^{\bullet}}) = 3{,}42$$

$$G(CO_2) = G_{{}^{\bullet}OH} = 2{,}62$$

$$G(H_2) = G_{H_2} = 0{,}44$$

d'où, en tenant compte des relations de bilan [3],

$$G_{e^-_{aq}} + G_{H^{\bullet}} = G(H_2O_2) - G(H_2) = 2{,}98$$

$$G_{H_2O_2} = 0{,}62$$

Les rendements sont exprimés en moléc./100 eV. On a ainsi déterminé les valeurs des deux rendements moléculaires G_{H_2} et $G_{H_2O_2}$, du rendement radicalaire $G_{{}^{\bullet}OH}$ et de la somme $(G_{e^-_{aq}} + G_{H^{\bullet}})$. Dans ce cas, il n'est pas possible de calculer les rendements respectifs de l'électron hydraté et de l'atome $H^{\bullet}$ puisqu'ils jouent ici le même rôle chimique.

Les valeurs de $G_{e^-_{aq}}$ et de $G_{H^{\bullet}}$ peuvent être déduites de la radiolyse γ de solutions aqueuses de méthanol désaérées et saturées de protoxyde d'azote N_2O (voir, par exemple, réf. 83). En effet, N_2O est un capteur spécifique de e^-_{aq} et on a :

$$N_2O + e^-_{aq} \rightarrow N_2 + {}^{\bullet}OH + OH^-$$

$${}^{\bullet}OH + CH_3OH \rightarrow {}^{\bullet}CH_2OH + H_2O$$

$$H^{\bullet} + CH_3OH \rightarrow {}^{\bullet}CH_2OH + H_2$$

Le radical organique disparaît principalement selon les deux réactions :

$$2\ {}^{\bullet}CH_2OH \rightarrow (CH_2OH)_2 \rightarrow H_2CO + CH_3OH$$

pour former des produits stables, l'éthylène glycol et le formaldéhyde (voir, par exemple, réf. 84). Les rendements d'azote et d'hydrogène, mesurés pour des solutions 10^{-3} M en N_2O et 0,1 M en méthanol, sont donnés par les relations (83) :

$$G(N_2) = G_{e^-_{aq}} = 2{,}8$$

$$G(H_2) = G_{H_2} + G_{H^{\bullet}} = 1{,}05$$

ou

$$G_{e^-_{aq}} = 2{,}8 \text{ et } G_{H^{\bullet}} = 0{,}6$$

On a

$$G_{e^-_{aq}} + G_{H^{\bullet}} = 3{,}4$$

en accord approximatif avec la détermination précédente concernant l'acide formique.

Le tableau 2 donne des estimations plus récentes des RRM, obtenues d'après les résultats de la radiolyse par les rayons γ de ^{60}Co ou les rayons X de même énergie,[15] de diverses solutions aqueuses neutres et diluées. En tenant compte de ce tableau, on peut adopter, pour le milieu neutre et l'ensemble des solutés, les valeurs suivantes (exprimées en moléc./100 eV) :[16]

[4] $G_{e^-_{aq}} = 2{,}65$ $G_{H^{\bullet}} = 0{,}60$ $G_{H_2} = 0{,}45$
$G_{{}^{\bullet}OH} = 2{,}80$ $G_{H_2O_2} = 0{,}68$ $G_{-H_2O} = 4{,}15$

Le fait de trouver des valeurs à peu près identiques pour les RRM, quelle que soit la nature du soluté, est en faveur du modèle précédemment évoqué, modèle que nous allons détailler ci-dessous. Nous serons aidés en cela par l'étude expérimentale de l'influence de la concentration du soluté sur la validité de l'équation [1].

En effet, lorsque la concentration d'un bon capteur de e^-_{aq} ou de $^{\bullet}OH$ est augmentée au delà de certaines limites, les valeurs des rendements moléculaires correspondants (c'est-à-dire, G_{H_2} et $G_{H_2O_2}$) ne sont plus constants et diminuent (pour une série de références sur ces expériences, voir réfs. 91–93). Ce fait peut être, par exemple, mis en évidence par le tracé, pour divers solutés S, du rapport $G_{H_2}/(G_{H_2})^0$ en fonc-

[14]Mentionnons le fait que les valeurs de ces rendements augmentent sensiblement avec la concentration d'acide formique utilisée, dans la gamme allant de 10^{-4} à 1 M (réfs. 35 et 40). Un tel effet peut être attribué, en partie, à une capture plus efficace des radicaux libres et également à une modification du mécanisme de formation de H_2 lorsque la concentration en acide formique augmente.

[15]Rappelons que, pour la gamme habituelle d'énergie (typiquement, de l'ordre du MeV), les rayons γ ou X interagissent avec la matière essentiellement par l'intermédiaire des électrons Compton.

[16]Comme nous le verrons plus loin, ces valeurs représentent les rendements des espèces ~10^{-7} s après le dépôt primaire d'énergie, c'est-à-dire à une échelle de temps correspondant à leur homogénéisation par diffusion dans l'ensemble de la solution.

© 1999 CNRC Canada

Tableau 2. Rendements[a] radicalaires et moléculaires de l'eau neutre, à la température ambiante, irradiée avec les rayons γ de ^{60}Co.

$G_{e^-_{aq}}$	$G_{H^\bullet}$	$G_{^\bullet OH}$	G_{H_2}	$G_{H_2O_2}$	G_{-H_2O}	Références
2,7	0,61	2,87[b]	0,43	0,61	4,14[c]	85
2,6	0,6	2,7	0,45	0,7	4,1	86
2,7	0,55	2,75	0,45	0,7	4,15	87
2,65	0,65	2,8	0,45[b]	0,7	4,2	88
2,64	0,57	2,82	0,45	0,68	4,14	89[d]
2,63	0,55	2,72	0,45	0,68	4,08[c]	90[e]

[a]Exprimés en moléc./100 eV.

[b]Valeur calculée d'après le bilan.

[c]Les auteurs ajoutent un rendement en radicaux $HO_2^\bullet$ de 0,026 moléc./100 eV.

[d]Ensemble de valeurs à 25°C.

[e]pH 3–11.

tion du logarithme du produit k_S[S], où $(G_{H_2})^0$ représente le rendement moléculaire d'hydrogène en l'absence de soluté, k_S la constante de vitesse de la réaction du soluté avec le radical réducteur (en M^{-1} s^{-1}) et [S] la concentration du soluté (en M). Ne disposant alors que de peu de données cinétiques expérimentales, Schwarz (91), dès 1955, a tracé en fait $G_{H_2}/(G_{H_2})^0$ en fonction de [X] = p[S], où p est un paramètre de normalisation caractéristique d'un soluté donné (p = 1 est choisi pour le soluté NO_2^-). Il a constaté que tous les points expérimentaux, après normalisation, se trouvaient sensiblement sur la *même* courbe (fig. 3). D'après l'analyse de cet auteur, les constantes de normalisation p doivent être égales aux rapports $k_S/k_{NO_2^-}$. Un tel résultat a amplement été confirmé par la suite et a justifié l'emploi extensif de cette représentation (voir, par exemple, réfs. 92–100).

Cette courbe, dite « courbe de Schwarz, » reflète le devenir du radical e^-_{aq}[17] en fonction de l'efficacité de sa capture par le soluté dans les zones hétérogènes. En résumé, ce destin consiste :

(*a*) soit à réagir avec lui-même ou avec les autres espèces radiolytiques présentes dans les zones hétérogènes;

(*b*) soit à réagir dans ces mêmes zones avec le soluté si la concentration de celui-ci est suffisamment grande;

(*c*) soit à diffuser dans la partie homogène.

D'après la figure 3, concernant l'hydrogène, il apparaît que l'action des solutés dans les zones hétérogènes est négligeable pour les faibles concentrations de ceux-ci (inférieures à ~10^{-3} M pour les bons capteurs de e^-_{aq}). Mais on voit également que le rendement moléculaire en H_2 ne peut plus être considéré comme constant lorsqu'augmente cette concentration. Le soluté intervient alors à un stade plus primaire. Des résultats analogues ont été établis pour H_2O_2 en tant que produit moléculaire (voir, par exemple, réfs. 91, 92 et 94).

L'étude de l'influence de la concentration du soluté était à l'époque le seul moyen d'obtenir des données sur les stades alors assez méconnus précédant l'homogénéisation.

B. Élaboration de modèles diffusionnels

Les hétérogénéités ainsi mises expérimentalement en évidence proviennent de deux origines : d'une part, de la répartition des ionisations dans la solution et, d'autre part, de la réponse de la matière à ces ionisations. À partir des années cinquante, des modèles ont été développés pour décrire ces phénomènes, modèles d'abord simples, puis de plus en plus élaborés.

Fig. 3. Effet, sous l'influence des rayons γ de ^{60}Co et pour des solutions aqueuses désaérées, de la concentration du soluté S sur le rendement moléculaire en H_2, exprimé sous la forme $G_{H_2}/(G_{H_2})^0$, où $(G_{H_2})^0$ représente le rendement d'hydrogène en l'absence de soluté. [X] = p[S], où $p = k_S/k_{NO_2^-}$, $k_{NO_2^-}$ = 4,1 × 10^9 M^{-1} s^{-1} (réf. 86) et k_S sont respectivement les constantes de vitesse des réactions de e^-_{aq} avec NO_2^- et avec le soluté S, et [S] est la concentration du soluté. La courbe est théorique. D'après réf. 91.

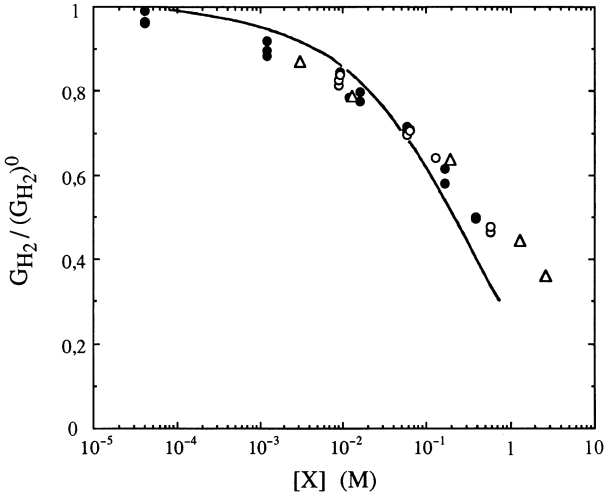

Pour obtenir la distribution énergétique initiale des électrons libérés lors des actes successifs d'ionisation, les calculs ont utilisé le plus souvent la formule de Møller donnant la section efficace différentielle $d\sigma = \sigma(Q)\, dQ$ pour une collision électron–électron où le transfert d'énergie est compris entre Q et $Q + dQ$ (en unités SI) (101) :

$$[5] \qquad d\sigma = \left(\frac{1}{4\pi\varepsilon_0}\right)^2 \frac{2\pi e^4}{m_0 v^2}\; A(Q)\; \frac{dQ}{Q^2} \quad (\text{m}^2/\text{électron})$$

où v est la vitesse de l'électron incident, e sa charge et m_0 la masse de l'électron au repos. $A(Q)$ est une fonction de Q et de l'énergie de l'électron incident, qui varie peu autour de 1 comparativement à $1/Q^2$ pour des énergies inférieures à ~1 MeV. D'après cette formule, $\sigma(Q)$ peut donc être considérée comme inversement proportionnelle au carré de l'énergie échangée. On s'attend, par conséquent, à une grande population d'électrons libérés de faible énergie, ainsi qu'il sera précisé plus loin (voir sect. IV-A).

Afin de traduire l'hétérogénéité spatiale des dépôts d'énergie, Magee et al. (102) ont distingué trois classes selon les valeurs des énergies échangées, classes qu'ils ont intitulées : « *spurs* » (ou grappes) (<100 eV), « *blobs* » (ou gouttes) (~100 à 500 eV) et « *short tracks* » (ou trajectoires

[17]Rappelons toutefois que l'entité réductrice donnant naissance à H_2 était assimilée jusqu'à la découverte de l'électron hydraté en 1962 à l'atome d'hydrogène. Ceci n'enlève rien aux conclusions que l'on peut retirer de la figure 3.

© 1999 CNRC Canada

courtes) (~500 eV à 5 keV).[18] Moyennant certaines hypothèses, ces auteurs ont calculé la distribution de ces trois classes qui serait, dans le cas de l'eau liquide et pour un électron d'énergie initiale de 1 MeV, respectivement 67 %, 11 % et 22 %.[19]

Il a été ensuite nécessaire d'estimer quel était, dans ces conditions, le devenir des espèces radiolytiques sachant que leur répartition initiale est conditionnée par l'hétérogénéité des ionisations.

Signalons que Samuel et Magee (105) avaient envisagé, dès 1953, la diffusion des radicaux dans ces zones hétérogènes qu'ils avaient déjà nommées *« spurs »* et définies comme des entités sphériques évoluant indépendamment les unes des autres. Dans la plupart des modèles, la distribution des radicaux dans les zones hétérogènes était supposée initialement gaussienne et il était le plus souvent admis qu'elle le restait pendant toute la diffusion. Cette hypothèse fut dite de la « diffusion prescrite », ou « approximation de Jaffé » (91, 97–99, 105–110).

On était ainsi amené à un système d'équations aux dérivés partielles, non linéaires, de résolution difficile, qui s'écrivait, par exemple pour les deux radicaux $H^\bullet$ et $^\bullet OH$, sous la forme :

$$[6]\quad \begin{cases} \dfrac{\partial[^\bullet OH]}{\partial t} = D_{^\bullet OH}\nabla^2[^\bullet OH] \\ \qquad\qquad - 2k_{^\bullet OH + ^\bullet OH}[^\bullet OH]^2 - k_{H^\bullet + ^\bullet OH}[H^\bullet][^\bullet OH] \\ \dfrac{\partial[H^\bullet]}{\partial t} = D_{H^\bullet}\nabla^2[H^\bullet] \\ \qquad\qquad - 2k_{H^\bullet + H^\bullet}[H^\bullet]^2 - k_{^\bullet OH + H^\bullet}[^\bullet OH][H^\bullet] \end{cases}$$

équations dans lesquelles les concentrations radicalaires $[^\bullet OH]$ et $[H^\bullet]$ sont fonctions à la fois des coordonnées d'espace *x, y, z* et de temps *t*, ∇^2 est l'opérateur Laplacien, $D_{^\bullet OH}$ et $D_{H^\bullet}$ désignent les coefficients de diffusion des espèces $^\bullet OH$ et $H^\bullet$, et $k_{^\bullet OH + ^\bullet OH}$, $k_{^\bullet OH + H^\bullet}$ et $k_{H^\bullet + H^\bullet}$ représentent respectivement les constantes de vitesse des réactions :

$$^\bullet OH + {}^\bullet OH \rightarrow H_2O_2$$

$$^\bullet OH + H^\bullet \rightarrow H_2O$$

$$H^\bullet + H^\bullet \rightarrow H_2$$

Indépendamment, en 1955, Fricke (108), Magee (109), et plus particulièrement Schwarz (91), considérèrent, dans ce cadre, l'action d'un soluté S dans les zones hétérogènes, ce qui revient à introduire un terme supplémentaire de la forme $k_{H^\bullet + S}[H^\bullet]$ [S] ou $k_{^\bullet OH + S}[^\bullet OH]$ [S] dans les équations [6]. La figure 3 montre la courbe d'inhibition du rendement d'hydrogène moléculaire, ainsi calculée analytiquement par Schwarz (91). Par la suite, divers auteurs ont repris et développé ce modèle diffusionnel en mettant en oeuvre, pour sa résolution, l'emploi de méthodes numériques (97–99, 110–114). C'est ainsi que, par exemple, Flanders et Fricke (111), en 1958, furent les premiers à utiliser un ordinateur (*« high-speed electronic computer »*) pour résoudre une équation cinétique analogue aux équations [6] mais écrite pour un seul radical et un soluté. Leurs résultats sont très voisins de ceux obtenus de façon analytique. Le problème de l'appauvrissement en soluté des zones hétérogènes a également été abordé (112), mais la prise en compte d'un tel effet s'est avérée inutile, sa participation n'entraînant qu'une correction de l'ordre de 1 % sur la fraction des radicaux réagissant avec le soluté. D'autres travaux, de la même époque, et notamment ceux de Kuppermann et Belford (113), Mozumder et Magee (98), Kuppermann (99) et Schwarz (114), ont aussi justifié, par l'emploi de méthodes numériques plus élaborées, la validité des approximations impliquées dans les traitements analytiques utilisés antérieurement pour interpréter l'évolution des radicaux.

L'ensemble de ces travaux a permis d'affiner la comparaison des courbes expérimentales et théoriques, traduisant l'action de solutés dans les zones hétérogènes, et de confirmer ainsi les résultats obtenus initialement par Schwarz (91). L'accord est relativement bon, excepté pour les concentrations importantes du soluté (>0,1 M), concentrations pour lesquelles des mécanismes supplémentaires de formation de l'hydrogène difficile à inhiber ont été invoqués (115). D'autres auteurs, tels que Sowden (116) et Mahlman (117), ainsi que Peled et Czapski (100), ont rapporté des observations identiques. Ces résultats ont conduit à adopter pour l'hydrogène difficile à capter un rendement égal à 0,15–0,2 moléc./100 eV (114, 118, 119). Ce rendement est inclus dans la valeur G_{H_2} = 0,45, préconisée plus haut pour le rendement moléculaire d'hydrogène dans le cas d'irradiations avec les rayons γ de ^{60}Co (voir éq. [4]). L'origine d'un tel rendement n'est toutefois pas encore élucidée (voir, par exemple, réfs. 89 et 120; voir aussi sect. IV-A).

Comme nous allons le voir, de nombreux autres résultats concernant les modèles diffusionnels ont été décrits par la suite tant au point de vue expérimental que théorique, et l'application récente des méthodes de simulation Monte-Carlo a permis en particulier d'obtenir un panorama valable des conséquences de l'irradiation, par des rayonnements à ionisations diffuses, des solutions aqueuses diluées.

C. Influence de divers paramètres sur les RRM

La description donnée précédemment pour la radiolyse γ ou X de l'eau neutre et de ses solutions diluées demande à être étendue à des conditions expérimentales différentes : variation importante de concentrations, solutions acides et alcalines, grands débits de dose, utilisation d'autres types de rayonnements, milieux aérés, et influences de la température, de la nature de la phase et de la pression. C'est ce que nous allons maintenant examiner successivement.

1. Influence de la concentration du soluté

(a) Exceptions aux courbes de dilution : Ainsi que nous l'avons déjà mentionné, pour les solutions diluées, les

[18]Pour des échanges supérieurs à 5 keV, l'électron éjecté donne un embranchement (ou *« branch track »*) dont la trajectoire est traitée théoriquement, comme celle de l'électron primaire, en y comptabilisant les échanges des trois classes précédentes. Ces électrons « secondaires », d'énergie de recul importante, sont parfois appelés « rayons δ ».

[19]Des calculs récents, utilisant les techniques de simulation Monte-Carlo, ont donné, pour la répartition des pertes d'énergie sous forme de grappes, gouttes et trajectoires courtes, des valeurs correspondantes de 75 %, 12 % et 13 % (réf. 103) et de 52 %, 19 % et 29 % (réf. 104), en accord relatif avec les valeurs de Magee et al. (réf. 102).

© 1999 CNRC Canada

courbes donnant le rendement de disparition du soluté en fonction de la concentration de celui-ci aboutissent à un palier traduisant la capture complète des radicaux (voir sect. II-D). La figure 2 schématise cet « effet de dilution ».

Tel n'est pas toujours le cas. Par exemple, le rendement de réduction par les rayons γ de ^{60}Co de l'ion cérium IV en milieu H_2SO_4 0,4 M aéré est donné par (voir sect. II-B et réfs. 28, 30, 37 et 38) :

$$G(-Ce^{IV}) = 2\ G_{H_2O_2} + G_{H^\bullet} - G_{^\bullet OH} = 2{,}45 \text{ moléc./100 eV}^{20}$$

relation traduisant le mécanisme

[7] $H^\bullet + O_2 \rightarrow HO_2^\bullet$

[8] $HO_2^\bullet + Ce^{IV} \rightarrow H^+ + O_2 + Ce^{III}$

[9] $^\bullet OH + Ce^{III} \rightarrow OH^- + Ce^{IV}$

[10] $H_2O_2 + Ce^{IV} \rightarrow Ce^{III} + H^+ + HO_2^\bullet$

Or, en la présence d'air, le rendement de formation de H_2O_2 dans l'eau de même acidité mais en l'absence d'autres solutés, est égal à la moitié du rendement de disparition de Ce^{IV} :

$$G(H_2O_2) = G_{H_2O_2} + (1/2)(G_{H^\bullet} - G_{^\bullet OH}) = 1{,}2 \text{ moléc./100 eV}$$

par suite du mécanisme

[7] $H^\bullet + O_2 \rightarrow HO_2^\bullet$

[11] $^\bullet OH + H_2O_2 \rightarrow HO_2^\bullet + H_2O$

[12] $HO_2^\bullet + HO_2^\bullet \rightarrow H_2O_2 + O_2$

Ainsi que l'a signalé Sworski (37), le rendement de réduction de l'ion cérium IV sera le même, que la réduction se produise par les réactions [7]–[10] ou [7] et [10]–[12]. Cette dernière voie subsiste pour des concentrations très faibles en Ce^{IV} et on n'observe donc pas de courbe de dilution, telle que nous l'avons définie ci-dessus.[21]

Un exemple de nature différente est donné par les réactions en chaîne initiées par le rayonnement. Elles conduisent expérimentalement à des rendements de transformation du soluté souvent bien supérieurs à ceux calculables à partir des RRM. Un seul radical assure alors la transformation d'un nombre important de molécules du soluté. Tel est le cas de la peroxydation (voir, par exemple, réf. 121) de certains produits organiques ou biologiques (représentés par RH), réaction qui peut s'écrire globalement :

$$RH + O_2 \rightsquigarrow ROOH$$

Cette réaction en chaîne peut être déclenchée par des radicaux $^\bullet OH$ provenant de la radiolyse de l'eau. On est alors amené, par exemple, au schéma simplifié suivant :

[13] initiation : $^\bullet OH + RH \rightarrow H_2O + R^\bullet$

[14] propagation : $R^\bullet + O_2 \rightarrow RO_2^\bullet$

[15] $RO_2^\bullet + RH \xrightarrow{k_p} ROOH + R^\bullet$

[16] terminaison : $2\ RO_2^\bullet \xrightarrow{k_t}$ produits non radicalaires

Le calcul basé sur l'état quasi stationnaire en radicaux libres $^\bullet OH$, $R^\bullet$ et $RO_2^\bullet$ conduit à (122) :

$$[17] \quad G(-RH) = G_{^\bullet OH} + \frac{k_p}{\sqrt{2\,k_t}}\sqrt{\frac{G_{^\bullet OH}}{I}}\,[RH]_0$$

où I est le débit de dose (ou intensité d'irradiation), k_p et k_t représentent les constantes de vitesse des réactions [15] et [16], et $[RH]_0$ est la concentration initiale en solutés peroxydables. Un calcul analogue aurait permis d'obtenir le rendement en hydroperoxyde :

$$[18] \quad G(ROOH) = \frac{k_p}{\sqrt{2\,k_t}}\sqrt{\frac{G_{^\bullet OH}}{I}}\,[RH]_0$$

$G(-RH)$ et $G(ROOH)$ sont donc fonctions linéaires de la concentration en solutés, et dans ce cas l'effet de dilution n'est pas observé.

(b) Utilisations des courbes de dilution : Comme il apparaît figure 2, pour les solutions très diluées, la courbe de dilution peut être confondue avec sa tangente à l'origine. Le rendement est alors proportionnel à la concentration. Par conséquent, dans cette zone, pour une dose donnée, il disparaît le même pourcentage de soluté, quelle qu'en soit la concentration (122; voir aussi réf. 123). Ceci est à prendre en considération lors de la radiolyse des solutions extrêmement diluées, en particulier lorsqu'on étudie l'autoradiolyse d'un système en solution aqueuse. En effet, un soluté radioactif ou une molécule marquée à forte activité spécifique peut subir des transformations dues aux produits de la radiolyse de l'eau provoquée par son propre rayonnement.

En général, c'est dans la zone de 10^{-5} à 10^{-3} M que peuvent être utilement étudiés les mécanismes de radiolyse et donc les propriétés des radicaux. Cette zone correspond souvent à un palier expérimental traduisant une capture totale des radicaux dans la zone homogène et une action encore négligeable du soluté dans les zones hétérogènes. Si l'on augmente la concentration (jusqu'à ~1 M) de ce dernier, la quasi-totalité des produits moléculaires peut alors être inhibée. Par ailleurs, une partie de plus en plus importante de l'ionisation se fait directement sur le soluté lui-même. On a ainsi un mélange d'effets direct et indirect (voir sect. II-D). Nous allons maintenant étudier plus précisément les caractéristiques de l'effet direct.

(c) Effet direct : Pour pouvoir étudier l'effet direct sur un soluté, il faut que celui-ci soit en concentration relativement élevée, disons supérieure à ~1 M (voir, par exemple, réf. 124). C'est ainsi qu'ont été examinés à ce point de vue des solutés à haute solubilité dans l'eau, tels que les anions nitrate (125, 126), perchlorate (127), chlorure (128, 129) et iodure (130), ainsi que l'acide sulfurique (131). Certains effets directs peuvent également être étudiés en utilisant comme

[20] La marge d'erreur sur cette valeur est de ±0,1 moléc./100 eV (réf. 30).
[21] Les valeurs des RRM concernant la radiolyse de l'eau en milieu acide sont données plus loin (voir sect. III-C.2).

© 1999 CNRC Canada

Fig. 4. Représentation schématique des effets direct et indirect. L'exemple présenté ici correspond au cas où $G_i^0 < G_d^0$. D'après réfs. 122 et 129.

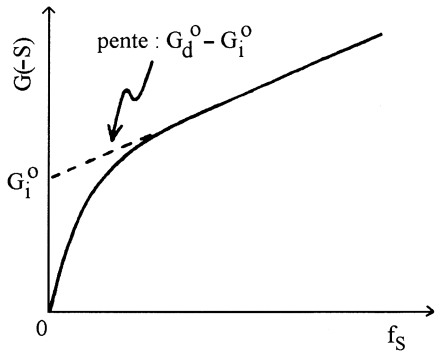

soluté un liquide organique miscible à l'eau, tel que l'acide formique (132).

Les difficultés sont les suivantes :

(*i*) Les espèces formées lors de l'irradiation de solutions concentrées résultent tout à la fois de l'effet direct et de l'effet indirect. Ces deux effets peuvent ne pas être additifs par suite de compétitions impliquant des réactions entre les produits de radiolyse de l'eau et du soluté.

(*ii*) L'utilisation de solutés en très grande concentration introduit une modification profonde de la structure des solutions, qui peut se traduire en particulier par une variation de la constante diélectrique et une influence de la force ionique sur les vitesses de réaction.

Ce n'est pourtant que lorsque effet direct et effet indirect sont additifs que le rendement global de transformation du soluté S peut être exprimé par l'équation (122, 129) :

$$G(-S) = f_S\ G_d^0 + (1 - f_S)\ G_i^0\ \varphi([S])$$

f_S est ici le rapport entre l'énergie directement absorbée par le soluté et l'énergie totale absorbée par la solution, rapport sensiblement égal à la fraction électronique de S. G_d^0 est le rendement de l'effet direct exprimé en moléc./100 eV absorbés par le soluté. Ce rendement est supposé indépendant de la concentration de S. G_i^0 est le rendement maximal de l'effet indirect et dépend du mécanisme de réaction des produits primaires de radiolyse de l'eau avec S pour donner la transformation considérée. La fonction de la concentration $\varphi([S])$ varie entre 0 et 1 et exprime la fraction de ces produits primaires effectivement utilisée pour cette transformation.

Pour les plus grandes concentrations de S, $\varphi([S]) = 1$, et l'équation précédente se ramène alors à la relation linéaire :

$$G(-S) = G_i^0 + f_S(G_d^0 - G_i^0)$$

Par conséquent, si l'on trace la courbe donnant la valeur du rendement expérimental en fonction de f_S, on obtiendra une courbe asymptotique à cette droite. D'après l'ordonnée à l'origine et la pente de la droite, on peut obtenir G_i^0 et G_d^0 et estimer donc la part de l'effet direct et celle de l'effet indirect (fig. 4) (122, 125, 130).

(d) Cas des macromolécules biologiques : L'irradiation des macromolécules et tout particulièrement des biopolymères in vivo présente un aspect plus complexe que les cas précédemment décrits, consistant à distinguer effets direct et indirect. Tout d'abord, la matière biologique humaine est formée, pondéralement, de ~70 % d'eau, ce qui entraîne que les deux effets peuvent se produire simultanément et donner lieu à des actions non additives. De plus, dans le cas de l'ADN cellulaire, la radiolyse peut s'effectuer sur des molécules d'eau liées à celui-ci (133, 134) conduisant à un effet dit *« quasi direct »* (135–137), effet qui peut se ramener à l'un ou à l'autre des cas précédents.

Par ailleurs, l'ionisation est parfois suivie d'un phénomène de transfert de charge intramoléculaire qui intervient lors de l'irradiation de certaines protéines (138, 139) et de l'ADN (137, 139–141), et qui peut ainsi modifier profondément les transformations mises en jeu. C'est dès 1965 qu'un tel phénomène a été envisagé (142); il a donné lieu à diverses études dont certaines continuent à se développer activement.

Tableau 3. Rendements[a] radicalaires et moléculaires de l'eau en milieu H_2SO_4 0,4 M, à la température ambiante, irradiée avec les rayons γ de ^{60}Co.

$G_{e^-_{aq}} + G_{H^\bullet}$	$G_{^\bullet OH}$	G_{H_2}	$G_{H_2O_2}$	G_{-H_2O}	Références
3,7	2,8	0,45	0,90	4,6	79
3,65	2,90	0,40	0,78	4,45[b]	90[c]
3,65	2,95	0,45	0,80	4,55	92, 143
3,68	2,96	0,45	0,81	4,58	144
3,66	2,97	0,40	0,76	4,50	145

[a]Exprimés en moléc./100 eV.

[b]Les auteurs ajoutent un rendement en radicaux $HO_2^\bullet$ de 0,008 moléc./100 eV.

[c]pH 0,46.

2. Influence du pH

Dès 1950, de nombreuses expériences de radiolyse γ et X ont concerné les milieux aqueux acides. En fait, elles ont été développées avant celles se rapportant aux solutions neutres précédemment décrites. Comme on l'a déjà vu, l'acide le plus souvent utilisé était dans ce cas l'acide sulfurique en solution aqueuse 0,4 M. Pour les RRM, les valeurs déduites de l'étude d'un grand nombre de systèmes minéraux et organiques en milieu acide présentent un accord remarquable, confirmant l'interprétation émise par Allen (75) en 1948 et concernant l'existence des zones d'hétérogénéité. Le tableau 3 indique, à titre d'exemple, cinq séries de valeurs obtenues par différents auteurs. En tenant compte de ce tableau, nous adopterons, pour le milieu H_2SO_4 0,4 M, les rayons γ de ^{60}Co et l'ensemble des solutés, les valeurs suivantes (exprimées en moléc./100 eV) (122) :

$$[19]\quad \begin{aligned} &G_{e^-_{aq}} + G_{H^\bullet} = 3{,}70 \quad G_{H_2} = 0{,}40 \\ &G_{^\bullet OH} = 2{,}90 \quad G_{H_2O_2} = 0{,}80 \quad G_{-H_2O} = 4{,}50 \end{aligned}$$

L'hypothèse le plus souvent avancée pour interpréter l'influence de l'acidité sur les RRM consiste évidemment à supposer que les ions H^+ captent, à ces concentrations, une grande partie, voire la totalité, des électrons hydratés situés dans les zones hétérogènes, en produisant des atomes $H^\bullet$ par la réaction :

$$[20]\quad e^-_{aq} + H^+ \rightarrow H^\bullet$$

© 1999 CNRC Canada

Tableau 4. Rendements[a] radicalaires et moléculaires de l'eau, à pH 13,5, irradiée à la température ambiante avec les rayons γ de ^{60}Co.

$(G_{e^-_{aq}} + G_{H^\bullet})$	$(G_{^\bullet OH} + G_{O^{\bullet-}})^b$	G_{H_2}	$(G_{H_2O_2} + G_{HO_2^-})^b$	G_{-H_2O}	Références
3,27	3,04	0,43	0,53	4,12	145
3,34[c]	3,01[c]	0,40	0,56[c]	4,14[c]	147
3,85	3,40	0,36	0,58	4,57	148
3,18[d]	2,72[d]	0,45[d]	0,68[d]	4,09[d]	35, 150

[a]Exprimés en moléc./100 eV.

[b]Nous avons indiqué les rendements en entités oxydantes par les expressions $(G_{^\bullet OH} + G_{O^{\bullet-}})$ et $(G_{H_2O_2} + G_{HO_2^-})$, afin de tenir compte des formes basiques de $^\bullet OH$ (pK_a = 11,9) et de H_2O_2(pK_a = 11,7), sans toutefois que les rôles de $O^{\bullet-}$ et de HO_2^- soient ici précisés.

[c]Valeur interpolée.

[d]3 < pH < 13.

Le rendement de l'entité réductrice radicalaire est alors représenté, pour chaque pH, par la somme $(G_{e^-_{aq}} + G_{H^\bullet})$. Selon Hayon (146), ces électrons donneraient préférentiellement en milieu neutre une réaction de recombinaison avec $^\bullet OH$, formant de l'eau :

[21] $e^-_{aq} + {}^\bullet OH \rightarrow OH^-$

En milieu acide, ce processus serait défavorisé par le fait que les atomes $H^\bullet$ qui remplacent e^-_{aq} sont moins réactifs vis-à-vis des radicaux $^\bullet OH$. Ces derniers, ainsi « protégés » de l'action des électrons hydratés, entraîneraient une augmentation du rendement de décomposition de l'eau (146, 147), comme le montre l'expérience (79, 90, 92, 143–145; voir aussi réfs. 35, 41 et 148–151). La validité d'un tel mécanisme est confirmée par des calculs récents de simulation Monte-Carlo (152) qui montrent qu'en milieu neutre la réaction [21] se produit effectivement de façon prédominante. Ces processus tendent en milieu acide à augmenter $G_{^\bullet OH}$ et aussi $G_{H_2O_2}$ (voir éqs. [4] et [19]), par suite de la dimérisation des radicaux $^\bullet OH$. Le fait que e^-_{aq} soit ainsi transformé en atome $H^\bullet$ rend par conséquent l'entité réductrice moins réactive, ce qui augmente bien $(G_{e^-_{aq}} + G_{H^\bullet})$ et donc G_{-H_2O} puisque le rendement en H_2 n'est que très faiblement modifié (voir éqs. [4] et [19]).

Ces expériences ont été étendues en milieu alcalin à des pH allant jusqu'à 14 (35, 145, 147, 148, 150, 153–156). Les valeurs des RRM ainsi déterminées restent constantes entre pH 4 et 11. En milieu fortement alcalin, on a trouvé des valeurs assez dispersées (voir, par exemple, réf. 147 et tableau 4). Mentionnons un certain nombre d'auteurs (35, 150, 154) qui suggèrent que les RRM demeurent constants depuis la neutralité jusqu'aux pH les plus élevés étudiés. L'existence de telles dispersions dans les déterminations de ces rendements provient en partie du fait que seul un petit nombre de solutés peut être étudiée commodément en ces milieux (156).

Cette dispersion des résultats expérimentaux pour des pH basiques rend difficile leur interprétation quantitative. On peut toutefois supposer, par analogie avec le milieu acide, que l'ion OH^- intervient dans les zones hétérogènes pour donner probablement la réaction (153) :

$$^\bullet OH + OH^- \rightarrow O^{\bullet-} + H_2O$$

Cette réaction, en milieu suffisamment alcalin, consomme vraisemblablement la quasi-totalité des radicaux $^\bullet OH$. L'eau oxygénée proviendrait alors uniquement de la dismutation de l'anion $O^{\bullet-}$ selon

[22] $$O^{\bullet-} + O^{\bullet-} \xrightarrow{H_2O} HO_2^- + OH^-$$

La réaction [22], moins rapide que son homologue $^\bullet OH + {}^\bullet OH \rightarrow H_2O_2$ (157), conduirait à une diminution de $(G_{H_2O_2} + G_{HO_2^-})$ par rapport au milieu neutre, en accord avec la majorité des auteurs (145, 147, 153, 155). En ce qui concerne la somme des rendements radicalaires réducteurs $(G_{e^-_{aq}} + G_{H^\bullet})$, le fait de remplacer $^\bullet OH$ par $O^{\bullet-}$ défavoriserait probablement la réaction de recombinaison :

$$e^-_{aq} + O^{\bullet-} \xrightarrow{H_2O} 2OH^- \quad (k = 2{,}31\times10^{10}\ M^{-1}\ s^{-1})$$

bien que la différence de sa constante de vitesse avec celle de la réaction [21] (k = 3,02 × 10^{10} M^{-1} s^{-1}) soit relativement faible (158). On s'attendrait ainsi à une augmentation de $(G_{e^-_{aq}} + G_{H^\bullet})$. Quant à la somme $(G_{^\bullet OH} + G_{O^{\bullet-}})$, elle tendrait à croître, de façon concomitante avec la diminution annoncée plus haut de $(G_{H_2O_2} + G_{HO_2^-})$. G_{H_2} étant inchangé, le rendement de décomposition de l'eau augmenterait donc, puisque l'écriture des équations de bilan :

$$G_{-H_2O} = (G_{e^-_{aq}} + G_{H^\bullet}) + 2\,G_{H_2}$$
$$= (G_{^\bullet OH} + G_{O^{\bullet-}}) + 2\,(G_{H_2O_2} + G_{HO_2^-})$$

doit être satisfaite. De tels résultats ne sont pas en contradiction avec les données expérimentales de Hayon (145) et de Haïssinsky (147).

Malheureusement, en milieu alcalin, les radicaux $O^{\bullet-}$ pourraient donner des réactions supplémentaires, notamment avec les solutés présents, soit pour capter les radicaux, soit pour ajuster le pH. Ceci expliquerait les divergences constatées entre certains auteurs, la nature de leurs solutions étant différentes.

Bien que le problème de l'influence de l'acidité ne soit pas encore totalement résolu, on voit que des interprétations peuvent être envisagées. Toutefois, des données expérimentales supplémentaires apparaissent nécessaires, afin de préciser en particulier, de façon définitive, la valeur des RRM en milieux alcalins et d'estimer quantitativement l'influence des divers paramètres intervenant. Les méthodes de simulation Monte-Carlo pourraient, à ce point de vue, apporter d'utiles renseignements.

3. Influence du débit de dose

Une influence du débit de dose est observée, en particulier, chaque fois qu'une réaction du premier ordre en radical est en compétition avec une réaction du deuxième ordre de

© 1999 CNRC Canada

Fig. 5. Variation de $G(-S)$ en fonction du débit de dose I, calculée à partir de l'équation [23] pour la série de données indiquée dans le texte (courbe en trait continu). La courbe en tirets représente la loi asymptotique en $1/\sqrt{I}$ obtenue d'après l'équation [24] pour des débits de dose suffisamment élevés.

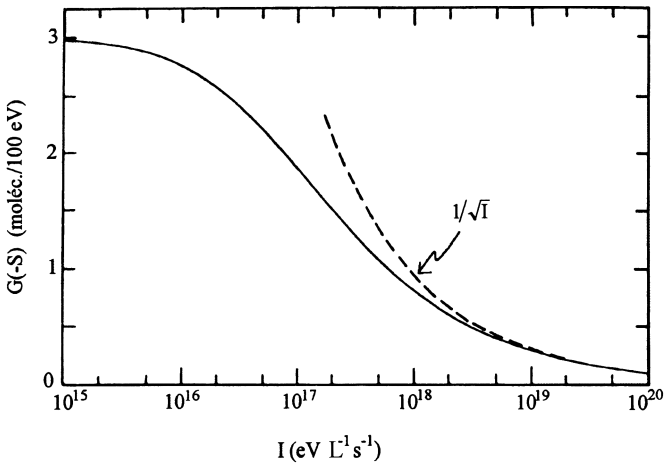

ce même radical (voir, par exemple, réf. 159). Un cas simple peut être traité, si l'on imagine, pour le radical $R^{\bullet}$ et un soluté S, les réactions suivantes :

$$R^{\bullet} + S \xrightarrow{k_1} \text{produit supposé non réagissant dans le système étudié}$$

$$R^{\bullet} + R^{\bullet} \xrightarrow{k_2} R_2$$

En écrivant l'état quasi stationnaire pour les radicaux $R^{\bullet}$, on obtient la relation suivante exprimant le rendement initial de disparition du soluté $G(-S)$:

$$[23] \qquad G(-S) = \left(\frac{k_1^{\,2}\,[S]_0^{\,2}}{4\,k_2\,I}\right)\left[\sqrt{1+\frac{8\,k_2\,I\,G_{R^{\bullet}}}{k_1^{\,2}\,[S]_0^{\,2}}}-1\right]$$

où k_1 et k_2 représentent les constantes de vitesse des deux réactions précédentes, $G_{R^{\bullet}}$ le rendement en radicaux $R^{\bullet}$, $[S]_0$ la concentration initiale du soluté et I le débit de dose (intensité d'irradiation). On voit que, dans ce cas, l'expression de $G(-S)$ est fonction de I.

Un exemple numérique peut être donné en prenant la série de valeurs : $k_1 = 10^6\ M^{-1}\ s^{-1}$, $k_2 = 10^{10}\ M^{-1}\ s^{-1}$, $G_{R^{\bullet}} = 3$ moléc./100 eV et $[S]_0 = 10^{-5}$ M. La figure 5 représente la variation de $G(-S)$ avec I (exprimé en eV $L^{-1}\ s^{-1}$) dans une échelle semi-logarithmique, telle qu'obtenue à partir de la relation [23] et des données précédentes. Il apparaît sur la figure que, pour les faibles valeurs de I, $G(-S)$ tend vers la valeur $G_{R^{\bullet}}$, indépendante de I; ce rendement diminue ensuite jusqu'à zéro en suivant, pour les débits de dose plus élevés, une loi asymptotique en $1/\sqrt{I}$:

$$[24] \qquad G(-S) \approx \sqrt{\frac{k_1^{\,2}\,[S]_0^{\,2}\,G_{R^{\bullet}}}{2\,k_2\,I}}$$

Des mécanismes analogues se retrouvent dans le cas des courbes de dilution. Une courbe de dilution, nous l'avons vu (voir sect. II-D), traduit le plus souvent des compétitions entre des réactions du soluté et des réactions biradicalaires; son allure est donc fonction de I, le palier étant atteint pour des concentrations d'autant plus faibles que I est faible. Ce n'est que quand tous les radicaux sont captés par le soluté que le rendement de transformation de celui-ci devient indépendant, dans de très larges limites, de I.

Un cas analogue se produit lors des réactions en chaîne telles que celles citées précédemment (voir sect. III-C.1-a), et pour lesquelles nous avons établi une dépendance du rendement en hydroperoxyde $G(ROOH)$ en $1/\sqrt{I}$ (voir éq. [18]). La chaîne est d'autant plus longue que le débit de dose est faible, puisque la réaction de terminaison est biradicalaire.

Lorsque le débit de dose atteint de très grandes valeurs (disons supérieures à 10^{25} eV $L^{-1}\ s^{-1}$), les zones d'hétérogénéité se recoupent dans l'ensemble de la solution irradiée, favorisant ainsi la formation de produits moléculaires qui survient alors de façon quasi homogène. Cette formation ne sera inhibée par le soluté que si celui-ci est en grande concentration. Pour les faibles concentrations, seuls réagiront avec le soluté les produits moléculaires formés, c'est-à-dire l'eau oxygénée (H_2 étant peu réactif). Les valeurs des RRM sont donc modifiées et ne doivent pas être confondues avec celles de la radiolyse γ classique (160).

À titre d'exemple, avec des débits de dose exceptionnellement élevés, Muller et al. (160) ont utilisé successivement comme capteurs de H_2O_2 les ions ferreux et le cérium IV. Le débit de dose était de 5×10^{30} eV $L^{-1}\ s^{-1}$ ($\sim 10^{12}$ Gy s^{-1}) pour une impulsion d'électrons de 2 MeV d'une durée de 50 ns. Pour de faibles concentrations en capteurs (10^{-3} M) et en milieu H_2SO_4 0,4 M désaéré, ces auteurs trouvent que :

$$G(Fe^{3+}) = G(Ce^{III}) = 2\,G(H_2O_2) = 1{,}4 \text{ moléc./100 eV}$$

L'égalité de ces trois rendements prouve que l'eau oxygénée est le seul produit réagissant. Pour des concentrations plus élevées, le calcul montre que $G(Fe^{3+})$ tend vers 4,6 moléc./100 eV, valeur résultant de la capture des radicaux $^{\bullet}OH$ par les ions ferreux dans les zones hétérogènes (160). Entre ces deux extrêmes, l'influence de la concentration en Fe^{2+} s'effectue selon les lois de compétition homogène.

Le fait de produire par radiolyse pulsée à haute intensité des concentrations homogènes d'eau oxygénée ($\sim 10^{-4}$ M) en quelques microsecondes permet d'étudier la physionomie cinétique de cette molécule dans des délais très brefs, ce qui constitue une application originale de cette méthode. C'est ainsi qu'on a pu mesurer directement la constante de vitesse de la réaction $H_2O_2 + VO_2^{+} \rightarrow VO_3^{+} + H_2O$, égale à $5{,}7 \times 10^3\ M^{-1}\ s^{-1}$ en milieu H_2SO_4 0,4 M (161).

Un problème important doit attirer l'attention : lorsqu'on réalise des simulations expérimentales d'irradiation, comme par exemple, le stockage de déchets radioactifs, le débit de dose est un paramètre dont les influences doivent être étudiées à la lumière des deux possibilités d'intervention précédentes.

Un travail réalisé par Fanning et al. (162), dans une perspective différente, a consisté à étudier, par radiolyse pulsée, l'influence de l'intensité d'irradiation sur l'évolution dans l'eau pure de l'électron hydraté. La gamme des doses étudiée allait jusqu'à 80 Gy pour des impulsions d'électrons de 20 ns. Il est apparu que la fraction de e^{-}_{aq} disparaissant à un temps donné dépend, à partir d'un certain seuil, de la dose délivrée par impulsion. Un tel seuil a été interprété

© 1999 CNRC Canada

Tableau 5. Influence de la nature du rayonnement (rayons γ de ^{60}Co et rayons α du polonium 210) sur les rendements[a,b] de radiolyse pour deux solutés (S) en solution aqueuse H_2SO_4 0,4 M désaérée.

S	$G(-S)_\gamma$	$G(-S)_\alpha$
Fe^{2+}	8,15 ± 0,15	3,60 ± 0,1[c]
Ce^{IV}	2,45 ± 0,1	3,20[c]

[a]Exprimés en moléc./100 eV.

[b]D'après réf. 30.

[c]Voir aussi réf. 168.

comme résultant d'un recoupement des zones hétérogènes. À partir des données ci-dessus, les auteurs (118, 162) ont pu obtenir certaines informations concernant la dimension des zones d'hétérogénéité et la distribution spatiale des électrons hydratés à l'intérieur de celles-ci.

4. Influence de la nature et de l'énergie du rayonnement

Nous avons vu que les premières expériences concernant la radiolyse de l'eau pure (1902–1914) ont été effectuées en employant comme sources surtout des émetteurs α, principalement le polonium 210 (voir sect. II-A et tableau 1). De tels émetteurs ont continué à être utilisés dans les travaux qui suivirent l'interruption due à la première guerre mondiale, développant ainsi l'aspect quantitatif de cette radiolyse (voir, par exemple, réfs. 27, 77 et 163–169). On s'est alors aperçu que les effets chimiques des rayons α étaient différents de ceux des rayons β^-, γ ou X, puisque, en l'absence d'air, ces derniers ne conduisaient pas, pour les doses habituelles, à une production mesurable de H_2O_2 et de H_2, tandis que ces deux produits s'accumulaient dans le cas des rayons α (170; voir aussi sect. II-A).

Ce résultat, ainsi que ceux concernant des irradiations utilisant d'autres types de rayonnements à ionisations denses, ont été considérés au début comme traduisant une différence de mécanismes, alors qu'ils provenaient en fait d'une différence dans les vitesses initiales de formation de H_2O_2 et de H_2. De même, les rendements de divers solutés irradiés en solutions aqueuses dans les mêmes conditions se sont avérés profondément distincts de ceux obtenus avec les rayons γ ou X. Le tableau 5 indique, à titre d'exemple et pour les rayons α, les rendements pour deux systèmes oxydo-réducteurs bien étudiés : Fe^{3+}/Fe^{2+} et Ce^{IV}/Ce^{III}. Soulignons néanmoins que, pour certains solutés, la dispersion des résultats expérimentaux, et donc des déterminations des valeurs des RRM à transfert d'énergie linéique élevé, est importante (30, 168; voir aussi réf. 171).

Cette influence de la nature du rayonnement provient en général du fait que, pour les rayonnements à ionisations denses, les rendements des produits moléculaires H_2O_2 et H_2 sont supérieurs à ceux mesurés pour les rayons γ, tandis que le contraire est constaté pour les produits radicalaires. C'est ainsi qu'en milieu aéré, le rapport $G(Fe^{3+})/G(Ce^{III})$ décroît, passant de 6,5 pour les rayons γ à environ 2 pour les rayons α émis par ^{210}Po (122). En effet, d'après leur schéma réactionnel, le rendement des ions ferriques en milieu H_2SO_4 0,4 M aéré soumis à l'action des rayons γ de ^{60}Co, $G(Fe^{3+}) = 2\,G_{H_2O_2} + G_{\bullet OH} + 3\,G_{H\bullet} = 15{,}6$ moléc./100 eV (voir sect. II-B et réf. 122), est très sensible à la valeur des rendements radicalaires. Au contraire, le rendement en cérium III, $G(Ce^{III}) = 2\,G_{H_2O_2} + G_{H\bullet} - G_{\bullet OH} = 2{,}45$ moléc./100 eV (voir sect. II-B et réf. 122), dépend, dans les mêmes conditions, principalement du rendement moléculaire en H_2O_2. Ces caractéristiques ont été attribuées à une hétérogénéité particulière intervenant au niveau des phénomènes primaires et due au recoupement des zones d'hétérogénéité déjà décrites (voir plus haut). Le paramètre choisi pour refléter cette hétérogénéité est le TEL, « transfert d'énergie linéique » ou « pouvoir d'arrêt » ($-dE/dx$) (172), traduisant la densité des actes primaires, ionisations et excitations, le long de chaque trajectoire. Le tableau 6 donne, à titre d'exemple, quelques valeurs de TEL dans l'eau pour diverses particules énergétiques.

Tableau 6. TEL,[a] pour l'eau, de différents types de rayonnement.

Rayonnement	TEL	Références
Rayons γ[b] de ^{60}Co	0,2–0,3	172, 173
Protons ($^1H^+$) de 100 MeV	0,65	173
Rayons β^- de 5,7 keV (^{3}H)	0,65	173
Rayons X[b] de 220 kV	0,7	173
Protons de 10 MeV	4,7	159
Deutons ($^2H^+$) de 18 MeV	5,2	92, 143
Hélions ($^4He^{2+}$) de 32 MeV	22,5	92, 143
Protons de 1 MeV	28	159
Ions $^{12}C^{6+}$ de 900 MeV	30	174
Protons de 100 keV	75	175
Rayons α de 5,3 MeV (^{210}Po)	92	176, 177
Rayons α de 1,5 MeV ($^{10}B(n,\alpha)^7Li$)	220	177
Ions $^{36}S^{16+}$ de 2,7 GeV	250	178
Ions $^{12}C^{6+}$ de 25 MeV	520	179
Ions $^{58}Ni^c$ de 40 MeV	5200	180, 181
Ions $^{238}U^c$ de 1250 MeV	17 000	181

[a]Valeurs « initiales », exprimées en keV/μm (voir, par exemple, réf. 168).

[b]Soulignons qu'il s'agit en fait du TEL des électrons éjectés lors de l'absorption du rayonnement γ ou X.

[c]Partiellement « épluchés ».

Les études précédentes ont été ainsi étendues, au fur et à mesure, à différents types de rayonnements. Citons les rayons α et les noyaux de lithium de recul de la réaction $^{10}B(n,\alpha)^7Li$ (voir, par exemple, réf. 182), les rayons β^- du tritium[22] en utilisant l'eau tritiée (40, 183, 184) et surtout les faisceaux d'ions accélérés. Il peut s'agir, par exemple, de protons d'énergie pouvant être inférieure à 600 keV (185), ou encore d'ions lourds énergétiques (179–181, 186, 187) ayant perdu (entièrement ou partiellement) leurs électrons et caractérisés alors par des valeurs de TEL élevées (voir tableau 6). Ainsi, pour les ions d'uranium 238, « épluchés » à un état de charge de +35 et accélérés à une énergie de 1250 MeV, le TEL obtenu est de 17 000 keV/μm (181). Par ailleurs, le rendement en radicaux $^{\bullet}OH$ a pu être mesuré en fonction du TEL à l'aide de divers capteurs (fig. 6) (187). Quant à l'électron hydraté (fig. 7), son rendement a été obtenu grâce à l'emploi de faisceaux pulsés de protons, de deutons et d'hélions (188–190).

[22]Rappelons que l'énergie maximale du spectre des rayons β^- du tritium (^{3}H ou T) est de 18,6 keV, avec une énergie moyenne de 5,7 keV.

© 1999 CNRC Canada

Fig. 6. Rendement en radicaux •OH (exprimé en moléc./100 eV) en fonction du TEL lors de la radiolyse de l'eau. D'après réf. 187.

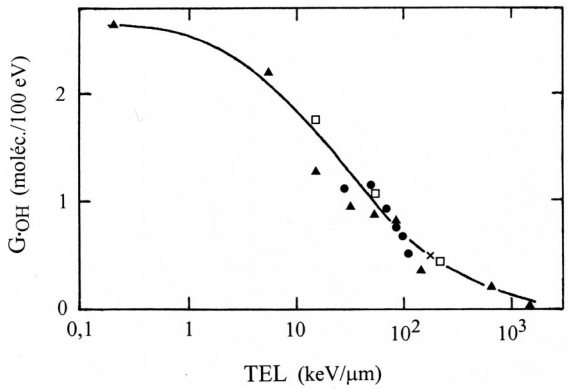

Fig. 7. Rendement en électrons hydratés (exprimé en moléc./100 eV) en fonction du TEL lors de la radiolyse pulsée (~10 μs) de l'eau à pH 7 par hélions (●) et par deutons (○). Les courbes sont théoriques. D'après réfs. 188 et 190.

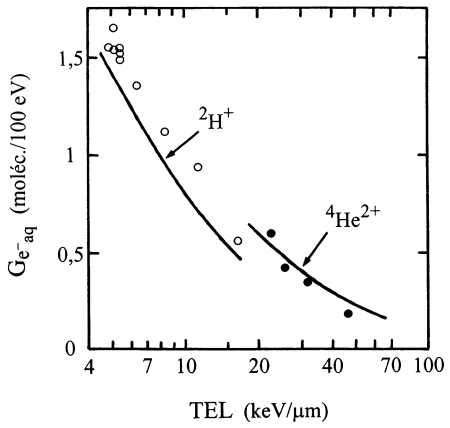

L'expérience a montré qu'il ne fallait pas se contenter de décalquer le modèle appliqué au cas des rayons γ, mais qu'on devait prendre en considération un rendement radicalaire G_{HO_2}•, même en l'absence d'oxygène. Ce rendement peut être révélé par le dégagement d'oxygène associé à la radiolyse de solutions acides Fe^{2+}/Cu^{2+}, dont le mécanisme est le suivant (191, 192) :

$$Fe^{2+} + {}^{\bullet}OH \rightarrow Fe^{3+} + OH^-$$

$$Fe^{2+} + H_2O_2 \rightarrow Fe^{3+} + {}^{\bullet}OH + OH^-$$

$$Cu^{2+} + H^{\bullet} \rightarrow Cu^{+} + H^{+}$$

$$Cu^{2+} + HO_2^{\bullet} \rightarrow Cu^{+} + H^{+} + O_2$$

$$Cu^{+} + Fe^{3+} \rightarrow Cu^{2+} + Fe^{2+}$$

Par conséquent,

$$G(O_2) = G_{HO_2}\bullet$$

On avait ainsi observé, dès 1955, pour les faibles TEL (~0,2 keV/μm), un très petit rendement G_{HO_2}• = 0,02 moléc./100 eV (191). Il a été constaté que ce rendement augmentait avec le TEL (178–180, 187, 188, 192–195), atteignant une valeur de 0,43 moléc./100 eV pour des ions

Fig. 8. Rendements différentiels en $HO_2^{\bullet}$ en fonction du TEL pour différents ions accélérés. La ligne en tirets donne le rendement limite (0,02 moléc./100 eV) obtenu avec des électrons rapides. D'après réf. 180.

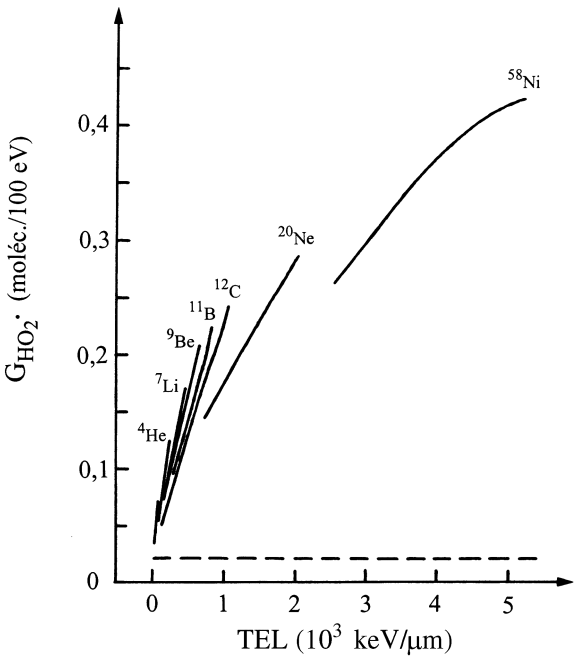

^{58}Ni de TEL égal à 5200 keV/μm (180). Ces résultats sont résumés figure 8, d'après LaVerne et Schuler (180).

Le premier modèle appliqué pour interpréter l'ensemble des résultats concernant l'influence du TEL fut celui, simpliste, du « collier de perles » (*« string of beads »*) (105, 110, 196) proposé dès 1953 pour décrire la distribution des zones hétérogènes le long des trajectoires des particules ionisantes. Bien que conduisant à des estimations géométriques vraisemblables, il fut vite abandonné.

On fut ensuite amené à supposer (40, 77, 167, 168, 191, 192, 197) que la grande densité des produits radiolytiques dans les trajectoires entraînait dans une zone périphérique les réactions suivantes entre radicaux et produits moléculaires :

[*a*] $${}^{\bullet}OH + H_2O_2 \rightarrow HO_2^{\bullet} + H_2O$$

[*b*] $${}^{\bullet}OH + H_2 \rightarrow H_2O + H^{\bullet}$$

[*c*] $$H^{\bullet} + H_2O_2 \rightarrow H_2O + {}^{\bullet}OH$$

ce qui explique tout à la fois la possibilité de formation de $HO_2^{\bullet}$ en l'absence d'air, la complexité de l'action des solutés qui, selon leur comportement cinétique, peuvent ou non interférer avec ces réactions à l'intérieur de la trajectoire, et enfin le fait que le TEL ne suffit pas à appréhender l'ensemble des phénomènes.

La description spatiale impliquée dans le mécanisme précédent a conduit à envisager au sein d'une même trajectoire deux zones coaxiales (196) (fig. 9) : (*i*) l'une, le « coeur », de forte densité en événements, où s'élaborent les produits moléculaires H_2 et H_2O_2; (*ii*) l'autre est une zone annulaire, dite « pénombre », où s'absorbent les électrons secondaires qui y forment majoritairement des produits radicalaires.

© 1999 CNRC Canada

Fig. 9. Représentation de la trajectoire d'une particule lourde chargée. D'après réf. 198.

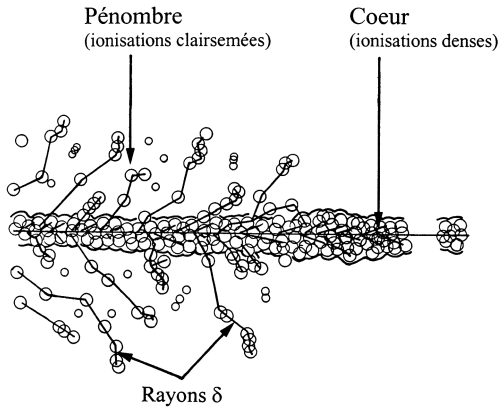

C'est donc le spectre de TEL qui définira mieux la radiolyse, spectre prenant en compte non seulement la trajectoire de la particule incidente, mais aussi celle des électrons éjectés avec suffisamment d'énergie.

Au cours de la diffusion, les réactions [*a*], [*b*] et [*c*] ont lieu dans la pénombre sauf si le soluté est trop concentré ou trop réactif avec les espèces intervenant. Pour les TEL pas trop élevés, la réaction [*a*] serait responsable de la formation de $HO_2^{\bullet}$, ou d'une partie de celle-ci, ainsi qu'il a été déjà proposé (191, 192). Pour les TEL élevés, il semble que la participation de la réaction [*a*] soit insuffisante pour expliquer, à elle seule, le rendement de $HO_2^{\bullet}$. Il est donc apparu nécessaire de faire intervenir d'autres mécanismes de formation de ce radical, tels que, par exemple, la production d'un atome d'oxygène susceptible de réagir avec $^{\bullet}OH$ (99, 194; voir aussi réf. 179), ou encore l'intervention d'ions de l'eau multichargés (199–202). Des calculs de simulation Monte-Carlo, développés récemment à partir des considérations précédentes, donnent des résultats encourageants (203).

Le problème de la radiolyse à haut TEL n'est toutefois pas encore pleinement résolu, mais l'intérêt de ses applications radiobiologiques incitent à en développer une meilleure compréhension.

5. Influence de la présence d'oxygène

(a) Introduction : Nous avons vu l'intérêt que présente l'étude de la radiolyse de solutions diluées. Elle permet en effet de caractériser, non seulement les espèces, radicalaires ou non, formées par radiolyse du solvant, mais aussi celles provenant de l'action de ces intermédiaires sur le soluté. La radiolyse de solutions d'oxygène est particulièrement riche en renseignements utiles et originaux. En effet, l'oxygène joue des rôles fondamentaux en biologie et en radiobiologie. Sa chimie concerne principalement les échanges d'électrons, et l'étude de la radiolyse des solutions aérées a développé considérablement nos connaissances concernant la chimie radicalaire de cet élément.

(b) Actions de l'oxygène sur la radiolyse de solutions diluées : Ce gaz est soluble dans de nombreux milieux et en particulier dans l'eau, c'est donc un vecteur d'oxydoréduction quasi universel. Si on ne prend pas de précautions particulières, la cible irradiée contient de l'oxygène. Par exemple, la concentration de celui-ci dans l'eau équilibrée avec l'air à pression atmosphérique et température ambiante est ~2,5 × 10^{-4} M.[23] Ceci indique qu'un soluté, bon capteur de O_2 ($k \sim 10^{10}$ M^{-1} s^{-1}, par exemple), en concentration suffisante, réagit dans ce milieu avec un temps de réaction de quelques microsecondes, permettant de développer certaines compétitions dans cette échelle de temps (205).

Tableau 7. Influence de l'oxygène sur les rendements[a] de radiolyse de divers solutés en solutions aqueuses irradiées par les rayons γ de ^{60}Co.

	G(–S)		
Soluté (S)	O_2 absent	O_2 présent	Références
Fe^{2+}	8,15[b]	15,6[b]	30
As^{III}	1,8[c]	3,5[c]	30
Ce^{IV}	2,45[b]	2,45[b]	28, 30, 37
Acide formique	3,2	2,6	40, 206
Éthanol	5,1	2,3	206

[a]Exprimés en moléc./100 eV.
[b]En solution aqueuse H_2SO_4 0,4 M.
[c]pH 2,5.

L'influence de l'oxygène, en radiolyse, a été rapidement mise en évidence. Ainsi, comme nous l'avons vu, le rendement d'oxydation des ions ferreux en solution aqueuse H_2SO_4 0,4 M, pour les rayons γ de ^{60}Co, est 15,6 moléc./100 eV en présence d'air et 8,15 en son absence (voir sects. II-B et III-C.4 et tableau 5) (30, 122). Le tableau 7 donne quelques exemples concernant les effets de O_2 en radiolyse. Le plus souvent, celui-ci augmente les rendements d'oxydation du soluté, mais il peut parfois les diminuer en jouant un rôle protecteur comme dans le cas de l'acide formique (40, 206) et de l'éthanol (206). Dans certains cas, les rendements (par exemple, pour Ce^{IV}) ne sont pas modifiés par la présence d'oxygène (28, 30, 37).

(c) Réactions gouvernant la radiolyse des solutions aérées :

La chimie de l'oxygène se caractérise par le fait qu'il peut échanger quatre électrons. La réaction globale :

[25] $O_2 + 4\ e^- + 4\ H^+ \rightarrow 2\ H_2O$

s'effectue souvent avec formation des intermédiaires suivants, dont deux sont radicalaires :

[26] $O_2 \rightarrow O_2^{\bullet -} \rightarrow H_2O_2 \rightarrow {}^{\bullet}OH \rightarrow H_2O$

Les potentiels de réduction des couples mis en jeu ont les valeurs suivantes, exprimées en volts, à pH 7 et 25°C, par rapport au potentiel standard d'électrode à hydrogène (207; voir aussi sect. IV-C.2) :

$O_2/O_2^{\bullet -}$ $E^{\circ\prime} = -0{,}33$ V

$O_2^{\bullet -}/H_2O_2$ $E^{\circ\prime} = 0{,}94$ V

$H_2O_2/{}^{\bullet}OH$ $E^{\circ\prime} = 0{,}46$ V

${}^{\bullet}OH/H_2O$ $E^{\circ\prime} = 2{,}18$ V

tandis qu'à pH 0, ils ont les valeurs (207) :

[23]La concentration d'une solution aqueuse saturée en oxygène, à température ambiante, est donc de $[O_2] \sim 1{,}25 \times 10^{-3}$ M (voir, par exemple, réf. 204).

© 1999 CNRC Canada

Fig. 10. Exemple de courbes de survie. D'après réf. 214.

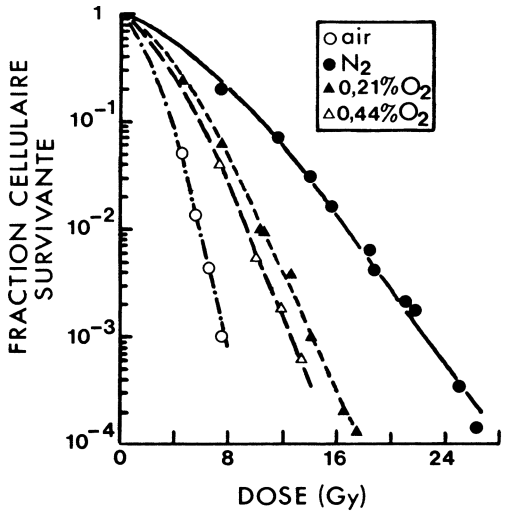

$O_2/HO_2^{\bullet}$	$E° = -0{,}05$ V
$HO_2^{\bullet}/H_2O_2$	$E° = 1{,}48$ V
$H_2O_2/^{\bullet}OH$	$E° = 0{,}87$ V
$^{\bullet}OH/H_2O$	$E° = 2{,}59$ V

Voyons, à titre d'exemple, le mécanisme mis en jeu dans le cas de la radiooxydation des ions ferreux en solution diluée aqueuse acide en l'absence ou en la présence d'air. En l'absence d'air, le rôle oxydant est joué par l'atome H. La séquence, impliquant une telle radiooxydation,

$$H^+ + H^{\bullet} + Fe^{2+} \rightarrow H_2 + Fe^{3+}$$

$$^{\bullet}OH + Fe^{2+} \rightarrow OH^- + Fe^{3+}$$

$$H_2O_2 + Fe^{2+} \rightarrow Fe^{3+} + {}^{\bullet}OH + OH^-$$

conduit à la réaction endergonique globale :

$$2\ H^+ + 2\ Fe^{2+} \rightarrow H_2 + 2\ Fe^{3+}$$

Cette réaction n'est pas thermodynamiquement possible de manière spontanée car le potentiel du couple mettant en jeu l'oxydant (H^+/H_2, $E° = 0$) est inférieur à celui du couple contenant le réducteur (Fe^{3+}/Fe^{2+}, $E° = 0{,}77$ V). Elle demande, dans les conditions standard, 1,54 eV (~148,6 kJ/mol), énergie qui est fournie dans ce cas par les espèces réactives formées par la radiolyse de l'eau (208).

En la présence d'air, les atomes $H^{\bullet}$ oxydants sont transformés en $HO_2^{\bullet}$ qui oxydent trois ions ferreux, ce qui conduit à la réaction globale (208) :

$$O_2 + 4\ H^+ + 4\ Fe^{2+} \rightarrow 2\ H_2O + 4\ Fe^{3+}$$

Cette réaction est responsable de ~71 % de la radiooxydation des ions Fe^{2+} en milieu aéré, le complément étant dû à l'action des radicaux $^{\bullet}OH$ et de H_2O_2. Elle diffère profondément de la précédente car elle dégage de l'énergie (1,84 eV en valeur absolue, soit ~177,5 kilojoules par mole d'oxygène consommée). Néanmoins, par suite de l'obstacle présenté par la faible valeur du potentiel $O_2/HO_2^{\bullet}$, elle ne se produit pas spontanément. Le pouvoir oxydant de l'oxygène est, en revanche, libéré par l'intervention des espèces transitoires produites par le rayonnement, celui-ci jouant ainsi le rôle de catalyseur de la réaction. Tel est souvent le cas lors de l'irradiation de milieux organiques ou biologiques (208). En particulier, les chaînes de peroxydation (121) représentent la catalyse par le rayonnement de la réaction exergonique (voir sect. III-C.1.a) :

Fig. 11. Variation du facteur d'amplification de l'oxygène (FAO) en fonction du TEL, pour un tissu de densité unité. D'après réf. 219.

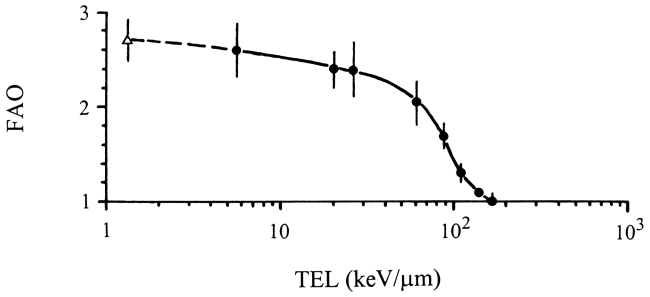

$$RH + O_2 \rightsquigarrow ROOH$$

où RH représente la molécule subissant la peroxydation.

(d) Action à l'échelle cellulaire : La première étude connue concernant l'intervention de l'oxygène en radiobiologie date de 1921 (209), bien que l'on doive rappeler ici les travaux de Gottwald Schwarz (210), qui avaient montré, dès 1909, un effet radioprotecteur de l'ischémie.[24] Cet *effet oxygène* fut depuis lors l'objet de nombreuses études (voir, par exemple, réfs. 26, 81, 211 et 212). Son rôle est d'importance primordiale lors de la plupart des actions biologiques des rayonnements ionisants.

C'est ainsi que, pour l'eau, O_2 peut réagir soit sur des radicaux primaires en transformant le couple $H^{\bullet}/e^-_{aq}$ en $HO_2^{\bullet}/O_2^{\bullet -}$, soit sur des radicaux ($R^{\bullet}$) provenant du soluté en donnant en particulier un peroxyradical $RO_2^{\bullet}$. Il peut aussi réagir sur un site radicalaire créé au sein d'une macromolécule. Pour l'ADN, il peut ainsi bloquer les processus de réparation (voir, par exemple, réf. 213).

À l'échelle cellulaire, les effets de l'oxygène sur la radiolyse sont souvent complexes. Ils se traduisent toujours par une radiosensibilisation que l'on caractérise par la mesure de l'influence de l'oxygène sur la survie cellulaire. Celle-ci est explicitée par les *courbes de survie* obtenues en portant le logarithme de la fraction cellulaire survivante (S/S_0) en fonction de la dose absorbée D (fig. 10) (voir, par exemple, réfs. 26, 81 et 212–217). Elles sont souvent paramétrées sous la forme :

$$[27] \quad S = S_0\, e^{-\alpha D - \beta D^2}$$

dite « forme linéaire-quadratique » (217). Ces courbes permettent d'estimer la valeur du « facteur d'amplification de

[24]L'ischémie caractérise l'état d'une cellule ou d'un tissu peu ou non oxygéné.

© 1999 CNRC Canada

l'oxygène » (FAO) (en anglais : *« oxygen enhancement ratio »* ou OER) (26, 81, 208, 212), qui est donné par :

$$\text{FAO} = \frac{\text{dose en l'absence d'air}}{\text{dose en la présence d'air}}$$

pour obtenir le même effet biologique (la même survie cellulaire) (218).

Pour les faibles TEL (électrons accélérés), le FAO reste voisin de 3 pour des doses comprises entre 2 et 20 Gy, et diminue quand augmentent le TEL (fig. 11) et le débit de dose. D'autre part, l'effet de l'oxygène croît pour des pressions partielles (pO_2) allant de 0 à ~30 Torr[25] (208). Pour des pO_2 plus élevées, le gain en radiosensibilité est très faible, même en utilisant des pressions hyperbares[25] (208; voir aussi réfs. 26 et 220).

Divers mécanismes ont été invoqués pour expliquer les effets biologiques de l'oxygène sous irradiation. Il a été montré par étude des mélanges O_2/N_2O que, au niveau cellulaire, ces effets sensibilisateurs n'étaient pas dus au simple remplacement de e^-_{aq} par $O_2^{\bullet-}$ et que le radical anion superoxyde $O_2^{\bullet-}$ ne semble pas indispensable à la radiosensibilisation (221). Il est apparu qu'au moins une partie de cet effet pourrait être attribuée à la réaction déjà évoquée du type

$$R^\bullet + O_2 \rightarrow RO_2^\bullet$$

conduisant à une inhibition par O_2 de la réparation de certains défauts radioinduits (213; voir aussi réf. 51). Le problème est toutefois loin d'être complètement résolu.

6. Influence de la température

Des études systématiques concernant les influences de la température sur les phénomènes de radiolyse n'ont été entreprises qu'assez tardivement. Elles ont été souvent impulsées par la nécessité de connaître les mécanismes de la radiolyse de l'eau se déroulant au sein de certains réacteurs nucléaires (voir, par exemple, réf. 222). Ces travaux se sont développés selon plusieurs directions : l'une d'elles s'intéresse à la variation, en fonction de la température, des rendements radicalaires et moléculaires, une autre concerne la modification du spectre de l'électron hydraté, la troisième enfin correspond à l'influence de la température sur les vitesses ou les équilibres des réactions mises en jeu.

(a) Variation des RRM en fonction de la température :
Depuis 1962 (223), un certain nombre de déterminations des RRM en fonction de la température a été publié; elles utilisent le plus souvent la méthode des solutés. Pour une bonne part, ces déterminations concernent les rayons γ ou les électrons accélérés et les milieux neutres (85, 224–229) ou parfois acides (H_2SO_4 0,4 M) (223, 230, 231), les températures étant situées dans la gamme 2–410°C. En comparant les résultats des divers auteurs, des dispersions expérimentales relativement importantes ont été constatées. Un intérêt particulier doit toutefois être accordé aux travaux récents d'Elliot et al. (89) aboutissant aux résultats suivants pour les RRM en milieu neutre entre 20 et 300°C (fig. 12) :

$$G_{e^-_{aq}} = 2{,}56 + (3{,}40 \times 10^{-3})\ t$$

Fig. 12. Variation des RRM (exprimés en moléc./100 eV), pour l'eau neutre irradiée avec les rayons γ de ^{60}Co ou des électrons accélérés, en fonction de la température t (exprimée en degrés Celsius). D'après réf. 89.

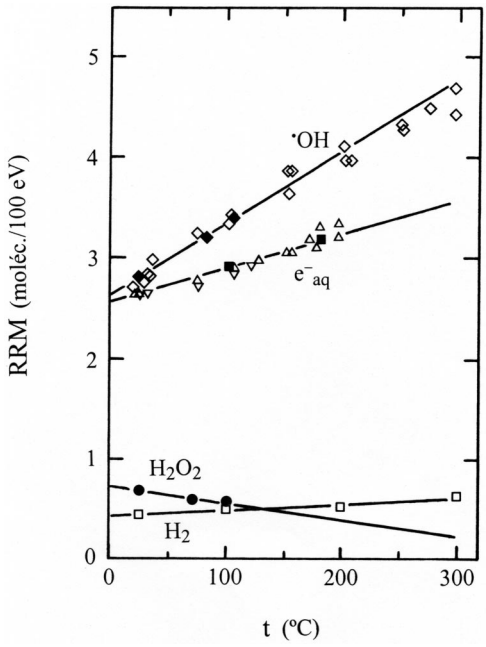

$$G_{\cdot OH} = 2{,}64 + (7{,}17 \times 10^{-3})\ t$$

$$G_{H_2} = 0{,}43 + (0{,}69 \times 10^{-3})\ t$$

$$G_{H\cdot} = 0{,}54 + (1{,}28 \times 10^{-3})\ t$$

$$G_{H_2O_2} = 0{,}72 - (1{,}49 \times 10^{-3})\ t$$

où t est la température, exprimée en degrés Celsius, et où les valeurs de G sont données en moléc./100 eV. On voit, d'après les relations précédentes, que les rendements radicalaires augmentent avec la température tandis que le rendement en H_2O_2 diminue, ce qui semble montrer que la distribution des espèces primaires est plus étalée quand croît la température (et donc la vitesse de diffusion) dans l'intervalle considéré. Une variation analogue a été trouvée par Kent et Sims (227). Elliot et al. (232) ont établi de même que, pour les deutons de 23 MeV et les ions $^7Li^{3+}$ de 157 MeV irradiant des solutions neutres, les rendements en radicaux $^\bullet OH$ et en e^-_{aq} croissent et celui de H_2O_2 diminue, dans la gamme 25–180°C.

Le rendement en H_2 dans la plupart des cas précédents pose problème puisqu'il semble varier en sens inverse de H_2O_2. Il a été suggéré que H_2 est formé unimoléculairement (85), par exemple à partir de la décomposition d'une molécule d'eau excitée électroniquement (89, 201, 233) :

$$H_2O^* \rightarrow H_2 + O$$

Cette suggestion a néanmoins été discutée par LaVerne et Pimblott (234). L'influence de la température sur les RRM

[25]1 bar = 10^5 Pa = 0,986 92 atm (1 atm = 760 Torr = 101 325 Pa), l'unité SI de pression étant le pascal (Pa) ou N/m^2. Les pressions dites hyperbares, parfois utilisées en radiothérapie, sont de l'ordre de 3 à 4 atm.

© 1999 CNRC Canada

Fig. 13. Spectres d'absorption de e^-_{aq} pour différentes valeurs de la température (exprimée en kelvins). Les valeurs donnent, en fonction de l'énergie *E* (exprimée en électron-volts), l'absorbance *A* normalisée par rapport au maximum d'absorption (A_{max}). Les fléches indiquent les positions (E_{max}) des maxima de A/A_{max} pour les différents spectres. Les spectres successifs ont été décalés de 0,2 unité vers le haut pour éviter les recouvrements. D'après réf. 242.

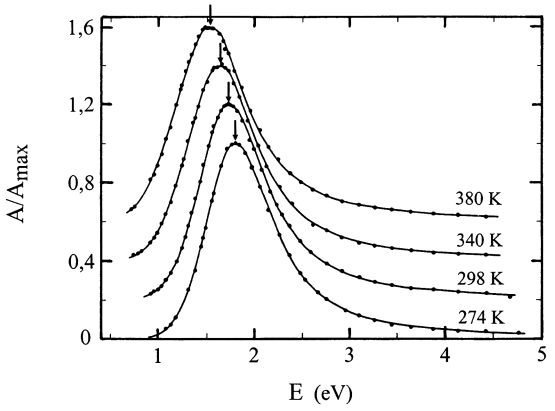

n'est donc pas clairement expliquée. En fait, plusieurs propriétés de l'eau, telles que la densité, la viscosité, la constante diélectrique et le produit ionique, doivent intervenir (85, 235). L'étude des effets de température sur la radiolyse de l'eau a été développée théoriquement par Swiatla-Wojcik et Buxton (233, 236), LaVerne et Pimblott (234) et Kabakchi et Bugaenko (237), à l'aide de modèles déterministes, et par Frongillo et al. (238) en utilisant les techniques de simulation Monte-Carlo. L'influence du TEL a, de plus, été estimée par différents auteurs (229, 236, 238), dans la gamme 25–300°C.

(b) Spectre d'absorption de e^-_{aq} en fonction de la température : Le spectre de l'électron hydraté se déplace vers le rouge (c'est-à-dire vers les énergies plus faibles) lorsque la température augmente (239–243; voir aussi réf. 72), comme on peut le constater sur la figure 13, d'après les résultats de Jou et Freeman (242). Ces derniers auteurs ont étudié les modifications du spectre entre 274 et 380 K et ont constaté que celui-ci demeure de forme gaussienne pour les énergies inférieures à E_{max} (énergie associée au maximum d'absorption) et de forme lorentzienne pour les énergies supérieures à E_{max}.[26] Comme le montre la figure 13, les déplacements spectraux sont différents pour les deux zones considérées, ce qui laisse à penser que l'on a affaire à des transitions de nature différente pour chacune d'elles (72). De plus, le produit $G_{e^-_{aq}}\varepsilon_{max}$ (où ε_{max} est le coefficient d'extinction molaire de e^-_{aq} au maximum du spectre, exprimé en M^{-1} cm^{-1}) varie très peu, de $50{,}4 \times 10^3$ moléc./(100 eV M cm) à 274 K à $51{,}8 \times 10^3$ moléc./(100 eV M cm) à 380 K (242). Comme $G_{e^-_{aq}}$ augmente avec la température (voir fig. 12), $\varepsilon_{max}(e^-_{aq})$ décroît avec celle-ci. Elliot et Ouellette (244) ont ainsi rapporté, pour des températures allant jusqu'à 200°C, une décroissance sensiblement linéaire de $\varepsilon_{max}(e^-_{aq})$ en fonction de la température, suivant la loi $\varepsilon_{max} = 20\,364 - 20{,}4\,t$ (où *t* est en degrés Celsius).

Au-dessus de 175°C, le maximum d'absorption continue à se déplacer vers les énergies plus faibles, mais avec un coefficient de température moindre; cette variation se poursuit jusqu'à la température critique de l'eau (~371°C pour D_2O[27]), et même au-delà (240, 241, 243). Ce déplacement peut être attribué à la modification des pièges électroniques due au changement progressif avec la température de la structure associative de l'eau.

Notons enfin que la simulation numérique du spectre d'absorption de e^-_{aq} pour diverses valeurs de la température (298, 340 et 373 K) (245) n'est pas pleinement en accord avec les résultats expérimentaux.

(c) Influence de la température sur diverses constantes de vitesse de réaction : La méthode de radiolyse a permis de mesurer en fonction de la température la constante de vitesse de certaines réactions rapides concernant entre autres : e^-_{aq} (158, 224, 239, 243, 244, 246–250), $O^{\bullet-}$ (251), $H^\bullet$ (158, 247, 252–256), ainsi que des radicaux produits secondairement par le rayonnement, tels que $N_3^\bullet$, $NO_2^\bullet$, $Br_2^{\bullet-}$, $I_2^{\bullet-}$ et $(SCN)_2^{\bullet-}$ (257). Pour cette dernière série, donnée ici à titre d'exemple, les énergies d'activation pour les réactions avec divers phénols et l'ion ascorbate sont comprises entre 7 et 41 kJ/mol, dans la gamme de températures 5–75°C. Les variations correspondantes de la constante de vitesse semblent dépendre, pour cette même série, à la fois de l'énergie d'activation et du facteur préexponentiel, cette dernière influence apparaissant jouer un rôle prédominant (257).

Des mesures récentes jusqu'à 300°C ont montré que, pour un certain nombre de réactions, l'énergie d'activation ne demeurait pas constante dans l'intervalle de température considéré (158, 224, 243, 247, 248, 256). Tel est le cas, entre autres, des réactions (158) :

$$^\bullet OH + {}^\bullet OH \rightarrow H_2O_2$$

$$e^-_{aq} + H_3O^+ \rightarrow H^\bullet$$

$$e^-_{aq} + {}^\bullet OH \rightarrow OH^-$$

$$H^\bullet + O_2 \rightarrow HO_2^\bullet$$

$$e^-_{aq} + O_2 \rightarrow O_2^{\bullet-}$$

Des valeurs négatives peuvent même être obtenues, par exemple dans le cas des réactions de e^-_{aq} avec NO_2^-, NO_3^-, SeO_4^{2-} (224, 248) et éventuellement avec lui-même (158, 243). Il a été montré que l'ensemble de ces situations pouvait être décrite adéquatement par l'équation de Noyes (258; voir aussi réfs. 158, 247 et 248) :

[28] $$1/k = 1/k_{diff} + 1/k_{réact}$$

où k_{diff} est la constante de vitesse de la réaction limitée par la diffusion et $k_{réact}$ est celle de la réaction chimique ultérieure (fig. 14). Lorsque $k_{diff} << k_{réact}$, l'étape limitante est la

[26]On sait que E_{max} est reliée à la longueur d'onde λ_{max} correspondant au maximum d'un spectre de e^-_{aq} par $E_{max} = 1240/\lambda_{max}$, où E_{max} est exprimée en eV et λ_{max} en nm. $T(K) = t(°C) + 273{,}15$.

[27]Notons que, afin de minimiser les pertes de lumière dues à l'absorption infrarouge, de l'eau lourde est le plus souvent employée pour l'étude des spectres d'absorption de e^-_{aq} au-dessus de 100°C (voir, par exemple, réf. 240).

© 1999 CNRC Canada

Fig. 14. Variation de k en fonction de $1/T$, dans une échelle semi-logarithmique, pour le cas de la réaction $e^-_{aq} + {}^\bullet OH \rightarrow OH^-$. D'après réfs. 158 et 244.

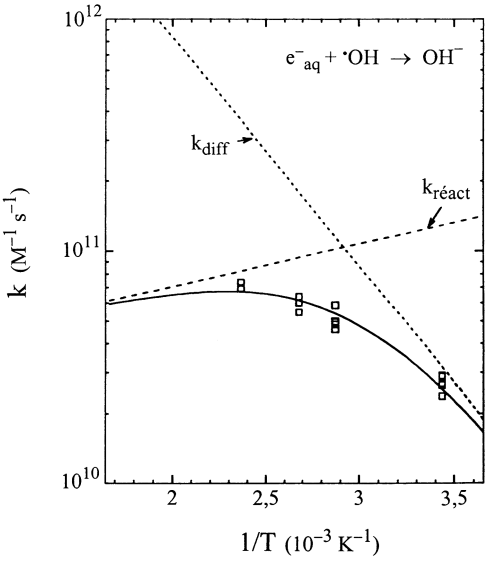

diffusion des espèces réagissantes et lorsque $k_{diff} >> k_{réact}$, c'est la réaction chimique qui impose sa vitesse (235).

7. Influence de la nature de la phase

Nous avons, jusqu'à présent, considéré la radiolyse de l'eau à l'état liquide. En effet, l'ensemble des données concernant la phase vapeur (voir, par exemple, réfs. 41 et 259–262) ou solide (voir, par exemple, réfs. 41 et 263–267) est relativement moins développé. Le fait que le stade de condensation ou d'agrégation du solvant joue sur les résultats expérimentaux doit cependant être envisagé. Par exemple, il semble logique d'admettre que la part des réactions biradicalaires, tout particulièrement la réaction $H^\bullet + {}^\bullet OH \rightarrow H_2O$, soit favorisée par la densité du milieu, produisant un effet de « cage » (268). Les rendements qui traduisent la radiolyse de l'eau seraient donc d'autant plus faibles que la phase est condensée, les mécanismes restant *grosso modo* qualitativement semblables.

La comparaison quantitative des rendements primaires entre les deux phases, vapeur et liquide, est toutefois difficile à établir. Les méthodes de simulation Monte-Carlo ont néanmoins permis de calculer le rendement initial de radiolyse de l'eau, dans l'une et l'autre phase, par des électrons d'énergie 10 keV. Pour la phase vapeur, les valeurs calculées du rendement de décomposition de l'eau ainsi obtenues : 7,87 (269), 6,33 (270), 7,21 (271) et 7 (272) moléc./100 eV, sont comparables aux résultats expérimentaux (7,5 ± 1 moléc./100 eV) (260–262; voir aussi tableau 8). Quant à l'eau liquide, par simulations Monte-Carlo, il a été obtenu des données : 7,67 (270), 7,47 (271), 7,2 (272) et 6,6 (273, 274) moléc./100 eV, qui supportent, elles aussi, la comparaison avec l'expérience (~5–7 moléc./100 eV) (118, 119, 130, 275–277). Ces résultats ont été discutés par Bednář (278), Sukhonosov (279) et Pimblott et Mozumder (280).

La comparaison des rendements vapeur/liquide de H_2 et H_2O_2 est également difficile à établir car les rendements mesurés de ces deux produits lors de la radiolyse de la vapeur d'eau sont peu élevés et correspondent probablement à des états quasi stationnaires relativement bas pour les débits de dose habituels (41, 261, 281, 282). Ceci présenterait une analogie qualitative avec l'eau liquide irradiée avec des rayonnements de faibles TEL (voir sect. II-A).

Tableau 8. Rendements[a] des processus primaires de la radiolyse de l'eau en phase vapeur, estimés par Willis et Boyd (réf. 261).

Processus primaires d'ionisation	Rendements
$H_2O \rightarrow H_2O^{\bullet+} + e^-$	1,99
$H_2O \rightarrow H^+ + {}^\bullet OH + e^-$	0,67
$H_2O \rightarrow OH^+ + H^\bullet + e^-$	0,57
$H_2O \rightarrow H_2 + O^{\bullet+}(^2D) + e^-$	0,06
$H_2O \rightarrow H_2^{\bullet+} + O + e^-$	0,01
	$G_{ionisation}$ = 3,30
Processus primaires d'excitation électronique	Rendements
$H_2O \rightarrow H^\bullet + {}^\bullet OH$	3,58
$H_2O \rightarrow H_2 + O$	0,45
	$G_{excitation}$ = 4,03

[a]Exprimés en moléc./100 eV.

En la présence de capteurs d'atomes $H^\bullet$ et d'électrons, on a toutefois mesuré, à ~120°C, un rendement G_{H_2} = 0,45 ± 0,1 (260, 282–285). Ce rendement « non captable » en H_2 a été attribué (voir, par exemple, réfs. 260 et 278) à une contribution des molécules d'eau excitées électroniquement, selon le processus : $H_2O^* \rightarrow H_2 + O$, ou à un mécanisme de capture électronique résonante dissociative : $H_2O + e^- \rightarrow H_2O^- \rightarrow H^- + {}^\bullet OH$, suivi de $H^- + H_2O \rightarrow H_2 + OH^-$, ou bien encore à la formation d'atomes d'hydrogène excités électroniquement ou « chauds », c'est-à-dire possédant suffisamment d'énergie cinétique, et pouvant participer à la réaction : $H^{\bullet *}$ (ou $H^\bullet_{\text{« chaud »}}$) + $H_2O \rightarrow H_2 + {}^\bullet OH$.

Les rendements ci-dessus évoqués s'appliquent particulièrement aux irradiations par électrons rapides et rayons γ ou X, mais ils sont à peu près indépendants du TEL au moins jusqu'aux irradiations par des produits de fission de ^{235}U (286). Ils ne sont, de plus, modifiés par la température qu'au delà de ~150°C (281, 287; voir aussi réf. 260).

Par ailleurs, pour des pressions suffisantes, l'électron peut former avec l'eau des agrégats gazeux négatifs (voir, par exemple, réf. 72; voir aussi réf. 288) :

$$e^- + (H_2O)_n \rightarrow (H_2O)_n^-$$

qui se comportent, vis-à-vis des différents solutés, de manière analogue à l'électron hydraté en phase liquide.

Pour la glace, le rendement de décomposition de l'eau diminue lorsque la température décroît : ainsi, il a été proposé (41) les valeurs (en moléc./100 eV) de 3,4 à –10°C, 1 à –78°C et 0,5 à –200°C. Selon les conditions d'irradiation, quatre espèces radiolytiques principales peuvent être piégées : les atomes $H^\bullet$, les radicaux ${}^\bullet OH$ et $HO_2^\bullet$ (ce dernier étant formé en petite quantité, probablement par la rencontre de ${}^\bullet OH$ et de H_2O_2), et les électrons (263, 264, 289–294). Ces espèces ont généralement été identifiées, et suivies cinétiquement en fonction de la température, par résonance paramagnétique électronique (RPE) ou par spectrophotométrie d'absorption optique. À 4,2 K, les rendements de $H^\bullet$ et de ${}^\bullet OH$ sont égaux à ~0,9 moléc./100 eV (264). À partir de 20 K, les atomes $H^\bullet$ deviennent mobiles et disparaissent rapidement au-dessus de 50 K (295). Quant aux radicaux ${}^\bullet OH$, ils

© 1999 CNRC Canada

commencent à migrer à compter de ~100 K (291). Les expériences de conductivité ont montré, d'autre part, que les électrons « en excès » quasi libres (ou « secs ») sont, dans la glace cristalline irradiée, formés avec une mobilité relativement grande (25 ± 10 cm^2 V^{-1} s^{-1}) et sensiblement constante entre –65 et –120°C (296–299). Le temps de vie (ou de piégeage) de ces électrons dépend fortement de la température : 250 ns à –80°C, 1 ns à –30°C et 100 ps à –5°C (297, 299, 300). Kevan (264) a souligné, par ailleurs, la possibilité d'une corrélation entre les températures de déclin des diverses espèces radicalaires formées et celles des réorganisations moléculaires de la glace cristalline.

Les électrons piégés (e^-_{vis}) ont été observés dans la glace neutre ou alcaline (264, 265) et sont caractérisés par une bande d'absorption dans le visible (avec un maximum situé autour de ~630–650 nm) (290, 293, 300–303), très similaire à celle de l'électron hydraté (72, 83; voir aussi réf. 293). On a ainsi été conduit à conclure que e^-_{vis} dans la glace a une structure analogue à celle de e^-_{aq} dans l'eau liquide (299, 304) et que les pièges correspondants pourraient être des lacunes du réseau, produites lors de l'irradiation (305, 306). De plus, le rendement de e^-_{vis} (en moléc./100 eV) est faible : 0,95 à –5°C (303), 0,05 à –50°C (303) et 10^{-4}–10^{-3} à –196°C (302). À très basse température, une bande d'absorption a également été observée dans l'infrarouge (~3600 nm) et attribuée à un autre type d'électrons piégés (e^-_{ir}) (306–308). Certains auteurs (306, 307) ont suggéré que les pièges associés à e^-_{ir} sont constitués par les cavités naturelles de la structure cristalline de la glace.

Les glaces alcalines irradiées pourraient conduire à la formation du « diélectron » (264), c'est-à-dire une espèce composée de deux électrons piégés dans le même site selon une structure qui serait analogue à celle des centres F′ rencontrés, par exemple, dans les halogénures alcalins.[28] L'existence transitoire d'une telle espèce a également été avancée, dans certains cas, lors de la radiolyse de l'eau liquide (255, 310–313).

Soulignons enfin divers travaux de désorption stimulée par impact d'électrons de faible énergie (3–150 eV) sur des couches minces solides d'eau (H_2O/D_2O), amorphes ou cristallines, déposées sur un substrat métallique, qui montrent la production de H_2/D_2 (314), $D^\bullet$ et O (315), H^-/D^- (316, 317), H^+/D^+ (318) et O_2 (319). L'interprétation de ces résultats s'appuie principalement sur les mécanismes (voir, par exemple, réf. 320) d'attachement dissociatif électronique (formation résonante d'ions négatifs transitoires), de dissociation dipolaire, ou encore d'excitation électronique (« excitons de Frenkel ») dissociative de H_2O. Ces travaux pourraient apporter d'utiles renseignements sur les interactions et le devenir des électrons secondaires, en fin de parcours dans les traces des rayonnements ionisants. Une large proportion de ces électrons possèdent, on le sait, des énergies inférieures à une centaine d'électron-volts (voir sect. III-B).

8. Influence de la pression

À 20°C, l'eau liquide subit, pour des pressions supérieures à ~1,5 kbar,[25] d'importants changements structuraux, l'eau semblant alors se comporter comme un fluide « simple » non associé (321). Un certain nombre d'expériences portent sur l'influence de la pression sur la radiolyse γ de l'eau et de solutions aqueuses, allant de 1 atm jusqu'à 8,7 kbar (pression pour laquelle le point de fusion de la glace est de 25°C). Hentz et al. (322–324) ont ainsi montré que, pour des solutions neutres ou acides et dans l'intervalle de pression considéré, les rendements primaires (RRM) de e^-_{aq}, $^\bullet OH$, $H^\bullet$, H_2 et H_2O_2 sont indépendants de la pression. Selon ces auteurs (323), ceci entraîne comme conséquence qu'une variation, en fonction de la pression, du rendement d'un produit de la radiolyse de ces solutions, ne pourrait provenir que de l'effet de la pression sur les constantes de vitesse relatives de certaines réactions secondaires. Une telle interprétation a permis la détermination des volumes molaires d'activation pour certaines réactions de l'électron hydraté et de l'atome $H^\bullet$, en particulier pour $H^\bullet + OH^- \rightarrow e^-_{aq} + H_2O$. À partir de ces données et moyennant certaines hypothèses concernant le complexe activé dans chaque cas, les volumes molaires partiels de e^-_{aq} et de $H^\bullet$ ont pu être estimés (324–326).

Citons également, parmi les résultats obtenus, l'influence de la pression sur le spectre de l'électron hydraté qui montre un déplacement du maximum vers le bleu (327–329; voir aussi réf. 72) (fig. 15).

Fig. 15. Spectres de e^-_{aq} à 29°C, pour diverses valeurs de la pression : ○, 1 atm, ●, 1,10 kbar, □, 2,13 kbar, ■, 3,53 kbar, △, 4,88 kbar et ▲, 6,26 kbar. Les spectres successifs ont été décalés de 0,2 unité vers le haut pour éviter les recouvrements. D'après réf. 328.

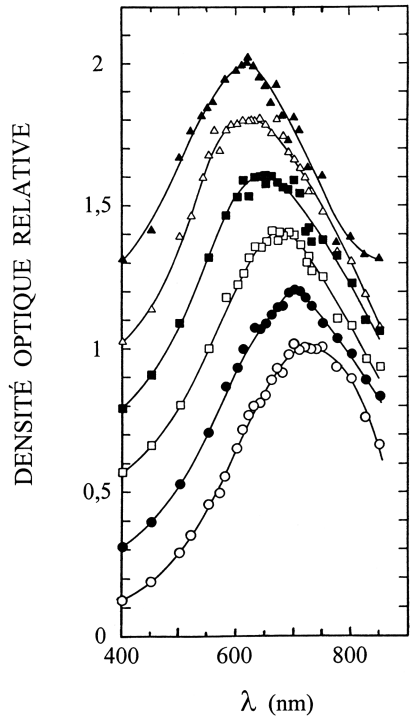

[28]Le centre F′ (ou F^-) est généralement considéré comme formé par un site anionique vacant ayant capté deux électrons (voir, par exemple, réf. 309).

© 1999 CNRC Canada

Fig. 16. Variation du rendement en radicaux •OH en fonction du temps lors de la radiolyse de l'eau par des électrons accélérés (voir texte). À noter que la courbe simulée (*c*) a été obtenue pour des répartitions spatiales initiales d'électrons hydratés et de radicaux •OH de formes gaussiennes, d'écarts-types respectivement égaux à $\sigma(e^-_{aq})$ = 40 Å et $\sigma(^\bullet OH)$ = 7,5 Å. D'après réf. 273.

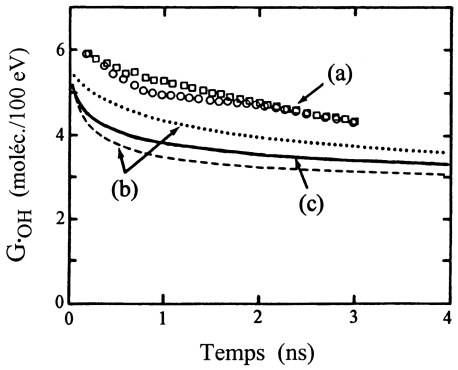

IV. Conclusion : la radiolyse de l'eau à l'orée du XXI^{ème} siècle

A. État actuel des connaissances

Nous avons vu comment, à partir des premières expériences concernant la radiolyse de l'eau et datant de 1902 (voir sect. II-A), nos connaissances ont pu s'élargir et se clarifier. Il est toutefois apparu que certains aspects quantitatifs de cette radiolyse ne sont pas encore pleinement résolus. Il serait intéressant que, dès les premières années du XXI^{ème} siècle, des progrès soient réalisés dans cette direction, progrès qui favoriseraient dans l'avenir les applications et les retombées de la radiolyse. C'est ainsi qu'un certain nombre de problèmes nous semblent appelés à de proches développements.

Un des plus importants parmi ceux-ci est sans doute le rôle joué par la distribution hétérogène de l'énergie, représentée schématiquement par le paramètre TEL (voir sect. III-C.4). En effet, s'il est apparu dès 1948 (75) que la répartition initiale des ionisations conditionnait une part importante des phénomènes ultérieurs, l'accord quantitatif n'est cependant pas toujours établi entre les mesures expérimentales, les calculs analytiques et l'application des méthodes Monte-Carlo. La figure 16 montre une telle comparaison en ce qui concerne les valeurs de $G_{\bullet OH}$ en fonction du temps, obtenues (*a*) par spectrophotométrie rapide à 280 nm d'après Jonah et al. (275), (*b*) par calculs semi-analytiques utilisant l'action sur le rendement radicalaire de divers solutés bons capteurs de •OH et la transformation de Laplace inverse (119, 273; voir aussi réf. 330), et (*c*) par calculs de simulation mettant en oeuvre la méthode des temps de réactions indépendants d'après Pimblott et LaVerne (273). On voit que l'accord est bon entre les courbes (*b*) et (*c*), mais que la courbe (*a*) donne des résultats différents. Ce même désaccord est retrouvé par d'autres auteurs (voir, par exemple, réfs. 152 et 331–334). Selon LaVerne et Pimblott (119, 273), le rendement en radicaux •OH à 200 ps ne serait d'ailleurs pas 5,9 moléc./100 eV comme rapporté par Jonah et Miller (275), mais plutôt ~4,4–4,6 moléc./100 eV tel qu'obtenu à partir des études avec des capteurs. D'autres expériences seraient nécessaires.

De plus, il semble que, lorsque le TEL augmente, de nouvelles réactions soient susceptibles d'entrer en jeu. C'est ainsi que, comme nous l'avons vu (voir sect. III-C.4), a été invoquée la production d'atomes d'oxygène pouvant réagir avec •OH (99, 178, 194), ou encore l'intervention d'ions de l'eau multichargés (200–202), réactions conduisant toutes deux à l'espèce radicalaire $HO_2^\bullet$. Des calculs préliminaires de simulation Monte-Carlo de la radiolyse de l'eau à haut TEL (203) ont été abordés récemment à ces points de vue.

Même pour les faibles TEL dont les effets ont été largement étudiés, certaines questions demeurent posées. Ainsi, les résultats concernant l'action de capteurs dans les zones hétérogènes indiqueraient que la contribution des réactions suivantes :

[29] $H^\bullet + e^-_{aq} \rightarrow H_2 + OH^-$

[30] $e^-_{aq} + e^-_{aq} \rightarrow H_2 + 2\ OH^-$

[31] $H^\bullet + H^\bullet \rightarrow H_2$

ne soit pas suffisante pour expliquer l'origine du rendement d'hydrogène « moléculaire » égal, on le sait, à G_{H_2} = 0,45 moléc./100 eV (89, 120; voir aussi réf. 35). En fait, il existerait un rendement *non captable* en H_2 de 0,15–0,2 moléc./100 eV (114, 118–120; voir aussi sect. III-B) qui pourrait provenir d'une contribution des molécules d'eau excitées électroniquement, soit directement, soit après recombinaison géminée d'un électron avec son cation parent H_2O^+ (voir, par exemple, réfs. 87, 152 et 335) :

$$H_2O^* \rightarrow H_2 + O$$

$$H_2O^+ + e^- \rightarrow H_2O^* \rightarrow H_2 + O$$

ou encore d'un mécanisme d'attachement électronique dissociatif (120, 320, 336–338), mis en évidence en phase condensée par Rowntree et al. (316) et étudié ensuite par plusieurs auteurs (314, 317), pour des électrons d'énergie comprise dans les deux gammes ~5,5–11 eV et ~18–32 eV :

$$H_2O + e^- \rightarrow H_2O^- \rightarrow H^- + {}^\bullet OH$$

suivi de la réaction

$$H^- + H_2O \rightarrow H_2 + OH^-$$ [29]

Par ailleurs, nous l'avons vu (voir sect. III-C.2), le problème de la radiolyse de l'eau aux grands pH n'est pas complètement résolu, les valeurs des RRM étant souvent, en milieu alcalin, en désaccord apparent, selon les auteurs.

Nous avons vu également que l'influence de la température est en cours d'étude (voir sect. III-C.6). Soulignons ici que des points d'interrogation peuvent demeurer, comme par exemple l'anomalie cinétique de la disparition de e^-_{aq} qui se manifeste par une valeur négative de l'énergie d'activation à partir de 150°C (158, 243). Une telle anomalie devrait se

[29]Peled et Czapski (réf. 100) ont de plus émis l'hypothèse que l'origine du rendement « non captable » en H_2 proviendrait des zones d'hétérogénéité contenant des concentrations initiales élevées en radicaux.

© 1999 CNRC Canada

Fig. 17. Distribution des pertes d'énergie pour des électrons incidents de 1 MeV dans l'eau liquide, d'après les calculs de simulation Monte-Carlo de LaVerne et Pimblott (réf. 104). La perte d'énergie la plus probable est égale à 22–23 eV, alors que la perte d'énergie moyenne est de ~57 eV. Le seuil à ~7,3 eV correspond au seuil d'excitation électronique de l'eau en phase condensée (voir réf. 344). D'après réf. 104.

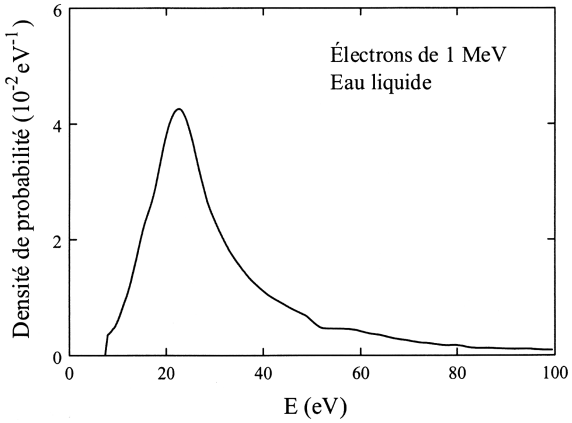

traduire par une modification concomitante du rendement en H_2 (233, 234, 236), ce qui ne paraît pas être observé (158). Le biélectron a été suggéré en tant qu'espèce transitoire intervenant au cours de ce processus, mais son existence n'a pas été établie (243, 255, 311–313). Une confirmation expérimentale de la valeur de la constante de vitesse de la réaction [30] en fonction de la température serait utile.

D'autres données expérimentales et (ou) théoriques auraient, elles aussi, besoin d'être déterminées. Citons un certain nombre d'entre elles.

Les sections efficaces d'interaction des électrons d'énergie inférieure à ~100 eV restent mal connues (152, 273, 280, 320, 333, 339–343). C'est pourtant dans cette zone que se fait une part importante des échanges d'énergie entre l'eau et les électrons incidents, comme on peut le voir figures 17 et 18. Cette dernière figure montre le spectre d'énergie des électrons secondaires, au moment de leur éjection, calculé par simulation Monte-Carlo pour des électrons incidents de 20 keV dans l'eau liquide (152) : une large proportion des électrons éjectés (88 %) a une énergie inférieure à 20 eV. La détermination de ces sections efficaces est indispensable pour assurer en particulier une bonne description des phénomènes par les méthodes de simulation Monte-Carlo. Les seuls résultats expérimentaux actuellement disponibles dans la littérature à ce sujet, pour l'eau en phase condensée, sont ceux de Michaud et Sanche (346; voir aussi réfs. 320, 338 et 343) pour des énergies de l'électron comprises entre 1 et 18 eV.

Un autre problème concerne la caractérisation de la distribution spatiale initiale (à ~10^{-12} s) des espèces créées par l'absorption du rayonnement. Cette distribution constitue, en effet, le point de départ de l'étape de chimie hétérogène au cours de laquelle les espèces qui résultent de la dissociation des molécules d'eau ionisées et (ou) excitées diffusent dans le milieu et réagissent entre elles. Si la position initiale des espèces telles que $^{\bullet}OH$, H_3O^+, $H^{\bullet}$ et H_2 découle directement du déploiement de la trajectoire des particules incidentes dans le milieu, les électrons éjectés lors des ionisations parcourent, quant à eux, une distance au cours de laquelle ils

Fig. 18. Spectre énergétique des électrons secondaires, au moment où ils sont éjectés par des électrons incidents de 20 keV dans l'eau liquide, d'après les calculs de simulation Monte-Carlo de Cobut et al. (réf. 152) : ▽, éjectés par les électrons primaires seulement; ●, éjectés à la fois par les électrons primaires et par toutes les générations d'électrons secondaires successives. Dans ce dernier cas, 64 % des électrons éjectés ont une énergie inférieure à 7,3 eV (seuil d'excitation électronique de l'eau en phase condensée; voir réf. 344), 70 % ont une énergie inférieure à ~8,8 eV (potentiel d'ionisation de l'eau liquide; voir réf. 345) et 88 % ont une énergie inférieure à 20 eV. Ces proportions demeurent approximativement les mêmes lorsque l'énergie des électrons primaires varie entre 5 et 150 keV. D'après réf. 152.

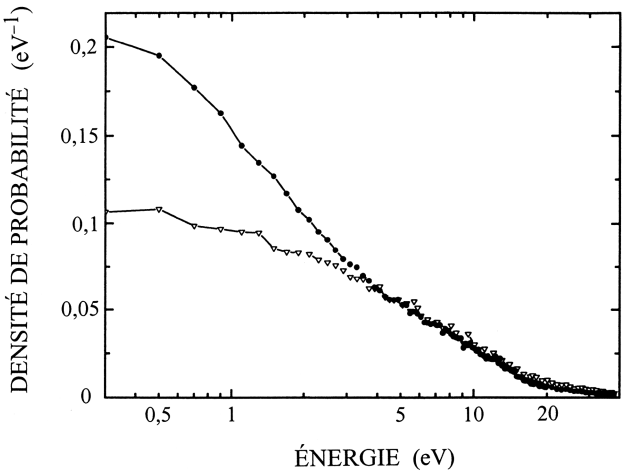

perdent progressivement leur énergie cinétique pour finalement se thermaliser, se localiser et s'hydrater. La distance radiale qui sépare les positions initiale et finale de l'électron est appelée « distance de thermalisation » (r_{th}), car on considère généralement que les électrons se localisent très rapidement à partir du moment où leur énergie cinétique devient comparable à l'énergie thermique. La connaissance de r_{th} conditionne ainsi grandement la distribution spatiale initiale de e^-_{aq} (347).

De nombreuses études ont porté sur la détermination de r_{th} pour l'eau liquide et ont conduit à une large gamme de valeurs, s'étendant de ~15 Å à plus de 100 Å (99, 105, 114, 118, 119, 152, 272, 273, 277, 331, 333, 334, 338, 347–359). Des calculs récents de simulation Monte-Carlo ont indiqué cependant qu'une bonne description du déclin mesuré des rendements en e^-_{aq} pour les trajectoires de rayonnement de faible TEL pouvait être obtenue avec des valeurs de r_{th} se situant entre ~69 Å (273) et ~90–100 Å (152, 333, 347).

À titre d'illustration, la géométrie de trois trajectoires de protons est représentée figure 19 pour trois valeurs de TEL initial différentes (152, 333). Un agrandissement du schéma indique la distribution spatiale, à ~10^{-12} s, des entités primaires.

Il a été montré que, non seulement pour l'eau mais aussi pour un grand nombre d'autres liquides, une corrélation existe entre r_{th} et la mobilité de l'électron thermique (352; voir aussi réf. 360), ce qui semble indiquer que la plus grande partie de la distance de thermalisation s'effectue alors que l'électron est suffisamment ralenti, proche de l'état thermalisé. Une meilleure caractérisation des propriétés des « électrons de subexcitation » (361), pour lesquels l'énergie

© 1999 CNRC Canada

Fig. 19. Géométries de trois trajectoires de protons, dans l'eau liquide, pour trois valeurs de TEL initial différentes (0,3, 8 et 20 keV/μm), d'après les calculs de simulation Monte-Carlo de Frongillo et al. (réf. 333; voir aussi réf. 152). La figure montre les projections, sur le plan *XY*, des positions des entités primaires produites à ~10^{-12} s. L'encadré du haut donne, à cette échelle de temps, un schéma agrandi d'une zone hétérogène (impliquant ici, à titre d'exemple, deux ionisations et une excitation électronique; voir, à ce sujet, réfs. 103, 280 et 340). r_{th} est la distance de thermalisation de l'électron secondaire éjecté lors d'une ionisation.

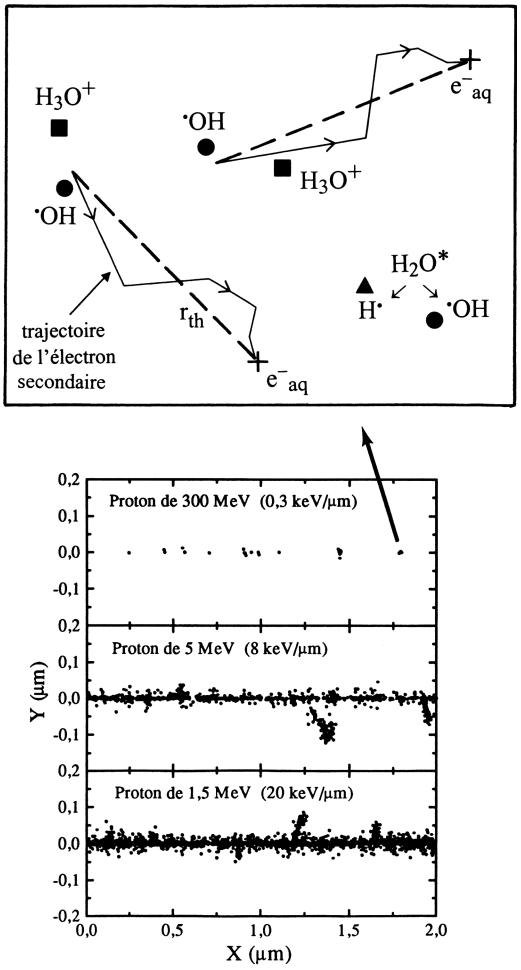

est inférieure au seuil d'excitation électronique de l'eau (~7,3 eV; voir réf. 344), apparaît ainsi souhaitable au niveau de la détermination de leurs paramètres de transport. De tels électrons, comme il a déjà été vu (120, 152, 314, 316, 317, 336–338), peuvent intervenir, en compétition avec la thermalisation, dans des réactions de capture résonante dissociative.

Les avancées récentes réalisées dans la production d'impulsions laser ultracourtes et dans les calculs de simulation utilisant les méthodes de dynamique moléculaire et (ou) Monte-Carlo associées aux intégrales de chemin de Feynman, ont permis de mieux cerner le mécanisme séquentiel et la dynamique du processus d'hydratation de l'électron (voir, par exemple, réf. 72; voir aussi réfs. 362 et 363). On a pu ainsi déterminer les cinétiques d'apparition (temps caractéristique : T_1 ~ 110–180 fs) et de relaxation (temps caractéristique : T_2 ~ 240–620 fs) du précurseur (e^-_{ir}) de e^-_{aq} (72), précurseur absorbant dans l'infrarouge. Si la plupart des auteurs privilégient un modèle d'hydratation, simple ou élaboré, mettant essentiellement en jeu les deux états électroniques e^-_{ir} et e^-_{aq}, la nature et le(s) mode(s) de déclin de e^-_{ir} restent l'objet de controverses (72, 362, 363). Il a aussi été suggéré que e^-_{ir} pourrait réagir avec H_2O selon la réaction (364, 365) :

$$e^-_{ir} + H_2O \rightarrow H^\bullet + OH^-$$

en compétition avec l'hydratation.

Nous venons d'attirer l'attention sur certains points qui semblent actuellement mériter de plus amples développements. Malgré le manque relatif de données, un panorama de la radiolyse de l'eau pure ou contenant divers solutés peut néanmoins être obtenu dans la plupart des cas, à condition de développer une analyse critique des paramètres intervenant. Cette analyse est facilitée par le fait que les valeurs des RRM sont bien établies pour les milieux neutre et acide, ainsi que nous l'avons vu précédemment (voir équations [4] et [19]).

B. Applications

La plupart des applications des radiations ionisantes sortent du cadre de cet article, car elles n'impliquent pas nécessairement la radiolyse de l'eau. Nous allons cependant en citer quelques-unes (impliquant ou non cette radiolyse), afin de souligner l'importance pratique du développement des travaux généraux portant sur l'effet chimique des radiations. On trouvera, dans un article récent de Draganić (366), un plus large aperçu sur ces problèmes.

Par exemple, 80 % des réacteurs nucléaires générateurs d'électricité sont refroidis à l'eau. Il faut donc connaître le comportement de celle-ci lorsqu'elle est soumise, à environ 300°C, à de grands flux de rayonnements. Des travaux sont en cours (voir, par exemple, réfs. 158, 222, 227, 229, 235 et 367).

Par ailleurs, les rayonnements ionisants, et tout particulièrement les électrons accélérés, sont utilisés comme méthode complémentaire des traitements classiques de recyclage des eaux usées et des boues résiduaires (voir, par exemple, réfs. 90 et 368). Les produits chlorés sont dégradés, les microorganismes tués et la germination des graines inhibée.

Le stockage des déchets radioactifs pose évidemment de très gros problèmes concernant d'une part, l'action des rayonnements sur les containers et le milieu environnant et d'autre part, la nature des dégagements gazeux associés (voir, par exemple, réfs. 369–371). Une des difficultés provient du fait qu'il n'est pas possible expérimentalement de comparer les résultats pour les mêmes débits de dose, étant donnée la durée importante des temps de stockage.

Un autre problème, lui aussi difficile à résoudre, consiste à évaluer les doses auxquelles sont soumis les astronautes. Ils reçoivent des électrons, des protons et des ions lourds de grande énergie et de diverses origines. Les mécanismes alors mis en jeu sont différents de ceux se produisant sur Terre (voir, par exemple, réfs. 198 et 372–375).

Disons pour terminer que les rayonnements sont utilisés pour la conservation des aliments (viandes en morceaux, graines, etc.) (voir, par exemple, réfs. 90 et 376) et la stérili-

© 1999 CNRC Canada

Fig. 20. Données thermodynamiques correspondant à la réduction de l'oxygène, par captures successives d'un électron, pour les systèmes O_2–H_2O et H_2O–H_2 (réfs. 51, 122, 207, 208 et 382–384). Les potentiels standard de réduction sont exprimés en volts, à pH 7 et 25°C, par rapport au potentiel normal d'électrode à hydrogène.

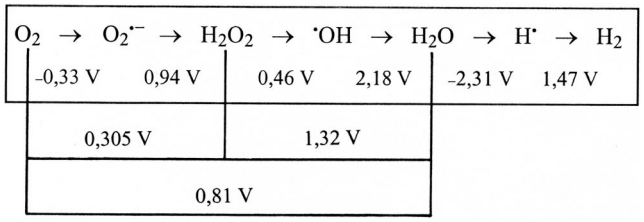

sation du matériel médical et des médicaments (voir, par exemple, réfs. 90 et 377).

Enfin, l'emploi des rayonnements se fait au stade industriel pour produire, dans de très bonnes conditions, des réactions de polymérisation ou de greffe (voir, par exemple, réfs. 90 et 378–381).

C. Retombées

Nous allons évoquer rapidement quelles sont actuellement les principales retombées de la radiolyse de l'eau.

1. Apport à l'étude des interactions matière – rayonnements ionisants

La radiolyse fournit des données concernant une interaction particulière entre l'énergie et la matière et complète ainsi celles apportées par la photolyse, la sonolyse, la thermolyse, l'électrolyse et même la voltolyse, qui constituent une partie importante de la chimie-physique tant théorique qu'expérimentale. Il est donc utile de connaître les mécanismes réactionnels, la nature des intermédiaires, les rendements des transferts d'énergie, etc., intervenant lors de la radiolyse de l'eau afin de les comparer à ceux gouvernés par d'autres échanges d'énergie impliquant eux aussi la décomposition de l'eau. Le développement de cette comparaison pourrait se révéler fructueux.

2. Chimie radicalaire

On sait que, dès 1914, Debierne (12) avait suggéré que le rayonnement décompose l'eau en atomes $H^\bullet$ et en radicaux $^\bullet OH$, hypothèse qui fut reprise plus tard (19–21; voir aussi sect. II-A). C'est ainsi qu'il a été admis que l'irradiation de l'eau liquide formait des intermédiaires radicalaires. Ces espèces furent ensuite identifiées et caractérisées, cinétiquement et thermodynamiquement.

La radiolyse est actuellement la méthode la plus utilisée pour l'étude des radicaux libres dérivés de l'oxygène. Ces différentes espèces sont les intermédiaires de la séquence conduisant de l'oxygène à l'hydrogène par captures successives d'un électron (fig. 20) (51, 122, 207, 208, 382–384; voir sect. III-C.5-c) et peuvent être formées par radiolyse de l'eau aérée ou désaérée.

En milieu acide, $O_2^{\bullet-}$ est remplacé par $HO_2^\bullet$, son acide conjugué, tandis que, en solution alcaline, $^\bullet OH$ et $H^\bullet$ sont transformés en leur base conjuguée, respectivement $O^{\bullet-}$ et e^-_{aq}. Les valeurs de pK_a correspondantes sont (82, 86, 122, 207) :

Fig. 21. Réduction des structures quinoniques. L'anion radicalaire semiquinone ($Q^{\bullet-}$) est obtenu à partir de la *p*-benzoquinone (Q) par addition d'un électron. La fonction quinonique peut interférer avec l'oxygène (O_2) et l'anion superoxyde ($O_2^{\bullet-}$) en donnant des réactions redox dont les caractéristiques sont fonctions de l'acidité du milieu et de la nature des substituants. D'après réf. 388.

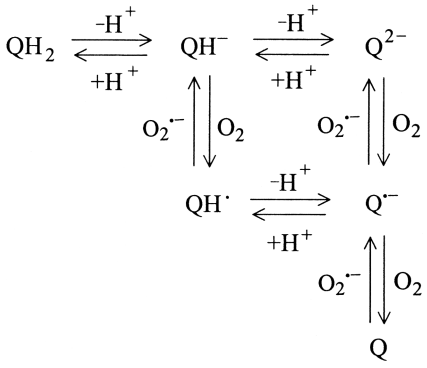

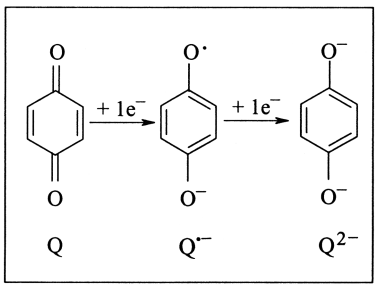

$$HO_2^\bullet \rightleftarrows O_2^{\bullet-} + H^+ \qquad pK_a = 4{,}8$$

$$H_2O_2 \rightleftarrows HO_2^- + H^+ \qquad pK_a = 11{,}7$$

$$^\bullet OH \rightleftarrows O^{\bullet-} + H^+ \qquad pK_a = 11{,}9$$

$$H^\bullet \rightleftarrows e^-_{aq} + H^+ \qquad pK_a = 9{,}6$$

On voit figure 20 que $O_2^{\bullet-}$ peut être oxydant ou réducteur, tandis que $^\bullet OH$ est très oxydant, son potentiel redox étant élevé.

Ces radicaux peuvent donner lieu, à leur tour, à des radicaux de 2ème génération (voir, par exemple, réfs. 51, 90 et 385–387). Ainsi, $^\bullet OH$ peut facilement arracher un atome d'hydrogène à une molécule organique RH et conduire au radical $R^\bullet$:

$$^\bullet OH + RH \rightarrow R^\bullet + H_2O$$

tandis que $O_2^{\bullet-}$ peut, entre autres, réduire les formes quinoniques et donner un radical semiquinone (fig. 21) (51, 387–390). Les structures quinoniques se rencontrent fréquemment dans des molécules présentant un intérêt biologique, telles que la vitamine K, certains transporteurs biologiques d'électrons, divers médicaments, etc. (389).

De nombreux autres radicaux peuvent également être obtenus par radiolyse pulsée ou continue. Parmi ceux les plus fréquemment rencontrés, citons $N_3^\bullet$ (radical azide), $Cl_2^{\bullet-}$, $Br_2^{\bullet-}$, $SO_4^{\bullet-}$, $(SCN)_2^{\bullet-}$, $RS^\bullet$ (radical thiyle), $COO^{\bullet-}$, $NO_2^\bullet$, $NH_2^\bullet$, etc.

© 1999 CNRC Canada

3. Chimie bioradicalaire

À la suite des travaux de McCord et Fridovich (391), il est apparu que, au cours de diverses oxydations biologiques, des radicaux libres, principalement $O_2^{\bullet-}$, pouvaient être formés in vivo. Ces espèces sont capables de conduire à d'autres radicaux qui, à leur tour, peuvent jouer un rôle soit bénéfique, soit délétère (voir, par exemple, réfs. 51, 122, 204, 387 et 392–394). Une enzyme, la *superoxyde dismutase* (391), est dédiée à la régulation de l'ion-radical $O_2^{\bullet-}$ dont la dismutation est très lente ($k < 0{,}3\ M^{-1}\ s^{-1}$) quand elle n'est pas catalysée (82).

C'est ainsi qu'il est nécessaire de tenir compte des mécanismes radicalaires intervenant, par exemple, au niveau mitochondrial (voir, par exemple, réf. 395) ou lors de l'ischémie-reperfusion, de la phagocytose, de l'inflammation (voir, par exemple, réfs. 392–394), du métabolisme de médicaments (389), ou encore lors de divers processus biologiques complexes tels que la mort cellulaire programmée (ou apoptose) (voir, par exemple, réf. 396). De plus, il faut souligner que l'organisme humain contient, pondéralement, ~70 % d'eau et que la radiolyse de l'eau joue probablement un rôle important en radiobiologie, en introduisant une part d'effet indirect et (ou) quasi direct (voir, par exemple, réfs. 134–137).

L'étude in vitro de la radiolyse de solutions aqueuses diluées apporte, à certains points de vue, des éléments originaux permettant de mieux comprendre la nature et l'évolution de tels processus.

Remerciements

J.-P. J.-G. a bénéficié du Programme d'échanges franco-canadien INSERM-CRM en recherche médicale, qui lui a permis d'effectuer un stage au Laboratoire de Chimie-Physique de l'Université Paris V. Il est reconnaissant des facilités qui lui ont ainsi été accordées. Il remercie également le Conseil de Recherches Médicales (CRM) du Canada pour son support financier (Subvention n° MT-14617).

Bibliographie

1. P. Curie et M^me S. Curie. C. R. Acad. Sci. Paris, **127**, 175 (1898). (On remarquera que « S » est mis pour Sklodowska).
2. P. Curie, M^me P. Curie et G. Bémont. C. R. Acad. Sci. Paris, **127**, 1215 (1898). Voir aussi : E. Demarçay. C. R. Acad. Sci. Paris, **127**, 1218 (1898).
3. F. Giesel. Ber. Dtsch. Chem. Ges. (Berlin), **35**, 3608 (1902); **36**, 342 (1903).
4. M^me P. Curie. Radioactivité. Hermann, Paris. 1935. p. 347.
5. W. Ramsay et F. Soddy. Proc. R. Soc. London, **72**, 204 (1903).
6. A. Debierne. C. R. Acad. Sci. Paris, **141**, 383 (1905).
7. E. Rutherford et T. Royds. Philos. Mag. **17**, 281 (1909).
8. W. Ramsay. J. Chem. Soc. Trans. **91**, 931 (1907).
9. A.T. Cameron et W. Ramsay. J. Chem. Soc. Trans. **91**, 1593 (1907); **93**, 966 (1908); **93**, 992 (1908).
10. F.L. Usher. Jahrb. Radioakt. Elektron. **8**, 323 (1911).
11. A. Debierne. Bull. Soc. Chim. Fr. **3**, 1 (1908); C. R. Acad. Sci. Paris, **148**, 703 (1909); Radium (Paris), **6**, 65 (1909).
12. A. Debierne. Ann. Phys. **2**, 97 (1914).
13. M. Kernbaum. C. R. Acad. Sci. Paris, **148**, 705 (1909); **149**, 116 (1909); Radium (Paris), **6**, 225 (1909); **7**, 242 (1910).
14. G. Friedlander, J.W. Kennedy, E.S. Macias et J.M. Miller. Nuclear and radiochemistry. 3ème éd. Wiley, New York. 1981; J.-P. Adloff et R. Guillaumont. Fundamentals of radiochemistry. CRC Press, Boca Raton, Fla. 1993.
15. O. Risse. Z. Phys. Chem. Abt. A : **140**, 133 (1929).
16. H. Fricke et E.R. Brownscombe. Phys. Rev. **44**, 240 (1933).
17. C. Runge et G. Bodländer. Drude's Ann. (Ann. Phys. (Leipzig)), **2**, 1 (1903).
18. W. Duane et O. Scheuer. Radium (Paris), **10**, 33 (1913).
19. O. Risse. Strahlentherapie, **34**, 578 (1929).
20. S. Gordon. *Dans* Early developments in radiation chemistry. *Édité par* J. Kroh. The Royal Society of Chemistry, Cambridge. 1989. p. 163; A.O. Allen. *Dans* Actions chimiques et biologiques des radiations. 5ème Sér. *Édité par* M. Haïssinsky. Masson, Paris. 1961. p. 9.
21. J. Weiss. Nature (London), **153**, 748 (1944).
22. H. Fricke. J. Chem. Phys. **2**, 349 (1934); **2**, 556 (1934).
23. P. Bonét-Maury et M. Frilley. C. R. Acad. Sci. Paris, **218**, 400 (1944).
24. P. Günther et L. Holzapfel. Z. Phys. Chem. Abt. B : **44**, 374 (1939).
25. E.R. Johnson et A.O. Allen. J. Am. Chem. Soc. **74**, 4147 (1952).
26. Z.-M. Bacq et P. Alexander. Principes de radiobiologie. Masson, Paris. 1955; M. Tubiana et A. Wambersie. *Dans* Actions chimiques et biologiques des radiations. 12ème Sér. *Édité par* M. Haïssinsky. Masson, Paris. 1968. p. 255. Voir aussi : C. Ferradini et J.-P. Jay-Gerin. Cah. Radiobiol. **2**, 17 (1995).
27. S.C. Lind. The chemical effects of alpha particles and electrons. The Chemical Catalog Company, New York. 1921.
28. C.J. Hochanadel et J.A. Ghormley. J. Chem. Phys. **21**, 880 (1953).
29. R.H. Schuler et A.O. Allen. J. Chem. Phys. **24**, 56 (1956); J.V. Davies, D. Greene, J.P. Keene, J. Law et J.B. Massey. Phys. Med. Biol. **8**, 97 (1963).
30. R. Bensasson, A. Bernas, M. Bodard, L. Bouby, M. Cottin, M. Duflo, F. Kieffer, A. Koulkès, N. Leray, J. Pucheault et C. Vermeil. *Dans* Tables de constantes et données numériques. Vol. 13. *Édité par* M. Haïssinsky et M. Magat. Pergamon, Oxford. 1963.
31. H. Fricke et S. Morse. Am. J. Roentgenol. Radium Ther. **18**, 426 (1927); **18**, 430 (1927); Philos. Mag. **7**, 129 (1929); H. Fricke et E.J. Hart. J. Chem. Phys. **3**, 60 (1935).
32. N.A. Shishacow. Philos. Mag. **14**, 198 (1932); F.H. Krenz. Can. J. Res. Sect. B : **26**, 647 (1948); N. Miller. Nature (London), **171**, 688 (1953).
33. H. Fricke et E.J. Hart. *Dans* Radiation dosimetry. 2ème éd. Vol. II. *Édité par* F.H. Attix et W.C. Roesch. Academic Press, New York. 1966. p. 167.
34. H. Fricke et B.W. Petersen. Am. J. Roentgenol. Radium Ther. **17**, 611 (1927); E.J. Hart. J. Chem. Educ. **34**, 586 (1957).
35. I.G. Draganić et Z.D. Draganić. The radiation chemistry of water. Academic Press, New York. 1971.
36. G.L. Clark et W.S. Coe. J. Chem. Phys. **5**, 97 (1937).
37. T.J. Hardwick. Can. J. Chem. **30**, 23 (1952); T.J. Sworski. J. Chem. Phys. **21**, 375 (1953); Radiat. Res. **4**, 483 (1956).
38. G.R.A. Johnson et J. Weiss. Proc. R. Soc. London, Ser. A : **240**, 189 (1957).
39. H. Fricke. Cold Spring Harbor Symp. Quant. Biol. **2**, 241 (1934); H. Fricke et E.J. Hart. J. Chem. Phys. **2**, 824 (1934); H. Fricke, E.J. Hart et H.P. Smith. J. Chem. Phys. **6**, 229 (1938).
40. E.J. Hart. J. Am. Chem. Soc. **73**, 68 (1951); J. Phys. Chem. **56**, 594 (1952); Radiat. Res. **1**, 53 (1954); J. Am. Chem. Soc. **76**, 4198 (1954); **76**, 4312 (1954); Annu. Rev. Phys. Chem. **5**, 139 (1954); J. Chem. Educ. **36**, 266 (1959).
41. J.W.T. Spinks et R.J. Woods. An introduction to radiation chemistry. 3ème éd. Wiley, New York. 1990.

© 1999 CNRC Canada

42. E.J. Hart et M.S. Matheson. Discuss. Faraday Soc. **12**, 169 (1952).
43. R.W. Hummel, G.R. Freeman, A.B. Van Cleave et J.W.T. Spinks. Science (Washington, D.C.), **119**, 159 (1954). Voir aussi : J.W.T. Spinks. *Dans* Early developments in radiation chemistry. *Édité par* J. Kroh. The Royal Society of Chemistry, Cambridge. 1989. p. 409.
44. J.P. Keene. Nature (London), **188**, 843 (1960); J. Sci. Instrum. **41**, 493 (1964).
45. E.J. Hart et J.W. Boag. J. Am. Chem. Soc. **84**, 4090 (1962); J.W. Boag. *Dans* Actions chimiques et biologiques des radiations. 6ème Sér. *Édité par* M. Haïssinsky. Masson, Paris. 1963. p. 4.
46. R.L. McCarthy et A. MacLachlan. Trans. Faraday Soc. **56**, 1187 (1960).
47. M.S. Matheson et L.M. Dorfman. J. Chem. Phys. **32**, 1870 (1960); L.M. Dorfman, I.A. Taub et R.E. Bühler. J. Chem. Phys. **36**, 3051 (1962); L.M. Dorfman. Science (Washington, D.C.), **141**, 493 (1963).
48. M. Ebert, J.P. Keene, A.J. Swallow et J.H. Baxendale (*Éditeurs*). Pulse radiolysis. Academic Press, London. 1965; L.M. Dorfman et M.S. Matheson. *Dans* Progress in reaction kinetics. Vol. 3. *Édité par* G. Porter. Pergamon Press, Oxford. 1965. p. 237; A.K. Pikaev. Pulse radiolysis of water and aqueous solutions. Indiana University Press, Bloomington, Ind. 1967.
49. J.W. Hunt et J.K. Thomas. Radiat. Res. **32**, 149 (1967); J. Chem. Phys. **46**, 2954 (1967).
50. J.H. Baxendale et F. Busi (*Éditeurs*). The study of fast processes and transient species by electron pulse radiolysis. D. Reidel, Dordrecht. 1982; L.M. Dorfman et M.C. Sauer, Jr. *Dans* Investigation of rates and mechanisms of reactions. *Édité par* C.F. Bernasconi. Wiley, New York. 1986. p. 493; Y. Tabata (*Éditeur*). Pulse radiolysis. CRC Press, Boca Raton, Fla. 1991.
51. R.V. Bensasson, E.J. Land et T.G. Truscott. Excited states and free radicals in biology and medicine. Contributions from flash photolysis and pulse radiolysis. Oxford University Press, Oxford. 1993.
52. M.J. Bronskill et J.W. Hunt. J. Phys. Chem. **72**, 3762 (1968); M.J. Bronskill, R.K. Wolff et J.W. Hunt. J. Phys. Chem. **73**, 1175 (1969); M.J. Bronskill, W.B. Taylor, R.K. Wolff et J.W. Hunt. Rev. Sci. Instrum. **41**, 333 (1970).
53. C.D. Jonah. Rev. Sci. Instrum. **46**, 62 (1975).
54. H. Kobayashi et Y. Tabata. Nucl. Instrum. Meth. **B10/11**, 1004 (1985); *Dans* Pulse radiolysis. *Édité par* Y. Tabata. CRC Press, Boca Raton, Fla. 1991. p. 11; Y. Tabata, H. Kobayashi, M. Washio, S. Tagawa et Y. Yoshida. Radiat. Phys. Chem. **26**, 473 (1985).
55. W.M. Dale. Biochem. J. **34**, 1367 (1940); **36**, 80 (1942); J. Physiol. **102**, 50 (1943); Br. J. Radiol. **16**, 171 (1943); W.M. Dale, W.J. Meredith et M.C.K. Tweedie. Nature (London), **151**, 280 (1943).
56. C.B. Allsopp. Trans. Faraday Soc. **40**, 79 (1944).
57. G. Czapski et A.O. Allen. J. Phys. Chem. **66**, 262 (1962).
58. E. Hayon et A.O. Allen. J. Phys. Chem. **65**, 2181 (1961); J. Jortner et J. Rabani. J. Am. Chem. Soc. **83**, 4868 (1961); J. Phys. Chem. **66**, 2078 (1962); **66**, 2081 (1962).
59. J. Weiss. Nature (London), **165**, 728 (1950); T. Rigg, G. Stein et J. Weiss. Proc. R. Soc. London, Ser. A : **211**, 375 (1952).
60. N.F. Barr et A.O. Allen. J. Phys. Chem. **63**, 928 (1959).
61. G. Czapski et H.A. Schwarz. J. Phys. Chem. **66**, 471 (1962).
62. E. Collinson, F.S. Dainton, D.R. Smith et S. Tazuké. Proc. Chem. Soc. London, 140 (1962).
63. G. Stein. Discuss. Faraday Soc. **12**, 227 (1952).
64. R.L. Platzman. *Dans* Physical and chemical aspects of basic mechanisms in radiobiology. Publication 305. *Édité par* J.L. Magee, M.D. Kamen et R.L. Platzman. National Research Council, Washington, D.C. 1953. p. 22.
65. J. Weiss. Annu. Rev. Phys. Chem. **4**, 143 (1953); Nature (London), **186**, 751 (1960).
66. C.W. Gilbert, J.P. Keene, P.F. Browne et T.J. Davy. British Empire Cancer Campaign, 38th Annu. Rep. Part II. 1960. p. 498; J.P. Keene. Discuss. Faraday Soc. **36**, 304 (1964).
67. J.P. Keene. Br. J. Radiol. **35**, 650 (1962); Nature (London), **197**, 47 (1963).
68. M.S. Matheson. Annu. Rev. Phys. Chem. **13**, 77 (1962).
69. J.W. Boag. The Silver Jubilee book of the Gray laboratory. Leveridge, London. 1982. p. 112; *Dans* Early developments in radiation chemistry. *Édité par* J. Kroh. The Royal Society of Chemistry, Cambridge. 1989. p. 7; E.J. Hart. The Silver Jubilee book of the Gray laboratory. Leveridge, London. 1982. p. 137.
70. J.W. Boag et E.J. Hart. Nature (London), **197**, 45 (1963).
71. J.L. Magee. Can. J. Phys. **68**, 853 (1990).
72. A. Bernas, C. Ferradini et J.-P. Jay-Gerin. Can. J. Chem. **74**, 1 (1996).
73. J.T. Allan et G. Scholes. Nature (London), **187**, 218 (1960); J. Rabani. J. Am. Chem. Soc. **84**, 868 (1962); J. Rabani et G. Stein. J. Chem. Phys. **37**, 1865 (1962).
74. A.O. Allen. Radiat. Res. **1**, 85 (1954); M. Cottin et M. Lefort. J. Chim. Phys. **52**, 545 (1955).
75. A.O. Allen. J. Phys. Colloid Chem. **52**, 479 (1948). Voir aussi : A.O. Allen. *Dans* Early developments in radiation chemistry. *Édité par* J. Kroh. The Royal Society of Chemistry, Cambridge. 1989. p. 1.
76. G.R. Freeman. *Dans* The study of fast processes and transient species by electron pulse radiolysis. *Édité par* J.H. Baxendale et F. Busi. D. Reidel, Dordrecht. 1982. p. 19.
77. J. Pucheault et C. Ferradini. Proceedings of the second United Nations international conference on the peaceful uses of atomic energy. Genève, septembre 1958. Vol. 29. P/1232. Pergamon, London. 1959. p. 24.
78. F.S. Dainton. J. Am. Chem. Soc. **78**, 1278 (1956).
79. J. Pucheault et C. Ferradini. J. Chim. Phys. **54**, 659 (1957).
80. J. Kroh (*Éditeur*). Early developments in radiation chemistry. The Royal Society of Chemistry, Cambridge. 1989.
81. M. Tubiana, J. Dutreix et A. Wambersie. Introduction to radiobiology. Taylor & Francis, London. 1990. Voir aussi : M.R. Raju. Heavy particle radiotherapy. Academic Press, New York. 1980; T.W. Griffin, A. Wambersie, G. Laramore et J. Castro. Int. J. Radiat. Oncol. Biol. Phys. **14**, S83 (1988); P. Chauvel. J. Chim. Phys. **88**, 1125 (1991); J.R. Castro. Radiat. Environ. Biophys. **34**, 45 (1995); E.A. Blakely et A. Kronenberg. Radiat. Res. **150**, S126 (1998) et références citées.
82. B.H.J. Bielski et A.O. Allen. J. Phys. Chem. **81**, 1048 (1977); A.O. Allen et B.H.J. Bielski. *Dans* Superoxide dismutase. Vol. I. *Édité par* L.W. Oberley. CRC Press, Boca Raton, Fla. 1982. p. 125; B.H.J. Bielski, D.E. Cabelli, R.L. Arudi et A.B. Ross. J. Phys. Chem. Ref. Data, **14**, 1041 (1985) et références citées.
83. E.J. Hart et M. Anbar. The hydrated electron. Wiley, New York. 1970.
84. C. Ferradini et J.-P. Jay-Gerin. Radiat. Phys. Chem. **48**, 473 (1996) et références citées.
85. W.G. Burns et W.R. Marsh. J. Chem. Soc. Faraday Trans. 1, **77**, 197 (1981).
86. G.V. Buxton, C.L. Greenstock, W.P. Helman et A.B. Ross. J. Phys. Chem. Ref. Data, **17**, 513 (1988); Site sur Internet : http://www.rcdc.nd.edu.

© 1999 CNRC Canada

87. N.V. Klassen. J. Chim. Phys. **88**, 747 (1991).
88. H.A. Schwarz. J. Phys. Chem. **96**, 8937 (1992).
89. A.J. Elliot, M.P. Chenier et D.C. Ouellette. J. Chem. Soc. Faraday Trans. **89**, 1193 (1993).
90. R.J. Woods et A.K. Pikaev. Applied radiation chemistry : radiation processing. Wiley, New York. 1994.
91. H.A. Schwarz. J. Am. Chem. Soc. **77**, 4960 (1955).
92. A.O. Allen. The radiation chemistry of water and aqueous solutions. D. Van Nostrand Co., Princeton, N.J. 1961.
93. T.J. Sworski. *Dans* Solvated electron. Adv. Chem. Ser. Vol. 50. *Édité par* E.J. Hart. American Chemical Society, Washington, D.C. 1965. p. 263.
94. H.A. Schwarz, J.M. Caffrey, Jr. et G. Scholes. J. Am. Chem. Soc. **81**, 1801 (1959).
95. D.A. Armstrong, E. Collinson et F.S. Dainton. Trans. Faraday Soc. **55**, 1375 (1959); F.S. Dainton. Radiat. Res. Suppl. **1**, 1 (1959).
96. C. Ferradini. Adv. Inorg. Chem. Radiochem. **3**, 171 (1961).
97. A. Kuppermann. *Dans* Actions chimiques et biologiques des radiations. 5ème Sér. *Édité par* M. Haïssinsky. Masson, Paris. 1961. p. 85; Nucleonics, **19**, 38 (1961).
98. A. Mozumder et J.L. Magee. Radiat. Res. **28**, 215 (1966).
99. A. Kuppermann. *Dans* Radiation research 1966. Proc. 3rd Int. Congr. Radiat. Res. Cortina d'Ampezzo, Italy. 26 juin – 2 juillet 1966. *Édité par* G. Silini. North-Holland, Amsterdam. 1967. p. 212.
100. E. Peled et G. Czapski. J. Phys. Chem. **74**, 2903 (1970).
101. Chr. Møller. Ann. Phys. **14**, 531 (1932); R.D. Evans. The atomic nucleus. McGraw–Hill, New York. 1955. p. 567; J. Pucheault. Actions chimiques des rayonnements sur la matière. Cours de Génie chimique des industries atomiques, I.N.S.T.N., Saclay. 1963–1964. p. 8.
102. J.L. Magee, K. Funabashi et A. Mozumder. Proc. 6th Jpn. Conf. Radioisotopes, 1964. Nippon Genshiryoku Sangyo Kaigi, Tokyo. 1965. p. 755; A. Mozumder et J.L. Magee. Radiat. Res. **28**, 203 (1966); J. Chem. Phys. **45**, 3332 (1966).
103. S.M. Pimblott, J.A. LaVerne, A. Mozumder et N.J.B. Green. J. Phys. Chem. **94**, 488 (1990).
104. J.A. LaVerne et S.M. Pimblott. Radiat. Res. **141**, 208 (1995); S.M. Pimblott. Radiat. Res. **147**, 511 (1997).
105. A.H. Samuel et J.L. Magee. J. Chem. Phys. **21**, 1080 (1953). Voir aussi : J.L. Magee. *Dans* Physical and chemical aspects of basic mechanisms in radiobiology. Publication 305. *Édité par* J.L. Magee, M.D. Kamen et R.L. Platzman. National Research Council, Washington, D.C. 1953. p. 51; Annu. Rev. Nucl. Sci. **3**, 171 (1953).
106. G. Jaffé. Radium (Paris), **10**, 126 (1913); Ann. Phys. **42**, 303 (1913); Phys. Z. **30**, 849 (1929).
107. D.E. Lea. Actions of radiations on living cells. 2ème éd. Cambridge University Press, London. 1955.
108. H. Fricke. Ann. N.Y. Acad. Sci. **59**, 567 (1955).
109. J.L. Magee. J. Chim. Phys. **52**, 528 (1955).
110. A.K. Ganguly et J.L. Magee. J. Chem. Phys. **25**, 129 (1956).
111. D.A. Flanders et H. Fricke. J. Chem. Phys. **28**, 1126 (1958).
112. H. Fricke et D.L. Phillips. J. Chem. Phys. **32**, 1183 (1960).
113. A. Kuppermann et G.G. Belford. J. Chem. Phys. **36**, 1412 (1962); **36**, 1427 (1962).
114. H.A. Schwarz. J. Phys. Chem. **73**, 1928 (1969).
115. J.W. Falconer, K.C. Kurien, F.W. Mellows et L.M. Theard (*Éditeurs*). Summary of Proc. 4th Informal Conf. Radiat. Chem. Water. University of Notre Dame, Notre Dame, Ind. 23–25 mars 1961. Sect. 3. p. 34.
116. R.G. Sowden. J. Am. Chem. Soc. **79**, 1263 (1957); Trans. Faraday Soc. **55**, 2084 (1959).
117. H.A. Mahlman. J. Chem. Phys. **32**, 601 (1960).
118. C.N. Trumbore, D.R. Short, J.E. Fanning, Jr. et J.H. Olson. J. Phys. Chem. **82**, 2762 (1978).
119. J.A. LaVerne et S.M. Pimblott. J. Phys. Chem. **95**, 3196 (1991); S.M. Pimblott et J.A. LaVerne. Radiat. Prot. Dosim. **52**, 183 (1994).
120. V. Cobut, J.-P. Jay-Gerin, Y. Frongillo et J.P. Patau. Radiat. Phys. Chem. **47**, 247 (1996).
121. R. Latarjet, T. Alper, J.A.V. Butler, P. Demerseman, P. Douzou, J. Durup, M. Durup, M. Ebert, L.H. Gray, V.J. Horgan, A. Howard, H. Marcovich, D. Maxwell, S. Okada, C. Paquot, J.St.L. Philpot, B.W. Porter, N. Rebeyrotte, D.B. Roodyn, F.H. Sobels, C. Vermeil et J. Weiss. Les peroxydes organiques en radiobiologie. Colloque sur les peroxydes organiques formés par les radiations et leur rôle en radiobiologie, Paris, 9–10 janvier 1957. Actions chimiques et biologiques des radiations. 4ème Sér. *Édité par* M. Haïssinsky. Masson, Paris. 1958; R.N. Feinstein (*Éditeur*). Implications of organic peroxides in radiobiology. Radiat. Res. Suppl. **3**, 1 (1963). Voir aussi : Z.B. Alfassi (*Éditeur*). Peroxyl radicals. Wiley, Chichester. 1997.
122. C. Ferradini et J. Pucheault. Biologie de l'action des rayonnements ionisants. Masson, Paris. 1983.
123. J.C. Muller et C. Ferradini. Radiochem. Radioanal. Lett. **5**, 171 (1970).
124. C. Vermeil. Int. J. Radiat. Biol. **3**, 307 (1961).
125. H.A. Mahlman. J. Phys. Chem. **67**, 1466 (1963).
126. M. Daniels et E.E. Wigg. J. Phys. Chem. **73**, 3703 (1969); M. Daniels. J. Phys. Chem. **73**, 3710 (1969); M. Faraggi, D. Zehavi et M. Anbar. Trans. Faraday Soc. **67**, 701 (1971).
127. M. Cottin. J. Chim. Phys. **53**, 903 (1956); D. Katakis et A.O. Allen. J. Phys. Chem. **68**, 3107 (1964); J. Konstantatos et D. Katakis. J. Phys. Chem. **71**, 979 (1967); D. Katakis et J. Konstantatos. J. Phys. Chem. **72**, 2054 (1968); C. Ferradini, J. Pucheault, R. Julien, L. Gilles et B. Lesigne. J. Chim. Phys. **72**, 121 (1975).
128. M. Anbar et J.K. Thomas. J. Phys. Chem. **68**, 3829 (1964); R.J. Woods, B. Lesigne, L. Gilles, C. Ferradini et J. Pucheault. J. Phys. Chem. **79**, 2700 (1975).
129. J. Pucheault, C. Ferradini, R. Julien, A. Deysine, L. Gilles et M. Moreau. J. Phys. Chem. **83**, 330 (1979).
130. A. Hadjadj, R. Julien, J. Pucheault, C. Ferradini et B. Hickel. J. Phys. Chem. **86**, 4630 (1982).
131. J.W. Boyle. Radiat. Res. **17**, 427 (1962); **17**, 450 (1962); F.S. Dainton, A.R. Gibbs et D. Smithies. J. Chem. Soc. A, 33 (1967); R.W. Matthews, H.A. Mahlman et T.J. Sworski. J. Phys. Chem. **76**, 1265 (1972); B. Lesigne, C. Ferradini et J. Pucheault. J. Phys. Chem. **76**, 3676 (1972); **77**, 2156 (1973).
132. D. Smithies et E.J. Hart. J. Am. Chem. Soc. **82**, 4775 (1960).
133. W. Saenger. Principles of nucleic acid structure. Springer-Verlag, New York. 1984.
134. C. von Sonntag. The chemical basis of radiation biology. Taylor & Francis, London. 1987.
135. D. Becker et M.D. Sevilla. Adv. Radiat. Biol. **17**, 121 (1993); M.D. Sevilla et D. Becker. *Dans* Electron spin resonance. Specialist periodical reports. Vol. 14. *Édité par* N.M. Atherton, M.J. Davies et B.C. Gilbert. The Royal Society of Chemistry, Cambridge. 1994. p. 130.
136. S.G. Swarts, M.D. Sevilla, D. Becker, C.J. Tokar et K.T. Wheeler. Radiat. Res. **129**, 333 (1992); S.G. Swarts. *Dans* Radiation research 1895–1995. Proc. 10th Int. Congr. Radiat. Res. Würzburg, 27 août – 1er septembre 1995. Vol. 2. *Édité par* U. Hagen, D. Harder, H. Jung et C. Streffer. 10th ICRR

© 1999 CNRC Canada

Society, Würzburg. 1995. p. 208; Radiat. Res. **147**, 516 (1997); S.G. Swarts, D. Becker, M. Sevilla et K.T. Wheeler. Radiat. Res. **145**, 304 (1996). Voir aussi : B. Boudaiffa, I. Ménard, D.J. Hunting et L. Sanche. Cah. Radiobiol. **6**, 3 (1997) et références citées.

137. M. Faraggi, C. Ferradini et J.-P. Jay-Gerin. New J. Chem. **19**, 1203 (1995) et références citées; J. Chim. Phys. **93**, 78 (1996).
138. C.C. Moser, J.M. Keske, K. Warncke, R.S. Farid et P.L. Dutton. Nature (London), **355**, 796 (1992); J.N. Onuchic, D.N. Beratan, J.R. Winkler et H.B. Gray. Annu. Rev. Biophys. Biomol. Struct. **21**, 349 (1992); M. Faraggi, C. Ferradini, C. Houée-Levin et M.H. Klapper. *Dans* Radiation research 1895–1995. Proc. 10th Int. Congr. Radiat. Res. Würzburg, 27 août – 1er septembre 1995. Vol. 2. *Édité par* U. Hagen, D. Harder, H. Jung et C. Streffer. 10th ICRR Society, Würzburg. 1995. p. 241; C. Capeillère-Blandin. Biochimie, **77**, 516 (1995); H.B. Gray et J.R. Winkler. Annu. Rev. Biochem. **65**, 537 (1996); D.S. Bendall (*Éditeur*). Protein electron transfer. BIOS Scientific, Oxford. 1996; J.-M. Lopez-Castillo, A. Filali-Mouhim, É. Nguyen Van Binh-Otten et J.-P. Jay-Gerin. J. Am. Chem. Soc. **119**, 1978 (1997) et références citées; I. Pecht et O. Farver. *Dans* Photochemistry and radiation chemistry. Complementary methods for the study of electron transfer. Adv. Chem. Ser. Vol. 254. *Édité par* J.F. Wishart et D.G. Nocera. American Chemical Society, Washington, D.C. 1998. p. 65.
139. M.C.R. Symons. Radiat. Phys. Chem. **45**, 837 (1995); Free Radical Biol. Med. **22**, 1271 (1997).
140. C.J. Murphy, M.R. Arkin, Y. Jenkins, N.D. Ghatlia, S.H. Bossmann, N.J. Turro et J.K. Barton. Science (Washington, D.C.), **262**, 1025 (1993); C.J. Murphy, M.R. Arkin, N.D. Ghatlia, S. Bossmann, N.J. Turro et J.K. Barton. Proc. Natl. Acad. Sci. U.S.A. **91**, 5315 (1994); M.R. Arkin, E.D.A. Stemp, R.E. Holmlin, J.K. Barton, A. Hörmann, E.J.C. Olson et P.F. Barbara. Science (Washington, D.C.), **273**, 475 (1996); D.B. Hall, R.E. Holmlin et J.K. Barton. Nature (London), **382**, 731 (1996); J.M. Warman, M.P. de Haas et A. Rupprecht. Chem. Phys. Lett. **249**, 319 (1996); D.N. Beratan, S. Priyadarshy et S.M. Risser. Chem. Biol. **4**, 3 (1997); E.J.C. Olson, D. Hu, A. Hörmann et P.F. Barbara. J. Phys. Chem. B. **101**, 299 (1997); F.D. Lewis, T. Wu, Y. Zhang, R.L. Letsinger, S.R. Greenfield et M.R. Wasielewski. Science (Washington, D.C.), **277**, 673 (1997); R.E. Holmlin, P.J. Dandliker et J.K. Barton. Angew. Chem. Int. Ed. Engl. **36**, 2714 (1997); E.K. Wilson. Chem. Eng. News, **76**, 51 (1998); K. Fukui et K. Tanaka. Angew. Chem. Int. Ed. Engl. **37**, 158 (1998); J. Jortner, M. Bixon, T. Langenbacher et M.E. Michel-Beyerle. Proc. Natl. Acad. Sci. U.S.A. **95**, 12 759 (1998); S.O. Kelley et J.K. Barton. Science (Washington, D.C.), **283**, 375 (1999); M.E. Nuñez, D.B. Hall et J.K. Barton. Chem. Biol. **6**, 85 (1999); H.-W. Fink et C. Schönenberger. Nature (London), **398**, 407 (1999).
141. P. O'Neill et E.M. Fielden. Adv. Radiat. Biol. **17**, 53 (1993); P. O'Neill, T. Melvin et S.W. Botchway. *Dans* Radiation damage in DNA : structure/function relationships at early times. *Édité par* A.F. Fuciarelli et J.D. Zimbrick. Battelle Press, Columbus, Ohio. 1995. p. 65; T. Melvin, S. Botchay, A.W. Parker et P. O'Neill. J. Chem. Soc. Chem. Commun. 653 (1995).
142. M.E. Winfield. J. Mol. Biol. **12**, 600 (1965).
143. M. Lefort. J. Chim. Phys. **54**, 782 (1957); Annu. Rev. Phys. Chem. **9**, 123 (1958).
144. H.A. Mahlman et J.W. Boyle. J. Am. Chem. Soc. **80**, 773 (1958).
145. E. Hayon. Trans. Faraday Soc. **61**, 723 (1965); **61**, 734 (1965); J. Phys. Chem. **69**, 2628 (1965); *Dans* Radiation chemistry of aqueous systems. *Édité par* G. Stein. The Weizmann Science Press of Israel, Jerusalem. 1968. p. 157.
146. E. Hayon. J. Phys. Chem. **68**, 1242 (1964).
147. M. Haïssinsky. J. Chim. Phys. **62**, 1141 (1965); **62**, 1149 (1965); *Dans* Actions chimiques et biologiques des radiations. 11ème Sér. *Édité par* M. Haïssinsky. Masson, Paris. 1967. p. 131.
148. F.S. Dainton et W.S. Watt. Nature (London), **195**, 1294 (1962); Proc. R. Soc. London, Ser. A : **275**, 447 (1963); T. Balkas, F.S. Dainton, J.K. Dishman et D. Smithies. Trans. Faraday Soc. **62**, 81 (1966).
149. C.H. Cheek, V.J. Linnenbom et J.W. Swinnerton. Radiat. Res. **19**, 636 (1963).
150. Z.D. Draganić, I.G. Draganić et M.M. Kosanić. J. Phys. Chem. **70**, 1418 (1966); I.G. Draganić, M.T. Nenadović et Z.D. Draganić. J. Phys. Chem. **73**, 2564 (1969).
151. G.V. Buxton. Radiat. Res. Rev. **1**, 209 (1968).
152. V. Cobut, Y. Frongillo, J.P. Patau, T. Goulet, M.-J. Fraser et J.-P. Jay-Gerin. Radiat. Phys. Chem. **51**, 229 (1998); Y. Frongillo, T. Goulet, M.-J. Fraser, V. Cobut, J.P. Patau et J.-P. Jay-Gerin. Radiat. Phys. Chem. **51**, 245 (1998).
153. A.-M. Koulkès-Pujo. C. R. Acad. Sci. Paris, **243**, 1865 (1956); Ann. Chim. **5**, 707 (1960). Voir aussi : C. Ferradini. *Dans* Actions chimiques et biologiques des radiations. 10ème Sér. *Édité par* M. Haïssinsky. Masson, Paris. 1966. p. 89; B. Hickel, H. Corfitzen et K. Sehested. J. Phys. Chem. **100**, 17 186 (1996).
154. C.H. Cheek et V.J. Linnenbom. J. Phys. Chem. **67**, 1856 (1963).
155. G.V. Buxton et F.S. Dainton. Proc. R. Soc. London, Ser. A : **287**, 427 (1965).
156. R. Julien et J. Pucheault. J. Chim. Phys. **64**, 725 (1967). Voir aussi : R. Julien. Thèse de Doctorat, Université de Paris (1965).
157. E. Bjergbakke, Z.D. Draganić, K. Sehested et I.G. Draganić. Radiochim. Acta, **48**, 65 (1989).
158. A.J. Elliot. Rate constants and *G*-values for the simulation of the radiolysis of light water over the range 0–300°C. Publication AECL-11073. Atomic Energy of Canada Ltd., Chalk River, Ont. 1994.
159. W.G. Burns et R. Barker. *Dans* Progress in reaction kinetics. Vol. 3. *Édité par* G. Porter. Pergamon, Oxford. 1965. p. 303.
160. J.C. Muller et C. Ferradini. Radiochem. Radioanal. Lett. **7**, 205 (1971); J.C. Muller, C. Ferradini et J. Pucheault. Int. J. Radiat. Phys. Chem. **7**, 635 (1975); **7**, 643 (1975).
161. J. Pucheault, C. Ferradini, M. Gardès, B. Lesigne, L. Gilles et J.C. Muller. Int. J. Chem. Kinet. **9**, 603 (1977); M. Gardès-Albert. Thèse de Doctorat, Université Paris V (1981).
162. J.E. Fanning, Jr., C.N. Trumbore, P.G. Barkley et J.H. Olson. J. Phys. Chem. **81**, 1264 (1977).
163. E. Wourtzel. Radium (Paris), **11**, 289 (1919); **11**, 332 (1919); J. Phys. Radium, **1**, 77 (1920).
164. C.E. Nurnberger. J. Phys. Chem. **38**, 47 (1934).
165. F.C. Lanning et S.C. Lind. J. Phys. Chem. **42**, 1229 (1938).
166. M. Lefort. J. Chim. Phys. **48**, 339 (1951); *Dans* Actions chimiques et biologiques des radiations. 1ère Sér. *Édité par* M. Haïssinsky. Masson, Paris. 1955. p. 93.
167. J. Pucheault. C. R. Acad. Sci. Paris, **246**, 409 (1958).
168. J. Pucheault. *Dans* Actions chimiques et biologiques des radiations. 5ème Sér. *Édité par* M. Haïssinsky. Masson, Paris. 1961. p. 31.
169. E. Collinson, F.S. Dainton et J. Kroh. Proc. R. Soc. London, Ser. A : **265**, 407 (1962).

© 1999 CNRC Canada

170. P. Bonét-Maury et M. Lefort. C. R. Acad. Sci. Paris, **226**, 1363 (1948); Nature (London), **162**, 381 (1948).
171. C.P. Ferradini et R.V. Bensasson. *Dans* Early developments in radiation chemistry. *Édité par* J. Kroh. The Royal Society of Chemistry, Cambridge. 1989. p. 99.
172. ICRU Report 16. Linear energy transfer. International Commission on Radiation Units and Measurements, Washington, D.C. 1970.
173. A.J. Swallow. Radiation chemistry. An introduction. Longman Group Ltd., London. 1973. p. 18.
174. G. Baldacchino, S. Bouffard, E. Balanzat, V. Mouton, M. Gardès-Albert, Z. Abedinzadeh, D. Jore, S. Deycard, D. Le Parc et B. Hickel. J. Chim. Phys. **94**, 200 (1997).
175. J. Pucheault et R. Julien. Radiochem. Radioanal. Lett. **2**, 27 (1969).
176. A. Appleby et E.A. Christman. Radiat. Res. **60**, 34 (1974).
177. J. Pucheault et P. Sigli. Int. J. Radiat. Phys. Chem. **8**, 613 (1976).
178. G. Baldacchino, D. Le Parc, B. Hickel, M. Gardès-Albert, Z. Abedinzadeh, D. Jore, S. Deycard, S. Bouffard, V. Mouton et E. Balanzat. Radiat. Res. **149**, 128 (1998). Voir aussi : G. Baldacchino, S. Bouffard, E. Balanzat, M. Gardès-Albert, Z. Abedinzadeh, D. Jore, S. Deycard et B. Hickel. Nucl. Instrum. Methods B : Phys. Res. **146**, 528 (1998); G. Baldacchino, V. Trupin, S. Bouffard, E. Balanzat, M. Gardès-Albert, Z. Abedinzadeh, D. Jore, S. Deycard et B. Hickel. J. Chim. Phys. **96**, 50 (1999).
179. J.A. LaVerne. Radiat. Phys. Chem. **34**, 135 (1989).
180. J.A. LaVerne et R.H. Schuler. J. Phys. Chem. **91**, 6560 (1987).
181. J.A. LaVerne et R.H. Schuler. J. Phys. Chem. **100**, 16 034 (1996).
182. P. Sigli et J. Pucheault. J. Chim. Phys. **65**, 1543 (1968); **70**, 717 (1973); P. Sigli, C. Ferradini et J. Pucheault. J. Chim. Phys. **67**, 412 (1970); P. Sigli. Thèse de Doctorat, Université Paris VI (1972) et références citées.
183. E. Collinson, F.S. Dainton et J. Kroh. Proc. R. Soc. London, Ser. A : **265**, 422 (1962); **265**, 430 (1962).
184. G. Lemaire, C. Ferradini et J. Pucheault. J. Phys. Chem. **76**, 1542 (1972) et références citées.
185. J. Pucheault, R. Julien et J. Chevrel. Rev. Phys. Appl. **2**, 137 (1967).
186. R.H. Bisby, R.B. Cundall, H.E. Sims et W.G. Burns. Faraday Discuss. Chem. Soc. **63**, 237 (1977).
187. W.G. Burns et H.E. Sims. J. Chem. Soc. Faraday Trans. 1, **77**, 2803 (1981).
188. M.C. Sauer, Jr., K.H. Schmidt, E.J. Hart, C.A. Naleway et C.D. Jonah. Radiat. Res. **70**, 91 (1977).
189. W.G. Burns, R. May, G.V. Buxton et G.S. Tough. Faraday Discuss. Chem. Soc. **63**, 47 (1977).
190. C.A. Naleway, M.C. Sauer, Jr., C.D. Jonah et K.H. Schmidt. Radiat. Res. **77**, 47 (1979).
191. E.J. Hart. Radiat. Res. **2**, 33 (1955); E. Bjergbakke et E.J. Hart. Radiat. Res. **45**, 261 (1971).
192. D.M. Donaldson et N. Miller. Trans. Faraday Soc. **52**, 652 (1956).
193. K.F. Baverstock et W.G. Burns. Nature (London), **260**, 316 (1976).
194. J.A. LaVerne, W.G. Burns et R.H. Schuler. J. Phys. Chem. **89**, 242 (1985); J.A. LaVerne et R.H. Schuler. J. Phys. Chem. **89**, 4171 (1985); **90**, 5995 (1986); **96**, 7376 (1992).
195. J.A. LaVerne, R.H. Schuler et W.G. Burns. J. Phys. Chem. **90**, 3238 (1986).
196. J.L. Magee et A. Chatterjee. J. Phys. Chem. **84**, 3529 (1980); A. Chatterjee et J.L. Magee. J. Phys. Chem. **84**, 3537 (1980); J.L. Magee et A. Chatterjee. *Dans* Kinetics of nonhomogeneous processes. *Édité par* G.R. Freeman. Wiley, New York. 1987. p. 171.
197. P.R.J. Burch. Radiat. Res. **11**, 481 (1959).
198. C. Ferradini. J. Chim. Phys. **76**, 636 (1979); *Dans* Actions biologique et chimique des radiations ionisantes. Vol. 1. *Édité par* B. Tilquin. Éditions Ciaco, Bruxelles. 1990. p. 52.
199. R. Katz et G.-R. Huang. Radiat. Phys. Chem. **33**, 345 (1989).
200. M. Gardès-Albert, D. Jore, Z. Abedinzadeh, A. Rouscilles, S. Deycard et S. Bouffard. J. Chim. Phys. **93**, 103 (1996).
201. C. Ferradini et J.-P. Jay-Gerin. Radiat. Phys. Chem. **51**, 263 (1998).
202. G.H. Olivera, C. Caraby, P. Jardin, A. Cassimi, L. Adoui et B. Gervais. Phys. Med. Biol. **43**, 2347 (1998).
203. Y. Frongillo, T. Goulet, M.-J. Fraser, J.-P. Jay-Gerin, V. Cobut et J.P. Patau. The effect of the radiation LET on the production of HO_2 radicals in irradiated liquid water : A Monte-Carlo simulation study. *Dans* Book of Abstracts, 45th Annu. Meet. Radiat. Res. Soc. Providence, R. I., 3–7 mai 1997. p. 81.
204. W.H. Koppenol. Free Radical Biol. Med. **25**, 385 (1998).
205. P. Howard-Flanders. Adv. Biol. Med. Phys. **6**, 553 (1958).
206. J.H. Baxendale. Radiat. Res. Suppl. **4**, 114 (1964).
207. W.H. Koppenol et J. Butler. Adv. Free Radical Biol. Med. **1**, 91 (1985).
208. E. Lartigau, M. Guichard et C. Ferradini. J. Chim. Phys. **91**, 1140 (1994). Voir aussi : E. Lartigau. Cah. Radiobiol. **1**, 7 (1995) et références citées.
209. H. Holthusen. Pflüger's Arch. Gesamte Physiol. Menschen Tiere, **187**, 1 (1921).
210. G. Schwarz. Münchener Med. Wochenschr. **56**, 1217 (1909).
211. E. Petry. Biochem. Z. **135**, 353 (1923); H.G. Crabtree et W. Cramer. Proc. R. Soc. London, Ser. B : **113**, 226 (1933); **113**, 238 (1933); J.C. Mottram. Br. J. Radiol. **9**, 606 (1936); A. Lacassagne. C. R. Acad. Sci. Paris, **215**, 231 (1942); H.M. Patt. Physiol. Rev. **33**, 35 (1953); L.H. Gray, A.D. Conger, M. Ebert, S. Hornsey et O.C.A. Scott. Br. J. Radiol. **26**, 638 (1953).
212. J. Kiefer. Biological radiation effects. Springer-Verlag, Berlin. 1990; E.J. Hall. Radiobiology for the radiologist. 4ème éd. J.B. Lippincott, Philadelphia. 1994.
213. J.E. Biaglow. *Dans* Radiation chemistry. Principles and applications. *Édité par* Farhataziz et M.A.J. Rodgers. VCH, New York. 1987. p. 527.
214. H.B. Michaels, E.R. Epp, C.C. Ling et E.C. Peterson. Radiat. Res. **76**, 510 (1978).
215. H.B. Hewitt et C.W. Wilson. Ann. N.Y. Acad. Sci. **95**, 818 (1961).
216. J. Gueulette, V. Grégoire et A. Wambersie. J. Chim. Phys. **91**, 1092 (1994).
217. R.J. Yaes, P. Patel et Y. Maruyama. Int. J. Radiat. Oncol. Biol. Phys. **20**, 1353 (1991); J.-M. Cosset, B. Dubray et H. Thames. Bull. Cancer/Radiother. **79**, 357 (1992); D.J. Brenner et E.J. Hall. Int. J. Radiat. Oncol. Biol. Phys. **23**, 252 (1992) et références citées; A. Courdi. J. Chim. Phys. **91**, 1025 (1994).
218. L.D. Skarsgard et I. Harrison. Radiat. Res. **127**, 243 (1991).
219. G.W. Barendsen, C.J. Koot, G.R. van Kersen, D.K. Bewley, S.B. Field et C.J. Parnell. Int. J. Radiat. Biol. **10**, 317 (1966).
220. K.N. Prasad. Handbook of radiobiology. 2ème éd. CRC Press, Boca Raton, Fla. 1995. p. 61.
221. A. Samuni et G. Czapski. Radiat. Res. **76**, 624 (1978); D. Ewing, T.M. Koval et H.L. Walton. Radiat. Res. **106**, 356 (1986).
222. W.G. Burns et P.B. Moore. Radiat. Eff. **30**, 233 (1976); P. Cohen. Water coolant technology of power reactors. American Nuclear Society, La Grange Park, Ill. 1980; G.V. Buxton. Int. J. Radiat. Biol. **59**, 1 (1991); H. Christensen. Nucl. Technol. **109**, 373 (1995).

© 1999 CNRC Canada

223. C.J. Hochanadel et J.A. Ghormley. Radiat. Res. **16**, 653 (1962).
224. G.V. Buxton. Water Chem. Nucl. React. Syst. **5**, 123 (1989); G.V. Buxton et N.D. Wood. Radiat. Phys. Chem. **34**, 699 (1989).
225. H. Shiraishi, Y. Katsumura, D. Hiroishi, K. Ishigure et M. Washio. J. Phys. Chem. **92**, 3011 (1988); H. Shiraishi, Y. Katsumura et K. Ishigure. Radiat. Phys. Chem. **34**, 705 (1989).
226. A.J. Elliot, M.P. Chenier et D.C. Ouellette. Can. J. Chem. **68**, 712 (1990).
227. M.C. Kent et H.E. Sims. Water Chem. Nucl. React. Syst. **6**, 153 (1992).
228. G.R. Sunaryo, Y. Katsumura, I. Shirai, D. Hiroishi et K. Ishigure. Radiat. Phys. Chem. **44**, 273 (1994); G.R. Sunaryo, Y. Katsumura, D. Hiroishi et K. Ishigure. Radiat. Phys. Chem. **45**, 131 (1995); G.R. Sunaryo, Y. Katsumura et K. Ishigure. Radiat. Phys. Chem. **45**, 703 (1995).
229. K. Ishigure, Y. Katsumura, G.R. Sunaryo et D. Hiroishi. Radiat. Phys. Chem. **46**, 557 (1995).
230. Y. Katsumura, Y. Takeuchi et K. Ishigure. Radiat. Phys. Chem. **32**, 259 (1988); Y. Katsumura, S. Yamamoto, D. Hiroishi et K. Ishigure. Radiat. Phys. Chem. **39**, 383 (1992).
231. A.J. Elliot, D.C. Ouellette, D. Reid et D.R. McCracken. Radiat. Phys. Chem. **34**, 747 (1989).
232. A.J. Elliot, M.P. Chenier, D.C. Ouellette et V.T. Koslowsky. J. Phys. Chem. **100**, 9014 (1996).
233. D. Swiatla-Wojcik et G.V. Buxton. J. Phys. Chem. **99**, 11 464 (1995).
234. J.A. LaVerne et S.M. Pimblott. J. Phys. Chem. **97**, 3291 (1993).
235. B. Hickel. J. Chim. Phys. **88**, 1177 (1991).
236. D. Swiatla-Wojcik et G.V. Buxton. J. Chem. Soc. Faraday Trans. **94**, 2135 (1998).
237. S.A. Kabakchi et V.L. Bugaenko. High Energy Chem. **26**, 319 (1992).
238. Y. Frongillo, T. Goulet, M.-J. Fraser, Ph. Bernat, J.-P. Jay-Gerin et A.J. Elliot. Étude par simulation Monte-Carlo de la radiolyse de l'eau pure en fonction de la température et à différents TEL. *Dans* Recueil des résumés des communications, 8èmes Journées d'études de chimie sous rayonnement. Orléans–Nouan-le-Fuzelier, France, 19–24 mai 1996. p. C-2.
239. W.C. Gottschall et E.J. Hart. J. Phys. Chem. **71**, 2102 (1967).
240. B.D. Michael, E.J. Hart et K.H. Schmidt. J. Phys. Chem. **75**, 2798 (1971).
241. R.S. Dixon et V.J. Lopata. Radiat. Phys. Chem. **11**, 135 (1978).
242. F.-Y. Jou et G.R. Freeman. J. Phys. Chem. **83**, 2383 (1979).
243. H. Christensen et K. Sehested. J. Phys. Chem. **90**, 186 (1986).
244. A.J. Elliot et D.C. Ouellette. J. Chem. Soc. Faraday Trans. **90**, 837 (1994).
245. A. Wallqvist, G. Martyna et B.J. Berne. J. Phys. Chem. **92**, 1721 (1988); E. Gallicchio et B.J. Berne. J. Chem. Phys. **105**, 7064 (1996).
246. B. Hickel. *Dans* Proc. 4th Tihany Symp. Radiat. Chem. Keszthely, Hungary. 1er–5 juin 1976. *Édité par* P. Hedvig et R. Schiller. Akadémiai Kiadó, Budapest. 1977. p. 801.
247. A.J. Elliot, D.R. McCracken, G.V. Buxton et N.D. Wood. J. Chem. Soc. Faraday Trans. **86**, 1539 (1990).
248. G.V. Buxton et S.R. Mackenzie. J. Chem. Soc. Faraday Trans. **88**, 2833 (1992).
249. H. Christensen, K. Sehested et T. Løgager. Radiat. Phys. Chem. **43**, 527 (1994).
250. H. Shiraishi, G.R. Sunaryo et K. Ishigure. J. Phys. Chem. **98**, 5164 (1994).
251. B. Hickel et K. Sehested. J. Phys. Chem. **95**, 744 (1991).
252. B. Hickel et K. Sehested. J. Phys. Chem. **89**, 5271 (1985).
253. K. Sehested and H. Christensen. Radiat. Phys. Chem. **36**, 499 (1990).
254. P. Han et D.M. Bartels. J. Phys. Chem. **94,** 7294 (1990).
255. P. Han et D.M. Bartels. J. Phys. Chem. **96**, 4899 (1992).
256. G.V. Buxton et A.J. Elliot. J. Chem. Soc. Faraday Trans. **89**, 485 (1993).
257. Z.B. Alfassi, R.E. Huie, P. Neta et L.C.T. Shoute. J. Phys. Chem. **94**, 8800 (1990).
258. R.M. Noyes. *Dans* Progress in reaction kinetics. Vol. 1. *Édité par* G. Porter et B. Stevens. Pergamon, Oxford. 1961. p. 129.
259. W. Mund. *Dans* Actions chimiques et biologiques des radiations. 2ème Sér. *Édité par* M. Haïssinsky. Masson, Paris. 1956. p. 1; S.C. Lind. Radiation chemistry of gases. Reinhold Publishing Corporation, New York. 1961.
260. R.S. Dixon. Radiat. Res. Rev. **2**, 237 (1970).
261. C. Willis et A.W. Boyd. Int. J. Radiat. Phys. Chem. **8**, 71 (1976).
262. D.A. Armstrong. *Dans* Radiation chemistry. Principles and applications. *Édité par* Farhataziz et M.A.J. Rodgers. VCH, New York. 1987. p. 263.
263. J.A. Ghormley et A.C. Stewart. J. Am. Chem. Soc. **78**, 2934 (1956).
264. L. Kevan. *Dans* Radiation chemistry of aqueous systems. *Édité par* G. Stein. The Weizmann Science Press of Israel, Jerusalem. 1968. p. 21; *Dans* Actions chimiques et biologiques des radiations. 13ème Sér. *Édité par* M. Haïssinsky. Masson, Paris. 1969. p. 57.
265. F. Kieffer. *Dans* The study of fast processes and transient species by electron pulse radiolysis. *Édité par* J.H. Baxendale et F. Busi. D. Reidel Publishing Co., Dordrecht. 1982. p. 363.
266. H.A. Gillis et I. Carmichael. Radiat. Phys. Chem. **22**, 981 (1983).
267. N.V. Klassen. Radiat. Phys. Chem. **48**, 281 (1996); R.E. Johnson et T.I. Quickenden. J. Geophys. Res. **102**, 10 985 (1997) et références citées.
268. J. Franck et E. Rabinowitsch. Trans. Faraday Soc. **30**, 120 (1934).
269. S. Ohno, H. Nagayama, K. Okazaki et S. Sato. Bull. Chem. Soc. Jpn. **48**, 2153 (1975).
270. J.E. Turner, H.G. Paretzke, R.N. Hamm, H.A. Wright et R.H. Ritchie. Radiat. Res. **92**, 47 (1982); H.G. Paretzke, J.E. Turner, R.N. Hamm, H.A. Wright et R.H. Ritchie. J. Chem. Phys. **84**, 3182 (1986).
271. I.G. Kaplan, A.M. Miterev et V.Ya. Sukhonosov. Radiat. Phys. Chem. **27**, 83 (1986); **36**, 493 (1990); I.G. Kaplan et V.Ya. Sukhonosov. Radiat. Res. **127**, 1 (1991).
272. E.A. Bigildeev et V. Michalik. Radiat. Phys. Chem. **47**, 197 (1996); V. Michalik, M. Begusová et E.A. Bigildeev. Radiat. Res. **149**, 224 (1998).
273. S.M. Pimblott et J.A. LaVerne. J. Phys. Chem. A. **101**, 5828 (1997).
274. S.M. Pimblott et J.A. LaVerne. Radiat. Res. **150**, 159 (1998).
275. C.D. Jonah et J.R. Miller. J. Phys. Chem. **81**, 1974 (1977); A.C. Chernovitz et C.D. Jonah. J. Phys. Chem. **92**, 5946 (1988); C.D. Jonah, D.M. Bartels et A.C. Chernovitz. Radiat. Phys. Chem. **34**, 145 (1989).
276. G.R. Freeman (*Éditeur*). Kinetics of nonhomogeneous processes. Wiley, New York. 1987. p. 277.
277. C. Ferradini et J.-P. Jay-Gerin. J. Chem. Phys. **89**, 6719 (1988).
278. J. Bednář. Radiat. Phys. Chem. **34**, 69 (1989); Theoretical foundations of radiation chemistry. Kluwer Academic Publishers, Dordrecht. 1990. p. 243. Voir aussi : I. Santar et J. Bednář. Collect. Czech. Chem. Commun. **32**, 953 (1967).
279. V.Ya. Sukhonosov. High Energy Chem. **29**, 5 (1995); **29**, 243 (1995).
280. S.M. Pimblott et A. Mozumder. J. Phys. Chem. **95**, 7291 (1991); A. Mozumder. *Dans* Proc. 7th Tihany Symp. Radiat.

© 1999 CNRC Canada

Chem. Balatonszéplak, Hungary. 9–14 septembre 1990. *Édité par* J. Dobó, L. Nyikos et R. Schiller. Hungarian Chemical Society, Budapest. 1991. p. 3.
281. R.F. Firestone. J. Am. Chem. Soc. **79**, 5593 (1957).
282. A.R. Anderson, B. Knight et J.A. Winter. Nature (London), **201**, 1026 (1964); Trans. Faraday Soc. **62**, 359 (1966). Voir aussi : A.R. Anderson. *Dans* Fundamental processes in radiation chemistry. *Édité par* P. Ausloos. Wiley, New York. 1968. p. 281.
283. J.H. Baxendale et G.P. Gilbert. J. Am. Chem. Soc. **86**, 516 (1964); Discuss. Faraday Soc. **36**, 186 (1964).
284. J.Y. Yang et I. Marcus. J. Am. Chem. Soc. **88**, 1625 (1966).
285. G.R.A. Johnson et M. Simic. J. Phys. Chem. **71**, 1118 (1967); *Dans* The chemistry of ionization and excitation. *Édité par* G.R.A. Johnson et G. Scholes. Taylor & Francis, London. 1967. p. 211.
286. A.W. Boyd et O.A. Miller. Can. J. Chem. **46**, 3773 (1968).
287. A.R. Anderson, B. Knight et J.A. Winter. Nature (London), **209**, 199 (1966).
288. P. Ayotte et M.A. Johnson. J. Chem. Phys. **106**, 811 (1997) et références citées.
289. L.H. Piette, R.C. Rempel, H.E. Weaver et J.M. Flournoy. J. Chem. Phys. **30**, 1623 (1959).
290. V.N. Shubin, V.A. Zhigunov, V.I. Zolotarevsky et P.I. Dolin. Nature (London), **212**, 1002 (1966).
291. S. Siegel, L.H. Baum, S. Skolnik et J.M. Flournoy. J. Chem. Phys. **32**, 1249 (1960); S. Siegel, J.M. Flournoy et L.H. Baum. J. Chem. Phys. **34**, 1782 (1961). Voir aussi : B.G. Ershov et A.K. Pikaev. Radiat. Res. Rev. **2**, 1 (1969).
292. J.A. Brivati, M.C.R. Symons, D.J.A. Tinling, H.W. Wardale et D.O. Williams. Trans. Faraday Soc. **63**, 2112 (1967).
293. K. Eiben et I.A. Taub. Nature (London), **216**, 782 (1967); I.A. Taub et K. Eiben. J. Chem. Phys. **49**, 2499 (1968).
294. J. Bednarek, A. Plonka, A. Hallbrucker, E. Mayer et M.C.R. Symons. J. Am. Chem. Soc. **118**, 9387 (1996); J. Bednarek, A. Plonka, A. Hallbrucker et E. Mayer. J. Phys. Chem. A. **102**, 9091 (1998).
295. J.M. Flournoy, L.H. Baum et S. Siegel. J. Chem. Phys. **36**, 2229 (1962).
296. J.B. Verberne, H. Loman, J.M. Warman, M.P. de Haas, A. Hummel et L. Prinsen. Nature (London), **272**, 343 (1978).
297. J.M. Warman, M.P. de Haas et J.B. Verberne. J. Phys. Chem. **84**, 1240 (1980).
298. J.M. Warman, M. Kunst, M.P. de Haas et J.B. Verberne. J. Electrost. **12**, 115 (1982).
299. M.P. de Haas, M. Kunst, J.M. Warman et J.B. Verberne. J. Phys. Chem. **87**, 4089 (1983).
300. J.M. Warman et C.D. Jonah. Chem. Phys. Lett. **79**, 43 (1981); J.M. Warman, M. Kunst et C.D. Jonah. J. Phys. Chem. **87**, 4292 (1983).
301. D. Schulte-Frohlinde et K. Eiben. Z. Naturforsch. **17A**, 445 (1962).
302. K. Kawabata. J. Chem. Phys. **55**, 3672 (1971).
303. G. Nilsson, H.C. Christensen, J. Fenger, P. Pagsberg et S.O. Nielsen. *Dans* Adv. Chem. Ser. Vol. 81. *Édité par* R.F. Gould. American Chemical Society, Washington, D.C. 1968. p. 71; G. Nilsson, H. Christensen, P. Pagsberg et S.O. Nielsen. J. Phys. Chem. **76**, 1000 (1972).
304. S. Pommeret et Y. Gauduel. J. Phys. Chem. **95**, 4126 (1991).
305. K. Kawabata, S. Okabe et H. Horii. Chem. Phys. Lett. **20**, 586 (1973); K. Kawabata. J. Chem. Phys. **65**, 2235 (1976).
306. G.V. Buxton, H.A. Gillis et N.V. Klassen. Can. J. Chem. **55**, 2385 (1977).
307. G.V. Buxton, H.A. Gillis et N.V. Klassen. Chem. Phys. Lett. **32**, 533 (1975); Can. J. Chem. **54**, 367 (1976).
308. K. Kawabata, G.V. Buxton et G.A. Salmon. Chem. Phys. Lett. **64**, 487 (1979); H.A. Gillis, G.G. Teather et C.K. Ross. J. Phys. Chem. **84**, 1248 (1980); G.J. Trudel, H.A. Gillis, N.V. Klassen et G.G. Teather. Can. J. Chem. **59**, 1235 (1981); Z. Wu, H.A. Gillis, N.V. Klassen et G.G. Teather. J. Chem. Phys. **78**, 2449 (1983); G.V. Buxton, M. Medley, G.A. Salmon, P.J. Baugh, R. Catterall et P.B. Williams. J. Chem. Soc. Faraday Trans. 1, **81**, 3067 (1985).
309. F. Seitz. Rev. Mod. Phys. **18**, 384 (1946); D. Saint-James. J. Phys. Radium, **18**, 260 (1956); V.J. Robinson et M.R. Chandratillake. *Dans* Radiation chemistry. Principles and applications. *Édité par* Farhataziz et M.A.J. Rodgers. VCH, New York. 1987. p. 435.
310. A. Ekstrom. Radiat. Res. Rev. **2**, 381 (1970).
311. H.-P. Kaukonen, R.N. Barnett et U. Landman. J. Chem. Phys. **97**, 1365 (1992).
312. C. Ferradini et J.-P. Jay-Gerin. Radiat. Phys. Chem. **41**, 487 (1993) et références citées.
313. K.H. Schmidt et D.M. Bartels. Chem. Phys. **190**, 145 (1995).
314. G.A. Kimmel, T.M. Orlando, C. Vézina et L. Sanche. J. Chem. Phys. **101**, 3282 (1994); G.A. Kimmel, R.G. Tonkyn et T.M. Orlando. Nucl. Instrum. Methods B : Phys. Res. **101**, 179 (1995); G.A. Kimmel et T.M. Orlando. Phys. Rev. Lett. **77**, 3983 (1996).
315. G.A. Kimmel et T.M. Orlando. Phys. Rev. Lett. **75**, 2606 (1995); G.A. Kimmel, T.M. Orlando, P. Cloutier et L. Sanche. J. Phys. Chem. B. **101**, 6301 (1997); T.M. Orlando et G.A. Kimmel. Surf. Sci. **390**, 79 (1997).
316. P. Rowntree, L. Parenteau et L. Sanche. J. Chem. Phys. **94**, 8570 (1991).
317. M. Tronc, R. Azria, Y. Le Coat et E. Illenberger. J. Phys. Chem. **100**, 14 745 (1996); W.C. Simpson, L. Parenteau, R.S. Smith, L. Sanche et T.M. Orlando. Surf. Sci. **390**, 86 (1997); W.C. Simpson, M.T. Sieger, T.M. Orlando, L. Parenteau, K. Nagesha et L. Sanche. J. Chem. Phys. **107**, 8668 (1997); W.C. Simpson, T.M. Orlando, L. Parenteau, K. Nagesha et L. Sanche. J. Chem. Phys. **108**, 5027 (1998).
318. M.T. Sieger, W.C. Simpson et T.M. Orlando. Phys. Rev. B: Condens. Matter, **56**, 4925 (1997) et références citées.
319. M.T. Sieger, W.C. Simpson et T.M. Orlando. Nature (London), **394**, 554 (1998).
320. L. Sanche. Radiat. Phys. Chem. **34**, 15 (1989); *Dans* Excess electrons in dielectric media. *Édité par* C. Ferradini et J.-P. Jay-Gerin. CRC Press, Boca Raton, Fla. 1991. p. 1.
321. R.A. Horne et D.S. Johnson. J. Phys. Chem. **70**, 2182 (1966).
322. R.R. Hentz, Farhataziz, D.J. Milner et M. Burton. J. Chem. Phys. **46**, 2995 (1967).
323. R.R. Hentz, Farhataziz, D.J. Milner et M. Burton. J. Chem. Phys. **46**, 4154 (1967); R.R. Hentz, Farhataziz et D.J. Milner. J. Chem. Phys. **47**, 4865 (1967).
324. R.R. Hentz et R.J. Knight. J. Chem. Phys. **52**, 2456 (1970).
325. R.R. Hentz, Farhataziz, D.J. Milner et M. Burton. J. Chem. Phys. **47**, 374 (1967); R.R. Hentz, Farhataziz et D.J. Milner. J. Chem. Phys. **47**, 5381 (1967); R.R. Hentz et D.W. Brazier. J. Chem. Phys. **54**, 2777 (1971).
326. R.R. Hentz, Farhataziz et D.J. Milner. J. Chem. Phys. **49**, 2153 (1968).
327. U. Schindewolf, H. Kohrmann et G. Lang. Angew. Chem. Int. Ed. Engl. **8**, 512 (1969).
328. R.R. Hentz, Farhataziz et E.M. Hansen. J. Chem. Phys. **55**, 4974 (1971).
329. M.G. Robinson, K.N. Jha et G.R. Freeman. J. Chem. Phys. **55**, 4933 (1971); F.-Y. Jou et G.R. Freeman. J. Phys. Chem. **81**, 909 (1977).

© 1999 CNRC Canada

330. S.M. Pimblott, J.A. LaVerne, D.M. Bartels et C.D. Jonah. J. Phys. Chem. **100**, 9412 (1996) et références citées.
331. M.A. Hill et F.A. Smith. Radiat. Phys. Chem. **43**, 265 (1994).
332. M. Domae, Y. Katsumura, K. Ishigure et V.M. Byakov. Radiat. Phys. Chem. **48**, 487 (1996).
333. Y. Frongillo, M.-J. Fraser, V. Cobut, T. Goulet, J.-P. Jay-Gerin et J.P. Patau. J. Chim. Phys. **93**, 93 (1996).
334. H. Tomita, M. Kai, T. Kusama et A. Ito. Radiat. Environ. Biophys. **36**, 105 (1997).
335. V.M. Byakov. Int. J. Radiat. Phys. Chem. **8**, 283 (1976).
336. R.L. Platzman. *Dans* Abstr. 2nd Int. Congr. Radiat. Res. Harrogate, Yorkshire, England. 5–11 août 1962. p. 128.
337. R.J. Hanrahan. *Dans* Proc. Workshop Interface Radiat. Chem. Radiat. Phys. Argonne, Ill. 9–10 septembre 1982. Publication ANL-82-88. *Édité par* M.A. Dillon, R.J. Hanrahan, R. Holroyd, Y.-K. Kim, M.C. Sauer, Jr. et L.H. Toburen. Argonne National Laboratory, Argonne, Illinois. 1983. p. 132.
338. T. Goulet et J.-P. Jay-Gerin. J. Phys. Chem. **92**, 6871 (1988); Radiat. Res. **118**, 46 (1989); T. Goulet, J.P. Patau et J.-P. Jay-Gerin. J. Phys. Chem. **94**, 7312 (1990); Radiat. Prot. Dosim. **31**, 33 (1990).
339. M. Inokuti. Radiat. Eff. Defects Solids, **117**, 143 (1991).
340. S.M. Pimblott et N.J.B. Green. *Dans* Research in chemical kinetics. Vol. 3. *Édité par* R.G. Compton et G. Hancock. Elsevier, Amsterdam. 1995. p. 117.
341. Atomic and molecular data for radiotherapy and radiation research. IAEA-TECDOC-799. International Atomic Energy Agency, Vienna. 1995.
342. M. Dingfelder, D. Hantke, M. Inokuti et H.G. Paretzke. Radiat. Phys. Chem. **53**, 1 (1998) et références citées.
343. A.D. Bass et L. Sanche. Radiat. Environ. Biophys. **37**, 243 (1998) et références citées.
344. M. Michaud, P. Cloutier et L. Sanche. Phys. Rev. A : Stat. Phys. Plasmas, Fluids, Relat. Interdiscip. Top. **44**, 5624 (1991).
345. T. Goulet, A. Bernas, C. Ferradini et J.-P. Jay-Gerin. Chem. Phys. Lett. **170**, 492 (1990); A. Bernas, C. Ferradini et J.-P. Jay-Gerin. Chem. Phys. **222**, 151 (1997); J. Photochem. Photobiol. A : **117**, 171 (1998). Voir aussi : A. Bernas, T. Goulet, J.-P. Jay-Gerin et C. Ferradini. *Dans* Proc. 7th Tihany Symp. Radiat. Chem. Balatonszéplak, Hungary, 9–14 septembre 1990. *Édité par* J. Dobó, L. Nyikos et R. Schiller. Hungarian Chemical Society, Budapest. 1991. p. 17.
346. M. Michaud et L. Sanche. Phys. Rev. A : Gen. Phys. **36**, 4684 (1987).
347. T. Goulet, J.-P. Jay-Gerin, Y. Frongillo, V. Cobut et M.-J. Fraser. J. Chim. Phys. **93**, 111 (1996) et références citées.
348. A. Mozumder. J. Chem. Phys. **50**, 3153 (1969).
349. A. Mozumder et J.L. Magee. Int. J. Radiat. Phys. Chem. **7**, 83 (1975); *Dans* Physical chemistry. An advanced treatise. Vol. VII. *Édité par* H. Eyring. Academic Press, New York. 1975. p. 699.
350. K. Kowari et S. Sato. Bull. Chem. Soc. Jpn. **51**, 741 (1978).
351. J.L. Magee et A. Chatterjee. Radiat. Phys. Chem. **15**, 125 (1980); J. Phys. Chem. **82**, 2219 (1978); J.E. Turner, J.L. Magee, H.A. Wright, A. Chatterjee, R.N. Hamm et R.H. Ritchie. Radiat. Res. **96**, 437 (1983); J.E. Turner, R.N. Hamm, H.A. Wright, R.H. Ritchie, J.L. Magee, A. Chatterjee et W.E. Bolch. Radiat. Phys. Chem. **32**, 503 (1988).
352. G.R. Freeman. Annu. Rev. Phys. Chem. **34**, 463 (1983); (*Éditeur*) Kinetics of nonhomogeneous processes. Wiley, New York. 1987. p. 19; *Dans* The liquid state and its electrical properties. *Édité par* E.E. Kunhardt, L.G. Christophorou et L.H. Luessen. Plenum, New York. 1988. p. 251.
353. J.A. LaVerne et A. Mozumder. Radiat. Phys. Chem. **23**, 637 (1984).
354. M. Zaider et D.J. Brenner. Radiat. Res. **100**, 245 (1984); D.J. Brenner. Radiat. Phys. Chem. **32**, 157 (1988); M. Zaider, M.G. Vracko, A.Y.C. Fung et J.L. Fry. Radiat. Prot. Dosim. **52**, 139 (1994).
355. V.V. Konovalov, A.M. Raitsimring et Yu.D. Tsvetkov. Radiat. Phys. Chem. **32**, 623 (1988); V.V. Konovalov et A.M. Raitsimring. Chem. Phys. Lett. **171**, 326 (1990); A.I. Kalugin, V.V. Konovalov, N.V. Shokhirev et A.M. Raitsimring. J. Electroanal. Chem. **359**, 63 (1993).
356. A. Beaudré. Thèse de Doctorat, Université de Toulouse (1988); M. Terrissol et A. Beaudré. Radiat. Prot. Dosim. **31**, 175 (1990).
357. S.V. Stepanov. J. Phys. IV, **3**, 41 (1993).
358. R.H. Ritchie, R.N. Hamm, J.E. Turner et W.E. Bolch. *Dans* Computational approaches in molecular radiation biology. Monte-Carlo methods. *Édité par* M.N. Varma et A. Chatterjee. Plenum, New York. 1994. p. 33 et références citées.
359. Dayashankar et M.A. Prasad. Radiat. Phys. Chem. **45**, 147 (1995); Dayashankar. *Dans* Proc. Trombay Symp. Radiation and Photochem. Trombay, Mumbai, India. 14–19 janvier 1998. Preprint Volume, Part II. p. 223.
360. J.-P. Jay-Gerin, T. Goulet et I. Billard. Can. J. Chem. **71**, 287 (1993).
361. R.L. Platzman. Radiat. Res. **1**, 558 (1954); **2**, 1 (1955). Voir aussi : J.L. Magee et M. Burton. J. Am. Chem. Soc. **73**, 523 (1951); J. Weiss. Nature (London), **174**, 78 (1954); J. Chim. Phys. **52**, 539 (1955); J.L. Magee. Can. J. Chem. **55**, 1847 (1977); M.A. Ishii, M. Kimura et M. Inokuti. Phys. Rev. A: Stat. Phys. Plasmas, Fluids, Relat. Interdiscip. Top. **42**, 6486 (1990); M. Inokuti. Appl. Radiat. Isot. **42**, 979 (1991) et références citées.
362. P.J. Rossky et J.D. Simon. Nature (London), **370**, 263 (1994) et références citées; E. Keszei, T.H. Murphrey et P.J. Rossky. J. Phys. Chem. **99**, 22 (1995); S. Bratos et J.-Cl. Leicknam. Chem. Phys. Lett. **261**, 117 (1996); **291**, 496 (1998); S. Bratos, J.-Cl. Leicknam, D. Borgis et A. Staib. Phys. Rev. E: Stat. Phys. Plasmas, Fluids, Relat. Interdiscip**.** Top. **55**, 7217 (1997); D. Borgis et S. Bratos. J. Mol. Structure **436–437**, 537 (1997); K. Drukker et S.W. de Leeuw. Chem. Phys. Lett. **291**, 283 (1998).
363. A. Reuther, A. Laubereau et D.N. Nikogosyan. J. Phys. Chem. **100**, 16 794 (1996); C. Pépin, T. Goulet, D. Houde et J.-P. Jay-Gerin. J. Phys. Chem. A, **101**, 4351 (1997); J.-P. Jay-Gerin. Can. J. Chem. **75**, 1310 (1997) et références citées; M. Assel, R. Laenen et A. Laubereau. J. Phys. Chem. A, **102**, 2256 (1998); A. Kummrow, M.F. Emde, A. Baltuška, M.S. Pshenichnikov et D.A. Wiersma. J. Phys. Chem. A, **102**, 4172 (1998); C. Silva, P.K. Walhout, K. Yokoyama et P.F. Barbara. Phys. Rev. Lett. **80**, 1086 (1998); K. Yokoyama, C. Silva, D.H. Son, P.K. Walhout et P.F. Barbara. J. Phys. Chem. A, **102**, 6957 (1998); T. Megyes et E. Keszei. J. Chim. Phys. **96**, 13 (1999); T. Goulet, C. Pépin, D. Houde et J.-P. Jay-Gerin. Radiat. Phys. Chem. **54**, 441 (1999); W. Marbach, A.N. Asaad et P. Krebs. J. Phys. Chem. A, **103**, 28 (1999).
364. G.A. Kenney-Wallace. Adv. Chem. Phys. **47**, 535 (1981).
365. C. Ferradini et J.-P. Jay-Gerin. Chem. Phys. Lett. **167**, 371 (1990).
366. I.G. Draganić. Radiochim. Acta, **70/71**, 317 (1995).
367. B. Pastina, J. Isabey et B. Hickel. J. Chim. Phys. **94**, 226 (1997); J. Nucl. Mater. **264**, 309 (1999).
368. N. Getoff. Radiat. Phys. Chem. **47**, 581 (1996).

© 1999 CNRC Canada

369. M. Fattahi, A. Eglem, C. Houée-Levin, C. Ferradini et P. Jacquier. J. Chim. Phys. **90**, 767 (1993).
370. Ph. Bernat. Thèse de Doctorat, Université Paris V (1994).
371. A. Saas. Clefs CEA **34**, 38 (1997); R. Turlay (*Éditeur*). Les déchets nucléaires : un dossier scientifique. Les Éditions de Physique, Les Ulis. 1997; Radioactive waste. Phys. Today, **50**, n° 6 (1997) (numéro spécial).
372. I.G. Draganić, Z.D. Draganić et J.-P. Adloff. Radiation and radioactivity on earth and beyond. 2ème éd. CRC Press, Boca Raton, Fla. 1993.
373. W. Schimmerling. Radioprotection, **28**, 173 (1993); Radiat. Environ. Biophys. **34**, 133 (1995).
374. G. Lemaire. J. Chim. Phys. **91**, 1176 (1994).
375. J.R. Letaw. *Dans* Fundamentals of space life sciences. Vol. 1. *Édité par* S.E. Churchill. Krieger Publishing Co., Malabar. 1997. p. 11.
376. A.J. Swallow. J. Chim. Phys. **88**, 1217 (1991); J. Raffi et P. Vincent. *Dans* Actions biologique et chimique des radiations ionisantes. Vol. II. *Édité par* B. Tilquin. Academia-Erasme, Louvain-La-Neuve. 1992. p. 91; G.A. Schreiber, N. Helle et K.W. Bögl. Int. J. Radiat. Biol. **63**, 105 (1993); J. Raffi et J.J. Belliardo. J. Chim. Phys. **90**, 1021 (1993); L. Saint-Lebe et J. Raffi. Cah. Nutr. Diét. **30**, 117 (1995); J. Farkas (*Éditeur*). Abstr. Symp. Curr. Aspects Food Irradiation. Budapest, Hungary, 30 juillet – 4 août 1995. Radiat. Phys. Chem. **48**, 357 (1996); H. Cerda, H. Delincée, H. Haine et H. Rupp. Mutat. Res. **375**, 167 (1997); J. Raffi. Trends Anal. Chem. **17**, 226 (1998).
377. F. Zeegers, A.-S. Crucq, M. Gibella et B. Tilquin. J. Chim. Phys. **90**, 1029 (1993); B. Tilquin et B. Rollmann. J. Chim. Phys. **93**, 224 (1996); J.L. Duroux, J.P. Basly et M. Bernard. J. Chim. Phys. **94**, 405 (1997); J.P. Basly, I. Longy et M. Bernard. Anal. Chim. Acta, **359**, 107 (1998); B. Tilquin et A.-S. Crucq. J. Chim. Phys. **96**, 167 (1999).
378. A. Chapiro. *Dans* Actions biologique et chimique des radiations ionisantes. Vol. II. *Édité par* B. Tilquin. Academia-Erasme, Louvain-La-Neuve. 1992. p. 50; Nucl. Instrum. Methods B : Phys. Res. **105**, 5 (1995). Voir aussi : A. Chapiro. *Dans* Early developments in radiation chemistry. *Édité par* J. Kroh. The Royal Society of Chemistry, Cambridge. 1989. p. 21.
379. A. Charlesby. Nucl. Instrum. Methods B : Phys. Res. **105**, 217 (1995).
380. Y. Tabata, Y. Ito et S. Tagawa (*Éditeurs*). CRC Handbook of radiation chemistry. CRC Press, Boca Raton, Fla. 1991. p. 721.
381. F. Balestic. Rayonnements et traitements ionisants. Masson, Paris. 1995. p. 145.
382. C. Ferradini. Biochimie, **68**, 779 (1986).
383. P. Wardman. J. Phys. Chem. Ref. Data, **18**, 1637 (1989); W.H. Koppenol. *Dans* Membrane lipid oxidation. Vol. I. *Édité par* C. Vigo-Pelfrey. CRC Press, Boca Raton, Fla. 1990. p. 1; D.T. Sawyer. Int. Rev. Experim. Pathol. **31**, 109 (1990); G.R. Buettner. Arch. Biochem. Biophys. **300**, 535 (1993); R.A. Larson. Naturally occurring antioxidants. Lewis Publishers, Boca Raton, Fla. 1997. p. 51.
384. H.A. Schwarz. J. Chem. Educ. **58**, 101 (1981).
385. G.V. Buxton. *Dans* The study of fast processes and transient species by electron pulse radiolysis. *Édité par* J.H. Baxendale et F. Busi. D. Reidel, Dordrecht. 1982. p. 267; *Dans* Radiation chemistry. Principles and applications. *Édité par* Farhataziz et M.A.J. Rodgers. VCH, New York. 1987. p. 321.
386. P. Wardman. *Dans* Radiation chemistry. Principles and applications. *Édité par* Farhataziz et M.A.J. Rodgers. VCH, New York. 1987. p. 565.
387. B. Halliwell et J.M.C. Gutteridge. Free radicals in biology and medicine. 3ème éd. Oxford University Press, Oxford. 1999.
388. A. Brunmark et E. Cadenas. Free Radical Biol. Med. **7**, 435 (1989).
389. C. Ferradini. J. Chim. Phys. **88**, 873 (1991).
390. M. Gardès-Albert. J. Chim. Phys. **88**, 889 (1991); M. Faraggi et C. Houée-Levin. J. Chim. Phys. **96**, 71 (1999).
391. J.M. McCord et I. Fridovich. J. Biol. Chem. **244**, 6049 (1969). Voir aussi : I. Fridovich. *Dans* Free radicals in biology. Vol. I. *Édité par* W.A. Pryor. Academic, New York. 1976. p. 239; *Dans* Superoxide dismutase. Vol. I. *Édité par* L.W. Oberley. CRC Press, Boca Raton, Fla. 1982. p. 1; J. Biol. Chem. **272**, 18 515 (1997).
392. M.-T. Droy-Lefaix, C. Ferradini et M. Gardès-Albert. Les radicaux libres en 10 questions. IPSEN, Paris. 1991; K. Yagi (*Éditeur*). Active oxygens, lipid peroxides, and antioxidants. Japan Scientific Societies Press, Tokyo. 1993; P.A. Riley. Int. J. Radiat. Biol. **65**, 27 (1994); D. Blake et P.G. Winyard (*Éditeurs*). Immunopharmacology of free radical species. Academic, London. 1995; M. Saran, C. Michel et W. Bors. Z. Naturforsch. C : Biosci. **53**, 210 (1998).
393. M.U. Dianzani. Boll. Soc. Ital. Biol. Sper. **68**, 491 (1992); J.P. Kehrer. Crit. Rev. Toxicol. **23**, 21 (1993); L. Montagnier, R. Olivier et C. Pasquier (*Éditeurs*). Oxidative stress in cancer, AIDS, and neurodegenerative diseases. Marcel Dekker, New York. 1998.
394. W.A. Pryor et G.L. Squadrito. Am. J. Physiol. : Lung Cell. Mol. Physiol. **268**, L699 (1995); J.S. Beckman et W.H. Koppenol. Am. J. Physiol. : Cell Physiol. **271**, C1424 (1996); H. Rubbo, V. Darley-Usmar et B.A. Freeman. Chem. Res. Toxicol. **9**, 809 (1996); W.H. Koppenol. *Dans* Free Radical Toxicology. *Édité par* K.B. Wallace. Taylor & Francis, Washington, D.C. 1997. p. 3; D.A. Wink et J.B. Mitchell. Free Radical Biol. Med. **25**, 434 (1998); M.B. Grisham, D. Jourd'heuil et D.A. Wink. Am. J. Physiol. : Gastrointest. Liver Physiol. **276**, G315 (1999).
395. M.K. Shigenaga, T.M. Hagen et B.N. Ames. Proc. Natl. Acad. Sci. U.S.A. **91**, 10 771 (1994).
396. M.D. Jacobson. Trends Biochem. Sci. **21**, 83 (1996); J. Mathieu, Y. Chancerelle, F. Hérodin, E. Multon, M. Drouet, J.-C. Mestries et J.-F. Kergonou. Ann. Pharmaceut. Fr. **54**, 193 (1996).

© 1999 CNRC Canada

Long chain β-aminoethanols as micellar catalysts for the hydrolysis of diphenyl-*p*-nitrophenyl phosphate. The observation of an unusual enhancement of catalysis in the presence of added polyols

H. Oumar-Mahamat, H. Ślebocka-Tilk, and R.S. Brown

Abstract: The hydrolysis of *p*-nitrophenyldiphenyl phosphate (PNPDPP, **7**) catalyzed by *N*-dodecylaminoethanol (**6a**), *N*-tetradecylaminoethanol (**6b**), *N*-methyl-*N*-tetradecylaminoethanol (**6c**), and *N*-hexadecylaminoethanol (**6d**) was investigated at 25°C at various pH values in aqueous media containing additives. Added ethanol or dimethoxyethane produces very little activity of **6a**, **b**, **c** toward **7**. The highest activities of **6a**, **b** were found at pH 8.0 and 8.5 in solvents containing 20% glycerol or ethylene glycol. Under no conditions was *N*-hexadecylaminoethanol (**6d**) found to be active. The kinetics of the reaction of **6b** with **7** were also investigated in a medium containing various amounts of glycerol, polyethylene glycol 400 (PEG 400), and water at pH 7.6–8.5. The best catalytic system comprised 3 mM **6b** in 20% aqueous ethylene glycol, pH 8.5, which accelerated the hydrolysis of **7** by ~1700-fold over the blank rate. Kinetic experiments conducted using [**7**]/[**6b**] = 1 and 2 demonstrate that **6b** exhibits true turnover catalysis. A mechanism for the catalyzed reaction is proposed.

Key words: β-aminoethanols, hydrolysis, *p*-nitrophenyldiphenyl phosphate, micelles, polyhydroxy alcohols.

Résumé : Opérant à 25°C, à divers pH, dans des milieux aqueux contenant des additifs, on a étudié l'hydrolyse du phosphate de diphényle et de *p*-nitrophényle (**7**) catalysée par *N*-dodécylaminoéthanol (**6a**), *N*-tétradécylaminoéthanol (**6b**), *N*-méthyl-*N*-tétradécylaminoéthanol (**6c**) et *N*-hexadécylaminoéthanol (**6d**). L'addition d'éthanol ou de diméthoxyéthane ne produise que de faibles activités des catalyseurs **6a**, **b**, **c** vis-à-vis de **7**. Les activités les plus élevées de **6a**, **b** ont été observées à des pH de 8,0 et 8,5, dans des solvants contenant 20% de glycérol ou d'éthylèneglycol. On n'a pas trouvé de conditions dans lesquelles le *N*-hexadécylaminoéthanol (**6d**) est actif. On a aussi examiné la cinétique de la réaction de **6b** avec **7** dans un milieu contenant diverses quantités de glycérol, de polyéthylèneglycol 400 (PEG 400) et d'eau, à des pH allant de 7,6 à 8,5. Le meilleur système catalytique est formé de 3 mM de **6b** dans de l'éthylèneglycol aqueux à 20%, à un pH de 8,5; dans ces conditions, l'hydrolyse de **7** se produit 1700 fois plus rapidement que dans l'essai à blanc. Des expériences cinétiques effectuées en utilisant un rapport [**7**]/[**6b**] = 1 et 2 démontre que le composé **6b** donne lieu à une réelle catalyse. On propose un mécanisme pour la réaction catalysée.

Mots clés : β-aminoéthanols, hydrolyse, phosphate de diphényle et de *p*-nitrophényle, micelles, alcools polyhydroxylés.

[Traduit par la Rédaction]

Introduction

Activated phosphate, phosphinate, and phosphonate esters of the general form **1** are potent acetylcholinesterase inhibitors (1). These include such substances as the insecticides parathion (RO = R = OEt; X = S; Y = $OC_6H_4NO_2$) and paraoxon (RO = R = OEt; X = O; Y = $OC_6H_4NO_2$), as well as the alkylphosphonofluoridate esters soman (RO = $(CH_3)_3CCH(CH_3)O$; R = CH_3; X = O; Y = F) and sarin (RO = $(CH_3)_2CHO$; R = CH_3; X = O; Y = F), the latter gaining their notoriety as organophosphorus nerve agents. Due to their potential toxicity, considerable attention has been directed toward methods of facilitating the hydrolysis or decomposition of organophosphates.

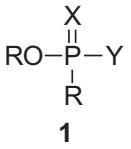

1

In some cases, metal chelates have been successfully shown to catalyze the hydrolysis of neutral phosphate and (or) phosphonate esters (2). More work has been directed to-

Received March 29, 1999.

H. Oumar-Mahamat, H. Ślebocka-Tilk, and R.S. Brown.[1] Department of Chemistry, Queen's University, Kingston, ON K6L 3N6, Canada.

[1]Author to whom correspondence may be addressed. Telephone: (613) 533-2616. Fax: (613) 533-6669. e-mail: rsbrown@chem.queens.ca

© 1999 NRC Canada

Scheme 1.

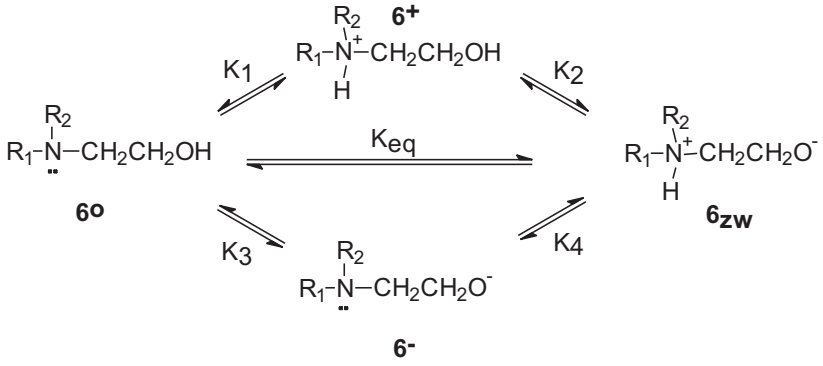

6a R_1=$C_{12}H_{25}$; R_2=H
b R_1=$C_{14}H_{29}$; R_2=H
c R_1=$C_{14}H_{29}$; R_2=CH_3
d R_1=C_{16}H33, R_2=H

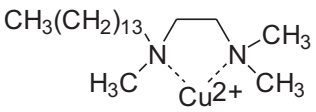

2

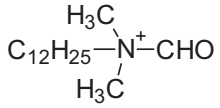

3

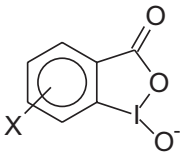

4

ward micelles (3) (which may (3*b–e*, *g–i*, *k*, *m*, *n*) or may not (3*a*, *f*) contain nucleophilic or general-base additives), functionalized micelles (4), and vesicular (5) means of decomposing organophosphate esters. Of the above surfactant systems, only a few exhibit true catalytic properties (2*e*, *f*, 3*e*, *k*, *m*, *o*, 4*g*, *o*, *q*). Perhaps the most efficacious are the systems initially discovered by Menger et al. (2*e*, *f*, 4*o*) (**2**, **3**), and Moss et al. (3*e*, *j–l*) (**4**), various derivatives of the latter being further investigated (6) due to the high reactivity attributable to the iodosobenzoates.

In general, functionalized quaternary ammonium materials containing a hydroxyethyl group (**5**) possess several important features that have been exploited for the reaction with phosphate esters. First, above the critical micelle concentration (CMC), hydrophobic substrates are attracted to the micellar pseudophase, which increases the local concentration and the likelihood of reaction with the polar head group. Second, the presence of the positively charged quaternary ammonium group electrostatically reduces the pK_a of the attached hydroxyethyl group, thereby creating appreciable quantities of $\mathbf{5_{ZW}}$ at reduced pH. For example, while the pK_a values for alcohols normally range from 15 to 19, those of choline and 2-(*N*,*N*,*N*-triethylammonium)ethanol are 12.8 (7) and 12.9 ± 0.3 (8), while those of micellar **5** (R = $C_{12}H_{25}$ and R = $C_{16}H_{33}$) are 12.9 and 12.4 (4*b*). Furthermore, zwitterionic $\mathbf{5_{ZW}}$ has been shown in several instances (4*b*, 8, 9) to be sufficiently nucleophilic to attack activated C and P esters.

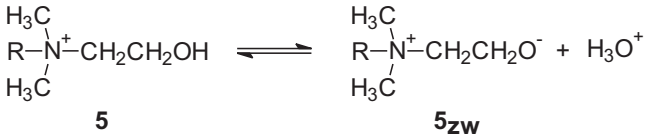

5 $\mathbf{5_{ZW}}$

Unfortunately, these hydroxyethyl quaternary ammonium species are not true catalysts in that they possess no internal means to subsequently regenerate **5** or $\mathbf{5_{ZW}}$ other than through attack of external OH^-. It appeared to us that one might expand the catalytic utility of such micelles by utilizing secondary or tertiary hydroxyethyl amines related to **5**. In principle, derivatives of **6** containing a long chain alkyl moiety should impart micellar characteristics. As shown in Scheme 1, such species can exist in aqueous media as a pH-dependent mixture of four species ($\mathbf{6^+}$, **6**°, $\mathbf{6_{ZW}}$, $\mathbf{6^-}$), the relative amounts of which are controlled by the four microscopic ionization constants K_1–K_4. Forms $\mathbf{6^+}$ and $\mathbf{6_{ZW}}$, in which the amine is protonated, formally resemble the charge types inherent in the more traditional quaternary ammonium micellar species **5**, $\mathbf{5_{ZW}}$. Following nucleophilic attack of the O^- of $\mathbf{6^-}$ or $\mathbf{6_{ZW}}$ on the activated phosphate, a possibility exists that the β-amino group, when deprotonated, might act as an internal nucleophile to displace phosphate to yield an aziridine, which, under the reaction conditions, could suffer nucleophilic ring opening to regenerate the catalyst.

Herein we describe our preliminary findings with surfactants in which four long chain alkyl substituted derivatives

© 1999 NRC Canada

of **6** are reacted with *p*-nitrophenyldiphenyl phosphate (**7**, PNPDPP) under various conditions of solvent composition and pH. Importantly, we have observed that the amino alcohols themselves are rather ineffective in promoting the hydrolysis of **7** unless added polyhydroxy cosolvents are present. In the presence of polyols such as glycerol, ethylene glycol, and even sorbitol, two of these derivatives, **6a**, **b**, probably as their zwitterionic forms, $\mathbf{6_{ZW}}$, appear to be effective nucleophiles toward PNPDPP, producing an *O*-phosphorylated intermediate. Furthermore, under the optimum conditions, **6b** is shown to be catalytically active due to its built-in turnover capabilities.

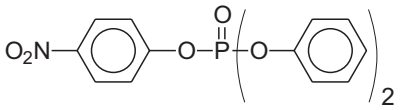

7

Experimental

a. Materials

p-Nitrophenyldiphenyl phosphate (**7**) was prepared as previously described (10). The amino alcohols **6a**–**d** were made by a generalized procedure (11) modified as follows. A 1130 mL acetone solution containing 300 mmol of 2-aminoethanol (or 2(*N*-methyl)aminoethanol) and 20 mmol of the C_{12}, C_{14}, or C_{16} primary alkyl bromide was heated at reflux for 15–18 h. After cooling, the acetone was removed at reduced pressure, and ether was added to the residue. The ether solution was twice washed with saturated $NaHCO_3$, and then H_2O. Following drying (Na_2SO_4) of the organic solution, the volatiles were removed to yield a semi-crystalline mass that was recrystallized from ether/pet. ether (1:1). The following physical properties were observed.

*2-(*N-*Dodecylamino)ethanol (**6a**)*: Yield 46.5%; mp 41–42°C; IR ($CHCl_3$ cast): 3282, 3120 cm^{-1}; ^1H NMR ($CDCl_3$) 80 MHz, δ: 3.64 (t, 2 H, CH_2OH), 2.78 + 2.62 (2 t, 4 H, CH_2NHCH_2), 1.97 (s, 2 H, NH + OH), 1.28 (bs, 20 H, $(CH_2)_{10}$), 0.88 (t, 3 H, CH_3). Anal. calcd. for $C_{14}H_{31}NO$: C 73.30, H 13.62, N 6.11; found: C 73.35, H 13.41, N 6.08.

*2-(*N-*Tetradecylamino)ethanol (**6b**)*: Yield 93% in methanol as solvent; mp 50–51°C; IR (KBr): 3492, 3272 cm^{-1}; ^1H NMR ($CDCl_3$) δ: 3.6 (t, 2 H, $NH_2CH_2CH_2OH$), 3.06 (bs, 2 H, NH + OH), 2.72 + 2.63 (2 t, 4 H, CH_2NHCH_2), 1.51 (m, 2 H, $-CH_2CH_2NHCH_2CH_2OH$), 1.28 (bs, 22 H, $(CH_2)_{11}$, 0.89 (t, 3 H, CH_3). Anal. calcd. for $C_{16}H_{35}NO$: C 74.64, H 13.70, N 5.44; found: C 74.82, H 13.79, N 5.26.

*2-(*N-*Methyl*-N-*tetradecylamino)ethanol (**6c**)*: Yield 19.2%; mp <25°C (crystallized from ether/pet. ether at low temperature and quickly filtered); IR ($CHCl_3$ cast): 3410 cm^{-1}; ^1H NMR ($CDCl_3$) δ: 3.54 (t, 2 H, CH_2OH), 2.99 (bs, 1 H, CH_2OH), 2.48 (t, 2 H, $N(CH_3)CH_2CH_2OH$), 2.37 (t, 2 H, $CH_2N(CH_3)CH_2CH_2OH$), 2.20 (s, 3 H, $N(CH_3)$), 1.43 (m, 2 H, $(CH_2)_{11}CH_2CH_2N$), 1.26 (s, 22 H, $(CH_2)_{11}$), 0.87 (t, 3 H, CH_3). Anal. calcd. for $C_{17}H_{37}NO$: C 75.21, H 13.74, N 5.16; found: C 74.61, H 13.74, N 4.94.

*2-(*N-*Hexadecylamino)ethanol (**6d**)*: Yield 54.5%; mp 49–50°C; IR ($CHCl_3$ cast): 3110, 3290 cm^{-1}; ^1H NMR ($CDCl_3$) δ: 3.62 (t, 2 H, $NHCH_2CH_2OH$), 2.75 (t, 2 H, $NHCH_2CH_2OH$), 2.60 (t, 2 H, $CH_2NHCH_2CH_2OH$), 2.36 (bs, 2 H, NH + OH), 1.48 (m, 2 H, $(CH_2)_{13}CH_2CH_2N$), 1.27 (bs, 26 H, $(CH_2)_{13}$), 0.88 (t, 3 H, CH_3). Anal. calcd. for $C_{18}H_{39}NO$: C 75.72, H 13.77, N 4.91; found: C 75.70, H 13.46, N 4.77.

b. Kinetics

Kinetics were monitored by observing the rate of formation of *p*-nitrophenoxide at 400 nm (T = 25°C) using a Hewlett–Packard 8451A diode array spectrophotometer or a Cary 210 UV-vis. spectrophotometer. Buffers employed were HEPPS (*N*-[2-hydroxyethyl]piperazine-*N*′-3-propanesulfonic acid), pH 7.5–8.5; CHES (cyclohexylaminoethanesulfonic acid), pH 8.5–10; and CAPS (cyclohexylaminopropanesulfonic acid), pH 10.5–11.5. Final buffer concentrations were 0.01 M, μ = 0.3 (KCl). pH values were measured using a Radiometer TTT2 titration unit with a Radiometer GK-2321C combination electrode, which was standardized using Fisher certified pH 7.00 and 10.00 buffers. pH values were simply measured from solutions that contained the organic cosolvents and amino alcohols and were not corrected. pH values measured before and after the reactions showed no significant deviations. Organic cosolvents were commercially available and used without further purification. Buffer solutions containing the amino alcohols at various concentrations and cosolvents were sonicated for 5 min, and then placed in 3 mL quartz cuvettes in the spectrophotometer cell holder for 20 min to allow thermal equilibration. Reactions were initiated by injecting 5 μL of a 3×10^{-2} M solution of PNPNPP (**7**) in ethanol or DME into the contents of the quartz cuvettes (final concentration of **7**, 5×10^{-5} M). Pseudo-first-order rate constants (k_{obs}) were evaluated by fitting the absorbance (Abs.) vs. time data to a standard exponential model via nonlinear least-squares treatment. Reactions were monitored in triplicate and followed to at least $3t_{1/2}$; in most cases the reactions displayed excellent first-order kinetics, and when they failed to do so, the reactions were repeated. Kinetic data for **6a**, **b**, **c** are presented in Tables 1–3, and the error limits presented are standard deviations.

c. Reactions in the presence of polyethylene glycols

One litre of polyethylene glycol (PEG) 400, having an average molecular weight of 400, was purified by mixing with 15 g of Celite followed by filtration through a medium pore sintered glass funnel. The material was then filtered through about 50 g of neutral alumina (~2 cm thick on sintered glass filtration funnel). The so-purified PEG was kept in a sealed bottle under Ar and thoroughly mixed before any use to ensure homogeneity. For kinetic runs, the solvent–PEG system requires the following protocol for ensuring clear solutions. (*i*) A 5×10^{-3} M mixture of **6b** was prepared in a solvent consisting of 20% v/v glycerol and 80% water containing 0.3 M KCl and 0.01 M HEPPS buffer, by shaking or sonication for 30 min at 50°C. (*ii*) To this solution was added, with agitation, the same volume of PEG 400 as the volume of glycerol added in part (*i*), resulting in a final composition of 16.5% PEG 400, 16.5% glycerol, and 67.5%

© 1999 NRC Canada

Table 1. Observed pseudo-first-order rate constants, $10^5 k_{obs}$ (s^{-1}), for the reaction of *p*-nitrophenyldiphenyl phosphate (**7**) with amino alcohols **6a**, **b** at 25°C in 33.3% ethylene glycol.[a]

10^3[**6a**] (M)	pH			
	8	9	10	11
0	0.54 ± 0.01	3.64 ± 0.02		
0.5	0.84 ± 0.01	9.45 ± 0.13	117.8 ± 0.4	149.6 ± 3.7
1.0	0.92 ± 0.03	43.77 ± 0.63	168.8 ± 1.4	282.8 ± 5.9
1.5	2.33 ± 0.05	134.0 ± 1.3	182.8 ± 2.5	286.2 ± 7.8
2.0	3.08 ± 0.08	169.1 ± 2.8	306.6 ± 2.1	340.9 ± 5.6
10^3[**6b**] (M)	pH			
	8	8.5	9	10
0	0.54 ± 0.01		3.64 ± 0.02	
0.5	47.3 ± 0.2		36.5 ± 1.9	18.1 ± 0.2
1.0	122.2 ± 1.0		120.6 ± 2.1	36.5 ± 1.5
1.5	210.3 ± 1.7	250 ± 9	200.0 ± 2.6	[b]
2	234.5 ± 1.4	307 ± 10	230.3 ± 9.9	[b]

[a]pH determined from measurement in cosolvent medium and is uncorrected; [**7**] = 5×10^{-5} M.

[b]Insoluble at these concentrations.

water (v/v). The pH of the resulting solution was adjusted to the desired value by addition of NaOH or HCl. Kinetic runs were undertaken using these mixtures as described above, and the results are presented in Table 4.

d. Turnover reactions

(*i*) To determine the catalytic ability of these amino alcohols a standard protocol of conducting the reaction in 20% (v/v) glycerol/H_2O media containing HEPPS (0.01 M, μ = 0.1 (KCl)), pH = 8.0, T = 25°C was investigated. The appearance of *p*-nitrophenoxide was monitored at 460 or 465 nm, and to maintain the final absorbance <1, the respective initial concentrations of DPPNPP (**7**) were 5×10^{-4} and 1×10^{-3} M. Two sets of experiments were conducted, one with sonication, and another without, but in each case the [**6b**] was 5×10^{-4} M. With sonication, the Abs. vs. time plots displayed an irregular and nonreproducible behavior, which is attributable to problems of turbidity. Without sonication, at [**6b**] = [**7**] = 5×10^{-4} M, the kinetics displayed an approximate first-order behavior, but with a small apparent burst of *p*-nitrophenoxide at the beginning of the reaction. Importantly, at the completion of the Abs. vs. time profile, the amount of *p*-nitrophenoxide liberated was (within experimental uncertainty) equal to the initial [PNPDPP]. When the [**7**] = 2[**6b**] ([**6b**] = 5×10^{-4} M), a burst in the production of *p*-nitrophenoxide (amounting to about 40% of the initial [PNPDPP] occurring within 160 min) was observed followed by a slower further release of *p*-nitrophenoxide, the final concentration of which was equivalent to the total initial [PNPDPP] (approximate time for completion of reaction 2000 min).

(*ii*) A series of turnover experiments was also conducted in a solvent system comprising 16.5% glycerol, 67% water, 16.5% PEG 400 (all v/v), 0.25 M KCl, and 0.01 M HEPPS, pH 8, T = 25°C containing three concentrations of **6b**, 1.1×10^{-3}, 2.8×10^{-3}, and 4.16×10^{-3} M. Three mL of the above solutions were inserted into a quartz cuvette in the spectrophotometer cell holder, which was then thermally equilibrated for 15 min. The reaction was initiated by sequential injection of $4 \times 25\mu$L of 3×10^{-2} M of DPPNPP in DME (final conc. of PNPDPP after four additions = 2×10^{-3} M). For the first injection, the Abs. vs. time profile was followed at 420 nm for $10t_{1/2}$ of reaction. The second to fourth portions were added to the same cell, and the Abs. vs. time profiles followed similarly but at 450, 460, and 470 nm, respectively, to keep the final absorbance less than 2.0. The pseudo-first-order rate constants for the individual runs were calculated as above and are presented in Table 5.

Results

a. Kinetics

Amino alcohols **6a**–**d** are not soluble in purely aqueous media and thus require organic cosolvents to attain sufficient solubility to conduct kinetic experiments with PNPDPP (**7**). The hexadecyl derivative (**6d**) is the least soluble of the series and requires at least 50% added ethanol or DME to attain a [**6d**] of 2×10^{-3} M. Even so, at pH 9 virtually no enhancement of the decomposition of **7** is observed in the presence of **6d** relative to the blank rate. Further studies with **6d** were abandoned.

Given in Tables 1–3 are the pseudo-first-order rate constants for the decomposition of **7** under a variety of conditions in the presence of **6a**, **b**, and **c**. In 33.3% EtOH or DME, **6b** is generally a better catalyst than is **6a**, but neither provides a dramatic enhancement of the decomposition of **7** at any pH between 8 and 11. However, as shown from the data in Tables 1 and 2, the presence of the polyhydroxy cosolvents ethylene glycol and glycerol leads to marked enhancement in the reactivity of both **6a** and **6b**. A comparison of these amino alcohols is given by the pseudo-first-order rate constants for decomposition of **7** in 33.3% ethylene glycol in Table 1. There is no linear pH dependent trend in the rate constants observed in the presence of either of **6a** or **6b**.

© 1999 NRC Canada

Table 2. Pseudo-first-order rate constants, $10^5 k_{obs}$ (s^{-1}), for the decomposition of **7** as a function of [**6b**] in various media at 25°C.[a]

(*a*) 33% DME

10^3 [**6b**] (M)	pH			
	8	9	10	11
0.0	0.41 ± 0.02	0.41 ± 0.01		
0.5	0.41 ± 0.01	1.76 ± 0.01	23.84 ± 0.14	49.77 ± 0.12
1.0	1.06 ± 0.01	13.84 ± 0.09	40.28 ± 0.41	71.52 ± 0.53
1.5	1.12 ± 0.01	20.08 ± 2.00	57.08 ± 0.69	94.17 ± 0.94
2.0	4.20 ± 0.03	37.10 ± 2.00	62.82 ± 1.94	102.86 ± 1.60

(*b*) 50% EtOH

10^3 [**6b**] (M)	pH				
	8.5	9	9[b]	10	11
0.0	0.19 ± 0.01	0.16 ± 0.01	0.33 ± 0.02	0.64 ± 0.02	2.78 ± 0.01
0.5	0.19 ± 0.01	0.21 ± 0.01	0.67 ± 0.01	0.78 ± 0.01	3.10 ± 0.01
1.0	0.22 ± 0.01	0.18 ± 0.01	1.03 ± 0.01	0.83 ± 0.02	3.14 ± 0.01
1.5	0.20 ± 0.01	0.24 ± 0.05	5.03 ± 0.01	1.03 ± 0.04	3.22 ± 0.01
2.0	0.23 ± 0.01	0.27 ± 0.01	8.07 ± 0.02	1.19 ± 0.03	3.3 ± 0.01

(*c*) 33.3% glycerol

10^3 [**6b**] (M)	pH		
	8	8.5	9.0
0.0	1.24 ± 0.04		3.43 ± 0.07
0.5	165.2 ± 5.2	73.8 ± 5.0	10.3 ± 0.1
1	245.9 ± 5.5	100.2 ± 5.2	15.5 ± 0.1
1.5	239.4 ± 6.0	196.5 ± 4.4	11.1 ± 0.1
2.0	263.2 ± 6.3	196.3 ± 12.9	19.1 ± 0.1
2.5	295.2 ± 30.8	101.1 ± 8.7	
3.0	282.1 ± 6.1		

(*d*) 20% glycerol

10^3 [**6b**] (M)	pH	
	7.5	8[c]
0.0		0.51 ± 0.01
0.5	147.2 ± 12.3	147 ± 1
1.0	235.7 ± 10.9	294 ± 11
1.5	272.2 ± 3.9	375 ± 13
2.0	276.9 ± 3.6	451 ± 19
2.5	295.6 ± 8.6	486 ± 4
3.0	300.0 ± 9.5	434 ± 4

(*e*) 20% ethylene glycol

10^3 [**6b**] (M)	pH 8.5[d]
0.0	0.44 ± 0.02
0.5	192.1 ± 8.0
1.0	380.7 ± 6.0
1.5	500.8 ± 8.4
2.0	671.7 ± 28.6[e]
2.5	693.6 ± 2.0
3.0	741.9 ± 13.7
3.5	675.4 ± 31.5

[a]pH measured by electrode immersed in solution and not corrected for added cosolvent; [**7**] = 5×10^{-5} M.

[b]pH 9; 33.3% EtOH.

[c]Maximum activity at pH 8; insoluble below pH 7 and above pH 8.5.

[d]At pH optimum for this medium.

[e]At pH 8.0, same conditions, k_{obs} = 456 ± 19 s^{-1}.

© 1999 NRC Canada

Table 3. Pseudo-first-order rate constants, $10^5 k_{obs}$ (s^{-1}), for the decomposition of **7** in the presence of **6c** in the presence of various solvents, T = 25°C.[a]

10^3[**6c**] (M)	50% EtOH[b]	33% EtOH[b]	33% DME[b]	33% ethylene glycol[b]	20% gycerol[c]
0.0	0.16 ± 0.01	0.33 ± 0.02	0.41 ± 0.01	3.64 ± 0.02	
0.5	0.34 ± 0.01	1.82 ± 0.11	7.58 ± 0.49	15.3 ± 0.1	73.4 ± 3.9
1.0	0.36 ± 0.01	6.38 ± 0.23	12.9 ± 0.5	48.1 ± 0.3	99.6 ± 14.8
1.5	0.40 ± 0.01	10.4 ± 0.3	18.8 ± 1.0	77.6 ± 0.7	122.3 ± 16.3
2.0	0.46 ± 0.01	13.3 ± 0.3	25.6 ± 1.0	87.4 ± 0.6	109.1 ± 7.8
2.5					120.7 ± 4.9
3.0					142.6 ± 8.6

[a]pH measured by electrode immersed in solution and is uncorrected for organic cosolvent. [**7**] = 5×10^{-5} M.
[b]pH 9.
[c]pH 8.

Fig. 1. A plot of k_{obs} for the hydrolysis of **7** vs. [**6b**] in various media at 25°C, μ = 0.3 (KCl), [buffer] = 0.01 M. (▲, 33% ethanol, pH 9; ■, 33% DME, pH 9; ▼, 20% glycerol, pH 8; ◆, 20% ethylene glycol, pH 8.5.)

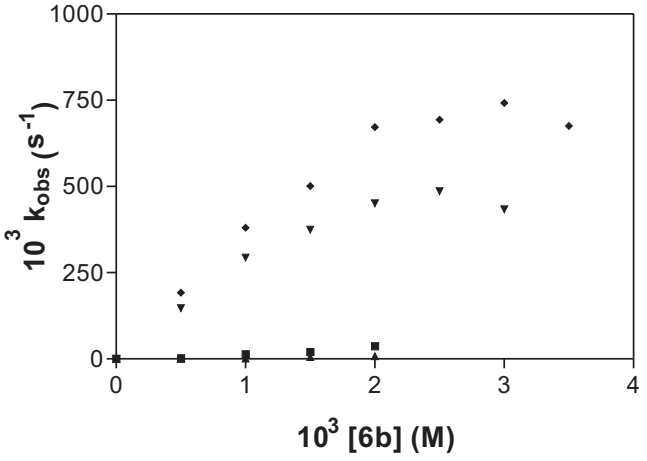

Shown in Fig. 1 are graphical representations of the pseudo-first-order rate constants for the decomposition of **7** as a function of [**6b**] at the optimum pH in various media. While we have not determined the critical micelle concentration (CMC) of any of these alcohols under the reaction conditions, the appearance of the k_{obs} vs. catalyst conc. plots with maxima at 2.5–3 mM strongly suggests micelle formation. For **6b**, ethylene glycol gives maximum activity at pH 8.5 when at 20% v/v, while 20% glycerol gives maximum activity at pH 8.0. Increasing or decreasing the amounts of these cosolvents leads to reduced activity, as do changes in the respective media pH. Given in Table 4 are rate constants for the reaction of **6b** with **7** in media containing polyethylene glycol (PEG 400) as a cosolvent. Up to half of the glycerol can be replaced by PEG 400 without noticeable drop in activity (relative to 33% glycerol), and the data show that when mixed with glycerol in a 1:1 ratio (16.5% v/v each), the k_{obs} for decomposition of **7** is about the same as with 33% glycerol at pH 8. In the absence of glycerol, 33% PEG 400 accelerates the reaction with 3.12×10^{-3} M **6b** by about 200-fold relative to the blank rate, while 16.5% each of added glycerol and PEG 400 accelerates the reaction with 3.33×10^{-3} M **6b** by about 400-fold. Methylated PEG 350, with the terminal OH groups replaced by CH_3O, seems to be as effective as PEG 400 in promoting the reactions of **6b** in glycerol media, pH 7.6–8.5 (see data in Table 4).

b. Control experiments

Under no conditions is the rate of decomposition of **7** accelerated markedly by simple medium effects in the absence of **6a**–**c**. The *N*-methyl derivative, **6c**, was investigated at the pH optima found for **6b** in solvents of different composition. The data for **6c** in Table 3 show similar overall trends to the reactions with **6b**, but in 20% ethylene glycol the maximum activity of **6c** is 2–4 times lower than that of **6b**, indicating that both secondary and tertiary amine are active. To investigate whether a simple N-substituted β-amino alcohol would exhibit a similar marked activity for the decomposition of **7** in 20% glycerol, the effects of 2×10^{-3} M added 2(*N*-methylamino)ethanol and 2(*N*,*N*-dimethylamino)ethanol were investigated at pH 8.0, T = 25°C, μ = 0.3 (KCl), [**7**] = 5×10^{-5} M. Under these conditions **7** was only slowly hydrolyzed, and the kinetic traces were clearly not first order. Although it is difficult to compare kinetics of dissimilar order, an approximate measure of the reactivity is the $t_{1/2}$ for appearance of the *p*-nitrophenoxide anion. In the presence of **6b**, **6c**, and 2(*N*-methylamino)ethanol, the respective halftimes (pH 8, 20% glycerol) were 2.55, 10.6, and 1667 min.

c. Turnover experiments

The reactions of equimolar and 1:2 stoichiometry of **6b**:**7** were investigated in 20% glycerol, pH 8, μ = 0.1 (KCl), 10^{-2} M HEPPS at 25°C where [**6b**] = 5×10^{-4} M. These conditions are not optimal, since the [**6b**] is roughly fourfold lower than for maximal activity. Nevertheless, they were chosen because the rate of appearance of *p*-nitrophenoxide could be monitored at 460 or 465 nm where the final absorbance was not greater than 1, (460 nm for [**7**] = 5×10^{-4} M; 465 nm for [**7**] = 1×10^{-3} M). Concentrations of **7** in excess of $1 \times l0^{-3}$ M could not be obtained for reasons of solubility.

Shown in Fig. 2 are the Abs. vs. time plots for the above experiments: for Fig. 2*a*, [**7**] = [**6b**] = 5×10^{-4} M, while for Fig. 2*b*, [**7**] = $1 \times l0^{-3}$ M = 2[**6b**]. The appearance of the plots, with the initial burst followed by nearly first-order production of *p*-nitrophenoxide, is consistent with a process involving phosphorylation of the amino alcohol to form an intermediate that decomposes on a similar time scale to regenerate the active amino alcohol.

© 1999 NRC Canada

Table 4. Pseudo-first-order rate constants, $10^4 k_{obs}$ (s^{-1}), for the decomposition of **7** by **6b** in the presence of PEG 400 under various conditions at T = 25°C, μ = 0.25 (KCl), [EPPS buffer] = 0.1 M.

16.5% glycerol, 16.5% PEG 400, 67% water			
10^3 [**6b**] (M)		pH	
	7.6	8.0	8.5
0.0	0.378 ± 0.003	0.574 ± 0.005	0.837 ± 0.04
1.0		48.2 ± 0.8	35.5 ± 0.5
1.25		141.8 ± 0.7	111.8 ± 0.9
2.50	198 ± 1	235 ± 2	206 ± 1
		25.2 ± 2[a]	243 ± 1[a]
3.33		263 ± 1	303 ± 1
4.16		337 ± 2	358 ± 1
15.5% glycerol, 61.5% water, 23.0% PEG 400			
10^3 [**6b**] (M)		pH	
	7.6	8.0	8.5
0.0		0.243 ± 0.005	0.387 ± 0.009
0.77		14.0 ± 0.1	
1.54		68.7 ± 0.2	54.3 ± 0.4
1.92	50.3 ± 0.8	82.7 ± 0.3	75.1 ± 0.5
2.31		105.3 ± 0.5	[b]
3.08		140.7 ± 0.6	[b]
3.85	92.3 ± 0.7	159.8 ± 0.9	[b]
0% glycerol, 67% water, 40% PEG 400			
10^3 [**6b**] (M)		pH	
	7.6	8.0	8.5
0.0	0.332 ± 0.004	0.430 ± 0.003	0.589 ± 0.003
1.04		16.0 ± 0.1	
2.08	24.1 ± 0.1	51.8 ± 0.8	38.4 ± 0.5
3.12		86.7 ± 0.7	74.1 ± 0.4
4.16	59.6 ± 0.6	118.2 ± 0.8	[b]
16.5% glycerol, 67% water, 16.5% MPEG[c]			
10^3 [**6b**] (M)		pH	
	pH 7.6	pH 8.0	pH 8.7 (CHES)
0.0	0.302 ± 0.009	0.481 ± 0.003	0.619 ± 0.002
1.04		56.8 ± 0.4	53.5 ± 0.9
1.56		85.3 ± 0.3	100.1 ± 0.9
4.16	218 ± 1	295 ± 1	291 ± 0.8

[a]Determined after allowing catalyst system to stand 24 h.

[b]Precipitates.

[c]Methyl PEG, average MW = 350, terminal groups methylated.

A second set of turnover experiments was conducted in the PEG containing solvents under more optimal conditions. Given in Table 5 are the pseudo-first-order rate constants for appearance of *p*-nitrophenoxide in the presence of **6b** in a solvent comprising 16.5% each of glycerol and PEG 400 and 67% water. To ensure that the reactions were done under homogeneous conditions, aliquots of 2.5×10^{-4} M **7** in DME were injected into the solutions and the absorbance vs. time profiles monitored for $10t_{1/2}$. After this time, another aliquot was added, and the process repeated. To ensure that the total absorbance of the solution did not exceed 2.0, progressively longer wavelengths (420–470 nm) for monitoring the reaction were used. The so-obtained Abs. vs. time data were analyzed to obtain the pseudo-first-order rate constants, which are seen to be the same for a given [**6b**], indicating that the catalyst must turn over during the time taken for the analysis.

Discussion

The choice of these long chain secondary and tertiary aminoethanols as potential micellar turnover catalysts for the decomposition of phosphate esters was dictated by several considerations including simplicity of preparation, ability to form micelles, possession of a nucleophilic pendant, and the requirement for turnover capabilities. From the observations and data given in the results section, **6b** possesses all of the above properties. The most surprising aspect, to our knowledge, is the marked enhancement in reactivity of **6b** in media containing 20–33% ethylene glycol or glycerol. Many

© 1999 NRC Canada

Table 5. Pseudo-first-order rate constants, $10^3 k_{obs}$ (s^{-1}), for the decomposition of **7** as a function of [**6b**] in 16.5% glycerol, 67% water, 16.5% PEG 400, μ = 0.25 (KCl), *T* = 25°C, [EPPS buffer] = 0.01 M, pH = 8.0.[a]

	[**6b**] (M)		
[DPPNPP **7**] (M)	1.1×10^{-3}	2.8×10^{-3}	4.16×10^{-3}
5×10^{-5}	0.83 ± 0.07	3.25 ± 0.03	3.37 ± 0.20
2.5×10^{-4}	0.852 ± 0.021		
5×10^{-4}	0.865 ± 0.025	3.23 ± 0.18	3.65 ± 0.28
7.5×10^{-4}	0.835 ± 0.041		
1×10^{-3}	1.035 ± 0.068[b]	3.25 ± 0.28	4.35 ± 0.52[b]
1.5×10^{-3}		2.98 ± 0.31	
2×10^{-3}		3.52 ± 0.48	

[a]pH measured from electrode immersed in solution and not corrected for cosolvent.

[b]Turbid solutions with precipitate at end of reactions.

reactions, including carboxyl (12), phosphoryl (13), and surfuryl (14) -group transfers are accelerated in going to less protic and less polar mixed solvent systems (15). The solvent effect generally results from either transition state (TS) stabilization or destabilization of the ground state consisting of nucleophile plus substrate. Poor solvation of anions in dipolar aprotic solvents leads to very marked acceleration of nucleophilic attack if charge is dispersed in the TS (15). Recently Bunton et al. (16) have investigated the attack of HO^- and the oximate of 2,3-butanedione on PNPDPP in water–CH_3CN and water–*t*-BuOH solvent mixtures. They found that the rates initially drop as the percentage of water decreases, but that further reductions in the water conc. led to increases in rate. This is rationalized by an initial stabilization of the nonionic PNPDPP followed by increasing destabilization of the anionic nucleophile resulting from its loss of hydration. Nevertheless, the total effects are far less than what is observed in the present study. Some work has been done on the effects of added DMSO on the hydrolysis of PNPDPP in media containing co-micelles of cetyltrimethylammonium bromide and diethylheptadecylimmidazolium ethylsulphate (4*r*), the net effect being that as the [DMSO] was increased to 90%, substantial increases in rates could be achieved.

Far less work appears to have been done on the effect of polyhydroxy additives on hydrolytic reactions (17). Nusselder and Engberts (17*a*) investigated the hydrolysis of three activated amides (1-acyl-1,2,4-triazoles) in aqueous media containing up to 4 mol% of carbohydrates such as maltose, glucose, and ribose. Although the effect of the additive was to slightly decrease the overall rate of reaction, there were substantial medium effects on the $\Delta S^{\ddagger}$ of reaction attributable to alterations in the three-dimensional H-bonded network in water. Cleve (17*b*) has looked at the hydrolysis of methyl trifluoromethylacetate in water containing alcohols such as butanol and found only modest effects on the reaction rates. Notably, in neither of these studies was there observed the sort of strong rate enhancements such as seen in the present study using the polyol additives, but the concentrations studied were far lower than is the case here.

The effect of the polyhydroxy solvents on the activity of **6b** toward **7** is probably not simple and likely results from a complex mixture of phenomena including changes in the micellar pseudophase, alteration of the pK_a values and K_{eq} associated with **6b** (Scheme 1), and hydrogen bonding by the cosolvent in a way that may lower the TS energy for phosphoryl group transfer from **7** to the O(H) of **6b**. Alternatively, it is possible that the polyhydroxy alcohols or PEGs provide the right environment to promote micellization of **6a**, **b**, and in their absence, no micelles are formed, but more work would be required to sort this out. It has been suggested that strong H bonds due to the hydroxy functions at the polar head groups of micelles are likely to be responsible for the binding of surfactants (4*b*, 8). The polyols in our case could provide such intermolecular H bonds, which transiently bind both the DPPNPP and **6b** thereby increasing the likelihood of productive encounters. However, since PEG 400 without glycerol and Methyl PEG 350 with 16.5% glycerol seem to promote the reactions, albeit somewhat less than with only glycerol or ethylene glycol, the additive cannot primarily be a H bond donor.

Fig. 2. Plots of the absorbance vs. time profiles for hydrolysis of **7** by **6b** in 20% glycerol (v/v), pH 8, μ = 0.1 (KC1), [buffer] = 0.01 M at 25°C. (*A*) [**6b**] = [**7**] = 5×10^{-4} M; (*B*) [**7**] = 2[**6b**] = 10^{-3} M.

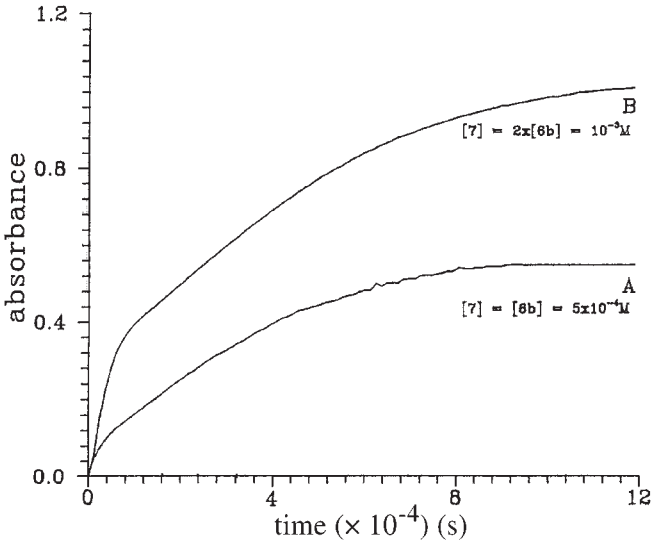

The enhancement of reactivity is not limited to the polyols ethylene glycol or glycerol, since 0.5 M sorbitol ($(HOCH_2CH(OH)CH(OH))_2$), pH 7.5, *T* = 25°C, and 2.5 mM **6b** gives a pseudo-first-order rate constant for reaction with **7** of 3.4×10^{-3} s^{-1}. By way of comparison, the system containing 20% ethylene glycol at pH 8.5 gives the highest k_{obs} of 7.42×10^{-3} s^{-1}. Thus, under the optimized conditions given in Table 2, at 3 mM added [**6b**], the ratio of the catalyzed to uncatalyzed process in 20% glycerol or 20% ethylene glycol ranges from 1000- to 1700-fold, pH 8–8.5.

Turnover

The additional point of interest in decomposition of **7** mediated by the micelles of **6b** relates to the turnover. Shown in Fig. 2 are absorbance vs. time plots for the reaction of **6b** with **7** under at relative concentration of 1:1 and 1:2, with [**6b**] = 5×10^{-4} M in 20% glycerol (v/v), pH 8, μ = 0.1 (KC1), buffer conc. = 0.01 M at 25°C. The plots are notable for an initial burst in the production of *p*-nitrophenoxide fol-

© 1999 NRC Canada

Scheme 2.

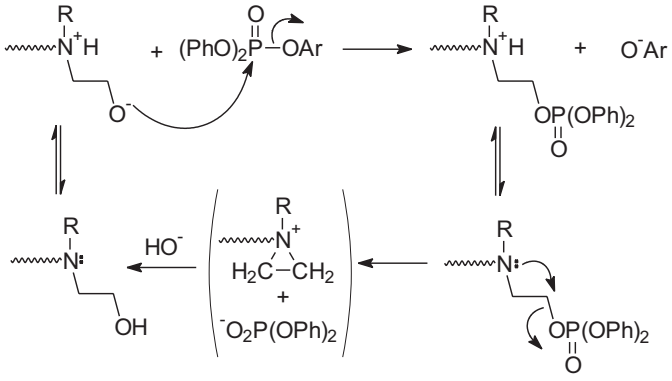

lowed by a slower process indicative of turnover. In that set of experiments, the [**6b**] was less than required for optimal activity due to the requirement of solubility and maintaining the final absorbance <1. In a second set of experiments using 1×10^{-3} to 4.2×10^{-3} M **6b** under more solubilizing conditions (16.5% glycerol, 67% water, 16.5% PEG 400, μ = 0.25 (KCl), T = 25°C, EPPS buffer conc. = 0.01 M, pH = 8.0) aliquots of 2.5×10^{-4} M **7** were added, and the successive pseudo-first-order rate constants for generation of *p*-nitrophenoxide were determined. From the data presented in Table 5 it is apparent that the rates of the reactions are the same up to the point of precipitate formation, indicating that the catalyst must be regenerating during the time of the individual rate experiments.

Since hydroxyethyl substituted quaternary ammonium micellar species (5) have not been demonstrated to have turnover capabilities other than through direct OH^--mediated hydrolysis (4*b*), the action of the free β-amino group in **6b** is implicated. Our belief in the free β-amino group as a potential mediator of turnover was guided by work reported by Heath (18), Baer (19), and Mannineu (20) detailing the reaction course for the decomposition of **8** (eq. [2] (18)) and **9** (eq. [3] (20)) as well as the known inability to produce a phosphorylethanolamine from base hydrolysis of **10** (eq. [4] (19)), the hydrolysis of which undoubtedly leads to aminoethanol. In the latter study (19*a*) the behavior of **10** toward base can be contrasted with that of diphenylphosphorylcholine, **13**, the hydrolysis of which yields phosphorylcholine, **14** (eq. [5] (19*b*)).

In an analogous process, the ability of a 2-amino group to act as a neighboring group in displacing $OSO_3^=$ from β-(aminoethyl)hydrogensulfate in NaOH solution forms the basis of the synthesis of aziridine (21). Finally, Lazarus and Benkovic (22) have reported a detailed analysis of the mechanism of hydrolysis of phosphorylethanolamine triesters, which reveals multiple catalytic effects of the intramolecular amino group, one of these being analogous to the process shown in eq. [3].

In view of the above, we envision the catalyzed decomposition of **7** by **6b** to follow the mechanism depicted in Scheme 2 where the zwitterionic form ($\mathbf{6_{ZW}}$) captures **7** to yield *p*-nitrophenoxide and the *O*-phosphorylated **6b**. Loss of the ammonium proton generates a free β-amino group, which is capable of an internal displacement of diphenyl phosphate to generate the aziridine/aziridinium, which subsequently reacts with OH^- to regenerate **6b**.

Finally, it is instructive to compare the reactivity of **6b** and other catalytic entities that have been reported to hydrolyze **7**. Given in Table 6 are the reported maximal observed pseudo-first-order rate constants, conditions, and $t_{1/2}$ values for hydrolysis of **7** mediated by various systems. It is clear that the best catalysts presently available are those related to the Moss' iodosobenzoates in cetyltrimethylammonium micelles (entries 5 (3*j*), 6 (3*d*), and 7 (6*e*) in Table 6) which are about two orders of magnitude better than the functionalized micelles. Of the remainder of the series, where a comparison can be made, the pseudo-first-order rate constants for the formulations reported to give maximal activity all lie within the same order of magnitude. Also, some of the better catalysts exhibit maximal activity at lower catalyst conc. than are required for our system. The Bunton surfactant

[2] 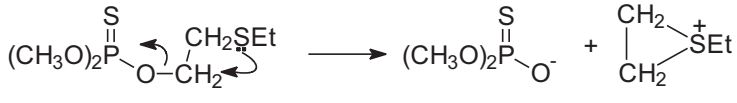

8

[3] 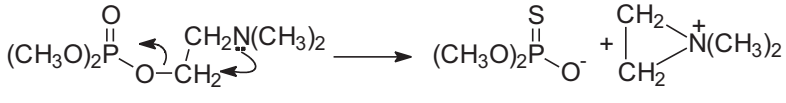

9

[4] 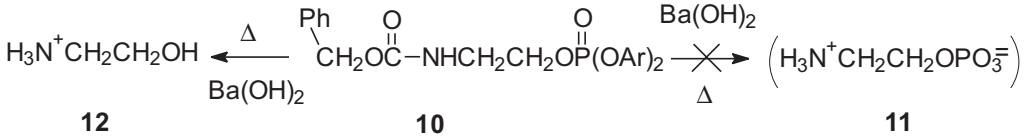

12 **10** **11**

[5] 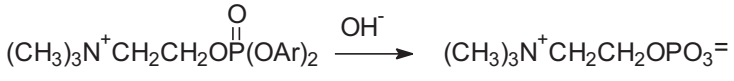

13 **14**

© 1999 NRC Canada

Table 6. Pseudo-first-order rate constants, conditions, and $t_{1/2}$ values for the hydrolysis of **7** mediated by various catalysts at T = 25°C.

Catalyst (conc. M)	Conditions	k_{obs} (s^{-1})	$t_{1/2}$ (s)	Reference
6b (3×10^{-3})	20% ethylene glycol pH 8	7.42×10^{-3}	93	This work
6b (2.5×10^{-3})	20% glycerol pH 8	4.85×10^{-3}	143	This work
2 (1.22×10^{-4})	pH 8, 10 mM *N*-ethylmorpholine	2.02×10^{-2}	34.2	2*e*
3 (8×10^{-3})	pH 9	2.0×10^{-2}	34.6	4*o*
4, X = H (1×10^{-4})	pH 8, 1 mM CTACl	6.45×10^{-2}	10.7	3*j*
4, X = $C_{16}H_{33}N^{+}Me_2(CH_2)_2OH$ (1×10^{-4})	pH 8, 0.2 mM CTACl	1.14	0.71	3*d*
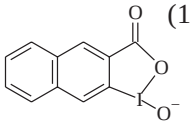 (1×10^{-4})	pH 8 0.02 M phosphate 5×10^{-3} M CTACl	0.26	2.7	6*e*
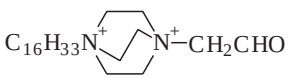 (3×10^{-3})	pH 9	8.2×10^{-3}	84.4	4*g*
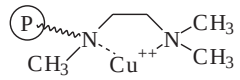 (1×10^{-3}) P = polymer	pH 8	~4.27×10^{-3}	~162	2*f*
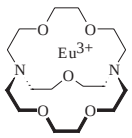 (1.6×10^{-3})	pH 9	1.8×10^{-3}	384	2*l*
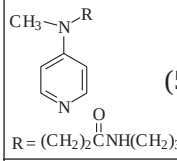 (5×10^{-4})	pH 9 5×10^{-4} M CTABr	~8.5×10^{-3}	~81	4*q*
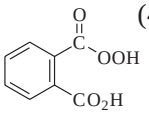 (4.5×10^{-4})	pH 8.5, 1 mM CTACl	2.4×10^{-2}	28.8	3*m*
$C_{16}H_{33}N^{+}Me_2(CH_2)_2OH$ (2.5×10^{-5})	0.01 M NaOH (pH 12)	~1.5	~0.5	4*b*

($C_{16}H_{33}N^{+}(CH_3)_2CH_2CH_2OH$) (entry 13 (4*b*)) is the most closely related to **6b** structurally and seems to be very reactive at pH 12, but the reactivity drops linearly with pH, so that at pH 8 it is the least effective of all the species in the table.

Conclusions

The above study indicates that formulations of the easily obtained **6b** in 20% ethylene glycol–H_2O or glycerol–H_2O at pH 8.5 or 8, respectively, provide a micellar catalyst system that reacts with **7**, giving a rate enhancement of ~1500-fold relative to spontaneous hydrolysis. The advantages of the present formulations with **6b** include ease of preparation, cost of the formulation, long-term stability, and low toxicity of the components. The activity of **6b** is critically dependent on the presence of polyols and (or) PEGs in the solution. The reasons for the marked enhancement in activity in the presence of these additives is not clear at present but could arise from medium effects, which favour the formation of micelles, or from a stabilization of the transition state for reaction brought about by transient H bonding with nucleophile and PNPDPP substrate. In addition, it has been shown that **6b** is catalytic in its reaction with PNPDPP, a phenomenon that we suggest arises from neighboring group assistance by the N in facilitating cleavage of the phosphorylated intermediate. It has been stated that

© 1999 NRC Canada

DPPNPP (**7**) is an attractive model for study because its spontaneous hydrolysis is slower than that of the more noxious phosphorus materials such as the nerve agents (2*e*, *f*). One expects that any catalyst capable of facilitating the hydrolysis of **7** should be effective for hydrolysis of the nerve agents. However, where direct comparison can be made, although certain catalysts (e.g., **4**) exhibit spectacular rate enhancements with **7**, their reactions with sarin and soman are somewhat less spectacular, being ~20–80-fold over the spontaneous hydrolysis (3*d*). Presumably this relates to differences in partitioning of **7** and sarin or soman between the aqueous and micellar pseudophase in which the catalytic entity resides, and TS energy differences for that reaction relative to cleavage of PNPDPP. In a given case the true test for a decontaminant is, of course, its reaction with the more noxious agent, and it remains to be determined how efficacious the **6b**–polyol systems are in this respect.

Acknowledgement

The authors gratefully acknowledge the financial support of the Defence Research Establishment Suffield (Supply and Services Canada contract no. W7702-9-R144/01-XSG).

References

1. (*a*) R.A. Main and F. Iverson. Biochem. J. **100**, 525 (1966); (*b*) J. Emsley and D. Hall. *In* The chemistry of phosphorus. Wiley, New York. 1976. p. 494.
2. (*a*) S.H. Gellman, R. Petter, and R. Breslow. J. Am. Chem. Soc. **108**, 2388 (1986); (*b*) R.S. Brown and M. Zamkanei. Inorg. Chim. Acta, **108**, 201 (1985); (*c*) R.A. Kenley, R.H. Flemming, R.M. Laine, D.S. Tse, and J.S. Winterle. Inorg. Chem. **23**, 1870 (1984); (*d*) B.S. Cooperman. *In* Metal ions in biological systems. Vol. 5. 1976. p. 79, and refs therein; (*e*) F.M. Menger, L.H. Gan, E. Johnson, and H.D. Durst. J. Am. Chem. Soc. **109**, 2800 (1987); (*f*) F.M. Menger and T. Tsuno. J. Am. Chem. Soc. **111**, 4903 (1989); (*g*) P. Scrimin, P. Tecilla, and U. Tonellato. J. Org. Chem. **56**, 161 (1991), and refs. therein; (*h*) F. Tafesse. Inorg. Chim. Acta, **269**, 287 (1998); (*i*) P. Scrimin, G. Ghinlanda, P. Tecilla, and R.A. Moss. Langmuir, **12**, 6235 (1996); (*j*) C.A. Bunton, P. Scrimin, and P. Tecilla. J. Chem. Soc. Perkin Trans. 2, 419 (1996); (*k*) Y. Fujii, T. Itoh, and K. Onodera. Chem. Lett. Jpn. 305 (1995); (*l*) S.J. Oh, C.W. Yoon, and J.W. Park. J. Chem. Soc. Perkin Trans. 2, 329 (1996).
3. (*a*) J.H. Fendler and E.J. Fendler. *In* Catalysis in micellar and macromolecular systems. Academic Press, New York (1975); (*b*) C.A. Bunton, E.J. Fendler, L. Sepulveda, and K.-U. Yang. J. Am. Chem. Soc. **90**, 5512 (1968); (*c*) C.A. Bunton, S. Diaz, J.M. Hellyer, Y. Ihara, and L.G. Ionescu. J. Org. Chem. **40**, 2313 (1975); (*d*) P.S. Hammond, J.S. Forster, C.N. Lieski, and H.D. Durst. J. Am. Chem. Soc. **111**, 7860 (1989); (*e*) R.A. Moss, K.W. Alwis, and G.O. Bizzigotti. J. Am. Chem. Soc. **105**, 681 (1983); (*f*) C.A. Bunton, Y.S. Hong, L.S. Romsted, and C. Quan. J. Am. Chem. Soc. **103**, 5788 (1981); (*g*) C.A. Bunton, G. Cerichelli, Y. Ihara, and L. Sepulveda. J. Am. Chem. Soc. **101**, 2429 (1979); (*h*) C.A. Bunton and L. Sepulveda. Israel J. Chem. **18**, 298 (1979); (*i*) C.A. Bunton, Y.S. Hong, L.S. Romsted, and C. Quan. J. Am. Chem. Soc. **103**, 5784 (1981); (*j*) R.A. Moss, B. Wilk, K. Krogh-Jespersen, J.T. Blair, and J.D. Westbrook. J. Am. Chem. Soc. **111**, 250 (1989); (*k*) R.A. Moss, S. Chatterjee, and B. Wilk. J. Org. Chem. **51**, 4303 (1986); (*l*) R.A. Moss, K.W. Alwis, and J.-S. Shin. J. Am. Chem. Soc. **106**, 2651 (1984); (*m*) S. Bhattacharaya and K. Snehalatha. J. Org. Chem. **62**, 2198 (1997); (*n*) Y.Y. Kim, K.H. Lim, and M.N. Khan. Colloids Surf. A, **121**, 239 (1997); (*o*) I.S. Ryzhkima, R.A. Shaqidullina, L.A. Ismaev, and I.B. Ivanov. Izv. Akad. Nauk, Ser. Khim. 242 (1995); Chem. Abstr. **123**, 83509e (1995).
4. (*a*) J.M. Brown, C.A. Bunton, S. Diaz, and Y. lham. J. Org. Chem. **45**, 4169 (1980); (*b*) C.A. Bunton and L.G. Ionescu. J. Am. Chem. Soc. **95**, 2912 (1973); (*c*) C.A. Bunton, L. Robinson, and M. Stam. J. Am. Chem. Soc. **92**, 7393 (1970); (*d*) J.M. Brown, C.A. Bunton, and S. Diaz. J. Chem. Soc. Chem. Commun. 971, (1974); (*e*) J. Epstein, J.J. Kaminski, N. Bodor, R. Enever, J...Sowa, and T. I-Iiguchi. J. Org. Chem. **43**, 2816 (1978); (*f*) C.A. Bunton, A.A. Kamego, M.J. Minch, and J.L. Wright. J. Org. Chem. **40**, 1321 (1975); (*g*). F.M. Menger and R.A. Persichetti. J. Org. Chem. **52**, 3451 (1987); (*h*) C.A. Bunton and S. Diaz. J. Am. Chem. Soc. **98**, 5663 (1976); (*i*) Ch. Rav-Acha, M. Chevion, J. Katzhendler, and J. Sarel. J. Org. Chem. **43**, 591 (1978); (*j*) T. Kunitake, S. Shinkai, and Y. Okahata. Bull. Chem. Soc. Jpn. **49**, 540 (1976); (*k*) T. Kunitake, Y. Okahata, and T. Sakamoto. J. Am. Chem. Soc. **98**, 7799 (1976); R.A. Moss, R.C. Nahas, and S. Ramaswami. J. Am. Chem. Soc. **99**, 627 (1977); (*m*) R.A. Moss, T.J. Lucas, and R.C. Nahas. J. Am. Chem. Soc. **100**, 5920 (1978); (*n*) C.D. Gutsche and G.C. Mei. J. Am. Chem. Soc. **107**, 7964 (1985); (*o*) F.M. Menger and L.G. Whitesell. J. Am. Chem. Soc. **107**, 707 (1985); (*p*) C.A. Bunton and G. Savelli. Adv. Phys. Org. Chem. **22,** 213 (1986), and refs. therein; (*q*) S. Bhattacharaya and K. Snehalatha. Langmuir, **11**, 4653 (1995); (*r*) L.G. Ionescu and E. Fatima de Souza. Surfactant Sci. Ser. **6**4 123 (1996).
5. (*a*) Y. Okahata, H. Ihara, and T. Kunitake. Bull. Chem. Soc. Jpn. **54**, 2072 (1981); (*b*) R.A. Moss and Y. Ihara. J. Org. Chem. **48**, 588 (1983); (*c*) R.A. Moss and S. Ganguli. Tetrahedron Lett. **30**, 2071 (1989); (*d*) R.A. Moss, P. Scrimin, S. Bhattacharya, and S. Swarup. J. Am. Chem. Soc. **109**, 6209 (1987), and refs. therein.
6. (*a*) R.A. Mackay, F.R. Longo, B.L. Knier, and H.D. Durst. J. Phys. Chem. **91**, 861 (1987); (*b*) A.R. Katritzky, B.L. DueIl, H.D. Durst, and B.L. Knier. Tetrahedron Lett. **28**, 3899 (1987); (*c*) J. Org. Chem. **53**, 3972 (1988); (*d*) R.A. Moss, K. Brachen, and T.J. Emge. *In* Proc. ERDEC Sci.: Conf. Chem. Biol. Def. Res. *Edited by* D.A. Berg. 413 (1995); (*e*) R.A. Moss, A.T. Kotchevar, B.D. Park, and P. Scrimin. Langmuir, **12**, 2200 (1996).
7. P. Haberfield and J. Pessin J. Am. Chem. Soc. **104**, 6191 (1982).
8. U. Tonellato. J. Chem. Soc. Perkin Trans. 2, 821 (1977).
9. (*a*) M. Chevion, J. Katzhendler, and S. Sarel. Israel J. Chem. **10**, 795 (1972); (*b*) V. Gani, C. Lapinte, and P. Viout. Tetrahedron Lett. 4435 (1973); (*c*) I. Tabushi and Y. Kuroda. Tetrahedron Lett. 3613 (1975); (*d*) G. Meyer. Tetrahedron Lett. 4581 (1972); (*e*) G. Meyer. Compt. Rend. **276C**, 1599 (1973); (*f*) K. Martinek, A.V. Levashov, and I.V. Berezin. Tetrahedron Lett. 1275 (1975); (*g*) R.C. Moss, R.C. Nahas, S. Ramaswami, and W.J. Sanders. Tetrahedron Lett. 3379 (1975).
10. W.M. Gulick, Jr., and D.H. Geske. J. Am. Chem. Soc. **88**, 2928 (1966).
11. R.A. Moss, S. Bhattachirjie, and S. Chaterjee. J. Am. Chem. Soc. **111**, 3686 (1989).
12. J. Cosby and G.E. Lienhard. J. Am. Chem. Soc. **92**, 5707 (1970).
13. W.Y. Abell and A.J. Kirby. Tetrahedron Lett. 1085 (1986).

© 1999 NRC Canada

14. B.D. Batts. J. Chem. Soc. B, 547 (1966).
15. A.J. Parker. Chem. Rev. **69**, 1 (1969).
16. C.A. Bunton, N.D. Gillitt, and A. Kumar. J. Phys. Org. Chem. **9**, 145 (1996).
17. (*a*) J.J.H. Nusselder and J.B.F.N. Engberts. J. Org. Chem. **52**, 3159 (1987); (*b*) N.J. Cleve. Finn. Chem. Lett. **14**, 49 (1987).
18. D.F. Heath. J. Chem. Soc. 1643 (1958).
19. (*a*) E. Baer and H.C. Stancer. Can. J. Chem. **34**, 436 (1956); (*b*) E. Baer. J. Am. Chem. Soc. **69**, 1253 (1947).
20. P.A. Mannineu. Acta Chem. Scand. **B32**, 269 (1978).
21. C.F.H. Allen, F.W. Spangler, and E.R. Webster. Org. Synth. Coll. vol. IV, 433 (1963).
22. R.A. Lazarus and S.J. Benkovic. J. Am. Chem. Soc. **101**, 4300 (1979).

© 1999 NRC Canada

Solubility of biphenyl in organic nonelectrolyte solvents. Comparison of observed versus predicted values based upon Mobile Order theory

Karina M. De Fina, Tina L. Sharp, and William E. Acree, Jr.

Abstract: Experimental solubilities are reported at 25.0°C for biphenyl dissolved in 26 different alkane, dialkyl ether, and alcohol solvents. Results of these measurements, combined with previously published biphenyl solubility data, are used to test the applications and limitations of expressions derived from Mobile Order theory. For the 40 solvents for which predictions could be made computations show that Mobile Order theory does provide fairly reasonable estimates of the saturation mole fraction solubilities. Average absolute deviation between predicted and observed values is 13.0%.

Key words: biphenyl solubilities, organic nonelectrolyte solvents, solubility predictions.

Résumé : Opérant à 25,0°C, on a déterminé les solubilités expérimentales du biphényl dissous dans 26 solvants différents comprenant des alcanes, des éthers et des alcools aliphatiques. Les résultats de ces mesures, combinées aux données de solubilité du biphényl publiées antérieurement, sont utilisés pour évaluer les applications et les limitations d'expressions dérivées de la théorie de l'ordre mobile. Pour les 40 solvants pour lesquels il était possible de faire de prédictions, les calculs montrent que la théorie de l'ordre fonctionnel conduit à des évaluations assez raisonnables des solubilités exprimées en fraction molaire de saturation. La déviation absolue moyenne entre les valeurs prévues et observées est de 13,0 %.

Mots clés : solubilités du biphényl, solvants organiques non électrolytiques, prédictions de la solubilité.

[Traduit par la Rédaction]

Introduction

Solid–liquid equilibrium data of organic nonelectrolyte systems are becoming increasingly important in the petroleum industry, particularly in light of present trends towards heavier feedstocks and known carcinogenicity/mutagenicity of many of the larger polycyclic aromatic compounds. Solubility data for a number of polycyclic aromatic hydrocarbons (e.g., anthracene and pyrene) and heteroatom polynuclear aromatics (e.g., carbazole, dibenzothiophene, and xanthene) have been published in the recent chemical literature (for listing of refs. see Acree (1–3)). Despite efforts by experimentalists and scientific organizations, both in terms of new experimental measurements and critically evaluated data compilations, there still exist numerous systems for which solubility data are not readily available.

To address this problem, researchers have turned to group contribution methods and semiempirical expressions to predict desired quantities. Group contribution methods have proved fairly successful in estimating solid solubility in pure and binary solvent mixtures from structural information (4–14). Group contribution methods typically predict solid–liquid equilibria and phase diagrams to within a root-mean-square deviation of 2 K. Practical application though, is limited to systems for which all group interaction parameters are known. Interaction parameters can be evaluated from liquid–vapor, liquid–liquid, and solid–liquid equilibria data. It is important that the database contain as many different functional groups as possible, preferably with adequate representation from both mono- and multifunctional solute/solvent molecules to permit evaluation of potential synergistic effects. The database should contain sufficient experimental values near infinite dilution in the event that one wishes to determine separate interaction parameters for finite concentration and infinite dilution activity coefficient predictions.

Abraham et al. (15, 16) recently developed a general solvation equation that can be used in the correlation and understanding of physico-chemical and biochemical phenomena. Physical properties that have been correlated include gas/solvent partition coefficients (as log L)

$$[1] \qquad \log L = c + rR_2 + s\pi_2^H + a\sum \alpha_2^H + b\sum \beta_2^H + \mathrm{d} \log L^{16}$$

and water/solvent partition coefficients (as log P)

$$[2] \qquad \log P = c + rR_2 + s\pi_2^H + a\sum \alpha_2^H + b\sum \beta_2^H + vV_x$$

Received March 22, 1999.

K.M. De Fina, T.L. Sharp, and W.E. Acree, Jr.[1]
Department of Chemistry, University of North Texas, Denton, TX 76203-5070, U.S.A.

[1]Author to whom correspondence may be addressed.
e-mail: acree@unt.edu

© 1999 NRC Canada

where R_2 and V_x refer to the excess molar refraction and McGowan volume of the solute, respectively, π_2^H is the solute dipolarity/polarizability descriptor, and $\sum \alpha_2^H$ and $\sum \beta_2^H$ are measures of the solute's hydrogen-bond acidity and hydrogen-bond basicity. For any given solvent, numerical values of the seven curve-fit coefficients (*c*, *r*, s, *a*, *b*, *d*, and *v*) are deduced by regressing experimental partition coefficient data in accordance with eqs. [1] and [2]. The input partition coefficients were sometimes calculated as the ratio of the solute molar solubilities in the organic solvent and water, $P = C_A^{org}/C_A^{aq}$, and as the ratio of the solute molar solubility in the organic solvent and vapor concentration, $L = C_A^{org}/C_A^{gas}$. Published papers have reported regression coefficients for water (15, 16) and a few select organic solvents (16).

To increase the solubility database available for developing group contribution methods and general solvation correlations, we are in the process of measuring solubility data for polycyclic aromatic hydrocarbons (PAHs) and polycyclic aromatic nitrogen heteroatoms (PANHs). In the present communication, we report biphenyl solubilities in 26 different alkanes, dialkyl ether, and alcohol solvents. Results of these measurements, combined with previously published biphenyl solubility data (17), are used to further test the applications and limitations of predictive expressions derived from Mobile Order theory. Subsequent studies will use the experimental biphenyl solubilities in developing gas/liquid partition and water/organic solvent partition correlations based upon eqs. [1] and [2].

Materials and methods

Biphenyl (Aldrich, 99%) was recrystallized several times from methanol. *n*-Nonane (TCI, 99+%), *n*-decane (TCI, 99+%), *n*-hexadecane (Aldrich, 99%), cyclooctane (Aldrich, 99+%), 2,2,4-trimethylpentane (Aldrich, HPLC), *tert*-butylcyclohexane (Aldrich, 99+%), dibutyl ether (Aldrich, 99%), methanol (Aldrich, 99.9+%), ethanol (Aaper Alcohol and Chemical Co., absolute), 1-propanol (Aldrich, 99+%, anhydrous), 2-propanol (Aldrich, 99+%, anhydrous), 1-butanol (Aldrich HPLC, 99.8+%), 2-butanol (Aldrich, 99+%, anhydrous), 1-pentanol (Aldrich, 99+%), 2-pentanol (Acros 99+%), 1-hexanol (Alfa Aesar, 99+%), 1-heptanol (Alfa Aesar, 99+%), 2-methyl-2-butanol (Acros, 99+%), 2-methyl-1-propanol (Aldrich, 99+%, anhydrous), 3-methyl-1-butanol (Aldrich, 99+%, anhydrous), 1-octanol (Aldrich, 99+%, anhydrous), 4-methyl-2-pentanol (Acros, 99+%), 2-ethyl-1-hexanol (Aldrich, 99+%), 2-methyl-1-pentanol (Aldrich, 99%), 2-methyl-2-propanol (Arco Chemicals, 99+%), and ethylene glycol (Aldrich, 99.8%, anhydrous) were stored over molecular sieves before use. Gas chromatographic analysis showed solvent purities to be 99.7 mol% or better.

Excess solute and solvent were placed in amber glass bottles and allowed to equilibrate in a constant temperature water bath at 25.0 ± 0.1°C for at least 3 days (often longer). Attainment of equilibrium was verified both by repetitive measurements after several additional days and by approaching equilibrium from supersaturation by pre-equilibrating the solutions at a higher temperature. Aliquots of saturated biphenyl solutions were transferred through a coarse filter into a tared volumetric flask to determine the amount of sample and diluted quantitatively with 2-propanol for spectrophotometric analysis at 250 nm on a Bausch and Lomb Spectronic 2000. Concentrations of the dilute solutions were determined from a Beer–Lambert law absorbance versus concentration working curve for nine standard solutions. The concentration of biphenyl in the standard solutions varied from 2.38×10^{-5} M to 1.19×10^{-4} M. The calculated molar absorptivity of the standard solutions varied slightly over the concentration range, from $\epsilon \approx 16\,500$ L mol^{-1} cm^{-1} (2.38×10^{-5} M) to $\epsilon \approx 16\,000$ L mol^{-1} cm^{-1} (1.19×10^{-4} M). Experimental molar concentrations were converted to (mass/mass) solubility fractions by multiplying by the molar mass of biphenyl, volume(s) of volumetric flask(s) used and any dilutions required to place the measured absorbances on the Beer–Lambert law absorbance versus concentration working curve, and then dividing by the mass of the saturated solution analyzed. Mole fraction solubilities were computed from (mass/mass) solubility fractions using the molar masses of the solute and solvent. Experimental biphenyl solubilities, X_A^{sat}, in 26 organic solvents studied are listed in Table 1. Numerical values represent the average of between four and eight independent determinations, with the measurements being reproducible to ±1.5%.

Results and discussion

Solubility data is available in the pharmaceutical literature for biphenyl dissolved in binary aqueous-methanol solvent mixtures. Khossravi and Connors (18) reported a molar solubility of $C_A^{sat} = 0.4245$ for biphenyl in neat methanol at 298.15 K. Molar solubilities can be converted to mole fractions using $V_{methanol} = 40.7$ cm^3 mol^{-1} and $V_{biph} = 149.4$ cm^3 mol^{-1} (16), and by assuming that the excess volume is negligible. Performing this computation, we calculate a mole fraction solubility of $X_A^{sat} = 0.018\,11$. Our experimental value of $X_A^{sat} = 0.018\,51$ differs from the published value by approximately 2%. Differences in chemical purities and experimental methodologies can lead to differences of a few percent between values determined by two different research groups.

Solvents listed in Table 1 include both noncomplexing alkanes and self-associating alcohols. Of the many solution models proposed in recent years, Mobile Order theory is perhaps the only one that is capable of describing solute behavior in such a wide range of solvent mixtures. The basic model (20–27) assumes that all molecular groups perpetually move, and that neighbours of a given kind of external atom in a molecule constantly change identity. All molecules of a given kind dispose of the same volume, equal to the total volume *V* of the liquid divided by the number N_A of molecules of the same kind, i.e., Dom A = V/N_A. The center of this domain perpetually moves. The highest mobile disorder is achieved whenever groups visit all parts of their domain without preference. Preferential contacts lead to deviations with respect to this "random" visiting. This is especially true in the case of hydrogen-bonding as specific interactions result in a specific orientation of the "donor" molecule with respect to an adjacent "acceptor" molecule.

In the case of an inert crystalline solute dissolved in a self-associating solvent, Mobile Order theory expresses the volume fraction saturation solubility, ϕ_A^{sat}, as

© 1999 NRC Canada

Table 1. Comparison between experimental biphenyl mole fraction solubilities and predicted values based upon Mobile Order theory.

Organic solvent	$(X_A^{sat})^{exp}$	Data ref.	$(X_A^{sat})^{calc}$	% dev.[a]
n-Hexane	0.124	17	0.1317	6.2
n-Heptane	0.138	17	0.1329	–3.7
n-Octane	0.147	17	0.1441	–2.0
n-Nonane	0.1551	This work	0.1593	2.7
n-Decane	0.1636	This work	0.1626	–0.6
n-Hexadecane	0.2151	This work	0.2001	–7.0
Cyclohexane	0.190	17	0.1780	–6.3
Methylcyclohexane	0.183	17	0.1758	–3.9
cis-1,2-Dimethylcyclohexane	0.195	17	0.2122	8.8
trans-1,2-Dimethylcyclohexane	0.183	17	0.2122	16.0
cis-1,3-Dimethylcyclohexane	0.172	17	0.2122	23.4
cis-1,4-Dimethylcyclohexane	0.182	17	0.2122	16.6
trans-1,4-Dimethylcyclohexane	0.173	17	0.2122	22.7
Cyclooctane	0.2194	This work	0.2096	4.5
tert-Butylcyclohexane	0.1740	This work	0.2002	15.1
2,2,4-Trimethylpentane	0.1094	This work	0.0996	–9.0
Benzene	0.381	17	0.3911	2.7
Toluene	0.377	17	0.3749	–0.6
Ethylbenzene	0.363	17	0.3686	1.5
Chlorobenzene	0.397	17	0.3892	–2.0
Dichloromethane	0.412	17	0.3935	–4.5
Chloroform	0.422	17	0.3934	–6.8
Carbon tetrachloride	0.342	17	0.3503	2.4
1,1-Dichloroethane	0.381	17	0.3894	2.2
1,2-Dichloroethane	0.397	17	0.3866	–2.6
1,2-Dibromoethane	0.389	17	0.3855	–0.9
Dibutyl ether	0.2660	This work	0.3414	28.3
Methanol	0.01851	This work	0.02429	31.2
Ethanol	0.03456	This work	0.04443	28.6
1-Propanol	0.04620	This work	0.05864	26.9
2-Propanol	0.03533	This work	0.06572	86.0
1-Butanol	0.05788	This work	0.07459	28.9
2-Butanol	0.05005	This work	0.06239	24.7
2-Methyl-1-propanol	0.03906	This work	0.05210	33.4
2-Methyl-2-propanol	0.04118	This work		
1-Pentanol	0.07573	This work	0.08253	9.0
2-Pentanol	0.06525	This work		
3-Methyl-1-butanol	0.05664	This work		
2-Methyl-2-butanol	0.07120	This work		
1-Hexanol	0.08592	This work	0.08177	–4.8
2-Methyl-1-pentanol	0.07216	This work		
4-Methyl-2-pentanol	0.06115	This work		
1-Heptanol	0.1001	This work	0.09205	–8.0
1-Octanol	0.1097	This work	0.1012	–7.7
2-Ethyl-1-hexanol	0.09481	This work		
Ethylene glycol	0.00269	This work	0.00268	–0.4
Carbon disulfide	0.369	17	0.3701	0.3

[a]Deviations (%) = $100[(X_A^{sat})^{calc} - (X_A^{sat})^{exp}]/(X_A^{sat})^{exp}$.

$$[3]\quad \ln \phi_A^{sat} = \ln a_A^{solid} - 0.5(1 - V_A/V_{solvent})\phi_{solvent} + 0.5 \ln [\phi_A^{sat} + \phi_{solvent}(V_A/V_{solvent})] - \phi_{solvent}^2 V_A(\delta'_A - \delta'_{solvent})^2(RT)^{-1} - r_{solvent}(V_A/V_{solvent})\phi_{solvent}$$

where the $r_{solvent}(V_A/V_{solvent})\phi_{solvent}$ term represents the contributions resulting from hydrogen-bond formation between the solvent molecules. For most of the published applications, $r_{solvent}$ was assumed to be unity for strongly associated solvents with single hydrogen-bonded chains such as monofunctional alcohols, to be two for water or diols, and to equal zero for nonassociated solvents such as saturated hy-

© 1999 NRC Canada

drocarbons. A more exact value for alcoholic solvents can be calculated based upon

$$[4] \quad r_{solvent} = (K_{solvent}\phi_{solvent}/V_{solvent})/(1 + K_{solvent}\phi_{solvent}/V_{solvent})$$

with a numerical value of $K_{solvent}$ = 5000 cm^3 mol^{-1} assumed for all mono-functional alcohols.

If complexation does occur between the crystalline solute and solvent

$$[5] \quad \ln \phi_A^{sat} = \ln a_A^{solid} - 0.5(1 - V_A/V_{solvent})\phi_{solvent} + 0.5 \ln [\phi_A^{sat} + \phi_{solvent}(V_A/V_{solvent})] - \phi_{solvent}^2 V_A(\delta'_A - \delta'_{solvent})^2(RT)^{-1} + \ln [1 + \phi_{solvent}(K_{ASolvent}/V_{solvent})]$$

then an additional term involving the solute–solvent equilibrium constant, $K_{ASolvent}$, must be introduced to describe the solubility enhancement that arises as a result of specific interactions. A slightly more complex expression applies in the case of solute complexation with a self-associating solvent. The symbols δ'_A and $\delta'_{solvent}$ denote the modified solubility parameters of the solute and solvent, respectively, V_i is the molar volume, and a_A^{solid} is the activity of the solid solute. This latter quantity is defined as the ratio of the fugacity of the solid to the fugacity of the pure hypothetical supercooled liquid. The numerical value of a_A^{solid} can be computed from

$$[6] \quad \ln a_A^{solid} = -\Delta H_A^{fus}(T_{mp} - T)/(RTT_{mp})$$

the solute's molar enthalpy of fusion, ΔH_A^{fus} at the normal melting point temperature, T_{mp}. Contributions from nonspecific interaction are incorporated into Mobile Order theory through the $\phi_{solvent}^2 V_A(\delta'_A - \delta'_{solvent})^2(RT)^{-1}$ term. Ruelle et al. (23–27) and Acree and co-workers (28–34) have presented an impressive set of comparisons between experimental and predicted values for anthracene, naphthalene, pyrene, biphenyl, carbazole, benzil, *p*-benzoquinone, tricosane, octacosane, 10-nonadecanone, 11-heneicosanone, 12-tricosanone, *trans*-stilbene, thioxanthen-9-one, and phenanthrene solubilities in a wide range of both noncomplexing and complexing solvents to document the predictive ability of Mobile Order theory.

Predictive application of eqs. [3] and [5] is relatively straightforward. First, an average numerical value of δ'_{biph} = 19.51 MPa$^{1/2}$ is computed by requiring that each equation (with $r_{solvent}$ = 0 and (or) $K_{ASolvent}$ = 0) perfectly describes biphenyl mole fraction solubility data in *n*-hexane (δ'_{biph} = 19.60 MPa$^{1/2}$), *n*-heptane (δ'_{biph} = 19.45 MPa$^{1/2}$), and *n*-octane (δ'_{biph} = 19.48 MPa$^{1/2}$). The numerical value of a_A^{solid} = 0.3844 is calculated using eq. [11] with ΔH_A^{fus} = 18 410 J mol^{-1} (35). A numerical value of V_{biph} = 149.4 cm^3 mol^{-1} (19) was used for the molar volume of the hypothetical subcooled liquid solute.

Table 1 summarizes the predictive ability of Mobile Order theory for the 40 different organic solvents for which both biphenyl solubility data and modified solubility parameters could be found. We could not find modified solubility parameters for all of the branched and secondary alcohol solvents. Solvent molar volumes and modified solubility parameters are listed in Table 2. The modified solubility parameters account for only nonspecific interactions, and in the case of the alcoholic solvents the hydrogen-bonding contributions have been removed. Numerical values of $\delta'_{solvent}$ were obtained from published compilations (23, 24, 26, 27), and were either deduced by regressing actual solubility data

Table 2. Solvent and solute properties used in Mobile Order predictions.

Component (*i*)	V_i/(cm^3 mol^{-1})	δ'_i/(MPa$^{1/2}$)[a]
n-Hexane	131.51	14.56
n-Heptane	147.48	14.66
n-Octane	163.46	14.85
n-Nonane	179.87	15.07
n-Decane	195.88	15.14
n-Hexadecane	294.12	15.61
Cyclohexane	108.76	14.82
Methylcyclohexane	128.32	15.00
cis-1,2-Dimethylcyclohexane	145.4	15.50
trans-1,2-Dimethylcyclohexane	145.4	15.50
cis-1,3-Dimethylcyclohexane	145.4	15.50
cis-1,4-Dimethylcyclohexane	145.4	15.50
trans-1,4-Dimethylcyclohexane	145.4	15.50
Cyclooctane	134.9	15.40
tert-Butylcyclohexane	173.9	15.50
2,2,4-Trimethylpentane	166.09	14.30
Benzene	89.4	18.95
Toluene	106.9	18.10
Ethylbenzene	123.1	18.02
Chlorobenzene	102.1	19.48
Dichloromethane	64.5	20.53
Chloroform	80.7	18.77
Carbon tetrachloride	97.8	17.04
1,1-Dichloroethane	84.8	18.51
1,2-Dichloroethane	78.8	20.99
1,2-Dibromoethane	87.0	20.75
Dibutyl ether	170.3	17.45
Methanol	40.7	19.25
Ethanol	58.7	17.81
1-Propanol	75.10	17.29
2-Propanol	76.90	17.60
1-Butanol	92.00	17.16
2-Butanol	92.4	16.60
2-Methyl-1-propanol	92.8	16.14
1-Pentanol	108.6	16.85
1-Hexanol	125.2	16.40
1-Heptanol	141.9	16.39
1-Octanol	158.3	16.38
Ethylene glycol	56.0	19.90
Carbon disulfide	60.0	20.50
Biphenyl[b]	149.4[c]	19.51[d]

[a]Tabulated values are taken from a compilation given in Ruelle et al. (23, 24, 26, 27).

[b]The numerical value of a_A^{solid} = 0.3844 was calculated from eq. [6] using ΔH_A^{fus} = 18 410 J mol^{-1} (35).

[c]Numerical value of V_{biph} = 149.4 cm^3 mol^{-1} was taken from the experimental data of Good et al. (19).

[d]Numerical value was calculated using the measured biphenyl mole fraction solubilities in *n*-hexane, *n*-heptane, and *n*-octane, in accordance with eqs. [3] and [5], with $r_{solvent}$ = 0 and (or) $K_{ASolvent}$ = 0.

© 1999 NRC Canada

of solid *n*-alkanes in organic solvents in accordance with the configurational entropic model of Huyskens and Haulait-Pirson (36) or estimated using known values for similar organic solvents. Examination of the entries in Table 1 reveals that Mobile Order theory does provide fairly reasonable estimates of the solubility behavior of biphenyl in a wide range of organic solvents. Average absolute deviation between predicted and observed values is 13.0%. The solvents hexane, heptane, and octane were excluded from the average deviation computation, since δ'_{biph} was based upon the measured biphenyl solubilities in these three alkane solvents. Expressed on a natural logarithmic mole fraction scale Mobile Order theory predicts the biphenyl solubilities to within ±0.12 ln units. It should be noted that Ruelle et al. (25) previously presented a similar comparison involving Mobile Order theory; however, the authors' solvent set included primarily saturated alkane hydrocarbons, benzene derivatives, and halogenated alkanes. Our comparison is more complete in that 19 additional solvents are considered. Readers are reminded that in evaluating the applicability of Mobile Order theory one must realize that many of these particular systems are highly nonideal, and that the experimental solubility data covers over a 150-fold range in mole fraction. Had an ideal solution been assumed, then the predicted mole fraction solubility would be $X_A^{sat} = a_A^{solid} = 0.3844$ for each solvent. The ideal solution approximation corresponds to a considerably larger average absolute deviation of 613% between predicted and observed values.

Acknowledgements

Tina Sharp thanks the University of North Texas and the U.S. Department of Education for support provided under the Ronald E. McNair Postbaccalaureate Achievement Program.

References

1. W.E. Acree, Jr. Polycyclic aromatic hydrocarbons in pure and binary solvents. IUPAC solubility data series. Vol. 54. Oxford University Press, Oxford, U.K. 1994.
2. W.E. Acree, Jr. Polycyclic aromatic hydrocarbons: binary nonaqueous systems: part 1 (solutes A–E). IUPAC solubility data series. Vol. 58. Oxford University Press, Oxford, U.K. 1995.
3. W.E. Acree, Jr. Polycyclic aromatic hydrocarbons: binary nonaqueous systems: part 2 (solutes F–Z). IUPAC solubility data series. Vol. 59. Oxford University Press, Oxford, U.K. 1995.
4. W.E. Acree, Jr. Int. J. Pharm. **18**, 47 (1984).
5. U. Domanska and T. Hofman. J. Solution Chem. **14**, 531 (1985).
6. U. Domanska. Fluid Phase Equilib. **35**, 217 (1985).
7. R.S. Basu, H. Pham, and D.P. Wilson. Int. J. Pharm. **7**, 319 (1986).
8. A.B. Ochsner and T.D. Sokoloski. J. Pharm. Sci. **74**, 634 (1985).
9. R. Carta and S. Dernini. J. Chem. Eng. Data, **28**, 328 (1983).
10. W.E. Acree, Jr., and J.H. Rytting. Int. J. Pharm. **13**, 197 (1983).
11. A. Martin, P.L. Wu, A. Adjei, A. Beerbower, and J.M. Prausnitz. J. Pharm. Sci. **70**, 1260 (1981).
12. C. Fiege, R. Joh, M. Petri, and J. Gmehling. J. Chem. Eng. Data, **41**, 1432 (1996).
13. T. Hofman, B. Borbes, and C. Casanova. Ber. Beunsenges. Phys. Chem. **102**, 25 (1998).
14. W.C. Moollan, U.M. Domanska, and T.M. Letcher. Fluid Phase Equilib. **128**, 137 (1997).
15. M.H. Abraham, H.S. Chadha, J.P. Dixon, and A.J. Leo. J. Phys. Org. Chem. **7**, 712 (1994).
16. M.H. Abraham, J. Andonian-Haftvan, J.P. Osei-Owasu, P. Sakellariou, J.S. Urieta, M.C. Lopez, and R. Fuchs. J. Chem. Soc. Perkin Trans. 2, 299 (1993).
17. W. Chang, Ph.D. Dissertation. North Dakota State University, Fargo, North Dakota. 1969.
18. D. Khossravi and K.A. Connors. J. Pharm. Sci. **82**, 817 (1993).
19. R.J. Good, E.E. Hard, A.M. Ellenburg, and H.B. Richards, Jr. J. Am. Chem. Soc. **75**, 436 (1953).
20. P.L. Huyskens and G.G. Siegel. Bull. Soc. Chim. Belg. **97**, 821 (1988).
21. G.G. Siegel, P.L. Huyskens, and G. Vanderheyden. Ber. Bunsenges. Phys. **94**, 549 (1990).
22. P.L. Huyskens. J. Mol. Struct. **274**, 223 (1992).
23. P. Ruelle, C. Rey-Mermet, M. Buchmann, H. Nam-Tran, U.W. Kesselring, and P.L. Huyskens. Pharm. Res. **8**, 840 (1991).
24. P. Ruelle, M. Buchmann, H. Nam-Tran, and U.W. Kesselring. Int. J. Pharm. **87**, 47 (1992).
25. P. Ruelle, M. Buchmann, and U.W. Kesselring. J. Pharm. Sci. **83**, 396 (1994).
26. P. Ruelle, E. Sarraf, and U.W. Kesselring. Int. J. Pharm. **104**, 125 (1994).
27. P. Ruelle, E. Sarraf, L. Van den Berge, K. Seghers, M. Buchmann, and U.W. Kesselring. Pharm. Acta Helv. **68**, 49 (1993).
28. J.R. Powell, D. Voisinet, A. Salazar, and W.E. Acree, Jr. Phys. Chem. Liq. **28**, 269 (1994).
29. K.A. Fletcher, K.S. Coym, L.E. Roy, C.E. Hernández, M.E.R. McHale, and W.E. Acree, Jr. Phys. Chem. Liq. **35**, 243 (1998).
30. K.A. Fletcher, M.E.R. McHale, K.S. Coym, and W.E. Acree, Jr. Can. J. Chem. **75**, 258 (1997).
31. C.E. Hernández and W.E. Acree, Jr. Can. J. Chem. **76**, 1312 (1998).
32. L.E. Roy, C.E. Hernández, and W.E. Acree, Jr. Polycyclic Aromat. Compds. **13**, 105 (1999).
33. L.E. Roy, C.E. Hernández, and W.E. Acree, Jr. Polycyclic Aromat. Compds. **13**, 205 (1999).
34. C.E. Hernández, K.M. De Fina, L.E. Roy, T.L. Sharp, and W.E. Acree, Jr. Can. J. Chem. **77**, 1465 (1999).
35. C. Plato and A.R. Glasgow, Jr. Anal. Chem. **41**, 330 (1969).
36. P.L. Huyskens and M.C. Haulait-Pirson. J. Mol. Liq. **31**, 135 (1985).

© 1999 NRC Canada

Étude de l'adsorption des hydrocarbures aromatiques polycycliques sur l'hydroxyde d'aluminium par chromatographie liquide à haute pression

Chakib Ameziane Hassani et Hugues Ménard

Résumé : L'étude par HPLC de l'adsorption des HAP dans le toluène sur l'hydroxyde d'aluminium calciné à des températures allant de 25 jusqu'à 700°C montre que le taux d'adsorption est maximal sur l'hydroxyde chauffé à 300°C. Les mesures du potentiel électrocinétique et de la surface spécifique sont en accord avec ces résultats. Les enthalpies d'adsorption des différents HAP sur l'hydroxyde chauffé à 300°C sont calculées, ceci nous a permis de mettre en évidence le phénomène de physisorption. Cette étude compare le pouvoir adsorbant élevé de l'hydroxyde d'aluminium vis-à-vis les HAP par rapport à celui d'autres matériaux réputés être potentiellement cancérigènes.

Mots clés : adsorption des HAP, hydroxyde d'aluminium.

Abstract: A study by high performance liquid chromatography of adsorption isotherm of HAP in toluene on $Al(OH)_3$ heated between 25 and 700°C shows that the rate of adsorption is maximal on the $Al(OH)_3$ heated at 300°C. The measurement of electrokinetic potential and the surface area of adsorbants approve this result. The determination of adsorption enthalpies of different HAP on the aluminium hydroxide has shown the existence of physical adsorption. The adsorbing power of $Al(OH)_3$ heated at 300°C is compared with that of other materials known or suspected very carcinogens.

Key words: adsorption isotherm of HAP, aluminium hydroxide.

Introduction

Il est généralement admis que l'inhalation des particules de dimension respirable dont les sources d'émission sont naturelles ou industrielles (Fonderie d'aluminium,[2] Fonderie de Fer (1)) peut avoir un effet sur la santé et le bien être des travailleurs. Ces particules interagissent avec les Hydrocarbures Aromatiques Polycycliques (HAP) au niveau pulmonaire et entraînent des maladies respiratoires en général et le cancer des poumons en particulier (2–5).

L'influence de la pollution de l'air sur l'apparition du cancer des poumons est encore un problème très discuté. Les HAP qui sont des produits potentiellement cancérigènes et mutagènes (6–8) constituent une importante catégorie des polluants chimiques rejetés dans l'atmosphère. À peu près tous les processus thermiques faisant intervenir des carburants organiques peuvent produire ces HAP. Une autre importante source de ces polluants est la fumée des cigarettes (9, 10).

En dehors des HAP d'autre corps sont suspect d'être initiateurs des tumeurs malignes, on citera l'amiante (11, 12), le noir de charbon et la silice (12).

Dans cette étude nous avons utilisé la chromatographie liquide à haute pression pour mesurer l'adsorption des différents HAP dans le toluène sur l'hydroxyde d'aluminium ayant subit des traitements thermiques allant de 25°C jusqu'à 700°C.

La mesure du potentiel électrocinétique et de la surface spécifique a permis d'expliquer la variation du taux d'adsorption des différents HAP sur les échantillons de l'hydroxyde d'aluminium.

Nous avons comparé les isothermes d'adsorption obtenues de l'hydroxyde d'aluminium avec les isothermes de l'amiante et des fibres de carbone.

Reçu 6 janvier 1999.

C.A. Hassani. Département de génie des procédés, École Supérieure de Technologie, Km 7 Routed'el jadida Oasis, Casablanca, Maroc.
H. Ménard.[1] Département de chimie, Université de Sherbrooke, Sherbrooke, QC J1K 2R1, Canada.

1. Auteur à qui adresser toute correspondance. Mél. : hmenard@courrier.usherb.ca
2. J. Lessage, G. Perrault et P. Duranol. IRSST, Montréal, Québec. Résultats non-publiés.

Partie expérimentale

Appareillage

Le système à chromatographie liquide à haute pression est constitué de plusieurs instruments. Nous avons utilisé une pompe Beckman modèle 100-A couplée à un détecteur ultraviolet (U.V.) de la compagnie Altex Hitachi, modèle 100–40 muni d'une cellule de détection de 10 μL. L'acquisition et le traitement des données sont faits à l'aide d'un microordinateur RX-8800 tel qu'utilisé par Noël (13).

© 1999 CNRC Canada

Fig. 1. Isothermes d'adsorption sur les différents échantillons de l'hydroxyde d'aluminium calciné du phénanthrène–toluène à débit constant 0,2 mL/min et température 20°C. Les températures de calcination sont (1) 100, (2) 150, (3) 700, (4) 400, (5) 250 et (6) 300°C.

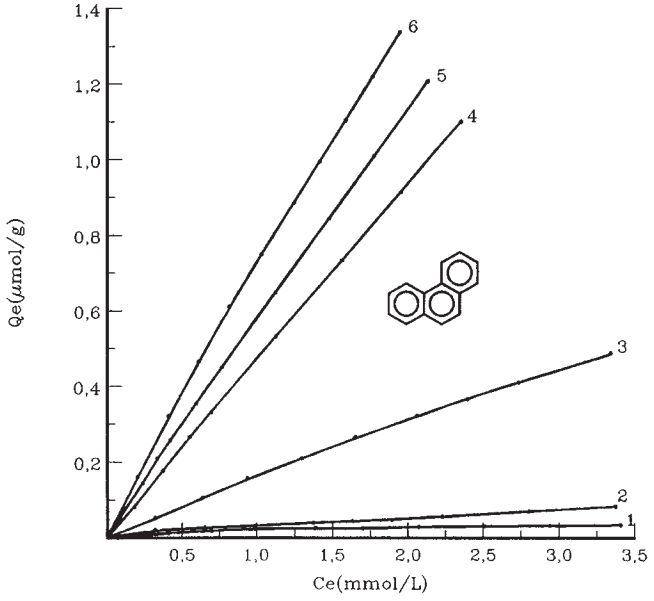

Deux systèmes d'injection sont utilisés, le premier est un système Rhéodyne, modèle 7125, le deuxième est un système Valco-valves, modèle C6W. Les boucles d'injection sont respectivement 20 et 50 μL.

Pour éviter les changements brusques de la température, nous avons utilisé un bain thermostable de la compagnie Haake, modèle FE-2 d'une précision de 0,01°C.

Les colonnes utilisées sont des tubes en acier inoxydable de la compagnie Swagelock ayant un diamètre interne de 4,6 mm et une longueur de 3,5 cm seulement.

Les tracés chromatographiques sont enregistrés simultanément par un intégrateur Hewlett Packard modèle 3390 A et un enregistreur Varian modèle 9176.

La mesure du potentiel électrocinétique est réalisée à l'aide d'un appareil de la compagnie Komlime-Sanderson modèle ZR-11. Les analyses sont effectuées dans une solution de KCl à pH neutre. Ce dernier est ajusté soit par HCl soit par KOH à une concentration de 10^{-3} M.

Les mesures de la surface spécifique sont effectuées par un appareil quantasorb-sorption de la compagnie Quantachrome Corp. modèle QS-10.

Réactifs

Les HAP utilisés sont l'anthracène (≥ 99,9 %), le pyrène (≥ 99 %), le benzo(e)pyrène (≥ 99 %) de la compagnie Aldrich Chemical Inc. et le phénanthrène (≥ 95 %) de la compagnie BDH.

L'hydroxyde d'aluminium utilisé comme support chromatographique est obtenu de la compagnie J.J. Baker Chemical Co. Il a subi des traitements thermiques allant de 25°C jusqu'à 700°C.

Nous avons utilisé comme éluant le toluène et l'hexane de qualité accuslov de la compagnie Anachemia, pour les sécher on ajoute dans une bouteille de 4 L, 40 g de tamis moléculaire (type 3A, grade 546) de la compagnie Fisher Scientific.

Tableau 1. Température de calcination, surface spécifique, potentiel électrocinétique, perte en poids et formule des différents échantillons de l'hydroxyde d'aluminium après calcination.

T (°C)	Σ (m^2/g)	ς (mV)	Perte en poids (%)	Formule
25	0,34	–32	0	Al_2O_3, 3 H_2O
100	0,40	–5	—	—
150	0,40	+19	0,03	Al_2O_3, 2,997 H_2O
250	282	+19	20,21	Al_2O_3, 1,2 H_2O
300	223	+15	27,85	Al_2O_3, 0,6 H_2O
400	188	+16	29,85	Al_2O_3, 0,4 H_2O
700	93	+13	34,37	Al_2O_3, 0,02 H_2O

Procédure

Tous les solvants utilisés pour le HPLC sont désoxygénés sous vide pendant une période de 15 min et une légère surpression d'azote sec circule au-dessus du solvant pendant la durée de l'expérience.

La colonne et la buse sont remplies et compactées à sec avec les supports utilisés et par la suite, de l'hexane est pompé sous pression à travers la colonne et la buse par une pompe Haskel. La colonne est placée dans un cylindre thermostable et reliée au HPLC. Le débit de l'éluant est de 0,2 mL/min.

Les échantillons calcinés de l'hydroxyde d'aluminium sont chauffés dans un four pendant 24 h à la pression atmosphérique.

Les différentes solutions des HAP sont préparées à partir d'une solution mère de 5×10^{-2} M et les quantités injectées varient entre 10 et 1000 nmol.

Les isothermes d'adsorption sont déterminées par la méthode de Chuduk et al. (14) et les énergies d'adsorption des HAP sur les différents supports sont calculées en appliquant l'équation de Takeuchi et al. (15) pour une série des isothermes obtenues à des températures variables. À partir des pics chromatographiques on peut obtenir Qe (concentration de la molécule sur l'absorbant) en fonction de la concentration en solution Ce (11).

Résolution et discussion

La figure 1 présente les isothermes d'adsorption du phénanthrène dans le toluène sur les différents échantillons de l'hydroxyde d'aluminium calcinés. Cette figure montre que le taux d'adsorption est pratiquement nul sur l'hydroxyde commercial (calciné à 25°C), il augmente à un maximum pour une température de traitement de 300°C puis diminue au-delà de cette température.

Le tableau 1 donne, en fonction de la température de calcination, les variations de la surface spécifique (Σ), le potentiel électrocinétique (ς), la perte en poids et les formules du solide après calcination.

Le tableau 1 montre que la surface spécifique (Σ) augmente de 0,34 m^2/g pour l'hydroxyde d'aluminium commercial à 282 m^2/g pour $Al(OH)_3$ chauffé à 250°C, et pour

© 1999 CNRC Canada

Fig. 2. Isothermes d'adsorption sur l'hydroxyde d'aluminium chauffé à 300°C du (1) anthracène–toluène; (2) phénanthrène–toluène; (3) pyrène–toluène; (4) pyrène–toluène à débit constant 0,2 mL/min et température de 20°C.

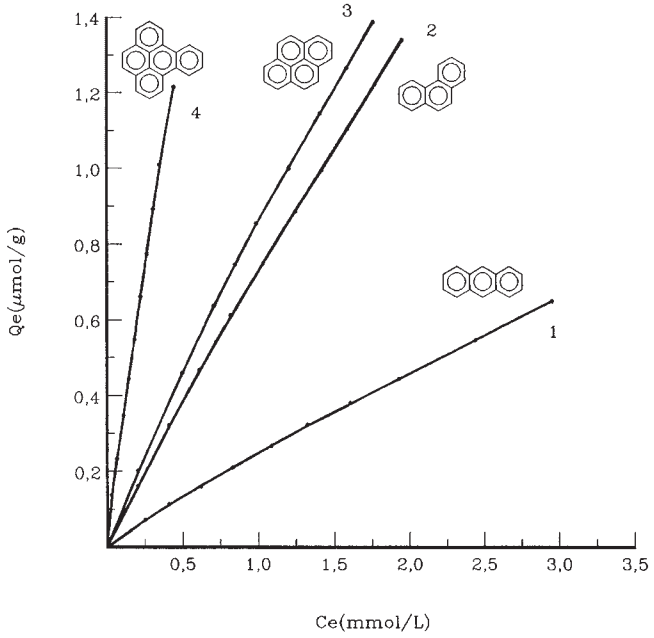

Fig. 3. Isothermes d'adsorption sur l'hydroxyde d'aluminium chauffé à 300°C du (1) phénanthrène–toluène; (2) phénanthrène–hexane à débit constant 0,2 mL/min et température de 20°C.

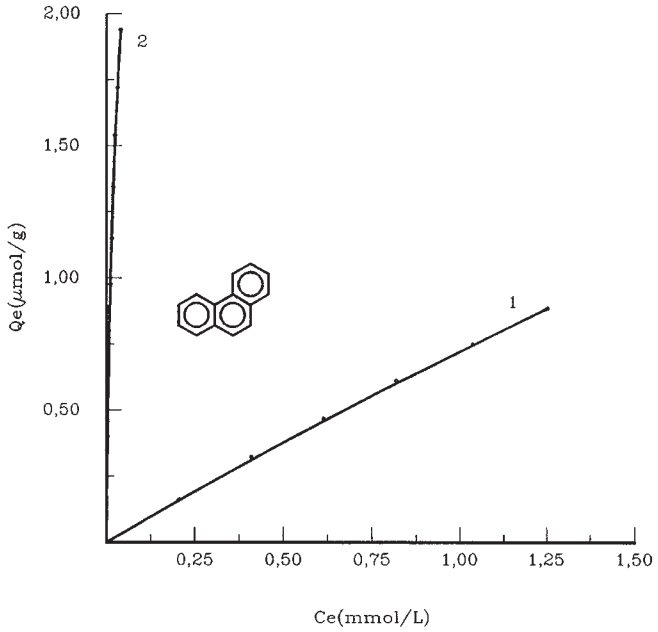

l'échantillon chauffé à 700°C cette valeur diminue à 93 m^2/g.

La variation du potentiel électrocinétique (ς) montre que sa valeur change de signe et devient positive à partir d'une température de 100°C. Ce changement de signe peut entraîner une augmentation du taux d'adsorption à cause de l'attraction des électrons Π des HAP par la surface de support chargée positivement.

Le tableau 1 montre aussi que la majeure partie de la perte en poids a lieu entre 250 et 300°C et correspond respectivement à 20,21 et 27,65 % ce qui donne les formules Al_2O_3, 1,2 H_2O pour l'hydroxyde chauffé à 250°C et Al_2O_3, 0,6 H_2O pour celui chauffé à 300°C.

Tous ces résultats montrent que l'hydroxyde d'aluminium atteint son activité maximale à une température comprise entre 250 et 300°C. Ceci justifie le grand taux d'adsorption des HAP sur l'échantillon calciné à 300°C.

La variation de la surface spécifique avec la température de traitement a déjà été trouvée par Sing (16) en faisant un traitement thermique sur la bayerite (forme cristalline de l'hydroxyde d'aluminium).

Rouquerol et al. (17), en faisant une étude sur la décomposition de l'hydrargillitte, a remarqué que la décomposition de celle-ci commence à une température de 183°C et se termine à 300°C avec des surfaces spécifiques respectives de 15,8 et 300 m^2/g. Sing (16) explique cette augmentation de la surface spécifique par la création des pores et la génération de la surface interne du solide à la suite du départ des groupements hydroxyles sous forme d'eau. La majeure partie de cette perte se produit entre 250 et 300°C. Dépassant cette température, le système subit le réarrangement spatial du réseau qui entraîne la fermeture des pores, et par conséquent la diminution de la surface spécifique (16, 18).

Cette phase active de l'hydroxyde d'aluminium que nous avons trouvée est mal connue jusqu'à présent. Trambouze et Courtial (19) l'ont préparé en chauffant le trihydrate à 236°C pendant 24 jours à la pression atmosphérique. Ils obtiennent un solide de formule Al_2O_3, 0,69 H_2O. Utilisant un dosage sélectif de bochmite, ils ont conclu que le solide est formé de bochmite et d'une phase amorphe répondant à la formule Al_2O_3, 0,48 H_2O, très voisine de celle trouvée par Papée et Tertian (20).

Ayant trouvé que le taux d'adsorption du phénanthrène dans le toluène est maximal sur l'hydroxyde $Al(OH)_3$ chauffé à 300°C, nous avons injecté sur ce support les différents HAP utilisés : l'anthracène, le pyrène et le benzo(e)pyrène. Les différentes injections ont donné les isothermes présentés à la figure 2. De cette figure on remarque que le taux d'adsorption augmente avec le nombre de cycles aromatiques de l'hydrocarbure, le benzo(e)pyrène soupçonné être le plus cancérigène est le plus fortement adsorbé.

La figure 3 illustre l'effet de la phase éluante sur l'adsorption des HAP sur $Al(OH)_3$ chauffé à 300°C. On remarque que l'utilisation de l'hexane au lieu du toluène comme éluant augmente le taux d'adsorption. Ce résultat s'explique par le fait que le toluène est un solvant plus polaire ayant une force d'élution nettement supérieure à celle de l'hexane.

Dans le but de savoir l'ordre d'énergie impliquée lors de l'adsorption des différents HAP sur $Al(OH)_3$ chauffé à 300°C nous avons appliqué la formule de Takeuchi et al. (15) pour une série d'isothermes obtenus à des températures variables. Selon Takeuchi et al. le facteur de capacité est relié à la température par la relation suivante:

$$\ln\ (K') = \frac{-\Delta H^\circ}{RT} + \frac{\Delta S^\circ}{R} + \ln\left(\frac{V_s}{V_M}\right)$$

© 1999 CNRC Canada

Tableau 2. Les enthalpies d'adsorption des différents HAP sur l'hydroxyde d'aluminium chauffé à 300°C.

Soluté	ΔH (kJ/mol)
Benzo(e)pyrène	–15,70 + 0,12
Pyrène	–11,66 + 0,31
Phénanthrène	–10,87 + 0,02
Anthracène	–2,22 + 0.03

$\Delta H°$ et $\Delta S°$ sont respectivement l'enthalpie et l'entropie lors du transfert du soluté de la phase mobile à la phase stationnaire, R la constante des gaz parfaits, T la température de la colonne, V_s le volume total de la phase stationnaire et V_m le volume du solvant dans la colonne. L'enthalpie d'adsorption est liée à la pente de la courbe donnant ln (K') en fonction de $1/T$.

Le tableau 2 présente les enthalpies d'adsorption des différents HAP sur $Al(OH)_3$ chauffé à 300°C. Ces résultats montrent que l'interaction des HAP avec la surface de support augmente avec le nombre de cycles que contient l'hydrocarbure. En plus nous remarquons que les énergies mises en jeu ne dépassent pas les 20 kJ/mol, ce qui permet de classer l'adsorption des HAP sur l'hydroxyde d'aluminium chauffé à 300°C dans la classe de physisorption.

La figure 4 permet de faire la comparaison de l'adsorption des HAP sur $Al(OH)_3$ chauffé à 300°C, l'amiante chrysotile et les fibres de carbone chauffées à 100°C. Elle présente les isothermes d'adsorption du phénanthrène dans le toluène sur les trois supports. Nous remarquons ici que $Al(OH)_3$ chauffé à 300°C adsorbe beaucoup plus que l'amiante soupçonné être très cancérigène.

Conclusions

Les tracés des isothermes par HPLC du phénanthrène sur les différents échantillons de $Al(OH)_3$ calcinés montrent que le taux d'adsorption est maximal sur l'hydroxyde chauffé à 300°C.

Les mesures du potentiel électrocinétique et de la surface spécifique effectuées sur les différents échantillons montrent que $Al(OH)_3$ atteint son activité maximale entre 250°C et 300°C; la surface devient chargée positivement et la surface spécifique atteint le maximum de 282 m^2/g.

La comparaison des isothermes d'adsorption des différents HAP sur $Al(OH)_3$ chauffé à 300°C révèle que le taux d'adsorption augmente avec le nombre de cycles aromatiques que contient l'hydrocarbure.

Le calcul des énergies d'adsorption des différents HAP sur $Al(OH)_3$ chauffé à 300°C a permis de classer l'adsorption dans la catégorie de physisorption.

La comparaison du pouvoir adsorbant de $Al(OH)_3$ chauffé à 300°C, l'amiante chrysotyle et les fibres de carbone montre que l'hydroxyde d'aluminium adsorbe les HAP beaucoup plus que l'amiante soupçonnée être très cancérigène.

Fig. 4. Isothermes d'adsorption sur (1) hydroxyde d'aluminium chauffé à 300°C; (2) amiante chrysotile; (3) fibres de carbone chauffés à 100°C à débit constant de 0,2 mL/min et température de 20°C.

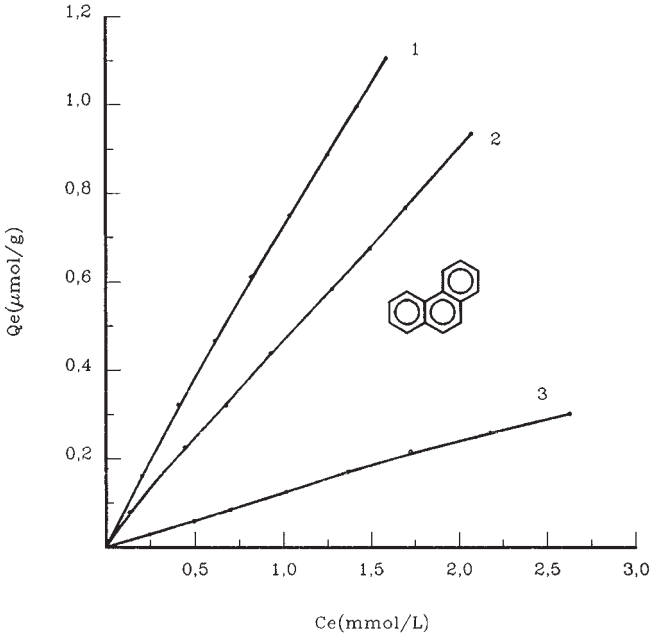

Remerciements

Les auteurs remercient, pour leur appui financier, l'Institut de Recherche en Santé et Sécurité au Travail (IRSST) et le Ministère d'Éducation du Québec.

Références

1. U. Knecht, H. Jelliehausen et H.J. Woitwidz. Brit. J. Ind. Med. **43**, 834 (1986).
2. J. Fournier et H. Pezerat. Environ. Res. **41**, 276 (1986).
3. J. Fournier et H. Pezerat. J. Chim. Phy. **79**, 589 (1980).
4. D.C. Topping et P. Nettesheim. J. Natl. Cancer Inst. **63**, 627 (1980).
5. M.C. Henry, G.D. Port et D.G. Kaufman. Nature (London), **201**, 916 (1975).
6. Publication du Centre National de Recherche Canadien N° 18982, Secrétariat de l'environnement. 1983.
7. Y.T. Woo et J.C. Arcos. Carcinogens in industry and the environment. Marcel Dekker, New York. 1981. Chap. 7.
8. D.M. Jerina, R.E. Lehr, H. Yagi, O. Hermandez, P. Dansette, P.G. Wislocki, A.W. Wood, R.L. Chang, W. Levin et A.H. Conney. In vitro metabolic activation in mutagenesis testing. Elsevier–North-Holland Biomedical Press, Amsterdam. 1976. pp. 159–177.
9. D. Hoffman et F.L. Wynder. Chemical carcinogens ACS monograph 173. American Chemical Society, Washington, D.C. 1976. pp. 324–365.
10. I.J. Selikoff, H. Seidman et E.C. Hammond. J. Natl. Cancer Inst. **65**, 507 (1975).
11. H. Ménard, L. Noel, F.M. Kimmerle, L. Tousignant et M. Lambert. Anal. Chem. **56**, 1240 (1984); **56**, 1240 (1984).
12. Publication du Centre National de Recherche Canadien N° 18565, Secrétariat de l'environnement. 1982.

© 1999 CNRC Canada

13. L. Noël. Thèse de doctorat. Université de Sherbrooke, Sherbrooke. 1986.
14. N.A. Ciiuduck, Y.A. Ettekov et A.V. Kiselev. J. Colloid Interface Sci. **84**, 149 (1981).
15. T. Takeuchi, M. Kumaki et D. Ishi. J. Chromatogr. **235**, 1358 (1982).
16. K.S.W. Sing. Colloq. Int. CNRS, 601 (1972).
17. F. Rouquerol, J. Rouquerol et B. Imelik. Bull. Soc. Chim. Fr. 3816 (1970).
18. J. Ffripiat, J. Chaudisson et A. Jelli. *Dans* Chimie physique des phénomènes de surface, applications aux oxydes et aux silicates. *Édité par* : Masson et Cie, Paris, France. 1971.
19. Y. Trambouze et R. Courtial. Bull. Soc. Chim. Fr. 1029 (1955).
20. D. Papée et R. Tertian. Bull. Soc. Chim. Fr. 983 (1955).

© 1999 CNRC Canada

Thermodynamic calculations for reactions involving hydrogen halide polymers, ions, and Lewis acid adducts. 4. The temperature dependence of some reactions of HF and HCl

Kathryn N. Rankin, W. David Chandler, and Keith E. Johnson

Abstract: Ab initio MP2/6-311++G(d,p) structure optimizations and frequency calculations have been carried out on 10 polymers, $(HX)_n$; on eight polyhalohydrogenate(1-) anions, $H_nX_{n+1}^-$, and on four polyhalohydrogen(I) cations, $H_{n+1}X_n^+$, (X = F and Cl) at a number of temperatures from 188 to 673 K, and at various total pressures. From the results, $\Delta G°$ and K values have been calculated for some reactions involving these species, and the relative amounts determined under a variety of conditions:

$$n\text{HX} \rightarrow (\text{HX})_n \qquad (n = 2\text{–}6)$$

$$\text{HX} + \text{H}_n\text{X}_{n+1}^- \rightarrow \text{H}_{n+1}\text{X}_{n+2}^- \qquad (n = 0\text{–}3)$$

$$\text{HX} + \text{H}_{n+1}\text{X}_n^+ \rightarrow \text{H}_{n+2}\text{X}_{n+1}^+ \qquad (n = 0, 1)$$

There are some marked differences between the fluorine and chlorine series, but generally, the relative amounts of the large molecules and ions decrease as the temperature increases. For all reactions, ln K can be expressed as function to the fourth power in $1/T$ indicating that $\Delta H°$ is more or less temperature dependent over a range of 400–500°.

Key words: ab initio, thermodynamics, HCl, HF.

Résumé : Opérant au niveau MP2/6-311++G(d,p), on a effectué une optimisation ab initio de structure et des calculs de fréquence pour dix polymères, $(HX)_n$; sur huit anions polyhalogénohydrogénate(–1), $H_nX_{n+1}^-$, et sur quatre cations polyhalogénohydrogène(I), $H_{n+1}X_n^+$, (X = F et Cl), à diverses températures entre 188 et 673 K et à diverses pressions totales. À partir des résultats de ces calculs, on a évalué les $\Delta G°$ et K de quelques réactions impliquant ces trois espèces et les valeurs relatives déterminées pour diverses conditions sont les suivantes

$$n\text{HX} \rightarrow (\text{HX})_n \qquad (n = 2\text{–}6)$$

$$\text{HX} + \text{H}_n\text{X}_{n+1}^- \rightarrow \text{H}_{n+1}\text{X}_{n+2}^- \qquad (n = 0\text{–}3)$$

$$\text{HX} + \text{H}_{n+1}\text{X}_n^+ \rightarrow \text{H}_{n+2}\text{X}_{n+1}^+ \qquad (n = 0, 1)$$

On observe des différences marquées entre les séries du fluor et du chlore, mais les quantités relatives des molécules et des ions plus importants diminuent généralement avec une augmentation de la température. Pour chacune des réactions, la valeur de ln K peut être exprimée en fonction de la quatrième puissance de $1/T$; ceci indique que, sur la plage de température allant de 400 à 500°, le $\Delta H°$ est plus ou moins dépendant de la température.

Mots clés : calculs ab initio, thermodynamique, HCl, HF.

Introduction

The formation and reactions of hydrogen halide polymers, $(HX)_n$, polyhalohydrogenate(1-) anions, $H_nX_{n+1}^-$, and polyhalohydrogen(I) cations, $H_{n+1}X_n^+$, (X = F, Cl) can proceed in the pure hydrogen halide or in mixtures of HX with $AlCl_3$ and ZCl, where ZCl is an alkali chloride or an organic chloride such as 1-ethyl-3-methyl-1*H*-imidazolium chloride (ImCl) (1). The optimized gas-phase structures and three general classes of reactions (reactions [1]–[3]) have been studied using data at 298 K obtained from MP2/6-311+G(d,p) calculations (1*d*–*f*). In those papers we have shown that, at 298 K, the gas phase formation of the polymers $(HF)_n$ (reaction [1]), has small and positive $\Delta G°$ values for n = 2–6; of

Received August 3, 1999.

K.N. Rankin. Department of Chemistry, Dalhousie University, Halifax, NS B3H 4J3, Canada.
W.D. Chandler[1] and K.E. Johnson. Department of Chemistry, University of Regina, Regina, SK S4S 0A2, Canada.

[1]Author to whom correspondence may be addressed. Telephone: (306) 585-4265. Fax: (306) 585-4894.
e-mail: chandler@cas.uregina.ca

 © 1999 NRC Canada

these clusters, only $(HF)_2$ does not exist in a cyclic structure. The standard reaction Gibbs energies for the corresponding HCl polymers (n = 2–4) are somewhat larger. By contrast, reaction series [2] and [3] are exergonic for all values of n studied and for both HF and HCl.

[1] $n\mathrm{HX} \rightarrow (\mathrm{HX})_n$

[2] $\mathrm{HX} + \mathrm{H}_n\mathrm{X}_{n+1}^- \rightarrow \mathrm{H}_{n+1}\mathrm{X}_{n+2}^-$

[3] $\mathrm{HX} + \mathrm{H}_{n+1}\mathrm{X}_n^+ \rightarrow \mathrm{H}_{n+2}\mathrm{X}_{n+1}^+$

Although the relevant literature relating to these complexes, anions, and cations was reviewed up to that time in our earlier work, there has been a fair amount of more recent interest in at least some of these species. There have been a variety of theoretical and (or) experimental assessments of the structures, energy surfaces, and bond energies (D_o and D_e), of IR and NMR spectra, and of solution equilibria for $(HF)_2$ (2), $(HF)_3$ (2*v*, 3), $(HF)_4$ (2*v*, 3), $(HF)_5$ (2*v*), $(HCl)_2$ (2*w*, *x*, 4), $(HCl)_3$ (4*c*), $(HCl)_4$ (4*c*), HF_2^- (5), $H_2F_3^-$ (5*d*–*f*, h), $H_3F_4^-$ (5*d*–*f*), and $H_4F_5^-$ (5*d*–*f*).

In this paper we discuss the results of ab initio MP2/6-311++G(d,p) structure optimizations and frequency calculations on 10 complexes, $(HX)_n$ (n = 2–6); on eight polyhalohydrogenate(1-) anions, $H_nX_{n+1}^-$ (n = 0–3), and on four polyhalohydrogen(I) cations, $H_{n+1}X_n^+$ (n = 0, 1), where X = F and Cl. The structures and thermodynamic data of $(HCl)_5$ and $(HCl)_6$ are reported for the first time. The frequency calculations were carried out at a number of temperatures from 188, the normal boiling point of HCl, to 673 K, and, in some cases, at various total pressures.

Most previous theoretical studies, with the exception of our earlier papers (1*d*–*f*), have tended to provide relative energies for some of these reactions at 0 K, (D_e), sometimes corrected for zero-point energies (D_o or the reaction internal energy, ΔU). However, if calculations are to be helpful in predicting the outcomes of reactions at equilibrium, they should provide standard reaction Gibb's energies, $\Delta G°$, or standard reaction enthalpies, $\Delta H°$, at useful temperatures. The difference between ΔH at 298 K and ΔU at 0 K, even with zero-point-energy differences taken into account, involves thermal energy (usually small) as well as the term ΔnRT, where Δn is the change in the total number of moles of gas during the reaction (eq. [4]). This PV work term, even at room temperature, can be as much as 12 kJ/mol for reactions we are interested in, although it more frequently is less than a quarter of that. At the same time, while $T\Delta S$, the energy change due to reactant/product entropy differences, can be as large as 80 kJ/mol in cluster formations, it is usually found to be less than 30 kJ/mol. Clearly the ΔE (D_e) or ΔU (D_o) values at 0 K, usually reported by theoreticians, while informative, simply do not provide the most reliable picture of how a chemical change should be viewed under equilibrium conditions. For example, the dimerization of HF has been well studied (eq. [1], X = F, n = 2, vide infra). The "best computed estimate" for D_e at 0 K is –19.1 ± 0.2 kJ/mol (2*aa*). Including the zero-point correction provides D_o or $\Delta U(0)$ of about –13 kJ/mol (2*x*, *z*). However, we will show that at 298 K $\Delta H°$ is –15.9 kJ/mol while $\Delta G°$ is +8.7 kJ/mol. For this reason, $\Delta G°$ and K values have been calculated for reactions [1]–[3], and the relative amounts of all species at equilibrium have been determined for the gas-phase reactions under a wide range of conditions of temperature and pressure.

The effect of temperature on the products and yields of inorganic and organic reactions can be dramatic. An excellent example of temperature dependence occurs in metal reductions as shown in Ellingham diagrams (9). It is our intention to illustrate how the temperature dependence of some relatively simple equilibria can be estimated from routine and readily available computational methods.

Calculations

Ab initio calculations were performed using GAUSSIAN 94 (6). Geometries of all species were optimized using the 6-311++G(d,p) basis set at the MP2 level. Vibrational frequencies were also obtained using the same computational model and basis set. From these latter calculations, it was possible (*a*) to determine that a structure represented a true minimum and not a saddle point in the energy surface, and (*b*) to obtain entropies (S), as well as zero-point energies and thermal corrections at the required temperature and pressure. All ab initio energies were corrected for thermal energies, including zero-point vibrations (Hartree–Fock zero-point energy values were scaled by 0.90 (7) and MP2 values by 0.95 (8), to give U values. Reaction internal energies (ΔU) were converted to reaction enthalpies (ΔH) by means of eq. [4], which assumes ideal gas behavior for all species (9). In Gaussian 94 the conversion of U to H, with thermal corrections, is carried out automatically. The ΔS values were computed using the S values resulting from frequency calculations.

[4] $\Delta H = \Delta U + \Delta nRT$

Results

The MP2/6-311++G(d,p) optimized structures of all species, except $(HCl)_5$ and $(HCl)_6$, which are new to this paper, are virtually the same as those given in the earlier papers (and references quoted therein) (1*e*, *f*) as well as in some of the more recent literature (2–5). While these are the structures or conformations with lowest energy in the gas phase and at 0 K, there are others, particularly for larger species, which are not much more energetic and which could be significantly populated in solution and at higher temperatures. One recent report suggests that the calculated structure of $(HF)_2$ is somewhat different when a counterpoise correction is included (2*y*). In particular, the FF distance becomes longer than that found experimentally or with computations that do not consider basis set superposition errors (BSSE). Table 1 provides the structural parameters calculated for all these molecules and ions along with experimental values where the latter are available. The agreement with experimental data is exceptionally good in most cases. The ions are essentially structures involving H^+ or X^- solvated by up to four molecules of the hydrogen halide. As a result, HF_2^- and HCl_2^- are linear. H_2F^+, H_2Cl^+, $H_2F_3^-$, and $H_2Cl_3^-$ are bent with C_{2v} symmetry. $H_3F_4^-$ and $H_3Cl_4^-$ have D_{3h} symmetry (trigonal planar). $H_4F_5^-$ has T_d symmetry while $H_4Cl_5^-$ is a distorted tetrahedron. Both $H_3F_2^+$ and $H_3Cl_2^+$ are structures

© 1999 NRC Canada

Table 1. Structural parameters calculated using MP2/6-311++G(d,p) optimizations.[a]

	X = F			X = Cl		
	H-X	X-X	<HXH	H-X	X-X	<HXH
HX	0.917			1.273		
	(0.917)[c]			(1.275)[c]		
H_2X^+	0.960		111.9	1.301		94.4
	(0.9577)[d]		(114.6)[d]	(1.304)[e]		(94.24)[e]
$H_3X_2^+$	0.941	2.281	118.3	1.289	3.119	97.5
		(2.30)[f]	(115.2)[f]			
HX_2^-	1.138	2.275	180.0	1.550	3.101	180.0
	(1.139)[g]	(2.278)[g]		(1.558)[h]	(3.117)[h]	
$H_2X_3^-$	0.997	2.347	133.3	1.350	3.251	118.9
$H_3X_4^-$	0.967	2.415	120.0	1.322	3.335	120.0
$H_4X_5^-$	0.951	2.482	109.5	1.309[b]	3.400[b]	109.8[b]
H_2X_2	0.920[b]	2.787	124.3	1.275[b]	3.937	104.3
		(2.72)[i]			(3.81)[j]	
H_3X_3	0.929	2.669	96.6	1.278	3.855	88.9
H_4X_4	0.937	2.583	109.6	1.278	3.810	100.1
H_5X_5	0.941	2.549	118.2	1.280[b]	3.791[b]	100.9[b]
H_6X_6	0.942	2.536	124.2	1.280	3.771	100.7
		(2.55)[k]				

[a]Distances in Å and angles in degrees. Values in parentheses are experimental ones.
[b]Average value.
[c]Reference 10.
[d]Reference 11.
[e]Reference 12.
[f]Reference 13.
[g]Reference 14.
[h]Reference 15.
[i]Reference 16. The calculated values of the two HFF bond angles are 121.3° (117 ± 6)° and 6.0° (10 ± 6)°.
[j]Reference 17.
[k]Reference 18.

Fig. 1. MP2/6-311++G(d,p) optimized structures of $(HCl)_5$ and $(HCl)_6$.

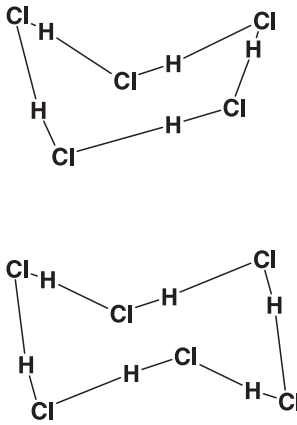

of H^+ sandwiched between two hydrogen halide molecules; however, the former is planar while the latter, with an H-Cl-Cl-H dihedral angle of 103.6°, is not. All the HF polymers as well as $(HCl)_n$, n = 2–4, are planar, and all except the dimers adopt a cyclic arrangement. The structures of $(HCl)_5$ and $(HCl)_6$, determined for the first time, are shown in Fig. 1. $(HCl)_5$ assumes a "half-chair" conformation in which the average H—Cl bond length is 1.279 Å, and the average HClH bond angle is 100.9°, although the angles vary between 97.4° and 104.3°. The optimized structure of $(HCl)_6$ is a symmetrical "chair" with H—Cl bond lengths of 1.280 Å. The HClH bond angles are identical at 100.7°. Unlike the fluorine analogues the "short" HCl bond in the series $(HCl)_n$ does not change significantly with n.

Table 2 is a list of the standard thermodynamic data ($\Delta H°$ and $\Delta G°$), calculated at 298 K, for the 24 reactions.

In all the reactions one side of the equilibrium is represented by an ion or molecule that is compounded from the species on the other side. As a result, energy calculations of the reactants and products involve differing numbers of basis functions so that energy differences will contain a basis set truncation error (BSTE). This BSTE can be split into two terms: (*i*) a basis set superposition error (BSSE), which can be approximated using a counterpoise (CP) correction, and (*ii*) a basis set incompleteness error (BSIE) that arises because the basis set used is never "complete." For the dimerization of HF (eq. [1], X = F, n = 2) Klopper and Lüthi (2*aa*) have estimated the BSSE and BSIE corrections using CCSD(T) calculations with a variety of basis sets. Their best estimate of D_e for the reaction, correcting for both the BSIE

© 1999 NRC Canada

Table 2. Standard thermodynamic data calculated at 298 K.[a]

	X = F		X = Cl	
	$\Delta H°$	$\Delta G°$	$\Delta H°$	$\Delta G°$
$HX + H^+ \rightarrow H_2X^+$	–485.7	–458.2	–570.5	–543.8
$HX + H_2X^+ \rightarrow H_3X_2^+$	–136.0	–102.7	–74.3	–41.3
$HX \rightarrow X^- + H^+$	1555.7	1531.6	1407.5	1385.0
$2HX \rightarrow H_2X_2$	–15.9	8.65	–5.96	13.7
$3HX \rightarrow H_3X_3$	–48.7	16.5	–19.7	30.8
$4HX \rightarrow H_4X_4$	–92.6	10.3	–32.5	44.4
$5HX \rightarrow H_5X_5$	–130.3	5.5	–42.0	59.6
$6HX \rightarrow H_6X_6$	–162.0	0.11	–51.2	76.1
$HX + X^- \rightarrow HX_2^-$	–189.3	–157.6	–104.0	–73.5
$HX + HX_2^- \rightarrow H_2X_3^-$	–114.7	–84.6	–58.1	–31.2
$HX + H_2X_3^- \rightarrow H_3X_4^-$	–88.7	–54.1	–52.3	–22.6
$HX + H_3X_4^- \rightarrow H_4X_5^-$	–62.6	–29.2	–42.2	–21.4

[a]All data were obtained using MP2/6-311++G(d,p) optimizations and frequency calculations and are quoted in kJ/mol.

and the BSSE, is –19.1 ± 0.2 kJ/mol. At the CCSD(T)/6-311++G(d,p) computational level, the CP correction is +4.6 kJ/mol, and the estimate of the BSIE correction is –3.5 kJ/mol. As the size of the basis set increases, both the CP and BSIE corrections get smaller, and their sum, the estimated BSTE error, becomes less consequential. For example, with the aug-cc-pVQz basis set these corrections are 1.0 and –0.3 kJ/mol, respectively. We have carried out counterpoise corrections on all the reactions studied. While some of these are significant, they become much less so when a larger basis set is used. For reactions [5] and [6] (X = F), MP2/6-311++G(d,p) CP corrections are +18.8 and +13.4 kJ/mol, respectively. However, MP2/aug-cc-pVQZ CP corrections are +4.6 and +2.8 kJ/mol, between 20 and 25% as large. We have assumed that, while the CP corrections can be large with the 6-311++G(d,p) basis set used in this work, the BSIE correction will also be large and of opposite sign. As a result, the BSTE error will be relatively inconsequential, particularly when compared with large values of the energies, and the data quoted do not include it. In those reactions for which we have used both the 6-311++G(d,p) and aug-cc-pVQZ basis sets in calculating thermodynamic parameters, the largest difference in $\Delta G°$ is 7.5%.

From the data of Table 2 it is possible to make some general conclusions:

(*i*) The formation of the polychlorohydrogenate(1-) anions, polychlorohydrogen(I) cations, and the HCl polymers is much less exothermic than the formation of the corresponding fluorine species with one notable exception; H_2Cl^+ is more stable than H_2F^+ relative to the hydrogen halide and proton.

(*ii*) Once the halide ion becomes available, the formation of the polyhalohydrogenate(1-) anions can proceed according to reaction [2]. Since $\Delta G°$ becomes less negative as *n* increases, any one or several of the four anions could occur depending on the relative amounts (pressures) of HX and X^-.

(*iii*) Once H^+ becomes available, the formation of the polyhalohydrogen(I) cations can proceed according to reaction [3]. Either or both the cations (*n* = 0 and 1) can exist depending on the conditions.

(*iv*) As *n* increases, the formation of the hydrogen halide polymers, according to reaction [1], becomes more exothermic. However, because of the unfavorable entropy term, at 298 K, these reactions are all endergonic. Interestingly, whereas the formation of the HCl clusters becomes increasingly unfavorable as the size increases, there is no comparable progression in $(HF)_n$ production; in fact, the preferred HF polymers are those with *n* = 5 and 6.

Our data agree extremely well with the recent ab initio and other calculations found in the literature (1–5), although, as noted earlier, some of the work does not involve zero-point energy corrections and most is reported at 0 K. In some cases experimental data are available. Our $\Delta H°$ of –189.3 kJ/mol at 298 K for reaction [5] (X = F) compares extremely well with the gas-phase fluoride ion affinity determinations of –162 ± 8 kJ/mol (19) and more recently of –192 ± 7 kJ/mol (at 298 K) (20). The calculated value of –104.0 kJ/mol for the corresponding chloride affinity of HCl (X = Cl, reaction [5]) is remarkably close to experimental values of –99.2 (21) and –96.7 kJ/mol (22).

[5] $\quad HX + X^- \rightarrow HX_2^-$

Proton affinities of HF (reaction [6], X = F) have been experimentally determined as –469 ± 8 (23) and 490 kJ/mol (24), in excellent agreement with the calculated $\Delta H°$ of –485.7 kJ/mol (Table 2). The corresponding proton affinities for HCl (reaction [6], X = Cl) are –538.1 (24) and –556.5 kJ/mol (25) as compared to our calculated $\Delta H°$ of –543.8 kJ/mol.

[6] $\quad HX + H^+ \rightarrow H_2X^+$

The formation of hydrogen fluoride polymers, particularly $(HF)_2$, has been the subject of a great deal of interest; recently, Quack and Suhm (2*e*) have published an excellent review of much of this work. Experimental estimates of the association energy of $(HF)_2$ (eq. [1], X = F, *n* = 2), such as –12.73 (17*b*), –12.41 (26), and the most recent –12.70 ± 0.01 kJ/mol (2*a*), correspond to computed D_o (ΔU at 0 K) values such as –12.8 (2*z*) and –12.6 kJ/mol (2*x*), and are in reasonable agreement with our calculated –15.9 kJ/mol at 298 K for $\Delta H°$. Reddington (27) estimated $\Delta H°$ to be –17.9 kJ/mol at 299 K by using a multi-parameter model to fit known properties of HF at that temperature. The same model

© 1999 NRC Canada

Table 3. Species present in pure HX at 1 atm.[a]

	Percentage			
	X = F		X = Cl	
	292 K	298 K	299 K[b]	188 K
HX	66.38	76.15	73.5	98.21
$(HX)_2$	1.52	1.77	0.8	1.74
$(HX)_3$	0.05	0.06	0.07	0.05
$(HX)_4$	0.62	0.54	0.8	0
$(HX)_5$	3.74	2.79	7.4	0
$(HX)_6$	27.69	18.69	17.4	0

[a]Calculated using thermodynamic data obtained from MP2/6-311++G(d,p) optimizations and frequency determinations.

[b]Data obtained using equilibrium constants available from ref. 27.

Fig. 2. Temperature dependence of the partial pressures of $(HF)_n$, n = 1–6, in pure HF at a total pressure of 1 atm. (○) HF; (□) $(HF)_2$; (◇) $(HF)_3$; (△) $(HF)_4$; (●) $(HF)_5$; (■) $(HF)_6$.

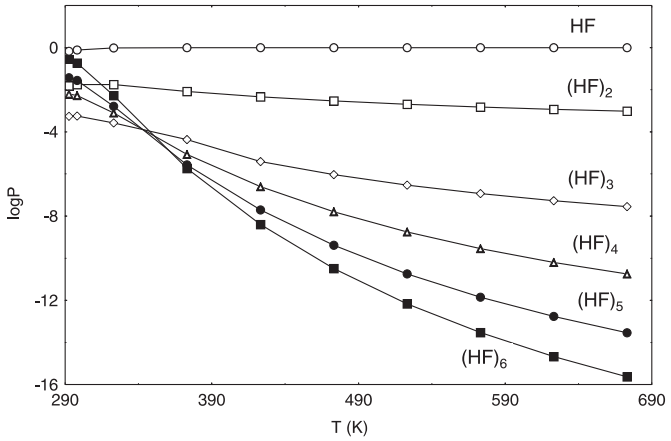

predicted $\Delta H°$ at 299 K to be –47.2, –97.1, –132.1, and –164.8 kJ/mol for the formation of the HF trimer, tetramer, pentamer, and hexamer, respectively. Our calculated values for the same set of complex formations, viz. –48.7, –92.6, –130.3, and –162.0 kJ/mol, are remarkably close.

Polymer formation in HCl is much less well studied. Our value of –5.96 kJ/mol for the standard formation enthalpy at 298 K of $(HCl)_2$ (eq. [1], X = Cl, n = 2) compares well with experimental association energy values of –5.15 ± 0.26 (17*b*) and –5.23 ± 0.01 kJ/mol (4*a*) and computed D_o value of –4.98 kJ/mol (2*x*).

Using equilibrium constant values, calculated at a particular temperature and pressure, it is possible to compute the relative pressures (amounts) of HX and the various polymers $(HX)_n$ present in an equilibrium mixture. These data are shown in Table 3 for the HF system at 292 K (the normal boiling point of pure HF) and 298 K, as well as for HCl at 188 K (its normal boiling point). The table also presents the corresponding data calculated using the equilibrium constants obtained by Reddington (27) from his experimentally based model. The percentages of the various species present in HF obtained from our ab initio calculations are surprisingly close to those estimated from Reddington's model. HF is the major species present at liquid HF temperature or at 298 K, but the hexamer, pentamer, and dimer are predicted to appear in significant amounts as well (20, 3, and 2%, respectively). For HCl, even at liquid temperature, 98% is monomeric HCl with less than 2% dimer. There is virtually nothing of the larger polymers. Figures 2 and 3 show the relative amounts of the species present in pure HF or HCl at various temperatures at 1 atm, calculated from our data. As the temperature rises, the amounts of the higher polymers, including the HF hexamer, which is so evident in liquid HF, decrease dramatically primarily as the result of the $T\Delta S°$ term in $\Delta G°$. Calculations of the percentage of each species present in HF at 292 K as a function of the total pressure show that the relative amount of the hexamer increases with pressure up to 5 atm. The amounts of the pentamer and tetramer increase up to a certain pressure and then decrease. The others species, including HF, decrease as the pressure increases above 1 atm. For example, at 5 atm, there is 5.5% HF, 0.3% dimer, 0.5% tetramer, 5.7% pentamer, and 88.0% hexamer.

Fig. 3. Temperature dependence of the partial pressures of $(HCl)_n$, n = 1–6, in pure HCl at a total pressure of 1 atm. (○) HCl; (□) $(HCl)_2$; (◇) $(HCl)_3$; (△) $(HCl)_4$; (●) $(HCl)_5$; (■) $(HCl)_6$.

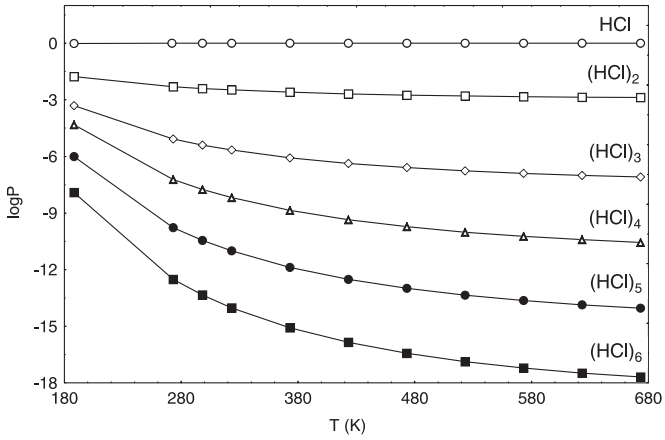

Fig. 4. Partial pressures of $H_nF_{n+1}^-$ species in a basic mixture (containing excess F^-) at 292 K. (○) HF; (□) HF_2^-; (◇) $H_2F_3^-$; (△) $H_3F_4^-$; (●) $H_4F_5^-$.

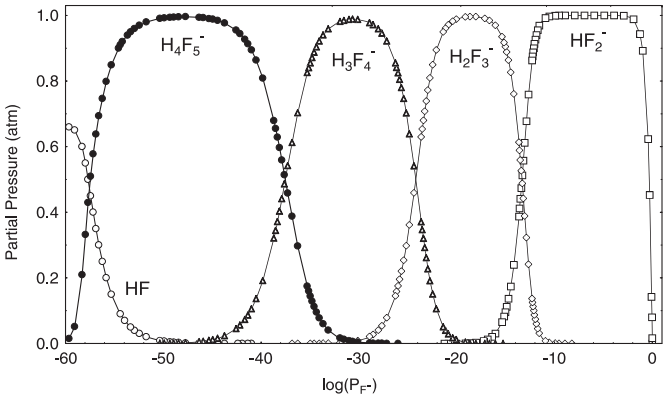

Using the equilibrium constants computed for reactions [1] and [2] at a number of temperatures between 188 and 673 K, it is also possible to calculate the relative amounts of the various species present in a basic mixture, one containing excess X^-. To illustrate, Figs. 4 and 5 are plots of partial pressures of

© 1999 NRC Canada

Fig. 5. Partial pressures of $H_nF_{n+1}^-$ species in a basic mixture (containing excess F^-) at 673 K. (○) HF; (□) HF_2^-; (◇) $H_2F_3^-$; (△) $H_3F_4^-$; (●) $H_4F_5^-$.

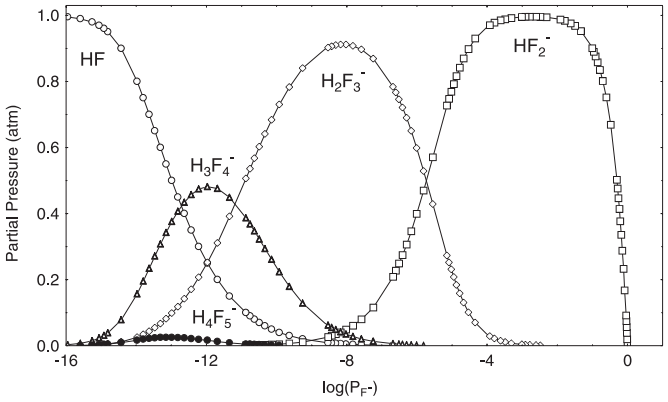

Fig. 6. Partial pressures of $H_nCl_{n+1}^-$ species in a basic mixture (containing excess Cl^-) at 188 K. (○) HCl; (□) HCl_2^-; (◇) $H_2Cl_3^-$; (△) $H_3Cl_4^-$; (●) $H_4Cl_5^-$.

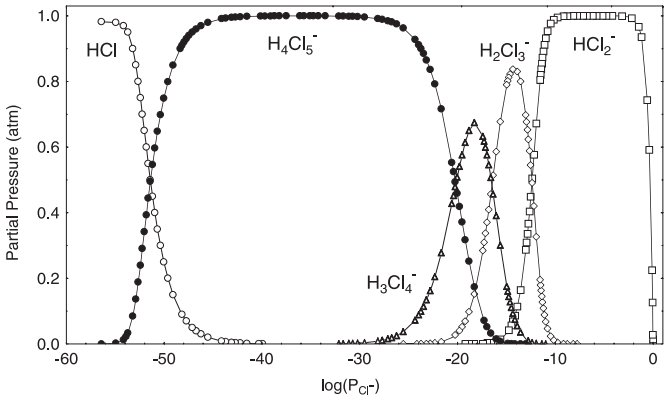

the species against the pressure of F^- at 292 and 673 K, respectively. At a F^- partial pressure approaching zero, HF and the polymers noted above predominate. As the pressure of F^- increases, the anion $H_4F_5^-$ begins to form, becoming the only species, and then disappearing as $H_3F_4^-$ forms. The process continues with the disappearance of $H_3F_4^-$, the consequent formation of $H_2F_3^-$ and then the formation of HF_2^- as the only species at higher fluoride ion pressures. Although these calculations are for gas phase reactions, they are entirely in accordance with solution experiments. For example, the NMR evidence, from mixtures of tetrabutylammonium fluoride with HF dissolved in a 1:2 mixture of CDF_3 and CDF_2Cl, indicates that at low HF concentration, HF_2^- is observed (5*f*). At higher HF concentrations the larger ions are formed. Ràfols et al. (5*d*) have studied the equilibria of HF in an ethanol–water mixture using conductiometric and potentiometric techniques. Their data give equilibrium constants quantitatively different from ours for reaction [2] (X = F, n = 0–3) but qualitatively in the same relative order. The authors also demonstrate that HF_2^- predominates in dilute HF solutions whereas HF and the larger anions predominate in solutions more concentrated in HF. A comparison of Figs. 4 and 5 also shows how the larger anions become less stable at higher temperature. For example, whereas at 292 K all ions could form depending on the conditions, at 673 K there should be almost no detectable $H_4F_5^-$

Fig. 7. Partial pressures of $H_{n+1}F_n^+$ species in an acidic mixture (containing excess H^+) at 292 K. (△) HF; (□) H_2F^+; (○) $H_3F_2^+$.

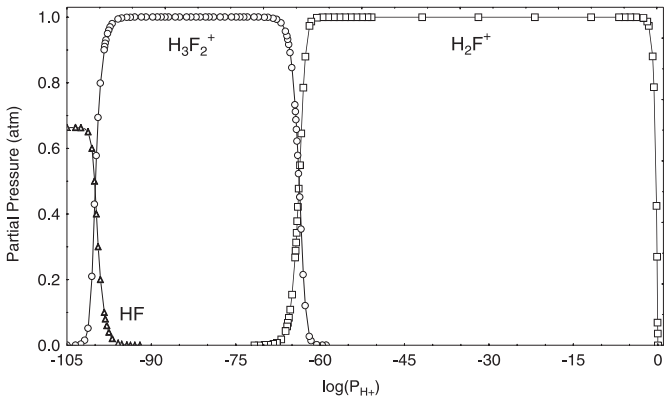

Fig. 8. Partial pressures of $H_{n+1}F_n^+$ species in an acidic mixture (containing excess H^+) at 673 K. (△) HF; (□) H_2F^+; (○) $H_3F_2^+$.

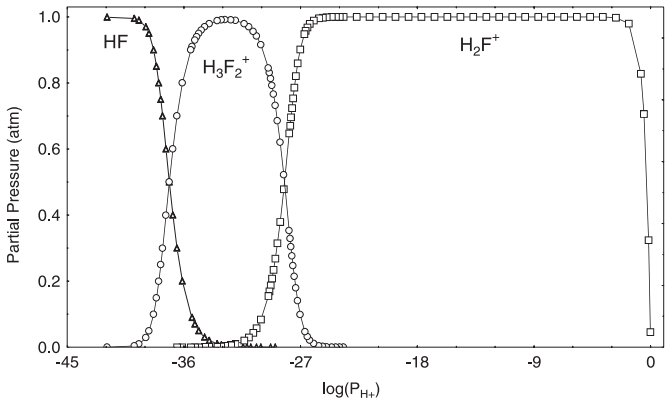

and little $H_3F_4^-$. As well, in going from 292 to 673 K, the range of F^- partial pressures needed to observe all the species present in solution decreases by many orders of magnitude.

Figure 6 is a partial pressure plot at 188 K for the comparable polychlorohydrogenate(1-) ions in solutions with an excess of Cl^-. Qualitatively, the figure is similar to those for the HF/F^- mixtures. However, at 188 K, the normal HCl boiling point, HCl, $H_4Cl_5^-$, and HCl_2^- are the predominant species. As the temperature rises, all of the larger anions become less stable so that at 673 K only HCl and (or) HCl_2^- should exist regardless of the amount of chloride ion present.

Plots of the partial pressures of HX and the two polyhalohydrogen(I) cations, $H_{n+1}X_n^+$, in acidic mixtures (excess H^+) at different temperatures are illustrated in Figs. 7–9. At very low H^+ pressures HX predominates. With increasing acidity the larger cations form, first $H_3X_2^+$, then H_2X^+. At higher temperatures the larger cation is less stable and less in evidence. In fact, at 673 K, only HCl and (or) H_2Cl^+ would be expected to exist regardless of the pressure of H^+.

The van't Hoff equation represents the temperature dependence of an equilibrium constant (9). Specifically, the derivative of ln K with respect to $1/T$ is $-\Delta H°/R$. For all the reactions represented by eqs. [1]–[3] a plot of ln K vs. $1/T$ is a concave curve that can be fitted to the expression [7] with high correlation coefficient (for example, Fig. 10) indicating that $\Delta H°$ is not temperature independent over the temperature range of 400–500°. The plots with the greatest curvature

© 1999 NRC Canada

Table 4. Values of ln K as a function of T^{-1}.[a]

	a	$b/10^3$	$c/10^4$	$d/10^7$
$HF + H^+ \rightarrow H_2F^+$	–13.2	60.1	–45.2	4.07
$HF + H_2F^+ \rightarrow H_3F_2^+$	–12.7	15.5	34.3	–4.19
$2HF \rightarrow H_2F_2$	–9.08	1.12	25.3	–2.72
$3HF \rightarrow H_3F_3$	–24.7	4.28	53.4	–6.02
$4HF \rightarrow H_4F_4$	–39.5	8.97	77.0	–8.98
$5HF \rightarrow H_5F_5$	–51.8	12.6	108	–12.5
$6HF \rightarrow H_6F_6$	–61.5	15.4	141	–16.0
$HF + F^- \rightarrow HF_2^-$	–13.6	23.2	–2.60	–0.721
$HF + HF_2^- \rightarrow H_2F_3^-$	–12.5	13.9	–0.462	–0.313
$HF + H_2F_3^- \rightarrow H_3F_4^-$	–13.0	9.76	29.7	–3.24
$HF + H_3F_4^- \rightarrow H_4F_5^-$	–12.0	6.17	41.2	–4.21
$HCl + H^+ \rightarrow H_2Cl^+$	–12.5	69.8	–27.5	1.80
$HCl + H_2Cl^+ \rightarrow H_3Cl_2^+$	–12.1	7.96	25.3	–2.12
$2HCl \rightarrow H_2Cl_2$	–6.96	–0.0102	17.7	–1.33
$3HCl \rightarrow H_3Cl_3$	–18.0	0.0578	43.9	–3.32
$4HCl \rightarrow H_4Cl_4$	–27.3	1.10	69.2	–5.30
$5HCl \rightarrow H_5Cl_5$	–36.0	1.17	95.4	–7.30
$6HCl \rightarrow H_6Cl_6$	–44.9	1.2	122	–9.31
$HCl + Cl^- \rightarrow HCl_2^-$	–12.0	12.1	12.3	–1.30
$HCl + HCl_2^- \rightarrow H_2Cl_3^-$	–10.9	6.95	2.51	–0.346
$HCl + H_2Cl_3^- \rightarrow H_3Cl_4^-$	–10.8	5.35	23.6	–1.86
$HCl + H_3Cl_4^- \rightarrow H_4Cl_5^-$	–7.05	4.01	26.3	–2.01

[a] $\ln K = a + b(T^{-1}) + c(T^{-2}) + d(T^{-3})$. Data obtained from MP2/6-311++G(d,p) calculations.

Fig. 9. Partial pressures of $H_{n+1}Cl_n^+$ species in an acidic mixture (containing excess H^+) at 673 K. (△) HCl; (□) H_2Cl^+; (○) $H_3Cl_2^+$.

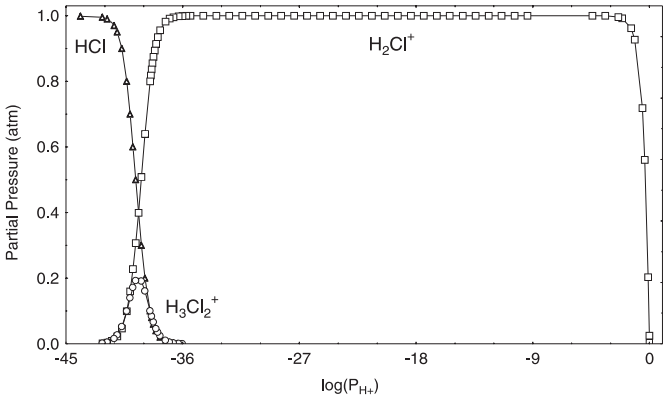

Fig. 10. Plot of ln K against $1/T$ for $(HCl)_2$.

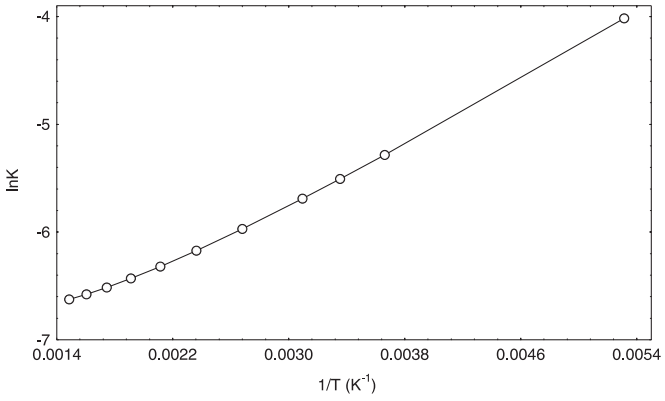

(the greatest temperature dependence of $\Delta H°$) are those obtained for the polymer formation reactions of HCl. Table 4 lists the coefficients for [7] found by nonlinear regression for all the equilibria studied.

$$[7] \qquad \ln K = a + bT^{-1} + cT^{-2} + dT^{-3}$$

Summary

Complete ab initio MP2/6-311++G(d,p) structure optimizations and frequency calculations have been carried out on 10 hydrogen halide polymers, $(HX)_n$; on eight polyhalohydrogenate(1-) anions, $H_nX_{n+1}^-$, and on four polyhalohydrogen(I) cations, $H_{n+1}X_n^+$, (X = F and Cl) at a number of temperatures ranging from 188 to 673 K, and at various total pressures. The structures predicted for these species agree with experimental results, where they are available, and with previously obtained calculations done at comparable or better computational levels. The structures of two of the polymers, $(HCl)_5$ and $(HCl)_6$, are reported for the first time. The former adopts a half-chair conformation, the latter a chair.

From the computational results, $\Delta H°$, $\Delta G°$, and K values have been calculated for 24 reactions involving these species. Our calculated values of $\Delta H°$ agree extremely well with the available experimental proton and halide affinities of HF and HCl. The formation of the polychlorohydrogenate(1-) anions, polychlorohydrogen(I) cations, and the HCl polymers is much less exothermic than the formation of the corresponding fluorine species with one notable exception; H_2Cl^+ is more stable than H_2F^+ relative to the hydrogen

© 1999 NRC Canada

halide and proton. Once halide ion or H^+ is available, the formation of the polyhalohydrogenate(1-) anions or polyhalohydrogen(I) cations can proceed. Since $\Delta G°$ becomes less negative as n increases, any one or several of the four anions or two cations in each series could occur depending on the relative amounts (pressures) of HX and ion. The percentages of the various species present in pure HF obtained from our ab initio calculations are surprisingly close to those estimated from a model proposed by Reddington (27). At low temperatures the HF and its hexamer predominate. However, as the temperature increases at constant pressure the hexamer partial pressure decreases until only HF is observed. With increasing H^+ or X^- partial pressure, HX disappears to be replaced by the largest cation or anion. Continued increase in ion pressure sees subsequent formation of the possible smaller anions or cations. There are some marked differences between the fluorine and chlorine series, but generally, the relative amounts of the large molecules, anions, and cations, and the range of partial pressures over which they are stable decrease as the temperature increases. For all reactions, ln K is not quite a linear function of $1/T$, indicating that $\Delta H°$ is temperature dependent over a range of 400–500°.

Acknowledgments

The authors thank the Natural Sciences and Engineering Research Council of Canada for support in the form of an operating grant to K.E.J.

References

1. (*a*) J.L.E. Campbell and K.E. Johnson. Inorg. Chem. **32**, 3809 (1993), and refs. therein; (*b*) J.L.E. Campbell, K.E. Johnson, and J.R. Torkelson. Inorg. Chem. **33**, 3340 (1994), and refs. therein; (*c*) J.L.E. Campbell and K.E. Johnson. J. Am. Chem. Soc. **117**, 7791 (1995), and refs. therein; (*d*) W.D. Chandler, K.E. Johnson, and J.L.E. Campbell. Inorg. Chem. **34**, 4943 (1995); (*e*) W.D. Chandler, K.E. Johnson, B.D. Fahlman, and J.L.E. Campbell. Inorg. Chem. **36**, 776 (1997); (*f*) W.D. Chandler and K. E. Johnson. Inorg. Chem. **38**, 2050 (1999).
2. (*a*) E.J. Bohac, M.D. Marshall, and R.E. Miller. J. Chem. Phys. **96**, 6681 (1992); (*b*) K.A. Peterson and T.H. Dunning, Jr. J. Chem. Phys. **102**, 2032 (1995); (*c*) W.C. Necoechea and D.G. Truhlar. Chem. Phys. Lett. **248**, 182 (1996); (*d*) A.V. Nemukhin, B.L. Grigorenko, and A.V. Savin. Chem. Phys. Lett. **250**, 226 (1996); (*e*) M. Quack and M.A. Suhm. Theor. Chim. Acta, **93**, 61 (1996); (*f*) J.J. Novoa, M. Planas, and M.C. Rovira. Chem. Phys. Lett. **251**, 33 (1996); (*g*) D.T. Anderson, S. Davis, and D.J. Nesbitt. J. Chem. Phys. **104**, 6225 (1996); (*h*) H.-C. Chang, and W. Klemperer. J. Chem. Phys. **104**, 7830 (1996); (*i*) S. Davis, D.T. Anderson, J.T. Farrell, Jr., and D.J. Nesbitt. J. Chem. Phys. **104**, 8197 (1996); (*j*) J.T. Farrell, Jr., M.A. Suhm, and D.J. Nesbitt. J. Chem. Phys. **104**, 9313 (1996); (*k*) R. Moszynski, T.G.A. Heijmen, and B. Jeziorski. Mol. Phys. **88**, 741 (1996); (*l*) D.T. Anderson, S. Davis, and D.J. Nesbitt. J. Chem. Phys. **105**, 4488 (1996); (*m*) W. Klopper, M. Quack, and M.A. Suhm. Chem. Phys. Lett. **261**, 35 (1996); (*n*) S. Davis, D.T. Anderson, and D.J. Nesbitt. J. Chem. Phys. **105**, 6645 (1996); (*o*) D.F.R. Brown, M.N. Gibbs, and D.C. Clary. J. Chem. Phys. **105**, 7597 (1996); (*p*) A.V. Nemukhin and B.L. Grigorenko. Int. J. Quantum Chem. **62**, 55 (1997); (*q*) Y. Volobuev, W.C. Necoechea, and D.G. Truhlar. J. Phys. Chem. A, **101**, 3045 (1997); (*r*) B.L. Grigorenko and A.V. Nemukhin. Chem. Phys. Lett. **270**, 103 (1997); (*s*) T.A. Wesolowski. J. Chem. Phys. **106**, 8516 (1997); (*t*) A. Niño and C. Muñoz-Caro. Comput. Chem. **21**, 143 (1997); (*u*) C.-C. Chuang, S.N. Tsang, W. Klemperer, and H.-C. Chang. J. Phys. Chem. A, **101**, 6702 (1997); (*v*) W. Klopper, M. Quack, and M.A Suhm. Mol. Phys. **94**, 105 (1998); (*w*) T. Yogi. J. Phys. Soc. Jpn. **67**, 1643 (1998); (*x*) Z. Bacic and Y. Qiu. Adv. Mol. Vib. Collision Dyn. **3**, 183 (1998); (*y*) P. Hobza and Z. Havlas. Theor. Chem. Acc. **99**, 372 (1998); (*z*) G.S. Tschumper, M.D. Kelty, and H.F. Schaefer III. Mol. Phys. **96**, 493 (1999); (*aa*) W. Klopper and H.P Lüthi. Mol. Phys. **96**, 559 (1999).
3. R. Ramaekers, D.M.A. Smith, J. Smets, and L. Adamowicz. J. Chem. Phys. **107**, 9475 (1997).
4. (*a*) H. Ni, J.M, Serafin, and J.J. Valentini. J. Chem. Phys. **104**, 2259 (1996); (*b*) Y. Qiu and Z. Bacic. J. Chem. Phys. **106**, 2158 (1997); (*c*) Z. Latajka and S. Scheiner. Chem. Phys. **216**, 37 (1997); (*d*) K. Liu, M. Dulligan, I. Bezel, A. Kolessov, and C. Wittig. J. Chem. Phys. **108**, 9614 (1998); (*e*) M. Kreissler, L. Lavialle, M. Boggio-Pasqua, and Y. Hannachi. J. Mol. Struct. (Theochem), **542**, 55 (1998); (*f*) K. Imura, T. Kasai, H. Ohoyama, and R. Naaman. J. Chem. Phys. **110**, 355 (1999).
5. (*a*) M.J. Bramley, G.C. Corey,and I.P. Hamilton. J. Chem. Phys. **103**, 9705 (1995); (*b*) P.G. Wenhold and R.R. Squires. J. Phys. Chem. **99**, 2002 (1995); (*c*) R.D. Harcourt. Int. J. Quantum Chem. **60**, 553 (1996); (*d*) C. Ràfols, K. Herodes, J.L. Beltrán, E. Bosch, and M. Rosés. J. Electroanal. Chem. **433**, 77 (1997); (*e*) T. von Rosenvinge, M. Parrinello, and M.L. Klein. J. Chem. Phys. **107**, 8012 (1997); (*f*) I.G. Shenderovich, S.N. Smirnov, G.S. Denisov, V.A. Gindin, N.S. Golubev, A. Dunger, R. Reibke, S. Kirpekar, O.L. Malkina, and H.-H. Limbach. Ber. Bunsenges. Phys. Chem. **102**, 422 (1998); (*g*) M.A. McAllister. J. Mol. Struct. (Theochem), **427**, 39 (1998); (*h*) K.M. Harmon, P.W. Brown, Jr., and S.H. Gill. J. Mol. Struct. **448**, 43 1998.
6. M.J. Frisch, G.W. Trucks, H.B. Schlegel, P.M.W. Gill, B.G. Johnson, M.A. Robb, J.R. Cheeseman, T. Keith, G.A. Petersson, J.A. Montgomery, K. Raghavachari, M.A. Al-Laham, V.G. Zakrzewski, J.V. Ortiz, J.B. Foresman, J. Cioslowski, B.B. Stefanov, A. Nanayakkara, M. Challacombe, C.Y. Peng, P.Y. Ayala, W. Chen, M.W. Wong, J.L. Andres, E.S. Replogle, R. Gomperts, R.L. Martin, D.J. Fox, J.S. Binkley, D.J. Defrees, J. Baker, J.P. Stewart, M. Head-Gordon, C. Gonzalez, and J.A. Pople, Gaussian 94, Revisions B.1 and E.1. Gaussian Inc., Pittsburgh, Pa. 1995.
7. J.A. Pople, H.B. Schlegel, R. Krishnan, D.J. DeFrees, J.S. Binkley, M.J. Frisch, R.A. Whiteside, R.F. Hout, and W.J. Hehre. Int. J. Quantum Chem. Symp. **15**, 269 (1981).
8. D. Heidrich, N.J.R. van Eikema Hommes, and P. von Ragué Schleyer. J. Comput. Chem. **14**, 1149 (1993).
9. P.W. Atkins. Physical chemistry. 6th ed. W.H. Freeman, New York. 1998.
10. K.P. Huber and G. Herzberg. Constants of diatomic molecules. Van Nostrand Reinhold, New York. 1979.
11. E. Schafer and R.I. Saykally. J. Chem Phys. **81**, 4189 (1984).
12. S.K. Lee, T. Amano, K. Kawaguchi, and M. Oldani. J. Mol. Spectrosc. **130**, 1 (1988).
13. D. Mootz and K. Bartmann. Angew. Chem. Int. Ed. Engl. **27**, 291 (1988).
14. K. Kawaguchi and E. Hirota. J. Chem. Phys. **87**, 6838 (1987).
15. J.L. Atwood, S.G. Bott, C.M. Means, A.W. Coleman, H.T. Zhang, and M.T. May. J. Am. Chem. Soc. **29**, 467 (1990).

© 1999 NRC Canada

16. B.J. Howard, T.R. Dyke, and W. Klemperer. J. Chem. Phys. **81**, 5417 (1984).
17. (*a*) N. Ohashi and A.S. Pine. J. Chem. Phys. **81**, 73 (1984); (*b*) A.S. Pine and B.J. Howard. J. Chem. Phys. **84**, 590 (1986); (*c*) G.A. Blake, K.L. Busarow, R.C. Cohen, K.B. Laughlin, Y.T. Lee, and R.J. Saykally. J. Chem. Phys. **89**, 6577 (1988).
18. J. Janzen and L. Bartell. J. Chem. Phys. **50**, 3611 (1969).
19. J.W. Larson and T.B. McMahon. Inorg. Chem. **23**, 2029 (1984).
20. P.G. Wenthold and R.R. Squires. J. Phys. Chem. **99**, 2002 (1995).
21. J.W. Larson and T.B. McMahon. J. Phys. Chem. **91**, 554 (1987).
22. R. Yamdagni and P. Kebarle. Can. J. Chem. **52**, 2449 (1974).
23. M.S. Foster and J.L. Beauchamp. Inorg. Chem. **14**, 1229 (1975).
24. S.G. Lias, J.E. Bartmoss, J.F. Liebman, J.L. Holmes, R.D. Levin, and W.G. Mallard. Gas phase ion and neutral thermochemistry. J. Phys. Chem. Ref. Data Suppl. **17**, 51 (1988).
25. N.G. Adams, D. Smith, M. Tichy, G. Javahery, N.D. Twiddy, and E.E. Ferguson. J. Chem. Phys. **91**, 4037 (1989).
26. D.C. Dayton, K.W. Jucks, and R.E. Miller. J. Chem. Phys. **90**, 2631 (1989).
27. R.L. Reddington. J. Phys. Chem. **86**, 553 (1982).

© 1999 NRC Canada

Excess molar volumes of methanol or ethanol + *n*-polyethers at 298.15 K

F.J. Carmona, F.J. Arroyo, I. García de la Fuente, J.A. González, and J.C. Cobos

Abstract: Excess molar volumes V_m^E at 298.15 K and atmospheric pressure for methanol and ethanol + 2,5-dioxahexane, + 3,6-dioxaoctane, + 2,5,8-trioxanonane, + 3,6,9-trioxaundecane, + 5,8,11-trioxapentadecane, + 2,5,8,11-tetraoxadodecane, and + 2,5,8,11,14-pentaoxapentadecane have been obtained from densities measured with an Anton–Paar DMA 602 vibrating-tube densimeter. All the excess volumes are negative over the whole mole fraction range. The V_m^E curves are shifted to the region rich in the alkanol, increasing their asymmetry with the number of oxygen groups in the polyethers. Results seem to remark the predominant contribution of free volume effects on interactional effects, particularly when the ethers are of the type CH_3-(O-$CH_2CH_2)_m$-CH_3. In the case of polyethers with longer *n*-alkyl chain ends, self-association of methanol and ethanol is more relevant. A short comparative study with results for mixtures with higher 1-alkanols and polyethers is also presented.

Key words: experimental, excess volumes, 1-alkanols, polyethers, self-association, free volume effects.

Résumé : Utilisant un densimètre à tube vibrant Anton–Paar DMS 602 et opérant à 298,15 K et à la pression ambiante, on a mesuré les densités du méthanol ainsi que de l'éthanol additionnés de 2,5-dioxahexane, 3,6-dioxaoctane, 2,5,8-trioxanonane, 3,6,9-trioxaundécane, 5,8,11-trioxapentadécane, 2,5,8,11-tétraoxadodécane et 2,5,8,11,14-pentaoxapentadécane et on en a déduit les volumes molaires en excès, V_m^E. Tous les volumes en excès sont négatifs pour l'ensemble des plages des fractions molaires. Les courbes des V_m^E sont déplacées vers les régions riches en alcanol et leur asymétrie augmente avec le nombre d'atomes d'oxygène dans les polyéthers. Les résultats semblent mettre en évidence la contribution prédominante des effets de volume libre sur les effets d'interaction, en particulier avec les éthers du type CH_3-(O-$CH_2CH_2)_m$-CH_3. Dans les cas de polyéthers dans lesquels les chaînes alkyles aux extrémités sont plus longues, l'autoassociation du méthanol et de l'éthanol est plus importante. On présente aussi une courte étude comparative avec les résultats obtenus avec des mélanges d'alcan-1-ols et de polyéthers de masses moléculaires plus élevées.

Mots clés : expérimental, volumes en excès, alcan-1-ols, polyéthers, autoassociation, effets des volumes libres.

[Traduit par la Rédaction]

1. Introduction

Mixtures containing oxygenated compounds, such as ethers (-O- group) and alkanols (-OH group), are of great importance from a practical point of view due to they are increasingly used as additives to gasoline owing to their octane-enhancing and pollution-reducing properties.

From a theoretical point of view, solutions involving oxaalkanes are of high interest because make possible the study of a number of effects (e.g., steric or proximity effects, cyclization) on the interactions present in the mixture considered. Binary systems of oxaalkanes and 1-alkanols are particularly interesting due to their complexity, consequence of the self-association of the alkanols partially destroyed by the active molecules of ethers, and of the new *intermolecular* OH---O bonds created. So, the treatment of this class of mixtures is a severe test for any theoretical model. Moreover, the analysis of the present systems is a previous step to study mixtures containing hydroxyethers, where the *intramolecular* effects between the -OH and -O- groups of cellosolves become of great importance (1, 2).

DISQUAC (3, 4), a purely physical model, has been successfully applied to the mixtures under study by considering structure-dependent interaction parameters (5). In this way, properties as excess molar enthalpies, H_m^E, or excess molar heat capacities at constant pressure, $C_{p,m}^E$, which are very sensitive to molecular structure are properly represented by DISQUAC. The Dortmund version of UNIFAC (6), which ignores proximity or steric effects fails to describe the mentioned properties (5). Unfortunately, both the DISQUAC and the UNIFAC models are based on rigid lattice theories and hence $V_m^E = 0$, a useful property to evaluate, e.g., changes in free volume or interstitial accommodation. The model more widely applied to represent simultaneously H_m^E and V_m^E is the so-called ERAS model (7), which combines the chemical, physical, and equation of state contributions, the two latter being expressed by the Flory equation of state (8). However,

Received February 22, 1999.

F.J. Carmona, F.J. Arroyo, I. García de la Fuente, J.A. González,[1] and J.C. Cobos. G.E.T.E.F., Departamento de Termodinámica y Física Aplicada, Universidad de Valladolid, E-47071 Valladolid, Spain.

[1]Author to whom correspondence may be addressed. Telephone: +34 983 42 65 03. Fax: +34 983 42 31 36. e-mail: jagl@termo.uva.es

© 1999 NRC Canada

Table 1. Source purity and density at 298.15 K and atmospheric pressure of pure compounds.

			ρ/kg m^{-3}	
Compound	Source	Purity (%)	Expt.	Literature
Methanol	Fluka	>99.5	786.69	786.37[a]
Ethanol	Fluka	Puriss p.a. >99.8	785.22	784.93[a]
2,5-Dioxahexane	Fluka	Purum ~99	861.53	863.70[a]
				861.55[b]
3,6-Dioxaoctane	Aldrich	98	835.67	835.10[a]
				836.07[b]
2,5,8-Trioxanonane	Fluka	Puriss p.a. >99.5	939.05	938.4[a]
				938.75[b]
3,6,9-Trioxaundecane	Fluka	Purum >98	903.90	903.3[c]
5,8,11-Trioxapentadecane	Fluka	Purum >98	878.62	878.30[b]
2,5,8,11-Tetraoxadodecane	Fluka	Purum >98	980.58	980.42[d]
				980.65[b]
2,5,8,11,14-Pentaoxapentadecane	Fluka	Purum >98	1006.53	1006.51[e]
				1006.20[d]

[a]Reference 37.
[b]Reference 15.
[c]Reference 38.
[d]Reference 39.
[e]Reference 40.

as far as we know, the ERAS model has been merely applied to mixtures of 1-propanol with 2,5,8-trioxanonane, or with 2,5,8,11-tetraoxadodecane (9). The lack of a systematic treatment of the present mixtures in the framework of the ERAS model underlines the difficulty in studying such mixtures.

As a continuation of our previous experimental studies on binary mixtures containing oxaalkanes and (or) 1-alkanols (10–21), and in order to extend the available database for 1-alkanols + polyethers mixtures, we report here V_m^E of systems formed by methanol or ethanol and 2,5-dioxahexane, 3,6-dioxaoctane, 2,5,8-trioxanonane, 3,6,9-trioxaundecane, 5,8,11-trioxapentadecane, 2,5,8,11-tetraoxadodecane, and 2,5,8,11,14-pentaoxapentadecane over the whole mole fraction range at atmospheric pressure and at 298.15 K. They will be useful to develop a further complete treatment of the present mixtures.

2. Experimental

An Anton–Paar DMA 602 vibrating-tube densimeter (22–24), operating under static conditions, was used to determine the densities, ρ, of the pure liquids and of their binary mixtures. The oscillation period τ (of about 3.6 ms) was measured with a Philips PM 6669 frequency meter. This was counted with eight digits, which were integrated and renewed every 10 s. Each value of τ was obtained from an average of 80 measurements, and for each pure liquid or mixture, three runs were developed. Protection against the generation of static electricity around the instrument and temperature stability were effective in maintaining an overall stable indication of $\Delta\tau = \pm 5$ ns, and hence $|\Delta\tau/\tau| = 1.4 \times 10^{-6}$. This gives a resolution in density of $|\Delta\rho/\rho| = 6 \times 10^{-6}$, where the errors due to calibration and the density of the references liquid are not taken into account. All the measuring operation and calculations were computer controlled.

Before each series of measurements the instrument was calibrated with doubly distilled and degassed water and "vacuum." The accuracy in the determination of ρ is believed to be less than $\pm 2 \times 10^{-2}$ kg m^{-3}. Hexane and acetone or ethanol were used for rinsing the cell tube between measurements. More details are given elsewhere (25). Temperature was evaluated by resistance measurement of an Anton–Paar thermistor (using a PM2534 Philips multimeter) previously tested against a HP-2804A quartz thermometer calibrated on the basis of the ITS-90 scale of temperature using the triple point of water. The densimeter was thermostated to ±0.003 K and measurements were carried out at 298.15 K and atmospheric pressure.

The source, purity, and experimental densities at 298.15 K of the pure compounds used are listed in Table 1. They are in good agreement with published values (Table 1). All liquids were carefully dried with molecular sieve (Union Carbide 4 Å, from Fluka) added to the chemicals, which were not degassed.

Binary mixtures were prepared by mass in small vessels of about 10 cm^3. Caution was taken to prevent evaporation, and the error in the final mole fraction is estimated to be less than ±0.0001. Conversion to molar quantities was based on the relative atomic mass table of 1985 issued by IUPAC (26).

The excess molar volumes were calculated from the densities of the pure liquids and their mixtures. As in order to obtain reliable results for V_m^E the absolute value of ρ are less important compared to the relative certainty in ρ (25), the accuracy in V_m^E is believed to be less than $\pm (0.01|V_{m,min}^E| + 0.005$ cm^{3}mol^{-1}), where $V_{m,min}^E$ denotes the minimum experimental value of the excess molar volume with respect to x_1.

3. Results

The results of V_m^E as a function of mole fraction of the alkanol, x_1, are collected in Table 2. The data were fitted by

© 1999 NRC Canada

Table 2. Excess molar volumes V_m^E for methanol (1) or ethanol (1) + linear polyethers (2) at 298.15 K and atmospheric pressure.

x_1	V_m^E (cm^3 mol^{-1})	x_1	V_m^E (cm^3 mol^{-1})	x_1	V_m^E (cm^3 mol^{-1})	x_1	V_m^E (cm^3 mol^{-1})
CH_3OH (1) + $CH_3OCH_2CH_2OCH_3$ (2)							
0.0251	–0.0444	0.3059	–0.4011	0.5931	–0.4984	0.8991	–0.2246
0.0550	–0.0942	0.3988	–0.4644	0.7004	–0.4557	0.9481	–0.1266
0.1198	–0.1918	0.4935	–0.4980	0.8017	–0.3665	0.9714	–0.0738
0.2123	–0.3100						
CH_3OH (1) + $CH_3CH_2OCH_2CH_2OCH_2CH_3$ (2)							
0.1151	–0.2765	0.4059	–0.6773	0.6952	–0.6543	0.8961	–0.3294
0.2110	–0.4556	0.4992	–0.7176	0.7749	–0.5651	0.9725	–0.1020
0.3052	–0.5864	0.5335	–0.7225				
CH_3OH (1) + $CH_3O(CH_2CH_2O)_2CH_3$ (2)							
0.0279	–0.0513	0.3090	–0.4637	0.5908	–0.6339	0.9028	–0.3242
0.0734	–0.1287	0.4056	–0.5520	0.6925	–0.6055	0.9511	–0.1880
0.1169	–0.1998	0.4249	–0.5672	0.7942	–0.5172	0.9741	–0.1063
0.2056	–0.3321						
CH_3OH (1) + $CH_3CH_2O(CH_2CH_2O)_2CH_2CH_3$ (2)							
0.0361	–0.0841	0.3135	–0.5929	0.5965	–0.7895	0.9011	–0.4072
0.0767	–0.1744	0.4064	–0.6985	0.7034	–0.7482	0.9487	–0.2428
0.1278	–0.2794	0.4979	–0.7686	0.7972	–0.6373	0.9726	–0.1402
0.2165	–0.4411						
CH_3OH (1) + $CH_3(CH_2)_3O(CH_2CH_2O)_2(CH_2)_3CH_3$ (2)							
0.0307	–0.0686	0.1357	–0.2733	0.5174	–0.6898	0.9004	–0.3329
0.0633	–0.1381	0.2272	–0.4255	0.5999	–0.6879	0.9504	–0.1902
0.0771	–0.1636	0.3202	–0.5474	0.6954	–0.6437	0.9745	–0.1055
0.1028	–0.2127	0.4045	–0.6269	0.7996	–0.5312		
CH_3OH (1) + $CH_3O(CH_2CH_2O)_3CH_3$ (2)							
0.0152	–0.029	0.2217	–0.393	0.6023	–0.765	0.9017	–0.444
0.0400	–0.076	0.3146	–0.528	0.6962	–0.748	0.9490	–0.271
0.0932	–0.177	0.4053	–0.637	0.8002	–0.659	0.9734	–0.157
0.1238	–0.232	0.5044	–0.718				
CH_3OH (1) + $CH_3O(CH_2CH_2O)_4CH_3$ (2)							
0.0376	–0.077	0.3171	–0.572	0.6918	–0.867	0.9013	–0.550
0.0587	–0.118	0.3928	–0.678	0.7976	–0.787	0.9488	–0.348
0.1230	–0.242	0.5039	–0.802	0.8500	–0.697	0.9733	–0.204
0.2208	–0.419	0.6001	–0.858				
CH_3CH_2OH (1) + $CH_3OCH_2CH_2OCH_3$ (2)							
0.0255	–0.0152	0.2174	–0.1191	0.6083	–0.1915	0.9033	–0.0818
0.0569	–0.0339	0.3131	–0.1575	0.7067	–0.1716	0.9473	–0.0476
0.0773	–0.0460	0.4097	–0.1818	0.7553	–0.1579	0.9782	–0.0211
0.1105	–0.0659	0.4977	–0.1941	0.8104	–0.1359		
CH_3CH_2OH (1) + $CH_3CH_2OCH_2CH_2OCH_2CH_3$ (2)							
0.0318	–0.051	0.2031	–0.267	0.5016	–0.432	0.8400	–0.268
0.1079	–0.156	0.3467	–0.381	0.6527	–0.412		
CH_3CH_2OH (1) + $CH_3O(CH_2CH_2O)_2CH_3$ (2)							
0.0151	–0.0110	0.1186	–0.0807	0.4173	–0.2377	0.8005	–0.2180
0.0280	–0.0204	0.1206	–0.0840	0.5029	–0.2593	0.8525	–0.1801
0.0423	–0.0306	0.2222	–0.1451	0.6012	–0.2657	0.8999	–0.1382
0.0685	–0.0497	0.3157	–0.1955	0.7068	–0.2512	0.9662	–0.0549
0.0896	–0.0634						
CH_3CH_2OH (1) + $CH_3CH_2O(CH_2CH_2O)_2CH_2CH_3$ (2)							
0.0223	–0.0316	0.2247	–0.2568	0.6004	–0.4388	0.8571	–0.2854
0.0410	–0.0514	0.3218	–0.3400	0.6487	–0.4349	0.9058	–0.2121
0.0682	–0.0874	0.4250	–0.4005	0.7082	–0.4128	0.9502	–0.1257
0.1485	–0.1825	0.5143	–0.4336	0.7502	–0.3875	0.9738	–0.0731
0.2109	–0.2456	0.5552	–0.4422	0.8064	–0.3438		

© 1999 NRC Canada

Table 2 (*concluded*).

x_1	V_m^E (cm^3 mol^{-1})	x_1	V_m^E (cm^3 mol^{-1})	x_1	V_m^E (cm^3 mol^{-1})	x_1	V_m^E (cm^3 mol^{-1})
CH_3CH_2OH (1) + $CH_3(CH_2)_3O(CH_2CH_2O)_2(CH_2)_3CH_3$ (2)							
0.0267	–0.0348	0.1177	–0.1414	0.4092	–0.3829	0.8522	–0.2856
0.0279	–0.0376	0.1917	–0.2214	0.5137	–0.4154	0.9030	–0.2121
0.0364	–0.0457	0.2363	–0.2611	0.6218	–0.4235	0.9476	–0.1310
0.0515	–0.0651	0.3026	–0.3198	0.7029	–0.3974	0.9485	–0.1303
0.0583	–0.0748	0.3100	–0.3244	0.7987	–0.3380	0.9505	–0.1258
0.0670	–0.0849						
CH_3CH_2OH (1) + $CH_3O(CH_2CH_2O)_3CH_3$ (2)							
0.0332	–0.0300	0.3125	–0.2526	0.6061	–0.3743	0.9022	–0.2056
0.0569	–0.0511	0.4152	–0.3166	0.7010	–0.3598	0.9506	–0.1204
0.1175	–0.1044	0.5053	–0.3509	0.8038	–0.3154	0.9734	–0.0711
0.2204	–0.1863						
CH_3CH_2OH (1) + $CH_3O(CH_2CH_2O)_4CH_3$ (2)							
0.0341	–0.035	0.3215	–0.308	0.6101	–0.456	0.9042	–0.275
0.0752	–0.078	0.4056	–0.366	0.7025	–0.452	0.9515	–0.166
0.1110	–0.116	0.5078	–0.435	0.8047	–0.401	0.9746	–0.097
0.2260	–0.222						

Fig. 1. V_m^E at 298.15 K and atmospheric pressure for methanol (1) + *n*-polyethers (2) mixtures. Solid lines, results from the smoothing eq. [1] with the coefficients listed in Table 3. Points, experimental data. (*a*) ● 2,5-dioxahexane; ▲ 2,5,8-trioxanonane; ◆ 2,5,8,11-tetraoxadodecane; ★ 2,5,8,11,14-pentaoxapentadecane. (*b*) ● 3,6-dioxaoctane; ▼ 3,6,9-trioxaundecane; ★ 5,8,11-trioxapentadecane.

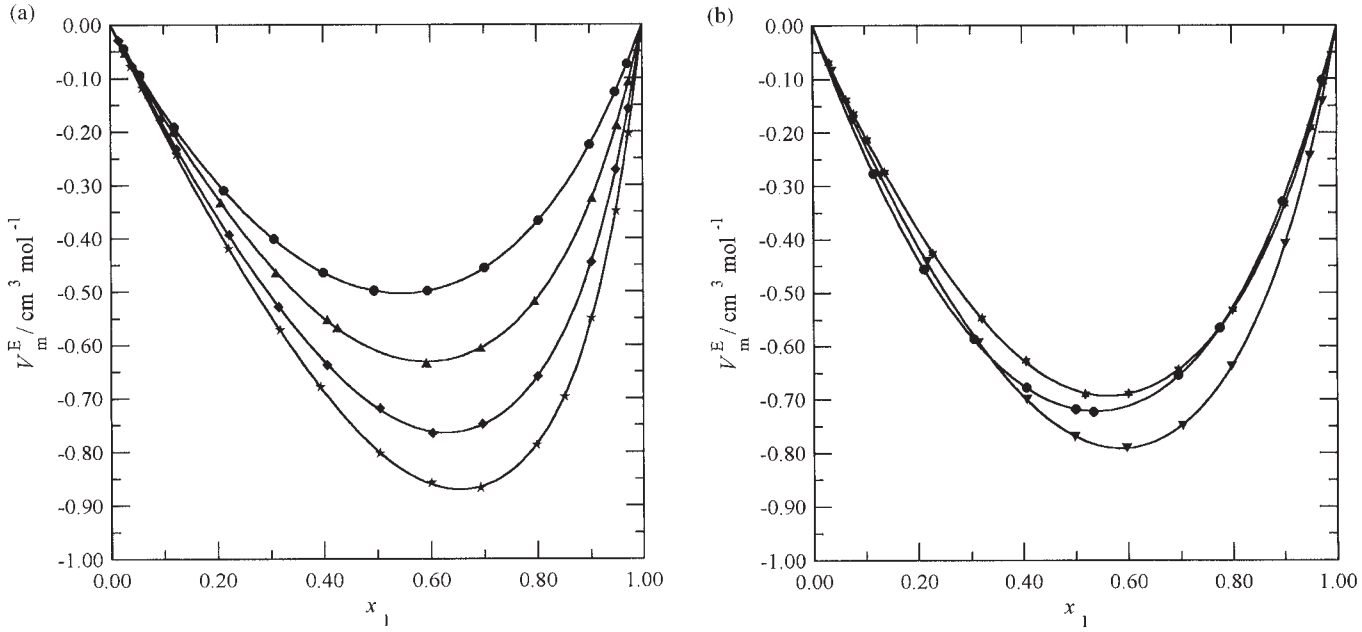

unweighted least-squares polynomial regression to the equation:

$$[1] \qquad V_m^E/\text{cm}^3\ \text{mol}^{-1} = x_1(1-x_1)\sum_{i=0}^{k} A_i(2x_1-1)^i$$

The number of coefficients k used in eq. [1] for each mixture was determined by applying an F test (27) at the 95% confidence level. Table 3 lists the parameters A_i obtained in the regression, together with the standard deviations σ, defined by

$$[2] \qquad \sigma(V_m^E)/\text{cm}^3\ \text{mol}^{-1} = [\sum (V_{m,\text{cal.}}^E - V_{m,\text{exp.}}^E)^2/(N-k)]^{1/2}$$

where N stands for the number of direct experimental values. For all the mixtures $\sigma(V_m^E)/|V_{m,\text{min}}^E| < 0.01$, in accord with the precision attainable with the instrument used. A graphical representation of the experimental results together with the smoothing curves are shown in Figs. 1 and 2.

For all the mixtures investigated, $V_m^E < 0$ over the whole mole fraction range. Systems with methanol show $|V_m^E|$ larger than those with ethanol. We note that the V_m^E curves are shifted to the region rich in alkanol, increasing their asymmetry with the number of oxygen groups in the polyether (see next section). V_m^E for methanol + 2,5-dioxahexane, + 3,6-dioxaoctane, + 2,5,8-trioxanonane, and + 5,8,11-trioxapentadecane and for ethanol + 3,6-dioxaoctane

© 1999 NRC Canada

Table 3. Coefficients A_i and standard deviations $\sigma(V_m^E)/cm^3\ mol^{-1}$ (eq. [2]) for representation of the V_m^E at 298.15 K and atmospheric pressure by eq. [1]. The error of the coefficients are given between brackets. N is the number of data points.

N	A_0	A_1	A_2	A_3	A_4	A_5	$\sigma(V_m^E)$
			CH_3OH (1) + $CH_3OCH_2CH_2OCH_3$ (2)				
13	–1.99651	–0.3345	–0.1935	–0.1219	–0.067		0.0004
	(0.0010)	(0.003)	(0.009)	(0.007)	(0.014)		
			CH_3OH (1) + $CH_3CH_2OCH_2CH_2OCH_2CH_3$ (2)				
10	–2.8700	–0.3832	–0.399	–0.226			0.0010
	(0.002)	(0.009)	(0.010)	(0.02)			
			CH_3OH (1) + $CH_3O(CH_2CH_2O)_2CH_3$ (2)				
13	–2.4461	–0.8260	–0.322	–0.426	–0.368		0.0019
	(0.005)	(0.015)	(0.05)	(0.03)	(0.08)		
			CH_3OH (1) + $CH_3CH_2O(CH_2CH_2O)_2CH_2CH_3$ (2)				
13	–3.0762	–0.9974	–0.355	–0.308	–0.535	–0.272	0.0013
	(0.004)	(0.018)	(0.03)	(0.10)	(0.05)	(0.11)	
			CH_3OH (1) + $CH_3(CH_2)_3O(CH_2CH_2O)_2(CH_2)_3CH_3$ (2)				
15	–2.7309	–0.635	–0.173	–0.386	–0.440		0.0016
	(0.004)	(0.013)	(0.04)	(0.03)	(0.06)		
			CH_3OH (1) + $CH_3O(CH_2CH_2O)_3CH_3$ (2)				
14	–2.8734	–1.361	–0.615	–0.32	–0.686	–0.59	0.002
	(0.005)	(0.03)	(0.05)	(0.14)	(0.08)	(0.16)	
			CH_3OH (1) + $CH_3O(CH_2CH_2O)_4CH_3$ (2)				
14	–3.1901	–1.778	–0.833	–0.52	–1.187	–0.93	0.002
	(0.006)	(0.03)	(0.06)	(0.15)	(0.09)	(0.17)	
			CH_3CH_2OH (1) + $CH_3OCH_2CH_2OCH_3$ (2)				
15	–0.7745	–0.1166	–0.0315	–0.085			0.0006
	(0.0014)	(0.005)	(0.006)	(0.011)			
			CH_3CH_2OH (1) + $CH_3CH_2OCH_2CH_2OCH_2CH_3$ (2)				
7	–1.731	–0.249	–0.178				0.002
	(0.006)	(0.012)	(0.03)				
			CH_3CH_2OH (1) + $CH_3O(CH_2CH_2O)_2CH_3$ (2)				
17	–1.0327	–0.369	–0.101	–0.168	–0.148		0.0013
	(0.003)	(0.010)	(0.03)	(0.02)	(0.05)		
			CH_3CH_2OH (1) + $CH_3CH_2O(CH_2CH_2O)_2CH_2CH_3$ (2)				
19	–1.7208	–0.517	–0.219	–0.237	–0.184		0.0017
	(0.004)	(0.012)	(0.03)	(0.03)	(0.06)		
			CH_3CH_2OH (1) + $CH_3(CH_2)_3O(CH_2CH_2O)_2(CH_2)_3CH_3$ (2)				
21	–1.6613	–0.439	–0.219	–0.355	–0.238		0.0016
	(0.004)	(0.011)	(0.04)	(0.02)	(0.05)		
			CH_3CH_2OH (1) + $CH_3O(CH_2CH_2O)_3CH_3$ (2)				
13	–1.4041	–0.654	–0.226	–0.294	–0.270		0.0019
	(0.005)	(0.016)	(0.05)	(0.04)	0.07)		
			CH_3CH_2OH (1) + $CH_3O(CH_2CH_2O)_4CH_3$ (2)				
13	–1.7055	–0.969	–0.255	0	–0.67	–0.657	0.003
	(0.008)	(0.018)	(0.08)		(0.11)	(0.06)	

and + 2,5,8-trioxanonane have been measured previously (28, 29). At x_1 = 0.5, data from Pal and Sharma (29) are about 3.5% larger than ours and are more scattered at low dilution of the alkanol, as the comparison of the respective V_m^E/x_1x_2 curves shows. Results at equimolar composition from Villamañán et al. (28) are also larger than those presented in this work (~5% for ethanol + 2,5,8-trioxanonane) except for the methanol + 2,5,8-trioxanonane system, which is lower (~3%).

4. Discussion

It is well known that V_m^E in 1-alkanols + *n*-alkanes mixtures is the result of several opposing effects: changes in self-association and physical interactions (dipole–dipole) between alkanol multimers and monomers lead to an increasing of volume; a decreasing of volume is obtained by changes of free volume and interstitial accomodation (30). So, for a given *n*-alkane, say *n*-heptane, V_m^E is positive over

© 1999 NRC Canada

Fig. 2. V_m^E at 298.15 K and atmospheric pressure for ethanol (1) + *n*-polyethers (2) mixtures. Solid lines, results from the smoothing eq. [1] with the coefficients listed in Table 3. Points, experimental data. (*a*) ● 2,5-dioxahexane; ▲ 2,5,8-trioxanonane; ◆ 2,5,8,11-tetraoxadodecane; ★ 2,5,8,11,14-pentaoxapentadecane. (*b*) ● 3,6-dioxaoctane; ▼ 3,6,9-trioxaundecane; ★ 5,8,11-trioxapentadecane.

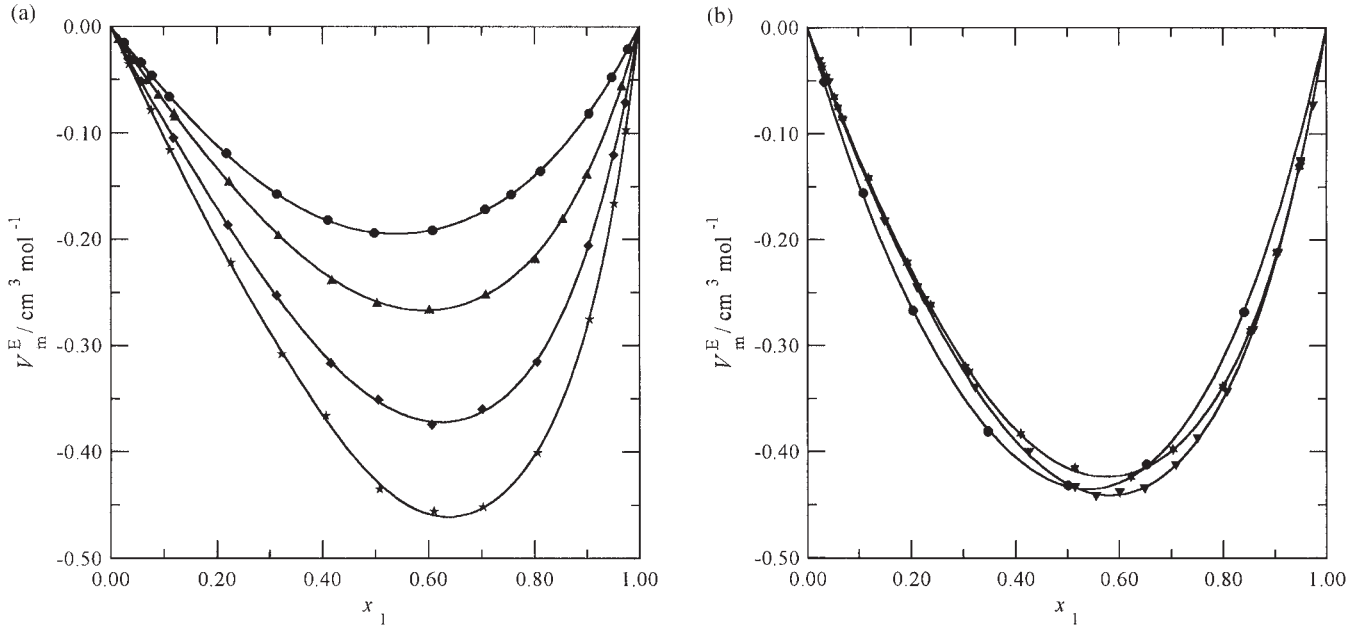

Table 4. H_m^E (J mol^{-1}) and V_m^E (cm^3 mol^{-1}) at equimolar composition, 298.15 K, and atmospheric pressure for several 1-alkanols + *n*-polyethers mixtures. Data are written as H_m^E/V_m^E.

	n-Polyether			
1-Alkanol	2,5-Dioxahexane	2,5,8-Trioxanonane	3,6-Dioxaoctane	3,6,9-Trioxaundecane
Methanol	338[a]/–0.499[b]	440[g]/–0.611[b]	344[g]/–0.720[b]	—/0.765[b]
Ethanol	803[a]/–0.194[b]	964[g]/–0.258[b]	737[g]/–0.433[b]	—/–0.430[b]
Propanol	1040[a]/–0.067[c]	1214[g]/–0.068[c]	870[g]/–0.385[c]	1123[i]/–0.304[c]
Butanol	1174[a]/—	—/—	842[h]/—	1254[i]/—
Pentanol	1264[a]/0.0645[d]	—/—	872[h]/—	1312[i]/—
Hexanol	1340[a]/0.1127[e]	—/0.2684[e]	941[g]/–0.3027[e]	—/–0.0283[e]
Heptanol	1433[a]/0.1685[f]	1626[g]/0.369[f]	—/—	1475[i]/—
Octanol	1517[a]/—	—/—	—/—	—/—
Nonanol	1588[a]/0.278[f]	—/0.559[f]	—/–0.183[f]	1637[i]/0.178[f]

[a]Reference 10.
[b]This work.
[c]Reference 15.
[d]Reference 29.
[e]Reference 21.
[f]Reference 20.
[g]Reference 41.
[h]Reference 42.
[i]Reference 11.

the whole range of concentration for lower 1-alkanols, and becomes sigmoid for longer alkanols (31). The magnitudes of these contributions are sensitive to the lengths of component molecules (31). For example, as the length of the 1-alkanol is increased, the negative effect accompanying the fitting of the *n*-alkane molecules into the alkanol multimer structure becomes progresively more important, and predominates for sufficient long alkanol molecules.

In systems of linear oxaalkanes and *n*-alkanes, the dipole–dipole interactions between ether molecules are weaken by the addition of the alkane. The sign of V_m^E depends on the relative size of the mixture components (32, 33). For di-*n*-propylether + *n*-heptane, where the molecular size of both components are similar, $V_m^E > 0$ over the whole range of concentration (32). In exchange, for systems comprising longer ether and shorter alkane molecules, e.g., di-*n*-butylether + *n*-hexane, free volumes contributions are relatively more important and $V_m^E < 0$ (33). The V_m^E of linear polyethers + *n*-alkanes are usually higher than those of linear ethers + *n*-alkanes, indicating larger differences between positive and

© 1999 NRC Canada

Fig. 3. V_m^E of 1-alkanol (1) + dioxaalkane (2) mixtures at 298.15 K, atmospheric pressure, and equimolar composition vs. *n*, the number of carbon atoms of the 1-alkanol: ● 2,5-dioxahexane; ◆ 3,6-dioxaoctane. Source of data: methanol and ethanol (this work); 1-propanol (15); 1-hexanol (21); 1-heptanol and 1-nonanol (20). Hollow symbols are corresponding data from literature: ○ 1-alkanol + 2,5-dioxahexane (29); ◇ 1-alkanol + 3,6-dioxaoctane (28).

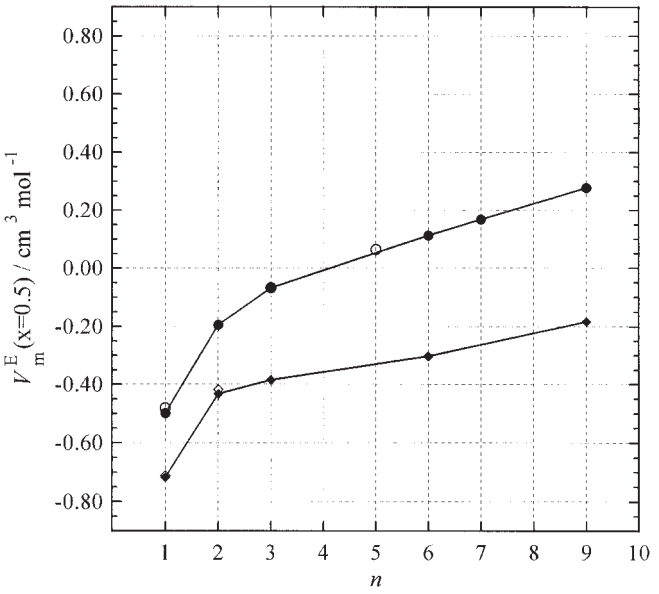

Fig. 4. V_m^E of 1-alkanol (1) + trioxaalkane (2) mixtures at 298.15 K, atmospheric pressure, and equimolar composition vs. *n*, the number of carbon atoms of the 1-alkanol: ▲ 2,5,8-trioxanonane; ▼ 3,6,9-trioxaundecane; ★ 5,8,11-trioxapentadecane. Source of data: methanol and ethanol (this work); 1-propanol (15); 1-hexanol (21); 1-heptanol and 1-nonanol (20). Hollow symbols are corresponding data from literature: △ 1-alkanol + 2,5,8-trioxanonane (28); ☆ 1-alkanol + 5,8,11-trioxapentadecane (29).

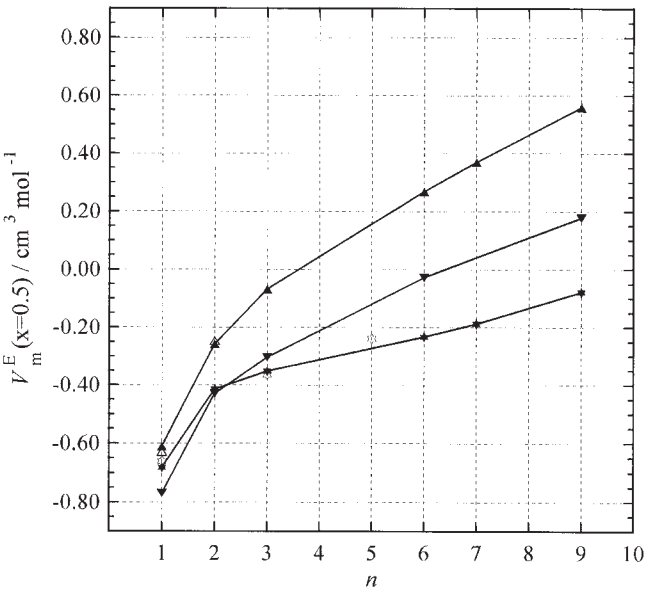

negative contributions (34). It is remarkable that in mixtures of CH_3-O-(CH_2-CH_2-O-)$_m$-CH_3 with *n*-pentane, V_m^E becomes S-shaped for m = 3, 4 (35).

For the mixtures under study, one must also take into account interactions between unlike molecules; i.e., the new OH---O bonds created, which contribute negatively to V_m^E.

From a purely interactional point of view, we note that H_m^E of solutions of methanol with polyethers are much lower than those of the remainder alkanols (Table 4), which actually show larger H_m^E than when are mixed with *n*-alkanes. So, polyethers are enough active to break the self-association of the alkanols (from ethanol) in such way that the number of broken H-bonds is not compensated by the new OH---O bonds formed. In the case of methanol, inmiscible with alkanes at room temperature, H_m^E is much lower, indicating stronger interactions between unlike molecules. Systems of 1-alkanols and *n*-alkanones behave similarly (36).

Now we'll examine qualitatively some of the main features found along our investigations on V_m^E of 1-alkanol + linear polyether mixtures.

4.1. Equimolar V_m^E values

4.1.1. *The effect of increasing the alkanol size for a given polyether*

In this case, V_m^E increases (Figs. 3–6), what may be due to (*i*) interactional effects as H_m^E also increases (Table 4); i.e., the number of broken hydrogen bonds is larger for longer alkanols and is not compensated by the OH---O bonds created; (*ii*) free volume effects, which are more important in mixtures containing short alcohol molecules. When both compounds are lengthened, the contribution from the interstitial accomodation might be enough negative and then V_m^E < 0. It occurs, e.g., in the 1-nonanol + 5,8,11-trioxapentadecane system (Fig. 4).

Systems of 1-alkanols and linear monoethers behave quite differently. For each monoether, V_m^E increases from methanol to ethanol or 1-propanol, and then decreases. H_m^E varies as in 1-alkanol + *n*-alkane mixtures when the *n*-alkane is fixed: increases from methanol to 1-propanol and then decreases rather slowly (14). It suggests that for longer alcohols the interactional contribution is practically the same, while the structural effects increase. Such different behaviour may be attributed to H_m^E is higher for the actual mixtures than for systems with monoethers, i.e., to a more important interactional contribution to V_m^E, in part due to the strong dipole–dipole interactions between polyether molecules.

4.1.2. The effect of increasing the n*-alkyl chain end length of the ether when the number of oxygen atoms and their relative position is fixed*

For a given alcohol, V_m^E is lower for the oxaalkane with the longer alkyl chain (except in some cases for methanol and ethanol; Figs. 3–4). This may be due to (*i*) H_m^E also decreases with the size of the ether (Table 4); i.e., ethers with larger *n*-alkyl chain ends are less active to break the self-association of the alcohol as the -O- groups are more hindered; (*ii*) free volume effects for shorter alcohols or interstitial accomodation for longer alkanols. The anomalous behaviour found for some mixtures with methanol or ethanol (Figs. 1*b*, 2*b*, 4, and 6) remarks the stronger self-association of these alcohols.

© 1999 NRC Canada

Fig. 5. V_m^E of 1-alkanol (1) + *n*-polyether (2) mixtures at 298.15 K, atmospheric pressure, and equimolar composition vs. *n*, the number of carbon atoms of the 1-alkanol: ● 2,5-dioxahexane; ▲ 2,5,8-trioxanonane; ◆ 2,5,8,11-tetraoxadodecane; ★ 2,5,8,11,14-pentaoxapentadecane. Source of data: methanol and ethanol (this work); 1-propanol (15); 1-hexanol (21); 1-heptanol and 1-nonanol (20). ○ 1-alkanol + 2,5-dioxahexane (29); △ 1-alkanol + 2,5,8-trioxanonane (28).

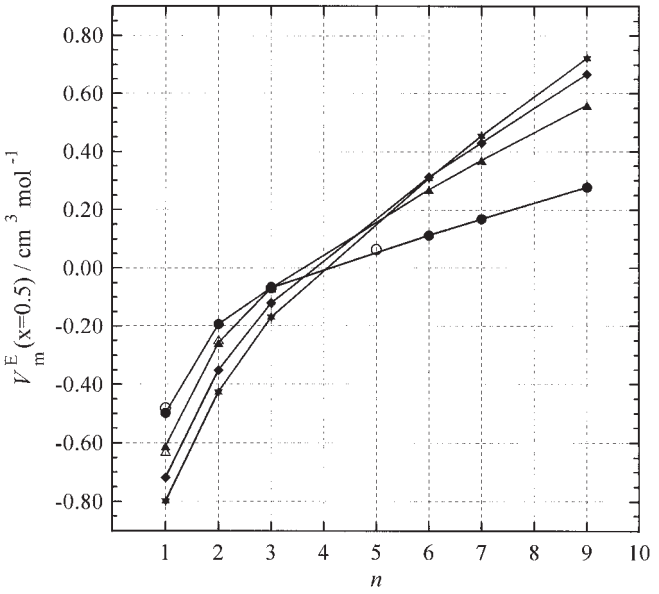

Fig. 6. V_m^E of 1-alkanol (1) + *n*-polyether (2) mixtures at 298.15 K, atmospheric pressure, and equimolar composition vs. *n*, the number of carbon atoms of the 1-alkanol: ● 3,6-dioxaoctane; ▼ 3,6,9-trioxaundecane. Source of data: methanol and ethanol (this work); 1-propanol (15); 1-hexanol (21); 1-nonanol (20). ○ 1-alkanol + 3,6-dioxaoctane (28).

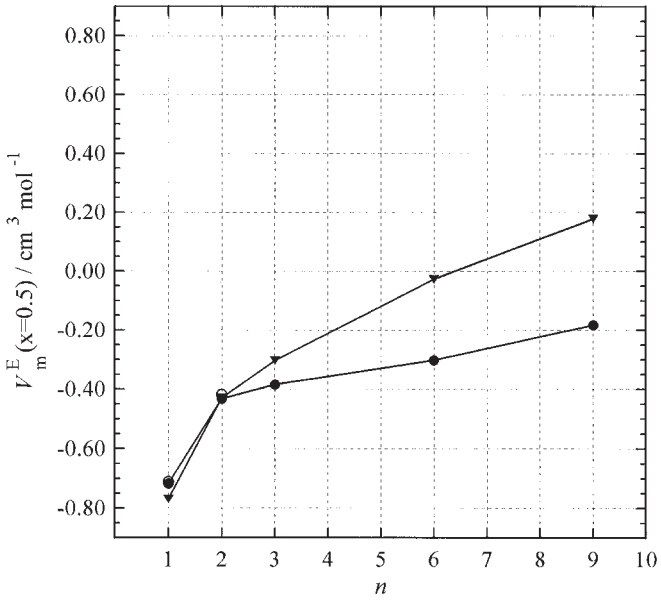

4.1.3. The effect of adding OCH_2CH_2 groups at the middle of the ether molecule when the n*-alkyl chain end is fixed*

We note that for short alkanol molecules, V_m^E decreases with the size of the ether (and $V_m^E < 0$; Figs. 5, 6). Longer 1-alkanols behave in opposite way, and the sign of V_m^E depends on the methyl or ethyl character of the polyether ends (Figs. 5, 6). As H_m^E (triether, e.g., CH_3CH_2-(O-$CH_2CH_2)_2$-O-CH_2CH_3) > H_m^E (diether; e.g., CH_3CH_2-O-CH_2CH_2-O-CH_2CH_3; see Table 4), this means that more H-bonds are disrupted, producing a positive contribution to V_m^E. As for the shorter alcohols V_m^E decreases, it must be due to free volume effects are predominant, particularly when the polyether ends are of ethyl character. In exchange, for longer 1-alkanols, when a less difference in size of the compounds exists, interactional effects become more important; e.g., at equimolar composition and 298.15 K, for the 1-heptanol + 2,5,8,11,14-pentaoxapentadecane system H_m^E/J mol^{-1} = 2056 (A. Roux, personal communication). Then the order of V_m^E is inverted (Figs. 5, 6).

We remark that, for CH_3-O-(CH_2-CH_2-O-)$_m$-CH_3 + alkane mixtures, $V_m^E(x = 0.5)$ behaves similarly with the size of the alkane (35).

4.2. The concentration dependence

The V_m^E curves are usually asymmetrical and shifted to higher concentration of alcohol. This may be attributed to free volume effects, as in this case the curves are shifted to the region rich in the compound of smaller molar volume. In exchange, the H_m^E curves are nearly symmetrical (11). For 1-alkanols + monoethers systems, the latter are skewed to low mole fractions of the alcohol and are also lower than for the systems treated here. It suggests that the self-association of alcohols is more important in solutions with monoethers than in those with polyethers.

We have also analysed the partial molar excess volume curves, V_i^E (i = 1, alcohol; i = 2, polyether) calculated from eq. [1] (and not shown in this work). The main difference between V_1^E and V_2^E is the changes in curvature found for V_1^E of methanol, ethanol, and 1-propanol, which can be related to their stronger self-association. For the longer alcohols, V_1^E results in more smoothed curves, in agreement with the fact that self-association is less important. The V_2^E curves show a very regular shape as polyethers are not self-associated. A similar behaviour is found for 1-alkanols + *n*-alkanes (30).

5. Conclusions

Data on V_m^E at 298.15 K and atmospheric pressure for methanol or ethanol + *n*-polyethers are reported. Results underline the predominant contribution of free volume effects on interactional effects, particularly for mixtures including polyethers of the type CH_3-(O-CH_2-$CH_2)_m$-CH_3. In systems with ethers of longer *n*-alkyl chain ends, self-association of methanol and ethanol is more relevant.

Acknowledgements

This work was supported by the Programa Sectorial de Promoción General del Conocimiento de la S.E.U.I. y D. del M.E.C. (Spain), Project ref. PB97–0488 and by the Consejería de Educación y Cultura de la Junta de Castilla y León, under the Project VA54/98. F.J.C. acknowledges the grants received from Junta de Castilla y León and from "Programa Nacional de Formación de Personal

© 1999 NRC Canada

Investigador" de la S.E.U.I. y D. del MEC. F.J.A. acknowledges the grant received from University of Valladolid.

References

1. J.C. Cobos. Ph.D. thesis. University of Valladolid, Spain. 1987.
2. J.C. Cobos and C. Casanova. Fluid Phase Equilib. **20**, 155 (1985); J.C. Cobos, I. García, C. Casanova, G. Roux-Desgranges, and J.-P.E. Grolier. Thermochim. Acta, **131**, 73 (1987); J.C. Cobos, C. Casanova, G. Roux-Desgranges, and J.-P.E. Grolier. J. Chem. Thermodyn. **19**, 791 (1987); J.C. Cobos, I. García, and C. Casanova. Can. J. Chem. **66**, 2618 (1988); M.A. Rubio, J.A. González, I. García de la Fuente, and J.C. Cobos. Fluid Phase Equilib. **143**, 111 (1998); J. Chem. Eng. Data, **43**, 811 (1998).
3. H.V. Kehiaian. Fluid Phase Equilib. **13**, 243 (1983).
4. H.V. Kehiaian. Pure Appl. Chem. **57**, 15 (1985).
5. S. Delcros, J.R. Quint, J.-P.E. Grolier, and H.V. Kehiaian. Fluid Phase Equilib. **113**, 1 (1995).
6. J. Gmehling, J. Li, and M. Schiller. Ind. Eng. Chem. Res. **32,** 178 (1993).
7. A. Heintz. Ber. Bunsenges. Phys. Chem. **89**, 172 (1985).
8. P.J. Flory. J. Am. Chem. Soc. **87**, 1833 (1965).
9. S. Mohren and A. Heintz. Fluid Phase Equilib. **133**, 247 (1997).
10. J.C. Cobos, M.A. Villamañán, and C. Casanova. J. Chem. Thermodyn. **16**, 861 (1984).
11. J.C. Cobos, I. García, J.A. González, and C. Casanova. J. Chem. Thermodyn. **22**, 383 (1990).
12. I. García de la Fuente, J.F. Rodríguez, J.A. González, J.C. Cobos, and C. Casanova. J. Solution Chem. **21**, 425 (1992).
13. I. García de la Fuente, J.F. Rodríguez, J.A. González, J.C. Cobos, and C. Casanova. J. Chem. Thermodyn. **24**, 23 (1992).
14. A. Serna, I. García de la Fuente, J.A. González, J.C. Cobos, and C. Casanova. Fluid Phase Equilib. **100**, 361 (1995).
15. A. Serna, I. García de la Fuente, J.A. González, and J.C. Cobos. Fluid Phase Equilib. **133**, 187 (1997).
16. U. Domańska and J.A. González. Fluid Phase Equilib. **119**, 131 (1996).
17. U. Domańska and J.A. González. Fluid Phase Equilib. **123**, 167 (1996).
18. U. Domańska and J.A. González. Fluid Phase Equilib. **129**, 139 (1997).
19. U. Domańska and J.A. González. Fluid Phase Equilib. **147**, 251 (1998).
20. F.J. Arroyo, F.J. Carmona, I. García de la Fuente, J.A. González, and J.C. Cobos. J. Solution Chem. In press.
21. A. Serna, I. García de la Fuente, J.A. González, and J.C. Cobos. Proc. 13th IUPAC Conf. Chem. Thermodyn. Clermont-Ferrand, France. July 17–22, 1994.
22. H. Stabinger, H. Leopold, and O. Kratky, Monatsh. Chem. **98**, 436 (1967).
23. O. Kratky, H. Leopold, and H. Stabinger. Z. Angew. Phys. **27**, 273 (1969).
24. H. Leopold. Elektronik, **19**, 297 (1970).
25. I. García de la Fuente, J.A. González, J.C. Cobos, and C. Casanova. J. Chem. Eng. Data, **37**, 535 (1992).
26. IUPAC commission on atomic weights and isotopic abundances 1985. Pure Appl. Chem. **58**, 1677 (1986).
27. P.R. Bevington. Data reduction and error analysis for the physical sciences. McGraw–Hill, New York. 1969. Chap. 10. p. 200.
28. M.A. Villamañán, C. Casanova, G. Roux-Desgranges, and J.-P.E. Grolier. Thermochim. Acta, **52**, 279 (1982).
29. A. Pal and S. Sharma. Fluid Phase Equilib. **145**, 151 (1998).
30. A.J. Treszczanowicz, O. Kiyohara, and G.C. Benson. Bull. Acad. Pol. Sci. Ser. Sci. Chim. XXIX, 103 (1981).
31. A.J. Treszczanowicz and G.C. Benson. J. Chem. Thermodyn. **10**, 967 (1978).
32. F. Kimura, A.J. Treszczanowicz, C.J. Halpin, and G.C. Benson. J. Chem. Thermodyn. **15**, 503 (1983).
33. K.N. Marsh, J.B. Ott, and M.J. Costigan. J. Chem. Thermodyn. **12**, 857 (1980).
34. A.J. Treszczanowicz, C.J. Halpin, and G.C. Benson. J. Chem. Eng. Data, **27**, 321 (1982).
35. L. Andreoli-Ball, L.M. Trejo, M. Costas, and D. Patterson. Fluid Phase Equilib. **147**, 163 (1998).
36. J.A. González. Can. J. Chem. **75**, 1412 (1997).
37. J.A. Riddick, W.B. Bunger, and T.K. Sakano. Organic solvents. *In* Physical properties and methods of purification, techniques of chemistry. Vol. II. *Edited by* A Weissberger. John Wiley & Sons, New York, 1986.
38. G. Roux, G. Perron, and J.E. Desnoyers. Can. J. Chem. **56**, 2808 (1978).
39. T. Treszczanowicz and D.J. Cieslak. J. Chem. Thermodyn. **25**, 661 (1993).
40. T. Treszczanowicz, G.C. Benson, and B.C.-Y. Lu. J. Chem. Eng. Data, **33**, 379 (1988).
41. M.A. Villamañán, C. Casanova, A.H. Roux, and J.-P.E. Grolier. J. Chem. Thermodyn. **14**, 251 (1982).
42. M. Pintos and M.I. Paz-Andrade. Int. Data Ser. Sel. Data Mixtures Ser. A, **1**, 25 (1979).

© 1999 NRC Canada

The effect of preparation and aging conditions on the internal environment of sol-gel derived materials as probed by 7-azaindole and pyranine fluorescence

Kulwinder K. Flora, Monika A. Dabrowski, Sean P. Musson, and John D. Brennan

Abstract: Sol-gel derived silicate materials were prepared by a two-stage processing method similar that commonly used for entrapment of biomolecules. In the first step, tetraethylorthosilicate (TEOS) was hydrolyzed by sonicating in the presence of water (molar ratio of H_2O:Si = 4:1) and 0.044 M HCl with no added alcohol. The hydrolyzed TEOS was then mixed with varying amounts of a buffer solution (1:1 up to 4:1 vol:vol of silane:buffer) to induce gelation, and the monoliths were aged at room temperature either in air or in buffer for several days, followed by prolonged drying in air over several months. The emission spectra of the entrapped probes 7-azaindole (7AI) and 8-hydroxy-1,3,6-trisulfonated pyrene (pyranine) were examined at various times during the aging process to monitor the effects of the H_2O:Si ratio on the evolution of the internal environment of the silicate materials. The results showed that (*i*) the internal environment of the silicate materials continued to evolve long after the drying of the matrix (as determined by mass changes) was complete; (*ii*) the internal structure of the silicate materials, as monitored by both 7AI fluorescence and infrared spectroscopy, was affected by the proportion of water used for gelation of dry-aged materials, but was similar for all wet-aged samples, and (*iii*) both wet-aged and dry-aged monoliths had a distribution of final environments present both during and after drying. The implications of these findings for protein entrapment are discussed.

Key words: fluorescence, sol-gel, silicate materials, aging conditions, biosensor.

Résumé : On a préparé des matériaux sol-gels dérivés de silicates en faisant appel à une méthode en deux étapes similaires à celle utilisée couramment pour l'encapsulation de biomolécules. Dans la première étape, on hydrolyse l'orthosilicate de tétraéthyle (OSTE) par sonification en présence d'eau (rapport molaire de H_2O:Si = 4:1) et 0,044 M HCl, sans addition d'alcool. On mélange ensuite l'OSTE hydrolysé à diverses quantités d'une solution tampon (de 1:1 à 4:1, vol:vol, de silane:tampon) afin d'induire la formation d'un gel, puis on fait vieillir les monolithes à la température ambiante, à l'air ou dans un tampon, pour plusieurs jours et finalement on fait sécher à l'air pendant plusieurs mois. Afin d'évaluer les effets du rapport H_2O:Si sur l'évolution de l'environnement interne des matériaux à base de silicate, on a ensuite examiné les spectres d'émission des sondes encapsulées (7-azaindole (7AI) et 8-hydroxy-pyrène-1,3,6-sulfoné (pyranine)) à divers moments du processus de vieillissement. Les résultats montrent que (*i*) l'environnement interne des matériaux à base de silicate continue d'évoluer même lorsque le séchage de la matrice est terminé (tel que déterminé par les changements de masses); (*ii*) la structure interne des matériaux à base de silicate, telle que déterminée par les spectroscopie de fluorescence et infrarouge du 7AI, est déterminée par la proportion d'eau utilisée lors de la formation du gel des matériaux vieillis et séchés, mais elle est la même pour tous les matériaux vieillis et humides et (*iii*) les monolithes vieillis, secs ou humides, comportent une distribution des environnements finals tant durant le séchage qu'après. On discute des implications de ces observations pour l'encapsulation des protéines.

Mots clés : fluorescence, sol-gel, matériaux à base de silicate, conditions de vieillissement, biosenseur.

[Traduit par la Rédaction]

Received February 17, 1999.

K.K. Flora and J.D. Brennan.[1] Department of Chemistry, McMaster University, Hamilton, ON L8S 4M1, Canada. **M.A. Dabrowski and S.P. Musson.** Department of Chemistry, Brock University, St. Catharines, ON L2S 3A1, Canada.

[1]Author to whom correspondence may be addressed. Telephone: (905) 525-9140 (ext. 27033). Fax: (905) 522-2509. e-mail: brennanj@mcmail.cis.mcmaster.ca

Introduction

In the past few years several reports have appeared describing a modified sol-gel processing method that is suitable for the encapsulation of biomolecules into materials derived from tetraethylorthosilicate (TEOS) or tetramethylorthosilicate (TMOS) (1–14). One modification involved the promotion of hydrolysis by sonication of TEOS or TMOS in the presence of water and acid, thereby removing the need for an alcohol co-solvent. A second modification was the ad-

© 1999 NRC Canada

dition of a buffered aqueous solution to the hydrolyzed silane to promote gelation. The buffer raised the pH to a value that was close to the physiological range and diluted the alcohol produced during hydrolysis of the alkoxysilane, resulting in an environment that was suitable for entrapped proteins (3–14). These modifications, combined with aging at low temperatures over a period of several days or weeks, have resulted in a large number of successful protein encapsulation protocols, as outlined in the review by Avnir et al. (11).

Efficient encapsulation of active biomolecules represents a major advance in the area of sol-gel science. However, little is known about the initial pore-liquid composition of materials processed in this manner, and how the internal environment evolves over time. Such information is critically important, since the pore-liquid will contain both alcohol and water, and the level of alcohol is important in determining the stability of entrapped biomolecules (1). Furthermore, the continued evolution of the matrix over periods of months can result in significant changes in the behaviour of entrapped proteins, making it difficult to develop analytical devices, such as biosensors, which rely on long-term stability of the entrapped protein. A detailed study of the changes in the chemical properties of sol-gel derived materials, prepared according to the standard procedures adopted for protein entrapment, is therefore required to optimize entrapment protocols.

In the present study, the fluorescent probes pyranine (8-hydroxy-1,3,6-trisulfonated pyrene) and 7-azaindole (7AI) were used to examine the internal environment of the sol-gel derived matrixes. Pyranine undergoes excited-state proton transfer reactions that depend on the pK_a of the solvent (15), and the emission of the probe is sensitive to trace amounts of water (16). Hence, pyranine provides quantitative information on ethanol:water ratios, giving useful information on pore-liquid composition (16, 17). The emission of 7AI is affected by pH (18, 19) and local dipolarity (20). The probe also undergoes specific hydrogen-bond mediated interactions in the presence of protonated species that result in the formation of an excited state tautomer with a unique emission wavelength of ca. 520 nm (21–23). Thus, 7AI can be used to obtain information regarding the presence of protonated species in the local microenvironment within the monolith. In the case of sol-gel derived silica, we show that 7AI also reports on the presence of silanol groups within the silicate matrix, causing the emission peak to shift to a characteristic wavelength between 410 and 415 nm, in agreement with a previous report of 7AI emission in silicate materials (24). Hence, 7AI can monitor changes in the relative amount of silanol groups within the matrix as a function of preparation and aging conditions. Based on the changes in the fluorescence emission of 7AI and pyranine as a function of the amount of water used for gelation and aging, an optimal set of processing conditions for the encapsulation of biomolecules is proposed.

Experimental

Chemicals

Tetraethylorthosilicate (TEOS, 99.999+%) was obtained from Aldrich Chemicals (Milwaukee, Wisconsin). 7-Azaindole and polymethacrylate fluorimeter cuvettes (1 cm^2) were obtained from Sigma Chemicals (St. Louis, Missouri). Pyranine (8-hydroxy-1,3,6-trisulfonated pyrene) and seminaphtharhodafluor-1 (SNARF-1) were obtained from Molecular Probes (Eugene, Oregon). Water used for preparation of buffers was distilled and deionized using a Milli-Q five-stage water purification system. All other chemicals were of analytical grade and were used without further purification.

Preparation of sol-gel derived monoliths

TEOS was hydrolyzed by mixing 9.0 mL of the silane, 2.8 mL of deionized water, and 0.2 mL of 0.1 N hydrochloric acid (molar ratio of H_2O:Si (R value) = 4.1) and sonicating the solution until a clear, single-phase solution was formed (approximately 2 h). The hydrolyzed solution was stored for 7 days at minus 20°C before use to ensure complete hydrolysis of the TEOS (25). Following hydrolysis, the silane solution was mixed with a phosphate buffer solution (10 mM, pH 8.20, 100 mM KCl) containing 20 μM of the appropriate fluorophore in a disposable polymethacrylate cuvette. The ratio of hydrolyzed TEOS to buffer was varied from 1:1 to 4:1 (by volume) while maintaining the total volume of the mixture at 1.5 mL. These ratios provided R values of 21, 13, 10, and 8 for the 1:1, 2:1, 3:1, and 4:1 mixtures, respectively. The TEOS:buffer mixture was vortexed at low speed to ensure proper mixing and was then allowed to gel with the cuvette in an upright position. Cuvettes containing dry-aged monoliths were capped with Parafilm and several small holes (ca. 1 mm diameter) were punched in the film. The monoliths were then allowed to dry at room temperature for a period of four months (125 days).

Wet-aged monoliths were prepared as outlined above, but had 2.0 mL of the phosphate buffer solution added approximately 10 min after gelation, resulting in R values of 64, 45, 39, and 28 for the 1:1, 2:1, 3:1, and 4:1 mixtures, respectively. The cuvettes containing these monoliths were then capped with Parafilm, and the samples were aged for 10 days in the buffer with an exchange of buffer each day. The buffer solutions used for the exchanges contained 20 μM of the appropriate probe to avoid leaching of the entrapped probe from the monoliths. After 10 days the buffer was removed, and the monoliths were allowed to dry for several months in a manner identical to that used for the dry-aged monoliths.

Fluorescence spectroscopy of sol-gel monoliths

Fluorescence spectra were collected using instrumentation that is described in detail elsewhere (25). Samples containing 7AI were excited at 290 nm with emission collected from 310 to 570 nm, those containing pyranine were excited at 351 nm with emission collected from 400 to 650 nm, while those containing SNARF-1 were excited at 514 nm with emission collected from 550 to 700 nm. All spectra were collected in 1 nm increments with 4 nm excitation and emission bandpasses. Appropriate blanks were subtracted from each sample, and the spectra were corrected for deviations in the emission monochromator throughput and photomultiplier tube response.

For dry-aged monoliths, spectra were collected on a daily basis at approximately 24 h intervals, starting 30 min after

© 1999 NRC Canada

gelation and continuing until there were no further changes in the mass of the samples (as determined daily using an analytical balance) or in the spectra (usually 25 days). Generally, fresh 1:1 TEOS:water samples weighed 2.04 ± 0.05 g, while the terminal mass was 0.39 ± 0.04 g, consistent with the expected 80% reduction in mass during drying (25). For wet-aged monoliths, spectra were collected daily from samples that had the surrounding phosphate buffer solution removed just prior to collection of spectra to minimize contributions from fluorophores that were present in solution. While it is possible that a residue of the probe may have remained adsorbed to the external surface of the monoliths, the strength of the fluorescence signal, which increased as the samples shrank and concentrated the entrapped probe, was sufficient to ensure that the spectra reflected the internal environment of the matrix. After collection of the spectra, 2 mL of a fresh phosphate buffer solution (containing 20 μM of the appropriate probe) was added to dilute any residual alcohol while avoiding leaching of the probes from the monoliths during aging. After 10 days (at which point no further changes in spectra were observed), the buffer was removed and the monoliths were capped with Parafilm (with a 1 mm hole punched in the film) and dried in air, with spectra collected every 2 or 3 days until no further changes in the size or mass of the monoliths occurred (ca. 30 days). Both wet-aged and dry-aged samples were left to age until a total of 125 days had elapsed since gelation, with spectra being collected at various times over this period.

Infrared spectroscopy

Representative infrared spectra were collected from wet-aged and dry-aged monoliths using a FTIR spectrometer (ATI-Mattson Research Series) with a diffuse reflectance accessory. The samples were prepared with 1:1 to 4:1 TEOS:buffer ratios and aged 125 days using the conditions described above. The samples were crushed and were degassed by heating at 120°C for 60 min before spectra were collected. A total of 1024 scans were collected in absorbance mode from 4000 to 400 cm^{-1} with a resolution of 4 cm^{-1} for each sample.

Results and discussion

Pyranine fluorescence

Pyranine has two emission peaks, one at 438 nm (protonated form, indicative of ethanol) and another at 518 nm (deprotonated form, indicative of water), which change in proportion as a function of the ratio of ethanol-to-water (16). The peak ratio was calibrated using standard ethanol:water mixtures, and was used to ascertain the volumetric ratio of ethanol:water in the freshly formed monoliths, and to monitor the evolution of the pore-liquid composition during aging and drying. The initial percentages of ethanol (by volume) were 36 ± 3, 46 ± 2, 54 ± 3, and 62 ± 3% for the dry-aged 1:1, 2:1, 3:1, and 4:1 TEOS:water systems, respectively. For the wet-aged samples, 2.0 mL of buffer was added to each sample after gelation. In this case, the percentages of ethanol were 10 ± 2% (1:1 ratio), 15 ± 2% (2:1 ratio), 21 ± 2% (3:1 ratio), and 28 ± 3% (4:1 ratio). Hence, a substantial dilution of the ethanol occurs immediately, as expected. Knowledge of the exact volumetric ratio of ethanol:water is important since many proteins remain stable at low ethanol concentrations (usually below ~20%), but become unstable at higher levels (1). The removal and replacement of the surrounding buffer at 24 h intervals resulted in further dilution of ethanol, with the percentage of ethanol being between 0% (1:1) and 10% (4:1) after the second buffer rinse, and zero for all samples after the third rinse. Thus, three rinses with buffer after gelation should remove all of the ethanol (provided equilibrium is reached) so that it would have no influence on the behaviour of entrapped proteins.

Fig. 1. Effect of aging conditions on pyranine emission ratio (438:514) during wet-aging for TEOS derived monoliths prepared with different TEOS:buffer ratios for gelation. (●) 1:1 TEOS:buffer, (■) 2:1 TEOS:buffer, (▲) 3:1 TEOS:buffer, (▼) 4:1 TEOS:buffer.

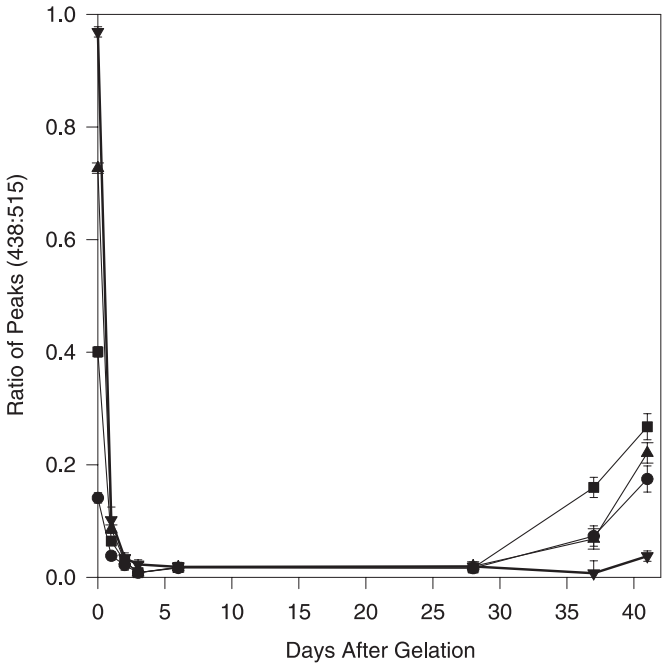

Continued aging of the wet-aged monoliths resulted in a long period during which there were no changes in pyranine fluorescence (about 28 days), followed by a slow increase in the ratio of protonated to deprotonated forms of the probe, as shown in Fig. 1. This spectral change indicates the slow loss of water from the interior of the monoliths, resulting in a re-emergence of the protonated form of the probe. The increase continued slowly until about day 125 (data not shown), even though the mass of the samples became constant by day 40. By day 125, the emission ratios of the different samples were all similar (values were between 0.89 and 0.93). The similarity in the emission ratios indicated that the final environment of all samples was similar, regardless of the initial amount of water used for gelation.

In the case of dry-aged monoliths, the loss of ethanol was much slower. Figure 2 shows the ratio of emission peaks corresponding to the protonated and deprotonated forms over the first 40 days of aging. As the monoliths aged, this ratio decreased for all samples, consistent with the preferential loss of ethanol from the interior of the matrix. This decrease continued for approximately 15 days for most

© 1999 NRC Canada

Fig. 2. Effect of aging conditions on pyranine emission ratio (438:514) during dry-aging for TEOS derived monoliths prepared with different TEOS:buffer ratios for gelation. (●) 1:1 TEOS:buffer, (■) 2:1 TEOS:buffer, (▲) 3:1 TEOS:buffer, (▼) 4:1 TEOS:buffer.

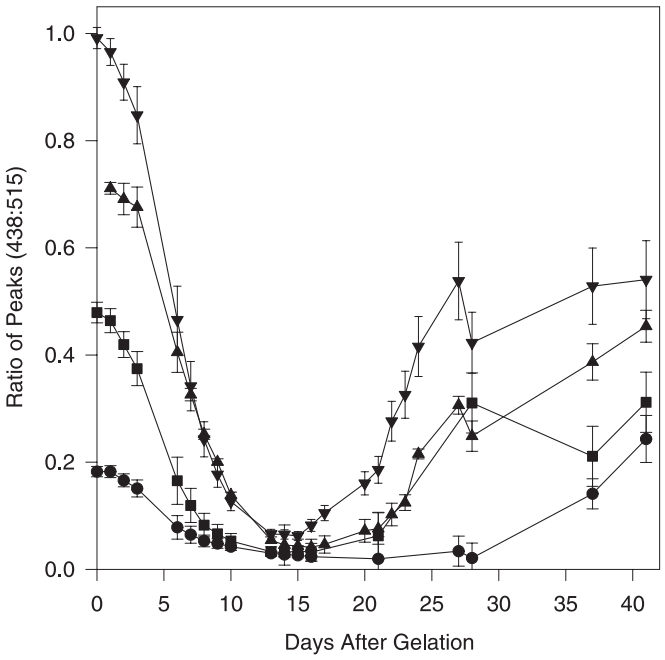

Fig. 3. Fluorescence spectra of 7AI collected at various times during wet-aging of TEOS derived monoliths prepared with a 3:1 TEOS:buffer ratio for gelation. The intensity values have been scaled to allow easier visualization of the differences between the spectra.

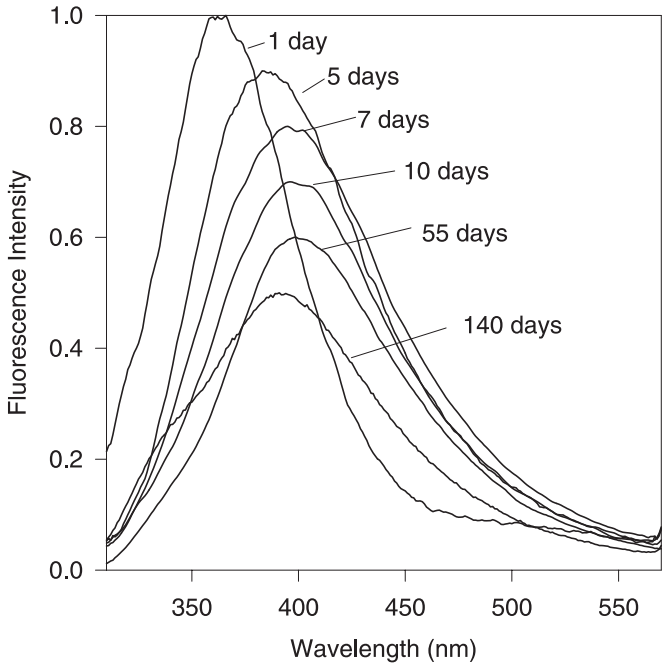

samples (about 20 days for the 1:1 ratio), showing that the loss of ethanol takes between 2 and 3 weeks, even when higher levels of water are initially present. Beyond about 15 days, the ratio began to increase slowly, in keeping with the trend observed from wet-aged samples. The increase in the spectral ratio continued for all samples up to and beyond day 40, indicative of a loss of internal water. Beyond day 40, trends became erratic. Each sample showed a large increase in the emission ratio, peaking at about day 90, indicative of a loss of water and a shift to a less polar environment. At day 90, the emission ratios were between 1.60 (1:1) and 2.25 (4:1), with the ratios increasing as water content decreased. Between days 90 and 125, the emission ratio of each sample first decreased and then increased again, likely signifying aggregation of the probe and (or) adsorption of the probe onto the surface of the silica. The only apparent trend during this period was that the samples prepared with less water (i.e., 4:1 sample) showed higher emission ratios than those made with more water (1:1 sample). Overall, the continuing changes in the ratio of the protonated and deprotonated forms of the probe indicates that changes in the internal environment of the matrix continue over periods of at least 12 weeks. Given that all of the dry-aged samples attained constant mass by day 28 (data not shown), the changes in the internal environment indicate that the internal structure of the silicate matrix, including condensation reactions which would reduce the number of SiOH groups and increase the number of water molecules, continue long after the mass of the sample becomes constant.

7-Azaindole fluorescence

7AI fluorescence emission spectra were monitored during aging of the sol-gel derived glasses to further examine how the internal environment of the glasses was affected by the preparation and aging conditions. Representative spectra of 7AI as a function of aging time for wet-aged monoliths formed with a silane:buffer ratio of 1:1 are shown in Fig. 3. The spectral properties (emission maximum and spectral full-width-at-half-maximum (FWHM)) measured at different times up to day 125 are listed in Table 1 for all wet-aged samples, and in Table 2 for dry-aged samples. In all cases, the initial fluorescence emission maxima were between 367 and 372 nm, while the FWHM values were between 71 and 75 nm. Comparison of these emission wavelength and FWHM values with those obtained from standard ethanol:water mixtures suggested an internal environment similar to that of a solution containing between 30% ethanol and 60% ethanol by volume, in agreement with the pyranine results. However, the emission maximum did not follow the trend expected based on the pyranine results (i.e., a blue-shift in the emission wavelength maximum as the TEOS:water ratio increased), suggesting that the 7AI emission was not reporting solely on the ethanol content of the pore liquid.

Figure 4 shows the evolution of the fluorescence emission maximum for 7AI during aging of each wet-aged system. For all TEOS:buffer ratios the fluorescence emission maximum red-shifted in a similar manner over the first seven days, evolving from ca. 370 nm to between 394 and 399 nm, after which the emission maximum remained constant. During this time, the FWHM value increased to ~101 nm for all systems, showing that a distribution of environments exists during the drying of the matrix, in agreement with previous reports (26). The wavelength shift and the increase in the FWHM value are consistent with the internal environment shifting toward higher polarity as ethanol is removed. How-

© 1999 NRC Canada

Table 1. Fluorescence characteristics of wet-aged TEOS derived monoliths containing 20 μM 7-azaindole as a function of drying time.

Aging time (days)	Wavelength or amplitude ratio 1:1[a,b]	Wavelength or amplitude ratio 2:1	Wavelength or amplitude ratio 3:1	Wavelength or amplitude ratio 4:1
Initial nm	368 (71)[c]	367 (73)	367 (72)	372 (72)
10[d]	394 (101)	397 (101)	398 (101)	399 (102)
25	396 (104)	397 (99)	396 (101)	396 (100)
55	403 (104)	401 (101)	400 (97)	398 (101)
90	386 (124)	391 (99)	393 (103)	400 (104)
104	392 (125)	396 (101)	397 (114)	389 (121)
116	395 (130)	396 (100)	394 (105)	391 (123)
125	389 (124)	394 (98)	393 (113)	391 (122)

[a]All values represent the average emission wavelength maximum and spectral full-width-at-half-maximum (FWHM) values from three different samples of identical composition.

[b]Typical errors in emission maxima for 7AI are ±1 nm or less, typical errors in FWHM for 7AI are ±3 nm or less.

[c]The number in brackets is the FWHM, in nanometers.

[d]Buffer was removed at day 10.

T**able 2.** Fluorescence characteristics of dry-aged TEOS derived monoliths containing 20 μM 7-azaindole as a function of drying time.

Aging time (days)	Wavelength or amplitude ratio 1:1[a,b]	Wavelength or amplitude ratio 2:1	Wavelength or amplitude ratio 3:1	Wavelength or amplitude ratio 4:1
Initial nm	371 (71)[c]	368 (73)	369 (71)	368 (75)
10	399 (104)	409 (104)	419 (100)	420 (102)
25	408 (96)	410 (94)	416 (90)	418 (95)
55	405 (96)	407 (98)	412 (97)	416 (97)
90	404 (88)	405 (99)	410 (86)	416 (95)
104	404 (89)	405 (100)	410 (97)	415 (96)
116	403 (95)	404 (99)	410 (96)	415 (95)
125	403 (99)	409 (98)	408 (98)	414 (96)

[a]All values represent the average emission wavelength maximum and spectral full-width-at-half-maximum (FWHM) values from three different samples of identical composition.

[b]Typical errors in emission maxima for 7AI are ±1 nm or less, typical errors in FWHM for 7AI are ±3 nm or less.

[c]The number in parentheses is the FWHM, in nanometers.

ever, two points merit further attention. Firstly, the 7AI wavelength shift requires 6 days to reach completion, even though the results obtained using pyranine clearly show that the ethanol is removed by day 3. Secondly, the final values for both the emission maximum and the FWHM are *larger* than the values obtained for 7AI in water. These results support the suggestion that 7AI does not report solely on the pore-liquid composition. This point is discussed in more detail later.

At day 10 the buffer was removed from the wet-aged monoliths and the monoliths were aged and dried in air. Table 1 shows that the emission maximum for all samples continues to shift over time, reaching values as high as 403 nm, with minimal changes in the FWHM over the first 55 days. Beyond day 55 the FWHM values increased for most samples while the emission maximum slowly blue-shifted, consistent with the slow loss of internal water, as indicated by pyranine. Given that this emission shift occurred only after the mass of the samples became constant, it is likely to be the result of both the continuing chemical evolution of the silica matrix (i.e., condensation of silanol groups to siloxanes) and the loss of entrapped water, in agreement with the results obtained from pyranine.

Figure 5 shows the changes in the emission wavelength for 7AI in dry-aged monoliths. In all cases the spectra red-shifted slightly over the first 6 days, with the emission maxima shifting by ~5 nm for each system and ending up between 375 and 380 nm. These spectral shifts are consistent with the preferential loss of ethanol from the matrix as determined using pyranine. Between days 6 and 10, the emission of 7AI in each system showed a broadening of the spectral contour and a large red-shift in the emission wavelength maximum, even though the pyranine spectra showed a steady loss of ethanol from all samples. It is likely that the loss of ethanol lowered the solubility of 7AI, causing the probe to either aggregate or adsorb to the surface of the evolving silica matrix, resulting in the broadening in the spectral contour.

Careful inspection of the changes in 7AI emission between days 6 and 10 reveal three points that warrant special attention. First, the emission wavelength of 7AI in all samples shifts to a value greater than 400 nm by day 10 and then

© 1999 NRC Canada

Fig. 4. Effect of aging conditions on 7AI emission wavelength during the first 25 days of wet-aging for TEOS derived monoliths prepared with different TEOS:buffer ratios for gelation. (●) 1:1 TEOS:buffer, (■) 2:1 TEOS:buffer, (▲) 3:1 TEOS:buffer, (▼) 4:1 TEOS:buffer. Representative error bars have been included for the 1:1 TEOS:buffer system. Similar error values are obtained for all other ratios.

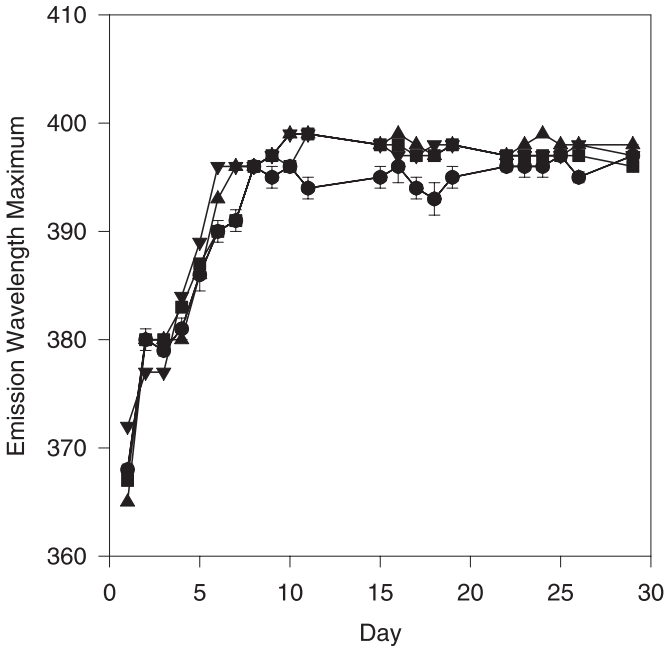

Fig. 5. Effect of aging conditions on 7AI emission wavelength during the first 25 days of dry-aging for TEOS derived monoliths prepared with different TEOS:buffer ratios for gelation. (●) 1:1 TEOS:buffer, (■) 2:1 TEOS:buffer, (▲) 3:1 TEOS:buffer, (▼) 4:1 TEOS:buffer. Representative error bars have been included for the 1:1 TEOS:buffer system. Similar error values are obtained for all other ratios.

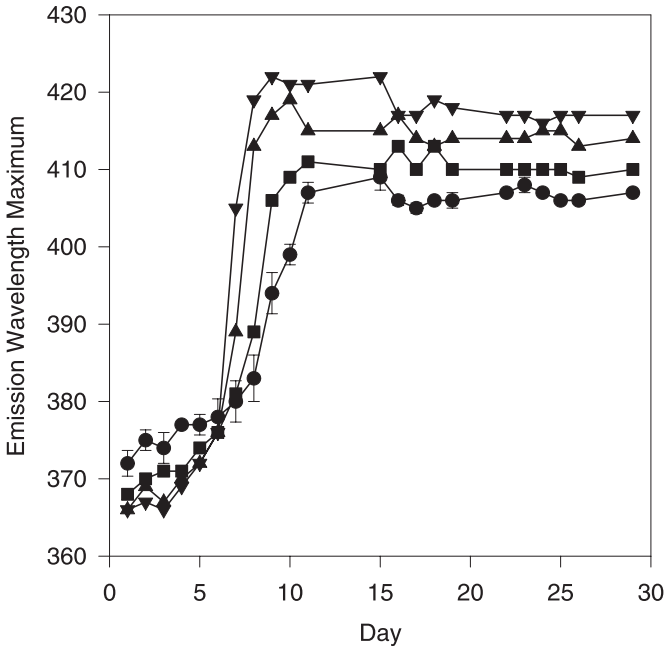

become constant. Given that the pyranine results show large changes in pore-liquid composition long after day 10, it is clear that 7AI is not sensitive only to pore-liquid composition. It is also clear that 7AI must undergo specific interactions with its surroundings, since the emission is substantially red-shifted compared to the values in water. The earlier time for the large spectra shift of 7AI as compared to pyranine is likely the result of poorer solubility of 7AI in water, resulting in adsorption of 7AI to the silicate at a higher water content than would occur for pyranine. Second, the FWHM values increase significantly to values that are ca. 25–30 nm broader than those obtained in water. Hence, the probe experiences a distribution of environments as the matrix evolves, as was the case with wet-aged materials. Third, the emission wavelength of 7AI at the completion of the wavelength shift (i.e., beyond day 10) is longer for systems that had a lower initial water content. For example, 7AI in the 4:1 TEOS:buffer system had an emission wavelength at 418 nm while the emission maximum of 7AI in the 1:1 system was 408 nm. These results indicated that the internal environment probed by 7AI changed as the amount of water used for gelation increased. Between days 10 and 125, the emission maximum of 7AI slowly shifted to shorter wavelengths and in most cases the spectra became more narrow, but the trend of shorter emission wavelength with higher R value remained, even up to day 125.

In comparing the wet-aged and dry-aged samples, three key observations can be made. First, it is noted that the final emission maxima of 7AI in dry-aged monoliths blue-shifted as the proportion of water used for gelation increased, while for wet-aged samples, the final emission maximum was the same regardless of the initial amount of water used for gelation. These results are in qualitative agreement with those obtained from pyranine, where wet-aged samples showed similar emission spectra while the spectra of dry-aged samples were dependent on the amount of water used for gelation. These results indicate that the final environment of wet-aged samples, which had R values of 28 or higher due to the presence of an excess amount of buffer during the first 10 days or aging, is not affected by the initial gelation conditions, while samples with $R < 28$ do depend on initial gelation conditions. Second, it is noted that the emission wavelength of 7AI in both wet-aged and dry-aged materials shifted to values beyond that obtained for the probe in water, but was always longer for dry-aged samples as compared to wet-aged samples. Hence, the proportion of water present during gelation affects the internal environment, but only when water levels are below an R value of 28. Finally, the final spectral widths after 125 days of drying were in all cases between 25 and 40 nm greater than the initial values, indicating that there was a distribution of final environments for the entrapped probe. However, the FWHM of 7AI in wet-aged monoliths was usually broader than in dry-aged samples, indicating a more uniform distribution of probe environments in dry-aged samples.

Both pyranine and 7AI indicate that the internal environment of both wet-aged and dry-aged sol-gel derived materials continues to evolve long after the samples have attained constant mass. The evolution of the internal environment continues for right up to 125 days for both wet-aged and

© 1999 NRC Canada

dry-aged samples. The length of time over which the samples change may cause some proteins to become inaccessible (25), or may alter protein binding constants (27, 28). It is also likely that the loss of water during the final stages of drying may result in dehydration and (or) denaturation of the entrapped proteins, causing loss of sensor function. The 7AI results also indicated the presence of a distribution of internal environments, even as early as 10 days into the aging step. The distribution of internal environments, and the change in this parameter over time, can lead to changes in sensor response times and sensitivity as the matrix ages, causing difficulties in sensor calibration (29). Hence, aging should be done only for 15 days for dry-aged samples, or 25 days for wet-aged samples, which correspond to the time at which constant mass is attained for the two types of samples. The samples should then be stored in a buffer solution to avoid the loss of entrapped water.

Origin of the 7AI spectral shift

A question that arises is the origin of the large red-shift for entrapped 7AI. The emission maximum is in all cases larger that that obtained for 7AI in water, therefore the spectral shift must be based on specific rather than general solvent effects (30). The red-shift for entrapped 7AI could in principle be due to a number of factors, including shifts in internal pH to values lower than ~5 (21), interaction of 7AI with buffer salts, which become more concentrated as the matrix dries, pressure-induced spectral shifts arising from the large capillary pressures, which would be between 19 and 36 MPa based on the typical pore sizes measured for such systems (25, 27), aggregation of the probe, or adsorption of the probe onto sites on the silica surface. To further examine these possibilities, several experiments were done. First, the internal pH of both wet-aged and dry-aged samples was measured by entrapping the pH sensitive fluorophore SNARF-1. The emission spectra indicated an internal pH of 6.5 ± 0.2, ruling out pH shifts as the basis of the 7AI red shift. Second, we measured the emission maximum of 7AI adsorbed onto the surface of phosphate or PIPES buffer salts. The emission maximum was 377 ± 2 nm regardless of the level of probe loading (1–20 μM), thus ruling out both interactions with buffer salts as the basis of the wavelength shifts. Third, emission spectra were collected from 7AI that was adsorbed onto quartz slides to eliminate pressure effects. 7AI was adsorbed onto either clean quartz slides, which had been soaked in hydrofluoric acid to provide a high surface silanol content, or onto quartz that was treated with trimethylchlorosilane (TMS) to cap the silanol groups. The emission maximum was between 408 and 415 nm on the HF treated slide, and was 392 nm on the TMS coated quartz slide. Hence, the large spectral shift for entrapped 7AI must be due to aggregation and (or) adsorption of the 7AI. It should be noted that red-shifts in both absorbance (31) and emission (32, 33) maxima are commonly observed for probes that are formed as Langmuir–Blodgett films or self-assembled monolayers, owing to specific interactions between the probe and the surface (33).

Matsui et al. (24) have also reported an emission maximum of between 415 and 420 nm for 7AI entrapped into TEOS derived materials. In this study, the absorbance, excitation, and emission spectra of the probe was investigated at several concentrations of entrapped 7AI to examine the question of whether 7AI was aggregated or adsorbed onto the silanol groups of the matrix. Their results clearly indicated that the red-shift in the 7AI emission spectra was due to adsorption of the probe onto silanol sites on the surface of the silica. To confirm this assertion, we collected infrared absorbance spectra for both the wet-aged and dry-aged samples that were prepared with a 1:1 to 4:1 TEOS:buffer ratio to determine if the silanol content was reflected by the 7AI emission data. Representative spectra collected for wet-aged and dry-aged materials prepared with a 3:1 TEOS:buffer ratio are shown in Fig. 6. The ratio of intensities in the SiOH stretching regions between 3000 and 3700 cm^{-1} and at 950 cm^{-1}, and the Si-O-Si stretching region at ~490 cm^{-1} (34) clearly show that the wet-aged sample had a lower proportion of SiOH groups (i.e., higher degree of crosslinking) as compared to the dry-aged sample. IR spectra collected for dry-aged samples prepared with different amount of water also indicated that the ratio of silanol groups to siloxane groups increased as the amount of water used for gelation decreased, suggesting that the use of larger amounts of water

Fig. 6. Diffuse reflectance infrared spectra of TEOS derived monoliths prepared with a 3:1 TEOS:buffer ratio for gelation. The samples were crushed to powder form and dried at 120°C for 60 min before spectra were collected. (*A*) wet-aged monolith, (*B*) dry-aged monolith.

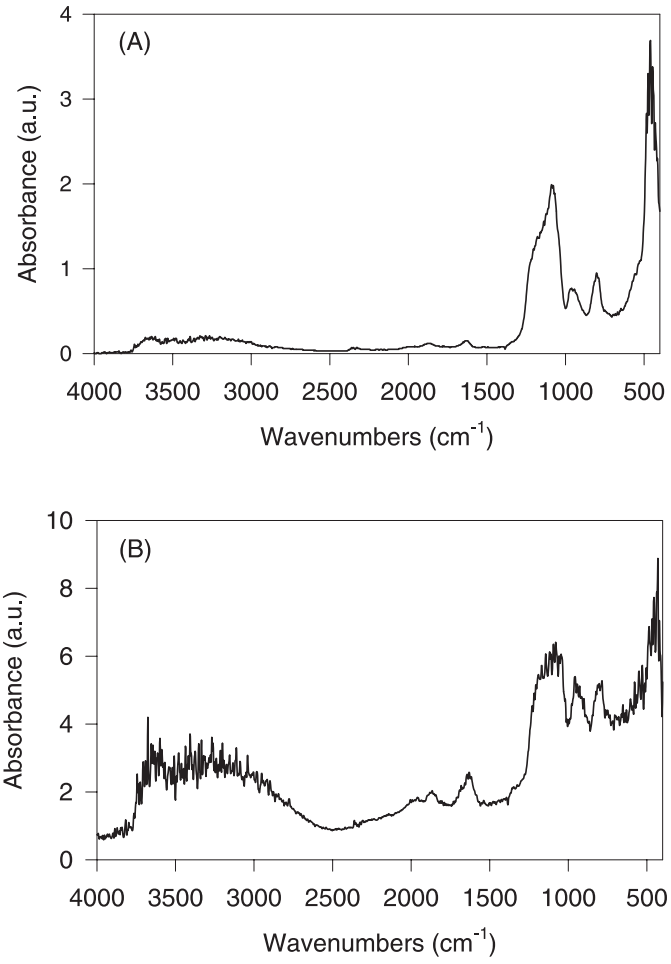

© 1999 NRC Canada

for gelation led to an increase in crosslinking. These results confirm that the 7AI emission spectral shifts reflect silanol content, and can therefore be used to qualitatively monitor the extent of cross-linking within sol-gel derived materials.

The sensitivity of 7AI emission to specific interactions involving silanol groups explains the emission red-shifts to values beyond those obtained in water, and is also in keeping with the shift of 7AI emission in the dry materials to shorter wavelengths as the level of water during aging increased. Increased levels of water during aging promote the dissolution and reprecipitation of silica, providing an increase in crosslinking through the process of coarsening and a corresponding decrease in silanol content (35–38). Hence, the 7AI emission spectra correspond well with the expected structure of the different silica matrixes. The finding that 7AI responds to silanol content is significant in that it shows 7AI to be a new and useful probe for examining the internal environment, the internal and external surface chemistry (assuming that some probes are likely adsorbed to the external surface of the matrix), and potentially the internal structure (i.e., silanol content) of sol-gel derived silicate materials.

Conclusions

The fluorescence of pyranine and 7AI were used to provide detailed information on the evolution of the internal environment of sol-gel derived silicate materials during aging and drying. Based on our studies, several useful conclusions can be drawn which have ramifications for the entrapment of biomolecules. First, it is advisable to use as high an *R* value as possible for gelation to reduce the initial level of ethanol, reducing the impact on the stability of entrapped proteins. Second, the buffer should be exchanged after gelation at least three times (i.e., samples should initially be wet-aged for at least three days, with daily buffer exchanges) to completely remove entrapped ethanol. Third, aging should be done only until there is an observable decrease in the amount of entrapped water. At this point there are shifts in both the FWHM value and emission wavelength maximum, and hence the distribution of environments, and the internal polarity. Based on emission data, these changes continue well beyond the point where the samples attain constant mass, indicating that the internal environment and structure continue to evolve for several months. Based on our observations, dry-aged samples should be aged for no more that 15 days, while wet-aged samples should be aged in air for no more than 25 days. After the initial period of aging the samples should be stored in a fully hydrated environment to avoid further losses of entrapped water. Such storage conditions should minimize further changes in the matrix, and thus maximize protein stability, in agreement with recent results from our laboratory (27, 28).

Acknowledgments

The authors wish to thank the Natural Sciences and Engineering Research Council of Canada and Research Corporation (Cottrell College Science Award to J.D.B.) for financial support of this work. We also wish to thank Human Resources and Development Canada for the provision of a Summer Career Placement award for M.A.D.

References

1. J.M. Miller, B. Dunn, J.S. Valentine, and J.I. Zink. J. Non-Cryst. Solids, **220**, 279 (1996).
2. S. Braun, S. Rappoport, R. Zusman, D. Avnir, and M. Ottolenghi. Mater. Lett. **10**, 1 (1990).
3. J.D. Jordan, R.A. Dunbar, and F.V. Bright. Anal. Chem. **67**, 2436 (1995).
4. S. Yamanaka, B. Dunn, J.S. Valentine, and J.I. Zink. J. Am. Chem. Soc. **117**, 9095 (1995).
5. J.S. Lundgren and F.V. Bright. Anal. Chem. **68**, 3377 (1996).
6. R. Wang, U. Narang, P.N. Prasad, and F.V. Bright. Anal. Chem. **65**, 2671 (1993).
7. B.C. Dave, H. Soyez, J.M. Miller, B. Dunn, J.S. Valentine, and J.I. Zink. Chem. Mater. **7**, 1431 (1995).
8. S.A. Yamanaka, F. Nishida, L.M. Ellerby, C.R. Nishida, B. Dunn, J.S. Valentine, and J.I. Zink. Chem. Mater. **4**, 495 (1992).
9. S. Braun, S. Shtelzer, S. Rappoport, D. Avnir, and M. Ottolenghi. J. Non-Cryst. Solids, **147**, 739 (1992).
10. B.C. Dave, B. Dunn, J.S. Valentine, and J.I. Zink. Anal. Chem. **66**, 1120A (1994).
11. D. Avnir, S. Braun, O. Lev, and M. Ottolenghi. Chem. Mater. **6**, 1605 (1994).
12. P.L. Edmiston, C.L. Wambolt, M.K. Smith, and S.S. Saavedra. J. Coll. Int. Sci. **163**, 395 (1994).
13. U. Narang, P.N. Prasad, F.V. Bright, K. Ramanathan, N.D. Kumar, B.D. Malhotra, M.N. Kamalasanan, and S. Chandra. Anal. Chem. **66**, 3139 (1994).
14. L.M. Ellerby, C.R. Nishida, F. Nishida, S.A. Yamanaka, B. Dunn, J.S. Valentine, and J.I. Zink. Science (Washington, D.C.), **225**, 1113 (1992).
15. E. Pines and D. Huppert. J. Phys. Chem. **87**, 4471 (1983).
16. V.R. Kaufman, D. Avnir, D. Pines, and D. Huppert. J. Non-Cryst. Solids, **99**, 379 (1988).
17. F. Nishida, J.M. McKiernan, B. Dunn, J.I. Zink, C.J. Brinker, and A.J. Hurd. J. Am. Ceram. Soc. **78**, 1640 (1995).
18. M. Negrerie, F. Gai, S.M. Bellefeuille, and J.W. Petrich. J. Phys Chem. **95**, 8663 (1991).
19. Y. Chen, R.L. Rich, F. Gai, and J.W. Petrich. J. Phys. Chem. **97**, 1770 (1993).
20. Y. Chen, F. Gai, and J.W. Petrich. J. Phys. Chem. **98**, 2203 (1994).
21. C.F. Chapman and M. Maroncelli. J. Phys Chem. **96**, 8430 (1992).
22. P. Avouris, L.L. Yang, and M.A. El-Bayoumi. Photochem. Photobiol. **24**, 211 (1976).
23. K.C. Ingham and M.A. El-Bayoumi. J. Am. Chem. Soc. **96**, 1674 (1974).
24. K. Matsui, T. Matsuzuka, and H. Fuijita. J. Phys. Chem. **93**, 4991 (1989).
25. L. Zheng, W.R. Reid, and J.D. Brennan. Anal. Chem. **69**, 3940 (1997).
26. U. Narang, J.D. Jordan, F.V. Bright, and P.N. Prasad. J. Phys. Chem. **98**, 8101 (1994).
27. K. Flora and J.D. Brennan. Anal. Chem. **70**, 4505 (1998).
28. L. Zheng, K. Flora, and J.D. Brennan. Chem. Mater. **10**, 3974 (1998).
29. R.A. Dunbar, J.D. Jordan, and F.V. Bright, Anal. Chem. **68**, 604 (1996).
30. J.R. Lakowicz. Principles of fluorescence spectroscopy. Plenum Press, New York. 1983.
31. K. Ochiai, M. Rikukawa, and K. Sanui. Chem. Commun. 867 (1999).

© 1999 NRC Canada

32. K. Ray, D. Bhattacharjee, and T.N. Misra, J. Chem. Soc. Faraday Trans. **93**, 4041 (1997).
33. R.S. Brown, J.D. Brennan, and U.J. Krull. J. Chem. Phys. **100**, 6019 (1994).
34. A. Bertoluzza, C. Fagnano, M.A. Morelli, V. Gottardi, and M. Guglielmi. J. Non-Cryst. Solids, **48**, 117 (1982).
35. L. Esquivias and J. Zarzycki. *In* Ultrastructure processing of advanced ceramics. *Edited by* J.D. Mackenzie and D.R. Ulrich. Wiley, New York. 1988. p. 255.
36. C.J. Brinker and G.W. Scherer. J. Non-Cryst. Solids, **70**, 301 (1985).
37. R.K. Iler. The chemistry of silica. Wiley, New York. 1979.
38. C.J. Brinker and G.W. Scherer. Sol-gel science. Academic Press, San Diego. 1990.

© 1999 NRC Canada

Estimation of particle size distribution in Athabasca oil sands by indirect instrumental neutron activation analysis

Robert Schutte, Gordon R. Thompson, Kingsley K. Donkor, M. John M. Duke, Roger Cowles, Xiu Ping Li, and Byron Kratochvil

Abstract: Instrumental neutron activation analysis (INAA) was used to predict the relative amounts of various sizes of fine particles in Athabasca oil sands. The method is based on regression analysis of element concentration data for 529 oil sand test portions, determined by INAA, against particle size distributions determined by three currently used methods. The most important elements for the estimation of particle sizes below 44 μm were found to be aluminum, sodium, and manganese. The INAA estimation method works because variation in elemental composition within particle size fractions in oil sands up to at least 44 μm is relatively small, whereas the variation between size fractions is significant. The new method does not involve the use of organic solvents, is faster and simpler to perform than the methods currently in use, and is comparable in precision. It has the added advantages that it can be readily automated, and concentrations of elements of special interest in oil sand processing, such as chlorine, are obtained simultaneously.

Key words: instrumental neutron activation analysis, oil sand, particle size distribution.

Résumé : On a utilisé l'analyse instrumentale par activation neutronique (AIAN) pour faire des prédictions concernant les quantités relatives des diverses tailles des particules fines des sables bitumineux de l'Athabasca. La méthode repose sur une analyse de régression des données relatives à la concentrations des éléments dans 529 portions analytiques de sables bitumineux, déterminées par AIAN, en fonction des distributions de tailles des particules déterminées par trois méthodes couramment utilisées. On a trouvé que les éléments les plus importants pour l'évaluation des tailles des particules en-dessous de 44 μm sont l'aluminium, le sodium et le manganèse. La méthode d'évaluation par AIAN est appropriée en raison de la faible variation de la composition élémentale dans des fractions dont la taille des particules dans les sables bitumineux est inférieure à 44 μm; par ailleurs, on note une variation importante entre des fractions de tailles différentes. La nouvelle méthode n'implique pas d'utilisation de solvants organiques et sa précision est comparable. De plus, on peut la rendre automatique et on peut obtenir de façon simultanée les concentrations d'éléments de sables bitumineux qui présentent un intérêt particulier, tel le chlore.

Mots clés : analyse instrumentale par activation neutronique, sable bitumineux, distribution de la taille des particules.

[Traduit par la Rédaction]

Introduction

In a previous study (1) on the variability of oil sands, it was shown that the fines concentration in the solids fraction of oil sands can be calculated from the concentrations of selected elements in the oil sand. This work follows that study, extending the method to other particle size ranges, addressing the basis for, and validation of, the method, and assessing the errors associated with it.

Information about the particle size distribution (PSD) of oil sand is essential to optimal extraction of bitumen from oil sands (2). It indicates ore quality, provides a measure of process performance during bitumen extraction, and provides information useful in the management of tailings (3). Oil sands with predominantly coarse particulates are usually rich in bitumen and easy to process in the conventional hot water extraction process. These ores do not require the addition of sodium hydroxide as a process aid, and tailings vol-

Received January 22, 1999.

R. Schutte. 4559 Seawood Terrace, Victoria, BC V8N 3W1, Canada.
G.R. Thompson. 6612-94 Ave., Edmonton, AB T6B 0XB, Canada.
K.K. Donkor. Department of Chemistry, College of New Caledonia, 3330-22nd Ave., Prince George, BC V2N 1P8, Canada.
M.J.M. Duke. SLOWPOKE Nuclear Reactor Facility, University of Alberta, Edmonton, AB T6G 2N8, Canada.
R. Cowles. Research Center, Syncrude Canada Ltd., 9417-17 Ave., Edmonton, AB T6N 1H4, Canada.
X.P. Li. 303, 345 Clarence St., Ottawa, ON K1N 5R5, Canada.
B. Kratochvil.[1] Department of Chemistry, University of Alberta, Edmonton, AB T6G 2G2, Canada.

[1]Author to whom correspondence may be addressed. Telephone: (780) 492-4665. Fax: (780) 492-8231.
e-mail: ron.kratochvil@ualberta.ca

© 1999 NRC Canada

umes are minimal. In contrast, high fines oil sands contain less bitumen, are difficult to process, require more water and sodium hydroxide, and longer residence times for extraction, yet still yield lower bitumen recoveries.

Process performance measures, such as froth quality and bitumen losses, are correlated with specific size fractions of the mineral components of oil sands. Particle size distribution also affects parameters such as wear on mining equipment, pressure drop in hydrotransport, flow rate in tailings disposal, and chloride content of produced bitumen. Furthermore, optimum tumbler residence time and middlings density during extraction depend on the fines (specifically clay) content of the ore. In light of the above there are incentives on the operations side to have particle size distribution information. On the laboratory side the incentives are to reduce the time and cost of PSD determinations, and to increase the reliability of the results.

The methods currently used in the oil sand industry for determining PSD are either a combination of screen/hydrometer separations (4), or laser scattering techniques with commercial Microtrac (model no. 7995, Leeds and Northrup, Florida, U.S.A.) or Coulter (model LS130, Coulter Corp., Florida, U.S.A.) instrumentation (4). These methods are time-consuming and laborious because they require removal of bitumen with organic solvents and wet screening prior to measurement. In addition, they are only applicable over a limited particle size range, and their sensitivity to particle shape leads to a bias in the estimation of the PSD. The method described here is rapid, simple to carry out, and does not involve use of organic solvents with attendant disposal problems.

The principle behind the method is the development of a set of correlations by applying regression analysis to a large set of PSD and elemental analysis data. To be useful the model must be significant and applicable to a wide variety of oil sand compositions. Therefore in this study an equal representation of all available oil sand facies (5) was employed to ensure wide applicability. The term facies is defined here as the sum total of features such as sedimentary rock type, mineral content, sedimentary structures, bedding characteristics, fossil content, etc., which characterizes a sediment as being deposited in a given environment (5).

Part 1. Basis for the method

Theory of the INAA method for PSD

To establish a basis for the INAA method, equations that express the amount of a component present in a sample as a function of the concentration of an element were derived. Later this result was modified to give the amount of a particle size fraction. The derivations use as key variables the concentrations of the elements in the total sample, as this is what is measured in the INAA method.

A two-component system can conveniently be used to arrive at the desired equations. Consider that one component is clay (weight fraction, x_1) and the other is pure quartz (SiO_2) (weight fraction, $1 - x_1$). The Al content of the clay is Al_c, and for a typical clay $Al_c = 0.159$ weight fraction. Initially, the aluminum content of the quartz is set at zero. The weight fraction of Al in the mixture is then

$$[1] \qquad Al = Al_c x_1$$

The amount of clay in the mixture as a function of the Al content is

$$[2] \qquad x_1 = \frac{Al}{Al_c}$$

To arrive at a more general case the aluminum content in quartz is introduced (weight fraction, Al_s). When irradiated in the SLOWPOKE reactor, silicon produces an aluminum signal due to the fast neutron induced transmutation reaction $^{28}Si(n, p)^{28}Al$. For the inner SLOWPOKE irradiation sites, the Si/Al interference factor is 207 ± 14 (6). That is, when analyzed under identical conditions, 207 μg Si produces the equivalent ^{28}Al activity as 1 μg Al. Thus, for the SLOWPOKE reactor, irradiation of pure quartz (SiO_2) produces an Al signal equivalent to 0.23% Al. The aluminum content of a mixture of SiO_2 and minerals containing Al is therefore the weighted sum of the Al in the two components. Equation [1] thus becomes

$$[3] \qquad Al = Al_c x_1 + Al_s(1 - x_1)$$

from which, through rearrangement, a new expression is obtained for the weight fraction of clay in the mixture as a function of the Al content:

$$[4] \qquad x_1 = \frac{Al - Al_s}{Al_c - Al_s} = \frac{-Al_s}{Al_c - Al_s} + \frac{Al}{Al_c - Al_s}$$

A plot of x_1 against Al yields a straight line with a non-zero intercept and a greater slope than in eq. [2]. The ratio (intercept/slope) = $-Al_s$.

Equation [4] implies that for the INAA method to work the concentrations of the elements must vary with component (as will be seen later, what is valid for components is equally valid for particle sizes). If element concentrations are equal, the weight fraction of each component becomes indeterminate. That elemental concentrations do vary with particle size fractions for oil sands is documented later.

Let us now introduce particle size distribution to the first example of clay in pure quartz. If a weight fraction p of the clay is $<q$ (size), and all the quartz is present in particles larger than q, then the weight fraction z of the sample $<q$ (size) as function of the Al content is given by

$$[5] \qquad z(<q) = px_1 = \frac{pAl}{Al_c}$$

When the quartz contains a fraction r of the $<q$ size class the equation becomes

$$[6] \qquad \begin{aligned} z(<q) &= px_1 + r(1 - x_1) \\ &= (p - r)x_1 + r \\ &= \frac{(p - r)Al}{Al_c} + r \end{aligned}$$

There is then a positive intercept for $Al = 0$ in the wt.% $<q$ vs. Al graph since $r \geq 0$.

When $p = r$ the coefficient of Al equals zero, and the element aluminum cannot be used to measure or calculate particle size $<q$ because under these conditions $<q$ is independent of sample composition. In the more general case where the quartz also contains, or appears to contain, aluminum, the

© 1999 NRC Canada

expression for the weight fraction of clay given by eq. [4] is substituted in eq. [6], giving as final result:

$$[7] \qquad z(<q) = \frac{(p-r)(Al - Al_s)}{Al_c - Al_s} + r$$

In general, the constants Al_s, Al_c, and the variables p and r in eq. [7] will not be known a priori for each geological deposit of interest. They are instead determined by regression analysis from an empirical set of data, a set large enough to provide acceptable confidence limits.

An improvement in the accuracy and precision of the determination of particle size can be achieved by incorporating additional elements. The derivation given above for the dependence of particle size $<q$ on the Al content can be applied to any element, so long as its concentration varies between the size fraction of interest and the remainder of the sample. In the ideal case the weight fraction of particles $<q$ may be determined independently n times from n elements. The multiple regression equation is a linear combination of the equations for the individual elements. Each element contributes a term of the form of eq. [7] multiplied by a weight factor that takes account of the covariance of the concentrations of the elements. In the simplest case of linear covariance between two size-determining elements, the weighting will be 0.5 for each of those elements.

Experimental

Samples and sample preparation

Two sets of samples representing a range of facies and oil content were provided by the Edmonton Research Laboratory of Syncrude Canada Ltd. These samples were obtained from the Athabasca oil sand deposit mined by Syncrude near Fort McMurray, Alberta. The first set consisted of 529 test portions of bulk oil sand and were analyzed as received. A second set of 10 samples, labelled X-5 through X-14, were sampled, the bitumen removed, and the solids separated into nine size fractions by sedimentation and sieving before analysis.

Prior to sizing, the second set was first homogenized with a Comil (Quadro Engineering, Waterloo, Ont.) at Syncrude's Edmonton Research Laboratory. Upon receipt, each sample was spread out in a layer about 2 cm thick and 1 g portions scooped from random locations to produce 100 g subsamples. Four subsamples were taken from each of the 10 bulk oil sands and Soxhlet-extracted to remove the bitumen and yield the solids (4). The solids were separated into size fractions and the particle size distribution and element concentrations determined as described in the next sections.

Separation by sieving/sedimentation and PSD analysis

Elutriation and sedimentation were explored for quantitative separations. Elutriation was found unsuitable because the excessive volume of liquid product streams obtained for each size fraction (about 6 L) required long run times, large glassware, and several days to evaporate the water. Sedimentation was therefore used for particle sizes below 44 μm (the fines fraction). Screening was employed for sizes >44 μm. Although screens are available for smaller sizes, sedimentation in water using a Stokes equivalent radius was considered more appropriate for oil sand samples because the important dimension for oil sand processing is the equivalent dimension in the water streams used for commercial extraction and tailings disposal.

A subsample of 84–86 g bitumen-free solids was first separated by sedimentation into fractions smaller and larger than 31 μm. To carry out the sedimentation, the sample was suspended in water in a glass beaker and stirred for 2–5 min. The solids were then allowed to settle for a predetermined time as estimated from Stokes equation. Times ranged from 2 min for the coarsest fraction to 15 min for the <3.9 μm fraction. A set volume of supernate was then transferred to a filter flask by suction. Since the slurry remaining in the beaker still contained particles of less than 31 μm, an amount of water equivalent to that removed was added to the beaker and the process repeated until the supernate appeared clear. About 10 repetitions were typically required. The sediment, of approximately 25 mL total volume and containing particles >31 μm, was air-dried and sieved, using a shaker (model RX-24 Tyler) and standard screens, into the size ranges >250, 180–250, 150–180, 90–150, 45–90, and 31–45 μm. A result of this procedure is that water soluble salts from the sample of oil sand solids end up in the <3.9 μm fraction. This may explain the very high Na and Cl levels in the <3.9 μm fraction from samples X-6 and X-8. Ultra pure water was used for samples X-11 to X-14 to avoid possible contamination from the distilled water but no difference was observed. In all, nine size fractions from each of the 10 oil sands were obtained by this method. The separated size fractions from all 10 oil sands were subsampled and their elemental composition determined by INAA.

All particle size distribution measurements were carried out at the Edmonton Research Laboratory of Syncrude using their screen/hydrometer and laser scattering equipment (Microtrac Model 7995 and Coulter Model LS130) and procedures (4, 7, 8). Statistical analysis of the data was carried out using the software program SIMSTAT (9) on an IBM Pentium computer.

INAA of elements that produce short-lived radionuclides

All irradiation and counting operations were performed at the University of Alberta SLOWPOKE-II Nuclear Reactor Facility. For the sized mineral fractions of the 10 oil sand solids, representative portions of 300–600 mg were accurately weighed into individual nitric acid washed 0.75 mL polyethylene irradiation vials. Standard reference materials from NIST, CANMET, and NRC were prepared in the same manner. The sized mineral fractions and standards were irradiated at a nominal thermal neutron flux of 1×10^{11} n cm^{-2} s^{-1} for 240 s in the inner site of the reactor. Following irradiation each sample was counted twice, initially for 300 s live-time after a decay time of ca. 15 min and a second time following a decay time of 30–60 min. The first count was performed at a sample-to-detector distance of 6 cm using a 19% hyperpure Ge detector with an automatic sample changer and PC-based multichannel analyzer (MCA) card. The second count was also performed at a sample-to-detector distance of 6 cm. However, for this count a 34% hyperpure Ge detector with automatic sample changer and PC-based MCA card was used.

© 1999 NRC Canada

Utilizing a dual counting scheme permits some optimization for those radionuclides with $T_{1/2} \leq 12$ min and for those with $T_{1/2} \geq 12$ min. From the initial count the elements Al, Ti, V, Ca, and Mn were quantified (Na and Dy may also be readily determined from the first count). The second count gives data on Dy, Sm, Eu, Ba, Na, K, Cl, and Mn. Element concentrations were determined by the semi-absolute method of INAA (10).

For the 529 bulk oil sand samples, portions of 10–12 g were packed in clean 7 mL polyethylene irradiation vials and individually irradiated for 4 min at a nominal thermal neutron flux of 2×10^{10} n cm^{-2} s^{-1} in an inner site of the reactor. Following a decay period of ca. 15 min each sample was counted for 5 min live-time at a sample-to-detector distance of 6 cm using a 19% hyperpure Ge detector. Following a decay period of not less than 30 min, each sample was recounted for 6 min live-time at a sample-to-detector distance of 6 cm, with a 34% hyperpure Ge detector. Again both γ-ray spectrometers were equipped with automatic sample changers and PC-based MCA cards. As for the mineral fractions, element concentrations were determined via the comparator semi-absolute method of INAA (10) using CANMET and NRC reference standards for comparison and quality control purposes. Utilizing the described analysis protocol the elements Ti, V, Al, Ca, Mn, K, Ba, Dy, Sm, Eu, and Cl were determined.

A stable, reproducible neutron flux is important in NAA, particularly when measuring short-lived radionuclides for quantitative elemental analysis. For SLOWPOKE II reactors operating at typical neutron flux levels of 1 to 10×10^{11} n cm^{-2} s^{-1}, the flux characteristics are reported to vary by $<\pm 2\%$ (2σ) over a period of several months (11). Data are not available, however, on flux stability at 2×10^{10} n cm^{-2} s^{-1}, the level used in this study. Therefore an Al standard was analyzed 15 times over a period of 5 weeks at a nominal flux of 2×10^{10} n cm^{-2} s^{-1}. Owing to the short half-life of ^{28}Al, multiple measurements could be made on the Al standard during extended runs on the same day as well as on separate days. The standard was also irradiated simultaneously with and without an oil sand sample in a second inner site to assess flux differences between sites; none were found. The variation in neutron flux at 2×10^{10} n cm^{-2} s^{-1} was found to be $\pm 1.35\%$ (1σ, $n = 15$), which was acceptable for this work.

Results and discussion

The model equations consider a mixture of particles as a two-component system, the components being those less than and those larger than a certain size. If all the particles contain an element of interest, for instance, clay contains silicon and so does quartz sand, then it is possible to separate the particles into two piles based on silicon concentration. Thus, a mixture, regardless of its complexity, is reducible to a two-component system. For another cutoff size, another system, with an associated regression analysis, is required.

The cumulative particle size distribution (PSD) by sedimentation and screening of the 10 oil sands is shown in Fig. 1 for the individual size fractions.[2] The data show that a range of particle sizes were obtained. The clay fraction (<3.9 μm) varied from 1% for X-10 to 10% for X-9 and X-14. The silt to fine sand fraction (45–90 μm) also varied considerably, ranging from 2.9 wt.% for X-8 to 27.9 wt.% for X-5. Sample X-8 contained 23 wt.% >250 μm sand, whereas all other samples contained less than 5.3% of this size fraction.

Fig. 1. Cumulative particle size distributions by sedimentation and screens.

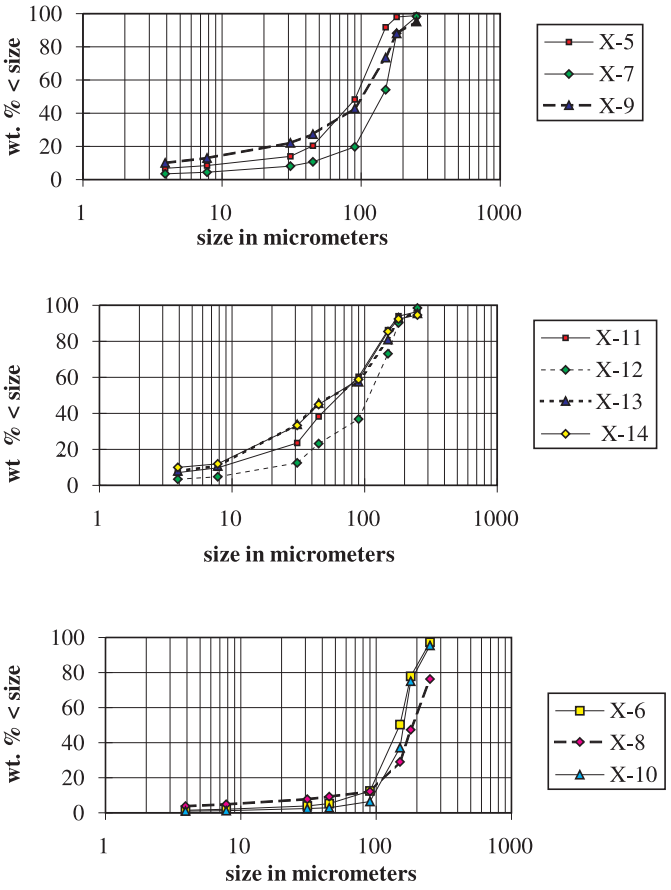

The cumulative data showed that total fines content (<45 μm) varied from 2.9% for X-10 to 45.6% for X-13 with a good distribution of values between. Total material <180 μm ranged from a low of 47% (X-8) to a high of 98% (X-5). It was important that the test oil sands covered a wide range of PSD so that the validity of the new method could be established over expected values.

Elemental analysis of size fractions by INAA

Twelve elements could be determined with reasonable precision by INAA using a short irradiation/count scheme. The average, standard deviation, and relative standard deviation (RSD) of the concentration of each element in the size fractions for the 10 oil sands are given in Table 1. The re-

[2] Complete data may be obtained from: The Depository of Unpublished Data, Document Delivery, CISTI, National Research Council Canada, Ottawa, Canada, K1A 0S2.

© 1999 NRC Canada

Table 1. INAA results for separated size fractions of 10 oil sands using short-lived radionuclides. All values are in μg/g except Al and Ca which are in wt.%.

Average concentration of elements in fractions from 10 oil sands												
Size, μm	Ti	V	Al%	Ca%	Dy	Sm	Ba	Eu	Na	Mn	K	Cl
<3.9	5270	109.0	11.20	0.195	4.62	8.0	358	1.40	10900	421	14800	5420
3.9–7.8	5810	88.4	9.02	0.193	5.45	9.1	421	1.66	1030	825	14800	76
7.8–31	5550	51.3	4.68	0.128	5.62	7.6	393	1.16	757	304	13200	79
31–45	6430	29.0	2.18	0.072	5.90	5.5	359	0.99	599	130	10600	35
45–90	4420	22.6	1.83	0.041	4.83	6.9	313	0.95	532	94	8670	34
90–150	1620	8.0	0.83	0.016	1.41	3.0	168	0.32	249	34	3510	26
150–180	500	4.4	0.68	0.016	0.86	1.7	140	0.19	198	26	2590	30
180–250	867	11.0	1.22	0.099	1.14	2.4	187	0.27	985	102	4310	48
>250	2970	40.3	2.93	0.332	2.92	4.1	222	0.60	693	359	6690	195
Standard deviation of average element concentration												
Size, μm	Ti	V	Al%	Ca%	Dy	Sm	Ba	Eu	Na	Mn	K	Cl
<3.9	1250	22.7	1.94	0.079	1.73	4.0	80	0.64	7990	186	4150	8570
3.9–7.8	1140	10.3	0.75	0.046	2.05	4.4	61	0.70	169	409	1590	63
7.8–31	831	8.8	1.61	0.075	1.62	3.6	171	0.53	177	113	4310	53
31–45	1280	2.2	0.57	0.030	2.35	2.3	224	0.35	270	49	6690	14
45–90	1560	4.1	0.48	0.012	2.50	3.2	145	0.41	162	23	4260	8
90–150	530	1.8	0.14	0.009	0.68	1.9	30	0.14	50	13	872	6
150–180	101	1.7	0.15	0.012	0.38	1.3	24	0.05	39	17	607	11
180–250	774	9.7	0.73	0.132	0.60	1.3	55	0.15	758	101	1580	53
>250	1650	20.8	1.56	0.668	1.33	1.9	68	0.27	349	291	2580	328
Relative standard deviation (RSD)												
Size, μm	Ti	V	Al%	Ca%	Dy	Sm	Ba	Eu	Na	Mn	K	Cl
<3.9	0.24	0.21	0.17	0.41	0.37	0.50	0.22	0.46	0.74	0.44	0.28	1.58
3.9–7.8	0.20	0.12	0.08	0.24	0.38	0.49	0.14	0.42	0.16	0.50	0.11	0.82
7.8–31	0.15	0.17	0.34	0.59	0.29	0.47	0.44	0.46	0.23	0.37	0.33	0.67
31–45	0.20	0.08	0.26	0.42	0.40	0.42	0.62	0.36	0.45	0.37	0.63	0.39
45–90	0.35	0.18	0.26	0.29	0.52	0.46	0.46	0.43	0.30	0.25	0.49	0.23
90–150	0.33	0.22	0.17	0.54	0.48	0.63	0.18	0.43	0.20	0.38	0.25	0.23
150–180	0.20	0.39	0.22	0.74	0.44	0.78	0.17	0.26	0.20	0.64	0.23	0.36
180–250	0.89	0.89	0.60	1.34	0.52	0.52	0.30	0.56	0.77	0.99	0.37	1.11
>250	0.56	0.52	0.53	2.01	0.45	0.47	0.31	0.44	0.50	0.81	0.39	1.68
Avg. RSD	0.35	0.31	0.29	0.73	0.43	0.53	0.32	0.42	0.40	0.53	0.34	0.79

sults of Table 1 show that for the <3.9 μm fraction the concentration of Ti, V, Al, and Ba vary little, with relative standard deviations of between 0.17 and 0.24, while the largest variation is shown by Cl(1.58), followed by Na(0.74). For the 31–45 μm (silt-size) fraction, the concentrations of the elements hardly vary. The RSDs for most of the elements are comparable to those for aluminum in the <3.9 μm fraction. Similarly, for the 150–180 μm (fine sand) fraction RSDs ranged from 0.17 for Ba to 0.78 for Sm. For the 180–250 and >250 μm fractions, the RSDs ranged from 0.30 to 2.01. In general, Al, V, and Ti had small RSDs for all size fractions; those for Dy, Sm, and Eu were somewhat larger, and those for Na and Cl the largest of all. With the exception of Na and Cl in the <3.9 μm fraction, none of the elements varied over wide ranges within a given size range.

For an element to be useful as a predictor of particle size, it is not sufficient for its concentration to be constant within a particle size fraction; it is also necessary that the concentration vary from one size fraction to another. This property is illustrated in Table 1, which summarizes the average concentrations for different size fractions. Titanium, barium, and dysprosium concentrations stay fairly constant up to 45 μm particle size. These elements therefore cannot discriminate between particle sizes below 45 μm, though they may provide some general differentiation between fine and coarse particles. In contrast, V, Al, Na, and K showed a steady decrease in concentration with increase in particle size and are therefore useful in discriminating among the size ranges of the finer particles. Such trends form the basis for the use of INAA for PSD measurements.

The other measurable elements — Ca, Sm, Eu, Mn, and Cl — displayed more irregular concentration/particle-size profiles, although the overall trend for all was towards lower concentrations in the larger particles. Standard deviations and RSDs for these elements (Table 1) show reasonable precision, confirming that the trends are real. These findings are

© 1999 NRC Canada

Fig. 2. Normalized element concentrations as a function of cumulative particle size for 10 oil sands.

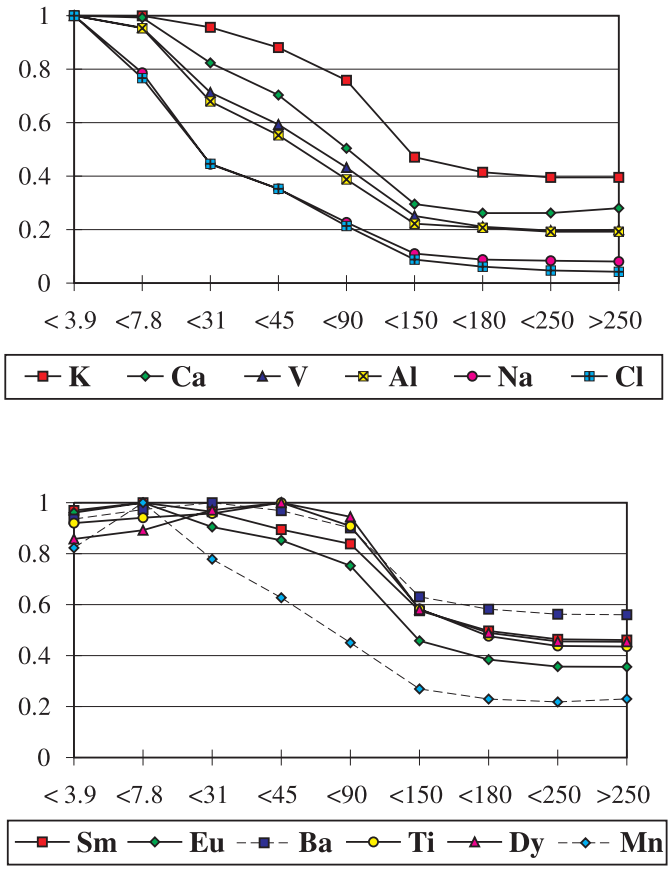

consistent with the role that these elements play in the model equations.

Evaluation of the soundness of the INAA prediction method should also include consideration of the composition of the cumulative particle size fractions. These compositions have been calculated, and the averages, standard deviations, and relative standard deviations of the concentrations are available.[2] Figure 2 illustrates the trends in the concentrations with cumulative particle size. To accommodate the wide range of absolute values of the averages, the averages were normalized by dividing them by the maximum average observed for each element. For six elements (K, Ca, V, Al, Na, and Cl), concentrations were greatest in the <3.9 μm fraction (Fig. 2). It is of note that Na and Cl normalized concentrations track together closely, as do V and Al. These elements appear closely associated with the clay size fraction. Because vanadium is present in oil sand in both the bitumen and the minerals, the V/Al ratios found here will not be the same as in bulk oil sand. Calcium and potassium showed the least variation with particle size. Manganese was at highest concentration in the <7.8 μm fraction. From that point on it showed considerable variation with particle size (Fig. 2, lower plot). The trend for K, Sm, Eu, Ba, Ti, and Dy was for little variation in concentrations in the finer particles, with significant decreases in concentrations in the >90 μm fraction. These elements appear to be predominantly associated with silt-size particles. All cumulative concentrations were essentially constant over the larger size ranges, therefore, the INAA method could not be applied to the prediction of PSD values for particles larger than about 150 μm. Particle sizes above 90 μm, do not, however, have a significant effect on the processibility of oil sands, and so their measurement is of lesser importance.

It should be noted that some fine particulates may be lost during the bitumen extraction step used to prepare the solids for screening. Previously, it was found that Soxhlet-extracted bitumen contained traces of the rare earth elements and aluminum, indicative of the presence of clay minerals (12). The extracted bitumen was not tested for these elements in this study.

Part 2. Application of the method

Development of regression equations for PSD from INAA

The method used to develop the model equations involved the following steps: finding the best fit equation, using multiple regression (least-squares) mathematical techniques, and relating element concentration to a given particle size range. Those terms in the equation that were redundant were deleted, and only those terms that improve the agreement between calculated and observed particle size measurements were retained.

Samples used to define and test the equations were obtained from two Syncrude mines (Base and Aurora), located about 35 km apart in the Athabasca deposit. Three data sets were used:

INAA, Microtrac, and Coulter data on 196 samples from the Base mine.

INAA, screen/hydrometer, and Coulter data on 129 samples from the Aurora mine.

INAA and Microtrac data on 214 samples from the Base mine. Of these, 112 samples included only <44, <22, and <11 μm size fraction data.

All of the INAA measurements were carried out under the same conditions as described earlier in this paper.

A preliminary cluster analysis was performed to provide insight into which of the particle sizes contained independent information about the sample. An analysis of the 214 Microtrac data set showed that particle sizes <3.9 μm correlated closely with each other, as do particle sizes in the 5.5–31 μm range. Based on these findings it was decided to study only four fines fractions, <3.9, 3.9–7.8, 7.8–31, and 31–44 μm in 10 samples (Part 1). Subsequently, because of a long Syncrude history of using <22, <11, <5.5, and <2.8 μm size ranges, these ranges were adopted for the INAA models. Cluster analysis for the Coulter data showed similarity in sizes to the Microtrac data; some differences appeared between 3.9 and 5.5 μm and between 22 and 31 μm. A break between 88 and 125 μm was found in the Microtrac but not in the Coulter data. This may be a result of a difference in the maximum particle size measurable by the two methods. The screen/hydrometer data showed little discrimination between fine size material, but breaks appeared between 44 and 75 μm, and between 75 and 125 μm.

Element correlation matrices provided insight into the number of independent variables available from the INAA data. For the Aurora mine, 32 of the 72 correlation coeffi-

© 1999 NRC Canada

Table 2. Coefficients of the linear model equations.

Microtrac equivalent particle sizes										
Size, μm	Constant	Al	Mn	Na	Ti	V	Ca	Ba	Eu	Dy
<44	1.0	4.89	0.0100	0.00857	0.00534					
<22	–3.1	6.87	0.0125	0.00575	0.000495				7.46	
<11	–2.6	5.99	0.00921	0.00574			–3.09			
<5.5	–4.6	2.91	0.00868	0.00356		0.139		–0.0100		
<2.8	–3.6	1.20	0.00369	0.00187		0.093				
<1.9	–3.3	0.655	0.00194	0.00097		0.0602				
<1.4	–1.0	0.253		0.000421		0.0244				
Coulter equivalent particle sizes										
Size, μm	Constant	Al	Mn	Na	Ti	V	Ca	Ba	Eu	Dy
<44	–2.7	6.43	0.0134	0.00577				–0.0224		7.43
<22	–5.4	5.99	0.0122	0.00545				–0.0245		4.13
<11	–0.5	5.05	0.00920	0.00390				–0.0176		2.20
<5.5	–0.8	3.20	0.00669	0.00259						1.11
<2.8	–0.2	2.01	0.00399	0.00187						0.633
<1.4	–0.2	1.07	0.00243	0.00101			1.26		2.99	
Screen and hydrometer equivalent particle sizes for use above limiting points										
Size, μm	Constant	Al	Mn	Na	Ti	V	Ca	Ba	Eu	Dy
<44 (screen)	–3.7	11.20	0.01048	0.00435				–0.0423		
<22 (hyd.)	2.3	9.63	0.00666					–0.0354		
<11	1.8	7.63	0.00860					–0.0361		
<5.5	2.0	5.80	0.00591					–0.0299		
<2.8	1.9	4.47	0.00328					–0.0224		

cients (*r*-values) calculated for 12 elements were <0.5. For the Base mine, 36 out of 72 were <0.5.

Model equations: testing and accuracy of the models

The principle behind the new INAA based method for particle size distribution is to use multiple linear regression analysis wherein the weight fraction smaller than a given size is the dependent variable, and the concentrations of elements, as measured by INAA on a sample of whole oil sand, are the independent variables. The statistically significant independent variables are kept, and the marginal and insignificant variables are omitted. The regression analysis is then rerun with only the significant variables. This fine tunes the values of the coefficients of the independent variables.

Each of the methods compared in this study (Coulter, Microtrac, and screen/hydrometer) has strengths and weaknesses for oil sands PSD determinations and yield differing results. Consequently, INAA equations must be derived from data obtained by each method. The constants and coefficients in the derived linear equations are given in Table 2. It is encouraging to see that the elements present in almost all equations (Al, Mn, and Na) are also amongst the elements that in the 10 oil sands tested show good variation of concentration with particle size, as required for successful size discrimination. The coefficients for Al in the Microtrac regression equations show an increase with cumulative particle size, as per eq. [7]. The coefficient for Al is 0.253 for <1.4 μm, 0.655 for <1.9 μm, 1.20 for <2.8 μm, 5.99 for <11 μm, and 6.87 for <22 μm. Only for the <44 μm fraction does the calculated value of 4.89 disagree with the trend. This may be due to an increase in the factor *r,* which may be appreciable for the non-Al containing fraction. In other words, the silica (quartz) sand in these solids has a sizable fraction of >22 and <44 μm particles. Another reason for the lower Al coefficient is that Ti was found to be a size discriminating element in the <44 μm fraction. Inclusion of Ti in the equations changed the coefficient for Al. Since the Al content of the non-clay component in most oil sands is expected to be smaller than that of the clay component, the intercept of a graph of wt.% particle size versus Al concentration will be <0, and the slope >0. The coefficient for Ba in the Coulter model for particles in the size ranges of <11, <22, and <44 μm was <0, which suggests Ba is more abundant in particles >11 μm than in those <11 μm. Observations on the 10 oil sands indicated that Ba, on a cumulative basis, peaks in the 7.8–32 μm fraction, providing support for this interpretation of the sign of the coefficient of individual elements.

As mentioned earlier, silicon produces an Al signal in INAA. If the Al/Si ratio of a sample is small, the correction to the Al result becomes important. Both slope and intercept of the model equations are affected. No correction for this interference was made in this work.

Table 3 gives values for correlation coefficients of the model equations of Table 2, along with the standard error of the estimate for the regression lines for each of the methods and particle sizes. A comparison of Table 3 with Table 4 shows that the standard error of the INAA method (0.090–6.69) is generally less than the standard error between the Microtrac and Coulter methods currently in use (4.85–8.08). From these data we conclude that overall the proposed INAA method is at least as good as, and in many ways better than, the PSD methods on which it is based.

Agreement of the models for the particle size ranges studied was good, as illustrated for the <44 μm fraction using equations derived from the coefficients in Table 2 for the Microtrac model (Fig. 3) and for the Coulter model (Fig. 4).

© 1999 NRC Canada

Table 3. Statistics of the model equations. (Numbers following method refer to the number of samples used in the model equations).

Method	<Size, μm	R^2	Standard error[a]
Microtrac (411)	44	0.925	5.68
	22	0.932	4.64
	11	0.929	3.99
	5.5	0.869	5.68
	2.8	0.784	3.44
	1.9	0.728	1.91
	1.4	0.611	0.90
Coulter (293)	44	0.923	6.69
	22	0.917	5.13
	11	0.902	3.86
	5.5	0.881	2.86
	2.8	0.859	1.99
	1.4	0.842	1.22
Screen (129)	44	0.928	4.04
Hydrometer (129)	22	0.920	3.42
	11	0.916	2.84
	5.5	0.905	2.74
	2.8	0.867	2.30

[a]The standard error of the estimate for the regression line, $S_{y\cdot x}$, defined by $S_{y\cdot x}^2 = \frac{N-1}{N-2}(S_y^2 - b^2 S_x^2)$ (see ref. 13).

Table 4. Comparisons between PSD methods. Standard errors from direct comparisons and from regression equations.

Methods compared	Size, μm	Standard error between methods	Standard error from reported values	Number of data pairs
Microtrac–Coulter	<44	7.22	8.08	196
	<22	5.96	6.71	196
	<11	4.22	5.55	196
	<5.5	3.43	4.85	196
	<2.8	1.94	4.98	196
	<1.4	0.64	6.80	196
Screen–Coulter	<44	7.06	11.36	129
Hydrometer–Coulter	<22	6.13	6.56	129
	<11	5.16	5.42	129
	<5.5	4.83	4.10	129
	<2.8	3.89	3.69	129
Microtrac–Microtrac	<44		5.6	89
	<22		5.5	89
	<11		3.1	89

The Coulter method was the only one used on both Base and Aurora mine samples. Prediction models based on the Coulter data were found to be equally applicable to both mines.

Results for the screen/hydrometer model, given in Fig. 5 for the <44 and <22 μm fraction, also show satisfactory reproducibility. Hydrometers are "blind" below certain concentrations, depending on particle size (see Table 5). By selecting hydrometer data above the minimum values in Table 5, the models improve but the results become less useful. Anytime the hydrometer-based INAA method predicts a particle size concentration below the limits shown in Table 5, the results should be treated with caution.

Precision of model equations, INAA, and oil sand sampling

A study was done on the precision of the proposed and existing methods to provide a basis for statistical comparison.

A set of equations was applied to the INAA data to determine particle size values for six size fractions for each method. Each equation was applied to three subsamples from each of six samples (X-5, X-6, X-7, X-8, X-9, X-10). Each of the three subsamples was then analyzed four times by INAA. This yielded a (3 × 4) matrix of particle size values for each size fraction and each oil sand. The standard deviation, average, and overall relative standard deviation

© 1999 NRC Canada

Fig. 3. Degree of fit. Microtrac model equivalent versus observed Microtrac PSD <44 μm, expressed as volume fraction (r = 0.93).

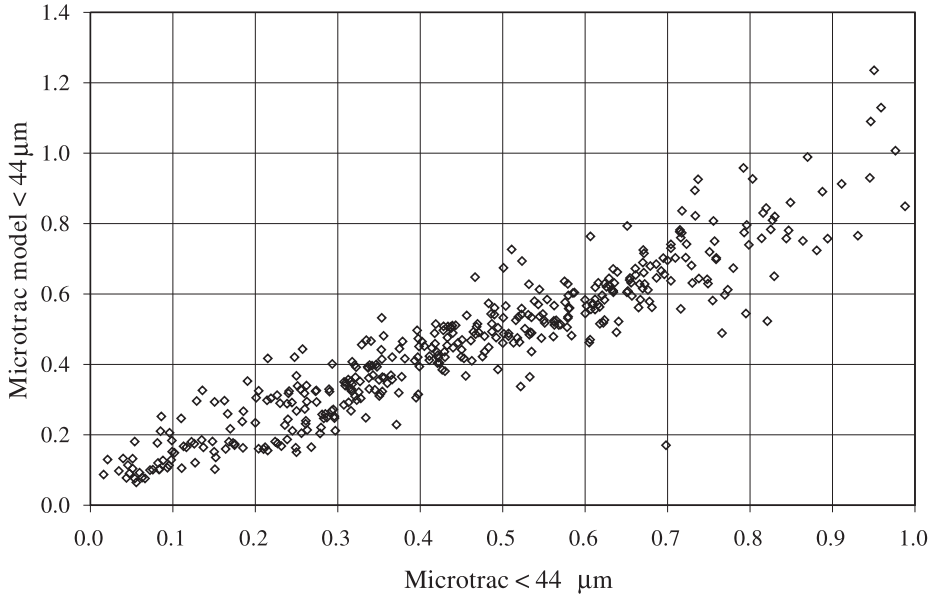

Fig. 4. Degree of fit. Coulter model equivalent versus observed Coulter PSD <44 μm, expressed as volume fraction (r = 0.96).

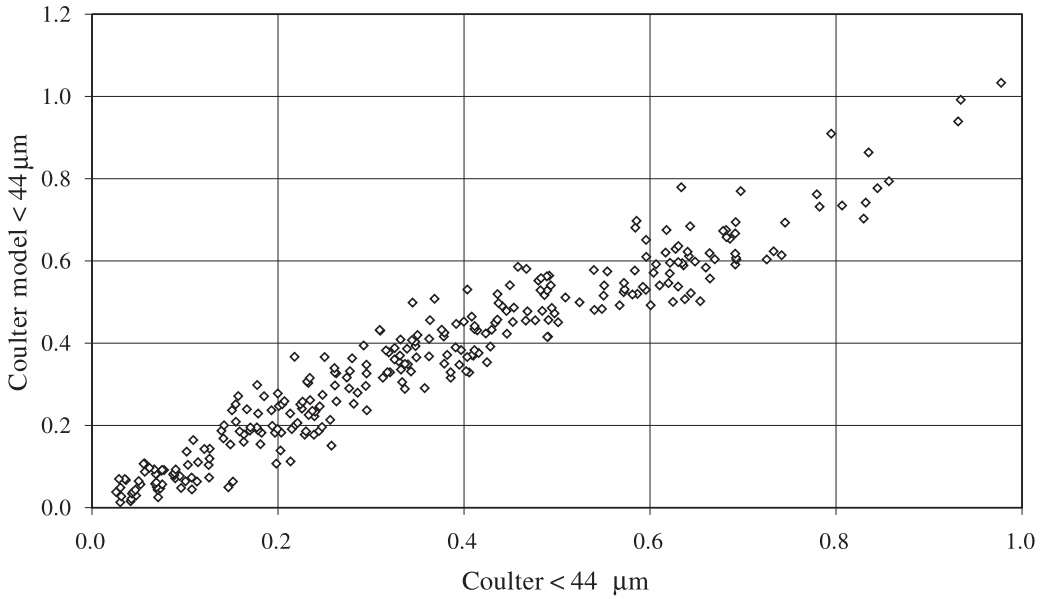

(RSD) were determined for each oil sand sample for the Microtrac and Coulter models. The four INAA measurements on each sample provided a measure of the repeatability (RSD*rep*) of the INAA technique for PSD measurement. The equations were later refined by inclusion of an additional 196 data sets; recommended coefficients for the terms are given in Table 2.

Three subsamples of each of six samples (X-5, X-6, X-7, X-8, X-9, X-10) were analyzed by INAA for elements via their short-lived radionuclides, then sent to the Syncrude Edmonton Research Laboratory for PSD measurement using Microtrac and Coulter instruments. At Syncrude the three approximately 12 g bulk oil sand subsamples from each sample were combined and the bitumen extracted. The cleaned solids were subdivided again into three portions and returned for INAA. After radioactive decay to essentially background levels the samples were returned to Syncrude for Microtrac and Coulter instrumental PSD determination. For each of the six oil sand samples, the standard deviation, mean, and relative standard deviation values were determined for both the Microtrac and Coulter data from the observations on the three subsamples to give overall RSD values.

A contributing factor to the overall uncertainty in the INAA prediction method is statistical counting variability in the INAA measurements. Conditions were adjusted to minimize this uncertainty. Uncertainties in the irradiation, decay, and counting times were estimated to be less than 1 in 2400, and that for counting geometry to be ≤1.5%. Uncertainty values for counting (1 SD) were determined at the time of measurement and are shown in Table 6 as RSD(c). It was

© 1999 NRC Canada

Table 5. Lower limits to which the hydrometer method measures particle concentrations.

Procedure	Cumulative size, μm	wt.%
Screen	<44	1.8
Hydrometer	<22	6.0
	<11	5.0
	<5.5	3.9
	<2.8	3.0

found that the uncertainty due to counting statistics amounts to only 1.5–2% of the overall uncertainty for PSD prediction by INAA.

Uncertainty values for measurements using the Microtrac and Coulter instruments and for the corresponding INAA procedure are summarized in Table 6. The results show that for all six particle sizes the INAA model has lower overall uncertainty than either of the Microtrac or Coulter methods. The repeatability of the INAA method falls between that of the Microtrac and Coulter methods, with the Coulter instrument having better repeatability and, with the exception of the <44 μm fraction, a lower overall uncertainty than the Microtrac instrument. It can be expected that for oil sands an INAA-based method for PSD determination at and below 44 μm will give results that are in all aspects comparable to either historic or current Microtrac and Coulter methods. It should be noted that in this study a recent model Coulter instrument (Model LS130) was being compared with an earlier Microtrac instrument (Model 7995).

The subsampling uncertainty for oil sand could be determined from the variability in concentration of the elements used in the model equations, Al, Eu, Mn, Na, Ti, V, Ba, Ca, and Dy. From the concentration data overall uncertainties, RSD(*o*), which include subsampling uncertainty and the uncertainty of the INAA measurement (repeatability) RSD(*m*), were calculated. From the values of RSD(*o*) and RSD(*m*) the uncertainty in the sampling operations, RSD(*s*), was obtained as the difference of the variances, where variance is the square of RSD. The results, summarized in Table 7, show that the sampling uncertainty for all the elements fell below 12% relative at the sample weights of approximately 12 g used for the INAA work. The last two columns in the table give the fraction of the overall uncertainty contributed by the measurement and sampling steps. The values indicate that for Al, Mn, Na, Ti, and Dy, sampling contributes more than 0.6 of the overall uncertainty. On the other hand, for Eu, V, Ba, and Ca, sampling contributes less than 0.4, indicating that sampling is not a major contributor to the overall uncertainty for these elements.

The overall uncertainty for the elements in cleaned solids was also determined by INAA in the same way as for the bulk oil sand and compared with the bulk oil sand results to provide insight into the relative uncertainty in subsampling whole oil sand as compared to clean solids. It was found that the latter operation had an uncertainty of about half that of subsampling whole oil sand.

Variability in elemental concentrations within and between facies

It was also of interest to determine the level of variability among samples of oil sand from the same facies. Samples

Fig. 5. Degree of fit. Screen/hydrometer model versus observed screen/hydrometer data: (*a*) <44 μm (r = 0.97) (*b*) <22 μm (r = 0.96).

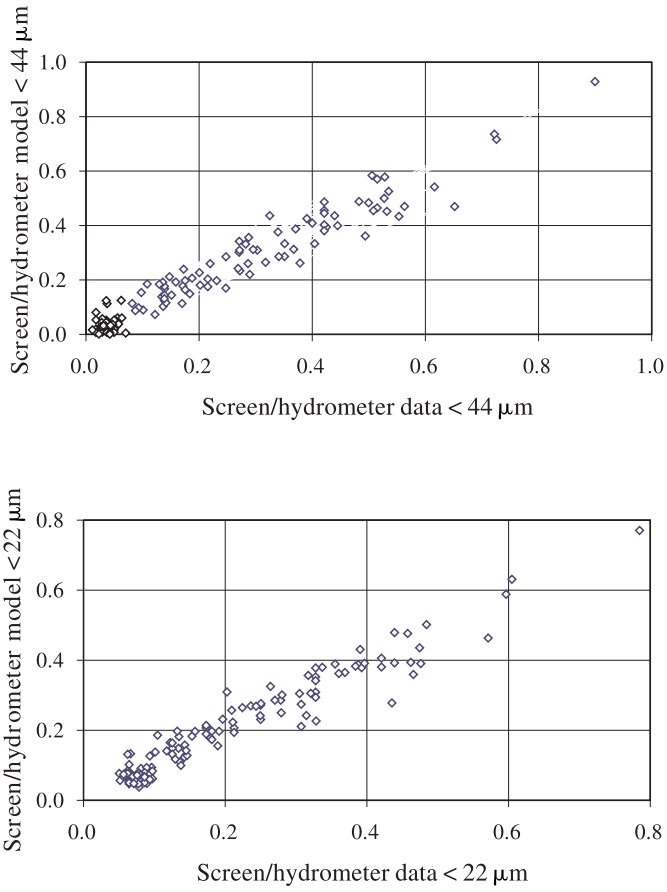

X-6, X-8, and X-10, all from facies 11, were used for this study. For a given oil sand facies, vanadium showed the least sampling uncertainty of the elements studied. The values for RSD(*s*) in Table 8 showed that for a particular facies the sampling contribution to the overall uncertainty varied widely from element to element, ranging from 2.0% for V to 49.2% for Mn. These results tend to parallel an earlier study of elemental variability across a transverse section of a single oil sand core (1, 12).

A single-factor analysis of variance (ANOVA) was performed on the original elemental concentrations of three selected samples of bulk oil sand, X-5, X-7, and X-10, from facies 10, 8, and 11, respectively. Table 9 summarizes the findings on the significance of the *F*-value for elements and samples. No consistent trend among elements was observed. For five of the elements, in two oil sands out of three, the between-sample heterogeneity did not differ from the within-sample heterogeneity. For Na, however, in two out of three oil sands, the between-sample heterogeneity differed from the within-sample heterogeneity, while for Ba and Eu, the three oil sand samples showed no difference. The most significant conclusions were that barium was constant in concentration from subsample to subsample within the uncertainty of the measurement, while Mn was variable. The conclusions reached from an analysis of variance were similar to the conclusions obtained from the uncertainty study on

© 1999 NRC Canada

Table 6. Summary of RSD values for Coulter LS130, Microtrac, and INAA models. RSD(*o*) = overall, RSD(*rep*) = repeatability, RSD(*c*) = counting.

		Microtrac					Coulter				
		Instrument		INAA model			Instrument		INAA model		
Size, μm	Sample	RSD(*o*)	RSD(*rep*)	RSD(*o*)	RSD(*c*)	RSD(*rep*)	RSD(*o*)	RSD(*rep*)	RSD(*o*)	RSD(*c*)	RSD(*rep*)
<44	5	0.044	0.013	0.031	0.0040	0.029	0.125	0.005	0.036	0.0037	0.034
	6	0.125	0.072	0.022	0.0053		0.077	0.011	0.035	0.0055	
	7	0.106		0.046	0.0046		0.143		0.048	0.0041	
	8	0.113		0.095	0.0054		0.137		0.143	0.0057	
	9	0.065		0.115	0.0047		0.080		0.109	0.0038	
	10	0.012		0.035	0.0064		0.070		0.031	0.0073	
Avg. RSD		0.078		0.057			0.105		0.067		
<22	5	0.084	0.025	0.046	0.0035	0.036	0.137	0.008	0.040	0.0049	0.037
	6	0.247	0.094	0.042	0.0053		0.099	0.015	0.041	0.0073	
	7	0.058		0.047	0.0046		0.154		0.042	0.0055	
	8	0.166		0.122	0.0051		0.153		0.152	0.0081	
	9	0.066		0.108	0.0036		0.079		0.102	0.0047	
	10	0.292		0.062	0.0067		0.078		0.036	0.0107	
Avg. RSD		0.152		0.071			0.117		0.069		
<11	5	0.044	0.05	0.047	0.0028	0.034	0.140	0.008	0.039	0.0044	0.034
	6	0.354	0.054	0.040	0.0045		0.100	0.015	0.038	0.0066	
	7	0.030		0.042	0.0044		0.151		0.040	0.0052	
	8	0.072		0.115	0.0042		0.155		0.136	0.0070	
	9	0.064		0.110	0.0028		0.079		0.101	0.0043	
	10	0.367		0.064	0.0071		0.082		0.039	0.0095	
Avg. RSD		0.155		0.070			0.118		0.066		
<2.8	5	0.299	0.136	0.019	0.0026	0.019	0.137	0.008	0.037	0.0028	0.029
	6	0.482	0.305	0.021	0.0029		0.081	0.013	0.029	0.0038	
	7	0.262		0.025	0.0029		0.130		0.039	0.0034	
	8	0.155		0.033	0.0030		0.139		0.105	0.0038	
	9	0.062		0.045	0.0030		0.070		0.092	0.0028	
	10	0.554		0.021	0.0035		0.107		0.035	0.0052	
Avg. RSD		0.302		0.027			0.111		0.056		
<1.4	5	0.868	0.447	0.061	0.0095	0.082	0.123	0.008	0.052	0.0059	0.039
	6	0.944	1.667	0.115	0.0173		0.107	0.010	0.043	0.0076	
	7	1.732		0.129	0.0162		0.087		0.047	0.0066	
	8	0.991		0.141	0.0152		0.102		0.116	0.0075	
	9	0.102		0.112	0.0083		0.064		0.095	0.0058	
	10	1.732		0.119	0.0214		0.187		0.062	0.0076	
Avg. RSD		1.062		0.113			0.112		0.069		

Table 7. Summary of uncertainty values calculated from actual concentrations of nine elements determined by INAA in bulk oil sand.

Element	RSD(*o*) (overall)	RSD(*m*) (measurement)	RSD(*s*) (sampling)	Fraction uncertainty from measurement	Fraction uncertainty from sampling
Al	0.060	0.030	0.052	0.25	0.75
Eu	0.125	0.100	0.075	0.64	0.36
Mn	0.065	0.026	0.060	0.16	0.84
Na	0.061	0.027	0.055	0.20	0.80
Ti	0.080	0.048	0.064	0.36	0.64
V	0.037	0.033	0.017	0.80	0.20
Ba	0.066	0.062	0.023	0.88	0.12
Ca	0.312	0.290	0.115	0.86	0.14
Dy	0.072	0.042	0.058	0.34	0.66

© 1999 NRC Canada

Table 8. Sampling uncertainty of elements in oil sand samples (X-6, X-8, X-10) from the same facies (facies 11). For each of the three oil sand samples, three subsamples were analyzed.

Element	Sampling uncertainty, RSD(*s*)
Al	0.060
Ba	0.131
Ca	0.473
Dy	0.228
Eu	0.247
Mn	0.492
Na	0.320
Ti	0.125
V	0.020

Table 9. Summary of ANOVA results for elements, analyzed in samples from three different facies.[a]

Element	X-5	X-7	X-10
Al	N	N	Y
Eu	N	N	N
Mn	Y	Y	Y
Na	Y	N	Y
Ti	Y	N	N
V	N	N	Y
Ba	N	N	N
Ca	N	N	Y
Dy	N	N	Y

[a]N, no significant difference between the *within*-sample heterogeneity (four repeats) and *between*-sample heterogeneity. 95% confidence limit. Y, significant difference.

elements, as expected. The uncertainty study identified Ca and Ba as elements for which the measurement uncertainty was large compared to the sampling uncertainty, and Na with Mn as elements for which the sampling uncertainty exceeded the measurement uncertainty.

Conclusions

A method has been developed for estimating particle size distribution (PSD) in bulk oil sand. Model equations were derived and tested for the prediction of PSD from the concentration of nine elements measured by INAA. Predicted particle size distributions compared favorably with results obtained by existing methods. Each of the three PSD methods currently in use could be simulated by the INAA method. The INAA-based model that predicts hydrometer equivalent data was only applicable above certain lower limits for the amount of the fine size fractions present because of the limited sensitivity of the hydrometer method for PSD determination of fine fractions. For all six particle sizes studied, the INAA model had lower overall uncertainty than the corresponding Microtrac and Coulter instrument methods; the instrument repeatability of INAA fell between those of Microtrac and Coulter, with the Coulter instrument having the best repeatability. For Athabasca oil sands, the INAA-based method outlined here for PSD determination at and below 44 μm gave results comparable to current Microtrac and Coulter methods.

Analysis of variance indicated that Ba and Eu tended to be constant in concentration in subsamples from a given oil sand, while Mn showed the greatest variability. The sampling uncertainty for cleaned solids was half that for bulk oil sand; the greatest contributor to uncertainty in the determination of element concentrations was the sampling of the oil sand itself.

The approach outlined in this paper may have application to particle size distribution estimation in other environmental systems such as soils, airborne particulates, or stream sediments.

Acknowledgements

The authors thank Syncrude Canada Ltd. for providing the oil sand samples used in this study, for performing the bitumen extractions, for the Microtrac and Coulter particle size measurements, and for permission to publish this work. Financial assistance was provided by Syncrude Canada Ltd., the University of Alberta Department of Chemistry, and the Natural Sciences and Engineering Research Council of Canada.

References

1. K.K. Donkor, B. Kratochvil, and M.J.M. Duke. Can. J. Chem. **74**, 583 (1996).
2. L.G. Hepler and C. Hsi (*Editors*). AOSTRA technical handbook on oil sands, bitumens and heavy oils, no 6. AOSTRA, Edmonton. 1989.
3. E.C. Sanford. Can. J. Chem. Eng. **61**, 554 (1983).
4. J.T. Bulmer and J. Starr (*Editors*). Syncrude analytical methods for oil sand and bitumen processing. AOSTRA, Edmonton. 1979.
5. D.G.A. Whitten and J.R.V. Brooks. The penguin dictionary of geology. Penguin Books, Middlesex. 1972.
6. G. Kennedy, J.L. Galinier, and L. Zikovsky. Can. J. Chem. **64**, 790 (1986).
7. E.C. Muly, N.H. Frock, and E.L. Weiss. J. Powder Bulk Solids Technol. **2**, 3 (1978).
8. P.E. Plantz. *In* Modern methods of particle size analysis. *Edited by* H.G. Barth. John Wiley, New York. 1984. Chap. 6.
9. N. Peladeau. SIMSTAT software. 1994. Montreal, Quebec.
10. C. Bergerioux, G. Kennedy, and L. Zikovsky. J. Radioanal. Chem. **50**, 229 (1979).
11. D.E. Ryan, D.C. Stuart, and A. Chattopadhay. Anal. Chim. Acta, **100**, 87 (1978).
12. K.K. Donkor. Ph.D. thesis. Department of Chemistry, University of Alberta, Edmonton. 1995.
13. W.J. Dixon and F.J. Massey, Jr. Introduction to statistical analysis. 3rd ed. McGraw–Hill, New York. 1969. p. 195.

© 1999 NRC Canada

Electron transfer reactions of bis(1,4,7-trithiacyclononane)palladium(III/II), -platinum(III/II), and -gold(III/II) complexes in aqueous solution and in acetonitrile

Mitsuru Matsumoto, Makoto Itoh, Shigenobu Funahashi, and Hideo D. Takagi

Abstract: The oxidation reactions of $Pd(ttcn)_2^{2+}$, $Pt(ttcn)_2^{2+}$, and $Au(ttcn)_2^{2+}$ (ttcn = 1,4,7-trithiacyclononane) complexes by a typical outer-sphere oxidizing reagent, $Ni(tacn)_2^{3+}$ (tacn = 1,4,7-triazacyclononane), were studied in aqueous acidic solution and in acetonitrile. The rate constants corresponding to the oxidation and reduction reactions were isolated for $Pd(ttcn)_2^{3+/2+}$ and $Au(ttcn)_2^{3+/2+}$ couples in both media. The electron exchange rate constants (k_{ex}) for $Pd(ttcn)_2^{3+/2+}$, $Pt(ttcn)_2^{3+/2+}$, and $Au(ttcn)_2^{3+/2+}$ couples at 25°C were estimated as 1.7×10^3, 59, 3.9×10^4 mol^{-1} dm^3 s^{-1} in aqueous solution and 6.7×10^3, 1.3×10^2, and 2.7×10^5 mol^{-1} kg s^{-1} in acetonitrile, respectively. An attempt to observe the reduction reaction of $Pt(ttcn)_2^{3+}$ was not successful because of the instability of $Pt(ttcn)_2^{3+}$ in aqueous solution. A comparison of the electron exchange rate constants of $Pd(tacn)_2^{3+/2+}$, $Pd(ttcn)_2^{3+/2+}$, $Pt(ttcn)_2^{3+/2+}$, and $Au(ttcn)_2^{3+/2+}$ couples in aqueous solution and in acetonitrile revealed that the inner-sphere contribution to the activation free energy for each reaction is identical in both solvents and that the self-exchange rate constants of these complexes directly reflect the structural differences of these complexes.

Key words: electron transfer, kinetics, Marcus theory, inner-sphere contribution.

Résumé : Opérant en solutions aqueuses acides et dans l'acétonitrile, on a étudié les réactions d'oxydation des $Pd(ttcn)_2^{2+}$, $Pt(ttcn)_2^{2+}$ et $Au(ttcn)_2^{2+}$ (ttcn = 1,4,7-trithiacyclononane) par un réactif oxydant typique de la couche externe, $Ni(tacn)_2^{3+}$. Pour chacun des milieux, on a pu isoler les constantes de vitesse correspondant aux réactions d'oxydation et de réduction des couples $Pt(ttcn)_2^{3+/2+}$ et $Au(ttcn)_2^{3+/2+}$. On a évalué que, à 25°C, les constantes de vitesse d'échange d'électron, ($k_{éch}$), pour les couples $Pd(ttcn)_2^{3+/2+}$, $Pt(ttcn)_2^{3+/2+}$ et $Au(ttcn)_2^{3+/2+}$ sont respectivement de $1,7 \times 10^3$, 59 et $3,9 \times 10^4$ mol^{-1} dm^3 s^{-1} en solution aqueuse et de $6,7 \times 10^3$, $1,3 \times 10^2$ et $2,7 \times 10^5$ mol^{-1} dm^3 s^{-1} en solution dans l'acétonitrile. Il n'a pas été possible d'observer la réaction de réduction du $Pt(ttcn)_2^{3+}$ en raison de l'instabilité du $Pt(ttcn)_2^{3+}$ en solution aqueuse. Une comparaison des constantes de vitesse d'échange d'électron des couples $Pd(tacn)_2^{3+/2+}$, $Pt(ttcn)_2^{3+/2+}$ et $Au(ttcn)_2^{3+/2+}$ en solutions dans l'eau ou dans l'acétonitrile indique que la contribution de la sphère interne à l'énergie libre d'activation de chaque réaction est identique pour chacun des solvants et que les constantes de vitesse d'autoéchange de ces complexes sont un reflet direct des différences de structure de ces complexes.

Mots clés : transfert d'électron, cinétiques, théorie de Marcus, contribution de la sphère interne.

[Traduit par la Rédaction]

Introduction

It is well known that 1,4,7-triazacyclononane (tacn) and 1,4,7-trithiacyclononane (ttcn) stabilize unusual oxidation states of metal ions, such as Ni(III), Pd(III), Au(II), and Pt(III) (1–6). However, the kinetic measurements of the electron transfer (ET) reactions involving these complexes have been limited to the $Ni(tacn)_2^{3+/2+}$ (7–9) and $Pd(tacn)_2^{3+/2+}$ couples (10) partly because of the stability of these compounds in solution and the lack of suitable oxidizing and reducing reagents. However, it seems essential to understand the precise reaction mechanism of the redox reactions involving these complexes for understanding the structure–reactivity relation in the outer-sphere electron transfer reactions.

Current interest in electron transfer chemistry is the quantitative examination of the magnitude of the activation barrier (11–13). The authors have been investigating the electron exchange reactions of Cu(I)/Cu(II) couples with various bidentate ligands for the better understanding of the structure–reactivity relation (14, 15). Marcus theory (16–19) pre-

Received May 25, 1999.

M. Matsumoto, M. Itoh, S. Funahashi, and H.D. Takagi.[1] Inorganic and Analytical Chemistry Division, Research Department of Chemistry and Physics, Graduate School of Sciences, Nagoya University, Furocho, Chikusa, Nagoya, 464-8602 Japan.

[1]Author to whom correspondence may be addressed. Telephone: +81-52-789-2470. Fax: +81-52-789-5473. e-mail: i45289a@nucc.cc.nagoya-u.ac.jp

 © 1999 NRC Canada

dicts that the outer-sphere reorganization energy is not very different for the ET reactions in the same solvent, especially when the ionic charges and sizes of the reactants are similar to each reaction couple. Therefore, the difference in the reactivity (i.e., the rates of ET) of metal complexes may be governed essentially by the internal reorganization barrier originating from the changes in nuclear coordinates that accompany the changes in the oxidation states, when the inner- and outer-sphere reorganizations take place concertedly (10, 20).

The $Pt(tacn)_2^{2+}$ and $Pd(tacn)_2^{2+}$ complexes are four-coordinate (3, 21, 22) with the square planar geometry typical of low-spin d^8 centers, while the corresponding tervalent d^7 complexes have six-coordinate distorted octahedral structure (23). The d^8 and d^7 palladium complexes with 1,4,7-trithiacyclononane were synthesized and characterized by Wieghardt et al. (24) and Schröder and co-workers (25, 26), and the structure of these complexes are similar to those of tacn complexes: $Pd(ttcn)_2^{2+}$ is square planar with a much shorter bond length between Pd and axial sulfur atoms than that between Pd and the axial nitrogen atoms in $Pd(tacn)_2^{2+}$, while $Pd(ttcn)_2^{3+}$ is tetragonally distorted octahedral with elongated bonds between Pd and the axially coordinated sulfur atoms. The gold(II) and -(III) complexes of ttcn were synthesized and characterized by Schröder and co-workers (27, 28) the d^9 gold(II) exhibits a tetragonally distorted octahedral structure, while the d^8 gold(III) has a structure similar to the corresponding Pd(II) complex. In case of Pt(II) complex, the structure is reported to be square pyramidal with elongated axial coordination of sulfur, while a distorted octahedral structure is suggested for Pt(III) complex from the ESR measurements (29). Therefore, structural changes in $Pd(ttcn)_2^{3+/2+}$, $Pt(ttcn)_2^{3+/2+}$, and $Au(ttcn)_2^{3+/2+}$ couples during the course of the electron exchange process are expected to be smaller than those observed for the $Pd(tacn)_2^{3+/2+}$ couple, when the reactions proceed through the outer-sphere process (10).

In this study, self-exchange rate constants were estimated for $Pd(ttcn)_2^{3+/2+}$, $Pt(ttcn)_2^{3+/2+}$, and $Au(ttcn)_2^{3+/2+}$ couples in aqueous acidic solution and in acetonitrile by using $Ni(tacn)_2^{3+}$ as the oxidizing reagent. $Ni(tacn)_2^{3+/2+}$ couple has been used in many studies as the typical outer-sphere electron transfer reagent because of the high oxidation potential and stability in aqueous acidic solutions and in organic solvents (7–9). Whether the solvent molecules play an important role in the activation process or not may be examined by comparing the activation barriers for the electron exchange reactions in aqueous solution and in acetonitrile. The structure–reactivity relation for $Pd(ttcn)_2^{3+/2+}$, $Pt(ttcn)_2^{3+/2+}$, and $Au(ttcn)_2^{3+/2+}$ couples is discussed in terms of the free energy required for the inner-sphere rearrangement.

Experimental

Materials

Triazacyclononane trihydrochloride and trithiacyclononane, obtained from Aldrich, were used without further purification. $[Ni(tacn)_2](ClO_4)_2$ and $[Ni(tacn)_2](ClO_4)_3$ were synthesized by the literature method (7, 8). Anal. calcd. for $NiC_{12}H_{30}N_6Cl_2O_8$: C 27.9, H 5.9, N 16.3; found: C 27.9, H 5.8, N 16.1. Anal. calcd. for $NiC_{12}H_{30}N_6Cl_3O_{12}$: C 23.4, H 4.9, N 13.7; found: C 23.4, H 5.0, N 13.6. (*Caution: Perchlorate salts of metal complexes with organic ligands are potentially explosive.*) $[Pd(ttcn)_2](PF_6)_2$ was prepared from potassium tetrachloropalladate (Wako Pure Chemicals Inc.) following the literature method (26). Anal. calcd. for $PdC_{12}H_{24}S_6P_2F_{12}$: C 19.0, H 3.2; found: C 19.0, H 3.0. $[Pt(ttcn)_2](PF_6)_2$ was synthesized from potassium tetrachloroplatinate (Wako) by the literature method (29). Anal. calcd. for $PtC_{12}H_{24}S_6P_2F_{12}$: C 17.0, H 2.9; found: C 16.9, H 2.7. $[Au(ttcn)_2](BF_4)_2$ was synthesized from potassium tetrachloroaurate (Fluka) using Schröder's method (27). Anal. calcd. for $AuC_{12}H_{24}S_6B_2F_8$: C 19.7, H 3.3; found: C 20.1, H 3.3. Tetra-*n*-butylammonium perchlorate (TBAP) was recrystallized twice from ethyl acetate – hexane mixture and dried under vacuum for 2 days. Acetonitrile (Wako) was twice distilled over P_2O_5 before use. The amount of water in thus purified acetonitrile was examined by a Mitsubishi Kasei Karl Fisher moisturemeter (<1 mmol kg^{-1}). Other chemicals were obtained from Wako (analytical grade) and used without further purification. Doubly distilled water was used for the preparation of aqueous solutions, and the ionic strength of the sample solutions was adjusted to 0.11 mol dm^{-3} by Na–$HClO_4$. The ionic strength of the acetonitrile solutions was adjusted to 0.10 mol kg^{-1} by TBAP.

Instruments

A Shimadzu UV-1600 spectrophotometer was used for the measurements of absorption spectra. Cyclic voltammograms were recorded by using a BAS-100B/W electrochemical analyzer. The temperature of the electrochemical cell was controlled at 25.0 ± 0.1°C. Kinetic measurements were carried out by a Unisoku RA401 stopped-flow spectrophotometer connected to a NEC PC computer via a Unisoku A/D converter. More than 10 traces were stored and analyzed for each run. The electron transfer reactions were observed under pseudo-first-order conditions at various temperatures (±0.1°C). The sample solutions were deaerated with N_2 or Ar before the measurements, and all measurements were carried out under N_2 or Ar atmosphere. The kinetic traces were analyzed by a nonlinear least-squares method using over 300 points for the 10 half-lives of the reactions. However, for some reactions, only three half-lives portion was used, because of the decomposition of the product through the succeeding reactions. Because of the instability of the M(III) states, the reactions of $Pt(ttcn)_2^{2+}$ and $Au(ttcn)_2^{2+}$ at higher temperatures were not so reliable as those obtained at relatively low temperatures. In such cases, the traces up to three half-lives were analyzed by the nonlinear least-squares method. However, the fits were excellent even in such cases. The second-order rate constants and the activation parameters were calculated from the linear least-squares analyses, and the errors were calculated by the standard procedure.

Results

Electrochemical measurements

To estimate the equilibrium constants for the redox reactions between $M(ttcn)_2^{2+}$ (M = Pd, Pt, Au) and $Ni(tacn)_2^{3+}$, the redox potentials of these couples were measured by cyclic voltammetry. $Ni(tacn)_2^{3+/2+}$ and $Au(ttcn)_2^{3+/2+}$ exhibited

© 1999 NRC Canada

Table 1. The redox potentials (in mV vs. NHE) for $Ni(tacn)_2^{3+/2+}$ and $M(ttcn)_2^{3+/2+}$ (M = Pd, Pt, Au) couples[a] and the equilibrium constants for the oxidation reactions of $M(ttcn)_2^{2+}$ by $Ni(tacn)_2^{3+}$.

Solvent	$Ni(tacn)_2^{3+/2+}$	$Pd(ttcn)_2^{3+/2+}$		$Pt(ttcn)_2^{3+/2+}$		$Au(ttcn)_2^{3+/2+}$	
	$E_{1/2}$/mV	$E_{1/2}$/mV	K	$E_{1/2}$/mV	K	$E_{1/2}$/mV	K
H_2O	952	1028	4.9×10^{-2}	757	2.0×10^{3}	899	7.9
Acetonitrile[b]	966	966	1.0	672	9.3×10^{4}	832	1.8×10^{2}

[a]Scan rate = 100 mV s^{-1}, Pt or GC disk working electrode and Pt wire counter electrode, and Ag/AgCl (in H_2O) or Ag^+/Ag (in AN) reference electrode were used. Typical error is within 2 mV except Pd complex in H_2O (see text).

[b]The potentials were corrected by use of $Fc^{+/0}$ (+400 mV vs. NHE).

quasi-reversible signals in aqueous acidic solution and in acetonitrile. The redox potential of $Pd(ttcn)_2^{3+/2+}$ in aqueous solution reported in Table 1 may be erroneous as the gradual decomposition of this complex was observed in water. The large peak to peak separation (100 mV) observed for the $Pt(ttcn)_2^{3+/2+}$ couple indicates that the electrode process is rather slow for this couple. These results and the equilibrium constants for the oxidation reactions of $M(ttcn)_2^{2+}$ with $Ni(tacn)_2^{3+}$ are summarized in Table 1.

Kinetic measurements in aqueous acidic solution

The oxidation reaction of $Pd(ttcn)_2^{2+}$ by $Ni(tacn)_2^{3+}$ was studied by observing the increase in the absorbance at 475 nm, which corresponds to the absorption maximum of the $Pd(ttcn)_2^{3+}$ species. The redox potentials reported in Table 1 indicate that the following reaction is not thermodynamically favored even with excess $Ni(tacn)_2^{3+}$ (K = 0.05).

$$[1] \quad [Pd(ttcn)_2]^{2+} + [Ni(tacn)_2]^{3+} \xrightarrow{k_f} [Pd(ttcn)_2]^{3+} + [Ni(tacn)_2]^{2+}$$

The rate law is complicated because of the reverse reaction even with excess $Ni(tacn)_2^{3+}$, and the forward rate constant, k_f, can be obtained only from the initial rate of the reaction. However, in the presence of an excess amount of one of the product, $Ni(tacn)_2^{2+}$, the rate law of reaction [1] becomes simple, and a pseudo-first-order kinetic trace is expected[2]:

$$[2] \quad \frac{d[Pd(ttcn)_2^{3+}]}{dt} = k_{obs}[Pd(ttcn)_2^{2+}] - k_b[Ni(tacn)_2^{2+}]_0[Pd(ttcn)_2^{2+}]_0$$

$$k_{obs} = k_f[Ni(tacn)_2^{3+}]_0 + k_b[Ni(tacn)_2^{2+}]_0$$

The reactions with excess amounts of $Ni(tacn)_2^{3+}$ and $Ni(tacn)_2^{2+}$ were excellently first order with respect to $Pd(ttcn)_2^{2+}$ for more than three half-lives. Plots of the pseudo-first-order rate constant, k_{obs}, against $[Ni(tacn)_2^{3+}]_0$ at various temperatures are shown in Fig. 1*a*. Second-order rate constants, k_f (forward) and k_b (backward), estimated from the slopes and intercepts of the plots, are summarized in Table 2. The k_b value obtained from the dependence of k_{obs} on $[Ni(tacn)_2^{2+}]_0$ (Fig. 2*a*) was (8.3 ± 0.2) × 10^3 mol^{-1} dm^3 s^{-1} at 25°C, which was in satisfactory agreement with the value obtained from the intercept of the plots shown in Fig. 1*a*, considering the fact that results obtained from the intercepts of plots are subject to large errors (Table SI).[3] The validity of eq. [2] was also confirmed by varying $[Ni(tacn)_2^{3+}]_0$ when $[Ni(tacn)_2^{2+}]_0 >> [Pd(ttcn)_2^{2+}]_0$, and by varying $[Pd(ttcn)_2^{2+}]_0$ when $[Ni(tacn)_2^{2+}]_0 >> [Ni(tacn)_2^{3+}]_0$. (Table SIX).

The oxidation reaction of $Pt(ttcn)_2^{2+}$ by $Ni(tacn)_2^{3+}$ was observed by the increase in the absorbance at λ = 400 nm, the absorption maximum of $Pt(ttcn)_2^{3+}$, under the conditions of $[Pt(ttcn)_2^{2+}]_0 >> [Ni(tacn)_2^{3+}]_0$. The reaction was first order for more than three half-lives. The plots of the conditional rate constants against the concentration of $Pt(ttcn)_2^{2+}$ were linear as shown in Fig. 1*b* at various temperatures. Therefore, the observed rate constant, k_{obs}, of the reaction was expressed by the following equation.

$$[3] \quad k_{obs} = k_f[Pt(ttcn)_2^{2+}]_0$$

The estimated second-order rate constants as well as the activation enthalpy and entropy are also listed in Table 2.

The oxidation reaction of $Au(ttcn)_2^{2+}$ by $Ni(tacn)_2^{3+}$ was monitored following the decrease of the absorbance at 404 nm, corresponding to the absorption maximum of $Au(ttcn)_2^{2+}$ species. Though the equilibrium constant of the reaction calculated from the redox potentials is 7.9 at 25°C, no meaningful intercept corresponding to the k_b process was observed under the experimental conditions, $[Ni(tacn)_2^{3+}]_0 >> [Au(ttcn)_2^{2+}]_0$. Therefore, the observed rate constant, k_{obs}, of the reaction was expressed by the following equation.

$$[4] \quad k_{obs} = k_f[Ni(tacn)_2^{3+}]_0$$

Although the slow decomposition of $Au(ttcn)_2^{2+}$ was observed in aqueous acidic solutions, the product of the decomposition reaction did not affect the kinetic data. As the

[2] When $[Ni^{3+}]_0$ and $[Ni^{2+}]_0 >> [Pd^{2+}]_0$, the rate of the oxidation reaction is expressed as below,
($[Pd^{3+}] = [Pd^{2+}]_0 - [Pd^{2+}]$)

$$\text{Rate} = k_f[Ni^{3+}]_0[Pd^{2+}] - k_b[Ni^{2+}]_0[Pd^{3+}]$$
$$= k_f[Ni^{3+}]_0[Pd^{2+}] - k_b[Ni^{2+}]_0\{[Pd^{2+}]_0 - [Pd^{2+}]\}$$
$$= \{k_f[Ni^{3+}]_0 + k_b[Ni^{2+}]_0\}[Pd^{2+}] - k_b[Ni^{2+}]_0[Pd^{2+}]_0$$

[3] The following have been deposited as supplementary material: observed rate constants for the oxidation reactions of $Pd(ttcn)_2^{2+}$, $Pt(ttcn)_2^{2+}$, and $Au(ttcn)_2^{2+}$ by $Ni(tacn)_2^{3+}$, listed in Tables SI–SXIV (10 pp.); Fig. SI: Dependence of the observed rate constants on the concentrations of the excess reagent; Fig. SII: The observed rate constants for the reverse reactions of (*a*) $Ni(tacn)_2^{3+}$ + $Pd(ttcn)_2^{2+}$ and (*b*) $Ni(tacn)_2^{3+}$ + $Au(ttcn)_2^{2+}$ in acetonitrile, I = 0.10 mol kg^{-1} (TBAP). Depository material may be purchased from: The Depository of Unpublished Data, Document Delivery, CISTI, National Research Council Canada, Ottawa, Canada, K1A 0S2.

© 1999 NRC Canada

Fig. 1. The observed rate constants for the oxidation reactions of (*a*) $Pd(ttcn)_2^{2+}$, (*b*) $Pt(ttcn)_2^{2+}$, and (*c*) $Au(ttcn)_2^{2+}$ by $Ni(tacn)_2^{3+}$ in aqueous solution under the pseudo-first-order conditions at various temperatures. $[H^+] = 1.0 \times 10^{-2}$ mol dm^{-3}, I = 0.11 mol dm^{-3} ($NaClO_4$). In (*a*), $[Ni(tacn)_2^{2+}]_0 = 1.0 \times 10^{-4}$ mol dm^{-3}.

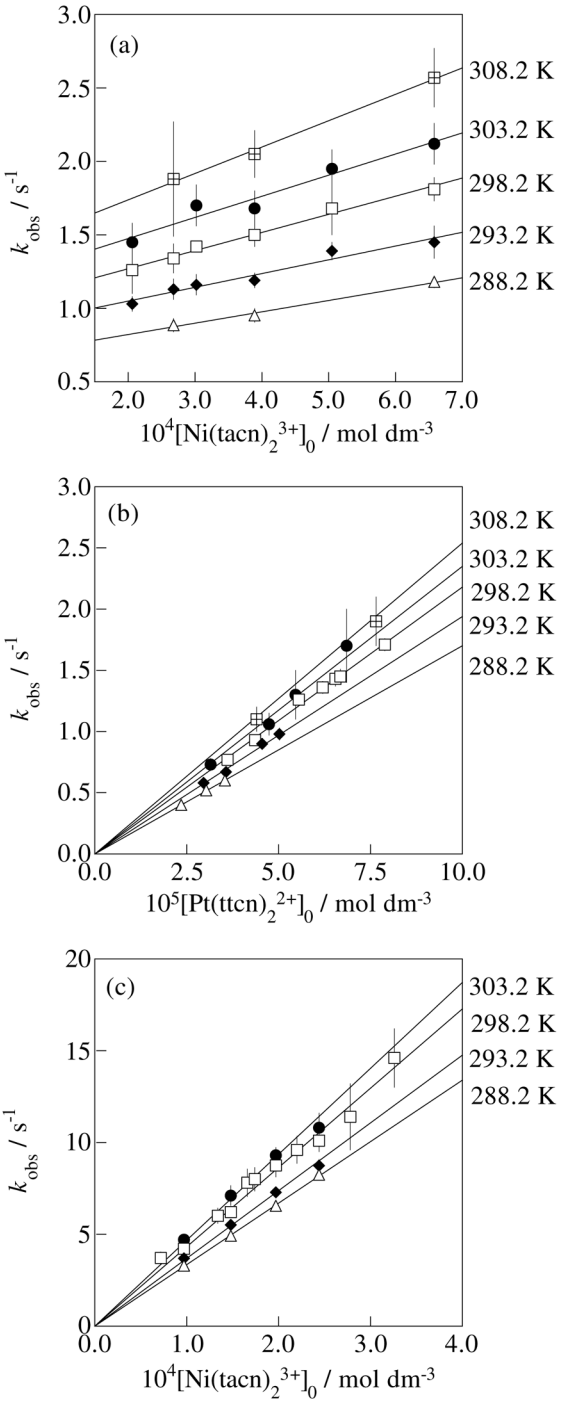

specific rate constant for the decomposition reaction lies between 3×10^{-4} and 8×10^{-4} s^{-1} under the experimental conditions, the sample solutions were freshly prepared prior to each run. Because of the auto-decomposition of the $Au(ttcn)_2^{3+}$ species, deviation from the typical first-order behavior was observed at the end of each reaction. The initial

Fig. 2. The observed rate constants for the reverse reactions of (*a*) $Ni(tacn)_2^{3+}$ + $Pd(ttcn)_2^{2+}$ and (*b*) $Ni(tacn)_2^{3+}$ + $Au(ttcn)_2^{2+}$ in aqueous solution, $[H^+] = 1.0 \times 10^{-2}$ mol dm^{-3}, I = 0.11 mol dm^{-3} ($NaClO_4$).

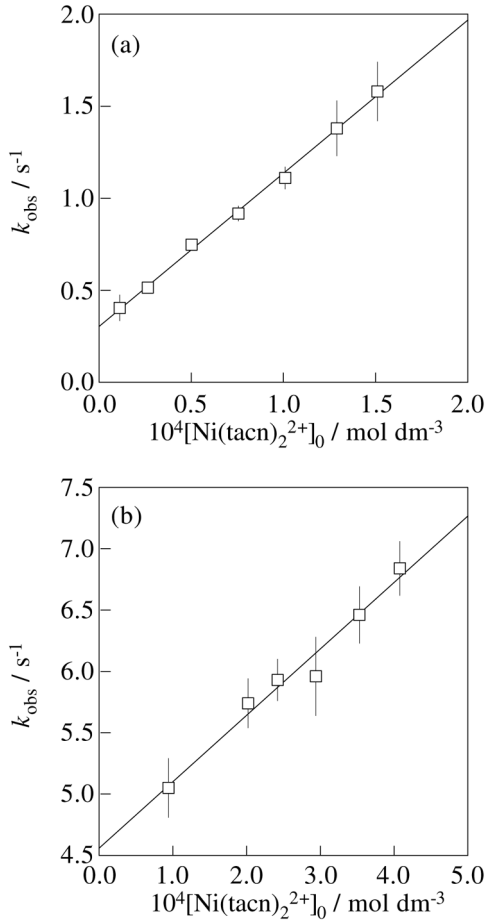

three half-life portions of each kinetic trace were therefore analyzed to determine the rate constants. The dependence of the pseudo-first-order rate constant, k_{obs}, on the initial concentration of $[Ni(tacn)_2^{3+}]_0$ is shown in Fig. 1*c*. An attempt was made to estimate the rate constant for the reverse reaction, by adding excess $Ni(tacn)_2^{2+}$ (eq. [2], Table SV[3]). The forward (k_f) and backward (k_b) rate constants so estimated are also listed in Table 2.

The dependence of the observed rate constants on pH was also examined (Tables SVI–SVIII)[3]. Though the pH range was limited because of the instability of $Ni(tacn)_2^{3+}$ at high pH, it was shown that the oxidation reactions of $Pd(ttcn)_2^{2+}$, $Pt(ttcn)_2^{2+}$, and $Au(ttcn)_2^{2+}$ by $Ni(tacn)_2^{3+}$ were independent of pH over the range of $2 < pH < 3$, indicating that there is no specific reaction pathway involving proton-dissociated species, such as $[Ni^{III}(tacn)(H_{-1}tacn)]^{2+}$, for the reactions examined in this study under the experimental conditions (30).

Kinetic measurements in acetonitrile

The absorption spectra of the reactants and products of the oxidation reactions of $Pd(ttcn)_2^{2+}$, $Pt(ttcn)_2^{2+}$, and $Au(ttcn)_2^{2+}$ by $Ni(tacn)_2^{3+}$ were examined in water and in acetonitrile. No significant shift of the absorption maxima of each species in the UV, visible, and near IR region in

© 1999 NRC Canada

Table 2. Second-order rate constants k_f and k_b, equilibrium constants K (= k_f/k_b), and the activation parameters for the oxidation reactions of $M(ttcn)_2^{2+}$ (M = Pd, Pt, Au) by $Ni(tacn)_2^{3+}$ in acidic aqueous solution.[a]

Parameters	T/K	$Pd(ttcn)_2^{2+}$	$Pt(ttcn)_2^{2+}$	$Au(ttcn)_2^{2+}$
$k_f/10^3$ mol^{-1} dm^3 s^{-1}	288.2	0.757 ± 0.072	17.0 ± 0.1	33.5 ± 0.2
	293.2	0.943 ± 0.104	19.4 ± 0.1	36.9 ± 0.5
	298.2	1.24 ± 0.07	21.8 ± 0.2	43.2 ± 0.9
	303.2	1.46 ± 0.21	23.5 ± 0.5	46.8 ± 0.9
	308.2	1.77 ± 0.13	25.4 ± 0.1	
$k_b/10^3$ mol^{-1} dm^3 s^{-1}	288.2	(6.68 ± 0.31)[b]		
	293.2	(8.49 ± 0.39)[b]		
	298.2	8.3 ± 0.2 (10.1 ± 0.8)[b]		5.42 ± 0.24
	303.2	(11.6 ± 0.8)[b]		
	308.2	(13.8 ± 0.6)[b]		
K	298.2	0.15 ± 0.01	—	8.0 ± 0.4
ΔH_f^*/kJ mol^{-1}		29.1 ± 1.3	12.3 ± 1.0	14.5 ± 1.4
ΔS_f^*/J mol^{-1} K^{-1}		–88.4 ± 4.2	–121 ± 3	–108 ± 5
ΔH_b^*/kJ mol^{-1}		24.1 ± 1[b]		
ΔS_b^*/J mol^{-1} K^{-1}		–89.4 ± 4[b]		

[a][H^+] = 1.00 × 10^{-2} mol dm^{-3}. Ionic strength of the solutions was adjusted 0.11 mol dm^{-3} by $NaClO_4$.
[b]Estimated from the intercepts of the plots (see text).

Table 3. Second-order rate constants k_f and k_b, equilibrium constants K (= k_f/k_b), and the activation parameters for the oxidation reactions of $M(ttcn)_2^{2+}$ (M = Pd, Pt, Au) by $Ni(tacn)_2^{3+}$ in acetonitrile.[a]

Parameters	T/K	$Pd(ttcn)_2^{2+}$	$Pt(ttcn)_2^{2+}$	$Au(ttcn)_2^{2+}$
$k_f/10^3$ mol^{-1} kg s^{-1}	278.2			222 ± 0.02
	283.2			274 ± 0.02
	288.2	3.49 ± 0.27	113 ± 3	334 ± 0.02
	293.2	5.41 ± 0.21	153 ± 2	403 ± 0.06
	298.2	6.48 ± 0.11	209 ± 6	475 ± 0.05
	303.2	9.08 ± 0.24	225 ± 9	
	308.2	11.0 ± 0.27	303 ± 11	
$k_b/10^3$ mol^{-1} kg s^{-1}	288.2	(5.3 ± 0.9)[b]		
	293.2	(5.7 ± 0.6)[b]		
	298.2	5.24 ± 0.10 (8.6 ± 0.3)[b]		8 ± 1
	303.2	(9.4 ±0.7)[b]		
	308.2	(13.5 ± 0.8)[b]		
K	298.2	1.2 ± 0.1	—	61 ± 7
ΔH_f^*/kJ mol^{-1}		39 ± 3	32 ± 3	23.9 ± 0.4
ΔS_f^*/J mol^{-1} K^{-1}		–41 ± 10	–35 ± 10	–56 ± 1
ΔH_b^*/kJ mol^{-1}		32 ± 5[b]		
ΔS_b^*/J mol^{-1} K^{-1}		–61 ± 16[b]		

[a]Ionic strength of the solutions was adjusted 0.10 mol kg^{-1} by TBAP.
[b]Estimated from the intercepts of the plots (see text).

acetonitrile and aqueous solutions indicates that the structures of these species in water are retained in acetonitrile, and that there is no specific solute–solvent interactions for these species in these two media.

All the oxidation reactions in acetonitrile were examined under pseudo-first-order conditions: $[Pd(ttcn)_2^{2+}]_0$, $[Ni(tacn)_2^{2+}]_0$ >> $[Ni(tacn)_2^{3+}]_0$, $[Pt(ttcn)_2^{2+}]_0$ >> $[Ni(tacn)_2^{3+}]_0$, $[Ni(tacn)_2^{3+}]_0$ >> $[Au(ttcn)_2^{2+}]_0$, for the oxidation reactions of $Pd(ttcn)_2^{2+}$, $Pt(ttcn)_2^{2+}$, and $Au(ttcn)_2^{2+}$ by $Ni(tacn)_2^{3+}$, respectively. For the reactions of $Au(ttcn)_2^{3+/2+}$, the reverse reaction was also investigated under the conditions of $[Ni(tacn)_2^{3+}]_0$, $[Ni(tacn)_2^{2+}]_0$ >> $[Au(ttcn)_2^{2+}]_0$. The dependence of the pseudo-first-order rate constant, k_{obs}, on the initial concentration of excess reagents is shown in Fig. 3. The estimated second-order rate constants as well as the activation enthalpy and entropy are summarized in Table 3.

Discussion

For the electron transfer reactions involving very large conformational change of one or both of the reactants, sluggish behaviors originating from the non-concerted inner- and outer-sphere reorganization processes may take place (31, 32). Examples of such cases have been reported as the "gated behavior" in some copper(II)/(I) couples for which a large structural inter-conversion of one of the reactants takes place prior to the ET process (33). The authors discussed the

© 1999 NRC Canada

Fig. 3. The observed rate constants for the oxidation of (*a*) $Pd(ttcn)_2^{2+}$, (*b*) $Pt(ttcn)_2^{2+}$, and (*c*) $Au(ttcn)_2^{2+}$ by $Ni(tacn)_2^{3+}$ in acetonitrile under the pseudo-first-order conditions at various temperatures. I = 0.10 mol kg^{-1} (TBAP). In (*a*), $[Ni(tacn)_2^{2+}]_0$ = 1.5 × 10^{-4} mol kg^{-1}.

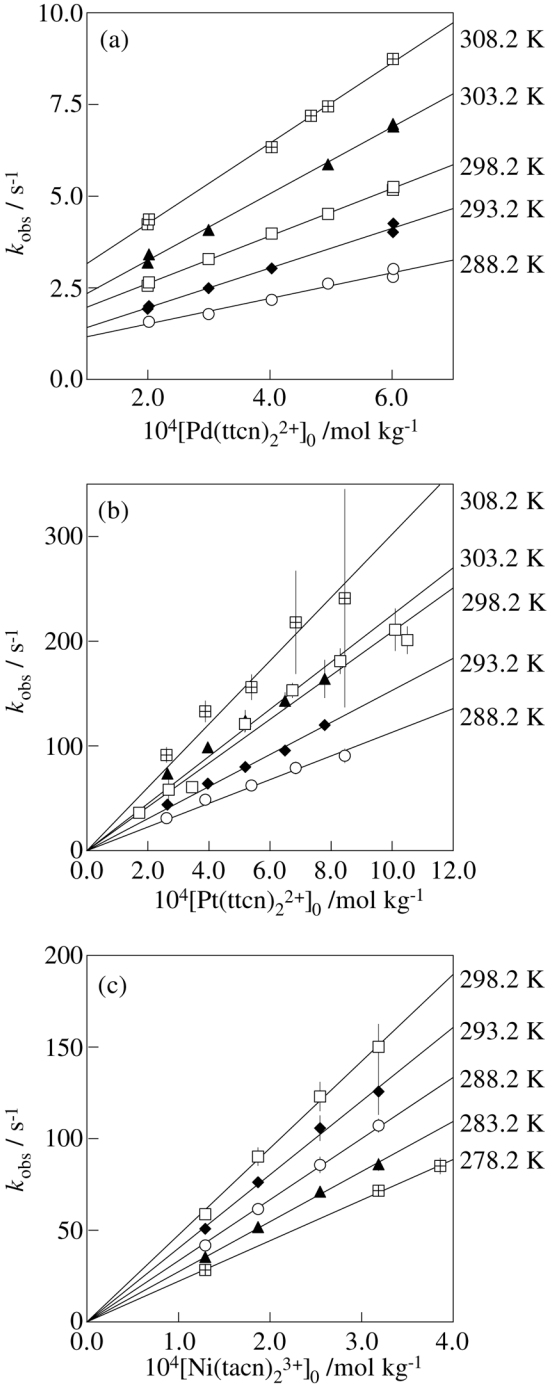

energetic origin of such a gated behavior (34) and concluded that the non-adiabaticity plays an important role in the hypothetical concerted electron transfer process of such redox couples and that the gated pathway opens up a lower-energy pathway than the direct concerted pathway.

Non-adiabaticity of a reaction originates from the poor electronic coupling between the reactants because of the effective shielding of the electronic orbitals, which are involved in the ET reactions, either by the outer shell electrons (35), by rather thick solvation sheaths (30), or by the very large energy gap between the donor and acceptor orbitals caused by the largely different coordination structures of the reactants as seen in the gated reactions (36).

Although a large negative activation entropy is expected for non-adiabatic electron exchange reactions (36), it seems that there are few experimental results that support this expectation (37). Several investigations of the outer-sphere self-exchange reactions in various solvents have not lead to simple relation between the activation entropy and the effect of solvents (38, 39). Tabulated results for the outer-sphere self-exchange reactions in water indicate that the activation entropies lie in the range of –50 to –130 J mol^{-1} K^{-1} (36). The activation volumes for such adiabatic outer-sphere self-exchange reactions are ca. –5 cm^3 mol^{-1} for most cases, and the exceptionally large activation volumes for $Co(ethylenediamine)_3^{3+/2+}$ and $Fe(CN)_6^{3-/4-}$ couples were attributed to the non-adiabaticity or to the cation effect, respectively (40, 41). Very few kinetic results concerning the outer-sphere self-exchange reactions in both water and non-aqueous solvents have been reported because of the instability of one of the species in certain solvents (42, 43). Results reported for $Fe(1,10\text{-penanthroline})_3^{3+/2+}$ in water and in acetonitrile (44) show that the activation enthalpy as well as the activation entropy varies in different solvents. Such a tendency has been observed for many outer-sphere ET reactions (45). However, it is now regarded that the linear isokinetic relation for such reaction systems may not lead to any fruitful conclusion (46). All these previously reported results indicate that the Marcus theory predicts the reliable activation free energies. However, the activation entropy certainly includes the information related to the numbers of the electronic states in the ground and activated levels related to the ET reaction. The discussion given below are, therefore, made on the basis of the activation free energies for each self-exchange reaction examined in this study.

ET reactions in aqueous acidic solution

The cross reaction rate constant, k_{et}, is related to the individual electron self-exchange rate constants, k_{11} and k_{22}, and the overall equilibrium constant, K_{12}, by the following Marcus cross relation (11, 47):

[5] $$k_{et} = \sqrt{k_{11}k_{22}K_{12}f}\,W_{12}$$

$$\ln f = \frac{[\ln K_{12} + (w_{12} - w_{21})/RT]^2}{4[\ln(k_{11}k_{22}/Z_{11}Z_{22}) + (w_{11} + w_{22})/RT]}$$

$$W_{12} = \exp\,[-(w_{12} + w_{21} - w_{11} - w_{22})/2RT]$$

$$w_{ij} = (Z_{11}Z_{22}e^2)/(D_s\sigma(1 + \beta\sigma I^{1/2}))$$

$$\beta = ((8\pi Ne^2)/(1000D_sk_BT))^{1/2}$$

where w_{ij}, Z_{ii} are the coulombic work required to bring the two species to a distance σ at which ET occurs with maximum probability, the diffusion rate of the species *ii*. N, k_B, and D_s are Avogadro's number, Boltzmann constant, and the static dielectric constant, respectively. From the rate constants, k_f, for the cross reactions of $Pd(ttcn)_2^{2+}$, $Pt(ttcn)_2^{2+}$,

© 1999 NRC Canada

Table 4. The used parameters and the calculated results by Marcus–Sutin model.

		$Pd(ttcn)_2^{3+/2+}$	$Pt(ttcn)_2^{3+/2+}$	$Au(ttcn)_2^{3+/2+}$
	a_{Ox}/a_{Red}[a]	450/470	480/530	480/470
	Δd[b]	41 (ax), 4 (eq)	120 (ax)[c]	10 (eq), –10 (ax)
In H_2O	k_{et}[d]	1.24×10^3	2.18×10^4	4.32×10^4
	K_{12}[e]	0.15 (k_f/k_b)	2.0×10^3 (CV)	7.9 (CV)
	W_{12}	1.02	1.05	1.03
	f	0.96	0.60	0.94
	k_{ex}[d]	1.7×10^3	59	3.9×10^4
	K_{os}[f]	0.18	0.33	0.22
	ΔG^*_{os}[g]	20.8	19.0	20.1
	ΔG^*_{is}[g]	29.6	42.1	23.0
In AN[h]	k_{et}[i]	6.48×10^3	1.63×10^5	4.75×10^5
	K_{12}	1.0 (CV)	8.0×10^4 (CV)	1.8×10^2 (CV)
	W_{12}	1.02	1.18	1.06
	f	1	0.31	0.65
	k_{ex}[i]	6.7×10^3	1.3×10^2	2.7×10^5
	K_{os}[j]	0.48	0.77	0.57
	ΔG^*_{os}[g]	19.9	18.2	19.3
	ΔG^*_{is}[g]	29.5	42.1	21.3

[a] a_{Ox} and a_{Red} correspond to the ionic radii of the oxidized and reduced forms of $M(ttcn)_2^{3+/2+}$ (pm).

[b] The changes of the M—S bond length from M^{3+} to M^{2+} in pm, which was estimated from the X-ray structural results (the structure of $Pt(ttcn)_2^{3+}$ was speculated by the ESR results). eq and ax denote the equatorial and axial positions, respectively.

[c] One of the axial M—S bonds is elongated in $Pt(ttcn)_2^{2+}$.

[d] mol^{-1} dm^3 s^{-1}.

[e] Kinetically (k_f/k_b) or electrochemically (CV) estimated K values (see text).

[f] mol^{-1} dm^3.

[g] kJ mol^{-1}.

[h] 1:1 ion pair was assumed, as the Fuoss-type equation estimates complete 1:1 ion-pair formation at the ionic strength used in this study.

[i] mol^{-1} kg s^{-1}.

[j] mol^{-1} kg.

and $Au(ttcn)_2^{2+}$ with $Ni(tacn)_2^{3+}$, the electron self-exchange rate constants for the $Pd(ttcn)_2^{3+/2+}$, $Pt(ttcn)_2^{3+/2+}$, and $Au(ttcn)_2^{3+/2+}$ couples were estimated as 5.2×10^3, 59, and 3.9×10^4 mol^{-1} dm^3 s^{-1} by using 6.0×10^3 mol^{-1} dm^3 s^{-1} as the self-exchange rate constant for the $Ni(tacn)_2^{3+/2+}$ couple (7, 9). The electron exchange rate constants for the $Pd(ttcn)_2^{3+/2+}$ and $Au(ttcn)_2^{3+/2+}$ couples were also estimated from the reverse reaction rate constants, k_b: $k_{Pd} = 620$ and $k_{Au} = 3.8 \times 10^4$ mol^{-1} dm^3 s^{-1}. The consistency of the calculated self-exchange rate constants from the forward and backward reactions is excellent for the $Au(ttcn)_2^{3+/2+}$ couple, while a rather poor agreement between the self-exchange rate constants from both directions was exhibited for the $Pd(ttcn)_2^{3+/2+}$ couple. Such an inconsistency may be attributed to the rather poor voltammogram for the latter couple, and the kinetically estimated equilibrium constant of reaction [1] ($k_f/k_b = 0.15$) seems more reliable. As a result, the value of 1.7×10^3 mol^{-1} dm^3 s^{-1} was taken as the electron exchange rate constant of the $Pd(ttcn)_2^{3+/2+}$ couple (Table 4).

The self-exchange rate constant for the $Pd(tacn)_2^{3+/2+}$ couple is reported by McAuley and Whitcombe (10) as 2×10^{-6} mol^{-1} dm^3 s^{-1}, which implies a substantial structural rearrangement in the course of the electron transfer process.

The semi-classical Marcus–Sutin model enables the theoretical calculation of electron exchange rate constants in solution (47). The adiabatic self-exchange rate constant, k_{ii}, is given by the product of the pre-equilibrium constant, K_0, the effective frequency of the nuclear vibrations, ν_n, and the nuclear factor, κ_n.

$$[6] \qquad k_{ii} = K_0 \nu_n \kappa_n$$

The pre-equilibrium constant may be expressed by the conventional Fuoss type equation, on the basis of the extended Debye–Hückel theory (48, 49). The effective frequency of nuclear vibration and the nuclear factor are given by the following equations (47):

$$[7] \qquad \nu_n^2 = \frac{\nu_{out}^2 \Delta G^*_{out} + \nu_{in}^2 \Delta G^*_{in}}{\Delta G^*_{out} + \Delta G^*_{in}}$$

$$[8] \qquad \kappa_n = \Gamma \exp\left[-(\Delta G^*_{out} + \Delta G^*_{in})/RT\right]$$

where ΔG^*_{in} and ΔG^*_{out} are the inner-sphere and outer-sphere contributions to the activation free energy, and ν_{in} and ν_{out} are the inner- and outer-sphere frequency terms representing the reduced metal-ligand stretching and solvent dipole orientation (typically 10^{11}–10^{12} s^{-1} for most liquids), respectively. ΔG^*_{in} and ΔG^*_{out} are given by eqs. [9] and [10] using the reduced force constant, f_i, the difference in the metal-ligand distance between reduced and oxidized forms of the ex-

© 1999 NRC Canada

Fig. 4. A comparison of the activation free energies in water and in acetonitrile, ΔG^* (H_2O).vs. ΔG^* (AN), for the self-exchange reactions of a series of $M(ttcn)_2^{3+/2+}$ (M = Pd, Pt, and Au) couples.

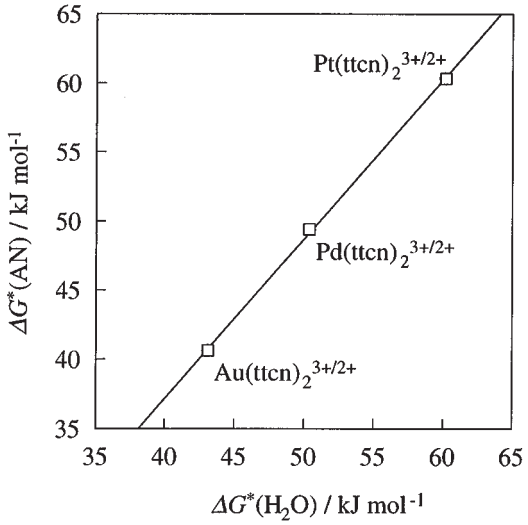

change couple, Δd_0, and the high- and low-frequency dielectric constants, D_{op} and D_s.

$$[9] \qquad \Delta G^*_{in} = \frac{1}{2} N \sum f_i \left(\frac{\Delta d_i}{2} \right)^2$$

$$[10] \qquad \Delta G^*_{out} = \frac{Ne^2}{16\pi\varepsilon_0} \left(\frac{1}{2a_1} + \frac{1}{2a_2} - \frac{1}{\sigma} \right) \left(\frac{1}{D_{op}} - \frac{1}{D_s} \right)$$

The nuclear tunneling factor, Γ, is usually expressed by the following Holstein's equation, and the value of Γ approaches unity at high temperature limit (47, 50). The value of ν_{in} is taken as being 1.5×10^{13} s^{-1} (47). Γ is close to unity when ΔG^*_{in} is less than ca. 30 kJ mol^{-1}.

$$[11] \qquad \Gamma = \exp \left[-\frac{\Delta G^*_{in}}{4h\nu_{in}} \right] \left(\tanh \frac{h\nu_{in}}{4kT} - \frac{h\nu_{in}}{4kT} \right)$$

When the solvent barrier is large, which is the case in most reactions in solution, ν_n can be replaced by the classical limit of the outer-sphere orientational frequency ν_{out}.

The effective radii a_i of the $M(ttcn)_2^{2+}$ and $M(ttcn)_2^{3+}$ complexes were estimated from the crystallographic data as 450/470 pm for Pd(III/II), 530/480 pm for Pt(III/II), and 480/470 pm for Au(III/II), respectively (24–29). By using these values, the application of the Marcus–Sutin model to the electron exchange reactions of $Pd(ttcn)_2^{3+/2+}$, $Pt(ttcn)_2^{3+/2+}$, and $Au(ttcn)_2^{3+/2+}$ couples, calculates the pre-equilibrium and outer-sphere contribution to the activation free energy, by the subtraction of which from the experimentally obtained total activation free energies the inner-sphere contributions to the activation free energies were roughly calculated as 30, 42, and 23 kJ mol^{-1} for $Pd(ttcn)_2^{3+/2+}$, $Pt(ttcn)_2^{3+/2+}$, and $Au(ttcn)_2^{3+/2+}$ couples, respectively (Table 4). These values are much smaller than that reported for the $Pd(tacn)_2^{3+/2+}$ couple (85 kJ mol^{-1}) (10).

For the electron exchange reaction between $Pd(tacn)_2^{2+}$ and $Pd(tacn)_2^{3+}$, ca. 135 pm was estimated for Δd_0, which involves the inversion process of two tacn rings around the axially positioned nitrogen atoms (22). However, Δd_0 values for the $Pd(ttcn)_2^{3+/2+}$ and $Au(ttcn)_2^{3+/2+}$ couples are merely 41–46 and 10 pm, respectively, even at the elongated axial positions. The oxidation of $Pt(ttcn)_2^{2+}$ involves an inversion of the ttcn ring around a non-coordinated sulfur atom, while another axial S atom is kept bound to the Pt center.

By using the reduced force constant for the M—S bond, ca. 100 Nm^{-1} (51), the free energy difference in internal rearrangements of the $Pd(ttcn)_2^{3+/2+}$ and $Au(ttcn)_2^{3+/2+}$ couples is estimated to be merely 2 kJ mol^{-1}, which may be compared with the calculated difference of 7 kJ mol^{-1} (ΔG^*_{in} values are 30 and 23 kJ mol^{-1} for $Pd(ttcn)_2^{3+/2+}$ and $Au(ttcn)_2^{3+/2+}$, respectively). It was suggested that the axially positioned nitrogen atoms in the square planar $Pd(tacn)_2^{2+}$ complex are also interacting with the Pd center so as to significantly influence the geometry in the equatorial plane, although the force constant for such interaction is fairly small (10 Nm^{-1}) (10). Similar situation may be expected for $Pt(ttcn)_2^{2+}$. The very large value of ΔG^*_{in} for the $Pd(tacn)_2^{3+/2+}$ may be partly attributed to the relatively large force constants between Pd and N atoms (51). A rapid fluxional behavior in $Pd(tacn)_2^{2+}$ ($>1 \times 10^5$ s^{-1}) was also reported by McAuley and co-workers (22). This fluxionality is obviously caused by the local concentration effect of the nearby uncoordinated nitrogen atoms with relatively low activation energy corresponding to the tacn ring inversion (32 kJ mol^{-1}) (52). Therefore, the very small electron exchange rate constant for the $Pd(tacn)_2^{3+/2+}$ couple is attributed largely to the inner-sphere contribution originates from the double inversion of the tacn rings in the activation process ($>2 \times 32$ kJ mol^{-1}). On the other hand, the electron exchange reactions are relatively fast for $Au(ttcn)_2^{3+/2+}$ and $Pd(ttcn)_2^{3+/2+}$ couples as the conformational changes required for the ET process are small, while an inversion (ca. 32 kJ mol^{-1}) around the uncoordinated S atom is involved in the $Pt(ttcn)_2^{3+/2+}$ electron exchange reaction. A larger interaction between Pt center and S atom than that for Pd center and S atom may also contribute to the larger inner-sphere activation free energy for the reaction of the $Pt(ttcn)_2^{3+/2+}$ couple.

ET reactions in acetonitrile

Because of the low dielectric constant of acetonitrile and the charge on the complex ions used in this study (3+/2+), the effect of the ion pair formation has to be taken into account. It is known that the metal(II) and -(III) complexes almost quantitatively form 1:1 ion pairs with ClO_4^- in acetonitrile. Applying the Marcus cross relation to the reactions in acetonitrile, we obtained k_{ex} for $M(ttcn)_2^{3+/2+}$ couples as $k_{Pd} = 6.7 \times 10^3$, $k_{Pt} = 1.3 \times 10^2$, $k_{Au} = 2.7 \times 10^5$ mol^{-1} kg s^{-1} from the oxidation reactions (the effect of the ion-pair formation was accounted for). By using the reverse reaction rate constant, k_b, the k_{Pd} and k_{Au} were calculated as 4.4×10^3 and 2.6×10^6, respectively. The larger k_{ex} in acetonitrile than in aqueous acidic solution is attributed to the difference of ΔG^*_{out} and K_0 in water and in acetonitrile. The activation free energies corresponding to the estimated self-exchange rate constants of each couple in acetonitrile at

© 1999 NRC Canada

25°C, ΔG^* (AN), are plotted against those in water, ΔG^* (H_2O), in Fig. 4. The plot is linear with unit slope (1.2 ± 0.1) as seen in Fig. 4. Such a linear relation implies that the difference in ΔG^*_{in} for various $M(ttcn)_2^{3+/2+}$ complexes is identical in water and acetonitrile. The intercept of the plot in Fig. 4 corresponds to the difference of the ΔG^*_{out} in H_2O and in acetonitrile. Therefore, specific solute–solvent interactions, such as the solvent intrusion to the vacant site of $M(ttcn)_2^{3+/2+}$ species, may not be significant in these reactions, which is also supported by the fact that no significant shift of the absorption maxima was observed for these species in water and in acetonitrile. As a result, the ET reaction rates for the species studied in this article are governed by the structural change of each species.

Conclusions

In this study, the electron exchange rate constants (k_{ex}) for $M(ttcn)_2^{3+/2+}$ couples (M = Pd, Pt, and Au) in H_2O and in acetonitrile were estimated. The difference between these k_{ex} values were explained by the difference in the inner-sphere contributions to the activation free energy (ΔG^*_{in}) of each redox couple. The relation between $\Delta G^*(H_2O)$ and $\Delta G^*(AN)$ indicates that there is no specific solute–solvent interactions involved these reactions. Unfortunately, the present study could not shed a light on the solution structures of the species involved in the ET reactions.

The free energy analysis of an ET reaction cannot tell if the reaction takes place in a concerted manner or not. However, a large structural change accompanying the ET process sometimes leads to sluggish electron transfer processes, such as gated or directional reactions (31–33, 53). It is a rather difficult task to distinguish gated and directional reactions from the concerted processes by means of the ordinary kinetic methods, as the activation free energies for gated and directional reactions also reflect the free energy barrier corresponding to the conformational change prior to the ET process (33). We anticipate that the mode of the inner-sphere activation process is the key to the understanding of the gated ET: the vibrationally coupled inner-sphere process (time scale is ca. 10^{13} s^{-1}) may lead the ordinary outer-sphere ET reactions in which the structural change takes place within the encounter complex, while the slower activation mode such as twisting or inversion cannot take place within the encounter complex and an intermolecular gated ET may become important. Studies at elevated pressures on the basis of the Stranks–Hush–Marcus–Swaddle theory (54, 55) are currently in progress, to clarify the involvement of non-adiabaticity and (or) the involvement of the gated process in these reaction systems.

Acknowledgment

This research was supported by the Grants-in-Aid for Scientific Research (grant nos. 05453042, 07554061, 07504003, and 10440193) from the Ministry of Education, Science and Culture of Japan. M.M. held a research fellowship from the Japan Society for the Promotion of Science for Young Scientists.

References

1. P. Chaudhuri and K. Wieghardt. Prog. Inorg. Chem. **35**, 329 (1987).
2. K. Wieghardt, W. Waltz, B. Nuber, J. Weiss, A. Ozarowski, H. Stratemeier, and D. Reinen. Inorg. Chem. **25**, 1651 (1986).
3. K. Wieghardt, M. Köppen, W. Swiridoff, and J. Weiss. J. Chem. Soc. Dalton Trans. 1869 (1983).
4. K. Wieghardt, H.-J. Küppers, and J. Weiss. Inorg. Chem. **24**, 3067 (1985).
5. K. Wieghardt, W. Schmidt, W. Herrman, and H.-J. Küppers. Inorg. Chem. **22**, 2953 (1983).
6. S.R. Cooper and S.C. Rawle. Struct. Bonding, **72**, 3 (1990).
7. A. McAuley, P.R. Norman, and O. Olubuyide. Inorg. Chem. **23**, 1938 (1984).
8. M.M. deMaine and D.M. Stanbury. Inorg. Chem. **30**, 2104 (1991).
9. A. McAuley, P.R. Norman, and O. Olubuyide. J. Chem. Soc. Dalton Trans. 1501 (1984).
10. A. McAuley and T.W. Whitcombe. Inorg. Chem. **27**, 3090 (1988).
11. B.S. Brunschwig, C. Creutz, D. Macartney, T.-K. Sham, and N. Sutin. Faraday Discuss. Chem. Soc. **74**, 113 (1982).
12. S.F. Nelsen, S.C. Blackstock, and Y.J. Kim. J. Am. Chem. Soc. **109**, 677 (1987).
13. D.K. Phelps, M.T. Ram, Y. Wang, S.F. Nelsen, and M.J. Weaver. J. Phys. Chem. **97**, 181 (1993).
14. H. Doine, Y. Yano, and T.W. Swaddle. Inorg. Chem. **28**, 2319 (1989).
15. P. Metelski, A.S. Hinman, H.D. Takagi, and T.W. Swaddle. Can. J. Chem. **73**, 61 (1995).
16. R.A. Marcus. Angew. Chem. Int. Ed. Engl. **32**, 1111 (1993).
17. R.A. Marcus. Electrochim. Acta, **13**, 995 (1968).
18. N.S. Hush. Prog. Inorg. Chem. **8**, 391 (1967).
19. R.A. Marcus. J. Chem. Phys. **24**, 966 (1956).
20. P.W. Crawford and F.A. Schultz. Inorg. Chem. **33**, 4344 (1994).
21. F.R. Hartley. The chemistry of platinum and palladium. Applied Science Publishers, London. 1973.
22. G. Hunter, A. McAuley, and T.W. Whitcombe. Inorg. Chem. **27**, 2634 (1988).
23. A.J. Blake, L.M. Gordon, A.J. Holder, T.I. Hyde, G. Reid, and M. Schröder. J. Chem. Soc. Chem. Commun. 1452 (1988).
24. K. Wieghardt, H.-J. Küppers, E. Raabe, and C. Krüger. Angew. Chem. Int. Ed. Engl. **25**, 1101 (1986).
25. A.J. Blake, A.J. Holder, T.I. Hyde, and M. Schröder. J. Chem. Soc. Chem. Commun. 987 (1987).
26. A.J. Blake, A.J. Holder, T.I. Hyde, Y.V. Roberts, A. Lavery, and M. Schröder. J. Organomet. Chem. **323**, 261 (1987).
27. A.J. Blake, J.A. Greig, A.J. Holder, T.I. Hyde, A. Taylor, and M. Schröder. Angew. Chem. Int. Ed. Engl. **29**, 197 (1990).
28. A.J. Blake, R.O. Gould, J.A. Greig, A.J. Holder, T.I. Hyde, and M. Schröder. J. Chem. Soc. Chem. Commun. 876 (1989).
29. A.J. Blake, R.O. Gould, A.J. Holder, T.I. Hyde, A.J. Lavery, M.O. Odulate, and M. Schröder. J. Chem. Soc. Chem. Commun. 118 (1987).
30. N. Koshino, S. Funahashi, and H.D. Takagi. J. Chem. Soc. Dalton Trans. 4175 (1997).
31. B.M. Hoffman and M.A. Ratner. J. Am. Chem. Soc. **109**, 6237 (1987).
32. B.S. Brunschwig and N. Sutin. J. Am. Chem. Soc. **111**, 7457 (1989).

© 1999 NRC Canada

33. C.A. Shalhi, Q. Yu, M.J. Heeg, N.M. Villeniuve, K.L. Juntunen, R.R. Schroeder, L.A. Ochrymowycz, and D.B. Rorabacher. Inorg. Chem. **34**, 6053 (1995).
34. N. Koshino, Y. Kuchiyama, S. Funahashi, and H.D. Takagi. Chem. Phys. Lett. **306**, 291 (1999).
35. V. Balzani, F. Scandola, G. Orlandi, N. Sabbatini, and M.T. Indelli. J. Am. Chem. Soc. **103**, 3370 (1981).
36. A.G. Lappin. Redox mechanisms in inorganic chemistry. Ellis Horwood, Chichester, U.K. 1994.
37. M.J. Weaver and E.D. Yee. Inorg. Chem. **19**, 1936 (1980).
38. S. Wherland. Coord. Chem. Rev. **123**, 169 (1993), and refs. therein.
39. N. Sutin and B.S. Brunschwig. Mechanistic aspects of inorganic reactions. *Edited by* D.B. Rorabacer and J.F. Endicott. ACS Symposium Series 198. ACS, Washington, D.C. 1982.
40. W.H. Jolley, D.R. Stranks, and T.W. Swaddle. Inorg. Chem. **29**, 385 (1990).
41. H. Takagi and T.W. Swaddle. Inorg. Chem. **31**, 4669 (1992).
42. J.D. Gribble and S. Wherland. Inorg. Chem. **29**, 1130 (1990).
43. H. Doine and T.W. Swaddle. Can. J. Chem. **68**, 2228 (1990).
44. H. Doine and T.W. Swaddle. Can. J. Chem. **66**, 2763 (1988).
45. T.W. Newton and F.B. Baker. Adv. Chem. **71**, 268 (1967).
46. R.G. Wilkins. Kinetics and mechanism of reactions of transition metal complexes. 2nd ed. VCH, Weinheim. 1991.
47. N. Sutin. Prog. Inorg. Chem. **30**, 442 (1983).
48. R.D. Cannon. Electron transfer reactions. Butterworth, London. 1980.
49. R.B. Jordan. Reaction mechanisms of inorganic and organometallic systems. Oxford University Press, New York. 1991.
50. B. Chance, D.C. DeVault, H. Frauenfelder, and R.A. Marcus. Tunneling in biological systems. *Edited by* N. Sutin. Academic Press, New York. 1979.
51. K. Nakamoto. Infrared and Raman spectra of inorganic and coordination compounds. 5th ed. John Wiley, New York. 1997.
52. F.A.L. Anet and J.S. Hartman. J. Am. Chem. Soc. **85**, 1204 (1963).
53. R. Bechtold, C. Kuehn, C Lepre, and S. Isied. Nature (London), **322**, 286 (1986).
54. D.R. Stranks. Pure Appl. Chem. **38**, 303 (1974).
55. T.W. Swaddle. Inorg. Chem. **29**, 5017 (1990).

© 1999 NRC Canada

Addition of cyclopentadiene derivatives on aromatic aldehydes or nitrosobenzene initiated by electrochemical reduction

F. Williot, M. Bernard, D. Lucas, Y. Mugnier, and J. Lessard

Abstract: The electrochemical reduction of nitrosobenzene (PhNO) in the presence of cyclopentadiene derivatives containing the indenyl group represented as In′H_2 (**10a**, **10b**, and **12b**) gives the imine derivatives PhN=In′. The process requires only a catalytic amount of electricity. When the electrolysis of aromatic aldehydes (ArCHO), 2,6-dichlorobenzaldehyde (**1a**), benzaldehyde (**1b**) and terephthalaldehyde (**2**), is performed in the presence of the In′H_2 derivatives, compounds ArCH=In′ are obtained in low yields. These compounds have been characterized by mass spectrometry and microanalysis. The overall process involves two consecutive chain reactions with regeneration of the anion In′H^-.

Key words: electrochemical reduction, nitrosobenzene, aromatic aldehydes, base catalysis, chain reaction.

Résumé : La réduction électrochimique du nitrosobenzène (PhNO) en présence de dérivés du cyclopentadiène contenant le groupe indényle symbolisé par In′H_2 (**10a**, **10b**, and **12b**) conduit à des dérivés de type imine, ArN=In′. Le processus ne requiert qu'une quantité catalytique d'électricité. Lorsque l'électrolyse d'aldéhydes aromatiques (ArCHO) comme le 2,6-dichlorobenzaldéhyde (**1a**), le benzaldéhyde (**1b**) et le téréphtalaldéhyde (**2**) est réalisée en présence des dérivés In′H_2, les composés ArCH=In′ sont obtenus en faible rendement. Ces derniers composés ont été caractérisés par spectrométrie de masse et microanalyse. Le processus global implique deux réactions en chaîne avec régénération de l'anion InH^-.

Mots clés : réduction électrochimique, nitrosobenzène, aldéhydes aromatiques, catalyse basique, réaction en chaîne.

Introduction

We have reported previously that the reaction between aromatic aldehydes (ArCHO), 2,6-dichlorobenzaldehyde (**1a**), benzaldehyde (**1b**), and terephtalaldehyde (**2**)[2], in the presence of indene (InH_2) gave the derivatives ($ArCH(InH)_2$), **10a**, **10b**, and **12b**, respectively, in a process involving three consecutive chain reactions (1): addition of electrochemically generated InH^- to ArCHO to form a carbinol, ArCH(OH)InH, with regeneration of InH^- (2, 3), base catalysed dehydration of the carbinol to the hydrocarbon ArCH=In, and finally, addition of InH^- to ArCH=In to give $ArCH(InH)_2$ with regeneration of InH^-. The latter chain reaction was a slow process requiring several hours (1). The ^{1}H-NMR spectra of **10a**, **10b**, and **12b** indicated that all the indenyl moieties exist in the γ form (a trisubstituted double bond and a methylene group) (1). This was confirmed by the X-ray structure of **12b** showing the four indenyl moieties in the γ form (1) (Scheme 1).

Results and discussion

Chain reactions initiated by electrochemical reduction of nitrosobenzene

The cyclic voltammogram of nitrosobenzene (ArNO) on a vitreous carbon electrode in DMF 0.2 M Bu_4NPF_6 at –20°C shows a reversible system A/A′ (Fig. 1). Peak A corresponds to the reduction of ArNO to its radical anion $ArNO^{\cdot-}$ and peak A′ to the oxidation of the anion (4). In the presence of 5 equiv. of **10a**, the voltammogram is changed: peak A decreases and peak A′ disappears (Fig. 1). The rapid drop of the current after the peak potential, resulting in a sharp, narrow, and symmetric peak A, is characteristic of a catalytic reaction occurring outside the diffusion layer (5). We have

Received May 3, 1999.

F. Williot, M. Bernard, D. Lucas, and Y. Mugnier.[1] Laboratoire de synthèse et d'électrosynthèse organométalliques, associé au Centre national de la recherche scientifique (Unité de recherche associé n° 5632), Faculté des Sciences Gabriel, 6 Boulevard Gabriel, 21000 Dijon, France.
J. Lessard.[1] Laboratoire d'Electrochimie et d'électrocatalyse, Département de Chimie, Université de Sherbrooke, Sherbrooke, J1K 2R1, Canada.

[1]Authors to whom correspondence may be adressed. JL: Telephone: (819) 821-7091. Fax: (819) 821-8017.
e-mail: jlessard@courrier.usherb.ca; YM: Telephone: (33) 03 80 39 60 91. Fax: (33) 03 80 39 60 91.
e-mail: yves.Mugnier@u-bourgogne.fr
[2]Numeric symbols for the compound names are continued from ref. 1.

 © 1999 NRC Canada

Scheme 1.

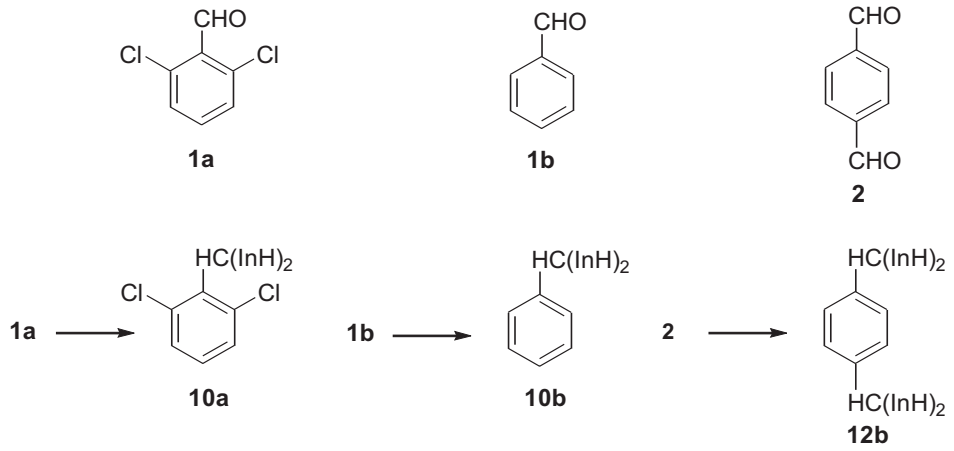

Table 1. Controlled potential electroreduction of ArNO in the presence of protons donors ($In'H_2$) on a mercury electrode in DMF/(n-Bu)$_4$NPF$_6$ (0.2 M) at –20°C followed by letting the solution stand at room temperature for several hours.[a]

Entry	E_w[b] (V)	$In'H_2$	$In'H_2$/ArNO (molar ratio)	mol e/mol ArNO ($\times 10^2$)	Solution color	Standing time (h)	Product(s) (% yield) Imine (ArN=In′)
1	–1	**10a**	4	6	Red	67	**13a** (21)
2	–1	**10b**	5	2.6	Red	72	**13b** (4)
3	–1	**12b**	2	11.7	Red	68	**14b** (9)

[a]The electrolyses were carried out under argon and the electrolysis solution was kept under argon after the current dropped to zero.

[b]Working potential vs. SCE.

Fig. 1. Cyclic voltammogram of nitrosobenzene in DMF/Bu$_4$NPF$_6$ solution at –20°C. Sweep rate: 0.1 V/s. Starting potential: +0.1 V. (*a*) ArNO alone; (*b*) in the presence of 5 equiv. of **10a**.

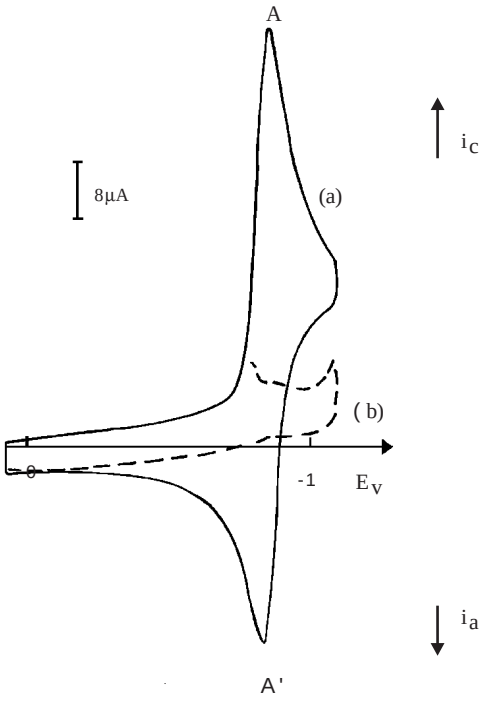

verified that **10a** does not react with ArNO when no potential was applied under the same experimental conditions.

When an electrolysis of ArNO was performed in the presence of 4 equiv. of **10a** at the potential of peak A and at –20°C, the current dropped to zero after the consumption of a catalytic amount of electricity (see Table 1). After the addition of water and extraction with methylene chloride, the crude product was purified by chromatography on silica gel (see Table 4) to give imine **13a** (see Table 1 and Scheme 2). Similar results were obtained from the electroreduction of ArNO in the presence of **10b** or **12b**, giving **13b** and **14b**, respectively. In all cases, azoxybenzene was also formed.

The voltammetric behaviour and the results of controlled potential electrolyses (Table 1) show that the electrochemical reduction of PhNO in the presence of **10a**, **10b**, or **12b** as proton donor induces a chain reaction giving an imine, ArN=In′ (**13a**, **13b**, or **14b**, respectively), and azoxybenzene. The mechanism of formation of these compounds is the same as that described previously for the electrochemically initiated reaction of PhNO with fluorene or indene (5, 6). No nitrone was isolated or detected in the reaction with **10a**, **10b**, or **12b**, whereas the formation of a nitrone was reported in the reaction with fluorene or indene (5). In all reactions of Table 1, only one of the indene rings (out of two in **10a** and **10b**, out of four in **12b**) did react with PhNO due to the fact that an excess of proton donors (**10a**, **10b**, or **12b**) has been used.

The reaction of nitrosoaromatic compounds with active methylene compounds in the presence of a basic catalyst to give anils (Erlich–Sachs reaction (7)) and nitrones has been known for a long time. The reaction gives either the anil or the nitrone or a mixture of both, depending on the active methylene compound, the basic catalyst, and the reaction conditions (8, 9).

© 1999 NRC Canada

Scheme 2.

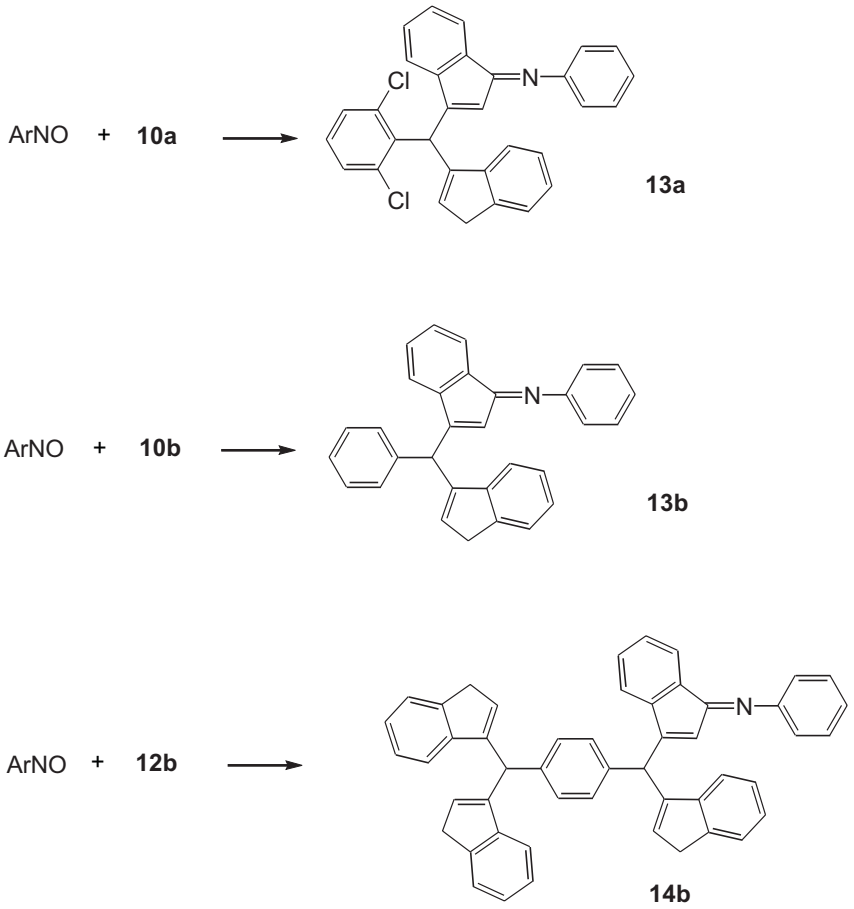

Scheme 3.

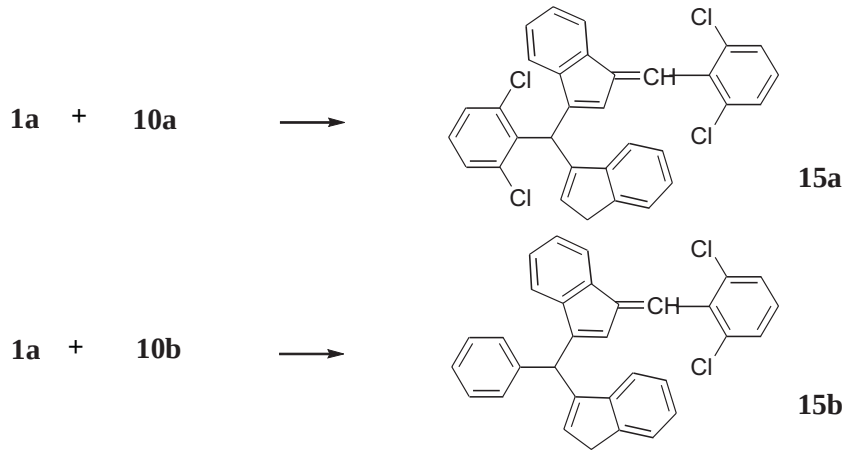

Chain reactions initiated by electrochemical reduction of aromatic aldehydes

It has long been known that indene or fluorene can be added to aldehydes, mainly aromatic aldehydes in the presence of a basic catalyst like potassium hydroxide (10, 11), sodium hydroxide (12, 13), KF-Al_2O_6 (14), or benzyltrimethylammonium hydroxide (triton B) (11).

As mentioned in the introduction, the reaction between InH_2 and aromatic aldehydes (ArCHO), initiated by electroreduction of the aldehyde, can give ArCH=In and (or) $ArCH(InH)_2$ through chain reactions. The latter was obtained after keeping the electrolysis solution at room temperature for several hours (1). The longer the standing time, the higher the yield of $ArCH(InH)_2$ (1).

We have examined the electrochemical behavior of aromatic aldehydes **1a**, **1b**, and **2** in the presence of proton donors **10a**, **10b,**or **12b** ($In'H_2$) in DMF 0.2 M Bu_4NPF_6 as supporting electrolyte with the aim of synthesizing the cor-

© 1999 NRC Canada

Scheme 4.

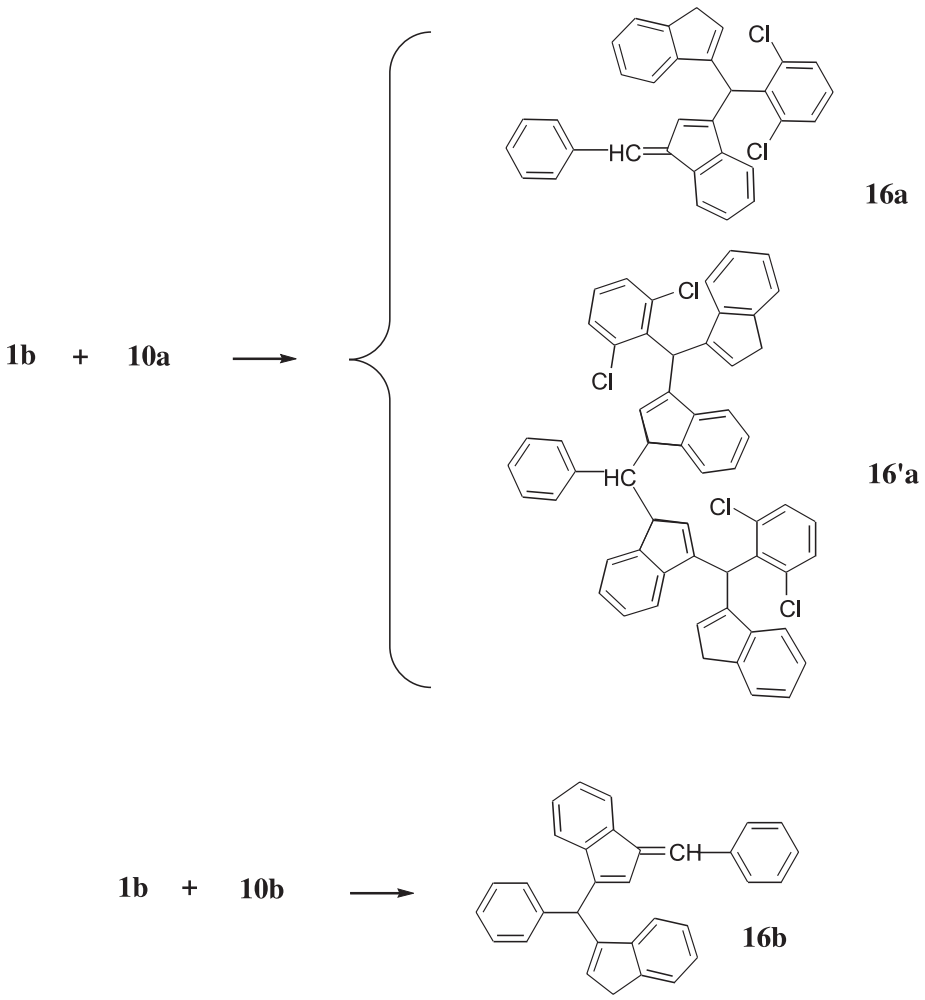

Table 2. Controlled potential electroreduction of aromatic aldehydes ArCHO in the presence of protons donors $In'H_2$ on a mercury electrode in DMF/$(n\text{-Bu})_4NPF_6$ (0.2 M) at –30°C followed by keeping the solution stand at room temperature for several hours.[a]

Entry	ArCHO	E_w[b] (V)	$In'H_2$	$In'H_2$/ArCHO (molar ratio)	mol e/mol ArCHO ($\times 10^2$)	Solution color	Standing time (h)	Product(s)	(% yield)
1	**1a**	–1.6	**10a**	4	11	Blue	24	**15a** (29)	
2	**1a**	–1.6	**10b**	5	5	Blue	20	**15b** (14)	
3	**1b**	–2	**10a**	4	8	Green	60	**16a** (9)	**16′a** (12)
4	**1b**	–2	**10b**	3.5	10	Blue	19	**16b** (10)	
5	**2**	–1.2	**10a**	6	4	Green	24	**17a** (19)	
6	**2**	–1.2	**10b**	6	4	Green	72	**17b** (8)	**17′b** (10)

[a]The electrolyses were carried out under argon and the electrolysis solution was kept under argon after the current dropped to zero.
[b]Working potential vs. SCE.

responding hydrocarbons ArCH=In′H (see for instance **15a**, **15b**, **16a**, **16b**, **17a**, and **17b** in Schemes 3–5). The controlled potential reduction of these aromatic aldehydes at –30°C consumed a catalytic amount of electricity varying from 0.11 to 0.04 equiv. of electron (see Table 2), indicating that a chain reaction occurred as with FlH_2 and InH_2. The electrolyzed solutions were then kept under argon at room temperature for 19–72 h before extraction to ensure a complete dehydration of the carbinols formed initially. After appropriate work-up and chromatographic separation, the hydrocarbons **15a** and **15b** (see Scheme 3) were obtained in low yields (29 and 14%, respectively) from reduction of **1a** in the presence of an excess of **10a** or **10b**, respectively (entries 1 and 2). Compounds **15a** and **15b** were characterized by mass spectrometry (see Table 3) and microanalysis (see Table 4). Only one isomer of **15a** and **15b** was isolated but its configuration (*E* or *Z*) could not be assigned.

The two other aldehydes **1b** and **2** behave similarly as aldehyde **1a**, giving products of addition involving the methylene groups of **10a** and **10b** (see Schemes 4 and 5) in the yields indicated in Table 2 (entries 3–6).

© 1999 NRC Canada

Scheme 5.

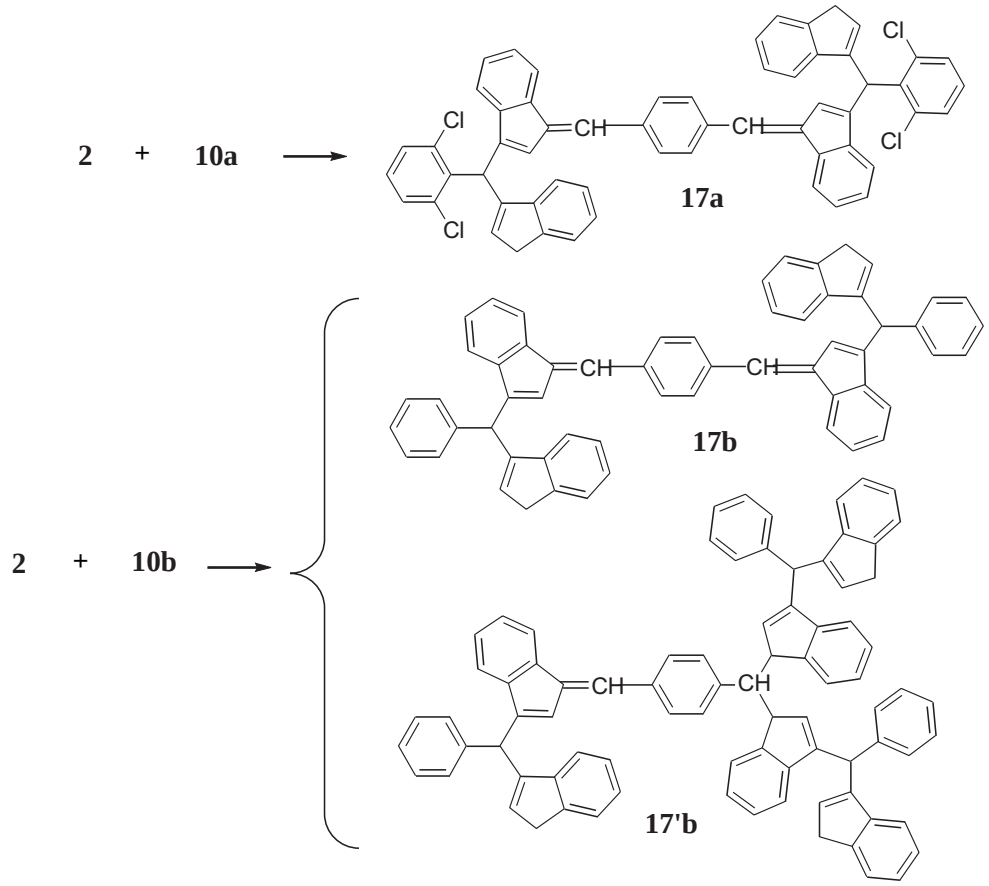

Interestingly, the reaction between **1b** and **10a** (Scheme 4) and between **2** and **10b** (Scheme 5) led to derivatives **16′a** (12% yield, entry 3) and **17′b** (10% yield, entry 6), respectively, after very long standing times (60 and 72 h). The formation of **16′a** can be explained by addition of **10a** onto **16a** and that of **17′b** by addition of **10b** onto **17b**.

The mechanism of formation of all compounds in Tables 1 and 2 involves base catalysed additions (chain reactions) of the type previously described for the formation of ArCH=In and $ArCH(InH)_2$ by electrochemical reduction of ArCHO in the presence of excess InH_2 (1).

Structure of products

To our knowledge all compounds are new. Imine derivatives ArN=In′ and hydrocarbon derivatives were characterized by mass spectrometry (see Table 3) and microanalytical data (see Table 4). In mass spectrometry, the molecular ion peak was observed for all derivatives (see Table 3).

Experimental part

The apparatus and techniques have been described previously (1). The reference electrode was an aqueous saturated calomel electrode (SCE) separated from the solution by a sintered glass disk. 2,6-Dichlorobenzaldehyde (**1a**), benzaldehyde (**1b**), terephtalaldehyde (**2**), and nitrosobenzene were commercially available products.

Typical electrolysis procedure

Formation of imine ArN=In′

Nitrosobenzene (75 mg, 0.6425 mmol) was electrolyzed on a mercury electrode at –0.95 V vs. SCE with **10a** (1 g, 2.57 mmol) in DMF (25 mL) containing $(n\text{-Bu})_4NPF_6$ (0.2 M) under argon atmosphere. The electrolysis was stopped when the current dropped to zero (0.06 electron per molecule of ArNO). The electrolyzed solution was stirred at room temperature under argon during 67 h (the color turned from brown to red) then poured into water and extracted with dichloromethane. Chromatography on silica gel with hexane–dichloromethane (1.85:1) as eluent gave compound **13b** in 21% yield.

Formation of derivative ArCH=In′

Benzaldehyde **1b** (95 μL, 0.90 mmol) was electrolyzed on a mercury electrode at –2 V vs. SCE with **10b** (1.01 g, 3.15 mmol) in DMF (25 mL) containing $(n\text{-Bu})_4NPF_6$ (0.2 M) under argon atmosphere. The electrolysis was stopped when the current dropped to zero (0.1 electron per molecule of ArCHO). The electrolyzed solution was stirred at room temperature under argon during 19 h (the color turned from green–brown to blue) then poured into water and extracted with dichloromethane. Chromatography on silica gel with pentane–acetone (9:1) as eluent gave compound **16b** in 10% yield.

© 1999 NRC Canada

Table 3. Mass spectrometry data.

Product	Molecular ion peak *m/z* (relative intensity, %)	Other peaks *m/z* (relative intensity, %)		
13a	477 (100)	442 (23)	385 (32)	115 (18)
			– C_6H_5NH	– InH
13b	409 (100)	294 (20)	115 (9)	
		– InH	– InH	
14b	651 (10)	448 (12)	332 (8)	115 (100)
		– $C_{15}H_9N$	– $C_{15}H_9N$	– InH_2
			– InH	
15a	544 (73)	474 (5)	385 (53)	115 (6)
		– Cl_2	– $C_7H_5Cl_2$	– InH
15b	476 (100)	361 (36)	205 (40)	
		– InH	– C_7H_6	
			– InH	
16a	476 (72)	385 (15)	115 (6)	
		– C_7H_7	– InH	
16′a	865 (5)	750 (2)	388 (43)	115 (35)
		– InH	$C_6H_5Cl_2CH(InH)_2$	– InH
16b	408 (100)	317 (50)	293(25)	
		– C_7H_7	– InH	
17a	874 (16)	115 (100)		
		– InH		
17b	738 (100)	623 (8)	115 (15)	
		– InH	– InH	
17′b	1058 (1)	944 (1)	738 (6)	205 (100)
		– In	– $C_6H_5CH(InH)_2$	$C_6H_5CH(InH)$

Table 4. Eluents for chromatographic separation, solvents for recrystallization, melting points, and microanalytical data.[a]

Product	Chromatography eluent	Recrystallization solvent	Melting point (°C)	Molecular formula	Microanalytical data					
					C (%)		H (%)		N (%)	
					Calcd.	Found	Calcd.	Found	Calcd.	Found
13a	1:CH_2Cl_2 1.85:hexane	—	118–125	$C_{31}H_{21}Cl_2N$	77.83	77.67	4.42	4.94	2.93	2.71
15a	1:CH_2Cl_2 4:hexane	Hexane/CH_2Cl_2	210	$C_{32}H_{20}Cl_4$	70.58	69.99	3.67	3.52		
15b	1:CH_2Cl_2 4:hexane	Hexane/CH_2Cl_2	172	$C_{32}H_{22}Cl_2$	80.67	80.22	4.62	4.64		
16a	1:CH_2Cl_2 4:hexane	Hexane	142–143	$C_{32}H_{22}Cl_2$	80.67	80.32	4.62	4.61		
16′a	1:CH_2Cl_2 4:hexane	Hexane	143–144	$C_{57}H_{40}Cl_4$	78.98	79.60	4.65	5.21		
16b	1:acetone 9:pentane	C_2H_5OH/H_2O	79	$C_{32}H_{24}$	94.11	93.36	5.88	5.78		
17a	1:CH_2Cl_2 2.33:hexane	Hexane/CH_2Cl_2	215	$C_{58}H_{38}Cl_4$	79.63	79.16	4.34	4.33		
17b	1:CH_2Cl_2 4:hexane	Hexane/CH_2Cl_2	146–148	$C_{58}H_{42}$	94.27	93.80	5.73	6.04		
17′b	1:CH_2Cl_2 4:hexane	Hexane/CH_2Cl_2	158	$C_{83}H_{62}$	94.10	93.89	5.90	6.25		

[a]Compounds **13b** and **14b** gave the correct ion peak in mass spectrometry (Table 3), but their microanalysis gave nonreproducible results. These microanalysis data are not included.

© 1999 NRC Canada

Acknowledgements

We are grateful to M.T. Compain for her technical assistance. We acknowledge financial support from the Ministère des Relations Internationales du Québec, the Fonds pour la Formation de Chercheurs et d'Aide à la Recherche (FCAR) du Québec, and the Natural Sciences and Engineering Research Council of Canada.

References

1. J.C. Gard, F. Williot, M. Bernard, P. Richard, M. Kubicki, D. Lucas, Y. Mugnier, and J. Lessard. New. J. Chem. **21**, 929 (1997).
2. J.C. Gard, B. Hanquet, Y. Mugnier, and J. Lessard. J. Electroanal. Chem. **365**, 299 (1994).
3. J.C. Gard, B. Hanquet, Y. Mugnier, and J. Lessard. Can. J. Chem. **74**, 55 (1996).
4. M.R. Asirvatham and M.D. Hawley. J. Electroanal. Chem. **57**, 179 (1974).
5. Y. Mugnier, J.C. Gard, Y. Huang, Y. Couture, A. Lasia, and J. Lessard. J. Org. Chem. **58**, 5329 (1993).
6. Y. Mugnier, E. Laviron, Y. Huang, and J. Lessard. J. Electroanal. Chem. **297**, 529 (1991).
7. P. Erlich and F. Sachs. Chem. Ber. **32**, 2341 (1899).
8. R.C. Azzam. Egypt. Acad. Sci. Proc. **9**, 89 (1953).
9. P.A.S. Smith. The chemistry of open-chain organic nitrogen compounds. Vol. 1.. W.A. Benjamin, Inc., New York. 1965. p. 368, and refs. therein.
10. E. Ghera and Y. Sprinzak. J. Am. Chem. Soc. **82**, 4945 (1960).
11. G. Kresze, H.G. Henkel, and H. Goetz. Ann. **18**, 674 (1964).
12. M. Avranoff and Y. Sprinsak. J. Am. Chem. Soc. **82**, 4953 (1960).
13. A. Sieglitz. Ber. Dtsch. Chem. Ges. B, **52**, 1513 (1919).
14. D. Villemin and M. Ricard. Tetrahedron Lett. **25**, 1059 (1984).

© 1999 NRC Canada

The photochemistry of 4-halobenzonitriles and 4-haloanisoles with 1,1-diphenylethene in methanol. Homolytic cleavage versus electron-transfer pathways[1]

Dino Mangion and Donald R. Arnold

Abstract: The photochemical reactivity of a series of 4-halobenzonitriles and 4-haloanisoles with 1,1-diphenylethene in a nucleophilic solvent (methanol) has been investigated. Analysis of the photochemical reactions involving the 4-halobenzonitriles revealed formation of alkene–methanol adducts, such as 1-methoxy-2,2-diphenylethane, 1-methoxy-2,2-diphenylethene, and 1,1-dimethoxy-2,2-diphenylethane, indicative of a photochemical electron-transfer mechanism. These products were not significant in the photochemical reactions involving the 4-haloanisoles. Both the 4-halobenzonitriles and the 4-haloanisoles produced an arene–alkene–methanol Markovnikov adduct, 1-aryl-2-methoxy-2,2-diphenylethane (aryl = 4-cyanophenyl or 4-methoxyphenyl). This compound was shown to undergo an acid-catalysed elimination to 1-aryl-2,2-diphenylethene under the reaction conditions, which subsequently underwent a 6π-electrocyclization to the 3-substituted(cyano or methoxy)-9-phenylphenanthrene. Possible mechanisms for the observed reactivity are discussed and evaluated.

Key words: photochemistry, photoinduced electron transfer, bond homolysis, radical ions, radicals, exciplexes.

Résumé : On a étudié la réactivité photochimique d'une série de 4-halogénobenzonitriles et de 4-halogénoanisoles avec le 1,1-diphényléthène, dans un solvant nucléophile (méthanol). L'analyse des réactions photochimiques impliquant les 4-halogénobenzonitriles a mis en évidence la formation d'adduits alcène–méthanol, tels que les 1-méthoxy-2,2-diphényléthane, 1-méthoxy-2,2-diphényléthène et 1,1-diméthoxy-2,2-diphényléthane; ces résultats suggèrent que le mécanisme de la réaction implique un transfert photochimique d'électron. Dans les réactions impliquant les 4-halogénoanisoles, la formation de ces produits n'est pas importante. Les 4-halogénobenzonitriles ainsi que les 4-halogénoanisoles conduisent tous à la formation d'un produit d'addition arène–alcène–méthanol selon la règle de Markovnikov, soit le 1-aryl-2-méthoxy-2,2-diphényléthane (aryl = 4-cyanophényl ou 4-méthoxyphényl). Il a été démontré que, dans les conditions de la réaction, ce produit subit une élimination acidocatalysée qui conduit au 1-aryl-2,2-diphényléthène et que ce dernier subit ensuite une électrocyclisation-6π avec formation d'un 9-phénylphénanthrène portant un substituant (cyano ou méthoxy) en position 3. On discute et on évalue divers mécanismes possibles pour la réactivité observée.

Mots clés : photochimie, transfert d'électron photoinduit, homolyse d'une liaison, ions radicaux, radicaux, exciplexes.

[Traduit par la Rédaction]

Introduction

A considerable portion of our recent research effort has been directed towards the elucidation of the electron-transfer photochemistry involving cyanoarene electron acceptors, olefinic electron donors, and nucleophiles (1, 2). Our most notable contribution in this area has been the development of the photoinduced nucleophile addition to aryl olefins (1) and the photochemical nucleophile–olefin combination, aromatic substitution (photo-NOCAS) reaction (2). The mechanisms for these reactions are well understood, as illustrated in Scheme 1. Both the photoinduced nucleophile addition to olefins and the photo-NOCAS reaction start off along a common mechanistic route and diverge along their specific pathways at a later stage, depending on the nature of the olefin.

Irradiation of the mixture of reactants leads initially to electronic excitation of the cyanoarene, here exemplified by 1,4-dicyanobenzene, to its first excited singlet state. Electron transfer with a ground state olefin gives a pair of radical ions. The olefinic radical cation may be trapped by the nucleophile, typically methanol, to give the more stable β-alkoxy radical. It is at this stage that the two reaction pathways diverge. If the olefin is aromatic, the β-alkoxy radical will have a reduction potential, which is low enough to al-

Received May 14, 1999.

D. Mangion and D.R. Arnold.[2] Department of Chemistry, Dalhousie University, Halifax, NS B3H 4J3, Canada.

[1]This is Part 47 of the series Radical Ions in Photochemistry. See refs. 1 and 2 for preceeding parts of this series.

[2]Author to whom correspondence may be addressed. Telephone: (902) 494-3714. Fax: (902) 494-1310. e-mail: arnold@ac.dal.ca

© 1999 NRC Canada

Scheme 1. Mechanism for the photoinduced nucleophile addition (R = aromatic) and photo-NOCAS reaction (R = aliphatic).

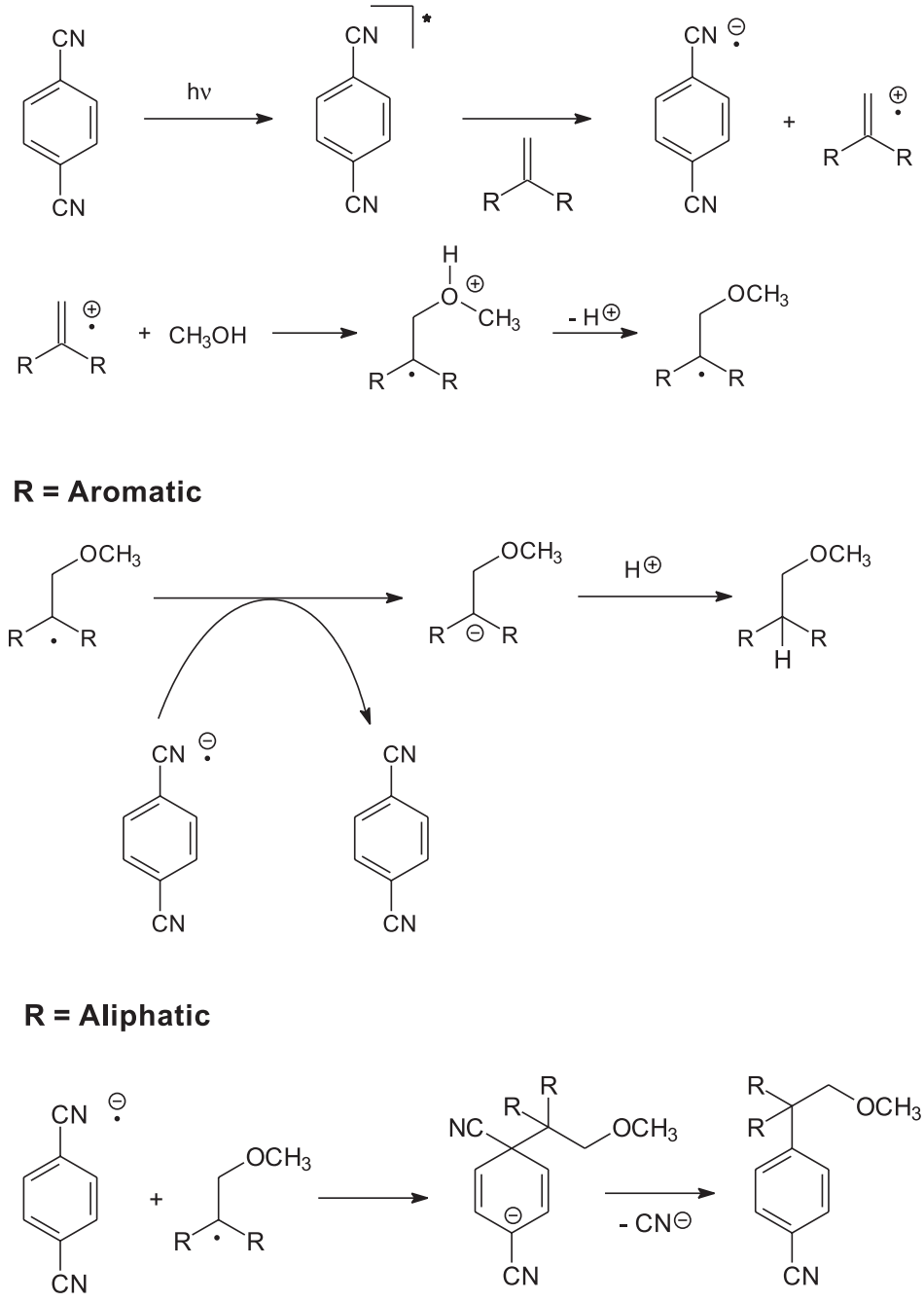

low reduction to the corresponding anion by the cyanoarene radical anion. The resulting β-alkoxy anion is subsequently protonated to give the ether product. On the other hand, if the olefin is aliphatic, then the intermediate β-alkoxy radical cannot be reduced to the corresponding anion; instead, the radical will add to the *ipso* position of the cyanoarene, expelling cyanide anion in order to rearomatize, and thus furnish the photo-NOCAS product. In both cases, the overall regioselectivity of the methanol addition is *anti*-Markovnikov; this is a direct consequence of the involvement of the olefin radical cation.

The scope and limitations of these reactions have been thoroughly investigated and documented, particularly with respect to the olefin and the nucleophile. Not much is known, however, about varying the electron acceptor, which in the past has invariably been a cyanoarene, commonly 1,4-dicyanobenzene, 1,4-dicyanonaphthalene, or 9,10-dicyanoanthracene.

The reasons for selecting these cyanoaromatics are manifold. The cyano function is strongly electron-withdrawing, imparting low reduction potentials to these compounds and thus making them good electron acceptors for the photoinduced electron transfer (PET) process. Unlike most other electron-withdrawing groups (such as carbonyl and nitro functions), the cyano group has no low-lying excited state of its own, and therefore, it does not exhibit its own

© 1999 NRC Canada

Scheme 2. Envisaged mechanism for the photochemical reaction between a cyanoarene bearing a cleavable group (X), an olefin, and methanol (CRIP, contact radical ion pair; SSRIP, solvent separated radical ion pair; FRI, free radical ions).

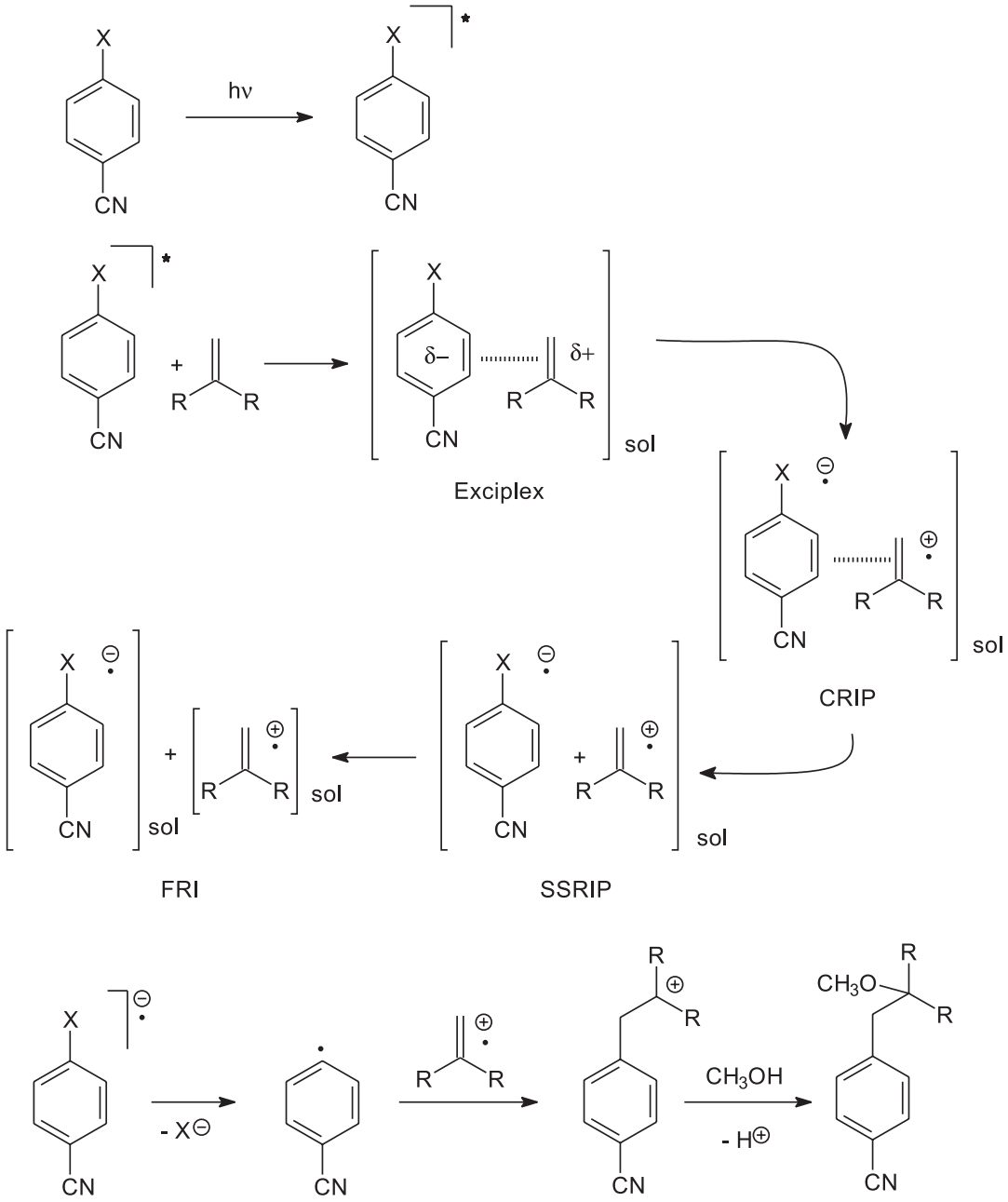

photochemistry. Furthermore, the cyanoarene radical anions resulting from the PET process are relatively stable and long-lived (as is evidenced by their fully reversible cyclic voltammetric scans), making the cyanoarenes particularly suitable as photosensitizers. In addition, when incorporated in the product (example, the photo-NOCAS reaction) the cyano substituent is a versatile function that can be readily converted into various other useful groups.

The aim of our current research is to investigate the effect of different electron acceptors on the outcome of these photochemical reactions. In particular, we are interested in altering the sequence of events in the mechanistic scheme by utilizing an electron acceptor that possesses an unstable, readily cleavable, radical anion. Rapid cleavage of the radical anion within the solvent cage would lead to the formation of an aryl radical in the vicinity of the olefinic radical cation. These highly reactive intermediates are expected to combine to give the more stable adduct cation, which will subsequently be trapped by a nucleophile, such as methanol, to give the final adduct. The proposed mechanism is illustrated in Scheme 2, utilizing a benzonitrile with a cleavable group (X) as the model compound.

The compounds selected for this investigation are a series of 4-halobenzonitriles (**1a**–**4a**), ranging from 4-fluoro- (**1a**) to 4-iodobenzonitrile (**4a**) (Fig. 1). There is considerable evidence in the literature that the radical anions of these species are unstable, due to cleavage of the aryl–halogen bond, giving the aryl radical and the corresponding halide anion

© 1999 NRC Canada

Fig. 1. Reactants (**1–7**) and products (**8–19**).

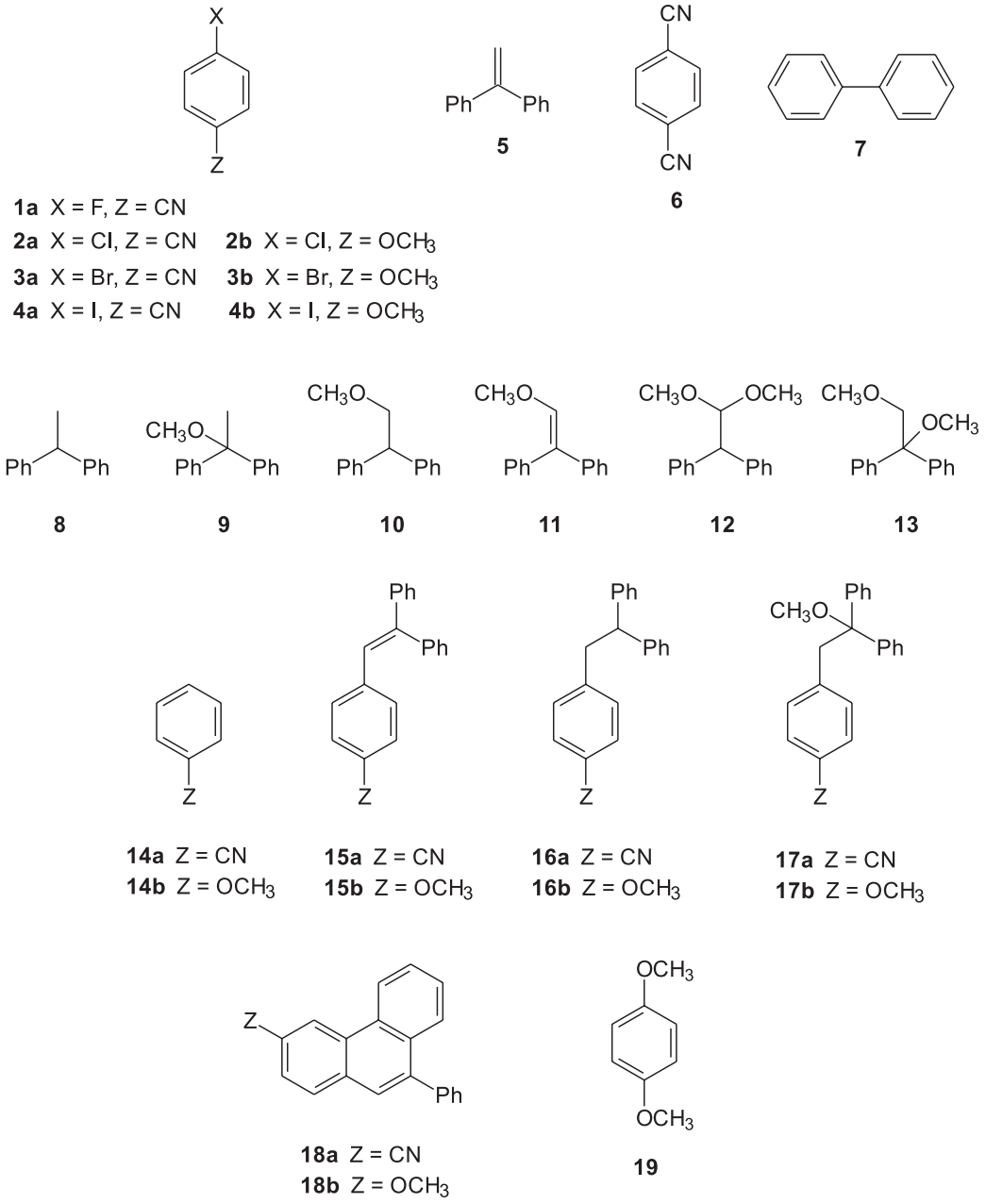

(3). Cleavage of haloarene radical anions has been extensively studied, primarily in connection with the photochemical (4) and electrochemical (5) unimolecular nucleophilic substitution reaction (via a radical intermediate; $S_{RN}1$). The olefin chosen as the model electron donor was 1,1-diphenylethene (**5**). A series of 4-haloanisoles (**2b**–**4b**), which are not expected to function as electron acceptors in the PET process, have also been investigated under similar conditions to provide additional insight into the mechanism.

Results

Irradiation of a methanol solution of 4-fluorobenzonitrile (**1a**) and 1,1-diphenylethene (**5**) leads solely to photoproducts (**8**–**10**) derived from the olefin without incorporation of the benzonitrile (Table 1, Reaction 1). The lack of photoreactivity of the fluoroarene **1a** was also observed upon irradiating **1a** in the absence of **5** in methanol using Pyrex ($\lambda > 280$ nm) or Quartz ($\lambda > 190$ nm) filters — no consumption of **1a** was observed in either case (Table 1, Reaction 2). In an attempt to explain the photoproducts observed in Reaction 1 and to define any alternative photochemical reactions of **5**, the olefin was irradiated in methanol in the absence of any cyanoarene (Table 1, Reaction 12). This led to a sluggish reaction, which delivered 1-methoxy-1,1-diphenylethane (**9**, 33%), 1,1-diphenylethane (**8**, 11%), and 1-methoxy-2,2-diphenylethane (**10**, 3%), as well as substantial polymerization after prolonged irradiation. This observation is in accord with results from a similar study reported in the literature (6). Furthermore,

© 1999 NRC Canada

Table 1. Photochemical reactions of cyanoarenes (**1a**–**4a**, **6**) and olefins (**5**, **10**, **15a**).

Reaction number	Cyanoarene (% consumed)	Olefin (% consumed)	% yield of products										
			8	**9**	**10**	**11**	**12**	**13**	**14a**	**15a**	**16a**	**17a**	**18a**
1	**1a** (0)	**5** (67)	2	10	21	—	—	—	—	—	—	—	—
2	**1a** (0)	—	—	—	—	—	—	—	—	—	—	—	—
3	**2a** (46)	**5** (78)	<2	2	26	7	6	2	—	3	12	17	—
4	**2a** (0)	—	—	—	—	—	—	—	—	—	—	—	—
5	**3a** (54)	**5**(90)	<2	2	17	4	5	<2	13	5	8	11	4
6	**3a** (100)	—	—	—	—	—	—	—	71	—	—	—	—
7	**4a** (100)	**5** (88)	<2	2	12	11	19	<2	23	38	5	5	21
8	**4a** (89)	—	—	—	—	—	—	—	85	—	—	—	—
9	—	**15a** (0)	—	—	—	—	—	—	—	—	—	—	—
10	**2a** (0)	**15a** (0)	—	—	—	—	—	—	—	—	—	—	—
11	**4a** (72)	**15a** (98)	—	—	—	—	—	—	80	—	—	—	98
12	—	**5** (81)	11	33	3	—	—	—	—	—	—	—	—
13[a]	**6** (8%)	**5** (100)	—	7	83	2	—	—	—	—	—	—	—
14	—	**11** (86)	—	—	—	—	40	23	—	—	—	—	—
15[a]	**6** (0)	**11** (92)	—	—	—	—	85	2	—	—	—	—	—

[a]Reactions contained biphenyl (**7**) as co-donor.

irradiation in the presence of the bona fide PET sensitization pair, 1,4-dicyanobenzene (**6**) and biphenyl (**7**), delivered ether **10** (83%), together with **9** (7%) and 1-methoxy-2,2-diphenylethene (**11**, 2%) (Table 1, Reaction 13). This reaction provides an enhanced yield as a result of the added co-donor **7** (1*a*).

Similar irradiation of a mixture of 4-chlorobenzonitrile (**2a**) and alkene **5** in methanol (Table 1, Reaction 3) afforded a series of olefin–methanol adducts — **9** (2%), **10** (26%), **11** (7%), and the diethers **12** (6%) and **13** (2%). In addition, products incorporating the 4-cyanophenyl moiety were now formed. The major adduct was 1-(4-cyanophenyl)-2-methoxy-2,2-diphenylethene (**17a**, 17%), with lesser amounts of 1-(4-cyanophenyl)-2,2-diphenylethane (**16a**, 12%) and 1-(4-cyanophenyl)-2,2-diphenylethene (**15a**, 3%). Adducts **16a** and **17a** are, to the best of our knowledge, new compounds.

To determine the mechanism for the formation of the diethers **12** and **13**, the methoxyalkene **11** was independently synthesized and subsequently subjected to irradiation in methanol (Table 1, Reaction 14). Under these conditions, **11** yielded 40% of the 1,1-diether **12** and 23% of the 1,2-isomer **13**. Furthermore, irradiation of **11** in the presence of the 1,4-dicyanobenzene (**7**) – biphenyl (**8**) PET-sensitization pair yielded 85% of **12** and 2% of **13** (Table 1, Reaction 15).

Irradiation of 4-bromobenzonitrile (**3a**) together with the olefin **5** gave a series of photoproducts similar to that obtained with the chloro derivative **2a** (Table 1, Reaction 5). In addition to the products observed previously, a considerable amount of benzonitrile (**14a**, 13%) was obtained as well as an additional product, identified as 3-cyano-9-phenylphenanthrene (**18a**, 4%). The structure of this new compound was firmly established by single-crystal X-ray crystallographic analysis (Fig. 2).[3]

Irradiation of 4-iodobenzonitrile (**4a**) in the presence of **5** resulted in a similar series of photoproducts. In this case, the major products were **15a** (38%) and **18a** (21%) (Table 1, Reaction 7).

Irradiation of the halobenzonitriles **2a**–**4a** in the absence of olefin **5** did not lead to any consumption of the starting material in the case of **2a** (Table 1, Reaction 4) but resulted in essentially quantitative conversions of **3a** and **4a** to benzonitrile (**14a**) (Table 1, Reactions 6 and 8).

The formation of **18a** was investigated by subjecting a pure sample of **15a** to irradiation in methanol. Alkene **15a** remained unconsumed when irradiated on its own (Table 1, Reaction 9) or in the presence of chlorobenzonitrile **2a** (Table 1, Reaction 10). However, **15a** was quantitatively converted (98%) to **18a** upon irradiation in the presence of **4a** (Table 1, Reaction 11). The 4-iodobenzonitrile (**4a**) was largely converted to benzonitrile (**14a**, 80%) under these conditions.

The 4-haloanisoles (**2b**–**4b**) were subjected to similar photochemical reaction conditions. Irradiation of 4-chloroanisole (**2b**) and olefin **5** in methanol led to a small amount of alkene:methanol adducts **9** (5%) and **10** (5%), together with a series of products incorporating the 4-methoxyphenyl moiety. 1-(4-Methoxyphenyl)-2,2-diphenylethene (**15b**) was the major product (40%), but considerable amounts of anisole (**14b**, 14%), 1-(4-methoxyphenyl)-2-methoxy-2,2-diphenylethane (**17b**, 4%), and 3-methoxy-9-phenylphenanthrene (**18b**, 8%) were also formed (Table 2, Reaction 16). Only a trace of 1-(4-methoxyphenyl)-2,2-diphenylethane (**15b**) was observed and its identification rests solely, though convincingly, on

[3] Crystallographic data has been deposited as supplementary material and may be purchased from: The Depository of Unpublished Data, Document Delivery, CISTI, National Research Council Canada, Ottawa, Canada, K1A 0S2. Details of data collection, structure analysis and refinement, and tables of interatomic distances and bond angles have also been deposited with the Cambridge Crystallographic Data Centre and can be obtained on request from: The Director, Cambridge Crystallographic Data Centre, University Chemical Laboratory, 12 Union Road, Cambridge, CB2 1EZ, U.K.

© 1999 NRC Canada

Fig. 2. Single-crystal X-ray crystallographic structure of 3-cyano-9-phenylphenanthrene (**18a**).

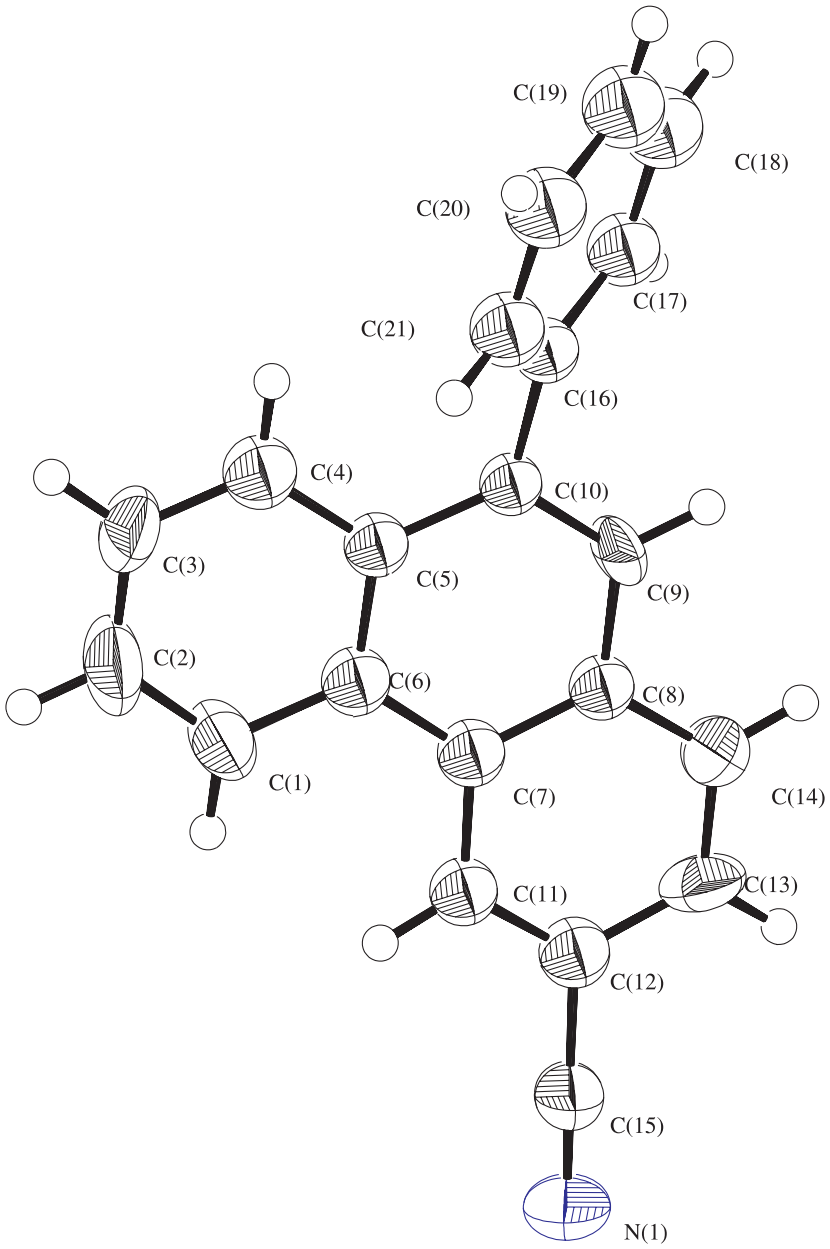

mass spectral data. 4-Bromoanisole (**3b**) and 4-iodoanisole (**4b**) reacted similarly (Table 2, Reactions 18 and 20).

Irradiation of the haloanisoles **2b**–**4b** in the absence of olefin **5** led to rapid consumption of the starting materials, coupled with the formation of **14b** (Table 2, Reactions 17, 19, and 21). In the case of 4-chloroanisole (**2b**), 1,4-dimethoxybenzene (**19**, 12%) was also formed.

Alkene **15b** was synthesized independently and subjected to irradiation in the presence of **4b** in methanol. Under these conditions, **15b** was quantitatively converted to **18b**. This was accompanied by considerable consumption of **4b** and the formation of **14b** (80%).

The ratio of **17**:**15** was observed to decrease in all the haloarene reaction mixtures as the irradiations progressed. This was shown to be due to an acid-catalysed thermal decomposition of **17** to **15**, implying that both **15** and **18** are secondary products, derived from **17**.

Discussion

Even though some of these photoinduced reactions deliver photoproduct **17**, consistent with the envisaged mechanism (Scheme 2), there are indications that in some cases the reaction may be more complex; in fact, an alternative mechanism might be operative. Rapid photoinduced homolytic cleavage of the haloarene carbon–halogen bond might preempt the PET process. Homolytic dissociation would furnish an aryl radical but would not produce the olefin radical cation. The direct photolysis of haloarenes has been extensively investigated, and reactions involving this process have found widespread application as reductive dehalogenation (7) and arylation (8) methods (Scheme 3).

Past studies involving the generation of haloarene radical anions, generally in connection with the $S_{RN}1$ mechanism, have circumvented the problem of competing homolytic

© 1999 NRC Canada

Table 2. Photochemical reactions of methoxyarenes (**2b**–**4b**) and olefins (**5**, **15b**).

Reaction number	Methoxyarene (% consumed)	Olefin (% consumed)	% yield of products								
			8	**9**	**10**	**14b**	**15b**	**16b**	**17b**	**18b**	**19**
16	**2b** (79)	**5** (78)	2	5	5	14	40	<2	4	8	<2
17	**2b** (88)	—	—	—	—	56	—	—	—	—	12
18	**3b** (100)	**5** (69)	—	2	—	29	30	<2	—	13	—
19	**3b** (100)	—	—	—	—	84	—	—	—	—	—
20	**4b** (100)	**5** (49)	—	—	—	22	40	<2	—	16	—
21	**4b** (64)	—	—	—	—	87	—	—	—	—	—
22	**4b** (79)	**15b** (96)	—	—	—	80	—	—	—	94	—

Table 3. Free energy changes ΔG_{PET} for the PET processes between 1,1-diphenylethene (**5**) and the listed electron acceptors (**1**–**4**, **6**).

Electron acceptor	Reduction potential $E_{1/2}^{red}$ (V)[a]	Excitation energy (kJ mol^{-1})		PET free energy ΔG_{PET} (kJ mol^{-1})[b]			Bond dissociation energy C_6H_5-X (kJ mol^{-1})[c]
		Singlet $E_{0,0}^{S}$	Triplet $E_{0,0}^{T}$	Acceptor excited singlet	Acceptor excited triplet	Donor excited singlet	
1,4-Dicyanobenzene (**6**)	–1.66[d]	406[d]	297[e]	–71	+39	–60	—
4-Fluorobenzonitrile (**1a**)	<–2.5	428[f]	324[f]	>–11	>+93	>+21	523 (X = F)
4-Chlorobenzonitrile (**2a**)	–2.07	410[f]	309[f]	–35	+66	–21	398 (X = Cl)
4-Bromobenzonitrile (**3a**)	–2.02	415[f]	308[f]	–45	+62	–26	313 (X = Br)
4-Iodobenzonitrile (**4a**)	–1.87	424[g]	—	–68	—	–40	268 (X = I)
4-Chloroanisole (**2b**)	<–2.5	406[g]	327[h]	>+11	>+90	>+21	398 (X = Cl)
4-Bromoanisole (**3b**)	<–2.5	406[g]	327[h]	>+11	>+90	>+21	313 (X = Br)
4-Iodoanisole (**4b**)	<–2.5	392[g]	—	>+25	—	>+21	268 (X = I)

[a]Measured by cyclic voltammetry vs. Standard Calomel Electrode (SCE) using 0.1 mol dm^{-3} tetraethylammonium perchlorate as supporting electrolyte in deoxygenated acetonitrile. The cathodic waves for the halobenzonitriles were irreversible, and the half-wave reduction potentials, $E_{1/2}^{red}$, were estimated by subtracting 0.03 V from the peak potentials obtained at a scan rate of 100 mV s^{-1} (12). Literature values for comparison include **2a**: –2.03 V (SCE, CH_3CN) (5*d*), –1.88 V (SCE, DMF) (3); **3a**: –1.83 V (SCE. DMF) (3); **4a**: –1.71 V (SCE, DMF) (3).

[b]Calculated using the Weller equation (9): $\Delta G_{PET} = F(E_{1/2}^{ox} - E_{1/2}^{red} - e/4\pi\varepsilon\alpha) - E_{0,0}$ kJ mol^{-1}; $E_{1/2}^{ox}$ for **5** = +1.88 V (SCE, CH_3CN) (13), Coulombic attraction term = 6.1 kJ mol^{-1} in methanol, singlet excitation energy $E_{0,0}^{S}$ for **5** = 396 kJ mol^{-1} (14).

[c]Reference 15.

[d]Reference 2*g*.

[e]Reference 16.

[f]Reference 17.

[g]The $E_{0,0}^{S}$ values for **4a** and **2**–**4b** were determined from the cut-off wavelengths in the electronic absorption spectra.

[h]Reference 18.

Scheme 3. Reductive dehalogenation and arylation reactions initiated by homolytic dissociation of a haloarene ArX (X = halogen).

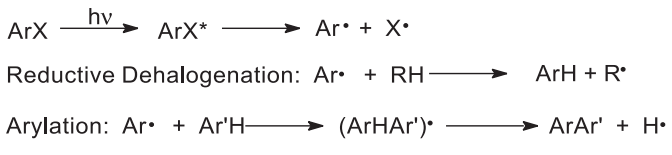

cleavage by avoiding the haloarene excited state. This was achieved by utilizing electrochemical techniques to generate the radical anion (5) or, in photochemical methods, by ensuring selective electronic excitation of the electron donor (commonly an enolate) or of a charge-transfer complex (4). Although PET involving an excited state haloarene has sometimes been proposed as the initiation step for the photochemical reactions, little is known about the exact nature of the photoinitiation mechanism (4*c*).

The primary requirement for an effective PET process involves the energetics. The electron-transfer process, as predicted by the Weller equation (9), must be exergonic. There is, however, a kinetic aspect that has to be considered as well. The lifetime of the excited state, the rate of electron transfer, and the concentration of the other constituent of the electron-transfer pair (i.e., the quencher) are all important in determining whether an excited state can partake in the electron-transfer process. The rate of PET depends on the energetics of the process, with a free energy for the PET process, ΔG_{PET}, more negative than –13 kJ mol^{-1} usually resulting in a diffusion-controlled rate (1.1×10^{10} M^{-1} s^{-1} in methanol) (9).

Examination of the electronic absorption spectra of the haloarenes (**1**–**4**) and 1,1-diphenylethene (**5**) indicates that these species will absorb competitively under the experimental conditions. Hence, it is not readily established which component is the light absorber and which excited state species is thus involved in the PET process (if such a process is occurring). Table 3 lists the calculated free energies, ΔG_{PET}, for the various possibilities. These values suggest that PET should occur at a diffusion-controlled rate with the halobenzonitriles **2a**–**4a** as well as with **6**, but should occur slowly, or not at all, with the fluorobenzonitrile **1a** or with the haloanisoles **2b**–**4b**, irrespective of whether it is the elec-

© 1999 NRC Canada

tron acceptor or the electron donor that is acting from its excited state.

The nature of the excited state is also an important factor. The haloarene singlets are expected to exhibit rapid intersystem crossing rates, i.e., short singlet excited state lifetimes. Chlorobenzene, for example, is reported to have a quantum yield of intersystem crossing of 0.7 (10) and a singlet lifetime of 0.74 ns (11). If we assume these values, we can conclude that, at a quencher concentration of 0.1 mol dm^{-3}, about 50% of the singlet excited states may live long enough to undergo electron transfer; 70% of the unquenched singlets will intersystem cross to the longer lived triplet state, but the loss in excitation energy on crossing to the triplet renders the electron-transfer process prohibitively endergonic (Table 3).

Deciding whether PET or photochemical homolytic dissociation is the predominant mechanism also depends upon the relative rates of the homolytic cleavage and the electron-transfer processes. Here we must recognize that PET is disadvantaged by the fact that this process is bimolecular and is thus restricted by the rate of diffusion through the medium and by the concentration of the electron-transfer partner. The efficiency of this process is also severely hindered by rapid back electron transfer. Homolytic cleavage, in its simplest form, is a unimolecular process, independent of the alkene, its concentration, and its rate of diffusion. One simple method that has been used to predict the likelihood of the homolytic dissociation is comparison of the energy of the reacting exciting state with the bond dissociation energy of the bond to be cleaved. Although the bond dissociation energies of the haloarenes involved in this study are not available, these energies can be approximated to the corresponding values for the halobenzenes (15), as displayed in Table 3. If we assume that the reacting excited state is the triplet then the values indicate that homolytic cleavage will probably be viable for the bromo (**3**) and iodo (**4**) derivatives, but is unlikely for the fluoro (**1**) and chloro (**2**) compounds. In the less probable situation that cleavage is rapid enough to occur from the singlet in competition with intersystem crossing, the chloro (**2**), bromo (**3**), and iodo (**4**) compounds are expected to undergo homolytic dissociation. These postulates were tested by a series of experiments involving irradiation of the haloarenes in pure methanol (Table 1, Reactions 2, 4, 6, and 8; Table 2, Reactions 17, 19, and 21). Whereas the bromo- (**3**) and iodoarenes (**4**) underwent extensive homolysis to give the corresponding dehaloarene (i.e., benzonitrile or anisole), the fluoro- (**1a**) and chlorobenzonitriles (**2a**) were stable under these conditions. These observations suggest that the observed homolysis, in these cases, occurs from the excited triplet state. 4-Chloroanisole (**2b**) exhibited appreciable cleavage despite the unfavourable energetics for the postulated pathway. Such apparently anomalous behaviour has been observed before with compounds such as 4-bromobiphenyl and 1-chloronaphthalene, where cleavage was attributed to the involvement of excimers, which facilitate the homolysis (19). The inefficacy of **2b** to undergo direct homolytic dissociation is highlighted by the formation of 1,4-dimethoxybenzene (**19**) via a photoinduced nucleophilic aromatic substitution (S_NAr) reaction. This reaction has been observed previously (20) and is an indication of the stability of the carbon–chlorine bond towards homolytic cleavage.

One of the strongest pieces of evidence for the PET mechanism is the observed formation, in all the halobenzonitrile reactions (Table 1, Reactions 1, 3, 5, and 7), of the alkene:methanol adduct, 1-methoxy-2,2-diphenylethane (**10**). The *anti*-Markovnikov regiochemistry of this adduct provides strong support for the involvement of the alkene radical cation. The high deuterium incorporation (47–86%) at the bisbenzylic position, when utilizing methanol-*O*-*d* as solvent, is a confirmation that the PET nucleophile addition outlined previously in Scheme 1 is operative. This mechanism requires a secondary electron transfer between the intermediate alkene:methanol adduct radical and the sensitizer radical anion in order to furnish the adduct anion, which is subsequently protonated to give the ether **10** as product. If we approximate the half-wave reduction potential $E_{1/2}^{red}$ of the 2-methoxy-1,1-diphenylethyl radical ($Ph_2C^{\cdot}CH_2OCH_3$) to that of the 1,1-diphenylethyl radical ($Ph_2C^{\cdot}CH_3$), which has been reported by Wayner et al. (21) as –1.34 V vs. SCE, we find that the reduction of the intermediate adduct radical by the sensitizer radical anion is highly exergonic with all the haloarene radical anions.

This process, however, requires the halobenzonitrile radical anion to survive long enough for this secondary electron transfer to occur, which is surprising, particularly since the rates of cleavage of the halobenzonitrile radical anion are extremely rapid in all cases except for the fluoro derivative, which is thought to be stable towards cleavage (although this is still the subject of debate) (22). The rates of cleavage of these radical anions have been determined by Saveant and co-workers (5*c*): 9×10^8 s^{-1} for $\mathbf{2a}^{\cdot-}$, 2×10^9 s^{-1} for $\mathbf{3a}^{\cdot-}$, and 2×10^{10} s^{-1} for $\mathbf{4a}^{\cdot-}$.

There is, however, evidence in the photochemical reactions for these species cleaving prior to the second electron transfer. In the photoreaction involving 1,4-dicyanobenzene (**6**) in methanol-*O*-*d*, the bisbenzylic position of the ether **10** exhibited 96% deuterium incorporation, indicating that reduction of the adduct radical to the corresponding anion and its subsequent protonation is essentially the sole pathway leading to the ether product (Scheme 1). However, in the case of the halobenzonitriles **1a**–**4a**, the deuterium incorporation percentage, albeit high, is appreciably lower (47–86%). This might reflect the unavailability of a proper reducing agent to complete the process. In such a situation, the 2-methoxy-1,1-diphenylethyl radicals have the option to undergo a disproportionation reaction to yield 1-methoxy-2,2-diphenylethane (**10**) (with no deuterium incorporation) and 1-methoxy-2,2-diphenylethene (**11**). In fact, considerable amounts of **11** have been observed in the chloro- (**2a**), bromo- (**3a**), and iodobenzonitrile (**4a**) reactions. This compound was shown to be photochemically active, reacting similarly to **5**. In a control experiment, **11** was observed to undergo an efficient PET methanol addition in the presence of the 1,4-dicyanobenzene (**6**) – biphenyl (**7**) pair, to give 1,1-dimethoxy-2,2-diphenylethane (**12**) in high yield (85%). Furthermore, **11** was shown to undergo methanol addition in the absence of a sensitizer to give the two isomeric diethers **12** and 1,2-dimethoxy-1,1-diphenylethane (**13**). Both of these products are found in the photochemical reactions involving the cleavable halobenzonitriles **2a**–**4a**.

As highlighted in the introduction, the major interest of this study is in those pathways that involve the co-reactivity

© 1999 NRC Canada

Scheme 4. 6π-Electrocyclization of **15** to **18**.

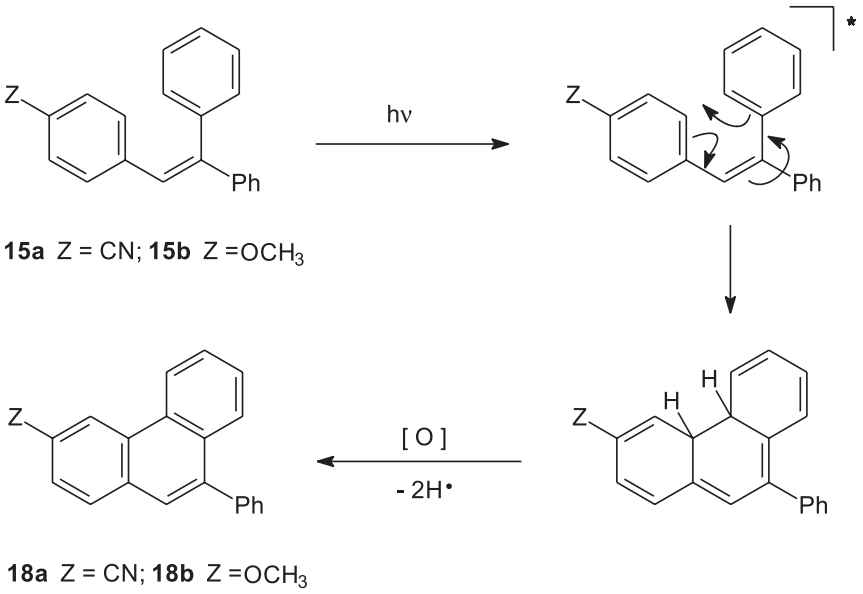

of the haloarene and the incorporation of the aryl moiety in the final products. Such products are absent in the 1,4-dicyanobenzene (**6**) reactions due to the stability of the 1,4-dicyanobenzene radical anion. For similar reasons, or possibly because PET is energetically unfavourable and does not occur, no such products were observed in the 4-fluorobenzonitrile (**1a**) reactions.

Analysis of the other haloarene photoreactions reveals the presence of four products resulting from the co-reaction of the alkene with the aryl fragment (**15**–**18**). In a series of separate experiments using **15a** and **15b** as starting materials, it was established that the phenanthrene derivatives **18a** and **18b** were secondary photoproducts arising from the photoinduced cyclization of **15a** and **15b**, respectively (Scheme 4). This 6π-electrocyclization reaction is well documented (23). Interestingly, this cyclization did not occur if **15a** or **15b** were irradiated in the absence of a haloarene. Addition of 4-chlorobenzonitrile (**2a**) to the solution also failed to affect the photocyclization, and in fact, none of this product was observed in the 4-chlorobenzonitrile (**2a**) photoreactions. However, irradiation of the solution upon addition of the iodoarenes **4a** or **4b** led to a quantitative conversion of **15a**–**b** to the phenanthrene derivatives **18a**–**b**. An explanation for this may be that the 6π-electrocyclization initially yields a 4*a*,4*b*-dihydrophenanthrene derivative that has to be oxidized to the final product. In the absence of a suitable oxidizing agent, this intermediate may undergo a photoinduced electrocyclic ring opening back to the starting material (23*a*). The introduction of **4a**–**b** provides a suitable oxidizing agent in the form of an iodine atom (or molecule) derived from the homolytic cleavage of the parent haloarene. No reactivity is observed in the presence of **2a**; this particular haloarene is resistant to homolytic cleavage and thus fails to provide a suitable oxidizing agent.

Control experiments have established that 1-(4-cyanophenyl)-2,2-diphenylethene (**15a**) and its methoxy analogue **15b** are secondary photoproducts arising from the acid-catalysed elimination of methanol from the corresponding ethers **17a** and **17b**, respectively. This provides a rational explanation for the fact that the ratios **15a**:**17a** and **15b**:**17b** increase in all reactions as the photoreaction proceeds. The photochemical reaction generates a hydrogen halide, and hence, the acidity of the medium increases as the reaction occurs. The larger ratios of **15**:**17** observed on going from chloro- to iodoarene might be due to the relative acidity of these halo acids.

The reactions of the halobenzonitriles are consistent with the previously proposed mechanism involving photoinduced electron transfer (Scheme 2). However, the fact that the 4-haloanisoles (**2b**–**4b**) also undergo an efficient reaction with 1,1-diphenylethene (**5**) to give a similar series of products (Table 2, Reactions 16, 18, and 20), despite unfavourable PET energetics (Table 3), is inconsistent with this mechanism. Therefore, we propose a modified, more general, mechanism in which the haloarene and the alkene initially form an exciplex of varying degree of charge separation, depending upon the constituents. If charge separation is considerable, then this initial exciplex might lead to a PET mechanism as suggested initially (Scheme 2). This will account for the formation of products, such as the alkene:methanol adducts **10**, **11**, and **12**, which are attributed to a PET mechanism. These products are only formed in the halobenzonitrile reactions in which appreciable charge separation is expected.

Alternatively, if charge separation in the exciplex is less favourable, the haloarene may undergo a homolytic dissociation, generating a halogen atom and an aryl radical, which will add to the neutral alkene to give the more stable radical (Scheme 5). This intermediate radical would then be trapped by the halogen atom, to give the 1-aryl-2-halo-2,2-diphenylethane, which may subsequently undergo an S_N1 reaction with methanol to furnish the observed products, ethers **17a**–**b**. This key halogen-containing intermediate compound has not been observed, however, its absence is consistent with its expected high S_N1 reactivity under these reaction conditions.

This exciplex-mediated pathway finds support upon consideration of the photochemistry of 4-chlorobenzonitrile (**2a**). This compound is stable to irradiation, on its own, in

© 1999 NRC Canada

Scheme 5. Proposed mechanism for the formation of products **17a** and **17b**.

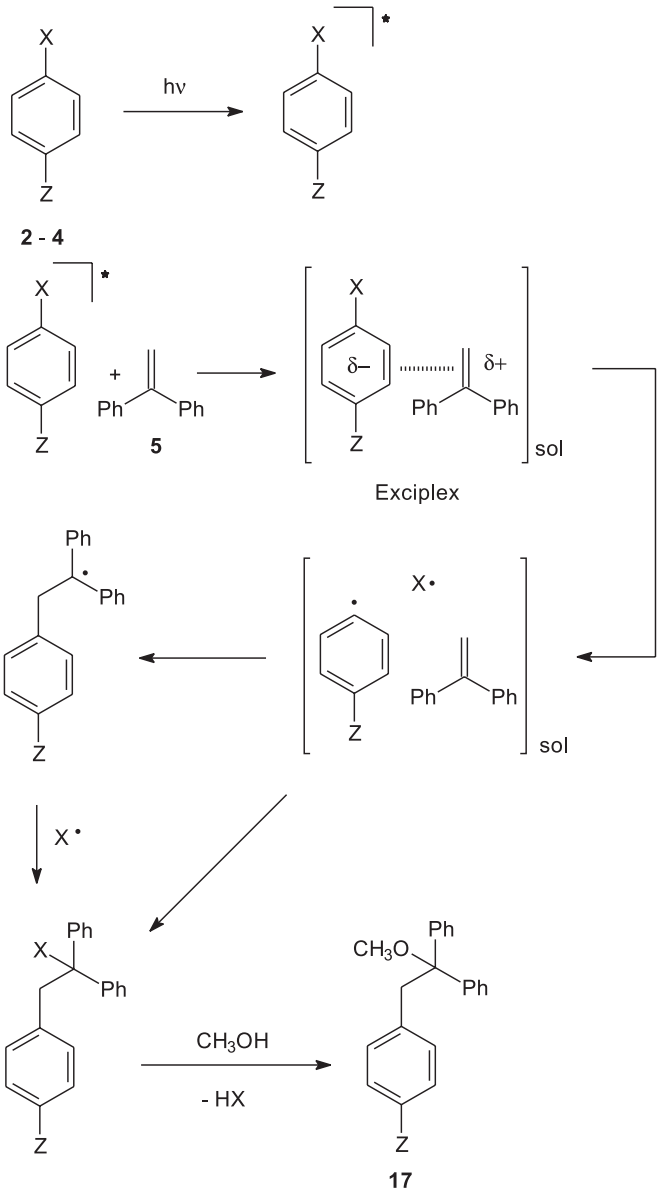

methanol (Table 1, Reaction 4), but does undergo a photoreaction in the presence of **5** (Table 1, Reaction 3), clearly indicating that the latter is necessary for reaction to occur. This rules out the possibility that a straightforward, unassisted homolytic cleavage of the carbon–chlorine bond is taking place in this case. The hypothesis that an exciplex, which activates the otherwise unreactive carbon–halogen bond towards homolysis, is a likely explanation for the observed reactivity. The role of exciplexes in similar situations involving haloarenes has been documented (24). In particular, the enhanced homolysis of the carbon–chlorine bond as a consequence of exciplex formation between chloroarenes and dienes has been firmly established (24*a*, *c*). However, no co-reaction between the two constituents was reported in these studies — the haloarenes were only observed to undergo a reductive dehalogenation.

Other photoproducts that we have observed in small quantities in all the reactions involving cleavable haloarenes are the 1-aryl-2,2-diphenylethanes **16a** and **16b**. Deuterium incorporation studies involving **16a** in methanol-*O*-*d* indicate deuterium incorporation (41–64%) at the bisbenzylic (C-2) position (Table 1, Reactions 3, 5, and 7), suggesting a 2-aryl-1,1-diphenylethyl anion as precursor. The plausible route to this species is via reduction of the corresponding radical (Scheme 6). Calculations suggest that this electron-transfer step is energetically viable when a halobenzonitrile radical anion acts as reducing agent. However, such a situation requires the halobenzonitrile radical anion to survive long enough for the electron transfer to occur. As previously mentioned, this is surprising in view of the short lifetimes of these species. Nevertheless, the variation in the yield of **16** in relation to the different haloarenes investigated does support this hypothesis. The 4-chlorobenzonitrile (**2a**) radical anion, which is the longest lived anion radical among all the cleavable haloarenes studied, does afford the greatest yield of **16a** (12%). This decreases in the case of the bromobenzonitrile **3a** (8%) and further in the case of the iodo derivative **4a** (5%). The haloanisoles **2b**–**4b** furnish only trace amounts (<2%) of the corresponding product **16b**, although in these cases, it is dubious whether the haloanisole radical anions are actually formed. This last point, as well as the incomplete deuterium incorporation in **16a** in the methanol-*O*-*d* reactions, requires a second reaction pathway that does not involve protonation of an anionic precursor. We suggest that this alternative route involves hydrogen atom abstraction by the 2-aryl-1,1-diphenylethyl radical (Scheme 6).

Conclusions

The involvement of a cyanoarene bearing a cleavable group has a drastic effect on the outcome of the photochemical reaction between cyanoarenes, olefins, and nucleophiles. The main photoproduct incorporating the cyanoaromatic moiety, i.e., 1-(4-cyanophenyl)-2-methoxy-2,2-diphenylethane (**17a**), possesses a Markovnikov regioselectivity, in contrast to the *anti*-Markovnikov regioselectivity characteristic of the otherwise similar photo-NOCAS product (2). This is a direct consequence of a different sequence of mechanistic events — cyanoarene moiety reacting with the olefin prior to trapping by the nucleophile, in contrast to the photo-NOCAS reaction where nucleophile and olefin combine before substituting on the cyanoarene.

The observed photoreactions are mechanistically quite complex. There is convincing evidence pointing towards both PET as well as direct photolytic carbon–halogen bond dissociation pathways. Both processes may be occurring competitively. Alternatively, an exciplex-mediated pathway, with varying degrees of charge separation, may be invoked to reconcile the observations, which might appear contradictory when considered from exclusively either the PET or the homolytic cleavage pathway.

Experimental section

General information

Photochemical reactions were monitored and analysed by gas chromatography – mass spectrometry (GC–MS) using an

© 1999 NRC Canada

Scheme 6. Proposed mechanism for the formation of products **16a** and **16b**.

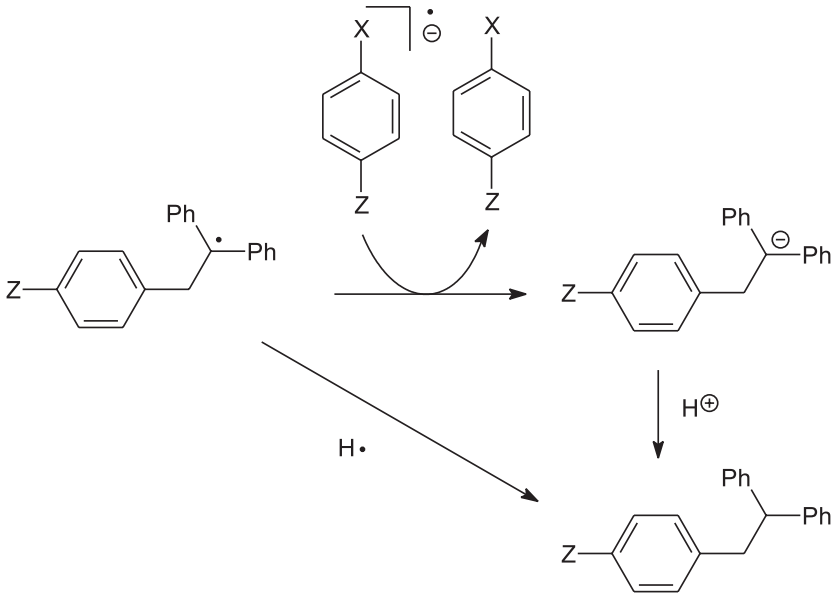

16a Z = CN, **16b** Z = OCH_3

HP 5890 gas chromatograph with a 5% phenylmethylsilicone fused silica WCOT column (25 m × 0.20 mm, 0.33 μm film thickness) and an HP 5970 mass selective detector. Deuterium incorporation studies were performed using single-ion monitoring mass spectrometry (sim-MS). Quantitative gas chromatographic analysis was performed on a Perkin Elmer AutoSystem gas chromatograph equipped with an autosampler, flame ionization detector (fid), and a DB-5 fused silica WCOT column (15 m × 0.25 mm, 1.5 μm film thickness).

Preparative separation of product mixtures was performed using flash chromatography (25) on a 15 × 5 cm silica gel (Aldrich, 230–400 mesh, 60 Å) column. This was generally followed by preparative, centrifugally accelerated, radial, thin-layer chromatography of the partially purified mixtures using a Chromatotron (Harrison Research) on 4, 2, or 1 mm silica gel (Aldrich, TLC grade 7749 with gypsum binder and fluorescent indicator) plates. The mobile phase was typically hexanes with increasing amounts of ethyl acetate. Collected fractions were analyzed by thin-layer chromatography using silica gel plates (Aldrich, 250 μm plate thickness, 5–17 μm, 60 Å, with fluorescent indicator) and (or) GC–MS.

All ^{1}H and ^{13}C NMR spectra were acquired on a Bruker AC 250F spectrometer at 250.13 MHz for ^{1}H and 62.90 MHz for ^{13}C. Chemical shifts are reported in ppm relative to tetramethylsilane (δ = 0 ppm) in ^{1}H NMR spectra and chloroform-*d* (δ = 77.0 ppm) in ^{13}C NMR spectra. Infrared spectra were recorded as films on sodium chloride plates on a Nicolet 205 FT-IR spectrophotometer and are reported in wave numbers (cm^{-1}) calibrated against the 1602 cm^{-1} polystyrene absorption. Ultraviolet-visible absorption spectra were recorded on a Hewlett–Packard (HP) 8452A diode-array spectrophotometer within a resolution of ±1 nm.

Melting points were determined using a Cybron Corporation Thermolyne apparatus equipped with a digital thermocouple (± 0.1°C) and are corrected. Elemental analysis was carried out by Canadian Microanalytical Service Ltd., Delta, B.C. High-resolution mass spectrometry (HRMS) for exact mass determination was performed on a CEC 21-110 mass spectrometer using an electron-impact energy of 70 eV. X-ray crystallographic analysis was performed on a Rigaku AFC5R diffractometer with graphite monochromated Cu-Kα radiation and a 12 kW rotating anode generator.

The cyclic voltammetry was performed on an EG&G PARC Potentiostat Model 173 and an EG&G PARC Universal Programmer Model 175. The measurements were done in a three-electrode electrochemical cell (5 mL volume) equipped with a spherical platinum working electrode, a platinum coil counter electrode, and a saturated calomel reference electrode (SCE). The acetonitrile solutions were deoxygenated by bubbling argon (presaturated with solvent) for 15 min prior to measurement. Tetraethylammonium perchlorate (0.1 mol dm^{-3}) was used as supporting electrolyte. The voltammograms were scanned at 100 mV s^{-1} and calibrated against the 1,4-dicyanobenzene reduction wave at –1.66 V (2*f*). In all cases, the electron transfer was irreversible and the half-wave potential was taken at 0.03 V before the peak potential (12).

Materials

1,4-Dicyanobenzene (98%, Aldrich) was purified by treatment with Norite in methylene chloride, followed by sublimation and recrystallization from 95% ethanol. 4-Iodobenzonitrile (Acros) and 4-bromobenzonitrile (98%, Aldrich) were recrystallized from hexanes while 4-chlorobenzonitrile (99%, Aldrich) was recrystallized from an ethanol–water mixture. Biphenyl (99%, Aldrich) was recrystallized from methanol. 4-Fluorobenzonitrile (99%, Aldrich), 4-chloroanisole (99%, Aldrich), 4-bromoanisole (99%, Aldrich), 4-iodoanisole (99%, Aldrich), and 1,1-diphenylethene (97%, Aldrich) were used as received.

Methanol was purified by reflux and fractional distillation over magnesium and stored over 3 Å molecular sieves (Aldrich). Hexanes for preparative chromatography were

© 1999 NRC Canada

fractionally distilled prior to use while ethyl acetate was used without further purification. Acetonitrile (anhydrous, Aldrich) for electrochemistry was used as received and transferred under nitrogen by cannula.

Irradiations

Investigative irradiations were performed in 2 mL sample volumes in 20 × 0.5 cm tubes using a 1 kW medium-pressure mercury-arc lamp (CGE) fitted with a Quartz water-cooled jacket immersed in a bath at 5°C. Reactions used for quantitative analyses were performed in 10 mL sample volumes in 20 × 1 cm tubes while large-scale preparative photochemical reactions were carried out in 20 × 2 cm tubes. All large-scale and quantitative-analysis reactions were deoxygenated by nitrogen ebullition for 15 min prior to irradiation. Tube distance from lamp axis was ca. 6 cm. Unless otherwise stated, all irradiations were carried out behind Pyrex ($\lambda > 280$ nm).

Dark control experiments were prepared for all major photochemical reaction mixtures. These consisted of solutions identical in composition to the ones being irradiated but stored in the dark. These controls were monitored after a time interval equal to that of the irradiated solutions and in no case was any reactivity observed, except where specifically mentioned.

Reaction details reported below are for the 10 mL quantitative-analysis samples unless otherwise stated. All yields were calibrated with respect to consumed starting material, i.e., the haloarene or 1,1-diphenylethene, depending on whether the product incorporates the 4-cyanophenyl/4-methoxyphenyl group or not. All quantitative-analysis GC runs were done in triplicate. Wherever relevant, isolated yields are also reported.

Irradiation of 1,1-diphenylethene (5) in methanol

A solution of 1,1-diphenylethene (**5**, 0.05 mol dm^{-3}) in methanol (10 mL) was irradiated for 300 h. Calibrated GC-fid analysis indicated that 81% of **5** was consumed, yielding 1,1-diphenylethane (**8**, 11%), 1-methoxy-1,1-diphenylethane (**9**, 33%), and 1-methoxy-2,2-diphenylethane (**10**, 3%). Appreciable polymerization was also noticed.

Pure samples of **8** and **9** were isolated from a large-scale photoreaction (100 mL) identical in composition to the above, while **10** was obtained from an alternative photoreaction (vide infra).

*1,1-Diphenylethane (**8**)*: Isolated yield: 10%, colourless oil. IR (film, NaCl) υ (cm^{-1}): 3061, 3026, 2967, 1600, 1493, 1450, 1026, 699; ^{1}H NMR spectrum in accordance with published data (26): ^{1}H NMR (250.13 MHz, $CDCl_3$, TMS) δ: 1.64 (d, 3H, J = 7.3 Hz), 4.15 (q, 1H, J = 7.3 Hz), 7.13–7.31 (m, 10H); ^{13}C NMR (62.90 MHz, $CDCl_3$) δ: 21.8 (q), 44.7 (d), 126.0 (d), 127.6 (d), 128.3 (d), 146.3 (s); MS *m/z* (rel. int.): 182(35), 167(100), 165(31), 103(5), 82(6).

*1-Methoxy-1,1-diphenylethane (**9**)*: Isolated yield: 22%, colourless oil. IR (film, NaCl) υ (cm^{-1}): 3089, 3059, 3025, 2981, 2935, 2825, 1492, 1446, 1104, 755, 699; ^{1}H NMR spectrum in accordance with published data (6): ^{1}H NMR (250.13 MHz, $CDCl_3$, TMS) δ: 1.56 (s, 3H), 3.16 (s, 3H), 7.22–7.38 (m, 10H); ^{13}C NMR (62.90 MHz, $CDCl_3$) δ: 25.1 (q), 50.6 (q), 80.8 (s), 126.77 (d), 126.74 (d), 127.9 (d), 146.4 (s); MS *m/z* (rel. int.): 212 (3), 197 (100), 180 (19), 165 (32), 135 (53), 105(31), 91(6), 77(53).

Irradiation of 1,4-dicyanobenzene (6), biphenyl (7), and 1,1-diphenylethene (5) in methanol

A solution of 1,4-dicyanobenzene (**6**, 0.02 mol dm^{-3}), biphenyl (**7**, 0.05 mol dm^{-3}), and 1,1-diphenylethene (**5**, 0.05 mol dm^{-3}) in methanol (10 mL) was irradiated for 6 h. Calibrated GC-fid analysis indicated 100% alkene consumption together with a 92% **6** recovery and an 84% **7** recovery. Products resulting from the photoreaction include 1-methoxy-1,1-diphenylethane (**9**, 7%), 1-methoxy-2,2-diphenylethane (**10**, 83%), and 1-methoxy-2,2-diphenylethene (**11**, 2%). A pure sample of **10** was obtained from a large-scale photoreaction (30 mL) identical in composition to the above.

The sim-MS of an identical photoreaction in methanol-*O-d* indicated 96% deuterium incorporation at the bisbenzylic position (C-2) of **10**.

*1-Methoxy-2,2-diphenylethane (**10**)*: Isolated yield: 81%, colourless oil. IR (film, NaCl) υ (cm^{-1}): 3087, 3061, 3027, 2982, 2922, 2874, 1601, 1495, 1451, 1121, 699; ^{1}H NMR spectrum in accordance with published data (27): ^{1}H NMR (250.13 MHz, $CDCl_3$, TMS) δ: 3.36 (s, 3H), 3.92 (d, 2H, J = 7.3 Hz), 4.29 (t, 1H, J = 7.3 Hz), 7.16–7.29 (m, 10H); ^{13}C NMR (62.90 MHz, $CDCl_3$) δ: 51.0 (d), 58.9 (q), 76.0 (t), 126.5 (d), 128.2 (d), 128.4 (d), 142.1 (s); MS *m/z* (rel. int.): 212 (4), 167 (100), 165 (36), 152 (19), 77(7).

Compound **11** was positively identified and characterized by alternative synthesis via a Wittig reaction from benzophenone and methoxymethyltriphenylphosphonium bromide, utilizing a literature procedure with minor modifications (28).

*1-Methoxy-2,2-diphenylethene (**11**)*: Colourless oil. IR (film, NaCl) υ (cm^{-1}): 3055, 3029, 2932, 2836, 1634, 1496, 1447, 1231, 1108, 764, 698; ^{1}H NMR (250.13 MHz, $CDCl_3$, TMS) δ: 3.76 (s, 3H), 6.45 (s, 1H), 7.18–7.40 (m, 10H); ^{13}C NMR (62.90 MHz, $CDCl_3$) δ: 60.6 (q), 120.5 (s), 126.4 (d), 126.6 (d), 127.6 (d), 128.0 (d), 128.2 (d), 128.3 (d), 129.8 (d), 137.6 (s), 140.4 (s), 146.4 (d); MS *m/z* (rel. int.): 210 (100), 167(98), 165(78), 139(7), 115(8), 89(7), 79(4).

Irradiation of 1-methoxy-2,2-diphenylethene (11) in methanol

A solution of 1-methoxy-2,2-diphenylethene (**11**, 0.05 mol dm^{-3}) in methanol (10 mL) was irradiated for 300 h. Calibrated GC-fid analysis of the photolysate indicated that 86% of the starting material (**11**) was consumed, yielding 1,1-dimethoxy-2,2-diphenylethene (**12**, 40%), and 1,2-dimethoxy-1,1-diphenylethane (**13**, 23%).

A pure sample of **13** was obtained from a large-scale photoreaction (60 mL) of identical composition to the above, while a pure sample of **12** was obtained from an alternative photoreaction (vide infra).

*1,2-Dimethoxy-1,1-diphenylethane (**13**)*: Isolated yield: 7%, colourless oil. IR (film, NaCl) υ (cm^{-1}): 3059, 3027, 2981, 2931, 2891, 1493, 1448, 1191, 1130, 1102, 1078, 756, 700; ^{1}H NMR (250.13 MHz, $CDCl_3$, TMS) δ: 3.23 (s, 3H), 3.33 (s, 3H), 4.11 (s, 2H), 7.23–7.38 (m, 10H); ^{13}C NMR (62.90 MHz, $CDCl_3$) δ: 51.6 (q), 59.6 (q), 76.3 (t), 82.2 (s),

© 1999 NRC Canada

127.1 (d), 127.3 (d), 128.0 (d), 143.1 (s); MS *m*/*z* (rel. int.): 210(6), 197(100), 105(71), 77(69).

Irradiation of 1,4-dicyanobenzene (6), biphenyl (7), and 1-methoxy-2,2-diphenylethene (11) in methanol

A solution of 1,4-dicyanobenzene (**6**, 0.02 mol dm^{-3}), biphenyl (**7**, 0.05 mol dm^{-3}), and 1-methoxy-2,2-diphenylethene (**11**, 0.05 mol dm^{-3}) in methanol (10 mL) was irradiated for 10 h. Calibrated GC-fid analysis of the final photolysate revealed that 92% of the starting alkene (**11**) was consumed while 100% of **6** and 79% of **7** remained unreacted. Products observed included 1,1-dimethoxy-2,2-diphenylethane (**12**, 85%) and 1,2-dimethoxy-1,1-diphenylethane (**13**, 2%).

A pure sample of **13** was isolated from a large-scale photoreaction (30 mL) identical in composition to the above.

*1,1-Dimethoxy-2,2-diphenylethane (**12**)*: Isolated yield: 56%, colourless oil. Spectral data in accordance with literature report (29): ^{1}H NMR (250.13 MHz, $CDCl_3$, TMS) δ: 3.31 (s, 6H), 4.23 (d, 1H, *J* = 7.6 Hz), 5.00 (d, 1H, *J* = 7.6 Hz), 7.18–7.33 (m, 10H); ^{13}C NMR (62.90 MHz, $CDCl_3$) δ: 54.0 (q), 54.5 (d), 106.4 (d), 126.4 (d), 128.3 (d), 128.7 (d), 141.1 (s); IR (film, NaCl) υ (cm^{-1}): 3030, 2930, 1601, 1495, 1450, 1120, 1062, 750, 700; MS *m*/*z* (rel. int.): 210(8), 167(12), 165(14), 152(6), 105(6), 77(6), 75(100).

Irradiation of 4-fluorobenzonitrile (1a) and 1,1-diphenylethene (5) in methanol

A solution of 4-fluorobenzonitrile (**1a**, 0.05 mol dm^{-3}) and 1,1-diphenylethene (**5**, 0.10 mol dm^{-3}) in methanol (10 mL) was irradiated for 75 h. Calibrated GC-fid analysis of the final photolysate revealed that 67% of **5** had been consumed while **1a** showed a 100% recovery. The products observed included 1,1-diphenylethane (**8**, 2%), 1-methoxy-1,1-diphenylethane (**9**, 10%), and 1-methoxy-2,2-diphenylethane (**10**, 21%).

The sim-MS of an identical photoreaction in methanol-*O-d* indicated 47% deuterium incorporation at the bisbenzylic position (C-2) of **10**.

Irradiation of 4-fluorobenzonitrile (1a) in methanol

A solution of 4-fluorobenzonitrile (**1a**, 0.05 mol dm^{-3}) in methanol (10 mL) was irradiated for 50 h. Calibrated GC-fid analysis of the final photolysate revealed no product formation together with 100% recovery of **1a**. Similar irradiation behind Quartz (λ > 190 nm) furnished identical results.

Irradiation of 4-chlorobenzonitrile (2a) and 1,1-diphenylethene (5) in methanol

A solution of 4-chlorobenzonitrile (**2a**, 0.05 mol dm^{-3}) and 1,1-diphenylethene (**5**, 0.10 mol dm^{-3}) in methanol (10 mL) was irradiated for 75 h. Calibrated GC-fid analysis of the final photolysate revealed that 78% of **5** and 46% of **2a** had been consumed. The products observed included 1-methoxy-1,1-diphenylethane (**9**, 2%), 1-methoxy-2,2-diphenylethane (**10**, 26%), 1-methoxy-2,2-diphenylethene (**11**, 7%), 1,1-dimethoxy-2,2-diphenylethane (**12**, 6%), 1,2-dimethoxy-1,1-diphenylethane (**13**, 2%), 1-(4-cyanophenyl)-2,2-diphenylethene (**15a**, 3%), 1-(4-cyanophenyl)-2,2-diphenylethane (**16a**, 12%), and 1-(4-cyanophenyl)-2-methoxy-2,2-diphenylethane (**17a**, 17%).

Pure samples of **16a** and **17a** were obtained from a large-scale photoreaction (60 mL) having an identical composition to the above. A pure sample of **15a** was obtained from an alternative photoreaction (vide infra).

The sim-MS of an identical photoreaction in methanol-*O-d* indicated 75% deuterium incorporation at the bisbenzylic position (C-2) of **10** and 64% deuterium incorporation at the bisbenzylic position (C-2) of **16a**.

*1-(4-Cyanophenyl)-2,2-diphenylethane (**16a**)*: Isolated yield: 2%, colourless oil. ^{1}H NMR (250.13 MHz, $CDCl_3$, TMS) δ: 3.41 (d, 2H, *J* = 7.8 Hz), 4.19 (t, 1H, *J* = 7.8 Hz), 7.07 (2H, half AA′BB′), 7.16–7.25 (m, 10H), 7.44 (2H, half AA′BB′); ^{13}C NMR (62.90 MHz, $CDCl_3$) δ: 42.2 (t), 51.5 (d), 119.0 (s), 122.8(s), 126.5 (d), 127.9 (d), 128.5 (d), 129.8 (d), 131.9 (d), 143.5(s), 145.9 (s); MS *m*/*z* (rel. int.): 167(100), 165(30), 152(17), 116(3), 89(3), 77(2); HRMS: calcd.: 283.1361, found: 283.1371.

*1-(4-Cyanophenyl)-2-methoxy-2,2-diphenylethane (**17a**)*: Isolated yield: 3%, white crystals, mp 147.1–148.3°C (corrected). IR (film, NaCl) υ (cm^{-1}): 3054, 3027, 2934, 2826, 2221, 1606, 1490, 1446, 1192, 1079, 826, 775, 751, 698; ^{1}H NMR (250.13 MHz, $CDCl_3$, TMS) δ: 3.15 (s, 3H), 3.63 (s, 2H), 6.83 (2H, half AA′BB′), 7.18–7.29 (m, 10H), 7.34 (2H, half AA′BB′); ^{13}C NMR (62.90 MHz, $CDCl_3$) δ: 42.0 (t), 51.0 (q), 83.4 (s), 109.8 (s), 119.2 (s), 127.1 (d), 127.5 (d), 127.9 (d), 131.1 (d), 131.2 (d), 142.8 (s), 143.8 (s); MS *m*/*z* (rel. int.): 281(5), 197(100), 165(5), 105(34), 77(28). Anal. (%) calcd.: C 84.31, H 6.11, N 4.47; found: C 84.04, H 6.06, N 4.37.

Irradiation of 4-chlorobenzonitrile (2a) in methanol

A solution of 4-chlorobenzonitrile (**2a**, 0.05 mol dm^{-3}) in methanol (10 mL) was irradiated for 50 h. Calibrated GC-fid analysis of the final photolysate revealed no product formation together with 100% recovery of **2a**.

Irradiation of 4-bromobenzonitrile (3a) and 1,1-diphenylethene (5) in methanol

A solution of 4-bromobenzonitrile (**3a**, 0.05 mol dm^{-3}) and 1,1-diphenylethene (**5**, 0.10 mol dm^{-3}) in methanol (10 mL) was irradiated for 75 h. Calibrated GC-fid analysis of the final photolysate revealed that 90% of **5** and 54% of **3a** had been consumed. The products observed included 1-methoxy-1,1-diphenylethane (**9**, 2%), 1-methoxy-2,2-diphenylethane (**10**, 17%), 1-methoxy-2,2-diphenylethene (**11**, 4%), 1,1-dimethoxy-2,2-diphenylethane (**12**, 5%), 1,2-dimethoxy-1,1-diphenylethane (**13**, <2%), benzonitrile (**14a**, 13%), 1-(4-cyanophenyl)-2,2-diphenylethene (**15a**, 5%), 1-(4-cyanophenyl)-2,2-diphenylethane (**16a**, 8%), 1-(4-cyanophenyl)-2-methoxy-2,2-diphenylethane (**17a**, 11%), and 3-cyano-9-phenylphenanthrene (**18a**, 4%).

Benzonitrile (**14a**) was identified by comparison with a commercial sample. A pure sample of **18a** was obtained from an alternative photoreaction (vide infra). The sim-MS of an identical photoreaction in methanol-*O-d* indicated 77% deuterium incorporation at the bisbenzylic position (C-2) of

© 1999 NRC Canada

10 and 50% deuterium incorporation at the bisbenzylic position (C-2) of **16a**.

Irradiation of 4-bromobenzonitrile (3a) in methanol

A solution of 4-bromobenzonitrile (**3a**, 0.05 mol dm^{-3}) in methanol (10 mL) was irradiated for 50 h. Calibrated GC-fid analysis of the final photolysate revealed 100% **3a** consumption and the formation of benzonitrile (**14a**) in 71% yield.

Irradiation of 4-iodobenzonitrile (4a) and 1,1-diphenylethene (5) in methanol

A solution of 4-iodobenzonitrile (**4a**, 0.05 mol dm^{-3}) and 1,1-diphenylethene (**5**, 0.10 mol dm^{-3}) in methanol (10 mL) was irradiated for 75 h. Calibrated GC-fid analysis of the final photolysate revealed that 88% of **5** and 100% of **4a** had been consumed. The products observed included 1-methoxy-1,1-diphenylethane (**9**, 2%), 1-methoxy-2,2-diphenylethane (**10**, 12%), 1-methoxy-2,2-diphenylethene (**11**, 11%), 1,1-dimethoxy-2,2-diphenylethane (**12**, 19%), 1,2-dimethoxy-1,1-diphenylethane (**13**, <2%), benzonitrile (**14a**, 23%), 1-(4-cyanophenyl)-2,2-diphenylethene (**15a**, 38%), 1-(4-cyanophenyl)-2,2-diphenylethane (**16a**, 5%), 1-(4-cyanophenyl)-2-methoxy-2,2-diphenylethane (**17a**, 5%), and 3-cyano-9-phenylphenanthrene (**18a**, 21%).

Pure samples of **15a** and **18a** were obtained from a large-scale photoreaction (60 mL) identical in composition to the above.

The sim-MS of an identical photoreaction in methanol-*O-d* indicated 86% deuterium incorporation at the bisbenzylic position (C-2) of **10** and 41% deuterium incorporation at the bisbenzylic position (C-2) of **16a**.

*1-(4-Cyanophenyl)-2,2-diphenylethene (**15a**)*: Isolated yield: 36%, white crystals, mp 116.5–117.1°C (corrected), lit. (30) mp 107–109°C. IR (film, NaCl) υ (cm^{-1}): 3057, 3026, 2225, 1601, 1499, 1444, 827, 765, 737, 698, 626; ^{1}H NMR (250.13 MHz, $CDCl_3$, TMS) δ: 6.94 (s, 1H), 7.06–7.41 (m, 14H); ^{13}C NMR (62.90 MHz, $CDCl_3$) δ: 109.7 (s), 119.0 (s), 126.1 (d), 127.8 (d), 128.1 (d), 128.3(d), 128.4(d), 218.9 (d), 129.9 (d), 130.1 (d), 131.7 (d), 139.4 (s), 142.1 (s), 142.5 (s), 146.2 (s); MS *m*/*z* (rel. int.): 281(100), 266(16), 203(29), 178(10).

*3-Cyano-9-phenylphenanthrene (**18a**)*: Isolated yield: 20%, white crystals, mp 136.0–136.6°C (corrected). IR (film, NaCl) υ (cm^{-1}): 3062, 3025, 2225, 1616, 1517, 1494, 1443, 1431, 1413, 889, 813, 770, 725, 702; ^{1}H NMR (250.13 MHz, $CDCl_3$, TMS) δ: 7.48–7.55 (m, 10H), 7.62 (app. t of d, 1H), 7.69 (s, 1H), 7.76 (app. t of d, 1H), 7.77 (d of d, 1H, J = 8.2, 1.5 Hz), 7.95 (d, 1H, J = 8.2 Hz), 8.71 (d, 1H, J = 8.2 Hz), 9.04 (s, 1H); ^{13}C NMR (62.90 MHz, $CDCl_3$) δ: 109.6 (s), 119.6 (s), 122.8 (d), 126.6 (d), 127.3 (d), 127.6 (d), 127.7 (d), 127.9 (d), 128.1 (d), 128.2 (d), 128.5 (d), 129.5 (d), 129.6 (s), 129.7 (s), 129.8 (d), 131.4 (s), 133.8 (s), 139.8 (s), 142.3 (s); MS *m*/*z* (rel. int.): 279(100), 125(19); X-ray crystallographic data: $C_{31}H_{13}N$, M = 279.34, primitive monoclinic, a = 7.817(4), b = 9.224(5), c = 20.638(6) Å, β = 99.43(4)°, U = 1468(1) $Å^3$ (by least-squares refinement on diffractometer angles for 21 carefully centered reflections), T = 296 K, λ = 0.710 69 Å, space group $P2_1/a$ (no. 14), Z = 4, D_C = 1.264 g/cm^3, F(000) = 584.00. Colourless needle with dimensions 0.06 × 0.17 × 0.30 mm, μ(M_O-Kα) = 0.73 cm^{-1}. Data were collected using a Rigaku AFC5R diffractometer in the range 8.56 < 2θ < 23.94°. Refinement was by full-matrix least-squares on F for 512 observed reflections and 117 variable parameters using teXsan crystallographic software package.[4] Some non-hydrogen atoms were refined anisotropically, while the rest were refined isotropically; the phenyl group was refined as a rigid body. Conventional R (for $I > 3\sigma(I)$) = 0.059 and R_w = 0.068. Largest difference peak and hole 0.21 and –0.22 e $Å^{-3}$.

Irradiation of 4-iodobenzonitrile (4a) in methanol

A solution of 4-iodobenzonitrile (**4a**, 0.05 mol dm^{-3}) in methanol (10 mL) was irradiated for 50 h. Calibrated GC-fid analysis of the final photolysate revealed 89% **4a** consumption and the formation of benzonitrile (**14a**) in 85% yield.

Irradiation of 1-(4-cyanophenyl)-2,2-diphenylethene (15a) in methanol

A solution of 1-(4-cyanophenyl)-2,2-diphenylethene (**15a**, 0.025 mol dm^{-3}) in methanol (2 mL) was irradiated for 6 h. No consumption of the starting material was observed. Similarly, a solution of **15a** (0.025 mol dm^{-3}) and 4-chlorobenzonitrile (**2a**, 0.025 mol dm^{-3}) in methanol (2 mL) did not result in any consumption of starting materials after 6 h of irradiation. Conversely, a solution of **15a** (0.025 mol dm^{-3}) and 4-iodobenzonitrile (**4a**, 0.025 mol dm^{-3}) in methanol (2 mL) resulted in 98% **15a** and 72% **4a** consumption after 6 h irradiation. Also observed was the formation of benzonitrile (**14a**, 80%) and 3-cyano-9-phenylphenanthrene (**18a**, 98%).

Irradiation of 4-chloroanisole (2b) and 1,1-diphenylethene (5) in methanol

A solution of 4-chloroanisole (**2b**, 0.05 mol dm^{-3}) and 1,1-diphenylethene (**5**) (0.10 mol dm^{-3}) in methanol (10 mL) was irradiated for 75 h. Calibrated GC-fid analysis revealed 78% consumption of **5** and 79% consumption of **2b** together with the formation of 1,1-diphenylethane (**8**, 2%), 1-methoxy-1,1-diphenylethane (**9**, 5%), 1-methoxy-2,2-diphenylethane (**10**, 5%), anisole (**14b**, 14%), 1-(4-methoxyphenyl)-2,2-diphenylethene (**15b**, 40%), 1-(4-methoxyphenyl)-2,2-diphenylethane (**16b**, <2%), 1-methoxy-2-(4-methoxyphenyl)-1,1-diphenylethane (**17b**, 4%), and 3-methoxy-9-phenylphenanthrene (**18b**, 8%).

Anisole (**14b**) was identified by comparison with a commercial sample. A pure sample of **15b** was obtained by an alternative synthesis method involving the dehydration of 2-(4-methoxyphenyl)-1,1-diphenylethanol (**20**), which was synthesized via a Grignard reaction between 4-methoxybenzylmagnesium chloride and benzophenone. The Grignard reagent was prepared according to a reported procedure (31). The intermediate alcohol **20** was subsequently dehydrated by refluxing with toluenesulphonic acid in benzene.

[4] teXsan for windows: crystal structure analysis package. Molecular Structure Corp. 1997.

© 1999 NRC Canada

*1-(4-Methoxyphenyl)-2,2-diphenylethene (**15b**)*: White crystals, mp 83.1–83.6°C (corrected), lit. (32) mp 83–84°C. IR (film, NaCl) υ (cm^{-1}): 3055, 3025, 2834, 1605, 1509, 1253, 1178, 1034, 699; ^{1}H NMR (250.13 MHz, $CDCl_3$, TMS) δ 3.75 (s,3H), 6.65–6.93 (4H, AA′BB′), 6.97 (s, 1H), 7.20–7.35 (m, 10H); ^{13}C NMR (62.90 MHz, $CDCl_3$) δ 55.2 (q), 113.4 (d), 127.2 (d), 127.3 (d), 127.4 (d), 127.7 (d), 128.2 (d), 128.7 (d), 130.1 (s), 130.4 (d), 130.8 (d), 140.58 (s), 140.63 (s), 143.6 (s), 158.4 (s); MS *m*/*z* (rel. int.): 165 (36), 286 (100).

A pure sample of (**17b**) was obtained by methylation of the alcohol **20** according to a published procedure (33).

*1-Methoxy-2-(4-methoxyphenyl)-1,1-diphenylethane (**17b**)*: White crystals, mp 102.8–103.7°C (corrected), lit. (34) mp 94–95°C. Spectroscopic data in agreement with published results (34): IR (film, NaCl) υ (cm^{-1}): 3057, 3024, 2936, 2831, 1611, 1513, 1245, 1179, 1077, 1036, 828, 755, 701; ^{1}H NMR (250.13 MHz, $CDCl_3$, TMS) δ 3.17 (s, 3H), 3.55 (s, 2H), 3.72 (s, 3H), 6.59–6.67 (4H, AA′BB′), 7.17–7.27 (m, 10H); ^{13}C NMR (62.90 MHz, $CDCl_3$) δ 40.5 (t), 50.8 (q), 55.0 (q), 83.4 (s), 112.8 (d), 126.7 (d), 127.6 (d), 127.7 (d), 128.7 (d), 131.3 (d), 144.8 (s), 157.8 (s); MS *m*/*z* (rel. int.): 77(31), 105(39), 197(100), 286(1).

Compound **16b** was present in too small amounts to be isolated and was identified by GC–MS only.

*1-(4-Methoxyphenyl)-2,2-diphenylethane (**16b**)*: MS *m*/*z* (rel. int.): 77(5), 121(100), 152(7), 165(13), 167 (25), 288(3).

A pure sample of **18b** was obtained from an alternative photoreaction (vide infra).

Irradiation of 4-chloroanisole (2b) in methanol

A solution of 4-chloroanisole (**2b**, 0.05 mol dm^{-3}) in methanol (10 mL) was irradiated for 75 h. Calibrated GC-fid analysis revealed 88% **2b** consumption together with the formation of anisole (**14b**, 56%) and 1,4-dimethoxybenzene (**19**, 12%).

Irradiation of 4-bromoanisole (3b) and 1,1-diphenylethene (5) in methanol

A solution of 4-bromoanisole (**3b**, 0.05 mol dm^{-3}) and 1,1-diphenylethene (**5**, 0.10 mol dm^{-3}) in methanol (10 mL) was irradiated for 75 h. Calibrated GC-fid analysis revealed 69% consumption of **5** and 100% consumption of **3b**, together with the formation of 1-methoxy-1,1-diphenylethane (**9**, 2%), anisole (**14b**, 29%), 1-(4-methoxyphenyl)-2,2-diphenylethene (**15b**, 30%), 1-(4-methoxyphenyl)-2,2-diphenylethane (**16b**, <2%), and 3-methoxy-9-phenylphenanthrene (**18b**, 13%).

Irradiation of 4-bromoanisole (3b) in methanol

A solution of 4-bromoanisole (**3b**, 0.05 mol dm^{-3}) in methanol (10 mL) was irradiated for 25 h. Calibrated GC-fid analysis revealed complete consumption of **3b** and the formation of 84% anisole (**14b**).

Irradiation of 4-iodoanisole (4b) and 1,1-diphenylethene (5) in methanol

A solution of 4-iodoanisole (**4b**, 0.05 mol dm^{-3}) and 1,1-diphenylethene (**5**,.0.10 mol dm^{-3}) in methanol (10 mL) was irradiated for 75 h. Calibrated GC-fid analysis indicated that 49% of **5** and 100% of **4b** had been consumed. Products observed included anisole (**14b**, 22%), 1-(4-methoxyphenyl)-2,2-diphenylethene (**15b**, 40%), 1-(4-methoxyphenyl)-2,2-diphenylethane (**16b**, <2%), and 3-methoxy-9-phenylphenanthrene (**18b**, 16%).

Irradiation of 4-iodoanisole (4b) in methanol

A solution of 4-iodoanisole (**4b**, 0.05 mol dm^{-3}) in methanol (10 mL) was irradiated for 75 h. Calibrated GC-fid analysis revealed 64% **4b** consumption together with the formation of 87% anisole (**14b**). The reaction turned dark red upon photolysis.

Irradiation of 1-(4-methoxyphenyl)-2,2-diphenylethene (15b)

A solution of 1-(4-methoxyphenyl)-2,2-diphenylethene (**15b**, 0.025 mol dm^{-3}) and 4-iodoanisole (**4b**, 0.025 mol dm^{-3}) in methanol (2 mL) resulted in 96% **15b** and 79% **4b** consumption after 6 h irradiation. Also observed was the formation of anisole (**14b**, 80%) and 3-methoxy-9-phenylphenanthrene (**18b**, 94%).

A pure sample of **18b** was isolated from a large-scale photoreaction (30 mL) of identical composition to the above.

*3-Methoxy-9-phenylphenanthrene (**18b**)*: Isolated yield: 60%, colourless oil. Spectroscopic data in agreement with published results (35): IR (film, NaCl) υ (cm^{-1}): 3057, 3022, 2932, 2833, 1621, 1598, 1503, 1439, 1429, 1253, 1221, 1177, 1036, 771, 701; ^{1}H NMR (250.13 MHz, $CDCl_3$, TMS) δ 4.02 (3H, s), 7.25 (dd, 1H, J = 8.5, 2.4 Hz), 7.43–7.63 (m, 8H), 7.80 (d, 1H, J = 8.5 Hz), 7.91 (d, 1H, J = 8.2 Hz), 8.07 (d, 1H, J = 2.4 Hz), 8.68 (d, 1H, J = 7.6 Hz); ^{13}C NMR (62.90 MHz, $CDCl_3$) δ 55.5 (q), 103.8 (d), 113.4 (d), 117.0 (d), 126.0 (d), 126.2 (s), 126.5 (d), 126.9 (d), 127.2 (d), 128.3 (d), 130.0 (s), 130.09 (d), 130.13 (d), 131.2 (s), 131.4 (s), 136.4 (s), 140.9 (s), 158.5 (s); MS *m*/*z* (rel. int.): 239 (42), 269 (30), 284 (100); HRMS: calcd.: 284.1201, found: 284.1196.

Thermal decomposition of 1-(4-cyanophenyl)-2-methoxy-2,2-diphenylethane (17a) and 1-methoxy-2-(4-methoxyphenyl)-1,1-diphenylethane (17b)

A solution of 1-(4-cyanophenyl)-2-methoxy-2,2-diphenylethane (**17a**, 0.025 mol dm^{-3}) in methanol (2 mL) was left to stand in the dark for 5 days. GC–MS analysis indicated partial conversion to 1-(4-cyanophenyl)-2,2-diphenylethene (**15a**). Upon addition of a drop of hydrochloric acid, GC–MS indicated almost complete conversion of **17a** to **15a**. 1-Methoxy-2-(4-methoxyphenyl)-1,1-diphenylethane (**17b**) underwent conversion to 1-(4-methoxyphenyl)-2,2-diphenylethene (**15b**) under similar conditions.

Acknowledgements

This work was supported financially by the Natural Sciences and Engineering Research Council of Canada. We thank Dr. D.L. Hooper at the Atlantic Regional Magnetic Resonance Center at Dalhousie University for help with the NMR spectra and with the preparation of the manuscript, Dr. T.S. Cameron at the X-Ray Crystallography Center at

© 1999 NRC Canada

Dalhousie University for the X-ray crystal structure and Dr. J.-H. Kim for the exact mass measurements. D.M. is grateful for a scholarship from the Izaak Walton Killam Memorial Foundation.

References

1. (*a*) R.A. Neunteufel and D.R. Arnold. J. Am. Chem. Soc. **95**, 4080 (1973); (*b*) A.J. Maroulis and D.R. Arnold. Synthesis, **10**, 819 (1979); (*c*) D.R. Arnold, X. Du, and J. Chen. Can. J. Chem. **73**, 307 (1995).
2. (*a*) R.M. Borg, D.R. Arnold, and T.S. Cameron. Can. J. Chem. **62**, 1785 (1984); (*b*) D.R. Arnold, K.A. McManus, and M.S.W. Chan. Can. J. Chem. **75**, 1055 (1997); (*c*) M.S.W. Chan and D.R. Arnold. Can. J. Chem. **75**, 1810 (1997); (*d*) H.J.P. de Lijser and D.R. Arnold. J. Org. Chem. **62**, 8432 (1997); (*e*) D.R. Arnold and K.A. McManus. Can. J. Chem. **76**, 1238 (1998); (*f*) D.A. Connor, D.R. Arnold, P.K. Bakshi, and T.S. Cameron. Can. J. Chem. **73**, 762 (1995).
3. D.E. Bartak, K.J. Houser, B.C. Rudy, and H.D. Hawley. J. Am. Chem. Soc. **94**, 7526 (1972).
4. (*a*) J.F. Bunnett. Acc. Chem. Res. **11**, 413 (1978); (*b*) C. Galli and J.F. Bunnett. J. Am. Chem. Soc. **103**, 7140 (1981); (*c*) M.A. Fox, J. Younathan, and G.E. Fryxell. J. Org. Chem. **48**, 3109 (1983); (*d*) R. Beugelmans. *In* CRC Handbook of photochemistry and photobiology. *Edited by* W.H. Horspool and P.-L. Song. CRC Press, New York. 1995. Chap. 88.
5. (*a*) J.M. Saveant. Acc. Chem. Res. **13**, 323 (1980); (*b*) C.P. Andrieux, J.M. Saveant, and D. Zann. Nouv. J. Chim. **8**, 107 (1984); (*c*) C. Amatore, M.A. Oturan, J. Pinson, J.M. Saveant, and A. Thiebault. J. Am. Chem. Soc. **107**, 3451 (1985); (*d*) Z. Chami, M. Gariel, J. Pinson, J.M. Saveant, and A. Thiebault. J. Org. Chem. **56**, 586 (1991).
6. J. Woning, A. Oudenampsen, and W.H. Laarhoven. J. Chem. Soc. Perkin Trans. 2, 2147 (1989).
7. (*a*) S. Davidson, J.W. Goodin, and G. Kemp. Adv. Phys. Org. Chem. **20**, 191 (1984); (*b*) P.K. Freeman, J.-S. Jang, and N. Ramnath. J. Org. Chem. **56**, 6072 (1991).
8. (*a*) J. Grimshaw and A.P. de Silva. Chem. Soc. Rev. **10**, 181 (1981); (*b*) S.V. Kessar and A.K. Singh Mankotia. *In* CRC Handbook of organic photochemistry and photobiology. *Edited by* W.H. Horspool and P.-L. Song. CRC Press, New York. 1995. Chap. 89; (*c*). M. D'Auria, E. De Luca, G. Mauriello, and R. Racioppi. J. Chem. Soc. Perkin Trans. 1, 271 (1998).
9. D. Rehm and A. Weller. Isr. J. Chem. **8**, 259 (1970).
10. T.F. Palmer and S.S. Parmar. J. Photochem. **31**, 273 (1985).
11. C.M. Previtali and T.W. Ebbesen. J. Photochem. **27**, 9 (1984).
12. (*a*) R.S. Nicholson and I. Shain. Anal. Chem. **36**, 706 (1964); (*b*) Anal. Chem. **37**, 178 (1965).
13. K. Gollnick, A. Schnatterer, and G. Utschick. J. Org. Chem. **58**, 6049 (1993).
14. H. Gorner. J. Phys. Chem. **86**, 20 (1986).
15. S.L. Murov, I. Charmichael, and G.L. Hug. Handbook of photochemistry. 2nd ed. Marcel Dekker, Inc. New York. 1993. p. 280.
16. P.J. Wagner and E.J. Siebert. J. Am. Chem. Soc. **103**, 7329 (1981).
17. T.P. Carsey, G.L. Findley, and S.P. McGlynn. J. Am. Chem. Soc. **101**, 4502 (1979).
18. S. Niizuma, L. Kwan, and N. Hirota. Mol. Phys. **35**, 1029 (1978).
19. N.J. Bunce. *In* CRC Handbook of photochemistry and photobiology. *Edited by* W.H. Horspool and P.-L. Song. CRC Press, New York. 1995. Chap. 86.
20. J.T. Pinhey and R.D.G. Rigby. Tetrahedron Lett. 1271 (1969).
21. D.D.M. Wayner, D.J. McPhee, and D. Griller. J. Am. Chem. Soc. **110**, 132 (1988).
22. D.B. Denney, D.Z. Denney, and S.P. Fenelli. Tetrahedron, **53**, 9835 (1996).
23. (*a*) K.A. Muszkat. Top. Curr. Chem. **88**, 89 (1980); (*b*) W.H. Laarhoven. Trav. Chim. Pays-Bas. **102**, 185 (1983); **102**, 241 (1983); (*c*) A. Gilbert. *In* CRC Handbook of photochemistry and photobiology. *Edited by* W.M. Horspool and P.-L. Song. CRC Press, New York. 1995. Chap. 23.
24. (*a*) W.K. Smothers, K.S. Schanze, and J. Saltiel. J. Am. Chem. Soc. **101**, 1895 (1979); (*b*) N.J. Bunce. J. Org. Chem. **47**, 1948 (1982); (*c*) N.J. Bunce and J.C. Gallacher. J. Org. Chem. **47**, 1955 (1982); (*d*) P.K. Freeman, R. Srinivasa, J.-A. Campbell, and M.L. Deinzer. J. Am. Chem. Soc. **108**, 5531 (1986).
25. W.C. Still, M. Kahn, and A Mitra. J. Org. Chem. **43**, 2923 (1978).
26. F. Weineit and H.J. Schnieder. J. Org. Chem. **56**, 5527 (1991).
27. W.A. Bonner and F.D. Mango. J. Org. Chem. **29**, 430 (1964).
28. G. Wittig and M. Schlosser. Chem. Ber. **94**, 1373 (1961).
29. T. Harada and T. Mukaiyama. Bull. Chem. Soc. Jpn. **66**, 882 (1993).
30. W. Tadros, Y. Akhnookh, and G. Aziz. J. Chem. Soc. 186 (1953).
31. K.V. Baker, J.M. Brown, N. Hughes, A.J. Skarnulis, and A. Sexton. J. Org. Chem. **56**, 698 (1991).
32. M. Kamata, K. Murayama, and T. Miyashi. Tetrahedron Lett. **30**, 4129 (1989).
33. J.W. Hilborn, E. MacKnight, J.A. Pincock, and P.J. Wedge. J. Am. Chem. Soc. **116**, 3337 (1994).
34. M. Freccero, A. Pratt, A. Albini, and C. Long. J. Am. Chem. Soc. **120**, 284 (1998).
35. F.I.M. van Ginkel, J. Cornelisse, and G. Lodder. J. Am. Chem. Soc. **113**, 4261 (1991).

© 1999 NRC Canada

Improved hydrophobic zeolites to fill silicone membranes for ethyl acetate extraction from water by pervaporation[1]

Hu Yang, Zhenghua Ping, Yingcai Long, and Quang Trong Nguyen

Abstract: Two types of hydrophobic zeolites Y were prepared by treating the NaY-type zeolite with $SiCl_4$, with or without subsequent hydrothermal treatment. X-ray diffraction analysis showed that the framework of the two modified zeolites Y are more perfect than that of the NaY one, and the Si/Al ratio is greatly enhanced by hydrothermal treatment. The determined sorption isotherms indicate an improvement of the ester-to-water sorption ratio with the increase in Si/Al ratio. When the zeolite-filled silicone membranes are used in separation of ethyl acetate – water mixture by pervaporation, both the total permeation flux and the selectivity to the ester are improved by the use of the hydrophobic zeolite Y as the filler in the membrane. The stronger the hydrophobicity of the zeolite Y, the higher the filled membrane selectivity.

Key words: hydrophobic zeolites Y, silicone-filled membranes, ethyl acetate – water mixture, sorption, pervaporation.

Résumé : On a préparé deux types de zéolithes Y hydrophobes par traitement du zéolithe de type NaY avec le $SiCl_4$, avec ou sans traitement hydrothermique subséquent. La diffraction des rayons X a montré que l'armature des zéolithes ainsi modifiés est plus parfaite que la structure du zéolithe NaY, et que le rapport Si/Al est fortement amélioré par traitement hydrothermique. Les isothermes de sorption déterminées indiquent une amélioration du rapport de la quantité d'ester sorbée à celle de l'eau avec l'augmentation du rapport Si/Al. Quand les membranes en silicone chargées de zéolithes sont utilisées en séparation du mélange eau – acétate d'éthyle par pervaporation, le flux total de perméation et la sélectivité à l'ester sont tous les deux améliorés par l'utilisation des zéolithes Y hydrophobes comme charge. Plus l'hydrophobie du zéolithe Y est élevée, plus la sélectivité de la membrane chargée de zéolithe est élevée.

Mots clés : zéolithes Y hydrophobes, membranes en silicone chargées, mélange eau – acétate d'éthyle, sorption, pervaporation.

Introduction

Since 1986, zeolite-filled polymer membranes have gained increasing attention in the separation of mixtures of water – volatile organic compounds (VOCs) by the pervaporation process (1–8). The separation by this membrane process is based on the difference in the permeation rates of the components, which are selectively sorbed at the membrane upstream face. The process is industrially used for alcohol dehydration and is attractive for the extraction of hydrophobic VOCs from water. It uses polymers with strong affinity to the compound to be preferentially permeated as membrane materials. For VOCs extraction from water, poly(dimethylsiloxane), or silicone rubber, is generally chosen as the membrane material. To improve its selectivity to VOCs, the latter can be filled with a zeolite. Zeolites are used for their high selectivity in catalysis or in separation as sorbent with fixed pore size. By mixing it with a polymer, improvements in membrane performances were observed.

According to its composition, zeolites exhibit different surface properties. For separation by pervaporation, membranologists focused on their hydrophobic and hydrophilic properties. Gao et al. (2) showed that PVC membranes filled with different hydrophilic zeolites to separate water–ethanol mixture improved the removal of water in pervaporation.

For the extraction of VOCs from water by pervaporation, hydrophobic zeolites (such as ZSM-5 or silicalite-1) as fillers impart good selectivity and permeation flux to silicone membranes (3–5). Smolders and co-workers (3) brought out a transport model to explain the function of silicalite in silicone membranes. According to this model, the hydrophobic silicalite-1 sorbs preferentially the organic solvent and prevents water molecules from entering the zeolite pores. The organic molecules can travel through zeolite pores and reach the downstream side of the membrane by less tortuous paths than water molecules.

The membrane performances depend strongly on the zeolite properties. In our previous works (9–11), we systemati-

Received March 24, 1999.

H. Yang, Z. Ping,[2] and Y. Long. Department of Macromolecular Science, Laboratory of Molecular Engineering of Polymers, Fudan University, 220 Handan Road, Shanghai, 200433, P.R. of China.
Q.T. Nguyen. Rouen University – UFR Sciences – UMR 6522, 76821 Mont St Aignan, France.

[1]See ref. 1.
[2]Author to whom correspondence may be addressed.
Telephone: (86-21)65642035. e-mail: zhping@fudan.edu.cn

© 1999 NRC Canada

cally investigated the relationship between the properties of the silicalite-1 filler and the resulting filled silicone membranes. The results showed that the membrane selectivity to ethanol increases with the silicon/aluminum (Si/Al) ratio of the ZSM-5 zeolite. Silicalite-1, an aluminum-free analogue of the ZSM-5 zeolite, which has the strongest affinity towards organic solvent, gave rise to a better membrane selectivity than ZSM-5. However, impurities coming from the raw materials are generally present in synthesized silicalite-1, and cause a loss in the zeolite affinity to the organic compounds. When such residual impurities are eliminated through acid and hydrothermal treatments (12), the silicalite hydrophobicity, and consequently the membrane selectivity, increase.

Besides the hydrophobicity, the zeolite pore size must be the other main factor that governs the membrane performances. However, no other types of hydrophobic zeolite were studied so far (except the ZSM-5). An interesting zeolite is the hydrophilic zeolite NaY; it belongs to faujasite (FAU) type framework. With a 12-oxygen ring and a pore size of ca. 0.8 nm, this zeolite has much larger pore than the common silicalite with 0.6 nm pore and 10-oxygen ring. Used as a filler in its hydrophobic form, one can expect to separate larger molecules or to have larger flux, compared with conventional silicalite-filled membranes. In general, the Si/Al ratio of the zeolite has a strong influence on the capacity of polar molecule sorption (13, 14). In the present work, hydrophobic zeolites Y were prepared by increasing the Si/Al ratio. To obtain the highest Si/Al ratio, we chose to combine two conventional chemical treatments, the $SiCl_4$ treatment (15, 16) and the hydrothermal treatment (17, 18). The structure of the obtained silicalites Y was studied with different techniques, and their characteristics in sorption and desorption of water and ethyl acetate were determined. In a last part, the separation performances of silicone membranes filled with different silicalites Y in the removal of ethyl acetate from water are compared together.

Experimental

Zeolite materials

The NaY zeolite powder was supplied by Wenzhou Corp. (China) with a Si/Al ratio of 2.5. The conversion of the hydrophilic NaY to a hydrophobic one was carried out according to a previously described procedure (16). It was first dehydrated at 502°C under nitrogen atmosphere, then contacted with a $SiCl_4$ saturated nitrogen stream at a flow ratio of 150 mL/min for 4 h at increasing temperatures (from 127 to 520°C). The chemically treated zeolite was flushed with dry nitrogen at 327°C for many hours to eliminate all residual reactant and gaseous reaction product, then cooled down to room temperature and washed with distilled water until pH = 7. Such a Si-enriched zeolite Y is called SY-1 in this work. When the SY-1 sample is hydrothermally treated at 802°C for 12 h, a second sample, SY-2, is obtained.

Characterization of zeolite structure

The powder X-ray diffraction patterns were acquired at room temperature on a Rigaku D-MAX/II A diffractometer at the frequency of the Cu-Kα radiation. The samples were dried at 300°C and then equilibrated in a desiccator containing saturated NaCl aqueous solution for 5 days. The Si was used as internal standard to correct the 2θ angles. The peaks at 2θ range of 50°–60°, such as (11,11,1), (15,3,3) reflection, were used to calculate the unit cell parameters of zeolites, and the least-squares method was used to adjust it. The starting materials were assumed to be 100% crystalline.

The ^{27}Al and ^{29}Si MAS NMR spectra were recorded using a Bruker MSL-300 spectrometer, whose ^{27}Al resonance frequency was 78.20 MHz. The rotor was spun at 3.5 kHz. The radio-frequency field was 45.5 kHz (corresponding to a $\pi/2$ pulse width of 5.5 μs); the recycle time is set at 100 ms. $AlCl_3(H_2O)_6$ (solid) was used as a reference. To make the structure analysis easier, the sample was presaturated with *acetylacetone* in a 50% ethanol solution in a reactor for a few days, then dried again. In the ^{29}Si MAS NMR measurement, the ^{29}Si resonance frequency used was 59.595 MHz. The rotor was spun at 3.0 kHz. The radio frequency field was 37.0 kHz (corresponding to a $\pi/3$ pulse width of 4.5 μs); the recycle time was set at 2 s; Q_8M_8 was used as a second reference for the ^{29}Si chemical shift.

The specific surface area and the pore volume were determined from N_2 adsorption isotherms at 77.35 K, using a Micrometric ASAP 2000 instrument.

Sorption and desorption measurements

The sorption isotherms of pure ethyl acetate and pure water vapors were measured in a Sartorius-7012 super-micro electrobalance at 25°C. The sample was activated in situ at 350°C under vacuum (<2.7 Pa) until complete desorption before the measurement. The vapor sorption capacity is expressed as the weight gain *per* 100 g of dry material.

Desorption was performed by thermogravimetric analysis (TGA) (with a NETZSCH TG-209 apparatus) on samples pre-equilibrated with a saturated solvent vapor at room temperature.

Preparation of zeolite Y – silicone membrane

The size of our FAU zeolite is about 1 μ, it is very hard to disperse, especially in high loading amount. So only 5% (w/w) filled PDMS was prepared. The membrane is prepared as the following. The zeolites were dehydrated at 500°C for 5 h before use. Ninety-five parts of a two- component silicone rubber (room temperature vulcanizable silicone rubber), 5 parts of zeolite, and 150 parts of solvent (cyclohexane) were mixed in a poly(ethylene) beaker until a homogeneous suspension was obtained. The suspension was then cast on a polyester film with a knife, and was left at room temperature for 48 h for vulcanization. The obtained composite membrane of ca. 200 μm thick was used in pervaporation without further treatment, and the SEM was used to characterize the structure of filled membrane.

Sorption and pervaporation measurements

The procedure for sorption in the membranes is the same as that for zeolites, except that the sample was activated at 50°C under vacuum (<2.7 Pa) before sorption. The pervaporation separation of a 1.23% ethyl acetate aqueous solution was measured at 30°C under 100 Pa pressure on the downstream side, using a stainless steel cell with an effective membrane area of 28 cm^2. The permeate collected in a trap cooled in liquid nitrogen for given time intervals was

© 1999 NRC Canada

Fig. 1. (*a*) XRD patterns in the 1.5–40° (2θ) range for different zeolites Y. (*b*) XRD patterns in the 50–60° (2θ) range for different zeolites Y.

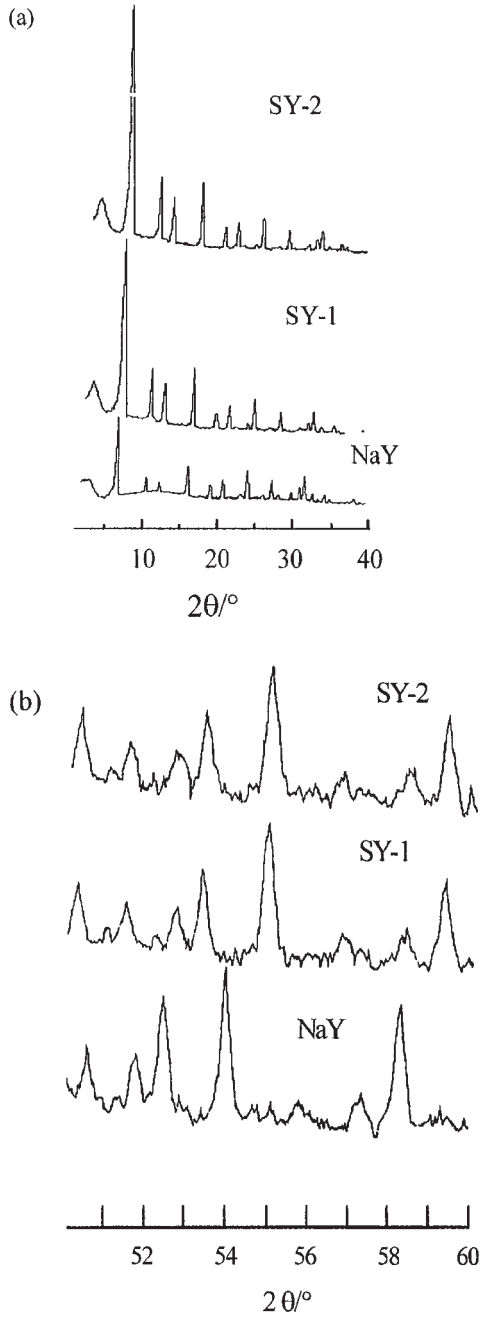

analyzed by gas chromatography. The permeation flux J and selectivity α were calculated as follows:

$$J = W_p/At$$

$$\alpha = (C_{ester}/C_w)^p/(C_{ester}/C_w)^f$$

where W_p is the weight of the permeate, A is the membrane area, t is the pervaporation time, C_{ester} and C_w are, respectively, the ester and the water weight fractions, and p, f superscripts refer to the permeate and the feed liquids, respectively.

Fig. 2. ^{29}Si MAS NMR spectra of FAU zeolite.

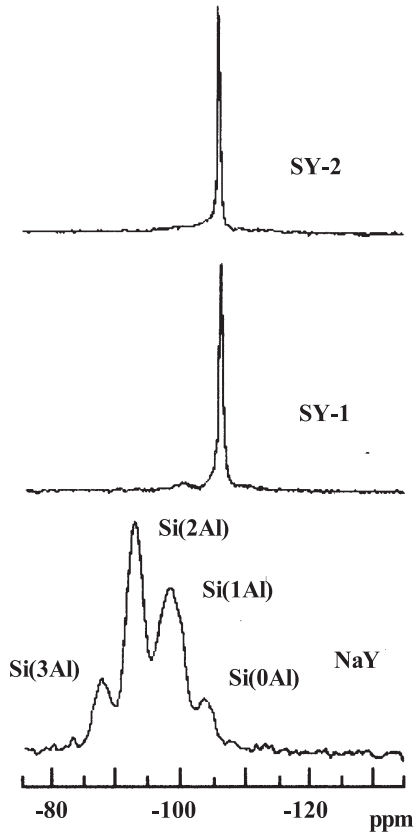

Results and discussion

Structure characterization of modified Y zeolites

The XRD (Fig. 1) shows that both samples maintain high crystallinity. Compared with the characteristic peaks in NaY, there are peak shifts toward higher angles; the peak shifts are larger for SY-2 than for SY-1, indicating a higher Si/Al ratio of SY-2.

In the ^{29}Si MAS NMR (Fig. 2), there still remains a Si(1Al) peak, –100 ppm for SY-1. The full width at half maximum of Si(0Al), –106.8 ppm, for SY-1 and SY-2 is 0.64 and 0.52 ppm, respectively. This indicates that the SY-2 framework has higher crystallinity. The ^{27}Al NMR was listed in Fig. 3. For SY-1, it contains mainly framework Al, 58.8 ppm, but for SY-2, there are mainly the octahedrally and tetrahedrally coordinated nonframework Al, 0.16 and 51.4 ppm (19–20). Such nonframework Al can be removed by acid treatment, its influence on the sorption property of zeolite is very limited (21).

The N_2 sorption curve is shown in Fig. 4. Almost no hysteresis is found in N_2 sorption–desorption cycles, indicating negligible second pore.

Sorption and desorption characteristics

The ethyl acetate sorption isotherms of in the SY-1 and SY-2 zeolites are illustrated in Fig. 5. The sorption amounts at saturation for the SY-1 and SY-2 zeolites (ca. 19 and 15 wt.%, respectively) are consistent with their specific surface area calculated from nitrogen sorption (Table 1): their ratio,

© 1999 NRC Canada

Fig. 3. ^{27}Al MAS NMR spectra of FAU zeolite.

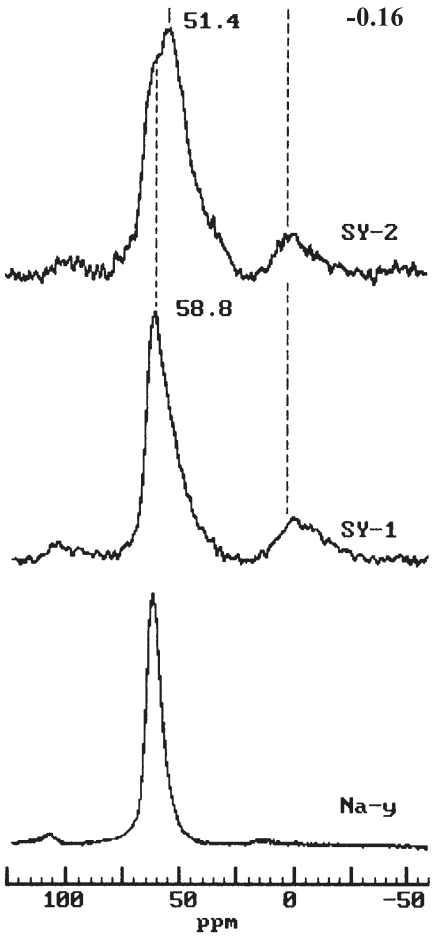

1.2, is practically the same as that of the BET surface areas obtained with nitrogen sorption. The decrease in the sorption amounts at saturation following the hydrothermal treatment corresponds to the pore volume reduction with the decrease in the Al content in the framework. The hydrophilic NaY sample also has strong ester sorption capacity, in spite of its hydrophilicity; this is due to the strong electrostatic interactions between the Na^+ cations and the polar ester molecules.

In the case of water sorption (Fig. 6), the hydrophilic zeolite NaY achieves sorption saturation at very low partial pressure, and reaches high sorption amounts. On the contrary, the dealuminated samples have much lower water sorption amounts compared with that of the zeolite NaY, and with the ester amounts sorbed in the SY samples. The SY-2 sample, which sorbs much less water than the SY-1, appears to have much more hydrophobic pores than SY-1, as the ratio of sorbed amounts is far below that of the BET surface areas. In other words, the pore surface of the SY-2 zeolite strongly repels water vapor, although the pores are fully accessible to the small water molecules. Such equilibrium behavior would favor a sorption-based separation of water – hydrophobic component mixtures. If we use the ratio of the sorption amount of ester to that of water at 0.05 relative vapor pressure to express the selectivity, the SY-2 sorption selectivity would be higher than 70.

Table 1. Some characteristics of studied zeolites Y: Si/Al ratio, BET surface area.

Zeolite type	NaY	SY-1	SY-2
Si/Al (XRD)	2.5	29.8	>100
BET surface area (m^2/g)	—	651	543

The desorption property of zeolite is another key factor for separation. It reflects the interaction energy between zeolite and the sorbed solvent. The higher the desorption temperature, the stronger the affinity of zeolite to the sorbed species. If the interaction is too strong, the sorbed solvent cannot be easily desorbed out of the membrane downstream side. The permeation flux of the species will decrease due to an extra resistance induced by the zeolite, and a smaller effect of the zeolite on the selectivity will result (22). The apparent endothermic effect can be observed in the DTA curves of NaY sorbed water and ester (see Fig. 7), which shows a very strong interaction existed between NaY and ester and water (electrostatic type). The strong interaction also reflects in the highest desorption T in NaY. The desorption temperature of ester on SY-2 zeolites lies in the medium, presenting both the character of a stronger affinity to ester and the easiness to desorb. SY-2 is the best sorbent for ester or organic VOCs among the studied zeolites.

Sorption and pervaporation characteristics of membrane

STM micrograph of the cross-section of the filled membrane is shown in Fig. 8. There are no apparent aggregates of the zeolite particles, and the adhesion between silicone and zeolite particles seem to be good, as there is no visible void space around the particles.

The sorption isotherms of ethyl acetate in pure silicone and zeolite-filled membranes are shown in Fig. 8. Zeolite particles, due to its high ester sorption capacity, increase the ester sorption extent of the membranes. However, the zeolite particles also act as physical crosslinks of the silicone polymer, thus reinforcing its elastic forces and its resistance to the swelling by solvent sorption. The final sorption capacity of filled membranes is the result of the balance of these trends. The data (Fig. 9) show that the filled membranes sorb more ester than the pure silicone membrane, with the highest sorption extents for the NaY-zeolite-filled membrane. Figure 10 shows the water absorption isotherms for different membranes. The NaY-filled membrane has by far the highest sorption extent. The membranes filled with the SY-1 and SY-2 zeolites absorb less water than the pure silicone membrane. Thus, the incorporation of hydrophobic zeolites into silicone rubber enhances the materials sorption selectivity, by improving the ester sorption while reducing water sorption. The sorption extent of ester in the composite membrane depends not only on the pore volume of the used zeolite, but also on its hydrophobicity. The latter property is probably the main factor for the selectivity change, as the water sorption is drastically reduced when the Si/Al ratio increases.

The pervaporation results of a 1.23 wt.% ester solution through the pure silicone membrane and the membranes filled with 5 wt.% of zeolite Y (Table 2) show that both the water and ethyl acetate fluxes through the filled membranes

© 1999 NRC Canada

Fig. 4. N_2 adsorption of dealuminated zeolite Y.

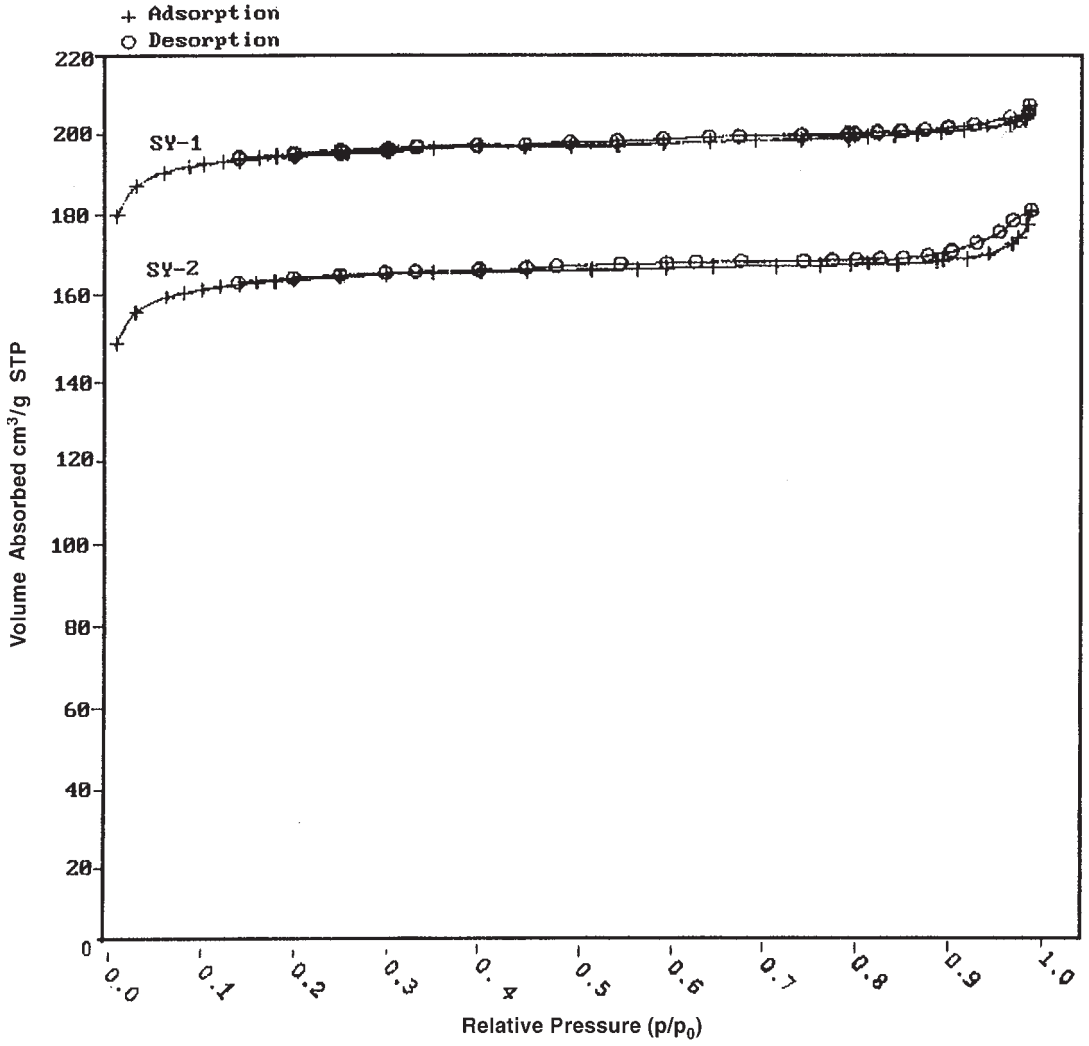

Fig. 5. Sorption isotherms of ethyl acetate in different zeolites Y at 25°C.

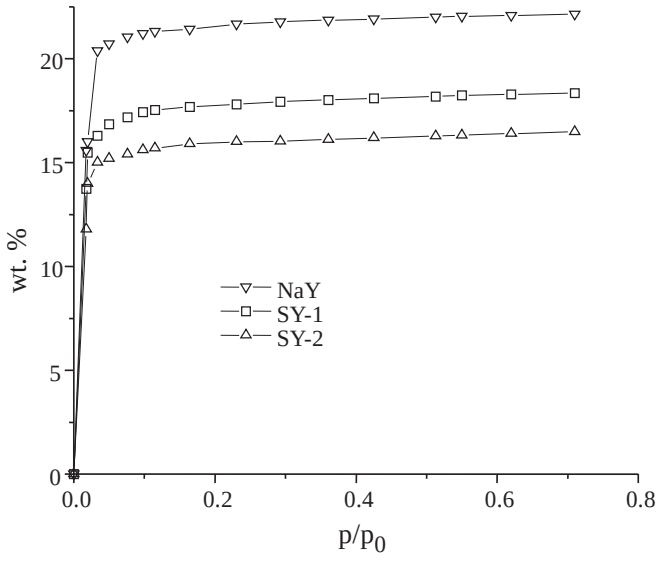

Fig. 6. Sorption isotherms of water in different zeolites Y at 25°C.

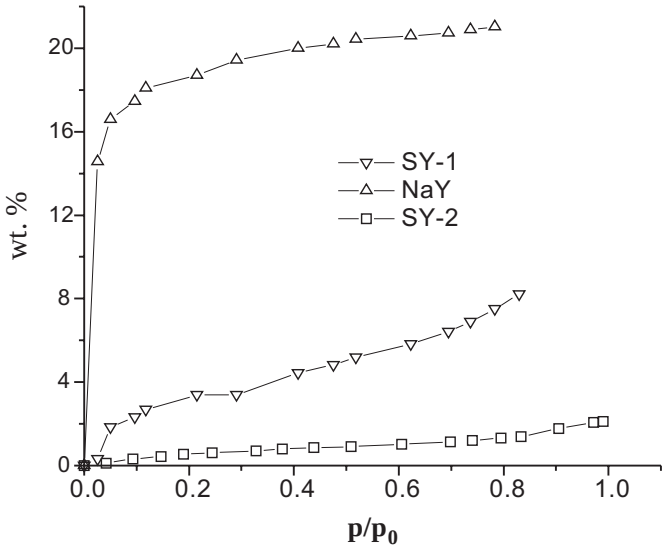

© 1999 NRC Canada

Fig. 7. TG/DTG/DTA curves of ester and water on zeolites Y. (—) DTG, (---) TG, (···) DTA, (↓) endothermic effect.

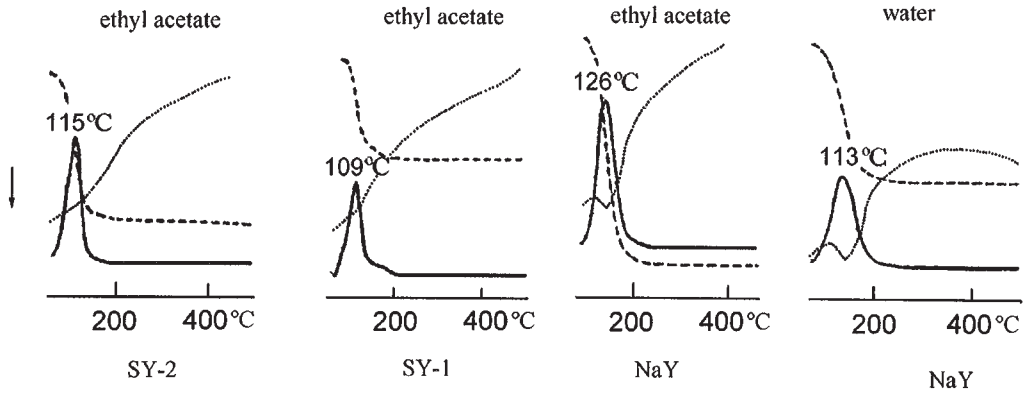

Fig. 8. SEM of the 5 wt.% SY-1-filled silicone rubber membrane.

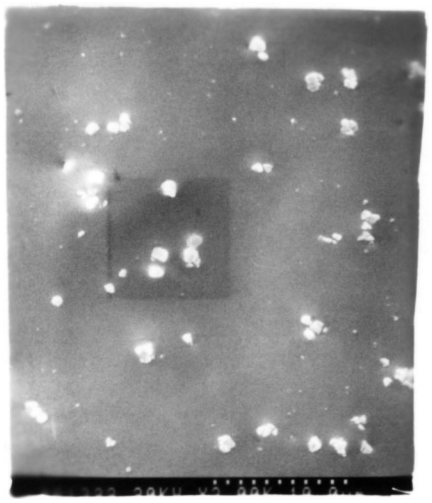

Fig. 9. Sorption isotherms of ethyl acetate in membranes filled with 5 wt.% of different zeolites Y.

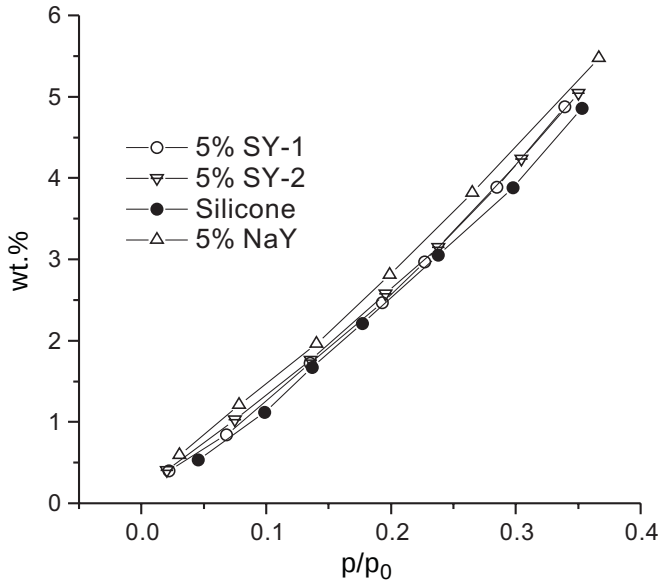

Fig. 10. Sorption isotherms of water in membranes filled with 5 wt.% of different zeolites Y.

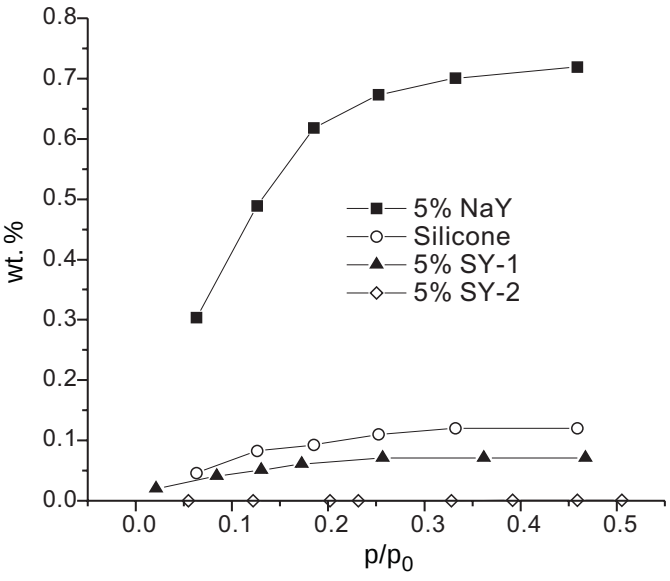

are higher than those through the pure silicone membrane. This can be explained by the increase in both the sorption and the overall diffusion coefficients of the ester molecules. Indeed, the diffusion of a molecule in a polymer is connected with the ability of the polymer to physically accommodate the permeate, and to continually provide opportunity, in the form of randomly generated void, for the permeants to progress (23). The ester molecules which are sorbed in the zeolite pores can be rapidly exchanged with the coming ester molecules. Although the free volume in the polymer phase would not change, this results in a faster migration down the chemical potential gradient, through the inter-particle polymer phase. As the sorption is selective in the SY-type zeolite, water molecules do not preferentially take the same paths through the zeolite particles due to the sorption selectivity and have to go around them in the polymer phase. Thus, the water flux decreases, and the ester flux increases, leading to an increase in the selectivity of the SY-zeolite-filled membranes. The increase in the total flux means that the gain in the ester flux is larger than the loss in water flux. Due to its higher hydrophobicity, the SY-2 gives rise to the most selective membrane. The situation is reversed for the membrane filled with the NaY zeolite. The latter zeolite is hydrophilic, thus favors water migration in its pores. However, the selectivity is only reduced from that

© 1999 NRC Canada

Table 2. Pervaporation characteristics of zeolite Y-filled silicone membranes.

		Membrane filled with		
	Unfilled	NaY	SY-1	SY-2
Total flux (g/m^2 h 100 μm)	279	288	296	293
Water flux (g/m^2 h 100 μm)	61	74	53	44
Selectivity	284	228	365	455

of the pure silicone membrane, but not reversed, due to the overall hydrophobicity of the filled membranes. It also appears that the sorption capacity of the zeolite is not the major factor in the selectivity improvement of the zeolite-filled membranes.

In conclusion, it appears that (*i*) the hydrophobic zeolites Y as fillers have a significant effect on the silicone membrane properties, even at a filler content level as low as 5 wt.%, and (*ii*) the ester sorption, permeation selectivity, and flux of the filled membranes increase with the filler Si/Al ratio.

Acknowledgements

The authors are grateful to the National Natural Science Foundation of China (grant CH 29236120-03) and to the AFCRST (grant PRA E 97-04) for their support of this work. The authors also wish to thank Prof. Ming Jian for his helpful suggestions.

References

1. M. Goldman, D. Frannkel, and G. Levin. J. Appl. Poly. Sci. **37**, 1791 (1989).
2. Z. Gao, Y. Yue, and W. Li. Zeolites, **16**, 70 (1996).
3. J.C.Te. Hennepe, D. Bargeman, M.H.V. Mulder, and C.A. Smolders. J. Membr. Sci. **35**, 39 (1987).
4. J.C.Te. Hennepe, W.B.F. Boswerger, D. Bargeman. M.H.V. Mulder, and C.A. Smolders. J. Membr. Sci. **89**, 185 (1994).
5. D. Jia, K.V. Peinemann, and R.D. Behling. J. Membr. Sci. **73**, 119 (1992).
6. F.J. Vankelecom, D. Depré, S.D. Beukelaer, and J.B. Uytterhoeven. J. Phys. Chem. **98**, 1230 (1994).
7. F.J. Vankelecom, D. Depré, S.D. Beukelaer, and J.B. Uytterhoeven. J. Phys. Chem. **99**, 1393 (1995).
8. Z-H. Ping, Y.C. Long, X. Chen, X.H. Chen, T.Q. Nguyen, and J. Néel. Récents Prog. Génie Proc. **6**, 395 (1992).
9. X. Chen, Z.-H. Ping, S.-K. Fu, and Y.-C. Long. Chem. J. Chin. Univ. **14**, 154 (1993) (in Chinese).
10. Y.-C. Long, X. Chen, Z.-H. Ping, S.-K. Fu, and Y.-J. Sun. Surf. Sci. Catal. **84**, 1083 (1994).
11. X. Chen, Zh.H. Ping, and Y.C. Long. J. Appl. Poly. Sci. **67**, 629 (1998).
12. Y.C. Long, M.Y. Jin, Y.J. Sun, T.L. Wu, L.P. Wang, and L. Fei. J. Chem. Soc. Faraday Trans. **92**, 1647 (1996).
13. J. Jänchen and H. Stach. Zeolites, **5**, 57 (1985).
14. H. Stach, U. Lohse, H. Thamm, and W. Schirmer. Zeolites, **6**, 74 (1986).
15. K. Beyer, I. Belenykaja, F. Hange, M. Tielen, P.J. Grobet, and P.A. Jacobs. J. Chem. Soc. Faraday Trans. 1, **81**, 2889 (1985).
16. M.W. Anderson and J. Klinowski. J. Chem. Soc. Faraday Trans. 1, **82**, 1449 (1986).
17. V. Patzelová, E. Drahorádová, and U. Lohse. Zeolites, **9**, 74 (1989).
18. T. Kerr. Zeolites, **9**, 350 (1989).
19. P.J. Grobet, P.A. Jacobs, and H.K. Beyer. Zeolites, **6**, 47 (1986).
20. J. Sanz, V. Fornés, and A. Corma. J. Chem. Soc. Faraday Trans. 1, **84,** 3113 (1988).
21. H. Yang, Q.T. Nguyen, Y.C. Long, Y.J. Sun, and Z.H. Ping. Phys. Chem. Chem. Phys. **1**, 2621 (1999).
22. R. Paul and D.R. Kemp. J. Polym. Sci. Symp. Ed. **41**, 79 (1973).
23. H.L. Frisch and S.A. Stern. Crit. Rev. Solid State Mater. Sci. **11**, 123 (1983/1984).

© 1999 NRC Canada

Thiol functionalization of surfaces for biosensor development

Mark E. McGovern and Michael Thompson

Abstract: The immobilization of biomolecules on substrate surfaces for biosensor development requires linking molecules that must meet a specific set of criteria. Two such agents based on bifunctional alkyltrichlorosilane structures, 1-bromo-11-(trichlorosilyl)-undecane and 1-(thiotrifluoroacetato)-11-(trichlorosilyl)-undecane, are employed to generate thiol-functionalized surfaces either by nucleophilic substitution followed by reduction (bromine-containing derivative) or deprotection (fluorine-containing compound). Both molecules have been attached to the surfaces of silicon wafers in conjunction with the diluent silane, octyltrichlorosilane. X-ray photoelectron spectroscopic analysis in the conventional and angle-resolved modes confirms that both silanization reactions were successful. The alkyl-bromine surfaces were subjected to treatment with a set of nucleophilic reactants followed by reduction and derivatization with trifluoroacetic anhydride. The latter in conjunction with surface analysis was used to estimate the level of thiol functionalization achieved. The fluorine-containing undecane surface has been studied by surface analysis both before and after deprotection of the thiol group by hydroxylamine solution. The results indicate that a high coverage of the surface was found for the protected moiety, with approximately 10% of the trifluoro acetate groups remaining after the deprotection procedure.

Key words: bifunctional silanes, thiol surface functionalization, biomolecule immobilization, X-ray photoelectron spectroscopy.

Résumé : Lors du développement de biosenseurs, l'immobilisation de biomolécules sur les surfaces de substrats requière la présence de molécules liantes qui répondent à un ensemble de critères bien définis. Pour générer des surfaces avec thiols fonctionnalisés, on a utilisé deux de ces agents comportant des structures alkyltrichlorosilanes bifonctionnelles, les 1-bromo-11-(trichlorosilyl)-undécane et 1-(trifluoroacétato)-11-(trichlorosilyl)-undécane, en faisant appel à une réaction de substitution nucléophile suivie d'une réduction (dérivé contenant du brome) ou une réaction de déprotection (composé contenant du fluor). Les deux molécules ont été liées aux surfaces de tranches silicium en même temps que le silane utilisé pour diluer, l'octyltrichlorosilane. Des analyses par spectroscopie photoélectronique de rayons X, dans les modes tant conventionnels que résolus en fonction de l'angle, confirment que les deux réactions de silanisation ont réussi. Les surfaces du bromure d'alkyle ont été soumises à un traitement par un ensemble de réactifs nucléophiles, suivi d'une réduction et d'une transformation en dérivé à l'aide de l'anhydride trifluoroacétique. Pour évaluer le degré de fonctionnalisation du thiol, on a fait appel à ce traitement combiné avec une analyse de surface. On a étudié la surface undécane contenant du fluor par une analyse de surface avant ainsi qu'après la déprotection du groupe thiol par une solution d'hydroxylamine. Les résultats indiquent que la portion protégée de la surface est bien recouverte; on a trouvé qu'environ 10 % des groupes trifluoroacétates sont encore présents après la déprotection.

Mots clés : silanes bifonctionnels, fonctionnalisation d'une surface de thiol, immobilisation de biomolécules, spectroscopie photoélectronique des rayons X.

[Traduit par la Rédaction]

Introduction

A key feature of the construction of biosensors is the immobilization of protein molecules or single strands of oligonucleotide to the surface of the device (1). Many strategies have been evolved for the immobilization of biomolecules in general to surfaces (2–11). One route to such a structure is that provided by bifunctional silanes, especially if the underlying device surface is amenable to silane chemistry. Such a moiety must contain a hydrocarbon chain of 8–18 carbons in length for the self-assembly process to function and be capable of synthesis and purification by relatively facile procedures (!12). An additional factor is the possibility for ease of surface characterization by X-ray photoelectron spectroscopic (XPS) analysis (13). The bifunctional trichlorosilanes constitute an attractive route for the immobilization of biomolecules on sensor surfaces.

Several reviews have been published recently regarding silane technology and self-assembled monolayers, and their many potential applications in science and industry (14–17).

Received August 10, 1999.

M.E. McGovern and M. Thompson.[1] Department of Chemistry, University of Toronto, 80 St. George Street, Toronto, ON M5S 3H6, Canada.

[1]Author to whom correspondence may be addressed. Telephone and fax: (416) 978-3575. e-mail: mikethom@chem.utoronto.ca

© 1999 NRC Canada

Trichlorosilanes can be synthesized by controlled reaction of a Grignard or alkyl lithium reagent with tetrachlorosilane or by hydrosilylation using trichlorosilane and a terminal alkene (13, 14). The latter is the preferred route because it produces a monoalkyltrichlorosilane in high yield, and is tolerant of many types of multifunctional molecules. Silanes with 11-, 16-, or 17-carbon chain lengths are most commonly used, both because they can undergo the self-assembly process, and the fact that intermediates are readily accessible. ω-Undecenyl alcohol or the carboxylic acid are both readily available at low cost and can be transformed into virtually any desired functionality. ω-Hexa- and ω-heptadecenyl intermediates are unavailable, but can be made by cross-coupling ω-undecenyl bromide with 1,5-bromopentane or 1,6-bromohexane to yield the long-chain bromides, which require extensive purification to be useable for hydrosilylation (13, 15). With respect to reaction with a biochemical species, the terminal group of a trichlorosilane can be employed as a nucleophile or act as a leaving group in an S_N2 environment. An example of a compound that can act in both capacities is 1-bromo-11-(trichlorosilyl)-undecane (BTU). (18–21). This molecule can be used to produce an alkylbromide functional surface, which reacts directly with nucleophile-bearing probes, or it can be transformed after the silanization reaction into a nucleophilic group such as a thiol. Other leaving groups such as the more reactive chloro and iodo acetates as well as benzylic bromides have been developed (22), but the main disadvantage with these molecules is their complex synthesis. An alternative pathway to the generation of thiol-functionalized silanes is the direct incorporation of a protected sulfur-containing functionality. Such an acetyl-protected thiol has been described in the literature (13), but appears to suffer from several drawbacks. Deprotection requires strongly basic conditions, which are detrimental to silane adhesion, and the deprotection step itself may be difficult to effect completely. Accordingly, we chose to synthesize a new silane 1-(thiotrifluoroacetato)-11-(trichlorosilyl)-undecane (TTU), which incorporates the trifluoroacetyl group (TFA). The trifluoroacetyl thiol esters are compounds known to be stable in the absence of moisture (23), and the TFA functionality is hydrolyzed in a facile manner, under mild conditions, resulting in greater yields in terms of deprotection. An added bonus with respect to surface immobilization with TTU is that XPS analysis of fluorine in the TFA moiety provides a highly sensitive method for surface characterization, especially if high dilution of the thiol-containing surface is envisaged.

In the present paper, we describe a comparison of the generation of thiol-functionalized surfaces using both BTU and TTU. After silanization with the former compound, the alkyl bromide group is converted to a thiol, whereas the analogous reaction with TTU followed by deprotection yields the same entity. To effect a direct comparison of surface population with these molecules, we have labelled the surface-bound thiol from the BTU procedure with trifluoroacetic anhydride (TFAA) (13). This protocol allows the facile XPS analysis of both surfaces, if the determination for TTU is conducted before the deprotection stage. The reason for the choice of XPS analysis of fluorine lies in the insensitivity of this technique for sulfur and, secondly, the coincidence of the S2*p* binding energy with a surface plasmon peak of substrate silicon. Finally, we note that the surface immobilizations for both TTU and BTU involve silanizing mixtures incorporating monofunctional silane.

Experimental

Materials

ω-Undecenyl alcohol 98%, potassium thioacetate 98%, trifluoroacetic anhydride 99+% (TFAA), hydrogen hexachloroplatinate (IV) hydrate 99.995%, trichlorosilane 99%, 97%, neutral alumina (standard grade, 150 mesh, 58 Å), silica gel (Merck, grade 9385, 230–400 mesh 60 Å), octadecyltrichlorosilane (OTS), octyltrichlorosilane (C8), potassium thiocyanate, tetrabutylammonium thiocyanate, hydroxylamine HCl, methanol, chloroform, dimethylformamide (DMF), 1 M lithium aluminum hydride in tetrahydrofuran (THF) were all obtained from Aldrich and used without further purification. Triphenylphosphine 98%, *N*-bromosuccinimide (NBS) 98%, anhydrous magnesium sulfate, phosphorus pentoxide, potassium hydroxide, hexanes, diethyl ether, tetrahydrofuran, isopropanol, methanol, and hydrochloric acid were purchased from BDH and were used without further purification. Dichloromethane and acetonitrile were purchased from BDH and were distilled over phosphorus pentoxide before use. Pyridine was obtained from BDH and was distilled over KOH before use. Toluene was distilled over Na under N_2 immediately before use. Hydrogen peroxide (30%) was obtained from Anachemia and was used as received. Magnesium nitrate hexahydrate was obtained from Sigma. Orvus soap was obtained from Stepan Canada Inc. under the product name "Stepanol WAC." Silicon wafers obtained from International Wafer Service were supplied approximately 0.4 mm thick and were polished on one side to a mirror finish. They were cut to a size of approximately 1 × 1 cm using a diamond-tipped pencil.

Instrumentation

NMR spectra are reported in units of δ and were recorded on either a Varian Gemini 200 spectrometer using a ^1H–^{13}C switchable probe, or on a Varian VXR400S spectrometer (^1H, ^{13}C, ^{19}F, ^{29}Si) using a 5 mm switchable probe. In the case of ^{29}Si, either inverse-gated decoupling or DEPT were used. The samples were dissolved in $CDCl_3$, which contained 0.03% tetramethylsilane (TMS). Both ^1H and ^{29}Si NMR spectra were referenced to TMS at 0.00 ppm, while ^{13}C NMR spectra were referenced to the center of the $CDCl_3$ triplet at 77.00 ppm. ^{19}F NMR spectra were calibrated using an external $CFCl_3$ standard (0.00 ppm).

Elemental analysis was performed by Canadian Microanalytical Service Ltd. (Delta, B.C.). The trichlorosilanes were handled in an inert atmosphere during various procedures. All elements except oxygen were determined for the TTU sample.

Fourier-transform infrared spectroscopy was performed on Nicolet 5DXB spectrophotometer using the manufacturer's software. Ten scans were collected and averaged at a resolution of 2 cm^{-1} and were referenced to polystyrene. The liquid samples were run neat on NaCl disks.

X-ray photoelectron spectra were recorded on a Leybold MAX-200 X-ray photoelectron spectrometer using an

© 1999 NRC Canada

Fig. 1. Synthetic pathways to BTU and TTU.

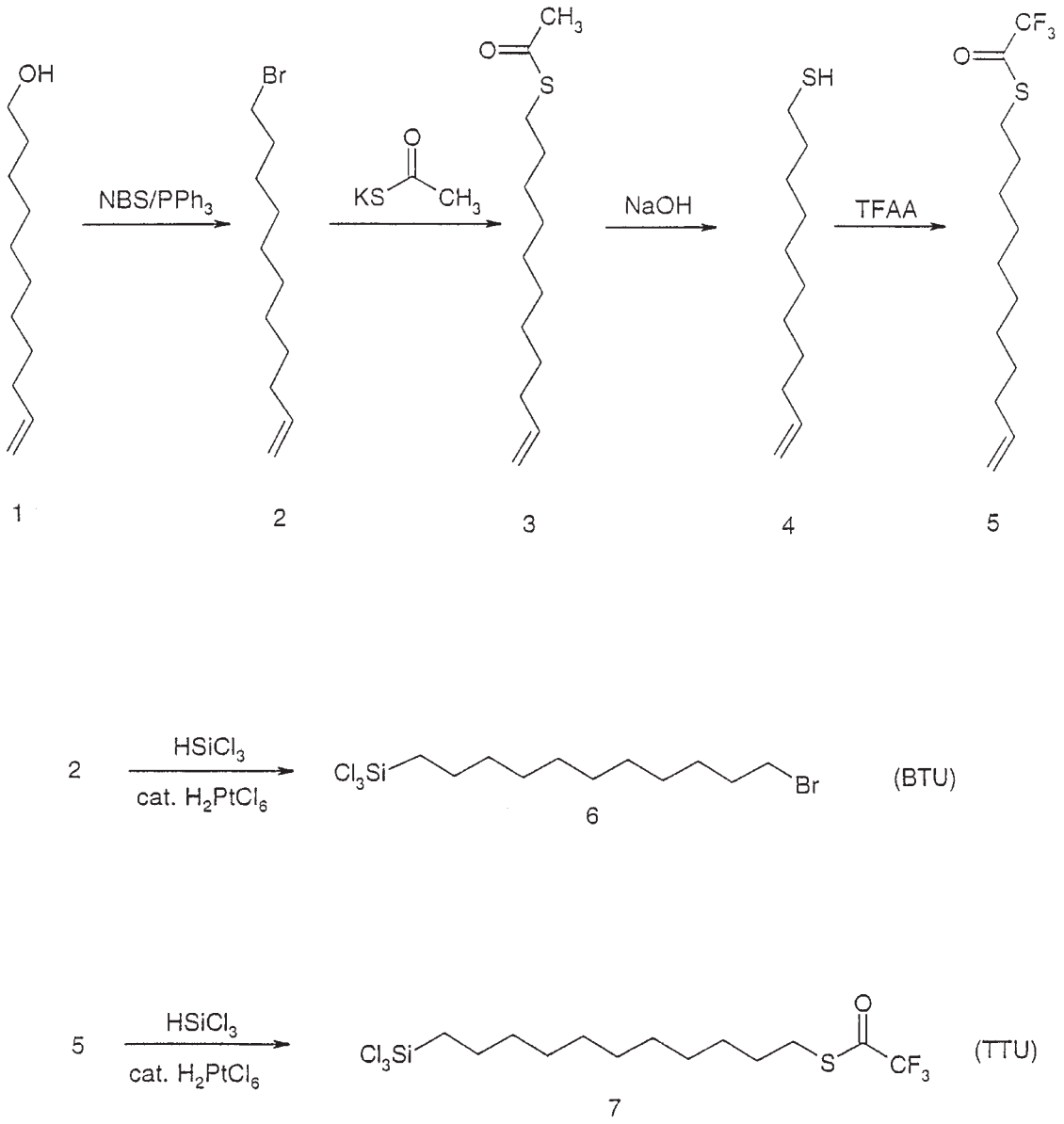

unmonochromatized Mg K_α source run at 15 kV and 20 mA. The energy scale of the spectrometer was calibrated to the Ag $3d_{5/2}$ and Cu $2p_{3/2}$ peaks at 368.3 and 932.7 eV, respectively. The binding energy scale was calibrated to 285 eV for the main C(1*s*) feature. For all samples, a survey run (pass energy = 192 eV, 0–1000 eV on the binding energy scale was recorded. X-ray analysis area was 4 × 7 mm, for determinations performed at a 90° angle relative to the electron detector). Angle-resolved XPS spectra were obtained using a 2 × 4 mm analysis area at various angles relative to the surface normal. Satellite subtraction and normalization were performed with software obtained from the manufacturer. Quantitation of spectra was performed using empirically derived sensitivity factors (obtained from the manufacturer), and for the Mg anode, the sensitivity factors were; C(1*s*) = 0.34, F(1*s*) = 1.00, O(1*s*) = 0.78, and Si(2*p*) = 0.4. Peak fitting and data analysis was performed using ESCA Tools software, which requires MATLAB (MS-windows version).

Optical microscopy was performed with a Sony CCD color video camera module XC-999/999P using a 10X Nikon lens with a separate fiber optic illumination from side angles. The images were displayed on a 13 in. (1 in. = 25.4 mm) Sony Trinitron monitor and were captured from the screen on standard black and white 400 ASA 35 mm film using a standard 35 mm camera. The magnification achieved was 260X.

Procedures

The various intermediates and silanes described in this work together with a summary of synthetic pathways are summarized in Fig. 1.

(1) Synthesis of intermediates

ω-*Undecenyl bromide (compound 2)*

In a flame-dried dual-necked 200 mL round-bottom flask with teflon coated magnetic stir bar, equipped with a con-

© 1999 NRC Canada

denser and N_2 inlet were placed 8.5 g (50 mmol) of ω-undecenyl alcohol **1** and 100 mL of dry dichloromethane. The flask was covered with aluminum foil and mixture stirred and cooled in a CCl_4 – dry ice bath (–23°C). Triphenylphosphine, 15.7 g (60 mmol), was added to the mixture and stirred until it dissolved. NBS, 9.8 g (55 mmol), was added to the mixture and stirred at –23°C for 1 h. The flask was removed from the cold bath and the mixture allowed to stir at room temperature for 30 min. The solution was transferred to a separatory funnel and washed with water saturated with sodium carbonate. The organic layer was dried with $MgSO_4$, filtered, and concentrated on a rotary evaporator. The purple precipitate was extracted with 3 × 50 mL aliquots of hexanes using a combination of mechanical stirring, heat, and sonification. The resulting suspension was filtered, and the hexanes removed on a rotary evaporator. The material was filtered through a short column of neutral alumina (5 cm ht., 3 cm diam.) using hexanes under vacuum and the product concentrated on a rotary evaporator to yield a clear liquid. Yield 10.64 g (91%); IR (neat): 3074, 2926, 1639, 1458, 999, 909 cm^{-1}; ^1H NMR (400 MHz, $CDCl_3$) δ: 5.79 (^1H, dddd, J = 17.2, 10.2, 7.0, 7.0 Hz), 4.93 (2H, m), 3.38 (2H, t), 2.02 (2H, dd, J = 6.2, 1.1. Hz), 1.83 (2H, m), 1.24–1.44 (12H, m); ^{13}C NMR (400 MHz, $CDCl_3$) δ: 139.03, 114.05, 33.93, 33.79, 32.86, 29.38, 29.08, 28.92, 28.76, 28.18.

*ω-Undecenyl thioacetate (compound **3**)*

In a 50 mL round-bottomed flask with teflon-coated magnetic stir bar, equipped with a condenser and N_2 inlet, were placed 3.50 g (15 mmol) of ω-undecenyl bromide (**2**), 1.71 g (15 mmol) of potassium thioacetate and 25 mL of 95% ethanol. The mixture was refluxed overnight after which the solution was transferred to a separatory funnel, 50 mL of water added and followed by extraction with 3 × 50 mL aliquots of hexanes. The organic layer was dried with $MgSO_4$, filtered, and concentrated on a rotary evaporator. Yield 3.32 g (97%); IR (neat): 3074, 2926, 1696, 1639, 1458, 1360, 1138, 999, 909 cm^{-1}, ^1H NMR (400 MHz, $CDCl_3$) δ: 5.79 (1H, ddd, J = 17.2, 10.2, 7.0, 7.0 Hz), 4.93 (2H, m), 2.85 (2H, t), 2.35 (3H, s), 2.02 (2H, dd, J = 6.2, 1.1 Hz), 1.55 (2H, m), 1.24–1.44 (12H, m); ^{13}C NMR (400 MHz, $CDCl_3$) δ: 195.91, 139.12, 114.07, 33.79, 30.62, 29.49, 29.39, 29.38, 29.14, 28.90, 28.79.

*ω-Undecenyl thiol (compound **4**)*

In a 50 mL round-bottomed flask with teflon-coated magnetic stir bar, equipped with condenser and N_2 inlet, were placed 2.0 g (8.76 mmol) of ω-undecenyl thioacetate (**3**), 20 mL of 95% ethanol, and 5 mL of 1 M NaOH. The mixture was refluxed for 1 h after which the solution was transferred to a separatory funnel, 50 mL of water added followed by extraction with 3 × 50 mL aliquots of hexanes. The organic layer was dried with $MgSO_4$, filtered, and concentrated on a rotary evaporator. Note: this material should be used immediately or stored in a frozen state. Yield 1.49 g (91%); IR (neat): 3074, 2926, 2550, 1639, 1458, 999, 909 cm^{-1}; ^1H NMR (400 MHz, $CDCl_3$) δ: 5.79 (1H, dddd, J = 17.2, 10.2, 7.0, 7.0 Hz), 4.93 (2H, m), 2.52 (2H, dd, 8.0, 4.0), 2.02 (2H, dd, J = 6.2, 1.1 Hz), 1.57 (1H,t), 1.24–1.44 (12H, m); ^{13}C NMR (400 MHz, $CDCl_3$) δ: 138.09, 114.07, 34.04, 33.78, 29.44, 29.39, 29.08, 29.04, 28.90, 28.36, 24.63.

*ω-Undecenyl thiotrifluoroacetate (compound **5**)*

In a 25 mL round-bottomed flask with teflon-coated magnetic stir bar were placed 0.939 g (3.33 mmol) of ω-undecenyl thiol (**4**) and 5 mL of dry pyridine. Trifluoroacetic anhydride, 0.699 g (0.33 mmol), was added, and the mixture stirred at room temperature for 30 min while stoppered. The pyridine was removed under vacuum and the solid material extracted with 3 × 20 mL aliquots of hexanes. The hexanes were removed with a rotary evaporator to yield an oil. The oil was distilled via Kugelrohr distillation apparatus, and a fraction was collected at 90°C at 0.1 mmHg (1 mmHg = 133.3 Pa). Yield 0.556 g (59%); IR (neat): 3074, 2926, 1704, 1639, 1458, 1285, 1203, 1162, 999, 909 cm^{-1}; ^1H NMR (400 MHz, $CDCl_3$) δ: 5.79 (1H, dddd, J = 17.2, 10.2, 7.0, 7.0 Hz), 4.93 (2H,m), 3.05 (2H, t), 2.02 (2H, dd, J = 6.2, 1.1 Hz), 1.55 (2H, m), 1.24–1.44 (12H, m); ^{13}C NMR (400 MHz, $CDCl_3$) δ: 184.81, 139.03, 114.11, 33.79, 29.43, 29.35, 29.32, 29.29, 28.95, 28.90, 28.67, 28.60, 24.66.

(2) Synthesis of silanes

*1-Bromo-(trichlorosilyl)-undecane (BTU, compound **6**)*

In a flame-dried heavy-walled ampoule were placed 2.03 g (8.7 mmol) of ω-undecenyl bromide (**2**), 1 mL of a 0.01 M H_2PtCl_6 sol in THF, and 1.35 g (10 mmol) of $HSiCl_3$. The ampoule was sealed at –195°C, and after thawing at room temperature, it was heated at 90°C overnight. The ampoule was opened at –195°C, and the remaining $HSiCl_3$ and THF removed under low vacuum. The main contents of the ampoule were distilled using a Kugelrohr distillation apparatus. The product distilled at 120–130°C at 0.4 mmHg. Yield 1.40g (69%); ^1H NMR (400 MHz, $CDCl_3$) δ 3.38 (2H, t), 1.84 (2H, m), 1.55 (2H, m), 1.24–1.44 (16H, m); ^{13}C NMR (400 MHz, $CDCl_3$) δ 34.05, 23.88, 31.84, 29.51, 29.43, 29.25, 29.04, 28.81, 28.23, 24.38, 22.31; ^{29}Si NMR (400 MHz, $CDCl_3$) δ 13.31.

*1-(Thiotrifluoroacetato)-11-(trichlorosilyl)-undecane (TTU, compound **7**)*

In a flame dried heavy-walled ampoule were placed 0.99g (3.5 mmol) of ω-undecenyl thiotrifluoroacetate (5), 0.47 g (3.5 mmol) of $HSiCl_3$, and 1 drop of a 4% sol of H_2PtCl_6 in isopropanol. The ampoule was sealed at –195°C and after thawing at room temperature, it was heated at 60°C overnight. The vial was then opened at –195°C and the remaining $HSiCl_3$ removed under low vacuum. The main contents of the ampoule were distilled using a Kugelrohr distillation apparatus. The product distilled at 140°C at 0.1 mmHg. Yield 1.17 g (80%); ^1H NMR (400 MHz, $CDCl_3$) δ: 3.05 (2H,t), 1.20–1.80 (20H, m); ^{13}C NMR (400 MHz, $CDCl_3$) δ: 184.90, 115.53, 31.82, 29.45, 29.35, 29.30, 29.00, 28.97, 28.68, 28.63, 24.32, 22.28; ^{29}Si NMR (400 MHz, $CDCl_3$) δ: 13.32; Elem. anal. calcd. (%): C 37.47, H 5.32, F 13.68, S 7.69, Cl 25.52, Si 6.74; found: C 38.91, H 5.58, F 8.32, S 9.05, Cl 21.92, Si 1.20.

(3) Silanization of silicon wafers

The wafers were first gently washed with Orvus soap solution by hand to gently remove large dust particles, then

© 1999 NRC Canada

rinsed copiously with distilled water and dried in air. The wafers were then washed with chloroform, blown dry with nitrogen, and then sonicated in 30% hydrogen peroxide for 30 min. They were rinsed five times with deionized water, and then were placed in an oven at 120°C for 30 min. The wafers were stored in a humidity chamber, which contained water saturated with $Mg(NO_2)_2$ overnight. The hydrated wafers were then quickly removed from the humidity chamber and placed into test tubes (previously silanized with OTS) and stoppered. A dry box filled with air (dried through a Drierite/molecular sieve train) was used to provide a low-moisture environment for the silanization reactions. The substrates were silanized for 2 h using 2 mL of a 1×10^{-3} M solution in dry toluene of one of the following mixtures: 50% BTU – 50% C8, or 50% TTU – 50% C8. The samples were then rinsed with dry toluene, then with chloroform before being dried under nitrogen.

(4) Thiol-functionalized surfaces and derivatization (BTU)

The 50% BTU – 50% C8 surfaces were placed individually into test tubes to be followed by treatment with 2 mL of a 1 M solution of either potassium thioacetate, potassium thiocyanate, or tetrabutylammonium thiocyanate in DMF for 1 h, and 4 h at room temperature, and for 1 h and 4 h at 60°C. After the reaction, the samples were rinsed five times with 2 mL of DMF, then three times with 2 mL of methanol.

To reduce the products obtained above, the samples were soaked in 2 mL of 1 M lithium aluminum hydride in THF under nitrogen for 1 h, rinsed with THF, soaked in 1 M HCl for 1 h, rinsed with deionized water, and then washed with methanol. The samples were then treated with 2 mL of 0.1 M TFAA in pyridine for 30 min, followed by a brief rinse with dry chloroform.

(5) Deprotection of thiol-functionalized surfaces (TTU)

Wafers with TTU immobilized on their surfaces were treated with 2 mL of 0.5 M NH_2OH in water (pH 8.5) for 2 h at room temperature. This was followed by rinsing with copious amounts of water before final washing with methanol and drying by a stream of N_2 gas.

Results and discussion

Strategy for silanization

Two aspects of the present work with regard to the overall protocols used for silanization deserve comment. Previous work in our laboratory has confirmed that the density of silane films deposited on glass is determined by the solvent extraction of surface moisture followed by silane hydrolysis prior to deposition. (Accordingly, geometric comparisons between the solvent molecule and silane hydrocarbon moiety should not be invoked to explain the formation of surface-bound silane films.) This observation leads to an optimum protocol for generating close-packed monolayers of silanes on hydroxylated substrates such as silicon, and this was employed in the present work. To achieve the formation of such layers, the silicon wafers were subjected to an atmosphere of controlled humidity prior to silanization involving anhydrous toluene as the reaction medium (24).

The second point concerns the dilution of the reacting bifunctional silanes, BTU and TTU, with octyltrichlorosilane to a level of 50% mol/mol total silane. This value represents a compromise deduced from observations made with respect to low XPS sensitivity at high levels of BTU dilution, and unwanted surface reactions at dilution values higher than 50%. With regard to the latter, increased proximity appears to result in cross-linking of thiol groups present in the monolayer by surface oxidation. Clearly, this is disadvantageous in terms of the subsequent reaction of surface functional groups with derivatized biological macromolecules. Finally, for surface analysis we required to maximize the detection of surface functional groups by XPS. This led us to the choice of 50% bifunctional silane, but this value can be adjusted with facility to allow control of the final population of thiol groups on the silanized surface.

Thiol-functionalized surfaces via BTU

X-ray photoelectron spectra of a silicon wafer recorded immediately after the substrate had been treated with a 50% mol/mol mixture of BTU and octyltrichlorosilane is shown in Fig. 2. Corresponding XPS high-resolution data together with peak identifications are presented in Table 1. The presence of covalently bound bromine confirms the successful silanization of the silicon surface.

X-ray photoelectron spectroscopy alone cannot provide an absolute value for the amount of BTU deposited on the surface per unit area. However, it is possible to compare the ratio of the bromine-to-carbon signal intensities (adjusted for sensitivity using Scofield parameters) obtained by experiment with those calculated on a theoretical basis for a self-assembled monolayer (of bifunctional silane and C8). Such a comparison can lead to an approximate measure of the yield with respect to attachment of covalently bound bromine groups to the wafer. This theoretical calculation, which is based on the premise that the silane mixture creates an "ideal" close-packed structure, can be presented in the following general format:

$$[1] \qquad \frac{E_{XPS}}{C_{XPS}} = \frac{(E \times f_1 \times f_2)}{(f_1 \times C_1 + (1 - f_1) \times C_2)}$$

where E_{XPS}/C_{XPS} is the theoretical ratio for a particular element to carbon, C_1 and C_2 are the numbers of carbon atoms in the active and diluent silanes, respectively, f_1 represents the weight fraction of active silane in the mixture and f_2 the purity of the active silane (usually assumed to be 1.0). Several assumptions are implicit in this model:

(*i*) Competition for film growth between active and diluent silanes is considered to be negligible, i.e., the surface ratio of the two silanes simply reflects their bulk solution conditions.

(*ii*) Other bromine or carbon-containing materials are absent in the system.

(*iii*) The film is a monolayer.

Experimentally, an XPS Br3*d*/Si2*p* average of 0.017 was obtained for two BTU and silane diluent controls, which should be compared with the theoretical value of 0.053 (E = 1, C_1 = 11, C_2 = 8, f_1 = 0.5, f_2 = 1.00). Therefore, the level of silanization with respect to the bromine moiety represents a yield of about 31%. Given that previous work has

© 1999 NRC Canada

Fig. 2. Peak fitted X-ray photoelectron spectra of 50% BTU – 50% C8 immobilized on a silicon substrate; (*A*) Ols, (*B*) C1*s*, (*C*) Si2*p*, (*D*) Br3*d*.

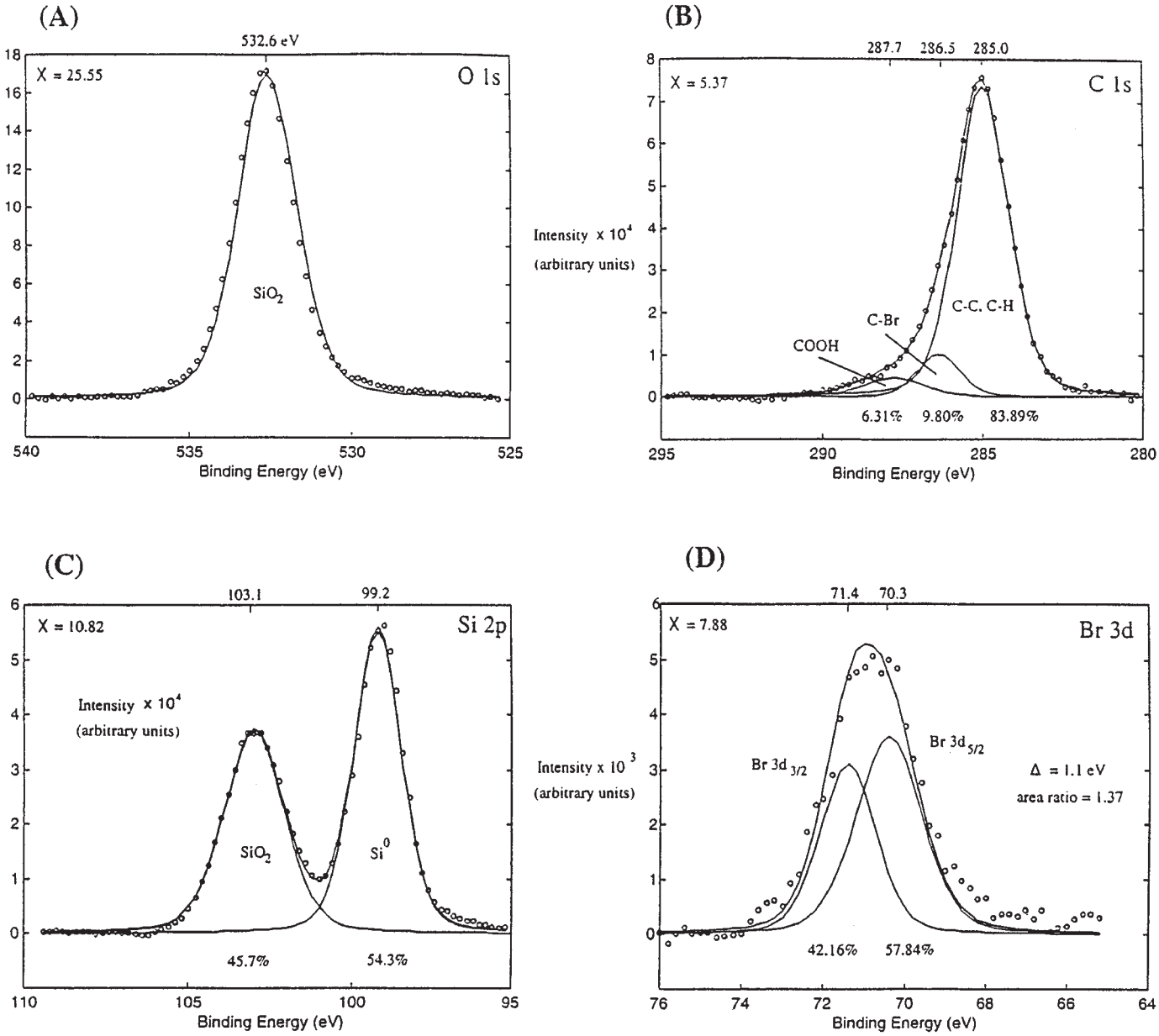

Table 1. High-resolution XPS analysis of 50% BTU – 50% C8 on silicon.

Signal	Binding energy (eV)	Atomic weight (%)	Ident.	Chi (χ) value[a]
O1*s*	532.6	100	SiO_2	25.55
C1*s*	285.0	83.9	C-C	5.37
	286.5	9.8	C-Br	
	287.7	6.3	COOH	
Si2*p*	99.2	54.3	Si°	10.82
	103.1	45.7	SiO_2	
Br3$d_{5/2}$	70.3	57.8	Br-C	7.88
Br3$d_{3/2}$	71.4	42.2	Br-C	

[a]χ = Gaussian curve-fitting parameter as determined by ESCA Tools software.

© 1999 NRC Canada

Table 2. XPS analyses (Br3*d*/Si2*p* ratio) of 50% BTU – 50% C8 surface subjected to nucleophilic substitution reactions.[a]

Conditions	Exp. Br3*d*/Si2*p*	Exp. yield (%)[b]
1 M KSCN in DMF		
22°C, 1 h	0.012	45
60°C, 4 h	0.006	71
60°C, 4 h	0.004	80
1 M TBASCN in DMF		
22°C, 1 h	0.031	14
22°C, 4 h	0.008	63
60°C, 1 h	0.017	19
60°C, 1 h	0.002	91
1 M $KSCOCH_3$ in DMF		
22°C, 1 h	0.006	73
22°C, 4 h	0.004	82
60°C, 1 h	0.003	85
60°C, 4 h	0.004	82

[a]Mean of two determinations.

[b]Yield calculated on the basis of the reduction in Br3*d* signal as compared with control BTU sample.

shown that carbon-based contamination on octadecyltrichlorosilane surfaces constitutes no more than approximately 5% of the total carbon analysis, it appears that an explanation based on this source of impurity does not explain the low yield for the BTU film (25). Competition between the two silanes is unlikely to be a significant factor, since the solubility of the two silanes in the reaction solvent is similar. A much more likely explanation for this result lies in the occurrence of a photochemical effect, which is responsible for a reduction in the level of bromine present on the substrate surface. Experiments involving exposure of BTU surfaces to light have confirmed that photochemical cleavage of bromine occurs. Furthermore, it is entirely possible that the XPS X-ray source can instigate similar photochemical processes during the actual surface analysis, since the unmonochromated magnesium X-ray source is also a source of ultraviolet light.

We now turn to a study of the conversion of the alkyl bromine moiety to thiolated surfaces through an initial reaction involving nucleophilic substitution reactions. The mixed silane surfaces were treated with two thiocyanates in addition to potassium thioacetate in dimethylformanide under various conditions of time and temperature. The results presented in Table 2 include the experimental Br to Si intensity ratios corrected for sensitivity factors for the different reactions. The experimental yield is calculated on the basis of the new Br/Si ratio compared to that for the silicon wafer with an intact mixed silane layer in place. In overall terms the results indicate that time of exposure to the three reagents employed is an important factor and that greater removal of Br occurs with the thioacetate anion. This observation likely reflects the enhanced nucleophilic activity of the thioacetate anion over thiocyanate, at least under the conditions employed here.

An additional observation made during these experiments was that a hazy film remained on the silicon wafers subsequent to nucleophile reagent treatment even after considerable solvent washing. These films, under the optical microscope, appeared to be composed of salt-like deposits of reagent, which adhered strongly to the substrate surface. In this regard, it is known that functionalized silane surfaces with medium to high polarity groups can serve as a nucleation site for crystal growth (20). The quantity of salt contaminant increases with reaction time and temperature. Since treatment with thioacetate for a shorter time at room temperature results in a high level of Br removal and minimal fouling, this protocol was employed for subsequent experiments leading to thiol functionalization and derivatization.

Two samples of silicon wafers with 50% BTU attached to their surfaces were exposed to 1 M potassium thioacetate for 2 h at room temperature in DMF. This was followed immediately by reduction with $LiAlH_4$, and after work-up, the thiol surface was derivatized with TFAA in pyridine. The introduction of the TFA group is confirmed by an XPS spectrum (not shown). Since, as mentioned above, the sensitivity of XPS for sulfur is too low to effect a quantitative analysis, the TFA functionality provides a convenient route to determine the thickness and degree of coverage of the BTU-derived thiol on the substrate surface. In the present work, the two samples were analyzed by angle-resolved XPS at four different take-off angles (20°, 30°, 45°, and 90°) with 90° being defined as the position at which the detector is normal to the plane of the sample surface. Fluorine, carbon, and silicon were the main elements of interest, and predictably, the percentage of fluorine was highest at 20°, while carbon and silicon were highest at 90°. To estimate the thickness and coverage of the films, the experimental ratios (F1*s*/C1*s*, C1*s*/Si2*p*, and F1*s*/Si2*p*) are compared to values calculated by a three-layer theoretical model. The following set of equations (eqs. [2]–[4]) (26) describes the relative attenuations experienced by photoelectrons ejected from three surface layers (A, B, and C):

$$[2]\qquad A(\theta) = [(1 - f_c) \times \lambda_a \times [1 - e^{(K_b(\theta))}]] + [f_c \times \lambda_a \times e^{(K_b(\theta))} \times e^{(K_c(\theta))}]$$

$$[3]\qquad B(\theta) = [(1 - f_c) \times \lambda_b \times [1 - e^{(K_b(\theta))}]] + [f_c \times \lambda_b \times [1 - e^{(K_b(\theta))}] \times e^{(K_c(\theta))}]$$

$$[4]\qquad C(\theta) = f_c \times \lambda_c \times [1 - e^{(K_c(\theta))}]$$

where the constants K_b and K_c are related to the particular take-off angle:

$$[5]\qquad K_b(\theta) = \frac{-t_b}{\lambda_b \times \sin\theta}$$

$$[6]\qquad K_c(\theta) = \frac{-t_c}{\lambda_c \times \sin\theta}$$

Where *A* represents the bottom layer, *B* the middle layer, and *C* the top layer. Theta (θ) is the photoelectron take-off angle, *f*(b or c) is the layer fraction coefficient, *t*(b or c) is the layer thickness, and lambda (λ) (a, b, or c) is each respective layer's mean free photoelectron path coefficient. To invoke this model, it was necessary to estimate the various mean free path values, since these are unavailable at the present time. However, for most films of an organic molecular type on an oxidized silicon surface, the mean free paths follow a particular trend. Electrons originating from the substate are

© 1999 NRC Canada

Table 3. Angle-resolved XPS of 50% BTU – 50% C8 on silicon modified with thioacetate anion followed by treatment with TFAA (three-layer model).

Take-off angle (°)	XPS signals	Exp. ratio	Fitted ratio
	Sample 1[a]		
20	F1*s*/C1*s*	0.06	0.07
	C1*s*/Si2*p*	3.12	2.92
	F1*s*/Si2*p*	0.19	0.19
30	F1*s*/C1*s*	0.05	0.05
	C1*s*/Si2*p*	2.57	2.31
	F1*s*/Si2*p*	0.13	0.12
45	F1*s*/C1*s*	0.06	0.04
	C1*s*/Si2*p*	1.97	1.75
	F1*s*/Si2*p*	0.12	0.08
90	F1*s*/C1*s*	0.05	0.04
	C1*s*/Si2*p*	1.26	1.75
	F1*s*/Si2*p*	0.07	0.05
	Sample 2[b]		
20	F1*s*/C1*s*	0.07	0.08
	C1*s*/Si2*p*	3.79	3.67
	F1*s*/Si2*p*	0.27	0.28
30	F1*s*/C1*s*	0.07	0.06
	C1*s*/Si2*p*	2.86	2.65
	F1*s*/Si2*p*	0.19	0.16
45	F1*s*/C1*s*	0.07	0.05
	C1*s*/Si2*p*	1.76	1.87
	F1*s*/Si2*p*	0.12	0.09
90	F1*s*/C1*s*	0.09	0.05
	C1*s*/Si2*p*	1.13	1.87
	F1*s*/Si2*p*	0.10	0.06

[a]Variables: λ_a = 28 Å, λ_b= 35 Å, λ_c = 44 Å; t_b = 2.5 Å, t_c = 1Å, f_c = 0.68.

[b]Variables: λ_a = 28 Å, λ_b= 35 Å, λ_c = 44 Å; t_b = 23 Å, t_c = 1Å, f_c = 0.78.

attenuated the most, and a value of 28 Å is typical, while electrons derived from the carbon layer have an intermediate level of attenuation, and so it was assigned a value of 35 Å. Fluorine is the least attenuated, since it is on top of the film, and was given a value of 44 Å. By varying these values 20%, it was discovered that even large errors in the estimates do not affect the modelled results significantly. Finally, three sets of ratios are generated, which correspond to the three possible combinations of observed values of element signals:

$$[7] \qquad F_{cb}(\theta) = \frac{C(\theta)}{B(\theta)}$$

$$[8] \qquad F_{ba}(\theta) = \frac{B(\theta)}{A(\theta)}$$

$$[9] \qquad F_{ca}(\theta) = \frac{C(\theta)}{A(\theta)}$$

For the work described here, the calculated ratios mentioned above (eqs. [7]–[9]) correspond to the experimental values for F1*s*/C1*s*, C1*s*/Si2*p*, and F1*s*/Si2*p*, respectively.

The fluorine layer was found to be 1 Å thick, and a coverage value of 0.73 was generated on average. The carbon layer was 25 Å thick, therefore, the total film thickness was determined to be 26 Å using the three-layer model. A summary of the experimental and theoretical values is presented in Table 3 (two samples).

The thickness values discussed above can also be evaluated in terms of molecular modelling for a two-component mixture. Since the active silane and the diluent silane are of different chain lengths, a weighted average length must be incorporated into such a model. Assuming that the surface is composed of an ideal, close-packed monolayer, then

$$[10] \qquad T_{avg} = \sin\theta[(t_1 \times f_1) + (t_2 \times (1 - f_1))]$$

In this expression, T_{avg} = the average film thickness in Angstroms, t_1 = the length of the active silane, f_1 = the percentage of active silane in mixture, t_2 = the length of the diluent silane, and theta (θ) = the angle at which the carbon chains may be tilted relative to the surface. The length of each silane was calculated by constructing a computer model and measuring the distance between two atoms, each at a distal end of the molecule. It has been demonstrated that the alkyl chains of an OTS film can be tilted at an angle as low as 75° relative to the normal (12). However, the orientations for these new films are not known, so theta (θ) was assumed to be 90°, and there is little difference between the numerical values for sin 75° (0.96) and sin 90° (1), in any case. Using t_1 = 17.15 Å, t_2 = 8.85 Å, and f_1 = 0.5, the average thickness was calculated to be 13 Å. Given the assumptions made in the three-layer and molecular model calculations, the comparison of values found from XPS data (26 Å) and from geometrical considerations (13 Å) is reasonable. The higher value for the former indicates, possibly, a tendency for several layer formation for the 50% BTU, 50% C8 silanization.

Thiol-functionalized surfaces via TTU

A survey XPS spectrum of a wafer treated with a 50% mixture of TTU and C8, in a similar fashion to that described above for BTU, is depicted in Fig. 3(*A*). Corresponding high-resolution data and peak identifications are given in Table 4. The trifluoromethyl group is found at 689.0 eV in the fluorine spectrum, but it is difficult to observe this group in the carbon spectrum, although it is partially resolved at 292.4 eV (Fig. 3(*B*)). The carbonyl group is observed at 289.0 eV, the carbon attached to sulfur is found at 286.9 eV, and the alkane carbons are found at 285.0 eV, which is also the peak used to calibrate the XPS spectra. The angle-dependent XPS silicon 2*s* spectrum (Fig. 4) shows well-resolved elemental and oxidized silicon peaks and two surface plasmons, which are produced by an energy-loss mechanism caused by silicon photoelectrons releasing a quantized amount of energy to the bulk silicon to produce mechanical motion. Unfortunately, "plasmon 1," occurring at 168.6 eV, obscures any sulfur 2*p* photoelectrons, which should be observed at 165 eV. Changing the angle to 20° improves the situation slightly, as shown in Fig. 4, and a small peak ascribed to sulfur at 164.1 eV can be seen, but is of insufficient magnitude to allow quantitative analysis.

Using a similar approach to that discussed for the BTU silanization, the F1*s*/C1*s* ratio from experimental work can be compared with a theoretical calculation based on eq. [1]. Two measurements made in this manner resulted in a mean

© 1999 NRC Canada

Fig. 3. X-ray photoelectron spectra of 50% TTU – 50% C8 immobilized on a silicon substrate; (*A*) survey spectrum; (*B*) deconvoluted C1*s* spectrum.

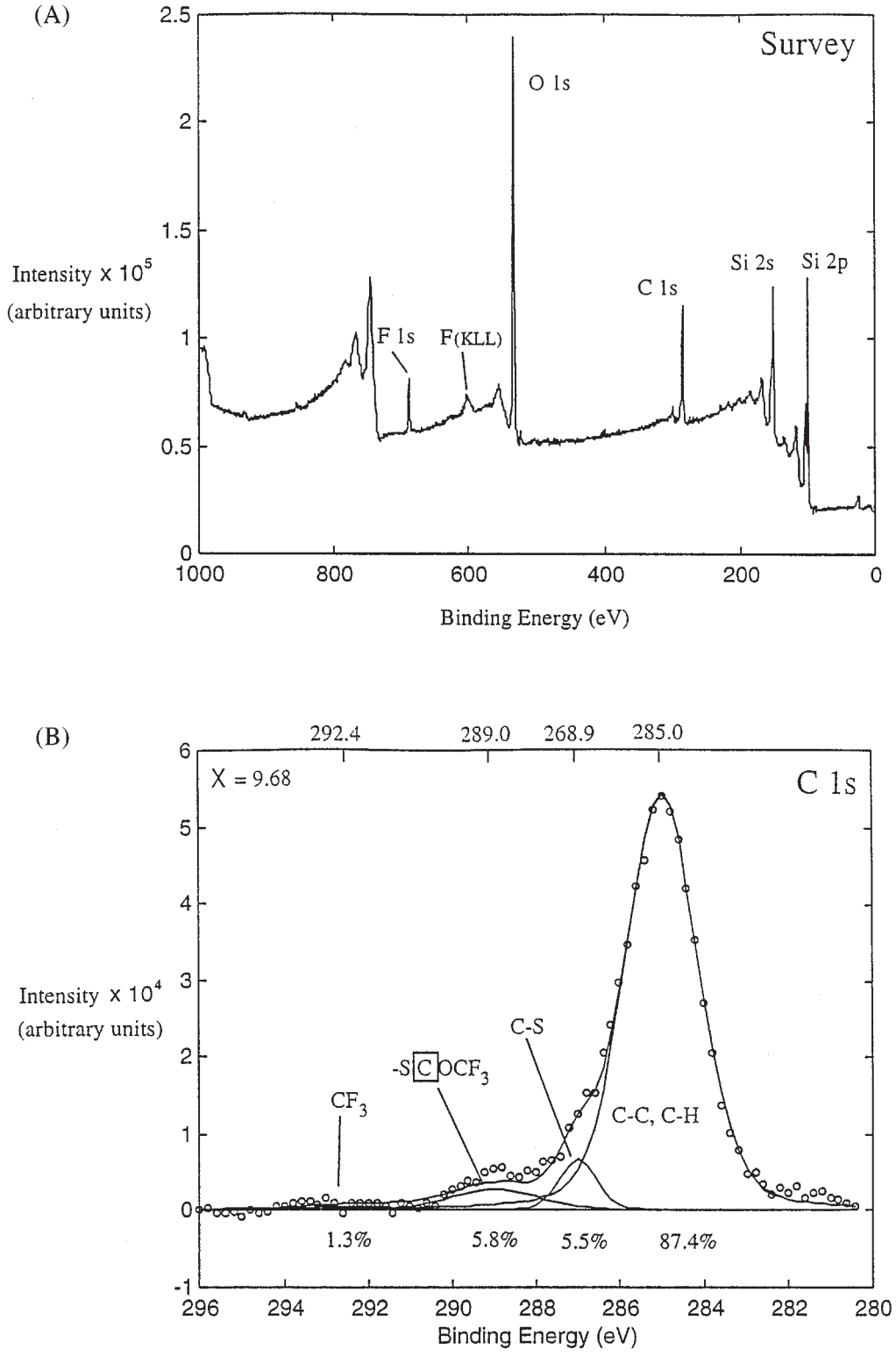

value of 0.12 (theoretical 0.14) corresponding to a yield of 86%. This result confirms the successful binding of the active silanizing agent to the wafer at a high surface density.

Turning to angle-resolved XPS, TTU provides an ideal benchmark for other thiol surfaces such as BTU that are derivatized with TFAA. Exponential and three-layer model results for TTU are given in Table 5 (two samples). For both samples, the thickness of the fluorine layer was 1 Å, and the degree of coverage was 0.91. The carbon layer was 15 Å thick, therefore the total film thickness was 16 Å. Given that

© 1999 NRC Canada

Table 4. High-resolution XPS analysis of 50% TTU – 50% C8 on silicon.

Signal	Binding energy (eV)	Atomic weight (%)	Ident.	Chi (χ)[a]
F1*s*	689.0	100	CF_3	11.10
O1*s*	532.6	100	$S1O_2$	14.97
C1*s*	285.0	87.4	C-C	9.68
	286.9	5.5	C-S	
	289.0	5.8	$SCOF_3$	
	292.4	1.3	CF_3	
Si2*p*	99.2	67.8	Si°	11.10
	103.0	32.2	SiO_2	
Si2*s*	150.8	42.6	Si°	
(TOA = 90°)	154.3	20.8	SiO_2	
	168.6	25.2	Plasmon 1	
	185.3	11.4	Plasmon 2	
Si2*s*	151.4	—	Si°	
(TOA = 20°)	154.9	—	SiO_2	
Si2*p*	165.1	—	CH_2SCOCF_3	

[a]χ = Gaussian curve-fitting parameter as determined by ESCA Tools software.

the error involved in both the XPS measurement and the modelling procedure is about ±2 Å, the experimental results are very close to the theoretical value of 13 Å. Good reproducibility was achieved, largely due to the efforts taken to control moisture in the silanization solvent, the use of a controlled humidity chamber to treat the silicon wafer, and the use of a low-moisture dry-box during the silanization process. Optical microscopy shows that no salt-like deposits are fouling an otherwise featureless surface.

Finally, we deal with the deprotection of TTU, that is, removal of the TFA functionality. Fortunately, assessment of the success of this type of reaction is a simple matter because the TFA group is easily observed in the XPS spectrum. Several deprotection schemes were tested, with the most advantageous being aqueous 0.5 M hydroxylamine (pH 8.5) for 2 h at room temperature. The experimental yield using this protocol (using an analogous calculation to that described for BTU above) was 9.8% (mean of several experiments). It is interesting to note that about 10% of the protecting groups are still attached to the surface after deprotection. Even if stronger nucleophiles or more basic conditions are employed, it is difficult to lower the yield, that is, remove all the TFA groups. We believe that the reason for this behaviour lies in the inaccessiblity of TTU species because they are embedded in pits on the silicon surface.

Conclusions

A number of the methods available for the attachment of biomolecules to substrate surfaces, such as chemisorption, cross-linking and encapsulation, complexation, and direct covalent binding, all suffer from several disadvantages. These are poor density of population of the surface, inadvertent wash-off, multi-point attachment leading to inaccessibility of tertiary structure, and the detrimental introduction of nonspecific binding sites for interfering materials. A goal of our work, in addition to work on proteins, is to produce linkers capable of the covalent, monolayer attachment of oligonucleotides to surfaces in the situation where low concentrations of nucleic acid are produced by synthesis, the immobilization is performed in water at pH 7 and at room temperature, there are no adverse efforts on the nucleic acid, and that the oligos can be attached in both permanent and reversible modes. These requirements are met by the new linking agent, TTU, which forms thiol-functionalized surfaces where the advantages of the thiol group lie in its ability to

Table 5. Angle-resolved XPS of 50% TTU – 50% C8 on silicon (three-layer model).

Take-off angle (°)	XPS signals	Exp. ratio	Fitted ratio
	Sample 1[a]		
20	F1*s*/C1*s*	0.10	0.11
	C1*s*/Si2*p*	2.62	2.73
	F1*s*/Si2*p*	0.27	0.30
30	F1*s*/C1*s*	0.12	0.09
	C1*s*/Si2*p*	1.86	1.64
	F1*s*/Si2*p*	0.22	0.15
45	F1*s*/C1*s*	0.12	0.08
	C1*s*/Si2*p*	1.26	1.06
	F1*s*/Si2*p*	0.15	0.09
90	F1*s*/C1*s*	0.16	0.08
	C1*s*/Si2*p*	0.71	0.70
	F1*s*/Si2*p*	0.11	0.05
	Sample 2[b]		
20	F1*s*/C1*s*	0.10	0.11
	C1*s*/Si2*p*	2.66	2.66
	F1*s*/Si2*p*	0.26	0.28
30	F1*s*/C1*s*	0.10	0.09
	C1*s*/Si2*p*	1.97	1.63
	F1*s*/Si2*p*	0.19	0.15
45	F1*s*/C1*s*	0.08	0.08
	C1*s*/Si2*p*	1.34	1.06
	F1*s*/Si2*p*	0.11	0.09
90	F1*s*/C1*s*	0.10	0.07
	C1*s*/Si2*p*	0.83	0.71
	F1*s*/Si2*p*	0.09	0.05

[a]Variables: λ_a = 28 Å, λ_b= 35 Å, λ_c = 44 Å; t_b = 15 Å, t_c = 1 Å, f_c = 0.91.

[b]Variables: λ_a = 28 Å, λ_b= 35 Å, λ_c = 44 Å; t_b = 15 Å, t_c = 1 Å, f_c = 0.89.

© 1999 NRC Canada

Fig. 4. High-resolution XPS spectra of silicon 2*s* and 2*p* and surface plasmons for 50% TTU – 50% C8 on silicon. Take-off angles as indicated.

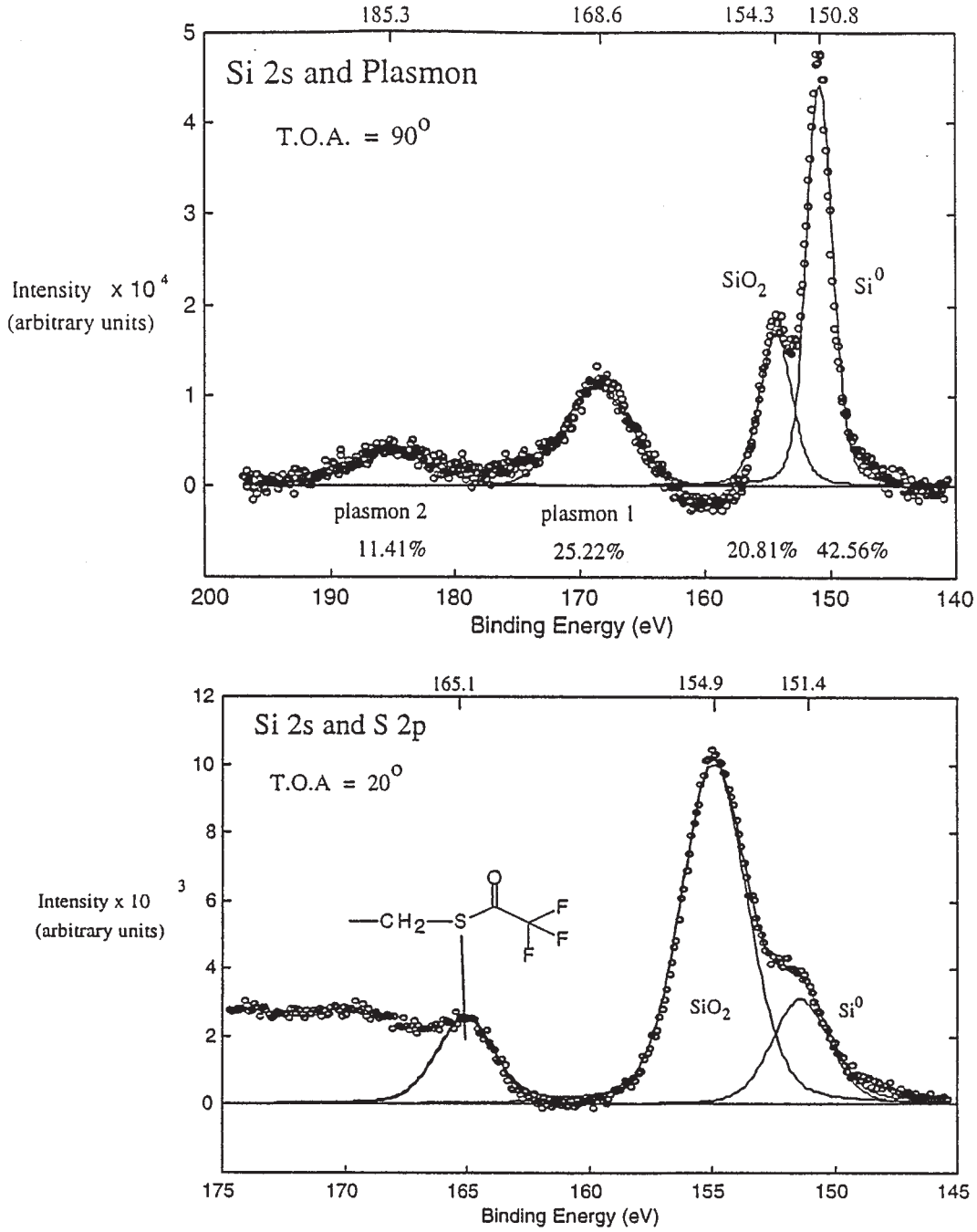

form two types of linkage, viz. disulfide and thioether. The disulfide bond can be created using the highly specific thiol–disulfide exchange process. The S_N2 reaction proceeds rapidly in water at neutral pH. Furthermore, asymmetrical disulfides can be prepared, which lead to the prevention of reverse reactions, and the disulfide moiety can be cleaved specifically under extremely mild conditions. A thioether bond can be formed easily via reagents that contain reactive-leaving functionalities. The resulting bond is very resistant to cleavage and is essentially permanent under physiological conditions. Accordingly, TTU offers a spectrum of possibilities for the attachment of nucleic acid through the special derivatization of oligonucleotides, DNA and RNA.

Acknowledgments

We are greatly indebted to the Natural Sciences and Engineering Research Council of Canada, and Materials and Manufacturing Ontario for support of this work. Also, we wish to thank Dr. R. Sodhi of the Centre for Biomaterials, University of Toronto, for assistance with the acquisiton of XPS data.

© 1999 NRC Canada

References

1. L. Bui, R. DeBono, V. Ghaemmaghami, K.M.R. Kallury, P. Li, N. McKeown, D. Stone, H. Su, L. Tessier, S. Vigmond, and M. Thompson. *In* Advances in biosensors. Vol 2. *Edited by* A.P.F. Turner. 1992. p. 18.
2. B. Mattiasson. J. Appl. Biochem. **3**, 183 (1981).
3. K. Mosbach (*Editor*). Methods in enzymology. Vol. 137. Academic Press, New York. 1988.
4. T.C.J. Gribnau (*Editor*). Coupling of effector-molecules to solid supports. Drukkerij van Mameren B.V., Nijmegen, The Netherlands. 1977.
5. P.D.G. Dean. Affinity chromatography: a practical approach. IRL, Oxford, U.K. 1985.
6. W.H. Scowten. Affinity chromatography: bioselective adsorption on inert matricies. Wiley, New York. 1986.
7. J. Meinkoth and G. Wahl. Anal. Biochem. **138**, 267 (1984).
8. M.I. Shtilman. Immobilization on polymers. VSP, Utrecht, The Netherlands. 1993.
9. R.B. Dunlap and P.T. Gilham. Advances in experimental medicine and biology. Vol. 42. 1973. pp. 173–180.
10. H. Schott. Affinity chromatography: template chromatography of nucleic acids and proteins, chromatographic science. Vol. 27. Marcel Dekker Inc., New York. 1984.
11. B. Johnsson, S. Lofas, and G. Lindquist. Anal. Biochem. **198**, 268 (1991).
12. M.E. Montgomery, M.A. Green, and M.J. Wirth. Anal. Chem. **64**, 1170 (1992).
13. S.R. Wasserman, Y.T. Tao, and G.M. Whitesides. Langmuir, **5**, 1074 (1989).
14. E.P. Plueddemann. Silane coupling agents. 2nd ed. Plenum Press, New York. 1991.
15. A. Ulman. Chem. Rev. **96**, 1533 (1996).
16. D.L. Allara. Crit. Rev. Surf. Chem. **2**, 199 (1993).
17. K.L. Mittal (*Editor*). Silanes and other coupling agents. VSP, Utrecht, The Netherlands. 1992.
18. N. Balachander, and C.N. Sukenik. Langmuir, **6**, 1621 (1990).
19. N.G. Cave and A.J. Kinloch. Polymer, **33**, 1162 (1992).
20. A.A. Campbell, G.E. Fryxell, G.L. Graff, P.C. Rieke, and B.J. Tarasevich. Scanning Microsc. **7**, 423 (1993).
21. M. Jiang, B. Nolting, P.S. Stayton, and S.G. Sligar. Langmuir, **12**, 1278 (1996).
22. Y.W. Lee, J. Reed-Mundell, C.N. Sukenik, and J.E. Zull. Langmuir, **9**, 3009 (1993).
23. P. Sleevi, T.E. Glass, and H.C. Dorn. Anal. Chem. **51**, 1931 (1979).
24. Canadian patent application no. 2,213,087 (1997); U.S. patent application no. 8,951,448 (1997).
25. M.E. McGovern. Monolayer chemistry-interaction of OTS with quartz/glass surfaces in various solvents probed by X-ray photoelectron spectroscopy and surface acoustic wave device. M.Sc. thesis. University of Toronto, Toronto. 1993.
26. J.D. Andrade (*Editor*). Surface and interfacial aspects of biomedical polymers. Vol. 1. *In* Surface chemistry and physics. Plenum Press, New York. 1985. Chap. 5, pp. 175–195.

© 1999 NRC Canada

New "molecular metals" based on symmetrically tetrasubstituted copper phthalocyanine complexes

B.N. Achar and P.K. Jayasree

Abstract: Pure copper(II) tetrasubstituted phthalocyanine complexes, CuPTX (where X = -NO_2, -NH_2, -SO_3H, and -OH) were synthesized. The electrical conductivity properties of these complexes were investigated both before and after iodine doping for the first time. Elemental, electronic, IR, magnetic susceptibility measurements, ESR, X-ray diffraction, and TGA analytical techniques were used to characterize and study the effect of substituents as well as iodine doping. Variation in the electrical conductivity of the copper phthalocyanine derivatives depends on the nature of the substituents and were found to show ~10^5 times improved electrical conductivity in comparison to parent unsubstituted copper phthalocyanine. Interestingly, these substituted complexes after iodine doping showed remarkably increased electrical conductivity nearly 10^{12} times that of unsubstituted copper phthalocyanine. This may be accounted for by the decrease in the metal–metal bond distance, increase in the approach of the ideal eclipsed system, or due to the combined effects of the above factors.

Key words: copper phthalocyanine, iodine doping, electrical conductivity.

Résumé : On a synthétisé des complexes purs de Cu(II) avec des phtalocyanines tétrasubstituées, CuPTX (dans lesquels X = NO_2, NH_2, SO_3H et OH). On a étudié les propriétés de conductivité électrique de ces complexes avant et après dopage par de l'iode. On a fait appel aux analyses élémentaires, aux spectres électroniques et IR, à des mesures de susceptibilité magnétique, à la résonance paramagnétique électronique, à la diffraction des rayons X et aux techniques analytiques thermogravimétriques pour les caractériser et pour étudier l'effet des substituants ainsi que le dopage par l'iode. La variation de la conductivité électrique des dérivés cuivrés de la phtalocyanine dépend de la nature des substituants et on a trouvé que la conductivité électrique est améliorée par un facteur de 10^5 par rapport à celle du complexe par du cuivre avec la phtalocyanine non substituée. Il est intéressant de noter que les complexes substitués, dopés à l'iode, présentent une conductivité électrique qui est pratiquement 10^{12} fois celle du complexe du cuivre avec la phtalocyanine non substituée. Cette observation pourrait être expliquée par la diminution de la longueur de la liaison métal–métal, une augmentation dans l'approche du système éclipsé idéal ou à une combinaison de ces facteurs.

Mots clés : complexe du cuivre et de la phtalocyanine, dopage à l'iode, conductivité électrique.

[Traduit par la Rédaction]

1. Introduction

Phthalocyanines have undergone world-wide intensive investigation because of their attractive properties like high tinctorial power, chemical inertness, thermal stability, electrical and catalytic properties (1–3). Electrical conductivity is one of the properties that attracted a great deal of interest since 1948 (4, 5). Enhancement of electrical conductivity of phthalocyanines by partial oxidation is now a well known phenomenon. Among the many oxidants used to study the effect on the electrical property of the phthalocyanine complexes, iodine has been used more frequently, and its effect on the electrical conductivity has been most extensively studied (6–8). Currently intensive research work is going on to produce useful electrically conducting phthalocyanine compounds, and phthalocyanines are now commercially used in many electronic devices (9–13). However, the electrical properties of the substituted metal phthalocyanines have been relatively little studied (14–17). The present work describes the synthesis of pure copper(II) tetrasubstituted complexes, CuPTX (where X = -NO_2, -NH_2, -SO_3H, and -OH), and their characterization both before and after iodine doping for the first time. The results are used to investigate the effects of substituents as well as iodine doping on the electrical properties of the complexes.

Received April 19, 1999.

B.N. Achar[1] and P.K. Jayasree. Department of Studies in Chemistry, University of Mysore, Mysore-57 006, Karnataka State, India.

[1]Author to whom correspondence may be addressed. Telephone: 0091-0821-516374. e-mail: bnachar@yahoo.com

2. Experimental

Methods

Elemental analyses for C, H, and N were made by the Regional Sophisticated Instrumentation Centre, C.D.R.I., Lucknow. The copper contents of the tetrasubstituted copper phthalocyanine complexes were determined by decomposing

© 1999 NRC Canada

a known amount of the complex using H_2SO_4–HNO_3 mixture followed by careful evaporation and calcination (18). The purity of the complexes was further checked by ceremetric titrations (19). Electronic absorption spectra were recorded on a JASCO model UVIDEC-610 UV-vis spectrophotometer in 15 M sulphuric acid. IR spectra were recorded using Shimadzu 8201 PC FT-IR spectrophotometer by KBr disc technique. The magnetic susceptibility measurements were done using a Gouy magnetic balance consisting of the type NP-53 electromagnets with dc power supply type MP-1053 and a Keroy semimicrobalance supplied by Universal Scientific Company, Bombay, India. Pure $HgCo(SCN)_4$ was synthesized and used as a calibration standard (20). A JEOL-JDX-8P X-ray diffractometer was used to study the powder X-ray diffraction pattern of the samples. TGA studies were carried out using a Dupont model 990 thermal analyzer with the following conditions: sample size 5–10 mg, temperature range ambient to 800°C, heating rate 10°C/min. Perkin Elmer KBr die, carver laboratory press model C-12 ton capacity was used to prepare the pellets. The diameter and thickness of the pellets were determined by using a screw gauge readable up to 0.005 cm. Conducting silver paint (ELTECKS conductive silver preparation no. 1228/C) was coated on both surfaces of the pellets, and the electrical contacts of the samples were made using the same silver paint to the electrodes. The electrical contacts were checked to verify the ohmic connection, and the electrical measurements were done at ambient temperature using the Philips model PM 6303 RCL meter.

Materials

Pure copper(II) 2,9,16,23-tetrasubstituted phthalocyanines (CuPTX, where X = $-NO_2$, $-NH_2$, $-SO_3H$, and -OH) were prepared by using procedures as described elsewhere (21–24). A brief outline of the procedures are given below. All chemicals used were of analytical grade.

Preparation of tetrasodium salt of copper(II) 2,9,16,23-tetrasulphophthalocyanine 2-hydrate, CuPTS

Finely ground mixture of copper sulphate pentahydrate (5.2 g), monosodium salt of 4-sulphophthalic acid (23.36 g), ammonium chloride (2 g), ammonium molybdate (0.3 g), and urea (30 g) was taken in a 250 mL three-necked flask containing nitrobenzene (20 mL) fitted with a thermometer, a condenser, and a mechanical stirrer. The mixture was heated slowly with stirring to 180°C and maintained at this temperature for 6 h. The product was washed with methanol to remove nitrobenzene and was then purified using hydrochloric acid (1.0 N) and sodium hydroxide (1.0 N). The filtered product was dried in vacuum desiccator. Yield 80%. IR absorption bands (cm^{-1}): 745m, 920w, 1022s, 1185m, 1316m, 1386m, 1555 (broad), 3000–3625 (broad). Anal. calcd. for CuPTS, $C_{32}H_{16}N_8O_{14}S_4Na_4Cu$: C 37.67, H 1.58, N 10.98, Cu 6.22; found: C 38.01, H 2.01, N 11.02, Cu 6.25.

Preparation of copper(II) 2,9,16,23-tetranitrophthalocyanine, CuPTN

This was prepared by using the procedure as explained above except for using 4-nitrophthalic acid (16.9 g) in place of 4-sulphophthalic acid. The temperature of the reaction was slowly increased to 185°C and maintained at 185 ± 5°C for 4–5 h. The complex was purified by using 1.0 N sodium hydroxide and hydrochloric acid, and finally washing with distilled water. The blue-coloured product was dried at 125°C for 1 h. Yield 68%. IR absorption bands (cm^{-1}): 760m, 855w, 935ws, 1058w, 1090m, 1120w, 1338s, 1512s, 1595w. Anal. calcd. for CuPTN, $C_{32}H_{12}N_{12}O_8Cu$: C 50.83, H 1.59, N 22.23, Cu 8.40; found: C 51.88, H 1.72, N 22.54, Cu 8.50.

Preparation of copper(II) 2,9,16,23-tetraaminophthalocyanine 2-hydrate, CuPTA

Copper(II) 2,9,16,23-tetranitrophthalocyanine (5 g) was placed in a three-necked flask containing water (150 mL). The flask was fitted with a mechanical stirrer, a thermometer, and a stopper. Sodium sulphide nonahydrate (25 g) was added to the flask, stirred at 50°C for 5 h. The product was separated and treated with 250 mL sodium hydroxide (1.0 N), stirred for 1 h, and centrifuged. The product was purified by repeated treatment with water until it was free from sodium hydroxide. The pure CuPTA was dried in a vacuum desiccator. Yield 60%. IR absorption bands (cm^{-1}): 730m, 745m, 830w, 865w, 950m, 1055m, 1095m, 1136m, 1250w, 1302w, 1345w, 1410m, 1605m, 1790w, 3280w. Anal. calcd. for CuPTA, $C_{32}H_{24}N_{12}O_2Cu$: C 57.20, H 3.60, N 25.00, Cu 9.60; found: C 57.80, H 4.00, N 25.20, Cu 9.75.

Preparation of copper(II) 2,9,16,23-tetrahydroxyphthalocyanine, CuPTOH

Finely ground copper(II) 2,9,16,23-tetraaminophthalocyanine was added to 25 mL of 1.0 N hydrochloric acid solution. The mixture was kept in a bath of crushed ice until the temperature of the solution fell below 5°C. To this cold solution, chilled aqueous solution of sodium nitrite (1.55 g/4 mL) was added in small portions (0.5–1.0 mL at a time) with constant stirring. Heat was evolved by the reaction. Temperature should not be allowed to raise above 10°C. The chilled copper(II) tetradiazonium hydrogen sulphate prepared as above with suitable modification was added slowly to 20.0 N sulphuric acid solution (8 mL), boiled further for 5 min, and then poured into ice-cold water (150 mL). The solution was stirred vigorously. The product was decanted and then purified by washing with 1.0 N sodium hydroxide, 1.0 N hydrochloric acid, and finally with water. It was dried at 75°C for 1 h. Yield 85%. IR absorption bands (cm^{-1}): 725m, 885w, 926w, 1040w, 1075m, 1106w, 2700–3600 (broad). Anal. calcd. for CuPTOH, $C_{32}H_{16}N_8O_4Cu$: C 60.04, H 2.52, N 17.51, Cu 9.23; found: C 59.98, H 2.66, N 17.65, Cu 9.31.

Doping procedure

The iodine doping procedure for unsubstituted nickel phthalocyanine as explained elsewhere (25) has been adapted to dope the substituted copper phthalocyanine complexes. A brief summary of the procedure is given below.

Finely ground (0.5 g) tetrasubstituted copper phthalocyanine complex (CuPTX, where X = -OH, $-NO_2$, $-NH_2$, or $-SO_3Na$) was taken in a closed container containing 100 mL iodine saturated chlorobenzene solution and stirred for 48 h. The iodinated copper tetrasubstituted complex was collected by centrifugation, washed with several portions of hexane, and dried in a vacuum desiccator.

© 1999 NRC Canada

Table 1. Magnetic susceptibility, electronic spectral (15 M H_2SO_4), ESR and electrical conductivity data of copper(II) tetrasubstituted phthalocyanine complexes (CuPTX, where X = -SO_3H, -NO_2, -NH_2, and -OH).[a]

Compound	Magnetic susceptibility: Field strength (kG)	Magnetic susceptibility: μ_{eff} (BM)	λ_{max} nm (log ε)	X-ray diffraction data, "*d*" (Å)	"*g*" values	Conductivity $(\Omega\ cm)^{-1}$
CuPc (40)	1.92	4.00	752 (4.31)*, 710 (4.41), 438 (4.34), 302 (4.87), 224 (4.82)	12.34, 8.01, 5.18, 3.35, 3.22, 3.09	g_{av} = 2.075	1.0×10^{-12}
	2.82	3.44				
	3.58	3.18				
	4.35	3.14				
$C_{32}H_{16}N_8O_{14}S_4Na_4Cu$ CuPTS	1.92	2.79 [3.26]	760 (5.03), 665 (4.88)*, 410 (4.74), 304 (4.89), 252 (4.57)* [763 (5.00), 664 (4.85)*, 304 (4.54), 226 (4.69)]	14.78, 3.62 [11.17, 3.31]	g_{av} = 2.0649 [2.0682]	2.76×10^{-6} [1.32×10^{-1}]
	2.82	2.62 [3.47]				
	3.58	2.42 [3.53]				
	4.35	2.32 [3.71]				
$C_{32}H_{12}N_{12}O_8Cu$ CuPTN	1.92	2.65 [2.56]	734 (4.59), 680 (4.42)*, 302 (4.91), 204 (4.80) [792 (5.05), 710 (4.63), 435 (4.53), 305 (4.88), 249 (4.78)*, 225 (4.86)*, 202 (5.03)*]	13.86, 12.32, 9.25, 6.18, 5.57, 3.62, 3.50, 3.31, 3.21 [10.09, 8.64, 7.41, 5.31, 3.62, 3.31, 3.21]	g_{11} = 2.1233 $g_{\perp r}$ = 2.0586 [g_{11} = 2.1260 $g_{\perp r}$ = 2.0586]	..3.28×10^{-9} [1.30×10^{-1}]
	2.82	2.39 [2.99]				
	3.58	2.26 [2.98]				
	4.35	2.13 [3.28]				
$C_{32}H_{24}N_{12}O_2Cu$ CuPTA	1.92	2.25 [3.24]	740 (4.28), 376 (4.17), 302 (4.51), 216 (4.92) [787 (5.04), 703 (4.71), 421 (4.51), 308 (5.03), 251 (4.69)*, 222 (4.99)]	13.86, 12.32, 9.25, 6.18, 3.50, 3.21 [13.86, 12.32, 3.21]	g_{av} = 2.0617 [2.0680]	3.58×10^{-5} [7.25×10^{-1}]
	2.82	2.21 [3.12]				
	3.58	2.04 [3.03]				
	4.35	1.84 [2.53]				
$C_{32}H_{16}N_8O_4Cu$ CuPTOH	1.92	2.07 [2.72]	752 (4.31), 410 (4.15)*, 304 (4.75) [788 (5.05), 704 (4.81)*, 416 (4.66), 305 (5.06), 251 (4.88), 225 (4.86)*, 202 (5.21)*]	15.83, 13.86, 10.09, 6.18, 3.99, 3.50 [15.83, 13.86, 12.32, 10.09, 6.96, 3.21]	g_{av} = 2.0586 [2.0601]	2.72×10^{-8} [4.43×10^{-2}]
	2.82	2.03 [2.64]				
	3.58	1.97 [2.51]				
	4.35	1.96 [2.47]				

[a]*, shoulder. Values inside the square brackets represent after iodine doping.

Fig. 1. Structure of copper(II) 2,9,16,23-tetrasubstituted phthalocyanine, CuPTX (where X = -NO_2, -NH_2, -SO_3H, and -OH).

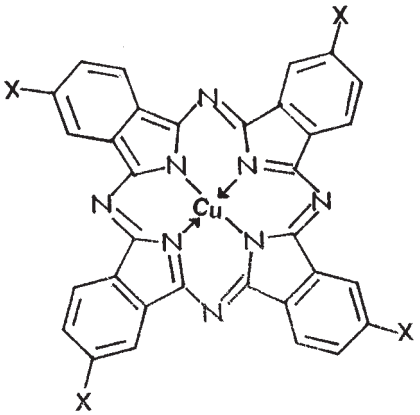

3. Results and discussion

The structure of copper(II) symmetrically tetrasubstituted phthalocyanine complex is shown in Fig. 1. Purity of the complexes are checked by elemental analysis, IR spectral data, and titrimetric analysis (19). The elemental analyses of C, H, N, and Cu agreed fairly well with the calculated values.

Electronic absorption spectra

The electronic transitions characteristics of phthalocyanine ring are assigned Q, B, N, L, and C bands (26). These characteristic absorption bands are also observed in the electronic absorption spectra of the tetrasubstituted copper phthalocyanine complexes (CuPTX, where X = -SO_3H, -NO_2, -NH_2, or OH) recorded in 15 M H_2SO_4 medium, Table 1. The Q band due to $a_{1u} \rightarrow e_g$ transition around 750 nm was found to show bathochromic shifts with hyperchromic effect in the case of all the three copper complexes, except in the case of CuPTS wherein the band showed hypsochro-

© 1999 NRC Canada

Fig. 2. Variations of magnetic moments with field strength: 1, CuPTS; 2, CuPTN; 3, CuPTA; and 4, CuPTOH. (*A*) Before I_2 doping and (*B*) after I_2 doping.

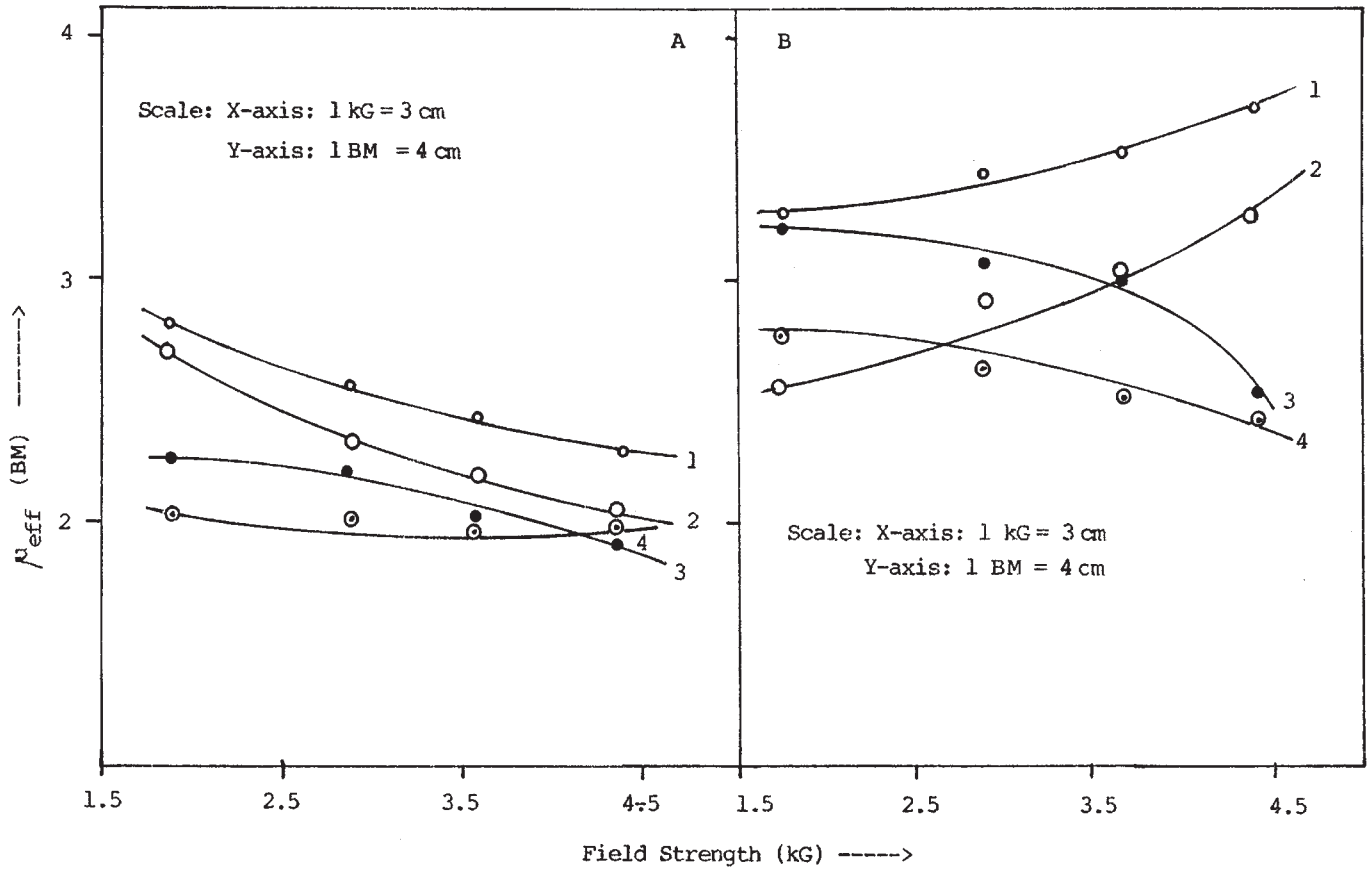

mic effect with respect to intensity after iodine doping. This band is due to monomeric species and found to be affected by the nature of the substituents. The multiplicity of this band towards the higher energy side in the region 665–704 nm observed for the complexes are due to the configurational interaction between the phthalocyanine molecules leading to the formation of dimeric species in solution. The intensity of this band depends upon the concentration of the dimer formed (27–29). All the complexes both before and after iodine doping showed absorptions around 376–435 nm of comparable intensity with Q band. This absorption is not observed in the vapour absorption spectrum of copper phthalocyanine (30). This is due to the change of the molecular symmetry from D_{4h} to C_{4v} in the strong acidic medium (31). The B (Soret) band around 305 nm, which can be assigned to the $a_{2u} \rightarrow e_g$ transition, was found to have not much affected with respect to positions but appeared broad due to the underlying $Np_\sigma \rightarrow e_g$ (π^*) transitions (32). The electronic absorption spectra of the complexes CuPTOH ad CuPTS showed the absence of L and C bands before iodine doping. But after iodine doping absorption due to C band appeared in CuPTOH but poorly resolved. This C band absorption is observed for the complex CuPTA before iodine doping found to disappear after iodine doping. The bands N and L are expected to observe between B and C, which are not well resolved in the solution spectra of the complexes both before and after iodine doping.

IR spectra

IR spectra of all the four complexes showed absorptions at 725–760, 748–891, 920–966, 1020–1060, 1075–1095, and 1106–1185 cm^{-1} assignable to phthalocyanine skeleton both before and after iodine doping (33). These absorptions are found to be unaffected with respect to their positions. But with respect to their intensity, they appeared broad with hypochromic effect.

Magnetic susceptibility measurements

The investigation on magnetic susceptibility properties of the tetrasubstituted copper(II) phthalocyanine complexes has been carried out in solid state at ambient temperature and varying magnetic field strengths from 1.92 to 4.35 kG (1 G = 0.1 mT), to know the effect of iodine doping. The magnetic moment, μ_{eff} values are calculated using the corrected susceptibility data for diamagnetism (34–35). Each value of magnetic moment calculated from the corrected susceptibility is an average of three independent determinations. The values are reproducible to ±0.1 BM. The plots of magnetic moment (μ_{eff}) values versus field strength are presented both before and after iodine doping, in Fig. 2. These complexes are paramagnetic in nature, which showed magnetic field dependent magnetic moment values both before and after iodine doping. The μ_{eff} values are found to decrease with increase in magnetic field strength before iodine doping, whereas these values are found to increase with increase in

© 1999 NRC Canada

Fig. 3. X-ray diffraction spectra: 1, CuPTA; 2, CuPTA (I_2 doped); 3, CuPTOH; and 4, CuPTOH (I_2 doped).

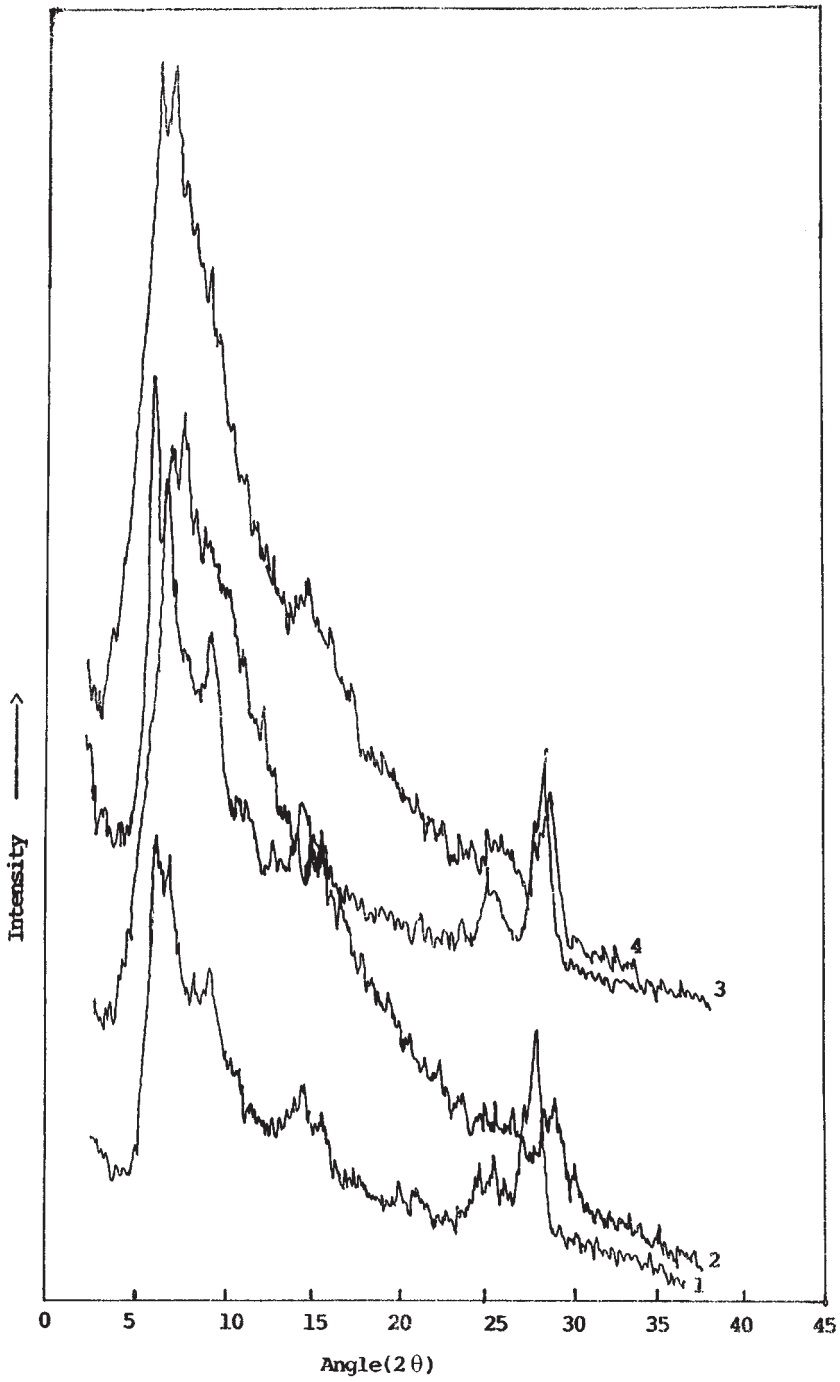

field strength after iodine doping except in the case of CuPTOH and CuPTA, which contain reactive hydroxy and amino substituted functional groups. These values and their variations with the magnetic field can be due to the combined effects of orbital contribution and intermolecular cooperative effects (21). The results presented in Table 1 indicate that there are two types of cooperative effects — positive and negative. The positive intermolecular cooperative effect leads to the increase in the magnetic moment values, and negative intermolecular cooperative effect leads to decrease in the magnetic moment values with increase in magnetic field strength. The difference in the magnetic moment field values of the copper complexes after iodine doping is due to the partial oxidation of phthalocyanine complexes as well as simultaneous adoption of a face-to-face stacking of the phthalocyanine structure (36). The most likely mechanisms for spin–spin coupling between adjacent copper atoms or superexchange through nitrogen atoms of the copper phthalocyanine macrocycle or direct exchange between the adjacent copper atoms. The former is the most feasible mechanism before iodine doping. The later mechanism seems to explain the magnetic susceptibility values af-

© 1999 NRC Canada

ter iodine doping. In conclusion, the variation of the susceptibility value with magnetic field strength and differences in them before and after iodine doping seem to be affected by the type of substituents at the peripheral benzene structures of the phthalocyanine molecule, ligand-based or metal-based partial oxidation, interplanar distance of the molecular stacks, and the types of intermolecular effects.

ESR studies

The calculated "*g*" values from the ESR spectra of all the complexes both before and after iodine doping are presented in Table 1. ESR spectral data of the complexes are in agreement with the magnetic susceptibility measurements with respect to the paramagnetic nature of the complexes. The nature of the spectra, both before and after iodine doping, indicates tetragonal site in all these complexes. All the complexes both before and after iodine doping showed a single relatively broad ESR signal, which can be explained as the sum of the contributions from all orientations of the molecule, wherein the hyperfine structures are obscured by electron–electron dipole interaction and exchange mechanism.

X-ray diffraction studies

The data of the powder X-ray diffraction study both before and after iodine doping are presented in Table 1. Typical X-ray diffraction spectra are given in Fig. 3. The interplanar spacings are calculated by using the Bragg's equation, $2d \sin \theta = n\lambda$. The nature of the powder X-ray diffraction spectra showed not much difference with respect to the appearance after iodine doping except with respect to the broadening of the Bragg's scattering. This indicates that the crystal lattice is not changed after iodine doping, and the broadening effect may be due to the partial transformation of the polycrystalline phase to the amorphous state.

Thermogravimetric Analytical (TGA) studies

The TGA analytical curves indicated the iodine contents in the doped tetrasubstituted copper phthalocyanine complexes are in the range 28–38%. This corresponds to the doping of iodine in these complexes to the extent of three iodine atoms per molecule. As per the TGA curve, the weight loss due to iodine is in between the temperature range 130–200°C. Iodine is found to be volatilizing slowly with time from the doped material. Because of this volatilization problem, iodine contents from TGA analytical data must be obtained soon after the synthesis of the doped complexes for getting reasonably accurate doped iodine contents.

Electrical conductivity studies

The measured electrical conductivity values both before and after doping with iodine of the complexes studied are reported in Table 1. Electrical conductivity of copper phthalocyanine is reported to be of the order 10^{-12}–10^{-13} $(\Omega\ \text{cm})^{-1}$ (37). These complexes showed 10^4–10^7 times improved electrical conductivity in comparison to the parent copper phthalocyanine. This may be due to the decrease in the metal–metal bond distance, increase in the overlap of the π electron system between the molecules or increase in the approach of the ideal eclipsed stacking systems or due to combined effects of the above factors. The substitution and the iodine doping found to increase the electrical conductivities remarkably ~10^{12} times in comparison to the parent copper phthalocyanine. The high electrical conductivity observed for the iodine doped phthalocyanine complexes shows the conductive path in these complexes does not depend on metal–metal overlap only but also on π–π and *d*–π overlaps. The "holes" for the charge carriers produced by the partial oxidation by iodine may either be at metal or ligand centered. The ESR data before and after iodine doping support the holes produced are ligand centered as the *g* values nearly equal to 2. When these complexes are partially oxidized with iodine, they become conducting while simultaneously adopting a face-to-face stacking of the phthalocyanine structure (36). Based on the observations and conclusions on the improved electrical conductivites of the doped unsubstituted metal phthalocyanine complexes by the other workers (37–39), similar conclusions can be drawn on the increased electrical conductivites observed after iodine doping in these complexes. That is, the improved electrical conductivites, firstly, must be due to the arrangement of the planar molecules in close facial proximity with sufficient intermolecular overlap and, secondly, due to the existence of fractional oxidation states in the arranged molecular stacking.

Acknowledgments

The authors thank Prof. A.S. Aravinda Murthy, Electrical and Electronics Department, National Institute of Engineering, Mysore, for the help in providing the necessary facility to carry out the electrical conductivity measurements.

References

1. F.H. Moser and A.L. Thomas. Phthalocyanine compounds. Reinhold Publishing Corp., New York. 1963.
2. F.H. Moser and A.L. Thomas. The phthalocyanines. Vols. 1 and 2. CRC Press, Boca Raton, Fla. 1983.
3. C.C. Leznoff and A.B.P. Lever. Phthalocyanines: properties and applications. Vols. 1 and 3. VCH, New York. 1989 and 1993.
4. D.D. Eley. Nature (London), **162**, 819 (1948).
5. A.T. Vartanyan. Zh. Fiz. Khim. **22**, 76 (1948).
6. K. Kasuga and M. Tsutusi. Coord. Chem. Rev. **32**, 67 (1980).
7. L. Kreja and W. Czerwinski. J. Mater. Sci. Lett. **11**(**9**), 538 (1992).
8. C. Park and Y.W. Park. Synth. Met. **71**(**1**–**3**), 2295 (1995).
9. K. Arishima, H. Hiratsuka, A. Tate, and T. Okada. Appl. Phys. Lett. **46**, 279 (1985).
10. M. Kato, Y. Nishioka, K. Kaifu, K. Kawamura, and S. Ohno. Appl. Phys. Lett. **46**, 196 (1985).
11. F.F. So and S.R. Forrest. J. Appl. Phys. **63**, 442 (1988).
12. L.R. Milgrom. PCT int. Appl. Wo9215.099 (Cl.HoB1/12) 03 Sept. 1992; G.B. Appl. 91/3, 99126 Feb. 1991.
13. T.L. Anderson, G.C. Komplin, and W.J. Piatro. J. Phys. Chem. **97**, 6577 (1993).
14. M. Hanack and M. Lang. Adv. Mater. **6**, 819 (1994).
15. R. Shankar, P. Vasudevan, P. Sharma, N.K. Jha, A. Cabrera, and N. Rosas. J. Mater. Sci. Lett. **15**, 1221 (1996).
16. M. Hanack, D. Oelkrug, and P. Haisch. Adv. Mater. **9**, 316 (1997).
17. L. Wing-Fong, K.M. Lui, and D.K.P. Ng. J. Mater. Chem. **7**, 2063 (1997).

© 1999 NRC Canada

18. N.P. Kanyev and A.A. Spryskov. Zhur. Priklad. Khim. **25**, 1220 (1952).
19. C.E. Dent, R.P. Linstead, and A.R. Lowe. J. Chem. Soc. 1033 (1934).
20. B.N. Figgis and R.S. Nyholm. J. Chem. Soc. 4190 (1958).
21. J.H. Weber and D.H. Busch. Inorg. Chem. **4**, 469 (1965).
22. B.N. Achar, G.M. Fohlen, and J.A. Parker. U. S. Pat. 4,499,260 (1985).
23. A.I. Vogel. Practical organic chemistry. 3rd ed. English Language Book Society, London. 1971.
24. J. Keshavayya. Ph.D. thesis. Studies on metal phthalocyanine complexes. Mysore University, Mysore. 1988.
25. C.J. Schramm, R.P. Scaringe, D.R. Stojakovic, B.M. Hoffman, J.M. Ibers, and T.J. Marks. J. Am. Chem. Soc. **102**, 6702 (1980).
26. L. Edwards and M. Gouterman. J. Mol. Spectrosc. **33**, 292 (1970).
27. K. Bernauer and S. Fallab. Helv. Chim. Acta, **44**, 1287 (1961).
28. D.W. Boyd and T.D. Smith. J. Chem. Soc. Dalton Trans. 839 (1972).
29. R.D. Farina, D.J. Halko, and J.H. Swinehart. J. Phys. Chem. **76**, 2343 (1972).
30. D. Eastwood, L. Edwards, M. Gouterman, and J. Steinfeld. J. Mol. Spectrosc. **20**, 381 (1966).
31. L. Edwards and M. Gouterman. J. Mol. Spectry. **33**, 292 (1970).
32. A.M. Schaffer, M. Gouterman, and E.R. Davidson. Theor. Chim. Acta, **30**, 9 (1973).
33. A.N. Sidorov and M.P. Kotliar. Opt. Spectrok. **11**, 175 (1961).
34. K. Lonsdale. J. Chem. Soc. 364 (1938).
35. P.W. Selwood. Magneto chemistry. 2nd ed. InterScience Publications Inc., New York. 1956.
36. E. Canadell and S. Alvarez. Inorg. Chem. **23**, 273 (1984).
37. C.G.B. Garret. *In* Semiconductors. Monograph 140. *Edited by* N.B. Honnay. ACS, Washington. 1959.
38. T.J. Marks. Ann. NY Acad. Sci. **313**, 594 (1978).
39. C.W. Dirk, E.A. Mintz, K.F. Schoch, Jr., and T.J. Marks. J. Macromol. Sci. Chem. **A16**(**1**), 275 (1981).
40. J.M. Bhandari. Ph.D. thesis. Metal phthalocyanine complexes. Mysore University, Mysore. 1992.

© 1999 NRC Canada

Preferred conformation and barriers to internal rotation of *ortho*-disubstituted cyclopropylbenzenes

Ludger Ernst, Thomas Rieck, and Mark Soliven

Abstract: Schaefer's "*J* method" was employed to show that 2-cyclopropyl-1,3-dimethylbenzene (**5**) in solution prefers the perpendicular conformation in which the torsional angle Θ between the C(1)—H bond of the cyclopropyl group and the plane of the benzene ring is 90°. This is opposed to the situation in cyclopropylbenzene (**3**) where the bisected conformer (Θ = 0°) prevails. From the value of –0.85 ± 0.01 Hz for ^6J(H-α,H-*para*) in **5** (for solutions in CS_2 and in acetone) a barrier to rotation about the cyclopropyl–aryl bond of 6.4 kJ/mol can be derived if a predominantly two-fold potential and a vanishing ^6J(H,H) for Θ = 0° are assumed. The introduction of the two *ortho*-methyl groups into **3** thus effectively interchanges the ground and transition state conformations of the internal rotation. This effect is well reproduced by ab initio (STO-3G and 6-31G*) and semiempirical (AM1) molecular orbital computations. The preference for the perpendicular conformation of an *ortho*-disubstituted cyclopropyl substituent was also demonstrated by a dynamic NMR study of 2-cyclopropyl-4-isopropyl-1,3,5-trimethylbenzene (**10**). Exchange-broadened ^{1}H spectra due to slow rotation of the cyclopropyl group were only obtained near the low-temperature limit of the spectrometer (–140°C), and the barrier to rotation is estimated to lie near 28 kJ/mol ($\Delta G^{\ddagger}$). MM3 molecular mechanics computations suggest that the rather large increase of the rotational barrier in **10** relative to **5** is caused by the combined buttressing effect of the isopropyl and the 5-methyl groups. The present findings explain why an earlier attempt (in 1970) to determine the rotational barrier in 2-cyclopropyl-1,3,5-trimethylbenzene by dynamic NMR was bound to fail.

Key words: conformation, cyclopropylbenzenes, *ortho*-disubstituted, NMR spectroscopy, rotational barrier.

Résumé : On a utilisé la méthode *J* de Schaefer pour montrer que, en solution, le 2-cyclopropyl-1,3-diméthylbenzène (**5**) adopte préférentiellement la conformation perpendiculaire dans laquelle l'angle de torsion Θ, entre la liaison C(1)—H du groupe cyclopropyle et le plan du noyau benzénique, est égal à 90°. Ce résultat est opposé à la situation qui prévaut dans le cyclopropylbenzène (**3**) dans lequel le conformère bissecté (Θ = 0°) prédomine. Pour la valeur de –0,85 ± 0,01 Hz pour ^6J(H-α,H-*para*) dans le composé **5** (pour des solutions dans le CS_2 et dans l'acétone), on évalue que la barrière à la rotation autour de la liaison cyclopropyle–aryle est égale à 6,4 kJ/mol si l'on fait l'hypothèse que la barrière de potentiel est principalement binaire et que ^6J(H,H) disparaît pour Θ = 0°. L'introduction des deux groupes méthyles en *ortho* du composé **3** provoque donc un échange effectif des conformations des états fondamental et de transition de la rotation interne. On peut très bien reproduire cet effet par des calculs d'orbitales moléculaires ab initio (STO-3G et 6-31G*) et semi-empiriques (AM1). Une étude de RMN dynamique du 2-cyclopropyl-4-isopropyl-1,3,5-triméthylbenzène (**10**) a aussi permis de mettre en évidence la préférence d'un substituant cyclopropyle *ortho*-disubstitué pour la conformation perpendiculaire. Ce n'est que près de la limite inférieure de température du spectromètre (–140°C) qu'on a pu obtenir des spectres RMN du ^{1}H élargis en raison d'une rotation lente du groupe cyclopropyle et on a évalué que la barrière à la rotation se situe près de 28 kJ/mol ($\Delta G^{\ddagger}$). Des calculs de mécanique moléculaire au niveau MM3 suggèrent que la forte augmentation de la barrière rotationnelle dans **10** par rapport à **5** est provoquée par l'effet combiné de compression des groupes isopropyle et 5-méthyle. Les résultats obtenus ici expliquent pourquoi, lors d'un essai antérieur (1970), il n'a pas été possible de déterminer la barrière rotationnelle dans le 2-cyclopropyl-1,3,5-trimétylbenzène par RMN dynamique.

Mots clés : conformation, cyclopropylbenzènes, *ortho*-disubstitution, spectroscopie RMN, barrière rotationnelle.

[Traduit par la Rédaction]

Received February 19, 1999.

This paper is dedicated to Professor Ted Schaefer in recognition of his contributions to NMR spectroscopy.

L. Ernst[1] and T. Rieck. Institut für Organische Chemie, Technische Universität Braunschweig, Hagenring 30, D-38106 Braunschweig, Germany.
M. Soliven. Department of Chemistry, University of Manitoba, Winnipeg, MB R3T 2N2, Canada.

[1]Author to whom correspondence may be addressed. Telephone: (+49-531) 391-5379. Fax: (+49-531) 391-5387. e-mail: L.Ernst@tu-bs.de

 © 1999 NRC Canada

Introduction

The preferred conformation of simple *sec*-alkylbenzenes, Ph-$C^{\alpha}HR^1R^2$, with respect to internal rotation about the C(sp^2)—C(sp^3) bond, has the C^{α}—H bond in the plane of the benzene ring (1). For the simplest and most prominent example, isopropylbenzene (**1**), this has been shown by numerous experimental techniques, among them ^{1}H NMR on **1** itself (2) and on the 3,5-dibromo derivative (3), or supersonic molecular jet spectroscopy (4). The energy minimum of the rotational potential is hence depicted by conformer **1a** in which the torsional angle Θ of the C^{α}—H bond out of the aromatic plane is 0°. The maximum of the rotation potential is computed to lie at Θ = 90° (**1b**) both by ab initio MO (2) and by MOMM (combined MO/molecular mechanics) calculations (5). The rotational barrier, i.e., the energy difference between **1b** and **1a**, has been determined by NMR to be 6.5–8.4 kJ/mol (2, 3) and has been computed by ab initio MO methods (2) to be 14.1 kJ/mol (geometry-optimized STO-3G) or 13.4 kJ/mol (6-31G), while the MOMM procedure gives 9.6 kJ/mol (5), in better agreement with the experimental finding. The shape of the rotational potential is predominantly twofold with a possible smaller contribution by a fourfold component (2). When the isopropyl group is flanked by two simple *ortho*-substituents such as methyl in 2-isopropyl-1,3,5-trimethylbenzene (**2**) (6) or when a dichloromethyl group is flanked by two *ortho*-chlorines as in 2,6-dichlorobenzal chloride (7), the minimum and maximum energy conformations still have Θ = 0° and 90°, respectively, but the rotational barrier is increased so much that slow rotation about the C(sp^2)—C(sp^3) bond can easily be observed in moderately low-temperature ^{1}H- (6) and ^{13}C-NMR (8) spectra. In **2**, for example, the rotational barrier, $\Delta G^{\ddagger}$, was determined to be 53.6 kJ/mol (6).

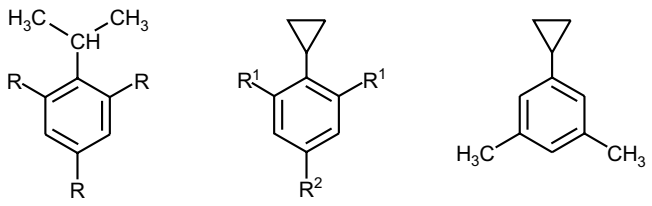

1, R = H
2, R = CH_3

3, $R^1 = R^2 = H$
4, $R^1 = R^2 = CH_3$
5, $R^1 = CH_3$, $R^2 = H$

6

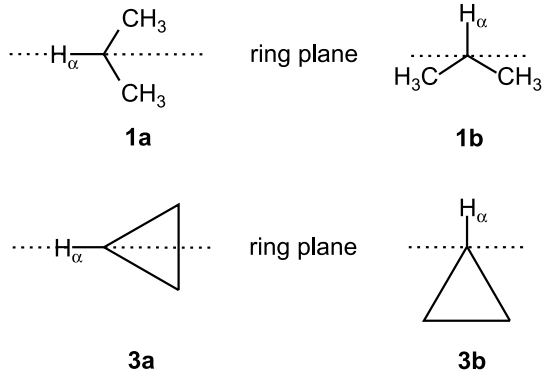

1a **1b**

3a **3b**

With respect to its preferred conformation and its barrier to internal rotation, cyclopropylbenzene (**3**) behaves very similarly to **1**. By applying the *J* method (9), Parr and Schaefer (10) determined the barrier in **3** to be 8.4 ± 1.3 kJ/mol and the preferred conformation to be the "bisected" one, **3a**. According to an X-ray crystallographic study (11), the molecule also assumes this conformation in the solid state. Earlier, presupposing the similar conformational behaviour of **1** and **3**, one of us had studied (6) an *ortho*-disubstituted derivative of **3**, viz. 2-cyclopropyl-1,3,5-trimethylbenzene (**4**), expecting that it would show hindered rotation in its ^{1}H NMR spectrum at moderately low temperatures as had been the case with **2**. However, within the limits of the available instrumentation at that time (spectrometer frequency: 90 MHz; lowest attainable temperature: –120°C), no decoalescence of the *ortho*-methyl signal could be observed, and it was concluded that the $\Delta G^{\ddagger}$ value of the rotational barrier was smaller than 31.4 kJ/mol. Our interest in the problem was stirred again when Drumright et al. (12) reported that, in the solid state, 9-chloro-10-cyclopropylanthracene prefers the "perpendicular" conformation corresponding to **3b** and that this was also borne out by MMX molecular mechanics computations on 9-cyclopropylanthracene. Also, Mislow and co-workers (13) had reported barriers to cyclopropyl rotation, determined by dynamic NMR spectroscopy, of 45.6 ± 2.1 and 41.4 ± 2.1 kJ/mol for 1,2-dicyclopropyl-3,4,5,6-tetraisopropylbenzene and 1,2,3,4-tetracyclopropyl-5,6-diisopropylbenzene, respectively. In these compounds, the cyclopropyl groups also assume the perpendicular conformation. We wondered whether there is generality to the finding that the addition of two *ortho*-substituents to the cyclopropyl group in cyclopropylarenes switches the favoured conformation from **3a** to **3b**. If so, our fruitless low-temperature ^{1}H NMR experiments on **4** could be explained not only (*i*) by too low a rotational barrier but also (*ii*) by the preference of **4** for the "wrong" (perpendicular) conformation. In the perpendicular conformation of **4**, the *ortho*-methyl groups are in symmetrical environments, and decoalescence of their signal cannot be expected on lowering the temperature. We therefore devised experiments, using more straightforward compounds than Mislow's, to find out whether explanation (*i*) or (*ii*) is appropriate or whether, possibly, (*i*) and (*ii*) hold simultaneously.

Results and discussion

Application of the *J* method to 2-cyclopropyl-1,3-dimethylbenzene (5)

Schaefer's *J* method (9) provides a way to determine the preferred conformation and the twofold barrier, V_2, to internal rotation (if it is small enough) in benzylic and benzalic compounds. It makes use of the $\sin^2 \Theta$ dependence of the six-bond spin–spin coupling, ^6J, between the nucleus in the *para* ring position and a nucleus bonded to the α position of the side chain:

$$[1] \qquad {}^6J = {}^6J_0 + {}^6J_{90} \langle \sin^2 \Theta \rangle$$

$^6J_0$ and $^6J_{90}$ are the values at Θ = 0° and 90°, and $\langle \sin^2 \Theta \rangle$ represents the value of $\sin^2 \Theta$ averaged over the hindered rotor states. If ^6J is accurately determined and $^6J_0$ and $^6J_{90}$ are known, $\langle \sin^2 \Theta \rangle$ can be calculated and, for a given tempera-

© 1999 NRC Canada

Table 1. ^{1}H NMR spectral parameters of compound **5**.

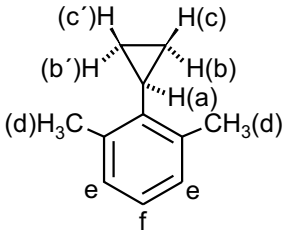

	Solvent[b]	
Parameter[a]	CS_2	Acetone
Cyclopropyl part		
δ(a)	1.594(0)	1.666(0)
δ(b)	0.932(0)	0.980(0)
δ(c)	0.443(0)	0.451(0)
^3J(a,b)	8.43(2)	8.46(1)
^3J(a,c)	5.82(2)	5.86(1)
^3J(b,b′)	9.20(2)	9.22(1)
^2J(b,c)	–4.37(2)	–4.31(1)
^3J(b,c′)	5.91(0)	5.93(0)
^3J(c,c′)	9.30(2)	9.29(1)
Aromatic part		
δ(d)	2.327(0)	2.363(0)
δ(e)	6.785(0)	6.913(0)
δ(f)	6.832(0)	6.947(0)
^5J(a,d)	–0.643(1)	–0.637(1)
^5J(a,e)	0.325(1)	0.321(1)
^6J(a,f)	–0.848(2)	–0.854(2)
^6J(d,d′)	—[c]	—[c]
^4J(d,e)	–0.695(2)	–0.706(3)
^6J(d,e′)	–0.544(1)	–0.556(2)
^5J(d,f)	0.330(1)	0.338(1)
^4J(e,e′)	—[c]	—[c]
^3J(e,f)	7.536(1)	7.549(1)

[a]For labelling of the protons, see the formula. Standard deviations of the parameters are given in parentheses after the values and refer to the last decimal quoted. Root mean square errors of the analyses were as follows. Cyclopropyl part: 0.040 Hz (CS_2 solution), 0.026 Hz (acetone-d_6 solution); aromatic part: 0.014 Hz (CS_2 solution), 0.012 Hz (acetone-d_6 solution).

[b]The "CS_2" solution consisted of **5**/CS_2/cyclohexane-d_{12}/hexafluorobenzene/tetramethylsilane in a molar ratio of 5/84.5/10/0.25/0.25. In the "acetone" solution, 84.5 mol% acetone-d_6 were used instead of CS_2.

[c]The values of these coupling constants are very strongly correlated ($r > 0.96$). Their individual values are determined by transitions of extremely small intensities that cannot be observed in the experimental spectrum. No values are therefore given.

Table 2. ^{1}H NMR spectral parameters of compound **6**.

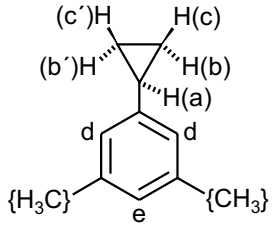

Parameter[a]	Value
δ(a)	1.804(0)
δ(b)	0.879(0)
δ(c)	0.614(0)
δ(d)	6.664(—)
δ(e)	6.734(—)
^3J(a,b)	8.415(2)
^3J(a,c)	5.092(1)
^4J(a,d)	–0.470(2)
^6J(a,e)	–0.182(3)
^3J(b,b′)	9.369(2)
^2J(b,c)	–4.348(3)
^3J(b,c′)	6.207(0)
^3J(c,c′)	9.366(2)
^4J(d,e)	1.67(—)

[a]For labelling of the protons, see the formula. The solution consisted of **6**/acetone-d_6/cyclohexane-d_{12}/hexafluorobenzene/tetramethylsilane in a molar ratio of 5/84.5/10/0.25/0.25. Standard deviations of the parameters are given in parentheses after the values and refer to the last decimal quoted. The root mean square error of the analysis was 0.013 Hz. Only the cyclopropyl proton transitions were assigned. The chemical shifts of the aromatic protons and their mutual coupling constant were determined "by hand" and kept constant during the iterative analysis. The methyl protons were decoupled.

ture and reduced moment of inertia, leads to the value of V_2 and discloses the nature of the rotational ground state (9). For benzalic compounds, the ground state conformation is bisected (**1a**, **3a**) if $\langle\sin^2\Theta\rangle$ is between 0 and 0.5, and it is perpendicular (**1b**, **3b**) if $\langle\sin^2\Theta\rangle$ is between 0.5 and 1. Good estimates are available for $^6J_0$ (0.0 Hz) and $^6J_{90}$ (–1.11 Hz) in cyclopropylbenzene from the earlier work by Parr and Schaefer (10), who have justified their choice in detail. These values are believed not be affected by methyl substitution on the benzene ring. A careful analysis of the ^{1}H NMR spectrum of 2-cyclopropyl-1,3-dimethylbenzene (**5**) was therefore undertaken in order to obtain the experimental value of ^6J(H,H). Both CS_2 and acetone solutions of **5** were studied, and the results of the iterative analysis are given in Table 1. Figure 1 shows the aromatic region of the experimental and the calculated ^{1}H NMR spectrum of **5** (CS_2 solution) to demonstrate the quality of the fit. For comparison, the spectrum of the unhindered 3,5-dimethyl derivative **6** was also recorded and analysed (Table 2) but only of an acetone solution because material was scarce.

The important coupling constant in **5**, ^6J(H-α,H-*para*), has virtually identical values in the two solutions, viz. –0.848(2) Hz (CS_2) and –0.854(2) Hz (acetone) so that it may be safely regarded as –0.85 ± 0.01 Hz. If we follow the earlier arguments (10) and accept the mentioned values for $^6J_0$ and $^6J_{90}$, the experimental coupling constant leads to $\langle\sin^2\Theta\rangle = -0.85/(-1.11) = 0.77$. A quantum mechanical solution to the hindered rotor problem (14) gives values of $\langle\sin^2\Theta\rangle$ as a function of temperatures, twofold barriers, and reduced moments of inertia, which have been tabulated (15) for easy use.[2] For $\langle\sin^2\Theta\rangle = 0.77$, a temperature of 300 K, and reduced moments of inertia between 1.0 and 4.0 × 10^{-38} g cm^2, these tables give a twofold barrier of 6.4 kJ/mol to rotation about the cyclopropyl–aryl bond in **5**. As $\langle\sin^2\Theta\rangle$ is

[2]We are grateful to Prof. T. Schaefer for a copy of this table.

© 1999 NRC Canada

Fig. 1. Aromatic region of the experimental (top) and calculated (bottom) 300 MHz ^{1}H NMR spectrum of a 5 mol% solution of **5** in CS_2.

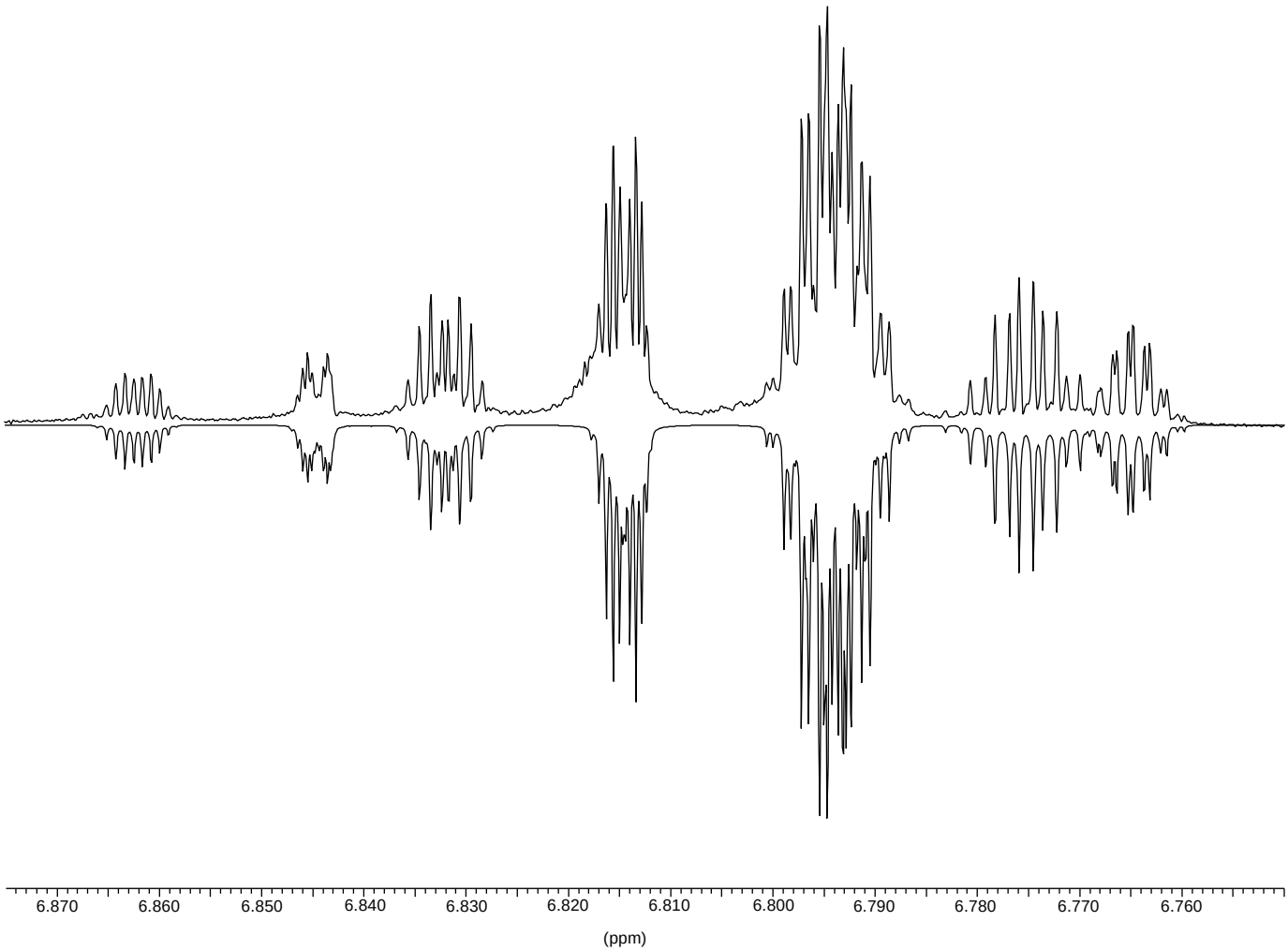

between 0.5 and 1.0, it also follows that the perpendicular conformation represents the ground state of the rotational potential. For the 3,5-dimethyl derivative **6**, the experimental coupling constant ^6J(H-α,H-*para*) of –0.18 Hz leads to $\langle \sin^2 \Theta \rangle = 0.16$, which proves the preference for the bisected conformation of this molecule and yields an estimate of 9.6 kJ/mol for the rotational barrier, of the same order of magnitude as the value for cyclopropylbenzene (**3**) itself which is 8.4 kJ/mol. Thus, the two important findings are: the rotational barrier in **5** is too small for dynamic NMR experiments on this compound to be successful, and the symmetry of the perpendicular ground state would preclude the observation of signal decoalescence even in case of a sufficiently high barrier. A referee has pointed out that the relative ^{1}H chemical shifts of the cyclopropyl protons H(a) ($\delta = 1.666$ in **5**, $\delta = 1.804$ in **6**) and of H(c) ($\delta = 0.451$ in **5**, $\delta = 0.614$ in **6**) are also consistent with the proposed conformational differences between **5** and **6**, as they are in line with the expected relative ring current effects of the phenyl group in the preferred conformations.

The conformational behaviour of **5** and **3** was qualitatively reproduced by molecular orbital computations. Ab initio computations of the rotational potential of **5** carried out for $\Theta = 0°$ to 90° in steps of 15° predict the energy maximum for $\Theta = 0°$ and a relatively flat energy minimum area extending from 60° to 90°, the 90° conformation lying slightly higher than the 60° conformation and the lowest energy occurring at $\Theta = 75°$ (Fig. 2*a*). The STO-3G and 6-31G* basis sets yield rotational barriers of 6.8 and 7.3 kJ/mol, respectively, in rather good agreement with the experimental result of 6.4 kJ/mol obtained by the *J* method. The semiempirical AM1 procedure predicts a similar shape of the barrier, although with $E(90°) < E(60°)$ and the minimum still at $\Theta = 75°$, but the barrier is overestimated almost exactly by a factor of two. The goodness of the agreement between experiment and ab initio computations is expressed by the $\langle \sin^2 \Theta \rangle$ values calculated for a temperature of 300 K and the shapes of the theoretical potentials, which contain a small fourfold and a negligible sixfold component. The calculated $\langle \sin^2 \Theta \rangle$ values are 0.74 for both the STO-3G and 6-31G* potentials, while the experimental finding was 0.77. The AM1 curve gives 0.85.

The reversal of the relative energies of the bisected and perpendicular conformations that follows from our present and from Parr's and Schaefer's (10) experiments is also reproduced by molecular orbital computations on cyclopropylbenzene (**3**), see Fig. 2*b*. Here, the bisected and perpendicular conformations correspond to an energy minimum and maximum, respectively, and the barrier is estimated to be 7.8 (6-31G*), 1.6 (STO-3G), or 10.0 kJ/mol

© 1999 NRC Canada

Fig. 2. Results of the molecular orbital computations of the internal rotation potential in 2-cyclopropyl-1,3-dimethylbenzene (**5**) (*a*) and in cyclopropylbenzene (**3**) (*b*). Θ is the torsional angle by which the cyclopropyl C(1)—H bond is twisted out of the plane of the benzene ring.

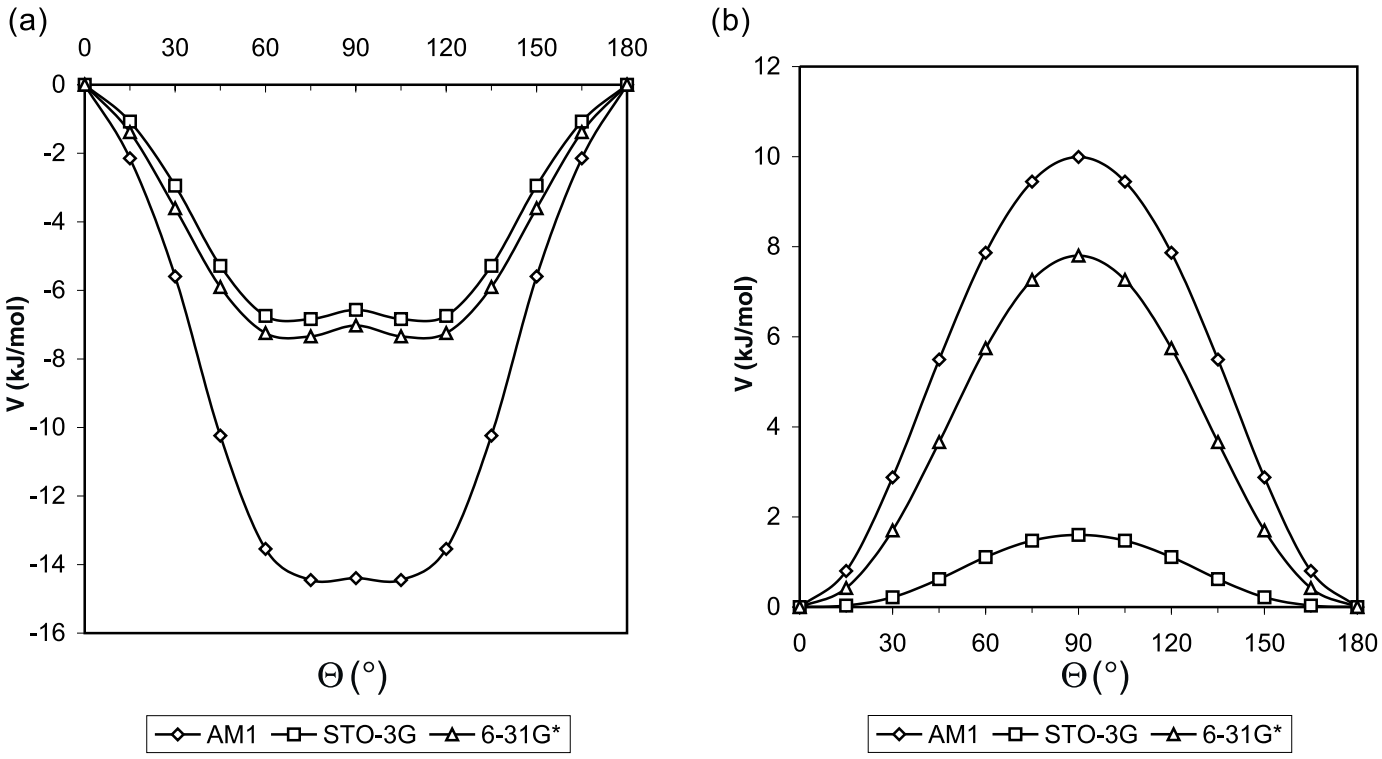

(AM1). The STO-3G result is clearly at variance with Parr's and Schaefer's (10) experimental finding (8.4 kJ/mol), but the 6-31G* value is similar to the experimental one, and the AM1 value also comes relatively close. To summarize the molecular orbital results, the three computational schemes agree (amongst themselves and with experiment) in the nature of the rotational ground and transition states for **3** and **5** and in the reversal of the stability of these states when two *ortho*-substituents are introduced into cyclopropylbenzene.

A comparison of the coupling constants in the cyclopropane ring of compounds **3** and **5** reveals one unexpected difference. While most of the *J*(H,H) values are very similar in the two compounds, i.e., they are unaffected by the substitution pattern of the phenyl group, the vicinal *trans* coupling constant involving H-1 [^3J(a,c) in Table 1] is distinctly affected, being 5.82 Hz (CS_2) or 5.86 Hz (acetone) in the 2,6-dimethyl derivative **5** and only 5.03 Hz (CS_2) in cyclopropylbenzene (**3**) itself (10), a difference of 14%. In the 3,5-dimethyl derivative **6** the coupling is 5.09 Hz (acetone, Table 2), similar to the value in **3**. As both **3** and **6** prefer the bisected conformation, which allows maximum cyclopropyl–aryl conjugation, while **5** favours the perpendicular conformation in which conjugation is minimal, these findings suggest that the coupling constant $^3J_{1,2}{}^{trans}$ in 1-substituted cyclopropanes is sensitive to conjugative effects exerted by the substituent. This coupling can possibly serve as an indicator of the preferred conformation in cyclopropanes carrying other conjugating substituents. The smaller values of $^3J_{1,2}{}^{trans}$ would point to a preference of the bisected conformation. This idea is supported by the small value of 4.89 Hz for $^3J_{1,2}{}^{trans}$ in vinylcyclopropane (16), in which the s-*trans* (= bisected) conformer predominates.

Application of dynamic NMR spectroscopy to 2-cyclopropyl-4-isopropyl-1,3,5-trimethylbenzene (10)

In a variable-temperature NMR experiment, a prochiral indicator group -CX_2Y in the *meta*-position of an *ortho*-dimethylated cyclopropylbenzene should, in principle, indicate by nonequivalence of the geminal X groups when cyclopropyl rotation becomes slow on the NMR timescale at low temperature if the preferred cyclopropyl conformation is perpendicular. We chose an isopropyl group as the prochiral indicator. As mentioned in the introduction, the rotation of an isopropyl group that is flanked by two *ortho*-substituents can be easily stopped, and in its preferred conformation the two methyl groups reside above and below the aromatic plane, respectively. They should therefore become nonequivalent when cyclopropyl rotation itself is slow and the three-membered ring favours the perpendicular conformation. We studied 2-cyclopropyl-4-isopropyl-1,3,5-trimethylbenzene (**10**), which was prepared as follows. In a Grignard reaction with acetaldehyde, bromo compound **7**, prepared from **2**, gave the secondary alcohol **8**, which was dehydrated with Al_2O_3 in vacuo at 100–150°C to give styrene **9**. This was converted into **10** by methylenation with $CH_2I_2/Al(CH_3)_3$ (17) (Scheme 1).

Low-temperature ^{1}H NMR spectra (Fig. 3*a*–*d*) were recorded of a solution of **10** in CBr_2F_2 containing 10% by volume of CD_2Cl_2 to provide a deuterium lock signal. On cooling the sample to temperatures below 0°C the signals

© 1999 NRC Canada

Scheme 1.

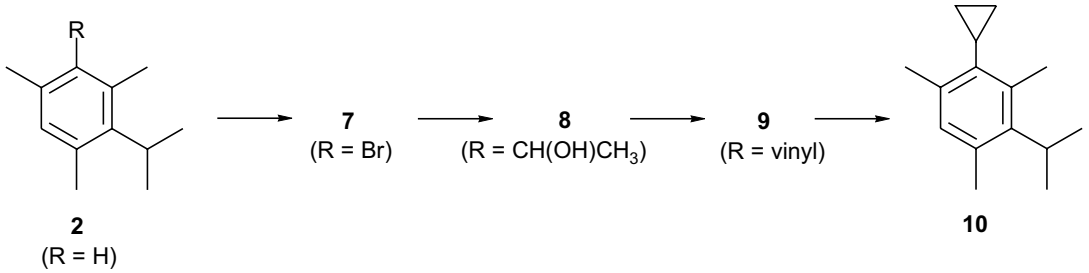

Fig. 3. Variable temperature ^{1}H NMR spectra of 2-cyclopropyl-4-isopropyl-1,3,5-trimethylbenzene in CBr_2F_2/CD_2Cl_2 (90:10, v/v). Experimental spectra shown were obtained at 23°C (*a*), –29°C (*b*), –80°C (*c*), –140°C (*d*). Theoretical spectrum (*e*), computed for rate constants of 0 and 18 s^{-1} for isopropyl and cyclopropyl rotation, respectively (see text).

© 1999 NRC Canada

Scheme 2.

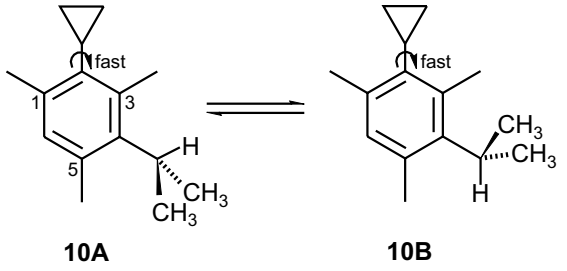

10A **10B**

Scheme 3.

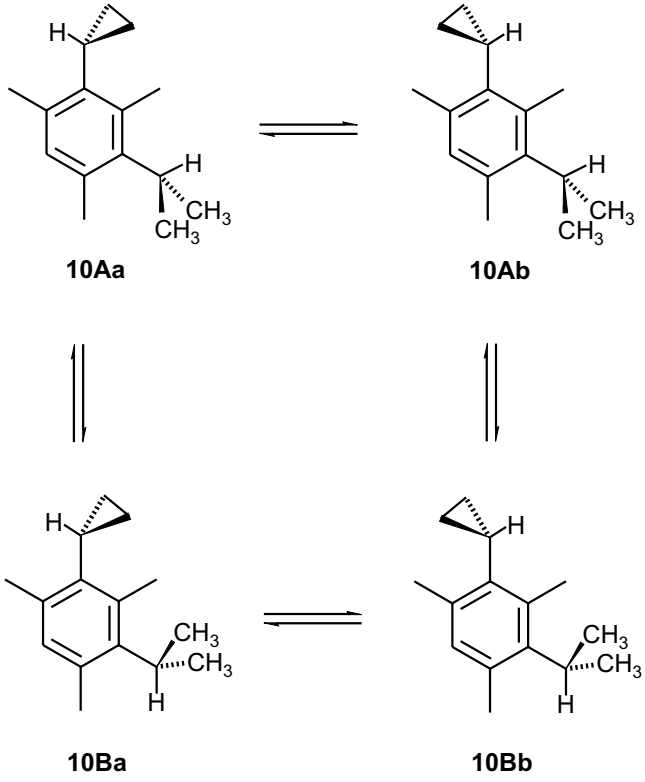

10Aa **10Ab**

10Ba **10Bb**

broadened (Fig. 3*b*; –29°C). Below –30°C the signals of the aromatic proton, of the three ring methyl groups, and the doublet of the isopropyl-CH_3 groups were doubled with a 1:1 ratio of the components (Fig. 3*c*; –80°C). The reason for this doubling of signals is slow rotation of the isopropyl group about the bond by which it is attached to the aromatic ring. Two rotamers are present which both have the C^{α}—H^{α} bond in the plane of the aromatic ring, pointing towards the 3-methyl group in one rotamer (**10A**) and to the 5-methyl group in the other (**10B**). Cyclopropyl rotation is still fast on the NMR timescale at this temperature (Scheme 2).

Apart from general signal broadening due to increasing sample viscosity and decreasing magnetic field homogeneity, an additional instance of line broadening was observed below –120°C, which can only be explained by cyclopropyl rotation also becoming slow. Eventually two broad signals (ratio ca. 3:1) emerged from both the isopropyl-CH_3 and the cyclopropyl-H-2^Z,3^Z (*cis* with respect to aryl) absorptions (Fig. 3*d*). These signals were neither well separated nor reasonably sharp at the low-temperature limit of the spectrometer (–140°C). The slow-exchange chemical shift differences could therefore not be determined. The ring-CH_3 and aryl-H resonances remained as six and two relatively sharp signals, respectively, apart from the accidental coincidence of two methyl lines. This shows that the cyclopropyl group does not adopt the two possible bisected conformations because in that case there should have been four sets of signals for each constitutionally different group in the molecule, i.e., 12 ring-CH_3 and 4 aryl-H singlets, and 4 isopropyl-CH_3 doublets. These four sets of signals would arise from the four possible combinations of bisected isopropyl (**A**, **B**) and bisected cyclopropyl (**a**, **b**) conformations as shown in formulae **10Aa**, **10Ab**, **10Ba**, and **10Bb** (Scheme 3).

Scheme 4.

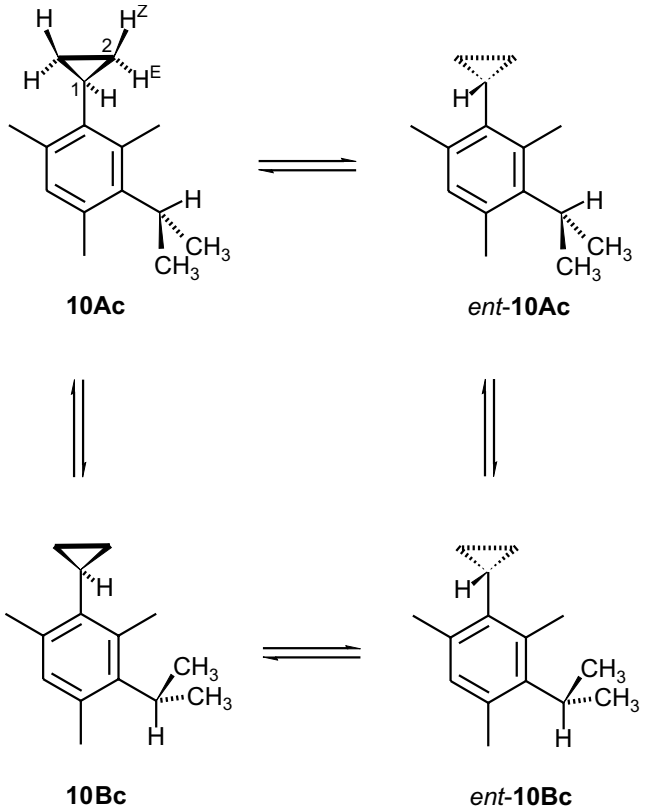

10Ac *ent*-**10Ac**

10Bc *ent*-**10Bc**

The case of only one pair of bisected cyclopropyl rotamers being populated (e.g., **10Aa**/**10Ba**) may be dismissed, as no exchange broadening would then have occurred below –120°C. The remaining possibility, viz. the perpendicular cyclopropyl conformation (**c**) combined with the two bisected isopropyl conformations (**A**, **B**) to give rotamers **10Ac** and **10Bc** is in full agreement with the number of observed ring-CH_3 and aryl-H signals. Cyclopropyl rotation by 180° in **10Ac** or **10Bc** exchanges the sites of the isopropyl-CH_3 and of the cyclopropyl-CH_2 groups yet transforms these rotamers only into their enantiomers, which explains the smaller number of signals relative to the situation involving **10Aa**, **10Ab**, **10Ba**, and **10Bb** (Scheme 4). The intensity ratio of ca. 3:1 for the partly separated isopropyl-CH_3 and cyclopropyl-H-2^Z signals in the exchange-broadened spectrum at –140°C must be interpreted by one of the four expected chemical shifts being separated from the other three that are close to each other. As the low-temperature

© 1999 NRC Canada

measurements could not be extended to a temperature beyond exchange broadening, only a rough estimate of the barrier to cyclopropyl rotation in **10** is possible. Taking a coalescence temperature of –135°C and a chemical shift difference between the cyclopropyl-H-2^Z signals of ca. 27 Hz leads to an approximate barrier $\Delta G^{\ddagger}$ at that temperature of 28 kJ/mol. Figure 3*e* is intended only to demonstrate that the lowest temperature spectrum can be simulated by selecting a small rate constant and a reasonable set of chemical shifts. However, other combinations of parameters will produce similar spectra, so not too much significance should be attributed to the rate constant of 18 s^{-1} employed.

The estimate, if rough, of 28 kJ/mol for cyclopropyl rotation in **10** contrasts with the value of 6.4 kJ/mol determined for **5**. MM3 molecular mechanics computations were carried out to explain this large difference. For **5**, the dihedral driver option was used to vary the angle of cyclopropyl rotation in 5° steps, and the rest of the molecular geometry was allowed to be minimized. Additionally, for **10**, the torsion of the isopropyl group was fixed in both of the possible bisected conformations. The computations did not provide quantitative agreement with the experimental results but gave the proper geometries of the minimum and maximum energy conformations. They predicted a lower rotational barrier (22 kJ/mol) for **5** than for **10** (30–34 kJ/mol depending on the orientation of the isopropyl group). The barrier increase in **10** relative to **5** is caused by the combined buttressing effects of the isopropyl and 5-methyl groups upon the 3-methyl group, increasing the interaction of the latter with the cyclopropyl group. A referee has kindly performed STO-3G calculations on **10** and obtained a barrier of ca. 30 kJ/mol, in good agreement with our experimental and MM3 results.

Conclusions

Using rather simple model compounds and applying two independent NMR methods, we have shown that the "bisected" conformation, which represents the favoured rotamer of cyclopropylbenzene, becomes the rotational transition state when two *ortho*-substituents of the size of methyl groups are added to the molecule. The symmetrical "perpendicular" conformation becomes the rotational ground state. This reversal of ground and transition states is reproduced by ab initio and semiempirical molecular orbital computations. Larger substituents or additional buttressing groups plus an unsymmetrical substitution pattern are required to make the rotational barrier accessible to dynamic NMR measurements.

Experimental

The melting point of **8** was determined on a Laboratory Devices Mel-Temp II apparatus. Infrared spectra were recorded on a Nicolet 320 FT-IR spectrometer, of substance films or of KBr disks as indicated. EI mass spectra (70 eV) were recorded on a MAT 8430 spectrometer. The ^{1}H NMR spectra for the iterative analyses of **5** and **6** were obtained on a Bruker AM300 spectrometer at 300 MHz and ambient temperature under the solution conditions given in Tables 1 and 2. These samples were degassed five times by the freeze–pump–thaw technique and then flame-sealed. Digital resolutions were better than 0.01 Hz per data point in the Fourier transformed spectra. The iterative analyses were carried out with the computer program NUMARIT (18), as modified by Marat and Sebastian (19). All other NMR spectra were obtained on a Bruker AM400 spectrometer at 400 MHz (^{1}H) or 101 MHz (^{13}C). Chemical shifts in the ^{1}H spectra were referenced to tetramethylsilane (δ = 0.000) or the residual proton signal of 1,1,2,2-tetrachloroethane-d_2 (δ = 5.98). Chemical shifts in the ^{13}C spectra were referenced to the solvent signal, $\delta(CDCl_3)$ = 77.05 or $\delta(C_2D_2Cl_4)$ = 73.79. The low-temperature ^{1}H NMR spectra of **10** were obtained from a dilute solution in CBr_2F_2/CD_2Cl_2 (9:1, by volume). The residual proton signal of CD_2Cl_2 was used as the chemical shift reference, δ = 5.32. The temperature display of the spectrometer was calibrated against the standard methanol sample (4% in methanol-d_4) (20). Elemental analyses were performed at the Institute of Inorganic and Analytical Chemistry of the Technical University of Braunschweig. Flash column chromatography was carried out using silica gel 60 for flash chromatography (Fluka).

Ab initio (STO-3G and 6-31G*) molecular orbital computations employed the program system Gaussian 94 (21). Internal rotational potentials were found by fixing the torsional angle Θ at values between 0° and 90° in steps of 15°, and optimizing the values of other angles and bond lengths, with the constraint, however, that the phenyl moiety remain planar. The semiempirical AM1 algorithm (22) was also used.

2-Cyclopropyl-1,3-dimethylbenzene (5)

This compound was prepared from 2-ethenyl-1,3-dimethylbenzene according to Brown and Cleveland (23). The ^{1}H NMR chemical shifts are similar to those given in ref. 23. For more detailed ^{1}H NMR data, see text, Table 1. ^{13}C NMR (101 MHz, $CDCl_3$, δ = 77.05) δ: 139.1 (s, C-2), 139.0 (s, C-1,3), 127.9 (d, C-4,6), 126.1 (d, C-5), 20.6 (q, 1,3-CH_3), 12.2 (d, *c*-Pr-C-1), 8.1 (t, *c*-Pr-C-2,3).

1-Cyclopropyl-3,5-dimethylbenzene (6)

To lithium granulates (0.96 g, 138.3 mmol) in dry ether (25 mL) under N_2 a solution of 1-iodo-3,5-dimethylbenzene (24) (14.39 g, 62.0 mmol) in dry ether (75 mL) was added dropwise with stirring during 45 min. Stirring was continued for another 30 min. To remove the excess lithium, the reaction mixture was transferred to a second flask by pouring it through a transfer piece filled with cotton wool. A solution of bromocyclopropane (1.50 g, 12.4 mmol) in dry ether (10 mL) was added dropwise and the mixture warmed to reflux for 15 h. The reaction mixture was poured onto ice water (100 mL), the organic phase separated, the aqueous phase extracted with ether, and the combined organic phases washed twice with water and dried over $MgSO_4$. The solvent was distilled off and the residue subjected to flash column chromatography (silica gel, *n*-pentane; R_f: 0.33) to give 178 mg (10%) of **6** as a colourless oil. The ^{1}H NMR chemical shifts are similar to those reported previously (25). For more detailed ^{1}H NMR data, see text, Table 2. ^{13}C NMR (101 MHz, $CDCl_3$, δ = 77.05) δ: 143.9 (s, C-1), 137.8 (s, C-3,5), 127.1 (d, C-4), 123.5 (d, C-2,6), 21.3 (q, 3,5-CH_3), 15.1 (d, *c*-Pr-C-1), 9.0 (t, *c*-Pr-C-2,3).

© 1999 NRC Canada

2-Bromo-4-isopropyl-1,3,5-trimethylbenzene (7)

To 2-isopropyl-1,3,5-trimethylbenzene (**2**) (26) (2.20 g, 13.6 mmol) and iron powder (30 mg) in dry CCl_4 (10 mL) was added bromine (1.72 g, 10.8 mmol) in dry CCl_4 (3 mL) at room temperature. Ten drops were added first and the remainder only when the formation of HBr gas was visible after the induction period. Stirring was continued overnight. The reaction mixture was diluted with CH_2Cl_2 (30 mL) and washed with 10% aqueous $NaHSO_3$ solution (20 mL), 10% aqueous NaOH solution (20 mL), and twice with water (20 mL). Drying over $MgSO_4$ and distilling off the solvent left a yellow oil. Flash column chromatography (silica gel, *n*-pentane; R_f 0.47) gave 2.6 g (99%) of **7** as a colourless oil. The NMR spectra of **7** and of the compounds described below were measured at elevated temperatures because coalescence phenomena led to broad lines in the room temperature spectra. IR (film) cm^{-1}: 2959 vs, 2931 s, 2876 m, 1463 s, 1460 s, 1452 s, 1388 m, 1365 m, 1189 m, 1073 m, 974 vs, 862 m, 722 w. ^1H NMR (400 MHz, 100°C, $C_2D_2Cl_4$, residual solvent signal, δ: 5.98) δ: 6.90 (s, 1H; H-6), 3.50 (sept, J = 7.3 Hz, 1H; i-Pr-CH), 2.54 (s, 3H; 3-CH_3), 2.39 (s, 3H; 1-CH_3), 2.34 (s, 3H; 5-CH_3), 1.37 (d, J = 7.3 Hz, 6H; i-Pr-CH_3). ^{13}C NMR (101 MHz, 100°C, $C_2D_2Cl_4$, δ: 73.79) δ: 143.5 (s, C-4), 135.6 (s, C-3), 135.0 (s, C-1), 134.4 (s, C-5), 131.0 (d, C-6), 127.1 (s, C-2), 30.0 (d, i-Pr-CH), 23.6 (q, 1-CH_3), 21.2 (q, 3-CH_3), 20.9 (q, 2C, i-Pr-CH_3), 20.7 (q, 5-CH_3); assignments by C,H-HETCOR, C,H-COLOC, and H,H-NOE. MS(EI) *m/z* (%): 242/240 (M^+, 38), 227 (96), 225 (100), 147 (18), 146 (52), 145 (16), 131 (17), 119 (14), 115 (10). Anal. calcd. for $C_{12}H_{17}Br$: C 59.76, H 7.10; found: C 59.36, H 7.09.

1-(3-Isopropyl-2,4,6-trimethylphenyl)-ethan-1-ol (8)

To a 30% lithium – mineral oil dispersion (506 mg) in dry ether (3 mL) was added dropwise a solution of **7** (2.40 g, 10.0 mmol) in dry ether (3 mL) under N_2 at room temperature. After addition of the first few drops, the reaction was started by gentle warming. When the addition of **7** was complete stirring was continued for 2.5 h at 30°C. The mixture was cooled to 0°C, and a solution of acetaldehyde (541 mg, 12.3 mmol) in dry ether (8 mL) was added dropwise. After stirring the reaction mixture for 30 min at 0°C and for 1h at room temperature it was poured onto ice water (30 mL), and the organic layer was separated. The aqueous phase was extracted twice with ether (30 mL), and the combined organic phases were washed with a saturated aqueous $NaHSO_3$ solution (25 mL) and thrice with water (10 mL). Drying over $MgSO_4$ and distilling off the solvent furnished a yellow oil (2.6 g) from which white crystals separated on standing in the refrigerator overnight. The crystals were collected and recrystallized from *n*-pentane to yield 1.12 g (55%) of **8**, mp 78°C. IR (KBr) cm^{-1}: 3315 vs, 2958 vs, 2933 vs, 2873 s, 1456 s, 1366 m, 1301 m, 1075 s, 1049 s, 895 m, 865 m, 706 w. ^1H NMR (400 MHz, 90°C, $C_2D_2Cl_4$, residual solvent signal, δ: 5.98) δ: 6.81 (s, 1H; H-5), 5.44 (q, J = 6.8 Hz, 1H; CH-O), 3.54 (sept, J = 7.3 Hz, 1H; i-Pr-CH), 2.48 (s, 3H; 2-CH_3), 2.42 (s, 3H; 6-CH_3), 2.38 (s, 3H; 4-CH_3), 1.75 (s, 1H; OH), 1.60 (d, J = 6.8 Hz, 3H; CH_3-CHO-), 1.404 (d, J = 7.3 Hz, 3H; i-Pr-CH_3), 1.402 (d, J = 7.3 Hz, 3H; i-Pr-CH_3). ^{13}C NMR (101 MHz, 90°C, $C_2D_2Cl_4$, δ: 73.79) δ: 142.9 (s, C-3), 139.0 (s, C-1), 134.8 (s, C-4), 134.0 (s, C-2), 132.5 (d, C-5), 132.4 (s, C-6), 67.7 (d, CHO), 28.9 (d, i-Pr-CH), 21.8 (q, -OCH-CH_3), 21.1 (q, 4-CH_3), 21.0 (q, 2C, i-Pr-CH_3), 20.2 (q, 6-CH_3), 16.8 (q, 2-CH_3); assignments by C,H-HETCOR and -COLOC. MS(EI) *m/z* (%): 206 (M^+, 58), 191 (100), 188 (50), 173 (60), 149 (24), 145 (22), 121 (40). Anal. calcd. for $C_{14}H_{22}O$: C 81.50, H 10.75; found: C 81.36, H 10.77.

2-Isopropyl-1,3,5-trimethyl-4-vinylbenzene (9)

To neutral Al_2O_3 (10 g, ICN, activity: "super I") **8** was added (900 mg, 4.4 mmol) and, at a pressure of 0.8 mbar (1 bar = 100 kPa), the mixture was heated to 100°C for 2.5 h and then to 150°C for 30 min. The product was collected in a cooling trap (liq. N_2) as a colourless liquid and purified by flash column chromatography (silica gel, *n*-pentane; R_f 0.27), yield 703 mg (86%). IR (film) cm^{-1}: 2960 vs, 2933 s, 2874 m, 1632 w, 1459 m, 1363 w, 995 m, 919 s, 865 m. ^1H NMR (400 MHz, 100°C, $C_2D_2Cl_4$, residual solvent signal, δ: 5.98) δ: 6.86 (s, 1H; H-6), 6.72 (dd, J = 17.9 and 11.4 Hz, 1H; -CH=), 5.54 (dd, J = 11.4 and 2.3 Hz, 1H; H_E of =CH_2), 5.20 (dd, J = 17.9 and 2.3 Hz, 1H; H_Z of =CH_2), 3.52 (sept, J = 7.3 Hz, 1H; i-Pr-CH), 2.38 (s, 3H; 1-CH_3), 2.36 (s, 3H; 3-CH_3), 2.27 (s, 3H; 5-CH_3), 1.40 (d, J = 7.3 Hz, 6H; i-Pr-CH_3). ^{13}C NMR (101 MHz, 100°C, $C_2D_2Cl_4$, δ: 73.79) δ: 141.7 (s, C-2), 137.0 (s, C-4), 136.6 (d, -CH=), 134.0 (s, C-1), 133.6 (s, C-3), 132.2 (s, C-5), 130.7 (d, C-6), 118.5 (t, =CH_2), 29.2 (d, i-Pr-CH), 21.0 (q, 3C, i-Pr-CH_3 and 1-CH_3), 20.3 (q, 5-CH_3), 17.8 (q, 3-CH_3); assignments by C,H-HETCOR and -COLOC. MS(EI) *m/z* (%): 118 (M^+, 58), 174 (14), 173 (100), 159 (14), 145 (43). Anal. calcd. for $C_{14}H_{20}$: C 89.30, H 10.70; found: C 89.47, H 10.91.

2-Cyclopropyl-4-isopropyl-1,3,5-trimethylbenzene (10)

To a solution of **9** (0.50 g, 2.7 mmol) and CH_2I_2 (2.1 g, 7.9 mmol) in dry *n*-hexane (5 mL) under N_2 a 2 M solution (6.64 mL) of $Al(CH_3)_3$ in toluene was added dropwise at room temperature. The progress of the reaction was monitored by GC. After 17 h, when the ratio of **9**/**10** was ca. 3:2, more CH_2I_2 (2.1 g, 7.9 mmol) was added followed by more (6.64 mL) of the $Al(CH_3)_3$ solution. After a reaction time of 90 h the ratio of **9**/**10** was ca. 1:22. The reaction mixture was then cooled to 0°C, and 10% aqueous NaOH (6 mL) was added cautiously with stirring. After stirring for another 20 min ether (20 mL) was added and the organic phase separated. The aqueous phase was extracted twice with ether (20 mL). The combined organic phases were washed with water (20 mL) and dried over $MgSO_4$. The solvent was distilled off, and a yellow oil (540 mg) remained. To remove the starting material, the raw product was dissolved in dry CCl_4 (7 mL) in a test tube, and a solution of one drop of bromine in CCl_4 (2 mL) was added at 0°C. After shaking for a short time CH_2Cl_2 (20 mL) was added and the solution washed twice with a saturated aqueous $Na_2S_2O_3$ solution (12 mL) and once with water (20 mL). Drying over $MgSO_4$ and distilling off the solvent left a black oil. Flash column chromatography (silica gel, *n*-pentane; R_f 0.27) yielded 188 mg (46%) of **10** as a colourless oil. IR (film) cm^{-1}: 3079 w, 3001 s, 2962 vs, 2928 s, 2872 m, 1459 m, 1033 m, 1016 m, 902 w, 864 w, 816 w. ^1H NMR (400 MHz, 100°C, $C_2D_2Cl_4$, residual solvent signal, δ: 5.98) δ: 6.80 (s, 1H; H-6), 3.52 (sept, J = 7.2 Hz, 1H; i-Pr-CH), 2.52 (s, 3H;

© 1999 NRC Canada

3-CH_3), 2.41 (s, 3H; 1-CH_3), 2.38 (s, 3H; 5-CH_3), 1.74 (m, 1H; *c*-Pr-H-1), 1.41 (d, J = 7.2 Hz, 6H; i-Pr-CH_3), 1.07 (m, 2H; *c*-Pr-H-2^E,3^E), 0.56 (m, 2H, *c*-Pr-H-2^Z,3^Z). ^{13}C NMR (101 MHz, 100°C, $C_2D_2Cl_4$, δ = 73.79) δ: 141.8 (s, C-4), 137.8 (s, C-2), 136.9 (s, C-3), 135.3 (s, C-1), 133.3 (s, C-5), 130.9 (d, C-6), 29.2 (d, i-Pr-CH), 21.0 (q, 2C, i-Pr-CH_3), 20.9 (q, 5-CH_3), 20.0 (q, 1-CH_3), 17.6 (q, 3-CH_3), 12.9 (d, *c*-Pr-CH), 8.8 (t, 2C, *c*-Pr-CH_2); assignments by C,H-HETCOR and -COLOC. MS(EI) *m/z* (%): 202 (M^+, 46), 188 (24), 187 (100), 173 (22), 159 (47), 145 (26). Anal. calcd. for $C_{15}H_{22}$: C 89.04, H 10.96; found: C 89.41, H 11.07.

Acknowledgements

We thank the Fonds der Chemischen Industrie, Frankfurt–Main, for partial support of this work. L.E. thanks Ted Schaefer for inviting him to his laboratory and for his hospitality during several weeks in the summer of 1996 when part of the present work was carried out. We thank one referee for useful comments on the chemical shifts of **5** and **6** and another referee for carrying out STO-3G calculations on **10** and relating to us his results of the rotational barrier.

References

1. E.L. Eliel, S.H. Wilen, and L.N. Mander. Stereochemistry of organic compounds. Wiley, New York. 1994. p. 626.
2. T. Schaefer, R. Sebastian, and G.H. Penner. Can. J. Chem. **66**, 1495 (1988).
3. T. Schaefer, W.J.E. Parr, and W. Danchura. J. Magn. Reson. **25**, 167 (1977).
4. J.I. Seeman, H.V. Secor, P.J. Breen, V.H. Grassian, and E.R. Bernstein. J. Am. Chem. Soc. **111**, 3140 (1989).
5. J. Kao. J. Am. Chem. Soc. **109**, 3817 (1987).
6. A. Mannschreck and L. Ernst. Chem. Ber. **104**, 228 (1971).
7. T. Schaefer, R. Schwenk, C.J. Macdonald, and W.F. Reynolds. Can. J. Chem. **46**, 2187 (1968).
8. L. Ernst and A. Mannschreck. Chem. Ber. **110**, 3258 (1977).
9. W.J.E. Parr and T. Schaefer. Acc. Chem. Res. **13**, 400 (1980).
10. W.J.E. Parr and T. Schaefer. J. Am. Chem. Soc. **99**, 1033 (1977).
11. J.S.A.M. de Boer, B.O. Loopstra, and C.H. Stam. Rec. Trav. Chim. Pays-Bas, **106**, 537 (1987).
12. R.E. Drumright, R.H. Mas, J.S. Merola, and J.M. Tanko. J. Org. Chem. **55**, 4098 (1990).
13. W. Weissensteiner, A. Gutiérrez, M.D. Radcliffe, J. Siegel, M.D. Singh, P.J. Tuohey, and K. Mislow. J. Org. Chem. **50**, 5822 (1985).
14. P.B. Ayscough, M.S. Brice, and R.E.D. McClung. Mol. Phys. **20**, 41 (1971).
15. T. Schaefer, J.B. Rowbotham, W.J.E. Parr, K. Marat, and A.F. Janzen. Can. J. Chem. **54**, 1322 (1976).
16. G. Schrumpf. Tetrahedron Lett. 2571 (1970).
17. K. Maruoka, Y. Fukutani, and H. Yamamoto. J. Org. Chem. **50**, 4412 (1985).
18. J.S. Martin, A.R. Quirt, and K.E. Worvill. The NMR program library. Daresbury Laboratory, Daresbury, U.K.
19. K. Marat and R. Sebastian. Bruker Report. Bruker Analytische Messtechnik, Rheinstetten, Germany. 1993. p. 42.
20. Bruker AM Series User's Manual. Bruker Analytische Messtechnik, Rheinstetten, Germany. 1987.
21. M.J. Frisch, G.W. Trucks, H.B. Schlegel, P.M.W. Gill, B.G. Johnson, M.A. Robb, J.R. Cheeseman, T.A. Keith, G.A. Petersson, J.A. Montgomery, K. Raghavachari, M.A. Al-Laham, V.G. Zakrzewski, J.V. Ortiz, J.B. Foresman, J. Cioslowski, B.B. Stefanov, A. Nanayakkara, M. Challacombe, C.Y. Peng, P.Y. Ayala, W. Chen, M.W. Wong, J.L. Andres, E.S. Replogle, R. Gomperts, R.L. Martin, D.J. Fox, J.S. Binkley, D.J. Defrees, J. Baker, J.P. Stewart, M. Head-Gordon, C. Gonzalez, and J.A. Pople. Gaussian 94, Revision B.2. Gaussian Inc., Pittsburgh, Penn. 1995.
22. M.J.S. Dewar, E.G. Zoebisch, E.F. Healy, and J.J.P. Stewart. J. Am. Chem. Soc. **107**, 3902 (1985).
23. H.C. Brown and J.D. Cleveland. J. Org. Chem. **41**, 1792 (1976).
24. R.J. Sundberg and R.W. Heintzelmann. J. Org. Chem. **39**, 2546 (1974).
25. I.B. Repinskaya, A.I. Rezvukhin, and V.A. Koptyug. J. Org. Chem. USSR (Engl. Transl.) **7**, 2225 (1971).
26. R. Adams and A. Ferretti. J. Am. Chem. Soc. **83**, 2559 (1961).

© 1999 NRC Canada

Stereochemical rearrangements in tricarbonylrhenium(I) halide complexes of the nonracemic chiral ligand 2-[(4*R*,5*R*)-dimethyl-1,3-dioxan-2-yl]pyridine (L): a dynamic NMR study

Peter J. Heard, Alex D. Bain, and Paul Hazendonk

Abstract: Tricarbonylrhenium(I) halide complexes of the nonracemic chiral ligand 2-[(4*R*,5*R*)-dimethyl-1,3-dioxan-2-yl]pyridine (L), namely *fac*-[ReX(CO)$_3$L] (X = Cl, Br, or I), have been prepared and their latent fluxionality studied by dynamic NMR techniques in the slow and intermediate exchange regimes. In solution, these complexes give rise to four diastereoisomers, depending on the configuration at the metal and at the acetal-carbon atom, respectively; the relative populations are in the order *SR* > *RR* >> *RS* > *SS*. At moderate temperatures, a reversible "acetal ring flip" leads to *formal* inversion of configuration at the acetal-carbon atom; the free energies of activation are in the range 84–88 kJ mol^{-1} at 298 K. Above ca. 370 K, reversible ligand dissociation also occurs, leading to an exchange of all four diastereoisomers on the NMR chemical shift time-scale.

Key words: dynamic NMR, fluxionality, tricarbonylrhenium(I) complexes, chiral acetal ligands.

Résumé : On a préparé les complexes d'halogénures du tricarbonylrhénium(I) avec le ligand chiral non racémique 2-[(4*R*,5*R*)-diméthyl-1,3-dioxan-2-yl]pyridine (L), soit les *fac*-[ReX(CO)$_3$L] (X = Cl, Br, ou I), et on a étudié leurs propriétés fluxionnelles latentes par des techniques de RMN dans des régimes d'échange lents et intermédiaires. En solution, ces complexes présentent quatre diastéréoisomères suivant, respectivement, la configuration au niveau du métal ou de l'atome de carbone de l'acétal; les populations relatives sont dans l'ordre *SR* > *RR* >> *RS* > *SS*. À des températures modérées, une inversion réversible du cycle de l'acétal conduit à une inversion *formelle* de configuration au niveau du carbone de l'acétal; les énergies libres d'activation sont de l'ordre de 84 à 88 kJ mol^{-1} à 298 K. Au-dessus d'environ 370 K, il se produit aussi une dissociation réversible du ligand qui, à l'échelle de temps des déplacements chimiques en RMN, conduit à un échange des quatre diastéréoisomères.

Mots clés : RMN dynamique, propriétés fluxionnelles, complexes du tricarbonylrhénium(I), ligands acétal chiraux.

[Traduit par la Rédaction]

Introduction

Nonracemic chiral ligands play an important role in organometallic chemistry, particularly in homogeneous catalysis (1); understanding the bonding in these complexes is therefore of importance. The systematic study of fluxional processes provides a sensitive method for probing bonding interactions, particularly where multiple mechanistic pathways are competing. We have demonstrated recently that nonracemic chiral ligands can be used to elucidate dynamic processes that are otherwise unobservable (2, 3), providing detailed information on the bonding between the metal and the fluxional ligand. This paper illustrates the power of such an approach for the study of complex fluxional organometallic systems.

The latent fluxionality of transition metal complexes of potentially *mer*-terdentate ligands in which the ligand is restricted to a bidentate bonding mode is of current interest (4, 5). The possible mechanisms of the dynamics are the subject of controversy (6, 7). Our approach has been to employ a nonracemic chiral oxazoline ligand (8); the spectroscopic handle provided by the asymmetric centres enables the mechanism to be determined unambiguously. We reported recently on the use of the C_2-symmetric bis(oxazolines), 2,6-

Received February 24, 1999.

This paper is dedicated to Professor Ted Schaefer in recognition of his outstanding contributions to Canadian chemistry.

P.J. Heard.[1] Department of Chemistry, Birkbeck College, University of London, Gordon House, 29 Gordon Square, London WC1H 0PP, U.K.
A.D. Bain and P. Hazendonk. Department of Chemistry, McMaster University, 1280 Main Street West, Hamliton, ON L8S 4M1, Canada.

[1]Author to whom correspondence may be addressed. e-mail: p.heard@chemistry.bbk.ac.uk

 © 1999 NRC Canada

Table 1. Analytical data for the complexes $[ReX(CO)_3L]$.

Complex	Yield[a]	Infrared data[b]/cm^{-1}	Mass spectral data[c]	Analyses[d] C	H	N
$[ReCl(CO)_3L]$	72	2031	484 $[M - H]^+$	29.81 (32.20)	2.25 (2.70)	2.36 (2.89)
		1925	450 $[M - Cl]^+$			
		1899				
$[ReBr(CO)_3L]$	60	2032	528 $[M - H]^+$	27.86 (29.50)	2.17 (2.47)	2.31 (2.64)
		1927	500 $[M - H - CO]^+$			
		1900	449 $[M - H - Br]^+$			
$[ReI(CO)_3L]$	39	2031	576 $[M - H]^+$	26.08 (27.09)	1.99 (2.27)	2.08 (2.43)
		1928	548 $[M - H - CO]^+$			
		1902	449 $[M - H - I]^+$			

[a]Percentage yield relative to $[ReX(CO)_5]$.

[b]Carbonyl stretching modes; recorded as CH_2Cl_2 solutions.

[c]LSIMS mass spectral data.

[d]Calculated analyses in parentheses; analytically pure samples could not be obtained (see text) and consequently good analytical figures for the complexes could not be obtained.

Fig. 1. Fluxional complexes of the C_2-symmetric nonracemic chiral ligands, 2,6-bis[(4*S*)-alkyloxazolin-2-yl]pyridine (alkyl = methyl or isopropyl), studied previously. The chirality at the carbon atoms enables the mechanisms of the fluxional processes to be determined unambiguously.

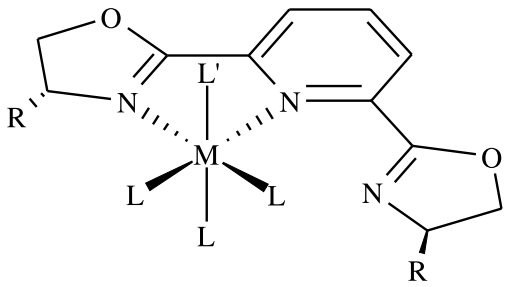

M = Re; L = CO; L' = Cl, Br or I
M = Pt; L = Me; L' = Cl, Br or I
M = Mo; L = L' = CO
M = W; L = L' = CO
R = Me or ^{i}Pr

bis[(4*S*)-alkyloxazolin-2-yl]pyridine (alkyl = methyl or isopropyl), as a mechanistic probe for the dynamic stereochemical rearrangements in complexes of the type shown in Fig. 1 (2, 3). This paper describes the results of a detailed dynamic NMR study on the tricarbonylrhenium(I) halide complexes of the closely related acetal ligand, 2-[(4*R*,5*R*)-dimethyl-1,3-dioxan-2-yl]pyridine (L), namely *fac*-$[ReX(CO)_3L]$ (X = Cl, Br, or I).

Experimental

Syntheses

All manipulations were performed using standard Schlenk techniques (9) under an atmosphere of dry, oxygen-free nitrogen. Solvents were dried (10) and degassed before use. The pentacarbonylrhenium(I) halides were prepared according to previously published procedures (11). (2*R*,3*R*)-Butanediol, 2-pyridinecarboxaldehyde, and 2,2-dimethoxypropane were purchased from Aldrich Chemical Company and were used without further purification. The compounds were prepared as described below. Analytical and ^{1}H NMR data are reported in Tables 1 and 2, respectively.

2-[(4*R*,5*R*)-Dimethyl-1,3-dioxan-2-yl]pyridine (L)

(See ref. 12.) 2-Pyridinecarboxaldehyde (1.0 cm^3, 10.5 mmol), (2*R*,3*R*)-butanediol (1.5 cm^3, 16.43 mmol), 2,2-dimethyoxypropane (1.5 cm^3, 16 mmol), and ca. 40 mg of *p*-toluenesulfonoic acid were refluxed for 48 h in toluene (30 cm^3). The toluene was then extracted with (*i*) aqueous Na_2CO_3 solution and (*ii*) water. After drying ($MgSO_4$), the toluene was concentrated in vacuo to yield an oil. The ligand, 2-[(4*R*,5*R*)-dimethyl-1,3-dioxan-2-yl]pyridine, was purified from hot hexane and characterized by ^{1}H NMR spectroscopy. Yield: 1.40 g, 75%.

The three complexes, $[ReX(CO)_3L]$ (X = Cl, Br, or I), were prepared similarly, as illustrated by the procedure for the complex X = Br.

{2-[(4*R*,5*R*)-Dimethyl-1,3-dioxan-2-yl]pyridine}bromotricarbonylrhenium(I)

$[ReBr(CO)_5]$, 100 mg (0.246 mmol), and 50 mg (0.279 mmol) of 2-[(4*R*,5*R*)-dimethyl-1,3-dioxan-2-yl]pyridine were refluxed for ca. 18 h in 20 cm^3 of benzene. The solvent was then removed in vacuo to yield an oil that was purified by precipitation from a CH_2Cl_2–hexane solvent mixture at –20°C. Yield: 72 mg, 60%.

Physical methods

Infrared spectra were recorded as CH_2Cl_2 solutions on a Nicolet 205 FT-IR spectrometer, operating in the region 4000–400 cm^{-1}. Elemental analyses were carried out at University College London. Mass spectra (LSIMS) were obtained at the London School of Pharmacy on a VG Analytical ZAB-SE instrument, using Xe^+ ion bombardment at 8 kV energy.

^{1}H NMR spectra were recorded in $[D]_2$-tetrachloroethane at McMaster University on a Bruker AM300 NMR spectrometer, operating at 300.13 MHz. Chemical shifts are quoted in ppm relative to tetramethylsilane as an internal standard. Probe temperatures were controlled by a standard

© 1999 NRC Canada

Table 2. ^{1}H NMR data[a] for the complexes [ReX(CO)$_3$L].

Complex	Diastereoisomer[b]	δ(acetal-C*H*$_3$)	δ(acetal ring-*H*)	δ(acetal C-*H*)	δ(pyridine-*H*)[c]
Ligand (L)[d]		1.32 (5.6); 1.27 (5.6)	3.79 (5.6; 7.6); 3.76 (5.6; 7.6)	5.91	8.55 (4.8); 7.66 (7.8; 7.5); 7.50 (7.8); 7.19 (4.8; 7.5)
[ReCl(CO)$_3$L]	*SR* (58)	1.56 (6.1); 1.36 (6.1)	4.01 (6.1; 8.6); 3.79 (6.1; 8.6)	6.61	8.75 (5.5); 7.99 (8); 7.63 (8; 8); 7.50 (8; 5.5)
	RR (37)	1.43 (6.1); 1.33 (6.1)	4.40 (6.1; 8.6); 4.03 (6.1; 8.9)	6.15	8.72 (5.5); 8.01 (8); 7.63 (8; 8); 7.47 (8; 5.5)
	RS (4.5)	1.51 (6.3); 1.30 (5.9)	4.24	6.73	
	SS (0.5)			6.08	
[ReBr(CO)$_3$L]	*SR* (54)	1.55 (6.2); 1.37 (6.1)	4.01 (6.2; 8.8); 3.79 (6.1; 8.8)	6.61	8.7 (5); 7.7 (7); 7.6 (6; 7); 7.5 (5; 7)
	RR (41)	1.41 (6.1); 1.34 (6.1)	4.43 (6.1; 9.0); 4.04 (6.1; 9.0)	6.13	8.7 (5); 8.1 (7); 7.6 (6; 7); 7.5 (5; 7)
	RS (4)	1.49 (6.3); 1.30 (5.8)	4.23; 3.86	6.73	
	SS (1)	1.60 (6.2)		5.94	
[ReI(CO)$_3$L]	*SR* (52)	1.53 (6.1); 1.38 (6.1)	4.00 (6.1; 8.6); 3.79 (6.1; 8.6)	6.55	8.76 (5.3); 7.96 (7.7); 7.60 (7.7; 8); 7.49 (8; 5.3)
	RR (44)	1.39 (6.1); 1.36 (6.1)	4.45 (6.1; 8.8); 4.05 (6.1; 8.8)	6.07	8.81 (5.1); 7.98 (7.7); 7.6 (7.7; 8); 7.46 (8; 5.1)
	RS (4)	1.47 (6.3); 1.30 (5.9)	4.20; 3.89	6.65	
	SS (<0.5)	1.59 (6.3)		~ 5.96[e]	

[a]Spectra recorded in $(CDCl_2)_2$ at 303 K; chemical shifts quoted in ppm relative to tetramethylsilane as an internal standard (see Fig. 2 for labelling of diastereoisomers); $^3J_{HH}$/Hz given in parentheses; not all signals due to the *RR* and *SS* diastereoisomers observed.

[b]Populations (%) given in parentheses.

[c]Approximate values only for complexes because of extensive overlap of the signals (see text).

[d]Recorded in $CDCl_3$ solution.

[e]Overlaps with the solvent signal.

B-VT 2000 unit and are considered accurate to within ±1°C. Standard one-dimensional variable temperature experiments were carried out in the temperature range 303–393 K; probe temperatures was allowed to equilibrate for ca. 20 min before each spectrum was recorded. Acquisition times were typically ca. 5 s, and a relaxation delay of 5 s was allowed between scans. Band shapes were analysed using the non-iterative simulation program MEX (13). Inversion-recovery experiments were carried out using the automation program INVREC2P (modified from the Bruker program INVREC), which generates the pulse sequence D1–90-τ-90-VD-90-free induction decay. For nonselective inversions the delay, τ, was 10 μs. For the selective experiments, the signal to be inverted was placed on resonance and τ was set at $1/(2\Delta\nu)$; $\Delta\nu$ is the frequency difference between the inverted and observed signals. The relaxation delay, D1, was 30 s. For the selective and nonselective inversions, respectively, 24–30 and 12–16 experiments (i.e., the number of delay times in the VD list) were carried out. Exchange rates were extracted from the longitudinal magnetizations using the program CIFIT (14). Two-dimensional exchange (EXSY) spectra, recorded using the Bruker automation program NOESYPH, were acquired prior to the selective inversions, to ascertain which signals were undergoing chemical exchange. Typical acquisition parameters for the EXSY experiment are described elsewhere (3). The rate constants obtained from the dynamic NMR experiments were used to calculate the Eyring activation parameters; the errors quoted are those defined by Binsch and Kessler (15).

Results

The three complexes, [ReX(CO)$_3$L] {X = Cl, Br, or I; L = 2-[(4*R*,5*R*)-dimethyl-1,3-dioxan-2-yl]pyridine}, were isolated as air-stable brown oils as described above. The mass spectra (LSIMS) of the complexes displayed strong peaks due to the species $[M - H]^+$, due to the loss of the acetal carbon – H, and $[M - X]^+$ (X = Cl, Br, or I); the observed and calculated isotope patterns are consistent. The infrared spectra (CH_2Cl_2 solution) displayed three carbonyl stretching bands in the region 1850–2050 cm^{-1}, as expected for a *fac*-octahedral tricarbonylrhenium(I) complex (16). Analytically pure samples could not be obtained; consequently, elemental analyses (C, H, and N) gave poor data. Data are reported in Table 1.

NMR studies

The ambient temperature (303 K) ^{1}H NMR spectra of the complexes, [ReX(CO)$_3$L] (X = Cl, Br, or I; L = 2-[(4*R*,5*R*)-dimethyl-1,3-dioxan-2-yl]pyridine), in [*D*]$_2$-tetrachloroethane displayed well-resolved signals due to the presence of four non-exchanging diastereoisomers (Fig. 2). The spectra of the three complexes were similar, and the results obtained for [ReBr(CO)$_3$L] will serve to illustrate the analysis of the problem.

The ^{1}H NMR spectrum of [ReBr(CO)$_3$L] at 303 K displayed signals in two regions of principal interest (Fig. 3): (*i*) acetal-methyl region (ca. δ = 1.1–1.7) and (*ii*) acetal-CH region (ca. δ = 6.0–7.0). The acetal-methyl region displayed

© 1999 NRC Canada

Fig. 2. The four diastereoisomers of the complexes $[ReX(CO)_3L]$, showing the interconversion pathways resulting from the acetal "ring flip" process. The letters *R* and *S* refer to the configuration at the metal and at the acetal carbon atom, respectively. The acetal-carbon atom is labelled C_1, and the acetal carbon-H is labelled H_A.

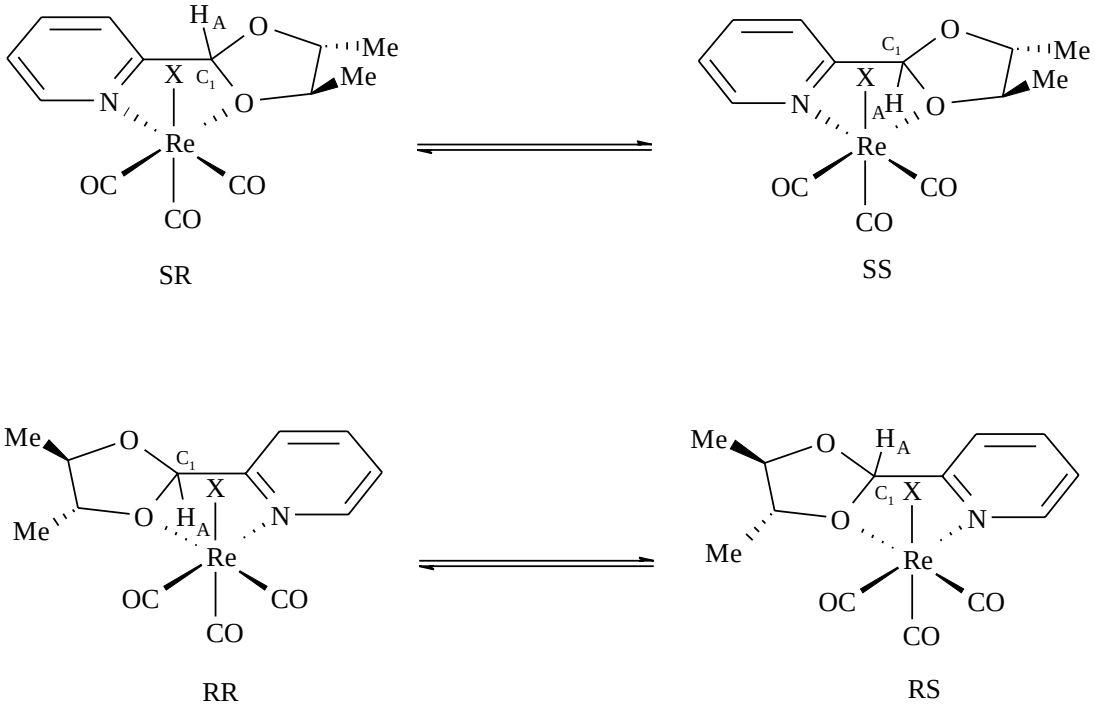

Fig. 3. ^1H NMR (300 MHz) spectrum of $[ReBr(CO)_3L]$ in $(CDCl_2)_2$, showing the acetal ring methyl and acetal carbon-H regions. See Fig. 2 for labelling. The broad signal denoted * is probably due to water.

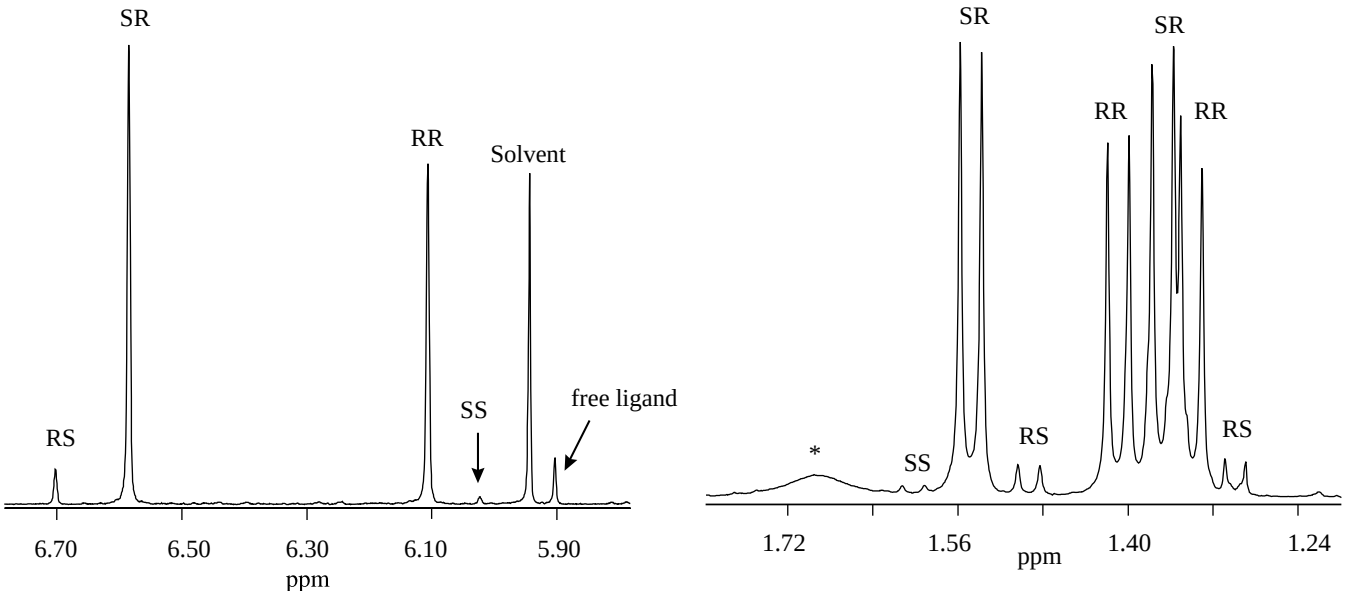

four pairs of doublets ($^3J_{HH} \approx 6$ Hz) of differing intensity. If it is assumed that inversion of configuration at the coordinated oxygen atom is rapid on the NMR chemical shift timescale (17, 18), the four pairs of doublets can be assigned to the four (non-exchanging) diastereoisomers shown in Fig. 2. These are labelled *SR*, *RR*, *RS*, and *SS* (depending on the configuration at the metal and at the acetal-carbon atom (C_1, see Fig. 2), respectively). The configuration at the metal (19) (*R* or *S*) was determined by viewing the molecule down the pseudo C_3 axis of symmetry (with the three CO ligands down) and assigning priorities to the three remaining ligands (halogen, oxygen, and nitrogen), according to the Cahn–Ingold–Prelog system (20).

The acetal-CH region displayed four broad singlets, assignable to the four diastereoisomers. The line broadening of these signals results from unresolved long-range couplings

© 1999 NRC Canada

Fig. 4. Spectra show the selective inversion of the signal of the acetal H of the *RR* diastereoisomer of the complex $[ReBr(CO)_3L]$ at 323 K. Delay times are shown alongside. See Fig. 2 for labelling of the diastereoisomers.

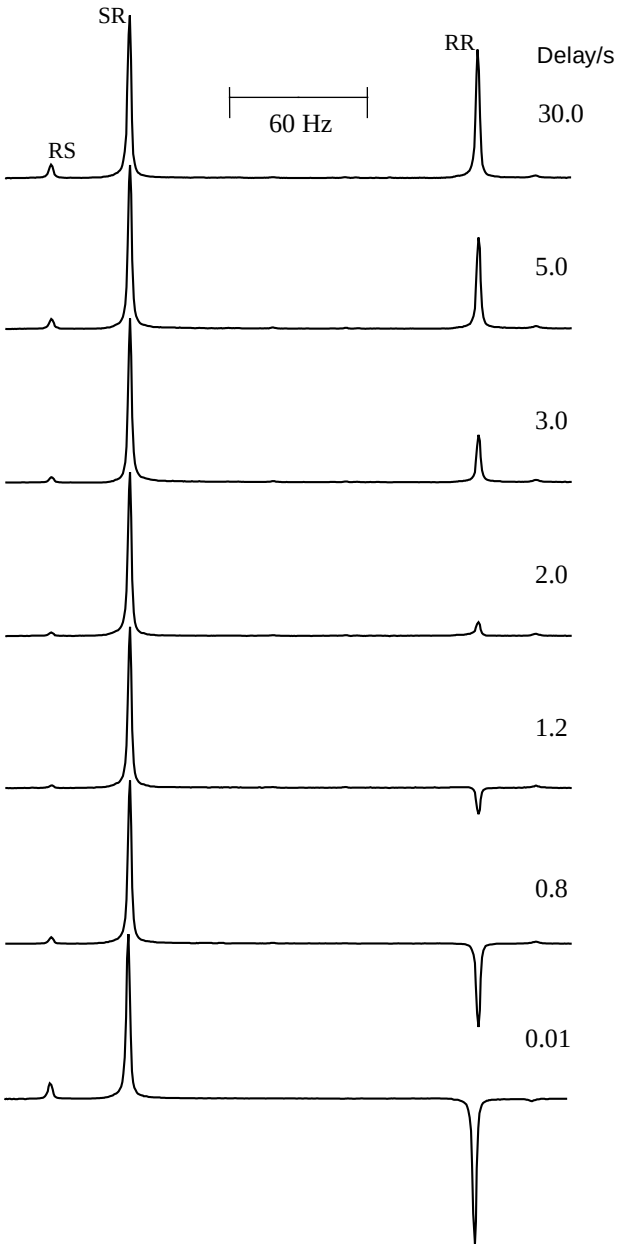

to the pyridine-H nuclides. The assignment of the major solution-state diastereoisomer was based on our results on the closely related complex, $[ReBr(CO)_3L^2]$ (L^2 = 2,6-bis[(4*R*,5*R*)-dimethyl-1,3-dioxan-2-yl]pyridine), which has four directly analogous diastereoisomers in solution. In the solid state $[ReBr(CO)_3L^2]$ exists exclusively as the *SR* diastereoisomer,[2] and (solid state and solution) ^{13}C NMR data indicate that it predominates in solution. The major solution-state species of the complex $[ReBr(CO)_3L]$ (L = 2-[(4*R*,5*R*)-dimethyl-1,3-dioxan-2-yl]pyridine) was therefore assigned as the *SR* diastereoisomer. The assignments of the remaining signals are based on the variable temperature ^1H NMR spectra (see below) and the relative chemical shifts of the acetal-CH signals. Exchange can occur between diastereoisomers (*SR* ⇆ *SS* and *RS* ⇆ *RR*) as a result of an "acetal ring flip" process, which leads to *formal* inversion of configuration at the acetal carbon atom, C_1 (see below). There is no exchange between these pairs because, at moderate temperatures (see below), there is no mechanism for *formal* inversion of configuration at the metal centre. The signal due to the *SS* diastereoisomer is thus readily identified because it exchanges with the signal due to the *SR* diastereoisomer (see above). The acetal-CH of the *SR* diastereoisomer is oriented on the same side as the halogen (Br) and resonates at higher frequency than the acetal-CH of the *SS* diastereoisomer. The acetal-CH of the *RS* diastereoisomer is also oriented on the same side as the halogen, so might be expected to resonate at higher frequency than the acetal-CH of the *RR* diastereoisomer. Thus, the high frequency acetal-CH signal of the *RR*/*RS* pair was assigned to the *RS* diastereoisomer. This is not unambiguous, but the *absolute* assignments do not affect the analysis of the dynamic exchange problem. The populations (Table 2), determined from the relative intensities of the acetal-CH signals, are in the order *SR* > *RR* >> *RS* > *SS*, and follow the trends expected on consideration of the different metal···ligand steric interactions.

The ^1H NMR spectrum of $[ReBr(CO)_3L]$ also displayed signals in the regions ca. δ = 3.6–4.6 and 7.2–9.0, due to the hydrogen nuclides of the acetal and pyridine rings, respectively. The signals of the four diastereoisomers are not well separated in these regions, frustrating complete assignment and accurate measurement of all chemical shifts and scalar couplings. ^1H NMR data for the ligand (L), 2-[(4*R*,5*R*)-dimethyl-1,3-dioxan-2-yl]pyridine, and the three complexes, $[ReX(CO)_3L]$ (X = Cl, Br, or I), are given in Table 2.

Variable-temperature dynamic ^1H NMR experiments were carried out on all three complexes in the temperature range 303–393 K. The signals of the acetal-CH nuclides (H_A, see Fig. 2) provide the most suitable spectroscopic handle on the kinetics. Above ca. 330 K, the acetal-CH signals due to the minor species (*RS* and *SS*) broaden quickly, as a consequence of exchange between pairs of diastereoisomers,. i.e., *SR* ⇆ *SS* and *RR* ⇆ *RS*. Rates were measured in the slow exchange regime by selective inversion experiments (21–24) and in the intermediate exchange regime by standard band shape analysis (25). The acetal-CH signals of the two major diastereoisomers, *SR* and *RR*, were selectively inverted at 323 and 328 K. At these temperatures, magnetization transfers were only observed between pairs of diastereoisomers (*SR* ⇆ *SS* and *RR* ⇆ *RS*), as a consequence of *formal* inversion of configuration at the acetal-carbon atom. This presumably arises from an "acetal ring flip" that leads to exchange of the coordinated and pendant oxygen atoms. No magnetization transfers were observed between the *SR*/*SS* pair and the *RR*/*RS* pair, showing clearly that there is no *formal* inversion of configuration at the metal centre (*R* ⇆ *S*) at these temperatures. Spectra for the selective inversion of the *RR* diastereoisomer at 323 K are shown in Fig. 4. Kinetic data are reported in Table 3.

[2] P.J. Heard, A.D. Bain, P. Hazendonk, and D.A. Tocher. J. Chem. Soc. Dalton Trans. Submitted.

© 1999 NRC Canada

Table 3. Kinetic data[a] for the complexes $[ReX(CO)_3L]$.

Temperature/K	$[ReCl(CO)_3L]$			$[ReBr(CO)_3L]$			$[ReI(CO)_3L]$[b]	
	SR ⇆ *SS*	*RR* ⇆ *RS*		*SR* ⇆ *SS*	*RR* ⇆ *RS*		*RR* ⇆ *RS*	
323[c]	0.05	0.16		0.05	0.09		0.09	
328[c]	0.10	0.27		0.09	0.14		0.18	
333	0.19	0.40		0.15	0.19		0.27	
338	0.30	0.70		0.23	0.32		0.44	
343	0.60	1.10		0.37	0.50		0.63	
348	1.00	1.70		0.61	0.79		0.85	
353	1.70	2.65		0.90	1.10		1.40	
358	2.60	3.60		1.40	1.70		2.20	
363	3.90	5.60		2.10	2.50		3.30	
373	11.2	12.4	0.40[d]	4.80	5.20	2.0[d]	7.10	
383	17.8	18.0	1.00[d]	10.0	10.5	6.5[d]	14.5	1.50[d]
393	28.0	26.0	1.80[d]	20.0	20.3	12.5[d]	28.5	3.50[d]

[a]First-order rate constants (s^{-1}) for the major → minor diastereoisomerizations; data from standard band shape analysis except those marked with footnote *c*.
[b]Independent rates for the *SR* ⇆ *SS* diastereoisomerization not measured (see text).
[c]Data from selective inversion experiments.
[d]Data refer to the reversible ligand dissociation process (see text).

Table 4. Eyring activation parameters[a] for the complexes $[ReX(CO)^3L]$.

Complex	Process	$\Delta H^{\ddagger}$/kJ mol^{-1}	$\Delta S^{\ddagger}$/J mol^{-1} K^{-1}	$\Delta G^{\ddagger}$/kJ mol^{-1}
$[ReCl(CO)_3L]$	*SR* ⇆ *SS*	104.0 (1.0)	52.0 (3.0)	88.4 (0.1)
	RR ⇆ *RS*	84.0 (0.6)	–1.0 (2.0)	84.20 (0.01)
	Ligand dissociation[b]	176		113
[Re $Br(CO)_3L$]	*SR* ⇆ *SS*	85.8 (0.5)	–4.0 (1.0)	87.0 (0.1)
	RR ⇆ *RS*	79.8 (0.7)	–19.0 (2.0)	85.5 (0.1)
	Ligand dissociation[b]	108		93
[Re $I(CO)_3L$][c]	*RR* ⇆ *RS*	82.0 (1.0)	–10.0 (3.0)	85.2 (0.1)
	Ligand dissociation[b]	103		95

[a]$\Delta G^{\ddagger}$ quoted at 298 K; errors, given in parentheses, are those defined by Binsch and Kessler (15); data refer to the major → minor diastereoisomerizations.
[b]Approximate values; estimated errors ca. ±10%; $\Delta S^{\ddagger}$ not calculated (considered unreliable due to narrow temperature range).
[c]Activation parameters for the *SR* ⇆ *SS* diastereoisomerization not calculated (see text).

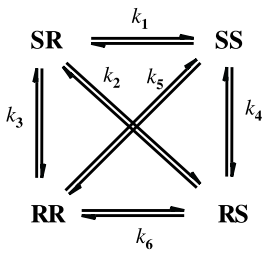

(I)

Analysis of the variable temperature ^{1}H NMR line shapes of the acetal-CH signals was carried out according to the dynamic spin system (**I**).

The six possible rate constants were treated as independent variables in the analysis. Below ca. 370 K, band shapes could be simulated accurately with only two nonzero rate constants, namely k_1 and k_6, corresponding to the *formal* inversion of configuration at C_1 (Fig. 2). At temperatures in excess of 370 K, the band shape analysis indicated the onset of a second dynamic process on the NMR chemical shift time scale. Accurate simulation of the high temperature spectra required the use of equal, non-zero rate constants for k_2, k_3, k_4, and k_5, in addition to the non-zero rates for k_1 and k_6. This second process is presumed to involve ligand dissociation; the process is fully reversible, and there was no evidence of decomposition. Twelve reliable fits were obtained, seven of which are shown in Fig. 5. Kinetic data are reported in Table 3, and the Eyring activation parameters are reported in Table 4. Band shape changes, consistent with the above analysis, were also observed in the other regions of the variable temperature ^{1}H NMR spectra (see above).

The compounds $[ReX(CO)_3L]$ (X = Cl or I; L = 2-[(4*R*,5*R*)-dimethyl-1,3-dioxan-2-yl]pyridine) behaved analogously to the bromo complex, and the dynamic NMR spectra were analysed on the same basis (see above). However, the signal due to the *SS* diastereoisomer of the iodide complex was obscured by the residual solvent signal (δ = 5.96), frustrating a full analysis of the *RS* ⇆ *SS* kinetics; acceptable fits of the experimental spectra were obtained using equal rates for the two independent acetal ring flip processes.

Discussion

Variable temperature ^{1}H NMR data show clearly that, at moderate temperatures, a (reversible) *formal* inversion of

© 1999 NRC Canada

Fig. 5. Experimental and computer simulated variable temperature ^{1}H NMR spectra of the complex [ReBr(CO)$_3$L]. Rate constants are reported in Table 4. The bands denoted * and ● are due to solvent and free ligand, respectively.

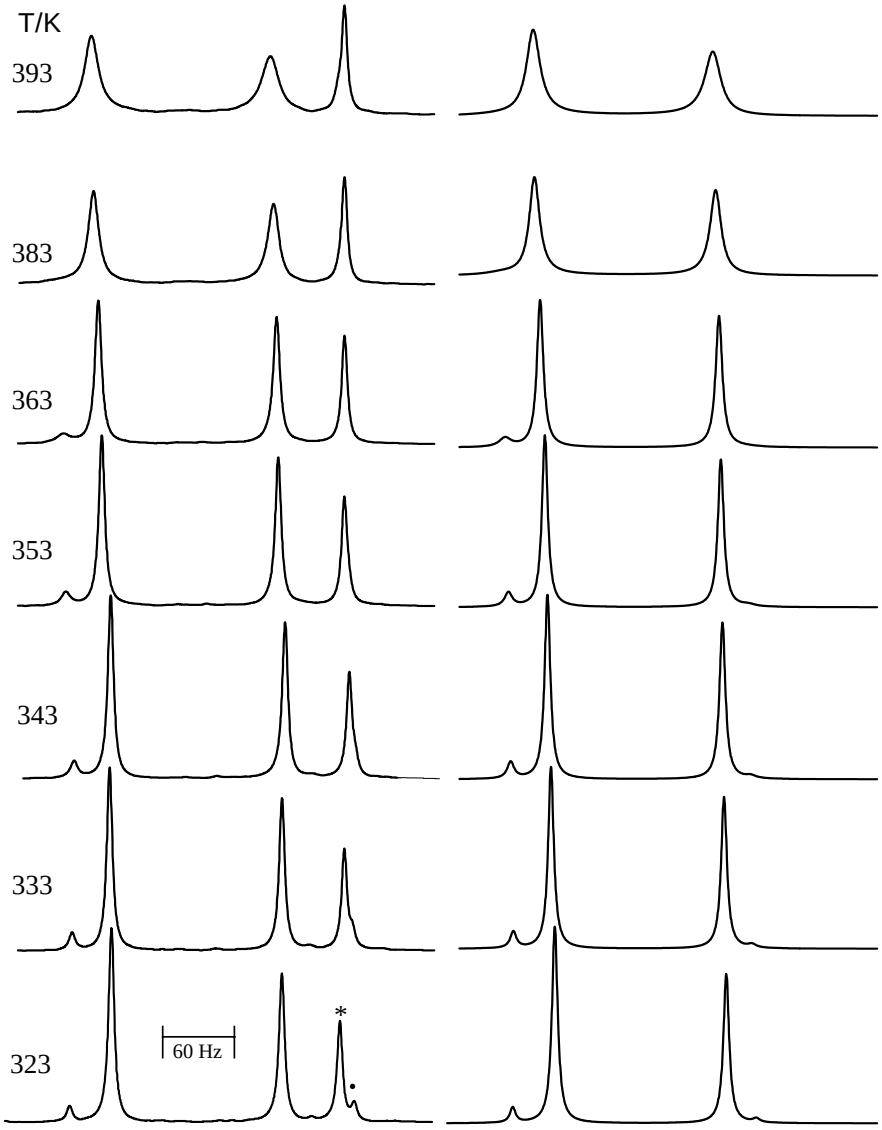

configuration occurs at the acetal-carbon atom, C_1, causing an interconversion between pairs of diastereoisomers (*SR* ⇆ *SS* and *RR* ⇆ *RS*). This formal inversion of configuration presumably results from an acetal ring flip process that exchanges the coordinated and pendant oxygen donor atoms. Two possible mechanisms, shown in Fig. 6, can be envisaged for the acetal ring flip. Mechanism (*i*) (Fig. 6) involves cleavage of the Re—O bond, yielding a five coordinate transition state, followed by the formation of a new Re—O bond. Mechanism (*ii*) involves a loosening of the Re—O bond, concomitant with the formation of a pseudo seven coordinate transition state. The small magnitudes for the entropy of activation, $\Delta S^{\ddagger}$, (Table 4) point towards an associated transition state of the type involved in mechanism (*ii*). Conversely, the free energies of activation ($\Delta G^{\ddagger}$(298 K) ≈ 84–88 kJ mol^{-1}) indicate that Re—O bond cleavage is involved; data are comparable to the activation energies for the cleavage of the Re—N bond in the closely related complexes [ReX(CO)$_3$L^3] (X = Cl, Br or I; L^3 = 2,6-bis[(4*S*)-methyloxazolin-2-yl]pyridine) (2). This suggests that mechanism (*i*) (Fig. 6) is preferred. Although entropy of activation data provide information about the structure of the transition state, they are a less reliable indicator than energy of activation data. For this reason we consider mechanism (*i*) (Fig. 6) most likely, but more work is clearly necessary to establish this. We are currently investigating complexes of the analogous ligand 2-[(4*R*,6*R*)-dimethyl-1,3-dioxan-2-yl]pyridine to gain further insight.

The magnitudes of the free energies of activation for the *SR* → *SS* processes are ca. 2–4 kJ mol^{-1} greater than for the *RR* → *RS* process. This may, in part, arise from a weakening of the Re—O bonding interaction, because of increased steric interactions between one of the ligand methyls and the metal moiety in the *RR* diastereoisomer. This would lead to a small increase in the ground state energy of the *RR* diastereoisomer and hence a lowering of the free energy of activation. However, the differences in $\Delta G^{\ddagger}$ are higher than expected from the relative ground-state energies of the two

© 1999 NRC Canada

Fig. 6. Two possible mechanisms for the acetal ring flip in the complexes $[ReX(CO)_3L]$.

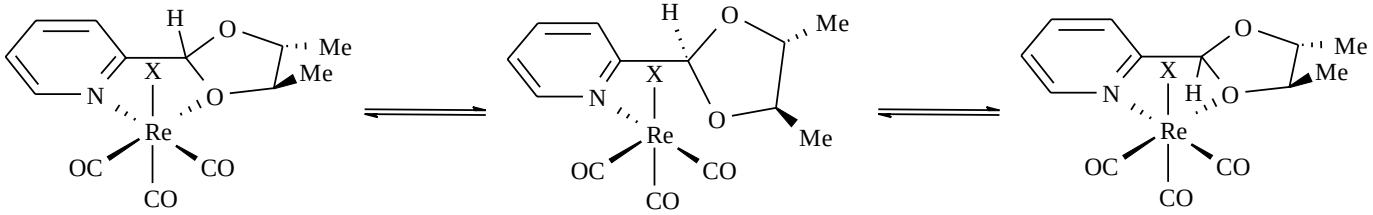

Mechanism (i)

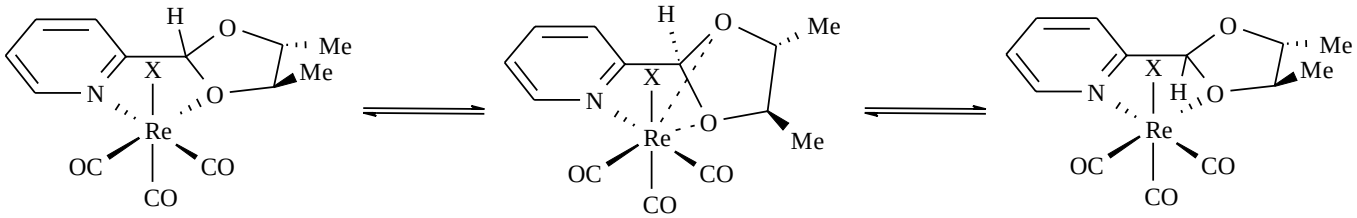

Mechanism (ii)

diastereoisomers. This tends to suggest that the transition-state species of the two processes are subtly different, which is difficult to rationalize, particularly in terms of mechanism (*i*). The effect of the halogen on the dynamics appears to be minimal; this is expected because the halide is *cis* to the fluxional ligand.

Ring flip processes of this type are novel in tricarbonylrhenium(I) halide complexes, but a similar behaviour has been observed previously in palladium(II) complexes of bipyrimidine (bipym) (26). The tricarbonylrhenium(I) halide complexes of bipym, *fac*-$[ReX(CO)_3(bipym)]$ (X = Cl, Br, or I), do not shown analogous fluxional behaviour at a measurable rate on the NMR time-scale.[3]

Above ca. 370 K, the band shape changes indicate that the ligand is undergoing a reversible dissociation from the metal centre (see above), leading to an averaging of all four diastereoisomers. Only two or three reliable rate constants were obtained for this process, and the energy data obtained must therefore be treated with some caution. The principle contribution to $\Delta G^{\ddagger}$ probably comes from the energy required to break the Re—N(pyridine) bond. The higher magnitudes for the ligand dissociation, compared to the acetal ring flip fluxion (see above), presumably reflect the differences in the Re—O and Re—N bond strengths. The considerably higher magnitude of $\Delta G^{\ddagger}$ obtained for the chloro complex is not thought significant; experimental errors, consequential of the narrow temperature range, are the most likely explanation.

Conclusions

The complexes $[ReX(CO)_3L]$ (X = Cl, Br, or I; L = 2-[(4*R*,5*R*)-dimethyl-1,3-dioxan-2-yl]pyridine) give rise to four diastereoisomers in solution. At moderate temperatures an acetal ring flip process leads to exchange of the pendant and coordinate oxygen atoms, causing formal inversion of configuration at the acetal carbon atom. The kinetics of the acetal ring flip were measured in the slow and intermediate exchange regimes, and the results indicate that the mechanism involves initial cleavage of the Re—O(acetal) bond, concomitant with the formation of a five coordinate transition state.

Acknowledgements

We are grateful to Birkbeck College, McMaster University, and the Natural Sciences and Engineering Research Council of Canada (NSERC) for the funding. Julie Nielsen is acknowledged for helpful discussion.

References

1. J.P. Collman, L.S. Hegedus, J.R. Norton, and R.G. Fink. Principles and applications of organotransition metal chemistry. University Science Books, California. 1987.
2. P.J. Heard and C. Jones. J. Chem. Soc. Dalton Trans. 1083 (1997).
3. P.J. Heard and D.A. Tocher. J. Chem. Soc. Dalton Trans. 2169 (1998).
4. A. Gelling, M.D. Olsen, K.G. Orrell, A.G. Osborne, and V. Šik. J. Chem. Soc. Dalton Trans. 3479 (1998), and refs. therein.
5. A. Gelling, K.G. Orrell, A.G. Osborne, V. Šik, M.B. Hursthouse, D.E. Hibbs, and K.M.A. Malik. J. Chem. Soc. Dalton Trans. 2151 (1998), and refs. therein.
6. E. Rotondo, G. Giordano, and D. Minniti. J. Chem. Soc. Dalton Trans. 253 (1996).

[3] E.W. Abel, P.J. Heard, and K.G. Orrell. Unpublished results.

© 1999 NRC Canada

7. E.W. Abel, A. Gelling, K.G. Orrell, A.G. Osborne, and V. Šik. J. Chem. Soc. Chem. Commun. 2329 (1996).
8. T.G. Gant and A.I. Meyers. Tetrahedron, **50**, 2297 (1994).
9. D.F. Shriver. Manipulation of air-sensitive compounds. McGraw–Hill, New York. 1969.
10. D.D. Perrin and W.L.F. Armarego. Purification of laboratory chemicals. Pergamon, Oxford. 1988.
11. S.P. Schmidt, W.C. Trogler, and F. Basolo. Inorg. Synth. **28**, 160 (1979).
12. F.A.J. Meskens. Syntheses, 501 (1981).
13. A.D. Bain and G.J. Duns. Can. J. Chem. **74**, 819 (1996).
14. A.D. Bain and J.A. Cramer. J. Magn. Reson. **118**, 21 (1996).
15. G. Binsch and H. Kessler. Angew. Chem. Int. Ed. Engl. **19**, 411 (1980).
16. D.A. Edwards and J. Marshalsea. J. Organomet. Chem. **131**, 73 (1977).
17. W. Cherry and N. Epiotis. J. Am. Chem. Soc. **98**, 1135 (1976).
18. R.F.W. Bader, J.R. Cheeseman, K.E. Laidig, K.B. Wiberg, and C. Breneman. J. Am. Chem. Soc. **112**, 6530 (1990).
19. E.W. Abel, K. Kite, and P.S. Perkins. Polyhedron, **6**, 319 (1987), and refs. therein.
20. E.L. Eliel and S.H. Wilen. Stereochemistry of organic compounds. Wiley, New York. 1994.
21. A.D. Bain and J.A. Cramer. J. Phys. Chem. **97**, 2884 (1993).
22. A.D. Bain and J.A. Cramer. J. Magn. Reson. **103 A**, 217 (1993).
23. S. Forsen and R.A Hoffman. J. Chem. Phys. **39**, 2892 (1963).
24. R.E. Hoffman and S. Forsen. Prog. Nucl. Magn. Reson. Spectrosc. **1**, 15 (1966).
25. J. Sandström. Dynamic NMR spectroscopy. Academic Press, New York. 1982.
26. J.G.P. Delis, P.G. Aubel, K. Vrieze, and P.W.N.M. van Leeuwen. Organometallics, **16**, 2948 (1997).

© 1999 NRC Canada

Qualitative analysis of complex mixtures of VOCs using the inside needle capillary adsorption trap

S. Shojania, M.E. McComb, R.D. Oleschuk, H. Perreault, H.D. Gesser, and A. Chow

Abstract: An alternative sampling technique for fingerprint analysis of complex mixtures of petroleum-based products is presented. Fingerprint chromatograms of the volatile organic compounds (VOCs) for class 0–5 accelerants can be readily obtained using the recently developed *inside needle capillary adsorption trap* (INCAT) device. The concentration of VOCs from the static headspace of these complex mixtures, onto the adsorbing carbon coating of the INCAT device, avoids some problems associated with conventional headspace gas chromatography (HS-GC). The INCAT sampling method is a solventless extraction technique in which the analytes adsorbed inside the device are thermally desorbed inside the heated injection port of a gas chromatograph (GC), or a gas chromatograph coupled with a mass spectrometer (GC–MS). The presented method of active sampling with the INCAT device was used to obtain fingerprint chromatograms of the headspace of various gasolines, paint thinners, and lighter fluids. The static headspace chromatograms, from active sampling with the INCAT device, were compared with direct liquid injection of the samples. The INCAT chromatograms showed preferential adsorption of aromatic compounds over lighter, more volatile, but less polar compounds. Each class of the accelerant can be positively identified from the fingerprint chromatogram using only a few characteristic peaks. In addition, the ability to detect these volatile components of gasoline in aqueous samples at environmentally significant levels was also investigated.

Key words: VOC, fingerprinting, INCAT, petroleum, headspace GC.

Résumé : On présente une technique d'échantillonnage alternative pour l'analyse des empreintes digitales de mélanges complexes de produits à base de pétrole. Utilisant le dispositif dénommé *piège d'adsorption capillaire inséré dans l'aiguille* (« INCAT ») développé récemment, on peut facilement obtenir des chromatogrammes d'empreintes digitales des composés organiques volatils (COV) des accélérants des classes 0 à 5. La concentration des COV contenus dans les gaz de confinement (l'espace de tête) statique de ces mélanges complexes sur la couche de carbone adsorbant du dispositif INCAT permet d'éviter certains problèmes associés à la chromatographie gazeuse des gaz de confinement conventionnelle (CG-ET). La méthode d'échantillonnage à l'aide de l'INCAT est une technique d'extraction sans solvant dans laquelle les produits à analyser adsorbés dans le dispositif sont désorbés thermiquement dans l'injecteur de l'échantillon d'un chromatographe en phase gazeuse (CG) ou d'un chromatographe en phase gazeuse couplé à spectromètre de masse (CG–SM). On a utilisé la méthode préposée d'échantillonnage actif à l'aide du dispositif INCAT pour obtenir des chromatogrammes d'empreintes digitales des gaz de confinement de diverses essences, diluants de peinture et d'essences à briquet. Les chromatogrammes des gaz de confinement statiques obtenus par échantillonnage actif à l'aide du dispositif INCAT ont été comparés à ceux obtenus par injection directe du liquide des échantillons. Les chromatogrammes INCAT mettent en évidence une adsorption préférentielle des composés aromatiques par rapport à celle des composés plus légers, plus volatiles, mais moins polaires. Chaque classe d'accélérant peut être identifiée de façon positive à partir du chromatogramme d'empreintes digitales en n'utilisant que quelques pics caractéristiques. De plus, on a aussi étudié la possibilité de détecter ces composants volatiles de l'essence dans des échantillons aqueux, à des niveaux significatifs d'un point de vue environnemental.

Mots clés : composés organiques volatiles (COV), empreintes digitales, piège d'adsorption capillaire inséré dans l'aiguille (INCAT), pétrole, CG des gaz de confinement (d'espace de tête).

[Traduit par la Rédaction]

Received March 8, 1999.

This paper is dedicated to Professor Ted Schaefer in recognition of his outstanding contributions to Canadian chemistry.

S. Shojania, M.E. McComb, H. Perreault, H.D. Gesser, and A. Chow.[1] Department of Chemistry, University of Manitoba, Winnipeg, MB R3T 2N2, Canada.
R.D. Oleschuk. Department of Chemistry, University of Alberta, Edmonton, AB T6G 2G2, Canada.

[1]Author to whom correspondence may be addressed. Telephone: (204) 474-9504. Fax: (204) 474-7608.
e-mail: achow@cc.umanitoba.ca

 © 1999 NRC Canada

Fig. 1. Schematic of the INCAT device.

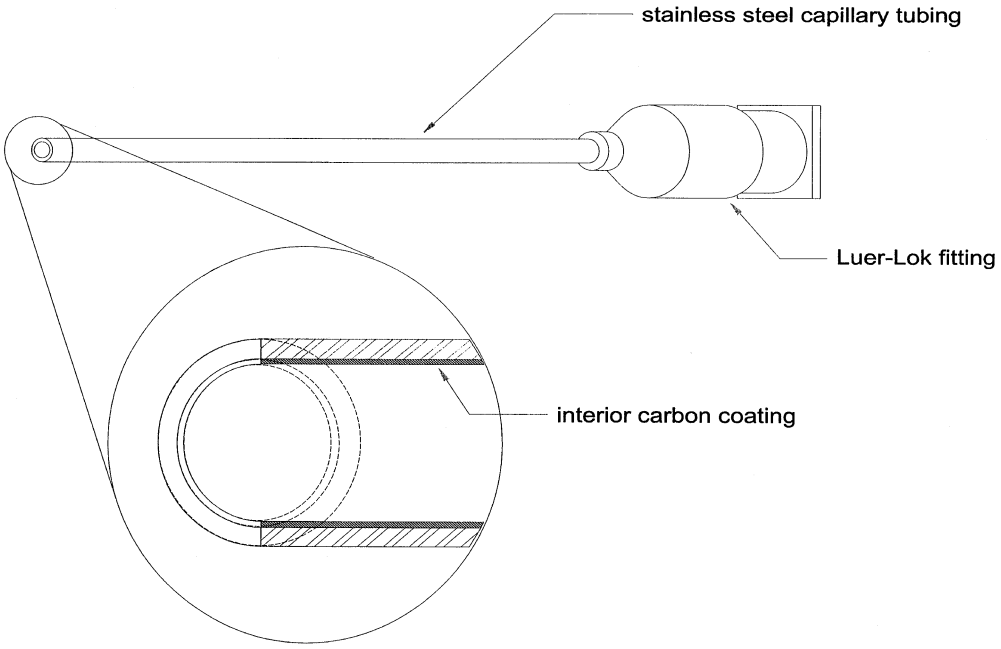

Introduction

Pattern recognition, or *fingerprint* analysis, is employed in the qualitative analysis of complex mixtures. Source identification of a sample can be determined by comparing a characteristic chromatogram of the sample to libraries of complex mixture chromatograms (1). In such analysis, the identification of the individual components is not necessary. The characteristic profile or *fingerprint* of the chromatogram allows for positive identification of the material. Fingerprint analysis by gas chromatography has been by itself sufficient for source identification of complex petroleum distillates in both forensic and environmental applications (1). For example, identification of arson accelerants can be achieved by comparing the chromatograms of the static headspace above fire debris with those of similarly obtained commercial reference accelerants (e.g., kerosene, gasoline, etc.). Environmental investigations of point source pollution may also be achieved by fingerprint analysis (2). Identification of the source of a spill may be possible by chromatographic comparison of a sample from the contaminated site with waste or products from suspected source points.

In the analysis of complex mixtures, such as petroleum distillates, the use of headspace gas chromatography (HS-GC) may often simplify the analysis by reducing the number of peaks in the chromatogram and showing distinctive differences between samples based on the levels of volatile organic compounds (VOCs) (2, 3). The VOCs in some liquid samples may be present in relatively low concentrations and thus be obscured by the more abundant nonvolatile components in the chromatogram. The VOCs that are part of these complex mixtures will partition between the liquid and vapor phases. If the sample is placed in a gas-tight container, an equilibrium between the liquid and vapor phases will be established. Most petroleum distillates contain many VOCs in characteristic quantities. Thus, a profile of the peaks from the static headspace of the sample will also serve as fingerprint of the sample.

Headspace sampling (static or dynamic) is advantageous over direct liquid sampling of complex mixtures of VOCs in cases when a liquid sample is not always available, or when the analytes are in a liquid matrix that would complicate GC analysis. The sampling of headspace is then advantageous for samples that would require solvent extraction (i.e., contaminated soil, water, foods, packaging materials, arson debris, etc.). Conventional methods for HS-GC usually involve cryogenic focusing of large volumes of the static headspace onto the GC column (2). Samples often require heating to increase the amount of analyte mass in the static headspace (3). However, depending on the nature of the mixture, thermal degradation of the sample may result upon heating of the sample, thereby producing compounds that may obscure the analysis.

Solid phase extraction (SPE) methods have been used to concentrate headspace components, which are then solvent desorbed from the solid phase (2, 4). A sample of the headspace is actively drawn through small packed columns or cartridges containing the solid phase adsorbent. The adsorbed analytes are then solvent desorbed, and a fraction of the solvent extract is introduced into the GC for analysis. Extraction of the analytes from the static headspace onto the solid phase avoids the necessity of cryogenic focusing of large headspace volumes, but usually requires a solvent extraction step. In some cases, there may be additional sample preparation steps required for the cartridges themselves.

The method of solid-phase microextraction (SPME) has been applied to the analysis of a variety of complex mixtures of VOCs (5–9). The SPME method uses a small fused silica fibre coated with a liquid phase sorbent. The coated fibre is introduced into the static headspace and allowed to reach equilibrium with the VOCs that are present. The headspace analytes are then concentrated onto the fibre coating. The

© 1999 NRC Canada

Table 1. Classification scheme for accelerants and the samples studied.

Class no.	Class	Samples studied
0	Unclassified	Escort camp fuel (Imperial Oil Ltd., Toronto, Ont.)
1	Light Petroleum Distillates (LPD)	Ronsonol pocket lighter fluid (Ronsonol Corporation of Canada, Mississauga, Ont.)
2	Gasoline	Shell octane rated gasolines: Bronze 87, Silver 89 and Gold 91 (Shell Canada Ltd., Calgary, Alta.)
3	Medium Petroleum Distillates (MPD)	Varsol® (Imperial Oil Ltd., Toronto, Ont.), generic paint thinner (Canadian Tire Corporation Ltd., Toronto, Ont.)
4	Kerosene	Kerosene (Reochem Inc., Toronto, Ont.)
5	Heavy Petroleum Distillates (HPD)	Shell diesel fuel (Shell Canada Ltd., Calgary, Alta.)

SPME device is then inserted into a GC or GC coupled to a mass spectrometer (GC–MS) system to thermally desorb the analytes directly onto the column. Thus, the SPME method is a solventless extraction technique.

A new method of solventless extraction of VOCs has been achieved using the *inside needle capillary adsorption trap* (INCAT) (10, 11). The INCAT device (Fig. 1) has an adsorbing carbon coating on the interior surface of a hollow stainless steel needle. This device is able to sample the static headspace of a sample both actively and passively (10). In the active sampling procedure, an aliquot of the static headspace volume is drawn through the device via a syringe. The volatile analytes are then adsorbed and concentrated inside the device. The INCAT device can then be inserted into a heated injection port of a GC to thermally desorb the analytes directly onto the GC column for separation. The concentration of analytes inside the INCAT device avoids the necessity for cryogenic focusing of large sample volumes onto the GC column, a method employed in most HS-GC analyses (3).

Other methods designed to increase headspace sensitivity, such as closed loop stripping (CLS) and purge-and-trap (P&T) methods, require larger headspace sample volumes for cryogenic focusing onto the GC column. The use of extraction devices such as SPE cartridges or SPME fibres increases the sensitivity of headspace sampling. The INCAT device can be used in a similar manner, without a solvent extraction step, and with no time required by the headspace analytes to reach equilibrium. To demonstrate these features, a simple application to qualitative analysis of samples of the six classes of accelerants (1) has been performed. The chromatograms of the static headspace of the six classes of accelerants, according to the ASTM forensic classification scheme (12), were obtained from active sampling with the INCAT device and compared to the chromatograms obtained from direct liquid injection of the samples. Samples included the following: light petroleum distillates (pocket lighter fluid), gasolines, medium petroleum distillates (paint thinner), kerosene, heavy petroleum distillates (diesel fuel), and unclassified accelerants (camp fuel). The BTEX compounds (benzene, toluene, ethyl benzene, and xylenes) present were used as target analytes to compare the different classes. In addition, aqueous samples with low levels of gasoline components were examined to determine the sensitivity of the technique and simulate environmentally significant levels.

Experimental

The INCAT devices used in this study were prepared from 50.8 mm long, 26 gauge (0.46 mm nominal o.d.; 0.25 mm nominal i.d.) hypodermic needles with metal Luer-Lok hub (Hamilton Co., Reno, Nev.). The needles were coated with one of three types of activated carbon blacks: Raven-15 (Columbian Carbon Co., New York, N.Y.), Super Sorb (Amoco Research Corp., Chicago, Ill.), and Saran from poly(vinylidene chloride) (RMC, Kingston, Ont.). The carbon blacks were suspended in 1% w/w solution of Silwet surfactant (Union Carbide, Danbury, Conn.) in isopropanol (Fisher Scientific Co., Fair Lawn, N.J.). The needles were coated using a syringe to draw a 1 mL volume of the carbon black suspension through the length of the needle, which was then pushed out. The coated devices were baked for 1 h at 300°C while passing helium gas through the length of the needle to ensure that no clogging occurred and to remove the suspension solvent. Once ready, the INCAT device was plugged with a small piece of septum at the Luer-Lok end, and inserted into the injection port of a GC to determine if any off-gassing occurred.

Direct liquid sampling and static headspace sampling (via the INCAT device) was performed on the samples listed in Table 1. For each sample, 2 mL of the liquid were placed in a 40 mL GC vial sealed with a screw-top septum containing cap for headspace sampling. A separate sample, with 2 mL in a 4 mL GC vial sealed with screw-top septum containing cap, was prepared for direct liquid sampling. Active sampling of the headspace with the INCAT device was performed by drawing 0.10 mL of the headspace through the device at an approximate rate of 0.35 mL/min, with a 0.50 mL gas-tight syringe (Hamilton Co., Reno, Nev.). The withdrawn headspace volume was then pushed out the device at the same rate. Thus, the 0.10 mL sample was allowed to pass over the coating twice. The Luer-Lok end of the INCAT device was then plugged with a small piece of septum. Subsequently, the INCAT device was immediately inserted into the injection port of the GC for thermal desorption.

Gas chromatography was performed using a Varian Star 3400 CX series GC (Varian Instrument Group, Walnut Creek, Calif.) with a flame ionization detector (FID). The samples were separated on a 15 m DB-1 megabore column (J&W Scientific Inc., Folsom, Calif.) of 100% dimethylpolysiloxane

© 1999 NRC Canada

Table 2. Means, standard deviations, and percent relative standard deviations of the response factors (R_f) and the retention times (R_t) from n = 4 liquid injections of the BTEX standard.

Compound	Mean R_f	Std. dev. R_f	% RSD R_f	Mean R_t	Std. dev. R_t	% RSD R_t
Benzene	1.109	0.014	1.28	6.264	0.013	0.204
Toluene	1.02	0.003	0.282	8.972	0.004	0.05
Ethyl benzene	1.048	0.011	1.086	11.29	0.004	0.035
m,p-Xylene	0.954	0.002	0.201	11.58	0.005	0.043
o-Xylene	0.948	0.004	0.393	12.07	0.008	0.064

(0.53 mm i.d., 5.00 μm film thickness). Analytes were thermally desorbed from the INCAT device in the heated injection port (210°C) of the GC for 2 min. The initial column temperature was held at 30°C for the 2 min injection time. The temperature of the column was ramped to 195°C at a rate of 8°C/min and held for 5 min. The column was then heated to a final temperature of 200°C at a rate of 20°C/min, and held at this temperature for 2 min. The detector temperature was 200°C. The entire run time for the separation was 30 min. A second thermal desorption injection of the device was performed to ensure that all of the sample had been desorbed in the first 2 min injection, and indicated that no carry-over occurred.

To estimate the sensitivity of the INCAT sampling method, and to demonstrate its usefulness in characterizing environmentally significant concentrations of VOCs, an aqueous solution saturated with Shell Bronze gasoline was prepared and an aliquot of this solution was diluted by a factor of 1000 with water. Initially, samples prepared with 2 mL of the aqueous solution in 40 mL vials were used, and 0.10 mL of the static headspace was actively sampled by the INCAT device. However, the chromatogram obtained for the saturated solution showed poor peak intensity. A second set of samples was prepared with 5 mL of the aqueous solution in 40 mL GC vials, and 10.0 mL of the headspace was actively sampled using a gas-tight syringe (Hamilton Co., Reno, Nev.). The rate of sampling with this 10.0 mL syringe was approximately 2.5 mL/min. The withdrawn volume was pushed out of the INCAT device at the same rate at which it was actively removed from the headspace, allowing the headspace sample volume to pass over the coating twice. The larger headspace volume for the aqueous gasoline solutions improved the sensitivity of the sampling method.

The retention times and response factors were determined for the BTEX compounds by repeated (n = 4) 0.10 μL liquid injections of the BTEX standard. The mean, standard deviation, and percent relative standard deviation (RSD) from the mean of the retention times and response factors for each of the BTEX compounds are listed in Table 2. The *meta* and *para* xylenes were not resolved as two distinct peaks with the DB-1 column.

Results and discussion

These experiments were designed to determine if the adsorptive coating of the INCAT device would improve the headspace sensitivity in direct gas sampling. Previously reported INCAT devices (10, 11) were made with a colloidal graphite coating as the carbon adsorbent. However, graphite has a very low surface area, and hence, a low capacity, which gave a variation in the relative amounts of adsorbed compounds as the device reached capacity (10). To improve the capacity of the devices, activated carbon coatings have been incorporated. Other methods designed to increase headspace sensitivity, such as closed loop stripping (CLS) and purge and trap (P&T) methods, require larger headspace sample volumes for cryogenic focusing onto the GC column (3). The use of extraction devices, like SPE cartridges or SPME fibres, increases the sensitivity of the headspace sampling. The INCAT device can be used in a similar manner, without a solvent extraction step, and with no time required to reach equilibrium with the headspace. To demonstrate these features, a simple application to qualitative analysis of the six classes of accelerants (1) has been performed.

The static headspace of the BTEX standard was actively sampled using INCAT devices with three different coatings. The chromatograms obtained for the liquid injection and the injection of INCAT sampled headspace of the standard are shown in Fig. 2. The Raven-15 coated INCAT (Fig. 2*b*) showed the best adsorption of the compounds. Using the change in mass from the uncoated needle and the internal surface area of the capillary, the coating contained 1.01 ± 0.03 mg/cm^2. The Saran and Super Sorb (Figs. 2*c* and *d*) coatings contained 0.28 ± 0.03 mg/cm^2 and 0.60 ± 0.03 mg/cm^2, respectively. The differences in the amount of carbon resulting from the coating process are likely due to the differences in the grain sizes among the three carbon blacks. To reduce the variation in the amount of carbon in each needle, it is necessary to have a uniform grain size for the different carbon blacks. The Raven-15 INCAT device was chosen for the remaining headspace samples due to the larger amount of carbon on the interior surface of the needle. It should also be noted that the tailing in the benzene peaks in Figs. 2*b–d* are the result of benzene diffusing onto the column during the 2 min injection. The initial column temperature during the injection was held at 30°C, but lower temperatures would be required to focus benzene at the top of the column for the entire injection time. Shorter injection times for the INCAT device at higher desorption temperatures would reduce the tailing of benzene. In addition, a lower initial column temperature would prevent benzene from moving through the column until the entire sample had been desorbed from the device. Thus, all of the analytes would be focussed at the top of the column until the temperature program begins upon completion of the injection. The lowering of the initial column temperature, coupled with an increase in the injection port temperature (reducing the desorption time), would then improve the chromatographic resolution. The entire sample would be desorbed before any of the analytes begin to diffuse onto the column — then all

© 1999 NRC Canada

Fig. 2. Comparison of the gas chromatograms obtained from sampling a mixture of BTEX compounds (16.7% v/v of each) by (*a*) direct liquid sampling (0.10 μL), attenuation 1280; (*b*) a Raven-15 coated INCAT (0.10 mL of headspace), attenuation 16; (*c*) a Saran coated INCAT (0.10 mL of headspace), attenuation 16; and (*d*) a Super Sorb coated INCAT (0.10 mL of headspace), attenuation 16.

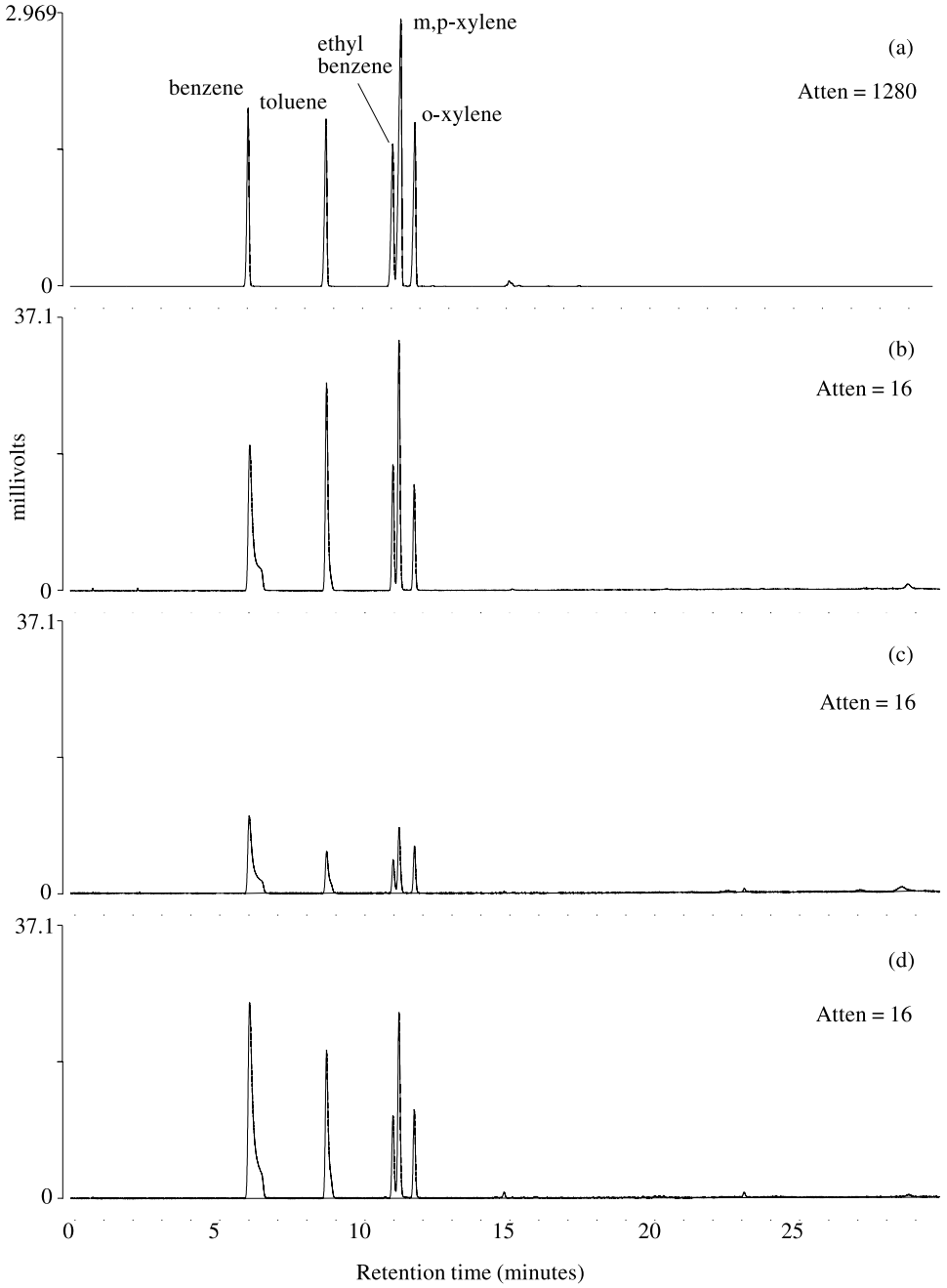

analytes would enter the column as a small "sample plug," as in liquid sample introduction.

To show that the INCAT device can be used to yield a reproducible fingerprint of a complex mixture, the Shell Bronze gasoline was sampled four times. The chromatograms shown in Fig. 3 were obtained from a 0.10 mL active sampled volume of the static headspace above 2 mL of gasoline in 40 mL containers, for four separate Shell Bronze gasoline samples. The BTEX peaks in the four chromatograms were used to measure the consistency of the sampling method. Table 3 lists the mean retention times and peak areas of the BTEX compounds for the four trials of the Shell Bronze gasoline using active sampling of the headspace with the Raven-15 INCAT device. The RSD for the BTEX peak areas ranged from 6.6 to 11.6%. There is a strong indication of preferential adsorption of aromatic compounds found in the headspace over lighter and more volatile compounds that are in high concentrations in gasoline. Although the presence of these lighter gasoline components is noticeable in the headspace chromatograms, the peak areas are not as high as expected.

Figures 4–9 show direct comparisons between chromatograms obtained using the INCAT to actively sample the headspace and direct liquid sampling for the samples

© 1999 NRC Canada

Fig. 3. Gas chromatograms illustrating the reproducibility in headspace sampling of Shell Bronze gasoline with a Raven-15 coated INCAT device (attenuation 4). Sampling conditions: 0.10 mL headspace sampled. BTEX compounds correspond to the retention times and area measurements shown in Table 3.

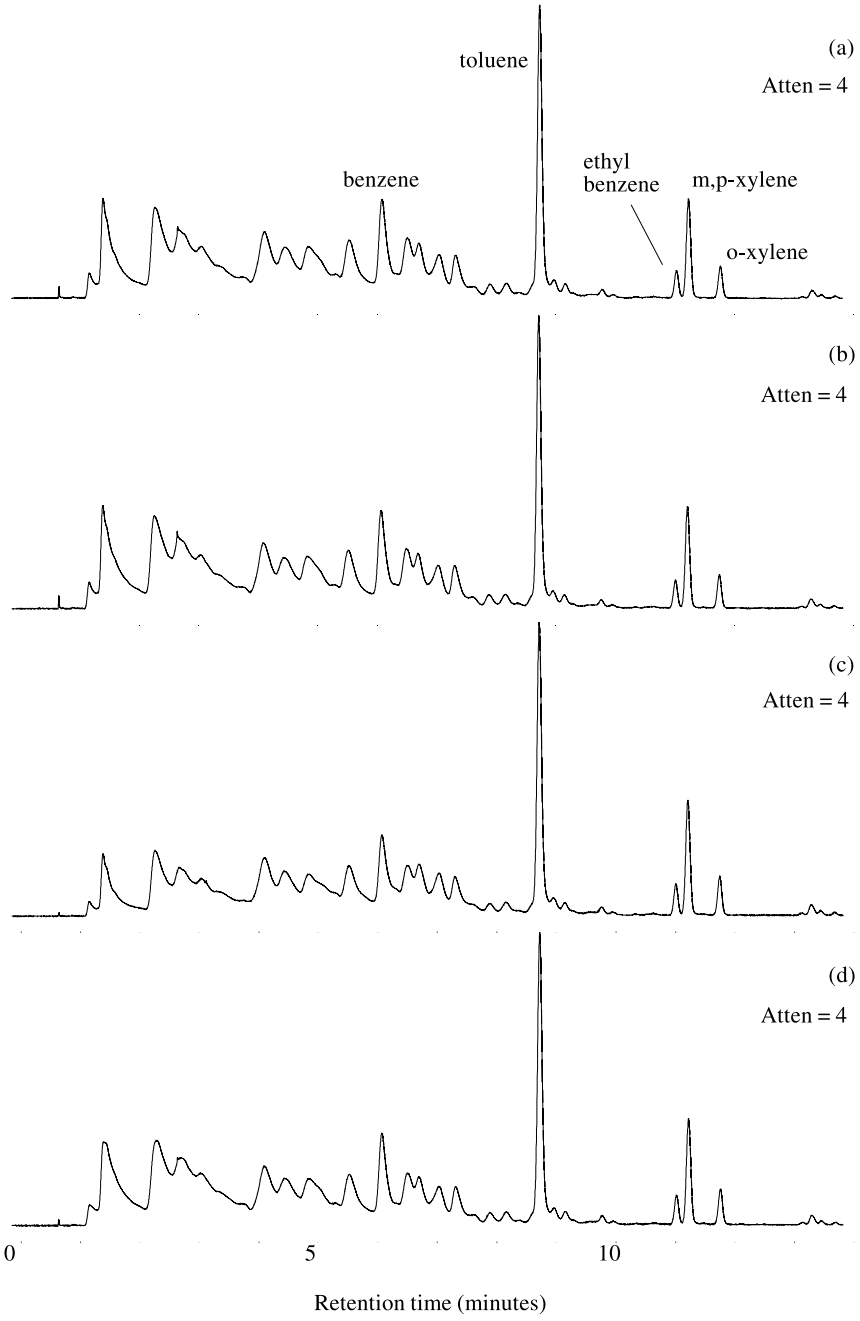

Table 3. Means, standard deviations, and percent relative standard deviations of the retention times and peak areas of the BTEX compounds from n = 4 trials of active sampling of 0.10 mL of the headspace of Shell Bronze gasoline.

Compound	Mean R_t	Std. dev. R_t	% RSD R_t	Mean peak area	Std. dev. area	% RSD area
Benzene	6.26	0.02	0.258	2732	317	11.6
Toluene	8.969	0.007	0.073	5389	603	11.2
Ethyl benzene	11.292	0.005	0.040	432.5	28.7	6.64
p,m-Xylene	11.574	0.005	0.044	1691	148	8.72
o-Xylene	12.067	0.007	0.058	529.8	58.4	11.0

© 1999 NRC Canada

Fig. 4. Comparison between the gas chromatograms of (*a*) the class 0 accelerant camp fuel, obtained from a direct liquid sample (0.10 μL), attenuation 559, and (*b*) a headspace sample using a Raven-15 coated INCAT device (0.10 mL), attenuation 4.

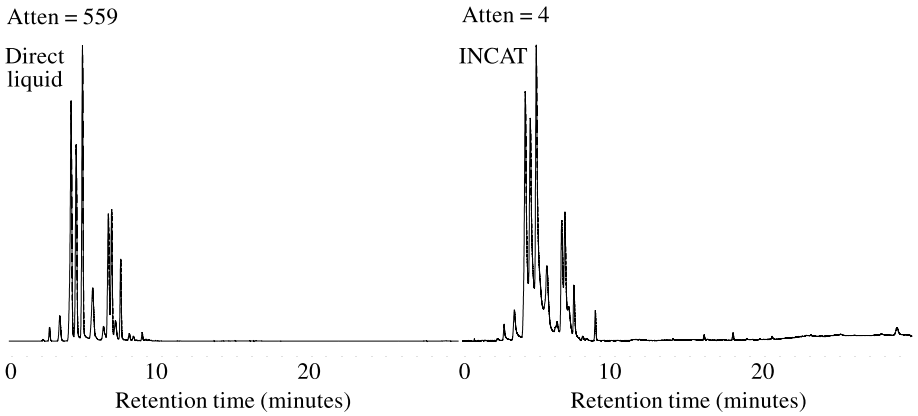

Fig. 5. Comparison between the gas chromatograms of (*a*) the class 1 accelerant Ronsonol pocket lighter fluid, obtained from a direct liquid sample (0.10 μL), attenuation 534, and (*b*) a headspace sample using a Raven-15 coated INCAT device (0.10 mL), attenuation 4.

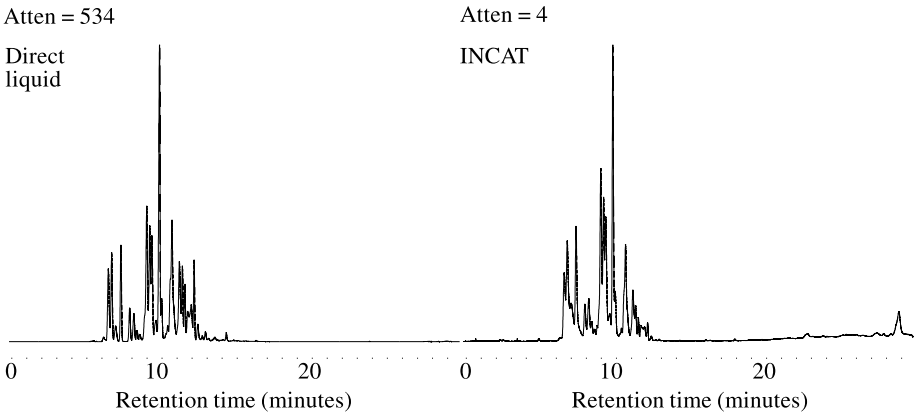

from each class of arson accelerants. The chromatograms have been normalized to percentage of the full scale for qualitative comparison of the fingerprints. The chromatograms obtained for classes 0 and 1 (camp fuel and pocket lighter fluid, Figs. 4 and 5) show only subtle differences between their respective liquid and headspace peak profiles. There are not many components in the mixtures (relative to gasoline) according to the liquid sample chromatograms (Figs. 4*a* and 5*a*), and very little BTEX compounds are present. The similarity between the profiles obtained for the liquid and INCAT headspace sampling suggest that in cases where a liquid sample is not available, the INCAT headspace sampling method can produce a characteristic peak profile of the sample for fingerprint identification.

The liquid and headspace sample chromatograms for the different grades of gasoline, shown in Fig. 6, again indicates the preferential adsorption for aromatic compounds on the coating inside the device. From these chromatograms, it is clear that the lighter components, appearing at shorter retention times, are not as abundant as expected in the headspace sample. BTEX compounds are more abundant than lighter and more volatile compounds when the INCAT device is used. This indicates that the Raven-15 coating has a greater affinity for the aromatic species in the headspace. The presence of BTEX compounds in headspace samples at different levels allows for differentiation of gasolines rated with specific octane numbers, from other classes of accelerants and from each other. However, it is likely that the differences in the relative amounts of BTEX compounds may be too subtle to positively identify a particular brand of gasoline among samples with the same octane rating. In such situations, the monitoring of a few more characteristic peaks would be required to positively identify the manufacturer of the gasoline.

The chromatograms obtained for the two paint thinner samples — the class 3 accelerants (Fig. 7) — show very similar amounts of BTEX components. The presence of BTEX components in this case is sufficient to positively identify the two samples as class 3 accelerants. However, Varsol® and the generic brand of paint thinner could not be differentiated on the basis of BTEX compounds alone. There are a few characteristic peaks in both the initial and final regions of the headspace chromatograms that do allow distinction between the samples.

Figure 8 shows the chromatograms obtained from direct liquid and headspace sampling of the class 4 accelerant, kerosene. As with the class 0 and class 1 accelerants, the chromatograms obtained for the liquid and headspace samples are very similar. The chromatograms can be distinguished based only on the differences in the relative amounts of a few peaks, one of which is the obvious benzene peak. The relative amounts of BTEX compounds in the headspace

© 1999 NRC Canada

Fig. 6. Comparison between the gas chromatograms of the class 2 accelerant gasoline, obtained from a direct liquid sample (0.10 μL) and a headspace sample using a Raven-15 coated INCAT device (0.10 mL), for (*a*) Shell Bronze (octane rating 87), attenuation 285 (liquid sample), attenuation 9 (INCAT sample); (*b*) Shell Silver (octane rating 89), attenuation 276 (liquid sample), attenuation 3 (INCAT sample); and (*c*) Shell Gold (octane rating 91), attenuation 572 (liquid sample), attenuation 4 (INCAT sample).

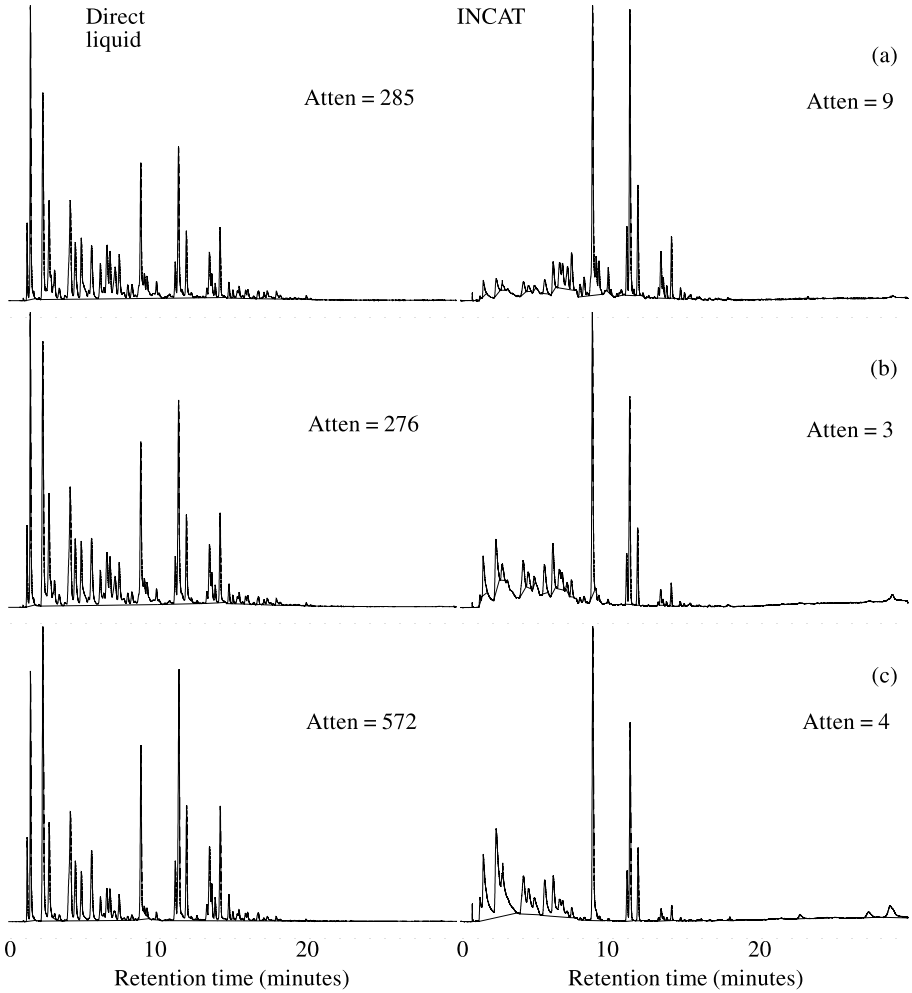

are present at characteristic levels relative to the other classes of accelerants. Therefore, the BTEX compounds can be used to distinguish kerosene from the other classes. In addition, the similarity between the two chromatograms of Fig. 8 once again illustrates how the INCAT device would be useful for sampling the headspace when a liquid sample is not available.

The chromatograms obtained from the liquid versus INCAT headspace sampling of diesel fuel (Fig. 9), a class 5 accelerant, show the most noticeable difference in the peak profiles. All of the BTEX compounds are present, and most are in greater amounts relative to their levels in gasoline samples. Only benzene is less abundant in diesel fuel than in the Bronze grade of gasoline, which contained the highest levels of BTEX compounds relative to accelerants from classes 0 to 4.

The bar chart shown in Fig. 10, represents the data for the absolute peak areas of BTEX compounds observed in the six classes of accelerants. From the relative amounts of BTEX compounds in representative samples for each class, it is possible to discriminate between the classes of accelerants. To distinguish between different brands of a sample within a specific class (e.g., Varsol® and the generic paint thinner), it would be necessary to monitor additional peaks. Since the aromatic components in these samples tend to be preferentially adsorbed by the Raven-15 adsorbent, it would be useful to identify a few more characteristic aromatic compounds by GC–MS.

The chromatograms in Fig. 11 were obtained with the INCAT device by active sampling of the static headspace of the aqueous solution saturated with Shell Bronze gasoline (Fig. 11*a*), the 1:1000 diluted solution of the latter (Figs. 11*b* and *c*), and a blank (Fig. 11*d*). The aqueous solution, saturated with gasoline (Fig. 11*a*), shows all of the BTEX compounds, as well as some of the other VOCs. This profile is not comparable to that of the Bronze gasoline, shown in Figs. 3 and 6, due to the different solubilities of the various components in water. The diluted aqueous gasoline solution chromatograms (Figs. 11*b* and *c*) are also shown to contain all of the BTEX compounds. The remaining peaks ($R_t \geq 20$) are likely to be the result of irreversible adsorption of some of the adsorbates, which may gradually lead to the formation of a tar on the adsorbing surface (13) — which is slowly decomposing upon repeated use of the

© 1999 NRC Canada

Fig. 7. Comparison between the gas chromatograms of the class 3 accelerant paint thinner, obtained from a direct liquid sample (0.10 μL) and a headspace sample using a Raven-15 coated INCAT device (0.10 mL), for (*a*) Varsol®, attenuation 430 (liquid sample), attenuation 1 (INCAT sample); and (*b*) a generic brand of paint thinner, attenuation 442 (liquid sample), attenuation 1 (INCAT sample).

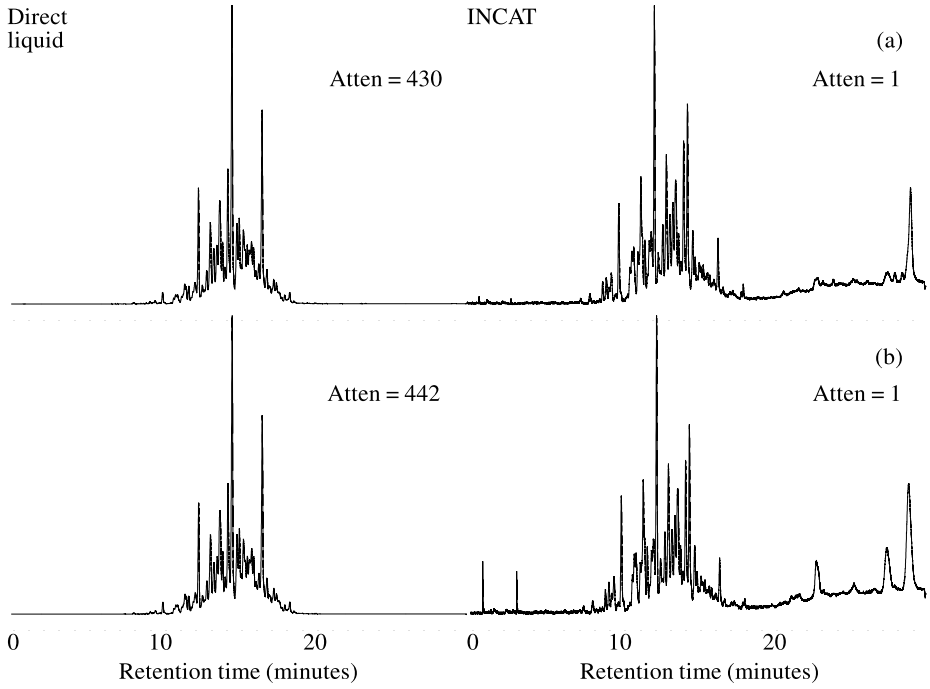

Fig. 8. Comparison between the gas chromatograms of the class 4 accelerant kerosene, obtained from a direct liquid sample (0.10 μL), attenuation 389, and a headspace sample using a Raven-15 coated INCAT device (0.10 mL), attenuation 1.

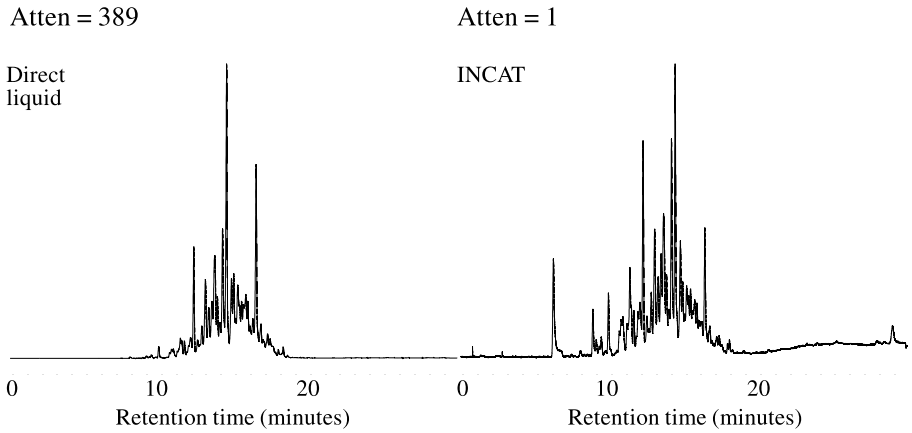

INCAT sampler. A more thorough cleaning step may be required to reduce the amount of tar buildup, such as passing a reactive gas through the device during the cleaning run, or a periodic longer baking period. It should be noted that during the course of these experiments, the Raven-15 INCAT device was used for more than 60 manual injections, and is still being used. It is not surprising then that there may be a gradual buildup of these irreversibly adsorbed compounds — the effects of which became more prevalent in the background with increased use of the device.

To estimate the amounts of the BTEX compounds present (an upper bound estimate), the solubilities of each of pure BTEX compounds in water can be used. Thus, the 1:1000 diluted solution is estimated to contain (w/v): 1.78 ppm of benzene, 0.515 ppm of toluene, 0.152 ppm of ethyl benzene, 0.198 ppm of *p*-xylene, 0.200 ppm of *m*-xylene, and 0.175 ppm of *o*-xylene. The other species present in gasoline will, however, affect the solubilities of the individual components. Pure benzene has a water solubility in the pure phase of 1780 ppm, but in the presence of the other components of gasoline, its solubility is reduced to 65 ppm (14). Thus, the upper bound estimate of the BTEX levels in the 1:1000 diluted solution of saturated aqueous gasoline is very generous. The INCAT device, when sampling at room temperature and sampling less than a third of the headspace volume (10.0 mL out of 35.0 mL of headspace), enabled detection of 65 ppb of benzene in the 1:1000 diluted solution. The limit of detection could still be reduced further by

© 1999 NRC Canada

Fig. 9. Comparison between the gas chromatograms of the class 5 accelerant diesel fuel, obtained from a direct liquid sample (0.10 μL), attenuation 55, and a headspace sample using a Raven-15 coated INCAT device (0.10 mL), attenuation 40.

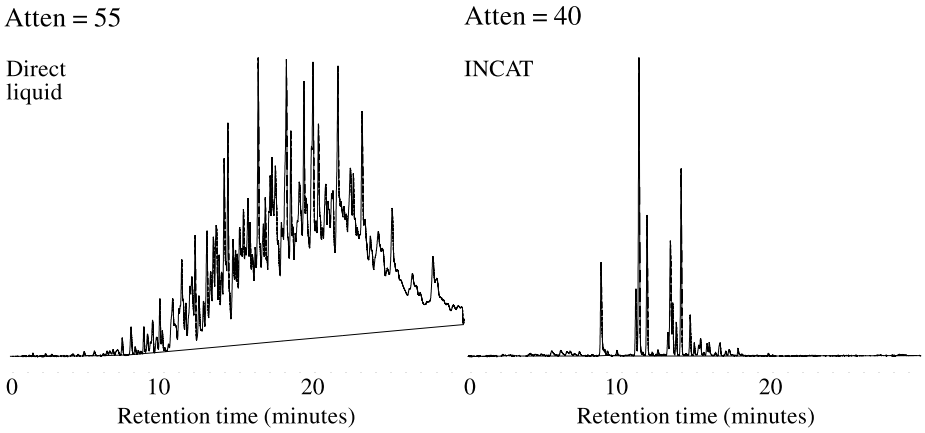

Fig. 10. Bar chart comparison of the absolute peak areas of BTEX compounds observed from static headspace sampling of the mixtures from the six classes of arson accelerants. Sampling conditions: 0.10 mL of static headspace sampled using a Raven-15 INCAT device.

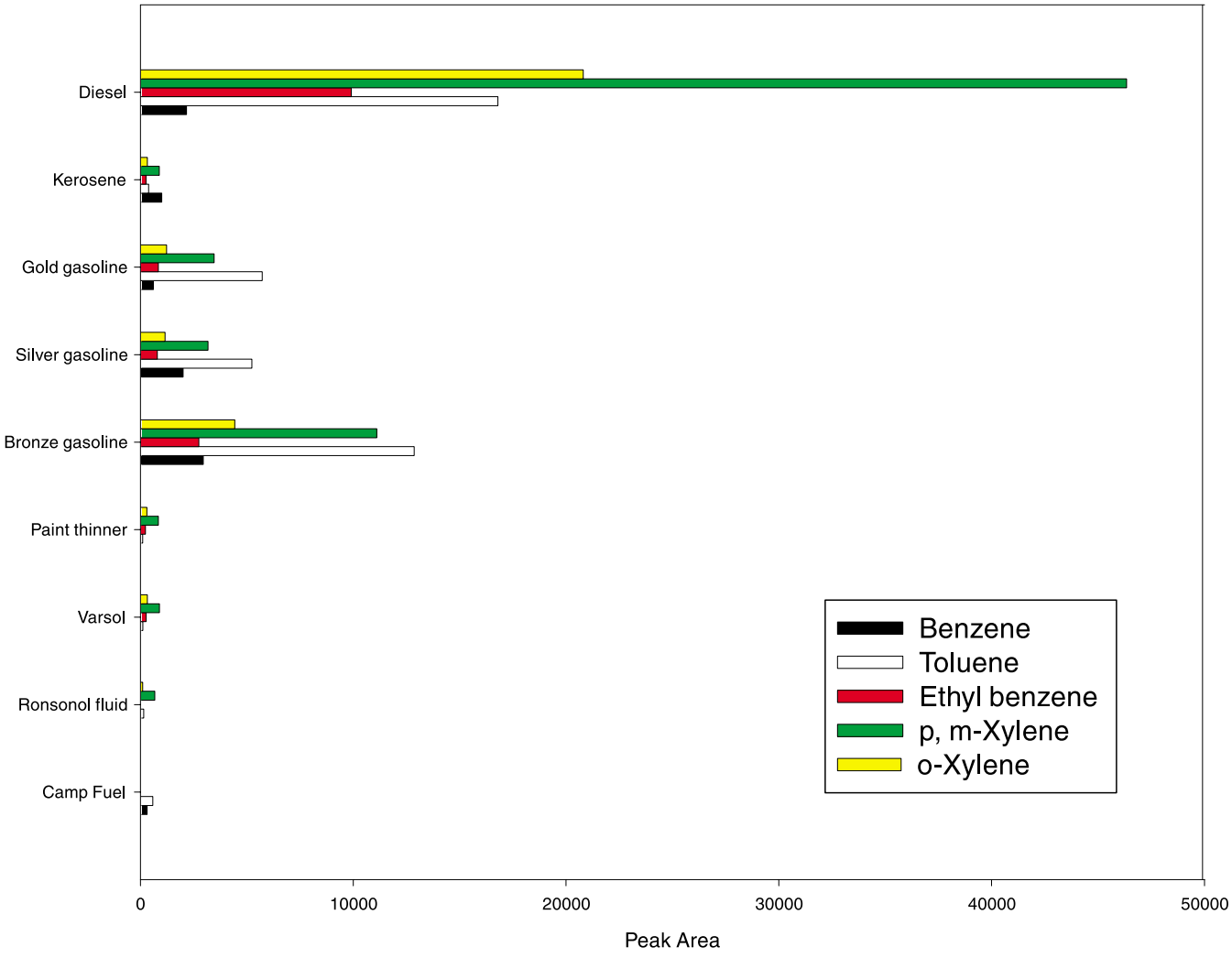

© 1999 NRC Canada

Fig. 11. Headspace analysis of (*a*) an aqueous solution saturated with Shell Bronze gasoline, attenuation 3; (*b*) a 1:1000 dilution of the aqueous solution saturated with Shell Bronze gasoline, attenuation 3; (*c*) the 1:1000 diluted solution, attenuation 1; and (*d*) a blank, attenuation 1. Sampling conditions: 10.0 mL headspace actively sampled using a Raven-15 coated INCAT device.

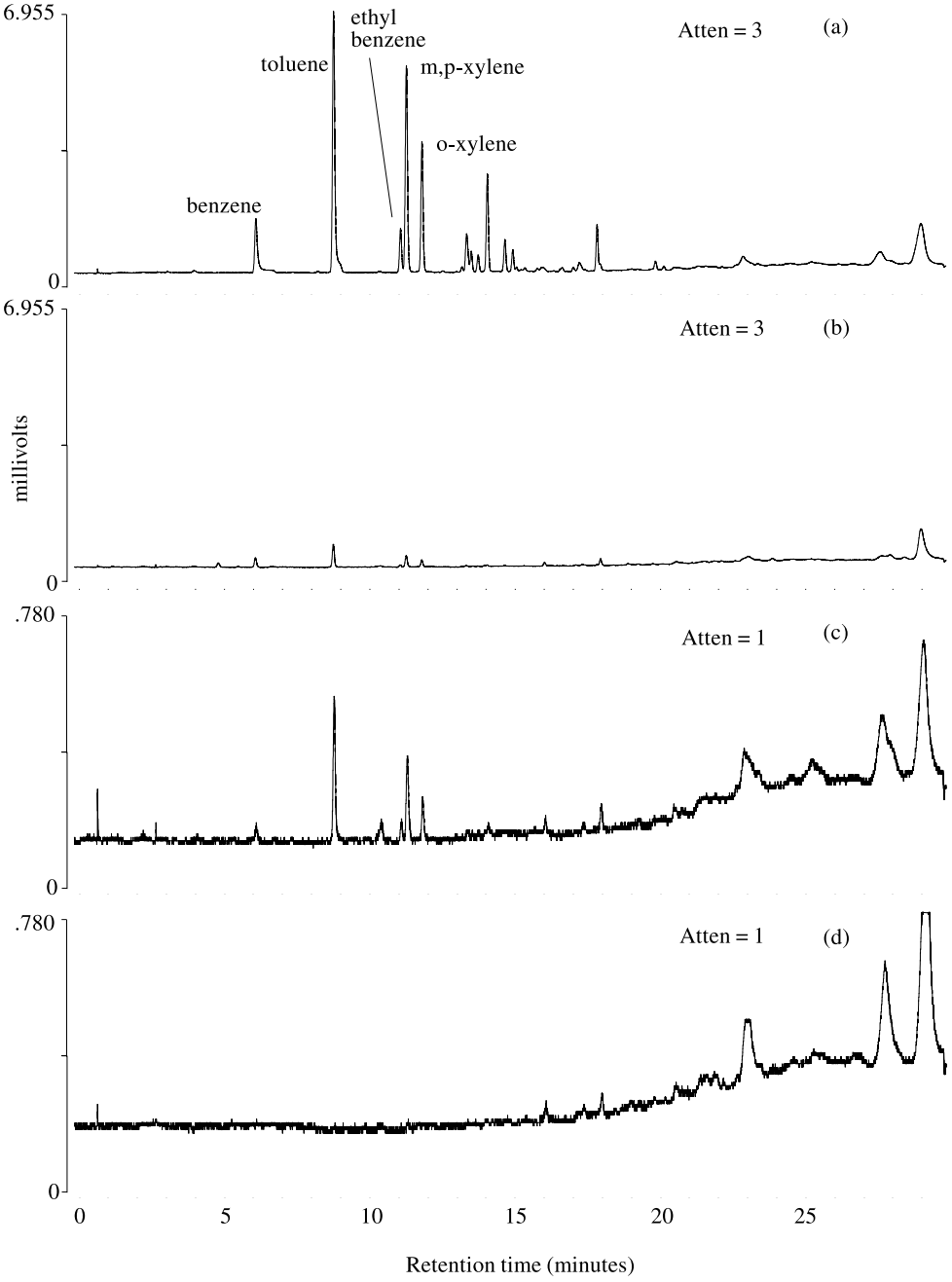

increasing the volume of the headspace that is actively sampled, or by heating the sample to increase the headspace concentration of the VOCs prior to sampling.

Conclusions

Static headspace sampling of complex mixtures is extremely useful for fingerprint identification of mixtures when liquid samples are not available. Sampling of the headspace above samples can be achieved without solvent extraction. The INCAT device can be used to sample the headspace of a sample and concentrate the analytes inside the device. Thermal desorption of the analytes from the INCAT directly into the GC simplifies the extraction and analysis procedure.

The INCAT device has been shown to enable reproducible GC fingerprints of complex mixtures of VOCs, with an average RSD of 9.8%. Using the INCAT device, the distinction between different classes of accelerants has been achieved using only five target peaks corresponding to BTEX compounds. The INCAT device provides a novel approach to the characterization of complex mixtures for fingerprint analysis. Concentration of the headspace analytes inside the device allows for larger volumes of the headspace to be sampled without requiring cryogenic focusing. The INCAT

© 1999 NRC Canada

sampling technique thus provides a sensitive alternative to the conventional methods of direct headspace sampling, like CLS and P&T methods. Moreover, the solventless extraction aspect of active sampling with the INCAT device simplifies the sampling method without requiring time to reach an equilibrium with the headspace analytes.

Acknowledgments

The authors thank L. Morton and D. Quin (RMC, Kingston, Ont.) for providing the carbon black Saran from poly(vinylidene chloride), E. Smirnova for use of the Varian Star GC, and K. Lalbiharie for helpful advice. We also acknowledge the Sustainable Development Innovations Fund of the Government of Manitoba, the University of Manitoba, and the Natural Sciences and Engineering Research Council of Canada (NSERC) for financial assistance.

References

1. F.J. Debbrect. *In* Modern practice of gas chromatography. 3rd ed. *Edited by* R.L. Grob. John Wiley and Sons, New York. 1995. Chap. 7.
2. J.M. Loeper. *In* Modern practice of gas chromatography. 3rd ed. *Edited by* R.L. Grob. John Wiley and Sons, New York. 1995. Chap. 14.
3. B. Kolb and L.S. Ettre. Static headspace gas chromatography: theory and practice. Wiley–VCH, New York. 1997. Chap. 8.
4. K. Robards, P.R. Haddad, and P.E. Jackson. Principles and practice of modern chromatographic methods. Academic Press, London. 1994. Chap. 8.
5. C.L. Arthur and J. Pawliszyn. Anal. Chem. **62**, 2145 (1990).
6. D. Louch, S. Motlagh, and J. Pawliszyn. Anal. Chem. **64**, 1187 (1992).
7. C.L. Arthur, L. Killam, K.D. Buchholz, D. Potter, M. Chai, Z. Zhang, and J. Pawliszyn. Environ. Lab. **11**, 10 (1992).
8. Z. Zhang and J. Pawliszyn. Anal. Chem. **65**, 1843 (1993).
9. C.L. Arthur, M. Chai, and J. Pawliszyn. J. Microcolumn Sep. **5**, 51 (1993).
10. S. Shojania, R.D. Oleschuk, M.E. McComb, H.D. Gesser, and A. Chow. Talanta, **50**, 193 (1999).
11. M.E. McComb, R.D. Oleschuk, E. Giller, and H.D. Gesser. Talanta, **44**, 2137 (1997).
12. T.A. Brettel. *In* Modern practice of gas chromatography. 3rd ed. *Edited by* R.L. Grob. John Wiley and Sons, New York. 1995. Chap. 13.
13. J.W. Hassler. Purification with activated carbon. Chemical Publishing Co., Inc., New York. 1974. pp. 65–68.
14. B. Bauman. EPA OUST Natl. Conf. Charlotte, N.C. March 1997.

© 1999 NRC Canada

Determination of proton exchange rates in aqueous solution using TOCSY

R.E.D. McClung, T.T. Nakashima, H. Yamamoto, and G. Kotovych

Abstract: A product operator description of the nuclei in an ensemble of molecules undergoing intermolecular exchange during the spin-lock period of TOCSY is presented. Experimental measurements of the transfer of magnetization from the CH_2 protons in *N*-acetylglycine to the solvent water protons, via exchange of the NH proton with water protons during the spin-lock period in TOCSY, are shown to be in agreement with theoretical predictions at lower pH values (7.85–9.54) where the rate constants for NH–water exchange are known. Measurements at higher pH (up to 11.03) indicate that the highest rate constant for exchange that can be determined by this technique is $\tau_A^{-1} \sim 4000\ s^{-1}$.

Key words: product operator, density matrix, intermolecular exchange, TOCSY, NMR.

Résumé : On présente une description d'un opérateur de produit du noyau dans un ensemble de molécules subissant un échange intermoléculaire au cours d'une période de spin bloqué de « TOCSY ». On démontre que, à des valeurs faibles de pH (7,85–9,54) pour lesquelles on connaît les constantes de vitesse d'échange NH–eau, il existe une bonne correspondance entre prédictions théoriques et les résultats expérimentaux relatifs du transfert de magnétisation de protons CH_2 de la *N*-acétylglycine aux protons de l'eau qui agit comme solvant, par le biais d'un échange du proton NH avec les protons de l'eau au cours d'une période de spin bloqué de « TOCSY ». Les mesures à des valeurs de pH plus élevées (allant jusqu'à 11,03) indiquent que la valeur la plus élevée pour une constante de vitesse qui puisse être déterminée par cette technique est $\tau_A^{-1} \approx 4000\ s^{-1}$.

Mots clés : opérateur de produit, matrice de densité, échange intermoléculaire, « TOCSY », RMN.

[Traduit par la Rédaction]

Introduction

In a recent communication (1) we reported the observation that the water "stripe" in TOCSY maps of aqueous solutions of compounds containing exchangeable protons (OH, NH, or SH) contained correlations at the resonance frequencies of the protons that were scalar coupled to the exchangeable protons. We suggested at that time that these correlations were attributable to TOCSY transfer of magnetization from nonexchanging protons to the exchangeable protons via scalar coupling, and exchange of magnetization between the exchangeable protons and the bulk water. One would therefore observe a correlation between a nonexchanging proton and water in the water stripe. The intensities of the correlations in the water stripe at the resonance frequencies of the scalar-coupled protons depends, not surprisingly, upon the magnitudes of the scalar couplings and the rate at which protons are transferred from OH, NH, or SH to water. These correlations may be observed even at higher exchange rates where the resonance lines of the exchangeable proton and the water proton have coalesced.

In biological systems, water plays an important role in the determination of the structure and function of biomolecules and the study of the water–biomolecule interaction is very important in understanding their three-dimensional structure in solution. One aspect of such investigations is the exchange processes involving exchangeable protons in the biological molecule and bulk water in order to probe solvent accessibility and solvent "hidden" sites. This gives some insight into the conformation of the biomolecules in solution. Previously, measurements of the rate constant for exchange of NH protons in proteins and peptides were limited to very slow exchange, which can be studied by deuterium substitution (2–5), and to slow exchange, which can be studied by water proton magnetization transfer experiments. In the latter category several methods are available (6–13). The water magnetization is perturbed by some presaturation or inversion sequence and the exchange rate is determined by monitoring the buildup of the resonance from the exchangeable proton as in Forsen–Hoffman type experiments (6). These experiments are limited to slow rates of exchange because the OH, NH, or SH lines must be distinct from the H_2O res-

Received March 22, 1999.

This paper is dedicated to Professor Ted Schaefer in recognition of his outstanding contributions to Canadian chemistry.

R.E.D. McClung,[1] T.T. Nakashima, H. Yamamoto,[2] and G. Kotovych. Department of Chemistry, University of Alberta, Edmonton, AB T6G 2G2, Canada.

[1]Author to whom correspondence may be addressed. Telephone: (780) 492-5489. Fax: (780) 492-8231.
[2]Present address: Department of Organic Materials, Osaka National Research Institute, AIST, Osaka, Japan.

 © 1999 NRC Canada

onance. In other studies (7–11), 1D and 2D techniques have been used to selectively excite the water magnetization, followed by selective detection of the resonances of only those protons arising from exchange with water. For the proton exchange reaction

$$[1] \qquad H^{*}_{(solute)} + H_{(solvent)} \underset{k}{\overset{k}{\rightleftarrows}} H_{(solute)} + H^{*}_{(solvent)}$$

where the asterisk is used only to distinguish the two protons, the rates of forward and reverse reactions are equal to $k\,[H_{(solute)}][H_{(solvent)}]$. It is conventional to report the reciprocal of the lifetime of the solute proton, τ_A^{-1}, which is equal to the pseudo-first-order rate constant for exchange of a proton from the solute to the solvent, $k[H_{(solvent)}]$, rather than the rate constant k. In previous studies (2–13), measurements of the rate constants for exchange were limited to $\tau_A^{-1} \lesssim 100\ s^{-1}$. While, in principle, exchange rate constants of 10^3–$10^4\ s^{-1}$ can be determined by NMR using lineshape analysis, this is only practical for systems where the exchanging sites have comparable populations. In the case of biomolecules, the exchangeable protons are present at mM concentrations in 90% H_2O – 10% D_2O solutions where the solvent proton concentration is ~100 M. This enormous population difference between the exchanging protons renders lineshape analysis impossible because of the predominance of the large water signal.

In the present report, we show that exchange rate constants greater than 1000 s^{-1} may be obtained using the information contained in the water "stripe" from TOCSY experiments even though the exchanging proton resonances have coalesced with that from water. As a model system we chose *N*-acetylglycine in which the rate constant for NH proton–water exchange has been measured over a broad pH range (14).

Experimental

pH measurements

All pH measurements were carried out at 298 K with a Fisher Scientific Accumet model 15 pH meter equipped with a standard glass electrode and a fiber-tip saturated calomel reference electrode. Standard buffers, pH 4.00, 7.00, and 10.00, were used to standardize the pH meter at ambient temperature.

NMR measurements

The samples for NMR spectroscopy contained 0.1 M *N*-acetylglycine (Aldrich Chemical Co.) in 0.6 M KNO_3 – H_2O solution. KOH was added to bring the solutions to the desired pH values. NMR spectra were obtained on a Varian Unity 500 NMR spectrometer at 298 K. All the TOCSY experiments (15) used a B_1 field for which γB_1 = 12.5 kHz and were recorded with 1024 complex points and 64 t_1 increments using the States–Haberkorn–Ruben (16) method. The water signal was attenuated using transmitter presaturation during the relaxation delay for 1.5 s using a saturation field B_1 for which γB_1 = 110 Hz. An external capillary of DMSO-d_6 was used to provide the deuterium lock signal. Accurate spin-locking times were calculated from the number of MLEV loops that were performed for the specified mixing times.

Spectral data were processed using standard Varian software. Zero-filling, exponential apodization, and Fourier transformation of the data were followed by integration of each peak from the f_2 slice through the TOCSY map at the intensity maximum of the CH_2 peak in f_1. No significant differences in the relative intensities of the peaks were obtained when peak volumes rather than peak areas from the f_2 slices were used to measure the peak intensities. Attempts to develop a 1D TOCSY experiment with selective excitation of the CH_2 resonance were unsuccessful.

Theory

In this section, a product operator description (17) of the behaviour of the magnetizations of the nuclei in molecules that are undergoing intermolecular exchange during a spin-lock period is presented. It is convenient to represent the density operator, $\rho(t)$, for the ensemble of spin systems as

$$[2] \qquad \rho(t) = \sum_M \sum_j b_{Mj}(t)\mathbf{B}_{Mj}$$

where the sum over M includes all types of molecules in the ensemble, $\{\mathbf{B}_{Mj}\}$ is the set of spherical-tensor basis product operators (18) for the spin system present in molecules of type M, and $\{b_{Mj}(t)\}$ is a set of complex time-dependent coefficients whose values indicate the types of coherences present at time t. During the spin-lock period, the spin Hamiltonian $H^{(M)}$ for each type of molecule M present in the sample is assumed to be of the form (19)

$$[3] \qquad H^{(M)} = 2\pi \sum_{p,m\neq p} J^{(M)}_{mp}\mathbf{I}^{(Mm)}\cdot\mathbf{I}^{(Mp)}$$

where $J^{(M)}_{mp}$ is the spin–spin coupling constant for the scalar coupling between spins m and p within a molecule of type M, since the spin-locking field effectively eliminates the Zeeman interactions. In the absence of chemical exchange, the equation of motion for the coefficient $b_{Mr}(t)$ is (20)

$$[4] \qquad \frac{db_{Mr}}{dt} = i2^{2-N_M}\sum_j Tr\ \{\mathbf{B}^{*}_{Mr}[\mathbf{B}_{Mj}, H^{(M)}]\}b_{Mj}$$

where N_M is the number of spin-1/2 nuclei in molecules of type M. This free precession results in the transfer of in-phase magnetization among the complete network(s) of mutually coupled spins in molecules of type M.

Intermolecular chemical exchange of nuclei between molecules of type M and molecules of type M' causes the transfer of coherence between the spin systems in the two types of molecules. In the exchange process, there will be $n_{MM'}$ nuclei in molecule M, which interchange with $n_{MM'}$ nuclei in molecule M'. In the interchange, the spin operators $\mathbf{I}^{(M1)}$, $\mathbf{I}^{(M2)}$, $\mathbf{I}^{(M3)}$, $\cdots$,$\mathbf{I}^{(Mn_{MM'})}$ for the exchanging nuclei in molecule M are interchanged with the respective spin operators $\mathbf{I}^{(M'1)}$, $\mathbf{I}^{(M'2)}$, $\mathbf{I}^{(M'3)}$, $\cdots$, $\mathbf{I}^{(M'n_{MM'})}$ for the exchanging nuclei in molecule M'. The rate of exchanges between M and M' is $k\,[M][M']$, where k is the rate constant for the exchange reaction, and the reciprocals of the average lifetimes of molecules of types M and M' are given by

© 1999 NRC Canada

$$[5]\qquad \tau_M^{-1} = \frac{\text{exchange rate}}{[M]} = k[M']$$

and

$$[6]\qquad \tau_{M'}^{-1} = \frac{\text{exchange rate}}{[M']} = k[M']$$

respectively (21). The coefficients of those product operators $\mathbf{B}_{Mq}$ for molecule M that contain any of the operators $\mathbf{I}^{(M1)}$, $\mathbf{I}^{(M2)}$, $\mathbf{I}^{(M3)}$, $\cdots$,$\mathbf{I}^{(Mn_{MM'})}$ and the coefficients of those product operators $\mathbf{B}_{M'q}$ for molecule M' which contain any of the operators $\mathbf{I}^{(M'1)}$, $\mathbf{I}^{(M'2)}$, $\mathbf{I}^{(M'3)}$, $\cdots$,$\mathbf{I}^{(M'n_{MM'})}$ will be affected by the interchange of the $n_{MM'}$ nuclei between M and M'. The rate at which the coefficient b_{Mq} changes is given by

$$[7]\qquad \left(\frac{db_{Mq}}{dt}\right)_{\text{exchange}} = -\tau_M^{-1} b_{Mq}\, \chi_{Mq\in\text{ exchanging}} + \sum_{M'} \tau_{M'}^{-1} \sum_{q'} b_{M'q'} \chi_{Mq\leftrightarrow M'q'} \chi_{Mq\in\text{ exchanging}}$$

where $\chi_{Mq\leftrightarrow M'q'} = 1$ if the product operator $\mathbf{B}_{M'q'}$ becomes product operator $\mathbf{B}_{Mq}$ when the $n_{MM'}$ nuclei on molecules M and M' are interchanged, and is zero otherwise; and $\chi_{Mq\in\text{ exchanging}} = 1$ if the operator $\mathbf{B}_{Mq}$ contains a spin operator for any of the exchanging nuclei and is zero otherwise.

For the solute–solvent proton exchange reaction [1], which is of primary interest in this article, the solvent (water) molecules have a single type of proton with spin operator $\mathbf{I}_{-1}^{\text{W}}$, and the *N*-acetylglycine solute molecules have 6 protons with spin operators $\mathbf{I}_{-1}^{\text{A NH}}$, $\mathbf{I}_{-1}^{\text{A CH}_2(1)}$, $\mathbf{I}_{-1}^{\text{A CH}_2(2)}$, $\mathbf{I}_{-1}^{\text{A CH}_3(1)}$, $\mathbf{I}_{-1}^{\text{A CH}_3(2)}$and $\mathbf{I}_{-1}^{\text{A CH}_3(3)}$. The rate equations that describe the effects of exchange on the coefficients b_{W}, $b_{\text{A NH}}$, $b_{\text{A CH}_2(1)}$, $b_{\text{A CH}_2(2)}$, $b_{\text{A CH}_3(1)}$, $b_{\text{A CH}_3(2)}$, and $b_{\text{A CH}_3(3)}$ associated with the transverse components of the proton magnetizations are

$$[8]\qquad \begin{aligned}
\left(\frac{db_{\text{W}}}{dt}\right)_{\text{exchange}} &= -\tau_{\text{W}}^{-1} b_{\text{W}} + \tau_{\text{A}}^{-1} b_{\text{A NH}}\\
\left(\frac{db_{\text{A NH}}}{dt}\right)_{\text{exchange}} &= -\tau_{\text{A}}^{-1} b_{\text{A NH}} + \tau_{\text{W}}^{-1} b_{\text{W}}\\
\left(\frac{db_{\text{A CH}_2(1)}}{dt}\right)_{\text{exchange}} &= 0\\
\left(\frac{db_{\text{A CH}_2(2)}}{dt}\right)_{\text{exchange}} &= 0\\
&\vdots\ \ \vdots\ \ \vdots\\
\left(\frac{db_{\text{A CH}_3(3)}}{dt}\right)_{\text{exchange}} &= 0
\end{aligned}$$

where $\tau_{\text{A}}^{-1} = 2k[\text{water}]$ and $\tau_{\text{W}}^{-1} = k[\text{acetylglycine}]$. When spin–spin coupling in acetylglycine is included, a large number of product operators are required, and the exchange effects on the corresponding coefficients fall into two categories:

$$[9]\qquad \left(\frac{db_{\text{A}\ell}}{dt}\right)_{\text{exchange}} = -\tau_{\text{A}}^{-1} b_{\text{A}\ell}$$

for product operators $\mathbf{B}_{\text{A}\ell}$ that contain $\mathbf{I}_{-1}^{\text{A NH}}$, and

$$[10]\qquad \left(\frac{db_{\text{A}\ell}}{dt}\right)_{\text{exchange}} = 0$$

for product operators $\mathbf{B}_{\text{A}\ell}$ that do not contain $\mathbf{I}_{-1}^{\text{A NH}}$. Since the product operator $\mathbf{B}_{\text{A}\ell}$ associated with coefficient $b_{\text{A}\ell}$ in eq. [9] contains $\mathbf{I}_{-1}^{\text{A NH}}$ and spin operators for other protons in the acetylglycine molecule, no transfer of coherence from the water proton to this coherence is possible. Therefore, exchange simply causes the coefficients associated with antiphase magnetizations and multiple quantum coherences involving the NH proton to decay.

The equation of motion, including spin–spin coupling and chemical exchange, for the coefficient b_{Mr} during the spin-lock period is

$$[11]\qquad \frac{db_{Mr}}{dt} = i2^{2-N_M} \sum_j Tr\,\{\mathbf{B}_{Mr}^*[\mathbf{B}_{Mj}, H^{(M)}]\} b_{Mj} - \tau_M^{-1} b_{Mq} \chi_{Mq\in\text{ exchanging}} + \sum_{M'} \tau_{M'}^{-1} \sum_{q'} b_{M'q'} \chi_{Mq\leftrightarrow M'q'} \chi_{Mq\in\text{ exchanging}}$$

In matrix form, this equation is

$$[12]\qquad \frac{d\mathbf{b}}{dt} = \mathbf{K}\cdot\mathbf{b}$$

where $\mathbf{b}$ is a vector containing the values of the coefficients $b_{11}(t)$, $b_{12}(t)$, $\cdots$, $b_{21}(t)$, $b_{22}(t)$, $\cdots$, $b_{31}(t)$, $b_{32}(t)$, $\cdots$, with the first index indicating the type of molecule, and the second index the product operator index for molecules of that type. The elements of the $\mathbf{K}$ matrix are

$$[13]\qquad K_{Mr;M's} = i2^{2-N_M} Tr\{\mathbf{B}_{Mr}^*[\mathbf{B}_{Ms}, H^{(M)}]\}\,\delta_{MM'} - \tau_M^{-1}\,\chi_{Mq\in\text{ exchanging}}\,\delta_{MM'}\delta_{rs} + \tau_{M'}^{-1}\chi_{Mq\leftrightarrow M'q'}\chi_{Mq\in\text{ exchanging}}$$

The solution to eq. [12] is

$$[14]\qquad \mathbf{b}(t) = \mathbf{U}\cdot\exp\,[\mathbf{\Lambda}t]\cdot\mathbf{U}^{-1}\cdot\mathbf{b}(0)$$

where $\mathbf{U}$ and $\mathbf{\Lambda}$ are the eigenvectors and eigenvalues of $\mathbf{K}$, and $\mathbf{U}^{-1}$ is the inverse of $\mathbf{U}$. $\mathbf{b}(0)$ describes the state of the ensemble of spin systems at the beginning of the spin-lock period, and $\mathbf{b}(t)$ describes the ensemble at the end of this period. The results of our product operator description of the intermolecular exchange problem (eqs. [12]–[14]) are consistent with the results of the more complicated density matrix description (21, 22). In the present development the transverse magnetization for a particular proton is equal to the coefficient associated with the spin operator $\mathbf{I}_{-1}$ for that proton. In the conventional density matrix description, which uses normalized density matrices (21) or operators (23), the transverse magnetization for that proton would be equal to the product of the concentration of molecules containing that spin and the coefficient associated with spin operator $\mathbf{I}_{-1}$ for that proton. If one sets the exchange rates to zero, the results of the product operator description of isotropic mixing dur-

© 1999 NRC Canada

Table 1. NH proton exchange rates for *N*-acetylglycine.

	τ_A^{-1} (s^{-1})	
pH	This work	Ref. 14 [a]
7.85	6	3
8.75	15	21
9.54	160	130
10.40	800	940 [b]
11.03	2000	4000 [b]

[a]Calculated from $\tau_A^{-1} = 3.75 \times 10^{-8}[H^+]$.

[b]Extrapolation of measured rates.

ing a spin-lock period can be used to reproduce the calculated coherence transfer amplitudes given by Cavanagh et al. (24).

In the TOCSY pulse sequence, the magnetizations are labelled by their chemical shifts during the t_1 evolution period at the beginning of the spin-lock period, and we are interested in the detected signals, which result from nuclei that had a particular chemical shift during t_1. Hence we focus our attention on those terms in the density operator at the beginning of the spin-lock period that represent the transverse magnetizations of a particular group of nuclei in one type of molecule, and determine the amplitudes of the transverse magnetizations present at the end of the spin-lock period. Since the coherence levels of all coherences in the ensemble are unchanged during a spin-lock period, only the –1 coherence level operators need be considered. In *N*-acetylglycine, 793 basis product operators (1 for each of the 792 possible single quantum transitions in the *N*-acetylglycine system with 6 coupled protons, plus 1 for the water proton) are required. To determine the fate of the C$\mathbf{H}_2$ magnetization as it evolves through the spin-lock period, one defines the initial conditions by setting the two elements of $\mathbf{b}(0)$ that correspond to the spin operators for the transverse magnetizations of the CH_2 protons of *N*-acetylglycine to 1, and all other elements to zero. The intensities of the various peaks in the slice through the 2D TOCSY contour map at the value of f_1 for the CH_2 protons of *N*-acetylglycine are proportional to the elements of $\mathbf{b}(t)$ for the spin operators for the corresponding transverse magnetizations. The sum of the elements that correspond to the operators for the CH_2 protons gives the intensity of the *N*-acetylglycine CH_2 peak, the element corresponding to the spin operator for the NH proton gives the intensity of the *N*-acetylglycine NH peak, the sum of the elements corresponding to the spin operators for the methyl protons gives the intensity of the *N*-acetylglycine CH_3 peak, and the element associated with the spin operator for the water proton gives the intensity of the water peak.

Results and discussion

To test the applicability of the theory presented above, we have studied the rate of exchange between the NH proton in *N*-acetylglycine with water. Rates from 5 to 95 s^{-1} have been determined as a function of pH by lineshape analysis (14). In that study, the collapse of the doublet of quartets arising from the resonance of the glycine methylene group to a single quartet as the pH increased was simulated using the Bloch equations modified for chemical exchange to extract the rate of exchange of the amide proton. The methylene resonance is split into a doublet from coupling to the amide proton (5.9 Hz) and is further split into a quartet by a 0.3Hz long-range coupling from the methyl protons of the acetate group. The relevant results of this study are summarized in Table 1.

Fig. 1. The f_2 trace of the TOCSY contour map at the f_1 position of the CH_2 resonance of *N*-acetylglycine for an aqueous solution of *N*-acetylglycine at pH 8.75. Mixing time 0.093 s. The dispersive signal at 4.3 ppm is due to the signal of external water in the capillary of DMSO-d_6 used for the lock signal.

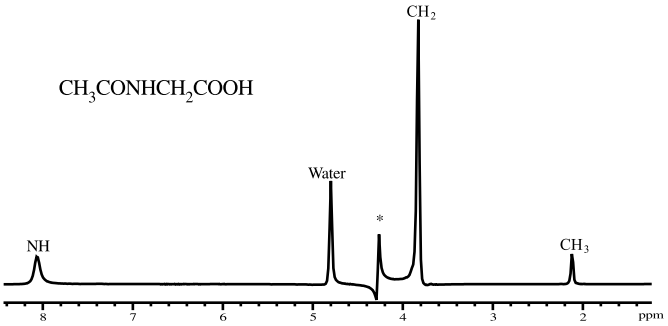

In the present investigation, we studied *N*-acetylglycine solutions at pH values that overlap the previous study so that the exchange theory could be tested. Measurements at higher pH values were also performed in order to determine the upper limit of exchange rates measurable with the current technique. TOCSY experiments were performed on each solution at a number of different mixing times and the transfer of the glycine CH_2 magnetization present at the end of the t_1 interval to other nuclei during spin-locking was determined from the f_2 slice of the 2D contour map at the f_1 frequency of the CH_2 resonance. A typical slice is shown in Fig. 1 for the pH 8.75 solution and a mixing time of 0.093 s. The integrals of the CH_2, NH, CH_3, and water resonances were determined at each mixing time for each pH value. The observed magnetization transfer data are compared in Fig. 2 with the intensities calculated using the theory in the previous section, with the value of the exchange rate constant, τ_A^{-1}, chosen to obtain reasonable agreement between observed and calculated peak intensities. The observed intensities were adjusted so that their sum remained equal to the sum for the shortest mixing time in order to minimize relaxation effects, which are not included in the theoretical description. The agreement between theory and experiment is quite good in all cases. At the slowest exchange rate studied here (pH 7.85), the experimental intensity of the CH_2 group is slightly higher than that predicted by the theory and that for the amide resonance is slightly lower than predicted. The experimental intensity of the NH resonance may be low because of T_2 effects. The exchange rate constants determined here are tabulated in Table 1 and these values agree, within experimental uncertainty, with those from Rabenstein's study (14). However, the present method allowed us to study exchange with rate constants as large as 2000 s^{-1}, while lineshape analysis was limited to rate constants of 100 s^{-1} or less.

It is apparent from Fig. 2 that the scalar coupling between the glycine CH_2 and NH protons gives rise to periodic transfer of magnetization between them during the spin-lock pe-

© 1999 NRC Canada

Fig. 2. Integrated intensities of peaks in the f_2 trace of the TOCSY contour maps at the f_1 position of the CH_2 resonance of *N*-acetylglycine at various spin-lock periods. □: CH_3 of *N*-acetylglycine; ■: water; O: NH of *N*-acetylglycine; ●: CH_2 of *N*-acetylglycine. (*a*) pH 7.85, τ_A^{-1} = 6 s^{-1}; (*b*) pH 8.75, τ_A^{-1} = 15 s^{-1}; (*c*) pH 9.54, τ_A^{-1} = 160 s^{-1}; (*d*) pH 10.40, τ_A^{-1} = 800 s^{-1}; solid lines show intensities calculated with J_{NH-CH_2} = 5.9 Hz and $J_{CH_3-CH_2}$ = 0.3 Hz and the values of τ_A^{-1} given.

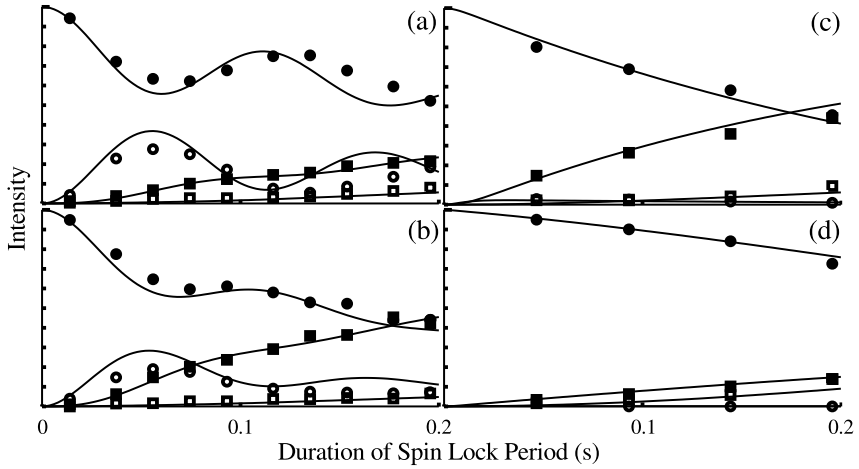

Fig. 3. Calculated TOCSY peak intensities as a function of exchange rate for the water peak and the NH, CH_2, and CH_3 peaks of *N*-acetylglycine for a spin-lock time of 0.150 s.

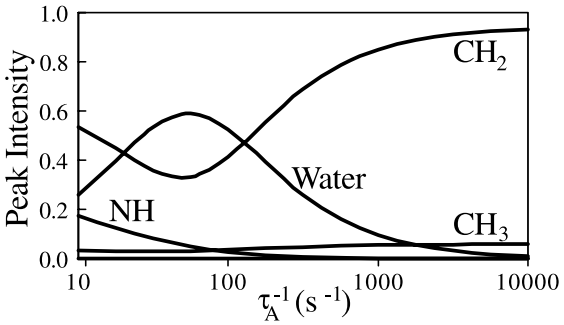

riod at slow exchange rates (Figs. 2*a* and 2*b*). As the exchange rate increases, magnetization transferred from CH_2 to NH via scalar coupling is transferred more rapidly to the water protons so that little of it remains for the scalar coupling to transfer back to the CH_2 protons at later times. In Fig. 2*c*, where τ_A^{-1} = 160 s^{-1}, there is essentially a monotonic decay of the CH_2 magnetization, with a concomitant growth in the magnetization transferred to the water protons by exchange, and the NH proton line has low intensity throughout the spin-lock period. At even faster exchange rates ($\tau_A^{-1} \gtrsim$ 600 s^{-1}), the NH resonance has coalesced with the water resonance and the rate of transfer of magnetization from the *N*-acetylglycine protons to water is much slower than at smaller values of τ_A^{-1}. This is to be expected since the scalar coupling between the NH and CH_2 protons is interrupted so frequently — exchange effectively decouples the NH and CH_2 protons — that little coherent magnetization transfer from CH_2 to NH can occur.

To delineate the variations in the magnitudes of the transferred magnetizations with τ_A^{-1}, the intensities of the spectral peaks at the end of a spin-lock period of 0.15 s were computed for 10 $s^{-1} \leq \tau_A^{-1} \leq$ 10 000 s^{-1}. The results are shown in Fig. 3. The NH intensity is reasonably large when τ_A^{-1} is small, but is very small for $\tau_A^{-1} \geq$ 100 s^{-1} as indicated above. The most striking feature shown in Fig. 3 is the variation of the magnitude of the magnetization transferred from the *N*-acetylglycine CH_2 protons to water with τ_A^{-1}. The intensity of the water peak goes through a maximum at $\tau_A^{-1} \cong$ 80 s^{-1}, and decreases slowly as τ_A^{-1} increases. The CH_2 peak goes through a minimum at $\tau_A^{-1} \cong$ 80 s^{-1}. It is unlikely that reliable measurements of the rate constants for NH–water exchange can be made for $\tau_A^{-1} \gtrsim$ 4000 s^{-1} since the water peak intensity will be too small for accurate measurement. The CH_3 peak intensity increases slowly with τ_A^{-1} above τ_A^{-1} = 80 s^{-1} because the small 0.3 Hz CH_2–CH_3 scalar coupling becomes more effective in transferring magnetization away from the CH_2 protons as the NH and CH_2 protons are increasingly decoupled by exchange. It should be pointed out that the intensity of the water peak is approximately proportional to the length of the spin-lock period in TOCSY for $\tau_A^{-1} >$ 80 s^{-1}. Furthermore, the results reported here are specific to the *N*-acetylglycine spin system, so only qualitative extensions of the conclusions reached here to other spin systems can be made. Calculations of the behaviour expected of other spin systems with exchangeable protons are straightforward.

In earlier work on proton magnetization transfer from nonexchangeable protons in amino acids and peptides to water during the spin-lock period in TOCSY (1), attention was focussed on the water stripe of the TOCSY map, i.e., the f_1 trace of the TOCSY map at the f_2 position of the water resonance. The results reported here have some implications for such studies. The water peak in the f_2 traces of the TOCSY contour maps at the f_1 position of the CH_2 used here is, in fact, the CH_2 peak in the water stripe used in the previous work. Hence the calculated intensities of the water peak shown in Fig. 3 are applicable to studies of the f_2 water stripe. The CH_2 peak of *N*-acetylglycine in the water stripe of the TOCSY map for a spin-lock time of 0.15 s will have maximum intensity when $\tau_A^{-1} \sim$ 80 s^{-1}, and one would expect to observe a CH_2 peak with significant intensity only if $\tau_A^{-1} \lesssim$ 4000 s^{-1}. When the CH_2 peak intensity in the water stripe is smaller than its maximum value, τ_A^{-1} is either greater than or

© 1999 NRC Canada

less than ~80 s^{-1}. If the exchange rate is slow ($\tau_A^{-1} \lesssim 80\ s^{-1}$), the NH resonance should be resolved; but when the exchange rate is fast ($\tau_A^{-1} \gtrsim 80\ s^{-1}$), the NH resonance will have coalesced with the water resonance.

Acknowledgments

We wish to thank the Natural Sciences and Engineering Research Council of Canada and the University of Alberta for financial support.

References

1. T.T. Nakashima, R.E.D. McClung, and G. Kotovych. J. Magn. Reson. **133**, 222 (1998).
2. G. Wagner and K. Wüthrich. J. Mol. Biol. **160**, 343 (1982).
3. L. Mayne, Y. Paterson, D. Cerasoli, and S. W. Englander, Biochemistry, **31**, 10 678 (1992).
4. H. Roder, G. Elove, and S.W. Englander. Nature (London), **335**, 700 (1988).
5. E. Tuchsen and C. Woodward. J. Mol. Biol. **185**, 405 (1985).
6. S. Forsen and R.A. Hoffman. J. Chem. Phys. **39**, 2892 (1963).
7. B. Adams and L. Lerner. J. Magn. Reson. **96**, 604 (1992).
8. E.R. Johnston and A.B. Little, Jr. J. Magn. Reson. Ser. A, **114**, 113 (1995).
9. C. Dalvit. J. Magn. Reson. Ser. A, **113**, 120 (1995).
10. S. Mori, M. O'Neal Johnson, J.M. Berg, and P.C.M. van Zijl. J. Am. Chem. Soc. **116**, 11 982 (1994).
11. T.-L. Hwang. P.C.M. van Zijl, and S. Mori. J. Biomol. NMR **11**, 221 (1998).
12. G. Gemmecher, W. Jahnke, and H. Kessler. J. Amer. Chem. Soc. **115**, 11 620 (1993).
13. S. Koide, W. Jahnke, and P.E. Wright. J. Biomol. NMR **6**, 306 (1995).
14. D.L. Rabenstein. Can. J. Chem. **50**, 1036 (1972).
15. A. Bax and D.G. Davis. J. Magn. Reson. **65**, 355 (1985); M.H. Levitt, R. Freeman, and T. Frenkiel. J. Magn. Reson. **47**, 328 (1982).
16. D.J. States, R.A. Haberkorn, and D.J. Ruben. J. Magn. Reson. **48**, 286 (1982).
17. O.W. Sorensen, G.W. Eich, M.H. Levitt, G. Bodenhausen, and R.R. Ernst. Prog. NMR Spectrosc. **16**, 163 (1983).
18. T.T. Nakashima and R.E.D. McClung. J. Magn. Reson. **70**, 187 (1986).
19. L Braunschweiler and R.R. Ernst. J. Magn. Reson. **53**, 521 (1983).
20. D.R. Muhandiram and R.E.D. McClung, J. Magn. Reson. **76**, 121 (1988).
21. J.L. Kaplan and G. Fraenkel. J. Am. Chem. Soc. **94**, 2907 (1972).
22. C.S. Johnson. *In* Advances in magnetic resonance. Vol. 1. *Edited by* J.Waugh. Academic Press, New York. 1965. p. 33.
23. N.R. Skrynnikov and R.R. Ernst. J. Magn. Reson. **137**, 276 (1999).
24. J. Cavanagh, W.J. Chazin, and M. Rance. J. Magn. Reson. **87**, 110 (1990).

© 1999 NRC Canada

Geometrical isomerism and ^{19}F NMR spectroscopy of octahedral perfluoroethyl- and perfluoropropyl-substituted β-diketonates and monothio-β-diketonates of rhodium(III)

Gary A. Stern and John B. Westmore

Abstract: In solution in acetone at room temperature, tris(perfluoropropanoyl and perfluorobutanoyl)benzoylmethanate complexes of rhodium(III) are shown by ^{19}F NMR spectroscopy to exist as nearly statistical 1:3 mixtures of their respective *fac* and *mer* octahedral isomers, whereas the analogous perfluoroalkanoylthiobenzoylmethanate complexes have a *fac*-octahedral structure. For all four complexes studied, vicinal F–F coupling constants are too small (0–3 Hz) to lead to resolved multiplet peaks, so that perfluoroethyl groups show singlet resonances for their CF_3 groups. Since four-bond coupling constants are significantly larger, ~9 Hz, perfluoropropyl groups show the expected multiplet resonances for their CF_3 groups. In acetone, AB patterns, with geminal coupling constants equal to ~270 Hz, are observed for the CF_2 groups next to the chelate ring (except for the perfluoropropanoylthiobenzoylmethanate complex). (These observations are modified by solvent. In toluene, one of the AB patterns of a *mer*-octahedral complex collapses to a single peak.) The AB spectra, which are subject to substituent and solvent effects, can be interpreted in terms of perfluoroalkyl groups rotating rapidly about the C_{ring}—C_{alkyl} bond, with an unsymmetric double potential well, giving unequal rotamer populations. Changes in the spectra were not noticeable over the temperature range accessible in the acetone and toluene solvents used.

Key words: rotation, perfluoroalkyl groups, fluorine NMR spectra, fluorine–fluorine coupling constants, fluorinated β-diketonate complexes, monothio-β-diketonates, rhodium complexes.

Résumé : Faisant appel à la spectroscopie RMN du ^{19}F, on montre que, en solution dans l'acétone, à la température ambiante, les complexes tris(perfluoropropanoyl et perfluorobutanoyl)benzoylméthanate de rhodium(III) existent sous la forme de mélanges 1:3 pratiquement statistiques de leurs isomères octaédriques *fac* et *mer* respectifs alors que les complexes perfluoroalcanoylthiobenzoylméthanates analogues existent sous la forme d'une structure octaédrique-*fac*. Pour chacun des quatre complexes étudiés, les constantes de couplage F–F vicinales sont trop faibles (0–3 Hz) conduire à des pics multiplets résolus; les groupes CF_3 des groupes perfluoroéthyles apparaissent donc comme singulets. Les constantes de couplage à travers quatre liaisons étant beaucoup plus importantes, ≈9 Hz, les groupes CF_3 des groupes perfluoropropyles se présentent sous la forme de multiplets attendue. Dans l'acétone, on observe des diagrammes AB, avec des constantes de couplage geminales d'environ 270 Hz, pour les groupes CF_2 adjacents du cycle du chélate (à l'exception du complexe perfluoropropanoylthiobenzoylméthanate). (Ces observations varient avec le solvant. Dans le toluène, l'un des diagrammes AB d'un complexe octaédrique-*mer* ne donne qu'un seul pic). Les spectres AB, qui sont soumis à des effets de substituant et de solvants, peuvent être interprétés en fonction de groupes perfluoroalkyles en rotation rapide autour de la liaison C_{cycle}—C_{alkyle} avec un puits de potentiel double et asymétrique conduisant à des populations inégales de rotamères. Dans le domaine de température accessible avec des solutions dans l'acétone ou le toluène, il n'a pas été possible de noter de différences dans les spectres.

Mots clés : rotation, groupes perfluoroalkyles, spectres RMN du fluor, constantes de couplage fluor–fluor, complexes β-dicétonates fluorés, monothio-β-dicétonates, complexes du rhodium.

[Traduit par la Rédaction]

Received November 5, 1998.

This paper is dedicated to Professor Ted Schaefer in recognition of his outstanding contributions to Canadian chemistry.

G.A. Stern[1] and J.B. Westmore.[2] Department of Chemistry, University of Manitoba, Winnipeg, MB R3T 2N2, Canada.

[1]Present address: Department of Fisheries and Oceans, Freshwater Institute, 501 University Crescent, Winnipeg, MB R3T 2N6, Canada.

[2]Author to whom correspondence may be addressed. Telephone: (204) 474-9761. Fax: (204) 474-7608. e-mail: westmor@cc.umanitoba.ca

 © 1999 NRC Canada

Introduction

Octahedral metal complexes having three unsymmetric bidentate ligands can adopt facial (*fac*) or meridional (*mer*) structures. While the *mer* isomer is statistically three times more likely to form than the *fac* isomer, the ratio is strongly influenced by thermodynamic parameters or by kinetics of the formation reactions. Under appropriate conditions, isomerism of such complexes can be studied by nuclear magnetic resonance spectroscopy. Our initial interest in this topic was prompted by our syntheses of fluorinated β-diketonate complexes of rhodium(III), which are sufficiently volatile for study by electron ionization mass spectrometry. We found, by single crystal X-ray diffraction (XRD), that tris(thioacetyltrifluoroacetonato)rhodium(III) adopts the *fac*-octahedral geometry (1). However, for the rhodium(III) complexes **1**–**4** to be described in this paper, XRD was not an option because we were unable to prepare single crystals of suitable quality. For these complexes, ^{19}F NMR spectroscopy shows that not only does the X substituent (O or S) influence geometrical isomerism but also, as a bonus, has led to some interesting conclusions regarding the rotational behavior of the perfluoroalkyl substituents.

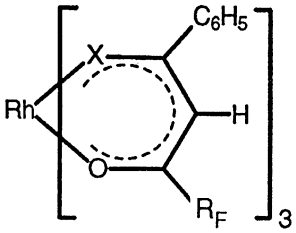

1. X = S, $R_F = C_2F_5$

2. X = S, $R_F = n\text{-}C_3F_7$

3. X = O, $R_F = C_2F_5$

4. X = O, $R_F = n\text{-}C_3F_7$

Because our description of the NMR spectra presented in this paper requires an interpretation of F–F coupling constants, we first present a brief summary of this topic, along with some key references. The coupling constant depends upon the number and nature of the bonds intervening between the coupled fluorine atoms, dihedral angles between bonds, substituent effects, and "through space" interactions. In particular, the near-zero values (<~1 Hz) observed for vicinal coupling constants (2–18) may be a consequence of the averaging effects of internal rotation about the C—C bond, and, in part, to cancellation of the orbital, spin-dipolar, and Fermi contact terms of nonuniform sign (19, 20). All three of these terms make significant contributions to geminal coupling constants (19, 20), which, experimentally, have wide variations (150–400 Hz), that have been attributed partly to the sensitivity of the Fermi contact term to changes in the FCF bond angles, and also partly to the sensitivity of the orbital and Fermi contact terms to substituent effects (21–24). In contrast to the near-zero coupling constants between vicinal fluorines, substantially larger values for coupling over four and five bonds have been observed (25–30).

The ^{19}F NMR spectra of many metal complexes containing perfluoroalkyl groups have been reported (31–37). The compounds include metal-alkyl bonded complexes of Mn, Re, Fe, and Co (31); Co and Rh (32); β-diketonate and (or) monothio-β-diketonate complexes of Ni, Pd, and Co (33); Be (34); Ru, Rh, Pd, and Pt (35); Ni, Pd, and Co (36); and Zn and Pd (37). In most cases the spectra were simply used for characterization purposes. In this paper, we report a more detailed analysis of the spectra of rhodium(III) β-diketonate and monothio-β-diketonate complexes containing perfluoroalkyl substituents. Not only do the spectra reveal the geometry of the complexes, but they also lead to some interesting conclusions about the rotational behavior of the perfluoroalkyl groups.

Experimental section

Syntheses

The four ligands needed to prepare complexes **1**–**4** were synthesized by published methods (38).

To prepare β-diketonate complexes **3** and **4**, $RhCl_3 \cdot H_2O$ (0.32 mmol), in 10 mL of ethanol, was added to a solution of the appropriate ligand (0.96 mmol) in 10 mL of ethanol. The solution was refluxed for 1 h, then cooled, and a small amount of water was added. This solution was then shaken with methylene chloride; the methylene chloride extract was dried over sodium sulfate. After evaporation of methylene chloride, the resulting oily red residue was added to a silica gel column (60–200 mesh) through which methylene chloride was passed. For each complex, two bands separated, while a portion of the sample still remained at the top of the column. The first band (red) eluted quite readily but did not contain the desired complex. The second band (yellow), which contained the desired product, eluted slowly, so that the silica from this part of the column was removed and the product was extracted from it with acetone. After evaporation of acetone, the residue was subjected to fractional sublimation, under roughing pump vacuum, to yield the desired rhodium chelate as a yellow sublimate. The molecular masses and fragmentation patterns determined by mass spectrometry (VG 7070E-HF mass spectrometer) supported assignment of the yellow products as monomeric tris-chelate complexes. Complex **3** *m*/*z*: 898 (100%), RhL_3^+ (898, calcd.); 848 (36%), $[RhL_3 - CF_2]^+$; 633 (57%), RhL_2^+; 181 (81%), $HRhC_6H_5^+$. Complex **4** *m*/*z*: 1048 (100%), RhL_3^+ (1048, calcd.); 733 (51%), RhL_2^+; 181 (65%), $HRhC_6H_5^+$.

The monothio-β-diketonate complexes **1** and **2** were prepared by the same procedure. The desired products were again found in the second band (red) on the silica gel column and were subjected to fractional sublimation, in vacuo, to yield the desired complexes as red sublimates. The assignments of the red products as monomeric tris-chelate complexes were supported by mass spectrometry. Complex **1** *m*/*z*: 946 (100%), RhL_3^+ (946, calcd.); 896 (17%), $[RhL_3 - CF_2]^+$; 665 (32%), RhL_2^+; 383 (49%), $[Rh(L - H)]^+$. Complex **2** *m*/*z*: 1096 (100%), RhL_3^+ (1096, calcd.); 765 (49%), RhL_2^+; 433 (55%), $[Rh(L - H)]^+$.

^{19}F nuclear magnetic resonance spectroscopy

Dilute solutions (5–7 mmol%) of the complexes were prepared in acetone or toluene to which a small amount of C_6F_6

© 1999 NRC Canada

Table 1. Fluorine chemical shifts (ppm) and coupling constants (Hz) for perfluoroethyl-substituted complexes **1** and **3**.[a]

		AB part					X_3 part		
Complex	Solvent	Sub-spectrum	$\delta_A(CF_2)$	$\delta_B(CF_2)$	$\Delta\upsilon_{AB}$ (Hz)	J_{AB}	Sub-spectrum	$\delta_X(CF_3)$	$J_{AX} = J_{BX}$
1 (X = S)	Acetone		–119.41	–119.41	0	—		–81.38	≤1.0
3 (X = O)[b]	Acetone	1	–118.201	–118.697	140	267.5	a	–81.72	~2.0
		2	–118.197	–118.883	194	266.5	b	–81.86	~2.7
		3	–118.342	–118.837	282	268.0	c (*fac*?)	–81.92	≤1.0
		4	–118.391	–118.821	121	268.0	d	–82.04	~3.0
3 (X = O)[b]	Toluene	1	–119.064	–119.543	135	269.0	a	–82.24	~1.7
		2	–119.054	–119.656	170	267.2	b	–82.37	~2.3
		3	–119.374	–119.722	98	267.3	c (*fac*?)	–82.56	≤1.0
		4	–119.557	–119.557	0	—	d	–82.45	~2.3

[a]Values of δ_X, J_{AX}, and J_{AB} are experimentally determined. The other NMR parameters emerge from the computer simulations for which a line width of 1.5 Hz was used. The uncertainties are estimated to be 0.002 ppm for δ_A and δ_B, 0.01 ppm for δ_X, and 0.3 Hz for J_{AB}. $\Delta\upsilon_{AB}$ (Hz) is the frequency difference between the A and B resonances.

[b]For complex **3**, sub-spectra 1–4 and a–d, respectively, are presented from low to high field. No match between a particular resonance occurring in the AB region with another in the CF_3 (X_3) region is implied.

was added to act as an internal chemical shift reference. In these solvents, $\delta_F(C_6F_6)$ was taken as –162.90 ppm with respect to $\delta_F(CFCl_3)$. Thus, the variations in δ_F that are reported for samples in the two solvents will be a combination of solvent effects for both the reference and the sample. The chlorinated solvents, chloroform and methylene chloride, were unsuitable because the complexes appeared to decompose slowly in them. The solutions were transferred to 5 mm o.d. NMR tubes, then degassed by the freeze–pump–thaw procedure; the sample tubes were then flame sealed. All ^{19}F NMR spectra were recorded with a Bruker AM300 spectrometer, at a frequency of 282.4 MHz, with fluorines decoupled from protons by broad-band irradiation. For detailed examinations of selected spectral regions, the spectral window was reduced, and the spectrum was accumulated with up to 500 free induction decays; Fourier transformation yielded spectra with a digital resolution of 0.076 Hz/point. The probe was at room temperature (~27°C) for the results described (we noticed no significant changes in the spectra over the high- or low-temperature range accessible with the acetone and toluene solvents).

The NMR spectra were analyzed with the assistance of the NUMARIT spectral simulation computer program (39)[3], which was extensively modified by R. Sebastian, formerly of this department.

Results and discussion

The ^{19}F NMR spectra of the monothio-β-diketonate complexes are simpler than those of the β-diketonates, so we shall discuss them first.

Monothio-β-diketonate complexes

The spectrum of complex **1** ($R_F = CF_2CF_3$), recorded in acetone at room temperature, consists of only two resonances, both appearing as singlets. The deceptive simplicity of this spectrum must be explained, for the CF_2 group could be an AB system because the plane of the chelate ring is not a molecular plane of symmetry. In addition, in separate experiments, we have observed that the ^{103}Rh–F coupling constant in the analogous complex when $R_F = CF_3$ is ~0.5 Hz, about the same as J_{HF} when not proton decoupled. However, in the spectra discussed in this paper, peak structure resulting from ^{103}Rh–F coupling was not resolved. The low-field resonance, at –81.38 ± 0.01 ppm (relative intensity = 3), and the high-field resonance, at –119.41 ± 0.01 ppm (relative intensity = 2), must be assigned to the fluorine atoms of the CF_3 and CF_2 groups, respectively. The full width at half maximum (FWHM) of each signal was ~2 Hz, i.e., not measurably greater than that of the C_6F_6 reference peak; combined with the lack of peak structure, and assuming that the CF_3 peak is no more than 0.5 Hz broader than the reference peak. This implies that the F–F vicinal coupling constant is no greater than 1 Hz, as anticipated from the introduction. The single-peak CF_2 resonance, unlike the AB patterns shown by complexes **2**–**4** (later), indicates that the chemical shifts of these two fluorines are identical, or nearly so, because geminal coupling constants are expected to be high (see Introduction). To permit easy comparison of NMR parameters of all complexes, the chemical shifts for complex **1** are included in Table 1.

The spectrum of complex **2** ($R_F = CF_2CF_2CF_3$), a potential seven-spin $ABMNX_3$ system, contains three major resonances, namely a triplet (centred on $\delta \approx -79.5$ ppm), a quintet (centred on $\delta \approx -117.7$ ppm), and a singlet ($\delta \approx -125.5$ ppm), with relative intensities of 3:2:2, respectively (Fig. 1). However, this spectrum is much simpler than its full analysis as an $ABMNX_3$ spectrum would require. The triplet must be assigned to the fluorine atoms of the CF_3 group. Assignment of the remaining resonances is consistent with both coupling constant and chemical shift evidence. We assign the singlet to the fluorines of the β-CF_2 group, since vicinal coupling constants between these fluorines and those of the adjacent CF_3 and α-CF_2 groups are expected, on the basis of the earlier discussion, to be very small. Furthermore, there is no evidence of any MN structure for this peak thus indicating that these fluorines have identical, or nearly identical, chemical shifts. *Consequently, we can interpret the other*

[3]Reworked by R. Sebastian and incorporated into the XSIM NMR computational package as NUMMRIT by K. Marat of this department, to whom queries should be addressed.

© 1999 NRC Canada

Fig. 1. $^{19}F\{^{1}H\}$ NMR spectrum of complex **2** in acetone.

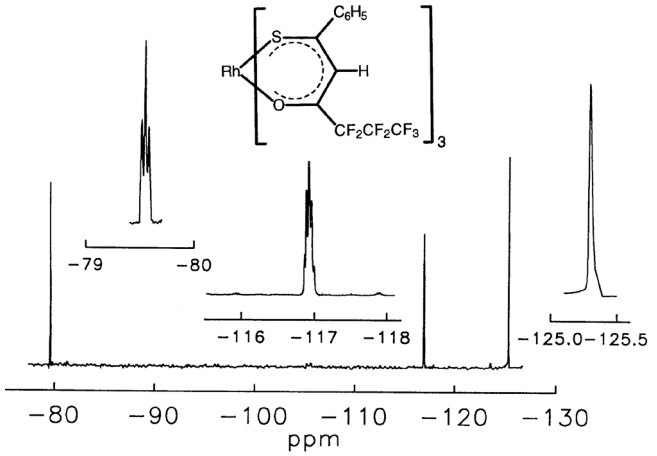

Fig. 2. CF_2 $^{19}F\{^{1}H\}$ spectral region (AB part) of complex **2**: (*a*) experimental spectrum in acetone, (*b*) simulated spectrum.

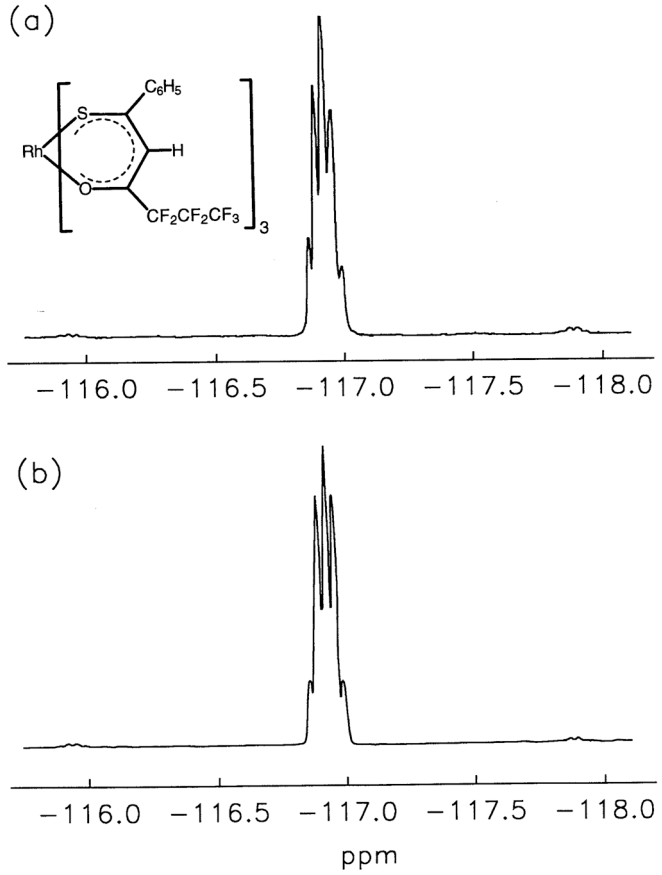

parts of the spectrum in terms of coupling between the α-CF_2 and CF_3 groups only. The remaining assignment of the quintet to the α-CF_2 group is also consistent with its chemical shift, which is similar to that of the CF_2 group of complex **1**. This is as expected because the electronic environment of the α-CF_2 group in complex **2** is similar to that of the CF_2 group in complex **1**, i.e., both are located between the ring carbon atom and a perfluoroalkyl group (the inductive effects of the CF_3 and CF_2CF_3 groups bound to the CF_2 group next to the ring should be very similar). On the other hand, the β-CF_2 group in complex **2** has a substantially different environment from the α-CF_2 group, and therefore a different chemical shift. Similar assignments have been made for the fluorine atoms in a metal complex containing the Mn-CO-$CF_2CF_2CF_3$ group (31). The quintet, with peak intensity ratios of 1.01:4.02:6.02:4.01:1.00, is associated with two outer sets, each of four low intensity peaks. The quintet and triplet splitting patterns exhibited by the α-CF_2 and CF_3 groups, respectively, are consistent with a special case of an ABX_3 spin system that we analyze as follows. In the general case (40), for an ABX_3 spin system, the AB part of the spectrum consists of 16 peaks, comprised of four AB sub-spectra of relative intensities 1:3:3:1, each with the same value of J_{AB}, but with effective chemical shift differences given by $\Delta^*\delta_{AB} = \Delta\delta_{AB} + m_s(J_{AX} - J_{BX})/f$, where $\Delta\delta_{AB}$ is the chemical shift difference between A and B; m_s is the resultant spin of the X_3 nuclei, with the values ±1/2, ±3/2; and f is the operating frequency of the spectrometer. The repeated spacings between the AB sub-spectra are equal to $1/2(J_{AX} + J_{BX})$. The X_3 part consists of 14 resolved peaks of which two together, containing half the total intensity of the X_3 region, are always separated by $(J_{AX} + J_{BX})$ (40). When $J_{AX} = J_{BX}$, as expected here for a $CF_2CF_2CF_3$ group with free rotation about the C—C bonds, the X_3 part collapses to a symmetrical 1:2:1 triplet with spacings equal to J_{AX}. The repeated spacings between the AB sub-spectra now equal J_{AX}, and the effective chemical shift differences all equal $\Delta\delta_{AB}$. The eight strong central peaks of the four AB sub-spectra can only collapse to the observed 1:4:6:4:1 quintet if $\Delta\upsilon = J_{AX}$, where $\Delta\upsilon$ is the common separation between the central peaks of the AB sub-spectra. The remaining eight weak peaks of the four AB sub-spectra are assigned to the two sets of four low-intensity outer peaks, with spacings equal to J_{AX}. Figure 2 shows a comparison between the AB portion of the experimental spectrum and a simulated spectrum (39) for which the input parameters δ_A, δ_B, δ_X, J_{AB}, J_{AX}, J_{BX} and line width were adjusted until the best match between the X_3 and AB regions of the experimental and simulated spectra was obtained. The resulting NMR parameters are presented in Table 2. The $^4J_{AX}$ and $^4J_{BX}$ values are 8.9 ± 0.3 Hz, i.e., significantly larger than the vicinal coupling constants. The J_{AB} value, 270.0 ± 0.3 Hz, is within the wide range of values (150–400 Hz), noted in the introduction, that have been observed for geminal coupling constants.

For either monothio-β-diketonate complex only one type of perfluoroalkyl group can be recognized from the NMR spectrum, and consequently, the three groups are equivalent. Therefore, both complexes have a *fac*-octahedral structure for which the perfluoroalkyl groups are necessarily equivalent, owing to the presence of a C_3 symmetry axis. (In contrast, for a *mer*-octahedral structure, which lacks a C_3 axis, the three perfluoroalkyl groups are non-equivalent, i.e., one of the three perfluoroacyl residues is *trans* to a benzoyl residue, while the other two are *trans* to each other but not equivalent by symmetry. Thus, each perfluoroalkyl group of the *mer* isomer has a distinct spectrum.) A *fac*-octahedral structure for the monothio-β-diketonate complexes agrees with our XRD structure determination (1) of tris(thioacetyltrifluoroacetonato)rhodium(III), and is consistent with structures of

© 1999 NRC Canada

Table 2. Fluorine chemical shifts (ppm) and coupling constants (Hz) for perfluoropropyl-substituted complexes **2** and **4**, in solution in acetone.[a]

	AB part						X_3 part		β-CF_2 part		
Complex	Sub-spectrum	δ_A(α-CF_2)	δ_B(α-CF_2)	$\Delta\upsilon_{AB}$ (Hz)	J_{AB}	$^4J_{AX} = {}^4J_{BX}$	Sub-spectrum	$\delta_X(CF_3)$	Sub-spectrum	δ(β-CF_2)	J(vic)
2 (X = S)		–116.781	–117.041	73	270.0	8.9		–79.55		–125.34	~1
4 (X = O)[b]	1	–115.462	–115.942	136	270.8	8.9	a	–79.43	w	–125.12	~0.9
	2	–115.518	–115.914	112	270.9	8.8	b	–79.52	x	–125.21	~0.9
	3	–115.718	–116.078	102	270.4	8.7	c	–79.56	y	–125.40	~1.9
	4	–115.743	–116.102	101	270.4	8.7	d	–79.45	z	–125.47	~1.6

[a]Values of δ_X, δ(β-CF_2), and J(vic) are experimentally measured. The other NMR parameters emerge from the computer simulations for which a line width of 1.5 Hz was used. The uncertainties are estimated to be 0.002 ppm for δ_A and δ_B, 0.01 ppm for δ_X, and 0.3 Hz for J_{AB}, $^4J_{AX}$, and $^4J_{BX}$. υ_{AB} (Hz) is the frequency difference between the A and B chemical shifts.

[b]For complex **4**, sub-spectra 1–4, a–b, and w–z, respectively, are listed from low to high field. No matches among particular absorptions occurring in the the three spectral regions are implied.

various other tris(monothio-β-diketonato)rhodium(III) complexes (35, 41).

β-Diketonate complex 3 ($R_F = C_2F_5$)

Spectra of this complex, shown in Fig. 3, were recorded in both toluene and acetone, in order to reinforce the correctness of the assignments given below. In both solvents, the spectra contain two groupings of peaks. One grouping (relative intensity = 3) occurs between –81.65 and –82.10 ppm (in acetone) or between –82.20 and –82.60 ppm (in toluene), and the other grouping (relative intensity = 2) occurs between –117.20 and –119.80 ppm (in acetone) or between –118.20 and –120.60 ppm (in toluene). These must be assigned to the fluorines of the CF_3 and CF_2 groups, respectively. In both solvents, the first set contains four major resonance peaks and a number of minor peaks, while the second set contains at least six major resonance peaks in acetone, seven in toluene, and a number of minor peaks. The minor peaks in the CF_3 region of the spectra are assigned to impurities that, despite several attempts, we failed to remove completely by column chromatography followed by fractional sublimation of the complex under roughing pump vacuum.

The observation of four major peaks in the CF_3 region indicates that both *fac* and *mer* isomers are present in solution. Three of these peaks, which are necessarily of equal intensity, can be assigned to the *mer* isomer and the fourth to the *fac* isomer. The relative areas of the shaded parts of the peaks (Fig. 4), starting from low field, are 1.05:1.01:0.85:1.00 (in acetone) and 1.05:1.00:0.85:1.01 (in toluene). These results suggest that the third peak, starting from low field, can be assigned to the *fac* isomer, even though the intensities of the three remaining peaks are not exactly equal (owing probably to contributions from impurities). The *fac*:*mer* ratio is close to the statistical 1:3 ratio, in contrast to the monothio-β-diketonate complexes **1** and **3** for which the *fac* isomer is formed exclusively.

Although no splitting of the four resonances in the CF_3 region is apparent, the peak widths differ. Thus, for the spectrum recorded in acetone solution, the approximate FWHM values are 4.0, 4.7, 2.0, and 5.0 Hz, from low to high field, respectively. If we interpret these peaks as the X_3 parts of four ABX_3 sub-spectra then, according to the analysis described above for complex **2**, each of these peaks corresponds to a symmetrical 1:2:1 triplet with spacings equal to $1/2(J_{AX} + J_{BX}) = J_{AX}$, since $J_{AX} = J_{BX}$. By noting that the FWHM value for the C_6F_6 resonance used for calibration is ~2 Hz, then we find upper limits for the respective values of J_{AX} to be ~2.0, 2.7, ≤1, and 3.0 Hz. Similarly, the FWHM values in toluene, i.e., 2.7, 4.3, 1.3, and 4.3 Hz, lead to the J_{AX} upper limit values 1.7, 2.3, ≤1, and 2.3 Hz, respectively. Based on the earlier discussion, these small coupling constants are as expected for coupling between vicinal fluorines. The NMR parameters for these resonance peaks (referred to as sub-spectra a–d) are summarized in Table 1.

Fig. 3. $^{19}F\{^1H\}$ NMR spectrum of complex **3** in (*a*) acetone (*b*) toluene.

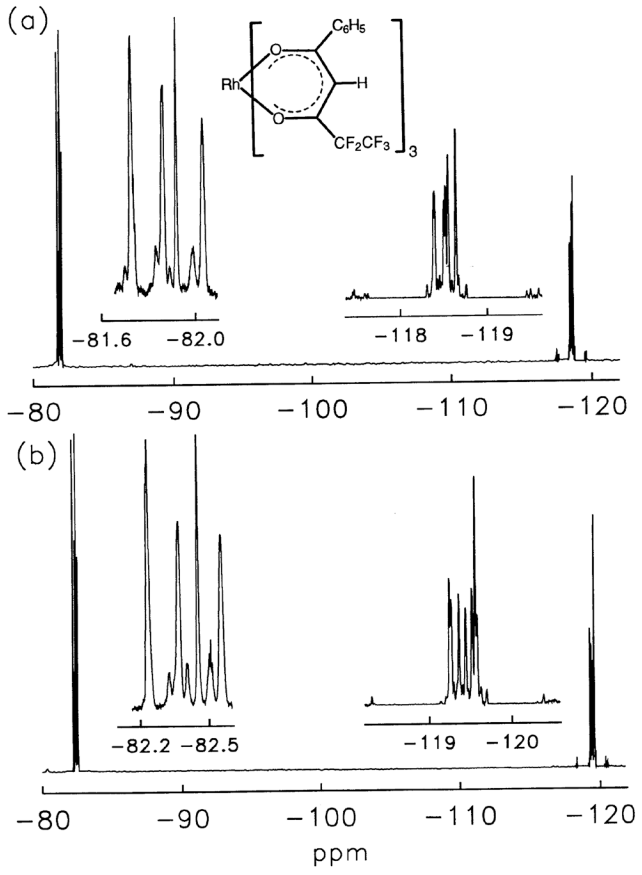

© 1999 NRC Canada

Fig. 4. CF_3 $^{19}F\{^1H\}$ spectral region (X_3 part) of.complex **3** in (*a*) acetone and (*b*) toluene. Not all impurities could be successfully be removed. Relative areas of the peaks are determined from the shaded portions.

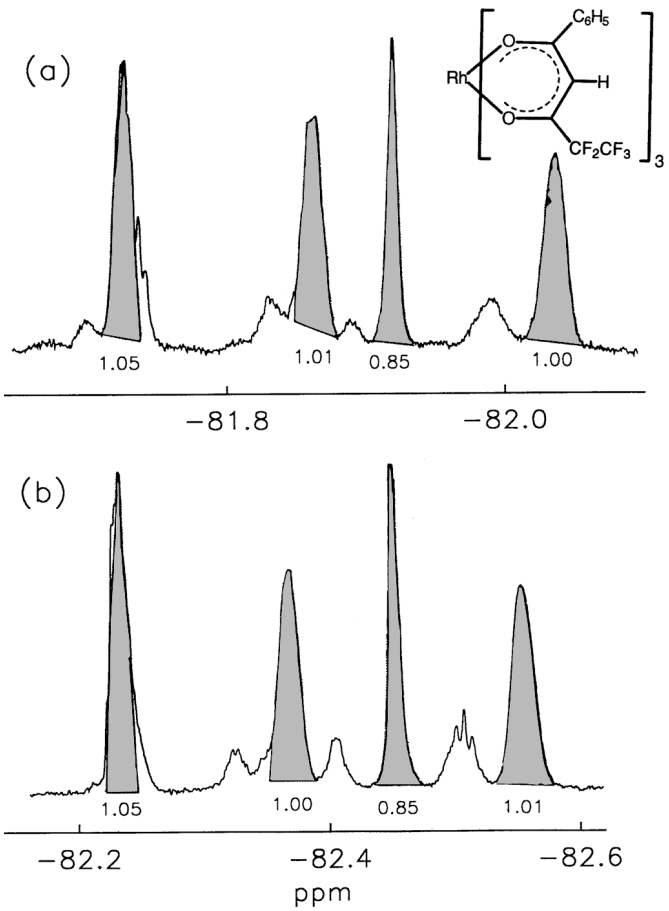

Fig. 5. CF_2 $^{19}F\{^1H\}$ NMR spectral region (AB part) of complex **3**: (*a*) experimental spectrum in acetone, (*b*) simulated spectrum. Not all impurities could be successfully be removed.

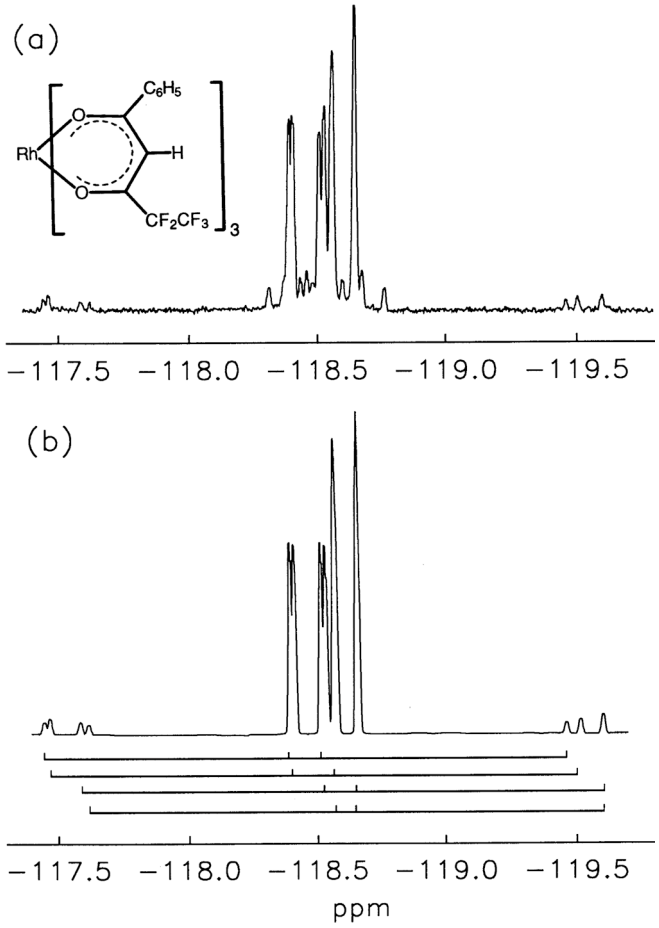

Strictly speaking, the CF_2 region of the spectrum should be interpreted as the AB parts of four ABX_3 spectra. However, in view of the small J_{AX} and J_{BX} coupling constants observed, it is more practical to regard this region as four overlapping AB sub-spectra, with the peaks broadened by the small vicinal couplings. Thus, we expect to observe eight strong peaks in this region, unless some of them are superimposed. The presence of small amounts of impurities as well as partial overlap of some peaks made it impossible to measure the relative intensities of peaks accurately and to associate them with a particular isomer. (As noted above, the intensities of the three resonances for the *mer* isomer should always be equal, and therefore, if one of the four signals is smaller or larger than the other three, it must be assigned to the *fac* isomer. In the present case, the intensities of the peaks in the X_3 region show that the intensities in the AB region will not be sufficiently different to allow us to assign signals in the AB region to a particular isomer.) These AB sub-spectra are therefore simply referred to as sub-spectra 1–4 (counting from low to high field). We have not matched these sub-spectra to any particular peak in the X_3 (CF_3) region of the spectrum. Figures 5 and 6 show expanded views of the AB (CF_2) spectral region, recorded in acetone and toluene, respectively. As before, these sub-spectra were analyzed, by simulation as four ABX_3 spectra, with the Numarit program (39) by using the NMR parameters and line width as input parameters that could be adjusted until a good match to the experimental spectrum was obtained. (In the form used, this program can simulate four ABX_3 spectra, but the four intensities must be equal, and the line widths in all spectra must be the same. This presents little difficulty in the present case because the four experimental spectra for the C_2F_5 groups are of approximately equal intensity, and the line width variations will not significantly influence the appearance of the spectrum. Because we could not match the peaks in the AB (CF_2) region to specific peaks in the X_3 (CF_3) region, we used as input the average δ_X value of the peaks in the CF_3 region, and also $J_{AX} = J_{BX} = 1.6$ Hz. The effect of this approximation on the accuracy of the simulations is, of course, minimal.) The experimental spectra, recorded in acetone and toluene, are compared to the simulated spectra in Figs. 5 and 6. The NMR parameters for the sub-spectra, labeled 1–4, recorded in both solvents, are given in Table 1.

The experimental spectra can now be explained. In acetone (Fig. 5), the two incompletely resolved peaks close to –118.40 ppm arise from the A parts of sub-spectra 1 and 2, while the two incompletely resolved peaks between –118.50 and –118.54 ppm are due to the B part of sub-spectrum 1

© 1999 NRC Canada

Fig. 6. CF_2 $^{19}F\{^1H\}$ NMR spectral region (AB part) of complex **3**: (*a*) experimental spectrum in toluene, (*b*) simulated spectrum. Not all impurities could be successfully be removed.

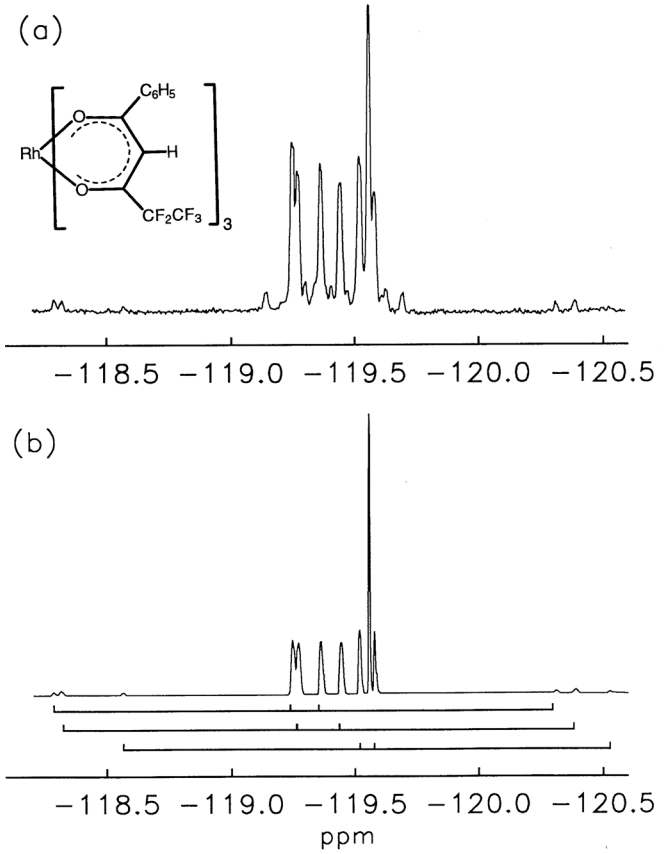

and the A part of sub-spectrum 3. The single peak at –118.56 ppm is the result of the B part of sub-spectrum 2 lying almost directly over the A part of sub-spectrum 4, while the remaining single peak at –118.65 ppm results from the superimposition of the B parts of sub-spectra 3 and 4. In toluene (Fig. 6), we observed only three small peaks on each side of the central region, implying that one of the potential AB sub-spectra has collapsed to a single peak. The two incompletely resolved peaks near –119.23 ppm correspond to the A parts of sub-spectra 1 and 2, while their B parts occur at –119.36 and –119.44 ppm, respectively. The peaks at –119.52 and –119.58 ppm correspond to the A and B parts, respectively, of sub-spectrum 3. Finally, the peak at –119.56 ppm corresponds to a CF_2 group, where geminal coupling is not observed (i.e., for spectrum 4, $\delta_A = \delta_B$).

β-Diketonate complex 4 (R_F = *n*-C_3F_7)

The spectrum of this complex, recorded in acetone (Fig. 7), consists of three groups of resonances falling in the spectral regions centered on $\delta \approx -79.54$ ppm (relative intensity = 3), $\delta \approx -115.80$ ppm (relative intensity = 2), and $\delta \approx -125.30$ ppm (relative intensity = 2). Thus, the resonances near $\delta \approx -79.54$ ppm, which show 12 resolved or nearly resolved peaks, must be assigned to the fluorine atoms of the CF_3 group. The resonances near $\delta \approx -115.80$ ppm show evidence of 16 peaks in the central part and 16, or more, small peaks in the outer parts. These are assigned to the α-CF_2 group and will be discussed later. The resonances near $\delta \approx$

Fig. 7. $^{19}F\{^1H\}$ NMR spectrum of complex **4** in acetone.

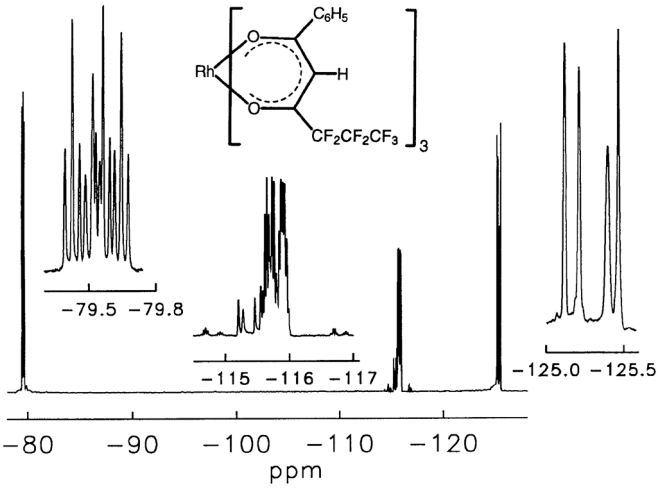

Fig. 8. β-CF_2 $^{19}F\{^1H\}$ NMR spectral region of complex **4** in acetone.

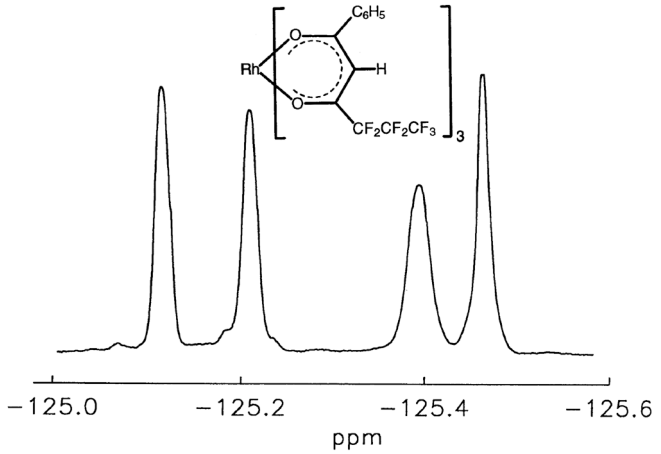

–125.30 ppm must therefore be assigned to the fluorines of the β-CF_2 groups and, because they are simplest, will be discussed first.

When the spectral region around $\delta \approx -125.3$ is expanded (Fig. 8), four peaks, none of which show evidence of splitting, become apparent. These peaks are assigned to the β-CF_2 group, in a mixture of *fac* and *mer* isomers. As noted above, such fluorine atoms are expected to have small, or zero, coupling to vicinal fluorines of the CF_3 and α-CF_2 groups. From low to high field, the FWHM values are 4.6, 4.6, 7.7, and 6.3 Hz, respectively. If we take the FWHM value of the C_6F_6 calibration peak as 2 Hz, then the upper limits for the vicinal coupling constants are 0.9, 0.9, 1.9, and 1.6 Hz, respectively. (This is based on the assumption that these peaks are unresolved 1:5:10:10:5:1 sextets formed by coupling of the β-CF_2 fluorines to the CF_3 and α-CF_2 fluorines, with both sets of vicinal coupling constants equal, and that the FWHM of the sextet equals $3J_{vic}$.) The relative areas of the four peaks (0.96:1.02:1.01:1.00 from low to high field) indicate that the *fac* and *mer* isomers are formed as a nearly statistical 1:3 mixture. These results are summarized as spectra w–z in Table 2.

© 1999 NRC Canada

Fig. 9. CF_3 $^{19}F\{^1H\}$ NMR spectral region (X_3 part) of complex **4** in acetone.

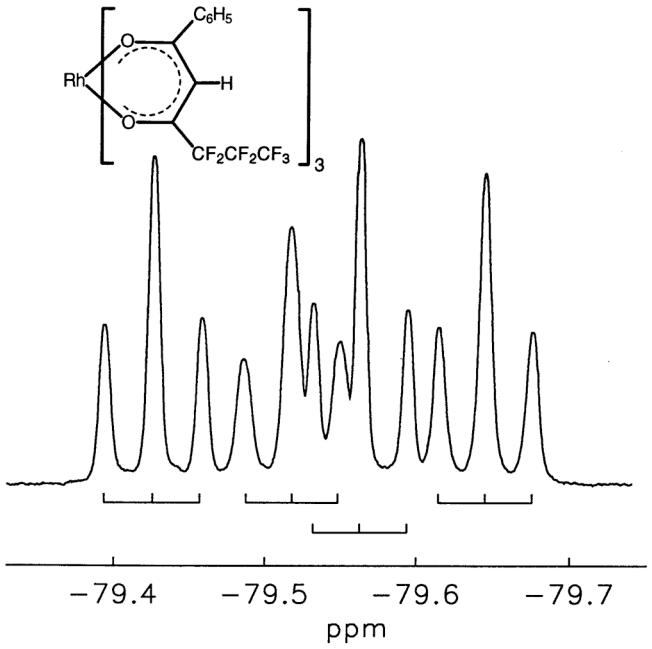

Figure 9 shows an expansion of the CF_3 region of the spectrum. The 12 peaks are easily analyzed as four symmetrical 1:2:1 triplets of nearly equal intensity. No further splitting of any of the peaks is apparent, but there are slight variations in peak width, which can be assigned to non-zero, but small, vicinal couplings, in agreement with the magnitude of the coupling constants deduced above from the β-CF_2 spectral region. To simplify the rest of the analysis, we have assumed that the only effect of the vicinal couplings is to broaden the peaks observed in the α-CF_2 and CF_3 spectral regions. As for complex **2**, a four-bond coupling between the CF_3 fluorines and α-CF_A and α-CF_B fluorines results in an ABX_3 spin system. When $J_{AX} = J_{BX}$, the X_3 spectrum collapses to the observed symmetrical 1:2:1 triplet. The NMR parameters for the CF_3 region of the spectrum, labeled as spectra a–d, are given in Table 2. Because the J_{AX} values are the same within experimental error for each of spectra a–d and w–z, it will not be possible to match the peaks in this region to those in the α-CF_2 region.

Based on the foregoing, the α-CF_2 region of the spectrum (Fig. 10) corresponds to the AB portions of four ABX_3 spectra of approximately equal intensity. Recalling the analysis given above for complex **2**, we see that, in the general case, each AB region would contain 16 peaks, corresponding to four AB sub-spectra with spacings equal to $1/2(J_{AX} + J_{BX})$, and of relative intensities 1:3:3:1, of which 8 strong peaks would be in the central region, and 4 small satellite peaks would be on either side. Thus, if the chemical shifts of the four AB sub-spectra are not very different, we expect 32 peaks in the central region, and 16 smaller peaks on each side. The number of peaks actually observed is much lower than the maximum. This can be attributed to accidental superimposition of some of the peaks and (or) to the equality of $\Delta\upsilon$ with $n\{1/2(J_{AX} + J_{BX})\}$ (n = 1, 2, 3, etc), within an AB sub-spectrum, where $\Delta\upsilon$ is the common separation between the central peaks of the AB sub-spectra, as before. This was

Fig. 10. α-CF_2 $^{19}F\{^1H\}$ NMR spectral region (AB part) of complex **4**: (*a*) experimental spectrum in acetone, (*b*) simulated spectrum.

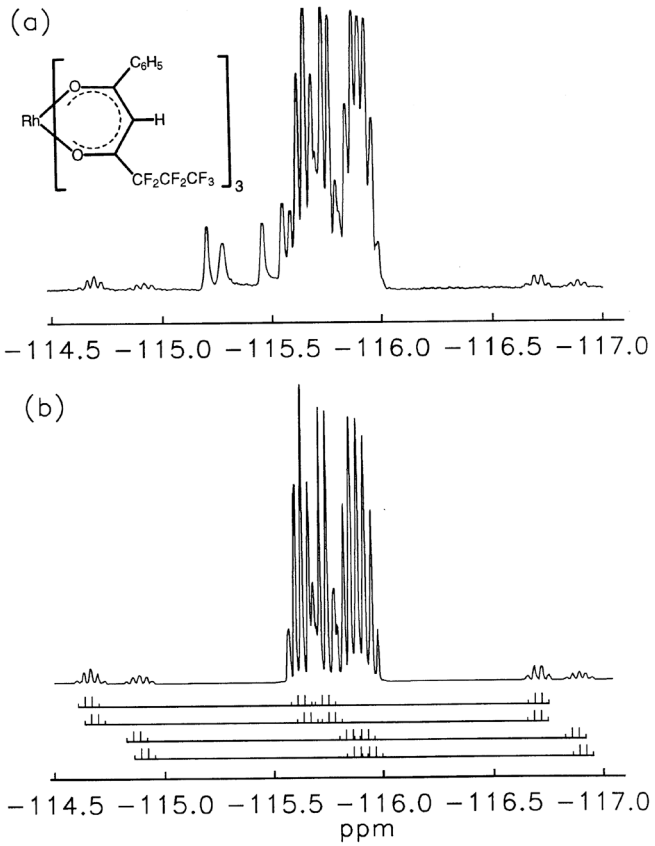

the case above for complex **2** (n = 1). Depending upon the value of $\Delta\upsilon_{AB}$, the two central quartets may overlap with one another. Thus, the complicated pattern of overlapping peaks observed in the central part of the experimental spectrum can be regarded as eight partially overlapping 1:3:3:1 quartets. Similarly, the outer peaks on each side correspond to four overlapping 1:3:3:1 quartets. From the recognizable patterns produced, it was possible to simulate the spectrum, and to obtain the various chemical shifts and coupling constants given in Table 2. Figure 10 shows the close correspondence between the experimental and the simulated (39) AB region of the spectrum, and also shows how the peaks in the experimental spectrum arise. The peaks between –115.61 and –115.74 ppm result from the partial overlap of the central A parts of sub-spectra 1 and 2, while those lying between –115.74 and –115.84 ppm arise from the overlap of the central B parts of sub-spectra 1 and 2, with coincidence of several of the peaks. Finally, the peaks between –115.84 and –116.10 ppm result from the closely overlapping central A and B parts of sub-spectra 3 and 4, again with coincidence of many peaks.

The spectrum (single peak or AB) of the CF_2 group adjacent to the chelate ring

The foregoing discussion has answered the question of the basic structures (i.e., *fac* or *mer* octahedral) of the complexes. However, the part of the spectrum exhibited by the CF_2 group next to the quasi-aromatic planar chelate ring de-

© 1999 NRC Canada

Fig. 11. Conformations considered as rotameric minima for the CF_2R group bound to the planar chelate ring.

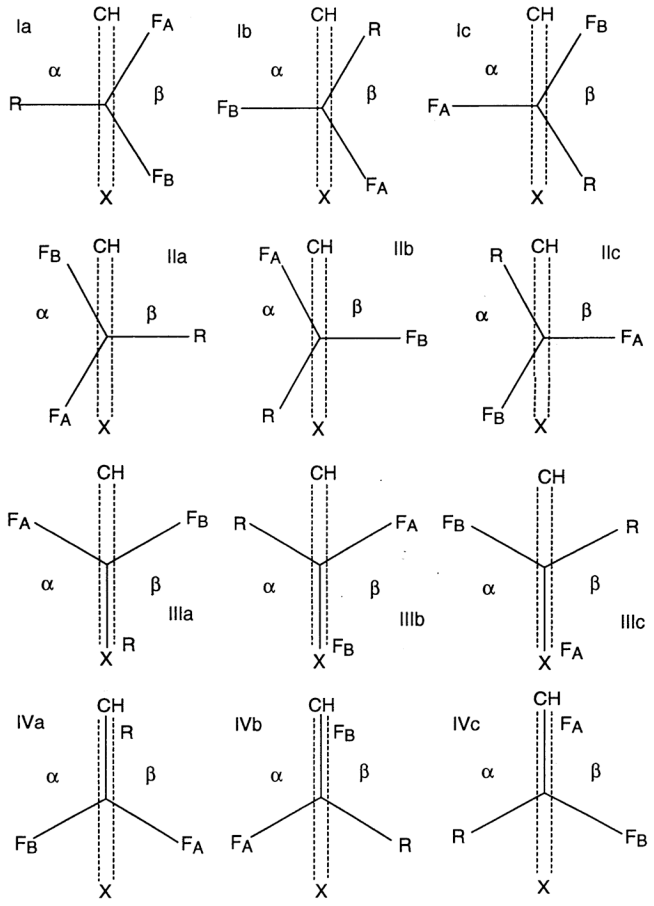

serves further analysis. The CF_2CF_3-substituted monothio-β-diketonate complex **1** yields a single-peak resonance for the CF_2 group, whereas the $CF_2CF_2CF_3$-substituted complex **2** exhibits an AB pattern for the α-CF_2 group. For the β-diketonate complex **3** in acetone, all four symmetrically non-equivalent CF_2CF_3 groups of the *fac* and *mer* isomers show AB patterns for the CF_2 group, but one of these AB patterns collapses to a single peak in toluene. Again, for the β-diketonate complex **4**, four AB sub-spectra are exhibited by the α-CF_2 parts of the four non-equivalent $CF_2CF_2CF_3$ substituents.

Without, for now, weighing their relative probabilities or rejecting unlikely conformations, we consider orientations of the CF_2R group with respect to the plane of the chelate ring that would reasonably correspond to energy minima; in Fig. 11 the view is along the C_{ring}—CF_2R bond, and the plane of the chelate ring is represented edgewise by the broken double line. The neighboring CH and X parts of the chelate ring are also shown. As depicted, conformations I(a–c) and II(a–c) have the projection of one of the bonds of the CF_2R group perpendicular to the plane of the chelate ring; conformations III(a–c) have one bond of the CF_2R group eclipsing the C—X bond of the chelate ring, while conformations IV(a–c) have one bond eclipsing the C—CH bond of the chelate ring. The planes of the chelate rings are not molecular planes of symmetry, either for chemically equivalent chelate rings of the *fac*-octahedral isomer or for any of the non-equivalent chelate rings of the *mer*-octahedral isomer. Thus, the two faces of the chelate ring, denoted as α and β, are not symmetrically equivalent, and in none of the 12 conformations are F_A and F_B equivalent.

We are now able to predict the type of spectrum exhibited by the α-CF_2 group for different limiting conditions of interconversion rates and probabilities of the conformations, and of the relative electronic environment of the two faces of the chelate ring. In the case of slow rotation (as set by the NMR experiment), each conformation present in significant amounts will contribute to the observed spectrum. If one conformation dominates, then an AB spectrum appropriate to that conformation will be observed; if several conformations have a significant presence, then a complex spectrum containing several overlapping AB contributions will be observed. A single-peak spectrum can result only if the chemical shifts of F_A and F_B are the same, as would be the case in conformations IIIa and IVa, if the two faces of the chelate ring should be insubstantially different. In fact, we shall show later that these conformations are unlikely.

In the case of rapid interconversion among conformations, the time-averaged chemical shifts of the two α-CF_2 fluorines will depend upon the chemical shifts in the conformations and upon their relative probabilities. Consequently, a single AB spectrum will normally result, although a single-peak resonance occurs under certain conditions. It is with the rapid interconversion scenario that the NMR spectra are consistent.

Preferred conformations and rotation of the perfluoroalkyl group

For simplicity, we confine the following discussion to the conditions most likely to prevail. We have found (1) for tris(thioacetyltrifluoroacetonato)rhodium(III) in the solid state that the orientation of the CF_3 group (i.e., R = F and X = S) corresponds to identical conformations IV(a, b, or c) (Fig. 11) in which a C—F bond eclipses the C–H part of the ring plane. The observed H···F separation of 226 pm is considerably less than the sum (270–305 pm) of the hydrogen and fluorine van der Waals radii, but also much larger than the sum (108 pm) of their covalent radii (42) and is within experimental error of their estimated[4] minimum separation (221 pm) for a rotating CF_3 group. If this result represents a genuine preference for this conformation, possibly as a result of hydrogen bonding, rather than an artifact of crystal packing, then it is reasonable to suppose that IVb and IVc represent low-energy conformations of the CF_2R group of the present molecules.

To assess the energy changes developed on rotation of the CF_2R group, we can note that in benzyl fluoride the conformer of greatest stability in the gas phase is an eclipsed form analogous to one of the equivalent forms IVa–c (R = F, Fig. 11) with a barrier to internal rotation of 1.17 kJ mol^{-1} (43); however, in acetonitrile and cyclohexane solvents a perpendicular conformer, analogous to one of the equivalent forms I/II (R = F), is more stable, with respective barriers to internal rotation of 3.22 and 0.72 kJ mol^{-1} in the two sol-

[4] Molecular Modeling Pro program. WindowChem Software Inc., Fairfield, Calif.

© 1999 NRC Canada

Fig. 12. Energy changes on rotation of the CF_2R group. 0° corresponds to conformation IVa in Fig. 11. The principal barrier is taken as 9 kJ mol^{-1} and the 180° barrier as 3 kJ mol^{-1} (see text).

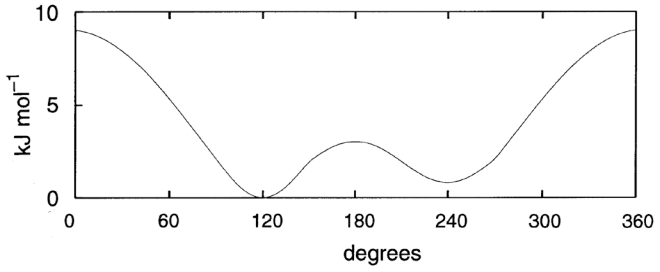

vents. In the case of 1,1,1-trifluoro-2-phenylethane, the stable conformer is a perpendicular form analogous to Ia/IIa (R = CF_3) with a solvent independent barrier to internal rotation of 9.02 kJ mol^{-1} (44).

It is clear from the foregoing discussion that conformer IVa represents the highest energy form (by ~9 kJ mol^{-1} with respect to the potential energy minimum), while all the remaining 11 conformers differ in energy by no more than ~3 kJ mol^{-1}. Less certain is the choice of low-energy conformations, though the crystal structure evidence favoring an eclipsed C—F bond, coupled with the preference noted above for a perpendicular orientation for the C—R bond, suggests that IVb and IVc are indeed favored choices. If so, the energy changes for rotation of the CF_2R group are of the form depicted in Fig. 12, where the minima (corresponding to the R group being on the α or β sides of the chelate ring) are shown with unequal depths. Interactions of a rotating CF_2R group, in most conformations of the R group with the X substituent, or with another chelate ring or its substituents, appear minimal, but interactions with solvent molecules (themselves influenced by their proximity to different parts of the complexes) could differ on either side of the chelate ring (the results do show that the spectra are, indeed, influenced by the solvent) and give the rationale for the unequal minima in Fig. 12.

This model can be used to explain the spectra generated by the CF_2R groups. When the minima are of unequal depth, the probability of the two low-energy conformers IVb and IVc are unequal, and consequently, the time-averaged chemical shifts of F_A and F_B will differ, and an AB spectrum will result. As the energies of the minima equalize, the probabilities of the conformers also equalize, the time-averaged chemical shifts equalize, and a single-peak spectrum results.

The scenario of rapid interconversion among conformations is consistent with observed chemical shifts. The values of $\Delta\upsilon_{AB}$ shown in Tables 1 and 2 range up to nearly 300 Hz. If these values represent the differences between time-averaged values of the A and B chemical shifts, weighted for different populations of conformations, it is reasonable to propose that the extreme chemical shift difference between A and B resonances in different conformations is not more than ~1000 Hz. Thus, interconversion among various conformations must occur faster than this, as is certainly the case. Even considering an unreasonably high rotational energy barrier of 15 kJ mol^{-1}, a very fast interconversion rate of ~1.5 × 10^{10} s^{-1} is predicted from rate = (kT/h) exp (–Ea/RT) where kT/h = 6.25 × 10^{12} at room temperature (45). Furthermore, the rate would still be very fast even at the lowest temperatures possible with the solvents used, in agreement with our variable temperature experiments.

Substituent and solvent effects

Chemical shift differences are smaller for the monothio-β-diketonate than for the β-diketonate complexes — compare **1** with **3**, Table 1, and **2** with **4**, Table 2 (the difference actually becomes zero for complex **1**). The ring substituent X could influence the results by producing intrinsic changes in the F_A and F_B chemical shifts and (or) by changes in the rotational relative energy minima (i.e., changes in relative rotamer probabilities. The chemical shift differences are also solvent dependent — compare the results for complex **2** in acetone and toluene (Table 1). In toluene, one potential AB spectrum for a perfluoropropyl group has collapsed to a single-peak resonance, thus implying that $\Delta\upsilon_{AB}$ for F_A and F_B is near zero in this solvent. It is more reasonable to attribute this result to a near equalization of conformation probabilities in toluene than to intrinsic changes in chemical shifts producing an accidental near-coincidence of F_A and F_B chemical shifts. These proposals are reminiscent of results obtained for substituted benzenes, as, for example, for benzyl alkyl ethers (29) where the conformations adopted are sensitive to substituent and solvent effects.

Comparisons with reported structures

In agreement with the observations in this paper, the structures of tris(monothio-β-diketonate) complexes of vanadium(III) (46), iron(III) (41, 47), cobalt(III) (46, 48), technetium(III) (49), ruthenium(III) (41), rhodium(III) (35, 41), and indium(III) (50) have all been reported as *fac*-octahedral. Similarly, bis(monothio-β-diketonates) of nickel(II) (41, 51–53), copper(II) (41), palladium(II) (41, 54), and platinum(II) (41, 54) have all been reported as *cis* square planar. On the other hand, tris complexes formed from unsymmetric β-diketones and cobalt(III) (46) or ruthenium(II) (55) adopt *mer*-octahedral, as well as *fac*-octahedral structures, with a preference for the *mer*-octahedral form of the cobalt(III) complex (46). Square planar complexes of copper(II) (56), palladium(II) (57–59), and platinum(II) (59) can adopt the *trans* as well as the *cis* form.

The preferred formation of *fac*-octahedral and *cis* square planar metal complexes from monothio-β-diketones has prompted the suggestion of weak nonbonding interactions between the sulfur atoms (46, 51). This proposal is consistent with the relatively short S···S distance (less than twice the van der Waals radius of sulfur) in a tris(monothio-β-diketonate) rhodium complex (1). In some complexes, the adoption of the *fac*-octahedral structure can also be assisted by better metal $d_\pi(t_{2g}) \rightarrow$ ligand π^* bonding between the metal and sulfur atoms when the three metal–sulfur bonds are mutually perpendicular. This is consistent with the observed shortening of the Rh—S bonds in a monothio-β-diketonate rhodium complex (1).

Conclusions

In acetone and toluene, tris(monothio-β-diketonates) of rhodium(III) exist as *fac*-octahedral complexes whereas

© 1999 NRC Canada

tris(β-diketonates) exist as nearly statistical mixtures of *fac*- and *mer*-octahedral complexes. The ^{19}F NMR spectra are consistent with rapid rotation of the pendant perfluoroalkyl groups.

Acknowledgements

We thank Dr. M. Das for gifts of the perfluorinated β-diketones, T. Wolowiec and M. Jang for recording the NMR spectra, C. Beaulieu for preparation of sample tubes, and the Natural Sciences and Engineering Research Council of Canada for financial support.

References

1. L.W. Tari, G.A. Stern, J.B. Westmore, and A.S. Secco. Acta. Crystallogr. Sect. C: Cryst. Struct. Commun. **C46**, 197 (1990).
2. L. Petrakis and C.H. Sederholm. J. Chem. Phys. **35**, 1243 (1961).
3. S. Ng and C.H. Sederholm. J. Chem. Phys. **40**, 2090 (1964).
4. R.J. Abraham and L. Cavalli. Mol. Phys. **9**, 67 (1965).
5. L. Cavalli and R.J. Abraham. Mol. Phys. **19**, 265 (1970).
6. L. Cavalli. J. Magn. Reson. **6**, 298 (1972).
7. D.F. Evans. Discuss. Faraday Soc. **34**, 139 (1962).
8. N. Boden, J. Feeney, and L.H. Sutcliffe. J. Chem. Soc. 3482 (1965).
9. K.L. Servis and J.D. Roberts. J. Am. Chem. Soc. **87**, 1339 (1965).
10. K.L. Williamson and B.A. Braman. J. Am. Chem. Soc. **89**, 6183 (1967).
11. M.L. Huggins. J. Am. Chem. Soc. **75**, 4123 (1953).
12. R.K. Harris and V.J. Robinson. J. Magn. Reson. **1**, 362 (1969).
13. N.F. Ramsey and E.M. Purcell. Phys. Rev. **85**, 143 (1952).
14. N.F. Ramsey. Phys. Rev. **91**, 303 (1953).
15. H.M. McConnell. J. Chem. Phys. **24**, 460 (1956).
16. M.J. Stephen. Proc. R. Soc. London Ser. A, **A243**, 274 (1957).
17. M. Karplus. J. Chem. Phys. **30**, 11 (1959).
18. H.S. Gutowski, M. Karplus, and D.M. Grant. J. Chem. Phys. **31**, 1278 (1959).
19. K. Hirao, H. Nakatsuji, H. Kato, and T. Yonezawa. J. Am. Chem. Soc. **94**, 4078 (1972).
20. K. Hirao, H. Nakatsuji, and H. Kato. J. Am. Chem. Soc. **95**, 31 (1973).
21. G.E. Maciel, J.W. McIver, N.S. Ostlund, and J.A. Pople. J. Am. Chem. Soc. **92**, 4151 (1970).
22. S.P.S. Porto. J. Mol. Spectrosc. **3**, 248 (1959).
23. W.F. Edgell, P.A. Kinsey, and J.W. Amy. J. Am. Chem. Soc. **79**, 2691 (1957).
24. R.D. Chambers, L.H. Sutcliffe, and G.J.T. Tiddy. Trans. Faraday Soc. **66**, 1025 (1970).
25. J. Hilton. J. Magn. Reson. **14**, 241 (1974).
26. C. Schumann and F. Cavagna. J. Magn. Reson. **18**, 172 (1975).
27. C.W. Haigh, J. Hilton, L.H. Sutcliffe, and G.J.T. Tiddy. J. Magn. Reson. **18**, 241 (1975).
28. S.L. Manatt and M.A. Cooper. J. Am. Chem. Soc. **99**, 4561 (1977).
29. T. Schaefer, W. Niemczura, C.-M. Wong, and K. Marat. Can. J. Chem. **57**, 807 (1979).
30. J.M. Miller, T.R.B. Jones, and G.B. Deacon. Inorg. Chim. Acta, **32**, L75 (1979).
31. E. Pitcher, A.D. Buckingham, and F.G.A. Stone. J. Chem. Phys. **36**, 124 (1962).
32. J.A. McCleverty and G. Wilkinson. J. Chem. Soc. 4200 (1964).
33. D.T. Haworth, J.W. Beery, and M. Das. J. Fluorine Chem. **20**, 599 (1982).
34. D.T. Haworth. J. Fluorine Chem. **26**, 331 (1984).
35. D.T. Haworth and M. Das. J. Fluorine Chem. **20**, 487 (1982).
36. M. Das and D.T. Haworth. J. Inorg. Nucl. Chem. **43**, 2317 (1981).
37. P.J. Toscano, C. Dettelbacher, J. Waechter, N.P. Pavri, D.H. Hunt, E.T. Eisenbraun, B. Zheng, and A.E. Kaloyeros. J. Coord. Chem. **38**, 319 (1996).
38. M. Das. Inorg. Chim. Acta, **48**, 33 (1981).
39. J.S. Martin, A.R. Quirt, and K.E. Worvill. The NMR program library. Daresbury Laboratory, Daresbury, U.K.
40. R.J. Abraham. The analysis of high resolution NMR spectra. Elsevier, New York. 1971.
41. M. Das, S.E. Livingstone, J.H. Mayfield, D.S. Moore, and N. Saha. Aust. J. Chem. **29**, 767 (1976).
42. J.E. Huheey, E.A. Keiter, and R.L. Keiter. Inorganic chemistry. Principles of structure. 4th ed. Harper Collins College Publishers, New York. 1993. p. 292.
43. T. Schaefer, C. Beaulieu, R. Sebastian, and G.H. Penner. Can. J. Chem. **68**, 581 (1990).
44. T. Schaefer, P. Hazendonk, and D.M. McKinnon. Can. J. Chem. **73**, 1387 (1995).
45. J.W. Emsley, J. Feeney, and L.H. Sutcliffe. High resolution nuclear magnetic resonance spectroscopy. Vol. 1. Pergamon Press, Oxford. 1965.
46. R.H. Holm, D.H. Gerlach, J.G. Gordon, and M.G. McNamee. J. Am. Chem. Soc. **90**, 4184 (1968).
47. B.F. Hoskins and C.D. Pannan. Inorg. Nucl. Chem. Lett. **11**, 409 (1975).
48. J. Ollis, M. Das, V.J. James, S.E. Livingstone, and K. Nimgirawath. Cryst. Struct. Commun. **5**, 679 (1976).
49. G. Bandoli, U. Mazzi, H. Spies, R. Münze, E. Ludwig, E. Uhlemann, and D. Scheller. Inorg. Chim. Acta, **132**, 177 (1987).
50. C. Sreelatha, V.D. Gupta, C.K. Narula, and H. Noth. J. Chem. Soc. Dalton Trans. 2623 (1985).
51. O. Siiman, D.D. Titus, C.D. Cowman, J. Fresco, and H.B. Gray. J. Am. Chem. Soc. **96**, 2353 (1974).
52. J. Sieler, P. Thomas, E. Uhlemann, and E. Höhne. Z. Anorg. Allg. Chem. **380**, 160 (1971).
53. D.C. Craig, M. Das, S.E. Livingstone, and N.C. Stephenson. Cryst. Struct. Commun. **3**, 283 (1974).
54. E.A. Shugam, L.M. Shkol'nikova, and S.E. Livingstone. Zh. Strukt. Khim. **8**, 550 (1967).
55. S. Aynetchi, P.B. Hitchcock, E.A. Seddon, K.R. Seddon, Y.Z. Yousif, J.A. Zora, and K. Stuckey. Inorg. Chim. Acta, **113**, L7 (1986).
56. P.-K. Hon, C.E. Pfluger, and R.L. Belford. Inorg. Chem. **5**, 516 (1966).
57. B. Wenclawiak, A.A. Pinkerton, and N.J. Terrill. Inorg. Chim. Acta, **149**, 213 (1988).
58. P.-K. Hon, C.E. Pfluger, and R.L. Belford. Inorg. Chem. **6**, 730 (1967).
59. S. Okeya, S. Ooi, K. Matsumoto, Y. Nakamura, and S. Kawaguchi. Bull. Chem. Soc. Jpn. **54**, 1085 (1981).

© 1999 NRC Canada

Time-reversal in NMR of solids[1]

Serge Lacelle

Abstract: The behavior of multiple spin dynamics under time-reversal excitation is investigated in strongly dipolar coupled spin networks. It is demonstrated that the typical physical intuition that NMR spectroscopists have of time-reversal in such systems is erroneous. By studying the equation of motion of the spin system in an infinite one-dimensional quantum spin chain with nearest-neighbor dipolar interactions and evolving under time-reversal excitation, a more appropriate physical picture emerges. Implications of these new findings are briefly discussed in the context of error propagation and teleportation in NMR quantum information processing.

Key words: time-reversal, NMR, nuclear spin dynamic, quantum information processing.

Résumé : On a étudié le comportement de la dynamique de spins multiples dans des conditions d'excitation à inversion de temps, dans des réseaux de spins couplés fortement dipolaires. On a démontré que l'intuition physique typique des spectroscopistes de la RMN, relative à l'inversion de temps dans de tels systèmes, est erronée. En étudiant l'équation de mouvement du système de spins, dans une chaîne de spins quantiques unidimensionnelle et infinie, comportant des interactions dipolaires avec le voisin le plus près et en évolution sous l'influence d'une excitation à inversion de temps, on observe une représentation physique plus appropriée. On discute brièvement des implications de ces nouvelles observations dans le contexte de la propagation et de la télécinétique des erreurs dans le traitement de l'information quantique en RMN.

Mots clés : inversion de temps, RMN, dynamique des spins nucléaires, traitement de l'information quantique.

[Traduit par la Rédaction]

1. Background

The second law of thermodynamics states that processes in isolated systems are possible only if the entropy increases or remains constant (1, 2). As a consequence, for real (i.e., irreversible) processes, entropy has been construed as "an arrow of time." Cosmological connotations and interpretations of this slogan abound in the popular and scientific literatures (3). In physical chemistry, the elimination of composition gradients by mutual diffusion and temperature gradients by thermal diffusion, as a function of increasing time, represent typical irreversible macroscopic behavior. However, reversibility is nevertheless possible on macroscopic scales; the "mixing-unmixing" experiment of E.L. Hahn (4) with glycerol and dye undergoing Couette flow in the annulus of two concentric cylinders is a case in point.

At the microscopic level, in classical mechanics Newton's equation of motion, $\boldsymbol{F} = m\mathrm{d}^2\boldsymbol{r}/\mathrm{d}t^2$, is invariant under the time-reversal operation, $t \rightarrow -t$. This symmetry implies that the inverse of a dynamical process is also a solution to Newton's equation (5). Likewise, in quantum mechanics (3, 6), time-reversal invariance is a property of the solutions to Schrödinger's time dependent equation, $i\hbar\partial\Psi(\boldsymbol{r}, t)/\partial t = H\Psi(\boldsymbol{r}, t)$. Thus, the reversible behavior of the equations of motion at the microscopic level appear superficially incompatible with the irreversible behavior observed on macroscopic scales.

This dichomotomy of macroscopic and microscopic behavior has occupied different generations of scientists over the last 130 years or so (7, 8). Numerous suggestions to resolve this apparent paradox have been proposed over time. Appeals to statistical mechanics have led the way to rationalize this problem. The dynamical equations of motion apply to individual microscopic states, while macroscopic behavior correspond to conditions of numerous microscopic states. Thus, in phase space, if an initial macroscopic condition is chosen to correspond to an "ordered state," with time the system will evolve in the direction of the more numerous "disordered states," which are compatible with the macroscopic constraints. Each of the microscopic trajectories that relate the macroscopic "ordered and disordered" states are dynamically reversible. However, since the final macroscopic state correponds to many more microscopic states than those found in the initial macroscopic state, the probability of observing a recurrence at the macroscopic level without external intervention, is prohibitively small indeed. For example, an estimate of Poincaré's recurrence time in dilute but macroscopic samples of gas with a number density

Received April 13, 1999.

This paper is dedicated to Professor Ted Schaefer in recognition of his outstanding contributions to Canadian chemistry.

S. Lacelle.[2] Département de Chimie, Université de Sherbrooke Sherbrooke, QC J1K 2R1, Canada.

[1]Presented in part at the Workshop for Quantum Information Processing and NMR at Harvard University, Cambridge, Mass., U.S.A., Feb. 22–24, 1999.

[2]Telephone: (829) 821-7823. Fax: (829) 821-8017. e-mail: slacelle@courrier.usherb.ca

© 1999 NRC Canada

of 10^{24} molecules/m^3 yields 10^{18} times the age of the universe (2). Hence, irreversibility observed on the macroscopic realm and reversibility of the microscopic dynamics are indeed compatible.

It is interesting to view NMR spin echoes in this context. In liquids of single or uncoupled spin systems, evolution in static inhomogeneous magnetic fields under the Hahn sequence, $90 - \tau - 180 - \tau$, produces an echo at 2τ for a system that was initially at thermal equilibrium. This behavior is understandable in terms of the deterministic dynamics of the spin isochromats if dissipation is lacking. Following the initial $\pi/2$ rf pulse, a free induction decay (FID) arises from the dephasing of the magnetization due to the differential precession in the spatially inhomogeneous magnetic field. A rewinding of the magnetization in the τ period subsequent to the π rf pulse, which reverses the sense of precession of the different isochromats, results in a spin echo at 2τ. In absence of dissipation, the entropy of the spin system remains constant, and the spin system recovers its initial nonequilibrium macroscopic state (i.e., the one following the initial $\pi/2$ rf pulse). The dynamical trajectories of the spin isochromats in the first and second τ periods are related by time-reversal symmetry; see for example the runners on a racetrack analogy of Brewer and Hahn (4).

Now consider rigid solids consisting of homonuclear dipolar coupled spin systems. In such instances, the Hahn sequence does not refocus the magnetization due to the bilinear character of the dipolar interactions among the spins. To obtain spin echoes, rf pulse sequences with propagators related by changes of signs in the Hamiltonians are needed.Thus, if in the first τ period, the spin density operator evolves under a dipolar Hamiltonian H, then at τ one finds,

$$[1] \qquad \rho(\tau) = U(\tau)\, \rho(0)\, U^{+}(\tau)$$

where $\rho(0)$ is the initial spin density operator, with

$$[2] \qquad U(\tau) = \exp\,(-iH\tau)$$

and $U^{+}(\tau)$ is the Hermitian conjugate of eq. [2]. In the second τ period, if the spin system evolves under a propagator $V(\tau)$ with a Hamiltonian $-H$, i.e., related by Hermitian conjugation to $U(\tau)$, then

$$[3] \qquad V(\tau) = \exp\,[-i(-H\tau)] = U^{+}(\tau)$$

As a consequence, the spin density operator at 2τ becomes

$$\begin{aligned}[4] \qquad \rho(2\tau) &= V(2\tau - \tau)\, \rho(\tau)\, V^{+}(2\tau - \tau) \\ &= V(\tau)\, U(\tau)\, \rho(0)\, U^{+}(\tau)\, V^{+}(\tau) \\ &= U^{+}(\tau)\, U(\tau)\, \rho(0)\, U^{+}(\tau)\, U(\tau) \\ &= \rho(0)\end{aligned}$$

since $U^{+}(\tau) = U^{-1}(\tau)$. Hence, the Hermitian conjugation relationship between the propagators in the first and second τ periods produces a spin echo in a dipolar coupled spin system. A change in the sign of the Hamiltonian would thus appear to be equivalent to time-reversal in the scheme of eq. [4].

Time-reversal excitation in NMR of solids was first suggested by Schneider and Schmiedel (9) as a possibility to observe FIDs of strongly dipolar coupled solids unencumbered by receiver dead-time limitations. It is noteworthy that this proposal originated from the curiosity of determining if it was possible to create an average dipolar Hamiltonian with a negative scaling factor.[3] Following this initial work, Rhim and Kesselmeier (10, 11), examined the consequences of such method with CW irradiation at the magic angle. Rhim et al. (12, 13) were the first to systematically implement and further elaborate pulse sequences with time-reversal excitation properties in solids. Initially, these experiments served to demonstrate the limitations of the spin thermodynamics approach, e.g., the FID of a strongly dipolar coupled spin system was viewed as an irreversible process during which the spin system achieved a quasi-equilibrium state. There was also initial hope that multiple pulse sequences, which exploited time-reversal excitation, could be tailored to achieve high-resolution in NMR of solids.

Fig. 1. Behavior of multiple-spin correlations or multiple quantum coherences (circles with radial filling) as a function of evolution time under $+H$ and $-H$, according to our typical preconceived notion of time-reversal with symmetric evolution and reversal.

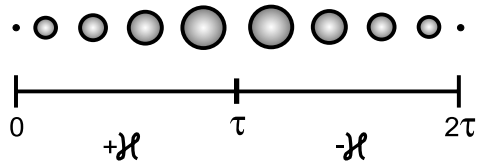

Further developments of time-reversal excitation procedures were proposed by Yen and Pines (14) in order to limit dipolar dephasing, which occurred during multiple quantum NMR experiments of solids. By using propagators for the preparation and mixing periods that were Hermitian conjugate to one another, the resulting multiple quantum coherences were generated and converted in such a way that in the corresponding spectra there was no cancellation of phases. Consequently, higher order multiple quantum coherences could be detected (indirectly) with greater ease in solids (15).

More recently, time-reversal excitation procedures have been devised to study a variety of polarization echoes (as opposed to coherence echoes) and transfers in homonuclear and heteronuclear spin systems in static and rotating solids (16–19). In these investigations, transfers of polarization through spin diffusion processes, multiple-spin order growth, and cross-polarization were all reversed, thereby showing the deterministic character of the many-body evolution in strongly dipolar coupled spin systems in absence of dissipation.

In view of this cultural background, the intuition of virtually every NMR spectroscopist of time-reversal excitation in dipolar coupled spin systems, corresponds to the cartoon depicted in Fig. 1. There, one observes the growth of multiple-spin correlations or multiple quantum coherences as a function of τ under $+H$ evolution. In the second τ period, evolution under $-H$ would produce a regression of growth to bring the system back to its initial state. Note the striking similarity of the behavior in Fig. 1 with the runners on a

[3] H. Schneider. Personal communication.

© 1999 NRC Canada

Fig. 2. Behavior of multiple-spin correlations or multiple quantum coherences (circles with radial filling for $0 < t < \tau$, and inverse radial filling for $\tau < t < 2\tau$) as a function of evolution time under $+H$ and $-H$, according to the time series expansion of the Liouville – von Neumann equation of motion for the spin density operator. The reciprocal relationship of the radial filling of the circles among the two evolution periods is to symbolize and emphasize the sign differences between the spin operators during these two time periods, and the ensuing time-reversal asymmetry.

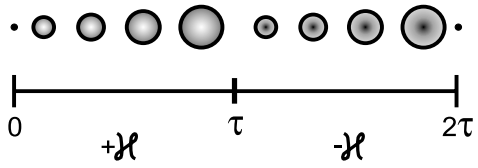

racetrack analogy of the spin echo in single or uncoupled spin systems (4). In the next section, I demonstrate that such physical intuition is wrong, and show the appropriate way to physically view the behavior of strongly dipolar coupled systems under time-reversal excitation. Two applications of this result in the context of quantum information processing in molecular systems are briefly discussed in Sect. 3. Finally, the last section summarizes our findings.

2. Results

A caricature of the physical intuition based on the result of the growth processes derived in this section for time-reversal excitation is shown in Fig. 2. One immediately notices the lack of the mirror image behavior, which is characteristic of the time-reversal interpretation in Fig. 1. Some consequences are obtained in this section, while some implications of Fig. 2 are discussed in the next section.

Our derivations are obtained from a model of an infinite one-dimensional (1-D) quantum spin chain with spins $I = 1/2$ and nearest-neighbor (nn) dipolar interactions. Initially at thermal equilibrium in a strong Zeeman field, the spin system is then driven by a propagator with a nonsecular average dipolar Hamiltonian, $H = H^{+2} + H^{-2}$, between 0 and τ, and $-H$ from τ to 2 τ; $H^{\pm 2}$ is a pure double quantum Hamiltonian given by

$$[5] \qquad H^{\pm 2} = -\frac{1}{2}\sum_{j<k} D_{jk}\, I_j^{\pm}\, I_k^{\pm}$$

with $I_j^{\pm}$ the raising and lowering spin angular momentum operators of spin j. The dipolar coupling constant, D_{jk}, between nearest-neighbor spins j and k is

$$[6] \qquad D_{jk} = D = \frac{\gamma^2 \hbar}{2 r_{jk}^3}(1 - 3\cos^2\theta_{jk})$$

with γ the magnetogyric ratio, r_{jk} the distance between spins j and k, and θ_{jk} the angle between the internuclear vector $\boldsymbol{r}_{jk}$ and the Zeeman field. The spin dynamics of this model were solved exactly for multiple quantum NMR experiments, and the theoretical results compared favorably to corresponding experiments on materials with quasi-1-D distributions of spins (20).

Instead of using the fermion field operator methodologies as in ref. 20, a Taylor series expansion of $\rho(\tau)$ about 0 and with $\rho(0) = I_Z$, and propagation under H will be performed for the first τ period. For the second evolution period, between τ and 2τ, the initial condition corresponds to $\rho(\tau)$, and the system is propagated under $-H$. The characteristics of the solutions of the Liouville – von Neumann equation (see eq. [1]) will become evident by examining just the first few orders of the expansion. The correspondence between the series expansion and the exact solution for this model has been verified in details in the limits when $\tau \to 0$, and when $\tau \to \infty$ in the context of multiple quantum NMR of 1-D quantum spin chains (20).

The series expansion of $\rho(\tau)$ in eq. [1] yields the nested commutator expansion,

$$[7] \qquad \rho(\tau) = \rho(0) - i\tau[H,\rho(0)] - \frac{\tau^2}{2}[H,[H,\rho(0)]] - i\frac{\tau^3}{6}[H,[H,[H,\rho(0)]]] + \ldots$$

Thus, for $\rho(0) = I_Z$, and $H = H^{+2} + H^{-2}$, one finds the evolution between 0 and τ with eq. [7],

$$[8] \qquad \rho(\tau) = I_z + iD\tau(I_j^+ I_{j+1}^+ - I_j^- I_{j+1}^-) - (D\tau)^2(I_j^+ I_{j+1}^z I_{j+2}^- - I_j^- I_{j+1}^z I_{j+2}^+) - i(D\tau)^3\frac{2}{3}(I_j^+ I_{j+1}^z I_{j+2}^z I_{j+3}^+ - I_j^- I_{j+1}^z I_{j+2}^z I_{j+3}^-) + \ldots$$

Implicit in this way of representing the solution $\rho(\tau)$ are sums over the lattice positions j, which are not shown explicitly. Furthermore, the growth of the multiple-spin coherences is symmetric in the lattice label (identified by subscripts on the spin operators) or direction, i.e., only the solutions in the direction of increasing j are shown explicitly in eq. [8], the corresponding solutions growing in the direction of decreasing j are not shown. This amounts to looking at the growth only along one direction of the chain. We also assume that $D\tau < 1$. As τ increases beyond the limit $D\tau = 1$, the violation of the inequality implies a breakdown of the successive approximation concept. In this limit, the question of convergence of the series expansion becomes questionable, and one needs to revert to the exact solution at the expense of simplicity in the mathematical treatment and in the physical reasoning, in order to verify the validity of the expansion in eq. [8] as was done in ref. 20. These simplifications change nothing of the spin dynamics and the results, but should help to lighten up the equations and the reasoning, so that only the essential physical characteristics of the solution remain.

Hence, with increasing time, one finds contributions from single-spin terms, two-spin terms, three-spin terms, ..., n-spin terms, ... which appear *sequentially* in eq. [8] with respective time dependence τ^0, τ^1, τ^2, ..., τ^{n-1}, ... This aspect of the solution is indicated graphically in Figs. 1 and 2 for the evolution between 0 and τ. Furthermore, each n-spin correlation is weighted by a product of $n - 1$ dipolar coupling constants; since only nn dipolar interactions are considered in the model, this product is D^{n-1}. Only zero- and two-quantum coherences are produced. There is also an obvious alterna-

© 1999 NRC Canada

tion between the zero- and two-quantum coherences, which leads to alternating and periodic oscillations of the intensities in the corresponding multiple quantum NMR spectra (20). Interestingly, the growth processes, induced by the average Hamiltonian H, occur by correlating a "new" spin at the (spatial) ends of the previous n-spin coherences, thereby producing $(n + 1)$-spin correlations.

The evolution of the spin system under $-H$ for the period from τ to 2τ proceeds from the initial condition given by eq. [8]. Introducing eq. [8] as initial condition into eq. [7] with $-H$ produces the solution for the second τ period; the time in this period is symbolized by t. To see how this solution comes about, we systematically calculate the different orders in an ascending fashion, starting with t^0. This corresponds to the same manner in which the different spin terms contribute to the solution as t increases between τ and 2τ. When $t = \tau$, a dipolar spin echo is produced.

The zeroth order contribution (t^0) is the initial condition given by the entire eq. [8]. Thus, the sum of all spin terms, which have been produced during the first τ period, is also present at the beginning of the second τ period, i.e., at $t = 0$.

The first-order contribution (t^1) is obtained by inserting I_Z from the initial condition (i.e., eq. [8]) into the first commutator in eq. [7]. This yields $it[H, \rho(0)]$. The sign of this contribution is the opposite of the corresponding two-spin term, which occurred during the first τ evolution period. Hence, for short time periods in both the first (τ) and second (t) period of evolution, these two-spin terms cancel, as it should be, since these are both the first multiple-spin terms to appear in each of these periods. Note that if the duration of the first period is τ, then to cancel exactly, the first-order contribution in the second period under $-H$ must also have a duration equal to τ. On the other hand, for a first evolution period of duration τ and for times $t < \tau$ during the second evolution period, a substantial cancellation will be produced initially only for the two-spin terms, as these are the ones that contribute the most at small t. To cancel higher order multiple-spin terms will require a longer evolution period, i.e., should occur on a time scale $t < t < \tau$, as these processes require higher orders of time to become observable.

The second-order contributions (t^2) come from two different sources. The first-order contribution $iD\tau(I_j^+I_{j+1}^+ - I_j^-I_{j+1}^-)$ from the initial condition (see eq. [8]), when inserted into the first-order commutator of eq. [7] with $-H$ yields $2D^2\tau t(I_j^+I_{j+1}^zI_{j+2}^- - I_j^-I_{j+1}^zI_{j+2}^+)$. The zeroth order contribution, I_Z from the initial condition (see eq. [8]), when inserted into the second-order commutator of eq. [7] with $-H$ produces $-(Dt)^2(I_j^+I_{j+1}^zI_{j+2}^- - I_j^-I_{j+1}^zI_{j+2}^+)$. Hence, the sum of the second-order contributions from the initial condition in eq. [8], i.e., $-(D\tau)^2(I_j^+I_{j+1}^zI_{j+2}^- - I_j^-I_{j+1}^zI_{j+2}^+)$, and the above terms generated under the $-H$ evolution, i.e., $2D^2\tau t(I_j^+I_{j+1}^zI_{j+2}^- - I_j^-I_{j+1}^zI_{j+2}^+)$, and $-(Dt)^2(I_j^+I_{j+1}^zI_{j+2}^- - I_j^-I_{j+1}^zI_{j+2}^+)$, will vanish identically only when the duration of the first and second evolution periods are identical, i.e., when $t = \tau$. However, when $t < \tau$, there is less cancellation of the three-spin terms due to the t^2-dependence, than the two-spin terms that have only a t-dependence.

Higher successive orders can be examined in a similar fashion, and taken to infinite order, the expansion would lead to the conclusion that $\rho(2\tau) = \rho(0) = I_Z$ as already noted from eq. [4]. However, we can already extract useful information and consequences from the behavior of the first few orders of the series expansion for time-reversal excitation.

As observed above, following an evolution period initially under a propagator with $+H$ and then $-H$, it is the lowest order terms that are the first ones to "disappear" to a very good approximation by mutual cancellation from both evolution periods. Consequently, the picture proposed in Fig. 2 is more appropriate to describe the behavior of a dipolar coupled spin systems evolving under time-reversal excitation.

Another important realization is the following: to cancel the contribution of a term of nth order (τ^n) produced during the $+H$ evolution period requires the contributions from all previous orders between τ^0 and τ^{n-1} during the $-H$ evolution. Furthermore, for times $\tau < \tau$ during the second evolution period, the different orders have the following time dependence, where the τ^r dependence arises from the second evolution period, while the τ^s dependence is inherited from the first evolution period: for the zeroth order terms, τ^0t^0; for the first-order terms, $t^0\tau^1$, $t^1\tau^0$; for the second-order terms, $t^0\tau^2$, $t^1\tau^1$, and $t^2\tau^0$; for the third-order terms, $t^0\tau^3$, $t^1\tau^2$, $t^2\tau^1$, and $t^3\tau^0$; and so on for higher order terms. When $t = \tau$, then each contribution to the nth order terms has the required τ^n dependence, and the sum of the different contributions to the nth order is identically zero, with the exception of the zeroth order $t^0\tau^0$, which is the sole survivor, thus yielding $\rho(2\tau) = \rho(0)$.

3. Discussion

The behavior of multiple-spin systems under time-reversal excitation as presented in the previous section imposes limitations on how one could possibly control such systems for quantum information processing purposes. In recent years, the field of quantum information processing has made major theoretical and experimental strides (21).[4] Through the manipulation of coherent superpositions of quantum states, there is the hope of exploiting quantum entanglements (nonseparable states), quantum interference, and parallelism in order to achieve potentially massive speedups in some computational tasks. Tremendous benefits, from skilful utilizations of quantum information in molecular systems, are also expected for technological issues related to miniaturization. Furthermore, in addition to the these features, the quantum computing paradigm offers the possibility to better understand quantum theory. Some excitement has been generated by these prospectives in NMR (22, 23). In this section, two applications, related to the behavior of quantum errors and quantum teleportation from the field of quantum information processing, are examined with the perspectives of taking advantage of time-reversal excitation in multiple-spin systems in these problems. Limitations imposed by the nature of the time-reversal behavior are discussed in light of the results from the preceeding section.

For a quantum computer to function successfully, some error correction and error prevention methodologies will be required due to the interactions of the quantum computer with the environment, and the inherent interactions among quantum bits (qubits) (21).[4] In a quantum computer's pro-

[4] J. Preskill. Unpublished lecture notes for a course on quantum computation, available from http://www.theory.caltech.edu/people/preskill/ph229/.

© 1999 NRC Canada

Fig. 3. The upper portion corresponds to the conventional scheme for quantum teleportation of an unknown quantum state ξ from Alice (A) to Bob (B) with channel resources for entanglement sharing (E) and classical communication (C). In the lower portion, both channels are replaced by a single channel, in this case, a 1-D quantum spin chain with nn dipolar interactions.

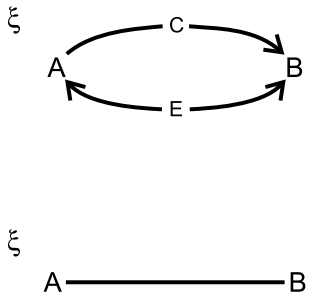

cessing and memory units, errors correspond to unwanted modifications in the amplitudes and the relative phases of coherent superpositions. Quite some efforts have already been dedicated toward such enterprise, and promising results have appeared (21)[4].

To control errors based on dipolar interactions among qubits in a quantum register of nuclear spins, we have strived at developing error correction and prevention strategies based on multiple pulse line narrowing sequences and time-reversal excitation.[5] As an illustration, imagine an ensemble quantum computer (22) consisting of an ensemble of 1-D infinite and rigid quantum spin chains with only nn dipolar interactions among spins on the same chain. If a computation, composed of quantum gates (combinations of rf pulses and evolution periods) is executed on such a system, with the simultaneous application of a multiple pulse line narrowing sequence in the background to eliminate dipolar interactions, after a period τ, one finds the quantum computer in the state QC(τ; ε_d). To remove determinisitic errors, ε_d, which might have accumulated due to residual dipolar interactions among qubits, one could imagine reversing only the part of the evolution due these interactions by using a time-reversal sequence (12, 13), thus producing QC(2τ). Hence, by alternating periods of computation with periods of error corrections, one could proceed to the final output of the computation.

Now suppose a nondeterministic error occurs, due to the interaction of a spin with the environment (i.e., a T_1 process) halfway ($\tau/2$) during a first evolution period under H in this system; moreover, assume that multiple-spin correlations involving from 2 to k spins have been excited at that point, and that the error appeared in the k-spin coherences. On further evolution, all higher order terms of n-spin coherences with $n \geq k$ become contaminated with the error. Thus, error propagation continues until τ, resulting in QC(τ, ε_k, ε_{k+1}, ε_{k+2},...), where the subscripts on the errors correspond to the size of the multiple-spin coherences in which they occur.

If a time-reversal sequence is applied for a second τ evolution period, it is interesting to calculate the effect of error propagation with both scenarios presented in Figs. 1 and 2. Halfway during the time-reversed period (i.e., at $3\tau/2$), one would find QC($3\tau/2$, ε_k) for the behavior dictated by the physical intuition based on Fig. 1. Due to the nondeterminisitic nature of the error, the time-reversal excitation sequence will not be able to correct the error ε_k. Further evolution would produce at 2τ, QC(2τ, ε_k, ε_{k-1}, ε_{k-2},...), i.e., the error would have propagated to n-multiple-spin coherences with $n \leq k$. Hence, refocusing is possible only for n-spin coherences with $n > k$. On the other hand, with the results obtained in the last section and depicted in Fig. 2, time-reversal excitation during the second evolution period would yield QC($3\tau/2$, ε_k) and QC(2τ, ε_k, ε_{k+1}, ε_{k+2},...) respectively at $3\tau/2$ and 2τ. Refocusing of the $n < k$ spin coherences would be possible, however, due to the error propagation, higher order ($n \geq k$) multiple-spin coherences could not be refocused.

Hence, in 1-D spin systems with nn dipolar interactions, error propagation to higher order multiple-spin correlations is a generic feature of multiple-spin dynamics. Current quantum error correcting strategies cannot deal with such detrimental behavior.[4] It would be interesting to determine the nature of error propagation in spin systems with $d = 1$ and dipolar interactions beyond nn, and for systems with $d > 1$. For systems with $d = 3$ and with full dipolar interactions, physical intuition would lead one to believe that sensitivity to initial conditions in the multiple-spin dynamics would produce error propagation from a single spin to many spins during evolution. A cellular automata model of this idea has been described for $d = 2$ spin systems with nn interactions (24).

Another potential application, where one could envision using time-reversal excitation in a spin system, is quantum teleportation (21)[4]. In this phenomenon, an unknown quantum state ξ is transported from one site A (Alice) to another B (Bob) by only exchanging information. The quantum teleportation protocol (see upper portion of Fig. 3) involves dual channels to allow information exchanges between Alice and Bob. In one channel, one spin each of an entangled pair of spins, such as $1/\sqrt{2}$ ($\alpha\alpha + \beta\beta$), is distributed to Alice and Bob. With the computational basis $0 = \alpha$, and $1 = \beta$, one can write the total state of the system (without the normalization constant) as $\xi_A(0_A0_B + 1_A1_B)$. This state can be expressed as $\phi^+_A\xi_B + \phi^-_A(\sigma_z\xi)_B + \psi^+_A(\sigma_x\xi)_B + \psi^-_A(-i\sigma_y\xi)_B$, where $\phi^\pm = (00 \pm 11)$ and $\psi^\pm = (01 \pm 10)$ correspond to the so-called Bell basis set, and σ_x, σ_y, and σ_z are the Pauli spin matrices. Alice makes a Bell measurement on her two particles (ξ and her spin of the entangled pair). Due to the orthogonality of the Bell basis set, the total state is collapsed by multiplying it with the conjugtate of the Bell state that Alice used, thus leaving Bob with its corresponding state $(\sigma\xi)_B$, where σ is either one of the Pauli matrices or the unit matrix. Alice then sends two bits of classical information to Bob through the classical channel (see upper portion of Fig. 3), telling him which Bell basis state she used, and then Bob obtains the state ξ by performing the appropriate conditional measurement, σ, on his particle. Thus, the quantum state ξ has been teleported from site A to site B. A NMR version of this protocol has been realized experimentally with three contiguous atoms using an ensemble quantum computer (i.e., with

[5] A. Blais and S. Lacelle. Unpublished work.

© 1999 NRC Canada

mixed states or a density matrix as opposed to pure states) (25).

In an effort to improve this teleportation scheme, one could imagine replacing both channels with a single channel (see lower portion of Fig. 3), along which entangled states and classical information would be transmitted. This would reduce the necessary transmission resources. Here, the single channel would be a 1-D quantum spin chain with nn dipolar interactions. Hence, teleportation could potentially be achieved over much longer distances than across three atoms.

The sharing of entangled states would be produced by driving the chain with $H = H^{+2} + H^{-2}$. By examining eq. [8], one finds that indeed, the growth of zero and double quantum coherences occurs only at the "ends" of the chain, so that in principle, it would be possible to bring to Alice and Bob each a spin from an entangled pair, i.e., a state of the form $(I_A^+ I_2^Z I_3^Z \ldots I_{n-1}^z I_B^+ - I_A^- I_2^Z I_3^Z \ldots I_{n-1}^z I_B^-)$ would connect Alice and Bob. Note that other double quantum/*k*-multiple-spin coherences, with $k < n$ would also be produced. To be more efficient, one could presumably devise a selective propagator for exciting only double quantum/*n*-multiple-spin coherences.[6]

Following the Bell measurement with mixed states, transmission of the classical information would be achieved by preparing a mixed state $(I_A I_{A'}, I_2^z I_3^z \ldots I_{n-1}^z I_B^z)$. In such a state, I_A and $I_{A'}$, spin states encoding one bit of information each, and I_B^z are produced by Alice and Bob who both use Stern–Gerlach type preparations to replace the end-atoms used in the entangled spin pair, which they received and retrieved from the *n*-multiple-spin coherence. Thus, by adding the prepared atoms $I_A I_A$ and I_B^z at their respective ends of the remaining $I_2^z I_3^z \ldots I_{n-1}^z$ chain state, and then time-reversing the evolution of this new state with some $-H$, according to the scenario of Fig. 1, a recession of growth in the opposite direction of the chain would be expected. In the end, Bob could receive Alice's bits of information. However, as shown in the previous section, time-reversal excitation proceeds according to the scenario displayed in Fig. 2, so that motion-reversal as proposed in Fig. 1 is not a valid method to transmit information.

At this point, some skeptical readers might be wondering "Where's the chemistry in these applications?" The chemical physics aspects consist of controlling and processing quantum information at the microscopic level, and its measurements and observation at the macroscopic level, with NMR methodologies in chemical systems.

4. Concluding remarks

As NMR spectroscopists, our interpretation of time-reversal excitation in strongly dipolar coupled spin systems is initially based on our previous experiences with spin echoes of single spin systems, reversibility, and irreversibility in macroscopic systems. Due to this cultural foundation, our physical intuition normally leads our preconceived notions to a mental picture like the one depicted in Fig. 1 in order to imagine and interpret the time-reversal of multiple-spin excitations. However, as shown in this work, in order to be consistent with the Liouville – von Neumann equation of motion, the manner in which time-reversal excitation proceeds in strongly dipolar coupled spin systems is more appropriately described by Fig. 2. As a result, attempts to exploit time-reversal excitation procedures, such as demonstrated with quantum error propagation and quantum teleportation in quantum information processing, should be based on the physically correct results associated and represented by Fig. 2. Finally, as an example of another potential avenue, our work suggests the possibility of devising a method in order to discriminate between multiple-spin correlations of different sizes, and thereby achieving a certain degree of selectivity towards higher multiple-spin correlations by using periods of time-reversal excitation with unequal durations[7] when relying on the behavior shown in Fig. 2 as a physical basis.

Acknowledgments

This paper is dedicated to Prof. T. Schaefer, one of the pioneers of NMR in chemistry in Canada. His work helped to open the way for other generations of NMR spectroscopists with different perspectives (as exemplified by the work presented here) and who collectively produce a rich and vibrant tapestry of NMR contributions to Canadian sciences. I would like to thank Prof. A. Pines and A. Blais for their suggestions, and Dr. L. Tremblay for his help with the figures. This work was supported by a grant from the Natural Sciences and Engineering Research Council of Canada.

References

1. I.N. Levine. Physical chemistry. 4th ed. McGraw–Hill, New York. 1995. pp. 95–97.
2. R.S. Berry, S. Rice, and J. Ross. Physical chemistry. John Wiley & Sons, New York. 1980. pp. 625–626, 636–643.
3. P.C.W. Davies. The physics of time asymmetry. University of California Press, Berkeley. 1977.
4. R.G. Brewer and E.L. Hahn. Sci. Am. **251**, 50 (1984).
5. A.P. French. Newtonian mechanics. W.W. Norton & Company, New York. 1971. pp. 178–180.
6. A. Peres. Quantum theory: concepts and methods. Kluwer Academics, Dordrecht. 1995. pp. 258–259, 341–346.
7. J.L. Lebowitz. *In* Lecture notes in physics, 25 years of nonequilibrium statistical mechanics. *Edited by* J.J. Brey, J. Marro, J.M. Rubi, and M. San Miguel. Vol. 445. Springer-Verlag, Berlin. 1995. pp. 1–20; Phys. Today, **46**, 32 (1993).
8. R.C. Tolman. The principles of statistical mechanics. Oxford University Press, Oxford. 1938. pp. 152–155, and refs. therein.
9. H. Schneider and H. Schmiedel. Phys. Lett. **30A**, 298 (1969).
10. W.K. Rhim and H. Kesselmeier. Phys. Rev. **B3**, 3655 (1971).
11. H. Kesselmeier and W.K. Rhim. Phys. Rev. **B5**, 761 (1972).
12. W.K. Rhim, A. Pines, and J.S. Waugh. Phys. Rev. Lett. **25**, 218 (1970).
13. W.K. Rhim, A. Pines, and J.S. Waugh. Phys. Rev. **B3**, 684 (1971).
14. Y.S. Yen and A. Pines. J. Chem. Phys. **78**, 3579 (1982).
15. J. Baum, M. Munowitz, A.N. Garroway, and A. Pines. J. Chem. Phys. **83**, 2015 (1985).

[6] A. Pines. Personal communication.
[7] A. Blais. Personal communication.

© 1999 NRC Canada

16. S. Zhang, B.H. Meier, and R.R. Ernst. Phys. Rev. Lett. **69**, 2149 (1992).
17. M. Tomaselli, S. Hedinger, D. Suter, and R.R. Ernst. J. Chem. Phys. **105**, 10 672 (1996).
18. S.M. De Paul, M. Tomaselli, A. Pines, M. Ernst, and B.H. Meier. J. Chem. Phys. **108**, 826 (1998).
19. M. Ernst, B.H. Meier, M. Tomaselli, and A. Pines. J. Chem. Phys. **108**, 9611 (1998).
20. E.B. Fel'dman and S. Lacelle. J. Chem. Phys. **107**, 7067 (1997).
21. C.H. Bennett. Phys. Today, **48**, 24 (1995).
22. D.G. Cory, A.F. Fahmy, and T.F. Havel. Proc. Natl. Acad. Sci. U.S.A. **94**, 1634 (1997).
23. N.A. Gershenfeld and I.L. Chuang. Science (Washington, D.C.), **275**, 350 (1997).
24. S. Lacelle. Adv. Magn. Opt. Res. **16**, 171 (1991).
25. M.A. Nielsen, E. Knill, and R. Laflamme. Nature (London), **396**, 52 (1998).

© 1999 NRC Canada

Electrospray ionization mass spectrometry and on-line capillary zone electrophoresis – mass spectrometry for the characterization of citrate synthase

Mark E. McComb, Lynda J. Donald, and Hélène Perreault

Abstract: The enzyme citrate synthase from *E. coli* is a protein with a molecular weight (M_r) of 47 885 Da (wild type). This enzyme has been studied extensively, and its amino acid sequence has been characterized. This model protein has been used in this work for development and validation of methods involving capillary electrophoresis (CE) and electrospray ionization mass spectrometry (ESI-MS). The M_r determinations were conducted using sample infusion ESI-MS, and the tryptic digestion products of wild-type citrate synthase were characterized by on-line CE–ESI-MS coupled with a sheathless interface. On-line experiments were conducted on two different mass spectrometers, a Quattro-LC triple quadrupole instrument equipped with a Z-Spray™ source (Micromass), and a reflecting time-of-flight (TOF) mass spectrometer built in-house in the Time-of-Flight Laboratory, Department of Physics, University of Manitoba. This is the first article to be written on the interfacing of a Z-Spray™ source with CE. Unmodified fused silica capillaries gold-coated sheathless interfaces were used. The on-line CE separations yielded theoretical plate numbers greater than 10^4 on average. Selected ion electrophorograms (SIE) of the tryptic peptides recorded on the Quattro-LC displayed *S*/*N* ratios ranging from ca. 14 to 120 on raw data. These SIE enabled identification of each peptide. The use of reflecting time-of-flight mass spectrometry (TOFMS) afforded mass resolution values of ca. 6000 ($m/\Delta m_{FWHM}$), which enabled isotopic resolution of the peptide components. CE–ESI-MS and CE–ESI-TOFMS experiments enabled the generation of a complete tryptic map of citrate synthase.

Key words: capillary electrophoresis, electrospray ionization, mass spectrometry, citrate synthase, tryptic digestion, triple quadrupole analyzer, time-of-flight analyzer.

Résumé : L'enzyme synthase du citrate, extraite d'*E. coli*, est une protéine de poids moléculaire (M_γ) de 47 885 Da. On a étudié cet enzyme de façon exhaustive et on a caractérisé sa séquence d'acides aminés. Cette protéine modèle a été utilisée dans ce travail réalisé pour développer et valider des méthodes impliquant l'électrophorèse capillaire (EC) et la spectrométrie de masse avec ionisation par électrovaporisation (« SM-IES »). Les déterminations de M_γ ont été effectuées en faisant appel à SM-IES par une infusion de l'échantillon et on a caractérisé les produits obtenus par digestion enzymatique de la synthase de citrate à l'aide de la trypsine en faisant appel à la SM-IES couplée à l'EC en ligne à l'aide d'une interface sans liquide de support. Les expériences en ligne ont été réalisées sur deux spectromètres de masse différents, un spectromètre de masse Quattro-LC muni d'un analyseur à triple quadripôle équipé d'une source Z-Spray™ et un spectromètre de masse à temps d'envol (« TOF ») muni d'un réflecteur construit dans le Time-of-Flight Laboratory du département de physique, de l'Université du Manitoba. Il s'agit du premier article publié sur le couplage d'une source Z-Spray™ avec un appareil d'EC. Des capillaires de silice fondue non modifiés et des interfaces sans liquide de support, plaquées or, ont été utilisées. En moyenne, les séparations EC en ligne donnent lieu à un nombre de plateaux théoriques supérieur à 10^4. Dans les électrophorogrammes d'ions présélectionnés (EIP) des peptides obtenus par hydrolyse à la trypsine, enregistrés sur le spectromètre de masse Quattro-LC, les rapports *S*/*B* s'étalent d'environ 14 à 120 sur les données brutes. Ces EIP ont permis d'identifier chacun des peptides. L'utilisation du spectrométrie de masse à temps d'envol (SM-TOF) muni d'un réflecteur permet d'obtenir des valeurs de résolution de masse d'environ 6000 ($m/\Delta m_{FWHM}$), ce qui rend possible la résolution isotopique des composants peptidiques. Les expériences de EC–SM-IES et de EC–SM-TOF-IES ont permis de générer une carte tryptique complète de la synthase du citrate.

Received February 24, 1999.

This paper is dedicated to Professor Ted Schaefer in recognition of his outstanding contributions to Canadian chemistry.

M.E. McComb, L.J. Donald, and H. Perreault.[1] Chemistry Department, University of Manitoba, Winnipeg, MB R3T 2N2, Canada.

[1]Author to whom correspondence may be addressed. Telephone: (204) 474-7418. Fax: (204) 474-4608.
e-mail: perreau@cc.umanitoba.ca

 © 1999 NRC Canada

Mots clés : électrophorèse capillaire, ionisation par électrovaporisation, spectrométrie de masse, synthase du citrate, digestion à la trypsine, analyseur à triple quadripôle, analyseur à temps d'envol.

[Traduit par la Rédaction]

Introduction

Mass spectrometry (MS) has been described as one of three key technologies available to probe cell proteins and to correlate the latter to their genes (1). Direct identification of proteins may be accomplished using a combination of enzymatic proteolysis, liquid chromatographic or capillary electrophoretic (CE) separations, and MS. Sample infusion electrospray ionization mass spectrometry (ESI-MS) and on-line CE–ESI-MS are now well implemented techniques in several laboratories specializing in protein and peptide analysis, and have been used in this work to confirm the molecular weight (M_r) and amino acid sequence of a biologically important enzyme, citrate synthase.

On-line CE–ESI-MS is a powerful method for the analysis of biological molecules, particularly proteins (2, 3). CE offers high-resolution separations, typically with theoretical plate counts ranging from 10^5 to 10^6, while ESI-MS allows for the characterization of a wide M_r range of peptides and proteins. On-line CE–ESI-MS allows for the analysis of exceedingly small volumes of solution, i.e., on the order of a few tens of nanoliters, which is advantageous, considering that sample sizes may be limited when dealing with biological materials.

Development of on-line methods and validation of their performance both require that these methods be tested with known compounds. A substance of choice for validation of the on-line CE–ESI-MS described in this article is citrate synthase, a protein of medium molecular weight (M_r = 47 885 Da, wild type). This protein was chosen as a model based on prior characterization by electrospray ionization time-of-flight mass spectrometry (ESI-TOFMS) (4) and matrix-assisted laser desorption/ionization time-of-flight mass spectrometry (MALDI-TOFMS) (5).

The use of different types of CE–MS interfaces has been discussed previously. Several groups have used a sheathless ESI design, which affords a stable electrospray and is relatively easy to manufacture (6–12). In this approach, electrical contact at the capillary terminus is provided through a conductive coating, typically gold. The same gold surface is used for production of the electrosprayed ions. Enhanced sensitivity, as well as the elimination of mixing problems associated with a sheath liquid, make the sheathless design favourable, and justify the use of this type of interface in the work presented here.

In the general analytical approach described in this article, mass spectra of intact citrate synthase were acquired first to obtain M_r information, and more complete mass spectral characterization was performed on tryptic peptides by on-line CE–ESI-MS. For these on-line experiments, a Quattro-LC triple quadrupole mass spectrometer (Micromass) and a home-built reflecting time-of-flight mass spectrometer were used.

It should be noted that this article is the first to describe the implementation of CE–MS using the Micromass Z-Spray™ source. Although Major and Ashcroft (13) reported on the use of a coaxial sheathflow CE–MS interface to analyze a standard peptide mixture on a Micromass Quattro-II instrument, this article constitutes the first report on sheathless CE–MS involving a Quattro-LC instrument. The detailed description of the interfacing process will be given in a publication that is currently in preparation.[2]

Experimental

Chemicals

Acetic acid (99.9985%) was used to make up solutions of the running electrolyte and was obtained from Alfa Aesar (Wordhill, Mass.). Hydrofluoric acid (HF), used to prepare the capillaries, was obtained from Fisher (Nepean, Ont.). Trypsin (TCPK treated), used for the digestion, was obtained from Sigma.

Citrate synthase

The protein was prepared from *E. coli* as described (14). Both the wild type and a mutant, L164A, were made available by Ayed and Duckworth (15). Samples for direct infusion ESI-MS measurements were dialyzed into 5 mM ammonium bicarbonate at pH 7.5 as described in an earlier publication (4). It should be noted that the calculated M_r value for wild-type citrate synthase derived from the SWISS-PROT sequence[3] is misleading, due to the following modifications: loss of N-terminal M, post-translational modification N11D (16), and sequencing error F289V (17). With these modifications, the M_r calculated for the wild-type protein is 47 885 Da. Thus, the calculated M_r value for the L164A mutant is 47 843 Da.

Tryptic digest of wild-type citrate synthase

The protein (1.0 mg/mL in 20 mM Tris–HCl and 1 mM EDTA, pH = 7.8) was incubated with 0.01 mg/mL TPCK-treated trypsin for 3 h at 37°C. It should be noted that dialysis (4) was omitted for citrate synthase samples subjected to enzymatic digestion.

Capillary zone electrophoresis

Fused silica capillaries with 50 μm i.d. and 350 μm o.d. were supplied by Polymicro Technologies (Phoenix, Ariz.). The total length of the capillaries used in this study was 40 cm. Capillary electrophoresis was performed using a Spellman CZE 1000R 30 kV power supply (Plainview, N.Y.) operated in the positive polarity mode. The electrospray potential at the cathodic end of the capillary was generated us-

[2] M.E. McComb and H. Perreault. In preparation.
[3] http://www.expasy.ch/sprot-yop.html

© 1999 NRC Canada

ing an EG&G Ortec no. 459 5 kV bias supply (Oak Ridge, Tenn.) operated in the positive polarity mode. Acetic acid (1–10% in water) was used as the running electrolyte.

Preparation of gold-coated capillaries

Preparation of the capillaries is described in detail elsewhere (18). In brief, the capillaries used for on-line CE–ESI-MS were prepared based on the sheathless ESI approach. Approximately 1 cm of the capillary terminus was etched in 40% HF to make a conical end. The capillary end was then cleaned with methanol and coated with gold by vapour deposition.

Sample-infusion ESI-MS

Direct sample infusion ESI-MS of citrate synthase was performed on a q-TOF instrument located at the Micromass factory (Micromass Inc., Manchester, U.K.). Spectra were acquired using a cone (declustering) voltage of 60 V.

CE–ESI-MS

These experiments were performed on a Quattro LC (Micromass, U.K.) mass spectrometer equipped with a Z-Spray™ interface. Spectral analysis was carried out using Mass-Lynx 3.0 software. Spectra were obtained using 8 points/Da with a scan rate of 500 Da/s over a 1000 Da range. This resulted in acquisition rate of 0.5 spectrum/s and yielded monoisotopic (unit mass) resolution within the mass range scanned. Electrospray was performed using an interface built in-house, complete details of which will be presented in a separate publication.[2] A 60 s hydrodynamic injection was used to load the sample onto the capillary, resulting in approximately 800 fmol of sample being introduced into the capillary.

CE–ESI-TOFMS

These experiments were performed on a reflecting TOF mass spectrometer, an instrument built in-house in the Time-of-Flight Laboratory, Physics Department, University of Manitoba. Spectral analysis was carried out using TOFMA software written in-house. Spectra were recorded in 2 ns channels. The instrument (19, 20) and interface (18) have been described in greater detail elsewhere. For these measurements, it was possible to acquire a complete mass spectrum at each time interval, but not to record it. The total ion electrophorogram (TIE) was thus recorded in one run, separately from the mass spectra. The latter were recorded in a subsequent run, over the duration of the whole CE separation, and summed over 1 min segments, to produce a total of ca. 20 spectra. The technology necessary to realize simultaneous acquisition of TIE and mass spectral data for large data sets associated with CE–MS (12, 21) is currently being installed. Implementations will include software design and storage capabilities.

Results and discussion

CE–ESI-MS and CE–ESI-TOFMS

The M_r measurements on different types of citrate synthase can be effected very efficiently by sample infusion ESI-MS, as shown in Fig. 1. The nominal M_r difference of 42 between the two types, wild type (*a*) and the L164A mutant (*b*), reflects the substitution of a leucine residue by alanine. The M_r measurements yielded 47 887.9 Da for wild-type citrate synthase, and 47 845.5 Da for the mutant. The corresponding calculated values (average mass) are 47 884.95 and 47 842.87, respectively. The error on these measurements is thus of the order of 40–60 ppm.

To characterize wild-type citrate synthase further, a 3 h tryptic digest was performed and the resulting peptides analysed by on-line CE–ESI-MS and CE–ESI-TOFMS. For both analyses, the injection volume was ca. 40 nL (by gravity), and the protein concentration was ca. 2×10^{-5} M resulting in ca. 800 fmol of each peptide being injected. The background electrolyte, 5% acetic acid, was chosen to minimize interaction of the peptides with the negatively charged silanol groups on the inner walls of the fused-silica capillary and to favour protonation of the analytes.

The TIE obtained by analyzing the tryptic digest on the Micromass triple quadrupole mass spectrometer is shown in Fig. 2*a*. Because of the large number of peptides present and the abundant chemical background associated with the separation buffer used, very little information could be obtained from the TIE, which exhibits a S/N value ≤5. Moreover, the S/N of this TIE trace was compromised by the presence of contaminants in the CE electrolyte. A reconstructed TIE excluding signals from impurities would feature a considerably higher S/N value. It should be noted that these results are the first to be published on the use of on-line CE–ESI-MS with a Z-Spray™ source for the characterization of a "real life" sample, and that the interface has not been fully optimized. We have used this interface to analyze standard peptide mixtures (22), and S/N values obtained were between 5 and 40 (TIE), with 400 fmol of the peptides being injected. Other reports on the use of sheathless interfaces give the following values: $S/N = 4$ on 4 fmol of myoglobin (23), $S/N = 5$ on 300 amol of leucine-enkephalin (24), and $S/N > 20$ on 30 fmol of digested cytochrome c (9). It is expected that our interface will allow for similar sensitivity levels once fully optimized.[2] The TIE obtained by CE–ESI-TOFMS of another citrate synthase digest was similar to that of Fig. 2*a*. The performance of the CE–ESI-TOFMS setup has been characterized (18) as yielding S/N values ≥30 in the TIE on 230 fmol of standard peptides.

Citrate synthase has a total of 44 possible tryptic cleavage sites. A large number of peptides may thus be obtained from a single digestion, which in turn provides for a difficult separation. However, it is possible to gain useful information on the peptide through selected reconstructed ion electrophorograms (SIE) as shown in Fig. 2*b*. The SIE traces thus obtained allow detection of single peptides among other components, thus facilitating their mass spectral identification. In total, 44 SIE were obtained with S/N varying from ca. 14 to 120 on raw data (not all shown). Additional peptides were identified from the digest, but due to poor signal intensity, they were not included here. The most intense signals were obtained for $[M + H]^+$ and $[M + 2H]^{2+}$ ions of peptides. The electrophoretic efficiency was relatively high, with theoretical plate counts (N) from ca. 8000 (m/z 633.4) to ca. 88 000 (m/z 540.9). The N values of less than 50 000 are attributed to peptide adsorption on bare fused silica, and to the use of an acidic separation buffer (5% acetic acid). Moreover, the Tris buffer used to perform the digestion has a

© 1999 NRC Canada

Fig. 1. Electrospray mass spectra of citrate synthase, obtained by direct sample infusion on: (*a*) wild type, (*b*) L164A mutant. The insets show the transformed data.

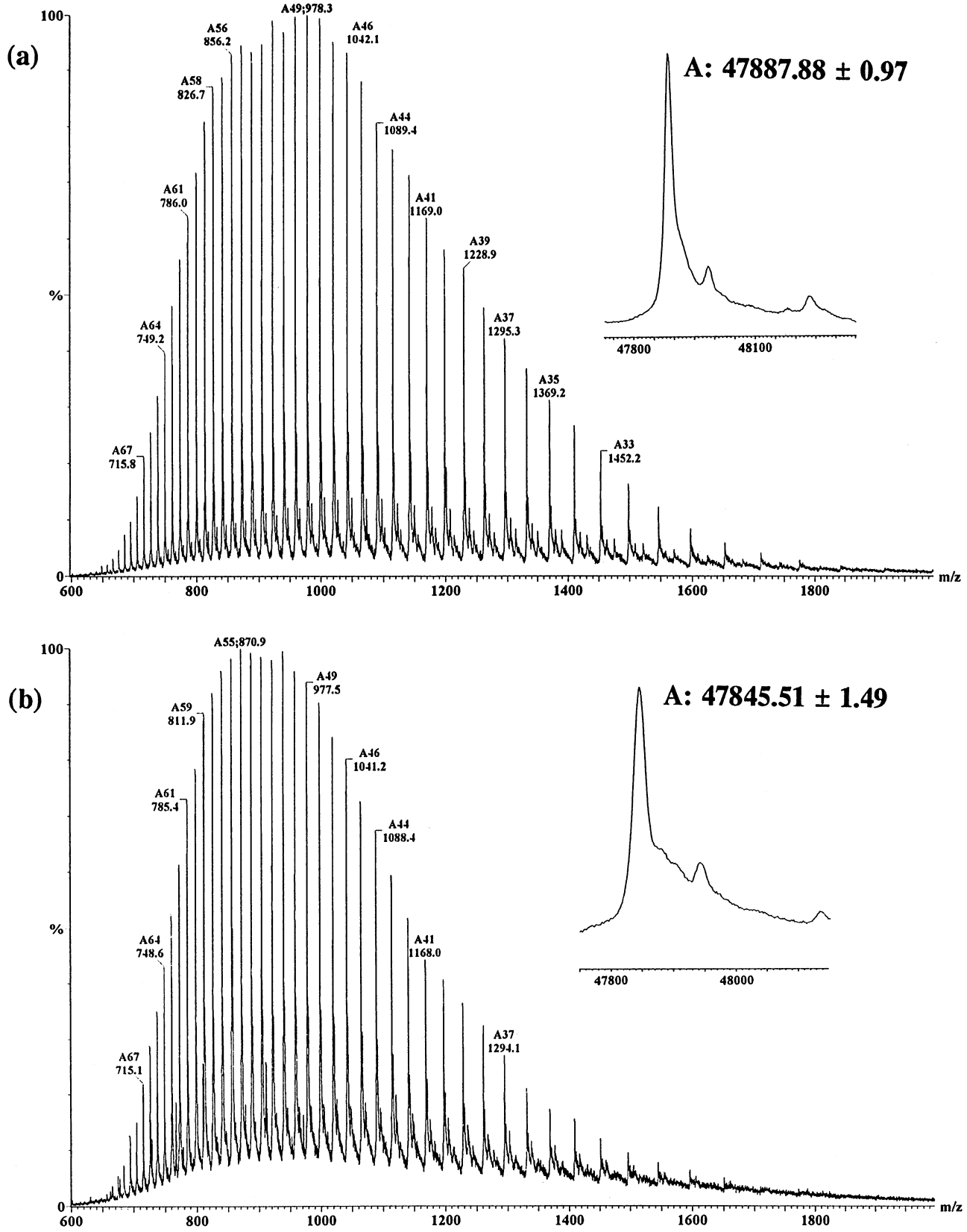

© 1999 NRC Canada

Fig. 2. On-line CE–ESI-MS electrophorograms obtained for the tryptic digestion products of wild-type citrate synthase. (*a*) Total ion electrophorogram (TIE), and (*b*) some selected reconstructed ion electrophorograms (SIE).

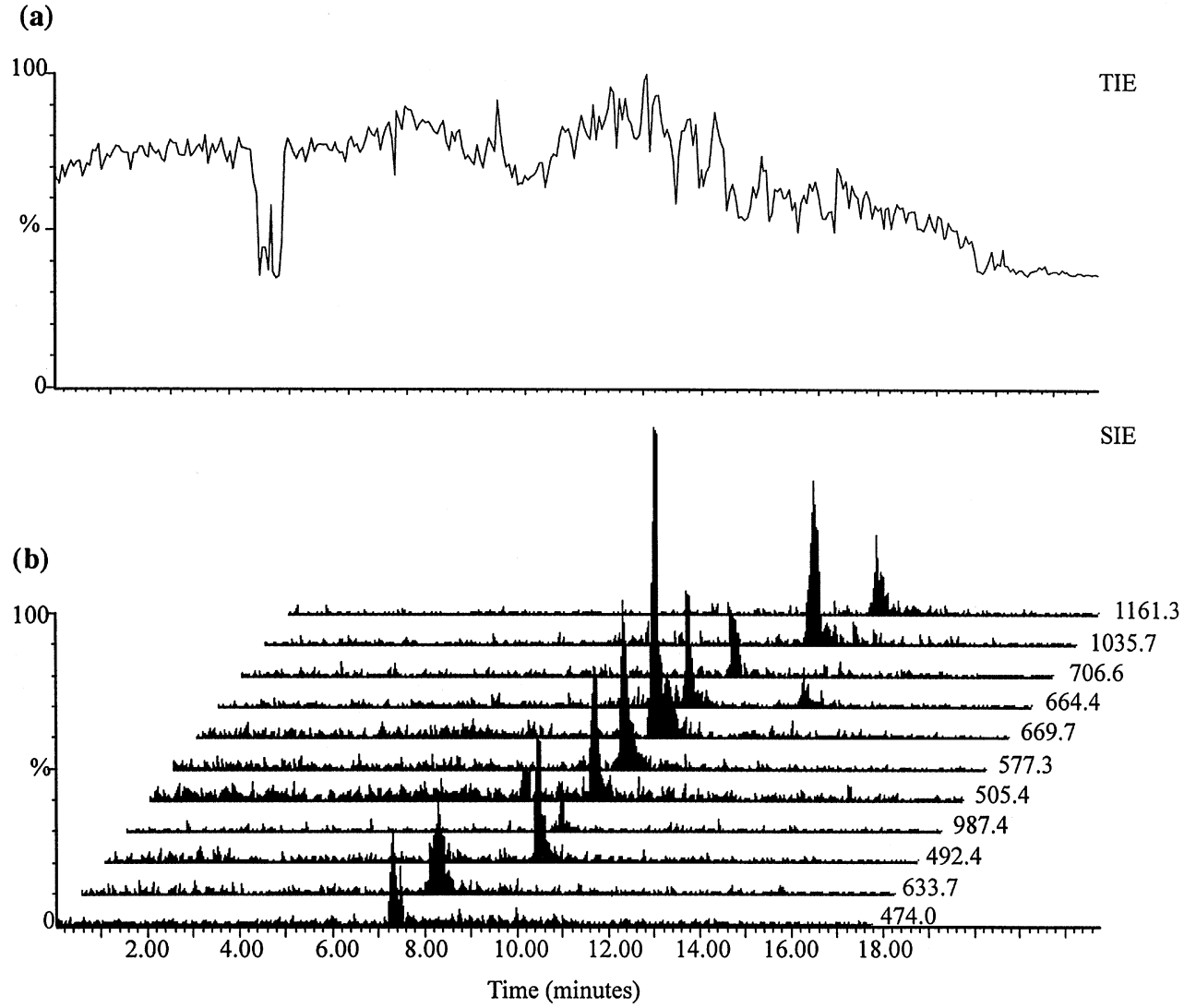

higher conductivity than 5% acetic acid, and thus sample stacking (isotachophoresis) will not have occurred. In general, the electrophorograms were reproducible in terms of migration order of the tryptic peptides, and average *N* values on CE peaks. The results presented here in Fig. 2 are representative of the CE–ESI-MS system used.

Some comparisons between the mass spectra (raw data) obtained on the two mass spectrometers are presented in Fig. 3. The mass resolution was superior with the TOF mass spectrometer than with the Quattro-LC instrument, and high resolution facilitated the assignment of multiply charged fragment ions. This performance was typical of the ESI-TOF instrument (19, 20) with mass resolution $\approx 6000(m/\Delta m_{FWHM})$, enabling baseline isotopic resolution. In comparison, the triple quadrupole analyzer was tuned for unit mass resolution. Although lower, the extent of resolution still allowed the identification of the peptides over the mass range investigated, albeit with more difficulty in the case of higher charge states. In general, sensitivity was higher on the TOF instrument than on the triple quadrupole instrument, and comparable CE efficiency was obtained on the two mass spectrometers (18).

Table 1 shows *S*/*N* and theoretical plate count values derived from three SIE traces shown in Fig. 3 (*m*/*z* 577.3, 633.4, and 1035.7). The mass spectra of the three peptides corresponding to these traces are shown in Fig. 3 (*b*, *d*, *f*). These values were typical of the peptides observed on the Quattro-LC. The comparative spectra in Fig. 3 (*a*, *c*, *e*) were obtained by CE–ESI-TOFMS.

A mass spectrum was obtained from each SIE, resulting in the identification of 44 tryptic fragments. These were tentatively identified and matched with literature values as shown in Table 2. It is noted that a few peptides were observed from their SIE, with *S*/*N* values less than 5, and were therefore not included in Table 2. In some cases, molecular ions corresponding to two charge states were observed for a single peptide, and these results were confirmed by similar SIE for each charge state. The charge states of molecular

© 1999 NRC Canada

Fig. 3. Comparison of mass spectral data obtained by on-line CE–MS obtained using the CE–ESI-TOFMS system (*a*, *c*, *e*) and the CE–ESI-MS (triple quadrupole) instrument (*b*, *d*, *f*).

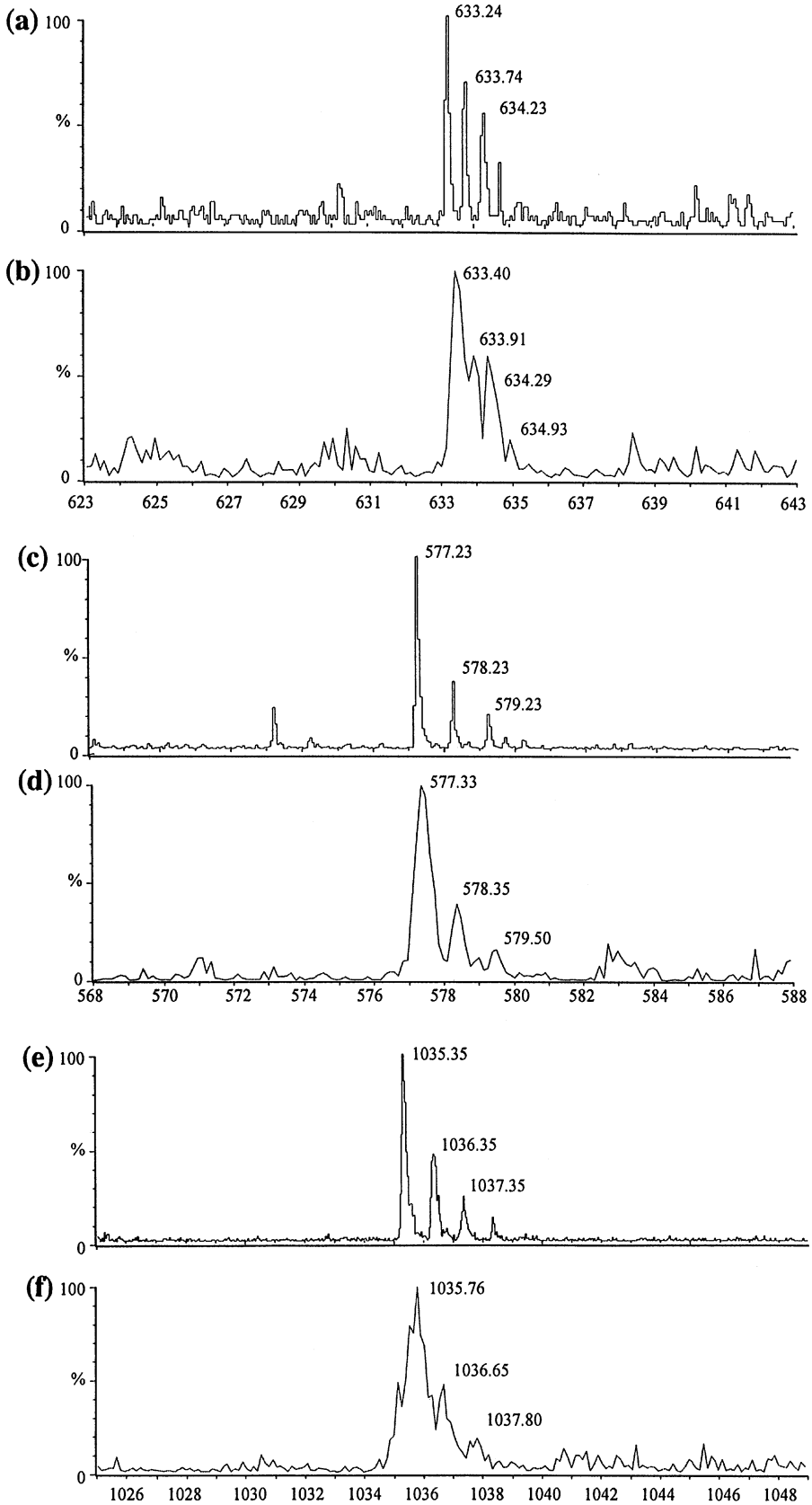

© 1999 NRC Canada

Table 1. Separation parameters for on-line CE–ESI-MS of the tryptic peptides of wild-type citrate synthase using a triple quadrupole mass spectrometer. Values are from Figs. 2 and 3.

Tryptic peptide	m/z	M_t (min)	FWHM (min)	N^a	S/N (SIE)^b
9	577.3	9.84	0.16	20953	53.1
10	633.4	7.81	0.21	7663	54.91
23	1035.7	12.01	0.22	16510	37.88

[a] $N = 5.54(M_t/\text{FWHM})^2$.

[b] $S/N = S/\text{RMS}$.

Table 2. Tryptic fragments of wild-type citrate synthase.

Tryptic fragment	Sequence	Calculated mass $[M + nH]^{n+}$	Observed mass $Q^3[M + nH]^{n+}$	n	% error	Observed mass TOF$[M + nH]^{n+}$	n	% error
1	1–4	434.23	434.3	1	0.01			
11–12	120–126	474.07	474	2	0.01			
20	218–221	492.22	492.4	1	0.04			
43–45	419–426	505.08	504.9	2	0.04			
5	33–37	505.08	505.4	1	0.06			
25–29	290–306	509.84	509.0	4	0.16			
24–25	283–290	527.62	527.3	2	0.06	527.23	2	0.07
40–41	405–417	532.62				532.20	3	0.08
26–28	291–299	541.09	540.9	2	0.04	538.22	2	0.53
9[a]	105–109	577.66	577.3	1	0.06	577.23	1	0.07
32[a]	315–319	577.73	577.3	1	0.07	577.23	1	0.09
40	405–409	612.75	613.9	1	0.19	612.28	1	0.08
25–28	290–299	619.18				618.24	2	0.15
10	110–119	633.74	633.4	2	0.05	633.24	2	0.08
39	388–404	658.42	658.3	3	0.02			
41–44	410–425	664.75	664.2	3	0.08			
31	310–314	664.70	664.4	1	0.05			
21	222–239	669.41	669.7	3	0.04			
32–34	315–332	682.81	682.2	3	0.09			
15	158–163	706.82	704.4	1	0.34	704.22	1	0.37
24–28	283–299	706.14	706.6	3	0.07			
22	240–273	785.88	786.1	4	0.03	784.20	4	0.21
11	120–125	790.94	791.5	1	0.07			
5–6	33–55	790.21	791.4	3	0.15			
16–17	164–177	795.04	795.2	2	0.02			
40–41	405–417	798.43	800.2	2	0.22	799.79	2	0.17
29–32	300–319	804.96	803.6	1	0.17			
25–30	290–309	809.61	811.4	3	0.22			
29	300–306	817.99	817.6	1	0.05	817.27	1	0.09
37	357–370	821.97	822.2	2	0.03	821.30	2	0.08
27–29	293–306	840.95	840.95	2	0.01			
19	189–217	842.46	841.0	4	0.01			
36–37	356–370	886.06	885.8	2	0.03			
6–7	38–69	886.47	886.5	4	0.00			
12–14	126–157	889.26	890.2	4	0.11			
24	283–289	898.05	897.6	1	0.05	897.37	1	0.08
38	371–387	916.14	916.5	2	0.04			
26–29	291–306	940.57	941.2	2	0.11	940.73	2	0.02
6	38–55	941.53	941.6	2	0.04			
23–29	274–306	983.90	982.0	4	0.19	984.30	4	0.04
39	388–404	987.13	987.4	2	0.03			
2–4	5–32	990.80	990.7	3	0.01			
21	222–239	1003.62	1003.9	2	0.03	1002.85	2	0.08
43–45	419–426	1009.15				1008.35	1	0.08
23	274–282	1036.24	1035.7	1	0.05	1035.35	1	0.09

© 1999 NRC Canada

Table 2 (*concluded*).

Tryptic fragment	Sequence	Calculated mass $[M + nH]^{n+}$	Observed mass $Q^3[M + nH]^{n+}$	*n*	% error	Observed mass TOF$[M + nH]^{n+}$	*n*	% error
22	240–273	1047.51	1047.5	3	0.00	1045.08	3	
24–25	283–290	1054.24				1053.41	1	0.08
33–36	320–356	1073.99	1073.7	4	0.03			
26–28	291–299	1081.17				1080.34	1	0.08
31–33	310–327	1082.25				1081.85	2	0.04
26–30[a]	291–309	1135.82				1136.84	2	0.09
23–26[a]	274–292	1135.86				1136.84	2	0.09
37–38[a]	357–387	1152.40	1152.9	3	0.04			
2–5[a]	5–37	1152.99	1152.9	3	0.01			
8–9	70–109	1161.29	1161.3	4	0.00			
4	22–32	1187.34				1186.40	2	0.08
18	178–188	1327.53				1326.39	1	0.09

[a]Peaks indicated may be assigned to more than one peptide.

ions observed on the two instruments varied. This was due, presumably, to different ESI and declustering potentials and different interface designs.

Fewer peptides were readily observed and identified in the TOF mass spectra, because not every possible spectrum could be obtained individually out of 1 min segments. Peptides with low *S*/*N* spectra were likely obscured by other abundant components or baseline noise. Also, the samples run by CE–ESI-MS and CE–ESI-TOFMS were digested separately and at different times, using enzymes from different batches. However, the ESI-TOFMS data obtained complemented the results obtained with the LC-Quattro and enabled complete characterization of the digest. In three cases, the assignments were ambiguous and could not be confirmed due to peptides that had similar *m*/*z* values, i.e., T9 and T32 at *m*/*z* 577.66 and 577.73. It was not possible to differentiate these peptides based on mass alone. Further characterization would require digestion with a different enzyme or the use of sequencing methods, which we are currently investigating. The use of tandem MS on-line with CE is also under investigation.

The *m*/*z* values in Table 2 indicate lower accuracy for CE–ESI-TOFMS measurements than for CE–ESI-MS experiments, due mainly to calibration drift of the TOF instrument, which may be corrected as long as calibrants are run immediately prior to analysis. In our case, the drift occurred during the time required to condition the system. Also, calibration was performed using sample infusion, which could have caused discrepancies vs. the use of CE introduction.

Mapping of the proteolytic fragments is useful for positive identification of the protein by database searching. Figure 4 shows the tryptic peptide map of synthase citrate based on the results shown in Table 2. A complete peptide map was obtained based solely on the CE–ESI-MS results, with the exception of Tryptic Fragment no. 19, which was observed only with the ESI-TOF mass spectrometer. The *m*/*z* values of the most intense singly charged peaks were used to perform an on-line database search, in order to investigate the possibility of identifying the protein using the peptide information alone. The search parameters were as follows: protein name: unknown; M_r range: 40 kDa ± 20%; species: *Escherichia coli*; peptide masses: 492.4, 505.4, 577.3, 613.9, 664.4, 791.5, 795.2, 822.2, 897.6, 1035.7; minimum number of peptides to match: 4; enzyme: trypsin; missed cleavage sites: 2; cysteine: reduced form. The search was performed on Feb. 8, 1999, SWISS-PROT Release 37, and updates up to Feb. 5, 1999: 78 197 entries. The search produced one protein match: score: 0.5; no. peptide matches: 6; accession no.: P00891; ID: CISY-ECOLI; description: CITRATE SYNTHASE (EC 4.1.3.7). The search was performed in less than 1 min on-line and resulted in a correct match for the protein studied. We note that a combination of limited search parameters must be used in order to minimize the number of results from the search. Eliminating the species name and M_r range of the intact protein resulted in over 100 search results, which would make the correct identification of the protein much more difficult.

Conclusions

ESI-MS using sample infusion produces very indicative values for the M_r of two very closely related citrate synthase species, the wild type and a mutant. On-line CE–ESI-MS and CE–ESI-TOFMS produced significant results for the separation and analysis of tryptic peptides of wild-type citrate synthase. It should be emphasized that CE–MS analyses were performed on nonpurified protein samples, which traditionally require extensive buffer exchange via dialysis prior to further characterization. This article is the first to demonstrate the coupling of sheathless CE with the Z-Spray™ ESI interface on the Micromass Quattro LC triple quadrupole mass spectrometer and its use for characterization of a large enzyme. We have confirmed the usefulness of on-line CE–MS, as performed on two different mass spectrometers, in enabling the complete sequence elucidation of wild-type citrate synthase.

Acknowledgments

We thank the members of the Time-of-Flight Laboratory, especially K.G. Standing and W. Ens, for helpful discussions, and for use of the ESI-TOF instrument. We express our thanks to R. Bordoli who obtained the q-TOF spectra by sample infusion at the Micromass factory. We acknowledge the Natural Sciences and Engineering Research Council of

© 1999 NRC Canada

Fig. 4. Citrate synthase map, generated with on-line CE–MS results. The assignments are based on values given in Table 2.

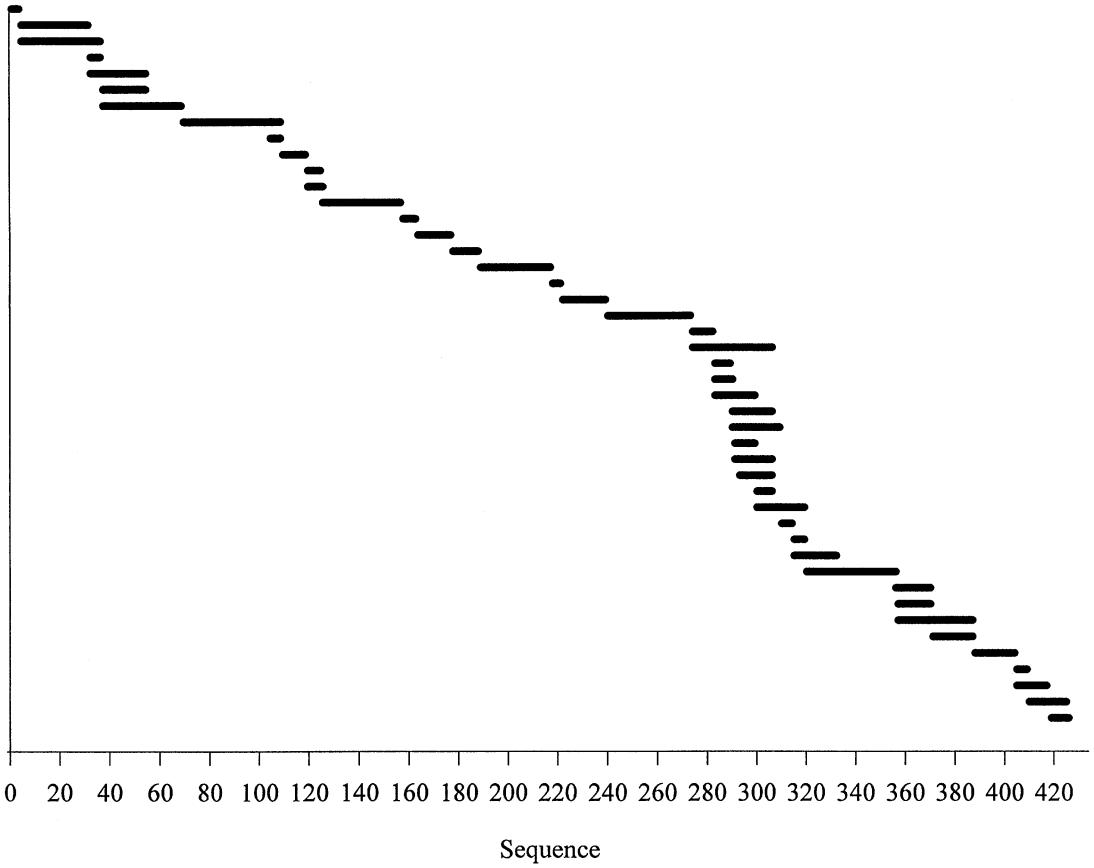

Canada (NSERC) for financial support, and the University of Manitoba for a graduate scholarship awarded to M.E. McComb. We sincerely thank H.W. Duckworth and A. Ayed for providing the citrate synthase samples.

References

1. J.R. Yates III. J. Mass Spectrom. **33**, 1 (1998).
2. J.C. Severs and R.D. Smith. *In* Handbook of capillary electrophoresis. *Edited by* J.P. Landers. CRC Press, New York. 1997. p. 791.
3. J.C. Severs and R.D. Smith. *In* Electrospray ionization mass spectrometry, fundamentals, instrumentation and applications. *Edited by* R.B. Cole. John Wiley & Sons, Inc., New York. 1997. p. 343.
4. A. Ayed, A. Krutchinski, W. Ens, K.G. Standing, and H.W. Duckworth. Rapid Commun. Mass Spectrom. **12**, 339 (1998).
5. M.E. McComb, R.D. Oleschuk, D.M. Manley, L.J. Donald, A. Chow, J.D.J. O'Neil, H.W. Duckworth, W. Ens, K.G. Standing, and H. Perreault. Rapid Commun. Mass Spectrom. **11**, 1716 (1997).
6. J.A. Olivares, N.T. Nguyen, C.R. Yonker, and R.D. Smith. Anal. Chem. **59**, 1230 (1987).
7. M.S. Kriger, K.D. Cook, and R.S. Ramsey. Anal. Chem. **67**, 385 (1995).
8. R.S. Ramsey and S.A. Mcluckey. J. Microcolumn Sep. **7**, 461 (1995).
9. J.H. Wahl, D.C. Gale, and R.D. Smith. J. Chromatogr. A, **659**, 217 (1994).
10. K.P. Bateman, R.L. White, and P. Thibault. Rapid Commun. Mass Spectrom. **11**, 307 (1997).
11. J.T. Wu, M.G. Qian, M.X. Li, L. Liu, and D.M. Lubman. Anal. Chem. **68**, 3388 (1996).
12. D.C. Muddiman, A.L. Rockwood, Q. Gao, J.C. Severs, H.R. Udseth, and R.D. Smith. Anal. Chem. **67**, 4371 (1995).
13. H.J. Major and A.E. Ashcroft. Rapid Commun. Mass Spectrom. **10**, 1421 (1996).
14. H.W. Duckworth and A.W. Bell. Can. J. Biochem. **60**, 1143 (1982).
15. A. Ayed and H.W. Duckworth. Protein Sci. **8**, 1116 (1999).
16. V. Bhayana and H.W. Duckworth. Biochemistry, **23**, 2900 (1984).
17. D.H. Anderson and H.W. Duckworth. J. Biol. Chem. **263**, 2163 (1988).
18. M.E. McComb, A.N. Krutchinsky, W. Ens, K.G. Standing, and H. Perreault. J. Chromatogr. A, **800**, 1 (1998).
19. I.V. Chernushevich, W. Ens, and K.G. Standing. *In* Electrospray ionization mass spectrometry, fundamentals, instrumentation and applications. *Edited by* R.B. Cole. John Wiley & Sons, Inc., New York. 1997. p. 203.
20. A.N. Verentchikov, W. Ens, and K.G. Standing. Anal. Chem. **66**, 126 (1994).
21. M.G. Quan, J. Wu, S. Parus, and D.M. Lubman. Rapid Commun. Mass Spectrom. **10**, 1209 (1996).
22. M.E. McComb, A.N. Krutchinski, W. Ens, K.G. Standing, and H. Perreault. Proc. 45th ASMS Conf. Mass Spectrom. Allied Topics, Orlando, Fla. May 31 – June 4, 1998. p. 1269.
23. P. Cao and M. Moini. J. Am. Soc. Mass Spectrom. **8**, 561 (1997).
24. D. Figeys, I. van Oostven, A. Ducret, and R. Aebersold. Anal. Chem. **68**, 1822 (1996).

© 1999 NRC Canada

NMR and molecular structure of partially oriented mono and *para* methyl- and chlorobenzenes dissolved in nematic liquid crystals

Raymond T. Syvitski and E. Elliott Burnell

Abstract: Spectral parameters, order parameters, and structural parameters, including the vibrationally corrected r_α structure of the partially oriented solutes *p*-xylene, *p*-chlorotoluene, *p*-dichlorobenzene, toluene, and chlorobenzene dissolved in three liquid crystal mixtures, are reported. For samples containing the three solutes *p*-xylene, *p*-dichlorobenzene, and 1,3,5-trichlorobenzene, multiple quantum (MQ) nuclear magnetic resonance was used to aid in the analysis of the complex high-resolution spectra of the *p*-xylene. The high-resolution spectra of 1,3,5-trichlorobenzene and *p*-dichlorobenzene were easily identified and analyzed once the calculated *p*-xylene spectrum was subtracted from the experimental one. The methyl groups of *p*-xylene, *p*-chlorotoluene, and toluene have similar geometries when the structure is determined from dipolar couplings corrected for harmonic vibrations.

Key words: nematic liquid crystal, NMR, molecular structure, order parameter.

Résumé : On a déterminé les paramètres spectraux, d'ordre et structuraux, y compris la structure r_α vibrationnellement corrigée de solutés partiellement orientés (*p*-xylène, *p*-chlorotoluène, *p*-dichlorobenzène, toluène et chlorobenzène) dissous dans trois mélanges de cristaux liquides. Pour les échantillons contenant le *p*-xylène, le *p*-dichlorobenzène et le 1,3,5-trichlorobenzène comme solutés, on a utilisé la résonance magnétique nucléaire à multiples quantum (MQ) comme aide dans l'analyse du spectre complexe du *p*-xylène à haute résolution. Les spectres à haute résolution du 1,3,5-trichlorobenzène et du *p*-dichlorobenzène sont facilement identifiables et on peut les analyser directement dès que le spectre calculé du *p*-xylène est soustrait du spectre expérimental. Les groupes méthyles du *p*-xylène, du *p*-chorotoluène et du toluène possèdent des géométries semblables quand on détermine la structure à partir des couplages dipolaires corrigés pour les vibrations harmoniques.

Mots clés : cristal liquide nématique, RMN, structure moléculaire, paramètre d'ordre.

[Traduit par la Rédaction]

1. Introduction

The NMR spectra of solute molecules dissolved and orientationally ordered in liquid-crystalline solvents can provide a wealth of valuable information. For example, this is one of the few methods available for obtaining accurate molecular structures in the liquid phase. In addition, directional properties such as anisotropies of chemical shifts and indirect spin–spin coupling constants, as well as dipolar and quadrupolar coupling constants, are measurable (1–3). Moreover, the average second-rank orientational order parameters that can be calculated from the dipolar or quadrupolar couplings provide information about the anisotropic intermolecular forces that are responsible for the orientational ordering (4).

There is general consensus that molecular size- and shape-dependent short-range interactions represent the dominant mechanism that is responsible for orientational ordering in nematic liquid crystals. However, additional interactions are known to be present, and their precise description is a matter of current controversy (4). Because the orientational ordering is dominated by short-range effects, it seems appropriate to choose for study probe solutes that have very similar sizes and shapes; differences in orientational order parameters might then reflect the effects of the additional, weak interactions. Hence, in this paper, we report on proton NMR experiments on a series of similar-shaped solutes in nematic liquid crystals. To compare results among solute molecules in as equivalent a manner as possible, several solutes are dissolved in the same sample tube. The manner in which we deal with the added complexity caused by superimposed spectra of several partially oriented solutes is one primary focus of this paper, and is discussed below in the section on spectral analysis. The other primary focus is the use of the dipolar couplings obtained from the spectra to determine vibrationally corrected molecular structures for the probe

Received February 22, 1999.

This paper is dedicated to Professor Ted Schaefer in recognition of his outstanding contributions to Canadian chemistry.

R.T. Syvitski and E.E. Burnell.[1] Department of Chemistry, University of British Columbia, 2036 Main Mall, Vancouver, BC V6T 1Z1, Canada.

[1]Author to whom correspondence may be addressed. Telephone: (604) 822-2603. Fax: (604) 822-2847. e-mail: elliott.burnell@ubc.ca

© 1999 NRC Canada

Fig. 1. The experimental high-resolution spectrum *C* is of Sample no. 8, partially oriented *p*-xylene–*p*-dichlorobenzene–TCB in 55 wt.% ZLI 1132–EBBA at 299 K. Spectrum *B* is the calculated spectrum of *p*-xylene from the fit to spectrum *C*. Spectrum *A* is a subtraction of the calculated from the experimental spectrum. Since experimental lines had a broad base, the subtraction was performed using a calculated spectrum in which the line shape is the addition of two Lorentzians with line broadenings of 1 and 4 Hz. Note that resonances corresponding to the external lock signal (acetone-d_6 in a capillary tube), TCB, and *p*-dichlorobenzene are clearly visible in the top spectrum. In the experimental spectrum *C*, the rolling base line, which is approximately 50 kHz wide, is from the liquid crystal. Lines from the TCB triplet have been truncated.

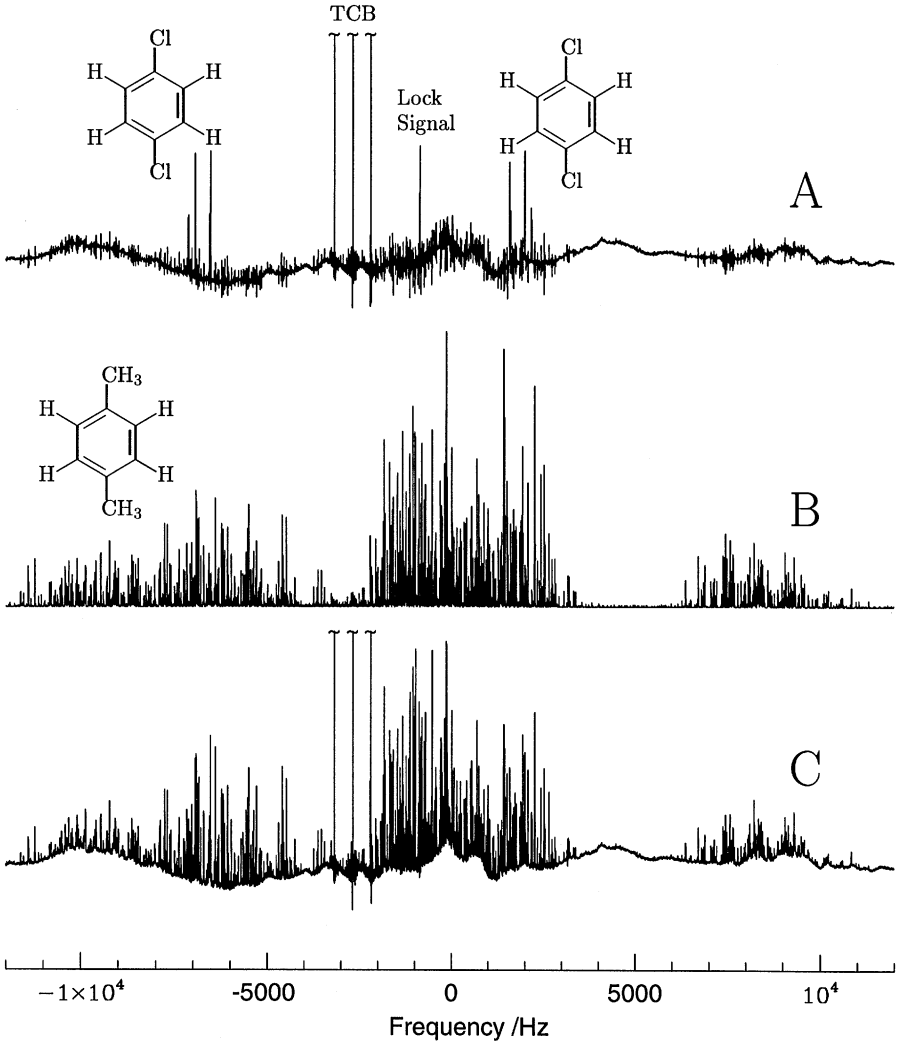

solutes. A detailed discussion of the order parameters that have not been corrected for the effects of molecular vibrations appears elsewhere (5).

The complexity of high-resolution NMR spectra of partially oriented molecules, and thus the ability to determine accurately spectral parameters such as chemical shifts and nuclear coupling constants from such spectra, depends on the flexibility and symmetry of the molecules and on the number and type of nuclear spins. For example, the proton NMR spectrum of complex liquid crystal molecules is typically broad and featureless and therefore impossible to analyze accurately; the rolling base line in the experimental spectrum of Fig. 1*C* is from the liquid crystal. Nuclear quadrupolar couplings from deuterium spectra (6) (and, in favorable cases, nuclear dipolar couplings from proton spectra (7–12)) of randomly or specifically deuterated molecules can be determined easily. However, these compounds are not readily available (the synthesis of a wide variety of such molecules is very time consuming and problematic (13)), and the accuracy of order parameters determined from such spectra is far less than that obtained from high-resolution proton NMR. As a consequence, it is common to utilize small protonated solute molecules for precise NMR studies involving liquid-crystalline solvents. Unfortunately, even with small solutes that contain ≥6 spins, determining spectral parameters from high-resolution spectra can be extremely difficult. In such cases, the use of two-dimensional multiple-quantum (MQ) NMR spectroscopy (14–16) is very helpful, since there are comparatively fewer lines in the spectra (17–22). However, the use of MQ spectra is not entirely straightforward; the intensities depend on both spectral and experimental parameters in such a complicated manner that they are not normally used for the analysis. In addition, care must be taken so that an incorrect and therefore mean-

© 1999 NRC Canada

Table 1. Solute and solvent sample composition.

Sample no.	Solutes	Liquid crystal solvent
1	Toluene–chlorobenzene–TCB[a]	ZLI 1132[b]
2	Toluene–chlorobenzene–TCB[a]	55 wt.% ZLI 1132–EBBA
3	Toluene–chlorobenzene–TCB[a]	EBBA
4	*p*-Chlorotoluene–*p*-dichlorobenzene–TCB[a]	ZLI 1132[b]
5	*p*-Chlorotoluene–*p*-dichlorobenzene–TCB[a]	55 wt.% ZLI 1132–EBBA
6	*p*-Chlorotoluene–*p*-dichlorobenzene–TCB[a]	EBBA
7	*p*-Xylene–*p*-dichlorobenzene–TCB[a]	ZLI 1132[b]
8	*p*-Xylene–*p*-dichlorobenzene–TCB[a]	55 wt.% ZLI 1132–EBBA
9	*p*-Xylene–*p*-dichlorobenzene–TCB[a]	EBBA

[a]TCB refers to the internal orientational standard 1,3,5-trichlorobenzene that was utilized for the scaling method described in ref. 5. Total solute concentration was <10 mol%.

[b]See ref. 23 for chemical composition.

ingless "fit" is not obtained. Nevertheless, the analysis is far easier than for the normal high-resolution spectra.

An additional problem with MQ NMR is the technical limitation that leads to spectra with broad peaks and therefore poor resolution. Thus, although the relatively few number of lines in the MQ spectrum can be advantageous, spectral parameters are not determined with high accuracy. Therefore, parameters determined from MQ spectra are used only as a starting point when analyzing high-resolution spectra. Despite the poor resolution of the MQ spectra, often only minor adjustments to parameters determined from such spectra are required in order to obtain a fit to the high-resolution spectrum (see refs. 19–22). High-resolution spectra can have many hundreds of lines, and thus, obtaining erroneous spectral parameters from a well fit spectrum is extremely unlikely.

Unlike microwave or electron diffraction data, dipolar couplings can provide accurate relative proton positions; by combining structural data from liquid crystal NMR and from microwave or from electron diffraction studies, it is possible to determine accurate molecular structures. However, since molecular vibrations affect the observed results, data should be vibrationally corrected before determining such structures. In this study, we analyze MQ and high-resolution proton NMR spectra of the partially oriented probe solutes: *p*-xylene, *p*-chlorotoluene, *p*-dichlorobenzene, toluene, and chlorobenzene. We determine spectral parameters, molecular order parameters, and internuclear distances, including the vibrationally corrected r_α structure for these solute molecules. It is interesting that there is variation in the methyl group geometries reported in the literature for this series of methylbenzenes. The technique used here (NMR spectroscopy of the five orientationally ordered solutes in the three nematic liquid crystal mixtures: Merck ZLI 1132 (see ref. 23 for chemical composition), 55 wt.% ZLI 1132–EBBA, and *N*-(*p*-ethoxybenzylidene)-*p*′-*n*-butylaniline (EBBA)) is an ideal tool for the investigation of such an interesting result.

2. Experiment

The nematic liquid crystal Merck ZLI 1132 and all solutes were used without further purification. The liquid crystal EBBA was synthesized (24) and purified by recrystallization from cold methanol. Each of nine samples was prepared by dissolving three solutes in one of the liquid crystal solvents: ZLI 1132, 55 wt.% ZLI 1132–EBBA, or EBBA. The composition of each sample is given in Table 1.

Proton NMR spectra of the nine samples were acquired at 299.6 ± 0.5 K on a Bruker AMX-500 spectrometer. Acetone-d_6 in a coaxial capillary provided the deuterium lock. For high-resolution proton NMR spectra, 32K point FIDs were acquired after a single pulse, zero filled to 64K points and processed using a Lorentzian line broadening of 1.0 Hz. Half-height line widths for these high-resolution spectra were typically 2–3 Hz. The spectrum obtained from Sample no. 8 is presented in Fig. 1, with an expanded region in Fig. 2. For samples containing *p*-xylene (Sample nos. 7–9, Table 1) two-dimensional MQ interferograms were acquired using the pulse sequence (25, 26)

$$[1]\qquad \left(\frac{\pi}{2}\right)_\phi - - - \tau - - - \left(\frac{\pi}{2}\right)_\phi - - - t_1 - - - \left(\frac{\pi}{2}\right) - - - t_2(\text{acquire})$$

with 1000–1500 increments in t_1, and for each t_1 increment 1024 points were collected in t_2; a one-dimensional MQ spectrum was produced by zero filling to 2048 in t_1, 2D magnitude Fourier transforming, and performing a summed projection onto the F1 axis. Selective detection of specific MQ coherences was accomplished by the repeated application of the pulse sequence [1] for each t_1 increment; after each application the phase ϕ of the first and second pulse was incremented relative to the third pulse (and receiver). To selectively detect the 7- or 8-quantum coherences, a 14 or 16 step phase cycle, where ϕ was incremented by 25.7° or 22.5°, was used. Alternate adding and subtracting within the phase cycle eliminates all but the ±7- or 8-quantum coherences (25, 26). While in principal this phase cycle also permits detection of $\pm k \times$ 7-quantum or $\pm k \times$ 8-quantum spectra, where k = 2, 3,..., this was not a problem since, for a n-spin-1/2 system, n is the highest attainable MQ order. For Sample nos. 7– 9, only *p*-xylene will contribute to the 7- and 8-quantum spectra, since the other two solutes have <7 spins. The intensity of MQ lines is highly dependent on the τ value, and therefore, at least two MQ spectra with τ values between 10 and 21 ms were acquired for each *p*-xylene sample in an attempt to detect all 7- or 8-quantum transitions.

© 1999 NRC Canada

Fig. 2. The top three spectra *A*, *B*, and *C* are an expansion of Fig. 1. Spectrum *D* is an expansion of the spectrum predicted from the fit to the 7-quantum spectrum. Note that the line positions and intensities between the 7-quantum prediction and the experimental spectra are in sufficiently good agreement that only minor adjustments to spectral parameters were required to fit the experimental spectrum. In the experimental spectrum, the average line width at half maximum height is 2–3 Hz. The intensities of the calculated spectrum closely correspond with those of the experimental one. In spectrum *A*, resonances indicated with an asterisk are from *p*-dichlorobenzene.

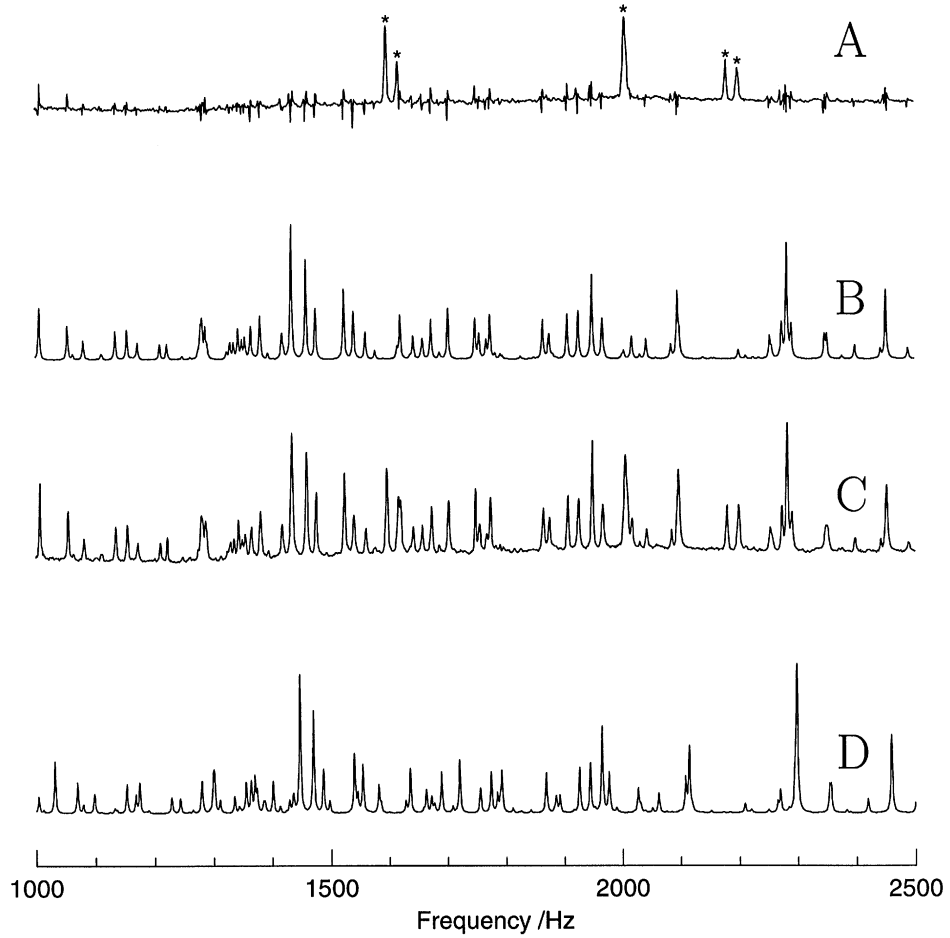

The recycling time was 4 s. The 7-quantum spectrum obtained from Sample no. 8 is presented in Fig. 3.

3. Spectral analysis

Since the component molecules of liquid crystal phases are undergoing random and rapid translational diffusion, intermolecular dipolar couplings are averaged to zero. However, due to anisotropic molecular reorientation, intramolecular dipolar couplings are averaged to a non-zero value. As a consequence, MQ and high-resolution NMR spectra contain only couplings between nuclei on the same molecule. Spectral parameters can be determined accurately by analyzing the experimental spectrum using the spin Hamiltonian

$$H = -\sum_i \nu_i I_i^Z + \sum_i \sum_{j>i} \left[(J_{ij} + 2D_{ij}) I_i^Z I_j^Z + \frac{1}{2}(J_{ij} - D_{ij})(I_i^+ I_j^- + I_i^- I_j^+) \right] \quad [2]$$

where ν_i is the resonance frequency of nucleus, *i*, J_{ij}, and D_{ij} are the indirect and direct (dipolar) coupling constants between nuclei *i* and *j* on the same molecule, and I^Z, I^+, and I^- are the spin operators.

For analysis of experimental spectra, initial estimates of spectral parameters ν_i, J_{ij}, and D_{ij}, either from previous studies or a "best guess," are required. The best guess may be values of ν_i and J_{ij} obtained from isotropic phase NMR spectra and values of D_{ij} calculated from

$$D_{ij} = -\frac{\mu_0 \hbar \gamma_i \gamma_j}{8\pi^2} \sum_{\beta\xi} S_{\beta\xi} \left\langle \frac{\cos\theta_\beta \cos\theta_\xi}{r_{ij}^3} \right\rangle \quad [3]$$

where the angle brackets indicate a statistical average over all intramolecular motions, β and ξ are the molecular fixed *x*, *y*, *z* axes, r_{ij} is the internuclear distance between nuclei *i* and *j*, θ_β and θ_ξ are the angles between the internuclear vector and the molecular β and ξ axes, and $S_{\beta\xi}$ is an element of the molecular order parameter matrix. Estimates of internuclear distances can be determined from general knowledge of structures or from previous structural studies. The molecular order parameter matrix,

© 1999 NRC Canada

Fig. 3. The experimental +7-quantum spectrum *A* is of Sample no. 8. Only resonances from *p*-xylene are observed; for an *n*-spin-1/2 system, *n* is the highest attainable MQ order. Spectrum *B* is the calculated +7-quantum spectrum of *p*-xylene. Note that the line width in the experimental spectrum is approximately 50 Hz, and the intensities of the calculated spectrum do not correspond with those of the experimental.

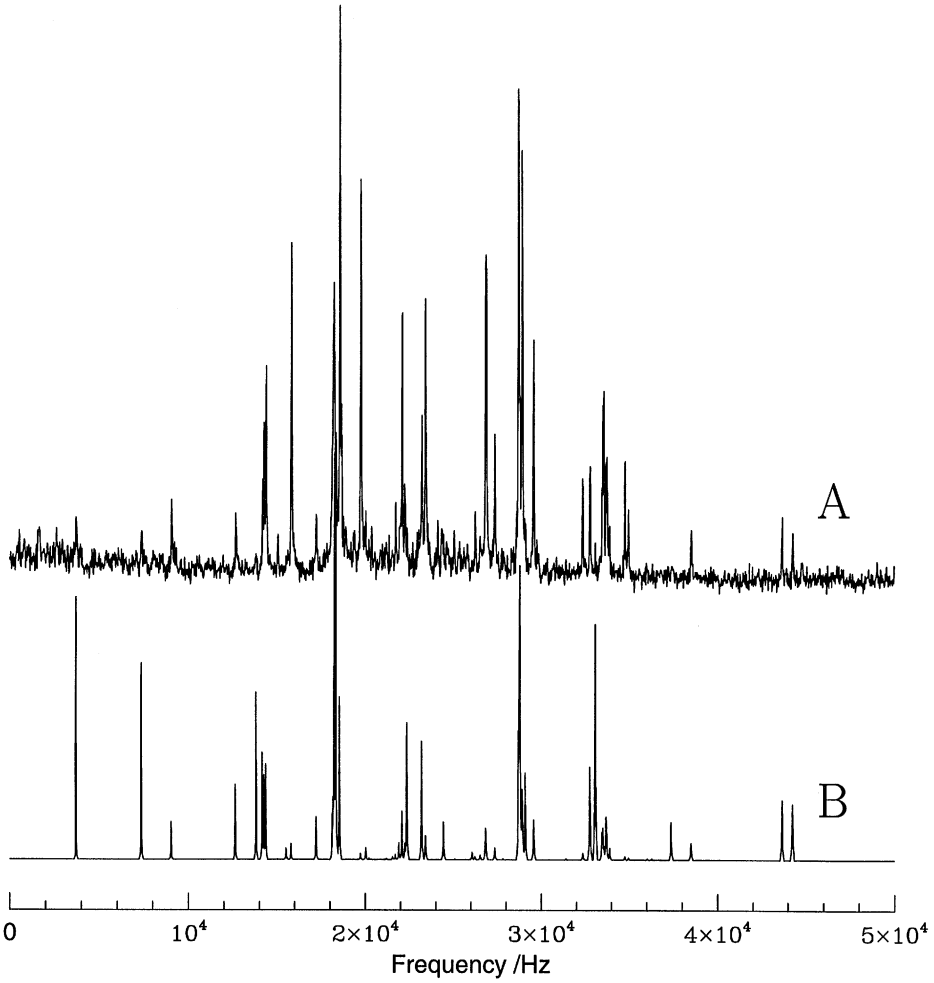

$$[4] \qquad S_{\beta\xi} = \frac{1}{2}\left\langle 3\cos\theta_{\beta Z}\cos\theta_{\xi Z} - \delta_{\beta\xi}\right\rangle$$

(where the angle brackets indicate a statistical average over all orientations of the molecules, and $\theta_{\beta Z}$ and $\theta_{\xi Z}$ are the angles between the magnetic field direction Z and molecular β and ξ axes), is inferred from studies of similar molecules or from calculations based on theories or models for the anisotropic intermolecular potential. Since there are no large-amplitude molecular motions which significantly affect the $S_{\beta\xi}$ or structural parameters (21), and orientational–vibrational correlations (27–29) are assumed to be negligible, the averages of the orientational and structural parameters have been separated in eq. [3].

From the estimates of the spectral parameters, a trial spectrum is calculated using eq. [2] and the appropriate selection rules for high-resolution or MQ spectra. Experimental and calculated spectra are compared, and ν_i and (or) D_{ij} are manually adjusted until the overall structure of the calculated spectrum is similar to the experimental. The calculated frequencies are then assigned to the experimental ones, and spectral parameters are adjusted by a least-squares fitting routine. Frequencies are repeatedly assigned and (or) unassigned and parameters adjusted until a reasonable fit to the experimental spectrum is obtained; this is the most time-consuming portion of spectral analysis. Assignment of calculated to experimental frequencies was performed with the aid of a cursor-controlled graphical interface program SM.[2] Care was taken to avoid assignment of overlapping or unresolvable lines. Frequencies were determined from a five-point weighted average about the maximum intensity point. In all cases, the frequencies were no more than 0.2 Hz different from a standard Bruker peak-picking routine for lines with half-height line width ≤3 Hz.

Without accurate estimates of spectral parameters, analysis of high-resolution spectra for molecules with ≥6 spins can be extremely difficult (30); this will be particularly true when there are resonances from other solutes in the spec-

[2] SM edition 2.2.0. Jan. 1992. SM is a configurable plotting program written by Robert Lupton (Princeton University, Princeton) and Patricia Monger (McMaster University, Hamilton).

© 1999 NRC Canada

trum. In an attempt to reduce analysis time of the complex high-resolution *p*-xylene spectra, MQ spectra were examined first. For Sample no. 7, the 7- and 8-quantum spectra were examined before good estimates of chemical shifts and D_{ij} could be determined, whereas only 7-quantum spectra were necessary for the other two samples containing *p*-xylene (Sample nos. 8 and 9). The experimental 7-quantum spectrum of Sample no. 8, along with the one calculated using the spectral parameters obtained from the analysis, are shown in Fig. 3. The agreement between experimental and calculated spectral line positions is excellent. It must be remembered that intensities in the calculated MQ spectrum are meaningless. The spectral parameters obtained from the fit to the MQ spectrum are then used to calculate the high-resolution NMR spectrum, and the result for Sample no. 8 is shown in Fig. 2*D*. Most peaks can be assigned immediately to lines in the experimental spectrum (compare Fig. 2*C* and *D*). As has been found for several other complicated spin systems (19, 21, 22), a correct fit to the MQ spectrum can give a prediction of the high-resolution spectrum that is amazingly close to that observed. In the current case, the fit to the high-resolution spectrum is complicated by the presence of lines from the extra two solutes that are present. Once spectral parameters for the MQ spectra were determined, the high-resolution spectra were analyzed within hours, and the spectral parameters obtained are given in Table 2. The spectrum calculated from the parameters in Table 2 for Sample no. 8 is presented in Figs. 1*B* and 2*B*. The excellent quality of the fit for *p*-xylene is demonstrated by subtracting the calculated (Figs. 1*B* and 2*B*) from the experimental (Figs. 1*C* and 2*C*) spectrum, the results being presented as Figs. 1*A* and 2*A*. The experimental *p*-dichlorobenzene and TCB spectra are easily observed and were analyzed without the aid of MQ NMR. For each sample that contained *p*-xylene, the complete determination of spectral parameters obtained by starting from the MQ spectra and then analyzing the high-resolution spectrum only required a month.

Spectra for samples that contained toluene–chlorobenzene–TCB and *p*-chlorotoluene–*p*-dichlorobenzene–TCB were analyzed without the aid of MQ NMR. Spectral parameters for the monomethylbenzenes (toluene and *p*-chlorotoluene) were determined first. A cluster of lines approximately 2000 Hz upfield from the main spectrum contained no frequencies from chlorobenzene or *p*-dichlorobenzene, and thus, many lines in this cluster could be assigned, and some D_{ij}, which are unique to the methylbenzene, could be determined; this allowed for easier assignment of lines within the main portion of the spectrum. Once spectral parameters for the methylbenzenes were determined (Table 2), the calculated spectra were subtracted from the experimental, and the spectra from the chlorobenzenes and 1,3,5-trichlorobenzene were easily identified and analyzed (Table 2).

4. Determination of molecular structure and molecular order parameters

Solute molecular order parameters and proton internuclear distances were calculated from a simultaneous fit to D_{ij} determined for the solute in all three liquid crystal mixtures (Tables 3 and 4); calculations were performed using the least-squares minimization routine NL2SNO (31), eq. [3], and a priori estimates (32) of proton–carbon bond distances and angles. A priori estimates are values that are adjusted in the least-squares routine; thus, the least-squares routine includes equations for both D_{ij} and geometrical parameters. The structure is allowed to deviate from that determined previously; however, large deviations are discouraged by the least-squares criteria. In previous studies (19, 22, 33–35) of solutes in liquid crystals, the structure of the benzene ring did not vary significantly from that determined by electron diffraction. Thus, during the least-squares minimization the benzene ring was fixed to the geometry determined previously. Values of D_{ij} between methyl and ring protons for toluene, *p*-chlorotoluene, and *p*-xylene were calculated for each 15° rotation of the methyl group using a sixfold potential $U = V/2(1 + \cos(6\theta))$ where V was fixed at 60 J/mol (36) and $\theta = 0$ is when one proton is in the plane of the benzene ring. No attempt was made to correlate methyl rotation and reorientational motion. In the approximation that a $P_2(\cos\theta)$ bond additive interaction (37) describes the orientational potential, and that the methyl group retains C_3 symmetry upon rotation, then the orientational potential is invariant to the methyl rotation.

The effects of vibrational motion on the experimental observations (and thus the molecular structure) are different for different experimental techniques. Therefore, in order to compare or combine structural information derived from various experimental methods, the observed data should be "vibrationally corrected." Electron diffraction and microwave techniques study molecules in the gas phase where molecular collisions and interactions are minimized. In comparison, in this study, molecules are in an anisotropic condensed phase, and the anisotropy of the phase affects vibrational motions (orientational–vibrational correlations). For orientational–vibrational correlations, it is assumed that the orienting forces alter the vibrational potential of the molecules, which affects the observed D_{ij}. Corrections have been calculated for certain molecules such as CH_4 (27), acetylene (29), benzene (34), chlorobenzene (34), and CH_3F (38). For molecules with a large $S_{\beta\xi}$, the orientational–vibrational correlations will have a very small effect (≈0.2%) on the observed D_{ij} (34, 39). Normal-mode bond vibrations have a larger effect (≈2.0%) on the observed D_{ij} (39), and thus, we have attempted to correct for these effects only. The average structure determined by subtracting the contributions from harmonic vibrations, the r_α structure, has been established as a suitable physical basis for comparing results (40–43). The average r_α structures determined from different techniques are usually in good agreement with each other.

A second calculation of order parameters and structural parameters was performed using a version of the least-squares routine modified to include the subroutine VICO (33, 44), which corrects for the non-negligible effects of molecular vibrations on D_{ij} (Tables 3 and 4). VICO calculates corrections using the Taylor expansion of D_{ij} about the equilibrium position

$$[5] \qquad D_{ij} = D_{ij}^{e} + \sum_{\delta}\left(\frac{\partial D_{ij}}{\partial \delta}\right)_{e}\langle\Delta\delta\rangle + \frac{1}{2}\sum_{\delta}\left(\frac{\partial^2 D_{ij}}{\partial \delta^2}\right)_{e}\langle\Delta\delta^2\rangle + \ldots$$

where D_{ij}^{e} is the dipolar coupling at equilibrium, δ is the x', y', and z' internuclear axis, $\langle\Delta\delta\rangle$ is the average vibrational

© 1999 NRC Canada

Table 2. Fitting parameters and rms errors from analysis of high-resolution and MQ NMR spectra.[a]

Solutes	Parameter[b]	Liquid crystal		
		Merck ZLI 1132	55 wt.% ZLI 1132–EBBA	EBBA
		Sample no. 1	Sample no. 2	Sample no. 3
Chlorobenzene	$D_{1,2}$	–1862.92(07)	–1282.57(06)	–1506.95(06)
	$D_{1,11}$	–280.89(16)	–187.54(21)	–199.17(46)
	$D_{1,3}$	–80.45(06)	–45.04(06)	–12.39(05)
	$D_{1,4}$	–43.01(24)	–9.12(36)	72.60(64)
	$D_{2,11}$	–624.69(18)	–352.96(24)	–99.53(40)
	$D_{2,3}$	–42.53(21)	–8.57(33)	71.44(67)
	$J_{1,2}$ [c]	7.608	7.608	7.608
	$J_{1,11}$ [c]	1.451	1.451	1.451
	$J_{1,3}$ [c]	0.864	0.864	0.864
	$J_{1,4}$ [c]	1.781	1.781	1.781
	$J_{2,11}$ [c]	7.280	7.280	7.280
	$J_{2,3}$ [c]	1.301	1.301	1.301
	ν_1 [d]	–3851.15(02)	–3976.17(03)	–2895.17(07)
	ν_2 [d]	–3870.82(02)	–3973.60(03)	–2880.10(07)
	ν_{11} [d]	–4019.38(01)	–4071.38(01)	–3011.00(01)
	rms error	0.298	0.330	0.289
	Number of assigned lines	39	39	35
Toluene	$D_{1,2}$	–1870.33(08)	–1262.18(02)	–1491.20(10)
	$D_{1,11}$	–279.68(13)	–186.31(03)	–206.09(18)
	$D_{1,3}$	–81.16(07)	–50.01(01)	–32.58(09)
	$D_{1,4}$	–46.31(13)	–21.90(03)	28.07(22)
	$D_{1,5}$	–617.57(05)	–407.24(01)	–426.78(09)
	$D_{2,11}$	–635.73(13)	–394.32(03)	–262.45(25)
	$D_{2,3}$	–46.37(14)	–21.76(03)	27.67(22)
	$D_{2,5}$	–176.35(06)	–118.11(02)	–134.67(11)
	$D_{5,11}$	–133.58(13)	–90.26(03)	–106.39(22)
	$D_{5,6}$	2464.93(03)	1662.25(01)	1963.05(04)
	$J_{1,2}$ [e]	8.00	8.00	8.00
	$J_{1,11}$ [e]	0.92	0.92	0.92
	$J_{1,3}$	0.94(16)	0.49(44)	0.37(25)
	$J_{1,4}$ [e]	1.86	1.86	1.86
	$J_{1,5}$	–0.72(08)	–0.69(02)	–0.58(13)
	$J_{2,11}$	7.28(20)	7.46(05)	7.27(48)
	$J_{2,3}$ [e]	1.11	1.11	1.11
	$J_{2,5}$	0.57(09)	0.34(03)	0.36(17)
	$J_{5,11}$	–1.28(27)	–0.56(08)	–0.54(43)
	ν_1 [d]	–3813.17(01)	–3912.96(01)	–2782.23(02)
	ν_2 [d]	–3869.13(01)	–3969.34(01)	–2840.32(02)
	ν_{11} [d]	–3971.21(02)	–4025.51(01)	–2927.76(02)
	ν_5 [d]	–1669.00(01)	–1681.38(01)	–562.88(01)
	rms error	0.510	0.110	0.660
	Number of assigned lines	171	151	149
TCB[f]	$D_{1,4}$	213.59(08)	147.67(06)	151.55(04)
	ν_1 [d]	–3707.32(02)	–3816.21(01)	–2689.23(01)
	rms error	0.199	0.136	0.109
	Number of assigned lines	3	3	3

© 1999 NRC Canada

Table 2 (*continued***).**

Solutes	Parameter[b]	Liquid crystal		
		Merck ZLI 1132	55 wt.% ZLI 1132–EBBA	EBBA
		Sample no. 4	Sample no. 5	Sample no. 6
p-Dichlorobenzene	$D_{1,2}$	–2411.29(07)	–2255.46(17)	–3035.20(15)
	$D_{1,3}$	–49.89(08)	–24.02(19)	27.68(16)
	$D_{1,4}$	56.36(08)	99.98(19)	254.98(15)
	$J_{1,2}$ [g]	8.55	8.55	8.55
	$J_{1,3}$ [g]	0.39	0.39	0.39
	$J_{1,4}$ [g]	2.57	2.57	2.57
	ν_1 [d]	–2621.48(09)	–2699.33(25)	–3058.53(22)
	rms error	0.186	0.620	0.531
	Number of assigned lines	8	10	10
p-Chlorotoluene	$D_{1,2}$	–2596.80(06)	–2323.54(07)	–2901.55(09)
	$D_{1,3}$	–41.16(06)	–23.24(08)	11.83(08)
	$D_{1,4}$	83.51(16)	102.78(20)	211.14(23)
	$D_{1,5}$	–707.50(07)	–605.32(09)	–673.78(11)
	$D_{2,3}$	83.30(17)	102.21(21)	210.49(23)
	$D_{2,5}$	–231.75(06)	–204.91(09)	–248.26(10)
	$D_{5,6}$	3424.82(04)	3063.94(04)	3828.14(05)
	$J_{1,2}$	8.52 (22)	8.42(66)	8.49(41)
	$J_{1,3}$ [h]	0.39	0.39	0.39
	$J_{1,4}$ [h]	2.58	2.58	2.58
	$J_{1,5}$	–0.64(08)	–0.58(12)	–0.64(13)
	$J_{2,3}$ [h]	2.58	2.58	2.58
	$J_{2,5}$	0.28(09)	0.36(13)	0.45(13)
	ν_1 [d]	–2537.69(17)	–2606.36(21)	–2934.16(26)
	ν_2 [d]	–2605.87(18)	–2688.29(24)	–3045.33(26)
	ν_5 [d]	–482.12(07)	–502.43(09)	–849.59(09)
	rms error	0.563	0.612	0.688
	Number of assigned lines	132	100	111
TCB[f]	$D_{1,4}$	203.29(01)	165.53(10)	156.51(01)
	ν_1 [d]	–2580.31(02)	–2664.43(25)	–3058.21(01)
	rms error	0.024	0.245	0.013
	Number of assigned lines	3	3	3
		Sample no. 7	Sample no. 8	Sample no. 9
p-Dichlorobenzene	$D_{1,2}$	–2403.92(05)	–2189.81(15)	–2702.88(14)
	$D_{1,3}$	–49.35(06)	–22.61(16)	23.80(16)
	$D_{1,4}$	57.21(06)	97.13(16)	225.83(16)
	$J_{1,2}$ [f]	8.55	8.55	8.55
	$J_{1,3}$ [f]	0.39	0.39	0.39
	$J_{1,4}$ [f]	2.57	2.57	2.57
	ν_1 [d]	–837.52(07)	–908.56(22)	–2755.40(21)
	rms error	0.196	0.531	0.521
	Number of assigned lines	12	10	10
p-Xylene[i]	$D_{1,2}$	–2670.51(04) [–2733.9]	–2229.24(08) [–2269.0]	-2369.51(04) [-2386.7]
	$D_{1,3}$	–39.60(05) [–39.8]	–27.47(08) [–28.0]	–8.58(04) [–4.6]
	$D_{1,4}$	87.97(05) [92.6]	85.13(09) [91.2]	131.66(04) [134.55]
	$D_{1,5}$	–714.82(03) [–727.1]	–585.03(06) [–593.3]	–580.35(03) [–582.6]

© 1999 NRC Canada

Table 2 (*concluded*).

Solutes	Parameter[b]	Liquid crystal		
		Merck ZLI 1132	55 wt.% ZLI 1132–EBBA	EBBA
	$D_{1,8}$	–235.24(03) [–241.4]	–195.37(07) [–201.7]	–203.74(04) [–204.0]
	$D_{5,6}$	3472.13(04) [3495.2]	2896.91(10) [2908.2]	3076.68(02) [3088.7]
	$D_{5,8}$	–121.38(25) [–124.2]	–101.24(05) [–102.9]	–107.58(02) [–109.9]
	$J_{1,2}$	7.93(14) [—]	8.16(47) [—]	7.59(20) [—]
	$J_{1,3}$	0.40(15) [—]	0.85(39) [—]	0.64(18) [—]
	$J_{1,4}$	2.04(19) [—]	1.57(45) [—]	1.49(21) [—]
	$J_{1,5}$	–0.61(06) [—]	–0.68(12) [—]	–0.79(06) [—]
	$J_{1,8}$	0.36(07) [—]	0.42(13) [—]	0.36(07) [—]
	$J_{5,8}$	0.56(05) [—]	0.57(10) [—]	0.60(05) [—]
	ν_1 [d]	–756.80(05) [–756.7]	–826.20(10) [–826.1]	–2662.65(05) [–2662.6]
	ν_5 [d]	1307.29(06) [1299.3]	1293.08(13) [1291.9]	–537.47(05) [–538.07]
	rms error	0.485 [5.113]	0.780 [4.303]	0.522 [9.636]
	Number of assigned lines	210 [44]	172 [34]	275 [30]
TCB[f]	$D_{1,4}$	202.66(01)	160.76(15)	139.70(01)
	ν_1 [d]	–795.85(01)	–873.33(38)	–2745.15(03)
	rms error	0.008	0.385	0.033
	Number of assigned lines	3	3	3

[a]For atom numbering refer to Fig. 4. Numbers in parentheses are errors (68% confidence) in the last two reported digits of varied parameters.
[b]Dipolar couplings, *J* couplings, chemical shifts, and rms errors are in Hz.
[c]Parameters not varied during analysis of spectrum. Values were determined from a separate analysis of chlorobenzene dissolved in the nematic phase of ZLI 1132.
[d]Frequency is referenced to an arbitrary zero and is increasing to high field. In principle, chemical shift anisotropies can be determined from isotropic–nematic frequency shifts; however, proton shifts are small, and the variation in anisotropic local solvent effects among chemically distinct protons makes such measurements impracticable (61).
[e]Parameters not varied during fitting of spectrum. Values taken from ref. 62.
[f]TCB refers to an internal orientational standard 1,3,5-trichlorobenzene.
[g]Parameters not varied during fitting of spectrum. Values taken from ref. 63.
[h]Parameters not varied during fitting of spectrum. Values taken from ref. 64.
[i]Values in square brackets are from analysis of the 7-quantum spectrum. *J* couplings were set to zero for the MQ analysis.

amplitude (anharmonic) in the δ direction, and $\langle\Delta\delta^2\rangle$ is the corresponding mean-square amplitude (harmonic). The r_α structure was determined by subtracting the harmonic contribution from D_{ij} and calculating the molecular order parameters and internuclear distances using these corrected dipolar couplings. Mean-square amplitudes $\langle\Delta\delta^2\rangle$ were calculated[3] from normal-mode vibrational analysis (46) using force constants from refs. 47 and 48).

5. Discussion

5.1. Molecular structure

Accurate molecular structure determination using proton NMR dipolar couplings faces the problem that the dipolar couplings are products of order and geometric parameters. Hence, only accurate relative proton coordinates are available. To determine the complete molecular structure, it is necessary to fit the proton geometry to the carbon skeleton. The error associated with the resulting structure is difficult to determine. Bond angles are probably not accurate to better than 0.2°, and CH bond distances to 0.01 Å. Thus, the statistical uncertainties (68% confidence level) reported in Table 3 are optimistic.

The relative values of the proton coordinates reported in Table 3 are from simultaneous fits to the dipolar couplings obtained in three different liquid crystals for each molecule. The use of more than one liquid crystal provides extra independent equations to the fitting procedure. The complete structure is then obtained by utilizing data from other studies (mainly gas-phase work) for geometric parameters. Some of these parameters are used as a priori estimates. It is noteworthy that most of the values so obtained do not differ significantly from the a priori estimates. For chlorobenzene, toluene, *p*-dichlorobenzene, and *p*-chlorotoluene, the $\angle_\alpha$(C3C2H1) is about 0.4° larger than the a priori estimate. This difference is ascribed to the difficulty associated with fitting the proton structure around the carbon skeleton, as discussed above. In the case of *p*-xylene, $\angle_\alpha$(C3C2H1) differs by 1° and r_α(C2—H1) by 0.013 Å from the a priori estimates, which are taken from gas-phase electron diffraction work. However, it is well known that proton coordinates are difficult to determine by electron diffraction, and the new NMR values are taken to be more reliable.

A glance at the a priori estimates for the methyl group geometry indicates that the methyl group structure appears to vary among the molecules studied. On the contrary, our results indicate that the methyl groups in the series of

[3]Program written by R.L. Hilderbrant utilizing the methods developed by Hilderbrant and Wieser (45).

© 1999 NRC Canada

Fig. 4. Coordinate system and atom numbering of solute molecules.

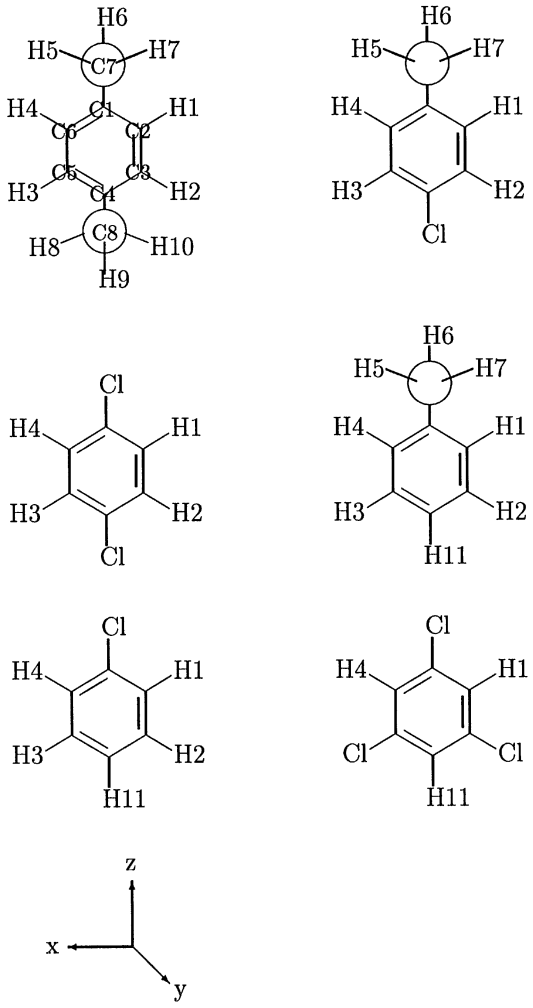

methylbenzenes (toluene, *p*-xylene, and *p*-chlorotoluene) have essentially the same r_α(C—H(Me)) bond length and $\angle_\alpha$(CCH(Me)) angle. The unexpected scatter among a priori estimates is likely a result of the different experimental techniques utilized for the various studies.

It is interesting that one effect of the vibrational corrections is that there is a slight improvement in the rms error over the fit without such corrections (*p*-xylene is an exception). In general, the vibrationally corrected structural parameters lie closer to the a priori estimates than do the noncorrected ones.

5.2. Order parameters

The main motivation behind the choice of solutes in this work is the investigation of the solute order parameters, and a discussion of the scaled order parameters that were not corrected for the minor effects of molecular vibrations is presented elsewhere (5). It is generally accepted that anisotropic short-range repulsive forces are primarily responsible for the orientational ordering of liquid crystals, i.e., forces that can be related to size, shape, and conformation of the molecules (49–52). Controversy has arisen over the importance of anisotropic long-range interactions (5, 53–55). The spectra in this paper have been recorded in such a manner that the order parameters obtained can be used to explore various models for the anisotropic potential. In many previous studies, solutes dissolved in the same liquid crystal were in different sample tubes; thus, to examine the order parameters of the molecules an orientational scaling parameter was required for each solute to account for different sample conditions (53, 56–60). In this study, several solutes are dissolved in the same sample (similar to the sample preparation described in ref. 58); order parameters among these solutes can be directly compared without scaling.

The order parameters calculated both with and without vibrational corrections are reported in Table 4. The vibrationally corrected values are consistently about 2% larger. Hence, the neglect of vibrational effects when utilizing order parameters to investigate intermolecular forces is justified, as it is unlikely that any current theory will be able to predict order parameters to the 2% level.

The solute molecules chosen for investigation represent two groups; solutes in each group are related by their similar size and shape (the mono- and *para*-substituted molecules), but solutes within the groups have different molecular multipole moments. The S_{zz} of the *para* group of molecules in the 55 wt.% liquid-crystal mixture are all similar (Fig. 5). As short-range interactions are expected to be similar for these molecules, the long-range interactions, which involve molecular quadrupoles and dipoles, appear to be negligible in this particular liquid-crystal mixture. In previous studies, the long-range interactions were also determined to be of minimal importance with D_2 and HD dissolved in this liquid-crystal mixture (4).

In previous studies, D_2 and HD were found to have a positive orientational order in the component liquid crystal ZLI 1132 and a negative orientational order in EBBA (4). The ordering was attributed to the molecular electric quadrupole of D_2 and HD interacting with the anisotropic electric field gradient experienced in the liquid-crystal environment. In ZLI 1132, the trend for the scaled values of S_{zz} is S_{zz}(*p*-xylene) > S_{zz}(*p*-chlorotoluene) > S_{zz}(*p*-dichlorobenzene). However, in EBBA this trend is reversed (Fig. 5). This is consistent with the sign and magnitude of the interaction found for D_2 and HD (4, 5). For toluene and chlorobenzene, the quadrupoles of these two molecules are very similar, and thus, the effect is not as prevalent.

Dipoles appear to have little effect on the ordering of the molecules. If dipoles were important, then *p*-chlorotoluene, which has a large dipole along the *z*-axis, should have a vastly different S_{zz} than do the other two *para*-substituted benzenes, which have zero dipole moment. However, S_{zz} of *p*-chlorotoluene lies between the values for *p*-xylene and *p*-dichlorobenzene in both EBBA and 1132 (Fig. 5).

6. Summary

In this paper, we have determined spectral parameters, order parameters, and structural parameters (including the vibrationally corrected structural parameters) of *para*- and mono-substituted benzenes dissolved in various liquid crystals. Spectral parameters for *p*-xylene were estimated by analyzing the MQ spectra first, then accurately determined using the high-resolution spectra. The spectra of TCB and *p*-dichlorobenzene were easily identified and analyzed once

© 1999 NRC Canada

Table 3. Structural parameters from fits to dipolar couplings.[a]

Parameter[b]		Chlorobenzene	Toluene	*p*-Dichlorobenzene	*p*-Chlorotoluene	*p*-Xylene	TCB[c]
r(C2—H1)	n	1.0812(04)	1.0838(15)	1.0760(04)	1.0792(53)	1.0914(11)	1.094
	v	1.0819(02)	1.0831(15)	1.0760(03)	1.0806(04)	1.0890(14)	—
r(C3—H2)	n	1.0803(05)	1.0824(14)	1.0760(04)	1.0737(63)	1.0914(11)	—
	v	1.0791(02)	1.0792(14)	1.0760(03)	1.0749(05)	1.0890(14)	—
r(C4—H11)	n	1.0803(04)	1.0742(17)	—	—	—	1.094
	v	1.0808(02)	1.0778(17)	—	—	—	—
r(C—H(Me))	n	—	1.0983(10)	—	1.1032(04)	1.1038(08)	—
	v	—	1.0929(11)	—	1.0986(04)	1.0988(11)	—
r(C—C(Me))	n	—	1.4896(51)	—	1.4898(06)	1.5066(16)	—
	v	—	1.5044(46)	—	1.4892(05)	1.5109(22)	—
∠(C3C2H1)	n	121.53(08)	120.11(09)	120.58(01)	118.84(05)	119.67(01)	121.0
	v	121.30(04)	120.27(09)	120.58(01)	119.31(04)	119.78(01)	—
∠(C4C3H2)	n	121.04(07)	120.53(10)	(119.99)[d]	120.27(07)	(118.93)[d]	121.0
	v	120.66(03)	120.41(10)	(119.95)[d]	120.41(05)	(118.82)[d]	—
∠(CCH(Me))	n	—	110.49(17)	—	110.12(05)	109.84(08)	—
	v	—	111.42(17)	—	111.50(04)	111.12(11)	—
∠(CCC(Me))	n	—	120.85	—	120.88	121.4	—
	v	—	120.85	—	120.90	121.4	—
rms error[e]		0.3098	0.3150	0.3121	0.2949	0.3867	—
rms error[f]		0.1601	0.3111	0.2195	0.2335	0.4795	—
A priori estimates[g]		[h]	[i]	[j]	[k]	[l]	[c]
r(C2—H1)		1.0823(02)	1.077(02)	1.076(02)	1.0811(02)	1.076(02)	1.094
r(C3—H2)		1.0787(02)	1.076(02)	1.076(02)	1.0745(02)	1.076(02)	—
r(C4—H11)		1.0808(02)	1.076(02)	—	—	—	1.094
r(C—H(Me))		—	1.113(02)	—	1.0989(02)	1.113(02)	—
r(C—C(Me))		—	1.516(05)	—	1.4891(02)	1.512(02)	—
∠(C3C2H1)		120.89(05)	119.70(05)	120.05(05)	118.90(05)	120.80(05)	121.0
∠(C4C3H2)		120.56(05)	120.10(05)	(120.48)[d]	120.40(05)	(117.8)[d]	121.0
∠(CCH(Me))		—	110.30(05)	—	111.17(05)	110.30(05)	—
∠(CCC(Me))[m]		—	120.70(—)	—	120.91(—)	121.4(—)	—
Fixed parameters		[h]	[i]	[j]	[k]	[l]	[c]
r(C1—C2)		1.389	1.388	1.395	1.406	1.405	1.3908
r(C2—C3)		1.394	1.388	1.391	1.404	1.392	1.3908
r(C3—C4)		1.393	1.383	1.395	1.400	1.405	1.3908
r(C—Cl)		1.739	—	1.729	1.72	—	1.7326
∠(C1C2C3)		119.04	120.90	119.47	121.52	121.40	118.0
∠(C2C3C4)		120.06	120.20	119.47	118.64	121.40	122.0
∠(C3C4C5)		120.23	119.50	121.06	121.48	117.10	118.0
∠(C3C4H11)		119.89	120.30	—	—	—	121.0
∠(CCCl)		119.27	—	119.47	119.26	—	119.0

[a]Refer to Fig. 4 for structure and atom numbering of molecules. Bond distances *r* in Å and bond angles ∠ in degrees. In the least-squares fit to experimental dipolar couplings, the weight given to each dipolar coupling is $(1/\text{error})^2$ where the errors are from Table 2. Numbers in parentheses are statistical errors (68% confidence) in the last two reported digits of varied parameters (see text).

[b]Parameters that are indicated with "n" are calculated with no vibrational corrections to dipolar couplings, whereas parameters indicated with "v" are calculated with vibrational corrections and are the r_α structural parameters.

[c]Structural parameters not adjusted. From ref. 65. TCB refers to an internal orientational standard 1,3,5-trichlorobenzene.

[d]Parameters are calculated from ∠(C1C2C3) and ∠(C3C2H1).

[e]The rms error in Hz between calculated and experimental dipolar couplings.

[f]The rms error in Hz between vibrationally corrected and experimental dipolar couplings.

[g]A priori estimates are from refs. 34, 63, 64, 66, 67, and the weight associated with the estimates is $(1/\text{error})^2$ where the errors are reported in parentheses.

[h]r_α structure determined from liquid-crystal NMR data, which has been corrected for normal-mode vibrations and orientational–vibrational correlations (34).

[i]From molecular orbital calculations using Gaussian 92 and HF/6-31G* theory/basis set (66).

[j]r_α structure from a joint analysis of liquid-crystal NMR, electron diffraction, and rotational spectroscopy data (63).

[k]r_α structure from liquid-crystal NMR data, which has been corrected for normal-mode vibrations (64).

[l]r_α structure from electron diffraction data (67).

[m]No error is associated with this parameter. This is adjusted so the C1—C7 (and C4—C8) bond directions are collinear with the *z* axis of the molecule.

© 1999 NRC Canada

Table 4. Order parameters from fits to dipolar couplings.[a]

Solute	Order parameter[b]		Liquid crystal		
			Merck ZLI 1132	55 wt.% ZLI 1132–EBBA	EBBA
			Sample no. 1	Sample no. 2	Sample no. 3
Chlorobenzene	S_{zz}	n	0.23724(26)	0.16334(18)	0.19191(21)
		v	0.23921(14)	0.16469(09)	0.19355(11)
	$S_{xx} - S_{yy}$	n	0.29192(15)	0.17442(10)	0.09667(13)
		v	0.29559(08)	0.17661(06)	0.09767(07)
Toluene	S_{zz}	n	0.23233(35)	0.15668(23)	0.18503(28)
		v	0.23539(35)	0.15874(23)	0.18747(28)
	$S_{xx} - S_{yy}$	n	0.29035(20)	0.18412(12)	–0.14883(23)
		v	0.29427(20)	0.18652(12)	–0.15017(24)
TCB[c]	S_{yy}	n	–0.28838	–0.19938	–0.20462
			Sample no. 4	Sample no. 5	Sample no. 6
p-Dichlorobenzene	S_{zz}	n	0.30854(20)	0.28860(19)	0.38838(25)
		v	0.31062(13)	0.29055(12)	0.39099(16)
	$S_{xx} - S_{yy}$	n	0.23495(07)	0.15805(17)	0.05427(16)
		v	0.23654(04)	0.15915(10)	0.05469(10)
p-Chlorotoluene	S_{zz}	n	0.32950(20)	0.29479(13)	0.36830(22)
		v	0.33489(16)	0.29961(14)	0.37432(18)
	$S_{xx} - S_{yy}$	n	0.21944(13)	0.16033(13)	0.09268(18)
		v	0.22247(10)	0.16259(10)	0.09416(14)
TCB[c]	S_{yy}	n	–0.27447	–0.22350	–0.21132
			Sample no. 7	Sample no. 8	Sample no. 9
p-Dichlorobenzene	S_{zz}	n	0.30761(12)	0.28021(11)	0.34586(14)
		v	0.30967(12)	0.28209(11)	0.34818(14)
	$S_{xx} - S_{yy}$	n	0.23307(04)	0.15293(11)	0.05006(09)
		v	0.23465(04)	0.15399(11)	0.05044(09)
p-Xylene	S_{zz}	n	0.33637(43)	0.28066(36)	0.29811(38)
		v	0.34157(59)	0.28500(49)	0.30272(52)
	$S_{xx} - S_{yy}$	n	0.21971(14)	0.16824(15)	0.12447(15)
		v	0.22495(19)	0.17226(21)	0.12756(21)
TCB[c]	S_{yy}	n	–0.27362	–0.21705	–0.18862

[a]For axes definitions see Fig. 4. For corresponding structural parameters refer to Table 3. Numbers in parentheses are errors (68% confidence) in the last two reported digits of varied parameters.

[b]Order parameters that are indicated with "n" are calculated with no vibrational corrections to dipolar couplings, whereas parameters indicated with "v" are calculated with vibrational corrections.

[c]TCB refers to an internal orientational standard 1,3,5-trichlorobenzene.

Fig. 5. Scaled, vibrationally corrected order parameters (S_{zz}) for the (*a*) *para*- and (*b*) mono-substituted benzenes. In calculating values for solutes in different sample tubes, the S_{zz} values were scaled using the ratio of TCB dipolar couplings from samples 7, 8, or 9 to TCB dipolar couplings in the sample of interest.

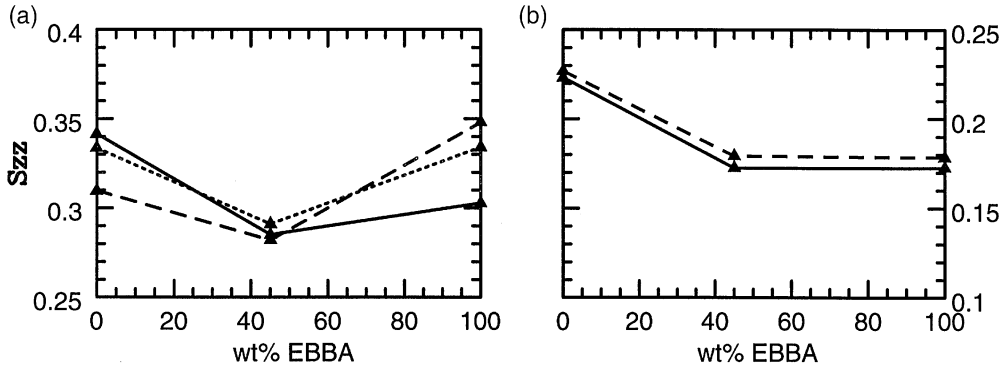

© 1999 NRC Canada

the calculated *p*-xylene spectrum was subtracted from the experimental. Spectral parameters for toluene, chlorobenzene, *p*-chlorotoluene, *p*-dichlorobenzene, and TCB were determined without the aid of MQ spectra. This is one of very few studies where many solutes were dissolved in a liquid-crystal mixture and where MQ spectroscopy was utilized in a successful attempt to simplify analysis of high-resolution spectra.

Proton positions were determined from at least three independent sets of dipolar couplings; only after dipolar couplings were corrected for vibrations did bond angles and lengths of the methyl groups on *p*-xylene, *p*-chlorotoluene, and toluene have similar values despite variations in a priori estimates.

Acknowledgments

We thank James M. Polson and Thambirajah Chandrakumar for their useful suggestions when analyzing the NMR spectra, and the Natural Sciences and Engineering Research Council of Canada for financial support. We are grateful to the E. Merck Company of Darmstadt, Germany, for their gift of the nematic liquid crystal Merck ZLI 1132.

References

1. A.D. Buckingham and K.A. McLauchlan. Prog. Nucl. Magn. Reson. Spectrosc. **2**, 63 (1967).
2. P. Diehl and C.L. Khetrapal. NMR basic principles and progress. Vol. 1. Springer-Verlag, Berlin. 1969. p. 1.
3. J.W. Emsley and J.C. Lindon. NMR spectroscopy using liquid crystal solvents. Pergamon Press, Oxford. 1975.
4. E.E. Burnell and C.A. de Lange. Chem. Rev. **98**, 2359 (1998).
5. R.T. Syvitski and E.E. Burnell. Chem. Phys. Lett. **281**, 199 (1997).
6. R.Y. Dong. Nuclear magnetic resonance of liquid crystals. 2nd ed. Springer-Verlag, New York. 1997.
7. T.P. Higgs and A.L. MacKay. Chem. Phys. Lipids, **20**, 105 (1977).
8. J.W. Emsley, G.R. Luckhurst, and C.P. Stockley. Mol. Phys. **44**, 565 (1981).
9. J.W. Emsley, B.M. Fung, N.J. Heaton, and G.R. Luckhurst. J. Chem. Phys. **87**, 3099 (1987).
10. B. Janik, E.T. Samulski, and H. Toriumi. J. Phys. Chem. **91**, 1842 (1987).
11. E.J. Delikatny and E.E. Burnell. Mol. Phys. **67**, 757 (1989).
12. M.E. Rosen, S.P. Rucker, C. Schmidt, and A. Pines. J. Phys. Chem. **97**, 3858 (1993).
13. C.L. Khetrapal. Int. J. Mod. Phys. B, **9**, 2573 (1995).
14. G. Drobny, A. Pines, S.W. Sinton, D.P. Weitekamp, and D. Wemmer. Faraday Symp. Chem. Soc. **13**, 33 (1979).
15. S.W. Sinton and A. Pines. Chem. Phys. Lett. **76**, 263 (1980).
16. W.S. Warren and A. Pines. J. Am. Chem. Soc. **103**, 1613 (1981).
17. G. Bodenhausen. Prog. Nucl. Magn. Reson. Spectrosc. **14**, 137 (1981).
18. C.P. Slichter. Principles of magnetic resonance. 3rd ed. Springer-Verlag, New York. 1990.
19. J.M. Polson and E.E. Burnell. J. Magn. Reson. Ser. A, **106**, 223 (1994).
20. J.C.T. Rendell and E.E. Burnell. J. Magn. Reson. Ser. A, **112**, 1 (1995).
21. J.M. Polson and E.E. Burnell. J. Chem. Phys. **103**, 6891 (1995).
22. T. Chandrakumar, J.M. Polson, and E.E. Burnell. J. Magn. Reson. Ser. A, **118**, 264 (1996).
23. J. Lounila and J. Jokisaari. Prog. Nucl. Magn. Reson. Spectrosc. **15**, 249 (1982).
24. P. Keller and L. Liebert. Solid State Phys. Suppl. **14**, 19 (1978).
25. A. Wokaun and R.R. Ernst. Chem. Phys. Lett. **52**, 407 (1977).
26. W.S. Warren, D.P. Weitekamp, and A. Pines. J. Chem. Phys. **73**, 2084 (1980).
27. J.G. Snijders, C.A. de Lange, and E.E. Burnell. Israel J. Chem. **23**, 269 (1983).
28. J. Lounila and P. Diehl. J. Magn. Reson. **56**, 254 (1984).
29. A.J. van der Est, E.E. Burnell, J.B.S. Barnhoorn, C.A. de Lange, and J.G. Snijders. J. Chem. Phys. **89**, 4657 (1988).
30. E.E. Burnell and P. Diehl. Mol. Phys. **24**, 489 (1972).
31. J.E. Dennis, D.M. Gay, and R.E. Welsch. ACM Trans. Math. Software, **7**, 3 (1981).
32. T.C. Wong and E.E. Burnell. J. Magn. Reson. **22**, 227 (1976).
33. P. Diehl and W. Niederberger. J. Magn. Reson. **9**, 495 (1973).
34. R. Wasser, M. Kellerhals, and P. Diehl. Magn. Reson. in Chem. **27**, 335 (1989).
35. J.C.T. Rendell and E.E. Burnell. Mol. Phys. **90**, 541 (1997).
36. D. Lister, J. MacDonald, and N. Owen. Internal rotation and inversion. Academic Press, London. 1978.
37. D.A. Long. Proc. R. Soc. London Ser. A, **217**, 203 (1953).
38. J.B.S. Barnhoorn and C.A. de Lange. Mol. Phys. **88**, 1 (1996).
39. J. Kaski, J. Vaara, and J. Jokisaari. J. Am. Chem. Soc. **118**, 8879 (1996).
40. N.D.J. Lucas. Mol. Phys. **22**, 147 (1971).
41. K. Kuchitsu and S.J. Cyvin. Molecular structure and vibrations. Elsevier, Amsterdam. 1972.
42. A.G. Robiette. Specialist periodical reports, molecular structure by diffraction methods. 1st ed. Chem. Soc., London. 1973.
43. J.W. Emsley and J.C. Lindon. Mol. Phys. **29**, 531 (1975), and refs. therein.
44. S. Sýkora, H. Bösiger, J. Vogt, and P. Diehl. J. Magn. Reson. **36**, 53 (1979).
45. R.L. Hilderbrant and J.D. Wieser. J. Chem. Phys. **55**, 4648 (1971); M. Toyama, T. Oka, and Y. Morino. J. Mol. Spectrosc. **13**, 193 (1964); Y. Morino and E. Hirota. J. Chem. Phys. **23**, 737 (1955).
46. S.J. Cyvin. Molecular vibrations and mean square amplitudes. Elsevier, Amsterdam. 1968.
47. J.R. Scherer. Spectrochim. Acta, **20**, 345 (1964).
48. J.A. Draeger. Spectrochim. Acta Part A, **41**, 697 (1985).
49. W.M. Gelbart. J. Phys. Chem. **86**, 4289 (1982).
50. D. Frenkel. Liq. Cryst. **5**, 929 (1989).
51. G.J. Vroege and H.N.W. Lekkerkerker. Rep. Prog. Phys. **55**, 1241 (1992).
52. G. Vertogen and W.H. de Jeu. Thermotropic liquid crystals, fundamentals. 2nd ed. Springer, Heidelberg. 1989.
53. A.F. Terzis, C.D. Poon, E.T. Samulski, Z. Luz, R. Poupko, H. Zimmermann, K. Müller, H. Toriumi, and D.J. Photinos. J. Am. Chem. Soc. **118**, 2226 (1996).
54. J.W. Emsley, W.E. Palke, and G.N. Shilstone. Liq. Cryst. **9**, 643 (1991).
55. A.F. Terzis and D.J. Photinos. Mol. Phys. **83**, 847 (1994).
56. C.T. Yim and D.F.R. Gilson. Can. J. Chem. **68**, 875 (1990).
57. D.J. Photinos, C.D. Poon, E.T. Samulski, and H. Toriumi. J. Phys. Chem. **96**, 8176 (1992).
58. J.B.S. Barnhoorn, C.A. de Lange, and E.E. Burnell. Liq. Cryst. **13**, 319 (1993).
59. D.J. Photinos and E.T. Samulski. J. Chem. Phys. **98**, 10 009 (1993).
60. D.S. Zimmerman and E.E. Burnell. Mol. Phys. **78**, 687 (1993).

© 1999 NRC Canada

61. E.E. Burnell and C.A. de Lange. Chem. Phys. Lett. **136**, 87 (1987), and refs. therein.
62. P. Diehl, H.P. Kellerhals, and W. Niederberger. J. Magn. Reson. **4**, 352 (1971).
63. S. Cradock, P.B. Liescheski, and D.W.H. Rankin. J. Magn. Reson. **91**, 316 (1991).
64. P. Diehl and F. Moia. Org. Magn. Reson. **15**, 326 (1981).
65. A. Almenningen and I. Hargittai. J. Mol. Struct. **116**, 119 (1984).
66. P.C. Chen and C.W. Wu. J. Phys. Chem. **99**, 15 023 (1995).
67. A. Domenicano, G. Schultz, M. Kolonits, and I. Hargittai. J. Mol. Struct. **53**, 197 (1979).

© 1999 NRC Canada

Modelling and calculation of dipole moment functions for XH bonds

Christopher D. Daub, Bryan R. Henry, Martin L. Sage, and Henrik G. Kjaergaard

Abstract: Two studies of aspects of modelling dipole moment functions of XH bonds in small molecules for use in calculating overtone intensities have been undertaken. The first study deals with the fitting of ab initio calculations of the dipole moment at discrete points to a functional form. The two methods that are compared are the use of least-squares regression and the use of interpolating polynomials. The interpolating polynomial method is deemed superior due to its greater efficiency in terms of the number of points necessary to obtain reasonable results. The second study attempts to explain the indifference of calculated overtone intensities to the inclusion of electron correlation in the ab initio calculation of the dipole moment function. It is found that in most cases the influence of electron correlation can be modelled as a function with a very small matrix element, which results in a very small contribution to the overtone intensity.

Key words: dipole moment function, vibrational overtone intensities, electron correlation, ab initio calculations.

Résumé : Nous présentons deux études de modèles pour la fonction du moment dipolaire dans les liens XH. La première a pour sujet le raccord à une forme fonctionnelle des calculations ab initio à des points discrets. Deux méthodes sont comparées, la régression des moindres carrées et l'interpolation polynomiale. On trouve que l'interpolation polynomiale est meilleure, parce qu'elle donne des résultats raisonnables plus efficacement. La deuxième étude essaie d'expliquer nos observations que l'intensité des transitions vibrationnelles à haute excitation n'est pas tellement affectée par l'inclusion de la corrélation entre les électrons dans nos calculs du moment dipolaire. On trouve que l'effet de la corrélation peut être modelé comme une fonction avec un élément de matrice minuscule, ayant pour résultat une petite contribution à l'intensité.

Mots clés : fonction du moment dipolaire, intensité des transitions vibrationelles, corrélation entre électrons, calculs ab initio.

Introduction

For the past several years, the HCAO (Harmonically Coupled Anharmonic Oscillators) model has been widely used to understand the observed energy levels in the vibrational spectra of XH_n groups, both qualitatively and quantitatively (1, 2). However, due to several factors, understanding the observed intensities has posed more of a challenge. First, experimental vibrational intensities are difficult to determine accurately, especially in the overtone region, due to the weakness of the highly vibrationally excited transitions. Second, the nature of the vibrational potential surface is uncertain, although a Morse potential seems to fit the energy levels very well for most of the spectroscopically relevant region. Third, an accurate dipole moment function (DMF) is required. It is the third requirement that we address in this paper.

Historically, the modelling of the DMF was done on the basis of ideas such as the bond-dipole approximation, which attempted to fit the DMF to a functional form. The function was chosen so that it displayed the physically correct limiting behaviour for a single XH bond at large bond displacements (3–5). There are two weaknesses in this approach. First, the DMF of a polyatomic molecule, even if it is only calculated along a single bond, is not independent of the rest of the molecular environment. Therefore, there is no reason to think that the limiting behaviour of a single XH bond should be transferable to an XH bond in a molecule (6), although it is possible that a functional form could be devised to suit the limiting behaviour of the remaining molecular

Received January 29, 1999.

This paper is dedicated to Professor Ted Schaefer, a wonderful colleague who was a continuous source of knowledge.

C.D. Daub. Guelph Waterloo Program for Graduate Work in Physics, University of Guelph, Guelph, ON N1G 2W1, Canada.
B.R. Henry.[1] Guelph Waterloo Program for Graduate Work in Physics and Guelph Waterloo Centre for Graduate Work in Chemistry, University of Guelph, Guelph, ON N1G 2W1, Canada.
M.L. Sage. Department of Chemistry, Syracuse University, Syracuse, NY 13244-4100, U.S.A.
H.G. Kjaergaard. Department of Chemistry, University of Otago, P.O. Box 56, Dunedin, New Zealand.

[1]Author to whom correspondence may be addressed. Telephone: (519) 824-4120, ext. 3804. e-mail: chmhenry@uoguelph.ca

 © 1999 NRC Canada

fragment. Second, there are external parameters in the functional form, which must be fit to the observed intensities in a post hoc fashion. This approach compromises the predictive power of the intensity calculation. In the last few years, advances in computing power have made the calculation of ab initio DMFs possible, even for quite large molecules (e.g., He @ C_{60} (7)). Despite the fact that the limiting behaviour of these DMFs is often unphysical, especially for Hartree–Fock calculations, their accuracy near the equilibrium bond length is quite good, and the calculated intensities tend to be within a factor of two of the observed values. Another interesting effect that we have noticed is the fact that, although increasing the basis set size almost universally improves our calculated intensities, any improvement on moving beyond the Hartree–Fock theory tends to be limited to the fundamental transition (8, 9).

The purpose of this paper is twofold. First, we wish to examine the various methods of converting discrete, ab initio values of the DMF to a useful functional form via a fitting procedure of some kind. This study is in many ways an extension of a previous paper (6). Second, we want to have a better understanding of why inclusion of electron correlation in the DMF has little effect on our calculations of overtone intensities.

Theory and computational methods

We express the intensity of a vibrational transition in terms of the oscillator strength *f*, given by (10)

$$[1] \qquad f_{e\leftarrow g} = \frac{4\pi m_e}{3e^2 h}\nu_{eg}\left|\vec{\mu}_{eg}\right|^2 = 4.702\times10^{-7}(\text{cm D}^{-2})\tilde{\nu}_{eg}\left|\vec{\mu}_{eg}\right|^2$$

where $\tilde{\nu}_{eg}$ is the transition frequency given in cm^{-1} and $\vec{\mu}_{eg} = \langle e|\vec{\mu}|g\rangle$ is the transition dipole moment matrix element in Debye (= $3.335\,64 \times 10^{-30}$ C m).

Dipole moment functions

The DMF $\vec{\mu}$ for an XH_n group is modelled as a polynomial expansion in the internal bond displacement coordinates q_j

$$[2] \qquad \vec{\mu}(q_1, q_2, \ldots, q_n) = \sum_{i_1 i_2 \ldots i_n} \vec{\mu}_{i_1 i_2 \ldots i_n} q_1^{i_1} q_2^{i_2} \ldots q_n^{i_n}$$

where

$$[3] \qquad \vec{\mu}_{i_1 i_2 \ldots i_n} = \frac{1}{i_1!\, i_2! \ldots i_n!} \frac{\partial \sum_{j=1}^{n} i_j \vec{\mu}}{\partial q_1^{i_1} \partial q_2^{i_2} \ldots \partial q_n^{i_n}}$$

In this paper, we wish to separate the fundamental problem of modelling the DMF from the complications of applying the model to a specific situation. Therefore, we will consider only the single bond one-dimensional DMF. This simplifies eqs. [2] and [3] considerably:

$$[2a] \qquad \vec{\mu}(q) = \sum_i \vec{\mu}_i q^i$$

and

$$[3a] \qquad \vec{\mu}_i = \frac{1}{i!}\frac{\partial^i \vec{\mu}}{\partial q^i}$$

For the same reason, we will ignore the problem of Eckart embedding (8–11).

The coefficients $\vec{\mu}_i$ are determined from ab initio calculations of the dipole moment at various bond displacements using the Gaussian 94 program (12) and numerical calculation of the derivatives.

Morse oscillator wave functions and matrix elements

The wave functions and matrix elements for the Morse oscillator were first derived by Rosen (13). However, they are given in a simpler form by Sage (3). Refer to ref. 3 for the definitions of the various quantities in eqs. [5], [7], and [8].

In the HCAO approach, Morse oscillator wave functions are used in $\vec{\mu}_{eg} \equiv \langle e|\vec{\mu}|g\rangle \equiv \langle v|\vec{\mu}|0\rangle$. The one-dimensional Morse oscillator potential is expressed as

$$[4] \qquad V(q) = D_e(e^{-aq} - 1)^2$$

where D_e is the dissociation energy and *a* is the Morse oscillator parameter with units of inverse length. The derivation of the wave functions is given elsewhere (3). The result is

$$[5] \qquad |v\rangle = N_v e^{-x/2} x^{C-v-1/2} L_v^{2C-2v-1}(x)$$

The energy eigenvalues for the Morse oscillator relative to the bottom of the potential well are given by (5)

$$[6] \qquad E_v/hc = (v+1/2)\tilde{\omega} - (v+1/2)^2\tilde{\omega}x$$

where $\tilde{\omega}$ and $\tilde{\omega}x$ are the Morse oscillator frequency and anharmonicity, respectively.

In most of our previous work, we have generated the various matrix elements of Morse oscillators using numerical integration methods. However, in this paper, an analytical expression for one matrix element in particular is needed, $\langle v|A(1 - e^{\gamma aq})|0\rangle$, where *A* and γ are adjustable parameters. The reasons for this will become clear later. For the present, we will only state the result.

Rewriting the matrix element, we have

$$[7] \qquad \langle v|A|0\rangle - A\langle v|e^{\gamma aq}|0\rangle = -A(2C)^{\gamma}\langle v|x^{-\gamma}|0\rangle$$

$\langle v|x^{-\gamma}|0\rangle$ has been evaluated previously (3). Using this result, we can write

$$[8] \qquad \langle v|A(1-e^{\gamma aq})|0\rangle = -A(2C)^{\gamma} N_v N_0 \binom{\gamma}{v} \Gamma(2C-\gamma-v-1)$$

Modelling of the DMF

The fundamental problem of modelling the DMF is how to obtain the coefficients $\vec{\mu}_i$ defined in eqs. [2*a*] and [3*a*]. There are two obvious choices to consider. The first possibility is a multivariate least-squares regression on the calculated ab initio points. The second is a numerical procedure to obtain an interpolating polynomial from the calculated ab initio points.

Our test system is the CH bond in CHD_2F. We have optimized the geometry at the Hartree–Fock level of theory using the 6-311++G(2d,2p) basis set. The Morse parameters for this bond are taken from experiment ($\tilde{\omega}$ = 3079 ± 6 cm^{-1} and $\tilde{\omega}x$ = 53.9 ± 1.5 cm^{-1} (14, 15)).

© 1999 NRC Canada

Table 1. Oscillator strengths for the CH-stretching transitions in CHD_2F based on the numerical integration of the transition dipole moment.

	Step size (Å)					
v	0.1	0.05	0.025	0.0125	Experimental[a]	Factor
1	6.058	6.078	6.078	6.078	6.48	10^{-6}
2	4.206	3.721	3.721	3.721	3.1	10^{-8}
3	12.34	8.365	8.364	8.365	11.3	10^{-9}
4	77.82	8.078	8.078	8.078	10.0	10^{-10}
5	2.073×10^4	8.517	8.519	8.517	6.2	10^{-11}
6	5.924×10^4	1.137	1.138	1.138		10^{-11}
7		1.952	1.951	1.952		10^{-12}
8		4.189	4.178	4.187		10^{-13}
9		1.072	1.070	1.072		10^{-13}
10		3.087	3.106	3.094		10^{-14}

[a]From refs. 14 and 15.

Fig. 1. Comparison of different orders in the polynomial expansion for the least-squares regression model of the DMF.

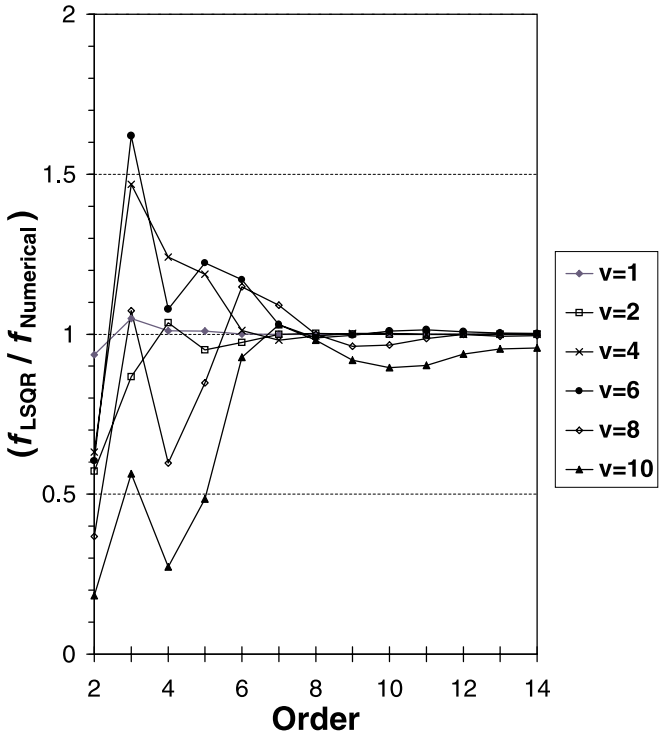

Fig. 2. Comparison of different orders in the polynomial expansion for the interpolating polynomial model of the DMF.

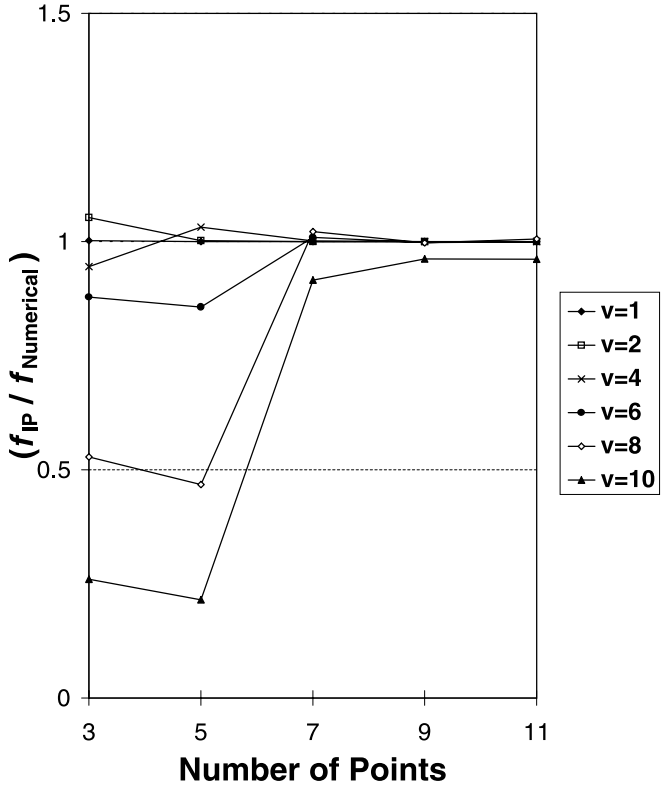

To make meaningful conclusions about the accuracy of the two methods, we need to compare them to an exact answer. An exact numerical result was obtained by numerically calculating $\vec{\mu}_{eg}$ directly from the ab initio results with decreasing step size until the calculation converged (Table 1). The integration converged to within 10% for a step size of 0.05 Å. However, we will compare our results to the smallest step size we considered (0.0125 Å). The numerical calculation was also used to determine the optimal integration range. We found that the range from $q = -0.5$ Å to $q = 0.9$ Å led to a relative error on the order of 10^{-4}, even for the worst case of the $0 \rightarrow 10$ transition.

Comparison of models

Before the two models could be compared, it was necessary to determine the optimal step size between data points. In the least-squares regression, a step size of 0.05 Å was sufficient. However, as in the numerical integration, we use the smallest step size (0.0125 Å). The range used in the regressions was the same as that used in the numerical integration. In the interpolating polynomial, since the data points must be equally spaced around $q = 0$, a smaller step size places limits on the range of points included in the model. A step size of 0.1 Å balances the need to sample a large enough range with the need for enough data points.

© 1999 NRC Canada

Fig. 3. Comparison of DMFs for CHD_2F, *x* component, for different levels of theory. All calculations used the 6-311++G(2d,2p) basis set.

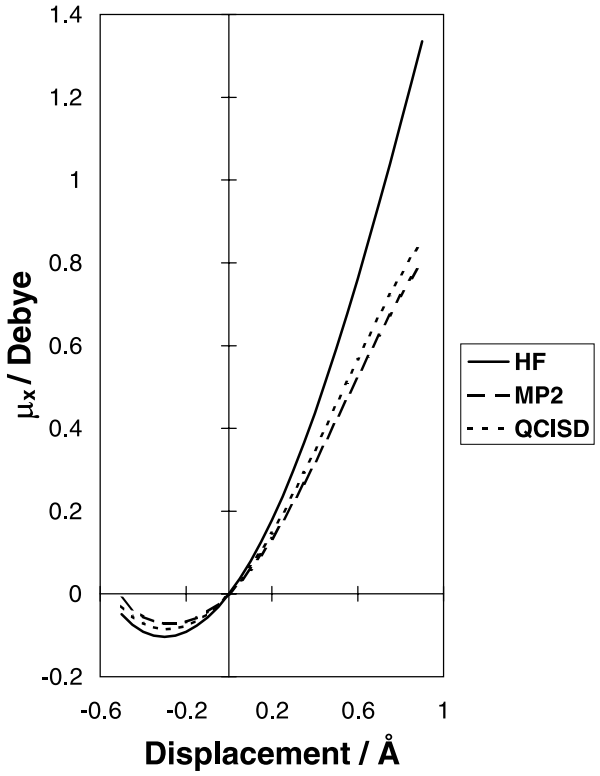

Once the details of the calculations were decided upon, we could perform the calculations for different polynomial orders and compare them to the exact numerical result. Figures 1 and 2 show the effect of differing polynomial orders in the regression and the interpolating polynomial, respectively.

Conclusions

Both methods produce good results, provided that the order of the polynomial generated is sufficiently high. Results within a few percent of the exact numerical results are obtained for all values of *v* with a DMF polynomial of at least sixth order from the interpolating polynomial method, and at least seventh order for the least-squares regression. This indicates that our usual practice of using a fourth order DMF polynomial may not be sufficient for accurately calculating overtone intensities above $v = 5$ or 6.

The results for the interpolating polynomial method are very good, especially given that useful results can be obtained from only a few data points. Thus, for practical reasons the interpolating polynomial method is better than the least-squares method. However, one should beware of the problems brought about by modelling high-order interpolating polynomials. Nonrealistic, rapid oscillations can occur between data points as the high-order terms attempt to fit between the data points (16). Since the DMF is so smooth, this is for the most part avoided unless the step size is small. The fact that the tenth order results show little improvement over the eighth order results is likely due to the onset of these oscillations combined with the lesser impact of very high-order terms.

The influence of electron correlation

The insensitivity of overtone intensities to the inclusion of electron correlation is now well established, at least for molecules with no unsaturated bonds (8, 9). However, what is still lacking is an understanding of the source of this insensitivity. Figure 3 shows that there are significant differences between a DMF calculated using Hartree–Fock theory and a DMF that accounts for electron correlation in some form. However, this difference in the DMF appears to cancel out in the final intensity calculation.

In our previous work, we attempted to explain this insensitivity using the idea that the inner wall of the potential might be more important for the calculation of overtone intensities, combined with the fact that the DMF over this inner part tends to be much less sensitive to electron correlation effects (8, 17). However, an examination of the value of the transition dipole moment calculated only over the inner wall compared to the value calculated over the outer wall shows that they are very nearly equal. The overtone intensity arises due to minute differences between the inner wall integration and the outer wall integration, and hence, the inner wall cannot be considered to be the only important region.

What we will present is a new method of analysing the insensitivity to electron correlation, based on a different model of the influence of electron correlation on the DMF.

Modelling electron correlation in the DMF

Consider two different dipole moments calculated at the same value of the bond coordinate *q*, one obtained using Hartree–Fock theory and one obtained using a theory including electron correlation. The influence of electron correlation is simply the difference between the two values. We want to fit this difference to a model. The natural choice is a polynomial expansion. However, examination of the difference over the important range of *q* suggests that some form of exponential type function may be more suitable. We have chosen to fit to the function $F(q) = A(1 - e^{\gamma q q})$, but there may be other possibilities. This function is nonlinear in the fitting parameters *A* and γ, and therefore requires an iterative approach to the best-fit parameters. The statistical procedure generates a fit to *A* and γa. A value for γ is obtained with a value for *a* derived from Morse parameters in (8), except for CHF_3 where the Morse parameters are derived from the polyad positions in (18) and for HCl and HF where the Morse parameters are taken from (19). Figure 4 shows the difference between the Hartree–Fock and the electron correlation DMF, as well as the least-squares fit to the function $F(q)$, for CHD_2F. Table 2 shows the values of the parameters *A* and γ for several XH bonds.

The matrix element for $F(q)$ is evaluated in eqs. [7] and [8]. We can gain more insight by considering the ratio of this matrix element for the *v*th overtone to the matrix element for the fundamental transition. We call this ratio $R_{F(q)}(v)$, where the symbol *R* is used to indicate a ratio, with the subscript indicating the function being ratioed. From the

© 1999 NRC Canada

Fig. 4. Comparison of the difference between the HF/6-311++G(2d,2p) and MP2/6-311++G(2d,2p) calculated DMF (x component) of CHD_2F with the model function $F(q)$. The fit is over the range of q = –0.3 Å to q = 0.4 Å with a step size of 0.05 Å.

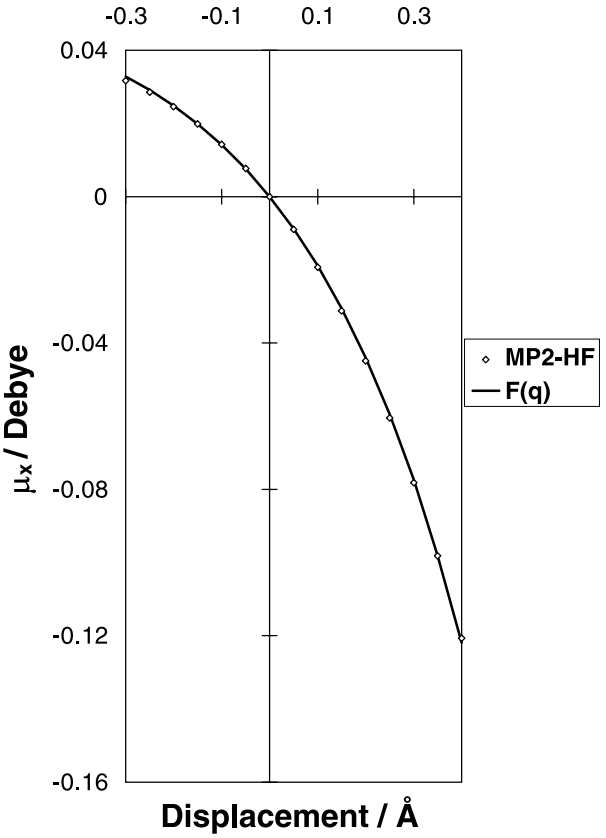

definitions of the gamma function and the binomial function (20), we can obtain

$$[9] \qquad R_{F(q)}(v) = \frac{\langle v|F(q)|0\rangle}{\langle 1|F(q)|0\rangle} = \sqrt{\left(\frac{4C(C-1)+2v(1-2C)+1}{(4C^2-8C+3)v!}\right)[(2C-2)\ldots(2C-v)]} \times \frac{(\gamma-1)\ldots(\gamma-v+1)}{(2C-\gamma-3)\ldots(2C-\gamma-v-1)}$$

The motivation for calculating this ratio is that we have an indication of how the influence of electron correlation changes with v. Furthermore, $R_{F(q)}(v)$ only depends on two parameters, the dimensionless anharmonicity $C = \omega/2\omega x$ and the fit parameter γ, which makes its general behaviour relatively simple to understand. Qualitatively, it is sufficient to study the factor appearing outside the root in eq. [9]. For all $v > 1$, integer values of $\gamma < v$ will correspond to roots of $R_{F(q)}(v)$. Thus, in the event that γ is close to an integer (which is the case for several of the examples in Table 2), the effects of electron correlation will be negligible for transitions to states with v greater than γ. Note that when $\gamma \approx 2$, the intensity of the first overtone (v = 2) can be affected by electron correlation, while higher overtones are unaffected.

To get more quantitative results, a criterion is needed for deciding how small $R_{F(q)}(v)$ must be in order for it to be considered negligible. An empirical rule is that the oscillator strength for the first overtone $f(2)$ tends to be a factor of 10^2 less than that of the fundamental transition $f(1)$, and falls by another order of magnitude for each subsequent overtone (21). If we call the ratio of oscillator strengths $R_{f_{\text{empirical}}}(v)$, we can write

$$[10] \qquad R_{f_{\text{empirical}}}(v) = \frac{f(v)}{f(1)} = \frac{1}{10^v}$$

We define a new parameter, ϵ, that corresponds to the fraction of oscillator strength due to electron correlation ($R_{f_{\text{EC}}}(v)$) that we are willing to allow. Thus, we write this criterion as

$$[11] \qquad R_{f_{\text{EC}}}(v) < \epsilon R_{f_{\text{empirical}}}(v) = \frac{\epsilon}{10^v}$$

Since the matrix element and the oscillator strength f are related by eq. [1], we can write

$$[12] \qquad R_{F(q)}(v) = \sqrt{\frac{\nu_{10}}{\nu_{v0}}}\sqrt{R_{f_{\text{EC}}}(v)} < \sqrt{\frac{\epsilon}{v}}\frac{1}{10^{v/2}}$$

where we have used as an approximation the fact that for a harmonic potential $\nu_{10}/\nu_{v0} = 1/v$.[2]

Figure 5 shows the area of parameter space where the criterion of eq. [12] is satisfied for several values of ϵ for $R_{F(q)}(3)$, i.e., for transitions to the v = 3 state. It also shows the parameters corresponding to some real XH bonds from Table 2.

Conclusions

Nearly all the XH bonds in Table 2 fit the form of $F(q)$ very closely upon the addition of electron correlation to the dipole moment calculation. There are a few exceptions, for example, the behaviour of the NH bond in NH_3 and the CH bond in CHF_3. In NH_3, the MP2 result in particular is atypical, while the QCISD result, when modelled using an interpolating polynomial, is virtually identical to the HF result except for the linear term. In CHF_3, on the other hand, the influence of electron correlation on the DMF is much less than in the rest of the species studied, which makes the lack of agreement with $F(q)$ that is present in this molecule unimportant.

Another interesting effect is the fact that the particular type of electron correlation has little effect on how well the bond fits the model. Even DFT methods seem to follow the

[2] Equation [12] should not be interpreted as a rigorous comparison of the relative contribution of electron correlation to the oscillator strength. Although we can model the DMF as $\vec{\mu} = \vec{\mu}_{\text{HF}} + F(q)$, and the matrix element as $\langle v|\mu|0\rangle = \langle v|\mu_{\text{HF}}|0\rangle + \langle v|F(q)|0\rangle$, once we calculate ratios, this easy comparison is lost. However, eq. [12] in combination with Fig. 5 still provides a useful estimate of the sensitivity of real XH bonds to the inclusion of electron correlation.

© 1999 NRC Canada

Table 2. Fit parameters for the function $F(q)$ of several single XH bonds.[a]

Molecule	Theory[b]	Component	A (Debye)[c]	γ[c,d]
CHD_2F[e]	MP2	x	0.057 ± 0.0012	1.658 ± 0.023
		z	(9.87 ± 0.46) × 10^{-3}	1.810 ± 0.053
	QCISD	x	0.031 ± 0.00065	2.006 ± 0.026
		z	(8.48 ± 0.49) × 10^{-3}	2.018 ± 0.070
	B3LYP	x	0.152 ± 0.011	1.578 ± 0.075
		z	0.124 ± 0.0052	1.139 ± 0.037
CH_4[f]	MP2	z	–0.084 ± 0.003	1.695 ± 0.042
	QCISD	z	–0.053 ± 0.002	1.745 ± 0.033
HF[f]	MP2	z	0.126 ± 0.003	1.009 ± 0.015
	QCISD	z	0.120 ± 0.0004	1.439 ± 0.003
HCl[f]	QCISD	z	0.059 ± 0.0005	1.954 ± 0.010
NH_3[g]	MP2	x	(–7.3 ± 2.2) × 10^{-3}	3.402 ± 0.391
		z	(–0.3 ± 2.0) × 10^{-3}	4.391 ± 8.520
	QCISD	x	0.327 ± 0.0097	0.142 ± 0.004
		z	2.845 ± 26.033	0.012 ± 0.107
CHF_3[f]	MP2	z	–0.204 ± 7.216	0.038 ± 1.342
	QCISD	z	–0.084 ± 0.065	0.177 ± 0.134

[a]The range of the fit in all cases is from q = –0.3 Å to q = 0.4 Å, with a step size of 0.05 Å.

[b]The 6-311++G(2d,2p) basis set is used in all cases, except for CHF_3 where the 6-311++G(d,p) basis set is used, and for HCl where the 6-311++G(3df,3pd) basis set is used.

[c]Uncertainties are one standard deviation.

[d]γ is dimensionless.

[e]The coordinate system has the z axis along the CF bond and the CH bond in the xz plane.

[f]The z axis is along the bond being modelled.

[g]The coordinate system has the z axis along the C_3 axis, with the chosen NH bond in the xz plane.

Fig. 5. Contour plot of $R_{F(q)}(3)$ with contours satisfying eq. [12] for values of ϵ = 0.1 (---), 0.05 (····), and 0.01 (—). Points correspond to some of the fit parameters from Table 2, with circles within ϵ = 0.01 and crosses between ϵ = 0.01 and 0.05.

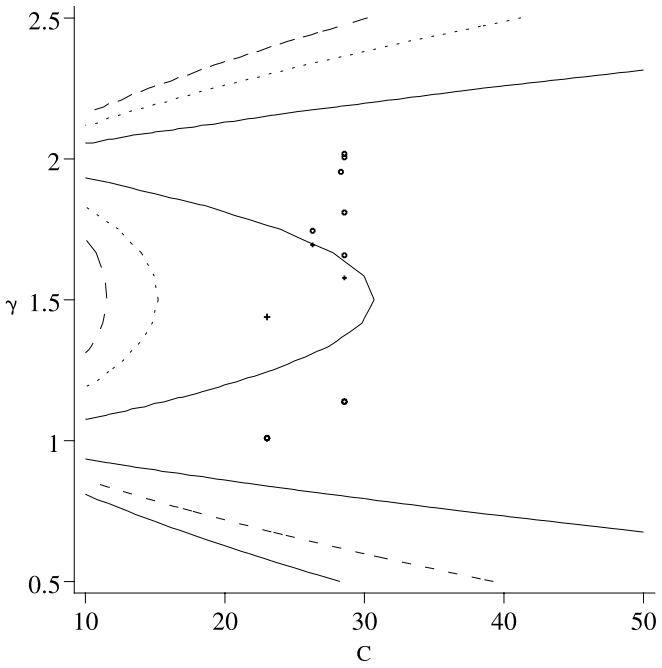

general trend, in agreement with recent results showing that DFT DMF calculations do not significantly alter overtone intensities calculated from a Hartree–Fock DMF. It appears that if one method of electron correlation can be fit to $F(q)$ for a particular bond, then other methods show the same behaviour.

If the bond under investigation does show a good fit to $F(q)$, the actual values of the fit parameters A and γ are relatively unimportant, especially for the higher overtones. A typical CH bond has a value of $\tilde{\omega}$ around 3000 cm^{-1}, and a value of $\tilde{\omega}x$ around 50 cm^{-1}. These values of the Morse parameters will give a value of C around 30, and other XH bonds will have dimensionless anharmonicities in this range as well. Figure 5 shows that a very wide range of values of γ will lead to a small contribution for $R_{F(q)}(3)$ at values of C of around 30. In the specific cases shown in Fig. 5, all points but three satisfy the criterion of ϵ = 0.01. The three remaining points are within the area satisfying ϵ = 0.05. From our calculations with eqs. [9] and [12], we have noted that this range widens even further for higher overtones, as expected.

Thus, a good approach would be to look at several types of XH bonds, and to determine how closely they agree with the model $F(q)$ in a small molecule upon the addition of electron correlation. When a similar type of bond occurs in a larger molecule, the result of the earlier calculation can be used to decide whether computational resources can be saved by ignoring electron correlation in the calculation on the larger molecule.

A further complication arises when considering molecules that contain unsaturated bonds, such as HCN. In our previous study (8), we noted that the influence of electron correlation was greater in HCN than in the other molecules under study. We believe that this difference arises due to the linearity of the DMF calculated at the Hartree–Fock level, which

© 1999 NRC Canada

leads to smaller intensities. Consequently, even though the influence of electron correlation on the DMF may be typical, the criterion of eq. [12] is no longer valid.

Despite the fact that we have obtained a reasonable mathematical framework for understanding the insensitivity of overtone intensities to the inclusion of electron correlation, we are still without a good physical explanation. A possible explanation could involve inspecting the electronic wave functions for the Hartree–Fock and the correlated calculations, and examining how they differ as q is changed. The fact that Hartree–Fock calculations tend to predict an ionic dissociation limit may be a factor.

As a referee has pointed out, it would be interesting to see the effect of extending the DMF calculation to a multiconfiguration approach (MCSCF). Normally, MCSCF becomes important for a reliable determination of the wave function when bond extensions are large. As we have noted above, the truly important region of the DMF for calculating intensities is determined by the overlap with the ground and excited state vibrational wave functions. Since the ground state wave function is centered at $q = 0$, the behaviour of the DMF at higher values of q is relatively unimportant. Nevertheless, it still may be worth investigating multi-reference effects to shed light on a physical picture for the observed insensitivity of the overtone intensities to the effects of electron correlation in the DMF.

Acknowledgments

Funding for this research has been provided by the Natural Sciences and Engineering Research Council of Canada.

References

1. O.S. Mortensen, B.R. Henry, and M.A. Mohammadi. J. Chem. Phys. **75**, 4800 (1981).
2. M.S. Child and R.T. Lawton. Faraday Discuss. Chem. Soc. **71**, 273 (1981).
3. M.L. Sage. Chem. Phys. **35**, 375 (1978).
4. R. Mecke. Z. Elektrochem. **54**, 38 (1950).
5. M.L. Sage and J. Jortner. Adv. Chem. Phys. **47**, 293 (1981).
6. H.G. Kjaergaard and B.R. Henry. J. Chem. Phys. **96**, 4841 (1992).
7. C.G. Gray, J.D. Goddard, S. Goldman, J. Yang, and J.D. Poll. Chem. Phys. Lett. **213**, 377 (1993).
8. H.G. Kjaergaard, C.D. Daub, and B.R. Henry. Mol. Phys. **90**, 201 (1997), and refs. therein.
9. H.G. Kjaergaard and B.R. Henry. Mol. Phys. **83**, 1099 (1994).
10. P.W. Atkins. Molecular quantum mechanics. 2nd ed. Oxford University Press, Oxford. 1983.
11. C. Eckart. Phys. Rev. **47**, 552 (1935).
12. M.J. Frisch, G.W. Trucks, H.B. Schlegel, P.M.W. Gill, B.G. Johnson, M.A. Robb, J.R. Cheeseman, T. Keith, G.A. Petersson, J.A. Montgomery, K. Raghavachari, M.A. Al-Laham, V.G. Zakrzewski, J.V. Ortiz, J.B. Foresman, J. Cioslowski, B.B. Stefanov, A. Nanayakkara, M. Challacombe, C.Y. Peng, P.Y. Ayala, W. Chen, M.W. Wong, J.L. Andres, E.S. Replogle, R. Gomperts, R.L. Martin, D.J. Fox, J.S. Binkley, D.J. Defrees, J. Baker, J.P. Stewart, M. Head-Gordon, C. Gonzalez, and J.A. Pople. Gaussian 94. Revision B.1. Gaussian, Inc., Pittsburgh, Pa. 1995.
13. N. Rosen. J. Chem. Phys. **1**, 319 (1933).
14. C. Kormann, M. Lewerenz, and M. Quack. Chem. Phys. Lett. **149**, 429 (1988).
15. T.-K. Ha, D. Luckhaus, and M. Quack. Chem. Phys. Lett. **190**, 590 (1992).
16. W.H. Press, B.P. Flannery, S.A. Teukolsky, and W.T. Vetterling. Numerical recipes in Pascal. Cambridge University Press, Cambridge. 1989.
17. K.K. Lehmann and A.M. Smith. J. Chem. Phys. **93**, 6140 (1990).
18. M. Quack. Annu. Rev. Phys. Chem. **41**, 839 (1990).
19. G. Herzberg. Molecular spectra and molecular structure I: spectra of diatomic molecules. 2nd ed. Van Nostrand, Princeton. 1950.
20. M. Abramovitz and I.A. Stegun (*Editors*). Handbook of mathematical functions. 10th printing. National Bureau of Standards, Washington, D.C. 1972.
21. B.R. Henry. The local mode model. *In* Vibrational spectra and structure. Vol. 10. Elsevier, Amsterdam. 1981.

© 1999 NRC Canada

Zinc-67 NMR study of tetrahedral and octahedral zinc sites with symmetrical oxygen, nitrogen, and sulfur ligands

Simon Sham and Gang Wu

Abstract: We report a ^{67}Zn nuclear magnetic resonance (NMR) study of compounds containing zinc ions coordinated by oxygen, nitrogen, and sulfur ligands. New information concerning ^{67}Zn nuclear quadrupole coupling constants (NQCC) and chemical shift was obtained from magic-angle spinning (MAS) spectra of solid compounds containing both natural abundance and enriched ^{67}Zn isotopes. Rapid ligand exchange processes of $[Zn(thiourea)_4]^{2+}$ in aqueous solutions were also observed.

Key words: ^{67}Zn NMR, nuclear quadrupolar coupling constant, ligand exchange.

Résumé : On a mesuré les spectres de résonance magnétique nucléaire (RMN) du ^{67}Zn de composés contenant des ions zinc coordinés à des ligands oxygénés, azotés et sulfurés. Grâce aux spectres obtenus par la technique de rotation à l'angle technique (magique) de composés solides contenant du ^{67}Zn en abondance naturelle ou enrichie, on a obtenu de nouvelles informations relatives aux constantes de couplage quadripolaire nucléaire (CCQN) et les déplacements chimiques du ^{67}Zn. On a aussi observé des processus d'échange rapide de ligand pour le $[Zn(thiourée)_4]^{2+}$.

Mots clés : RMN du ^{67}Zn, constante de couplage quadripolaire nucléaire, échange de ligands.

[Traduit par la Rédaction]

Introduction

Zinc is among the most important metal elements in biology and is an integral constituent of a large number of enzymes (1, 2). To study the catalytic or structural role of zinc ions in these enzymes, it is important to have a means of probing the nature of the zinc binding site. In the absence of X-ray crystallographic data, direct detection of diamagnetic d^{10} Zn^{2+} ions in biological systems is difficult because of the lack of a suitable spectroscopic probe. From an NMR perspective, ^{67}Zn (the only NMR-active zinc isotope) is among a number of potentially important but insensitive metal nuclei such as ^{43}Ca and ^{25}Mg. The insensitivity of ^{67}Zn NMR arises from the fact that ^{67}Zn is a quadrupolar nucleus (spin 5/2, $Q = 0.15 \times 10^{-28}$ m^{-2}) with low natural abundance (4.11%) and a small magnetogyric ratio ($\gamma = 1.6768 \times 10^7$ rad T^{-1} s^{-1}). Consequently, ^{67}Zn NMR experiments are remarkably difficult. In addition to the low intrinsic sensitivity, solution state ^{67}Zn NMR is further hampered by the fact that molecular tumbling motion always induces efficient ^{67}Zn quadrupole relaxation, resulting in short life times of Zeeman energy levels, which lead to broad NMR lines. To date, ^{67}Zn NMR of liquid samples has been limited to studies of either highly symmetric species or unsymmetrical complexes undergoing rapid exchange with large excessive $[Zn(H_2O)_6]^{2+}$ (3–6). Despite the biological relevance of zinc ions, the aforementioned practical difficulties have made ^{67}Zn NMR a nearly forgotten area. In the past, NMR studies of the metal binding sites in zinc-containing proteins have essentially relied on the utility of a surrogate nuclear probe, ^{113}Cd (7).

Solid-state NMR represents a useful approach to obtaining high-resolution NMR spectra for quadrupolar nuclei. In many aspects, it is more advantageous to study quadrupolar nuclei in the solid state than in solution. Since molecular motion is largely restricted in solids, quadrupole relaxation is not as efficient as in solution. As a result, the intrinsic resolution of solid-state NMR spectra is not limited by the lifetime of the quadrupole energy levels. However, solid-state ^{67}Zn NMR studies are still rare. Two solid-state ^{67}Zn NMR studies have appeared in the literature (8, 9); but the compounds under study are of cubic symmetry, so the electric field gradient (EFG) at the zinc site vanishes. The ^{67}Zn NMR study of $Zn(CH_3COO)_2 \cdot 2H_2O$ by Oldfield and coworkers (10) is the first report dealing with a noncubic zinc compound in the solid state. Later, Bastow and Stuart (11) obtained ^{67}Zn NMR spectra of both single-crystal and powdered ZnO samples. Recently, we reported some preliminary results of a natural abundance ^{67}Zn NMR study of zinc compounds with both tetrahedrally and octahedrally coordinated

Received March 22, 1999.

This paper is dedicated to Professor Ted Schaefer in recognition of his outstanding contributions to Canadian chemistry.

S. Sham and G. Wu.[1] Department of Chemistry, Queen's University, Kingston, ON K7L 3N6, Canada.

[1]Author to whom correspondence may be addressed. Telephone: (613) 533-2644. Fax: (613) 533-6669. e-mail: gangwu@chem.queensu.ca

 © 1999 NRC Canada

oxygen ligands (12). Here we extend our solid-state ^{67}Zn NMR study to compounds where the zinc center is coordinated by either nitrogen or sulfur ligands. To the best of our knowledge, ^{67}Zn nuclear quadrupole coupling constants (NQCC) have not been determined for any noncubic zinc center coordinated by nitrogen and sulfur ligands.

Experimental section

All solid-state NMR spectra were obtained on a Bruker Avance-400 NMR spectrometer operating at 25.036 MHz for ^{67}Zn nuclei. Solution NMR spectra were obtained on Bruker Avance-500 and Avance-400 spectrometers. All ^{67}Zn chemical shifts were referenced to an external sample of 1.0 M $Zn(NO_3)_2$ aqueous solution (δ_{iso} = 0 ppm). Magic-angle spinning (MAS) ^{67}Zn NMR experiments were performed using a probe purchased from Doty Scientific Inc. (Columbia, S.C.). Powder samples were packed into zirconium oxide rotors (5 mm o.d.). Typical sample spinning speeds were between 7 and 9 kHz. A pulse width of 5 μs was used, and the recycle time was between 1 and 10 s. Samples of ZnSe and $Zn(CH_3COO)_2{\cdot}2H_2O$ were obtained from commercial sources and used without further purification. Anhydrous $Zn(CH_3COO)_2$ was obtained by heating the corresponding hydrate sample in oven for 2 days at 80°C. ZnO (88% ^{67}Zn-enriched) was purchased from Trace Science International (Toronto, Ont.). Crystals of $^{67}Zn(ClO_4)_2{\cdot}6H_2O$ were formed by dissolving 25 mg of ^{67}ZnO in 3.6 mL of 0.25 M $HClO_4$. A solid sample of tetrakis(imidazole)zinc(II) perchlorate, $Zn[ImH]_4(ClO_4)_2$ (ImH = imidazole), was then obtained by slow evaporation of a 1:4 molar ratio mixture of $^{67}Zn(ClO_4)_2{\cdot}6H_2O$ and imidazole (81 mg) from 1 mL of 95% ethanol. An aqueous solution of $^{67}Zn(NO_3)_2$ was prepared by dissolving 24 mg of ^{67}ZnO in 1.1 mL of 0.5 M HNO_3. To this solution, 93 mg of thiourea, $SC(NH_2)_2$, in 1 mL of distilled H_2O was added. Crystals of tetrakis(thiourea)zinc(II) nitrate, $^{67}Zn[SC(NH_2)_2]_4(NO_3)_2$, were then formed by slow evaporation of the solvent. For concentration-dependent experiments, the concentration of $[Zn]^{2+}$ was kept constant at 0.65 mM, and an appropriate amount of thiourea was added to the solution to form a specific $[Zn]^{2+}$ to thiourea concentration ratio. Solution ^{67}Zn NMR experiments were carried out at room temperature (298.5 K), using a pulse width of 55.0 μs and a recycle delay of 100 ms. Typically, 2000–3000 scans were collected. Prior to Fourier Transformation (FT), FIDs were left-shifted to remove data points due to probe ring-down, followed by 200–250 Hz exponential line broadening. Simulations of solid-state NMR spectra were performed on a Pentium 200 personal computer using the SOLIDS program package kindly provided by Dr. Klaus Eichele and Professor Rod Wasylishen (Dalhousie University, Halifax, N.S.).

Results and discussion

Figure 1 shows ^{67}Zn MAS spectra of solid ZnSe and $Zn(ClO_4)_2{\cdot}6H_2O$ obtained at 9.4 T. The cubic structure of ZnSe (13) yields a negligible ^{67}Zn NQCC at the zinc center, and therefore, the MAS spectrum of ZnSe shows a sharp isotropic peak centered at 276 ppm with a full width at the half-height (FWHH) of 16 Hz. Interestingly, this value is even smaller than that observed for the standard reference sample, $Zn(NO_3)_2$ (aq), which has a line width of 80 Hz. In an early study, Haller et al. (8) reported a 50 Hz line width for the ^{67}Zn NMR signal from a stationary ZnSe sample. Close inspection of the spectrum presented in Fig. 1(*a*) showed no indication of any indirect spin–spin coupling (J) between ^{67}Zn and ^{77}Se (spin 1/2, natural abundance = 7.58%) nuclei, suggesting that $^1J(^{67}Zn, ^{77}Se)$ must be smaller than the observed line width.

Fig. 1. ^{67}Zn MAS spectra of (*a*) natural abundance ZnSe (number of scans, 360; recycle delay, 1 s; spinning rate, 5.0 kHz) and (*b*) ^{67}Zn-enriched $Zn(ClO_4)_2{\cdot}6H_2O$ (number of scans, 128; recycle delay, 10 s; spinning rate, 6.0 kHz). Spinning sidebands are marked as "ssb."

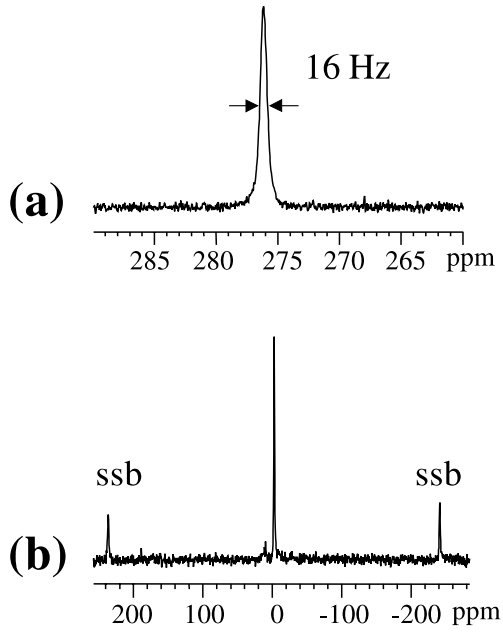

The isotropic ^{67}Zn chemical shift observed for solid $^{67}Zn(ClO_4)_2{\cdot}6H_2O$ is –3 ppm, which suggests a similar zinc environment in both solid and solution state. The crystal structure of $Zn(ClO_4)_2{\cdot}6H_2O$ at room temperature (space group $P6_3mc$) (14) reveals that the zinc ion is coordinated by six water molecules with a nearly perfect O_h site symmetry. The Zn—O distances are 2.123 and 2.152 Å. The O-Zn-O angles are very close to those expected for a regular octahedron, e.g., 86.3°, 179.0°, 94.4°, and 84.9°. From the line width observed in the ^{67}Zn MAS spectrum, it is estimated that e^2qQ/h is less than 0.2 MHz.

Figure 2(*a*) shows the natural abundance ^{67}Zn MAS spectrum of $Zn(CH_3COO)_2$. The spectrum exhibits a typical line shape arising from the second-order quadrupolar interaction (15). The isotropic ^{67}Zn chemical shift of $Zn(CH_3COO)_2$ is found to be 245 ppm, which is similar to that found for ZnO (11, 12) where the zinc atom is tetrahedrally bonded to four oxygen atoms. No solution ^{67}Zn NMR data are available in the literature for zinc centers coordinated to four oxygen ligands. The crystal structure of $Zn(CH_3COO)_2$ (space group *Fdd*2) indicates that the zinc ion is in a slightly distorted tetrahedral environment (16). The Zn—O bond length varies from 1.914 to 1.955 Å, and the O-Zn-O angle ranges from

© 1999 NRC Canada

Fig. 2. Experimental (solid lines) and calculated (broken lines) ^{67}Zn MAS spectra of (*a*) natural abundance $Zn(CH_3COO)_2$ (number of scans, 32 225; spinning rate, 8.5 kHz; recycle delay, 1 s), (*b*) ^{67}Zn-enriched $Zn(imidazole)_4(ClO_4)_2$ (number of scans, 16 774; recycle time, 1 s; spinning rate, 8.1 kHz), and (*c*) ^{67}Zn-enriched $Zn(thiourea)_4(NO_3)_2$ (number of scans, 19 188, recycle time, 2 s; spinning rate, 9.1 kHz).

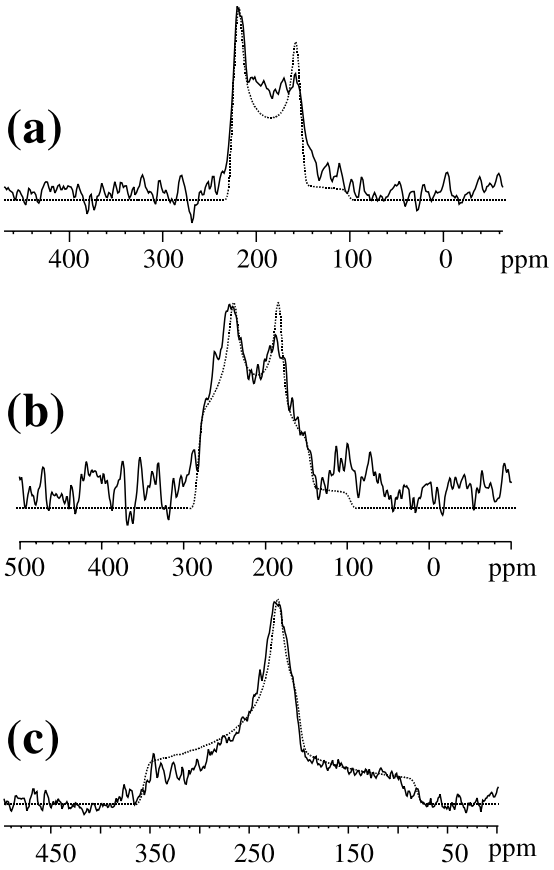

102.2° to 115.9°. Analysis of the MAS line shape shown in Fig. 2(*a*) yields that e^2qQ/h = 2.42 MHz and η = 0.1.

To explore the sensitivity enhancement by isotopic enrichment, we prepared two ^{67}Zn-enriched compounds: $^{67}Zn[ImH]_4(ClO_4)_2$ and $^{67}Zn[SC(NH_2)_2]_4(NO_3)_2$. The enrichment level is about 88% for both compounds. Figures 2(*b*) and (*c*) show the ^{67}Zn MAS spectra of the two ^{67}Zn-labeled compounds. For $^{67}Zn(ImH)_4(ClO_4)_2$, the isotropic ^{67}Zn chemical shift is 291 ppm, which is comparable to the value of 264 ppm observed in acetone solution. The ^{67}Zn chemical-shift value for zinc ions coordinated by four nitrogen ligands is also in agreement with that observed in $[Zn(NH_3)_4]^{2+}$ from solution ^{67}Zn NMR studies (3). However, both the line width and peak position of the solution state ^{67}Zn spectrum of $^{67}Zn(ImH)_4(ClO_4)_2$ were found to be solvent dependent. For example, the ^{67}Zn NMR spectrum of $Zn(ImH)_4(ClO_4)_2$ in methanol exhibits a peak at 280 ppm with a much larger line width, 2500 Hz, than that found in acetone, 500 Hz. Furthermore, we did not observe any ^{67}Zn NMR signal from an aqueous solution of $Zn(ImH)_4(ClO_4)_2$, presumably due to rapid ligand exchange (vide infra). The crystal structure of $Zn(ImH)_4(ClO_4)_2$ (space group *C*2/*c*) shows that the zinc ion lies on a crystallographic C_2 axis and is tetrahedrally coordinated by four nitrogen atoms from the imidazole molecules (17). The two independent Zn—N(imidazole) bond lengths are nearly identical, 1.997 and 2.001 Å. The N-Zn-N angles range from 105.3° to 113.3°. Analysis of the ^{67}Zn MAS line shape shown in Fig. 2(*b*) also yields that e^2qQ/h = 2.80 MHz and η = 0.4. To our knowledge, $Zn(ImH)_4(ClO_4)_2$ represents the only example where the ^{67}Zn NQCC for a ZnN_4 coordination environment is determined.

Figure 2(*c*) shows the ^{67}Zn MAS spectrum of $^{67}Zn[SC(NH_2)_2]_4(NO_3)_2$. The isotropic ^{67}Zn chemical shift is 359 ppm, which is in agreement with those reported for zinc sites coordinated by four sulfur atoms (3). From analysis of the ^{67}Zn MAS spectrum, we obtained that the ^{67}Zn NQCC is 3.15 MHz with η = 1. The crystal structure of $Zn[SC(NH_2)_2]_4(NO_3)_2$ (space group *Pnaa*) indicates that the zinc ions are coordinated by four sulfur atoms from the thiourea ligands (18). The two Zn—S distances are 2.324 and 2.361 Å, which are considerably longer than the Zn—N distances in the zinc–imidazole complex. The S-Zn-S angle between the two longer Zn—S bonds is 100.0°, and the angle between the two shorter Zn—S bonds is 121.5°, both of which deviate considerably from the perfect tetrahedral angle. It is also noted that the ^{67}Zn EFG tensors in $Zn(ImH)_4(ClO_4)_2$ and $Zn[SC(NH_2)_2]_4(NO_3)_2$ exhibit very different asymmetry parameters. This observation is somewhat surprising, since the two compounds have a similar tetrahedral arrangement at the zinc center.

Compared with the ^{67}Zn MAS spectrum of natural abundance $Zn(CH_3COO)_2$, as shown in Fig. 2(*a*), the overall sensitivity enhancement in the ^{67}Zn MAS spectra of the two ^{67}Zn-enriched compounds does not appear as dramatic as expected from the enrichment level, i.e., a factor of 20. Although solution ^{67}Zn NMR did prove that the ^{67}Zn enrichment procedure was successful, several other factors may contribute to the apparent lack of full signal enhancement in the ^{67}Zn spectra of $^{67}Zn(ImH)_4(ClO_4)_2$ and $^{67}Zn[SC(NH_2)_2]_4(NO_3)_2$. First, the molecular size of $Zn(ImH)_4(ClO_4)_2$ (FW = 536) and $Zn[SC(NH_2)_2]_4(NO_3)_2$ (FW = 493) is larger than that of $Zn(CH_3OO)_2$ (FW = 183). Second, in the case of $^{67}Zn(ImH)_4(ClO_4)_2$, a small sample of the enriched compound (ca. 50 mg) was used, which is much less than ca. 150 mg used for the natural abundance $Zn(CH_3COO)_2$ sample. Third, the ^{67}Zn spin-lattice relaxation time (T_1) is much longer in $^{67}Zn(ImH)_4(ClO_4)_2$ and $^{67}Zn[SC(NH_2)_2]_4(NO_3)_2$ than in $Zn(CH_3COO)_2$. By performing ^{67}Zn MAS experiments with different recycle delays, we were able to provide an estimate for ^{67}Zn T_1 in $^{67}Zn[SC(NH_2)_2](NO_3)_2$, $T_1 \approx 2$ s. In $Zn(CH_3COO)_2$, however, the T_1 was estimated to be less than 0.5 s (12). After considering all these factors, the sensitivity enhancement in Figs. 2(*b*) and (*c*) seems reasonable. It is worth pointing out that our attempts to record ^{67}Zn MAS spectra for natural abundance samples of $Zn(ImH)_4(ClO_4)_2$ and $Zn[SC(NH_2)_2]_4(NO_3)_2$ were unsuccessful, presumably due to the long T_1 values.

Similar to the case of the zinc imidazole complex, we also observed rapid ligand exchange in the aqueous solution of $Zn[SC(NH_2)_2]_4(NO_3)_2$. Figure 3 shows the result of the concentration study to examine the rapid ligand exchange process in $Zn[SC(NH_2)_2]_4(NO_3)_2$. When the concentration of thiourea is low, the ^{67}Zn chemical shift is close to 0 ppm, in-

© 1999 NRC Canada

Table 1. Solid-state ^{67}Zn NMR data for zinc compounds.

Compound	Zinc coordination	δ_{iso} (ppm)	e^2qQ/h (MHz)	η	Ref.
ZnO (hexagonal)	ZnO_4	240.1	2.407	0.0	11
		240	2.40	0.0	12
ZnS (cubic)	ZnS_4	378	0	—	8
		380.5	0	—	11
		381.9	0	—	12
ZnS (hexagonal)	ZnS_4	365	<0.5	0	11
		364.5	<0.4	0	12
ZnSe (cubic)	$ZnSe_4$	273	—	—	8
		276	—	—	This work
ZnTe (cubic)	$ZnTe_4$	85	—	—	8
$K_2Zn(CN)_4$ (cubic)	ZnC_4	291	0	—	9
$Zn(CH_3COO)_2\cdot 2H_2O$	ZnO_6	0	5.3	0.85	10
$ZnSO_4\cdot 7H_2O$	ZnO_6	10	1.70	0.2	12
$Zn(CH_3COO)_2$	ZnO_4	245	2.42	0.1	This work
$Zn(imidazole)_4(ClO_4)_2$	ZnN_4	291	2.80	0.4	This work
$Zn(thiourea)_4(NO_3)_2$	ZnS_4	359	3.15	1.0	This work
$Zn(ClO_4)_2\cdot 6H_2O$	ZnO_6	–3.0	<0.2	—	This work

Fig. 3. ^{67}Zn NMR spectra of aqueous solutions of $Zn(NO_3)_2$ and thiourea at different thiourea conc./$[Zn^{2+}]$ ratios. The pH value of the solution varies from 4.20 (1:1) to 3.78 (1:9).

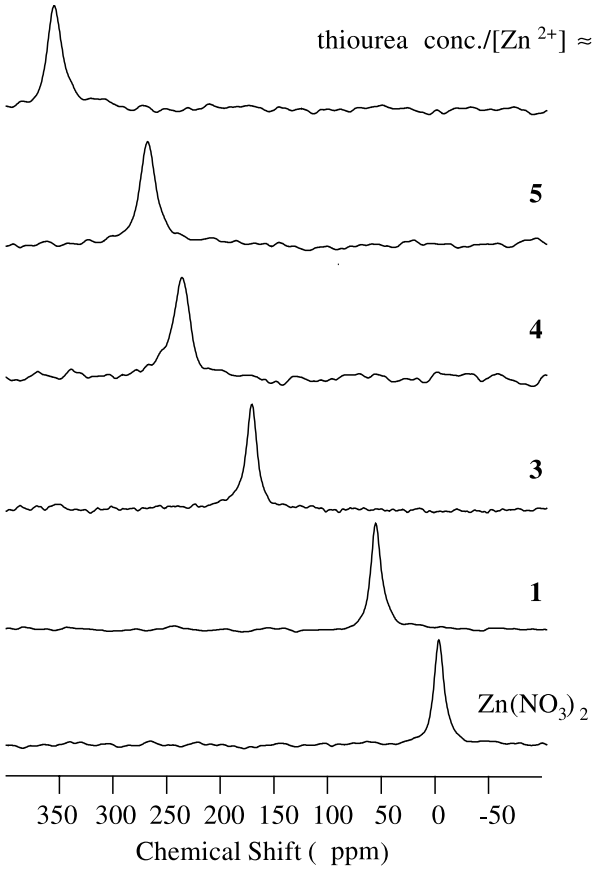

dicating the existence of $[Zn(H_2O)_6]^{2+}$ species. As the concentration of the thiourea ligand is increased, the ^{67}Zn NMR signal is shifted toward higher frequencies. At the highest metal–ligand ratio used in this study, thiourea conc./$[Zn^{2+}] \approx 9$, the ^{67}Zn chemical shift of 355 ppm for the solution sample is practically identical to that observed in the solid state, 359 ppm.

To examine possible trends in solid-state ^{67}Zn NMR parameters, we summarize in Table 1 the presently available data in the literature for zinc compounds. It is noted that the ^{67}Zn NQCC has also been determined in zinc metal, e^2qQ/h = 11.983 MHz (19–21); however, it is reasonable not to compare this value with those obtained for zinc compounds. With this exception, the largest ^{67}Zn NQCC found in zinc compounds is that in $Zn(CH_3COO)_2\cdot 2H_2O$, e^2qQ/h = 5.3 MHz (10). The crystal structure of $Zn(CH_3COO)_2\cdot 2H_2O$ (22) indicates that the zinc ion is coordinated by six oxygen atoms in a very distorted octahedral environment. Four of the six oxygen atoms are from the acetate groups. The other two oxygen atoms are those from the water molecules. Whereas, the Zn—O bond length varies slightly from 2.14 to 2.18 Å, a significant distortion from perfect O_h symmetry exists in the O-Zn-O bond angles. For example, large distortions are found when the two mutually *trans* oxygen atoms are due to the acetate and water, respectively, i.e., O(Ac)-Zn-O(W) = 152°, or when the two *cis* oxygen atoms are from the same acetate group, O(Ac)-Zn-O(Ac) = 61°. The distortion is, however, smaller when the two *cis* oxygen atoms arise from the acetate and water, respectively, i.e., O(Ac)-Zn-O(W) = 108°. To study the possible correlation between ^{67}Zn NQCC and molecular structure, we have used a parameter called the mean deviation of bond angles as a measure of the degree of deviation of the zinc site of interest from a perfect symmetry, T_d or O_h. The mean deviation of bond angles can be defined for a tetrahedral site as

$$[1] \qquad \Delta(T_d) = \frac{1}{4}\sum_i \left| \theta_i - 109.5° \right|$$

where θ_i is the ith bond angle across the zinc center. In a similar fashion, one can define a mean deviation of bond angles for an octahedral site using 90° and 180° as perfect angles. In Fig. 4, ^{67}Zn NQCC is plotted against the mean deviation of bond angles as defined in eq. [1] for presently available ^{67}Zn NMR data. As seen in Fig. 4, the octahedral

© 1999 NRC Canada

Fig. 4. Plot of ^{67}Zn NQCC versus mean bond angle deviation from perfect T_d (■) and O_h (●) symmetry.

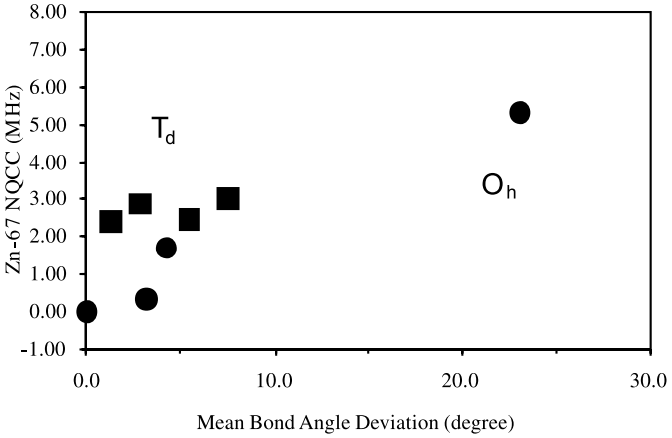

compounds appear to show a correlation between the magnitude of the ^{67}Zn NQCC and the degree of deviation from the O_h symmetry, whereas the tetrahedral compounds are insensitive to the mean deviation of bond angles, at least within the presently available data. It is also somewhat surprising that a very small distortion from the perfect T_d symmetry in ZnO (O-Zn-O: 108.14° and 110.77°) (23) results in a reasonably large ^{67}Zn NQCC, 2.40 MHz. However, $ZnSO_4 \cdot 7H_2O$ exhibits larger distortion (O-Zn-O: 80.6°, 97.5°, 172.3°) than ZnO but has a smaller ^{67}Zn NQCC, 1.7 MHz. It is clear that using the mean deviation of bond angles alone to explain the results may be oversimplified because the model does not consider the nature of the Zn—ligand bond. For the octahedral compounds examined in this study, the zinc ions are coordinated to six oxygen atoms with similar bond lengths, 2.09 ± 0.10 Å. Thus, it is perhaps not surprising that a reasonable correlation is observed among octahedral compounds. However, the Zn—ligand distance for the tetrahedral compounds varies from 1.914 to 2.000 to 2.361 Å for Zn—O (acetate), Zn—S (thiourea), and Zn—N (imidazole), respectively. This discrepancy may be responsible for the lack of correlation between ^{67}Zn NMR parameters and molecular structure among tetrahedral compounds. Nevertheless, more investigations are definitely required before one can draw any conclusion about the correlation between ^{67}Zn NMR parameters and molecular structure.

Based on the presently available solid-state ^{67}Zn NMR data, it seems that the value of 5.3 MHz found in $Zn(CH_3COO)_2 \cdot 2H_2O$ may represent an upper limit of the ^{67}Zn NQCC for zinc ions coordinated octahedrally by *symmetrical* ligands but a lower limit for octahedral compounds with *unsymmetrical* ligands. The zinc binding geometry in the zinc–insulin complex belongs to the latter case, since each of the two zinc sites in the two-zinc insulin hexamer is coordinated by three imidazolyl nitrogen atoms and three water oxygen atoms (24). In light of the new solid-state ^{67}Zn NMR data, it appears that the value of 1.86 MHz suggested for the ^{67}Zn NQCC in insulin by Shimizu and Hatano (25) may be grossly underestimated.

Conclusions

In this study, we have focused on the solid-state ^{67}Zn NMR spectra of tetrahedral and octahedral zinc centers that are symmetrically coordinated by water, acetate, imidazole, and thiourea ligands. It is well known that the active zinc sites in metalloproteins usually contain *unsymmetrical* ligands. Therefore, it would be desirable, although technically challenging, to extend these solid-state ^{67}Zn NMR studies to some model compounds where the zinc center resembles those in zinc-containing proteins. Unfortunately, to this date, our efforts in recording solid-state ^{67}Zn NMR signals for unsymmetrical zinc sites have been unsuccessful, presumably due to the large quadrupole coupling constants associated with those sites. It should be noted that the solid-state ^{67}Zn NMR results reported in this study were obtained at a relatively low magnetic field, 9.4 T. Since the second-order quadrupolar broadening is inversely proportional to the applied magnetic field strength, the availability of very high-field instrument (18.8 T or greater) holds the promise of making unsymmetrical coordination zinc sites accessible.[2]

Acknowledgments

This research was supported by research and equipment grants from the Natural Sciences and Engineering Research Council of Canada (NSERC).

References

1. S.J. Lippard and J.M. Berg. Principles of bioinorganic chemistry. University Science Books, Mill Valley, Calif. 1994.
2. J.J.R. Frausto da Silva and R.J.P. Williams. The biological chemistry of the elements. Oxford University Press, Oxford. 1991.
3. P. Granger. *In* Transition metal nuclear magnetic resonance. *Edited by.* P.S. Pregosin. Elsevier Science Publishers B.V., Amsterdam, The Netherlands. 1991. pp. 285–346.
4. M. Kodaka, T. Shimizu, and M. Hatano. Inorg. Chim. Acta, **78**, L55 (1983).
5. T. Shimizu and M. Hatano. Inorg. Chem. **24**, 2003 (1985).
6. A. Delville and C. Detellier. Can. J. Chem. **64**, 1845 (1986).
7. K. McAteer, A.S. Lipton, and P.D. Ellis. *In* Encyclopedia of nuclear magnetic resonance. *Edited by* D.M. Grant and R.K. Harris. Wiley, Chichester, U.K. 1996. pp. 1085–1091.
8. M. Haller, W.E. Hertler, O. Lutz, and A. Nolle. Solid State Commun. **33**, 1051 (1980).
9. G. Wu, S. Kroeker, and R.E. Wasylishen. Inorg. Chem. **34**, 1595 (1995).
10. A.C. Kunwar, G.L. Turner, and E. Oldfield. J. Magn. Reson. **69**, 124 (1986).
11. T.J. Bastow and S.N. Stuart. Phys. Status Solidi B: **145b**, 719 (1988).
12. G. Wu. Chem. Phys. Lett. **298**, 375 (1998).
13. R.W.G. Wyckoff. Crystal structure. Wiley, New York. 1963.
14. S. Ghosh, M. Mukherjee, A. Seal, and S. Ray. Acta Crystallogr. Sect. B: Struct. Sci. **B53**, 639 (1997).

[2] After the submission of this manuscript, two solid-state ^{67}Zn NMR studies have appeared in the literature (26, 27).

© 1999 NRC Canada

15. E. Kundla, S. Samoson, and E. Lippmaa. Chem. Phys. Lett. **83**, 229 (1981).
16. A.V. Capilla and R.A. Aranda. Cryst. Struct. Comm. **8**, 795 (1979).
17. C.A. Bear, K.A. Duggan, and H.C. Freeman. Acta Crystallogr. Sect. B: Struct. Crystallogr. Cryst. Chem. **B31**, 2713 (1975).
18. R. Vega, A. López-Castro, and R. Márquez. Acta Crystallogr. Sect. B: Struct. Crystallogr. Cryst. Chem. **B34**, 2297 (1978).
19. H. Herberg, J. Abart, and J. Voitländer. Z. Naturforsch. A: Phys. Chem. Kosmophys. **34A**, 1029 (1979).
20. J. Goyette and R.V. Pound. Phys. Rev. B: Condens. Matter, **B35**, 391 (1987).
21. T.J. Bastow. J. Phys.: Condens. Matter, **8**, 11309 (1996).
22. J.N. van Niekerk, F.R.L. Schoening, and J.H. Talbot. Acta Crystallogr. **6**, 720 (1953).
23. H. Schulz and K.H. Thiemann. Solid State Commun. **32**, 783 (1979).
24. M.J. Adams, T.L. Blundell, E.J. Dodson, G.G. Dodson, M. Vijayan, E.N. Baker, M.M. Harding, D.C. Hodgkin, B. Rimmer, and S. Sheat. Nature (London), **224**, 491 (1969).
25. T. Shimizu and M. Hatano. Inorg. Chim. Acta, **76**, L177 (1983).
26 T. Vosegaard, U. Andersen, and H.J. Jakobsen. J. Am. Chem. Soc. **121**, 1970 (1999).
27 F.H. Larsen, A.S. Lipton, H.J. Jakobsen, N.C. Nielsen, and P.D. Ellis. J. Am. Chem. Soc. **121**, 3783 (1999).

© 1999 NRC Canada

Solvent dependence of rotational energetics and formyl-proton long-range spin–spin coupling behavior of 2,6-dichloro- and 2,6-dinitrobenzaldehydes using dipolar couplings and temperature dependence of long-range couplings

Juhani Lounila, Yrjö Hiltunen, Kari Tuppurainen, Anja Pulkkinen, and Reino Laatikainen

Abstract: The formyl rotational energetics, solvent effects on the energetics and formyl-proton spin–spin coupling behavior of 2,6-dichlorobenzaldehyde were studied by using dipolar couplings analysis and the temperature dependence of the spin–spin couplings. The general form of the rotational potential was taken from molecular mechanics and the conjugative $\sin^2 \Theta$-type component (where Θ is the formyl-ring dihedral angle) was then optimized using the dipolar couplings obtained by analyzing ^{1}H NMR and ^{13}C proton satellite spectra in a liquid crystal solvent. The optimization based on the dipolar couplings gave the following rotational free energy potential: $V(\Theta) = 4.5 \cos^6 \Theta + 10.7\ (\pm 2.0) \sin^2 \Theta$, in kJ/mol. The analysis based on the temperature dependence of ^6J data allowed estimation of solvent effects on the potential. For example, the potentials in acetone and in acetonitrile differ by a $1.0 \sin^2 2\Theta$ (in kJ/mol). The chloroform solvent effect can be described by term of $-1.0 \cos^6 \Theta$. When the formyl-proton six-bond coupling data was fit, assuming it obeyed the expression $^6J(\Theta) = {}^6J_{90} \sin^2 \Theta + {}^6J_0$ and assuming $^6J_0 = 0.015$ Hz, the analysis yielded $^6J_{90}$ of –0.48 (± 0.03) Hz. The scalar coupling temperature dependence method was applied also to the conformational analysis of 2,6-dinitrobenzaldehyde.

Key words: spin–spin coupling, dipolar coupling, solvent effect, rotational barrier, benzaldehyde.

Résumé : Faisant appel à une analyse du couplage dipolaire et de l'influence de la température sur les constantes de couplage, on a étudié les énergies associées à la rotation du formyle, les effets de solvant sur ces énergies ainsi que le comportement de couplage spin–spin formyle-proton du 2,6-dichlorobenzaldéhyde. La forme générale du potentiel de rotation a été tirée de calculs de mécanique moléculaire et on a ensuite optimisé la composante de conjugaison de type $\sin^2 \Theta$ (dans lequel Θ est l'angle dièdre entre le formyle et le noyau) à l'aide des couplages dipolaires obtenus en analysant les spectres RMN du ^{1}H et les satellites du proton dans les spectres du ^{13}C mesurés dans un solvant cristal liquide. L'optimisation réalisée en se basant sur les couplages dipolaires conduit au potentiel d'énergie libre de rotation suivant: $V(\Theta) = 4{,}5 \cos^6 \Theta + 10{,}7\ (\pm 2{,}0) \sin^2 \Theta$, en kJ/mol. L'analyse résultant de la variation des valeurs de ^6J en fonction de la température permet d'évaluer les effets de solvant sur le potentiel. Par exemple, les potentiels dans l'acétone et dans l'acétonitrile diffèrent par $1{,}0 \sin^2 2\Theta$ (en kJ/mol). L'effet de solvant du chloroforme peut être décrit en termes de $-1{,}0 \cos^6 \Theta$. Quand on a ajusté les données de couplage formyle-proton à travers six liaisons en faisant l'hypothèse que $^6J(\Theta) = {}^6J_{90} \sin^2 \Theta + {}^6J_0$ et $^6J_0 = 0{,}015$ Hz, l'analyse conduit à une valeur de $^6J_{90}$ de –0,48 (± 0,03) Hz. On a aussi appliqué la méthode de la variation du couplage scalaire en fonction de la température à l'analyse conformationnelle du 2,6-dinitrobenzaldéhyde.

Mots clés : couplage spin–spin, couplage dipolaire, effet de solvant, barrière à la rotation, benzaldéhyde.

[Traduit par la Rédaction]

Received June 17, 1999.

This paper is dedicated to Professor Ted Schaefer in recognition of his outstanding contributions to Canadian chemistry.

J. Lounila and A. Pulkkinen. Department of Physical Sciences, University of Oulu, P.O. Box 3000, FIN-90401 Oulu, Finland.
Y. Hiltunen,[1] K. Tuppurainen, and R. Laatikainen.[2] Kuopio University NMR Research Group, Department of Chemistry, University of Kuopio, P.O. Box 1627, FIN-70211 Kuopio, Finland.

[1]Present address: Raahe Institute of Computer Engineering, FIN-92101 Raahe, Finland.
[2]Author to whom correspondence may be addressed. Telephone: +358-17-163248. Fax: +358-17-163259.
e-mail: reino.laatikainen@uku.fi

 © 1999 NRC Canada

Introduction

The experimental characterization of rotational energetics in solution, and especially a determination of the solvent dependence of the energetics, are difficult tasks although there are a number of methods available, the most common being the infrared, Raman and dynamic NMR spectroscopies (1, 2). The former methods suffer from experimental problems, DNMR suits only for relatively large rotational barriers, and all of them produce only little information about the shape of the barrier. The DNMR barrier is usually interpreted by using two parameters, $\Delta H^{\#}$ and $\Delta S^{\#}$, although the relationship between them and the shape of barrier is not straightforward (3). The problems of the optical spectroscopies have been reviewed by Jorgensen (2). For these reasons the studies on solvent effects on low rotational barrier are rather scarce, if the studies on systems containing nitrogen or sulphur are ignored. In aromatic systems, also the *J*-method, the conformational dependence of spin–spin couplings of benzylic protons, can also be used for very low barriers (4). The *J*-method has been developed and widely applied by Ted Schaefer for estimation of rotational energetics in aromatics. In this paper we show that significant information about the formyl-ring torsion barrier in 2,6-dichlorobenzaldehyde (26DCBA) and 2,6-dinitrobenzaldehyde (26DNBA) can be derived using dipolar couplings obtained in a liquid crystal solvent and by examining the temperature dependence of the formyl proton long-range couplings in various isotropic solvents. The theory and applications of the dipolar coupling method has been previously discussed by Emsley (5).

It has been found previously, for example, that a change of solvent from CS_2 to DMSO stabilizes the CF-off-planar conformation of benzyl fluoride by 2 kJ/mol (6), a value typically found by other means (2). An opposed change is indicated by the ^6J data for benzyl alcohol (7) while the data for ethylbenzene imply practically no solvents effects (8). Medium effect analyses based on the *J*-method have been carried out also for some other alkoxy benzenes (9), benzal fluoride (10), 3,5-dichlorobenzyl fluoride (11), and fluorobenzyl fluorides (12). The solvent effect on the relatively low barrier of 2,6-fluorobenzaldehydes was studied by DNMR (13). The results suggest that the electrostatic interactions play a role, but not straightforward, in the phenomenon. In general, a polar solvent favors conformations of larger dipole or higher moments although the packing effects may also be significant when the barrier is flat (2), as it is in our case. For 26DCBA, another electrostatic mechanism may also operate: the barrier contains a significant contribution from the chlorine–oxygen Coulombic repulsion. This contribution depends on the medium around the molecules and should be reduced in a medium of higher dielectric constant. We have used the explanation for the behavior of some methylene malonaldehydes (14), and it has also been examined theoretically (15). The solvent may operate also by entropic mechanism (16).

The *J*-method can be used only if the conformational behavior of the coupling is known. This is the case with CH_2-type protons, but not with a formyl proton. The problem can be solved and also more information about the energetics is obtained by using the temperature dependence of the spin–spin couplings, "the temperature dependent *J*-method" (17). In our case, the determination of the conformational behavior of the formyl proton in benzaldehydes offers a challenge, because being usually very small, the couplings are difficult to determine, and on the other hand, the formyl proton spin–spin coupling behavior differs interestingly from that of the methyl, methylene, and vinyl protons (18–20): it is known that $^6J_{90}$ in the well-known expression for benzylic six-bond coupling (4)

$$[1] \qquad {}^6J(\Theta) = {}^6J_{90} \sin^2 \Theta + {}^6J_0$$

is abnormally small, maybe –0.30 to –0.500 Hz (19, 20), whereas it is ca. –1.2 Hz for toluene (21). Θ is the dihedral angle between the ring and the benzylic proton. It has been also shown that the value of $^6J_0$ is, unexpectedly, positive for some *meta*-substituted benzaldehydes (22) and, probably, for 2-chlorobenzaldehyde (19), while for other CH protons it can be assumed to be zero or negative. The estimation of $^6J_{90}$ is difficult because the conjugation holds the formyl group tightly in the ring plane, and the group is not easily twisted out of plane even by large substituents. The largest known values have been reported for 2,6-dinitrobenzaldehyde, –0.230 Hz, and 2,6-dichlorobenzaldehyde, –0.156 Hz (23). Because the potential is a sum of opposing conjugational and steric (including Coulombic) terms and because the Coulombic terms depend also on the solvent, it is also difficult to predict $\langle \sin^2 \Theta \rangle$ (= the expectation value of $\sin^2 \Theta$) with theoretical methods. In 26DNBA there are three rotors and a reliable estimation of $\langle \sin^2 \Theta \rangle$ is theoretically even more difficult.

The low torsion barrier of 26DCBA offers a good probe for study of the solvents effects on the torsion barrier. In this work, the dipolar coupling method and the "temperature dependent *J*-method" were used to study the formyl torsion energetics and the barrier shape of 26DCBA in various isotropic solvents. An estimate of $^6J_{90}$ was also obtained.

Experimental

The samples for isotropic spectra were prepared as ca. 10 wt.%/vol.%, degassed and measured in a routine way (19). The spectra were measured on a Bruker AM 400WB spectrometer. The temperatures were determined by the methanol method (24).

The liquid crystal solvent was a mixture composed of 42 wt.% Phase IV (eutectic mixture of *p*-methoxy-*p*′-*n*-butylazoxybenzenes by Merck) and 58 wt.% ZLI 1167 (eutectic mixture of 4-*trans* cyano, 4′-*trans* alkyl bicyclohexyls (alkyl = propyl, pentyl, and heptyl) by Merck). The liquid crystal sample contained 5 wt.% of 2,6-dichlorobenzaldehyde. The ^1H and ^{13}C NMR spectra were recorded at 399.8 and 100.5 MHz, respectively, on a JNM-GX400 spectrometer (at about 300 K) from a coaxial double tube (outer diameter 5 mm) with $CDCl_3$ as a locking substance in the interwall space. The indirect spin–spin coupling constants, J_{ij}, of 26DCBA were measured in the isotropic phase of the Phase IV – ZLI 1167 mixture (at about 350 K).

A rotation barrier calculation with full geometry optimisations at the HF/6-31G* level was done using the Gaussian98 program (25) running on IBM RISC/6000 320 workstation.

© 1999 NRC Canada

Fig. 1. The geometry and numbering of 2,6-diclorobenzaldehyde.

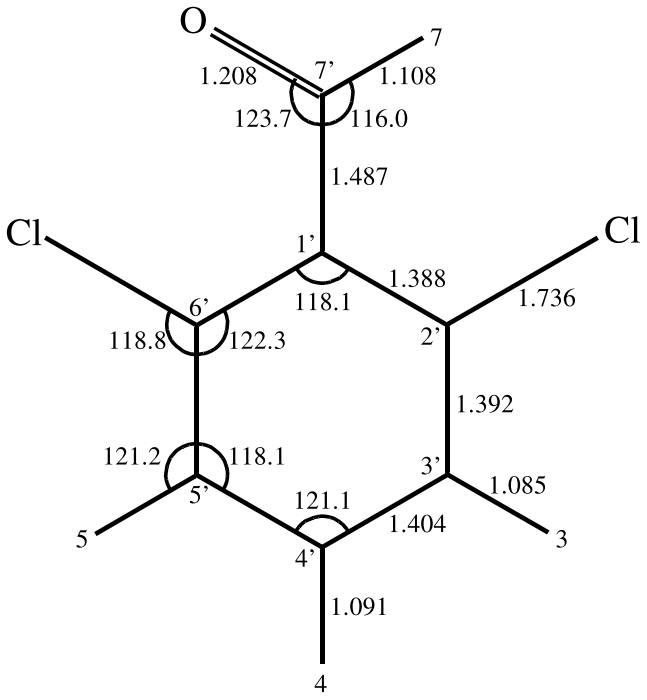

Table 1. Spectral parameters (in Hz) of 2,6-dichlorobenzaldehyde in the mixed nematic phase (42% Merck phase IV + 58% Merck ZLI 1167).

i, *j*	D_{ij}[a]	J_{ij}
3, 4	–950.775(3)	8.1
3, 5	–201.413(8)	1.3
3, 7	–84.103(5)	0.4
3, 1′	–82.30(10)	5.8
3, 2′	–304.03(10)	0.0
3, 3′	–2766.51(9)	170.7
3, 4′	–396.26(9)	0.0
3, 5′	–101.78(10)	7.6
3, 6′	–65.58(12)	0.0
3, 7′	–29.36(14)	0.0
4, 7	–48.695(8)	–0.1
4, 1′	–47.62(16)	0.0
4, 2′	–75.42(9)	11.7
4, 3′	–314.62(10)	0.0
4, 4′	–2040.63(12)	167.9
4, 7′	–17.82(14)	0.0
7, 1′	–172.5(3)	24.5
7, 2′	–88.45(10)	0.0
7, 3′	–31.30(12)	0.0
7, 4′	–21.39(19)	0.0
7, 7′	–716.81(14)	188.84

[a]The numbers in parentheses give the 90% confidence limits in the last significant numbers of the spectral parameters, arising from the random errors. The total errors are somewhat larger, as they contain also systematic contributions arising from the uncertainties in the fixed values of the *J*-couplings.

Spectral analysis

The numbering of the nuclei of 26DCBA is shown in Fig. 1.

The spectra measured in the isotropic and nematic phases of the Phase IV – ZLI 1167 mixture were analysed by the computer program LEQUOR (26). The spin–spin coupling constants J_{ij} obtained in the isotropic phase were kept constant in the refinements of the dipolar couplings D_{ij}. The resulting *J* and *D* couplings are shown in Table 1.

The isotropic spectra were analyzed with the current version of the program PERCHit (27). The resulting spectral parameters of 26DCBA are given in Table 2. The analyses yielded also the values of dipolar couplings between the aromatic protons. The phenomenon has been explained previously for some aromatics (28): the larger absolute values of the dipolar couplings in benzene solution arise from parallel stacking of the benzene and 26DCBA. Because the *D* couplings correlate rather strongly with the ^3J coupling, especially for those spectra approaching the AX_2 type, we bound the values of the *D*-couplings to each other by the constraining equation $D_{meta} = 0.192\ D_{ortho}$, arising from the geometry of aromatic ring (28). The constraint reduced the confidence limits of all the couplings by 20–80%. The spectrum of 26DNBA was close to an AX_2 system and did not allow the determination of the dipolar couplings (Table 3).

Results and discussion

The molecular mechanics of 2,6-dichlorobenzaldehyde

A STO-3G calculation has given the rotational potential $V(\Theta) = 2.7 \sin^2 \Theta - 2.8 \sin^2 2\Theta$ (in kJ/mol) (20). In the same way, a fitting to seven energy values calculated at the HF/6-31G* level gave $V(\Theta) = 3.0 \sin^2 \Theta - 3.2 \sin^2 2\Theta$ or $V(\Theta) = 15.8 \sin^2 \Theta + 12.8 \cos^4 \Theta$. The rms value was 0.03 kJ/mol for both of the fittings. The potential in benzaldehyde is markedly higher than the first terms; the $\sin^2 \Theta$ terms do not represent a pure conjugational effect but are sums of a positive conjugational and a negative term arising from formyl-ring steric interactions. In general, also more sophisticated ab initio methods give rather poor results for the formyl rotational energetics in benzaldehydes (29–31), and the uncertainties of less than 1 kcal/mol (proposed recently (31)) are too large for estimation of $\langle \sin^2 \Theta \rangle$ when the barriers are as low as they are in this case. Because molecular mechanics allows a separation of the conjugational and steric terms, it was used in this work to find the shapes of the terms, which were then optimized on the basis of the experimental data.

Because the standard MMP2 parametrisation (32) gives 28.3 kJ/mol for the rotational barrier for benzaldehyde, which is close to the observed values in solution, reviewed in ref. 29, the method is expected to give a rather realistic picture about the barrier. We decomposed the computed rotational energy function of 26DCBA into two parts, first, into the conjugational component:

$$[2] \qquad V_c = 29.27 \sin^2 \Theta - 16.38$$

and, second, into the steric part:

$$[3] \qquad V_{st} = 17.14 \cos^2 \Theta + 4.51 \cos^6 \Theta + 23.34$$

The rms values of the fits were 0.07 and 0.02 kJ/mol, for eqs. [2] and [3], respectively. The first terms of the equations partly cancel each other, explaining thus the lowness of the

© 1999 NRC Canada

Table 2. ^{1}H NMR spectral parameters (in Hz) of 2,6-dichlorobenzaldehyde.[a]

T (K)	$\nu_{3,5} - \nu_4$	$^3J_{34}$	D_{34}	$^5J_{37}$	$^6J_{47}$	rms/n[b]
10% (v/v) in acetonitrile-d_3						
298	8.165	8.1452(5)	–0.0056(2)	0.3998(6)	–0.1303(8)	0.0004/13
310	7.531	8.1447(4)	–0.0054(3)	0.4001(8)	–0.1329(12)	0.0005/12
330	6.434	8.1434(3)	–0.0047(2)	0.4007(7)	–0.1385(11)	0.0005/13
345	5.433	8.1404(4)	–0.0042(3)	0.4013(9)	–0.1416(13)	0.0005/11
10% (v/v) in acetone-d_6						
267	22.863	8.1444(4)	–0.0059(2)	0.4018(4)	–0.1325(4)	0.0003/16
285	22.403	8.1422(5)	–0.0054(2)	0.4024(5)	–0.1363(5)	0.0003/16
305	21.522	8.1402(5)	–0.0049(2)	0.4031(4)	–0.1402(5)	0.0003/16
330	20.386	8.1372(3)	–0.0043(2)	0.4036(3)	–0.1456(3)	0.0002/16
10% (v/v) in $C_6D_6/CDCl_3$ (1:9)						
305	14.189	8.1124(5)	–0.0048(3)	0.3983(4)	–0.1242(5)	0.0002/10
310	15.240	8.1111(8)	–0.0049(4)	0.3988(6)	–0.1260(9)	0.0003/10
328	16.647	8.1086(6)	–0.0045(3)	0.4000(4)	–0.1290(9)	0.0002/10
330	16.940	8.1081(4)	–0.0044(2)	0.4000(4)	–0.1303(4)	0.0003/14
10% (v/v) in $C_6D_6/CDCl_3$ (1:1)						
287	–66.286	8.1140(7)	–0.0069(4)	0.3990(3)	–0.1222(2)	0.0002/14
305	–63.932	8.1116(13)	–0.0064(6)	0.4001(5)	–0.1272(4)	0.0003/14
317	–62.745	8.1098(4)	–0.0059(2)	0.4009(2)	–0.1300(2)	0.0001/14
330	–61.564	8.1084(7)	–0.0057(4)	0.4016(3)	–0.1328(2)	0.0002/14
345	–60.408	8.1055(5)	–0.0051(3)	0.4027(2)	–0.1365(2)	0.0002/16
10% (v/v) in $C_6D_6/CDCl_3$ (9:1)						
298	–107.898	8.1117(13)	–0.0076(6)	0.4033(4)	–0.1297(4)	0.0003/16
300	–107.775	8.1121(14)	–0.0076(7)	0.4041(4)	–0.1303(5)	0.0003/16
310	–104.909	8.1110(20)	–0.0077(10)	0.4031(6)	–0.1314(6)	0.0005/16
320	–102.375	8.1088(10)	–0.0069(5)	0.4041(3)	–0.1348(3)	0.0002/16
330	–99.907	8.1069(9)	–0.0063(5)	0.4040(3)	–0.1369(3)	0.0002/16
345	–96.798	8.1053(6)	–0.0062(3)	0.4047(2)	–0.1396(2)	0.0001/14
10% (v/v) in CCl_4/C_6D_6 (8:2)						
305	–19.808[c]	8.0996(8)	–0.0055(4)	0.4046(8)	–0.1301(9)	0.0006/10
315	–22.135	8.0988(5)	–0.0055(4)	0.4045(4)	–0.1329(4)	0.0003/16
325	–22.853	8.0972(5)	–0.0052(3)	0.4051(5)	–0.1357(5)	0.0003/15
330	–21.248[c]	8.0977(9)	–0.0050(3)	0.4057(7)	–0.1366(9)	0.0007/12
335	–23.625	8.0965(4)	–0.0050(3)	0.4052(3)	–0.1376(3)	0.0001/15

[a]The numbers in parentheses give the 90% confidence limits in the last significant numbers of the spectral parameters.

[b]The residual root mean square/number of the frequencies used in the fitting. Very weak or strongly overlapping lines were ignored.

[c]Another sample, with slightly different concentration, was used at 305 and 330 K.

barrier. If the $\sin^2\Theta$ and $\cos^2\Theta$ terms are combined and the constant term (having no effect on $\langle\sin^2\Theta\rangle$) is ignored,

$$[4] \qquad V_{MM} = 12.14\ \sin^2\Theta + 4.51\ \cos^6\Theta$$

The first term contains now the conjugational energy and the $\cos^2\Theta$-shaped steric energy, the second one contains the $\cos^6\Theta$-shaped steric interactions. The theoretical barriers are depicted in Fig. 2.

The rotational potential and dipolar couplings

The anisotropy of the potential energy of a molecule in the average field generated by its neighbors distinguishes liquid crystals from ordinary liquids. The resulting anisotropy of the molecular motion leads to large intramolecular magnetic dipole–dipole interactions between nuclei, and to corresponding structure in the NMR spectrum. The resulting dipolar couplings D_{ij} contain detailed information on the geometry and potential energy functions of the molecule (33).

In the mean field approximation the external anisotropic forces acting on a molecule in a uniaxial liquid crystal environment are specified by the single particle potential energy U_{ext}. Its truncated series expansion in terms of the direction cosines of the director in the molecular frame, $\cos\theta_\alpha$, defines the symmetric and traceless *interaction tensor* $A_{\alpha\beta}$ (34):

$$[5] \qquad U_{ext} = -\frac{3}{2}\sum_{\alpha,\beta} A_{\alpha,\beta}\ \cos\theta_\alpha\ \cos\theta_\beta$$

The problem of describing the interaction between a nonrigid molecule and the liquid crystal mean field is essentially that of describing the dependence of $A_{\alpha\beta}$ on the molecular geometry. A straightforward solution is the hypothesis of

© 1999 NRC Canada

Table 3. Long-range spin–spin couplings (in Hz) of formyl proton in 2,6-dinitrobenzaldehyde.

Solvent	Temperature	$^6J_{74}$[a]	$^5J_{73}$[a]
Acetonitrile-d_3	303	(–)0.2327(4)	0.3710(6)
	336	(–)0.2292(12)	0.3745(20)
Acetone-d_6[b]	303	(–)0.2256(3)	0.3721(5)
	335	(–)0.2227(3)	0.3755(5)
$CDCl_3$/acetone-d_6	303	(–)0.2297(10)	0.3691(16)
(3:1, v/v)	336	(–)0.2233(11)	0.3735(19)
CD_2Cl_2	303	(–)0.2304(14)	0.3698(23)
C_6D_6	303	(–)0.2175(20)	0.3719(32)
	336	(–)0.2213(3)	0.3736(4)

[a]The numbers in parentheses give the 90% confidence limits in the last significant numbers of the spectral parameters.

[b]The relative shifts were ν(CHO) = 2.482, ν(3, 5) = 0.000, and ν(4) = 0.515 ppm. J_{34} = 8.268 Hz.

segment additivity of $A_{\alpha\beta}$: the interaction is built up from the contributions associated with the rigid segments of the molecule, considered as isolated entities. If the principal axis systems of the segmental interaction tensors are known, they are completely specified by two independent parameters each. These parameters are $\Delta A = A_3 - (A_1+A_2)/2 = 3A_3/2$, the *anisotropy* of the tensor, and $\eta = (A_1 - A_2)/A_3$, its *asymmetry*, where A_1, A_2, and A_3 are the principal values of the tensor (35). As these parameters are treated as geometry-independent constants, the dependence of the *molecular* $A_{\alpha\beta}$ on the geometry arises entirely from the rotations of the principal axes of the segmental tensors with respect to the molecule fixed frame. Thus, the external potential energy of each segment is separately described by the function [5], which can be written as

$$[6] \qquad U_{ext} = -\frac{\Delta A}{2}(3\cos^2\theta - 1 + \eta\sin^2\theta\cos 2\phi)$$

in which θ and ϕ are the spherical polar angles of the liquid crystal director in the principal axis system of the segmental $A_{\alpha\beta}$.

This so-called "zero-order" segment additivity has been used extensively to describe the anisotropic forces acting on non-rigid molecules in liquid crystals. Originally, Marcelja (36) generalized the Maier–Saupe theory of liquid crystals (37) by assuming an additive dispersive interaction between the mean field and each segment of mesogenic molecules consisting of rigid cores and flexible alkyl chains. Subsequently, Emsley et al. (38) extended this approach to a general second-order mean field interaction using essentially the spherical tensor equivalent of eq. [5]. Photinos et al. (39) proposed a more sophisticated additivity approach for alkyl chains, wherein the elementary rigid segments are the chords joining the midpoints of adjacent CC bonds, together with the terminal segments parallel with the CC bonds at the ends of the chain. The additivity scheme has been reasonably successful in its liquid crystal applications, that is, in studying the interactions associated with large-amplitude conformational changes in various mesogens and solutes (5) as well as with small-amplitude vibrational motions in solute molecules (40).

Fig. 2. The rotational barrier of 2,6-diclorobenzaldehyde predicted by (*a*) STO-3 G method, (*b*) HF/6-31G* method, (*c*) MM2 method, (*d*) the dipolar coupling analysis, (*e*) the *J*-method for acetone-d_6, (*f*) the *J*-method for $CDCl_3$ + benzene (9:1), and (*g*) the *J*-method for CCl_4 + benzene (9:1) solutions.

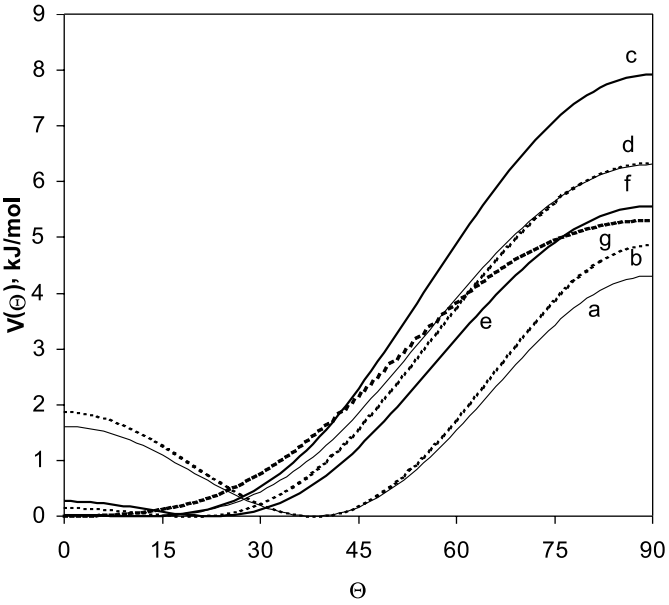

In 26DCBA, the rigid segments are the aromatic ring and the formyl group. As the isolated aromatic ring has C_{2v} symmetry, the directions of the principal axes of its interaction tensor are known: the axes 1 and 3 are taken to be in the plane of the ring, with the 3 axis along the *para* HC-CC direction. Thus, the interactions of the ring (denoted as R) are specified by the parameters ΔA_R and η_R. The principal axes of the formyl group are not completely determined by its symmetry. However, if the hydrogen is assumed to have a negligible effect on U_{ext}, then the interaction tensor of the formyl group can be taken to be cylindrically symmetric about the CO bond, and hence, its interactions are described by the single parameter ΔA_{CO}. This common approximation should be apt for the present case, because previous investigations (41) have indicated that in the particular liquid crystal solvent used in this study the determined values of ΔA_{CH} of the CH bonds of solute molecules are generally small. Thus, the external forces acting on 26DCBA can be characterized by a total of three independent parameters, ΔA_R, η_R, and ΔA_{CO}.

The total potential energy of the molecule is the sum

$$[7] \qquad U_{tot}(\theta, \phi, \Theta) = U^R_{ext}(\theta, \phi) + U^{CO}_{ext}(\theta, \phi, \Theta) + U_{int}(\Theta)$$

Here, $U_{ext}{}^R$ and $U_{ext}{}^{CO}$ are the external potential energies of the aromatic ring and the formyl group (CO bond), respectively, and U_{int} is the internal conformational energy of the molecule. The variables θ and ϕ are the spherical polar angles of the director in the ring fixed principal axis system 1, 2, 3 defined above, and Θ is the rotational angle between the planes of the ring and the formyl group. According to eq. [6], $U_{ext}{}^{CO}$ is a function of the single variable θ', the angle between the CO bond and the director (as η_{CO} is taken to be zero), which can be expressed as a function of θ, ϕ, and Θ.

© 1999 NRC Canada

The parameters specifying U_{tot}, i.e., ΔA_R, η_R, and ΔA_{CO}, and the coefficients of the rotational potential energy U_{int} can be determined from the experimental dipolar couplings D_{ij} between the magnetic nuclei i and j. The observable D_{ij} is the average value of the function

$$[8] \qquad d_{ij}\ (\theta, \phi, \Theta) = -P_2\ (\cos\ \alpha)\ K_{ij}\ \frac{P_2\ (\cos\ \Theta_{ij})}{r_{ij}^3}$$

over the reorientational and internal motions of the molecule (42). In eq. [8], $P_2(x) = (3x^2 - 1)/2$ is the second-order Legendre polynomial, α is the angle between the director and the applied magnetic field direction, Θ_{ij} is the angle between the director and the internuclear vector $\boldsymbol{r}_{ij}$ (of length r_{ij}), and $K_{ij} = \mu_0\, h\gamma_i\, \gamma_j/(16\pi^3)$. where μ_0 is the permeability in vacuo and γ_i is the magnetogyric ratio of the nucleus i. The angle Θ_{ij} is a function of θ and ϕ; in addition, Θ_{ij} and generally also r_{ij} depend on the rotational angle Θ, if one of the nuclei i, j is the formyl proton. Thus, if the motions of the molecule are treated by the classical Boltzmann statistics (as in the approaches of Marcelja (36), Emsley et al. (38), and Photinos et al. (39)), then the dipolar couplings can be computed by equations

$$[9] \qquad D_{ij} = \frac{1}{Z}\int_0^{\pi} d\theta \sin\theta \int_0^{2\pi} d\phi \int_0^{2\pi} d\Theta\, d_{ij}(\theta, \phi, \Theta) e^{-U_{tot}(\theta,\phi,\Theta)/kT}$$

where Z is the partition function:

$$[10] \qquad Z = \int_0^{\pi} d\theta \sin\theta \int_0^{2\pi} d\phi \int_0^{2\pi} d\Theta\ e^{-U_{tot}(\theta,\phi,\Theta)/kT}$$

If the molecular geometry is fixed, the theoretical expressions, eq. [9], are fitted to the experimental values of the dipolar couplings by the least squares adjustment of the parameters specifying U_{tot}.

The rotational potential from the dipolar couplings

Despite the number of the dipolar couplings (Table 1), it was necessary to apply severe constraints in the least-squares refinement of the parameters. The molecular geometry was kept fixed to the values given in Fig. 1, obtained by structural studies on similar compounds. The structure of the aromatic ring was taken to be identical with that of 1,3-dichlorobenzene as determined by a combined analysis of electron diffraction, rotation constant, and liquid crystal NMR data (43). The bond lengths and angles of the formyl group were taken from an electron diffraction study of terephthalaldehyde (44). The latter study indicates also that the formyl group leaves the geometry of the aromatic ring almost unchanged, thus lending support to the reliability of the present combined geometry.

As a matter of fact, the structure of the formyl group reported in ref. 44 is based on the set of average internuclear distances (r_g structure), while the ring geometry reported in ref. 43 is based on the average nuclear positions (r_α structure). In the present work the vibrational averaging effects were ignored (except for the one-bond couplings D_{CH}, see below), and thus the small differences between the r_g and r_α structures can be disregarded. However, it is well known (45) that the dipolar couplings between directly bonded nuclei involving a proton are significantly influenced by the vibrational motions. In particular, in various substituted benzene derivatives the harmonic vibrational corrections for the one-bond D_{CH} couplings in the ring are normally of the order of 9%. In fact, the values of these corrections are remarkably insensitive to the type of the substitution and liquid crystal solvent (except in anomalous cases where D_{CH} is very small due to an opportune orientation of the nuclear pair). For these reasons the one-bond D_{CH} couplings of 26DCBA were in the present work multiplied by a correction factor of 1.09. All the other vibrational corrections are much smaller, normally significantly less than 3%, corresponding to errors of less than 1% in the internuclear distances. As the relative errors in the fixed molecular geometry are probably larger than 1%, such small vibrational corrections are irrelevant. In any case, incorporation of accurate vibrational corrections in the analysis would necessitate also the incorporation of the so-called deformational corrections, which are due to the orientation-dependent distortions of the solute molecule in the liquid crystal environment (34, 35, 46). This in turn would increase the number of adjustable parameters (because the intermolecular interactions are then built up from the contributions associated with the individual *bonds* of the molecule), and the least-squares fit of the couplings would not result in well determined values for the parameters. Because the rotational effects on the formyl-ring geometry are similar in magnitude with the other vibrational corrections, no rotational corrections were done on the geometry. For example, our HF/6-31G* calculations indicate that the rotational effects on the formyl-ring CC bond are small; the bond-length grows from 1.501 to 1.511 Å when Θ grows from 0° to 90°. The corresponding effects on the C1′-C7-H7 and C2′-C1′-C7′ angles were +1.1° and +1.4°, respectively.

Only one coefficient in the rotational potential energy function U_{int} was sufficiently well determined to allow its refinement. Hence, the results of the molecular mechanics calculations described in the preceding section were used to write the dependence of U_{int} on the rotational angle Θ as

$$[11] \qquad U_{int}(\Theta) = V_2\ \sin^2\ \Theta + V_6\ \cos^6\ \Theta$$

where V_2 was an adjustable parameter, and V_6 was constrained to the calculated value of 4.51 kJ/mol (see eq. [4]).

The constrained fits of the 21 dipolar couplings resulted in well determined values for the four remaining parameters: $\Delta A_R = (29.1 \pm 1.2) \times 10^{-22}$ J, $\eta_R = 3.27 \pm 0.06$, $\Delta A_{CO} = (8.0 \pm 0.7) \times 10^{-22}$ J, and $V_2 = 10.7 \pm 0.9$ kJ/mol. With these values, the couplings are reproduced within 3.7% (the average deviation between the calculated and experimental couplings being 1.7%) except for the small long-range couplings $D_{37'}$ and $D_{47'}$ which have deviations of 6.1 and 4.6% (1.8 and 0.8 Hz), respectively. Hence, the level of agreement between the calculated and experimental data is within the uncertainty resulting from the fixed molecular geometry, together with the vibrational and deformational contributions. To allow for the effects of these systematic uncertainties on the error limits of the resulting parameters, standard deviations of 2% were assigned to the experimental couplings in the error analysis of the fitting procedure. Thus, the uncertainties

© 1999 NRC Canada

Table 4. Fitting of the ^6J data with various values of V_{st} (in kJ/mol) and $^6J_0$ (Hz).

	Model				
Parameter	A	B1	B[b]	B2	s (90%)[a]
V_c	8.9 $\sin^2\Theta$	9.3 $\sin^2\Theta$	9.8 $\sin^2\Theta$	10.8 $\sin^2\Theta$	0.2
V_{st}	4.5 $\cos^6\Theta$	4.5 $\cos^6\Theta$	4.5 $\cos^6\Theta$	5.5 $\cos^6\Theta$	Not opt.
$V_s(CD_3CN)$	1.0 $\sin^2 2\Theta$	1.0 $\sin^2 2\Theta$	1.0 $\sin^2 2\Theta$	0.9 $\sin^2 2\Theta$	<0.1
V_s(acetone)	0	0	0	0	
$V_s(C_6H_6/CDCl_3$, 1:9)	2.1 $\sin^2 2\Theta$	–0.9 $\cos^6\Theta$	–1.0 $\cos^6\Theta$	–0.9 $\cos^6\Theta$	<0.1
$V_s(C_6H_6/CDCl_3$, 1:1)	1.7 $\sin^2 2\Theta$	–0.8 $\cos^6\Theta$	–0.8 $\cos^6\Theta$	–0.8 $\sin^6\Theta$	<0.1
$V_s(C_6H_6/CDCl_3$, 9:1)	1.1 $\sin^2 2\Theta$	–0.5 $\cos^6\Theta$	–0.6 $\cos^6\Theta$	–0.5 $\sin^6\Theta$	<0.1
$V_s(CCl_4/C_6D_6$, 8:1)	1.2 $\sin^2 2\Theta$	1.2 $\sin^2 2\Theta$	1.2 $\sin^2 2\Theta$	1.1 $\sin^2 2\Theta$	<0.1
$^6J_{90}$	–0.469	–0.489	–0.483	–0.508	10
$^6J_0$	0.015	0.015	0	0.015	Not opt.
rms[c]	0.00040	0.00031	0.00032	0.00031	

[a]The 90% confidence limits, which are negligible when compared with the uncertainty arising from the uncertainty of the model.

[b]The best model. The models B1 and B2 are for an examination of the sensitivity of the solution for the assumptions done in the model B.

[c]The rms error (Hz) of the model.

of the parameters quoted above are the standard deviations propagating from these enlarged errors of the couplings.

The resulting $V_2 = 10.7 \pm 0.9$ kJ/mol is in good agreement with the values of 12.1 and 9.8 ± 1.0 kJ/mol obtained by the molecular mechanics calculation and the temperature dependence of the ^6J (see below), respectively. The result, together with the theoretical barriers and that based on the *J*-method, is presented in Fig. 2.

Estimation of rotational energetics and $^6J_{90}$ using temperature and solvent dependence of ^6J

Although all the spectral parameters of 26DCBA (Table 2) appeared solvent and temperature dependent, the relative variation (totally 14%) in ^6J is far larger than in the others (0.6% in ^3J and 1.7% in ^5J) and can be thus accounted for mostly by the solvent dependence of the conformational freedom of the formyl group. Our data offers thus an opportunity for estimation of solvent effects on low rotational potentials in solution.

For the data fitting we assumed that the rotational potential follows the function described above with

$$[12] \quad V = V_c \sin^2\Theta + V_{st} \cos^6\Theta + V_s$$

where the last term V_s arises from solvent and, that ^6J behaves as given by eq. [1]. $^6J_0$ is of ca. +0.01 Hz in 2-chlorobenzaldehyde, in benzaldehyde it is probably closer to zero (19), and thus if the substituent effects are additive, $^6J_0$ of 26DCBA should fall well into the range from 0 to 0.03 Hz. Although $^6J_0$ is sensitive to *meta* substitution (22), the equality of the coupling in benzaldehyde and salicylaldehyde (47) indicates no strong *ortho* substituent effect.

If we assume that potential terms are intrinsically solvent and temperature independent, we have five parameters (V_c, V_s, V_{st}, $^6J_{90}$, and $^6J_0$) to be fitted into the data. Because $^6J_0$ and $^6J_{90}$ correlate strongly, one of them must be fixed. Because $^6J_0$ is obviously rather close to zero or slightly positive (19), we fitted the data keeping $^6J_0$ fixed and just tested the sensitivity of the result to its value. Also V_{st} and V_c values correlate strongly. Therefore, V_{st} was fixed to 4.51 kJ/mol, as obtained by molecular mechanics. The fitting was done with program FUNNY using "classical averaging" in computing the ensemble of the $\sin^2\Theta$ term for eq. [1], as has been described before (17).

If the solvent potential is kept the same (i.e., $V_s = 0.0$) for all of the solvents, the rms error of the fit is 0.0048 Hz. The goodness of the fit depends also on the form of V_s: if it has the $\sin^2\Theta$ shape, the rms error is 0.00046 Hz, while 0.00041 or 0.00040 Hz are obtained by using $\cos^6\Theta$ or $\sin^2 2\Theta$ shaped V_s, respectively. The parameters obtained using the last one are given by the model A in Table 4. An inspection of the fits reveals some systematic trends in the calculated–observed differences. These are removed and the rms error is reduced to 0.0003 Hz by using different forms of V_s for each solvent. Admitting $^6J_{90}$ to be different in the polar (acetone and acetonitrile) and non-polar solvents does not improve the fit and the $^6J_{90}$ values do not differ significantly. The result of the last model, varying also V_{st} and $^6J_0$ are also given in Table 4. In the final fitting 27 observations were used, and the number of optimized parameters was seven.

We may conclude now, *first*, that the value of $^6J_{90}$ is not sensitive to the value V_{st} (an uncertainty of ca. 25% in latter causes 0.025 Hz uncertainty in $^6J_{90}$), and because $^6J_0$ is rather well defined, its uncertainty does not affect $^6J_{90}$ too much, *second*, that the solvent effects are insensitive of the approximations and are well described by 1–2 kJ/mol high terms, *third*, that the shape of V is not sensitive to the value of $^6J_0$ and V_{st} and is similar to that obtained with the other methods used in this work. If we assume that $V_6 = 4.51$ kJ/mol, the resulting V_2 term of 9.8 kJ/mol is in agreement with the above value of 10.7 kJ mol, obtained from the dipolar couplings. *Fourth*, the solvent effects do not follow the dielectricity of the solvent: the solvents effects of CD_3CN and CCl_4 are similar and different from that of acetone. This is in accordance with the predictions of Jorgensen (2): for flat barriers also the solvent-packing effects can be significant. The barrier is lowered in $CDCl_3$ suggesting that chloroform forms a hydrogen bond simultaneously to the formyl oxygen and the aromatic chlorine.

© 1999 NRC Canada

Conformational dependence of ^3J and ^5J

Although the variation of ^6J is far larger than that of ^3J and. ^5J, a part of the variation of the latter may arise from the formyl torsion. When ^3J is plotted vs. T or ^6J, the rms error is as large as 0.016 Hz. When a solvent effect J_s is included, the rms error is reduced to 0.0011 Hz with

[13] $$^3J = 8.1909(14) + 0.359(50)\ ^6J + J_s$$

J_s (zero for acetone) varies between 0.001 and –0.045 Hz, which is ca. 0.5% of the total value. The numbers in parentheses give the standard deviations of the coefficients. The result indicates that the conformational variation contribution is ca. 30% of that of ^6J. The corresponding plot for ^5J gives rms error of 0.0004 Hz with

[14] $$^5J = 0.3810(30) - 0.156(21)\ ^6J + J_s$$

where J_s varies between –0.003 and 0.002 Hz, which is ca. 1% of the total value. The rather small coefficient of the ^6J term reflects the so-called π-contribution to the ^5J (48, 49). Assuming $^6J_{90}$ of 0.48 Hz the contribution can be described with a term of 0.06 $\sin^2\Theta$, which is clearly smaller than the terms of 0.34 $\sin^2\Theta$ and 0.24 $\sin^2\Theta$ proposed for toluoic (49) and styrenoic systems (50), respectively.

Conformational analysis of 2,6-dinitrobenzaldehyde

The solvent and temperature behavior of the long-range couplings of 26DNBA are somewhat perplexing (Table 3). Anyhow, ^6J varies much more than ^5J suggesting that a great deal of the ca. 5% variation of the former (at 303 K) arises from conformational flexibility. The corresponding ca. 1% variation of ^5J does not correlate with that of ^6J and must thus be explained with an intrinsic solvent effect, which is not unexpected with the nitro groups. Because the equilibrium position of the formyl group, indicated by ^6J, and even the direction of the temperature dependence of ^6J depends on such a weak perturbation as solvent, we conclude that the rotational free energy potential at the equilibrium position is rather flat.

To estimate the formyl torsion barrier we parameterized MMP2 molecular mechanics to give a torsion barrier of 28.5 kJ/mol for benzaldehyde and barriers of 11 and 14 kJ/mol for nitrobenzene (the average value of the three literature values given in ref. 51 is 12.5 kJ/mol). All the four combinations of the parameters gave very flat potentials with $\langle\sin^2\Theta\rangle$ between 0.35 and 0.80; the average of 0.55 gave $^6J_{90}$ of –0.42 Hz. The result is sensitive to the force field parameters, and we may only conclude that $^6J_{90}$ is somewhere between –0.300 and –0.500 Hz.

Conclusions

All the methods used here agree that the rotational barrier of 2,6-dichlorobenzaldehyde is rather low, see Fig. 2. The solvent effect can be described with terms of 1–2 kJ/mol in size as presumed on the basis of Monte Carlo calculations (2) for flat potentials or as found experimentally (6–12). The changes in the shapes and values of the solvent effects cannot be explained by the polarity alone; also, packing effects seem to have some contribution to the solvent effects. Together with previous studies (17), we believe that there is enough evidence that the solvent and temperature dependence of long-range spin–spin couplings offers a sensitive tool also for study of weak solvent–solute interaction.

The above analysis indicates that $^6J_{90}$ of 2,6-dichlorobenzaldehyde is ca. –0.48 ± 0.03 Hz. The data of ^5J(CHO, H_m) suggest also that the expression for the coupling contains a 0.06 $\sin^2\Theta$ term, which is relatively smaller than for the toluoic (49) and styrenoic systems (50).

References

1. S. Mizushima. Structure of molecules and internal rotation. Academic Press, New York. 1954; R.J. Abraham and E. Bretschneider. *In* Internal rotation in molecules. *Edited by* W.J. Orville-Thomas. J. Wiley and Sons, New York. 1974. pp. 481–576.
2. W.L. Jorgensen. J. Phys. Chem. **87**, 5304 (1983).
3. A. Peyman and H.D. Beckhaus. Comput. Chem. **14**, 201 (1990).
4. W.J.E. Parr and T. Schaefer. Acc. Chem. Res. **13**, 400 (1980).
5. J.W. Emsley. *In* Encyclopedia of nuclear magnetic resonance. *Edited by* D.M. Grant and R.K. Harris. John Wiley & Sons, Chichester. 1996. pp. 2781–2787.
6. T. Schaefer, J. Peeling, and R. Sebastian. Can. J. Chem. **63**, 3219 (1985); T. Schaefer, C. Beaulieu, R. Sebastian, and G.H. Penner. Can. J. Chem. **68**, 581 (1990).
7. T. Schaefer, R. Sebastian, J. Peeling, G.H. Penner, and K. Koh. Can. J. Chem. **67**, 1015 (1989).
8. T. Schaefer, G.H. Penner, and R. Sebastian. Can. J. Chem. **65**, 873 (1986).
9. T. Schaefer, K.J. Cox, C.L. Morier, C. Beaulieu, R. Sebastian, and G.H. Penner. Can. J. Chem. **68**, 1553 (1990).
10. T. Schaefer, G.M. Bernard, Y. Bekkali, and D. McKinnon. Can. J. Chem. **74**, 1626 (1996).
11. T. Schaefer, J.R. Mansfield, F.E. Hruska, and R. Sebastian. Can. J. Chem. **70**, 1750 (1992).
12. T. Schaefer, R.W. Schurko, R. Sebastian, and F.E. Hruska. Can. J. Chem. **73**, 816 (1995).
13. T. Schaefer, C.S. Takeuchi, G.M. Bernard, and F.E. Hruska. Can. J. Chem. **73**, 106 (1995).
14. R. Laatikainen and V. Kral. J. Chem. Soc. Perkin Trans. 2, 1091 (1985); K. Tuppurainen and R. Laatikainen. J. Mol. Struct. (Theochem), **281**, 15 (1993).
15. M.W. Wong, M.J. Frisch, and K.B. Wiberg. J. Am. Chem. Soc. **113**, 4776 (1991); for later theoretical studies see also J.B. Foresman, T.A. Keith, K.B. Wiberg, J. Snoonian, and M.J. Frisch. J. Phys. Chem. **100**, 16 098–16 104 (1996).
16. A.D. Bain and P. Hazendonk., J. Phys. Chem. A, **101**, 7182 (1997).
17. R. Laatikainen. Magn. Res. Chem. **24**, 588 (1986); R. Laatikainen and K. Tuppurainen. Magn. Res. Chem. **24**, 595 (1986); R. Laatikainen, E. Kolehmainen, T. Kuokkanen, and K. Tuppurainen. J. Magn. Reson. **78**, 9 (1988).
18. R. Laatikainen, V. Kral, and P. Äyräs. J. Magn. Reson. **74**, 12 (1987), and refs. therein.
19. R. Laatikainen, K. Tuppurainen, Y. Hiltunen, S. Lötjönen. Magn. Reson. Chem. **28**, 939 (1990).
20. T. Schaefer, J. Peeling, G.H. Penner, A. Lemire, and R. Laatikainen. Can. J. Chem. **64**, 1859 (1986).
21. T. Schaefer, R. Sebastian, and G.H. Penner. Can. J. Chem. **63**, 2597 (1985).
22. T. Schaefer and G.S. Takeuchi. Can. J. Chem. **67**, 827 (1989).
23. C.L. Bell, S.S. Danyluk, and T. Schaefer. Can. J. Chem. **47**, 3529 (1969).
24. A.L. van Geet. Anal. Chem. **40**, 2227 (1968).

© 1999 NRC Canada

25. M.J. Frisch, G.W. Trucks, H.B. Schlegel, G.E. Scuseria, M.A. Robb, J.R. Cheeseman, V.G. Zakrzewski, J.A. Montgomery, Jr., R.E. Stratmann, J.C. Burant, S. Dapprich, J.M. Millam, A.D. Daniels, K.N. Kudin, M.C. Strain, O. Farkas, J. Tomasi, V. Barone, M. Cossi, R. Cammi, B. Mennucci, C. Pomelli, C. Adamo, S. Clifford, J. Ochterski, G.A. Petersson, P.Y. Ayala, Q. Cui, K. Morokuma, D.K. Malick, A.D. Rabuck, K. Raghavachari, J.B. Foresman, J. Cioslowski, J.V. Ortiz, B.B. Stefanov, G. Liu, A. Liashenko, P. Piskorz, I. Komaromi, R. Gomperts, R.L. Martin, D.J. Fox, T. Keith, M.A. Al-Laham, C.Y. Peng, A. Nanayakkara. Gaussian 98. Revision A.5, C. Gonzalez, M. Challacombe, P.M.W. Gill, B. Johnson, W. Chen, M.W. Wong, J.L. Andres, M. Head-Gordon, E.S. Replogle, and J.A. Pople. Gaussian 98, Revision A.5. Gaussian, Inc., Pittsburgh, Pa. 1998.
26. P. Diehl, H.P. Kellerhals, and W. Niederberger. J. Magn. Reson. **4**, 352 (1971).
27. R. Laatikainen. J. Magn. Reson. **92**, 1 (1991); R. Laatikainen, M. Niemitz, U. Weber, J. Sundelin, T. Hassinen, and J. Vepsäläinen. J. Magn. Reson. **A120**, 1 (1996).
28. R. Laatikainen, J. Ratilainen, R. Sebastian, and H. Santa. J. Am. Chem. Soc. **117**, 11006 (1995), and refs. therein.
29. G.H. Penner, P. George, and C.W. Bock. J. Mol. Struct. (Theochem), **152**, 201(1987).
30. R.J. Meier. J. Phys. Chem. **97**, 10248 (1993); M. Head-Gordon and J. Pople. J. Phys. Chem. **97**, 10250 (1993); K.B. Borisenko, C.W. Bock, and I. Hargittai. J. Phys. Chem. **100**, 7426 (1996).
31. M.R. Nelson and R.F. Borkman. Theochem. **432**, 247 (1998).
32. J.T. Sprague, J.C. Tai, Y. Yuh, and N.L. Allinger. J. Comput. Chem. **8**, 581 (1987).
33. Nuclear magnetic resonance of liquid crystals. *Edited by* J.W. Emsley. Reidel, Dordrecht. 1985.
34. J. Lounila and P. Diehl. J. Magn. Reson. **56**, 254 (1984).
35. J. Lounila and P. Diehl. Mol. Phys. **52**, 827 (1984).
36. S. Marcelja. J. Chem. Phys. **60**, 3599 (1974).
37. W. Maier and A. Saupe. Z. Naturforsch. A, **14**, 882 (1959).
38. J.W. Emsley, G.R. Luckhurst, and C.P. Stockley. Proc. Roy. Soc. London Ser. A, **381**, 117 (1982).
39. D.J. Photinos, E.T. Samulski, and H. Toriumi. J. Phys. Chem. **94**, 4688 (1990).
40. P. Diehl. *In* Encyclopedia of nuclear magnetic resonance. *Edited by* D.M. Grant and R.K. Harris. John Wiley & Sons, Chichester. 1996. pp. 4591–4602.
41. J. Lounila, M. Ala-Korpela, and J. Jokisaari. J. Chem. Phys. **93**, 8514 (1990), and refs. therein.
42. J. Lounila and J. Jokisaari. Progr. NMR Spectrosc. **15**, 249 (1982).
43. D.G. Anderson, S. Cradock, P.B. Liescheski, and D.W.H. Rankin. J. Mol. Struct. **216**, 181 (1990).
44. C.W. Bock, A. Domenicano, P. George, I. Hargittai, G. Portalone, and G. Schultz. J. Phys. Chem. **91**, 6120 (1987).
45. S. Sýkora, J. Vogt, H. Bösiger, and P. Diehl. J. Magn. Reson. **36**, 53 (1979).
46. J. Lounila. Mol. Phys. **58**, 897 (1986).
47. T. Schaefer, R. Sebastian, R. Laatikainen, and S.R. Salman. Can. J. Chem. **62**, 326 (1986).
48. R. Wasylishen and T. Schaefer., Can. J. Chem. **50**, 1852 (1972); T. Schaefer, J. Peeling, and G.H. Penner. Can. J. Chem. **61**, 2773 (1983).
49. T. Schaefer and R. Laatikainen. Can. J. Chem. **61**, 2785 (1983).
50. E. Kolehmainen, R. Laatikainen, and V. Kral. Magn. Reson. Chem. **24**, 498 (1986).
51. G.H. Penner. J. Mol. Struct. (Theochem), **137**, 121(1986).

© 1999 NRC Canada

Controlled molecular design of ether- and ester-bridged norbornenes and their ring-opening metathesis polymerizations

Alaa S. Abd-El-Aziz, Andrea L. Edel, Leslie J. May, Karen M. Epp, and Harold M. Hutton

Abstract: A series of functionalized polynorbornenes containing pendent ether- or ester-bridged poly(aromatic ether) chains were prepared. The ether-bridged norbornene complex was synthesized via cyclopentadienyliron-mediated nucleophilic aromatic substitution reactions. This methodology, combined with that of dicyclohexylcarbodiimide-mediated coupling, allowed for the formation of novel oligomeric aryl ether and ester substituted norbornene complexes. Photolytic demetallation gave the monomers in good yields. Structural identification of the *exo* and *endo* isomers of both the metallated and demetallated norbornene derivatives was accomplished using HH and CH COSY NMR techniques. Ring-opening metathesis polymerization (ROMP) of these monomers using $RuCl_3$(hydrate) and $(Cy_3P)_2Cl_2Ru$=CHPh allowed for the preparation of the functionalized polynorbornenes. Thermal analysis of the resulting polymeric materials demonstrated greater thermal stability as the number of aryl ether groups increased.

Key words: aromatic ethers, cyclopentadienyliron, polynorbornene, ROMP, ruthenium catalysts.

Résumé : On a préparé une série de polynorbornènes fonctionnalisés comportant des chaînes pendantes (latérales) poly(éthers aromatiques) à pont éther ou ester. On a synthétisé le complexe du norbornène à pont éther par le biais de réactions de substitutions aromatiques nucléophiliques catalysées par le cyclopendiénylfer. Cette méthodologie, combinée à celle du couplage catalysé par le dicyclohexylcarbodiimide, permet de former de nouveaux complexes oligomères du norbornène substitué par des esters ou des éthers aromatiques. La démétallation photolytique conduit aux monomères avec des bons rendements. On a déterminé la structure des isomères tant *exo* qu'*endo* des dérivés norbornènes métallés et démétallés en faisant appel aux techniques RMN « COSY » HH et CH. En soumettant ces monomères à une réaction de polymérisation par ouverture de cycle accompagnée d'une métathèse à l'aide de $RuCl_3$(hydrate) et de $(Cy_3P)_2Cl_2Ru$=CHPh, permet de préparer des polynorborbènes fonctionnalisés. Une analyse thermique des matériaux polymériques qui en résultent a permis de démontrer que la stabilité thermique augmente avec une augmentation du nombre de groupes éthers aromatiques.

Mots clés : éthers aromatiques, cyclopentadiénylfer, polynorbornène, « ROMP », catalyseurs de ruthénium.

[Traduit par la Rédaction]

Introduction

Polynorbornene, first prepared in the early 1960's by Truett et al. (1), has seen numerous applications in industry due its high tear strength and dynamic-damping properties (2–5). As the demand for higher temperature applications has increased, there have been attempts to modify polynorbornene via functionalization of the polymer backbone (6–9). Poly(aromatic ethers) are of particular importance due to their high thermal stability (10–14). In addition, ester derivatives of polynorbornene warrant investigation due to their potential as thermoplastic resins (2, 3). It has therefore been of interest to functionalize polynorbornene with pendent aryl ether chains bridged to the norbornene unit either through an ether or ester linkage.

Ring-opening metathesis polymerization (ROMP) of highly strained bicyclo[2.2.1]heptenes using classical initiators has been well established in the literature (1–5). A drawback of these initiators is their low tolerance for monomers containing polar functional groups, which results in appreciable catalyst deactivation during polymerization (5). However, recent developments in ROMP catalysts have allowed for the incorporation of polar functionalities such as chloro, fluoro, hydroxyl, nitrile, ester, and imide groups into the norbornene unit (15–24). Two classes of catalytic systems have been developed and adopted as the primary cata-

Received April 29, 1999.

This paper is dedicated to Professor Ted Schaefer in recognition of his outstanding contributions to Canadian chemistry.

A.S. Abd-El-Aziz,[1] A.L. Edel, L.J. May, K.M. Epp, and H.M. Hutton. Department of Chemistry, University of Winnipeg, Winnipeg, MB R3B 2E9, Canada.

[1]Author to whom correspondence may be addressed. Telephone: (204) 786-9335. Fax: (204) 775-2114. e-mail: abdelaziz@uwinnipeg.ca

 © 1999 NRC Canada

Scheme 1.

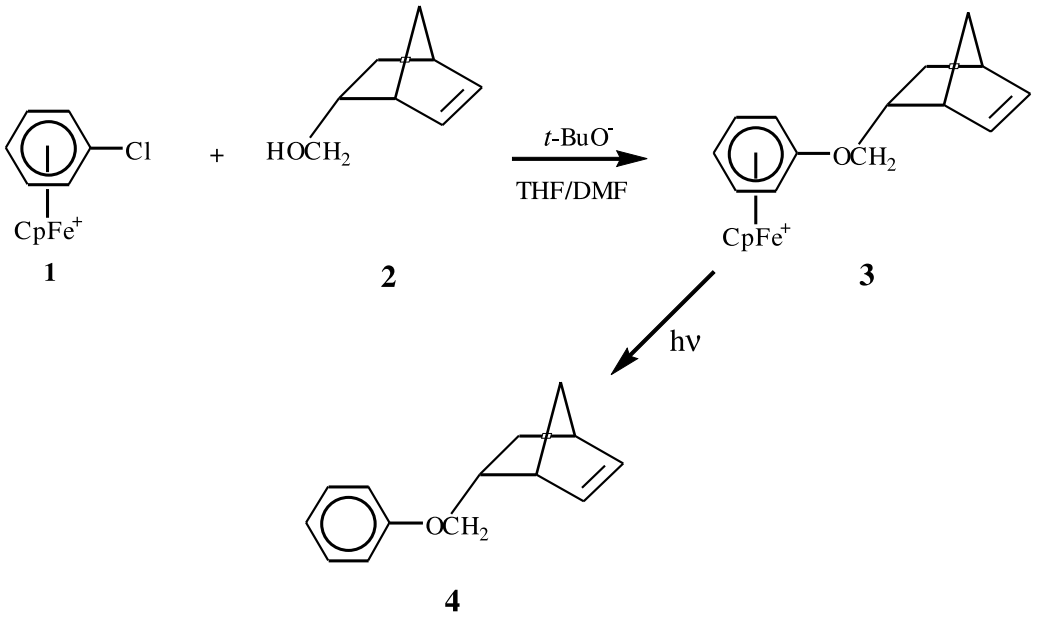

lysts used in the ROMP of polar norbornene monomers. These include ruthenium carbene complexes (9, 25–39) as well as molybdenum and tungsten alkylidene complexes (6–8, 17, 18, 21, 23, 40–50). Ruthenium-based systems have found greater industrial application due to their ability to facilitate ROMP in the presence of oxygen and protic environments, as well as their increased tolerance towards a large variety of polar functional groups. Recently, Grubbs and coworkers (29) developed a highly reactive ruthenium-based benzylidene catalyst, which allows for the living ring-opening metathesis polymerization of a variety of functionalized norbornene monomers in both organic and aqueous solvents. This catalyst, known as bis(tricyclohexylphosphine)benzylidene ruthenium(IV) dichloride or "Grubbs' catalyst," has proven to be extremely effective in the ROMP of highly strained bicyclic olefins (29, 30, 32, 39).

Our success in the preparation of poly(aromatic ethers) via cyclopentadienyliron ($CpFe^+$)-mediated nucleophilic aromatic substitution reactions (51–58) has prompted our investigation into the controlled molecular design of norbornene monomers containing pendent aryl ether and (or) ester chains. Recently, we communicated our initial results of the cyclopentadienyliron-complexed norbornenes and their subsequent polymerizations (59). Here, we report the full synthesis and characterization of these substituted norbornene monomers, as well as their ROMP using either $RuCl_3$(hydrate) or $(Cy_3P)_2Cl_2Ru$=CHPh catalysts.

Results and discussion

Monomer syntheses

Norbornene monomers containing ether and (or) ester bridges were synthesized using metal-mediated nucleophilic aromatic substitution (S_NAr). This methodology was used to prepare poly(aromatic ether) chains pendent to norbornene monomers, which would otherwise be difficult to prepare using traditional organic methods (60). This report details the synthesis of two new classes of norbornene monomers, the first containing an ether bridge between the norbornene unit and the aromatic ether side chain, and the second containing an ester bridge.

Preparation of the etheric linked monomer was readily performed via S_NAr of the chloroarene complex (**1**) with an excess of *exo*,*endo*-5-norbornene-2-methanol (**2**), as shown in Scheme 1. Generation of the nucleophile under an inert nitrogen atmosphere for 1 h, followed by the addition of η^6-chlorobenzene-η^5-cyclopentadienyliron hexafluorophosphate (**1**) dissolved in a mixture of *N*,*N*-dimethylformamide (DMF) and THF yielded the product (**3**) in 85% yield after reacting for 16 h at room temperature.

Preparation of the ester-bridged complexes was accomplished via the condensation reaction of 5-norbornene-2-methanol (**2**) with the benzoic acid complexes as described in Scheme 2. (Benzoic acid)$CpFe^+$ (**5**) and (*p*-chlorobenzoic acid)$CpFe^+$ (**6**) were prepared using the methodology established by Nesmeyanov et al. (61). Condensation of these acid complexes with **2** in the presence of dicyclohexylcarbodiimide (DCC) and pyridine in dichloromethane afforded the ester-functionalized norbornene complexes **7** and **8**, in 62 and 70% yields, respectively.

This methodology was further extended towards the preparation of norbornene complexes containing two or three pendent metal moieties within the aryl ether chain. The synthesis of these aryl ether derivatives involved the initial preparation of the terminal phenoxy complexes (**14, 15**), as detailed in Scheme 3. This was accomplished by reacting the bimetallic arene complex (**12**), for example, with an excess of hydroquinone (**13**) in a THF–DMF solvent mixture for 16 h. The resulting yellow precipitate was isolated in 90% yield for complex **15**. Characterization of the bimetallic complex (**15**) was readily accomplished using ^{1}H NMR spectroscopy. The two Cp resonances, appearing as distinct singlets at 5.31 and 5.25 ppm, indicated successful preparation of the desired product. Further verification resulted from the analysis of the ^{13}C NMR spectrum, which also showed two Cp resonances at 78.80 and 78.13 ppm.

© 1999 NRC Canada

Scheme 2.

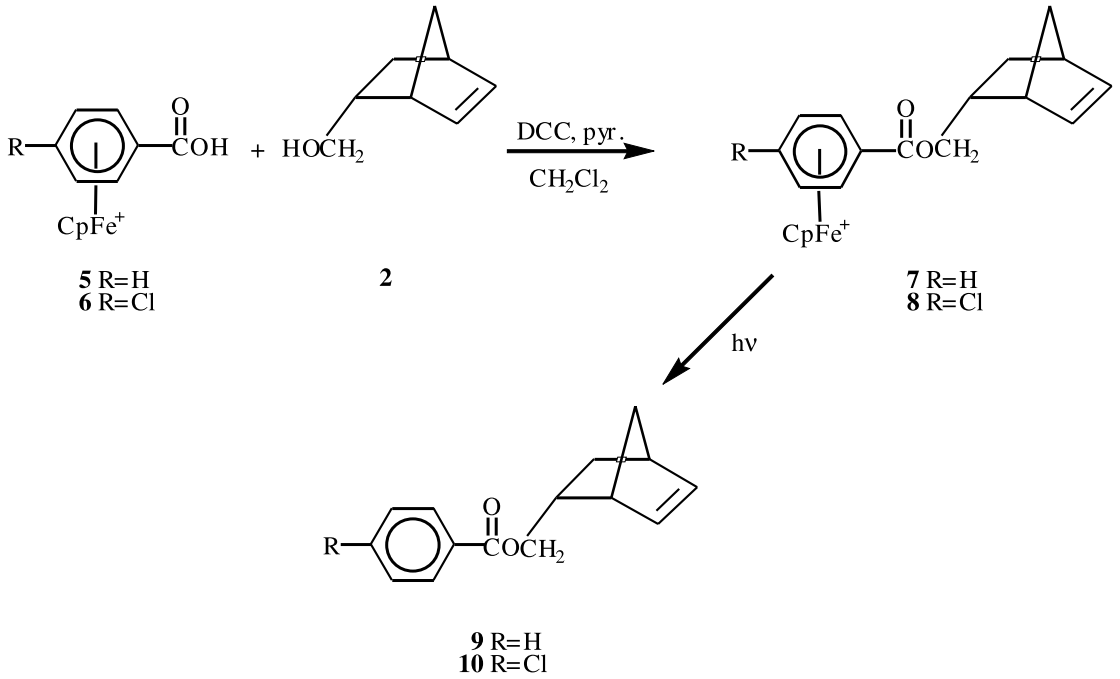

5 R=H
6 R=Cl

2

7 R=H
8 R=Cl

9 R=H
10 R=Cl

Scheme 3.

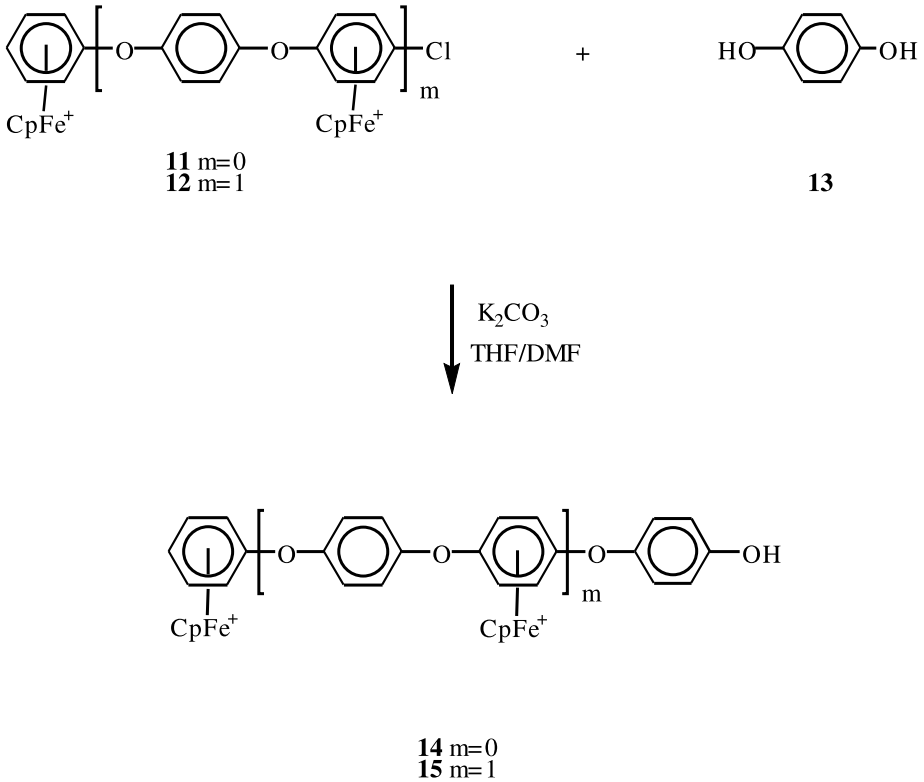

11 m=0
12 m=1

13

14 m=0
15 m=1

Nucleophilic aromatic substitution was used to prepare the bi- (**16**) and tri-metallic (**17**) norbornene complexes. This was done by reacting a 1:1 molar ratio of complex **14** or **15** with **8** in the presence of excess base in DMF, as described in Scheme 4. The resulting yellow precipitates were consistently isolated in high yields ranging from 81–86%. Confirmation of the structure of the trimetallic complex (**17**) was obtained using one-dimensional NMR techniques. Three Cp resonances in the ^{1}H NMR spectrum appearing at 5.34, 5.32, and 5.26 ppm and in the ^{13}C NMR at 79.60, 78.97, and 78.08 ppm were consistent with the proposed structure.

Isolation of the organic monomers from their cyclopentadienyliron moieties was achieved via photolytic demetallation (62). Complexes **3**, **7**, **8**, **16**, and **17** were each

© 1999 NRC Canada

Scheme 4.

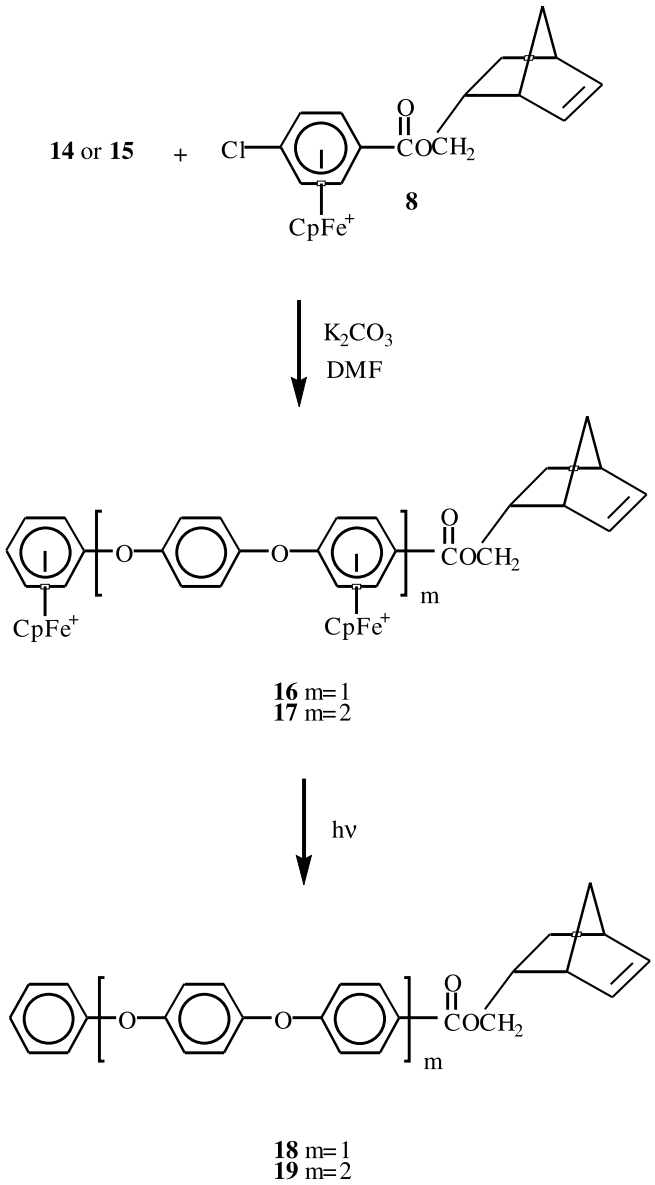

dissolved in a 1:4 ratio of acetonitrile to dichloromethane, followed by irradiation under a xenon lamp for 4–8 h, the length of time increasing as the number of $CpFe^+$ moieties increased. The organic monomers **4**, **9**, **10**, **18**, and **19**, were isolated by this process in good yields.

Monomer characterization

Structural analysis of the functionalized norbornene molecules (**3**, **4**, **7**–**10**, **16**–**19**) was accomplished using NMR, IR, C-H analysis and MS. One- and two-dimensional NMR spectroscopic techniques were extremely valuable in the characterization process due to the complicated *exo*, *endo* isomeric mixture of the products. As the 1-D NMR spectra were quite complex, homonuclear correlation spectroscopy (HH COSY) was employed as a means to identify proton–proton connectivities and chemical shifts. Once all of the protons were assigned to the *exo* or *endo* isomers, hetero-

Fig. 1. ^1H and ^{13}C NMR spectra of complex **8**.

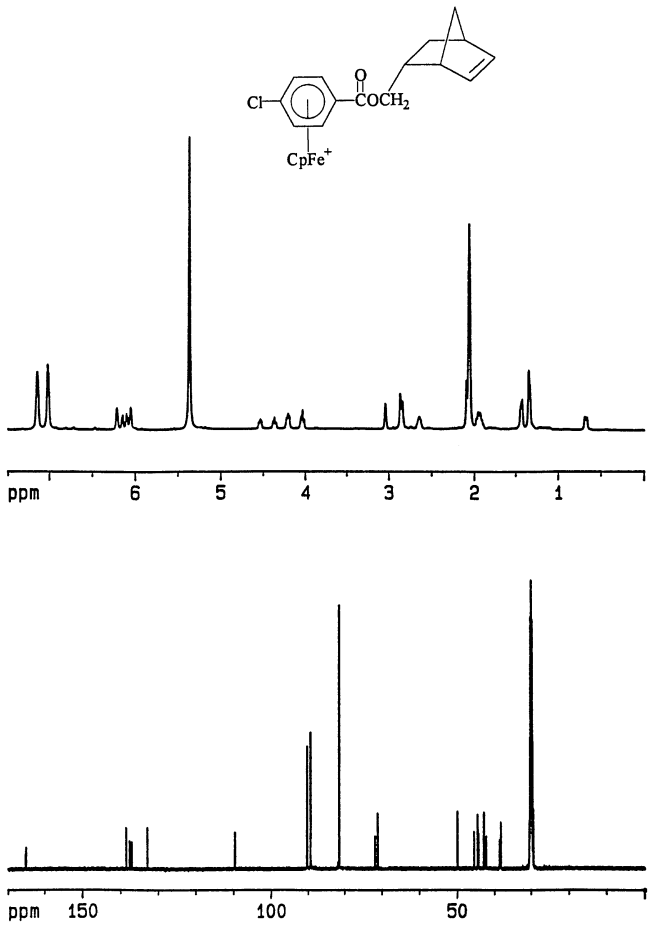

nuclear correlation spectroscopy (CH COSY) was used to locate the ^{13}C NMR chemical shifts.

Cyclopentadienyl resonances, which appear from 5.4 to 5.0 ppm in the ^1H NMR spectra and from 82 to 78 ppm in the ^{13}C NMR spectra, were instrumental in confirming the structure of the complexed norbornenes **3**, **7**, **8**, **16**, and **17**. Complex **3** showed a strong singlet at 5.14 ppm and at 77.06 ppm in the ^1H NMR and ^{13}C NMR spectra, respectively, representative of the cyclopentadienyl resonance. In the ester-bridged derivatives, the Cp resonance was identified further downfield than in the ether-bridged complex due to the stronger electron-withdrawing capability of the carbonyl group. Therefore, the Cp resonance in complex **8** appeared as a single peak at 5.36 ppm and at 81.47 ppm in the ^1H and ^{13}C NMR spectra, respectively (Fig. 1). The appearance of only one Cp signal for the two isomers in both of these complexes was attributed to the large separation between the norbornene unit and the Cp ring. This distance provided sufficient spacing between the two groups such that the electronic effects of the *exo*, *endo* isomerism at C-2 did not influence the Cp protons. Although only one Cp was present for these complexes, evidence for the presence of two isomers was observed with respect to the number of methylene protons (norbornene–CH_2O) and vinyl protons. With respect to the methylene protons, four resonances at 4.20 and 4.03 ppm and at 4.53 and 4.36 ppm in **8** for the

© 1999 NRC Canada

Fig. 2. HH COSY NMR of complex **8** showing relevant connectivities for *exo* and *endo* isomer determination.

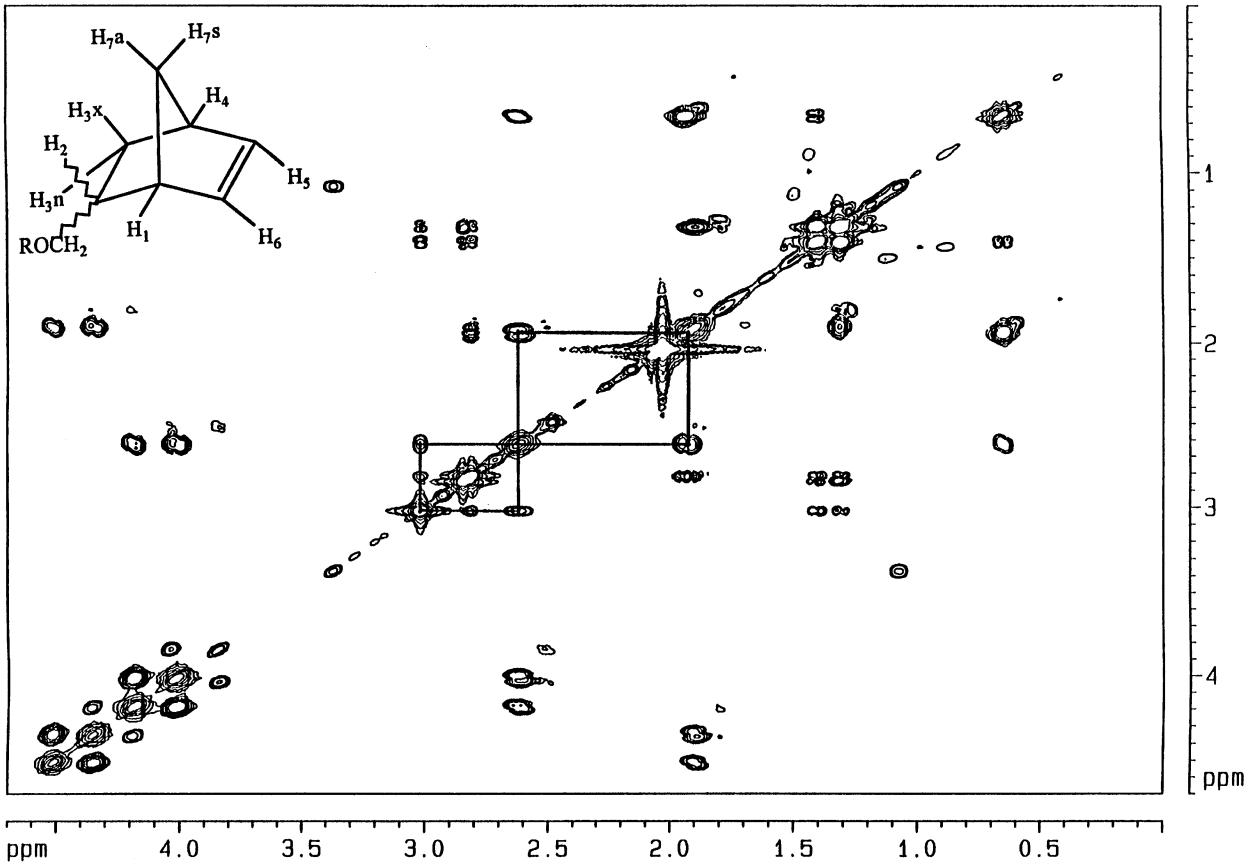

endo and *exo* isomers, respectively, were observed. The vinyl protons at 6.21 and 6.05 ppm for the *endo* H_5 and H_6 protons and at 6.14 and 6.10 ppm for the *exo* H_5 and H_6 protons, as described in Fig. 1.

Previous NMR studies involving substituted bicyclo[2.2.1]heptenes have detailed the identification of the *exo* and *endo* isomers relative to several key couplings located for certain proton resonances (63–70). These correspond to the H-1, H-2, H-3x, and H-3n protons, as identified in Fig. 2. Location of the *endo* isomer was assigned based upon the coupling between the *exo* H-2 and the bridgehead H-1 protons and (or) for the *exo* H-3x proton to the bridgehead H-4 proton, showing moderate intensity in their contours. Although these couplings could not be measured due to peak broadness, their connectivities were observed in the HH COSY NMR spectrum, as shown in Fig. 2 for complex **8**. Literature values for this particular coupling report *J* values in the range of 3.2–3.9 Hz, which verifies the modest coupling for these protons (67). As for the *exo* isomer, no coupling or connectivity was observed for the *endo* H-2 proton to H-1, or for the *endo* H-3n proton to H-4. This observation is in agreement with previous investigations of the *endo* H-2 and H-3n resonances in *exo* substituted norbornene derivatives (67). Strong coupling between the two *exo* protons H-2 and H-3x was identified in the HH COSY, indicating the presence of the *endo* isomer. Complex **8** had a calculated *J* value of 8.9 Hz for this coupling, which is also shown in the HH COSY spectrum. Musher (65) has reported more intense coupling between two *exo* protons (H-2 and H-3x) than between two *endo* protons (H-2 and H-3n) despite identical dihedral angles. This allowed for further distinction between the *exo* and *endo* isomers. Once these well-defined couplings were located, the rest of the protons could be identified based upon their connectivities as determined by the HH COSY spectrum.

Photolytic demetallation of complexes **3**, **7**, **8**, **16**, and **17** led to the isolation of the substituted norbornene monomers **4**, **9**, **10**, **18**, and **19** in good yields. NMR, IR, C-H analysis, and MS techniques were used to confirm the structures of the demetallated products. In the ^{1}H NMR spectrum of compound **4**, as an example, the absence of the Cp resonance at 5.14 ppm observed in complex **3** indicated the loss of the metallic moiety. Further evidence for the liberation of the organic monomer was observed in the upfield shift of the methylene resonances (norbornene–CH_2O) from 4.38 to 3.87 ppm in **3** to 4.05–3.57 ppm in **4**. A downfield shift of the aromatic protons from their original positions at 6.40–6.30 and 6.20–6.16 ppm in the starting material, to 7.50–6.70 ppm in the spectrum of the photolyzed product, was also observed. Similar chemical shift trends were identified for the ester-containing norbornene derivatives. Further spectral identification of all the products is listed in the experimental section.

Polymer syntheses

Ring-opening metathesis polymerizations were performed using ruthenium-based catalysts, namely $RuCl_3$(hydrate) and $(Cy_3P)_2Cl_2Ru$=CHPh. Polymerization of monomer **4** was ex-

© 1999 NRC Canada

Scheme 5.

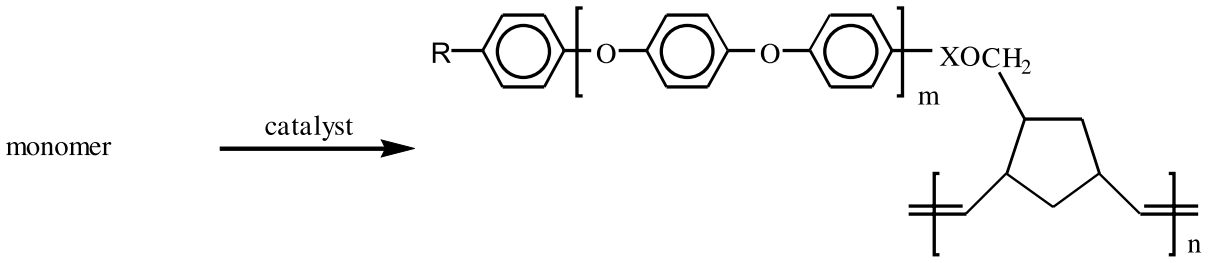

monomer	catalyst	polymer	R	X	m
4	$RuCl_3$(hydrate)	**20**	H	direct link	0
9	$(Cy_3P)_2Cl_2Ru{=}CHPh$	**21**	H	C=O	0
10	$(Cy_3P)_2Cl_2Ru{=}CHPh$	**22**	Cl	C=O	0
18	$(Cy_3P)_2Cl_2Ru{=}CHPh$	**23**	H	C=O	1
19	$(Cy_3P)_2Cl_2Ru{=}CHPh$	**24**	H	C=O	2

Table 1. $RuCl_3$(hydrate) polymerizations of compound **4** using [M]:[I] ratios of 100:1.

Solvent ratio (mL)	Mw[a]	Mn[b]	PDI[c]	Yield (%)
1.0 EtOH	298 000	87 000	3.4	32
0.97 EtOH/0.03 H_2O	328 000	125 000	2.6	45
0.5 EtOH/0.5 H_2O	535 000	248 000	2.1	73
1.0 H_2O	397 000	177 000	2.2	82

[a]Weight-average molecular weight.

[b]Number-average molecular weight.

[c]Polydispersity index.

Table 2. ROMP results for polymers **21**–**24** using Grubbs' catalyst with [M]:[I] ratios of 100:1.

Polymer	Mw[a]	Mn[b]	PDI[c]	Yield (%)
21	108 000	57 000	1.9	71
22	462 000	195 000	2.4	74
23	145 000	87 000[d]	1.7	73
24	74 000	49 000[d]	1.5	66

[a]Weight-average molecular weight.

[b]Number-average molecular weight.

[c]Polydispersity index.

[d]Molecular weights are representative of the soluble portions of the polymer.

amined using a monomer to initiator ratio ([M]:[I]) of 100:1 with $RuCl_3$(hydrate) as the catalyst. The catalyst was prepared by stirring ruthenium trichloride hydrate in ethanol for 2 h; this solution was then added to monomer **4** and heated at 60°C for 24 h yielding an off-white, fibrous solid (**20**) following precipitation into methanol. Previous investigations using ruthenium chloride(hydrate) as a catalyst detail the advantages of using ethanol–water solvent mixtures, as it has been noted that an increased amount of water yields higher molecular weight polymers with lower polydispersities (PDI) (71, 72). In keeping with this methodology, polymerizations were carried out using varying ratios of ethanol to water as observed in Table 1. Molecular weight determination of the resulting polymeric materials was accomplished using gel permeation chromatography (GPC). A weight-average molecular weight (Mw) of 298 000 was observed when using 100% EtOH, which increased up to 535 000 with a 50:50 EtOH/H_2O mixture. Polymerization was also successful when using 100% water, yielding a molecular weight of 397 000.

Ring-opening metathesis polymerization of the ester-containing monomers with both ruthenium catalysts was also attempted. Under analogous conditions to those employed for monomer **4**, monomer **9** was subjected to ROMP using $RuCl_3$(hydrate). Numerous attempts to polymerize this monomer using this catalyst were unsuccessful. The recent development of ruthenium benzylidene catalysts, namely $(Cy_3P)_2Cl_2Ru{=}CHPh$, by Grubbs and co-workers (29), has led to the availability of a highly active metathesis catalyst. This ruthenium-based system is of significant interest as it offers mild reaction conditions and affords high conversion rates of the monomer to the polymer. These catalysts also show a marked improvement in their functional group tolerance, prompting our investigation into the polymerization of the ester-bridged norbornene monomers.

The general methodology used in the preparation of these polymeric materials involved the initial transfer of the catalyst to the round-bottomed flask in a glove box. Initially, the catalyst was dissolved in CH_2Cl_2, which was then added to a CH_2Cl_2 solution of the monomer (**9**, **10**, **18**, **19**). The resulting mixture was stirred at room temperature under a nitrogen atmosphere until a gelatinous material formed, generally within 1 h. An excess of ethyl vinyl ether was then added to cleave the catalyst from the polymer chain. Subsequent precipitation from methanol gave off-white, fibrous polymeric materials (**21**–**24**), as described in Scheme 5, in yields ranging from 66 to 74%. GPC analyses of the polymers are described in Table 2, showing Mw's ranging from 74 000 to 462 000 for the variously functionalized polynorbornenes, with PDIs from 1.5 to 2.4.

© 1999 NRC Canada

Table 3. Various [M]:[I] ratios comparing Mw, Mn, PDI, and yield for polymer **21**.

[M]:[I]	Mw[a]	Mn[b]	PDI[c]	Yield (%)
25:1	8 400	3 900	2.2	59
50:1	16 000	6 500	2.5	52
100:1	108 000	57 000	1.9	71
150:1	511 000	168 000	3.0	80

[a]Weight-average molecular weight.

[b]Number-average molecular weight.

[c]Polydispersity index.

In an attempt to obtain higher molecular weight polymers with narrow polydispersities, the reaction conditions were altered by varying the [M]:[I] ratios to 25-, 50-, 100-, and 150:1 using monomer **9** as a model for these experiments (Table 3). Ratios of 25:1 and 50:1 yielded fairly low molecular weight polymers with Mw's of 8400 and 16 000 with PDIs of 2.2 and 2.5, respectively. Polymerizations performed using ratios of 100:1 yielded higher molecular weight polynorbornenes (108 000) with polydispersities of 1.9. When a ratio of 150:1 was used, a significant increase in the molecular weight was obtained (511 000), although the PDI was 3.0. As a result of these observations, polymerizations were consistently performed using [M]:[I] ratios of 100:1 with the purpose of maintaining high molecular weight polymers with low polydispersities.

To obtain a living polymer, complete consumption of the monomer must be accomplished in such a way that initiation proceeds faster than propagation (73). In an attempt to determine whether or not the ruthenium benzylidene polymerizations were living, a ROMP reaction was conducted with the intention of forming a homopolymer using monomer **9**. This proceeded with the withdrawal of a small portion of polymer solution 1 h after the initial ROMP reaction commenced. A second aliquot of monomer **9** was then added to the stirring polymer solution as a means to facilitate chain growth by the continued propagation of the monomer. GPC analysis of the polymer removed from solution after 1 h was compared to the final polymer. Based upon the trace provided from the GPC plot, two significantly different peaks were present for each of the polymers. The initial aliquot of polymer removed from the reaction flask had a much lower weight-average molecular weight (Mw = 22 600 g/mol, PDI = 2.8) than the final polymer (Mw = 108 000 g/mol, PDI = 1.9). This increase in molecular weight provided definitive evidence that the polymerization was living.

Polymer characterization

Solubility studies of the ether- and ester-bridged polymers were performed as a means to assess their processability. Chloroform ($CHCl_3$), dimethylacetamide (DMAc), dimethylformamide (DMF), and dimethylsulfoxide (DMSO) were all examined to determine their suitability as solvents for dissolving the functionalized polynorbornenes. Polymers **20**–**22**, containing single aromatic groups pendent to the polynorbornene backbone, demonstrated good solubility in $CHCl_3$ and DMAc at room temperature. However, DMF and DMSO only partially solubilized the polymeric materials. With respect to the longer pendent aromatic ether chains, it was found that as the length of the chain increased, the solubility of the polymeric materials decreased. Polymers **23** and **24** demonstrated minimal solubility in $CHCl_3$ at room temperature and only partial solubility when refluxed for 1 h. Low solubility of the polymers was observed in both DMAc and DMF; however, in DMSO, they remained completely insoluble.

Structural characterization of the polymers was most effectively carried out using ^1H and HH COSY NMR spectroscopy. As the monoarene-substituted polymers **20**–**22** demonstrated greater solubility in organic solvents in comparison to the oligoether polynorbornenes, higher resolution NMR spectra could be obtained. The broadness of the aromatic peaks located between 8.05 and 7.95 ppm and between 7.60 and 7.30 ppm in **21** is characteristic of the broadening effects associated with polymerization. More importantly, successful polymerization was readily identifiable by the shifting of the olefinic resonances from 6.20 to 6.01 ppm in the monomer (**9**) to 5.40–5.20 ppm in the polymer (**21**). As this resonance appeared as a single broad band and knowing that $(Cy_3P)_2Cl_2Ru{=}CHPh$ yields the *trans* microstructure, it can be said with confidence that the vinylene units exist in the *trans* configuration (32, 47).

FT-IR spectroscopy was useful in estimating the microstructure of the polymeric materials by looking at the respective *cis* and *trans* absorptions. Previous studies involving the geometry of polynorbornene and its derivatives have found that *cis* in-plane = C-H bending occurs at 1404 and 740 cm^{-1}, with the *trans* appearing at 960 cm^{-1} (22, 74, 75). Comparison of monomer **9** with its respective polymer (**21**), allowed for the peak at 969 cm^{-1} to be assigned to the *trans* = C-H bending absorption. In addition, the absence of absorption in the regions of 1404 and 740 cm^{-1} confirmed the lack of the *cis* configuration within the polymer.

Thermal analysis of the polymeric materials was performed using differential scanning calorimetry (DSC) and thermogravimetric analysis (TGA). In comparison to polynorbornene, which has a glass transition temperature (Tg) of 35°C (74), it was found that as the length of the aryl ether chain increased, a noticeable increase in the Tg's was obtained. The results showed that the polymers containing single arene units pendent to the polynorbornene backbone (**20**, **21**) displayed a well-defined Tg at 55°C. Examination of the penta-arene functionalized polymer (**24**) showed that the Tg increased to 73°C, as shown in Table 4. The DSC thermogram further verified the amorphous nature of the *trans*-rich polynorbornene derivative, as no crystalline melting peaks were observed, which is consistent with previous studies of *trans* polynorbornenes (73).

Polymer degradation was also investigated using TGA. It was determined that as the number of aryl ether linkages in the monomer increased, the polymeric material exhibited higher thermal stability. This is in agreement with previous findings for industrially prepared engineering thermoplastics such as PEEK or PEKK, which demonstrate increased thermal stability resulting from the high number of aromatic ethers in the polymer backbone (10–12). Our results revealed that this increase in aryl ether groups pendent to the polynorbornene backbone allowed for greater thermal stability, as defined by the increase in polymer degradation from 417°C for polymer **21** to 460°C for polymer **24**. Further thermal decomposition data is given in Table 4.

© 1999 NRC Canada

Table 4. Thermal degradation temperatures for polymers **20**–**24**.

DSC (°C)		TGA (°C)		
Polymer	Tg[a]	T_{onset}	$T_{midpoint}$	T_{endset}
20	54.9	374.6	418.7	461.2
21	54.7	385.3	417.0	450.6
22	65.3	354.3	401.9	427.5
23	67.6	393.9	422.4	456.8
24	73.3	408.5	460.2	509.6

[a]Glass transition temperatures (Tg's) are reported as the midpoint.

Experimental section

General

^1H and ^{13}C NMR spectra were recorded at 200 and 50 MHz on a Gemini 200 NMR spectrometer and at 500 and 125 MHz on a Bruker 500 spectrometer, respectively. Chemical shifts were calculated from the solvent that was used as the internal reference and coupling constants were calculated in Hz. IR spectra were recorded on a Bomem FT-IR spectrophotometer. Mass spectra were obtained on a Hewlett–Packard 5890 Series II mass spectrometer as well as on a Hewlett–Packard 5989A mass spectrometer. Molecular weight analyses by GPC were performed using a BL-gel mixed D column (Phenomenex) equipped with a CH-30 column heater (Eppendorf) and a PL-DCU (Polymer Laboratories) detection system, with $CHCl_3$ as the eluent at a flow rate of 0.7 mL per min. Calibration of the instrument was accomplished using polystyrene standards. Glass transition temperatures were determined using differential scanning calorimetry (DSC) performed on a Mettler DSC 25 at a heating rate of 10°C/min, taking the midpoint of the transition from the second heating. Thermogravimetric analysis (TGA) was recorded on a Mettler Toledo TGA/SDTA851 with a heating rate of 10°C/min under a steady stream of nitrogen (20 mL/min).

Materials

Preparation of the starting complex **1** was performed via the previously reported ligand exchange reaction (76, 77). Complexes **5** and **6** were prepared by the ligand exchange of toluene and *p*-chlorotoluene, respectively, and their subsequent oxidation was previously described by Nesmeyanov et al. (61). Complexes **12** and **14** were synthesized using previously reported methodologies (51). Anhydrous aluminum chloride, aluminum powder, ferrocene, chloroarenes, ammonium hexafluorophosphate, hydroquinone, 98%-*exo*,*endo*-5-norbornene-2-methanol, dicyclohexylcarbodiimide, ruthenium(III) chloride hydrate, and bis(tricyclohexylphosphine)benzylidene ruthenium(IV) dichloride are all commercially available and were used without further purification. Pyridine was vacuum distilled over calcium chloride and dried over 4 Å molecular sieves. All solvents (reagent grade) were used without further purification, with the exception of tetrahydrofuran, which was distilled over sodium metal under nitrogen gas. Silica gel 60–100 mesh, was used in the column chromatographic purification of the liberated arenes. Prior to polymerization, dichloromethane was dried over calcium chloride, distilled, and then degassed by several freeze–pump–thaw repetitions.

Monomer syntheses

*Nucleophilic substitution reaction. Preparation of complex **3***

Into a 50 mL round-bottom flask, 2.1 mmol (0.25 mL) of **2**, 2.5 mmol (0.281 g) of potassium *tert*-butoxide, and 3 mL of THF were stirred at room temperature for 1 h under a nitrogen atmosphere. Subsequently, 1.0 mmol (0.378 g) of **1** dissolved in 3 mL of THF and 1 mL of DMF was added to the reaction flask and stirred for 16 h at room temperature under nitrogen. The resulting solution was then filtered through a sintered glass crucible into a 10% (v/v) HCl solution, resulting in the generation of a yellow solution. After rinsing the reaction flask and crucible with a small amount of CH_2Cl_2, a concentrated aqueous solution of NH_4PF_6 was added. This solution was then extracted with CH_2Cl_2 (4 × 50 mL) and the organic layer dried over $MgSO_4$, filtered, and the solvent removed by rotary evaporation. The resulting dark orange oil (**3**) was rinsed with several aliquots of diethyl ether and dried under vacuum: 0.396 g (85%). ^1H NMR (500 MHz, CD_3COCD_3): (*endo*) δ (ppm): 6.40–6.30 (br m, 3H, ArH), 6.22 (m, 1H, J = 3.0 Hz and J = 5.3 Hz, H_5), 6.20–6.16 ppm (br d, 2H, ArH), 6.02 (m, 1H, J = 2.6 and 5.3 Hz, H_6), 5.14 (br s, 5H, Cp), 4.02 (t, 1H, J = 9.1 Hz, nor-CH_2O), 3.87 (t, 1H, J = 7.1 Hz, nor-CH_2O), 3.02 (br s, 1H, H_1), 2.85 (br s, 1H, H_4), 2.62–2.63 (br s, 1H, H_2) 1.92–1.94 (br m, 1H, H_{3x}), 1.45 (br d, 1H, J = 7.8 Hz, H_{7s}), 1.34 (br d, 1H, J = 7.8 Hz, H_{7a}), 0.70 (m, 1H, J = 11.6 and 2.6 Hz, H_{3n}); (*exo*) δ (ppm): 6.40–6.30 (br m, 3H, ArH), 6.20–6.16 (br d, 2H, ArH), 6.15 (m, 1H, H_5), 6.13 (m, 1H, H_6), 5.14 (br s, 5H, Cp), 4.38 (t, 1H, J = 9.2 Hz, nor-CH_2O), 4.19 (t, 1H, J = 6.5 Hz, nor-CH_2O), 2.88 (br s, 2H, H_1 and H_4), 2.06–2.04 (br m, 1H, H_{3x}), 1.90–1.92 (br, 1H, H_2), 1.49 (br d, 1H, H_{7s}), 1.35 (br d, 1H, H_{7a}), 1.31 (m, 1H, H_{3n}). ^{13}C NMR (125 MHz, CD_3COCD_3): (*endo*) δ (ppm): 138.49 (1C, C_5), 135.04 (1C, quat ArC), 132.53 (1C, C_6), 87.34 (2C, ArC), 84.65 (1C, ArC), 77.06 (5C, Cp), 75.31 (2C, ArC), 73.87 (1C, nor-CH_2O), 49.73 (1C, C_7), 44.36 (1C, C_1), 42.78 (1C, C_4), 38.58 (1C, C_2), 28.95 (1C, C_3); (*exo*) δ (ppm): 137.64 (1C, C_6), 136.70 (1C, C_5), 135.13 (1C, quat ArC), 87.34 (2C, ArC), 84.65 (1C, ArC), 77.06 (5C, Cp), 75.31 (2C, ArC), 74.41 (1C, nor-CH_2O), 45.30 (1C, C_7), 44.17 (1C, C_1), 42.22 (1C, C_4), 38.91 (1C, C_2), 29.51 (1C, C_3). Anal. calcd. for $C_{19}H_{21}F_6FeOP$: C 48.95, H 4.54; found: C 48.75, H 4.61.

*Condensation reaction. Preparation of complexes **7** and **8***

Into a 25 mL round-bottom flask was placed 1.00 mmol (0.422 g) of **5** or **6**, 1.00 mmol (0.206 g) of DCC, and 1.654 mmol (0.20 mL) of **2**. To this was added 10 mL of CH_2Cl_2 followed by four drops of pyridine. The reaction mixture was gently stirred at room temperature for 7 h (**7**) or 3 h (**8**), resulting in the formation of a heterogeneous yellow solution. Due to the precipitation of dicyclohexylurea (DCU) from the reaction mixture, the solution was gravity filtered, rinsed with 2 × 10 mL portions of CH_2Cl_2, and then rotovaped to dryness. The resulting yellow viscous material was dissolved in a minimal amount of acetone and filtered once again to remove the remaining DCU. Precipitation of the crude product into diethyl ether and subsequent cooling in the freezer overnight yielded the pure complex as a yellow semi-crystalline material.

© 1999 NRC Canada

*Complex **7***: 0.306 g (62%). IR (cm^{-1}): 1733 (CO). ^1H NMR (200 MHz, CD_3COCD_3): (*endo*) δ (ppm): 7.05 (d, 2H, ArH), 6.72 (m, 3H, ArH), 6.23 (m, 1H, H_5), 6.08 (m, 1H, H_6), 5.28 (s, 5H, Cp), 4.23 (q, 1H, nor-CH_2O), 4.05 (t, 1H, nor-CH_2O), 3.07 (br s, 1H, H_1), 2.84 (br s, 1H, H_4), 2.66 (m, 1H, H_2), 1.97 (br m, 1H, H_{3x}), 1.46 (br s, 1H, H_{7s}), 1.34 (br d, 1H, H_{7a}), 0.73 (m, 1H, H_{3n}); (*exo*) δ (ppm): 7.05 (d, 2H, ArH), 6.72 (m, 3H, ArH), 6.15 (m, 1H, H_5), 6.14 (m, 1H, H_6), 5.28 (s, 5H, Cp), 4.56 (q, 1H, nor-CH_2O), 4.39 (t, 1H, nor-CH_2O), 2.89 (br s, 2H, H_1 and H_4), 2.13 (br m, 1H, H_{3x}), 1.93 (br m, 1H, H_2), 1.45 (br s, 1H, H_{7s}), 1.37 (br d, 1H, H_{7a}), 1.31 (br m, 1H, H_{3n}). ^{13}C NMR (50 MHz, CD_3COCD_3): (*endo*) δ (ppm): 165.96 (1C, CO), 138.50 (1C, C_5), 132.78 (1C, C_6), 90.94 (1C, ArC), 89.96 (2C, ArC), 89.40 (2C, ArC), 79.21 (5C, Cp), 70.83 (1C, nor-CH_2O), 49.91 (1C, C_7), 44.64 (1C, C_1), 42.94 (1C, C_4), 38.36 (1C, C_2), 29.79 (1C, C_3); (*exo*) δ (ppm): 166.02 (1C, CO), 137.69 (1C, C_6), 132.78 (1C, C_5), 90.94 (1C, ArC), 89.96 (2C, ArC), 89.40 (2C, ArC), 79.21 (5C, Cp), 71.51 (1C, nor-CH_2O), 45.52 (1C, C_7), 44.39 (1C, C_1), 42.35 (1C, C_4), 38.73 (1C, C_2), 29.40 (1C, C_3). Anal. calcd. for $C_{20}H_{21}F_6FeO_2P$: C 48.61, H 4.28; found: C 48.37, H 4.33.

*Complex **8***: 0.370 g (70%). IR (cm^{-1}): 1733 (CO). ^1H NMR (500 MHz, CD_3COCD_3): (*endo*) δ (ppm): 7.14 (d, 2H, *J* = 6.7 Hz, ArH), 7.01 (d, 2H, *J* = 6.7 Hz, ArH), 6.21 (m, 1H, *J* = 3.1 and 5.5 Hz, H_5), 6.05 (m, 1H, *J* = 2.6 and 5.5 Hz, H_6), 5.36 (s, 5H, Cp), 4.20 (q, 1H, *J* = 6.8 and 10.5 Hz, nor-CH_2O), 4.03 (t, 1H, *J* = 9.5 and 10.5 Hz, nor-CH_2O), 3.04 (br s,1H, H_1), 2.84 (br s, 1H, H_4), 2.64 (m, 1H, H_2), 1.96 (m,1H, *J* = 3.7 and *J* = 8.9 Hz, H_{3x}), 1.42 (d, 1H, H_{7s}), 1.32 (d, 1H, H_{7a}), 0.67 (m,1H, *J* = 2.4 and 11.7 Hz, H_{3n}); (*exo*) δ (ppm): 7.14 (d, 2H, *J* = 6.7 Hz, ArH), 7.01 (d, 2H, *J* = 6.7 Hz, ArH), 6.14 (m, 1H, *J* = 2.3 Hz, H_5), 6.10 (m, 1H, *J* = 2.3 Hz, H_6), 5.36 (s, 5H, Cp), 4.53 (q, 1H, *J* = 6.8 and 10.8 Hz, nor-CH_2O), 4.36 (t, 1H, *J* = 9.1 Hz, nor-CH_2O), 2.86 (br s, 2H, H_1 and H_4), 2.15 (br, 1H, H_{3x}), 1.92 (m, 1H, H_2), 1.41 (br d, 1H, H_{7s}), 1.33 (br d, 1H, H_{7a}), 1.30 (m, 1H, H_{3n}). ^{13}C NMR (125 MHz, CD_3COCD_3): (*endo*) δ (ppm): 165.09 (1C, CO), 138.45 (1C, C_5), 132.79 (1C, C_6), 109.58 (1C, quat ArC), 90.19 (2C, ArC), 89.28 (2C, ArC), 81.47 (5C, Cp), 71.12 (1C, nor-CH_2O), 49.92 (1C, C_7), 44.59 (1C, C_1), 42.90 (1C, C_4), 38.26 (1C, C_2), 29.77 (1C, C_3); (*exo*) δ (ppm): 165.19 (1C, CO), 137.57 (1C, C_6), 136.93 (1C, C_5), 109.58 (1C, quat ArC), 90.19 (2C, ArC), 89.28 (2C, ArC), 81.47 (5C, Cp), 71.78 (1C, nor-CH_2O), 45.50 (1C, C_7), 44.37 (1C, C_1), 42.31 (1C, C_4), 38.60 (1C, C_2), 29.46 (1C, C_3). Anal. calcd. for $C_{20}H_{20}ClF_6FeO_2P$: C 45.44, H 3.81; found: C 45.70, H 4.00.

*Nucleophilic substitution reactions. Preparation of complex **15***

Into a 50 mL round-bottom flask, 1.00 mmol of **12** was combined with 8.00 mmol (0.881 g) of hydroquinone (**13**) and 2.00 mmol (0.276 g) of potassium carbonate. These reagents were stirred and refluxed for 16 h at 65°C in 16 mL of THF and 4 mL of DMF under an inert N_2 atmosphere. After cooling to room temperature, the reaction mixture was poured into 10% (v/v) HCl, and to this was added a concentrated solution of NH_4PF_6. Immediate precipitation of the product as a yellow solid allowed for isolation of the complex in very high yield.

*Complex **15***: 0.811 g (90%). ^1H NMR (200 MHz, CD_3COCD_3): δ (ppm): 8.72 (s, 1H, -OH), 7.55 (s, 4H, uncomplexed ArH), 7.19 (d, 2H, *J* = 6.9 Hz, uncomplexed ArH), 7.00 (d, 2H, *J* = 7.6 Hz, uncomplexed ArH), 6.45–6.23 (br m, 9H, complexed ArH), 5.31 (s, 5H, Cp), 5.25 (s, 5H, Cp). ^{13}C NMR (50 MHz, CD_3COCD_3): δ (ppm): 156.30 (1C, uncomplexed quat C), 152.32 (1C, uncomplexed quat C), 151.57 (1C, uncomplexed quat C), 146.45 (1C, uncomplexed quat C), 134.51 (1C, complexed quat C), 132.98 (1C, complexed quat C), 131.70 (1C, complexed quat C), 124.42 (2C, uncomplexed ArC), 124.11 (2C, uncomplexed ArC), 122.90 (2C, uncomplexed ArC), 117.87 (2C, uncomplexed ArC), 87.80 (2C, complexed ArC), 85.81 (1C, complexed ArC), 78.80 (5C, Cp), 78.13 (5C, Cp), 77.58 (2C, complexed ArC), 75.71 (2C, complexed ArC), 74.79 (2C, complexed ArC). Anal. calcd. for $C_{34}H_{28}F_{12}Fe_2O_4P_2$: C 45.26, H 3.13; found: C 45.37, H 3.31.

*Nucleophilic substitution reactions. Preparation of complexes **16** and **17***

Typically, 1.00 mmol of the phenolic complex (**14** or **15**) was added to 1.00 mmol of **8** along with 2.50 mmol of potassium carbonate. To this was added 10 mL of DMF, and the reaction mixture was allowed to stir at room temperature under a N_2 atmosphere for 16 h. The resulting solution was then poured into 10% (v/v) HCl and formed a yellow precipitate upon addition of a concentrated solution of NH_4PF_6.

*Complex **16***: 0.495 g (81%). IR (cm^{-1}): 1732 (CO). ^1H NMR (200 MHz, CD_3COCD_3): (*endo*) δ (ppm): 7.55 (br s, 4H, uncomplexed ArH), 7.05 (br s, 2H, complexed ArH), 6.67 (br s, 2H, complexed ArH), 6.46 (br s, 5H, complexed ArH), 6.33 (m, 1H, H_5), 6.08 (m, 1H, H_6), 5.33 (s, 5H, Cp), 5.26 (s, 5H, Cp), 4.23 (q, 1H, nor-CH_2O), 4.07 (t, 1H, nor-CH_2O), 3.06 (br s,1H, H_1), 2.82 (br s, 1H, H_4), 2.66 (m, 1H, H_2), 1.97 (m,1H, H_{3x}), 1.46 (br d, 1H, H_{7s}), 1.36 (br d,1H, H_{7a}), 0.73 (m,1H, H_{3n}); (*exo*) δ (ppm): 7.55 (br d, 4H, uncomplexed ArH), 7.05 (s, 2H, complexed ArH), 6.67 (s, 2H, complexed ArH), 6.46 (br s, 5H, complexed ArH), 6.24 (m, 1H, H_5), 6.14 (m, 1H, H_6), 5.33 (s, 5H, Cp), 5.26 (s, 5H, Cp), 4.55 (q, 1H, nor-CH_2O), 4.42 (t, 1H, nor-CH_2O), 2.88 (br s, 2H, H_1 and H_4), 2.15 (br m, 1H, H_{3x}), 1.95 (m, 1H, H_2), 1.44 (br d, 1H, H_{7s}), 1.38 (br d, 1H, H_{7a}), 1.30 (m, 1H, H_{3n}). ^{13}C NMR (50 MHz, CD_3COCD_3): (*endo*) δ (ppm): 165.62 (1C, CO), 151.92 (1C, uncomplexed quat ArC), 151.40 (1C, uncomplexed quat ArC), 138.46 (1C, C_5), 136.25 (1C, complexed quat ArC), 134.65 (1C, complexed quat ArC), 132.85 (1C, C_6), 124.67 (2C, uncomplexed ArC), 124.56 (2C, uncomplexed ArC), 88.34 (2C, complexed ArC), 87.87 (2C, complexed ArC), 85.87 (1C, complexed ArC), 79.71 (5C, Cp), 78.19 (5C, Cp), 77.99 (2C, complexed ArC), 77.67 (2C, complexed ArC), 70.86 (1C, nor-CH_2O), 49.94 (1C, C_7), 44.69 (1C, C_1), 42.92 (1C, C_4), 38.36 (1C, C_2), 29.81 (1C, C_3); (*exo*) δ (ppm): 165.71 (1C, CO), 151.92 (1C, uncomplexed quat ArC), 151.40 (1C, uncomplexed quat ArC), 137.59 (1C, C_6), 136.99 (1C, C_5), 136.25 (1C, complexed quat ArC), 134.65 (1C, complexed quat ArC), 124.67 (2C, uncomplexed ArC), 124.56 (2C, uncomplexed ArC), 88.34 (2C, complexed ArC), 87.87 (2C, complexed

© 1999 NRC Canada

ArC), 85.87 (1C, complexed ArC), 79.71 (5C, Cp), 78.19 (5C, Cp), 77.99 (2C, complexed ArC), 77.67 (2C, complexed ArC), 71.52 (1C, nor-CH_2O), 45.56 (1C, C_7), 44.45 (1C, C_1), 42.35 (1C, C_4), 38.74 (1C, C_2), 29.42 (1C, C_3). Anal. calcd. for $C_{37}H_{34}F_{12}Fe_2O_4P_2$: C 47.06, H 3.63; found: C 47.34, H 3.61.

Complex ***17***: 1.02 g (86%). IR (cm^{-1}): 1732 (CO). ^1H NMR (200 MHz, CD_3COCD_3): (*endo*) δ (ppm): 7.64 (br s, 4H, uncomplexed ArH), 7.61 (br s, 4H, uncomplexed ArH), 7.18 (br s, 2H, complexed ArH), 7.05 (br s, 2H, complexed ArH), 6.68–6.31 (br m, 9H, complexed ArH), 6.28 (m, 1H, H_5), 6.13 (m, 1H, H_6), 5.34 (s, 5H, Cp), 5.32 (s, 5H, Cp), 5.26 (s, 5H, Cp), 4.24 (m, 1H, nor-CH_2O), 4.01 (br t, 1H, nor-CH_2O), 3.08 (br s,1H, H_1), 2.81 (br s, 1H, H_4), 2.76 (br m, 1H, H_2), 2.00 (m, 1H, H_{3x}), 1.53 (br d, 1H, H_{7s}), 1.35 (br d, 1H, H_{7a}), 0.71 (m, 1H, H_{3n}); (*exo*) δ (ppm): 7.64 (br s, 4H, uncomplexed ArH), 7.61 (br s, 4H, uncomplexed ArH), 7.18 (br s, 2H, complexed ArH), 7.05 (br s, 2H, complexed ArH), 6.68–6.31 (br m, 9H, complexed ArH), 6.22 (m, 1H, H_5), 6.20 (m, 1H, H_6), 5.34 (s, 5H, Cp), 5.32 (s, 5H, Cp), 5.26 (s, 5H, Cp), 4.56 (m, 1H, nor-CH_2O), 4.37 (t, 1H, nor-CH_2O), 2.87 (br s, 2H, H_1 and H_4), 2.13–2.04 (br m, 1H, H_{3x}), 1.93 (br m, 1H, H_2), 1.44 (br d, 1H, H_{7s}), 1.37 (br d, 1H, H_{7a}), 1.34 (br m, 1H, H_{3n}). ^{13}C NMR (50 MHz, CD_3COCD_3): (*endo*) δ (ppm): 165.59 (1C, CO), 152.30 (1C, uncomplexed quat ArC), 152.03 (1C, uncomplexed quat ArC), 151.61 (1C, uncomplexed quat ArC), 151.36 (1C, uncomplexed quat ArC),138.47 (1C, C_5), 136.34 (1C, complexed quat ArC), 134.68 (1C, complexed quat ArC), 132.88 (1C, C_6), 132.25 (2C, complexed quat ArC), 124.68 (2C, uncomplexed ArC), 124.62 (2C, uncomplexed ArC), 124.50 (2C, uncomplexed ArC), 124.46 (2C, uncomplexed ArC), 88.26 (2C, complexed ArC), 87.76 (2C, complexed ArC), 85.77 (1C, complexed ArC), 79.60 (5C, Cp), 78.97 (5C, Cp), 78.08 (5C, Cp), 77.71 (2C, complexed ArC), 77.39 (2C, complexed ArC), 75.36 (2C, complexed ArC), 75.34 (2C, complexed ArC), 70.81 (1C, nor-CH_2O), 49.95 (1C, C_7), 44.64 (1C, C_1), 42.94 (1C, C_4), 38.35 (1C, C_2), 29.81 (1C, C_3); (*exo*) δ (ppm): 165.69 (1C, CO), 152.30 (1C, uncomplexed quat ArC), 152.03 (1C, uncomplexed quat ArC), 151.61 (1C, uncomplexed quat ArC), 151.36 (1C, uncomplexed quat ArC), 137.53 (1C, C_6), 136.99 (1C, C_5), 136.34 (1C, complexed quat ArC), 134.68 (1C, complexed quat ArC), 132.25 (2C, complexed quat ArC), 124.68 (2C, uncomplexed ArC), 124.62 (2C, uncomplexed ArC), 124.50 (2C, uncomplexed ArC), 124.46 (2C, uncomplexed ArC), 88.26 (2C, complexed ArC), 87.76 (2C, complexed ArC), 85.77 (1C, complexed ArC), 79.60 (5C, Cp), 78.97 (5C, Cp), 78.08 (5C, Cp), 77.71 (2C, complexed ArC), 77.39 (2C, complexed ArC), 75.36 (2C, complexed ArC), 75.34 (2C, complexed ArC), 71.47 (1C, nor-CH_2O), 46.56 (1C, C_7), 44.42 (1C, C_1), 42.36 (1C, C_4), 38.75 (1C, C_2), 29.42 (1C, C_3). Anal. calcd. for $C_{54}H_{47}F_{18}Fe_3O_6P_3$: C 46.51, H 3.40; found: C 46.49, H 3.56.

Photolytic demetallation. Preparation of compounds ***4***, ***9***, ***10***, ***18***, *and* ***19***

Each of the complexes, **3**, **7**, **8**, **16**, and **17**, were dissolved in a 4:1 mixture of CH_2Cl_2:CH_3CN, and transferred to a Pyrex photolytic tube. The reaction tube was then fitted into a photochemical apparatus equipped with a xenon lamp and irradiated at room temperature for 4–8 h, the time increasing as the number of metal moieties increased. After this time, the solvent was removed by rotary evaporation, and the contents were dissolved in $CHCl_3$ and washed with several aliquots of water (3 × 50 mL). The resulting solution was dried over $MgSO_4$, gravity filtered, and then evaporated under reduced pressure. Using a minimal amount of CH_2Cl_2 (1–2 mL), the crude product was transferred to a silica gel column, which was eluted first with hexane and then $CHCl_3$. Once again, the solvent was removed by rotary evaporation, liberating the arene–norbornene derivatives in good yields.

Compound ***4***: 0.166 g (83%). ^1H NMR (500 MHz, $CDCl_3$): (*endo*) δ (ppm): 7.50–6.70 (5H, ArH), 6.19 (m, 1H, *J* = 3.0 and 5.6 Hz, H_5), 5.98 (m, 1H, *J* = 2.9 and 5.6 Hz, H_6), 3.73 (t, 1H, *J* = 9.3 Hz, nor-CH_2O), 3.57 (t, 1H, *J* = 6.5 Hz, nor-CH_2O), 3.07 (br s, 1H, H_1), 2.87 (br s, 1H, H_4), 2.62–2.56 (m, 1H, *J* = 6.5 Hz, H_2) 1.97–1.91 (m, 1H, *J* = 9.4, 11.6, and 2.6 Hz, H_{3x}), 1.51 (br s, 1H, *J* = 2.6 and 8.1 Hz, H_{7s}), 1.33 (br s, 1H, *J* = 8.1 Hz, H_{7a}), 0.70 (m, 1H, *J* = 4.3, 11.6, and 2.6 Hz, H_{3n}); (*exo*) δ (ppm): 7.50–6.70 (5H, ArH), 6.18 (m, 1H, H_5), 6.13 (m, 1H, H_6), 4.05 (t, 1H, *J* = 9.1 Hz, nor-CH_2O), 3.87 (t, 1H, *J* = 6.2 Hz, nor-CH_2O), 2.90 (br s, 1H, H_4), 2.87 (br s, 1H, H_1), ~1.92 (m, 1H, H_2), 1.50 (br s, 2H, H_{7s} and H_{7a}), 1.37 (m, 1H, H_{3n}), 1.27 (m, 1H, H_{3x}). ^{13}C NMR (125 MHz, $CDCl_3$): (*endo*) δ (ppm): 159.21 (1C, quat ArC), 137.45 (1C, C_5), 132.37 (1C, C_6), 129.43 (2C, ArC), 120.55 (1C, ArC), 115 (2C, ArC), 71.38 (1C, nor-CH_2O), 49.41 (1C, C_7), 43.96 (1C, C_1), 41.65 (1C, C_4), 38.42 (1C, C_2), 29.06 (1C, C_3); (*exo*) δ (ppm): 159.21 (1C, quat ArC), 136.78 (1C, C_6), 136.47 (1C, C_5), 129.43 (2C, ArC), 120.55 (1C, ArC), 114.61 (2C, ArC), 72.24 (1C, nor-CH_2O), 45.10 (1C, C_7), 43.78 (1C, C_4), 42.29 (1C, C_1), 38.65 (1C, C_2), 29.72 (1C, C_3). MS, *m*/*z*; M^+ 200. Anal calcd. for $C_{14}H_{16}O$: C 83.96, H 8.05; found: C 83.81, H 8.12.

Compound ***9***: 0.160 g (70%). IR (cm^{-1}): 1714 (CO). ^1H NMR (500 MHz, $CDCl_3$): (*endo*) δ (ppm): 8.07 (d, 2H, *J* = 8.0 Hz, ArH), 7.55 (t, 1H, *J* = 7.2 Hz, ArH), 7.44 (t, 2H, *J* = 8.1 Hz, ArH), 6.20 (m, 1H, *J* = 3.0 and 5.7 Hz, H_5), 6.01 (m, 1H, *J* = 2.8 and 5.7 Hz, H_6), 4.13 (q, 1H, *J* = 10.8 Hz, nor-CH_2O), 3.91 (t, 1H, *J* = 10.8 Hz, nor-CH_2O), 2.99 (br s, 1H, H_1), 2.85 (br s, 1H, H_4), 2.55 (m, 1H, H_2) 1.90 (m, 1H, H_{3x}), 1.49 (br d, 1H, H_{7s}), 1.30 (br d, 1H, H_{7a}), 0.67 (m, 1H, *J* = 2.6, 4.2, and 11.7 Hz, H_{3n}); (*exo*) δ (ppm): 8.07 (d, 2H, *J* = 8.0 Hz, ArH), 7.55 (t, 1H, *J* = 7.2 Hz, ArH), 7.44 (t, 2H, *J* = 8.1 Hz, ArH), 6.13 (m, 1H, *J* = 3.1 and 5.6 Hz, H_5), 6.11 (m, 1H, *J* = 2.9 and 5.6 Hz, H_6), 4.42 (q, 1H, *J* = 10.9 Hz, nor-CH_2O), 4.22 (t, 1H, *J* = 10.9 Hz, nor-CH_2O), 2.88 (br s, 1H, H_4), 2.82 (br s, 1H, H_1), 1.90 (m, 1H, H_2), 1.40 (br s, 2H, H_{7s} and H_{7a}), 1.34 (m, 1H, H_{3n}), 1.26 (m, 1H, H_{3x}). ^{13}C NMR (125 MHz, $CDCl_3$): (*endo*) δ (ppm): 166.45 (1C, CO), 137.57 (1C, C_5), 132.73 (1C, ArC), 132.16 (1C, C_6), 130.54 (1C, quat ArC), 129.50 (2C, ArC), 128.26 (2C, ArC), 68.26 (1C, nor-CH_2O), 49.35 (1C, C_7), 43.95 (1C, C_1), 42.19 (1C, C_4), 37.88 (1C, C_2), 28.93 (1C, C_3); (*exo*) δ (ppm): 166.55 (1C, CO), 136.92 (1C, C_6), 136.19 (1C, C_5), 132.73 (1C, ArC), 130.46 (1C, quat ArC), 129.50 (2C, ArC), 128.26 (2C, ArC), 68.94 (1C, nor-CH_2O), 44.97 (1C, C_7), 43.71 (1C, C_1), 41.59 (1C, C_4), 38.08 (1C, C_2), 29.56 (1C, C_3). MS,

© 1999 NRC Canada

m/*z*: M^+ 228. Anal. calcd. for $C_{15}H_{16}O_2$: C 78.92, H 7.06; found: C 78.54, H 7.12.

Compound ***10***: 0.168 g (64%). IR (cm^{-1}): 1715 (CO). ^1H NMR (500 MHz, $CDCl_3$): (*endo*) δ (ppm): 7.97 (d, 2H, ArH), 7.39 (d, 2H, ArH), 6.17 (m, 1H, H_5), 5.98 (m, 1H, H_6), 4.09 (q, 1H, *J* = 6.6 and. 10.9 Hz, nor-CH_2O), 3.88 (t, 1H, *J* = 9.3 Hz, nor-CH_2O), 2.94 (br s, 1H, H_1), 2.83 (br s, 1H, H_4), 2.52 (m, 1H, H_2) 1.89 (m, 1H, H_{3x}), 1.46 (br s, 1H, H_{7s}), 1.28 (br s, 1H, H_{7a}), 0.63 (m, 1H, H_{3n}); (*exo*) δ (ppm): 7.97 (d, 2H, ArH), 7.39 (d, 2H, ArH), 6.11 (m, 1H, H_5), 6.10 (m, 1H, H_6), 4.38 (q, 1H, *J* = 10.1 Hz, nor-CH_2O), 4.20 (t, 1H, *J* = 6.6 Hz, nor-CH_2O), 2.85 (br s, 1H, H_4), 2.77 (br s, 1H, H_1), 1.86 (m, 1H, H_2), 1.37 (br s, 2H, H_{7s} and H_{7a}), 1.32 (m, 1H, H_{3n}), 1.27 (m, 1H, H_{3x}). ^{13}C NMR (125 MHz, $CDCl_3$): (*endo*) δ (ppm): 165.42 (1C, CO), 139.05 (1C, quat ArC), 137.56 (1C, C_5), 131.99 (1C, C_6), 130.80 (2C, ArC), 128.80 (1C, quat ArC), 128.50 (2C, ArC), 68.40 (1C, nor-CH_2O), 49.28 (1C, C_7), 43.86 (1C, C_1), 42.11 (1C, C_4), 37.77 (1C, C_2), 28.85 (1C, C_3); (*exo*) δ (ppm): 165.52 (1C, CO), 139.12 (1C, quat ArC), 136.86 (1C, C_6), 136.04 (1C, C_5), 130.80 (2C, ArC), 128.88 (1C, quat ArC), 128.50 (2C, ArC), 69.09 (1C, nor-CH_2O), 44.88 (1C, C_7), 43.60 (1C, C_1), 41.50 (1C, C_4), 37.96 (1C, C_2), 29.48 (1C, C_3). MS, *m*/*z*: M^+ 262. Anal. calcd. for $C_{15}H_{15}ClO_2$: C 68.57; H. 5.75; found: C 68.23, H 5.95.

Compound ***18***: 0.210 g (51%). IR (cm^{-1}): 1707 (CO). ^1H NMR (200 MHz, $CDCl_3$): (*endo*) δ (ppm): 8.05 (br d, 2H, ArH), 7.38 (br, 2H, ArH), 7.15–6.98 (br m, 9H, ArH), 6.21 (m, 1H, H_5), 6.02 (m, 1H, H_6), 4.10 (q, 1H, nor-CH_2O), 3.90 (t, 1H, nor-CH_2O), 2.98 (br s, 1H, H_1), 2.87 (br s, 1H, H_4), 2.55 (m, 1H, H_2), 1.91 (br m, 1H, H_{3x}), 1.50 (br d, 1H, H_{7s}), 1.32 (br s, 1H, H_{7a}), 0.64 (m, 1H, H_{3n}); (*exo*) δ (ppm): 8.05 (br d, 2H, ArH), 7.38 (br d, 2H, ArH), 7.15–6.98 (br m, 9H, ArH), 6.13 (m, 1H, H_5), 6.11 (m, 1H, H_6), 4.40 (q, 1H, nor-CH_2O), 4.21 (t, 1H, nor-CH_2O), 2.89 (br s, 1H, H_4), 2.82 (br s, 1H, H_1), 1.84 (br m, 1H, H_2), 1.40 (br s, 2H, H_{7s} and H_{7a}), 1.34 (br m, 1H, H_{3n}), 1.25 (br m, 1H, H_{3x}). ^{13}C NMR (50 MHz, $CDCl_3$): (*endo*) δ (ppm): 165.98 (1C, CO), 162.05 (1C, quat ArC), 157.36 (1C, quat ArC), 153.75 (1C, quat ArC), 150.93 (1C, quat ArC), 137.61 (1C, C_5), 132.19 (1C, C_6), 131.66 (2C, ArC), 129.79 (2C, ArC), 124.62 (1C, quat ArC), 123.28 (1C, ArC), 121.51 (2C, ArC), 120.36 (2C,ArC), 118.56 (2C, ArC), 116.79 (2C, ArC), 68.17 (1C, nor-CH_2O), 49.35 (1C, C_7), 43.95 (1C, C_1), 42.19 (1C, C_4), 37.89 (1C, C_2), 28.92 (1C, C_3); (*exo*) δ (ppm): 166.04 (1C, CO), 162.05 (1C, quat ArC), 157.36 (1C, quat ArC), 153.75 (1C, quat ArC), 150.93 (1C, quat ArC), 136.96 (1C, C_6), 136.22 (1C, C_5), 131.66 (2C, ArC), 129.79 (2C, ArC), 124.71 (1C, quat ArC), 123.28 (1C, ArC), 121.51 (2C, ArC), 120.36 (2C,ArC), 118.56 (2C, ArC), 116.79 (2C, ArC), 68.84 (1C, nor-CH_2O), 44.99 (1C, C_7), 43.69 (1C, C_1), 41.60 (1C, C_4), 37.89 (1C, C_2), 28.92 (1C, C_3). MS, *m*/*z*: M^+ 412. Anal. calcd. for $C_{27}H_{24}O_4$; C 78.62, H 5.86; found: C 78.84, H 5.80.

Compound ***19***: 0.275 g (46%). IR (cm^{-1}): 1716 (CO). ^1H NMR (200 MHz, $CDCl_3$): (*endo*) δ (ppm): 8.02 (br d, 2H, ArH), 7.33 (br d, 2H, ArH), 7.09–6.92 (br m, 17H, ArH), 6.20 (m, 1H, H_5), 6.00 (m, 1H, H_6), 4.10 (q, 1H, nor-CH_2O), 3.89 (t, 1H, nor-CH_2O), 2.97 (br s, 1H, H_1), 2.86 (br s, 1H, H_4), 2.54 (br m, 1H, H_2), 1.90 (br m, 1H, H_{3x}), 1.48 (br s, 1H, H_{7s}), 1.30 (br s, 1H, H_{7a}), 0.66 (br m, 1H, H_{3n}); (*exo*) δ (ppm): 8.02 (br d, 2H, ArH), 7.33 (br, 2H, ArH), 7.09–6.92 (br m, 17H, ArH), 6.12 (m, 2H, H_5 and H_6), 4.39 (q, 1H, nor-CH_2O), 4.21 (t, 1H, nor-CH_2O), 2.88 (br s, 1H, H_4), 2.80 (br s, 1H, H_1), 1.88 (br m, 1H, H_2), 1.40 (br s, 2H, H_{7s} and H_{7a}), 1.34 (br m, 1H, H_{3n}), 1.27 (br m, 1H, H_{3x}). ^{13}C NMR (50 MHz, $CDCl_3$): (*endo*) δ (ppm): 165.98 (1C, CO), 162.08 (1C, quat ArC), 162.06 (1C, quat ArC), 157.72 (1C, quat ArC), 154.34 (1C, quat ArC), 153.33 (1C, quat ArC), 153.11 (1C, quat ArC), 152.58 (1C, quat ArC), 150.72 (1C, quat ArC), 137.61 (1C, C_5), 132.18 (1C, C_6), 131.63 (2C, ArC), 129.70 (2C, ArC), 122.86 (1C, ArC), 121.63 (2C, ArC), 120.45 (2C, ArC), 120.20 (2C, ArC), 119.86 (2C, ArC), 119.83 (2C, ArC), 119.69 (2C, ArC), 118.20 (2C, ArC), 116.74 (2C, ArC), 68.18 (1C, nor-CH_2O), 49.35 (1C, C_7), 43.94 (1C, C_1), 42.19 (1C, C_4), 37.87 (1C, C_2), 28.92 (1C, C_3); (*exo*) δ (ppm): 166.04 (1C, CO), 162.08 (1C, quat ArC), 162.06 (1C, quat ArC), 157.72 (1C, quat ArC), 154.34 (1C, quat ArC), 153.33 (1C, quat ArC), 153.11 (1C, quat ArC), 152.58 (1C, quat ArC), 150.72 (1C, quat ArC), 136.95 (1C, C_6), 136.21 (1C, C_5), 131.63 (2C, ArC), 129.70 (2C, ArC), 122.86 (1C, ArC), 121.63 (2C, ArC), 120.45 (2C, ArC), 120.20 (2C, ArC), 119.86 (2C, ArC), 119.83 (2C, ArC), 119.69 (2C, ArC), 118.20 (2C, ArC), 116.74 (2C, ArC), 68.84 (1C, nor-CH_2O), 44.98 (1C, C_7), 43.69 (1C, C_1), 41.59 (1C, C_4), 37.87 (1C, C_2), 28.92 (1C, C_3). MS, *m*/*z*: M^+ 597. Anal. calcd. for $C_{39}H_{32}O_6$: C 78.51, H 5.41; found: C 78.28, H 5.49.

Polymer syntheses

$RuCl_3$(hydrate) polymerization. Preparation of polymer ***20***

In a 10 mL round-bottom flask, 1 mol % of $RuCl_3$(hydrate) was stirred in the previously described ethanol or water solvent system (71, 72). Generation of the catalyst proceeded under a nitrogen atmosphere for 2–3 h, after which it was added to the monomer (**4**). The resulting solution was heated at 60°C for a 24 h period, yielding a viscous material. After dissolution in $CHCl_3$, the polymer was precipitated into methanol with vigorous stirring. A fibrous, off-white solid was obtained following this purification process. IR (cm^{-1}): 1714 (CO), 969 (*trans* olefin). ^1H NMR (200 MHz, $CDCl_3$): δ (ppm): 7.30–7.10 (br s, 2H, ArH), 6.90–6.70 (br s, 3H, ArH), 5.40–5.25 (br s, 2H, olefinic H), 3.90–3.60 (br d, 2H, poly-CH_2O), 2.90–1.10 (br peaks, 7H, aliphatic ring protons).

$(Cy_3P)_2Cl_2Ru{=}CHPh$ polymerizations. Preparation of polymers ***21–24***

Using [M]:[I] ratios of 100:1, the catalyst was weighed out in a glove box and transferred to a 10 mL RBF. To this flask was added 0.5 mL of CH_2Cl_2 for every 100 mg of monomer used. Outside of the glovebox, another equivalent of CH_2Cl_2 (0.5 mL/100 mg) was added to a second 10 mL round-bottom flask containing the monomer under a N_2 atmosphere. Using an airtight syringe, the catalyst solution was then transferred under N_2 to the vigorously stirring monomer. The polymerization reaction proceeded for approximately 1 h, giving a gelatinous material. To this, a small volume of ethyl vinyl ether was added. The polymer

© 1999 NRC Canada

was then dissolved in either CH_2Cl_2 or $CHCl_3$ and precipitated into methanol yielding a fibrous, off-white material.

*Poymer **21***: 0.220 g (71%). IR (cm^{-1}): 1714 (CO), 969 (*trans* olefin). ^1H NMR (500 MHz, $CDCl_3$): δ (ppm): 8.05–7.95 (br s, 2H, ArH), 7.60–7.30 (br, 3H, ArH), 5.40–5.20 (br s, 2H, olefinic H), 4.40–4.05 (br d, 2H, poly-CH_2O), 3.10–1.19 (br peaks, 7H, aliphatic ring protons).

*Polymer **22***: 0.270 g (74%). IR (cm^{-1}): 1715 (CO), 969 (*trans* olefin). ^1H NMR (200 MHz, $CDCl_3$): δ (ppm): 8.01–7.90 (br s, 2H, ArH), 7.45–7.35 (br s, 2H, ArH), 5.40–5.20 (br s, 2H, olefinic H), 4.35–4.05 (br d, 2H, poly-CH_2O), 3.09–1.04 (br peaks, 7H, aliphatic ring protons).

*Polymer **23***: 0.316 g (73%). IR (cm^{-1}): 1712 (CO), 967 (*trans* olefin). ^1H NMR (200 MHz, $CDCl_3$): δ (ppm): 8.00–7.80 (br s, 2H, ArH), 7.40–6.75 (br s, 11H, ArH), 5.45–5.25 (br s, 2H, olefinic H), 4.35–4.05 (br d, 2H, poly-CH_2O), 3.00–0.90 (br peaks, 7H, aliphatic ring protons).

*Polymer **24***: 0.186 g (66%). IR (cm^{-1}): 1714 (CO), 964 (*trans* olefin). ^1H NMR (200 MHz, $CDCl_3$): δ (ppm): 8.00–7.85 (br s, 2H, ArH), 7.35–6.75 (br s, 19H, ArH), 5.45–5.20 (br s, 2H, olefinic H), 4.40–4.10 (br s, 2H, poly-CH_2O), 3.00–0.90 (br peaks, 7H, aliphatic ring protons).

Acknowledgements

Financial support for this work provided by the Natural Sciences and Engineering Research Council of Canada (NSERC), American Chemical Society – Petroleum Research Funds (ACS–PRF), and Manitoba Hydro is gratefully acknowledged. A.L.E. and K.M.E. (graduate students, University of Manitoba) also thank the Department of Chemistry at the University of Manitoba. Mettler Toledo is also gratefully acknowledged.

References

1. W.L. Truett, D.R. Johnson, I.M. Robinson, and B.A. Montague. J. Am. Chem. Soc. **82**, 2337 (1960).
2. K.J. Ivin and J.C. Mol. Olefin metathesis and metathesis polymerization. Academic Press, Inc., San Diego. 1997.
3. K.J. Ivin and T. Saegusa (*Editors*). Cycloalkenes and bicycloalkenes – ring-opening polymerization. Vol. 1. Elsevier, London. 1984.
4. G. Odian. Principles of polymerization. 3rd ed. John Wiley & Sons, Inc., New York. 1991.
5. B.M. Novak, W. Risse, and R.H. Grubbs. Adv. Polym. Sci. **102**, 47 (1992).
6. C. Pugh, J. Dharia, and S.V. Arehart. Macromolecules, **30**, 4520 (1997).
7. Z. Komiya, C. Pugh, and R.R. Schrock. Macromolecules, **25**, 3609 (1992).
8. C. Pugh, J. Shao, J.J. Ge, and S.Z.D. Cheng. Macromolecules, **31**, 1779 (1998).
9. B.R. Maughon, M. Weck, B. Mohr, and R.H. Grubbs. Macromolecules, **30**, 257 (1997).
10. R.J. Cotter. Engineering plastics: a handbook of polyarylethers. Gordon and Breach Publishers, Basel. 1995.
11. Z.Y. Wang and P.W. Broughton. Can. J. Chem. **75**, 1346 (1997).
12. J.E. Douglas and Z.Y. Wang. Can. J. Chem. **75**, 1340 (1997).
13. P.M. Hergenrother, B.J. Jensen, and S.J. Havens. Polymer, **88**, 358 (1988).
14. M. Ueda and F. Ichikawa. Macromolecules, **23**, 926 (1990).
15. S. Matsumoto, K. Komatsu, and K. Igarashi. Ring-opening Polym. Int. Symp. ACS Symp. Ser. (303) 1977.
16. R. Madan, R.C. Anand, and I.K. Varma. Ind. J. Chem. Tech. **5**, 74 (1998).
17. S.C.G. Biagini, M.P. Coles, V.C. Gibson, M.R. Giles, E.L. Marshall, and M. North. Polymer, **39**, 1007 (1998).
18. V. Heroguez, S. Breunig, Y. Gnanou, and M. Fontanille. Macromolecules, **29**, 4459 (1996).
19. B.S. Heinz, W. Heitz, S.A. Krugel, F. Raubacher, and J.H. Wendorff. Acta. Polym. **48**, 385 (1997).
20. M.A. Tlenkopatchev, S. Fomine, L. Fomina, R. Gavino, and T. Ogawa. Polym. J. **29**, 622 (1997).
21. M.R. Buchmeiser, N. Atzl, and G.K. Bonn. J. Am. Chem. Soc. **119**, 9166 (1997).
22. R. Madan, R.C. Anand, and I.K. Varma. J. Polym. Sci. Part A: Polym. Chem. **35**, 2917 (1997).
23. D. Albagli, G.C. Bazan, R.R. Schrock, and M.S. Wrighton. J. Am. Chem. Soc. **115**, 7328 (1993).
24. P. Lecomte, D. Mecerreyes, P.Dubois, A. Demonceau, A.F. Noels, and R. Jerome. Polym. Bull. **40**, 631 (1998).
25. S.T. Nguyen. L.K. Johnson, and R.H. Grubbs. J. Am. Chem. Soc. **114**, 3974 (1992).
26. S.T. Nguyen and R.H. Grubbs. J. Am. Chem. Soc. **115**, 9858 (1993).
27. S. Kanaoka and R.H. Grubbs. Macromolecules, **28**, 4707 (1995).
28. C. Fraser and R.H. Grubbs. Macromolecules, **28**, 7248 (1995).
29. P. Schwab, M.B. France, J.W. Ziller, and R.H. Grubbs. Angew. Chem. Int. Ed. Engl. **34**, 2039 (1995).
30. D.M. Lynn, S. Kanaoka, and R.H. Grubbs. J. Am. Chem. Soc. **118**, 784 (1996).
31. M. Weck, P. Schwab, and R.H. Grubbs. Macromolecules, **29**, 1789 (1996).
32. P. Schwab, R.H. Grubbs, and J.W. Ziller. J. Am. Chem. Soc. **118**, 100 (1996).
33. M. Weck, B. Mohr, B.R. Maughon, and R.H. Grubbs. Macromolecules, **30**, 6430 (1997).
34. D.M. Lynn, B. Mohr, and R.H. Grubbs. J. Am. Chem. Soc. **120**, 1627 (1998).
35. E.L. Dias and R.H. Grubbs. Organometallics, **17**, 2758 (1998).
36. T. Weskamp, W.C. Schattenmann, M. Spiegler, and W.A. Hermann. Angew. Chem. Int. Ed. Engl. **37**, 2490 (1998).
37. A.W. Stumpf, E. Saive, A. Demonceau, and A.F. Noels. J. Chem. Soc. Chem. Commun. 1127 (1995).
38. H. Katayama and F. Ozawa. Chem. Lett. 67 (1998).
39. V. Percec and D. Schlueter. Macromolecules, **30**, 5783 (1997).
40. R.R. Schrock, J. Feldman, L.F. Cannizzo, and R.H. Grubbs. Macromolecules, **20**, 1172 (1987).
41. G.C. Bazan, E. Khosravi, R.R. Schrock, W.J. Feast, V.C. Gibson, M.B. O'Regan, J.K. Thomas, and W.M. Davis. J. Am. Chem. Soc. **112**, 8378 (1990).
42. G.C. Bazan, R.R. Schrock, H.N. Cho, and V.C. Gibson. Macromolecules, **24**, 4495 (1991).
43. G.C. Bazan, J.H. Oskam, H-N Cho, L.Y. Park, and R.R. Schrock. J. Am. Chem. Soc. **113**, 6988 (1991).
44. D. Albagli, G. Bazan, M.S. Wrighton, and R.R. Schrock. J. Am. Chem. Soc. **114**, 4150 (1992).
45. J.H. Oskam and R.R. Schrock. J. Am. Chem. Soc. **115**, 11 831 (1993).
46. D.H. McConville, J.R. Wolf, and R.R. Schrock. J. Am. Chem. Soc. **115**, 4413 (1993).

© 1999 NRC Canada

47. R.O'Dell, D.H. McConville, G.E. Hofmeister, and R.R. Schrock. J. Am. Chem. Soc. **116**, 3414 (1994).
48. J-K. Lee, R.R. Schrock, D.R. Baigent, and R.H. Friend. Macromolecules, **28**, 1966 (1995).
49. T.J. Boyd, Y. Geerts, J-K. Lee, D.E. Fogg, G.G. Lavoie, R.R. Schrock, and M.F. Rubner. Macromolecules, **30**, 3553 (1997).
50. C. Pugh, J-Y. Bae, J. Dharia, J.J. Ge, and S.Z.D. Cheng. Macromolecules, **31**, 5188 (1998).
51. A.S. Abd-El-Aziz, C.R. de Denus, L.R. McGillivray, and M.J. Zaworotko. J. Chem. Soc. Dalton Trans. 3375 (1995).
52. A.S. Abd-El-Aziz, E.K. Todd, and K.M. Epp. J. Inorg. Organomet. Polym. **8**, 127 (1998).
53. A.S. Abd-El-Aziz, K.M. Epp, and C.R. de Denus. Polym Prepr. Am. Chem. Soc. Div. Polym. Chem. **29**, 408 (1998).
54. A.S. Abd-El-Aziz, D.A. Armstrong, S. Bernardin, and H.M. Hutton. Can. J. Chem. **74**, 2073 (1996).
55. A.S. Abd-El-Aziz, E.K. Todd, and K.M. Epp. Polym. Prepr. Am. Chem. Soc. Div. Polym. Chem. **29**, 300 (1998).
56. A.S. Abd-El-Aziz, Y. Lei, and C.R. de Denus. Polyhedron, **14**, 1585 (1995).
57. A.S. Abd-El-Aziz, K.M. Epp, C.R. de Denus, and G. Fisher-Smith. Organometallics, **13**, 2299 (1994).
58. A.S. Abd-El-Aziz and C.R. de Denus. J. Chem. Soc. Chem. Commun. 663 (1994).
59. A.S. Abd-El-Aziz, A.L. Edel, K.M. Epp, and H.M. Hutton. New J. Chem. **23**, 569 (1999).
60. A. Moroz and M.S. Shvartsberg. Russ. Chem. Rev. (Engl. Transl.), **43**, 679 (1974).
61. A.N. Nesmeyanov, N.A. Vol'kenau, E.I. Sirotkina, and V.V. Deryabin. Dokl. Akad. Nauk SSSR, **177**, 1110 (1967).
62. A.N. Nesmeyanov, N.A. Vol'kenau, and E.I. Sirotkina. Dokl. Akad. Nauk SSSR, **190**, 857 (1970).
63. J. Fisher and M.J. Gradwell. Magn. Reson. Chem. **29**, 1068 (1991).
64. R.R. Fraser. Can. J. Chem. **40**, 78 (1962).
65. J.I. Musher. Mol. Phys. **6**, 93 (1963).
66. K.L. Williamson. J. Am. Chem. Soc. **85**, 516 (1963).
67. P. Laszlo and P. von Rague Schleyer. J. Am. Chem. Soc. **86**, 1171 (1964).
68. E.W.C. Wong and C.C. Lee. Can. J. Chem. **42**, 1245 (1964).
69. E.I. Snyder and B. Franzus. J. Am. Chem. Soc. **86**, 1166 (1964).
70. P. Laszlo and P. von Rague Schleyer. J. Am. Chem. Soc. **85**, 2709 (1963).
71. B.M. Novak and R.H. Grubbs. J. Am. Chem. Soc. **110**, 960 (1988).
72. M. Lautens, A.S. Abd-El-Aziz, and J. Reibel. Macromolecules, **22**, 4133 (1989).
73. R.P. Quirk and B. Lee. Polym. Int. **27**, 359 (1992).
74. F. Cataldo. Polym. Int. **57**, 49 (1994).
75. W.J. Feast and L.A. Shahada. Eur. Polym. J. **27**, 27 (1991).
76. A.N. Nesmeyanov, N.A. Vol'kenau, and I.N. Bolesova. Tetrahedron Lett. 1725 (1963).
77. I.U. Khand, P.L. Pauson, and W.F. Watts. J. Chem. Soc. C, 2261 (1968).

© 1999 NRC Canada

On combination lines in the NMR spectra of strongly coupled spin systems

Alex. D. Bain

Abstract: Strongly coupled spin systems provide many curious and interesting effects in NMR spectra, one of which is the presence of unexpected (from a first-order viewpoint) lines. A physical reason is given for the presence of these combination lines. The X part of the spectrum of an ABX spin system is analysed as an example. For an ABX system, it is well known that the AB nuclei give a spectrum consisting of two AB-type spectra, corresponding to the two orientations of the X nucleus. It can also be shown that the X part of the spectrum corresponds to the X nucleus undergoing a transition in the presence of an AB-like spin system. For weakly coupled systems, the four observed lines correspond to the four different orientations of the A and B nuclei. For a strongly coupled system, two additional lines may appear, the combination lines. The resulting six lines correspond to the four spin orientations, plus the two zero-quantum transitions. It is shown that these six lines are such that there is no net excitation of the AB-like spin system associated with the X transitions. There is no AB coherence created directly by a pulse applied to X. AB coherence is created as the system evolves, and this is responsible for many of the curious effects. This is shown to be true for all spin sub-systems, which are weakly coupled to a strongly coupled sub-system.

Key words: NMR, strong coupling, second-order spectra, ABX spin system, combination lines, spectral analysis.

Résumé : Les spectres RMN des systèmes de spin fortement couplés fournissent des effets intéressants et curieux; l'un d'eux est la présence de raies inattendues d'un point de vue du premier ordre. On présente une raison physique pour la présence de ces raies de combinaison. À cette fin, on analyse la partie X du spectre d'un système de spin ABX. Pour un système ABX, il est bien connu que les noyaux AB donnent un spectre correspondant à deux spectres de type AB qui correspondent aux deux orientations du noyau X. On peut aussi montrer que la partie X du spectre correspond au noyau X subissant une transition en présence d'un système de spin de type AB. Pour les systèmes faiblement couplés, les quatre raies observées correspondent aux quatre orientations différentes des noyaux A et B. Pour un système fortement couplé, deux raies supplémentaires apparaissent; les raies de combinaison. Les six raies qui en résultent correspondent aux quatre orientations de spin, en plus des deux transitions de quantum nul. On montre que ces six raies sont telles qu'il n'y a pas d'excitation nette du système de spin de type AB associé aux transitions X. Aucune cohérence AB n'est créée directement par une pulsation appliquée à X. La cohérence AB est créée lorsque le système évolue et elle est responsable de plusieurs effets curieux. On montre que ceci est vrai pour tous les sous systèmes de spin faiblement couplés à un sous système fortement couplé.

Mots clés : RMN, couplement fort, spectre du seconde ordre, système de spin ABX, raies de combinaison, analyse spectral.

[Traduit par la Rédaction]

Introduction

The ABX spin system is a classic part of NMR (1–4). It is a spin system that can be solved analytically, yet it illustrates many important features of NMR spectra. These range from simple first-order, weakly coupled, spectra (AMX), through to magnetic equivalence (A_2X). When the system is strongly coupled, the phenomena of combination lines, deceptively simple spectra (5), and virtual coupling (6) can be seen. The ABX system is the simplest example in which the relative signs of couplings become visible and important. The pedagogical value of the ABX system has long been recognised (7–9). It is tempting to think, in the days of high-field magnets, that strong coupling is no longer important, but we will always have AA′X systems. For all these reasons, the ABX spin system is still an important one to understand.

Further phenomena can be seen in pulse experiments. If the X part of a weakly coupled heteronuclear AMX system undergoes a spin echo, the signal simply decays as T_2. However, if the A and B are strongly coupled, the signal can undergo substantial modulations as a function of echo time (10, 11). Phase and intensity distortions may also be expected in other experiments (12, 13). In a deceptively simple case, it has been shown that although the observed splittings

Received March 4, 1999.

This paper is dedicated to Professor Ted Schaefer in recognition of his outstanding contributions to Canadian chemistry.

A.D. Bain.[1] Dept. of Chemistry, McMaster University, 1280 Main St. W., Hamilton ON L8S 4M1, Canada.

[1]Fax: (905) 522 2509. e-mail: bain@mcmaster.ca

 © 1999 NRC Canada

are small (due to opposite signs of couplings), the DEPT experiment responds to the true couplings (14).

Since there is an analytical solution (1, 15, 16), all of these effects can be readily calculated and simulated. In this paper, we seek to give some less mathematical rationalizations, in order to gain some more insight.

The ABX spin system

It is useful to start with the AB spin system. The wave functions are well known (1). They are mixtures of the basic wave functions, governed by the angle θ defined by eq. [1]:

$$[1] \qquad \tan(2\theta) = J/(\nu_A - \nu_B)$$

In this equation, J is the coupling, and ν_A and ν_B are the resonance frequencies of the two nuclei. The density matrix for the AB spin system is made from all possible combinations (as kets and bras) of these four wave functions. This leads to 16 density matrix elements: four level populations, one pair of zero-quantum transitions, four pairs of single-quantum transitions, and one pair of double-quantum transitions. The pairs arise because all the transitions have a non-zero frequency, so they can precess in either the positive or negative sense.

The ABX spin system is a combination of the AB and the X spin system. This is obvious in the AB part, which consists of two AB patterns, each with a different value of θ, denoted by θ_+ and θ_-. If J_{AX} is not equal to J_{BX}, then the difference in magnetic field experienced by A and B depends on the orientation of the X nucleus. The AB part of the spectrum has two AB patterns, depending on the *z* component of the X spin.

Although it is not obvious, a similar statement holds for the X part of the spectrum. In the case of equivalent spins, or weak coupling, the four lines in the X part of the spectrum represent the four orientations of the A and B nuclei. For strong coupling, we need to expand the idea of orientations to the more general concept of coherence level zero. There are four level populations for AB, but six coherence-level-zero density matrix elements, since the zero-quantum transitions must be included. The six lines in the X part of a general ABX spectrum map onto the six coherence level zero density matrix elements.

How is this mapping done? Some heroic algebra shows that the density matrix for an ABX system can be factored into an X part and an AB part (15). However, the AB part depends on the state of the X nucleus. A single spin, X, has four density matrix elements, corresponding to the unit operator, *1*, and the operators I_z, I_+, I_-, as in eq. [2]:

$$[2] \qquad 1 = |0) = \frac{1}{\sqrt{2}}\{|\alpha><\alpha| + |\beta><\beta|\}$$

$$I_+ = |1_{+1}) = |\alpha><\beta|$$

$$\sqrt{2I_z} = |1_0) = \frac{1}{\sqrt{2}}\{|\alpha><\alpha| - |\beta><\beta|\}$$

$$I_- = |1_{-1}) = |\beta><\alpha|$$

In superspin terms, these correspond to $|1_0)$, $|1_{+1})$, $|1_{-1})$, and $|0)$, where the subscript is the coherence level of each density matrix element. Note that if the kets and bras are identical, there is no coherence. If the coherence level of the X nucleus is zero, then the AB part of this part of the factored density matrix is just an AB density matrix with the appropriate value of θ. This is the mathematical description of the two AB patterns in that region of the spectrum. However, when the X spin has coherence,. i.e., we are looking in the X part of the spectrum, life gets more interesting.

Just as the AB part of an ABX spectrum is factored according to the orientation of the X spin, so also the X part of the spectrum can be factored according to a rather special AB-type spin system. An AB density matrix can always be constructed from a ket–bra combination of the AB wave functions. When the X spin has coherence, the AB part of an ABX is slightly different: the ket has one of the values of θ, say θ_+, and the bra has the *other* angle, θ_-. In other words, during an X transition, the AB part of the density matrix "jumps" from one value of θ to the other (6). In this unusual AB-type density matrix, what used to be a level population now has coherence, since the two θ values are different. The role of the zero-quantum transitions, the combination lines, is to cancel out this coherence.

There is a fundamental principle that physics should be local. That is, a ^{13}C transition should not create coherence in the spectrum of two ^{31}P nuclei making up the AB part of an ABX. This is rigorously true for all spin systems — a non-selective pulse applied to one region of the spectrum will not excite any of the other regions. In terms of the density matrix, the element that corresponds to the total X spectrum has no coherence associated with the AB part. Although strongly coupled spin systems must obey this principle before any evolution, they find it difficult to adhere to it as a function of time.

The density matrix element representing the total X spectrum is the sum of the elements that represent the individual transitions. In a weakly coupled AMX system, there is no AM coherence associated with any of the individual X transitions. Therefore, the total X spectrum will have no AM coherence. However, for an ABX system, the density matrix elements for the individual transitions *have* AB coherence (17). The X transition is represented by the operator I_+, or superspin $|1_{+1})$, combined with a ket–bra density matrix element for the AB system. In weak coupling, the ket and bra are identical, so there is no coherence associated. In strong coupling, the ket and bra are different, so there must be AB coherence. This difference in wave function creates the AB coherence associated with that X transition. This cancels out only in the sum of all the transitions.

The pattern of combination lines in a strongly coupled spin system is therefore the one that gives no *net* coherence to the AB part of the spectrum. In weak coupling each of the individual X transitions has no AM coherence. This is no longer possible for strong coupling, since the X spin affects the AB part of the spectrum. The physical principle of no AB coherence only applies to the sum. The interesting effects, such as echo modulation, show up as the spin system evolves in time. As time progresses, the density matrix elements oscillate at different frequencies, so the coherence cancellation in the AB part of the spectrum no longer occurs. The various consequences are predictable, but may be counter-intuitive.

For the ABX spin system, the coherences can be calculated explicitly. This makes it easy to see the creation of AB

© 1999 NRC Canada

coherence following the excitation of the X spin alone. However, there is nothing in this discussion that restricts the phenomenon to the ABX spin system. Any time there is a strongly coupled spin subsystem, M, which is weakly coupled to another subsystem, N, similar results will occur. Excitation of the N subsystem will not create M coherence immediately, but such coherence will arise during the evolution. As with the ABX system, curious and unexpected results may occur.

Conclusions

The ABX spin system can be factored into an AB part and an X part. The AB part of the spectrum depends on the orientation of the X spin, as is well-known. Similarly, the X part of the spectrum depends on the AB part, provided that the nature of the AB part is generalized. The six transitions in the X part of the spectrum map onto the six coherence-level-zero density matrix elements of the generalized AB part. These coherence-level-zero elements can be regarded as combinations of four level populations and two zero-quantum transitions. Their intensities are governed by the principle that there should be no net excitation of the AB spins when X is excited. However, the cancellation is true only at time zero. If an ABX system is subjected to a sequence of pulses and evolutions, the coherences no longer cancel as time progresses. This is responsible for all the peculiar effects. The phenomenon is not restricted to the ABX spin system, but will arise any time a subsystem of the total system is strongly coupled.

Acknowledgements

I would like to thank the Natural Sciences and Engineering Research Council of Canada (NSERC) for financial support, and Ted Schaefer for many “stimulating” discussions.

References

1. J.A. Pople, W.G. Schneider, and H.J. Bernstein. High-resolution nuclear magnetic resonance. McGraw–Hill Book Company, Inc., New York. 1959.
2. H.J. Bernstein, J.A. Pople, and W.G. Schneider. Can. J. Chem. **35**,.65 (1957).
3. J.A. Pople and T. Schaefer. Mol. Phys. **3**, 547 (1961).
4. T. Schaefer. Can. J. Chem. **40**, 1678 (1962).
5. R.J. Abraham and H.J. Bernstein. Can. J. Chem. **39**, 216 (1961).
6. J.I. Musher and E.J. Corey. Tetrahedron, **18**, 791 (1962).
7. R.S. Reid. J. Chem. Educ. **66**, 344 (1989).
8. W.H. Hersh. J. Chem. Educ. **74**, 1485 (1997).
9. M. Edgar, J.W. Emsley, and M.I.C. Furby. J. Magn. Reson. **128**, 105 (1997).
10. A. Kumar and R.R. Ernst. J. Magn. Reson. **24**, 425 (1976).
11. A. Kumar and R.R. Ernst. Chem. Phys. Lett. **37**, 162 (1976).
12. G.E. Bigam, R.E.D. McClung, T.T. Nakashima, C.M. Angelov, and R.G. Cavell. Magn. Reson. Chem. **35**, 502 (1997).
13. J. Natterer, O. Schedletzky, J. Barkemeyer, J. Bargon, and S.J. Glaser. J. Magn. Reson. **133**, 92 (1998).
14. A.D. Bain, E. Wolf, D.W. Hughes, and I.D. Spenser. Croat. Chem. Acta, **69**, 681 (1996).
15. A.D. Bain. J. Magn. Reson. **37**, 209 (1980).
16. L.E. Kay and R.E.D. McClung. J. Magn. Reson. **77**, 258 (1988).
17. A.D. Bain. J. Magn. Reson. **39**, 335 (1980).

© 1999 NRC Canada

A solid state NMR and molecular orbital study of hydroxylammonium chloride

Glenn H. Penner, Y.C. Phillis Chang, and H. Michelle Grandin

Abstract: Deuterium and nitrogen-15 NMR spectroscopy has been used to measure the ^{2}H quadrupolar coupling and ^{15}N chemical shift tensors in solid hydroxylammonium chloride, $NH_3OH^+Cl^-$, (HAC). In addition, the NH_3 and OH dynamics have been investigated by variable temperature ^{2}H line shapes and T_1 measurements. The Arrhenius activation energy for NH_3 rotation is 22.5 ± 1.8 kJ/mol with a pre-exponential factor of $8 \pm 3 \times 10^{12}$ s^{-1} from line shapes and 21.3 ± 2 kJ/mol with an infinite temperature correlation time, τ_∞, of $5.0 \pm 0.4 \times 10^{-14}$ s from the T_1 analysis. The latter value corresponds to a pre-exponential factor of $6.7 \pm 0.5 \times 10^{12}$ s^{-1}, if a three-site exchange is assumed. There was no evidence for OH reorientation up to 405 K, indicating a rather strong OH···Cl hydrogen bond. Previously reported inconsistencies between crystal structure and molecular orbital derived N—O bond lengths are cleared up by performing geometry optimizations with large basis sets and taking electron correlation into account. The internal rotational potential for the isolated HA cation is calculated to be 5.8 kJ/mol at the MP2/6-31G** level, with the *trans* geometry preferred. Calculations that employ the neutron diffraction geometry and include the Cl^- anions that surround the HA^+ cation yield an upper limit for the activation energy for NH_3 group rotation of 62 kJ/mol. Analysis of the deuterium spectrum and T_1 data yield nuclear quadrupolar coupling constants of 160 ± 5 kHz and 194 ± 5 kHz (η = 0.50 ± 0.05) for the ND_3 and OD deuterons, respectively. Density functional calculations of the deuterium and nitrogen-14 nuclear quadrupolar coupling constants at the B3LYP level show that it is necessary to include the influence of the surrounding chloride anions. We have also shown that it is possible to obtain accurate proton chemical shifts from the deuterium MAS spectrum of solid HAC-d_4.

Key words: solid state NMR, molecular dynamics, nitrogen 15 chemical shift anisotropy.

Résumé : On a utilisé la spectroscopie RMN du ^{2}H et du ^{15}N pour mesurer le couplage quadripolaire du ^{2}H et les tenseurs des déplacements chimiques du ^{15}N dans le chlorure d'hydroxylammonium solide, $NH_3OH^+Cl^-$ (CHA). De plus, on a étudié la dynamique du NH_3 et du OH à l'aide de mesures de T_1 et des formes des raies du ^{2}H à température variable. En se basant sur les formes des raies, l'énergie d'activation d'Arrhenius pour la rotation du NH_3 est de 22,5 ± 1,8 kJ/mol avec un facteur préexponentiel de $8 \pm 3 \times 10^{12}$ s^{-1}; l'analyse des valeurs de T_1 conduit à une valeur de 21,3 ± 2 kJ/mol avec une température infinie de temps de corrélation de, τ_{inf}, de $5{,}0 \pm 0{,}4 \times 10^{-14}$. Cette dernière valeur correspond à un facteur préexponentiel de $6{,}7 \pm 0{,}5 \times 10^{12}$ s^{-1} si l'on fait l'hypothèse que l'échange se fait sur trois sites. Aucune donnée ne permet de laisser croire qu'il se produit une réorientation du OH jusqu'à 405K; ceci suggère l'existence d'une forte liaison hydrogène OH···Cl. En procédant à des optimisations de la géométrie à l'aide d'ensembles de bases élargies et en tenant compte de la corrélation électronique, on a pu corriger les incohérences qui avaient été rapportées antérieurement relativement aux longueurs des liaisons N—O observées dans la structure cristalline et les valeurs obtenues par calculs d'orbitales moléculaires. On a calculé que le potentiel de rotation interne du cation HA isolé est égal à 5,8 kcal/mol au niveau MP2/6-31G** et que la géométrie *trans* est privilégiée. Des calculs qui font appel à la géométrie déterminée par diffraction de neutrons et qui incluent les anions Cl^- qui entourent le cation HA^+ permettent d'établir que la limite supérieure pour l'énergie d'activation pour la rotation du NH_3 est de 62 kcal/mol. L'analyse du spectre du deutérium et les données de T_1 permettent de déterminer que les constantes de couplage quadripolaire nucléaire des deutérons du ND_3 et du OD sont respectivement de 160 ± 5 kHz et 194 ± 5 kHz (η = 0,50 ± 0,05). Des calculs de densité fonctionnelle des constantes de couplage quadripolaire nucléaire du ^{2}H et du ^{14}N au niveau B3LYP montrent qu'il est nécessaire d'inclure l'influence des anions chlorures avoisinants. On a aussi montré qu'il est possible d'obtenir des valeurs exactes pour les déplacements chimiques du spectre d'après la technique de rotation à l'angle technique (magique) du CHA-d_4.

Mots clés : RMN à l'état solide, dynamique moléculaire, anisotropie du déplacement chimique du ^{15}N.

[Traduit par la Rédaction]

Received March 8, 1999.

This paper is dedicated to Professor Ted Schaefer in recognition of his outstanding contributions to Canadian chemistry.

G.H. Penner,[1] Y.C.P. Chang, and H.M. Grandin. Department of Chemistry and Biochemistry, University of Guelph, Guelph, ON N1G 2W1, Canada.

[1]Author to whom correspondence may be addressed. Telephone: (519) 824-4120 ext. 2602. Fax: (519) 766-1499. e-mail: penner@chembio.uoguelph.ca

 © 1999 NRC Canada

Fig. 1. Simulated deuterium NMR powder spectra for η values of (*a*) 0.0, (*b*) 0.5, and (*c*) 1.0.

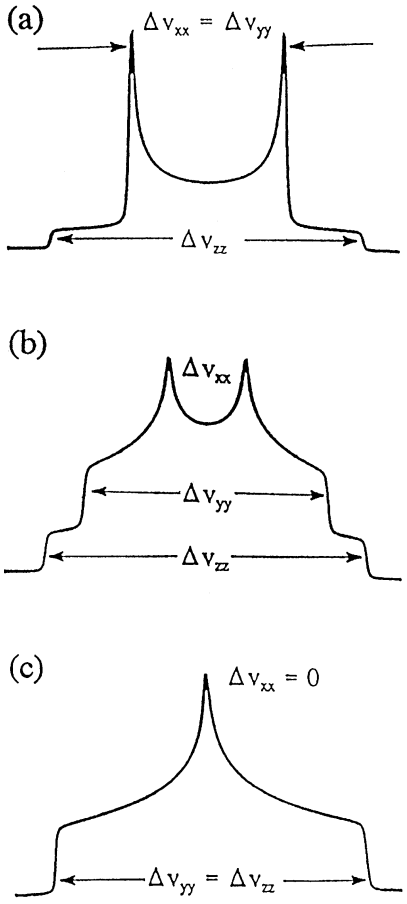

Introduction

The purpose of this study is twofold. We are primarily interested in the measurement of the ^{15}N chemical shift and ^{2}H nuclear quadrupole interactions in HAC, comparison of these with the values obtained from ab initio molecular orbital calculations and the uses of the temperature dependent ^{2}H line shapes and T_1 to investigate the dynamics of the HA cation in solid HAC. Our second goal is to obtain reliable molecular orbital calculations of the optimum geometry of HA^+. There has been considerable disagreement in the past as to the length of the N—O bond in HA^+. Neutron diffraction (1) and X-ray studies (2–4) give very different results and previous MO calculations at the HF level yield results that are rather dependent on basis set (3). No calculations of the optimized geometry have been reported in the last decade nor have any calculations employed computational methods that included electron correlation.

Theoretical background

Deuterium line shapes

The solid state deuterium NMR spectral line shape is dominated by the quadrupolar interaction. This is the interaction between the nuclear quadrupole moment, *eQ*, and the electric field gradient (efg) tensor at the nucleus. The quadrupolar coupling constant, χ, which is a measure of the strength of the quadrupolar interaction is given as

$$[1] \qquad \chi = \frac{e^2 q_{zz} Q}{h}$$

The line shape is also influenced by the asymmetry parameter of the efg tensor, η, which is defined as the difference between the two smaller principal components of the diagonalized electric field gradient tensor, eq_{xx} and eq_{yy}, with respect to the largest component, eq_{zz}.

$$[2] \qquad \eta = \frac{eq_{zz} - eq_{xx}}{eq_{zz}} = \frac{\Delta\nu_{yy}\Delta\nu_{xx}}{\Delta x_{zz}}$$

where $|eq_{xx}| < |eq_{yy}| < |eq_{zz}|$ and $eq_{xx} + eq_{yy} + eq_{zz} = 0$.

The quadrupolar coupling constant and asymmetry parameter are related to the three separations, or splittings, in the powder spectrum, $\Delta\nu_{xx}$, $\Delta\nu_{yy}$, and $\Delta\nu_{zz}$, which are shown in Fig. 1. The splitting are related to the quadrupolar coupling constant, χ.

$$[3] \qquad \begin{aligned} \Delta\nu_{xx} &= 3/4\chi(1-\eta) \\ \Delta\nu_{yy} &= 3/4\chi(1+\eta) \\ \Delta\nu_{zz} &= 3/2\chi \end{aligned}$$

In many cases the efg tensor is nearly axially symmetric about along the X—D bond, and the value of η is rather small (<0.1). Then the powder spectrum is a typical Pake doublet with a characteristic splitting between peaks of 3χ/4 and shoulders separated by 3χ/2. The effects of motion on the deuterium powder spectrum are twofold. First the width of the spectral line is narrowed by the motion. In the case of a jumping motion of the X—D bond between three or more equally populated sites, as is expected for ND_3 groups, η is averaged to zero, and if the motion is fast compared to the quadrupolar interaction (i.e., $>10^6$ s^{-1}), the quadrupolar splitting, Δν, is reduced to

$$[4] \qquad \Delta\upsilon_{\text{eff}} = \frac{3\chi}{8}(3\cos^2\theta - 1)$$

where θ is the angle between the X—D bond and the rotational axis. Secondly, if the motional rate, *k*, is of the order of χ (~10^4 –10^6 s^{-1}) the spectral line shape is severely distorted due to the large T_2 anisotropy associated with the dynamic process. The distorted line shapes can readily be simulated for a given combination of χ, θ, and *k*.

Deuterium spin-lattice relaxation

The spin-lattice relaxation time, T_1, characterizes the return of the bulk magnetization to its equilibrium state after a perturbing pulse. Relaxation is stimulated by time dependent nuclear spin interactions, and is most efficient when these fluctuations occur at the resonance frequency of the nucleus. For deuterons, the primary source of these fluctuating fields is the time dependent part of the quadrupolar interaction.

When the reorientational motion can be described by an exponential correlation function, and the temperature dependence of the correlation time follows Arrhenius behaviour, the rate of relaxation may be fit to the following equations (5):

© 1999 NRC Canada

Fig. 2. Simulated ^{15}N NMR powder spectra for η values of (*a*) 0.0, (*b*) 0.5, and (*c*) 1.0.

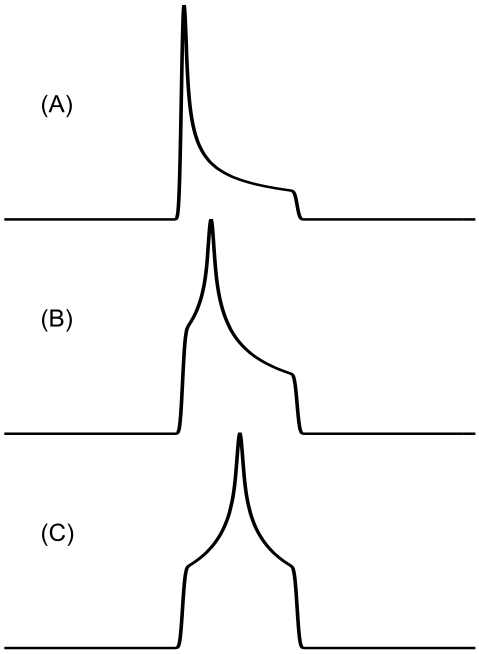

$$[5] \qquad \frac{1}{T_1} = K\left(\frac{\tau_c}{1+\omega_0^2\tau_c^2} + \frac{4\tau_c}{1+4\omega_0^2\tau_c^2}\right)$$

$$[6] \qquad \tau_c = \tau_\infty \exp\left(\frac{E_a}{RT}\right)$$

where τ_c is the correlation time for the motion ($\tau_c \therefore \beta 5\ k^{-1}$), τ_∞ is its value at infinite temperature, and ω_0 is the Larmor precession frequency. In addition, E_a is the activation energy for the motion influencing T_1, and K depends on the strength of the dominant nuclear spin interaction (in this case χ^2) and the exact nature of the reorientational motion. For jumps of the X—D bond between three or more equivalent positions oriented at an angle θ about the rotational axis, K is given by

$$[7] \qquad K = \frac{9\pi^2\chi^2}{20}(3\cos^2\theta - 1)^2$$

In this case, if a plot of ln (T_1) vs. inverse temperature is made, one often sees a V-shaped curve, with a T_1 minimum at $\omega_0\tau_c = 0.62$. There is, in general, much information to be extracted from this T_1 plot. The slope of the curve on either side of the T_1 minimum is characteristic of the activation energy for the motion influencing T_1. The intercept at $1/T = 0$ yields a value for τ_∞, while the depth of the minimum can be used to determine a value for the effective quadrupolar coupling constant. Note that knowledge of τ_∞ and E_a allows calculation of the motional rate at any temperature, through eq. [6]. The relaxation rate was not the same across the powder spectrum indicating an orientational dependence of the T_1. This T_1 anisotropy is consistent with our assumption of a three-site jump rotational model (6).

Nitrogen-15 powder line shapes

In an applied magnetic field, B_0, a magnetic nucleus in a molecule experiences an effective magnetic field, B_{eff}, due to the shielding effect of the surrounding electrons. This shielding is anisotropic and thus depends on the orientation of the molecule in the applied magnetic field. The dependence of the observed spectral frequency is given by

$$[8] \qquad \nu(\theta,\phi) = \nu_0 - \nu_0(\sigma_{11}\sin^2\theta\cos^2\phi + \sigma_{22}\sin^2\theta\cos^2\phi + \sigma_{33}\cos^2\theta)$$

where the two angles, θ and φ, describe the orientation of the shielding tensor with respect to B_0 and σ_{ii} is the *i*th principal component of the shielding tensor. The principal components of the shielding tensor are usually reported as chemical shifts, δ_{ii}, with respect to a reference. The commonly accepted convention is that $\delta_{11} > \delta_{22} > \delta_{33}$.

Powder samples contain many small crystallites that are randomly oriented with respect to B_0. As a result the powder spectrum consists of a broad line shape spanning the range of chemical shifts for every possible orientation. Three typical powder spectra are shown in Fig. 2. The powder spectrum is usually characterized by the chemical shift anisotropy, Δδ, and the asymmetry parameter, η.

If

$$[9] \qquad \left|\delta_{11} - \delta_{isotropic}\right| > \left|\delta_{33} - \delta_{isotropic}\right|$$

then

$$[10] \qquad \Delta\delta = \delta_{11} - (\delta_{22} + \delta_{33})/2$$

and

$$[11] \qquad \eta = \frac{\delta_{22} - \delta_{33}}{\delta_{11} - \delta_{isotropic}}$$

If

$$[12] \qquad \left|\delta_{11} - \delta_{isotropic}\right| < \left|\delta_{33} - \delta_{isotropic}\right|$$

δ_{11} and δ_{33} in eqs. [10] and [11] are exchanged.

The isotropic shift, observed in solution or in the magic angle spinning spectra of solids, is

$$[13] \qquad \delta_{isotropic} = (\delta_{11} + \delta_{22} + \delta_{33})/3$$

Experimental

Samples of $^{15}NH_3OHCl$ (99% ^{15}N) and ND_3ODCl (98% D) were purchased from MSD isotopes and Aldrich, respectively.

The deuterium spectra were recorded on a Bruker ASX-200 NMR spectrometer operating at 30.7 MHz, using the quadrupolar echo pulse sequence: $(\pi/2)_x - \tau_Q - (\pi/2)_y - \tau_Q -$ acquire (7). The length of the π/2 pulse was approximately 2.5 μs. At each temperature, the echo signals were collected for a τ_Q value of 40 μs. The echo signals were Fourier transformed to obtain the deuterium NMR spectra. The temperature of the sample chamber was electronically regulated by a Eurotherm B-VT 2000 temperature controller to within ±0.2°C over the course of a measurement. The true temperature of the sample was recorded just prior to each measurement by lowering a copper-constantan thermocouple down

© 1999 NRC Canada

Table 1. Structural parameters for NH_3OH^+.

	X-ray[a]	Neutron diff.[b]	MP2/6-31G**[c]	MP4/6-311++G**[c]	QCI(SD)/6-31G**[c]	B3LYP/D95**	MP2/6-31G** *trans* state
r(NO)	1.411[d]	1.369 (1.383)	1.409	1.408	1.411	1.41	1.413
$r(NH_a)$	—	1.024 (1.047)	1.027	1.031	1.027	1.034	1.027
$r(NH_b)$	—	1.017 (1.046)	1.027	1.031	1.027	1.034	1.027
$r(NH_c)$	—	1.019 (1.039)	1.026	1.029	1.025	1.032	1.025
r(OH)	—	0.985 (0.996)	0.975	0.979	0.973	0.979	0.973
$a(ONH_a)$	—	110.8	111.9	112.2	111.9	112.4	107.4
$a(ONH_b)$	—	110.2	111.9	112.2	111.9	112.4	107.4
$a(ONH_c)$	—	109.4	104.2	104.9	104.3	104.6	113.8
a(NOH)	—	107.2	106.6	106.3	106.8	107.2	107.3
$d(H_aNOH_d)$	—	53.6	62.6	62.1	62.4	62.6	121.1
$d(H_bNOH_d)$	—	—	—	—	–62.4	–62.6	–121.1
$d(H_cNOH_d)$	—	180	180	180	180	180	0

[a]From ref. 3.

[b]From ref. 1.

[c]All calculated geometries gave a plane of symmetry passing through H_c-N-O-H_d.

[d]X-ray structures of the NO_3^- and ClO_4^- salts gave r(NO) values of 1.40 and 1.41 Å, respectively (4, 2).

Fig. 3. The structure of the NH_3OH^+ cation.

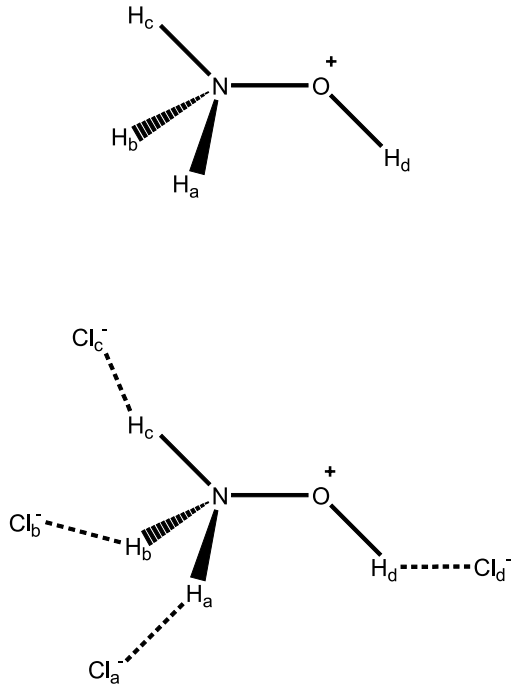

the gas venting tube until it came into contact with the sample coil. The estimated uncertainty of the recorded sample temperature was about ±0.5°C.

The deuterium T_1 data were acquired using an inversion recovery pulse sequence modified for quadrupolar nuclei: $(\pi)_x - \tau - (\pi/2)_{\pm x} - \tau_Q - (\pi/2)_y - \tau_Q$ – acquire (8). Typically, 12 values of τ were used to determine T_1 at each temperature. The pulse spacing, τ_Q, for the T_1 determination was 40 μs. The time between repetitions of the pulse sequence was always greater than $5T_1$. The data were fit using a nonlinear least-squares algorithm employing an exponential fitting function to obtain the relevant relaxation time parameters.

Deuterium MAS spectra were obtained with a sample spinning speed of 5 kHz using single pulse excitation and a pulse width of 3.0 μs. The chemical shifts were referenced to $[(CD_3)_3Si]_4C$, which has a chemical shift of 0.23 ppm with respect to liquid TMS.

Magic angle and static ^{15}N cross polarization (9) experiments were performed with a contact time of 10 ms and a 90° pulse of 5.5 μs. Chemical shifts were referenced to the nitrate peak of $^{15}NH_4{}^{15}NO_3$, which has a chemical shift of –4.0 ppm with respect to liquid nitromethane (10).

Quadrupolar echo spectra were simulated by standard methods using the program MXQET (11). Simulated spectra were visually matched to experimental line shapes. The T_1 data were least-squares fit to the BPP spectral density function, to obtain the activation energy, E_a, the correlation time at infinite temperature, τ_∞, and the effective quadrupolar coupling constant, χ_{eff}.

Molecular orbital calculations were performed using GAUSSIAN 98W (12) on a 300MHz Pentium II personal computer. Computed ^{15}N chemical shielding values, σ, were converted to the chemical shift, δ, scale using the equation (14):

$$[14] \quad \delta = -135.8 - \sigma$$

Deuterium and ^{14}N nuclear quadrupolar coupling constants were obtained from the computed electric field gradient values using the equation (15):

$$[15] \quad \chi(\text{MHz}) = -237 Q q_{zz}$$

were Q is the nuclear quadrupolar moment in units of barns (1 barn = 10^{-28} m^2) and q_{zz} is the largest component of the efg tensor at the nucleus and is given in atomic units. The values of $Q(^{14}N)$ = 20.1 and $Q(^2H)$ = 2.86 were taken from the compilation of Pyykkö (15).

Results and discussion

The structure of NH_3OH^+

The structure of HA^+ is depicted in Fig. 3. Table 1 shows the structural parameters of the HA cation in HAC as obtained from diffraction experiments together with geometry optimized structures of HA^+ at various levels of molecular

© 1999 NRC Canada

Fig. 4. Experimental and simulated deuterium powder spectra for HAC-d_4.

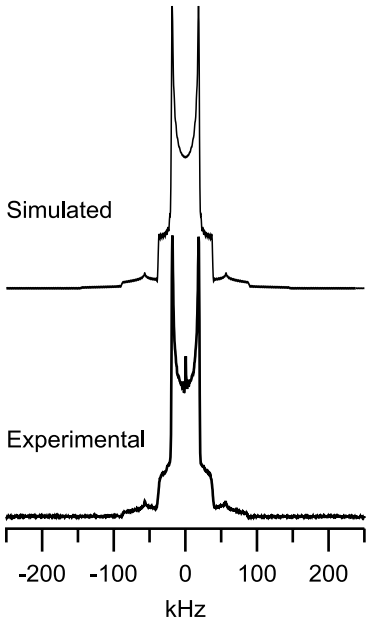

orbital theory. As can be seen, the computed NO bond lengths are in good agreement with the X-ray values for solid HAC and the nitrate and perchlorate salts. Since X-rays are diffracted by electron density, hydrogen positions can not be reliably determined. On the other hand, if a deuterated sample can be obtained, neutron diffraction structures can yield accurate deuteron positions. A comparison of the optimized and neutron diffraction structures show reasonable agreement with the exception of r(NO) and a(ONH_c). The neutron diffraction NO bond length is significantly shorter than the X-ray or optimized values. The optimized O-N-H bond angle for the N—H bond *trans* to the O—H bond, a(ONH_c), is consistently and significantly smaller than the expected tetrahedral angle at all levels of theory employed in this study.

Deuterium line shapes

The ^2H spectrum of a fully deuterated sample of HAC is shown in Fig. 4. This spectrum is clearly a composite of two Pake doublets, one with a small effective χ and one with a large χ value. The narrower line shape is due to the ND_3 group, and the broader component is due to the OD deuteron. Figure 4 also shows a simulation of the ^2H spectrum and yields values of χ_{eff} = 53 ± 1.5 kHz and η_{eff} = 0.0 for the narrow component and χ_{eff} = 194 ± 5 kHz and η_{eff} = 0.50 ± 0.05 for the broad component.These χ values are consistent with rapid rotation of the ND_3 group and a static OD deuteron at room temperature. Figure 5 shows the ^2H line shape as a function of temperature. The ND_3 line shape changes below 200 K but the OD part of the spectrum is unchanged. The ND_3 part of the spectrum can be simulated, and these are also shown in Fig. 5 for different rates of the three-site jumping motion of the ND_3 deuterons. A fit of the temperature dependent rates to the Arrhenius equation yields an activation energy of 22.5 ± 1.8 kJ/mol and a pre-exponential factor of 8 ± 3 × 10^{12} s^{-1} and an unaveraged χ value of 160 ± 5 kHz. The OD part of the line shape does not change up to 405 K.

Fig. 5. The deuterium powder spectra for HAC-d_4, together with simulations, as a function of temperature.

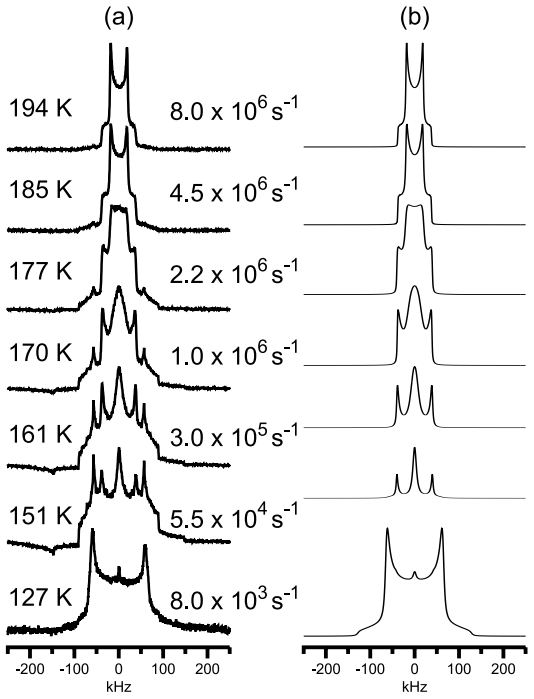

Fig. 6. The deuterium T_1 curve for solid HAC-d_4 as a function of inverse temperature. The solid curve is a least-squares fit of the points to eqs. [5] and [6].

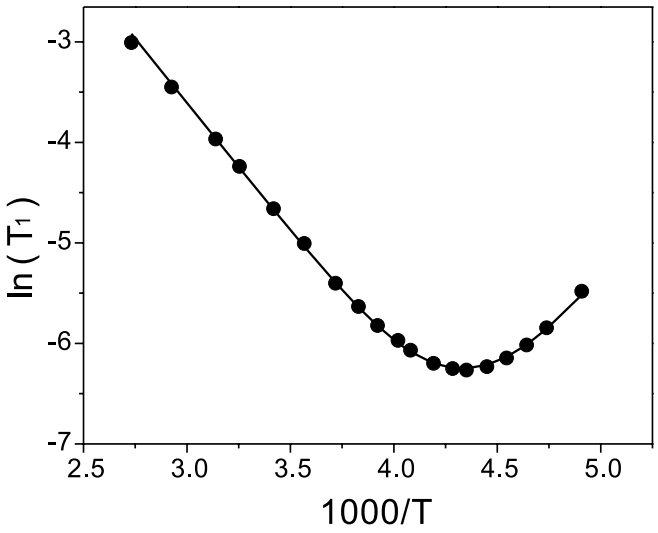

Deuterium spin-lattice relaxation

The ^2H T_1 as a function of temperature is presented in Fig. 6. As the OD deuteron is static throughout the temperature range studied, the curvature in the ln (T_1) vs. 1/T plot is entirely due to the change in the reorientational rate of the ND_3 group. A fit of the experimental data to eqs. [5] and [6] yields E_a = 21.3 ± 2 kJ/mol, τ_∞ = 5.0 ± 0.4 × 10^{-14} s, and χ = 155 ± 5 kHz. An earlier proton T_1 study gave E_a = 18.0

© 1999 NRC Canada

Table 2. Calculation of the ^{15}N chemical shift components, δ_{11}, δ_{22}, and δ_{33}, for NH_3OH^+.

	r(NO) = 1.369 Å			r(NO) = 1.411 Å		
	δ_{11}	δ_{22}	δ_{33}	δ_{11}	δ_{22}	δ_{33}
HF/6-31G**	–314	–316	–388	–312	–317	–388
B3LYP/6-31G**	–292	–294	–377	–290	–293	–378
B3LYP/D95**	–281	–284	–371	–280	–282	–372
MP2/6-31G**	–313	–315	–395	–312	–315	–396
Observed	–257	–257	–320	–257	–257	–320
	r(NH) = 1.04 Å			r(NH) = 1.00 Å		
	δ_{11}	δ_{22}	δ_{33}	δ_{11}	δ_{22}	δ_{33}
HF/6-31G**	–307	–311	–382	–317	–323	–394
B3LYP/6-31G**	–284	–287	–371	–296	–300	–384
B3LYP/D95**	–273	–276	–365	–286	–290	–379
MP2/6-31G**	–307	–310	–390	–317	–320	–401
Observed	–257	–257	–320	–257	–257	–320

Fig. 7. Simulated and experimental ^{15}N powder spectra of solid HAC-^{15}N.

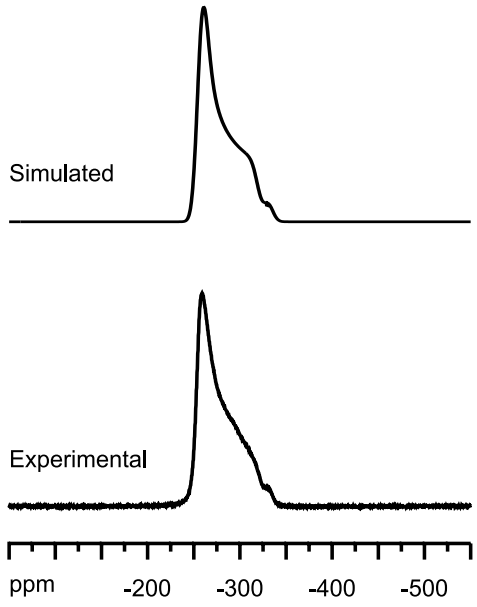

kJ/mol and $\tau_\infty = 2.3 \times 10^{-14}$ s (16). The value of χ also agrees with that obtained from the line shape analysis. For a three-site jumping motion the rotational correlation time and jumping rate are related by $\tau = 1/(3k)$. Using the infinite temperature rate constant from the line shape analysis a τ_∞ value of $(3.0 - 6.7) \times 10^{-14}$ s is obtained, in good agreement with the deuterium and proton T_1 results. Our E_a values are about 20–25% higher than that of the proton study. This effect has been previously reported (17), and it has been attributed to a shifting of the torsional energy levels towards the bottom of the potential well due to an increase in the moment of inertia upon deuteration. The predicted result is an increase in the energy difference between the zero-point energy and the energy maximum for NH_3 rotation.

Internal rotation

The calculated value of E_a for internal rotation in isolated NH_3OH^+ is 5.8 kJ/mol. At the MP2/6-31G** level with geometry optimization. The value changes to 6.6 kJ/mol if the neutron diffraction structure is used. Both of these values are significantly smaller than the activation energy for NH_3 rotation measured in solid HAC. Evidently there are important intermolecular interactions affecting the rotational barrier. The neutron diffraction structure shows relatively short N-H···Cl distances, indicative of hydrogen bonding. If the NH_3 end of the HA^+ cation is surrounded by three Cl^- anions, arranged according to the neutron diffraction structure, E_a goes up to 62 kJ/mol. Although this is now significantly higher than the measured values, it does represent an upper limit, since the geometry of the $[NH_3OH^+\ Cl_3^-]^{-2}$ complex was not allowed to relax during these calculations.

The ^{15}N chemical shift tensor

The experimental and simulated ^{15}N spectra for a non-spinning sample of ^{15}N enriched HAC are shown in Fig. 7. The chemical shift tensor components are $\delta_{11} = \delta_{22} = -267 \pm 1$ ppm and $\delta_{33} = -330 \pm 1$ ppm with respect to pure CH_3NO_2. The observed chemical shift anisotropy, $\Delta\delta$, is 63 ppm with an asymmetry parameter, η, of 0.0. Rapid rotation of the NH_3 group insures that η is negligible. A small (less than 1% of the total intensity) featureless peak appears at –341 ppm and is due to a small amount of NH_4Cl in the sample. Table 2 gives the ^{15}N tensor components calculated at various levels and with different basis sets for several structures of the isolated NA^+ cation and the neutron diffraction structure of the $[NH_3OH^+Cl_3^-]^{-2}$ cluster. The tabulated results show clearly that the calculated chemical shift components are rather insensitive to a change of NO or NH bond length. The set of calculated tensor components for isolated HA^+ that are closest to the experimental values are those calculated at the B3LYP level of density functional theory using the D95** basis set. DFT calculations at the B3LYP/D95** level employing solid state diffraction structures have been in good agreement with measured values for a series of nitrogen heterocycles (18) and for nitrobenzene derivatives.[2] A further calculation on $[NH_3OH^+Cl_3^-]^{-2}$ yields values of δ_{11}

[2] G.H. Penner, Y.-C.P. Chang, A. Barrett, and R.E. Wasylishen. Unpublished results.

© 1999 NRC Canada

Fig. 8. The deuterium MAS spectrum of HAC-d_4. The inset shows the central set of peaks.

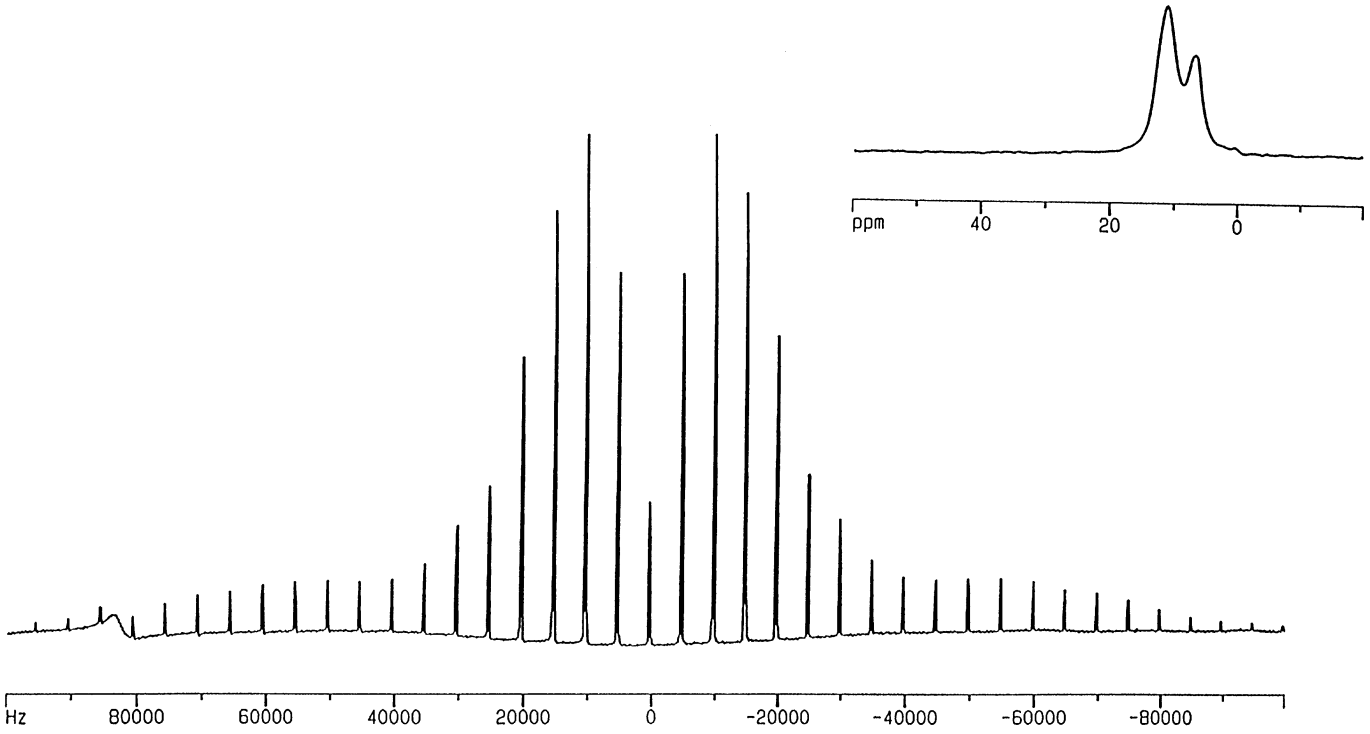

= –280 ppm, δ_{22} = –285 ppm, and δ_{33} = –340 ppm. This calculation yields a δ_{33} value that is much closer to experiment and the best calculated value of $\Delta\delta$ but slightly poorer agreement for δ_{11} and δ_{22}. The NH_3OH^+ cation is unique among ammonium cations in that is has by far the largest chemical shift anisotropy reported to date.

Calculation of nuclear quadrupolar coupling constants

Our experimental values for the deuterium nuclear quadrupolar coupling constants, χ(OD) and $\chi(ND_3)$, are 194 ± 5 kHz and 155–160 kHz, respectively, the latter value being a motional average over all three ND deuterons. The corresponding, calculated values for free HA^+, using the neutron diffraction geometry are 251 kHz (η = 0.26) and 221 kHz. These values were obtained from B3LYP/6-31G** calculations, which have been shown to give χ(D) values in excellent agreement with gas phase experimental values (19). These values are strongly dependent on X—D bond lengths, the χ values decreasing with elongation of the bond. Calculations for the $[NH_3OH^+Cl_4^-]^{-3}$ cluster give values of 233 (η = 0.27) and 217 kHz, in slightly better agreement with experiment. If one then corrects for thermal motion (1) (r_{OD} = 0.996 and r_{ND} = 1.045) a significantly better agreement is achieved with χ(OD) = 205 (η = 0.29) and χ(ND) = 179 kHz.

The ^{14}N quadrupolar coupling constant has been measured in solid HAC by nuclear quadrupole resonance spectroscopy (20). A $\chi(^{14}N)$ value of 4.0 MHz and an asymmetry value of 0.04 were obtained. Calculations on free HA^+, using all of the geometries and basis sets of Table 2 gave values in the rather narrow range of 2.8 ± 0.2 MHz with η values of less than 0.05. The value of χ as in poor agreement with the NQR experiment. On the other hand MP2/6-31G** calculations on $[NH_3OH^+Cl_3^-]^{-2}$ gave $\chi(^{14}N)$ = 4.3 MHz and η = 0.04. A B3LYP/D95** calculation on $[NH_3OH^+Cl_4^-]^{-3}$ gave $\chi(^{14}N)$ = 4.0 MHz and η = 0.10 in very good agreement with the experimental values. Obviously, the inclusion of the chloride ions around the HA^+ cation strongly affects the efg at the nitrogen nucleus.

Isotropic deuterium chemical shifts

The accurate determination of proton chemical shifts in solids has been notoriously difficult. Two techniques have contributed significantly to overcoming these difficulties. The CRAMPS experiment removes the strong homonuclear dipolar coupling while maintaining chemical shift information (21). Very fast magic angle spinning will remove the homonuclear couplings and anisotropic chemical shift interaction. The combination of these two can yield high-resolution ^{1}H spectra for solid samples. Unfortunately, CRAMPS is a fairly demanding experiment, and ultrafast MAS requires special equipment. Alternatively, one can obtain comparable resolution by performing a simple ^{2}H MAS experiment at typical spinning speeds. Isotropic chemical shifts can be obtained from an MAS spectrum of a uniformly deuterated polycrystalline sample provided that the deuterons are not involved in an exchange process with rates on the order of the quadrupolar coupling constant (10^3–10^5 s^{-1}). A deuterium MAS spectrum is shown in Fig. 8. There are two isotropic peaks with chemical shifts of 11.4 ± 0.1 ppm and 6.9 ± 0.1 ppm with respect to TMS. The assignment, while not agreeing with the expected intensities, is based on the fact that the peak at 11.4 ppm is associated with a much broader manfold of spinning sidebands. We as-

© 1999 NRC Canada

sign the more intense peak at 11.4 ppm to the OD deuteron. Unfortunately, our calculations (B3LYP/D95**) on $[NH_3OH^+Cl_4^-]^{-3}$ yield isotropic NH_3 and OH chemical shifts that differ by less than 1 ppm.

Summary

We have determined the deuterium quadrupolar coupling constant, χ, for the ND_3 and OD deuterons in solid HAC-d_4. In addition, the temperature dependent rates and activation energy for ND_3 group rotation have been determined. These are in good agreement with an earlier proton NMR study. Analysis of the ^{15}N powder spectrum of HAC-^{15}N provides the ^{15}N chemical shift tensor components. Calculation of the ^{15}N shift tensor gave the best agreement with experiment for B3LYP calculations using the neutron diffraction structure. Molecular orbital calculations of $\chi(^2H)$ and $\chi(^{14}N)$ in isolated HA^+ are in poor agreement with the experimental numbers. Including the effects of the surrounding Cl^- anions results in a significant improvement. Similarly, calculations on the E_a for NH_3 rotation are more realistic if the N-H···Cl hydrogen bonding interactions are included. Finally, we show that a deuterium MAS experiment can distinguish the ND_3 and OD deuterons providing solid state proton chemical shifts for *solid* HAC.

Acknowledgments

We wish to thank the Natural Sciences and Engineering Research Council of Canada (NSERC) for financial support. Dr. Nick Taylor of the University of Waterloo is also thanked for help with interpreting the neutron diffraction structure.

References

1. V.M. Padmanabhan, H.G. Smith, and S.W. Peterson. Acta Crystallogr. **22**, 928 (1967).
2. B. Dickens. Acta Crystallogr. Sect. B, **25**, 1875 (1969).
3. K.-L. Shi, R.-Q. Wang, and T.C.W. Mak. J. Mol. Struct. **160**, 109 (1987).
4. A.R. Rheingold, J.T. Cronin, and T.B. Brill. Acta. Crystallogr. Sect. C, **43**, 402 (1987).
5. N. Bloembergen, E.M. Purcell, and R.V. Pound. Phys. Rev. **73**, 679 (1948).
6. D.A. Torchia and A. Szabo. J. Magn. Reson. **49**, 107 (1987).
7. J.H. Davis, K.R. Jeffrey, M. Bloom, M.I. Valic, and T.P. Higgs, Chem. Phys. Lett. **42**, 390 (1976).
8. D.E. Demco, P. van Hecke, and J.S. Waugh. J. Magn. Reson. **16**, 16 (1974).
9. A. Pines, M.G. Gibby, and J.S. Waugh. J. Chem. Phys. **59**, 569 (1973).
10. T.M. Duncan. A compilation of chemical shift anisotropies. Farragut Press, Chicago. 1990.
11. M.S. Greenfield, A.D. Ronemus, R.L. Vold, R.R. Vold, P.D. Ellis, and T.R. Raidy. J. Magn. Reson. **72**, 89 (1987).
12. M.J. Frisch, G.W. Trucks, H.B. Schlegel, G.E. Scuseria, M.A. Robb, J.R. Cheeseman, V.G. Zakrzewski, J.A. Montgomery, Jr., R. E. Stratmann, J.C. Burant, S. Dapprich, J.M. Millam, A.D. Daniels, K.N. Kudin, M.C. Strain, O. Farkas, J. Tomasi, V. Barone, M. Cossi, R. Cammi, B. Mennucci, C. Pomelli, C. Adamo, S. Clifford, J. Ochterski, G.A. Petersson, P.Y. Ayala, Q. Cui, K. Morokuma, D.K. Malick, A.D. Rabuck, K. Raghavachari, J.B. Foresman, J. Cioslowski, J.V. Ortiz, B.B. Stefanov, G. Liu, A. Liashenko, P. Piskorz, I. Komaromi, R. Gomperts, R.L. Martin, D. J. Fox, T. Keith, M.A. Al-Laham, C.Y. Peng, A. Nanayakkara, C. Gonzalez, M. Challacombe, P.M.W. Gill, B. Johnson, W. Chen, M.W. Wong, J.L. Andres, C. Gonzalez, M. Head-Gordon, E.S. Replogle, and J.A. Pople. Gaussian 98, Revision A.3. Gaussian, Inc., Pittsburgh, Pa. 1998.
13. C.J. Jameson and J. Mason. *In* Multinuclear NMR. *Edited by* J. Mason. Plenum, New York. 1987.
14. T.-K. Ha. Chem. Phys. Lett. **107**, 117 (1986).
15. P. Pyykkö. Z. Naturforsch. **47a**, 189 (1992).
16. F. Köksal. J. Phys. Chem. Solids, **45**, 1201 (1984).
17. J. Tang, L. Sterna, and A. Pines. J. Magn. Reson. **41**, 289 (1980).
18. M.S. Solum, K.L. Altmann, M. Strohmeier, D.A. Berges, Y. Zhang, J.C. Facelli, R.J. Pugmire, and D.M. Grant. J. Am. Chem. Soc. **119**, 9804 (1997).
19. W.C. Bailey. J. Mol. Spect. **190**, 318 (1998).
20. R.A. Marino and O. Tõnis. Chem. Phys. Lett. **4**, 489 (1970).
21. B.C. Gerstein. Phil. Trans. Roy. Soc. London, **A299**, 521 (1981).

© 1999 NRC Canada

Synthesis and X-ray structural characterization of the ruthenium β-diketonato complexes: $Ru(hfac)_3$, *cis*-$Ru(hfac)_2(MeCN)_2$, and *cis*-$Ru(hfac)(acac)(MeCN)_2$

Ian R. Baird, Steven J. Rettig, Brian R. James, and Kirsten A. Skov

Abstract: $Ru(hfac)_3$ (**2**) was synthesized via peroxide oxidation of the Ru(II) species $[Na][Ru(hfac)_3]$ (**1**) (hfac = 1,1,1,5,5,5-hexafluoroacetylacetonate). Treatment of either **1** or **2** with CF_3SO_3H in MeCN generated *cis*-$Ru(hfac)_2(MeCN)_2$ (**3**). $Ru(acac)_2(hfac)$ (**4**) (acac = acetylacetonate) was generated by addition of hfac to an EtOH solution of *cis*-$[Ru(acac)_2(MeCN)_2][CF_3SO_3]$. Subsequent treatment of **4** with CF_3SO_3H in MeCN yielded *cis*-$Ru(acac)(hfac)(MeCN)_2$ (**7**). Syntheses of $[Na][Ru(hfac)_2(acac)]$ (**5**) and $Ru(hfac)_2(acac)$ (**6**) are also reported. The complexes were characterized generally by elemental analysis, cyclic voltammetry, UV-vis, NMR, and IR spectroscopies. The structures of **2**, **3**, and **7** were established by X-ray crystallographic analyses. Crystals of **2** are monoclinic with a = 8.7781(4), b = 13.0760(11), c = 19.1857(5) Å, β = 92.2275(5)°, Z = 4, and space group $P2_1/n$; those of **3** are monoclinic with a = 25.731(4), b = 8.8332(13), c = 18.1955(4) Å, β = 93.3395(6)°, Z = 8, and space group $C2/c$; and those of **7** are triclinic with a = 7.6812(9), b = 10.680(2), c = 12.578(2) Å, α = 88.062(6)°, β = 83.874(3)°, γ = 69.5898(15)°, Z = 2, and space group $P\bar{1}$. The structures were solved by Patterson methods and refined by full-matrix least-squares procedures to $R(F)$ = 0.036, 0.035, and 0.068 ($R_w(F^2)$ = 0.061, $R_w(F)$ = 0.052, and $R_w(F)$ = 0.089), respectively.

Key words: ruthenium, β-diketonato complexes, acetylacetonate, 1,1,1,5,5,5-hexafluoroacetylacetonate, acetonitrile complexes.

Résumé : On a synthétisé le $Ru(hfac)_3$ (**2**) par le biais d'une oxydation au peroxyde de l'espèce Ru(II) suivante: $[Na][Ru(hfac)_3]$ (**1**) (hfac = 1,1,1,5,5,5-hexafluoroacétonylacétonate). Le traitement des composés **1** ou **2** avec du CF_3SO_3H dans du MeCN conduit au *cis*-$Ru(hfac)_2(MeCN)_2$ (**3**). On a généré du $Ru(acac)_2(hfac)$ (**4**) (acac = acétylacétonate) par addition de hfac à du *cis*-$[Ru(acac)_2(MeCN)_2][CF_3SO_3]$ en solution dans EtOH. Un traitement subséquent du produit **4** avec du CF_3SO_3H dans du MeCN conduit au *cis*-$Ru(acac)(hfac)(MeCN)_2$. On rapporte aussi les synthèses de $[Na][Ru(hfac)_2(acac)]$ (**5**) et $Ru(hfac)_2(acac)$ (**6**). Les complexes ont généralement été caractérisés par analyse élémentaire, voltampérométrie cyclique et par spectroscopies UV-vis, RMN et IR. Les structures **2**, **3** et **7** ont été confirmées par diffraction des rayons X. Les cristaux du composé **2** sont monocliniques, groupe d'espace $P2_1/n$, avec a = 8,7781(4), b = 13,0760(11) et c = 19,1857(5) Å, β = 92,2275(5)° et Z = 4; ceux du composé **3** sont monocliniques, groupe d'espace $C2/c$, avec a = 25,731(4), b = 8,8332(13) et c = 18,1955(4) Å, β = 93,3395(6)° et Z = 8 et ceux du composé **7** sont tricliniques, groupe d'espace $P\bar{1}$, avec a = 7,6812(9), b = 10,680(2) et c = 12,578(2) Å, α = 88,062(6)°, β = 83,874(3)° et γ = 69,5898(15)° et Z = 2. Les structures ont été résolues par les méthodes de Patterson et affinées par les méthodes des moindres carrés (matrice complète) jusqu'à des valeurs de $R(F)$ = 0,036, 0,035 et 0,068 ($R_w(F^2)$ = 0,061, $R_w(F)$ = 0,052 et $R_w(F)$ = 0,089) respectivement.

Mots clés : ruthénium, complexes β-dicétonato, acétylacétonate, 1,1,1,5,5,5-hexafluoroacétylacétonate, complexes d'acétonitrile.

[Traduit par la Rédaction]

Received April 28, 1998.

This paper is dedicated to Professor Ted Schaefer in recognition of his outstanding contributions to Canadian chemistry.

I.R. Baird, S.J. Rettig, and B.R. James.[1] Department of Chemistry, University of British Columbia, Vancouver, BC V6T 1Z1, Canada.
K.A. Skov. Advanced Therapeutics, British Columbia Cancer Research Centre, Vancouver, BC V5Z 1L3, Canada.

[1]Author to whom correspondence may be addressed. Telephone: (604) 822-4217. Fax: (604) 822-2847. e-mail: brj@chem.ubc.ca

 © 1999 NRC Canada

Introduction

1,1,1,5,5,5-Hexafluoroacetylacetonate (hfac) and other β-diketonates constitute a class of chelating ligands that has been widely employed; their coordination chemistry with Ru(II) and Ru(III) has been widely studied (1–7), with stable, six-membered chelate rings being formed. Variation of the substituents at the 1 and 5 positions of hfac leads to numerous ligand possibilities (8–11). Many research groups, especially Shimizu's, have studied the electrochemical and chemical properties of tris(β-diketonato) ruthenate(II) and ruthenium(III) complexes, including the effects of such substituents (6, 8, 9–16). Patterson and Holm (15) reported that the half-wave reduction potentials span a large range from +0.726 V for $Ru(hfac)_3$ to –0.728 V for $Ru(acac)_3$ (vs. SCE).

Typically, the synthesis of Ru(III) tris(β-diketonato) complexes is performed by reacting the β-diketone with $RuCl_3 \cdot 3H_2O$ in H_2O:EtOH (1:2) (i.e., via a "Ru blue" intermediate) (3) or in 10% aqueous HCl and Na_2CO_3 (1). However, for isolation of mixed-ligand β-diketonato complexes, such syntheses are limited, and yield only a small amount of a mixture of the tris and the mixed-ligand species, which must be isolated chromatographically (7). The synthesis of tris(β-diketonato) complexes with asymmetric ligands (where R ≠ R′ for R(CO)CH(CO)R′) has also been reported, but a mixture of optical isomers with *mer*- and *fac*- configurations resulted, making subsequent purification difficult (17).

In one instance, the mixed-ligand complexes $Ru(hfac)_2(acac)$ and $Ru(acac)_2(hfac)$ were prepared by refluxing $Ru(hfac)_3$ and $Ru(acac)_3$ in toluene for days, but neither complex was isolated pure (15); however, $Ru(acac)_2(hfac)$ has been isolated via a Ru blue route (10) and from *cis*-$Ru(acac)_2(MeCN)_2$ (18). Substitution of a β-diketonate ligand by two MeCN ligands in the presence of a strong acid, such as CF_3SO_3H, yields [Ru(β-diketonato)$_2$(MeCN)$_2$][CF_3SO_3] species which are useful precursors for the synthesis of other mixed-ligand, β-diketonato complexes (18–20).

Here we report the synthesis and structural characterization of $Ru(hfac)_3$ (**2**), the new complex *cis*-$Ru(hfac)_2(MeCN)_2$ (**3**) and *cis*-Ru(hfac)(acac)$(MeCN)_2$ (**7**). The NMR, IR, UV-vis, and CV data are reported for all the complexes. Only elemental analysis data for **7** were previously reported. The syntheses and characterizations of [Na][$Ru(hfac)_2(acac)$] (**5**) and pure $Ru(acac)_2(hfac)$ (**4**) and $Ru(hfac)_2(acac)$ (**6**) are also reported. These complexes have been used as precursors for syntheses of various Ru-imidazole species that are of interest biologically (21–23).

Experimental

Hacac, Hhfac, and $NaHCO_3$ (Aldrich products) were used as received, as were anhydrous MeCN (Aldrich) and benzene (Fisher). Other solvents were dried using the appropriate drying agent: MeOH (Mg), EtOH (Mg), acetone (K_2CO_3), and CH_2Cl_2 (CaH_2). d_6-Acetone and $CDCl_3$ were obtained from CIL, Inc.

UV-vis absorption spectra were recorded in MeOH on an HP 8452A diode array spectrophotometer and are given as λ_{max} (nm) ($\varepsilon_{max} \times 10^{-3}$ (M^{-1} cm^{-1})), sh = shoulder. IR spectra (as KBr pellets) were recorded as cm^{-1} on an ATI Mattson Genesis FTIR instrument (only the relatively intense bands are reported), and ^1H and $^{19}F\{^1H\}$ NMR spectra were recorded on Bruker AC200F or Varian XL300 spectrometers. ^1H shifts are referenced to the residual proton shift of the internal deuterated solvent, and ^{19}F shifts are referenced to trifluoroacetic acid. Electrochemistry was performed on 10^{-3} M solutions (MeCN) in 0.1 M TBAP (tetrabutylammonium perchlorate) on a Pine biopotentiostat model AFCBP1; the working and counter electrodes were Pt plates (6 mm^2) and the reference electrode was Pt wire. Reduction potentials are reported vs. SCE, the values being determined by reference to a measured ferrocene/ferrocenium couple. TLC was run on precoated (0.2 mm) silica gel 60 F_{254} plates (E.M. Laboratories, Inc). LR–MS (+ LSIMS) data were obtained in this department on a KRATOS Concept IIHQ instrument. All the spectra, CV data, and procedures were done at room temperature (r.t.). Elemental analyses were performed here by Mr. P. Borda.

cis-[Ru(acac)$_2$(MeCN)$_2$][CF_3SO_3]

This precursor was synthesized using a modification of a procedure reported for the synthesis of the analogous perchlorate salt (19). This same synthesis for the triflate, starting from the $Ru(acac)_3$ precursor, appeared in the literature during the course of our work on such systems (20). Data for *cis*-[$Ru(acac)_2(MeCN)_2$][CF_3SO_3]: yield 96% (cf. lit. yield of 70% (20)). Anal. calcd. for $C_{15}H_{20}N_2O_7SF_3Ru$: C 33.96, H 3.80, N 5.28; found: C 34.18, H 3.87, N 4.97. LR–MS (+ LSIMS): 382 (M^+), 341 (M^+ – MeCN), 300 (M^+ – 2MeCN). IR: 3469 (O-H); 3098, 2990, 2931 (C-H); 2326 ($C{\equiv}N_{asym.}$); 2296 ($C{\equiv}N_{sym.}$); 1524 (C=O); 1428, 1329, 1265, 1157, 1030, 939, 639. UV-vis: 214 (11.6), 282 (9.67), 318 (5.12), 552 (1.40). ^1H NMR (300 MHz, $CDCl_3$) δ: 37.53 (br s, 6H, *Me*CN), –23.46 (s, 6H, acac-*Me*), –27.22 (s, 6H, acac-*Me*). $^{19}F\{^1H\}$ NMR (188 MHz, $CDCl_3$) δ: –1.89 (s, $CF_3SO_3^-$). The IR and ^1H NMR data are similar to those reported for the analogous perchlorate salt (19). $E_{1/2}$ = –77 ± 3 mV.

[Na][Ru(hfac)$_3$] (1)

The synthesis of [K][$Ru(hfac)_3$] was previously reported (9). Here, we report a new route to the analogous sodium salt. In a Schlenk tube, a solution of $RuCl_3 \cdot 3H_2O$ (4.015 g, 0.0162 mol) in 30 mL EtOH was stirred at 75°C for 4 h under a steady stream of H_2. $NaHCO_3$ (4.615 g, 0.0549 mol) was added slowly to the resulting Ru blue solution, followed by addition of Hhfac (7.76 mL, 0.0549 mol). The reaction vessel was sealed under 1 atm N_2 and the mixture then stirred for 16 h at r.t. The final solution was purple–pink, and TLC analysis revealed the major product as a pink band (**1**), which was separated by column chromatography (silica gel; CH_2Cl_2:MeOH, 20:1) to yield a purple–black solid (~8 g), which was further purified via vacuum sublimation at 100°C (7.576 g, 65%). Anal. calcd. for $C_{15}H_3O_6F_{18}RuNa$: C 24.18, H 0.41; found: C 24.07, H 0.50. IR: 1555 (C=O); 1526, 1447, 1333, 1265, 1221, 1150, 820, 698, 606. UV-vis: 210 (8.01), 236 (8.89), 290 (17.4), 490 (11.6), 528 (13.9). ^1H NMR (200 MHz, d_6-acetone) δ: 6.19 (s, hfac-*H*). $^{19}F\{^1H\}$ NMR (188 MHz, d_6-acetone) δ: 2.18 (s, -CF_3), not previously reported. The other spectroscopic data are in good agreement with those previously reported for the K salt (9). $E_{1/2}$ = 718 ± 3 mV.

© 1999 NRC Canada

$Ru(hfac)_3$ (2)

The compound **2** was synthesized according to a modified literature procedure (9). Compound **1** (1.05 g, 1.41 mmol) was suspended in H_2O:benzene (200 mL, 1:1) to give a red–brown biphasic system. H_2O_2 (1% aqueous, 5 mL) was added dropwise and the mixture stirred at r.t. for 2 h; the resulting aqueous phase was opaque, yellow–brown, while the organic layer was deep red. The aqueous phase was separated and washed with benzene (2 × 40 mL). The organic washings were taken to dryness at r.t., and the crude **2** was purified by sublimation at 60°C to yield red crystals (0.776 g, 76%). Anal. calcd. for $C_{15}H_3O_6F_{18}Ru$: C 24.95, H 0.42; found: C 25.07, H 0.60. IR: 1582 (C=O); 1539, 1421, 1348, 1266, 1210, 1149, 822, 698, 601. UV-vis: 216 (12.5), 274 (14.5), 376 (6.65), 524 (1.87). ^{1}H NMR (300 MHz, $CDCl_3$) δ: –41.67 (s, hfac-*H*). $^{19}F\{^1H\}$ NMR (188 MHz, $CDCl_3$) δ: –11.49 (s, -CF_3), not previously reported. The other spectroscopic data agree well with those previously reported (9). $E_{1/2}$ = 721 ± 3 mV.

***cis*-$Ru(hfac)_2(MeCN)_2$ (3)**

Compound **1** (4.00 g, 5.54 mmol) was dissolved in 150 mL MeCN to give a purple–pink solution. The mixture, heated slowly during dropwise addition of CF_3SO_3H (0.865 mL, 6.09 mmol), quickly turned red–brown, this being accompanied by much fuming. The solution was refluxed for 1 h in air during which the colour turned dark brown. TLC analysis revealed a number of side-products and a brown band (R_f = 0.90; CH_2Cl_2:MeOH, 50:1), which was separated by column chromatography (silica gel; CH_2Cl_2) to give pure **3** as a brown solid (2.709 g, 95%). Suitable crystals for X-ray analysis were obtained from slow evaporation of a concentrated MeOH solution of **3**. Anal. calcd. for $C_{14}H_8N_2O_4F_{12}Ru$: C 28.15, H 1.35, N 4.69; found: C 28.35, H 1.33, N 4.62. LR–MS (+ LSIMS): 598 (M^+), 516 (M^+ – 2MeCN). IR: 2357 ($C{\equiv}N_{asym.}$); 2285 ($C{\equiv}N_{sym.}$); 1576, 1546 (C=O); 1482, 1475, 1335, 1262, 1212, 1195, 1153, 1095, 798, 696. UV-vis: 218 (17.1), 286 (16.8), 418 (6.10), 470 (8.43). ^{1}H NMR (200 MHz, d_6-acetone) δ: 6.20 (s, 2H, hfac-*H*), 2.87 (s, 6H, *Me*CN). $^{19}F\{^1H\}$ NMR (188 MHz, d_6-acetone) δ: 0.98 (s, -CF_3), 0.38 (s, -CF_3). $E_{1/2}$ = 1143 ± 3 mV. Of note, **3** could also be synthesized from **2** in relatively high yield (75%) using conditions identical to those reported above for the synthesis from **1**.

$Ru(acac)_2(hfac)$ (4)

In a Schlenk tube, *cis*-$[Ru(acac)_2(MeCN)_2][CF_3SO_3]$ (2.45 g, 4.61 mmol) was dissolved in 30 mL EtOH. $NaHCO_3$ (0.433 g, 5.16 mmol) and Hhfac (725 μL, 5.12 mmol) were then added, and the reaction mixture was heated to reflux under air (~80°C). After 1.5 h, the mixture, originally navy blue, became dark red. The solvent was removed and the residue was loaded onto a silica gel column and eluted quickly (CH_2Cl_2:MeOH, 25:1) by flash chromatography to remove any low R_f side-products. The first band (dark red) yielded a solid, which was dissolved in acetone, and the solution was then transferred to a sublimation flask equipped with a cold finger and heated to 100°C under vacuum; the dark red product, which sublimed onto the cold finger, was transferred to a sample vial and dried in vacuo at r.t. (1.75 g, 75%). (**4** is hygroscopic and must be transferred quickly when handling in air. Because **4** sublimes at ~60°C under vacuum, the removal of acetone solvate, prior to elemental analysis, was not possible.) Anal. calcd. for $C_{15}H_{15}O_6F_6Ru{\cdot}0.5C_3H_6O$: C 37.02, H 3.39; found: C 37.02, H 3.26. IR: 1543, 1521 (C=O); 1420, 1340, 1259, 1201, 1146, 1099, 1025, 934, 808, 693. UV-vis: 210 (13.4), 284 (13.6), 332 (6.43), 502 (2.38). ^{1}H NMR (300 MHz, d_6-acetone) δ: –8.82 (s, 6H, acac-*Me*), –9.01 (s, 6H, acac-*Me*), –28.45 (s, 1H, hfac-*H*), –38.95 (s, 2H, acac-*H*). $^{19}F\{^1H\}$ NMR (188 MHz, d_6-acetone) δ: –9.71 (s, -CF_3), not previously reported. The spectroscopic data generally agree well with those previously reported (10), but δ for hfac-*H* in $CDCl_3$ is reported at –35.10. $E_{1/2}$ = –232 ± 3 mV.

[Na][$Ru(hfac)_2(acac)$] (5)

In a Schlenk tube, **3** (0.300 g, 0.502 mmol) was dissolved in 10 mL EtOH to give a dark brown solution. $NaHCO_3$ (0.0534 g, 0.636 mmol) and Hacac (60 μL, 0.584 mmol) were added, and the mixture was heated to reflux (~80°C) in air. The reaction was monitored using TLC as no colour change was observed; the concentration of **3** decreased while a new pink band appeared after ~2 h. After 7 h the solvent was removed under reduced pressure, and then CH_2Cl_2 (20 mL) was added. The mixture was sonicated for 5 min, yielding a dark purple solid, which was collected and washed with CH_2Cl_2 (3 × 10 mL). The crude solid was purified by column chromatography (silica gel; CH_2Cl_2:acetone, 20:1) to yield a pink–purple solid (0.0986 g, 32%). Anal. calcd. for $C_{15}H_9O_6F_{12}RuNa$: C 28.27, H 1.42; found: C 28.06, H 1.38. IR: 1550, 1521 (C=O); 1466, 1391, 1323, 1264, 1198, 1146, 940, 808, 695. UV-vis: 210 (8.06), 248sh (11.1), 278 (18.2), 380 (2.01), 478 (7.59). ^{1}H NMR (200 MHz, d_6-acetone) δ: 5.77 (s, 2H, hfac-*H*), 5.00 (s, 1H, acac-*H*), 1.86 (s, 6H, acac *Me*). $^{19}F\{^1H\}$ NMR (188 MHz, d_6-acetone) δ: 2.50 (s, -CF_3), 2.48 (s, -CF_3). $E_{1/2}$ = 284 ± 3 mV.

$Ru(hfac)_2(acac)$ (6)

Compound **5** (0.0550 g, 0.0863 mmol) was suspended in an H_2O (20 mL):benzene (20 mL) mixture to give a dark purple, biphasic system. This was stirred at r.t. in air, and H_2O_2 (1% aqueous, 5 mL) was added dropwise, the mixture becoming green. The aqueous phase was pale yellow while the organic layer was dark green. After 1 h, the organic phase was separated and the benzene removed via rotary evaporation at 20°C. The crude **6** was purified by sublimation at 60°C to give a green–black solid (0.0423 g, 80%). Anal. calcd. for $C_{15}H_9O_6F_{12}Ru$: C 29.33, H 1.48; found: C 28.99, H 1.49. IR: 1583, 1579 (C=O); 1553, 1520, 1436, 1344, 1264, 1207, 1152, 807, 699, 598. UV-vis: 248sh (11.1), 286 (19.2), 376 (8.25), 556 (1.67). ^{1}H NMR (300 MHz, $CDCl_3$) δ: –14.34 (s, 6H, acac *Me*), –31.82 (s, 1H, acac-*H*), –56.72 (s, 2H, hfac-*H*). $^{19}F\{^1H\}$ NMR (188 MHz, $CDCl_3$) δ: –6.71 (s, -CF_3), –8.06 (s, -CF_3). $E_{1/2}$ = 289 ± 3 mV.

***cis*-$Ru(acac)(hfac)(MeCN)_2$ (7)**

Compound **7** was synthesized according to a modified literature procedure (18). Compound **4** (0.159 g, 0.313 mmol) was dissolved in 10 mL MeCN and the mixture heated in air to 70°C yielding a red solution to which CF_3SO_3H (44 μL,

© 1999 NRC Canada

Scheme 1. Synthesis of *cis*-Ru(acac)(hfac)$(MeCN)_2$ from $Ru(acac)_2(hfac)$ (**4**); **7**: *cis*-$[Ru(acac)_2(MeCN)_2][CF_3SO_3]$ = 1.0 (path *A*) and 0.1 (path *B*).

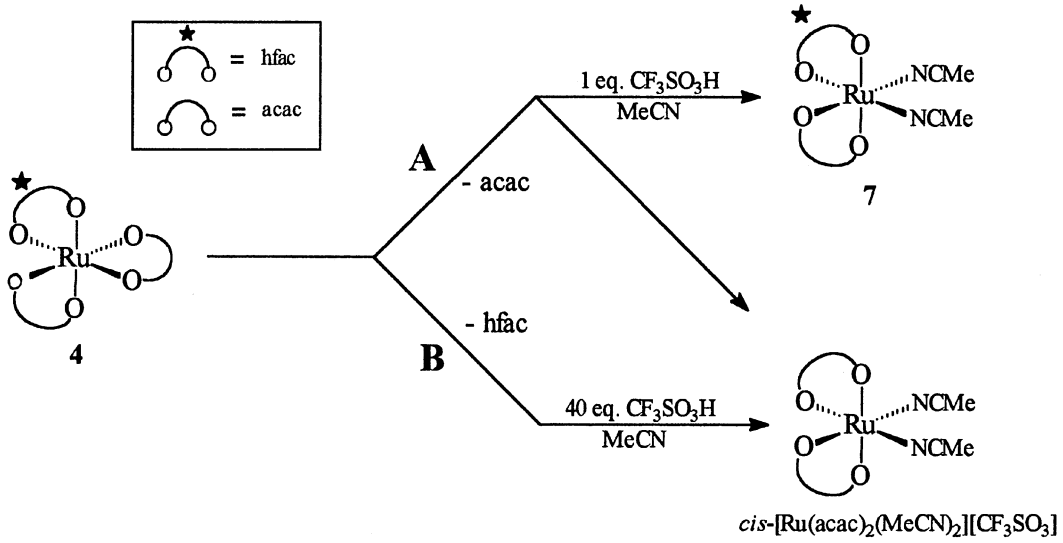

Scheme 2. Attempted synthesis of *cis*-Ru(acac)(hfac)$(MeCN)_2$ (**7**) from $Ru(hfac)_2(acac)$ (**6**).

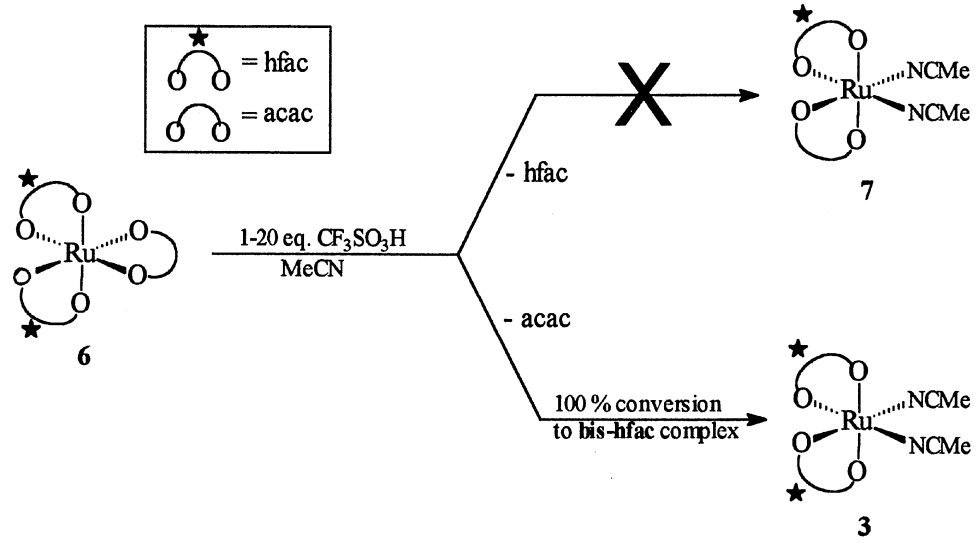

0.313 mmol) was then added. TLC analysis after 2 h revealed that $acac^-$ and $hfac^-$ displaced products ((**7**) and *cis*-$[Ru(acac)_2(MeCN)_2][CF_3SO_3]$, respectively) were formed in equal amounts. The mixture was purified using preparative TLC (CH_2Cl_2:MeOH, 20:1); the band corresponding to **7** yielded a red–brown solid (0.0746 g, 49%). Crystals suitable for X-ray analysis were obtained via slow evaporation of a concentrated MeOH solution of **7**. Anal. calcd. for $C_{14}H_{14}N_2O_4F_6Ru$: C 34.46, H 2.88, N 5.72; found: C 34.38, H 2.88, N 5.42. IR: 2993, 2930 (C-H); 2346 ($C{\equiv}N_{asym.}$); 2270 ($C{\equiv}N_{sym.}$); 1567, 1547 (C=O); 1406, 1261, 1200, 1147. UV-vis: 228 (15.8), 276 (14.1), 352 (4.07), 482 (4.67). ^1H NMR (200 MHz, d_6-acetone) δ: 6.04 (s, 1H, hfac-*H*), 5.37 (s, 1H, acac-*H*), 2.76 (s, 3H, *Me*CN), 2.69 (s, 3H, *Me*CN), 1.94 (s, 3H, acac *Me*), 1.93 (s, 3H, acac *Me*). $^{19}F\{^1H\}$ NMR (188 MHz, d_6-acetone) δ: 2.29 (s, -C*F*$_3$), 2.09 (s, -C*F*$_3$). $E_{1/2}$ = 544 ± 3 mV. Only the elemental analysis data were previously reported (18).

This reaction was repeated using a ratio of 1:40 for **4**:CF_3SO_3H, which yielded results different from those described above. The major product here was *cis*-$[Ru(acac)_2(MeCN)_2][CF_3SO_3]$ as determined by TLC and ^1H NMR, while only ~10% of **7** was present, showing that the stoichiometry of the reactants is important in determining the reaction path (see Scheme 1). The synthesis of **7** was also attempted starting from either **5** or **6**, following the same reaction conditions as described above; however, only **3** was produced (see Scheme 2).

X-ray crystallographic analyses of 2, 3, and 7

Crystallographic data for **2**, **3**, and **7** appear in Table 1, and the respective structures are shown in Figs. 1–3. The final unit-cell parameters were obtained by least squares on the setting angles for 13 128 reflections with 2θ = 4.0°–61.0° for **2**, 14 188 reflections with 2θ = 4.0°–60.1° for **3**, and 9023 reflections with 2θ = 4.0°–60.1° for **7**. The

© 1999 NRC Canada

Table 1. Crystallographic data.

Compound	**2**[a–c]	**3**[b,d,e]	**7**[a,b,f]
Formula	$C_{15}H_3F_{18}O_6Ru$	$C_{14}H_8F_{12}N_2O_4Ru$	$C_{14}H_{14}F_6N_2O_4Ru$
fw	722.23	597.28	489.34
Crystal system	Monoclinic	Monoclinic	Triclinic
Space group	$P2_1/n$ (no. 14)	$C2/c$ (no. 15)	$P\bar{1}$ (no. 2)
a, Å	8.7781(4)	25.731(4)	7.6812(9)
b, Å	13.0760(11)	8.8332(13)	10.680(2)
c, Å	19.1857(5)	18.1955(4)	12.578(2)
α,°	—	—	88.062(6)
β,°	92.2275(5)	93.3395(6)	83.874(3)
γ,°	—	—	69.5898(15)
V, Å^3	2200.5(2)	4128.5(7)	961.5(2)
Z	4	8	2
ρ_{calc}, g/cm^3	2.180	1.922	1.690
$F(000)$	1388	2320	484
μ, cm^{-1}	8.97	8.90	8.92
Crystal size, mm	0.25 × 0.25 × 0.07	0.25 × 0.35 × 0.40	0.45 × 0.35 × 0.10
Transmission factors	0.80–1.00[g]	0.82–1.00[g]	0.83–1.00[g]
Scan type	φ, ω sweeps	φ, ω sweeps	φ, ω sweeps
Scan range, deg in ω	0.5	0.5	0.5
Data collected	462 frames, 16 s/frame	462 frames, 45 s/frame	462 frames, 30 s/frame
$2\theta_{max}$, deg	61	60.1	60.1
Total reflections	20189	19530	9023
Unique reflections	5883	5100	4382
R_{merge}	0.039	0.047	0.037
No. with $I \geq 3\sigma(I)$	3416	5100	4363
No. of variables	389	325	256
$R(F)$ ($I \geq 3\sigma(I)$)	0.036	0.035	0.068
$R_w(F)$ ($I \geq 3\sigma(I)$)	0.028	0.052	0.089
$R(F^2)$ (all data)	0.063	—	—
$R_w(F^2)$ (all data)	0.061	—	—
gof	1.34	1.23	1.25
Max Δ/σ (final cycle)	0.007	0.01	0.00
Residual density e/Å^3	–1.43 to 1.22	–1.19 to 1.18	–0.92 to 0.97

[a]Rigaku/ADSC CCD diffractometer.

[b]Temperature 180 K, Mo K_α (λ = 0.71069 Å), graphite monochromator, takeoff angle 6.0°, aperture 94.0 × 94.0 mm at a distance of 38.9 mm (for **2**) and 39.2 mm (for **3** and **7**) from the crystal. All data used in the refinement.

[c]Function minimized $\Sigma w(F_o^2 - F_c^2)^2$ where $w = 1/\sigma^2(F_o^2)$, $R = \Sigma||F_o| - |F_c||/\Sigma|F_o|$, $R_w = [\Sigma w(F_o^2 - F_c^2)^2/\Sigma w(F_o^2)^2]^{1/2}$, and gof = $[\Sigma w(F_o^2 - F_c^2)^2/(m - n)]^{1/2}$.

[d]Rigaku AFC6S diffractometer.

[e]Function minimized $\Sigma w(|F_o^2| - |F_c^2|)^2$ where $w = 1/\sigma^2(F_o^2)$, $R = \Sigma||F_o^2| - |F_c^2||/\Sigma|F_o^2|$, $R_w = [\Sigma w(|F_o^2| - |F_c^2|)^2/\Sigma wF_o^4]^{1/2}$, and gof = $[\Sigma w(|F_o^2| - |F_c^2|)^2/(m\text{-}n)]^{1/2}$.

[f]Function minimized $\Sigma w(|F_o| - |F_c|)^2$ where $w = 1/\sigma^2(F_o^2)$, $R = \Sigma||F_o| - |F_c||/\Sigma|F_o|$, $R_w = [\Sigma w(|F_o| - |F_c|)^2/\Sigma wF_o^2]^{1/2}$, and gof = $[\Sigma w(|F_o| - |F_c|)^2/(m - n)]^{1/2}$.

[g]Includes crystal decay, absorption, and scaling corrections.

data processed,[2] corrected for Lorentz and polarization effects, and absorption.

The structures were solved by Patterson methods and expanded using Fourier techniques. Complex **2** crystallized in the monoclinic space group $P2_1/n$. The Λ enantiomer is seen here, but both stereoisomers must be present in the unit cell; the Δ isomer was illustrated for the previously reported X-ray structure of $Ru(acac)_3$ (3), which crystallized in the $P2_1/c$ space group. Complex **3** crystallized in the monoclinic space group $C2/c$. Complex **7** crystallized in the triclinic space group $P\bar{1}$. The CF_3 groups at C(6) and C(10) for **2** and **3**, respectively, were modelled as 1:1 two-fold disordered. Population parameters for the disordered atoms were adjusted to give roughly equivalent isotropic thermal parameters. For **2** and **3** the non-hydrogen atoms were refined anisotropically while for **7** some of the atoms were refined isotropically. Hydrogen atoms were fixed in calculated positions with C—H = 0.98 Å and $B_H = 1.2B_{bonded\ atom}$. Neutral atom scattering factors for all atoms and anomalous dispersion corrections for the non-hydrogen atoms were taken from Standard Tables (24). Final atomic coordinates and equivalent isotropic thermal parameters, selected bond lengths and bond angles appear in Tables 2–4, respectively. Hydrogen atom parameters, anisotropic thermal parameters,

[2] d*TREK: area detector software. Version 3.13. Molecular Structure Corp., The Woodlands, Tex. 1998; teXsan: crystal structure analysis package. Unix version 1.8. Molecular Structure Corp. The Woodlands, Tex. 1997.

© 1999 NRC Canada

Fig. 1. ORTEP view of $Ru(hfac)_3$ (**2**); 50% probability thermal ellipsoids are shown.

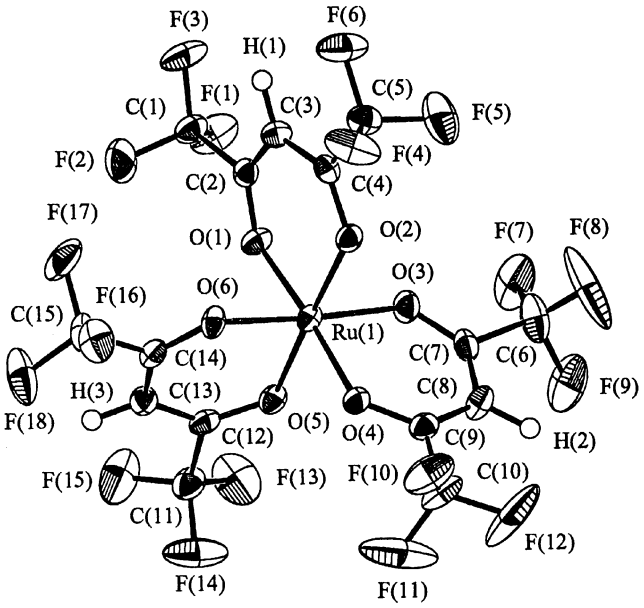

Fig. 2. ORTEP view of *cis*-$Ru(hfac)_2(MeCN)_2$ (**3**); 50% probability thermal ellipsoids are shown.

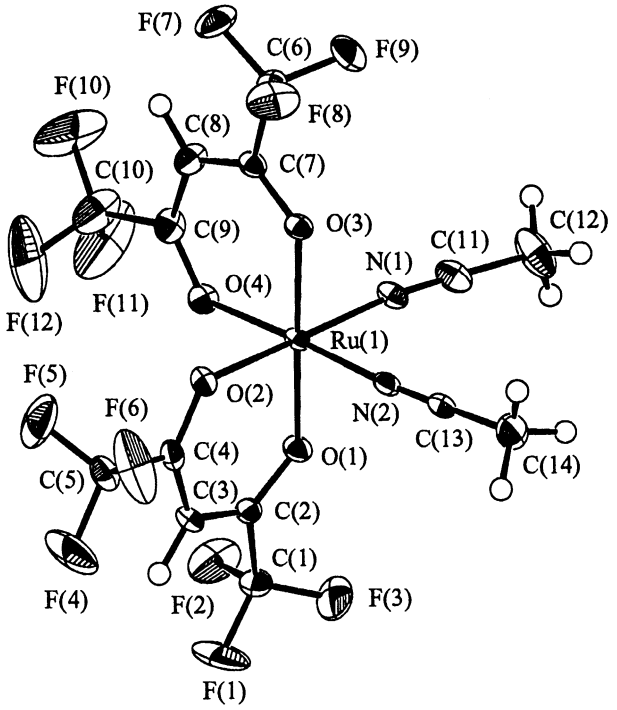

complete listing of bond lengths and angles, torsion angles, intermolecular contacts, and least-squares planes are included as supplementary material.[3]

Fig. 3. ORTEP view of *cis*-$Ru(acac)(hfac)(MeCN)_2$ (**7**); 50% probability thermal ellipsoids are shown.

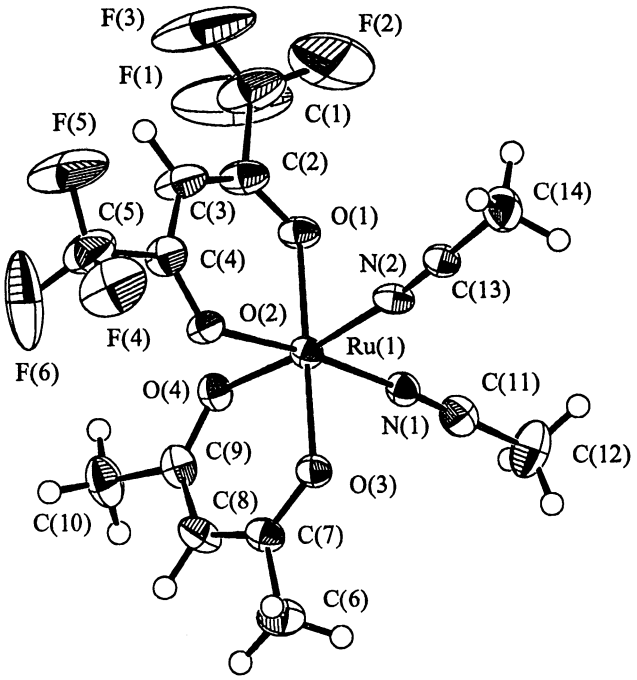

Results and discussion

Series of Ru(III) tris(β-diketonato) complexes have been synthesized previously (14, 15), and such species have been used as catalysts, e.g., $Ru(acac)_3$ effects the hydrogenation of nitroarenes to amines (25). Our interest was more in their use as precursors for synthesizing nitroimidazole derivatives (see Introduction). Because of the substitution – inert nature of the Ru tris(β-diketonato) complexes, more useful precursors for introduction of further mono- and bidentate ligands via ligand substitution were needed. Kobayashi et al. (18) initially reported that bis(MeCN)bis(β-diketonato)ruthenium(II) complexes could be prepared by reducing the corresponding tris(β-diketonato)ruthenium(III) with zinc amalgam in an MeCN–EtOH–H_2O mixture, and that these bis-MeCN complexes were useful intermediates for the synthesis of mixed-ligand β-diketonato ruthenium(III) complexes. Kasahara et al. (19) then reported the preparation of bis(MeCN)bis(β-diketonato)ruthenium(III) species through a ligand displacement reaction of tris(β-diketonato)ruthenium(III) complexes, induced by strong acid. $Ru(acac)_3$ has been shown to be stable under basic and neutral conditions, while introduction of acid leads to protonation of an acac ligand (26).

To synthesize mixed β-diketonato Ru(III) complexes, the appropriate homoleptic β-diketonato complexes were first required. $Ru(hfac)_3$ (**2**) could not be directly synthesized from an EtOH Ru blue solution in the presence of $NaHCO_3$, as previously described (3) for $Ru(acac)_3$, because of in situ re-

[3] Copies of material on deposit may be purchased from: The Depository of Unpublished Data, Document Delivery, CISTI, National Research Council Canada, Ottawa, Canada, K1A 0S2. Tables of hydrogen atom coordinates and bond lengths and angles involving hydrogen atoms have also been deposited with the Cambridge Crystallographic Data Centre and can be obtained on request from: The Director, Cambridge Crystallographic Data Centre, University Chemical Laboratory, 12 Union Road, Cambridge, CB2 1EZ, U.K.

© 1999 NRC Canada

Table 2. Final atomic coordinates (fractional) and B_{eq} (10^3 Å^2).[a]

Atom	*x*	*y*	*z*	B_{eq}	Occ.
2					
Ru(1)	0.47142(3)	0.51053(2)	0.227564(15)	1.748(5)	
F(1)	0.4268(2)	0.83468(15)	0.32557(12)	3.97(6)	
F(2)	0.5454(3)	0.7439(2)	0.40285(12)	5.14(7)	
F(3)	0.6673(2)	0.85231(14)	0.34254(12)	3.74(6)	
F(4)	0.9754(2)	0.55083(15)	0.16592(13)	4.29(6)	
F(5)	0.8538(3)	0.6459(2)	0.09299(12)	4.99(7)	
F(6)	0.9753(2)	0.7118(2)	0.17944(13)	4.52(6)	
F(7)	0.1954(14)	0.6787(7)	0.0561(5)	6.0(2)	0.59(2)
F(7a)	0.159(2)	0.657(2)	0.0530(10)	10.5(6)	0.41
F(8)	0.3296(15)	0.602(2)	–0.0187(7)	8.5(5)	0.59
F(8a)	0.3702(12)	0.6675(12)	0.0184(11)	6.6(3)	0.41
F(9)	0.1151(10)	0.5490(6)	0.0081(7)	5.6(2)	0.59
F(9a)	0.227(5)	0.5520(8)	–0.0224(8)	10.5(7)	0.41
F(10)	0.5636(2)	0.20879(15)	0.10617(13)	4.32(6)	
F(11)	0.3435(3)	0.1850(2)	0.1437(2)	8.29(10)	
F(12)	0.3711(4)	0.2238(2)	0.0388(2)	8.33(10)	
F(13)	–0.0024(2)	0.4753(2)	0.31532(13)	5.38(7)	
F(14)	0.0698(2)	0.3273(2)	0.34603(15)	5.77(7)	
F(15)	0.0801(2)	0.4506(2)	0.41828(13)	6.01(8)	
F(16)	0.7611(2)	0.3579(2)	0.40578(11)	3.42(5)	
F(17)	0.7195(2)	0.5095(2)	0.44183(11)	4.42(6)	
F(18)	0.5939(2)	0.3827(2)	0.48218(12)	5.00(7)	
O(1)	0.4656(2)	0.64111(15)	0.27960(12)	2.04(5)	
O(2)	0.6666(2)	0.54635(15)	0.18299(11)	1.90(5)	
O(3)	0.3569(2)	0.5736(2)	0.14549(12)	2.26(5)	
O(4)	0.4743(2)	0.37309(15)	0.18088(12)	2.03(5)	
O(5)	0.2725(2)	0.47438(15)	0.26934(12)	1.98(5)	
O(6)	0.5926(2)	0.4562(2)	0.30892(11)	1.93(5)	
C(1)	0.5551(4)	0.7852(3)	0.3394(2)	2.49(9)	
C(2)	0.5794(4)	0.7000(2)	0.2860(2)	1.83(7)	
C(3)	0.7155(4)	0.6968(2)	0.2514(2)	2.03(8)	
C(4)	0.7450(4)	0.6230(2)	0.2018(2)	1.82(7)	
C(5)	0.8920(4)	0.6319(3)	0.1609(2)	2.57(9)	
C(6)	0.2492(6)	0.5944(4)	0.0333(2)	3.86(12)	
C(7)	0.3201(4)	0.5243(3)	0.0911(2)	2.17(8)	
C(8)	0.3377(4)	0.4225(3)	0.0756(2)	2.65(9)	
C(9)	0.4121(3)	0.3546(2)	0.1213(2)	2.02(8)	
C(10)	0.4230(5)	0.2419(3)	0.1017(2)	3.50(10)	
C(11)	0.0995(4)	0.4256(3)	0.3531(2)	2.77(9)	
C(12)	0.2626(4)	0.4476(2)	0.3319(2)	1.96(7)	
C(13)	0.3811(4)	0.4326(2)	0.3819(2)	2.11(8)	
C(14)	0.5326(4)	0.4379(2)	0.3664(2)	1.97(7)	
C(15)	0.6542(4)	0.4211(3)	0.4249(2)	2.71(9)	
H(1)	0.7934	0.7486	0.2624	2.4	
H(2)	0.2965	0.3968	0.0307	3.2	
H(3)	0.3549	0.4175	0.4300	2.5	
3					
Ru(1)	0.117317(7)	0.08910(2)	0.180137(9)	1.139(6)	
F(1)	0.09616(9)	–0.4694(2)	0.27965(12)	4.77(6)	
F(2)	0.16861(10)	–0.4176(2)	0.23531(11)	4.27(6)	
F(3)	0.14916(10)	–0.3197(2)	0.33702(9)	4.57(5)	
F(4)	–0.03090(8)	–0.3111(2)	0.11089(11)	5.05(6)	
F(5)	–0.00757(9)	–0.1691(3)	0.02583(9)	5.10(6)	
F(6)	–0.05149(9)	–0.0805(2)	0.11131(14)	5.46(6)	

© 1999 NRC Canada

Table 2 (*continued*).

Atom	*x*	*y*	*z*	B_{eq}	Occ.
F(7)	0.12310(8)	0.4963(2)	–0.03331(8)	3.36(4)	
F(8)	0.06129(8)	0.5104(2)	0.04013(9)	3.72(5)	
F(9)	0.13844(10)	0.5722(2)	0.07789(11)	3.83(5)	
F(10)	0.2069(6)	0.054(2)	–0.0731(7)	8.4(4)	0.50
F(10a)	0.1884(6)	0.025(2)	–0.0831(6)	7.3(3)	0.50
F(11)	0.2276(5)	–0.1038(13)	0.0057(5)	8.1(3)	0.50
F(11a)	0.2465(4)	–0.0193(11)	0.0083(7)	7.8(3)	0.50
F(12)	0.1555(4)	–0.1276(12)	–0.0461(6)	9.3(3)	0.50
F(12a)	0.1831(5)	–0.1624(7)	–0.0169(6)	7.7(3)	0.50
O(1)	0.13423(7)	–0.1058(2)	0.23605(9)	1.60(4)	
O(2)	0.05185(7)	0.0009(2)	0.12815(8)	1.51(4)	
O(3)	0.10304(7)	0.2867(2)	0.12462(8)	1.41(4)	
O(4)	0.15802(7)	–0.0017(2)	0.09778(9)	1.68(4)	
N(1)	0.18032(9)	0.1845(2)	0.23242(11)	1.60(4)	
N(2)	0.07570(8)	0.1686(2)	0.26171(10)	1.49(4)	
C(1)	0.12963(12)	–0.3577(3)	0.27183(14)	2.27(6)	
C(2)	0.10631(10)	–0.2225(3)	0.22884(12)	1.55(5)	
C(3)	0.05953(11)	–0.2422(3)	0.18688(13)	1.75(5)	
C(4)	0.03673(10)	–0.1319(3)	0.14080(13)	1.55(5)	
C(5)	–0.01368(11)	–0.1720(3)	0.09705(14)	2.08(6)	
C(6)	0.11061(12)	0.4731(3)	0.03616(13)	2.10(6)	
C(7)	0.12169(10)	0.3115(3)	0.06287(13)	1.41(5)	
C(8)	0.14984(11)	0.2164(3)	0.01946(13)	2.05(6)	
C(9)	0.16416(12)	0.0702(3)	0.03864(14)	1.97(6)	
C(10)	0.1927(2)	–0.0240(4)	–0.0173(2)	4.20(10)	
C(11)	0.21031(11)	0.2445(3)	0.26948(15)	2.27(6)	
C(12)	0.24757(13)	0.3242(4)	0.3197(2)	3.71(8)	
C(13)	0.05440(10)	0.2211(3)	0.30914(13)	1.75(5)	
C(14)	0.02774(13)	0.2902(4)	0.36895(15)	3.04(7)	
7					
Ru(1)	0.20695(5)	0.14390(4)	0.25742(3)	1.987(8)	
F(1)	0.2765(10)	0.4950(6)	0.0344(3)	12.7(2)	
F(2)	0.4682(9)	0.4651(7)	0.1417(5)	13.6(2)	
F(3)	0.2210(9)	0.6248(5)	0.1610(4)	11.7(2)	
F(4)	–0.2279(8)	0.4349(6)	0.5051(4)	6.46(15)	0.75
F(5)	–0.2249(9)	0.6083(6)	0.4250(7)	10.3(2)	0.75
F(6)	–0.3732(10)	0.4815(11)	0.3666(7)	9.8(3)	0.75
F(7)	–0.212(4)	0.504(3)	0.493(2)	10.7(8)	0.25
F(8)	–0.316(3)	0.604(2)	0.3479(13)	6.6(4)	0.25
F(9)	–0.352(4)	0.452(3)	0.401(2)	5.8(5)	0.25
O(1)	0.2894(4)	0.2882(3)	0.1782(2)	2.54(7)	
O(2)	–0.0114(4)	0.2787(3)	0.3448(2)	2.35(7)	
O(3)	0.1259(4)	0.0012(3)	0.3374(2)	2.23(7)	
O(4)	0.0328(4)	0.1643(3)	0.1430(2)	2.33(7)	
N(1)	0.4089(5)	–0.0015(4)	0.1730(3)	2.21(8)	
N(2)	0.3827(5)	0.1435(4)	0.3672(3)	2.31(9)	
C(1)	0.2898(12)	0.5021(7)	0.1350(6)	6.1(2)	
C(2)	0.2025(8)	0.4100(5)	0.1988(4)	3.23(12)	
C(3)	0.0495(8)	0.4706(5)	0.2689(4)	4.00(14)	
C(4)	–0.0464(7)	0.4019(5)	0.3349(4)	3.16(12)	
C(5)	–0.2231(10)	0.4873(7)	0.4052(6)	5.3(2)	
C(6)	–0.0418(7)	–0.1433(5)	0.3796(4)	3.56(13)	
C(7)	–0.0040(6)	–0.0354(5)	0.3117(3)	2.42(10)	
C(8)	–0.1094(7)	0.0144(5)	0.2241(3)	3.03(12)	
C(9)	–0.0874(6)	0.1072(5)	0.1475(3)	2.75(11)	
C(10)	–0.2189(7)	0.1455(6)	0.0585(4)	3.70(13)	

© 1999 NRC Canada

Table 2. (*concluded*).

Atom	*x*	*y*	*z*	B_{eq}	Occ.
C(11)	0.5206(7)	–0.0910(5)	0.1307(4)	2.88(12)	
C(12)	0.6639(8)	–0.2044(6)	0.0769(4)	4.36(14)	
C(13)	0.4872(6)	0.1527(5)	0.4201(3)	2.31(10)	
C(14)	0.6205(7)	0.1689(5)	0.4864(4)	3.65(13)	

[a] $B_{eq} = (8/3)\pi^2\Sigma\Sigma(U_{ij}a_ia_j(\boldsymbol{a}_i\cdot\boldsymbol{a}_j))$.

Table 3. Selected bond lengths (Å) with estimated standard deviations in parentheses.[a]

Bond	Length	Bond	Length
2			
Ru(1)—O(1)	1.980(2)	O(1)—C(2)	1.263(3)
Ru(1)—O(2)	2.000(2)	O(2)—C(4)	1.261(3)
Ru(1)—O(3)	2.012(2)	O(3)—C(7)	1.258(4)
Ru(1)—O(4)	2.009(2)	O(4)—C(9)	1.270(4)
Ru(1)—O(5)	2.006(2)	O(5)—C(12)	1.256(4)
Ru(1)—O(6)	1.986(2)	O(6)—C(14)	1.264(4)
3			
Ru(1)—O(1)	2.034(2)	Ru(1)—O(2)	2.038(2)
Ru(1)—O(3)	2.040(2)	Ru(1)—O(4)	2.042(2)
Ru(1)—N(1)	2.016(2)	Ru(1)—N(2)	2.007(2)
O(2)—C(4)	1.261(3)	O(1)—C(2)	1.259(3)
O(4)—C(9)	1.267(3)	O(3)—C(7)	1.266(3)
N(2)—C(13)	1.147(3)	N(1)—C(11)	1.127(3)
C(13)—C(14)	1.454(4)	C(11)—C(12)	1.466(4)
7			
Ru(1)—O(1)	2.053(3)	Ru(1)—O(2)	2.030(3)
Ru(1)—O(3)	2.036(3)	Ru(1)—O(4)	2.023(3)
Ru(1)—N(1)	2.006(4)	Ru(1)—N(2)	2.030(3)
O(2)—C(4)	1.253(6)	O(1)—C(2)	1.259(6)
O(4)—C(9)	1.268(5)	O(3)—C(7)	1.266(4)
N(2)—C(13)	1.127(4)	N(1)—C(11)	1.140(6)
C(13)—C(14)	1.445(5)	C(11)—C(12)	1.451(7)

[a] In **2**, **3**, and **7**, the "external" C—C bond distances (i.e., outside of the chelate rings) of the hfac and acac ligands are in the range 1.502–1.551 Å, while those within the delocalized ring systems are 1.365–1.415 Å. The C—F bond lengths, excluding data for the disordered F-atoms, are 1.269–1.346 Å.

duction to the air-stable, Ru(II) species [Na][Ru(hfac)$_3$] (**1**). The H_2O_2 oxidation of **1** to **2** followed that reported previously by Endo et al. (9) who reported **2** to be unstable, even under N_2 in the absence of light. In the present work, **2** was, however, found to be stable for long periods in air. Its X-ray structure (Fig. 1, Table 3) reveals average O-Ru-O intra- and inter-ring bond angles of 92.58°and 88.26°, respectively, and the average Ru—O bond length (1.999 Å) is the same as that of the acac structure (3), implying that the electron-withdrawing CF_3 groups have surprisingly little effect on the interaction of these β-diketonate ligands with Ru(III). There are strong intramolecular interactions between the methyne CH atoms and adjacent F-atoms of both CF_3 groups: the H···F distances are ~2.35 Å, while the C···F distances are ~2.71 Å and the C···H···F angles are close to 100°.

The mixed-ligand complexes containing both acac and hfac were isolated, but not without some difficulty. Patterson and Holm (15) reported the synthesis of Ru(acac)$_2$(hfac) (**4**) and Ru(hfac)$_2$(acac) (**6**), by refluxing Ru(acac)$_3$ and Ru(hfac)$_3$ (1:1) in toluene for 7 days (15), but the products were not isolated and purified. Compound **4** has been isolated, albeit in only 7% yield, from a Ru blue route (10). The bis-MeCN complexes, *cis*-[Ru(acac)$_2$(MeCN)$_2$][CF_3SO_3], and *cis*-Ru(hfac)$_2$(MeCN)$_2$ (**3**), were thus developed as synthetic precursors as they gave less complicated product mixtures in much higher yields.

Complex **4** was synthesized by treating *cis*-[Ru(acac)$_2$(MeCN)$_2$][CF_3SO_3] with about one equiv. each of Hhfac and $NaHCO_3$; the reaction proceeded rapidly giving a high yield (75%), presumably because of the relatively labile nitrile ligands and the entropically favoured chelate formation. Kobayashi et al. (18) have synthesized **4** from the Ru(II) precursor *cis*-Ru(acac)$_2$(MeCN)$_2$ in 32% yield.

Synthesis of **6** required a two-step procedure: ligand substitution in **3** to form [Na][Ru(hfac)$_2$(acac)] (**5**) followed by a Ru(II) → Ru(III) oxidation step using H_2O_2. The reaction to generate **5** required longer times and gave only 32% yield in comparison to the synthesis of **4**; i.e., the displacement of two MeCN ligands by acac$^-$ at Ru(II) is more difficult than the corresponding displacement by hfac$^-$ at Ru(III). Using the same reaction conditions for the transformation of **1** to **2**, H_2O_2 oxidation of **5** proceeded quickly. This corresponding oxidation is more efficient than for the synthesis of **2** as the final aqueous phase was pale yellow, suggesting all of **5** had been oxidized and transferred to the organic phase. The final green product (**6**), not previously isolated (10), was purified via sublimation and obtained in 80% yield.

The IR spectra of metal acetylacetonato complexes show a strong, characteristic $\nu_{C=O}$ stretching mode near 1570 cm^{-1} (27, 28). The $\nu_{C=O}$ and $\nu_{C=C}$ bands of Ru(III) β-diketonato complexes typically appear in the 1510–1620 and the 1420–1580 cm^{-1} regions, respectively, and are substituent-dependent, the hfac complexes displaying higher values than the acac complexes. These shifts can be explained in terms of the electron-withdrawing CF_3 group, and the consequent strengthening of the C=O and C=C bonds. For example, for Ru(hfac)$_2$(acac) (**6**), the $\nu_{C=O}$ bands appear at 1583 and 1579 cm^{-1}, corresponding to the hfac and acac ligands, respectively. Correspondingly, the Ru(II) complex [Na][Ru(hfac)$_2$(acac)] (**5**) has C=O bands at 1550 and 1521 cm^{-1}, the shift of the bands to lower energy being due to the lower oxidation state of the metal. The higher $\nu_{C=O}$ (1582 cm^{-1}) for Ru(hfac)$_3$ (**2**) (vs. the value of 1555 cm^{-1} for the Ru(II) analogue, [Na][Ru(hfac)$_3$] (**1**)) coincides with the value previously reported (9).

Ru(III) complexes often give very broad, poorly resolved ^{1}H NMR signals as a result of rapid nuclear spin relaxation induced by the paramagnetism (2), but examples of interpretable ^{1}H NMR data for Ru(III) species have appeared (29–31), and these studies on the β-diketonate complexes provide further examples. Table 5 summarizes the chemical

© 1999 NRC Canada

Table 4. Selected bond angles (deg) with estimated standard deviations in parentheses.[a]

Bonds	Angle (deg)	Bonds	Angle (deg)
2			
O(1)-Ru(1)-O(2)	93.05(8)	O(1)-C(2)-C(1)	112.2(3)
O(1)-Ru(1)-O(3)	91.11(9)	O(1)-C(2)-C(3)	128.9(3)
O(1)-Ru(1)-O(4)	176.08(9)	C(1)-C(2)-C(3)	119.0(3)
O(1)-Ru(1)-O(5)	87.80(8)	C(2)-C(3)-C(4)	122.4(3)
O(1)-Ru(1)-O(6)	86.32(9)	O(2)-C(4)-C(3)	129.4(3)
O(2)-Ru(1)-O(3)	88.83(9)	O(2)-C(4)-C(5)	111.9(3)
O(2)-Ru(1)-O(4)	89.60(8)	C(3)-C(4)-C(5)	118.7(3)
O(2)-Ru(1)-O(5)	178.23(9)	O(3)-C(7)-C(6)	111.9(3)
O(2)-Ru(1)-O(6)	88.76(9)	O(3)-C(7)-C(8)	130.4(3)
O(3)-Ru(1)-O(4)	91.85(9)	C(6)-C(7)-C(8)	117.6(3)
O(3)-Ru(1)-O(5)	89.60(9)	C(7)-C(8)-C(9)	122.3(3)
O(3)-Ru(1)-O(6)	176.37(9)	O(4)-C(9)-C(8)	128.3(3)
O(4)-Ru(1)-O(6)	89.63(9)	O(4)-C(9)-C(10)	112.1(3)
O(4)-Ru(1)-O(6)	90.85(8)	C(8)-C(9)-C(10)	119.5(3)
O(5)-Ru(1)-O(6)	92.84(9)	O(5)-C(12)-C(11)	114.0(3)
Ru(1)-O(1)-C(2)	122.6(2)	O(5)-C(12)-C(13)	128.1(3)
Ru(1)-O(2)-C(4)	122.1(2)	C(11)-C(12)-C(13)	117.9(3)
Ru(1)-O(3)-C(7)	122.9(2)	C(12)-C(13)-C(14)	122.9(3)
Ru(1)-O(4)-C(9)	124.0(2)	O(6)-C(14)-C(13)	129.6(3)
Ru(1)-O(5)-C(12)	122.7(2)	O(6)-C(14)-C(15)	111.4(3)
Ru(1)-O(6)-C(14)	121.7(2)		
3			
O(1)-Ru(1)-O(2)	93.19(7)	O(1)-Ru(1)-O(3)	177.98(7)
O(1)-Ru(1)-O(4)	86.03(7)	O(1)-Ru(1)-N(1)	88.55(8)
O(1)-Ru(1)-N(2)	91.94(7)	O(2)-Ru(1)-O(3)	88.70(7)
O(2)-Ru(1)-O(4)	87.40(7)	O(2)-Ru(1)-N(1)	177.54(7)
O(2)-Ru(1)-N(2)	90.84(7)	O(3)-Ru(1)-O(4)	93.33(7)
O(3)-Ru(1)-N(1)	89.59(7)	O(3)-Ru(1)-N(2)	88.76(7)
O(4)-Ru(1)-N(1)	94.46(8)	O(4)-Ru(1)-N(2)	177.24(7)
N(1)-Ru(1)-N(2)	87.36(8)	Ru(1)-O(1)-C(2)	122.5(2)
Ru(1)-O(2)-C(4)	121.76(15)	Ru(1)-O(3)-C(7)	121.36(15)
Ru(1)-O(4)-C(9)	121.4(2)	Ru(1)-N(1)-C(11)	169.3(2)
Ru(1)-N(2)-C(13)	175.5(2)	O(1)-C(2)-C(1)	112.4(2)
O(1)-C(2)-C(3)	128.8(2)	C(1)-C(2)-C(3)	118.8(2)
C(2)-C(3)-C(4)	124.1(2)	O(2)-C(4)-C(3)	129.6(2)
O(2)-C(4)-C(5)	112.5(2)	C(3)-C(4)-C(5)	117.9(2)
O(3)-C(7)-C(6)	111.7(2)	O(3)-C(7)-C(8)	129.7(2)
C(6)-C(7)-C(8)	118.6(2)	C(7)-C(8)-C(9)	124.3(2)
O(4)-C(9)-C(8)	129.6(2)	O(4)-C(9)-C(10)	112.3(2)
C(8)-C(9)-C(10)	118.0(2)	N(1)-C(11)-C(12)	177.6(3)
N(2)-C(13)-C(14)	179.0(3)		
7			
O(1)-Ru(1)-O(2)	93.59(12)	O(1)-Ru(1)-O(3)	179.45(11)
O(1)-Ru(1)-O(4)	87.03(11)	O(1)-Ru(1)-N(1)	91.40(14)
O(1)-Ru(1)-N(2)	86.98(12)	O(2)-Ru(1)-O(3)	86.20(12)
O(2)-Ru(1)-O(4)	86.99(11)	O(2)-Ru(1)-N(1)	174.46(14)
O(2)-Ru(1)-N(2)	91.31(13)	O(3)-Ru(1)-O(4)	93.48(11)
O(3)-Ru(1)-N(1)	88.82(13)	O(3)-Ru(1)-N(2)	92.51(12)
O(4)-Ru(1)-N(1)	90.89(12)	O(4)-Ru(1)-N(2)	173.66(14)
N(1)-Ru(1)-N(2)	91.33(14)	Ru(1)-O(1)-C(2)	120.5(3)
Ru(1)-O(2)-C(4)	121.7(3)	Ru(1)-O(3)-C(7)	123.6(3)
Ru(1)-O(4)-C(9)	123.1(3)	Ru(1)-N(1)-C(11)	174.6(4)
Ru(1)-N(2)-C(13)	172.0(3)	O(1)-C(2)-C(1)	112.8(5)
O(1)-C(2)-C(3)	130.7(5)	C(1)-C(2)-C(3)	116.5(5)
C(2)-C(3)-C(4)	124.2(5)	O(2)-C(4)-C(3)	129.3(5)

© 1999 NRC Canada

Table 4 (*concluded*).

Bonds	Angle (deg)	Bonds	Angle (deg)
O(2)-C(4)-C(5)	113.6(4)	C(3)-C(4)-C(5)	117.1(5)
O(3)-C(7)-C(6)	115.7(4)	O(3)-C(7)-C(8)	125.3(4)

[a]Excluding data for disordered F-atoms, the F-C-F angles are in the range 104.1–109.0°, while the F-C-C angles are 108.8–115.6°.

Table 5. ^{1}H and $^{19}F\{^{1}H\}$ NMR data for the Ru(III) tris(β-diketonato) complexes.[a]

Complex	δ_H Me (acac)	δ_H CH (acac)	δ_H CH (hfac)	δ_F
$Ru(acac)_3$	–7.11	–30.25	—	—
$Ru(acac)_2(hfac)$, **4**	–8.82, –9.01	–38.95	–28.45	–9.71
$Ru(hfac)_2(acac)$, **6**	–14.34	–56.72	–31.82	–6.71, –8.06
$Ru(hfac)_3$, **2**	—	—	–41.67	–11.49

[a]At r.t.; in $CDCl_3$ for **2**, **6**, and $Ru(acac)_3$, and in d_6-acetone for **4**.

Fig. 4. ^{1}H NMR spectrum of $Ru(hfac)_2(acac)$ (**6**) in $CDCl_3$ at r.t.

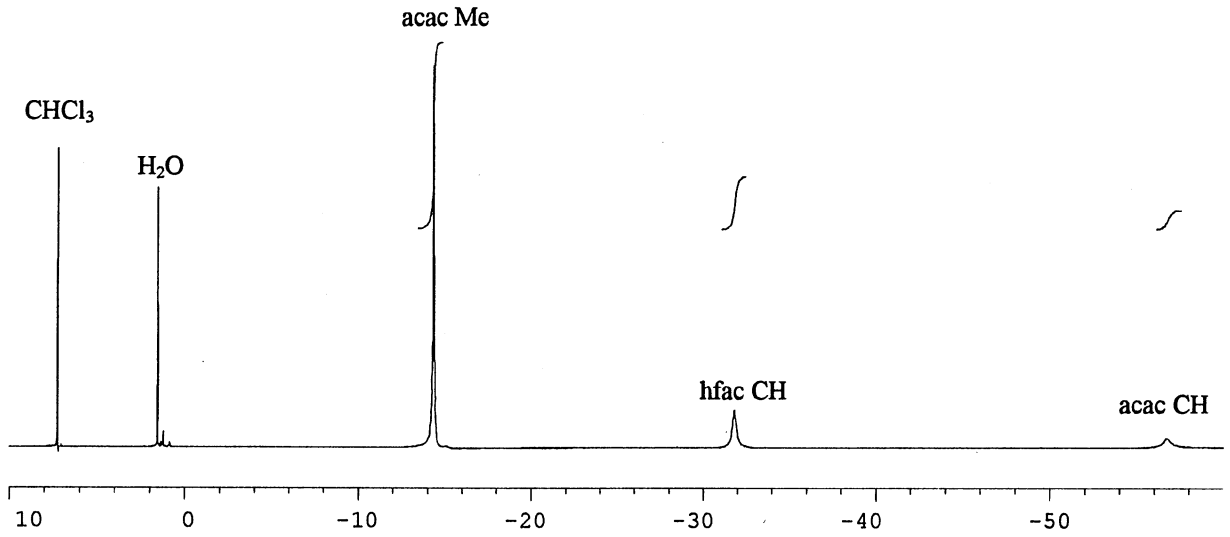

shifts for the three tris(β-diketonato) complexes. The δ values for the Me signals of the coordinated acac ligands reveal an upfield shift (compared to a "diamagnetic value") due to interaction with the paramagnetic Ru(III) centre. The "stronger electron-withdrawing hfac ligand" shifts the Me signals further upfield. Complex **4** has two Me group signals, one from a moiety *trans* to the hfac ligand and one from a moeity *trans* to an acac ligand. Complex **6** has only one signal for the Me groups due to its increased symmetry with regard to the methyls. The signals for the methyne protons of acac and hfac exhibit even more significant upfield shifts. This is consistent with electronic delocalization on the chelated ligand across the methyne proton, that produces an even greater electron spin imbalance between the ligand and the metal and hence a greater isotropic shift (2). Again, the more hfac ligands, the greater the upfield shift. This effect is more pronounced for the acac methyne signal as substitution of two acac ligands of $Ru(acac)_3$ by hfac (to give **6**) renders a chemical shift change of ~26 ppm, while the reverse process (from **2** to **4**) produces a chemical shift change of ~13 ppm. A representative ^{1}H NMR spectrum illustrating the upfield shifts is shown in Fig. 4 for complex **6**; δ assignments were made according to integration ratios. The signals of the methyne protons that are bonded directly to the chelate ring are always relatively broad in Ru(III) species, and indeed, in some acac/nitroimidazole derivatives, the signals are not observed.

The $^{19}F\{^{1}H\}$ NMR spectra (Table 5) show that $Ru(hfac)_3$, with magnetically equivalent CF_3 groups, has the highest upfield signal (δ –11.49). Substitution of one hfac by acac results in a downfield shift for **6**, with two signals at δ –6.71 and –8.06, comparable to the Me proton signals of acac in **4**. The non-regular trend in δ_F with number of hfac ligands may result from a solvent effect ($CDCl_3$ vs. d_6-acetone).

The Ru(III) → Ru(II) $E_{1/2}$ values for **2**, **6**, and **4** (721, 289, and –232 mV vs. SCE in MeCN, respectively) compare reasonably well with those previously reported by Patterson and Holm (15) (726 in MeCN, 332 and –184 mV in DMF, respectively), noting that data for **6** and **4** had been determined using a mixture of the species. $E_{1/2}$ data reported by Hoshino et al. (10) appear to be in error, but in all cases, relative stabilization of Ru(II) increases markedly with increasing number of hfac ligands.

The reaction of $Ru(hfac)_3$ with CF_3SO_3H in MeCN, in an attempt to generate *cis*-$[Ru(hfac)_2(MeCN)_2][CF_3SO_3]$ analogous to the acac species (19), formed *cis*-$Ru(hfac)_2(MeCN)_2$

© 1999 NRC Canada

(**3**), implying an in situ reduction of Ru(III) to diamagnetic Ru(II). The electron-accepting CF_3 substituents clearly stabilize the Ru(II) oxidation state, thus promoting reduction of Ru(III), presumably by residual H_2O introduced by either the MeCN solvent or the hygroscopic CF_3SO_3H. Compound **3** was also readily synthesized from [Na][Ru(hfac)$_3$] (**1**). The geometry of **3** is *cis*, according to the IR, NMR, and X-ray crystallographic data. The two ν_{CN} bands for **3** (at 2357 and 2285 cm^{-1}) and for the corresponding bis-acac complex (at 2326 and 2296 cm^{-1}) (cf. 2254 cm^{-1} for free MeCN) are consistent with the absence of $d\pi \rightarrow p\pi$ backbonding from Ru. The ^1H NMR data (singlets at δ 6.20 and 2.87 corresponding to the hfac methyne proton and Me of MeCN, respectively) do not distinguish the geometry of the complex, but the $^{19}F\{^1H\}$ NMR spectrum (singlets at δ 0.98 and 0.38 for two inequivalent CF_3 groups) supports the *cis* formulation in solution, as the *trans* isomer would have revealed only one singlet. The X-ray structure (Fig. 2) reveals the *cis* geometry. The Ru—O distances average 2.038(2) Å, and the two Ru—N distances average 2.011(2) Å (Table 3). The nitriles exhibit a lengthening of the Ru—N bonds compared to those, for example, in [Ru(MeCN)(PPh$_3$)]$_2$(μ-$O_2CC_6H_4$-*p*-NO_2)$_4$(μ-H_2O) (Ru—N 1.98 Å) (32), suggesting a stronger *trans* influence for hfac versus carboxylate. Both Ru—N bonds are longer than 2.0 Å, the sum of the estimated single covalent radii (33), implying little Ru(II)$\rightarrow$N, $d\pi \rightarrow p\pi$ backbonding. The C—N bond lengths average 1.137(2) Å, slightly shorter than the 1.157 Å calculated for MeCN in the gas phase (34). Shortening of the C—N bond is commonly observed in both transition metal (35) and main group (36) nitrile complexes and is evidence against any π-backbonding in the metal–ligand interaction; this correlates well with the positive infrared shift of ν_{CN} for **3**. Intramolecular methyne CH$\cdots$F interactions are again evident, as noted for **2**.

The synthesis of *cis*-Ru(acac)(hfac)(MeCN)$_2$ (**7**) was attempted from the two mixed-ligand Ru(III) precursors **4** and **6**; however, only one of the reactions was moderately successful (involving in situ reduction of Ru(III)). Addition of 1 equiv. of triflic acid to an MeCN solution of **4** revealed rapid formation of *cis*-[Ru(acac)$_2$(MeCN)$_2$][CF_3SO_3] and **7** in approximately equal amounts (Scheme 1). Use of 40 equiv. of triflic acid resulted in a lower yield of **7**, thus displaying the acid dependence of the reaction: at higher acid concentration, the hfac ligand is preferentially displaced. This observation is opposite to that reported by Kobayashi et al. (18) where for a number of mixed Ru(III) β-diketonato complexes (not involving hfac) the more basic acac ligand was preferentially displaced. These workers also reported the synthesis of **7** by treatment of **4** with a refluxing mixture of EtOH, MeCN, and H_2O (10:1:1) in the presence of zinc amalgam for 2 h; the yield was 39% versus the 49% reported here. Attempts to form **7** from **6** via triflic acid treatment in MeCN gave complete conversion to **3** whatever concentration of acid was used (Scheme 2); i.e., the acac is now preferentially displaced. There is clearly a delicate balance between factors affecting acid cleavage of the Ru—O bonds. Structural data for **7** (Table 3) show Ru—O_{hfac} bond lengths of 2.053 and 2.030 Å, and Ru—O_{acac} lengths of 2.036 and 2.023 Å, with the shorter bond in each set being *trans* to MeCN. The factors involved include: the relative basicities of acac and hfac, the relative strengths of the Ru—O bonds as reflected in ratios of kinetic labilities, and the stage at which reduction to Ru(II) occurs. Of note, attempts to synthesize **7** from the Ru(II) starting material [Na][Ru(hfac)$_2$(acac)] (**5**) were also unsuccessful.

X-ray analysis of **7** (Fig. 3) revealed essentially octahedral bonding at the metal within the *cis* geometry. The Ru—N(1) bond distance is 2.006(4) Å for MeCN *trans* to hfac while that of Ru—N(2) for MeCN *trans* to acac is 2.030(3) Å, any *trans* influencing effects being small. As in **3**, the C—N bond lengths (average 1.133(5) Å) are shorter than that of free MeCN and indicate zero π-backbonding in the ligand–metal interaction. Of note, the average Ru^{II}—O_{hfac} bond lengths in **7** (2.041 Å) and **3** (2.038 Å) are significantly longer than the average Ru^{III}—O_{hfac} bond length in **2** (1.999 Å), and the difference is typical of that usually found between corresponding bond lengths in Ru^{II} and Ru^{III} complexes (37).

The ^1H NMR spectrum of **7** supports a *cis* geometry in solution. Thus, two signals for the coordinated MeCN ligands are observed (δ 2.76 and 2.69), and the methyne ^1H signal for hfac is further downfield than the corresponding signal for acac (δ 6.04 and 5.37, respectively) due to the electron-withdrawing property of the CF_3 substituents. The IR spectrum correspondingly shows two ν_{CN} bands at 2346 and 2270 cm^{-1}, in the range observed for *cis*-[Ru(acac)$_2$(MeCN)$_2$][CF_3SO_3] and **3**.

A comparison of UV-vis spectra of the Ru(II) complexes **3** and **7** shows the effect of replacement of hfac by acac on the MLCT band of these complexes; the energy for this electronic transition increases, λ_{max} shifting from 418 to 352 nm for **3** and **7**, respectively. The LMCT band for the Ru(III) species, *cis*-[Ru(acac)$_2$(MeCN)$_2$][CF_3SO_3], was observed at 318 nm.

The Ru(III)$\rightarrow$Ru(II), $E_{1/2}$ reduction potentials for *cis*-[Ru(acac)$_2$(MeCN)$_2$][CF_3SO_3], *cis*-Ru(acac)(hfac)(MeCN)$_2$ (**7**), and *cis*-Ru(hfac)$_2$(MeCN)$_2$ (**3**) are –77, +544, and +1143 mV (vs. SCE), respectively, again demonstrating relative stabilization of Ru(II) with increasing number of hfac ligands. The stepwise increase in $E_{1/2}$ for the bis-MeCN complexes is ~610 mV, greater than that observed for the series of tris(β-diketonato) Ru(III) species (see above). The data also show that replacement of an hfac ligand by two MeCN ligands increases $E_{1/2}$ by up to ~420 mV, while corresponding replacement of an acac increases $E_{1/2}$ by up to ~775 mV. Such increases in $E_{1/2}$ on coordination of MeCN to Ru are well documented (20, 32, 38, 39); one of these reports states that a single MeCN ligand stabilizes the +2 oxidation state by ~0.4 V (39). The in situ reduction that occurs during the synthesis of **7** from a Ru(III) precursor resembles that seen in formation of **3** from Ru(hfac)$_3$ (**2**) or Ru(hfac)$_2$(acac) (**6**) and is considered to be due to the presence of residual H_2O.

Acknowledgements

This work was supported by the Natural Sciences and Engineering Research Council of Canada (research grant to B.R.J. and a postgraduate fellowship to I.R.B.). Johnson Matthey, Ltd. and Colonial Metals Inc. kindly donated the $RuCl_3 \cdot 3H_2O$.

© 1999 NRC Canada

References

1. H. Veening, W.E. Bachman, and D.M. Wilkinson. J. Gas Chromatogr. 248 (1967).
2. A. Johnson and G.W. Everett, Jr. J. Am. Chem. Soc. **94**, 1419 (1972).
3. T.S. Knowles, M.E. Howells, B.J. Howlin, and G.W. Smith. Polyhedron, **13**, 2197 (1994).
4. K. Hiroaki and K. Saito. Bull. Chem. Soc. Jpn. **52**, 3545 (1979).
5. A. Endo, K. Shimizu, G.P. Satô, and M. Mukaida. Chem. Lett. 437 (1984).
6. A. Endo, K. Shimizu, and G.P. Satô. Chem. Lett. 581 (1985).
7. Y. Hoshino, Y. Yukawa, A. Endo, K. Shimizu, and G.P. Satô. Chem. Lett. 845 (1987).
8. Y. Satsu, A. Endo, K. Shimizu, G.P. Satô, K. Ono, I. Watanabe, and S. Ikeda. Chem. Lett. 585 (1986).
9. A. Endo, M. Kajitani, M. Mukaida, K. Shimizu, and G.P. Satô. Inorg. Chim. Acta, **150**, 25 (1988).
10. Y. Hoshino, Y. Yukawa, T. Maruyama, A. Endo, K. Shimizu, and G.P. Satô. Inorg. Chim. Acta, **174**, 41 (1990).
11. Y. Hoshino, R. Takahashi, K. Shimizu, G.P. Satô, and K. Aoki. Inorg. Chem. **29**, 4816 (1990).
12. A. Endo, Y. Hoshino, K. Hirakata, Y. Takeuchi, K. Shimizu, Y. Furushima, H. Ikeuchi, and G.P. Satô. Bull. Chem. Soc. Jpn. **62**, 709 (1989).
13. A. Endo, M. Watanabe, S. Hayashi, K. Shimizu, and G.P. Satô. Bull. Chem. Soc. Jpn. **51**, 800 (1978).
14. A. Endo. Bull. Chem. Soc. Jpn. **56**, 2733 (1983).
15. G.S. Patterson and R.H. Holm. Inorg. Chem. **11**, 2285 (1972).
16. J. Tang, K. Shimizu, and R.A. Osteryoung. Inorg. Chem. **31**, 2328 (1992).
17. K. Kobayashi, Y. Satsu, Y. Hoshino, S. Arai, K. Hatakeyama, A. Endo, K. Shimizu, and G.P. Satô. Bull. Chem. Soc. Jpn. **62**, 3252 (1989).
18. T. Kobayashi, Y. Nishina, K. Shimizu, and G.P. Satô. Chem. Lett. 1137 (1988).
19. Y. Kasahara, Y. Hoshino, K. Shimizu, and G.P. Satô. Chem. Lett. 381 (1990).
20. K. Oomura, D. Ooyama, Y. Satoh, N. Nagao, H. Nagao, F.S. Howell, and M. Mukaida. Inorg. Chim. Acta, **269**, 342 (1998).
21. I.R. Baird, S.J. Rettig, B.R. James, and K.A. Skov. Can J. Chem. **76**, 1379 (1998).
22. P.K.L. Chan, P.K.H. Chan, D.C. Frost, B.R. James, and K.A. Skov. Can. J. Chem. **66**, 117 (1988).
23. P.K.L. Chan, B.R. James, D.C. Frost, P.K.H. Chan, H.-L. Hu, and K.A. Skov. Can. J. Chem. **67**, 508 (1989).
24. (*a*) International tables for X-ray crystallography. Vol. IV. Kynoch Press, Birmingham, U.K. (present distributor Kluwer Academic Publishers. Boston, Mass. U.S.A.) 1974. pp. 99–102; (*b*) International tables for crystallography. Vol. C. Kluwer Academic Publishers, Boston, Mass. U.S.A. 1992. pp. 200–206.
25. J.F. Knifton. J. Org. Chem. **41**, 1200 (1976).
26. A.M.W. Cargill Thompson, D.A. Bardwell, J.C. Jeffery, L.H. Rees, and M.D. Ward. J. Chem. Soc. Dalton Trans. 721 (1997).
27. H.F. Holtzclow, Jr., and J.P. Collman. J. Am. Chem. Soc. **79**, 3318 (1957).
28. K. Nakamoto, Y. Morimoto, and A. Martell. J. Am. Chem. Soc. **83**, 4533 (1961).
29. O.M. Ni Dhubhghaill, W.R. Hagen, B.K. Keppler, K.-G. Lipponer, and P.J. Sadler. J. Chem. Soc. Dalton Trans. 3305 (1994).
30. C. Anderson and A.L. Beauchamp. Inorg. Chem. **34**, 6065 (1995).
31. M.J. Clarke, V.M. Bailey, P.E. Doan, C.D. Hiller, K.J. LaChance-Galang, H. Dhaghlian, S. Mandal, C.M. Bastos, and D. Lang. Inorg. Chem. **35**, 4896 (1996).
32. B.K. Das and A.R. Chakravarty. Inorg. Chem. **30**, 4978 (1991).
33. G.E. Rodgers. Introduction to coordination, solid state, and descriptive inorganic chemistry. McGraw–Hill, New York. 1994. p. 164.
34. C.C. Costain. J. Chem. Phys. **29**, 864 (1958).
35. H. Endres. *In* Comprehensive coordination chemistry. Vol. 2. *Edited by* G. Wilkinson, R.D. Gillard, and J.A. McCleverty. Pergamon Press, Oxford, U.K. 1987. p. 264.
36. B. Swanson, D.F. Shriver, and J.A. Ibers. Inorg. Chem. **8**, 2182 (1969).
37. H.C. Stynes and J.A. Ibers. Inorg. Chem. **10**, 2304 (1971).
38. W.F. DeGIovani and A. Deronzier. J. Chem. Soc. Chem. Commun. 1461 (1992).
39. I. Rapaport, L. Helm, A.E. Merbach, P. Bernhard, and A. Ludi. Inorg. Chem. **27**, 873 (1988).

© 1999 NRC Canada

Symmetry in double-diffusive convection

Brian Pettitt and Werner Danchura

Abstract: A theoretical treatment of the double-diffusive convection instability is presented, with a focus on the isothermal case of two solutes in a common solvent, initially forming a distinct interface. Linear stability analysis is used to determine the wave number of the marginal mode and symmetry properties of the corresponding fluid flow for realistic values of two control parameters: (*i*) the ratio of the diffusion coefficient of the solute in the lower solution to that in the upper solution (τ_d), and (*ii*) the ratio of the excess densities (relative to the solvent) of the upper to the lower solutions (τ_ρ). It is shown that the instability has two regimes: (*i*) $\tau_d^{-3/2} < \tau_\rho < \tau_d^{-1}$ in which diffusion precedes convection, and (*ii*) $\tau_d^{-1} < \tau_\rho < 1$ in which convection is immediate. The two regimes are separated by a point ($\tau_\rho = \tau_d^{-1}$) through which the wavelength diverges and the fluid velocity undergoes a continuous symmetry change. Above this point, columns of alternating up-and-down flow fade continuously into the solutions above and below the original interface. Below it, the flow within a column undergoes at least one reversal. The horizontal nodal plane associated with such a reversal should be observable.

Key words: double-diffusive convection, fluid instability, pattern formation, solutions.

Résumé : On présente un traitement théorique à l'instabilité de convection à double diffusion en mettant l'accent sur le cas isothermique de deux solutés dans un solvant commun qui forment initialement une interface distincte. On a utilisé l'analyse de stabilité linéaire pour déterminer le nombre d'onde du mode marginal et les propriétés de symétrie de l'écoulement du fluide correspondant pour des valeurs réalistes de deux paramètres de contrôle: (*i*) le rapport du coefficient de diffusion du soluté dans la solution inférieure par rapport à celui dans la solution supérieure (τ_d) et (*ii*) le rapport des excès de densités (par rapport au solvant) de la solution supérieure par rapport à la solution inférieure (τ_ρ). On a démontré que l'instabilité a deux régimes: (*i*) $\tau_d^{-3/2} < \tau_\rho < \tau_d^{-1}$ dans lequel la diffusion précède la convection et (*ii*) $\tau_d^{-1} < \tau_\rho < 1$ dans lequel la convection est immédiate. Les deux régimes sont séparés par un point ($\tau_\rho = \tau_d^{-1}$) à travers lequel la longueur d'onde diverge et la vitesse du fluide subit un changement continu de symétrie. Au-dessus de ce point, il se produit un déplacement vertical continu et alternant des colonnes au-dessus et en-dessous de l'interface originale. En-dessous de ce point, l'écoulement dans une colonne subit au moins une inversion. On devrait pouvoir observer le plan nodal horizontal associé avec cette inversion.

Mots clés : convection à double diffusion, instabilité fluide, patron de formation, solutions.

[Traduit par la Rédaction]

Introduction

An inhomogeneous solution containing two solutes, which is initially stable in the sense that its density decreases upward, can develop a convective flow pattern in regions where small vertical velocity disturbances are amplified by lateral diffusive fluxes. If an element of the fluid, suddenly displaced upward by such a disturbance, contains an excess of the solute with the larger diffusion constant, buoyancy is created in it by a net transport of molecules out. The neighboring element, displaced downward by the initial disturbance, is driven further by the net transport of molecules into it. Along with the analogous case of heat and one solute, this isothermal fluid instability is referred to as double-diffusive convection (1–3). Most work on this class of problems has involved heat transport, with model applications in oceanography (3, 4), geology and minerology (3, 5), and fluid mechanics (6). Diffusion/convection effects are important in the pattern formation produced by autocatalytic reactions (7) and some electrochemical reactions (8, 9), but there is little in the way of detailed theories coupling the hydrodynamics and chemical kinetics of processes as complicated as these.

In this paper we present a thorough linear stability analysis of double-diffusive hydrodynamics for two solutes evolving out of an initially discrete horizontal interface, which goes beyond the usual assumptions of linear concentration gradients, prescribed instability heights, and rigid boundary conditions. The presentation includes enough basic fluid mechanics to reveal the main features of the model and the approximations needed to make it tractable, in a way that emphasizes its general properties and leads to some new results. Part of this analysis is similar to that of Sartory (10), but it differs extensively in basic descriptive features (such as dimensionless groups), numerical methods, results, and interpretation. One of our objectives is to show that geometric features of this instability are suggestive of a rich variety

Received May 4, 1999.

This paper is dedicated to Professor Ted Schaefer in recognition of his outstanding contributions to Canadian chemistry.

B. Pettitt[1] and W. Danchura. Department of Chemistry, University of Winnipeg, Winnipeg, MB R3B 2E9, Canada.

[1]Author to whom correspondence may be addressed. Telephone: (204) 786-9732. Fax: (204) 775-2114. e-mail: pettitt@uwinnipeg.ca

© 1999 NRC Canada

of patterns (11, 12), even within the linearized hydrodynamic regime.

Double-diffusive hydrodynamics

The initial system is a solution with concentration c_l^0 of a solute (diffusion constant D_l) overlaid by a solution of a second solute with concentration c_u^0 (diffusion constant $D_u < D_l$) (10). The pure solvent (with density ρ_0 and kinematic viscosity ν_0) is the same in both layers, and the density of this system is assumed to be described by an equation-of-state that is linear in the solute concentrations:

$$[1] \qquad \rho(\vec{r},t) = \rho_0(1 + \beta_l c_l(\vec{r},t) + \beta_u c_u(\vec{r},t))$$

with constant coefficients $\beta_i = \rho_0^{-1}\partial\rho/\partial c_i$. Static stability of this state requires that the density of the lower layer be greater than that of the upper layer ($\rho_0\beta_l c_l^0 = \delta\rho_l^0 > \delta\rho_u^0 = \rho_0\beta_u c_u^0$). It is well known that aqueous solutions with distinctly different densities can be layered with sharp interfaces if care is taken to avoid turbulent mixing. The idealized initial state is a model for such systems. It is perhaps best visualized in terms of removal of a thin, horizontal membrane initially separating the two layers. For mathematical simplicity, the layers are regarded as infinitely thick and wide. In practical terms, this means that they must be thick enough to exceed the vertical range of an instability at its onset and extend horizontally on a scale much larger than the wavelength. For aqueous solutions, this is typically a few centimeters. Evolution out of this state is described by the concentrations

$$[2] \qquad c_i(\vec{r},t) = c_i^{\mathrm{d}}(\vec{r},t) + \delta c_i(\vec{r},t)$$

and the velocity field $\vec{v}(\vec{r},\, t)$, where c_i^{d} and δc_i are diffusive and convective contributions, respectively. The pressure in the fluid is similarly partitioned as

$$[3] \qquad p(\vec{r},t) = p^{\mathrm{d}}(\vec{r},t) + \delta p(\vec{r},t)$$

It is assumed that the reference state is described by simple independent diffusion of the solute molecules, such that a perturbation analysis of the δc_i's, $\vec{v}$, and δp is capable of revealing the simplest features of the instability.

If the initially sharp interface is the horizontal plane $z = 0$ (in a lab-fixed frame to which all subsequent equations apply), the diffusive parts are

$$[4] \qquad \begin{aligned} c_l^{\mathrm{d}}(\vec{r},t) &= \frac{1}{2}c_l^0 \ \ \mathrm{erfc}(z/\sqrt{4D_l t}) \\ c_u^{\mathrm{d}}(\vec{r},t) &= \frac{1}{2}c_u^0 \ \ \mathrm{erfc}(-z/\sqrt{4D_u t}) \end{aligned}$$

for this constant-volume process, well away from any vertical walls and assuming that there are always regions of the original solutions above and below the active region. The corresponding vertical gradients are

$$[5] \qquad \begin{aligned} \gamma_l(z,t) &= \frac{\partial c_l^{\mathrm{d}}}{\partial z} = -\frac{c_l^0}{h_l} \ \ \exp(-\pi z^2/h_l^2) \\ \gamma_u(z,t) &= \frac{\partial c_u^{\mathrm{d}}}{\partial z} = \frac{c_u^0}{h_u} \ \ \exp(-\pi z^2/h_u^2) \end{aligned}$$

The quantities $h_i = \sqrt{4\pi D_i t}$ are distances that represent the diffusive broadening of the concentration profiles of the two species during the time t.

Convection is assumed to arise out of this diffusive state with the appearance of a zone in the mixing layer within which the fluid becomes dynamically unstable by the mechanism described in the introduction. The relevant hydrodynamical equations (13) are the equation of continuity

$$[6] \qquad \frac{\partial\rho}{\partial t} + \nabla\cdot(\rho\vec{v}) = 0$$

the Navier–Stokes equation (for a spatially uniform shear viscosity, $\eta = \rho\nu$)

$$[7] \qquad \rho\left(\frac{\partial}{\partial t} + \vec{v}\cdot\nabla - \nu\nabla^2\right)\vec{v} = -\nabla p - g\rho\hat{z}$$

and the diffusion equations for solutes undergoing independent diffusion (14)

$$[8] \qquad \left(\frac{\partial}{\partial t} + \vec{v}\cdot\nabla - D_i\nabla^2\right)c_i = 0$$

g is the acceleration of gravity and $\hat{z}$ is a unit vector upward. A tractable model of double-diffusive convection is obtained using the incompressibility condition, $\nabla\cdot\vec{v} = 0$, rather than the full continuity equation, and by adopting the Boussinesq approximations (13) for the Navier–Stokes equation (i.e., using the solvent values for the density and the viscosity everywhere except in the gravitational force-density, $-g\rho\hat{z}$). The Navier–Stokes and diffusion equations then reduce to the following forms for the convective parts:

$$[9] \qquad \begin{aligned} &\left(\frac{\partial}{\partial t} + \vec{v}\cdot\nabla - \nu_0\nabla^2\right)\vec{v} = -\frac{1}{\rho_0}\nabla\delta p - g\hat{z}\sum_i \beta_i\delta c_i \\ &\left(\frac{\partial}{\partial t} + \vec{v}\cdot\nabla - D_i\nabla^2\right)\delta c_i = -\gamma_i v_z \end{aligned}$$

where v_z is the vertical component of the local velocity. These approximate equations are valid for more than two solutes and for other initial states if the concentration gradients are adapted accordingly.

Linear stability analysis

For cases where the velocity field grows from an infinitesimal disturbance, there is a linear regime in which the operator $(\vec{v}\cdot\nabla)$ can be ignored in the description of the onset of an instability. With this assumption, and some lengthy but standard vector analysis to remove the pressure (13), the previous equations reduce to

$$[10] \qquad \begin{aligned} &\left(\frac{\partial}{\partial t} - \nu_0\nabla^2\right)\nabla^2\vec{v} = -g\sum_i \beta_i\left(\hat{z}\nabla^2\delta c_i - \frac{\partial}{\partial z}\nabla\delta c_i\right) \\ &\left(\frac{\partial}{\partial t} - D_i\nabla^2\right)\delta c_i = -\gamma_i v_z \end{aligned}$$

with the form

© 1999 NRC Canada

$$[11]\quad \left(\frac{\partial}{\partial t}-\nu_0\nabla^2\right)\nabla^2 v_z = -g\sum_i \beta_i\left(\frac{\partial^2}{\partial x^2}+\frac{\partial^2}{\partial y^2}\right)\delta c_i$$

for the vertical component being of particular importance. These equations are fairly general, in that they apply to cases with physical boundaries (free or rigid for the velocity and no flux for the solutes) as well as the infinitely extended model, provided the amplitudes are small enough to be described by linearized perturbation analysis.

Diffusion is assumed to progress in the time interval $0 \le t \le t_d$, during which $\vec{v} = 0$ and $\delta c_i = 0$ and after which growth of a mode in the disturbance

$$[12]\quad \begin{aligned} v_z &= W(z)\,\sin(k_x x)\,\sin(k_y y)\,e^{\zeta(t-t_d)} \\ v_x &= \frac{1}{k^2}\frac{\partial^2 v_z}{\partial x \partial z} \\ v_y &= \frac{1}{k^2}\frac{\partial^2 v_z}{\partial y \partial z} \\ \delta c_i &= \Theta_i(z)\,\sin(k_x x)\,\sin(k_y y)\,e^{\zeta(t-t_d)} \end{aligned}$$

with $k_x^2 + k_y^2 = k^2$, occurs at a rate ζ for an interval during which the concentration gradients are frozen at $\gamma_i(z) \equiv \gamma_i(z, t_d)$. With the definition

$$[13]\quad d_k^2 = \frac{d^2}{dz^2} - k^2$$

the equations reduce to the forms

$$[14]\quad \begin{aligned} (d_k^2 - \zeta/\nu_0)d_k^2 W(z) &= -\frac{gk^2}{\nu_0}\sum_i \beta_i \Theta_i(z) \\ (d_k^2 - \zeta/D_i)\Theta_i(z) &= \frac{\gamma_i(z)}{D_i}W(z) \end{aligned}$$

After additional manipulations, this set can be summarized in the single form (written for the velocity, but common to all three quantities)

$$[15]\quad \begin{aligned} &(d_k^2 - \zeta/D_l)(d_k^2 - \zeta/D_u)(d_k^2 - \zeta/\nu_0)d_k^2 W(z) \\ &= -k^2 R(z)(d_k^2 - \zeta/D(z))W(z) - 2k^2 R'(z)W'(z) - k^2 R''(z)W(z) \end{aligned}$$

where the primes denote derivatives in z, and the new quantities are

$$[16]\quad R(z) = \frac{g}{\nu_0}\left(\frac{\beta_l \gamma_l(z)}{D_l} + \frac{\beta_u \gamma_u(z)}{D_u}\right)$$

and

$$[17]\quad D(z) = \frac{\beta_l D_u \gamma_l(z) + \beta_u D_l \gamma_u(z)}{\beta_l \gamma_l(z) + \beta_u \gamma_u(z)}$$

$D(z)$ is undefined where the concentration gradients vanish (notably for $z >> h_l$), but no difficulty results from this property because $R(z)$ and $R(z)/D(z)$ vanish in this limit, as do $R'(z)$ and $R''(z)$. Thus, $W(z)$ and $\Theta_i(z)$ have asymptotic forms that are, in general, linear combinations of $\exp(\pm kz)$, $\exp\left(\pm\sqrt{k^2 + \zeta/\nu_0 z}\right)$ $\exp\left(\pm\sqrt{k^2 + \zeta/D_u z}\right)$, and $\exp\left(\pm\sqrt{k^2 + \zeta/D_l z}\right)$.

A convective mode grows out of a disturbance if $\zeta > 0$, and it is damped out if $\zeta < 0$. The stationary states with $\zeta = 0$ thus represent the margin between stability and instability, where this linear model of the process is most reasonable. For these marginal states, eqs. [14] simplify to

$$[18]\quad \begin{aligned} \left(\frac{d^2}{dz^2} - k^2\right)^2 W(z) &= -\frac{gk^2}{\nu_0}\sum_i \beta_i \Theta_i(z) \\ \left(\frac{d^2}{dz^2} - k^2\right)\Theta_i(z) &= \frac{\gamma_i(z)}{D_i}W(z) \end{aligned}$$

with the solutions behaving as $\exp(-k|z|)$ as $z \to \pm\infty$. These equations and boundary conditions are the foundation of the analysis and calculations on the characteristic properties of double-diffusive convection presented in the rest of this work. Most of the literature on this problem is concerned with the analogous process in water layers driven by *linear* thermal and salt gradients, with prescribed boundary conditions at the top and bottom of a distinct layer.

Dimensional analysis and interpretation

It is appropriate to use $h_l = \sqrt{4\pi D_l t_d}$ as a unit of distance, this being a measure of the extent of diffusion by the more mobile species up to time t_d, and leading to dimensionless distances $s = z/h_l$ and wave numbers $\kappa = kh_l$. It is convenient to define the ratio of the diffusion constants $\tau_d = D_l/D_u > 1$ and the ratio of the initial excess densities $\tau_\rho = \delta\rho_u^0/\delta\rho_l^0 < 1$ (two parameters open to experimental control), and the dimensionless number

$$[19]\quad R = \frac{g\delta\rho_l^0 h_l^3}{\nu_0 \rho_0 D_l} \propto t_d^{3/2}$$

The last quantity is analogous to the Rayleigh number, with the crucial difference that, unlike the case of a fluid layer with a given height (heated from below), there are no distinct horizontal boundaries. In terms of these quantities, eqs. [18] for the marginal states become

$$[20]\quad \begin{aligned} \left\{\frac{d^2}{ds^2} - \kappa^2\right\}^2 w(s) &= -R\kappa^2[\theta_l(s) + \tau_\rho \theta_u(s)] \\ \left\{\frac{d^2}{ds^2} - \kappa^2\right\}\theta_l(s) &= -\exp(-\pi s^2)\,w(s) \\ \left\{\frac{d^2}{ds^2} - \kappa^2\right\}\theta_u(s) &= \tau_d^{3/2}\exp(-\pi\tau_d s^2)\,w(s) \end{aligned}$$

where $w = W \cdot h_l/D_l$, $\theta_l = \Theta_l/c_l^0$, and $\theta_u = \Theta_u/c_u^0$ are dimensionless velocity and convective concentration profiles behaving as $\exp(-\kappa|s|)$ as $s \to \pm\infty$.

© 1999 NRC Canada

The distance $h_0 = (\nu_0 \rho_0 D_l / g \delta \rho_l^0)^{1/3}$ is characteristic of the initial state of the lower solution, and it is related to h_l by $R = (h_l/h_0)^3$. Thus, $z_s = R^{1/3}s$ and $k_s = R^{-1/3}\kappa$ are positions and wave numbers in units of h_0 and h_0^{-1}, respectively. These are natural units for comparing the marginal states of systems with the same lower solution, especially those with different concentrations of the solute in the upper layer.

These considerations indicate that the (s, κ) form of the equations is suitable for solving the problem, but interpretation of the results (especially those to do with the geometry of the flow) is more appropriate in terms of the (z_s, k_s) variables. The equations, with the appropriate boundary conditions, represent a transcendental relationship between κ and R. That is, the equations can be solved for R with varying values of κ, the lowest positive value of R permitting such a solution corresponding to the time at which this mode becomes unstable. The minimum such value of R (corresponding to the shortest evolution under pure diffusion) identifies the mode of convection that first grows out of the diffusive state. The initial state is inherently unstable with respect to convection if the limit $\kappa \to 0$ gives $R \to 0$ but a well-defined value of $k_s = \kappa/R^{1/3}$. In this manner, the behavior of the marginal states can be mapped for varying values of the excess-density ratio (τ_ρ) and the diffusion-constant ratio (τ_d).

Symmetry and boundary conditions

Only the relative amplitudes of $w(s)$, $\theta_l(s)$, and $\theta_u(s)$ are determined by their equations (eq. [20]), which constitute a linear, non-autonomous set of (4 + 2 + 2)th = 8th-order differential equations with an eigenvalue (R). The lowest eigenvalue is not necessarily positive, but the lowest positive eigenvalue necessarily corresponds to the marginal state (because of the relationship between R and h_l). Because these linearized equations do not determine the amplitudes or the growth rates, they only describe the shape and the range of the vertical flow initiated by passage through a marginal state. The corresponding wave vector, through the relation $k^2 = k_x^2 + k_y^2$ and the associated rotational symmetry around the vertical axis, gives an infinitely degenerate set of flow patterns in the horizontal plane (13).

That s appears in the operators of these equations as s^2 indicates that the solutions divide into even and odd classes (i.e., $w(-s) = \pm w(s)$ and similarly for the concentrations). It is convenient to scale the amplitudes for the even class with $w(0) = 1$. Other symmetry properties of the system are revealed by combining eqs. [20] into the single equation

$$[21] \quad \left\{\frac{d^2}{ds^2} - \kappa^2\right\}^3 w(s) = R\kappa^2 \{\exp(-\pi s^2) - \tau_\rho \tau_d^{3/2} \exp(-\pi \tau_d s^2)\} w(s)$$

For even $w(s)$ the left-hand-side is negative at $s = 0$, and $R > 0$ therefore requires $1 - \tau_\rho \tau_d^{3/2} < 0$ for the right-hand-side to be negative. The resulting condition, $\tau_\rho > \tau_d^{-3/2}$, for convection to be possible was derived heuristically by Huppert and Manins (15), who gave experimental evidence for its validity. It was shown to be obeyed in a variety of aqueous solutions by Huppert and Hallworth (16), who also noted an equivalent form in the work of Sartory (10). If both solutes are strong electrolytes, the effects of off-diagonal terms in the diffusion matrix are important (17).

Multiplication of eq. [21] by $w(s)$, and integration by parts gives the relation

$$[22] \quad -\int_0^\infty \{[w'''(s)]^2 + 3\kappa^2[w''(s)]^2 + 3\kappa^4[w'(s)]^2 + \kappa^6[w(s)]^2\} ds = -R\kappa^2 \int_0^\infty \{\mathrm{erf}(\sqrt{\pi} s) - \tau_\rho \tau_d \, \mathrm{erf}(\sqrt{\pi \tau_d} s)\} w(s) w'(s) ds$$

thus imposing the symmetry condition (for positive R)

$$[23] \quad \int_0^\infty \{\mathrm{erf}(\sqrt{\pi} s) - \tau_\rho \tau_d \, \mathrm{erf}(\sqrt{\pi \tau_d} s)\} \, w(s) w'(s) ds > 0$$

on the solutions to this problem. For a function with the symmetry properties $0 \le w(z) \le 1$ and $w'(z) \le 0$, and no other restrictions, this condition is satisfied if the factor within the brackets of the integrand is negative on the entire range. This being true only if $\tau_\rho > \tau_d^{-1}$, the point $\tau_\rho = \tau_d^{-1}$ is associated with a change in the basic symmetry of the vertical velocity profile.

There is an alternative to imposing the boundary conditions in the asymptotic region, where all three functions decay exponentially. Where s is large enough for the right-hand sides of eqs. [20] to be negligible, the functions have the forms (for $s >> 0$)

$$[24] \quad \begin{aligned} \theta_l(s) &= A_l \exp(-\kappa s) \\ \theta_u(s) &= A_u \exp(-\kappa s) \\ w(s) &= (w_0 + w_1 s + w_2 s^2) \exp(-\kappa s) \\ &= -\frac{R}{4\kappa}[\theta_l(s) + \tau_\rho \theta_u(s)] - \frac{2}{\kappa} w'(s) - \frac{1}{\kappa^2} w''(s) \end{aligned}$$

With these conditions, it must be decided where s is large enough for them to be applicable. With the purely exponential forms, it must be decided where s is effectively infinite. The results must be the same for these two approaches, a feature that can be used for checking calculations.

Computational method

The set of eqs. [20] was converted to the equivalent set of eight first-order equations and the supplementary condition $dR/ds = 0$ on the eigenvalue. The solutions were divided into even ($w(-s) = w(s)$) and odd ($w(-s) = -w(s)$) classes and solved for $s \ge 0$, subject to the following sets of nine conditions within each class.

Even (at $s = 0$)	Odd (at $s = 0$)	Even and odd (as $s \to \infty$)
$w = 1$	$w = 0$	$w' + \kappa w = 0$
$w' = 0$	$w' = 1$	$w'' - \kappa^2 w = 0$
$w''' = 0$	$w'' = 0$	$\theta_l' + \kappa \theta_l = 0$
$\theta_l' = 0$	$\theta_l = 0$	$\theta_u' + \kappa \theta_u = 0$
$\theta_u' = 0$	$\theta_u = 0$	

The last two conditions for $s \to \infty$ also apply to the alternate set for s large, but the first two are replaced with

© 1999 NRC Canada

Fig. 1. Characteristic dependence of the eigenvalue (R) on the wave number (k_s) above (*a*) and below (*b*) the divergence for $\tau_d = 3.0$. The mode of marginal stability has the limiting wave number $k_m = 0.4543$ for $\tau_\rho = 0.5$ in (*a*) and the value at the minimum, $k_m = 0.1390$, for $\tau_\rho = 0.3$ in (*b*). The units are explained in the text.

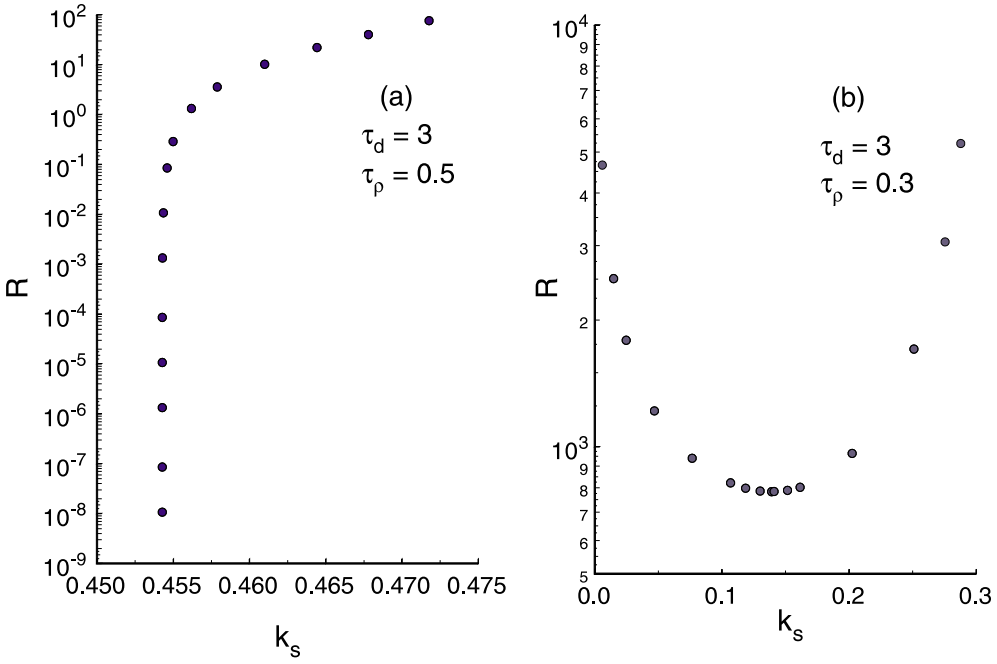

$$w + \frac{R}{4\kappa}[\theta_l + \tau_\rho \theta_u] + \frac{2}{\kappa} w' + \frac{1}{\kappa^2} w'' = 0$$

$$w' - \frac{R}{4}[\theta_l + \tau_\rho \theta_u] + \frac{2}{\kappa} w'' + \frac{1}{\kappa^2} w''' = 0$$

The equations were solved with a shooting method (18), programmed in such a way as to allow extensive control of the input and inspection of the results. Fourth-order Runge–Kutta integration with adaptive grid-spacing projected the initial values and guesses at $s = 0$ (for either symmetry class) to the long-range region (where both types of boundary conditions were applied). A Newton–Raphson procedure refined the initial guesses, and iterative solutions were sought (in double precision) such that the error in the eigenvalue, R, was insensitive to the initial guesses and the limit of the integration to within 1 ppm. The corresponding velocity profile, $w(s)$, was inspected graphically. Extensive calculations showed that the same results were obtained with both types of boundary conditions, but the exponential forms were slightly easier to implement. In all cases studied, the lowest non-negative eigenvalue appeared in the class of even functions.

Results and discussion

We treated the excess-density ratio, τ_ρ, as a control parameter for a given value of the ratio of the diffusion constants, τ_d, and looked for the lowest positive eigenvalue (R) as a function of k_s. Two characteristic behaviors were exhibited, as illustrated in Fig. 1 for $\tau_d = 3$, which corresponds approximately to aqueous solutions of sucrose over NaCl (19). For $\tau_\rho = 0.5$ (Fig. 1*a*), k_s has the limiting value $k_m = 0.4543$ for $R \rightarrow 0$. As the figure shows, for $R << 1$ the disturbance with this wave number is a well-defined state, which we have interpreted to mean that the initial interface is inherently unstable at k_m. The corresponding vertical velocity profile, illustrated in Fig. 2, is symmetric and nodeless. For $\tau_\rho = 0.3$, states with this symmetry or a single node at $z_s = 0$ exist only for $R < 0$. The dependence of R on k_s for the next state is shown in Fig. 1*b*, and the corresponding vertical velocity profile is included in Fig. 2. The minimum in Fig. 1*b* is at $R_m = 783.103$ for the corresponding wave number $k_m = 0.1390$. The initially stable interface evolves by diffusion for the corresponding minimum time before the onset of convection through marginal Fourier components with this wave number.

The spatial symmetries of these two representative marginal states are further illustrated in Fig. 3 so as to show the relationships of their vertical ranges to their lateral periodicities. For this figure, the cellular fluid flow was assumed to have a square planform ($k_x = k_y = k/\sqrt{2}$), which is the simplest approximation to the irregular forms observed for sucrose–NaCl solutions (21). The contours connect points with equal values of the vertical velocity, $w(z)\ \sin(k_x x)\ \sin(k_y y)$, across the middle of a cell ($k_x x = \pi/2$). Whereas the disturbance for $\tau_\rho = 0.5$ fades monotonically into the solutions above and below the interfacial zone of cellular up and down flow, that for $\tau_\rho = 0.3$ has a prominent central zone with distinct counter-rotating zones above and below it that fade into the solutions.

The unit of distance in these figures is h_0. For example, in dilute aqueous NaCl ($D_l \approx 1.5 \times 10^{-9}$ m^2 s^{-1} and $\nu_0 \approx 1 \times 10^{-6}$ m^2 s^{-1}) with $\delta\rho_l^0/\rho_0 = 0.02$ (i.e., 0.48 M), this has the value $h_0 = 20\ \mu$m. The wavelengths exhibited in Fig. 3 correspond to 0.4 mm ($\tau_\rho = 0.5$) and 1.3 mm ($\tau_\rho = 0.3$) for 0.065 and 0.045 M sucrose in the upper layer, respectively (20). The former case is expected to be immediately unstable with respect to regular columns of alternating up-and-down flow,

© 1999 NRC Canada

Fig. 2. Vertical velocity profiles above ($\tau_\rho = 0.5$) and below ($\tau_\rho = 0.3$) the divergence for $\tau_d = 3$, corresponding to the marginal modes defined in Fig. 1. The curves represent the relative speed of the fluid along a vertical line at the center of the upward-flowing half of a cell.

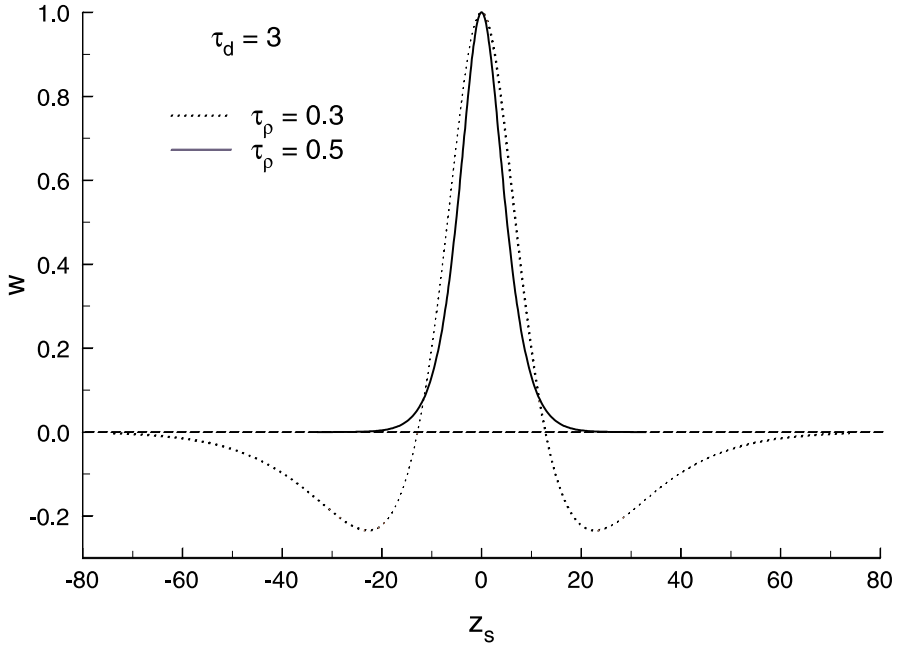

Fig. 3. Contour plots of the vertical component of the fluid velocity in vertical cross-sections of square-planform cells for the modes shown in Figs. 1 and 2. The horizontal and vertical distance scales are the same in each figure. The arrows indicate the relative magnitude and the direction of the flow, and the contours illustrate the symmetry difference above (*a*) and below (*b*) the divergence.

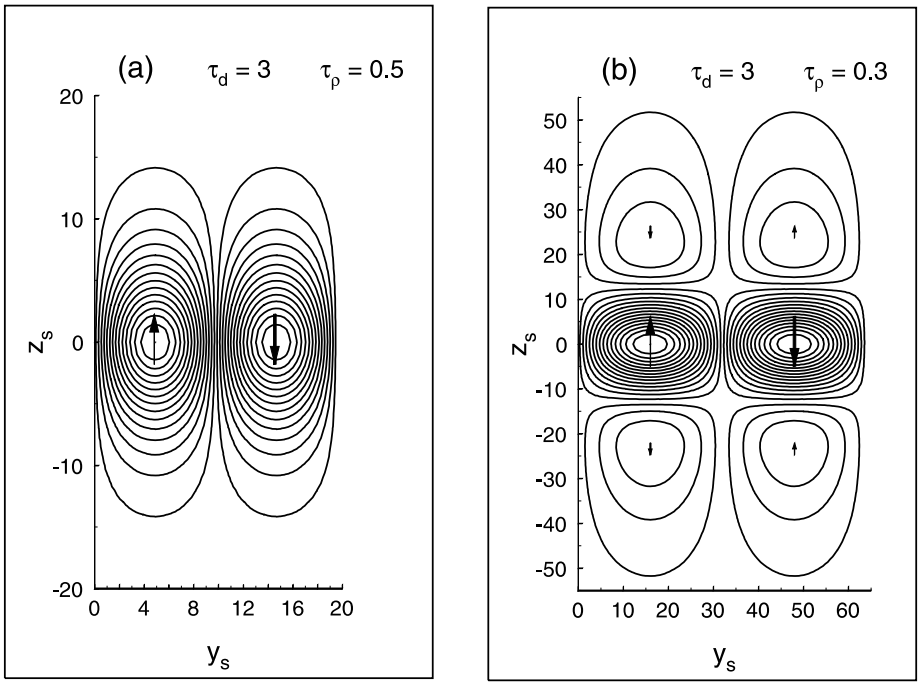

and the latter to evolve under diffusion for 2 s before an instability appears with weaker counter-rotating components capping and underlying such columns.

These examples also serve to illustrate that the layers do not have to be very deep for the neglect of upper and lower surfaces to be valid. While the length and time scales are only approximate, the distinctly different symmetry signatures of these two cases are definite predictions of the linear analysis. We are not aware of any clear experimental evidence for this symmetry difference, but the dominant milli-

© 1999 NRC Canada

Fig. 4. The wave number of the marginal mode (k_m) as a function of excess-density ratio (τ_ρ) for diffusion-constant ratios $\tau_d = 3.0$ and 1.25. The circles are results of numerical calculations, the lines represent the 1/3 power law of eq. [26], and the squares are the threshold values $\tau_\rho = \tau_d^{-3/2}$. The divergent points appear at $\tau_\rho = \tau_d^{-1}$.

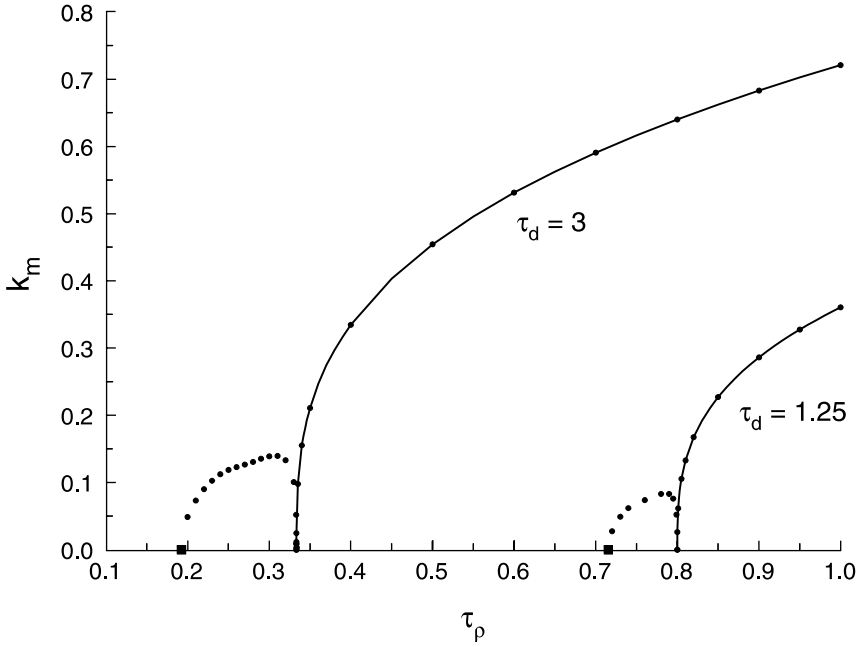

Fig. 5. Wave numbers (k_m) and eigenvalues (R_m) of marginal states as functions of excess-density ratio (τ_ρ) for diffusion-constant ratio $\tau_d = 3.0$. The wave number graph is expanded from Fig. 4.

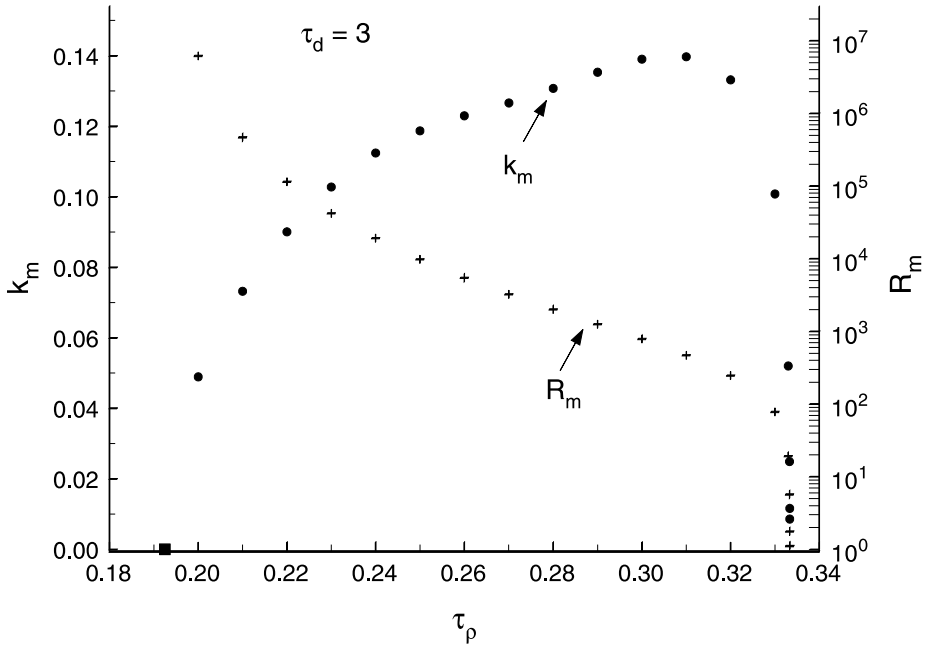

meter wavelength scale for this system is exhibited in the work of Shirtcliffe and Turner (21) on solutions with large τ_ρ (immediate convection).

Figure 4 shows the behavior of k_m as a function of τ_ρ for $\tau_d = 3$ and $\tau_d = 1.25$, and Fig. 5 expands part of the $\tau_d = 3$ data so as to observe the corresponding behavior of R_m. These graphs illustrate the main properties of the marginal states, and they are best interpreted by considering a sequence of sucrose solutions with increasing concentrations over samples from a stock solution of NaCl. For very low sucrose concentrations, such that $\tau_\rho < \tau_d^{-3/2} \approx 0.19$, diffusion alone drives the system to equilibrium. For sucrose concentrations such that the excess density is in the range $\tau_d^{-3/2} < \tau_\rho < \tau_d^{-1}$, a decreasing interval of diffusion precedes the onset of marginal states of convection with wave numbers approaching zero at the two ends of the range. As τ_ρ increases in the range $\tau_d^{-1} < \tau_\rho < 1$, convection is immediate in a marginal mode with increasing wave number (decreasing wave-

© 1999 NRC Canada

length and vertical range) and the symmetry of Fig. 3(*a*). Velocity profiles for $\tau_\rho \to \tau_d^{-1}$ (from below) exhibit a continuous change of symmetry from that of Fig. 3(*b*) to that of Fig. 3(*a*).

If τ_ρ is regarded as a control parameter for these two-layer initial states, then our calculations indicate that $\tau_\rho = \tau_d^{-1}$ is a unique point in their stability, through which the wavelength of the lateral periodicity ($2\pi/k_m$) diverges. Analyzed with the equation

$$[25] \qquad k_m = A_\pm \left| \tau_\rho - \tau_d^{-1} \right|^{a_\pm}$$

near the two sides of this point, our data for both values of τ_d in Fig. 4 gave an exponent $a_+ = 1/3$ to within 2 ppm. The fit is described by

$$[26] \qquad k_m^3 = \frac{3}{16}(\tau_d \tau_\rho - 1)$$

with the error in the amplitude also within 2 ppm, over the entire range $\tau_d^{-1} < \tau_\rho < 1$. The behavior on the other side of this point is much more complicated, giving a limiting value of $a_- \approx 0.332$ from the $\tau_d = 3$ data.

The range of excess densities within which diffusion precedes convection, $\tau_d^{-1} - \tau_d^{-3/2}$, has a maximum value of 4/27, which occurs for $\tau_d = 2.25$. For very large values of τ_d, this range is very small and the initial state is inherently unstable for nearly all values of τ_ρ. As $\tau_\rho \to \tau_d^{-3/2}$ (from above), the eigenvalue (R_m) increases rapidly (Fig. 5), and more nodes appear in $w(z)$ (not shown). For example, $R_m = 6.1875 \times 10^6$ for $\tau_d = 3$ and $\tau_\rho = 0.2$, corresponding to a diffusion time of 12 min for the system ($\delta\rho_1^0/\rho_0 = 0.02$) that takes only 2 s at $\tau_\rho = 0.3$. The wavelength of the corresponding square flow field is 3.6 mm, and the vertical profile exhibits a dominant central zone with a sequence of progressively weaker oscillations (with four nodes) above and below it before decaying exponentially. The height of the central zone, defined as the distance between the first nodes above and below $z = 0$ is 1. 7 mm, and the fluid velocity outside this zone is everywhere less than 3% of its maximum at $z = 0$. These small amplitude oscillations and the associated large eigenvalues make it difficult to calculate the marginal states in this region, just above the threshold for double-diffusive convection.

The position of this threshold ($\tau_\rho = \tau_d^{-3/2}$) was shown to arise from a symmetry condition, and the detailed calculations (illustrated in Figs. 4 and 5) indicate that the wavelength of the instability and the diffusion time decrease rapidly on passing through it. The point $\tau_\rho = \tau_d^{-1}$ was shown to be associated with a symmetry change in the vertical velocity profile and the detailed calculations reveal this to be a point around which the system is inherently unstable with respect to long-wavelength disturbances. Although the initial state of a perfectly sharp interface is artificial, the limiting behavior of k_m (Fig. 1*a*) shows that this feature is not responsible for the divergence. The diffusive concentration profiles for any $t_d > 0$ (however small) evolving out of this initially sharp state are the same as if the initial state was any one in the earlier time-course of this evolution. The absence of any containing boundaries for the fluid is implicated in the divergence only to the extent that they must be well beyond the wavelength and vertical range of the marginal disturbance. Within the approximations of linear stability analysis, this behavior is an inherent feature of this system of two solutes in a common solvent. There must be a critical matching of the initial diffusive fluxes, which tend to overturn the stable density gradient, for long-wavelength disturbances to be released by the viscous damping of the solution.

The most interesting result of this work is the prediction of a distinct symmetry change in the pattern of fluid flow across the point at $\tau_\rho = \tau_d^{-1}$. Above this point, alternating columns of up-and-down flow fade montonically away from the original interface. Below it, the columns contain more complex patterns, the simplest being a single reversal in the sense of the flow above and below a prominant central zone. These counter-rotating components of the columns are strongest for the short-wavelength instabilities of this type. The horizontal nodal planes of these reversals should be observable in the refractive index gradients of aqueous layers of sugar over salt, and other systems.

The theory outlined above provides a coherent, approximate scheme for calculating the effects of viscosity, densities, and diffusion coefficients on pattern formation by double-diffusive convection. It is reasonable to expect that patterns set by passage through marginal states will be preserved to some extent in growing modes (11). Dynamical nonlinearities, nonlinear equations-of-state, concentration-dependence of viscosity and diffusion coefficients, more general initial states, and finite boundaries are expected to complicate the observable features of such patterns, perhaps leading to secondary instabilities similar to those of Rayleigh–Bénard convection (13, 22–24). The general problem of pattern formation by multicomponent chemical and thermal fluxes coupled by diffusion and chemical reactions, a central one in several sciences (12), is usefully approached through simplified models in which precise calculations can be made.

Acknowledgments

We are very pleased to dedicate this paper to our friend and teacher, Ted Schaefer.

References

1. J.S. Turner. Ann. Rev. Fluid Mech. **17**, 11 (1985).
2. P.L. Vitagliano, L. Ambrosone, and V. Vitagliano. J. Phys. Chem. **96**, 1431 (1992).
3. A. Brandt and H.J.S. Fernando. (*Editors*). Double-diffusive convection. American Geophysical Union (Geophysical Monograph 94), Washington. 1995.
4. R.W. Schmitt. Ann. Rev. Fluid Mech. **26**, 255 (1994).
5. O.M. Phillips. Flow and reactions in permeable rocks. Cambridge University Press, New York. 1991.
6. J. Tanny, C.C. Chen, and C.F. Chen. J. Fluid Mech. **303**, 1 (1995).
7. P.K. Maini, K.J. Painter, and H.N.P. Chau. J. Chem. Soc. Faraday Trans. **93**, 3601 (1997).
8. S. Nakabayashi, M. Yanagida, and K. Uosaki. J. Phys. Chem. **100**, 714 (1996).
9. J.A. Pojman, A. Komlósi, and I.P. Nagy. J. Phys. Chem. **100**, 16 209 (1996).
10. W.K. Sartory. Biopolymers, **7**, 251 (1969).

© 1999 NRC Canada

11. M.C. Cross and P.C. Hohenberg. Rev. Mod. Phys. **65**, 851 (1993).
12. C. Bowman and A.C. Newell. Rev. Mod. Phys. **70**, 289 (1998).
13. S. Chandrasekhar. Hydrodynamic and hydromagnetic stability. Oxford University Press, London. 1962.
14. E.L. Cussler. Diffusion: mass transfer in fluid systems. 2nd ed. Cambridge University Press, Cambridge. 1997.
15. H.E. Huppert and P.C. Manins. Deep-Sea Res. **20**, 315 (1973).
16. H.E. Huppert and M.A. Hallworth. J. Phys. Chem. **88**, 2902 (1984).
17. D.G. Miller and V. Vitagliano. J. Phys. Chem. **90**, 1706 (1986).
18. W.H. Press, S.A. Teukolsky, W.T. Vettering, and B.P. Flannery. Numerical recipes in fortran. 2nd ed. Cambridge University Press, New York. 1992.
19. J.A. Rard, J.G. Albright, D.G. Miller, and M.E. Zeidler. J. Chem. Soc. Faraday Trans. **92**, 4187 (1996).
20. R.C. Weast (*Editor*). CRC handbook of chemistry and physics. 55th ed. CRC Press, Cleveland. 1974.
21. T.G.L. Shirtcliffe and J.S. Turner. J. Fluid Mech. **41**, 707 (1970).
22. E.L. Koschmieder. Bénard cells and taylor vortices. Cambridge University Press, Cambridge. 1993.
23. M. Assenheimer and V. Steinberg. Phys. Rev. Lett. **76**, 756 (1996).
24. A. La Porta and C.M. Surko. Phys. Rev. Lett. **80**, 3759 (1998).

© 1999 NRC Canada

Collagen remodeling in the extracellular matrix of the cardiomyopathic Syrian hamster heart as assessed by FTIR attenuated total reflectance spectroscopy

Pamela S. Bromberg, Kathleen M. Gough, and Ian M.C. Dixon

Abstract: Collagen type I and III deposition in the cardiac extracellular matrix contributes significantly to myocardial dysfunction. Diffuse and focal fibrosis is believed to accompany human congestive cardiomyopathy (CCM) associated with congestive heart failure (CHF). The left ventricle collagen remodeling that occurs in the hamster model of CCM is marked by left ventricle fibrosis, hypertrophy and dilation, proceeded by CHF post 150 days of age. The objectives of our study were to (*i*) evaluate changes in collagen deposition in the right (RV) and left (LV) ventricular tissue of cardiomyopathic (CMP) and control (CON) myocardium using FTIR ATR spectroscopy, (*ii*) classify the normal and diseased heart tissue using linear discriminant analysis (LDA) aided by a genetic algorithm (GA) selection of spectroscopically diagnostic regions in the mid-IR region, (*iii*) rationalize the spectroscopic differences between left/right ventricle tissue as well as CON/CMP tissue according to the pathophysiology documented for the UM-X7.1 strain of CMP hamsters. The presence of collagen in the tissue was confirmed spectroscopically by observation of the collagen IR fingerprint in the 1000–1800 cm^{-1} region. Difference spectroscopy was utilized to substantiate which tissue under comparison exhibited pronounced collagen content. Multivariate analysis (LDA) was carried out on user-selected spectral subregions and compared to class separation based on spectral subregions chosen nonsubjectively by a GA. Our study confirmed that the animals experienced LV collagen remodeling denoted by focal rather than diffuse fibrosis. In addition, RV collagen remodeling, denoted by decreased RV collagen content, appeared to accompany the increased LV collagen deposition found for the CMP animals.

Key words: FTIR spectroscopy, collagen, cardiomyopathy, genetic algorithm, linear discriminant analysis.

Résumé : Les dépôts de collagènes de type I et III dans la matrice cardiaque extracellulaire apporte une contribution importante au dysfonctionnement du myocarde. On croit généralement que la fibrose diffuse et focale accompagne la cardiomyopathie humaine congestive (CMC) associée à l'insuffisance cardiaque globale (ICG). Le remodelage du collagène du ventricule gauche qui se produit lors d'une CMC dans un hamster servant de modèle est caractérisé par une fibrose, une hypertrophie et une dilatation du ventricule gauche qui est suivi d'une ICG pour les sujets de plus de 150 jours. Les objectifs de notre étude étaient (*i*) d'évaluer les changements dans les dépôts de collagène dans les tissus des ventricules gauche (VG) et droit (VD) de myocardes cardiomyophatique (CMP) et de contrôle (CON) à l'aide de la spectroscopie « ATR FTIR », (*ii*) de classifier les tissus cardiaques normaux et malades en faisant appel à une analyse discriminante linéaire (ADL) s'appuyant sur une sélection à algorithme génétique (AG) de régions de l'IR moyen pouvant servir de diagnostique spectroscopique, (*iii*) de rationaliser les différences spectroscopiques entre les tissus des ventricules gauche et droit ainsi que entre les tissus CON et CMP suivant les pathophysiologies reconnues pour la souche UM-X7.1 de hamsters CMP. On a pu confirmer spectroscopiquement la présence de collagène dans les tissus par l'observation des empreintes digitales du collagène dans la région 1000–1800 cm^{-1} de l'IR. On a utilisé la spectroscopie différentielle pour établir quel tissu comportait la quantité la plus élevée de collagène. On a effectué une analyse discriminante linéaire à plusieurs variables sur des sous régions spectrales choisies par l'utilisateur et on l'a comparée à une séparation de classe effectuée sur la base de sous régions spectrales choisies de façon non subjective par un AG. Notre étude confirme que les animaux subissent un remodelage du collagène du VG caractérisé par une fibrose focale plutôt que diffuse. De plus, il semble que le remodelage du collagène du VD, caractérisé par une diminution dans la teneur en collagène dans le VD, accompagne l'augmentation du dépôt de collagène dans le VG qui a été observée avec les animaux CMP.

Received March 22, 1999.

This paper is dedicated to Professor Ted Schaefer in recognition of his outstanding contributions to Canadian chemistry.

P.S. Bromberg and K.M. Gough.[1] Department of Chemistry, University of Manitoba, Winnipeg, MB R3T 2N2, Canada.
I.M.C. Dixon. Institute of Cardiovascular Sciences, St. Boniface General Hospital Research Centre, University of Manitoba, Winnipeg, MB R2H 2A6, Canada.

[1]Author to whom correspondence may be addressed. Telephone: (204) 474-6262. Fax: (204) 474-7608.
e-mail: kmgough@ms.umanitoba.ca

© 1999 NRC Canada

Mots clés : spectroscopie IR à transformation de Fourier, collagène, cardiomyopathie, algorithme génétique, analyse discriminante linéaire.

[Traduit par la Rédaction]

Introduction

Cardiomyopathy has an ill-defined etiology and a clinical treatment strategy has yet to be clearly defined. Several cardiomyopathies are inheritable or induced by alcohol toxicity, malnutrition or viral infection, however, idiopathic congestive cardiomyopathy (CCM), classified as either hypertrophic or dilated cardiomyopathy, is of unknown etiology in humans (1). The incidence of CCM has been reported to be 5–8 cases/100 000 population annually with a 5 year mortality of nearly half of those afflicted (2). CCM is typically diagnosed by the presence of dilation and systolic dysfunction in the left ventricle when congenital, coronary, valvular, hypertensive or pericardial heart disease is not a predisposing factor (1). Essentially, CCM leads to left ventricle dysfunction and decreases the heart's efficiency to eject oxygenated blood into the arterial circulation, causing progressive accumulation of fluid in the lungs (congestion) and subsequent congestive heart failure. Histopathologically, CCM reveals myocyte hypertrophy and atrophy, myofilament loss, lymphocyte infiltration, intracellular changes such as large irregularly shaped nuclei and lipid droplet deposition as well as diffuse and focal fibrosis (predominantly collagen type I and III) (1). Remodeling of the major components of the cardiac extracellular matrix (ECM), such as collagen, is believed to play a pivotal role in myocardial dysfunction, such that the change in the collagen content of a ventricle may compromise the stiffness, contractility and electrical properties of the heart muscle (3).

Over the last three decades, Fourier transform infrared (FTIR) spectroscopy has been successfully implemented in studies concerning the interaction, structure and dynamics of isolated tissue components such as proteins, (4) lipids, (5) carbohydrates, (6) and nucleic acids (7). The wealth of information accumulated on isolated tissue components, and combinations thereof, has facilitated the spectroscopic examination of select tissue components in their native environments, namely in cells and tissues (8). Furthermore, the spectral comparison of normal and diseased tissue provides a method by which the pathology may be objectively addressed in concordance with the disease state itself (8).

Since the early sixties, attenuated total reflectance (ATR) spectroscopy in the mid-IR region has been applied to the structural analysis of a variety of materials (bulk, thin films, liquids, solids, gases) (9). The attraction that lies in the use of ATR spectroscopy on bulk materials, such as tissues, is that in comparison to conventional transmission mid-IR spectroscopy, sample preparation is easy and nondestructive and spectral contrast is typically better. The former benefit is due to the sampling of the material in its natural state, while the latter improvement in spectral quality is due to the absence of the interference fringes and atmospheric bands commonly observed in traditional transmission spectroscopy (9). In the mid sixties, the biological and medical application of ATR spectroscopy was explored, and the possibility of creating an ATR accessory in the form of a hypodermic needle using fibre optic technology for in vivo blood and tissue analysis was under contention (10, 11). Recent advances in the area of in vivo analysis of blood components (glucose, haemoglobin, O_2, CO_2) using fibre optics have mainly concerned the near IR region, but have included measurements acquired by both transmission and reflection spectroscopy (12–14). Therefore, FTIR spectroscopy utilizing an ATR accessory offers a valuable alternative to conventional transmission spectroscopy for the examination of tissues and disease at the macromolecular level.

When one takes the traditional histological findings into account, an IR spectrum of CCM heart tissue may in turn show appreciable alterations in protein, carbohydrate, lipid, and nucleic acid content and (or) structure when compared to that of normal heart tissue. Recently, the absorption band assignment of collagen type I in the mid-IR spectra of human breast tissue (15) and infarcted rat heart tissue (16) has been documented. The latter investigators demonstrated that differences in the spectra of infarcted rat left ventricle, in comparison to that of control rats, were attributable to an increased deposition of collagen type I in the cardiac ECM as well to subtle differences in the lipid and nucleic acid content of the respective tissues (16). Characteristic IR absorption bands between 1000 and 1400 cm^{-1} were assigned to the C–O stretching vibrations of the carbohydrate residues attached to collagen (1032 and 1082 cm^{-1}) and the amide III and CH_2 wagging vibrations of collagen (1202, 1240, 1283, 1315, and 1338 cm^{-1}) (16). It has also been established that the amide I band profile (1610–1690 cm^{-1}) of collagen type I triple helix is distinct and can be characterized by predominant absorptions near 1662 and 1628 cm^{-1}, where absorptions from the 3_1 helices and intermolecular hydrogen bonding interactions of collagen chains, respectively, are thought to occur (15, 16). Normal cardiac tissue can therefore be differentiated from diseased cardiac tissue with elevated collagen deposition simply by the simultaneous evaluation of the deviation of the amide band profile from a maximum near 1655 cm^{-1}, due to predominant contributions from α-helical proteins, to that expected for the collagen triple helix and inspection of the 1000–1400 cm^{-1} region of the spectrum.

In the present study, ATR–FTIR spectroscopy was utilized to monitor collagen-related changes/pathology in the cardiac extracellular matrix of a strain of cardiomyopathic hamsters. Substantial documentation is available denoting the predictable pathological course of progressive cardiomyopathy in the line of hamsters used in this study, such as dilation, left ventricle hypertrophy, left ventricle collagen deposition, and congestive heart failure (17–20). To facilitate objective classification of the cardiac tissue as cardiomyopathic (CMP) or as normal (CON) the spectra were subjected to multivariate analysis using a linear discriminant algorithm (8, 21). LDA is a complex statistical analysis that takes into account within-group and between-group variance to discriminate between assigned classes, resulting in an overall (%) separation of classes. Moreover, two methods were used to discriminate the most spectroscopically diagnostic subregions,

© 1999 NRC Canada

namely user-selected subregions and genetic algorithm-selected subregions for subjective and nonsubjective classification, respectively. In this manner, the spectral subregions that yielded the highest linear discriminant analysis (LDA) separation between left and right ventricular tissue and between CMP and CON tissue could be evaluated in terms of collagen remodeling in this animal model.

Materials and methods

Materials and IR spectroscopy

The UM-X7.1 strain of Syrian hamsters, supplied by the laboratory of Dr. Ian Dixon (Division of Cardiovascular Science, St. Boniface General Hospital and Research Centre, Winnipeg, Manitoba), was used in this study as a paradigm of human congestive cardiomyopathy. The excised hearts of male hamsters (controls, four animals, 200 days old. Cardiomyopathic, four animals, 200 days old) were stored on dry ice prior to dissection. The left and right ventricular tissue was cut free of atria and spectra were collected from left and right ventricles (LV and RV, respectively) of cardiomyopathic (CMP, N_{LV} = 30, N_{RV} = 27 spectra) and control (CON, N_{LV} = 20, N_{RV} = 15 spectra) hearts. Mid-IR spectra (1000–4000 cm^{-1}) were acquired from randomly sampled tissue (sample size ca. 2 × 2 × 2 mm^3) using a Bio-Rad FTS-40A infrared spectrometer equipped with a "Split Pea" single reflection ATR accessory (Harrick Scientific). For each sample 256 interferograms were acquired, signal-averaged and Fourier transformed to generate spectra with a nominal resolution of 2 cm^{-1}. Spectra were then truncated between 1000–1800 cm^{-1} and the area under the curve normalized to an arbitrary numerical value of 10 to compensate for inconsistencies in tissue volume sampled. Second derivative spectra of the normalized raw data were then calculated prior to their use in multivariate analysis (LDA).

Data analysis

In the preliminary analysis, class average spectra were calculated as the arithmetic mean of all spectra in each of the following designated classes: LV(CON), LV(CMP), RV(CON), and RV(CMP). Difference spectra[2] between ventricles of the same tissue class (CON or CMP) and between tissue classes of the same ventricle (LV or RV) were calculated to ascertain the most diagnostic regions of the mid-IR. The difference spectra were utilized only as a guide to user-selection of diagnostic subregions for multivariate analysis. It was established that the 1000–1800 cm^{-1} region, particularly subregions within this range, illustrated the most prominent differences between the class average spectra. Further data reduction methodologies were then investigated to prepare the normalized, second derivatives of the raw spectra for LDA.

Two data reduction methodologies were used: manual splicing of the derivative spectra and the use of a genetic algorithm. Data reduction was necessary due to the restriction of the LDA program, which required that the number of attributes (data points) be less than the number of spectra under comparison. In the first approach, spectral subregions within the 1000–1800 cm^{-1} fingerprint region were manually chosen on the basis of spectroscopic assignments. Spectral regions with observable differences of diagnostic significance were identified in the class average spectra (Figs. 1–4). The corresponding regions in the second derivative spectra of the normalized raw data were selected as input for the LDA to discriminate between the following two-class problems:

LV(CON) vs. RV(CON)

LV(CMP) vs. RV(CMP)

RV(CMP) vs. RV(CON)

LV(CMP) vs. LV(CON)

This manual splicing (data reduction) was continued on each of the four two-class problems until a high LDA separation (>80%) was achieved. In the second data reduction approach, the normalized, derivative spectra were subjected to a genetic algorithm (22) to determine spectral subregions that were most diagnostic as inputs for LDA. Genetic algorithm (GA) selected subregions for LDA served in the nonsubjective classification of the cardiac tissue in the four two-class problems defined previously. The GA was programmed to choose less than 10 spectral subregions within 50 iterations of the program until the LDA separation between the chosen classes was optimized. For each spectral subregion chosen by the GA, the program automatically averaged the data points to one value (attribute) prior to feed into the LDA algorithm.[3]

Results and discussion

The class average spectra for LV(CON), RV(CON), LV(CMP), and RV(CMP) along with the relevant difference spectra are shown in Figs. 1–4. The visual inspection of the 1000–1800 cm^{-1} portion of the spectra revealed subtle differences in several spectral subregions, mainly those concerning absorptions due to collagen, carbohydrate, and lipid. Although differences were evident in the amide I (~1650 cm^{-1}) and amide II (~1545 cm^{-1}) band profiles of the groups under comparison, these spectral subregions exhibited a high within-group standard deviation especially in the LV(CMP) group (data not shown). Therefore, the amide I and amide II spectral subregions were left out of the user-selected subregion data reduction methodology. Sharp peaks in difference spectra are most likely due to variance in the signal-to-noise quality of the spectra rather than poor water vapor compensation, since the ATR technique does not typically suffer from the atmospheric bands seen in traditional transmission spectroscopy. The user-selected subregions utilized in the LDA of the four defined two-class problems and the LDA results are summarized in Table 1. The spectral subregions chosen nonsubjectively by the genetic algorithm and utilized as input for LDA are summarized in Table 2.

[2] *A* minus *kB* where *k* is a constant near unity chosen so that the baseline is flat and near zero.

[3] The GA and LDA programs were both developed "in house" by the Informatics Division of the Institute for Biodiagnostics (IBD), National Research Council of Canada (NRCC) in Winnipeg, Manitoba.

© 1999 NRC Canada

Fig. 1. Differences between the class average spectra from the left and right ventricles of the control animals illustrate between-group variances. Difference spectra were not used in the statistical analyses (LDA). (*a*) Class average spectra; RV(CON), solid line; LV(CON), broken line.

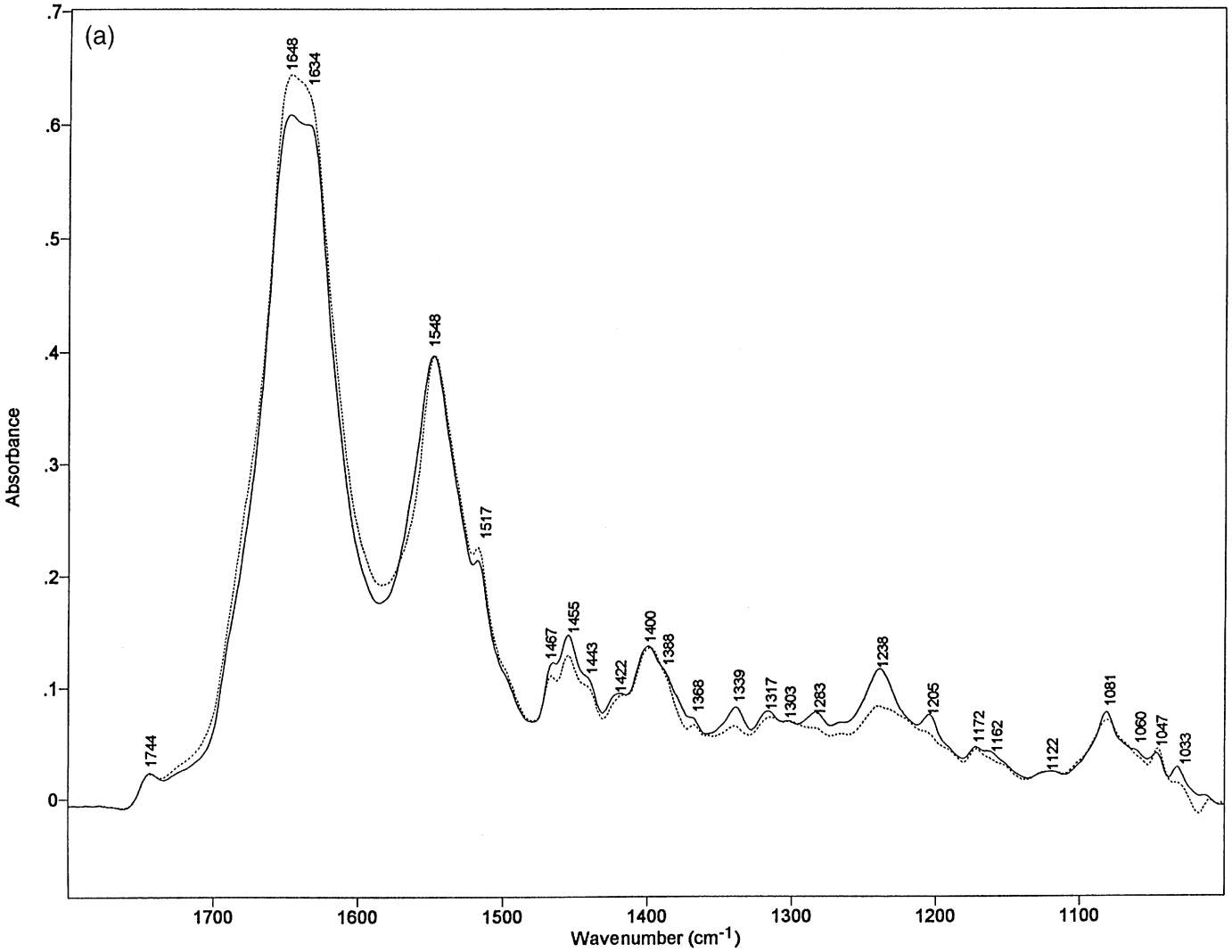

Visual comparison of the class average spectra for the left and right ventricles of control hamster hearts (Fig. 1*a*) suggested that compositional differences, especially in terms of collagen content, existed between the two ventricles of the normal heart. The difference spectrum, shown in Fig. 1*b*, illustrated that the collagen type I content of control right ventricles was greater than that of the control left ventricles. Absorption bands that may be assigned to the C–O stretching vibrations of the carbohydrate residues attached to collagen (1031 and 1081 cm^{-1}) and the amide III and CH_2 wagging vibrations of collagen (1204, 1239, 1280, 1318, 1338, and 1380 cm^{-1}) were greater in RV(CON) than in LV(CON). Secondly, the relative intensity of the CH_2 scissoring vibration (~1466 cm^{-1}) to the COO^- symmetric stretch (~1400 cm^{-1}), upon visual inspection of the two class average spectra, was found to be greater in RV(CON) than in LV(CON). The high proline/hydroxyproline and glycine content of collagen (nearly 60% of the amino acid composition of collagen) in comparison to the lower aspartate/glutamate content may serve as an explanation for the enhancement of the CH_2 bending vibration over that of the COO^- symmetric stretching absorption (15). The difference spectrum (Fig. 1*b*) also revealed that a lower frequency amide I component near 1631 cm^{-1} was more prevalent in RV(CON) than in LV(CON), which may be tentatively assigned to an amide I feature representative of the influence of strong intermolecular H-bonding between collagen chains (16). The hydroxyl groups of the hydroxyproline residues stabilize the collagen triple helix by the formation of interchain hydrogen bonds (23).

Confirmation for the distinction of RV(CON) from the LV(CON) class in terms of collagen content was provided by the LDA separation (92.5%) between the classes when regions of the second derivative spectra, representative of the amide III/CH_2 wagging subregion (1200–1285 cm^{-1}), were manually spliced together and used in the analysis (Table 1). Therefore, variations existed in the ventricular collagen content of control hearts in which the right ventricle contained a greater quantity of collagen in its ECM. The right ventricle, a smaller chamber with thinner walls than that of the left,

© 1999 NRC Canada

Fig. 1 (*concluded*). (*b*) Difference spectrum RV(CON) minus LV(CON).

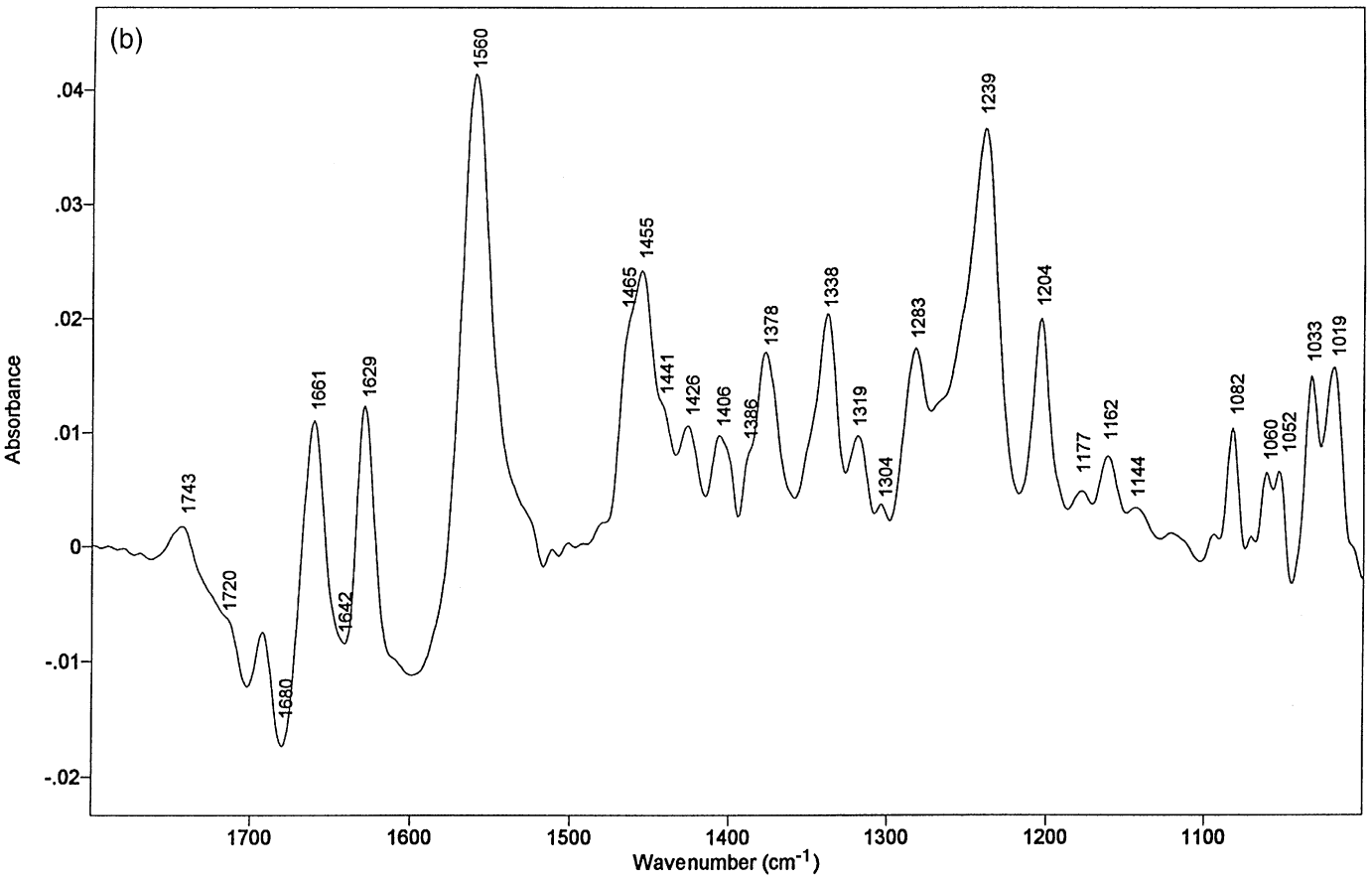

Table 1. LDA results for the manually spliced subregions.

Groups	Number of spectra	Number of attributes	Subregions selected (cm^{-1})	Assignment	LDA separation (%)
LV(CON) vs. RV(CON)	35	24	1275–1285	Amide III/proline CH_2 wagging	92.5
			1235–1240		
			1205–1210		
LV(CMP) vs. RV(CMP)	57	40	1720–1735	Side of phospholipid C=O stretch	85.8
			1330–1335	Amide III/proline CH_2 wagging	
			1310–1315		
			1020–1030	C–O–C stretching region due to carbohydrates or carbohydrate residues on collagen	
RV(CMP) vs. RV(CON)	42	21	1735–1740	Phospholipid C=O stretch	98.1
			1205–1208	Amide III/proline CH_2 wagging	
			1155–1165	C–OH stretching region due to carbohydrates or hydroxyproline residues on collagen	
LV(CMP) vs. LV(CON)	50	31	1735–1745	Phospholipid C=O stretch	98.3
			1455–1465	CH_3 bending and CH_2 scissoring region	
			1320–1325	Amide III/proline CH_2 wagging	
			1203–1205		

© 1999 NRC Canada

Fig. 2. Differences between the class average spectra from the left and right ventricles of the cardiomyopathic animals illustrate between-group variances. Difference spectra were not used in the statistical analyses (LDA). (*a*) Class average spectra; LV(CMP), solid line; RV(CMP), broken line.

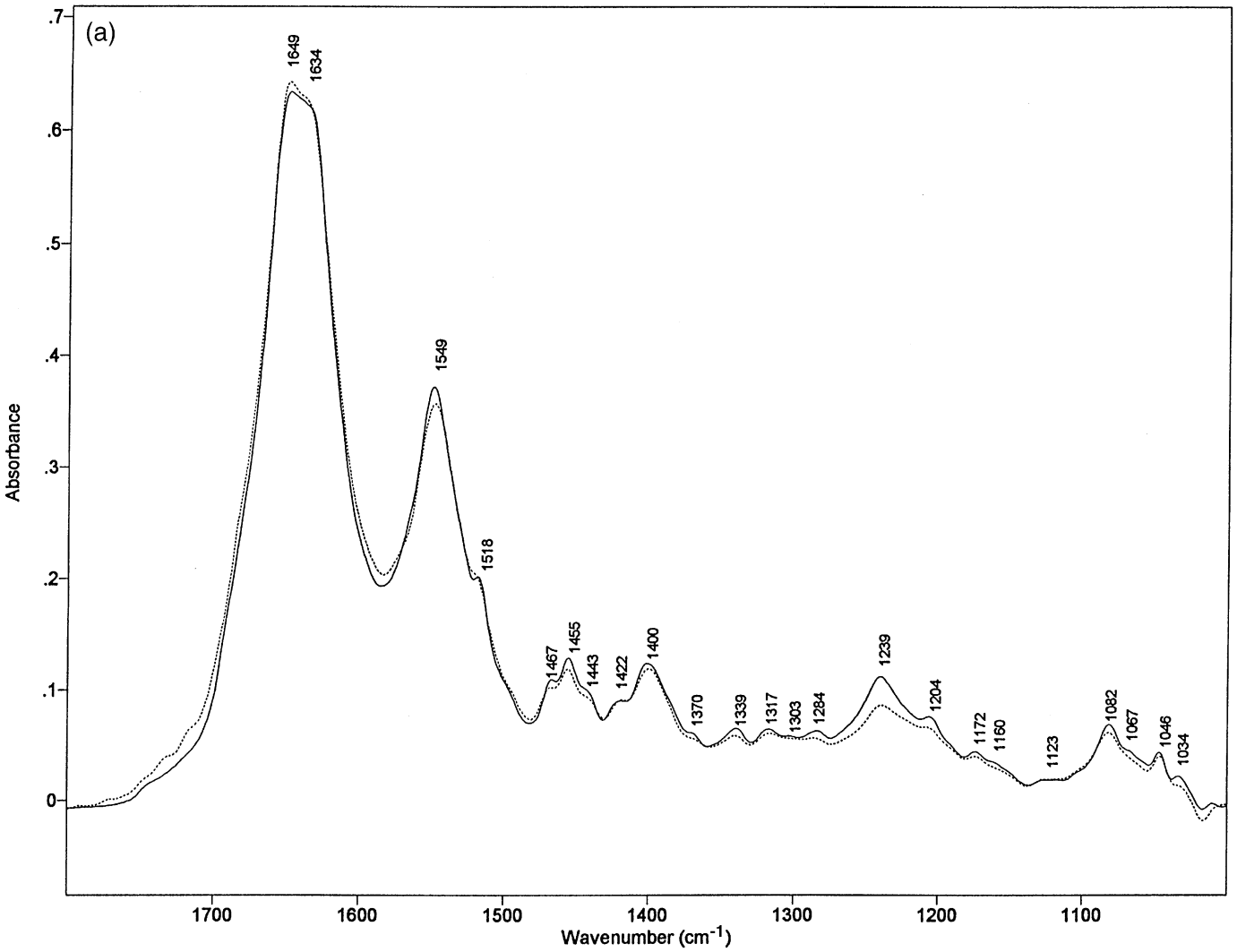

may require greater collagen in its ECM perhaps as a means to increase the ventricular tensile strength and thus enhance the contraction and relaxation phases of the ventricle. Greater collagen content in the right ventricle as opposed to the left ventricle of control rat hearts, detected by biochemical assay of the 4-hydroxyproline concentration of the myocardium, has been noted in other studies (19, 24, 25).

The nonsubjective classification of the control heart tissue as either left or right ventricle, using spectral subregions selected by a genetic algorithm, yielded a 100% LDA separation based on attributes derived from spectral regions where the collagen signature in RV(CON) was found. The GA had a tendency to pick subregions that were found to lie upon the side of an absorption or between absorptions rather than centred upon a peak (Table 2). For instance, the subregions 1431–1432, 1112–1114, and 1001–1013 cm^{-1} may be considered as subregions between the CH_2 scissoring and the COO^- symmetric stretching vibrations and subregions within or along the sides of the various C–O stretching vibrations of carbohydrates, respectively. However, the GA did select a spectral subregion (1276–1289 cm^{-1}) centred about an absorption of the amide III mixing with the proline side chain and glycine backbone CH_2 wagging vibrations (15). Furthermore, the GA also chose spectral subregions, which did not correspond to those chosen subjectively for the LDA above. For example, the GA selected the subregion 1507–1513 cm^{-1}, which lies upon the side of the absorption that one would see for the residue tyrosine (1517 cm^{-1}) as well as that assigned to the side of the nucleoside base C=O stretch of nucleic acids (1708–1720 cm^{-1}). The absorption for tyrosine ring vibration would normally be expected to be of higher relative intensity in tissue containing a lower proportion of collagen (i.e., LV(CON) as opposed to RV(CON) in this instance), since tyrosine is not a recurrent residue found in the collagen protein (15). The weak C=O absorption due to nucleic acids has been reported to appear at 1721 cm^{-1}, and in infarcted tissue this absorption is expected to be attenuated because extensive collagen type I deposition occurs after phagocytosis of cellular debris (8). However, the difference spectrum between LV(CON) and RV(CON) in Fig. 1*a* does

© 1999 NRC Canada

Fig. 2 (*concluded*). (*b*) Difference spectrum LV(CMP) minus RV(CMP).

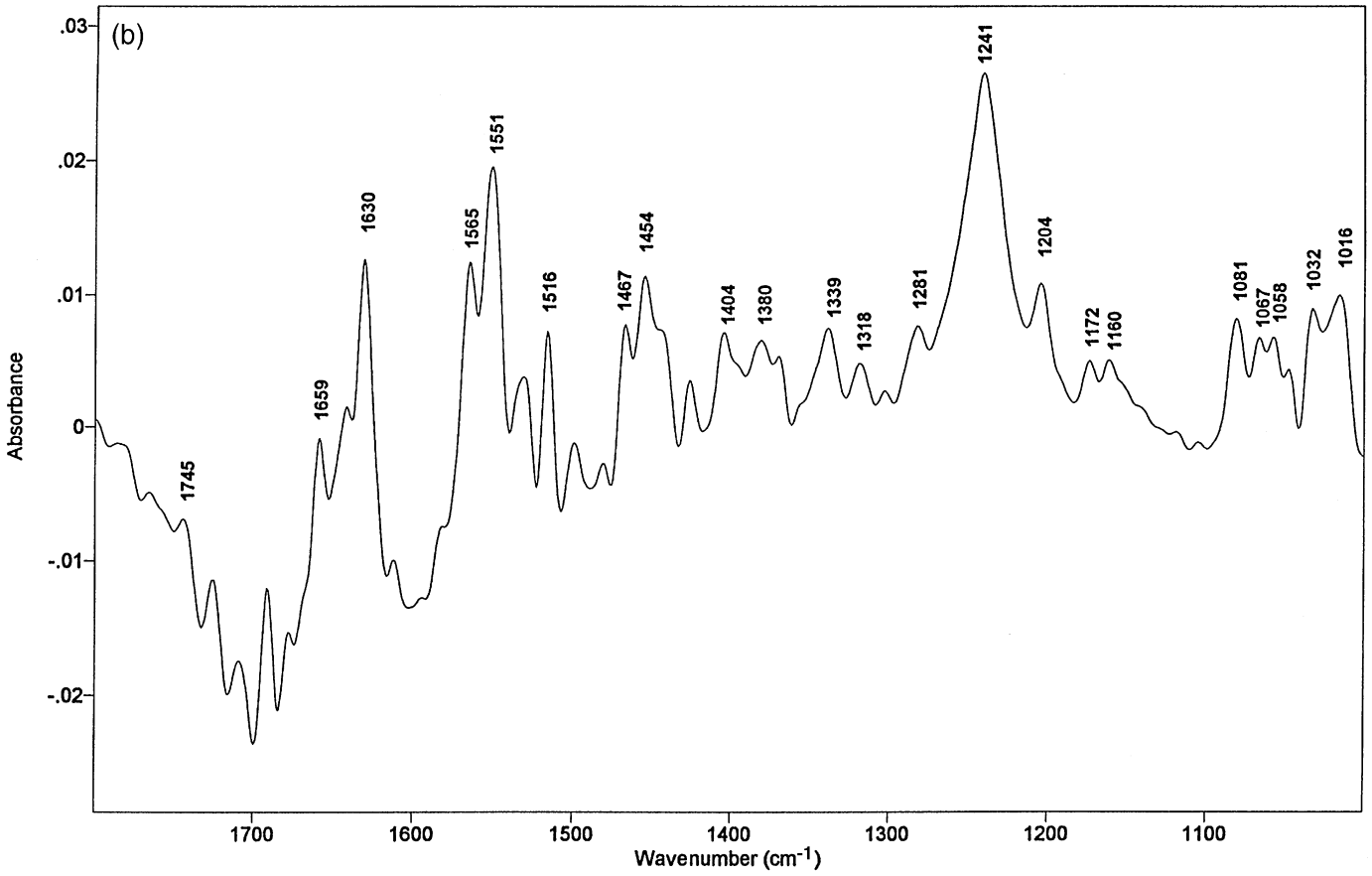

not provide any significant information about whether the left or right ventricle contains more tyrosine or nucleic acids. The GA also selected the subregion corresponding to the C–OH stretching vibration (1155–1164 cm^{-1}). Absorptions in this subregion are commonly seen in the spectra of carbohydrates or of proteins high in hydroxyproline content, such as collagen, or proteins that contain a number of serine or threonine residues (16). Furthermore, Liu et al. (16) found that the ratio of the 1159:1172 cm^{-1} absorptions was greatly increased in infarcted rat heart as opposed to that of control, suggesting that the 1159 cm^{-1} feature was due specifically to the C–OH stretching of hydroxyproline. Although this C–OH stretching subregion did not enhance the LDA separation when significant spectroscopically diagnostic subregion were user-selected, comparison of RV(CON) and LV(CON) revealed that the 1162:1172 cm^{-1} ratio was slightly greater in RV(CON) (Fig. 1*a*). Therefore, the GA not only provided a nonsubjective classification of control ventricular tissue, but it also utilized subregions for LDA classification that were more subtly distinct than those chosen manually.

In contrast to the differences observed in the class average spectra of the control ventricular tissue, the cardiomyopathic ventricular tissue spectra were not as distinct upon visual comparison (Fig. 2*a*). The difference spectrum between the class average spectra for the groups LV(CMP) and RV(CMP), shown in Fig. 2*b*, illustrated the minute difference in collagen content of the two ventricles. Both class average spectra, LV(CMP) and RV(CMP), displayed the collagen fingerprint (i.e., absorption bands at 1032, 1082, 1202, 1240, 1283, 1315, and 1338 cm^{-1}). However, the difference spectrum (Fig. 2*b*) indicated a slight difference between these spectral subregions of the two class average spectra, whereby the collagen fingerprint was found to be slightly more pronounced in the LV(CMP) class average spectrum. Upon subtraction of RV(CMP) from LV(CMP), a collagen-like fingerprint remained just above a zero difference. Furthermore, the difference spectrum illustrated a less prominent phospholipid ester C=O stretching vibration (~1745 cm^{-1}) in LV(CMP). The phospholipid content of a tissue typically decreases when the content of another component (i.e., collagen) increases. The LDA separation using the user-selected subregions to classify the groups LV(CMP) and RV(CMP) was satisfactory (85.8%) when subregions such as those representing the phospholipid ester C=O (1720–1735 cm^{-1}), amide III/CH_2 wagging (1310–1315 and 1330–1335 cm^{-1}) and C–O stretching of carbohydrates (1020–1030 cm^{-1}) were used in (Table 1). The collagen content in the ECM of the left and right ventricles of the CMP hearts does not differ to the extent observed with the control ventricles. This is perhaps due to collagen remodeling in both ventricles wherein the left ventricular collagen increased and the right ventricular collagen remained similar to control levels or decreased.

The nonsubjective classification of the CMP tissue yielded a 100% separation of subregions that were GA-selected.

© 1999 NRC Canada

Fig. 3. Differences between the class average spectra from the right ventricles of the cardiomyopathic and control myocardium are indicative of decreased collagen deposition in the right ventricles of the CMP hearts. Difference spectra were not used in the statistical analyses (LDA). (*a*) Class average spectra; RV(CON), solid line; RV(CMY), broken line.

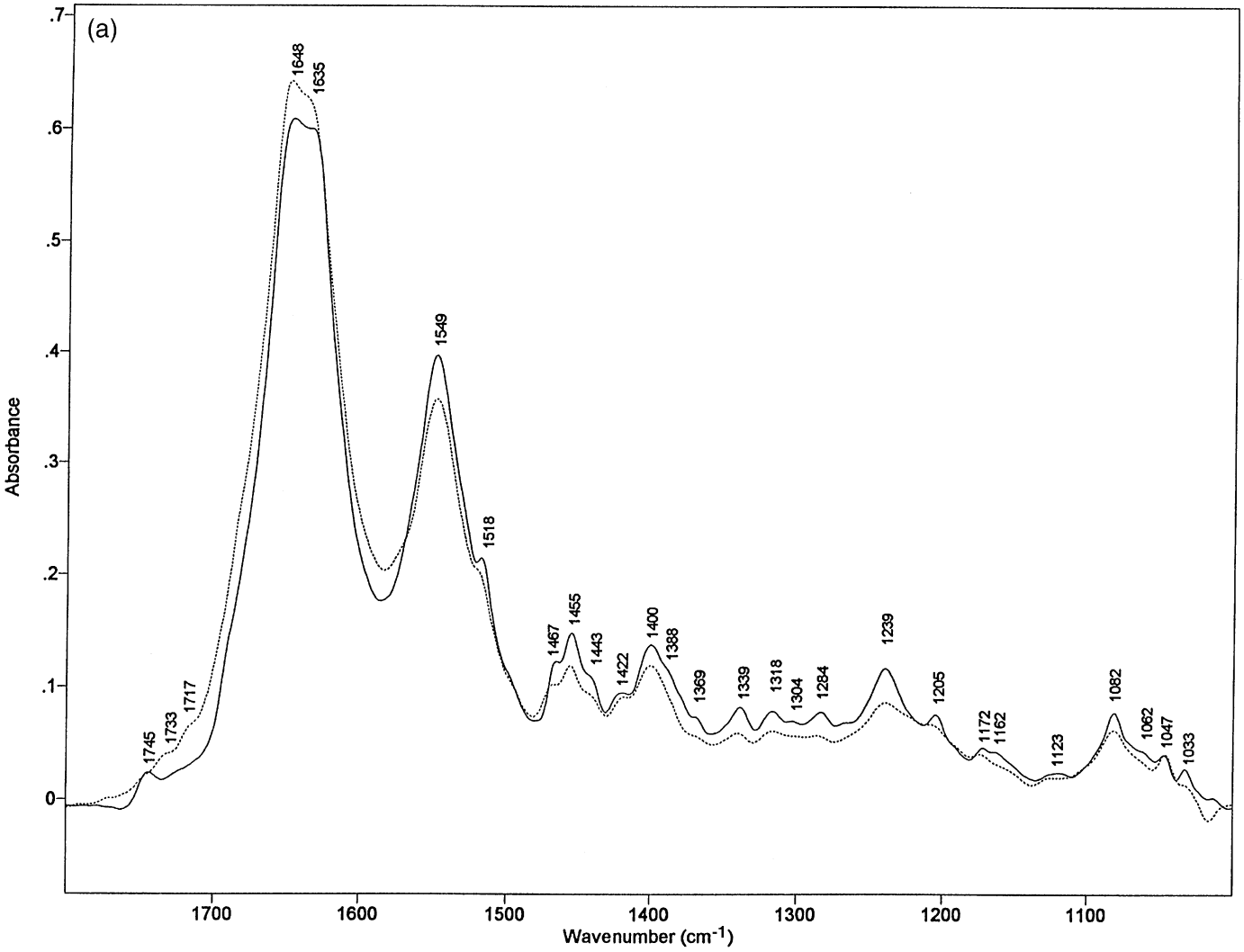

However, in contrast to the subregions chosen by the GA for the control spectra, the CMP spectral subregions were of rather a broad range (>30 cm^{-1}) such that classification was based on nearly the entire fingerprint region (Table 2). Since the GA program "averaged" each spectral range to a single point (attribute), the GA/LDA 100% separation of the LV(CMP) group from the RV(CMP) group may have been an artifact. The rather large subregions selected by the GA that generated a 100% separation between the left and right CMP ventricles included the lipid/nucleic acid C=O stretching subregion (1713–1743 cm^{-1}), the amide I and II band profiles (1511–1712 cm^{-1}), the subregion between the CH_2 scissoring and the amide II (1474–1500 cm^{-1}), the subregion containing the COO^- symmetric stretching vibration (1364–1436 cm^{-1}), the amide III/proline CH_2 wagging subregion (1316–1350 and 1205–1238 cm^{-1}) and the C–O stretching subregion of carbohydrates or carbohydrate residues of collagen (1000–1032 and 1070–1112 cm^{-1}). Therefore, although the GA was a useful method for reduction of the number of spectral attributes and for selection of less obvious distinctions between spectra for LDA input, manual selection of spectral subregions that exhibited observable differences between the class average spectra was necessary to avoid possible artifactual distinctions between groups under comparison.

Verification of collagen remodeling in the right ventricle of cardiomyopathic hamster hearts involved the direct comparison of the groups RV(CMP) and RV(CON). Visually, the most apparent differences between the class average spectra RV(CMP) and RV(CON) concern the IR subregions where absorptions due to phospholipid and collagen occur (Fig. 3). The subregions chosen and manually spliced for LDA input that generated an LDA separation between classes of 98.1% are shown in Table 1. Absorptions in the subregions 1735–1740 cm^{-1} (side of lipid C=O), 1205–1208 cm^{-1} (amide III/CH_2 wagging) and the ratio of the 1162:1172 cm^{-1} (contribution from the C–OH stretching of hydroxyproline) were greater in RV(CON) than in RV(CMP). Further differences between the groups RV(CMP) and RV(CON) were noted upon visual inspection of Fig. 3; the C–O stretching of car-

© 1999 NRC Canada

Fig. 3 (*concluded*). (*b*) Difference spectrum RV(CON) minus RV(CMP).

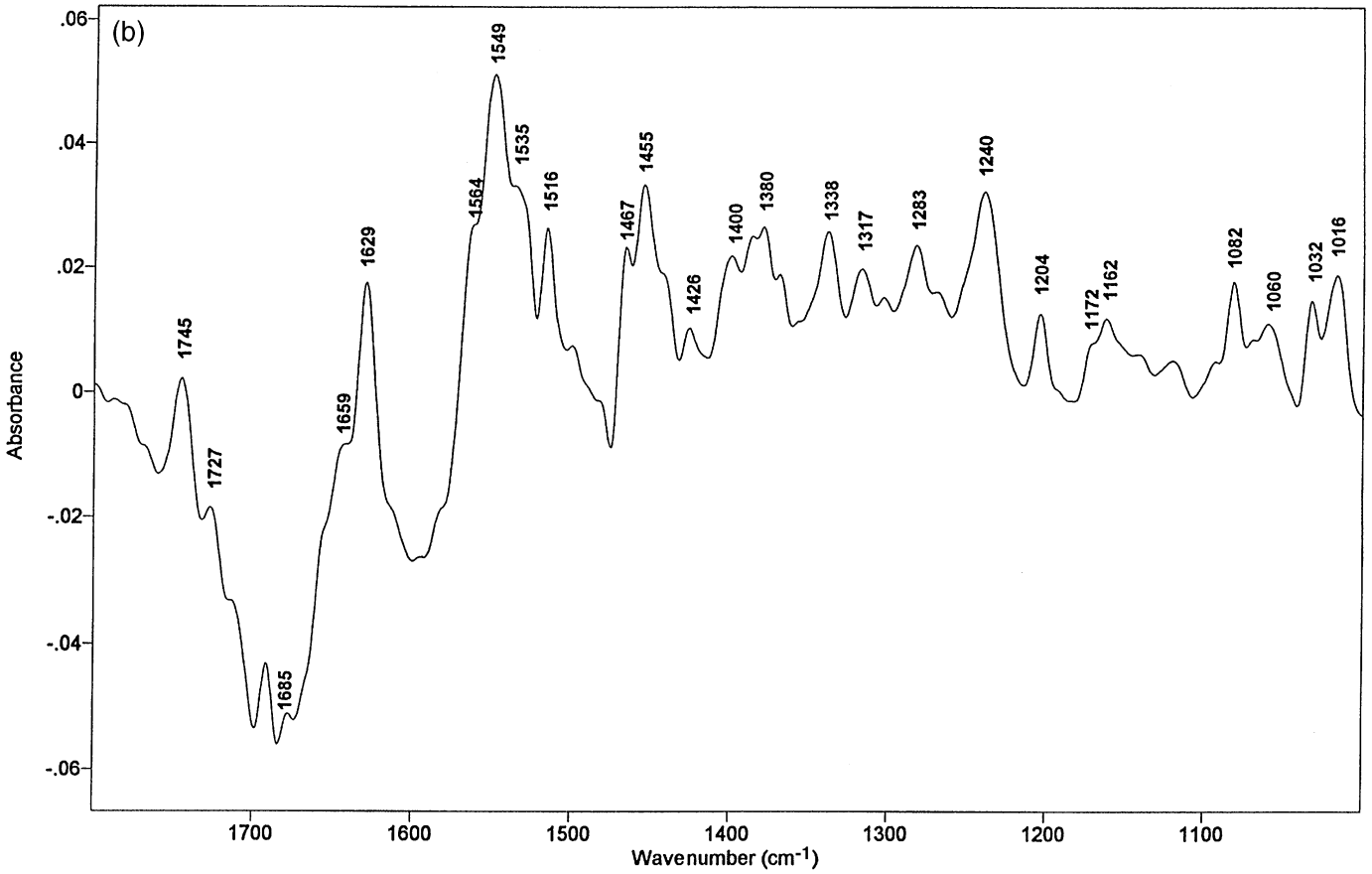

bohydrates or carbohydrate residues attached to collagen (1031 and 1081 cm^{-1}) was more prevalent in RV(CON); the CH_2 scissoring (1466 cm^{-1}) was greater than the COO^- symmetric stretch (1398 cm^{-1}) in RV(CON); and the amide I maximum had shifted to lower frequency in RV(CON) in comparison to RV(CMP). Thus, although the model used in this study was expected to be a paradigm of LV cardiomyopathy in which collagen remodeling of the ECM occurs primarily in the left ventricle, the greater phospholipid and collagen type I content in the right ventricle of control rather than in right ventricle of the CMP hearts, supported the likelihood of collagen remodeling of the ECM of the right ventricle as well. However, while RV(CMP) was found to have decreased collagen deposition in comparison to RV(CON), little difference was found in the collagen deposition of RV(CMP) and LV(CMP) in comparison to the noticable difference between RV(CON) and LV(CON). Therefore, the decrease in RV collagen deposition in the CMP hearts was not great enough to augment the difference in collagen deposition between the two ventricles of the CMP hearts beyond that found for the two ventricles of the control hearts.

The nonsubjective classification of the right ventricles as either CON or CMP, using GA-selected subregions, yielded a 100% LDA separation based on attributes derived from spectral subregions that mainly involved absorptions due to collagen (Table 2). In contrast to the subregions chosen manually, the GA did not select the lipid C=O absorption. The GA, however, did choose the C–OH stretching subregion due to carbohydrates and (or) hydroxyproline (1156–1188 cm^{-1}) and the amide III/proline CH_2 wagging subregion (1294–1335 and 1201–1238 cm^{-1}), similar to those subregions selected by the manual splicing methodology. In addition, the GA selected subregions in the C–O stretching region due to carbohydrates or carbohydrate residues on collagen (1084–1127 and 1022–1071 cm^{-1}), the side of the COO^- symmetric stretch (1360–1404 cm^{-1}), and the amide I and amide II band profiles (1592–1670 and 1497–1578 cm^{-1}, respectively), all of which were found to differ between RV(CMP) and RV(CON) as illustrated in the difference spectrum in Fig. 3*b*.

Finally, evidence for collagen remodeling in the left ventricle of the cardiomyopathic hamster hearts was derived initially from the direct comparison of the groups LV(CON) and LV(CMP). Visual comparison of the fingerprint region of the class average spectra for LV(CON) and LV(CMP) revealed that the groups differed predominantly in spectral subregions where absorptions due to collagen and phospholipid occur (Fig. 4*a*). For instance, deposition of a greater amount of collagen in the group LV(CMP) was inferred from the presence of more prevalent absorptions in the amide III/proline CH_2 wagging region (1339, 1283, 1240, 1204 cm^{-1}) and by attenuation of the phospholipid C=O (1745 cm^{-1}) stretching absorption in LV(CMP). In addition, the enhanced relative intensity of the CH_2 scissoring absorption (1467 cm^{-1}) to the COO^- symmetric stretching

© 1999 NRC Canada

Fig. 4. Differences between the class average spectra from the left ventricles of the cardiomyopathic and control myocardium are indicative of increased collagen deposition in the left ventricles of the CMP hearts. Difference spectra were not used in the statistical analyses (LDA). (*a*) Class average spectra; LV(CMP), solid line; LV(CON), broken line.

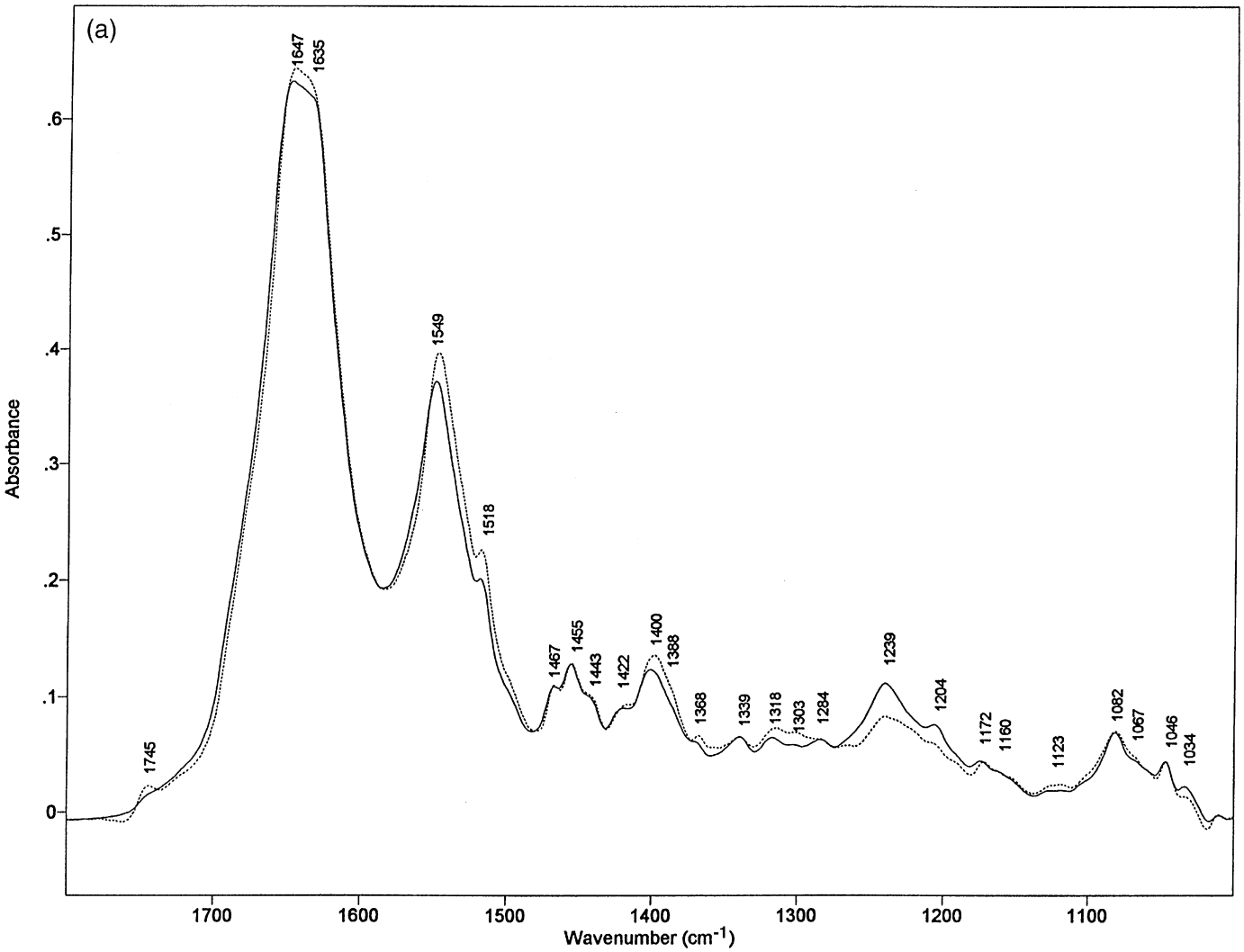

absorption (1400 cm^{-1}) in LV(CMP), visually detected upon comparison of the group-mean spectra further supported elevated collagen deposition in LV(CMP). The CH_3 bending/CH_2 scissoring subregion (1455–1465 cm^1), sides of bands within the amide III/proline CH_2 wagging subregion (1320–1325 and 1203–1205 cm^{-1}) and the C=O stretching subregion (1735–1745 cm^{-1}) were found to augment the separation between classes in the LDA resulting in a LDA class separation of 98.3% (Table 1). Differences in the C–O and C–OH stretching regions (1030–1175 cm^{-1}) and in the absorption due to tyrosine (1515 cm^{-1}), wherein the former was found to be greater in LV(CMP), and the latter was found to be greater in LV(CON), could be detected visually (difference spectrum, Fig. 4*b*) but were not found to further enhance the LDA separation between the classes beyond that reported.

Nonsubjective classification of the left ventricles as either CON or CMP, using GA-selected subregions, generated a 100% LDA separation based on attributes derived from spectral subregions that contained collagen absorptions (Table 2). Analogously to the manual-splicing methodology for data reduction, the GA selected the CH_3 bending/CH_2 scissoring region (1455–1468 cm^{-1}). Although it was not detected visually, the relative intensity of the CH_2:CH_3 absorptions has been found to increase in infarcted tissue where increased collagen deposition may be found (16). Moreover, the GA selected a subregion containing the procession of CH_2 scissoring vibrations (1429–1440 cm^{-1}), as well as a region centred about the COO^- symmetric stretching vibration (1397–1413 cm^{-1}). Therefore, the LDA that utilized the GA-selected subregions may have also classified upon differences in the relative intensity of CH_2 scissoring (proline/glycine) to the COO^- symmetric stretching (aspartate/glutamate) in tissue with elevated collagen deposition due to the high glycine and proline residue count in the collagen sequence. Contrary to the subregions chosen manually, the GA did select the subregions due to the C–O stretching of carbohydrates and carbohydrate residues on collagen and the C–OH stretching of carbohydrates and (or) hydroxyproline (1088–1177 cm^{-1}) to distinguish between the

© 1999 NRC Canada

Fig. 4 (*concluded*). (*b*) Difference spectrum LV(CMP) minus LV(CON).

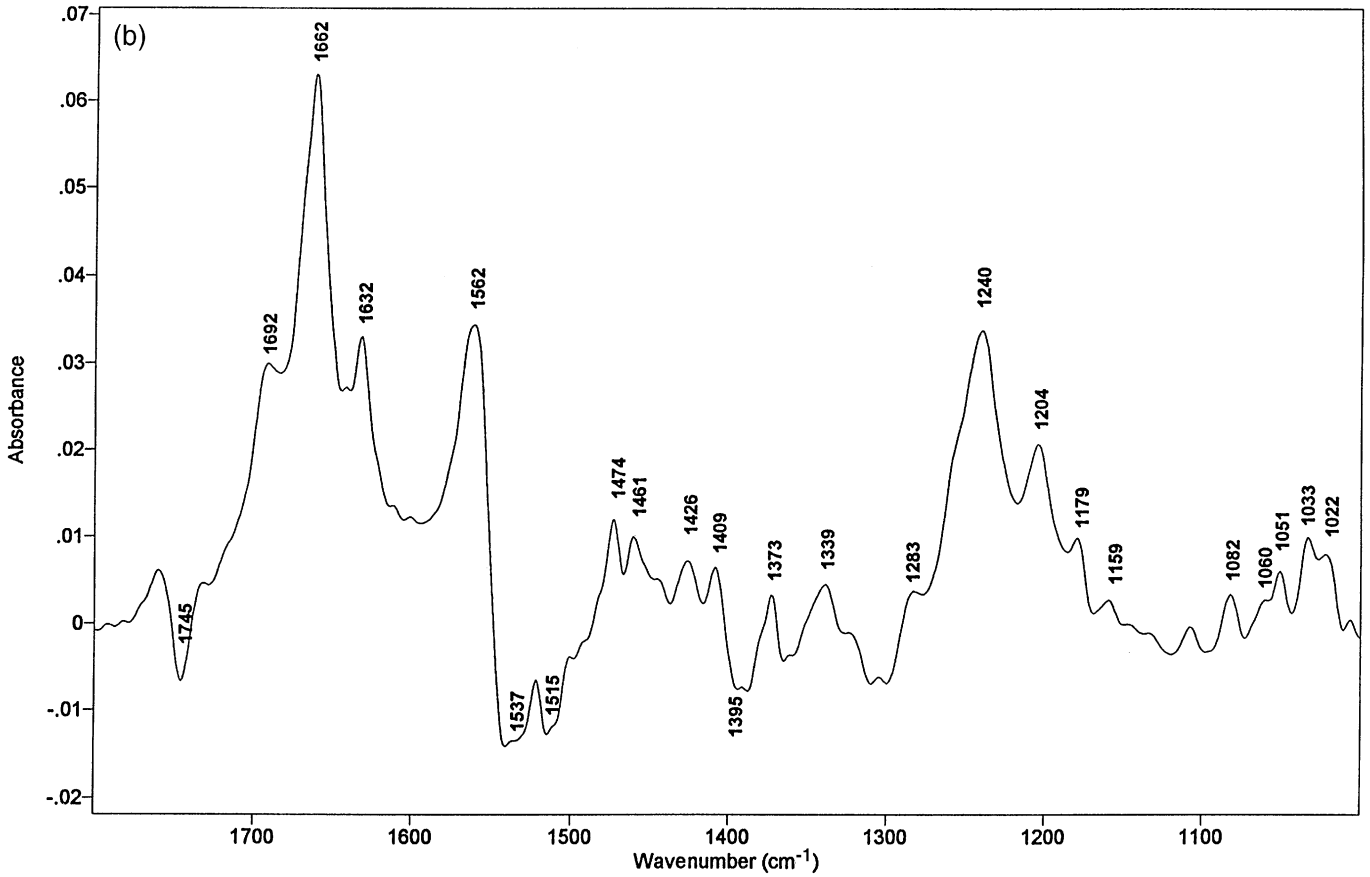

classes, while it did not select the lipid C=O subregion nor the amide III/proline CH_2 wagging subregion (Table 2). Although the latter regions were not chosen by the GA, both the difference spectrum (Fig. 4) and the LDA performed upon the user-selected subregions (Table 1) validated that class distinction could be augmented by use of these regions. Instead of subregions containing absorptions reflective of phospholipid content or absorptions containing the slew of overlapping bands due to the amide III/proline CH_2 wagging vibrations, the GA chose subregions that contained the amide I absorption (1597–1633 and 1634–1711 cm^{-1}), which were not utilized in the LDA performed on the manually-spliced spectral subregions. The LV(CMP) group exhibited a high standard deviation in the amide I subregion (data not shown), thus this subregion was not considered as reliable in class distinction strategies as some of the other spectral subregions already mentioned. However, the difference spectrum in Fig. 4*b* supported the GA selection of subregions within the amide I absorption for LDA separation of the LV(CMP) and LV(CON) classes, since the greatest difference was found to lie within the amide I band profile. In Fig. 4*b* the amide I region of LV(CMP) contained significant contributions from components that may be attributed to structure of the collagen triple helix. For instance, the enhanced absorptions near 1632 and 1662 cm^{-1} in LV(CMP) as opposed to LV(CON) were representative of the amide I absorptions due to the cross-linking intermolecular hydrogen bonding network between collagen chains and the 3_1-helix structural motif of collagen, respectively (16). Therefore, implementation of difference spectroscopy in combination with the utilization of a genetic algorithm to select spectroscopically diagnostic subregions of spectra for comparative purposes such as LDA allowed for distinction of the two classes LV(CMP) and LV(CON) based upon collagen deposition. The cardiomyopathic left ventricular tissue exhibited elevated collagen content in the extracellular matrix, which would progressively worsen until the contractility of the left ventricle was so compromised that congestive heart failure would ensue.

Conclusions

The results of the current study illustrated that the use of a genetic algorithm to select diagnostic spectral subregions of tissues with varied composition coupled to multivariate analysis (LDA) was a successful approach for 100% objective classification of the cardiac tissue. The reliability of the GA–LDA results was tested through the manual splicing of spectra to generate spectral subregions to classify by LDA in the user-selected methodology. The analysis of cardiac collagen deposition by IR spectroscopy confirmed those found by other studies of the hamster paradigm of congestive cardiomyopathy that utilized biochemical assays, while in some instances further information was acquired. Specifically, left ventricular collagen remodeling in the cardiomyopathic ECM was denoted by localized elevated collagen deposition rather than by diffuse fibrosis. Furthermore, the decreased collagen deposition observed in the

© 1999 NRC Canada

Table 2. Genetic algorithm-selected spectral subregions that lead to nonsubjective classification of the heart tissue.

CON tissue (LV vs. RV) subregions (cm^{-1})	CMP tissue (LV vs. RV) subregions (cm^{-1})	RV tissue (CMP vs. CON) subregions (cm^{-1})	LV tissue (CMP vs.CON) subregions (cm^{-1})	Assignment
	1713–1743			C=O (nucleic acids) to C=O (lipids)
1708–1720				C=O (nucleic acids)
	1634–1712	1592–1670	1634–1711	Sides of amide I
1667–1680				High frequency side of the amide I: β-sheet (high frequency component), turns or 1662 cm^{-1} due to 3_1-helix (structural motif in collagen)
			1597–1633	Low frequency side of amide I: β-sheet (low frequency component) and intermolecular H-bonding between collagen chains (cross-linking)
1507–1513	1511–1633			Side of tyrosine absorption (~1517 cm^{-1}) and structural motifs associated with the low frequency side of the amide I
	1474–1500			Between CH_2 scissoring and amide II
		1497–1578		Amide II region
			1455–1468	CH_3 asymmetric bend (1457 cm^{-1}) and CH_2 scissoring (1467 cm^{-1})
1431–1432			1429–1440	Procession of the CH_2 bending vibrations
	1364–1436	1360–1404	1397–1413	Centred or upon side of the COO^- symmetric stretch
1276–1289	1316–1350	1294–1335		Amide III/proline CH_2 wagging
	1205–1238	1201–1238		
1155–1164		1156–1188	1160–1177	C–OH stretching due to Ser, Thr, and carbohydrates and (or) hydroxyproline residues on collagen
1112–1114	1070–1112	1084–1127	1088–1159	C–O–C stretching region due to carbohydrates or carbohydrate residues on collagen
1001–1013	1000–1032	1022–1071		

right ventricles of cardiomyopathic hearts in comparison to control samples indicated that right ventricular collagen remodeling accompanied left ventricular collagen remodeling in this animal model. This observation of decreased collagen deposition in the CMP right ventricle was opposite to that found in a recent FTIR microspectroscopic study of hearts of the same hamster line. That is, Liu et al. (26), found increased focal fibrosis in the RV of the CMP hamster heart tissue examined at a spatial resolution of $50 \times 50\ \mu m^2$ by IR microspectroscopy. It would be of particular interest to further investigate the localized deposition of collagen deposition in this hamster model by IR microscopy of thin sections of the heart myocardium (epicardium to the endocardium) at a greater spatial resolution (i.e., $10 \times 10\ \mu m^2$) by utilizing a synchrotron-generated source in the IR microspectroscopy.

Acknowledgements

Special thanks to the Informatics Division of the Institute for Biodiagnostics (IBD), NRCC for development of the programs for the GA and LDA, the Molecular Spectroscopy Division of the IBD, NRCC for technical expertise and availability of the instrumentation, and the University of Manitoba Graduate Fellowship (Duff Roblin fund), and the Gorden P. Osler Graduate Scholarship for student support. This work was supported by the Natural Sciences and Engineering Research Council of Canada (NSERC) (K.M. Gough) and the Heart and Stroke Foundation of Manitoba (I.M.C. Dixon). I.M.C.D. is a scholar of the Medical Research Council – PMAC program (Astra Pharma, Inc.).

References

1. R.C. Schlant and R.W. Alexander. Hurst's, the heart. 8th ed. McGraw–Hill Inc. 1994. pp. 1585–1590, 1609–1619.
2. E. Braunwald. Heart disease: a textbook of cardiovascular medicine. W.B. Saunders Co., Philadelphia. 1997. pp. 1407–1408.
3. V. Pelouch, I.M.C. Dixon, L. Golfman, R.E. Beamish, and N.S. Dhalla. Role of extracellular matrix proteins in heart function. Mol. Cell. Biochem. **129**, 101 (1994).
4. M. Jackson and H.H. Mantsch. The use and misuse of FTIR spectroscopy in the determination of protein structure. Crit. Rev. Biochem. Mol. Biol. **30**(**2**), 95 (1995).
5. H.H. Mantsch and R.N. McElhaney. Phospholipid transitions in model and biological membranes as studied by IR spectroscopy. Chem. Phys. Lipids, **57**, 213 (1991).
6. P.T.T. Wong, M. Cadrin, and S.W. French. Distinctive infrared spectral features in liver tumor tissue of mice: evidence of structural modifications at the molecular level. Exp. Mol. Pathol. **55**, 269 (1991).
7. E. Taillandier and F. Liquier. Infrared spectroscopy of DNA. Meth. Enzymol. **211**, 307 (1992).
8. M. Jackson and H.H. Mantsch. FTIR spectroscopy in the clinical sciences. *In* Biomedical applications of spectroscopy. *Edited by* R.J.H. Clark and R.E. Hester. John Wiley and Son Ltd., Chichester. 1996. pp. 185–215.
9. N.J. Harrick. Internal reflection spectroscopy. Interscience Publishers, New York. 1967. pp. 217–222.
10. F.S. Parker and R. Ans. Infrared studies of human and other tissues by the attenuated total reflection technique. Anal. Biochem. **18**, 414 (1967).

© 1999 NRC Canada

11. D.F. Capellaro and N.S. Kapny. A hypodermic probe using fibre optics. Nature (London), **191**, 927 (1961).
12. M.R. Robinson, R.P. Eaton, D.M. Haaland, G.W. Koepp, E.V. Thomas, B.R. Stallard, and P.L. Robinson. Non-invasive glucose monitoring in diabetic patients: a preliminary evaluation. Clin. Chem. **38**(**9**), 1618 (1992).
13. F. Faris, P. Rolfe, M. Thorniley, Y. Wickramasinghe, R. Houston, M. Doyle, and S. O'Brien. Non-invasive optical monitoring of cerebral blood oxygenation in the foetus and newborn: a preliminary investigation. J. Biomed. Eng. **14**(**4**), 303 (1992).
14. E.J. Fogt. Continuous ex vivo and in vivo monitoring with chemical sensors. Clin. Chem. **36**(**8**), 1573 (1990).
15. M. Jackson, L-P. Choo, P.H. Watson, W.C. Halliday, and H.H. Mantsch. Beware of connective tissue proteins: assignments and implications of collagen absorptions in infrared spectra of human tissues. Biochim. Biophys. Acta, **1270**, 1 (1995).
16. K.Z. Liu, M.J. Jackson, M.G. Sowa, I.M.C. Dixon, and H.H. Mantsch. Modification of the extracellular matrix following myocardial infarction monitored by FTIR spectroscopy. Biochim. Biophys. Acta, **1315**, 73 (1996).
17. E.W. Gertz. Cardiomyopathic Syrian hamster: a possible model of human disease. Progr. Exp. Tumor Res. **16**, 242 (1972).
18. G. Jasmin and L. Proschek. Hereditary polymyopathy and cardiomyopathy in the Syrian hamster. I. Progression of heart and skeletal muscle lesions in the UM-X7.1 line. Muscle and Nerve, **5**, 20 (1982).
19. G. Davison, C.S. Hall, J.G. Miller, M. Scott, and S.A. Wickline. Cellular mechanisms of captopril-induced matrix remodeling in Syrian hamster cardiomyopathy. Circulation, **90**, 1334 (1994).
20. I.M.C. Dixon, H. Ju, N.L. Reid, T. Scammell La Fleur, J.P. Werner, and G. Jasmin. Cardiac collagen remodeling in the cardiomyopathic Syrian hamster and the effect of losartan. J. Mol. Cell. Cardiol. **29**(**7**), 1837 (1997).
21. G.J. McLachlan. Discriminant analysis and statistical pattern recognition. Wiley, New York. 1992.
22. A.S. Bangalore, R.E. Shaffer, G.W. Small, and M.A. Arnold. Genetic algorithm-based method for selecting wavelengths and model size for use with partial least-squares regression: application to near-infrared spectroscopy. Anal. Chem. **68**(**23**), 4200 (1996).
23. T.E. Creighton. Proteins. Structures and molecular properties. 2nd ed. W.H. Freeman and Co., New York. 1993. pp.196–197.
24. V. Pelouch, I.M.C. Dixon, R. Sethi, and N.S. Dhalla. Alteration of collagenous protein profile in congestive heart failure secondary to myocardial infarction. Mol. Cell. Biochem. **129**, 121 (1994).
25. V. Robert, N. Van Theim, S.L. Cheav, C. Mouas, B. Swynghedauw, and C. Deleayre. Increased cardiac type I and III collagen mRNAs in aldosterone-salt hypertension. Hypertension, **24**, 30 (1994).
26. K.Z. Liu, I.M.C. Dixon, and H.H. Manstch. Distribution of collagen deposition in cardiomyopathic hamster hearts determined by infrared microscopy. Cardiovas. Pathol. **8**, 41 (1999).

© 1999 NRC Canada

Chelated fluoroboron cations. I. Synthesis and NMR studies involving the tertiary-amine ligands *N*,*N*,*N*′,*N*′-tetramethylethylenediamine and *N*,*N*,*N*′,*N*″,*N*″-pentamethyldiethylenetriamine

James A.W. Shoemaker and J. Stephen Hartman

Abstract: Several possible methods of synthesis of chelated fluoroboron cations are explored, using the *tert*-amines *N*,*N*,*N*′,*N*′-tetramethylethylenediamine (Me_4en) and *N*,*N*,*N*′,*N*″,*N*″-pentamethyldiethylenetriamine (Me_5dien) as model chelating ligands. Both ligands displace pyridine from $(pyr)_2BF_2^+$ (as its PF_6^- salt) to form the bidentate $(Me_4en)BF_2^+$ and $(Me_5dien)BF_2^+$ cations. The same cations, as well as the corresponding $BFCl^+$ and $BFBr^+$ cations, can also be prepared by displacement of the donor molecule (D = pyridine or isoxazole) and the heavy halide ion (Cl^- or Br^-) from the neutral $D{\cdot}BF_2X$ and $D{\cdot}BFX_2$ adducts. The central nitrogen of Me_5dien becomes chiral when it and one terminal nitrogen are coordinated, and the prochiral and magnetically nonequivalent fluorines of $(Me_5dien)BF_2^+$ give ^{19}F NMR signals separated by 1.2 ppm. In $(Me_5dien)BFCl^+$ the boron is a second chiral centre and the two diastereomers, distinguishable by NMR with ^{19}F chemical shifts differing by 3.0 ppm, form in a 3:1 ratio. The bidentate $BFBr^+$ cations of Me_4en and Me_5dien are insoluble in non-coordinating solvents but have been detected by positive ion FAB mass spectrometry and ^{11}B MAS NMR. The tridentate complex $(Me_5dien)BF^{+2}$ does not form under our conditions.

Key words: *N*,*N*,*N*′,*N*′-tetramethylethylenediamine, *N*,*N*,*N*′,*N*″,*N*″- pentamethyldiethylenetriamine, chelated fluoroboron cations, fluorine-19 NMR, boron-11 NMR, pyridine, isoxazole, chiral, magnetically nonequivalent.

Résumé : Utilisant les amines tertiaires *N*,*N*,*N*′,*N*′-tétraméthyléthylènediamine (Me_4en) et *N*,*N*,*N*′,*N*″,*N*″-pentaméthyldiéthylènetriamine (Me_5dien) comme ligands chélatants modèles, on a exploré plusieurs méthodes de synthèse de cations fluorobores chélatés. Les deux ligands déplacent la pyridine du $(pyr)_2BF_2^+$ (sous forme de sel PF_6^-) pour conduire aux cations bidentates $(Me_4en)BF_2^+$ et $(Me_5dien)BF_2^+$. On peut préparer ces mêmes cations, ainsi que les cations correspondants $BFCl^+$ et $BFBr^+$, en déplaçant la molécule donneur (D = pyridine ou isoxazole) et l'ion halogénure lourd (Cl^- ou Br^-) des adduits neutres $D{\cdot}BF_2X$ et $D{\cdot}BFX_2$. Quand un azote terminal et l'azote central du Me_5dien sont coordinés simultanément, ce dernier devient chiral et, en RMN du ^{19}F, les atomes de fluor prochiraux et magnétiquement inéquivalents du $(Me_5dien)BF_2^+$ donnent des signaux séparés par 1,2 ppm. Dans le $(Me_5dien)BFCl^+$, le bore est un deuxième centre chiral et les deux diastéréoisomères, que l'on peut distinguer par RMN avec des déplacements chimiques du ^{19}F de 3,0 ppm, sont présents dans un rapport de 3:1. Les cations bidentates $BFBr^+$ du Me_4en et Me_5dien sont insolubles dans les solvants qui ne peuvent donner lieu à de la coordination; on peut toutefois les détecter par spectrométrie de masse par bombardement avec des atomes rapides et la RMN du ^{11}B par la technique « MAS ». Dans nos conditions réactionnelles, le complexe tridentate $(Me_5dien)BF^{+2}$ ne se forme pas.

Mots clés : *N*,*N*,*N*′,*N*′-tétraméthyléthylènediamine, *N*,*N*,*N*′,*N*″,*N*″-pentaméthyldiéthylènetriamine, cations fluorobores chélatés, RMN du fluor-19, RMN du bore-11, pyridine, isoxazole, chiral, magnétiquement inéquivalent.

[Traduit par la Rédaction]

Introduction

Boron trifluoride adducts of Lewis bases (electron pair donors D) normally have the covalent structure $D{\cdot}BF_3$, which forms very rapidly, usually with no activation barrier, from D and BF_3. However ionic coordination isomers $D_2BF_2^+{\cdot}BF_4^-$, as well as $D_3BF^{+2}{\cdot}(BF_4^-)_2$ and $D_4B^{+3}{\cdot}(BF_4^-)_3$, are also possible; indeed we have prepared $(quinuclidine)_2BF_2^+{\cdot}BF_4^-$ (1). Occasionally the $D_2BF_2^+{\cdot}BF_4^-$ coordination isomer forms spontaneously, when both donor sites are part of the same chelating ligand. The prototype case was reported by Wiberg and Buchler (2) in 1963, and included an early use of ^{11}B

Received April 14, 1999.

This paper is dedicated to Professor Ted Schaefer in recognition of his outstanding contributions to Canadian chemistry.

J.A.W. Shoemaker and J.S. Hartman.[1] Department of Chemistry, Brock University, St. Catharines, ON L2S 3A1, Canada.

[1]Author to whom correspondence may be addressed. Telephone: (905) 688-5550, ext. 3849.
e-mail: shartman@chemiris.labs.brocku.ca

© 1999 NRC Canada

and ^{19}F as well as ^{1}H NMR to prove the structure. However it is still true that only a few chelated BF_2^+ cations are known (2–6), although there are many neutral BF_2 chelated species, for example, dipyrromethene boron difluoride derivatives with interesting fluorescence properties (7). Attempts at forming chelated BF_2^+ cations with bidentate N-donor ligands have been reported sporadically over the past 30 years (2–6, 8, 9). Typically the reaction with *tert*-amine chelating donors has been carried out in dry ether (2, 8, 9) or $CHCl_2F$ (4), with 1–4 equiv. of $Et_2O{\cdot}BF_3$ at room temperature (2, 8, 9), or with BF_3 at –196°C followed by slow warming (2, 4, 9). During the reaction, fluorine must be transferred between boron atoms in order to form a BF_2^+ cation and BF_4^- anion from two BF_3 units (reaction [1]). In general,

[1] 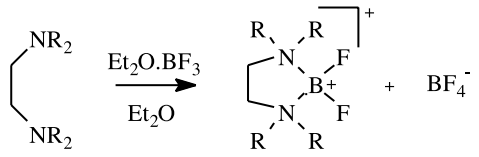

R = H or Me

these methods have been successful if the amine chelating ligands are rigid (compounds **1**–**5**) (2, 4). However, with more flexible ligands, even "textbook" chelating ligands such as ethylenediamine (en) and *N*,*N*,*N*′,*N*′-tetramethylethylenediamine (Me_4en), only non-chelated products

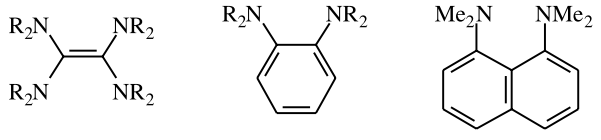

R = H or Me

1,2 **3,4** **5**

are formed: the mono and bis BF_3 adducts of the ligands (8, 9). Although the chelate effect should stabilize the ionic coordination isomer, the activation barrier to transfer of a fluoride ion apparently interferes, and the simpler process of covalent BF_3 adduct formation occurs instead. It seems that only when the two donor sites are held in close proximity is there a good chance of forming the ionic isomer. To further study these systems, alternative approaches to the synthesis of chelated $D_2BF_2^+$ ions are needed.

Our recent studies of the formation of four-coordinate fluoroboron cations (1, 10–12) are based on reactions of the mixed boron trihalide adducts (13). These precursors form fluoroboron cations via heavy halogen displacement:

[2] $D.BF_2X + D' \longrightarrow DD'BF_2^+ + X^-$

$D.BFX_2 + D' \longrightarrow DD'BFX^+ + X^-$

[3] $DD'_2BF^{2+} + X^-$

B—Cl, B—Br, and B—I bonds are much weaker than B—F bonds (444, 368, and 267 kJ/mol, respectively, compared to 646 kJ/mol for B—F in the boron trihalides (14), and the same trend occurs in four-coordinate boron), so the heavy halides are much more easily displaced than fluoride, and this is the basis of our systematic formation of $D_2BF_2^+$, $DD'BF_2^+$, and D_2BFX^+ ions (1, 10–12). We now report the first application of these methods to the synthesis of chelated fluoroboron cations, and the first systematic synthesis of the previously elusive chelated-ethylenediamine class of fluoroboron cations.

Experimental section

Materials

Materials were handled with standard inert-atmosphere Schlenk line and glove bag techniques. Boron trifluoride etherate (Aldrich), ethylenediamine (en) (J.T. Baker Chemical Co., 100.4%), isoxazole (Aldrich, 99%), Me_4en (Aldrich, 99%), and Me_5dien (Aldrich, 99%), and crude *N*,*N*,*N*″,*N*″-tetraethyldiethylenetriamine (Et_4dien) (Aldrich, 90%) were used without further purification. Boron trifluoride etherate was stored at –20°C until use. The bases were dried over 3 Å Molecular Sieves that had been heated in a muffle furnace at 400°C for more than 3 h and cooled over a period of 0.5 h in a vacuum desiccator. Boron trifluoride (Aldrich, 99.5%), boron trichloride (Matheson, 99.5%), boron tribromide (Aldrich, 99.9%), ammonium hexafluorophosphate (Aldrich, 95+%), and pyridine (Aldrich, 99.5%) were all handled as described previously (10, 11). Acetone (Caledon, HPLC grade), chloroform (Caledon, hydrocarbon stabilized, 99.8%), chloroform-d_1 (Cambridge Isotope Laboratories, 99.8%), nitromethane (Fisher Scientific Co.), and sulpholane (BDH) were dried over 3 Å Molecular Sieves. Hexane (Caledon, HPLC grade) was dried over sodium wire. All solvents were used without further purification.

Mixed boron halide adducts and salts

The pyr·BF_nCl_{3-n} (n = 0–3) adduct system was prepared by the method used previously (10), and the same method was used to prepare the ISOX·BF_nX_{3-n} systems (ISOX is isoxazole, **6**). ^{11}B and ^{19}F NMR parameters for the ISOX·BF_nX_{3-n} adducts in chloroform are as follows: ISOX·BF_3: ^{11}B, –0.6 ppm,

6

^{19}F, –149.0 ppm, $^1J_{BF}$ not resolved; ISOX·BF_2Cl: ^{11}B, 2.6 ppm, ^{19}F, –130.9 ppm, $^1J_{BF}$ = 32.9 Hz; ISOX·$BFCl_2$: ^{11}B, 4.9 ppm, ^{19}F, –123.4 ppm, $^1J_{BF}$ = 61.0 Hz; ISOX·BCl_3: ^{11}B, 4.9 ppm; ISOX·BF_2Br: ^{11}B, 0.4 ppm, ^{19}F, –124.3 ppm, $^1J_{BF}$ = 45.1 Hz; ISOX·$BFBr_2$: ^{11}B, –3.1 ppm, ^{19}F, –117.3 ppm, $^1J_{BF}$ = 81.4 Hz; ISOX·BBr_3: ^{11}B, –13.4 ppm.

$(pyr)_2BF_2^+{\cdot}PF_6^-$ was prepared by a modification of the method used previously (10), involving precipitation from a 1:1 chloroform:ethanol solution. $(pyr)_2BF_2^+{\cdot}PF_6^-$ decomposes at 95°C. Its NMR parameters in acetone-d_6 are as follows: ^1H: 9.16 ppm (s), 8.70 ppm, $^3J_{HH}$ = 7.2 Hz (t), and 8.20 ppm, $^3J_{HH}$ = 7.0 Hz (t); ^{11}B: 3.0 ppm, $^1J_{BF}$ = 23.2 Hz;

© 1999 NRC Canada

Table 1. NMR parameters of haloboron cations.

	^{19}F chemical shift (ppm) in		^{11}B chemical shift (ppm) in		$^1J_{BF}$ (Hz) in	
	$CDCl_3$	Acetone	$CDCl_3$	Acetone	$CDCl_3$	Acetone
$(pyr)(Me_4en)BF_2^+$	–160.8	–158.7			29.0	29.2
$(pyr)(Me_5dien)BF_2^+$	–160.5	–158.7			28.8	27.4
$(en)BF_2^+$		–156.2				32.6
$(Me_4en)BF_2^+$	–156.6	–154.7	3.7	4.4	32.7	31.4
$(Me_5dien)BF_2^{+a}$	–153.9	–152.0	3.5	4.6	32.9	32.9
	–155.1	–153.0			32.9	32.9
$(Me_4en)BFCl^+$	–139.9	–137.5[b]	8.8	9.2[b]	60.5	58.6[b]
$(Me_5dien)BFCl^+$	–137.5	–135.1[b]	8.8	9.4[b]	61.0	60.2[b]
	–140.6	–137.7[b]	8.8	9.3[b]	61.0	60.2[b]

[a]Coupling constants ($^1J_{BF}$) obtained from the ^{11}B spectra are somewhat larger than those determined from the ^{19}F spectra: 33.5 Hz in $CDCl_3$, 34.5 Hz in acetone.

[b]Insoluble in acetone; obtained in 3:1 acetone:sulpholane.

^{13}C: 147.5, 144.8, and 128.9 ppm; ^{19}F: –70.6 ppm, $^1J_{PF}$ = 707.2 Hz, and –153.4 ppm, $^1J_{BF}$ = 23.2 Hz; and ^{31}P: –140.8 ppm, $^1J_{PF}$ = 707.2 Hz.

Instrumentation

Most ^{19}F, ^{11}B, and all ^{31}P NMR spectra were obtained on a Bruker AC-200 4.7 T multinuclear Fourier Transform NMR spectrometer operating at 188.31 MHz (^{19}F), 64.20 MHz (^{11}B), and 81.01 MHz (^{31}P), using 5 mm NMR tubes. ^{19}F spectra were obtained with 16K FIDs, 16K zero-filling, and spectral windows of up to 35 000 Hz, with between 256 and 4096 30° pulses and a relaxation delay of 1.0 s. The 90° pulse length was 6.6 μs. ^{19}F chemical shifts are accurate to ±0.1 ppm and were internally referenced to C_6F_6 as a secondary standard (–162.7 ppm from $CFC1_3$), and are reported in ppm from $CFC1_3$. $^1J_{BF}$ coupling constants are accurate to ±1 Hz. ^{11}B spectra were obtained with 16K FIDs, 16K zero-filling, and spectral windows of up to 6400 Hz, with between 256 and 4096 30° pulses and a relaxation delay of between 0.5 and 10 s. The 90° pulse length was 17.1 μs. ^{11}B chemical shifts are accurate to ±0.1 ppm and were externally referenced to $Et_2O{\cdot}BF_3$. ^{31}P spectra were obtained with 16K FIDs, 16K zero-filling, and spectral windows of up to 36 000 Hz, with between 4096 and 64K 30° pulses and a relaxation delay of 0.5 s. The 90° pulse length was 17.1 μs. ^{31}P chemical shifts are accurate to ±0.1 ppm and were externally referenced to 85% H_3PO_4.

Some ^{19}F, ^{11}B, $^{11}B\{^{19}F\}$, ^{19}F–^{19}F COSY, and ^{11}B–^{19}F HETCOR NMR spectra were obtained at 30°C on a Bruker DRX-500 11.7 T multinuclear Fourier Transform NMR spectrometer (McMaster University) operating at 470.53 MHz (^{19}F) and 160.46 MHz (^{11}B) using between 40 and 128 30° pulses with 32K FIDs. The 90° pulse durations were 7.5 μs (^{19}F) and 15.0 μs (^{11}B). Spectral windows of 42 016 Hz (^{19}F) and 40 000 Hz (^{11}B) were used. $^{11}B\{^{19}F\}$ decoupling experiments used selective and broad band decoupling pulse power between 25 and 35 dB. ^{19}F–^{19}F COSY experiments were performed using the Bruker cosy45 pulse program, with a 2.0 s relaxation delay. ^{11}B–^{19}F HETCOR experiments used the Bruker hxcocp pulse program, with the BIRD sequence removed. The BIRD sequence was removed because there was no $^3J_{HB}$ or $^4J_{HF}$ coupling visible, and the sequence induced T_1 artifacts in our spectra. The relaxation delay was 1.0 s.

^{11}B solid-state magic angle spinning (MAS) NMR spectra of the samples were obtained on a Bruker DPX-300 7.4 T multinuclear Fourier Transform NMR spectrometer operating at 96.29 MHz, using a Bruker MAS probe with 4 mm spinners (capacity ~100 mg) and spin rates of 5–12.5 kHz. From 256 to 2048 scans were obtained, with relaxation delays of between 0.5 to 5.0 s between scans. 32K data points were obtained, and Fourier transformed with 5–15 Hz of line broadening. Trimethyl borate was used as the external standard, with its chemical shift being set to 18.3 ppm from $Et_2O{\cdot}BF_3$.

Routine ^1H, ^1H–^1H COSY, and ^{13}C spectra were obtained on the Bruker DPX-300 7.4 T multinuclear Fourier Transform NMR spectrometer operating at 300.13 and 75.45 MHz, respectively, and referenced to internal TMS.

Positive and negative ion FAB spectra were obtained on a Concept 1S double beam mass spectrometer with 8 kV accelerating voltage, using Xe collision gas at 7.5 W power. 3-nitrobenzyl alcohol (NBA) was used as the liquid matrix. Data were collected on a Kratos DART data system with SUN Spectrostation 10, using XMACH3 software.

Semi-empirical calculations at the PM3 level were performed via MacSpartan 1.7.1 software on an Apple 7600 Power PC with a 233 MHz processor.

Results

(a) The pyr·BF_nCl_{3-n} system: reactions with Me_4en

Addition of 2.5 mol equiv. of Me_4en to a pyr·BF_nCl_{3-n} (BF_3:BCl_3 = 1:1.5) solution in chloroform gives initially $(pyr)(Me_4en)BF_2^+$ from pyr·BF_2Cl. Its NMR parameters are given in Table 1. The singly coordinated Me_4en then readily displaces the remaining pyridine, giving chelated $(Me_4en)BF_2^+$ (**7**) (eq [4]). The cation **7** precipitates from chloroform as the white chloride salt, identified by its positive ion FAB mass spectrum: $(Me_4en)BF_2^+$ (165 *m/z* (100%)) and ion clusters $((Me_4en)BF_2^+)_2(Cl^-)$ (365 *m/z* (5.6%)), $((Me_4en)BF_2^+)_3(Cl^-)_2$ (565 *m/z*), and $((Me_4en)BF_2^+)_4(Cl^-)_3$ (767 *m/z*) (Fig. 1) and elemental analysis: C calcd. = 35.97%, found = 36.13%; N calcd. = 13.98%, found = 14.09%; H calcd. = 8.05%, found = 8.30%.

A side reaction occurs: displacement of pyr from pyr·BF_3 to form the monodentate $Me_4en{\cdot}BF_3$ adduct (Table 2). This reaction is selective and attacks only the BF_3 adduct, as we

© 1999 NRC Canada

Fig. 1. Positive ion fast atom bombardment mass spectrum of $(Me_4en)BF_2^+ \cdot Cl^-$ in a 3-nitrobenzyl alcohol (NBA) matrix, showing the ion cluster signals C_nA_{n-1} (C = cation, A = anion).

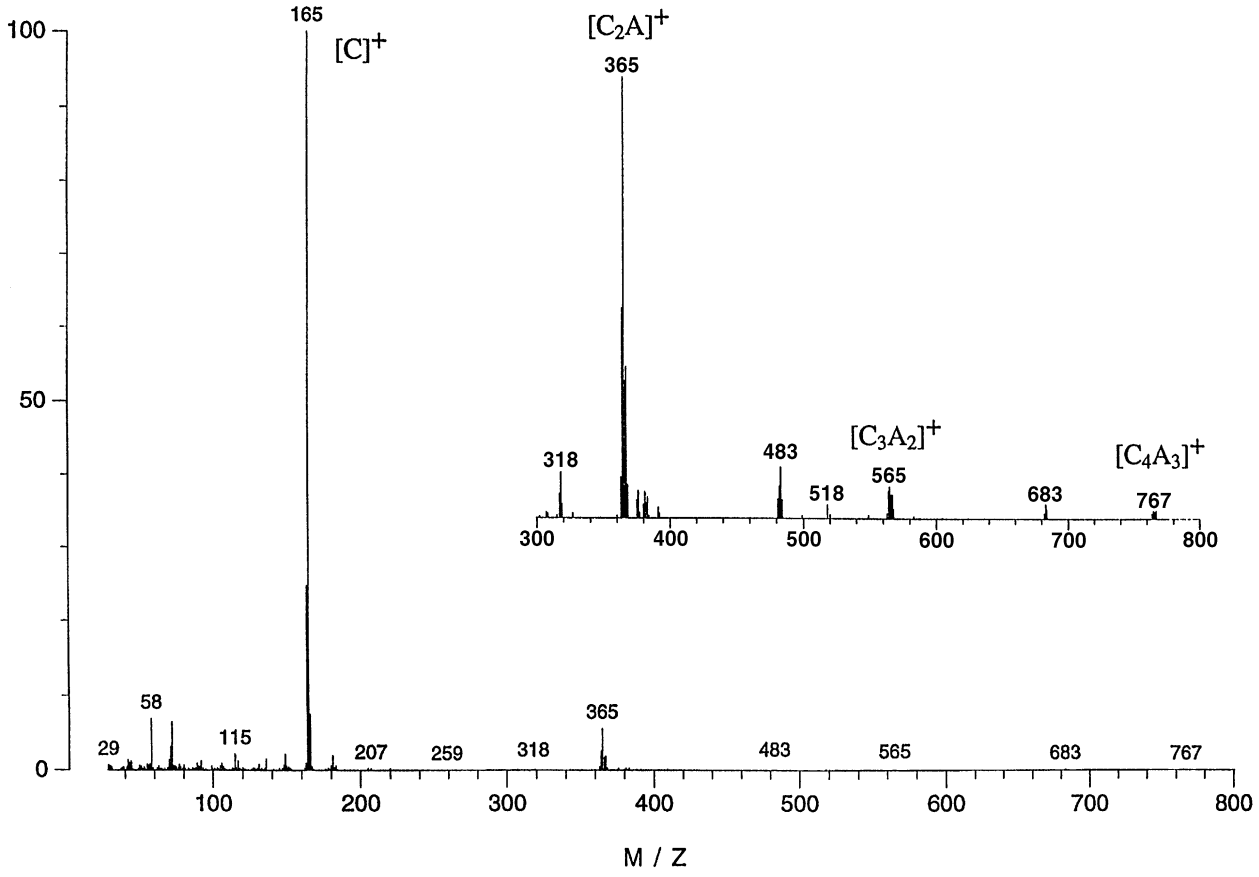

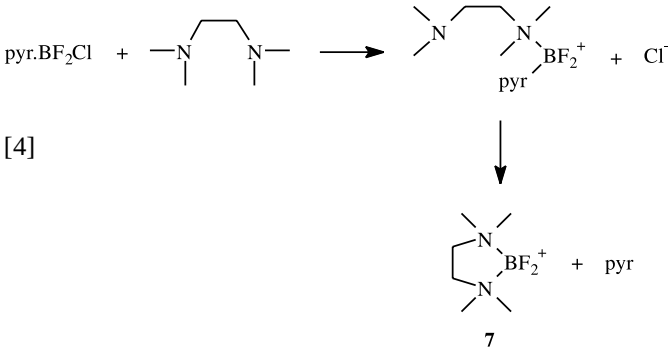

[4]

7

have observed in similar adduct systems (12). Although both nitrogen atoms of Me_4en are available to coordinate to BF_3 (8, 9) (see $Et_2O \cdot BF_3$ section below) only the mono-BF_3 adduct forms in detectable amounts by displacement of pyr from $pyr \cdot BF_3$. This reaction is troublesome because it occurs faster than the formation of our desired $(Me_4en)BF_2^+$ cation, and gives a large amount of uncomplexed pyridine in solution, which then reacts with $pyr \cdot BF_2Cl$ to form $(pyr)_2BF_2^+$ (10). To compensate, a large excess of Me_4en must be added to compete effectively with the displaced pyr. Even so, the best yield of $(Me_4en)BF_2^+$ obtainable is about 60%.

On standing for several days at room temperature this problem rights itself, for the $(pyr)_2BF_2^+$ so formed is used up by reaction with Me_4en, and $(Me_4en)BF_2^+$ continues to precipitate as the chloride salt. A positive ion FAB mass spectrum of the mother liquor after a week confirms this, for only the $(Me_4en)BF_2^+$ and $(Me_4en)BFCl^+$ (see below) cations are detected. Thus, there are rapid initial reactions followed by much slower reactions, as we have noted before in other haloboron adduct–cation systems (12).

As well as the slow formation of more $(Me_4en)BF_2^+$ from $(pyr)_2BF_2^+$, there is also the slow formation of $(Me_4en)BFCl^+$ from $pyr \cdot BFCl_2$ (eq. [3]), and again there is competition from free pyr, which generates $(pyr)_2BFCl^+$ from $pyr \cdot BFCl_2$: confirmed by its NMR data (10) and by a low-intensity peak at 223 *m/z* in the FAB mass spectrum of the solution after standing for 1 week.

(b) The $pyr \cdot BF_nCl_{3-n}$ system: reactions with Me_5dien

Addition of 2.5 mol equiv. of Me_5dien to a $pyr \cdot BF_nCl_{3-n}$ (BF_3:BCl_3 = 1:1.5) solution in chloroform leads to results similar to those described above for Me_4en except that none of the products precipitate from solution, which allows monitoring by solution NMR (Fig. 2). Initial formation of $(pyr)(Me_5dien)BF_2^+$ from $pyr \cdot BF_2Cl$ occurs readily. The coordinated Me_5dien then displaces pyr from the mixed-donor cation, giving the desired chelated $(Me_5dien)BF_2^+$ cation **8**

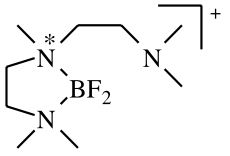

8

© 1999 NRC Canada

Table 2. NMR parameters of boron trihalide adducts.

	^{19}F chemical shift (ppm) in		^{11}B chemical shift (ppm) in		$^{1}J_{BF}$ (Hz) in	
	$CDCl_3$	CH_3NO_2	$CDCl_3$	CH_3NO_2	$CDCl_3$	CH_3NO_2
$Me_4en{\cdot}BF_3$	–162.3	–157.6	0.1	1.1	15.5	15.4
$Me_5dien{\cdot}BF_3$[a]	–162.0	–158.8	–0.2		15.9	15.9
$Me_5dien{\cdot}BF_3$[b]	–160.8	–158.7	–0.2		15.5	
$Me_4en{\cdot}(BF_3)_2$	–158.6	–157.2			15.5	15.1
$Me_5dien{\cdot}(BF_3)_2$[c]		–158.1				15.5
$Me_5dien{\cdot}(BF_3)_2$[d]		–156.9				15.5
$Me_5dien{\cdot}(BF_3)_3$		–151.8 (3F)				15.5
		–157.3 (6F)				15.0
$Me_4en{\cdot}BF_2Cl$		–135.1		5.6		43.9
$Me_4en{\cdot}BFCl_2$		–123.3		9.4		70.3
$Me_5dien{\cdot}BFCl_2$	–126.9	–124.9	8.4	9.4	70.2	70.8
$Me_4en{\cdot}BCl_3$			10.2	11.1		
$Me_5dien{\cdot}BCl_3$			10.0	11.1		

[a]Coordination at an end nitrogen.

[b]Coordination at middle nitrogen.

[c]Dicoordination at both end nitrogen atoms.

[d]Dicoordination at the middle and one end nitrogen. ^{19}F chemical shifts of the centre and end coordinated BF_3 overlap with a separation of only 0.05 ppm at 188.31 MHz.

Fig. 2. 188.31 MHz ^{19}F NMR spectra of a $CDCl_3$ solution of $pyr{\cdot}BF_nCl_{3-n}$ (mole ratio pyr:BF_3:BCl_3 = 2.5:1:1.5). (*a*) Initial solution; (*b*) after Me_5dien addition (same number of moles as moles pyr present); (*c*) after standing for 2.3 h; (*d*) after standing for 13.8 h.

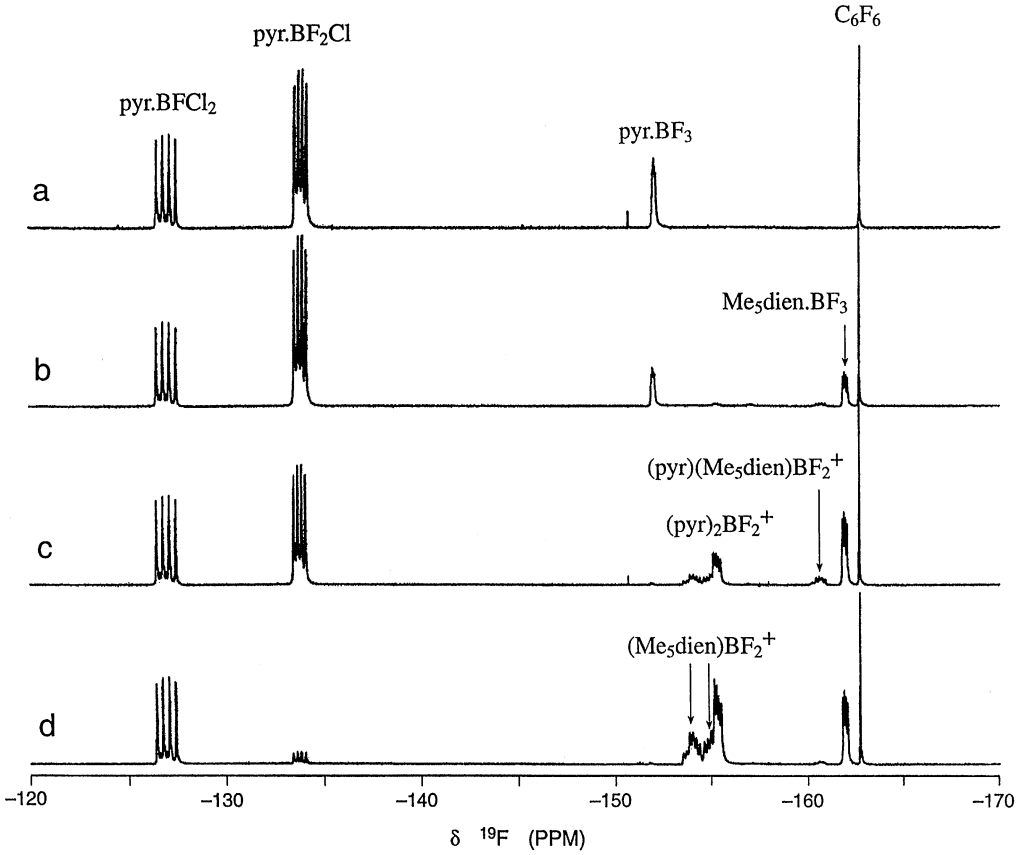

(Table 1 and Fig. 2). The centre nitrogen of Me_5dien becomes chiral upon formation of the +1 cation, making the BF_2 fluorines prochiral and magnetically nonequivalent. These fluorines are distinctive in a ^{19}F–^{19}F COSY NMR spectrum (Fig. 3) as the only fluorine signals that give cross peaks, since this is the only compound in the complex mixture with two nonequivalent fluorines. The $^{2}J_{FF}$ value of 61.2 Hz is comparable to the few available literature values for geminal FBF coupling (15, 16). The presence of $(Me_5dien)BF_2^+$ was confirmed by a positive ion FAB mass spectrum obtained di-

© 1999 NRC Canada

Fig. 3. 470.53 MHz partial ^{19}F–^{19}F COSY NMR spectrum of $(Me_5dien)BF_2^+$ and other species present in a solution of 4-Mepyr·BF_nCl_{3-n} following reaction with Me_5dien and standing for 3 months. Some fluorine-containing impurity species do not give rise to signals on the diagonal, apparently because of their longer spin-lattice relaxation times.

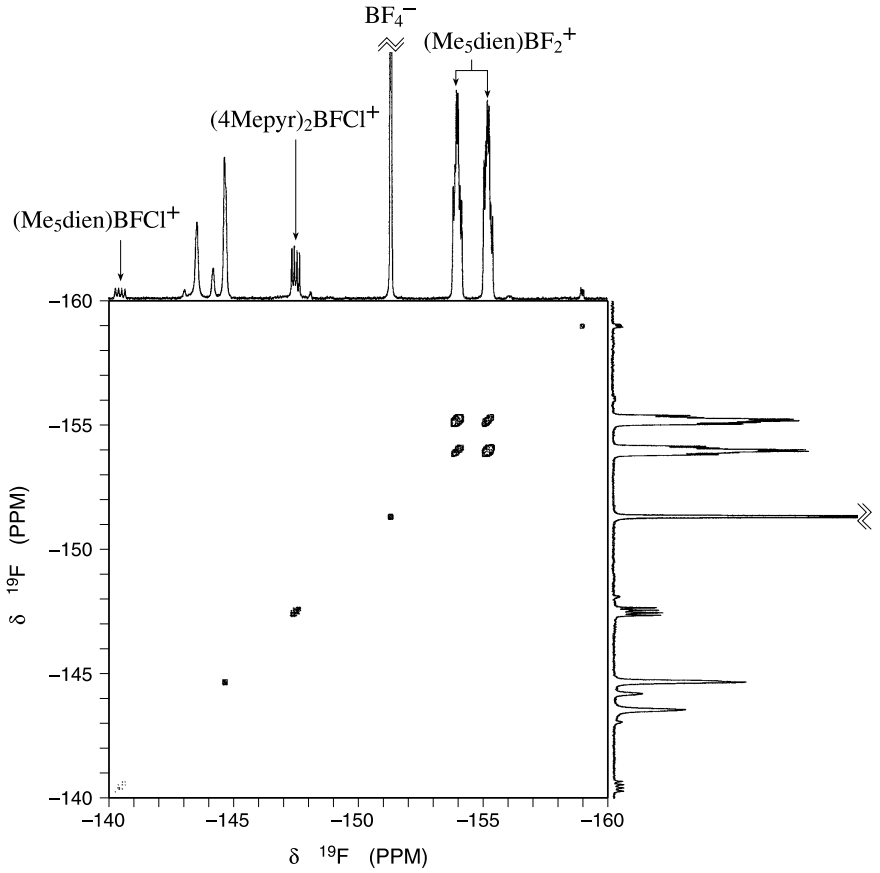

rectly from the chloroform solution introduced into an NBA matrix: parent ion at 221 (12.5%) and 222 (49.7%) *m/z*; $Me_5dien·H^+$ was the ion of greatest intensity.

Like Me_4en, Me_5dien readily displaces pyr from pyr·BF_3, forming a monodentate $Me_5dien·BF_3$ adduct (Fig. 2 and Table 2). Either an end nitrogen or the centre nitrogen of Me_5dien can be the donor site, and we detect both isomers of the mono-BF_3 adduct by reaction of Me_5dien with $Et_2O·BF_3$ (see below), but the ^{19}F chemical shift indicates that only the end nitrogen displaces pyr from pyr·BF_3, consistent with the greater steric hindrance of the centre nitrogen. As with the Me_4en system described above, this side reaction is troublesome because the liberated pyridine competes with Me_5dien in forming fluoroboron cations. The initial reactions occurring on the scale of hours, illustrated in Fig. 2, are followed by slower reactions requiring several days. This is a characteristic of many of our mixed boron trihalide – fluoroboron cation systems: many different reactions can occur, some fast and others extremely slow (11, 12). Figure 4 shows ^{19}F NMR monitoring of the later stages of this reaction. As in the Me_4en system, several things happen. Me_5dien slowly displaces pyridine from $(pyr)_2BF_2^+$ so that eventually the only remaining BF_2^+ cation is $(Me_5dien)BF_2^+$. Also $(Me_5dien)BFCl^+$ forms very slowly, over many days, from pyr·$BFCl_2$. Both boron and the central nitrogen of bidentate Me_5dien are chiral, and the well-separated ^{19}F 1:1:1:1 quartets at –137.5 and –140.5 ppm, are assigned to the two diastereomers of $(Me_5dien)BFCl^+$, which form at a ratio of about 1:3 in chloroform. The presence of $(Me_5dien)BFCl^+$ is confirmed by a positive ion FAB mass spectrum taken directly from the same chloroform solution: parent ion at 237 (2.4%) and 238 (8.2%) *m/z*.

Not only $(Me_5dien)BFCl^+$ but also $(pyr)_2BFCl^+$ forms from pyr·$BFCl_2$. The presence of these two cations, after the complete loss of $(pyr)_2BF_2^+$, complicates the system. $(pyr)_2BFCl^+$, unlike $(pyr)_2BF_2^+$, does not undergo appreciable pyridine displacement by Me_5dien, and the presence of this second $BFCl^+$ cation has prevented isolation of $(Me_5dien)BFCl^+$. These two species, along with $(Me_5dien)BF_2^+$, persist in solution for many months. A ^{11}B–^{19}F HETCOR NMR spectrum (Fig. 5), of a solution that had been standing at room temperature for 3 months (and involved the 4-Mepyr rather than the pyr adduct system; the behavior is essentially identical), displays the magnetically nonequivalent fluorine atoms of the $(Me_5dien)BF_2^+$ cation, both correlating to the same ^{11}B 1:2:1 triplet. (Only one diasteoremer of $(Me_5dien)BFCl^+$ is visible in this spectrum.)

We have not found any evidence for tridentate coordination of Me_5dien, i.e., $(Me_5dien)BF^{2+}·Cl^-_2$, which would form by displacement of a further Cl^- from $(Me_5dien)BFCl^+$. This species would have distinctive ^{19}F NMR parameters (10, 11), but FAB mass spectrometry would not distinguish the $(Me_5dien)BFCl^+$ cation from an ion pair containing a tridentate $(Me_5dien)BF^{+2}$ cation and a Cl^- counterion. One of

© 1999 NRC Canada

Fig. 4. 188.31 MHz ^{19}F NMR spectra of the same solution as in Fig. 2 (2.5:1:1.5 mol pyr·BF_nCl_{3-n} + 2.5 mol Me_5dien), showing the appearance of further new fluorine-containing species after long reaction times at room temperature. The reaction times are (*a*) 2, (*b*) 4, (*c*) 6, (*d*) 8, (*e*) 10 days.

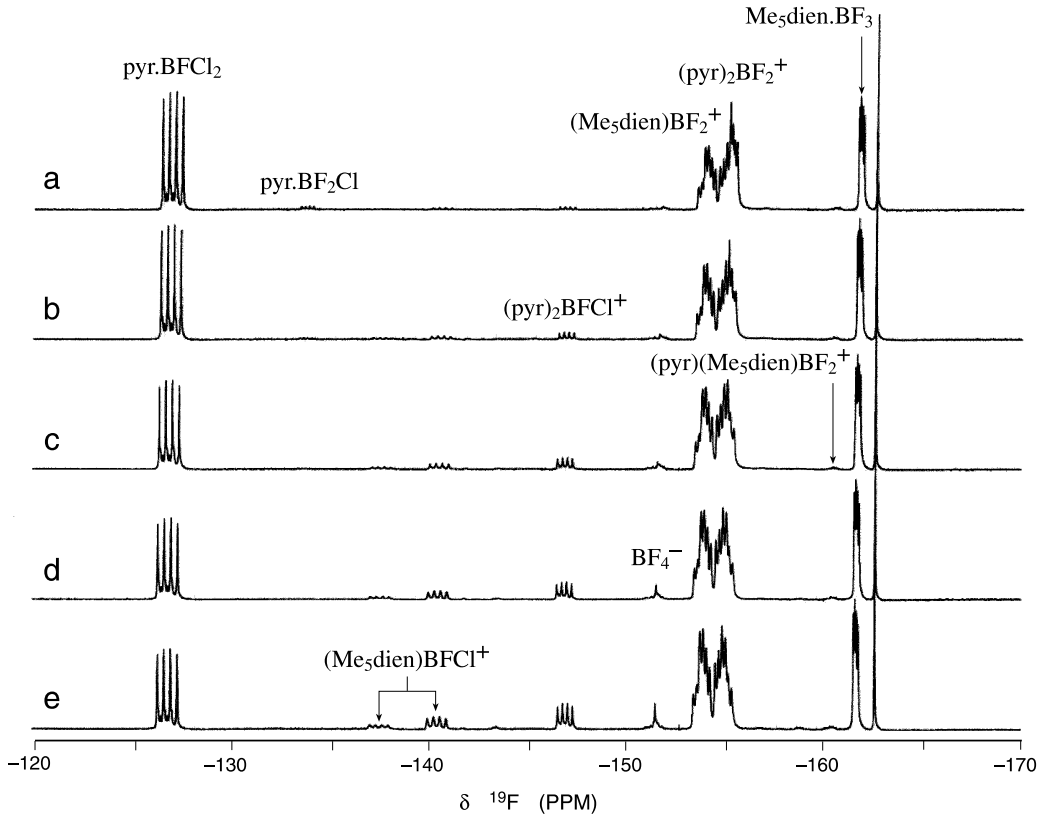

Fig. 5. 11.7 T partial ^{11}B–^{19}F HETCOR NMR spectrum of species formed from a solution of 4-methylpyridine to which Me_5dien had been added, after standing for 3 months. The signals of both magnetically nonequivalent BF_2 fluorines correlate with the ^{11}B 1:2:1 triplet of $(Me_5dien)BF_2^+$.

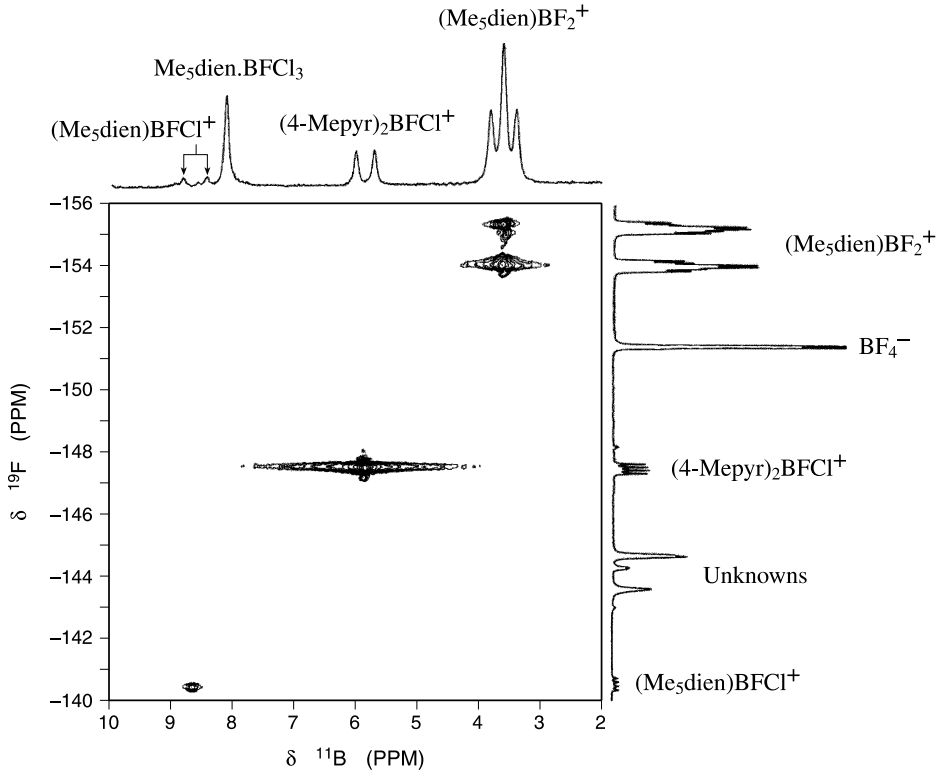

© 1999 NRC Canada

the objectives of the studies described below, involving mixed boron trihalide adducts of isoxazole, which is a much weaker donor than pyridine, and Br as well as Cl as the heavy halogen since Br^- is a better leaving group than Cl^-, was to obtain the fully chelated (tridentate) species.

(c) The ISOX·BF_nX_{3-n} (X = Cl, Br) systems: reactions with Me_4en

Addition of 2.0 and 4.0 mol equiv. Me_4en to chloroform solutions of ISOX·BF_nCl_{3-n} (ISOX:BF_3:BCl_3 = 2:1:1 and 4:1:3 mol, respectively) caused the colourless solutions to immediately turn yellow, and an orange solid to form at the top. ^{19}F and ^{11}B NMR spectra of the solutions, after standing for 24 h, contained signals of Me_4en·BF_3, Me_4en·$BFCl_2$, (Me_4en)$BFCl^+$, and Me_4en·BCl_3, and for the solution richer in BCl_3, a small amount of (Me_4en)BF_2^+ (Tables 1 and 2). The orange solid, after drying, gave positive ion FAB mass spectra showing the presence of (Me_4en)BF_2^+ (165 *m/z* (100%)) and (Me_4en)$BFCl^+$ (181 *m/z* (16 and 43% in the two samples)). The orange solid, dissolved in 1:1 acetone:sulpholane or nitromethane, gave ^{11}B and ^{19}F NMR signals of the same four species as the yellow solution, plus (Me_4en)BF_2^+ and (or) Me_4en·BF_2Cl. (The former, as its chloride salt, is very insoluble in chloroform; the latter is detected only rarely because chloride is displaced very readily by the uncoordinated nitrogen of Me_4en, giving chelated (Me_4en)BF_2^+.)

The ISOX·BF_nCl_{3-n} system's behavior with Me_4en differs greatly from that of the pyr·BF_nCl_{3-n} system described above, apparently due to the much weaker basicity of ISOX (pK_b = 12.7) than pyridine (pK_b = 8.8). Me_4en (pK_b^1 = 5.0) (17) readily displaces ISOX from all of the ISOX·BF_nCl_{3-n} adducts, giving the full series of Me_4en·BF_nCl_{3-n} adducts (in which Me_4en is monodentate), followed by chelate ring closure with expulsion of Cl^- to give the BF_2^+ (reaction [5]) and $BFCl^+$ cations, which occurs especially readily for Me_4en·BF_2Cl. In contrast, in the pyr·BF_nCl_{3-n} system described above, Me_4en preferentially displaces Cl^- rather than pyr. Furthermore, the displaced ISOX, unlike pyr, is inert and does not cause undesirable side reactions. These differences have important implications for synthesis.

Br^- is a much better leaving group than Cl^- in mixed boron trihalide adducts, so fluoroboron cations form much more rapidly from BF_2Br adducts than from the corresponding BF_2Cl adducts (1). Thus we have explored the ISOX·BF_nBr_{3-n} system, with its two very easily displaceable groups ISOX and Br^-, as a possible starting material for preparing chelated fluoroboron cations. However, in the ISOX system the crucial BF_2Br and $BFBr_2$ adducts form in far less than their statistical proportions at equilibrium compared to the unmixed-halogen adducts, as is commonly observed in mixed boron trihalide adduct systems involving "soft" donors (13).

Addition of 5.0 and 4.0 mol equiv. Me_4en to chloroform solutions of ISOX·BF_nBr_{3-n} (ISOX:BF_3:BBr_3 = 5:2:3 and 4:1:3 mol equiv., respectively) caused the colourless solution to immediately turn yellow, and a brown solid to form at the top. ^{19}F and ^{11}B NMR of the solutions detected only a very small amount of Me_4en·$BFBr_2$ and (Me_4en)BF_2^+ in addition to some unreacted ISOX·BF_3 and an unidentified ^{19}F singlet at –151.3 ppm. The brown solid, after drying, gave FAB mass spectra showing the presence of Me_4en·H^+ (117 *m/z* (100%)), (Me_4en)BF_2^+ (165 *m/z* (22 and 27%)), Me_4en·H·HBr^+ (197 *m/z* (5 and 7%)), and (Me_4en)$BFBr^+$ (225 *m/z* (Br-rich sample only; 5%)). Most of the solid was insoluble in nitromethane, acetone, acetone–sulpholane, and acetonitrile, and the small amount that did dissolve gave only the NMR signals seen in the chloroform mother liquor. ^{11}B MAS NMR spectra of a similar solid are described below.

(d) The ISOX·BF_nX_{3-n} (X = Cl, Br) systems: reaction with Me_5dien

Addition of 2.0 and 4.0 mol equiv. Me_5dien to chloroform solutions of ISOX·BF_nCl_{3-n} (ISOX:BF_3:BCl_3 = 2:1:1 and 4:1:3 mol, respectively) caused the colourless solutions to immediately turn orange, and a red solid to form at the top. ^{19}F and ^{11}B NMR spectra of the solutions, after standing for 24 h, contained signals of the (Me_5dien)BF_2^+ and (Me_5dien)$BFCl^+$ cations (both diastereomers of the latter, in a 1:3 ratio), as well as Me_5dien·BF_3, Me_5dien·$BFCl_2$, and Me_5dien·BCl_3 (Tables 1 and 2). The ^{19}F spectrum also included five singlets in the –150 to –160 ppm range, arising from unknown species, without any corresponding ^{11}B signals. Positive ion FAB mass spectra of the solution included peaks consistent with (Me_5dien)BF_2^+ (222 *m/z* (42.3%)), (Me_5dien)$BFCl^+$ (238 *m/z* (13.3%)), and Me_5dien·H^+ (174 *m/z* (100%)). Positive ion FAB mass spectra of the red solid, after drying, showed the presence of (Me_5dien)BF_2^+ (222 *m/z* (62 and 52%)) and (Me_5dien)$BFCl^+$ (238 *m/z* (24 and 31%)), and Me_5dien·H^+ (174 *m/z* (100%)). The red solid partially dissolved in 1:1 acetone:sulpholane and nitromethane, and ^{11}B and ^{19}F NMR spectra of the solution showed the same species as were present in the mother liquor.

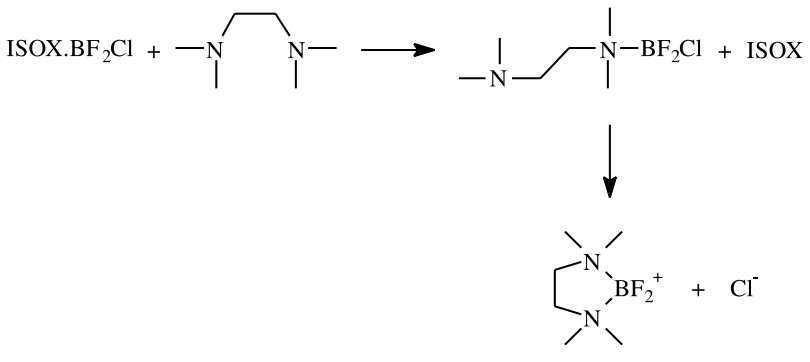

[5]

7

© 1999 NRC Canada

Fig. 6. 96.29 MHz ^{11}B MAS NMR spectra of the insoluble material formed from the reaction of Me_5dien with $ISOX{\cdot}BF_nBr_{3-n}$ solutions of initial proportions of $ISOX:BF_3:BBr_3$ of (*a*) 5:2:3, (*b*) 4:1:3.

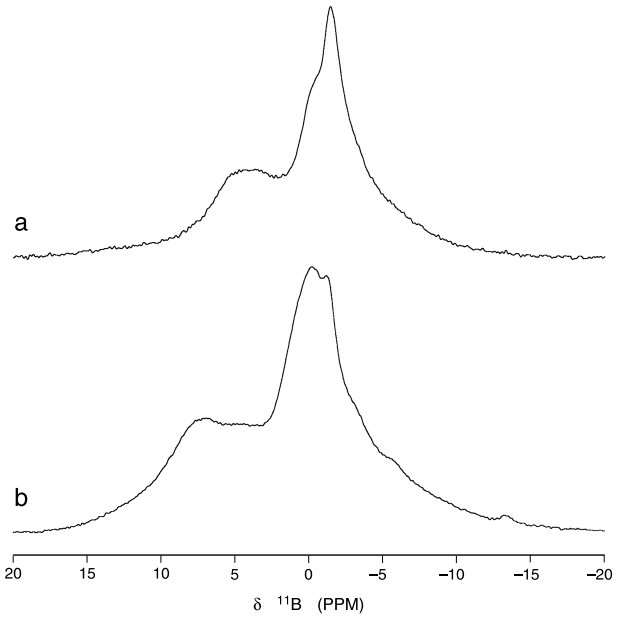

Addition of 5.0 and 4.0 mol equiv. Me_5dien to chloroform solutions of $ISOX{\cdot}BF_nBr_{3-n}$ ($ISOX:BF_3:BBr_3$ = 5:2:3 and 4:1:3 mol, respectively) caused the colourless solutions to immediately turn yellow, and a brown solid to form at the top. ^{19}F and ^{11}B NMR of the chloroform solutions gave a small signal of $Me_5dien{\cdot}BF_3$, and other ^{19}F peaks in the –150 to –160 ppm region arising from unknown species. The brown solid, after drying, gave positive ion FAB mass spectra showing the presence of $Me_5dien{\cdot}H^+$ (174 *m*/*z* (100%)), $(Me_5dien)BF_2^+$ (222 *m*/*z* (9 and 6%)), $Me_5dien{\cdot}H{\cdot}HBr^+$ (254 *m*/*z* (18 and 25%)), and $(Me_5dien)BFBr^+$ (282 *m*/*z* (2%)). No new NMR signals were obtained on attempts to dissolve the solid in nitromethane, acetone, 1:1 acetone:sulpholane, or acetonitrile.

^{11}B MAS NMR of the solid gives further information, despite broadening by dipolar coupling to ^{19}F and quadrupolar broadening (Fig. 6). The solids from the Me_4en and the Me_5dien systems give similar spectra. We have shown (unpublished work) that there is a good correlation between solution and solid-state ^{11}B chemical shifts of fluoroboron adduct and cation species, with the solid NMR signal being a few ppm to lower frequency (higher field) than the solution signal. Despite the poor resolution, Fig. 6 clearly shows differences in relative peak intensities with increased Br enrichment. $D{\cdot}BF_nBr_{3-n}$ adducts absorb in the 2 to –10 ppm range while $D_2BF_nBr_{2-n}^+$ cations absorb in the 10–2 ppm range, and there are strong signals in both regions, with the sample prepared from the more bromine-rich mixture (Fig. 6*b*) having much more intensity at lower field corresponding to the presence of a larger proportion of $BF_nBr_{2-n}^+$ cations. This is consistent with the positive ion FAB spectra in which relative peak intensities suggest greater cation intensity, especially the $BFBr^+$ cation, when the starting materials are more bromine-rich.

(e) Stepwise displacement of pyr from $(pyr)_2BF_2^+{\cdot}PF_6^-$

Excess Me_4en (from 2 to 64 mol equiv.), added to acetone solutions containing 20 mg/mL of $(pyr)_2BF_2^+{\cdot}PF_6^-$, reacts over several hours to give first the nonchelated $(pyr)(Me_4en)BF_2^+$, detectable by NMR but never present in high concentrations, and finally chelated $(Me_4en)BF_2^+$. The higher the excess of Me_4en, the greater the yield of the $(Me_4en)BF_2^+$, up to about a 16 mol equivalent excess, beyond which the overall yield stayed constant at about 50–60%, with or without heating to 50°C to accelerate the reaction. Positive ion FAB mass spectra confirmed the existence of $(Me_4en)BF_2^+$ in the acetone solution. However impurities form as well.

Excess Me_5dien (from 2 to 16 mol equiv.), added to acetone solutions containing 20 mg/mL of $(pyr)_2BF_2^+{\cdot}PF_6^-$, reacts over several hours to give first the nonchelated $(pyr)(Me_5dien)BF_2^+$, which never builds up to high concentrations but reacts to give bidentate $(Me_5dien)BF_2^+$. ^{19}F NMR monitoring of the reaction is shown in Fig. 7. The greater the excess of Me_5dien, the greater the yield of $(Me_5dien)BF_2^+$, up to 35–40% when the molar excess is 10 or greater. Positive ion FAB mass spectra of the acetone solution confirm the existence of $(Me_5dien)BF_2^+$.

However in both systems, ^{19}F spectra show that the formation of fluorine-containing impurities competes with the formation of the chelated cations (Fig. 7). There are four significant ^{19}F impurity signals: δ –138.4 ppm (unknown, though likely $BF_2OH_2^-$ (18)), –144.7 ppm, $^1J_{BF}$ = 13.5 Hz (BF_3OH^- (18)), $pyr{\cdot}BF_3$ and BF_4^-. Work on minimizing the formation of these species is in progress. The BF_3OH^- and (tentative) $BF_2OH_2^-$ ^{19}F signals vary in chemical shift by a few ppm in different samples.

Ethylenediamine (en) and *N*,*N*,*N*″,*N*″-tetraethyldiethylenetriamine (Et_4dien) were also reacted with the $(pyr)_2BF_2^+{\cdot}PF_6^-$ salt at 2 and 10 mol excess concentrations, with and without heating to 50°C. Ethylenediamine, when present in a twofold molar excess, forms the desired $(en)BF_2^+$ (Table 1) in very small quantity at room temperature. Its NMR parameters match those previously obtained, in preliminary experiments at the University of Manitoba, from a minor (less than 1%) product that formed, in addition to the major product $en{\cdot}(BF_3)_2$, from the reaction of BF_3 with a mixture of en and $(en{\cdot}2H)^{2+}{\cdot}(BF_4^-)_2$ (19). Et_4dien gave no NMR evidence of coordination. Both of these bases give much more rapid formation of the same impurity species described above, than are obtained when reacting Me_4en and Me_5dien, and this indicates that N—H bonds, not present in the latter bases, favour the formation of the impurities.

(f) Reaction of chelating donors with $Et_2O{\cdot}BF_3$

In a 1:1 ($Me_4en:Et_2O{\cdot}BF_3$) solution in chloroform, both $Me_4en{\cdot}BF_3$ and $Me_4en{\cdot}(BF_3)_2$ (Table 2) were visible by ^{19}F NMR after 24 h at room temperature. A white precipitate formed over this period of time. It was dried and dissolved in nitromethane, and gave ^{19}F signals of both the mono and bis BF_3 adducts. In $Et_2O{\cdot}BF_3$-rich solutions ($Me_4en:Et_2O{\cdot}BF_3$ = 1:2 and 1:3), only a very small amount of the bis BF_3 adduct was detectable after 24 h. Again the

© 1999 NRC Canada

Fig. 7. 188.31 MHz ^{19}F NMR spectra of an acetone solution of $(pyr)BF_2^+ \cdot PF_6^-$ (10 mg in 500 μL) to which a 16-fold excess of Me_5dien had been added. The PF_6^- fluorine signals (doublet at δ –70.6 ppm; $^1J_{PF}$ = 707 Hz) are not shown. (*a*) Initial spectrum, and following reaction at room temperature for (*b*) 0.8, (*c*) 3.2, (*d*) 6.3, (*e*) 12.6, (*f*) 25.3, (*g*) 50.5 h.

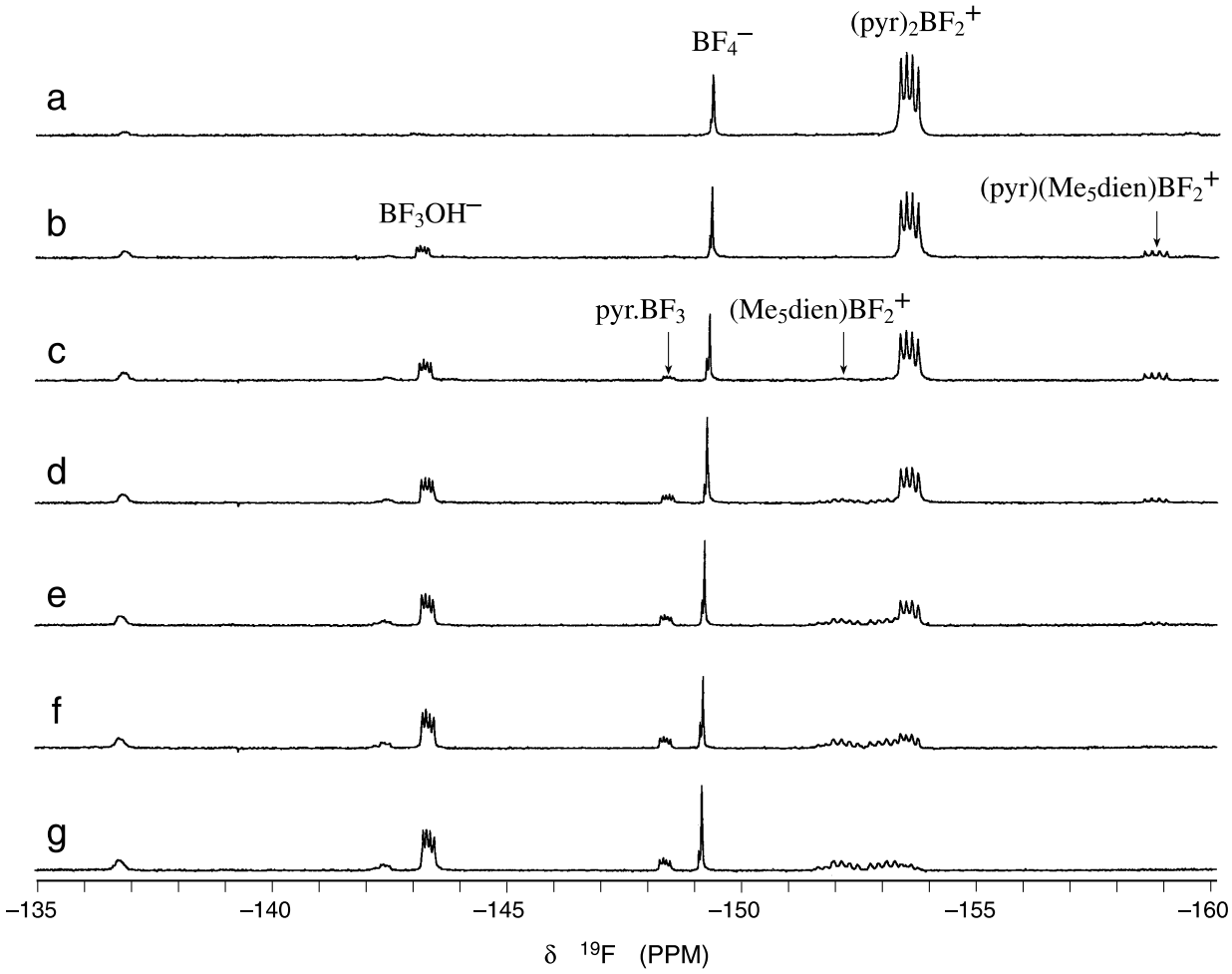

white precipitates, dried and dissolved in nitromethane, gave ^{19}F signals of only the mono and bis BF_3 adducts. There was no indication of $(Me_4en)BF_2^+$, consistent with the work of Brown et al. (8) and Singaram and Pai (9).

In a 1:1 (Me_5dien:$Et_2O \cdot BF_3$) solution in chloroform, both isomers of $Me_5dien \cdot BF_3$ (bonded through the end nitrogen and through the centre nitrogen) were detected by ^{19}F NMR after 24 h. A small signal at –147.4 ppm ($^1J_{BF}$ = 14.2 Hz), consistent with BF_3OH^-, and a few unidentified singlets in the –140 to –150 ppm region, were also visible. The dried white precipitate, dissolved in nitromethane, gave ^{19}F signals for both mono-BF_3 adducts. In a 1:2 Me_5dien:$Et_2O \cdot BF_3$ solution, only the mono-BF_3 adduct bonded through the centre nitrogen was detectable by ^{19}F NMR in solution after 24 h. The white precipitate, dissolved in nitromethane, gave ^{19}F signals that we assign to the bis BF_3 adduct of Me_5dien, with BF_3 coordinated to the two terminal nitrogen atoms (i.e., only one ^{19}F signal); and to the tris BF_3 adduct (two ^{19}F signals, in a 2:1 ratio). In a 1:3 Me_5dien:$Et_2O \cdot BF_3$ solution in chloroform, no adducts could be detected by ^{19}F NMR of the solution after 24 h. The precipitate, dissolved in nitromethane, gave ^{19}F signals corresponding to the tris BF_3 adduct and the bis BF_3 adduct with one terminal nitrogen and the central nitrogen coordinated (two ^{19}F signals, in a 1:1 ratio). A 1:6 Me_5dien:$Et_2O \cdot BF_3$ solution gave the same results as the 1:3 solution: no adduct ^{19}F signals detectable in the solution, and the same species detected in the precipitate. As with the Me_4en:$Et_2O \cdot BF_3$ system, no fluoroboron cations could be detected. The NMR signals of these species were assigned by using chemical shift trends based on steric hindrance of tertiary-amine donors (16), as well as relative peak intensities.

Discussion

(a) Reactivity trends and implications for synthesis

Heavy halide ion and donor molecule displacement from $D \cdot BF_2X$ (D = pyridine or isoxazole) gives the chelated BF_2^+ cations of Me_4en and Me_5dien that are not accessible from $Et_2O \cdot BF_3$. Pyridine displacement from $(pyr)_2BF_2^+$ provides an alternative but less efficient route. The $BFCl^+$ and $BFBr^+$ cations form similarly, but much less readily, by displacement from $D \cdot BFX_2$, which reacts much less readily than the corresponding $D \cdot BF_2X$ when it reacts at all (1, 10–12). Me_5dien behaves like monodentate *tert*-amines, but unlike pyridines and amidines (10, 11), in being unable to displace

© 1999 NRC Canada

the second heavy halogen of $D{\cdot}BFX_2$, so the tridentate $(Me_5dien)BF^{2+}$ does not form. Me_5dien is a versatile tridentate chelating ligand and coordinates to many elements (20), but there is only one report of tridentate chelation to boron: Kelly and co-workers (21) prepared $[(Me_5dien)BH]^{2+}$ by displacement of Me_3N and two iodide ions from $Me_3N{\cdot}BHI_2$. Iodide is by far the best halide leaving group, and displacement from a $D{\cdot}BFI_2$ adduct would have the greatest likelihood of giving tridentate $(Me_5dien)BF^{+2}$. However, $D{\cdot}BFI_2$ adducts are not readily accessible. The formation of mixed F, I boron trihalide adducts is very unfavourable, with only traces forming from the reaction of $D{\cdot}BF_3$ with BI_3, a consequence of Pearson's "symbiotic principle" that we have discussed previously (16).

The much slower displacement of pyridine compared to isoxazole from $D{\cdot}BF_nX_{3-n}$ is consistent with the much higher basicity of pyridine. Pyridine's basicity also complicates the system because the displaced pyridine competes with the chelating donor. Isoxazole's ease of displacement and its inability to participate in further displacement reactions makes the $ISOX{\cdot}BF_nX_{3-n}$ adducts particularly useful in fluoroboron cation synthesis, and further studies are under way. Isoxazole displacement from the $ISOX{\cdot}BF_nX_{3-n}$ adducts also allows the formation of monodentate BF_2X and BFX_2 adducts of the chelating ligands, inaccessible by our usual method of BF_nX_{3-n} adduct formation, which requires an excess boron trihalide stage for halogen redistribution. The monodentate BCl_3 and BBr_3 adducts of Me_4en and Me_5dien adducts also form readily by isoxazole displacement from the corresponding ISOX adducts, but do not form chelated BCl_2^+ or BBr_2^+ cations under our conditions that readily displace heavy halide from the mixed fluorine, heavy halogen adducts.

Chelated $(Me_4en)BF_2^+$ and $(Me_5dien)BF_2^+$ can also be formed by stepwise displacement of pyridine from $(pyr)_2BF_2^+{\cdot}PF_6^-$, but the reaction requires weeks at room temperature. Raising the temperature is not an option, since this increases the proportion of undesirable side products. Displacement of isoxazole from $(ISOX)_2BF_2^+{\cdot}PF_6^-$ would be much faster, but isoxazole is too weak a base to displace heavy halide ion from $ISOX{\cdot}BF_2X$, so we cannot prepare $(ISOX)_2BF_2^+$. The ideal base, still being sought, would be sufficiently strong to form $D_2BF_2^+$ but sufficiently weak and low in steric hindrance to be more easily displaced than pyridine.

(b) Reaction pathways

Our work confirms the reports of Brown et al. (8) and Singaram and Pai (9) that chelated BF_2^+ species are not formed by reaction of Me_4en or similar bases with $Et_2O{\cdot}BF_3$. We could not detect even trace amounts by ^{19}F NMR, but only the mono- and bis-BF_3 adducts and for Me_5dien the tris-BF_3 adduct. This can be explained by considering the reaction paths available.

While heavy halide ion is a favourable leaving group, it is well established that fluoride ion must be transferred among other species and does not exist independently in solvents such as $CHCl_3$ (22). Thus, the second nitrogen donor site cannot close the chelate ring by simply driving off fluoride ion, analogous to the loss of chloride or bromide ion. Following formation of the mono-BF_3 adduct, a second BF_3 can either coordinate to the second nitrogen or to a fluorine of the already coordinated BF_3 to give an intermediate B---F---BF_3 bridge, a requirement for fluoride transfer between boron atoms and formation of the chelated BF_2^+ cation as its BF_4^- salt. The bond enthalpy of the nitrogen–boron bond is so much greater than that of the B---F bridge bond (129.3 kJ/mol for $Me_3N{\cdot}BF_3$ vs. 15.25 kJ/mol for bridging B---F (23)) that the second possibility cannot compete, so chelated BF_2^+ cations of the ethylenediamine class of donors do not form from $Et_2O{\cdot}BF_3$. Extreme crowding, such as in an initial BF_3 adduct with the rigid bidentate ligand 1,10-phenanthroline, could change the situation however, and 1,10-phenanthroline apparently interacts directly with BF_3 to form $(1,10\text{-phen})BF_2^+{\cdot}BF_4^-$ (5, 6, 24).

Although fluoride is not a leaving group in the $D{\cdot}BF_nX_{3-n}$ adducts, the presence of fluoride greatly accelerates the loss of the heavy halide ion, rates of halide loss always varying in the order $D{\cdot}BF_2X >> D{\cdot}BFX_2 >> D{\cdot}BX_3$ (1, 10–12). We have previously discussed the mechanistic implications of this in terms of π bonding in the transition state (10). We rarely detect loss of heavy halide from $D{\cdot}BX_3$ under our conditions but Ryschkewitsch and co-workers (25), using stronger conditions, have studied a wide range of such reactions.

Reaction trends involving the chelating ligands are similar to the trends we have observed earlier for substitution of monodentate ligands in $D{\cdot}BF_nX_{3-n}$ adducts, i.e., there seems to be a complex interplay of steric effects, ligand basicity effects, and differential stabilization of the transition state by π bonding to boron from ligands that remain attached throughout the reaction. A similar pattern applies to ligand displacement from $(pyr)_2BF_2^+$ and related $D_2BF_2^+$ ions by monodentate ligands (12) and now by Me_4en and Me_5dien. Me_4en and Me_5dien (pK_b[1] values: 5.0 and 4.6, respectively (17)) are more basic than pyridine but displacement of pyridine is slow, consistent with *tert*-amine steric hindrance as observed previously (1). The intermediate non-chelated $(pyr)(DD)BF_2^+$ species is detected so the reaction must be stepwise, but the intermediate never builds up to high concentrations. Chelate ring closure is evidently favoured, since even a very large excess of chelating donor does not give detectable amounts of the bis(monodentate) species $(Me_4en)_2BF_2^+$ or $(Me_5dien)_2BF_2^+$.

(c) NMR parameters

The wide range of ^{19}F chemical shifts and ^{11}B–^{19}F coupling constants, and their systematic variation with ligand steric hindrance, make NMR the most useful empirical tool in monitoring and interpreting these complex systems. Aside from ^{19}F and ^{11}B chelation shifts of several ppm to high frequency and $^1J_{BF}$ values several Hz smaller than those of corresponding non-chelated systems (Table 1), trends in systems involving Me_4en and Me_5dien are much the same as in previously reported systems. Thus the ^{19}F NMR parameters of the monodentate (pyr)(chelating ligand)BF_2^+ cations (Table 1) are consistent with those of our previously reported $(pyr)(R_3N)BF_2^+$ species (–160.4 to –162.5 ppm; $^1J_{BF}$ = 28.5–29.7 Hz) (1). $(Me_4en)BF_2^+$ and $(Me_5dien)BF_2^+$ ^{19}F chemical shifts and $^1J_{BF}$ values (Table 1) can be compared to the nonchelated $(R_3N)_2BF_2^+$ values (–158.9 to –165.4 ppm; $^1J_{BF}$ = 36.2–39.5 Hz) (1). The NMR parameters of $(en)BF_2^+$,

© 1999 NRC Canada

$(Me_4en)BF_2^+$, and $(Me_5dien)BF_2^+$ (Table 1) are typical of a series of increasing steric hindrance, the ^{19}F signal shifting to higher frequency as steric hindrance increases. The NMR parameters of the mono-adducts of Me_4en and Me_5dien with BF_nCl_{3-n} are consistent with those of simple trialkylamines (16) and match those of the Me_2NEt adducts the most closely, supporting our conclusion that Me_5dien coordinates preferentially through an end nitrogen.

These trends allow us to assign the ^{19}F NMR signals of the nonequivalent BF_2 fluorines of $(Me_5dien)BF_2^+$ and of the major and minor (3:1 ratio) diastereomers of $(Me_5dien)BFCl^+$ (Fig. 4). Fluorine F_a of $(Me_5dien)BF_2^+$, *cis* to two methyl groups, is in an environment very similar in steric hindrance to the $(Me_4en)BF_2^+$ fluorines, while F_b, *cis*

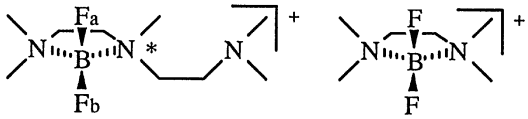

to a methyl group and the more bulky $CH_2CH_2NMe_2$ group, is deshielded. We can therefore assign the –153.9 ppm signal to F_b and the –155.1 ppm signal, very similar in chemical shift to $(Me_4en)BF_2^+$, to F_a. Similarly, the fluorine of one diastereomer of $(Me_4en)BFCl^+$ (**9**) has an environment similar to the fluorine of $(Me_4en)BFCl^+$, whereas the fluo-

9 **10**

rine of the other diastereomer (**10**) is more hindered and should appear at higher frequency. Since the major isomer and $(Me_4en)BFCl^+$ have very similar ^{19}F chemical shifts, while the minor isomer is shifted approximately 2 ppm to higher frequency, the major isomer is **9** and the minor isomer is **10**. In contrast the ^{11}B chemical shifts of fluoroboron cations are not very sensitive to the nitrogen substituents, so **9** and **10** have ^{11}B chemical shifts differing by only 0.1 ppm.

Formation of **9** and **10** in a 3:1 ratio probably reflects differences in steric hindrance in the transition state, since steric hindrance greatly affects rates of substitution at tetrahedral boron in fluoroboron systems (10). However, we cannot dismiss the possibility that their relative thermodynamic stabilities might determine the ratio. Semi-empirical calculations at the PM3 level give a negligible energy difference between **9** and **10**, only 0.18 kJ/mol with **9** lower in energy whereas the experimental error in the calculation of conformational energy differences at the PM3 level is typically about 4 kJ/mol (26). The observed 3:1 ratio of diastereomers would correspond to an energy difference (2.7 kJ/mol, neglecting entropy effects), which is less than the experimental error. Higher level calculations would be instructive.

Solid-state NMR has great potential in these systems because some key species, especially bromine-containing ones, are insoluble in any non-coordinating solvent. ^{11}B and ^{19}F MAS NMR spectra of fluoroboron cations including $(pyr)_2BF_2^+$, as their PF_6^- salts, are poorly resolved but give chemical shifts similar to solution values.[2] Despite the poor resolution, apparently arising from strong dipolar coupling to ^{19}F (27), ^{11}B MAS NMR spectra of the insoluble material formed in the reaction of Me_5dien with $ISOX{\cdot}BF_nBr_{3-n}$ (Fig. 6) confirm that the expected $BF_nBr_{2-n}^+$ cations (10–2 ppm (10, 24)) and BF_nBr_{3-n} adducts (2 to –10 ppm (16)), are present, and that their relative intensities vary in the expected manner with changes in the proportions of F to Br. High-power proton decoupling has little effect on the resolution. High-power ^{19}F decoupling will be required to obtain high-resolution spectra. ^{19}F MAS NMR can be informative, despite serious broadening due to ^{19}F–^{19}F dipolar interactions, and would be much more useful with sample spinning at sufficiently high speeds to eliminate the dipolar interactions (28), or with use of the CRAMPS (combined rotation and multiple pulse spectroscopy) sequence (29). We are exploring these possibilities as we study the formation of a variety of chelated fluoroboron systems, including those involving chiral chelating ligands with possible applications in stereoselective catalysis.

Conclusions

Chelated fluoroboron cations of Me_4en and Me_5dien are accessible by displacement reactions from mixed boron trihalide adducts and by displacement of pyridine from $(pyr)_2BF_2^+$, but not by reaction of the chelating ligands with $Et_2O{\cdot}BF_3$ or $ISOX{\cdot}BF_3$. Mixed boron trihalide adducts of isoxazole are a particularly convenient starting material for the preparation of chelated fluoroboron cations.

Acknowledgments

We thank Tim Jones and Dr. Jhansi Lakshmi for assistance with the instrumentation, W.R. (Rick) Szerminski and Paul Ragogna for synthesis of $(pyr)_2BF_2^+{\cdot}PF_6^-$, Prof. Alex F. Janzen (University of Manitoba) for helpful discussions, Dr. Ayaaz Pirani and Prof. Gary J. Schrobilgen (McMaster University) for technical advice, Dr. Don Hughes and Brian Sayer (McMaster University) for assistance with the 11.7 T NMR instrument, and the Natural Sciences and Engineering Research Council of Canada for financial support.

References

1. M.J. Farquharson and J.S. Hartman. Can. J. Chem. **67**, 1711 (1989).
2. (*a*) N. Wiberg and J.W. Buchler. Chem. Ber. **96**, 3000 (1963); (*b*) J. Am. Chem. Soc. **85**, 243 (1963).
3. N.M.D. Brown and P. Bladon. J. Chem. Soc. A, 526 (1969).
4. T. Onak, H. Rosendo, G. Siwapinyoyos, R. Kubo, and L. Linun. Inorg. Chem. **18**, 2943 (1979).
5. K.R. Koch and S. Madelung. Polyhedron, **10**, 2221 (1991).
6. D.D. Axtell, A.V. Campbell, P.C. Keller, and J.V. Rund. J. Coord. Chem. **5**, 129 (1976).
7. (*a*) J. Karolin, L.B.-A. Johannson, L. Strandberg, and T. Ny. J. Am. Chem. Soc. **116**, 7801 (1994); (*b*) F. Li, S.I. Yang, Y. Ciringh, J. Seth, C.H. Martin III, D.L. Singh, D. Kim, R.R.

[2] J.S. Hartman and W.R. Szerminski, Brock University, St. Catharines. Unpublished work. 1998.

© 1999 NRC Canada

Birge, D.F. Bocian, D. Holten, and J.S. Lindsey. J. Am. Chem. Soc. **120**, 10 001 (1998); (*c*) X. Song, J. Nolan, and B.I. Swanson. J. Am. Chem. Soc. **120**, 11 514 (1998).
8. (*a*) H.C. Brown, B. Singaram, and J.R. Schwier. Inorg. Chem. **18**, 51 (1979); (*b*) H.C. Brown and B. Singaram. Inorg. Chem. **18**, 53 (1979).
9. B. Singaram and G.G. Pai. Hetrocycles, **18**, 387 (1982).
10. M.J. Farquharson and J.S. Hartman. Can. J. Chem. **74**, 1309 (1996).
11. J.S. Hartman, Z. Yuan, A. Fox, and A. Nguyen. Can. J. Chem. **74**, 2131 (1996).
12. J.S. Hartman, E.I. Ilnicki, J.A.W. Shoemaker, W.R. Szerminski, and Z. Yuan. Can. J. Chem. **76**, 1317 (1998).
13. J.S. Hartman and J.M. Miller. Adv. Inorg. Chem. Radiochem. **21**, 147 (1978).
14. N.N. Greenwood and A. Earnshaw. Chemistry of the elements. Pergamon Press, Oxford. 1984. Table 6.3.
15. (*a*) J.S. Hartman and P. Stilbs. J. Chem. Soc. Chem. Commun. 566 (1975); (*b*) M. Appel and W. Beck. J. Organomet. Chem. **319**, C1 (1987).
16. A. Fox, J.S. Hartman, and R.E. Humphries. J. Chem. Soc. Dalton Trans. 1275 (1982).
17. D.R. Perrin. Dissociation constants of organic bases in aqueous solutions. Butherworths, London. 1965.
18. (*a*) R.E. Mesmer and A.C. Rutenberg. Inorg. Chem. **12**, 699 (1973); (*b*) K. Kuhlmann and D.M. Grant. J. Phys. Chem. **68**, 3208 (1964).
19. J.S. Hartman, A.F. Janzen, and X. Ou. 79th Annu. Canadian Chem. Conf. Paper 57. St. John's, Newfoundland. June 23–26, 1996.
20. (*a*) G. Fraenkel and W.R. Winchester. J. Am. Chem. Soc. **110**, 8720 (1988); (*b*) D. Hoffmann, W. Bauer, F. Hampel, N.J.R. van Eikema Hommes, P. von Ragué Schleyer, P. Otto, U. Pieper, D. Stalke, D.S. Wright, and R. Snaith. J. Am. Chem. Soc. **116**, 528 (1994); (*c*) M. Kotowski, S. Begum, I.G. Leipoldt, and R. van Eldik. Inorg. Chem. **27**, 4472 (1988); (*d*) E. Kimra, T. Koike, M. Kodama, and D. Meyerstein. Inorg. Chem. **28**, 2998 (1989); (*e*) J.L. Atwood, K.D. Robinson, C. Jones, and C.L. Raston. J. Chem. Soc. Chem. Commun. 1697 (1991).
21. S.A. Genchur, G.L. Smith, and H.C. Kelly. Can. J. Chem. **49**, 3165 (1971).
22. A. F. Janzen. Coord. Chem. Rev. **130,** 355 (1994).
23. X. Ou, R. Wallace, and A.F. Janzen. Can. J. Chem. **71**, 51 (1993).
24. (*a*) J.A.W. Shoemaker. M.Sc. thesis. Brock University, St. Catharines, Ont. 1999; (*b*) J.S. Hartman and J.A.W. Shoemaker. Paper 1031. 82nd Annu. Canadian Chem. Conf. Toronto, Ont. May 30 – June 2, 1999; (*c*) Part II of this series: J.S. Hartman and J.A.W. Shoemaker. Polyhedron. In press.
25. (*a*) C.W. Makosky, G.L. Galloway, and G.E. Ryschkewitsch. Inorg. Synth. **12,** 141 (1970); (*b*) G.E. Ryschkewitsch. *In* Boron hydride chemistry. *Edited by* E.L. Muetterties. Academic Press, New York. 1975. Chap. 6; (*c*) M.A. Mathur and G.E. Ryschkewitsch. Inorg. Chem. **19**, 3054 (1980).
26. MacSpartan plus tutorial and user's guide. Wavefunction, Inc., Irvine, Calif. 1996. Sect. 13, Table 13-3.
27. C.A. Fyfe. Solid state NMR for chemists. CFC Press, Guelph, Ont. 1983. Chap. 1.
28. (*a*) U. Scheler. Solid state NMR, **12**, 9 (1998); (*b*) P.K. Isbester, J.L. Brandt, T.A. Kestner, and E.J. Munson. Macromolecules, **31**, 8192 (1998); (*c*) K.K.S. Lau and K.K. Gleason. J. Phys. Chem. B, **102**, 5977 (1998).
29. J.M. Miller. Progr. NMR Spect. **28**, 255 (1996).

© 1999 NRC Canada

A ^{19}F nuclear magnetic resonance study of the conjugate Brönsted–Lewis superacid HSO_3F–SbF_5. Part 1

Dingliang Zhang, Markus Heubes, Gerhard Hägele, and Friedhelm Aubke

Abstract: The Brönsted–Lewis superacid HSO_3F–SbF_5 or "magic acid" is re-investigated by modern ^{19}F NMR methods over a wide concentration range. The system is found to be considerably more complex than had been assumed previously. A total of 13 different anions are identified of which only five have previously been identified in magic acid. With increasing SbF_5 contents the concentration of monomeric anions like $[SbF_6]^-$, $[SbF_5(SO_3F)]^-$, *cis*- and *trans*-$[SbF_4(SO_3F)_2]^-$, and *mer*-$[SbF_3(SO_3F)_3]^-$ gradually decreases. Except for $[Sb_2F_{11}]^-$, which is present in very small concentrations only, the formation of oligomers involves exclusively μ-fluorosulfato bridges. In addition to donor $(SO_3F)^-$ and acceptor (SbF_5) complex formation to give $[SbF_5(SO_3F)]^-$ and possibly ligand redistribution, the solvolysis of SbF_5 or $SbF_4(SO_3F)$ in HSO_3F appears to be the principal formation reaction for polyfluorosulfatofluoroantimonate(V) anions. In glass (NMR tubes) the solvolysis product HF is converted to the oxonium ion $[H_3O]^+$, which has previously been identified by ^1H NMR and structurally characterized as $[H_3O][Sb_2F_{11}]$ by us.

Key words: magic acid, conjugate superacid, fluorosulfuric acid, ^{19}F NMR spectra.

Résumé : On a réétudié l' « acide magique » (superacide de Brönsted–Lewis), HSO_3F–SbF_3 en faisant appel à la RMN du ^{19}F et en opérant sur une grande plage de concentrations. On a trouvé que le système est beaucoup plus complexe que ce qui avait été envisagé auparavant. On a identifié un total de 13 anions différents, dont seulement cinq avaient été identifiés antérieurement dans l'acide magique. Avec une augmentation de la concentration de SbF_5, il y a diminution de la concentration des anions monomères, du type $[SbF_6]^-$, $[SbF_5(SO_3F)]^-$, *cis*- et *trans*-$[SbF_4(SO_3F)_2]^-$ et *mer*-$[SbF_3(SO_3F)_3]^-$. À l'exception du $[Sb_2F_{11}]^-$ dont la concentration est très faible, la formation d'oligomères implique exclusivement des ponts μ-fluorosulfato. En plus de la formation de complexes provenant du donneur $(SO_3F)^-$ et de l'accepteur (SbF_5) conduisant au $[SbF_5(SO_3F)]^-$ ou de la possibilité d'une redistribution de ligands, il semble que la solvolyse du SbF_5 ou du $SbF_4(SO_3F)$ dans le HSO_3F soit la réaction principale de formation des anions polyfluorosulfatofluoroantimonantes(V). En présence de verre (tubes de RMN), le HF produit par solvolyse se transforme en ion oxonium $[H_3O]^+$ qui a été identifié antérieurement par RMN du ^1H et pour lequel on a caractérisé la structure, $[H_3O][Sb_2F_{11}]$.

Mots clés : acide magique, superacide conjugué, acide fluorosulfurique, spectre RMN du ^{19}F.

[Traduit par la Rédaction]

Introduction

The conjugate Brönsted–Lewis superacid HSO_3F–SbF_5 or "magic acid" (1) has found in the past extensive use as reaction medium for the generation and stabilization of a wide range of highly electrophilic, long-lived cations. Well documented examples extend from inorganic main group cations (1–3) to a large number of carbocations (1, 4). The reasons for the enormous versatility of magic acid are its outstanding solvent characteristics, in particular its ionizing and protonating abilities, which allow the dissolution of a large number of substrates (1–4). The proton acidity of magic acid is only exceeded by that of the related conjugate superacid HF–SbF_5 (1, 2). This is altogether not surprising because the constituent Brönsted acids fluorosulfuric acid (5) and anhydrous hydrogen fluoride (6) are the strongest simple protonic acids with identical Hammett (7) acidity function values of $-H_0 = 15.1$ (1, 2, 8), while the Lewis superacid SbF_5 is ranked as the strongest molecular Lewis acid (9).

For magic acid Hammett acidity function studies (7) are reported (10–13) for concentrations up to 80 mol% SbF_5. A comparison between HF–SbF_5 and HSO_3F–SbF_5 (14, 15)

Received March 8, 1999.

This paper is dedicated to Professor Ted Schaefer in recognition of his outstanding contributions to Canadian chemistry.

D. Zhang and F. Aubke.[1] Department of Chemistry, The University of British Columbia, 2036 Main Mall, Vancouver, BC V6T 1Z1, Canada.
M. Heubes and G. Hägele.[1] Institut für Anorganische Chemie und Strukturchemie I, Heinich-Heine-Universität Düsseldorf, Universitätsstr.1, D-40225 Düsseldorf, Germany.

[1]Authors to whom correspondence may be addressed. FA: Telephone: (604) 822-3817. Fax: (604) 822-2847. e-mail: aubke@chem.ubc.ca; GH: Telephone: ++49-211-8112288. Fax: ++49-211-8113085. e-mail: haegele@uni-duesseldorf.de

 © 1999 NRC Canada

suggests that at 0.5 mol % SbF_5, the former is more acidic by a factor of approximately 10^4 (15). It is not immediately obvious why this should be, since the constituent Brönsted acids have identical -H_0 values (1, 2, 9) and SbF_5 is common to both superacid systems.

To probe the composition of HSO_3F–SbF_5, several ^{19}F NMR studies (16–19) have been reported between 1965 and 1978. Because of the limited resolution and sensitivity of NMR spectra at that time, accurate assignments of the signals have been difficult and some disagreement is found among the reported studies (16–19). There is however general agreement that very complex equilibria are encountered, which will be discussed subsequently. The situation is much simpler in the HF–SbF_5 system, where in addition to $[SbF_6]^-$ oligomeric *cis*-fluorine bridged anions like $[Sb_2F_{11}]^-$, $[Sb_3F_{16}]^-$, etc. are present at high SbF_5 concentrations and detected by ^{19}F NMR (20). Since these early studies the resolution, sensitivity, and evaluation of NMR spectra have all significantly improved by the introduction of pulse spectroscopy and Fourier transformation in one- and two-dimensional techniques (21). We have applied state of the art NMR methods to reinvestigate the HSO_3F–SbF_5 system with two objectives:

(*i*) to obtain more precise structural information on the anionic species present and

(*ii*) to suggest plausible pathways of formation of these anions from the interaction of HSO_3F with SbF_5.

We present here a ^{19}F NMR study of the HSO_3F–SF_5 superacid system over a wide concentration range with SbF_5 molar fractions *x* between 0.001 and 0.795. The techniques employed include high resolution ^{19}F 1D- and 2D NMR methods of the type ^{19}F–^{19}F COSY and ^{19}F *J* resolved spectra at 181 MHz.

Experimental

Preparation of NMR samples

The purity of freshly distilled fluorosulfuric acid was checked by conductometry and by NMR. Purified antimony pentafluoride was transferred in vacuo into a 50 mL vial fitted with a Teflon stopcock. The amount of the antimony pentafluoride transferred was determined by difference weighing. Inside a dry box, freshly distilled fluorosulfuric acid was pipetted into the reactor. The amount of fluorosulfuric acid was also determined by difference weighing. The mixture was then stirred magnetically for ca. 15 min. About 0.4 mL of the solution was pipetted into an NMR tube. A sealed capillary tube containing a solution of 5% (w/w) $CFCl_3$ in CD_3COCD_3 was inserted into the NMR tube in order to provide chemical shift references and a field lock. The NMR tube was attached to a B10–B10 adapter fitted with a Kontes Teflon stem stopcock and then taken out of the dry box. The NMR tube was evacuated after it was cooled to –95 ~ –100°C in an ethanol – dry ice slurry bath. The sample was degassed by three freeze–pump–thaw cycles. The NMR tube was then flame-sealed under vacuum. Samples were checked immediately after preparation by ^1H-NMR in Vancouver and then shipped to Düsseldorf for ^{19}F-NMR studies. All samples were kept at room temperature. Repeated NMR measurements spanning a period of several months showed the stable, equilibrated state of NMR samples discussed in this paper.

^{19}F NMR spectroscopy

Both 1D and 2D ^{19}F NMR spectra were acquired at low temperatures (see text) using a Bruker AM 200 NMR spectrometer equipped with a Bruker variable temperature unit B-VT 1000. For each 1D ^{19}F NMR spectrum, 64K memory size was used for data storage (TD = 64K) and 1024 scans were acquired (NS = 1024) for each Free Induction Decay (FID). No zero-filling was applied to the FIDs before Fourier transformation. For ^{19}F–^{19}F COSY NMR, a standard program, COSY.AUR, was used with the following pulse sequence:

[1] Relaxation time t_1 – 90° pulse – evolution time τ – 45° pulse – FID

TD = 2 K and NS = 32 were used and 512 experiments were measured for every 2D spectrum. For 2D *J*-resolved NMR, a standard program, JRES.AUR, was used and the following pulse sequence was implemented:

[2] Relaxation time t_1 – 90° pulse – evolution time τ – 180° pulse – evolution time *t* – FID

TD = 4 K along the F_1 axis and TD = 128 along the F_2 axis were used, and 64 experiments were measured for each 2D spectrum. The FIDs for 1D NMR were processed using the Bruker Win-NMR software on an IBM-compatible PC and the FIDs for 2D NMR were processed with the program UXNMR running on a UNIX workstation (ASPECT).

Results and discussion

An already published (22) observation, made at the outset of this study, will be briefly summarized. All samples prepared as described in the experimental section are found to exhibit in the ^{19}F NMR spectrum a resonance line at ~–162 ppm, which is attributed to dissolved SiF_4. The ^1H NMR spectrum, in addition to the main resonance due to exchange between HSO_3F and the acidium ion $H_2SO_3F^+$, a second single resonance between ~9.5 and ~8.0 ppm, which is assigned to the oxonium ion H_3O^+. The intensity of both resonances increases with increasing SbF_5 contents. From NMR tubes with a SbF_5 content of 20 mol% or higher a white crystalline solid is obtained, which is identified by vibrational spectroscopy as $[H_3O][Sb_2F_{11}]$ and structurally characterized by single crystal X-ray diffraction. It is concluded, that magic acid contains variable amounts of HF, which will react with glass to give H_3O^+. Evidence for this view is obtained in a recently completed ^{19}F NMR study[2] of magic acid in tubes made from fluoroplastics, where the SiF_4 resonance is absent in the ^{19}F NMR spectrum and the H_3O^+ resonance is of exceedingly low intensity. The commonly held view (1), that HSO_3F–SbF_5, just like pure HSO_3F and SbF_5 will not attack glass must be seriously questioned.

[2] J.H. Kühn-Velten, M. Bodenbinder, G. Hägele, and F. Aubke. To be submitted.

© 1999 NRC Canada

Fig. 1. ^{19}F NMR spectrum of the HSO_3F–SbF_5 system with x_{SbF_5} = 0.342 at 213 K.

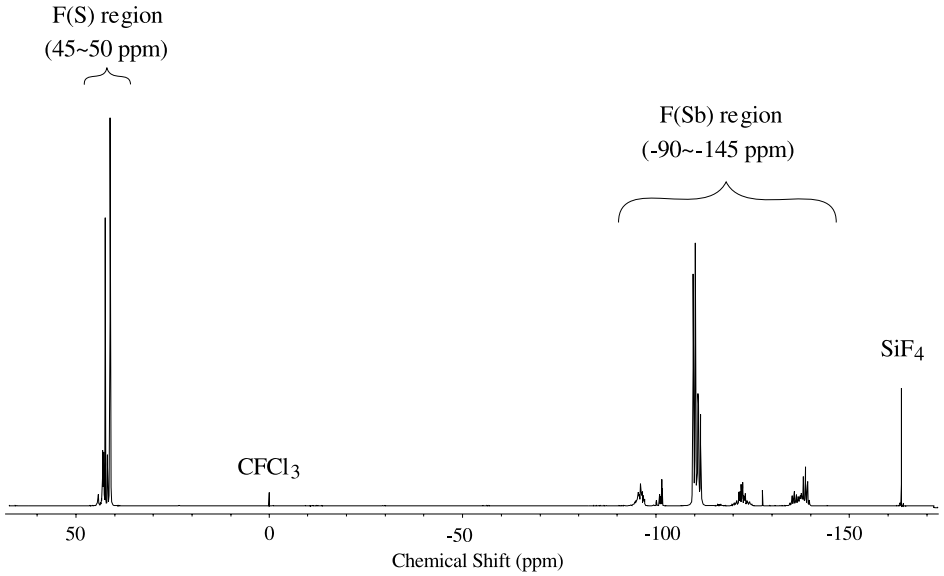

1D and 2D ^{19}F–^{19}F COSY spectroscopy

The first ^{19}F NMR study of the HSO_3F–SbF_5 system is reported by Thompson et al. (16). Due to the limited sensitivity and resolution, only two partially overlapped AX_4 spin systems are observed from the spectrum of a 1.7 mol kg^{-1} solution of SbF_5 in HSO_3F (x_{SbF_5} = 0.15). They are assigned to monomeric $[SbF_5(SO_3F)]^-$ and the SO_3F-bridged dimer $[Sb_2F_{10}(SO_3F)]^-$, and the following mechanism for their formation is proposed:

[3] $SbF_5 + HSO_3F \rightleftarrows H[SbF_5(SO_3F)]$

[4] $H[SbF_5(SO_3F)] + HSO_3F \rightleftarrows H_2SO_3F^+ + [SbF_5(SO_3F)]^-$

[5] $2H[SbF_5(SO_3F)] \rightleftarrows H_2SO_3F^+ + [Sb_2F_{10}(SO_3F)]^-$

Commeyras and Olah (17) extend the ^{19}F NMR investigation of the HSO_3F–SbF_5 system to a wider SbF_5/HSO_3F ratio range of 0~1.4 (x_{SbF_5} = 0~0.58) and support the earlier assignments (16). In addition, they observe signals due to the monomer $[SbF_6]^-$ (–120 ppm) and F-bridged dimer $[Sb_2F_{11}]$- (–115 ppm) as well as two unassigned signals at –122 and –124 ppm. To explain the formation of the perfluoroantimonate(V) species, the existence of polysulfuric acids is proposed according to

[6] $2SbF_5 + 2HSO_3F \rightleftarrows H_2SO_3F^+ + [Sb_2F_{11}]^- + SO_3$

[7] $SO_3 + HSO_3F \rightleftarrows HS_2O_6F$

[8] $SO_3 + HS_2O_6F \rightleftarrows HS_3O_9F$

This proposal is subsequently disputed by Dean and Gillespie (18). To decrease the viscosity of the system in order to improve the resolution of the spectrum, these authors use sulfuryl chlorofluoride (SO_2ClF) as a diluent for the HSO_3F–SbF_5 system with the SbF_5:HSO_3F ratio at 0.92:1.00 (x_{SbF_5} = 0.48). Besides the signals observed previously, two A_2X_2 spin systems due to *cis*-$[SbF_4(SO_3F)_2]^-$ units and two singlets due to *trans*-$[SbF_4(SO_3F)_2]^-$ units are also observed. Therefore, they argue that $[SbF_6]^-$ and $[Sb_2F_{11}]$- are formed more likely through ligand redistribution such as

[9] $2[SbF_5(SO_3F)]^- \rightleftarrows [SbF_4(SO_3F)_2]^- + [SbF_6]^-$

rather than by decomposition of HSO_3F as suggested in reactions [6]–[8]. More recently, Brunel et al. (19) have carried out ^{19}F NMR studies of the HSO_3F–SbF_5 and HSO_3CF_3–SbF_5 systems, using sulfuryl difluoride (SO_2F_2) as an internal reference. They conclude that the *cis*-F-bridged $H[Sb_nF_{5n}(SO_3F)]$ (n = 0–5) species are the main species in high SbF_5 concentration ranges and that the SO_3F-bridged dimer $[Sb_2F_{10}(\mu\text{-}SO_3F)]^-$ is present in low concentration only in systems with low x_{SbF_5}. This conclusion is contradictory to previous studies (16, 18), which indicate the 1:1 and 2:1 complexes $H[SbF_5(SO_3F)]$ and $H[Sb_2F_{10}(\mu\text{-}SO_3F)]$ are the principal species.

In summary, previous ^{19}F NMR studies of the HSO_3F–SbF_5 system differ in many aspects: the SbF_5 concentrations chosen, the use of diluents, the spectra observed, and the spectral interpretations. The approach in the present study is to start with the HSO_3F–SbF_5 system with x_{SbF_5} as low as possible, provided that reasonable spectra can be acquired. The monomeric antimony(V) species are most likely present at low x_{SbF_5}. The mole fraction of SbF_5 is gradually increased to observe oligomerization and the changes in relative concentrations of species. To avoid any possible interference, no diluent was added into the HSO_3F–SbF_5 system in this study.

General features of 1D ^{19}F NMR spectra of the HSO_3F–SbF_5 system

As an example, the ^{19}F NMR spectrum of an HSO_3F–SbF_5 system with x_{SbF_5} = 0.35 is shown in Fig. 1.

The spectrum may be divided into two regions: the F(S) region (δ C*F*Cl_3 = 40~45 ppm), where the signals due to fluorines of SO_3F groups are observed, and the F(*Sb*).region (δ C*F*Cl_3 = –80~–150 ppm) where signals due to fluorines

© 1999 NRC Canada

bonded to Sb(V) are observed. In addition, there is a sharp singlet at ca. –162 ppm, which is attributed to $SiF_{4(solv)}$.

Apparently, there is a trace amount of HF that reacts with SiO_2, the main component of glass, to produce SiF_4 according to

[10] $4HF + SiO_2 \rightarrow 2H_2O + SiF_4$

The other product, H_2O, is a strong base in the system and is protonated to form the oxonium ion H_3O^+, which is observable using ^1H NMR spectroscopy. Its salt with weakly nucleophilic $[Sb_2F_{11}]^-$ as the counter anion has been isolated as discussed (22). The other possible route for the production of H_2O, dehydration of HSO_3F according to

[11] $2HSO_3F \rightleftarrows H_2O + S_2O_5F_2$

is unlikely because the signal due to $S_2O_5F_2$ at 47~48.5 ppm (23, 24) is not observed in the ^{19}F NMR spectra of all samples studied by us here. Evidence for reaction [10] also comes from the visual observation of etching of NMR tubes and capillary tubes after several weeks.

The mechanism for the generation of HF in magic acid is not obvious. The observation of progressively increasing amounts of SiF_4 with increasing x_{SbF_5} in the system suggests that the trace amounts of HF may be introduced as an impurity in SbF_5. However, as discussed in the following sections, partial solvolysis of SbF_5 in HSO_3F according to

[12] $SbF_5 + HSO_3F \rightleftarrows SbF_4(SO_3F) + HF$

[13] $SbF_4(SO_3F) + HSO_3F \rightleftarrows SbF_3(SO_3F)_2 + HF$

is a much more likely source for HF.

This proposal is based on the assumption that SbF_5 or $SbF_4(SO_3F)$ are more readily solvolyzed by HSO_3F than coordinatively saturated anions like $[SbF_6]^-$ and $[SbF_5(SO_3F)]^-$. Since SiF_4 is also observed by ^{19}F NMR spectroscopy for the neat solvent HSO_3F, it is also possible that some HF may be formed by the self dissociation of HSO_3F ($K < 3 \times 10^{-7}$):

[14] $HSO_3F \rightleftarrows SO_3 + HF$

(see ref. 25) or may be present as an impurity in HSO_3F. It is not at all uncommon to observe SiF_4 as well as BF_3 in the gas phase of freshly distilled HSO_3F or introduced with HSO_3F as an impurity.

Figure 2 illustrates the ^{19}F NMR spectra of pure HSO_3F and HSO_3F–SbF_5 systems with various x_{SbF_5} values in the F(S) region (δ C*F*Cl_3 = 40~45 ppm).

In this region, all signals are singlets. For the solvent and solutions with low SbF_5 content, intense signals due to HSO_3F dominate the region. A main peak due to F-$^{32}SO_3H$ and a weak satellite peak due to F-$^{34}SO_3H$ can be observed (26, 27). For example, in the 1D ^{19}F NMR spectrum of fluorosulfuric acid (see Fig. 2), the very intense peak at 41.98 ppm and a weak satellite peak at 41.94 ppm are observed. The isotope shift is 0.044 ppm, in agreement with the previous studies (26, 27). For less intense F(S) signals, the satellite peak (*F*-$^{34}SO_3$) is not observed. Long-range couplings of the types ^{19}F-S-O-Sb-^{19}F and ^{19}F-S-O-Sb-O-S-^{19}F are not observed for any samples in this study. Consequently, little information about the structures of the fluorosulfato-antimonate(V) species can be extracted from the signals in the F(S) region, and no assignment of resonances in this region will be made.

In contrast, the F(Sb) region (δ C*F*Cl_3 = –80~–150 ppm) (see Fig. 3) provides a great deal of structural information. The observed splitting of the signals results from the coupling between non-equivalent fluorines bonded to the same antimony atom. The complex spectral feature of this region indicates complicated equilibria of various chemical species in the system. The overlap of signals is sometimes so severe that an analysis based solely on traditional 1D ^{19}F NMR spectra remains ambiguous. Even with the assistance of 2D NMR methods, the spectral analysis is occasionally inconclusive.

Significant signal broadening begins to be observed in the spectra of the HSO_3F–SbF_5 system with $x_{SbF_5} \geq 0.500$. The spectra in the F(Sb) region of the systems with x_{SbF_5} = 0.649 and 0.795 are dominated by broad peaks. Such signal broadening precludes any detailed analysis in terms of individual species. Therefore, the assignment of signals discussed in the following sections will focus on the F(Sb) region in the spectra of solutions with low SbF_5 content ($0.000\,999 \leq x_{SbF_5} \geq 0.342$). For the convenience, the following notation system for the assignable signals in the F(Sb) region is used. The signals in the F(Sb) region are labeled according to their multiplicity: S for singlet, D for doublet, T for triplet, Q for quartet, q for quintet, s for sextet, etc. For signals of the same multiplicity, a number is attached in the order of their appearance from low field to high field.

The increasing viscosity of the system, as the SbF_5 content increases, may not be the only factor responsible for the broadness of signals, because a number of relatively sharp lines are also observed as well in the F(Sb) region. The oligomeric structures of $(SbF_5)_m$ and possibly $H[Sb_mF_{5m}(SO_3F)]$ or $H[Sb_mF_{5m+1}]$, as well as ligand exchange, may contribute to the broadness of the signals. The sharp lines are probably from some relatively small complex anions. Among these sharp lines, the most intense signals labeled T3 and T6 can be assigned to *cis*-$[SbF_4(SO_3F)_2]^-$, S8 to $[SbF_6]^-$, and Q1 to $[Sb_2F_{11}]^-$.

As reported previously (16–19), the proton exchange between the Sb(V) species and HSO_3F appears to be rapid and only averaged signals of both complex acids and their conjugate anions are observed in the ^{19}F NMR spectra. For convenience, the anionic formulation is used to represent both forms in the discussion. The assignment of segments (monomeric Sb(V) moieties), $SbF_n(SO_3F)_{5-n}$ μ-(SO_3F), and μ-$(SO_3F)SbF_n(SO_3F)_{4-n}$ μ-(SO_3F), in the oligomeric species will be discussed below. To distinguish the segments from monomeric species (both complex acids and conjugate anions), the segments are formulated as neutral fragments.

Assignment of monomeric species

In the ^{19}F NMR spectra (F(Sb) region) of the HSO_3F–SbF_5 system with x_{SbF_5} = 0.000 999 (see Fig. 3*a*), there are a number of multiplets in addition to two singlets. Apparently, several chemical species are present in the system. The possible monomers of the type $[SbF_n(SO_3F)_{6-n}]^-$ are illustrated in Fig. 4.

In these species, antimony(V) is assumed to be octahedrally coordinated by fluoro and fluorosulfato ligands.

© 1999 NRC Canada

Fig. 2. Low temperature ^{19}F NMR spectra from the F(S) region of the HSO_3F–SbF_5 system.

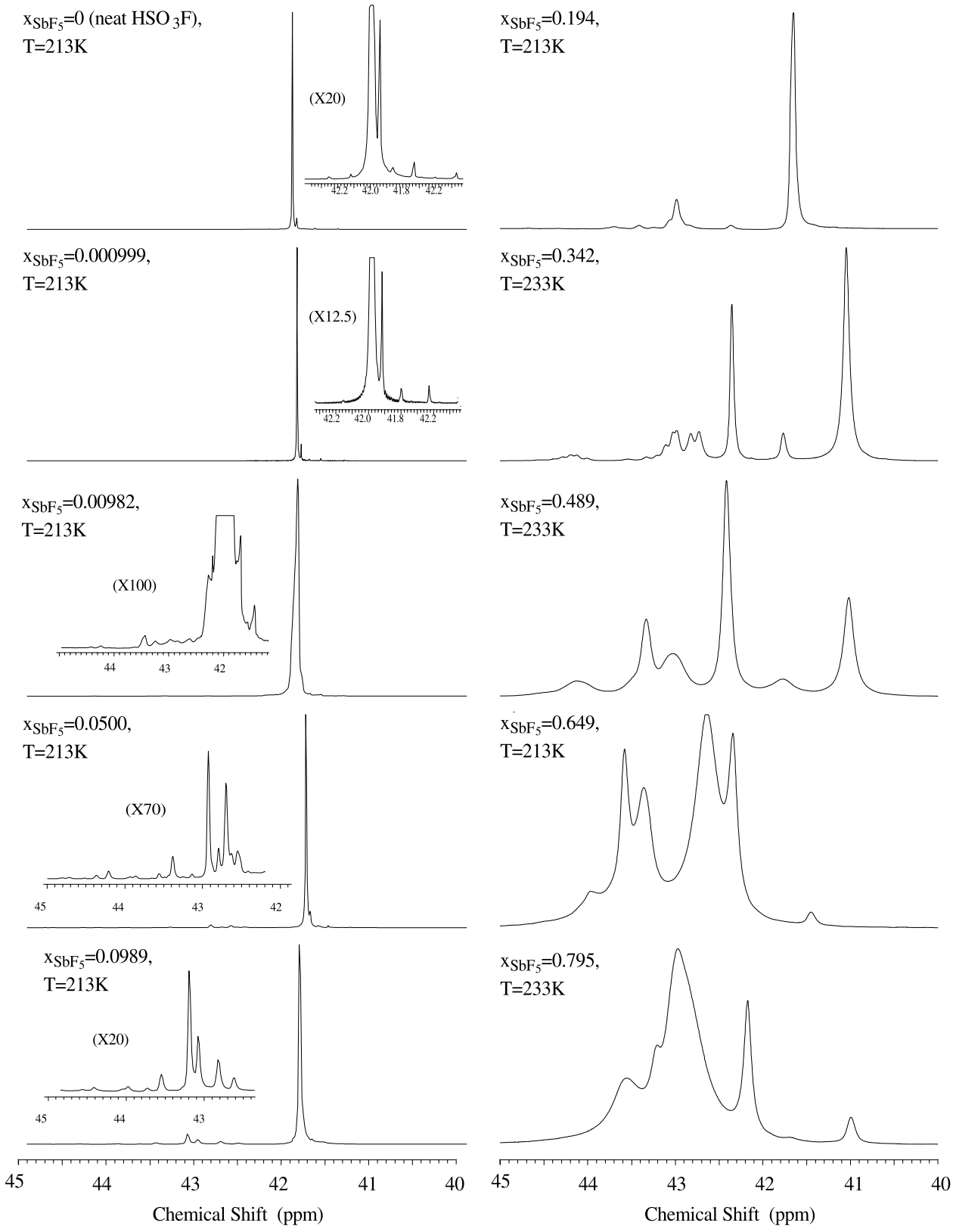

From the coupling patterns and relative intensities of the signals, they can be readily assigned to some of the monomeric species expected to be present. With the assistance of 2D ^{19}F–^{19}F COSY NMR, the analysis becomes more straightforward and definitive. In the 2D ^{19}F–^{19}F COSY spectrum (F(Sb) region) of the HSO_3F–SbF_5 system

© 1999 NRC Canada

Fig. 3. ^{19}F NMR spectra from the F(Sb) region of the $HSO_3F–SbF_5$ system.

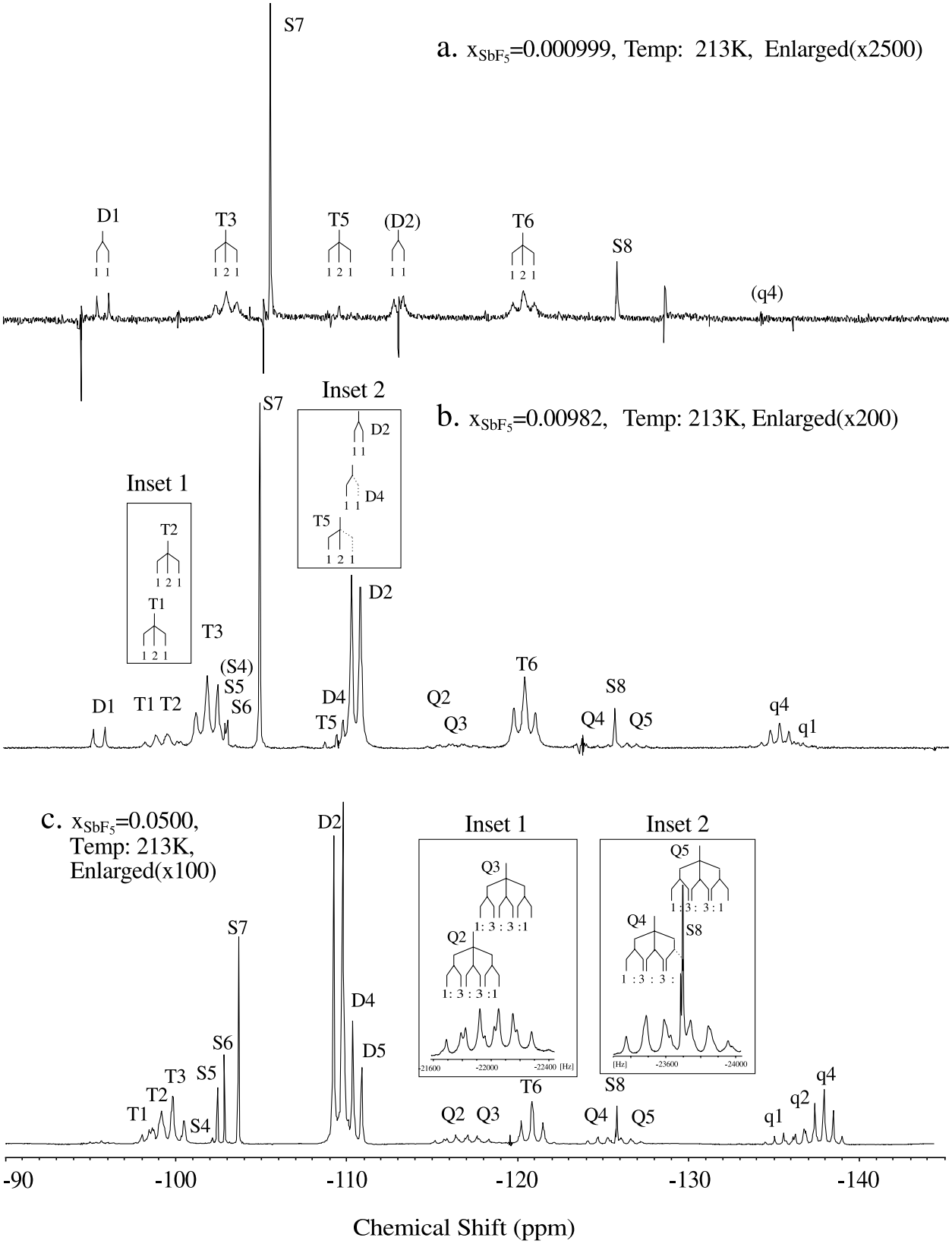

© 1999 NRC Canada

Fig. 3 (*continued*).

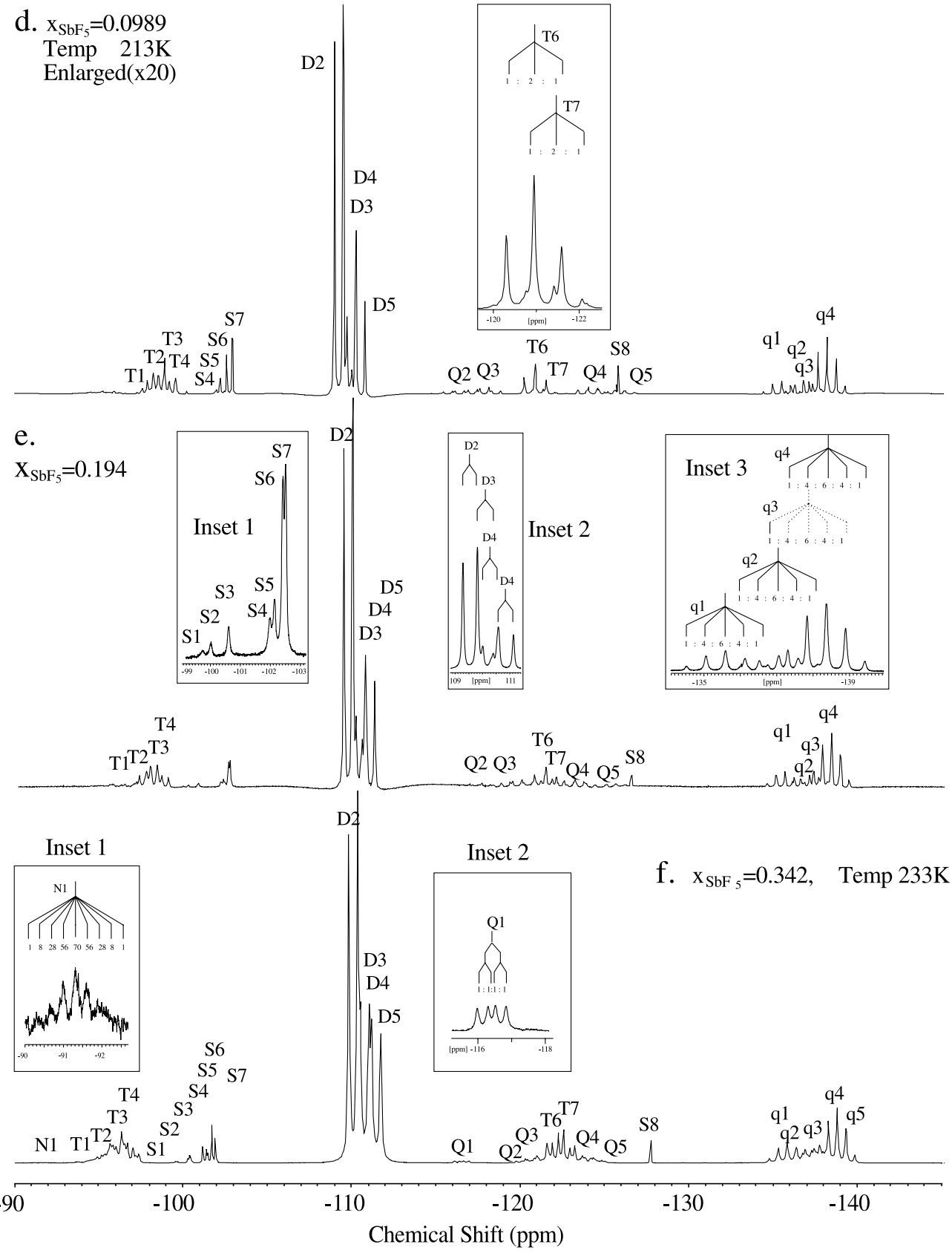

© 1999 NRC Canada

Fig. 3. (*concluded*).

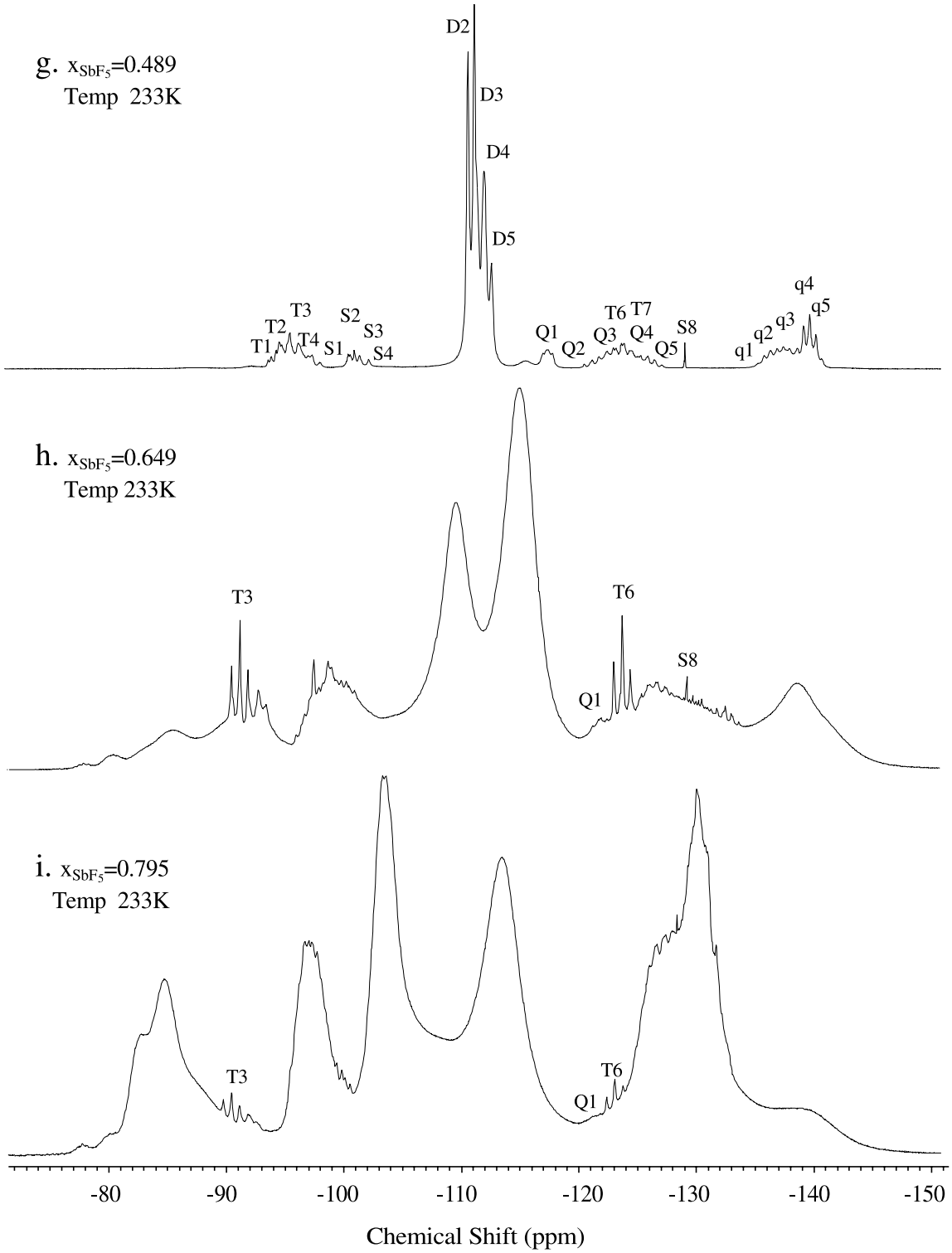

with x_{SbF_5} = 0.000 999 (see Fig. 5), the cross-peaks D1T5 and T3T6 clearly indicate the correlation between doublet D1 and triplet T5, and between triplet T3 and triplet T6.

Thus, we can unequivocally assign D1 and T5 (AX_2 spin system) to *mer*-$[SbF_3(SO_3F)_3]^-$ and T3 and T6 (A_2X_2 spin system) to *cis*-$[SbF_4(SO_3F)_2]^-$.

The singlets in the F(Sb) region may be assigned to species containing chemically equivalent fluorines, namely $[SbF_6]^-$, *trans*-$[SbF_4(SO_3F)_2]^-$, *fac*-$[SbF_3(SO_3F)_3]^-$, *trans*- and *cis*-$[SbF_2(SO_3F)_4]^-$, and $[SbF(SO_3F)_5]^-$ (see Fig. 4). In previous ^{19}F NMR studies of HSO_3F–SbF_5 systems with high SbF_5:HSO_3F ratios, Commeyras and Olah (17) assign the signal at $CFCl_3$ = –120 ppm to $[SbF_6]^-$. In the present study, however, no singlet at –120 ppm is observed. Dean and Gillespie (18) observe two singlets at –102~–104 ppm in the spectrum of a sulfuryl chlorofluoride solution of

© 1999 NRC Canada

Fig. 4. Monomeric species of the type $[SbF_n(SO_3F)_{6-n}]^-$ (n = 0–6) and corresponding spin systems in the F(Sb) region.

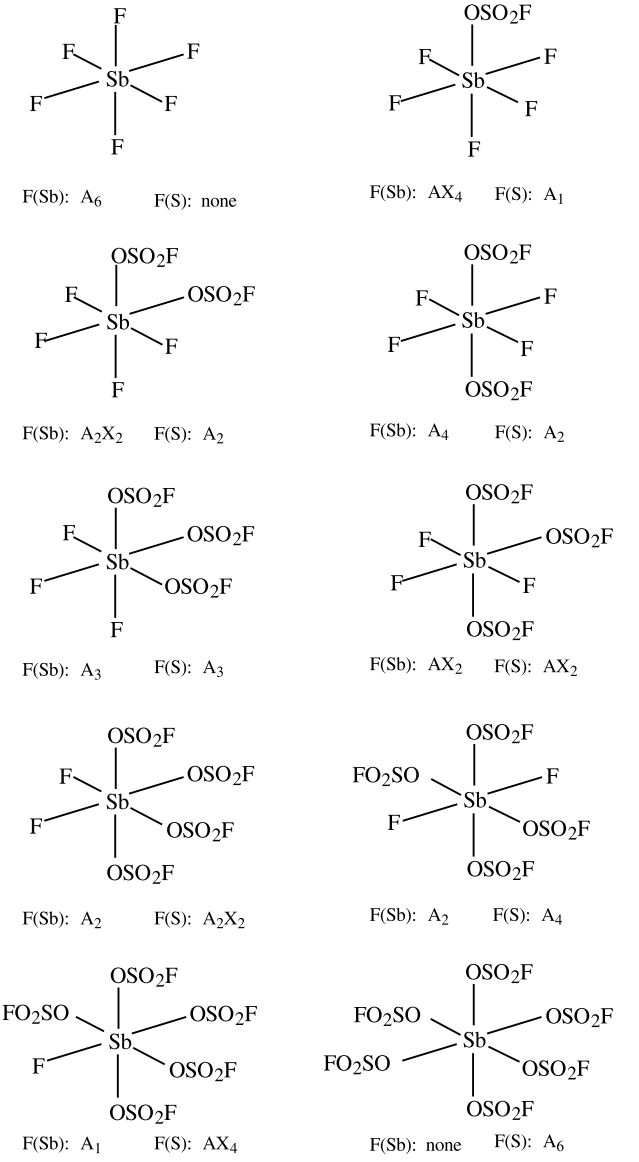

SbF_5:HSO_3F (0.92:1.00) recorded at –100°C and assign both of them to *trans*-$[SbF_4(SO_3F)_2]$ units. Brunel et al. (19) assign a high-field singlet at δ C*F*Cl_3 = –115.8 ppm to $[SbF_6]^-$ and the low-field singlet at δ C*F*Cl_3 = –91.9 ppm to *trans*-$[SbF_4(SO_3F)_2]^-$. Following these previous assignments, the high-field sharp line S8 at –125.6 ppm is assigned to $[SbF_6]^-$ and the other singlet S7 at –105.0 ppm is assigned to *trans*-$[SbF_4(SO_3F)_2]^-$.

As x_{SbF_5} increases from 0.000 999 to 0.009 82 (see Fig. 3*b*), D2 and q4 become considerably more intense in the spectrum. The relative intensities and distinct splitting patterns in the 1D ^{19}F NMR spectrum and the cross-peak D2q4 in the ^{19}F–^{19}F COSY spectrum (see Fig. 6) clearly indicate that the two signals represent an AX_4 spin system.

This AX_4 spin system can be assigned to monomeric $[SbF_5(SO_3F)]^-$, which is in agreement with the previous studies (16–19).

Fig. 5. ^{19}F–^{19}F COSY NMR spectrum of the HSO_3F–SbF_5 system with x_{SbF_5} = 0.000 999.

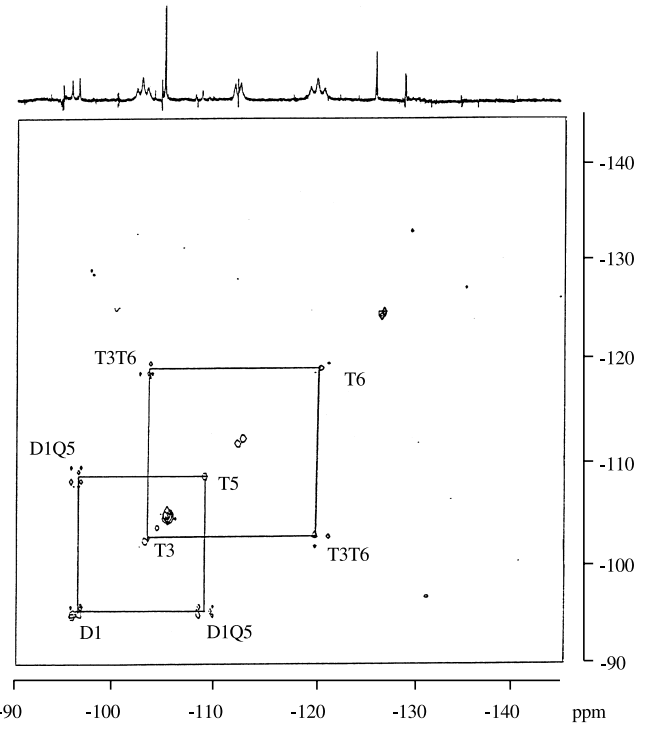

All signals assigned to monomeric species are observable in the HSO_3F–SbF_5 system at least up to x_{SbF_5} = 0.489 except D1 and T5, which is only barely observable for x_{SbF_5} = 0.0500 and is absent in the systems with higher x_{SbF_5}. This observation suggests that the monomeric *mer*-$[SbF_3(SO_3F)_3]^-$, which has the highest SO_3F content among all species observed in this study, exists only at very low SbF_5 concentration. It has not been observed in the previous NMR studies of HSO_3F–SbF_5 systems with high HSO_3F:SbF_5 ratios. However, it has been reported by Thompson et al. (16) for the HSO_3F–$SbF_4(SO_3F)$ and HSO_3F–SbF_5–SO_3 systems. It was reported that, based on cryoscopic measurements, the freshly distilled HSO_3F contains ~0.0006 mol kg^{-1} of SO_3 (25), which is comparable with the concentration of SbF_5 in the x_{SbF_5} = 0.000 999 system. Therefore, the insertion reaction of SO_3 with SbF_5 in HSO_3F (16) may have contributed to the formation of species with high SO_3F/F ratios.

The chemical shifts and coupling constants of signals assigned to monomeric species in the HSO_3F–SbF_5 system with x_{SbF_5} = 0.009 84 are summarized in Table 1.

In spite of some variations in chemical shifts for the signals with increasing x_{SbF_5}, the following general correlation between the ^{19}F chemical shifts and their chemical environment is observed:

(*i*) For the fluorine *trans* to a fluorosulfato group, the signal shifts to low field as *cis* fluorines are sequentially replaced by fluorosulfato groups in fluoro-fluorosulfatoantimonate(V).

(*ii*) Similarly, the signal of the fluorine *cis* to another fluorine shifts to low field as *cis* fluorines are sequentially replaced by fluorosulfato groups in fluoro-fluorosulfatoantimonate(V).

© 1999 NRC Canada

Fig. 6. ^{19}F–^{19}F COSY NMR spectrum of the HSO_3F–SbF_5 system with x_{SbF_5} = 0.009 84.

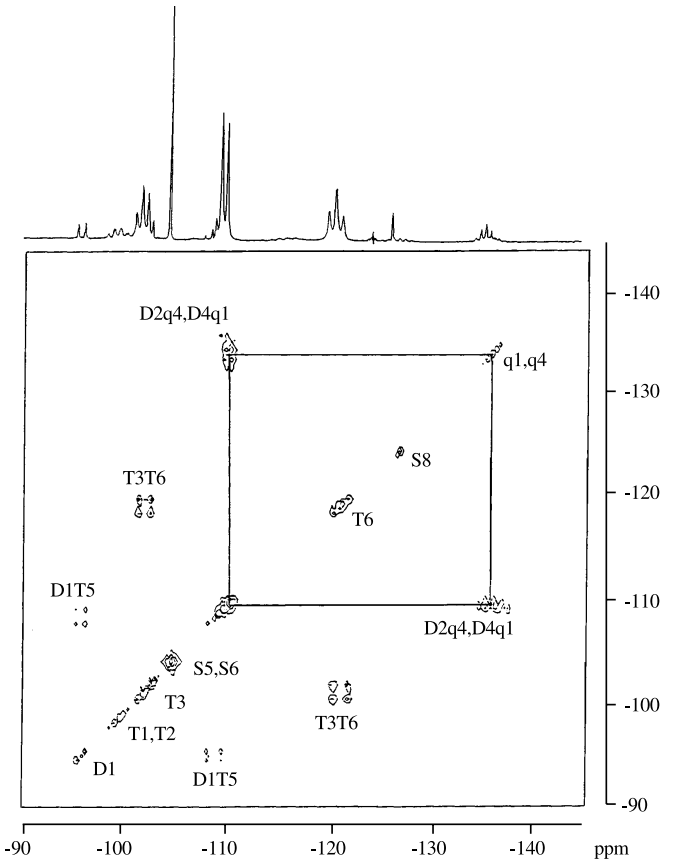

Fig. 7. (*a*) *J*-resolved ^{19}F NMR spectrum of the HSO_3F–SbF_5 system with x_{SbF_5} = 0.0500. (*b*) ^{19}F–^{19}F COSY NMR spectrum of the HSO_3F–SbF_5 system with x_{SbF_5} = 0.0500.

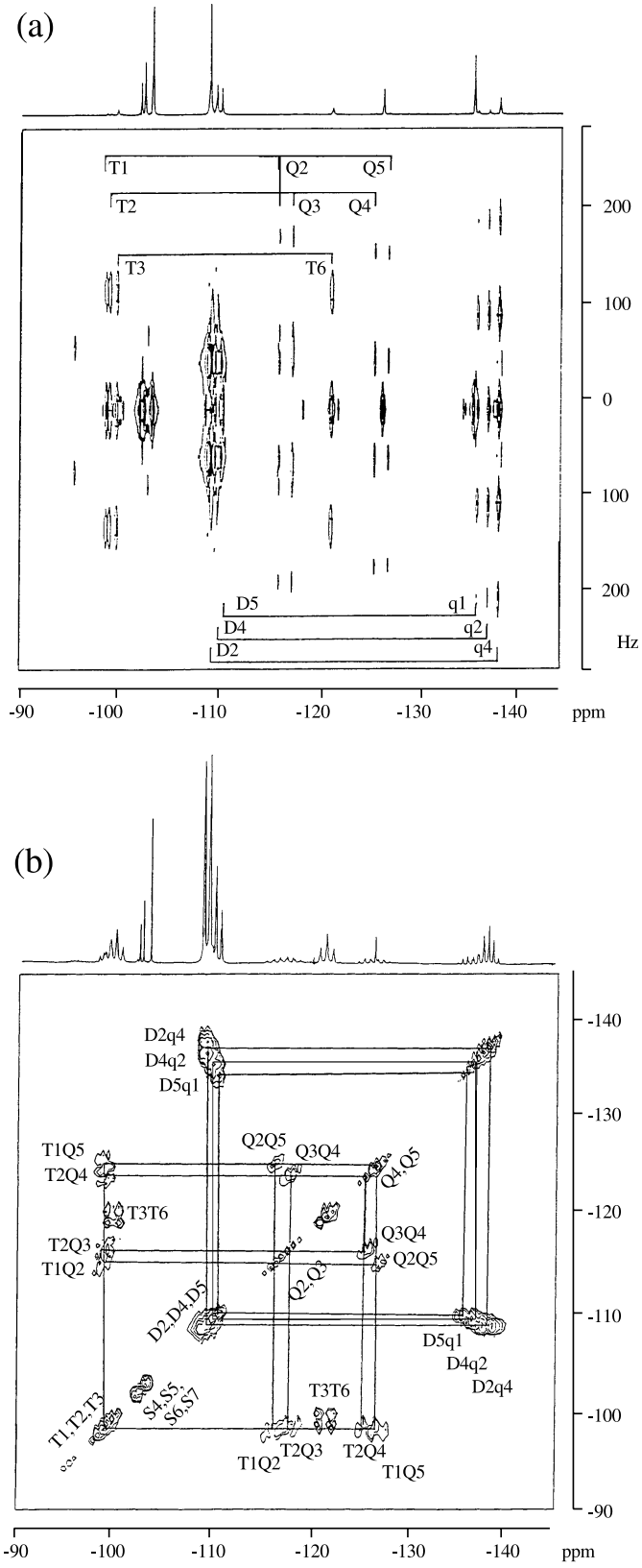

(*iii*) In the same fluoro-fluorosulfato-antimonate(V), signals due to fluorines *trans* to fluorine appear at lower fields than those *trans* to fluorosulfate.

These trends agree in general with the empirical equation established for substituted perfluoro complex anions of the type $[EF_nL_{6-n}]^{m-}$ (E = Ti, W, Sn; m = 2 and E = P; m = 1) (28)

$$[15] \quad \Delta_F = pC + qT$$

In this equation, Δ_F is the difference in chemical shift of a signal between the fully fluorinated and partly substituted species. *C* and *T* are constants for the particular substituent and central atom. The quantities *p* and *q* are the number of substituents *cis* and *trans*, respectively, to the fluorines whose shifts are calculated. However, attempts to quantitatively fit the data with the equation were not successful. A possible explanation is, that the data collected from this system are the averaged chemical shifts of the complex acids and their conjugate anions.

Based on integration of the signals, about 27% of the Sb(V) species is estimated to be present as $[SbF_5(SO_3F)]^-$, 52% as $[SbF_4(SO_3F)_2]^-$, 4% as $[SbF_3(SO_3F)_3]^-$, and less than 1% as $[SbF_6]^-$ in the system with x_{SbF_5} = 0.009 82. This result is not consistent with initial formation of $[SbF_5(SO_3F)]^-$, by direct combination of SbF_5 with HSO_3F (eqs. [3] and [4]) and subsequent ligand redistribution reactions according to

© 1999 NRC Canada

Table 1. Assignment of monomeric species for a HSO_3F–SbF_5 system with x_{SbF_5} = 0.009 82. Chemicals shifts δ_F (ppm), coupling constants J_{FF} (Hz).

Species	Structure	F(Sb) signal	Sb(V) mol %
$[SbF_6]$	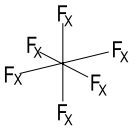	X_6 System X: -125.64 (**S8**)	<1
$[SbF_5(SO_3F)]$	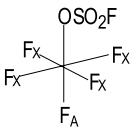	AX_4 System A: -135.24 (**q4**) X: -110.55 (**D2**) J_{AX} 100	27
cis-$[SbF_4(SO_3F)_2]$	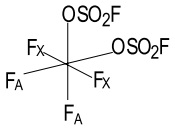	A_2X_2 System A: -120.36 (**T6**) X: -101.89 (**T3**) J_{AX} 120	39
trans-$[SbF_4(SO_3F)_2]$	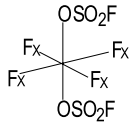	X_4 System X: -104.95 (**S7**)	13
mer-$[SbF_3(SO_3F)_3]$	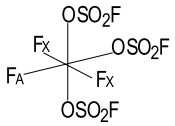	AX_2 System A: -109.44 (**T5**) X: -96.65 (**D1**) J_{AX} 127	4

[16] $2[SbF_5(SO_3F)]^- \rightleftarrows [SbF_4(SO_3F)_2]^- + [SbF_6]^-$

[17] $2[SbF_4(SO_3F)_2]^- \rightleftarrows [SbF_3(SO_3F)_3]^- + [SbF_5(SO_3F)]^-$

The insertion reaction of residual SO_3 and SbF_5 in HSO_3F may contribute partly to the formation of species with a high SO_3F contents in the system with x_{SbF_5} = 0.000 999. For the systems with $x_{SbF_5} \geq 0.009\ 82$, such a contribution seems too small, when the extremely low concentration of SO_3 is considered. Solvolysis of SbF_5 in HSO_3F as shown in eqs. [12] and [13] appears to have occurred. Otherwise, a higher concentration of $[SbF_6]^-$ would have been anticipated.

Assignment of segments in the oligomeric species

Although oligomerization is expected as the SbF_5 content increases, it is still surprising that it occurs in the system with an SbF_5 concentration as low as x_{SbF_5} = 0.009 82. It is noted from the spectrum of the system with x_{SbF_5} = 0.009 82 (see Fig. 3*b*) that three small peaks just downfield of D2 do not belong to the same multiplet. The separation from the central peak is 100 and 50 Hz for the lower field and higher field peaks, respectively. Moreover, the intensity of the peak at higher field to the central peak is approximately twice the intensity expected for a triplet. As illustrated in Inset 2 in Fig. 3*b*, where the expected but unobserved peaks are indicated by broken lines, it is likely that the first two peaks on the left belong to a triplet T5 with one peak of the multiplet buried in the intense D2, and the high-field peak is one half of a doublet D4, again, with the other half buried in D2. From the corresponding ^{19}F–^{19}F COSY spectrum (see Fig. 6), D4 is correlated with a quintet q1, which is partially overlapped with the intense q4, to form another AX_4 spin system. It can be assigned to a segment of the type $[SbF_5\text{-}(\mu\text{-}SO_3F)^-]$.

In the 1D NMR spectrum of the HSO_3F–SbF_5 system with x_{SbF_5} = 0.009 82 (see Fig. 3*b*), the signals at –97.5~–101 ppm are apparently two triplets, T1 and T2, with close chemical shifts and slightly different coupling constants. This is much clearer in the 1D ^{19}F NMR spectrum (see Fig. 3*c*) and ^{19}F *J*-resolved spectrum (F(Sb) region) of the HSO_3F–SbF_5 system with x_{SbF_5} = 0.0500 (see Fig. 7*a*).

In the 1D spectrum (see Fig. 3*c*), the signals in the region –97~–101 ppm are resolved into three triplets T1, T2, and T3. The ^{19}F–^{19}F COSY spectrum (F(Sb) region) (see Fig. 7*b*) indicates T1 and T2 are correlated with Q2 and Q5, Q3, and Q4, respectively. In the 1D ^{19}F NMR spectrum, the quartets Q2 and Q3 are partially overlapped to form a "sextet" with the area ratio of 1:3:4:4:3:1 in the region –115~–118.5 ppm (see Inset 1, Fig. 3*c*). The other two quartets, Q4 and Q5, form another "sextet" at –123.5~–127.5 ppm (see Inset 2, Fig. 3*c*), which is overlapped with the readily recognizable singlet S8 at –125.8 ppm assigned to $[SbF_6]^-$. Careful inspection of the frequencies and area ratios of the peaks sug-

© 1999 NRC Canada

Fig. 8. ^{19}F–^{19}F COSY NMR spectrum of the HSO_3F–SbF_5 system with x_{SbF_5} = 0.194.

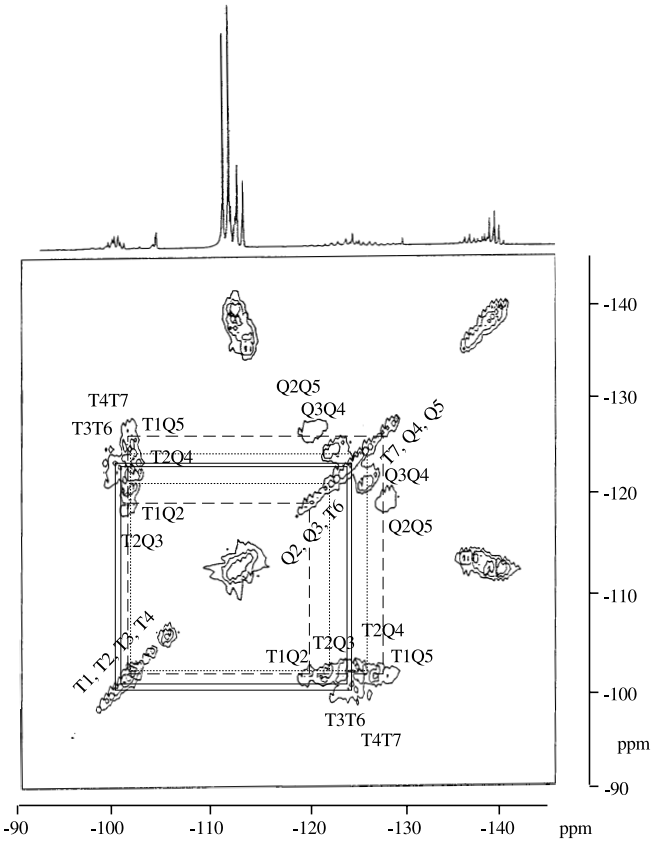

gests that each of them results from A or M of two AMX_2 spin systems T1Q2Q5 and T2Q3Q4, respectively. These two AMX_2 systems can be assigned to the segments of the type *cis*-[$(SO_3F)SbF_4$-(μ-SO_3F)-], or of the type *cis*-[-(μ-SO_3F)-SbF_4-(μ′-SO_3F)-]with two different terminal segments on each side.

It is also evident from the *J*-resolved spectrum of the x_{SbF_5} = 0.0500 system (see Fig. 7*a*) that the signals at –134~–139 ppm are three overlapped quintets, q1, q2, and q4. In the ^{19}F–^{19}F COSY spectrum, the cross peaks D2q4, D4q2, and D5q1 indicate that q4, q2, and q1 are coupled with three partially overlapped doublets D2, D4, and D5, respectively, to form three AX_4 systems. One of the AX_4 systems, D2q4, has been assigned to monomeric $[SbF_5(SO_3F)]^-$. The other two may be assigned to a segment of the type $[SbF_5$(-SO_3F)-] with different segments on the other side of the bridging fluorosulfato group.

In the ^{19}F NMR spectrum of the HSO_3F–SbF_5 system with x_{SbF_5} = 0.009 82 (see Fig. 3*b*), the weak signals at –103.50 ppm are recognized as three singlets, and based on similarities in chemical shifts, are possibly the same singlets as S4, S5, and S6 observed for the x_{SbF_5} = 0.0500 system (see Fig. 3*c*). They can be assigned to segments of the type *trans*-[(SO_3F)-SbF_4-(μ-SO_3F)-]. At high x_{SbF_5}, there are additional three singlets (S1, S2, and S3) at lower field (see Inset 1, Figs. 3*e* and 3*f*), which may be better assigned to segments of the type *trans*-[-(μ-SO_3F)-SbF_4-(μ′-SO_3F)-] in trimers or higher oligomeric species. The assignment of these singlets to monomers with high SO_3F/F ratios, such as *fac*-$[SbF_3(SO_3F)_3]$, $[SbF_2(SO_3F)_4]$, and $[SbF(SO_3F)_5]$, is less likely because:

(*i*) the relative intensity of S4, S5, and S6 increase as the SbF_5 concentration increases, which is contrary to what is expected for the monomers with a high SO_3F/F ratio. As the x_{SbF_5} increases from 0.000 999 to 0.009 82, in fact, the signals D1 and T5 due to *mer*-$[SbF_3(SO_3F)_3]^-$ are barely observable, and the relative intensities of S7 due to *trans*-$[SbF_4(SO_3F)_2]^-$ and T3T6 due to *cis*-$[SbF_4(SO_3F)_2]^-$ are reduced significantly; and

(*ii*) singlets S4, S5, and S6 cannot be observed even in the spectrum of the HSO_3F–SbF_5 system with x_{SbF_5} = 0.000 999, which has a high HSO_3F–SbF_5 mole ratio. Singlets S1, S2, and S3 are observed only in the HSO_3F–SbF_5 system with low HSO_3F–SbF_5 mole ratios ($x_{SbF_5} \geq 0.194$).

For the same reasons, assignment of these singlets to segments with a high SO_3F content, such as *trans*-$[(SO_3F)_3SbF_2$-(μ-SO_3F)-] and $[(SO_3F)_4SbF$-(μ-SO_3F)-], seems implausible.

Two triplets, T4 and T7, emerge in the ^{19}F NMR spectrum of the system with x_{SbF_5} = 0.0989 (the inset in Fig. 3*d*) and higher. Parallel to triplets T3 and T6, which are attributed to the monomeric species *cis*-$[SbF_4(SO_3F)_2]^-$, T4 and T7 are also correlated to each other as seen from the ^{19}F–^{19}F COSY spectrum (see Fig. 8).

They compose another A_2X_2 spin system, which is better attributed to a segment, *cis*-[-(μ-SO_3F)-SbF_4-(μ-SO_3F)-], linking two identical moieties.

A glimpse at the signals at –109~–111 ppm in spectra of the systems with x_{SbF_5} = 0.0989 and 0.194 may give the impression that they are three overlapped doublets. However, the separation between the two peaks of lowest intensity varies from 55 Hz for x_{SbF_5} = 0.0989–72 Hz for x_{SbF_5} = 0.194. Both these separations are lower than all the coupling constants found for terminal fluorines in this particular system. Analysis of the intensities of the signals suggests that they may be composed of four doublets. In the spectrum of the HSO_3F–SbF_5 system with x_{SbF_5} = 0.194, for example, these signals were analyzed by deconvolution into the following four doublets: D2 (109.6 ppm, $^2J_{FF}$ = 99 Hz), D3 (110.1 ppm, $^2J_{FF}$ = 100 Hz), D4 (110.3 ppm, $^2J_{FF}$ = 100 Hz), and D5 (110.9 ppm, $^2J_{FF}$ = 100 Hz) (see Inset 2, Fig. 3*e*). From the ^{19}F–^{19}F COSY spectrum (see Figs. 7 and 9), these doublets are correlated to the quintets q1, q2, q3, and q4 at –134~–140 ppm, respectively. Signal q3, which is correlated to the weakest of the doublets, D3, is so weak that it cannot be clearly observed in the spectrum of the x_{SbF_5} = 0.0989 system. As shown in Inset 3 of Fig. 3*e*, only one peak remains unassignable to either q1, q2, or q4 and therefore is assigned to q3 while the rest of q3 is buried in the intense signal due to q4. Among four AX_4 spin systems, D2q4 has been assigned to the monomer $[SbF_5(SO_3F)]^-$. The other three AX_4 systems can be attributed to fragments of the type $[SbF_5$-(*m*-SO_3F)-].

A quartet, Q1, with the area ratio of 1:1:1:1 appears at ~–116.4 ppm in the spectra of the systems with $x_{SbF_5} \geq 0.342$. It can be assigned to the eight fluorines *cis* to the bridging fluorine in $[Sb_2F_{11}]^-$. As sketched in Inset 2 of Fig. 3*f*, the signal is split into two lines with a 1:1 ratio by a terminal fluorine ($^2J_{FF}$ = 102 Hz) and then further split by the bridging fluorine ($^2J_{FF}$ = 60 Hz). Only the most intense portion of the nonet N1, due to the bridging fluorine, is barely observ-

© 1999 NRC Canada

Fig. 9. ^{19}F–^{19}F COSY NMR spectrum of the HSO_3F–SbF_5 system with x_{SbF_5} = 0.342.

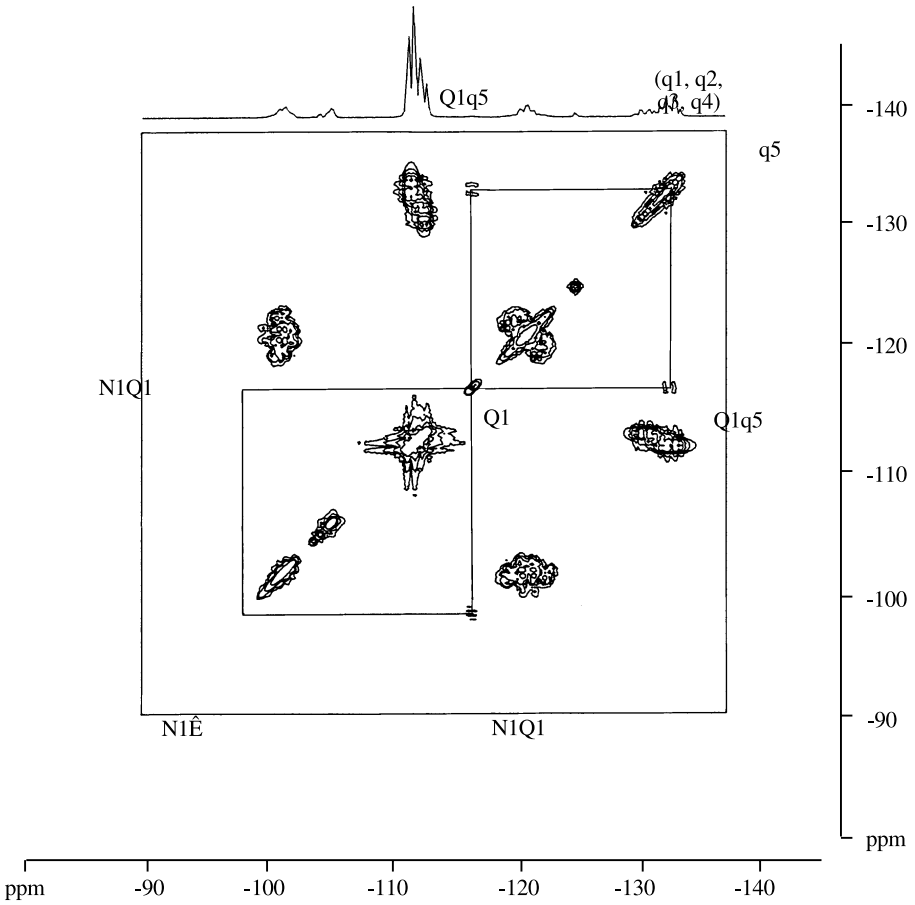

able at –91.0 ppm (see Inset 1, Fig. 3*f*). The quintet q5, due to the two terminal fluorines, falls into the q1q2q3q4 region. The correlation between N1, Q1, and q5, however, is very clear from the corresponding ^{19}F–^{19}F COSY spectrum (see Fig. 9).

The assignments discussed above are summarized in Table 2. Some variations in chemical shifts are observed for the signals as x_{SbF_5} changes. The data listed in Table 2 are measured from the spectrum of the HSO_3F–SbF_5 system with x_{SbF_5} = 0.0989 except signals due to *trans*-[-(μ-SO_3F)-SbF_4-(μ′-SO_3F)-] and the dimer $[Sb_2F_{11}]^-$, which can only be clearly observed for HSO_3F–SbF_5 systems with $x_{SbF_5} \geq 0.194$ and for systems with $x_{SbF_5} \geq 0.342$, respectively.

With the assignments proposed above, it is possible to estimate the relative concentrations of different segments in the HSO_3F–SbF_5 system with $x \leq 0.342$. The results are presented in Table 3. Due to the signal overlap and possible inaccurate baseline settings over the wide frequency range, integration errors inevitably occur to some extent. The errors are small for intense, narrow peaks and large for weak, broad peaks. The estimation of concentration of segments is not feasible for the systems with $x_{SbF_5} \geq 0.489$, since integration of the individual signals from overlapped, broadened peaks is not reliable.

Possible oligomeric species in the HSO_3F–SbF_5 system

As the concentration of the Lewis acid SbF_5 increases, it is expected that oligomeric antimony(V) species should begin to appear. The relative concentration of oligomeric species is expected to increase while the relative concentration of monomeric antimony(V) species decreases accordingly. Among the monomeric species observed, $[SbF_3(SO_3F)_3]^-$ has the highest SO_3F content. Therefore, the dimeric species would likely be limited to the types $[Sb_2F_{11-n}(SO_3F)_n]$ (n = 0–3), formed by the following dimerizations by addition of SbF_5 to the monomeric species:

[18] $[SbF_6]^- + SbF_5 \rightleftarrows [Sb_2F_{11}]^-$

[19] $[SbF_5(SO_3F)]^- + SbF_5 \rightleftarrows [Sb_2F_{10}(SO_3F)]^-$

[20] $[SbF_4(SO_3F)_2]^- + SbF_5 \rightleftarrows [Sb_2F_9(SO_3F)_2]^-$

[21] $[SbF_3(SO_3F)_3]^- + SbF_5 \rightleftarrows [Sb_2F_8(SO_3F)_3]^-$

Dimeric SO_3F-containing species are unlikely to be linked by F-bridges. Studies of ternary fluoride fluorosulfates based on vibrational spectra indicate that fluorosulfate always takes precedence over fluoride as a bridging ligand (29–33). Moreover, F-bridged dimers would have spin systems of three or more different types of fluorines, which should result in more complicated ^{19}F NMR spectra. In this study, simple splitting patterns are observed, which can be interpreted either in terms of monomeric species or in terms of segments linked by SO_3F-bridges. Most spin systems observed consist of one or two different types of fluorines. Two AMX_2 spin systems are satisfactorily assigned to seg-

© 1999 NRC Canada

Table 2. Assignment of ^{19}F NMR signals (F(Sb) region) to segments in oligomeric fluoro-fluorosulfato-antimonate(V) species in the HSO_3F–SbF_5 system with x_{SbF_5} = 0.0989. Chemical shifts δ_F [ppm], coupling constants J_{FF} [Hz].

Structure of segment	Structure of segment	^{19}F chemical shift [ppm] coupling constant [Hz]
$[SbF_5(\mu\text{-}SO_3F)]^-$	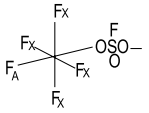	AX_4 Systems: A: -137.8 (q3), X: -109.8 (D3), J_{AX} 100 A: -137.0 (q2), X: -110.1 (D4), J_{AX} 100 A: -135.6 (q1), X: -110.7 (D5), J_{AX} 100
cis-$[(\mu\text{-}SO_3F)SbF_4(SO_3F)]^-$ or *cis*-$[(\mu\text{-}SO_3F)SbF_4(\mu'\text{-}SO_3F)]^-$	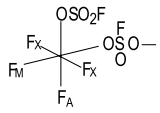	AMX_2 Systems: A: -126.1 (Q5), M: -116.7 (Q2), X: -98.1 (T1), J_{AM} 114, J_{AX} 100 A: -124.5 (Q4), M: -118.2 (Q3), X: -98.3 (T2), J_{AM} 115, J_{AX} 102
cis-$[(\mu\text{-}SO_3F)SbF_4(\mu'\text{-}SO_3F)]^-$	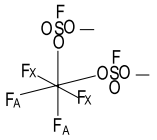	A_2X_2 System: A: -121.6 (T7), X: -98.7 (T4), J_{AX} 124
trans-$[(SO_3F)\text{-}SbF_4(\text{-}(\mu\text{-}SO_3F)\text{-}]$	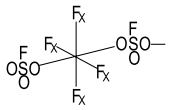	X_4 Systems: X: -102.1 (S4) X: -102.4 (S5) X: -102.7 (S6)
trans-$[\text{-}(\mu\text{-}SO_3F)\text{-}SbF_4\text{-}(\mu'\text{-}SO_3F)\text{-}]$ (x_{SbF_5}= 0.194)	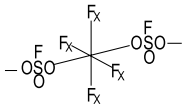	X_4 Systems: X: -99.8 (S1) X: -102.0 (S2) X: -102.6 (S3)
dimer $[SbF_5\text{-}(\mu\text{-}F)\text{-}SbF_5]^-$ (x_{SbF_5}= 0.342)	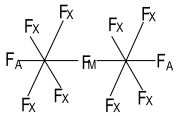	$[AX_4]_2M$ System: A: ? , M: -91.0 (N1), X: -116.4 (Q1), J_{AX} 102, J_{MX} 60

ments of the types *cis*-$[SbF_4(SO_3F)\text{-}(\mu\text{-}SO_3F)\text{-}]$ or *cis*-$[\text{-}(\mu\text{-}SO_3F)\text{-}SbF_4\text{-}(\mu'\text{-}SO_3F)\text{-}]$. Coupling constants observed for most multiplets (98~120 Hz) point to terminal rather than bridging fluorines. The only exceptions are N1 and Q1 for which smaller coupling constants (60 Hz) are observed. Indeed, N1 and Q1 are due to the F-bridged perfluoro anion $[Sb_2F_{11}]^-$, where no SO_3F^- competes with F^- as the bridging ligand. The small coupling constant (60 Hz) results from the coupling between the bridging fluorine and *cis*-terminal-fluorines (equatorial fluorines).

Illustrated in Fig. 10 are all possible dimeric isomers of the types $[Sb_2F_{11-n}(SO_3F)_n]$ (n = 0–3).

The last three isomers of the type $[Sb_2F_8(SO_3F)_3]^-$ have two terminal fluorosulfates on the same antimony. Each of the three isomers has an AX_2 spin system. According to eq. [20], these isomers should have formed from the direct combination of *mer*-$[SbF_3(SO_3F)_3]^-$ and SbF_5. However, signals due to AX_2 spin systems other than those assigned to the monomer *mer*-$[SbF_3(SO_3F)_3]^-$, are not observed in the F(Sb) region. This suggests they may have rearranged to other isomers. Thus, the possible dimeric Sb(V) species are limited to $[Sb_2F_{11}]^-$, $[Sb_2F_{10}(\mu\text{-}SO_3F)]^-$, *cis*- and *trans*-$[Sb_2F_9(SO_3F)_2]^-$, and *cis*,*cis*-, *cis*,*trans*-, and *trans*,*trans*-$[SbF_4(SO_3F)\text{-}(\mu\text{-}SO_3F)\text{-}SbF_4(SO_3F)]^-$.

Since the fluorine on the bridging SO_3F^- does not couple with other fluorines, information about connectivity between different segments of SO_3F-bridged oligomers is unavailable. Only for the F-bridged dimer $[Sb_2F_{11}]^-$ is the connectivity manifested in a unique nonet due to the coupling of the bridging fluorine to eight equivalent terminal *cis*-fluorines. In the spectrum of the system with x_{SbF_5} = 0.342 (see Fig. 3*f*), only a portion of the characteristic nonet N1 centered at δ C*F*Cl_3 = –91.0 ppm can be observed because of its low intensity, but the correlated Q1 at δ C*F*Cl_3 = –116.4 ppm due to eight *cis*-fluorines is clearly observed.

Among the four AX_4 spin systems, D2q4 has been assigned to the monomer $[SbF_5(SO_3F)]^-$. D5q1 is tentatively assigned to the dimer $[Sb_2F_{10}(\mu\text{-}SO_3F)]^-$ and D4q2 to the segment $[SbF_5\text{-}(\mu\text{-}SO_3F)\text{-}]$ in both *cis*- and *trans*-$[SbF_5\text{-}(\mu\text{-}SO_3F)\text{-}SbF_4(SO_3F)]^-$. It is noted that the appearance of the AX_4 spin system D3q3 is accompanied by the emergence of the A_2X_2 spin system T4T7 and three singlets S1, S2, and S3. T4T7 can be assigned to a segment *cis*-$[(\text{-}(\mu\text{-}SO_3F)\text{-}SbF_4\text{-}(\mu\text{-}SO_3F)\text{-}]$ linking two identical moieties at each end. S1, S2, and S3 are assigned to segments of the type *trans*-$[\text{-}(\mu\text{-}SO_3F)\text{-}SbF_4\text{-}(\mu\text{-}SO_3F)\text{-}]$, which link either identical or different moieties at each end. The coincident appearance of these spin systems suggests the formation of various trimeric

© 1999 NRC Canada

Fig. 10. Dimeric species of the type $[Sb_2F_{11-n}(SO_3F)_n]^-$ (n = 0–3) and corresponding spin systems in the F (Sb) region.

$[Sb_2F_{11}]^-$

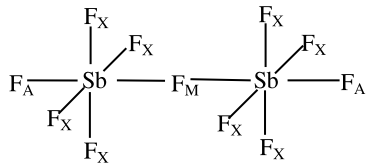

F(Sb): $[AX_4]_2M$

SO_3F-bridged $[Sb_2F_9(SO_3F)_2]^-$

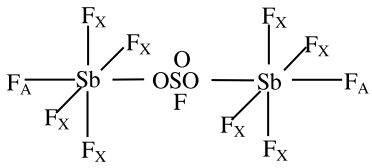

F(Sb): AX_4

Possible SO_3F-bridged dimers of the type $[Sb_2F_9(SO_3F)_2]^-$

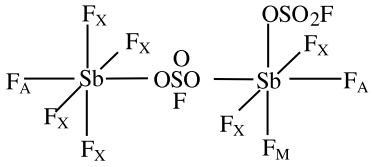

F(Sb): AX_4 and AMX_2

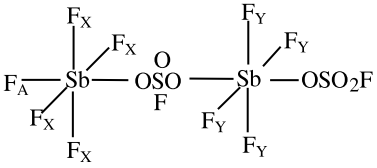

F(Sb): AX_4 and Y_4

Possible SO_3F-bridged dimers of the type $[Sb_2F_8(SO_3F)_3]^-$

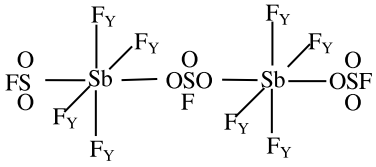

F(Sb): Y_8

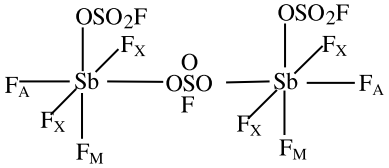

F(Sb): AMX_2

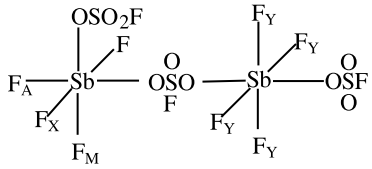

F(Sb): AMX_2 and Y_4

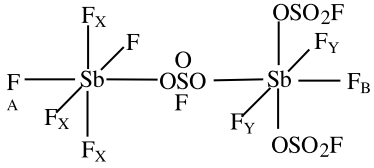

F(Sb): AX_4 and BY_2

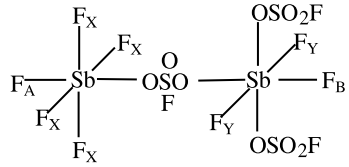

F(Sb): AX_4 and BY_2

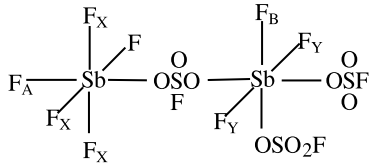

F(Sb): AX_4 and BY_2

fluoro-fluorosulfato-antimonate(V) species, e.g., *cis*- and *trans*-$[SbF_5$-(μ-SO_3F)-SbF_4-(μ-SO_3F)-$SbF_5]^-$. However, it must be pointed out that the possibility of the existence of higher oligomeric species cannot be excluded, particularly in the systems with high SbF_5/HSO_3F ratios.

The most intense signal of the four singlets at low field (–100~–105 ppm), S7, has been assigned to the monomeric $[SbF_4(SO_3F)_2]^-$. The remaining three singlets are assigned to the fragments of the type *trans*-$[SbF_4(SO_3F)$-(μ-SO_3F)-]. S4 is tentatively assigned to *trans*-$[SbF_5$-(μ-SO_3F)-SbF_4-$(SO_3F)]^-$, S5 to *cis, trans*-$[SbF_4(SO_3F)$-(μ-SO_3F)-$SbF_4(SO_3F)]$, and S6 to *trans, trans*-$[SbF_4(SO_3F)$-(μ-SO_3F)-$SbF_4(SO_3F)]$.

Of the two AMX_2 spin systems, T2Q3Q4 and T1Q2Q5, either can be assigned to the segment *cis*-$[SbF_4(SO_3F)$-(μ-SO_3F)-] in the dimer *cis*-$[SbF_5$-(μ-SO_3F)-$SbF_4(SO_3F)]^-$ and the other to the segment *cis*-$[SbF_4(SO_3F)$-(μ-SO_3F)-] in the dimers *cis,cis*- and *cis,trans*-$[SbF_4(SO_3F)$-(μ-SO_3F)-$SbF_4(SO_3F)]^-$ or vice versa. The analysis of relative concentrations of segments favors the assignment of T2Q3Q4 to the dimer *cis*-$[SbF_5$-(μ-SO_3F)-$SbF_4(SO_3F)]^-$ and T1Q2Q5 to the dimers *cis,cis*- and *cis,trans*-$[SbF_4(SO_3F)$-(μ-SO_3F)-$SbF_4(SO_3F)]^-$. It is entirely possible that, at high x_{SbF_5}, terminal fluorosulfato groups in the fragments of the type *cis*-$[SbF_4(SO_3F)$-(μ-SO_3F)-] may transform into bridging fluorosulfato groups to form fragments of the type *cis*-[-(μ-SO_3F)-SbF_4-(μ'-SO_3F)-], which then link two non-equivalent terminal segments to form trimers or even higher oligomers. However, there is no definitive evidence for such transformations in the ^{19}F NMR spectra. The variation in chemical shifts of the signals may also be attributed to the shifts of the equilibria between complex acids and their conjugate anions and to the change of the medium.

© 1999 NRC Canada

Table 3. Relative concentrations of monomeric species and segments in oligomeric species in the HSO_3F–SbF_5 system.

		Molar fraction of SbF_5, x_{SbF_5}					
		0.000999	0.00982	0.0500	0.0989	0.194	0.342
Species	Signals	Relative concentration, Sb(V) mol %					
Monomeric species							
$[SbF_6]^-$	S8	2	<1	<1	<1	<1	<1
$[SbF_5(SO_3F)]^-$	D2q4	15	27	36	42	45	37
cis-$[SbF_4(SO_3F)_2]^-$	T3T6	48	39	20	12	8	7
trans-$[SbF_4(SO_3F)_2]^-$	S7	21	13	5	3	1	<1
mer-$[SbF_3(SO_3F)_3]^-$	D1T5	14	4	2	0	0	0
Segments in oligomeric species							
$[SbF_5$-(μ-F)]	Q1	0	0	0	0	0	<1
	D3q3	0	0	0	3	6	15
$[SbF_5$(μ-$SO_3F)]$	D4q2	0	0	10	10	7	4
	D5q1	0	3	7	12	15	17
cis-$[SbF_4$(μ-$SO_3F)_2]$	T4T7	0	0	0	<1	4	8
cis-$[SbF_4(SO_3F)$(μ-$SO_3F)]$ or	T1Q2Q5	0	6	8	4	5	2
cis-$[SbF_4$(μ-$SO_3F)$(μ′-$SO_3F)]$	T2Q3Q4	0	6	8	10	8	6
	S1	0	0	0	0	<1	<1
trans-$[SbF_4(SO_3F)$(μ-$SO_3F)]$	S2	0	0	0	0	<1	<1
or	S3	0	0	0	0	<1	<1
trans-$[SbF_4$(μ-$SO_3F)$(μ′-$SO_3F)]$	S4	0	1	<1	<1	<1	<1
	S5	0	<1	2	1	<1	<1
	S6	0	<1	2	2	1	1

Table 4. Proposed principal species and their relative concentrations in HSO_3F–SbF_5 system.

	Molar fraction of SbF_5, x_{SbF_5}					
	0.000999	0.00982	0.0500	0.0989	0.194	0.342
	Sb(V) mol %					
Constituent species						
$[SbF_6]^-$	2	<1	<1	<1	<1	<1
$[SbF_5(SO_3F)]^-$	15	20	36	42	45	37
cis-$[SbF_4(SO_3F)_2]^-$	48	39	20	12	9	7
trans-$[SbF_4(SO_3F)_2]^-$	21	13	5	3	1	<1
mer-$[SbF_3(SO_3F)_3]^-$	14	4	2	0	0	0
Total of monomeric species	100	76[a]	63	57	54	44
$[Sb_2F_{11}]^-$	0	0	0	0	0	<1
$[SbF_5$-(μ-$SO_3F)$-$SbF_5]^-$	0	3	7	12	15	17
trans-$[SbF_5$-(μ-$SO_3F)$-$SbF_4(SO_3F)]^-$	0	3	<1	<1	1	1
cis-$[SbF_5$-(μ-$SO_3F)$-$SbF_4(SO_3F)]^-$	0	11	17	20	14	10
trans,*trans*-$[SbF_4(SO_3F)$-(μ-$SO_3F)$-$SbF_4(SO_3F)]^-$	0	<1	2	2	1	1
cis,*cis*-$[SbF_4(SO_3F)$-(μ-$SO_3F)$-$SbF_4(SO_3F)]^-$	0	5	6	3	5	2
cis,*trans*-$[SbF_4(SO_3F)$-(μ-$SO_3F)$-$SbF_4(SO_3F)]^-$	0	2	4	2	<1	<1
Total of dimeric species	0	24[a]	36	39	36	31
cis-$[SbF_5$-(μ-$SO_3F)$-SbF_4-(μ-$SO_3F)$-$SbF_5]^-$, other trimers, and higher oligomers	0	0	0	4	10	24
Total of oligomeric species	0	24[a]	36	43	46	55

[a]From T2Q3Q4 + S4 = 7, it is expected that ca. 7% Sb(V) species may exist as the fragment $[SbF_5$-(μ-$SO_3F)$-] in *cis*- and *trans*-$[Sb_2F_{10}(SO_3F)]^-$. The signals D4q2 due to the -SbF_5 moiety (an AX_4 spin system) is overlapped with D2q4 due to another AX_4 spin system by coincidence.

Based on these assignments, it is possible to estimate the relative concentrations of the proposed oligomeric species by analysis of the relative concentration of segments. The results for HSO_3F–SbF_5 systems with $x_{SbF_5} \leq 0.342$ are listed in Table 4.

Such an estimation is not feasible for HSO_3F–SbF_5 systems with $x_{SbF_5} \geq 0.342$ because it is impossible to obtain integral values for each of the overlapped, broad signals. However, it can be roughly estimated that about 67% of Sb(V) species exist as $[SbF_5]$- moieties, 25% as *cis*-$[SbF_4]$-

© 1999 NRC Canada

moieties, 4.5% as *trans*-[SbF_4]- moieties, and 3.5% as $[Sb_2F_{11}]^-$ in the x_{SbF_5} = 0.489 system.

Summary and conclusion

The results presented here depart from previous work by Commeyras et al. (17, 19) in two important aspects:

(*i*) Concentrations of the monomeric anions *cis*- and *trans*-$[SbF_4(SO_3F)_2]^-$ are at any mole fraction of SbF_5 considerably higher than the concentration of $[SbF_6]^-$ (see Table 3). Hence, formation of the bis-fluorosulfato anions $[SbF_4(SO_3F)_2]^-$ solely by ligand redistribution of $[SbF_5(SO_3F)]^-$ (eq. [9]) becomes improbable. Instead solvolysis of SbF_5 or possibly of $SbF_4(SO_3F)$ in HSO_3F (eqs. [12] and [13]) and subsequent complex formation with either SO_3F^- or F^- is much more likely. The byproduct HF is rapidly converted by reaction with glass to H_2O (eq. [12]), which functions as a base to give the oxonium ion $[H_3O]^+$. The $[H_3O]^+$ ion is identified by ^1H NMR and structurally characterized as $[H_3O][Sb_2F_{11}]$ (22).

(*ii*) In oligomeric anions or in segments of oligomers, bridging by μ-SO_3F groups, originally suggested by Gillespie et al. (16, 18) for dilute solutions is now observed even at high SbF_5 concentrations. A μ-fluoro group is only found in $[Sb_2F_{11}]^-$. Oligomeric anions with fluorobridges and terminal SO_3F-groups of the type $[(SbF_5)_n(SO_3F)]^-$ (n = 2–4) all previously identified by Commeyras and co-workers (19) are not detectable with modern NMR techniques.

Their postulated formation by reaction of *cis*-F-bridged oligomeric $(SbF_5)_n$ (n = 2–4) with the selfionization SO_3F^- according to

$$[22] \quad (SbF_5)_n + SO_3F^-_{(solv)} \xrightarrow[HSO_3F]{} [(SbF_5)_n(SO_3F)]^- \qquad n = 2\text{–}4$$

is not supported by our findings. The *cis*-F-bridges found in liquid SbF_5 do not persist in magic acid, when samples are prepared as described in the experimental section. Our results are consistent with spectroscopic findings for the ansolvo species $SbF_4(SO_3F)$ (29, 30), $SbF_3(SO_3F)_2$ (30), and others (31–33) where in all instances only fluorosulfato bridges are observed.

The evidence for solvolysis of the Lewis acids SbF_5 and $SbF_4(SO_3F)$ (eqs. [12] and [13]) with HF and, via interaction with glass, of H_2O as intermediates, presented here and elsewhere (22), is reason for concern. Protonation of H_2O, which is a base in HSO_3F, is expected to reduce the proton acidity of magic acid drastically.

It is conceivable, that the difference in proton acidity between HF–SbF_5 and HSO_3F–SbF_5 noted by Sommer et al. (14, 15) is due to water formed in these side reactions. In spite of this limitation, the convenience of working in glass outweighs in most cases the slight reduction in proton acidities (14, 15). To study the effect water has on the types and concentrations of anions observable by ^{19}F NMR in magic acid we have recently completed an identical study in a glass free environment[2] and will report shortly on the results.

Acknowledgements

Thanks are due to the Fonds der Chemischen Industrie e. V. for material support (G.H.), the Natural Sciences and Engineering Research Council of Canada for operating funds (F.A.), and the NATO for a collaborative grant (G.H. and F.A.).

References

1. G.H. Olah, G.K.S. Prakash, and J. Sommer. *In* Superacids. J. Wiley, New York. 1985, and refs. therein.
2. T.A. O'Donnell. *In* Superacids and acidic melts as inorganic chemical reaction media. VCH Publishers, New York. 1993, and refs. therein.
3. R.J. Gillespie. Acc. Chem. Res. **1**, 202 (1968).
4. G.H. Olah and P. von R. Schleyer. *In* Carbonium ions. Vols. 1–5. Wiley Interscience, New York. 1968, 1970, 1973, 1973, and 1976.
5. R.C. Thompson. *In* Inorganic sulphur chemistry. *Edited by* G. Nickless. Elsevier, Amsterdam. 1968. p. 587.
6. M.F.A. Dove and A.F. Clifford. *In* Chemistry in non-aqueous ionizing solvents. *Edited by* J. Jander, H. Spandau, and C.C. Addison. Vieweg, Braunschweig/Wiesbaden. 1971, and refs. therein.
7. L.P. Hammett and A.J. Deyrup. J. Am. Chem. Soc. **54**, 2721 (1932).
8. R.J. Gillespie and J. Liang. J. Am. Chem. Soc. **110**, 6037 (1988).
9. P.L. Fabré, J. Devynk, and B. Tremillon. Chem. Rev. **82**, 591 (1982), and refs. therein.
10. R.J. Gillespie and P.E. Peel. J. Am. Chem. Soc. **95**, 5173 (1973).
11. R.J. Gillespie and P.E. Peel. Adv. Phys. Org. Chem. **9**, 1 (1972).
12. V. Gold, K. Laali, K.P. Morris, and L.Z. Zdunek. J. Chem. Soc. Chem. Commun. 769 (1981).
13. V. Gold, K. Laali, K.P. Morris, and L.Z. Zdunek. J. Chem. Soc. Perkin Trans. 2, 859 (1985).
14. J. Sommer, P. Canivet, S. Schwartz, and P. Rimmelin. J. Am. Chem. Soc. **100**, 2576 (1978).
15. J. Sommer, P. Canivet, S. Schwartz, and P. Rimmelin. Nouv. J. Chim. **5**, 45 (1981).
16. R.C. Thompson, J. Barr, R.J. Gillespie, J.B. Milne, and R.A. Rothenbury. Inorg. Chem. **4**, 1641 (1965).
17. A. Commeyras and G.A. Olah. J. Am. Chem. Soc. **91**, 2929 (1969).
18. P.A.W. Dean and R.J. Gillespie. J. Am. Chem. Soc. **91**, 7264 (1969).
19. D. Brunel, A. Germain, and A. Commeyras. Nouv. J. Chim. **2**, 275 (1978).
20. J. Bacon, P.A.W. Dean, and R.J. Gillespie. Can. J. Chem. **48**, 3413 (1970).
21. J.K.M Sanders and B.K. Hunter. Modern NMR spectroscopy: a guide for chemists. 2nd ed. Oxford University Press, Oxford. 1993.
22. D. Zhang, S.J. Rettig, J. Trotter, and F. Aubke. Inorg. Chem. **35**, 6113 (1996).
23. R.J. Gillespie and E.A. Robinson. Can. J. Chem. **40**, 675 (1962).
24. M. Lustig. Inorg. Chem. **4**, 1828 (1965).
25. R.J. Gillespie, J.B. Milne, and R.C. Thompson. Inorg. Chem. **5**, 468 (1966).
26. R.A. Stewart, S. Fujiwara, and F. Aubke. J. Chem. Phys. **49**, 965 (1968).
27. R.J. Gillespie and J.W. Quail. J. Chem. Phys. **39**, 2555 (1963).

© 1999 NRC Canada

28. P.J. Chevrier and S. Brownstein. J. Inorg. Nucl. Chem. **42**, 1397 (1980).
29. R.J. Gillespie and R.A. Rothenbury. Can. J. Chem. **42**, 416 (1964).
30. W.W. Wilson and F. Aubke. J. Fluorine Chem. **13**, 431 (1979).
31. H. Imoto and F. Aubke. J. Fluorine Chem. **15**, 59 (1980).
32. D. Zhang and F. Aubke. J. Fluorine Chem. **58**, 81 (1992).
33. H. Willner, F. Mistry, and F. Aubke. J. Fluorine Chem. **59**, 333 (1992).

© 1999 NRC Canada

Temperature dependence of the creatine kinase reaction measured in rat brain in vivo by ^{31}P NMR saturation transfer

Richard Buist, Scott Kroeker, and James Peeling

Abstract: Creatine kinase (CK) catalyzes the reversible phosphorylation of MgADP by phosphocreatine and thus regulates cellular concentrations of ADP and ATP. The temperature dependence of this reaction has been determined in rat brain in vivo between 30 and 40°C using ^{31}P NMR saturation transfer measurements. The pseudo-first-order rate constant for the forward CK reaction, k_f, varies little with temperature over this range, with an apparent activation energy E_a = 14.2 ± 4.9 kJ/mol. This is considerably lower than the values of E_a for isolated CK enzymes. However, when changes in [MgADP] and [H^+] with temperature are considered, a substrate concentration-independent value of E_a = 65.3 ± 9.7 kJ/mol is obtained for the maximum forward reaction velocity V_{max}. This agrees well with literature values for the isolated brain-type isoform of CK.

Key words: creatine kinase, activation energy, temperature, brain, rat.

Résumé : La kinase de créatine (KC) catalyse la phosphorylation réversible de MgADP par la phosphocréatine et régularise ainsi les concentrations cellulaires des di- et triphosphates d'adénosine. Faisant appel à des mesures de transfert de saturation en RMN du ^{31}P, on a déterminé la dépendance de cette réaction sur la température dans un cerveau de rat, in vivo, entre 30 et 40°C. Sur cette plage de températures, la constante de vitesse de pseudo-premier ordre pour la réaction normale de la KC, k_f, ne varie que très peu et son énergie d'activation apparente, E_a = 14,2 ± 4,9 kJ/mol. Cette valeur est de beaucoup inférieure aux valeurs de E_a mesurées avec des enzymes KC isolés. Toutefois, lorsqu'on considère les variations de [MgADP] et de [H^+] en fonction de la température, on obtient une E_a qui est indépendante de la concentration de substrat et dont la valeur est égale à 65,3 ± 9,7 kJ/mol pour la valeur maximale de la vitesse de la réaction normale, V_{max}. Cette valeur est en bon accord avec les valeurs rapportées dans la littérature pour des isoformes de KC isolées du cerveau.

Mots clés : kinase de créatinine, énergie d'activation, température, cerveau, rat.

[Traduit par la Rédaction]

Introduction

The creatine kinase (CK; EC 2.7.3.2) reaction (eq. [1]):

[1] $$PCr^{2-} + MgADP^{-} + H^{+} \rightleftarrows Cr + MgATP^{2-}$$

where PCr is phosphocreatine and Cr is creatine, plays an important role in regulating in vivo concentrations of ADP and ATP (1–4). The major isoenzymes of CK found in the brain are brain-type CK (BB-CK) and mitochondrial CK (mito-CK) (5), although recently, the presence of small amounts of muscle-type CK (MM-CK) has been reported in discrete areas of human (6), chicken (7), and rat (6) brain.

Measurements of the temperature dependence of CK activity in vitro yield Arrhenius activation energy (E_a) values in the range of 42–142 kJ/mol (8–13) for the forward rate constant k_f. For the related enzyme arginine kinase (AK), measurements of the temperature dependence of k_f in vitro give values for E_a ranging from 42 to 100 kJ/mol. E_a = 46.8 kJ/mol for k_f of AK in intact crayfish (14) and 126 kJ/mol in crab muscle (15) in vivo, while in vivo measurements on tail muscle in shrimp (16) and ex vivo measurements on single barnacle muscle fibers (17) show little temperature dependence of k_f.

The in vivo temperature dependence of the creatine kinase reaction in brain has not been characterized, but may give insight into the temperature dependence of cerebral oxygen metabolic rate and energy utilization rate. The results of an in vivo ^{31}P NMR spectroscopy saturation-transfer study of the creatine kinase reaction in rat brain from 30–40°C are described here.

Received April 16, 1999.

This paper is dedicated to Professor Ted Schaefer in recognition of his outstanding contributions to Canadian chemistry.

R. Buist.[1] Department of Radiology, University of Manitoba, 770 Bannatyne Avenue, Winnipeg, MB R3E 0W3, Canada.
S. Kroeker and J. Peeling. Department of Chemistry, University of Winnipeg, 515 Portage Avenue, Winnipeg, MB R3B 2E9, Canada.

[1]Author to whom correspondence may be addressed. Department of Pharmacology & Therapeutics, A006 Chown Building, The University of Manitoba, 770 Bannatyne Ave., Winnipeg, MB R3E 0W3, Canada. e-mail: rbuist@ms.umanitoba.ca

 © 1999 NRC Canada

Fig. 1. ^{31}P NMR spectra of rat brain saturated at the γ-ATP resonance (top) and at the mirror position about the PCr resonance (bottom). Saturation positions are indicated by arrows.

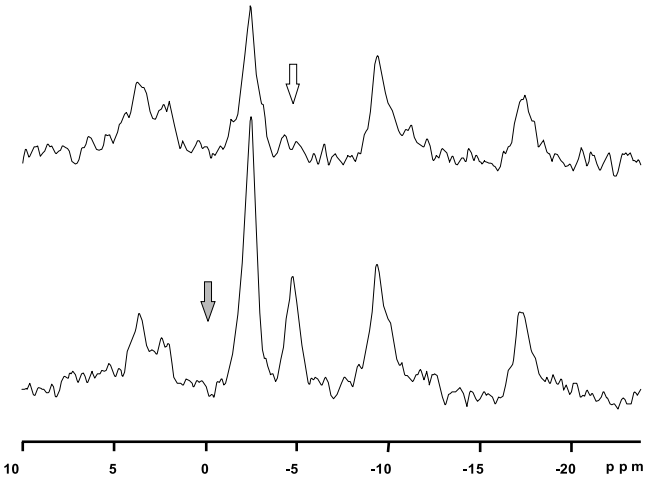

Experimental

The experiments used 14 adult male Sprague–Dawley rats weighing 300–350 g, handled and cared for in accordance with the guidelines of the Canadian Council on Animal Care. Each rat was used for a maximum of three separate sessions with measurements being made at 1–4 temperatures each time. For each experimental session, the rat was mechanically ventilated using 1.0% halothane, 30% O_2, and balance N_2O. An arterial line was placed in either the tail artery or a femoral artery to monitor blood pressure and blood gases. Arterial blood pressure was recorded once during each acquisition. Blood gases and blood pH were normalized by adjusting ventilator parameters before beginning a series of acquisitions at each temperature. The alpha-stat model of acid–base balance at temperatures differing from normal was used to regulate ventilation (18). This model requires that blood pH vary with temperature such that when normal body temperature is restored, normal blood gases and pH are obtained.

A thermocouple was inserted into the inner ear through the tympanic membrane to monitor brain temperature (19). Brain temperature was adjusted and maintained using a cylindrical thermostatted water bath about the head and a thermostatted water blanket for the body, together with air cooling and heating. Body temperature was monitored using a rectal probe, and the rectal temperature corresponded closely to the brain temperature.

NMR spectroscopy experiments were carried out on a Bruker Biospec 7 T, 21 cm horizontal bore scanner using a 1.5 × 2 cm elliptical surface coil tuned to the ^{31}P resonance frequency (121.5 MHz) sewn onto the scalp in an identical position relative to the brain of the rat for each experiment. No changes in the adjustable matching capacitors, and only small changes in tuning, were required for different rats and different temperatures, so that an identical pulse length (80 μs) was used for each experiment to ensure localization to the same part of the brain each time. ^{1}H MR images obtained with a surface coil of identical dimensions but tuned to the proton frequency showed that the contribution of underlying scalp and temporalis muscle to the spectra was minimal (20). Shimming was carried out to obtain a water ^{1}H NMR line width of 0.3–0.4 ppm using the ^{31}P coil to observe the water proton signal.

The saturation rf power level was carefully adjusted to completely eliminate the γ-ATP resonance while having a minimal direct saturation effect on the PCr resonance. To correct for direct saturation, a control spectrum was obtained with irradiation for an identical length of time at the mirror position as shown in Fig. 1. A saturation time of 4 s just prior to acquisition and a recycle delay of 6 s were used. At each temperature, three pairs of spectra were obtained at each saturation position using 64 averages for each spectrum. Thus the total acquisition time for a rate constant determination at a given temperature was 19.2 min. An acquisition size of 1024 points was used with a sweep width of 10 kHz. The FIDs were Fourier transformed after zero-filling to 2048 points and applying exponential line-broadening of 30 Hz. The intensity ratios from the three pairs of phased spectra were averaged to yield the final estimate of the extent of saturation transfer.

Preliminary experiments were carried out using similar parameters to those described above but with several different values for the saturation time t (0.1, 0.25, 0.5, 1, 2, and 4 s). A non-linear three-parameter fit to eq. [2] was carried out,

$$[2] \qquad M_t = M_\infty(1 + k_f T_1^{PCr} \exp(-t/T_{1app}^{PCr}))$$

where M_t and M_∞ represent the PCr magnetization at t and ∞, T_1^{PCr} is the longitudinal relaxation time for PCr in the absence of exchange but in the presence of saturation, and T_{1app}^{PCr} is the relaxation time of PCr in the presence of exchange and saturation. T_1 was not dependent on temperature in the range 30°C to 40°C (p = 0.39), with an average T_1^{PCr} = 2.44 s, in agreement with previously reported values (21, 23–25). Subsequently, k_f was calculated using this value of T_1^{PCr} and eq. [3] (26):

$$[3] \qquad k_f = \left(\frac{M_0}{M_\infty} - 1\right) \frac{1}{T_1^{PCr}}$$

where M_0 is the magnetization of PCr in the presence of the mirror saturation.

Intracellular pH could not be determined accurately from the ^{31}P NMR spectra due to the low signal-to-noise ratio and overlap of the broad inorganic phosphate (P_i) peak with neighbouring peaks (21, 27). However, under the alpha-stat regime of pH management, intracellular pH, pH_i, decreases with increasing temperature, with d(pH)/dT = –0.011 U/°C and normothermic pH = 7.06 in rat brain (22). These data were used to calculate [H^+] at each experimental temperature. To determine [PCr] and [MgADP] at each temperature, [PCr]/[ATP] was measured directly from the experimental spectra at each temperature by curve-fitting the PCr and ATP peaks using the deconvolution software built into the spectrometer system. Lorentzian line-shapes were used throughout. [ATP] was assumed to be 4.6 mM (21) and to be independent of temperature (28), and total creatine concentration (Cr plus PCr) was assumed to be 15.0 mM (21) and

© 1999 NRC Canada

Table 1. Physiological data from the experimental rats. Values shown are mean ± SEM.

Temperature (°C)	Mean arterial blood pressure (mmHg)[a]	Arterial $P(CO_2)$ (mmHg)	Arterial $P(O_2)$ (mmHg)	Arterial pH
30.04 ± 0.02	109.1 ± 5.8	48.8 ± 3.5	144 ± 10	7.35 ± 0.01
31.03 ± 0.04	107.1 ± 2.4	43.0 ± 2.5	115 ± 20	7.34 ± 0.03
32.06 ± 0.02	126.0 ± 4.0	48.0 ± 3.3	158 ± 14	7.33 ± 0.03
33.01 ± 0.05	108.9 ± 6.1	41.1 ± 1.9	115 ± 15	7.38 ± 0.02
34.06 ± 0.02	112.5 ± 2.5	47.8 ± 2.2	133 ± 10	7.33 ± 0.03
35.04 ± 0.02	116.6 ± 5.6	48.0 ± 3.2	121 ± 21	7.32 ± 0.03
36.01 ± 0.05	104.5 ± 5.9	38.2 ± 1.8	147 ± 23	7.37 ± 0.01
37.03 ± 0.05	108.7 ± 7.9	36.8 ± 2.8	137 ± 13	7.34 ± 0.04
39.02 ± 0.04	98.2 ± 9.3	37.4 ± 0.6	136 ± 13	7.34 ± 0.02
40.00 ± 0.01	98.2 ± 8.4	40.3 ± 1.9	123 ± 11	7.35 ± 0.02

[a]1 mmHg = 133.3 Pa.

independent of temperature (28). [MgADP] at each temperature was calculated using the CK equilibrium constant K_{eq} = 1.66 × 10^9 M^{-1} at 38°C (29) and the van't Hoff equation with ΔH = –2 kJ/mol (22). The concentration of free Mg^{2+} was assumed to be temperature independent.

The CK rate equation, eq. [4] (21, 30, 31), was used to calculate the temperature dependence of enzyme activity independent of substrate concentration.

$$[4] \qquad v_{for} = k_{for}[PCr] = \frac{V_{max}[ADP][PCr]}{DK_m(ADP)K_i(PCr)}$$

where

$$D = 1 + \frac{[ADP]}{K_i(ADP)} + \frac{[PCr]}{K_i(PCr)} + \frac{[ATP]}{K_i(ATP)} + \frac{[Cr]}{K_i(Cr)} + \frac{[ADP][PCr]}{K_m(ADP)K_i(PCr)} + \frac{[ATP][Cr]}{K_m(ATP)K_i(Cr)} + \frac{[ADP][Cr]}{K_m(ADP)K_i(Cr)}$$

v_{for} is the forward velocity, V_{max} is the maximum forward reaction velocity independent of substrate concentration, K_m are Michaelis constants and K_i are inhibition constants for the substrates (indicated in parentheses). The values for K_m and K_i were taken from ref. 21 with the exception of K_m(ADP) for which a value of 27 μM was used (13, 32). V_{max} at each temperature was calculated from these equations.

Data were obtained from 3–6 rats at each temperature. The mean values of k_f and V_{max} obtained at each temperature were fit to Arrhenius plots to obtain activation parameters.

The dependence of blood gas parameters and blood pressure on temperature was tested using one-way ANOVA followed by Scheffé's post-hoc comparisons. The dependence of k_f on blood gas parameters and blood pressure was tested using multi-way ANOVA with temperature as one of the variables. Parameters derived from linear regression are shown with standard errors calculated from the standard errors of the fitted parameters. The *p*-value shown is that for the comparison with a slope of zero, and *R* is the correlation coefficient.

Fig. 2. Plot of $\log_{10}(V_{max})$ vs. T^{-1} for the maximum forward reaction velocity of the creatine kinase reaction in rat brain between 30 and 40°C. The solid line is the least-squares best fit to the data, giving E_a = 65.3 ± 9.7 kJ/mol (p = 0.0002, R = 0.92).

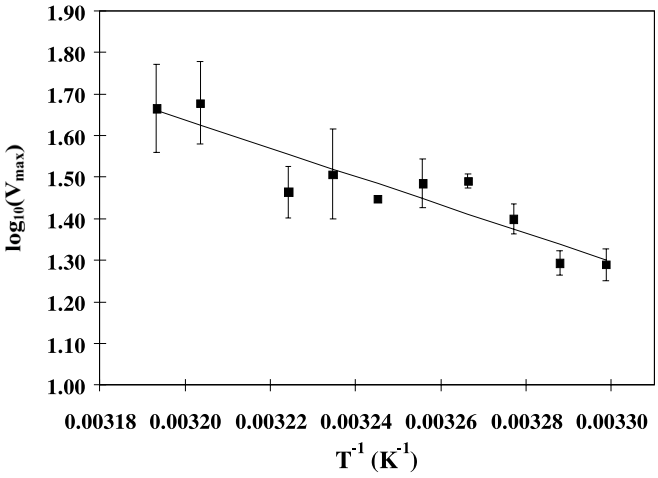

Results

Physiological parameters are listed in Table 1. Blood gas parameters and blood pressure were independent of temperature; k_f was not correlated with any physiological parameter besides temperature.

Typical ^{31}P spectra of rat brain with and without saturation of the γ-ATP resonance are shown in Fig. 1. An average reduction in PCr peak height of 55 ± 4 (mean ± SD)% was observed in the γ-ATP saturated spectrum compared to control.

[PCr]/[ATP] varied significantly with temperature (p = 0.011, R = 0.76), as shown in Fig. 2. Average values for k_f, [MgADP], and V_{max} at each temperature are given in Table 2 along with the number of determinations at each temperature. Each determination at a given temperature represents data from a different rat.

A linear least-squares fit of $\log_{10}(k_f)$ vs. T^{-1} gave E_a = 14.2 ± 4.9 kJ/mol significantly different from zero (p = 0.021, R = 0.71). The temperature dependence of V_{max} is shown in Fig. 3. A linear least-squares fit of $\log_{10}(V_{max})$ vs. T^{-1} gave E_a = 65.3 ± 9.7 kJ/mol (p = 0.0002, R = 0.92).

© 1999 NRC Canada

Table 2. Mean (± SEM) values for k_f, [MgADP], and V_{max} for the indicated number of animals (N) studied at each temperature, T.

T (°C)	k_f (s^{-1})	[MgADP] (μM)	V_{max} (mM/s)	N
30.04 ± 0.02	0.454 ± 0.014	0.027 ± 0.002	20.0 ± 1.9	6
31.03 ± 0.04	0.485 ± 0.020	0.029 ± 0.003	20.2 ± 1.3	3
32.06 ± 0.02	0.467 ± 0.028	0.021 ± 0.002	25.6 ± 2.1	5
33.01 ± 0.05	0.529 ± 0.021	0.020 ± 0.002	31.5 ± 1.2	6
34.06 ± 0.02	0.569 ± 0.019	0.022 ± 0.002	31.0 ± 4.4	6
35.04 ± 0.02	0.543 ± 0.021	0.023 ± 0.003	28.3 ± 0.5	4
36.01 ± 0.05	0.488 ± 0.037	0.020 ± 0.003	32.3 ± 10.3	4
37.03 ± 0.05	0.514 ± 0.057	0.022 ± 0.002	29.2 ± 4.5	5
39.02 ± 0.04	0.534 ± 0.033	0.013 ± 0.002	47.4 ± 14.1	5
40.00 ± 0.01	0.511 ± 0.006	0.014 ± 0.002	45.8 ± 16.9	5

Fig. 3. Temperature dependence of [PCr]/[ATP] measured from the mirror saturation spectra.

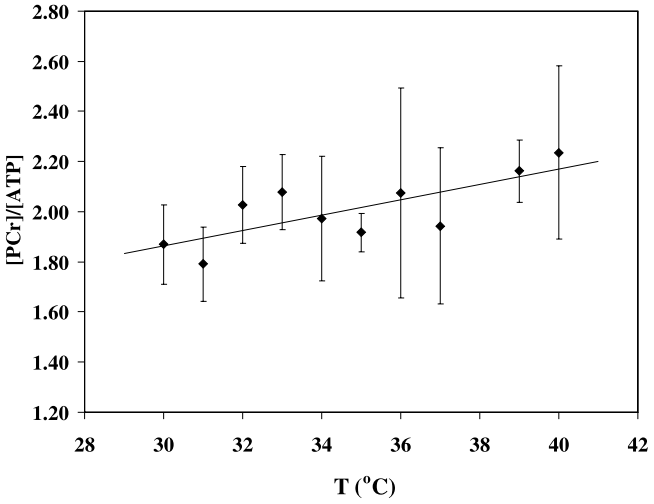

Discussion

The values for k_f obtained in this study (0.43–0.55 s^{-1}) fall into the range of k_f values for the CK reaction in rat and mouse brain (0.31–0.68 s^{-1}) reported in the literature (21, 23–25, 33). Similarly, the average value found for T_1 for PCr (2.44 s) is in accord with literature values (1.7–3.9 s) (21, 23–25).

The k_f data show little temperature dependence. This differs from the results of studies carried out on isolated CK enzymes in vitro for which E_a ranges from 50–142 kJ/mol (8–12), and from a study on perfused rat heart, which found E_a = 42 kJ/mol (13). However, k_f measured in vivo for the related enzyme AK also has a small temperature dependence in shrimp (16) and barnacle (17) muscle, although there may be a pronounced species dependence for AK activity (14, 15).

The regulation of the CK reaction in vivo and in vitro has been studied in detail (13, 21, 30, 32, 34, 35). A change in [MgADP] with temperature will change the value of k_f directly as can be seen from eq. [4], the CK rate equation. This can obscure the true temperature dependence of enzyme activity. Indeed, pH decreases in rat brain in vivo as temperature increases (22), and the observed significant increase with temperature in the [PCr]/[ATP] ratio suggests a substantial decrease in [MgADP] with temperature. When the temperature dependence of [MgADP] is considered, the calculated value of V_{max} is temperature dependent with E_a = 65.3 ± 9.7 kJ/mol. This falls into the range measured in vitro for BB-CK, 58–72 kJ/mol (8–10). It should be noted that the calculated V_{max} = 30 mM/s at 37°C (using K_m = 27 μM), a value that is very close to the in vitro value for BB-CK (21). The value for E_a is not strongly dependent on the value of K_m(ADP); for K_m(ADP) = 11 or 110 μM, the extreme range of values reported in the literature (36, 37), E_a changes from 58.8 to 70.0 kJ/mol, respectively.

The values for the concentration ratio [PCr]/[ATP] determined in this study, ranging from 1.8 at 30°C to 2.2 at 40°C, are in good agreement with the results of previous studies (21, 22). However, the increase in [PCr]/[ATP] with increasing temperature is at variance with other literature data. In rat brain, previous studies have shown [PCr]/[ATP] to decrease slightly (28) or to remain constant (38) over a temperature range similar to that in this study. The reason for these differences is not clear but may relate to differences in experimental conditions.

In addition to altering the CK equilibrium position, changes in pH can also have a direct intrinsic effect on CK enzyme activity (39–41), perhaps by inducing conformational changes or hydrogen bonding changes that alter the active site. This too could affect the measured activation energy. Using the previously reported temperature dependence of pH in rat brain (22) and published data showing the dependence of enzyme activity on pH in vitro (39), the direct effect of pH may increase the activation energy by about 4 kJ/mol.

One limitation of this study is the possible contribution to the observed NMR signal of resonances from phosphorus metabolites in muscle adjacent to the brain. NMR images obtained with a coil of identical size to that used for the spectroscopy measurements showed that the contribution of such muscle to the ^{31}P NMR spectra was small. This was confirmed by the experimental value of 2.0 (averaged over all experiments) for [PCr]/[ATP], a value in agreement with literature values for rat brain (21, 22). A larger value for [PCr]/[ATP] is observed for muscle (21), and any significant contribution of muscle to the spectra would have increased the value of [PCr]/[ATP] above that observed. At any rate, any small undetected contribution of muscle to the spectra would be similar at each temperature and for each experi-

© 1999 NRC Canada

mental animal, and it is unlikely that this would dramatically alter the temperature dependence of the rate constant, and hence E_a.

Another possible source of error in this study is the use of a constant value for T_1^{PCr} over the temperature range 30–40°C. Although no temperature dependence was observed experimentally, the data were not precise enough to exclude a small temperature dependence. Previous studies have shown T_1^{PCr} to increase slightly with increasing temperature for the isolated enzyme (11) and in perfused rat heart (13). The effect of a similar (undetected) small temperature dependence in the present study would be to decrease the calculated value of k_f with increasing temperature (eq. [3]) and therefore decrease E_a for k_f and V_{max}. However, since the temperature dependence of T_1^{PCr} is small, any effect on E_a is likely to be less than about 10 kJ/mol.

In conclusion, the experimental values of the rate constant for the creatine kinase forward reaction in rat brain have a very small temperature dependence in vivo over the range 30–40°C. When the temperature dependence of the substrate concentration is considered, V_{max} for this enzyme in vivo depends on temperature with a value for E_a, which agrees well with the literature values for the enzyme in vitro.

Acknowledgements

This study was funded by a grant from the Heart and Stroke Foundation of Canada. Fang-Wei Yang, Yan Fan, and Mark Campbell provided valuable technical assistance. We thank Dr. V. Kuprianov for valuable discussions.

References

1. D.L. Friedman and R. Roberts. J. Comp. Neurol. **343**, 500 (1994).
2. H.L. Sweeney. Med. Sci. Sports Exerc. **26**, 30 (1994).
3. R.A. Meyer, H.L. Sweeney, and M.J. Kushmerick. Am. J. Physiol. **246**, C365 (1984).
4. T. Wallimann, M. Wyss, D. Brdiczka, K. Nicolay, and H.M. Eppenberger. Biochem. J. **281**, 21 (1992).
5. W. Hemmer and T. Wallimann. Dev. Neurosci. **15**, 249 (1993).
6. R.J. Hamburg, D.L. Friedman, E.N. Olson, T.S. Ma, M.D. Cortez, C. Goodman, P.R. Puleo, and M.B. Perryman. J. Biol. Chem. **265**, 6403 (1990).
7. W. Hemmer, E. Zanolla, E.M. Furter-Graves, H.M. Eppenberger, and T. Wallimann. Eur. J. Neurosci. **6**, 538 (1994).
8. W. Stein, J. Bohner, R. Steinhart, and M. Eggstein. Clin. Chem. **28**, 19 (1982).
9. U. Hagelauer and U. Faust. J. Clin. Chem. Clin. Biochem. **20**, 633 (1982).
10. K. Okano, K. Yamamoto, Y. Ohba, K. Matsumura, and T. Miyaji. Clin. Chim. Acta, **169**, 159 (1987).
11. H. Eldar and H. Degani. Magn. Reson. Med. **11**, 121 (1989).
12. J.-F. Goudemant, L. VanderElst, B. Dupont, Y. VanHaverbeke, and R.N. Muller. NMR Biomed. **7**, 101 (1994).
13. P.M. Matthews, J.L. Bland, and G.K. Radda. Biochim. Biophys. Acta, **763**, 140 (1983).
14. K.W. Butler, R. Deslauriers, Y. Geoffrion, J.M. Storey, K.B. Storey, I.C.P. Smith, and R.L. Somorjai. Eur. J. Biochem. **149**, 79 (1985).
15. R.W. Briggs, G.K. Radda, and K.R. Thulborn. Biochim. Biophys. Acta, **845**, 343 (1985).
16. T.W.M. Fan, R.M. Higashi, and A.N. Lane. Biochim. Biophys. Acta, **1135**, 44 (1992).
17. R. Alvarez, M. Luxoro, V. Nassar-Gentina, and G. Szklarz. Quart. J. Exp. Physiol. **65**, 199 (1980).
18. R.B. Reeves. *In* Acid-base regulation and body temperature. *Edited by* H. Rahn and O. Prakash. Martinus Nijhoff Publishers, Boston. 1985. Chap. 2.
19. G.R. Sutherland, H. Lesiuk, P. Hazendonk, J. Peeling, R. Buist, P. Kozlowski, A. Jazinksi, and J.K. Saunders. Can. J. Neurol. Sci. **19**, 317 (1992).
20. R. Tyson. Ph.D. thesis. University of Manitoba, Winnipeg. 1996.
21. J.A. Bittl, J. DeLayre, and J.S. Ingwall. Biochemistry, **26**, 6083 (1987).
22. D.C. Johnson, M. Nishimura, P. Okunieff, H. Kazemi, and B. Hitzig. J. Appl. Physiol. **67**, 2527 (1989).
23. M. Tsuji, E. Allred, F. Jensen, and D. Holtzman. Brain Res. Dev. Brain Res. **85**, 192 (1995).
24. A. Sauter and M. Rudin. J. Biol. Chem. **268**, 13166 (1993).
25. M. Rudin and A. Sauter. J. Pharmacol. Exp. Ther. **251**, 700 (1989).
26. S.B. Perry, J. McAuliffe, J.A. Balschi, P.R. Hickey, and J.S. Ingwall. Biochemistry, **27**, 2165 (1988).
27. D.D. Gilboe, D.B. Kintner, M.E. Anderson, and J.H. Fitzpatrick, Jr. J. Neurochem. **71**, 2542 (1998).
28. M. Hägerdal, J. Harp, and B.K. Siesjö. J. Neurochem. **24**, 743 (1975).
29. J.W. Lawson and R.L. Veech. J. Biol. Chem. **254**, 6528 (1979).
30. V.V. Kupriyanov, A. Ya Steinschneider, E.K. Ruuge, V.I. Kapel'ko, M. Yu Zueva, V.L. Lakomkin, V.N. Smirnov, and V.A. Saks. Biochim. Biophys. Acta, **805**, 319 (1984).
31. J.F. Morrison and W.W. Cleland. J. Biol. Chem. **241**, 673 (1966).
32. P.M. Matthews, J.L. Bland, D.G. Gadian, and G.K. Radda. Biochim. Biophys. Acta, **721**, 312 (1982).
33. C.D. Smith, W. Landrum, J.M. Carney, P.W. Landfield, and M.J. Avison. Neurobiol. Aging, **18**, 617 (1997).
34. V.V. Kupriyanov, R.S. Balaban, N.V. Lyulina, A.Y. Steinschneider, and V.A. Saks. Biochim. Biophys. Acta, **1020**, 290 (1990).
35. V.V. Kupriyanov, N.V. Lyulina, A.Y. Steinschneider, M.Y. Zueva, and V.A. Saks. FEBS Lett. **208**, 89 (1986).
36. C.T. Basson, A.M. Grace, and R. Roberts. Mol. Cell. Biochem. **67**, 151 (1985).
37. H.D. Orth. *In* Creatine kinase isoenzymes. Pathophysiology and clinical application. *Edited by* H. Lang. Springer–Verlag, Berlin. 1981. Chap. 2.
38. M. Verhaegen, P. Iaizzo, M. Todd, P.A. Iaizzo, and M.M. Todd. Anesthesiology, **82**, 1208 (1995).
39. G.D. Williams, B. Enders, and M.B. Smith. Biochem. Int. **26**, 35 (1992).
40. P.F. Cook, G.L. Kenyon, and W.W. Cleland. Biochemistry, **20**, 1204 (1981).
41. M. Wyss, J. Smeitink, R.A. Wevers, and T. Wallimann. Biochim. Biophys. Acta, **1102**, 119 (1992).

© 1999 NRC Canada

Solid-state nuclear magnetic resonance studies of triphenylsilyl-, triphenyltin-, and triphenyllead(pentacarbonyl)manganese(I) complexes

Dharamdat Christendat, Ian S. Butler, Denis F.R. Gilson, and Frederick G. Morin

Abstract: The solid-state CP MAS (^{29}Si, ^{119}Sn, and ^{207}Pb) NMR spectra of the triphenylsilyl-, triphenyltin-, and triphenyllead(pentacarbonyl)manganese(I) complexes, $(Ph_3E)Mn(CO)_5$ (E = Si, Sn, Pb), have been analyzed to give the chemical shifts, one-bond spin–spin coupling constants, $^1J_{E-Mn}$, the "effective-dipolar" coupling constants ($D - \Delta J/3$), the chemical shift tensors, and the spin–spin anisotropy (ΔJ), where the analysis permits. For the tin and lead compounds, three and four sets of chemical shifts, respectively, were observed, and two different polymorphs occur for the lead complex, depending on the solvent used for recrystallization. The average values of the reduced coupling constants, $^1K_{Mn-Si}$ (2.64×10^{20} T^2 J^{-1}), $^1K_{Sn-Mn}$ (1.25×10^{20} T^2 J^{-1}), and $^1K_{Pb-Mn}$ (4.18×10^{20} T^2 J^{-1}) showed a linear correlation with the *s*-electron densities at the respective metal nuclei. The principal components of the chemical shift tensors have been determined for the tin and lead compounds.

Key words: manganese-group-14 compounds, solid-state ^{29}Si, ^{119}Sn, and ^{207}Pb CP MAS NMR, spin–spin coupling, chemical shift anisotropy, quadrupole coupling.

Résumé : On a analysé les spectres RMN (^{29}Si, ^{119}Sn et ^{207}Pb) obtenus à l'état solide, à l'aide de la technique de CPMAS, pour les complexes triphénylsilyl-, triphénylétain- et triphénylplomb(pentacarbonyl)manganèse(I), $(Ph_3E)Mn(CO)_5$ (E = Si, Sn, Pb) et, dans les cas où cela était possible, on en a tiré les déplacements chimiques, les constantes de couplage spin–spin à travers une liaison, $^1J_{E-Mn}$, les constantes de couplage « dipolaires effectives » ($D - \Delta J/3$), les tenseurs des déplacements chimiques et l'anisotropie spin–spin (ΔJ). Dans les cas des composés de l'étain et du plomb, on a observé respectivement trois et quatre ensembles de déplacements chimiques et on a observé deux polymorphes différents pour le complexe du plomb suivant la nature du solvant utilisé pour la recristallisation. Les valeurs moyennes des constantes de couplage réduites, $^1K_{Mn-Si}$ ($2{,}64 \times 10^{20}$ T^2 J^{-1}), $^1K_{Sn-Mn}$ ($1{,}25 \times 10^{20}$ T^2 J^{-1}) et $^1K_{Pb-Mn}$ ($4{,}18 \times 10^{20}$ T^2 J^{-1}) donnent une corrélation linéaire avec les densités d'électrons-*s* au niveau des noyaux des métaux respectifs. On a déterminé les principales composantes des tenseurs des déplacements chimiques pour les composés de l'étain et du plomb.

Mots clés : composés du manganèse-éléments du groupe 14; RMN (^{29}Si, ^{119}Sn et ^{207}Pb) à l'état solide, à l'aide de la technique de CPMAS; constante de couplage; anisotropie du déplacement chimique; couplage quadripolaire.

[Traduit par la Rédaction]

Introduction

Magic-angle spinning (MAS) is a technique commonly used for averaging anisotropic interactions in solid-state nuclear magnetic resonance experiments, but if a spin-1/2 nucleus is bonded to a quadrupolar nucleus, spin > 1/2, then a residual coupling remains, due to second order contributions involving the product of the dipolar and nuclear quadrupolar coupling constants (1–3). By using the resonance of the spin-1/2 nucleus as a probe, it is possible to determine the spin–spin coupling constant, *J*, and the nuclear quadrupole coupling constant, χ, and, at slow spinning speeds, the chemical shift anisotropy of the probe nucleus. These quantities are not usually obtainable from solution state NMR spectra of either the spin-1/2 or the quadrupolar nucleus since rapid relaxation of the quadrupolar nucleus leads to decoupling.

The purpose of the present work was to examine the various parameters obtained from the solid-state CP MAS NMR

Received May 12, 1999.

This paper is dedicated to Professor Ted Schaefer in recognition of his outstanding contributions to Canadian chemistry.

D. Christendat, I.S. Butler,[1] D.F.R. Gilson,[1] and F.G. Morin. Department of Chemistry, McGill University, 801 Sherbrooke St. West, Montreal, QC H3A 2K6, Canada.

[1]Authors to whom correspondence may be addressed. DFRG: Telephone: (514) 398-6908. e-mail: gilson@omc.lan.mcgill.ca; ISB: Telephone: (514) 398-6910. e-mail: butler@omc.lan.mcgill.ca

 © 1999 NRC Canada

Table 1. NMR data for triphenyltinmanganesepentacarbonyl, $Ph_3SnMn(CO)_5$.

	Site A[a]	Site B	Site C
δ_{iso} (solution) (ppm)		–11.93 (±.05)	
δ_{iso} (ppm)[b]	–13.6	2.8	5.6
$^1J_{Sn–Mn}$ (Hz)	135 (±1)	142 (±2)	141 (±1)
$^1K_{Sn–Mn}$[c]	1.21	1.27	1.27
d[a] (Hz)	34.4 (±0.5)	34.3 (±0.3)	30.3 (±3.3)
δ_{11} (ppm)	72	81	89
δ_{22} (ppm)	3	50	47
δ_{33} (ppm)	–115	–123	–120
$\Delta\delta$ (ppm)[d]	–152	–188	–188
χ (MHz)[e]		18.33 (±0.03)	
D (Hz)	466 (±7)	465 (±7)	411(±45)
D (Hz)	584 (±4)	584 (±4)	580 (±4)
ΔJ (Hz)	353 (±8)	345 (±8)	507 (±55)

[a]Two coincident chemical shifts for this site.

[b]Uncertainties are ±0.3 and ±3.0 ppm for the isotropic chemical shifts and chemical shift tensors, respectively.

[c]In $10^{21} \times T^2 J^{-1}$.

[d]Anisotropy parameter $\Delta\delta = \delta_{33} - 1/2 (\delta_{11} + \delta_{22})$.

[e]Value taken from ref. 6.

spectra of triphenylsilyl-, triphenyltin-, and triphenyllead complexes of (pentacarbonyl)manganese(I), $(Ph_3E)Mn(CO)_5$ (E = Si, Sn, Pb), where ^{55}Mn (S = 5/2, NA = 100%) is the quadrupolar nucleus. The other member of group 14, germanium, has no spin-1/2 isotope. These covalent bimetallic compounds offer a unique opportunity to examine the chemical shift anisotropy and the spin–spin coupling between the elements of a main group and a transition metal. The crystal structures of the silicon and tin compounds have been determined previously (4, 5), and the nuclear quadrupole coupling constants have been measured by solid-state, broadline ^{55}Mn NMR spectroscopy of single crystals of the triphenylgermanium, triphenyltin, and triphenyllead complexes (6). However, no NMR or NQR results have been reported for the triphenylsilyl complex.

Experimental

The triphenylsilane complex was prepared by the reaction of dimanganese decacarbonyl and triphenylsilane in an evacuated tube at 250°C (7) and the tin complex by reacting triphenyltin chloride with the sodium pentacarbonylmanganese salt (8). Triphenyllead acetate was reacted with sodium pentacarbonylmanganese in tetrahydrofuran solvent at room temperature to give the lead compex. The complexes were recrystallized from either octane or a benzene–octane mixture. Solution state NMR spectra were obtained for concentrated $CDCl_3$ solutions at room temperature (21°C) on a Varian XL-300 spectrometer operating at a field strength of 7.05 T. Solid-state, proton decoupled, CP MAS spectra were obtained using a Chemagnetics CMX-300 spectrometer operating at 59.5, 111.7, and 62.7 MHz, for the ^{29}Si, ^{119}Sn, and ^{207}Pb resonances, respectively. Spectra were also recorded for ^{29}Si at 19.8 MHz using a Chemagnetics CMX-100 spectrometer. Powdered samples were contained in 7.5 mm diameter zirconia pencil-type rotors. Spinning rates in the range 3.0–5.0 kHz were used to identify the isotropic chemical shifts. Experimental details, contact times, pulse delays, and number of transients are given in the figure captions. The chemical shifts of the ^{29}Si, ^{119}Sn, and ^{207}Pb nuclei were referenced to external tetramethylsilane, tetramethyltin, and tetramethyllead, respectively, using the chemical shifts of 2,2-dimethyl-2-silapentane-5-sulfonate (0.80 ppm), tetracyclohexyltin (–97.0 ppm), and tetraphenyllead (–135.0 ppm) as external secondary references for the solid-state measurements. Line broadening of 0 and 10 Hz was applied, and the FIDs were zero filled to 8 and 4 K data points on the Chemagnetics CMX-300 and CMX-100 instruments, respectively, before transformation. The resonance lines in all sidebands were fitted with Lorentzian line shapes using the program Peakfit (Jandel Scientific) and the errors given in Tables 1 and 2 are from the averages of the fitted parameters. Calculation of the shift tensors was performed with the aid of a computational package developed by Kentgens et al. (9). X-ray diffraction measurements were made using a Rigaku AFC6S diffractometer at 20°C with Mo-Kα radiation (λ = 0.7107 Å).

Results and discussion

Provided the ratio of the nuclear quadrupole coupling constant, χ, to the resonance frequency, ν_S, is small, i.e., $\chi/4S(2S - 1)\nu_S << 1$, then the splittings that are retained in the solid-state spectra obtained under magic-angle-spinning conditions are given (2) by eq. [1]

$$[1] \qquad \Delta\nu_m = -mJ + (3\chi D''/10\nu_s)[S(S + 1) - 3m^2]/[S(2S - 1)]$$

where D'' is the effective dipolar coupling constant, modified by an angular term, eq. [2]

$$[2] \qquad D'' = 1/2(D - \Delta J/3)(3\cos^2\beta^D - 1 + \eta\sin^2\beta^D\cos 2\alpha^D)$$

D is the direct dipole coupling constant, $(\mu_0/4\pi)(h\gamma_I\gamma_S/r_{IS}^3)$, ΔJ is the anisotropy in the spin–spin coupling, α^D and β^D are, respectively, the azimuthal and polar angles relating the internuclear vector to the principal axes of the electric field

© 1999 NRC Canada

Table 2. NMR data for triphenylleadmanganesepentacarbonyl, $Ph_3PbMn(CO)_5$, recrystallized from octane and benzene–octane solutions.

	Site A	Site B	Site C	Site D
From octane				
δ_{iso} (solution) (ppm)		48.4 (±0.1)		
δ_{iso} (ppm)	70.1	72.4	105.8	112.2
$^1J_{Pb-Mn}$ (Hz)	250 (±4)	253 (±4)	275 (±8)	274 (±7)
$^1K_{Pb-Mn}$	3.99	4.04	4.44	4.43
d (Hz)	2.30 (±0.6)	9.19 (±0.74)	11.4 (±0.5)	2.26 (±0.1)
δ_{11} (ppm)	–65	–54	–96	–75
δ_{22} (ppm)	59	57	180	187
δ_{33} (ppm)	216	214	233	224
$\Delta\delta$ (ppm)	219	213	191	168
χ (MHz)[a]	12.04 (±0.01)		10.6 (±0.4)	
D″ (Hz)	47.4 (±12.4)	190 (±15)	267 (±22)	52.9 (±4.3)
From benzene–octane				
δ_{iso} (solution) (ppm)		48.4 (±0.1)		
δ_{iso} (ppm)	61.0	63.2	112.0	115.5
$^1J_{Pb-Mn}$ (Hz)	251(±1)	247(±1)	273 (±3)	274 (±1)
$^1K_{Pb-Mn}$	4.06	3.99	4.41	4.43
d (Hz)	2.41 (±0.02)	3.19 (±0.11)	4.14 (±0.15)	2.25 (±0.06)
δ_{11} (ppm)	–58	–70	–91	–87
δ_{22} (ppm)	33	62	167	196
δ_{33} (ppm)	208	197	261	238
$\Delta\delta$ (ppm)	221	200	213	183
D″	49.7(0.4)	65.8(2.3)	97.0(6.5)	52.7(2.2)

[a]Value taken from ref. 6.

Fig. 1. ^{29}Si CP-MAS spectra of $Ph_3SiMn(CO)_5$, (*a*) at 19.85 MHz: contact time 2 ms; pulse delay 30 s; spinning speed 3.0 kHz; 2000 transients, and (*b*) at 59.4 MHz: contact time 3 ms; pulse delay 60 s; spinning speed 2.0 kHz; 1150 transients.

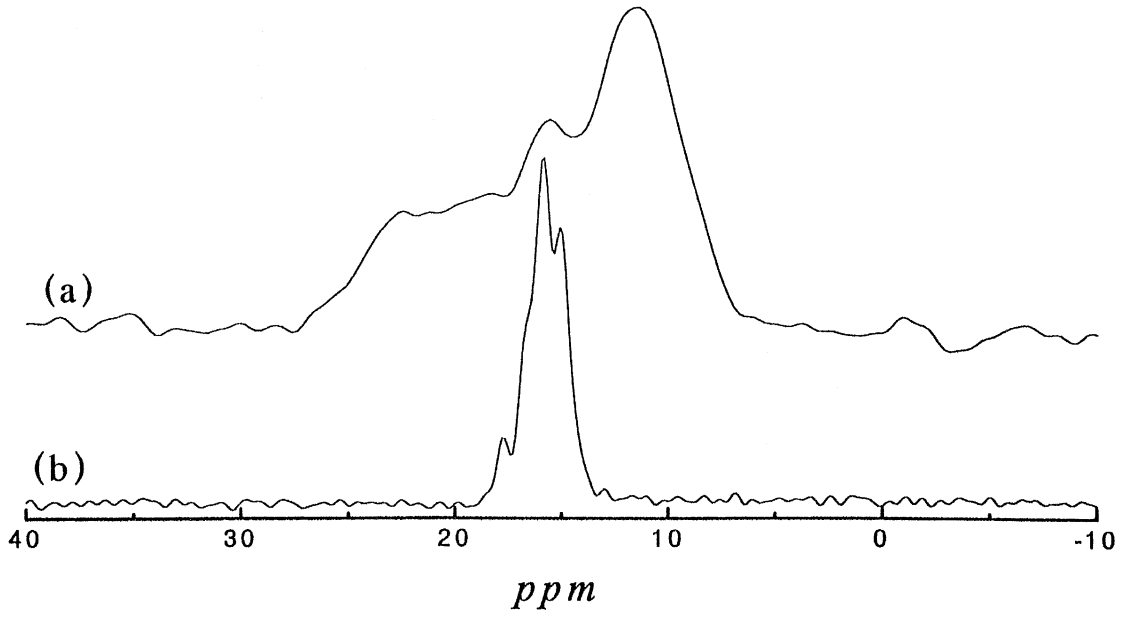

gradient, and η is the asymmetry in the field gradient. For ^{29}Si and ^{119}Sn, where the magnetogyric ratios are negative, the modified form (3) of eqs. [1] and [2] was used. The local symmetry about the Mn—E bonds in the $(Ph_3E)Mn(CO)_5$ complexes is sufficiently high that the angle β^D is equal to 0°, and thus eq. [2] is reduced to a much simpler form

[3] $$D'' = (D - \Delta J/3)$$

© 1999 NRC Canada

Table 3. NMR data for triphenylsilylmanganesepentacarbonyl, $Ph_3SiMn(CO)_5$.

	At 59.4 MHz		At 19.85 MHz	
	Site A	Site B	Site A	Site B
δ_{iso} (solution)		17.9		
δ_{iso} (ppm)	15.8	17.0	15.5	16.9
$^1J_{Mn-Si}$ (Hz)	15.9 (±2)	15.3 (±2)	16.7 (±2)	12.9 (±2)
$^1K_{Mn-Si}$[a]	–0.27	–0.26	–0.28	–0.22
d (Hz)	–39.1	–35.2	–118.0	–104.9
χ (MHz)[b]	25.9	23.0	25.9	22.7
D (Hz)	–375 (±2)	–380 (±2)	–375 (±2)	–380 (±2)

[a]In $10^{21} \times T^2 J^{-1}$.

[b]Values were obtained with the assumption of $\Delta J = 0$.

Fig. 2. Solid-state CP-MAS ^{119}Sn spectrum of $Ph_3SnMn(CO)_5$ at 111.7 MHz. Contact time 1 ms; pulse delay 10 s; spinning speed 4.5 kHz; 6000 transients.

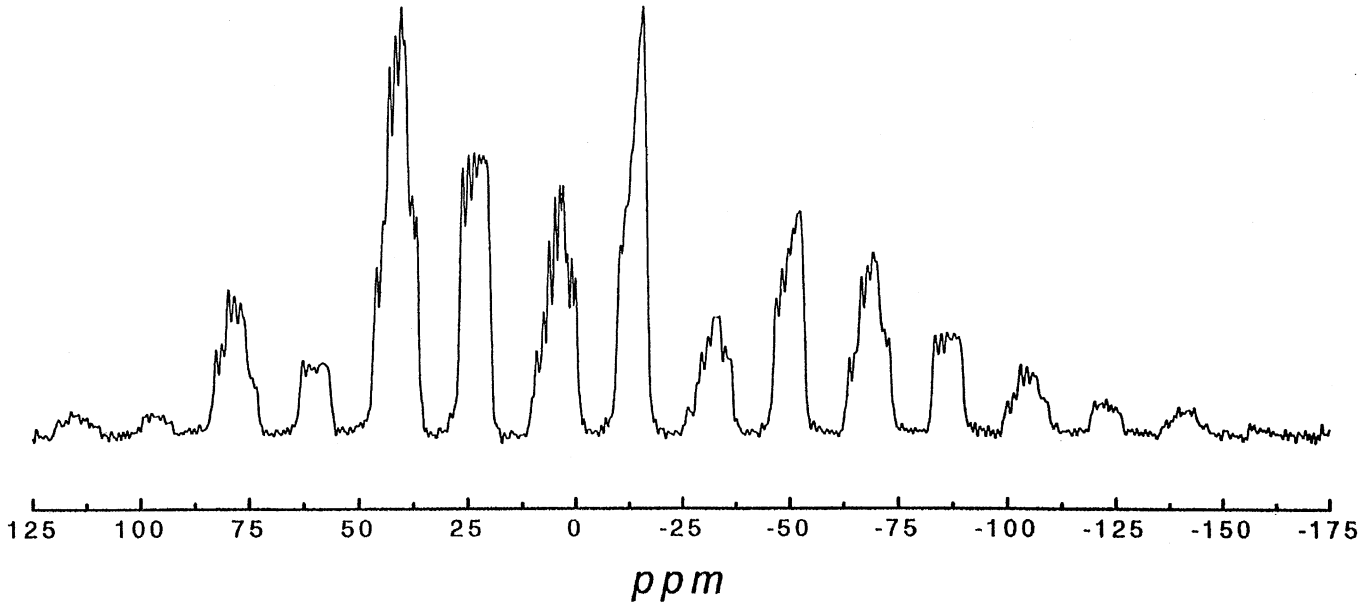

The CP MAS spectra of the triphenylsilyl complex are shown in Fig. 1 and the NMR parameters are given in Table 3, together with the solution-state chemical shifts. The chemical shift anisotropy is too small and spinning sidebands were not obtained, and therefore, the shift anisotropy could not be determined. The crystal structure (5) showed that two molecules occur in the asymmetric unit cell, and so, two chemical shifts and a total of 12 lines are expected in the spectrum. Clearly, the solid-state NMR spectrum cannot be fitted easily; therefore, the spectrum was also measured at 19.8 MHz where the second-order splitting is increased by a factor of three while the chemical shift dispersion, in Hz, is reduced by a factor of three (the perturbation condition still holds at the lower field). The extra information this provides made it possible to fit both spectra and obtain consistent values for the second-order splitting, the spin–spin coupling, and the chemical shifts (Table 3).

The spectrum of the tin complex, Figs. 2 and 3, shows that there are three chemical shifts, but the highest field centre band arises from the overlap of two resonances. This is consistent with the crystal structure (4), where there are four molecules in the asymmetric unit. The differences in the molecular structures lie in the variations in the dihedral angles of the phenyl rings. These lie in quite narrow ranges, but are associated with two pairs of molecules (4). Two of the dihedral angles, at 41° and 60°, are within 1° for all four molecules, but the third rings are at 66° in one pair and 59° in the other. These differences are the probable cause of the different chemical shifts.

The spectra of the lead complex, Figs. 4 and 5,were also complicated by the presence of crystallographically induced chemical shift differences, with four sets of chemical shifts for both polymorphs, which, like the tin complex, occur in pairs and result in two sets of 12 peaks. The spin–spin couplings of the high-field resonances were 22 Hz smaller than those of the low-field centre band, Table 2, and were assigned the larger value of the nuclear quadrupole coupling constant, 12.04 MHz, rather than the value of 10.6 MHz (6). This distinction was based on the fact that the ^1J coupling is inversely proportional to the nuclear quadrupole coupling

© 1999 NRC Canada

Fig. 3. The centre band of the CP-MAS ^{119}Sn NMR spectrum of $Ph_3SnMn(CO)_5$ at 111.7 MHz, showing three chemical shifts. Low-field isotropic centre bands are due to overlap of two slightly different tin chemical shifts.

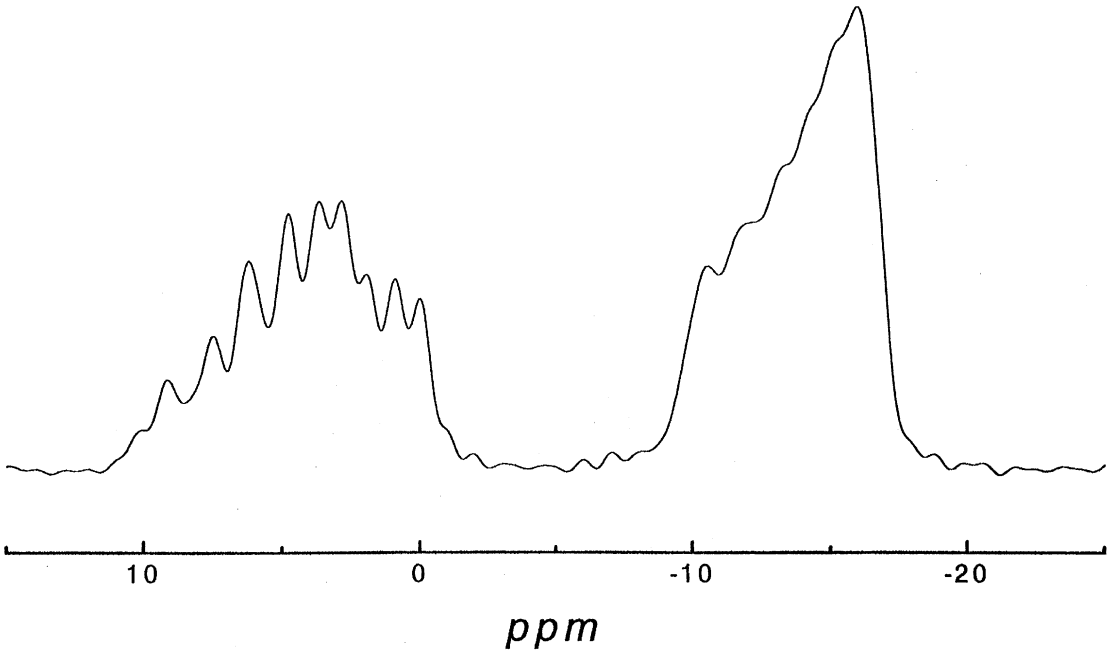

Fig. 4. Solid-state CP-MAS ^{207}Pb spectrum of $Ph_3PbMn(CO)_5$ at 62.7 MHz. Low-field and high-field isotropic centre bands are due to two slightly different lead chemical shifts, resulting in sets of 12 peaks in each centre band. (*a*) Recrystallized from octane; contact time 2 ms; pulse delay 25 s; spinning speed 5.0 kHz; 4000 transients. (*b*) Recrystallized from 50/50 benzene/octane mixed solvent; contact time 2 ms; pulse delay 25 s; spinning speed 5.0 kHz; 4000 transients.

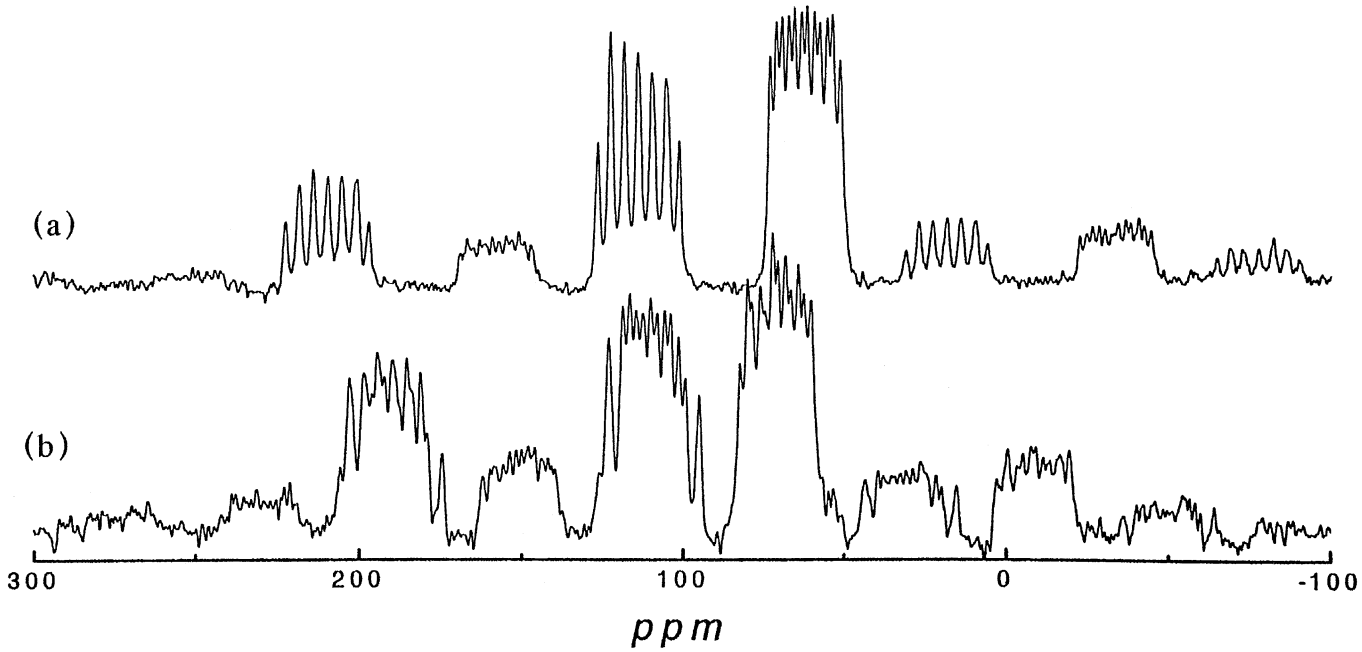

constant (10, 11) if the Fermi contact term is the dominant mechanism of spin–spin coupling (12). It was suggested, from the results of the single-crystal broad-line ^{55}Mn NMR experiment (6), that this triphenyllead-(pentacarbonyl)manganese(I) complex would crystallize in a monoclinic space group and have 2/*m* symmetry with two crystallographically independent sites across a mirror plane. In the present work, it was found that the ^{207}Pb chemical shifts for the lead complex recrystallized from octane differed from those obtained from a sample recrystallized from a 50/50 mixture of benzene and octane. A determination of the crystal structures of these two different polymorphs was attempted, but sample decomposition and persistent twinning prevented the determination of the full structures, but unit cell dimensions

© 1999 NRC Canada

Fig. 5. The centre band of the CP-MAS ^{207}Pb NMR spectra of $Ph_3PbMn(CO)_5$ at 62.7 MHz, showing four chemical shifts. (*a*) Recrystallized from octane. (*b*) Recrystallized from benzene–octane.

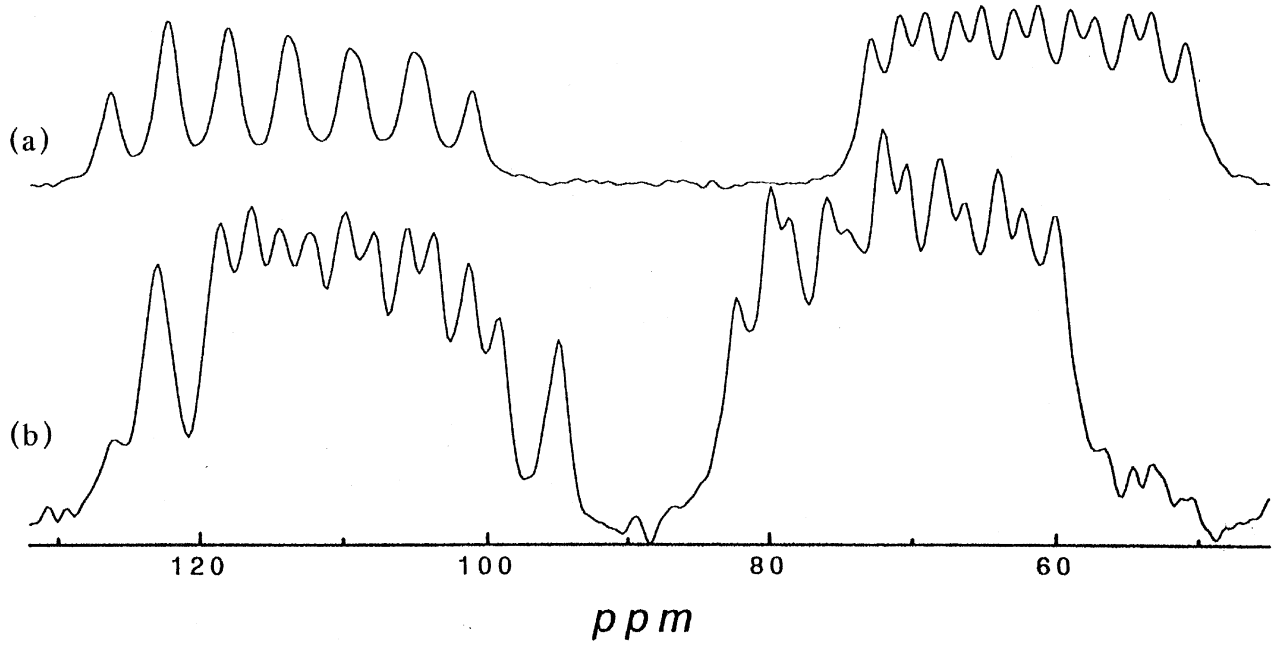

Fig. 6. Plot of the one-bond reduced spin–spin coupling constants $|^1K_{Mn-E}|$ (in $10^{21} \times T^2\ J^{-1}$) vs. electron density, $|\Psi(0)|^2$ at the Group 14 (IVA) nucleus.

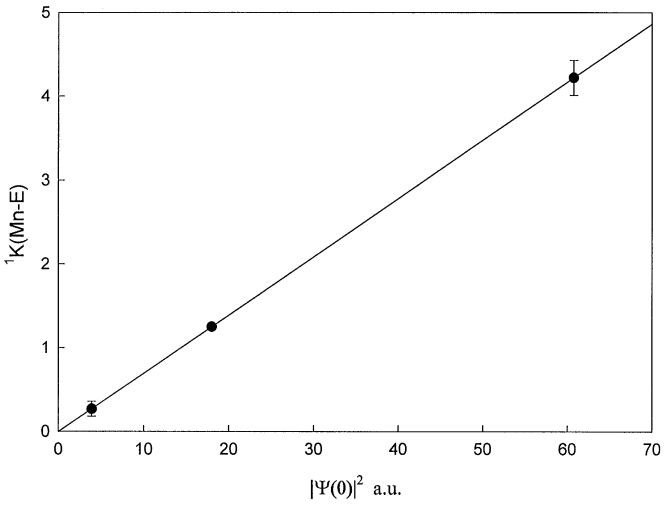

were obtained. The complex crystallized in two different space groups; *I*2/*m* from octane, a = 12.2090(3) Å, b = 64.5767(6) Å, c = 11.4994 Å, β = 90.70°, Z = 16 with four molecules in the asymmetric unit, and $P2_1$ from a benzene–octane mixture, a = 12.221(5) Å, b = 32.262(8) Å, c = 11.508(6) Å, β = 90.54(4)°, Z = 8, with four molecules in the asymmetric unit. Thus the difference in the two structures is a doubling of the *b* direction of the unit cell. The triphenylgermanium complex is also capable of crystallizing in two different forms (13, 14).

The lack of accurate Pb—Mn bond lengths precluded the calculation of the direct dipole coupling constant and a complete analysis of the data. However, Harris and co-workers (15) have shown that the effective dipolar coupling constant, *D*″, can be obtained from an analysis of chemical shift anisotropy for each of the spinning sideband manifolds. A plot of the shift anisotropy, determined from the Herzfeld–Berger analysis, versus the spin state, m, of the S nucleus will give a slope of $2(D - \Delta J/3)$ and an intercept of $\Delta\delta$. The components of the shift tensors for the tin and lead complexes, Tables 1 and 2, show that the differences between the solid state chemical shifts arise primarily from changes in the δ_{22} components. The spans of the chemical shift tensors, $\delta_{33} - \delta_{11}$, for triorganolead(IV) compounds (16–18), are typically larger than 600 ppm. The values obtained in our studies are the smallest observed for Ph_3PbX (when X ≠ Ph). Comparison of the spans for the tin and lead complexes showed the expected increase as the size of the valence *p*-electron radius, $\langle r^{-3}\rangle_{np}$ increases and the ratio of the spans, 1.5, is in good agreement with the ratio $\langle r^{-3}\rangle_{6p}/\langle r^{-3}\rangle_{5p}$. The span for the silyl complex is very small and could not be determined from the ^{29}Si CP MAS experiment.

The contributions to the coupling arise from the diamagnetic spin-orbit (DSO), paramagnetic spin-orbit (PSO), spin dipolar (SD), and Fermi contact (FC) interactions. The first two terms are usually much smaller and of opposite sign (19) than the latter two, which are the major terms. To compare the spin–spin coupling constants without the dependence on the nuclear properties, it is necessary to use the reduced coupling constants, $K_{Mn-E} = 4\pi^2 J_{Mn-E}/(h\gamma_{Mn}\gamma_E)$, which are proportional to the product of the *s*-electron densities at the nuclei and the *s*-character of the hybrid orbitals used to form the bond and divided by an average excitation energy, ΔE, (12, 19, 20). Using the *s*-electron densities given by Pyykko and Weisenfeld (21), with a non-relativistic value for silicon and relativistic values for the heavier elements, a plot of the reduced couplings, $|K_{Mn-E}|$, against the *s*-electron densities, $|\Psi(0)|^2$, for the silicon, tin, and lead nuclei,

© 1999 NRC Canada

Fig. 6, gave a linear relationship, indicating that the FC term dominates the coupling, and the *s*-bond order and the average excitation energy are nearly the same in all cases. However, the results obtained for the tin complex showed that the anisotropy in the coupling constants is finite and, therefore, the FC/SD contribution is still important.

Acknowledgments

This work was supported by grants from the Natural Sciences and Engineering Research Council of Canada (NSERC) and Fonds pour la formation de chercheurs et l'aide à la recherche (Québec) (FCAR). We thank Dr. A.M. Lebuis for assistance in examining the crystal structures and Professor R.E. Wasylishen for the HBA program.

References

1. A.C. Olivieri. J. Magn. Reson. **81**, 201 (1989).
2. R.K. Harris and A.C. Olivieri. Prog. Nucl. Magn. Res. **24**, 435 (1992).
3. A.C. Olivieri. Magn. Reson. Chem. **34**, 365 (1996).
4. H.P. Weber and R.F. Bryan. Acta Crystallogr. **22**, 822 (1967).
5. A.-M. Lebuis, D. Christendat, D.F.R. Gilson, and I.S. Butler. Acta Crystallogr. Sect C: Cryst. Struct. Commun. **C53**, 1206 (1997).
6. J.L. Slater, M. Pupp, and R.K. Sheline. J. Chem. Phys. **57**, 2105 (1972).
7. R.D. Gorsich. J. Am. Chem. Soc. **84**, 2486 (1962).
8. W. Jetz, P.B. Simons, J.A.J. Thompson, and W.A.G. Graham. Inorg. Chem. **5**, 2217 (1966).
9. A.P. Kentgens, W. Power, and R.E. Wasylishen. HBLQFIT Sideband analysis. Version 2.2. Dalhousie University, Halifax. 1991.
10. D.F.R. Gilson. J. Chem. Phys. **43**, 312, (1965).
11. D. Christendat, I. Wharf, F.G. Morin, I.S. Butler, and D.F.R. Gilson. J. Magn. Reson. **131**, 1 (1998).
12. C. Juan and H.S. Gutowsky. J. Chem. Phys. **37**, 2198 (1962).
13. Y.T. Struchkov, K.N. Anisimov, O.P.Osipova, N.E. Kolobova, and A.N. Nesmeyanov. Proc. Acad. Sci. U.S.S.R. Chem. (Engl. transl.) **172**, 15 (1967).
14. B.T. Kilbourn, T.I. Blundell, and H.M. Powell. Chem. Commun. 444 (1965).
15. R. Gobetto, R.K. Harris, and D.C. Apperley. J. Magn. Res. **96**, 119 (1992).
16. J.R. Ascenso and R.K. Harris. J. Organomet. Chem. **301**, C23 (1986).
17. U. Behrens, A.K. Brimah, T.M. Sollman, R.D. Fischer, D.C. Apperley, N.A. Davis, and R.K. Harris. Organomet. **11**, 1718 (1992).
18. R.K. Harris and A. Sebald. Magn. Reson. Chem. **28**, 81 (1989).
19. J.A. Gonzalez, G.A. Aucar, M.C. Ruiz, and R.H. Contreras. Int. J. Quantum Chem. **66**, 823 (1997).
20. C.J. Jameson. Multinuclear NMR spectroscopy. Chap. 4. *Edited by* J. Mason. Plenum, New York. 1987.
21. P. Pyykko and L. Weisenfeld. Mol. Phys. **43**, 557 (1981).

© 1999 NRC Canada

Probing the motion of the η^2-dideuterium ligand by solution and solid-state ^{2}H NMR spectroscopy[1]

Glenn A. Facey, Tina P. Fong, Dmitry Gusev, Peter M. Macdonald, Robert H. Morris, Marcel Schlaf, and Wei Xu

Abstract: Variable temperature ^{2}H NMR is used to measure the T_1^{min} values of the η^2-D_2 and D ligands in *trans*-$[M(\eta^2\text{-}D_2)(D)(dppe)_2]^+$, M = Ru (**1**) and Os (**2**) in solution. The rapid spinning motion of the η^2-D_2 ligand results in a much longer T_1^{min} than that of the terminal deuteride. The quadrupole coupling constant (C_Q) for the terminal deuteride is calculated to be 79 kHz for **1** and 81 kHz for **2** while motion-reduced coupling constant (C_Q^{eff}) for the D in the η^2-D_2 ligands in **1** and **2** are in the range 19–22 and 27–31 kHz, respectively. The actual C_Q for these ligands with short D—D distances (<1 Å) should be at least $2C_Q^{eff}$ and probably greater than that of the terminal deuteride but less than that of D_2(g), 227 kHz. A fast spinning (>>61 MHz) and tilting of the primary electric field gradient component of between 90° and 60° or between 50° and 40° with respect to the axis of D_2 rotation is an explanation for the small C_Q^{eff}. Therefore neither D—D nor M—D bonding dominates the electric field gradient direction in these M(η^2-D_2) bonds. The complex $[RuD_2(C_5Me_5)(dppm)]^+$ **3**, which exists in solution as a 3.3:1 mixture of Ru(D···D) (**3a**) and $Ru(D)_2$ (**3b**) tautomers, has T_1^{min}(D) values that provide C_Q^{eff} values of 66 kHz for **3a** and 71 kHz for **3b**. The elongated D···D ligand in **3a** with d(D···D)≅ 1.10 Å may be "static" compared to the 61.4 MHz ^{2}H spectrometer frequency and therefore have "compressed dihydride" character and display similar Ru—D bonds as in **3b**. However, it is more likely that the static C_Q for the D of **3a** is much larger than that of a terminal Ru-D but averaged to 66 kHz by a 180° flip of the D_2 as observed in **7**. The complexes *trans*-$[M(D\cdots D)(Cl)(dppe)_2]PF_6$, M = Ru (**4**), Os (**5**), and Ru(η^2-D_2)(dppb)(μ-Cl)$_3$RuCl(dppb) (**6**) also have motion-reduced C_Q values. Some ^{2}H NMR quadrupole echo wide-line spectra of **1**, **4**, and $Os(D\cdots D)(Cl)_2(CO)(P^iPr_3)_2$ (**7**) (contaminated with 20% Os(H···D)) were recorded in the solid phase from 293 to 123 K. These also indicate that the C_Q^{eff} of the D in the D_2 ligands are motion-reduced. Simulation of the spectra of **7** are suggestive of a twofold reorientation of a D_2 ligand with a static C_Q value in the range of 120–167 kHz, a tilt angle of the electric field gradient of about 50°, and an asymmetry parameter near to zero. Significantly, the MAS ^{2}H spectrum of **7** has a broad doublet, possibly due to a non-averaged D–D dipolar/quadrupolar interference phenomenon; this is first time this has been observed. Variable temperature T_1 data for solid **7** are also reported, which allow the evaluation of the activation barrier to the twofold flipping motion of the D_2; the only other way of quantifying such an energy barrier is by use of an inelastic neutron scattering method.

Key words: dihydrogen, deuterium, NMR, ruthenium, osmium, complexes, dynamics, hydride, bonding.

Résumé : On a fait appel à la RMN du ^{2}H à température variable pour mesurer les valeurs de T_1^{min} des ligands η^2-D_2 et D dans les *trans*-$[M(\eta^2\text{-}D_2)(D)(dppe)_2]^+$, M = Ru (**1**) et Os (**2**), en solution. Le mouvement de rotation rapide du ligand η^2-D_2 fait que la valeur de T_1^{min} est beaucoup plus élevée que dans le cas d'un deutérure terminal. On a calculé que la constante de couplage quadripolaire (C_Q) d'un deutérure terminal est égale à 79 kHz pour le produit **1** et de 81 kHz pour le produit **2** alors que la constante de couplage réduite du mouvement (C_Q^{eff}) du D dans les ligands η^2-D_2 des produits **1** et **2** sont respectivement de l'ordre de 19 à 22 et de 27 à 31 kHz. Les valeurs minimales réelles de C_Q pour ces ligands comportant de faibles distances D—D (<1 Å) devraient être égales à $2C_Q^{eff}$, probablement plus

Received May 12, 1999.

This paper is dedicated to Professor Ted Schaefer in recognition of his outstanding contributions to Canadian chemistry.

G.A. Facey. Department of Chemistry, University of Ottawa, Department of Chemistry, 10 Marie Curie, Ottawa, ON K1N 6N5, Canada.
T.P. Fong, P.M. Macdonald, and R.H. Morris.[2] Department of Chemistry, University of Toronto, 80 St. George St., Toronto, ON M5S 3H6, Canada.
D.G. Gusev. Chemistry Department, Sir Wilfred Laurier University, Waterloo, ON N2L 3C5, Canada.
M. Schlaf. Department of Chemistry, University of Guelph, Guelph, ON N1G 2W1, Canada.
W. Xu. Nova Research, 2928 16th St N.E., Calgary, AB T2E 7K7, Canada.

[1]Some of this work was presented at the symposium on the "Role of Spectroscopic Methods in Modern Inorganic Chemistry," PACIFICHEM'95 Conference, Honolulu, December 1995.

 © 1999 NRC Canada

grandes que celles d'un deutérure terminal, mais inférieure à celle du D_2(g), 227 kHz. Pour expliquer la faible valeur du C_Q^{eff}, il faut faire appel à une rotation rapide (>>61 MHz) et à une inclinaison de la composante du gradient du champ électrique primaire d'une valeur allant de 90° à 60° ou de 50° à 40° par rapport à l'axe de rotation de D_2. En conséquence, dans ces liaisons M(η^2-D_2), aucune des liaisons D—D ou M—D ne domine la direction du gradient du champ électrique. Le complexe $[RuD_2(C_5Me_5)(dppm)]^+$ (**3**), qui existe en solution sous la forme d'un mélange 3,3:1 des tautomères Ru(D···D) (**βa**) et $Ru(D)_2$ (**3b**), présente des valeurs de T_1^{min}(D) qui permettent de déduire des valeurs de C_Q^{eff} de 66 kHz pour **3a** et de 71 pour **3b**. Le ligand D···D allongé de **3a**, pour lequel la *d*(D···D) = 1,10 Å, peut être « statique » par comparaison avec la fréquence du spectromètre ^{2}H (61,4 MHz), il peut présenter un caractère de « dihydrure comprimé » et il peut présenter des longueurs de liaisons Ru—D qui sont semblables à celles observées avec **3b**. Toutefois, il est vraisemblablement plus probable que la valeur de C_Q statique du D de **3a** est beaucoup plus grande que celle du Ru-D terminal, mais que sa valeur moyenne est ramenée à 66 kHz par une inversion de 180° du D_2, telle qu'on peut l'observer avec **7**. Les complexes du *trans*-$[M(D\cdots D)(Cl)(dppe)_2]PF_6$, M = Ru (**4**), Os (**5**), et ceux du Ru(η^2-D_2)(dppb)(μ-$Cl)_3$RuCl(dppb) (**6**) possèdent aussi des valeurs de C_Q réduites pour le mouvement. Opérant à l'état solide, de 293 à 123 K, on a enregistré quelques spectres RMN du ^{2}H à bandes larges avec écho quadripolaire pour les composés **1**, **4** et $Os(D\cdots D)(Cl)_2(CO)(P^iPr_3)_2$ (**7**) contaminé avec 20% de Os(H···D). Ceux-ci indiquent que les valeurs de C_Q^{eff} du D dans les ligands de D_2 sont réduites par le mouvement. Une simulation du spectre du produit **7** suggère qu'il se produit une réorientation binaire du ligand D_2 avec une valeur de C_Q statique de l'ordre de 120 à 167 kHz, un angle d'inclinaison du gradient du champ électrique d'environ 50° et un paramètre d'asymétrie pratiquement égal à zéro. Il est significatif que le spectre ^{2}H « MAS » du composé **7** présente un large doublet qui pourrait résulter d'un phénomène d'interférence dipolaire/quadripolaire D–D pour lequel il ne s'est pas établi de moyenne. On a aussi déterminé les valeurs de T_1 par RMN à température variable du solide **7**; elles permettent d'évaluer la barrière d'activation pour le mouvement d'inversion binaire de D_2. La seule autre façon de quantifier une telle barrière d'énergie est d'utiliser la méthode de dispersion inélastique de neutrons.

Mots clés : dihydrogène, deutérium, RMN, ruthénium, osmium, complexes, dynamique, hydrure, liaison.

[Traduit par la Rédaction]

Introduction

Transition metal dihydrogen complexes (1–4) display a fascinating range of dynamic properties including torsional libration, rapid spinning, and quantum mechanical tunnelling as detected by ^{1}H NMR and inelastic neutron scattering (5–7). Deuterium NMR provides valuable dynamic information for many systems (8) but has so far only been applied to a few dihydrogen complexes (9–13). Table 1 lists the deuterium quadrupole coupling constants determined in two types of investigations: solid-state ^{2}H NMR and solution ^{2}H NMR. The complex W(η^2-D_2)$(CO)_3(P^iPr_3)_2$ is reported to have a quadrupole coupling constant ($C_Q = e^2q_{zz}Q/h$) of 124 kHz on the basis of a width of 62 kHz between singularities in the wide-line spectrum at room temperature and the assumption of large angle motion of the D_2 ligand (9). A more thorough variable temperature study with line-fitting analysis is needed to determine C_Q for this complex. However for comparison purposes in Table 1, we calculate the effective (motion-averaged) quadrupole coupling (C_Q^{eff}) to be 62 × 4/3 = 83 kHz on the basis of the reported splitting. For comparison, a terminal W—D bond has a C_Q^{eff} of about 55 kHz (Table 1) as determined in a study of T_1 of $WD(CO)_2(NO)(PMe_3)_2$ in solution. The solution T_1 studies of the D_2 ligand in some Re and Os complexes suggest C_Q^{eff} in the range of 60–74 kHz (Table 1) (11–13). These are thought to be motion-averaged values. The true values are thought to be greater than the C_Q for terminal Re-D or Os-D (65–75 or 87 kHz, see Table 1) and possibly to be in the range 120–175 kHz depending on assumptions about the spinning motion, the asymmetry parameter η, and the angle between the D–D vector and the major axis of the electric field gradient (12). The C_Q values of other classical deuteride ligands in transition metal complexes range from 55 to 158 kHz depending on the ionic character of the bond and the M—D bond distance (13). Ab initio calculation by Guo et al. (10) of the C_Q of Rb(η^2-D_2) with *d*(Rb—D) = 1.75 Å, *d*(D—D) = 0.85 Å gives a value of about 155 kHz with η 0.62. This work also shows that the C_Q undergoes a dramatic change from 225 kHz for free D_2(g) to 155 kHz for Rb(η^2-D_2) and then to 20 kHz for the product of oxidative addition, $DRbD^+$, as the D—D distance changes from 0.74 to 0.85 Å and then to greater than 0.85 Å. The true C_Q value for a dihydrogen complex is therefore expected to fall between that of free D_2 and of a dideuteride complex with no D—D bonding (Fig. 1). The direction of q_{zz} should change from along the D—D bond in free D_2 to some intermediate angle in the M(η^2-D_2) complex and finally along the M—D bond in the dideuteride. Therefore, these parameters should be sensitive indicators of D—D and M—D bonding. Little is known about the relative importance of these components in M(η^2-H_2) bonding.

However the determination of the true C_Q value instead of the motion-averaged one is still a challenge because not enough is known about the exact motion of the D_2 ligand in the complexes described so far. Fortunately the D_2 ligands in the complexes *trans*-$[M(D_2)D(dppe)_2]^+$ M = Ru (**1**) and Os (**2**), dppe = $PPh_2CH_2CH_2PPh_2$ (Fig. 2), in solution should have well-defined motion: "fast spinning" (>>400 MHz) internal motion superimposed on isotropic tumbling of the molecule, on the basis of previous ^{1}H T_1 studies of the hydrogen-containing isotopomers (14–16). A good contrast to these compounds is $[Ru(D\cdots D)(C_5Me_5)(dppm)]^+$ (**3a**) dppm = $PPh_2CH_2PPh_2$; the hydrogen analog has an H_2 ligand elongated to 1.10 Å and static in solution with respect to the motion of the molecule (17). A useful property of this complex for

© 1999 NRC Canada

Table 1. Effective deuterium quadrupole coupling constants and other properties of deuterated dihydrogen and hydride complexes.

Complex	C_Q^{eff}, kHz	*d*(D—D), Å[a]	*d*(M—D), Å	Reference
$W(D_2)(CO)_3(P^iPr_3)_2$	83[b]	0.85	1.9	9
$WD(CO)_2(NO)(PMe_3)_2$	55		1.73	13
$[Re(\eta^2\text{-}D_2)D(CO)(NO)(PMe_3)_2]^+$	≈74			13
cis-$[Re(\eta^2\text{-}D_2)(CO)(PMe_3)_4]^+$	>61	0.96		13
$ReDL_5$[c]	65–75		1.69–1.77	13
$Os(\eta^2\text{-}D_2)D(CO)(Cl)(P^iPr_3)_2$	74	0.90		11
$Os(\eta^2\text{-}D_2)D(CO)(Cl)(P^iPr_3)_2$	87			11

[a]Calculated from literature ^1J(HD) values using *d*(HH) = 1.42–0.0167*J*(HD) (18).

[b]Calculated from the reported splitting of 62 kHz. This value is very tentative because a long 6 μs pulse was used at 30 MHz. (9).

[c]Various neutral ligands.

Fig. 1. The expected properties of D_2 upon coordination and then oxidative addition to a metal complex.

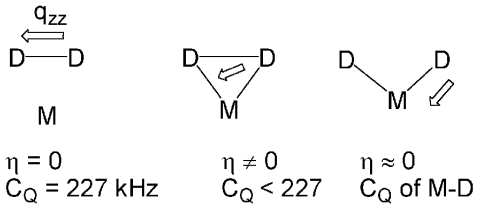

comparison purposes is that it exists in solution as a mixture of **3a** and its dideuteride tautomer $[Ru(D)_2(C_5Me_5)(dppm)]^+$ (**3b**). An intriguing type of H_2 motion occurs in the complex *trans*-$[Os(H\cdots H)(Cl)(dppe)_2]^+$ where the dihydrogen ligand has a frequency of motion similar to that of the tumbling of the complex in solution (18). Therefore the complexes *trans*-$[M(D\cdots D)(Cl)(dppe)_2]^+$ M = Ru (**4**) and Os (**5**) are also worth studying. The structures of all of these compounds have been determined by NMR methods as well as single crystal X-ray and neutron diffraction methods (except **4**) (18, 19). Very low temperature (down to 5 K) spectra of **4** provide evidence for tunneling of the D nuclei (20). Also included in the present study is an interesting dimeric complex $Ru(\eta^2\text{-}D_2)(dppb)(\mu\text{-}Cl)_3RuCl(dppb)$ (**6**) (dppb = $PPh_2(CH_2)_4PPh_2$); the H_2 complex was described by Joshi and James (21). A more comprehensive solid-state NMR study on $Os(D\cdots D)(Cl)_2(CO)(P^iPr_3)_2$ (**7**) is described here, which provides evidence for a twofold reorientation of the elongated D_2 ligand. The evidence for the 1.1 Å D···D distance in this complex comes from ^{1}H NMR studies (22), since no single crystal structure determination has been done. In **4**, **5**, and **7** the D···D distances are elongated because they are *trans* to the weak field chloride ligand (23, 24).

Experimental section

General

All of the experiments were performed under a dry D_2 or Ar atmosphere by use of standard Schlenk techniques. All of the samples were handled under an Ar atmosphere and exposed to D_2 before NMR measurements. All of the solvents were dried by standard methods and freshly distilled before use. ^{1}H, ^{2}H, and ^{31}P NMR spectra of solutions were obtained on Varian Unity-400 and Varian Gemini-300 spectrometers.

Fig. 2. Structures of the non-classical dideuterium complexes.

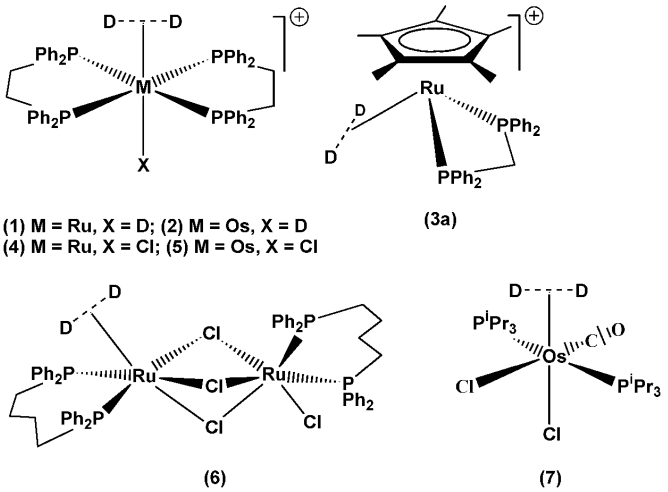

The purity of the samples was verified by ^{1}H, ^{31}P{^{1}H} NMR and ^{2}H NMR measurements.

Sample preparation

trans-*[Ru(D$_2$)D(dppe)$_2$]PF$_6$*, ***1***

This was prepared from *trans*-$[Ru(H_2)H(dppe)_2]PF_6$ by H/D exchange with D_2 at room temperature in CH_2Cl_2 (16). Some deuteration occurred at the CH_2 and Ar-H groups of the phosphine ligands. ^{2}H NMR (CH_2Cl_2) δ: 7.5 (br, Ar-D), 2.0 (br, CDH), –5 (br, η^2-D_2), and –10.5 (br, RuD). Temp. (K)/T_1D$_2$/T_1D (ms): 295/1167 ± 10/62 ± 10; 253/572 ± 1/32 ± 1; 233/413 ± 1/22 ± 1; 213/255 ± 1/15 ± 1; 193/181 ± 1/15 ± 1; 183/196 ± 1/29 ± 1.

trans-*[Os(D$_2$)D(dppe)$_2$]PF$_6$*, ***2***

A mixture of *cis*-$OsBr_2(dppe)_2$ (560 mg, 0.49 mmol) (18), NaO-*t*-Bu (50 mg, 0.5 mmol) and $NaPF_6$ (350 mg, 2 mmol) in 20 mL THF and 20 mL of CH_2Cl_2 was stirred under an excess of D_2(g) (1 atm) for 5 h. The solvent was evaporated in vacuo. The residue was dissolved in 15 mL CH_2Cl_2 and filtered to remove NaBr/$NaPF_6$. The addition of 40 mL hexanes caused the precipitation of the product as an off-white solid (yield 370 mg, 68%). ^{31}P{^{1}H} NMR (CD_2Cl_2) –103.6 ppm (s). There were small impurity peaks at 25 (s, $[Os(O_2)(D)(dppe)_2]^+$ (25) and 18 (s) ppm that were not removed by recrystallization from CH_2Cl_2/Et_2O. ^{1}H NMR: no

© 1999 NRC Canada

hydride peaks. ^{2}H NMR (CH_2Cl_2, 253 K): –6.6 (br, η^2-D_2), –8.8 (br, OsD). Temp. (K)/T_1D_2/T_1D (ms): 253/76/44; 238/100/19; 223/98/15; 208/94/14; 193/115/21; 183/172/not observed.

[Ru(D$_2$)(C$_5$Me$_5$)(dppm)]BF$_4$, ***3a***

A 100 mL Schlenk tube was charged with RuCl(C_5Me_5)(dppm) (0.4 g, 0.56 mmol) (26), $AgBF_4$ (0.11 g, 0.56 mmol) and CH_2Cl_2 (15 mL). This mixture was stirred vigorously under an N_2 atmosphere for 1 h. Then the Schlenk tube was put under vacuum and refilled with D_2 with stirring. The same procedure was repeated after 0.5 h and the stirring was continued for another 0.5 h. The AgCl was removed by filtration. Et_2O was diffused into the filtrate slowly. A light yellow solid (0.22 g, 88%) was obtained, which was washed with Et_2O and dried under vacuum. ^{2}H NMR (CH_2Cl_2), 293 K: –5.9 (23% **3b**, T_1 164 ms), –6.7 (77% **3a**, 178 ms); 273 K: –5.8 (20%, 100 ms), –6.6 (80%, 135 ms); 253 K: –5.9 (19%, 60 ms), –6.6 (81%, 84 ms); 233 K: –5.9 (19%, 38 ms), –6.6 (81%, 51 ms); 213 K: –5.9 (20%, 23 ms), –6.5 (80%, 30 ms); 193 K: –5.9 (shoulder on **3a** peak, 18 ms); –6.4 (**3a**, 21 ms); 183 K: –6.3 (br, 23 ms).

trans-*[Ru(D$_2$)Cl(dppe)$_2$]PF$_6$,* ***4***

Under Ar, [RuCl(dppe)$_2$]PF_6 (2.0 g, 1.8 mmol) (27) was dissolved in 30 mL CH_2Cl_2. The resulting red solution was cooled to 248 K (monitored with a thermometer) using a dry ice – acetone bath. Deuterium gas was bubbled into the solution until the color changed to yellow (approx. 5 min). Then Ar was immediately purged through the system to remove the excess deuterium gas. Diethyl ether (100 mL) that had been precooled to 248 K was quickly added to precipitate the product. When the precipitate settled, the ether was syringed out, and the cream-colored product was dried under a stream of Ar. ^{2}H NMR (CH_2Cl_2, 253 K): –12.4 ppm (s). When the sample was warmed to 293 K or if the sample was prepared at room temperature, the ^{2}H NMR also revealed resonances at 7.3 and 1.5 ppm caused by D/H exchange between the Ru(D_2) and C-H sites. Temp. (K)/T_1D_2 (ms): 294/272 ± 6; 253/127 ± 2; 233/88 ± 3; 213/54 ± 3; 193/48 ± 3; 183/54 ± 4.

trans-*[Os(D$_2$)Cl(dppe)$_2$]PF$_6$,* ***5***

D_2(g) was reacted with [OsCl(dppe)$_2$]PF_6 in CH_2Cl_2 (18). ^{2}H NMR (CH_2Cl_2): –11.5 (br). Temp. (K)/T_1D_2 (ms): 253/76 ± 7; 233/37 ± 3; 213/19 ± 2; 193/25 ± 2; 178/23 ± 4.

(η^2-D$_2$)(dppb)Ru(μ-Cl)$_3$Ru(Cl)(dppb), ***6***

The same method that was used for the η^2-H_2 complex was followed starting from (dppb)Ru(μ-Cl)$_3$Ru(Cl)(dppb) (21) but under a D_2 atmosphere. Some deuteration occurred at the CH_2 and Ar-H groups. ^{2}H NMR (CH_2Cl_2) δ: 2.0 (br), –11.3 (br). Temp. (K)/δ D_2/T_1D_2 (ms): 293/–11.3/245 ± 5; 273/–11.3/158 ± 1; 253/–11.4/93 ± 1; 233/–11.5/60 ± 1; 213/–11.6/46 ± 1; 193/–11.7/53 ± 1; 183/–11.7/54 ± 4.

Os(D$_2$)(Cl)$_2$(CO)(P^{i}Pr$_3$)$_2$, ***7***

The reported preparation of Os(HD)Cl_2(CO)(P^{i}Pr$_3$)$_2$ from Os(D)Cl(CO)(P^{i}Pr$_3$)$_2$ (80% OsD, 20% OsH) (22), was used with the following modification: 37 wt.% DCl in D_2O (99.5 atom % D, Aldrich) was used instead of HCl in toluene. ^{1}H NMR (C_6D_6 under D_2) –7.46 (residual η^2-HD, 1:1:1 t, J_{HD} 20.1 Hz, 0.2 H). Therefore, the sample was 20% Os(HD) and 80% Os(D_2) as determined by integration.

Solution NMR deuterium T_1 measurements

The measurement of T_1 of concentrated samples in CH_2Cl_2 was done on a Varian Unity-400 spectrometer using the inversion-recovery method (π-τ-π/2). A nonlinear three-parameter fitting routine of the spectrometer was used to calculate the T_1 values. The pulses were calibrated at each probe temperature. The errors of such T_1 determinations were lower than 5% and the relaxation rates were mono-exponential. The temperatures were calibrated by ^{1}H NMR with a standard methanol sample.

Solid-state deuterium NMR spectroscopy

Deuterium NMR spectra of **1, 3**, and **4** were recorded on a Chemagnetics CMX300 spectrometer operating at 45.98 MHz, using a Chemagnetics broadline deuterium probe equipped with a 5 mm diameter solenoid coil. The quadrupolar echo pulse sequence (90*x*–τ–90*y*–τ–acq) (28) was employed using quadrature detection with complete phase cycling of the pulse pairs. The 90° pulse length was 2 μs, the interpulse delay was 30 μs, the recycle delay was 5 s, the spectral width was 1 MHz, and the data size was 2K. The samples (~200 mg) sealed in 5 mm tubes were cooled to the desired temperature using the boil-off from liquid nitrogen, and regulated at that temperature using a feedback loop controlled resistive heater. Samples were temperature equilibrated for at least 30 min prior to beginning data acquisition.

Compound **7** (150 mg) was sealed in a standard 5 mm NMR tube 30 mm in length under 1 atm N_2 gas. The spectra for **7** were collected on a Bruker ASX 200 NMR spectrometer. The ^{2}H CPMAS spectrum was acquired by placing the sample tube into a Bruker 7 mm o.d. zirconia stretch rotor. The Hartman Hahn match was set directly on the sample. The ^{1}H 90° pulse was 4.5 μs, and the contact time was 4 ms, 8K time domain points were collected for 3860 scans with a sweep width of 0.25 MHz using a 2 s relaxation delay. The spinning speed was 5.000 kHz and was stable to within 1 Hz. The ^{2}H wideline spectra were acquired with the quadrupolar echo sequence using a Bruker wideline probe with a 5 mm insert. The 90° pulses were 3.5 μs and the echo delays were 35 μs. The temperature was regulated with the instrument's variable temperature unit to within 1 K, but the temperature of the sample was measured directly with a thermocouple inserted at the top of the magnet bore such that it was in contact with the coil of the probe. The accuracy of the measured temperatures was within 1 K. The T_1 relaxation times were measured using the inversion recovery method with the 90° read pulse replaced with a quadrupolar echo. Each measurement was made with 12 τ values. All simulations were carried out on an SGI Indigo using the MXET1 program kindly provided by Dr. R.R. Vold.

Calculations

The calculation of C_Q (eq. [1]) from the minimum T_1 with respect to temperature of the deuterium in a complex isotropically tumbling in solution has been described previously (13). The temperature dependence of T_1 is given by eqs. [2] and [3].

© 1999 NRC Canada

Fig. 3. Definition of the angle Δ in a fast-spinning D_2 complex.

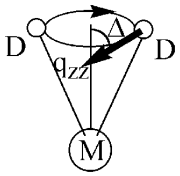

$$[1] \qquad C_Q = \frac{e^2 q_{zz} Q}{h}$$

$$[2] \qquad \frac{1}{T_1(D_2)} = 0.3\pi^2(1+\eta^2/3)(C_Q)^2\left\{A\frac{\tau_c}{1+\tau_c{}^2\omega^2} + A\frac{4\tau_c}{1+4\tau_c{}^2\omega^2}\right\}$$

$$[3] \qquad \tau_c = \tau_o e^{(E_a/RT)}$$

where C_Q is the static quadrupole coupling constant, $\eta = (\Delta\nu_{yy} - \Delta\nu_{xx})/\Delta\nu_{zz}$ is the asymmetry parameter of the electric field gradient, A is 1 for the case of a deuterium nucleus tumbling with the molecule with no additional internal motion, τ_c is the correlation time of the molecule, and ω is $2\pi\nu$, where ν is the spectrometer frequency. For $\tau_c = 0.62/\omega$ the spectral density function $J(\omega) + 4J(2\omega)$ reaches a maximum value which leads in turn to a T_1 minimum. Equation [2] then simplifies to eq. [4] where ν is in MHz and $T_1{}^{min}$ is in seconds (12).

$$[4] \qquad (C_Q)^2 = 1.489(\nu/(T_1{}^{min}(1 + \eta^2/3)))$$

The value of η is usually not known but ranges from 0 to 1. This leads to an uncertainty in the value of C_Q of 10% or less.

This equation needs to be modified for the case of rapid spinning (or rapid, random reorientation in a plane) of a D_2 ligand with the q_{zz} of each D oriented at an angle Δ with respect to the coordination axis, which is also the axis of rotation (Fig. 3). Because the $M(D_2)$ bonding involves both D-D and M-D components, at least for short D—D distances, then Δ will not in general be equal to 90°. If there is no D—D bonding (i.e., a dihydride structure) then q_{zz} would be expected to point along the M—D bond. Therefore, a determination of the angle Δ would provide valuable information about the bonding.

Woessner (29, 30) has provided the spectral density functions to describe axially symmetrical internal motion superimposed on isotropic molecular tumbling with an axis of relaxation at an angle Δ with respect to the axis of rotation or other symmetrical motion. There are three additive functions of the diffusion constants of motion that contain coefficients $A = (3\cos^2\Delta - 1)^2/4$, $B = 3\sin^2\Delta\cos^2\Delta$, and $C = 3(\sin^4\Delta)/4$, respectively. With rapid internal rotation or diffusion of the nucleus, the functions with the B and C terms become very small and leave the spectral density function as in eq. [5].

$$[5] \qquad J(\omega) = \frac{(3\cos^2\Delta - 1)^2}{4}\,\frac{\tau_c}{1+\tau_c{}^2\omega^2}$$

Fig. 4. Relationship between the angle Δ and the factor $(1/A)^{1/2}$ from eq. [6].

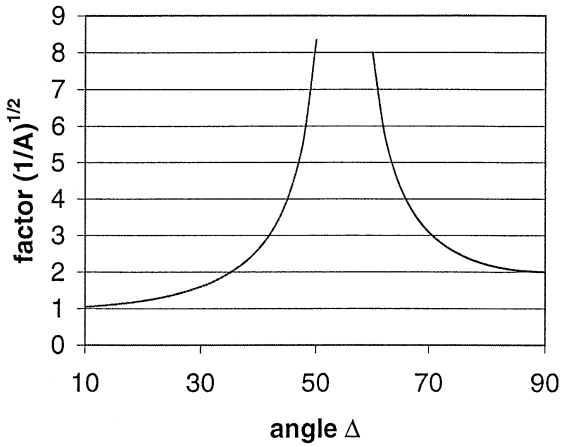

When Δ is 90°, the well-known result of $A = (3\cos^2\Delta - 1)^2/4 = 0.25$ is obtained. This factor has been used to correct $T_1{}^{min}$ values of ^1H in "fast-spinning" dihydrogen complexes where the dipolar relaxation is at 90° to the axis of rotation (15). Equation [4] now becomes eq. [6].

$$[6] \qquad C_Q = 1.220(1/A)^{1/2}(\nu/(T_1{}^{min}(1 + \eta^2/3)))^{1/2}$$

The remarkable dependence of the factor $(1/A)^{1/2}$ on the angle Δ is illustrated in Fig. 4. As Δ approaches the "magic angle" of 54° this factor becomes enormous. Equation [6] is not accurate near the singularity. However, it illustrates that large corrections may be needed to calculate C_Q from $T_1{}^{min}$ if there is rapid, symmetrical motion with an angle involving q_{zz} between 40° and 70°.

Results and discussions

Preparation of the deuterated materials

All of the complexes except **7** could be prepared from deuterium gas by various synthetic methods. Complexes **4**–**6** could be prepared by direct reaction of $D_2(g)$ with solutions of the unsaturated starting complexes $[MCl(dppe)_2]^+$ or $Ru_2Cl_4(dppb)_2$. The ruthenium complexes in solution gradually become deuterated at some of the methylene and aromatic C—H bonds. The deuteration of the methylene C-H likely requires the dissociation of a Ru—P bond and coordination of the C—H bond to allow exchange with Ru—D bonds (31).

Complex **1** was prepared by displacement of H_2 and then HD ligands from *trans*-$[Ru(H_2)H(dppe)_2]^+$ by use of excess $D_2(g)$. This reaction proceeds via intermediate formation of $[Ru(D_2)H(dppe)_2]^+$ with the release of H_2 (16). Intramolecular exchange of H and D produces $[Ru(HD)(D)(dppe)_2]^+$, which reacts with D_2 releasing HD(g) and producing **1**. Some deuteration of both aromatic and methylene C—H bonds also occurred by an uncharacterized mechanism.

Since the η^2-D_2 ligand of *trans*-$[Os(H_2)H(dppe)_2]^+$ is not very labile a bromide displacement route was employed to make the deuterated analogue **2**. We have shown that *cis*-$OsBr_2(dppe)_2$ is an excellent starting material for osmium dppe chemistry (18). In particular, it can be converted into the required complex **2** in one pot (eq. [7]) (32) while avoid-

© 1999 NRC Canada

Table 2. T_1^{min} (D) and relevant data for complexes **1**–**7**.

Compounds	^{2}H T_1^{min} [a] (ms)	Temp (K)	C_Q^{eff} [b] (kHz)	C_Q^{eff} S. S.[c] (kHz)	d(DD)[d] (Å)	d(MD)[d] (Å)	DMD (°)
[Ru(D)(D_2)(dppe)$_2$]BPh$_4$ **1**	181	193	19–22	48	0.94	1.81	30
[Ru(D)(D_2)(dppe)$_2$]BPh$_4$ **1**	15	193	79	~75		1.64	
[Os(D)(D_2)(dppe)$_2$]PF$_6$ **2**	94	193	27–31		0.96	1.74	32
[Os(D)(D_2)(dppe)$_2$]PF$_6$ **2**	14	193	81			1.62	
[Ru($D\cdot\cdot D$)Cp*(dppm)]BF$_4$ **3a**	21	193	57–66		1.1	1.66	38
[Ru(D)$_2$Cp*(dppm)]BF$_4$ **3b**	18	193	71				
trans-[Ru(D_2)Cl(dppe)$_2$]PF$_6$ **4**	47	193	38–44	54,[f] 107[g]	1.0[e]	1.65[i]	35[i]
trans-[OsCl($D\cdot\cdot D$)(dppe)$_2$]PF$_6$ **5**	20	193	59–68		1.22	1.58	45
(D_2)(dppb)Ru(μ-Cl)$_3$Ru(Cl)(dppb) **6**	48	213	38–44		0.93[e]	1.6	
Os($D\cdot\cdot D$)(Cl)$_2$(CO)(P^{i}Pr$_3$)$_2$ **7**	20[h]	260		120–167	1.1[e]	1.6[i]	40[i]

[a]Measured at 61.45 MHz, samples in CH_2Cl_2.
[b]Calculated by use of eq. [4] with η = 0 for M—D bonds and η ranging from 0 to 1 for M(D_2) bonds.
[c]Estimated from singularities in the 143 K spectra run at 46 MHz.
[d]From neutron diffraction studies unless indicated otherwise.
[e]Calculated from J(HD).
[f]123 K.
[g]5 K.
[h]Measured in the solid state at 30.7 MHz.
[i]Estimated value.

ing protic reagents that might cause unwanted hydrogen incorporation (excess $NaPF_6$ is actually required for this reaction).

[7] $$OsBr_2(dppe)_2 + NaPF_6 + NaO\text{-}t\text{-}Bu + 2D_2 \rightarrow [Os(D_2)D(dppe)_2]PF_6 + 2NaBr + DO\text{-}t\text{-}Bu$$

The deuteration to produce complex **3** proceeded via displacement of dinitrogen by D_2 from [Ru(C_5Me_5)(N_2)(dppm)]BF_4 that was first generated in situ from Ru(C_5Me_5)Cl(dppm) and $AgBF_4$ (33). It is interesting that there appears to be a significant isotope effect on the equilibrium constant between the Ru(D···D) and Ru(D_2) isotopomers. Integration of the solution ^{2}H NMR signals provides a ratio of 3.3:1 for Ru(D···D): Ru(D_2) at 20°. The ratio for Ru(H···H): Ru(H_2) was reported to be 2:1 (34).

The deuteration in **7** relied on the addition of DCl to Os(D)Cl(CO)(P^{i}Pr$_3$)$_2$/Os(H)Cl(CO)(P^{i}Pr$_3$)$_2$ (80/20%). Complex **7** was found to contain 80% D_2 and 20% HD ligand.

Solid-state deuterium NMR results

Some preliminary attempts were made to obtain C_Q from wide-line solid-state spectra (see Table 2). It must be born in mind that such spectra will be super-positions of signals from all deuterons in the sample and that the detailed line shapes will reflect all motions present including those of the deuterons themselves as well as the molecules to which they are attached.

Figure 5 shows the spectra of **1** at 293 and 143 K. At 293 K the spectrum appears to be characteristic of intermediate time scale motional narrowing. Distinct spectral components for the two types of deuterons (Ru-D and Ru-D_2) cannot be resolved, making assignments or analysis difficult. At 143 K an additional broad component appeared, likely attributable to a slow moving component. A reasonable interpretation is that the broad component is associated with the Ru—D bond

Fig. 5. ^{2}H wide-line spectra of **1** at 46 MHz, 143 K (bottom) and 293 K (top).

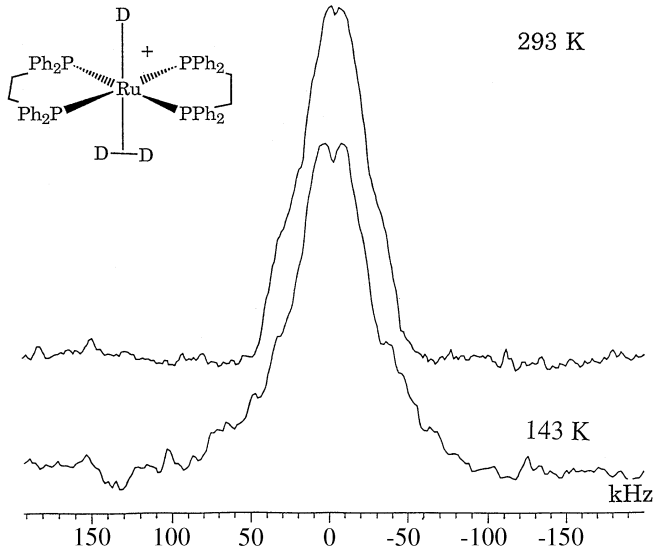

with a C_Q of about 75 kHz (cf. solution study of **1** below) while the narrow central component is due to the mobile D_2 group with a motion-reduced C_Q (cf. the fast-exchange spectra of **7** in Fig. 8 below). Only one spectrum was recorded for **3** at 143 K. This also appeared to have narrow and broad components, somewhat similar to the fast exchange spectra of **7**.

The spectra of **4** are shown in Fig. 6. There are clearly two components in these spectra as well. At the higher temperature (243 K) the spectrum is dominated by a component having a non-zero asymmetry parameter ($\eta \approx 0.7$) and $C_Q \approx$ 50 kHz. Evidently, there is motion of the deuterons, but it cannot be stated whether it is due to D–D rotation/libration and (or) flexing of the rest of the molecule. At the lower

© 1999 NRC Canada

Fig. 6. Variable temperature ^{2}H wide-line spectra of **4** at 46 MHz.

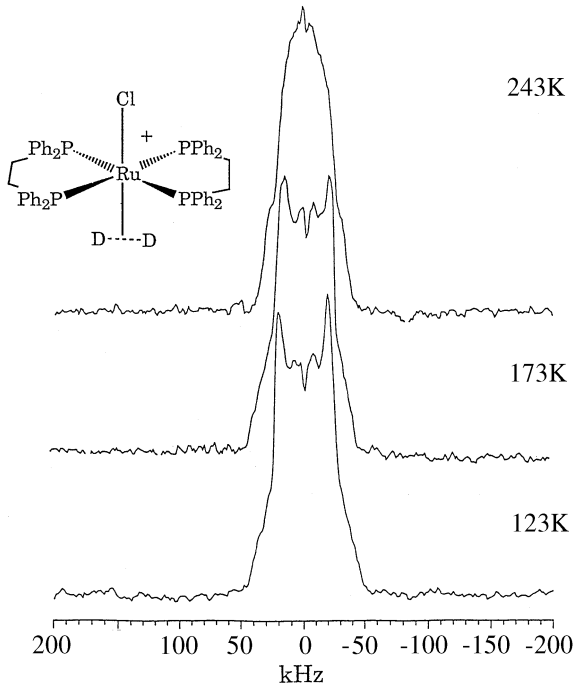

temperature (123 K) the spectrum is dominated by a component having an asymmetry parameter near zero ($\eta \approx 0.15$) and C_Q equal to 54 kHz. More recent results of Buntkowsky et al. (20) indicate that there continue to be line shape changes down to 5 K with the static C_Q evaluated to be 107 kHz, and the primary electric field gradient tilted at $\Delta = 45°$ and $\eta < 0.1$. This analysis indicates that the motion is some combination of rotational diffusion and twofold reorientation of the D_2 ligand.

To obtain more detailed information from the spectra of **1** and **3** regarding mechanisms and rates of motion, detailed temperature-dependent relaxation time and line shape analyses will be necessary.

A more detailed study of **7** was conducted. The ^{2}H CPMAS spectrum of the solid containing 80% Os(D_2), 20% Os(HD) is shown in Fig. 7. Each band in the spectrum consists of a narrow signal ($\Delta\nu_{1/2}$ = 80 Hz) and a broad doublet signal reminiscent of a partially averaged powder pattern with a width of 890 Hz at the inner singularities and 1680 Hz at the base. Both signals are centred at ~–8 ppm in the centre band. There is no evidence for a peak at ~1 ppm for CD bonds that might have formed as a result of H/D exchange. One can see that the envelope of spinning sidebands is the same for both signals and that it does not approximate a Pake doublet. This indicates that there is an anisotropic motion of the HD and D_2 ligands and (or) that the electric field gradient tensor, $\boldsymbol{V_{ii}}$, of the deuterium atoms has a large asymmetry parameter, η. The overall width of the sideband envelope (~80 kHz) suggests that the former is true. The intensity ratio of the broad to narrow components agrees fairly closely with that measured from the solution spectrum despite the fact the CPMAS spectrum is difficult to integrate as all of the sidebands must be considered, there is overlap between the signals and the CP experiment is not quantitative.

Fig. 7. ^{2}H CPMAS spectrum at 30.7 MHz of solid **7** containing 80% Os(D_2), 20% Os(HD). The top spectrum shows the complete spinning side band envelope, while the bottom spectrum shows the incompletely averaged D-D dipolar powder pattern at the base of the peak at –8 ppm.

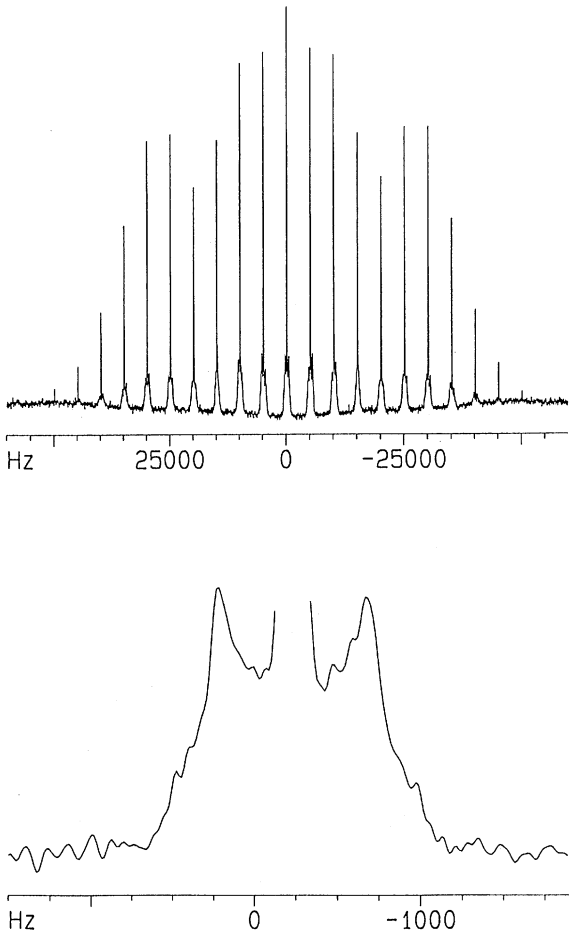

Therefore, one can assign the broad component to the D_2 ligand and the narrow component to the HD ligand. For the HD ligand, magic angle spinning and high power proton decoupling will eliminate the first-order quadrupolar interaction, the dipolar coupling between the H and D nuclei and the indirect *J* coupling; thus, a single isotropic line is expected. The situation is much more complicated for the D_2 ligand. In this case magic angle spinning will not completely remove the second-order quadrupolar interaction, and the effects will be evident in the spectrum through the homonuclear dipolar coupling between the two deuterons (2.13 kHz based on a 1.1 Å separation). This phenomenon has been reviewed for the case of heteronuclear spin 1/2 – quadrupolar spin pairs and is referred to as "residual dipolar coupling" (35). The MAS spectra of the spin 1/2 isotopes in these cases exhibit residual powder patterns resulting from the second-order quadrupolar interaction of the quadrupolar nucleus and the heteronuclear dipolar interaction. To our knowledge the case of a D–D spin pair has not been studied in this regard but it is expected that the second-order quadrupolar effects will show up in the spectrum as a result of the homonuclear dipolar coupling between the deuterons. We have not, as yet, undertaken a detailed analysis of the

© 1999 NRC Canada

Fig. 8. Wide line ^{2}H NMR spectra of **7** at 30.7 MHz. Observed spectra are on the left and simulated spectra are on the right with model 1: C_Q = 120 kHz, η = 0, Δ = 52.5°; and model 2: C_Q = 166.7 kHz, η = 0.28, Δ = 49.7°.

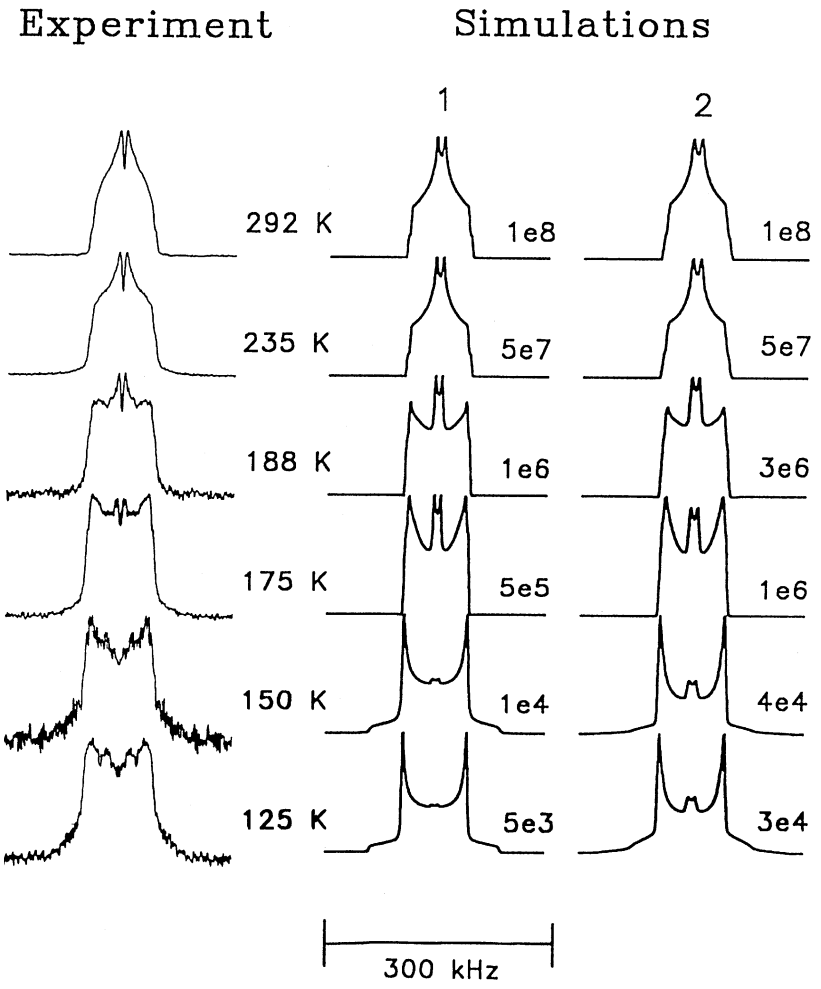

spectrum. It is complicated by the effects of molecular motion and the possible interference between this motion and the MAS. We do not expect the indirect *J* coupling to have a significant effect as it is very small. Preliminary experiments have revealed that the appearance of the spectrum is dependent on both spinning speed and field strength. Further study is required to completely understand the spectrum.

Wide line ^{2}H NMR spectra **7** were collected as a function of temperature and are shown in Fig. 8. One can see that the line shapes are very temperature dependent, indicating without doubt that the D_2 ligand is mobile. The interpretation of this data is made difficult, since one does not have available the static quadrupolar coupling constant, C_Q, asymmetry parameter, η, nor the orientation of the electric field gradient tensor, $\boldsymbol{V}_{ii}$, with respect to the molecule. Despite this lack of information one can conclude with certainty that the D_2 moiety is not undergoing an equally populated *n* site rotation ($n \geq 3$) about the coordinating axis. This would give rise to an axially symmetric spectrum, which is not the case. The spectrum recorded at 292 K is a fast motion limit spectrum, whereas all spectra recorded at lower temperatures are distorted by the molecular motion occurring at a rate comparable to the reciprocal of the static quadrupolar coupling constant. The frequency difference between one pair of singularities in each spectrum remains constant throughout the entire temperature range; thus, one component of the electric field gradient tensor must be unaffected by the motion. This would be the case for a twofold flip about the coordinating axis where the component of the electric field gradient tensor perpendicular to the Os D–D plane would remain constant. Furthermore, the spectra agree qualitatively with those previously calculated for similar complexes (36) assumed to show a mutual incoherent exchange of the deuterons.

The spectra were fit to a two-site model where the dihydrogen moiety undergoes 180° flips about the coordinating axis (Fig. 9*a*). To fit the data we had to guess at C_Q as our equipment does not permit us to record spectra at temperatures where the motion would be frozen out. We also had to provide an estimate for Δ, the angle between the largest component of the electric field gradient tensor, $\boldsymbol{V}_{zz}$, and the axis of the motion (see Fig. 9*b*). Typically $\boldsymbol{V}_{zz}$ lies along an X—D bond, however, in this case where the deuterons participate in a three centre interaction, one would expect that $\boldsymbol{V}_{zz}$ would be directed at a point on the coordinating axis intermediate between the midpoint of the D—D bond and the Os atom. Therefore, the angle Δ is restricted to values be-

© 1999 NRC Canada

Fig. 9. (*a*) Axis system defining the electric field gradient components. (*b*) Δ, the angle between the largest component of the electric field gradient tensor, V_{zz}, and the axis of the motion.

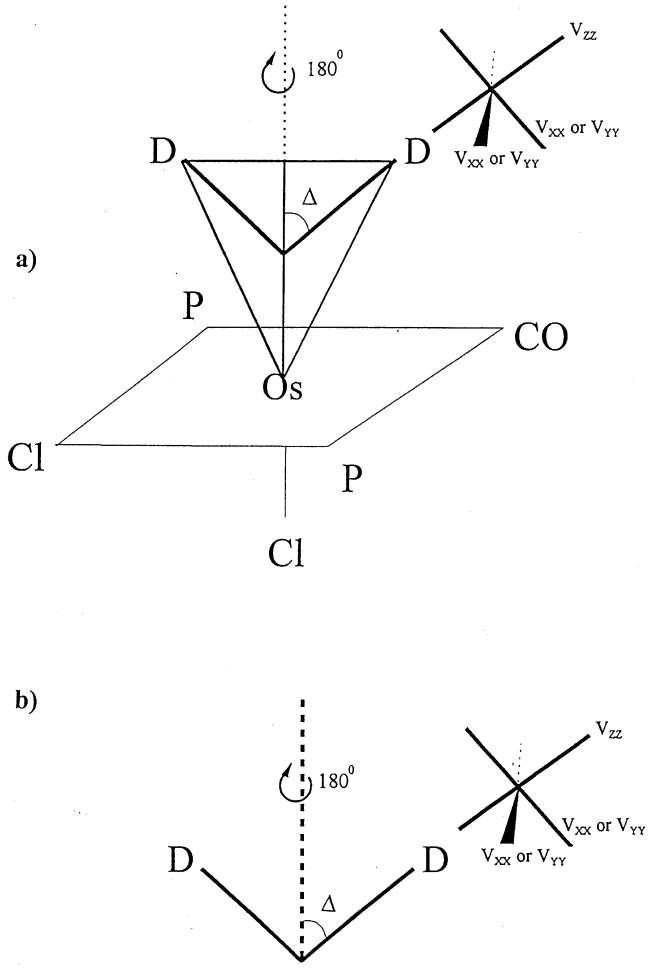

tween 19.7° and 90°, since the D—D bond length was estimated to be 1.1 Å by use of ^{1}H T_1 and J(HD) data, and the Os—D bond is estimated to be ~1.63 Å.

A series of ^{2}H line-shape simulations (37) were carried out varying C_Q, η, Δ, and the rate of the motion. The best fits are shown in Fig. 8(1) and (2). At temperatures greater than ~175 K, the fits are very nearly identical. At the lower temperatures however there are considerable differences. Unfortunately, spectra with high signal to noise ratios are difficult (i.e., time consuming) to acquire at low temperatures due to attenuated echo signals arising from the intermediate rate motion, long T_1's, and small amounts of deuterium. As a result, we are unable to distinguish between the two cases but believe that these data support the two-site reorientation model for the D_2 moiety. Other motions not included in the simulation to account for the differences are torsional libration of the D_2 and tunneling of the D nuclei through the rotational barrier. In addition, broadening of the peaks may be caused by a distribution of activation barrier energies due to solid-state effects.

According to the fitting procedure, the values of C_Q might range from 120 to 167 kHz depending on the asymmetry parameter and angle Δ. This magnitude of C_Q is greater than

Fig. 10. Observed and calculated temperature dependence of T_1 of the D in solid **7**.

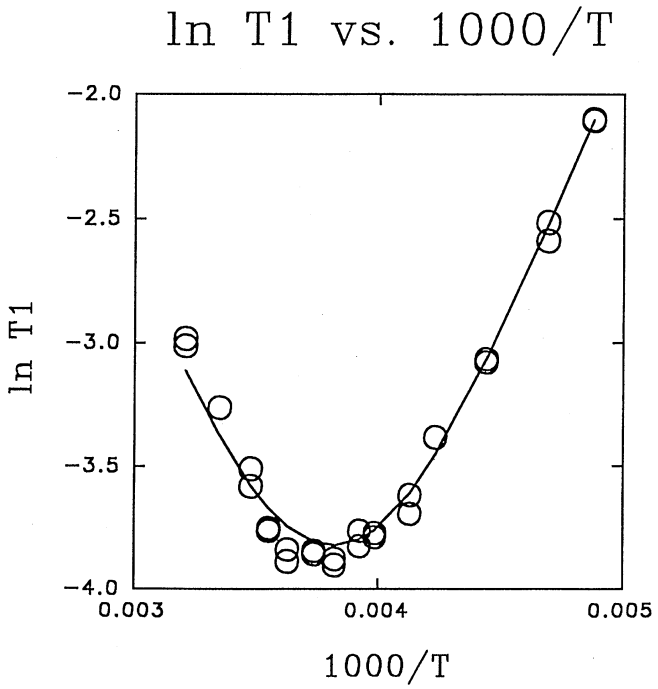

the 87 kHz reported for the terminal Os—D bond in Os(η^2-D_2)D(CO)(Cl)(P^{i}Pr$_3$)$_2$ (Table 1) as expected because of the D—D bonding character in **7**. The C_Q for **7** is also greater than the C_Q^{eff} = 74 kHz for the D_2 ligand of the osmium complex in Table 1 and the C_Q^{eff} = 59–68 kHz for the D_2 ligand in **5** (Table 2). This indicates that the static quadrupole coupling constant for the D_2 ligands in Os(η^2-D_2)D(CO)(Cl)(P^{i}Pr$_3$)$_2$ and **5** must be greater than the motion-reduced C_Q^{eff} value. The value Δ of 49°–53° is also indicative of some D—D and some Os—D bonding. A D_2 ligand with the primary electric field gradient tilted at such an angle should experience a large increase in T_1(D) if rotation (or torsional libration) about the Os–D_2 coordination axis contributes to the overall motion (cf. Fig. 4).

^{2}H T_1 relaxation times were measured as a function of temperature and are plotted in Fig. 10. The T_1 data were fit with the BPP spectral density function, eq. [8] (38), and the Arrhenius

$$[8] \qquad \frac{1}{T_1} = C\left(\frac{\tau_c}{1+\omega^2\tau_c^{\,2}} + \frac{2\tau_c}{1+4\omega^2\tau_c^{\,2}}\right)$$

relation (eq. [3]) to obtain the activation energy, E_a, for the D_2 reorientation. The fitted curve is represented by the solid line in Fig. 10. The activation energy was found to be 19.7 ± 0.5 kJ/mol. This low barrier is consistent with the gradual line shape changes observed over a wide temperature range (Fig. 8). The activation energy is higher than those measured by inelastic neutron scattering (<10 kJ/mol) (6, 39) for dihydrogen complexes with H—H distances of 0.85–1.0 Å. This indicates that the complex studied here has a considerable degree of dihydride character. The T_1 goes through a minimum at 260 K when $1/\tau_c$ is approximately $2\pi\nu \approx 10^8$ Hz, where ν is the spectrometer frequency of 30.7 MHz. The fact

© 1999 NRC Canada

Fig. 11. The temperature dependence of the 400 MHz ^{1}H T_1 of the H_2 ligand in $[Ru(H_2)(Cl)(dppe)_2]^+$ (●) compared to that of the 61.4 MHz ^{2}H T_1 of **4** (■).

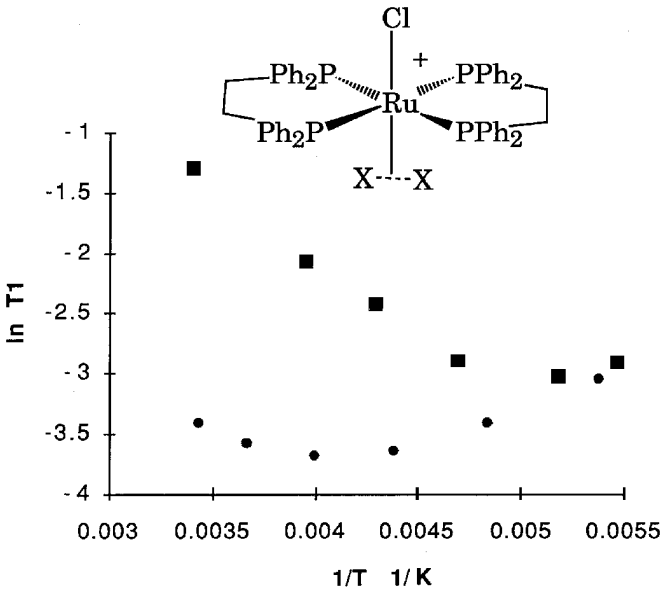

that the rate of twofold reorientation at this temperature is of this magnitude (see Fig. 8) is consistent with our interpretation of the motion of the deuterium. It is clear that the D_2 motion causes a significant increase in the T_1 value over that expected for a "static" deuterium nucleus with a C_Q of 120–167 kHz. For example, the observed T_1^{min}(D) is 20 ms at 260 K, 30.7 MHz, while that calculated by use of eq. [4] is approx. 3 ms (with C_Q = 120 MHz). It is interesting that a pure twofold reorientation would have no influence on the T_1 of the hydrogen nuclei in a dihydrogen ligand since the flip is along the same axis as the dipole–dipole relaxation vector. Therefore, D NMR is a better probe of motion in this regard. Equation [6], which refers to a free rotor motion, is not applicable to the flipping D_2 motion in **7**.

Solution deuterium NMR results

The T_1 of a deuterium resonance can be conveniently measured by a standard inversion-recovery pulse sequence, and its value reflects the quadrupole interaction (eq. [2]). Locating the minimum T_1 is a challenge. Because of the small gyromagnetic ratio of deuterium relative to hydrogen, T_1^{min} occurs at a lower temperature for deuterium than hydrogen. For example, Fig. 11 compares the temperature dependence of the 400 MHz ^{1}H T_1 of the H_2 ligand in $[Ru(H_2)(Cl)(dppe)_2]^+$ compared to that of the 61.4 MHz ^{2}H T_1 of **4**; the lower frequency D nucleus has a minimum T_1 at a much lower temperature than the ^{1}H T_1. However, we have found that the use of concentrated solutions increases solution viscosity and significantly increases the correlation time of the molecule.[3] Therefore, our investigations were done using concentrated CH_2Cl_2 solutions of the complexes (150–200 mg/mL).

Fig. 12. Observed ^{2}H T_1 for D_2 (■) and D (▲) of **1** in CH_2Cl_2 at 61.4 MHz.

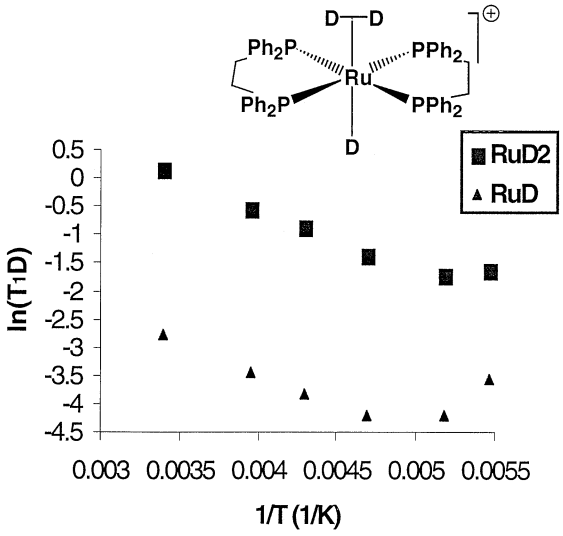

The T_1 data for both D_2 and D ligands of complex **1** are plotted in Fig. 12. The T_1^{min} and C_Q values are listed in Table 2. The D_2 ligands in **1** and **2** have dramatically longer T_1^{min} than the terminal deuteride (by a factor of 12.3 and 6.7, respectively). Therefore fast motion (>>61 MHz) must be influencing the relaxation of the D_2 ligands. The quadrupole coupling constant for the terminal deuteride is calculated by use of eq. [4] with $\eta = 0$ to be 79 kHz for **1** and 81 kHz for **2**, while motion-averaged C_Q^{eff} for the η^2-D_2 ligands in **1** and **2** could range from 19 ($\eta = 1$) to 22 ($\eta = 0$) and from 27 ($\eta = 1$) to 31 ($\eta = 0$) kHz, respectively. If D—D bonding were to dominate q_{zz} then the angle Δ would be 90° and the correction factor $(1/A)^{1/2} = 2$. In this case $C_Q = 2C_Q^{eff}$ = 44 and 62 for **1** and **2**, respectively with $\eta = 0$. These are the minimum possible values of C_Q for the complexes, but they seem unlikely because they are smaller than the coupling constant of a terminal deuteride. The actual C_Q for the deuterons in these ligands with short D—D distances (<1 Å) should probably be greater than that of the terminal deuteride but less than that of D_2(g), 227 kHz. Since it is known that the hydrogen analogues of **1** and **2** have rapidly spinning (>>400 MHz) H_2 ligands it is reasonable to use to eq. [6] to account for the motion-reduction of the C_Q value. Therefore the multiplying factor $(1/A)^{1/2}$ should likely be between 79/21 and 227/21 for C_Q of the D in the D_2 ligand in **1**. By use of Fig. 4 this corresponds to two possible ranges of angles Δ: either between 59° and 66° or 45° and 51°. Similarly for **2**, the factor $(1/A)^{1/2}$ falls between 81/30 and 227/30 and the angle ranges are 61°–71° or 40°–49°. If M—D bonding were to dominate then the angle would be half of the DMD bond angle (15° for **1** and 16° for **2**, see Table 2). Therefore, neither D—D nor M—D bonding dominates the electric field gradient direction as shown in Fig. 1. Complex **1** has more D-D character than complex **2** on the basis of longer M—H distances and a shorter H—H distance (Table 2). Also, the unexpectedly weak acidity of **1** and **2** implies the presence of a strong H—H bond (40). One might

[3] For example the ^{1}H T_1^{min} at 400 MHz of the H_2 ligand of $[Ru(H)(H_2)(dppe)_2]BPh_4$ in a concentrated CD_2Cl_2 solution (150 mg/1 mL) occurs at 273 K, while a dilute solution occurs at 40° lower. Both determinations give the same value of T_1 = 20 (± 2) ms.

© 1999 NRC Canada

expect **1** to have the larger C_Q and Δ values, but the uncertainties in the values are too large to make a conclusion.

Complex **3a** that contains an elongated 1.1 Å D···D ligand has an effective quadrupole coupling constant (66 kHz with $\eta = 0$) of magnitude near to that of the terminal Ru—D bonds in **3b** and **1** (71–79 kHz). The D···D ligand in **3a** may be "static" compared to the 61.4 MHz ^{2}H spectrometer frequency, considering that the H···H ligand in [Ru(H···H)Cp*(dppm)]BF_4 has no internal motion that influences T_1(H) relative to the ca. 400 MHz frequency of molecular tumbling (17). Therefore, the C_Q^{eff} value suggests that the bond has mainly Ru-D character and that **3a**-(H···H) is a "compressed dihydride." This interpretation is supported by the fact that the pK_a of this complex is also dihydride-like (40). On the other hand, the T_1(H) studies would not have detected a pure 180° flip of the H_2 ligand, since the dipolar relaxation vector is colinear with this motion. If such a rapid twofold reorientation of the D_2 ligand is occurring, then the static C_Q value for **3a** might be much larger than 66 kHz. The one solid-state spectrum of **3a** has features of such a motion. Also we have evidence that D···D distances of 1.0–1.1 Å should give C_Q >100 kHz on the basis of the work with **4** and **7**.

Complexes **4**–**6** have small C_Q^{eff} values, which are also likely to be motion-averaged values. This is certainly true for **4** where C_Q^{eff} is about 40 kHz while the static C_Q is 107. T_1 studies of their hydrogen analogues suggest that in all of these complexes the H_2 ligands reorient with frequencies comparable or greater than 400 MHz (7). The nature of the motion is unknown but could involve wide angle libration or hopping between fourfold sites of unequal population (7). One feature of the T_1^{min} value of complex **6** is that it occurs at a temperature that is 20° higher than those of the other complexes of Table 2. This is consistent with the larger size and correlation time of this dimeric molecule.

Conclusions

A range of dideuterium complexes **1**–**7** that are suitable for study by solid and solution ^{2}H NMR spectroscopy has been prepared by different synthetic routes. The great difference in relaxation time between the terminal deuteride and dideuterium ligands in complexes **1** and **2** clearly demonstrates that internal motion of the η^2-D_2 ligand is rapid and that the major component of the electric field gradient is not directed along the D–D vector but is instead probably tilted toward the metal. A range of possible tilt angles can be estimated by use of eq. [6] to solve for the factor *A*. These angles indicate that there is a major concentration of electron density at the center of the MD_2 triangle for these complexes with H—H distances of less than one Å. The T_1^{min} values of the terminal deuterium ligands in **1** and **2** lead to reasonable Ru-D and Os-D C_Q values of 79 and 81 kHz, respectively. The elongated dideuterium complex **3a** has C_Q^{eff} = 66 kHz, similar to the C_Q of its dideuteride tautomer (**3b**) according to the T_1^{min} measurements on solutions. The D···D ligand in **3a** might be "static" compared to the 61.4 MHz ^{2}H spectrometer frequency. In this case the C_Q^{eff} value results from the Ru-D character and therefore **3a**-(H···H) is a "compressed dihydride." A more likely possibility is that the D_2 ligand undergoes rapid 180° flips even at 143 K so that a large static C_Q > 100 kHz is motion-averaged to C_Q^{eff} = 66 kHz. The complexes **4**–**6** also have motion-reduced C_Q values.

The ^{2}H NMR quadrupole echo wide-line spectra of **1**, **4**, and **7** also indicate that the C_Q of the D in the D_2 ligands in these complexes are motion-reduced in the solid state at room temperature. The estimates for the static C_Q of 107 kHz for **4** and 120–167 kHz for **7** are the first such determinations for dideuterium complexes. The determination of the barrier to twofold orientation of the D_2 ligand of 19.7 kJ/mol for **7** is the first such determination by a method other than inelastic neutron scattering (INS). The D NMR method is an attractive method of obtaining such information because the amount of sample required is much less than INS (0.1–0.2 g vs. 1–2 g) and more accessible equipment is available. However, it is likely that these two methods will be complementary, with the INS providing barriers for sample when less than 10 kJ/mol, while D NMR, when greater than 10 kJ/mol.

The first MAS D NMR spectrum has been recorded of a D_2 complex. The first evidence has been provided for an incompletely averaged D–D dipolar interaction.

Acknowledgments

We thank Prof. B.R. James for providing the precursor to complex **6**, Dr. G. Kubas for sending the spectrum of $W(D_2)(CO)_3(P^iPr_3)_2$, Nick Plavac for some solution D NMR spectra, and Prof. R. Hembre for details on the synthesis of **3**. We thank Dr H. Grondey, Dr. G. Buntkowsky, and Prof. H.-H. Limbach for useful suggestions. This research was supported by a grant to R.H.M. and a postdoctoral fellowship to W.X. from the Natural Sciences and Engineering Research Council of Canada (NSERC) and by a loan of platinum metals from Johnson–Matthey.

References

1. G.J. Kubas. Acc. Chem. Res. **21**, 120 (1988).
2. D.G. Hamilton and R.H. Crabtree. J. Am. Chem. Soc. **110**, 4126 (1988).
3. P.G. Jessop and R.H. Morris. Coord. Chem. Rev. **121**, 155 (1992).
4. D.M. Heinekey and W.J.J. Oldham. Chem. Rev. **93**, 913 (1993).
5. H.H. Limbach, S. Ulrich, S. Grundemann, G. Buntkowsky, S. Saboetienne, B. Chaudret, G.J. Kubas, and J. Eckert. J. Am. Chem. Soc. **120**, 7929 (1998).
6. V. Rodriguez, S. Sabo-Etienne, B. Chaudret, J. Thoburn, S. Ulrich, H.H. Limbach, J. Eckert, J.C. Barthelat, K. Hussein, and C.J. Marsden. Inorg. Chem. **37**, 3475 (1998).
7. R.H. Morris and R.J. Wittebort. Magn. Res. Chem. **35**, 243 (1997).
8. L.G. Butler and E.A. Keiter. J. Coord. Chem. **32**, 121 (1994).
9. G.J. Kubas, C.J. Unkefer, B.I. Swanson, and E. Fukushima. J. Am. Chem. Soc. **108**, 7000 (1986).
10. K. Guo, W.L. Jarrett, and L.G. Butler. Inorg. Chem. **26**, 3001 (1987).
11. V.I. Bakhmutov, J. Bertran, M.A. Esteruelas, A. Lledos, F. Maseras, J. Modrego, L.A. Oro, and E. Sola. Chem. Eur. J. **2**, 815 (1996).
12. V.I. Bakhmutov and V.E.V. Rev. Inorg. Chem. **18**, 183 (1998).

© 1999 NRC Canada

13. D. Nietlispach, V.I. Bakhmutov, and H. Berke. J. Am. Chem. Soc. **115**, 9191 (1993).
14. K.A. Earl, G. Jia, P.A. Maltby, and R.H. Morris. J. Am. Chem. Soc. **113**, 3027 (1991).
15. M.T. Bautista, K.A. Earl, P.A. Maltby, R.H. Morris, C.T. Schweitzer, and A. Sella. J. Am. Chem. Soc. **110**, 7031 (1988).
16. M.T. Bautista, E.P. Cappellani, S.D. Drouin, R.H. Morris, C.T. Schweitzer, A. Sella, and J. Zubkowski. J. Am. Chem. Soc. **113**, 4876 (1991).
17. W.T. Klooster, T.F. Koetzle, G. Jia, T.P. Fong, R.H. Morris, and A. Albinati. J. Am. Chem. Soc. **116**, 7677 (1994).
18. P.A. Maltby, M. Schlaf, M. Steinbeck, A.J. Lough, R.H. Morris, W.T. Klooster, T.F. Koetzle, and R.C. Srivastava. J. Am. Chem. Soc. **118**, 5396 (1996).
19. A. Albinati, W. Klooster, T.F. Koetzle, J.B. Fortin, J.S. Ricci, J. Eckert, T.P. Fong, A.J. Lough, R.H. Morris, and A. Golombek. Inorg. Chim. Acta, **259**, 351 (1997).
20. G. Buntkowsky, F. Wehrmann, T.P. Fong, R.H. Morris, and H.-H. Limbach. Phys. Chem. Chem. Phys. **1**, 4033 (1999).
21. A.M. Joshi and B.R. James. J. Chem. Soc. Chem. Commun. 1785 (1989).
22. M. Esteruelas, F.J. Lahoz, E. Onate, L.A. Oro, C. Valero, and B. Zeier. J. Am. Chem. Soc. **117**, 7935 (1995).
23. N.S. Hush. J. Am. Chem. Soc. **119**, 1717 (1997).
24. R.H. Morris. *In* Transition metal sulphides. Chemistry and catalysis. *Edited by* T. Weber, R. Prins, and R.A. van Santen. Kluwer Acad. Pub., London. 1998. pp. 57–89.
25. T.Y. Bartucz, A. Golombek, A.J. Lough, P.A. Maltby, R.H. Morris, R. Ramachandran, and M. Schlaf. Inorg. Chem. **37**, 1552 (1998).
26. G. Jia, A.J. Lough, and R.H. Morris. Organometallics, **11**, 161 (1992).
27. B. Chin, A.J. Lough, R.H. Morris, C.T. Schweitzer, and C. Dagostino. Inorg. Chem. **33**, 6278 (1994).
28. J.H. Davis, K.R. Jeffrey, M. Bloom, M.I. Valic, and T.P. Higgs. Chem. Phys. Lett. **42**, 390 (1976).
29. D.E. Woessner. J Chem. Phys. **36**, 1 (1962).
30. D.E. Woessner. J. Chem. Phys. **37**, 647 (1962).
31. M. Ogasawara and M. Saburi. Organometallics, **13**, 1911 (1994).
32. E.P. Cappellani, P.A. Maltby, R.H. Morris, C.T. Schweitzer, and M.R. Steele. Inorg. Chem. **28**, 4437 (1989).
33. R.T. Hembre and S. McQueen. J. Am. Chem. Soc. **116**, 2141 (1994).
34. G. Jia and R.H. Morris. J. Am. Chem. Soc. **113**, 875 (1991).
35. R.K. Harris and A.C. Olivieri. Prog. NMR Spectr. **24**, 435(1992).
36. G. Buntkowsky, H.H. Limbach, F. Wehrmann, I. Sack, H.M. Vieth, and R.H. Morris. J. Phys. Chem. A, **101**, 4679 (1997).
37. M.S. Greenfield, A.D. Ronemus, R.L. Vold, R.R. Vold, P.D. Ellis, and T.E. Raidy. J. Magn. Reson. **72**, 89 (1987).
38. N. Bloembergen, E.M. Purcell, and R.V. Pound. Phys. Rev. **73**, 679 (1948).
39. J. Eckert and G.J. Kubas. J. Phys. Chem. **97**, 2378 (1993).
40. E.P. Cappellani, S.D. Drouin, G. Jia, P.A. Maltby, R.H. Morris, and C.T. Schweitzer. J. Am. Chem. Soc. **116**, 3375 (1994).

© 1999 NRC Canada

Symmetry, disorder, and dynamics in solid crown ether complexes: ^{2}H NMR studies of 15-crown-5·NaI, 15-crown-5·$NaClO_4$, and 21-crown-7·KI

G.W. Buchanan, M. Gerzain, and C.I. Ratcliffe

Abstract: ^{2}H NMR line shapes have been obtained as a function of temperature for partially deuteriated 15-crown-5·NaI, 15-crown-5·$NaClO_4$ and 21-crown-7·KI. Sudden changes in the line shapes above 330 K correspond to phase transitions: DSC shows transitions at 338, 347 K for 15-crown-5·NaI, and 356, 374, 383 K for 15-crown-5·$NaClO_4$. The ^{2}H NMR line shapes for the room temperature (RT) phases show the onset of a motion of the macrocycles above 200K, which is rapid a little above room temperature. Through detailed analysis of the complicated line shapes it has been shown that the most consistent interpretation of the dynamics in these RT phases is a "merry-go-round" type of motion similar to that found for 18-crown-6 and 12-crown-4 complexes in which O-CH_2-CH_2 units exchange sites around the ring, simultaneously adjusting their conformation to fit the site. In the high-temperature phases of all three complexes all the ring atoms are dynamically equivalent. This can only happen through a combination of increased symmetry and disorder for which possible models have been devised.

Key words: ^{2}H NMR, crown ether complexes, dynamics, disorder.

Résumé : On a déterminé les formes des bandes des spectres RMN du ^{2}H en fonction de la température pour des 15-couronne-5·NaI, 15-couronne-5·$NaClO_4$ et 21-couronne-7·KI partiellement deutérées. Les changements brusques qui se produisent dans les formes des bandes au-dessus de 330 K correspondent à des transitions de phases: l'analyse calorimétrique différentielle met en évidence la présence de transitions à 338 et 347 K pour la 15-couronne-5·NaI et à 356, 374 et 383 K pour la 15-couronne-5·$NaClO_4$. Les formes des bandes des spectres RMN du ^{2}H pour les phases qui existent à la température ambiante mettent en évidence la mise en route d'un mouvement des macrocycles au-dessus de 200 K et celui-ci devient rapide au-dessus de la température ambiante. Une analyse détaillée des formes de bandes compliquées, a permis de suggérer que l'interprétation la plus appropriée pour la rythmique des ces phases implique un mouvement de type carrousel semblable à celui observé avec les complexes des 18-couronne-6 et 12-couronne-4 dans lequel les unités O-CH_2-CH_2 changent de sites autour du cycle, avec un ajustement simultané de leur conformation pour équilibrer le site. Dans les phases à températures élevées, tous les atomes cycliques des trois complexes sont dynamiquement équivalents. Ceci ne peut se réaliser que par la combinaison d'une augmentation de la symétrie et du désordre pour lesquels on a développé divers modèles possibles.

Mots clés : RMN du ^{2}H, complexes d'éthers couronnes, dynamique, désordre.

[Traduit par la Rédaction]

Introduction

Complexes of crown ethers and their derivatives are widely recognised as simple model systems for molecular recognition (for reviews see refs. 1, 2). The great flexibility of many of the crowns means that they can adapt their conformation to achieve optimum complexation of a guest atom or molecule via their O atoms, Fig. 1.

Very many crystal structures of such complexes have been determined and the fact that the atoms are usually located at specific sites may give the impression that in their crystalline complexes the macrocycles are static. In fact, in recent studies of molecular complexes of 18-crown-6 and 12-crown-4 it has become apparent that in the solid state these macrocycles have considerable motional freedom. From ^{13}C CP/MAS, ^{1}H, and ^{2}H NMR studies, evidence was found that 18-crown-6 invariably undergoes a large amplitude motion in the neighbourhood of room temperature (3–5). For the malononitrile

Received August 19, 1999.

This paper is dedicated to Professor Ted Schaefer in recognition of his outstanding contributions to Canadian chemistry.

G.W. Buchanan and M. Gerzain.[1] Ottawa–Carleton Chemistry Institute, Department of Chemistry, Carleton University, 1125 Colonel By Drive, Ottawa, ON K1S 5B6, Canada.
C.I. Ratcliffe.[2] Steacie Institute for Molecular Sciences, National Research Council, 100 Sussex Drive, Ottawa, ON K1A 0R6, Canada.

[1]Present address: Patent Division, ECM, Munich, Germany.
[2]Author to whom correspondence may be addressed.
Telephone: (613) 991-1240. Fax: (613) 954-5242.
e-mail: cir@ned1.sims.nrc.ca

© 1999 NRC Canada

Fig. 1. A 15-crown-5·Na^+ complex showing the Na^+ coordinated by the O atoms of the five -O-CH_2-CH_2- units that constitute the macrocycle.

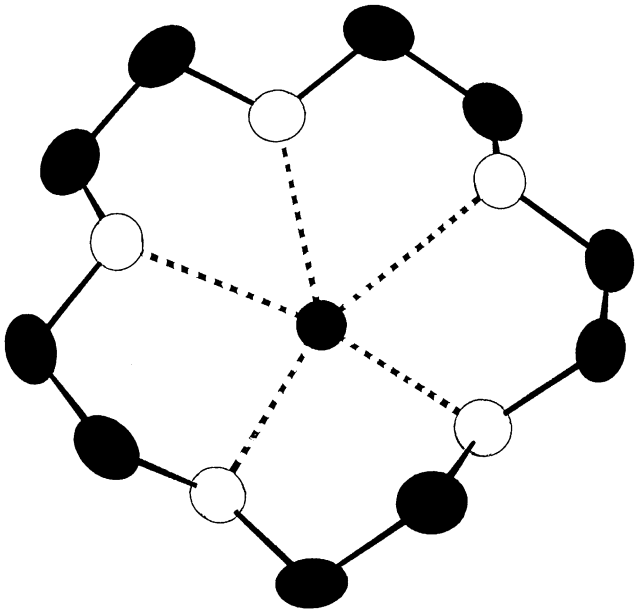

complex 18-crown-6·2$CH_2(CN)_2$, in which the macrocycle adopts a pseudo-D_{3d} conformation, it was demonstrated by means of ^{2}H NMR that the whole ring rotates within itself with an activation energy of 47.6 kJ/mol. (5). Each -O-CH_2-CH_2- unit visits six sites around the ring, simultaneously adjusting its conformation to suit each crystallographic site being visited. The motion resembles that of a "merry-go-round," as each C atom moves up or down on either side of the plane of the ring as it goes from site to site, and is essentially invisible in X-ray diffraction studies. The solid complex of 12-crown-4·LiNCS also shows a similar kind of motion, but complicated by a 50:50 disorder in the C atom positions, which gives rise to a concomitant up-down flip motion as the carbons jump between the disordered sites independently of the rotation of the ring (6). Effects of the ring dynamics on the ^{23}Na and ^{133}Cs NMR spin-lattice relaxation times in Cs^+(18-crown-6)$_2Na^-$ and Cs^+(15-crown-5)$_2Na^-$ have also been reported (7) from which activation energies of 31.2 and 35.4 kJ/mol. respectively were determined.

The current paper extends ^{2}H NMR studies to the complexes 15-crown-5·NaI, 15-crown-5·$NaClO_4$, and 21-crown-7·KI, which have odd numbers of -O-CH_2-CH_2- units, with a view to determining whether merry-go-round (m-g-r) dynamics is a general feature of all unsubstituted crown ether complexes.

Experimental

Synthesis

The partially deuteriated materials 15-crown-5-d_8·NaI, 15-crown-5-d_4·$NaClO_4$, and 21-crown-7-d_{12}·KI were synthesised as outlined in Scheme 1. The preparations followed literature precedents for 15-crown-5 (8–13) and 21-crown-7 (14).

Solid-state NMR

^{2}H NMR powder spectra were recorded on a Bruker AMX 300 spectrometer at 46.05 MHz as a function of temperature by using a variable temperature N_2 gas-flow probe (5 mm sample) with a Eurotherm temperature controller. A phase alternated quadrupole echo pulse sequence (15) was used with a delay time of 35 μs between X and Y pulses of 2.6–3.0 μs duration. Variable temperature ^{13}C CP/MAS NMR spectra were obtained at 45.26 MHz on a Bruker CXP-180 spectrometer using a Doty Scientific Inc. 7mm VT Probe (spin rates 3–4kHz).

Differential scanning calorimetry

DSC was performed using a Seiko SSC5200 instrument with a heating rate of 10° per minute from 273–373 K, with a nitrogen flow rate of 50 mL per minute.

^{2}H NMR background

The following provides a short description of the underlying principles of ^{2}H NMR line-shape analysis. All the basic theory has been described in detail elsewhere (16–21), and we will follow the same treatment as before (5). Briefly, ^{2}H (spin $I = 1$) NMR in solids is dominated by a perturbation of the Zeeman interaction by the quadrupole coupling tensor, which itself arises from the interaction of the nuclear quadrupole moment (Q) with the electric field gradient (eq) around the nucleus. The ^{2}H powder line shape, which is a summation of resonance line pairs for a distribution over all crystallite orientations, has either two or three pairs of characteristic features (edges, shoulders and peaks) separated by frequencies

$$\Delta\upsilon_{zz} = 3\chi/2$$

$$\Delta\upsilon_{yy} = 3\chi(1 + \eta)/4 \quad [1]$$

$$\Delta\upsilon_{xx} = 3\chi(1 - \eta)/4$$

where χ is the quadrupole coupling constant = e^2qQ/h in Hz and the asymmetry parameter $\eta = (\Delta\upsilon_{yy} - \Delta\upsilon_{xx})/\Delta\upsilon_{zz}$. The $\Delta\upsilon_{ii}$ are proportional to the principal axis components of the effective quadrupole coupling tensor, but information regarding signs of these is lost.

Molecular motion at sufficiently high rates can cause changes in the ^{2}H NMR line shape. Differing degrees of line shape averaging are observed depending on the rate of reorientation and the orientations of the principal axes of the e.f.g. tensor relative to the rotation axis. In the fast motion limit (f.m.l.) at reorientation rates about 10^7 jumps/s or faster, analytical expressions for the line shapes are relatively easy to obtain (17, 18, 21). The orientation of the tensor must first be described in a final reference frame in terms of the Euler angles

$$V(\alpha, \beta, \gamma) = RV_{pas}R^{-1} \quad [2]$$

where R is the Euler angle rotation matrix describing the coordinate transformation and V_{pas} is the tensor in its principal axis system. The fast motion line shape is then given by an effective tensor, which is the population weighted average of the tensor components in the final frame for all the sites (orientations) visited during the motion.

© 1999 NRC Canada

Scheme 1.

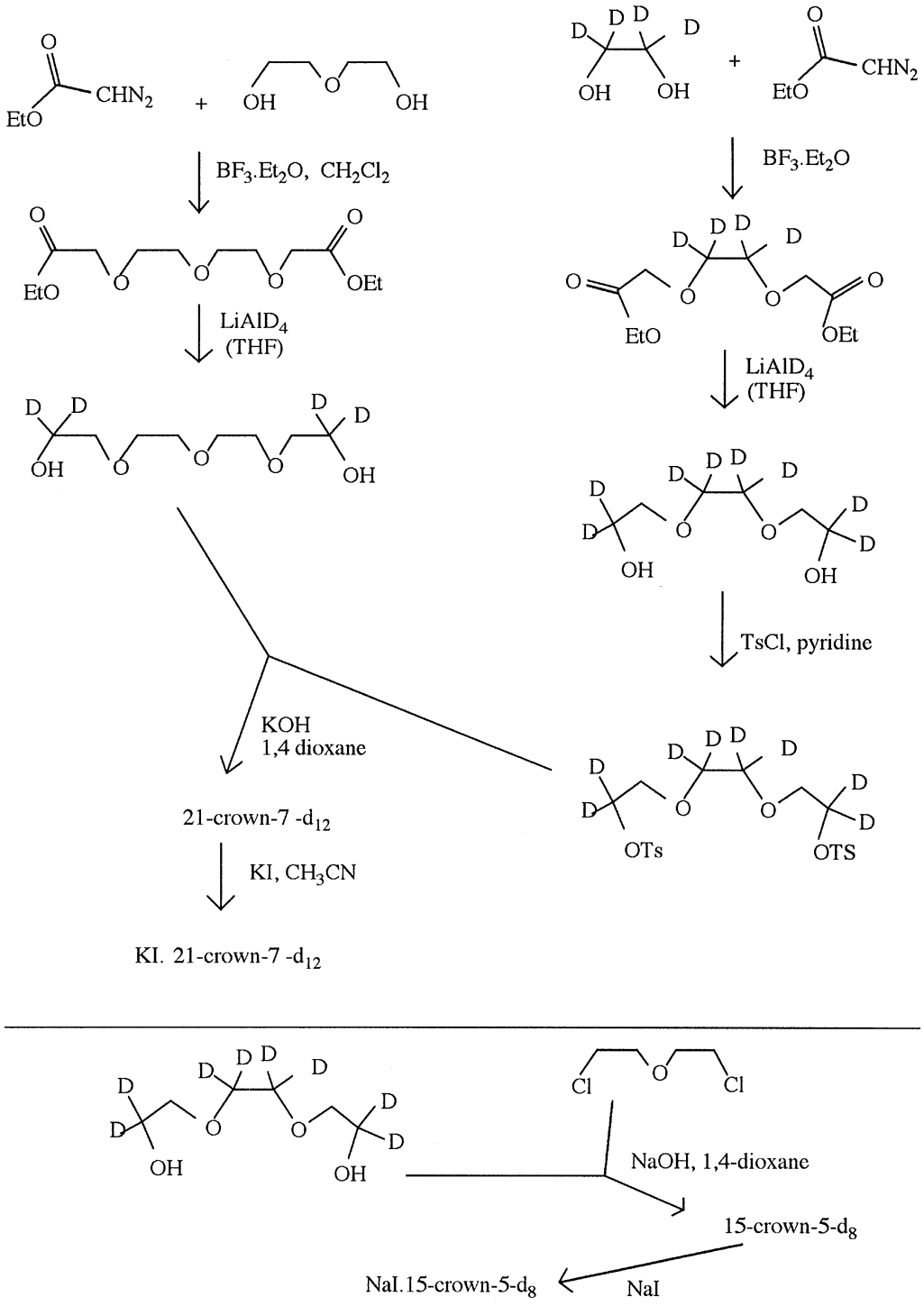

[3] $V_{eff} = \Sigma_{i=1,n} V_i(\alpha, \beta, \gamma) p_i / \Sigma_{i=1,n} p_i$

where p_i is the population factor of site i.

Intermediate rate line shapes depend on the specific rate of motion and the experimental details (e.g., on the echo delay time), and have to be calculated numerically. Methods for doing this are well established (17–20). Calculations were performed using a much modified version of an algorithm originally due to Vega and Luz (20).

Results and discussion

DSC results

It was immediately apparent from inspection of the ^2H NMR line shapes that all three complexes showed at least one phase transition (characterized by a sudden change in the line shape with temperature), and possibly more (suggested by more subtle but unexpected changes in line shape). DSC scans on the 15-crown-5 complexes, Fig. 2, indeed

© 1999 NRC Canada

confirmed the sharp transitions and located others: 15-crown-5·NaI has 2 transitions peaking at 338 K (onset ~302 K) and 347 K; 15-crown-5·$NaClO_4$ has three transitions peaking at ~356, 374, and 383 K.

^{13}C NMR spectra

The ^{13}C CP/MAS NMR spectra of 15-crown-5·NaI were examined between 210–330 K. There is a single isotropic resonance over this range with no spinning sidebands (chemical shift 70.1 ppm at room temperature). A dramatic line-broadening occurs as the temperature decreases; halfwidths were 12 Hz at 330 K and 230 Hz at 210 K. This behaviour is characteristic of the fade-out effect seen previously for 18-crown-6 complexes (4), and is explained by interference of the incoherent averaging processes caused by dynamics of the macrocycle with the coherent averaging effects of the ^{1}H decoupling, as first described by Rothwell and Waugh (22).

^{2}H NMR spectra

The ^{2}H NMR spectra of 15-crown-5·NaI, 15-crown-5·$NaClO_4$ and 21-crown-7·KI as a function of temperature are shown in Figs. 3, 4, 5 and the widths of the numerous measurable line-shape features (peaks, edges) are plotted in Figs. 6, 7, 8 respectively. All three complexes show sharp isotropic lines in the centre of the spectra at temperatures above about 250 K, which are interpreted as solution spectra arising from traces of occluded solvent. The room temperature phases of all three complexes appear to be stable at least down to the temperatures where essentially static limit line shapes are observed; at 238, 225, and 206 K, respectively. These static line-shape parameters are given in Table 1. Also included in Table 1 for comparison are the values for the 18-crown-6·$2CH_2(CN)_2$ complex (5). As the temperature increases, all show pronounced changes in line shape and intensity, which are consistent with intermediate rate dynamics, and line shapes corresponding to the fast motion limit are achieved a little above room temperature (by about 327, 306, and 302 K, respectively). These f.m.l. line shapes are very complicated, showing numerous identifiable features that must arise from several overlapping powder patterns. The development of the intermediate rate and the f.m.l. line-shape patterns are very similar for the two 15-crown-5 complexes, though the changes for the NaI complex are offset by about 20° to higher temperature than in the $NaClO_4$ complex.

In all three cases there are sharp changes in line shape due to phase transitions: 15-crown-5·NaI between 337–345 K (cf. 338 K, DSC); 15-crown-5·$NaClO_4$ at 374 K (cf. 374 K, DSC); 21-crown-7·KI at 338 K. Above these transitions the line shapes for both 15-crown-5 complexes are axially symmetric, whereas that for the 21-crown-7 complex has a large asymmetry parameter (parameters in Table 1). More significantly these high-temperature line shapes represent a single tensor indicating that all the deuteriums have become dynamically equivalent! There is no significant further change in the line shapes for the 15-crown-5 complexes even on passing through the next higher phase transitions at 347 (15-crown-5·NaI) and 383 K (15-crown-5·$NaClO_4$).

Hysteresis is observed in 15-crown-5·NaI, which, on cooling, shows the high-temperature line shape down to 322 K (and down to 312 K in the presence of the room temperature phase), and similarly for 15-crown-5·$NaClO_4$ down to 369 K. 21-crown-7·KI shows mixed phases on cooling below 338 K and slowly transforms at 335 K.

Fig. 2. DSC scans for (top) 15-crown-5·NaI and (bottom) 15-crown-5·$NaClO_4$. Repeat scans for the latter (offset scales) are also shown (dashed and dotted curves).

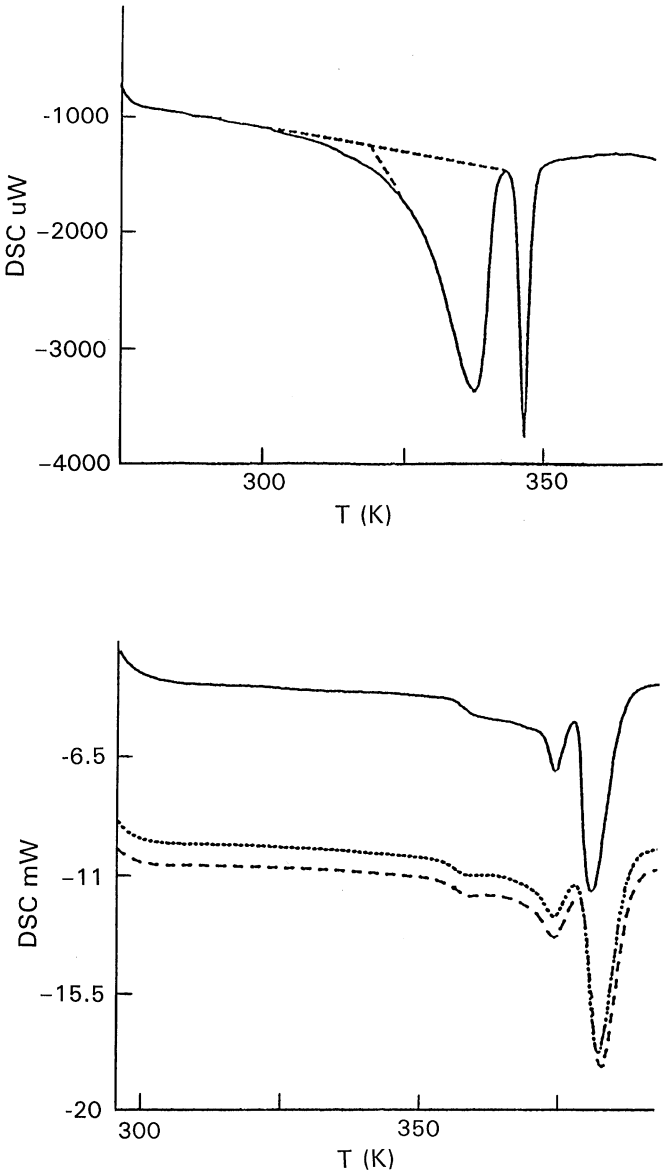

15-Crown-5·$NaClO_4$ also shows subtle changes in the line shapes in the region of 348–359 K (best seen in the feature width versus temperature plot, Fig.7), which can be associated with the 356 K phase transition.

The line shapes for 15-crown-5·$NaClO_4$ and 21-crown-7CKI also display a significant temperature dependence of the feature widths in the intermediate temperature region between room temperature and the HT phase transitions, Figs. 7, 8.

Analysis and model

With the knowledge of the components of the static quadrupole coupling tensors it now remains to find dynamic

© 1999 NRC Canada

Fig. 3. ^{2}H NMR line shapes as a function of temperature for 15-crown-5·NaI. The spectrum at 317 K (bottom right) was obtained after cooling from the HT phase and shows signals from both the room temperature and HT phases.

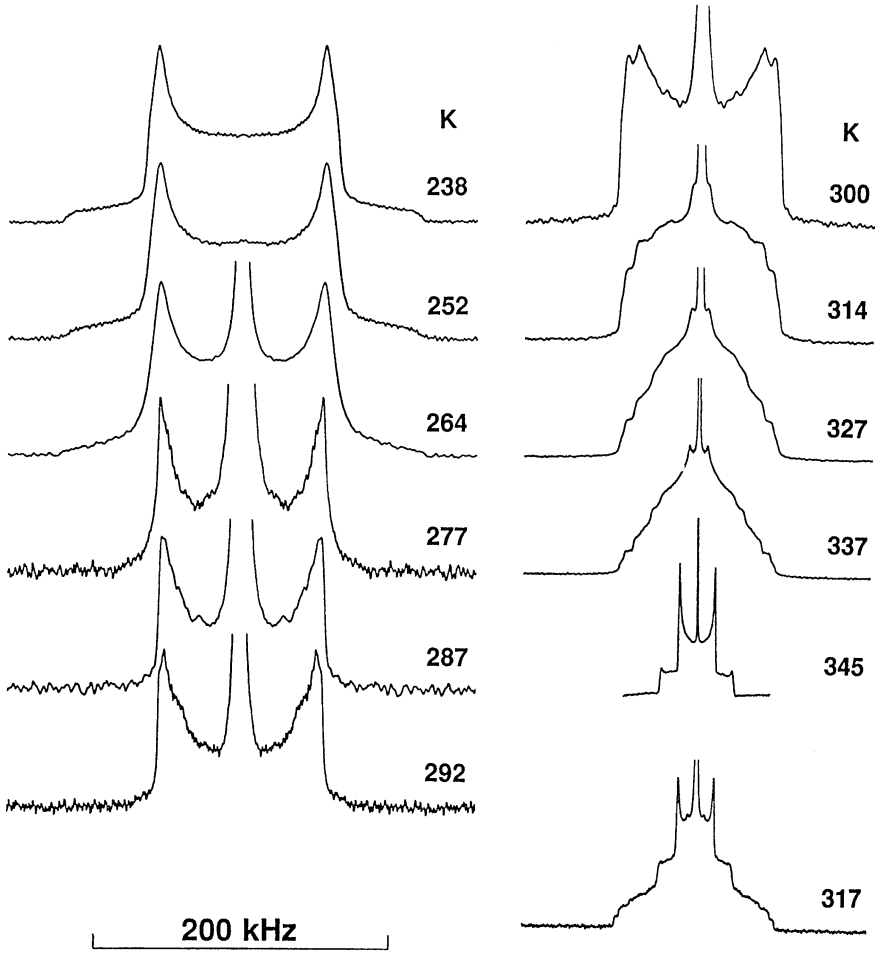

Table 1. Summary of ^{2}H NMR line-shape parameters for the RT phases (static limit) and HT phases (f.m.l.) of 15-crown-5·NaI, 15-crown-5·$NaClO_4$, and 21-crown-7·KI.

	T (K)	Dynamic state	Feature width (kHz)			χ (kHz)	η
			$\Delta\upsilon_{xx}$	$\Delta\upsilon_{yy}$	$\Delta\upsilon_{zz}$		
15-crown-5·NaI	238	Static	112.6	130.4	243.0	162.0	0.073
	345	f.m.l.	25.3	25.3	50.6	33.7	0
	359	f.m.l.	25.0	25.0	50.0	33.3	0
15-crown-5·$NaClO_4$	225	Static	112.0	129.5	241.5	161.0	0.073
	375	f.m.l.	27.4	27.4	54.8	36.5	0
	400	f.m.l.	26.8	26.8	53.6	35.7	0
21-crown-7·KI	206	Static	113.0	131.0	244.0	162.7	0.074
	340	f.m.l.	3.5	29.5	33.0	22.0	0.788
	407	f.m.l.	2.0	26.0	28.0	18.7	0.857
18-crown-6·2$CH_2(CN)_2$	198	Static	114.3	131.8	246.1	164.1	0.071
Ref. 5	373	f.m.l.	34.8	34.8	69.6	46.4	0

models, which give averaged line shapes consistent with the experimental data. Our analysis will focus largely on (*a*) the room temperature (RT) phases and (*b*) the high-temperature (HT) phases where the ^{2}H NMR line shape has simplified to a single component. It is not possible to extract much useful information from the spectra in the short temperature regions corresponding to the intermediate phases of 15-crown-5·$NaClO_4$, though one might expect the dynamics to be intermediate between those of the RT and HT phases.

Room temperature phases

The X-ray diffraction structures are known for both 15-crown-5·NaI at 193 K (23) and 15-crown-5·$NaClO_4$ at room temperature (24). The ring conformation in both structures

© 1999 NRC Canada

Fig. 4. ^{2}H NMR line shapes as a function of temperature for 15-crown-5·$NaClO_4$.

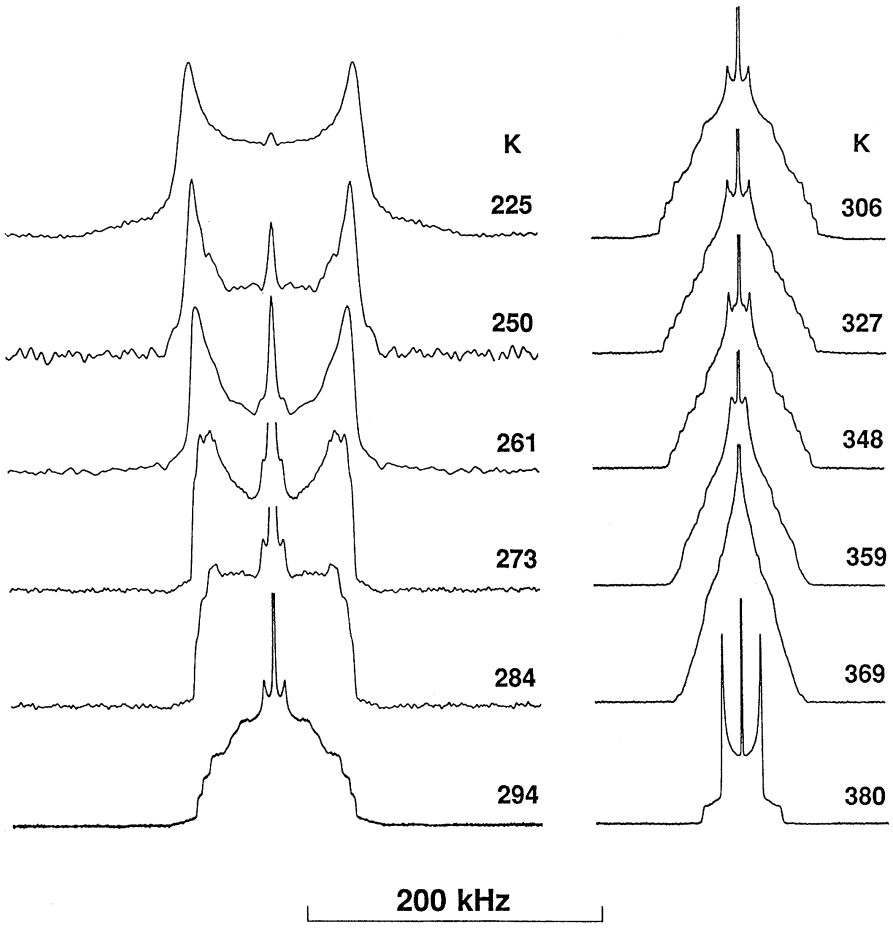

Fig. 5. ^{2}H NMR line shapes as a function of temperature for 21-crown-7·KI.

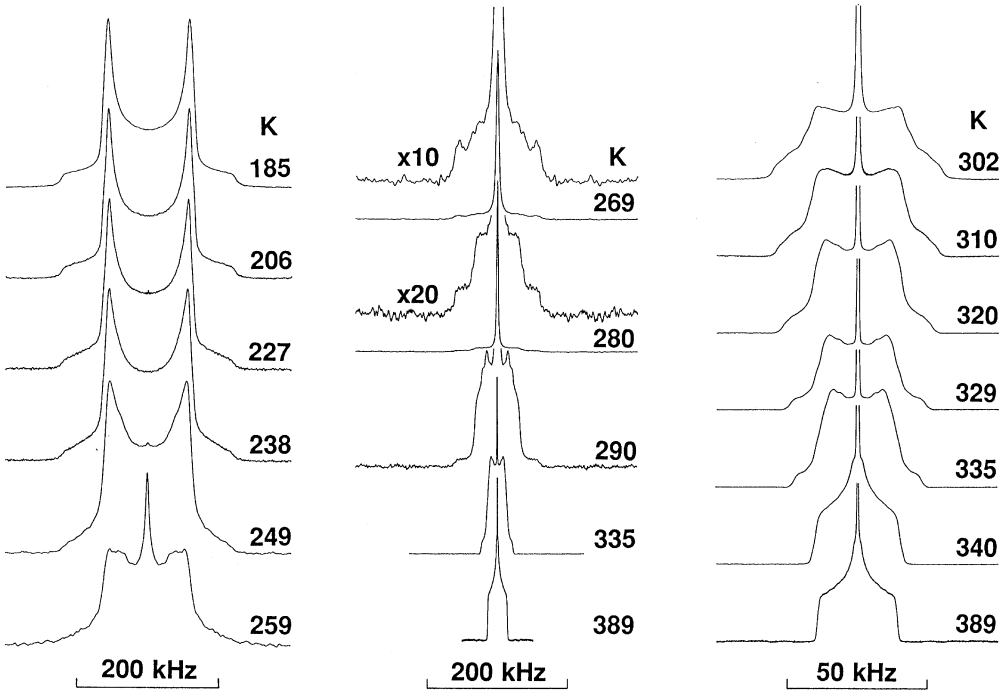

© 1999 NRC Canada

Fig. 6. Widths of the measureable features (shoulders, peaks) of the ^{2}H NMR line shapes as a function of temperature for 15-crown-5·NaI. The dotted connecting lines are a visual aid to indicate where there is an apparent continuity of the measured feature between one temperature and the next.

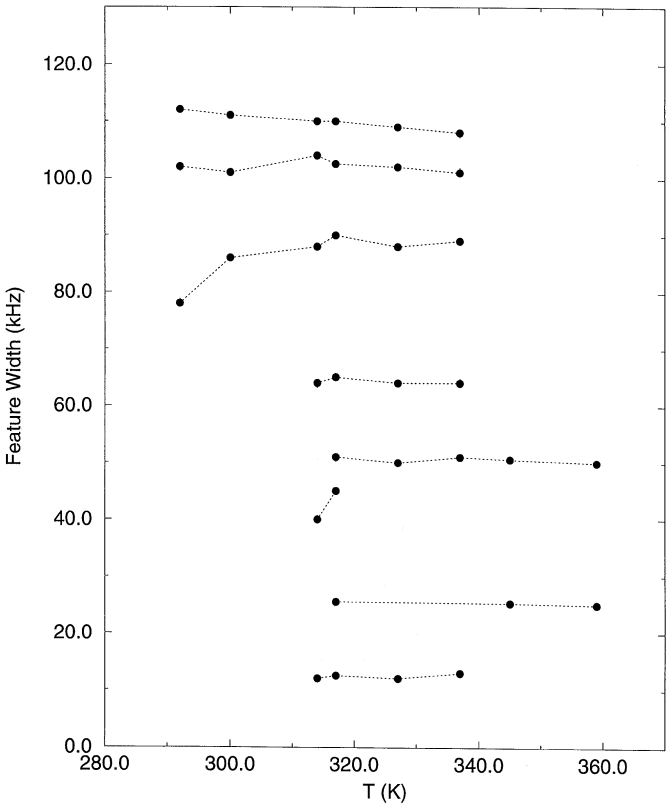

Fig. 7. Widths of the measureable features (shoulders, peaks) of the ^{2}H NMR line shapes as a function of temperature for 15-crown-5·$NaClO_4$. The dotted connecting lines are a visual aid to indicate where there is an apparent continuity of the measured feature between one temperature and the next.

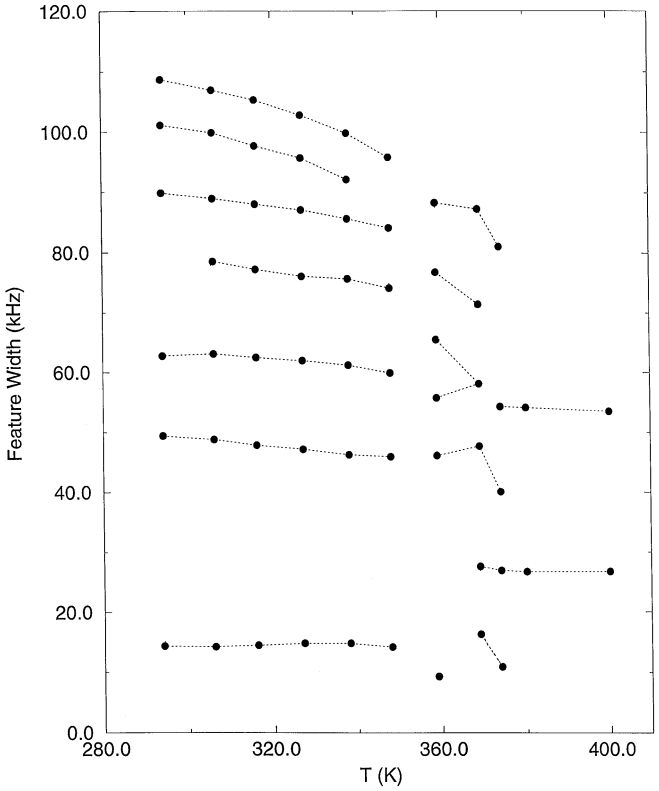

apparently corresponds to the one that is most commonly found for 15-crown-5·Na^+ complexes and which calculations also show to have the lowest energy (25). An important point to note from the start is that all the deuterons are involved in the dynamics, since there are no traces of the static ^{2}H line shape in the f.m.l. spectra.

Two dynamic models that might lead to the very complicated f.m.l. ^{2}H line shapes in the RT phases were considered:

(1) The first model has no ring reorientation but individual CD_2 groups undergoing up-down flips through different angles. There would therefore be 10 pairs of exchanging sites (note the two Ds on the same C must flip through the same angle), resulting in a superposition of 10 distinct averaged line shapes. However, this model was rejected on two counts: (*a*) The X-ray diffraction structures do not show any kind of disorder, which would be an implicit requirement for such a two-site flip, i.e., the CD_2 groups only have one site if the ring is not rotating; (*b*) if such up-down flips were to occur then, no matter what the flip angle between the two sites, the averaged line shapes should always have one component with a width roughly half of the static line shape's widest component (the XX component of the static tensor should be largely unaffected by the averaging, since it is known (5) to be perpendicular to the DCD plane). Consequently, considerable intensity should build at the position of this feature (width about 110–112 kHz). No such strong feature is observed, and in fact nearly all the line-shape components observed are narrower than this.

(2) The second model is the merry-go-round type of motion, and the following detailed analysis ultimately leads to the conclusion that this is the best model consistent with the experimental data. In the m-g-r motion each O-CD_2-CD_2 unit exchanges among all O-CD_2-CD_2 sites around the ring, changing its conformation to fit the site it currently sits on. However, because the four Ds within each unit cannot physically exchange with each other the ring reorientation always implies averaging of four independent sets of Ds giving four distinct averaged line shapes, i.e., there are four sets of 5D in 15-crown-5, or four sets of 7D in 21-crown-7. In both of the 15-crown-5 complexes studied the crystal symmetry of the RT phase is such that the four sets of exchanging Ds are inequivalent. Consequently the f.m.l. line shape could have up to 12 distinct pairs of features, though this number will likely be reduced because of overlaps.

Since the crystal structures are known for the two 15-crown-5 complexes it is possible to calculate the averaging effects of the m-g-r motion on the ^{2}H NMR line shapes for the specific geometries of the macrocycle, and thus verify if this model is consistent with the experimental results. This requires the orientations of the principal tensor components

© 1999 NRC Canada

Fig. 8. Widths of the measureable features (shoulders, peaks) of the ^{2}H NMR line shapes as a function of temperature for 21-crown-7·KI. The dotted connecting lines are a visual aid to indicate where there is an apparent continuity of the measured feature between one temperature and the next.

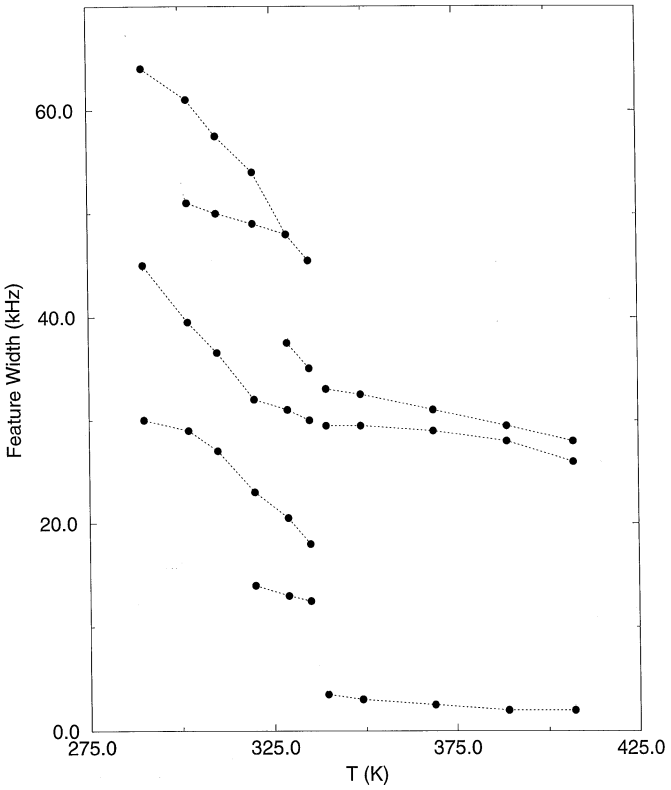

for all the D atom sites to be defined. In the case of C—D bonds the principal ZZ axis of the electric field gradient and quadrupole coupling tensors is, to a first approximation, oriented along the bond direction, and in the present case it can be assumed that the XX component of the tensor will be perpendicular to the CD_2 plane (a result of the 18-crown-6 analysis (5)). Unfortunately the exact orientation of the C—D bonds is not known because the diffraction does not permit good refinement of the H positions. However, based on the crystal structures of the two complexes, the orientations of all the C—D bonds were estimated by assuming a D-C-D angle of 100°, with the 2 D atoms in a plane at right angles to the O-C-C plane and equally displaced on either side of the OCC bisector. (In the 18-crown-6 analysis this was a successful approximation.) Euler angles were then calculated (for each D atom) to transform the ^{2}H quadrupole coupling tensors into the chosen reference frame, which was arbitrarily defined in the case of 15-crown-5C$NaClO_4$ by a mean plane containing the O atoms and the perpendicular to this plane as the *Z* axis, and in the case of 15-crown-5C·NaI the Na—-I axis was chosen as the *Z* axis.

Dynamic averaging via the merry-go-round motion was then calculated, using the observed low-temperature static ^{2}H NMR line-shape parameters for the starting tensor, for each of the four sets of 5 D sites. The averaged tensors were diagonalised to obtain the principal components for the f.m.l. powder line shape. The resulting numbers are given in

Table 2. Calculated averaged line-shape components (kHz) for 15-crown-5·NaI for the four sets of exchanging deuterons.[a]

Tensor	$\Delta\upsilon_{xx}$	$\Delta\upsilon_{yy}$	$\Delta\upsilon_{zz}$
1	12.9 (13)	89.1 (89)	102.0 (102)
2	0.2 (14)	60.8 (50)	61.0 (64)
3	9.1 (9)	101.4 (101)	110.5 (110)
4	5.2 (12)	99.2 (88)	104.4 (100)

[a]Based on crystal structure with <DCD = 100°. Values in parentheses are one set of adjusted values that produce a line shape that reasonably approximates the observed shape of the spectra at 327–337 K.

Table 3. Calculated averaged line-shape components (kHz) for 15-crown-5·$NaClO_4$ for the four sets of exchanging deuterons.[a]

Tensor	$\Delta\upsilon_{xx}$	$\Delta\upsilon_{yy}$	$\Delta\upsilon_{zz}$
1	6.0 (14)	60.8 (49)	66.8 (63)
2	5.4 (10.5)	84.0 (78.5)	89.4 (89)
3	1.8 (10.5)	75.0 (78.5)	76.8 (89)
4	16.0 (9)	104.0 (99)	120.0 (108)

[a]Based on crystal structure with <DCD = 100°. Values in parentheses are one set of adjusted values that produce a line shape that reasonably approximates the observed shape of the spectra at 306–348 K.

Fig. 9. Simulated fast motion limit line shapes for the merry-go-round motion in 15-crown-5·$NaClO_4$: (top) based on the crystallographic data with <DCD = 100°; (bottom) based on slightly modified averaged tensors.

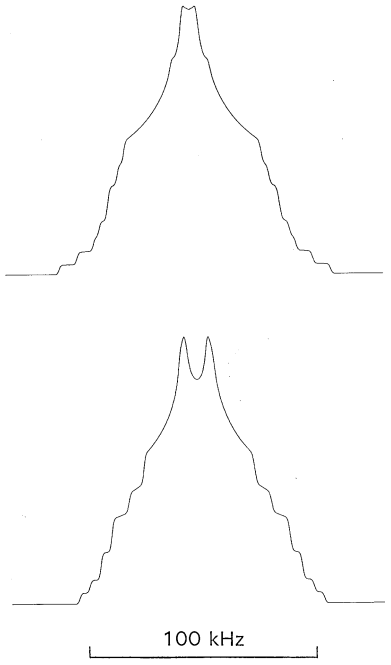

Tables 2, 3. The final calculated spectrum was then obtained by superimposing the four averaged line shapes, see Fig. 9, top, for 15-crown-5·$NaClO_4$.

The comparisons with the fast motion limit experimental spectra are very encouraging and, since we do not really expect that all the C—D bonds will have the orientations artificially defined by the <DCD = 100°, it is not too unreasonable to expect that small changes should bring the observed and calculated patterns into agreement. Indeed, in

© 1999 NRC Canada

Fig. 10. Simulated line shapes for the merry-go-round motion in 15-crown-5·NaI as a function of jump rate (s^{-1}), based on the crystallographic data with <DCD = 100°.

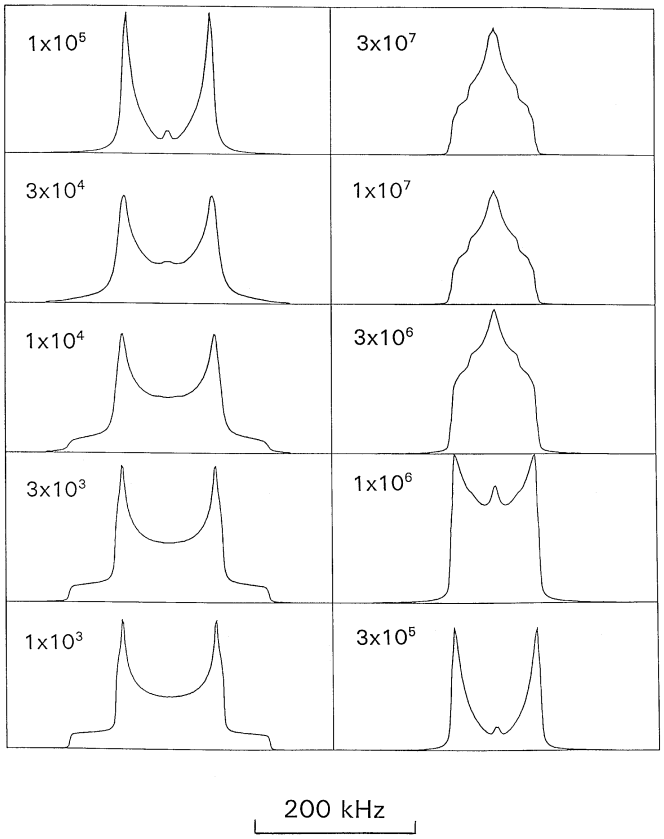

this regard the simulations are very useful in that they indicate how the features of the observed spectra might be broken down into four overlapping tensor line shapes. Possible tensors, determined in this way, are given in parentheses in Tables 2, 3, and the corresponding simulated line shapes for both complexes compare very favourably with experiment, e.g., compare Fig. 9, bottom with Fig. 4.

Further support for the model comes from a comparison of the behaviour of the intermediate rate line shapes. Simulations were performed (with the <DCD = 100° orientations) using a kinetic exchange matrix that allowed jumps between adjacent -OCD_2CD_2- sites and results are shown for 15-crown-5·NaI in Fig. 10. The observed and calculated spectra both follow the same basic development: There is an initial loss of intensity of the wings and centre of the static spectrum to form a two-horned line shape, followed by a gradual in-filling of the centre of the spectrum to form a block shape and eventually the multi-featured f.m.l. line shape, which has an overall conical–pyramidal appearance.

What this exercise has shown is that the ^2H NMR line shapes for the RT phases of the 15-crown-5 complexes are consistent with the merry-go-round motion. The consistency of this model, together with the precedent of m-g-r motion in 18-crown-6 and 12-crown-4 complexes and the fact that no other motion that could fit the observables has been conceived, gives confidence that this model is indeed correct. In this work the analysis has had to be rather more qualitative than quantitative because of the complexity of the problem: due to the lack of simplifying symmetry there are just too many unknowns for a rigorous solution.

Unfortunately the RT structure of 21-crown-7·KI is not available, so interpretation of the NMR data is therefore more speculative. Of the very few crystal structures known, none have 21-crown-7 complexed with Na^+ (26–28). However, all of these structures have the 21-crown-7 in an elongated and distinctly non-planar rather than circular form, and in general 21-crown-7 would be expected to have considerably more possible conformations than 15-crown-5. The ^2H NMR results again indicate that all D atoms are involved in the dynamics of the RT phase, however, the line shapes develop a little differently from the 15-crown-5 complexes. In the f.m.l. for the RT phase there are four pairs of strong features that cannot be matched to two distinct tensors and closer inspection reveals other weaker features. This suggests that the spectrum is a composite of more than two averaged line shapes. The spectra are too narrow for up/down CD_2 flips, so once again the most probable motion is m-g-r. There is in fact no reason to expect the line shapes to develop in the same way as the 15-crown-5 complexes that were similar by virtue of their very similar conformations. Furthermore the equivalence of all the D atoms in the HT phase requires m-g-r motion to be involved in the overall dynamics of this phase (see below). The fairly strong temperature dependence of the f.m.l. line shapes between 290 K and the phase transition may be explained by a gradually changing conformation.

High-temperature phases

The HT phases are quite remarkable in having dynamic equivalence of all the deuterons. In terms of the ^2H NMR this means that the 4 independent sets of exchanging D sites are all behaving identically. It remains to answer how this can happen. Structural information would help, but unfortunately none of the HT phase crystal structures are known. However, clues can be found by observing how equivalence is achieved in the 18-crown-6·$2CH_2(CN)_2$ and 12-crown-4·LiCNS complexes. (Note that the statements made below refer to equivalence under m-g-r motion and do not necessarily apply to the static molecule):

In 18-crown-6·$2CH_2(CN)_2$ the symmetry alone (pseudo-D_{3d}) makes the 4 sets of 6 exchanging sites equivalent. Each C-D is either axial or equatorial and during each site-to-neighbouring-site jump switches from one to the other. Mirror planes perpendicular to the ring make the 2 C atoms in the O-CD_2-CD_2 unit equivalent, and an inversion centre ensures that "top" and "bottom" D atoms are equivalent, i.e., both sides of the ring are identical. No disorder is necessary.

In 12-crown-4·LiCNS the dynamically averaged spectrum shows a superimposition of two nonaxially symmetric line shapes, which indicates that there are two distinct groups of deuteron sites. A mirror plane perpendicular to the ring ensures equivalence of the 2 C atoms, but in this case it also creates a 50:50 positional disorder. This makes pairs of sets equivalent. The two faces of the 12-crown-4 ring are not identical (the ring coordinates to Li^+ positioned at the top side), so the pairs of sets correspond to Ds on the top or on the bottom.

Contrast these with the RT phases of the 15-crown-5 complexes where the ring has no symmetry: The Na^+ is to one

© 1999 NRC Canada

Table 4. Comparison of factors involved in the dynamics of several crown ether complexes.

Crown complex	Equivalence of four sets of D	Top/bottom equivalence	Disorder	No. of sites for each D
18-Crown-6·$2CH_2(CN)_2$ (5)	All equivalent			6
12-Crown-4·LiCNS (6)	Two pairs equivalent			8
15-Crown-5·NaI or $NaClO_4$ RT phases	All *non*-equivalent			5
15-Crown-5·NaI or $NaClO_4$ HT phases	All equivalent			$n \times 10^a$, $n > 2$
21-Crown-7·KI HT phase	All equivalent			14 or $n \times 14$

[a]Multiple of 10 required to account for axial symmetry.

side of the ring, so top and bottom faces are different, and there is no mirror plane, so the 2 C are inequivalent. All four sets of D remain inequivalent.

Thus it can be seen that various combinations of symmetry and dynamic disorder produce different degrees of equivalence. To make all four sets of exchanging D dynamically equivalent there are two major requirements:

(*a*) the two C atoms in an O-CD_2-CD_2 unit must be made equivalent.

(*b*) the top and bottom faces of the ring must be made equivalent.

The first can be achieved by having *(i) a mirror plane perpendicular to the ring*, and in many cases this will imply a positional disorder. The second can be achieved in several ways *(ii) an inversion centre*; *(iii) a mirror plane in the ring plane*; *(iv) a C_2 axis in the ring plane.* In some cases this will impart disorder.

Clearly (*a*) and (*b*) must apply to the HT phases of 15-crown-5·NaI, 15-crown-5·$NaClO_4$ and 21-crown-7·KI. For the 15-crown-5 complexes the averaged HT line shape is also axially symmetric. Axial symmetry in an averaged line shape is generally indicative of reorientation about an *n*-fold axis ($n > 2$). It is possible that this could be from a fivefold symmetric molecular conformation, but in general fivefold conformations are not energetically favoured (25, 29), although one complex, (15-crown-5)$_2$·$BaBr_2$·$2H_2O$, with a pseudo-C_5 conformation is known (30). Also, true fivefold symmetry in crystals is not common. A more likely alternative is to have dynamic disorder of a non-fivefold molecular conformation about a crystal symmetry axis with $n > 2$; quite possibly $n = 4$, perhaps in a tetragonal structure. For the 21-crown-7 complex the averaged HT line shape is non-axially symmetric with ~1, so this cannot have any *n*-fold symmetry. This is in keeping with the elongated forms of the known structures. Table 4 compares the factors involved in dynamic averaging in all the crown complexes discussed above. Another point of interest is that in transforming from the RT to HT phases there will have to be a rearrangement of the guest atoms so that both faces of the ring are identical.

Conclusions

It has been shown that the solid crown ether complexes 15-crown-5·NaI, 15-crown-5·$NaClO_4$, and 21-crown-7·KI have several solid phases.

^{2}H NMR line-shape studies of the room temperature phases show onset of a crown motion above 200 K that is rapid, with respect to the reciprocal of the static quadrupolar coupling constant, a little above room temperature. Detailed analysis leads to the conclusion that this motion is similar to the merry-go-round motion observed in 18-crown-6 complexes, where O-CH_2-CH_2 units exchange sites around the ring, simultaneously adjusting their conformation to fit the site. The rather complicated line shapes are composed of four superimposed line shapes that arise from four inequivalent sets of exchanging deuterons.

In the high-temperature phases all the deuteron sites around the rings become dynamically equivalent, and, though the structures are not known, it has been demonstrated how this may be brought about through a combination of crystal symmetry and disorder on top of the m-g-r motion. It is likely that the 15-crown-5 dynamics involve reorientation about an *n*-fold ($n > 2$) crystal axis involving disorder. It would be very interesting, though experimentally challenging, to obtain the HT X-ray crystal structures to confirm these inferences.

It is remarkable that motion in these large macrocycles is so easy in the solid state, and it is probably the fact that the molecule rotates within itself that allows this to occur with a relatively small activation energy.

Finally, these complexes will make fine new additions to the rides at "the molecular fairground."

Acknowledgements

G.W.B. thanks the Natural Sciences and Engineering Research Council of Canada (NSERC) for continued financial support via an operating grant. M.G. also thanks NSERC for a fellowship. We thank Prof. Z.Y.Wang for access to the DSC facility and Pierre Moulinie for technical assistance. C.I.R. would like to thank Dr. J.A. Ripmeester for helpful discussions.

References

1. J.S. Bradshaw, R.M. Izatt, A.V. Bordunov, C.Y. Zhu, and J.K. Hathaway. *In* Comprehensive supramolecular chemistry. Vol. 1. *Edited by* J.L. Atwood, J.E.D. Davies, D.D. MacNicol, F. Vogtle, J.-M. Lehn, and G.W. Gokel. Pergamon, New York. 1996. Chap. 2.
2. I. Goldberg. *In* Inclusion compounds. Vol. 2. *Edited by* J.L. Atwood, J.E.D. Davies, and D.D. MacNicol. Academic Press, London. 1984. Chap. 9.
3. G.W. Buchanan, R.A. Kirby, J.A. Ripmeester, and C.I. Ratcliffe. Tetrahedron Lett. **28**, 4783, (1987).
4. G.W. Buchanan, C. Morat, C.I. Ratcliffe, and J.A. Ripmeester. J. Chem. Soc. Chem. Commun. 1306 (1989).
5. C.I. Ratcliffe, J.A. Ripmeester, G.W. Buchanan, and J.K. Denike. J. Am. Chem. Soc. **114**, 3294 (1992).
6. C.I. Ratcliffe, G.W. Buchanan, and J.K.Denike. J. Am. Chem. Soc. **117**, 2900 (1995).

© 1999 NRC Canada

7. M.J. Wagner, L.E.H. McMills, A.S. Ellaboudy, J.L. Eglin, J.L. Dye, P.P. Edwards, and N.C. Pyper. J. Phys. Chem. **96**, 9656 (1992).
8. G.E. Pacey, Y.P. Wu, and B.P. Bubnis. Synth. Commun. **11**, 323 (1981).
9. B.R. Bowsher and A.J. Rest. J. Chem. Soc. Dalton Trans. 1157 (1981).
10. G.W. Gokel, D.J. Cram, C.L. Liotta, H.P. Harris, and F.L.Cook. J. Org. Chem. **39**, 2445 (1974).
11. R.N. Greene. Tetrahedron Lett. 1793 (1972).
12. G. Johnes, C.J. Ransom, and C.B. Reese. Synthesis, 515 (1976).
13. F.L. Cook, J.C. Caruso, M.P. Byrne, C.W. Bowers, D.H. Speck, and C.L. Liotta. Tetrahedron Lett. 4029 (1974).
14. P.L. Kuo, M. Miki, and M. Okahara. Bull. Soc. Chem. Jpn. **53**, 1689 (1981).
15. J.H. Davis, K.R. Jeffrey, M. Bloom, M.I. Valic, and T.P. Higgs. Chem. Phys. Lett. **42**, 390 (1976).
16. R.G. Barnes. *In* Advances in nuclear quadrupole resonance. *Edited by* J.A.S. Smith. Heyden, London. **1**, 335 (1974).
17. R.J. Wittebort, E.T. Olejniczak, and R.G. Griffin. J. Chem. Phys. **86**, 5411 (1987).
18. M.S. Greenfield, A.D. Ronemus, R.L. Vold, R.R. Vold, P.D. Ellis, and T.E. Raidy. J. Magn. Reson. **72**, 89 (1987).
19. H.W. Spiess and H. Sillescu. J. Magn. Reson. **42**, 381 (1981).
20. A.J. Vega and J. Luz. J. Chem. Phys. **86**,1803 (1987).
21. C.I. Ratcliffe. J. Phys. Chem. **91**, 6464 (1987).
22. W.P. Rothwell and J.S. Waugh. J. Chem. Phys. **74,** 2721 (1981).
23. G.W. Buchanan, M. Gerzain, and C. Bensimon. Acta Cryst. **C50**, 1016 (1994).
24. G. Shoham and N. Cohen. Acta Cryst. **C45**, 1154 (1989).
25. M.D. Paulsen and B.P. Hay. J. Mol. Struct. (Theochem), **429**, 49 (1998).
26. P. Groth. Acta Chem. Scand. **A35**, 541 (1981).
27. P.C. Junk and J.L. Atwood. J. Chem. Soc. Chem. Commun. 1551 (1995).
28. P.C. Junk and J.L. Atwood. J. Chem. Soc. Dalton Trans. 4393 (1997).
29. M.D. Paulsen, J.R. Rustad, and B.P. Hay. J. Mol. Struct. (Theochem), **397**, 1 (1997).
30. J. Feneau-Dupont, E. Arte, J.P. Declercq, G. Germain, and M. Van Meerssche. Acta Cryst. **B35**, 1217 (1979).

© 1999 NRC Canada

Assignment of ^{1}H and ^{13}C spectra for polyprenol-12, a molecule with severe ^{1}H and ^{13}C spectral crowding, with the aid of high-resolution, ^{13}C-detected, ^{13}C–^{1}H shift correlation spectra

William F. Reynolds, Stewart McLean, Helen Jacobs, and Wayne W. Harding

Abstract: Polyprenol-12 contains a linear sequence of 12 isoprene units. As a result, there is severe crowding in several regions of the ^{1}H and ^{13}C spectra. Nevertheless, it is possible to assign a substantial majority of individual resonances as well as to confirm the number and sequence of *E* and *Z* isoprene units with the aid of high-resolution (0.001 ppm along each axis) ^{13}C-detected ^{13}C–^{1}H shift correlation spectra. By contrast, the corresponding ^{1}H-detected sequences (e.g., HSQC and HMBC) do not have sufficient resolution to allow these assignments, in spite of their higher sensitivity.

Key words: ^{13}C-detected 2D shift correlation, polyprenol 12, spectral assignments.

Résumé : Le polyprénol-12 comporte une séquence linéaire de 12 unités isopréniques. Il en résulte que, pour ce composé, plusieurs régions des spectres RMN du ^{1}H et du ^{13}C présentent un important encombrement. Faisant appel aux spectres du ^{13}C, à haute résolution (0,001 ppm sur chacun des axes), avec corrélation ^{13}C–^{1}H des déplacements, il est toutefois possible de faire l'attribution de la majorité des résonances individuelles. Toutefois, malgré leur sensibilité plus élevée, les spectres des séquences correspondantes avec détection du ^{1}H (par exemple, « HSQC » et « HMBC ») ne conduisent pas à des résolutions qui permettent de faire ces attributions.

Mots clés : corrélation bidimensionnelle des déplacements de raies de ^{13}C observées, polyprénol 12, attributions spectrales.

[Traduit par la Rédaction]

Introduction

Due to their significant sensitivity advantages, ^{1}H-detected ^{13}C–^{1}H shift correlation sequences such as HSQC (1), HMQC (2), and HMBC (3) have largely replaced the earlier ^{13}C-detected versions of these experiments. However, the price that one pays for the higher sensitivity is that the intrinsic resolution obtainable with the former sequences (particularly along the F_1 or ^{13}C axis) is poorer than with ^{13}C-detected sequences. First, the ^{1}H multiplet structure for each cross-peak also appears along the F_1 axis in HMQC and HMBC (but not HSQC) spectra (4). Second, with ^{1}H-detected sequences, it is the much wider ^{13}C axis that is time-incremented, increasing the difficulty of obtaining excellent ^{13}C resolution. The latter problem can be partially overcome by using forward linear prediction to increase the number of t_1 data points (5). However, even with very extensive linear prediction (e.g., prediction of 256 F_1 data out to 4096 with zero filling to 8192 for an HSQC spectrum with a ^{13}C spectral window of 6300 Hz (5)), we find that the best obtainable ^{13}C resolution using linear prediction is ca. 4 Hz. This is considerably broader than typical natural line widths of ^{13}C peaks, suggesting a not surprising limitation in the ability of linear prediction to precisely define line shapes. The limiting ^{13}C resolution is generally much worse for HMQC and HMBC spectra where it is determined by ^{1}H multiplet widths. These multiplet widths also determine effective F_2 resolution in many cases.

On the other hand, ^{13}C-detected sequences with ^{1}H decoupling during acquisition provide singlets along the F_2 (^{13}C) axis. Since the acquisition time is usually a small fraction of the experiment time, one can acquire a large number of t_2 data points to give excellent ^{13}C resolution without paying a high cost in time. By contrast, doubling the

Received June 17, 1999.

This paper is dedicated to Professor Ted Schaefer in recognition of his outstanding contributions to Canadian chemistry.

W.F. Reynolds[1] and S. McLean. Department of Chemistry, University of Toronto, Toronto, ON M5S 3H6, Canada.
H. Jacobs[1] and W.W. Harding. Department of Chemistry, University of the West Indies, Mona Campus, Kingston, Jamaica.

[1]Authors to whom correspondence may be addressed. WFR: Telephone and fax: (416) 978-3563; e-mail: bgranozi@alchemy.chem.utoronto.ca; HJ: Telephone: (876) 927-1910. Fax: (876) 977–1835. e-mail: hjacobs@uwimona.edu.jm

 © 1999 NRC Canada

number of t_1 (^{13}C) increments in a ^1H-detected 2D experiment doubles the experiment time. Second, several of the ^{13}C-detected sequences provide partial or full ^1H–^1H decoupling along the F_1 (^1H) axis. For example, inclusion of a BIRD pulse (6) in the basic HETCOR sequence (7) eliminates all ^1H–^1H coupling except geminal coupling between non-equivalent methylene protons (8). Alternatively, we have developed a constant time version of HETCOR that provides full ^1H–^1H decoupling (9). For *n*-bond (n = 2 or 3) correlation experiments, Kessler's constant time COLOC sequence (10) provides full ^1H–^1H decoupling while our FLOCK sequence (11) provides partial ^1H–^1H decoupling.

Thus, it is possible with ^{13}C-detected sequences to obtain high-resolution ^{13}C–^1H shift correlation spectra with each peak being a singlet along F_1 and a singlet or partially collapsed multiplet along F_2. While the improved resolution that these sequences provide is often not needed, in some cases it is absolutely essential for structural and (or) spectral assignments (12). Furthermore, we have recently shown that the use of modern microprobe and microtube technology can significantly reduce the amount of sample needed for these experiments (13). We now provide a particularly striking example of the use of ^{13}C-detected experiments to determine the structure and to assign almost all resolved carbons of a natural product with severe ^1H and ^{13}C spectral crowding. The compound is the polyprenol, **1**, composed of a chain of 12 isoprene units.

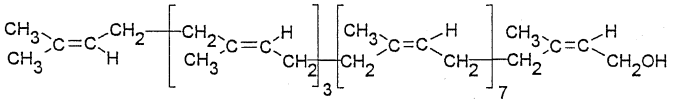

1

Results and discussion

After isolation (see Experimental), **1** was initially characterized in $CDCl_3$ solution by a combination of ^1H, ^{13}C, and DEPT-edited ^{13}C spectra. Although showing severe overlap in several ^1H and ^{13}C spectral regions, the spectra suggested that **1** was composed of a chain of isoprene units, including terminal isoprene units **2A** and **2B** and a number of internal *E* (**2C**) and *Z* (**2D**) units.

The integrated ^1H spectrum suggested the presence of 13 CH_3 groups, i.e., a total of 12 isoprene units. This was confirmed by a high-resolution mass spectrum that showed a parent ion corresponding to $C_{60}H_{98}O$. The ^{13}C spectra showed weak overlapping peaks near δ 16 and δ 40, respectively consistent with the chemical shifts of CH_3 groups and CH_2 groups *gem* to CH_3 in *E* units (14). The areas of these peaks relative to other resolved CH_3 and CH_2 signals suggested the presence of 2 or more likely 3 *E* units, with the ambiguity due to the spectral overlaps.

A search of the literature suggested that **1** was a member of a class of compounds called polyprenols (15). Polyprenols from plant sources usually have 9–13 isoprene units with 11 or 12 being most common (15). Due to the biosynthetic origin of these compounds (16), they typically have a sequence of 2 or 3 *E* units adjacent to the ω terminal isoprene unit, **2A**, followed by a number of *Z* units and terminated by a hydroxylated isoprene unit, **2B**. However, polyprenols with only *E* units are also known (15).

Characterization of these polyprenols has relied heavily on empirical ^1H (16) and ^{13}C (14) chemical shift correlations. It has been demonstrated that the ^1H spectra of polyprenols, particularly in the CH_3 region, are much better resolved in C_6D_6 than in $CDCl_3$ (17). However, there have been no attempts to carry out complete and rigorous spectral assignments for these polyprenols or to use detailed 2D investigations to confirm stereochemical sequences. Consequently, we decided to investigate the extent to which it was possible to assign the structure and the ^1H and ^{13}C spectra of **1**, with the aid of high-resolution ^{13}C-detected ^1H–^{13}C shift correlation sequences.

Spectra were obtained at 500 MHz (^1H) and 125 MHz (^{13}C) at 25°C, using a 3 mm microprobe optimized for ^{13}C detection. The sample contained 12 mg of **1** dissolved in ca. 160 μL of C_6D_6, with 0.1% TMS as internal standard. A microprobe was used since, in our experience (13), this gives better resolution than a 5 mm probe and high resolution was considered critical. The observed ^1H resolution, non-spinning, was 0.42 Hz for the TMS signal. The ^1H spectrum for the CH_3 region showed reasonable spectral dispersion (see Fig. 1*a*). $CDCl_3$:C_6D_6 solvent mixtures were also tried but they gave poorer resolution of overlapping peaks. Decoupling in the center of the olefinic region combined with resolution enhancement allowed clear resolution of 9 of the 13 CH_3 signals while the other 4 seemed completely overlapped. (See Fig. 1*b*). However, the olefin and methylene proton regions were still badly overlapped, in part due to the presence of vicinal coupling. By contrast, a preliminary ^{13}C spectrum suggested that the individual peaks were very narrow. Consequently, we obtained a ^{13}C spectrum with unusually good data point resolution (65 536 data points for a spectral window of 18 431 Hz, with zero-filling to 524 288). While zero filling to 524 288 gives a data point resolution of ca. 0.07Hz/point, defining resolved line positions to better than 0.001 ppm, zero filling beyond a factor of two does not result in any further line narrowing of resolved lines (18). Consequently, the narrowest observable lines should be about 18 431/65 536 ≈ 0.3 Hz. In fact, the average observed line width (with no weighting function) was 0.4 Hz for CH_3 carbons and non-protonated olefinic carbons and 0.6 Hz for the remaining carbons. This is considerably less than one would normally expect for protonated carbons in a compound of over 800 molecular weight, suggesting a high degree of internal chain motion in **1**. This is not surprising, since **1** resembles a short segment of natural rubber. It has long been known that internal chain mobility allows one to observe relatively sharp ^{13}C lines even in a solid sample of

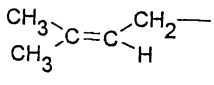

2A

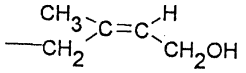

2B

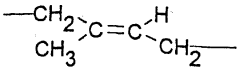

2C

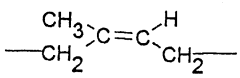

2D

© 1999 NRC Canada

Fig. 1. (*a*) Integrated ^{1}H spectrum of CH_3 region of **1**. (*b*) Corresponding 1H spectrum with resolution enhancement and decoupling in the middle of the olefinic ^{1}H signals.

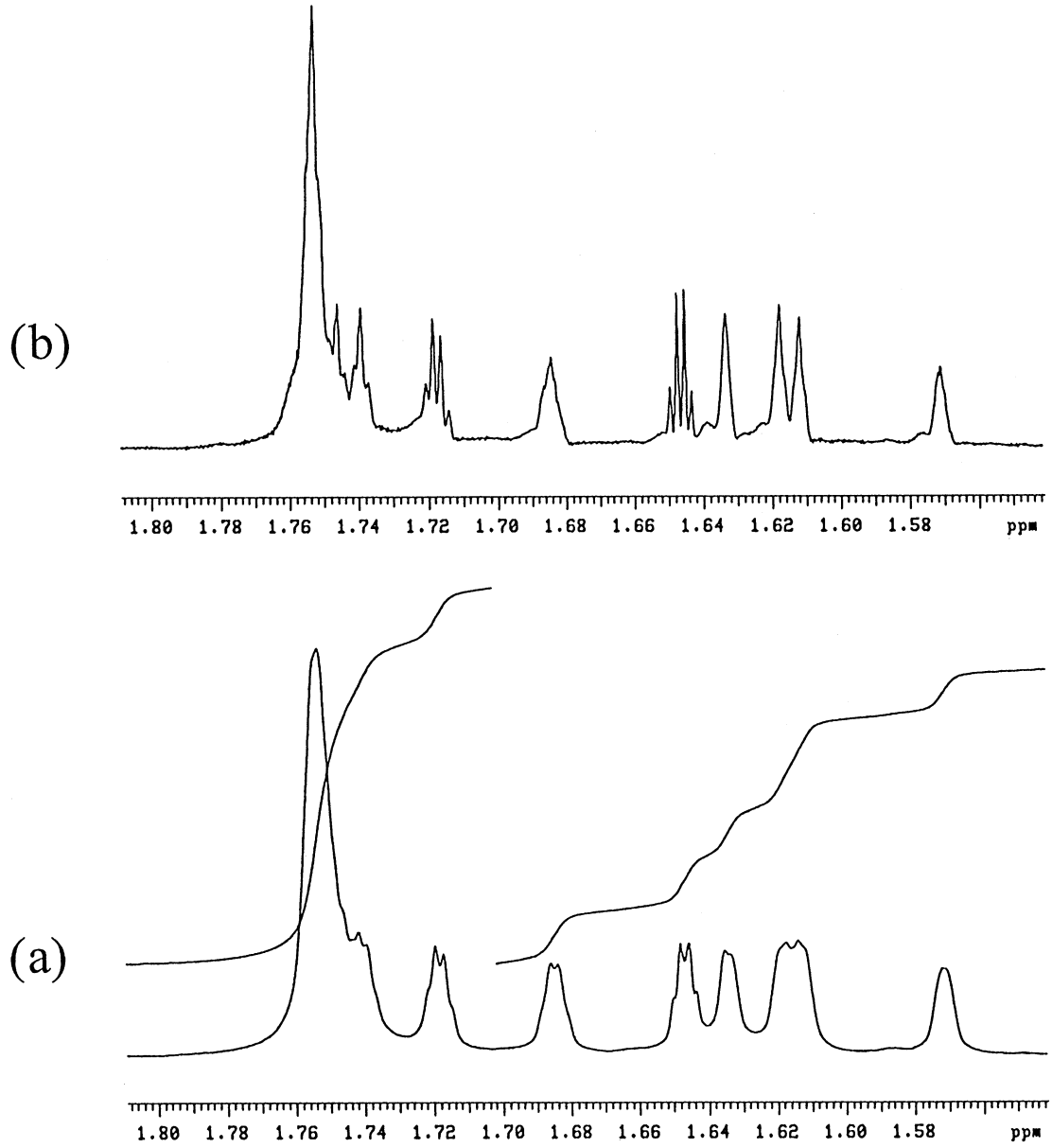

natural rubber (19). The excellent resolution allowed the observation of three completely resolved CH_3 signals between δ 16.124–16.140, i.e., within two Hz at 125 MHz. This and the observation of three resolved CH_2 signals in the range δ 40.206–40.250 confirmed the presence of 3 *E* isoprene units. Overall, 47 of the possible 60 ^{13}C signals were observed, including 11 of 12 non-protonated olefinic ^{13}C signals and 10 of 12 protonated olefinic ^{13}C signals. Figure 2 shows an expansion of part of the non-protonated olefinic region. Six signals are observed in a region of only 0.11 ppm, five corresponding to single carbons and the sixth corresponding to two unresolved carbons. The resolution of CH_2 and CH_3 signals is not as complete with 9 of 13 CH_3 signals and 17 of 23 CH_2 signals observed. The partial overlap is not surprising since the proposed structure has a sequence of seven identical *Z* isoprene units.

A series of ^{13}C-detected ^{1}H–^{13}C shift correlation spectra was next acquired in an attempt to assign ^{1}H and ^{13}C spectral peaks for **1** as completely as possible, as well as to confirm the presumed sequence of internal *E* and *Z* units. First, two one-bond ^{1}H–^{13}C shift correlation spectra were obtained using the version of HETCOR incorporating a BIRD pulse (8). Since **1** contains no chiral carbons, this sequence provides a singlet for each ^{1}H signal. One spectrum covered the aliphatic carbon – proton spectral regions while the second covered the olefinic carbon/proton spectral windows. In each case, the data point resolution was better than 0.01 ppm along each spectral axis (see Experimental for details). Two spectral expansions from the aliphatic carbon/proton spectrum are illustrated in Figs. 3 and 4, respectively corresponding to *E* CH_2 units at δ_C 40.2 and *E* CH_3 units at δ_C 16.1. These illustrate the excellent resolution obtainable for both

© 1999 NRC Canada

Fig. 2. (*a*) Signals for non-protonated olefinic carbons of **1**. (*b*) Expansion of the spectrum in Fig. 2*a*. (*c*) Further expansion of the same spectrum.

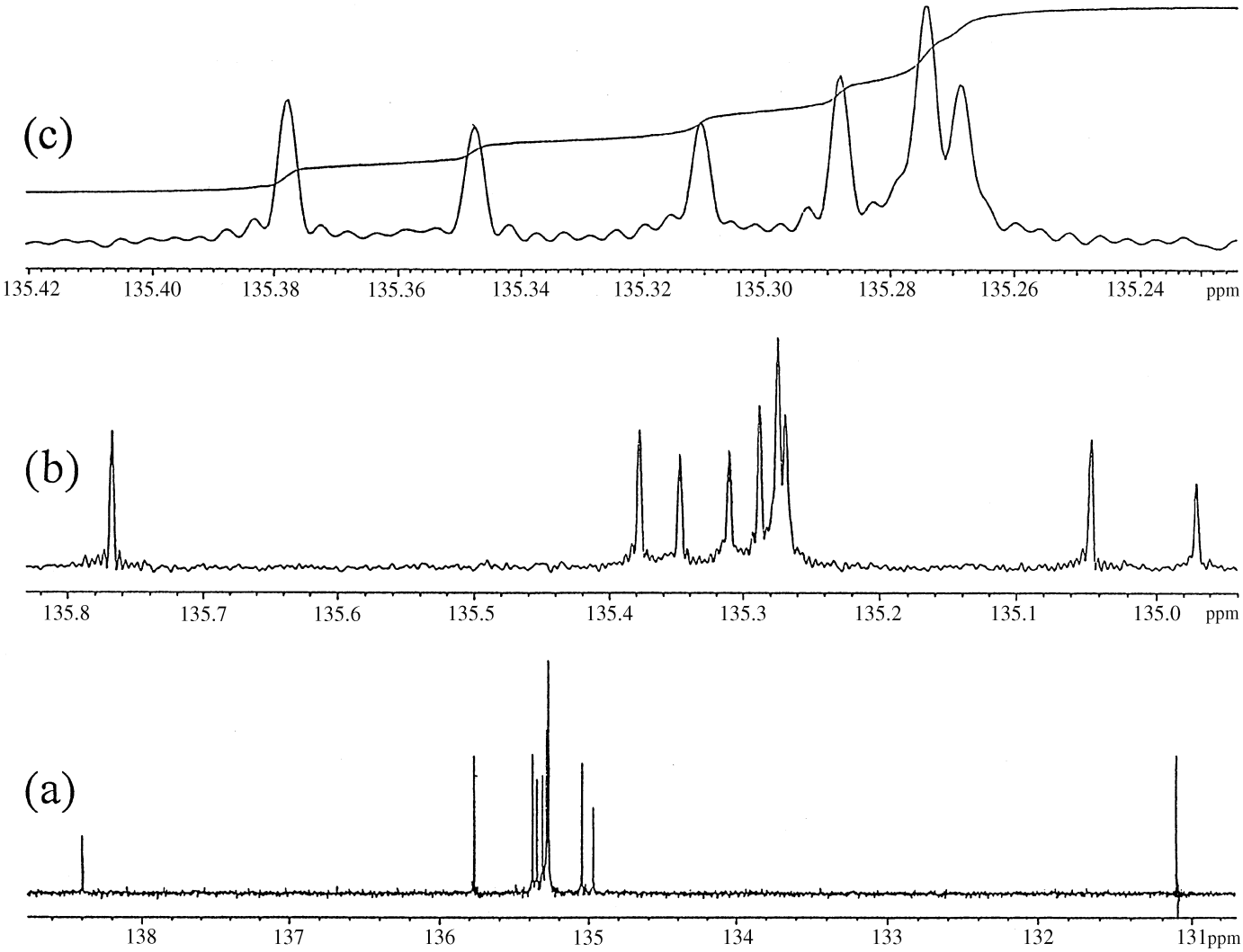

^{1}H and ^{13}C axes using the ^{13}C-detected sequence. In fact, due to full ^{1}H–^{1}H decoupling by the BIRD pulse, the ^{1}H resolution is actually better for the 2D spectra than for the corresponding 1D spectra where ^{1}H–^{1}H multiplet structure leads to spectral overlap, particularly for CH_2 protons. To confirm the resolution advantages of the ^{13}C-detected spectra, a pair of HSQC spectra were obtained for the same spectral regions, making use of extensive linear prediction to give comparable data point resolution along the two axes (see Experimental for details). The inferior resolution of the ^{1}H-detected HSQC spectra is obvious in Figs. 3 and 4. This reflects (*i*) the intrinsically limited ^{13}C resolution with HSQC (see above) and (*ii*) the presence of ^{1}H–^{1}H multiplet structure along the ^{1}H axes of the HSQC spectra, particularly for CH_2 groups. Obviously, it is possible to make spectral assignments from the HETCOR spectra, which are impossible with the HSQC spectrum. It should be noted that the spectral resolution would be even worse with an HMQC spectrum due to the presence of ^{1}H–^{1}H multiplet structure along both F_1 and F_2. Finally, it should also be noted that the HETCOR spectrum was obtained in absolute value mode while the HSQC spectrum was obtained in phase sensitive mode. The latter should give better resolution due to the better line shapes in phase sensitive mode. Thus, the resolution advantages of HETCOR should be even greater if the spectrum were obtained in phase sensitive mode.

The HETCOR spectra allowed assignment of ^{1}H chemical shifts of protons to their directly bonded carbons. Next, to complete the assignments of carbons and hydrogens to individual isoprene units as well as the sequences of isoprene units, two *n*-bond (n = 2 or 3) ^{13}C-detected ^{13}C–^{1}H shift correlation spectra were obtained. These were obtained using the phase-sensitive version (20) of our FLOCK sequence (11). Arguably, there are advantages to using COLOC (10) over FLOCK, since each proton signal appears as a singlet with COLOC, while FLOCK provides only partial ^{1}H–^{1}H decoupling. However, there also disadvantages to COLOC (11). COLOC is a "constant time" sequence in which ^{1}H chemical shift information is generated by incrementally moving a pair of ^{1}H and ^{13}C 180° pulses through the evolution period prior to polarization transfer from ^{1}H to ^{13}C. For ^{1}H singlets, optimum polarization transfer occurs when the

© 1999 NRC Canada

Fig. 3. (*a*) Expansion of BIRD-decoupled HETCOR spectrum of **1**, illustrating resolved cross-peaks for CH_2 groups from *E* isoprene units. (*b*) The corresponding HSQC spectrum for the same region.

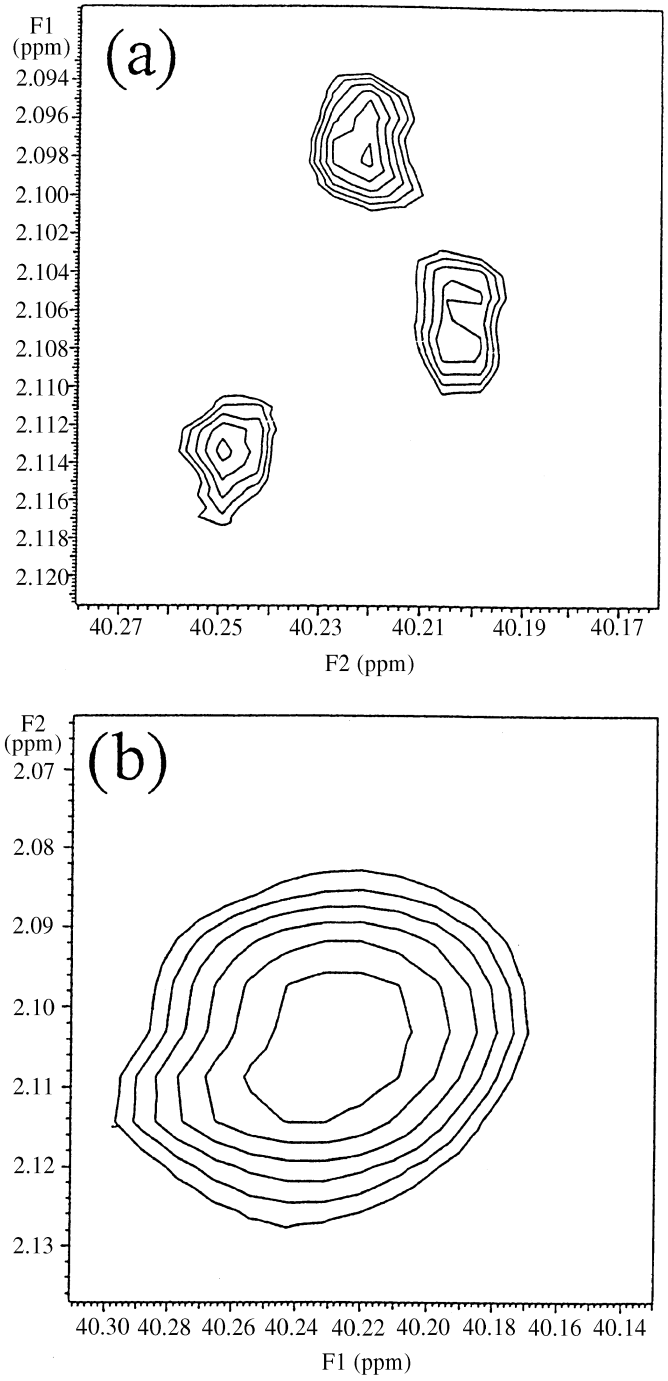

Fig. 4. (*a*) Expansion of BIRD-decoupled HETCOR spectrum of **1**, illustrating resolved cross-peaks for CH_3 groups from *E* isoprene units. (*b*) The corresponding HSQC spectrum for the same region.

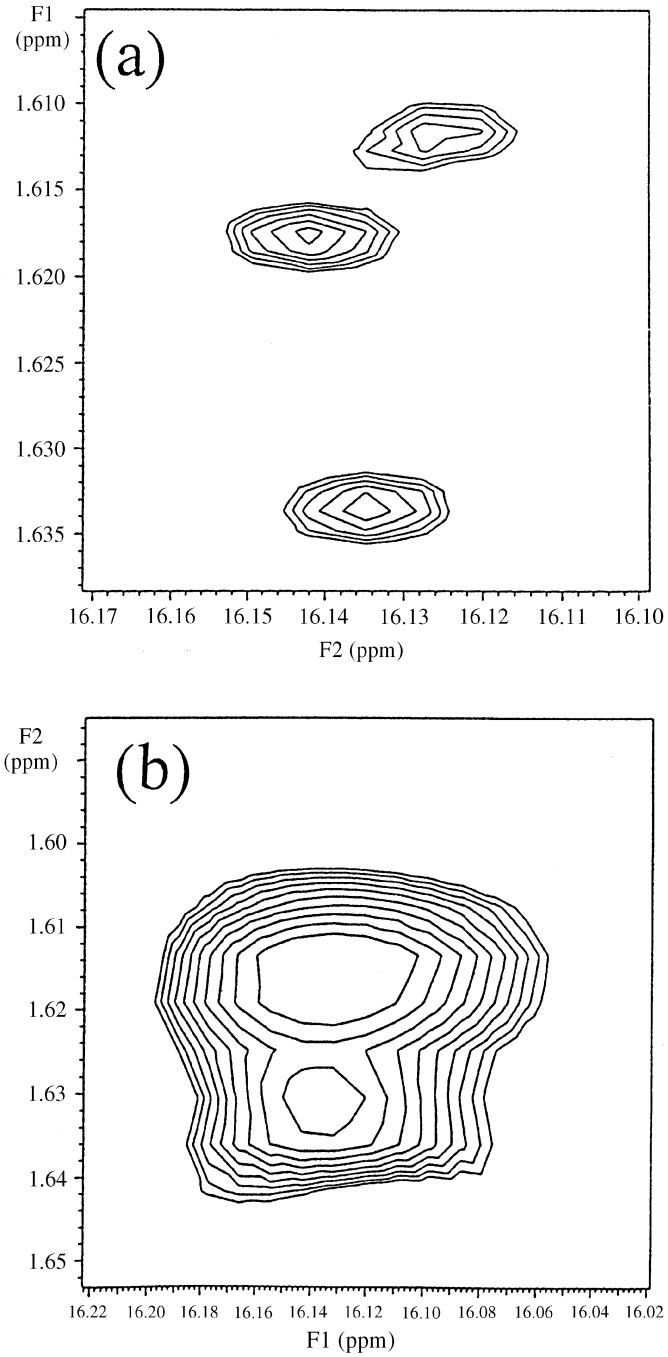

constant time, $T \approx (1/2)^n J_{CH}$. However, for ^1H multiplets, proton coupling vectors also evolve and signal intensity disappears if $T = (1/2)^n J_{HH}$. Since $^n J_{CH}$ and $^n J_{HH}$ are similar in magnitude in **1** and since there is a range of $^n J_{CH}$ values, it is difficult to find an optimum value for *T*. While these problems can be minimized by choosing a value of *T* that is considerably smaller than 1/2 $^n J_{CH}$, this severely limits the attainable $F_1(^1H)$ resolution. Second, in order to obtain a phase sensitive spectrum, it is necessary that no ^1H chemical shift evolution occurs at $t_1 = 0$. In the case of COLOC, this requires that the pair of 180° pulses be initially at the midpoint of *T*, further limiting the attainable F_1 resolution.

© 1999 NRC Canada

Fig. 5. Expansion of phase-sensitive FLOCK spectrum of **1**, illustrating two-bond cross-peaks between CH_3 groups and non-protonated olefinic carbons.

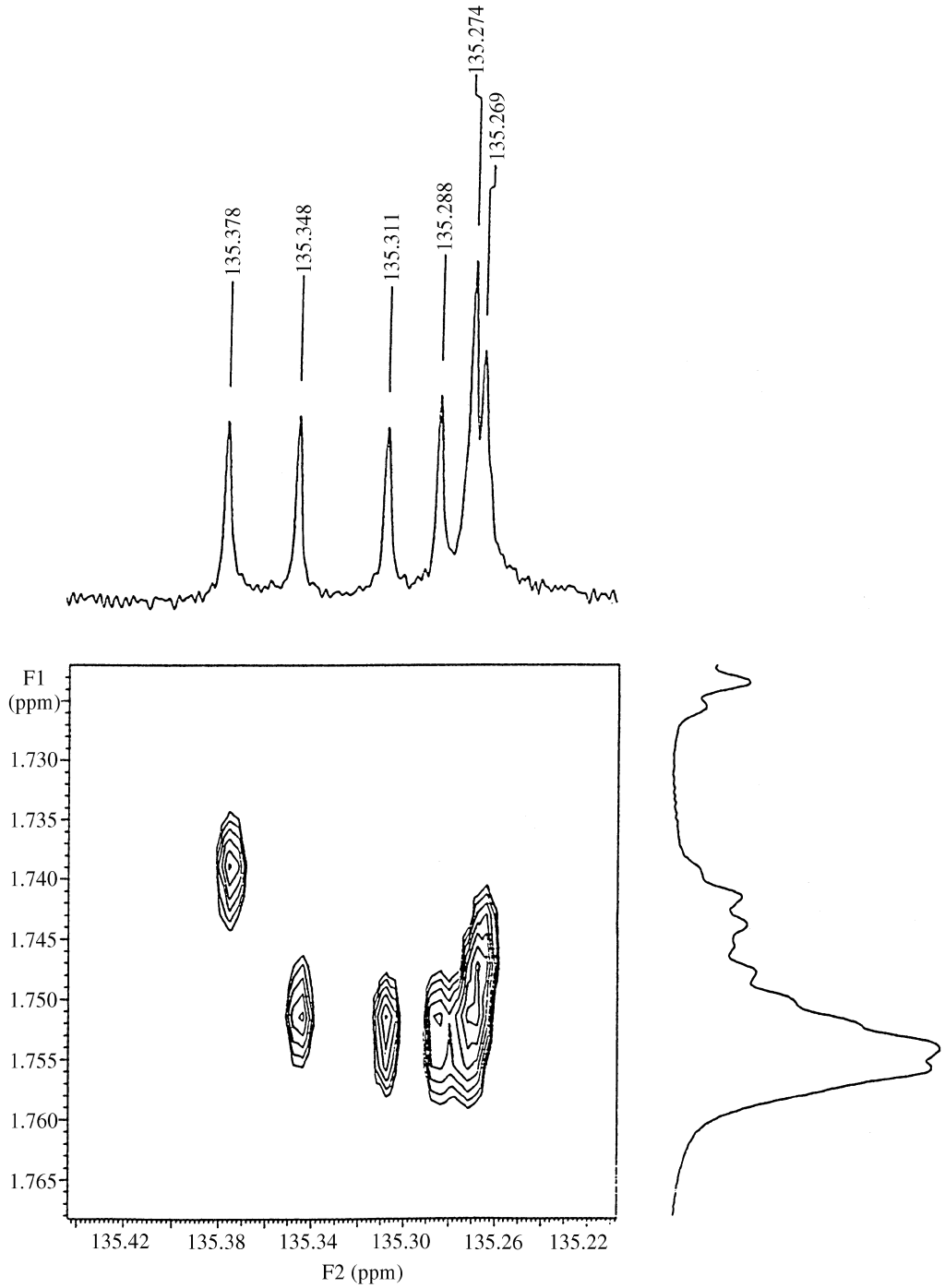

Therefore, we chose phase sensitive FLOCK that has no intrinsic limitations on the attainable F_1 resolution.

Two FLOCK spectra were recorded. In each case, the full ^1H spectral window was used while the ^{13}C spectral window was narrowed on either the aliphatic or olefinic ^{13}C spectral window. As a result of the wider ^1H spectral window, this ^1H resolution was slightly poorer than for the HETCOR spectra (or 2 Hz/point, i.e., 0.004 ppm/point), but still with excellent ^1H resolution. In each case, the ^{13}C resolution was identical to that in the HETCOR spectrum for the same carbon region (see Experimental for details).

A representative expansion of one of the FLOCK spectra is illustrated in Fig. 5. This illustrates the cross-peaks between CH_3 protons and some of the olefinic carbons. As a result of this spectral expansion and similar expansions for other olefinic carbons, it was possible to correlate 9 of 13

© 1999 NRC Canada

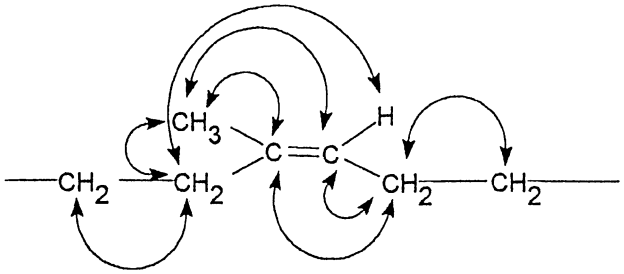

3

CH_3 ^1H signals with pairs of olefinic carbons in individual isoprene units. The remaining four CH_3 signals could not be definitively assigned since their chemical shifts were identical (see Fig. 1). Other regions of the two FLOCK spectra establish correlations for CH_3 protons to geminal CH_2 carbons, CH_2 protons to olefinic carbons, and ^1H–^{13}C correlations within coupled CH_2–CH_2 units, (see **3** for an illustration of key *n*-bond cross-peaks). The former cross-peaks allowed completion of the ^1H and ^{13}C assignments for eight of the 12 isoprene units, while the two-bond ^1H–^{13}C correlations within coupled CH_2–CH_2 units allowed determination of the sequence of isoprene units.

For the remaining four internal isoprene units, ^1H chemical shifts for corresponding protons in the four units are identical within 0.01 ppm. Thus, even though there is partial resolution of olefinic carbons, it is not possible to unambigously assign these carbons to individual isoprene units. Nevertheless, the fact that one can assign so many of the carbon and hydrogen signals in a compound with such severe spectral crowding, clearly demonstrates the great value of ^{13}C-detected shift correlation sequences for this kind of assignment problem. The completed assignments are given in Table 1.

Experimental

Extraction and isolation

The compound was isolated from *Guarea Jamaicensis* (Meliaceae). The plant material was collected at Gourie Forest, Manchester, Jamaica, in September 1996. Voucher specimens are preserved in the Herbarium, University of the West Indies, Mona, Jamaica. Dried, milled leaves and twigs of *G. Jamaicensis* (2.1 kg) were percolated with hexane (3 × 4 L) and the combined hexane solutions concentrated in vacuo to yield a green gum (20 g). The gum was subjected to column chromatography in acetone–hexane mixtures (5–20% acetone). The residue from the fractions eluted with 5% acetone–hexane (1.33 g) was rechromatographed by column chromatography in 3% ethyl acetate–hexane to provide polyprenol-12 (439 mg) as a colourless viscous oil.

NMR spectroscopy

Initial ^1H and ^{13}C spectra were obtained at 200 MHz (50 MHz for ^{13}C) on a Varian GEMINI-200 spectrometer, using 50 mg of **1** in 1 mL of $CDCl_3$ in a 5 mm tube at ambient temperature. Most subsequent spectra were obtained on a Varian Unity 500 spectrometer equipped with a 3 mm Nalorac microprobe optimized for ^{13}C detection (^{13}C 90° pulse width = 6.5 μs, ^1H decoupler 90° pulse width = 10 μs). Comparison HSQC and HMBC spectra were obtained with a 3 mm Nalorac inverse detection probe. Twelve milligrams of **1** were dissolved in ca. 160 μL of $CDCl_3$ containing 0.1% tetramethylsilane. Spectra were acquired under variable temperature control at 25°C. ^1H (500 MHz) and ^{13}C (125 MHz) spectra were respectively obtained with a 3240 Hz spectral window with 32 758 data points (zero filled to 131 072) and for an 18 431 Hz spectral window with 65 536 data points (zero filled to 524 288). No weighting was initially used for either spectrum but the ^1H spectrum was subsequently reprocessed with a resolution enhancement function. The 2D BIRD-decoupled HETCOR spectrum for the aliphatic region had a ^{13}C (F_2) spectral window of 3737 Hz and a ^1H (F_1) spectral window of 595 Hz with 4096 data points (zero filled to 8192), 256 time increments, 24 transients per increment, and a relaxation delay of 0.75 s. The spectrum was acquired in absolute value mode with ^1H WALTZ decoupling during acquisition. The 256 F_1 increments were linearly predicted to 512 points with zero filling to 1024 points. π/3 shifted sine bell processing was applied along each axis. For the olefinic HETCOR spectra, the ^{13}C spectral window was 532 Hz and the ^1H spectral window was 335 Hz with 512 data points (zero filled to 1024) and 256 time increments, linearly predicted to 512 points with zero filling to 1024 points. Two phase sensitive FLOCK spectra were obtained. The spectrum for the ^{13}C aliphatic region used the same ^{13}C spectral window and data points as the corresponding HETCOR spectrum as previously. However, the spectrum covering the ^{13}C olefinic region used a ^{13}C spectral width of 2058 Hz (with 2048 data points zero filled to 4096) to include both protonated and non-protonated olefinic carbons. A common ^1H spectral window of 2149 Hz with 2 × 256 time increments with linear prediction of each data set to 1024 and zero filling to 2048. Sixty-four transients were collect per time increments and Gaussian weighting was applied along each axis.

The comparison HSQC and HMBC spectra were obtained using a Nalorac inverse detection 3 mm microprobe. In each case, parameters were chosen to give the same data point resolution as the corresponding ^{13}C detected experiments, e.g., for the phase sensitive HSQC spectrum for the aliphatic region, the ^1H (F_2) spectral width was 595 Hz with 512 data points (zero filled to 1024) while the ^{13}C (F_1) spectral window was 3737 Hz with 2 × 512 time increments, with each data set linearly predicted to 4096 points and zero filled to 8192. GARP ^{13}C decoupling was applied during acquisition and Gaussian weighting was used for each axis.

Acknowledgments

Dr. George R. Proctor and Mr. Jonathan Littau assisted with the plant collection and identification. Financial assistance from the Natural Sciences and Engineering Research Council of Canada (NSERC) (W.F.R.), the CIDA–UWI Institutional Strengthening fund (W.W.H.), and the UWI Research Fund (H.J.) is gratefully acknowledged. Finally, W.F.R. acknowledges his great debt to Professor Ted Schaefer for introducing him to NMR spectroscopy and for encouraging him to pursue a career in research.

© 1999 NRC Canada

Table 1. Assigned ^{13}C and ^{1}H chemical shifts[a] for polyprenol-12, **1**, in C_6D_6.

Isoprene unit[b]	Carbon[c]	δ_C	δ_H	Isoprene unit	Carbon	δ_C	δ_H
1	1	17.757[d]	1.571	6–9	1	32.624[e]	2.170
	2	131.101	—		1	32.603	2.170
	3	124.927	5.240		2	135.348	—
	4	27.227	2.182		2	135.311	—
	5	25.877	1.684		2	135.288	—
					2	135.274	—
2	1	40.223	2.112		3	125.599[e]	5.280
	2	134.970	—		3	125.582	5.278
	3	124.792	5.291		4	26.928[f]	2.220
	4	27.124	2.198		5	23.709[f]	1.753
	5	16.124	1.613				
3	1	40.206	2.103	10	1	32.642	2.175
	2	135.046	—		2	135.269	—
	3	124.760	5.296		3	125.508	5.252
	4	27.124	2.209		4	26.859	2.185
	5	16.140	1.617		5	23.705	1.747
4	1	40.250	2.118	11	1	32.529	2.110
	2	135.274	—		2	135.768	—
	3	124.668	5.31		3	125.241	5.164
	4	27.083	2.179		4	26.789	2.098
	5	16.134	1.633		5	23.583	1.718
5	1	32.367	2.165		1	32.510	2.032
	2	135.378	—	12	2	138.394	—
	3	125.512	5.278		3	125.950	5.412
	4	26.920	2.220		4	59.046	4.020
	5	23.702	1.739		5	23.525	1.647

[a]Chemical shifts in δ scale, relative to internal $Si(CH_3)_4$. Chemical shifts are quoted to 0.001 ppm, since data point resolution was better than 0.001 ppm/Hz. Repeat measurements indicated a reproducibility of ±0.003 ppm.

[b]Number of isoprene units is shown below.

[c]Numbering of carbons within isoprene units is shown below.

[d]CH_3 group *Z* with respect to CH_2 group in isoprene unit 1 (**2A**).

[e]Three overlapping carbons.

[f]Four overlapping carbons.

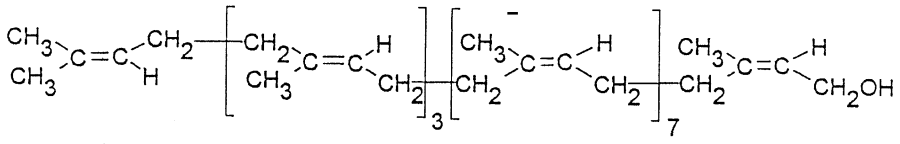

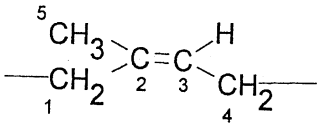

References

1. G. Bodenhausen and D.J. Ruben. Chem. Phys. Lett. **69**, 185 (1980).
2. A. Bax and S. Subramanian. J. Magn. Reson. **67**, 565 (1986).
3. A. Bax and M.F. Summers. J. Am. Chem. Soc. **108**, 2093 (1986).
4. (*a*) A. Bax, M. Ikura, L.E. Kay, D.A. Torchia, and R. Tschudin. J. Mag. Reson. **86**, 304 (1990); (*b*) W.F. Reynolds, S. McLean, L.-L. Tay, M. Yu, R.G. Enriquez, D.M. Estwick, and K.O. Pascoe. Magn. Reson. Chem. **35**, 455 (1992).
5. W.F. Reynolds, M. Yu, R.G. Enriquez, and I. Leon. Magn. Reson. Chem. **35**, 505 (1997).
6. J.R. Garbow, D.P. Weitekamp, and A. Pines. Chem. Phys. Lett. **93**, 504 (1982).
7. A. Bax and G.A. Morris. J. Magn. Reson. **42**, 501 (1981).
8. A. Bax. J. Magn. Reson. **53**, 517 (1983).

© 1999 NRC Canada

9. W.F. Reynolds, S. McLean, M. Perpick-Dumont, and R.G. Enriquez. Magn. Reson. Chem. **26**, 1068 (1988).
10. H. Kessler, C. Griesinger, J. Zarbock, and H.R. Loosli. J. Magn. Reson. **57**, 331 (1984).
11. W.F. Reynolds, S. McLean, M. Perpick-Dumont, and R.G. Enriquez. Magn. Reson. Chem. **27**, 162 (1989).
12. S. McLean, W.F. Reynolds, J.-P. Yang, H. Jacobs, and L.L. Jean-Pierre. Magn. Reson. Chem. **32**, 422 (1994).
13. W.F. Reynolds, M. Yu, and R.G. Enriquez. Magn. Reson. Chem. **35**, 614 (1997).
14. Y. Tanaka and H. Sato. Polymer, **17**, 113 (1976).
15. F.W. Hemming. Terpenoids in Plants. Academic Press, New York. 1967.
16. J. Feeney and F.W. Hemming. Anal. Biochem. **20**, 1 (1969).
17. Y. Tanaka and H. Hirasawa. Chem. Phys. Lipids, **51**, 183 (1989).
18. E. Bartholdi and R.R. Ernst. J. Magn. Reson. **11**, 9 (1973).
19. M.W. Duch and D.M. Grant. Macromolecules, **3**, 165 (1990).
20. K.A. Carpenter, W.F. Reynolds, J.-P. Yang, and R.G. Enriquez. Magn. Reson. Chem. **30**, S35 (1992).

© 1999 NRC Canada

Tris{(diphenylphosphino)dimethylsilyl}methane: a sterically hindered tripod

Dawn M. Friesen, Robert McDonald, and Lisa Rosenberg

Abstract: The synthesis and characterization of a new tripodal tris(phosphine) molecule, $HC(Me_2SiPPh_2)_3$ (**3**) is described. The impact of dimethylsilyl "elbows" on the conformational preferences of this tris(dimethylsilyl)methane core in solution and in the solid state was assessed for **3** and its precursor $HC(Me_2SiBr)_3$ (**2**). Hindered rotation around the "arms" of **3**, evident from its solid state structure, has been probed in solution by variable temperature, $^1H\{^{31}P\}$ NMR spectroscopy, and molecular modelling studies based on the solid state structure of **2** also indicate significant barriers to rotation in this molecule. The susceptibility of **3** to cleavage of the P—Si bonds by protic reagents is described.

Key words: tripodal tris(phosphine), polyphosphine, trisilylmethane, C_3-symmetry.

Résumé : On décrit la synthèse et la caractérisation d'une nouvelle molécule tris(phosphine) tripodale, $HC(Me_2SiPPh_2)_3$ (**3**). On a évalué l'impact des « coudes » diméthylsilyles du composé **3** et de son précurseur, $HC(Me_2SiBr)_3$ (**2**), sur les préférences conformationnelles de ce noyau tris(diméthylsilyl)méthane en solution et à l'état solide. La rotation empêchée autour des « bras » du composé **3**, évidente dans la structure à l'état solide, a été étudiée en solution à l'aide de la spectroscopie RMN du $^1H\{^{31}P\}$ à température variable; des études de modélisation moléculaire sur la structure du composé **2** à l'état solide indiquent qu'il existe aussi des barrières importantes à la rotation dans cette molécule. On décrit la susceptibilité du composé **3** au clivage des liaisons P-Si par des réactifs protiques.

Mots clés : tris(phosphine) tripodale, polyphosphine, trisilylméthane, symétrie C_3.

[Traduit par la Rédaction]

Introduction

The rich transition metal chemistry of tripodal tris(phosphine) ligands has evolved from a desire to exploit the general utility of the ancillary phosphine while establishing a greater degree of control over coordination environment during the activation of small molecules at metal centres (see, for example ref. 1). These facially-binding, chelating ligands promote reactivity at the coordinated metal centre by directing incoming substrates to coordination sites that are mutually *cis* and that are *trans* to the strongly labilizing phosphines. However, dissociation of a single arm of the coordinated phosphine during catalysis or stoichiometric reactions of tripodal phosphine complexes, (1*o*, 1*p*, 2) while in some cases necessary to allow coordination of substrate molecules, can complicate the reaction mechanisms and result in a loss of stereocontrol. The ease of this dissociation may be encouraged by flexibility at the "elbows" of tripodal ligands: rotation around bonds to the central atom of the tripod (and (or) around the P—X bonds) is required to allow the dissociated phosphine arm to move out of the metal's coordination sphere. If the barriers to such rotations can be increased, dissociation of a single arm should become entropically disfavoured. The conformational rigidity of such P_3 units may also be exploited to enforce specific macromolecular geometries, through their incorporation in larger organic or inorganic frameworks. We have begun investigating the effect of substituents at these elbows on the barriers to rotation in the arms of tripodal phosphine molecules, and report here the synthesis and characterization of a new tripod, tris{(diphenylphosphino)dimethylsilyl)}methane (**3**), which exhibits hindered rotation at its elbows as a result of the methyl substituents at silicon.

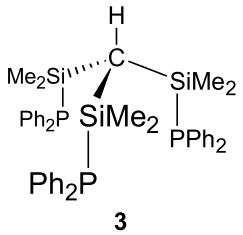

3

Received June 18, 1999.

This paper is dedicated to Professor Ted Schaefer in recognition of his outstanding contributions to Canadian chemistry.

D.M. Friesen and L. Rosenberg.[1] Department of Chemistry, University of Manitoba, Winnipeg, MB R3T 2N2, Canada.
R. McDonald. X-ray Crystallography Laboratory, Department of Chemistry, University of Alberta, Edmonton, AB T6G 2G2, Canada.

[1]Author to whom correspondence may be addressed. Telephone: (204) 474-8548. Fax: (204) 474-7608. e-mail: rosenber@cc.umanitoba.ca

© 1999 NRC Canada

[1]

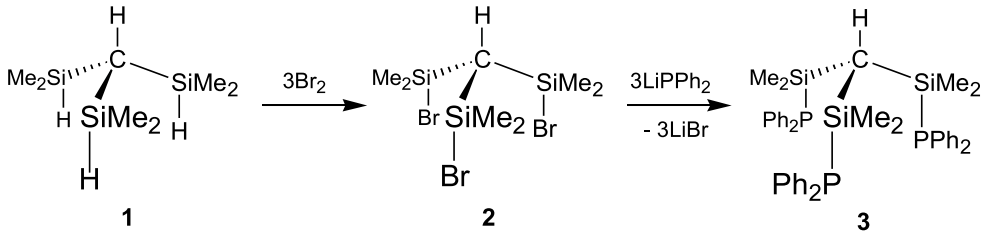

1 2 3

Results and discussion

Synthesis of tris{(diphenylphosphino)dimethylsilyl}methane, 3

The tris-brominated trisilylmethane fragment, **2**, was used previously to prepare a range of tridentate amide ligands for early transition metals and complexes of the group 14 elements (4). Addition of three equivalents of lithium diphenylphosphide to **2** gives quantitative conversion, as determined by NMR spectroscopy, to tris{(diphenylphosphino)dimethylsilyl}methane, **3**, which can be isolated as a white powder in 62% yield after toluene extraction from the reaction residue (eq. [1]).[2]

Tripod **3** has some solubility in non-polar hydrocarbons and is extremely soluble in aromatic hydrocarbons, ethers, and chlorinated solvents. While only mildly susceptible to oxidation, both in solution and in the solid state, **3** does slowly decompose in air via hydrolysis of the P—Si bonds (vide infra).

The effect of the $SiMe_2$ elbows on tripod conformation

Triphos ($H_3CC\{CH_2PPh_2\}_3$) and related tripodal tris(phosphine) ligands typically exhibit relatively unhindered rotation about the C—P bonds of each arm, which manifests itself in average solution structures of C_{3v} symmetry (5). Crystallographic studies of these molecules generally show unsymmetric solid state structures where inequivalent conformations at each of the three arms are attributed to solid state effects (6). An interesting exception is the structure of $HC(CH_2PPh_2)_3$ (**4**), an analogue of **3** with CH_2 elbows, in which a staggered conformation along each $C_{methine}$—CH_2 bond, with gauche $H_{methine}$-C-C-P torsion angles,[3] gives rise to a molecule of pseudo C_3 symmetry (7). The handedness of the resulting chiral conformation of this molecule is evident from the clockwise distribution of phosphine groups around the base of the tripod (anti-clockwise for the other enantiomer, which is present in equal abundance). Maximum separation of the phenyl rings in this C_3-symmetric structure is manifest in a "gearing" of the PPh_2 groups. However, the ^1H and $^{31}P\{^1H\}$ NMR spectra of **4** are consistent with its C_{3v} symmetry in solution, similar to other tripodal P_3 molecules. As described below, the decreased rotational barriers that should result from replacing C—P bonds in this molecule with Si—P bonds, as in **2** and **3** (an average bond lengthening of about 0.42 Å), appear to be offset by the steric requirements of the methyl substituents on silicon in these compounds.

Fig. 1. Molecular structure of $HC(Me_2SiBr)_3$ (**2**). Non-hydrogen atoms are represented by Gaussian ellipsoids at the 20% probability level. Hydrogen atoms are shown with arbitrarily small thermal parameters.

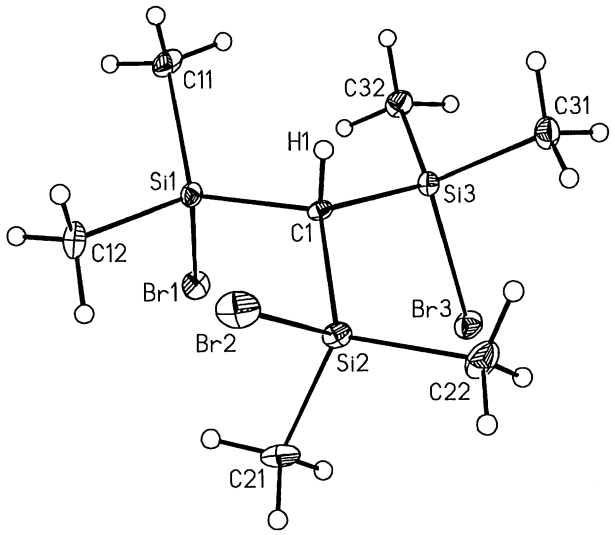

The precursor tripod, $HC(Me_2SiBr)_3$ (**2**) exhibits free rotation around bonds to the $SiMe_2$ elbows in solution. ^1H NMR spectra of **2** at varying temperatures as low as 90°C show negligible peak broadening, and the sharp singlet due to equivalent SiMe groups is consistent with an average structure of high symmetry (C_{3v}) for this molecule in solution. However, an X-ray crystallographic study of a single crystal of **2** shows it to be less symmetric in the

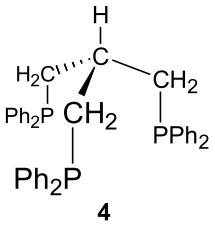

4

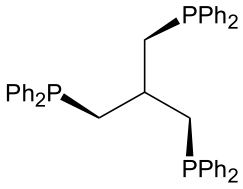

top view, solid state

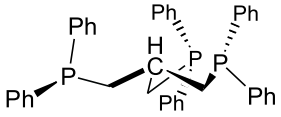

side view, solid state

[2] An alternative synthesis of **3**, and some of its properties, were reported while this manuscript was in preparation. The authors report an 89% yield, but microanalysis indicates the presence of impurities (1.5% high in carbon, 1.3% low in phosphorus) (3*a*).
[3] In **4** these torsion angles are 48.5°, 51.0°, and 44.8°.

© 1999 NRC Canada

Table 1. Crystallographic experimental details for compound **2**.

(*a*) Crystal data	
Compound	**2**
Formula	$C_7H_{19}Br_3Si_3$
Formula weight	427.22
Crystal dimensions (mm)	0.69 × 0.24 × 0.12
Crystal system	monoclinic
Space group	$P2_1/n$ (a nonstandard setting of $P2_1/c$ (no. 14))
Unit cell parameters[a]	
a (Å)	10.0709 (4)
b (Å)	14.4133 (7)
c (Å)	11.6023 (5)
β (deg)	111.270 (3)
V (Å^3)	1569.41 (12)
Z	4
ρ_{calcd} (g cm^{-3})	1.808
μ (mm^{-1})	11.45
(*b*) Data collection and refinement conditions	
Diffractometer	Siemens P4/RA[b]
Radiation (λ (Å))	Graphite-monochromated Cu Kα (1.54178)
Temperature (°C)	–60
Scan type	θ–2θ
Data collection 2θ limit (deg)	115.0
Total data collected	2259 ($-11 \le h \le 0$, $-15 \le k$ 0, $-11 \le l \le 12$)
Independent reflections	2126
Number of observations (NO)	1955 ($F_o^2 \ge 2\sigma(F_o^2)$)
Structure solution method	Direct methods (SHELXS-86)[c]
Refinement method	Full-matrix least-squares on F^2 (SHELXL-93)[d]
Absorption correction method	Semiempirical (Ψ scans)
Range of transmission factors	0.6030–0.1136
Data/restraints/parameters	2126 ($F_o^2 \ge -3\sigma(F_o^2)$) / 0 / 119
Extinction coefficient (*x*)[e]	0.0036 (3)
Goodness-of-fit (*S*)[f]	1.158 ($F_o^2 \ge -3\sigma(F_o^2)$)
Final *R* indices[g]	
$F_o^2 > 2\sigma(F_o^2)$	R_1 = 0.0552, wR_2 = 0.1519
All data	R_1 = 0.0598, wR_2 = 0.1557
Largest difference peak and hole	0.897 and –0.992 e Å^{-3}

[a]Obtained from least-squares refinement of 54 reflections with $54.0° < 2\theta < 60.3°$.

[b]Programs for diffractometer operation, data collection, data reduction, and absorption correction were those supplied by Siemens.

[c]Reference 15.

[d]G.M. Sheldrick. SHELXL-93. Program for crystal structure determination. University of Göttingen, Germany. 1993. Refinement on F_o^2 for all reflections (all of these having $F_o^2 \ge -3\sigma(F_o^2)$). Weighted *R*-factors wR_2 and all goodnesses of fit *S* are based on F_o^2; conventional *R*-factors R_1 are based on F_o, with F_o set to zero for negative F_o^2. The observed criterion of $F_o^2 > 2\sigma(F_o^2)$ is used only for calculating R_1, and is not relevant to the choice of reflections for refinement. *R*-factors based on F_o^2 are statistically about twice as large as those based on F_o, and *R*-factors based on ALL data will be even larger.

[e]$F_c^* = kF_c[1 + x\{0.001F_c^2\lambda^3/\sin(2\theta)\}]^{-1/4}$ where *k* is the overall scale factor.

[f]$S = [\Sigma w(F_o^2 - F_c^2)^2/(n-p)]^{1/2}$ (*n* = number of data; *p* = number of parameters varied; $w = [\sigma^2(F_o^2) + (0.0808P)^2 + 13.8082P]^{-1}$ where $P = [\max(F_o^2, 0) + 2F_c^2]/3$).

[g]$R_1 = \Sigma||F_o| - |F_c||/\Sigma|F_o|$; $wR_2 = [\Sigma w(F_o^2 - F_c^2)^2/\Sigma w(F_o^4)]^{1/2}$.

solid state, having a *syn–anti–anti* orientation of the bromine substituents with respect to the central methine proton. (See Fig. 1 for the molecular structure of **2**, Table 1 for crystallographic data, Table 2 for positional and thermal parameters for the individual atoms, and Table 3 for some representative bond distances and angles,

© 1999 NRC Canada

Table 2. Atomic coordinates and equivalent isotropic displacement parameters for compound **2**.[a]

Atom	*x*	*y*	*z*	U_{eq}, Å^2
Compound **2**				
Br1	0.34378(11)	0.32805(7)	–0.20305(9)	0.0339(4)*
Br2	0.38177(12)	0.37758(8)	–0.67748(10)	0.0431(4)*
Br3	0.47196(11)	0.08961(7)	–0.28964(10)	0.0362(4)*
Si1	0.2182(3)	0.3448(2)	–0.4078(2)	0.0229(6)*
Si2	0.4400(2)	0.2716(2)	–0.5247(2)	0.0249(6)*
Si3	0.2601(2)	0.1274(2)	–0.4354(2)	0.0215(6)*
C1	0.2736(8)	0.2486(5)	–0.4908(7)	0.018(2)*
C11	0.0250(10)	0.3400(7)	–0.4294(9)	0.035(2)*
C12	0.2560(12)	0.4639(6)	–0.4473(10)	0.040(2)*
C21	0.5884(10)	0.3222(7)	–0.3905(10)	0.040(3)*
C22	0.5006(12)	0.1714(7)	–0.5937(11)	0.045(3)*
C31	0.2235(11)	0.0401(6)	–0.5608(9)	0.035(2)*
C32	0.1297(10)	0.1113(7)	–0.3591(10)	0.035(2)*

[a]Anisotropically-refined atoms are marked with an asterisk (*). The form of the anisotropic displacement parameter is exp $[-2\pi^2(h^2a^{*2}U_{11} + k^2b^{*2}U_{22} + l^2c^{*2}U_{33} + 2klb^*c^*U_{23} + 2hla^*c^*U_{13} + 2hka^*b^*U_{12})]$.

Table 3. Selected interatomic distances (Å), interatomic angles (deg), and torsional angles (deg) for compounds **2** and **3**.

Compound **2**					
Br1—Si1	2.263(3)	Si1—C11	1.871(9)	Si2—C22	1.857(10)
Br2—Si2	2.251(3)	Si1—C12	1.852(9)	Si3—C1	1.883(8)
Br3—Si3	2.257(3)	Si2—C1	1.885(7)	Si3—C31	1.857(9)
Si1—C1	1.884(8)	Si2—C21	1.871(10)	Si3—C32	1.846(9)
Br1-Si1-C1	107.6(3)	Br2-Si2-C21	107.0(3)	Br3-Si3-C32	104.7(3)
Br1-Si1-C11	107.2(3)	Br2-Si2-C22	102.7(4)	C1-Si3-C31	112.4(4)
Br1-Si1-C12	105.8(4)	C1-Si2-C21	113.4(4)	C1-Si3-C32	115.6(4)
C1-Si1-C11	113.0(4)	C1-Si2-C22	114.2(4)	C31-Si3-C32	108.5(5)
C1-Si1-C12	115.4(4)	C21-Si2-C22	111.9(5)	Si1-C1-Si2	115.4(4)
C11-Si1-C12	107.3(5)	Br3-Si3-C1	108.3(3)	Si1-C1-Si3	115.9(4)
Br2-Si2-C1	106.6(3)	Br3-Si3-C31	106.7(3)	Si2-C1-Si3	114.4(4)
H1-C1-Si1-Br1	165.08	H1-C1-Si2-Br2	38.6	H1-C1-Si3-Br3	156.6
H1-C1-Si1-C11	47.0	H1-C1-Si2-C21	156.0	H1-C1-Si3-C31	38.9
H1-C1-Si1-C12	–77.1	H1-C1-Si2-C22	–74.2	H1-C1-Si3-C32	–86.4
Compound **3**					
P1—Si1	2.2827(10)	P3—Si3	2.2722(8)	Si2—C1	1.894(2)
P1—C11	1.845(2)	P3—C51	1.834(2)	Si2—C4	1.871(3)
P1—C21	1.837(3)	P3—C61	1.832(2)	Si2—C5	1.873(2)
P2—Si2	2.2794(10)	Si1—C1	1.906(2)	Si3—C1	1.900(2)
P2—C31	1.835(2)	Si1—C2	1.870(3)	Si3—C6	1.869(3)
P2—C41	1.836(3)	Si1—C3	1.875(3)	Si3—C7	1.878(2)
Si1-C1-Si2	114.34(12)	Si3-P3-C61	106.75(8)	P2-Si2-C5	111.17(9)
Si1-C1-Si3	111.84(11)	C51-P3-C61	101.94(11)	C1-Si2-C4	111.25(11)
Si2-C1-Si3	115.03(11)	P1-Si1-C1	107.28(8)	C1-Si2-C5	115.84(11)
Si1-P1-C11	97.72(8)	P1-Si1-C2	106.53(9)	C4-Si2-C5	106.31(13)
Si1-P1-C21	106.80(9)	P1-Si1-C3	109.58(10)	P3-Si3-C1	107.82(7)
C11-P1-C21	103.29(11)	C1-Si1-C2	110.83(11)	P3-Si3-C6	103.40(8)
Si2-P2-C31	99.03(8)	C1-Si1-C3	117.71(11)	P3-Si3-C7	109.98(8)
Si2-P2-C41	108.41(8)	C2-Si1-C3	104.40(13)	C1-Si3-C6	111.38(11)
C31-P2-C41	101.75(11)	P2-Si2-C1	108.10(8)	C1-Si3-C7	116.28(10)
Si3-P3-C51	101.10(7)	P2-Si2-C4	103.49(10)	C6-Si3-C7	107.23(12)
H1-C1-Si1-P1	–37.1	H1-C1-Si2-P2	–48.3	H1-C1-Si3-P3	–47.3
H1-C1-Si1-C2	–153.0	H1-C1-Si2-C4	–161.3	H1-C1-Si3-C6	–160.0
H1-C1-Si1-C3	87	H1-C1-Si2-C5	77.2	H1-C1-Si3-C7	76.7

© 1999 NRC Canada

Fig. 2. Two views of the molecular structure of $HC(Me_2SiPPh_2)_3$ (**3**) (with methyl and phenyl hydrogen atoms omitted). The view on the right, approximately along the methine H1—C1 bond, illustrates the geared conformation of the PPh_2 groups, resulting in a pseudo-C_3 symmetry of the molecule.

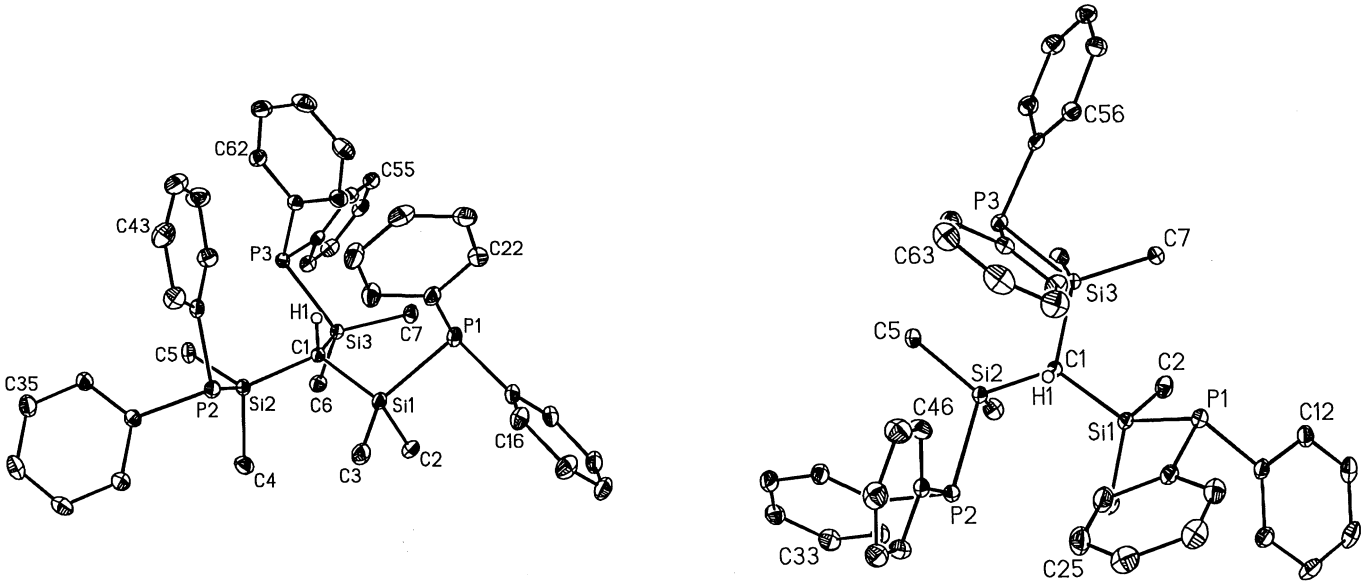

and torsional angles.)[4] Molecular models of **2** built and minimized with HyperChem software (AM1) suggest the solid state structure is one of two lowest energy conformers, the second having a *syn–syn–anti* conformation. Both of these structures maximize the distance between $SiMe_2$ protons, alleviating steric repulsions around the Si_3 base of the tripod. Conformational stability of approximately 2–3 kcal/mol is thus obtained, relative to a more symmetric structure in which all three Si–Br's eclipse the central C—H bond (all *syn*) or one in which the Br's are all *anti* to the central C—H bond. Based on the crystallographically-determined molecular structure of **2**, the calculated barrier to rotation around a single arm ($C_{central}$–Si) of **2** is approximately 5 kcal/mol. The impact of the methyl substituents on silicon in this molecule is further demonstrated by a widening and flattening of the Si_3 tripodal base in its solid state structure: the Si-C-Si bond angles have widened from typical tetrahedral values to an average value of 115.2(4)°, the basal plane containing the three silicon atoms being only 0.418(8) Å from the central carbon. Such splaying of the three C—Si bonds has been observed for a tripodal tris(amine) compound and other molecules containing this tris(dimethylsilyl)methane core,(4*b*, 3*b*) while normal tetrahedral angles are observed at the central carbon for the less bulky $HC(CH_2PPh_2)_3$ (**4**) ($C\text{-}C_{central}\text{-}C$ (avg) = 110.3°) (7).

The steric effects of the $SiMe_2$ groups in the tris(dimethylsilyl)methane core are amplified upon replacement of the bromines in **2** with diphenylphosphine moieties. An X-ray crystallographic study of a single crystal of **3**[4,5] shows that in the solid state, the tripod exhibits pseudo-C_3 symmetry, similar to the molecular structure of $HC(CH_2PPh_2)_3$ (**4**). (Views of one of the two enantiomeric forms of **3** (present in equal abundance in the crystal lattice) are shown in Fig. 2, and some relevant bond distances and angles, and torsional angles are shown in Table 3.) As for **4**, this pseudo-chirality arises from gauche conformations along each of the three H–C–Si–P fragments, and is accompanied by a "geared" distribution of phenyl substituents on phosphorus, around the base of the tripod. Staggered conformations along the C—Si bonds in this structure direct one silylmethyl group on each arm toward the lone pair on phosphorus on the adjacent arm. The second silylmethyl group on each arm points down, approximately *anti* to the $H_{methine}$. Maximum distance between phenyl and methyl substituents is thus achieved. As for compound **2**, a widening of the Si···Si distances in **3** to accomodate the methyl substituents on silicon gives an average Si-C-Si angle of 113.74(11)° and the central carbon is just 0.484(2) Å from the plane containing all three silicons.

The solid state, geared structure of **3** appears to be maintained in solution: variable temperature, $^1H\{^{31}P\}$ NMR spec-

[4] Tables of atomic coordinates for all atoms, a complete listing of bond lengths and angles, torsional angles, least-squares planes, anisotropic thermal parameters, derived positions for the hydrogen atoms, and ORTEP diagrams for the structures of compounds **2** and **3** are available as supplementary material and may be purchased from: The Depository of Unpublished Data, Document Delivery, CISTI, National Research Council Canada, Ottawa, Canada, K1A 0S2. Bond lengths and angles and hydrogen positions for compound **2** have also been deposited with the Cambridge Crystallographic Data Centre and can be obtained on request from: The Director, Cambridge Crystallographic Data Centre, University Chemical Laboratory, 12 Union Road, Cambridge, CB2 1EZ, U.K. Structure factors are no longer being deposited and can be obtained on request from the author.

[5] The X-ray structure of **3** reported here is identical to one published by Avent et al. (3) while this manuscript was in preparation. To simplify our discussion of the solid state and solution structures of **3**, and our comparison of the solid state structures of **2** and **3**, we have included some details of our crystallographic results.

© 1999 NRC Canada

Table 4. Phosphorus–silicon bond cleavage reactions.

Expt.	Concentration of **3** (M)	Solvolysis conditions[a]	Result
1	0.057	H_2O, 100 equiv.[b], 25°C	14% cleavage in 7.5 h 100% cleavage in 3.5 days
2	0.057	H_2O, 100 equiv.[b], 123°C	100% cleavage in 6.5 h
3	0.051	CH_3OH, 100 equiv., 25°C	26% cleavage in 4 h 100% cleavage in 3 days
4	0.051	CH_3OH, 100 equiv., 123°C	100% cleavage in 3.5 h
5	0.057	0.01 M HCl (aq)[c], 25°C	100% cleavage in 4 h

[a]All solvolysis reactions carried out in d_8-toluene in sealed NMR tubes.

[b]Total H_2O in sealed sample, both dissolved and undissolved in d_8-toluene.

[c]100 equiv. H_2O[b].

Fig. 3. The SiMe region of the $^1H\{^{31}P\}$ NMR spectrum of **3** at 190 K: the upper trace is the calculated spectrum, the lower is the experimentally observed spectrum (an asterisk marks the signal due to the $H_{methine}$).

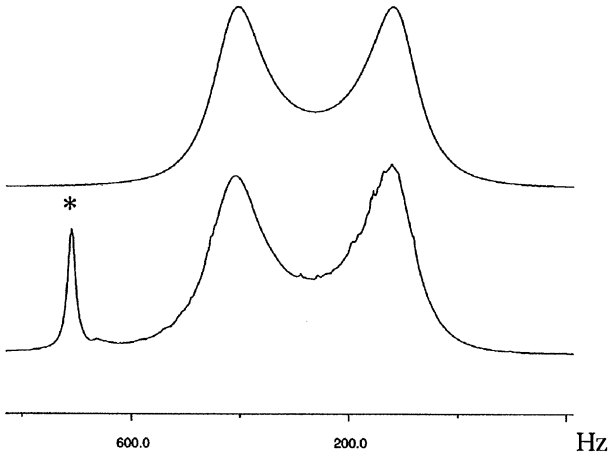

troscopy (500 MHz) confirms the mutual exchange of silylmethyl groups between two diastereotopic sites on each of the three $SiMe_2$ moieties in the molecule, consistent with a ground state solution conformation of C_3 symmetry. When a sample of **3** in d_8-toluene is cooled, the slightly broad singlet observed at 0.53 ppm in the room temperature spectrum undergoes decoalescence at about 195 K. Two broad singlets of equal relative intensity and centred around the original signal are observed in the spectrum of the sample at 180 K, the lowest temperature studied. At no temperature are signals observed by ^1H or $^{31}P\{^1H\}$ NMR that correspond to a less symmetric solution conformation, such as the solid state, *syn–anti–anti* conformation of compound **2**. The H_{ortho} and H_{meta} signals in the aromatic region of the $^1H\{^{31}P\}$ NMR spectrum of **3** also decoalesce as the sample temperature is lowered, while the H_{para} signal remains unchanged, apart from very slight broadening. Due to the complexity of overlapping signals in this region, only the H_{ortho} signals are clearly resolved at the low-temperature limit: again, the low-temperature pattern is consistent with a simple two-site exchange.[6]

The observed exchange of silylmethyl groups between diastereotopic sites in a ground state, C_3-symmetric conformation represents conversion between the two atropisomers of **3**, which are present in equal amounts (ie. the molecule is not optically active in solution). Such exchange requires rotation around the three $C_{methine}$—Si bonds in **3**, and the barrier to this rotation was evaluated through line-shape analysis of the SiMe peaks in the $^1H\{^{31}P\}$ NMR spectra recorded for **3** at low temperature. (See, for example, Fig. 3.) Rate constants calculated for the exchange process at various temperatures gave an energy of activation (E_a) for the two site exchange of 10.9 kcal/mol, when substituted into the Arrhenius equation. An Eyring plot gave activation parameters for the exchange: $\Delta H^{\ddagger}$ = 10.5 kcal/mol, $\Delta S^{\ddagger}$ = 9.1 cal/K mol, and therefore $\Delta G^{\ddagger}$ (300 K) = 7.7 kcal/mol. These values are consistent with a thermodynamically-enforced conformational preference for **3** in solution: it is an unusually rigid tripodal framework.

Reactivity studies

Of concern in the synthesis and subsequent reactivity of transition metal complexes of **3** is the generally-accepted sensitivity of P—Si bonds to cleavage by water and protic solvents (8). To gauge the tolerance of **3** for such reagents, we undertook a series of reactivity studies. The tripod is not soluble in water or methanol, and shows only slight degradation when stirred as a suspension in either solvent. The sensitivity of **3** to these protic reagents in solution was probed by NMR experiments in which approximately 100 equiv of water, methanol, or dilute HCl(aq) was added to **3** in d_8-toluene. The results (summarized in Table 4) indicate that P—Si bond cleavage occurs relatively slowly for **3** in the presence of water or methanol, with quantitative conversion to cleavage products requiring approximately three days at room temperature (Expts. 1 and 3, Table 4). These rates are accelerated at higher temperatures, with quantitative conversion to cleavage products occurring in 3–6 h in samples heated to 123°C (Expts. 2 and 4, Table 4). Slightly slower rates observed for water relative to methanol in these reactions are probably due to its lower solubility in toluene. (We observe signals in the ^1H NMR spectra due to both dissolved and undissolved water.) The rate of hydrolysis also accelerates with the addition of a catalytic amount of acid (Expt. 5, Table 4), whereupon complete cleavage of the P—Si bonds in **3** occurs at room temperature within 4 h.

[6] $\Delta G^{\ddagger}$ values for decoalescence of the H_{ortho} and SiMe signals (calculated simply from coalescence temperatures and peak separations at the low-temperature limit) are equal within experimental error, suggesting both decoalescences arise from the same exchange process. See the experimental section for details.

© 1999 NRC Canada

Scheme 1.

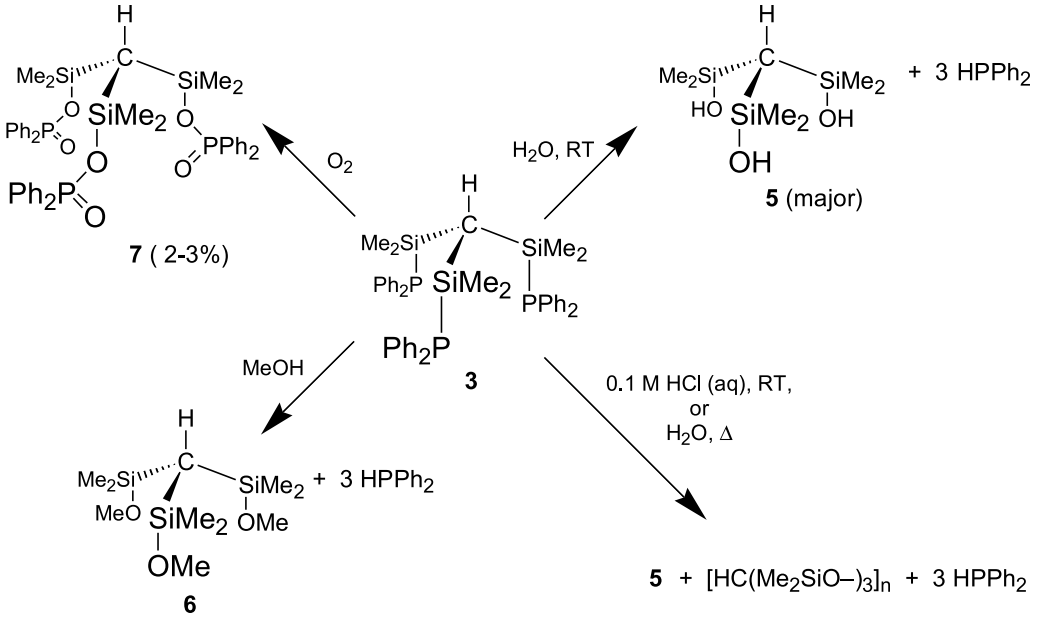

In the above solvolysis reactions, $HPPh_2$ is the phosphorus-containing cleavage product, but the fate of the silicon-containing tripodal core depends on the reagents and reaction conditions (Scheme 1). At room temperature, hydrolysis of the P—Si bond in **3** produces principally the tris(silylalcohol), $HC\{(CH_3)_2Si(OH)\}_3$ (**5**) (9), as determined by ^1H NMR spectroscopy. However, self condensation of the SiOH groups in **5** gives some oligomeric siloxane impurities, resulting in a range of small peaks from 0–0.1 ppm in the ^1H NMR spectrum, and a slight cloudiness in the sample.[7] When the reaction is carried out at high temperature, monomeric **5**, initially the major product, undergoes more extensive oligomerization, as determined by relative integration of SiMe signals in the ^1H NMR spectra before and after complete hydrolysis. The formation of polysiloxanes in this reaction is also evident from the appearance of a gelatinous white precipitate in the NMR tube. Similarly, in the reaction of **3** with dilute acid, the initial hydrolysis product, **5**, is rapidly joined in the reaction mixture by oligomerization products, which give broad peaks due to SiMe and SiOH groups (0–0.6 ppm) in the ^1H NMR spectrum and a slight cloudiness in the NMR sample. In the presence of excess methanol, **3** is cleanly converted to $HPPh_2$ and $HC\{Me_2Si(OMe)\}_3$, **6**, at room temperature or higher (9). Compound **6** does not oligomerize, and could probably be isolated from larger scale reaction mixtures by fractional distillation. While the tripod is sensitive enough to these reagents that we must avoid their use in the preparation of metal complexes of **3**, these reactivity studies suggest that if we wish to capitalize on the conformational rigidity of **3** in the templated incorporation of three phosphine units into a variety of macromolecular structures, we may cleave and recover the trisilylmethane core in a controlled manner via methanolysis.

Despite the complexity of the ^1H NMR spectra acquired during the hydrolysis of **3**, we observed no intermediate, partially hydrolyzed, podand species in these reactions: the $^{31}P\{^1H\}$ NMR spectra were clean and simple, showing only unreacted tripodal starting material and free diphenyl phosphine. In the methanolysis reactions (room temperature and high temperature), traces of a possible, unidentified intermediate are observed in the initial NMR spectra.[8] The observed signals account for less than 2% of the total phosphorus-containing material, and disappear before P–Si cleavage is complete.

As described earlier, the tris(phosphine) **3** is relatively stable to oxidation both in the solid state and in solution (Scheme 1). Bubbling oxygen through solutions of **3** (or passing oxygen over a solid sample of **3**) for 15 min gives only trace amounts of the oxidation product $HC(Me_2SiOP(=O)Ph_2)_3$ (**7**) (10), as determined by ^1H and ^{31}P NMR spectroscopy.[9]

Conclusions

Steric hindrance arising from the introduction of dimethylsilyl elbows in a tripodal molecule has given a significantly rigid tris(phosphine) compound (**3**). We are currently exploring the coordination chemistry of this chelating ligand. While the sensitivity of the P—Si bonds to cleavage by protic reagents limits the range of solvents available for reactions of **3** with transition metals, clean methanolysis of these bonds will allow the recovery of the tripodal core. Future work will capitalize on this feature of the reactivity of **3** in synthetic strategies requiring the regio- or stereospecific delivery of three phosphine units into a variety of macromolecular structures.

[7] This cloudiness is in addition to that due to the emulsion arising from the low solubility of water in toluene.
[8] $^{31}P\{^1H\}$: δ –50.6 ppm, ^1H: δ 0.20 ppm (SiMe).
[9] Hydrolysis by trace water in the oxygen gas gives some P–Si cleavage (3%).

© 1999 NRC Canada

Experimental

General procedures and reagent syntheses

Unless otherwise noted, all reactions and manipulations were done under an N_2(g) atmosphere in a glovebox or using conventional Schlenk techniques. Hexanes, ether, and THF were purified by distillation from sodium/benzophenone under argon, toluene was distilled from sodium under argon, benzene was vacuum transferred from over sodium/benzophenone, and methanol was purified by distillation from Mg under nitrogen. Deuterated solvents were purchased from Cambridge Isotopes, degassed and vacuum transferred from over sodium/benzophenone (d_6-benzene, d_8-toluene) or calcium hydride (d_1-chloroform). Tris(dimethylsilyl)methane (4*a*, 9), lithium diphenylphosphide (11), and *tert*-butylchloride (12) were prepared according to literature procedures. Bromine (≥ 99.5%) was purchased from Anachemia and used as received without further purification.

NMR spectra were obtained on a Bruker AM 300 operating at 300.133 MHz for ^{1}H, 121.496 MHz for ^{31}P, 75.469 MHz for ^{13}C, and 59.6 MHz for ^{29}Si, or on a Bruker AMX 500 operating at 500.13 MHz for ^{1}H and 202.46 MHz for ^{31}P. Chemical shifts are reported (in ppm) for 300 K unless otherwise stated. ^{1}H chemical shifts are referenced to residual protonated solvent peaks at 7.15 ppm (C_6D_5H), 2.09 ppm ($PhCD_2H$), and 7.29 ppm ($CHCl_3$). ^{13}C chemical shifts are referenced to C_6D_6 at 128.0 ppm and $CDCl_3$ at 77.5 ppm. Both ^{1}H and ^{13}C chemical shifts are reported relative to tetramethylsilane. ^{31}P chemical shifts are reported relative to 85% H_3PO_4(aq). Microanalysis was performed by Guelph Chemical Laboratories Ltd., Guelph, Ontario, Canada. Mass spectroscopic analysis was carried out by Mr. Wayne Buchannon, in the Department of Chemistry, University of Manitoba.

Modified synthesis of $HC(Me_2SiBr)_3$, 2 (22, 38)

A 3.0 M solution of bromine in benzene was added dropwise over 3 h to a solution of $HC(Me_2SiH)_3$ (**1**, 10.46 g, 54.91 mmol) in benzene (10.0 mL). A stream of nitrogen was passed through the flask and allowed to exit via a dispersion tube submerged in a 0.85 M solution of *cis*-cyclooctene in toluene (400 mL), to trap product HBr(g) and any unreacted Br_2(g). The addition of Br_2 was stopped when the orange colour of bromine persisted in the reaction mixture (total volume 35 mL, 105 mmol Br_2). The solvent was removed in vacuo to give a pale beige paste, which was dissolved in ether or benzene (3.0 mL) for transfer by syringe to a distillation flask. Distillation under reduced pressure gave the product, a white crystalline solid that solidified in the condenser and had to be transferred over using a heat gun; bp 70–87°C (0.1 mmHg) (1 mmHg = 133.3 Pa). Yield: 42.5% (9.97 g). ^{1}H NMR (300 MHz, C_6D_6, δ): 0.67 (s, 18H, SiCH_3), 0.27 (s, 1H, C*H*). ^{13}C{^{1}H} NMR (75 MHz, C_6D_6, δ): 15.15 (s, *C*H), 7.47 (s, SiCH_3).

Synthesis of $HC(Me_2SiPPh_2)_3$, 3

In a 100 mL two-neck round-bottom flask equipped with an air-cooled reflux condenser, PPh_3 (9.7 g, 37 mmol) was dissolved in THF (25 mL). To this solution was added lithium metal (0.51 g, 74 mmol) in thin strips, and the mixture was left stirring until most of the lithium had been consumed. After 2 h, *tert*-butylchloride (4.0 mL, 37 mmol) was added slowly to the dark red $LiPPh_2$ solution by syringe, giving a white ppt and the evolution of gaseous isobutene. A 250 mL, two-neck round-bottom flask equipped with a pressure-equalizing dropping funnel and an air-cooled reflux condenser was charged with **2** (5.3 g, 12 mmol) in THF (25 mL). The $LiPPh_2$ solution was filtered by cannula into the dropping funnel, and added dropwise to the solution of **2** in THF over 30 min, giving a yellow solution with a white precipitate. The clear yellow solution was filtered by cannula into a small Schlenk tube, the solvent was removed in vacuo and the residue extracted with toluene (75 mL). The resulting solution was filtered through Celite on a sintered glass frit, and the toluene removed under vacuum. The product, a white powder, was washed with pentane (3 × 10 mL), and dried under vacuum. Yield: 62% (5.68 g); mp (uncorrected) 197–203°C. ^{1}H NMR (300 MHz, C_6D_6, δ): 7.53 (br m, 12H, *o*-C_6H_5), 7.01 (br m, 18H, *p*-, *m*-C_6H_5), 1.20 (q, $^3J_{PH}$ = 3.5 Hz, 1H, C*H*), 0.53 (br s, 18H, SiCH_3). ^{1}H NMR (300 MHz, $CDCl_3$, δ): 7.30–7.40 (m, 12H, *o*-C_6H_5), 7.10–7.20 (m, 18H, *p*-, *m*-C_6H_5), 0.85 (q, $^3J_{PH}$ = 3.5 Hz, 1H, C*H*), 0.39 (br s, 18H, SiCH_3). ^{13}C NMR (75 MHz, C_6D_6, δ): 134.68, 128.81 (m, C_6H_5), 2.10 (m, 6C, SiCH_3). ^{13}C NMR (75 MHz, $CDCl_3$, δ): 135.85 (m, *ipso*-C_6H_5), 134.22 (m, *o*-C_6H_5), 128.42 (m, *m*-C_6H_5), 127.45 (s, *p*-C_6H_5), 1.86 (m, SiCH_3), 1.24 (q, $^2J_{PC}$ = 10.7 Hz, *C*H). ^{31}P{^{1}H} NMR (121 MHz, C_6D_6, δ): –51.1 (s, 3P, PPh_2). ^{31}P{^{1}H} NMR (121 MHz, $CDCl_3$, δ): –51.3 (s, *P*Ph_2). ^{29}Si{^{1}H} NMR (60 MHz, C_7D_8, δ): 7.8–8.4 (br m). Anal. calcd. for $C_{43}H_{49}P_3Si_3$: C 69.51, H 6.65; found: C 69.28, H 6.74. MS (EI, 70 eV) *m*/*z*: 557 [M – PPh_2], 372 [M – 2 PPh_2], 186 [M – 3 PPh_2]. See Table 5 and text for variable temperature NMR data for **3**.

Reaction of $HC(Me_2SiPPh_2)_3$ (3) with H_2O

(a) At room temperature

Tris{(diphenylphosphino)dimethylsilyl}methane (**3**) (0.5 mL of a 0.0644 M standard solution in d_8-toluene, 0.032 mmol) was placed in a sealable NMR tube, which was attached to the vacuum line via a needle valve adapter. Deionized water (60 μL, 3.32 mmol, degassed by three freeze–pump–thaw cycles) was added under a flow of nitrogen, the mixture was degassed by one freeze–pump–thaw cycle, and the sample was sealed under vacuum. The progress of the reaction was monitored by ^{31}P{^{1}H} and ^{1}H NMR spectroscopy. For $HC(Me_2SiOH)_3$ (**5**): ^{1}H NMR (300 MHz, C_7D_8, δ): 0.37 (s, 3H, SiO*H*), 0.27 (s, 18H, SiCH_3), –0.11 (s, 1H, C*H*).

(b) At 123°C

A sealed NMR tube containing **3** (0.50 mL of a 0.0644 M standard solution in d_8-toluene, 0.032 mmol) and deionized water (60 μL, 3.32 mmol), prepared as described above, was placed in an oil bath at 123°C and was removed periodically for assessment of the progress of reaction by ^{31}P{^{1}H} and ^{1}H NMR spectroscopy.

Reaction of $HC(Me_2SiPPh_2)_3$ (3) with CH_3OH

(a) At room temperature

A sealed NMR tube containing **3** (0.5 mL of a 0.0644 M standard solution in d_8-toluene, 0.032 mmol) and methanol (130 μL, 3.23 mmol) was prepared as described above. The

© 1999 NRC Canada

Table 5. Variable temperature $^1H\{^{31}P\}$ NMR data[a] for **3** (500 MHz, C_7D_8).

T (K)	$SiCH_3$	CH	PPh_2
220	0.53, br s, 18H, 11.8	1.32, s, 1H	7.46, d, 12H, 7.3[b] 6.98, t, 6H, 7.6[c] 6.93, m, 12H[d]
210	0.53, br s, 18H, 27.0	1.35, s, 1H	7.48, br d, 12H, 6.8[b] 6.99, t, 6H, 7.6[c] 6.87–6.96, br m, 12H[d]
200	0.50, br s, 18H, 108.2	1.38, br s, 1H, 6.8	7.48, br s, 12H, 23.0[b] 6.98, br t, 6H, 7.3[c] 6.92, br s, 12H, 22.7[d]
190	0.36, br s, 9H, 145.3 0.83, br s, 9H, 145.3	1.42, br s, 1H, 20.3	7.48, br s, 12H, 139.0[b] 6.97, br t, 12H, 6.8[c] 6.91, br s, 12H, 105.8[d]
180	0.20, br s, 9H, 39.8 0.89, br s, 9H, 59.7	1.41, br s, 1H, 37.8	[e] 7.62, br s, 6H, 35.8[b] 7.33, br s, 6H, 27.9[b] 6.75, br s, 6H, 37.8[d]

[a]δ (ppm), multiplicity, RI, J_{H-H} or $\omega_{1/2}$ (Hz).
[b]H_o.
[c]H_p.
[d]H_m.
[e]Some peaks were lost under solvent signals.

progress of the reaction was monitored by $^{31}P\{^1H\}$ and ^1H NMR spectroscopy. For $HC(Me_2SiOMe)_3$ (**6**): ^1H NMR (300 MHz, C_7D_8, δ): 3.22 (s, 9H, $SiOCH_3$), 0.21 (s, 18H, $SiCH_3$), 0.01 (s, 1H, C*H*).

(b) At 123°C

A sealed NMR tube containing **3** (0.50 mL of a 0.0644 M standard solution in d_8-toluene, 0.032 mmol) and methanol (130 μL, 3.23 mmol), prepared as described above, was placed in an oil bath at 123°C and was removed from the bath periodically to assess the progress of reaction by $^{31}P\{^1H\}$ and ^1H NMR spectroscopy.

Reaction of $HC(Me_2SiPPh_2)_3$ (3) with 0.1 M HCl (aq), at 25°C

A sealed NMR tube containing **3** (0.50 mL of a 0.0644 M standard solution in d_8-toluene, 0.032 mmol) and 0.1 M HCl (60 μL, 3.3 mmol H_2O, 0.006 mmol H_3O^+, degassed by three freeze–pump–thaw cycles) was prepared as described above. The progress of the reaction was monitored by $^{31}P\{^1H\}$ and ^1H NMR spectroscopy.

Reaction of $HC(Me_2SiPPh_2)_3$ (3) with O_2

(a) In the solid state

In a Schlenk, solid tris{(diphenylphosphino)dimethylsilyl}methane, **3** (20 mg, 0.03 mmol), was placed under an atmosphere of oxygen gas (99.9%) for 15 min, then the oxygen was removed under vacuum. The sample was dissolved in d_6-benzene (0.6 mL) and the solution was transferred to an NMR tube, for analysis by ^1H and $^{31}P\{^1H\}$ NMR spectroscopy. For $HC(Me_2SiP\{=O\}Ph_2$: ^1H NMR (300 MHz, C_6D_6, δ): 0.41 (s, 18H, $SiCH_3$), other peaks were lost in the baseline; $^{31}P\{^1H\}$ NMR (121 MHz, $CDCl_3$, δ): 98.9 (s, $P(=O)Ph_2$).

(b) In solution

Oxygen gas (99.9%) was bubbled through a solution of **3** (20 mg, 0.03 mmol) in toluene (5.0 mL) in a Schlenk for 15 min. After removal of the oxygen and toluene under vacuum, a white, oily, solid residue was dissolved in d_6-benzene (0.6 mL) and transferred to an NMR tube for analysis by ^1H and $^{31}P\{^1H\}$ NMR spectroscopy.

Molecular modeling of $HC(Me_2SiBr)_3$ (2)

Atomic coordinates from the crystallographically-determined molecular structure of **2** were imported into the HyperChem modeling program.[10] This structure was used as the starting point for semi-empirical, AM1 calculations, employing a Polak–Ribiere conjugate gradient for geometry minimization. To determine the barrier to rotation around the $C_{methine}$—Si bonds, one torsional angle (H1-C1-Si2-Br2) was varied between 0° and 360°: for each calculation the rest of the molecule was allowed to relax around this constrained angle. Once the minimization was complete, the torsion constraint was removed and the heat of formation was calculated. Rotational barriers were determined from a plot of the heat of formation versus torsion angle.

Line-shape analysis of 3 and related calculations

Line-shape analysis was carried out on the SiMe region of $^1H\{^{31}P\}$ NMR (500 MHz) spectra recorded for compound **3** in d_8-toluene at 220, 210, 200, and 190 K, using XSIM[11] and a modified version of DNMR3 (13). Rate constants (*k*) for the two-site exchange were determined iteratively at each

[10]Hypercube, Inc., Gainesville, Fla.
[11]K. Marat. Winnipeg, 1999.

© 1999 NRC Canada

temperature, giving well-matched simulated and experimental spectra (see Fig. 3). Estimated errors in k varied from 2–6%, temperatures are ±5 K. Thermodynamic parameters were obtained from the slope and intercept of an Eyring plot (ln (k/T) vs. 1/T, R = 1.000): $\Delta H^{\ddagger}$ = 10.5 kcal/mol, $\Delta S^{\ddagger}$ = 9.1 cal/K mol. These yielded $\Delta G^{\ddagger}$(300 K) = 7.7 kcal/mol (± 2.5%). Energy of activation, E_a = 10.9 kcal/mol, was determined from the slope of an Arrhenius plot (ln k vs. 1/T, R = 1.000) (14).

$\Delta G^{\ddagger}$ was also calculated for decoalescence of both the H_{ortho} and SiMe signals in the variable temperature $^1H\{^{31}P\}$ NMR (500 MHz) spectra recorded for compound **3** using the value for the rate constant k_C (where $k_C = \pi\Delta\nu_C/(2)^{1/2}$) in the Eyring equation

$$\Delta G^{\ddagger} = -RT_C \ln [k_C h)/(k_B T_C)]$$

where R = the gas constant, T_C = coalescence temperature, $\Delta\nu_C$ = peak separation at the low-temperature limit, h = Planck's constant, and k_B = Boltzmann constant (14). For the two-site exchange of (*i*) H_{ortho} groups: T_C = 185 ± 5 K, $\Delta\nu_C$ = 145 Hz, $\Delta G^{\ddagger}$ = 8.5 ± 0.2 kcal/mol; (*ii*) SiMe groups: T_C = 195 ± 5 K, $\Delta\nu_C$ = 395 Hz, $\Delta G^{\ddagger}$ = 8.6 ± 0.2 kcal/mol.

Acknowledgements

Funding for this work from the Natural Sciences and Engineering Research Council of Canada (research grant to L.R., postgraduate scholarship to D.M.F.) and from the University of Manitoba's University Research Grants Program is gratefully acknowledged. The authors thank Dr. Kirk Marat for assistance with analysis of the variable temperature NMR data and for helpful discussions.

References

1. (*a*) H.A. Mayer and W.C. Kaska. Chem. Rev. **94**, 1239 (1994); (*b*) L. Sacconi and F. Mani. Transition Met. Chem. **8**, 179 (1982); (*c*) C. Bianchini and A. Meli. Acc. Chem. Res. **31**, 109 (1999); (*d*) C. Bianchini, A. Meli, M. Peruzzini, F. Vizza, and F. Zanobini. Coord. Chem. Rev. **120**, 193 (1992); (*e*) C. Bianchini, S. Moneti, M. Peruzzini, and F. Vizza. Inorg. Chem. **36**, 5818 (1997); (*f*) C. Bianchini, A. Marchi, L. Marvelli, M. Peruzzini, A. Romerosa, and R. Rossi. Organometallics, **15**, 3804 (1996); (*g*) K. Heinze, G. Huttner, and O. Walter. Eur. J. Inorg. Chem. 593 (1999); (*h*) P. Schober, R. Soltek, G. Huttner, L. Zsolnai, and K. Heinze. Eur. J. Inorg. Chem. 1407 (1998); (*i*) K. Heinze, G. Huttner, L. Zsolnai, and P. Schober. Inorg. Chem. **36**, 5457 (1997); (*j*) S. Mann, G. Huttner, L. Zsolnai, and K. Heinze. Angew. Chem. Int. Ed. **35**, 2808 (1996); (*k*) T. Seitz, A. Asam, G. Huttner, O. Walter, and L. Zsolnai. Z. Naturforsch. **50b**, 1287 (1995); (*l*) L.F. Rhodes and L.M. Venanzi. Inorg. Chem. **26**, 2692 (1987); (*m*) J. Ott, L.M. Venanzi, C.A. Ghilardi, S. Midollini, and A. Orlandini. J. Organomet. Chem. **291**, 89 (1985); (*n*) W.O. Siegl, S.J. Lapporte, and J.P. Collman. Inorg. Chem. **12**, 674 (1973); (*o*) G.G. Johnston and M.C. Baird. J. Chem. Soc. Chem. Commun. 1008 (1989); (*p*) E.G. Thaler, K. Folting, and K.G. Caulton. J. Am. Chem. Soc. **112**, 2664 (1990).
2. (*a*) O. Siegl, S.J. Lapporte, and J.P. Collman. Inorg. Chem. **10**, 2158 (1971); (*b*) E.G. Thaler and K.G. Caulton. Organometallics, **9**, 1871 (1990); (*c*) D.J. Rauscher, E.G. Thaler, J.C. Huffman, and K.G. Caulton. Organometallics, **10**, 2209 (1991); (*d*) G. Kiss and I.T. Horváth. Organometallics, **10**, 3798 (1991); (*e*) C. Landgrafe, W.S. Sheldrick, and M. Südfeld. Eur. J. Inorg. Chem. 407 (1998).
3. (*a*) A.G. Avent, D. Bonafoux, C. Eaborn, S.K. Gupta, P.B. Hitchcock, and D.J. Smith. J. Chem. Soc. Dalton Trans. 831 (1999); (*b*) C. Eaborn, P.B. Hitchcock, and P.D. Lickiss. J. Organomet. Chem. **269**, 235 (1984).
4. (*a*) L.H. Gade and C. Becker. Inorg. Chem. **32**, 2308 (1993); (*b*) H. Memmler, L.H. Gade, and J.W. Lauher. Inorg. Chem. **33**, 3064 (1994); (*c*) K.W. Hellmann, P. Steinert, and L.H. Gade. Inorg. Chem. **33**, 3859 (1994); (*d*) K.W. Hellmann, S. Friedrich, L.H. Gade, W.-S. Li, and M. McPartlin. Chem. Ber. **128**, 29 (1995); (*e*) H. Memmler, K. Walsh, L.H. Gade, and J.W. Lauher. Inorg. Chem. **34**, 4062 (1995); (*f*) K.W. Hellmann, L.H. Gade, O. Gevert, P. Steinert, and J.W. Lauher. Inorg. Chem. **34**, 4069 (1995); (*g*) H. Memmler, U. Kauper, L.H. Gade, D. Stalke, and J.W. Lauher. Organometallics, **15**, 3637 (1996).
5. C. Moberg. Angew. Chem. Int. Ed. Engl. **37**, 248 (1998).
6. (*a*) C. Mealli. Acta Cryst. **B38**, 1040 (1982); (*b*) T.R. Ward, L.M. Venanzi, A. Albinati, F. Lianza, T. Gerfin, V. Gramlich, and G.M.R. Tombo. Helv. Chim. Acta, **74**, 983 (1991); (*c*) A. Muth, O. Walter, G. Huttner, A. Asam, L. Zsolnai, and C. Emmerich. J. Organomet. Chem. **468**, 149 (1994); (*d*) B.C. Janssen, V. Sernau, G. Huttner, A. Asam, O. Walter, M. Büchner, and L. Zsolnai. Chem. Ber. **128**, 63 (1995).
7. B.C. Janssen, A. Asam, G. Huttner, V. Sernau, and L. Zsolnai. Chem. Ber. **127**, 501 (1994).
8. (*a*) S. Trippett. *In* Halogenophosphines and related compounds. Vol. 1. *Edited by* S. Trippett. The Chemical Society, London. 1970; (*b*) J. Thottathil. *In* Developments in the preparation and use of silicon-containing organophosphorus compounds. *Edited by* R. Engel. Marcel Dekker, Inc., New York. 1992; (*c*) D.M. Schubert and A.D. Norman. Inorg. Chem. **23**, 4130 (1984).
9. C. Eaborn, P.B. Hitchcock and P.D. Lickiss. J. Organomet. Chem. **252**, 281 (1983).
10. E.W. Abel and I.H. Sabherwal. J. Chem. Soc. A,. 1105 (1968).
11. G.W. Luther and G. Beyerle. Inorg. Synth. **17**, 186 (1977).
12. C. Weygand. *In* Weygand/Hilgetag preparative organic chemistry. *Edited by* G. Hilgetag and A. Martini. Wiley, New York. 1972. p. 219.
13. D.A. Kleier and G. Binsch. J. Mag. Res. **3**, 146 (1970).
14. H. Günther. NMR spectroscopy: an introduction. John Wiley & Sons, Chichester. 1980.
15. G.M. Sheldrick. Acta Crystallogr. Sect. A, **A46**, 467 (1990).

© 1999 NRC Canada

Nuclear magnetic resonance investigations of azo-hydrazone, acid–base equilibria of FD&C Yellow No. 5 (tartrazine)

Eugene P. Mazzola, Sandra J. Bell, Saleh A. Turujman, Julie N. Barrows, John E. Bailey, Jr., Joseph B. McMahon, Tania K. Germann, and William F. Reynolds

Abstract: Azo-hydrazone, acid–base equilibria were examined for the water-soluble, food color additive FD&C Yellow No. 5 (Y5), with the observation of dynamic NMR effects near, and at, pH 10, where the food colorant converts from a predominantly hydrazone tautomer (acidic to moderately basic pH) to a prevailing azo-anion resonance hybrid (high pH). Potentiometric titrations further indicate that the pK_a of Y5 is ca. 10. These data suggest that observed NMR line broadening is due to slow proton transfer between a hydrazone-NH and water.

Key words: ^{1}H, ^{13}C, and ^{15}N NMR, azo-hydrazone/acid–base equilibria, FD&C Yellow No. 5.

Résumé : On a étudié l'équilibre acide–base, azo-hydrazone, du colorant jaune FD&C No. 5 (Y5) qui est soluble dans l'eau et qui est utilisé comme additif alimentaire. À cette fin, on a fait appel aux effets RMN dynamiques à (ou près d') un pH de 10 auquel le colorant passe d'une forme tautomère hydrazone prédominante (pH acide à modérément basique) à un hybride de résonance azo-anionique (pH élevé). Des mesures de titrages potentiométriques indiquent de plus que le pK_a du Y5 est d'environ 10. Ces données suggèrent que l'élargissement des raies observées dans les spectres RMN résulte d'un transfert lent de proton entre l'eau et un NH de l'hydrazone.

Mots clés : RMN du ^{1}H, du ^{13}C et du ^{15}N, équilibre acide–base/azo-hydrazone, jaune FD&C No. 5.

[Traduit par la Rédaction]

Compounds exhibiting azo-hydrazone tautomerism have been extensively investigated in a variety of organic solvent systems (1). However, partly because of the difficulty of obtaining IR spectra of aqueous solutions, their water-soluble analogs have still received limited attention. Several years ago the azo-hydrazone, acid–base equilibria of FD&C Yellow No. 5 (Y5, **1**) was examined by ^{15}N NMR, and significant change was observed from pH 7 to 12 (2). At pH 7, chemical shift values were –168.9 and –11.2 ppm (relative to $NH_4{}^{15}NO_3$). The former is typical of those reported for hydrazone sp^3-hybridized nitrogens, whereas the latter is characteristic of imino nitrogens (3). These resonances were assigned to the α- and β-nitrogens, respectively, and were interpreted as evidence that Y5 exists predominantly as a hydrazone below pH 9, as shown in the *anti*-configuration, **1a**.

At pH 12, signals were observed at 40.5 and 97.5 ppm (also relative to $NH_4{}^{15}NO_3$) (2), which are in the range found for azo compounds (4). They were assigned by comparison with the chemical shift of the β-^{15}N-labeled isotopomer of Y5 ([β-^{15}N]-Y5), which appears at 97.0 ppm. The resonance at 97.5 ppm was, therefore, assigned to the β-nitrogen. These chemical shifts were interpreted as demonstrating that Y5 occurs almost exclusively as an azo-anion, e.g., **1b**, above pH 11. The extremely large changes in ^{15}N chemical shifts with pH (ca. 210 ppm for N_α), corresponding to a major fraction of the total ^{15}N chemical shift range (5), supported the belief that deprotonation in Y5 is associated with substantial electronic reorganization. More recently we have determined the ^{15}N NMR spectra of the bisaryl compound FD&C Yellow No. 6 (Y6, **2**) at neutral and basic pH and found that it exhibits similar behavior (6). We now report on the complete investigation of the azo-hydrazone, acid–base equilibria of Y5. ^{13}C NMR was used to characterize Y5 at a variety of pH values between 2 and 12. Total proton and carbon NMR signal assignments were

Received May 20, 1999.

This paper is dedicated to Professor Ted Schaefer in recognition of his outstanding contributions to Canadian chemistry.

E.P. Mazzola,[1] J.B. McMahon, and T.K. Germann. Joint Institute for Food Safety and Applied Nutrition, Department of Chemistry, University of Maryland, College Park, MD 20742, U.S.A.
S.J. Bell, S.A. Turujman, J.N. Barrows, and J.E. Bailey, Jr. Center for Food Safety and Applied Nutrition, Office of Cosmetics & Colors, U.S. Food and Drug Administration, 200 C St., S.W., Washington, DC 20204, U.S.A.
W.F. Reynolds. Department of Chemistry, University of Toronto, Toronto, ON M5S 3H6, Canada.

[1]Author to whom correspondence may be addressed. Telephone: (301) 405-1826. Fax: (301) 314-9121.
e-mail: em105@umail.umd.edu

 © 1999 NRC Canada

Table 1. ^{1}H and ^{13}C NMR data[a] for compounds **1a** and **1b**.

	1a[b]		**1b**[c]	
Position	^{1}H	^{13}C	^{1}H	^{13}C
3		140.8		146.9
4		126.2		123.2
5		163.4		157.4
6		165.8		171.8
1′		140.1		141.8
2′/6′	7.79 d (9.1)	120.4	7.92 s	122.8
3′/5′	7.80 d (9.1)	127.3	7.92 s	127.3
4′		140.4		140.2
1″		143.7		156.7
2″/6″	7.37 d (8.4)	117.5	7.79 d (8.6)	121.9
3″/5″	7.71 d (8.4)	128.0	7.87 d (8.6)	127.4
4″		140.6		141.4

[a]Chemical shifts referenced to dioxane at 3.70 ppm (^{1}H) and 67.4 ppm (^{13}C); coupling constants are in parentheses.

[b]In D_2O at pH 7.

[c]In D_2O at pH 12.

made, and the pK_a value for Y5 was determined potentiometrically.

Results and discussion

^{13}C and ^{1}H NMR spectra and signal assignments

The ^{13}C NMR spectra of Y5, at 20 MHz, exhibit similar behavior, with changing pH, to those of Y6, i.e., as the pH is increased from 2 to 10, most of the ^{13}C NMR signals exhibit broadening along with either upfield or downfield shifts, and maximum line broadening occurs at pH 10. As the solution pH is further increased to 12, the broadened resonances sharpen and continue their respective migrations. This dynamic behavior suggests, as is the case for Y6, the existence of one or more intermediate (on the NMR timescale) equilibrium processes (7).

Assignment of the ^{13}C and ^{1}H NMR signals of Y5 was complicated by the existence of two *p*-sulfophenyl groups (rings A and C) whose ^{13}C and ^{1}H NMR resonances are very similar (Table 1). In addition, the carbons of the pyrazole (B) ring and that of its only substituent (the carboxylate group at C-3) are all quaternary, thus eliminating the possibility of their chemical shift assignments via long-range proton–carbon connectivities. However, the β-^{15}N-labeled isotopomer of Y5 was easily prepared. Observed ^{15}N–^{13}C couplings in this compound together with (*i*) pyrazolone model compounds (8), and (*ii*) direct heteronuclear (HETCOR) and long-range, heteronuclear chemical shift correlation (FLOCK) (9) experiments permitted assignment of all the carbon and proton NMR signals of Y5. The assignment of these resonances is described below.

Comparison of the ^{13}C NMR spectra of Y5 and [β-^{15}N]-Y5 at pH 7 revealed four couplings between the ^{15}N-nucleus and carbons in the A- and B-rings (Table 2). The signal at 163.4 ppm was assigned to the B-ring, oxygen-bearing C-5, thus distinguishing it from the carboxy C-6. The resonance at 143.7 ppm was ascribed to the A-ring, nitrogen-bearing carbon (1″), the double-intensity signal at 117.5 ppm to C-2″/6″, and the most shielded (quaternary) resonance at 126.2 ppm to the imino C-4 (10).

Table 2. Y5 ^{13}C–^{15}N coupling constants.[a]

Position	pH 7	pH 12
3	0	5
4	6.4	3
5	11.8	2.5
1″	6	5.5
2″/6″	<1	4
3″/5″	0	1.2
4″	0	<1

[a]Taken from the dissertation submitted in partial fulfillment of the requirements for the Ph.D. degree (S.J.B.) awarded by The George Washington University, Washington, D.C.

A HETCOR experiment permitted assignment of the signal at 7.37 ppm to H-2″/6″, and the *ortho*-coupled (8.4-Hz) resonance at 7.71 ppm was then attributed to H-3″/5″. The HETCOR experiment now allowed assignment of the double-intensity signal at 128.0 ppm to C-3″/5″. Additionally, a FLOCK experiment showed 3-bond connectivities between H-2″/6″ and C-4″ at 140.6 ppm and H-3″/5″ and C-1″ (143.7 ppm) thus completing the assignments of the A-ring. The HETCOR experiment further demonstrated direct couplings between the proton signals at 7.79 and 7.80 ppm and the carbon resonances at 120.4 and 127.3 ppm, respectively. Moreover, the FLOCK experiment revealed 3-bond connectivities between (*i*) the proton resonance at 7.79 ppm and the carbon at 140.4 ppm and (*ii*) the proton signal at 7.80 ppm and the carbon resonance at 140.1 ppm.

Without corresponding isotopic enrichment at N-1, unequivocal assignments for the C-ring protons and single- and double-intensity carbons could not be made. However, signals at 127.3 ppm, which are pH-invariant over the range 2–12, have been observed for carbons 3′/5′ of pyrazolone T (**3**), which are similar to C-3′/5′ of Y5 (8). The resonances of Y5 at 127.3 ppm, at pH 7 and 12, were, therefore, also assigned to C-3′/5′. The rest of the signals of the C-ring are then as given in Table 1. Finally, the remaining resonances at 140.8 ppm (pH 7) and 146.9 ppm (pH 12) can be ascribed to C-3 by default. The signals of Y5 at pH 12 (Table 1) were assigned by means of similar ^{15}N–^{13}C couplings (Table 2) and chemical shift correlation experiments described above.

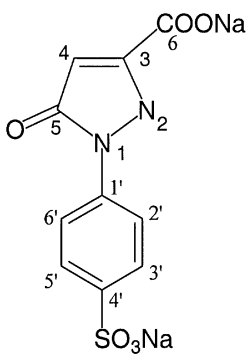

3

© 1999 NRC Canada

Scheme 1.

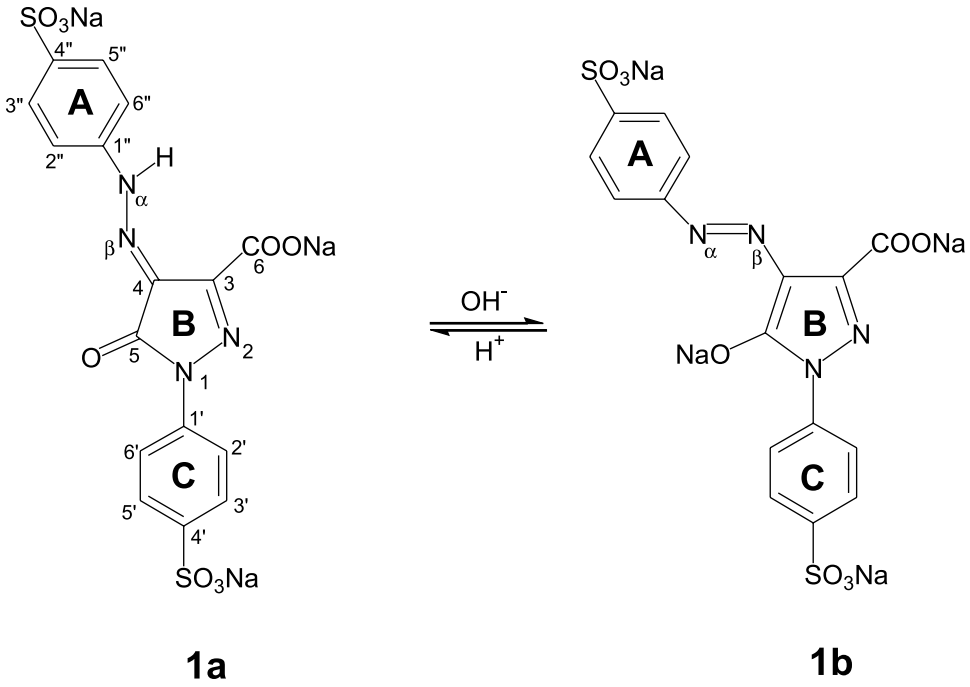

1a 1b

Scheme 2.

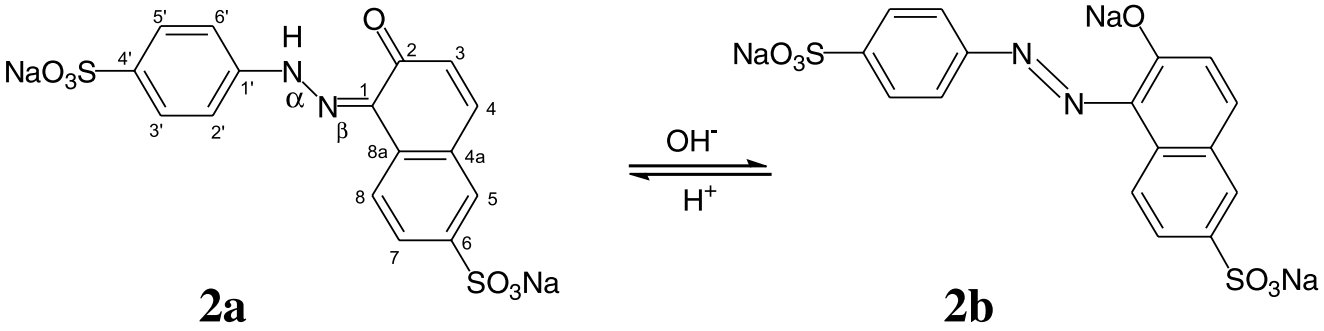

2a 2b

Molecular conformations and configurations

^{13}C and ^{15}N NMR spectra have provided evidence that Y5 exists predominantly as a hydrazone at neutral pH (vide supra). Further information concerning the geometry about the hydrazone linkage was obtained by examination of the 2-bond, ^{15}N–^{13}C coupling constants between the β-nitrogen and carbons 3 and 5 in the ^{13}C NMR spectrum of [β-^{15}N]-Y5 at pH 7. An 11.8 Hz coupling was observed to C-5 and essentially no coupling to C-3 (Table 2). The difference in magnitude between these two coupling constants indicates that C-5 is situated *cis* to the lone-pair electrons of the β-nitrogen (11). Y5, therefore, occurs as the *anti*-hydrazone (**1a**) at pH 7.

Y5 has also been inferred to be present as an azo-anion species at basic pH. The corresponding couplings between the β-nitrogen of [β-^{15}N]-Y5 and carbons 3 and 5 at pH 12 are the following: 5 Hz to C-3 and 2.5 Hz to C-5 (Table 2). These data suggest that the overall shape of the Y5 molecule has changed in going from neutral to high pH 12, viz. C-3 is now located *cis* to the β-nitrogen lone-pair electrons (11). Y5 thus exists as the *trans*-azo compound (**1b**) at pH 12.

Dynamic NMR effects

As previously mentioned, at 20 MHz the ^{13}C NMR spectra of Y5 exhibit significant line broadening between pH 9 and 11. This signal broadening can be ascribed to an acid–base equilibrium, involving species **1a** and **1b** (Scheme 1), in a manner similar to that seen for the dye, Y6 (**2**) in Scheme 2 (6). This interpretation is supported by the pK_a of Y5, which has been determined potentiometrically to be 10.03.[2] Interestingly, at 100 MHz, *separate* signals for the azo and hydrazone species are observed for the ^{13}C NMR spectra of Y5 at pH values close to the pK_a. Apparently, the fivefold increase in resonance frequency provides just enough chemical shift separation to move the equilibrium process from the *near-fast* exchange regime at 20 MHz to the *intermediate* exchange regime at 100 MHz. Like Y6, the Y5 system is atypical in that the azo-anion conjugate base

[2] Microlit Laboratories, Madison, N.J.

© 1999 NRC Canada

Table 3. Y5 azo-hydrazone average lifetime calculations.

Position	$W_{H/2}$ (pH 7)	$W_{H/2}$ (pH12)	$W_{H/2}$ (pH10)	$\Delta\nu$ (Hz)	τ (ms)
3′/5′	3.2	4.0	4.1	0	[a]
4′	1.7	3.2	2.8	4	[a]
3″/5″	4.3	4.4	4.8	12	60[b]
4″	2.2	3.2	[c]	16	—
1′	1.8	3.3	5.8	34	23
2′/6′	3.5	3.2	10.1	48	23
4	2.4	[c]	[c]	60	—
2″/6″	4.5	3.4	27.7	88	24
6	2.3	3.2	[d]	120	—
5	2.5	3.1	[d]	120	—
3	[c]	3.1	[d]	122	—
1″	2	2.9	[d]	260	—

[a]Not exchange broadened.

[b]Considerable error due to slight broadening and very small $\Delta\delta$.

[c]Obscured.

[d]Not observed.

(**1b**) is considerably different structurally from the hydrazone acid (**1a**) from which it is derived. The relatively slow (on the ^{13}C NMR timescale) proton transfer for this nitrogen–acid system (between the hydrazone-NH and water) was not completely unexpected, since NH–OH exchange is anticipated to be slower than the more commonly encountered OH–OH exchange in oxygen acids.

The existence of line broadening in the 20 MHz, ^{13}C NMR spectra permits calculation of average lifetimes for the hydrazone and azo-anion species. The standard practice of variable-temperature experiments is largely precluded in these systems because of the temperature dependence of solution pH. In addition, more accurate line widths could be determined for exchange-broadened, *averaged* signals at 20 MHz than for *individual* ones at 100 MHz. Therefore, as an approximate alternative, the line widths of four carbon resonances were measured at pH 7, 10, and 12. If the assumption is made that the pK_a occurs at pH 10, these line widths, together with the chemical shift separations, can be inserted into the following equation for the *near-fast* exchange regime (12):

$$(T_2)^{-1} = N_A(T_{2_A})^{-1} + N_B(T_{2_B})^{-1} + N_A^2N_B^2\,(\omega_A - \omega_B)^2\,(\tau_A + \tau_B)$$

where N_A and N_B are the respective mole fractions of the hydrazone and azo species, T_{2_A} and T_{2_B} are the natural line widths (widths at half-height), ω_A and ω_B represent the chemical shift separation, $T_{2'}$ is the line width at pH 10, and τ_A and τ_B are the lifetimes. Three average lifetimes ($1/2[\tau_A + \tau_B]$) were obtained, which are in excellent agreement with each other (Table 3) and are, for the sake of consistency, also in the range of $0.1–10^{-5}$ s, where dynamic NMR effects are observed (7*c*).

Analysis of ^{13}C NMR line broadenings for the hydrazone and azo species of Y5 and Y6 yields average lifetimes of ca. 23 and 2 ms (6), respectively. In addition, the pK_a values of Y5 and Y6 were determined to be 10 and 12 (6), respectively. The kinetic and thermodynamic acidities of the hydrazone NHs are, therefore, seen to be reversed in the two dyes.

Experimental

The trisodium salt of 4,5-dihydro-5-oxo-1-(4-sulfophenyl)-4-(4-sulfophenyl)azo-1*H*-pyrazole-3-carboxylic acid (Y5, **1**) (Hilton–Davis) was used without further purification. The β-^{15}N-labeled isotopomer ([β-^{15}N]-Y5) was prepared by diazotization of 4-amino-benzenesulfonic acid (Fisher) with $Na^{15}NO_2$ (95 at.% ^{15}N, Merck) and coupling to the disodium salt of 4,5-dihydro-5-oxo-1-(4-sulfophenyl)-1*H*-pyrazole-3-carboxylic acid (Hilton–Davis).

Proton, ^{13}C, and ^{15}N NMR spectra were recorded at 400, 100, and 40 MHz, respectively, in D_2O on a Varian NMR Instruments VXR-400S spectrometer. In addition, ^{13}C NMR spectra were obtained at 20 MHz in D_2O on a Varian NMR Instruments FT-80A spectrometer. Both ^{13}C (at 100 MHz) and proton chemical shifts are reported relative to TMS (Table 1). ^{15}N chemical shifts are reported relative to the $^{15}NO_3^-$ resonance using aqueous, saturated ammonium [^{15}N]nitrate solution as the external standard.

Directly bonded, heteronuclear chemical shift correlation (HETCOR) NMR spectra were obtained at 100 MHz with spectral widths of 1300 and 250 Hz in the carbon and proton dimensions, respectively, and with 256 data points in the ^{13}C dimension. Sixty-four incremented ^{13}C spectra of 32 scans each were acquired by using 11.5 μs (90°) ^1H pulse widths and a 1 s repetition rate. Free-induction decays in both dimensions were processed as a 128 × 512 matrix with appropriate zero filling and modified pseudo-echo weighting. The value $^1J(CH)$ = 165 Hz was used for calculating the delays Δ_1 and Δ_2.

Long-range, heteronuclear chemical shift correlation (FLOCK) NMR spectra were recorded at 100 MHz with spectral widths of 6000 and 250 Hz in the carbon and proton dimensions, respectively, and with 1024 data points in the ^{13}C dimension; 192 incremented ^{13}C spectra of 256 scans each were acquired by using 11.5 μs (90°) ^1H pulse widths and a 1 s repetition rate. Free-induction decays in both dimensions were processed as a 512 × 2048 matrix with appropriate zero filling and modified pseudo-echo weighting. The value $^nJ(CH)$ = 7.5 Hz was used for calculating the delays Δ_1 and Δ_2, and $^1J(CH)$ = 165 Hz was used for τ in the bilinear rotation decoupling (BIRD) (13) pulses.

References

1. (*a*) P. Ball and C.H. Nichols. Dyes Pigm. **3**, 5 (1982); (*b*) A. Lycka. Annu. Rep. Nucl. Magn. Reson. Spectrosc. **26**, 247 (1993).
2. S.J. Bell, E.P. Mazzola, and B. Coxon. Dyes Pigm. **11**, 93 (1989).
3. P.W. Westerman, R.E. Botto, and J.D. Roberts. J. Org. Chem. **43**, 2590 (1978).
4. (*a*) N.A. Porter, G.R. DuBay, and G.J. Green. J. Am. Chem. Soc. **100**, 920 (1978); (*b*) R.O. Duthaler and J.D. Roberts. J. Am. Chem. Soc. **100**, 4969 (1978).
5. G.C. Levy and R.L. Lichter. Nitrogen-15 nuclear magnetic resonance spectroscopy. Wiley–Interscience, New York. 1979. Chap. 3.

© 1999 NRC Canada

6. E.P. Mazzola, S.A. Turujman, S.J. Bell, J.N. Barrows, J.E. Bailey, Jr., E.G. Mouchahoir, S. Prescott, M.D. Archer, M. Oliver, W.F. Reynolds, and K.W. Nielsen. Tetrahedron, **52**, 5691 (1996).
7. (*a*) H S. Gutowsky and C.H. Holm. J. Chem. Phys. **25**, 1228 (1956); (*b*) H.M. McConnell. J. Chem. Phys. **28**, 430 (1958); (*c*) R.S. Drago. Physical methods for chemists. 2nd ed. Saunders, New York. 1992. pp. 95–98.
8. S.J. Bell, E.P. Mazzola, M.J. DiNovi, W.F. Reynolds, and K.W. Nielsen. J. Heterocycl. Chem. **28**, 641 (1991).
9. W.F. Reynolds, S. McLean, M. Perpick, and R.G. Enriquez. Magn. Reson. Chem. **27**, 162 (1989).
10. (*a*) R.G. Rees and M.J. Green. J. Chem. Soc. B, 387 (1968); (*b*) G.E. Hawkes, E.W. Randall, J. Elguero, and C.J. Marzin. J. Chem. Soc. Perkin Trans. 2, 1024 (1977); (*c*) S.P. Singh, S.A. Farnum, V.I. Stenberg, and S.S. Parmar. J. Pharm. Sci. **68**, 470 (1979).
11. (*a*) P.S. Pregosin, E.W. Randall, and A.I. White. J. Chem. Soc. Perkin Trans. 2, 1 (1972); (*b*) G.W. Buchanan and B.A. Dawson. Can. J. Chem. **55**, 1437 (1977); (*c*) Org. Magn. Reson. **13**, 293 (1980).
12. R.S. Drago. Physical methods for chemists. 2nd ed. Saunders, New York. 1992. pp. 290–295.
13. J.R. Garbow, D.P. Weitekamp, and A. Pines. Chem. Phys. Lett. **93**, 504 (1982).

© 1999 NRC Canada

The second dielectric virial coefficient of the dipolar Gay–Berne fluid

A.D. Buckingham and Y. Tantirungrotechai

Abstract: We report the second dielectric virial coefficient B_ε of a nonpolarizable dipolar Gay–Berne fluid. The second dielectric virial coefficient is evaluated for several sets of shape parameters and temperature. The second dielectric virial coefficient for rodlike molecules is negative while it is large and positive for disklike molecules. It decreases to zero on increasing the temperature.

Key words: dipolar fluids, dielectric constant, intermolecular forces, shape parameters.

Résumé : On a mesuré le deuxième coefficient du viriel diélectrique, B_ε, d'un fluide dipolaire non polarisable de Gay–Berne. On a évalué le deuxième coefficient du viriel diélectrique pour plusieurs ensembles de paramètres de forme et de température. Pour les molécules en forme de tige, le deuxième coefficient du viriel diélectrique est négatif alors que sa valeur est positive et élevée pour les molécules en forme de disque. Il tend vers zéro par augmentation de température.

Mots clés : fluids dipolaires, constante diélectrique, forces intermoléculaires, paramètres de forme.

[Traduit par la Rédaction]

Introduction

At low densities, the Clausius–Mossotti function of a fluid can be written as a virial expansion of the total dielectric polarization ${}_TP$ in the density $\rho = V_m^{-1}$ where V_m is the molar volume (1)

$$[1] \qquad {}_TP = \frac{\varepsilon_r - 1}{\varepsilon_r + 2}\rho^{-1} = A_\varepsilon + B_\varepsilon\rho + C_\varepsilon\rho^2 + \ldots$$

ε_r is the dielectric constant of the fluid and A_ε, B_ε, C_ε, $\cdots$ are the first, second, third dielectric virial coefficients. The first dielectric virial coefficient A_ε consists of two terms, one representing the polarization due to the polarizability and the other the orientation polarization

$$[2] \qquad A_\varepsilon = \frac{N_A}{3\varepsilon_0}(\bar{\alpha} + \frac{\mu^2}{3k_BT})$$

where N_A is Avogadro's number and ε_0 is the permittivity of a vacuum. Measurements of A_ε as a function of temperature yield the molecular dipole moment μ and the static polarizability $\bar{\alpha}$ (2). The second dielectric virial coefficient B_ε relates to pair interactions, which are absent in the ideal gas, and can be written (1) as

$$[3] \qquad B_\varepsilon = \frac{N_A^2}{3 \cdot \Omega \cdot \varepsilon_0}\int d(12)\,\frac{1}{2}[\Delta\bar{\alpha} + \frac{\Delta\mu^2}{3k_BT}]\exp(-\frac{W_{12}}{k_BT})$$

where W_{12} is the dimer interaction energy, $\Delta\bar{\alpha} = (\alpha_{12,\alpha\alpha} - \alpha^{(0)}_{1,\alpha\alpha} - \alpha^{(0)}_{2,\alpha\alpha})/3$, $\Delta\mu^2 = (\boldsymbol{\mu}_1 + \boldsymbol{\mu}_2)^2 - \mu_1^{(0)2} - \mu_2^{(0)2}$ and $\int d(12) = V_m\,\Omega$ (1). This integration is performed over all possible dimer separations and orientations and for linear molecules $d(12) = R^2\,dR\,\sin\theta_1\,d\theta_1\,\sin\theta_2\,d\theta_2\,d\phi$ with the coordinates defined as in Fig. 1, so $\Omega = 2$. As for A_ε, the contributions to B_ε consist of two similar terms but in the form of the changes in the mean polarizability and mean-square dipole moment due to the pair interaction. For dipolar fluids, the orientation contribution $\Delta\mu^2/3k_BT$ is generally much larger than that due to the induced polarizability $\Delta\bar{\alpha}$ and may be positive or negative (1). A comprehensive review of this field of study up to 1970 has been given by Sutter (3).

Molecular shape is known to play an important role in B_ε (1). Several models have been proposed to take into account the anisotropic potential, such as the Kihara model (4), the shape factor proposed by Buckingham and Pople (1, 5), the "off-centre" dipole model of Lawley and Sutton (6), the asymmetrical hard dumbbell model of Ohba and Nomura (7), and the hard ellipsoid model of Muckenfuss, Curtiss, and Bird (8). This last model coupled with a point dipole was used by Joslin to study the effect of molecular shape on the second virial coefficients of the pressure, dielectric constant, Kerr effect, and the depolarized light scattering (9). In this paper, we report a study of B_ε of the nonpolarizable dipolar Gay–Berne fluid.

Received March 3, 1999.

This paper is dedicated to Professor Ted Schaefer in recognition of his outstanding contributions to Canadian chemistry.

A.D. Buckingham[1] and Y. Tantirungrotechai. Department of Chemistry, University of Cambridge, Lensfield Road, Cambridge CB2 1EW, U.K.

[1]Author to whom correspondence may be addressed. Telephone:+44 1223 336458. Fax:+44 1223 336362. e-mail: adb1000@cam.ac.uk

© 1999 NRC Canada

Fig. 1. The intermolecular coordinates used to define the relative molecular position and orientation. Molecule 1 is fixed in the *xz* plane. θ_1 and θ_2 are the angles of the symmetry axes of molecules 1 and 2 measured from the *z*-axis. ϕ denotes the torsional angle of molecule 2 with respect to the *xz* plane. *R* is the intermolecular distance between the origins in molecules 1 and 2.

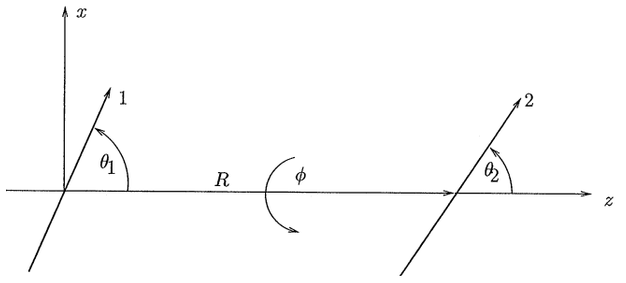

Gay and Berne have modified the overlap potential between two ellipsoidal Gaussians of Berne and Pechukas (10) that leads to the single-site orientation-dependent potential (11). The so-called Gay–Berne potential takes the form (12)

$$[4] \qquad W_{GB}\,(\boldsymbol{r}_{12},\,\boldsymbol{e}_1,\,\boldsymbol{e}_2) = 4\varepsilon(\hat{\boldsymbol{r}}_{12},\boldsymbol{e}_1,\,\boldsymbol{e}_2)[\rho_{12}^{-12}-\rho_{12}^{-6}]$$

where $\boldsymbol{e}_1$, $\boldsymbol{e}_2$ are orientation unit vectors of the axially symmetric particles 1 and 2 separated by the intermolecular vector $\boldsymbol{r}_{12} = r_{12}\,\hat{\boldsymbol{r}}_{12}$. The shifted-distance ρ_{12} is $(r_{12} - \sigma\,(\hat{\boldsymbol{r}}_{12},\,\boldsymbol{e}_1,\,\boldsymbol{e}_2) + \sigma_0)/\sigma_0$ where $\sigma(\hat{\boldsymbol{r}}_{12},\,\boldsymbol{e}_1,\,\boldsymbol{e}_2)$ is the distance for a given orientation at which the potential is zero. This orientation-dependent impact parameter $\sigma(\hat{\boldsymbol{r}}_{12},\,\boldsymbol{e}_1,\,\boldsymbol{e}_2)$ takes the form

$$[5] \qquad \sigma(\hat{\boldsymbol{r}}_{12},\,\boldsymbol{e}_1,\,\boldsymbol{e}_2)$$

$$= \sigma_0\left\{1-\frac{\chi}{2}\left[\frac{(\hat{\boldsymbol{r}}_{12}\cdot\boldsymbol{e}_1+\hat{\boldsymbol{r}}_{12}\cdot\boldsymbol{e}_2)^2}{1+\chi(\boldsymbol{e}_1\cdot\boldsymbol{e}_2)}+\frac{(\hat{\boldsymbol{r}}_{12}\cdot\boldsymbol{e}_1-\hat{\boldsymbol{r}}_{12}\cdot\boldsymbol{e}_2)^2}{1-\chi(\boldsymbol{e}_1\cdot\boldsymbol{e}_2)}\right]\right\}^{-1/2}$$

where $\chi = (\kappa^2 - 1)/(\kappa^2 + 1)$, $\kappa = \sigma_{\parallel}/\sigma_{\perp}$ is a parameter defining the molecular length over the molecular diameter, and σ_0 is a constant defining the length scale that is equal to the cross-sectional diameter $\sigma_{\perp}$. The orientation-dependent well depth $\varepsilon\,(\hat{\boldsymbol{r}}_{12},\,\boldsymbol{e}_1,\,\boldsymbol{e}_2)$ is given by

$$[6] \qquad \varepsilon(\hat{\boldsymbol{r}}_{12},\boldsymbol{e}_1,\boldsymbol{e}_2) = \varepsilon^0\,\varepsilon_1^{\nu}(\boldsymbol{e}_1,\boldsymbol{e}_2)\,\varepsilon_2^{\mu}(\hat{\boldsymbol{r}}_{12},\boldsymbol{e}_1,\boldsymbol{e}_2)$$

$$[7] \qquad \varepsilon_1(\boldsymbol{e}_1,\boldsymbol{e}_2) = [1-\chi^2(\boldsymbol{e}_1\cdot\boldsymbol{e}_2)^2]^{-1/2}$$

$$[8] \qquad \varepsilon_2(\hat{\boldsymbol{r}}_{12},\boldsymbol{e}_1,\boldsymbol{e}_2)$$

$$=1-\frac{\chi'}{2}\left[\frac{(\hat{\boldsymbol{r}}_{12}\cdot\boldsymbol{e}_1+\hat{\boldsymbol{r}}_{12}\cdot\boldsymbol{e}_2)^2}{1+\chi'(\boldsymbol{e}_1\cdot\boldsymbol{e}_2)}+\frac{(\hat{\boldsymbol{r}}_{12}\cdot\boldsymbol{e}_1-\hat{\boldsymbol{r}}_{12}\cdot\boldsymbol{e}_2)^2}{1-\chi'(\boldsymbol{e}_1\cdot\boldsymbol{e}_2)}\right]$$

where $\chi' = (\kappa'^{1/\mu} - 1)/(\kappa'^{1/\mu} + 1)$, $\kappa' = \varepsilon_{ss}/\varepsilon_{ee}$. ε_{ss} and ε_{ee} are the well depths of side-by-side and end-to-end configurations, and ε^0 is a parameter setting the energy scale of this potential. The original set of parameters, $\kappa = 3$, $\kappa' = 5$, $\nu = 1$, and $\mu = 2$, was obtained by fitting this potential form to the site–site potential of a four-site Lennard-Jones molecule (11). Other sets of parameters have been proposed since then, for example, the new set of exponents of Luckhurst et al. (13) and the "disk-like" parameters of Emerson et al.

Fig. 2. The reduced rodlike Gay–Berne potential $W^* = W/\varepsilon^0$ as a function of the reduced intermolecular distance $R^* = R/\sigma_<$ and shape parameters κ and κ'. Plots in long-dashed, broken, dotted, and solid lines are used to represent $(\kappa, \kappa') = (1.0, 1.0)$, (1.5, 2.0), (2.0, 3.0), and (3.0, 5.0), respectively. The dimer relative configurations are defined by $(\theta_1, \theta_2, \phi)$ as in Fig. 1.

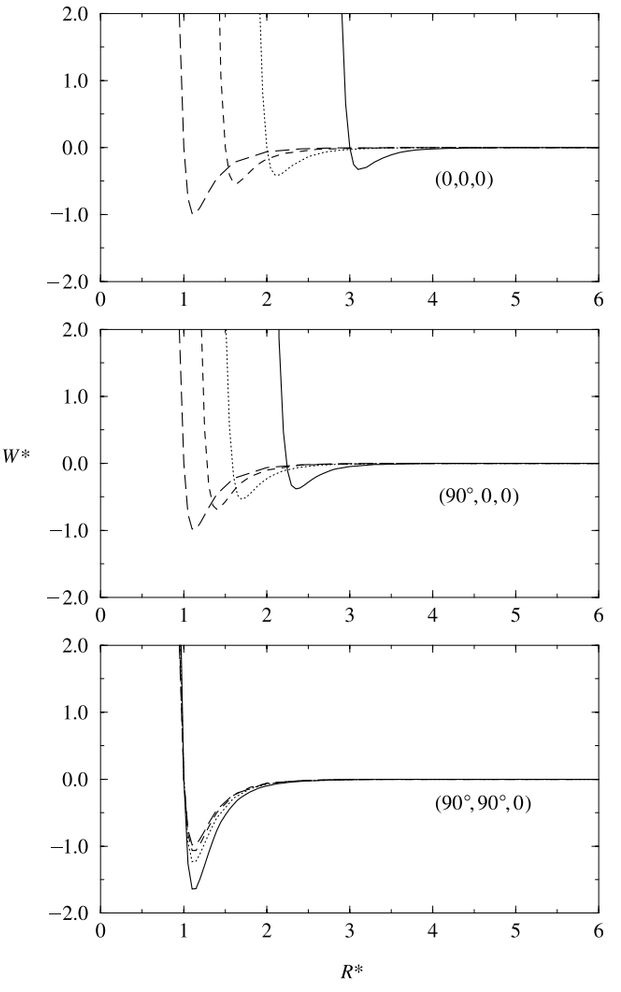

(14). We keep $\nu = 1$, $\mu = 2$ and vary κ and κ'. An extension and generalization of this model has been made by Cleaver et al. (15). These authors give the general expression for the interaction between two nonequivalent uniaxial particles; they report parameters for a rod–disk dimer obtained from the interaction energy of *p*-terphenyl and triphenylene.

The Gay–Berne potential has been employed extensively in the simulation of liquid crystals in which the anisotropic potential is crucial (13, 14). Satoh et al. studied mesophase formation of the dipolar Gay–Berne fluid using the Monte Carlo technique (16).

Model

For the nonpolarizable dipolar fluid we can write B_ε as

$$[9] \qquad B_\varepsilon = \frac{N_A^2}{3\cdot\Omega\cdot\varepsilon_0}\int d(12)\left[\frac{\boldsymbol{\mu}_1\cdot\boldsymbol{\mu}_2}{3k_BT}\right]\exp\left(-\frac{W_{12}}{k_BT}\right)$$

© 1999 NRC Canada

Table 1. The reduced second dielectric virial coefficient $B_\varepsilon^* = B_\varepsilon/(N_A^2\sigma_<^6)$ of the dipolar Gay–Berne rod- and disklike fluids as functions of $T^* = k_BT/\varepsilon^0$ and $\mu^{2*} = \mu^2/(4\pi\varepsilon_0\varepsilon^0\sigma_<^3)$.

	$\kappa = 3, \kappa' = 5$					$\kappa = 1/3, \kappa' = 1/5$				
μ^{2*}/T^*	0.5	1.0	1.5	2.0	3.0	0.5	1.0	1.5	2.0	3.0
0.25	–1.31	–0.146	–0.052	–0.027	–0.011	1.82×10^4	7.40	0.581	0.152	0.034
0.5	–5.35	–0.585	–0.209	–0.107	–0.043	7.59×10^4	29.8	2.33	0.609	0.136
1.0	–23.2	–2.38	–0.843	–0.429	–0.174	3.62×10^5	1.23×10^2	9.36	2.45	0.545
1.5	–59.7	–5.51	–1.92	–0.970	–0.392	1.10×10^6	2.90×10^2	21.5	5.55	1.23
2.0	-1.29×10^2	–10.2	–3.46	–1.74	–0.700	2.87×10^6	5.53×10^2	38.9	9.97	2.19
2.5	-2.56×10^2	–16.7	–5.53	–2.75	–1.10	7.21×10^6	9.45×10^2	62.8	15.8	3.43
3.0	-4.99×10^2	–25.5	–8.15	–4.01	–1.59	1.79×10^7	1.52×10^3	93.9	23.1	4.98

Fig. 3. The reduced disklike Gay–Berne potential $W^* = W/\varepsilon^0$ as a function of the reduced intermolecular distance $R^* = R/\sigma_<$ and shape parameters κ and κ'. Plots in long-dashed, broken, dotted, and solid lines are used to represent $(\kappa,\kappa') = (1.0, 1.0)$, (2/3, 1/2), (1/2, 1/3), and (1/3, 1/5), respectively.

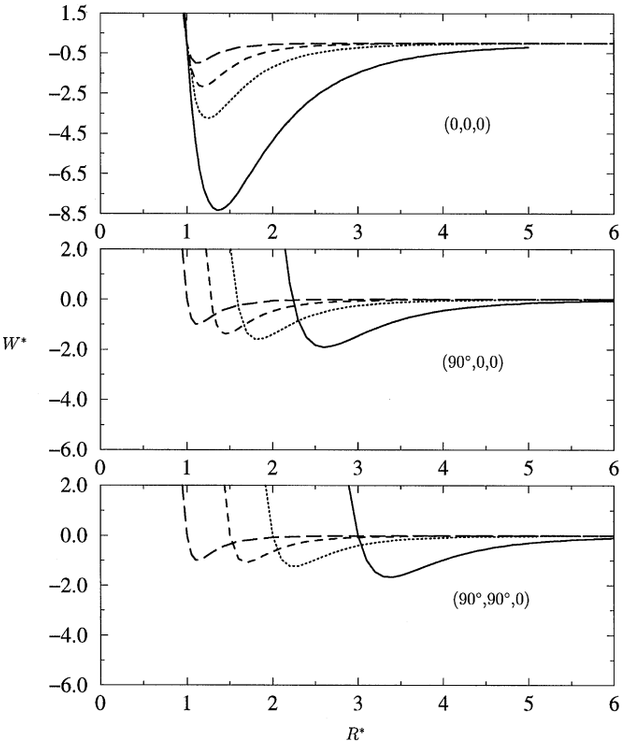

Following the suggestion of Joslin (9), we modified this formula to reduce the errors of the numerical integration

$$[10] \qquad B_\varepsilon = \frac{N_A^2}{3\cdot\Omega\cdot\varepsilon_0}\int d(12)\left[\frac{\boldsymbol{\mu}_1\cdot\boldsymbol{\mu}_2}{3k_BT}\right]\left\{\exp\left(-\frac{W_{12}}{k_BT}\right)-1\right\}$$

We report all quantiites in the reduced dimensionless units, which are defined as

$$T^* = \frac{k_BT}{\varepsilon^0}, \quad \mu^{2*} = \frac{\mu^2}{4\pi\varepsilon_0\varepsilon^0\sigma_<^3}, \quad B_\varepsilon^* = \frac{B_\varepsilon}{N_A^2\sigma_<^6}$$

where $\sigma_<$ is $\sigma_\perp$ for rodlike molecules and $\sigma_\parallel$ for disklike molecules. In our study, the interaction energy of the Gay–Berne nonpolarizable dipolar fluid is the same as used by Satoh et al. (16) and is given by

$$[11] \qquad W_{12} = W_{GB} + W_{elec}$$

where W_{GB} is defined as in eq. [4] and

$$W_{elec} = -\frac{1}{4\pi\varepsilon_0}\frac{\{3(\mu_{1\alpha}R_\alpha)(\mu_{2\beta}R_\beta) - R^2(\mu_{1\alpha}\mu_{2\alpha})\}}{R^5}$$

We use the original set of parameters $(\kappa,\kappa', \nu, \mu)$ suggested by Gay and Berne (11) in this study. Other sets of (κ, κ') for rodlike molecules are obtained from a linear interpolation between $(\kappa = 3, \kappa' = 5)$ and $(\kappa = 1, \kappa' = 1)$. Parameters of disklike molecules are the inverse of those of rodlike molecules.

In the case of disklike molecules we fix $\sigma_\parallel$ at the same value as the $\sigma_\perp$ of the rodlike molecules, hence requiring σ_0 (disk) = σ_0 (rod) κ(rod). Plots of Gay–Berne potentials in reduced units for selected sets of shape parameters and orientations are shown in Figs. 2 and 3 for rodlike and disklike molecules, respectively.

The second dielectric virial coefficient (see eq. [10]) is evaluated numerically in two steps. The angular integration is performed first using the Monte Carlo technique with a quasi-random generator (Sobol sequence) (17). The radial integration is performed afterwards with the Romberg integration scheme (17). The second dielectric virial coefficients B_ε are calculated for several sets of μ^{2*}, T^*, and (κ, κ'). These results are given in Tables 1–4.

Results and discussion

For both the rodike and disklike molecules considered, the second dielectric virial coefficient increases in magnitude as μ^{2*} increases and decreases exponentially to zero on increasing T^*. The results (see Tables 1–3) show that rodlike molecules ($\kappa > 1$) have negative B_ε while disklike molecules have positive B_ε for all μ^{2*}, T^* considered. This implies that rodlike molecules statistically favour side-by-side configurations while the disklike favour end-to-end configurations. The magnitude of B_ε for the rodlike molecules is less than that of their complimentary disklike molecules. This is due to a much deeper well in the Gay–Berne potential of the disklike molecules than for the rodlike molecules. Another factor contributing to a larger magnitude of B_ε for a disklike fluid is the dipole–dipole interaction energy in which a head-

© 1999 NRC Canada

Table 2. The reduced second dielectric virial coefficient $B^*_\varepsilon = B_\varepsilon/(N_A^2\sigma_<^6)$ of the dipolar Gay–Berne rod- and disklike fluids as functions of $T^* = k_BT/\varepsilon^0$ and $\mu^{2*} = \mu^2/(4\pi\varepsilon_0\varepsilon^0\sigma_<^3)$.

	$\kappa = 2, \kappa' = 3$					$\kappa = 1/2, \kappa' = 1/3$				
μ^{2*}/T^*	0.5	1.0	1.5	2.0	3.0	0.5	1.0	1.5	2.0	3.0
0.25	–0.933	–0.109	–0.039	–0.020	–0.008	28.6	0.564	0.115	0.045	0.014
0.5	–3.83	–0.436	–0.155	–0.079	–0.032	1.20×10^2	2.28	0.464	0.180	0.056
1.0	–17.0	–1.79	–0.626	–0.317	–0.127	5.81×10^2	9.45	1.89	0.725	0.225
1.5	–45.1	–4.18	–1.44	–0.719	–0.288	1.81×10^3	22.7	4.36	1.66	0.510
2.0	-1.01×10^2	–7.86	–2.61	–1.30	–0.515	5.03×10^3	44.2	8.05	3.02	0.915
2.5	-2.11×10^2	–13.2	–4.21	–2.06	–0.811	1.41×10^4	77.7	13.3	4.85	1.45
3.0	-4.29×10^2	–20.7	–6.30	–3.03	–1.18	4.12×10^4	1.31×10^2	20.3	7.23	2.12

Table 3. The reduced second dielectric virial coefficient $B^*_\varepsilon = B_\varepsilon/(N_A^2\sigma_<^6)$ of the dipolar Gay–Berne rod- and disklike fluids as functions of $T^* = k_BT/\varepsilon^0$ and $\mu^{2*} = \mu^2/(4\pi\varepsilon_0\varepsilon^0\sigma_<^3)$.

	$\kappa = 3/2, \kappa' = 2$					$\kappa = 2/3, \kappa' = 1/2$				
μ^{2*}/T^*	0.5	1.0	1.5	2.0	3.0	0.5	1.0	1.5	2.0	3.0
0.25	–0.676	–0.074	–0.026	–0.013	–0.005	3.72	0.177	0.046	0.020	0.007
0.5	–2.81	–0.299	–0.103	–0.052	–0.020	15.9	0.720	0.186	0.0813	0.028
1.0	–12.6	–1.23	–0.418	–0.208	–0.082	83.3	3.12	0.776	0.332	0.114
1.5	–34.7	–2.91	–0.962	–0.473	–0.186	2.90×10^2	7.90	1.85	0.773	0.260
2.0	–82.1	–5.52	–1.76	–0.855	–0.334	9.28×10^2	16.6	3.58	1.45	0.475
2.5	-1.81×10^2	–9.43	–2.86	–1.37	–0.527	3.03×10^3	32.1	6.20	2.41	0.766
3.0	-3.95×10^2	–15.2	–4.32	–2.02	–0.763	1.06×10^4	59.9	10.2	3.75	1.15

Table 4. The reduced second dielectric virial coefficient $B^*_\varepsilon = B_\varepsilon/(N_A^2\sigma_0^6)$ of a Stockmayer fluid ($\kappa = 1.0$, $\kappa' = 1.0$) as a function of $T^* = k_BT/\varepsilon^0$ and $\mu^{2*} = \mu^2/(4\pi\varepsilon_0\varepsilon^0\sigma_0^3)$.

	T^*				
μ^{2*}	0.5	1.0	1.5	2.0	3.0
0.25	0.022	0.0007	0.0001	0.0000	0.0000
0.5	0.384	0.0111	0.002	0.0005	0.0001
1.0	7.89	0.190	0.030	0.009	0.002
1.5	61.1	1.08	0.160	0.046	0.009
2.0	3.50×10^2	4.00	0.545	0.151	0.028
2.5	1.83×10^3	12.1	1.47	0.392	0.070
3.0	9.60×10^3	32.8	3.47	0.875	0.149

to-tail ($\rightarrow\cdots\hookrightarrow$) dipole alignment is more stable than an antiparallel ($\uparrow\cdots\downarrow$) alignment at the same separation. In other words, the most stable configuration in a dimer of disklike molecules is the most stable configuration in both the Gay–Berne potential and the dipolar potential, whereas the most stable configuration in a dimer of rodlike molecules is the most stable configuration in the Gay–Berne potential but a local minimum configuration on the dipolar surface. In a dipolar nonpolarizable soft sphere fluid (see Table 4), the dipole–dipole interaction energy is the factor determining the relative orientation. This leads to the positive B^*_ε at all μ^{2*} and T^* (1) and possibly to the nonexistence of the liquid phase in dipolar hard sphere fluids when the dipole strength is large (18).

Plots of the reduced angular integrand of B^*_ε as a function of $R^* = R/\sigma_<$ for ($T^* = 1.0$, $\mu^{2*} = 1.0$) are shown in Fig. 4. This reduced angular integrand B^*_ε(ang) is related to B^*_ε by $B^*_\varepsilon = \int B^*_\varepsilon(\text{ang})\, R^{2*}\, dR^*$. B^*_ε arises mostly from B_ε(ang) in the R^* region from ~1 to $1.5\sigma_<$. For rodlike molecules with large κ, B^*_ε(ang) is negative for all R^*. This reflects the dominant shape effect upon the dipolar (head-to-tail) interaction. As κ decreases, B^*_ε(ang) at large R^* becomes positive, i.e., the dipole term becomes important and configurations other than side-by-side become more accessible, and the minimum shifts toward small R^*. The maximum of B^*_ε(ang) of the disklike molecules increases as κ decreases to zero since the Gay–Berne energy is more attractive and configurations other than head-to-tail or head-to-head or tail-to-tail are less accessible. For small κ (large anisotropy), both the Gay–Berne energy and the electrostatic energy favour the head-to-tail configuration, leading to the large positive B^*_ε(ang) at large R^*. As κ increases towards 1, other configurations become more accessible, which leads to small negative values at large R^*. When $\kappa = 1$, which is the case for a Stockmayer fluid (19), the molecular shape becomes unimportant in determining B_ε; therefore B^*_ε(ang) becomes positive for all R^* due to a favorable dipolar head-to-tail configuration.

Conclusions

Second dielectric virial coefficients of the nonpolarizable dipolar Gay–Berne fluid are reported for several shape parameters and temperatures. The anisotropic repulsion, reflecting the effect of molecular shape, is crucial for the sign of B_ε, i.e., dipolar disklike and spherical dipolar molecules have a positive sign while dipolar rodlike molecules have a negative sign. The attractive term in the Gay–Berne potential increases the magnitude of B_ε, especially in disklike molecules. In real molecules, however, there are other long-range interactions in addition to the simple dipole–dipole interaction described in this work. For example, HCN, although a rodlike molecule, should have a positive B_ε at low temperatures due to the strong hydrogen bond that

© 1999 NRC Canada

Fig. 4. The reduced angular integrand of B_ε^* for the Gay–Berne fluid with different shape parameters κ and κ' as a function of the reduced intermolecular distance $R^* = R/\sigma_<$ at $T^* = 1.0$ and $\mu^{2*} = 1.0$.

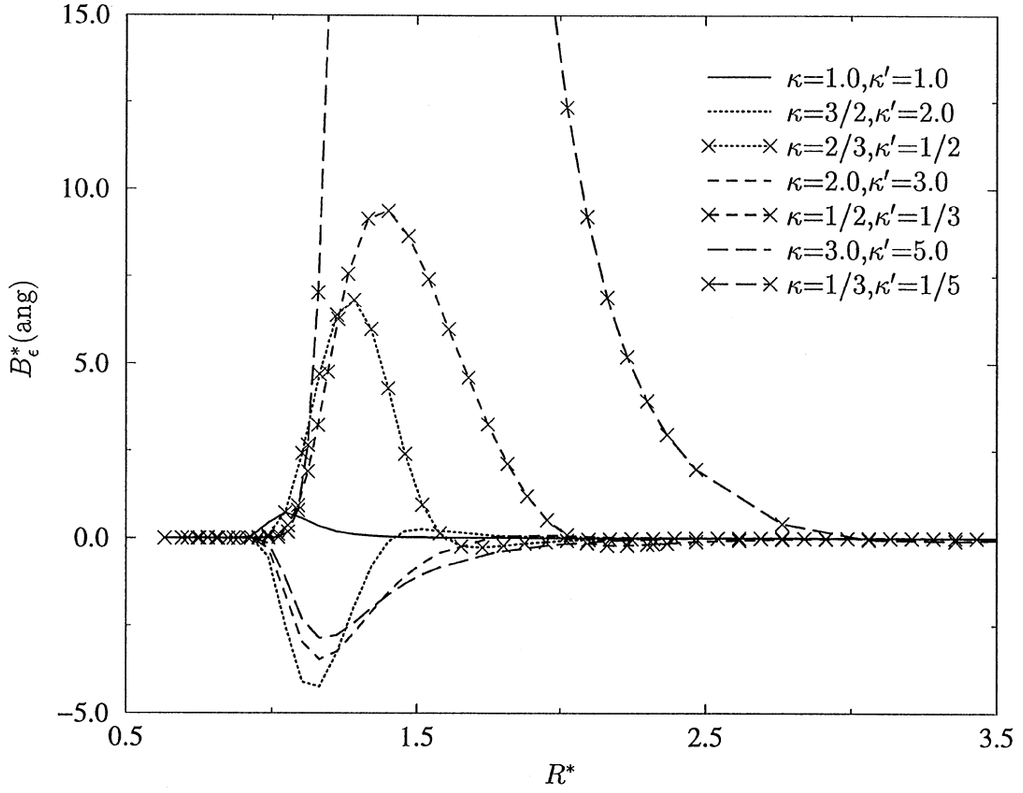

favors a head-to-tail configuration (20),[2] and polarizability can have a major effect on B_ε for dipolar fluids (1).

Since molecular shape is important to the second dielectric virial coefficient, it is interesting to anticipate the B_ε for mixtures of molecules of different shape. Using the generalization of Cleaver et al. (15), results have been obtained and will be published separately.

Acknowledgements

The authors would like to thank Dr. A.J. Stone for suggestions on the computer implementation. Y.T. acknowledges the receipt of a Thai Government scholarship.

References

1. A.D. Buckingham and J.A. Pople. Trans. Faraday Soc. **51**, 1029 (1955); **51**, 1179 (1955).
2. P. Debye. Polar molecules. Chemical Catalog Co., U.S.A. 1929.
3. H. Sutter. Dielectr. Relat. Mol. Processes. **1**, 65 (1972).
4. T. Kihara. J. Phys. Soc. Jpn. **6**, 289 (1951).
5. A.D. Buckingham and J.A. Pople. Discuss. Faraday Soc. **22**, 17 (1956).
6. K.P. Lawley and L.E. Sutton. Trans. Faraday Soc. **59**, 2680 (1963).
7. M. Ohba and H. Nomura. Mol. Phys. **70**, 729 (1990).
8. C. Muckenfuss, C.F. Curtiss, and R.B. Bird. J. Chem. Phys. **23**, 1542 (1955).
9. C.G. Joslin. Mol. Phys. **47**, 771 (1982).
10. B.J. Berne and P. Pechukas. J. Chem. Phys. **56**, 4213 (1972).
11. J.G. Gay and B.J. Berne. J. Chem. Phys. **74**, 3316 (1981).
12. J.T. Brown, M.P. Allen, E.M. del Río, and E. de Miguel. Phys. Rev. E: Stat. Phys. Plasmas, Fluids, Relat. Interdiscip. Top. **57**, 6685 (1998).
13. G.R. Luckhurst, R.A. Stephens, and R.W. Phippen. Liq. Cryst. **8**, 451 (1990).
14. A.P.J. Emerson, G.R. Luckhurst, and S.G. Whatling. Mol. Phys. **82**, 113 (1994).
15. D.J. Cleaver, C.M. Care, M.P. Allen, and M.P. Neal. Phys. Rev. E: Stat. Phys. Plasmas, Fluids, Relat. Interdiscip. Top. **54**, 559 (1996).
16. K. Satoh, S. Mita, and S. Kondo. Liq. Cryst. **20**, 757 (1996).
17. W.H. Press, S.A. Teukolsky, W.T. Vetterling, and B.P. Flannery. Numerical recipes in Fortran. 2nd ed. Cambridge University Press, U.K. 1992.
18. R. van Roij. Phys. Rev. Lett. **76**, 3348 (1996).
19. W.H. Stockmayer. J. Chem. Phys. **9**, 398 (1941).
20. A.D. Buckingham. Annu. Rev. Phys. Chem. **49**, xiii (1998).

[2] Also, A.D. Buckingham and Y. Tantirungrotechai, unpublished results.

© 1999 NRC Canada

^{31}P chemical shielding as a function of bond angle: phosphorus chemical shielding surface of phosphinoborane $R_2PBR'_2$

Michael J.T. Ditty and William P. Power

Abstract: The phosphorus chemical shielding surface of phosphinoborane $R_2PBR'_2$ has been investigated via molecular orbital theory calculation and experimental measurement of selected derivatives. Ab initio calculations of phosphorus chemical shielding tensors were determined for the phosphinoboranes H_2PBH_2 and $(CH_3)_2PB(CH_3)_2$. Changes in the angle from planarity, i.e., that between the P-BR'_2 plane and the bisector of the RPR angle, are reflected in the orientations and magnitudes of the three principal components of the phosphorus chemical shielding tensor. To determine the validity of the calculated phosphorus chemical shielding surface, three phosphinoborane compounds with different angles from planarity were synthesized and studied by solid-state ^{31}P NMR spectroscopy. The ^{31}P NMR powder patterns provided experimental magnitudes of the principal components of the phosphorus chemical shielding tensor for each compound, which compared well to the calculated predictions; where orientations of these tensors could be determined experimentally, they also agreed well with the calculated results. The combined experimental and theoretical results provide a good description of the effects on changes in bond angle on phosphorus chemical shielding as the molecule is distorted from a planar to folded geometry.

Key words: chemical shielding, solid-state NMR, phoshinoborane, ab initio calculations.

Résumé : On a étudié la surface de blindage chimique du phosphore dans des $R_2PBR'_2$ par le biais de calculs d'orbitales moléculaires et de mesures expérimentales sur des dérivés choisis. Faisant appel à des calculs ab initio, on a déterminé les tenseurs du blindage chimique du phosphore dans les phosphinoboranes, H_2PBH_2 et $(CH_3)_2PH(CH_3)_2$. Les changements dans l'angle de planarité, c'est-à-dire l'angle entre le plan du P-BR'_2 et la bissectrice de l'angle RPR, se reflètent dans les orientations et les amplitudes des trois principales composantes du tenseur de blindage chimique du phosphore. Afin de déterminer la validité de la valeur calculée de la surface de blindage chimique du phosphore, on a réalisé la synthèse de trois composés phosphinoboranes présentant des déviations différentes de planarité et on les a étudiés par spectroscopie RMN du ^{31}P à l'état solide. Les patrons des spectres RMN du ^{31}P des poudres permettent d'obtenir les amplitudes expérimentales des principales composantes du tenseur de blindage chimique du phosphore pour chacun des composés et ces valeurs se comparent bien avec les valeurs calculées; dans les cas où les orientations de ces tenseurs peuvent être déterminées de façon expérimentale, elles sont aussi en bon accord avec les résultats des calculs. Une combinaison des résultats expérimentaux et théoriques permet d'obtenir une bonne description des effets des changements dans l'angle de liaison sur le blindage chimique du phosphore lorsqu'on déforme la molécule d'une géométrie plane à une autre repliée.

Mots clés : blindage chimique, RMN à l'état solide, phosphinoborane, calculs ab initio.

[Traduit par la Rédaction]

Introduction

Phosphorus chemical shielding has been the focus of much recent interest, particularly in terms of efforts to reliably predict its values through ab initio approaches in a variety of different environments (1–10). These efforts have resulted from an attempt to rationalize the general trends observed in ^{31}P NMR, predominantly using the isotropic chemical shift values obtained in solution NMR studies (11–13). What has become evident is that the changes in phosphorus chemical shielding are best reflected in changes of the complete chemical shift (or shielding) tensor, as the isotropic average of this tensor often masks clear trends in the changes of individual principal components of the tensor (14, 15). In one such effort, we have recently shown the effect of changes in bond length on the phosphorus chemical shielding of a series of isoelectronic R_3PX compounds, where X = BH_3, CH_2, NH, and O (16). That study indicated the phosphorus

Received June 10, 1999.

This paper is dedicated to Professor Ted Schaefer in recognition of his outstanding contributions to Canadian chemistry.

M.J.T. Ditty and W.P. Power.[1] Department of Chemistry, University of Waterloo, Waterloo, ON N2L 3G1, Canada.

[1]Author to whom correspondence may be addressed. Telephone: (519) 888-4567, ext. 3626. Fax: (519) 746-0435. e-mail: william.power@uwaterloo.ca

 © 1999 NRC Canada

Fig. 1. Structures of the compounds investigated either computationally or experimentally through the course of this study: **1**, H_2PBH_2; **2**, $(CH_3)_2PB(CH_3)_2$; **3**, Mes_2PBMes_2 (Mes = mesityl); **4**, Ph_2PBMes_2 (Ph = phenyl); **5**, (1-Ad)(H)$PBMes_2$ (1-Ad = 1-adamantyl).

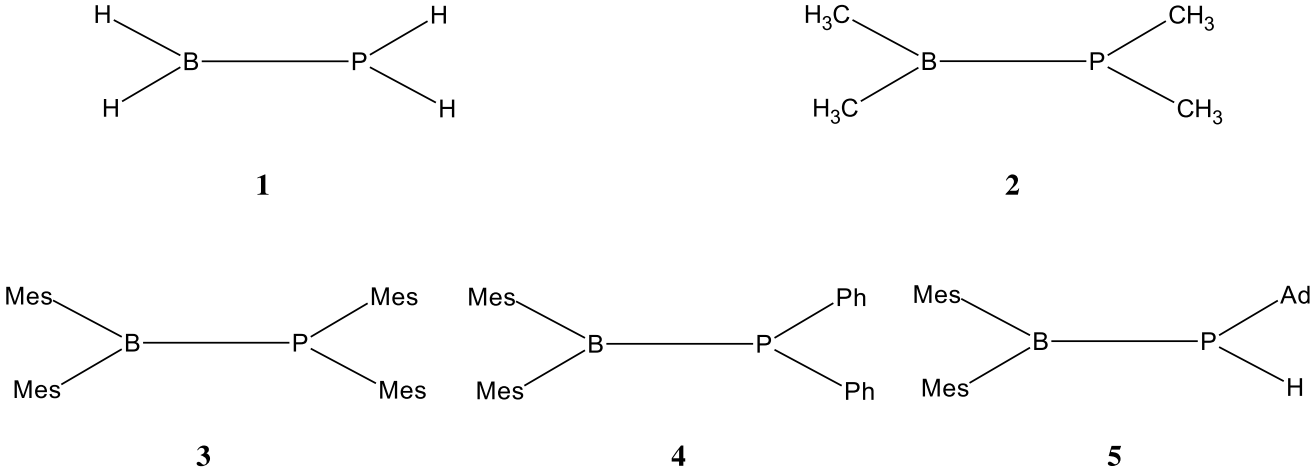

1 **2**

3 **4** **5**

chemical shielding of each compound followed the same general chemical shielding surface, and changes in the shielding were due to the changes in P–X bond length through the series.

In this article, we demonstrate a similar approach to the effects of bond angle on phosphorus chemical shielding, through calculation of the chemical shielding surface in phosphinoborane, $R_2PBR'_2$, where R = R′ = H (**1**), CH_3 (**2**), and experimental measurements of the phosphorus chemical shift tensors in $(2,4,6\text{-}(CH_3)_3C_6H_2)_2PB(2,4,6\text{-}(CH_3)_3C_6H_2)_2$ (Mes_2PBMes_2, **3**), $(C_6H_5)_2PB(2,4,6\text{-}(CH_3)_3C_6H_2)_2$ (Ph_2PBMes_2, **4**), and $(C_{10}H_{13})(H)PB(2,4,6\text{-}(CH_3)_3C_6H_2)_2$ ((1-Ad)(H)$PBMes_2$, **5**). The structures of these five compounds are given in Fig. 1. The compounds characterized experimentally (**3**–**5**), originally by Pestana and Power, (17) exhibit a range of angles ϕ between the PBR'_2 and the bisector of the R-P-R angle, ranging from 2° (planar molecule) to 62°, with minimum twist angles (<8°) about the P—B bonds. The experimental results show that the predictions from ab initio methods are reliable models of the changes in phosphorus chemical shielding when the angle ϕ is varied between 0° (planar geometry) and 90° (folded geometry). The phosphinoborane system is an interesting example of changes in phosphorus chemical shielding because, in addition to the range of ϕ angles these compounds demonstrate, there is also a significant change in the degree to which the phosphorus "lone pair" and the vacant B 2*p* orbital can interact.

Experimental

Calculations

Computational methods used to calculate phosphorus chemical shielding tensors were based solely on Gaussian 94 (18), which utilizes the gauge invariant (including) atomic orbital method (GIAO) (19). All calculations were completed using a Silicon Graphics Indigo^2 XL workstation. Two geometry parameter sets were utilized to create the chemical shielding surfaces (*i*) an optimized geometry for each molecule (frozen geometry) H_2PBH_2 and $(CH_3)_2PB(CH_3)_2$ changing only the angle ϕ between the P—B bond plane and the PR_2 plane and (*ii*) optimized geometries, for each molecule, at each angle ϕ. Calculations utilized the B3LYP hybrid method for the geometry optimization and Hartree–Fock (HF) method for the ^{31}P NMR shielding calculations, using the basis set 6-311+G(3d,2p) for all atoms.

Sample preparation

All synthetic procedures were performed using modified Schlenk techniques. Solvents were distilled under nitrogen from sodium metal and benzophenone. The compounds 1-adamantyl dichlorophosphonic acid ((1-Ad)$P(O)Cl_2$) (20), 1-adamantyl phosphine ((1-Ad)PH_2) (20), chlorobis(mesityl)phosphine (Mes_2PCl) (21, 22), dimesityl phosphine (Mes_2PH) (22), (dimesitylphosphino)dimesitylborane (Mes_2PBMes_2, **3**) (17), (diphenylphosphino)dimesitylborane (Ph_2PBMes_2, **4**) (17, 23), and (1-adamantylphosphino)dimesitylborane ((1-Ad)(H)$PBMes_2$, **5**) (17) were prepared according to literature methods. Diphenylphosphine (Ph_2PH), dimesitylboron fluoride (Mes_2BF), *n*-butyllithium (*n*-BuLi, 1.6 M in hexanes), 2-mesitylmagnesium bromide (MesMgBr, 1 M in tetrahydrofuran, THF), 1-adamantyl bromide ($C_{10}H_{13}Br$), phosphorus trichloride (PCl_3), aluminum bromide ($AlBr_3$), and lithium aluminum hydride ($LiAlH_4$) were obtained from the Aldrich Chemical Company. Samples for subsequent solid-state NMR spectroscopy (**3**–**5**) were characterized by high resolution ^1H and ^{31}P NMR, electron ionization mass spectrometry and melting points, which all matched literature data (17).

Solid-state NMR spectroscopy

All solid-state NMR spectra were obtained at 11.75 T and 295 K on a Bruker AMX-500 NMR spectrometer, operating at 202.46 MHz for ^{31}P and 500.13 MHz for ^1H. The ^{31}P NMR spectra were referenced to an external sample of solid $NH_4H_2PO_4$, which has a chemical shift of +0.81 ppm with respect to 85% H_3PO_4(aq). All ^{31}P solid-state NMR spectra were obtained with cross-polarization (CP) and high-power ^1H decoupling, with ^1H 90° pulse widths of 4–5 μs and contact times of 5 ms. Simulated spectra were obtained on a PC microcomputer using the WSOLIDS computer program of Eichele and Wasylishen (24) incorporating the POWDER interpolation scheme (25).

© 1999 NRC Canada

Table 1. Structural parameters for the phosphinoboranes H_2PBH_2 (**1**) and $(CH_3)_2PB(CH_3)_2$ (**2**) obtained from geometry optimization using Gaussian-94 with the B3LYP density functional method and 6-311+G(3d,2p) basis sets for all atoms. Bond lengths are given in angstroms; bond angles in degrees. Note: C_3 symmetry of the CH_3 groups was maintained throughout the geometry optimizations of **2**.

Angle ϕ	Bond			Angle	
H_2PBH_2					
68.16	P—B	H—B	H—P	H-B-H	H-P-H
	1.8667	1.1861	1.4082	120.75	100.23
				H-B-P	H-P-B
				119.63	103.80
$(CH_3)_2PB(CH_3)_2$					
62.67	P—B	C—B	C—P	C-B-C	C-P-C
	1.9016	1.5783	1.8563	121.75	102.38
				C-B-P	C-P-B
				119.13	106.72
		C_B—H	C_P—H	H-C_B-H	H-C_P-H
		1.0889	1.0889	106.98	108.49
				H-C-B	H-C-P
				111.86	110.44

Results

The primary goal of this study was to correlate the effects of structural changes, specifically bond angles, on phosphorus chemical shielding. We have used a combination of theoretical predictions and experimental measurements to provide a proper description of these effects, and we illustrate the results of the theoretical predictions first.

Computational

The model phosphinoboranes investigated by ab initio methods were H_2PBH_2 (**1**) and $(CH_3)_2PB(CH_3)_2$ (**2**), chosen for reasons of computational accessibility. A general view of their structures is provided in Fig. 1. Each of these molecules was subjected to a geometry optimization that resulted in the structural parameters outlined in Table 1; these results agreed well with previous calculations performed on this class of compounds (26). Since our focus was the effect of bond angle changes at phosphorus, we manipulated the structures of these molecules as a function of the angle ϕ, where this angle lies between the P—B bond direction and the bisector of the HPH (or CPC) bond angle. Structural "surfaces" were achieved by varying this angle in 10° steps between a planar geometry (ϕ = 0°) and a folded geometry (ϕ = 90°) in two distinct fashions. In the first case, that of a "frozen" geometry, the structural parameters other than the angle ϕ were held at their optimized values. In the second, called an "optimized" geometry, the structure was allowed to relax to a minimum energy for the defined value of ϕ. The construction of these two surfaces was undertaken to separate the influence of strict bond angle changes from the aspects of the phosphinoborane structure covariant with this changing angle. The frozen geometry implies no change in the structure save for that of the angle from planarity. The optimized geometry displayed systematic variation in several structural parameters, most notably in the P—B and P—H (or P—C) bond lengths, and the HBH and HPH (or CPC) bond angles. Details are provided in Table 2. All other structural parameters were invariant to within 0.5% of their fully optimized values.

The results from these two geometric surfaces were then used to predict the magnetic shielding properties of phosphorus as a function of the angle from planarity ϕ. The results from these calculations are given in Fig. 2. While it is normal to report chemical shielding in terms of the standard definitions, $\sigma_{11} \leq \sigma_{22} \leq \sigma_{33}$, we have opted to use, as an alternative, a molecular reference frame that is more meaningful for comparisons detailed in this investigation (see Fig. 3). In this molecular fixed frame, the *z* axis lies along the bisector of the HPH (or CPC) angle, the *y* axis lies in the HPH (or CPC) plane perpendicular to *z*, and *x* lies perpendicular to the HPH (or CPC) plane. Consequently, in the planar geometry (ϕ = 0°), *x* lies perpendicular to the plane of the molecule, while *y* lies in the molecular plane and perpendicular to the P—B bond. In the folded geometry (ϕ = 90°), *y* still lies perpendicular to the P—B bond, and *x* lies along the P—B bond. While these directions provide a good reference with respect to the changes in molecular structure, the results from the calculations show that the principal components of the phosphorus chemical shielding tensor do not follow these directions rigorously. In fact, the rotation of the tensor about the *y* direction, implied by the rotation of the HPH (or CPC) plane about this axis, is restricted to a large degree, such that the tensor follows the same sense of rotation but at a slower rate. Hence, as the angle ϕ is increased, the principal components σ_x and σ_z deviate from the *x* and *z* axes by values indicated in Fig. 2.

There are three key areas of interest on the H_2PBH_2 and $(CH_3)_2PB(CH_3)_2$ surfaces. These are the data points where the tensor components correspond to the planar angles, ϕ = 2.2, 42.1, and 61.6°. These data points are of special interest because the three phosphinoborane compounds, Mes_2PBMes_2 (**3**), Ph_2PBMes_2 (**4**), and (1-Ad)(H)$PBMes_2$ (**5**), demonstrate the corresponding angles from planarity.

© 1999 NRC Canada

Table 2. Selected structural parameters for the geometries of H_2PBH_2 (**1**) and $(CH_3)_2PB(CH_3)_2$ (**2**) optimized at each value of the angle from planarity ϕ. Bond lengths are given in angstroms; bond angles in degrees. Parameters not given have not deviated significantly from the optimized structure values.

H_2PBH_2					
Angle ϕ	P—B bond	H—B bond	H—P bond	H-B-H angle	H-P-H angle
0	1.8017	1.1819	1.3805	123.55	110.42
10	1.8043	1.1820	1.3809	123.47	110.13
20	1.8120	1.1821	1.3823	123.20	109.28
30	1.8244	1.1824	1.3846	122.78	107.89
40	1.8408	1.1829	1.3876	122.21	106.05
50	1.8594	1.1835	1.3909	121.53	103.87
60	1.8794	1.1841	1.3950	120.86	101.71
70	1.8985	1.1848	1.3991	120.24	99.7
80	1.9150	1.1854	1.4031	119.77	98.01
90	1.9295	1.1858	1.4071	119.44	96.7
$(CH_3)_2PB(CH_3)_2$					
Angle ϕ	P—B bond	C—B bond	C—P bond	C-B-C angle	C-P-C angle
0	1.8176	1.5969	1.8418	122.72	112.23
10	1.8213	1.5963	1.8421	122.71	111.70
20	1.8320	1.5946	1.8426	122.72	110.21
30	1.8489	1.5921	1.8437	122.67	108.07
40	1.8702	1.5893	1.8456	122.58	105.72
50	1.8932	1.5869	1.8488	122.32	103.61
60	1.9160	1.5854	1.8540	121.86	101.98
70	1.9390	1.5850	1.8611	121.03	100.87
80	1.9655	1.5861	1.8708	119.64	100.24
90	2.0021	1.5895	1.8827	117.47	100.24

The importance of these compounds is that they will provide experimental data to test the predictive potential of the chemical shielding surfaces.

Experimental

The solid-state ^{31}P CP static NMR spectra of **3**–**5** are given in Fig. 4, together with their best-fit simulations. The relevant spectral parameters resulting from these simulations are listed in Table 3. The anisotropic ^{31}P NMR line shapes $\nu_P(\theta, \varphi)$ arise from the orientation dependence (given in spherical polar coordinates by the polar and azimuthal angles θ and φ with respect to B_o, the magnetic field direction) of the ^{31}P anisotropic chemical shift and the ^{31}P–^{11}B direct dipolar coupling, as well as the relative orientation of these two interactions (27), given by the equation

$$[1]\quad \nu(\theta, \varphi) = \nu_o[1 - (\sigma_{11}\sin^2\theta\cos^2\varphi + \sigma_{22}\sin^2\theta\sin^2\varphi + \sigma_{33}\cos^2\theta)] + m_B R_{PB}[3(\sin\beta\sin\theta\cos(\alpha - \varphi) + \cos\beta\cos\theta)^2 - 1]$$

where ν_o is the ^{31}P Larmor frequency, σ_{ii} (i = 1, 2, 3) are the principal components of the ^{31}P chemical shielding tensor, m_B = +3/2, +1/2, –1/2, –3/2 are the equally probable spin states of the adjacent ^{11}B (I = 3/2) nucleus, R_{PB} is the ^{31}P–^{11}B dipolar coupling constant, and the angles α and β are the azimuthal and polar angles, respectively, describing the orientation of the P–B dipolar vector (i.e., the P—B bond) in the principal axis system of the ^{31}P chemical shielding tensor. The quality of the spectral simulations for all three compounds was markedly improved if the contributions from the 19.58% naturally-abundant ^{10}B(I = 3) nuclear isotope were included as well, with a ^{31}P–^{10}B dipolar coupling constant of 0.334 87 (i.e., $\gamma(^{10}B)/\gamma(^{11}B)$) of that of ^{31}P–^{11}B dipolar coupling. There was no evidence of indirect P–B J coupling in any of the ^{31}P solid-state NMR spectra, although the ^{31}P CPMAS NMR spectrum of **3** (Fig. 4*a*) showed substantial residual dipolar coupling to the quadrupolar boron isotopes directly adjacent to phosphorus, in spite of rapid sample rotation of 9.5 kHz. The centreband at 20 ± 20 ppm, spans 7000 Hz. In the planar geometry in which this molecule is found, the electric field gradient around boron must be very large, resulting in a ^{11}B quadrupolar coupling constant of approximately 400 MHz.[2]

In practice, absolute chemical shielding values, expressed in ppm with respect to a bare ^{31}P nucleus, are not measured; rather, the chemical shifts relative to an accepted reference compound are determined. Thus the principal components of the ^{31}P chemical shift tensor, given by δ_{ii} (i = 1, 2, 3), are determined experimentally, where δ_{11} corresponds to the least shielded component σ_{11}, etc., in accord with convention (28). The chemical shift values with respect to 85%

[2] M.J.T. Ditty and W.P. Power. Unpublished results.

© 1999 NRC Canada

Fig. 2. Phosphorus chemical shielding surfaces for **1** and **2** in frozen and optimized geometries. The fully optimized geometries, including optimum values of the angle from planarity, ϕ, are included for H_2PBH_2 at 68.16° and $(CH_3)_2PB(CH_3)_2$ at 62.67°. The chemical shielding surfaces display the dependence of the molecular-frame principal components (σ_x, ◆; σ_y, ▲; σ_z, ■; these directions are defined in the text and in Fig. 3) of the phosphorus chemical shielding tensor as a function of the angle from planarity, ϕ. Also included with the symbol × are the deviation angles of the *x* and *z* shielding components from the *x* and *z* molecular axes; the vertical scale on the right pertains to these values only.

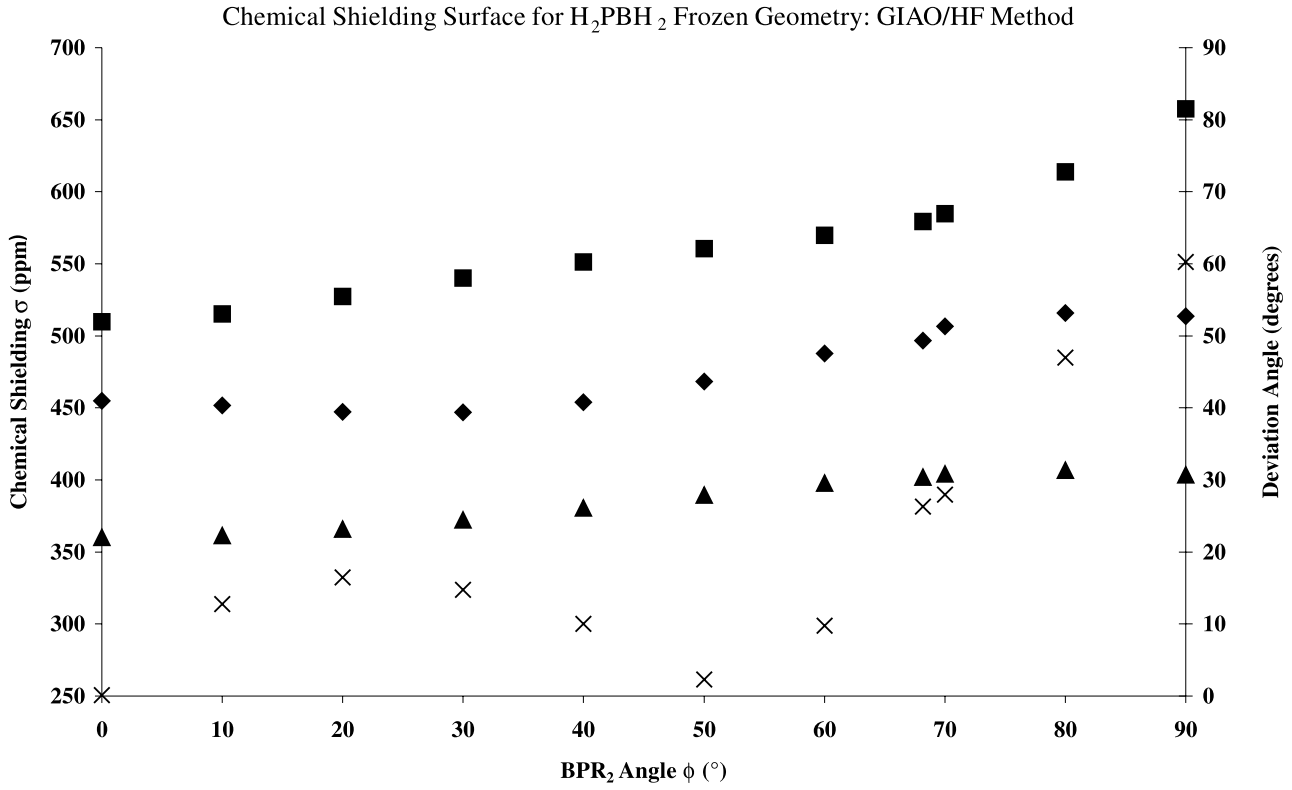

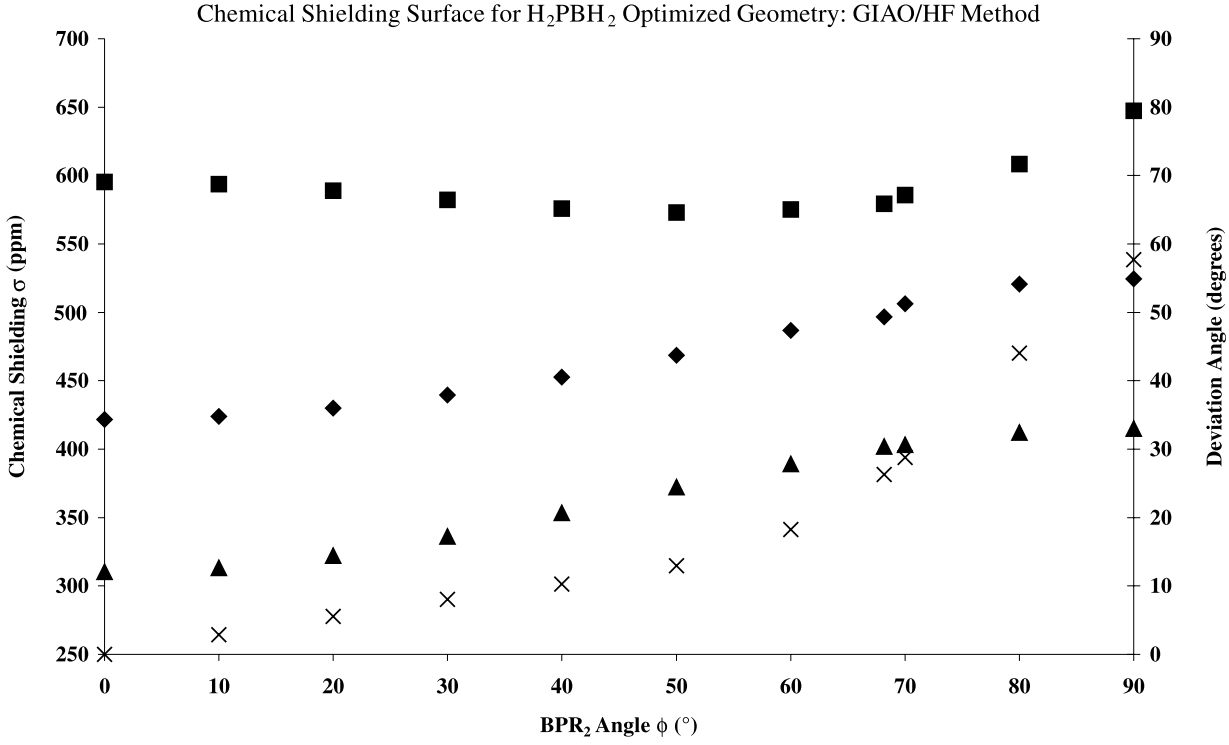

© 1999 NRC Canada

Fig. 2 (*concluded*).

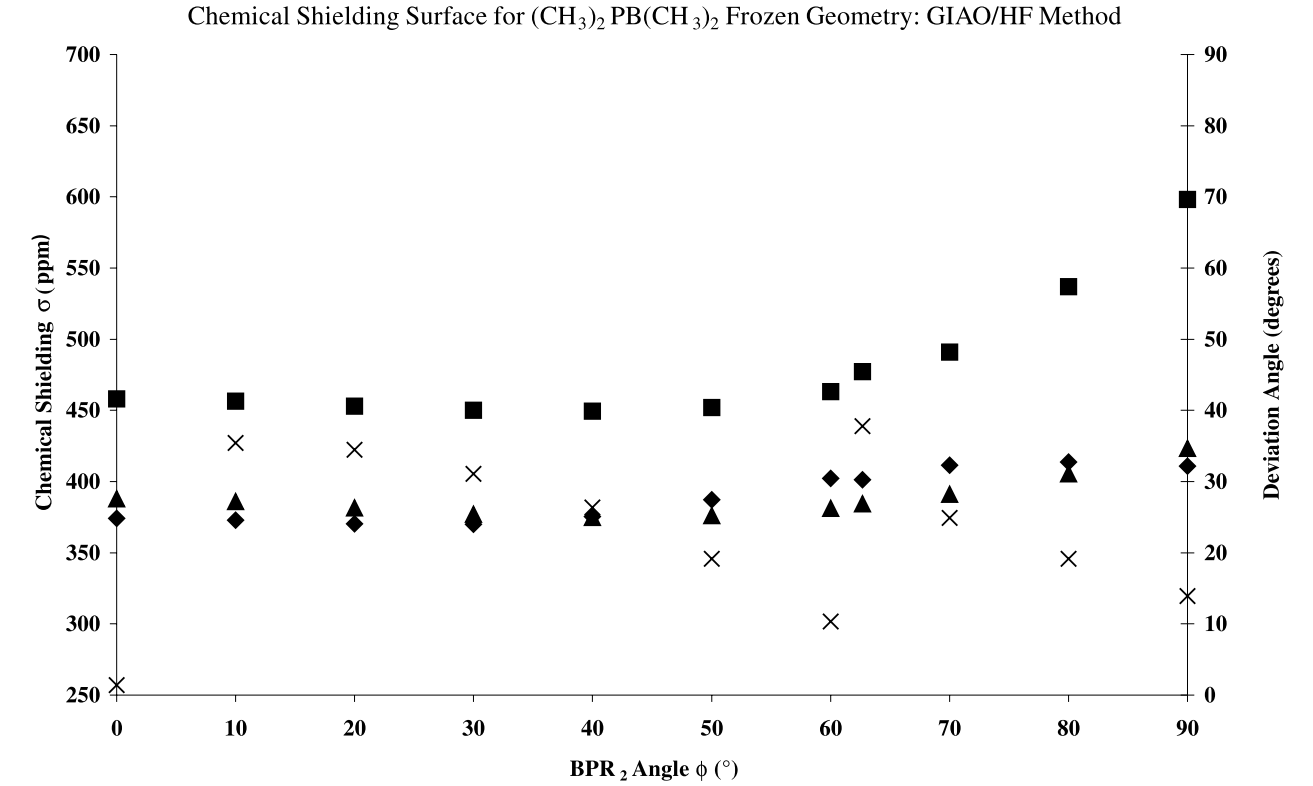

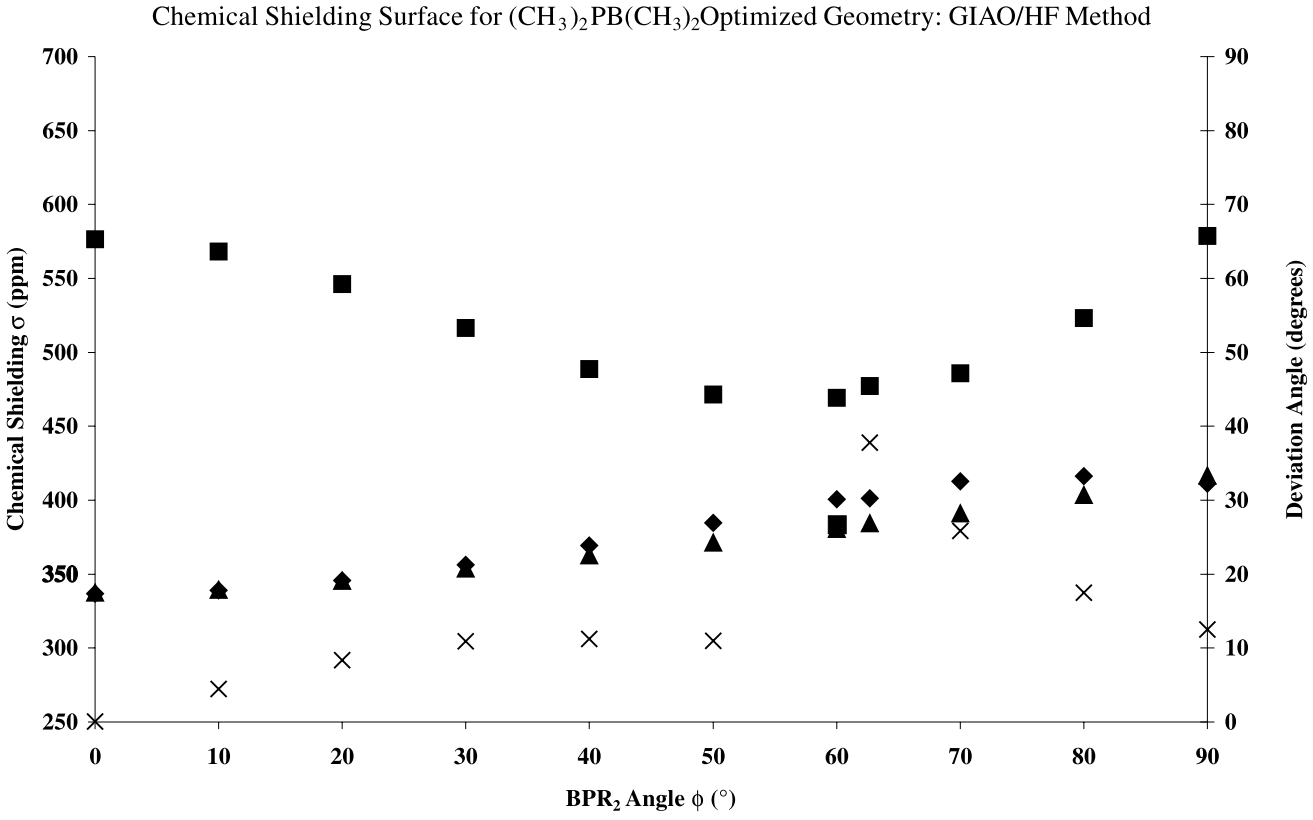

© 1999 NRC Canada

Fig. 3. Definition of the (*x, y, z*) molecular-frame axis system, as well as the molecular-frame principal components (σ_x, σ_y, σ_z) of the phosphorus chemical shielding tensor. The deviation angle lies between the *x* (*z*) axis and the σ_x (σ_z) components.

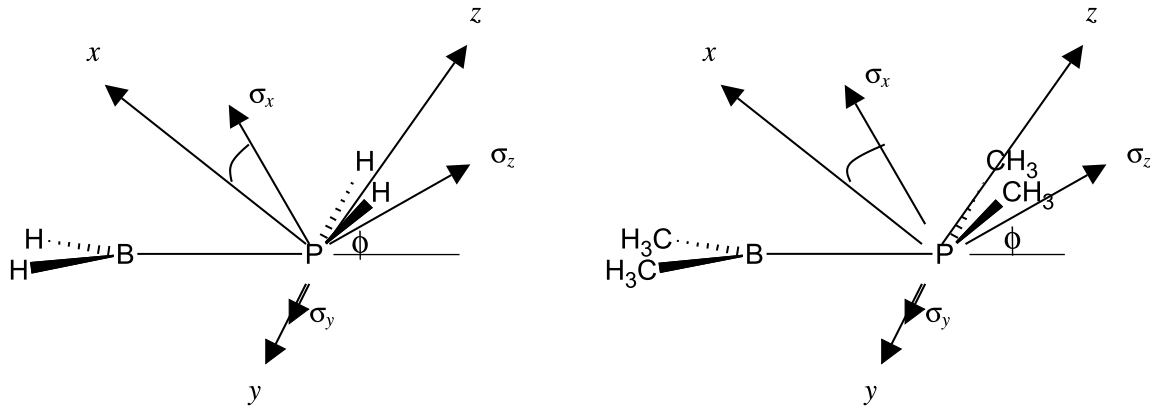

H_3PO_4(aq) may be converted to chemical shielding using the absolute chemical shielding scale for phosphorus established by Jameson et al. (29) given by

[2] $\sigma_{ii} = 328.35 \text{ ppm} - \delta_{ii}$

where *ii* = 11, 22, 33, or *iso*.

The ^{31}P solid-state NMR spectra display significant chemical shift anisotropies, ranging in spans ($\delta_{11} - \delta_{33}$) from 182 ppm for **3**, to 98 ppm for **4**, and to 194 ppm for **5**. Compounds **3** and **4** display approximately axially symmetric phosphorus chemical shift tensors, although with the sense of the axial symmetry reversed between the two. Compound **5** displays complete nonaxial symmetry of its phosphorus chemical shift tensor. The ^{31}P–^{11}B dipolar coupling constants, which depend on the internuclear separations of the two nuclear isotopes, become smaller in magnitude as the geometry of these molecules move further from planarity, in accord with expectations based on the bond length changes observed through this series by X-ray crystallography (17).

Compounds **3**–**5** are air sensitive compounds, decomposing to the corresponding phosphine and boryloxide upon prolonged contact with air (30). To limit this process, the samples were packed and sealed in MAS rotors under a nitrogen atmosphere prior to spectral acquisition. In addition, it was difficult to completely purify these compounds from their parent phosphines. Consequently, the spectra of **3** (see Fig. 4*a*), in particular, contain some spectral intensity at low frequencies corresponding to the phosphine Mes_3P (–39 ppm) (21). The ^{31}P static NMR spectrum of the solid phosphine Mes_3P overlaps partially with that of the phosphinoborane. The identity of this impurity was confirmed by solid-state ^{31}P NMR of the pure phosphine (spectrum not shown), and simulation of the relevant phosphinoborane was completed by exclusion of the phosphine's spectrum from the fitting analysis. Since this impurity masks the low frequency end of the anisotropic ^{31}P NMR powder pattern of **3**, the errors in both δ_{33} and β are larger than the other parameters. The broad feature near 30 ppm is particularly sensitive to the value of α.

Discussion

The chemical shielding surface generated by calculation enables us to evaluate the relative magnitude of the anisotropy over a range of angles. It is believed that this chemical shielding surface can be used as a predictive tool, of anisotropy and magnitudes of tensor components for similar phosphorus compounds. Chemical shielding calculations for H_2PBH_2 and $(CH_3)_2PB(CH_3)_2$ revealed that changes in the angle from planarity affected the orientations and magnitudes of the three principal components of the chemical shielding tensor significantly. The first set of calculations used the frozen geometry parameters over the entire range of ϕ. A significant trend that is observed for both H_2PBH_2 and $(CH_3)_2PB(CH_3)_2$ is that they converge to a minimum anisotropic span at their fully optimized geometries 177 ppm at $\phi = 68.16°$ and 93 ppm at $\phi = 62.67°$, respectively.

The tensor component σ_y that is perpendicular to the phosphorus–boron bond and is coplanar with the boron substituents is governed by the movement of the substituents on the phosphorus atom out of the P—B bond plane. Its orientation is unchanged and its magnitude becomes progressively more shielded as the angle is increased. The tensor component σ_z that is oriented as the bisector of the PR_2 plane, and parallel to the phosphorus–boron bond, initially has a large shielding value that decreases sharply until 60°; its shielding changes very little after this angle. The tensor component σ_x that is oriented along the phosphorus lone pair increases linearly until an angle of 60°; at angles greater than 60° the shielding increases rapidly.

The second set of shielding calculations utilized the optimized geometry parameters (frozen geometry) of the respective molecule for each calculation. It has been observed, that as the planar angle was changed from 0 to 90° some of the bonding angles and bond lengths change. The changes include an increase in both the P—B bond length and the P—H bond lengths with a concomitant decrease in the H-P-H angle. These trends are also observed in the crystallographic data reported by Pestana and Power (17).

Both the frozen and optimized geometry chemical shielding surfaces for H_2PBH_2 display nonaxially symmetric powder patterns. The main differences between the two surfaces are the greater shielding for all tensor components in the frozen geometry surface and the angle at which the minimum chemical shielding anisotropy is produced, at 0° for the frozen geometry compared to fully optimized angle on the optimized geometry surface. Also, an identical trend to that encountered in a frozen geometry is followed by the σ_z

© 1999 NRC Canada

Fig. 4. $^{31}P\{^{1}H\}$ cross-polarization solid-state NMR spectra of polycrystalline phosphinoboranes at 11.75 T and 295 K: (*a*) **3**, Mes_2PBMes_2; with MAS at 9.5 kHz, experimental static, and calculated static (*b*) **4**, Ph_2PBMes_2, experimental and calculated static.

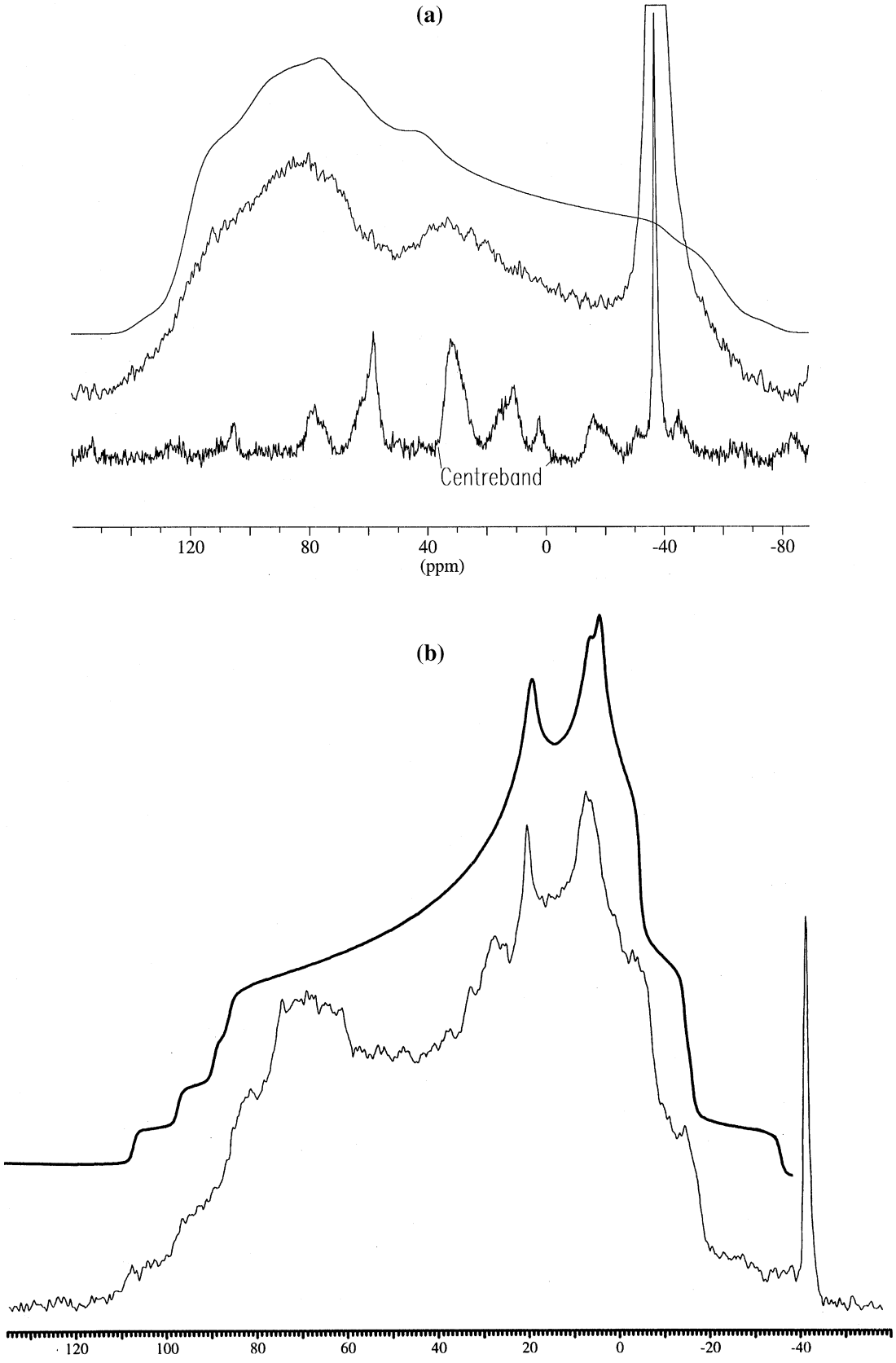

© 1999 NRC Canada

Fig. 4 (*concluded*). (*c*) **5**, (1-Ad)(H)PBMes$_2$, experimental and calculated static parameters used to generate the calculated spectra are given in Table 3.

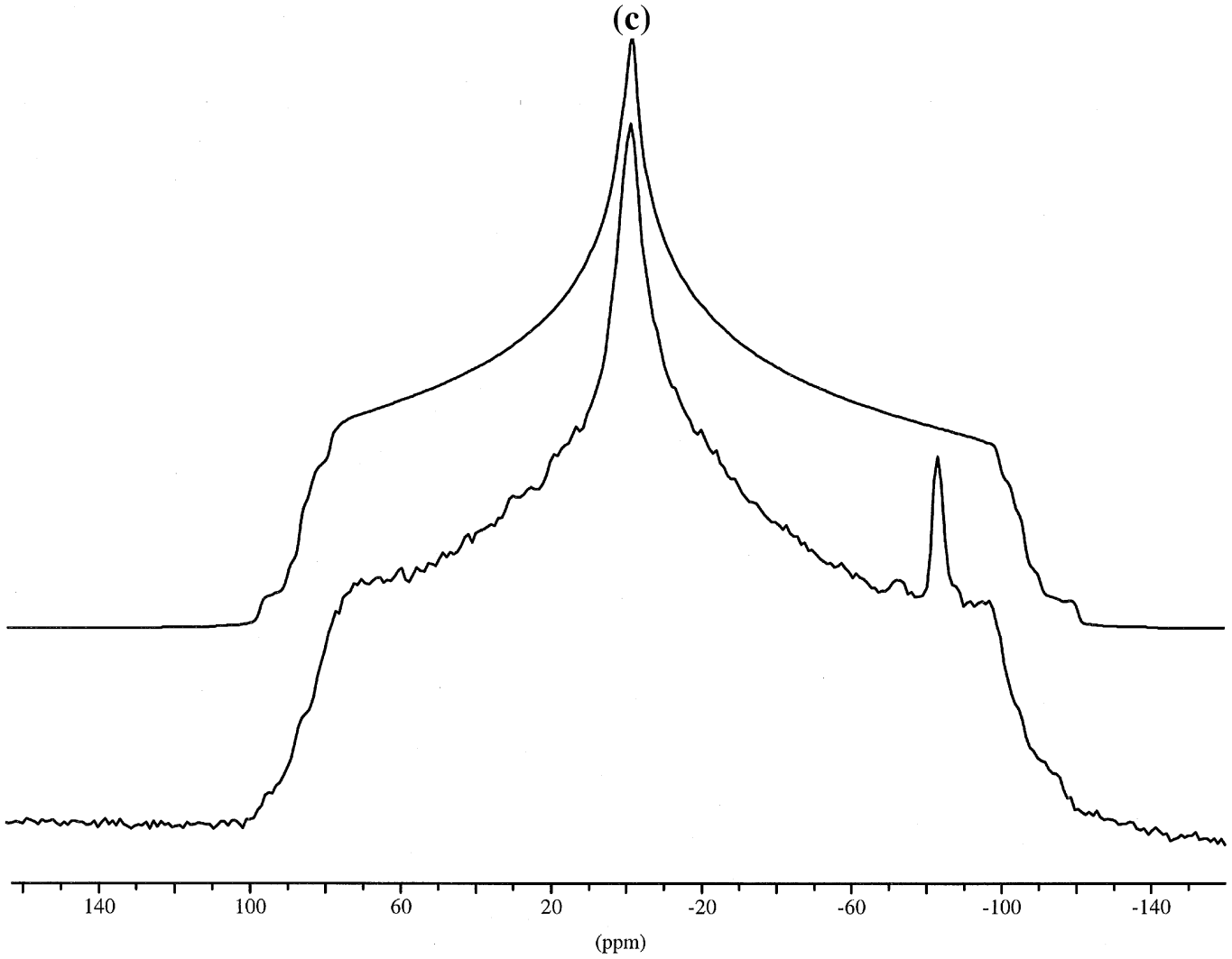

tensor component in the optimized geometry surface. Since a frozen geometry was used, changes in the degree of phosphorus lone pair donation to the empty boron 2*p* orbital do not play a key role in the shielding of the σ_y or σ_z tensor components. This set of calculations with a "frozen" structure did not permit a "relaxation" of the structure with concomitant changes in the character of the lone pair. The lone pair remains localized on phosphorus and resulting in very little change in the shielding of these components. Much the same trends can be deduced for the calculations involving **2**, the methylated phosphinoborane.

The most relevant test of the calculated surfaces involves comparison to experimental values obtained for phosphinoboranes with different angle of planarity, and it was on this basis that compounds **3**–**5** were chosen for investigation. Ideally, the calculated surfaces should provide some predictive value for phosphorus chemical shielding. The experimental and calculated results compare well, providing some support for the validity of the trends extracted from the calculated surfaces. The magnitudes of the chemical shielding principal components are lower (less shielded) in the compounds characterized experimentally. This is a consequence of the difference in the attached R and R′ groups (H, CH_3 vs. Mes, Ph, 1-Ad) between the calculated and experimental compounds. The trend to decreased shielding with bulkier substitution is properly represented between the H and CH_3 surfaces, so this difference is consistent with the calculations. More significant are the relative trends, in terms of the orientations of the various principal components as the angle from planarity is changed. Here, the agreement between the two calculated surfaces, and between the calculated surfaces and experimental results, is quite reasonable. For the planar molecule, **3**, the anisotropic chemical shielding spans 182 ppm; as the angle is increased to 42°, this span is significantly reduced to 98 ppm for **4**; and the span increases markedly beyond that, to 194 ppm for **5**, where the angle from planarity is 62°. The orientations of the principal components follow those predicted from the surface. For compound **3**, the P—B bond lies perpendicular to the most shielded principal component, in accord with the calcula-

© 1999 NRC Canada

Table 3. Spectral parameters used to provide best-fit simulations of the experimental ^{31}P CP static NMR spectra of solid samples of Mes_2PBMes_2 (**3**), Ph_2PBMes_2 (**4**), and (1-Ad)(H)$PBMes_2$ (**5**). Phosphorus chemical shift (or chemical shielding) values are given in ppm with respect to 85% H_3PO_4(aq) (or the bare nucleus, respectively). Errors in the chemical shifts (chemical shieldings) are less than ±3 ppm, unless indicated otherwise. R_{PB} denotes the strength of the ^{31}P–^{11}B direct dipolar coupling constant, with an error of less than ±60 Hz; the dipolar coupling to ^{10}B (I = 3, 19.58% natural abundance) was also included in the calculated spectra, with a magnitude of 0.33487 × R_{PB}. Errors in the angles α and β are less than ±7° and ±3°, respectively, unless indicated otherwise. Line broadening of 500–1000 Hz was applied to each calculated spectrum to improve the fit to the experimental spectrum.

Compound	Mes_2PBMes_2, **3**	Ph_2PBMes_2, **4**	(1-Ad)(H)$PBMes_2$, **5**
Angle φ	2.2°	42.1°	61.6°
δ_{11} (σ_{11}) (ppm)	122 (206)	87 (241)	87 (241)
δ_{22} (σ_{22}) (ppm)	75 (253)	0 (328)	–3 (331)
δ_{33} (σ_{33}) (ppm)	–60 ± 10 (388)	–6 (334)	–107 (435)
R_{PB} (Hz)	2400	2430	1900
α (degrees)	75 ± 5	0	60
β (degrees)	90 ± 10	20	40

tions. However, the calculations fail to correctly predict the orientation of the least shielded component, σ_z; the calculations place this component along the P—B bond, whereas it lies 75° from this vector in **3**. This is probably due to the substituents, most notably the twists experienced by the mesityl rings in the crystal lattice (17). As the angle is increased to approximately 40°, the calculations predict that σ_x and σ_z deviate from the molecular *x*, *y*, *z* axes, by about 10°, resulting in an expected value for β of 40° – 10° = 30°, in accord with the experimental results for **4**. The intermediate component, σ_y in the calculated surfaces and δ_{22} in the experimental results, is substantially more shielded in the experimental results, a difference that is most likely due to the different identity of the substituents on phosphorus between the calculated and experimental molecules. Finally, at the largest experimental angle of 62°, the orientation of the most shielded component for **5** is in accord with the expectations from the surface, when the angle from planarity and the deviation angle of the σ_x and σ_z components from the *x* and *z* axes are taken into account. The sole discrepancy here is the apparent interchange of the orientations of the δ_{11} and δ_{22} components. This interchange can be attributed to the substitution of phosphorus in **5**, since hydrogen is one substituent. It can be argued that the H_2PBH_2 is a better model of the surface for this molecule than $(CH_3)_2PB(CH_3)_2$, in which case these components (σ_y and σ_z) are anticipated to follow this trend. It is clear that the general features of the calculated chemical shielding surfaces, large anisotropy at a planar geometry, reducing to a minimum value near the optimized geometry, then increasing significantly at angles beyond.

Conclusions

The phoshorus chemical shielding surface for phosphinoboranes of the form $R_2PBR'_2$ have been investigated from a calculated and experimental viewpoint. The calculations show clear trends in the phosphorus shielding as the bond angles at phosphorus are changed, from a planar molecule to a folded form. Experimental data obtained for compounds that sample different regions of this surface provide support for the predictive value of the calculated surface. It is hoped that these ongoing contributions involving calculated and experimental values of phosphorus chemical shielding tensors in a variety of different molecules and geometries will provide further insights into the factors influencing the wide range of phosphorus chemical shifts.

Acknowledgments

The authors would like to thank Prof. R.T. Oakley and Dr. G. Lesley for their invaluable assistance with the synthetic aspects of this work. We acknowledge also the financial support of the Natural Sciences and Engineering Research Council of Canada (NSERC) in the form of research and equipment grants.

References

1. P. Lazzeretti and R. Zanasi. J. Chem. Phys. **72**, 6768 (1980).
2. D.B. Chesnut and C.K. Foley. J. Chem. Phys. **85**, 2814 (1986).
3. U. Fleischer, M. Schindler, and W. Kutzelnigg. J. Chem. Phys. **86**, 6337 (1987).
4. T.D. Bouman and Ae.E. Hansen. Chem. Phys. Lett. **175**, 292 (1990).
5. C.J. Jameson, A.C. de Dios, and A.K. Jameson. J. Chem. Phys. **95**, 9042 (1991).
6. D. Gudat, W. Hoffbauer, E. Niecke, W.W. Schoeller, U. Fleischer, and W. Kutzelnigg. J. Am. Chem. Soc. **116**, 7325 (1994).
7. J.A. Tossell and P. Lazzeretti. Chem. Phys. Lett. **140**, 37 (1987).
8. T.C. Farrar and J.D. Trudeau. Nuclear magnetic shieldings and molecular structure. *In* NATO ASI series C: mathematical and physical sciences. Vol. 386. *Edited by* J.A. Tossell. Kluwer Academic Publishers, Dordrecht, The Netherlands. 1993. p. 27.
9. W. Kutzelnigg, U. Fleischer, and M. Schindler. *In* NMR basic principles and progress. Vol. 23. *Edited by* P. Diehl, E. Fluck, and R. Kosfeld. Springer–Verlag, Berlin. 1990. p. 165.
10. D.B. Chesnut. J. Am. Chem. Soc. **120**, 10504 (1998).
11. J.H. Lechter and J.R. Van Wazer. J. Chem. Phys. **44**, 815 (1966).
12. P.S. Pregosin and R.W. Kunz. *In* NMR basic principles progress. Vol. 16. *Edited by* P. Diehl, E. Fluck, and R. Kosfeld. Springer–Verlag, Berlin. 1979.
13. D.G. Gorenstein. Prog. NMR Spectrosc. **16**, 1 (1983).
14. J.A. Davies and S. Dutremez. Coord. Chem. Rev. **114**, 61 (1992).
15. G.H. Penner, W.P. Power, and R.E. Wasylishen. Solid State Nucl. Magn. Reson. **1**, 85 (1992).

© 1999 NRC Canada

16. W.P. Power. J. Am. Chem. Soc. **117**, 1800 (1995).
17. D.C. Pestana and P.P. Power. J. Am. Chem. Soc. **113**, 8426 (1991).
18. M.J. Frisch, G.W. Trucks, H.B. Schlegel, P.M.W. Gill, B.G. Johnson, M.A. Robb, J.R. Cheeseman, T. Keith, G.A. Peterson, J.A. Montgomery, K. Raghavachari, M.A. Al-Laham, V.G. Zakrzewski, J.V. Ortiz, J.B. Foresman, J. Cioslowski, B.B. Stefanov, A. Nanayakkara, M. Challacombe, C.Y. Peng, P.Y. Ayala, W. Chen, M.W. Wong, J.L Andres, E.S. Replogle, R. Gomperts, R.L. Martin, J.S. Binkley, D.J. Defrees, J. Baker, J.P. Stewart, M. Head-Gordon, C. Gonzalez, and J.A. Pople. Gaussian 94, Revision D.4. Gaussian, Inc., Pittsburgh, Pa. 1995.
19. R. Ditchfield. Mol. Phys. **27**, 789 (1974).
20. H. Stetter and W.D. Last. Chem. Ber. **102**, 3357 (1969).
21. H. Schmidbaur and S. Schnatter. Chem. Ber. **116**, 1947 (1983).
22. R.A. Bartlett, M.M. Olmstead, P.P. Power, and G.A. Sigel. Inorg. Chem. **26**, 1941 (1987).
23. X. Feng, M.M. Olmstead, and P.P. Power. Inorg. Chem. **25**, 4615 (1986).
24. K. Eichele and R.E. Wasylishen. J. Magn. Reson. **A106**, 46 (1994).
25. D.W. Alderman, M.S. Solum, and D.M. Grant. J. Chem. Phys. **84**, 3717 (1986).
26. P.P. Power. Angew. Chem. Intl. Ed. Engl. **29**, 449 (1990), and refs. therein.
27. W.P. Power and R.E. Wasylishen. Annu. Rep. NMR Spectrosc. **23**, 1 (1991).
28. J. Mason. Solid State Nucl. Magn. Reson. **2**, 285 (1993).
29. C.J. Jameson, A. de Dios, and A.K. Jameson. Chem. Phys. Lett. **167**, 574 (1990).
30. (*a*) H.C. Brown and V.H. Dodson. J. Am. Chem. Soc. **79**, 2302 (1957); (*b*) K.J. Weese, R.A. Bartlett, B.D. Murray, M.M. Olmstead, and P.P. Power. Inorg. Chem. **26**, 2409 (1987).

© 1999 NRC Canada

A multinuclear magnetic resonance study of crystalline tripotassium tetracyanocuprate

Scott Kroeker and Roderick E. Wasylishen

Abstract: Direct NMR observation of copper-63/65 nuclei in solid $K_3Cu(CN)_4$ provides the first experimental example of anisotropic copper chemical shielding. Axially symmetric by virtue of the space group symmetry, the shielding tensor spans 42 ppm, with the greatest shielding when the unique axis is perpendicular to the applied magnetic field. The nuclear quadrupole coupling constant is also appreciable, $C_Q(^{63}Cu)$ = –1.125 MHz, reflecting a deviation of the $Cu(CN)_4^{3-}$ anion from pure tetrahedral symmetry. Spin–spin coupling to ^{13}C nuclei in an isotopically enriched sample is quantified by line-shape simulations of both ^{13}C and $^{63/65}Cu$ magic-angle spinning (MAS) NMR spectra to be 300 Hz. It is shown that this information is also *directly* available by $^{63/65}Cu$ triple-quantum (3Q) MAS NMR. The relative merits of these three approaches to characterizing spin–spin couplings involving half-integer quadrupolar nuclei are discussed. Chemical shielding tensors for nitrogen-15 and carbon-13 are obtained from NMR spectra of non-spinning samples, and are compared to those of tetrahedral group 12 tetracyanometallates. Finally, $^2J(^{63/65}Cu,^{15}N)$ detected in ^{15}N MAS experiments are found to be 19 and 20 Hz for the two crystallographically distinct cyanide ligands.

Key words: NMR, quadrupolar nucleus, chemical shielding tensor, multiple-quantum magic-angle spinning, metal cyanide, spin–spin coupling.

Résumé : Une observation RMN directe des noyaux cuivre-63/65 du $K_3Cu(CN)_4$ est le premier exemple expérimental du blindage chimique anisotrope du cuivre. De symétrie axiale en raison de la symétrie de son groupe d'espace, le tenseur de blindage s'étale sur 42 ppm; le blindage le plus important se produit lorsque l'axe unique est perpendiculaire au champ magnétique appliqué. La constante de couplage quadripolaire nucléaire est importante, $C_Q(^{63}Cu)$ = –1,125 MHz et elle est un reflet d'une déviation de l'anion $Cu(CN)_4^{3-}$ par rapport à une symétrie tétraédrique pure. Sur la base de la simulation de la forme des bandes des spectres RMN du ^{13}C et du $^{63/65}Cu$ par rotation à l'angle magique (« MAS »), on a pu établir que la valeur du couplage spin–spin avec le noyau ^{13}C d'un échantillon isotopiquement enrichi est égale à 300 Hz. On a démontré que cette information est aussi disponible *directement* par RMN MAS à triple quantum (3Q) du $^{63/65}Cu$. On discute des mérites relatifs de ces trois approches pour la caractérisation des couplages spin–spin impliquant des noyaux quadripolaires à demi-unités. On a obtenu les tenseurs de blindage chimique de l'azote-15 et du carbone-13 à partir de spectres RMN d'échantillons immobiles et on les a comparés à ceux des tétracyanométallates tétraédriques du groupe 12. Enfin, on a trouvé que les constantes $^2J(^{63/65}Cu,^{15}N)$ détectées lors d'expériences MAS du ^{15}N sont égales respectivement à 19 et 20 Hz pour les deux ligands cyanures cristallographiquement distincts.

Mots clés : RMN, noyau quadripolaire, tenseur de blindage chimique, rotation à l'angle magique à multiples quanta, cyanure métallique, couplage spin–spin.

[Traduit par la Rédaction]

Introduction

Simple inorganic salts containing cyanide ligands complexed to copper(I) combine in a variety of ratios, displaying diverse structural characteristics (1). Potassium dicyanocuprate, for example, comprises spiralling polymer chains of composition $[Cu(CN)_2^-]_\infty$ (2) and $KCu_2(CN)_3\cdot H_2O$ forms two-dimensional sheets involving $[Cu_2(CN)_3^-]_\infty$ (3). By contrast, $K_3Cu(CN)_4$ consists of discrete $Cu(CN)_4^{3-}$ tetrahedra (4). In terms of copper coordination, the one-to-one complex, CuCN, contains two-coordinate copper atoms (5–7), whereas both $KCu(CN)_2$ and $KCu_2(CN)_3\cdot H_2O$ possess copper centres bound to three cyanide ligands in a nearly trigonal planar arrangement, and $K_3Cu(CN)_4$ includes four copper–carbon linkages. Given this diversity, these systems serve as excellent model compounds for studying geometric effects on the carbon and nitrogen NMR parameters.

In addition to their attractiveness as well-characterized model compounds, the chemistry of cyanometallates, in general, is a popular means of constructing supramolecular as-

Received January 29, 1999.

This paper is dedicated to Professor Ted Schaefer in recognition of his outstanding contributions to Canadian chemistry.

S. Kroeker and R.E. Wasylishen.[1] Department of Chemistry, Dalhousie University, Halifax, NS B3H 4J3, Canada.

[1]Author to whom correspondence may be addressed. Telephone: (902) 494-2564. Fax: (902) 494-1310.
e-mail: Roderick.Wasylishen@Dal.ca

 © 1999 NRC Canada

semblies (8). The particular utility of tetracyanocuprate tetrahedra as building blocks has been highlighted in a recent review (9). Since then, other related reports have appeared. The reaction of $K_3Cu(CN)_4$ with Me_3SnCl and 4,4′-bipyridine produces a porous structure of $[Cu_2(\mu\text{-}CN)_2(CN)_2]$ sheets bridged by bipyridine "pillars" (10). One- and two-dimensional materials result from hydrothermal reactions of CuCN and $Cu(NO_3)_2\cdot 2.5H_2O$ with organonitrogen ligands (11).

Toward the development of a more systematic understanding of NMR parameters in cyanocuprates, a comprehensive investigation of crystalline tripotassium tetracyanocuprate, $K_3Cu(CN)_4$, has been performed. The structure of this compound consists of distorted tetrahedral $Cu(CN)_4^{3-}$ units in the solid phase, with a C_3 rotation axis defining the unique Cu—C—N bond (4). This geometric arrangement simplifies the analysis of NMR line shapes by fixing the orientation of certain tensor components.

The relatively high symmetry at the copper centre also makes it possible to directly probe the metal using copper NMR. Both naturally occurring isotopes, ^{63}Cu (69.1%) and ^{65}Cu (30.9%), are spin-3/2. Their magnetogyric ratios, γ, are comparable to that of carbon-13. They have sizeable quadrupole moments, eQ, with the consequence that their powder NMR spectra are observed only when the nucleus is situated in a symmetrical environment where the electric field gradient (EFG) is small. There are a number of reports of copper NMR in solutions (12, 13), but few in solid samples. In spite of the inherent challenges of copper NMR, interesting experiments have been successfully performed on systems ranging from simple cubic ionic solids (14) to high-T_c cuprate superconductors (see ref. 15 for example). Of particular relevance to the present work, copper-63/65 NMR has been used to probe cyanide ordering in the host/guest framework compounds "$N(CH_3)_4CuM(CN)_4\cdot G$," where M = Zn, Cd, Pt and G = CCl_4, $CHCl_3$, CH_3CCl_3, and $CHBr_3$ (16). A principal objective of these studies was to unambiguously identify Cu–C–N–Zn connectivities in $N(CH_3)_4CuZn(CN)_4$ by NMR of both copper-63/65 and carbon-13 (16*a*). For that compound, copper atoms exist in perfectly tetrahedral environments, rendering the EFG at that site zero, and its line shape isotropic. Less definitive were copper-63 NMR studies of some of the other compounds, where second-order quadrupolar line shapes compromised site distinction (16*b*).

The work presented herein concerns a cyanocuprate of *known* structure, which may be used to assess the sensitivity of the quadrupole coupling to deviations from cubic symmetry. Moreover, $K_3Cu(CN)_4$ is an ideal model for evaluating the feasibility of triple-quantum magic-angle spinning investigations involving nearly tetrahedral copper centres, in view of the growing importance of this structural motif.

Experimental

Materials

Tripotassium tetracyanocuprate was prepared by addition of CuCN to an aqueous solution containing a stoichiometric excess of KCN. Small, white crystals formed as the water evaporated. Isotopically enriched samples were prepared using an appropriate ratio of ^{13}C-, ^{15}N-, or ^{13}C^{15}N-enriched and natural abundance KCN. The resulting solids were characterized by Raman spectroscopy, using the well-documented cyanide stretching frequency as a means to establish chemical identity and purity (17). Some difficulties were encountered in isolating $K_3Cu(CN)_4$ crystals free from $KCu(CN)_2$ and $KCu_2(CN)_3\cdot H_2O$ contaminants. Repeated recrystallization resulted in a mixture of $K_3Cu(CN)_4$ and $KCu(CN)_2$ estimated to be 4:1. Although the copper quadrupolar interaction in the latter compound is too large to adversely affect the copper-63/65 NMR spectra of $K_3Cu(CN)_4$ (18, 19), its presence interfered with the analysis of carbon-13 and nitrogen-15 NMR spectra. This problem was resolved by subtracting the MAS NMR spectra of nearly pure $KCu(CN)_2$ from those of impure $K_3Cu(CN)_4$.

NMR spectroscopy

Spectra were acquired using Bruker spectrometers and probes: an MSL-200 operating at 4.7 T with a 7 mm double-bearing magic-angle spinning (MAS) probe and an AMX-400 at 9.4 T with a 4 mm double-bearing triple-resonance MAS probe. Although $K_3Cu(CN)_4$ is a piezoelectric material (vide infra), we did not encounter problems with acoustic ringing (20). Carbon-13 and nitrogen-15 NMR spectra were acquired using single-pulse excitation, with 60° pulses and recycle delays of 90 s or longer, due to long spin-lattice relaxation times. Carbon-13 chemical shifts are referenced with respect to TMS using solid adamantane as a secondary reference. Nitrogen-15 chemical shifts are reported with respect to liquid ammonia, referenced using solid $^{15}NH_4NO_3$, which has a shift of +23.80 ppm relative to liquid ammonia at 20°C.

Copper-63/65 single-pulse excitation MAS spectra of the central transition were collected using pulse durations which maximized the signal amplitude of the central transition — typically 2 μs. For $^{63/65}$Cu MAS NMR spectra of the satellite transitions and for non-spinning samples, very short pulses (<1 μs) were applied to minimize inhomogeneous radiofrequency (rf) excitation over the spectral region of interest. Triple-quantum (3Q) MAS experiments were performed using strong rf pulses ($\nu_{rf} \approx 167$ kHz), the durations of which were adjusted to provide optimal excitation (4.0 μs) and transfer (1.2 μs) of 3Q coherences. A six-phase cycle designed to simultaneously select the echo and anti-echo coherence pathways was employed (21). The 1D isotropic projection was constructed by plotting the echo maximum for each t_1 slice as a function of the total evolution time, $t_1 + t_2$, prior to Fourier transformation (22). Copper-63/65 chemical shifts are referenced to an aqueous solution containing KCN/NaCN/CuCN corresponding to a CN:Cu molar ratio of about six, to ensure that $Cu(CN)_4^{3-}$ is the predominant copper–cyanide species present (23). The copper chemical shift of this system is reported to be 494 ppm with respect to 1.0 M $[Cu(NCCH_3)_4][BF_4]$ in acetonitrile (24).

Line-shape simulations

Spectral calculations were carried out using programs developed in this laboratory. WSOLIDS is a Windows-based C++ program designed to compute frequency–domain NMR line shapes resulting from the influence of a variety of spin interactions. The following models were employed in this study: (*a*) central transition MAS line shape of a $^{63/65}$Cu nucleus accounting for, where necessary, spin–spin coupled ^{13}C

© 1999 NRC Canada

Fig. 1. Copper-63 MAS NMR spectra of the central transition in natural abundance $K_3Cu(CN)_4$ at 4.7 and 9.4 T. Experimental spectra are the result of 1000 transients at a sample spinning frequency of 6.45 kHz (4.7 T) and 128 transients at 8.00 kHz (9.4 T). Displayed regions at both fields span 4 kHz.

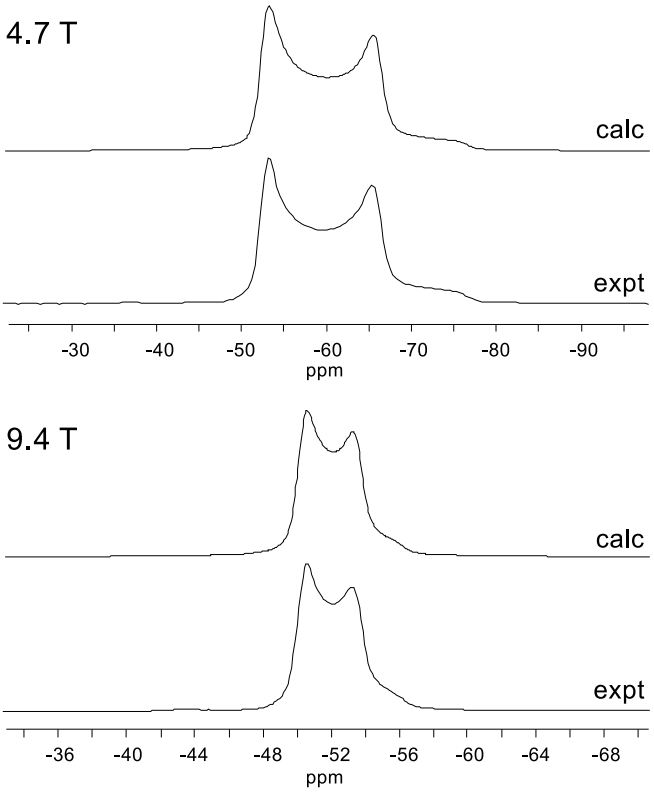

nuclei; (*b*) line shape of the $^{63/65}$Cu central transition in a non-spinning sample, subject to anisotropic chemical shielding and quadrupolar interactions; (*c*) MAS spectral line shape of ^{13}C and ^{15}N nuclei, spin–spin coupled to quadrupolar $^{63/65}$Cu spins, including residual dipolar effects as a first-order perturbation to the pure *J*-split multiplets. A second program, QUADSPIN, includes some extensions of the models described above, and was used for (*a*) calculating stationary spectra of ^{13}C and ^{15}N spin–spin coupled to quadrupolar nuclei ($^{63/65}$Cu and (or) ^{14}N), quadrupolar perturbations accounted for by first-order perturbation theory, and (*b*) the time-domain calculation of an isolated copper-63/65 nucleus evolving under the influence of both anisotropic shielding and first-order quadrupolar effects, subject to MAS at any speed (i.e., spinning sidebands). Essential to both programs is the POWDER algorithm of Alderman et al. (25), which provides an efficient means to simulate a powder pattern for which all possible crystallite orientations must be considered. All frequency–domain MAS line shapes are computed under the "infinite spinning speed" assumption, which does not account for the spinning sidebands generally observed when the spinning frequency is less than the inhomogeneously broadened powder pattern. Hence, in order to establish meaningful comparisons between experimental and calculated spin-1/2 MAS line shapes, it was necessary to construct an "isotropic MAS powder spectrum" by adding the spinning sidebands to the centreband (26).

Results and discussion

Copper NMR

Copper-63 MAS NMR spectra[2] of the central (1/2 ↔ –1/2) transition (27–30) of $K_3Cu(CN)_4$ in natural elemental abundance are shown in Fig. 1, along with the best-fit calculated spectra. A single copper site with an isotropic chemical shift of –49 ppm (corrected for second-order quadrupolar effects) is observed by NMR, consistent with the crystal structure (4). Also in agreement with the crystal structure is the presence of an axially symmetric EFG at the copper nucleus, manifesting in a line shape that is characteristic of the second-order quadrupolar interaction (27, 28). The space group for this compound includes a C_3 axis along one of the Cu—CN bonds ($r_{Cu—C}$ = 2.014 ± 0.011 Å; angle CuCN 180°), with slight structural differences between this and the other three ligands ($r_{Cu—C}$ = 1.992 ± 0.007 Å; angle CuCN 173.7° ± 0.6°) (4). This minor distortion from tetrahedral symmetry, however, is sufficient to induce a substantial electric field gradient at the copper, resulting in a quadrupole coupling constant, C_Q, of magnitude 1.125 ± 0.010 MHz for ^{63}Cu and 1.040 ± 0.010 MHz for ^{65}Cu. Since C_Q reflects the product of eQ and the largest component of the EFG at the nucleus, V_{33}, these experimental values testify to the extreme sensitivity of copper quadrupole coupling constants to molecular symmetry. This deviation from pure tetrahedral symmetry is also evident from its piezoelectric (31) and pyroelectric properties (32).

In fact, the copper quadrupole coupling tensor in this compound was first determined in 1951 by Becker (33), who analyzed the orientation-dependence of a 3.5 cm long by 1.4 cm diameter cylindrical crystal with respect to a 1.1 T magnetic field. Quadrupole coupling constants of 1.113 ± 0.003 and 1.030 ± 0.003 MHz were reported for the two isotopes. The differences between values obtained in the present study and those of the previous study are not *statistically* significant; however, if these values are suggestive of a true disparity, it may reside in Becker's failure to account for anisotropic chemical shielding. These effects would be very small (~500 Hz) at such a low applied field, but could skew the analysis subtly. The ratio of the quadrupole coupling constants in both studies agrees with that anticipated on the basis of the quadrupole moments: $Q(^{63}Cu)/Q(^{65}Cu)$ = 1.081 (34).

Copper-63/65 NMR spectra of the central transition in a non-spinning sample of $K_3Cu(CN)_4$ were also acquired at 4.7 and 9.4 T. Figure 2 contains the experimental spectra along with the best-fit calculations for ^{63}Cu, incorporating, in addition to the quadrupolar interaction as determined by MAS NMR, effects due to anisotropic chemical shielding (Table 1). Whereas there is generally no a priori justification for assuming coincidence of the interaction tensor orientations (35), full advantage was taken in these analyses of the

[2] Analogous spectra were collected and analysed for the copper-65 isotope, and yielded results consistent with the ratios of their respective magnetogyric ratios, $\gamma(^{63}Cu)/\gamma(^{65}Cu)$ = 0.933 53, and quadrupole moments, $Q(^{63}Cu)/Q(^{65}Cu)$ = 1.081 (34).

© 1999 NRC Canada

Table 1. Nuclear magnetic resonance data for $K_3Cu(CN)_4$.

		δ_{iso}/ppm[a]	$\delta_\perp$/ppm[b]	$\delta_\parallel$/ppm[b]	$J(^{63}Cu, X)$/Hz[e]	C_Q/MHz[f]
^{13}C	1	161.4	275[c]	–65[d]	300 ± 2	—
	2	162.4			298 ± 2	—
^{15}N	1	282.5	450[c]	–45[d]	19 ± 1	—
	2	288.5			20 ± 1	—
^{63}Cu		–49 ± 1	–63 ± 1	–21 ± 1	—	–1.125
^{65}Cu		–49 ± 1	–63 ± 1	–21 ± 1	—	–1.040

[a]From MAS NMR spectra, estimated uncertainty ±0.2 ppm, except where noted.

[b]From NMR spectra of non-spinning samples, estimated uncertainty ±5 ppm, except where noted.

[c]Individual sites not resolved.

[d]Calculated from δ_{iso} and $\delta_\perp$.

[e]From MAS NMR spectra of spin-1/2 nuclei.

[f]Magnitude from $^{63/65}Cu$ MAS NMR, sign from ^{13}C MAS NMR spectra, estimated uncertainty ±0.010 MHz.

Fig. 2. Copper-63 NMR spectra of the central transition for a non-spinning natural abundance sample of $K_3Cu(CN)_4$. The experimental spectrum at 4.7 T represents the coaddition of 500 transients, whereas at 9.4 T, 15 787 transients were acquired. Displayed regions in all spectra span 10 kHz.

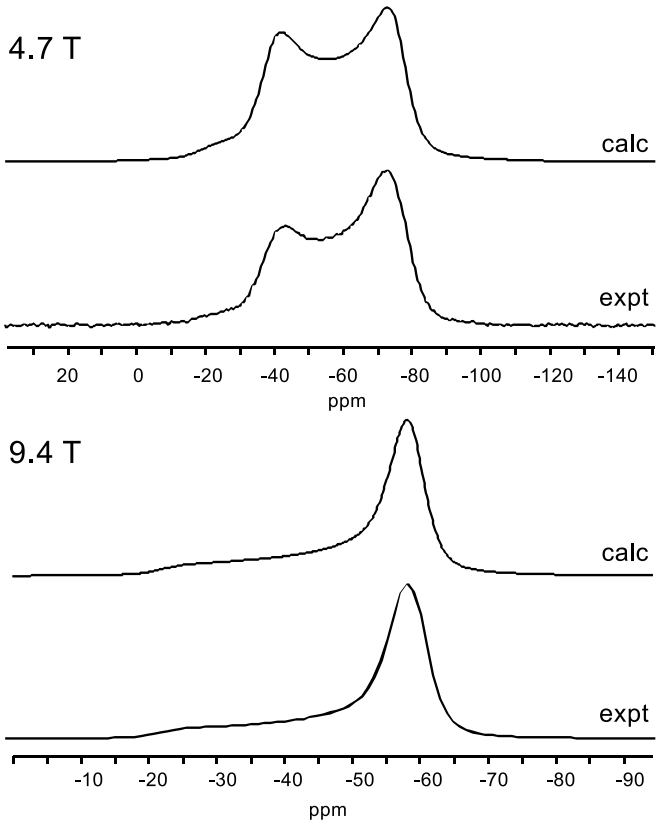

molecular three-fold rotational symmetry in identifying the mutual EFG and shielding tensor orientation. The presence of a C_3 axis demands that the unique component of the axially symmetric interaction tensors be aligned with the rotation axis. Because the EFG tensor is traceless, the largest component is unique; its orientation in the molecular frame is fixed. For the magnetic shielding tensor, however, the

Fig. 3. Schematic of anion structure in crystalline $K_3Cu(CN)_4$. Also depicted are the copper EFG and chemical shielding tensor orientations.

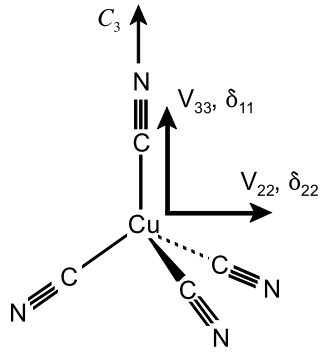

unique component may be the most- or least-shielded element, corresponding to $\kappa = +1$ or -1, respectively:

$$[1] \qquad \kappa = \frac{3(\delta_{22} - \delta_{iso})}{\delta_{11} - \delta_{33}}$$

where the most shielded direction is along δ_{33} and the least shielded direction lies along δ_{11}. If $\kappa = +1$, for instance, the unique components of the EFG and shielding tensors are coincident, whereas if $\kappa = -1$, V_{33} and δ_{11} are aligned with the rotation axis. The choice between these possibilities is straightforward based on the observed line shapes (36). It is found that the copper shielding tensor spans 42 ± 1 ppm, the least shielded component lying parallel to V_{33}. This is depicted in Fig. 3. Simulated spectra illustrating how the quadrupolar and shielding interactions combine are presented in Fig. 4. This appears to be the first experimental determination of anisotropic nuclear magnetic shielding for copper. The anisotropic character is relatively small compared to the total range of copper shielding, estimated to be about 1000 ppm (12). This is not surprising, based on the nearly tetrahedral symmetry at the copper centre, and can be contrasted with the shielding anisotropy of approximately 1200 ppm in gas-phase CuCl, as calculated from $^{63/65}Cu$ spin–rotation data (37).[3]

[3] S. Kroeker and R.E. Wasylishen. Unpublished results.

© 1999 NRC Canada

Fig. 4. NMR central transition line-shape simulations for copper-63 in a non-spinning $K_3Cu(CN)_4$ powder sample depicting the orientation dependence of the two dominant internal interactions: quadrupolar (Q), shielding (S), and their combined effect (Q + S). The Larmor frequency is 53.10 MHz, corresponding to ^{63}Cu at 4.7 T, and 106.05 MHz for ^{63}Cu at 9.4 T (see Fig. 1). The orientation of the unique tensor component with respect to the applied magnetic field direction is indicated by θ for selected spectral features. The isotropic chemical shift is denoted by the broken vertical line.

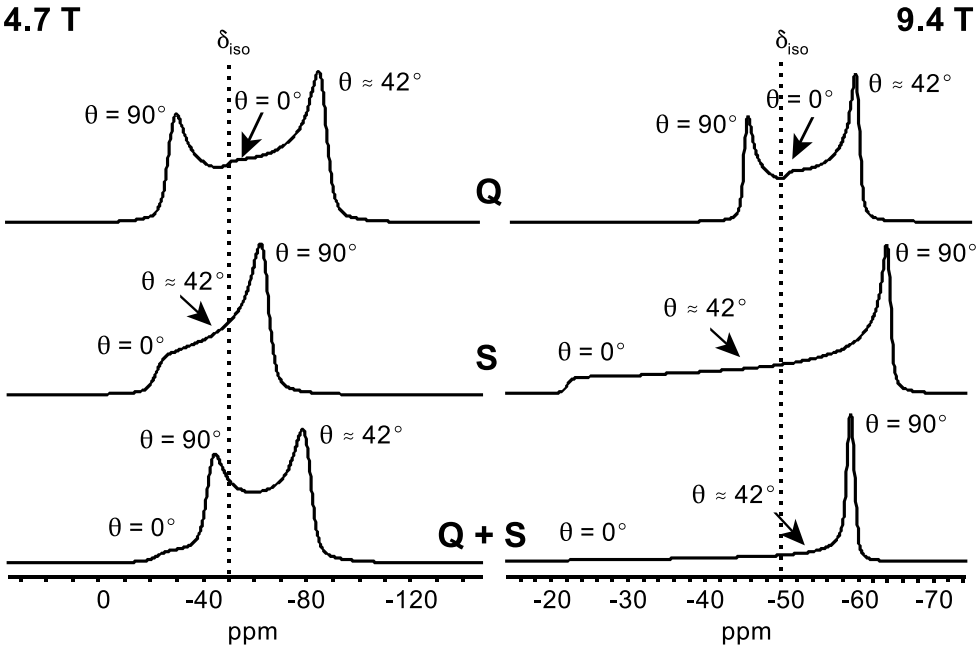

Also apparent from Fig. 4 is the opposite magnetic field dependence of the second-order quadrupolar and chemical shielding interactions. At 4.7 T, second-order quadrupolar effects are marginally more prominent, whereas at 9.4 T, anisotropic shielding clearly dominates the line shape. This differing field dependence implies that reliable characterizations of shielding and quadrupole coupling tensors are aided by analyzing spectra acquired at multiple magnetic fields — especially when tensor orientations are not fixed by crystal symmetry. Moreover, it is likely that shielding tensors of quadrupolar nuclei will be more frequently reported, as the magnetic field strength available for NMR continues to increase.

In spite of generally good agreement between the calculated and experimental spectra, a slight discrepancy is observed in the intensities of the stationary 4.7 T spectrum (Fig. 2). A likely explanation involves consideration of weak spin–spin coupling interactions between copper nuclei and surrounding ^{14}N nuclei. Two-bond *J*-couplings are 14 Hz (vide infra), and dipolar couplings, $R_{DD}(^{63}Cu,^{14}N)$, are calculated from the internuclear separation, $r_{Cu,N}$, to be about 75 Hz:

$$[2] \qquad R_{DD}(I, S) = \left(\frac{\mu_0}{4\pi}\right)\left(\frac{\hbar}{2\pi}\right)\gamma(I)\gamma(S)\left\langle r_{I,S}^{-3}\right\rangle$$

Although these constants are small in comparison with the quadrupolar and shielding interactions, their effects will be magnified by two factors. First, ^{14}N has a spin, $S = 1$, so the copper signal will be split into three subspectra (i.e., $2S + 1$). Second, the high natural abundance of ^{14}N (99.63%) implies that each copper centre will be coupled to four nitrogen-14 nuclei. These effects may result in nearly 1 kHz of additional broadening. More importantly, however, the splitting due to dipolar coupling depends on the orientation, β, of the copper–nitrogen internuclear vector with respect to the applied magnetic field. To a good approximation, the magnitude of the ^{14}N,$^{63/65}$Cu dipolar splitting varies as $(1/2)R_{DD}(3\cos^2\beta - 1)$. Thus, for crystallite orientations where the rotation axis (that is, V_{33} and δ_{11}) is parallel to the field direction ($\theta = 0°$), three chemically equivalent ^{14}N nuclei will be situated with $\beta \approx 70°$, and the dipolar splitting will be scaled by –0.3. By contrast, for $\theta = 90°$, the three ^{14}N nuclei will be nearly aligned with the field, $\beta \approx 20°$, and the scaling of R_{DD} will be minimal, 0.85. The low-frequency feature represents orientations with V_{33} and δ_{11} at 42°, for which the other three ^{14}N nuclei will have β ranging from 30° to 70°, bracketing the magic angle, where R_{DD} is scaled to zero. Of course, these "splittings" are too small to be observed, but their net effect is a broadening which will be more effective for some orientations than others. With reference to Fig. 2, greater broadening at the singularity corresponding to $\theta = 90°$ may manifest as an *apparent loss* of signal intensity with respect to the singularity at $\theta = 42°$, where less dipolar "broadening" will result in an *apparent augmentation* of the intensity. Thus, the observed line shape of the stationary sample may be accounted for by consideration of the second-order quadrupolar interaction, anisotropic copper shielding, *and* heteronuclear spin–spin interactions between copper-63/65 and nitrogen-14.

Another approach to the characterization of quadrupolar and chemical shielding tensors in solids is satellite transition spectroscopy (SATRAS). Originally proposed as a more precise measurement of the quadrupole coupling tensor than central transition line-shape modelling (38), this technique has developed into a valuable means for obtaining detailed

© 1999 NRC Canada

Fig. 5. Copper-65 MAS NMR spectrum of the central and satellite transitions in $K_3Cu(CN)_4$ at 9.4 T. (Spinning rate: 12.00 kHz; number of transients: 2560) The calculated spectrum is based on a time-domain calculation involving anisotropic shielding and the first-order quadrupolar interaction, according to the tensors determined from non-spinning samples. The central transition in both traces is truncated to exhibit the spinning sideband envelope of the satellite transitions.

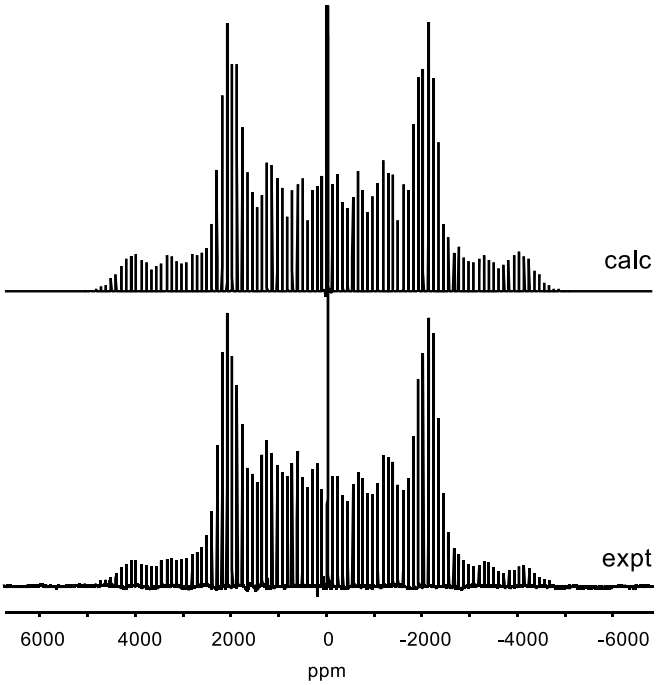

Fig. 6. Copper-63 MAS NMR spectra of the central transition in 30% ^{13}C-enriched $K_3Cu(CN)_4$ at 4.7 and 9.4 T. At 4.7 T, 1200 transients were collected with a 3.00 kHz spinning speed; 32 transients were acquired at 9.4 T, with a spinning frequency of 6.40 kHz. The depicted regions each span 4 kHz.

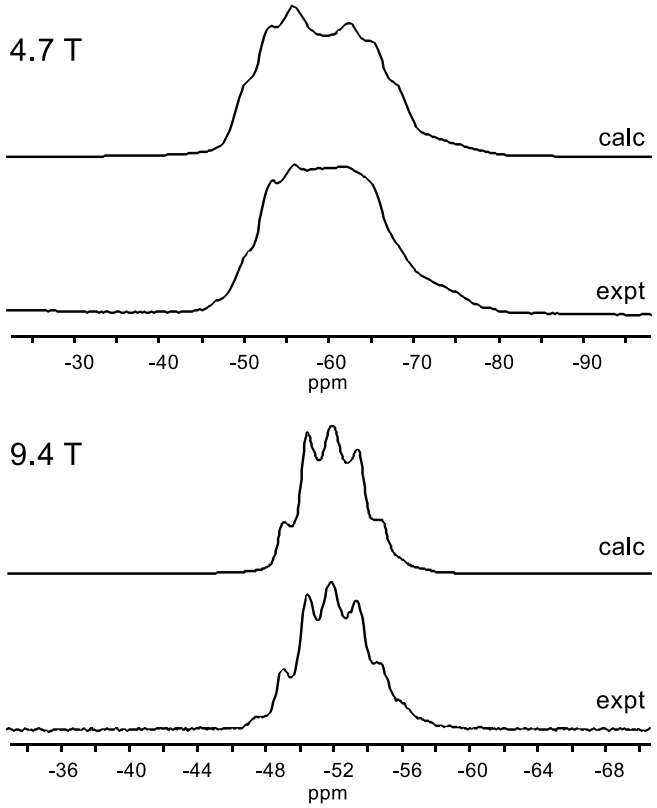

information about the magnitudes and relative orientation of shielding and quadrupole coupling tensors (39). Figure 5 depicts the spinning sideband (ssb) manifold for the copper-65 satellite transitions (+3/2 ↔ +1/2, –1/2 ↔ –3/2) along with simulations based on the parameters given in Table 1. Although the agreement appears to be quite good, a number of considerations, both experimental and theoretical, limit the usefulness of this method in the present case. For example, instrumental demands include spinning rates that are high and very stable, and rf pulses that are strong and homogeneous over the entire detection range. In this case, a strong, broad signal due to the presence of copper in the probe is observed 1500 ppm to high frequency of aqueous $Cu(CN)_4^{3-}$. While this interference has been artificially "removed" in the data processing stage, spinning sideband intensities in the region of overlap may be unreliable. From the programming point of view, only first-order quadrupolar effects were considered in the simulation, with the consequence that no second-order line shapes or peak shifts due to quadrupolar effects are calculated. This approximation substantially reduces the required computation time, while still yielding a useful simulation of the data (39*b*, 40). Fundamentally, however, the chemical shielding interaction in this compound is simply too small relative to the quadrupolar interaction for the satellite transition ssb calculations to be sensitive to modifications of its magnitude or orientation. Line-shape modelling of the central transition in a non-spinning sample is the best way to characterize the shielding tensor in this case. In spite of these limitations, Fig. 5 illustrates that high-quality copper-63/65 SATRAS NMR spectra may be obtained, confirming the quadrupolar parameters obtained from the central transition. The utility of this method for gaining precise information from calculations of the spinning sidebands may be profitably applied in select cases where the quadrupolar and shielding interactions are of comparable magnitude, or where the shielding can be neglected altogether.

Given the relative ease with which one may observe copper-63/65 NMR signals in this sample, how easy is it to measure *J*-couplings by directly probing the copper nucleus? A sample of $K_3Cu(CN)_4$, enriched to about 30% in ^{13}C, was analyzed by MAS NMR at 4.7 and 9.4 T. From the spectra in Fig. 6, it is apparent that the line shape loses its characteristic definition, becoming a series of humps and shoulders about 800 Hz wide. These spectra represent the superposition of overlapping copper sites weighted by the statistical abundances of copper nuclei coupled to zero, one, two, three, and four carbon-13 nuclei (0.24:0.41:0.26:0.08:0.01). With the knowledge of C_Q and δ_{iso} gained from NMR analyses of the unlabelled compound, these line shapes may be simulated to obtain estimates of *J*, assuming as a first approximation that coupling to zero and one ^{13}C nucleus dominate the observed peaks at this level of isotopic enrichment. However, because of the lack of definition in the line shape, reasonable fits can be obtained for a range of subspectral

© 1999 NRC Canada

Fig. 7. Isotropic reconstruction of ^{63}Cu triple-quantum MAS NMR data in 30% ^{13}C-enriched $K_3Cu(CN)_4$. Two-hundred forty transients were collected for each of the 128 t_1 slices. The interpulse delay was incremented by 25.7 μs. The central peak has been set to zero for convenience.

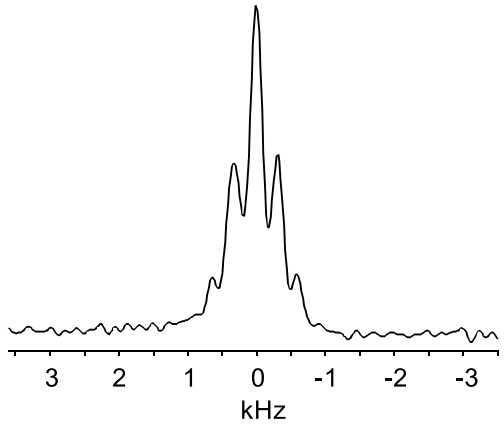

amplitudes and positions, yielding $^1J(^{63}Cu,^{13}C)$ = 300 ± 15 Hz. Additional complications resulting from residual dipolar coupling to ^{14}N nuclei may also influence the spectral appearance, especially at lower field, resulting in experimental line shapes which are difficult to calculate without introducing a variety of additional parameters and assumptions.

Recent progress has made it possible to obtain "high-resolution" NMR spectra of half-integer quadrupolar nuclei in solids (41–43). The thrust of these advances is the averaging of residual anisotropic line shapes generally observed even under conditions of magic-angle spinning, leaving only isotropic peaks. Essential to one such technique is its utilization of single- and multiple-quantum coherences under MAS to produce an *echo* corresponding to complete removal of orientation-dependent line-shape contributions at a particular point in the time evolution of the spin system (44). Multiple-quantum (MQ) MAS takes advantage of the fact that anisotropic contributions to symmetric transitions under rapid sample rotation are multiplied by a factor which depends only on the spin, S, and the $m \leftrightarrow -m$ transition of interest (denoted simply by m) (44):

$$[3] \qquad A_4(S, m) = 2m[18S(S+1) - 34m^2 - 5]$$

The sign of this coefficient may be changed by selecting the opposite coherence pathway, $p = 2m$, with the consequence that the time evolution of orientation-dependent terms is effectively "undone" by an appropriate choice of coherences. In practice, the experiment consists of an initial excitation pulse designed to generate MQ coherence followed by a variable delay, t_1, and a second pulse for converting the MQ coherence into the single-quantum ($p = -1$) central transition for detection. The echo is observed at a time, t_2, corresponding to the refocussing of all anisotropic contributions:

$$[4] \qquad t_2 = \frac{-A_4(S, m)}{A_4(S, -1/2)} t_1 = kt_1$$

When performed in a standard two-dimensional manner with regular increments of t_1, this approach yields purely isotropic peaks.

An idiosyncracy of this technique is that peak positions in the isotropic spectrum are not simply their chemical shifts, but are modified by both chemical shift and quadrupolar effects. Moreover, it was recently shown that splittings due to J-coupling, "J_{MQ}," are no longer equal to the value of J, but depend on both S and the MQ coherence chosen to effect the desired averaging (45):

$$[5] \qquad J_{MQ} = \left(\frac{k - 2m}{1 + k}\right) J$$

For triple-quantum MAS (3QMAS) of a spin-3/2 nuclide (m = –3/2), J-coupling will manifest in the isotropic spectrum as a splitting 2.125 times[4] the true value of J (45). Thus, 3QMAS aids in the direct observation of J-coupling both by elimination of quadrupolar "broadening" and by an amplification of J.

In Fig. 7, the ^{63}Cu 3QMAS spectrum of the ^{13}C-enriched sample exhibits a central peak representing uncoupled copper-63 nuclei, flanked by a doublet with a splitting of 640 Hz. $^1J(^{63}Cu,^{13}C)$ can be computed from this splitting to be 301 Hz. Also observed in this spectrum are smaller peaks separated by 1260 Hz, which can be attributed to copper-63 coupled to *two* carbon-13 nuclei. The advantage of this approach is that the J-coupling can be obtained directly — aside from a constant factor — from the isotropic spectrum, without requiring tedious line-shape fitting or prior knowledge of the quadrupolar parameters.

Carbon-13 NMR

Carbon-13 MAS NMR spectra of a $K_3Cu(CN)_4$ sample enriched to 30% in $^{13}C^{15}N$ were acquired at both 4.7 and 9.4 T (Fig. 8). To a first approximation, the observed line shapes represent two sites, each coupled to a spin-3/2 nucleus with isotropic J-couplings given by the separation between peaks. The isotropic chemical shifts are the average value of the four peaks, amounting to a difference of one ppm between the sites. The intensities of the interleaved quartets clearly identify the sites as arising from the cyanide ligand lying along the rotation axis ("site 1"), and the three remaining chemically equivalent cyanides ("site 2").

A more detailed analysis reveals that the splittings between adjacent peaks for a given site are unequal. These subtleties may be understood in terms of first-order perturbation theory as residual dipolar shifts originating in the quadrupolar nature of the coupled copper nuclei (46):

$$[6] \qquad \Delta\nu_m = \left(\frac{3R_{DD}C_Q}{20\nu_L}\right)\left[\frac{S(S+1) - 3m^2}{S(2S-1)}\right] \times (3\cos^2\beta - 1 + \eta\sin^2\beta\cos 2\alpha)$$

[4] It should be noted that different data processing conventions have been propagated in the literature, which will influence the magnitude of this multiplicative constant. It is, therefore, essential to use the factor that is appropriate to the method of processing spectral data. See ref. 22 for a comprehensive discussion of this matter.

© 1999 NRC Canada

Fig. 8. Carbon-13 MAS NMR spectra of 30% $^{13}C^{15}N$-enriched $K_3Cu(CN)_4$ at 4.7 and 9.4 T. For the experimental spectrum at 4.7 T, 208 transients were acquired at a 3.50 kHz rotation rate. For the 9.4 T spectrum, 608 transients were collected at a rotation rate of 8.00 kHz.

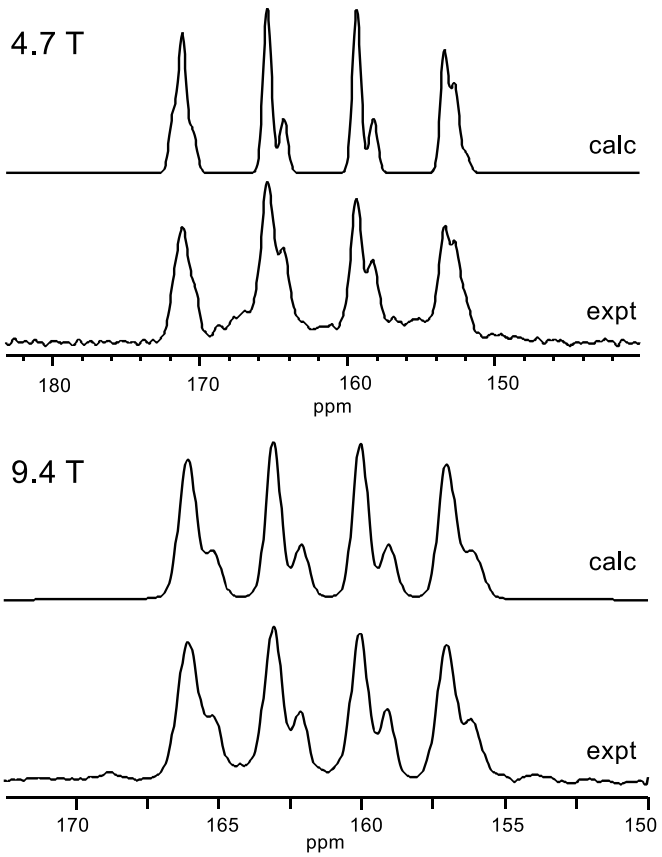

Fig. 9. Nitrogen-15 MAS NMR spectra of 75% ^{15}N-enriched $K_3Cu(CN)_4$ at 4.7 and 9.4 T. Forty-six and 16 transients were coadded for the 4.7 and 9.4 T spectra, respectively. The spinning rates were 2.91 and 10.00 kHz.

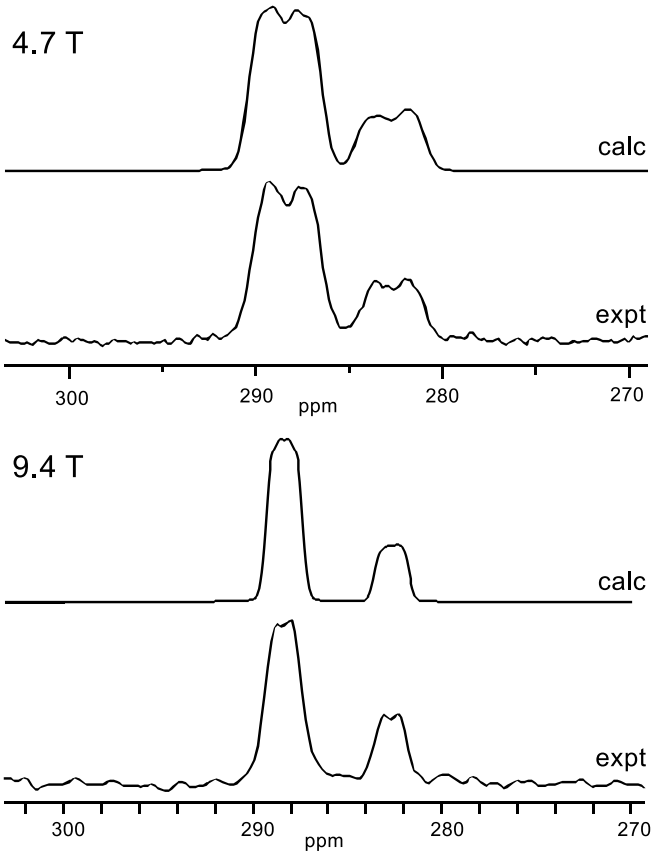

where (α, β) are polar angles defining the orientation of the copper-carbon internuclear vector in the EFG principal axis system, and η designates the *asymmetry* of the EFG tensor in terms of the principal elements, ($|V_{33}| \geq |V_{22}| \geq |V_{11}|$), $\eta = (V_{11} - V_{22})/V_{33}$. The Larmor frequency of the quadrupolar nucleus is denoted by ν_L. Employing the approach of Olivieri et al. (47), these line-shape distortions may be precisely simulated, yielding the values listed in Table 1.

It is important to emphasize that successful calculations of this sort rely on a great deal of prior information. In this case, the crystal structure provides estimates of the dipole–dipole coupling constants, R_{DD}, which were calculated from internuclear separations to be 983 and 1015 Hz to copper-63 for sites 1 and 2, respectively (see eq. [2]).[5] The molecular symmetry inherent in the crystal structure also fixed the relative orientations of the internal interactions, and the orientation of $r_{Cu,C}$ relative to V_{33} was determined from the bond angles. Although coupling to both spin-active copper nuclei was included, parameters were varied according to the ratio of their magnetogyric ratios, $\gamma(^{63}Cu)/\gamma(^{65}Cu) = 0.933\,53$ (34). Finally, the magnitude of C_Q determined from copper-63/65 MAS NMR was used in the calculations.

A careful inspection of eq. [6] reveals that in addition to J and δ_{iso}, this analysis yields information about the relative signs of R_{DD} and C_Q. For this particular case, axial symmetry ($\eta = 0$) and the spin factors ($S = 3/2$; $m = \pm 1/2, \pm 3/2$) may be introduced to simplify expression [6]:

$$[7] \qquad \Delta\nu_{\pm 1/2} = +\left(\frac{3R_{DD}C_Q}{20\nu_L}\right)(3\cos^2\beta - 1)$$

$$[8] \qquad \Delta\nu_{\pm 3/2} = -\left(\frac{3R_{DD}C_Q}{20\nu_L}\right)(3\cos^2\beta - 1)$$

The dipolar coupling constant being positive by virtue of like signs for $\gamma(^{63/65}Cu)$ and $\gamma(^{13}C)$ (eq. [2]), and the orientational term depending in a predictable fashion on the struc-

[5] These values of R_{DD} are upper limits, since any librational motion of the anion or cyano groups will lead to an averaging and hence a reduction of dipolar interactions. Unfortunately, reliable anisotropic thermal parameters are unavailable for $K_3Cu(CN)_4$ (4). Furthermore, NMR experiments are sensitive not to R_{DD} itself, but to an *effective* dipolar coupling constant, R_{eff}, modified by the anisotropy in the ***J*** tensor (48). Since excellent spectral fits were achieved by assuming $R_{eff} = R_{DD}$ (calculated from X-ray data (4)), it appears that any librational motions result in minimal motional averaging of dipolar coupling constants and that the anisotropy in the indirect spin–spin coupling constant is small compared to R_{DD}.

© 1999 NRC Canada

ture, the sign of C_Q governs the direction of the line shifts. Since the high-frequency peak splitting for site 1 is stretched, and the low-frequency splitting squeezed, C_Q must be negative. For site 2, the sign of the orientational term is negative ($\beta = 70°$), justifying the observation that the high-frequency splitting is squeezed, leading again to a negative quadrupole coupling constant. On the other hand, the sign of *J* is not available from calculations based on first-order perturbation theory (46).

The values of $^1J(^{63/65}Cu,^{13}C)$ obtained from copper-63/65 NMR experiments must be re-evaluated in light of the information garnered from carbon-13 MAS NMR spectra. The most glaring difference is that neither $^{63/65}Cu$ MAS nor 3QMAS could resolve couplings to the two crystallographically distinct carbon nuclei present in solid $K_3Cu(CN)_4$, whereas even a cursory examination of the carbon-13 MAS spectra makes this obvious. A second difference is that the uncertainties in *J* estimated from line-shape modelling of carbon-13 MAS spectra are ±2 Hz, much smaller than those of the copper NMR spectra, estimated to be ±15 Hz for both 1D MAS and 2D 3QMAS. (Uncertainties in the 3QMAS spectra are mainly due to low digital resolution, and could be improved at the expense of total experiment time by decreasing the t_1 increment.) These advantages may be offset, however, by the stringent symmetry requirements and high degree of prior knowledge necessary for reliable line-shape calculations of ^{13}C MAS spectra in the presence of coupled quadrupolar nuclei. Copper-63/65 MAS spectral calculations yield reasonable estimates of *J*, but are limited as a general strategy by the need to have control over the level of isotopic enrichment so as to obtain the quadrupolar parameters in an independent experiment. It should also be emphasized that copper-63/65 chemical shifts are more sensitive than ^{13}C or ^{15}N shifts to thermal gradients due to rapid rotation of the sample (49). The effect of this temperature dependence is to "smear out" the line shape so that the singularities are less well-defined, and simulations less precise. Another interesting contrast is that whereas spin-1/2 MAS spectra may be perturbed by spin–spin coupling to a quadrupolar nucleus, the symmetric transitions involved in 3QMAS are free from distortions arising from the dipolar interaction, in the limit of first-order perturbation theory (50). What emerges from this comparison is that choosing the ideal experiment to obtain a given parameter will depend critically on the particularities of the spin system as well as on the available experimental resources.

A ^{13}C NMR spectrum of a non-spinning sample of 30% ^{13}C-labelled $K_3Cu(CN)_4$ was also acquired at 4.7 T (not shown). The powder pattern is indicative of an axially symmetric shielding tensor, with the chemical shift for perpendicular orientations, $\delta_\perp$, easily identified. Given the complexity of the spin system (i.e., simultaneous coupling to both $^{63/65}Cu$ and ^{14}N), no attempt was made to calculate the spectrum; however, $\delta_\perp$ was estimated to be 275 ± 5 ppm. Individual carbon-13 sites are not resolved, suggesting that the *local* molecular symmetry of site 2 is sufficient to produce essentially axial symmetry in the shielding tensor, even though it is not dictated by the space group symmetry. From the measured values of δ_{iso} and $\delta_\perp$, $\delta_\parallel$ may be calculated to yield a span, $\Omega = \delta_\perp - \delta_\parallel$, for the cyano ^{13}C shielding tensors of 340 ± 5 ppm.

The carbon shielding in $K_3Cu(CN)_4$ may be compared with other cyanide-containing compounds. First, the isotropic chemical shifts of 161 and 162 ppm agree with the value obtained in aqueous solution, δ_{iso} = 161.6 ppm (51). These shifts appear to be more deshielded than any other organic or inorganic cyanide compound investigated in the solid phase by NMR (52), and slightly more *shielded* than the "free" CN anion in solution (166.2 ppm) (51). Whereas organic nitriles tend to appear around 120 ppm, the tetrahedral group 12 tetracyanometallates possess δ_{iso} between 148 and 153 ppm (53). The similar species, $N(CH_3)_4CuZn(CN)_4$, exhibits an isotropic shift of 157 ppm (16*a*). Even more shielded are the square-planar group 10 tetracyanometallates, having δ_{iso} ranging from 128 to 139 ppm (54). The spans of the related tensors exhibit less variability and correspondingly less obvious trends, with organic nitriles generally having $\Omega \approx 320$ ppm and the tetracyanometallates displaying spans of approximately 330 ppm (group 12 tetrahedra) and 350 ppm (group 10 square-planars). For $Cu(CN)_4^{3-}$ tetrahedra in $N(CH_3)_4CuZn(CN)_4$ and $K_3Cu(CN)_4$, the spans fall between these values. By implication, these general observations suggest that *all* carbon-13 shielding tensor elements are modified on moving from organic- to metal-bound cyanides.

Nitrogen-15 NMR

A 75% ^{15}N-enriched sample of $K_3Cu(CN)_4$ was prepared and analyzed by ^{15}N NMR. Figure 9 depicts the isotropic powder line shapes under conditions of MAS at 4.7 and 9.4 T. The two types of chemically equivalent cyanide ligands are clearly evident from the 1:3 intensity ratio, the more shielded lying along the symmetry axis. The difference in the isotropic ^{15}N chemical shifts is larger than the ^{13}C shift difference by a factor of six. Indeed, nitrogen shifts are generally more sensitive to structural differences than carbon shifts, manifesting in a larger overall range of nitrogen-15 chemical shifts (52). In constrast to the ^{13}C NMR results, the isotropic chemical shifts of 282.5 and 288.5 ppm are less shielded than the "free" cyanide ligand in water, 274.2 ppm (55).

Fine structure is observed in the individual line shapes corresponding to the two sites. Since 98.9% of the carbon in the sample is the spin-inactive isotope carbon-12, these features must be due to two-bond *J*-coupling to copper-63/65. Following the same protocol as for the carbon-13 MAS spectra, simulations yield $^2J(^{63}Cu,^{15}N)$ = 19.0 ± 1 and 20.0 ± 1 Hz for sites 1 and 2, respectively. Dipolar coupling constants, $R_{DD}(^{63}Cu,^{15}N)$, calculated from structural data are –107 and –104 Hz, according to eq. [2].

Spectra of the non-spinning sample were also acquired, with results similar to the carbon-13 spectra (not shown). The low-frequency end of the axially symmetric powder pattern lacks definition, and the two chemically distinct sites are unresolved, but $\delta_\perp$ may be easily extracted. Calculating $\delta_\parallel$ as above, the nitrogen-15 shielding tensor spans nearly 500 ppm (Table 1), with the most shielded component aligned with the Cu—C—N bond.

These NMR results may be compared with those obtained for solid $K_2Hg(CN)_4$ (26), in which the mercury atom occupies a site of pure tetrahedral symmetry. The isotropic ^{15}N chemical shift is 280.9 ppm in this compound, very similar to the values 282.8 and 288.5 ppm found for $K_3Cu(CN)_4$.

© 1999 NRC Canada

The measured shielding anisotropies are also similar, (477 ppm in $K_2Hg(CN)_4$ from a Herzfeld–Berger analysis (56) of spinning sideband intensities), with the same tensor orientation. The shielding results for tetrahedral cyanometallates contrast with organic nitriles, which typically exhibit spans of 400 ppm and isotropic shifts near 260 ppm (52). The origin of these differences appears to lie in lower shielding perpendicular to the M—C—N bond for cyanometallates than for R—C—N moieties.

Conclusions

Tripotassium tetracyanocuprate has been thoroughly examined by a variety of NMR methods to characterize chemical shielding tensors for carbon-13, nitrogen-15, and copper-63/65, as well as quadrupole coupling tensors for the latter. This appears to be the first example of copper shielding anisotropy determined by NMR. Isotropic one- and two-bond *J*-couplings to the copper centre have been measured for both cyanide sites. This comprehensive investigation of NMR properties in a "simple" model compound of known crystal structure is suggestive of the powerful capacity of NMR in the characterization of supramolecular framework materials based on tetrahedral $Cu(CN)_4^{3-}$ building blocks. Where multiple copper sites exist in a given solid, triple-quantum MAS appears to be a viable method for resolving individual resonances, given its capacity to resolve splittings arising from *J*-coupling. Solid $K_3Cu(CN)_4$ exhibits excellent NMR sensitivity, is straightforward to prepare, and may serve as a useful standard for copper-63/65 NMR of solids. These results also underscore the merits of utilizing modest levels of $^{13}C^{15}N$-enrichment to obtain high-quality carbon-13 and nitrogen-15 MAS NMR spectra, while simultaneously simplifying the ^{13}C spectral analysis by removing quadrupole-perturbed ^{13}C–^{14}N dipolar interactions (16*a*). In combination with a related study of solid CuCN (5), the work decribed here represents a starting point for a systematic study of copper(I) cyanide complexes.

Acknowledgements

We are grateful to the Natural Sciences and Engineering Research Council (NSERC) of Canada for supporting this work through research and equipment grants. S.K. thanks NSERC, the Walter C. Sumner Foundation and the Izaak Walton Killam Trust for postgraduate scholarships. R.E.W. is grateful to the Canada Council for a Killam Research Fellowship. NMR spectra were obtained at the Atlantic Region Magnetic Resonance Centre, generously supported by NSERC of Canada. Dr. Klaus Eichele is acknowledged for assistance in MQMAS spectral processing.

References

1. F.A. Cotton and G. Wilkinson. Advanced inorganic chemistry. 5th ed. John Wiley and Sons, Toronto, 1988. p. 757.
2. D.T. Cromer. J. Phys. Chem. **61**, 1388 (1957).
3. D.T. Cromer and A.C. Larson. Acta Crystallogr. **15**, 397 (1962).
4. R.B. Roof, Jr., A.C. Larson, and D.T. Cromer. Acta Crystallogr. Sect. B, **B24**, 269 (1968).
5. S. Kroeker, R.E. Wasylishen, and J.V. Hanna. J. Am. Chem. Soc. **121**, 1582 (1999).
6. G.A. Bowmaker, B.J. Kennedy, and J.C. Reid. Inorg. Chem. **37**, 3968 (1998).
7. T.L. Stemmler, T.M. Barnhart, J.E. Penner-Hahn, C.E. Tucker, P. Knochel, M. Böhme, and G. Frenking. J. Am. Chem. Soc. **117**, 12489 (1995).
8. (*a*) T. Iwamoto. *In* Inclusion compounds. *Edited by* J.L. Atwood, J.E.D. Davies, and D.D. MacNicol. Academic Press, London. 1984. Chap. 2. p. 29; (*b*) T. Iwamoto. *In* Comprehensive supramolecular chemistry. Vol. 6. *Edited by* J.L. Atwood, J.E.D. Davies, D.D. MacNicol, and F. Vögtle. Elsevier Scientific Ltd., Amsterdam. 1996. Chap. 19. p. 643; (*c*) S.R. Batten and R. Robson. Angew. Chem. Int. Ed. Engl. **37**, 1461 (1998).
9. A.M.A. Ibrahim. J. Organomet. Chem. **556**, 1 (1998).
10. A.M.A. Ibrahim, E. Siebel, and R.D. Fischer. Inorg. Chem. **37**, 3521 (1998).
11. D.J. Chesnut and J. Zubieta. Chem. Commun. 1707 (1998).
12. R.J. Goodfellow. *In* Multinuclear NMR. *Edited by* J. Mason. Plenum Press, New York, 1987. p. 564.
13. P. Granger. *In* Transition metal nuclear magnetic resonance. *Edited by* P.S. Pregosin. Elsevier, New York. 1991. p. 264.
14. E.R. Andrew, J.L. Carolan, and P.J. Randall. Chem. Phys. Lett. **11**, 298 (1971).
15. (*a*) C.H. Pennington, D.J. Durand, C.P. Slichter, J.P. Rice, E.D. Bukowski, and D.M. Ginsberg. Phys. Rev. B, **39**, 274 (1989); (*b*) C.H. Pennington, D.J. Durand, C.P. Slichter, J.P. Rice, E.D. Bukowski, and D.M. Ginsberg. Phys. Rev. B, **39**, 2902 (1989); (*c*) S.E. Barrett, D.J. Durand, C.H. Pennington, C.P. Slichter, T.A. Friedmann, J.P. Rice, and D.M. Ginsberg. Phys. Rev. B, **41**, 6283 (1990).
16. (*a*) R.D. Curtis, C.I. Ratcliffe, and J.A. Ripmeester. Chem. Commun. 1800 (1992); (*b*) S. Nishikiori, and C.I. Ratcliffe. Disord. Mater. **10**, 9 (1995); (*c*) J.A. Ripmeester and C.I. Ratcliffe. *In* Comprehensive supramolecular chemistry. Vol. 8. *Edited by* J.L. Atwood, J.E.D. Davies, D.D. MacNicol, and F. Vögtle. Elsevier Scientific Ltd., Amsterdam. 1996. Chap. 8. p. 323.
17. M.J. Reisfeld and L.H. Jones. J. Mol. Spectrosc. **18**, 222 (1965).
18. H. Krüger and U. Meyer-Berkhout. Z. Phys. **132**, 171 (1952).
19. G.L. McKown and J.D. Graybeal. J. Chem. Phys. **44**, 610 (1966).
20. E. Fukushima and S.B.W. Roeder. Experimental pulse NMR — a nuts and bolts approach. Addison–Wesley Publishing Co., Inc., London. 1981. p. 463.
21. R. Ernst, G. Bodenhausen, and A. Wokaun. Principles of NMR in one and two dimensions. Oxford University Press, New York. 1987.
22. P.P. Man. Phys. Rev. B, **58**, 2764 (1998).
23. T. Yamamoto, H. Haraguchi, and S. Fujiwara. J. Phys. Chem. **74**, 4369 (1970).
24. K. Endo, K. Yamamoto, K. Deguchi, and K. Matsushita. Bull. Chem. Soc. Jpn. **60**, 2803 (1987).
25. D.W. Alderman, M.S. Solum, and D.M. Grant. J. Chem. Phys. **84**, 3717 (1986).
26. G. Wu and R.E. Wasylishen. J. Phys. Chem. **97**, 7863 (1993).
27. H.J. Behrens and B. Schnabel. Physica B, **114**, 185 (1982).
28. E. Kundla, A. Samoson, and E. Lippmaa. Chem. Phys. Lett. **83**, 229 (1981).
29. P.C. Taylor, J.F. Baugher, and H.M. Kriz. Chem. Rev. **75**, 203 (1975).
30. B.C. Gerstein and C.R. Dybowski. Transient techniques in NMR of solids. Academic Press, Orlando, Fla. 1985.
31. E. Staritzky and F.H. Ellinger. Anal. Chem. **28**, 422 (1956).
32. E.G. Cox, W. Wardlaw, and K.C. Webster. J. Chem. Soc. 775 (1936).

© 1999 NRC Canada

33. G. Becker. Z. Phys. **130**, 415 (1951).
34. P. Raghavan. Atom. Data Nucl. Data Tab. **42**, 189 (1989).
35. S. Kroeker, K. Eichele, R.E. Wasylishen, and J.F. Britten. J. Phys. Chem. B, **101**, 3727 (1997).
36. R.W. Schurko, R.E. Wasylishen, and A.D. Phillips. J. Magn. Reson. **133**, 388 (1998).
37. K.D. Hensel, C. Styger, W. Jäger, A.J. Merer, and M.C.L. Gerry. J. Chem. Phys. **99**, 3320 (1993).
38. H.J. Jakobsen, J. Skibsted, H. Bildsøe, and N.C. Nielsen. J. Magn. Reson. A, **85**, 173 (1989).
39. (*a*) J. Skibsted, N.C. Nielsen, H. Bildsøe, and H.J. Jakobsen. Chem. Phys. Lett. **188**, 405 (1992); (*b*) J. Skibsted, N.C. Nielsen, H. Bildsøe, and H.J. Jakobsen. J. Magn. Reson. A, **95**, 88 (1991); (*c*) C. Jäger. *In* NMR basic principles and progress: solid-state NMR II. Vol. 31. *Edited by* P. Diehl, E. Fluck, H. Günther, R. Kosfeld, and J. Seelig (guest editor: B. Blümich). Springer–Verlag, Berlin. 1994. p. 133.
40. D. Massiot, C. Bessada, J.P. Coutures, and F. Taulelle. J. Magn. Reson. **90**, 231 (1990).
41. L. Llor and J. Virlet. Chem. Phys. Lett. **152**, 248 (1988).
42. A. Samoson, E. Lippmaa, and A. Pines. Mol. Phys. **65**, 1013 (1988).
43. (*a*) L. Frydman and J.S. Harwood. J. Am. Chem. Soc. **117**, 5367 (1995); (*b*) A. Medek, J.S. Harwood, and L. Frydman. J. Am. Chem. Soc. **117**, 12779 (1995).
44. J.P. Amoureux. Solid State NMR, **2**, 83 (1993).
45. G. Wu, S. Kroeker, R.E. Wasylishen, and R.G. Griffin. J. Magn. Reson. **124**, 237 (1997).
46. R.K. Harris and A.C. Olivieri. Prog. NMR Spectrosc. **24**, 435 (1992).
47. (*a*) A.C. Olivieri, L. Frydman, and L.E. Diaz. J. Magn. Reson. **75**, 50 (1987); (*b*) A.C. Olivieri, L. Frydman, M. Grasselli, and L. Diaz. Magn. Reson. Chem. **26**, 615 (1988); (*c*) A.C. Olivieri. J. Magn. Reson. **81**, 201 (1989).
48. (*a*) R.E. Wasylishen. *In* Encyclopedia of nuclear magnetic resonance. *Edited by* D.M. Grant and R.K. Harris. John Wiley and Sons, Chichester. 1996, p. 1685; (*b*) S. Kroeker, J.V. Hanna, R.E. Wasylishen, E.W. Ainscough, and A.M. Brodie. J. Magn. Reson. **135**, 208 (1998).
49. L.C.M. van Gorkom, J.M. Hook, M. Logan, J.V. Hanna, and R.E. Wasylishen. Magn. Reson. Chem. **33**, 791 (1995).
50. G. Wu and R.E. Wasylishen. Mol. Phys. **95**, 1177 (1999).
51. J.J. Pesek and W.R. Mason. Inorg. Chem. **18**, 924 (1979).
52. T.M. Duncan. Principal components of chemical shift tensors: a compilation. 2nd ed. The Farragut Press, Chicago. 1994.
53. G. Wu, S. Kroeker, and R.E. Wasylishen. Inorg. Chem. **34**, 1595 (1995).
54. A.J. Kim and L.G. Butler. Inorg. Chem. **32**, 178 (1993).
55. R.E. Wasylishen. Can. J. Chem. **60**, 2194 (1982).
56. J. Herzfeld and A.E. Berger. J. Chem. Phys. **73**, 6021 (1980).

© 1999 NRC Canada

Solid-state phosphorus-31 NMR study of phosphine- and phosphite-substituted cobaloximes

Robert W. Schurko, Roderick E. Wasylishen, Scott J. Moore, Luigi G. Marzilli, and John H. Nelson

Abstract: Solid-state ^{31}P NMR spectra of two phosphite- and 17 phosphine-substituted cobaloximes have been acquired under conditions of magic-angle spinning (MAS) and cross polarization (CP) at two applied magnetic fields. In the majority of cases, eight-peak multiplets are observed in the ^{31}P CPMAS NMR spectra, arising from one-bond indirect spin–spin coupling to cobalt (spin S = 7/2). The spacings between adjacent peaks gradually increase or decrease from low to high frequency, due to the presence of residual dipolar coupling between the cobalt and phosphorus nuclei. Values of $^1J(^{59}\text{Co},^{31}\text{P})$ were estimated from the spacing between the central peaks of the eight-peak multiplets. For the phosphine-substituted cobaloximes, values of $^1J(^{59}\text{Co},^{31}\text{P})$ range from 225 to 372 Hz, while in the phosphite derivatives this coupling is considerably larger, from 420 to 615 Hz. From comparison with cobaloximes for which the cobalt nuclear quadrupole coupling interaction is fully characterized, the residual dipolar shift, d, and sense of the ^{31}P NMR spectrum can be utilized to infer the electric field gradient (EFG) orientations at the cobalt nucleus in cobaloximes for which such data are unavailable. The magnitudes of $^1J(^{59}\text{Co},^{31}\text{P})$ and d, as well as the sense of the spectra, are shown to be dependent upon the nature of the axially-substituted ligands. Phosphorus-31 CPMAS NMR spectra of several cobaloximes exhibit broad peak shapes at room temperature. Variable-temperature ^{31}P NMR experiments reveal that the cobalt nucleus is effectively self-decoupled at room temperature; however, splittings due to $^1J(^{59}\text{Co},^{31}\text{P})$ were observed in spectra acquired at low temperatures.

Key words: solid-state ^{31}P NMR, ^{59}Co–^{31}P spin–spin coupling constants, ^{59}Co electric field gradient tensors, cobaloximes.

Résumé : Opérant à l'état solide, dans des conditions de rotation à l'angle magique (« MAS ») et de polarisation croisée (« CP ») de deux champs magnétiques appliqués, on a déterminé les spectres RMN du ^{31}P de dix-neuf cobaloximes, dont deux substituées par du phosphite et dix-sept portant des phosphines substituées. Dans la majorité des cas, les spectres RMN « CPMAS » du ^{31}P présentent tous des multiplets à huit pics qui découlent du couplage spin–spin indirect à travers une liaison avec le cobalt (spin S = 7/2). En raison des couplages dipolaires résiduels entre les noyaux de cobalt et de phosphore, les séparations entre les pics adjacents augmentent ou diminuent graduellement en passant des basses aux hautes fréquences. On a déterminé les valeurs de $^1J(^{59}\text{Co},^{31}\text{P})$ à partir des séparations entre les pics centraux des multiplets à huit pics. Pour les cobaloximes substituées par des phosphines, les valeurs de $^1J(^{59}\text{Co},^{31}\text{P})$ varient entre 225 et 372 Hz alors que, pour les dérivés portant des phosphites, cette valeur est beaucoup plus élevée, allant de 420 à 615 Hz. Par comparaison avec des cobaloximes pour lesquelles l'interaction de couplage quadripolaire nucléaire du cobalt a été bien caractérisée, le déplacement dipolaire résiduel, d, et le sens du spectre RMN du ^{31}P peuvent être utilisés pour déduire les orientations du gradient du champ électrique (GCE) au niveau du noyau de cobalt des cobaloximes pour lesquelles de telles données sont disponibles. On a démontré que les amplitudes de $^1J(^{59}\text{Co},^{31}\text{P})$ et de d ainsi que le sens des spectres dépendent de la nature des ligands substitués de façon axiale. À la température ambiante, les spectres RMN « CPMAS » du ^{31}P de plusieurs cobaloximes se présentent sous la forme de pics à larges bandes. Des expériences de RMN du ^{31}P à température variable mettent en évidence que, à la température ambiante, le noyau de cobalt s'autodécouple efficacement; toutefois, à l'aide des spectres acquis à basse température, on peut observer les dédoublements provoqués par le couplage $^1J(^{59}\text{Co},^{31}\text{P})$.

Mots clés : RMN du ^{31}P à l'état solide, constantes de couplage spin–spin ^{59}Co–^{31}P, tenseurs du gradient du champ électrique dans ^{59}Co, cobaloximes.

[Traduit par la Rédaction]

Received May 10, 1999.

This paper is dedicated to Professor Ted Schaefer in recognition of his outstanding contributions to Canadian chemistry.

R.W. Schurko and R.E. Wasylishen.[1] Department of Chemistry, Dalhousie University, Halifax, NS B3H 4J3, Canada.
S.J. Moore and L.G. Marzilli. Department of Chemistry, Emory University, Atlanta, GA 30322, U.S.A.
J.H. Nelson. Department of Chemistry, University of Nevada, Reno, NV 89557, U.S.A.

[1]Author to whom correspondence may be addressed. Telephone: (902) 494-2564. Fax: (902) 494-1310.
e-mail: Roderick.Wasylishen@Dal.ca

© 1999 NRC Canada

Fig. 1. Structure of cobaloximes, where L = neutral ligands (i.e., phosphines, phosphites) and X = anionic species (i.e., Cl^-, Br^-, N_3^-, and Me^-).

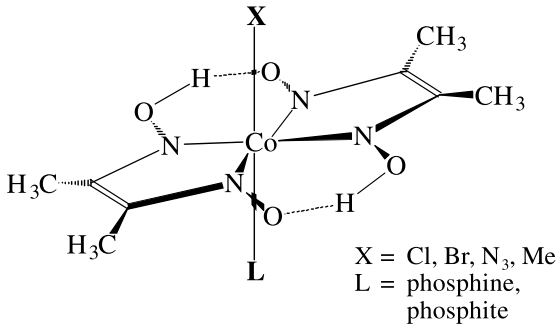

Introduction

Recently, there has been much interest in solid-state NMR spectra of spin-1/2 nuclei which are spin-coupled to quadrupolar nuclei (spin $S \geq 1$) (1–3). One reason for this interest is that acquisition of solid-state magic-angle spinning (MAS) NMR spectra allows for the measurement of indirect spin–spin couplings (*J*-couplings), which are not readily available from analogous solution NMR experiments. In solution, the relaxation of quadrupolar nuclei is generally very efficient, resulting in "self-decoupling" of the quadrupolar nucleus (4). As a consequence, sharp transitions corresponding to the discrete spin states of the quadrupolar nucleus are not observed in the spin-1/2 NMR spectrum.

A second reason for interest in such spin pairs is the appearance of residual dipolar coupling in the spin-1/2 MAS NMR spectra. In general, the spin states of a quadrupolar nucleus are not quantized exactly along the direction of the magnetic field because of perturbations from the quadrupolar interaction. Consequently, the spin states of the quadrupolar nucleus must be described by mixing of the pure Zeeman spin states. In such cases, MAS fails to completely average the dipolar interaction between the *I* and *S* nuclei, due to the presence of non-secular terms in the dipolar hamiltonian. Residual dipolar coupling is manifested in the MAS NMR spectrum as a "distortion" in the multiplet resulting from *J*-coupling between the *I* and *S* nuclei; that is, rather than observing $2S + 1$ evenly-spaced peaks in the multiplet, the peaks are shifted such that there is either a uniform decrease or increase in spacing between adjacent peaks on going from low to high frequency across the multiplet (vide infra). Analysis of spectra exhibiting these quadrupolar induced distortions may provide information about the orientation of the electric field gradient (EFG) tensor at the quadrupolar nucleus, the magnitude and sign of the quadrupolar coupling constant, C_Q, and in some cases, the asymmetry parameter, η. First-order perturbation (5–7) and exact (8, 9) theories have been developed to treat this problem.

The phosphorus–cobalt spin pair in a series of phosphine- and phosphite-substituted cobaloximes is considered in this paper. Cobaloximes are pseudo-octahedral complexes with two bidentate dimethylglyoxime (DH) moieties in a rectangular planar arrangement about the central cobalt atom (Fig. 1). A variety of ligands can be substituted into the axial positions, with typical cobaloximes possessing one neutral ligand (L) and one anionic ligand (X). Cobaloximes have been widely studied for over 40 years (10), due to their diverse coordination chemistry (11), interesting reactivity in solution (12), and potential as model complexes for larger, biologically-relevant molecules such as cobalamine (vitamin B_{12}), and methylcobalamin B_{12} (13). A number of solution NMR studies have been conducted on the cobaloximes (14), and several solid-state NMR studies have been reported in the literature, including a preliminary investigation of the ^{31}P, ^{59}Co spin pair in cobaloximes by our group (15), a solid-state ^{59}Co NMR study of cobaloximes and related complexes (16), and a recent letter discussing solution and solid-state NMR of triphenylphosphine-substituted cobaloximes (17).

In this paper, which is an extension of our previous work (15), we present solid-state ^{31}P CPMAS NMR spectra of cobaloximes, $LCo(DH)_2X$, where X = Cl^-, Br^-, N_3^-, and Me^- (Me = methyl), and L is a phosphine or phosphite ligand. Values of one-bond indirect spin–spin coupling constants, $^1J(^{59}Co,^{31}P)$, are estimated directly from the MAS NMR spectra. Well-characterized cobaloximes, i.e., cobaloximes for which there are ^{59}Co nuclear quadrupolar parameters and crystallographic data, are discussed first, as independent knowledge of these parameters aids in ensuring proper spectral analysis. Discussion is then extended to systems for which there is an absence of such data. Difficulties associated with multiparameter spectral analysis where two or more parameters are covariant are addressed. Variations in $^1J(^{59}Co,^{31}P)$ for the series of compounds investigated here are discussed qualitatively in terms of conventional steric and electronic effects arising from particular axial ligands. Finally, variable-temperature solid-state ^{31}P CPMAS NMR spectra of two cobaloximes are presented, which exhibit clearly resolved multiplets at low temperatures, and self-decoupling of ^{59}Co at room temperature. A rough estimate of the upper limit of the ^{59}Co spin-lattice relaxation time at room temperature can be obtained from measurements of the peak widths.

Experimental

Cobaloximes were synthesized using standard literature methods (13*c*, 18–20) and new procedures described elsewhere (21). Solid-state ^{31}P NMR spectra were acquired at 81.033 MHz (4.7 T) and 161.982 MHz (9.4 T) on Bruker MSL-200 and AMX-400 spectrometers, under conditions of cross-polarization, magic-angle spinning, and high-power proton decoupling. Microcrystalline samples were thoroughly powdered and packed into 4 mm (9.4 T) and 7 mm (4.7 T) o.d. zirconium oxide rotors. Typical pulse widths, contact times, and relaxation delays were 5 μs, 5 ms, and 4 s, respectively. Spinning rates for the 7 mm rotors ranged from 2.0 to 4.5 kHz, and for the 4 mm rotors from 3.0 to 9.0 kHz. Experiments required the acquisition of 500–8000 scans, depending on the amount of sample available. All ^{31}P NMR spectra were referenced with respect to 85% H_3PO_4 (aq) by setting the phosphorus resonance of solid $NH_4H_2PO_4$ to 0.81 ppm. Low-temperature NMR experiments were performed by passing dry nitrogen gas from liquid N_2 boil-off. Dry N_2 was passed through a heat-exchange coil that was

© 1999 NRC Canada

Table 1. Phosphorus-31 NMR parameters for well-characterized cobaloximes.[a]

$LCo(DH)_2X$ (L, X)	δ_{iso} (ppm)	R_{eff} (Hz)[b]	$^1J(^{59}Co,^{31}P)$ (Hz)	β^D (°)	α^D (°)	$C_Q(^{59}Co)$ (MHz)[c]	η^c	d (Hz)[d]
PBu_3, Cl (**I**)[e]								
Site 1	31.2(1)	995(15)	350(3)	90	90	–41.5	0.2	+79
Site 2	29.8(1)	978(15)	352(3)	90	90	–40.9	0.35	+86
PPh_3, Me (**II**)[e]	17.6(2)	810(20)	225(2)	90	0	28.1	0.77	–8
PPh_3, Cl (**III**)[f]	23.7(1)	910(20)	371(2)	90	90	–60.45	0.81	+158

[a]Spectra of **II** and **III** acquired at 294 K, spectra of **I** acquired at 155 K. Uncertainties are in parentheses.

[b]$R_{eff} = R_{dd} - \Delta J/3$, with R_{dd} calculated from known bond distances.

[c]From ref. 26. Errors in C_Q are ±0.01 MHz. Measurements made at room temperature.

[d]Calculated for spectra at 9.4 T (ν_S = 94.48 MHz).

[e]From ref. 15.

[f]This work.

immersed in liquid nitrogen. The temperature of the sample was controlled by carefully adjusting the gas flow and heater in a complementary fashion, and was stable to within ±3 K. Temperatures inside of the MAS rotors were not calibrated with an internal NMR standard. The spinning sidebands were summed to produce an isotropic MAS pattern representative of the centreband at an infinite spinning rate (22). All spectra were analyzed with the WSolids program, which was developed in this laboratory, and incorporates the POWDER routine of Alderman et al. (23) for the efficient calculation of solid-state NMR powder patterns.

Results and discussion

First-order perturbation treatment of residual dipolar coupling

A treatment based on first-order perturbation theory has been developed by Olivieri et al. (5, 7, 24) and others (6), which is valid in the limit $C_Q/(4S(2S-1)) << \nu_S$, where ν_S is the Larmor frequency of the quadrupolar nucleus. Thus, for ^{59}Co (S = 7/2), the first-order perturbation approach is valid provided that $C_Q/84\nu_S << 1$, which is the case for the majority of complexes examined here. The transition frequencies in the MAS spectrum of a spin-1/2 nucleus, ν_m, are displaced by a residual dipolar shift, d, such that

$$[1] \qquad \nu_m = \nu_{iso} - m_S J_{iso} + \frac{S(S+1) - 3m_S^2}{S(2S-1)} d$$

where J_{iso} is the isotropic indirect spin–spin coupling constant, $m = S, S-1, ..., -S$, and

$$[2] \qquad d = \left(\frac{3C_Q R_{eff}}{20\nu_S}\right)[(3\cos^2\beta^D - 1) + \eta\sin^2\beta^D\cos^2\alpha^D]$$

In eq. [2], β^D and α^D are polar angles describing the orientation of the I–S dipolar vector, r_{IS}, with respect to the EFG tensor at the S nucleus. It is impossible to separate contributions from dipolar coupling and the anisotropy of the J-coupling (25); thus, the effective dipolar coupling constant, $R_{eff} = R_{dd} - \Delta J/3$, where $R_{dd} = (\mu_0/4\pi)(\gamma_I\gamma_S\hbar/2\pi)\langle r_{IS}^{-3}\rangle$, and $\Delta J = J_{\parallel} - J_{\perp}$. The quadrupolar coupling constant and asymmetry parameter are defined as $C_Q = eQV_{33}/h$ (where Q is the nuclear quadrupole moment) and $\eta = (V_{11} - V_{22})/V_{33}$. The V_{ii} are principal components of the EFG in its principal axis system, defined such that $|V_{33}| \geq |V_{22}| \geq |V_{11}|$. Thus, increased distortions resulting from residual dipolar coupling are directly proportional to the magnitude of C_Q and R_{eff}, and inversely proportional to the strength of the applied magnetic field. The sense of the spectrum (i.e., the direction in which the spacings between adjacent peaks are increasing) is defined as follows: if the spacings between adjacent peaks increase from high to low frequency, the sense of the spectrum is positive, and d is positive. Alternatively, if the spacings decrease from high to low frequency, the spectral sense and d are negative. Note that our definition of d differs in sign from some previous studies. This is irrelevant provided that one is consistent.

Well-characterized cobaloximes

In previous work by our group, the cobaloximes $PBu_3Co(DH)_2Cl$ (**I**) (Bu = *n*-butyl) and $PPh_3Co(DH)_2Me$ (**II**) were characterized by solid-state ^{31}P CPMAS NMR experiments (15). Both of these complexes have also been studied by ^{59}Co nuclear quadrupole resonance (NQR), from which values of C_Q and η were obtained (26). From a combination of these data, it was found that in **I**, the intermediate component of the EFG tensor, V_{22}, is directed along the Co, P bond, whereas in **II**, the smallest component, V_{11}, adopts this orientation (see Table 1). The remaining components lie in the plane of the DH moieties, oriented such that one bisects the N-Co-N angle of the heterocyclic ring, and the other bisects the inter-ring N-Co-N angle. Clearly, substitution of different ligands into the axial positions have significant effects on the EFG tensor orientation. Thus, if the magnitude of C_Q and η are known, and the dipolar coupling constant can be calculated from known interatomic distances, analysis of the MAS spectrum of the spin-coupled spin-1/2 nucleus can yield information on the orientation of the EFG tensor at the quadrupolar nucleus, as well as the sign of C_Q.

$PPh_3Co(DH)_2Cl$ (**III**) has been characterized by both ^{59}Co NQR and NMR (26, 27), and X-ray crystallographic studies (28). LaRossa and Brown (26, 27) report C_Q = +60.45 MHz and η = 0.81, with the proposed sign of C_Q determined via an empirical partial field gradient model described in their papers. Using this model, they also suggest that the largest component of the EFG tensor, V_{33}, is oriented along the direction of the Co, P bond. The Co, P internuclear distance is reported as 2.327 Å (28) from which R_{dd} is calculated to be

© 1999 NRC Canada

Fig. 2. Experimental and calculated ^{31}P CPMAS NMR spectra of $PPh_3Co(DH)_2Cl$ (**III**) at (A) 4.7 and (B) 9.4 T. Some small peaks resulting from sample impurity are observed in (A).

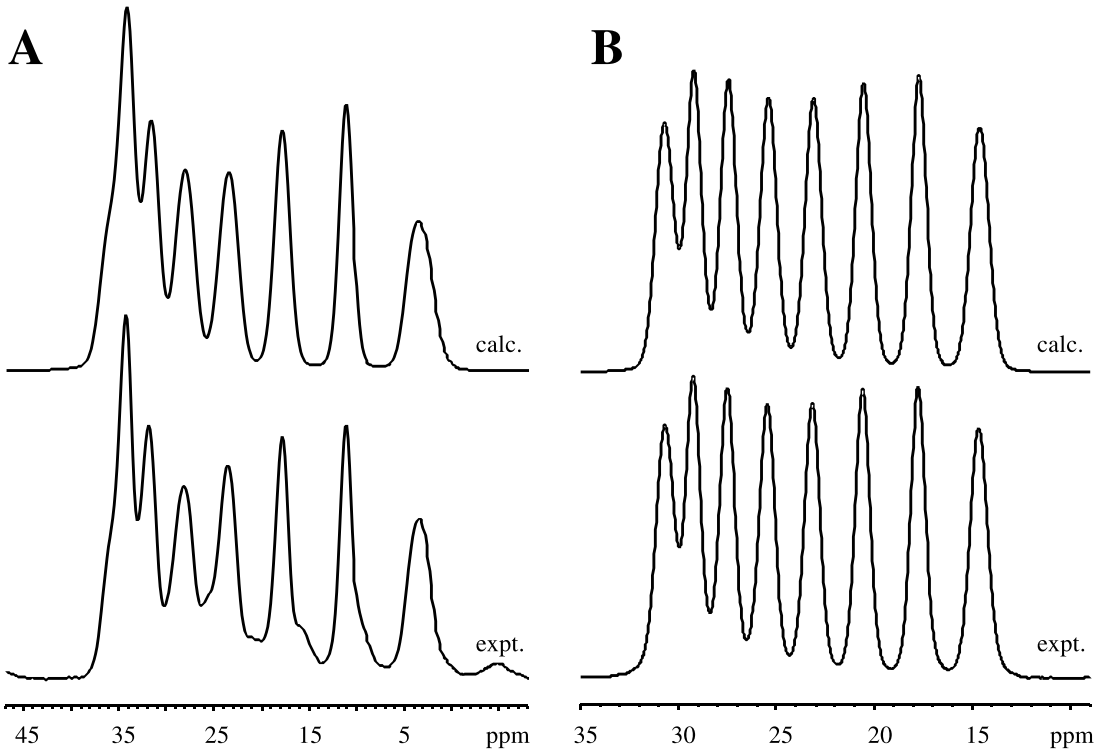

910 Hz. The *J*-coupling can be measured from the central spacing of the ^{31}P CPMAS NMR spectra (Fig. 2); $^1J(^{59}Co,^{31}P)$ = 371 Hz. Using the positive sign of C_Q proposed by LaRossa and Brown, the spectra cannot be simulated with $\beta^D = 0°$; however, with C_Q = –60.45 MHz, β^D = 90°, and α^D = 90°, an excellent fit can be obtained. This corresponds to the intermediate component of the EFG tensor, V_{22}, being aligned along the Co, P bond. Similar disagreement in the sign of C_Q and orientation of the EFG tensor was found for $PPh_3Co(DH)_2Me$ (**II**) in our previous work (15).

There are several interesting observations to make regarding the data in Table 1. First, the presence of the methyl group (X = Me^-) results in a large decrease in $^1J(^{59}Co,^{31}P)$ compared to the chloro-substituted cobaloximes. Changing the nature of the phosphorus ligand results in much smaller variation in $^1J(^{59}Co,^{31}P)$. The sense of the spectra for **II** is negative (as indicated by *d*), whereas for **I** and **III** the senses are positive. The magnitude of the residual dipolar shift is largest for **III**, which has the largest $|C_Q|$. However, other factors determine the size of *d*, such as R_{eff}, the EFG tensor orientation and η; thus, direct correlation between the magnitudes of *d* and C_Q cannot be assumed. If $\boldsymbol{r}_{Co,P}$ were coincident with V_{33} (i.e., $\beta^D = 0°$), then such correlations may exist (vide infra).

The uncertainties in R_{eff} given in Table 1 reflect the degree to which R_{eff} can be varied while simulating the spectra without creating any apparent differences between the calculated and experimental spectra. The residual dipolar shifts observed in the MAS spectra are not very sensitive to small changes in R_{eff} of ca. 20 or 30 Hz. If ΔJ is smaller than or on the order of $^1J(^{59}Co,^{31}P)$, the maximum contribution would be ca. 100–125 Hz, which would be detectable given the uncertainties in R_{eff}. If there is a contribution to R_{eff} from ΔJ, it must be less than 90 Hz (contribution to R_{eff} is $\Delta J/3$ = 30 Hz). For the purposes of this work, it is assumed that $R_{eff} \simeq R_{dd}$.

Cobaloximes for which quadrupolar data are unknown

If ^{59}Co quadrupolar data are unavailable, or reasonable assumptions cannot be made regarding the EFG tensor orientation, the only parameters available from the ^{31}P MAS NMR spectrum are δ_{iso}, $^1J(^{59}Co,^{31}P)$, and *d*. The residual dipolar shift is proportional to C_Q, R_{eff}, and the angular factor in eq. [2], whose magnitude is dependent upon η, β^D, and α^D. The covariance of these parameters means that it is possible to calculate identical MAS NMR spectra using substantially different parameters. As an example, for a hypothetical Co, P spin pair with $^1J(^{59}Co,^{31}P)$ = 350 Hz and R_{eff} = 900 Hz, spectra may be calculated which appear almost identical using C_Q = +40 MHz and $\beta^D = 0°$ or C_Q = –80 MHz and β^D = 90° ($\alpha^D = 0°$, $\eta = 0$). In systems where the EFG tensor orientation is given by $\beta^D = 0°$, the parameters α^D and η do not play a role in determining the magnitude of *d*. In such cases, it is possible to gain information on either R_{eff} or C_Q if one of these parameters is known independently. However, the EFG tensor orientation was found to vary in the three well-characterized cobaloximes, so general assumptions permitting this type of analysis are not possible. Nevertheless, valuable information is still available from these spectra.

First, cobaloximes with chloride or azide anions as the anionic axial species are considered. No structural or quadrupolar data are available for $P(tol)_3Co(DH)_2Cl$ (**IV**) (tol = tolyl); however, the only difference between $PPh_3Co(DH)_2Cl$

© 1999 NRC Canada

Fig. 3. Experimental and calculated ^{31}P CPMAS NMR spectra of P(*p*-tol)$_3$Co(DH)$_2$Cl (**IV**) at (A) 4.7 and (B) 9.4 T and PPh$_3$Co(DH)$_2$N$_3$ (**V**) at (C) 4.7 and (D) 9.4 T.

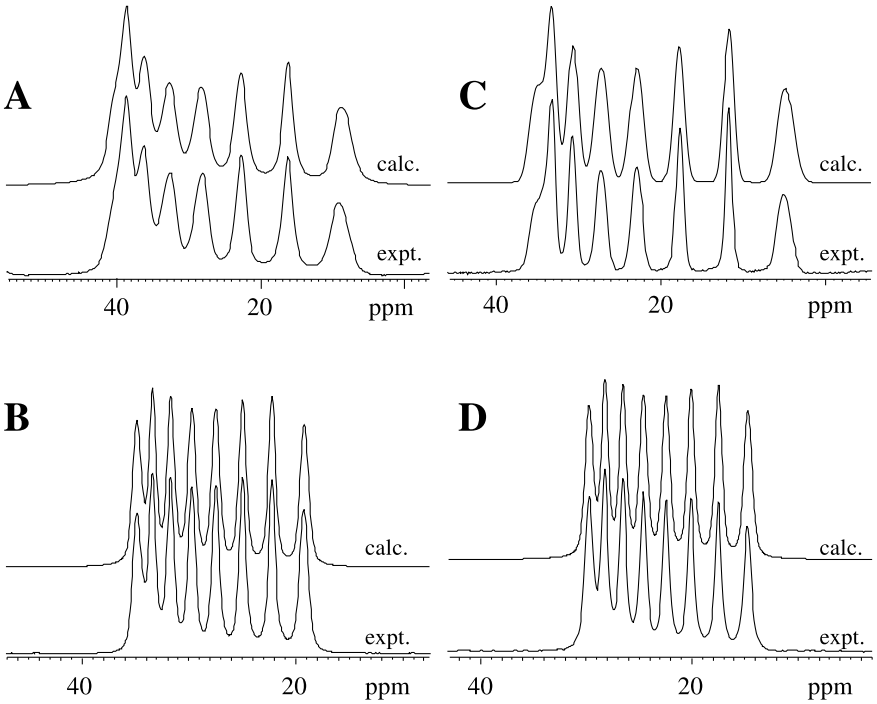

(**III**) and **IV** is the presence of the *para*-methyl groups on the phenyl rings of the phosphine ligand. The spectra of **IV** (Fig. 3A, B) are remarkably similar to those of **III** (Fig. 2), as evidenced by the spectral parameters (see Table 2). The isotropic chemical shifts and $^1J(^{59}Co,^{31}P)$ are also very similar in these complexes. Another structurally similar cobaloxime is PPh$_3$Co(DH)$_2$N$_3$ (**V**). In the crystal structure of this compound, the reported Co, P bond length is 2.311(1) Å (29), which corresponds to R_{dd} = 929(1) Hz. It has been suggested that the Co, P bond length is very similar to that in **III** since the N_3^- species is a weak *trans*-influencing ligand (30, 31) similar to Cl^- (29), and hence, should have comparable effects on overall molecular structure. The spectra of **III**, **IV,** and **V** (Fig. 3C, D) have positive residual dipolar shifts, similar δ_{iso}, and comparable $^1J(^{59}Co,^{31}P)$ values. Given the structural similarity of these cobaloximes, it is likely that the EFG orientation is the same in all three complexes (i.e., β^D = 90°, α^D = 90°, V_{22} along the Co, P bond).

Parameters for several other chloro- and azidocobaloximes are presented in Table 2. The magnitude of $^1J(^{59}Co,^{31}P)$ and the δ_{iso} for PMePh$_2$Co(DH)$_2$Cl (**VI**) and PMe$_2$PhCo(DH)$_2$N$_3$ (**VII**) coincide with prior examples. Comparing PBz$_3$Co(DH)$_2$Cl (**VIII**) and PBz$_3$Co(DH)$_2$N$_3$ (**IX**) (Bz = benzyl), reductions in both $^1J(^{59}Co,^{31}P)$ and *d* are observed in the azidocobaloxime, similar to that observed for **III** and **V**.

The ^{31}P CPMAS NMR spectra of methyl-substituted cobaloximes are now discussed. Alkyl groups are strong electronic *trans*-influencing ligands (30, 31) compared to the halide and azide anions. The presence of the axially-substituted methyl group results in a lengthening of the Co, L bond; this has been documented for a number of cobaloximes involving both phosphorus- and nitrogen-coordinated ligands (10, 32). Accordingly, R_{dd}(Co,P) is generally smaller (ca. 10–15%) in phosphorus-substituted alkyl cobaloximes.

Quadrupolar data are not available for PMe$_3$Co(DH)$_2$Me (**X**). The Co, P bond length is reported as 2.293(1) Å (33), corresponding to R_{dd} = 951(1) Hz. This bond length is significantly shorter than average Co, P bond lengths in phosphorus-substituted alkylcobaloximes ($r_{Co,P} \geq 2.41$ Å) due to the small size of the PMe$_3$ ligand. As a result, R_{dd} is on the order of those observed in the halogen- and azido-substituted cobaloximes. The value of $^1J(^{59}Co,^{31}P)$ is ca. 70 Hz less than the smallest *J*-coupling in the halide- and azide-substituted cobaloximes, demonstrating that a shorter Co, P bond length does not necessarily lead to an increased value of $^1J(^{59}Co,^{31}P)$.

The X-ray crystal study of **X** reveals that there are two crystallographically distinct molecules in the unit cell. This is also evident in the ^{31}P CPMAS NMR spectra of **X** (Fig. 4), as two sites with distinct isotropic chemical shifts are resolved. It is noted that the sense of the spectrum is negative, as is the case for PPh$_3$Co(DH)$_2$Me (**II**), and the remainder of the spectra of the alkyl-substituted cobaloximes discussed in this paper (vide infra). The phosphorus nucleus in **X** is the most shielded of all the examples reported in this paper. This is reasonable given that the phosphorus nucleus in uncoordinated PMe$_3$ is more shielded than in other phosphine ligands considered here (34).

In Table 2, spectral data are presented for several alkylcobaloximes, which are similar to **II**, such as P(*p*-FC$_6$H$_4$)$_3$Co(DH)$_2$Me (**XI**), P(*p*-ClC$_6$H$_4$)$_3$Co(DH)$_2$Me (**XII**), P(Me$_2$Ph)Co(DH)$_2$Me (**XIII**), and P(Et$_2$Ph)Co(DH)$_2$Me (**XIV**) (see Fig. 5 for spectra of **XII**, **XIII**, and **XIV**). In **XI** and **XII**, $^1J(^{59}Co,^{31}P)$, δ_{iso} and *d* are very similar to those ob-

© 1999 NRC Canada

Table 2. Phosphorus-31 NMR parameters for phosphine- and phosphite-substituted cobaloximes, $LCo(DH)_2X$, and uncoordinated neutral ligands, L.

Cobaloxime $LCo(DH)_2X$ (L, X)	δ_{iso}, cobaloxime (ppm)	δ_{iso}, free ligand (ppm)	Δ (ppm)	$^1J(^{59}Co,^{31}P)$ (Hz)	d (Hz)[a]
PBu_3, Cl (**I**)[b,c] Site 1	31.2(1)	–30.9[f]	62.1	350(3)	+79
Site 2	29.8(1)		60.7	352(3)	+86
PPh_3, Me (**II**)[b]	17.6(2)	–10.3	27.9	225(2)	–8
PPh_3, Cl (**III**)[b]	23.7(1)	–10.3	34	371(2)	+158
P(*p*-tol)$_3$, Cl (**IV**)	27.9(2)	–10.4	38.3	362(1)	+147
PPh_3, N_3 (**V**)	23.0(1)	–10.3	33.3	348(2)	+122
$PMePh_2$, Cl (**VI**)	22.3(1)	–26.8[f]	49.1	351(2)	+114
PMe_2Ph, N_3 (**VII**)	32.1(2)			344(3)	+121
PBz_3, Cl (**VIII**)	27.3(2)			357(2)	+116
PBz_3, N_3 (**IX**)	24.0(2)			345(5)	+72
PMe_3, Me (**X**) Site 1	–3.5(1)	–63[g]	59.5	275(2)	–19
Site 2	–1.7(1)		64.7	275(2)	–20
P(*p*-$FC_6H_4)_3$, Me (**XI**)	20.87(3)			226(2)	–12
P(*p*-$ClC_6H_4)_3$, Me (**XII**)	27.10(5)			228(2)	–24
$P(Me_2Ph)$, Me (**XIII**)	10.15(3)			255(2)	–92
$P(Et_2Ph)$, Me (**XIV**)	22.89(3)			254(1)	–72
$P(OEt)_3$, N_3 (**XV**)	82.6(2)	139.2[f]	–56.6	615(2)	+80
$P(OPh)_3$, Me (**XVI**) Site 1	108.2(1)	119[h]	–10.9	430(3)	–59
Site 2	106.8(2)		–12.2	420(2)	–61
PPh_3, Br (**XVII**)[d]	24.3(3)	–10.3	34.6	372(9)	—
PEt_3, Me (**XVIII**)[c,d]	6.5(3)	–30.9[f]	37.4	250(5)	—
PBu_3, N_3 (**XIX**)[c]	28.5(2)	–18.6[f]	47.1	345(3)	+55

[a]Calculated for spectra at 9.4 T (ν_S = 94.48 MHz). Errors in d are as high as ±15 Hz for spectra acquired at room temperature, and ±35 Hz for low temperature spectra, due to the broadened peaks.

[b]NQR data available.

[c]Spectra acquired at 155 K.

[d]Spectra cannot be calculated using first-order perturbation theory.

[e]δ_{iso} from solid-state NMR measurements (50).

[f]δ_{iso} from solution NMR measurements (14*f*).

[g]δ_{iso} from solid-state NMR measurements (34).

[h]δ_{iso} from solid-state NMR measurements (51).

Fig. 4. Experimental and calculated ^{31}P CPMAS NMR spectra of $PMe_3Co(DH)_2Me$ (**X**) at (A) 4.7 and (B) 9.4 T.

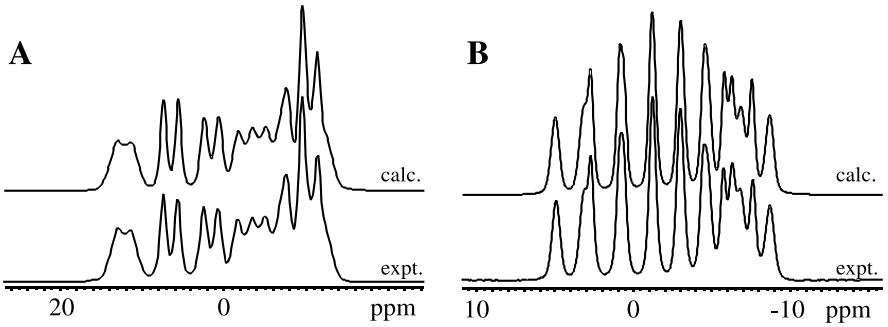

served for **II**. In the latter complexes, which have significantly different phosphine groups, the magnitude of $^1J(^{59}Co,^{31}P)$ increases slightly, with a larger residual dipolar shift in comparison to **II**, **XI**, and **XII**. This is indicative of either a substantial increase in C_Q, or a change in the orientation of the EFG tensor. In all cases, the values of $^1J(^{59}Co,^{31}P)$ in the alkylcobaloximes are significantly smaller than in the chloro- and azide-substituted species. Possible reasons for this are discussed below.

Phosphite-substituted cobaloximes have very different NMR spectra than phosphine-substituted cobaloximes. $P(OEt)_3Co(DH)_2N_3$ (**XV**) was considered in our first study on the cobaloximes, and was found to have $^1J(^{59}Co,^{31}P)$ = 615(2) Hz, the largest for all of the cobaloximes considered

© 1999 NRC Canada

Fig. 5. Experimental and calculated ^{31}P CPMAS NMR spectra of P(*p*-ClC_6H_4)$_3$Co(DH)$_2$Me (**XII**) at (A) 4.7 and (B) 9.4 T, P(Me_2Ph)Co(DH)$_2$Me (**XIII**) at (C) 4.7 and (D) 9.4 T, and P(Et_2Ph)Co(DH)$_2$Me (**XIV**) at (E) 4.7 and (F) 9.4 T.

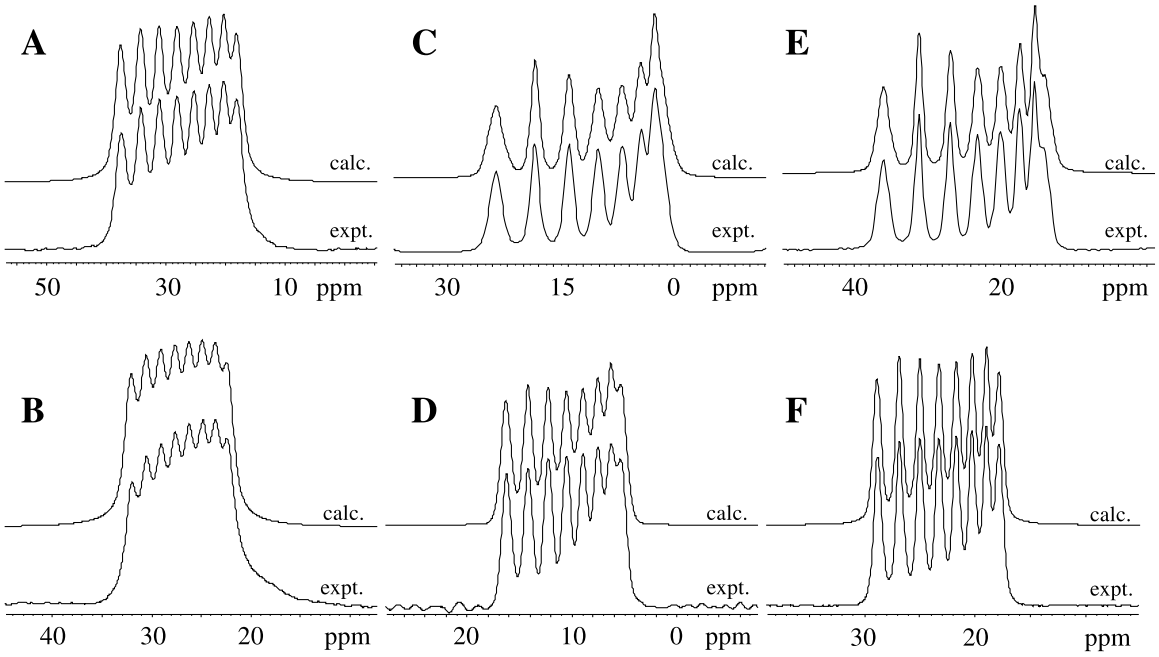

Fig. 6. Experimental and calculated ^{31}P CPMAS NMR spectra of P(OPh)$_3$Co(DH)$_2$Me (**XVI**) at 9.4 T.

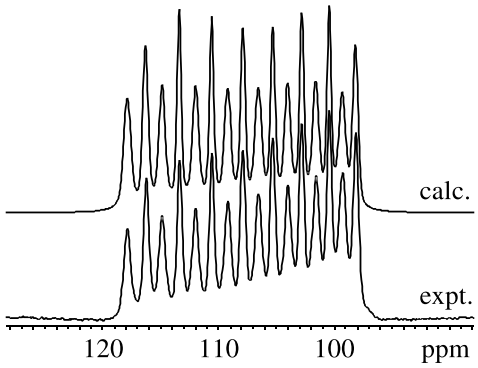

Fig. 7. Experimental ^{31}P CPMAS NMR spectra of PPh$_3$Co(DH)$_2$Br (**XVII**) at (A) 4.7 and (B) 9.4 T.

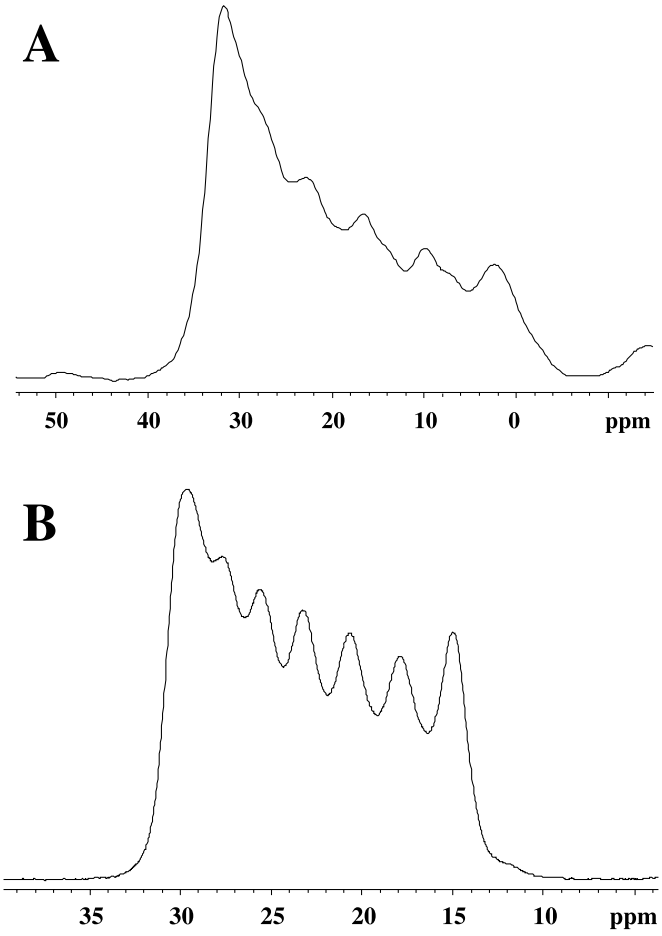

(15). In addition, the phosphorus nucleus is deshielded by ca. 50 ppm relative to the range of δ_{iso} reported for the phosphine-substituted cobaloximes, in accordance with trends previously observed in solution ^{31}P NMR studies (10, 14*f*). Neither crystallographic nor quadrupolar data have been obtained for P(OPh)$_3$Co(DH)$_2$Me (**XVI**). The spectra of **XVI** reveal that there are two crystallographically non-equivalent sites, with $^1J(^{59}Co,^{31}P)$ = 430(2) Hz and 420(2) Hz, and δ_{iso} = 108.2(1) ppm and 106.8(1) ppm, respectively (Fig. 6). The values of $^1J(^{59}Co,^{31}P)$ are large enough that the transitions arising from the two sites are completely resolved, unlike in the spectra of **X** (Fig. 4). The value of $^1J(^{59}Co,^{31}P)$ is reduced compared to **XV**, undoubtedly due to the substitution of the Me into the axial position; notwithstanding, $^1J(^{59}Co,^{31}P)$ in **XVI** is still larger than those for all of the phosphine cobaloximes. In addition, the residual dipolar shifts are of opposite sign in **XV** and **XVI**, indicating either that the EFG tensor orientations and (or) the signs of C_Q are different.

© 1999 NRC Canada

Finally, we consider systems where the first-order perturbation treatment appears to fail. Phosphorus-31 CPMAS NMR spectra of $PPh_3Co(DH)_2Br$ (**XVII**) acquired at both 4.7 and 9.4 T display an interesting anomaly (Fig. 7): at the lower field, there are only six peaks resolved, and at the higher field, only seven. Eight peaks are resolved in the high-field spectra of all of the other cobaloximes, with seven or eight peaks resolved at the lower field, depending on the degree of residual dipolar coupling and the magnitude of $^1J(^{59}Co,^{31}P)$. Attempts to simulate the spectra of **XVII** at both fields were unsuccessful, as the degree of distortion in peak spacings could not be duplicated exactly with the expressions derived from first-order perturbation theory. This result was also observed for **XVII** by Asaro et al. (17) in their recent work. Calculations using full theory were unsuccessful; however, we are presently limited to spectral simulations involving full diagonalization of the combined Zeeman and quadrupolar hamiltonian for cases in which $\eta = 0$. Interestingly, the crystal structure obtained for this compound reveals that $r_{Co,P}$ is almost identical to that in $PPh_3Co(DH)_2Cl$ (**III**), with no significant differences in molecular structure (35). As well, the values of $^1J(^{59}Co,^{31}P)$ in **III** and **XVII** are very similar. The magnitude of C_Q is assumed to be quite large in **XVII**, resulting in the severely distorted multiplet, though the source of the increase in V_{33} is unknown. Similar difficulties in calculating spectra using the first-order perturbation approach were encountered with $PEt_3Co(DH)_2Me$ (**XVIII**), which is one of the complexes exhibiting temperature-dependent ^{59}Co self-decoupling (vide infra).

General trends in the NMR parameters obtained in this study are as follows:

1. The magnitude of $^1J(^{59}Co,^{31}P)$ is significantly reduced if the anionic species, X, is an alkyl group, for both phosphine- and phosphite-substituted cobaloximes.

2. Examination of the complexes with the same L ligands and X = Cl^- or N_3^- (i.e., **III** and **V**, L = PPh_3; **VIII** and **IX**, L = PBz_3; **I** and **XIX**, L = PBu_3), reveals that there is a small reduction in $^1J(^{59}Co,^{31}P)$ in the azidocobaloximes compared to the corresponding chloro species (ca. 2 to 5%).

3. For the phosphine alkylcobaloximes, $^1J(^{59}Co,^{31}P)$ increases with decreasing steric bulk of the phosphine.

4. Values of $^1J(^{59}Co,^{31}P)$ in phosphite-substituted cobaloximes are much larger than in phosphine-substituted cobaloximes.

5. The isotropic coordination chemical shifts are as follows: for phosphines, the coordination chemical shift, $\Delta = \delta_{iso}(\text{coord.}) - \delta_{iso}(\text{free ligand})$ is positive (i.e., the ^{31}P nucleus becomes deshielded upon coordination to the cobaloxime). For the phosphites, it is negative. This is in accord with ^{31}P coordination shifts measured in solution (14*f*).

6. Isotropic ^{31}P chemical shifts in the cobaloximes behave in an identical fashion to those of the corresponding uncoordinated ligands. The phosphorus becomes deshielded in the phosphite-substituted cobaloximes and the span of the chemical shift tensor increases. Phosphorus nuclei are most shielded with small phosphine groups and X = Me^-.

7. In chloro- and azidocobaloximes the residual dipolar shift, *d*, is positive; for alkylcobaloximes, *d* is negative, and for several compounds, quite small.

The small negative values of the residual dipolar shift, *d*, in the alkylcobaloximes likely result from a reduced angular factor ($3\cos^2\beta^D - 1 + \eta\sin^2\beta^D\cos 2\alpha^D$), and not simply from decreased $C_Q(^{59}Co)$ in these compounds. If $\beta^D = 90°$ and $\alpha^D = 0°$, as in the case of **II**, the angular factor is $-1 + \eta$, which can be quite small. Alternatively, if $\beta^D = 90°$ and $\alpha^D = 90°$, as in **I** and **III**, the angular factor is $-1 - \eta$. The fact that *d* is consistently positive and larger for the chloro- and azido-substituted cobaloximes, and negative and smaller for the majority of the methyl-cobaloximes, suggests that the EFG tensor orientations may be similar within each series of compounds.

Interpretation of the indirect spin–spin coupling constants, $^1J(^{59}Co,^{31}P)$

Indirect spin–spin couplings between phosphorus and metal nuclei have often been interpreted in terms of the Fermi-contact mechanism, which is the dominant coupling mechanism for light nuclei such as protons and first-row nuclei (36). The interactions between the nuclear spins are mediated by electrons, and are described by a non-relativistic hyperfine hamiltonian which, according to Ramsey (37), can be decomposed into terms characterizing individual contributions from (*i*) the orbital motion of the electrons (orbital mechanism, OB), (*ii*) nuclear and electron spin dipolar interaction (spin–dipolar mechanism, SD), and (*iii*) the Fermi-contact (FC) mechanism, which accounts for direct coupling between the electron and nuclear spins. There is also a FC, SD cross term that makes no contribution to J_{iso}, but can make significant contributions to the ***J*** tensor. The Fermi contact term is isotropic, and contributions from this mechanism reflect the unpaired electron populations of *s* atomic orbitals of nuclei involved in the coupling (36, 38).

The assumption of the direct correspondence between *s*-character of involved nuclei and the magnitude of J_{iso} must be regarded with caution, since certain *J*-couplings between phosphorus and heavy nuclei which had previously been assumed to be dominated by the FC mechanism have been shown to have large contributions from other coupling mechanisms (vide infra). It has been proposed that the lengthening of the M, P bond (M = metal, e.g., Pt or Hg), say from the presence of a strong *trans*-influencing ligand, results in a reduction of *s*-character of the M atom involved in the M, P bond, leading to a decrease in the magnitude of J_{iso} (assuming that *J* is dominated by the FC mechanism) (39). Changes in the magnitude of J_{iso} have also been attributed to decreasing or increasing *s*-character resulting from different hybrid molecular orbitals at the metal nucleus, which are dependent on the coordination number and electron-donating abilities of the coordinated ligands (39; see for example, ref. 40). Solid-state ^{31}P NMR experiments on powder samples and single crystals have demonstrated that there are significant *J*-anisotropies, and therefore contributions from mechanisms other than the FC mechanism in $^1J(^{195}Pt,^{31}P)$ in square planar complexes (41), $^1J(^{199}Hg,^{31}P)$ in tetrahedral mercury phosphines (42) and $^1J(^{63/65}Cu,^{31}P)$ in linear copper(I) phosphines (43). In heavy atoms, relativistic effects, which may make a contribution to J_{iso}, cannot be ignored (44).

As discussed above, spectral calculations for cobaloximes in which dipolar and quadrupolar coupling constants are known reveal that ΔJ is probably less than 90 Hz; hence, it is possible that the FC mechanism is dominant in $^1J(^{59}Co,^{31}P)$.

© 1999 NRC Canada

Table 3. Comparison of $^1J(^{59}Co,^{31}P)$ and $^1J(^{103}Rh,^{31}P)$ in cobaloximes and rhodoximes ($LRh(DH)_2X$).

$LM(DH)_2X$ M= Co, Rh L, X	$^1J(^{59}Co,^{31}P)$ (Hz)	$^1K(^{59}Co,^{31}P)$ (N A^{-2} m^{-3}) × 10^{21}	$^1J(^{103}Rh,^{31}P)$ (Hz)[a]	$^1K(^{103}Rh,^{31}P)$ (N A^{-2} m^{-3}) × 10^{21}	$^1J(^{59}Co,^{31}P)/4.38$ (Hz)
PPh_3, Me	225	1.96	–66	4.28	51.4
PMe_3, Me	275	2.4	–78.1	5.07	62.8
$P(OPh)_3$, Me	430	3.75	–116.6	7.57	98.2
PPh_3, Cl	371	3.24	–120	7.79	84.7

[a]Data from ref. 47.

Fig. 8. Variable-temperature ^{31}P CPMAS NMR of (A) $PEt_3Co(DH)_2Me$ (**XVIII**) and (B) $PBu_3Co(DH)_2N_3$ (**XIX**) at 9.4 T. All spectra of **XVIII** acquired with ν_{rot} = 4136 Hz. Spectrum marked with asterisk was acquired with ν_{rot} = 5383 Hz; for other spectra of **XIX**, ν_{rot} = 4000 Hz.

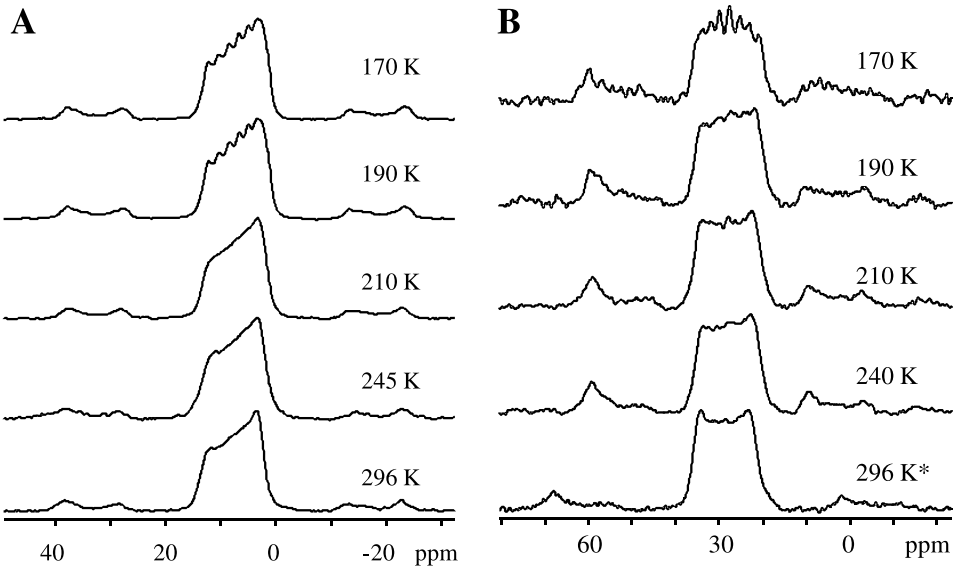

However, the exact contributions of the SD and OB terms, which affect both the anisotropic and isotropic components of the ***J***-tensor, to $^1J(^{59}Co,^{31}P)$ are unknown at this time. If the FC mechanism is dominant, a qualitative explanation of the changes in $^1J(^{59}Co,^{31}P)$ may be formulated as follows: the presence of a methyl group, which is a strong σ-donor and *trans*-influencing ligand, may result in a decrease in the 4*s*-electron density concentrated in the Co, P bond, resulting in a reduced value of $^1J(^{59}Co,^{31}P)$. Similarly, the presence of a phosphite ligand may result in an increase in the 4*s*-electron density in the Co, P bond, resulting in an augmented value of $^1J(^{59}Co,^{31}P)$. Comparable effects of methyl, halide, phosphine and phosphite ligand substitution on $^1J(M,^{31}P)$ have been observed in a large number of cases for phosphorus bonded to transition metals (39). Some examples include $^1J(^{195}Pt,^{31}P)$ in square planar phosphine- and phosphite-substituted platinum(II) complexes (45), $^1J(^{183}W,^{31}P)$ in octahedral phosphine- and phosphite-substituted pentacarbonyl tungsten compounds (46) and the very close correspondence with $^1J(^{103}Rh,^{31}P)$ from ^{31}P NMR studies of the rhodium analogs of the cobaloximes, the rhodoximes (vide infra) (47).

In isostructural complexes with different metals in the same group of the periodic table, indirect spin–spin coupling constants, $^1J(M,^{31}P)$, are normally compared by two different methods. The first is to consider the reduced coupling constants, $K(N,N') = 4\pi^2 J(N,N')/(h\gamma_N\gamma_{N'})$, which eliminates the dependence of the *J*-coupling on the magnitudes and signs of the magnetogyric ratios (48). It has also been proposed that $^1J(M,^{31}P)$ for two different metals should be equivalent to the ratio of their *s*-electron densities and magnetogyric ratios, $\gamma|s(0)|^2$ (39). Comparing *J*-couplings to phosphorus involving ^{59}Co and ^{103}Rh, $^1J(^{59}Co,^{31}P)$ is predicted to be approximately 4.38 times larger than $^1J(^{103}Rh,^{31}P)$ (49). In Table 3, $^1J(^{59}Co,^{31}P)$ and $^1J(^{103}Rh,^{31}P)$ are compared in several analogous cobaloximes and rhodoximes. The reduced coupling constants are two times as large in the rhodoximes, whereas the ratio of $\gamma|s(0)|^2$ underestimates $^1J(^{59}Co,^{31}P)$. Qualitatively, $^1K(^{59}Co,^{31}P)$ and $^1K(^{103}Rh,^{31}P)$ increase by the same factors in the alkylated cobaloximes and rhodoximes. The reduced coupling constant increases as the atomic number of the metal, *Z*, increases in a series of isostructural compounds (48). This is thought to be due to increasing $|s(0)|^2$ upon descending any group of the periodic table.

Temperature-dependent self-decoupling of cobalt

Previously, we observed the manifestation of self-decoupling of the ^{59}Co nucleus in the ^{31}P CPMAS NMR spectra of $PBu_3Co(DH)_2Cl$ (**I**) acquired at room temperature (4). The fine structure resulting from the *J*-coupling is not

© 1999 NRC Canada

present in these spectra; rather, broad resonances are observed. Additional examples are presented here (Fig. 8), for $PEt_3Co(DH)_2Me$ (**XVIII**) and $PBu_3Co(DH)_2N_3$ (**XIX**). As the samples are cooled down to 170 K, the multiplet structure is observed in both cases. The self-decoupling of the cobalt nucleus is attributed to shorter values of the cobalt spin-lattice relaxation times, $T_1(^{59}Co)$, at higher temperatures. Since the ^{31}P nucleus is indirectly spin–spin coupled to a rapidly relaxing quadrupolar nucleus (^{59}Co) through an interaction of the form $J\mathbf{I}\cdot\mathbf{S}$, scalar relaxation of the second kind becomes the dominant spin–spin relaxation mechanism at the ^{31}P nucleus. If the ^{59}Co nucleus has a short relaxation time, $T_1(^{59}Co)$, compared with the magnitude of $J(^{59}Co,^{31}P)^{-1}$, then fluctuating magnetic fields arise which induce efficient spin–spin relaxation of ^{31}P. As a result, the ^{31}P NMR spectra do not exhibit the expected multiplet structure, but have broadened lineshapes indicating self-decoupling of the ^{59}Co nucleus. Rough deconvolution of the powder patterns provides estimates of individual peak widths, from which upper limits on $T_1(^{59}Co)$ of 8 and 9 ms are calculated for **XVIII** and **XIX**, respectively. It is not surprising that self-decoupling is observed in **XIX**, since the neutral ligand in this complex (PBu_3) is the same as that in **I**. However, for **XVIII**, which is similar to $PMe_3Co(DH)_2Me$ in structure, the observance of the self-decoupling phenomenon is somewhat more surprising. Self-decoupling at room temperature was also observed in the ^{31}P CPMAS NMR spectra of $PBu_3Co(DH)_2Me$ and $P(OMe)_3Co(DH)_2N_3$; however, variable-temperature NMR spectra of these complexes are not presented here.

The ^{31}P CPMAS NMR spectra of $P(p\text{-}ClC_6H_4)_3Co(DH)_2Me$ (**XII**) are quite broad at room temperature (see Fig. 5A, B), though multiplet structure is discernible. Low-temperature experiments conducted on this sample down to 165 K revealed no significant changes in the linewidths of the peaks. Peak-broadening mechanisms in the ^{31}P CPMAS NMR spectra of the cobaloximes must arise from sources other than the quadrupolar-dominated spin-lattice relaxation of the cobalt nucleus (e.g., sample non-crystallinity, magnetic susceptibility effects, etc.). Given the variety of the ligands present in complexes which exhibit the temperature-dependent self-decoupling phenomenon, the exact nature of the molecular motion giving rise to fluctuating EFGs at the cobalt nucleus (which induce efficient spin-lattice relaxation) is unknown at this time.

Conclusions

NMR parameters determined from the ^{31}P CPMAS NMR spectra of 19 cobaloximes have been presented. The ^{59}Co quadrupolar parameters and EFG tensor orientations vary with substitution of different axial ligands. The orientations of the EFG tensors determined for three "well-characterized" cobaloximes provide information on possible EFG tensor orientations in cobaloximes for which structural and quadrupolar data are not available. For example, in phosphine-substituted alkylcobaloximes, d is negative, suggesting an orientation in which V_{11} is along the Co, P bond. In several of the phosphine-substituted chloro- and azidocobaloximes, d is positive, intimating that V_{22} is along the Co, P bond.

The magnitude of $^1J(^{59}Co,^{31}P)$ varies according to the nature of the neutral and anionic axial ligands. Specific trends in $^1J(^{59}Co,^{31}P)$ can be qualitatively related to the steric bulk and electronic nature of the neutral ligands and the *trans*-influencing ability of the anionic species. No correlation is found between the Co, P internuclear distance and the magnitude of $^1J(^{59}Co,^{31}P)$. The Fermi-contact mechanism can be used to qualitatively explain why $^1J(^{59}Co,^{31}P)$ is reduced in methylcobaloximes and increased in phosphite-substituted cobaloximes.

Variable-temperature ^{31}P NMR experiments reveal that ^{59}Co is partially self-decoupled at room temperature, and "re-coupled" at temperatures on the order of 170 K or lower, opposite to trends observed in the extreme-narrowing limit in solution. Upper limits on $T_1(^{59}Co)$ are estimated from the line widths of the ^{31}P MAS NMR spectra, assuming that scalar relaxation of the second kind is operative at the phosphorus nuclei.

Acknowledgments

We thank the Natural Sciences and Engineering Research Council (NSERC) of Canada for funding (R.E.W.) and the Atlantic Regional Magnetic Resonance Centre (ARMRC) for the solid-state NMR facilities. R.W.S. thanks the Killam Foundation and Walter C. Sumner Foundation for graduate fellowships. R.E.W. thanks the Canada Council for a Killam Research Fellowship. We are very grateful to Dr. Klaus Eichele for the development of the WSolids software package. We thank Ms. Myrlene Gee, Dr. Michael D. Lumsden, Mr. Guy M. Bernard, Mr. David L. Bryce, and Dr. Scott Kroeker for many helpful comments, Ms. Elinor Cameron for crystal structure database searches, and Dr. T.S. Cameron for assistance with the variable-temperature experiments.

References

1. R.K. Harris and A.C. Olivieri. Progr. NMR Spectrosc. **24**, 435 (1992).
2. (*a*) R.K. Harris. *In* Encyclopedia of nuclear magnetic resonance. *Edited by* D.M. Grant and R.K. Harris. John Wiley & Sons, Chichester, U.K. 1996, pp. 2909–2914; (*b*) C.A. McDowell. *In* Encyclopedia of nuclear magnetic resonance. *Edited by* D.M. Grant and R.K. Harris. John Wiley & Sons, Chichester, U.K. 1996, pp. 2901–2908.
3. P. Grondona and A.C. Olivieri. Concepts Magn. Reson. **5**, 319 (1993).
4. (*a*) J.A. Pople. Mol. Phys. **1**, 168 (1958); (*b*) J.C.P. Sanders and G.J. Schrobilgen. *In* Multinuclear magnetic resonance in liquids and solids — chemical applications. NATO ASI Series. Series C: mathematical and physical sciences. Vol. 322. *Edited by* P. Granger and R.K. Harris. Kluwer Academic Publishers, Dordrecht, The Netherlands. 1990. pp. 157–186.
5. A.C. Olivieri, L. Frydman, and L.E. Diaz. J. Magn. Reson. **75**, 50 (1987).
6. D.C. Apperly, B. Haiping, and R.K. Harris. Mol. Phys. **68**, 1277 (1989).
7. A.C. Olivieri. J. Magn. Reson. **81**, 201 (1989).
8. E.M. Menger and W.S. Veeman. J. Magn. Reson. **46**, 257 (1982).
9. S.H. Alarcón, A.C. Olivieri, and R.K. Harris. Solid State Nucl. Magn. Reson. **2**, 325 (1993).

© 1999 NRC Canada

10. N. Bresciani-Pahor, M. Forcolin, L.G. Marzilli, L.Randaccio, M.F. Summers, and P.J. Toscano. Coord. Chem. Rev. **63**, 1 (1985).
11. P.J. Toscano and L.G. Marzilli. Progr. Inorg. Chem. **31**, 105 (1984).
12. N.M. Samus and A.V. Ablov. Coord. Chem. Rev. **28**, 177 (1979).
13. (*a*) L. Randaccio, N. Bresciani-Pahor, E. Zangrando, and L.G. Marzilli. Chem. Soc. Rev. **18**, 225 (1989); (*b*) R.G. Finke, D.A. Schiraldi, and B.J. Mayer. Coord. Chem. Rev. **54**, 1 (1984); (*c*) G.N. Schrauzer and R.J. Windgassen. J. Am. Chem. Soc. **88**, 3738 (1966).
14. (*a*) H.A.O. Hill and K.G. Morallee. J. Chem. Soc. A, 554 (1969); (*b*) W.C. Trogler, R.C. Stewart, L.A. Epps, and L.G. Marzilli. Inorg. Chem. **13**, 1564 (1974); (*c*) P.L. Gaus and A.L. Crumbliss. Inorg. Chem. **15**, 739 (1976); (*d*) R.C. Stewart and L.G. Marzilli. Inorg. Chem. **16**, 424 (1977); (*e*) A.V. Cartano and L.L. Ingraham. Bioinorg. Chem. **7**, 351 (1977); (*f*) J.A. Kargol, R.W. Crecely, J.L. Burmeister, P.J. Toscano, and L.G. Marzilli. Inorg. Chim. Acta, **40**, 79 (1980); (*g*) J. Huet and A. Gaudemer. Org. Magn. Reson. **20**, 4 (1982); (*h*) C. Tavagnacco, G. Balducci, G. Costa, K. Täschler, and W. von Philipsborn. Helv. Chim. Acta, **73**, 1469 (1990); (*i*) K.L. Brown and S. Satyanarayana. J. Am. Chem. Soc. **114**, 5674 (1992); (*j*) S.J. Moore, M. Iwamoto, and L.G. Marzilli. Inorg. Chem. **37**, 1169 (1998).
15. R.W. Schurko, R.E. Wasylishen, and J.H. Nelson. J. Phys. Chem. **100**, 8057 (1996).
16. A. Medek, V. Frydman, and L. Frydman. Proc. Natl. Acad. Sci. U.S.A. **94**, 14237 (1997).
17. F. Asaro, R. Gobetto, L. Liguori, and G. Pellizer. Chem. Phys. Lett. **300**, 414 (1999).
18. P.J. Toscano, C.C. Chiang, T.J. Kistenmacher, and L.G. Marzilli. Inorg. Chem. **20**, 1513 (1981).
19. R.C. Stewart and L.G. Marzilli. J. Am. Chem. Soc. **100**, 817 (1978).
20. W.C. Trogler, R.C. Stewart, L.A. Epps, and L.G. Marzilli. Inorg. Chem. **13**, 1564 (1974).
21. S.J. Moore and L.G. Marzilli. Inorg. Chem. **37**, 5329 (1998).
22. G. Wu and R.E.Wasylishen. J. Phys. Chem. **97**, 7863 (1993), and refs. therein.
23. D.W. Alderman, M.S. Solum, and D.M. Grant. J. Chem. Phys. **84**, 3717 (1986).
24. A.C. Olivieri. Magn. Reson. Chem. **34**, 365 (1996).
25. R.E. Wasylishen. *In* Encyclopedia of nuclear magnetic resonance. *Edited by* D.M. Grant and R.K. Harris. John Wiley & Sons: Chichester, U.K. 1996, pp. 1685–1695.
26. R.A. LaRossa and T.L. Brown. J. Am. Chem. Soc. **96**, 2072 (1974).
27. T.L. Brown. Acc. Chem. Res. 408 (1974).
28. S. Brückner and L. Randaccio. J. Chem. Soc. Dalton Trans. 1017 (1974).
29. J.H. Nelson, N.E. Takach, N. Bresciani-Pahor, L. Randaccio, and E. Zangrando. Acta Crystallogr. **C40**, 742 (1984).
30. T.G. Appleton, H.C. Clark, and L.E. Manzer. Coord. Chem. Rev. **10**, 335 (1973).
31. S.S. Zumdahl and R.S. Drago. J. Am. Chem. Soc. **90**, 6669 (1968), and refs. therein.
32. A. Bigotto, E. Zangrando, and L. Randaccio. J. Chem. Soc. Dalton Trans. 96 (1976).
33. N. Bresciani-Pahor, L. Randaccio, P.J. Toscano, A.C. Sandercock, and L.G. Marzilli. J. Chem. Soc. Dalton Trans. 129 (1982).
34. C.J. Jameson, A. de Dios, and A.K. Jameson. Chem. Phys. Lett. **167**, 575 (1990).
35. N. Bresciani-Pahor, M. Calligaris, G. Nardin, and L. Randaccio. Gazz. Chim. Ital. **111**, 147 (1981).
36. (*a*) J. Kowalewski. Ann. Rep. NMR Spectrosc. **12**, 81 (1982); (*b*) R.H. Contreras and J.C. Facelli. Ann. Rep. NMR Spectrosc. **27**, 255 (1993).
37. N.F. Ramsey. Phys. Rev. **91**, 303 (1953).
38. (*a*) H.M. McConnell. J. Chem. Phys. **24**, 460 (1956); (*b*) J.A. Pople and D.P. Santry. Mol. Phys. **8**, 1 (1964).
39. P.S. Pregosin and R.W. Kunz. ^{31}P and ^{13}C NMR of transition metal complexes. *In* NMR basic principles and progress. Vol. 16. *Edited by* P. Diehl, E. Fluck, and R. Kosfeld. Springer–Verlag, Berlin. 1979. pp. 1–153.
40. H.B. Buergi, R.W. Kunz, and P.S. Pregosin. Inorg. Chem. **19**, 3707 (1980), and refs. therein.
41. W.P. Power and R.E. Wasylishen. Inorg. Chem. **31**, 2176 (1992).
42. (*a*) M.D. Lumsden, R.E. Wasylishen, and J.F. Britten. J. Phys. Chem. **99**, 16602 (1995); (*b*) W.P. Power, M.D. Lumsden, and R.E. Wasylishen. J. Am. Chem. Soc. **113**, 8257 (1991); (*c*) G.H. Penner, W.P. Power, and R.E. Wasylishen. Can. J. Chem. **66**, 1821 (1988).
43. S. Kroeker, J.V. Hanna, R.E. Wasylishen, E.W. Ainscough, and A.M. Brodie. J. Magn. Reson. **135**, 208 (1998).
44. P. Pyykkö. Chem. Rev. **88**, 563 (1988).
45. (*a*) F.H. Allen and A. Pidcock. J. Chem. Soc. A, 2700 (1968); (*b*) S.O. Grim, R.L. Keiter, and W. McFarlane. Inorg. Chem. **6**, 1133 (1967); (*c*) N. Ahmad, E.W. Aiscough, T.A. James, and S.D. Robinson. J. Chem. Soc. Dalton Trans. 1148 (1973).
46. (*a*) S.O. Grim, D.A. Wheatland, and W. McFarlane. J. Am. Chem. Soc. **89**, 5573 (1967); (*b*) S.O. Grim, P.R. McAllister, and R.M. Singer. J. Chem. Soc. Chem. Commun. 38 (1969).
47. (*a*) F. Asaro, R.D. Garlatti, G. Pellizer, and G. Tauzher. Inorg. Chim. Acta, **211**, 27 (1993); (*b*) M. Ludwig, L. Öhrström, and D. Steinborn. Magn. Reson. Chem. **33**, 984 (1995).
48. C.J. Jameson. Multinuclear NMR. *Edited by* J. Mason. Plenum Press, New York. 1987. pp. 89–131.
49. R.J. Goodfellow. Multinuclear NMR. *Edited by* J. Mason. Plenum Press, New York. 1987. pp. 521–561.
50. G.H. Penner and R.E. Wasylishen. Can. J. Chem. **67**, 1909 (1989).
51. Y. Huang, H.L. Uhm, D.F.R. Gilson, and I.S. Butler. Inorg. Chem. **33**, 804 (1994).

© 1999 NRC Canada

A comparison of NMR distance determinations in the solid state by cross polarization, REDOR, and TEDOR techniques

Colin A. Fyfe, Andrew R. Lewis, and Jean-Michel Chézeau

Abstract: Solid-state NMR distance determinations using Hartmann–Hahn cross polarization between spin-1/2 nuclei ($^{19}F/^{29}Si$) are reported. $^{19}F \rightarrow {}^{29}Si$ polarization transfer for the T-1 silicon site in the clathrasil octadecasil shows an oscillatory behaviour as a function of the contact time. These oscillations were observed for non-spinning powder samples and also for different spinning speeds at the various MAS sideband matching conditions. Three analytical functions that allow efficient nonlinear least-square regression analyses of the experimental data to determine the internuclear distances for non-spinning powder samples as well as at the ±1 and ±2 MAS sideband matching conditions are reported. Using these functions, a $^{19}F—^{29}Si$ distance of 2.53 ± 0.04 Å was determined for the T-1 silicon in octadecasil from fitting of the oscillatory behaviour. This distance is in good agreement with that known from the X-ray structure and the previous $^{19}F/^{29}Si$ REDOR and TEDOR distance measurements. The advantages and limits of the different dipolar-based NMR techniques for heteronuclear distance determinations are examined and discussed.

Key words: cross polarization (CP), NMR distance measurements, octadecasil, $^{19}F—^{29}Si$ distances, REDOR, TEDOR.

Résumé : La polarization croisée, dans les conditions de résonance de Hartmann–Hahn, est utilisée pour mesurer des distances entre noyaux de spin 1/2 ($^{19}F/^{29}Si$) par RMN à l'état solide. Le transfert de polarisation $^{19}F \rightarrow {}^{29}Si$, pour les atomes en site T-1 dans le clathrasil octadecasil, présente des oscillations jusqu'à des temps de contact d'environ 10 ms. Ces oscillations, observées en absence de rotation de l'échantillon, mais également pour différentes vitesses de rotation à l'angle magique, ont été paramètrées. Les fonctions qui permettent l'analyse de la courbe expérimentale par régression non-linéaire des moindres carrés sont données pour les diverses conditions expérimentales : échantillon statique et, lors de la rotation à l'angle magique, accord sur les bandes latérales ±1 et ±2 par rapport aux conditions statiques. La distance $^{19}F—^{29}Si$ obtenue, 2,53 ± 0,04 Å, est en bon accord avec les précédentes déterminations par diffraction des rayons X et par les méthodes REDOR et TEDOR. Les avantages et les limites des différentes méthodes de RMN permettant de déterminer des distances par mesure du couplage dipolaire hétéronucléaire sont examinés et discutés.

Mots clés : polarisation croisée (CP), détermination des distances par RMN, octadecasil, distances $^{19}F—^{29}Si$, REDOR, TEDOR.

Introduction

Solid-state NMR spectroscopy has considerable potential in solid-state structure investigations via the direct determination of internuclear distances from experiments based on the through-space dipolar interactions between selected pairs of nuclei. The dipolar coupling, D, between two nuclei, I and S, depends on the gyromagnetic ratios of the two nuclei, γ_I, γ_S, and on the internuclear distance r (eq. [1]) (1).

$$[1] \qquad D = \mu_0 \gamma_I \gamma_S h/(16\pi^3 r^3)$$

In eq. [1] μ_0 is the magnetic field constant in a vacuum, and h is Planck's constant. Furthermore, since $D \propto r^{-3}$, moderately accurate values of dipolar couplings can yield very accurate values for the corresponding internuclear distances, with the most unambiguous distance measurements coming from systems where I and S interact as isolated spin pairs.

In high-resolution solid-state NMR, magic angle spinning (MAS) is used to narrow the otherwise extremely broad (up to several kHz) resonances. Under MAS conditions the heteronuclear dipolar interaction becomes time dependent (eq. [2]) (1),

Received February 15, 1999.

This paper is dedicated to Professor Ted Schaefer in recognition of his outstanding contributions to Canadian chemistry.

C.A. Fyfe,[1] and A.R. Lewis.[2] Department of Chemistry, University of British Columbia, 2036 Main Mall, Vancouver, BC V6T 1Z1, Canada.
J.M. Chézeau. Laboratoire de Matériaux Minéraux, UPRES-A 7016 CNRS, Ecole Nationale de Supérieure de Chimie de Mulhouse, Université de Haute-Alsace, 3 rue Alfred Werner, 68093 Mulhouse Cedex, France.

[1]Author to whom correspondence may be addressed. Telephone: (604) 822-2293. Fax: (604) 822-2847. e-mail: fyfe@chem.ubc.ca.
[2]Present address: Laboratoire de Matériaux Minéraux, UPRES-A 7016 CNRS, Ecole Nationale de Supérieure de Chimie de Mulhouse, Université de Haute-Alsace, 3 rue Alfred Werner, 68093 Mulhouse Cedex, France.

 © 1999 NRC Canada

[2] $$D(\alpha, \beta, t) = 0.5D[\sin^2 \beta \cos 2(\alpha + \omega_r t) - \sqrt{2} \sin 2\beta \cos (\alpha + \omega_r t)]$$

α and β are the polar angles describing the orientation of the *I–S* internuclear vector with respect to a MAS rotor-fixed coordinate system with its *z*-axis along the spinning axis. MAS does not remove the dipolar interaction, but averages the effective dipolar coupling to zero over each complete rotor cycle (1). Thus, in its simplest form, the use of MAS precludes a direct measurement of *D*.

Recently, there has been considerable interest in heteronuclear distance determinations using the Rotational-Echo Double Resonance (REDOR) (1, 2) and Transferred-Echo Double Resonance (TEDOR) (3, 4) experiments introduced by Schaefer and co-workers. These employ radio frequency (r.f.) pulses applied at specific points in each rotor period to prevent the complete averaging out of the dipolar interactions, and thus allow the effects of dipolar dephasing to accumulate. Using appropriate analysis (1, 4–10), the magnitudes of the dipolar couplings can be experimentally measured and accurate interatomic distances determined. Because these techniques are based on the dipolar interaction that acts through space, there is no requirement that the nuclei be chemically bonded.

REDOR and TEDOR have been applied to amino acids (1–4), peptides (4, 6, 11), proteins (7, 12), semiconductors (13), oxides (14), polymers (15), and molecular sieve frameworks (16–21). In cases where the distances are known independently from X-ray diffraction measurements, those obtained from REDOR and TEDOR experiments are in very good agreement (2, 11, 16).

In the cross polarization (CP) experiment, spin polarization, and thus net magnetization, is transferred via dipolar interactions from abundant *I* spin system (usually ^{1}H) to the dilute *S* spins (e.g., ^{13}C, ^{15}N, or ^{29}Si). The *S* spin FID is then recorded with decoupling applied to the *I* spins. Often, there are significant sensitivity gains associated with the use of CP. These arise because of the enhancement of the order of γ_I/γ_S (compared to a one-pulse NMR experiment on the *S* spins), and the ability to use shorter recycle delays if the T_1 of the *I* spins is less than that of the *S* spins.

Commonly, CP experiments are carried out where the signal intensity is monitored as a function of the contact time τ. The initial build-up of intensity is related to the strength of the *I–S* dipolar couplings, and thus analysis of CP experiments should permit discrimination between different *I–S* distances and, ideally, yield quantitative estimates for these distances if the spins are sufficiently isolated. Measurements of average *I–S* dipolar couplings or distances determined from CP have been reported in the literature (22–26).

In cases where there are a large number of *I* spins coupled to each *S* spin, oscillations at many frequencies interfere, and the signal intensity observed for the *S* spins exhibits an exponential rise to a maximum followed by an exponential decay (27, 28). The dynamics of this process have been extensively described in the literature (27, 29–33).

Oscillations in the ^{1}H/^{13}C cross polarization signal intensity were first reported for a single crystal of ferrocene by Müller et al. (34). Similar oscillations have since been reported in the literature for non-spinning powder samples (23, 35), liquid crystals (36), and oriented lipid bilayers (25). Müller et al. (34) presented a theoretical description of this behaviour and showed that the frequency of this transient oscillation is related to the heteronuclear dipolar coupling constant. An oscillatory behaviour as a function of contact time should be observable whenever the *IS* dipolar interaction is dominated by a few nearest neighbour *I* spins; effectively meaning isolated I_NS spin systems with *N* less than about four (23). However, these oscillations can be damped by other heteronuclear and homonuclear interactions (32).

Stejskal and Schaefer (27, 37) reported transient oscillations under MAS in ^{1}H/^{13}C/^{15}N double cross polarization experiments, and demonstrated the effects of MAS on the CP matching condition. Since then, only relatively few examples of oscillatory behaviour in CP MAS experiments have been reported (23, 24, 26, 38–40). In some cases (24, 26, 39), the authors used slight modifications of the equation derived for the stationary single crystal case by Müller et al., but the modifications proposed ignored the effects of MAS or powder averaging. Consequently, the dipolar couplings and distance information obtained must be viewed as invalid. Hawkes et al. (38) recognized the need to include the effects of MAS on the dipolar coupling (eq. [2]), but did not give an explicit equation describing the CP behaviour.

Recently, Hediger (23, 41) incorporated the effects of sideband matching, powder averaging and MAS for spin-1/2 systems using Floquet theory (42, 43) and applied it to determine the ^{1}H/^{13}C dipolar coupling in a powder sample of co-crystallized C_{60}(ferrocene)$_2$. This sound theoretical analysis means that the CP MAS experiment should now be a viable method for heteronuclear distance determinations in systems of isolated spin pairs.

In previous work we reported ^{19}F—^{29}Si distance determinations in octadecasil by REDOR and TEDOR experiments, and noted that an oscillatory behaviour was observed for the T-1 Si during ^{19}F/^{29}Si CP experiments (16). In the present paper the results of our investigation of this system using ^{19}F/^{29}Si cross polarization are presented. Three analytical functions were derived, which allow efficient nonlinear least-square regression analysis of the experimental data to determine the internuclear distances for non-spinning powder samples as well as at the sideband matching conditions under MAS. The advantages and limits of the different dipolar-based heteronuclear distance determination experiments are also discussed.

Experimental

The pure, highly crystalline octadecasil sample (crystal size 80 μm), was kindly provided by Dr. P. Caullet. The structure was checked by powder X-ray diffraction, ^{19}F, and ^{29}Si MAS NMR measurements, all of which agreed with previously reported results (44, 45). Fluorine contents in these materials are usually in the range 2.3–2.6% (45), which corresponds to occupancies of 80–100% of the D4R units by fluoride ions. The idealized elemental composition of octadecasil is $Si_{20}O_{40}\cdot 2(Q^+F^-)$ where Q^+ is the quinuclidinium cation.

All experiments were carried out using a Bruker MSL-400 spectrometer. The Bruker MAS probe was modified by tuning the high-frequency channel to 376.44 MHz. Approxi-

© 1999 NRC Canada

Fig. 1. (*a*) Schematic representation of the framework structure of octadecasil showing the packing arrangement of the two types of cages: the large [$4^6 6^{12}$]-cages and the small [4^6]-cages (D4R units). Each vertex represents a silicon atom, and oxygen atoms (not shown) lie approximately midway between these. Thick lines indicate connections closer to the viewer. (*b*) Portion of the octadecasil framework showing the four D4R units surrounding each T-2 silicon. T-1 silicons are connected to three other T-1 sites in the same D4R unit and to one T-2 silicon. Fluoride anions, which lie at the center of approximately 90% of the D4R units, are 2.63 Å from each T-1 silicon and 5.69 Å from the nearest T-2 silicon. The distance between fluoride anions in adjacent D4R units is 9.33 Å.

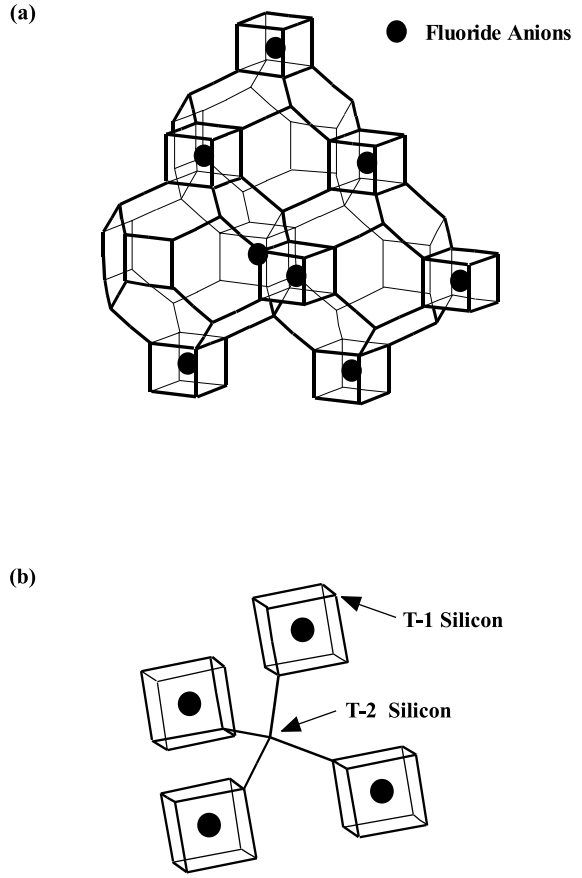

mately 250 mg of sample was packed in a 7 mm diameter rotor and spinning speeds in the range of 2.0–4.2 kHz were used. The ^{19}F r.f. field was generated by amplifying a frequency-tripled 125.48 MHz signal. In some cases external attenuators were necessary to attain the r.f. powers needed to observe the different matching conditions. The reflected power was monitored on both channels throughout the experiments to ensure the probe remained matched and tuned. The experimental data were integrated to determine peak areas and nonlinear least-squares fitting was performed as described below.

Programs were written using Mathematica software (46) to simulate the *IS* spin behaviour in terms of both numerical integration and Bessel functions, the latter being much more efficient. In the actual functions used to fit the data, a scaling factor (which was optimized during the fitting) was used to match the theoretical and experimental intensities. Initial visual fitting was done to find suitable starting values for the various parameters, and in some cases, it was necessary to hold one or more parameters constant to ensure convergence.

Results and discussion

Structure of octadecasil

Figure 1(*a*) shows the structure of completely siliceous octadecasil, as determined by single crystal X-ray diffraction (45). The framework can be built by linking octadecahedral [$4^6 6^{12}$] cages through all their common six-membered ring faces. Since these octadecahedral cages do not completely fill three-dimensional space, another type of void, the very small [4^6]-cage or double four-membered ring (D4R) unit, is created. When prepared from a fluoride-containing medium, the product crystallizes in a tetragonal phase (space group *I*4/*m*, no. 87), with the quaternary ammonium templating cation (quinuclidinium in this case) in the large cages, and the fluoride ion in the D4R units. The fluoride ion is needed to balance the positive charge of the organic cation. The octadecasil framework contains two types of T-sites: the vertices of the D4R units (designated as T-1), and the vertices that are shared by four six-rings (T-2 sites). Each T-2 Si is connected to T-1 silicons from four different D4R units (Fig. 1(*b*)). These sites occur in the ratio 4 T-1:1 T-2, which means there are 16 T-1 and 4 T-2 sites per unit cell. Elemental analysis indicates that ca. 90% of the D4R units contain a fluoride ion. From the X-ray crystal structure data, the T-1 silicons are 2.63 Å from the fluoride ion inside their D4R unit and more than 7 Å from the fluoride ions in the adjacent D4R units. The T-2 silicons are 5.69 Å from (up to) four equivalent fluoride ions, and the closest F—F distance is 9.33 Å. Because of the distances involved and the low natural abundance of ^{29}Si (4.8%), the ^{19}F/^{29}Si interactions for the T-1 silicons approximate well the case of isolated spin pairs.

The quantitative ^{29}Si MAS NMR spectrum shows two sharp resonances as expected from the structure (Fig. 2), and based on their relative intensities, these can be unambiguously assigned as indicated. For a non-spinning sample, a symmetrical, featureless peak with a full width at half-height of 6200 Hz is observed. The ^{19}F MAS NMR spectrum (not shown) consists of a single sharp resonance at –38.2 ppm with respect to $CFCl_3$, which is consistent with its location within the D4R unit in the structure (44, 45, 47).

Hartmann–Hahn matching profiles

For spin-1/2 nuclei, efficient *I*–*S* magnetization transfer occurs in a stationary sample when the standard Hartmann–Hahn matching condition (29) (eq. [3]) is fulfilled (31).

$$[3] \qquad \omega_{1I} = \omega_{1S}$$

Here $\omega_{1I} = -\gamma_I B_{1I}$, $\omega_{1S} = -\gamma_S B_{1S}$, and B_{1I}, B_{1S} are the radio frequency fields applied to the *I* and *S* spins, respectively. However, when MAS is used, Stejskal et al. (27) showed that under certain conditions, the matching condition centered at $\omega_{1I} = \omega_{1S}$ splits into narrow sideband matching conditions $\omega_{1I} = \omega_{1S} + n\omega_r$ (n = 0, ±1, ±2, ±3,...) separated by the rotation frequency ω_r. These sideband matching conditions will appear whenever the MAS frequency is comparable to, or exceeds, the width of the abundant *I* spin

© 1999 NRC Canada

Fig. 2. Quantitative ^{29}Si MAS NMR spectrum of octadecasil showing the two resonances assigned to the T-1 and T-2 silicons, respectively. The relative peak intensities (4:1) are as expected from the crystal structure. The spectrum was acquired using 48 scans, a spinning speed of 2.2 kHz, pulse width of 8 μs, and a 110 s relaxation delay. No ^{1}H or ^{19}F decoupling was used.

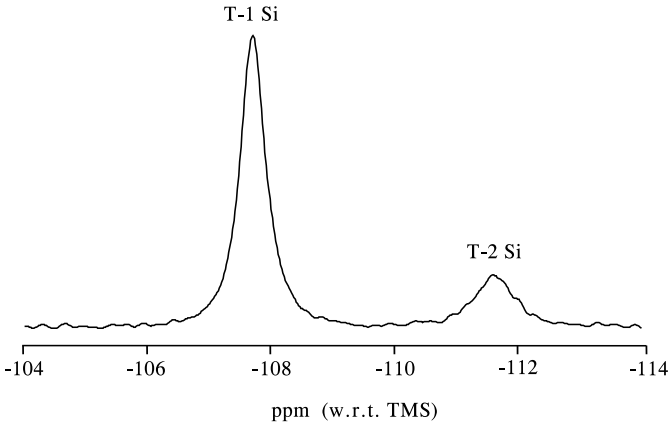

resonance and the heteronuclear dipolar coupling frequencies (27, 37, 48). If the MAS frequency is slow compared to the homogeneous line width of the abundant *I* spins, sample spinning does not significantly influence the polarization transfer obtained by Hartmann–Hahn cross polarization (HHCP) (27, 48).

For systems of isolated *IS* spin pairs spinning sufficiently rapidly to reach the fast MAS regime ($\omega_r/2\pi >> D$), Hediger et al. (41) has shown that for HHCP between spin-1/2 nuclei, the matching condition splits into only four sideband matching conditions described by eq. [4].

$$[4] \qquad \omega_{1I} = \omega_{1S} + f\omega_r, \qquad f = \pm 1 \text{ or } \pm 2$$

An identical result was derived by Marks and Vega (49). These sidebands arise because MAS modulates the dipolar interactions by ω_r and $2\omega_r$ (eq. [2]) (27). No polarization transfer is expected at the centerband position ($f = 0$), although this is sometimes observed due to flip-flop processes between remote *I* spins (27, 50), and due to polarization transfer through heteronuclear scalar (*J*) coupling (48, 51). This effect had been previously observed by Schaefer et al. (37) in their double cross polarization experiment on ^{13}C-^{15}N labelled glycine and asparagine.

Figure 3 shows the matching profiles obtained for a powder sample of octadecasil using ^{19}F–^{29}Si Hartmann–Hahn CP. These profiles were determined by measuring the peak area(s) in the ^{29}Si NMR spectra as a function of the ^{29}Si r.f. field strength, with the contact time and ^{19}F field strength held constant. For non-spinning samples, a single match condition was found (Fig. 3(*a*)) that corresponded to the exact Hartmann–Hahn condition (eq. [3]) as expected. Under MAS almost no polarization transfer was observed at the exact Hartmann–Hahn match, but up to four other matching conditions separated by integral multiples of the spinning speed were found, as expected (Figs. 3(*b*, *c*)). For the highest spinning speeds used the available ^{29}Si r.f. power was not sufficient to observe all four matching conditions. The

Fig. 3. Hartmann–Hahn ^{19}F–^{29}Si CP matching profiles for the two T-sites in octadecasil: (*a*) non-spinning sample, (*b*) 3.37 kHz MAS, and (*c*) 4.15 kHz MAS. The ^{19}F r.f. field strength was 17 kHz, and contact times of 2 ms and 10 ms were used for the static and MAS experiments, respectively. For the MAS experiments, the sideband matching conditions, *f*, are also indicated.

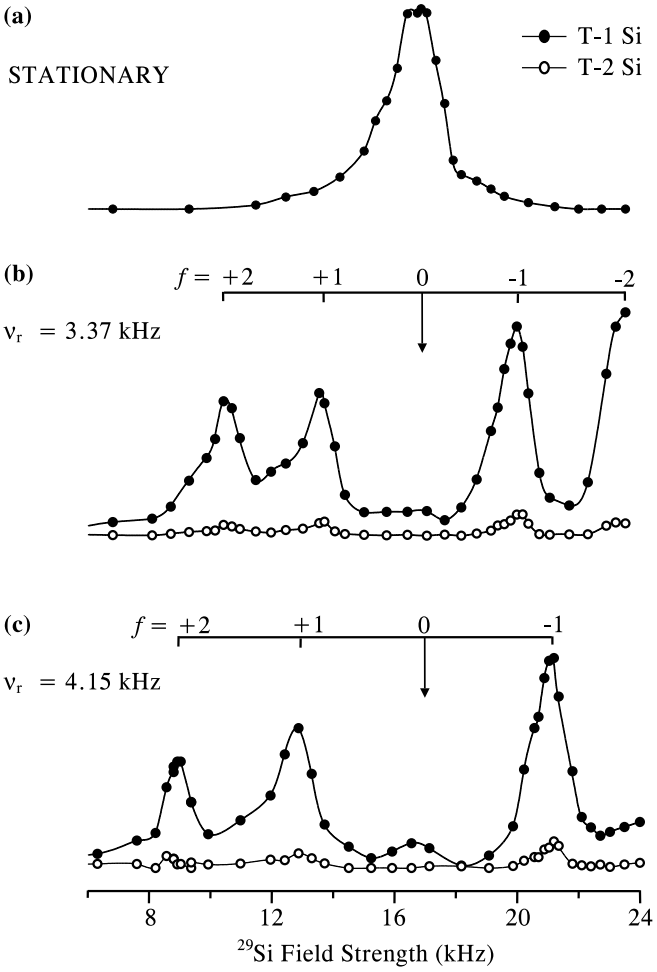

matching profiles for the T-2 Si seem to mimic the behaviour seen for the T-1 Si (Figs. 3(*b*, *c*)), however the signal to noise ratio for the T-2 Si was quite poor at the 10 ms contact time employed.

According to several authors (27, 52, 53), the relative intensities of the peaks in the Hartmann–Hahn matching profile should be symmetrical about the center-matching condition, $\omega_{1I} = \omega_{1S}$. However, Hartmann–Hahn matching profiles reported in the literature rarely show this, and in the present case, a very non-symmetrical profile was observed (Fig. 3). Although some of this asymmetry could perhaps arise from experimental artifacts (for example, the behaviour of the NMR probe, filters, attenuators and amplifiers used), Ding and McDowell (50, 54) have attributed this effect to the magnitude of the applied r.f. fields. They report that the cross relaxation rate has a direct dependence on the product of the r.f. amplitudes of the spin locking fields on both the *I* and *S* nuclei, and the magnitude of this factor will therefore change because the strength of one of the r.f. fields is varied.

© 1999 NRC Canada

Table 1. Functions describing HHCP behaviour for isolated *IS* spin pairs in powder samples at various matching conditions.[a]

Matching condition	Function	Exact integral	In terms of Bessel functions
Stationary sample	$g_0(\tau)$	$\frac{1}{2}\int_0^{\pi}\cos[\pi D\tau(3\cos^2\beta-1)]\sin\beta\,d\beta$	$\cos\left(\frac{\pi D\tau}{2}\right)J_0\left(\frac{3\pi D\tau}{2}\right) - 2\sum_{k=1}^{\infty}\left[\frac{1}{(4k^2-1)}J_k\left(\frac{3\pi D\tau}{2}\right)\cos\left(\frac{\pi D\tau}{2}+\frac{k\pi}{2}\right)\right]$
MAS $f = \pm 1$	$g_{\pm1}(\tau)$	$\frac{1}{2}\int_0^{\pi}\cos\left[\frac{\pi D\tau}{\sqrt{2}}\sin 2\beta\right]\sin\beta\,d\beta$	$J_0\left(\frac{\pi D\tau}{\sqrt{2}}\right)+2\sum_{k=1}^{\infty}\left[\frac{1}{(1-4(2k)^2)}J_{2k}\left(\frac{\pi D\tau}{\sqrt{2}}\right)\right]$
MAS $f = \pm 2$	$g_{\pm2}(\tau)$	$\frac{1}{2}\int_0^{\pi}\cos\left[\frac{\pi D\tau}{2}\sin^2\beta\right]\sin\beta\,d\beta$	$\cos\left(\frac{\pi D\tau}{2}\right)J_0\left(\frac{\pi D\tau}{2}\right) - 2\sum_{k=1}^{\infty}\left[\frac{(-1)^k}{(1-4k^2)}J_k\left(\frac{\pi D\tau}{2}\right)\cos\left(\frac{\pi D\tau}{2}+\frac{k\pi}{2}\right)\right]$

[a] D in Hz, τ is the contact time in seconds, k is an integer.

In the present case, it was the ^{29}Si field strength that was varied, and the intensity of the matching conditions increased with increasing r.f. field strengths.

Although the spinning speeds employed were only about three times greater than the largest ^{19}F–^{29}Si dipolar coupling calculated from the crystal structure (1230 Hz for the T-1 Si), the matching profiles indicate that ^{29}Si nuclei in both T-sites are behaving as isolated I_NS spin systems to a good approximation. This is in agreement with the previous REDOR and TEDOR experiments (16). The small amount of polarization transfer observed at the centerband ($f = 0$) matching condition may be due to flip-flop processes between remote ^{19}F spins or polarization transfer mediated through heteronuclear *J*-coupling.

Theoretical Hartmann–Hahn cross polarization behaviour for powder samples

In their investigation of the ^{1}H–^{13}C polarization transfer in a stationary single crystal of ferrocene, Müller et al. (34) showed that the oscillatory behaviour of the ^{13}C magnetization M as a function of the contact time τ could be described by

$$[5]\qquad M(\tau) = M_0\,[1 - 0.5\exp(-k_1\tau)\cos[0.25D(1 - 3\cos^2\theta)\tau] - 0.5\exp(-k_2\tau)]$$

where M_0 is the equilibrium I spin magnetization obtained by a single $\pi/2$ pulse, k_1 and k_2 are first-order rate constants that describe the decay of the transient oscillation and the increase in the net magnetization respectively, and θ is the angle between the *I–S* internuclear vector and the magnetic field direction vector. In eq. [5] the effects of decay due to spin lattice relaxation of the *I* spins in the rotating frame are assumed to be negligible (i.e., $T_{1\rho} \rightarrow \infty$). Müller et al. assumed that the spin system could be described by a Hamiltonian limited to the strongly coupled *IS* spin pair, with the effect of more remote *I* spins represented by an isotropic random-field spin–diffusion relaxation mechanism. These authors also set $k_1 = 3k_2/2$, but Hediger (23) has since shown that these rate constants are better treated as independent variables in order to fit the behaviour at longer contact times. Equation [5] is only valid if the rate constant describing the *I* spin diffusion is smaller than the heteronuclear couplings. If this is not the case then the spin system will be dominated by homonuclear interactions and no transient oscillations will be seen (23).

Hediger (23) has reported that, considering the *S* spin quasi-equilibrium polarization at long times ($\langle S_z\rangle_{qe}$), eq. [5] can be extended to the case of a stationary powder sample by including the effect of the individual crystallites' orientations. This yields eq. [6]

$$[6]\qquad \langle Sz\rangle(\tau) = \omega_{0I}\left\{0.5[1-\exp(-k_1\tau)g_0(\tau)] + \left[\frac{\langle S_z\rangle_{qe}}{\omega_{0I}} - 0.5\right][1-\exp(-k_2\tau)]\right\}$$

Here $\langle S_z\rangle(\tau)$ is the expectation value of the polarization on the *S* spin, ω_{0I} is Larmor frequency of the *I* spins, and $\langle S_z\rangle_{qe}$ is defined by eq. [7] (23).

$$[7]\qquad \langle S_z\rangle_{qe} = N\omega_{0I}/(N+1)$$

For truly isolated *IS* spin pair, $N = 1$, and thus $\langle S_z\rangle_{qe} = \omega_{0I}/2$, which means that half of the initial polarization on the *I* spin is transferred to the *S* spin, and that there is no spin diffusion with remote *I* spins (i.e., no k_2 term). However in a "real" isolated spin system where there is a strongly coupled *IS* spin pair and *N*-1 remote (weakly coupled) *I* spins, $\langle S_z\rangle_{qe}$ can have values between $\omega_{0I}/2$ (ideal two-spin system, no k_2) and ω_{0I} (*N* large; as assumed by Müller et al. in the derivation of eq. [6]).

The function $g_0(\tau)$ in eq. [6] that describes the oscillatory behaviour of the polarization as it shuttles between the *I* and *S* spin is given in Table 1 and corresponds to the calculation of *D* averaged for a powder. This powder average normally involves integration over two angles (α and β) (1), however in this case (isolated spin pairs), it is only necessary to integrate over a single angle (β) because it is not possible to detect the phase of the dipolar coupling (S. Hediger, personal communication, 1997).

Assuming that the decay is dominated by $T_{1\rho}$ relaxation of either the *I* or *S* spins, the effect of $T_{1\rho}$ relaxation can be incorporated (26) in eq. [6], giving

© 1999 NRC Canada

$$[8]\qquad \langle S_z\rangle(\tau) = \omega_{0I}\left\{0.5[\exp(-\tau / T_{1\rho}) - \exp(-k_1\tau)g_0(\tau)] + \left[\frac{\langle S_z\rangle_{qe}}{\omega_{0I}} - 0.5\right][\exp(-\tau / T_{1\rho}) - \exp(-k_2\tau)]\right\}$$

Hediger also derived equations that describe the HHCP behaviour of isolated spin-1/2, *IS* spin pairs under MAS conditions. In the high-speed limit ($\omega_r/2\pi >> D$), eq. [8] can be extended to the case of a powder undergoing MAS by replacing the oscillatory term $g_0(\tau)$ with the appropriate function $g_f(\tau)$ to yield eq. [9] (23).

$$[9]\qquad \langle S_z\rangle(\tau) = \omega_{0I}\left\{0.5[\exp(-\tau / T_{1\rho}) - \exp(-k_1\tau)g_f(\tau)] + \left[\frac{\langle S_z\rangle_{qe}}{\omega_{0I}} - 0.5\right][\exp(-\tau / T_{1\rho}) - \exp(-k_2\tau)]\right\}$$

The evolution of the spin system will be different at the $|f| = 1$ and $|f| = 2$ matching conditions, but identical when $f = 1$ or –1, and when $f = 2$ or –2. The two functions $g_f(\tau)$ (23) that describe the oscillation of the polarization between the *I* and *S* spins at the four MAS matching conditions described by eq. [4] are given in Table 1. These functions incorporate the effects of MAS on the dipolar coupling and the averaging of the *I*–*S* internuclear vectors over the crystallite orientations in a powder sample.

The functions $g_0(\tau)$ and $g_f(\tau)$ may be evaluated using numerical integration but this can be computationally intensive. However, using the general methodology reported by Mueller (5), it is possible to re-express these integrals in terms of Bessel functions of the first kind. These functions were derived and are given in Table 1. The function for the non-spinning sample is has the same form as that reported previously for the SEDOR experiment, (5) and that for the $f = \pm 1$ MAS matching condition corresponds to that reported for the Double Cross Polarization experiment by Vogt et al. (55) although the arguments are different due to the different nature of the experiments. To our knowledge, the equation describing the HHCP behavior at $f = \pm 2$ MAS matching condition in terms of Bessel functions has not been presented elsewhere. When expressed in this form, nonlinear least-squares fitting of the experimental data using eqs. [8] and [9] becomes much more efficient.

Variable contact time experiments on stationary samples

Figure 4 shows the area of the ^{29}Si resonance for a stationary sample as a function of the contact time. At short contact times a clear oscillatory behavior is seen, which is progressively damped at longer times. A slight upward trend is also apparent with increasing contact time. Although this resonance includes signals from both of the T-1 and T-2 silicons, the contribution to the total area from the T-2 silicons is expected to be small enough to neglect. In fact, for contact times up to 10 ms under MAS conditions (where the two T-sites are well resolved), the T-2 signal intensity is less than 10% that of the T-1 Si (Fig. 5). This is about the same as the uncertainty in the peak area determined by integration for the stationary sample, and on this basis, the analysis and fitting of the data in terms of only the T-1 silicons is considered valid. Note that efficient (and maximum) polarization transfer is obtained using a relatively short contact time (ca. 0.5 ms). Significant decay due to $T_{1\rho}$ relaxation effects was observed at long contact times as can be seen in Fig. 5.

Fig. 4. ^{19}F–^{29}Si CP behaviour for the T-1 Si in a stationary octadecasil (powder) sample as a function of the contact time. The line shows the fit calculated using eq. [8] with D = 1440 Hz, $\langle S_z\rangle_{eq}/\omega_{0I}$ = 0.9, k_1^{-1} = 2.2 ms, k_2^{-1} = 25.5 ms, and $T_{1\rho}$ = 2 s. The ^{19}F r.f. field strength was 17 kHz.

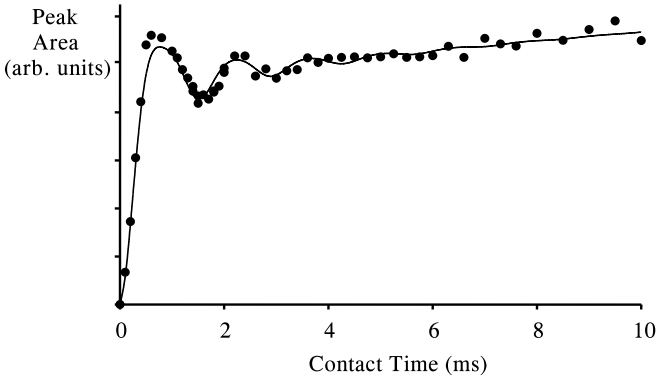

The increase in the signal amplitude as the contact time was increased up to 10 ms indicates that there is additional polarization transfer from other, more distant ^{19}F nuclei, and therefore, the spin system cannot be considered as a *completely* isolated spin pair. This implies that $\langle S_z\rangle_{qe}/\omega_{0I}$ must be greater than 0.5. However, $\langle S_z\rangle_{qe}$ and k_2 are strongly correlated (eq. [8]). For this reason the value of $\langle S_z\rangle_{qe}/\omega_{0I}$ was held constant in order to ensure reliable fitting between different data sets. From the X-ray structure of octadecasil, it was determined that there are (up to) eight fluoride ions within a 12 Å-radius sphere surrounding a T-1 silicon (corresponding to ^{19}F–^{29}Si dipolar couplings >15 Hz). Using eq. [7], and taking into consideration the statistical occupancy of the D4Rs (ca. 90%), a value of 0.9 was found for $\langle S_z\rangle_{qe}/\omega_{0I}$.

The ^{19}F–^{29}Si dipolar coupling was determined by fitting the experimental data to eq. [8] using the procedure described above. The best fit was obtained with k_1^{-1} = 2.2 ms, k_2^{-1} = 25.5 ms, and $T_{1\rho}$ = 2 s. The actual values of these parameters do not affect the dipolar coupling since this is defined by the period of the oscillations. Once suitable values for these five parameters were found, nonlinear least-squares regression gave D = 1440 Hz, corresponding to a Si—F distance of 2.49 Å (eq. [1]), which is slightly shorter than the 2.63 Å determined from X-ray diffraction. The resulting theoretical curve calculated using these values is overlaid on the experimental data in Fig. 4 and is in quite good agreement. The largest discrepancies occur at contact times up to 1 ms, and are attributed to the slight variation (decrease) in the output of the ^{19}F amplifier power with increasing contact time. In this case the Hartmann–Hahn match had been optimized for a 2 ms contact time. It is interesting to note that it

© 1999 NRC Canada

Fig. 5. ^{19}F–^{29}Si CP behaviour for the two T-sites in octadecasil under MAS conditions as a function of the contact time at the $f = -1$ sideband matching condition. The oscillatory behaviour for the T-1 Si and the decay due to $T_{1\rho}$ are clearly seen. The theoretical fit calculated using eq. [9] for the T-1 Si with D = 1360 Hz is also shown.

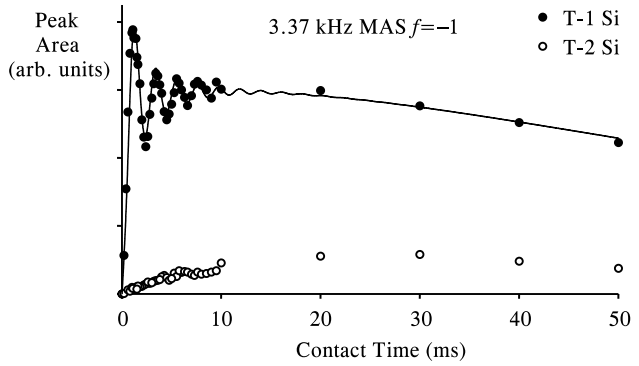

Fig. 6. ^{19}F–^{29}Si CP behaviour for the T-1 Si in octadecasil at the $|f| = 1$ sideband matching conditions under various MAS speeds. Curves calculated using eq. [9] with D = 1340 Hz (ν_r = 3.37 kHz, $f = -1$), D = 1380 Hz (ν_r = 3.37 kHz, $f = +1$), and D = 1360 Hz (ν_r = 4.66 kHz, $f = -1$) are overlaid. The intensities have been arbitrarily scaled to separate the curves.

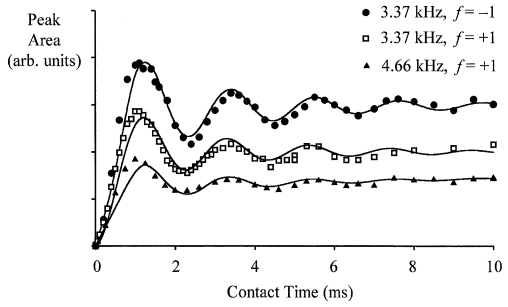

was possible to determine this distance although there was no obvious dipolar structure in the ^{29}Si spectrum of the stationary sample. The slightly larger dipolar coupling found from fitting of the experimental data may reflect the contribution from fluoride ions in other D4R's, and to a lesser extent the T-2 intensity.

MAS experiments at the $f = \pm1$ and $f = \pm2$ sideband matching conditions

Under MAS conditions, the transient oscillations became significantly more pronounced than for the stationary sample as can be seen by a comparison of Figs. 4–7. The oscillatory behaviour at the $f = +1$ sideband matching condition should be identical to that observed when the $f = -1$ match is used, and the period should be independent of the spinning speed. As seen in Fig. 6, the periodicity of the transient oscillations observed for the T-1 silicons is very similar at equivalent sideband matching conditions and different spinning speeds, in good agreement with the theoretical predictions.

Fitting of the experimental data to eq. [9] (expressed in terms of Bessel functions) was done as described for the non-spinning data. Because the oscillations are quite clearly defined at contact times of up to 8–10 ms, more periods of the oscillations are available to check the goodness of fit for given dipolar couplings, which reduces the uncertainty in the final D values. The reduction in the rate of damping of the oscillatory behavior with increasing spinning speed (and the corresponding increase in the values of k_1 used in the fitting) is as anticipated: at higher spinning speeds the effects of the relatively weak ^{19}F–^{19}F interactions are progressively "spun out."

Values of the parameters determined from the fittings were $T_{1\rho}$ = 70–400 ms, k_1^{-1} = 3.5–6 ms, and k_2^{-1} = 20–80 ms with $\langle S_z \rangle_{qe}/\omega_{0I}$ fixed at 0.9. In Figs. 5 and 6 the data from three experiments are presented with the theoretical curves determined from the nonlinear regression analyses. Because of the hardware limitations, the CP matching conditions were optimized using a 10 ms contact time to ensure that good matching was maintained over the period of the oscillations and also at the longer contact times (50–60 ms) required to observe the effects of $T_{1\rho}$ decay. This compromise results in a poor fit to the data acquired at very short (<1 ms) contact times, but does not affect the distance determination from fitting of the oscillatory behaviour. The dipolar couplings determined from fits to seven experimental data sets acquired at the $f = +1$ and -1 matching conditions range from D = 1330 to 1400 Hz with a mean of 1360 Hz and estimated standard deviation of 50 Hz. This corresponds to a Si—F distance of 2.54 (0.03) Å, which is slightly shorter than the distance determined from X-ray diffraction.

The oscillatory behaviour at the $f = +2$ and -2 sideband matching conditions should have a longer period compared to those observed at the $f = \pm1$ matches, exactly as was observed in the experimental data acquired for the T-1 Si under MAS conditions with appropriately adjusted r.f. field strengths. Fitting of the data to eq. [9] with the appropriate function $g_f(\tau)$ was carried out as described above and similar values of the various parameters were found. Experimental data obtained for the T-1 Si at the $f = +2$ matching condition for a spinning speed of 4.15 kHz are shown in Fig. 7 together with the curve calculated using the parameters listed in the caption. As previously, the matching was optimized for the time period in which the oscillatory behaviour is observed at the expense to the goodness of fit to the initial part of the curve. At the $f = +2$ matching condition only two periods of the oscillation were observed up to a contact time of 10 ms compared with the three to four seen when $f = \pm1$ (Figs. 5, 6). For this reason the uncertainty in the dipolar couplings is increased somewhat compared to those obtained from data acquired at the $f = \pm1$ matching conditions, and is closer to that determined from the stationary sample data.

The CP behavior observed for the T-2 Si at the $f = -1$ sideband matching condition is shown in Fig. 5. Similar behavior was observed at the other MAS matching conditions. No clear (reproducible) oscillatory behavior was seen for these silicons. For the T-2 silicons, a Si—F distance of 5.69 Å was calculated from the X-ray structure. However, depending on the exact occupancy of the D4R units, there can be up to four fluoride anions in a (partial) tetrahedral arrangement around each T-2 Si (and thus equidistant from it). This represents a much more complicated case than for the T-1 silicons because the experiment no longer involves isolated ^{19}F–^{29}Si spin pairs. Assuming a binomial distribution with 90% occupancy of each D4R unit by a fluoride ion, the probabilities that four, three, two, one, or none of the D4R

© 1999 NRC Canada

Table 2. ^{19}F–^{29}Si dipolar couplings and interatomic distances in octadecasil determined using various methods.

T-site	Parameter[a]	CP[a,b]	REDOR[a,b]	TEDOR[a,b]	XRD[b,c]
T-1	*D* (Hz)	1380 (80)	1150 (50)	1130 (50)	1230 (5)
	r (Å)	2.53 (0.04)	2.69 (0.04)	2.70 (0.04)	2.632 (0.003)
T-2	*D* (Hz)	n.d.[d]	120 (20)[e,f]	120 (20)[e,f]	122 (5)
	r (Å)	n.d.[d]	5.7 (0.4)[e,f]	5.7 (0.4)[e,f]	5.688 (0.003)

[a]Dipolar couplings (*D*) determined from nonlinear least-squares fitting of experimental data and internuclear distances (*r*) calculated from these.

[b]Standard deviations given in parentheses.

[c]Distances determined from the single crystal X-ray data of Caullet et al. (45) and *D* calculated from these.

[d]Not determined.

[e]*D* determined from visual fitting of experimental data and *r* calculated from this.

[f]Standard deviation estimated from visual fitting.

Fig. 7. ^{19}F–^{29}Si CP MAS behaviour for the T-1 Si in octadecasil at the $f = +2$ sideband matching condition. The line shows the fit calculated using eq. [9] with $D = 1400$ Hz, $\langle S_z \rangle_{eq}/\omega_{0I} = 0.9$, $k_1^{-1} = 6$ ms, $k_2^{-1} = 13$ ms, and $T_{1\rho} = 125$ ms. The spinning speed was 4.15 kHz and the ^{19}F r.f. field strength was 17 kHz.

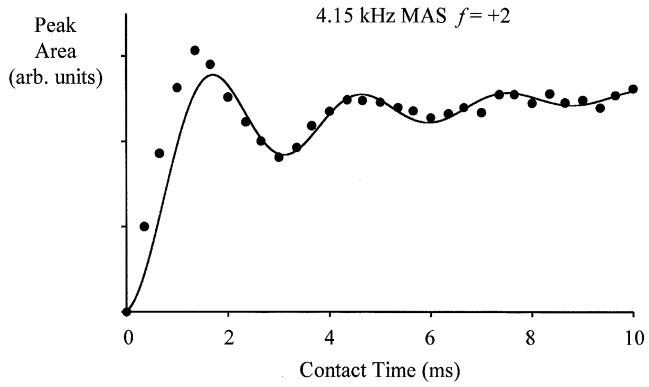

units surrounding a given T-2 Si are occupied are 0.6561, 0.2916, 0.0486, 0.0036, and 0.0001, respectively (16).

Oscillatory HHCP behavior has been observed previously in a few systems, which most probably contain I_NS spin systems with $N \leq 4$ (24, 26, 40). The (apparent) lack of oscillations in the T-2 CP data as a function of contact time may be a consequence of the significantly lower signal-to-noise ratio for this peak, but may also result from "destructive interference" of the oscillations expected for the I_NS spin systems (N = 1–4). Fitting of T-2 data was not attempted.

In light of the analysis presented by Vogt et al. (55) the application of non linear least-squares fitting succeeds in the present case as a result of the high signal-to-noise ratio in the experimental data, which means that the oscillations are very clearly defined. In cases where the data are not of such high quality, the use of an alternative approaches (such as the Tikhonov regularization method) may permit the dipolar couplings, and subsequently the internuclear distances, to be determined (55).

Comparison with distance determinations from other NMR techniques

The average of the dipolar couplings determined from fitting of the CP data at the five possible matching conditions (stationary and MAS) for the T-1 Si is given in Table 2 together with the Si—F distances determined from REDOR, TEDOR, and X-ray diffraction experiments. Comparison of these data reveals that, for isolated spin pairs, analyses of variable contact time HHCP experiments can yield heteroatomic distances almost as reliable and accurate as REDOR and TEDOR experiments provided clear oscillatory behaviour is observed. In general, REDOR and TEDOR will be affected by the finite pulse lengths, r.f. field inhomogeneities, and variations in the spinning speed, all of which will reduce the efficiency of the evolution of the dipolar dephasing, and yield a smaller dipolar coupling and larger distances. Cross polarization experiments are less affected by the rotor period related effects, and as expected give shorter distances than REDOR and TEDOR (Table 2). Compared to the X-ray diffraction distance, *r* measured from CP experiments is somewhat shorter. This is probably due to the $1/r^3$ based averaging over motions of the fluoride ion for the CP measurements whereas diffraction uses a simple unweighted averaging, placing the fluoride ion at the center of the D4R units (45). It is expected that the motions of the fluoride ion will be larger than, for example, covalent bond vibrations.

The choice of the most appropriate experiment in a given situation will depend on a number of factors. The relaxation characteristics of the nuclei are important parameters that should be carefully considered. All three NMR techniques are affected by the T_1 value of the excited nuclei. In addition, CP will be limited by very short $T_{1\rho}$ values, REDOR by the *S* spin T_2 value, and TEDOR by the T_2 values of both *I* and *S* spins. In cases where there are a number of different *S* spins and more than one *I* spin, but still isolated *IS* pairs, CP and TEDOR will be preferred over REDOR as they can easily be extended to multidimensional experiments because they involve *I* to *S* coherence transfer (19, 56). Furthermore, because TEDOR and CP involve polarization transfer, only signals from *S* spins coupled to *I* spins are observed, and there is no need to acquire two experiments per data point to achieve normalization as is the case for REDOR experiments.

Hardware considerations are also important; CP is demanding in terms of r.f. stability, particularly if relatively small dipolar couplings are being measured since relatively long contact times will be necessary. All three techniques are sensitive to variations in the spinning speed during the experiment. Changes in the spinning speed will cause mismatching of the r.f. field strengths during the HHCP experiment, which will directly affect the efficiency of the polarisation transfer. For REDOR and TEDOR, the r.f. pulses will no longer be rotor-synchronized, and as a conse-

© 1999 NRC Canada

quence, the dephasing observed will be smaller than it should be. At very high MAS speeds REDOR and TEDOR experiments are not feasible due to finite pulse lengths (10, 57), however, several variations of the CP experiment have been developed that are less sensitive to the matching conditions and are still applicable under these conditions (40, 41, 48, 58–61).

The amplitude of the oscillations in the HHCP experiments is larger than for REDOR and TEDOR, which in principle allows the dipolar coupling to be measured more reliably from fitting of the experimental data. In general HHCP experiments to determine *I–S* distances in spin pairs will be best when done at the $f = \pm 1$ matching conditions under MAS for three reasons. Firstly, greatly improved spectral resolution may be achieved using MAS. Secondly, the intensity of the signal should be greater at the $f = \pm 1$ matching conditions than at $f = \pm 2$. Thirdly, the higher frequency of the oscillations compared to that for stationary samples and at $f = \pm 2$ (which should permit more periods to be observed and thus increase the reliability of the dipolar coupling determination).

For the T-2 silicon in octadecasil, the curves calculated assuming the correct statistical occupancy and spatial arrangement of the ^{19}F spins fit multi-spin TEDOR and REDOR data well (see Table 2) (16, 62). And although it is possible to calculate the CP behavior for small spin clusters (63) as can be done for REDOR and TEDOR (6, 62, 64), such calculations require the explicit knowledge of the number of spins as well as the geometry of the spin system. This is information that will usually not be known a priori and without this, distance determinations in multiple spin systems will not be possible. Recently Gullion and Pennington (65) reported a modified REDOR experiment, θ-REDOR. In theory, this technique allows the behaviour for I_NS spin systems to be separated into a linear combination of two-spin *I–S* systems. θ-REDOR may thus provide a possible solution to the problem of determining heteronuclear distances in multiple-spin systems. At present it is very difficult to extract this information from analysis of CP data.

Conclusions

The present work demonstrates that accurate heteronuclear distances (which are in good agreement with those obtained from X-ray diffraction) can be measured in the solid state from cross polarization NMR experiments on spin-1/2 nuclei. These measurements were successfully carried out for stationary powder samples and also under MAS conditions. Previously, the only reliable CP distance determinations reported for powder samples undergoing MAS were average distances (23, 24, 26). Expressions describing the HHCP behaviour for both non-spinning and MAS conditions were derived in terms of Bessel functions. These equations permit efficient nonlinear least-squares regression analysis of experimental data, and allow the *I–S* dipolar couplings and distances to be determined.

The choice of which dipolar-based heteronuclear distance determination technique (CP, REDOR, or TEDOR) is most appropriate for a given sample requires consideration of the relative magnitudes of the various nuclear relaxation parameters (T_1, T_2, and $T_{1\rho}$) in addition to the performance (and limitations) of the available NMR hardware. As for REDOR and TEDOR, the distances obtained from fitting of the oscillatory CP behavior are only reliable if the spin system under investigation can be considered (or closely approximates) an *isolated IS* spin pair. Verification that this is indeed the case must come from independent sources (e.g., samples prepared with specific isotopic labelling, or physical dilution in unlabelled compound, etc.) as the presence of oscillations in CP, REDOR, or TEDOR data does not by itself prove that this situation exists.

Acknowledgements

C.A.F. acknowledges the financial support of the Natural Sciences and Engineering Research Council of Canada (NSERC) in the form of operating and equipment grants. J.-M.C. thanks the fondation pour l'Ecole de Chimie de Mulhouse for financial support. The authors are grateful to Dr. P. Caullet, Laboratoire de Matériaux Minéraux, Ecole Nationale de Supérieure de Chimie de Mulhouse, France, for kindly providing the sample of octadecasil used in this work, and to Mr. T. Markus for invaluable assistance with probe and spectrometer electronics. Dr. S. Hediger is thanked for providing a copy of her excellent thesis, and for helpful discussions.

References

1. T. Gullion and J. Schaefer. Adv. Magn. Reson. **13**, 57 (1989).
2. Y. Pan, T. Gullion, and J. Schaefer. J. Magn. Reson. **90**, 330 (1990).
3. A.W. Hing, S. Vega, and J. Schaefer. J. Magn. Reson. **96**, 205 (1992).
4. A.W. Hing, S. Vega, and J. Schaefer. J. Magn. Reson. Ser. A, **103**, 151 (1993).
5. K.T. Mueller. J. Magn. Reson. Ser. A, **113**, 81 (1995).
6. A. Naito, K. Nishimura, S. Tuzi, and H. Saitô. Chem. Phys. Lett. **229**, 506 (1994).
7. L.M. McDowell, D. Barkan, G.E. Wilson, and J. Schaefer. Solid State Nucl. Magn. Reson. **7**, 203 (1996).
8. K.T. Mueller, T.P. Jarvie, D.J. Aurentz, and B.W. Roberts. Chem. Phys. Lett. **242**, 535 (1995).
9. K.T. Mueller, T.P. Jarvie, D.J. Aurentz, and B.W. Roberts. Chem. Phys. Lett. **254**, 281 (1996).
10. A. Naito, K. Nishimura, S. Kimura, S. Tuzi, M. Aida, N. Yasuoka, and H. Saitô. J. Phys. Chem. **100**, 14995 (1996).
11. S.M. Holl, G.R. Marshall, D.D. Beusen, K. Kociolek, A.S. Redlinski, M.T. Leplawy, R.A. McKay, S. Vega, and J. Schaefer. J. Am. Chem. Soc. **114**, 4830 (1992).
12. G.R. Marshall, D.D. Beusen, K. Kociolek, A.S. Redlinski, M.T. Leplawy, Y. Pan, and J. Schaefer. J. Am. Chem. Soc. **112**, 963 (1990).
13. S. Holl, T. Kowalewski, and J. Schaefer. Solid State Nucl. Magn. Reson. **6**, 39 (1996).
14. L.-S. Du, F. Wang, and C.P. Grey. J. Solid State Chem. **140**, 285 (1998).
15. Y. Pan. Solid State Nucl. Magn. Reson. **5**, 263 (1995).
16. C.A. Fyfe, A.R. Lewis, J.M. Chézeau, and H. Grondey. J. Am. Chem. Soc. **119**, 12210 (1997).
17. A.L. Blumenfeld and J.J. Fripiat. J. Phys. Chem. B, **101**, 6670 (1997).

© 1999 NRC Canada

18. C. Fernandez, D.P. Lang, J.P. Amoureux, and M. Pruski. J. Am. Chem. Soc. **120**, 2672 (1998).
19. C.A. Fyfe, K.C. Wong-Moon, Y. Huang, H. Grondey, and K.T. Mueller. J. Phys. Chem. **99**, 8707 (1995).
20. C.A. Fyfe, K.T. Mueller, H. Grondey, and K.C. Wong-Moon. Chem. Phys. Lett. **199**, 198 (1992).
21. C.A. Fyfe, K.T. Mueller, H. Grondey, and K.C. Wong-Moon. J. Phys. Chem. **97**, 13484 (1993).
22. P.P. Aroca. Ph.D. thesis. University of British Columbia, Vancouver. 1995.
23. S. Hediger. Ph.D. dissertation. Eidgenössische Technische Hochschule Zürich, Zürich. 1997.
24. C.H. Klein Douwel, W.E.J.R. Maas, W.S. Veeman, G.H. Werumeus Buning, and J.M.J. Vankan. Macromolecules, **23**, 406 (1990).
25. F. Tian and T.A. Cross. J. Magn. Reson. **127**, 220 (1997).
26. K.L. Walther, A. Wokaun, and A. Baiker. Mol. Phys. **71**, 769 (1990).
27. E.O. Stejskal, J. Schaefer, and J.S. Waugh. J. Magn. Reson. **28**, 105 (1977).
28. R. Voelkel. Angew. Chem. Int. Ed. Engl. **27**, 1468 (1988).
29. S.R. Hartmann and E.L. Hahn. Phys. Rev. **128**, 2042 (1962).
30. D.E. Demco, J. Tegenfeldt, and J.S. Waugh. Phys. Rev. B, **11**, 4133 (1975).
31. A. Pines, M.G. Gibby, and J.S. Waugh. J. Chem. Phys. **59**, 569 (1973).
32. M. Mehring. Principles of high-resolution NMR in solids. Springer–Verlag, Berlin. 1983.
33. E.O. Stejskal and J.D. Memory. High resolution NMR in the solid state — fundamentals of CP/MAS. Oxford University Press, New York. 1994.
34. L. Müller, A. Kumar, T. Baumann, and R.R. Ernst. Phys. Rev. Lett. **32**, 1402 (1974).
35. T.H. Walter, G.L. Turner, and E. Oldfield. J. Magn. Reson. **76**, 106 (1988).
36. R. Pratima and K.V. Ramanathan. J. Magn. Reson. Ser. A, **118**, 7 (1996).
37. J. Schaefer, E.O. Stejskal, J.R. Garbow, and R.A. McKay. J. Magn. Reson. **59**, 151 (1984).
38. G.E. Hawkes, M.D. Mantle, K.D. Sales, S. Aime, R. Gobetto, and C.J. Groombridge. J. Magn. Reson. Ser. A, **116**, 251 (1995).
39. E.W. Hagaman, P.C. Ho, L.L. Brown, F.M. Schell, and M.C. Woody. J. Am. Chem. Soc. **112**, 7445 (1990).
40. S. Hediger, B.H. Meier, and R.R. Ernst. Chem. Phys. Lett. **240**, 449 (1995).
41. S. Hediger, B.H. Meier, and R.R. Ernst. Chem. Phys. Lett. **213**, 627 (1993).
42. J.H. Shirley. Phys. Rev. B. **138**, 979 (1965).
43. S. Vega, E.T. Olejniczak, and R.G. Griffin. J. Chem. Phys. **80**, 4832 (1984).
44. L. Delmotte, M. Soulard, F. Guth, A. Sieve, A. Lopez, and J.L. Guth. Zeolites, **10**, 778 (1990).
45. P. Caullet, J.L. Guth, J. Hazm, J.M. Lamblin, and H. Gies. Eur. J. Solid State Inorg. Chem. **28**, 345 (1991).
46. S. Wolfram. The mathematica book. 3rd ed. Cambridge University Press, Cambridge. 1996.
47. H. Kessler, J. Patarin, and C. Schott-Darie. Stud. Surf. Sci. Catal. **85**, 75 (1994).
48. S. Hediger, B.H. Meier, and R.R. Ernst. J. Chem. Phys. **102**, 4000 (1995).
49. D. Marks and S. Vega. J. Magn. Reson. Ser. A, **118**, 157 (1996).
50. S. Ding, C.A. McDowell, and C. Ye. J. Magn. Reson. Ser. A, **109**, 6 (1994).
51. A. Verhoeven, R. Verel, and B.H. Meier. Chem. Phys. Lett. **266**, 465 (1997).
52. F. Engelke, T. Kind, D. Michel, M. Pruski, and B.C. Gerstein. J. Magn. Reson. **95**, 286 (1991).
53. R. Wind, S.F. Dec, H. Lock, and G.E. Maciel. J. Magn. Reson. **79**, 136 (1988).
54. S. Ding, C.A. McDowell, and C. Ye. J. Magn. Reson. Ser. A, **109**, 1 (1994).
55. F.G. Vogt, D.J. Aurentz, and K.T. Mueller. Mol. Phys. **95**, 907 (1998).
56. A.J. Vega. J. Am. Chem. Soc. **110**, 1049 (1988).
57. R. Fu, S.A. Smith, and G. Bodenhausen. Chem. Phys. Lett. **272**, 361 (1997).
58. R. Fu, P. Pelupessy, and G. Bodenhausen. Chem. Phys. Lett. **264**, 63 (1997).
59. H. Geen, J.J. Titman, and H.W. Spiess. Chem. Phys. Lett. **213**, 145 (1993).
60. X. Wu and K.W. Zilm. J. Magn. Reson. Ser. A, **104**, 154 (1993).
61. T.M. Babara and E.H. Williams. J. Magn. Reson. **99**, 439 (1992).
62. A.R. Lewis. Ph.D. thesis. University of British Columbia, Vancouver. 1998.
63. S. Ray, V. Ladizhansky, and S. Vega. J. Magn. Reson. **135**, 427 (1998).
64. J.M. Goetz and J. Schaefer. J. Magn. Reson. **127**, 147 (1997).
65. T. Gullion and C.H. Pennington. Chem. Phys. Lett. **290**, 88 (1998).

© 1999 NRC Canada

A nuclear magnetic resonance investigation of the micellar properties of a series of sodium cyclohexylalkanoates

Judith A. MacInnis, R. Palepu, and D. Gerrard Marangoni

Abstract: The micellar properties of a family of surfactants, the sodium cyclohexylalkanoates, have been investigated in aqueous solution using multinuclear NMR spectroscopy. C-13 chemical shift measurements have been used to determine both the cmc values and the micellar aggregation numbers (N_s values) of these surfactants. The cmc values and the degrees of counterion binding were estimated from ^{23}Na chemical shift measurements. The critical micelle concentrations (cmc's) and the aggregation numbers determined from the NMR experiments indicate that these amphiphiles have high cmc's and low aggregation numbers when compared to other single-headed surfactants (most notably the sodium alkanoates). The conformational changes incurred by the carbon atoms upon micelle formation have been deduced from the ^{13}C chemical shift differences ($\delta_{surf,mic} - \delta_{surf,aq}$). These results are used to discuss the formation of the aggregates of the sodium cyclohexylalkanoate surfactants as a function of the length of the alkanoate side chain.

Key words: micelles, surfactants, NMR spectroscopy, chemical shifts, aggregation numbers, degree of counterion binding, conformational changes.

Résumé : Opérant en solutions aqueuses et faisant appel à la spectroscopie RMN multinucléaire, on a étudié les propriétés micellaires d'une famille d'agents de surface, les cyclohexylalcanoates de sodium. On a utilisé des mesures de déplacement chimique du ^{13}C pour déterminer les valeurs des concentrations micellaires critiques (cmc) et les nombres d'agrégation micellaire (valeurs N_s) de ces agents de surface. Les valeurs des cmc et les degrés d'agrégation des contre-ions ont été évalués à l'aide de mesures de déplacement chimique du ^{23}Na. Les cmc et les nombres d'agrégation déterminés à l'aide de la RMN indiquent que, pour ces amphiphiles, les valeurs des cmc sont élevées et celles des nombres d'agrégation sont faibles lorsqu'on les compare à celles d'autres agents de surface à une seule tête (en particulier, les alcanoates de sodium). On a fait appel aux différences de déplacements chimiques du ^{13}C ($\delta_{surf.mic} - \delta_{surf.aq}$) pour déduire les changements conformationnels subis par les atomes de carbones lors de la formation des micelles. On utilise ces résultats pour discuter de la formation des agrégats des agents de surfaces des cyclohexylalcanoates de sodium en fonction de la longueur de la chaîne latérale alcanoate.

Mots clés : micelles, agents de surface, spectroscopie RMN, déplacements chimiques, nombres d'agrégation, degré d'agrégation du contre-ion, changements conformationnels.

[Traduit par la Rédaction]

Introduction

Surfactants (surface active agents) contain mainly a polar or ionic head group and a linear or branched hydrocarbon or fluorocarbon chain. The unusual behaviour of surfactants in solution can be attributed to the amphiphilic nature of the surfactant monomer. The polar or ionic headgroup interacts with its aqueous environment and is solvated due to dipole–dipole or ionic-dipole interactions. The nonpolar chain interacts very weakly with water resulting in the formation of ordered water molecules in the area surrounding the nonpolar chains (hydrophobic effect). This subtle interplay of attractive and repulsive forces leads to the formation of aggregates after a certain concentration of surfactant is reached. This concentration is known as the critical micelle concentration (cmc). It has been found that a large number of experimental observables change rapidly over a very narrow concentration range (the cmc region).

The bulk properties of sodium *n*-alkanoates have been extensively reported in the literature (1, 2) but very little attention has been given to the physicochemical properties of compounds that contain a cyclohexyl ring in the place of a long hydrocarbon or fluorocarbon chain. The generic structure of this surfactant family is given below.

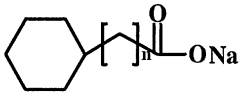

Received May 18, 1999.

This paper is dedicated to Professor Ted Schaefer in recognition of his outstanding contributions to Canadian chemistry.

J.A. MacInnis, R. Palepu, and D.G. Marangoni.[1]
Department of Chemistry, St. Francis Xavier University, PO Box 5000, Antigonish, NS B2G 2W5, Canada.

[1]Author to whom correspondence may be addressed.
Telephone: (902) 867-2324. Fax: (902) 867-2414.
e-mail: gmarango@stfx.ca

© 1999 NRC Canada

Fig. 1. ^{13}C NMR spectrum of sodium cyclohexylbutanoate (SChBu).

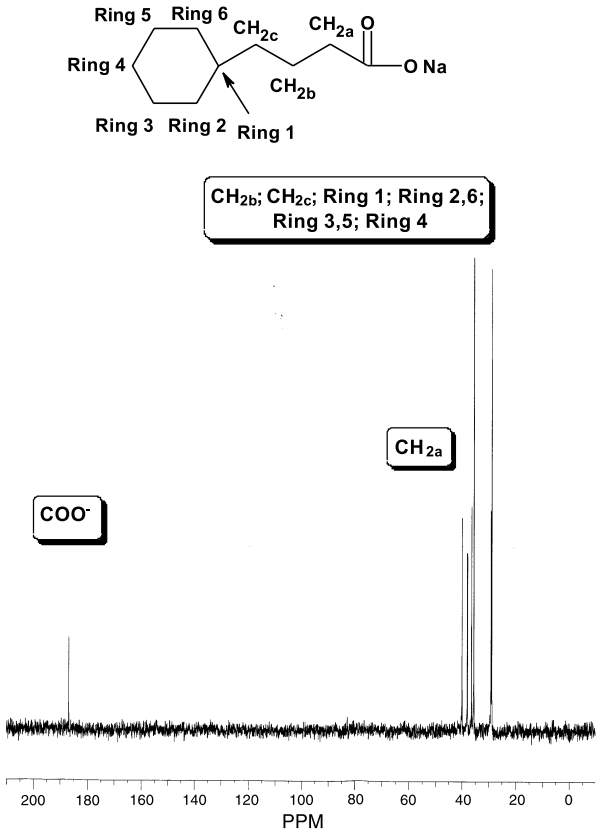

The main area of interest for these compounds is the presence of the cyclohexyl ring, as these surfactants are similar in molecular structure to compounds that are found in petroleum products (3). These petroleum acids, containing mainly short chain alkyls attached to saturated, partially saturated, or aromatic structures, have been postulated to play an important role in the reduction of interfacial tensions during alkaline water flooding of oil reservoirs (3). Hence, a comprehensive study of the properties of these surfactants may be important in the determination of their structure/performance relationships.

Nuclear magnetic resonance is a powerful tool that can be used to investigate the physicochemical properties of micellar systems (4–28). The transfer of monomer from the bulk solution into the micellar phase is generally accompanied by changes in a number of NMR parameters (e.g., chemical shifts and relaxation rates). These changes can be used to estimate a variety of parameters that characterize the micelle formation process (cmc values (4–8), counterion binding (7–11), aggregation numbers (6, 12–15), and the degree of solubilization of additives (16–19). In addition, conformational changes upon micellisation have been investigated using ^{13}C chemical shift changes and paramagnetic relaxation enhancement experiments (6, 12, 15, 20). The dynamics of the chains within the micellar interior have been determined by NMR ^{13}C, ^{31}P, ^{2}H, and ^{14}N relaxation time measurements (21–24). The application of NMR spectroscopy to the study of the formation of micelles and other aggregated systems has been the subject of several excellent reviews (25–28).

The purpose of this paper is to characterize the aggregation properties of the sodium cyclohexylalkanoate surfactants. ^{13}C and ^{23}Na chemical shift measurements were used to obtain the cmc values, the surfactant aggregation number and the degree of counterion binding for the sodium cyclohexylalkanoate surfactants in water. Conformational changes upon micelle formation have been determined from the ^{13}C chemical shift changes after the onset of micellisation. These results have been used to probe the effect of the increase in the length of the alkanoate side chain on the formation of aggregates of the sodium cyclohexylalkanoates.

2. Experimental

Preparation and purification of surfactants

Cyclohexylalkanoic acid, purchased from Aldrich (99% purity, used as received), were dissolved in triply deionized water and converted to the corresponding sodium salts by neutralization with analytical grade NaOH to pH ≅ 10. The surfactants (SChAc ≡ Sodium cyclohexylacetate, SChPr ≡ sodium cyclohexylpropanoate, SChBu ≡ sodium cyclohexylbutanoate, SChPe ≡ sodium cyclohexylpentanoate) were recovered by carefully removing the solvent under vacuum and extracting the solid with diethyl ether for 2–5 days. The surface tensions vs. log ($C_{surf,t}$) (where $C_{surf,t}$ is the total concentration of the surfactant) plots were free of any minima, indicating that the final product was free of surface-active impurities.

NMR experiments

The NMR spectra (^{1}H and proton decoupled ^{13}C) were obtained on a Bruker AC-200 at St. F.X. University and a Bruker AC-250 NMR at the Atlantic Region Magnetic Resonance Centre (ARMRC) at Dalhousie University. A typical ^{13}C spectrum for the cyclohexylalkanoate surfactants is presented in Fig. 1. ^{23}Na chemical shifts were obtained on a Bruker AMX-400 NMR spectrometer at the ARMRC. Homonuclear and heteronuclear 2-D NMR spectra (COSY and ^{13}C-detected HETCORR) were obtained on the AC-200 spectrometer using the standard pulse programs from the Bruker software library in order to assign the proton and the carbon peaks of the surfactants. Deuterium oxide (D_2O) was used as a solvent for all NMR experiments. The ^{1}H spectra were referenced to the HOD peak ($\delta = 4.81$ ppm) while the ^{13}C chemical shift signals were referenced to the deuterium lock signal using the method of Söderman and Guering (12). The ^{23}Na chemical shifts were measured with a 1.00 M solution of NaCl as the reference, and are reported with respect to the chemical shift of the counterion at infinite dilution.

3. Results and discussion

A. cmc values

The cmc values for the sodium cyclohexylalkanoates were obtained from ^{13}C and ^{23}Na chemical shift measurements. The methodology for the determination of the cmc values from the ^{13}C chemical shift measurements will be described in this section first.

For the ^{13}C measurements, if we assume that the surfactant ion exists in two states, the "free" state (in the aque-

© 1999 NRC Canada

Table 1. Micellar properties of sodium cyclohexylalkanoate surfactants as a function of the alkyl chain length.

Surfactant	cmc values[1]/M (^{13}C δ values)	cmc values[1]/M (^{23}Na δ values)	$\beta\delta_{Na,mic}$	β	N_s
SChAc	1.02	0.89	0.33	0.45	4 ± 2
SChPr	0.37	0.33	0.34	0.47	7 ± 2
SChBu	0.25	0.22	0.33	0.45	10 ± 2
SChPe	0.12	0.13	0.39	0.54	14 ± 2

Fig. 2. ^{13}C chemical shifts (ppm) vs. the inverse of the surfactant concentration for the methylene carbon adjacent to the cyclohexyl ring of the sodium cyclohexylbutanoate.

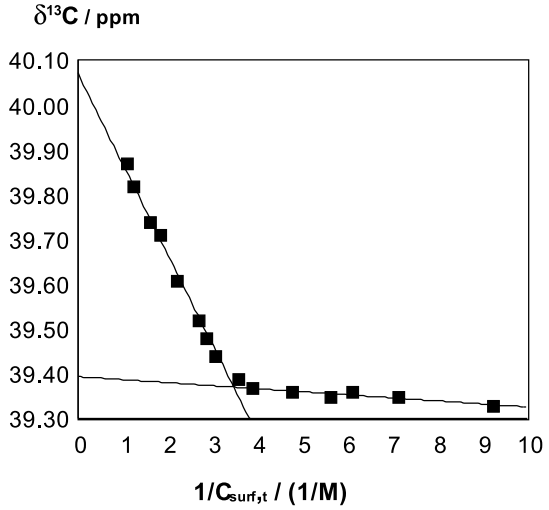

ous phase) and the "bound" state (in the micellar phase), the observed ^{13}C chemical shifts can be written as follows

$$[1] \qquad \delta_{surf,obs} = p\,\delta_{surf,mic} + (1 - p)\delta_{surf,aq}$$

where $\delta_{surf,obs}$ is the averaged (observed) chemical shift of the surfactant ion, $\delta_{surf,aq}$ is the ^{13}C NMR chemical shift of the surfactant ion in the aqueous phase, and $\delta_{surf,mic}$ is the NMR chemical shift of the surfactant ion in the micellar phase. If we define the *p* value of the surfactant as

$$[2] \qquad p = \frac{C_{surf,mic}}{C_{surf,tot}}$$

and substituting the definition of the *p* value into the two-site model (eq. [1] above), we obtain the following for the ^{13}C or the counterion chemical shifts.

$$[3] \qquad \delta_{surf,obs} = \left(\frac{C_{surf,mic}}{C_{surf,t}}\right)\delta_{surf,mic} + \left(\frac{C_{surf,aq}}{C_{surf,t}}\right)\delta_{surf,aq}$$

where $C_{surf,t}$ is the total concentration of the surfactant, $C_{surf,aq}$ and $C_{surf,mic}$ are the concentrations of the surfactant ion or counterion in the aqueous phase ("free") and the micellar phase ("bound"). For the surfactant ions, a plot of the observed ^{13}C chemical shift vs. the inverse of total surfactant concentration should, therefore, yield two linear regions that intersect at the inverse of the critical micelle concentration for the surfactant. A sample plot of the observed ^{13}C chemical shifts against the inverse of the total surfactant concentration is given in Fig. 2 for the methylene carbon adjacent to the cyclohexyl ring of the sodium cyclohexylbutanoate. The averaged cmc values for the sodium cyclohexylalkanoates were obtained from the breaks in the ^{13}C vs. the inverse of the surfactant concentration for each of the carbon resonance's for the n = 1–4 cyclohexyl alkanoates. These values are given in Table 1. It should be noted that these values are in excellent agreement with those reported in the literature (3).

B. Degree of counterion binding: β

The degree of counterion binding of a surfactant (the β value) is defined as

$$[4] \qquad \beta = \frac{C_{c,mic}}{C_{surf,mic}}$$

where $C_{c,mic}$ is the concentration of the counterion absorbed at the micellar surface. For a sodium ion (counterion) under conditions of fast exchange between the aqueous phase and the micellar phase, the observed counterion chemical shifts ($\delta_{c,obs}$) can be written as follows.

$$[5] \qquad \delta_{c,obs} = \left(\frac{C_{c,mic}}{C_{c,t}}\right)\delta_{c,mic} + \left(\frac{C_{c,aq}}{C_{c,t}}\right)\delta_{c,aq}$$

where $C_{c,t}$ is the total concentration of the counterion, $C_{c,aq}$ and $C_{c,mic}$ are the concentrations of the counterion in the free and bound states, respectively. Hence, the combination of eq. [5] with eq. [4] (definition of the β value) yields the following for the ^{23}Na chemical shifts.

$$[6] \qquad \delta_{c,obs} = \delta_{c,aq} + \beta(\delta_{c,mic} - \delta_{c,aq})\left(1 - \frac{cmc}{C_{c,t}}\right)$$

A plot of the observed ^{23}Na chemical shifts vs. the inverse of the total counterion concentration should yield two linear regions that intersect at the inverse of the cmc value of the surfactant. The ^{23}Na chemical shift data are given in Fig. 3*a* for the SChAc and the SChPr surfactants and Fig. 3*b* for the SChBu and the SChPe systems. To be consistent with refs. 7 and 8, these chemical shifts are plotted relative to the chemical shift of a sodium counterion at infinite dilution. The cmc values obtained from the breaks in these plots are also given in Table 1. We note that the agreement between the cmc values from the ^{13}C chemical shifts and the ^{23} Na chemical shifts is reasonable. However, since the cmc value is not a true critical point, we do not expect perfect agreement between the cmc values measured from different experimental methods (29).

© 1999 NRC Canada

Fig. 3. ^{23}Na chemical shifts (ppm) vs. the inverse of the surfactant concentration. (A) ● SChAc, ◆ SChPr; (B) ■ SChBu, ▲ SChPe.

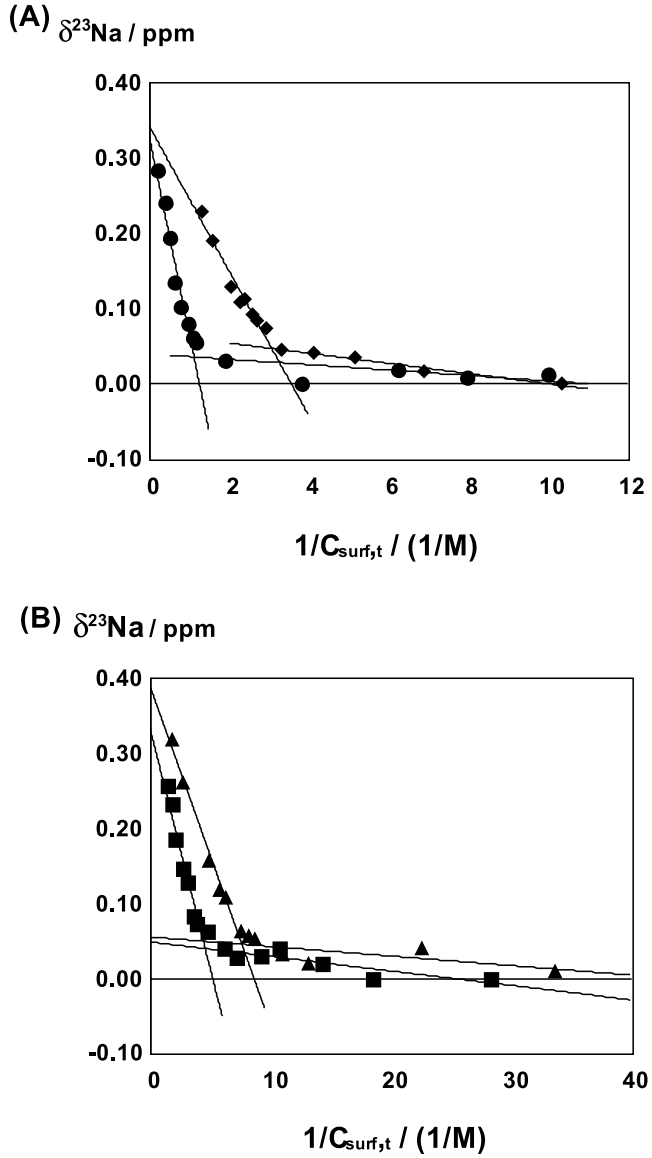

With an estimate of the counterion NMR chemical shift in the micellar phase, $\delta_{c,mic}$, the degree of counterion binding can be determined from eq. [5]. The slopes and the intercepts of the plots of the counterion chemical shift vs. inverse counterion concentration above the cmc value yield the product of $\beta\delta_{Na,mic}$; these are also reported in Table 1. As we clearly see from Table 1, the product $\beta\delta_{Na,mic}$ does not change significantly in value as the length of the alkyl chain in the sodium cyclohexylalkanoates is increased. This is also the case for single-headed and two-headed surfactants of comparable chain length (7, 8, 15). In the work of Gustavsson and Lindman (7, 8), the $\beta\delta_{Na,mic}$ values of alkyl sulfates were observed to be constant (–0.28 ± 0.04) as the chain length of the surfactant increased. Hence, we can assume that the electronic environment of the ^{23}Na counterion in the cyclohexylalkanoate aggregates does not change significantly as we increase the alkyl chain length. We have calculated our values of β employing the $\delta_{Na,mic}$ values for the alkyl carboxylate micelles obtained by Gustavsson and Lindman (7, 8). These counterion binding values are also presented in Table 1. It appears that the sodium cyclohexylalkanoates are characterized by very large cmc values and small degrees of counterion binding. It would follow, therefore, that this family of surfactants have small aggregation numbers.

It is generally assumed that the chemical shift changes of the counterion are dominated by changes in the paramagnetic shielding term of the ion at infinite dilution. For a hydrated, monatomic counterion, the paramagnetic shielding term is mostly due to the overlap of the outer orbitals of the sodium counterion and the oxygen of the hydrating water molecule i.e., direct ion-ion interactions are usually unimportant. For these surfactants, the electronic environment of the headgroup leads to significant positive values of the product $\beta\delta_{Na,mic}$. These large, positive values are consistent with the sodium ion bound at the carboxylate micellar surface undergoing a significant amount of polarisation, likely due to the H-bonding between the negatively charged O atom in the carboxylate anion and the protons on the water molecules surrounding the counterion. Since the $\beta\delta_{Na,mic}$ values for the cyclohexylalkanoates are not much different from those of the straight chain alkanoates, it is safe to assume that the chemical shift of the sodium counterion at the micellar surface is the same for both surfactant families, and that the small differences are due to the difference in the degree of counterion binding between both sets of surfactants. We note that the β values determined from conductivity experiments are indeed smaller for the cyclohexyl surfactants compared to the straight chain alkanoates.[2] Hence, our assumption that the $\delta_{Na,mic}$ values are the same for both of these carboxylate surfactants is reasonable.

Using the cmc values and the β values of these surfactants from the NMR experiments,

we have calculated the Gibbs energy of micellisation ($\Delta_{mic}G°$ values) using the charged pseudo-phase model of micelle formation (31), which for a single headed surfactant with monovalent counterions is as follows.

$$[7] \qquad \Delta_{mic}G° = RT(1 + \beta) \ln X_{cmc}$$

The $\Delta_{mic}G°$ values for the cyclohexylalkanoate surfactants are given in Table 2 and plotted in Fig. 4 as a function of the surfactant chain length. The slope of the plot of the $\Delta_{mic}G°$ values against the total number of carbon atoms in the surfactant yields an estimate of –3.0 kJ/mol for the Gibbs energy of transfer of a CH_2 group from the aqueous phase to the micellar interior, which agrees well with the literature values (1, 30). The $\Delta_{mic}G°$ values of the sodium alkylcarboxylates, the sodium alkylsulfates, and the sodium alkylsulfonates are also plotted in Fig. 5. When we compare the $\Delta_{mic}G°$ values of the cyclohexylalkanoates with those of the straight chain alkanoates, we see, for example, that the SChAc surfactant (a total of 8 carbon atoms) has a $\Delta_{mic}G°$ value that is ≈ 6 kJ/mol less than that of sodium octanoate;

[2] J.A. MacInnis, D.G. Marangoni, and R. Palepu. J. Colloid Interface Sci. Submitted July 1999.

© 1999 NRC Canada

Table 2. $\Delta_{mic}G°$ values (kJ/mol) for different families of one-headed surfactants.

Number of carbon atoms	Sodium alkanoates	Sodium alkyl sulfates	Sodium alkyl sulfonates	Sodium cyclohexyl alkanoates
7	–23.1	—	—	—
8	–26.8	–33.7	–30.5	–20.6
9	–30.0	–36.5	—	–23.5
10	–33.0	–40.9	–37.6	–25.4
12	—	–46.4	–44.6	–29.9

Fig. 4. $\Delta_{mic}G°$ values for various surfactant families. ● Sodium cyclohexyalkanoates; ◆ sodium alkanoates; ■ sodium alkyl sulfates; ▲ sodium alkyl sulfonates.

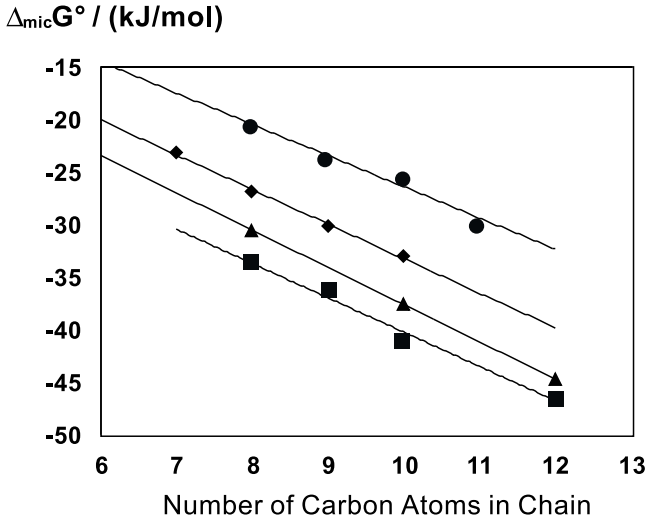

Fig. 5. Plot of the calculated chemical shifts (from eq. [10]) as a function of the inverse surfactant concentration for the CH_{2c} carbon of SChBu.

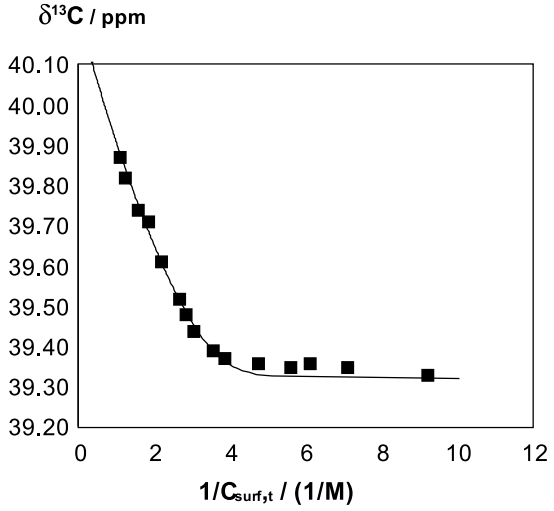

the SChBu surfactant (10 carbon atoms) has a $\Delta_{mic}G°$ value ≈ 6 kJ/mol less than that of sodium decanoate. Hence, we can conclude from the Gibbs energies for micelle formation that the cyclohexyl ring appears to behave as a four carbon chain (i.e., a difference of two CH_2 groups), indicating that the presence of the six carbon ring structure makes micelle formation thermodynamically less favourable for the sodium cyclohexylalkanoate surfactants vs. the well-known sodium alkanoate surfactants having the same total number of carbon atoms.

C. Surfactant aggregation numbers

Aggregation numbers can also be determined from ^{13}C chemical shifts. This is based on several assumptions (12–14, 25). A simplified situation is said to exist where the surfactant is present in only two forms — either as a free monomer or in a micelle with aggregation number, N_s. The chemical shifts are different in the two states and the monomer and micelle shift, $\delta_{surf,aq}$ and $\delta_{surf,mic}$, are assumed to be independent of surfactant concentration. The mean aggregation numbers of the surfactants were estimated from the ^{13}C chemical shift data from the mass action model, employing the method outlined by Lang (13) and Gao et al. (14). With the above assumptions in mind, the equilibrium between the surfactant monomers in the aqueous phase and the micellar phase can be written as follows

$$[8] \qquad N_s S \Leftrightarrow S_{N_s}$$

Here, N_s is the surfactant aggregation number and S_{N_s} and S represent the surfactant in aggregated form and in aqueous solution, respectively. The equilibrium constant for the above reaction is written (neglecting activity corrections)

$$[9] \qquad K = \frac{C_{mic}}{(C_{surf,aq})^{N_s}}$$

where C_{mic} is the concentration of aggregates having an aggregation number N_s (i.e., $C_{mic} = C_{surf,mic}/N_s$) and $C_{surf,aq}$ is the concentration free monomer in solution. The free monomer concentration is written in terms of the total surfactant concentration, $C_{surf,t}$. Since $C_{surf,t} = C_{surf,mic} + C_{surf,aq}$, the equilibrium constant expression is rewritten as follows.

$$[10] \qquad K = \frac{C_{surf,t} - C_{surf,aq}}{N_s(C_{surf,aq})^{N_s}}$$

If the observed chemical shift is written in terms of the total surfactant concentration according to eq. [3], then substituting for $C_{surf,aq}$ in eq. [8] yields

$$[11] \qquad \frac{1}{C_{surf,t}} = (KN_s)^{\frac{1}{N_s-1}}(\delta_{surf,mic} - \delta_{surf,aq})^{-1} \times (\delta_{surf,mic} - \delta_{surf,obs})^{\frac{N_s}{N_s-1}}(\delta_{surf,obs} - \delta_{surf,aq})^{\frac{1}{1-N_s}}$$

© 1999 NRC Canada

Fig. 6. Plot of the chemical shift change upon micelle formation ($\delta_{surf,mic} - \delta_{surf,aq}$) as a function of carbon number for ● SChAc, ◆ SChPr, ■ SChBu, ▲ SChPe.

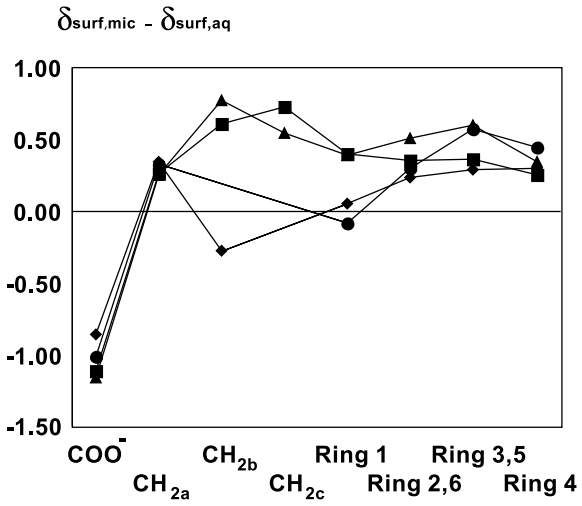

The aggregation number is then deduced from the variation of the ^{13}C $\delta_{surf,obs}$ values as a function of $C_{surf,t}$. By fitting eq. [11] to the concentration dependence of the observed shifts, it is possible to extract an estimate of N_s, the micellar aggregation number. A plot of the experimental chemical shifts fitted to eq. [10] is presented in Fig. 5 for a carbon contained in the cyclohexyl ring of sodium cyclohexylpropanoate. The aggregation numbers are shown in Table 1. It is clear from this table that the aggregate formed by the sodium cyclohexylalkanoates are indeed small, and as such, cannot be considered true micelles. It is also clear however, that as the chain length increases, the aggregate size increases, and the self-assembled units likely take on some of the characteristics of true micelles. It should be pointed out that the use of ^{13}C chemical shifts to obtain surfactant aggregation numbers from the application of the mass action model has been criticized by several authors as yielding low aggregation numbers for typical surfactants (like sodium dodecylsulfate (12)). However as a function of the carbon chain length, it does qualitatively predict the trends in the aggregation number. It should be noted that these values are in good agreement with the aggregation numbers determined via viscosity measurements.[2]

D. Chemical shift changes upon micelle formation

The ^{13}C chemical shift changes upon micellisation can give qualitative information about conformational changes that surfactant molecules undergo when forming micelles. Generally, a high frequency shift is associated with an increase in the number of *trans* conformers, whereas a low frequency shift is interpreted in terms of an increasing probability of *gauche* configurations (4–7, 12, 25). It should be noted that there are other contributions to the chemical shift changes upon micelle formation including headgroup interactions and hydration changes (31), but that the conformational arguments for the chemical shift changes upon micelle formation appear to be supported by other experimental techniques (32, 33). The ^{13}C chemical shift changes upon micelle formation, $\delta_{surf,mic} - \delta_{surf,aq}$, are plotted in Fig. 6 and given in Table 3 for all the sodium cyclohexylalkanoates. It can be seen from Fig. 6 that for all the sodium cyclohexylalkanoate surfactants studied, the carboxylate carbon undergoes a low frequency shift on micelle formation and the first methylene group on the chain (CH_{2a}) undergoes a high frequency shift change upon micelle formation. For the remaining alkyl chain carbons and the ring carbons however, there appear to be two definite patterns for the ^{13}C chemical shift changes upon micelle formation. In the case of the SChAc and the SChPr, the first carbon atom on the ring (Ring 1) is characterized by a very slight change in its chemical shift upon micelle formation. In addition, the chemical shift changes for the ring carbons for the SChAc and the SChPr tend to increase towards a maximum value near the end of the cyclohexyl ring. In the case of the second methylene group on the carboxylate chain (CH_{2b}) for the SChPr, we observe a large negative chemical shift change upon micelle formation. In addition, for the headgroup carbon, the ^{13}C chemical shift differences appear to be relatively constant upon increasing the length of the carboxylate chain in the surfactant.

Table 3. Chemical shift changes ($\delta_{surf,mic} - \delta_{surf,aq}$) upon micelle formation for sodium cyclohexylalkanoate surfactants.

Carbon group	SChAc	SChPr	SChBu	SChPe
COO^-	–1.01	–0.86	–1.11	–1.16
CH_{2a}	0.33	0.35	0.27	0.26
CH_{2b}	—	–0.27	0.61	0.78
CH_{2c}	—	—	0.73	0.55
Ring 1	–0.08	0.06	0.40	0.39
Ring 2, 6	0.30	0.24	0.36	0.51
Ring 3, 5	0.58	0.29	0.37	0.60
Ring 4	0.45	0.30	0.26	0.35

With the assumption that the shift changes upon micelle formation are due to conformational changes and (or) hydration differences only, it appears that the shift changes indicate a different mode of aggregation for the two lower members of the sodium cyclohexylalkanoates. A less strained configuration for the ring carbons (i.e., an increase in the number of *trans* conformers) is predicted as the carboxylate carbon chain length increases. According to Grant and Cheney (34), the ^{13}C chemical shift would change by a maximum of 4.8 ppm for a complete *gauche – trans* isomerisation. Hence, in the case of the cyclohexylalkanoate surfactants, we propose that the first carbon of the cyclohexylalkanoates (the headgroup carbon) has a predominately *gauche* configuration, and that the carbons bearing the headgroups do not suffer significant changes in their micellar environment as the alkyl chain length increases. We note that for the cyclohexyl ring carbons, the chemical shift changes upon micelle formation are essentially all positive and that there is a definite increase in the magnitude of the $\Delta\delta$ values for the surfactant ring carbons as the alkanoate chain length increases. Given the ^{13}C chemical shift differences, the small aggregation numbers, and the high cmc values of the SChAc and the SChPr, we conclude that these surfactants form very loose, heavily hydrated aggregates that possibly employ a stack-like aggregation process. The longer members of this family have a more normal pattern of $\Delta\delta$ values, and hence a more

© 1999 NRC Canada

typical (more micellar like) aggregation process ensues. Note that the $\delta_{surf,mic} - \delta_{surf,aq}$ values for the ring carbons appear to increase with an increasing number of methylene groups in the carboxylate chain. This is likely due to more motional freedom in the interior of the cyclohexylalkanoate aggregate, resulting from the differences in the mode of aggregation of the longer chain sodium cyclohexylalkanoate surfactants. We are currently determining the dynamics of the carbon nuclei inside the micelle via NMR ^{13}C spin-lattice relaxation time measurements. These results will be the subject of a future paper.

4. Conclusions

Multi-nuclear NMR spectroscopy has been used to obtain the equilibrium micellar properties (the critical micelle concentration, the degree of counterion binding and surfactants aggregation numbers) of the sodium cyclohexylalkanoates as a function of the length of the alkanoate chain attached to the cyclohexyl ring. The environment of the counterion at the micellar surface has been probed using surfactant counterion chemical-shift measurements. These surfactants resemble the long chain sodium alkanoate surfactants in that the cmc values decrease and the aggregation numbers increase with an increase in the total number of carbon atoms in the surfactant. In terms of the Gibbs energy of micelle formation, these surfactants are identical to a sodium alkanoate surfactant with two less CH_2 groups. The ^{13}C chemical shift measurements indicate the aggregation process differs for the first two members of the series (SChAc and SChPr) than for the other two higher chain length members investigated. This is due to the fact that as CH_2 groups are added to the alkyl chain, the cyclohexyl ring carbons appear to obtain more conformational freedom upon aggregate formation. This indicates that as the length of the alkanoate side chain increases, the cyclohexyl rings experience a more nonpolar environment in the interior of the micelle.

Acknowledgements

The financial support of the Natural Sciences and Engineering Research Council of Canada (NSERC) (research grants D.G.M. and R.P.) and the St. F.X. University Council for Research is greatly appreciated. The authors are grateful to Don Hooper and Mike Lumsden at the Atlantic Region Magnetic Resonance Centre for some of the NMR work in this paper and for valuable discussions.

References

1. B. Lindman and H. Wennerstrom. Top. Curr. Chem. **87**, 1 (1980).
2. D.G. Hall and G.J.T. Tiddy. *In* Anionic surfactants (physical chemistry of surfactant action). Vol. 11. *Edited by* E.H. Lucassen-Reynders. Marcel Dekker, New York. 1981. Chap. 2. p. 55.
3. A. Skauge and J.J. Spitzer. J. Phys. Chem. **87**, 2398 (1983).
4. S. Mazumdar. J. Phys. Chem. **94,** 5947 (1990).
5. Y. Chevalier and C. Chachaty. Colloid Polym. Sci. **262,** 489 (1984).
6. B.D. Perrson, T. Drakenberg, and B. Lindman. J. Phys. Chem. **83**, 3011 (1987).
7. H. Gustavsson and B. Lindman. J. Am. Chem. Soc. **97**, 3923 (1975).
8. H. Gustavsson and B. Lindman. J. Am. Chem. Soc. **100**, 4647 (1978).
9. I.D. Robb. J. Colloid Interface Sci. **37**, 521 (1971).
10. P. Stilbs and B. Lindman. J. Phys. Chem. **85**, 2587 (1981).
11. M. Jansson and P. Stilbs. J. Phys. Chem. **89**, 4868 (1985).
12. O. Söderman and P. Guering. Colloid Polym. Sci. **265**, 76 (1987).
13. J. Lang. J. Phys. Chem. **86**, 992 (1982).
14. Z. Gao, R.E. Wasylishen, and J.C.T. Kwak. J. Colloid Interface Sci. **137,** 137 (1990).
15. P. Stilbs. J. Colloid Interface Sci. **87**, 385 (1982).
16. G.D. Boucher, A.C. MacDonald, B.E. Hawrylak, and D.G. Marangoni. Can. J. Chem. **76**, 1266 (1998).
17. Z. Gao, R.E. Wasylishen, and J.C.T. Kwak. J. Phys. Chem. **93**, 2190 (1989).
18. J.C.T. Kwak and D.G. Marangoni. Langmuir, **7**, 2083 (1991).
19. D.G. Marangoni, A.P. Rodenhiser, J.M. Thomas, and J.C.T. Kwak. ACS Symp. Series, **501**, 194 (1992).
20. M. Jansson, P. Li, and P. Stilbs. J. Phys. Chem**. 91,** 5279 (1987).
21. C. Chachaty, T. Ahlnäs, B. Lindstrom, H. Nery, and A.M. Tistchenko. J. Colloid Interface Sci. **122**, 406 (1988).
22. O. Söderman, M. Monduzzi, A. Ceglie, and B. Lindman. J. Colloid Interface Sci. **136**, 113 (1990).
23. A. Ceglie, M. Monduzzi, and O. Söderman. J. Colloid Interface Sci. **142**, 129 (1991).
24. O. Söderman, E. Hansson, and M. Monduzzi. J. Colloid Interface Sci. **141**, 512. (1991).
25. C. Chachaty. Progress NMR Spectrosc. **19**, 183 (1987).
26. P. Stilbs. Progress NMR Spectrosc. **19**, 1 (1987).
27. O. Söderman and P. Stilbs. Progress NMR Spectrosc. **26**, 445 (1994).
28. O. Söderman and U. Olsson. Curr. Opin. Colloid Interface Sci. **2**, 131 (1996).
29. P. Mukerjee and K.J. Mysels. Critical micelle concentrations for aqueous surfactant systems US-NBS. No. 36. U.S. GPO, Washington, D.C. 1971.
30. C. Tanford. The hydrophobic effect: the formation of micelles and biological membranes. 2nd. ed. John Wiley, New York. 1980.
31. T. Ahlnäs and O. Söderman. Colloids Surf. **12**, 125 (1984).
32. R.G. Griffin, L. Powers, and P.S. Pershan. Biochemistry, **17**, 2718 (1978).
33. B. Faucompré and B. Lindman. J. Phys. Chem. **91**, 383 (1987).
34. D.M. Grant and B.V. Cheney. J. Am. Chem. Soc. **89**, 5319 (1967).

© 1999 NRC Canada

1999 Pure or Applied Inorganic Chemistry Award Lecture
Curves in chemistry: supramolecular materials taking shape[1,2]

Geoffrey A. Ozin

Abstract: A large part of the development of mathematics was driven by the desire to understand why objects in nature are found in a myriad of shapes and sizes and why certain forms are preferred over others. The area of mathematics called the calculus of variations has been utilized to handle the optimal forms in geometry and nature. It has been used to comprehend morphogenesis and the similarity, yet variety, of forms in the natural world. The mathematical underpinnings of natural form are beginning to influence the inorganic materials world, especially the unusual morphologies that arise in the field of self-assembly. These morphologies often exhibit curved shapes resembling those of minimal surfaces rather than familiar Platonic, polyhedral crystal habits. The curved shapes of mesostructured inorganic materials synthesized by supramolecular templating are striking examples of minimal surface area and energy principles at work in their growth and form.

Key words: mesoporous materials, morphosynthesis, silica, supramolecular.

Résumé : Une grande partie du développement des mathématiques a été stimulée par le désir de comprendre pourquoi les divers objets que l'on retrouve dans la nature adoptent une myriade de formes et de tailles et pourquoi il y a une préférence pour certaines formes. La partie des mathématiques que l'on nomme calcul des variations a été utilisée pour traiter de la question des formes optimales en géométrie et dans la nature. On l'a utilisée pour comprendre la morphogénèse et la similarité dans la variété des formes que l'on rencontre dans la nature. Les bases mathématiques de la forme naturelle commencent à influencer le monde des matériaux inorganiques, particulièrement les morphologies inhabituelles que l'on rencontre dans le domaine des autoassemblages. Ces morphologies présentent souvent des formes arrondies qui ressemblent à celles des surfaces minimales plutôt qu'aux formes cristallines polyédriques platoniques familières. Les formes arrondies des matériaux inorganiques à structures méso obtenus à l'aide de matrices supramoléculaires sont des exemples frappants de la mise en oeuvre des principes de minimisation de l'énergie et de la superficie de la surface lors de leur croissance et leur formation.

Mots clés : matériaux mésoporeux, morphosynthèse, silice, supramoléculaire.

[Traduit par la Rédaction]

Introduction

On viewing the unusually curved silica shape displayed in Fig. 1, Jean Marie Lehn commented "you have synthesized a facsimile of a Brancusi sculpture that I have just seen in the New York museum of modern art." This brought to mind Jean Marie Lehn's axiom in his classic text Supramolecular Chemistry (1), "if it exists it can be synthesized." Having synthesized such uniquely curved shapes we felt compelled to investigate their growth and form, and coined the term morphosynthesis (2). This is what my group has been working on for the past few years. A brief personal perspective of this research forms the subject of my award lecture presentation and paper. The reader is directed to the original references of our published papers to appreciate the analytical details underlying our contributions to this emerging and highly active field of materials chemistry.

Planes and curves

Both of the materials shown in Fig. 1 are composed only of silica. The one on the top is dodecasil 3C and the one on the bottom is hexagonal mesoporous silica. Notably, the familiar octahedral shape with planar faces, sharp edges, and

Received June 2, 1999.

G.A. Ozin. Materials Chemistry Research Group, Chemistry Department, 80 St. George Street, University of Toronto, Toronto, ON M5S 3H6, Canada.

[1]This is an invited paper based on the Pure or Applied Inorganic Chemistry Award Lecture presented at the Chemical Institute of Canada Conference, Toronto, June 1999.

[2]Dedicated to Charles T. Kresge, an inventor of supramolecular templating to mesoporous silica materials, a great friend and colleague, and champion of our materials chemistry research.

© 1999 NRC Canada

Fig. 1. SEM images of (A) dodecasil 3C and (B) hexagonal mesoporous silica.

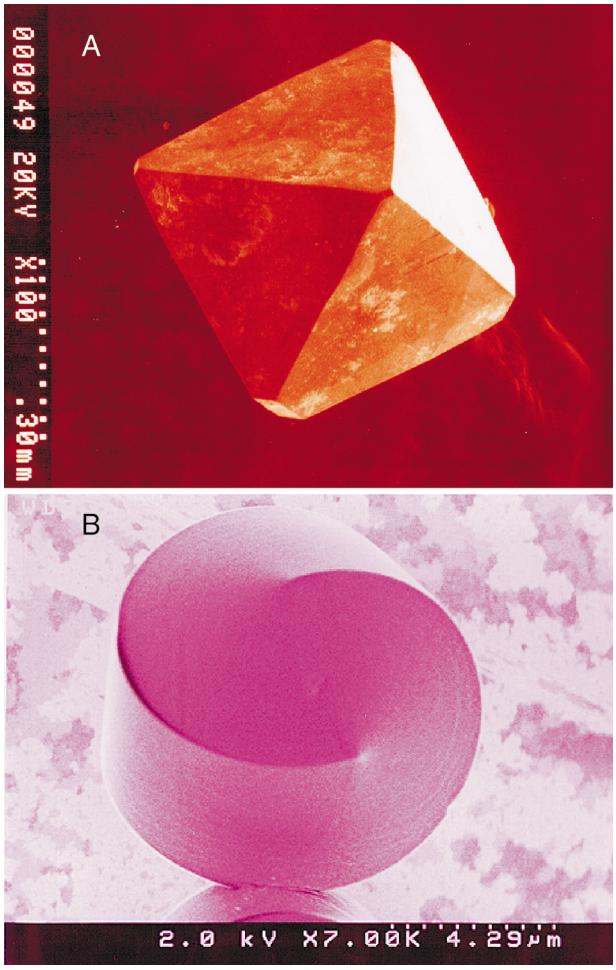

Fig. 2. (A) Hexagonal lyotropic mesophase and (B) hexagonal mesoporous silica replica.

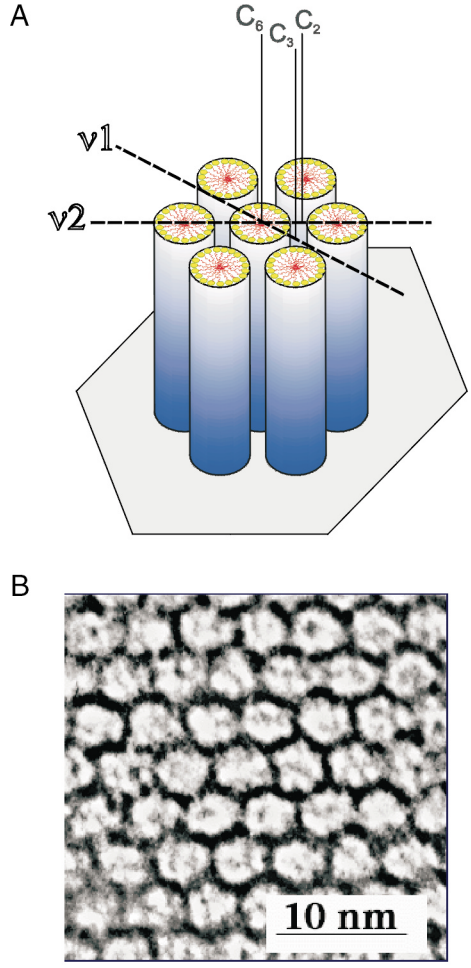

pointed apices has crystalline microporosity (IUPAC convention, length scale of pores <2 nm), while the unfamiliar curved object has crystalline mesoporosity (2–50 nm) but is amorphous at the microscale. Single organic molecules facilitate the production of micropores in dodecasil 3C, whereas a supramolecular assembly of organic amphiphiles enables the creation of ordered mesopores in silica. The morphology and microstructure of the former is determined by crystallographic physics, space groups, planar symmetry elements, and thermodynamics and kinetics of crystal nucleation and growth. Traditional concepts of this type, however, do not explain the periodic mesoscale porosity, growth, and highly curved form of the latter.

Supramolecular materials taking shape

Presented is a synopsis of our work aimed at elucidating principles that underpin the growth and form of hexagonal mesoporous silica over all three spatial dimensions. The research required a paradigmatic shift in materials synthesis and the development of a "language of shape" to explain morphogenesis of inorganic materials with curved form. It brings complexity into inorganic chemistry and introduces hierarchy to inorganic materials. The thinking behind the work can be traced to the idea that a noncovalently bound assembly of surfactant molecules, like the one illustrated in Fig. 2A, can direct the organization and hydrolytic polycondensation of silicate species to create silica replicas of the templating mesophase (3*a*). A transmission electron micrograph (TEM) image that clearly displays a hexagonal close-packed array of 5-nm-diameter channels in a surfactant-templated, hexagonal symmetry mesoporous silica is shown in Fig. 2B.

Research scientists at Mobil first demonstrated that this kind of self-assembly synthesis can be orchestrated to yield silica materials with hexagonal, cubic, and lamellar mesostructures, as well as various disordered versions of these basic structures (3*a*). At that time the mechanism of formation of these materials was proposed to involve the co-assembly of inorganic and organic building units with charge, geometrical, and structural complementarity at the interface between interacting moieties. Subsequently, others researchers extended the paradigm of surfactant templating of silica species through judicious variations of pH (acid and base catalysis); the nature of the surfactant (cationic, neutral, anionic); the relative concentration of precursors; and the use of aqueous, nonaqueous solvents, co-solvents and co-surfactants, to create silica mesostructures (3*b*).

The resemblance of the supramolecular templating pathway to organic matrix-mediated biomineralization processes

© 1999 NRC Canada

Fig. 3. Schematic summary of morphology control achieved with hexagonal mesoporous silica synthesized under acidic conditions.

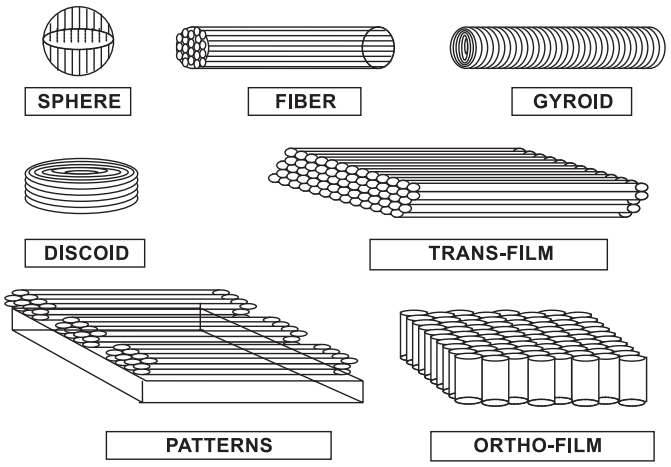

in nature is important and inspires a biomimetic way of thinking about the synthesis of hierarchical structures on length scales unparalleled in inorganic materials chemistry (4, 5). Interactions between inorganics and organics comprising the supramolecular assembly are envisioned to be of the electrostatic, ion pair, metal–ligand, covalent and hydrogen-bonding type and has become the accepted way to describe the chemistry involved in the self-assembly synthesis of a cornnucopia of mesostructured materials (6).

Studies on the mode of formation of the hexagonal symmetry form of mesoporous silica are founded on the co-assembly of silica-based moieties with surfactant micellar and liquid crystal species. Mechanistic studies, for example by in situ EXAFS, EPR, and fluorescence probe techniques, although differing slightly in detail, more-or-less support the co-assembly scheme. These studies, however, are not able to say anything about the shape of the resulting mesoporous silica material (7).

Our research effort has focused not only on shape control of mesoporous silica but also on morphogenesis, the origin and growth of a particular form (2, 4, 5, 8). An illustration of hexagonal mesoporous silica morphologies that we have managed to synthesize, in a reproducible fashion, from initially clear dilute aqueous solutions of surfactant and silica reagents under acid catalyzed conditions are shown in Fig. 3. These comprise fibers, supported oriented film at solid–liquid interfaces, free-standing oriented film at air–liquid interfaces, spheres, highly curved and patterned shapes, Archimedian screws, and micron scale soft lithographically defined patterns on gold surfaces (9–19).

The research necessitated crossing boundaries between subdisciplines of chemistry. It depended on an integration of chemical and physical concepts, synthetic methods, processing strategies, and analytical techniques in surfactant, sol–gel, liquid crystal, surface, colloid, and crystal growth sciences. This entailed taking command over topological defects, director fields, surface charge, elastic deformations, and differential contraction of polymerizable silicate micelles and liquid crystals. With this knowledge it proved possible to control the co-assembly of surfactants and silicates over three spatial dimensions and angstrom to millimetre length scales, to yield a desired morphology of hexagonal mesoporous silica. Key relations between synthesis conditions, mesostructure, and morphology were established by different kinds of microscopy, diffraction, spectroscopy, thermal, and adsorption analytical techniques. This research led to examples of mesostructured inorganic materials with hierarchical architectures and complex form. It led to the concept of "panoscopic materials" and a new materials chemistry tool box in which materials synthesis is conducted over "all" length scales (20). Thinking of this type inspired ideas about the potential utility of mesostructured materials in a diversity of areas from catalysis to bone implants, chemical delivery systems to membranes, batteries to fuel cells, and electronics to photonics (20, 21).

Synthesis-shape diagrams

To develop a model for the nucleation, growth, and form of hexagonal mesoporous silica curved shapes we first investigated the relations between synthesis conditions and the emergence of a particular shape (14, 16). This involved establishing a novel kind of synthesis-shape "phase diagram" for mesoporous silica morphologies. No additives, co-solvents, or salts were used in these preparations. The synthesis was based on quiescent, acidic, aqueous ambient temperature and pressure conditions, with only pH control over the notably narrow range of –1 to +1. These acidities are below the isoelectric point of silica (pH < 2–3) and therefore the chemistry involves acid-catalyzed condensation polymerization of protonated silicates in the microphase-separated domains of a lyotropic silicate mesophase.

In all of the work described in this paper, the material that forms is exclusively the hexagonal form of mesoporous silica with essentially the same composition and channel structure. It is found that fiber, gyroid/discoid, and sphere morphologies are favored in greater than 90% yield in specified regions of the synthesis-space diagram. Fiber shapes are formed under the most acidic conditions. The range of acidity in which these shapes are formed is only two pH units. This illustrates the sensitivity of the system on the acid side to small changes in pH. Interestingly, hybrid mesoporous silica morphologies such as "tadpoles" and "telephones," composed of fibers growing off one of two gyroids, are formed in regions of the diagram that lie between particular shapes. Above pH ~ 1, which favors spheres, the material that forms is amorphous silica, devoid of a mesostructure or a recognizable shape. On moving to the basic pH range, one again observes the formation of hexagonal mesoporous silica with interesting morphologies. Hence there is a range of pH between ~1 and 10 in which the interactions between the micellar assembly and the silica species is insufficient to support a silica-based mesophase and cannot lead to a hexagonal mesoporous silica replica.

© 1999 NRC Canada

Fig. 4. Representative SEM images of mesoporous (A) fiber, (B) discoid, and (C) sphere morphologies,

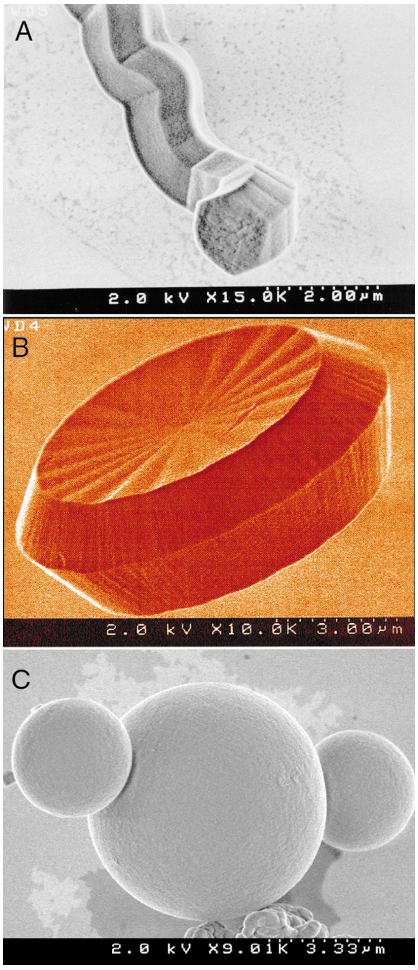

Fig. 5. Representative TEM images of whole mounted hexagonal mesoporous fiber (A) and discoid morphologies (B). The silica channel walls are spaced by about 5 nm.

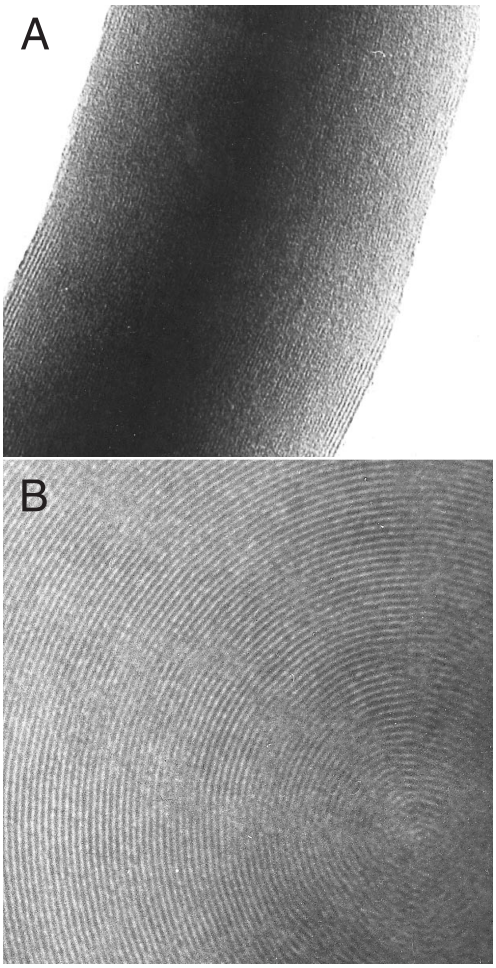

Some representative examples of scanning electron micrographs (SEMs) that demonstrate morphology control of hexagonal mesoporous silica are shown in Fig. 4. The relation between morphology and mesostructure for some of these shapes can be determined from TEM images of whole mounted specimens (Fig. 5). A summary of the results of SEM, TEM, and atomic force microscopy (AFM) imaging studies depict the relation between surface topology, mesostructure, and morphology. The relative disposition of the channels in the surface and bulk regions, the root mean square surface roughness, and the texture of these shapes provide valuable information on the processes responsible for morphogenesis. The channels run down the axis of the fibers and whirl concentrically around the axis of the gyroids/discoids, and both of these morphologies have very smooth bodies with a 5- to 10-nm surface mesostructure that mirrors that of the bulk. These shapes are to be contrasted with the spheres formed under the least acidic conditions, which display a granular texture with a less ordered channel structure. The spheres have an order of magnitude rougher surface (~50 nm) composed of ~50-nm grains with a ~5-nm surface mesostructure. They are best described as hexagonal mesoporous silica in the form of a nanocrystalline flocculate.

Shapes in time

This work led to the first experiments designed to probe nucleation and growth processes that are responsible for a particular mesoporous silica shape (15). Morphokinetics, a term coined to describe the nucleation and growth of these mesoporous silica shapes, was probed through a combination of dynamic light scattering (DLS) and the time dependence of crystalline mass yield, together with AFM and TEM studies of the earliest stage growth nuclei. Results of DLS for fiber, gyroid/discoid, and sphere syntheses are expressed graphically in terms of the evolution of the hydrodynamic radius of a specific mesoporous silica shape. This is obtained from the Stokes–Einstein equation, where the diffusion coefficient is calculated from the autocorrelation function of the scattered light. The DLS results reveal the existence of an embryonic species with an initial diameter of around 7 nm. This species grows in size by about 1 nm during an "incubation time," which increases in magnitude as the acidity decreases, and preferentially forms fibers, then gyroids/discoids, and finally spheres.

Representative results for the temporal dependence of the crystalline mass yield of mesoporous silica fiber and

© 1999 NRC Canada

Fig. 6. Morphokinetics, time dependence of the crystalline mass yield of hexagonal mesoporous silica fibers and gyroids/discoids.

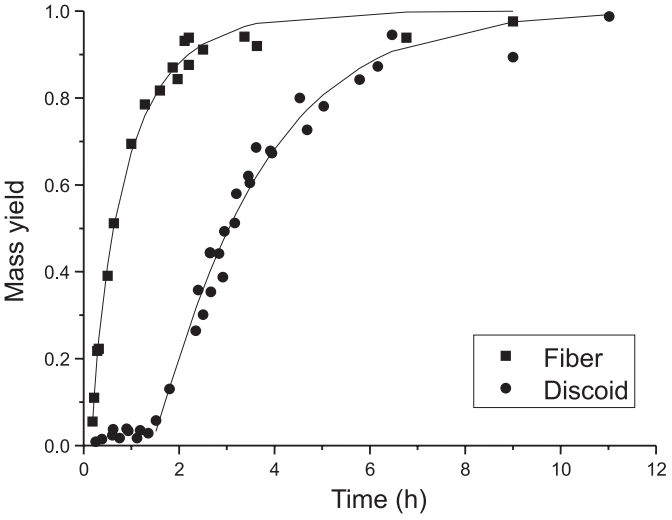

Fig. 7. Tapping mode AFM image with phase detection of the earliest stage growth nuclei on freshly cleaved graphite observed in a hexagonal mesoporous silica fiber synthesis.

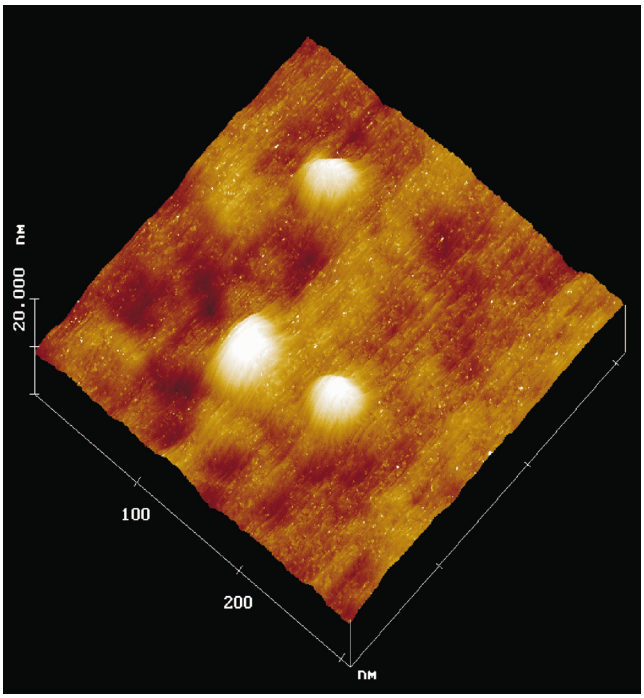

gyroid/discoid shapes is displayed in Fig. 6. The data fit well to the three-parameter Avrami equation, which is usually expressed in the following form:

$$[1] \qquad m(t)/m(\infty) = 1 - \exp\,[-k(t - \tau)^n]$$

where k is the crystallization rate constant, τ is the incubation time, and n is the dimensionality index of the growth process. This equation is often applied in the literature to describe the nucleation and crystallization of polymers, and was deemed a reasonable starting model to explain the nucleation, silicification, and growth of hexagonal mesoporous

Fig. 8. TEM image of the earliest stage growth nuclei on a copper grid observed in a hexagonal mesoporous silica fiber synthesis.

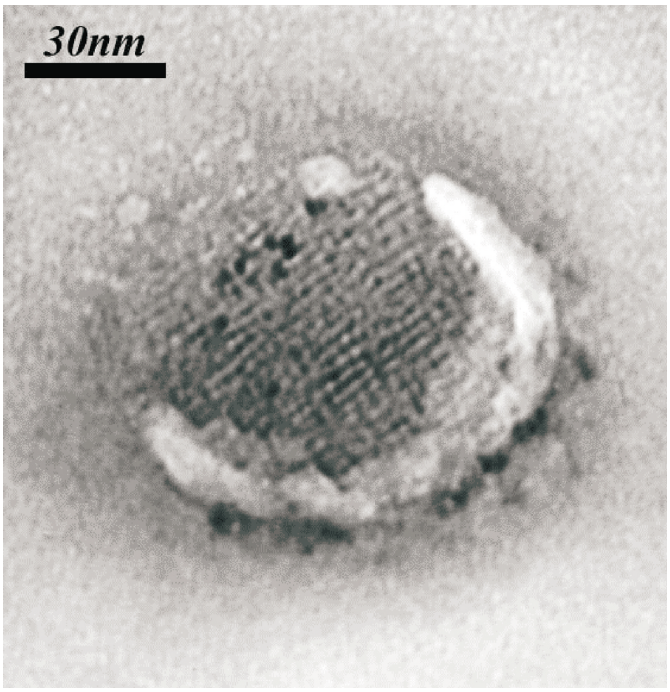

silica shapes. The extracted crystallization rate constants (k) were found to be 1.33 ± 0.05 and 0.41 ± 0.06 for the fiber and discoid/gyroid shapes. Corresponding incubation times (τ) were 0.18 ± 0.02 and 1.42 ± 0.13 h, and the Avrami dimensionality indices (n) were 0.77 ± 0.06 and 1.09 ± 0.11. The value of n turns out to reflect one- and two-dimensional growth processes, which is expected for the fiber and discoid/gyroid shapes, respectively.

Incubating the seed

Experiments were designed to look for viable growth nuclei at early times of the synthesis to probe their size, shape, rigidity, and mesostructure, and the presence of defects (15). The approach for sample preparation, although not ideal, involved dipping a piece of freshly cleaved graphite or a copper TEM grid into synthesis mixtures of different hexagonal mesoporous silica shapes at the earliest possible stage of a preparation. A tapping mode AFM image using phase detection reveals soft objects of around 50–70 nm in diameter (Fig. 7). This is the gentlest way of imaging and interrogating the mechanical properties of a fragile object with minimal perturbation of the structure. TEM images of these early stage species reveal roughly 50- to 70-nm-diameter "mesostructured nanoparticles," which seem to be best described as silicate liquid crystal growth nuclei (Fig. 8).

The collective results of these morphokinetic studies allow the formulation of a scheme to describe the growth of mesoporous silica shapes under quiescent dilute aqueous acidic synthesis conditions (Fig. 9). In the case of the gyroid/discoid shapes the steps that occur during the incubation period τ are described in order: (*i*) spontaneous assembly of ~7-nm-diameter cetyltrimethylammonium chloride

© 1999 NRC Canada

Fig. 9. Morphogenesis of a hexagonal mesoporous silica gyroid shape.

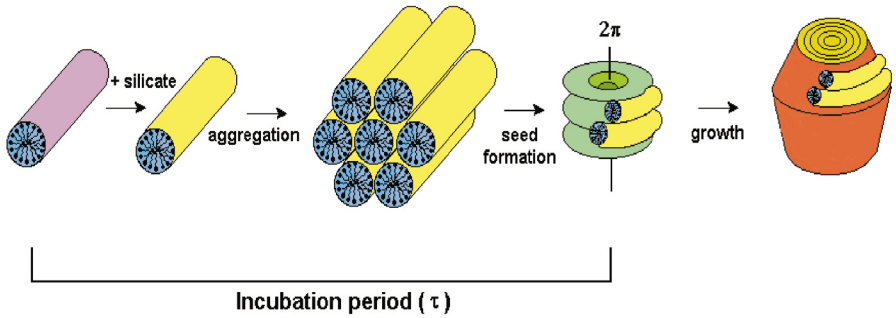

rod micelles and acid-catalyzed hydrolysis of tetraethoxyorthosilicate to soluble silicate species, (*ii*) incorporation of silicate into the headgroup region to form ~ 8-nm-diameter silicate rod micelles, (*iii*) aggregation of silicate micelle rods, and (*iv*) genesis of a gyroid/discoid-shaped silicate liquid crystal seed of size ca. 50–70 nm with a concentric director field whirling around the main rotation axis.

Processes that lead to the observed crystalline mass yield $m(t)/m(\infty)$ are described in order: (*v*) continuous accretion through "side-on" planar anchoring of silicate micelle rods on the surface mesostructure of the silicate liquid crystal seed, (*vi*) simultaneous polymerization of silicate in the microphase separated region between silicate micelles, and (*vii*) formation of rigid mesoporous silica with a well-defined gyroid/discoid shape.

The computed Avrami index *n* falls in the range expected for such a two-dimensional growth process that is to be anticipated for the morphogenesis of a gyroid/discoid shape. Similar considerations apply to the formation of fiber morphologies, except that the lower pH favors "end-on" homeotropic anchoring of the silicate micelle rods to a silicate liquid seed. Once the shape of the mesoporous silica has been established in the incubation stage, the surface mesostructure can be considered to template the growth of that shape.

Topological defects

Studies of the synthesis, bulk and surface mesostructure, morphology, and morphokinetics of hexagonal mesoporous silica emphasize the pervasive occurrence of curved shapes. This raises the issue of the origin of the curvature. A likely place to start looking for the origin of curves in this kind of materials chemistry is the deformation of an elastic liquid crystal medium. The role of splay, twist, and bend deformations of liquid crystals is well documented and usually treated by the theory of elasticity (22). Free energy minimization of the mesophase in terms of the three basic types of distortion yields patterns of stable director fields, topological defects, and optical birefringence textures for different classes of liquid crystals.

Topological defects can be line disclinations and dislocations, with micron dimensions and small energies of formation. They control the properties of liquid crystals and can be expected to play an important role in the nucleation, growth, and form of hexagonal mesoporous silica from silicification of a lyotropic hexagonal liquid crystal.

Fig. 10. Maltese cross optical birefringence pattern observed for a surfactant-free and annealed hexagonal mesoporous silica discoid between crossed polars in an optical microscope.

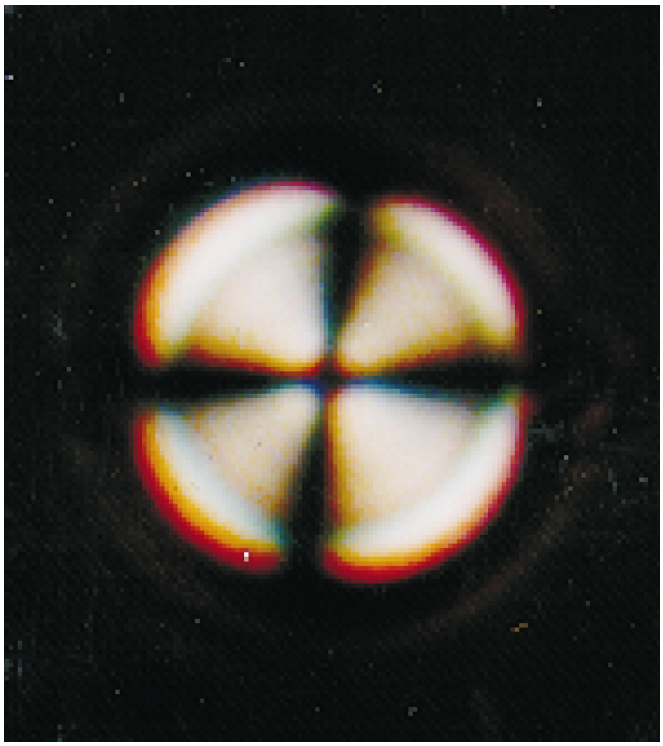

Topological defects manifest themselves in interesting ways for liquid crystals in complex geometries (23). Specifically, liquid crystal droplets show distinct director field patterns for different energy topological defects. Such defects and director field patterns may be preserved in silicate liquid crystal droplets through silicification. It is possible to envision that the growth of a particular mesoporous silica shape might be initiated by a specific kind of topological defect in a silicate liquid crystal droplet. This could apply to the early growth nuclei described above.

In this context, a relation has been found to exist between a specific type of defect and a particular mesoporous silica shape (16). Silicification essentially quenches the topological defect and its associated director field pattern as a mesoporous silica replica. An example of this is seen in the Maltese Cross optical birefringence pattern of a hexagonal

© 1999 NRC Canada

Fig. 11. Effect of the degree of surface positive charge on the structure of a hexagonal lyotropic liquid crystal growth nucleus: (A) highly protonated and (B) lightly protonated.

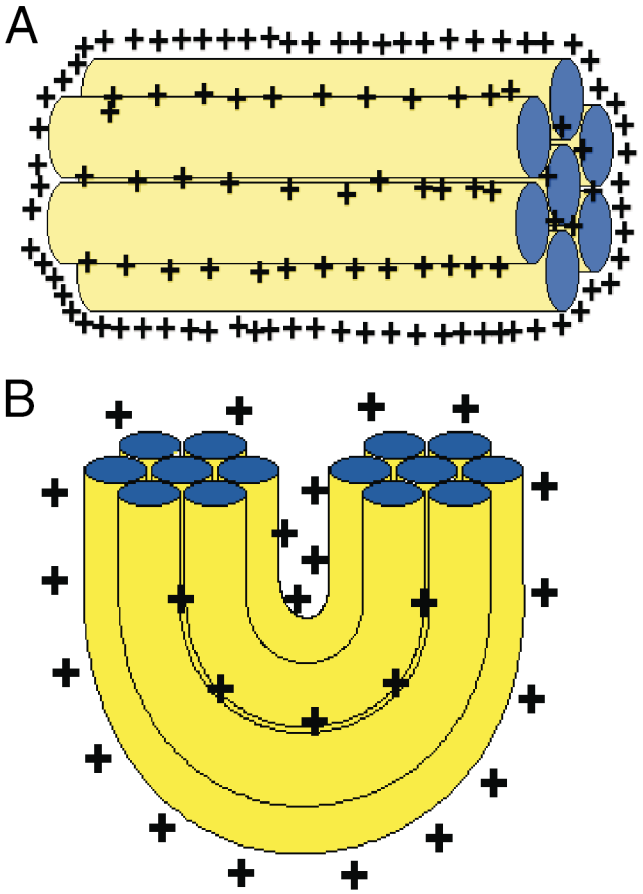

mesoporous silica discoid shape from which the surfactant had been removed and that had been annealed at 600°C to remove any micelle or strain based anisotropy (Fig. 10). The observed optical anisotropy and birefringence of the discoid must arise from the polarization response of an average electron density distributed around a concentric coaxial array of hexagonal close-packed channels. From the results it can be deduced that the surface director field of a silicate liquid crystal droplet serves to template its own polymerization and growth. The surface charge on the silicate liquid crystal and the nature of the growth medium act to control which defect is favored. In the simplest terms, a strongly acidic environment promotes a high electrical double layer repulsion and the formation of less curved shapes like fibers, while lower acidity surroundings promote more curved shapes like gyroids/discoids.

Colloidal crystallization

Collecting together the results of the above studies enables the formulation of a detailed mechanism for the growth and form of mesoporous silica shapes that is based upon the concept of colloidal crystallization. The model is founded upon the Derjaguin–Landau–Verwey–Overbeek (DLVO) theory of colloidal interactions and control of the electrical double-layer repulsion between colloidal dimension silicate micelles and silicate liquid crystal growth nuclei (24). To amplify, it is known that the ionic atmosphere around a charged colloidal particle in solution develops an electrical potential Ψ that decreases exponentially with distance z from the surface of the particle according to the Poisson–Boltzmann equation:

Fig. 12. Growth of hexagonal mesoporous silica fiber and gyroid/discoid morphologies. (A) "End-on" homeotropic addition of a highly charged silicate rod micelle to a highly charged silicate/silica fiber shaped seed. (B) "Side-on" planar addition of a lightly charged silicate rod micelle to a highly charged silicate/silica gyroid/discoid-shaped seed.

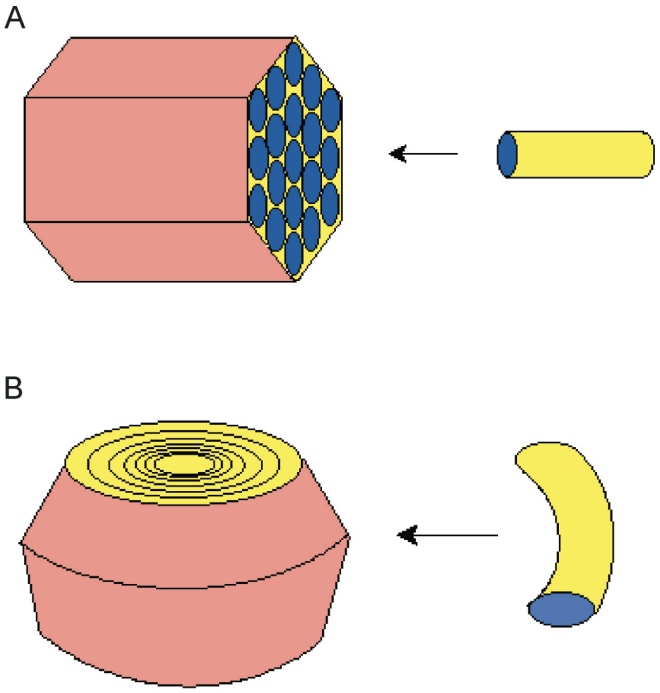

$$[2] \qquad \Psi = \Psi^{\circ} \exp(-\kappa z)$$

where κ^{-1} denotes the electrical double-layer thickness:

$$[3] \qquad \kappa^{-1} = \epsilon kT/e^2 \Sigma c_i^2 z_i^2$$

This shows that the electrical double-layer thickness can be reduced, by increasing the ionic strength $\Sigma c_i^2 z_i^2$, decreasing the dielectric constant ϵ, or decreasing the temperature T of the medium. It suggests that these synthetic parameters are "adjustable" and play an important role in the mechanism of formation of a mesoporous silica. The concept of colloidal crystallization provides a rational way of probing morphogenesis in this archetypal system, that is, experiments intentionally designed to establish the origin and growth of a particular curved shape.

This idea brings forth the relation between surface charge and shape of silicate liquid crystal growth nuclei. The concept is expressed in Fig. 11, which implies under strongly acidic conditions the elastically deformable cylindrical micelle assembly is heavily protonated and hence bears a strong positive charge. Bending is unfavorable under these conditions owing to unfavorable electrostatic repulsion, and

© 1999 NRC Canada

Fig. 13. (A) SEM, (B) TEM, and (C) POM images of radially patterned hexagonal mesoporous silica discoids.

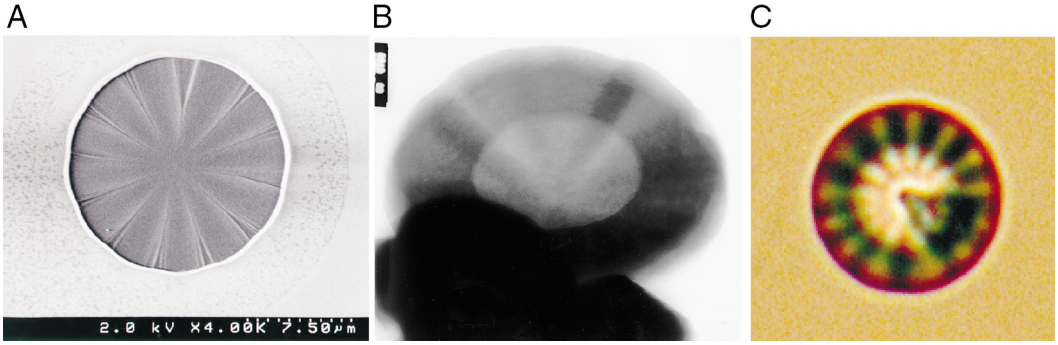

so silicate micelle growth nuclei tend towards fiber shapes. Using less acidic conditions, the micelle assembly is lightly protonated and less positively charged and is able to bend due to favorable Van der Waals attraction, so silicate micelle growth nuclei move towards discoid shapes.

The implication of the model, in the language of liquid crystals, is that at higher acidity the growth process is based upon the "end-on" homeotropic addition of silicate micelle rods to a fiber-shaped, silicate liquid crystal growth nucleus. By contrast lower acidity favors the addition of micelle rods in a "side-on" planar fashion to a discoid-shaped growth nucleus, as illustrated in Fig. 12. A colloidal crystallization description of the growth and form of fiber and gyroid/discoid mesoporous silica shapes leads naturally to the idea that at the lowest acidities a low electrical double-layer repulsion favors flocculation of silicate liquid crystal seeds. Conditions of lower acidity favor a slower rate of polymerization and a higher elasticity for the silicate mesophase. This allows the flocculate to minimize the surface-free energy and emerge as a mesoporous silica sphere shape as observed in practice.

Further evidence in support of the colloidal crystallization growth mechanism is obtained by systematically varying the electrical double-layer repulsion between silicate micelle rods and liquid crystal seeds by changing the ionic and dielectric strength of the synthesis medium. Addition of increasing amounts of a lower dielectric constant solvent than water, like ethanol, reduces the electrical double-layer repulsion and smoothly transforms a fiber preparation first to one that favors a gyroid/discoid and then to one that promotes a sphere shape. Similarly, the addition of increasing quantities of a large polarizable cation, like tetraethylammonium, to a fiber preparation creates a lower charge density in the Stern layer of the colloidal reactant particles, which results in a lower electrical double-layer repulsion, and the formation of gyroids/discoids and then spheres. Therefore the outcome of decreasing the dielectric constant and ionic strength is the same as decreasing the degree of protonation of the silicates in the micelle rods and liquid crystal seeds. The results provide compelling support for the colloidal crystallization mechanism for the formation of hexagonal mesoporous silica (14, 16).

Patterning

Intriguing designs have been found on the surface of mesoporous silica shapes (17). Radial patterns observed on discoid and gyroid morphologies are particularly impressive, as judged from the examples given in Fig. 13. While the aforementioned studies of the relation between bulk and surface mesostructure, optical birefringence, and morphology provided a useful insight into morphogenesis of curved mesoporous silica shapes, the origin of surface patterns remained an enigma and a challenge for materials chemistry.

A representative SEM image of a radially patterned discoid, bearing 12 nodes is shown in Fig. 13A. Analysis of the radial patterns of a large number of discoids showed the nodal frequency spans from 0 to over 100 with no obvious trend in the observed values. A TEM image of a whole mounted discoid specimen that displays the concentric channel structure in relation to its morphology is displayed in Fig. 13B. The optical birefringence pattern of a radially patterned discoid observed between crossed polars in an optical microscope is displayed in Fig. 13C. It is interesting to note that periodic variations in the channel director field appear to be mirrored by the frequency of radial surface patterns on a discoid and can be readily visualized in the polarizing optical microscope (POM); however they are less apparent when viewed in the electron microscope. Clearly, any periodic undulation of the channels as they whirl around the rotation axis of a discoid must be small.

Complexity

Upon thinking about an inherently simple system like the nucleation of a silicate mesophase that can grow by the accretion of silicate micelle rods and simultaneously polymerize, it is worth considering three physicochemical phenomena that could give rise to complex radial patterns on mesoporous silica discoid shapes (18). They are based on coupled chemical reactions involving activation and inhibition steps, thermally excited surface vibrational waves, and elastic deformations in a silicate liquid crystal. While these are all potentially pattern-generating systems, it is not immediately obvious which applies best and which stage in the growth process the pattern is created and rigidified as a mesoporous silica discoid.

To gain an insight into the morphogenesis of radial patterns in mesoporous silica discoid shapes, the theory of elasticity for nematics with some modification is considered a logical starting point (17). The standard model deals with a liquid crystal and a director field without a boundary. In the case of the hexagonal lyotropic silicate mesophase a boundary does exist and it turns out to be very important for the

© 1999 NRC Canada

Fig. 14. Discoid-shaped hexagonal liquid crystal with a 2π line disclination lying along the unique rotation axis *z*.

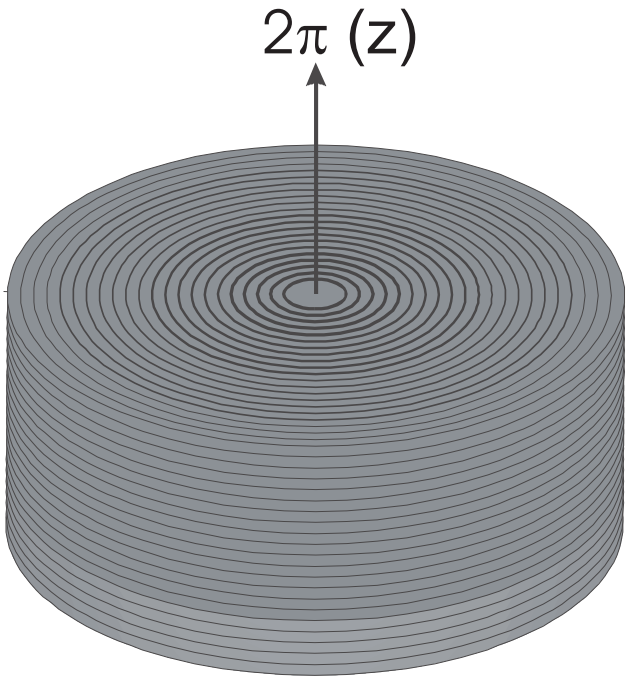

Fig. 15. Representative example of a calculated elastic distortion radial pattern of a discoid- shaped hexagonal liquid crystal.

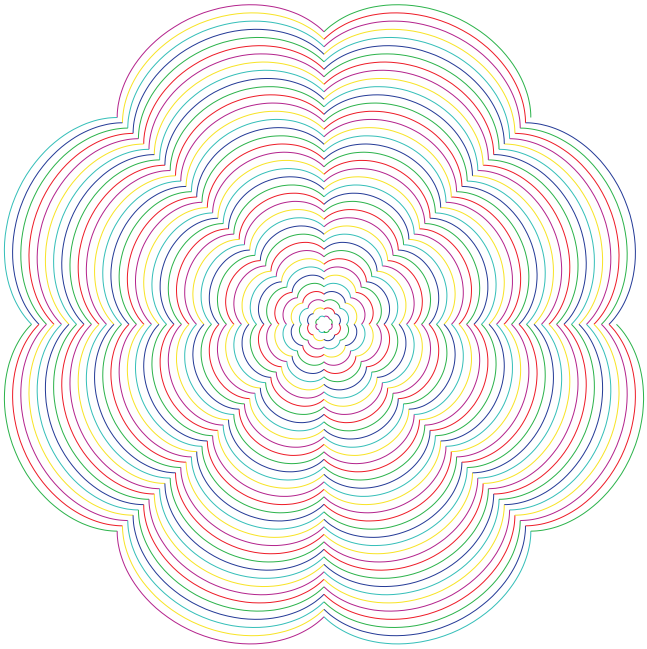

Fig. 16. (A) Observed and (B) calculated discoid hexagonal mesoporous silica morphologies with sunken shapes.

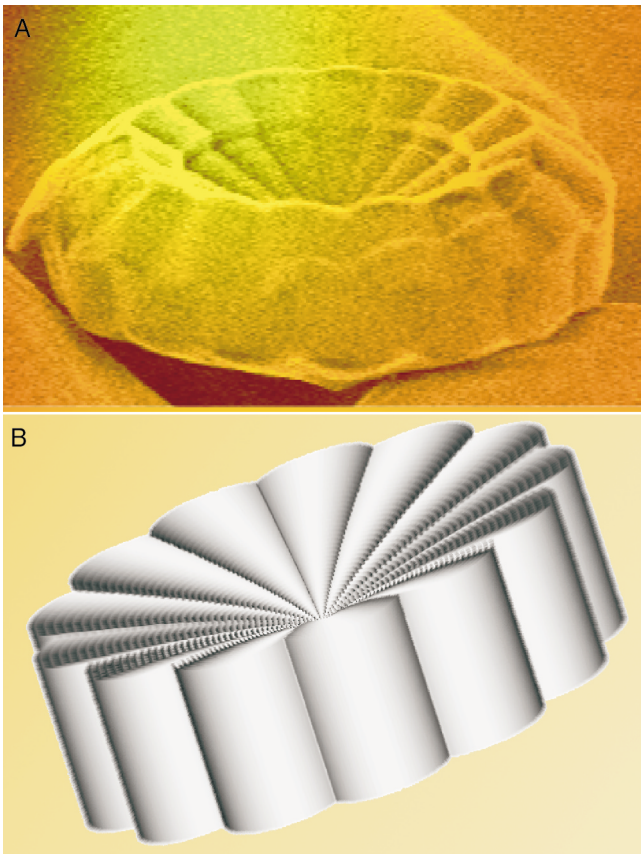

study of shape (Fig. 14). Therefore the surface tension contribution to the overall shape is considered in determining the free energy of the discoid mesophase. The equilibrium shape of a hexagonal silicate mesophase confined to a regular discoid geometry has been obtained by integrating the free energy density F_d over the volume of the liquid crystal, taking into account the surface tension term:

$$[4] \qquad F_d = \int \left\{ \frac{K_1}{2} (\mathrm{div}\,\vec{n})^2 + \frac{K_2}{2} (\vec{n}\, rot\, \vec{n})^2 + \frac{K_3}{2} (\vec{n}\, rot\, \vec{n})^2 \right\} dV + \sigma \int_{\text{surface}} \frac{|\nabla \vec{n}|}{2}\, dS$$

In this equation, K_1, K_2, and K_3 represent the splay, twist, and bend elastic deformation constants, σ is the surface tension constant, and *n* is the unit vector of the director field. It is found that the minimum energy of the regular discoid mesophase shown in Fig. 14 is attained by an elastic deformation to create a discoid with a nodal pattern, such as that illustrated in Fig. 15. Patterns of this type are similar to radial patterns observed on mesoporous silica discoid shapes.

Although calculations predict that radial patterns can appear on a planar discoid, it is found experimentally that radial patterns often occur on corrugated and (or) sunken discoid shapes (Fig. 16). Clearly, some other distortion is operative in the silicate discoid mesophase besides just spontaneous elastic deformation and that has not been taken into account in the free energy calculations.

This missing contribution to the growth process is believed to originate from longitudinal and radial differential contraction of micelle rods that comprise the liquid crystal discoid and that is induced by polymerization of silicate to silica. Because growth of a discoid is imagined to occur from the center and radially outwards, the inner portion of the discoid is expected to be more polymerized than the outer region. The outcome of including polymerization-induced differential contraction effects into the calculation

© 1999 NRC Canada

Fig. 17. (A–C) Hollow helicoid (Archimedian screw) and (D) hollow cylinder shapes of hexagonal mesoporous silica.

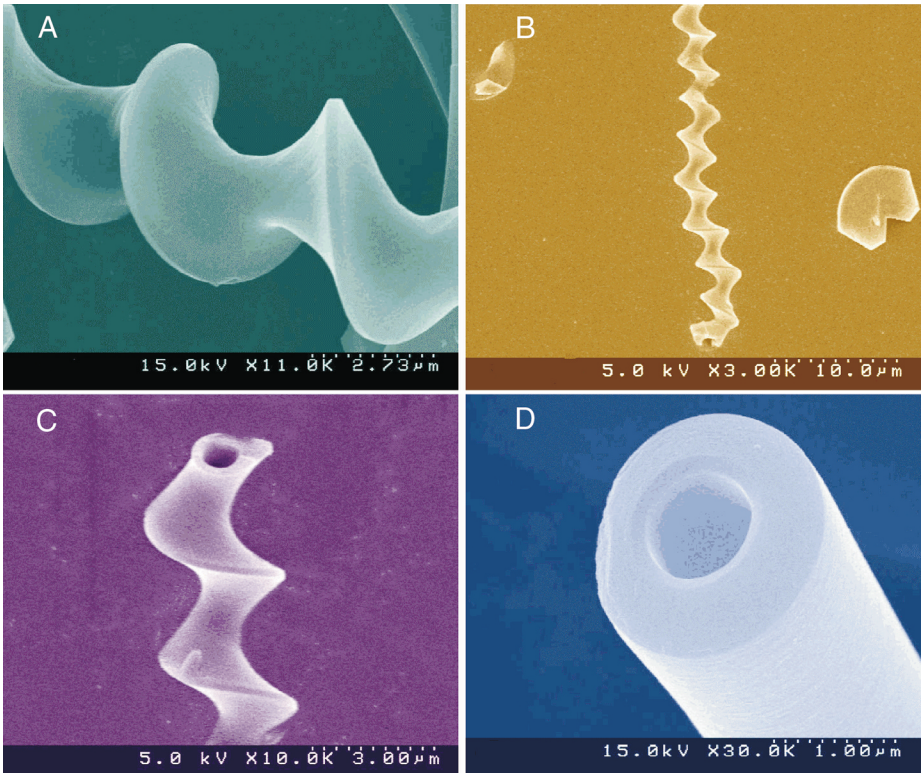

Fig. 18. TEM image of a whole mounted hexagonal mesoporous silica hollow helicoid. (A) Low magnification image of the entire morphology. (B) High magnification image depicting the mesoscale channels that follow the helicoid-generating curve of the Archimedian screw shape.

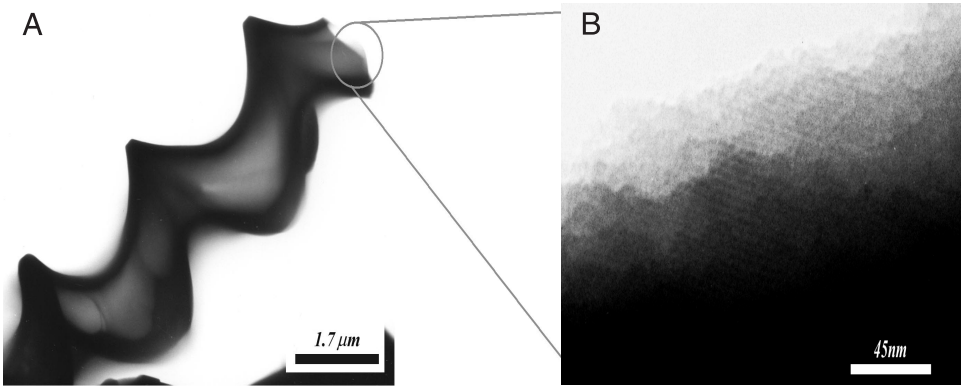

of the shape of the radially patterned mesoporous silica discoid is to create sunken discoid shapes like those shown in Fig. 16.

Supramolecular origami

Similar kinds of polymerization-induced differential contractions but now confined to a patch of hexagonal mesoporous silica film has been found to be responsible for the morphogenesis of hollow helicoids of mesoporous silica (19). It is found that a low acidity and high ionic strength medium favor a slow rate of silicification in a patch of mesoporous silca film. Hence polymerization-induced differential contraction of silicate micelle rods becomes influential in the formation of hollow helicoids rather than the formation of a mesoporous silica film (9, 10). Powder X-ray diffraction (PXRD) clearly defines the materials as hexagonal mesoporous silica and SEM images reveal morphologies consisting of extraordinary hollow helicoid shapes that resemble a screw thread (Fig. 17). TEM images recorded for whole-mounted helicoids reveal that they are hollow with a ca. 1-µm-thick "shell" (Fig. 18). They are composed of hexagonally close-packed ca. 5-nm-diameter channels which have an ca. 1-nm silica wall and appear to spiral around the major axis of the helicoid.

The dimensions of a significant collection of hollow helicoids have been analyzed by measurements of SEM images (Fig. 19A). It is striking that diagnostic dimensions of the screw, namely pitch width and angle, flute width, and inside and outside diameter, are found to span a rather narrow

© 1999 NRC Canada

Fig. 19. Screw parameters of (A) a mesoporous silica hollow helicoid and (B) histogram of number of right- and left-handed forms observed in a synthesis.

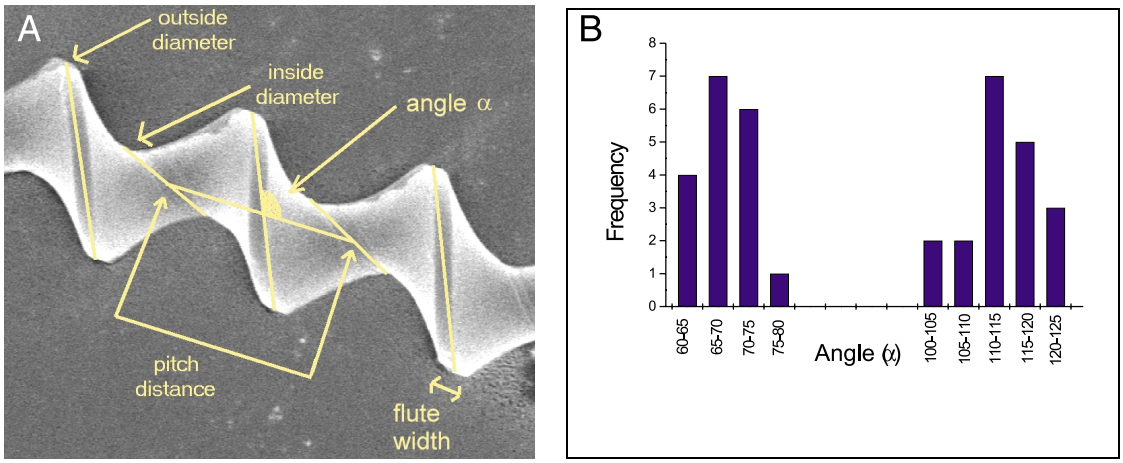

range. Notably, the pitch angle α centers around 70 and 110°, which respectively correspond to left- and right-handed helices that occur in essentially equal numbers within the same synthesis batch (Fig. 19B).

In developing a model for the morphogenesis of mesoporous silica hollow helicoids it is noted that in a synthesis they are typically accompanied by a larger yield of open-ended mesoporous silica hollow cylinders. SEM and TEM images of whole mounted specimens define well-ordered channels whirling concentrically around the axis of the cylinder. One also notices the co-existence of folded sheets, helical ribbons, hollow cones, and incomplete tubes. All of these objects are composed of the same hexagonal mesoporous silica material. Selected area electron diffraction (SAED) defines the relation between the hexagonal channel structure and morphology of a folded sheet. From the collective evidence we conclude that helical hollow cylinders originate from polymerization-induced differential contraction of a silicate liquid crystal "patch," which contracts further into hollow helicoids made of mesoporous silica (Fig. 20).

The folding mechanism emerges from both radial and longitudinal contractions across and parallel to the rods and channels, respectively, both of which are induced by polymerization of a hexagonal silicate mesophase to mesoporous silica. As the patch grows in area and thickness, older rods must undergo more polymerization and contraction than younger ones. Provided radial and longitudinal differential contractions in thickness are considered, they lead to diagonal bending of the patch because these two contractions act in mutually orthogonal directions. Within this diagonally folded patch, the volume of the micelle rods changes solely by contraction but not deformation. Therefore, the folded patch is stress free, that is, an energetically favorable configuration.

Parameters for such a configuration emerge from a purely geometrical approach and turn out to be a cylinder in which the micellar rods are pitched with a constant angle α relative to the principal axis:

$$[5] \qquad \alpha = \arctan\frac{1-\gamma_L}{1-\gamma_R}$$

Fig. 20. Supramolecular origami: polymerization-induced differential contraction and folding of a patch of hexagonal silicate liquid crystal film to give a mesoporous silica hollow cylinder.

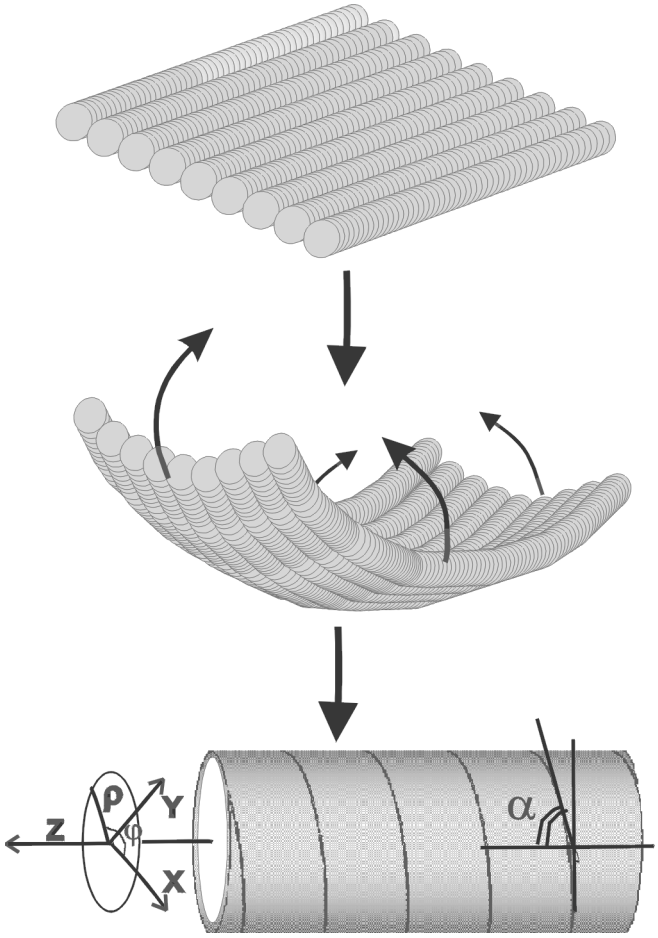

© 1999 NRC Canada

Fig. 21. Supramolecular origami: polymerization-induced differential contraction and folding of a patch of hexagonal silicate mesophase to give a mesoporous silica hollow helicoid: (A) linear and (B) quadratic contraction factor.

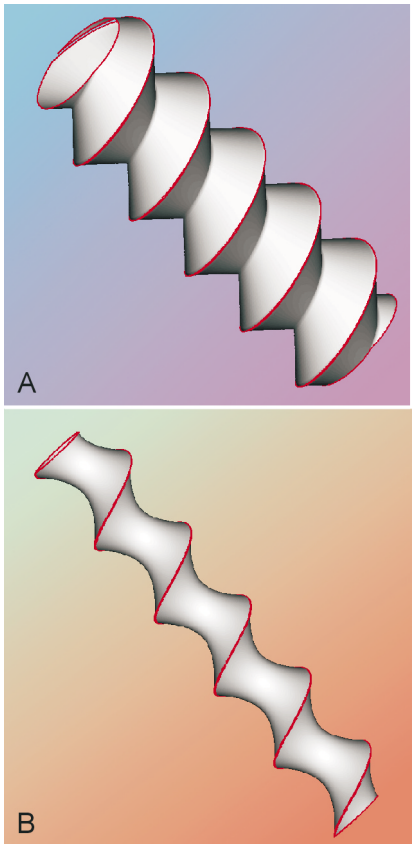

$$[6] \qquad \gamma_R \equiv \frac{\gamma_R(R_{in})}{\gamma_R(R_{out})}$$

$$[7] \qquad \gamma_L \equiv \frac{\gamma_L(R_{in})}{\gamma_L(R_{out})}$$

where γ_L and γ_R are longitudinal and radial contraction factors, and R_{in} and R_{out} are internal and external radii of the resultant cylinder, respectively. The contraction factor γ_R has been obtained from X-ray diffraction data, which provides the rod center-to-center distance before and after polymerization. It is estimated to be in the range from 0.6 to 1. The value of γ_L is obtained from the contraction expected for the condensation process SiOH + HOSi $\rightarrow$ SiOSi. It is estimated around 0.6 for complete polymerization.

To understand the case of both orthogonal and parallel differential contractions with respect to the surface of the patch, it is convenient to artificially separate the effect of bending due to polymerization in these two directions. This is possible because the configuration is free of internal stresses and therefore one stage is unlikely to influence the other. Orthogonal differential contraction gives the aforementioned hollow helical cylinder constructed from a set of N rods and described by the following set of equations:

$$[8] \qquad x_i = \rho \cos \varphi$$

$$[9] \qquad y_i = \rho \sin \varphi$$

$$[10] \qquad z_i = \left(\varphi + \sum_{k=1}^{i} \frac{d}{\rho \cos \alpha} \right) \frac{\rho}{\tan \alpha} = \frac{\rho \varphi}{\tan \alpha} + \frac{id}{\sin \alpha}$$

where i = 1, 2, 3...N is the rod number and d is the rod diameter.

Consider next differential contraction parallel to the surface of the cylinder. If we consider an infinite cylinder in which the contraction is independent of the position on the rod, then each point on the rod experiences the same tension in opposite directions. Therefore only rearrangements perpendicular to the rods, in the radial direction of the cylinder, can occur. From this one can derive that $\rho_i/(\tan \alpha_i)$ is independent of i, where ρ_i and α_i are the helicoid radius and angle of the ith rod just after beginning the second stage. From the geometry of the hollow helical cylinder the radius of the ith rod must change according to $\rho_{Li} \rightarrow \gamma_{Li}\rho$. Taking all of these into account one can obtain the equation of the contracted hollow tube:

$$[11] \qquad x_i = \gamma_{Li}\rho \cos \varphi$$

$$[12] \qquad y_i = \gamma_{Li}\rho \sin \varphi$$

$$[13] \qquad z_i = \left(\varphi + \sum_{k=1}^{i} \frac{d}{\gamma_{Li}\rho \cos \alpha} \right) \frac{\rho}{\tan \alpha}$$

An example of this simulation for linear and quadratic contractions is shown in Fig. 21. One can see an obvious resemblance to the experimental images.

In the past, helical shapes in nature have inspired such inventions as the water screw for agriculture, the retaining screw for wine presses, and architectural designs for spiral staircases. Today similarly helical-shaped DNA, proteins, and carbon nanotubes evoke great interest in biotechnology and nanotechnology. Also biomimetic synthesis of helical morphologies of calcium carbonate, barium sulfate, and silica provides insight into morphogenesis of mineralized spiral forms in biology and suggests new opportunities in materials science (19). In our work we have discovered a self-organizing synthesis involving a new kind of growth mechanism that reproducibly produces hollow helicoids of hexagonal mesoporous silica.

The understanding that has emerged from this study may reveal new ways of controlling the growth and form of composite inorganic–organic mesostructured materials with novel topologies. Siliceous hollow helicoids with spiraling channels may find utility for separating viral or bacterial particles, in chiral catalysis of macromolecules, and as micromolds for the fabrication of magnetically activated screws in microelectromechanical, microfluidic, and microanalytical devices. The ability to intentionally synthesize micron-sized shaped objects, like mesoporous silica fibers, discoids, gyroids, toroids, spheres, hollow cylinders, and hollow helicoids, begins to point the way to the idea of self-assembling "synthetic" microelectromechanical machines (SMEMS), like the one imagined in Fig. 22. One might be able to employ SMEMS as an alternative or adjunct to currently employed MEMS techniques, which rely on the fabrication of components. This paradigm raises some intriguing possibilities for future research aimed at the organization and inte-

© 1999 NRC Canada

Fig. 22. Futuristic concept of synthetic microelectromechanical machines (SMEMS).

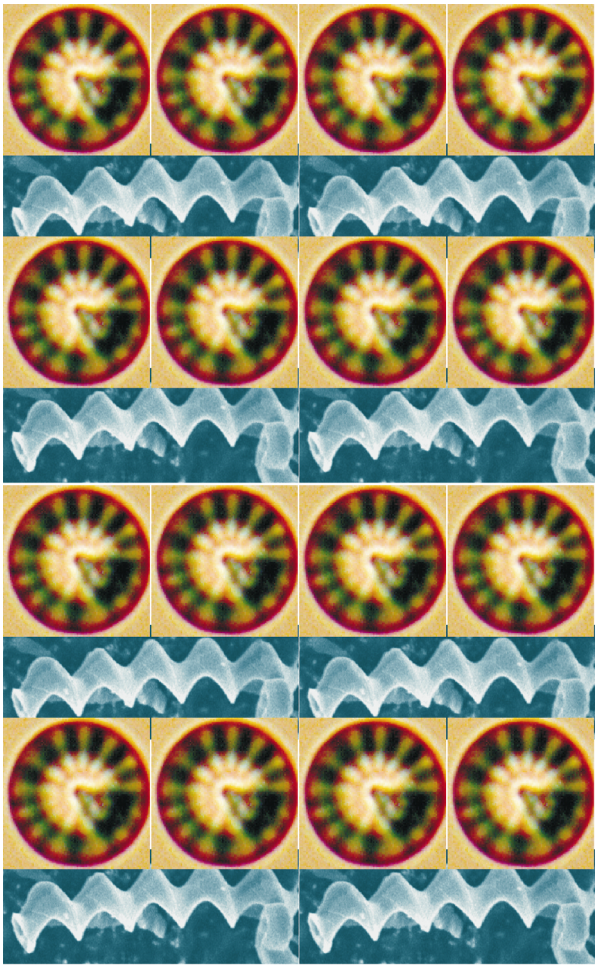

gration of synthetically shaped materials for functional devices (20, 21, 25).

Language of shape

Research on morphogenesis of mesoporous silica curved shapes required the crossing of boundaries between subdisciplines of chemistry. It involved the integration of chemical and physical concepts, synthetic methods, processing strategies, and analytical techniques, in surfactant, sol–gel, liquid crystal, surface, colloid, and crystal growth science. This entailed an appreciation of the role of topological defects, director fields, surface charge, elastic deformations, and polymerization-induced differential contraction in the nucleation and growth of mesoporous silica from a silicate mesophase.

A "language of shape" has emerged from studies of morphogenesis of mesoporous silica. The alphabet and words, sentences and paragraphs, and the pages of this story are laid out below.

Co-assembly
- Silicate rod micelles
- Silicate liquid crystal seeds

Growth nuclei
- Soft silicate mesophase, defects, director field patterns
- Initiates and directs growth to a particular shape

Growth
- Seed–rod, planar or homeotropic anchoring
- Seed–seed flocculation

Morphology and patterns
- Electrical double-layer effects
- Colloidal crystallization growth mechanism
- Elastic deformation surface patterns
- Polymerization induced differential contraction distortions

Hierarchy
- Distinct building rules at increasing length scales
- Shape and pattern generation
- Integration of structural components

Value of form

Ultimately, the scientific and technological impact of any new class of materials depends on the ability to control the size, morphology, and aggregate structure of primary particles. Self-assembling supramolecular materials are no exception in this respect. They introduce hierarchy for the first time into materials chemistry and bode well for the development of materials with novel properties, new functions, and perceived utility in a range of applications. Possibilities include mesostructured materials for large molecule catalysis, membrane separation and sensing, fuel cell electrodes, battery electrolytes, solar cells, chromatography supports, chiral separation stationary phases, bone implants, chemical delivery vehicles, enzyme immobilization, polymer composites, toxic cleanup of water streams, and acoustic and thermal insulation. The future looks very bright for self-assembling supramolecular materials.

Acknowledgements

The research described in this summary of my Pure or Applied Inorganic Chemistry Award Lecture has profoundly influenced my way of thinking about materials chemistry. Novel concepts in self-assembly, hierarchy, complexity, and topology that could lead to the networking of structural components over different length scales, to ultimately create a purely synthetic integrated chemical system, have been introduced and hopefully will make a difference to the way materials research evolves in the new millennium.

None of this would have been possible without the contributions of my co-workers Drs. Hong Yang, San Ming Yang, Neil Coombs, and Igor Sokolov who challenged me every day with important, insightful and creative ideas and suggestions. Dr. Charles Kresge championed the mesochemistry research in the group from 1994 to 1999 and was a regular visitor in Toronto for many memorable brainstorming sessions, both in the laboratory and at Avalon. During this exciting period of research, G.A.O. was awarded an Issac Walton Killam Memorial Fellowship from the Canada Council and H.Y. was awarded the 1998 NSERC Prize for the top Ph.D. Thesis in Canadian Natural Sciences. G.A.O. is also grateful to the Natural Sciences and Engineering Research

© 1999 NRC Canada

Council for financial support of this phase of the work. The sustained support and encouragement from the Chairman of the Chemistry Department, Dr. Martin Moskovits, is appreciated. G.A.O. is deeply indebted to Dr. Alan MacKay of Birkbeck College London University for stimulating discussions in the early stages of morphosynthesis and for translating the last book of Ernst Haeckel, Crystal Souls, an important work in the history of morphology (26). And last, but not least, I wish to express my gratitude to my best friend Linda Ozin who tries to make my writing more lucid.

References

1. J.M. Lehn. Supramolecular chemistry, concepts and perspectives. VCH, Weinheim, 1995.
2. G.A. Ozin. Morphogenesis of biomineral and morphosynthesis of biomimetic forms. Acc. Chem. Res. **30**, 17 (1997).
3. (*a*) C.T. Kresge, M. Leonowicz, W.J. Roth, J.C. Vartuli, and J.C. Beck. Ordered mesoporous molecular sieves synthesized by a liquid-crystal template mechanism. Nature (London), **359**, 710 (1992); (*b*) J.Y. Ying, C.P. Mehnert, and M.S. Wong. Synthesis and applications of supramolecular-templated mesoporous materials. Angew. Chem. Int. Ed. Engl. **38**, 56 (1999), and refs. therein.
4. G.A. Ozin and S. Mann. Synthesis of inorganic materials with complex form. Nature (London), **382**, 313 (1996).
5. G.A. Ozin, D. Khushalani, S. Oliver, G.C. Shen, I. Sokolov, and H. Yang. Blueprints for inorganic materials with natural form: inorganic liquid crystals and a language of inorganic shape. J. Chem. Soc. Dalton Trans., Spec. Issue Bioinorg. Chem., 3941 (1997).
6. P. Behrens. Voids in variable chemical surroundings: mesoporous metal oxides. Angew. Chem. Int. Ed. Engl. **35**, 515 (1996).
7. R. Zana, J. Frasch, M. Soulard, B. Lebeau, and J. Patarin. Fluorescence probing investigations of the mechanism of formation of organized mesoporous silica. Langmuir, **15**, 2603 (1999).
8. G.A. Ozin, H. Yang, and N. Coombs. Morphogenesis of shapes and surface patterns in mesoporous silica. Nature (London), **386**, 692 (1997).
9. H. Yang, N. Coombs, A. Kuperman, S. Mamiche-Afara, and G.A. Ozin. Synthesis of oriented mesoporous silica film on mica. Nature (London), **379**, 703 (1996).
10. G.A. Ozin, H. Yang, and N. Coombs. Free-standing and oriented mesoporous silica films grown at the air-water interface. Nature (London), **381**, 589 (1996).
11. G.A. Ozin, N. Coombs, I. Sokolov, and H. Yang. Shell mimetics. Adv. Mater. (Weinheim Ger.), **9**, 662 (1997).
12. G.A. Ozin, N. Coombs, and H. Yang. Mesoporous silica with micron scale designs. Adv. Mater. (Weinheim Ger.), **9**, 811 (1997).
13. G.A. Ozin, H. Yang, N. Coombs, and I. Sokolov. Synthesis of mesoporous silica spheres under quiescent aqueous acidic conditions. J. Mater. Chem. **8**, 743 (1998).
14. G.A. Ozin, C.T. Kresge, and H. Yang. Nucleation growth and form of mesoporous silica: role of defects and language of shape. Stud. Surf. Sci. Catal. **117**, 119 (1998).
15. G.A. Ozin, C.T. Kresge, S.M. Yang, H. Yang, N. Coombs, and I. Sokolov. Morphokinetics: growth of mesoporous silica curved shapes. Adv. Mater. (Weinheim Ger.), **11**, 52 (1999).
16. G.A. Ozin, C.T. Kresge, and H. Yang. The role of defects in the formation of mesoporous silica fibers, films and curved shapes. Adv. Mater. (Weinheim Ger.), **10**, 883 (1998).
17. G.A. Ozin, C.T. Kresge, H. Yang, and I. Sokolov. Radial patterns in mesoporous silica. Adv. Mater. (Weinheim Ger.), **11**, 636 (1999).
18. G.M. Whitesides and R.F. Ismagilov. Complexity in chemistry. Science (Washington, D.C.), **284**, 89 (1999).
19. G.A. Ozin, S.M. Yang, I. Sokolov, and N. Coombs. Supramolecular origami, hollow helicoids of mesoporous silica. Adv. Mater. (Weinheim Ger.), In press. (1999).
20. G.A. Ozin. Panoscopic materials: synthesis over "all" length scales. J. Chem. Soc. Chem. Commun. In press. (1999).
21. G.A. Ozin, E. Chomski, D. Khushalani, and M.J. MacLachlan. Mesochemistry. Curr. Opin. Coll. Interface Sci. **3**, 181 (1998).
22. L.D. Landau and E.M. Lifshitz. Theory of elasticity. Pergamon Press, New York. 1972.
23. G.P. Crawford and S. Zumer. Liquid crystals in complex geometries formed by polymer and porous networks. Taylor and Francis, London. 1996.
24. D.H. Everett. Basic principles of colloid science. Royal Society of Chemistry Paperbacks, Royal Society of Chemistry, Cambridge. 1994.
25. P. Day. Room at the bottom. Chem. Br., July, 29 (1999).
26. A. Mackay. "Crystal souls - Ernst Haeckel and biological forms." Society for Science on Form, Japan. Forma, **14**, 1999.

© 1999 NRC Canada

Spectroscopic conformational study of PMS 952, a specific imidazoline ligand. Experimental results

Marie-Hélène Baron, Sabine Halut-Desportes, Hai-Fen Ye, Jack Huet, and Edith Favre

Abstract: X-ray analysis of PMS 952 displays two kinds of very strong hydrogen bonds, an intramolecular one stabilizing the conformer **A** and an intermolecular one that associates conformers **A** to form two infinite chains. The ^{1}H NMR study of vicinal coupling constants based on dihedral angle values, evidences that PMS 952 takes up an eclipsed conformation, in CCl_4 and $CDCl_3$ solutions, closely related to the conformation in solid state. Deuterium exchange in methanol-d_4 points out the presence of a tautomeric form. However, as there is spectral evidence neither from NMR nor from FTIR studies for such a tautomer, this specie cannot be taken into account to explain the complexity of the FTIR spectra. NMR data also reveal that the imidazoline ring freely rotates while FTIR analysis allows characterizing two conformers (**A** and **B**), with lifetime shorter than NMR time scale. These two conformers are stabilized by two different intramolecular H-bonds. Taking into account that conformer **A** could exist in two states (monomer **A** and $\mathbf{(A)}_n$-chains), an equilibrium between **A**, $\mathbf{(A)}_n$, and **B** entities allowed the assignment of all main bands of the IR spectra, assigned to νNH, νOH, νCH, and νCN modes. The strength of hydrogen bonds is solvent dependent. Polar solvents, either proton donor or acceptor stabilized the conformer **A**, while CCl_4 favors the conformer **B**.

Key words: hydrogen bonds, X-ray, NMR, FTIR, imidazoline derivative.

Résumé : L'analyse du PMS 952 par diffraction X met en évidence deux types de liaisons hydrogène très fortes. Une liaison intramoléculaire stabilise les molécules sous forme de conformères **A** qui s'associent par liaisons intermoléculaires en deux chaînes paralèlles. L'étude RMN montre que dans un solvant apolaire ou peu polaire la conformation de la molécule dans le solide est conservée, alors que dans le méthanol, qui pertube les liaisons hydrogène il n'y a plus de rotamère privilégié. L'échange de protons dans le méthanol deutérié met en évidence une forme tautomère mais en quantité trop faible pour être décelée par spectroscopies RMN ou IR. Enfin l'équivalence magnétique des protons des deux méthylènes du cycle imidazolinique montre que celui-ci tourne librement, l'échelle de temps de la RMN ne permettant pas d'identifier des rotamères. Cette caractérisation se fait cependant par analyse IR qui met en évidence deux conformères **A** et **B** stabilisés par deux liaisons hydrogène intramoléculaires différentes. Le conformère **A** pouvant exister sous forme de monomère et sous forme associée $\mathbf{(A)}_n$, l'équilibre entre les espèces **A**, $\mathbf{(A)}_n$ et **B** permet d'attribuer les principales bandes des spectres aux modes νNH, νOH, νCH et νCN des différentes espèces. La polarité des solvants module la force des liaisons hydrogène intramoléculaires, les solvants polaires stabilisent le conformère **A**, alors que le CCl_4 stabilise le conformère **B**.

Mots clés : liaisons hydrogène, diffraction X, spectroscopies RMN, IRTF, dérivé imidazolinique.

Introduction

A vast array of α and β-adrenoceptor agonists and antagonists (α_1, α_2, β_1, β_2, β_3, and their subtypes) have been synthesized for decades. These compounds present many different pharmacological applications, i.e., antihypertension, obesity, non insulino dependant diabetes, analgesia, depression, etc., (1). On the other hand, over the past it has been established that many of adrenergic agents can interact with discrete imidazoline receptors I_1 and 1_2, named Imidazoline Prefering Binding Sites (IPBS) (2). The ubiquitous affinity on α and I receptors of the main part of these molecules makes the interpretation of the mechanism inducing the therapeutical effects difficult.

Received April 4, 1999.

E. Favre,[1] J. Huet, and H.-F. Ye. Laboratoire de Pharmacochimie Moléculaire et Systèmes membranaires, Casier 70 66 Université Denis Diderot-Paris 7, 2 Place Jussieu, 75251 Paris, cedex 05, France.
S. Halut-Desportes. Laboratoire de Chimie Inorganique et Matériaux Moléculaires Université P&M Curie-Paris 6, ESA CNRS 7071, 4 Place Jussieu, 75252 Paris, cedex 05, France.
M.-H. Baron. Laboratoire de Dynamique, Interactions et Réactivité. CNRS, UPR 2631 Université P&M Curie-Paris 6, 2 rue Henri Dunant, 94320 Thiais, France.

[1]Author to whom correspondence may be addressed. Telephone: 33 1 44 27 60 49. Fax: 33 1 44 27 56 41.
e-mail: favre@paris7.jussieu.fr

 © 1999 NRC Canada

Table 1. Crystallographic data.

Formula	$C_{13}H_{16}N_2O$
Fw	216.28
Crystal system	Monoclinic
a (Å)	9.169(2)
b (Å)	6.940(2)
c (Å)	18.446(3)
β (deg)	102.70(1)
V (Å^3)	1145(1)
Z	4
Space group	$P2_1/c$
Crystal shape	Parallelepiped
Crystal colour	Colourless
Linear absorption coefficient μ (cm^{-1})	0.75
Density ρ (g cm^3)	1.25
Diffractometer	CAD4, Enraf–Nonius
Radiation	MoKα (λ = 0.71069 Å)
Scan type	ω/2θ
Scan range (°)	0.8 + 0.345 tan θ
θ limits (°)	1–25
Temperature of measurement	Room temperature
Octants collected	h, –10, 10; *k*, 0.8; *l*, 0.21
No. of data collected	2347
No. of unique data collected	2016
Merging *R*	0.02
No. of unique data used for refinement	707 $(F_o)^2 > 3\sigma(F_o)^2$
Decay of standard reflections (%)	None
$R = \Sigma\|F_o - \|F_c\|\|/\Sigma F_o$	0.058
$Rw = [\Sigma w(F_o - \|F_c\|)^2/\Sigma w F_o^2]^{1/2}$	0.052
Extinction parameter	8.5
Goodness of fit	1.9
No. of variables	81
$\Delta\rho_{min}$ (e/Å^3)	–0.20
$\Delta\rho_{max}$ (e/Å^3)	0.25

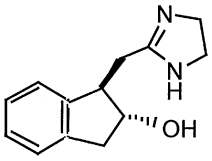

PMS 952

PMS 952 or 1-(2′-methylimidazolyl)-2-hydroxyindane presents interesting in vitro results, highly potent on I_1-PBS with an inhibition constant of 22 nM, and a significant specificity versus α_2 affinity (I_1/α_2 = 145).

The originality of this molecule is due to the presence of a hydroxyl group, generally absent of such potent molecules, except in the natural ligands (epinephrine and norepinephrine). The current paper is focused on conformational study. Structurally, hydrogen bondings may occur between this hydroxyl group and either NH entity or sp^2 nitrogen atom of the imidazoline ring. X-ray diffraction and spectroscopic studies were performed on PMS 952 to investigate this possible competition. Analysis of ^{1}H NMR spectra were carried out to reveal possible favored conformations, and FTIR spectroscopy is performed to study the occurrence and the strength of the H-bonds. Moreover, the very low time scale in IR allows characterizing conformers, which cannot be identified by NMR.

Experimental

For spectroscopic experiments deuterated solvents, CD_3OD, $CDCl_3$, CD_3CN, and DMSO-d_6 from SdS Company (France) were directly used. CCl_4 from Prolabo was dried on 5 Å molecular sieves.

PMS 952 was prepared by Ye (3).

X-ray analysis

A single crystal was selected and mounted on an automatic CAD-4F diffractometer using monochromated Mo Kα radiation. Unit cell dimensions with estimated standard deviations were obtained from least-squares refinements of the setting angles of 25 well-centered reflections. The intensities of two standard reflections, measured every hour throughout the data collection, show nonsignificant decay. Crystallographic data and other information are summarized in Table 1.

© 1999 NRC Canada

Table 2. Fractional atomic coordinates.

Atom	*x*/*a*	*y*/*b*	*z*/*c*	*U*(iso)	*U*(eq)
N(1)	0.4818(6)	0.7839(8)	0.0854(3)		0.0524
N(3)	0.4235(5)	0.4778(8)	0.1028(3)		0.0511
O(1)	0.5635(5)	0.1528(6)	0.1561(2)		0.0581
C(1)	0.6663(6)	0.4335(9)	0.2355(3)	0.039(2)	
C(2)	0.6954(7)	0.2470(9)	0.1946(3)	0.047(2)	
C(3)	0.7874(7)	0.120(1)	0.2540(3)	0.052(2)	
C(4)	0.9960(7)	0.231(1)	0.3654(4)	0.055(2)	
C(5)	1.0538(8)	0.384(1)	0.4105(4)	0.064(2)	
C(6)	0.9869(7)	0.564(1)	0.4004(4)	0.056(2)	
C(7)	0.8605(7)	0.5911(9)	0.3439(3)	0.051(2)	
C(8)	0.8036(7)	0.4390(9)	0.2977(3)	0.040(2)	
C(9)	0.8712(6)	0.2576(9)	0.3095(3)	0.043(2)	
C(10)	0.6411(6)	0.6156(9)	0.1894(3)	0.045(2)	
C(2′)	0.5125(7)	0.6194(9)	0.1262(3)	0.040(2)	
C(4′)	0.3142(7)	0.539(1)	0.0363(4)	0.055(2)	
C(5′)	0.3380(7)	0.761(1)	0.0322(4)	0.060(2)	

Corrections were made for Lorentz and polarization effects. An extinction correction was necessary. Computations were performed by using the PC version of CRYSTALS (4). Atomic form factors for neutral O, N, C, and H were taken from ref. 5. Real and imaginary parts of anomalous dispersion were taken into account. The structure was solved by direct methods using the SHELXS86 program (6) and successive Fourier maps. All hydrogen atoms have been located on difference maps, their positions were not refined, and they were given an overall thermal parameter.

Because of the few number of reflections only nitrogen and oxygen atoms were anisotropically refined, the other atoms were refined with an isotropic thermal parameter. Full matrix least-squares refinements were carried out by minimizing the function $\Sigma w(|F_o| - |F_c|)^2$, where F_o and F_c are the observed and calculated structure factors. Models converged with $R = \Sigma(||F_o| - |F_c||)/\Sigma|F_o|$ and $Rw = [\Sigma w(|F_o| - |F_c|)^2/\Sigma w(F_o)^2]^{1/2}$ to values listed in Table 1.

In the last stages of the refinement, each reflection was assigned a weight unity. Criteria for a satisfactory complete analysis were the ratio of rms shift to standard deviations being less than 0.2, and no significant features in the final difference map.

Atomic coordinates are given in Table 2.

Supplementary material available includes interatomic distances and bond angles, tables of anisotropic thermal parameters, coordinates of hydrogen atoms, bond distances and angles concerning hydrogen atoms and temperature factors.[2]

NMR experiments

^{1}H NMR spectra were recorded for CD_3OD, $CDCl_3$, and CCl_4 solutions using hexamethyldisyloxane as internal standard on a Bruker AC-200 FT instrument. For deuterium exchange experiments a 4.60×10^{-2} mol L^{-1} CD_3OD solution was used.

Transmission FTIR

FTIR spectra were recorded on a Perkin Elmer 1720 instrument equipped with a DTGS detector. Resolution was set at 4 cm^{-1}, using boxcar. A Balston air dryer from Whatman (U.K.) dried before and during measurements the spectrometer. Solutions at various concentrations from 10^{-3} to 10^{-1} mol L^{-1} were introduced into CaF_2 cells with 100, 200, or 500 μm spacers. For the solid phase, suspensions in Nujol/Fluorolub dispersives were inserted between two CaF_2 plates without spacer. A KBr pellet was also prepared with the powdered compound. For the solutions, difference spectra were computed between spectra of solutions and corresponding solvents. The spectral decomposition of the difference spectra were performed in the 2500–3480 cm^{-1} spectral range with a least-squares iterative program (Levenberg–Marquardt) (7). For these decompositions the number of bands and their frequencies at maximum were measured on second derivative spectra. Self-deconvolution procedure gave the same number of spectral components at similar frequencies, respectively (7). In most cases it has been possible to maintain close frequencies and specific empirical half-band width at half-band height for each kind of absorption bands, as CH and bonded or unbounded OH and NH groups. Lorentzian band profile was introduced for any band. Thus, only the area of each peak was adjusted to fit the overall spectra range. Changes in relative intensity according to solvent are qualitatively related to conformation changes.

Results and discussion

Crystallography

Structural analysis of PMS 952 shows a *trans* configuration for the methylene C10 and the hydroxyl group linked to the indane backbone. The OH group is involved in an intramolecular hydrogen bond with the N3 atom, forming a seven-membered ring.

[2] Supplementary material may be purchased from: The Depository of Unpublished Data, Document Delivery, CISTI, National Research Council Canada, Ottawa, Canada, K1A 0S2. With the exception of tables of anisotropic thermal parameters and temperature factors, these have also been deposited with the Cambridge Crystallographic Data Centre and can be obtained on request from: The Director, Cambridge Crystallographic Data Centre, University Chemical Laboratory, 12 Union Road, Cambridge, CB2 1EZ, U.K.

© 1999 NRC Canada

Fig. 1. Perspective view of the structure of PMS 952.

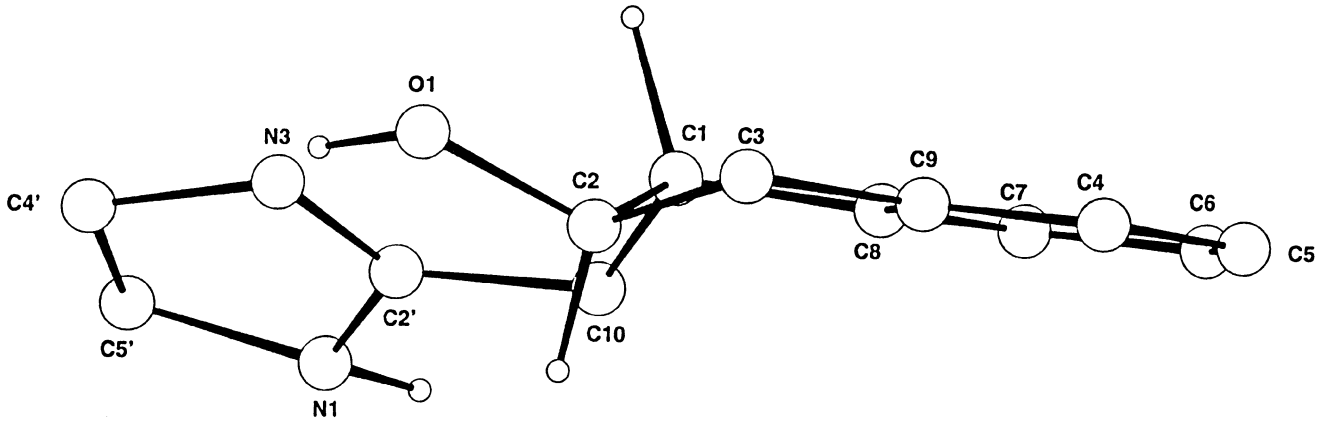

Fig. 2. Projection on *bc* plane showing chains including hydrogen bonds.

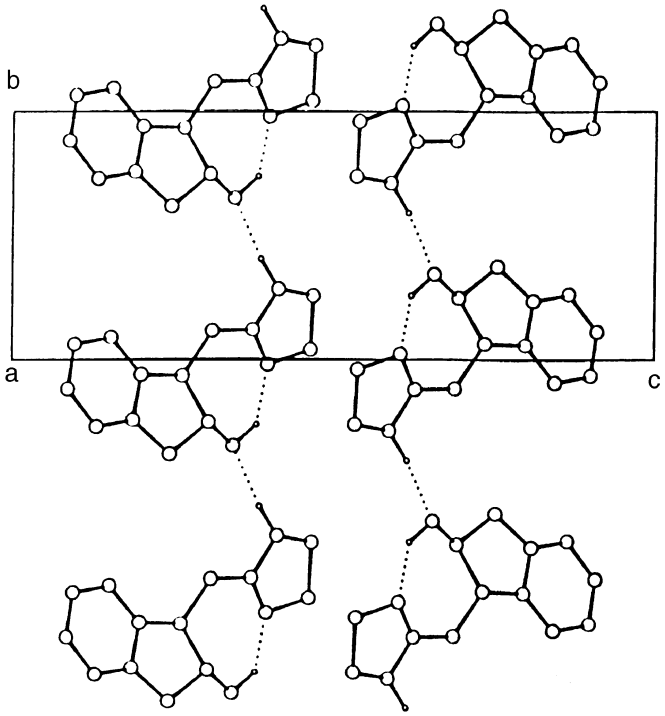

The molecule is shown on Fig. 1 with atom numbering using CAMERON (8).

The overall geometry is characterized by two main planes defined respectively by the atoms C1, C3, and the phenyl ring and by the atoms of imidazoline. The seven-membered ring connects these two planes (Fig. 1).

Eight over the nine atoms of the indane backbone are coplanar, the maximum distances to the plane being –0.017 Å for C1 and 0.024 Å for C8. The ninth atom C2 is located 0.451 Å out of the plane inducing an envelope conformation. The imidazoline ring is almost planar with distances to the plane: 0.087 Å for C5′ and 0.076 Å for C4′. The angle between this plane and the indane backbone is 151°. The seven-membered ring has a cycloheptane chair like conformation, C1, C10, C2′, and N3 being nearly coplanar. Within this ring the hydrogen atom H201 is involved in a strong intramolecular hydrogen bond with a distance H201···N3 = 1.77 Å and an angle N3···H201-O1 = 143°. In addition there is an intermolecular hydrogen bond between H200 atom (linked to N1) and O1 atom to form two infinite chains parallel to the *b* axis (distance H200···O1 = 1.88 Å and angle N1-H200···O1 = 168°). Figure 2 displays the molecular arrangement with inter- and intramolecular hydrogen bonds.

As a conclusion, PMS 952 appears conformationally blocked in the solid state, NMR and IR studies providing dynamic aspects in solutions are described hereafter.

NMR study

Spectra were recorded in three solvents, CD_3OD, $CDCl_3$, and CCl_4. Table 3 displays chemical shifts (^1H, δ ppm) and geminal coupling constants (^2J, Hz) for diasterotopic protons linked to C3 and C10 carbon atoms, and Fig. 3 gives atom positions and numbering. Signal assignments for spectra recorded in CD_3OD was readily achieved as all signals were clearly discernible, except for the H10 signal, which partially overlaps with the residual CH_3OH peak. In addition, the total deuterium exchange of H100 and H101 simplified the spectrum. Irradiation of the signal at 854 Hz, relative to H20, allowed assigning the singlet at 3.38 ppm to H10 unambiguously and also confirmed chemical shifts for H30 and H31 that appeared as two doublets. There is an overall similarity between proton chemical shifts and splitting patterns observed in CD_3OD, $CDCl_3$, and CCl_4, then the assignment of proton resonances for $CDCl_3$ and CCl_4 solutions was achieved by a comparison with chemical shifts observed for CD_3OD solutions. To control these attributions, the spectrum of PMS 952 with fully deuterated methylene C10 was also run in $CDCl_3$, and irradiation of H20 was performed.

A noteworthy detail is that the four imidazoline protons give rise to a singlet in the three solvents used. The magnetic equivalence of these protons implies that imidazoline ring freely rotates around the C10—C2′ bond on NMR time scale (ca. 10^{-6} s).

The general coupling pattern is observed for the diasterotopic protons of methylenes C3 and C10. Table 4 displays experimental and theoretical values of dihedral angles and vicinal coupling constants. Theoretical values were computed (PC MODEL program)[3] from the fractional parameters

[3] PCMODEL, V6.0. Serena Software, Box 3076, Bloomington, Ind. 47402-3076, U.S.A.

© 1999 NRC Canada

Table 3. Chemical shifts δH (ppm) and geminal coupling constants ^2J (Hz) of ABX systems.[a]

	$CDCl_3$		CCl_4		CD_3OD	
H	δ (ppm)	^2J (Hz)	δ (ppm)	^2J (Hz)	δ (ppm)	^2J (Hz)
H100	2.26 (dd)	17	1.93 (dd)	17.2	2.43 (dd); 2.66 (dd)	16
H101	2.66 (dd)		2.57 (dd)			
H30	2.88 (dd)	15.5	2.82 (dd)	15.5	2.83 (dd); 3.25 (dd)	15
H31	3.20 (dd)		3.17 (dd)			
H10	3.30 (m)		3.13 (m)		3.38 (m)	
H20	4.26 (m)		4.07 (m)		4.27 (m)	
H40′–41′, H50′–51′	3.58 (s)		3.29 (s)		3.63 (s)	
HAr	7.09 (m)		6.87 (m)		7.21 (m)	

[a]dd, doublet of doublet; m, multiplet; s, singlet.

Table 4. Theoretical and experimental vicinal coupling constants ^3J (Hz).

	^3J (Hz)	Theoretical values		Experimental values			
		Dihedral angle (°) PCMODEL	^3J (Hz) PCMODEL	Dihedral angle (°) (RX)	^3J (Hz) $CDCl_3$	^3J (Hz) CCl_4	^3J (Hz) CD_3OD
a	$^3J_{H20,H30}$	143	7.6	142.0	7.7	7.7	5.7; 6.6
b	$^3J_{H20,H31}$	26	8.9	25.7	9.0	9.2	
c	$^3J_{H10,H20}$	147.1	6.8	147.3	6.4	6.4	—
d	$^3J_{H10,H100}$	74.5	1.5	74.7	3.0	2.6	8.8; 6.3
e	$^3J_{H10,H101}$	5.2	11.9	5.1	11.7	11.9	

Fig. 3. Cameron view of PMS 952 with atom numbering.

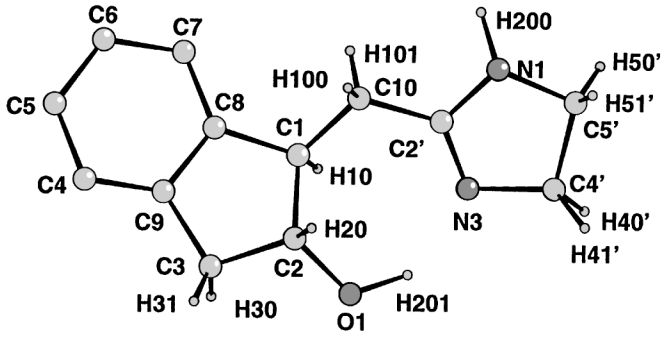

determined by X-ray analysis, according to Karplus rule. As expected dihedral angle values from PC MODEL program and those from X-ray analysis, both deriving from the same X-ray parameters, give the same results. Interestingly, theoretical coupling constants and experimental ones relative to $CDCl_3$ and CCl_4 solutions fit perfectly for all vicinal protons. In methanol solutions no correlation exists.

PMS 952 spectra display two ABX systems, (H30, H31, H20) and (H100, H101, H10). The protons of the first system are bonded to the semi-rigid part (five-membered ring) of the indane backbone, and then the relative dihedral angles (H30-C3-C2-H20) and (H31-C3-C2-H20) cannot freely fluctuate, resulting in experimental ^3J values ($^3J_{H20,H30}$ and $^3J_{H20,H31}$) in the same range for $CDCl_3$ and CCl_4 solutions (Table 4, entries *a*, *b*). These dihedral angle values of 142° and 26°, respectively, are relevant with the envelope conformation of the cyclopentane ring pointed out by X-ray analysis. This also holds true for the dihedral angle (H10-C1-C2-H20) of 147° (Table 4, entry *c*).

In the second ABX system, free rotation round C1—C10 bond may be allowed. But, in fact, a favored conformation exists in $CDCl_3$ and CCl_4 solutions, this conformation in dilute solutions is closely related to the conformation in solid state as stated by the similarity with theoretical and experimental ^3J values relative to $^3J_{H10,H100}$ and $^3J_{H10,H101}$ (Table 4, entries *d*, *e*). Such similarity in conformation between solution and crystalline state had been observed with norepinephrine (1). According to dihedral angles values θ (for H101-C10-C1-H10) of 5.1°, the conformation observed in $CDCl_3$ and CCl_4 solutions is eclipsed (**a**).

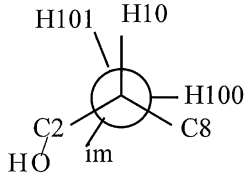

(**a**)

© 1999 NRC Canada

Fig. 4. FTIR transmission spectra of PMS 952. Fluorolub mull until 1300 cm^{-1}, then Nujol mull (*a*); difference spectra for solutions 10^{-2} mol L^{-1} in CD_3CN (*b*), in CCl_4 (*c*).

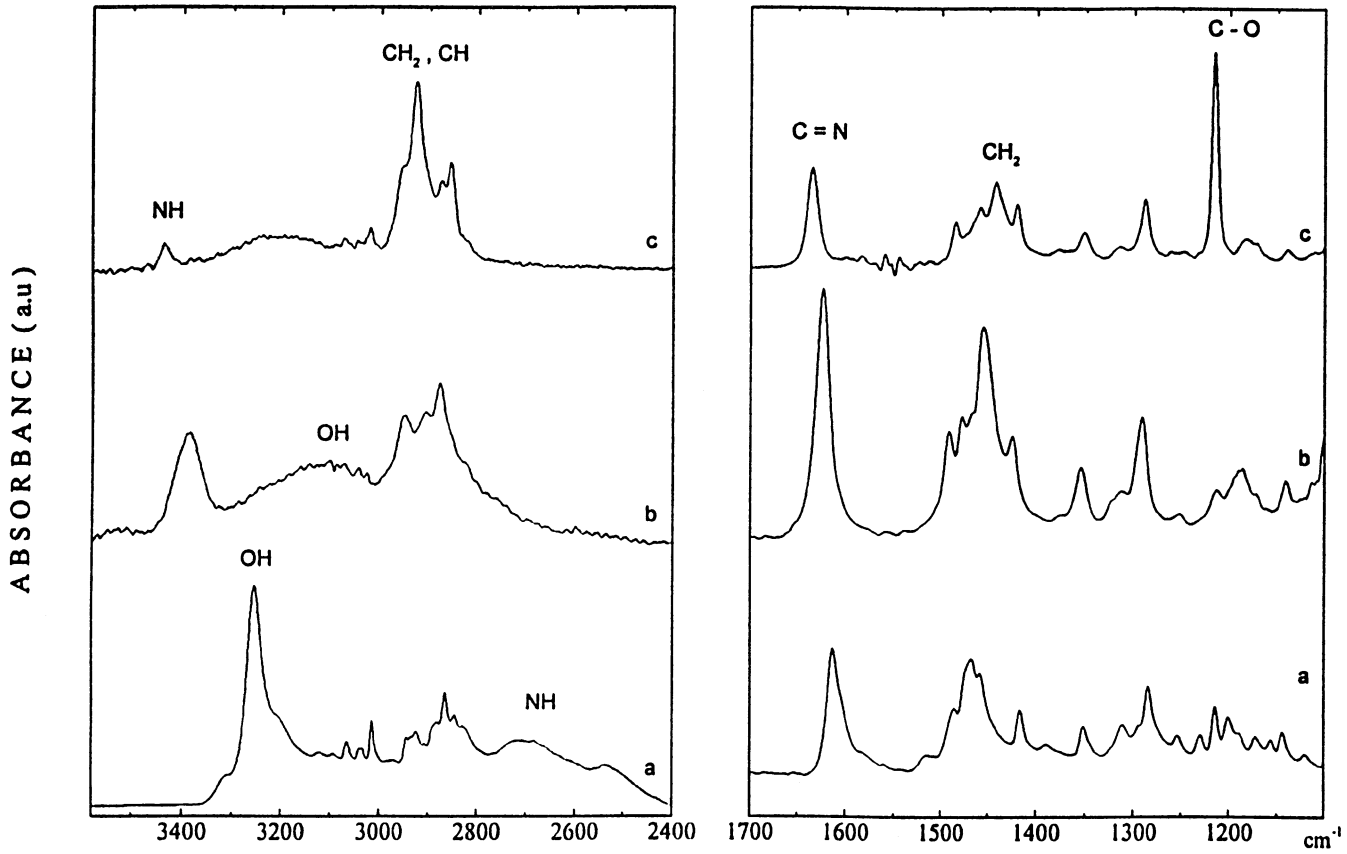

In this conformation H100 is distorted from the eclipsed position with a dihedral angle θ (H100-C10-C1-H10) of 74.6°.

Taking into account, on one hand, the experimental values of the vicinal coupling constants ^3J (11.7 and 3 Hz) and the values of the chemical shifts (2.26 and 2.66 ppm) of H100 and H101 and, on the other hand, the values of dihedral angle (5.1° and 74.6° from X-ray or theoretical data), we can state that H100 rises at 2.26 ppm and H101 at 2.66 ppm. Exactly similar reasoning shows that H30 rises at 2.88 ppm and H31 at 3.20 ppm.

In methanol solutions the experimental values of vicinal coupling constants do not fit with any dihedral angle or theoretical coupling constant values. This is related to an average value between several rotamers, resulting in the impossibility to attribute the coupling constant values $^3J_{H20,H30}$ and $^3J_{H20,H31}$ (Table 4, entries *a*, *b*) and $^3J_{H10,H100}$ and $^3J_{H10,H101}$ (Table 4, entries *d*, *e*). This could be due to the perturbation of the intramolecular H-bonds induced by methanol, when this solvent interacts either with the N3 atom (CD_3O-D···N3) or with the O1 atom (CD_3O-D···O1).

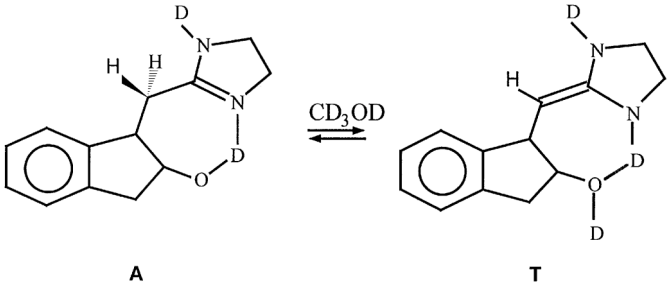

The deuterium exchange in CD_3OD of the protons H100 and H101, used for signal assignment, also pointed out the existence of a tautomeric form **T** in equilibrium with form **A**.

However, no olefinic proton resonance is detected in the 4–7 ppm range. The tautomeric form should exist in a very small amount, lower than 5%, as usually observed for enol form in keto–enol equilibrium when enol is not stabilized. This parallelism may be carried on, as the deuterium exchange was slow. The decrease of integrated signals versus time shows that the two diasterotopic protons H100 and H101 exchange at different rate. From kinetic curves $t_{1/2}$ = 6 h for the proton at 2.43 ppm and 12 h for the second one at 2.66 ppm.

FTIR vibrational analysis

Solid state

X-ray analysis of PMS 952 in the crystalline state points out the occurrence of strong intra and intermolecular hydrogen bonds. As expected, FTIR spectra of KBr pellet or fluorolub dispersion display these hydrogen bonds (Fig. 4*a*). Because it becomes much weaker on spectra for the solutions (see further), the very broad band centered at 2700 cm^{-1} is assigned to the NH stretching mode of the imidazoline ring involved in the intermolecular hydrogen bond (N1-H200···O1) described in X-ray study. The sharper band at 3255 cm^{-1} is attributed to the stretching vibration (νOH) of the OH group involved both in intra (O1-H201···N3) and

© 1999 NRC Canada

Fig. 5. FTIR transmisson difference spectra of PMS 952 in solution 2×10^{-2} mol L^{-1}. The spectral decompositions were performed following the procedure described in the experimental section.

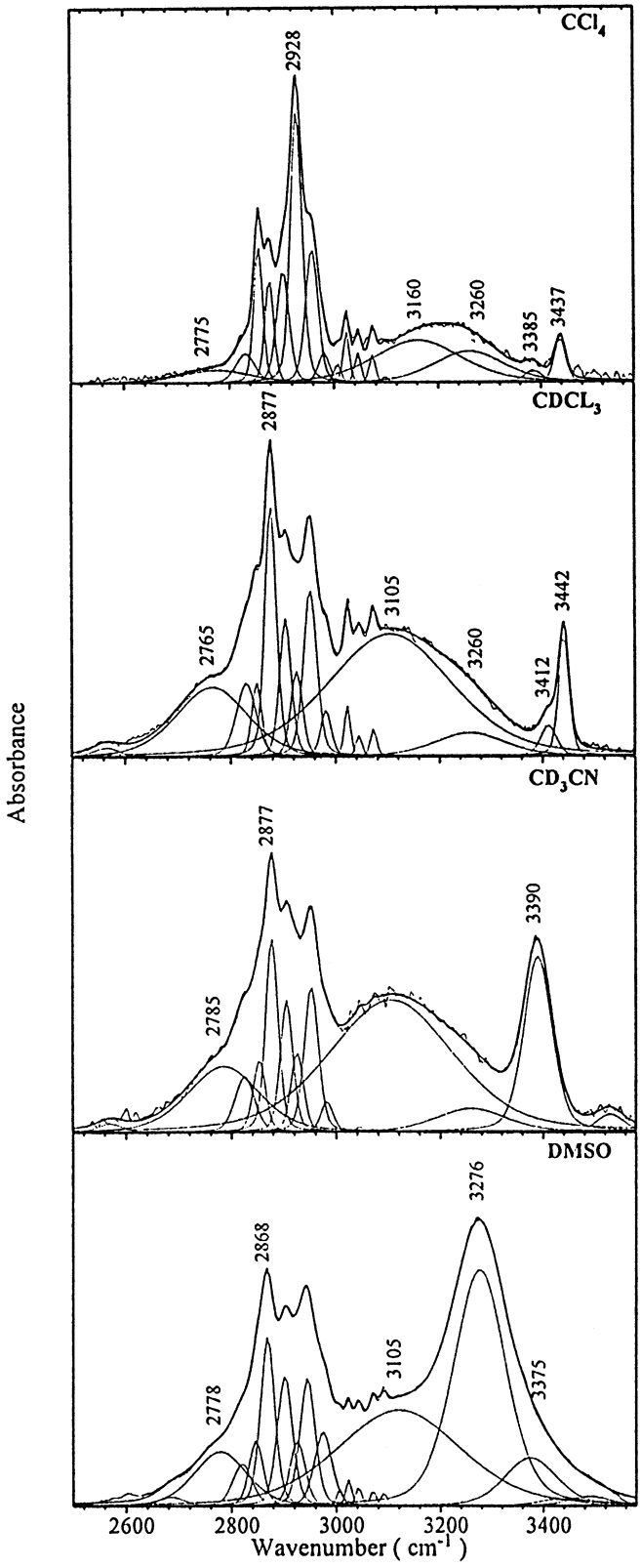

intermolecular (N1-H200···O1) bonds. Two shoulders are also detected in this spectral range. The one at 3208 cm^{-1} should also correspond to OH groups but only involved in the intramolecular hydrogen bond for molecules standing at the end of the polymeric chains described in X-ray analysis (Fig. 2). Compared to the other νOH mode the 47 cm^{-1} downshift reflects an enhancement of the strength of the intramolecular H-bond when the O1 oxygen atom is no more influenced by the intermolecular H-bond. The other shoulder at 3360 cm^{-1} might correspond to the free NH group on molecules located at the other extremity of the polymeric chains.

In the 1100–1700 cm^{-1} range the ν(C=N) mode arises at 1613 cm^{-1}. This low value for a ν(C=N) mode is relevant with a (N1-C2′-N3) conjugated system in this imidazoline ring, as currently observed in conjugated imine (9, 10).

Solutions

Spectra are recorded for solutions in CCl_4, as apolar solvent, $CDCl_3$, as proton donor, and CD_3CN and DMSO-d_6, as proton acceptor solvents.

Spectra for $CDCl_3$ (not shown) and CD_3CN (Fig. 4*b*) solutions display similar absorption profiles. DMSO only induces band broadening and frequency shifts. In CCl_4 large intensity changes are denoted (Fig. 4*c*). For a better identification of the individual vibrational modes, all absorption profiles have been decomposed in the 3000–3400 cm^{-1} range (Fig. 5). The number of bands for OH and NH modes largely exceeded that expected for a single molecular entity. Added to changes in relative intensity depending on solvents, the overall features reflect the presence of different species in equilibrium (see further for the detailed FTIR spectral analysis). From the X-ray and solid state FTIR analyses, the major species in the solid state is the conformer **A** in self-associated form $\mathbf{(A)}_n$, stabilized by both intramolecular H-bond (O1-H201···N3) and intermolecular H-bond (N1-H200···O1), giving the bands νOH and νNH at 3255 cm^{-1} and ca. 2700 cm^{-1}, respectively. In solution at 10^{-2} mol L^{-1} concentration, the conformer **A** could stay partly self-associated $\mathbf{(A)}_n$ via the intermolecular H-bond (N1-H200···O1), in agreement with a remaining component centered ca. 2700 cm^{-1}. In $CDCl_3$, CD_3CN, and DMSO-d_6 no significant spectral change was observable with the PMS 952 dilution from 10^{-1} to 10^{-3} mol L^{-1}, suggesting that such dilutions do not notably modify the molecular structure of the product. (In the apolar solvent CCl_4, PMS 952 was not soluble at 10^{-1} mol L^{-1}). In any solvent, spectra recorded at 10^{-3} mol L^{-1} were too weak to evaluate the expected decrease of the 2700 cm^{-1} shoulder.

Besides, NMR study has shown that in solution imidazole ring rotates around the C10—C2′ bond. This rotation could allow the formation of a second type of conformer, conformer **B**, stabilized by the intramolecular H-bond between H200 and O1 atoms (N1-H200···O1), instead of the exclusive (O1-H201···N3) intramolecular H-bond evidenced by X-ray for the solid. Indeed, in absence of self-association, the ratio between **A** and **B** species differing only by intramolecular linkages should be concentration independent. For polar solvents PMS 952 spectra are similar for 10^{-1} and 10^{-2} mol L^{-1}, indicating that A/B ratio is not significantly modified. This is in agreement with only a few amounts of self-associated species in these solvents. NMR would not detect the con-

© 1999 NRC Canada

Table 5. Vibrational frequencies for conformers **A** and **B**.

	Conformer **A**					Conformer **B**			
	Solid state	CCl_4	$CDCl_3$	CD_3CN	DMSO-d_6	CCl_4	$CDCl_3$	CD_3CN	DMSO-d_6
ν N-H	3360a	3437	3442	3390	3276	3260	3260	3260	≈3276
ν N-H[b]	2700	2775	2765	2785	2778	—	—	—	—
ν O-H	3255, 3208[a]	3160	3105	3105	3105	3385	3412	≈3390	3375
ν C=N	1613	1635	1629	1624	1618	1635	1629	1624	1618
ν C-H[c]	—	2786w	2877S	2877S	2868S	2928S	2925w	2925w	2925w

[a]Shoulder.

[b]N-H involved in intermolecular H-bond observed in self-associated species $(\mathbf{A})_n$.

[c]Refers to ν C-H, which intensities are strongly solvent dependent. S, strong; w, weak.

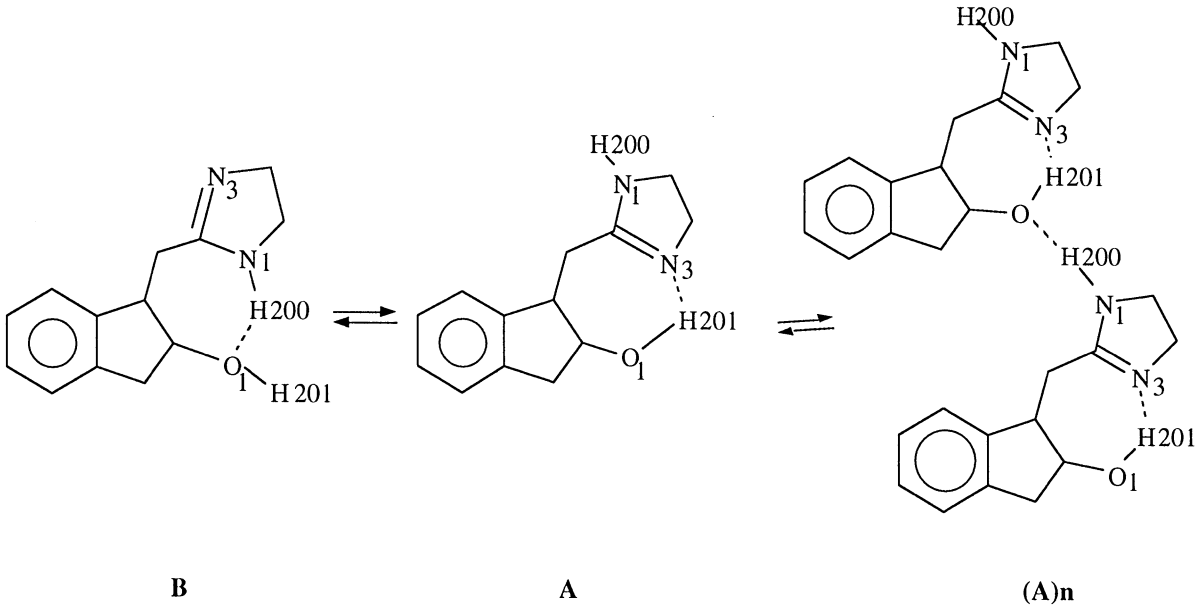

B **A** **(A)n**

former **B** due to a too short lifetime for NMR time scale (ca. 10^{-6} s). Conversely, it could be detected by the IR technique characterized by a much shorter time scale (ca. 10^{-13} s). An equilibrium between three species effectively fit the overall set of NH and OH stretching vibrations observed for OH and NH groups involved, or not, into hydrogen bonds:

A "free" NH group and an OH function involved in the intramolecular (O1-H201···N3) bond are both associated to the monomeric conformer **A**.

Intra (O1-H201···N3) and intermolecular (N1-H200···O1) H-bonds and "free" NH groups are attributed to self-associated conformers $(\mathbf{A})_n$.

The NH group involved in an intramolecular H-bond (N1-H200···O1) is associated to conformer **B**. In this case the oxygen atom becomes an acceptor site for H200. Then, for conformer **B**, not only bonded N1-H, but also O1-H and C-O1 stretching modes, are modified with respect to conformer **A**.

N-H stretching modes: Spectra shown in Fig. 5 display relatively sharp bands standing between 3442 and 3390 cm^{-1}. They are assigned to the νNH mode of the conformer **A** (Table 5). Compared to the νNH frequency for the solution in CCl_4 (3437 cm^{-1}) the weak increase with $CDCl_3$ (3442 cm^{-1}) implies a direct influence of this proton donor solvent on the hybridization state at the N1 nitrogen level (11). The down-shift of the νNH frequency to 3390 cm^{-1} with CD_3CN results from a direct H-bond of H200 with the C≡N moiety of this solvent (N1-H200···N≡C). Such H-bond increases with DMSO (N1-H200···O=S) as shown by the enhanced intensity and larger down shift of the νNH vibration (3276 cm^{-1}) (12).

The broad absorption bands in the 2800–2700 cm^{-1} range are assigned to the νN1-H200···O1 modes of self-associated conformers $(\mathbf{A})_n$ (Fig. 5). In the solid state, for $(\mathbf{A})_n$ species, this band raises ca. 2700 cm^{-1} (see above). In solutions this interaction is slightly solvent dependent (Table 5). It is noteworthy that dilution to 10^{-2} mol L^{-1} does not wholly prevent PMS 952 from self-association, via intermolecular H-bond, even in the very polar solvent such as DMSO.

The broad and relatively weaker absorption centered at 3260 cm^{-1} for the solutions in CCl_4, $CDCl_3$, and CD_3CN are associated to NH groups involved in the intramolecular N1-H200···O1 hydrogen bond in conformers **B** (Table 5). With DMSO this νNH mode for the conformer **B** could be overlapped by the νNH mode of the conformer **A** when its NH is bonded to the solvent.

O-H stretching modes: The broad bands in the 3100–3200 cm^{-1} range (Fig. 5) are assigned to the νOH mode for the H-bonded OH group of the conformer **A** (O1-H201···N3) (Table 5). In the solid state the corresponding band is not only sharper, but also at higher frequency (3255 cm^{-1})

© 1999 NRC Canada

because the O1 atom is simultaneously proton donor and electron acceptor when conformers **A** are self-associated (Fig. 2 and 4*a*). In solution the proportion of monomers over oligomers is much larger, and a mixture of **A** and $\mathbf{(A)}_n$ species explains the averaged increase of the internal H-bond strength and the broadness of the bands.

The νOH mode, centered at 3160 cm^{-1} for the CCl_4 solution, is shifted down to 3105 cm^{-1} with CD_3CN and DMSO. This means that the intramolecular H-bond (O1-H201···N3) is stronger in the proton acceptor solvents than in the apolar solvent. It should be related to the direct interaction of acetonitrile or DMSO with the N1-H group, increasing the local electron donor character on the conjugated N3 nitrogen on the imidazoline ring (12)..

The νOH mode for conformer **A** arises in the same range (3105 cm^{-1}) in the proton donor solvent $CDCl_3$. Compared to CCl_4 the increase of the strength of the intramolecular (O1-H201···N3) bond in $CDCl_3$ is this time, connected to the interaction of chloroform on the N1 atom. This entails a change in the hybridization state on the N1 atom, also influencing the conjugated (N1-C2′-N3) system (11).

In the 3400 cm^{-1} range, spectra for CCl_4 and $CDCl_3$ solutions display a weak and narrow band assigned to the νOH mode of conformer **B**. With CCl_4 this mode arises at 3385 cm^{-1}, while it is at slightly higher frequency with $CDCl_3$ (3412 cm^{-1}). Direct proton donor effect of chloroform on O1 is assumed, as on N1, for the conformer **A**, to explain this 17 cm^{-1} shift. At lower frequency, with increased intensity and strong broadening, the band in DMSO at 3375 cm^{-1} accounts for the relatively strong H-bond expected between the OH group and this basic solvent for the conformer **B**. In CD_3CN this band is assumed to be overlapped by the N-H stretching mode of the conformer **A** (3390 cm^{-1}).

Comparing intensities of bands relative to the intramolecular bonded νOH and νNH assigned to conformers **A** and **B**, respectively, it appears that the ratio A/B is smaller in CCl_4 than in $CDCl_3$ or CD_3CN solutions. The shift of the conformational equilibrium from conformer **A** to conformer **B** in CCl_4 is relevant with the weaker strength in this solvent, of the intramolecular (O1-H201···N3) bond relative to conformer **A**, which should facilitate the rotation of the imidazoline ring.

C-H stretching modes: The dependence on solvents of the A/B conformer ratio is connected with large intensity changes in the spectral range related to the aliphatic CH stretching modes (3000–2800 cm^{-1}). Accounting for the number of aliphatic CH of PMS 952, a tenth of individual νCH modes is expected for each conformer. However, only seven peaks are intense and resolved enough to be clearly identified on the second derivative absorption profiles. Only slight frequency shifts have been detected depending on solvents. However, the intensity of two components (2877 and 2928 cm^{-1}) is obviously solvent dependent. The component at 2877 cm^{-1}, relatively strong for $CDCl_3$, CD_3CN, and DMSO solutions, has a much weaker relative intensity for the CCl_4 solution. Conversely, the component at 2928 cm^{-1} weak for the solutions in polar solvents becomes strong in the apolar solvent. Accounting for the increase of the conformer **B** ratio versus **A** in CCl_4, the 2928 cm^{-1} band is assigned to conformer **B**, the 2877 cm^{-1} band to conformer **A** (Fig. 5, Table 5). Accordingly, changes associated to CH_2 deformation modes occur in the 1450 cm^{-1} spectral range (Fig. 4).

Compared to the solid state, no significant change occurs in the 3000–3100 cm^{-1} range for any solution corresponding to aromatic and ethylenic νC-H modes. This is relevant with NMR data: a significant amount of tautomer **T** should have resulted in the appearance of a specific ethylenic νC-H band.

C-O stretching mode: A band at 1216 cm^{-1} is strongly enhanced in CCl_4 (Fig. 4*b* and 4*c*). It might be assigned to the νC-O mode. Its strong enhancement when the proportion of the conformer **B** increases over conformer **A** might be due to an important electronic change on the C-OH functional group. Instead of being proton donor in the intramolecular O1-H···N3 of conformer **A**, the O1 atom becomes proton acceptor in the N1-H···O1 linkage for conformer **B**.

C=N stretching mode: According both to NMR and IR results excluding the presence of a significant amount of tautomer species, only one double bond is detected in the 1600–1700 cm^{-1} range. The band arising ca. 1620 cm^{-1} is assigned to the νC=N stretching mode of both conformers **A** and **B** and not to the νC=C mode of the tautomer.

No splitting is detected for νC=N vibration that could be related to the A/B conformational equilibrium. Indeed, this mode is expected to be much less sensitive to the H-bond network than the νOH and νNH modes. However, the νC=N frequency decreases with polar solvents (Table 5). So far this is relevant to a decrease of C=N bond order related to specific effects of the solvents on the conjugated N1-C-N3 system, already mentioned. Once more the affinity of $CDCl_3$ (proton donor) for the N1 nitrogen atom and the affinity of basic solvents for N1-H200 proton have qualitatively similar electronic consequences.

Conclusions

Intra and intermolecular hydrogen bonds pointed out by X-ray analysis of PMS 952 in the solid state appeared to be very strong. They are still observed by FTIR spectroscopy in solutions, even in polar solvents. Furthermore, ^1H NMR study of vicinal coupling constants, based on dihedral angle values, evidences that the conformation about C1—C10, C1—C2, and C2—C3 bonds in CCl_4 and $CDCl_3$ solutions are closely related to the conformation in solid state. So, little changes in solvent polarity do not affect the rigidity of this part of the molecule. However the restricted rotation are not observed in methanol, which is a competing agent for H-bonds. In addition, NMR spectra show that, for all solvents used, the imidazoline ring freely rotates around the C2′—C10 bond on NMR time scale, but this rotation does not notably modify dihedral angle values. On the other hand, the FTIR analysis pointed out the occurrence of two species, **A** and **B** conformers, deducing each other by a rotation around the C2′—C10 bond, and stabilized by two kinds of intramolecular hydrogen bonds. These entities should have too short lifetime to be detected by NMR. Their ratio depends on solvent effects. Polar solvents, either proton donor or acceptor, increase the strength of the (O1-H201···N3) intramolecular H-bond, versus the (N1-H200···O1) one, favouring conformer **A** over **B**. Conversely conformer **B** is

© 1999 NRC Canada

stabilized in the apolar solvent CCl_4. This emphasizes that structurally and electronically the imidazoline side of PMS 952 displays a large adaptability to various binding sites. This is relevant to its ability to bind I_1, I_2, α_1, and α_2 receptors, even if it is much more efficient on the I_1 binding site.

Acknowledgments

Financial support from Institut de Recherche Servier is acknowledged. The authors thank Dr. G. Chassaing for useful discussions, and Dr. N. Goasdoué for helpful comments on the manuscript. We are grateful to Dr. J.E. Ombetta in using PCMODEL for the theoretical coupling constant determinations, and Dr. A. Ensuque and M. Revault for technical assistance in printing IR spectra.

References

1. R.R. Ruffolo, Jr., W. Bondinell, and J.P. Hieble. J. Med. Chem. **38**, 3681 (1995).
2. S. Regunathan and D.J. Reis. Annu. Rev. Pharmacol. Toxicol. **36**, 511 (1996).
3. H.-F. Ye. Ph.D. thesis. (T. Paris-7 1998 163) Université Denis Diderot, Paris. 1998.
4. D.J. Watkin, J.R. Carruthers, and P.W. Betteridge. CRYSTALS, an advanced crystallographic computer program. Chemical Crystallography Laboratory, Oxford. 1988.
5. International tables for X-ray crystallography. Vol. IV. Kynoch Press, Birmingham, U.K. England. 1974.
6. G.M. Sheldrick. SHELXS86. Program for solution of crystal structures. University of Göttingen, Germany. 1986.
7. D. Baron. *In* Logiciels pour la chimie. Societé française de Chimie, Paris. 1991. p. 282.
8. L.J. Pearce and D.J. Watkin. Chemical Crystallography Laboratory, Oxford. 1992.
9. J. Favrot, D. Vocelle, and C. Sandorfy. Photochem. Photobiol. **30**, 417 (1979).
10. S. Gerscher, M. Mylrajan, P. Hildebrandt, M.H. Baron, R. Müller, and M. Engelhard. Biochemistry, **36**, 11 012 (1997).
11. A. Piart-Goypiron, M.H. Baron, H. Zine, J. Belloc, and M.J. Coulanges. Spectrochim. Acta, **49A**, 103 (1993).
12. H. Zine, M.H. Baron, and A. Piart-Goypiron. Spectrochim. Acta, **3**, 457 (1995).

© 1999 NRC Canada

Preparation of *N*-aryl-substituted spiro-β-lactams via Staudinger cycloaddition

Victor Barba, Cecilia Hernández, Susana Rojas-Lima, Norberto Farfán, and Rosa Santillan

Abstract: The interest in the study of β-lactams continues due to their therapeutic importance as antibiotics. In this work, six spiro-β-lactams (**7a**–**7c**, **8a**–**8c**) have been prepared using the [2+2] cycloaddition of isomaleimides to acid chlorides. The heterobicyclic structures obtained have been characterized by mass spectrometry, IR, NMR spectroscopy, and for compounds **7a**, **7b**, and **8b** the X-ray crystallographic study showed a nearly planar arrangement for the β-lactam ring.

Key words: β-lactams, azetidinone, isomaleimides, ketenes, X-ray crystallography.

Résumé : L'intérêt dans l'étude des β-lactames se maintient en raison de leur importance thérapeutique comme antibiotiques. Dans ce travail, on a préparé six spiro-β-lactames (**7a**–**7c**, **8a**–**8c**) en faisant appel à une cycloaddition [2+2] d'isomaléimides sur des chlorures d'acyles. Les structures hétérobicycliques obtenues ont été caractérisées par spectrométrie de masse, IR, spectroscopie RMN et, pour les composés **7a**, **7b** et **8b**, une étude par diffraction des rayons X montre que le cycle β-lactame existe dans un arrangement pratiquement plan.

Mots clés : β-lactames, azétidinone, isomaléimides, cétènes, diffraction des rayons X.

[Traduit par la Rédaction]

Introduction

Although a number of pharmacologically active mono- and bicyclic β-lactams are known (1–3), the interest in the synthesis of these types of heterocycles continues and various elegant preparative methods have been developed (4–7). Among the numerous methods for the synthesis of monocyclic β-lactams, the ketene–imine cycloaddition or its equivalent, the acid chloride – imine method, has proven to be an exceedingly effective route for the asymmetric construction of the azetidinone nuclei (8–11); specially, the β-lactams with defined stereochemistry represent an important synthetic target for a number of biologically active compounds containing this heterocyclic framework (12).

In the search for new 2-azetidinone nuclei, several spiro-β-lactams derived from [2+2] cycloaddition reaction of iminolactones with ketenes have been recorded in the literature (13–16). In this work we report the synthesis of four new spiro-β-lactams (**7c**, **8a**–**8c**) derived from isomaleimides (**4a**–**4c**) with acid chloride **5** or **6** by using the Staudinger reaction. Furthermore, the X-ray analysis for **8b** and two previously reported spiro-β-lactams (**7a**, **7b**) (13) was obtained.

Received June 18, 1999.

V. Barba, C. Hernández, N. Farfán, and R. Santillan.[1] Departamento de Química, Centro de Investigación y de Estudios Avanzados del IPN, Apdo. postal 14-740, 07000, México D.F., México.
S. Rojas-Lima. Universidad Autónoma del Estado de Hidalgo, Centro de Investigaciones Químicas, Carretera Pachuca-Tulancingo Km. 4.5, Ciudad Universitaria, Pachuca de Soto, Hidalgo, C.P. 42076, México.

[1]Author to whom correspondence may be addressed. Telephone: 52-5-747-3800, ext. 4055. Fax: 52-5-747-7113. e-mail: rsantill@mail.cinvestav.mx

Experimental

Instrumentation

^{1}H- and ^{13}C NMR spectra, in $CDCl_3$ and DMSO-d_6, were recorded on Jeol GSX-270 MHz and Jeol Eclipse +400 MHz NMR spectrometers. Special techniques (COSY, HETCOR, NOESY) were applied when necessary to assign the spectra adequately. Chemical shifts (ppm) are relative to $(CH_3)_4Si$. Coupling constants are quoted in Hz. Infrared spectra were recorded on a Perkin–Elmer 16F-PC FT-IR spectrophotometer. Melting points were obtained on a Gallenkamp MFB-595 apparatus and are uncorrected. Ultraviolet spectra were recorded on a Perkin–Elmer UV–vis λ 2S spectrophotometer from ethanol solutions. Mass spectra were recorded on a Hewlett–Packard 5989A spectrometer. Elemental microanalyses were determined by Oneida Research Services, Whitesboro, New York. Crystals suitable for X-ray diffraction of compounds **7a**, **7b**, and **8b** were obtained when the products were recrystallized from a mixture of ethyl ether – hexane.

X-ray diffraction studies of monocrystals were determined on an Enraf–Nonius CAD4 diffractometer (λ_{MoK_α} = 0.71073 Å, monochromator: graphite, T = 293 K, ω-2θ scan). Crystals were generally mounted in Lindeman tubes. Absorption correction was not necessary; corrections were made for

 © 1999 NRC Canada

Lorentz and polarization effects. Solution and refinement: direct methods (SHELXS-86) for structure solution and SHELXS (version 1.8, 1993) software package for refinement and data output. Hydrogen atoms were determined by difference Fourier maps and their positions as well as one overall isotropic thermal parameter were refined.

Reagents

All starting materials were commercially available. Solvents were used without further purification, but single crystals were grown from spectrophotometric-grade solvents.

General procedure for the preparation of arylmaleamic acids 3a–3c

To prepare the arylmaleamic acids **3a**–**3c**, equimolar quantities of the corresponding arylamine with maleic anhydride were mixed in 30 mL of dry THF at 0°C and stirred for 2 h at room temperature. The solvent was removed by filtration and the solid washed with THF; the product obtained was used without further purification. The preparation and spectroscopic data have already been published (17–18).

*4-(Phenylamino)-4-oxo-(Z)-2-butenoic acid (**3a**)*: mp 220–221°C (lit (17) = 196°C).

*4-(4′-Methoxy-phenylamino)-4-oxo-(Z)-2-butenoic acid (**3b**)*: mp = 213–214°C (lit (18) = 181–182°C).

*4-(4′-Hydroxy-phenylamino)-4-oxo-(Z)-2-butenoic acid (**3c**)*: mp = 220–223°C (lit (17) = 210°C).

General procedure for the preparation of isomaleimides 4a–4b

Arylmaleamic acids **3a**–**3b** were dissolved in 50 mL of dry dichloromethane, and dicyclohexylcarbodiimide was added with magnetic stirring at –78°C. The solution was stirred for 3–4 h at room temperature and the solvent was evaporated under reduced pressure; the solid obtained was washed with dry dichloromethane and used without further purification. The preparation and spectroscopic data have already been published (16, 19).

N-*Phenylisomaleimide (**4a**)*: mp 61–62°C (lit (19) = 57–62°C).

N-P-*Methoxy-phenylisomaleimide (**4b**)*: mp 70–73°C (lit (16) = 73–74°C).

N-P-*Acetoxy-phenylisomaleimide (**4c**)*: A solution containing 3 g (14 mmol) of compound **3c** and 10 mL (105 mmol) of acetic anhydride in 20 mL of dry dichoromethane was stirred at –78°C for 1 h, followed by the addition of 6 g (29 mmol) of dicyclohexylcarbodiimide. The mixture was stirred for 24 h at room temperature to give, after work-up, a yellow solid (2.35 g, 10 mmol) mp 127–129°C, 70% yield. EI (70 eV) *m/z* (%): 231 (M^+, 10), 190 (12), 189 (100), 145 (15), 119 (24), 99 (1), 77 (2), 54 (21); IR (KBr): 3082, 1792, 1680, 1198 cm^{-1}; ^1H NMR (270 MHz, $CDCl_3$) δ: 7.43 (2H, d, *J* = 9.0, H-2′,6′), 7.34 (1H, d, *J* = 5.5, H-3), 7.08 (2H, d, *J* = 9.0, 3′,5′), 6.63 (1H, d, *J* = 5.5, H-2), 2.26 (3H, s, CO—CH_3) ppm; ^{13}C NMR (67.8 MHz, $CDCl_3$) δ: 169.3 (C-1), 167.1 (OCO), 150.1 (C-4), 148.2 (C-4′) 143.3 (C-3), 141.1 (C-1′), 130.8 (C-2), 124.7 (C-2′,6′), 121.9 (C-3′,5′), 21.1 (CH_3) ppm.

General procedure for the preparation of β-lactams 7a–7c and 8a–8c

To a stirred solution of isomaleimide **4a**–**4c** in anhydrous dichloromethane at –78°C was added dropwise a solution of acid chloride in 10 mL of dry dichloromethane, followed by dropwise addition of a solution of triethylamine in dichloromethane. The reaction mixture was maintained at –78°C for 2 h, the resulting suspension was left to warm to room temperature and stirred for 36 additional hours.

The reaction mixture was brought to neutral pH and poured into dichloromethane and washed with water, the organic layer was separated, dried over magnesium sulfate, and evaporated under reduced pressure. The resulting crude product was purified by column chromatography using silica gel and hexane – ethyl acetate, 8:2, as the eluent. The preparation and spectroscopic data (IR, ^1H NMR) of **7a** and **7b** have been reported (16).

*3-Chloro-1-phenyl-5-oxa-1-azaspiro[3,4]oct-7-en-2,6-dione (**7a**)*: Compound **7a** was prepared from 0.5 g (2.9 mmol) of compound **4a** and 0.8 mL (10 mmol) of chloroacetyl chloride. The resulting product obtained was a colorless solid (0.24 g, 0.96 mmol) mp 132–133°C (lit (16) = 127–128°C), 33% yield. EI (70 eV) *m/z* (%): 249 (M^+, 6), 130(8.4), 119(100), 117(2), 102(9), 91(19), 77(11), 51(10); UV (EtOH) λ_{max}: 245 nm (log ε = 4.1); ^{13}C NMR (100 MHz, $CDCl_3$) δ: 167.53 (C-6), 157.77 (C-2), 149.93 (C-8), 134.84 (C-1′), 129.61 (C-3′,5′), 127.89 (C-7), 126.73 (C-4′), 118.46 (C-2′,6′), 96.34 (C-4), 64.66 (C-3) ppm.

*3-Chloro-1-*p*-methoxyphenyl-5-oxa-1-azaspiro[3,4]oct-7-en-2,6-dione (**7b**)*: Compound **7b** was prepared from 0.5 g (2.5 mmol) of compound **4b** and 0.51 mL (6.4 mmol) of chloroacetyl chloride. The product obtained was a colorless solid (0.23 g, 0.82 mmol) mp 128–130°C (lit (16) 132–133°C), 33% yield. EI (70 eV) *m/z* (%) : 279 ($M^{+\cdot}$, 7), 203 (2), 188 (2), 160 (2), 149 (100), 134 (37), 106 (13), 78 (11). UV (EtOH) λ_{max}: 258 nm (log ε = 4.1); ^{13}C NMR (100 MHz, $CDCl_3$) δ: 167.62 (C-6), 158.28 (C-2), 157.71 (C-4′), 149.81 (C-8), 127.79 (C-7), 127.37 (C-1′), 120.97 (C-2′,6′), 114.76 (C-3′,5′), 96.62 (C-4), 64.58 (C-3), 55.52 (OMe) ppm.

*3-Chloro-1-*p*-acetoxyphenyl-5-oxa-1-azaspiro[3,4]oct-7-en-2,6-dione (**7c**)*: Compound **7c** was prepared from 0.5 g (2.16 mmol) of compound **4c** and 0.51 mL (6.4 mmol) of chloroacetyl chloride. The product obtained was a colorless solid (0.22 g, 0.72 mmol) mp 118–119°C, 33% yield. EI (70 eV) *m/z* (%) : 307 (M^+, 3), 265 (13), 135 (100), 107 (6), 52 (2), 43 (13); UV (EtOH) λ_{max}: 249 nm (log ε = 4.1); IR (KBr): 3110, 1790, 1514, 1394 cm^{-1}; ^1H NMR (270 MHz, $CDCl_3$), δ: 7.56 (1H, d, *J* = 5.7, H-8), 7.28 (2H, d, *J* = 8.6, H-2′,6′), 7.05 (2H, d, *J* = 8.6, H-3′,5′), 6.58 (1H, d, *J* = 5.7, H-7), 5.32 (1H, s, H-3), 2.27 (3H, s, $OCOCH_3$) ppm; ^{13}C NMR (67.8 MHz, $CDCl_3$) δ: 169.2 (C-6), 167.4 (OCO), 157.7 (C-2), 149.8 (C-8), 148.8 (C-4′), 132.3 (C-1′), 128.1 (C-7), 122.9 (C-3′,5′), 119.7 (C-2′,6′), 96.3 (C-4), 64.8 (C-3), 21.0 (CH_3) ppm. Anal. calcd. for $C_{14}H_{10}ClNO_3$: C 54.72, H 3.25, N 4.56; found: C 54.71, H 3.18, N 4.57.

© 1999 NRC Canada

Scheme 1. Reagents: (*i*) THF, RT, 2 h. (*ii*) Dicyclohexylcarbodiimide (DCC), CH_2Cl_2, RT, 3 h, for **4c** 1 equiv. of acetic anhydride was used. (*iii*) CH_2Cl_2, triethylamine, –70°C, 2 h to RT 30–36 h.

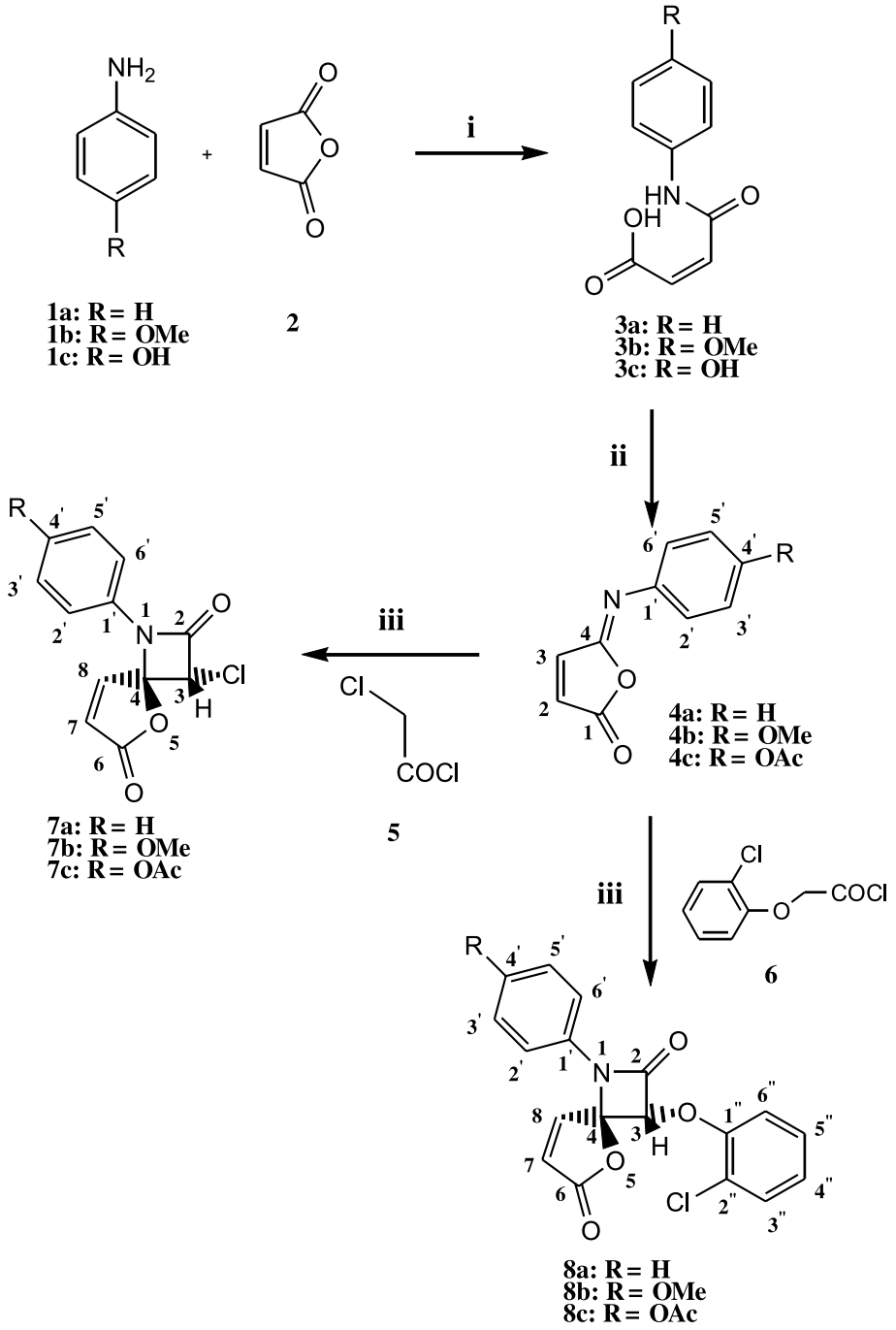

*3-o-Chlorophenoxy-1-phenyl-5-oxa-1-azaspiro-[3,4]oct-7-en-2,6-dione (**8a**)*: Compound **8a** was prepared from 0.5 g (2.9 mmol) of compound **4a** and 1.2 g (5.85 mmol) of *o*-chlorophenoxy-acetyl chloride. The product obtained was a colorless solid (0.29 g, 0.85 mmol) mp 181–182°C, 30% yield. EI (70 eV) *m/z* (%): 341 (M^+, 13), 306 (2), 278 (3), 224 (25), 222 (74), 187 (100), 159 (16), 131 (14), 119 (16), 91 (20), 77 (36); UV (EtOH) λ_{max}: 241 nm (log ϵ = 4.20); IR (KBr): 3110, 1782, 1588, 1514 cm^{-1}; ^1H NMR (400 MHz, $CDCl_3$) δ: 7.70 (1H, d, *J* = 5.7, H-8), 7.38 (1H, dd, *J* = 8.0, 1.4, H-3″), 7.33–7.39 (4H, m, H-2′,3′,5′,6′), 7.26 (1H, m, H-4′), 7.24 (1H, ddd, *J* = 8.0, 7.7, 1.4, H-5″), 7.09 (1H, dd, *J* = 8.0, 1.4, H-6″), 7.04 (1H, ddd, *J* = 8.0, 7.7, 1.4, H-4″), 6.49 (1H, d, *J* = 5.7, H-7), 5.74 (1H, s, H-3) ppm; ^{13}C NMR (100 MHz, $CDCl_3$) δ: 168.1 (C-6), 159.4 (C-2), 152.2 (C-1″), 150.1 (C-8), 135.0 (C-1′), 128.2 (C-4′), 129.6 (C-3′,5′), 130.8 (C-3″), 127.7 (C-7), 126.6 (C-5″), 124.2 (C-4″), 123.3 (C-2″), 118.5 (C-2′,6′), 115.7 (C-6″), 97.0 (C-4), 88.5 (C-3) ppm. Anal. calcd. for $C_{18}H_{12}ClNO_4$: C 63.34, H 3.51, N 4.10; found: C 63.32, H 3.65, N 4.12.

© 1999 NRC Canada

3-o-*Chlorophenoxy-1*-p-*methoxyphenyl-5-oxa-1-azaspiro[3,4]oct-7-en-2,6-dione (**8b**)*: Compound **8b** was prepared from 0.5 g (2.46 mmol) of compound **4b** and 1.2 g (5.85 mmol) of *o*-chlorophenoxyacetyl chloride. The product obtained was a colorless solid (0.26 g, 0.7 mmol) mp 136–137°C, 28% yield. EI (70 eV) *m/z* (%): 371 (M^+, 9), 224 (2), 222 (7), 203 (9), 187 (18), 149 (100), 134 (23), 106 (8), 77 (8); UV (EtOH) λ_{max}: 252 nm (log ϵ = 4.21); IR (KBr): 3104, 1780, 1718, 1248 cm^{-1}; ^1H NMR (400 MHz, $CDCl_3$) δ: 7.66 (1H, d, *J* = 5.7, H-8), 7.36 (1H, dd, *J* = 8.0, 1.4, m, H-3″), 7.25 (1H, d, *J* = 8.8, H-2′,6′), 7.22 (1H, ddd, *J* = 8.0, 7.3, 1.4, H-5″), 7.07 (1H, ddd, *J* = 8.0, 1.4, 1.0, H-6″), 7.01 (1H, ddd, *J* = 8.0, 7.3, 1.4, H-4″), 6.84 (1H, d, *J* = 8.8, H-3′,5′), 6.49 (1H, d, *J* = 5.7, H-7), 5.71 (1H, s, H-3), 3.77 (3H, s, OMe) ppm; ^{13}C NMR (100 MHz, $CDCl_3$) δ: 168.2 (C-6), 159.3 (C-2), 158.1 (C-4′), 152.2 (C-1″), 150.0 (C-8), 130.7 (C-3″), 128.1 (C-5″), 127.6 (C-7), 124.1 (C-4″), 123.3 (C-1′), 122.0 (C-2″), 121.0 (C-2′, 6′), 115.6 (C-6″), 114.7 (C-3′, 5′), 97.2 (C-4), 88.3 (C-3), 55.5 (OMe) ppm. Anal. calcd. for $C_{19}H_{14}ClNO_5$: C 61.45, H 3.77, N 3.77; found C 61.08, H 3.72, N 3.74.

3-o-*Chlorophenoxy-1*-p-*acetoxyphenyl-5-oxa-1-azaspiro[3,4]oct-7-en-2,6-dione (**8c**)*: Compound **8c** was prepared from 0.5 g (2.16 mmol) of compound **4c** and 1.2 g (5.85 mmol) of *o*-chlorophenoxyacetyl chloride. The product obtained was a colorless solid (0.30 g, 0.75 mmol) mp 122–123°C, 34% yield. EI (70 eV) *m/z* (%): 399 (M^+, 7), 356 (18), 224 (24), 222 (68), 189 (25), 187 (68), 159 (10), 135 (73), 107 (10), 77 (10), 69 (20), 43 (100); UV (EtOH) λ_{max}: 245 nm (log ϵ = 4.19); IR (KBr): 3088, 1766, 1516, 1482 cm^{-1}; ^1H NMR (400 MHz, $CDCl_3$), δ: 7.67 (1H, d, *J* = 5.6, H-8), 7.36 (1H, dd, *J* = 8.0, 1.6, H-3″), 7.33 (2H, d, *J* = 8.9, H-2′,6′), 7.23 (1H, ddd, *J* = 8.0, 7.3, 1.6, H-5″), 7.06 (2H, d, *J* = 8.9, H-3′,5′), 7.02 (2H, ddd, *J* = 8.0, 7.3, 1.4, H-4″,6″), 6.54 (1H, d, *J* = 5.6, H-7), 5.73 (1H, s, H-3), 2.28 (3H, s, $OCOCH_3$) ppm; ^{13}C NMR (100 MHz, $CDCl_3$) δ: 169.2 (C-6), 167.0 (OCO), 159.2 (C-2), 152.1 (C-1″), 149.9 (C-8), 132.4 (C-1′), 148.5 (C-4′), 130.7 (C-3″), 128.1 (C-5″), 127.8 (C-7), 124.2 (C-4″), 123.2 (C-2″), 122.8 (C-3′,5′), 119.6 (C-2′,6′), 115.6 (C-6″), 96.9 (C-4), 88.4 (C-3), 21.0 (CH_3) ppm. Anal. calcd. for $C_{20}H_{14}ClNO_6$: C 60.15, H 3.50, N 3.50; found C 59.97, H 3.54, N 3.50.

Results and discussion

When the arylamines **1a**–**1c** are treated with maleic anhydride (**2**), the arylmaleamic acids (**3a**–**3c**) are formed in excellent yields (17–18). The reaction of these acids with dicyclohexylcarbodiimide affords isomaleimides **4a**–**4c** in good yields (16, 19). In no case was the formation of *N*-arylmaleimides observed under these conditions.

The isomaleimides **4a**–**4c** underwent [2+2] cycloaddition reaction (Staudinger reaction) with two acid chlorides (**5**, **6**) in the presence of triethylamine to give regioselectively the spiro-β-lactams (**7a**–**7c** and **8a**–**8c**) in 27–34% yields (Scheme 1). The structure of these compounds was confirmed by mass spectrometry where molecular ions were detected in all cases.

The structures of β-lactams **7a**–**7c** and **8a**–**8c** were established by ^1H and ^{13}C NMR spectroscopy. ^1H NMR analysis of products **7a**–**7c** and **8a**–**8c** showed a singlet in the range of 5.31–5.74 ppm corresponding to H-3 of the β-lactam ring. Comparison of the ^1H NMR data for this signal shows that in the case of compounds **8a**–**8c** the signal is shifted to higher field ($\Delta\delta \approx 4$ ppm) than for **7a**–**7c**. These differences are due to the presence of electron-donating or -withdrawing substituents at the C-3 position (chlorine for **7a**–**7c** and oxygen for **8a**–**8c**). All of them display signals for vinylic protons (AB system) between 6.54 and 7.59 ppm for **7a**–**7c** and 6.49 and 7.70 ppm for **8a**–**8c**, with a coupling constant from 5.6 to 5.8 Hz; this AB system remained intact in the course of the cyclization.

The ^{13}C NMR spectra exhibited two carbonyl signals at 167–169 and 157–159 ppm for C-6 and C-2, respectively. The most interesting observation is the extreme high-field shift of the C-3 (88.5, 88.3, 88.4 ppm, for **8a**–**8c**) compared with the downfield shift for the same carbon in **7a**–**7c** (64.7, 64.6, 64.8 ppm). The susbtituent effects may explain these differences.

The relative configuration at C-3 and C-4 was established on the basis of evidence from NMR spectra and NOE studies. Thus, the proton attached to C-8 in **7b** showed NOE interaction with H-2′ in the 400 MHz NOESY spectrum. The fact that no effect was observed between H-8 and H-3 supports the conclusion that the chlorine atom at C-3 and the oxygen atom at C-4 have a *trans* relationship.

The structures of **7a**, **7b**, and **8a** were determined by X-ray crystallography, which confirmed the structures and stereochemistries of these compounds. The molecular structures of **7a**, **7b,** and **8a** are shown in Figs. 1–3. The crystal data are summarized in Table 1. Selected bond angles, interatomic distances, and torsion angles are given in Tables 2 and 3 and have been deposited.[2]

The X-ray analysis shows that the arrangement of bonds around the nitrogen atom is approximately planar. The C(12)—N(1) bond distances are 1.416(4)/1.412(4), 1.415(3)/1.414(3), and 1.426(6) Å for **7a**, **7b,** and **8b**, respectively, and are considerably shorter than the usual value of 1.47 Å, and indicate double bond character. Similar bond lengths (1.41(1) and 1.409(4) Å) have been reported for two similar β-lactams, **9** and **10** (20, 21) (Scheme 2). Additionally, the C(2)—N(1) bond distances of 1.383(4)/1.375(4), 1.377(3)/1.374(3), and 1.369(6) Å for **7a**, **7b,** and **8b**, respectively, are consistent with N=C double bonding. These results are in accordance with the observation than the C(12)-N(1)-C(2) bond angle is 3° larger than the corresponding bond angle for the C(12)-N(1)-C(4) fragment, which can be attributed to π-delocalization between the amide group and the aromatic ring.

The high ring strain can be seen from the internal angles, which show that the larger bond angle is C(2)-N(1)-C(4),

[2] Suplementary material may be purchased from: The Depository of Unpublished Data, Document Delivery, CISTI, National Research Council of Canada, Ottawa, Canada, K1A 0S2. These have also been deposited with the Cambridge Crystallographic Data Center, and can be obtained on request from: The Director, Cambridge Crystallographic Data Center, University Chemical Laboratory, 12 Union Road, Cambridge, CB2 1EZ, U.K.

© 1999 NRC Canada

Fig. 1. Molecular structure of compound **7a**; the thermal ellipsoid probability level is 25%.

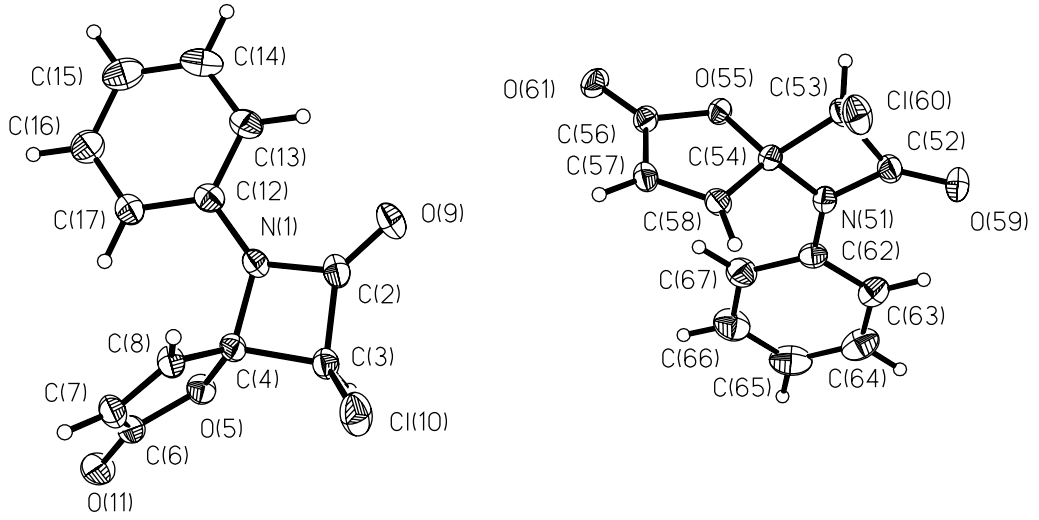

Fig. 2. Molecular structure of compound **7b**; the thermal ellipsoid probability level is 25%.

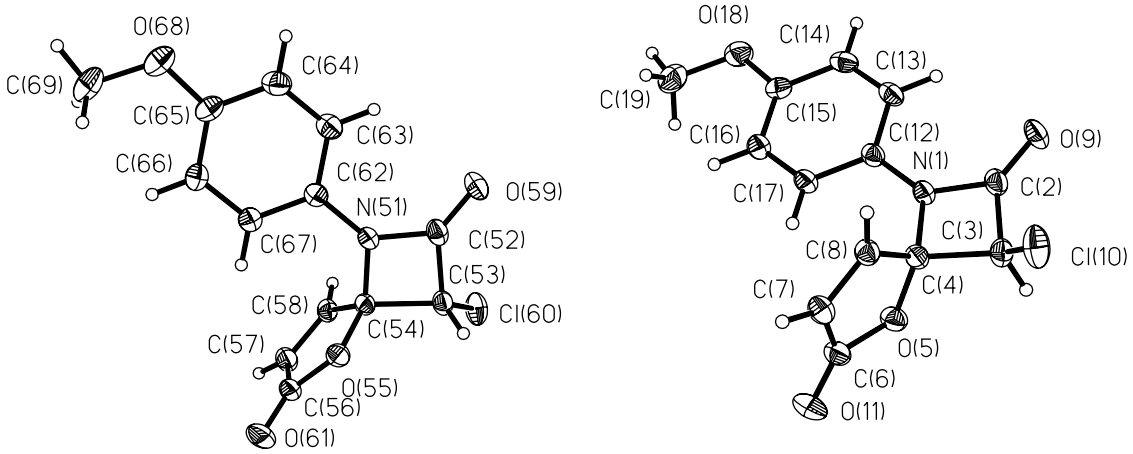

Fig. 3. Molecular structure of compound **8b**; the thermal ellipsoid probability level is 25%.

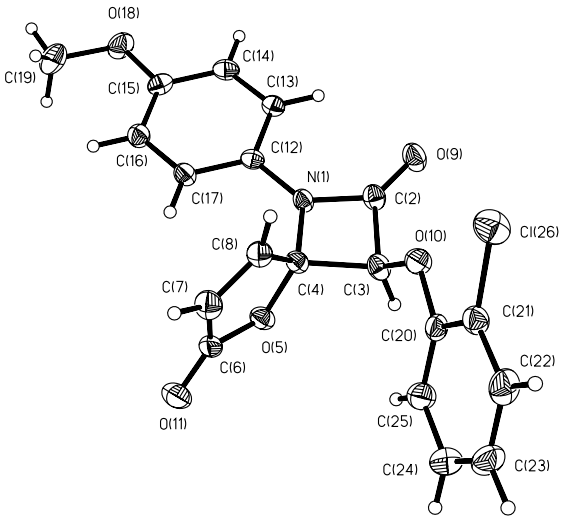

94.6(2)/94.9(2), 94.8(2)/95.0(2), and 95.2(3)° and the smaller bond angle is C(2)-C(3)-C(4), 86.2(2)/85.6(2), 86.0(2)/85.6(2), and 85.7(3)° for **7a**, **7b**, and **8b,** respectively.

The internal torsion angles indicate the nonplanarity of the β-lactam ring, in agreement with literature data on structural analogues (12, 20–22). The torsion angles in the β-lactam ring range from 4.6 to 9.1° (in absolute values). The dihedral angles between the plane of the phenyl ring and the β-lactam ring are 3.4/1.2, –1.2/7.5, and 2.9° for C(2)-N(1)-C(12)-C(13) and –2.3/7.9, –7.9/11.9, and –4.2° for C(4)-N(1)-C(12)-C(17), corresponding to **7a**, **7b**, and **8b**, respectively.

© 1999 NRC Canada

Table 1. Crystallographic data of compounds **7a**, **7b**, and **8b**.[a]

	7a	**7b**	**8b**
Formula	$C_{12}H_8ClNO_3$	$C_{13}H_{10}ClNO_4$	$C_{19}H_{14}ClNO_5$
Crystal size (mm)	0.40 × 0.30 × 0.20	0.24 × 0.24 × 0.18	0.3 × 0.3 × 0.24
Crystal system	Triclinic	Triclinic	Monoclinic
fw (g mol^{-1})	249.64	279.67	371.76
Space group	$P\bar{1}$	$P\bar{1}$	$P2_1/c$
Cell parameters			
a (Å)	7.393(1)	7.635(2)	7.397(1)
b (Å)	9.005(2)	10.061(2)	6.774(1)
c (Å)	17.681(4)	18.019(4)	33.924(7)
α (°)	94.63(3)	96.25(3)	90.00
β (°)	95.07(3)	101.01(3)	92.15(3)
γ (°)	102.75(3)	110.83(3)	90.00
V (Å^3)	1137.5(4)	1246.1(5)	1698.6(5)
Z	4	4	4
μ (mm^{-1})	0.330	0.316	0.256
ρ_{calcd} (g cm^{-3})	1.458	1.491	1.454
Data collection			
$2\theta_{max}$ (°)	44	46	44
Total reflections	2744	6904	4023
Unique reflections	2514	3452	2079
R_{merge}	0.0128	0.02	0.07
Refl. with $I > 4\sigma(I)$	1903	2541	1490
Refinement			
$R/R_w(F)$[b,d]	0.0343/0.0868	0.035/0.0892	0.0521/0.1306
$R/R_w(F^2)$ (all data)[c]	0.0567/0.0962	0.0572/0.1002	0.0816/0.1420
No. of variables	307	343	235
Gof[d]	0.999	1.027	1.188
Max Δ/σ (final cycle)	0.001	0.001	0.001
$\Delta\rho_{min}$ (e Å^{-3})	–0.224	–0.254	–0.216
$\Delta\rho_{max}$ (e Å^{-3})	0.208	0.309	0.420

[a]Temperature 293 K, Enraf Nonius CAD4 diffractometer, MoK_α (λ = 0.71073) radiation, graphite monochromator.
[b]$R(F) = \Sigma||F_o| - |F_c|| / \Sigma|F_o|$, $R_w(F) = [\Sigma\, w(|F_o| - |F_c|)^2 / \Sigma\, w|F_o|^2]^{1/2}$.
[c]$R(F^2) = \Sigma||F_o^2| - |F_c^2|| / \Sigma|F_o^2|$, $R_w(F^2) = [\Sigma\, w(|F_o^2| - |F_c^2|)^2 / \Sigma\, w|F_o^2|^2]^{1/2}$.
[d]Values given for R, R_w, and gof are based on those reflections with $I > 4\sigma(I)$.

Scheme 2.

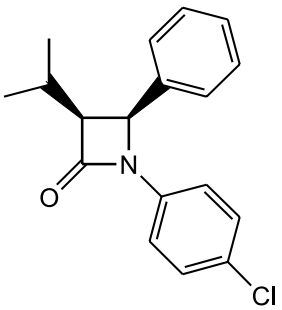

9

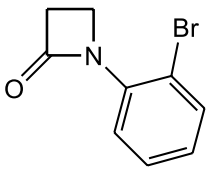

10

The mean values of the internal bond angles in the β-lactam ring are 89.6/89, 89.85/ 89.87, and 89.82° for **7a**, **7b**, and **8b**, respectively, indicating that the ring strain is very similar in these heterocycles.

In conclusion, the regioselective synthesis of four new spiro-β-lactams with a *trans* stereochemistry was shown by NOE experiments and X-ray diffraction analysis. The molecular perspective of these compounds shows a nearly planar arrangement for the β-lactam ring and the *N*-phenyl group.

Acknowledgments

Financial support from Consejo Nacional de Ciencia y Tecnología (CONACYT) is acknowledged.

© 1999 NRC Canada

Table 2. Selected bond lengths and bond angles of compounds **7a**, **7b**, and **8b**.

	7a/**7a′**	**7b**/**7b′**	**8b**
Bond lengths (Å)			
N(1)—C(12)	1.416(4)/1.412(4)	1.415(3)/1.414(3)	1.426(6)
N(1)—C(4)	1.457(4)/1.454(4)	1.460(3)/1.456(3)	1.463(6)
N(1)—C(2)	1.383(4)/1.375(4)	1.377(3)/1.374(3)	1.369(6)
C(2)—C(3)	1.514(5)/1.510(4)	1.510(4)/1.512(4)	1.531(7)
C(3)—C(4)	1.541(4)/1.560(4)	1.552(3)/1.559(3)	1.546(7)
C(4)—O(5)	1.418(3)/1.429(3)	1.419(3)/1.424(3)	1.428(6)
O(5)—C(6)	1.383(4)/1.380(4)	1.388(3)/1.384(3)	1.380(6)
C(6)—C(7)	1.453(5)/1.452(4)	1.459(4)/1.453(4)	1.463(8)
C(7)—C(8)	1.307(4)/1.306(4)	1.311(3)/1.312(3)	1.313(7)
C(8)—C(4)	1.482(4)/1.485(4)	1.484(3)/1.493(4)	1.483(7)
C(3)—Cl(10)[a]	1.755(3)/1.757(3)	1.754(3)/1.761(3)	1.409(6)
C(2)—O(9)	1.200(4)/1.207(4)	1.207(3)/1.201(3)	1.191(6)
C(6)—O(11)	1.196(4)/1.199(3)	1.185(3)/1.194(3)	1.200(6)
Bond angles (°)			
C(12)-N(1)-C(2)	134.0(3)/133.8(3)	134.1(2)/134.3(2)	133.8(4)
C(12)-N(1)-C(4)	131.3(3)/131.0(2)	131.0(2)/130.6(2)	130.9(4)
N(1)-C(2)-C(3)	90.7(2)/91.8(2)	91.7(2)/91.9(2)	91.2(4)
N(1)-C(2)-O(9)	132.1(3)/132.3(3)	132.4(3)/132.6(3)	133.1(5)
N(1)-C(4)-C(3)	86.9(2)/86.9(2)	86.9(2)/87.0(2)	87.2(3)
N(1)-C(4)-O(5)	114.2(2)/113.1(2)	113.7(2)/113.2(2)	113.3(4)
N(1)-C(4)-C(8)	116.8(3)/119.0(2)	117.4(2)/118.1(2)	117.6(4)
C(2)-N(1)-C(4)	94.6(2)/94.9(2)	94.8(2)/95.0(2)	95.2(3)
C(2)-C(3)-Cl(10)[a]	117.8(2)/115.6(2)	115.9(2)/115.5(2)	111.8(4)
C(2)-C(3)-C(4)	86.2(2)/85.6(2)	86.0(2)/85.6(2)	85.7(3)
C(3)-C(2)-O(9)	137.1(3)/135.8(3)	135.8(3)/135.5(2)	135.7(5)
C(3)-C(4)-O(5)	114.6(2)/113.9(2)	114.0(2)/113.5(2)	114.1(4)
C(3)-C(4)-C(8)	119.0(3)/118.6(3)	119.0(2)/119.8(2)	119.4(4)
C(3)-O(10)-C(20)	—	—	117.3(4)

[a]O(10) for **8b**.

Table 3. Selected torsion angles (°) for compounds **7a**, **7b**, and **8b**.[a]

	7a	**7b**	**8b**
C(12)-N(1)-C(2)-O(9)	7.9/–4.9	5.7/–3.5	2.3
C(12)-N(1)-C(2)-C(3)	–173.6/178.7	–177.5/178.0	–176.9
C(12)-N(1)-C(4)-C(3)	173.6/–178.6	177.5/–178.0	176.8
C(2)-N(1)-C(12)-C(13)	3.4/1.2	–1.2/7.5	2.9
C(4)-N(1)-C(12)-C(17)	–2.3/7.9	–7.9/11.9	–4.1
N(1)-C(2)-C(3)-C(4)	–9.1/6.3	–5.9/4.9	–6.7
C(2)-C(3)-C(4)-N(1)	8.6/–6.0	5.6/4.6	6.2

[a]A positive rotation is counterclockwise from atom 1, when viewed from atom 3 to atom 2.

References

1. W. Dürckheimer, J. Blumbach, R. Lattrell, and K. Scheunemann. Angew. Chem. Int. Ed. Engl. **24**, 180 (1985).
2. S. Anklam and J. Liebscher. Tetrahedron, **54**, 6369 (1998).
3. X.F. Ren, M.I. Konaklieva, and E. Turos. J. Org. Chem. **63**, 8898 (1998).
4. A.K. Mukerjee and R.C. Srivastava. Synthesis, 327 (1973).
5. F.P. Cossío, J.M. Odriozola, M. Oiarbide, and C. Palomo. J. Chem. Soc., Chem. Commun. 2, 74 (1989).
6. N.S. Isaccs. Chem. Soc. Rev. **76**, 181 (1976).
7. A.K. Mukerjee and A.K. Singh. Tetrahedron, **34**, 1731 (1978).
8. C. Palomo, F.P. Cossío, J.M. Ontoria, and J.M. Odriozola. Tetrahedron Lett. **32**, 3105 (1991).
9. R.C. Thomas. Tetrahedron Lett. **30**, 5239 (1989).
10. I. Ojima, T. Komata, and X.J. Qui. J. Am. Chem. Soc. **112**, 770 (1990).
11. C. Palomo, F.P. Cossío, and C. Cuevas. Tetrahedron Lett. **32**, 3109 (1991).
12. G. Barbaro, A. Battaglia, A. Guerrini, C. Bertucci, and S. Geremia. Tetrahedron Asymm. **9**, 3041 (1998), and refs. therein.
13. H.G. Capraro, G. Rihs, and P. Martin. Helv. Chim. Acta, **66**, 633 (1983).
14. M. Roth. Helv. Chim. Acta, **62**, 1966 (1979).
15. M. Roth. Helv. Chim. Acta, **64**, 1930 (1981).
16. H.G. Capraro, T. Winkler, and P. Martin. Helv. Chim. Acta, **66**, 362 (1983).

© 1999 NRC Canada

17. A. Boucherle, G. Carraz, A.M. Revol, and J. Dodu. Bull. Soc. Chim. France, 106, 500 (1960).
18. A.C. Tomé, J.A.S. Cavaleiro, F.M.J. Dominguez, and R.J. Cremlyn. Phosphorus Sulfur Silicon Relat. Elem. **79**, 187 (1993).
19. R.J. Cotter, C.K. Sauers, and J.M. Whelan. J. Org. Chem. **26**, 10 (1961).
20. R. Parthasarathy. Acta Cryst. **B24**, 1283 (1970).
21. H. Fujiwara, R.L. Varley, and J.M. van der Veen. J. Chem. Soc., Perkin Trans. 2, 547 (1977).
22. E.F. Paulus, D. Kobelt, and H. Jensen. Angew. Chem. Int. Ed. Engl. **8**, 990 (1969).

© 1999 NRC Canada

Cationic iron(III) complex with a hexadentate N_2,N'_2,O_2-aminopyridylphenolate ligand

Ika A. Setyawati, Steven J. Rettig, and Chris Orvig

Abstract: Iron(III) complexation with potentially hexadentate H_2bbpen (*N*,*N*′-bis(2-hydroxybenzyl)-*N*,*N*′-bis(2-methylpyridyl)ethylenediamine) was studied. The resulting monocationic complex, $[Fe(bbpen)]^+$ as its NO_3^- and PF_6^- salts, was characterized by infrared spectroscopy, mass spectrometry, elemental analyses, cyclic voltammetry, and X-ray crystallographic analysis. Crystals of $[Fe(bbpen)]NO_3 \cdot CH_3OH$ are monoclinic, space group $P2_1/c$, a = 10.2640(13), b = 14.7526(10), c = 18.3172(5) Å, β = 97.904(1)°, and Z = 4. The structure was solved by heavy-atom Patterson methods and refined to an R factor of 0.039 for 3526 reflections with $I > 3\sigma(I)$. The structure of the $[Fe(bbpen)]^+$ cation showed that the ligand is bound in a hexadentate fashion to the central Fe(III) ion, resulting in a distorted octahedral geometry. Magnetic susceptibility measurements indicated the presence of a high-spin Fe(III) ion, and the UV–vis spectrum of $[Fe(bbpen)]NO_3$ exhibits absorption maxima, λ_{max}, at 575 nm (ε = 5400 M^{-1} cm^{-1}), 323 (8900), and 275 (13 500). The cyclic voltammogram of $[Fe(bbpen)]NO_3$ showed a quasi-reversible, one-electron process corresponding to $[Fe^{III}(bbpen)]^+ + e^- \leftrightarrow [Fe^{II}(bbpen)]$ at –0.47 V vs. SCE.

Key words: cationic, iron(III), phenolate, pyridyl, hexadentate.

Résumé : On a étudié la complexation du fer(III) avec le H_2bbpen (*N*,*N*′-bis(2-hydroxybenzyl)-*N*,*N*′-bis(2-méthylpyridyl)éthylènediamine) qui peut être hexadentate. Faisant appel à la spectroscopie infrarouge, à la spectrométrie de masse, aux analyses élémentaires, à la voltampérométrie cyclique et à la diffraction des rayons X, on a caractérisé le complexe monocationique qui en résulte, $[Fe(bbpen)]^+$, sous la forme de ses sels NO_3^- et PF_5^-. Les cristaux de $[Fe(bbpen)]NO_3 \cdot CH_3OH$ sont monocliniques, groupe d'espace $P2_1/c$, avec a = 10,2640(13), b = 14,7526(10) et c = 18,3172(5) Å, β = 97,904(1)° et Z = 4. On a résolu la structure par la méthode des atomes lourds de Patterson et on l'a affinée jusqu'à un facteur R de 0,039 pour 3526 réflexions avec $I \geq 3\sigma(I)$. La structure du $[Fe(bbpen)]^+$ montre que le ligand est lié au Fe(III) central d'une façon hexadentate et que la géométrie octaédrique est déformée. Des mesures de susceptibilité magnétique suggèrent la présence d'un ion Fe(III) à spin élevé et le spectre UV–vis du $[Fe(bbpen)]NO_3$ présente des maxima d'absorption, λ_{max}, à 575 nm (ε = 5400 M^{-1} cm^{-1}), 323 (8900) et 275 (13 500). Le voltampérogramme cyclique du $[Fe(bbpen)]NO_3$ met en évidence un processus à un électron pratiquement réversible correspondant à $[Fe(III)(bbpen)]^+ + e^- \leftrightarrow [Fe(II)(bbpen)]$, à –0,47 V vs. SCE.

Mots clés : cationique, fer(III), phénolate, pyridyle, hexadentate.

[Traduit par la Rédaction]

Introduction

In iron-tyrosinate proteins, the interactions of iron with one or more phenolate moieties of the amino acid tyrosine play important roles in the functions and the stabilization of the geometries of the active sites. Some examples of iron-tyrosinate proteins are transferrin (1, 2), lactoferrin (3, 4), catecholate dioxygenases (5, 6), and purple acid phosphatases (7–10). Model compounds have been synthesized to mimic the environment in the active sites of iron-tyrosinate proteins (1, 2, 6, 9, 11–14). Most of the model small molecules studied contain ligands with nitrogen (aliphatic and (or) aromatic) and oxygen (phenolate and (or) carboxylate) donor atoms. Pyridyl (py) groups have been used in metalloprotein modeling studies as a mimic of the histidine amino acid in the active sites (11–13); moreover, polypyridyl ligands also have a potential application as heavy-metal chelators in biochemical studies. *N*,*N*,*N*′,*N*′-Tetrakis(2-pyridylmethyl)ethylenediamine (tpen) was used in studies of the effect of iron-chelating agents on the toxicity of doxorubicin to MCF-7 human breast cancer cells (15). In a recent in vitro study, Fe^{II}-tpen was found to exhibit a hepatoprotective effect on CCl_4-induced liver injury in rats (16).

In this paper, the coordination chemistry of Fe(III) with potentially hexadentate H_2bbpen (*N*,*N*′-bis(2-hydroxybenzyl)-*N*,*N*′-bis(2-methylpyridyl)ethylenediamine) is presented. This ligand contains three types of donor atoms (tertiary amine nitrogen, pyridyl nitrogen, and phenolate oxygen atoms), which may serve as a potential model of iron tyrosinate proteins. The reactions of Ga(III) and In(III) with H_2bbpen, H_2Clbbpen, and H_2Brbbpen ligands were previously undertaken in our group (17), resulting in the formation of monocationic $[M(L)]^+$ complexes (M = Ga, In). Model com-

Received June 29, 1999.

I.A. Setyawati, S.J. Rettig, and C. Orvig.[1] Medicinal Inorganic Chemistry Group, Department of Chemistry, University of British Columbia, 2036 Main Mall, Vancouver, BC V6T 1Z1, Canada.

[1]Author to whom correspondence may be addressed. Telephone: (604) 822-4449. Fax: (604) 822-2847. e-mail: orvig@chem.ubc.ca

 © 1999 NRC Canada

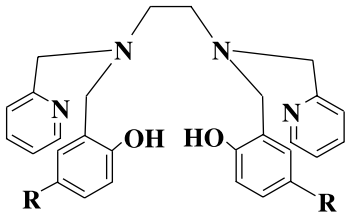

R = H, H_2bbpen
= Cl, H_2Clbbpen
= Br, H_2Brbbpen

pound studies of metalloenzymes incorporating manganese (18) and vanadium (19–22) with H_2bbpen have also been reported.

Experimental

Materials

Hydrated iron(III) nitrate, ethylenediamine, salicylaldehyde, sodium borohydride, 2-picolyl chloride hydrochloride, hexadecyltrimethylammonium bromide, anhydrous sodium acetate, sodium hexafluorophosphate, and tetra-*n*-butylammonium hexafluorophosphate [(TBA)PF_6] were obtained from Aldrich or Alfa and used without further purification. *N*,*N*′-Bis(salicylidene)ethylenediamine (H_2salen) (23), *N*,*N*′-bis(2-hydroxybenzyl)ethylenediamine (H_2bben), and *N*,*N*′-bis(2-hydroxybenzyl)-*N*,*N*′-bis(2-methylpyridyl)ethylenediamine (H_2bbpen) were prepared as described in the literature (17).

Instrumentation

IR (infrared) spectra were recorded as KBr discs, in the range 4000–500 cm^{-1}, on a Galaxy Series 5000 FTIR spectrometer. Mass spectra (Cs^+, LSIMS (Liquid Secondary Ion Mass Spectrometry)) were obtained on a Kratos Concept II H32Q, with thioglycerol as the matrix. C, H, and N analyses were performed by Mr. Peter Borda, in this department. The room temperature magnetic susceptibility was measured on a Johnson Matthey magnetic susceptibility balance using $Hg[Co(NCS)_4]$ as the susceptibility standard. UV–vis spectra were recorded on a Shimadzu UV-2100 spectrophotometer using acetonitrile. Electrochemical measurements were conducted on a Pine AFCBP1 bipotentiostat using a Pt disc working electrode, Pt coil wire-counter electrode, and Ag wire-reference electrode. Cyclic voltammetry experiments were performed at room temperature in CH_3CN solutions containing 0.25 M [(TBA)PF_6] as supporting electrolyte. Decamethylferrocene was used as an internal standard ($E_{1/2}$ = –0.12 V vs. SCE (Standard Calomel Electrode)), and the $E_{1/2}$ value is reported referenced against SCE.

Synthesis of metal complexes

[Fe(bbpen)]NO_3·CH_3OH

To a mixture of H_2bbpen (89 mg, 0.19 mmol) and NaOAc (sodium acetate) (34 mg, 0.41 mmol) in 5 mL methanol, solid $Fe(NO_3)_3.9H_2O$ (80 mg, 0.20 mmol) was added. Upon this addition, the solution turned purple immediately, and the solution was stirred for 30 min at room temperature. Suitable crystals for X-ray structural analysis were obtained by slow evaporation of the solvent at room temperature. The resulting purple solid was removed by filtration, yielding 35 mg (29%). IR (cm^{-1}, KBr disk): 1605(m), 1594(m), 1476(s), 1453(s) ($\nu_{C=N,\ C=C}$); 1289(s), 1270(s) (δ_{C-O}); 1382(s) (free ν_{NO3}-). UV-vis (in CH_3CN): λ_{max} (ε, M^{-1} cm^{-1}): 575 nm (5400), 323 (8900), 275 (13 500). $E_{1/2}$ = –0.47 V vs. SCE. Mass spectrum (LSIMS), *m*/*z*: 508 ([Fe(bbpen)]$^+$), 402 ([Fe($C_{21}H_{22}N_4O$)]$^+$), 296 ([Fe($C_{14}H_{16}N_4$)]$^+$). Anal. calcd. (found) for [Fe(bbpen)]NO_3·CH_3OH ($C_{29}H_{32}FeN_5O_6$): C 57.82 (58.04); H 5.35 (5.11); N 11.62 (11.65).

Table 1. Selected crystallographic data for [Fe(bbpen)]NO_3·CH_3OH.

Formula	$C_{29}H_{32}FeN_5O_6$
fw	602.45
Crystal system	Monoclinic
Space group	$P2_1/c$
a, Å	10.2640(13)
b, Å	14.7526(10)
c, Å	18.3172(5)
β, deg	97.904(1)
V, Å^3	2747.3(3)
Z	4
ρ_{calc}, g/cm^3	1.456
T, °C	–93
Radiation	Mo Kα
λ, Å	0.71069
μ, cm^{-1}	6.02
Transmission factor	0.8581–1.0000
R^a	0.039
$R_w{}^a$	0.033

$^aR = \Sigma||Fo| - |Fc|| / \Sigma|Fo|$. $Rw = (\Sigma w(|Fo| - |Fc|)^2 / \Sigma w|Fo|^2)^{1/2}$.

[Fe(bbpen)]PF_6

H_2bbpen (140 mg, 0.31 mmol) and NaOAc (56 mg, 0.68 mmol) were dissolved in a solution of warm methanol (5 mL). To this mixture, $Fe(NO_3)_3·9H_2O$ (120 mg, 0.30 mmol) was added, and stirring was continued at room temperature for 15 min. $NaPF_6$ (76 mg, 0.45 mmol) was then added, and the solution was stirred for another 30 min. The resulting purple solid was removed by filtration, yielding 125 mg (63%). IR (cm^{-1}, KBr disk): 1605(m), 1594(m), 1478(s), 1451(s) ($\nu_{C=N,\ C=C}$); 1291(s), 1270(s) (δ_{C-O}); 841(s) (free $\nu_{PF_6^-}$). Mass spectrum (LSIMS), *m*/*z*: 508 ([Fe(bbpen)]$^+$), 402 ([Fe($C_{21}H_{22}N_4O$)]$^+$), 296 ([Fe($C_{14}H_{16}N_4$)]$^+$). Anal. calcd. (found) for [Fe(bbpen)]PF_6 ($C_{28}H_{28}F_6FeN_4O_2P$): C 51.47 (51.08), H 4.32 (4.22), N 8.58 (8.45). The solid-state magnetic moment was 5.91 BM.

X-ray crystallographic analyses

Selected crystallographic data are presented in Table 1. The final unit-cell parameters were based on 14 343 reflections with 2θ = 4.0–61.6°. The data were processed[2] and corrected for Lorentz and polarization effects. The structure was solved by heavy-atom Patterson methods and expanded using Fourier techniques. The oxygen atom of the methanol molecule was modeled as twofold disordered. The non-hydrogen atoms were refined anisotropically. Methanol O-H hydrogen atoms were placed in difference map positions, but

[2] *teXsan*: Crystal structure analysis package, Molecular Structure Corp., The Woodlands, Tex. 1992.

© 1999 NRC Canada

Table 2. Selected bond lengths (Å) and bond angles (deg) in the cation of [Fe(bbpen)]NO_3·CH_3OH.

Fe(1)—O(1)	1.8610(14)	N(2)—C(16)	1.485(3)
Fe(1)—O(2)	1.8855(15)	N(2)—C(22)	1.487(3)
Fe(1)—N(1)	2.234(2)	N(3)—C(4)	1.339(3)
Fe(1)—N(2)	2.228(2)	N(4)—C(17)	1.352(3)
Fe(1)—N(3)	2.135(2)	C(1)—C(2)	1.511(3)
Fe(1)—N(4)	2.135(2)	C(3)—C(4)	1.500(3)
O(1)—C(11)	1.336(3)	C(9)—C(10)	1.505(3)
O(2)—C(24)	1.338(3)	C(10)—C(11)	1.415(3)
N(1)—C(1)	1.490(3)	C(16)—C(17)	1.493(3)
N(1)—C(3)	1.484(3)	C(22)—C(23)	1.502(3)
N(1)—C(9)	1.496(3)	C(23)—C(24)	1.422(3)
N(2)—C(2)	1.495(3)		
O(1)-Fe(1)-O(2)	103.64(6)	Fe(1)-N(1)-C(1)	107.04(13)
O(1)-Fe(1)-N(1)	88.91(6)	Fe(1)-N(1)-C(3)	111.51(14)
O(1)-Fe(1)-N(2)	165.52(7)	Fe(1)-N(1)-C(9)	109.33(12)
O(1)-Fe(1)-N(3)	93.80(7)	C(1)-N(1)-C(3)	110.2(2)
O(1)-Fe(1)-N(4)	93.21(7)	C(1)-N(1)-C(9)	108.7(2)
O(2)-Fe(1)-N(1)	164.93(7)	C(3)-N(1)-C(9)	110.0(2)
O(2)-Fe(1)-N(2)	88.77(7)	Fe(1)-N(2)-C(2)	106.65(13)
O(2)-Fe(1)-N(3)	93.37(7)	Fe(1)-N(2)-C(16)	110.50(13)
O(2)-Fe(1)-N(4)	96.88(7)	Fe(1)-N(2)-C(22)	108.94)13)
N(1)-Fe(1)-N(2)	80.04(7)	C(2)-N(2)-C(16)	110.7(2)
N(1)-Fe(1)-N(3)	77.28(7)	C(2)-N(2)-C(22)	109.2(2)
N(1)-Fe(1)-N(4)	90.59(7)	C(16)-N(2)-C(22)	110.7(2)
N(2)-Fe(1)-N(3)	92.85(7)	Fe(1)-N(3)-C(4)	118.2(2)
N(2)-Fe(1)-N(4)	77.71(7)	Fe(1)-N(3)-C(8)	122.6(2)
N(3)-Fe(1)-N(4)	165.86(7)	Fe(1)-N(4)-C(17)	118.0(7)
Fe(1)-O(1)-C(11)	134.70(14)	Fe(1)-N(4)-C(21)	123.4(2)
Fe(1)-O(2)-C(24)	133.48(14)		

were not refined. The remaining hydrogen atoms were fixed in calculated positions with C—H = 0.98 Å, thermal parameters 1.2 times those of the parent atoms, and methyl group orientations based on difference map peak positions. Neutral atom scattering factors for all atoms and anomalous dispersion corrections for the non-hydrogen atoms were taken from the *International Tables for X-Ray Crystallography* (24). Final atomic coordinates and equivalent isotropic thermal parameters appear in Table 2. Complete tables of crystallographic data, hydrogen atom parameters, anisotropic thermal parameters, bond lengths, bond angles, torsion angles, intermolecular contacts, and least-squares planes have been deposited as supplementary material.[3]

Results and discussion

The deep purple coloured monocationic $[Fe(bbpen)]^+$ complex was prepared from reactions of hydrated iron(III) nitrate with one equivalent of H_2bbpen and two equivalents of sodium acetate in methanol. Both the nitrate and hexafluorophosphate salts of this complex were isolated, and the latter was synthesized to obtain a higher yield of the monocationic complex for the measurement of its magnetic moment. Both salts are soluble in common organic solvents, such as methanol, acetonitrile, and acetone. They were characterized by spectroscopic methods (IR, LSIMS, UV–vis), elemental analyses, and magnetic and electrochemical techniques, and the nitrate salt by X-ray crystallography.

The IR spectra of the monocationic complex in each salt show medium bands around 1600 cm^{-1} and strong bands between 1480–1450 cm^{-1} corresponding, respectively, to C=N (py) and C=C stretching vibrations of the aromatic rings. These are consistent with the reported values for the analogous Ga(III) and In(III) complexes (17). The deformation bands of the phenolate C-O group appear in the range 1290–1279 cm^{-1}, similar to those found in the Ln(III) complexes[4]. The free (uncoordinated) anionic NO_3^- and PF_6^- have stretching vibrations at 1382 and 860 cm^{-1}, respectively.

The LSI-mass spectra show the $[Fe(bbpen)]^+$ parent peak, as well $[Fe(C_{21}H_{22}N_4O)]^+$ and $[Fe(C_{14}H_{16}N_4)]^+$ fragments, consistent with the loss of one and two phenolate arms, respectively, from the parent ion. This type of fragmentation is also observed in the Ln(III) [4] and $[Re^{V}O]^{3+}$ [5] complexes with the same ligand.

[3] Supplementary material may be purchased from: The Depository of Unpublished Data, Document Delivery, CISTI, National Research Council of Canada, Ottawa, Canada K1A 0S2. Tables of bond lengths and angles have also been deposited with the Cambridge Crystallographic Data Centre and can be obtained on request from: The Director, Cambridge Crystallographic Data Centre, 12 Union Road, Cambridge, CB2 1EZ, U.K.

[4] I.A. Setyawati, S. Liu, S.J. Rettig, and C. Orvig. Manuscript submitted for publication.

[5] L. Xu, I.A. Setyawati, J. Pierreroy, S.J. Rettig, and C. Orvig. Manuscript in preparation.

© 1999 NRC Canada

Fig. 1. ORTEP drawing of the $[Fe(bbpen)]^+$ cation in $[Fe(bbpen)]NO_3 \cdot CH_3OH$ showing the crystallographic numbering. Thermal ellipsoids for the non-hydrogen atoms are drawn at the 33% probability level.

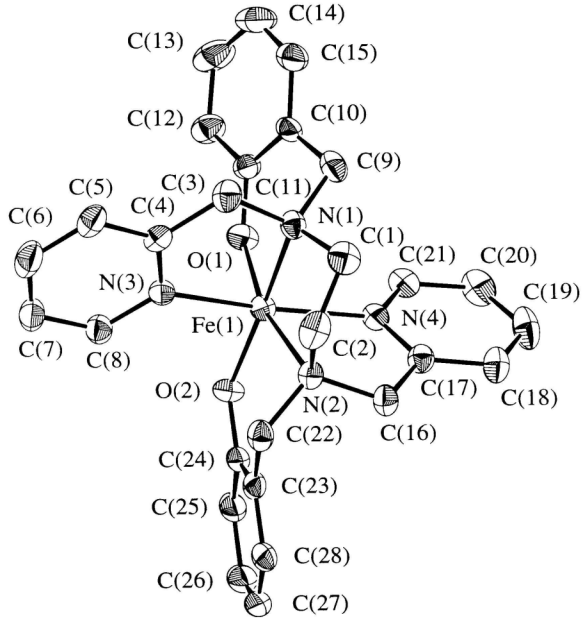

Crystals of $[Fe(bbpen)]NO_3 \cdot CH_3OH$ suitable for X-ray analysis were grown by slow evaporation of a methanol solution at room temperature. An ORTEP drawing of the cation in $[Fe(bbpen)]NO_3 \cdot CH_3OH$ is shown in Fig. 1.

The structure shows that hexadentate $bbpen^{2-}$ is bound to the central Fe(III) ion via two amine nitrogen atoms (ethylenediamine backbone), two pyridyl nitrogen atoms, and two phenolate oxygen atoms, the six atoms of which comprise a distorted octahedral geometry. Each half of the ligand forms a *fac*-N_2O arrangement: N1, N3, O1 being one face of the octahedron, while N2, N4, and O2 being the other face. The two amine nitrogen atoms and the two phenolic oxygen atoms are each *cis* pairs, and they form an equatorial plane, relative to which the two pyridyl nitrogen atoms are *trans* in axial positions. This structure is essentially identical to the Mn(III) (18), V(III) (19), Ga(III), and In(III) (17) analogues. The structure of $[Ru(bbpen)]^+$, however, showed two amine nitrogen, two pyridyl nitrogen, and two phenolate oxygen atoms, all as *cis* pairs (25).

Selected bond lengths and bond angles are listed in Table 2. The Fe—O bond lengths have an average of 1.873 Å, similar to those in bis(methanol)bis[2-(5-methylpyrazol-3-yl)phenolato]iron(III) nitrate (1.888 Å) (26), and in a trigonal bipyramidal iron(III) complex with a tetradentate tripodal amine phenolate (NO_3 donor set) and monodentate methylimidazole ligand ($[Fe\{N(CH_2\text{-}O\text{-}C_6H_4O)_3\}(1\text{-}Meim)]$) (1.876 Å). (27). The average Fe—N(amine) bond length of 2.231 Å and Fe—N(py) bond length of 2.135 Å in $[Fe(bbpen)]^+$ are comparable to those found in the dinuclear iron complexes with H_3bhpp (1,3-bis[(2-hydroxybenzyl)(2-pyridylmethyl)amino]-2-propanol) and H_3bhpmp (2,6-bis[(2-hydroxybenzyl)(2-pyridylmethyl)aminomethyl]-4-methylphenol) (11).

The three *trans* angles O1-Fe-N2, O2-Fe-N1, and N3-Fe-N4 are 165.52(7)°, 164.93(7)° and 165.86(7)°, respectively, a deviation of ~15° from 180°. The *cis* N1-Fe-N2 (amines) angle is 80.04(7)°, and the *cis* N(amine)-Fe-N(py) angles (N1-Fe-N3 and N2-Fe-N4) within the two five-membered chelate rings are 77.28(7)° and 77.71(7)°, respectively. All other *cis* angles in the complex are close to 90°, except the *cis* O1-Fe-O2 angle of 103.64(6)°, a deviation of ~14° from 90°. This deviation is similar to that found in the V(III) (19) and In(III) congeners (17), but was not observed in the Ga(III) (17) and Mn(III) (18) analogues, even though the ionic radius of high-spin Fe(III) (0.643 Å) is similar to those of Ga(III) (0.62 Å), V(III) (0.640 Å), and Mn(III) (0.645 Å), but significantly smaller than that of In(III) (0.800 Å) (28).

The solid-state magnetic moment of $[Fe(bbpen)]PF_6$ at room temperature was measured to be 5.91 BM. This value is in excellent agreement with the spin-only value of 5.92 BM for a high-spin Fe(III) ion.

The electronic spectrum of $[Fe(bbpen)]NO_3$ in CH_3CN is presented in Fig. 2. It consists of three maxima (λ_{max}) at 575 nm (ε = 5400 M^{-1} cm^{-1}), 323 (8900), and 275 (13 500). The electronic spectrum of H_2bbpen does not show any absorption maximum above 300 nm (18); thus, the two lower energy bands are assigned as ligand-to-metal charge-transfer bands (LMCT). Due to the intense LMCT bands, spin forbidden *d–d* transitions in the high-spin d^5 Fe(III) ion were not observed in this complex.

The 575 nm band is assigned to the charge-transfer transition from the $p\pi$ orbital of the phenolate oxygen to the $d\pi^*$ orbital of Fe(III) (11, 26, 29, 30). This band is similar to that in the dinuclear iron(III) complex with $bhpp^{3-}$ and two diphenyl phosphato ligands, λ_{max} = 586.5 (sic) nm (ε = 1150 M^{-1} cm^{-1}/Fe); the geometry around each iron(III) center was octahedral with a N_2O_4 donor set (two oxygen atoms from two diphenyl phosphato ligands) (11). However, the $p\pi \rightarrow d\pi^*$ transition is at a lower energy compared to that in the iron(III) complex of tetradentate *N,N′*-bis(2-hydroxybenzyl)ethylenediamine (H_2bben) and two monodentate imidazole ligands (490 nm) (26). Ainscough et al. (26) suggested a structure for $[Fe(bben)(Im)_2]^+$ with two *cis* phenolate oxygen atoms and two *trans* imidazole nitrogen atoms, similar to that of $[Fe(bbpen)]^+$, reported herein, with the *trans* pyridyl nitrogen atoms replacing those of imidazole in the former. The bathochromic shift of the charge-transfer bands of $[Fe(bbpen)]^+$ is consistent with the tighter bonding of the hexadentate ligand $bbpen^{2-}$, which gives a better phenolate-iron overlap, compared to a combination of one tetradentate (N_2O_2) and two monodentate imidazole ligands. The ligand field strengths of imidazole and pyridyl ligands may also play a role in this red-shifted absorption maximum. A relationship between the energy of the phenolate to iron(III) charge-transfer transition and the field strength of ligands coordinated to iron(III) has been observed previously (26, 31).

Another similar complex, that of iron(III) with the linear N_4O_2 amine phenolate ligand (26) (1,12-bis(2-hydroxyphenyl)-2,5,8,11-tetraazadodecane, also known as H_2bad (32)), has λ_{max} = 507 nm. By analogy to the structure of the Ga(III) complex with hexadentate bad^{2-} (32), the Fe(III) structure with the same ligand (26) can be postulated to have a similar distorted octahedral geometry, in which all four adjacent amine nitrogen atoms are *cis* to one another because of the steric constraints of the trien (triethylenetetra-

© 1999 NRC Canada

Fig. 2. UV–visible spectrum of 62 μM [Fe(bbpen)]NO_3 in acetonitrile.

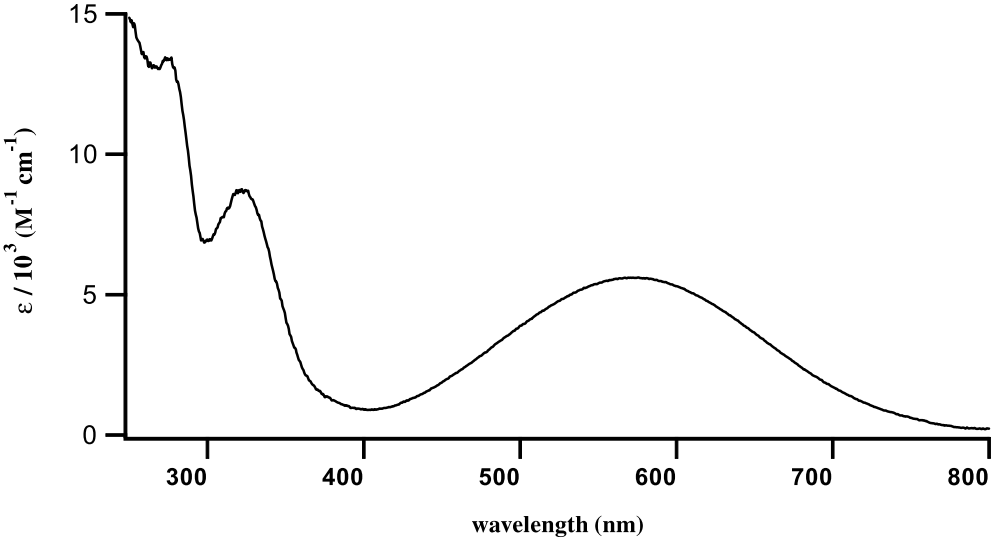

Fig. 3. Cyclic voltammogram of [Fe(bbpen)]NO_3 in CH_3CN (0.25 M (TBA)PF_6), scan rate is 100 mV s^{-1}.

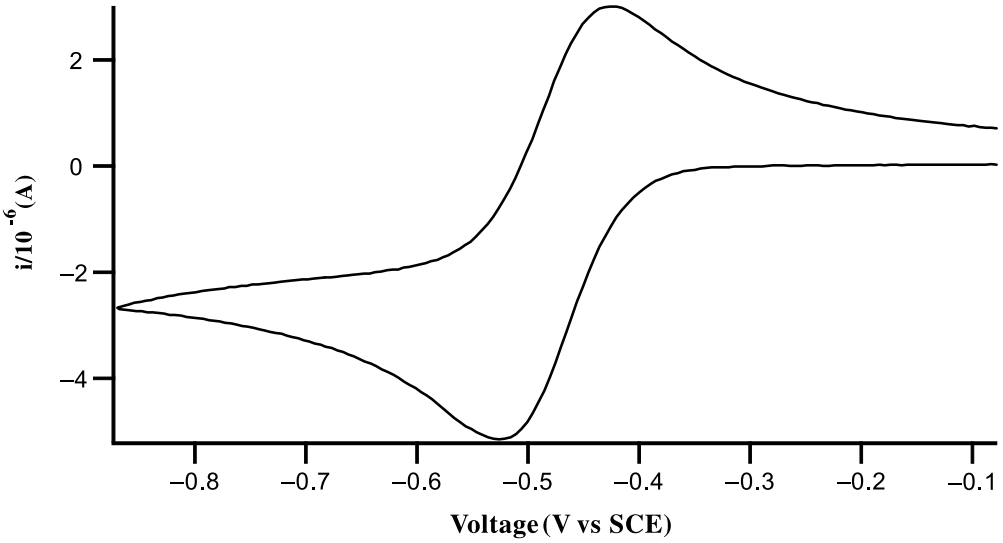

mine) backbone. If this were the case, the N_4O_2 donor atom set of $[Fe(bad)]^+$ (26) would be similar to that of $[Fe(bbpen)]^+$; however, the former would have a more sterically constrained structure, dictated by the presence of three five-membered chelate rings instead of two in the latter complex. The reduced steric strain in $[Fe(bbpen)]^+$ should improve the phenolate to iron orbital overlap, thus facilitating the charge-transfer transition, giving a lower energy LMCT band.

The higher energy LMCT band at 323 nm is associated with the transition from the phenolate $p\pi$ orbital to iron(III) $d\sigma^*$ orbital (11, 26, 29, 30). The energy difference between the two LMCT bands (~13 500 cm^{-1}) is a measure of 10 Dq for this octahedral complex. This value is similar to that of octahedral $[Fe(EDDHA)]^-$ complex (~11 000 cm^{-1}) (29) and $[Fe(OH_2)_6]^{3+}$ (13 700 cm^{-1}) (33).

The cyclic voltammogram of [Fe(L1)]NO_3 was recorded in acetonitrile in the range of –0.9 to 0.1 V versus SCE (Fig. 3). It exhibits a reversible reduction wave at $E_{1/2}$ = –0.47 V ($\Delta E\ p$ = 100 mV). This quasi-reversible one-electron redox process is assigned to $[Fe^{III}(L1)]^+ + e^- \leftrightarrow [Fe^{II}(L1)]$.

Conclusions

Monocationic $[Fe(bbpen)]^+$ was isolated with two different counter anions (NO_3^- and PF_6^-). Magnetic susceptibility measurements confirmed the presence of a high-spin iron(III) ion. The crystal structure of [Fe(bbpen)]$NO_3 \cdot CH_3OH$ showed a distorted octahedral geometry around iron(III) with two *cis* amine nitrogen atoms, two *cis* oxygen phenolate atoms, and two *trans* pyridyl nitrogen atoms, an arrangement similar to those found in the V(III) (19), Mn(III) (18), Ga(III), and In(III) congeners (17). The electronic absorption spectrum of [Fe(bbpen)]NO_3 exhibited two LMCT bands at 575 and 323 nm. The 575 nm band is similar to that noted in model studies of purple acid phosphatases'

© 1999 NRC Canada

active sites (11); however, it is at a lower energy compared to other iron(III) complexes with small ligands, used as models of transferrin and lactoferrin active sites (26, 29). The 10 Dq value of octahedral $[Fe(bbpen)]^+$ is calculated to be approximately 13 500 cm^{-1}, in good agreement with other iron(III) octahedral complexes (29, 33).

Acknowledgments

The authors gratefully acknowledge DuPont Pharmaceuticals for support, and the Natural Sciences and Engineering Research Council of Canada for both a graduate fellowship (I.A.S.) and operating grants. We also thank Dr. M.O. Wolf for the use of his electrochemistry instrument and Y. Zhu for his assistance.

References

1. D.C. Harris and P. Aisen. *In* Iron carriers and iron proteins. *Edited by* T.M. Loehr. VCH, New York. 1989. p. 239.
2. P. Aisen. *In* Iron carriers and iron proteins. *Edited by* T.M. Loehr. VCH, New York. 1989. p. 353.
3. R.E. Feeney and S.S. Komatsu. Struct. Bonding (Berlin), **1**, 149 (1966).
4. P.F. Hennart, D.J. Brasseur, J.B. Delogne-Desnoeck, M.M. Dramaix, and C.E. Robyn. Am. J. Clin. Nutr. **53**, 32 (1991).
5. L. Que, Jr. *In* Iron carriers and iron proteins. *Edited by* T.M. Loehr. VCH, New York. 1989. p. 467.
6. L. Que, Jr. and R.Y.N. Ho. Chem. Rev. **90**, 2607 (1990).
7. K. Doi, B.L. Antanaitis, and P. Aisen. Struct. Bonding (Berlin), **70**, 1 (1988).
8. L. Que, Jr. and A.E. True. Prog. Inorg. Chem. **38**, 97 (1990).
9. J.B. Vincent, G.L. Olivier-Lilley, and B.A. Averill. Chem. Rev. **90**, 1447 (1990).
10. R. Than, A.A. Feldmann, and B. Krebs. Coord. Chem. Rev. **182**, 211 (1999).
11. B. Krebs, K. Schepers, B. Bremer, G. Henkel, E. Althaus, W. Müller-Warmuth, K. Griesar, and W. Haase. Inorg. Chem. **33**, 1907 (1994).
12. A. Neves, M.A. De Brito, I. Vencato, V. Drago, K. Griesar, and W. Haase. Inorg. Chem. **35**, 2360 (1996).
13. E. Lambert, B. Chabut, S. Chardon-Noblat, A. Deronzier, G. Chottard, A. Bousseksou, J.-P. Tuchagues, J. Laugier, M. Bardet, and J.-M. Latour. J. Am. Chem. Soc. **119**, 9424 (1997).
14. R. Viswanathan, M. Palaniandavar, T. Balasubramanian, and T.P. Muthiah. Inorg. Chem. **37**, 2943 (1998).
15. J.H. Doroshow. Biochem. Biophys. Res. Commun. **135**, 330 (1986).
16. J.-O. Moon, S.-K.Park, and T. Nagano. Biol. Pharm. Bull. **21**, 284 (1998).
17. E. Wong, S. Liu, S.J. Rettig, and C. Orvig. Inorg. Chem. **34**, 3057 (1995).
18. A. Neves, S.M.D. Erthal, I. Vencato, A.S. Ceccato, Y.P. Mascarenhas, O.R. Nascimento, M. Hörner, and A.A. Batista. Inorg. Chem. **31**, 4749 (1992).
19. A. Neves, A.S. Ceccato, S.M.D. Erthal, I. Vencato, B. Nuber, and J. Weiss. Inorg. Chim. Acta, **187**, 119 (1991).
20. A. Neves, A.S. Ceccato, I. Vencato, Y.P. Mascarenhas, and C. Erasmus-Buhr. J. Chem. Soc., Chem. Commun. 652 (1992).
21. A. Neves, A.S. Ceccato, C. Erasmus-Buhr, S. Gehring, W. Haase, H. Paulus, O.R. Nascimento, and A.A. Batista. J. Chem. Soc. Chem. Commun. 1782 (1993).
22. A. Neves, S.M.M. Romanowski, I. Vencato, and A.S. Mangrich. J. Chem. Soc. Dalton Trans. 617 (1998).
23. D. Diehl and C.C. Hach. Inorg. Synth. **3**, 196 (1950).
24. (*a*) International tables for X-ray crystallography. Vol. IV. Kynoch Press, Birmingham, U.K. (present distributor Kluwer Academic Publishers, Boston, Mass. U.S.A.) 1974. p. 99–102; (*b*) International tables for X-ray crystallography. Vol. C. Kluwer Academic Publishers, Boston, Mass. U.S.A. 1992. p. 200–206.
25. A. Neves, M.A. De Brito, G. Oliva, O.R. Nascimento, E.H. Panepucci, and A.A. Batista. Polyhedron, **14**, 1307 (1995).
26. E.W. Ainscough, A.M. Brodie, J.E. Plowman, K.L. Brown, A.W. Addison, and A.R. Gainsford. Inorg. Chem. **19**, 3655 (1980).
27. J. Hwang, K. Govindaswamy, and S.A. Koch. J. Chem. Soc. Chem. Commun. 1667 (1998).
28. R.D. Shannon. Acta Crystallogr. Sect. A: Cryst. Phys. Diffr. Theor. Gen. Crystallogr. **A32**, 751 (1976).
29. B.P. Gaber, V. Miskowski, and T.G. Spiro. J. Am. Chem. Soc. **96**, 6868 (1974).
30. S. Wang, L. Wang, X. Wang, and Q. Luo. Inorg. Chim. Acta, **254**, 71 (1997).
31. J.W. Pyrz, L. Roe, L.J. Stern, and L. Que., Jr. J. Am. Chem. Soc. **107**, 614 (1985).
32. E. Wong, S. Liu, T. Lügger, F.E. Hahn, and C. Orvig. Inorg. Chem. **34**, 93 (1995).
33. H.B. Gray and H.J. Schugar. *In* Inorganic biochemistry. *Edited by* G.I. Eichhorn. Elsevier, Amsterdam. 1973.

© 1999 NRC Canada

Fluctuations in aqueous methanol, ethanol, and propan-1-ol: amplitude and wavelength of fluctuation

Yoshikata Koga

Abstract: Density, heat capacity, and isentropic compressibility data for aqueous methanol, ethanol, and propan-1-ol by Benson's group were used to evaluate two kinds of fluctuations; mean-square fluctuation densities; and (mean-square) normalized fluctuations, respectively, in volume, entropy, and cross (entropy/volume) effect. The mean-square fluctuation densities provide measures for the amplitude (intensity) of the fluctuation, while the normalized fluctuations contain information regarding the wavelength (extensity) of the fluctuation. Furthermore, their composition derivatives, the partial molar fluctuations of alcohols were calculated. These quantities signify the effect of additional solute on the respective fluctuations. These data were interpreted in terms of mixing schemes learned earlier in this laboratory by using the data of excess partial molar enthalpy, entropy, and volume, and the respective alcohol–alcohol interaction functions, i.e., the composition derivatives of partial molar quantities.

Key words: aqueous methanol, ethanol, and propan-1-ol; fluctuation density; normalized fluctuation; partial molar fluctuations of alcohol.

Résumé: Utilisant des données relatives à la densité, la capacité calorifique et la compressibilité isoentropique de solutions aqueuses de méthanol, éthanol et propan-1-ol, obtenues par le groupe du professeur Benson, on a évalué deux types de fluctuations, soit les fluctuations quadratiques moyennes de la densité ainsi que les fluctuations (quadratiques moyennes) normalisées respectivement pour le volume, l'entropie et l'effet croisé (entropie/volume). Les fluctuations quadratiques moyennes de la densité donnent des mesures de l'amplitude (intensité) de la fluctuation alors que les fluctuations normalisées comportent des informations relatives à l'influence de la longueur d'onde sur la fluctuation. De plus, on a calculé les dérivées de composition, les fluctuations molaires partielles des alcools. Ces grandeurs indiquent l'effet de soluté additionnel sur les fluctuations respectives. On a interprété ces données en fonction de schémas de mélanges développés antérieurement dans ce laboratoire en utilisant les données d'enthalpie, d'entropie et de volume molaires partiels en excès et les fonctions respectives d'interaction alcool–alcool, c'est-à-dire les dérivées de composition des quantités molaires partielles.

Mots clés : aqueux, méthanol, éthanol, propan-1-ol; fluctuation de densité; fluctuation normalisée; fluctuations molaires partielles d'alcool.
[Traduit par la Rédaction]

1. Introduction

It is fair to state that Canadian researchers including Benson, Desnoyers, Hepler, and Patterson have made important contributions in the thermodynamic studies of aqueous solutions. Their data are precise and thorough, and have provided keys to deepen the insights into this mysterious system, the aqueous solution. Their papers are too numerous to quote here.

In this paper, we limit our attention to a series of three papers by Benson et al. (1–3) on aqueous solutions of methanol (Me), ethanol (Et), and propan-1-ol (1P). For the three alcohols (AL), the densities were measured at several temperatures (1). Heat capacities (2), and isentropic compressibilities (3) were obtained at 25°C. All of these data were determined accurately and in small increments in the mole fraction of alcohol. From the volume data at 15, 25, and 35°C, thermal expansivities, α_p, can be calculated at 25°C. Thus, all three response functions, C_p, κ_T, and α_p can be obtained at 25°C accurately and in small increments of the mole fraction of AL, x_{AL} (AL = Me, Et, or 1P). They are all proper thermodynamic functions for the Gibbs (p, T, n_i) system, in a sense that they are all second derivatives of G with respect to the independent variables (p, T, n_i), where n_i is the amount of the ith component.

Response functions are related to mean-square fluctuations through standard statistical thermodynamics (4). Implicit in the derivation of such relationships, however, is that a local *thermodynamic value* must be determined in a coarse grain, the size of which must be large enough for a *thermodynamic quantity* to be defined but small enough so that the fluctuation can be detected. The appropriate size may depend on the situation in question and may not be fixed universally. Hence when a mean-square fluctuation is cited, the size of the coarse grain must be specified. The problem is that we do not know

Received March 15, 1999

This paper is dedicated to Professor G.C. Benson.

Y. Koga. Department of Chemistry, The University of British Columbia, 2036 Main Mall, Vancouver, B.C. V6T 1Z1, Canada.
Telephone: (604) 822-3491; **FAX:** (604) 822-2847; **e-mail:** koga@chem.ubc.ca

© 1999 NRC Canada

Table 1. Response functions and fluctuations: H_2O vs. *n*-hexane.

	Eq. no.	H_2O	*n*-Hexane
V_m ($cm^3\ mol^{-1}$)		18.07	135.3
κ_T (TPa^{-1})		452.5	1567.2
C_p ($J\ K^{-1}\ mol^{-1}$)		75.15	196.4
α_p ($10^{-4}\ K^{-1}$)		2.572	12.88
For N_z = 1 mole			
$< (\Delta V)^2 > /k$	1	2.44×10^6	63.2×10^6
$< (\Delta S)62 > /k$	2	75.15	196.4
$< (\Delta S)(\Delta V) > /k$	3	46.47×10^{-4}	1742.7×10^{-4}
${}^{V}\delta$	4	1.35×10^5	4.67×10^5
${}^{S}\delta$	5	4.16	1.45
${}^{SV}\delta$	6	1.38	51.93
${}^{V}\Delta$	8b	0.0624	0.0287
${}^{S}\Delta$	9b	1.91	0.0891
${}^{SV}\Delta$	10b	0.0353	0.0236

its proper size a priori. This difficulty may be circumvented by using mean-square fluctuation densities, in which the size of the coarse grain becomes implicit. As discussed below, fluctuation densities provide a measure for fluctuation amplitude, or intensity of fluctuation. However, the peculiar characteristics of liquid H_2O may be a manifestation of the collective fluctuations in the hydrogen-bond network involving a large number of H_2O molecules (5–8). Namely, the wavelength, or the extensity of fluctuation may be larger in H_2O than in a normal liquid. Hence, it would be convenient to have some information about the size of the coarse grain that is related to the wavelength (or the extent) of the fluctuation. The normalized fluctuations introduced by us earlier (9–12) serve this purpose, as discussed below.

Aqueous alcohols (AL) have been studied extensively and the papers up to the early 1980's have been comprehensively reviewed (13). Our more recent studies (14–16) basically supported earlier understandings (13). Additional findings may include

(*a*) AL forms the so-called iceberg in its immediate vicinity with concomitant reduction in the hydrogen-bond probability of bulk H_2O away from AL.

(*b*) Up to a threshold value of x_{AL}, the hydrogen-bond probability of bulk H_2O is still high enough to retain the hydrogen-bond connectivity throughout the entire bulk of H_2O, i.e., the hydrogen-bond percolation is intact. We call this mode of mixing, "mixing scheme I".

(*c*) Above the threshold value of x_{AL}, the percolation nature of H_2O is lost and the solution consists of two kinds of clusters rich in H_2O and AL, respectively. This is called mixing scheme II.

(*d*) The transition from mixing scheme I to scheme II is associated with anomalies in the third derivatives of G. It takes place within a small x_{AL} region. The transition starts at point X and ends at point Y. We interpret this as that at point X the strongest hydrogen bonds in the distribution reach the percolation threshold, while the weakest hydrogen bonds lose percolation nature at point Y. Hence, beyond point Y, there is no hydrogen-bond connectivity and the solution consists of two kinds of clusters, i.e., mixing scheme II.

(*e*) The larger the hydrophobic moiety, the lower the x_{AL} value of the boundary region.

2. Fluctuations

Mean-square fluctuations related to the response functions in the Gibbs variable system are written as (4),

$$[1] \qquad \frac{< (\Delta V)^2 >}{k} = T < V > \kappa_T$$

$$[2] \qquad \frac{< (\Delta S)^2 >}{k} = < C_p >$$

$$[3] \qquad \frac{< (\Delta V)(\Delta S) >}{k} = T < V > \alpha_p$$

where $< V >$ and $< C_p >$ are the average values in the coarse grain containing N_z molecules. The problem is that we do not know the proper size of the coarse grain, N_z, a priori. When a comparison is made between H_2O and *n*-hexane, for example, we are forced to choose arbitrarily $N_z = 1$ mole, say, for both. Table 1 shows the mean-square fluctuations, eqs.[1]–[3], comparing H_2O and *n*-hexane. Due to forcing N_z to be equal for both cases, mean-square fluctuations look larger for *n*-hexane than for H_2O, which seems to be against our common understanding since the bent hydrogen bond model (5). Thus, N_z must be larger for H_2O than for *n*-hexane. Indeed, recent molecular dynamics simulations (6,7) and an X-ray scattering study (8) indicated that collective fluctuations involving a large number of H_2O molecules are prevalent in liquid H_2O.

The mean-square fluctuation densities, below, make N_z implicit, and thus show a measure of the amplitude, or the intensity, of respective fluctuations.

$$[4] \qquad {}^{V}\delta \equiv \frac{< (\Delta V)^2 >}{(k < V >)} = T\kappa_T$$

$$[5] \qquad {}^{S}\delta \equiv \frac{< (\Delta S)^2 >}{(k < V >)} = \frac{< C_p >}{< V >}$$

$$[6] \qquad {}^{SV}\delta \equiv \frac{< (\Delta S)(\Delta V) >}{(k < V >)} = T\alpha_p$$

The partial-molar mean-square fluctuation densities are defined as,

$$[7] \qquad {}^{q}\delta_i \equiv N\left(\frac{\partial^q \delta}{\partial n_i}\right)_{p,T,nj} = (1 - x_i)\left(\frac{\partial^q \delta}{\partial x_i}\right)$$

©1999 NRC Canada

where $q = V$, S, or SV. These quantities signify the effect of incoming ith component on ${}^{q}\delta$. We note that ${}^{q}\delta$'s do not contain information about N_z. Earlier, we introduced the (mean square) normalized fluctuations ${}^{q}\Delta$'s as eqs. [8b]–[10b] below (9–12). First we normalized the deviation of a local value (a value in a coarse grain) from its global average by the mean volume of the coarse grain, and then took its mean-square.

$$[8a] \quad \left\langle \left(\frac{\Delta V}{< V >} \right)^2 \right\rangle = \frac{kT\kappa_T}{< V >}$$

$$[9a] \quad \left\langle \left(\frac{\Delta S}{< V >} \right)^2 \right\rangle = \frac{k < Cp >}{< V >^2}$$

$$[10a] \quad \left\langle \left(\frac{\Delta V}{< V >} \right) \left(\frac{\Delta S}{< V >} \right) \right\rangle = \frac{kT\alpha_p}{< V >}$$

By taking N_z arbitrarily equal to 1 mole and converting k to R we defined ${}^{q}\Delta$'s as (9-12)

$$[8b] \quad {}^{V}\Delta \equiv \frac{RT\kappa_T}{V_m}$$

$$[9b] \quad {}^{S}\Delta \equiv \frac{RC_{pm}}{V_m^2}$$

$$[10b] \quad {}^{SV}\Delta \equiv \frac{RT\alpha_p}{V_m}$$

where V_m is the molar volume and C_{pm} is the molar heat capacity. The partial-molar normalized fluctuations of the ith component, ${}^{q}\Delta_i$, were defined as (9,11,12),

$$[11] \quad {}^{q}\Delta_i \equiv (1 - x_i)\left(\frac{\partial {}^{q}\Delta}{\partial x_i} \right)$$

In eqs. [8]–[10], the right-hand sides, after averaging, contain N_z-dependent $< V >$, or V_m for $N_z = 1$ mole, in the denominator. This fact turned out to be convenient for conveying qualitative information about the appropriate size of N_z, and hence the wavelength, or the extensity, of fluctuation. When making a comparison between H_2O and *n*-hexane, for example, we have no other choice but choose the same value for N_z, say 1 mole. If the appropriate size of N_z is in fact larger for H_2O, we are dividing in eqs. [8]–[10] by an unduly smaller value of $< V >$ for H_2O, and hence the value of ${}^{q}\Delta$ becomes apparently larger for H_2O than otherwise if the appropriately larger value for N_z was used. Thus, ${}^{q}\Delta$ for H_2O conveys qualitative information that H_2O has a larger fluctuation than *n*-hexane in terms of wavelength as well as amplitude.

We now turn to aqueous methanol, ethanol, and propan-1-ol. We calculate ${}^{q}\delta$, eqs. [4]–[6], and ${}^{q}\delta_i$, eq. [7], to gain information about the amplitude of fluctuations, and ${}^{q}\Delta$, eqs. [8b]–[10b], and ${}^{q}\Delta_i$, eq. [11] for the amplitude plus the wavelength of respective fluctuations. We thus attempt to gain a deeper insight into the mixing schemes (mixing scheme I in particular) of these aqueous solutions. We note in passing that the coarse grain in aqueous AL solutions must be chosen such that the numbers of AL and H_2O molecules in the coarse grain, N_{AL}^Z and N_{W}^Z, ($N_Z = N_{\mathrm{AL}}^Z + N_{\mathrm{W}}^Z$) are in the same composition as the global one. Namely, $N_{\mathrm{AL}}^Z/(N_{\mathrm{AL}}^Z + N_{\mathrm{W}}^Z) = x_{\mathrm{AL}}$. Since we are in the Gibbs ensemble, the independent variables, p, T, and n_i are kept fixed.

Fig. 1. Excess partial molar volumes of methanol (Me), ethanol (Et) and propan-1-ol (1P) at 25°C. •, Methanol; ■, ethanol; ▲, propan-1-ol.

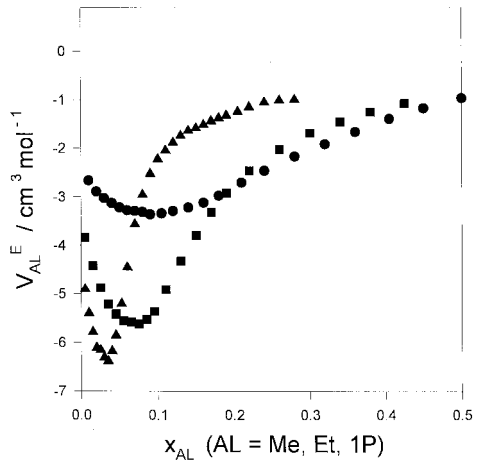

Fig. 2. Volume fluctuations at 25°C. (*a*) Mean-square volume fluctuation density, ${}^{V}\delta$. (*b*) Mean-square normalized volume fluctuation, ${}^{V}\Delta$. •, Methanol; ■, ethanol; ▲, propan-1-ol.

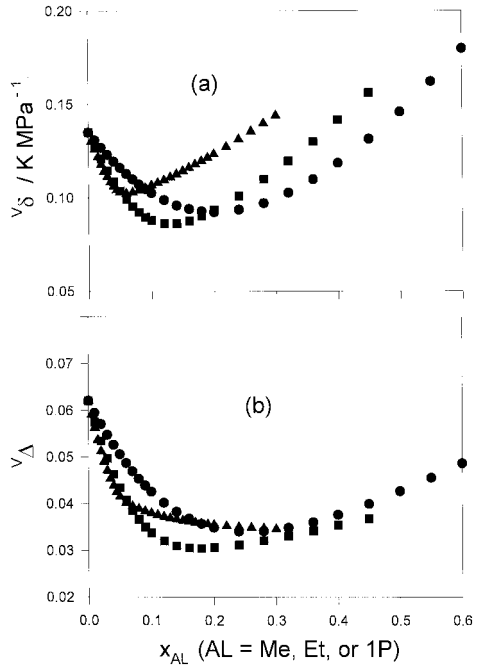

©1999 NRC Canada

Fig. 3. Partial molar volume fluctuations at 25°C. (*a*) ${}^{V}\delta_{\mathrm{AL}}$. (*b*) ${}^{V}\Delta_{\mathrm{AL}}$. •, Methanol; ■, ethanol; ▲, propan-1-ol. $\mathbf{X}_{\mathrm{AL}}$, the onset of the transition from mixing scheme I to II for AL (= Me, Et, or 1P); $\mathbf{Y}_{\mathrm{AL}}$, the end point of the transition for AL.

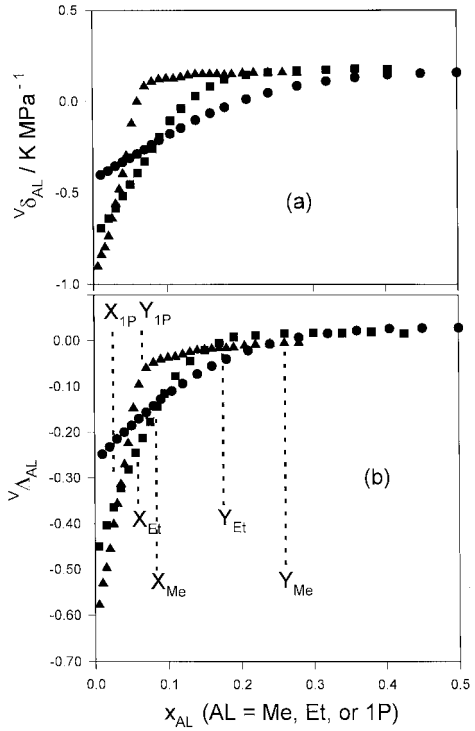

Fig. 4. Entropy fluctuations at 25°C. (*a*) Mean-square entropy fluctuation density, ${}^{S}\delta$. (*b*) Mean-square-normalized entropy fluctuation, ${}^{S}\Delta$. •, Methanol; ■, ethanol; ▲, propan-1-ol.

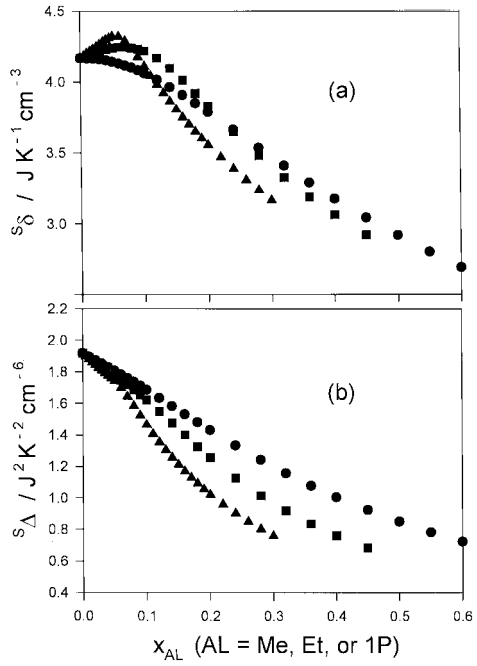

3. Data analysis and results

The first step is to draw a smooth curve through all the data points (1)–(3), and to read values off the smooth curve drawn at fixed predetermined increments. We used the following method to avoid losing the number of significant figures in the graphical smoothing process. A simple function, $f(x_i)$ was devised such that the residuals from data points $y_i(x_i)$, $r_i = y_i - f(x_i)$, are all within the last three significant figures, while the data themselves, y_i, have typically five to six significant figures. The values of r_i were plotted, and a smooth curve was drawn through all the (x_i, r_i) data points. The values of r_j were then read off the smooth curve drawn at x_j in predetermined increments, and the values of y_j were recovered using $y_j = r_j + f(x_j)$. All the smoothed values of V_m^E at 15, 25, and 35°C, C_p and κ_S at 25°C, are listed in the Supplementary Table deposited in CISTI.[1] The α_p data at 25°C were calculated using V_m data at 15, 25, and 35°C (8), and the κ_T data at 25°C using κ_S, V_m, C_p, and α_p. The α_p and κ_T data are also listed in the supplementary table.

From V_m^E data at 25°C, the excess partial molar volume of AL, V_{AL}^E, were calculated and are shown in Fig. 1. Using the proper response functions listed in Table 1, the mean-square volume-, entropy-, and cross fluctuation densities ${}^{V}\delta$, ${}^{S}\delta$, and ${}^{SV}\delta$ were calculated using eqs. [4]–[6]. Also the normalized volume, entropy, and cross fluctuations, ${}^{V}\Delta$, ${}^{S}\Delta$, ${}^{SV}\Delta$ were calculated using eqs. [8b]–[10b]. The effect of additional AL on the respective fluctuations, the partial molar fluctuations of AL were calculated using eqs. [7] and [11]. All these fluctuations and partial molar fluctuations are shown in Figs. 2–9.

4. Discussion

Our general understanding of the mixing schemes of aqueous alcohols mentioned briefly in the introduction was based on the composition and temperature dependency of the excess partial molar enthalpy, $H_{\mathrm{AL}}^{\mathrm{E}}$; entropy, $S_{\mathrm{AL}}^{\mathrm{E}}$; and volume, $V_{\mathrm{AL}}^{\mathrm{E}}$ of solute AL, which are other second derivatives of G. Furthermore, we used their composition derivatives (third derivatives of G) as a measure of solute–solute interaction. For example, the enthalpic interaction function, $H_{\mathrm{AL-AL}}^{\mathrm{E}}$, among alcohol molecules is defined as

$$[12] \qquad H_{\mathrm{AL-AL}}^{\mathrm{E}} \equiv N\left(\frac{\partial H_{\mathrm{AL}}^{\mathrm{E}}}{\partial n_{\mathrm{AL}}}\right) = (1 - x_{\mathrm{AL}})\left(\frac{\partial H_{\mathrm{AL}}^{\mathrm{E}}}{\partial x_{\mathrm{AL}}}\right)$$

This quantity signifies the effect of incoming AL on the partial molar enthalpy, i.e., the actual enthalpic situation, of AL. If $H_{\mathrm{AL-AL}}^{\mathrm{E}} < 0$, incoming AL molecules make the enthalpic situation of existing AL more favourable and thus we say the AL–AL interaction is attractive in terms of enthalpy. Similarly, a positive $H_{\mathrm{AL-AL}}^{\mathrm{E}}$ indicates a repulsive enthalpic in-

[1] Supplementary table,"Smoothed volumes at 15, 25, and 35°C and response functions at 25°C, for aqueous methanol, ethanol, and propan-1-ol." has been deposited in CISTI. Copies of the material on deposit may be purchased from the Depository of Unpublished Data, Document Delivery, CISTI, National Research Council Canada, Ottawa, ON K1A 0S2, Canada.

©1999 NRC Canada

Fig. 5. Partial molar entropy fluctuations at 25°C. (*a*) ${}^{S}\delta_{AL}$. (*b*) ${}^{S}\Delta_{AL}$. •, Methanol; ■, ethanol; ▲, propan-1-ol. $\mathbf{X}_{AL}$, the onset of the transition from mixing scheme I to II for AL (= Me, Et, or 1P); $\mathbf{Y}_{AL}$, the end point of the transition for AL.

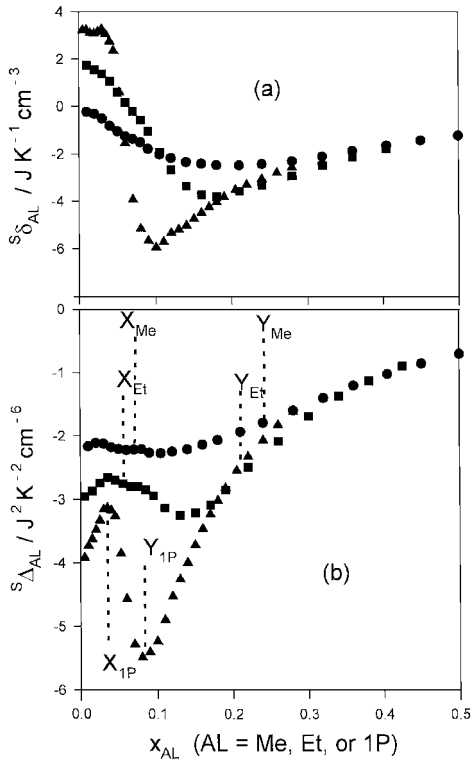

Fig. 6. Cross (entropy–volume) fluctuations at 25°C. (*a*) Mean-square cross fluctuation density, ${}^{SV}\delta$. (*b*) Mean-square normalized cross fluctuation, ${}^{SV}\Delta$. •, Methanol; ■, ethanol; ▲, propan-1-ol.

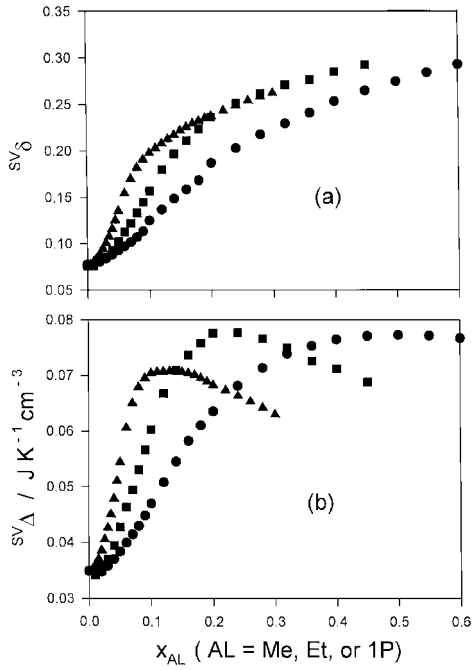

Fig. 7. Partial molar cross (entropy-volume) fluctuations of methanol at 25°C. (*a*) ${}^{SV}\delta_{Me}$. (*b*) ${}^{SV}\Delta_{Me}$. Circle, ${}^{SV}\delta_{Me}$ or ${}^{SV}\Delta_{Me}$; square, H^{E}_{Me-Me}. $\mathbf{X}_{Me}$, the onset of the transition from mixing scheme I to II; $\mathbf{Y}_{me}$, the end point of the transition for methanol.

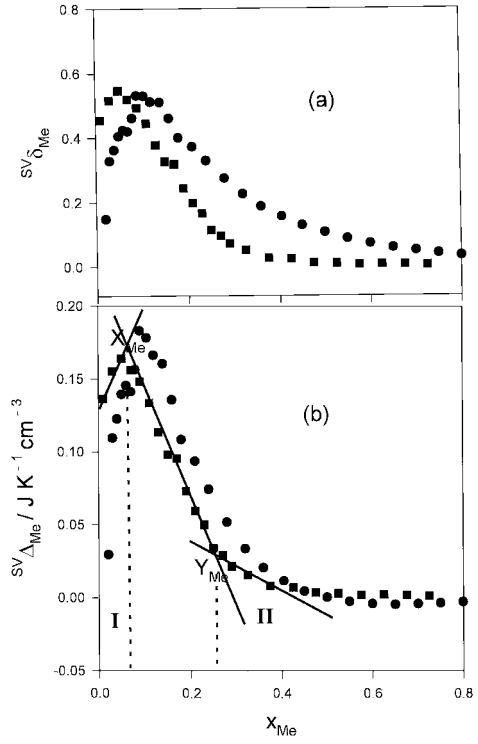

teraction between AL molecules. This together with entropy and volume analogs were used to gain an understanding of the mixing schemes, particularly for aqueous *tert*-butanol and 2-butoxyethanol (14,15).

As for methanol, ethanol, and propan-1-ol, the excess partial molar enthalpy data (16) behaved in the same way. The excess chemical potential and hence entropy data (17, see also footnote [2]) also showed the same trend. The excess partial molar volume data, V^{E}_{AL}, shown in Fig. 1 also display the same dependence as for higher alcohols (18). Hence, the general mixing schemes and the transition between two mixing schemes mentioned above in the introduction is indeed applicable to lower alcohols also. In particular, the fact that V^{E}_{AL} shows the initial decrease on addition of AL supports the fact that AL, even methanol, forms an "iceberg" in its immediate vicinity but reduces the hydrogen-bond network of bulk H_2O away from AL molecules, as discussed at some length earlier (14,15). Briefly, the excess partial molar volume of AL is negative due primarily to the size difference between AL and H_2O. However, H_2O is not just small solvent molecules but makes the hydrogen-bond network. Thus, H_2O is bulkier than the size determined by Van der Waals' radius. Due to the H_2O's bulkiness, there is a positive contribution resulting in the still

[2] J. Hu, C.A. Haynes, and Y. Koga. Manuscript in preparation

©1999 NRC Canada

Fig. 8. Partial molar cross (entropy–volume) fluctuations of ethanol at 25°C. (*a*) ${}^{SV}\delta_{Et}$. (*b*) ${}^{SV}\Delta_{Et}$. Circle, ${}^{SV}\delta_{Et}$ or ${}^{SV}\Delta_{Et}$; square, H^{E}_{Et-Et}. $\mathbf{X}_{Et}$, the onset of the transition from mixing scheme I to II; $\mathbf{Y}_{Et}$, the end point of the transition for ethanol.

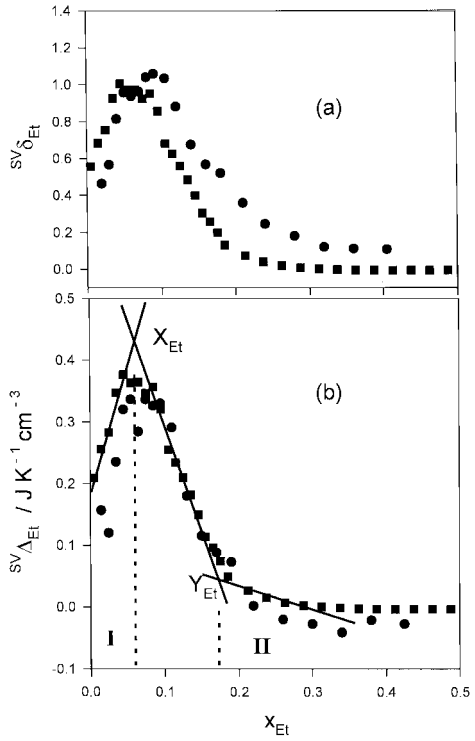

Fig. 9. Partial molar cross (entropy–volume) fluctuations of propan-1-ol at 25°C. (*a*) ${}^{SV}\delta_{1P}$. (*b*) ${}^{SV}\Delta_{1P}$. Circle, ${}^{SV}\delta_{1P}$ or ${}^{SV}\Delta_{1P}$; square, H^{E}_{1P-1P}. $\mathbf{X}_1$, the onset of the transition from mixing scheme I to II; $\mathbf{Y}_{1P}$, the end point of the transition for propan-1-ol.

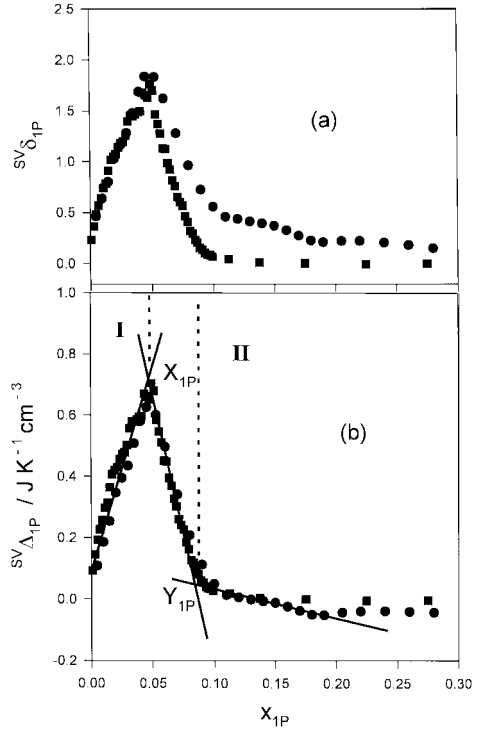

negative net value of V^{E}_{AL} at infinite dilution. As x_{AL} increases, the positive contribution is progressively reduced, (hence V^{E}_{AL} decreases), since the hydrogen-bond probability in the bulk H_2O away from existing solute AL is progressively reduced. This trend turns around at about the onset of the transition from mixing scheme I to scheme II.

Figure 2 shows the volume fluctuations, ${}^{V}\delta$ (amplitude) and ${}^{V}\Delta$ (amplitude as well as wavelength) decrease on increasing x_{AL}. This indicates that the tendency of putative momentary formation and destruction of icelike patches decreases on addition of AL. The effect is stronger for larger alcohols. This suggests two points:

(1) The iceberg formed in the immediate vicinity of AL is rigid enough not to participate in fluctuations.

(2) The hydrogen-bond probability in the bulk H_2O away from the iceberg is decreasing progressively to reduce the tendency of putative momentary formation and destruction of icelike patches.

The effects are apparent for both the amplitude and wavelength of the fluctuations. The partial molar volume fluctuations (Fig. 3) suggest that for both amplitude and wavelength the effect of incoming AL on the volume fluctuations is initially negative, but becomes less negative reaching almost zero, particularly for ${}^{V}\Delta_{AL}$ at the completion of the transition to mixing scheme II, point Y_{AL} in Fig. 3.

Figure 4 shows the entropy fluctuations. The amplitude of the entropy fluctuation, ${}^{S}\delta$, increases on addition of AL in mixing scheme I with less increase for smaller alcohols and with almost zero increase for methanol. ${}^{S}\Delta$, the amplitude and the wavelength, on the other hand, decreases as x_{AL} increases. The entropy fluctuation $< (\Delta S)^2 >$ can be translated as the fluctuation of the hydrogen-bond strength in aqueous solutions, since $T^2 < (\Delta S)^2 > = < (\Delta H)^2 >$. In terms of the bent-hydrogen-bond model, $< (\Delta S)^2 >$ reflects how widely the hydrogen bonds bend. Thus, H_2O molecules in the bulk that are fluctuating are perhaps forced to bend more near the icebergs, causing the hydrogen bonds to break more easily. At the same time, the wavelength of the fluctuation must be diminishing rapidly to compensate for the initial increase in amplitude, ${}^{S}\delta$. Figure 5 shows the transition from point X_{AL} to Y_{AL} as a shift of the branch in ${}^{S}\delta_{AL}$, and ${}^{S}\Delta_{AL}$ from mixing scheme I to mixing scheme II.

The peculiarity of H_2O is most conspicuous in the cross fluctuation, in that there is a negative contribution in the product $(\Delta S)(\Delta V)$ unlike normal liquids. Namely, the volume increase in fluctuation due to putative and momentary formation of icelike patches is associated with a negative ΔS. Thus, Fig. 6 indicates that the negative contribution diminishes rapidly on increasing x_{AL} for both ${}^{SV}\delta$ and ${}^{SV}\Delta$. The rate of decrease in the negative contribution, or that of increase in ${}^{SV}\delta$ and ${}^{SV}\Delta$,

©1999 NRC Canada

slows down quickly at about the boundary between mixing schemes I and II. This is more clearly seen in the partial molar cross fluctuations of methanol (Fig.7), ethanol (Fig. 8), and propan-1-ol (Fig. 9). The effect of AL on the negative contribution to the cross fluctuations decreases as x_{AL} increases up to the onset of transition, point X_{AL}, then drops sharply to the end point of transition, Y_{AL}. In the figures the enthalpic AL–AL interactions, H^{E}_{AL-AL}, are also plotted with an arbitrary scaling factor. The match between the partial molar cross fluctuation and the enthalpic AL–AL interaction is striking for propan-1-ol, (particularly for ${}^{SV}\Delta_{1P}$, Fig. 9*b*) while those for methanol and ethanol are not as impressive. The same exact match was observed for aqueous *tert*-butanol (12), but for aqueous 2-butoxyethanol they are only similar (11). Considering the uncertainties in both third-derivative quantities (a few per cent at best), and that there could be unknown systematic errors in the original data of the second derivatives, it may be safe to state that the x_{AL} dependence is similar between H^{E}_{AL-AL} and ${}^{SV}\delta_{AL}$ or ${}^{SV}\Delta_{AL}$. This could mean that the AL–AL interaction in terms of enthalpy (and of entropy also) and the AL's contribution to the cross fluctuations share the same fundamental cause. We suggest that the AL–AL interaction is operative via the bulk H_2O in solution, where putative occurrence of icelike patches causes the negative contribution to ${}^{SV}\delta$ and ${}^{SV}\Delta$. In mixing scheme I, the bulk H_2O remains still waterlike with the hydrogen bond probability high enough for bond percolation, and the interactions between iceberg clad AL's are operative through fluctuating bulk H_2O.

Acknowledgement

I would like to thank Professor G.C. Benson for his continuing understanding and support towards our works. This work was financed by the Natural Sciences and Engineering Reseach Council of Canada.

References

1. G.C. Benson and O. Kiyohara. J. Solution Chem. **9**, 791 (1980).
2. G.C. Benson, P.J. D'Arcy, and O. Kiyohara. J. Sol. Chem. **9**, 931 (1980).
3. O. Kiyohara and G.C. Benson. J. Solution Chem. **10**, 281 (1981).
4. L.D. Landau and E.M. Lifsfits. *In* Statistical physics. Pergamon, Oxford. 1980. Chap. XII.
5. J.D. Bernal and R.H. Fowler. J. Chem. Phys. **1**, 515 (1933).
6. T. Tanaka and I. Ohmine. J. Chem. Phys. **87**, 6128 (1987).
7. I. Ohmine. J. Phys. Chem. **99**, 6767 (1995).
8. T. Iijima and K. Nishikawa. J. Chem. Phys. **101**, 5017 (1994).
9. Y. Koga, Chem. Phys. Lett. **240**, 340 (1995).
10. Y. Koga, P. Westh, S. Sawamura, and Y. Taniguchi. J. Chem. Phys. **105**, 2028 (1996).
11. Y. Koga and P. Westh. Bull. Chem. Soc. Jpn. **37**, 172 (1996).
12. K. Tamura, A. Osaki, and Y. Koga. Phys. Chem. Chem. Phys. **1**, 121 (1999).
13. F. Franks and J.E. Desnoyers. Water Sci. Rev. **1**, 175 (1985).
14. Y. Koga. J. Crystallogr. Soc. Jpn. **37**, 172 (1995).
15. Y. Koga. J. Phys. Chem. **100**, 5172 (1996).
16. S.H. Tanaka, H.I. Yoshihara, A.W.-C. Ho, F.W. Lau, P. Westh, and Y. Koga. Can. J. Chem. **74**, 713 (1996).
17. E.C.H. To. J. Hu, C.A. Haynes, and Y. Koga. J. Phys. Chem. **102**, 10 958 (1998).
18. Y. Koga. J. Phys. Chem. **96**, 10 466 (1992).

©1999 NRC Canada

Temperature and pressure dependence of the volumetric properties of binary mixtures containing polyhaloalkanes

Carmen Jarne, Manuela Artal, José Muñoz Embid, Inmaculada Velasco, and Santos Otín

Abstract: Densities of binary mixtures of 1,1,2-trichlorotrifluoroethane + dibromomethane, + bromochloromethane, or + bromotrichloromethane were measured over their entire composition ranges at 288.15 and 308.15 K. Thermal expansion coefficients (α) and excess molar volumes (V^{E}_{m}) were calculated. Moreover, densities at 298.15 K and pressures up to 80 bar (1 bar = 100 kPa) were determined for these same mixtures. Isothermal compressibilities (κ_T) of the pure liquids and their mixtures were obtained.

Key words: density, excess volume, thermal expansion coefficient, isothermal compressibility.

Résumé : Opérant à 288,15 et à 308,15 K, on a mesuré les densités des mélanges binaires du 1,1,2-trichlorotrifluoroéthane avec le dibromométhane, le bromochlorométhane ou le bromotrichlorométhane sur l'ensemble des compositions. On a calculé les coefficients d'expansion thermique (α) et les volumes molaires en excès, (V^{E}_{m}). De plus, opérant sur les mêmes mélanges, on a mesuré les densités à 298,15 K à des pressions allant jusqu'à 80 bar (1 bar = 100 kPa). On en a déduit les compressibilités isothermiques (κ_T) des liquides purs et de leurs mélanges.

Mots clés : densité, volume en excès, expansion thermique, compressibilité isothermique.

[Traduit par la Rédaction]

Introduction

The thermodynamic study of different halogenated aliphatic compounds and their mixtures is of both theoretical and industrial interest. To correlate the structures of molecules with the thermodynamic properties of their mixtures it is necessary to have systematic information on the behaviour of substances with different specific groups. On the other hand, monohaloalkanes and different types of polyhaloalkanes represent a class of technically important compounds, used in industry as either intermediates or final products (refrigerants, blood substitutes, fire extinguishers, surfactants for extraction processes involving supercritical fluids, etc.). In view of the variety of possible mixtures, a large number of systems should be experimentally investigated in order to obtain the data necessary for the design of distillation columns and other stills for chemical plants.

Experimental data of the thermodynamic properties of polyhaloalkane binary mixtures with different halogen atoms in the same molecule are very scarce (1–6). In this work, the densities of binary mixtures of 1,1,2-trichlorotrifluoroethane + dibromomethane, + bromochloromethane, or + bromotrichloromethane were measured at 288.15 and 308.15 K, and thermal expansion coefficients (α) and excess molar volumes (V^{E}_{m}) were calculated over the entire composition range. Moreover, densities of these same mixtures at 298.15 K and pressures up to 80 bar were determined. Isothermal compressibilities (κ_T) of the pure liquids and their mixtures were calculated.

Received March 22, 1999.

C. Jarne, M. Artal, J.M. Embid, I. Velasco, and S. Otín.[1] Departamento de Química Orgánica – Química Física, Facultad de Ciencias, Universidad de Zaragoza, 50009-Zaragoza, Spain.

[1]Author to whom correspondence may be addressed. Telephone: 34.976.76.11.99. Fax: 34.976.76.12.02. e-mail: santos@posta.unizar.es

Experimental

The liquids used were dibromomethane (99 mol%), bromochloromethane (>98 mol%), and 1,1,2-trichlorotrifluoroethane (99.5 mol%), obtained from Fluka AG Buchs, and bromotrichloromethane (99 mol%), obtained from Aldrich. All the liquids were used without further purification. The densities of the pure liquids are listed in Table 1.

The excess molar volumes V^{E}_{m} were calculated for T = 288.15 K and T = 308.15 K from density measurements obtained by a vibrating-tube digital densimeter (Anton–Paar model DMA 60) equipped with a DMA 602 cell. The densimeter calibration was performed at atmospheric pressure using doubly distilled and degassed water, benzene, and tetrachloromethane using TRC references data (7). The vibrating-tube temperature was measured by an Anton–Paar DM 100-30 digital thermometer and was regulated to better than ±0.01 K using a Neslab RTE-210 thermostat. The thermometer was previously checked against the vapor pressure of benzene (Merck, >99.9%) along with the equation of Ambrose (8) relating temperature (T_{68}) with pressure by means of a sum of Chebyshev polynomials up to degree six (as recommended by IUPAC (9)).

 © 1999 NRC Canada

Table 1. Densities, ρ, of the pure liquid at 298.15 K.

	ρ (g cm^{-3})	
Substance	Experimental	Literature (7)
Dibromomethane	2.48083	2.4842
Bromochloromethane	1.92246	1.923
Bromotrichloromethane	2.00109	2.001
1,1,2-Trichlorotrifluoroethane	1.56327	1.5643

The mixtures were gravimetrically prepared and the mole-fraction error was estimated to be less than $\pm 10^{-4}$. Duplicate densities of the pure liquids and mixtures studied agreed to within 2×10^{-5} g cm^{-3}.

The densities (ρ) of the pure components and binary mixtures over the complete composition range were measured at T = 298.15 K and pressure range 3–80 bar, using the same vibrating-tube digital densimeter with a DMA 512 high pressure cell. High pressure was generated by a pressure amplifier (model AA-30; Haskel Inc.). Pressure was measured with a pressure gauge (CBI200; E. Cella S.P.A.). The accuracy on measured pressures is about 0.4 bar. The oscillation period (τ) of sample in the vibrating U tube was converted into density (ρ) via

$$[1] \qquad \rho = A(\tau^2 - B)$$

where A and B are instrument constants determined, at high pressure, by using isooctane (10), pure water (11), and 1,2-dichloroethane (10) as standard fluids. The values of parameter A, determined from the calibration, were treated as a function of pressure:

$$A = 0.652\,85 - 3.17(10^{-6})\,P$$

B is assumed to be temperature and pressure-independent (B = 15.1489).

The accuracy of the reported densities was estimated to be 1×10^{-4} g cm^{-3}.

Results and discussion

The calculated values of the excess molar volume V^{E}_{m} for the studied mixtures are listed in Tables 2–4 and plotted against x in Fig. 1. Each set of results was fitted by the ordinary (unweighted) least-squares method to a polynomial of the form:

$$[2] \qquad V^{E}_{m}/(\text{cm}^3\ \text{mol}^{-1}) = x(1-x)\ \Sigma\, A_i\ (2x-1)^i$$

where x is the mole fraction.

The values of the coefficients A_i determined by the least-squares analysis and the standard deviations σ given by

$$[3] \qquad \sigma(V^{E}_{m}) = [\Sigma(V^{E} - V^{E}_{exp})^2 / (N - M)]^{1/2}$$

where N is the number of experimental points and M is the number of fitting coefficients, are reported in Table 5.

To obtain the thermal expansion coefficients of the pure liquids, the experimental values of the obtained densities for each system, along with those published previously (5), have been fitted to a polynomial function:

$$[4] \qquad \rho/(g\ cm^{-3}) = \sum_{i=1}^{3}\sum_{j=1}^{3} A_{ij}(T - T_0)^{j-1} x^{i-1}$$

Fig. 1. Excess molar volumes, V^{E}_{m}, as a function of mole fraction: $(1 - x)$ 1,1,2-trichlorotrifluoroethane + x dibromomethane (circles), + x bromochloromethane (squares), or + x bromotrichloromethane (triangles). Open points, T = 288.15 K; closed points T = 308.15 K. Broken lines previous measurements (5) at T = 298.15 K.

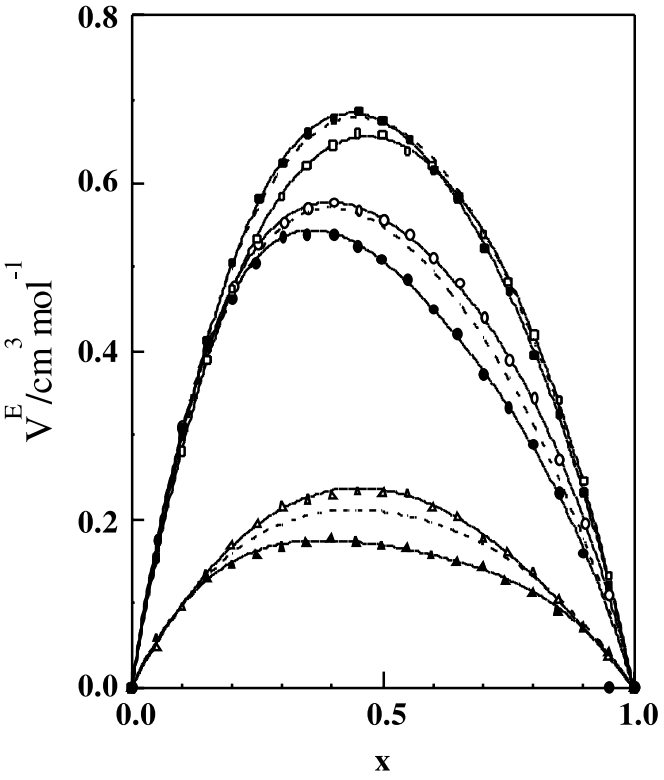

where T_0 = 278.15 K.

The coefficients A_{ij} are reported in Table 6.

The thermal expansion coefficients α are therefore obtained at T = 298.15 K by using the equation:

$$[5] \qquad \alpha/K^{-1} = -1/\rho\ (\delta\rho/\delta T)_P$$

We have obtained the following values of α for pure liquids: $\alpha(CH_2Br_2) = 1.211 \times 10^{-3}$ K^{-1}; $\alpha(CH_2BrCl) = 1.369 \times 10^{-3}$ K^{-1}; $\alpha(CBrCl_3) = 1.260 \times 10^{-3}$ K^{-1}; $\alpha(C_2Cl_3F_3) = 1.700 \times 10^{-3}$ K^{-1}. Figure 2 shows the values of α for the studied systems at the temperature 298.15 K.

The measured densities for the pure liquids and binary mixtures at 298.15 K and pressure range 3–80 bar are reported in Tables 7–9. The isothermal compressibilities, $\kappa_T = -V^{-1}(\delta V/\delta P)_T$, were obtained at 298.15 K and 1 bar, and are reported in Table 10.

The "excess" compressibility, defined as

$$[6] \qquad \kappa^{E} = -V^{-1}\ (\delta V^{E}/\delta P)_T = \kappa - \phi_1\kappa_1 - \phi_2\kappa_2$$

where ϕ_1 and ϕ_2 are the volume fractions, is widely used. The values of κ^{E} of the studied systems are plotted against x in Fig. 3.

As shown in Fig. 2 and Table 10, dibromomethane and 1,1,2-trichlorotrifluorethane respectively exhibit the minima and maxima values of the thermal expansion coefficient and isothermal compressibility. This behaviour points to a relation between the increase in the molecular complexity of the

© 1999 NRC Canada

Table 2. Densities, ρ, and excess molar volumes, V_m^E, for $(1 - x)$ 1,1,2-trichlorotrifluoroethane + (x) dibromomethane.

288.15 K			308.15 K		
x	ρ (g cm^{-3})	V_m^E (cm^3 mol^{-1})	x	ρ (g cm^{-3})	V_m^E (cm^3 mol^{-1})
0.0000	1.58925	0.000	0.0000	1.53630	0.000
0.0517	1.61538	0.175	0.0517	1.56210	0.176
0.1028	1.64282	0.310	0.1008	1.58807	0.309
0.1533	1.67161	0.410	0.1509	1.61621	0.406
0.2031	1.70168	0.478	0.2006	1.64594	0.462
0.2534	1.73372	0.528	0.2492	1.67648	0.506
0.3021	1.76655	0.554	0.3013	1.71102	0.537
0.3508	1.80106	0.569	0.3488	1.74443	0.541
0.4031	1.84012	0.578	0.4011	1.78314	0.540
0.4527	1.87941	0.567	0.4508	1.82208	0.526
0.5027	1.92105	0.558	0.4993	1.86210	0.510
0.5525	1.96493	0.539	0.5506	1.90687	0.486
0.6028	2.01191	0.511	0.5990	1.95175	0.451
0.6517	2.06019	0.482	0.6489	2.00048	0.422
0.7024	2.11342	0.442	0.6995	2.05330	0.374
0.7512	2.16809	0.390	0.7495	2.10858	0.333
0.8016	2.22784	0.344	0.8007	2.16887	0.290
0.8513	2.29139	0.272	0.8494	2.23047	0.231
0.9012	2.35955	0.197	0.9001	2.29928	0.161
0.9497	2.43081	0.111	0.9500	2.37192	0.089
1.0000	2.51081	0.000	1.0000	2.45067	0.000

Table 3. Densities, ρ, and excess molar volumes, V_m^E, for $(1 - x)$ 1,1,2-trichlorotrifluoroethane + (x) bromochloromethane.

288.15 K			308.15 K		
x	ρ (g cm^{-3})	V_m^E (cm^3 mol^{-1})	x	ρ (g cm^{-3})	V_m^E (cm^3 mol^{-1})
0.0000	1.58925	0.000	0.0000	1.53630	0.000
0.0499	1.59742	0.155	0.0497	1.54453	0.154
0.1011	1.60664	0.282	0.1016	1.55368	0.301
0.1515	1.61637	0.389	0.1517	1.56334	0.412
0.2003	1.62651	0.474	0.2009	1.57349	0.505
0.2496	1.63761	0.535	0.2534	1.58517	0.582
0.2997	1.64962	0.585	0.3015	1.59684	0.623
0.3501	1.66254	0.622	0.3511	1.60956	0.660
0.4006	1.67641	0.645	0.4025	1.62378	0.677
0.4507	1.69106	0.659	0.4518	1.63826	0.687
0.5007	1.70679	0.657	0.5013	1.65397	0.676
0.5504	1.72365	0.637	0.5533	1.67164	0.653
0.6002	1.74144	0.622	0.6022	1.68956	0.617
0.6512	1.76127	0.584	0.6513	1.70861	0.582
0.7003	1.78170	0.540	0.7022	1.73007	0.523
0.7509	1.80441	0.483	0.7514	1.75210	0.472
0.8009	1.82857	0.420	0.8020	1.77683	0.397
0.8504	1.85454	0.342	0.8511	1.80249	0.326
0.9002	1.88305	0.246	0.9014	1.83127	0.231
0.9504	1.91449	0.133	0.9505	1.86198	0.123
1.0000	1.94865	0.000	1.0000	1.89582	0.000

© 1999 NRC Canada

Table 4. Densities, ρ, and excess molar volumes, V^{E}_{m}, for (1 – *x*) 1,1,2-trichlorotrifluoroethane + (*x*) bromotrichloromethane.

288.15 K			308.15 K		
x	ρ (g cm^{-3})	V^{E}_{m} (cm^3 mol^{-1})	*x*	ρ (g cm^{-3})	V^{E}_{m} (cm^3 mol^{-1})
0.0000	1.58925	0.000	0.0000	1.53630	0.000
0.0507	1.60710	0.050	0.0503	1.55386	0.061
0.1007	1.62501	0.097	0.1504	1.59037	0.132
0.1495	1.64287	0.137	0.1997	1.60908	0.148
0.1993	1.66152	0.170	0.2488	1.62812	0.159
0.2512	1.68141	0.196	0.2989	1.64793	0.169
0.3005	1.70070	0.217	0.3488	1.66812	0.172
0.3504	1.72076	0.225	0.3974	1.68811	0.178
0.4000	1.74111	0.230	0.4479	1.70943	0.174
0.4504	1.76216	0.236	0.4969	1.73051	0.171
0.5008	1.78374	0.233	0.5473	1.75263	0.166
0.5502	1.80525	0.232	0.5975	1.77514	0.160
0.6003	1.82776	0.215	0.6464	1.79757	0.150
0.6500	1.85042	0.204	0.6986	1.82190	0.144
0.7001	1.87396	0.178	0.7448	1.84407	0.128
0.7489	1.89720	0.161	0.7979	1.87002	0.113
0.7997	1.92197	0.138	0.8482	1.89524	0.093
0.8496	1.94700	0.106	0.8990	1.92126	0.073
0.8990	1.97232	0.071	0.9486	1.94742	0.044
0.9493	1.99857	0.039	1.0000	1.97538	0.000
1.0000	2.02576	0.000	—	—	—

Table 5. Parameters A_i of eq. [2] for studied mixtures and standard deviations σ (V^{E}_{m}).

System	*T* (K)	A_0	A_1	A_2	A_3	σ(V^{E}_{m}) (cm^3 mol^{-1})
(1 – *x*) 1,1,2-Trichlorotrifluoroethane	288.15	2.233±0.005	–0.69±0.01	0.88±0.02	—	0.003
+ (*x*) dibromomethane	308.15	2.032±0.007	–0.94±0.01	0.89±0.03	—	0.004
(1 – x) 1,1,2-Trichlorotrifluoroethane	288.15	2.614±0.005	–0.26±0.01	0.48±0.02	—	0.003
+ (*x*) bromochloromethane	308.15	2.695±0.006	–0.62±0.02	0.37±0.03	0.29±0.06	0.003
(1 – *x*) 1,1,2-Trichlorotrifluoroethane	288.15	0.942±0.004	–0.18±0.01	—	—	0.003
+ (*x*) bromotrichloromethane	308.15	0.679±0.005	–0.18±0.01	0.40±0.02	—	0.003

Table 6. Coefficients A_{ij} of eq. [4] and standard deviations (σ).

(1 – *x*) 1,1,2-Trichlorotrifluoroethane + (*x*) dibromomethane			
i	*j* = 1	2	3
1	1.61945	–0.00184	-2.052×10^{-5}
2	0.39150	–0.00200	4.424×10^{-5}
3	0.52351	–0.00023	3.39×10^{-6}
		σ = 6.1×10^{-3}	
(1 – *x*) 1,1,2-Trichlorotrifluoroethane + (*x*) bromochloromethane			
i	*j* = 1	2	3
1	1.62079	–0.00265	—
2	0.09227	0.00099	-2.506×10^{-5}
3	0.25594	–0.00120	3.102×10^{-5}
		σ = 3.1×10^{-3}	
(1 – *x*) 1,1,2-Trichlorotrifluoroethane + (*x*) bromotrichloromethane			
i	*j* = 1	2	3
1	1.61511	–0.00247	-4.56×10^{-6}
2	0.34098	–0.00037	1.390×10^{-5}
3	0.09791	–0.00017	2.75×10^{-6}
		σ = 3.7×10^{-4}	

© 1999 NRC Canada

Table 7. Densities, ρ (g cm^{-3}), for (1 – *x*) 1,1,2-trichlorotrifluoroethane + (*x*) dibromomethane at 298.15 K.

	x						
P (bar)[a]	0.0000	0.2011	0.3503	0.5009	0.6499	0.8002	1.0000
3.0	1.5634	1.6724	1.7732	1.8908	2.0297	2.1973	2.4802
6.0	1.5644	1.6734	1.7741	1.8917	2.0306	2.1982	2.4809
9.0	1.5652	1.6743	1.7751	1.8926	2.0314	2.1989	2.4815
12.0	1.5659	1.6752	1.7760	1.8935	2.0322	2.1997	2.4819
15.0	1.5667	1.6760	1.7767	1.8942	2.0330	2.2004	2.4823
20.0	1.5680	1.6774	1.7781	1.8956	2.0343	2.2017	2.4831
25.0	1.5694	1.6794	1.7795	1.8969	2.0355	2.2029	2.4840
30.0	1.5708	1.6802	1.7808	1.8981	2.0367	2.2040	2.4848
35.0	1.5721	1.6814	1.7820	1.8993	2.0377	2.2050	2.4856
40.0	1.5733	1.6826	1.7831	1.9006	2.0388	2.2058	2.4862
45.0	1.5745	1.6838	1.7844	1.9014	2.0397	2.2067	2.4871
50.0	1.5760	1.6849	1.7854	1.9024	2.0407	2.2075	2.4879
55.0	1.5771	1.6861	1.7865	1.9033	2.0415	2.2082	2.4887
60.0	1.5784	1.6870	1.7875	1.9042	2.0422	2.2088	2.4895
65.0	1.5796	1.6879	1.7883	1.9050	2.0428	2.2095	2.4902
70.0	1.5808	1.6889	1.7892	1.9057	2.0435	2.2098	2.4909
75.0	1.5823	1.6898	1.7899	1.9063	2.0440	2.2103	2.4917
80.0	1.5832	1.6905	1.7907	1.9069	2.0444	2.2105	2.4925

[a]1 bar = 100 kPa

Fig. 2. Thermal expansion coefficient, α, as a function of mole fraction at 298.15 K: (1 – *x*) 1,1,2-trichlorotrifluoroethane + *x* dibromomethane (squares), + *x* bromochloromethane (circles), or + *x* bromotrichloromethane (triangles).

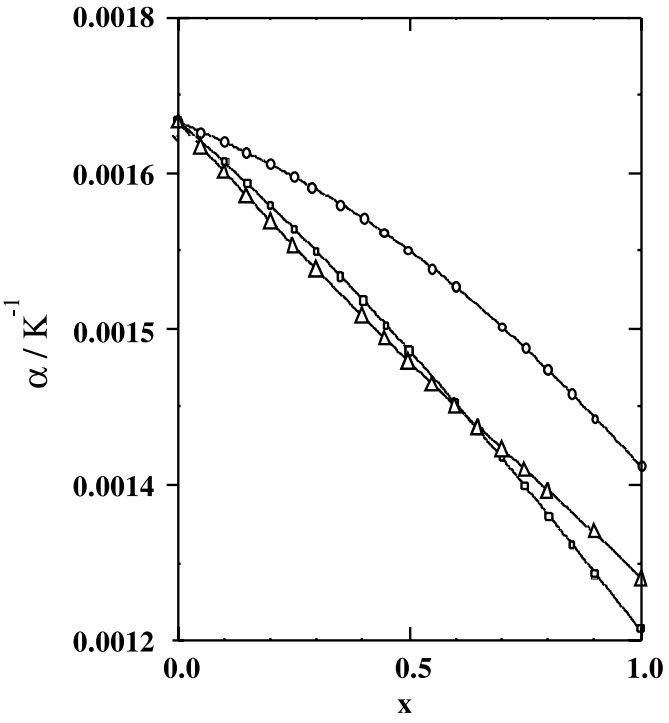

Fig. 3. Excess isothermal compressibility, κ^E, as a function of mole fraction at 298.15 K: (1 – *x*) 1,1,2-trichlorotrifluoroethane + *x* dibromomethane (—), + *x* bromochloromethane (---), or + *x* bromotrichloromethane (–·–·–).

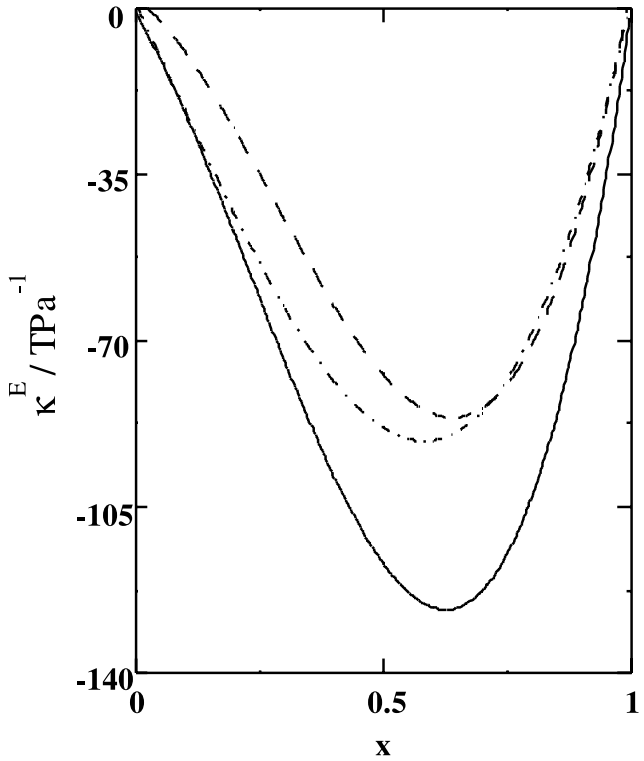

haloalkane (number of different halogen atoms in the molecule) and the corresponding increase of α and κ_T values. On the other hand, the density of these haloalkanes seems to change in the opposite direction to that of isothermal compressibility, demonstrating that any increase in the density of the haloalkane could decrease the intermolecular free space and thereby the molecule's ability to be compressed.

© 1999 NRC Canada

Table 8. Densities, ρ (g cm^{-3}), for (1 – *x*) 1,1,2-trichlorotrifluoroethane + (*x*) bromochloromethane at 298.15 K.

	x						
P (bar)[a]	0.0000	0.2024	0.3509	0.5005	0.6508	0.8001	1.0000
3.0	1.5634	1.5995	1.6367	1.6766	1.7349	1.8025	1.9227
6.0	1.5644	1.6005	1.6375	1.6774	1.7357	1.8033	1.9232
9.0	1.5652	1.6014	1.6384	1.6782	1.7364	1.8038	1.9236
12.0	1.5659	1.6022	1.6392	1.6790	1.7374	1.8045	1.9241
15.0	1.5667	1.6030	1.6400	1.6796	1.7378	1.8051	1.9245
20.0	1.5680	1.6044	1.6413	1.6809	1.7391	1.8063	1.9253
25.0	1.5694	1.6059	1.6427	1.6822	1.7402	1.8074	1.9261
30.0	1.5708	1.6072	1.6440	1.6833	1.7413	1.8084	1.9269
35.0	1.5721	1.6084	1.6453	1.6844	1.7424	1.8094	1.9276
40.0	1.5733	1.6096	1.6463	1.6855	1.7433	1.8103	1.9283
45.0	1.5745	1.6109	1.6475	1.6864	1.7443	1.8112	1.9291
50.0	1.5760	1.6120	1.6486	1.6875	1.7452	1.8119	1.9299
55.0	1.5771	1.6132	1.6497	1.6884	1.7461	1.8127	1.9306
60.0	1.5784	1.6142	1.6506	1.6893	1.7468	1.8135	1.9313
65.0	1.5796	1.6152	1.6515	1.6901	1.7476	1.8140	1.9319
70.0	1.5808	1.6161	1.6524	1.6908	1.7483	1.8145	1.9328
75.0	1.5823	1.6171	1.6533	1.6916	1.7489	1.8151	1.9335
80.0	1.5832	1.6180	1.6541	1.6912	1.7494	1.8156	1.9341

[a]1 bar = 100 kPa.

Table 9. Densities, ρ (g cm^{-3}), for (1 – *x*) 1,1,2-trichlorotrifluoroethane + (*x*) bromotrichloromethane at 298.15 K.

	x						
P (bar)[a]	0.0000	0.1968	0.3484	0.5005	0.6513	0.8000	1.0000
3.0	1.5634	1.6352	1.6947	1.7584	1.8262	1.8971	2.0007
6.0	1.5644	1.6361	1.6956	1.7593	1.8270	1.8979	2.0013
9.0	1.5652	1.6370	1.6965	1.7601	1.8278	1.8986	2.0018
12.0	1.5659	1.6379	1.6973	1.7609	1.8286	1.8994	2.0023
15.0	1.5667	1.6387	1.6981	1.7616	1.8293	1.9000	2.0028
20.0	1.5680	1.6402	1.6994	1.7629	1.8305	1.9013	2.0037
25.0	1.5694	1.6415	1.7007	1.7642	1.8317	1.9024	2.0046
30.0	1.5708	1.6428	1.7020	1.7654	1.8328	1.9034	2.0055
35.0	1.5721	1.6440	1.7032	1.7665	1.8338	1.9044	2.0062
40.0	1.5733	1.6454	1.7043	1.7675	1.8348	1.9053	2.0070
45.0	1.5745	1.6463	1.7054	1.7686	1.8358	1.9062	2.0078
50.0	1.5760	1.6475	1.7065	1.7696	1.8367	1.9070	2.0087
55.0	1.5771	1.6487	1.7074	1.7705	1.8376	1.9078	2.0095
60.0	1.5784	1.6496	1.7084	1.7713	1.8383	1.9085	2.0103
65.0	1.5796	1.6505	1.7092	1.7721	1.8389	1.9092	2.0111
70.0	1.5808	1.6514	1.7101	1.7730	1.8397	1.9098	2.0118
75.0	1.5823	1.6522	1.7109	1.7736	1.8404	1.9102	2.0127
80.0	1.5832	1.6531	1.7116	1.7742	1.8408	1.9107	2.0135

[a]1 bar = 100 kPa.

Table 10. Isothermal compressibility, κ_T (T Pa^{-1}), for studied mixtures at 298.15 K.

	x						
System	0.00	0.20	0.35	0.50	0.65	0.80	1.00
(1 – *x*) 1,1,2-trichorotrifluoroethane + (*x*) dibromomethane	1773	1576	1407	1246	1066	882	664
(1 – *x*) 1,1,2-trichorotrifluoroethane + (*x*) bromochloromethane	1773	1624	1502	1319	1195	1048	823
(1 – *x*) 1,1,2-trichorotrifluoroethane + (*x*) bromotrichloromethane	1773	1577	1423	1276	1138	1024	881

© 1999 NRC Canada

The excess molar volumes (V_m^E) for all the studied mixtures are positive and increase according to the sequence: 1,1,2-trichlorotrifluoroethane + bromochloromethane > + dibromomethane > + bromotrichloromethane. Although in principle this volumetric behaviour is qualitatively similar to the calorimetric one (12), the geometrical ("free volume") effects in the mixture might be important contributors to V_m^E. The excess isothermal compressibilities (κ^E) are negative; however, the mixture 1,1,2-trichlorotrifluoroethane + dibromomethane shows the maximum deviation from the ideal. The explanation of this behaviour is difficult to provide with only these kinds of measurements, given the variety and complexity of the interactional and geometrical effects present in the pure polyhaloalkanes.

References

1. M. Artal, J. Muñoz Embid, S. Otín, and I. Velasco. J. Chem. Thermodyn. **27**, 191 (1995).
2. M. Artal, J. Muñoz Embid, S. Otín, and I. Velasco. J. Chem. Thermodyn. **27**, 399 (1995).
3. M. Artal, J. Muñoz Embid, I. Velasco, and S. Otín. J. Chem. Thermodyn. **27**, 475 (1995).
4. M. Artal, J. Muñoz Embid, I. Velasco, and S. Otín. J. Solution Chem. **26**, 355 (1997).
5. J. Boquera, M. Artal, I. Velasco, and S. Otín. J. Chem. Thermodyn. **30**, 161 (1998).
6. M. Artal, J. Muñoz Embid, S. Otín, and I. Velasco. Fluid Phase Equilib. **154**, 223 (1999).
7. TRC Thermodynamics tables of non-hydrocarbons. Thermodynamics Research Center, The Texas A & M University System: College Station, Texas. 1994.
8. D. Ambrose. Pure Appl. Chem. **49**, 1437 (1977).
9. K.N. Marsh. IUPAC recommended reference materials for the realization of physicochemical properties. Blackwell, Oxford. 1987.
10. G. Hahn, K. Ulcay, P. Svejda, and M.A. Siddiqi. J. Chem. Eng. Data, **41**, 319 (1996).
11. G.S. Kell and E. Whalley. J. Chem. Phys. **62**, 3496 (1975).
12. J. Boquera. M.Sc. thesis. University of Zaragoza, Spain. 1997.

© 1999 NRC Canada

Semiempirical quantum chemical PM3 computations and evaluations of redox potentials, basicities, and dipole moments of the diphenylamine series as analytical reagents

Alexei N. Pankratov[1] and Andrew E. Shchavlev

Abstract: By evaluating the obtained results of PM3 computations, the following correlations were found: (*i*) the diarylamines redox potentials (*E*) with the first ionization potentials (*I*); (*ii*) the pK_a values characterizing both the amines nitrogen protonation and the carboxy substituted reagents dissociation via the COOH group, with the proton affinities of the corresponding diphenylamines and COO^--containing anions; (*iii*) the experimental values of the molecules dipole moments (μ) with the theoretical ones. The feasibility of the simple semiempirical quantum chemical evaluation of *E*, pK_a, and μ of the diphenylamine series as redox reagents was determined.

Key words: diphenylamine series, redox potential, pK_a, dipole moment, semiempirical quantum chemical evaluation.

Résumé : L'évaluation des résultats de calculs PM3 a permis d'établir les corrélations suivantes: (*i*) les potentiels redox de diarylamines (*E*) avec les premier potentiels d'ionisation (*I*); (*ii*) les valeurs de pK_a qui caractérisent la protonation de l'azote d'amines ainsi que la dissociation de réactifs portant des groupes carboxy via le groupe COOH avec les affinités protoniques des diphénylamines et des anions COO^- correspondants; (*iii*) les valeurs expérimentales des moments dipolaires des molécules (μ) et les valeurs théoriques. On a mis en évidence la possibilité de faire une évaluation chimique quantique semiempirique simple des paramètres *E*, pK_a et μ de la série diphénylamine comme réactifs redox.

Mots clés : série de la diphénylamine, potentiel redox, pK_a, moment dipolaire, évaluation chimique quantique semiempirique.

[Traduit par la Rédaction]

Introduction

Diphenylamine (DPA) and its substituted derivatives are widely distributed analytical redox reagents (1–4), antioxidants (5, 6), and drugs (7–9).

Homogeneous catalytic reactions of diarylamines oxidation catalyzed by copper(II), gold(III), manganese(II), ruthenium(IV), and iridium(IV) compounds are used for highly-sensitive, selective kinetic determination of these elements with the content level of 10^{-2} down to 10^{-6}% in different subjects, the lower limit of detectable concentrations being 1×10^{-3} down to 1×10^{-6} mg/mL. The corresponding techniques are characterized by a relative standard deviation s_r of 0.01 up to 0.13 and distinguished for the simple experimental procedures (3, 4, and refs. therein). The mechanism of the above catalytic processes includes most likely an increase in oxidation number of the element-catalyst (it's just an element to be determined) when interacting with an oxygen-containing large oxidant anion ($S_2O_8^{2-}$, VO_3^-, $Cr_2O_7^{2-}$, IO_3^-, IO_4^-). The catalyst with a greater oxidation number reacts with a DPA series compound to produce a deeply colored *N,N′*-diaryl-*p*-diphenoquinonediimine dication (1, 10–14). The analytical signal is registered spectrophotometrically.

Thus, the diphenylamines application is based on their oxidation reactions. The analytical significance of DPA derivatives, their selectivity to different oxidants (including the catalysts for the metals kinetic determination) and other important properties are due to the standard redox potentials $E°$ (instead of those, essentially the same formal potentials E^f found by the Walden method (15) are often used).

The diarylamines and their structural analogs capability for being oxidized in acidic media depends on the amines basicity, which is responsible for their reactive particles state, as well as for the reaction mechanism details (1, 10–14, 16, 17). The chemical behaviour of the carboxy substituted re-

Received May 10, 1999.

A.N. Pankratov[1] and A.E. Shchavlev. Department of Chemistry, N. G. Chernyshevskii Saratov State University, 83 Astrakhanskaya Street, Saratov 410026, Russia.

[1]Author to whom correspondence may be addressed. Telephone: ++7(8452)721491. Fax: ++7(8452)240446. e-mail: PankratovAN@info.sgu.ru

 © 1999 NRC Canada

agents on the oxidation in alkaline solutions is influenced by the acidic dissociation via the carboxy group (2, 18).

The diarylamines reactivity is also caused by their hydration (solvation), nonspecific contribution to which is related to the molecules dipole moments (μ). The μ values allow one to conclude on the feasibility and character of the interaction between the reactive species of any polarity.

Computational methods

The computations by means of the SCF MO LCAO PM3 method (19) were performed using the software from the MOPAC package (20, 21) with the complete geometry optimization (Broyden–Fletcher–Goldfarb–Shanno function minimizer) (22) involving Thiel's fast minimization algorithm (23). The preliminary optimization was realized by the molecular mechanics method (the MMX procedure) (24) with the software of the PCMODEL complex (24). In quantum chemical computations, the condition of the gradient norm not exceeding 0.02 kcal mol^{-1} $Å^{-1}$ was preset. In some cases, a sufficient decrease in gradient norm was achieved by means of abandonment of the Thiel's fast minimization routine (the key word NOTHIEL of the MOPAC package was applied), or under optimization with the Davidon–Fletcher–Powell method (key word DFP) (22), or by conducting double precision calculations (key word PRECISE), as well as using combined approaches involving the key words NOTHIEL, DFP, and PRECISE.

In calculating the rotational contributions to thermodynamic functions the symmetry number was taken as unity.

In the case of diphenylamines, whose molecules contain primary amino group NH_2, the primary nitrogen was considered to be protonated (25).

The linear regression analysis was performed with a confidence level of 0.95.

Results and discussion

The controlled-property molecular design of diphenylamines involves a priori evaluation of $E°$ (E^f), pK_a (K_a is either the acidity constant of the organic reagent's conjugate acid or the dissociation constant of diarylamine by the COOH group) and μ. Moreover, the aforesaid values measurement is often related to the experimental difficulties.

Protolytic, oxidative-reductive and polar properties of amino compounds could be predicted by means of quantum chemical methods. Earlier (26) we have found a correlation of the E^f values for DPA and its derivatives with the differences in total energies (computed by the INDO method) between cation radicals (oxidation intermediates in acidic media) and molecules. The polarographic oxidation half-wave potentials depend linearly upon the higher occupied molecular orbitals energies of depolarizers (27) and, hence, in accordance with Koopmans theorem (28), also upon their ionization potentials (I). An analogous relationship between $E°$ (E^f) and I may be reasonably suggested. The pK_a value can be determined to a significant extent by proton affinity (PA). The latter represents reaction enthalpy for a proton breaking-off in the gaseous phase:

$$BH^+ \rightarrow B + H^+$$

and is calculated by the formula (29, 30):

$$PA = \Delta H_f\ (B) + \Delta H_f\ (H^+) - \Delta H_f\ (BH^+)$$

where ΔH_f (H^+) = 367.163 kcal/mol (29, 30). When considering the amines protonation, we will assume B to be a reagent molecule. On studying the carboxy substituted diphenylamines dissociation, B means an anion with a COO^- group.

The aim of the present work is to reveal correlations between: (*i*) the experimental redox potentials (E) for the diphenylamine derivatives and the computed values of the first ionization potentials; (*ii*) pK_a for the diphenylamine series compounds and proton affinities; (*iii*) μ_{exper} and μ_{theor}.

The validity of the PM3 quantum chemical computations performed is confirmed for DPA by the reproduced standard gaseous-phase thermodynamic quantities: heat of formation (ΔH_f), entropy (S), Gibbs energy of formation (ΔG_f):

	ΔH_f, kcal/mol	S, cal mol^{-1} K^{-1}	ΔG_f, kcal/mol
Experiment (31)	48.20	97.5	82.00
Computed	51.33	102.6	83.59

Besides, for the series of organic compounds belonging to different classes and possessing various functional groups, we have established an accuracy of the most important thermodynamic and molecular characteristics reproduction by the MNDO, AM1 and PM3 methods (32, 33), as well as of the electronegativity, inductive and mesomeric parameters of the atomic groups (34). Among the mentioned methods, PM3 seems to provide satisfactory results in obtaining the heats of formation for nitro derivatives (19, 32) and dimethylsulphone (32). Many of the NO_2 and SO_2 group containing species are the subjects of our investigation. That is the reason for selecting the PM3 method for the purposes of this work.

The results obtained in the present work are shown in Tables 1–4.

We have found the following correlations (m is the number of considered points, r is the correlation coefficient, s_0^2 is the adequacy variance, e is the electron charge):

[1] $pK_a = A + B \times PA$ (kcal/mol)
$m = 10$, $A = -119.28 \pm 27.10$
$B = 0.5510 \pm 0.1259$ (mol/kcal)
$r = 0.9627$, $s_0^2 = 0.4280$

(for protonation of the nitrogen atom)

[2] $pK_a = A + B \times PA$ (kcal/mol)
$m = 7$, $A = -90.20 \pm 41.48$
$B = 0.2830 \pm 0.1241$ (mol/kcal)
$r = 0.9348$, $s_0^2 = 0.0436$

(for dissociation of the carboxylic group)

[3] $E = A + BI$
$m = 32$, $A = -2.4594 \pm 0.5347$ (V)
$B = 0.3822 \pm 0.0641$ (e^{-1})
$r = 0.9121$, $s_0^2 = 0.0039$

(for diarylamines)

© 1999 NRC Canada

Table 1. Computed heats of formation of molecular (B) and protonated (BH^+) forms, proton affinities and experimental pK_a values.

Compound	Heat of formation, kcal/mol		PA, kcal/mol	pK_a[a]
	ΔH_f (B)	ΔH_f (BH^+)		
DPA	51.33	200.98	217.51	0.78
4-Methyl-DPA	41.97	190.26	218.88	1.26
N-Methyl-DPA	54.35	203.17	218.34	1.71
4-Hydroxy-DPA	6.39	154.01	219.54	1.54
4-Methoxy-DPA	13.48	160.55	220.09	1.33
2-Carboxy-DPA	7.24	161.27	213.13	–1.37
4-Carboxy-DPA	–38.59	115.23	213.34	–1.24
4-Nitro-DPA	43.68	200.71	210.13	–2.78
2-Carboxy-3′-nitro-DPA	–45.54	111.37	210.25	–4.05
2-Carboxy-4′-arsono-DPA	–164.94	–9.20	211.42	–3.83

[a]Taken from refs. 35 and 36. Experimental pK_a values of conjugate acid dissociation for the diphenylamine series determined by spectrophotometric technique in sulphuric acid solutions.

Table 2. Computed heats of formation of anions (B) and molecules (BH^+) of carboxy substituted diarylamines, proton affinities and experimental pK_a values of COOH groups dissociation.

Compound	Heat of formation, kcal/mol		PA, kcal/mol	pK_a[a]
	ΔH_f (B)	ΔH_f (BH^+)		
2-Carboxy-DPA	–70.01	–35.84	332.99	3.99
2-Carboxy-2′-methyl-DPA	–76.33	–45.70	336.53	4.90
2-Carboxy-3′-methyl-DPA	–79.49	–45.97	333.64	3.94
2-Carboxy-3′-methoxy-DPA	–107.82	–73.18	332.52	4.18
2-Carboxy-4′-methoxy-DPA	–107.73	–74.78	334.21	4.44
2,2′-Dicarboxy-DPA	–153.48	–123.02	336.70	5.26
2-Carboxy-2′-nitro-DPA	–75.41	–40.90	332.65	3.85

[a]Taken from ref. 36. Experimental pK_a values determined by spectrophotometric method (for 2,2′-dicarboxy-DPA, by potentiometric technique).

[4] $E = A + BI$
$m = 34$, $A = -0.7085 \pm 0.2452$ (V)
$B = 0.1183 \pm 0.0199$ (e^{-1})
$r = 0.9058$, $s_0^2 = 0.0035$

(for diarylammonium cations)

[5] $\mu_{exper} = B\mu_{theor}$,
$m = 37$, $B = 0.9675 \pm 0.0737$
$r = 0.9337$, $s_0^2 = 0.7755$

The occurrence of the [1] and [2] type dependences is remarkable (in spite of the fact that 24 and 6 compounds, respectively (35, 36, 41, 46), were not included in the above relationships), because, in general, there is no simple relationship between acid–base properties of protolytes in aqueous solutions and proton affinities in the gaseous phase due to a substantial role played by the medium.

The linear correlation of redox potentials (35–46) with the amines' conjugate acids is ionization potentials is in agreement with the data from (1, 10, 11) concerning the participation of the reagents' protonated forms in redox reactions taking place in acidic media.

The μ_{exper} and μ_{theor} values for 3-nitro-DPA, 2,2′-dihydroxy-DPA, 2-nitro-*N*-methyl-DPA, 2,2′-dicarboxy-DPA, 4,4′-dicarboxy-DPA, and 2,2′-dinitro-4-methyl-4′-methoxy-DPA were excluded from the correlation series $\mu_{exper} = B\mu_{theor}$ because for the listed reagents the discrepancy between the experimental and theoretical dipole moments is close to 2D (in the case of 2-nitro-*N*-methyl-DPA) or exceeds 2D. Therefore, agreement between experimental and computed dipole moments was used as a criterion for inclusion of the compounds in the correlation calculations. The above mentioned discrepancy may well be due to factors not taken into account in the computations, such as atomic vibrations, internal rotation of the molecules, and the possibility of the latters' existence as mixtures of conformers.

Using eqs. [1]–[5], one can predict the *E*, pK_a, and μ values for the DPA series redox reagents, construct the compounds with the desired protolytic, oxidative–reductive properties, as well as polarity. The relatively high dipole moments of the diphenylamine molecules serve as a premise to the facilitated amines interaction with charged or polar oxidant species, to the amines effective solvation by polar solvents and, therefore, to the oxidation mechanisms' similarity with respect to different diarylamines (1, 10–14).

We have demonstrated the predictive power of eqs. [3] and [4] on the following example. Recently Mushtakova et al. (51) synthesized new redox reagents 4-sulphotriphenylamine (**1**), 4,4′-disulphotriphenylamine (**2**), 2-nitro-4′-sulpho-DPA (**3**), 3-nitro-4′-sulpho-DPA (**4**), 4-nitro-4′-sulpho-DPA (**5**), and determined their E^f_{exper} values. Using the PM3 method, for compounds **1**–**5** and their conjugate acids we computed first ionization potentials. Inserting the latter in [3] and [4] lets one obtain E^f_{theor} values, which are in good agreement with the experimental data:

© 1999 NRC Canada

Table 3. Computed first ionization potentials and experimental values of redox potentials for diphenylamine derivatives.

Compound	*I*, eV		$E°$ (E^f), V		
	Diarylamine molecule	Diarylammonium cation	Value	Conditions	Ref.
DPA	8.43	—	0.76	1 M H_2SO_4	35
4-Methyl-DPA	8.37	11.49	0.74	1 M H_2SO_4	35
N-Methyl-DPA	8.47	13.74	0.84	1 M H_2SO_4	35
4-Amino-DPA	8.09	—	0.604	pH 2	37
4-Acetylamino-DPA	8.22	12.17	0.70	1 M H_2SO_4	38
2-Methoxy-DPA	8.23	—	0.59	1 M H_2SO_4	35
4-Methoxy-DPA	8.24	—	0.59	1 M H_2SO_4	35
4-Carboxy-DPA	—	13.88	0.97	1 M H_2SO_4	35
2-Nitro-DPA	8.84	13.89	0.94	1 M H_2SO_4	35
3-Nitro-DPA	—	13.78	0.86	1 M H_2SO_4	35
4-Nitro-DPA	9.08	—	1.06	1 M H_2SO_4	35
4-Sulpho-DPA	—	13.43	0.84	1 M H_2SO_4	35
2,4-Diamino-DPA	—	11.94	0.75	1 M H_2SO_4	39
2-Amino-4′-methoxy-DPA	8.22	11.59	0.615	pH 2	37
4-Amino-4′-methyl-DPA	8.03	11.61	0.620	pH 2	37
4,4′-Diamino-DPA	7.93	10.69	0.598	pH 2	37
4-Amino-3-methoxy-DPA	7.95	11.57	0.636	pH 0–1, 50% acetone	40
4-Amino-4′-methoxy-DPA	7.97	11.44	0.64	1 M H_2SO_4	35
4-Amino-4′-nitro-DPA	—	12.08	0.670	pH 2	37
2-Carboxy-4′-methoxy-DPA	8.58	—	0.94	4.5 M H_2SO_4	36
2,2′-Dicarboxy-DPA	—	13.35	0.93	4.5 M H_2SO_4	36
2,3′-Dicarboxy-DPA	8.80	13.68	0.90	4.5 M H_2SO_4	36
2-Carboxy-3′-nitro-DPA	9.09	14.34	1.00	4.5 M H_2SO_4	36
2-Carboxy-4′-nitro-DPA	9.19	14.29	1.00	7 M H_2SO_4	36
2-Carboxy-4′-phosphono-DPA	8.83	13.01	0.93	4.5 M H_2SO_4	41
2-Carboxy-4′-arsono-DPA	—	12.55	0.85	1 M H_2SO_4	42
4-Amino-2-methyl-4′-methoxy-DPA	—	11.47	0.686	pH 0	43
2,4-Diamino-4′-methoxy-DPA	8.08	11.27	0.532	pH 0	43
2-Hydroxy-4-amino-4′-methoxy-DPA	8.03	11.42	0.565	pH 2	37
4-Amino-2,4′-dimethoxy-DPA	7.93	11.59	0.636	pH 0	43
4-Amino-3,4′-dimethoxy-DPA	7.89	11.37	0.530	pH 2	44
2-Chloro-4-amino-4′-methoxy-DPA	8.13	11.56	0.615	pH 2	37
4-Amino-2-carboxy-4′-methoxy-DPA	8.23	11.57	0.692	pH 2	44
Anilide of 4-amino-2-carboxy-4′-methoxy-DPA	8.21	11.07	0.754	pH 0	43
4-Amino-2-carbomethoxy-4′-methoxy-DPA	8.18	11.46	0.693	pH 2	44, 45
4-Amino-2′-nitro-4′-methoxy-DPA	8.45	11.53	0.645	pH 2	37
4-Amino-2-sulpho-4′-methyl-DPA	8.33	11.62	0.645	pH 2	37
4-Amino-2-sulpho-4′-methoxy-DPA	—	11.47	0.673	pH 2	44
Anilide of 4-amino-2-sulpho-4′-methoxy-DPA	8.29	—	0.788	pH 0	43
Anisidide of 4-amino-2-sulpho-4′-methoxy-DPA	8.23	—	0.780	pH 0	43
4-Amino-2-sulphomethoxy-4′-methoxy-DPA	8.22	—	0.678	pH 2	44
2-Carboxy-4-sulphamido-2′-methoxy-DPA	—	12.40	0.80	8.5 M H_2SO_4	46
4-Amino-2′,4′-dinitro-DPA	—	12.34	0.718	pH 2	37

Compound	Molecular form		Protonated form		E^f_{exper}, V[a]
	I, eV	E^f_{theor}, V	*I*, eV	E^f_{theor}, V	
1	8.89	0.94	13.66	0.91	0.89[b]
2	9.05	1.00	13.78	0.92	0.94[b]
3	9.24	1.07	14.09	0.96	0.91[c]
4	9.45	1.15	14.24	0.98	0.93[d]
5	9.46	1.16	14.29	0.98	1.1[d]

[a]Reference 51. [b]In 4 M H_2SO_4. [c]In 10 M H_2SO_4. [d]In 5 M H_2SO_4.

Incorporating the E^f_{exper} and *I* values into the eqs. [3] and [4] leads to the following linear dependences parameters:

$$E = A + BI$$
$$m = 37,\ A = -1.9588 \pm 0.4296\ (V)$$
$$B = 0.3212 \pm 0.0507\ (e^{-1})$$
$$r = 0.9084,\ s_0^2 = 0.0047$$

(for amino compounds)

$$E = A + BI$$
$$m = 39,\ A = -0.7215 \pm 0.2130\ (V),$$
$$B = 0.1194 \pm 0.0170\ (e^{-1}),$$
$$r = 0.9195,\ s_0^2 = 0.0036$$

(for the amines' conjugate acids)

© 1999 NRC Canada

Table 4. Experimental and computed dipole moments of diarylamine molecules.

Compound	μ_{exper}, D[a]	Conditions	μ_{theor}, D
DPA	0.95	Hexane, 293 K	0.877
N-Methyl-DPA	1.55	Benzene, 298 K	1.18
Triphenylamine	0.7	Hexane, 293 K	0.668
4-Anisyl-DPA	2.09	Benzene	0.920
4-Amino-DPA	2.07	Benzene	0.652
3-Hydroxy-DPA	1.98	Benzene, 298 K	1.50
4-Hydroxy-DPA	1.95	Benzene, 298 K	1.63
3-Methoxy-DPA	1.70	Benzene, 298 K	1.34
4-Methoxy-DPA	1.79	Benzene, 298 K	1.54
N-Acetyl-DPA	3.81	Benzene, 298 K	2.48
2-Carboxy-DPA	2.49	Dioxane, 298 K	3.75
N-Nitroso-DPA	3.33	Benzene, 298 K	3.14
2-Nitro-DPA	4.15	Benzene, 298 K	4.90
3-Nitro-DPA	4.66	Benzene, 298 K	2.31
4-Nitro-DPA	6.46	Benzene	6.89
2,2′-Dihydroxy-DPA	3.69	Benzene, 298 K	1.24
4,4′-Dihydroxy-DPA	3.50	Benzene, 298 K	2.16
4-Methoxytriphenylamine	2.09	Benzene, 298 K	1.70
4-Hydroxy-4′-methoxy-DPA	2.32	Benzene, 298 K	2.04
4,4′-Dimethoxy-DPA	2.06	Benzene, 298 K	2.12
4,4′-Difluoro-DPA	2.11	Benzene, 298 K	1.63
2-Carboxy-2′-methyl-DPA	2.60	Dioxane, 298 K	1.48
2-Carboxy-4′-methyl-DPA	2.32	Dioxane, 298 K	1.40
2-Carboxy-2′-methoxy-DPA	2.26	Dioxane, 298 K	2.20
2-Carboxy-4′-methoxy-DPA	2.94	Dioxane, 298 K	1.98
2-Nitro-*N*-methyl-DPA	3.64	Benzene, 298 K	5.60
4-Nitro-*N*-methyl-DPA	6.64	Benzene, 298 K	7.29
4-Acetyl-*N*-acetyl-DPA	4.14	Benzene, 298 K	3.03
2,2′-Dicarboxy-DPA	4.31	Dioxane, 298 K	2.13
4,4′-Dicarboxy-DPA	4.55	Dioxane, 298 K	2.37
2-Carboxy-2′-nitro-DPA	5.24	Dioxane, 298 K	5.09
2-Carboxy-4′-nitro-DPA	6.79	Dioxane, 298 K	7.63
2-Nitro-*N*-acetyl-DPA	5.76	Benzene, 298 K	7.29
3-Nitro-*N*-acetyl-DPA	5.67	Benzene, 298 K	6.05
4-Nitro-*N*-acetyl-DPA	6.16	Benzene, 298 K	4.89
2-Nitro-*N*-nitroso-DPA	5.80	Benzene, 298 K	5.49
3-Nitro-*N*-nitroso-DPA	4.79	Benzene, 298 K	5.84
4-Nitro-*N*-nitroso-DPA	4.10	Benzene, 298 K	5.27
2,2′-Dinitro-DPA	6.28	Dioxane, 298 K	7.66
4,4′-Dinitro-DPA	5.13	Dioxane, 298 K	4.35
4,4′-Dimethoxytriphenylamine	2.49	Benzene, 298 K	1.37
4,4′-Diacetyl-*N*-acetyl-DPA	4.50	Benzene, 298 K	3.00
2,2′-Dinitro-4-methyl-4′-methoxy-DPA	6.47	Benzene, 298 K	8.56

[a]Taken from refs. 47–50. Measured by the second Debye method.

The proposed approach in the present work for estimating *E*, pK_a, and μ values of the diarylamines aims to evaluate the molecular structure and may possibly be extended to other classes of analytical reagents and organic compounds in general.

Acknowledgement

The research described in this publication was made possible in part by grants no. d96-16 and no. d97-1381 from the International Soros Science Education Program, presented to Professor Dr. Sc. Alexei N. Pankratov. The authors would like to thank Professor Dr. Sc. Svetlana P. Mushtakova and post-graduate student Peter G. Nikonorov for valuable advice and discussion, and Dr. Olga M. Tsivileva for technical assistance.

References

1. E. Bishop (*Editor*). Indicators. Pergamon Press, Oxford, New York, Toronto, Sydney, Braunschweig. 1972.
2. N.S. Frumina. Theory and practice of application of the diphenylamine class reagents in analysis (in Russian). Saratov University Press, Saratov. 1976.
3. S.P. Mushtakova, N.N. Gusakova, A.N. Pankratov, E.E. Fedorov, and L.A. Gribov. Zh. Anal. Khim. **39**, 1010 (1984).

© 1999 NRC Canada

4. S.P. Mushtakova, A.P. Gumenyuk, O.A. Bilenko, A.N. Pankratov, L.F. Kozhina, and S.S. Khmelev. Zh. Anal. Khim. **50**, 732 (1995).
5. N.M. Emanuel', E.T. Denisov, and Z.K. Maizus. Chain reactions of hydrocarbons oxidation in the liquid phase (in Russian). Nauka, Moscow. 1965.
6. E.G. Rozantsev. Free iminoxyl radicals (in Russian). Khimiya, Moscow. 1970.
7. M. Kasai, M. Hirota, Y. Hamada, and H. Matsuoka. Tetrahedron, **29**, 267 (1973).
8. A.C. Mehta and S.G. Schulman. Talanta, **20**, 702 (1973).
9. J.F. McConnell and F.Z. Company. Cryst. Struct. Commun. **5**, 861 (1976).
10. K. Sriramam. Talanta, **24**, 31 (1977).
11. A.N. Pankratov, V.I. Morozov, S.P. Mushtakova, and A.V. Il'yasov. Izv. Akad. Nauk SSSR Ser. Khim. 1483 (1984).
12. A.N. Pankratov, S.P. Mushtakova, and L.A. Gribov. Zh. Anal. Khim. **42**, 352 (1987).
13. A.N. Pankratov. J. Mol. Struct. (Theochem), **315**, 179 (1994).
14. A.N. Pankratov, S.L. Shmakov, and A.E. Shchavlev. Croat. Chem. Acta, **68**, 325 (1995).
15. G.H. Walden, L.P. Hammett, and R.P. Chapman. J. Am. Chem. Soc. **55**, 2649 (1933).
16. A.N. Pankratov, I.M. Uchaeva, and A.N. Stepanov. Can. J. Chem. **71**, 674 (1993).
17. A.N. Pankratov and A.N. Stepanov. Croat. Chem. Acta, **70**, 585 (1997).
18. S.P. Mushtakova, N.S. Frumina, L.A. Gribov, and L.N. Kharlamova. Zh. Anal. Khim. **29**, 226 (1974).
19. J.J.P. Stewart. J. Comput. Chem. **10**, 209 (1989); **10**, 221 (1989).
20. J.J.P. Stewart. MOPAC, a semi-empirical molecular orbital program. QCPE. Program no. 455. 1983.
21. T. Clark. A handbook of computational chemistry. A practical guide to chemical structure and energy. Wiley–Interscience, John Wiley and Sons, New York, Chichester, Brisbane, Toronto, Singapore. 1985.
22. J.E. Dennis and R.B. Schnabel. Numerical methods for unconstrained optimization and nonlinear equations. Prentice–Hall, Inc., Englewood Cliffs, N.J. 1983.
23. W. Thiel. J. Mol. Struct. (Theochem), **163**, 415 (1988).
24. U. Burkert and N.L. Allinger. Molecular mechanics. ACS monograph 177. American Chemical Society, Washington, D.C. 1982.
25. P. Sykes. A guidebook to mechanism in organic chemistry. Longman Scientific & Technical, London; John Wiley & Sons, Inc., New York. 1986.
26. A.N. Pankratov, S.P. Mushtakova, and L.A. Gribov. Zh. Anal. Khim. **40**, 1128 (1985).
27. M.M. Baizer and H. Lund (*Editors*). Organic electrochemistry. An introduction and a guide. Marcel Dekker, Inc., New York, Bazel. 1983.
28. M.D. Newton. J. Chem. Phys. **48**, 2825 (1968).
29. R. De Kock and C. Jasperse. Inorg. Chem. **22**, 3839 (1983).
30. S. Olivella, F. Urpi, and J. Vilarrasa. J. Comput. Chem. **5**, 230 (1984).
31. D.R. Stull, E.F. Westrum, and G.C. Sinke. The chemical thermodynamics of organic compounds. John Wiley & Sons, Inc., New York, London, Sydney, Toronto. 1969.
32. A.N. Pankratov and A.E. Shchavlev. J. Mol. Struct. (Theochem) **392**, 137 (1997).
33. A.N. Pankratov. J. Mol. Struct. (Theochem), **453**, 7 (1998).
34. A.N. Pankratov and A.E. Shchavlev. Monatsh. Chem. **129**, 1007 (1998).
35. N.S. Frumina and E.G. Tregub. Zh. Anal. Khim. **26**, 669 (1971).
36. M.L. Nikurashina. Substituted phenylanthranilic acids as analytical reagents (in Russian). Dissert. Cand. Chem. Sci. Saratov University Press, Saratov. 1970.
37. L. Erdey, I. Kása, P. Klatsmányi, and T. Meisel. Acta Chim. Acad. Sci. Hung. **26**, 53 (1961).
38. G.H. Walden and S.M. Edmonds. Chem. Rev. **16**, 81 (1935).
39. M. Lederer and E.L. Ward. Anal. Chim. Acta, **6**, 1 (1952).
40. L.F. Oldfield and J.O'M. Bockris. J. Phys. Colloid Chem. **55**, 1255 (1951).
41. S.N. Eremenko, S.P. Mushtakova, N.N. Gusakova, A.M. Lukin, and N.S. Frumina. Zh. Anal. Khim. **30**, 2299 (1975).
42. M.L. Nikurashina, S.N. Eremenko, N.S. Frumina, and V.A. Shevko. Zavod. Lab. **38**, 903 (1972).
43. L. Erdey, É. Bányai, and É.B. Gere. Talanta, **3**, 54 (1959).
44. L. Erdey, É. Bányai, E. Zalay, and M. Tésy. Acta Chim. Acad. Sci. Hung. **15**, 65 (1958).
45. W.M. Clark. Oxidation–reduction potentials of organic systems. The Williams & Wilkins Company, Baltimore. 1960.
46. N.N. Gusakova, S.P. Mushtakova, M.A. Chernova, N.S. Frumina, T.V. Chernyshova, and A.N. Gaidukevich. *In* Chemical reagents and special purity grade substances: Proceedings of Scientific-Research Institute of Chemical Reagents and Special Purity Grade Substances (IREA) (in Russian). Moscow. 1981. No. 43. pp. 73–81.
47. O.A. Osipov, V.I. Minkin, and A.D. Garnovsky. Reference Book on Dipole Moments (in Russian). Vysshaya Shkola, Moscow. 1971.
48. A.E. Lutskii and V.N. Konel'skaya. Zh. Fiz. Khim. **35**, 1938 (1961).
49. A.E. Lutskii, L.A. Kochergina, and P.M. Bugai. Zh. Obshch. Khim. **33**, 985 (1963).
50. V.V. Prezhdo, E.E. Fedorov, S.N. Eremenko, and N.S. Frumina. Zh. Obshch. Khim. **45**, 1125 (1975).
51. P.G. Nikonorov, L.F. Kozhina, and S.P. Mushtakova. *In* New achievements in organic chemistry: collection of scientific works (in Russian). Saratov University Press, Saratov. 1997. p. 75–76.

© 1999 NRC Canada

Reactions of monovalent ions with a versatile building block $[Cr(phen)(C_2O_4)_2]^-$. Molecular and crystal structures of $NaCr(phen)(C_2O_4)_2 \cdot 3H_2O$, $KCr(phen)(C_2O_4)_2 \cdot DMF \cdot 0.5H_2O$, 4-$NH_3py[Cr(phen)(C_2O_4)_2] \cdot 2H_2O$, *N*-(*n*-butyl)$_4[Cr(phen)(C_2O_4)_2]$, and $PPh_4[Cr(phen)(C_2O_4)_2]$

Fernande D. Rochon and Gassan Massarweh

Abstract: The molecular and crystal structures of the products of the reaction between the building block $[Cr(phen)_2(C_2O_4)_2)]^-$ and several monovalent ions, two from the alkaline group (Na^+, K^+) and 4-NH_3pyridine$^+$, *N*-(*n*-butyl)$_4^+$, and PPh_4^+ were studied by crystallographic methods. $Na(Cr(phen)_2(C_2O_4)_2) \cdot 3H_2O$ (**1**) is monoclinic, $P2_1/c$, a = 9.129(2), b = 13.867(2), c = 17.934(5) Å, β = 117.52(2)°, Z = 4 and R = 0.0623. The sodium atom is surrounded by six oxygen atoms at distances between 2.363(6) and 2.484(8) Å. The Na···Na distance is 3.693(7) Å. The compound has an extended structure forming layers, held together by H bonds. $K(Cr(phen)_2(C_2O_4)_2) \cdot DMF \cdot 0.5H_2O$ (**2**) is monoclinic, $P2_1/n$, a = 11.298(2), b = 14.048(5), c = 14.240(5) Å, β = 108.19(2)°, Z = 4 and R = 0.0647. The material also possesses an extended 2D structure, but quite different from the one of the sodium compound. The coordination number around the K atom is 6 with K—O distances between 2.663(13) and 2.920(9) Å. The K···K distance is 3.939(9) Å. The other crystals 4-NH_3py$[Cr(phen)_2(C_2O_4)_2] \cdot 2H_2O$ (**3**), *N*-(*n*-butyl)$_4[Cr(phen)_2(C_2O_4)_2]$ (**4**), and $PPh_4[Cr(phen)(C_2O_4)_2]$ (**5**) have simple discrete ionic structures. Crystal **3** is monoclinic, *Cc*, a = 17.282(5), b = 15.037(3), c = 9.563(2) Å, β = 115.25(2)°, Z = 4, and R = 0.0386. The ions are held together by an extensive hydrogen bonding system involving the two molecules of water located in the lattice. Crystal **4** is monoclinic, $P2_1/c$, a = 12.329(3), b = 14.471(3), c = 18.181(3) Å, β = 97.75(2)°, Z = 4, and R_1 = 0.076 and finally, **5** is monoclinic, $P2_1/c$, a = 13.231(2), b = 14.410(2), c = 18.758(4) Å, β = 106.00(1)°, Z = 4, and R_1 = 0.0517.

Key words: crystal structure, chromium, oxalato, phenanthroline, sodium, potassium, 4-aminopyridinium, tetrabutylammonium, tetraphenylphosphonium.

Résumé : Les structures moléculaires et cristallines des produits de réaction entre la brique $[Cr(phen)_2(C_2O_4)_2]^-$ et plusieurs ions univalents, dont deux du groupe alkalin (Na^+ et K^+) et 4-NH_3pyridine$^+$, *N*-(*n*-butyl)$_4^+$, et PPh_4^+ ont été déterminées par diffraction des rayons-X. La réaction avec l'ion sodium a produit un composé contenant une structure étendue, formant des feuillets liés par des ponts hydrogènes. $Na(Cr(phen)_2(C_2O_4)_2) \cdot 3H_2O$ (**1**) est monoclinique, $P2_1/c$, a = 9.129(2), b = 13.867(2), c = 17.934(5) Å, β = 117.52(2)°, Z = 4 et R = 0.0623. Les atomes de sodium sont entourés de six atomes d'oxygène à des distances variant de 2.363(6) à 2.484(8) Å. La distance Na···Na est 3.693(7) Å. $K(Cr(phen)_2(C_2O_4)_2) \cdot DMF \cdot 0.5H_2O$ (**2**) est monoclinique, $P2_1/n$, a = 11.298(2), b = 14.048(5), c = 14.240(5) Å, β = 108.19(2)°, Z = 4 et R = 0.0647. Ce produit possède aussi une structure étendue 2D, mais différente de celle du cristal **1**. Le nombre de coordination du K est 6, avec des distances K—O de 2.663(13) à 2.920(9) Å. La distance K···K est 3.939(9) Å. Les autres cristaux 4-NH_3py$[Cr(phen)_2(C_2O_4)_2] \cdot 2H_2O$ (**3**), *N*-(*n*-butyl)$_4[Cr(phen)_2(C_2O_4)_2]$ (**4**) et $PPh_4[Cr(phen)_2(C_2O_4)_2]$ (**5**) possèdent des structures ioniques simples. Le cristal **3** est monoclinique, *Cc*, a = 17.282(5), b = 15.037(3), c = 9.563(2) Å, β = 115.25(2)°, Z = 4 et R = 0.0386. Les ions sont liés par un système important de ponts hydrogènes impliquant les deux molécules d'eau du réseau. Le cristal **4** est monoclinique, $P2_1/c$, a = 12.329(3), b = 14.471(3), c = 18.181(3) Å, β = 97.75(2)°, Z = 4 et R_1 = 0.076 et finalement, **5** est monoclinique, $P2_1/c$, a = 13.231(2), b = 14.410(2), c = 18.758(4) Å, β = 106.00(1)°, Z = 4 et R_1 = 0.0517.

Mots clés : structure cristalline, chrome, oxalato, phénanthroline, sodium, potassium, 4-aminopyridinium, tétrabutylammonium, tétraphénylphosphonium.

Received March 1, 1999.

F.D. Rochon[1] and G. Massarweh. Département de chimie, Université du Québec à Montréal, C. P. 8888, Montréal, QC H3P 3P8, Canada.

[1]Author to whom correspondence may be addressed. Telephone: (514) 987-3000, ext. 4896. Fax: (514) 987-4054. e-mail: rochon.fernande@uqam.ca

 © 1999 NRC Canada

Introduction

The search for new molecular based magnets (1) and precursors in the synthesis of superconducting materials (2) has recently greatly increased the interest in 2D and 3D oxalato-bridged compounds. Several homometallic (3–8), heterometallic (9–12) and mixed-valent complexes have lately been reported (13).

We have recently started a study on the ability of a new building block for the design of heteropolymetallic magnetic systems. This versatile building block, $[Cr(AA)(C_2O_4)_2]^-$ (AA = bipy or phen) is able to generate extended structures systems with quite novel topologies of the metallic centers (14, 15). The synthetic approach takes advantage of the well known bridging ability of the oxalato groups and of the relative inertness of the chromium(III) complexes towards substitution reactions. The synthetic route is straightforward and consists normally in reacting a barium-chromium precursor with the appropriate metal sulfate. We have shown (14, 15) that the $[Cr(bipy)(C_2O_4)_2]^-$ complex anion can efficiently act as a ligand towards bivalent cations (Ba^{2+}, Mn^{2+}, Co^{2+}, and Cu^{2+}), leading to completely different structures, in spite of the stoichiometric similarity of some of the crystalline materials: $MCr_2(bipy)_2(C_2O_4)_4(H_2O)_n{\cdot}mH_2O$, M = Ba(II), Co(II), Cu(II), $n = 2$, $m = 1$ (1.5 for Cu(II)); M = Mn(II), $n = 0$, $m = 0$. The overall structures of these heterometallic systems are strongly influenced by the coordination number of the bivalent metal ion. The barium derivative is a scaffolding-like material with a three-dimensional structure and 10-coordinated barium atoms, the manganese derivative exhibits a new type of heterobimetallic chains with octacoordinated manganese atoms, whereas the structures of the cobalt(II) and copper(II) compounds consist in discrete linear Cr-M-Cr trinuclear species and hexacoordinated metal atoms.

To study the role of the oxidation state of the assembling cation on the coordinating properties of the building block $[Cr(phen)(C_2O_4)_2]^-$, we have undertaken a study on monovalent cations. We have already studied the influence of the stoichiometry on the overall structure of the heterometallic system, with the reaction with a monovalent cation, namely silver(I) with the $[Cr(bipy)(C_2O_4)_2]^-$ brick. The results have shown that the crystal contains discrete tetranuclear cycles formed by two chromium and two silver atoms bridged by the oxalato groups (15). The silver atoms are pentacoordinated, exhibiting distorted trigonal bipyramidal geometries. It became interesting to determine how other monovalent ions, especially the non-transitional metals, can influence the self-assembling process. The product of the reaction of the $[Cr(bipy)(C_2O_4)_2]^-$ brick with sodium was recently reported (16). The results have shown that the product has a two-dimensional structure. We have now studied a similar reaction between the $[Cr(phen)(C_2O_4)_2]^-$ brick with five monovalent non-transitional ions; two from the alkaline group (Na and K ions) and three organic ions: 4-aminopyridinium, tetra-*n*-butylammonium and tetraphenylphosphonium. The Na and K ions are smaller in size than the Ba atom. The 4-aminopyridinium ions are interesting since they can form bonds with metallic centers and they also usually form H bonds with the oxalato ligands. Tetraalkylammonium or tetraphenylphosphonium ions, on the contrary, cannot bind to metals nor form any H bonds. But, the latter crystals could contain molecules of solvent able to generate H-bonding systems. Even without the presence of solvation, the results on discrete structures present some interest for comparison with extended structures. The results of this study on the reactions of these five univalent ions with the building block $[Cr(phen)(C_2O_4)_2]^-$ are described below.

Experimental

The chemicals were purchased from Aldrich and all manipulations were performed using materials as received. The IR spectra (KBr pellets) were recorded on a Perkin–Elmer 783 spectrometer. The two compounds, $Ba(Cr(phen)(C_2O_4)_2)_2{\cdot}4H_2O$ and $KCr(phen)(C_2O_4)_2$ were synthesized as described in the literature (17, 18). The K compound was recrystallized from a 1:1 mixture solution of DMF and H_2O and crystals identified by crystallographic methods as $K(Cr(phen)_2(C_2O_4)_2){\cdot}DMF{\cdot}0.5H_2O$ (**2**) were isolated. The Na compound (**1**) was also isolated following the same method used to prepare the K compound, substituting $K_2C_2O_4$ by $Na_2C_2O_4$. It was recrystallized in water.

$M(Cr(phen)(C_2O_4)_2)$ (M = Na (1), K (2)):

The Na and K compounds were also prepared by this second method. A suspension of $Ba(Cr(phen)(C_2O_4)_2)_2{\cdot}4H_2O$ (0.5 mmol) in 50 mL of water was reacted with a stoichiometric amount of M_2SO_4 dissolved in 10 mL of water. The mixture was then stirred at room temperature for about 15 h to promote the complete precipitation of barium sulfate, which was removed by filtration. Reddish crystals were obtained by slow concentration of the aqueous solution. The yields were about 80%. The compounds were recrystallized from water (**1**) or from a mixture of water and DMF (**2**).

A third method was used, especially for the preparation of the 4-pyNH$_3$ (**3**), (n-butyl)$_4$) (**4**) and the PPh$_4$ compounds (**5**). A suspension of $Ba(Cr(phen)(C_2O_4)_2)_2{\cdot}4H_2O$ (0.05 mmol) in 20 mL of water was reacted with a stoichiometric amount of Ag_2SO_4 dissolved in 10 mL of water. The mixture was then stirred at room temperature for about 15 h to promote the complete precipitation of barium sulfate, which was removed by filtration. A methanol solution (0.12 mmol) of the chloride salt of 4-pyNH$_3^+$ (for **3**), (n-butyl)$_4^+$ (for **4**)$^+$, or PPh$_4^+$ (for **5**) was then added and the AgCl precipitate removed by filtration. Red crystals were obtained by slow evaporation of the H_2O–CH_3OH solution. Crystals adequate for crystallographic studies were grown from H_2O–CH_3OH (**4** and **5**), water (**3**), or DMF (**4**).

*$Na(Cr(phen)_2(C_2O_4)_2){\cdot}3H_2O$ (**1**)*: IR data (cm^{-1}): 3450m, 1720s, 1710s, 1679vs, 1670vs, 1585vw, 1530vw, 1522m, 1518w, 1510w, 1428m, 1382s, 1340m, 1258vw, 1245m, 1225w, 1210w, 852m, 810m, 720m, 542m.

*$K(Cr(phen)_2(C_2O_4)_2){\cdot}DMF{\cdot}0.5H_2O$ (**2**)*: IR data (cm^{-1}): 3490m, 3084w, 3070w, 1720s, 1712s, 1680s, 1676s, 1610vw, 1586vw, 1522w, 1499vw, 1490vw, 1425m, 1373s, 1339w, 1313vw, 1258w, 1234m, 1225vw, 1150w, 1109w, 888w, 875w, 852m, 804m, 779vw, 736w, 719m, 660vw, 649w, 540m.

*$4\text{-}pyNH_3[Cr(phen)_2(C_2O_4)_2]{\cdot}2H_2O$ (**3**)*: IR data (cm^{-1}): 3400m, 3150m, 3100m, 3020w, 2980w, 2964w, 1730s, 1718s, 1677s,

© 1999 NRC Canada

1667s, 1587vw, 1538m, 1530m, 1522m, 1430m, 1400m, 1360s, 1316w, 1260w, 1220m, 1202w, 950w, 805m, 785vw, 720m, 650w, 542m.

*(*n*-Butyl)$_4$[Cr(phen)$_2$(C$_2$O$_4$)$_2$] (**4**):* IR data (cm^{-1}): 3440m, 3099vw, 3088w, 3010w, 2958s, 2940m, 2890vw, 2879m, 1720s, 1710vs, 1685vs, 1675vs, 1650w, 1640w, 1582w, 1515m, 1468m, 1460m, 1425m, 1412w, 1360s, 1345vs, 1338s, 1218s, 1105w, 900vw, 878w, 872w, 858m, 800s, 735w, 725m, 542m.

*P(Ph)$_4$[Cr(phen)$_2$(C$_2$O$_4$)$_2$] (**5**):* IR data (cm^{-1}): 3460m, 3090w, 3060m, 1730vs, 1710vs, 1690vs, 1675vs, 1665vs, 1640w, 1630w, 1610w, 1588m, 1520m, 1518m, 1495w, 1485m, 1445m, 1439m, 1430m, 1410w, 1355vs, 1316w, 1225m, 1215m, 1168w, 1143w, 1110s, 1079vw, 1033vw, 998m, 900vw, 873m, 855m, 803s, 798w, 785w, 765m, 750w, 737w, 721s, 689s, 663vw, 652w, 613w, 555m, 545s, 465w, 435w, 415m.

Crystallographic measurements and structure resolution

The crystals were selected after examination under a polarizing microscope for homogeneity. The data collection was made at room temperature on a Siemens P4 diffractometer with graphite-monochromatized MoKα radiation (λ = 0.71073 Å). The Siemens XSCANS program was used for the data collection. The unit cell parameters were obtained by least-squares refinement of the angles 2θ, ω and χ for about 40 well-centered reflections. Crystal **4** (*N*-Bu$_4^+$ salt) was smaller than the other crystals and it appeared of poorer quality. Attempts to obtain better crystals were not successful. Two different crystals were measured and the results presented here are those which gave the best results. The K$^+$ compound (crystal **2**) was not stable and decomposed regularly on the diffractometer. A great number of crystals coated with different kinds of grease or glue were studied without success. Finally one crystal gave suitable data. The data collection stopped when the three standard reflections were below 50% of their initial intensity. About 65% of the data collection had then been measured. Therefore, the structure was solved and refined with a partial data collection. The high-angle reflections were missing. For this reason, the number of observed data is limited, but the results are excellent considering the problems encountered. An absorption correction based on the equations of the crystal faces was made for crystal **2**.

The coordinates of the heavy atoms were determined from direct methods and the positions of all the other non-hydrogen atoms were found by the usual Fourier methods. The refinement of the structures was done by full-matrix least-squares analysis, except for crystal **2** (K$^+$ compound) which was refined in blocks due to the limited number of observed data and the high number of parameters. All the non-H atoms were refined anisotropically. The H atoms, except those of the water molecules, were fixed at their calculated positions (riding model). Most of the H atoms on the water molecules were located and refined. Crystal **1** contains three water molecules. W1 and W3 are located in the crystal lattice while W2 was found in the close environment of the Na atom, disordered on two close positions with occupation factors of 0.6 and 0.4. W3 is also disordered on three positions with occupation factors of 0.4, 0.3, and 0.3. Crystal **2** contains one molecule of DMF in the close environment of K and 0.5 molecule of water in the lattice close to an inversion centre, while crystal **3** contains two lattice molecules of water. The calculations were done on a SHELXTL[2] system. The refinement was done on F for crystals **1**, **2**, **3** and on F^2 for crystals **4** and **5**. The crystallographic data and the most pertinent information are summarized in Table 1.[3]

Results and discussion

Our synthetic approach towards monovalent ion–chromium(III) complexes, involve the reaction of the Ba(Cr(phen)(C$_2$O$_4$)$_2$)$_2$ precursor with a stoichiometric quantity of the corresponding sulfate salt. This method is very simple and seems to have a large applicability with almost any monovalent or divalent ions.

$$\mathrm{Ba(Cr(phen)(C_2O_4)_2)_2 + M_2SO_4 \rightarrow 2MCr(phen)(C_2O_4)_2 + BaSO_4}$$

The Na$^+$ and K$^+$ complexes were prepared following this method. If the metal is Ag, it can, in a further step, be precipitated with the chloride salt of the required cation as follows:

$$\mathrm{AgCr(phen)(C_2O_4)_2 + MCl \rightarrow MCr(phen)(C_2O_4)_2 + AgCl}$$

Crystals **3** (4-NH$_3$py), **4** (*n*-butyl)$_4$), and **5** (PPh$_4$) were prepared following this procedure.

The sodium compound was also synthesized directly by the method reported for the preparation of the K$^+$ compound (17, 18) in a 1:1 DMF–H$_2$O mixture. The 4-aminopyridinium compound was also obtained in an attempt to isolate a nickel compound. NiSO$_4$ was added to Ba(Cr(phen)(C$_2$O$_4$)$_2$)$_2$ and after the removal of BaSO$_4$, 4-aminopyridine was added to the solution. Crystals which proved to be 4-NH$_3$py [Cr(phen)(C$_2$O$_4$)$_2$]·2H$_2$O (**3**) were characterized by crystallographic methods. All these compounds are relatively easy to prepare, but crystals suitable for crystallographic analysis are difficult to prepare.

The results of the crystallographic studies of the Na$^+$ and K$^+$ compounds have shown that the materials are different even if the size of the two ions are not very different. The coordination number around the alkali metal is the same but the binding mode of the Cr-oxalato group is quite different.

[2] SHELXTL PLUS (PC version, 1990–1993). Siemens Analytical Instruments Inc., Madison, Wis.

[3] The following tables have been deposited: positional parameters, anisotropic thermal factors, bond distances and angles, and H coordinates and may be purchased from: The Depository of Unpublished Data, Document Delivery, CISTI, National Research Council Canada, Ottawa, Canada, K1A 0S2. Tables of bond distances and angles and H coordinates have also been deposited with the Cambridge Crystallographic Data Centre and can be obtained on request from: The Director, Cambridge Crystallographic Data Centre, University Chemical Laboratory, 12 Union Road, Cambridge, CB2 1EZ, U.K.

© 1999 NRC Canada

Table 1. Summary of the crystallographic data.

	Crystal				
	1	**2**	3	4	**5**
Formula	$C_{16}H_{14}CrN_2NaO_{11}$	$C_{19}H_{16}CrN_3KO_{9.5}$	$C_{21}H_{19}CrN_4O_{10}$	$C_{32}H_{44}CrN_3O_8$	$C_{40}H_{28}CrN_2O_8P$
M_w	485.3	529.4	539.4	650.7	747.61
Crystal system	Monoclinic	Monoclinic	Monoclinic	Monoclinic	Monoclinic
Space group	$P2_1/c$	$P2_1/n$	Cc	$P2_1/c$	$P2_1/c$
a (Å)	9.129(2)	11.298(3)	17.282(5)	12.329(3)	13.231(2)
b (Å)	13.867(2)	14.048(5)	15.037(3)	14.471(3)	14.410(2)
c (Å)	17.934(5)	14.240(5)	9.563(2)	18.181(3)	18.758(4)
β (°)	117.52(2)	108.19(2)	115.25(2)	97.75(2)	106.00(1)
Volume (Å^3)	2013.4(9)	2147.2(13)	2247.6(9)	3214.1(12)	3437.8(10)
Z	4	4	4	4	4
F(000)	988	1080	1108	1380	1540
ρ_{calcd} (mg m^{-3})	1.601	1.638	1.594	1.345	1.444
μ(MoKα) (mm^{-1})	0.653	0.787	0.576	0.410	0.438
R ($F > 4\sigma(F)$)[a]	0.0623	0.0647	0.0386		
R_1 ($I > 2\sigma(I)$)[a]				0.0762	0.0517
R_w[b]	0.0564	0.0533	0.0395		
wR_2 (all data)[c]				0.1277	0.0986
Goodness-of-fit	1.29	1.42	1.29	1.028	1.073

[a] $R = R_1 = \Sigma||F_o| - |F_c|| / \Sigma|F_o|$.

[b] $R_w = [\Sigma w(|F_o| - |F_c|)^2 / \Sigma|F_o|^2]^{1/2}$.

[c] $wR_2 = [\Sigma w(F_o^2 - F_c^2)^2 / \Sigma w(F_o^2)^2]^{1/2}$.

Fig. 1. Drawing of $NaCr(phen)(C_2O_4)_2 \cdot 3H_2O$ (**1**) showing the environment around the Na atoms, with the atom-numbering scheme. For clarity, only the main component is shown for the aqua ligand (W(21)). (The ellipsoids correspond to 30% probability.)

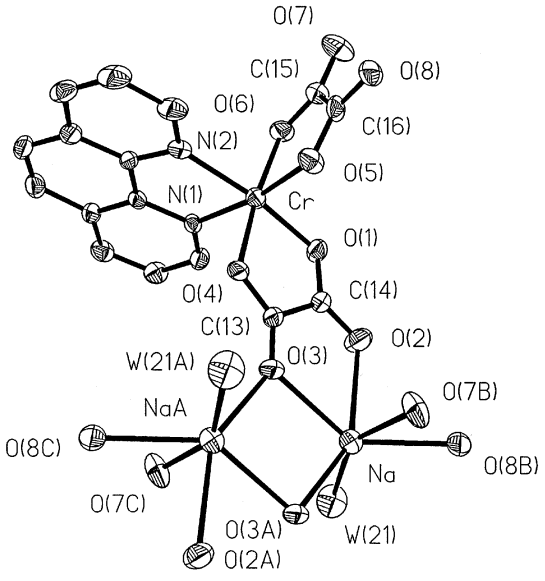

$Na(Cr(phen)(C_2O_4)_2) \cdot 3H_2O$ (1)

Crystals of the sodium compound $Na(Cr(phen)(C_2O_4)_2) \cdot 3H_2O$ (**1**) have an extended layer structure, where the sodium atoms join the chromiun complexed ions. The inversion center is between the two Na atoms. The Na···Na distance is relatively short, 3.693(7) Å. A labelled diagram showing the environment around the Na atoms is shown in Fig. 1. The environment of the sodium atoms has a distorted octahedral geometry with five short Na···O(oxalato) distances from 2.363(6) to 2.484(8) Å. One of the oxalato oxygen atoms, O(3), forms a bridge between the two Na atoms at distances Na—O(3) = 2.456(7) Å and Na—O(3A) = 2.363(6) Å. The sixth position is occupied by an aqua ligand which is disordered on two close positions with Na—W2 distances = 2.447(13) and = 2.367(20) Å. Selected bond distances and angles are shown in Table 2. The Cr—O bonds vary between 1.952(5) and 1.967(5) Å, while the Cr—N bonds are 2.051(7) and 2.080(7) Å. The angles around Cr are normal with chelate angles being smaller (O-Cr-O = 83.0(2)°, 83.6(3)°, and N-Cr-N = 79.8(3)°) than the other angles, as expected.

There are two different modes of bonding for the oxalato ligands (Scheme 1). The first type is the normal bridging bidentate mode, while in the second type, one O atom (O(3)) forms a further bond with the second metallic center of the pillar. There are two types of C—O bonds in the oxalato ligands. Those bonded to Cr have an average bond length of 1.285(9), while those in the close environment of the Na atoms are shorter, with an average value of 1.223(10) Å, indicating a lower multiplicity of the C—O bonds attached to Cr than those around the Na atoms. The O(3)—C(13) bond forming the bridge between the two Na atoms is not different 1.220(9) Å. The angles around O(3) are Na-O(3)-C(13) = 115.4(5)°, Na-O(3)-NaA = 100.1(2)°, and NaA-O(3)-C(13) = 144.4(5)°.

The 2D structure of the compound is quite interesting. The two oxalato ligands act as bridges between the sodium and the chromium atoms with Cr···Na distances of 5.570, 5.713, and 5.865 Å. One sheet of material can be seen in Fig. 2, which shows only the Na and Cr atoms. The two Na atoms can be considered as forming a pillar and have been

© 1999 NRC Canada

Fig. 2. Diagram of one sheet in the crystal $NaCr(bipy)(C_2O_4)_2 \cdot 3H_2O$ (**1**) showing only the Cr and Na atoms. The two Na atoms 3.693(7) Å apart have been joined and are in the center of the elongated parallelograms.

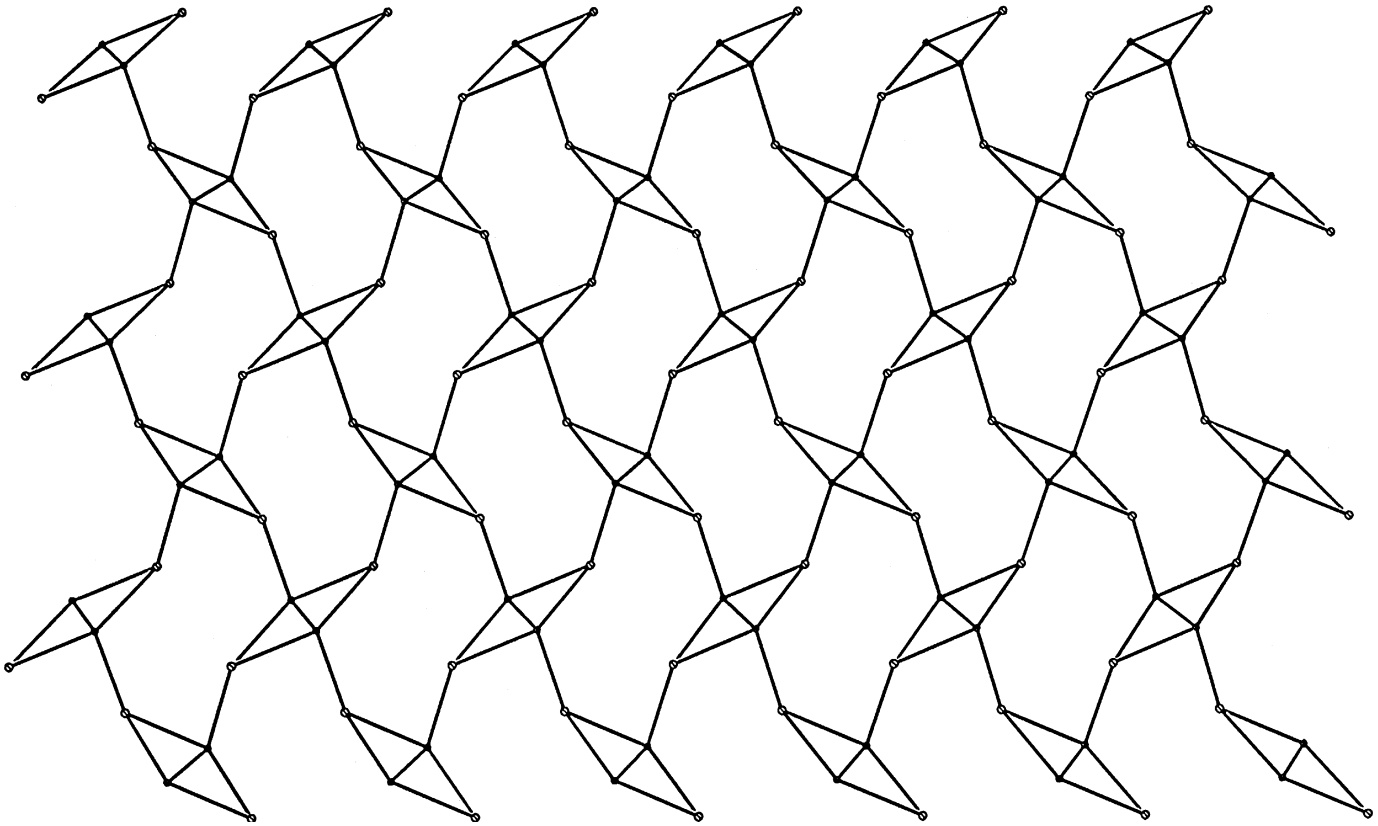

joined in the middle of the elongated parallelograms. The inversion center is also in the center of the two Na atoms. Large cycles containing four Cr and four Na atoms form large cavities (see Fig. 2) where the phenanthroline ligands are located (not shown in the figure). This structure could be compared to the 3D structure of the Ba-Cr(bipy) compound where the Ba and Cr atoms form chicken-wire sheets (14) which are further interconnected forming a 3D structure. The barium atoms have a coordination number of 10. Sodium atoms are smaller and should possess a lower coordination number. Therefore it cannot form a 3D structure, like the barium compound. In the present structure, the coordination number of the Na atoms is six including one aqua ligand.

Hydrogen bonds play an important stabilizing role in the crystal packing energy. The H-bonding system involving the lattice molecules of water and the aqua ligand with the oxalato O atoms is particularly important. The lattice molecules of water are located between the sheets, holding the different layers together. The O···O distances are acceptable but most of the molecules of water are disordered. Aromatic π–π stacking interaction of the phenanthroline ligands seem also to play an important role. The distances between the aromatic planes is about equal to the distance of the Na···Na atoms (3.7 Å).

$K(Cr(phen)(C_2O_4)_2)\cdot DMF\cdot 0.5H_2O$ (2)

$K(Cr(phen)(C_2O_4)_2)\cdot DMF\cdot 0.5H_2O$ is unstable and it proved difficult to obtain a suitable set of data. This material crystallized with a molecule of DMF, bonded to the K atom through the O atom and 0.5 molecule of water located in the lattice, close to an inversion center. A labelled diagram showing the environment around the K atoms is shown in Fig. 3. The K atoms have a coordination number of six forming a very distorted octahedron. There are five O atoms from the oxalato ligands with K—O distances between 2.713(10) and 2.981(11) Å and the sixth K—O(DMF) bond is 2.663(13) Å. The K···K distance is quite short, 3.939(9) Å, and the center of inversion is located between the two K atoms, which can be described again as a pillar. This pillar is longer than the one in the Na compound (3.693(7) Å, but shorter than the one observed in the Ba-Cr(bipy) compound (4.138(3) Å) (14).

The K atoms are bridged by the chromium(III) complexed ions. There are two different bridging modes of the oxalato groups as shown in Scheme 1. Contrary to the Na compound, each oxalato ligand binds the two different K atoms which form the pillars. One oxalato ligand bonded to Cr through O(3) and O(4) is bonded to two different K atoms through O(7) and O(8). The second oxalato ligand, which is bonded to Cr through O(1) and O(2) is also bonded to two different K atoms through O(5) and O(6). Furthermore, O(6) is bonded to the second K atom of the pillar forming a bridge between the two K atoms (Fig. 3).

Selected bond distances and angles are shown in Table 2. The Cr—O bonds vary between 1.963(8) and 1.997(10) Å, while the Cr—N bonds are 2.092(7) and 2.083(9) Å. The angles around Cr are normal with chelate angles being smaller

© 1999 NRC Canada

Fig. 3. Structure of $KCr(phen)(C_2O_4)_2 \cdot DMF \cdot 0.5H_2O$ (**2**) showing the environment around the Na atoms, with the atom-numbering scheme (only the N of phen are shown).

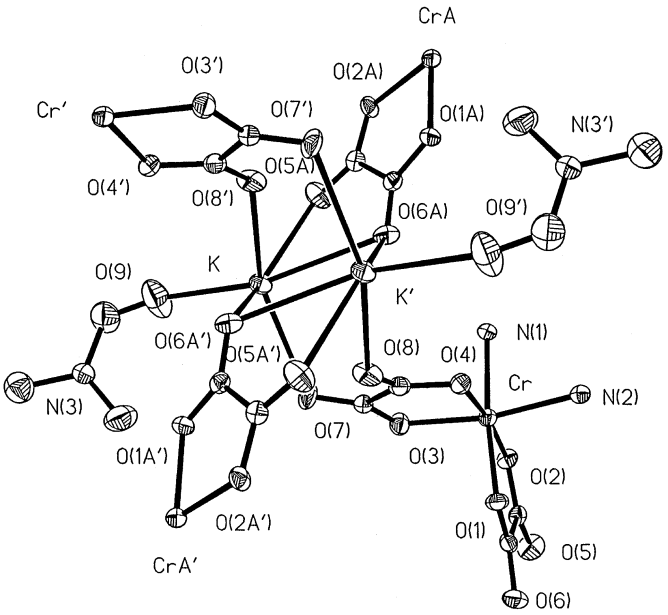

(O-Cr-O = 83.7(4)°, 82.8(4)°, and N-Cr-N = 80.0(3)°) than the other angles, as expected.

The structure of the compound consists in infinite thick layers parallel to the ab plane. The 2D network containing only the Cr and the K atoms is shown in Fig. 4. The two K atoms forming the pillar are connected by four oxalato bridges to four different Cr atoms. The eight bridging K···Cr units form a four-tipped star around the K···K pillars. The K···Cr distances are 5.812 and 6.125 Å. These thick sheets are very similar to the ones found in the 3D compound $(BaCr_2(bipy)_2(C_2O_4)_4(H_2O))_n \cdot nH_2O$ described recently (14). In the latter structure, the Ba and Cr atoms form chicken-wire sheets, which are further inter-connected by second layers which are formed of four-tipped stars around the Ba···Ba pillars resulting in a scaffolding material with a unique neutral three-dimensional framework. The latter second sheets are exactly the same as those found in the K compound (crystal **2**). Barium atoms can accept a large coordination number because of its larger size. In this particular case, it is ten. The number of Cr-oxalato bridges between the Ba atoms is twice as large as the number found in the alkali compounds. It is quite remarkable that the K compound is so similar to the Ba complex, except for the third dimension, which is absent in the K compound.

The two differences between the Ba material (14) and the K and Na compounds described here, are the charges on the ions and their sizes. It would be most pertinent now to prepare a larger alkali compound (Rb or Cs) where the metal size would be closer to the one of the Ba compound. This work is in progress.

The K compound crystallized with a disordered molecule of water in the lattice close to an inversion center. Therefore, the occupation factor of the molecule is 0.5. The positions of the two H atoms of the water molecules seem to be disordered. The DMF ligands bonded to the K atoms are oriented towards the outside of the layers where the water molecules are also located. The water molecules form H bonds be-

Fig. 4. Diagram of one layer in the crystal $KCr(phen)(C_2O_4)_2 \cdot DMF \cdot 0.5H_2O$ (**2**) showing only the Cr and K atoms.

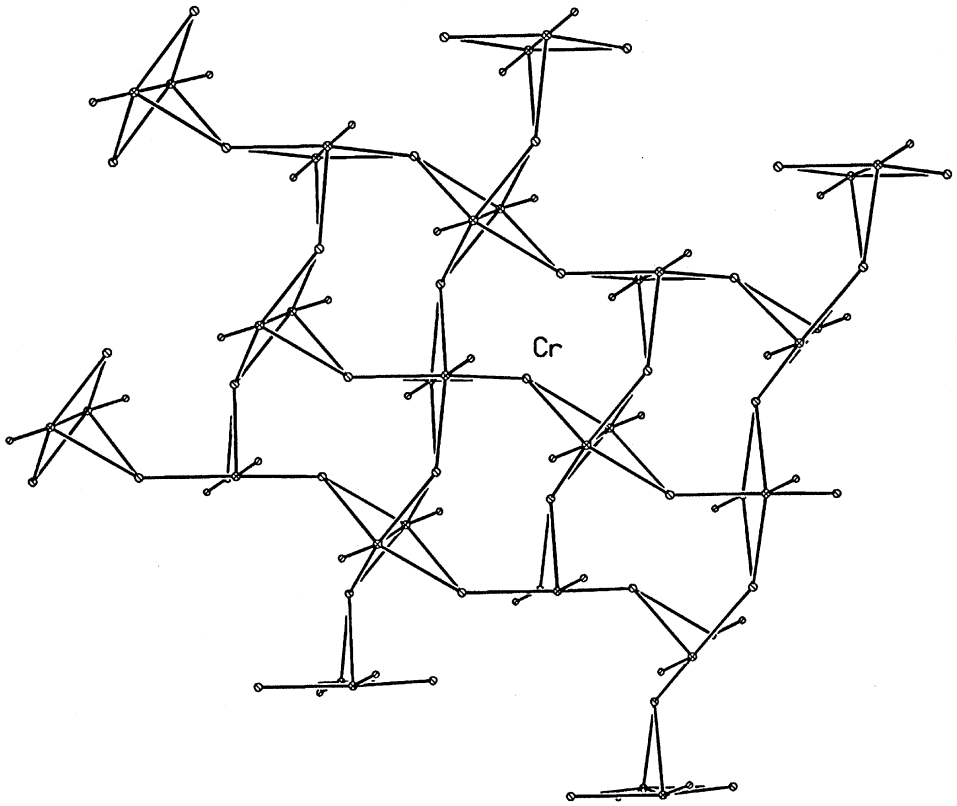

© 1999 NRC Canada

Fig. 5. Molecular structure of 4-NH_3py[Cr(phen)(C_2O_4)$_2$]·2H_2O (**3**) with the atom-numbering scheme. (The ellipsoids correspond to 30% probability.)

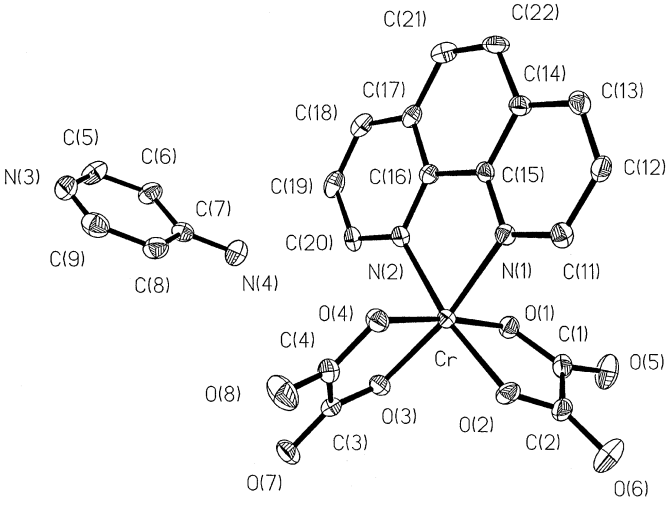

tween the different layers with W···O distances of 2.888 and 3.065 Å.

4-NH_3py[Cr(phen)(C_2O_4)$_2$]·2H_2O (3)

The structure of **3** consists of discrete 4-aminopyridinium and [Cr(phen)(C_2O_4)$_2$]$^-$ ions and two molecules of water located in the crystal lattice. A labelled diagram of the ions is shown in Fig. 5. Selected bond distances and angles are collected in Table 2. The geometry around Cr is a distorted octahedron with Cr—O bond distances between 1.945(4) and 1.980(4) Å and Cr—N bonds of 2.073(4) and 2.079(4) Å. The oxalato chelate angles are 82.7(1)° and 82.5(1)°, while the N-Cr-N angle is 79.9(2)°. The other *cis* angles are slightly greater than 90°, while the *trans* angles vary between 169.7(1)° and 174.2(1)°. The [Cr(phen)(C_2O_4)$_2$]$^-$ ions contain terminal oxalato ligands. As expected, the C—O bonds which are coordinated to Cr are significantly longer (avg. 1.293(5) Å) than the terminal C—O bonds (avg. 1.221(6) Å).

Surprisingly, the proton could not be located even if the structure was well refined and the residual electronic density was found quite low (<0.28 e Å^{-3}). The amino group (N(4)) on the pyridine ligand is the most basic, but only two H atoms were located and refined. The angles C(7)-N(4)-H are 115.4(12)° and 118.0(12)°. These larger values seem to confirm that the additional proton is effectively on the amino group. A free pair of electrons on N(4) would reduce the C(7)-N(4)-H angles to <109°. The internal angle at the pyridine N atom is 120.6(4)°. The pyridine ring is planar and N(4) is also in the same plane. The C(7)—N(4) bond is 1.323(5) Å and the internal angle around C(7) is slightly smaller (117.4(4)°) than the five others (119.6(5)–121.5(5)°).

The ions are held together by an elaborate hydrogen bonding system involving the two molecules of water located in the lattice, forming an extensive H-bonded 3D network. The protonated amino group is hydrogen bonded to O(6) (N(4)···O(6) = 2.950 Å) and to one molecule of water (N(4)···W(1) = 2.847 Å) with reasonable angles C(7)-N(4)···W(1) = 127.9° and C(7)-N(4)···O(6) = 114.9°. W(1) is also H-bonded to O(8) (distance = 2.854 Å) and to the second molecule of water (W(1)···W(2) = 2.938 Å). There are three other short contacts around W(2) with O(7) at 2.807 and 2.870 Å and with N(3) at 2.801 Å. Aromatic stacking interactions seem to play a stabilizing role in the crystal packing. The phenanthroline planes are all parallel to the *b* axis.

Fig. 6. Labelled diagram of the complexed anion in PPh_4[Cr(phen)(C_2O_4)$_2$] (**5**). The ellipsoids correspond to 30% probability. The labelling scheme for the Cr(III) anion is the same in crystal **4**.

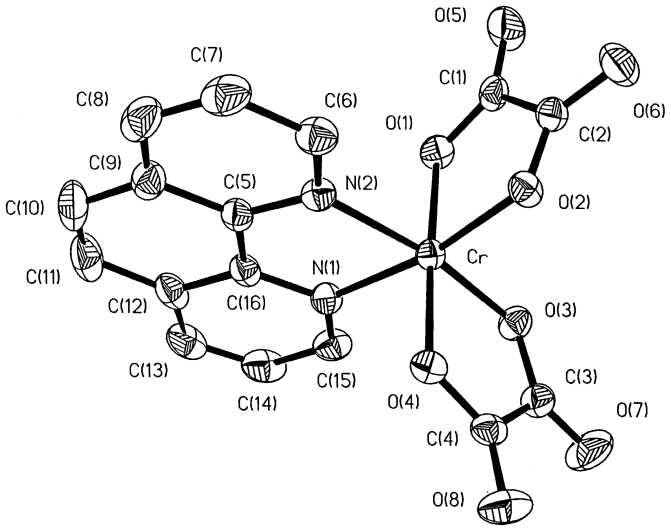

N-(*n*-Butyl)$_4$[Cr(phen)(C_2O_4)$_2$] (4) and PPh_4[Cr(phen)(C_2O_4)$_2$] (5)

The structure of crystals **4** and **5** consists of discrete (*N*-(*n*-butyl)$_4$)$^+$ or (P(Ph)$_4$)$^+$ and [Cr(phen)(C_2O_4)$_2$]$^-$ ions, but it crystallized without any molecules of solvent. These crystals were recrystallized from a mixture of H_2O–CH_3OH. Identical crystals of **4** were also obtained from a DMF solution. Therefore, no H-bonds are expected in these crystals. A labelled diagram of the [Cr(phen)(C_2O_4)$_2$]$^-$ ion in **5** is shown in Fig. 6. The selected bond distances and angles are shown in Table 2. The same labelling scheme was used for the anions in crystals **4** and **5**. The results on both crystals are very similar, except for the higher standard deviations of crystal **4**, due to the limited number of observed data, as discussed in the experimental section.

As for the other crystals, the geometry around Cr is a distorted octahedron with Cr—O bond distances between 1.939(3)–1.960(4) Å for **4** and 1.941(2)–1.954(2) Å for **5**. The Cr—N bonds are 2.077(4), 2.104(4) Å, and 2.065(2), 2.087(2) Å for **4** and **5** respectively. The oxalato chelate angles are 82.8(2)°, 83.0(2)°, and 83.08(8)°, 82.96(8)°, while the N-Cr-N angle is 77.9(7)° and 79.62(9)° for **4** and **5** respectively. The other *cis* angles are close or slightly greater than 90°, while the *trans* angles vary between 170.8(2)° and 176.5(2)° for **4** and between 170.51(8)° and 177.68(8)° for **5**.

The [Cr(phen)(C_2O_4)$_2$]$^-$ ions contain terminal oxalato ligands. The C—O bonds coordinated to Cr are significantly longer (avg. 1.288(7) Å for **4** and 1.292(3) Å for **5**) than the terminal C—O bonds (avg. 1.216(6) and 1.211(3) Å, respec-

© 1999 NRC Canada

Table 2. Selected distances (Å) and angles (°).

$Na(Cr(phen)(C_2O_4)_2)\cdot 3H_2O$ (**1**)			
Cr—O(1)	1.962(6)	Cr—O(4)	1.967(5)
Cr—O(5)	1.961(6)	Cr—O(6)	1.952(5)
Cr—N(1)	2.051(7)	Cr—N(2)	2.080(7)
Na—O(2)	2.455(6)	Na—O(3)	2.456(7)
Na···NaA	3.693(7)	Na—O(3A)	2.363(6)
Na—O(7B)	2.484(8)	Na—O(8B)	2.408(6)
Na—W(21)	2.447(13)	Na—W(22)	2.367(20)
O(1)—C(14)	1.266(9)	O(2)—(14)	1.236(11)
O(3)—C(13)	1.220(9)	O(4)—C(13)	1.278(10)
O(5)—C(16)	1.305(8)	O(6)—C(15)	1.289(11)
O(7)—C(15)	1.225(9)	O(8)—C(16)	1.211(11)
O(1)-Cr-O(4)	83.0(2)	O(5)-Cr-O(6)	83.6(3)
O(1)-Cr-O(5)	95.3(2)	O(1)-Cr-O(6)	92.8(2)
O(4)-Cr-O(5)	91.5(2)	O(4)-Cr-O(6)	173.2(2)
O(1)-Cr-N(1)	93.9(3)	O(4)-Cr-N(1)	91.7(2)
O(5)-Cr-N(1)	170.7(3)	O(6)-Cr-N(1)	94.0(2)
O(1)-Cr-N(2)	172.4(2)	O(4)-Cr-N(2)	93.0(2)
O(5)-Cr-N(2)	91.3(3)	O(6)-Cr-N(2)	91.7(2)
N(1)-Cr-N(2)	79.8(3)	O(2)-Na-O(3)	68.7(2)
O(2)-Na-O(3A)	148.6(3)	O(3)-Na-O(3A)	79.9(2)
O(2)-Na-O(7B)	92.4(3)	O(3)-Na-O(7B)	83.8(3)
O(3A)-Na-O(7B)	86.8(2)	O(2)-Na-O(8B)	82.5(2)
O(3)-Na-O(8B)	139.4(2)	O(3A)-Na-O(8B)	125.7(3)
O(7B)-Na-O(8B)	68.9(2)	O(2)-Na-W(21)	101.0(3)
O(3)-Na-W(21)	122.4(3)	O(7B)-Na-W(21)	153.5(3)
O(8B)-Na-W(21)	90.1(3)	Na-O(3)-NaA	100.1(2)
Na-O(3)-C(13)	115.4(5)	NaA-O(3)-C(13)	144.4(5)
$K(Cr(phen)(C_2O_4)_2)\cdot DMF\cdot 0.5H_2O$ (**2**)			
Cr—O(1)	1.968(7)	Cr—O(2)	1.997(10)
Cr—O(3)	1.963(8)	Cr—O(4)	1.975(10)
Cr—N(1)	2.092(7)	Cr—N(2)	2.083(9)
K—O(5A)	2.920(9)	K—O(6A′)	2.874(9)
K—O(7)	2.756(8)	K—O(8′)	2.713(10)
K—O(9)	2.663(13)	K—O(6A)	2.981(11)
O(1)—C(1)	1.317(16)	O(2)—C(2)	1.300(11)
O(3)—C(3)	1.256(16)	O(4)—C(4)	1.286(12)
O(5)—C(2)	1.239(16)	O(6)—C(1)	1.239(12)
O(7)—C(3)	1.212(13)	O(8)—C(4)	1.234(17)
O(9)—C(7)	1.216(18)	C(7)—N(3)	1.348(14)
N(3)—C(5)	1.455(16)	N(3)—C(6)	1.411(16)
K···KA	3.939(9)		
O(1)-C-O(2)	83.7(4)	O(1)-Cr-O(3)	95.3(3)
O(1)-Cr-O(4)	90.2(4)	O(2)-Cr-O(3)	93.5(4)
O(2)-Cr-O(4)	172.6(3)	O(3)-Cr-O(4)	82.8(4)
O(1)-Cr-N(1)	174.3(3)	O(2)-Cr-N(1)	95.0(4)
O(3)-Cr-N(1)	90.3(3)	O(4)-Cr-N(1)	91.4(4)
O(1)-Cr-N(2)	94.5(3)	O(2)-Cr-N(2)	90.2(4)
O(3)-Cr-N(2)	169.9(3)	O(4)-Cr-N(2)	94.6(4)
N(1)-Cr-N(2)	80.0(3)	K-O(6A)-K′	84.5(2)
K′-O(6A)-C(1A)	112.4(7)	K-O(6A)-C(1A)	126.9(10)
C(5)-N(3)-C(6)	119.0(9)	C(5)-N(3)-C(7)	118.7(10)
C(6)-N(3)-C(7)	122.0(10)	N(3)-C(7)-O(9)	124.1(12)
$4\text{-}NH_3Py[Cr(phen)(C_2O_4)_2]\cdot 2H_2O$ (**3**)			
Cr—O(1)	1.954(3)	Cr—O(2)	1.945(4)
Cr—O(3)	1.980(4)	Cr—O(4)	1.970(3)
Cr—N(1)	2.073(4)	Cr—N(2)	2.079(4)

© 1999 NRC Canada

Table 2 (*concluded*).

O(1)—C(1)	1.315(6)	O(2)—C(2)	1.291(5)
O(3)—C(3)	1.288(4)	O(4)—C(4)	1.279(6)
O(5)—C(1)	1.203(5)	O(6)—C(2)	1.223(7)
O(7)—C(3)	1.235(6)	O(8)—C(4)	1.223(5)
N(4)—C(7)	1.323(5)	N(4)—HN(41)	0.922(15)
N(4)—HN(42)	0.777(11)	W(1)—HW(11)	1.296(10)
W(1)—HW(12)	0.981(15)	W(2)—HW(21)	0.831(12)
W(2)—HW(22)	0.897(15)		
O(1)-Cr-O(2)	82.7(1)	O(3)-Cr-O(4)	82.5(1)
O(1)-Cr-O(3)	94.3(1)	O(1)-Cr-O(4)	174.2(1)
O(2)-Cr-O(3)	94.4(2)	O(2)-Cr-O(4)	92.7(1)
O(1)-Cr-N(1)	91.5(1)	O(2)-Cr-N(1)	93.4(2)
O(3)-Cr-N(1)	170.8(1)	O(4)-Cr-N(1)	92.2(1)
O(1)-Cr-N(2)	89.7(1)	O(2)-Cr-N(2)	169.7(1)
O(3)-Cr-N(2)	93.1(2)	O(4)-Cr-N(2)	95.3(1)
N(1)-Cr-N(2)	79.9(2)		

N-(*n*-Bu)$_4$[Cr(phen)$_2$(C$_2$O$_4$)$_2$] (**4**) and PPh$_4$[Cr(phen)$_2$(C$_2$O$_4$)$_2$] (**5**)

	4	**5**
Cr—O(1)	1.960(4)	1.941(2)
Cr—O(2)	1.939(3)	1.946(2)
Cr—O(3)	1.942(4)	1.954(2)
Cr—O(4)	1.951(4)	1.951(2)
Cr—N(1)	2.077(4)	2.065(2)
Cr—N(2)	2.104(4)	2.087(2)
O(1)—C(1)	1.277(6)	1.284(3)
O(2)—C(2)	1.302(7)	1.289(3)
O(3)—C(3)	1.288(7)	1.297(3)
O(4)—C(4)	1.284(6)	1.298(3)
O(5)—C(1)	1.228(6)	1.208(3)
O(6)—C(2)	1.218(6)	1.215(3)
O(7)—C(3)	1.206(7)	1.209(3)
O(8)—C(4)	1.214(6)	1.213(3)
O(1)-Cr-O(2)	82.8(2)	83.08(8)
O(3)-Cr-O(4)	83.0(2)	82.96(8)
O(1)-Cr-O(3)	94.0(2)	95.43(8)
O(1)-Cr-O(4)	176.5(2)	177.68(8)
O(2)-Cr-O(3)	95.7(2)	94.01(8)
O(2)-Cr-O(4)	95.6(2)	95.35(8)
O(1)-Cr-N(1)	92.0(2)	90.26(8)
O(2)-Cr-N(1)	170.9(2)	170.51(8)
O(3)-Cr-N(1)	92.2(2)	93.34(9)
O(4)-Cr-N(1)	89.9(2)	91.49(8)
O(1)-Cr-N(2)	89.3(2)	90.50(8)
O(2)-Cr-N(2)	93.3(2)	93.63(9)
O(3)-Cr-N(2)	170.8(2)	170.84(9)
O(4)-Cr-N(2)	93.9(2)	91.31(8)
N(1)-Cr-N(2)	79.1(2)	79.62(9)

tively) as observed in **3**. It is interesting to compare these distances with those observed in the sodium and potassium materials. In crystals **1** and **2**, the C—O bonds in the close environment of the alkali metals are also shorter (avg. 1.223(10) Å for **1** and 1.231(14) Å for **2**) than those bonded to Cr (avg. 1.285(9) Å for **1** and 1.290(14) Å for **2**). The values observed for the bonds in the close environment of the alkali metals seem very slightly longer than the terminal bonds observed in crystals **4** and **5**. But the standard deviations on several values are quite high and the small observed differences are not significant at the moment. Further work is needed to confirm this hypothesis.

The (*N*-(*n*-butyl)$_4$)$^+$ ions seem normal. They are slightly flattened in order to occupy more space as shown by the slightly larger angles, especially those far from the N atom. The PPh$_4^+$ ions seem normal with an average P—C bond distance of 1.793(3) Å, and an average C-P-C angle of 109.45(13)°. Aromatic stacking interactions of the phenanthroline ligands seem to play a stabilizing role in the crystal packing as observed in other crystals.

© 1999 NRC Canada

Scheme 1.

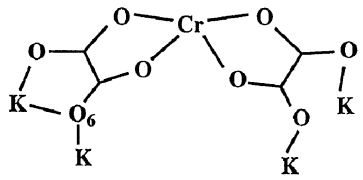

K-Cr

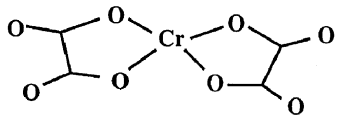

4-NH_3py-Cr NBu_4-Cr

PPh_4-Cr

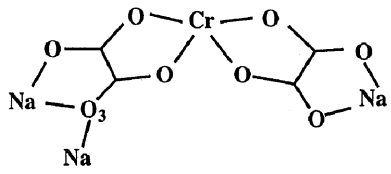

Na-Cr

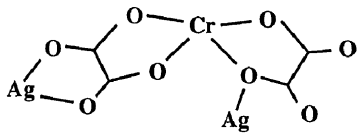

Ag-Cr

Conclusions

In this paper, we have illustrated some new examples of the self-assembly of the building block $[Cr(phen)(C_2O_4)_2]^-$ with different univalent ions. The presence of metallic ions is an excellent synthetic strategy towards the preparation of heteronuclear complexes with extended structure and generates a rich coordination chemistry. Alkali metals like sodium and potassium studied in this work have produced very interesting 2D networks. The coordination number around the alkali metals in these compounds is six. The size of the metals is probably too small to produce 3D materials. Work is underway on the study of the reactions with heavier alkali metals. Organic ions like 4-aminopyridinium seem interesting, because of their abilities to form H-bonds and in some cases to bind metals, while other ions like tetraalkylammonium or tetraphenylphosphine ions, which cannot bind metals nor form H-bonds, are not useful in generating extending structures. But the crystallographic results of the ionic entities are useful for comparison with the extended structures. For example, these results have shown that the terminal C=O bonds of the oxalato ligands seem very slightly shorter than those coordinated to the alkali metals, although the differences might not seem significant at the moment.

The variety of structures described here and in the two previous papers (14, 15) on the reactions of metals with the building block $[Cr(bipy)(C_2O_4)_2]^-$ show the importance of the four following factors: the size, the stereochemical preference and the oxidation state of the assembling cation, and the very versatile coordination behavior of the oxalato ion. Scheme 1 illustrates all the different functions identified in the products of the reaction of the monovalent ions with the building block $[Cr(A\text{-}A)_2(C_2O_4)_2)]^-$ characterized by our research group.

Further types of oxalato bonding were observed in compounds containing bivalent cations (Ba^{2+}, Mn^{2+}, Co^{2+}, Cu^{2+}) which we have reported with the bipyridine brick $[Cr(bipy)(C_2O_4)_2]^-$ (14,15). Other factors, like hydrogen bonding and aromatic stacking interactions, can also play an important stabilizing role in the overall crystal architecture of these materials.

Acknowledgment

The authors are grateful to the Natural Sciences and Engineering Research Council of Canada for financial support.

References

1. O. Kahn. Molecular magnetism. VCH, New York. 1993.
2. A. Bouayad, J.C. Trombe, and A. Gleizes. Inorg. Chim. Acta, **230**, 1 (1995).
3. G. De Munno, R. Ruiz, F. Lloret, J. Faus, R. Sessoli, and M. Julve. Inorg. Chem. **34,** 408 (1995).
4. G. De Munno, M. Julve, F. Nicolo, F. Lloret, R. Ruiz, and E. Sinn. Angew. Chem. Int. Ed. Engl. **32**, 613 (1993).
5. S. Decurtins, H.W. Schmalle, P. Schneuwly, and H.R. Oswald. Inorg. Chem. **32**, 1888 (1993).
6. H. Oshio and U. Nagashima. Inorg. Chem. **31**, 3295 (1992).
7. D. Deguenon, G. Bernardinelli, J.P. Tuchagues, and P. Castan. Inorg. Chem. **29**, 3031 (1990).
8. S. Decurtins, H.W. Schmalle, P. Schneuwly, L.M. Zheng, J. Ensling, and A. Hauser. Inorg. Chem. **34**, 5501 (1995).
9. S. Decurtins, H.W. Schmalle, H.R. Oswald, A. Linden, J. Ensling, P. Gütlich, and A. Hauser. Inorg. Chim. Acta, **216**, 65 (1994).
10. S. Decurtins, H.W. Schmalle, P. Schneuwly, J. Ensling, and P. Gütlich. J. Am. Chem. Soc. **116**, 9521 (1994).
11. H. Tamaki, Z.J. Zhong, N. Matsumoto, S. Kida, M. Koikawa, N. Achiwa, Y. Hashimoto, and H. Okawa. J. Am. Chem. Soc. **114**, 6974 (1992).
12. M. Verdaguer, M. Julve, A. Michalowicz, and O. Kahn. Inorg. Chem. **22**, 2624 (1983).
13. C.J. Nuttall, C. Bellito, and P. Day. J. Chem. Soc. Chem. Commun. 1513 (1995).
14. F.D. Rochon, R. Melanson, and M. Andruh. Inorg. Chem. **35**, 6086 (1996).
15. M. Andruh, R. Melanson, C.V. Stager, and F.D. Rochon. Inorg. Chim. Acta, **251**, 309 (1996).
16. M.C. Munoz, M. Julve, F. Lloret, J. Faus, and M. Andruh. J. Chem. Soc. Dalton Trans. **18**, 3125 (1998).
17. J.A. Broomhead. Aust. J. Chem. **15**, 228 (1962).
18. J.A. Broomhead and F.D. Dwyer. Aust. J. Chem. **14**, 250 (1961).

© 1999 NRC Canada

Lifetimes and UV-visible absorption spectra of benzyl, phenethyl, and cumyl carbocations and corresponding vinyl cations. A laser flash photolysis study

Frances L. Cozens, V.M. Kanagasabapathy, Robert A. McClelland, and Steen Steenken

Abstract: Benzyl (4-MeO, 4-Me, and 4-methoxy-1-naphthylmethyl), phenethyl (4-Me_2N, 4-MeO, 3,4-$(MeO)_2$, 4-Me, 3-Me, 4-F, 3-MeO, 2,6-Me_2, parent, and 4-methoxy-1-naphthylethyl) and cumyl (4-Me_2N, 4-MeO, 4-Me, parent) cations have been studied by laser flash photolysis (LFP) in 2,2,2-trifluoroethanol (TFE) and 1,1,1,3,3,3-hexafluoroisopropanol (HFIP). In most cases styrene or α-methylstyrene precursors were employed for the phenethyl and cumyl ions, the intermediate being obtained by solvent protonation of the excited state. Benzyl cations were generated by photoheterolysis of trimethylammonium and chloride precursors. While a 4-MeO substituent provides sufficient stabilization to permit observation of cations in TFE, cations with less stabilizing substituents usually require the less nucleophilic HFIP. Even in this solvent, the parent benzyl cation is too short-lived (lifetime <20 ns) to be observed. When generated in HFIP, phenethyl cations can be seen to react with unphotolyzed styrene, giving rise to dimer cations that are observed to grow in as the initial phenethyl cation decays. The dimer cations, in common with the oligomer cations seen in cationic styrene polymerization, have a λ_{max} 15–20 nm higher than the monomer and react with both solvent and styrene several orders of magnitude more slowly. This stabilization relative to the phenethyl may reflect an interaction with the aryl group present at the γ-carbon. Cations 4-$MeOC_6H_4C^+(R)$-CH_3 (R = Me, Et, i-Pr, *t*-Bu, cyclopropyl, C_6H_5, 4-$MeOC_6H_4$) were generated in TFE via the photoprotonation route. The alkyl series shows that steric effects are important in the decay reaction. The cation with R = cyclopropyl is a factor of 1.5 less reactive than the cation where R = phenyl. Several vinyl cations have also been generated by photoprotonation of phenylacetylenes. $ArC^+=CH_2$ has a reactivity very similar to that of its analog ArC^+H-CH_3, the vinyl cation being slightly (factors of 2–5) shorter-lived. For the various series of cations, including vinyl, substituents in the aryl ring have a consistent effect on the λ_{max}, a shift to higher wavelength relative to hydrogen of 15 nm for 4-Me, 30 nm for 4-MeO, and 50 nm for 4-Me_2N.

Key words: photogenerated carbocations, carbocation lifetime, styrene, photoprotonation.

Résumé : Faisant appel à la photolyse éclair au laser (« LFP »), on a étudié les cations de type benzyles (4-MeO et 4-Me ainsi que 4-méthoxy-1-naphtylméthyle), phénéthyle (4-Me_2N, 4-MeO, 3,4-$(MeO)_2$, 4-Me, 3-Me, 4-F, 3-MeO, 2,6-Me_2 et le fondamental ainsi que le 4-méthoxy-1-naphtyléthyle) et cumyle (4-Me_2N, 4-MeO, 4-Me et le fondamental) dans le 2,2,2-trifluoroéthanol (TFE) et le 1,1,1,3,3,3-hexafluoroisopropanol (« HFIP »). Dans la plupart des cas, des précurseurs de type styrène ou α-méthylstyrène ont été utilisés pour les ions de type phénéthyle et cumyle, obtenus par solvatation de l'état excité à l'aide d'un solvant. Les cations de type benzylique ont été générés par photohétérolyse de précurseurs triméthylammonium et chlorure. Un substituant 4-MeO fournit assez de stabilisation pour permettre d'observer les cations dans le TFE; toutefois, pour observer des cations portant des substituants moins stabilisants, il faut utiliser le « HFIP » qui est moins nucléophile. Même dans ce solvant, le temps de vie du cation benzyle fondamental est trop court (<20 ns) pour qu'on puisse l'observer. Quand on les génère dans le « HFIP », on peut observer la réaction des cations phénéthyles avec le styrène qui n'a pas réagi; cette réaction donne lieu à la formation de cations dimères dont on observe la croissance avec la décroissance du cation phénéthyle initial. Les cations dimères, comme les cations oligomères observés lors de la polymérisation cationique du styrène, ont un λ_{max} de 15 à 20 nm plus élevé que celui du monomère et leurs vitesses de réaction avec le solvant et le styrène sont de plusieurs ordres de grandeur plus faibles. La stabilisation relative du phénéthyle peut être un reflet d'une interaction avec le groupe aryle

Received April 19, 1999.

F.L. Cozens, V.M. Kanagasabapathy, and R.A. McClelland.[1] Department of Chemistry, University of Toronto, Toronto, ON M5S 3H6, Canada.
S. Steenken. Max-Planck-Institut fur Strahlenchemie, D-45413 Mulheim, Germany.

[1]Author to whom correspondence may be addressed. Telephone: (416) 978-3592. Fax: (416) 978-3592. e-mail: rmcclell@alchemy.chem.utoronto.ca

 © 1999 NRC Canada

présent sur le carbone γ. On a généré les cations 4-$MeOC_6H_4C^+(R)$-CH_3 (R = Me, Et, i-Pr, *t*-Bu, cyclopropyle, C_6H_5, 4-$MeOC_6H_4$) dans le TFE par le biais d'une réaction de photoprotonation. Les séries alkyles montrent que les effets stériques sont importants dans la réaction de désactivation. La réactivité du cation avec R = cyclopropyle est 1,5 fois moins grande que celle du cation dans lequel R = phényle. On a aussi généré plusieurs cations vinyliques par photoprotonation de phénylacétylènes. La réactivité d'ion $ARC^+=CH_2$ est très semblable à celle de son analogue ArC^+H-CH_3, le temps de vie du cation vinylique étant légèrement plus court (de 2 à 5 fois plus court). Pour les diverses séries de cations, y compris le cation vinyle, les substituants du cycle aromatique apportent un effet régulier sur le λ_{max}, soit des déplacements d'environ 15 nm (pour le 4-Me), 30 nm (pour le 4-MeO) et de 50 nm (pour le 4-Me_2N) vers une longueur d'onde plus grande par rapport au produit fondamental, portant un hydrogène.

Mots clés : carbocations photogénérés, temps de vie d'un carbocation, styrène, photoprotonation.

[Traduit par la Rédaction]

Laser flash photolysis (LFP) has been employed for a number of years for the observation of reactive intermediates and for the direct measurement of rate constants of their decay reactions. Photolyzing some precursor with a laser pulse initiates a rapid photochemical transformation to the reactive species of interest. This is detected by some method, in most cases absorption spectroscopy, and the decay directly monitored. In recent years, a number of applications involving carbocations have appeared, with the intermediate being generated and directly studied under normal solvolytic conditions, i.e., with water or an alcohol as solvent (1, 2). In this respect, detailed studies have been reported involving species such as xanthylium (3, 4), triarylmethyl (5–8), diarylmethyl (6–11), and fluorenyl cations (12–14). These ions are relatively conjugated, with the formal cationic center bearing at least two aromatic rings. Carbenium ions bearing a single stabilizing aryl ring are inherently more reactive, and thus in principle more difficult to study. In spite of this, such cations are accessible by LFP under appropriate conditions, and in two preliminary communications we have outlined aspects of this work (15, 16). This paper provides the full details, with a discussion of the photochemical methods employed to generate such cations in LFP experiments, and a comparison of the effect of solvent, cation structure, and aryl substituent. Comparisons with analogous vinyl cations are also presented.

Results and discussion

In total, 32 cations have been investigated. Table 1 provides their structure, absorption maxima, and decay rate constants in 2,2,2-trifluoroethanol (TFE) and (or) 1,1,1,3,3,3-hexafluoroisopropanol (HFIP). These solvents are necessary with most of the ions in Table 1, since their lifetimes in more nucleophilic solvents such as methanol, ethanol and water are less than 20 ns, the limit of detection with our LFP apparatus. Even then a 4-methoxy substituent (or 4-Me_2N) is usually required for the cation to be observed in TFE, and the less stabilized ones require HFIP. Changing from TFE to HFIP increases the lifetime by a factor of 10^3–10^4. Water, on the other hand, is three orders of magnitude more reactive than TFE.

4-Methoxyphenethyl cation

Two general photochemical routes were employed, styrene photoprotonation and photoheterolysis, and the results with the 4-methoxyphenethyl cation are typical. Photoprotonation, where it can be used, is the better method. This possibility was suggested through the observation of Markovnikov hydration upon irradiation of styrenes in aqueous acid, with the proposed mechanism involving protonation of the excited styrene to give intermediate phenethyl cations (17–19). With TFE (and HFIP) as solvent, addition proceeds smoothly without added acid, as illustrated in Scheme 1 for 4-methoxystyrene **1** where the ether **3** is the only product (Scheme 1). The protonation must be occurring with the solvent OH proton. This is perhaps not surprising, since the protonation of excited styrenes is general-acid catalyzed with a relatively small Bronsted α value (19).

Scheme 1.

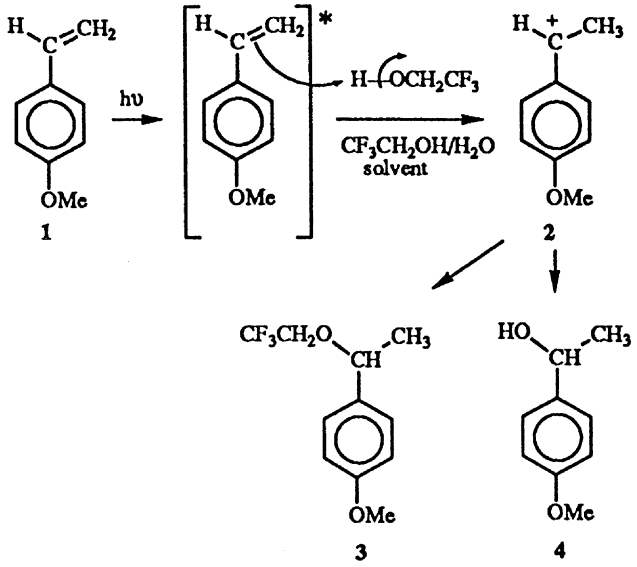

LFP of 4-methoxystyrene in TFE reveals a relatively strong transient with λ_{max} at 340 nm, coupled with significant negative optical density below 300 nm (Fig. 1A). The bleaching signal is the negative of the spectrum of 4-methoxystyrene and arises from use of the precursor solution as the optical density reference. The absorbance changes measured immediately after the laser pulse at both 340 and 255 nm are linear in laser intensity, indicating the occurrence of a monophotonic process. The absorbance above 300 nm decays to essentially zero at all wavelengths with the same rate constant of $(3.9 \pm 0.3) \times 10^5$ s^{-1}. This implies a single transient, and we assign this to the 1-(4-methoxy-

© 1999 NRC Canada

Table 1. Absorption maxima and rate constants (20°C) for cumyl, phenethyl, benzyl and 1-phenylvinyl cations obtained by 248 nm laser flash photolysis.

Ar-subst.	R_1, R_2	λ_{max},[a] (nm)	k_{TFE} (s^{-1})	k_{HFIP} (s^{-1})	k_{nuc} (M^{-1} s^{-1})
Cumyl and phenethyl cations $ArC^+(R_1)$-CH_3[b]					
4-Me_2N[c]	Me	380	(1.5×10^2)[d]	$<10^2$	2.4×10^7 (N_3^-)[d]
4-Me_2N	H	360	(4.0×10^1)[e]	$<10^2$	1.6×10^7 (N_3^-)[e]
4-MeO	4-$MeOC_6H_4$	330 (w), 490	1.3×10^2	$<10^2$	8.2×10^8 (N_3^-)[f]
4-MeO	cycPr[g]	380	3.3×10^2	$<10^2$	2.5×10^9 (N_3^-)[f]
4-MeO	C_6H_5	320 (w), 440	5.1×10^2	$<10^2$	2.7×10^9 (N_3^-)[f]
4-MeO	i-Pr	365	3.0×10^3	$<10^2$	5.0×10^7 (Br^-)[h,i]
4-MeO	Et	365	9.0×10^3	$<10^2$	1.2×10^8 (Br^-)[h,i]
4-MeONap[j]	H	320, 420	7.5×10^3	$<10^2$	5.1×10^9 (N_3^-)[f]
4-MeO	Me	360	1.6×10^4 (4×10^7)[d,k]	$<10^2$	1.1×10^8 (Br^-)[h,i]
4-MeO	*t*-Bu	370	1.6×10^4	$<10^2$	2.2×10^8 (Br^-)[h,i]
H	Ph	310 (w), 420	1.5×10^5	3×10^2	2.1×10^9 (Br^-)[h]
3,4-$(MeO)_2$	H	345, 430 (w)	2.1×10^5	2×10^2	2.5×10^9 (Br^-)[h]
4-MeO	H	340	3.9×10^5	2×10^2	4.5×10^9 (Br^-)[h]
4-Me	Me	340, 380 (sh)	1.0×10^7	6×10^2	1.3×10^9 (Br^-)[l]
H	Me	325, 400 (w)	$>5 \times 10^7$	9×10^3	6.7×10^9 (Br^-)[l]
2,6-Me_2	H	315, 475 (w)	$>5 \times 10^7$	3×10^4	9.8×10^9 (Br^-)[l]
4-Me	H	325, 390 (w)	$>5 \times 10^7$	7×10^4[m]	7.1×10^9 (Br^-)[l]
4-F	H	320	$>5 \times 10^7$	2×10^5[m]	8.9×10^9 (Br^-)[l]
3-Me	H	320, 430 (w)	$>5 \times 10^7$	2×10^5[m]	9.7×10^9 (Br^-)[l]
H	H	315, 410 (w)	$>5 \times 10^7$	4×10^5[m]	8.2×10^9 (Br^-)[l]
3-MeO	H	335, 390 (sh)	$>5 \times 10^7$	5×10^5	5.8×10^9 (Br^-)[l]
Benzyl cations $ArCH_2^+$					
4-MeONap[j,n]		305, 400	1.8×10^5	—[o]	4.9×10^9 (N_3^-)[f]
4-MeO[n]		320, 360 (sh)	4.3×10^6	3×10^2	4.8×10^9 (Br^-)[l]
4-Me[p]		310, 410 (w)	$>5 \times 10^7$	2×10^6	1.0×10^{10} (Br^-)[l]
1-Phenylvinyl cations $ArC^+=CR_1R_2$					
4-MeO[q]	Ph, Ph	340	1.4×10^4	$<1 \times 10^2$	6×10^6 (Br^-)[h]
4-MeO[q]	Me, Me	330	2.3×10^5	$<1 \times 10^2$	2.2×10^8 (Br^-)[h]
4-MeO[r]	H, H	335	1.3×10^6	3×10^2	2.3×10^9 (Br^-)[h]
H[q]	Ph, Ph	310, 410 (w)	$>5 \times 10^7$	2×10^4	8.2×10^8 (Br^-)[l]
2,4,6-Me_3[r,s]	H, H	305, 420 (w)	$>5 \times 10^7$	4×10^4	4.8×10^9 (Br^-)[l]
4-Me[r]	H, H	315, 350 (sh)	$>5 \times 10^7$	3×10^5	9.2×10^9 (Br^-)[l]
H[r]	H, Ph	310, 390 (w)	$>5 \times 10^7$	6×10^5	1.1×10^{10} (Br^-)[l]
H[r]	H, H	295, 360 (w)	$>5 \times 10^7$	2×10^6	1.0×10^{10} (Br^-)[l]

[a] w = weak; sh = shoulder.

[b] Precursor unless otherwise noted is $ArC(R)=CH_2$.

[c] Precursor is 4-$Me_2NC_6H_4CMe_2CMe_2C_6H_5$.

[d] Solvent is 2:1 (v:v) water:acetonitrile. Note that a similar value for k_s is expected in pure water, since k_{decay} in water:acetonitrile does not vary a great deal with solvent composition (ref. 6).

[e] Solvent is 50:50 water:TFE.

[f] Solvent is 10:90 water:TFE.

[g] Cyclopropyl.

[h] In TFE.

[i] Addition of bromide is reversible.

[j] 4-Methoxy-1-naphthyl.

[k] Precursor is $(4\text{-}MeOC_6H_4CMe_2)_2$.

[l] In HFIP.

[m] Based on extrapolation to zero styrene concentration.

[n] Precursor is trimethylammonium BF_4^- salt.

[o] Not examined.

[p] Precursor is 4-$MeC_6H_4CH_2Cl$.

[q] Precursor is $ArC(Br)C=CH_2$.

[r] Precursor is $ArC\equiv CR_1$.

[s] Identical behavior from $ArC\equiv CH$ and $ArC(Cl)C=CH_2$.

© 1999 NRC Canada

Fig 1. Transient spectra following 248 nm laser irradiation of 0.1 mM 4-methoxystyrene (A) and 1 mM 1-(4-methoxyphenyl)ethyl acetate (B – D) in TFE. Spectra B – D were obtained on the same solution; B, at a laser dose of 6 mJ and with oxygen saturation, C, 6 mJ and with argon, and D, 75 mJ and with oxygen saturation. Spectrum A was obtained at 25 mJ and with argon saturation. This spectra was unchanged on saturating with oxygen. The spectra in C and D, and the initial spectra in A and B were obtained at 50–100 ns after the laser pulse. The final spectra in A and B were obtained at 25–30 μs.

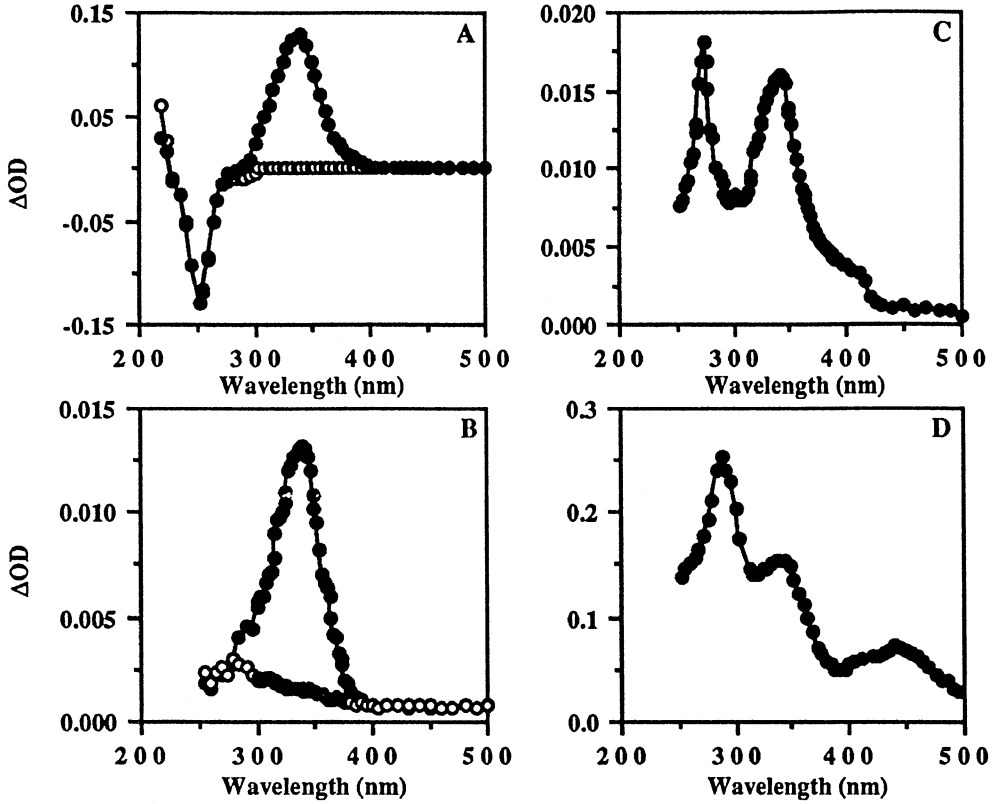

Scheme 2.

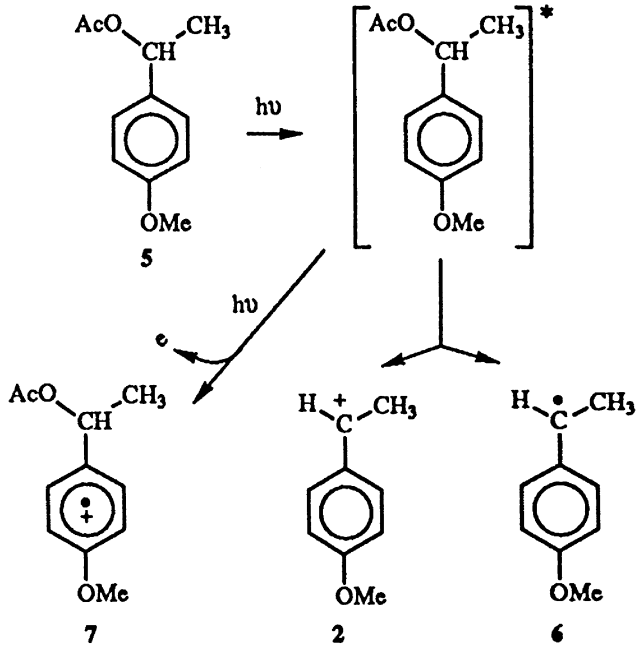

phenyl)ethyl cation **2** implicated by the Markovnikov ether photo-product **3**. The transient does exhibit kinetic behavior characteristic of carbocations (2), being quenched by nucleophiles such as bromide and azide, while oxygen has no effect.

Additional evidence is the observation of the same intermediate from a different precursor, 1-(4-methoxyphenyl)ethyl acetate **5** (Scheme 2). The photochemical reaction here is a photoheterolysis, and, as is typical of this route (2, 6), there are competing photo-reactions. Thus, as shown in Fig. 1C, irradiation of the ester results in two transients, the one with λ_{max} at 340 nm and a second at 275 nm. The former is the same as the transient from the styrene precursor. It has an identical spectrum, decays in TFE alone with the same rate constant, $(4.2 \pm 0.4) \times 10^5$ s^{-1}, and is quenched in an identical manner by bromide and azide ions. The 275 nm transient does not decay by exponential kinetics in argon-saturated solution and, while nucleophiles have no effect, oxygen is a very effective quencher. In fact, in the experiment in oxygen-saturated TFE, the 275 nm signal is no longer seen (Fig. 1B). This intermediate can be assigned as the 1-4-methoxyphenethyl radical **6**, the result of a competing photohomolysis. At higher laser doses additional absorbances appear: a band with λ_{max} near 295 nm and a second smaller broad peak at 400–500 nm. The 295 signal overlaps that of the radical but can be seen clearly in experiments with oxygen saturation (Fig. 1D). The two new bands appear to represent the same intermediate, since they decay with the same rate constant, with $k \sim 1 \times 10^5$ s^{-1}. A clue to the identity is the square dependence on the laser dose of the

© 1999 NRC Canada

Table 2. Effect of water on the irradiation of 4-methoxystyrene.

%(v/v) TFE	k_{decay} (s^{-1})	% Ether product	Initial OD (340 nm)[a]
100	4.0×10^5	100	1.00
95	1.5×10^6	90	0.85
90	3.6×10^6	80	0.70
80	6.3×10^6	40	0.60
70	9.6×10^6	Trace	0.50
60	1.3×10^7	0	0.40

[a]Relative to 100% TFE. This is equivalent to a relative quantum yield, since the measurements involve solutions of the same concentration of styrene being irradiated at 248 nm under identical conditions.

optical densities measured at 420 nm. This points to a biphotonic process, and suggests that this intermediate is the cation radical **7**, the result of a two-photon ionization. In fact the spectrum is that expected for the cation radical of an anisole derivative (20). The 340 nm transient on the other hand follows a linear dependence on laser intensity. Thus, as summarized in Scheme 2, the initial excited state, presumably the singlet, reacts to produce the cation and radical and, in competition, is further excited resulting in electron ejection. These experiments do not distinguish mechanisms for the formation of the cation and radical. There is the suggestion with benzyl carboxylates, including 4-methoxybenzyl acetate, that the primary event is photohomolysis with the cation being subsequently produced by electron transfer within the so-formed radical pair (21, 22).

A important feature with the styrene precursor is that there is no return of the absorbance below 300 nm as the cation decays back to the baseline above 300 nm. This is consistent with studies of thermal alkene additions that show that protonation in general is irreversible (23). In other words, the cation reacts predominantly by solvent addition, with little styrene being regenerated by elimination of a proton at the β-position.

As expected, addition of water significantly increases the rate constant for the decay of the cation. In addition, the alcohol **4** is produced at the expense of the ether (Table 2). Interestingly, the initial increase in rate constant is much greater than predicted on the basis of the amount of alcohol product. For example, 10% water results in only 20% of the alcohol product, but the rate constant for the decay of the cation is increased by almost 10-fold. This is consistent with a mechanism where, in addition to its direct nucleophilic combination, water accelerates the decay of the cation by acting as a general base to assist the TFE addition (24). Water also decreases the quantum yield for photoprotonation, as shown in the last column of Table 2. Coupled with the rate accelerating effect, this makes it increasingly difficult to study the cation in highly aqueous mixtures.

Substituted phenethyl cations by styrene protonation

In the same way, other phenethyl and cumyl cations are observed upon irradiation of the appropriate substituted styrene in TFE and (or) HFIP. Spectra of three cumyl cations and a naphthalene derivative are shown in Figs. 2 and 3A respectively. The other examples are available as supplementary material.[2] These show the same features discussed above for 4-methoxystyrene — a positive absorbance above 300 nm representing a single intermediate as shown by common decay kinetics across the entire spectrum,[3] effective quenching by bromide[4] and (or) azide ion, and bleaching due to depletion of the precursor. Spectra under stable ion conditions are available for the cumyl cation, λ_{max} = 326 and 390 nm (ε = 11 000 and 1400 respectively) and the 1,1-diphenylethyl cation, λ_{max} = 312 and 422 nm, (ε = 11 050 and 37 000 respectively) (25). The essentially identical spectra obtained here provide further confidence in the assignment of cation intermediates (see the spectrum for the cumyl ion in Fig. 2).

A further feature in common with 4-methoxystyrene is the lack of return of the bleaching as the absorbance of the cation decays. Thus the cations in general react by solvent addition. One exception is the 2,6-dimethylphenethyl cation where a competing deprotonation is indicated by the significant return of the precursor absorbance at the same rate constant as that obtained for cation decay. This aspect of 2,6-dimethyl systems has been recently demonstrated in a study of solvolysis of cumyl derivatives (26). While solvent addition is retarded by the steric effect of the *ortho* substituents, the rate constants for elimination are actually increased relative to analogs without the 2,6-dimethyl groups (26).

Styrene dimerization

The other exception occurs in HFIP with styrene and its 3- and 4-substituted derivatives. One indication of the difference is that the rate constants depend on the precursor concentration. This dependence is linear (eq. [1]), implicating a reaction of unphotolyzed precursor with the cation. With the

[2] Supplementary material may be purchased from: The Depository of Unpublished Data, Document Delivery, CISTI, National Research Council Canada, Ottawa, Ontario, Canada, K1A 0S2.

[3] The one exception is α-*tert*-butyl-4-methoxystyrene, where the decay requires fitting to a double exponential, with rate constants of 7×10^5 and 1.6×10^4 s^{-1}. The spectrum of the intermediate responsible for the slow decay, obtained at longer times when the faster one is complete, shows a λ_{max} of 370 nm. This is assigned to the α-*tert*-butyl-4-methoxyphenethyl cation on the basis of the close similarity with the spectra of the other α-alkyl-4-methoxyphenethyl derivatives. The faster decaying transient has its λ_{max} between 330 and 340 nm and has not been identified.

[4] With some of the cations, bromide addition shows reversible behavior. This has been seen previously (5) and occurs when the ionization of the bromide product has a rate constant similar to the quenching rate constant. With the very stable cations where ionization of the C—Br bond becomes faster than nucleophile–cation combination, bromide does not react at all. These cations are still quenched by azide ion.

© 1999 NRC Canada

Fig. 2. Spectra of cumyl cations 4-$XC_6H_4C^+(CH_3)_2$ obtained upon 248 nm laser irradiation of ~0.1 mM solutions of 4-$XC_6H_4C(CH_3)=CH_2$ — (A) X = H in HFIP, (B) X = Me in HFIP, and (C) X = MeO in TFE. ΔOD values have been adjusted so that the maximum is 0.1 in each case.

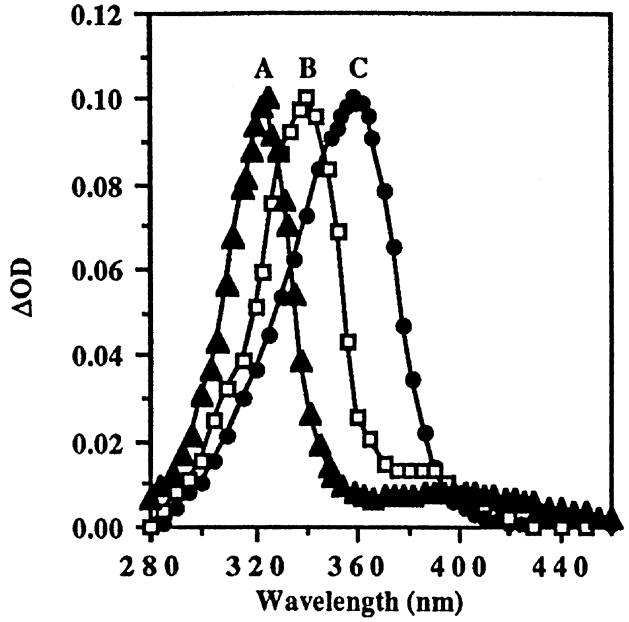

Table 3. Rate constants (20°C) for the reaction of phenethyl cations X-$C_6H_4CH^+$-CH_3 with the styrene X-$C_6H_4CH=CH_2$ in HFIP.

X	k^1_{sty} (M^{-1} s^{-1})
H	1.0×10^9
3-Me	9.4×10^8
4-F	4.3×10^8
4-Me	3.4×10^8
4-MeO	1.3×10^6

Fig. 3. Transient spectra following 248 nm irradiation of ~0.0001 M 4-methoxy-1-vinylnaphthalene (A) and 4-methoxy-1-napthylmethylammonium acetate (B) in argon-saturated TFE. Data points were obtained immediately after the laser pulse and at the completion of the exponential decay.

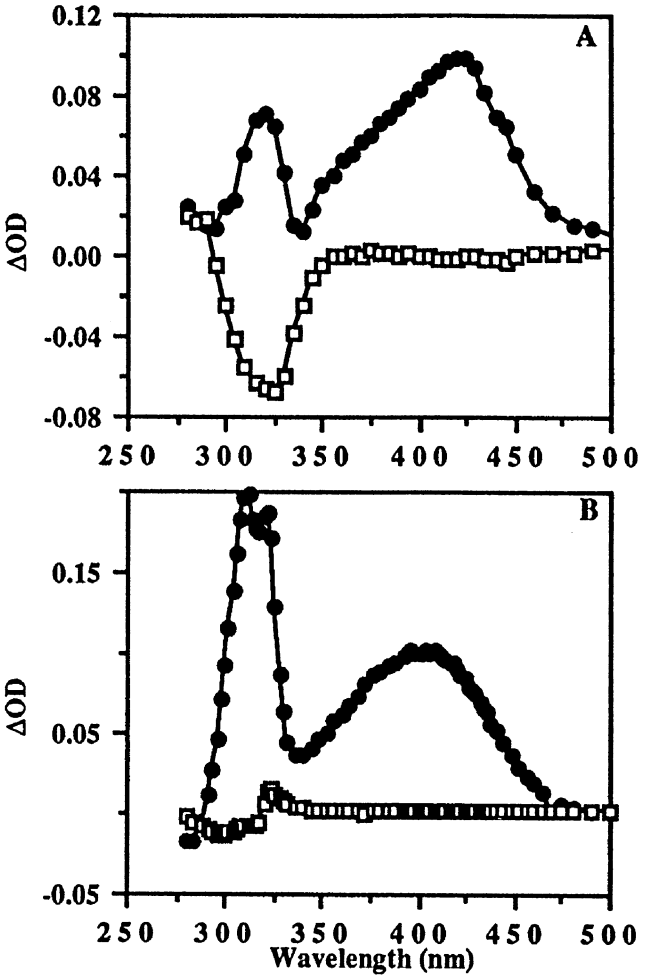

assumption (see Experimental) that the concentration of styrene is effectively unchanged in the laser pulse, the slopes of these plots (Table 3) are the second-order rate constants for the dimerization. The intercepts are the rate constants for the solvent reaction (the numbers in Table 1 for these cations).

$$[1] \qquad k_{obs}/s^{-1} = k_{HFIP} + k^1_{sty}[ArCH=CH_2]$$

Spectral changes provide further evidence. Figure 4 shows an example where dimerization dominates and a high laser intensity is employed to provide strong signals. After the initial "prompt" bleaching at 240 nm, there is a further exponential decay occurring at the same rate as at the higher wavelengths. Thus additional styrene is reacting. Moreover as the cation decays, a new species appears. There is considerable overlap, but it is clear that this absorbs at a slightly higher wavelength, with a λ_{max} around 345 nm for the product in Fig. 4. Similar observations are made with the other $ArCH=CH_2$, with a shift of ~20–30 nm in each case. The new absorbance is much more stable than the original one but there is decay at very long times, for example, with styrene (at 340 nm) with a rate constant of ~0.1 s^{-1}. (This is only approximate because of detector instability at very long times).

A similar situation has been observed for cations generated in strong acid solution. For example, when styrene is added to 98–100% sulfuric acid, the species observed is the bis-styryl cation, not the initially-formed phenethyl cation (27, 28). With α-methylstyrene, the cumyl cation is sufficiently stable to be seen, but it is not stable, reacting to give a new, long-lived, species with a higher λ_{max} identified as the bis-cumyl cation (27, 28). In a similar manner, we propose that phenethyl cations **9**, when generated by styrene photoprotonation in HFIP, react in part with residual styrene forming much more stable bis-styryl cations **10** (Scheme 3).

The dimerization is obviously the first step in the propagation sequence of the acid-initiated polymerization of styrenes. The dimer ions **10** in fact appear similar to the oligomeric **11** that have been detected during polymerization. With styrene, for example, the propagating cation has a λ_{max} of 340 nm (29, 30), the same as the cation **10** (X = H) observed in this work. One interesting observation is that the monomer ions **9** have a slightly slower λ_{max}. A possible explanation is that

© 1999 NRC Canada

Fig. 4. Transient spectra following 248 nm irradiation of 0.0004 M 4-methylstyrene in HFIP. The open circles were obtained immediately after the laser pulse and the closed circles at the completion (40 μs) of the exponential process. The other two traces were obtained at intermediate times. The Inset shows the absorbance change at the three indicated wavelengths. The rate constants (s^{-1}) are 1.6×10^5 (240 nm), 2.0×10^5 (320 nm) and 1.85×10^5 (360 nm).

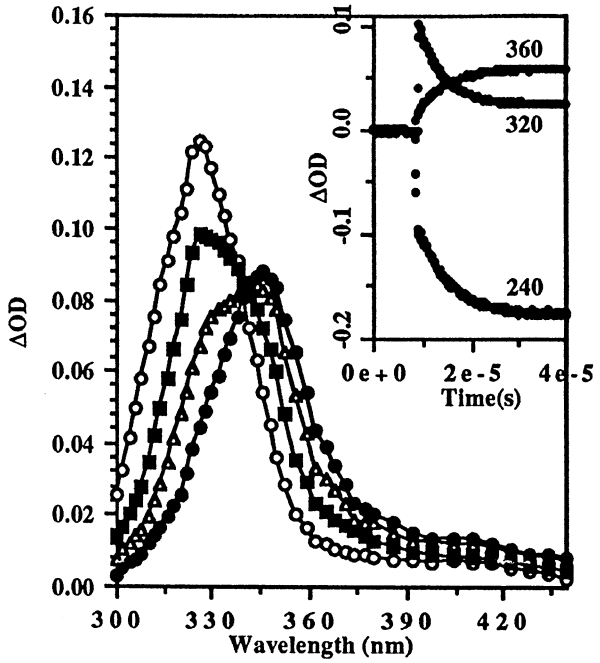

in **10** and **11** there is an interaction of the aryl group at the γ carbon with the positive charge at the α-carbon, as shown in structures in Scheme 3. Another interesting feature is that the dimer cation is much more stable than the monomer. This is also true of the oligomer. The rate constant for styrene propagation (k_{sty}^{pr} of Scheme 3) is ~10^5 M^{-1} s^{-1} at 20°C (29, 30), four orders of magnitude slower than the rate constant k_{sty}^{1} for the phenethyl cation reacting with styrene. It is interesting that the difference in stability between phenethyl and dimer/oligomer cations was suggested in 1968, and the interaction with the adjacent phenyl group in the latter proposed as the explanation (27).

We can be confident that it is the dimer cation **10** being observed at the end of the exponential process in the LFP experiments, and not an oligomer. One argument is based on the observation (Fig. 4) that the "slow" decay of styrene follows clean exponential kinetics, moreover reaching a stable absorbance at the completion of the change. If styrene were continually adding to a growing oligomeric cation, one would have expected a downward drifting absorbance. The other argument is that subsequent reactions with styrene are much slower than the first one, as discussed above. In other words, the reaction of the dimer cation with further styrene occurs on a much longer time scale than the initial reaction. Experimental limitations unfortunately preclude observation at long times at the lower wavelengths, i.e., where further depletion of styrene would be observed.

Cumyl cations do not show any sign of reacting with the residual α-methylstyrene in HFIP. This would appear to be a

Scheme 3.

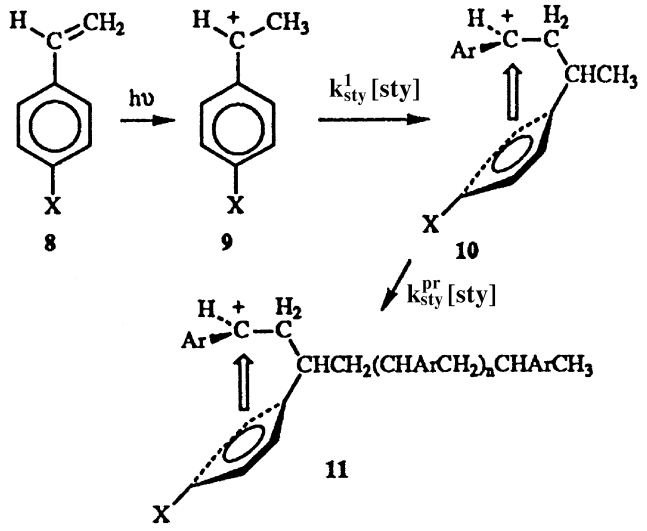

steric effect, since the reactivities of both the cation and the nucleophile are not that different from the those in the $ArCH{=}CH_2$ series. There is no dimerization with any of the cations in TFE. Here the more nucleophilic solvent can successfully compete with the low concentrations of precursor.

Benzyl cations

Styrene photoprotonation cannot be applied for the generation of $ArCH_2^+$; therefore we were forced to return to photoheterolysis. For 4-methoxybenzyl, both chloride and trimethylammonium (BF_4^- salt) precursors give a transient that can be assigned to the cation, although the former is limited to TFE solutions containing greater than 50% acetonitrile because of rapid ground state solvolysis. The cation is identified by several criteria. Its λ_{max} (320 nm, Fig. 5A) fits in a comparison with the 4-methoxyphenethyl (340 nm) and 4-methoxycumyl (360 nm) cations. The decay kinetics are typical of cations, a very efficient quenching by bromide, and a large difference between HFIP and TFE (Table 1). The same transient is observed with the two precursors, with the same decay rate constant, 9.0×10^6 s^{-1} and 8.6×10^6 s^{-1} for the chloride and ammonium salt respectively in 1:3 TFE:acetonitrile. Finally, product analysis following irradiation of the ammonium salt in TFE shows the presence of 4-methoxybenzyl 2,2,2-trifluoroethyl ether, the product derived from trapping of the cation by solvent. The other product formed in about the same amount is 4-methylanisole. This indicates the presence of a radical intermediate as well (31, 32), and, in argon-saturated solvents, LFP of both precursors shows a large band with λ_{max} at 290 nm, presumably due to the 4-methoxybenzyl radical. With 4-methoxybenzyl acetate in TFE, only the 290 absorbance of the radical is seen at low laser doses, while, like the phenethyl analog, absorbance for a cation radical dominates at higher intensities. Thus, this precursor results in so little cation that the intermediate cannot be detected in competition with the other pathways. In fact, 4-methoxybenzyl acetate is known to result in only low yields of photosolvolysis product when irradiated in alcohol solvents (22, 33).

© 1999 NRC Canada

Fig. 5. Transient spectra following 248 nm irradiation of ~0.001 M 4-methoxybenzyl chloride (A) and 4-methylbenzyl chloride (B) in oxygen-saturated 1:3 TFE: acetonitrile and HFIP respectively. Triangles are the ΔOD immediately after the laser pulse, and squares, ΔOD at the completion of the exponential decay that is observed. The crosses are the difference in the two.

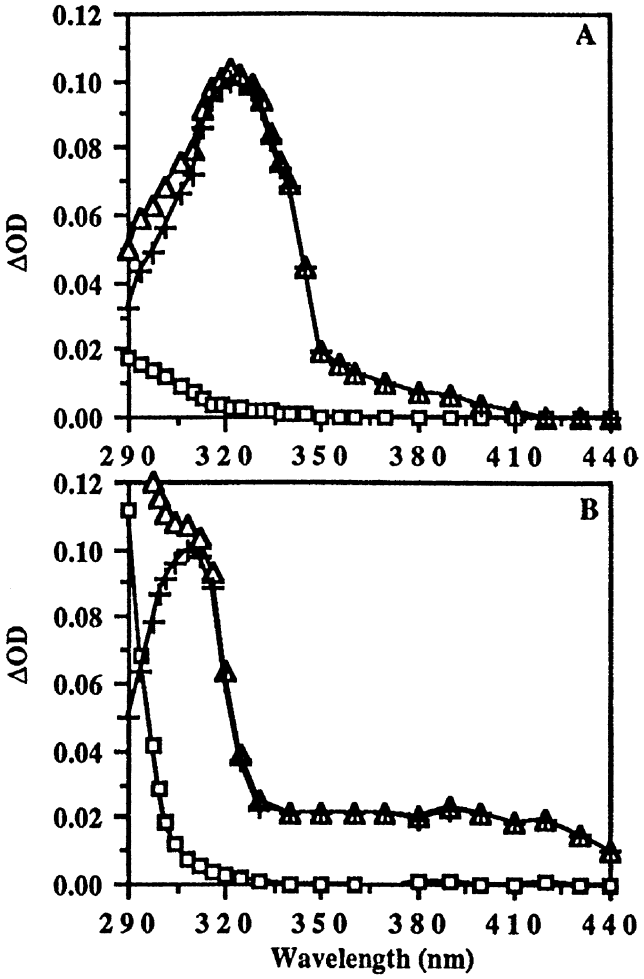

As shown in Fig. 3B, the 4-methoxy-1-naphthylmethyltrimethylammonium ion gives a strong signal that can be assigned to the primary cation. The evidence here is the efficient quenching by nucleophiles and the close similarity with the secondary cation obtained by photoprotonation. There is little indication of the presence of radical intermediate, as shown by very similar spectra being obtained under argon and oxygen.

For the 4-methylbenzyl cation, the chloride could be used as a precursor in HFIP. Spectra in oxygen-saturated solvent are shown in Fig. 5B. Below 300 nm a large non-decaying band of uncertain origin is observed. A shoulder above 300 nm does decay in an exponential fashion. By taking the difference between the initial and final absorbances, this species is found to have a λ_{max} of 310 nm with a weaker absorbance extending out above 400 nm. As will be discussed, this fits the expectation for this cation. The absorbance at 310 is quenched by bromide ion, with the ratio k_{Br}:k_{HFIp} equal to 5.0×10^3 M^{-1}. This allows for confirmation that this is due to the cation, through a comparison

Scheme 4.

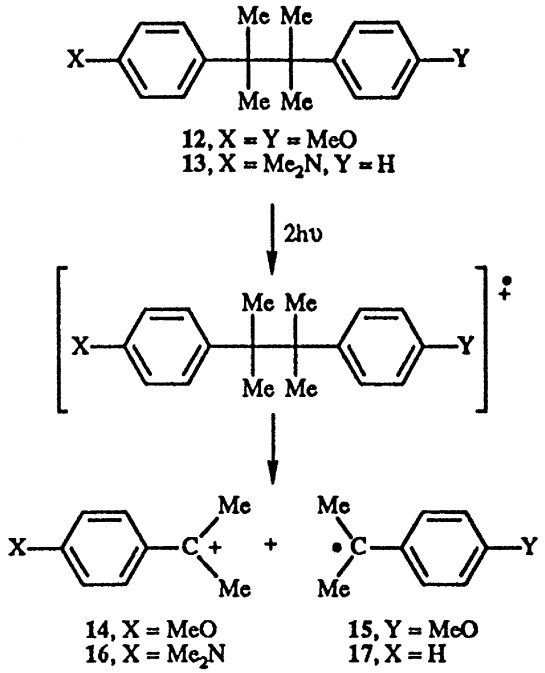

Table 4. Rate constants at 25°C for the solvolysis of 4-methylbenzyl bromide (20 μM) in HFIP in the presence of tetrabutylammonium bromide.

$[Bu_4N^+ Br^-]$	k_{solv} (s^{-1})
0	2.01×10^{-4} [a]
0.0003	8.26×10^{-5}
0.0006	5.15×10^{-5}
0.0009	3.92×10^{-5}
0.0012	2.94×10^{-5}
0.0015	2.32×10^{-5}

[a]Based on initial rate.

with a ratio obtained from the kinetics of ground state solvolysis of 4-methylbenzyl bromide in HFIP. As shown in Table 4, added bromide results in significant common ion inhibition. By fitting to $k_{solv} = k_{ion}$:$(1 + k_{Br}$:$k_{HFIP}[Br])$, k_{Br}:k_{HFIP} is found to be $(4.8 \pm 0.2) \times 10^3$, the same number obtained from the transient spectroscopy.

All attempts to generate detectable amounts of the parent benzyl cation in HFIP failed to provide any evidence of the cation. Precursors of benzyl chloride, benzyl bromide and benzyl acetate were employed. There were transients, but these could be attributed to radicals, or products from the radicals. A comparison of the 4-H and 4-Me derivatives in the phenethyl and cumyl series (Table 1) suggests that the benzyl cation is at least an order of magnitude more short-lived than 4-methylbenzyl. Thus the lifetime of $PhCH_2^+$ in HFIP is less than 50 ns. Even if this were the lifetime, the cation would be very difficult to detect unless the photochemical route to it was very efficient.

Radical cation fragmentation

By using photoprotonation, the 4-methoxycumyl cation can be studied in aqueous TFE until about 70% water is

© 1999 NRC Canada

Fig. 6. Transient spectra following 248 nm irradiation of 4-dimethylaminobiscumene **13** in oxygen-saturated 2:1 water:acetonitrile. Closed circles obtained immediately after the laser pulse are attributed to the cation radical $\mathbf{13}^{+\bullet}$. Open circles obtained near the end of the completion of the exponential decay are due to the 4-dimethylaminocumyl cation **16**. Rate constants measured at 275, 380 and 500 nm are respectively 8.8×10^4, 1.12×10^5, and 1.03×10^5 s^{-1}, respectively.

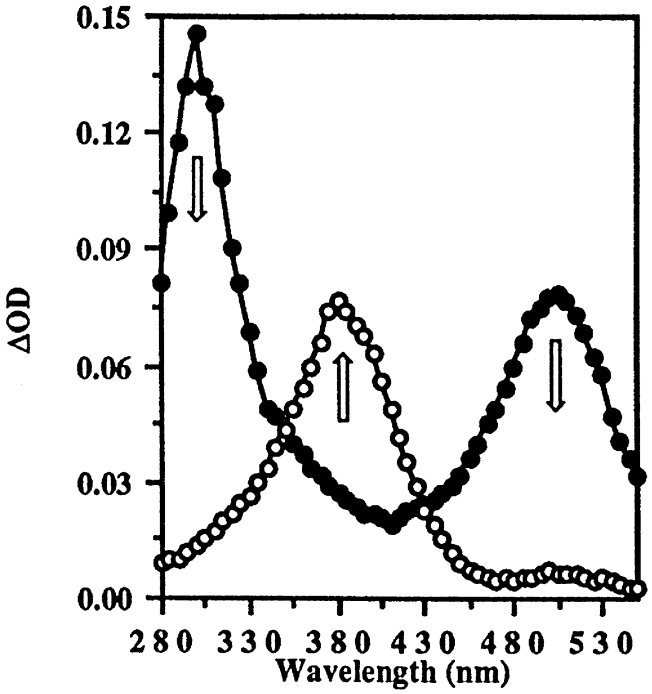

present. At this point the cation decays with a rate constant of 7.9×10^6 s^{-1}, still below the 20 ns limit. However, the amount of intermediate being produced upon irradiation is so small that further increases in water content are not possible. To obtain a water rate constant, we turned to bis-4-methoxycumene **12** as a precursor (Scheme 4). The photochemistry here involves a two photon ionization to the cation radical, which fragments within the laser pulse to cation **14** and radical **15** (34). With 2:1 water:acetonitrile as solvent, the cation can just be detected, with a decay of $\sim 4 \times 10^7$ s^{-1}. While the acetonitrile is required in this experiment to dissolve the precursor, a similar decay is expected in pure water, because rate constants in water:acetonitrile do not vary a great deal with solvent composition (6).

The very stable 4-dimethylaminocumyl cation is generated from the biscumene **13** in the same water:acetonitrile mixture. In this case the cation radical is much more stable so that it is this species that is present after the laser pulse, and the fragmentation occurs on the microsecond time scale (Fig. 6). This observation has been reported previously (35), although the fragmentation of $\mathbf{13}^{+\cdot}$ in the aqueous solvent of the present study is significantly faster than that for the same cation radical in solvents previously used. The 4-dimethylaminocumyl cation can be observed to grow in as the cation radical decays. This has a λ_{max} at 380 nm (382 nm, ref. 35), and a lifetime in the aqueous solvent of 7 ms.

Fig. 7. Spectra of vinyl cations $4\text{-}XC_6H_4C^+{=}CH_2$ obtained upon 248 nm laser irradiation of ~0.1 mM solutions of $4\text{-}XC_6H_4C{\equiv}CH$ — (A) X = H in HFIP, (B) X = Me in HFIP and (C) X = MeO in TFE. ΔOD values have been adjusted so that the maximum is 0.1 in each case.

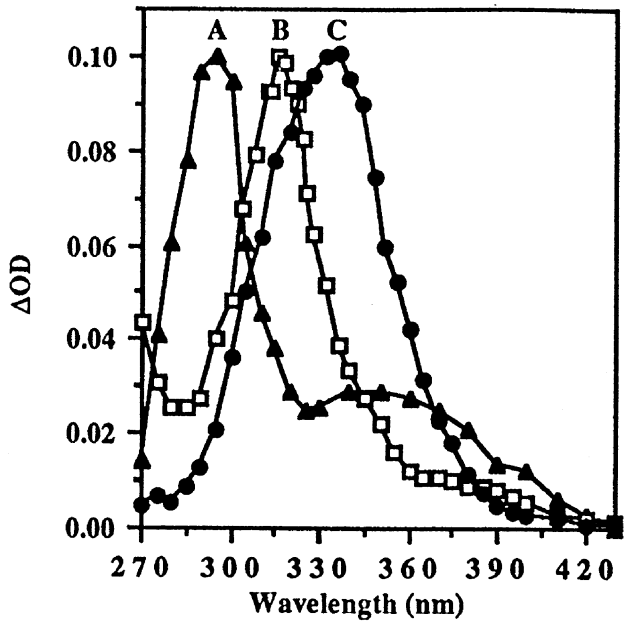

Scheme 5.

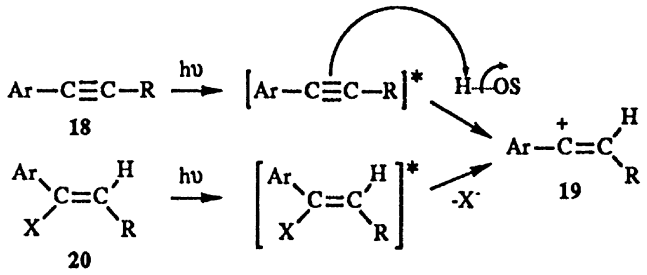

Phenylacetylenes as precursors of vinyl cations

Laser flash photolysis of *p*-methoxyphenylacetylene in both TFE and HFIP, and *p*-methylphenylacetylene, 2,4,6-trimethylphenylacetylene, diphenylacetylene, and phenylacetylene itself in HFIP results in transient spectra (see Fig. 7) that can be assigned to vinyl cations produced by photoprotonation (Scheme 5). With each precursor, there is a single intermediate, as shown by the absorbance above 300 nm decaying to near zero with the same rate constant at all wavelengths. Nucleophiles such as bromide ion have a pronounced quenching effect, evidence that these are cations. Vinyl cations, usually with two substituents on the β-carbon, have been produced in the past by photoheterolysis of halide precursors (36–39). As seen in Table 1, the 1-(4-methoxyphenyl)vinyl cation produced from the acetylene has a similar λ_{max} to that of the 2,2-dimethyl analog produced from the bromide. Even more compelling is the case of the 2,4,6-trimethylphenyl derivative, where the same cation was produced in the two different ways. Like styrenes, substituted phenylacetylenes have been shown to undergo photo-

© 1999 NRC Canada

Fig. 8. Substituent effect on the λ_{max} for benzyl, phenethyl, cumyl, 1-phenylvinyl, and 2,2-diphenyl-1-phenylvinyl cations. See text for explanation of *x* axis. Lines have been drawn with a slope of unity.

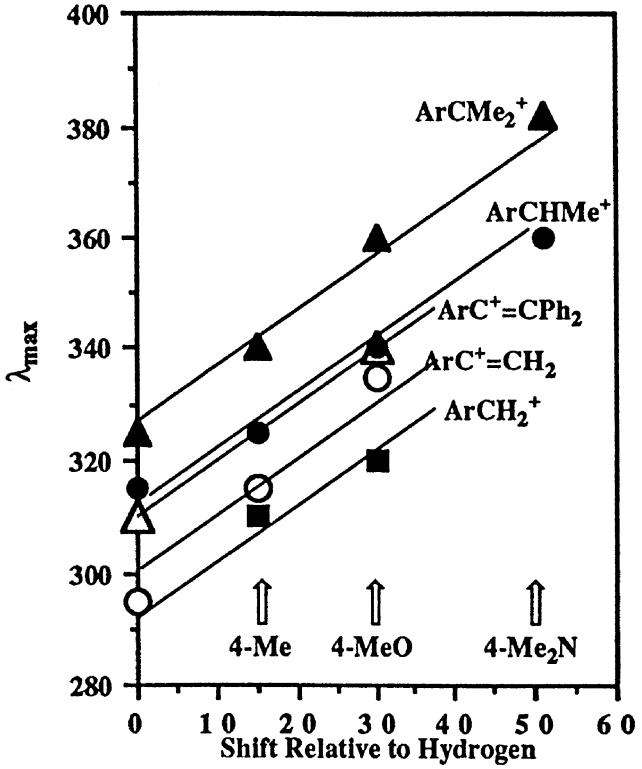

hydration in aqueous acids, with the ultimate product an acetophenone (17, 18). Flash photolysis investigations have revealed the presence of the enol intermediate (40–42), the immediate product of the hydration of the vinyl cation. The cations themselves were not detected. As discussed above, they would be too short-lived in water for detection by ns LFP.

Absorption maxima

Substituents affect λ_{max} in the order H < 4-Me < 4-MeO < 4-Me_2N. The effect is essentially the same for a given type of cation with, on average, a shift relative to H of 15 nm for 4-Me, 30 nm for 4-MeO, and 50 nm for 4-Me_2N. This is demonstrated in Fig. 8 where the observed λ_{max} are plotted against these factors. Recognizing that λ_{max} is only determined to ±5 nm, the correlations are excellent. Also apparent from this figure are the similar λ_{max} values for the vinyl and benzylic series. This was previously commented upon in a comparison of the 4-methoxy-substituted ions (15). In an arylvinyl cation, the π systems of the aryl ring and the alkene are orthogonal to one another (43). Thus the aryl ring interacts with the formally empty *p* orbital on the α-carbon in exactly the same way as it does in a benzylic cation.

For the same aryl group, the order of λ_{max} is $ArCH_2^+$ < $ArCHMe^+$ < $ArCMe_2^+$, with about a 20 nm difference between each pair. A weaker absorbance at higher wavelength is also apparent with some of the systems. The trend appears to be exactly opposite that of the larger absorbance at lower wavelength, and this is true both in terms of the aryl substituent and the α-methyl substituents. In fact the band at higher wavelength is usually not visible for the 4-MeO and 4-Me_2N substituted cations.

There has been some question as to the spectrum of the parent benzyl cation. An early theoretical calculation showed bands at 400–500 nm and 300 nm, with the latter being significantly stronger (44). This paper also suggested that a report of the benzyl cation in strongly acidic solutions (45) was incorrect. In agreement with the more intense absorbance, a band at 290 nm assigned to the cation was observed in an experiment involving photodissociation in a mass spectrometer (46). A more recent pulse radiolysis experiment in neat benzyl chloride is also in agreement, suggesting a strong band at 303 ± 2 nm and a weak band near 500 nm (47). In contrast, there have been several assignments to the benzyl cation where the λ_{max} is around 360 nm. These are based upon experiments by Dorfmann and coworkers who claimed to have generated the benzyl cation by pulse radiolysis in chlorocarbon solvents (48–50). The basis of this assignment was quenching of the observed transient by nucleophiles, and the fact that the approach does work for the triphenyl- and diphenylmethyl cations. A similar band was then observed and assigned to the benzyl cation following photoionisation of benzyl bromide in an argon matrix (51), and upon photolysis of dibenzyl ketone in vacuum-dried Nafion membranes (52).

While the parent cation has not being observed in this work, the data in Table 1 clearly shows that it must have λ_{max} around 300 nm with a weaker absorbance extending into the visible spectrum. This is in agreement with the first set of results discussed in the previous paragraph. The ~360 nm transient cannot be the benzyl cation. The pulse radiolysis approach requires fragmentation of a cation radical and we suspect that under the conditions employed by Dorfman and coworkers this is not occurring. In fact this is exactly what happens when precursors of the 9-fluorenyl cation are employed; there is no fragmentation and the intermediate that is observed is the cation radical of the precursor (13). Based on estimated pK_R values, the 9-fluorenyl cation is more stable than benzyl (53). Thus, if the approach does not work for 9-fluorenyl it is unlikely to have worked for benzyl. It can also be noted that the nucleophilic reactivities of the 360 nm transient have been criticized as not being appropriate for the benzyl cation (54). As a final comment, we note that even in those cases where the ~300 nm absorbance for the benzyl cation has been observed, this is clearly not the only species present. In other words there has not yet being a study showing a clean spectrum of this cation.

Substituent effects on rate constants

(a) Vinyl vs. phenethyl cations

As was noted previously in the case of the 4-methoxy derivatives (15) there is remarkably little difference in the lifetime of a vinyl cation $ArC^+=CH_2$ relative to that of a phenethyl cation $ArC^+H\text{-}CH_3$ with the same aryl group. The vinyl cation is slightly more reactive, but the differences are only 3.3 (TFE) and 1.4 (HFIP) for Ar = 4-$MeOC_6H_4$, 4.4 for 4-MeC_6H_4 in HFIP, and 2.5 for C_6H_5 in HFIP. As with the explanation for the similar spectra, this is consistent with the idea that the aryl ring interacts with the *p*-orbital on the α-carbon in exactly the same way in the two series.

© 1999 NRC Canada

Fig. 9. Correlation of log k_{TFE} for 4-$MeOC_6H_4C^+(R)CH_3$ vs. $E_s(R)$.

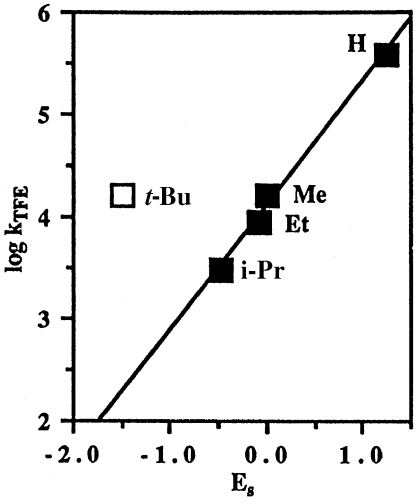

(b) α-Alkyl effects

For a given aryl group the rate constant for solvent addition follows the expected order cumyl < phenethyl < benzyl. Interestingly, the second methyl group exerts a greater kinetic stabilization than the first. In the 4-methoxy series in TFE, for example, there is a 11-fold difference between benzyl and phenethyl, but this increases to 24-fold for phenethyl and cumyl. The same comparisons for the 4-Me cations in HFIP lead to ratios of 28 and 120. This suggests that it is unlikely that it is electron donation alone that is important. A steric effect would account for the difference, the second methyl group increasing the steric bulk around the α-carbon to such a degree that nucleophilic addition is hindered to an extent greater than that of the first methyl substitution.

While there is insufficient data to perform a detailed breakdown into steric and electronic contributions, steric effects are clearly important. As shown in Fig. 9, there is a good correlation of the data for 4-methoxyphenethyl cations in TFE against the Taft steric parameter E_s, and this includes the point for the secondary cation. The correlation against the polar parameter σ^* is marginally poorer. In particular, this requires a difference in rate constant smaller than the one observed between i-Pr and Et.

An additional steric effect is probably responsible for the deviation of the point for the *tert*-butyl derivative. In this case, unfavorable interactions between the *ortho* hydrogens and the *tert*-butyl group twist the aryl ring, diminishing the resonance interaction with the *p* orbital on the α carbon. In fact MM2 calculations indicate a twist of 80 degrees. This argument is reinforced by the slow rate of solvolysis of 3,3-dimethyl-2-phenyl-2-chlorobutane, which has also been attributed to steric inhibition of resonance (55).

(c) Cyclopropyl versus phenyl

While an α-cyclopropyl group on a carbocation is strongly stabilizing, there has been some dispute whether the effect is greater or less than that of phenyl (56). In terms of the reactivities of fully-formed cations, a series $ArCH^+$-R where R = phenyl and cyclopropyl have been compared by LFP in TFE (57). For a given Ar, the reactivities are similar. However the phenyl series shows a greater effect of changing substituents in Ar. The result is that the cyclopropyl cation is slightly more stable (kinetically) when Ar is phenyl, but less stable when Ar is 4-methoxyphenyl.

The difference in the latter comparison is a factor of 10 (**21** vs. **22** in Scheme 6). Interestingly, the methylated analogs **23** and **24** studied in this work show a slightly greater stabilization (1.5-fold) for the cyclopropyl system. This can be traced to the substitution of α-hydrogen with methyl resulting only in a threefold rate constant diminution in the diarylmethyl cation, but a 42-fold diminution in the arylcyclopropyl pair. We attribute this to steric inhibition of resonance in the former. In these cations, maximum stabilization occurs when both aromatic rings are fully planar with the plane of the α-carbon. We suspect that methyl substitution results in additional twisting, so that while there is electronic and steric stabilization due to the methyl group, this is compensated by some loss of resonance interaction. The steric problem is not as severe in the cyclopropyl series, since the cyclopropyl is perpendicular to the π system.

Table 5. Values of ρ^r, ρ^n, and r^+ obtained by fitting rate constants for solvent capture of 1-arylethyl cations to eqs. [2] and [3].

Parameter	HFIP	TFE:water[a]
ρ^r	4.7	6.1
ρ^n	2.7	2.7
r^+	1.7	2.3

[a]Reference 58, as corrected in ref. 14.

Scheme 6.

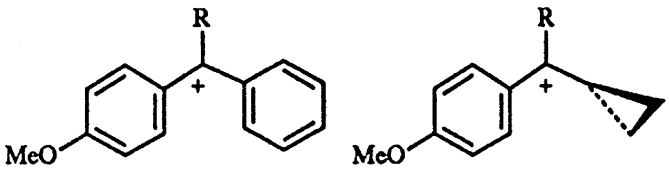

21, R = H, $k_{TFE} = 1.5 \times 10^3$ **22**, R = H, $k_{TFE} = 1.4 \times 10^4$
23, R = Me, $k_{TFE} = 5.1 \times 10^2$ **24**, R = Me, $k_{TFE} = 3.3 \times 10^2$

(d) Aryl substituent effects

Since the initial studies of Richard et al. (58) it has been known that rate constants for solvent capture of benzylic carbocations do not correlate with σ^+, as might have been expected. This has been observed now with several systems (2). What occurs is that σ^+ considerably underestimates the stabilizing effect of *para* π-donors like 4-methoxy. This is revealed by fitting to the two parameter Yukawa–Tsumo equation (eq. [2]), where r^+ values significantly greater than 1 result. Fitting to the modified eq. [3] (18), ρ_r is found to be larger than ρ_n.

$$[2] \qquad \log (k/k_o) = \rho\{\sigma + r^+(\sigma^+ - \sigma)\}$$

$$[3] \qquad \log (k/k_o) = \rho_n\sigma^n + \rho_r(\sigma^+ - \sigma^n)$$

The study of Richard et al. (58) actually involved 1-arylethyl cations, with the rate constants being obtained through use of the azide-clock method in 1:1 TFE:water as solvent. Six

© 1999 NRC Canada

such cations were studied directly in HFIP in this work (Table 5). A comparison of the parameters obtained by fitting to the above equations is given in Table 5. Since the two series do not involve the same substituents, and, moreover, since there are a limited number of substituents in each, the two sets of parameters can be regarded as being equivalent. This is perhaps surprising since the cations are 10^6-fold less reactive in HFIP.

(e) Styrene dimerization

For the reaction of a substituted phenethyl cation with its precursor styrene, there is a decrease in rate constant with increased electron donation (Table 3). Because of the manner in which this experiment is performed, the substituent is changing in both the electrophile and the nucleophile, and thus there will be compensating effects. Increased electron donation will stabilize the cation but at the same time increase nucleophilicity of the styrene. What the data show is that the former is more important. This is consistent with studies of benzylic-type cations where data are available for the reaction in both the formation and decay directions, in particular the finding that there is imbalance in the reaction coordinate (2, 58). In the direction where the cation is the reagent, the resonance interaction has decreased at the transition state to a greater extent than bond making. The reverse is true in the direction forming the cation, where the developing resonance interaction in the cation lags. In the present case, it can be seen that a benzylic-type cation (**9** in Scheme 3) is being replaced by a benzylic-type cation (**10**) where the positive charge is stabilized by the same aryl group. What we argue is that in the transition state, the resonance interaction in the reagent cation has diminished to a greater extent than the resonance interaction in the product cation that has developed. Thus, in changing from styrene to 4-methoxystyrene, the stabilizing effect of the 4-methoxy group is more important in the starting cation than it is in on the developing cation in the transition state. Thus, the initial state is stabilized more than the transition state and the reaction is slower.

Experimental section

TFE and HFIP were dried over 4 Å molecular sieves and distilled under nitrogen through a 40 cm Vigreux column prior to use. Water was purified with a Millipore-Q system. The nucleophiles tetrabutylammonium bromide and sodium azide were used as received.

Table 6 provides the precursors that were employed and their sources. In most cases the compounds were commercially available or were prepared by a literature method. Where the compounds were solids the mp was in agreement with values in the literature. The ^{1}H NMR spectra were in all cases fully consistent with the structure.

4-Methoxy-1-vinylnapthalene was prepared from 4-methoxy-1-napthaldehyde by reacting Tebbe's reagent following standard procedures (77–79). ^{1}H NMR ($CDCl_3$) δ (ppm): 3.99 (s, 3H), 5.33–5.39 (dd, 1H), 5.64–5.74 (dd, 1H), 6.79 (dd, 1H), 7.32–7.57 (m, 2H), 8.04–8.32 (m, 4H). HRMS: 184.0886 (calcd.: 184.0888). Anal. calcd.: C 84.75, H 6.56; found: C 84.70, H 6.60.

α-Isopropyl-4-methoxystyrene was prepared by reacting Tebbe's reagent with 2-methyl-4′-methoxyacetophenone. ^{1}H NMR ($CDCl_3$) δ (ppm): 1.10 (d, 6H), 2.82 (sept., 1H), 3.82 (s, 3H), 4.97 (dd, 1H), 5.10 (dd, 1H), 6.86 (d, 2H), 7.31 (d, 2H). Elem. anal. calcd.: C 81.77, H 9.15; found: C 81.44, H 9.02.

4-Methoxybenzyl 2,2,2-trifluoroethyl ether was prepared by adding 4-methoxybenzyl chloride to 2,2,2,-trifluoroethanol containing pyridine. After removal of the solvent, the residue was taken up in ether, washed with water, dilute HCl, and water. The ether was dried over $MgSO_4$, and after filtering to remove the drying agent, the solvent removed. ^{1}H NMR ($CDCl_3$) δ (ppm): 3.75 (q, 2H), 3.79 (s, 3H), 6.90 (d, 2H), 7.28 (d, 2H). EIMS (70 ev), *m*/*z*: 220 (30%, M^+), 189 (8%, $M^+ - OCH_3$), 135 (12%, $M^+ - CH_2CF_3$), 121 (100%, $M^+ - OCH_2CF_3$).

4-Methoxyphenethyl 2,2,2-trifluoroethyl ether was prepared by irradiating a solution of 4-methoxystyrene in 2,2,2-trifluoroethanol until there was no more styrene left. The ether was isolated as described in the previous paragraph. ^{1}H NMR ($CDCl_3$) δ (ppm): 1.45 (d, 3H), 3.65 (q, 2H), 3.81 (s, 3H), 4.56 (q, 1H), 6.90 (d, 2H), 7.28 (d, 2H). EIMS (70 ev), *m*/*z*: 234 (32%, M^+), 219 (100%, $M^+ - CH_3$), 135 (80%, $M^+ - OCH_2CF_3$).

Laser flash photolysis experiments were carried out with equipment in Mulheim and in Toronto. The carbocation precursors were photolyzed with 20 nanosecond pulses, typically of 30 mJ, of 248 (KrF^*) or 308 nm ($XeCl^*$) monochromatic light. A pulsed Xenon light provided the monitoring beam. This was passed through the cuvette containing the substrate, then through a monochromator onto a photomultiplier tube. The signal was digitized by Tektronix 7612 and 7912 transient recorders, and the digitized signal sent to various computers for data analysis. Stock solutions of the substrates of concentrations 0.1–0.01 M were prepared in acetonitrile or dichloromethane. A small amount of this solution was then added to the appropriate TFE, HFIP, or aqueous solution. This was then introduced into a flow cell apparatus, where, if desired, the solution was saturated with argon or oxygen by bubbling with the appropriate gas for 5–10 min. Absorption spectra were constructed point-by-point, with the solution being flowed through the cuvette so that there was unreacted substrate of the same concentration at each wavelength. The average optical density over a small time period was then determined at each wavelength and plotted against the latter to generate the spectrum. Rate constants were obtained by fitting the decay data to the exponential equation. five to seven kinetic runs were performed with each solution and the rate constants averaged. Observed rate constants refer to 20 ± 2°C, and were reproducible to ±2% in TFE and ±10% in HFIP. The nucleophile quenching experiments involved 5–6 solutions of tetrabutylammonium bromide or sodium azide varying in concentration from 5×10^5 to 0.001 M. Plots of the observed rate constant were linear in the concentration of the added nucleophile. The second-order rate constants were obtained as the least-squares slopes. The rate constants for the styrene quenching in Table 3 were obtained with initial styrene concentrations of 5×10^{-5} to 5×10^{-4} M. A low laser dose (5–10 mJ) was em-

© 1999 NRC Canada

Table 6. Cation precursors.

Cation	Precursor	Reference[a]
4-$Me_2NC_6H_4C^+(CH_3)_2$	4-$Me_2NC_6H_4C(CH_3)_2C(CH_3)_2C_6H_5$	59
4-$Me_2NC_6H_4CH^+CH_3$	4-$Me_2NC_6H_4CH{=}CH_2$	60
$(4\text{-}MeOC_6H_4)_2C^+CH_3$	$(4\text{-}MeOC_6H_4)_2C{=}CH_2$	61
4-$MeOC_6H_4C^+$(cycPr)CH_3[b]	4-$MeOC_6H_4C^+$(cycPr)$=CH_2$	62
4-$MeOC_6H_4C^+(C_6H_5)CH_3$	4-$MeOC_6H_4C^+(C_6H_5){=}CH_2$	64
4-$MeOC_6H_4C^+$(i-Pr)CH_3	4-$MeOC_6H_4C^+$(i-Pr)$=CH_2$	New
4-$MeOC_6H_4C^+$(Et)CH_3	4-$MeOC_6H_4C^+$(Et)$=CH_2$	65
4-MeONapCH^+CH_3[c]	4-MeONap$CH{=}CH_2$	New
4-$MeOC_6H_4C^+(CH_3)_2$	4-$MeOC_6H_4C(CH_3){=}CH_2$	66
	$\{4\text{-}MeOC_6H_4C(CH_3)_2\}_2$	67
4-$MeOC_6H_4C^+$(*t*-Bu)CH_3	4-$MeOC_6H_4C^+$(*t*-Bu)$=CH_2$	68
$Ph_2C^+CH_3$	$Ph_2C{=}CH_2$	Comm.
3,4-$(MeO)_2C_6H_3CH^+CH_3$	3,4-$(MeO)_2C_6H_3CH{=}CH_2$	Comm.
4-$MeOC_6H_4CH^+CH_3$	4-$MeOC_6H_4CH{=}CH_2$	Comm.
	4-$MeOC_6H_4CH(OCOCH_3)CH_3$	69
4-$MeC_6H_4C^+(CH_3)_2$	4-$MeC_6H_4C(CH_3){=}CH_2$	Comm.
$C_6H_6C^+(CH_3)_2$	$C_6H_5C(CH_3){=}CH_2$	Comm.
2,6-$Me_2C_6H_3CH^+CH_3$	2,6-$Me_2C_6H_3CH{=}CH_2$	Comm.
4-$MeC_6H_4CH^+CH_3$	4-$MeC_6H_4CH{=}CH_2$	Comm.
4-$FC_6H_4CH^+CH_3$	4-$FC_6H_4CH{=}CH_2$	Comm.
3-$MeC_6H_4CH^+CH_3$	3-$MeC_6H_4CH{=}CH_2$	Comm.
$C_6H_5CH^+CH_3$	$C_6H_5CH{=}CH_2$	Comm.
4-$MeOC_6H_4CH^+CH_3$	4-$MeOC_6H_4CH{=}CH_2$	Comm.
4-MeONapCH_2^+[c]	4-MeONap$CH_2N^+Me_3{\cdot}^-OAc$	32
4-$MeOC_6H_4CH_2^+$	4-$MeOC_6H_4CH_2N^+Me_3{\cdot}BF_4^-$	70
	4-$MeOC_6H_4CH_2Cl$	Comm.
4-$MeC_6H_4CH_2^+$	4-$MeC_6H_4CH_2Cl$	Comm.
4-$MeOC_6H_4C^+{=}CPh_2$	4-$MeOC_6H_4CBr{=}CPh_2$	71
4-$MeOC_6H_4C^+{=}CMe_2$	4-$MeOC_6H_4CBr{=}CMe_2$	72
4-$MeOC_6H_4C^+{=}CH_2$	4-$MeOC_6H_4C{\equiv}CH$	73
$C_6H_5C^+{=}CPh_2$	$C_6H_5CBr{=}CPh_2$	74
2,4,6-$Me_3C_6H_2C^+{=}CH_2$	2,4,6-$Me_3C_6H_2C{\equiv}CH$	75
	2,4,6-$Me_3C_6H_2CCl{=}CH_2$	75
4-$MeC_6H_4C^+{=}CH_2$	4-$MeC_6H_4C{\equiv}CH$	76
$C_6H_5C^+{=}CHPh$	$C_6H_5C{\equiv}CC_6H_5$	Comm.
$C_6H_5C^+{=}CH_2$	$C_6H_5C{\equiv}CH$	Comm.

[a]Comm. = commercially available.
[b]cycPr = cyclopropyl.
[c]Nap = naphthyl.

ployed to minimize depletion of the precursor. This was verified by observing that the rate constants did not depend significantly on laser dose.

Acknowledgements

Financial support from the Natural Sciences and Engineering Research Council of Canada is gratefully acknowledged. We also thank Jim Pincock (4-methoxy-1-naphthylmethylammonium acetate) and Joggi Wirz (4-dimethylaminostyrene) for initial gifts of compounds.

References

1. P.K. Das. Chem. Rev. **93**, 119 (1989).
2. R.A. McClelland. Tetrahedron, **52**, 6823 (1996).
3. R.A. McClelland, N. Banait, and S. Steenken. J. Am. Chem. Soc. **111**, 2929 (1989).
4. R.E. Minto and P.K. Das. J. Am. Chem. Soc. **111**, 8858 (1989).
5. R.A. McClelland, N. Banait, and S. Steenken. J. Am. Chem. Soc. **108**, 7023 (1986).
6. R.A. McClelland, V.M. Kanagasabapathy, N. Banait, and S. Steenken. J. Am. Chem. Soc. **111**, 3966 (1989).
7. R.A. McClelland, V.M. Kanagasabapathy, N. Banait, and S. Steenken. J. Am. Chem. Soc. **113**, 1009 (1991).
8. R.A. McClelland, V.M. Kanagasabapathy, N. Banait, and S. Steenken. J. Am. Chem. Soc. **114**, 1816 (1992).
9. R.A. McClelland, V.M. Kanagasabapathy, and S. Steenken. J. Am. Chem. Soc. **110**, 6913 (1988).
10. J. Bartl, S. Steenken, H. Mayr, and R.A. McClelland. J. Am. Chem. Soc. **112**, 6918 (1990).
11. E.O. Alonso, L.J. Johnston, J.C. Scaiano, and V.G. Toscano. J. Am. Chem. Soc. **112**, 1270 (1990).
12. S.L. Mecklenburg and E. Hilinski. J. Am. Chem. Soc. **111**, 5471 (1989).
13. R.A. McClelland, N. Mathivanan, and S. Steenken. J. Am. Chem. Soc. **112**, 4857 (1990).

© 1999 NRC Canada

14. F.L. Cozens, N. Mathivanan, R.A. McClelland, and S. Steenken. J. Chem. Soc. Perkin Trans. 2, 2083 (1992).
15. R.A. McClelland, F. Cozens, and S. Steenken. Tetrahedron Lett. **31**, 2821 (1990).
16. R.A. McClelland, C. Chan, F. Cozens, A. Modro, and S. Steenken. Angew. Chem. Int. Ed. Engl. **30**, 1337 (1991).
17. P. Wan, S. Culshaw, and K. Yates. J. Am. Chem. Soc. **104**, 2509 (1982).
18. P. Wan and K. Yates. J. Org. Chem. **48**, 869 (1983).
19. J. McEwan and K. Yates. J. Am. Chem. Soc. **109**, 5800 (1987).
20. P. O'Neill, S. Steenken, and D. Schulte-Frohlinde. J. Phys. Chem. **79**, 2773 (1975).
21. D.P. DeCosta and J.A. Pincock. J. Am. Chem. Soc. **111**, 8948 (1989); **115**, 2180 (1989).
22. J.A. Hilburn, E. MacKnight, J.A. Pincock, and P.J. Wedge. J. Am. Chem. Soc. **116**, 3337 (1994).
23. T.H. Lowry and K.S. Richardson. *In* Mechanism and theory in organic chemistry. 3rd ed. Harper and Row, New York. 1987. pp. 571–573.
24. T.W. Bentley and Z.H. Ryu. J. Chem. Soc. Perkin Trans 2, 761 (1994).
25. G.A. Olah, C.P. Pittman, Jr., R. Waack, and M. Doran. J. Am. Chem. Soc. **88**, 1488 (1966).
26. T.L. Amyes, T. Mizerski, and J.P. Richard. Can. J. Chem. **5**, 922 (1998).
27. V. Bertoli and P.H. Plesch. J. Chem. Soc. B, 1500 (1968).
28. S. Bywater and D. J. Worsfold. Can. J. Chem. **44**, 1671 (1966).
29. M. Villesange, A. Rives, C. Bunel, J.-P. Vairon, M. Froeyen, M. Van Beylen, and A. Persoons. Makromol. Chem. Makromol. Symp. **47**, 271 (1991).
30. T. Kunitake and K. Takarabe. Macromolecules, **12**, 1061, 1067 (1979).
31. M.A. Ratcliff and J.K. Kochi. J. Am. Chem. Soc. **93**, 3112 (1971).
32. B. Foster, B. Gaillard, N. Mathur, A.L. Pincock, J.A. Pincock, and C. Sehmbey. Can. J. Chem. **65**, 1599 (1987).
33. H.E. Zimmerman and V.R. Sandel. J. Am. Chem. Soc. **85**, 915 (1963).
34. J.L. Faria and S. Steenken. J. Phys. Chem. **97**, 10869 (1992).
35. P. Maslak, W.H. Chapman, Jr., T.M. Vallombroso, Jr., and B.A. Watson. J. Am. Chem. Soc. **117**, 12380 (1995).
36. W. Schnabel, I. Naito, T. Kitamura, S. Kobayashi, and H. Taniguchi. Tetrahedron, **36**, 3229 (1980).
37. S. Kobayashi, T. Kitamura, H. Taniguchi, and W. Schnabel. Chem. Lett. 117, (1983), 2101 (1984).
38. F.I.M. Van Ginkel, R.J. Visser, C.A.G.O. Varma, and G. Lodder. J. Photochem. **30**, 453 (1985).
39. S. Kobayashi, Q.Q. Zhu, and W. Schnabel. Naturforsch. Teil B, **42**, 825 (1988).
40. Y. Chiang, A.J. Kresge, M. Capponi, and J. Wirz. Helv. Chim. Acta, **69**, 1331 (1986).
41. Y. Chiang, A.J. Kresge, J.A. Santabello, and J. Wirz. J. Am. Chem. Soc. **110**, 5506 (1988).
42. T. Hochstrasser, A.J. Kresge, N.P. Schepp, and J. Wirz. J. Am. Chem. Soc. **110**, 7875 (1988).
43. P.J. Stang, Z. Rappoport, M. Haneck, and L.R. Subramanian. *In* Vinyl cations. Academic Press, New York. 1979. p. 16.
44. I. Hanazaki and S. Nagakura. Tetrahedron, **21**, 2441 (1965).
45. J.A. Grace and M.C.R. Symons. J. Chem. Soc. 958 (1959).
46. D.A. McCrery and B.S. Freiser. J. Am. Chem. Soc. **100**, 2902 (1978).
47. N. Fujisaki, P. Comte, and T. Gaumann. J. Chem. Soc. Chem. Commun. 848 (1993).
48. R.L. Jones and L.M. Dorfman. J. Am. Chem. Soc. **96**, 5717 (1974).
49. L.M. Dorfman, R.J. Sujdak, and B. Bockrath. Acc. Chem. Res. **9**, 352 (1976).
50. Y. Wang and L.M. Dorfman. Macromolecules, **13**, 63 (1980).
51. L. Andrews and B.W. Keelan. J. Am. Chem. Soc. **103**, 99 (1981).
52. V. Wintgens and J.C. Scaiano. Can. J. Chem. **65**, 2131 (1987).
53. D.D.M. Wayner, D.J. McPhee, and D. Griller. J. Am. Chem. Soc. **110**, 132 (1988).
54. H. Mayr, R. Schneider, B. Irrgang, and C. Schade. J. Am. Chem. Soc. **112**, 4460 (1990).
55. H.C. Brown, K.J. Morgan, and F.J. Chloupek. J. Am. Chem. Soc. **87**, 2137 (1965).
56. G.A. Olah, V.P. Reddy, and G.K.S. Prakash. Chem. Rev. **92**, 69 (1992).
57. W. Kirmse, B. Krzossa, and S. Steenken. J. Am. Chem. Soc. **118**, 7473 (1996).
58. J.P. Richard, M.E. Rothenberg, and W.P. Jencks. J. Am. Chem. Soc. **106**, 1361 (1984).
59. P. Maslak and S.L. Asel. J. Am. Chem. Soc. **110**, 8260 (1988).
60. H.K. Hall, L.C. Dunn, and A.B. Padias. J. Am. Chem. Soc. **45**, 835 (1980).
61. C.D. Hurd and T. Iwashige. J. Org. Chem. **24**, 1321 (1959).
62. R.R. Kostikov, A.P. Molchanov, and S.M. Nagi. J. Org. Chem. U.S.S.R. (Engl. Trans.) **19**, 1291 (1983).
63. D.H.R. Barton, L. Bohe, and X. Lusinchi. Tetrahedron, **46**, 5273 (1990).
64. C.D. Hurd and C.N. Webb. J. Am. Chem. Soc. **49**, 546 (1927).
65. J.T. Gupton and W.J. Layman. J. Org. Chem. **52**, 3683 (1987).
66. D. Seymour and K.B. Wolfstirn. J. Am. Chem. Soc. **70**, 1177 (1948).
67. S. Perrier, S. Sandkararaman, and J.K. Kochi. J. Chem. Soc. Perkin Trans. 2, 825 (1993).
68. G.A. Olah, M.B. Comisarow, and C.J. Kim. J. Am. Chem. Soc. **91**, 1458 (1969).
69. V.M. Potopov, V.M. Dem'yanovich, V.A. Khlebnikov, and S.S. Koval'skaya. J. Org. Chem. U.S.S.R. (Engl. Trans.) **21**, 1602 (1985).
70. E. Hilhurst, A.S. Iskander, T.B.R.A. Chen, and U.K. Pandit. Tetrahedron, **50**, 8863 (1994).
71. L.L. Miller and D.A. Kaufman. J. Am. Chem. Soc. **90**, 7282 (1968).
72. Z. Rappoport and J. Kaspi. J. Am. Chem. Soc. **96**, 4518 (1974).
73. M. Hanack and E. Weber. Chem. Ber. **116**, 777 (1983).
74. R.E. Buckles. J. Am. Chem. Soc. **71**, 1157 (1949).
75. T.H. Vaughn and J.A. Nieuwland. J. Am. Chem. Soc. **56**, 1207 (1934).
76. T.H. Vaughn. J. Am. Chem. Soc. **56**, 2064 (1934).
77. F.N. Tebbe, G.W. Parshall, and G.S. Reddy. J. Am. Chem. Soc. **100**, 3611 (1978).
78. S.H. Pine, R. Zahler, D.A. Evans, and R.H. Grubbs. J. Am. Chem. Soc. **102**, 3270 (1980).
79. S.H. Pine, R.J. Pettit, G.B. Geib, S.G. Cruz, C.H. Gallego, T. Tijerna, and R.D. Pine. J. Org. Chem. **50**, 1212 (1985).

© 1999 NRC Canada

Consideration of end effects of DNA hybridization in selection of fluorescent dyes for development of optical biosensors

S.C. Jakeway and U.J. Krull

Abstract: Intercalating fluorescent dyes are in widespread use to detect the presence of double-stranded DNA. Applications include the development of biosensors that rely on the attachment ("tethering") of a dye molecule by a short hydrocarbon chain to the terminus of a strand of DNA so that dye is continuously available and the biosensor is fully reversible. Double strands of DNA have end effects that limit the stability of hybridization and dye intercalation near the termini of the duplexes. Therefore, the selection of the dye must be based on consideration of spectroscopic properties and also issues associated with tether length and the stoichiometry of the binding of the dye with double- and single-stranded DNA. Ethidium bromide (EB) has been used extensively to detect hybridization of DNA in applications such as electrophoresis, gene chips, and biosensors. A number of dyes with greater quantum efficiency than EB for detection of hybridization have been reported. Furthermore, other practical spectroscopic advantages can be gained in terms of improved S/N by use of dyes that have excitation that is red shifted relative to EB. Pyrilium iodide has been disclosed as an intercalator of high quantum efficiency and long excitation wavelength. This work investigates pyrilium iodide in comparison to EB as a candidate for preparation of a tethered dye for detection of hybridization of DNA 20-mers.

Key words: biosensors, DNA, hybridization, fluorescence, end effects.

Résumé : L'utilisation de colorants fluorescents intercalés pour détecter la présence d'ADN à double brin est très répandue. Les applications comprennent le développement de biosenseurs qui dépendent de la fixation d'une molécule de colorant à une extrémité d'un brin d'ADN à l'aide de courtes chaînes d'hydrocarbures de façon à rendre le colorant continuellement disponible; le biosenseur est entièrement réversible. L'ADN à doubles brins conduit à des effets dus aux extrémités qui limitent la stabilité de l'hybridation et de l'intercalation du colorant près des extrémités des duplexes. Il en résulte que la sélection du colorant doit être faite sur la base d'une considération des propriétés spectroscopiques ainsi que des questions associées à la longueur de l'attache et à la stoechiométrie de la fixation du colorant sur l'ADN à un et à deux brins. Le bromure d'éthidium (« EB ») est couramment utilisé pour détecter l'hybridation de l'ADN dans des applications telles que l'électrophorèse, les puces géniques et les biosenseurs. Un certain nombre de colorants d'efficacité quantique supérieure à celle d'EB pour la détection de l'hybridation ont été suggérés. De plus, on peut obtenir des avantages spectroscopiques pratiques en termes d'amélioration du rapport S/N en utilisant des colorants pour lesquels l'excitation est déplacée vers le rouge par rapport au EB. Il a été démontré que l'iodure de pyrilium peut être utilisé pour intercaler avec une efficacité quantique et une longueur d'onde d'excitation élevées. Dans ce travail, on a comparé l'iodure de pyrilium et l'EB comme candidats pour la préparation d'un colorant fixé permettant de détecter l'hybridation d'ADN 20mères.

Mots clés : biosenseurs, ADN, hybridation, fluorescence, effets des extrémités.

[Traduit par la Rédaction]

Introduction

The use of DNA as a chemically selective "receptor" for the detection of complementary DNA or RNA has been proposed as the basis for development of gene chips and biosensors. Early work was pioneered in the area of electrochemistry where reduction of adenine and cytosine residues, and oxidation of guanine residues were shown to permit detection of DNA (1). Significant extension of early efforts had already been reported by the mid-1980s for a number of sensor platforms (2), and more recently work has focused on biosensors and gene chips (3, 4). In many methods, hybridization of a target strand of nucleic acid is detected by use of a reagent that interacts with double-stranded DNA. Intercalating dyes represent one type of reagent that has been widely used for detection of hybridization. One example is based on the development of a fibre-optic DNA biosensor where the surface of a cleaned optical fibre is derivatized

Received June 8, 1999.

S.C. Jakeway and U.J. Krull.[1] Chemical Sensors Group, Department of Chemistry, University of Toronto at Mississauga, 3359 Mississauga Road North, Mississauga, ON L5L 1C6, Canada.

[1]Author to whom correspondence may be addressed. Telephone: (905) 828-5437. Fax: (905) 828-5425. e-mail: ukrull@credit.erin.utoronto.ca

 © 1999 NRC Canada

Fig. 1. Structures of the dyes that were investigated.

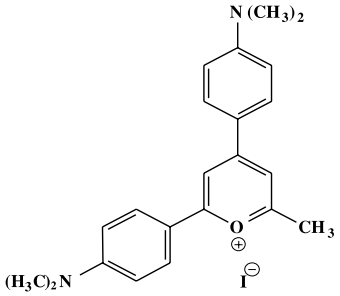

pyrylium iodide (PYI)

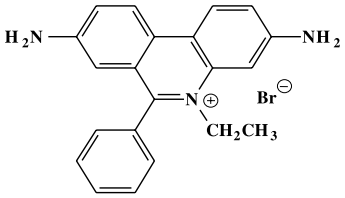

ethidium bromide (EB)

with a linker onto which a 20-mer of single-stranded DNA (ssDNA) is grown through automated synthesis (5, 6). A fluorescent intercalating dye such as ethidium bromide (EB) can be present in solution or tethered covalently to the ssDNA. The concept of a tether is based on localization of the dye near where intercalation occurs, and has been demonstrated in principle by attachment of EB by a hydrocarbon chain to the terminus of immobilized dT_{20} (6). The dye can intercalate if hybridization of target strands from a sample solution occurs with the ssDNA on the surface of the fibre. The dye can emit fluorescence if it is exposed to excitation radiation that is passed through the optical fibre, and fluorescence can be captured by the optical fibre and carried to a detector such as a photomultiplier tube (5). Interesting questions arise from the consideration of how many dye molecules should be tethered per oligomer. For example, can incorporation of dye at high density into double-stranded DNA (dsDNA) lead to unwanted effects such as self-quenching, can the selectivity that is associated with hybridization be altered, and can high local concentrations of dye lead to predominance of association with DNA by processes other than intercalation?

A wide variety of fluorescent dyes have been used to detect the presence of dsDNA. These include dyes such as EB (5), 4,6-diamidino-2-phenylindole (DAPI) (7), fluorescein (8), and thiazole orange (9). The majority of these fluorescent probes are deficient in one or more characteristics when considering their use in a biosensor where real world samples are to be analyzed. For example, real world samples contain both AT and GC base pairs in varying ratios and varying sequences. Hoechst 33258 preferentially binds to AT-rich regions in dsDNA, and this would lead to a different response from different samples based on the availability of AT sites rather than on the concentration of dsDNA alone. Biological samples may also contain several constituents that could potentially cause background fluorescence. Biological samples often contain species such as tryptophan or porphyrins, which can emit fluorescence when stimulated by UV and visible radiation. To reduce the background observed from other biological molecules, spectral absorption and emission characteristics of the probe should be selected to lie towards the red or near-IR wavelength region (10).

We have investigated the use of pyrylium iodide (Fig. 1) in contrast to the commonly used intercalator EB (Fig. 1), as a fluorophore for the detection of DNA hybridization, with the long-term goal being development of a tethered dye. Pyrylium iodide (PYI) was chosen because it is an intercalator, the emission and excitation spectra are red shifted with respect to EB, it has a larger fluorescence enhancement than EB (quantum yield not reported), emission results in a large Stokes' shift (65 nm) that is significant for provision of wavelength windows to separate emission from excitation radiation, and it binds preferentially to dsDNA (11). This dye maybe preferred to EB for use in the biosensor developed by Piunno et al. (5, 6, 12). The fluorescence properties of PYI and the optimal number of probe molecules that bind to dsDNA needs to be investigated to establish conditions for use in biosensors.

Our experiments have measured the fluorescence enhancement of PYI in solution to be about 4000% greater than EB under similar conditions involving intercalation into dsDNA in solution. Taken together with the red-shifted spectral characteristics and minimal binding to ssDNA, PYI appears to be a better choice of probe than EB. Our results suggest that the optimal loading ratio of PYI to a 20-mer of DNA is 1:1, as suited for a tethered dye, whereas the optimal loading ratio for EB to a 20-mer of DNA is in a higher range of at least 2:1 (dye:DNA). We have also observed that the bases near the terminal ends of the double-stranded oligonucleotide 20-mers may not hybridize with the same thermodynamic stability as areas towards the centre of the duplex, thus leading to a reduction of the number of dye molecules that can intercalate into the duplex.

Experimental

Chemicals

Ammonia solution (concd.) and boric acid were obtained from BDH (Toronto, Ont.). Rhodamine 6G, formamide, and bromophenol blue (Aldrich Canada, Oakville, Ont.), and xylene cyanole FF, Tris base, and EDTA (Sigma Canada, Oakville, Ont.) were used as received. Polyacrylamide and sodium chloride were obtained from Caledon (Georgetown, Ont.). All phosphoramidites were supplied by Dalton Chemical Laboratories Inc. (Toronto, Ont.). EB was purchased from Molecular Probes, Inc. (Eugene, Oreg,). PYI was a generous gift from Canon Research Centre (Japan). Sterile water was produced using glass double-distilled water by treatment with diethyl pyrocarbonate (Sigma) and autoclaving (120ºC and 4 atm (1 atm = 101 kPa)).

© 1999 NRC Canada

Fig. 2. Spectral overlap of excitation and emission curves for PYI and EB when in the presence of dT_{20} with dA_{20} (i.e., dsDNA). The oligomers and dye were each at a concentration of 3×10^{-6} M.

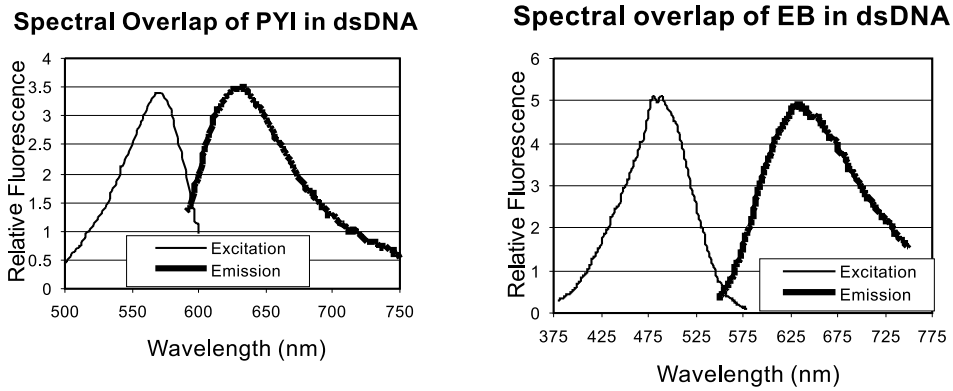

Purification of dT_{20} for use in hybridization studies

Oligonucleotide composed of 20 identical nucleotides was prepared by automated synthesis using an Applied Biosystems 391 DNA synthesizer PCR-MATE (Applied Biosystems Inc., Mississauga, Ont.), using the standard phosphoramidite method provided by ABI (13). The ssDNA was removed from the support (control pore glass, CPG) by using concentrated ammonia solution for 1 h. Gel electrophoresis was used to purify ssDNA. The concentration of each fraction was determined by absorption spectroscopy (A_{260}). The purified DNA was stored in at –20°C until further use.

Dye fluorescence in the presence of DNA

One litre of hybridization buffer was made by dissolving 58.44 g sodium chloride, 2.99 g NaH_2PO_4 (BDH), and 3.45 g $NaHPO_4 \cdot H_2O$ (BDH) or 3.89 g sodium dihydrogen orthophosphate (BDH) in 1 L of water. The pH was set to 7.0. The dyes (Fig. 1) and ssDNA were dissolved in hybridization buffer until the desired concentration of 3×10^{-6} M was reached for each. The fluorescence spectra of the dyes in solution were collected using a spectrofluorimeter (SLM–Aminco 8100, SLM Instruments, Urbana, Ill.) using 4-nm slit widths and a temperature of 20°C. The reference channel was based on use of 3 g/L of rhodamine dye in ethanol. Fluorescence spectra for the dyes were first collected in the absence of DNA. Fluorescence spectra of the dyes were then obtained in the presence of 20-mer ssDNA, and the concentration of dye and ssDNA was kept constant when the complementary strand of DNA replaced the portion of hybridization buffer. Finally, fluorescence spectra were obtained in the presence of ssDNA and complementary DNA (cDNA), and the ratio of dye:DNA was varied in the range from 1:1 to 6:1.

Results and discussion

The selection of a dye for study was based on avoiding certain factors that could limit analytical applications. Dyes with small Stokes' shifts (less than about 35 nm) were of little interest due to the difficulty of signal isolation from excitation wavelengths. It was also recognized that a small Stokes' shift could lead to a significant spectral overlap integral, thereby increasing the probability of self-quenching of the probe. Groove binding dyes were not used in this particular study because of their preference for DNA sequences rich in AT base pairs (14). EB was used for the purpose of comparison in these experiments because it has very well established binding properties, no sequence selectivity, and is currently used as the fluorescent probe to detect DNA hybridization for the biosensors that are being studied in our research group.

The expected spectral shifts were noted for both EB and PYI (11, 15) when the spectrum of the dye in solution was compared with the spectrum of the dye in dsDNA. The presence of the spectral shifts indicated that the dye was in a different environment from that in aqueous solution and consistent with the intercalation of the dyes into dsDNA. When EB was placed in solution with dsDNA at a 1:1 ratio, the excitation spectra red-shifted 15 nm with respect to the free dye, while the emission spectrum blue-shifted 10 nm with respect to the free dye in solution. At a 1:1 ratio of EB to ssDNA, the observed fluorescence in ssDNA (dT_{20} or dA_{20}) was not significantly different from the fluorescence of the free dye.

The emission from EB showed a larger Stokes' shift than that from PYI (134 nm compared with 61 nm, respectively). The spectral overlap of the excitation and emission spectra provides an indication of the potential for self-quenching.It was determined that the spectral overlap of EB was less than 0.5%, whereas that of PYI was 5.4% (Fig. 2). Therefore, self-quenching and inner-filter effects would be of greater consequence to calibration and sensitivity by a factor of approximately 10 when using PYI instead of EB.

Little or no fluorescence intensity increase was expected when the PYI was in contact with ssDNA (dT_{20}, dA_{20}, dG_{20}, or dC_{20}). PYI showed a dramatic increase in fluorescence intensity when bound to dsDNA relative to that of EB. The excitation maximum for PYI in dsDNA was 570 nm, which represents at least a 65-nm red shift in contrast to the corresponding experimentally determined value for EB.

The intensity of fluorescence was observed to increase by a factor of 47.7 ± 1.7 over that of the free dye in solution when PYI was added to a 1M hybridization buffer solution containing dT_{20} and dA_{20} in a 1:1:1 ratio (Fig. 3). PYI in the presence of dT_{20} showed a fluorescence intensity increase of 2.6 relative to that of the free dye in the absence of the ssDNA, and similarly, a twofold increase was observed from

© 1999 NRC Canada

Fig. 3. Emission spectra of PYI in solution (-) compared with PYI that had associated with dsDNA (-). The ratio of dye:dsDNA was 1:1 and the concentrations of each species in all cases was 3×10^{-6} M.

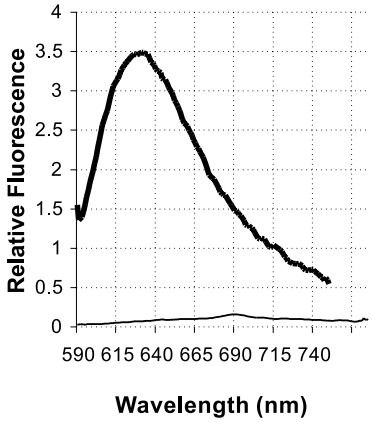

PYI in the presence of dA_{20}. An important point to consider when doing quantitative comparisons is that the excitation wavelength was held constant (suitable for maximum absorption of free dye in solution) when measuring the emission spectra of free dye in solution, dye with ssDNA, and dye with dsDNA. This implies that the fluorescence intensity enhancement is reported on the basis of what might be observed from a biosensor that is set to operate at fixed excitation wavelength, using a wavelength that is set to maximize signal for a background reference.

An examination of the effect of varying the ratio of PYI:dsDNA in the range 1:1 to 6:1, resulted in the fluorescence enhancements shown in Fig. 4 (relative enhancements based on comparison to free dye without any DNA at 632 nm). The reduction of fluorescence enhancement that is seen in Fig. 4 can be explained in terms of self-quenching. Self-quenching can be a result of spectral overlap and distance-dependent quenching phenomena such as coulombic (Förster) interactions (16).

Figure 4 suggests that the maximum number of PYI dye molecules that can intercalate into a dsDNA 20-mer would be 3, based on the lack of change in fluorescence when the dye concentration is increased from 4:1 to 6:1. The length of a dsDNA 20-mer is on the order of 68 Å, suggesting an average separation distance between the dye molecules of 23 Å (assuming an even distribution of dye throughout the double helix). However, if end effects (discussed below) are taken into account, the average distance between intercalated dye molecules might be as small as 13 Å. The optimum ratio of dye molecules for short dsDNA complexes is 1:1 to maximize S/N, based on the experimentally determined ratio of relative fluorescence of bound to free dye, which is an ideal ratio for a tethered dye. Experiments were not conducted where the ratio of dye:dsDNA was less than 1:1 because at least one dye molecule is needed to detect every DNA hybridization (recognition) event in the case where tethered dye is used for biosensor preparation.

EB on average intercalates into every fifth base pair in long DNA duplexes (17). EB usually intercalates into dsDNA, but at very high concentrations of EB there is evidence of a second form of interaction in which EB binds to

Fig. 4. The ratio of the relative fluorescence intensity at 632 nm between PYI in the presence of dsDNA and the dye in solution, for various dye:dsDNA concentrations. Excitation was held at 568 nm for all cases.

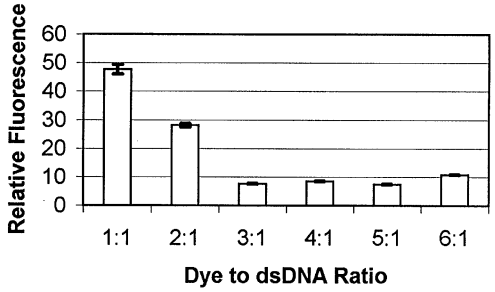

Fig. 5. The ratio of the relative fluorescence intensity at 623 nm between EB in the presence of dsDNA and the dye in solution, for various dye:dsDNA concentrations. Excitation was held constant at 500 nm for all cases.

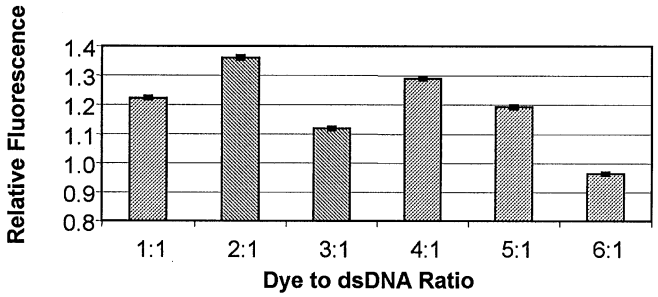

dsDNA in the major groove (17). The results of Fig. 5 indicate that the largest increase of fluorescence intensity occurs at a molar ratio of 2:1, for EB:dsDNA. In terms of device construction, a tethering protocol that provides two intercalants per immobilized ssDNA would be more difficult to achieve than for the 1:1 dye:DNA system.

It is well known that the terminal base pairs of dsDNA are not as thermodynamically stable and rigidly confined to the double helix structure, and the dynamics of "breathing" are greater than for the corresponding base pairs located away from the ends of dsDNA (18). End effects would be expected to have a proportionally larger impact on smaller dsDNA strands than for longer dsDNA strands on the presumption that the number of bases involved in the end effects remains constant regardless of strand length. An extrapolation of the work of Waring (17) suggests that a 20-mer might be able to accommodate up to four molecules of EB. However, the results obtained here suggest that a maximum of three EB molecules in a dA_{20}:dT_{20} structure is possible under the conditions used herein before a second competitive binding motif became significant. This would suggest that the effective length of the hybridized DNA 20-mer may be on the order of 12–16 base pairs, and 4–8 base pairs at the ends of dsDNA may not be sufficiently bound as complementary pairs to fully stabilize intercalation of EB. Dye molecules that do intercalate into a region that experiences end effects may provide a lesser fluorescence enhancement. The breathing of the DNA duplex would reduce the average quantum yield and therefore the fluorescence intensity from dye that binds near the ends of the dsDNA. The

© 1999 NRC Canada

determination that end effects may include perhaps three to four nucleotides at the end of dsDNA provides insight into the length of the tether that is required for attachment of dye to the terminus of DNA for development of a biosensor.

The increase in fluorescence intensity that is seen when the ratio of EB:dsDNA is increased to 4:1 can be explained by the secondary binding of EB to dsDNA. Waring suggests that secondary binding of EB becomes more prominent when the ratio of dye to base pairs becomes more than 1:5. Dye bound in this second motif would not have the same orientation as dye molecules that are intercalated into the double helix and thus would not be quenched with the same efficiency because of distance and the different orientations of the dipoles.

Conclusions

Pyrylium iodide showed several traits that would make it a favourable substitute for EB. The excitation maximum was experimentally confirmed to be 65 nm longer than the excitation maximum for EB. Our work showed that the fluorescence enhancement of PYI when intercalated into dsDNA was almost 4000% greater than that for EB at similar dye:dsDNA ratios. The maximum loading of PYI in a dA_{20}:dT_{20} duplex was determined to be three dye molecules. Importantly, the maximum response from PYI occurred when the ratio of dye:dsDNA was 1:1, which is optimal for tethering where one dye molecule would be attached to each immobilized ssDNA. The maximum loading ratio of EB to a 20-mer was determined to be three dye molecules for a mechanism involving intercalation. In the case of EB, the maximum fluorescence intensity enhancement occurred at a dye:dsDNA ratio of 2:1 (for a 20-mer). The end effects occurring at the termini of the short dsDNA used in this work reduced the extent of average binding of EB to oligonucleotides by intercalation.

A further series of experiments are underway in which base pair mismatches are deliberately positioned near the ends of 20-mer dsDNA. Measurements of the variations in the melt curves from these systems will help to quantitatively establish the energetics of end effects (thermodynamic effects), as well as the distance that end effects can extend from the termini of short strands of dsDNA.

Acknowledgements

We are grateful to the Natural Sciences and Engineering Research Council of Canada for financial support of this work, and to P.A.E. Piunno and J.H. Watterson for discussion. We thank Drs. Tadashi Okamoto and Nobuko Yamamoto of the Canon Research Center, Japan, for providing the PYI that we used in our experiments.

References

1. E. Palecek. Bioelectrochem. Bioeng. **15**, 275 (1986).
2. M.E. Downs, S. Kobayashi, and I. Karube. Anal. Lett. **20**, 1897 (1987).
3. Z. Junhui, C. Hui, and Y. Ruifu. Biotechnol. Adv. **15**, 43 (1997).
4. G. Ramsey. Nature Biotechnol. **16**, 40 (1998).
5. P.A.E. Piunno, U.J. Krull, R.H.E. Hudson, M.J. Dahma, and H. Cohen. Anal. Chem. **67**, 2635 (1995).
6. U.J. Krull, P.A.E. Piunno, C. Wust, A. Li, A. Gee, and H. Cohen. NATO ASI Ser. Ser. 2 Environ. **38**, 67 (1997).
7. W.D. Wilson, F.A. Tanious, H.J. Barton, L. Strekowski, D.W. Boykin, and R.L. Jones. J. Am. Chem. Soc. **111**, 5008 (1989).
8. M.U. Kumke, L. Shu, L.B. McGown, G.T. Walker, J.B. Pitner, and C.P. Linn. Anal. Chem. **69**, 500 (1997).
9. H.S. Rye, M.A. Quesada, K. Peck, R.A. Mathies, and A.N. Glazer. Nucleic Acids Res. **19**, 327 (1991).
10. S.A. Soper, J.H. Flanagan, Jr., B.L. Legendre, Jr., D.C. Williams, and R.P. Hammer. IEEE J. Select. Topics Quant. Electron. **2**, 1129 (1996).
11. N. Yamamoto, T. Okamoto, and M. Kawaguchi. Nucleic Acids Symp. Ser. **29**, 83 (1993).
12. A.H. Uddin, P.A.E. Piunno, R.H.E. Hudson, M.J. Damha, and U.J. Krull. Nucleic Acids Res. **25**, 4139 (1997).
13. Anonymous. PCR-Mate EP model 391 DNA synthesizer, user's manual version 1.00, Revision B. Applied Biosystems Inc., Mississauga, Ont. 1991.
14. S.K. Kim, S. Eriksson, M. Kubista, and B. Nordén. J. Am. Chem. Soc. **115**, 3441 (1993).
15. R.P. Haugland. Handbook of fluorescent probes and research chemicals. Molecular Probes, Inc. Eugene, Oreg. 1992.
16. H.H. Cheung. *In* Topics in fluorescence spectroscopy. Vol. 2. *Edited by* J.R. Lakowicz. Plenum Press, New York. 1991.
17. M.J. Waring. J. Mol. Biol. **13**, 269 (1965).
18. J. SantaLucia, Jr. Proc. Natl. Acad. Sci. U.S.A. **95**, 1460 (1998).

© 1999 NRC Canada

Crystal structure and solution studies of the product of the reaction of β-mercaptoethanol with vanadate

Sudeep Bhattacharyya, Raymond J. Batchelor, Frederick W.B. Einstein, and Alan S. Tracey

Abstract: Reaction of β-mercaptoethanol with vanadate under slightly alkaline conditions provided a crystalline complex that was characterized by X-ray diffraction and FTIR spectroscopy. The complex was dimeric in structure with a central $[VO]_2$ core and a pentacoordinate, crudely trigonal bipyramidal arrangement about each vanadium atom with a sulphur occupying a pseudo-axial position. A single ^{51}V NMR signal was observed for this complex when dissolved in water, chloroform or acetonitrile. A large influence of acetonitrile on the vanadium chemical shift suggested the possibility of reaction with acetonitrile. FTIR showed the presence of two complexes in acetonitrile solution but only one in chloroform or water. Mixed solvent studies were carried out in an effort to further characterize the solution complexes. Crystal structure of $[\{VO_2(OC_2H_4S)\}_2][NEt_4]_2$: monoclinic, space group $P2_1/n$,. a = 8.3451(17), b = 16.954(4), c = 10. 2064(25) Å; β = 101. 271(18)°; V = 1416.2 Å^3; Z = 2; R_F = 0.048 for 1355 data ($I_o \geq 2.5\sigma(I_o)$) and 147 variables.

Key words: mercaptoethanol, vanadate, vanadium NMR, X-ray diffraction, FTIR, thiolate.

Résumé : La réaction du β-mercaptoéthanol avec du vanadate dans des conditions faiblement alcalines conduit à la formation d'un complexe cristallin dont on a déterminé la structure par diffraction des rayons X et par spectroscopie IR à transformée de Fourier. Le complexe a une structure dimère avec un noyau central $[VO]_2$ et un arrangement pentacoordiné vaguement trigonal bipyramidal autour de chaque atome de vanadium dans lequel un soufre occupe une position pseudo-axiale. Pour ce complexe en solution dans l'eau, le chloroforme ou l'acétonitrile, on n'a observé qu'un seul signal en RMN du ^{51}V. La spectroscopie IR par TF met en évidence la présence de deux complexes dans l'acétonitrile et seulement un en solution dans le chloroforme ou l'eau. Afin de mieux caractériser les complexes en solution, on a effectué des études dans des solvants mixtes. Les cristaux du $[\{VO_2(OC_2H_4S)\}_2][NEt_4]_2$ sont monocliniques, groupe d'espace $P2_1/n$, avec a = 8,3451(17), b = 16,954(4) et c = 10,2064(25)Å; β = 101,271(18)°; V = 1416,2Å^3; Z = 2; R_F = 0,048 pour 1355 observations (avec $I_o \geq 2{,}5\sigma(I_o)$) et 147 variables.

Mots clés : mercaptoéthanol, vanadate, RMN du vanadium, diffraction des rayons X, IR à transformée de Fourier, thiolate.

[Traduit par la Rédaction]

Introduction

The aqueous chemistry of vanadium sulphur compounds has been attracting increasing attention over recent years (1–3). Amongst other things, sulphovanadium complexes are found in certain nitrogen-fixing enzymes where they provide an alternative to the more frequently encountered molybdenum-dependent nitrogenases (4). Furthermore, sulphur is frequently encountered (as the thiol group in cysteine) in the active site of enzymes that are inhibited by vanadate or vanadate complexes (5). Of paramount interest in this class of enzymes are the protein tyrosine phosphatases (PTPases) which are key regulators of many fundamental cell processes including cell mitosis, T-cell activation, and insulin responses (6, 7). Vanadate is a well known potent inhibitor of PTPases. X-ray characterization of PTPase/vanadate complexes shows vanadate in a pentacoordinate trigonal bipyramidal structure with the sulphur of the active site cysteine being covalently bound in an apical position. The three equatorial positions and the remaining apical position are occupied by oxo and hydroxo ligands that in turn donate or accept hydrogen bonds from adjacent active site residues (8).

Although the insulin-mimetic influences of vanadium are well known and attempts are being made to exploit this in therapeutic applications (9), there are many unanswered questions concerning the aqueous vanadate sulphur chemistry of relevance to such an application. Indeed, there is a marked paucity of information available. Our understanding

Received September 25, 1999.

S. Bhattacharyya and A.S. Tracey.[1] Department of Chemistry and Institute of Molecular Biology and Biochemistry, Simon Fraser University, Burnaby, BC V5A 1S6, Canada.
R.J. Batchelor and F.W.B. Einstein. X-ray Crystal Laboratory, Department of Chemistry, Simon Fraser University, Burnaby, BC V5A 1S6, Canada.

[1]Author to whom correspondence may be addressed. Telephone: (604) 291-4464. Fax: (604) 291-3765. e-mail: tracey@sfu.ca

 © 1999 NRC Canada

of the influences of ligands that contain sulphhydryl groups on the aqueous chemistry of vanadium in its higher oxidation states of vanadium is clouded. The statement or inference that vanadate (V(V)) is rapidly reduced to vanadyl (V(IV)) by sulphhydril groups is very frequently encountered. It is virtually dogma that in vivo vanadate is reduced fully to vanadyl by cellular glutathione. This tenet has been disputed and a number of factors regulating the redox equilibrium pointed out (10). More recently, evidence suggesting that the efficacy of reduction is lower than is frequently assumed has been presented (11).

Recently we have shown that, although peroxovanadate rapidly oxidizes the thiol groups of dithiothreitol, oxidation in the presence of the vanadate ion tends to be quite slow, particularly above neutral pH (12). Instead of rapid oxidation, a complexation reaction leading to formation of two products, both of V_2L stoichiometry was observed. The generation of a $[VO]_2$ cyclic core with the sulphhydryl group complexed in an auxiliary position was proposed for these materials (12). On the basis of a close correspondence in vanadium chemical shifts and because product formation is favored, a similar coordination, in a V_2L_2 stoichiometry was proposed for the product of the reaction of β-mercaptoethanol with vanadate (12). Somewhat inadvertently, during studies of the reactions of hydroxamidovanadate complexes with sulphur-containing ligands (13), a β-mercaptoethanol complex that contained no hydroxylamine and had a V_2L_2 stoichiometry was obtained in crystalline form. Better methods for its preparation were developed and its structure was established by X-ray crystallography. NMR studies of the dissolution of this product were carried out in an effort to obtain a correspondence between the solution and solid structures.[2]

Experimental section

Materials

All chemicals used in this work are reagent grade. Divanadium(V) pentoxide and β-mercaptoethanol (Aldrich Chemical Co.), tetraethylammonium hydroxide (20% aqueous solutions) (Sigma Chemical Co.) were used without further purification. Unless mentioned otherwise, all the solutions were prepared in dry solvents in a millimolar scale.

Synthesis of $[\{VO_2(OC_2H_4S)\}_2][(NEt_4)_2]$

A solid sample of V_2O_5 (0.10 g, 0.55 mmol) was added to a mixture of 20% aqueous solution of tetraethylammonium hydroxide (1 mL) and water (2 mL). The resultant slurry was warmed to 60°C with continuous stirring to obtain a clear colorless solution of tetraethylammonium vanadate. The pH of this solution was about 11.0. A stoichiometric amount of β-mercaptoethanol (0.1 mL, 1.43 mmol), was added in a dropwise fashion. The solution color immediately changed to orange. The pH of the resultant solution was maintained at about pH 8.5. An excess of tetraethylammonium chloride (0.5 g, 3 mmol) was added to this solution and it was kept standing overnight under a stream of air for rapid evaporation. A yellowish crystalline solid of the desired product was obtained after 10 h. The product was filtered, washed with acetone and ether, and finally dried in vaccuo. The crude product was recrystallized from acetonitrile. Yield: 0.22 g (35%). Anal. calcd. for $C_{20}H_{48}N_2O_6S_2V_2$: C, 41.5, H, 8.3, N, 4.8; found: C, 41.78, H, 8.30, N, 4.72.

Preparation of chloroform solutions

To about 0.05 g (~0.1 mmol) of $[\{VO_2(OC_2H_4S)\}_2][(NEt_4)_2]$, suspended in 5 mL of chloroform, was added a stoichiometric amount of bis(triphenylphosphoranyl)iminium chloride. The compound immediately dissolves with formation of a yellow solution with subsequent precipitation of $(NEt_4)Cl$. The solution was filtered and stored.

Spectroscopy

^{51}V NMR spectra were obtained from a Bruker AMX400 NMR spectrophotometer operating at 105.2 MHz at ambient temperature in the unlocked mode. Vanadium chemical shifts are reported relative to the chemical shift of $VOCl_3$ at 0 ppm. The following NMR parameters were used: pulse width 60° (20 μs); spectral width 62.5 kHz; aquisition time 0.065 s; line broadening, 40.0 Hz; frequency domain size 8 K. FTIR spectra were obtained from a BOMEM MB-102 instrument. All solution spectra were observed with a 0.15 mm zinc selenide cell. Aqueous solutions were prepared with water at pH 7.0. In each of the mixed solutions spectra, the aborbance of individual solvent mixtures were recorded and used as reference.

UV–vis spectra of the product complex, 0.69 mM in dimethylformamide, were obtained (1 cm pathlength cell) from an HP8452A diode array spectrophotometer.

X-ray diffraction

Crystals, which slowly decompose in air, were gently wedged and then sealed in glass capillaries, using a trace of epoxy glue as an adhesive. This was the method that yielded the final sample used. Several attempts using different methods of mounting did not produce a stable arrangement. The probable reason for this is the slow degradation of the crystals, producing a thin liquid layer on the surface. Even the best mounting attained required regular reorientation during data acquisition. Data were recorded with an Enraf Nonius CAD4F diffractometer using graphite monochromatized Mo Kα radiation. Data reduction included corrections for Lorentz and polarization effects.

Anisotropic displacement parameters were refined for the non-hydrogen atom sites. Hydrogen atoms were placed in calculated positions and were made to ride on their respective carbon atoms during refinement. Isotropic thermal parameters for all methylene hydrogen atoms were constrained

[2] Tables of crystallographic details, atomic coordinates, anisotropic displacement parameters, and bond distances and angles have been deposited and may be purchased from: The Depository of Unpublished Data, Document Delivery, CISTI, National Research Council Canada, Ottawa, Ontario, Canada, K1A 0S2. Tables of bond distances and angles and H coordinates have also been deposited with the Cambridge Crystallographic Data Centre and can be obtained on request from: The Director, Cambridge Crystallographic Data Centre, University Chemical Laboratory, 12 Union Road, Cambridge, CB2 1EZ, U.K.

© 1999 NRC Canada

Table 1. Crystallographic data for the structure determination of $[\{VO_2(OC_2H_4S)\}_2][NEt_4]_2$.

Formula	$V_2S_2O_6N_2C_{20}H_{48}$
fw	289.31
a (Å)[a]	8.3451(17)
b (Å)	16.954(4)
c (Å)	10.2064(25)
β (°)	101.271(18)
V (Å^3)	1416.2
Z	2
Temperature (K)	293
Observed reflns.[e]	1355
Crystal system	Monoclinic
Space group	$P2_1/n$
ρ_c (g cm^{-3})	1. 357
λ(Mo $K_{\alpha 1}$) (Å)	0.70930
μ(Mo K_α) (cm^{-1})	8.1
Min–max 2θ (°)	4–50
Transmission[b]	0.75–0.85
R_F[c]	0.048
R_{wF}[d]	0.058
Parameters	147

[a]Cell dimensions were determined from 26 reflections ($32° < 2\theta < 43°$).

[b]The data were not corrected for the effects of absorption. The maximum possible error in $|F_o|$ is ± 3.4%.

[c]$R_F = \Sigma(|F_o| - |F_c|) / \Sigma|F_o|$, for observed data.

[d]$R_{wF} = [\Sigma(w(|F_o| - |F_c|)^2) / \Sigma(wF_o^2)]^{1/2}$ for observed data.

[e]$I_o \geq 2.5\sigma(I_o)$.

to have identical shifts during refinement, as were those for all methyl hydrogen atoms.

The data collection was performed using the program DIFRAC[3]. The programs used for absorption corrections, data reduction, structure solution and graphical output were from the NRCVAX Crystal Structure System (14). Full matrix least-squares refinement was carried out using CRYSTALS[4]. Complex scattering factors for neutral atoms (15) were used in the calculation of structure factors. Computations were carried out on a Pentium computer. Crystal data and experimental details are given in Table 1. The atomic coordinates, equivalent isotropic thermal parameters and site occupancies for the non-hydrogen atoms are listed in Table 2.

Results and discussion

$[\{VO_2(OC_2H_4S)\}_2]^{2-}$ was obtained as a crystalline tetraethylammonium salt by reacting tetraethylammonium vanadate and β-mercaptoethanol in a 1:1 mol ratio in water under slightly alkaline conditions. The crystals are hygroscopic and lose their sharpness overnight on being exposed to air. The compound is quite soluble in water, other protic solvents, and in acetonitrile. The compound was found to have low solubility in nonprotic solvents such as chloroform, acetone, and dichloromethane. A chloroform solution was, however, prepared by changing the cation as described in the experimental section. In water, the complex undergoes hydrolysis to establish an equilibrium between complex, vanadate, and free ligand as observed in the ^{51}V NMR spectra. In solvents such as acetonitrile and chloroform, it has sufficient stability (>2 h) to allow investigation of its solution state characteristics.

Table 2. Fractional atomic coordinates and equivalent isotropic or isotropic displacement parameters (Å^2)for the non-hydrogen atom sites of $[\{VO_2(OC_2H_4S)\}_2][NEt_4]_2$.

Atom	*x*	*y*	*z*	U_{eq}[a]
V	0.99781(11)	0.08243(6)	0.08428(9)	0.0301
S	1.26262(20)	0.13893(9)	0.14879(17)	0.0448
O(1)	0.9170(5)	0.16220(22)	0.0126(4)	0.0408
O(2)	0.9343(5)	0.0712(3)	0.2236(4)	0.049
O(3)	1.1390(4)	–0.00592(21)	0.0348(4)	0.0358
N	0.7132(6)	0.3248(3)	0.1939(5)	0.037
C(1)	1.3753(7)	0.0476(4)	0.1669(6)	0.045
C(2)	1.3097(6)	–0.0043(3)	0.0511(5)	0.035
C(11)	0.8765(7)	0.3435(4)	0.2807(6)	0.044
C(12)	1.0183(8)	0.2954(5)	0.2527(8)	0.068
C(21)	0.6711(7)	0.2390(4)	0.2058(7)	0.046
C(22)	0.6642(9)	0.2107(4)	0.3431(7)	0.064
C(31)	0.5898(8)	0.3766(3)	0.2437(6)	0.043
C(32)	0.4163(9)	0.3710(4)	0.1692(8)	0.068
C(41)	0.7148(9)	0.3399(4)	0.0494(6)	0.056
C(42)	0.7593(12)	0.4228(5)	0.0163(7)	0.091

[a]U_{eq} is the mean of the principal axes of the displacement ellipsoid.

Fig. 1. Stereoscopic view of $[\{VO_2(OC_2H_4S)\}_2]$. The planarity of the four-membered ring of the $[VO]_2$ core and the nonplanar five-membered ring formed by the chelated β-mercaptoethanol ligand are evident in this view. 50% probability thermal ellisoids are shown for nonhydrogen atoms.

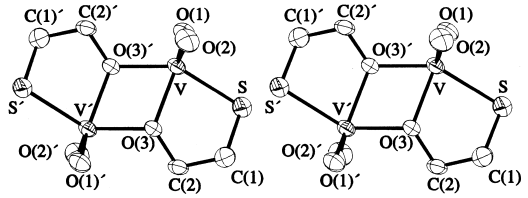

The crystal structure

A stereographic representation of the molecular structure of the $[\{VO_2(OC_2H_4S)\}_2]^{2-}$ anion is shown in Fig. 1. The anion has crystallographic inversion symmetry and the tetraethylammonium cation is in a general position. The only intermolecular distances significantly less than the sums of the appropriate accepted van der Waals radii are between the sulphur atom and one of the ethyl groups of the cation (S—C(12) 3.319(8) Å and S—C(21) 3.373(7) Å) and are not unusual.

A set of unique bond distances and bond angles for the anion are listed in Table 3. The bonds from vanadium to the

[3] E.J. Gabe, P.S. White, and G.D. Enright. *DIFRAC.* A Fortran 77 control routine for 4-circle diffractometers. National Research Council, Ottawa. 1995.

[4] D.J. Watkin, J.R. Carruthers, and P.W. Betteridge. CRYSTALS Chemical Crystallography Laboratory, University of Oxford, Oxford. 1984.

© 1999 NRC Canada

Table 3. Selected intramolecular distances (Å) and angles (°) for $\{VO_2(OC_2H_4S)\}_2^{2-}$.

Distances			
V—S	2.3803(19)	V—O(1)	1.621(4)
V—O(2)	1.622(4)	V—O(3)	2.029(4)
V—O(3)′ [a]	1.980(4)	S—C(1)	1.802(7)
O(3)—V′	1.980(4)	O(3)—C(2)	1.402(6)
C(1)—C(2)	1.489(8)		
Angles			
S-V-O(1)	94.08(15)	S-V-O(2)	104.45(15)
S-V-O(3)	79.23(11)	S-V-O(3)′	145.70(13)
O(1)-V-O(2)	108.39(22)	O(1)-V-O(3)	135.58(19)
O(1)-V-O(3)′	97.48(17)	O(2)-V-O(3)	115.84(19)
O(2)-V-O(3)′	102.30(19)	O(3)-V-O(3)′	69.93(14)
V-S-C(1)	96.89(21)	V-O(3)-V′	110.07(16)
V-O(3)-C(2)	125.6(3)	V′-O(3)-C(2)	122.4(3)
S-C(1)-C(2)	108.9(4)	O(3)-C(2)-C(1)	108.2(5)

[a] ′ represents the symmetry operation $2 - x, -y, -z$.

bridging oxygen atom are slightly but significantly asymmetric (V—O(3) 2.029(4) Å; V—O(3)′ 1.980(4) Å, where ′ represents the symmetry operation $2 - x, - y, -z$). The V-S-C(1)-C(2)-O(3) ring has an envelope conformation with C(1) constituting the flap (cf. the bond torsion angles: S-V-O(3)-C(2) = –0.3(2)°, O(3)-V-S-C(1) = –22.2(2)°, V-S-C(1)-C(2) = 44.2(3)°, V-O(3)-C(2)-C(1) = 29.2(3)°, S-C(1)-C(2)-O(3) = –48.6(3)°). The arrangement around O(3) is also close to planar (cf. the sum of the three bond angles at O(3) is 358.1°).

The structure shows two identical dioxovanadium centers, bridged to each other by the oxygen of the β-mercaptoethanol ligand to form a core $[VO]_2$ cyclic structural element. The coordination about vanadium is pentacoordinate in a crude trigonal bipyramidal arrangement about each vanadium atom. A pseudo-axial sulphur occupies one coordination site on each vanadium. The central $[VO]_2$ core is planar while the five-membered ring generated by the chelating ligand is highly distorted from planarity as can be judged from the stereoscopic representation of the structure (Fig. 1). Though several thiolato bound monooxovanadates have been reported (2, 3), the dioxovanadium center of this complex so far is unique to this thiolate ligand although it has previously been suggested for other thiolate ligands (12).

The axial coordination of the sulphur atom in trigonal bipyramidal coordination is a structural property also found in vanadate bound in the active site of protein tyrosine phosphatases (8, 16). The V—S bond length measured here (2.3803(19) Å) is considerably longer than that in a number of dithiolates (2.249 Å) where the sulphur occupies an equatorial location in the complexes (2, 3). The V—S bond length measured here is a little shorter than that reported for the V—S distance of the apical sulphur in the two protein tyrosine phosphatases, 2.5 Å (16), and 2.4 Å (8) under the much poorer resolution conditions of the protein structure determination.

^{51}V NMR and FTIR

Dissolution studies of the crystalline compound have been carried out in water and organic solvents. ^{51}V NMR and the FTIR (V=O stretching) spectroscopic studies were carried out in these solvents with a view toward obtaining information about structural changes in the molecule by monitoring the electronic environment around the metal center as reflected, for example, on the V=O stretching frequency. The results are collected in Table 4.

In aqueous solution, $[\{VO_2(OC_2H_4S)\}_2]^{2-}$ gives a ^{51}V NMR signal at –362 ppm (Fig. 2*a*) in the range typical for a thiol-coordinated vanadium center of this type (17). Other ^{51}V signals (Fig 2, insert) occur in the upfield range and correspond to vanadate and various of its oligomers that are produced by dissociation of the complex (18). A time course study showed that, in a dilute aqueous solution (~1–2 mM), the dissociation process required about 1 h to reach its endpoint. Since dissociation requires about an hour and, as there is no observable change in the ^{51}V chemical shift, it is likely that the solution NMR signal corresponds to the dimeric product of the solid state structure. Also, the observation of only one signal at –362 ppm throughout the hydrolysis process strongly suggested that the two dioxovanadium centres remain chemically equivalent until dissociation occurs. It is not very likely that dissociation to a monomer is fast while hydrolysis of the monomer is slow. In fact, it most likely is the cyclic $[VO]_2$ core that provides the stability to the complex. In the similar situation with glycolato complexes based on nucleosides, dimerization to afford the $[VO]_2$ core certainly is a major driving force for product formation (19). This $[VO]_2$ structural motif is a frequently encountered one and seems to be one of the defining properties of vanadate chemistry (20).

When a more concentrated solution (~50 mM) was studied, it was observed to maintain an equilibrium between initial complex and vanadate and its oligomers for several days. Generation of a green solution showed that oxidative decomposition occurred during this time period, but clearly, decomposition was not a rapid process. These observations suggest that the dimeric complex itself is oxidatively quite stable and that the oxidative decomposition of mercaptoethanol, and possibly similar ligands, by vanadate may involve minor or intermediate complexes generated during the

© 1999 NRC Canada

Table 4. NMR and IR data for the $[\{VO_2(OC_2H_4S)\}_2][(NEt_4)_2]$ complex in the solid and in solution.

	^{51}V NMR	FTIR	
	δ (ppm)[a]	ν (cm^{-1}) of O=V=O	Intensity ratio
Crystal	—	910	—
$CHCl_3$	–376	910	—
CH_3CN	–385	909, 930	10:9
Water	–362	912	—
$CHCl_3$ in acetonitrile			
(*i*) 25%	–382	909, 930	10:8
(*ii*) 50%	–380.5	909, 930	10:5
(*iii*) 100%	–376	910	—
Water in acetonitrile			
(*i*) 0.1%	–384	910, 928	10:9
(*ii*)1.0%	–382	910, 926	10:9
(*iii*) 5.0%	–377	910, 920	10:7
(*iv*) 10.0%	–376	910	—
(*v*) 50.0%	–370.5	910	—

[a]Chemical shifts are referenced to external $VOCl_3$ at 0 ppm.

Fig. 2. ^{51}V NMR spectrum of $[\{VO_2(OC_2H_4S)\}_2][NEt_4]_2$ (*a*) in 50 mM aqueous solution at pH 7.0; (*b*) in acetonitrile. The inset identifies the products of partial hydrolysis.

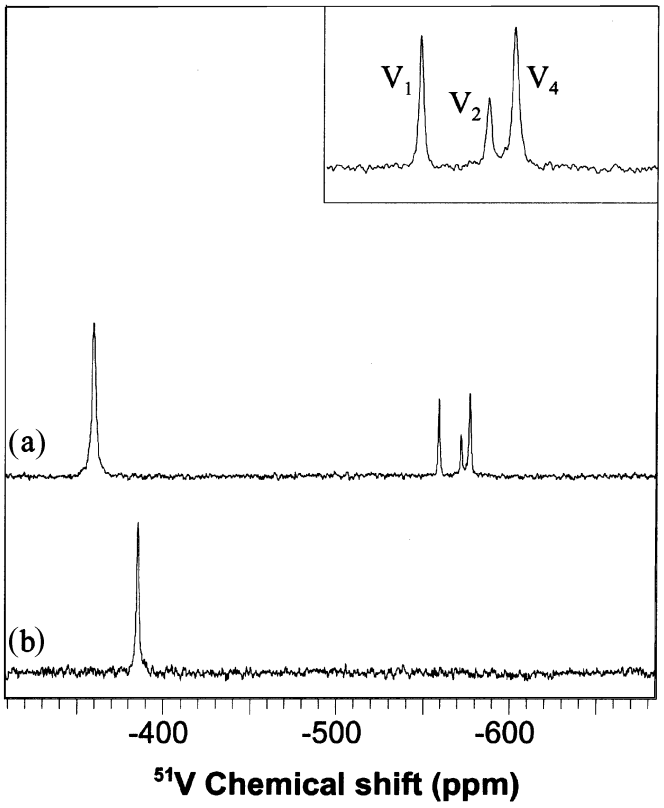

complexation process. Having started here from the pure complex, such compounds would be formed only after a degree of initial dissociation followed by a reassociative process. Under different conditions, oxidation of the ligand by vanadate could well be rapid. Certainly, it would be expected to be so under even moderately acid conditions.

In acetonitrile a single resonance, at –385 ppm (Fig. 2*b*), is observed and it remains unaltered for a prolonged period of time. Compared to water, this signal is shifted upfield by ca. 23 ppm. This seems a bit large to be accounted for by a solvation effect. In the noncoordinating chloroform solvent, the corresponding signal occurs at –376 ppm. The question then arises as to whether these three chemical shifts represent unique structural species or not. When mixtures of acetonitrile and chloroform, in different proportions, were used, a single signal but with a systematic change in chemical shift was observed (Table 4). This, however, does not exclude the possibility of two species which are in rapid interconversion. In this case, the rate of this interconversion is faster than the time scale of these NMR experiments (millisecond timescale). If, in fact, there are two species, one would expect to see them by employing an instrument with a time resolution faster than the rate of this interconversion.

Solution studies were therefore carried out using FTIR spectroscopy. Initial studies in chloroform solution suggested that there was no change in structure from that of the solid state. In both cases the V=O stretching band appears as a singlet, at 910 cm^{-1}. On the other hand, a solution of the β-mercaptoethanol complex in acetonitrile has a second stretching vibration at 930 cm^{-1} with an intensity comparable to the 910 cm^{-1} signal (Fig. 3*a*). Stepwise addition of chloroform (Table 4) into the acetonitrile solution causes a systematic decrease in intensity of the 930 cm^{-1} signal (Fig. 3). This gives strong support to the proposal that two independent species are found in acetonitrile solution. One of these (910 cm^{-1}) apparently has a structural form similar to that in the solid state (Fig. 1) while the second is dependent on the availability of the acetonitrile in the solution.

FTIR absorbances at 937 cm^{-1} have been observed for V(IV) thiolate complexes (21). However, we have observed absorbances close to 930 cm^{-1} for V(V) complexes other than those studied here. The finding that the 930 cm^{-1} absorbance decreases in intensity in a systematic way with addition of chloroform to an acetonitrile solution of the complex certainly mitigates the possibility that what is being observed actually is a V(IV) complex. It seems very unlikely that the oxidation state would be significantly influenced by going from an acetonitrile to chloroform solution. Also, the

© 1999 NRC Canada

Fig. 3. FTIR spectrum of $[\{VO_2(OC_2H_4S)\}_2][NEt_4]_2$ in (*a*) pure acetonitrile; (*b*) acetonitrile with 25% chloroform; (*c*) acetonitrile–chloroform 1:1 mixture.

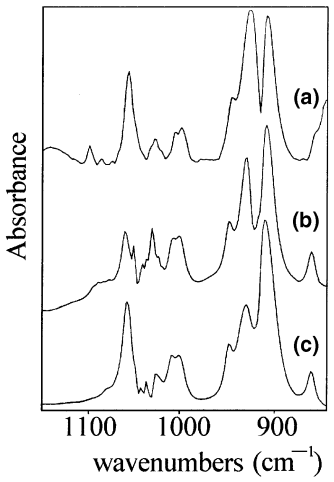

solutions are only slightly yellow and a V(IV) complex would be expected to be highly coloured because of intense transition bands in the visible region of the spectrum. For the above reasons, and also because the crystalline material was itself obtained from an acetonitrile solution, the 930 cm^{-1} frequency is assigned to a V(V) not a V(IV) complex.

In an attempt to learn more about the second species, FTIR dissolution studies were extended to a mixed water–acetonitrile system. In pure water, the complex gives a relatively broad stretching band at ca. 912 cm^{-1} which gradually loses its intensity and breaks into multiplets as it hydrolyzes to generate other vanadates, as confirmed in the NMR spectra (Fig. 2*a*). The close correspondence of this V=O vibration to that in $CHCl_3$ or KBr (910 cm^{-1}) suggests that a structure similar to the solid state is also present in water. In the mixed water–acetonitrile solvent system, two FTIR signals similar to those in pure acetonitrile (Fig. 3*a*) are obtained when the quantity of water is low. When the percentage of water in the solution is increased, the V=O stretching band at 910 cm^{-1} is unaltered (Table 4) but the 930 cm^{-1} signal decreases in intensity, indicating the loss of the second product. This is reminiscent of the chloroform–acetonitrile experiment. However, unlike in the chloroform–acetonitrile system, the 930 cm^{-1} signal also undergoes a gradual increase in wavelength and shifts toward the 910 cm^{-1} band and ultimately coalesces with it (Fig. 4) at a water concentration of about 10%.

The interconversion process between the two species in acetonitrile solvent is quite fast. Judging from the ^{51}V NMR chemical shifts observed in water and in acetonitrile and from the observation of only a single signal in the mixed solvent system, an interconversion rate faster than about 10^4 s^{-1} can be deduced. In the FTIR spectrum the two V=O stretches clearly are observed but the timescale here is in the picosecond range. The rate of the interconversion process suggests that any major structural changes arising from rearrangement of ligands is unlikely. Still, a possibility such as ring opening followed by accepting an acetonitrile molecule into the coordination sphere may describe what is happening. Alternative structures that do not invoke acetonitrile

Fig. 4. FTIR of $[\{VO_2(OC_2H_4S)\}_2][NEt_4]_2$ in acetonitrile with 10% water.

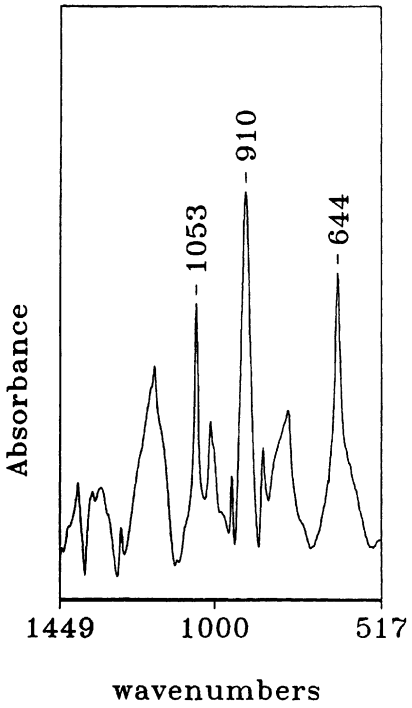

complexation, such as a macrocyclic structure similar to that seen with a chloroalkoxovanadate (22), seem unlikely although they have been invoked in order to explain the rather slow chemical exchange observed in glycolatovanadate systems (20, 23).

The UV–vis spectrum of the mercaptoethanol complex in dimethylformamide showed a single absorbance with a maximum at 286 nm (ε = 4850 M^{-1} cm^{-1}). The solutions of this complex and also those formed with dithiothreitol (12) are pale yellow. This contrasts with that reported for the highly coloured vanadium complex formed with $(HSCH_2CH_2)_3N$ where strong charge transfer bands at 375 and 500 nm were observed (3). Apparently, it is the multiple sulphur ligation in this latter complex that leads to the strong absorbance in the visible region.

Conclusions

Reaction of vanadate with β-mercaptoethanol in aqueous solution yielded a solid crystalline compound of moderate stability. The crystal structure revealed two thiolato bound dioxovanadium centers coupled through a $[VO]_2$ core. The $[VO]_2$ core in this molecule helps stabilize the complex in a manner not well known in vanadium-thiolate chemistry but that is, however, frequently encountered with bidentate oxygen donors (24) and apparently is one of the more important structural motifs of vanadium(V) chemistry.

In chloroform, FTIR spectroscopy suggests there is a close structural correspondence between the solid and solution structures (V=O stretch, 910 cm^{-1}). In acetonitrile the complex exists in two different structural forms, one of which appears to be similar to that found in the solid state. The second species requires the presence of acetonitrile and, in view of the lack of viable structural alternatives, this im-

© 1999 NRC Canada

plies that the acetonitrile is coordinated. In water and mixed acetonitrile/water solvents the frequency of the FTIR signal suggests an aqueous structure that corresponds to the solid state structure. Unfortunately, the results are somewhat equivocal as the signal of the acetonitrile-derived complex (930 cm^{-1}) does not only decrease in intensity but it also shifts in position with increase in water content until it overlaps the second V=O signal (910 cm^{-1}). This raises the possibility that water can replace acetonitrile in the 930 cm^{-1} complex. Unfortunately, because of the shift in signal position with increase in water content, the juxtaposition of the FTIR signals of the solid and aqueous solution at 910 cm^{-1} cannot be taken to be a good indicator of the coordination in aqueous solution. Indeed, the observation of a reaction with the weakly complexing solvent, acetonitrile, makes it very difficult to rule out the possibility that there is a coordination change from the solid state structure when the complex is dissolved in water. However, the loss in intensity of the 930 cm^{-1} that accompanies its frequency shift with increase in water content suggests conversion to the 910 cm^{-1} (crystal) structure probably is completed at high water concentrations.

Acknowledgments

Thanks are gratefully extended to the Natural Sciences and Engineering Research Council of Canada for its financial support of this work.

References

1. A. Butler and C.J. Carrano. Coord. Chem. Rev. **109**, 61 (1991).
2. C.R. Cornman, T.C. Stauffer, and P.D. Boyle. *In* Vanadium compounds: chemistry, biochemistry and therapeutic applications. ACS Symp. Ser. 711. *Edited by* A.S. Tracey and D.C. Crans. American Chemical Society, Washington. 1998. pp. 71–81.
3. K.K. Nanda, E. Sinn, and A.W. Addison. Inorg. Chem. **35**, 1 (1996).
4. R.E. Eady. Met. Ions Biolog. Syst. **31**, 363 (1995).
5. G. Huyer, S. Liu, J. Kelly, J. Moffat, P. Payette, B. Kennedy, G. Tsaprailis, M.J. Gresser, and C. Ramachandran. J. Biol. Chem. **272**, 843 (1997).
6. Z. Jia. Biochem. Cell Biol. **75**, 17 (1997).
7. E.B. Fauman and M.A. Saper. Trends Biochem. Sci. **21**, 413 (1996).
8. A.D.B. Pannifer, A.J. Flint, N.K. Tonks, and D. Barford. J. Biol. Chem. **273**, 10454 (1998).
9. A.S. Tracey and D.C. Crans (*Editors*). Vanadium compounds: chemistry, biochemistry and therapeutic applications. ACS Symp. Ser. 711. American Chemical Society, Washington. 1998.
10. N.D. Chasteen, J.K. Grady, and C.E. Holloway. Inorg. Chem. **25**, 2754 (1986).
11. J. Li, G. Elberg, D.C. Crans, and Y. Shechter. Biochemistry, **35**, 8314 (1996).
12. P.C. Paul and A.S. Tracey. J. Biol. Inorg. Chem. **2**, 644 (1997).
13. F. Nxumalo and A.S. Tracey. J. Biol. Inorg. Chem. **3**, 527 (1998).
14. E.J. Gabe, Y. LePage, J.-P. Charland, F.L. Lee, and P.S. White. J. Appl. Crystallogr. **22**, 384 (1989).
15. International tables for X-ray crystallography. IV. Kynoch Press, Birmingham. 1975.
16. J.M. Denu, D.L. Lohse, J. Vijayalakshmi, M.A. Saper, and J.E. Dixon. Proc. Natl. Acad. Sci. U.S.A. **93**, 2493 (1996).
17. D. Rehder, W. Priebsch, and M. von Oeynhausen. Angew. Chem. Int. Ed. Engl. **28**, 1221 (1989).
18. A.S. Tracey, J.S. Jaswal, and S.J. Angus-Dunne. Inorg. Chem. **34**, 5680 (1995).
19. A.S. Tracey, J.S. Jaswal, M.J. Gresser, and D. Rehder. Inorg. Chem. **29**, 4283 (1990).
20. S.J. Angus-Dunne, R.J. Batchelor, A.S. Tracey, and F.W.B. Einstein. J. Am. Chem. Soc. **117**, 5292 (1995).
21. T.-B. Wen, J.-C. Shi, X. Huang, Z.-N. Chen, Q.-T. Liu, and B.-S. Kang. Polyhedron, **17**, 331 (1998).
22. D.C. Crans, R.A. Felty, and M.M. Miller. J. Am. Chem. Soc. **113**, 265 (1991).
23. W.J. Ray, Jr., D.C. Crans, J. Zheng, J.W. Burgner II, H. Deng, and M. Mahroof-Tahir. J. Am. Chem. Soc. **117**, 6015 (1995).
24. F.W.B. Einstein, R.J. Batchelor, S.J. Angus-Dunne, and A.S. Tracey. Inorg. Chem. **35**, 1680 (1996).

© 1999 NRC Canada

Schiff base insertion in titanium alkyls; reduction of imine functions by benzyl addition

Simon J. Coles, Michael B. Hursthouse, David G. Kelly, Andrew J. Toner, and Neil M. Walker

Abstract: $TiBz_4$ reacts with *N*-2-fluorenyl(salicylideneimine) to afford a crystallographically characterized titanium(IV) complex containing two conventional bidentate Schiff base ligands and two O-bound ligands in which the imine function has been reduced by the addition of benzyl and hydrogen moieties.

Key words: insertion, nucleophilic additions, Schiff bases, titanium

Résumé : Le $TiBz_4$ réagit avec la *N*-2-fluorényl(salicylidèneimine) pour conduire à un complexe du titane(IV), caractérisé cristallographiquement, qui contient deux bases de Schiff bidentates conventionnelles comme ligands et deux ligands liés à l'oxygène dans lesquels la fonction imine a été réduite par l'addition de benzyle et d'hydrogène.

Mots clés : insertion, additions nucléophiles, bases de Schiff, titane.

[Traduit par la Rédaction]

The application of titanium complexes as asymmetric catalysts is developing quickly (1), and producing renewed interest in titanium–salen derivatives (2). Studies of organometallic Schiff base complexes have focused on tetradentate N_2O_2 Schiff base ligands and employed two synthetic strategies: group 4 complexes with Schiff base and chloride ligands have been alkylated with s-block alkylating agents (3, 4) or $AlMe_3$ (5); and alternatively, group 4 alkyls have been reacted directly with Schiff bases (6). Three basic forms of reactivity are observed: metal-centred alkylation, combined metal–ligand alkylation, and alkylation–reduction (Fig. 1). Dialkylated species are often the primary goal of studies, since such complexes have been demonstrated to function as active ethylene polymerization catalysts in both homogeneous and heterogeneous studies (6–8). To understand the relationship between catalytically active and inactive complexes, and the deactivation pathways of the former, it is essential to fully elucidate the potential reactivity of alkyl/aryl functions and Schiff base ligands within the group 4 coordination sphere. It has already been demonstrated that complexes in the +4 oxidation state, as depicted in Fig. 1, often undergo thermally induced migrations to fluxional and uncharacterizable products at or below ambient temperature. In some instances such products are obtained without the isolation of stable and well-defined intermediates. Reactions are presumed to result from alkyl migration to the Schiff base imine function (4*a*, 6). The present work identifies a new alternative form of reactivity in which benzyl and hydrogen moieties are added to the coordinated Schiff base ligand reducing the C=N function to a secondary amine.

Reaction of *N*-2-fluorenyl(salicylideneimine) (flusalH) with a –20°C hexane solution of $TiBz_4$ results in the precipitation of a brown solid. The ^1H NMR spectrum (270 MHz, benzene-$^2H_6$) of this material is complex, but presumably contains both *bis*-alkylated metal and reduced ligand species. Other groups have encountered similar spectra in their attempts to isolate group 4 organometallic Schiff base complexes (4*a*, 6). In our own experiments similar reactivity occurs between $TiBz_4$ and the tetradentate Schiff base ligands $salenH_2$ and $salphenH_2$, but the latter systems have proved as resistant to characterization as those considered by other workers. In contrast, extraction of the solid obtained from the $TiBz_4$–flusalH reaction with toluene results in its transformation to **1**; an orange crystalline complex which is isolated in a yield of 25% with respect to flusalH. Single crystal X-ray diffraction analysis indicates the presence of two deprotonated bidentate Schiff base ligands coordinated as conventional N,O chelates (Fig. 1). The remaining sites

Received June 6, 1999.

S.J. Coles and M.B. Hursthouse. Department of Chemistry, University of Southampton, Highfield, Southampton SO17 1BJ, U.K. **D.G. Kelly,[1] A.J. Toner, and N.M. Walker.**. Department of Chemistry and Materials, The Manchester Metropolitan University, Chester Street, Manchester M1 5GD, U.K.

[1]Author to whom correspondence may be addressed. Telephone: +44 161 247 1425. Fax: +44 161 247 6357. e-mail: d.g.kelly@mmu.ac.uk

 © 1999 NRC Canada

Fig. 1. Examples of organometallic titanium Schiff base complexes.

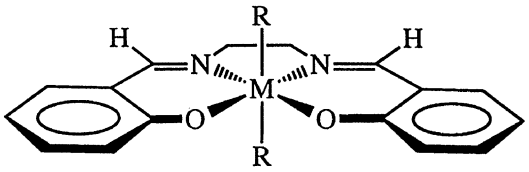

M = Ti^{4+}, R = Me (see ref. 3)

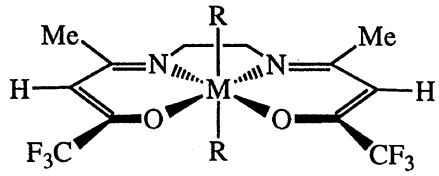

M = Zr^{4+}, R = CH_2Ph, CH_2CMe_3 (see ref. 6)

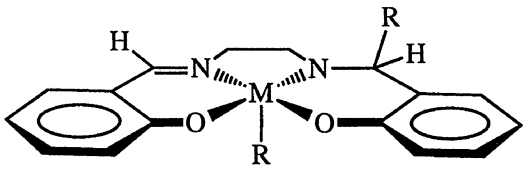

M = Ti^{4+}, R = Mesityl (see ref. 4a)

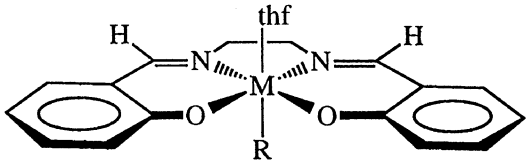

M = Ti^{3+}, R = Me (see ref. 5b)

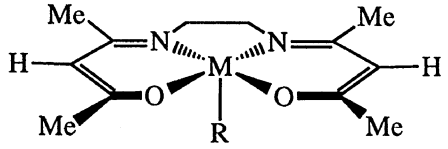

M = Ti^{3+}, R = CH_2Ph, Ph (see ref. 4b)

completing the octahedral geometry are occupied by O-bound reduced Schiff bases.[2]

Whilst hydrogen atoms are not detected in the crystallographic determination of **1**, comparison with free ligand structures, such as that of salenH_2 (9), clearly indicates a shift from double bond imine to single bond amine character. The coordinated C=N distance in **1** is 1.317(10) Å and that of the free amine 1.449(10) Å. Infrared spectroscopy and ^{1}H NMR are also indicative of coordinated imine and free amine functions in **1**. Titanium coordination geometry and the remaining bond lengths and angles within Schiff base and reduced Schiff base ligands are typical of such species.[3]

[2] Crystal data, **1**: 0.5 C_7H_8, $C_{100}H_{72}N_4O_4Ti$, M = 1441.52, monoclinic, space group $C2/c$, a = 14.526(4), b = 19.753(4), c = 26.753(10) Å, β = 93.307(10)°, V = 7663.5(39) Å^3, Z = 4, T = 293(2) K, μ = 0.170 mm^{-1}, 12 443 measured reflections were reduced to 5505 independent reflections of $I > 2\sigma(I)$. Final R = 0.0620, wR = 0.0850. Data collection and structure solution were carried out by published methods (2*c*). All non-hydrogen atoms were refined anisotropically, hydrogens were refined in positions and with thermal parameters defined by their respective hydrogen bearing atoms. Complete X-ray data are available as supplementary material and may be purchased from: The Depository of Unpublished Data, Document Delivery, CISTI, National Research Council Canada, Ottawa, Canada, K1A 0S2. Crystallographic data have also been deposited with the Cambridge Crystallographic Data Centre as supplementary publication no. CCDC-111691. Copies of the data may be obtained free of charge on application to The Director, Cambridge Crystallographic Data Centre, University Chemical Laboratory, 12 Union Road, Cambridge, CB2 1EZ, U.K. (fax: (+44)1223-336-033; e-mail: deposit@ccdc.cam.ac.uk).

[3] Synthesis. FlusalH was isolated from the conventional condensation of amine and salicylaldehyde followed by recrystallization and characterization by ^{1}H and elemental analysis. **1** was prepared by the following procedure: in an N_2 atmosphere, flusalH (500 mg, 1.75 mmol) was added in a single portion to a hexane solution (20 mL) of $TiBz_4$ (870 mg, 2.10 mmol) at –20°C. The dark brown precipitate which formed over 0.5 h was filtered, washed with hexane, and extracted with toluene. The resultant brown solution became progressively pale orange. Addition of hexane and storage at –20°C affords toluene solvated **1** over ca. 3 days. Satisfactory elemental analysis. ^{1}H NMR (270 MHz, $CDCl_3$) δ: 3.22 (m, 4H, PhCH_2CHNH), 3.72 (s, 4H, 9-fluorene CH_2), 3.96 (s, 4H, 9-fluorene CH_2), 4.18 (s, 2H, PhCH_2CH*NH*), 4.60 (m, 2H, PhCH_2*CH*NH), 6.67–7.86 (m, 54H, aromatic), 8.75 (s, 2H, *CH*) ppm; IR (Nujol, cm^{-1}): ν(C=N) 1612 (s) cm^{-1}, ν(N-H) 3376 (s), 3389 (s) cm^{-1}.

© 1999 NRC Canada

Scheme 1. Formation of **1**, full molecule generated by C_2 rotation.

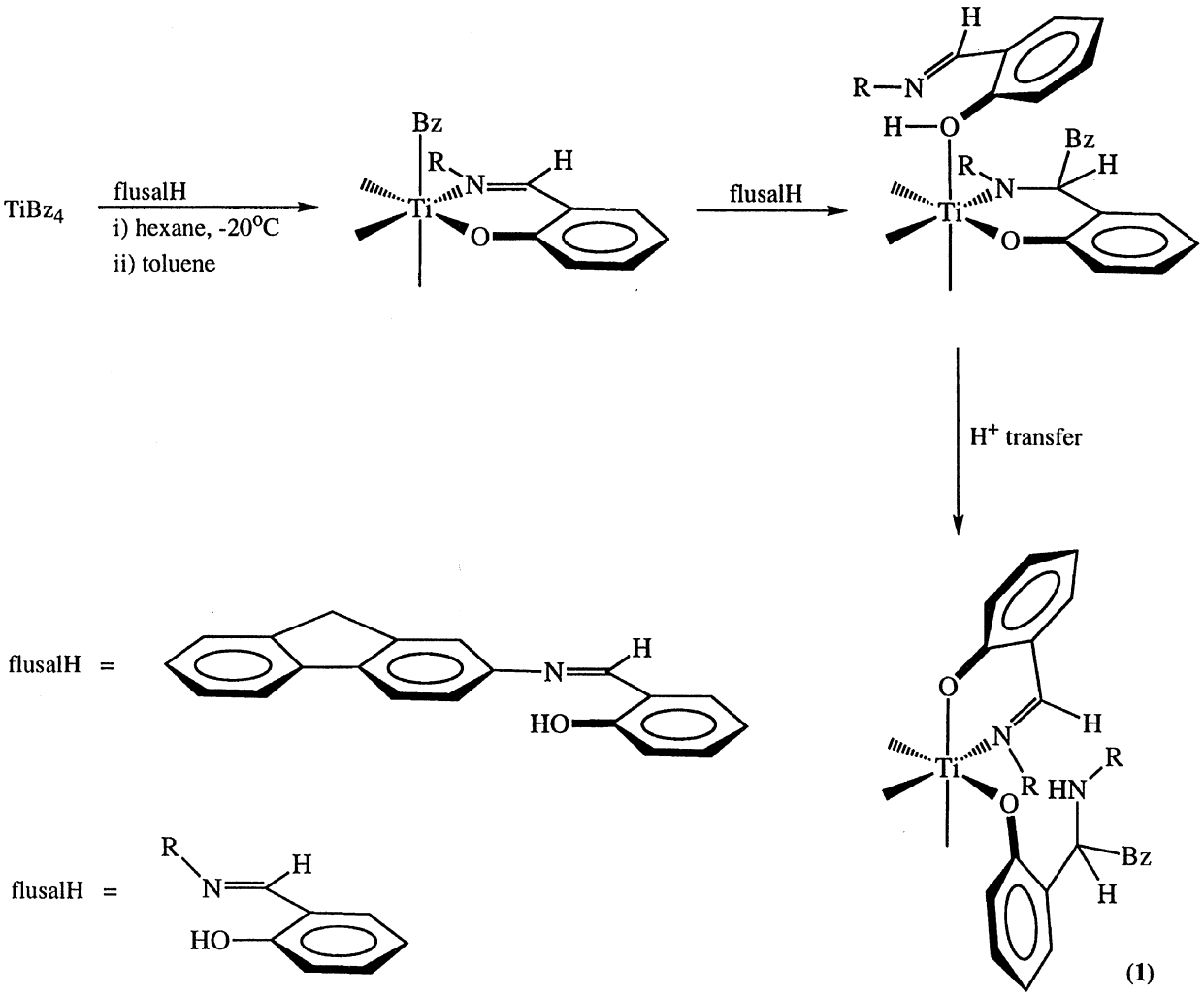

Although the formation of **1** cannot be followed mechanistically due to the complex spectrum attributed to the intermediate brown product(s), it is feasible to postulate a realistic reaction mechanism in harness with previous results involving similar transformations (3–6) (Scheme 1). Thus initial reactivity may be viewed as Schiff base insertion into a Ti–Bz moiety, or alkyl migration to a coordinated Schiff base. There are numerous examples of the former in which insertion into C≡O and C≡NR affords acyl or iminoacyl species, respectively (10). For the latter mechanistic approach, supporting evidence may be obtained from a similar migration in the reaction of MesMgBr and [$TiCl_2$(salen)] which is thought to result in the observed [TiMes(Mes-salen)] (4*a*). In this reaction the steric bulk of the mesityl ligand was considered to be significant in stabilizing the complex towards further reactivity or decomposition. In the formation of **1** the steric influence of the flusalH ligand may be equally important, with this sterically demanding Schiff base ligand inducing congestion at the metal centre and providing an alternative ligand-based coordination site to relieve this congestion. Similar transformations may occur with other ligands, but it is significant that **1** can be isolated and characterized when similar reactions result in intractable materials. Again the presence of the fluorenyl substituent may be crucial; π–π interactions between these planar substituents producing the unusual *cis* orientated reduced ligands which are evident in **1** (Fig. 1). These interactions appear to lock the molecule, preventing the fluxional behaviour and further reactivity which has plagued the characterization of other complexes.

The formation of **1** inevitably involves protonation of the alkylated imine function. This affords the characterized amine complex, rather than the imines observed in other group 4 species (Fig. 1). The hydroxyl group of flusalH is identified in Fig. 2 as the proton source. Concern always arises from the potential for reactivity with adventitious moisture. However, in this instance, the preparation and manipulation of the highly moisture sensitive $TiBz_4$ using identical solvents and procedures offers circumstantial support for the successful exclusion of moisture.

The formation of **1** and the observed reduction of imines to amines defines a further form of reactivity or deactivation for group 4 Schiff base complexes. Moreover, this reactivity may be applicable to a wider range of complexes which are not as readily characterized as the *N*-fluorenyl system employed here. Whilst there is no evidence that **1** is itself an

© 1999 NRC Canada

Fig. 2. Structure of **1**. Selected bond lengths (Å) and angles (°): Ti(1)—O(1) 1.840(5), Ti(1)—O(2) 1.875(6), Ti(1)—N(1) 2.281(7), N(1)—C(7) 1.449(10), N(1)—C(8) 1.379(12), N(2)—C(41) 1.317(10), N(1)—C(82) 1.409(10), O(1)-Ti(1)-O(2) 94.8(2), O(1)-Ti(1)-N(2) 90.9(2), O(2)-Ti(1)-N(2) 85.5(3).

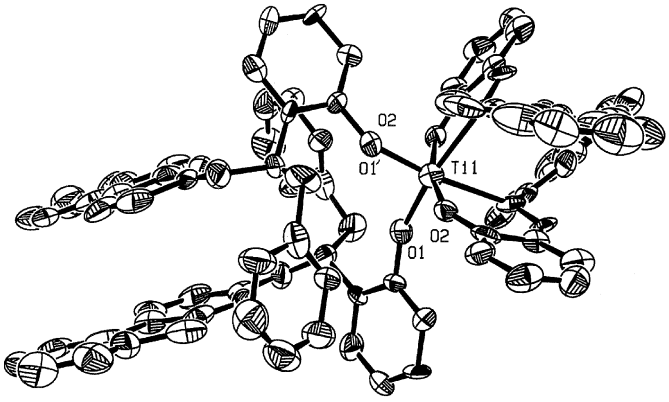

active ethylene polymerization catalyst, its structure and reactivity are of relevance to the closely related species which do perform such catalysis.

References

1. S.G. Nelson. Tetrahedron: Asymmetry, **9**, 357 (1998).
2. (*a*) V.I. Tararov, D.E. Hibbs, M.B. Hursthouse, N.S. Ikonnikov, K.M. Abdul Malik, M. North, C. Orizu, and Y.N. Belokon. J. Chem. Soc. Chem. Commun. 387 (1998); (*b*) H. Chen, P.S. White, and M.R. Gagné. Organometallics, **17**, 5358 (1998); (*c*) S.J. Coles, M.B. Hursthouse, D.G. Kelly, A.J. Toner, and N.M. Walker. J. Chem. Soc. Dalton Trans. 3489 (1998).
3. C. Floriani, E. Solari, F. Corazza, A. Chiesi-Villa, and C. Guastini. Angew. Chem. Int. Ed. Engl. **28**, 64 (1989).
4. (*a*) E. Solari, C. Floriani, A. Chiesi-Villa, and C. Rizzoli. J. Chem Soc. Dalton Trans. 367 (1992); (*b*) J.-M. Rosset, C. Floriani, M. Mazzanti, A. Chiesi-Villa, and C. Guastini. Inorg. Chem. **29**, 3991 (1990).
5. (*a*) S.J. Coles, M.B. Hursthouse, D.G. Kelly, A.J. Toner, and N.M. Walker. Polyhedron, **15**, 4307 (1996); (*b*) J. Organomet. Chem. **580**, 304 (1999).
6. E.B. Tjaden, D.C. Swenson, R.F. Jordan, and J.L. Petersen. Organometallics, **14**, 371 (1995).
7. T. Repo, M. Klinga, P. Pietikainen, M. Leskela, A.M. Uusitalo, T. Pakkanen, K. Hakala, P. Aaltonen, and B. Lofgren. Macromolecules, **30**, 171 (1997).
8. J.P. Corden, W. Errington, P. Moore, and M.G.H. Wallbridge. J. Chem. Soc. Chem. Commun. 323 (1999).
9. N. Bresciani-Pahor, M. Calligaris, G. Nardin, and L. Randaccio. Acta. Crystallogr. Sect. B: Struct. Sci. **34**, 1360 (1978).
10. (*a*) K.-H. Thiele, C. Kruger, A. Sarkau, I. Ötvös, T. Bartik, and G. Pályi. Organometallics, **6**, 2290 (1987); (*b*) S.L. Latesky, A.K. McMullen, and I.P. Rothwell. Organometallics, **4**, 1896 (1985); (*c*) M. Bochmann, L.M. Wilson, M.B. Hursthouse, and M. Motevalli. Organometallics, **7**, 1148 (1988).

© 1999 NRC Canada

Influence des ions fluorure et de la silice amorphe sur la solubilité des gels de zircone et caractérisation des fluoro-complexes de zirconium en milieu moyennement acide

Rémi Valéro, Bernard Durand, Jean-Louis Guth et Thierry Chopin

Résumé : La solubilité des gels de zircone en fonction du pH est étudiée afin d'appréhender d'abord l'influence des ions F^- seuls, puis l'influence de la présence simultanée d'ions F^- et de silice amorphe. Deux concentrations [F^-] sont choisies, 0,094 et 0,314 mol L^{-1}, correspondant à des rapports molaires initiaux F/Zr = 0,6 et 2,0. Les fluorocomplexes métalliques formés aux pH 0,5 et 2,5 sont caractérisés par ^{19}F RMN. L'influence des ions fluorures sur la solubilité du zircon est aussi étudiée. Il est montré que la formation de complexes siliciques riches en fluor déplace les équilibres entre les fluorocomplexes de zirconium vers les complexes pauvres en fluor et que, en présence de F^-, la synthèse hydrothermale est susceptible d'engendrer la cristallisation du zircon pour tous les pH compris entre 0 et 10.

Mots clés : gel de zircone, silice, zircon, ions fluorure, solubilité, ^{19}F RMN.

Abstract: The solubility of zirconia gels versus pH is studied in order to state first the influence of F^- ions alone, then the influence of the simultaneous presence of F^- and amorphous silica. Two concentrations of F^- ions are chosen, 0.094 and 0.314 mol L^{-1}, corresponding to initial molar ratios F/Zr = 0.6 and 2.0. Metal fluorocomplexes formed at pH 0.5 and 2.5 are characterized by ^{19}F NMR. The influence of F^- on the solubility of zircon is also studied. It is shown that the formation of silicon complexes rich in fluorine shifts the equilibriums between the zirconium fluorocomplexes toward the complexes poor in fluorine and that, in the presence of F^-, the crystallization of zircon by hydrothermal synthesis can be forecasted, for pH values in the range 0–10.

Key words: zirconia gels, silica, zircon, fluoride ions, solubility, ^{19}F NMR.

1. Introduction

Seulement quelques articles concernaient la synthèse hydrothermale du zircon et impliquaient des traitements mettant en jeu soit des pressions dépassant 500 bars (1 bar = 100 kPa) (1–3), soit des durées de plusieurs centaines d'heures (2, 4) soit des températures largement supérieures à 200°C (1–3, 5). Collette et Frondel (2) remarquaient cependant dès 1957, que la formation de zircon était favorisée par l'addition d'ions fluorure au milieu hydrothermal.

Il était bien connu en effet, qu'en l'absence d'ions fluorure, la silice amorphe ne présente une solubilité appréciable, qu'aux pH basiques supérieurs à 9, due à la formation d'ions $Si(OH)_3O^-$ par des réactions de dépolymérisation de la silice (6). Dixon (7) indiquaient aussi, dès 1946, que l'addition d'ions fluorure augmente la solubilité à pH acide ou neutre. Marcuccilli (8) a cependant montré que, pour des valeurs très faibles de [F^-], la solubilité peut être inférieure à ce qu'elle est en l'absence d'anion fluorure, en raison de la fixation superficielle d'atomes de fluor qui rend la silice hydrophobe. Pour des valeurs plus élevées de [F^-], l'augmentation de solubilité est attribuée principalement à la formation d'ions hexafluorosilicate SiF_6^{2-} (9). Toutefois, Ciavatta et al. (10), puis Marcuccilli (8) ont mis en évidence, par RMN du fluor 19, la présence à côté des ions SiF_6^{2-} d'espèces siliciques hexacoordinées hydrofluorées et aquofluorées. Selon Marat et Janzen (11) les échanges intermoléculaires d'ions fluorure entre les fluorocomplexes de silicium sont catalysés par la présence d'acide fluorohydrique et d'eau et, en l'absence de ces deux réactifs considérés comme des impuretés, les échanges intermolculaires rapides d'ions fluorure dans les systèmes SiF_4 – SiF_5^-, SiF_5^- – SiF_6^{2-} et SiF_4 – SiF_6^{2-} sont correlés à des changements de coordination selon les équilibres [1]; ils impliquent la formation intermédiaire de complexes disiliques à fluor pontant.

[1] Si4 ⇄ 5 ⇄ 6 – F1 ⇄ 2

Reçu le 21 juillet 1999.

R. Valéro, B. Durand[1] et J.L. Guth. Laboratoire de Matériaux Minéraux, URA 428, École Nationale Supérieure de Chimie de Mulhouse, 3, rue Alfred Werner, 68093 Mulhouse Cedex, France.
T. Chopin. Centre de Recherches Rhône Poulenc, 52 rue de la Haie Coq, 93308 Aubervilliers, France.

1.Auteur auquel la correspondance doit être adressée : Adresse actuelle : Laboratoire de Chimie des Matériaux Inorganiques et Énergétiques (LCMIE), Université Paul Sabatier, 118 route de Narbonne, 31062 Toulouse Cedex 4, France.
Tél. : 33 05 61 55 61 40. Téléc. : 33 05 61 55 61 63.

 © 1999 CNRC Canada

Axon et Klinowski (12) ont confirmé que, dans les milieux renfermant des ions fluorure et de la silice, un équilibre est rapidement établi entre le solide et la solution dans lequel la silice est dépolimérisée par les ions fluorure. Un rapport F/Si en solution proche de 5 leur a fait envisager l'existence d'espèce $SiF_5(H_2O)^-$ ou la présence en quantités équivalentes des espèces hexacoordinées SiF_6^{2-} et $SiF_4(H_2O)_2$ impliquées dans l'équilibre [2].

[2] $$SiF_6^{2-} \rightleftarrows SiF_5(H_2O)^- \rightleftarrows SiF_4(H_2O)_2 \rightleftarrows SiF_3(H_2O)_2\ (OH)$$

La largeur des pics RMN ^{29}Si et ^{19}F attribués à l'espèce SiF_6^{2-} est interprétée par un échange dynamique rapide d'ions fluorure entre les différentes espèces de l'équilibre [2]; des espèces à fluor pontant peuvent aussi se former.

D'après plusieurs auteurs (9, 13, 14), en l'absence d'anion fluorure, les gels de zircone sont essentiellement solubles en milieu très acide, la concentration [Zr] pouvant atteindre 10^{-2} à 10^{-1} mol L^{-1} à pH 0 et environ 10^{-3} mol L^{-1} à pH 1. Entre les pH 3 et 9, la solubilité devient quasiment nulle ($[Zr] < 2 \times 10^{-5}$ mol L^{-1}); elle augmente faiblement au-delà de pH 9 sans dépasser 2×10^{-2} mol L^{-1} même à pH 14. Dans les solutions aqueuses diluées et acides, les espèces solubles du zirconium sont généralement polynucléaires (15–17). L'espèce prédominante est le tétramère cyclique caractérisé par Clearfield (18). Une espèce monomérique du type $[Zr(H_2O)_nCl_m]^{(4-m)}$ se forme en milieu HCl concentré et différentes espèces plus condensées sont engendrées par hydrolyse du tétramère lorsque le pH augmente (19). Dans des solutions renfermant des ions nitrate, des polycations linéaires ont été mis en évidence (20). Dans les milieux aqueux renfermant des ions fluorure les espèces polymériques du zirconium sont détruites. Livage et al. (21) suggèrent qu'à pH acide les anions fluorure pénètrent dans la première sphère de coordination du zirconium en formant des espèces monomériques, mais qu'ils ne sont plus complexants au-delà de pH 5. Aja (14) confirme, d'une part, que la stoechiométrie des espèces fluorées dépend du pH et de l'activité des anions fluorure dans le milieu et, d'autre part, que lorsque le pH augmente la diminution du pouvoir complexant des anions fluorure provoque, selon leur concentration, soit la gélification de la solution, soit la formation intermédiaire d'espèces hydroxyzirconiques solubles. Des stoechiométries allant de ZrF^{3+} à ZrF_7^{3-} ont été proposées, mais seule l'espèce hexafluorée ZrF_6^{2-} a été précisément identifiée par spectrométrie Raman (22, 23) et ^{19}F RMN (22).

Aucune information précise concernant la solubilité des gels de zircone en milieu aqueux fluoré n'avait été trouvée dans la littérature. Avant d'aborder l'étude de la synthèse hydrothermale du zircon, sous pression autogène et à des températures situées dans la gamme 100 à 200°C, dans le but d'en déterminer le mécanisme (24), il était utile de préciser le rôle des ions fluorure sur la solubilité des gels de zircone et sur celle du zircon. Il importait aussi d'appréhender l'effet de la présence de silice amorphe dans le milieu hydrothermal sur la solubilité des gels de zircone. Ce mémoire présente également la caractérisation des espèces dissoutes du zirconium par RMN du fluor 19.

2. Techniques expérimentales et analytiques

Les gels de zircone ont été préparés à partir de solutions aqueuses renfermant 0,16 mol L^{-1} d'oxychlorure de zirconium (Fluka), par addition d'ammoniaque (Fluka 20%) jusqu'à pH 4. La teneur en zirconium déterminée par analyse chimique dans les xérogels est $4{,}4 \times 10^{-3}$ mol g^{-1}. Pour les préparations mettant en jeu simultanément zirconium et silicium, de la silice amorphe (Aérosil 130 Degussa) a été introduite dans la solution d'oxychlorure de zirconium de façon à obtenir un milieu équimolaire en Zr et Si, puis le pH a été comme auparavant ajusté à 4. Les ions fluorure ont été introduits par dissolution de fluorure d'ammonium avant la neutralisation à pH 4; deux concentrations ont été utilisées : 0,094 et 0,314 mol L^{-1}. Dans la suite, l'expression « ions fluorure » désignera l'ensemble des espèces dissoutes du fluor, à l'exception des complexes fluorés du zirconium ou du silicium : HF, F^-, FHF^- ou $F(HF)_n^-$. Les mélanges réactionnels, versés dans des flacons en polyéthylène ont été chauffés à l'étuve à 60°C pendant 24 h. Le pH a été maintenu constant pendant les expériences par addition d'ammoniaque (20%) ou d'acide chlorhydrique (37%). Les études de solubilité du zircon ont été conduites à partir de suspensions renfermant 0,16 mol L^{-1} de zircon (Aldrich), traitées comme les milieux précédents pour introduire des ions fluorure et ajuster le pH.

Les solubilités ont été déterminées par mesure des concentrations en zirconium et silicium. Pour le zirconium, il a été fait appel à la colorimétrie du complexe Zr (8–hydroxyquinolinol) qui possède une bande d'absorption à 395 nm (25, 26) et pour le silicium à l'absorption atomique. Dans les deux cas, les ions fluorure et le deuxième métal n'interfèrent pas.

Les spectres RMN ont été enregistrés sur un spectromètre Brucker AC250 opérant à une fréquence de 235 MHz et avec un angle d'inclinaison de 70°. Ils ont été accumulés en utilisant des impulsions de 4 μs et des délais de recyclage de 6 s. Pour les déplacements chimiques $CFCl_3$ a été pris comme référence. Les échantillons ont été préparés à partir d'une solution aqueuse de $ZrOCl_2$ (4.66×10^{-2} mol L^{-1}) à laquelle ont été ajoutées des quantités appropriées de NH_4F pour obtenir des rapports molaires F/Zr dans la gamme 3,0 à 6,5. Pour spectres tracés en présence de SiO_2, de la silice amorphe (Aérosil 130) a été ajoutée en proportion équimolaire au zirconium. Le pH a été ajusté soit à 0,5 soit à 2,5 et les échantillons ont été maintenus pendant 24 h à température ambiante.

3. Études de solubilité

3.1. Influence des ions fluorure sur la solubilité des gels de zircone en milieu aqueux

La solubilité des gels zircone, analysée dans la gamme de pH 1 à 11 (fig. 1), est accrue aux pH acides et moyennement basiques, par la formation de fluorocomplexes de zirconium, de façon d'autant plus importante que la concentration initiale en ions fluorure est élevée

Avec la concentration en ions fluorure la plus faible, 0,094 mol L^{-1}, la solubilité à pH 1,5, $2{,}5 \times 10^{-2}$ mol L^{-1}, correspond à une concentration spécifique de 3,75 F^- par Zr

© 1999 CNRC Canada

Fig. 1. Solubilité du gel de zircone en fonction du pH : (*a*) [F⁻] = 0,314 mol L^{-1}, (*b*) [F⁻] = 0,094 mol L^{-1}.

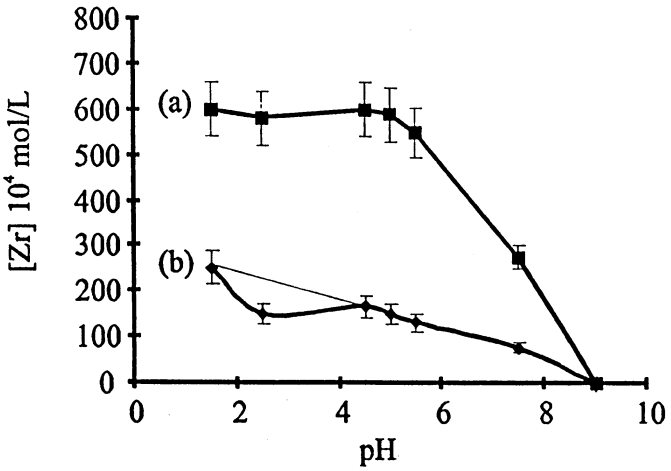

Fig. 2. Influence de la silice amorphe sur la solubilité du gel de zircone en fonction de pH avec [F⁻] = 0,094 mol L^{-1} : (*a*) [Zr], (*b*) [Si].

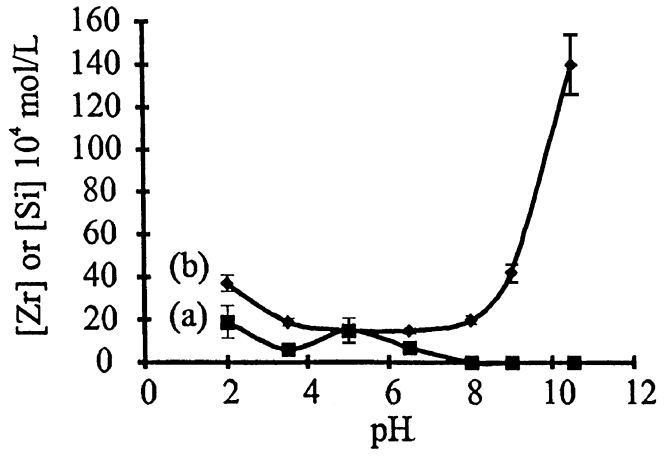

dissous. L'évolution générale avec l'augmentation du pH est une diminution linéaire de la solubilité qui atteint une valeur quasiment nulle à pH 9. Conformément aux observations de Aja (14) et Livage (21), la diminution de la solubilité est attribuée à une baisse du pouvoir complexant des anions fluorure et à une évolution de la stoechiométrie des fluorocomplexes du zirconium au fur et à mesure que le pH augmente. La valeur anormalement faible de la solubilité à pH 2,5, $1,5 \times 10^{-2}$ mol L^{-1}, pourrait être expliquée par une diminution de la concentration en ions fluorure due à la formation de fluorocomplexes de zirconium riches en fluor. La concentration spécifique en F^- atteint alors 6,25. Babu et al. (27) remarquent en effet que ces complexes se forment avec une cinétique maximale au voisinage de ce pH.

Avec la concentration en ions fluorures la plus élevée, 0,314 mol L^{-1}, la formation de fluorocomplexes de zirconium riches en fluor permet d'atteindre une solubilité de $5,8 \times 10^{-2}$ mol L^{-1} à pH 1,5. La concentration spécifique est alors voisine de 5,4 et la solubilité conserve la même valeur jusqu'à pH 5. Au-delà, les fluorocomplexes deviennent

Fig. 3. Influence de la silice amorphe sur la solubilité du gel de zircone en fonction du pH avec [F⁻] = 0,314 mol L^{-1} : (*a*) [Zr], (*b*) [Si].

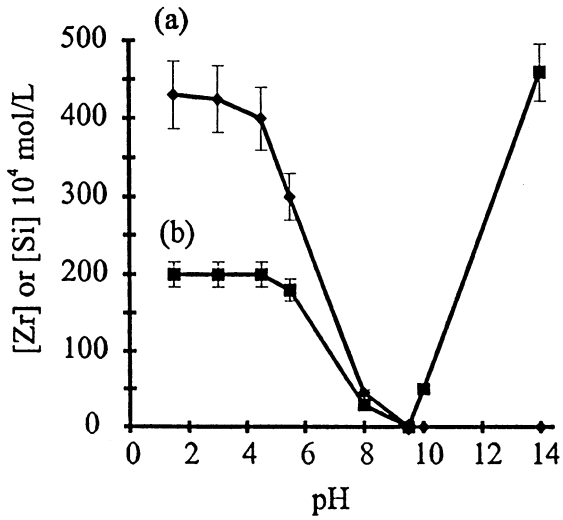

instables et la solubilité chute rapidement pour atteindre une valeur quasiment nulle également à pH 9.

3.2. Influence de la présence de silice sur la solubilité des gels de zircone en milieu aqueux fluoré

Pour la concentration en anions fluorure de 0,094 mol L^{-1}, l'introduction de silice dans le milieu hydrothermal n'affecte pas l'allure générale de la courbe de solubilité du gel de zircone (fig. 2, courbe *a*), mais diminue la concentration en zirconium dissous d'un facteur 10. Ainsi cette concentration diminue de 2×10^{-3} mol L^{-1} à une valeur pratiquement nulle lorsque le pH augmente de 2 à 8. La solubilité reste cependant plus élevée que celle observée pour un gel de zircone seul en l'absence d'anion fluorure qui selon Adair (9) est inférieure à 10^{-4} mol L^{-1} dans la même gamme de pH. En dessous de pH 8, la solubilité de la silice (fig. 2, courbe *b*) semble légèrement supérieure à celle du gel de zircone, mais l'écart ne devient appréciable qu'aux pH plus basiques. En outre, la comparaison avec les résultats obtenus par Iler (6), pour la silice seule, montre que la présence d'anions fluorure à faible concentration et de gel de zircone ne modifie ni l'allure de la courbe, ni les valeurs des concentrations en silicium dissous.

Pour la concentration en anions fluorure de 0,314 mol L^{-1}, l'apport de silice dans le milieu hydrothermal ne change pas non plus l'allure de la courbe de solubilité du gel de zircone (fig. 3, courbe *a*), mais la diminution de la concentration en zirconium dissous est moins accentuée. [Zr] conserve une valeur voisine de $4,2 \times 10^{-2}$ mol L^{-1} entre les pH 2 et 5, puis diminue régulièrement pour devenir quasiment nulle au-delà de pH 9,5. L'augmentation de la concentration en ions fluorure multiplie environ par 10 la solubilité de la silice (fig. 3, courbe *b*). [Si] atteint alors des valeurs moitié moindres que [Zr] lorsque le pH augmente de 1,5 à 9,5. Aux pH plus élevés la solubilité de la silice augmente, alors que celle du gel de zircone reste négligeable. Entre les pH 2 et 5, la concentration spécifique en ions F^- est voisine de 7,8 ou 5,2 selon qu'elle soit rapportée à la seule concentration en Zr ou à la somme des concentrations en Zr et Si. Si l'on as-

© 1999 CNRC Canada

Fig. 4. Solubilité du zircon en fonction du pH avec [F^-] = 0,094 mol L^{-1} : (*a*) [Zr], (*b*) [Si].

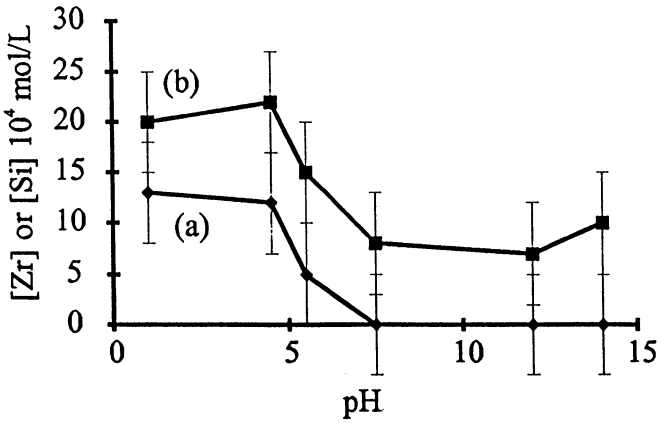

Fig. 5. Solubilité du zircon en fonction du pH avec [F^-] = 0,314 mol L^{-1} : (*a*) [Zr], (*b*) [Si].

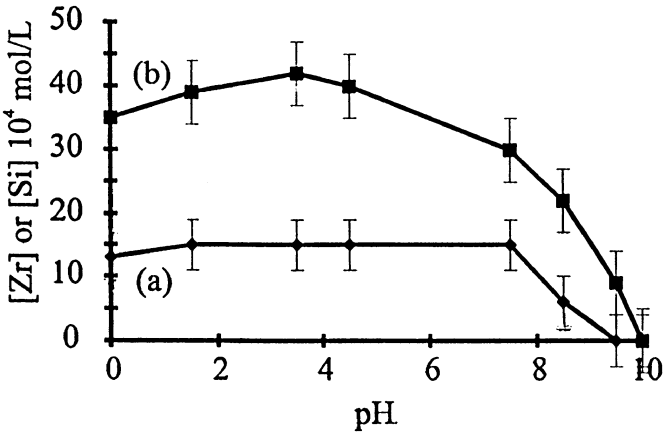

sume que le silicium est complexé sous la forme d'ions SiF_6^{2-} et qu'il ne se forme pas d'acide fluorhydrique, la concentration spécifique en ion F^- par rapport au zirconium dissous est voisine de 4,6.

3.3. Influence des ions fluorure sur la solubilité du zircon

En l'absence d'ion fluorure, le zircon est quasiment insoluble, quel que soit le pH dans la gamme 0 à 14. La teneur en silicium dissous est en de ça de la limite de détection (5×10^{-4} mol L^{-1}). Des traces de zirconium dissous sont décelées (environ 10^{-5} mol L^{-1}).

L'addition d'ions fluorure à la concentration de 0,094 mol L^{-1} accroît la solubilité à une valeur voisine de $1,5 \times 10^{-3}$ mol L^{-1} pour les pH compris entre 1 et 4 (fig. 4). Pour les pH plus élevés, la solubilité diminue. Les profils des courbes de variation en fonction du pH de [Zr] et [Si] sont similaires et [Si] (courbe *b*) semble supérieure à [Zr] (courbe *a*), mais le recouvrement des intervalles d'incertitude ne permet pas de conclure à une dissolution non congruente. L'augmentation de [F^-] à 0,314 mol L^{-1} accroît beaucoup plus fortement [Si] que [Zr] (fig. 5) et révèle indubitablement une dissolution non congruente pour les pH dans la gamme 0–9.

Dans les deux cas, la comparaison des figures, 2 et 4 d'une part, et 3 et 5 d'autre part, révèle une solubilité plus faible pour le zircon que pour le gel de zircone et la silice amorphe avec des écarts plus ou moins importants selon le pH et la concentration [F^-].

Fig. 6. Spectre ^{19}F RMN d'une solution d'oxychlorure de zirconium $4,66 \times 10^{-2}$ M contenant des ions F^- : F/Zr = 4, pH = 2,5.

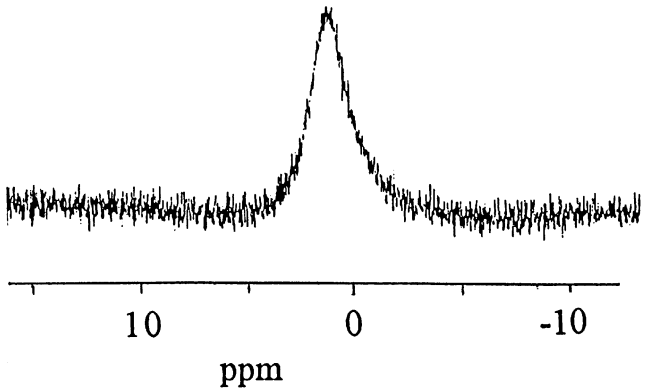

Fig. 7. Spectre ^{19}F RMN d'une solution d'oxychlorure de zirconium $4,66 \times 10^{-2}$ M en présence d'ions F^- et de silice amorphe : F/Zr = 4, Si/Zr = 1, pH = 2,5.

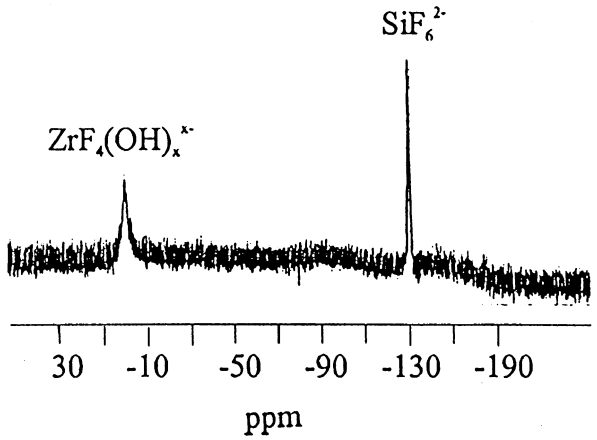

4. Caractérisation des fluorocomplexes du zirconium par ^{19}F RMN

4.1. Résultats

En l'absence de silice et pour les deux pH étudiés (0,5 et 2,5), les spectres RMN ne présentent qu'un seul pic large quel que soit le rapport F/Zr des concentrations dans l'intervalle 3,5 à 6,5, comme le montre la figure 6 pour pH = 2,5 et F/Zr = 4,0. A température ambiante, le déplacement chimique rapporté à $CFCl_3$ varie de +10 à –35 ppm lorsque le rapport F/Zr augmente de 3,5 à 6,5 pour la solution à pH 0,5 (fig. 9, courbe *b*) et de +3 à –19 ppm pour la solution à pH 2,5 (24). Simultanément la largeur à mi-hauteur du signal s'accroît (fig. 8). Pour les rapports F/Zr < 5,8 l'abaissement du pH de 2,5 à 0,5 ne modifie pas le profil des courbes; seule, une très faible augmentation des largeurs à mi-hauteur est observée. Par contre, pour les rapports F/Zr > 5,8, la largeur à mi-hauteur accuse une très forte élévation.

En présence de silice, le pic caractéristique des fluorocomplexes du zirconium est conservé, mais il apparaît quel

© 1999 CNRC Canada

Fig. 8. Influence du rapport F/Zr sur la largeur à mi-hauteur du signal RMN des fluorocomplexes du zirconium dans une solution 4,66 $\times 10^{-2}$ M d'oxychlorure de zirconium : (✹) solution à pH = 0,5, (Δ) solution à pH = 2,5, (▼) solution à pH 2,5 et renfermant de la silice amorphe en proportion équimolaire au zirconium.

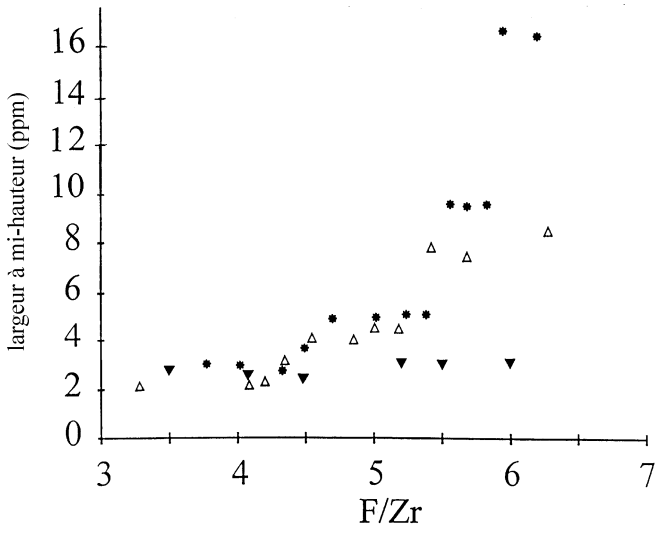

que soit le pH, mais uniquement pour les rapports F/Zr > 4, un second signal plus étroit au voisinage de –131 ppm, ainsi qu'en témoigne la figure 7 pour F/Zr = 4,0 et pH = 2,5. La variation du déplacement chimique du signal des fluorocomplexes est très significativement réduite puisqu'il n'évolue plus qu'entre +5 et –2,5 ppm lorsque le rapport F/Zr croît de 3,5 à 6,5 dans le milieu à pH 0,5 (fig. 9, courbe *a*). À pH 2,5, la réduction est moindre, le déplacement chimique passant de 0 à –12 ppm (24). Quant à la largeur du signal à mi-hauteur, elle demeure, quelque soit le pH, pratiquement constante et voisine de 2 ppm sur tout l'intervalle comme le montre la figure 8 (courbe ▼) ; elle a une valeur sensiblement égale à celle observée en l'absence de silice pour les plus petites valeurs du rapport F/Zr.

4.2. Discussion

À température ambiante, la RMN du fluor 19 ne permet pas de séparer les espèces dissoutes du fluor, autres que les fluorocomplexes métalliques : F^-, HF, FHF^-, $F(HF)_n^-$: elles se manifestent toutes par un seul signal situé habituellement au voisinage de –120 ppm. Aucun signal n'ayant été observé dans cette région, il semble donc que la majeure partie des ions fluorure introduits dans le milieu se combinent aux métaux pour former des fluorocomplexes et participent à des échanges dynamiques rapides entre différents fluorocomplexes.

Par ^{19}F RMN, le signal caractéristique des ions SiF_6^{2-} est fréquemment obtenu vers –128 ppm. Le pic au voisinage de –131 ppm dans les spectres des milieux renfermant de la silice et pour les rapports F/Zr > 4, doit donc être attribué à l'existence de fluorocomplexes de silicium hexacoordinés. Sa faible largeur à mi-hauteur pourrait traduire la prédominance de l'ion SiF_6^{2-}. Toutefois, la formation d'aquofluorocomplexes en équilibre avec SiF_6^{2-} selon [2] ainsi que celle de complexes siliciques à fluor pontant ne peuvent être exclues.

Fig. 9. Influence de la présence de silice amorphe sur l'évolution du déplacement chimique, en fonction du rapport F/Zr, du signal ^{19}F RMN des fluorocomplexes de zirconium, dans une solution 4,66 $\times 10^{-2}$ M d'oxychlorure de zirconium : (*a*) courbe tracée en présence de silice en proportion équimolaire au zirconium, (*b*) courbe tracée en absence de silice.

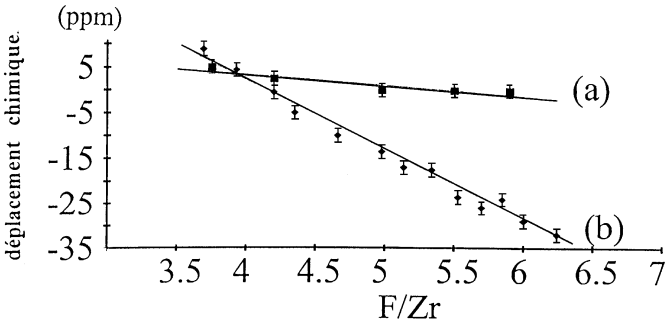

Par analogie avec les interprétations proposées par Janzen et al. (11) et Axon et al. (12) pour les fluorocomplexes de silicium, les largeurs à mi-hauteur élevées des pics caractéristiques des fluorocomplexes de zirconium peuvent être imputées à des échanges inter- et intramoléculaires dynamiques rapides d'ions fluorure entre différents fluorocomplexes du zirconium coexistant en équilibre dynamique complexe dans la solution. Ces échanges impliquent probablement la formation intermédiaire de complexes polyzirconiques à fluor pontant. En l'absence de silicium, l'augmentation du déplacement chimique au fur et à mesure que le rapport des concentrations F/Zr croît traduit vraisemblablement une évolution de la coordination du zirconium de 4 vers 6, voire 7 avec des changements de coordination Zr: $4 \rightleftarrows 5 \rightleftarrows 6 \rightleftarrows 7$ et F: $1 \rightleftarrows 2$. Une explication de l'augmentation simultanée de la largeur à mi-hauteur pourrait être que le déplacement des équilibres vers les complexes riches en fluor réduit la concentration des autres fluorozirconates impliqués dans la formation des espèces intermédiaires à fluor pontant, Zr···F···Zr. Les échanges d'ions fluorures devraient alors être nécessairement ralentis. On pourrait aussi avancer que l'acroissement du rapport F/Zr multiplie le nombre des fluorocomplexes susceptibles d'être formés et qu'il en résulte une augmentation de la largeur à mi-hauteur.

La réduction considérable des effets provoqués par l'augmentation du rapport F/Zr, lorsque de la silice est ajoutée dans le milieu en quantité équimolaire au zirconium, pourrait être interprétée en admettant, qu'aux faibles concentrations (F/Zr < 4), les ions F^- sont consommés pour former des fluorocomplexes de zirconium pauvres en fluor ($ZrF_4(OH)_x^{x-}$) préférentiellement à des fluorocomplexes de silicium, d'où l'absence de signal caractéristique de ces derniers. Pour les concentrations plus élevées (F/Zr ≥ 4) la formation d'ions hexafluorosilicate à côté des fluorocomplexes zirconiques pauvres en fluor consomme des quantités importantes d'ions F^- et s'oppose au déplacement des équilibres vers les fluorocomplexes zirconiques riches en fluor. La stabilité thermodynamique des ions SiF_6^{2-} serait alors intermédiaire entre celle des ions $ZrF_4(OH)_x^{x-}$ et celles des espèces zirconiques plus riches en fluor.

Une autre interprétation, plus conforme aux travaux de Janzen et al. (11) reviendrait à considérer qu'aux pH acides,

© 1999 CNRC Canada

l'acide fluorhydrique réagit avec la silice amorphe pour produire SiF_4 et que les réactions de SiF_4 avec les fluorocomplexes de zirconium riches en fluor aboutissent à un enrichissement en fluor des fluorocomplexes de silicium et un appauvrissement en fluor des fluorocomplexes de zirconium. Ces réactions impliqueraient la formation intermédiaire de complexes bimétalliques à fluor pontant selon par exemple les équations [3] et [4].

[3] $$ZrF_7^{3-} + SiF_4 \rightleftarrows F_6Zr\cdots F\cdots SiF_4 \rightleftarrows ZrF_6^{2-} + SiF_5^-$$

[4] $$ZrF_6^{2-} + SiF_5^- \rightleftarrows F_5Zr\cdots F\cdots SiF_5 \rightleftarrows ZrF_5^- + SiF_6^{2-}$$

Des réactions analogues pourraient être écrites pour ZrF_6^{2-} et ZrF_5^-.

5. Conclusion

En l'absence d'ion fluorure, la synthèse hydrothermale n'est susceptible de produire du zircon qu'aux pH basiques, la solubilité des deux précurseurs étant en effet plus importante que celle du zircon. En milieu moyennement acide (pH 2–7), les solubilités sont du même ordre de grandeur. En milieu plus acide (pH 0–2), la solubilité du gel de zircone est cent fois supérieure à celle de la silice amorphe.

Pour les pH moyennement acides, l'addition d'ions fluorure au milieu accroît la solubilité des gels de zircone, d'autant plus que leur concentration est élevée, par formation de fluorocomplexes de zirconium monomères. Leur stoechiométrie dépend d'autant plus du pH que la concentration en ions fluorure est faible. L'augmentation du pH au-delà de 4,5 à 5 déstabilise les fluorocomplexes et favorise la formation d'espèces polymères qui provoque une diminution de la solubilité du gel ; elle devient quasi nulle lorsque le pH dépasse 9.

L'introduction de silice amorphe dans le milieu hydrothermal diminue la solubilité du gel de zircone de façon d'autant plus significative que la concentration en ions fluorure est faible. Aux faibles concentrations ($[F^-]$ = 0,094 mol L^{-1}), la solubilité de la silice n'est pas modifiée et seuls des fluorocomplexes de zirconium pauvres en fluor semblent se former. Pour les concentrations plus élevées ($[F^-]$ = 0,314 mol L^{-1}), les mesures de solubilité et la caractérisation des espèces dissoutes par RMN du fluor 19 fournissent des résultats concordants prouvant que la formation de fluorocomplexes de silicium riches en fluor (SiF_6^{2-}) déplace les équilibres entre les fluorocomplexes de zirconium vers les complexes tétrafluorés.

En présence d'anions fluorure, la synthèse hydrothermale sera susceptible de produire du zircon, quel que soit le pH dans la gamme 0 à 10. Du côté acide, le gel de zircone et la silice amorphe présentent des solubilités très supérieures à celle du zircon. Cependant, en raison de la dissolution non congruente du zircon, des zircons non stoechiométriques déficitaires en silicium pourront cristalliser. Du côté basique, l'anticipation est plus difficile car la solutilité des deux précurseurs est fortement diminuée par la déstabilisation des fluorocomplexes. Les solubilités demeurant toutefois légèrement supérieures à celle du zircon, la cristallisation de zircons stoechiométriques pourrait se produire. L'investigation des possibilités de synthèse hydrothermale du zircon en présence d'anions fluorure et sous pression autogène à 150°C a confirmé ces prévisions en montrant notamment que des fluorozircons, dont le déficit en tétraèdres SiO_4 est compensé par des nids tétraédriques $[F_4 (OH)_{4-n}]$, cristallisent à pH acide (24, 28) alors que des zircons stoechiométriques exempts de fluor et à morphologie inédite se forment en milieu basique (24, 29).

Références

1. R. Caruba, A. Baumer et G. Turco. Geochim. Cosmochim. Acta, **39**, 11 (1975).
2. R.L. Collette et C. Frondel. Am. Mineral. **42**, 759 (1957).
3. A. Mumptonf et R. Roy. Geochim. Cosmochim. Acta, **21**, 217 (1961).
4. A. Mosset, P. Baules, P. Lecante, J.C. Trombe, H. Ahamdane et F. Bensamka. J. Mater. Chem. **6**, 1527 (1996).
5. V.V. Siorchuk et V.M. Certov. Izv. Akad. Nauk SSSR, Neorg. Mater. **25**, 622 (1989).
6. R.KJ. Iler. The chemistry of silica. Vol. 42. John Wiley and Son Ed. Chichester, England. 1979.
7. P. Dixon. Commonw. Aust. Sci. Ind. Res. **19**, 331 (1946).
8. F. Marcuccilli. Thèse, Université Haute Alsace, France (1992).
9. J.H. Adair, R.P. Denkewicz, F.J. Arriagada et K. Osseoasare. Ceram. Trans. **135** (1988).
10. L. Ciavatta, M. Iliano et R. Porto. Polyhedron, **7**, 1773 (1988).
11. R.K. Marat et A.F. Janzen. Can. J. Chem. **55**, 3845 (1977).
12. S.A. Axon et J. Klinowski. J. Chem. Soc. Faraday Trans. **89**, 4245 (1993).
13. H. Bilinski et M. Branica. Acta Chem. Scand. **20**, 853 (1966).
14. S.U. Aja, S.A. Wood et A.E. Williams-Jones. Appl. Geochem. **10** (6), 603 (1995).
15. M. Aberg. Acta Chem. Scand. **3**1, 171 (1977).
16. E. Barry Scheetz, W.B. White et S.D. Atkinson. Nucl. Technol. **56**, 289 (1982).
17. A. Clearfield et A. Vaughan. Acta Crystallogr. **9**, 555 (1956).
18. A. Clearfield. Rev. Pure Appl. Chem. 14, 91 (1964); Ind. Chem. **3**, 146 (1964).
19. S. Hannane, F. Bertin et J. Bouix. Bull. Soc. Chim. Fr. **127**, 43 et 50 (1990).
20. J. Livage, M. Henry et C. Sanchez. Prog. Solid State. Chem. **18**, 259 (1988).
21. J. Livage, M. Chatry, M. Henry et F. Tautelle. Mater. Res. Soc. Symp. Proc. **271**, 201 (1992).
22. P.A.W. Dean et D.F. Evans. J. Chem. Soc. A, **698** (1967).
23. W.P. Griffith et T.D. Wickins. J. Chem. Soc. A, **675** (1967).
24. R. Valéro. Thèse, Université Haute Alsace, France (1997).
25. R.T. Van Santen, J.H. Schlewitz et H. Toy. Anal. Chim. Acta, **33**, 593 (1965).
26. H.O. Schneider et M.E. Roselli. An. Asoc. Quim. Argent. **57**, 39 (1969).
27. C.A. Babu, B. Ayengar, K.B. Lal and R.V. Amalraj. Waste Manage. **13**, 279 (1993).
28. R. Valéro, L. Delmotte, J.L. Paillaud, B. Durand, J.L. Guth et T. Chopin. J. Mater. Chem. **9**, 117 (1999).
29. R. Valéro, B. Durand, J.L. Guth et T. Chopin. Microporous Mesoporous Mater. 29, 311 (1999).

© 1999 CNRC Canada

Temperature-dependent structural properties of a solid urea inclusion compound containing chiral guest molecules: 2-bromotetradecane/urea

Lily Yeo and Kenneth D.M. Harris

Abstract: Periodic structural properties of the 2-bromotetradecane/urea inclusion compound have been investigated as a function of temperature. Differential scanning calorimetry between 298 and 98 K identified three well-defined regimes, denoted the high-, intermediate-, and low-temperature phases. The structural properties of each phase (at 293, 207, and 142 K, respectively) have been investigated by single crystal X-ray diffraction. In the high-temperature phase, the inclusion compound has the hexagonal urea tunnel structure ($P6_122$) characteristic of the conventional urea inclusion compounds, with substantial orientational disorder of the guest molecules. In the intermediate-temperature phase, the symmetry is lowered to orthorhombic ($C222_1$), although the host structure remains close to the hexagonal tunnel structure of the high-temperature phase and there is no clear evidence for increased orientational ordering of the guest molecules. In the low-temperature phase, the urea tunnel structure is monoclinic ($P2_1$), and is based on a $2 \times 2 \times 1$ supercell of the hexagonal cell of the high-temperature structure. There are four independent types of tunnel, three of which are strongly distorted from hexagonal geometry. Within these distorted tunnels, there is a comparatively narrow distribution of guest molecule orientations, which correlate well with the observed distortions of the tunnels. The 2-bromotetradecane/urea inclusion compound highlights several issues of wider relevance concerning the structural properties of solid inclusion compounds.

Key words: urea inclusion compounds, X-ray diffraction, phase transitions, chiral recognition, incommensurate solid, 2-bromotetradecane/urea.

Résumé : On a étudié les propriétés structurales périodiques du composé d'inclusion 2-bromotétradécane/urée en fonction de la température. La calorimétrie à balayage différentielle entre 298 et 98 K permet d'identifier trois régimes bien définis dénommés phases à haute température, à température intermédiaire et à basse température. On a étudié les propriétés structurales de chacune des phases (à 293, 207 et 142 K, respectivement) à l'aide de la diffraction des rayons X par un cristal unique. Dans la phase à haute température, le composé d'inclusion comporte une structure hexagonale ($P6_122$) avec tunnel d'urée qui est caractéristique des composés d'inclusions usuels de l'urée. Dans la phase de température intermédiaire, la symétrie est abaissée à orthorhombique ($C222_1$) même si la structure hôte reste toujours proche de la structure hexagonale à tunnel de la phase à haute température; de plus, rien ne suggère que l'orientation des molécules incluses est augmentée. Dans la phase de basse température, la structure du tunnel d'urée est monoclinique ($P2_1$) et elle est basée sur une supercellule $2 \times 2 \times 1$ de la cellule hexagonale de structure à température élevée. On observe quatre types différents de tunnels, dont trois sont fortement déformés par rapport à la symétrie hexagonale. Dans ces tunnels déformés, la distribution des orientations des molécules incluses est relativement étroite en bonne corrélation avec les distorsions observées des tunnels. Le composé d'inclusion 2-bromotétradécane/urée illustre plusieurs points qui présentent une importance plus générale concernant les propriétés structurales des composés d'inclusion solides.

Mots clés : composés d'inclusion d'urée, diffraction des rayons X, transitions de phase, reconnaissance chirale, solide incommensurable, 2-bromotétradécane/urée.

[Traduit par la Rédaction]

1. Introduction

There is currently considerable interest in the diverse range of physicochemical properties associated with solid urea inclusion compounds (1–3). In conventional urea inclusion compounds, the urea molecules form a hydrogen-bonded host structure that contains linear, parallel tunnels (4, 5). This urea tunnel structure is stable only when the tunnels are filled with a dense packing of guest molecules. The effective diameter of the urea tunnel (defined on the basis of van der Waals radii) varies between about 5.5 and 5.8 Å as a function of position along the tunnel (6), and as a consequence of this rather confined geometry, only guest molecules based on a sufficiently long *n*-alkane chain and with a sufficiently

Received March 25, 1999.

L. Yeo and K.D.M. Harris.[1] School of Chemistry, University of Birmingham, Edgbaston Birmingham B15 2TT, United Kingdom.

[1]Author to whom correspondence may be addressed. Telephone: +44-121-414-7474. Fax: +44-121-414-7473.

 © 1999 NRC Canada

small degree of substitution are able to form these inclusion compounds with urea.

Several structural aspects of urea inclusion compounds are of interest, including: (*i*) the nature of the host structure and its dependence on temperature; (*ii*) the mode of ordering of the guest molecules within the host structure (in some cases there is only one-dimensional ordering of the guest molecules along the tunnels, whereas in other cases well-defined modes of inter-tunnel ordering also exist); (*iii*) the structural relationship between the host and guest subsystems, concerning mainly the commensurate versus incommensurate nature of the inclusion compound; (*iv*) the conformational properties of the guest molecules; (*v*) the orientational characteristics of the guest molecules with respect to reorientation about the tunnel axis; and (*vi*) for unsymmetric guest molecules of the type $X(CH_2)_nY$, the question of the orientation ($X(CH_2)_nY$ or $Y(CH_2)_nX$) adopted by the guest molecules along the tunnel, leading to different possible types of end-group interaction (X···X, Y···Y, and X···Y). In this paper we focus on issues relating to (*i*), although the work reported here also sheds light on some of the other structural aspects highlighted above.

To a first approximation, the space group of the average urea host structure in the conventional urea inclusion compounds at ambient temperature is $P6_122$ or $P6_522$ (see refs. 5 and 7 for detailed discussion of structural and symmetry properties of urea inclusion compounds). The urea tunnel is constructed from hydrogen bonded spirals of urea molecules, and a single crystal either contains only right-handed spirals (space group $P6_122$) or only left-handed spirals (space group $P6_522$). The chirality of the urea tunnel structure is generated spontaneously during crystal growth, and there is clearly considerable potential to exploit this property of urea inclusion compounds. For chiral guest molecules, such opportunities devolve upon the extent of chiral recognition between the host structure and the two enantiomers of a chiral guest species (which could be a reactant molecule, a transition state, or a reaction product). Among the potential applications, asymmetric synthesis could be achieved by carrying out a chemical reaction between achiral guest molecules to generate an enantiomeric excess of a chiral product guest molecule, with the chiral host environment influencing the preferred production of one enantiomer of the chiral product. Applications based on separation of the two enantiomers of a chiral guest may also be achieved. The opportunity to exploit the chiral nature of the urea tunnel structure in such applications depends on the extent to which the interaction between the host tunnel of a given chirality (e.g., $P6_122$) is different for the two enantiomers (*R* and *S*) of a chiral guest (note that the *R*-guest/($P6_122$)-host and *S*-guest/($P6_122$)-host systems have a diastereoisomeric relationship, and therefore correspond (in general) to different energies). Recent computational studies (8, 9) have provided insights into the characteristics of host-guest interaction that underlie this chiral recognition. For example, for chiral 2-bromoalkane guest molecules in the $P6_122$ urea tunnel structure, a clear preference for the *R* enantiomer over the *S* enantiomer is found.

In general, the opportunities to exploit the chirality of urea inclusion compounds are limited by the difficulty of accommodating, within the urea tunnel, guest molecules containing a side-group on the *n*-alkane chain (as required to have a chiral centre). Early work by Schlenk (10–14) demonstrated experimentally that urea inclusion compounds can indeed exhibit some degree of chiral recognition, but almost all subsequent studies of urea inclusion compounds (1) have focused on achiral guest molecules. Recently, in conjunction with our computational studies (8, 9) discussed above, we have prepared the urea inclusion compound containing the chiral guest molecule 2-bromotetradecane, and have begun a series of investigations into the physicochemical properties of this material. In this paper, we focus on the structural properties of the 2-bromotetradecane/urea inclusion compound, and particularly the temperature dependence of these properties. We note that, at a sufficiently low temperature, most urea inclusion compounds undergo phase transitions which, in general, are associated with changes in the symmetry of the host structure (15–18) and changes in the dynamic properties of the guest molecules (16, 19–23). Here we focus on structural aspects of these phase transitions in the 2-bromotetradecane/urea inclusion compound.

2. Experimental

Crystals of the 2-bromotetradecane/urea inclusion compound were prepared from commercially available reagents using the following method. A racemic sample of 2-bromotetradecane was added in excess (with respect to the expected guest/host molar ratio in the inclusion compound) to a saturated solution of urea in methanol in a conical flask under ultrasonic agitation at 55°C. A sufficient amount of 2-methylbutan-2-ol was added to render the liquid 2-bromotetradecane completely miscible with the methanol (we note that neither of the solvent molecules (methanol and 2-methylbutan-2-ol) used here is known to form a stable inclusion compound with urea, and there is no evidence (from other studies) for co-inclusion of these solvent molecules within the urea tunnel structure in the 2-bromotetradecane/urea inclusion compounds prepared here). Crystals (urea inclusion compound) that precipitated immediately at this stage were dissolved by adding a further small amount of methanol. The flask was then transferred to an incubator, in which it was cooled systematically from 55 to 15°C over 24 h, and then left at 15°C for several days. When sufficiently large crystals had grown, they were collected and washed with 2,2,4-trimethylpentane.

The crystals were long hexagonal needles, and their behaviour in the polarizing microscope was consistent with conventional urea inclusion compounds (hexagonal crystal system). Powder X-ray diffraction confirmed that the crystals had the conventional urea tunnel structure at ambient temperature, and that the sample did not contain any significant amount of the "pure" crystalline phase of urea (the crystal structure of which differs substantially from the urea substructure in urea inclusion compounds).

Differential scanning calorimetry was carried out on a Perkin–Elmer DSC-7 instrument, with the polycrystalline sample subjected to cooling and heating cycles at a rate of 10 K min^{-1}. The differential scanning calorimetry results identify three different temperature regimes (see Sect. 5.1), and our diffraction studies have been carried out for each of these phases.

© 1999 NRC Canada

Table 1. Data collection parameters for single crystal X-ray diffraction experiments.

	Temperature (K)		
	293	207	142
Number of frames recorded	18	23	23
Oscillation angle per frame (°)	10	8	8
Exposure time per frame (min)	10	15	10
Crystal-to-detector distance (mm)	120	80	90

Single crystal X-ray diffraction experiments were carried out using graphite-monochromated MoK_α radiation (λ = 0.710 73 Å) on a Rigaku R-Axis II diffractometer equipped with an area detector. For experiments below ambient temperature, a standard MSC low-temperature device (temperature stability ca. ±2 K) was used. There is no evidence that the phase transitions are associated with crystal twinning, allowing the structural properties to be investigated readily from single crystal diffraction data (note that crystal twinning is often found to accompany transitions from high-temperature to low-temperature phases in such systems). At each temperature, about 2 h was allowed for the crystal to reach thermal equilibrium before starting the X-ray diffraction measurements.

To provide an initial qualitative understanding of the diffraction patterns, single crystal X-ray diffraction rotation photographs were recorded at ambient temperature (293), 207, and 142 K, with the oscillation axis parallel to the needle axis of the crystal morphology (tunnel axis of the urea host structure). Single crystal X-ray diffraction data collections were carried out at ambient temperature (293), 207, and 142 K. Parameters relating to the data collections at each temperature are summarized in Table 1. Different crystals were used for the experiments at each temperature.

3. Structural description of conventional urea inclusion compounds

For most urea inclusion compounds, there is an incommensurate relationship between the periodic repeat distances of the host and guest substructures (denoted c_h and c_g, respectively) along the tunnel axis (classically, for an incommensurate system, sufficiently small integers p and q cannot be found for which $pc_h \approx qc_g$). Although the host and guest substructures are chemically distinguishable from each other, and possess different structural periodicities, these two substructures are not independent, and through their mutual interaction each substructure must exert a structural perturbation (modulation) on the other substructure. As the basic periodicities (c_h and c_g) of the two substructures are incommensurate, the modulation exerted upon a given substructure must be incommensurate with the basic periodicity of that substructure. Thus, the host substructure can be considered in terms of a "basic structure" (with period c_h along the tunnel) which is subjected to an incommensurate modulation (with period c_g along the tunnel) through its interaction with the guest substructure. The basic structure can be described using conventional crystallographic principles (e.g., three-dimensional space group symmetry). Similarly, the guest substructure can be considered in terms of an incommensurately modulated "basic structure." The incommensurate modulations describe perturbations to the basic structures that result from host-guest interaction.

Considering both the host and guest components together in a unified description of the crystal structure, four basis lattice vectors $\{\boldsymbol{a}_h, \boldsymbol{b}_h, \boldsymbol{c}_h, \boldsymbol{c}_g\}$ are required to define the periodicity of the composite inclusion compound (as the system is incommensurate, the value of c_h/c_g is irrational, or approximated by a rational number with high denominator). Correspondingly, the symmetry of the composite inclusion compound is described by a four-dimensional superspace group (7, 24). On transforming this structural description to reciprocal space, the diffraction pattern is described by four basis reciprocal lattice vectors $\{\boldsymbol{a}_h^*, \boldsymbol{b}_h^*, \boldsymbol{c}_h^*, \boldsymbol{c}_g^*\}$ and four integer Miller indices ($hklm$). Thus, a reciprocal lattice vector $\boldsymbol{S}$ is defined by the linear combination

$$\boldsymbol{S} = h\,\boldsymbol{a}_h^* + k\,\boldsymbol{b}_h^* + l\,\boldsymbol{c}_h^* + m\,\boldsymbol{c}_g^*$$

with integer coefficients h, k, l and m. Previously (5), the term "h" (host) diffraction pattern has been used to refer to the ($hkl0$) subset of the complete diffraction pattern, which arises from diffraction by the basic host structure (and by the incommensurate modulation to the basic guest structure). Similarly, the term "g" (guest) diffraction pattern has been used to refer to the ($hk0m$) subset of the complete diffraction pattern, which arises from diffraction by the basic guest structure (and by the incommensurate modulation to the basic host structure). In addition, the subset of the diffraction pattern comprising reflections ($hklm$) with $l \neq 0$ and $m \neq 0$ arises from the intermodulation of the host and guest substructures, and conveys important information on this structural aspect.

Descriptions of the symmetry properties of incommensurate urea inclusion compounds in superspace groups have been developed (7), and an attempt to determine the modulations in the host and guest substructures of an *n*-alkane/urea inclusion compound, by solving the structure in a superspace group, has been reported (25). Much recent research (26–28, footnote 2) has been devoted to studies of all aspects of the diffraction patterns from incommensurate urea inclusion compounds (particularly *n*-alkane/urea inclusion compounds), including measurement of incommensurate satellite reflections and detailed characterization of different forms of diffuse scattering.

4. Analysis of the h diffraction data

The single crystal X-ray diffraction data measured in this work constitutes the h diffraction pattern (($hkl0$) reflections). As discussed in ref. 5, structure determination calculations using the h diffraction data allow the basic host structure to be determined, and also provide some information concerning the guest substructure. First, the ($hk00$) reflections (which are common to both the h and g diffraction patterns) provide two-dimensional information on the basic guest structure projected on to the plane perpendicular to the

[2] C.L. Bauer, B.M. Kariuki, and K.D.M. Harris. Unpublished results.

© 1999 NRC Canada

tunnel axis. Second, the h reflections ($hkl0$) with $l \neq 0$ convey information on the incommensurate perturbations to the basic guest structure (these perturbations arise from host-guest interaction and have the same periodicity (c_h) as the basic host structure). This "perturbation electron density" represents the difference in electron density between the true guest substructure averaged over the periodicity of the basic host structure and the basic guest structure averaged over the periodicity of the basic host structure. Although this perturbation electron density conveys important structural information, it is more satisfactory to obtain a comprehensive understanding of the incommensurate modulations in incommensurate inclusion compounds by structure determination of the composite inclusion compound in a 4-dimensional superspace group. However, such analysis is not feasible in the present case as there are no sharp Bragg diffraction maxima of significant intensity in the g diffraction pattern. In summary, structure determination calculations using the h diffraction data yield: (*i*) the average basic host structure; and (*ii*) an averaged guest electron density (averaged over the periodicity of the basic host structure) which has a straightforward physical interpretation when projected on to the plane perpendicular to the tunnel axis.

In structure refinement, the method for introducing the contributions to the h diffraction pattern due to scattering from the guest molecules requires special attention, and the following strategy was followed. For the non-hydrogen atoms of the urea molecules, positional parameters (taken initially from the structure solution) and anisotropic displacement parameters were refined in the conventional manner. The difference Fourier map for this "host-only" structural model contains significant maxima located within the tunnel, representing guest electron density (as discussed above). A carbon atom was added in the position of the highest maximum in the difference Fourier map, and its positional parameters and isotropic displacement parameter were refined together with the parameters for the non-hydrogen atoms of the host structure (as expected, the refined values of the isotropic displacement parameters for the carbon atoms in the tunnel are significantly higher than the equivalent isotropic displacement parameters for the atoms of the urea molecules). This procedure was repeated, adding one carbon atom at a time, until the highest peak in the difference Fourier map represented a hydrogen atom of a urea molecule. Finally, hydrogen atoms were added to the urea molecules according to standard geometries and were refined using a "riding" model in which the same coordinate shifts are applied to a hydrogen atom and the nitrogen atom to which it is bonded. For each hydrogen atom, the isotropic displacement parameter was taken as 1.2 times the equivalent isotropic displacement parameter of the nitrogen atom to which it is bonded.

Structure solution calculations were carried out using the direct methods program SIR-92 (29), and structure refinement calculations were carried out using the SHELXL-93[3] program. Standard agreement factors R and R_w were considered.

5. Results and discussion

5.1 Identification of phase transition temperatures

Differential scanning calorimetry data (Fig. 1) were recorded[4] for a polycrystalline sample of 2-bromotetradecane/urea subjected to a cycle of cooling from 298 to 98 K and then heating from 98 to 298 K. On cooling the sample from 298 K, an exotherm is observed at 235 K (enthalpy change –0.029 J g^{-1}) and two further exotherms (which overlap significantly) are observed in the region between 198 and 168 K. As the latter exotherms overlap each other significantly, it is not possible to establish reliable enthalpy changes, and we have not attempted to investigate the structural properties at temperatures between 198 and 168 K. On subsequently warming the sample to ambient temperature, two endotherms (again overlapped significantly) are observed in the region between 186 and 200 K and one endotherm is observed at 256 K (enthalpy change 0.022 J g^{-1}). Clearly there is significant hysteresis in these transitions. The differential scanning calorimetry results identify three temperature regimes, which we denote the high-temperature phase (above 235 K on cooling), the intermediate-temperature phase (between 235 and ca. 198 K on cooling) and the low-temperature phase (below ca. 168 K on cooling). Further studies are required to elucidate the behaviour of the system between ca. 198 and 168 K, in the region of the two overlapping transitions.

We now focus on the structural properties in the high-temperature, intermediate-temperature and low-temperature phases.

5.2 Structural properties of the high-temperature phase

At ambient temperature (293 K), powder X-ray diffraction indicates that the 2-bromotetradecane/urea inclusion compound has the hexagonal basic host structure characteristic of conventional urea inclusion compounds. The single crystal X-ray diffraction rotation photograph for 2-bromotetradecane/urea at ambient temperature is shown in Fig. 2. The structure determined from the measured h diffraction data is shown, viewed along the tunnel axis, in Fig. 3 and structural parameters are listed in Table 2. This structure is completely consistent with the conventional hexagonal urea tunnel structure determined previously (4, 5) for urea inclusion compounds containing other types of guest molecules. From assessment of the Flack parameter,[3] no reliable information on the absolute configuration of the crystal may be obtained.

From the rotation photograph, no discrete diffraction maxima are discernible within the g diffraction pattern, which comprises only diffuse layer lines (suggesting that there is no long-range three-dimensional ordering of the guest molecules). The diffuse scattering comprises sheets in reciprocal space perpendicular to the tunnel axis, implying that the guest molecules exhibit an average periodicity along the tunnel but do not exhibit long-range ordering in other directions (i.e., no inter-tunnel ordering). The average periodicity along the tunnel (ca. 19.7 Å) is close to the length of one guest molecule in the type of extended conformation required to fit

[3] G.M. Sheldrick. SHELX 93, Program for crystal structure determination. University of Göttingen, Germany. 1993.
[4] L. Yeo, K.D.M. Harris, and E.H. Bocanegra. Manuscript in preparation.

© 1999 NRC Canada

Fig. 1. Differential scanning calorimetry data for the 2-bromotetradecane/urea inclusion compound: (*a*) for cooling between 298 and 98 K, and (*b*) for warming between 98 and 298 K.

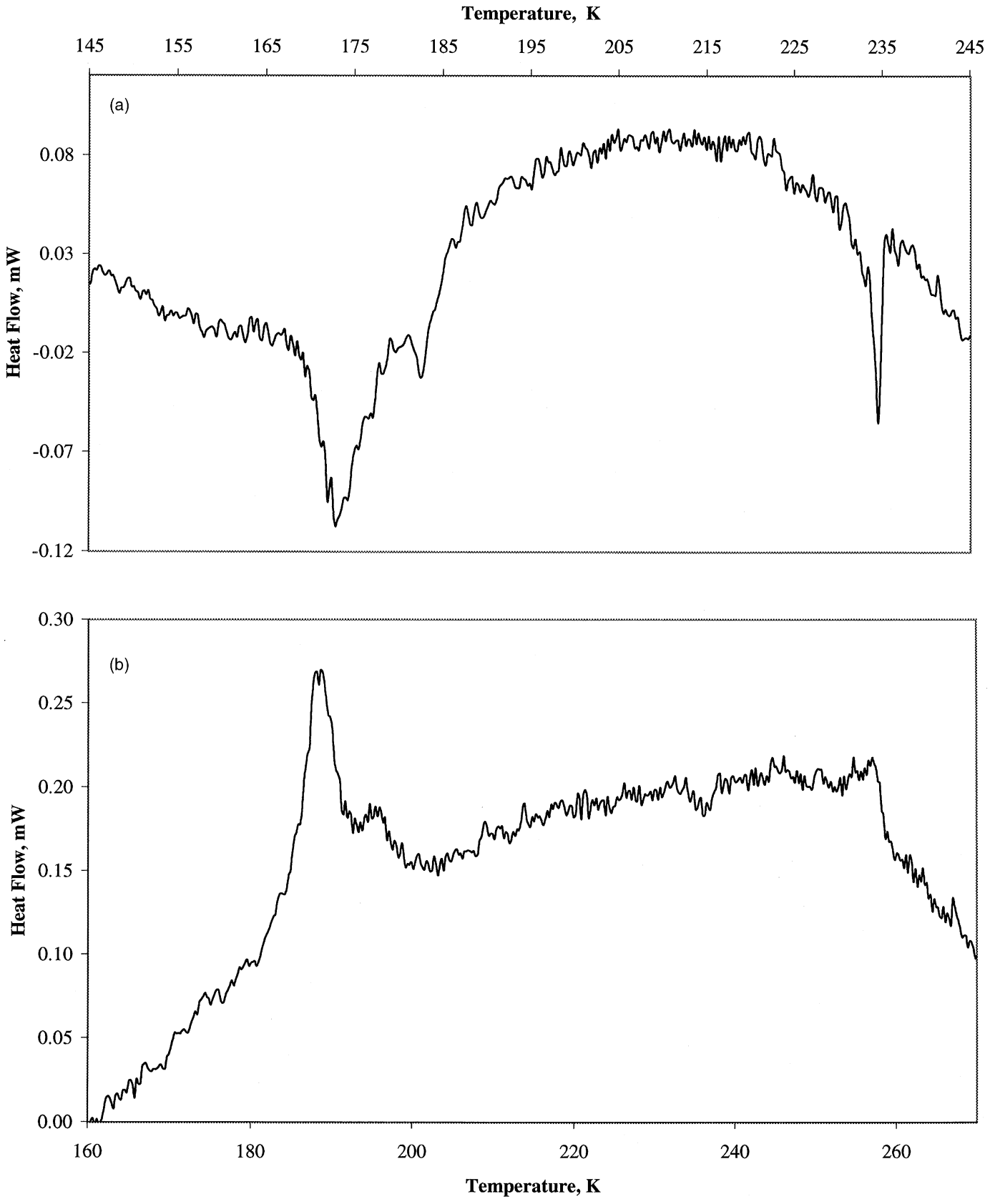

© 1999 NRC Canada

Fig. 2. Single crystal X-ray diffraction rotation photograph, recorded at 293 K, for the 2-bromotetradecane/urea inclusion compound rotating about the tunnel axis. Layer lines of the h diffraction pattern are indexed (the X-ray scattering between these layer lines represents the g diffraction pattern).

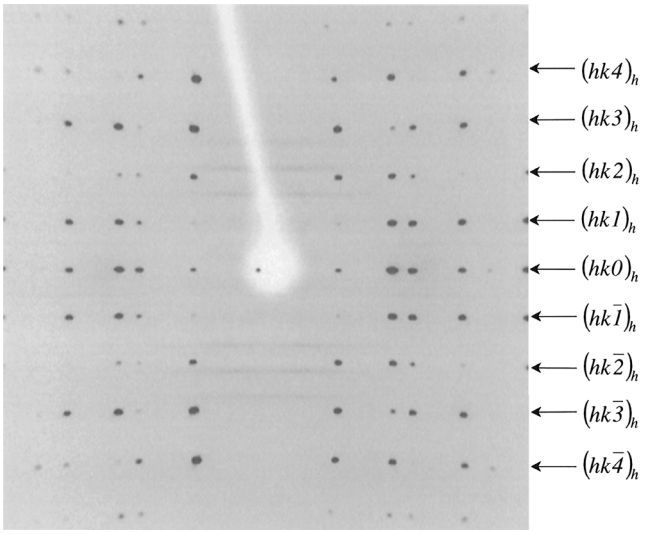

inside the urea tunnel structure. The intensity of scattering in the g diffraction pattern is substantially weaker than the intensities of the Bragg diffraction maxima in the h diffraction pattern.

5.3 Structural properties of the intermediate-temperature phase

The single crystal X-ray diffraction rotation photograph recorded at 207 K is shown in Fig. 4, from which there is no evidence for any decrease in crystal quality on entering the intermediate-temperature phase. The h diffraction pattern recorded at this temperature does not contain any additional layer lines, indicating that there is no superstructure along the tunnel direction in the intermediate-temperature phase. The number and arrangement of discrete diffraction maxima within each layer line in the h diffraction pattern is very similar to that for the high-temperature phase. Although no sharp Bragg diffraction maxima are discernible, regions of locally increased intensity are observed within the diffuse scattering in the g diffraction pattern, suggesting the introduction of some extent of weak inter-tunnel ordering of the guest molecules.

Within experimental errors in the single crystal X-ray diffraction data collection for the h diffraction pattern, the metric symmetry of the basic host structure in the intermediate-temperature phase is hexagonal, with essentially the same unit cell as the high-temperature phase. However, although the Laue symmetry of h diffraction data for the intermediate-temperature phase fairly closely approximates 6/*mmm* (as for the high-temperature phase), it is more correctly described as *mmm*. We recall that a lattice with hexagonal metric symmetry may be described alternatively on a C-centred orthorhombic (orthohexagonal) unit cell. Following transformation to this orthorhombic description, the h diffraction data are found to be most consistent with space group is $C222_1$.

Fig. 3. Structure of the 2-bromotetradecane/urea inclusion compound (space group $P6_122$), determined at 293 K, viewed along the tunnel axis ($\boldsymbol{c}_h$ axis). The atoms within the tunnel have been added to represent the contribution to the h diffraction pattern from scattering by the guest molecules — the physical significance of these atom positions is discussed in Sect. 4.

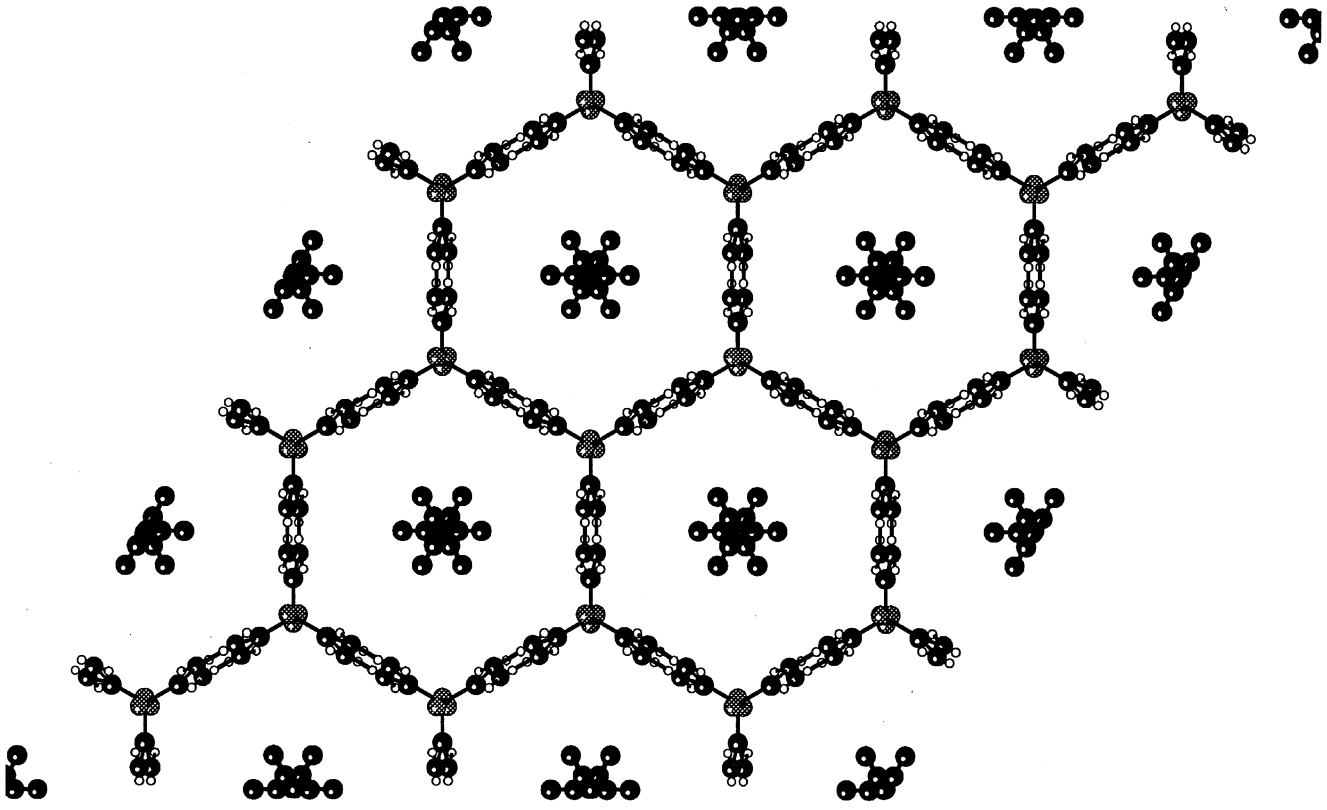

© 1999 NRC Canada

Table 2. Structural parameters determined from the h diffraction pattern for the 2-bromotetradecane/urea inclusion compound at 293 K, and other information relating to the structure refinement calculations.[a]

(A) Atom data

Atom	x	y	z	U_{iso} (Å^2)	U_{11} (Å^2)	U_{22} (Å^2)	U_{33} (Å^2)	U_{23} (Å^2)	U_{13} (Å^2)	U_{12} (Å^2)
O1	0.6421(4)	0.3210(2)	0.0833(0)	—	0.048(2)	0.059(1)	0.033(1)	0.001(1)	0.0000(0)	0.0242(8)
N1	0.9128(4)	0.4360(4)	0.1864(2)	—	0.047(1)	0.081(2)	0.037(2)	0.001(1)	–0.0034(9)	0.024(1)
C1	0.8175(5)	0.4087(3)	0.0833(0)	—	0.044(2)	0.049(2)	0.033(2)	–0.003(1)	0.0000(0)	0.022(1)
C2	0.944(5)	–0.056(5)	0.1667(0)	0.37(2)	—	—	—	—	—	—
C3	1.134(4)	0.134(4)	0.1667(0)	0.42(2)	—	—	—	—	—	—
C4	1.008(5)	0.004(3)	0.0833(0)	0.33(2)	—	—	—	—	—	—

(B) Bond length data (Å)

C1—O1	1.255(5)
C1—N1	1.333(3)

(C) Bond angle datum (°)

O1-C1-N1	120.7(2)

(D) Other information

Space group	$P6_122$
Lattice parameters	$\|a_h\|$ = 8.2582(9) Å
	$\|c_h\|$ = 10.9937(9) Å
No. of unique reflections with $\|F_o\| > 4\sigma(F_o)$	390
R	0.0669
R_w	0.2032
Weight	$1/[\sigma(F_o)^2 + (0.1397 \times P)^2 + 0.34 \times P]$ where P = [max. $(F_o^2, 0) + 2F_c^2]/3$
No. of parameters refined	26

[a]C2 to C4 denote carbon atoms introduced within the tunnel to represent the contribution to the h diffraction pattern from scattering by the guest molecules. The asymmetric unit of the host structure comprises one half urea molecule, with its C=O bond lying on a 2-fold axis (special position (2x, x, 1/12)). There are six urea molecules in the unit cell.

© 1999 NRC Canada

Fig. 4. Single crystal X-ray diffraction rotation photograph, recorded at 207 K, for the 2-bromotetradecane/urea inclusion compound rotating about the tunnel axis. Layer lines of the h diffraction pattern are indexed (the X-ray scattering between these layer lines represents the g diffraction pattern).

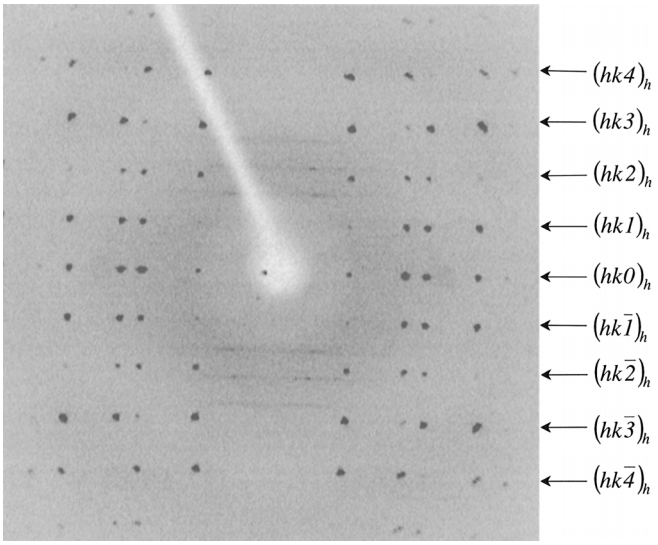

The structure determined (in space group $C222_1$) from the h diffraction data at 207 K is viewed along the tunnel axis in Fig. 5. As discussed above, although the Laue symmetry is strictly orthorhombic *mmm*, the deviations from hexagonal Laue group 6/*mmm* are relatively minor, and not surprisingly the host structure determined in space group $C222_1$ for the intermediate-temperature phase remains very close to the hexagonal tunnel structure of the high-temperature phase. Indeed, attempts to refine the structure of the intermediate-temperature phase using space group $P6_122$ (as for the high-temperature phase) also proceeded satisfactorily. Given the approximations inherent in the approach used here (for example, the method for introducing contributions to the h diffraction data due to scattering from the guest molecules), it is perhaps not surprising that subtle structural issues such as this may be difficult to resolve.

From the structure (Fig. 5) determined from the h diffraction data, there is no clear evidence that the guest molecules are more ordered in the intermediate-temperature phase than the high-temperature phase, although we recall (see Sect. 4) that the h diffraction data convey only limited information concerning the nature of the guest substructure. Presumably the lowering of the symmetry from hexagonal (high-temperature phase) to orthorhombic (intermediate-temperature phase) originates from some aspect that influences the h diffraction data sufficiently to detect the lowering of symmetry, but does not express a major effect on the basic host structure. The dynamic properties of the guest molecules, or other aspects of ordering of the guest molecules, may be important in this regard. The subtle structural distinction between the high-temperature and intermediate-temperature phases clearly merits more detailed investigations using other experimental techniques (for example, optical microscopy (to distinguish whether the crystals are uni-axial or bi-axial in the intermediate temperature phase) and high-resolution solid state ^{13}C NMR (which may be able to indicate directly the number of

Fig. 5. Structure of the 2-bromotetradecane/urea inclusion compound (space group $C222_1$), determined at 207 K, viewed along the tunnel axis ($\boldsymbol{c}_h$ axis). The atoms within the tunnel have been added to represent the contribution to the h diffraction pattern from scattering by the guest molecules — the physical significance of these atom positions is discussed in Sect. 4.

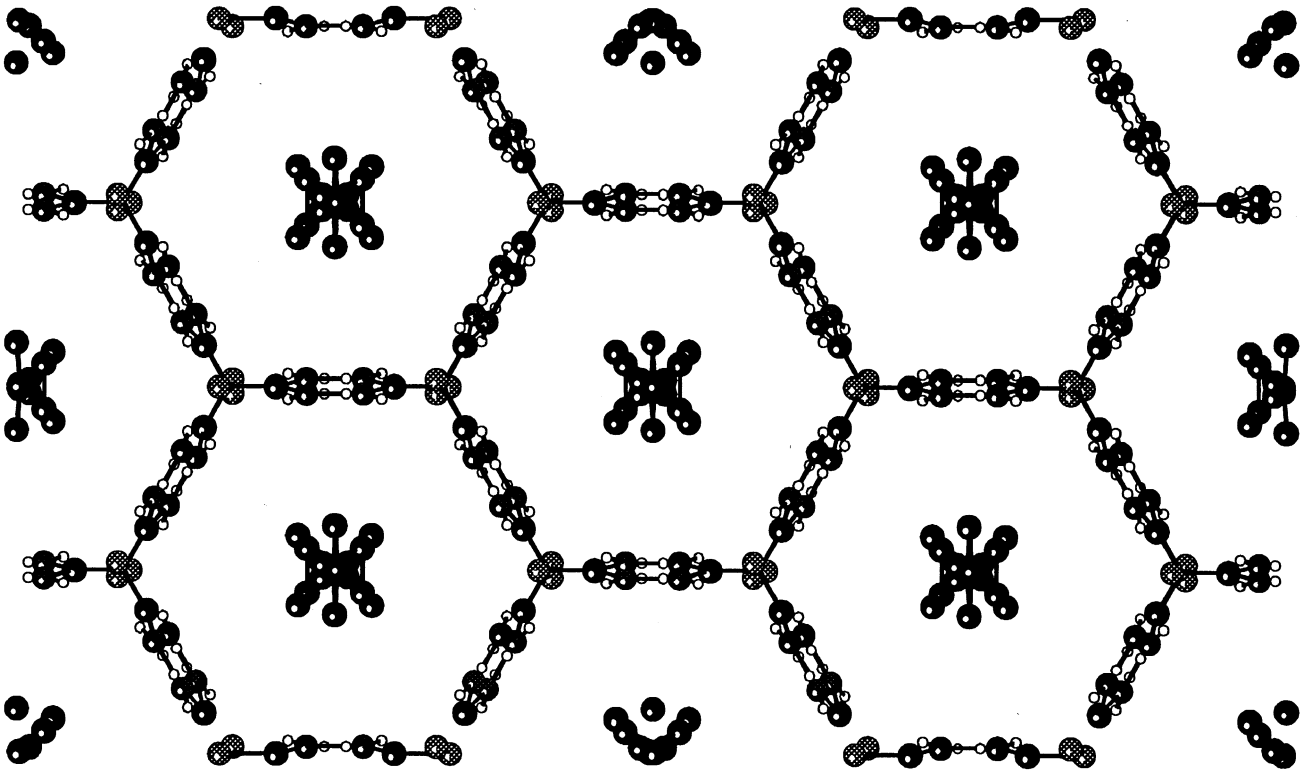

© 1999 NRC Canada

Fig. 6. Single crystal X-ray diffraction rotation photograph, recorded at 142 K, for the 2-bromotetradecane/urea inclusion compound rotating about the tunnel axis. Layer lines of the h diffraction pattern are indexed (the X-ray scattering between these layer lines represents the g diffraction pattern).

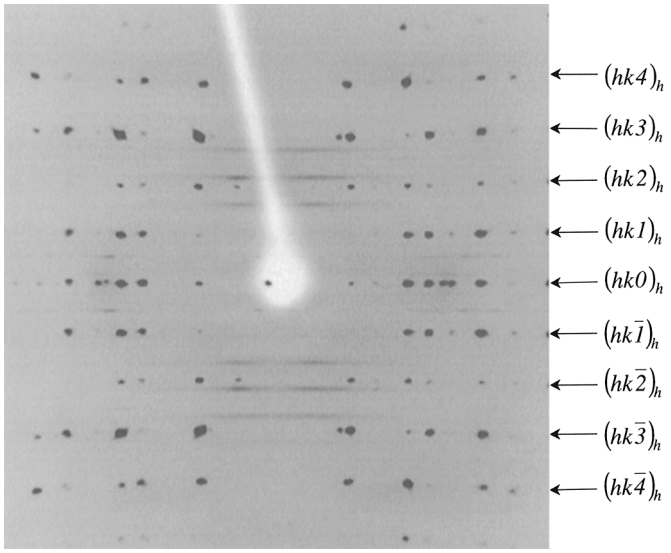

urea molecules in the asymmetric unit (1 urea molecule for $P6_122$; 1.5 urea molecules for $C222_1$)).

5.4 Structural properties of the low-temperature phase

The single crystal X-ray diffraction rotation photograph recorded at 142 K is shown in Fig. 6. From this photograph, there is no significant decrease in crystal quality on entering the low-temperature phase. The h diffraction pattern at 142 K does not contain any new layer lines (in addition to those for the intermediate-temperature and high-temperature phases), indicating that no new superstructure is generated along the tunnel direction in the low-temperature phase. On the other hand, the number and arrangement of discrete diffraction maxima within each layer line in the h diffraction pattern is very different from that in the high-temperature and intermediate-temperature phases.

The g diffraction pattern for the low-temperature phase has increased localization of intensity within the diffuse bands (compared with the high-temperature phase), suggesting that there is some increase in the extent of three-dimensional ordering of the guest molecules. However, the data do not allow a reliable assessment of the mode of inter-tunnel ordering (as defined by the parameter Δ_g (30)) of the guest molecules. The relative positions of the layer lines for the h and g diffraction patterns in Fig. 6 implies that there is an incommensurate relationship between the periodicities of the host and guest substructures along the tunnel axis in the low-temperature phase, with no evidence that the host and guest substructures lock into a commensurate relationship at any temperature studied.

From analysis of the h diffraction pattern, the metric symmetry of the basic host structure in the low-temperature phase is monoclinic, and represents an approximate $2 \times 2 \times 1$ supercell of the hexagonal cell of the basic host structure in the high-temperature phase. The Laue group is $2/m$ and the diffraction data are consistent with space group $P2_1$.

The structure determined from the measured h diffraction data at 142 K is viewed along the tunnel axis in Fig. 7, and structural parameters are listed in Table 3. From assessment of the Flack parameter,[3] no reliable information on the absolute configuration of the crystal could be obtained. The host structure contains four independent types of tunnel (parallel to the *b* axis) per unit cell, with irregular hexagonal geometry when projected on to the plane perpendicular to the tunnel axis (***ac*** plane). In contrast, the corresponding projections for the high-temperature phase and the intermediate-temperature phase are regular hexagons (exact for the high-temperature phase, and a close approximation for the intermediate-temperature phase). The degree of distortion of the tunnels in the low-temperature phase may be assessed by considering the "diameters" (see Fig. 8) between opposite corners of the irregular hexagonal projections. For three of the four independent types of tunnel (type A), one diameter is significantly longer than the other two, whereas for the other type of tunnel (type B), all three diameters are approximately the same. For tunnels of type A, we may expect that the planes of the guest molecules should be oriented (in projection) along the long diameter. For tunnels of type B, on the other hand, there may be no preferred orientation (in projection) of the planes of the guest molecules. These expectations are supported by the projection of the guest electron density (determined from the h diffraction pattern, see Sect. 4) on to the plane perpendicular to the tunnel axis, from which it is evident that the geometric distortions of the host tunnels are related to orientational ordering of the guest molecules. Thus, there is a significant increase in the orientational ordering of the guest molecules in the low-temperature phase, although we recall that several other aspects of disorder must remain in the guest substructure (see Sect. 5.5). The distribution of guest molecule orientations observed in tunnels of type B may represent a static average of three orientations related by 120° rotation about the tunnel axis.

5.5 Comments on disorder within the guest substructure

The lack of significant three-dimensional ordering of the guest molecules in the 2-bromotetradecane/urea inclusion compound is not unexpected in view of the different contributions to disorder that are known to exist in the guest substructure. First, the 2-bromotetradecane/urea inclusion compound studied here was prepared from a racemic sample of 2-bromotetradecane, and thus, although a given single crystal will have a preference to incorporate one particular enantiomer of 2-bromotetradecane (as discussed in Sect. 1), it is probable that each crystal contains a significant proportion of each enantiomer (we note that the chiral discrimination on forming urea inclusion compounds with chiral guest molecules is less than 100% (10–14)). Second, it is already known from bromine K-edge EXAFS spectroscopy (31) and Raman spectroscopy[5] of the 2-bromotetradecane/urea inclusion compound that there is disorder in the conformational properties of the -$CH(Br)CH_3$ end-group of the guest mole-

[5] L. Elizabé, F. Guillaume, K.D.M. Harris, and L. Yeo. Manuscript in preparation.

© 1999 NRC Canada

Fig. 7. Structure of the 2-bromotetradecane/urea inclusion compound (space group $P2_1$), determined at 142 K, viewed along the tunnel axis ($\boldsymbol{b}_h$ axis). The atoms within the tunnel have been added to represent the contribution to the h diffraction pattern from scattering by the guest molecules — the physical significance of these atom positions is discussed in Sect. 4.

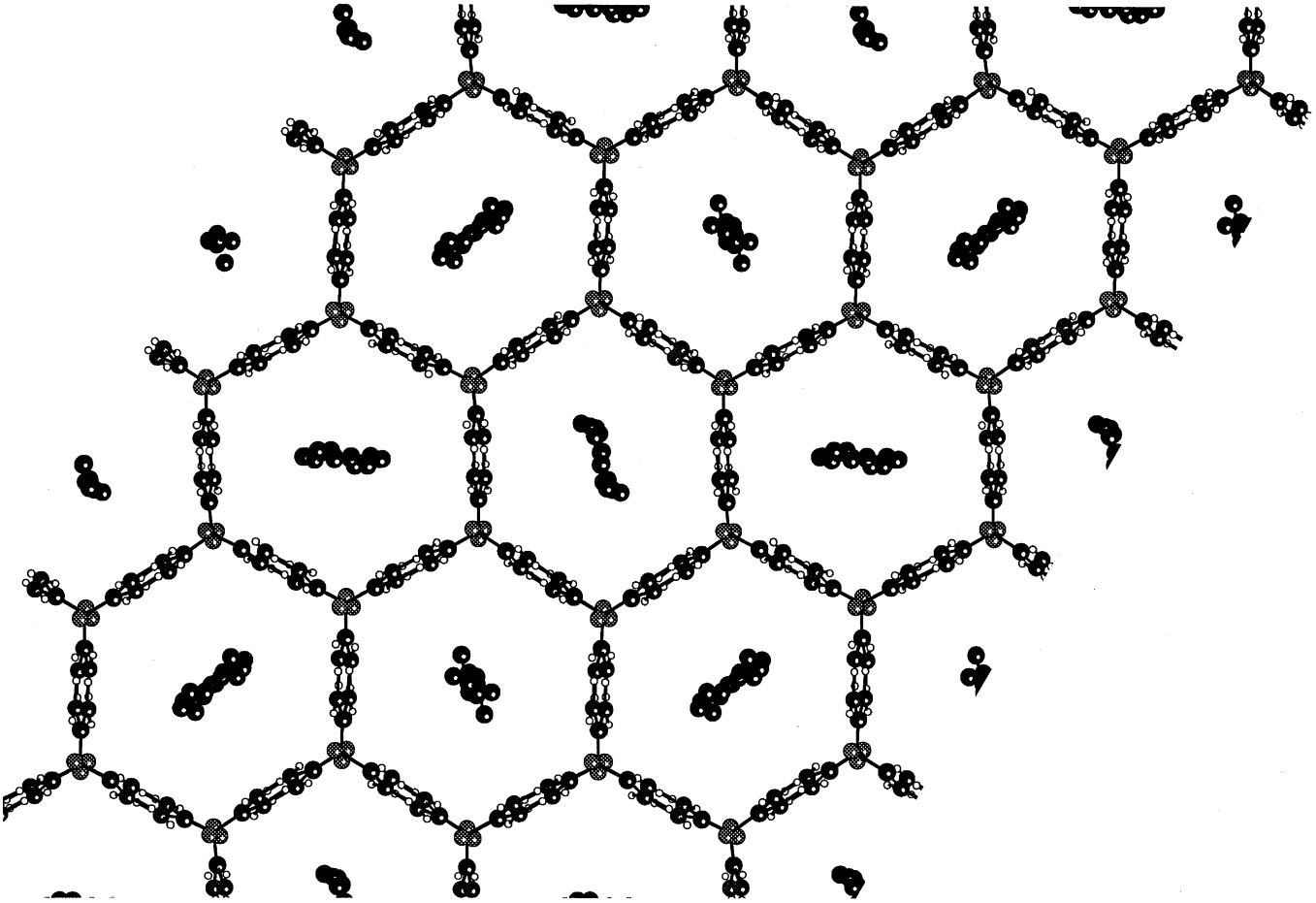

Fig. 8. Geometric characteristics of the "distorted" host tunnel structure in the 2-bromotetradecane/urea inclusion compound at 142 K.

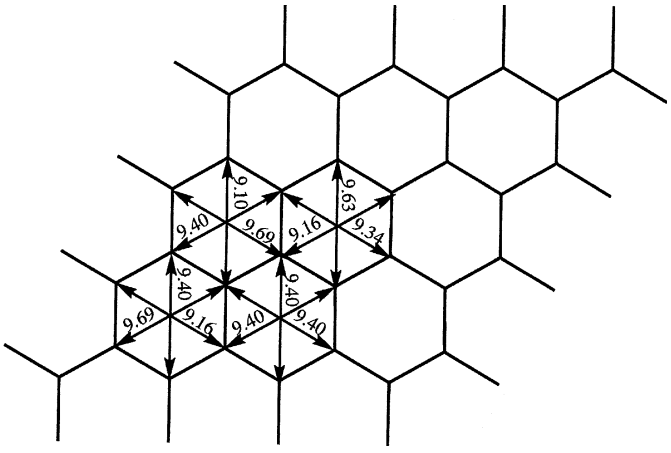

cules, with substantial populations of guest molecules in the conformation with the CH_3 substituent trans and substantial populations of guest molecules in the conformation with the Br substituent trans. Third, 2-bromotetradecane is an unsymmetric guest of the general type $X(CH_2)_nY$ discussed in Sect. 1 (X = H_3C-, Y = -$CH(Br)CH_3$). Thus, in general, disorder concerning the orientation of the guest molecules along the tunnel may be expected, together with disorder in the types of end-group interactions. Solid state NMR studies should provide more insight into this structural aspect of the 2-bromotetradecane/urea inclusion compound. Fourth, in most urea inclusion compounds the guest molecules undergo a variety of dynamic processes at sufficiently high temperature. Although the dynamic properties of 2-bromoalkane/urea inclusion compounds have not yet been investigated, it is plausible that there is some degree of dynamic disorder within the guest substructure, at least in the higher temperature phases.

6. Concluding remarks

In general, the phase transitions in urea inclusion compounds reflect the cooperative behaviour of the host and guest components. At ambient temperature, the high symmetry (hexagonal) of the average host structure reflects the time-averaged and space-averaged distribution of the guest molecules. At sufficiently low temperature, the guest molecules adopt a well-defined orientation (or a restricted set of orientations) with respect to the host, as a consequence of a diminution in the dynamics of the guest molecules. Concom-

© 1999 NRC Canada

Table 3. Structural parameters determined from the h diffraction pattern for the 2-bromotetradecane/urea inclusion compound at 142 K, and other information relating to the structure refinement calculations.[a]

(A) Atom data

Atom	*x*	*y*	*z*	U_{iso} (Å^2)	U_{11} (Å^2)	U_{22} (Å^2)	U_{33} (Å^2)	U_{23} (Å^2)	U_{13} (Å^2)	U_{12} (Å^2)
O1	0.3290(4)	0.7824(5)	0.8546(4)	—	0.029(3)	0.021(3)	0.040(3)	–0.005(3)	–0.010(3)	–0.004(3)
O2	–0.3498(4)	0.2813(5)	0.6574(5)	—	0.044(4)	0.023(3)	0.067(4)	–0.004(4)	–0.041(3)	–0.003(3)
O3	0.1579(5)	0.6158(6)	0.6830(4)	—	0.055(4)	0.0330(4)	0.034(3)	–0.001(4)	–0.010(3)	–0.006(4)
O4	0.3513(4)	0.1162(6)	0.3215(4)	—	0.043(3)	0.025(3)	0.050(4)	0.010(4)	–0.027(3)	0.001(3)
O5	0.1574(4)	0.2814(5)	0.1720(4)	—	0.052(4)	0.024(3)	0.027(3)	0.004(3)	–0.022(3)	–0.006(3)
O6	0.3289(4)	0.4475(5)	0.3429(4)	—	0.029(3)	0.018(3)	0.064(4)	–0.008(3)	–0.032(3)	0.001(3)
O7	0.3083(4)	0.4492(6)	0.8531(4)	—	0.036(3)	0.035(4)	0.035(3)	0.011(3)	–0.004(3)	0.004(4)
O8	0.182(4)	0.9454(6)	0.6613(5)	—	0.035(3)	0.025(3)	0.059(4)	0.002(3)	–0.019(3)	–0.009(3)
O9	0.3306(4)	0.1147(5)	0.8313(4)	—	0.027(3)	0.022(3)	0.033(3)	–0.006(3)	–0.010(2)	0.004(3)
O10	0.1611(5)	1.2827(6)	0.6628(5)	—	0.044(4)	0.022(3)	0.066(4)	0.004(4)	–0.024(4)	–0.007(3)
O11	–0.1816(4)	0.4508(6)	0.8279(4)	—	0.037(3)	0.030(3)	0.027(3)	–0.005(3)	–0.015(3)	–0.005(3)
O12	0.1597(4)	0.6149(5)	1.1935(4)	—	0.048(3)	0.025(3)	0.035(3)	0.012(3)	–0.030(3)	–0.003(3)
N1	–0.0454(6)	0.5513(6)	0.7726(5)	—	0.050(5)	0.004(3)	0.053(5)	–0.013(3)	–0.024(4)	0.003(3)
N2	0.2385(6)	0.1771(6)	0.2288(6)	—	0.089(6)	0.008(4)	0.071(6)	0.006(4)	–0.070(5)	0.000(4)
N3	0.4675(5)	0.5522(8)	0.2772(6)	—	0.030(4)	0.040(5)	0.055(5)	0.001(4)	–0.012(4)	0.008(4)
N4	–0.0410(6)	0.3435(7)	0.7498(5)	—	0.049(5)	0.038(5)	0.044(5)	–0.014(4)	–0.025(4)	–0.001(4)
N5	0.2468(6)	0.7198(6)	0.5467(6)	—	0.060(5)	0.007(4)	0.060(5)	–0.005(4)	–0.029(4)	0.009(4)
N6	0.2112(6)	1.38523(7)	0.7488(6)	—	0.056(5)	0.029(5)	0.063(5)	0.004(4)	–0.038(5)	–0.015(4)
N7	0.2385(7)	0.7187(7)	1.0530(5)	—	0.087(6)	0.030(5)	0.020(4)	0.013(3)	–0.019(4)	–0.015(5)
N8	0.0447(6)	1.0515(7)	0.7084(5)	—	0.038(4)	0.053(6)	0.042(4)	0.005(4)	–0.021(4)	–0.004(4)
N9	0.2735(6)	0.2206(8)	0.459(6)	—	0.053(5)	0.035(5)	0.054(5)	0.004(4)	–0.030(4)	0.012(4)
N10	0.2759(7)	0.0104(6)	0.970(5)	—	0.095(7)	0.002(3)	0.025(4)	0.012(3)	–0.014(4)	0.003(4)
N11	–0.2865(6)	0.3851(7)	0.7331(7)	—	0.067(6)	0.038(5)	0.078(6)	–0.014(4)	–0.062(5)	–0.006(4)
N12	0.0437(6)	0.8435(6)	0.7309(6)	—	0.061(5)	0.005(4)	0.068(5)	–0.010(4)	–0.037(5)	0.004(4)
N13	0.4655(5)	0.3450(7)	0.2579(6)	—	0.035(4)	0.014(4)	0.081(6)	0.001(4)	–0.030(4)	0.004(3)
N14	0.2269(6)	0.5113(8)	0.5452(6)	—	0.041(4)	0.042(5)	0.050(5)	0.005(4)	–0.018(4)	0.002(4)
N15	0.2725(6)	0.8872(6)	0.7719(6)	—	0.063(6)	0.013(4)	0.054(5)	–0.001(4)	–0.029(4)	0.003(4)
N16	0.2558(6)	0.2171(7)	0.9673(5)	—	0.075(6)	0.028(5)	0.028(4)	0.009(4)	–0.015(4)	0.007(4)
N17	0.4469(5)	0.3442(7)	0.7694(6)	—	0.031(4)	0.021(4)	0.060(5)	0.007(4)	–0.013(4)	–0.008(4)
N18	0.2520(5)	0.6784(6)	0.7941(5)	—	0.040(4)	0.024(4)	0.036(4)	0.004(3)	–0.019(3)	–0.006(3)
N19	0.4477(6)	0.5500(7)	0.7909(6)	—	0.033(4)	0.024(4)	0.061(5)	–0.002(4)	–0.011(4)	–0.007(4)
N20	0.2218(6)	0.3847(7)	0.2479(6)	—	0.050(5)	0.025(5)	0.065(6)	0.015(4)	–0.030(4)	0.000(4)
N21	0.2938(5)	0.0133(6)	0.4575(5)	—	0.031(4)	0.007(4)	0.053(5)	–0.002(3)	–0.021(4)	0.005(3)
N22	0.2303(6)	1.1767(7)	0.7305(6)	—	0.066(6)	0.032(5)	0.051(5)	0.006(4)	–0.032(5)	–0.003(4)
N23	–0.2661(6)	0.1777(6)	0.7106(6)	—	0.074(6)	0.014(4)	0.074(6)	–0.002(4)	–0.056(5)	–0.011(4)
N24	0.2145(6)	0.5117(7)	1.0568(6)	—	0.063(5)	0.018(4)	0.047(5)	0.009(4)	–0.026(4)	–0.004(4)
C1	0.0939(7)	0.9505(9)	0.7004(7)	—	0.048(6)	0.022(5)	0.058(6)	–0.024(5)	–0.021(5)	0.021(5)
C2	–0.3027(7)	0.284(1)	0.7010(7)	—	0.047(5)	0.040(6)	0.046(5)	–0.021(5)	–0.030(5)	–0.013(5)
C3	0.2882(6)	0.1104(8)	0.9216(5)	—	0.038(5)	0.012(4)	0.028(4)	–0.005(4)	–0.004(4)	–0.009(4)
C4	0.2085(6)	0.6133(8)	0.5965(7)	—	0.031(4)	0.008(4)	0.067(6)	–0.023(5)	–0.025(4)	0.015(4)
C5	0.1988(6)	1.282(1)	0.7135(6)	—	0.028(4)	0.061(7)	0.038(5)	0.008(5)	–0.013(4)	0.012(5)

© 1999 NRC Canada

Table 3 (*continued*).

(A) Atom Data

Atom	*x*	*y*	*z*	U_{iso} (Å^2)	U_{11} (Å^2)	U_{22} (Å^2)	U_{33} (Å^2)	U_{23} (Å^2)	U_{13} (Å^2)	U_{12} (Å^2)
C6	0.4185(6)	0.4489(8)	0.2939(6)	—	0.035(4)	0.028(5)	0.043(5)	0.020(4)	–0.026(4)	0.006(5)
C7	0.2873(5)	0.7808(8)	0.8093(5)	—	0.022(4)	0.020(4)	0.021(4)	–0.015(4)	0.007(3)	0.001(4)
C8	0.2044(6)	0.6185(9)	1.1020(5)	—	0.040(5)	0.037(5)	0.019(4)	0.020(4)	–0.012(3)	0.003(5)
C9	0.2049(6)	0.2790(8)	0.2139(6)	—	0.053(5)	0.013(4)	0.036(5)	0.012(4)	–0.027(4)	–0.008(4)
C10	0.3070(6)	0.1165(8)	0.4098(7)	—	0.028(4)	0.019(4)	0.066(6)	0.026(5)	–0.032(4)	–0.013(4)
C11	–0.0933(6)	0.4483(8)	0.7877(5)	—	0.064(6)	0.021(4)	0.020(4)	–0.022(4)	–0.033(4)	0.015(5)
C12	0.4005(5)	0.4490(8)	0.8058(6)	—	0.020(4)	0.026(5)	0.047(5)	0.004(4)	–0.013(4)	–0.006(4)
C13	0.454(6)	0.922(9)	0.018(5)	0.39(4)	—	—	—	—	—	—
C14	0.507(3)	0.361(4)	0.487(3)	0.17(1)	—	—	—	—	—	—
C15	–0.058(3)	0.469(5)	0.517(3)	0.28(2)	—	—	—	—	—	—
C16	0.051(4)	0.713(7)	0.504(4)	0.37(3)	—	—	—	—	—	—
C17	0.078(2)	0.279(3)	0.497(2)	0.19(1)	—	—	—	—	—	—
C18	–0.006(2)	0.158(3)	–0.027(2)	0.148(9)	—	—	—	—	—	—
C19	–0.073(2)	–0.070(4)	0.504(2)	0.20(1)	—	—	—	—	—	—
C20	0.005(2)	0.137(3)	0.061(2)	0.19(1)	—	—	—	—	—	—
C21	0.013(2)	–0.164(3)	0.504(2)	0.16(1)	—	—	—	—	—	—
C22	0.445(4)	1.108(6)	0.066(4)	0.31(2)	—	—	—	—	—	—
C23	0.576(2)	0.474(4)	0.424(2)	0.21(1)	—	—	—	—	—	—
C24	0.015(2)	0.147(3)	0.498(2)	0.17(1)	—	—	—	—	—	—
C25	0.48(1)	0.79(2)	0.016(9)	0.6(1)	—	—	—	—	—	—
C26	0.544(3)	0.248(6)	0.434(4)	0.31(2)	—	—	—	—	—	—
C27	0.036(4)	0.497(7)	0.017(4)	0.34(3)	—	—	—	—	—	—
C28	0.502(3)	0.158(5)	–0.017(3)	0.24(2)	—	—	—	—	—	—
C29	0.008(3)	–0.018(4)	0.016(3)	0.22(2)	—	—	—	—	—	—
C30	–0.034(4)	0.263(6)	–0.053(4)	0.34(3)	—	—	—	—	—	—
C31	0.494(2)	0.631(3)	0.514(2)	0.142(8)	—	—	—	—	—	—
C32	0.510(4)	0.823(5)	–0.003(4)	0.21(2)	—	—	—	—	—	—
C33	–0.003(2)	0.325(2)	–0.001(2)	0.138(8)	—	—	—	—	—	—
C34	0.464(3)	0.493(5)	0.549(3)	0.29(2)	—	—	—	—	—	—
C35	0.521(3)	1.013(5)	–0.026(3)	0.24(2)	—	—	—	—	—	—
C36	0.531(4)	0.803(7)	0.447(4)	0.38(3)	—	—	—	—	—	—
C37	0.031(3)	0.539(5)	0.483(3)	0.24(2)	—	—	—	—	—	—
C38	0.039(5)	0.350(8)	0.037(5)	0.43(4)	—	—	—	—	—	—
C39	0.556(3)	0.629(6)	0.430(4)	0.30(2)	—	—	—	—	—	—

(B) Bond length data (Å)

C1—O8	1.25(1)	C5—O10	1.26(1)	C9—O5	1.27(1)
C1—N8	1.33(1)	C5—N6	1.34(1)	C9—N2	1.32(1)
C1—N12	1.38(1)	C5—N22	1.35(1)	C9—N20	1.37(1)
C2—O2	1.29(1)	C6—O6	1.27(1)	C10—O4	1.25(1)
C2—N23	1.35(1)	C6—N3	1.33(1)	C10—N9	1.34(1)
C2—N11	1.31(1)	C6—N13	1.34(1)	C10—N21	1.33(1)

© 1999 NRC Canada

Table 3 (*concluded*).

C3—O9	1.280(9)	C7—O1	1.23(1)	C11—O11	1.25(1)
C3—N10	1.30(1)	C7—N15	1.39(1)	C11—N1	1.33(1)
C3—N16	1.35(1)	C7—N18	1.34(1)	C11—N4	1.38(1)
C4—O3	1.23(1)	C8—O12	1.295(9)	C12—O7	1.304(9)
C4—N5	1.38(2)	C8—N7	1.31(1)	C12—N17	1.34(1)
C4—N14	1.34(1)	C8—N24	1.35(1)	C12—N19	1.30(1)

(C) Bond angle data (°)

N8-C1-O8	125(1)	N6-C5-O10	121(1)	N2-C9-O5	122.8(8)
N12-C1-O8	118.2(8)	N22-C5-O10	121(1)	N20-C9-O5	120.2(8)
N12-C1-N8	116.8(8)	N22-C5-N6	118.8(9)	N20-C9-N2	117.0(7)
N11-C2-O2	123(1)	N13-C6-O6	119.7(8)	N21-C10-O4	120.3(9)
N23-C2-O2	117.8(8)	N3-C6-O6	121.6(8)	N9-C10-O4	121.3(8)
N23-C2-N11	119.7(8)	N13-C6-N3	118.7(7)	N21-C10-N9	118.3(8)
N10–C3-O9	123.8(8)	N18-C7-O1	122.8(9)	N1-C11-O11	119.9(8)
N16-C3-O9	116.3(8)	N15-C7-O1	121.4(8)	N4-C11-O11	123.1(8)
N16-C3-N10	119.9(7)	N18-C7-N15	115.8(8)	N1-C11-N4	116.8(8)
N14-C4-O3	123.3(9)	N7-C8-O12	123.6(9)	N17-C12-O7	119.6(8)
N5-C4-O3	120.3(8)	N24-C8-O12	116.7(8)	N19-C12-O7	120.7(8)
N5-C4-N14	116.3(8)	N24-C8-N7	119.7(7)	N19-C12-N17	119.7(7)

(D) Other parameters

Space group	$P2_1$
Lattice parameters	$\|a_h\|$ = 16.338(1) Å
	$\|b_h\|$ = 10.9665(8) Å
	$\|c_h\|$ = 16.338(1) Å
	β = 60.00(0)°
No. of unique reflections with $\|F_o\| > 4\sigma(F_o)$	5217
R	0.1317
R_w	0.3848
Weight	$1/[\sigma(F_o)^2 + (0.2079 \times P)^2 + 10.49P]$ where P = [max. $(F_o^2, 0) + 2F_c^2]/3$
No. of parameters refined	541

[a]C13 to C39 denote carbon atoms introduced within the tunnel to represent the contribution to the h diffraction pattern from scattering by the guest molecules. The asymmetric unit of the host structure comprises 12 independent urea molecules, giving a total of 24 urea molecules in the unit cell.

© 1999 NRC Canada

itantly, the host structure distorts to a lower symmetry that reflects the static orientational distribution of the guest molecules. The intimate interplay of both host and guest components is crucial in controlling the overall behaviour of these phase transitions.

In view of this synergy between host and guest properties, it is not surprising that the mode of distortion of the host structure in the low-temperature phases of urea inclusion compounds is found to depend critically on the type of guest molecule. At a qualitative level, the alkane/urea (32) and α,ω-dibromoalkane/urea (33) inclusion compounds behave in a similar way with respect to the phase transitions. In both cases, the host structure in the low-temperature phase is orthorhombic and is based on a distortion from the orthohexagonal description of the high-temperature structure. The 1,10-decanedicarboxylic acid/urea inclusion compound, on the other hand, exhibits more complicated structural behaviour in the low-temperature phase (34), with the formation of a large superstructure in directions perpendicular to the tunnel axis — this superstructure contains four independent types of tunnel exhibiting different modes of distortion. The structural properties of the 2-bromotetradecane/urea inclusion compound reported here represent another illustration of diversity of low-temperature structural properties for different types of guest molecules in urea inclusion compounds. Clearly the subtle interactions between the host and guest subsystems, which depend critically on the molecular structure of the guest, are crucial in controlling the evolution of the structural properties of these inclusion compounds with temperature.

Given the interest in the chiral recognition properties of 2-bromoalkane/urea inclusion compounds, knowledge of the structural properties (reported here) and the conformational properties of the guest molecules (reported elsewhere (31, footnote 5)) are important pre-requisites before the chiral recognition properties can be understood in depth.

Acknowledgements

We are grateful to Ciba Specialty Chemicals and the University of Birmingham for the award of a studentship to L.Y. We thank Dr. Eduardo Bocanegra (Universidad del Pais Vasco, Spain) for recording the differential scanning calorimetry data discussed in the text.

References

1. M.D. Hollingsworth and K.D.M. Harris. *In* Comprehensive supramolecular chemistry. Vol. 6. *Edited by* D.D. MacNicol, F. Toda, and R. Bishop. Pergamon Press, Oxford. 1996. p. 177.
2. K.D.M. Harris. J. Mol. Struct. **374**, 241 (1996).
3. K.D.M. Harris. Chem. Soc. Rev. **26**, 279 (1997).
4. A.E. Smith. Acta Crystallogr. **6**, 224 (1952).
5. K.D.M. Harris and J.M. Thomas. J. Chem. Soc. Faraday Trans. **86**, 2985 (1990).
6. A.R. George and K.D.M. Harris. J. Mol. Graphics, **13**, 138 (1995).
7. S. van Smaalen and K.D.M. Harris. Proc. R. Soc. London Ser. A, **452**, 677 (1996).
8. L. Yeo and K.D.M. Harris. Tetrahedron: Asymmetry, **7**, 1891 (1996).
9. L. Yeo and K.D.M. Harris. J. Chem. Soc. Faraday Trans. **94**, 1633 (1998).
10. W. Schlenk. Experientia, **8**, 337 (1952).
11. W. Schlenk. Justus Liebigs Ann. Chem. **7**, 1145 (1973).
12. W. Schlenk. Justus Liebigs Ann. Chem. **7**, 1156 (1973).
13. W. Schlenk. Justus Liebigs Ann. Chem. **7**, 1179 (1973).
14. W. Schlenk. Justus Liebigs Ann. Chem. **7**, 1195 (1973).
15. K.D.M. Harris, I. Gameson, and J.M. Thomas. J. Chem. Soc. Faraday Trans. **86**, 3135 (1990).
16. A.E. Aliev, S.P. Smart, I.J. Shannon, and K.D.M. Harris. J. Chem. Soc. Faraday Trans. **92**, 2179 (1996).
17. Y. Chatani, Y. Taki, and H. Tadokoro. Acta Crystallogr. Sect. B: Struct. Crystallogr. Cryst. Chem. **B33**, 309 (1977).
18. Y. Chatani, H. Anraku, and Y. Taki. Mol. Cryst. Liq. Cryst. **48**, 219 (1978).
19. H.L. Casal, D.G. Cameron, and E.C. Kelusky. J. Chem. Phys. **80**, 1407 (1984).
20. K.D.M. Harris and P. Jonsen. Chem. Phys. Lett. **154**, 593 (1989).
21. A. El Baghdadi, E.J. Dufourc, and F. Guillaume. J. Phys. Chem. **100**, 1746 (1996).
22. F. Guillaume, C. Sourisseau, and A.-J. Dianoux. J. Chim. Phys. Phys.-Chim. Biol. **6**, 2169 (1991).
23. S.P. Smart, F. Guillaume, K.D.M. Harris, and A.-J. Dianoux. J. Phys.: Condens. Matter, **6**, 2169 (1994).
24. S. van Smaalen. Crystallogr. Rev. **4**, 79 (1995).
25. R. Lefort, J. Etrillard, B. Toudic, F. Guillaume, T. Breczewski, and P. Bourges. Phys. Rev. Lett. **77**, 4027 (1996).
26. T. Weber, H. Boysen, M. Honal, F. Frey, and R.B. Neder. Z. Kristallogr. **211**, 238 (1996).
27. T.R. Welberry and S.C. Mayo. J. Appl. Crystallogr. **29**, 353 (1996).
28. R. Lefort. Ph.D. thesis. Université de Rennes, Rennes. 1998.
29. M.C. Burla, M. Camalli, G. Cascarano, C. Giacovazzo, G. Polidori, R. Spagna, and D. Viterbo. J. Appl. Crystallogr. **22**, 389 (1989).
30. K.D.M. Harris and M.D. Hollingsworth. Proc. R. Soc. London Ser. A, **431**, 245 (1990).
31. L. Elizabé, L. Yeo, K.D.M. Harris, G. Sankar, and J.M. Thomas. Chem. Mater. **10**, 1220 (1998).
32. L. Yeo, B.M. Kariuki, H. Serrano-González, and K.D.M. Harris. J. Phys. Chem. B, **101**, 9926 (1997).
33. L. Yeo and K.D.M. Harris. Acta Crystallogr. Sect. B: Struct. Sci. **B53**, 822 (1997).
34. L. Yeo, K.D.M. Harris, and F. Guillaume. J. Solid State Chem. **128**, 273 (1997).

© 1999 NRC Canada

Canadian Journal of Chemistry

Author Index
Volume 77, 1999

Revue canadienne de chimie

Index des auteurs
Volume 77, 1999

Abd-EI-Aziz, A.S., 1797
Achar, B.N., 1690
Acree, W.E., 1214, 1465, 1537, 1589
Adamson, J.G., 271
Addison-Jones, B., 326
Ahlberg, P., 628
Aicart, E., 348
Allen, A.D., 802
Alvarez-Cisneros, C., 130
Amyes, T.L., 922
Andraos, J., 459, 565
Andreana, P.R., 463
Andrews, D.T., 391, 523
Angel, A.J., 94
Aquino, M.A.S., 378
Argyropoulos, D.S., 667
Armesto, X.L., 997
Arnold, B., 1655
Arroyo, F.J, 1608
Artal, M., 2046
Asres, D.D., 319
Aubke, F., 1869
Austin, P.A., 830
Awitor, K.O., 243
Ayer, W.A., 1514
Azran, C., 537
Bader, R.F.W., 86
Bailey, J.E., Jr., 1941
Bain, A.D., 1340, 1707, 1810
Baird, I.R., 1821
Baltzer, L., 990
Banerjee, R., 451
Baonza, V.G., 348
Barba, V., 2025
Barber, S.E., 792
Baron, M.-H., 2015
Baronnet, F., 1177
Barré, C., 263
Barrie, P.J., 1050
Barros, C.M.F., 401
Barrows, J.N, 1941
Basch, H., 537
Batchelor, R.J., 2088
Baudy-Floc'h, M., 263
Baumstark, A.L., 308
Beam, C.F., 94
Beauchemin, D., 409
Bell, R.A., 146
Bell, S.J, 1941
Bender, T.P., 1444
Benedict, H., 943
Bennour, S., 760
Bernard, L., 243
Bernard, M., 1648
Bernasconi, C.F., 584
Berry, R.M., 667
Berthelette, C., 12
Betty, K.R., 1405
Bhattacharya, A.K., 451
Bhattacharyya, S., 2088
Biradha, K., 1196, 1327, 1436
Blackmann, A.G., 178
Blagoeva, I.B., 849
Böhme, D.K., 1453
Bohne, C., 1356
Bonnin, O., 243
Boucher, D., 687
Boucher, G.D., 340
Boukherroub, R., 1136
Boyd, M.J., 950
Bradaric, C.J., 1136
Brahma, G.S., 451
Brancaleon, L., 787
Breeze, S.R., 1424
Brennan, J.D., 1617
Broderick, T.L., 1249
Brodovitch, J.C., 326
Bromberg, P.S., 1843
Brondino, C., 57
Brönstrup, M., 774
Broo, A., 628
Broo, K.S., 990
Brossard, L., 1225
Brousmiche, D., 787
Brown, K.C., 1295
Brown, M.A., 502
Brown, R.S., 1005, 1577
Buchanan, G.W., 1911
Buckingham, A.D., 1946
Buist, R., 1887
Bunce, N.J., 1281, 1366
Buncel, E., 903
Bunton, C.A., 895
Burnell, E.E., 1761
Butler, I.S., 1892
Bytautas, L., 875
Cameron, N.S., 1311
Cameron, T.S., 378
Canle, L.M., 997
Cao, W., 1009
Capponi, M., 605
Caram, J.A., 511
Carmona, F.J., 1608
Caron, D., 223
Carret, S., 263
Carter, J., 806
Castro, J.A., 502
Castronuovo, G., 1218
Cavigliasso, G., 24
Chahoua, L., 1148
Chandler, W.D., 1599
Chang, Y.C.P., 1813
Chan-Shing, E.S., 687
Chen, X., 584
Chen, Y., 1471
Chen, Z., 291
Chênevert, R., 223
Chézeau, J.-M., 1984
Chiang, Y., 459, 1148
Choi, K.S., 1405
Choi, S.-Y., 1123
Chong, D.P., 24
Chopin, T., 2099
Chow, A., 1716
Chow, Y.L., 1374
Christendat, D., 1892
Chubb, F.L., 1057
Claridge, R.P., 647
Clark, C.R., 178
Cleland, W.W., 967
Cleverley, J.A., 842
Cobos, J.C., 1608
Coles, S.J., 155, 2095
Comuñas, M.J., 299
Conradie, J., 378
Cooley, J.M., 391, 523
Corbierre, M.K., 1311
Coupat, B., 243
Couture, P., 1340
Cowles, R., 1626

© 1999 NRC Canada

Cox, R.A., 649, 709
Coym, K.S., 1214
Cozens, F.L., 2069
Crampton, M.R., 639
Cremer, S.E., 1274
Crugeiras, J., 530
Cserti, C.C., 1136
Cyr, A., 1225
Dabo, P., 1225
Dabrowski, M.A., 1617
Daier, V., 57
Danchura, W., 1834
Dash, A.C., 451
da Silva, F.M., 624
Dasser, M., 223
Daub, C.D., 1775
Dean, K.E.S., 792
Decker, S.A., 65
De Fina, K.M., 1465, 1537, 1589
Demir, A.S., 1336
Deng, L., 1476
Denisov, G.S., 943
de Rossi, R.H., 860
Descarsin, M.T., 1349
Desjardins, P., 1444
Diallo, A.O., 122
Dickson, K.C., 146
Ditty, M.J.T., 1951
Dixon, I.M.S., 1843
Dixon, W.J., 1035
Dodier, M., 12
Donald, L.J., 1752
Donkor, K.K., 1626
Drake, J.E., 356, 1262
Drake, R.J., 356
Driedzic, W.R., 1249
D'Souza, M.J., 1118
Dubé, L., 12
Ducharme, Y., 1410
Duke, M.J.M., 1626
du Plessis, W.C., 378
Duran, M., 1476
Durand, B., 2099
Duygu, N., 1336
Earnhardt, J.N., 726
Edel, A.L., 1797
Edward, J.T., 1057
Einstein, F.W.B., 2088
Eisenberg, A., 1311
El-Bindary, A.A., 1305
El-Sonbati, A.Z., 1305
Elia, V., 1218
Eliason, R., 744
Embid, J.M., 2046
Engell, K.M., 978
Enright, G.D., 313
Epp, K.M., 1797
Epstein, N.A., 1249
Erasmus, J.C., 378
Erden, I., 1009
Ernst, L., 1697
Escandar, G.M., 1492
Esposito, A., 1108
Eustace, S.J., 459
Everall, C.J., 1405
Facey, G.A., 1899
Fallis, A.G., 159
Fanwick, P.E., 1274
Farfán, N., 2025
Fauvarque, J.F., 1349
Favre, E., 2015
Fenster, M., 667
Fenwick, M.H., 806
Fernández, J., 299
Ferradini, C., 1542
Fiakpui, C.Y., 216
Finefrock, A.E., 94
Finnin, M.S., 557
Fischer, M., 868
Fishbein, J.C., 1148
Fletcher, K.A., 1214
Flora, K.K., 1617
Fong, T.P., 1899
Foray, G.S., 676
Foroudian, H.J., 895
Fournier, J.P., 243
Fox, M.A., 1077
Frascaroli, M.I., 57
French, K.L., 94
Frey, J., 719
Friesen, D.M., 1931
Frutos, A., 1492
Fu, S., 281
Funahashi, S., 1498, 1638
Fyfe, C.A., 1984
Galezowski, W., 1042
García, J., 299
Garcia, V., 997
García de la Fuente, I., 1608
Gercek, Z., 1336
Germann, T.K., 1941
Gerzain, M., 1911
Gesser, H.D., 1716
Ghandi, K., 326
Gillitt, N.D., 895
Gilson, D.F.R., 1057, 1892
Glyde, R.W., 842
Göktürk, S., 1208
Golchoubian, H., 37
Golubev, N.S., 943
Gomes, A.K., 624
Gomes, M.T.S.R., 401
González, J.A., 1608
Gough, K.M., 1843
Grandin, H.M., 1813
Greedan, J.E., 1424
Grimmett, M.R., 178
Grindley, T.B., 481
Grow, R.H., 1009
Grünefeld, J., 439
Grunwald, E., 1097
Grzeskowiak, I., 1042
Guerro, M., 263
Gunn, J.R., 367
Gusev, D., 1899
Gut, I.G., 605
Guth, J.-L., 2099
Guthrie, J.P., 934
Hägele, G., 1869
Haget, Y., 332
Halut-Desportes, S., 2015
Harding, W.W., 1922
Harris, K.D.M., 2105
Harrison, K.A., 1410
Hartman, S.J., 1856
Harvey, P.D., 16
Hassani, C.A., 1594
Hawrylak, B.E., 1241
Hazendonk, P., 1340, 1707
Heard, P.J., 1707
Hellrung, B., 605
Hennigar, T.L., 1249
Henry, B.R., 1775
Henselwood, T.L., 281
Hernández, C., 2025
Hernández, C.E., 1214, 1465
Heubes, M., 1869
Hibbert, F., 1035
Hiltunen, Y., 1788
Hirai, K., 1066
Holland, H.L., 463
Hone, D.C., 842
Hou, Y., 960
Houk, K.N., 540, 875
Hoz, S., 537
Huang, W.-w., 806
Huang, Y., 495
Huber, S.N., 237
Huet, J., 2015
Humeres, E., 1050
Hurst, D.R., 94
Hursthouse, M.B., 2095
Hutton, H.M., 1797
Hynes, R.C., 1057
Ider, S., 249
Igdar, A.C., 1336
Iiba, E., 1066
Ishiyama, J., 1374

© 1999 NRC Canada

Itoh, M., 1638
Iyama, T., 1419
Jacobs, H., 1922
Jakeway, S.C., 2083
James, B.R., 182, 1821
Jamieson, H.E., 409
Jarczewski, A., 1042
Jarne, C., 2046
Jayasree, P.K., 1690
Jay-Gerin, J.P., 1542
Jędral, W., 1281
Jenkins, H.A., 155
Jiang, F., 1327
Jiang, W., 879
Jiang, Z., 495
Joe, K.S., 1405
Johnson, K.E., 1599
Johnston, A.N., 1366
Johnston, L.J., 787
Jones, J., 624
Joseph-Nathan, P., 130
Junquera, E., 348
Kakkar, A.K., 205
Kameyama, H., 258
Kanagasabapathy, V.M., 2069
Karlsson, A., 628
Kazmaier, P., 903
Keeffe, J.R., 1009
Kelly, D.G., 2095
Kera, H.M., 1305
Ketner, R.J., 584
Kevill, D.N., 1118
Khan, A., 1005
Khasrou, L.N., 1262
Kiehlmann, E., 1436
Kimura, A., 416
Kirby, A.J., 792, 849
Kjaergaard, H.G., 1775
Kliegel, W., 439
Klobukowski, M., 65
Klug, M., 1050
Kluger, R., 271
Knaus, E.E., 216
Kochi, J.K., 913
Koedjikov, A.H., 849
Koeppl, G.W., 695
Koga, Y., 2039
Konstantinov, A.D., 1366
Koshino, N., 1498
Kotovych, G., 1728
Kovac, F., 308
Kratochvil, B., 1626
Kreevoy, M.M., 733, 943
Kresge, A.J., 459, 1528
Kroeker, S., 1887, 1962
Krull, U.J., 2083
Kuchiyama, Y., 1498
Kumar, A., 895
Kumar, D., 1288
Kuznetsov, A.M., 1085
Laatikainen, R., 1788
Lacelle, S., 1745
Lait, S., 1281
Lamprecht, G.J., 378
Le Grel, P., 263
Lee, H.S., 738
Lee, H.-W., 659
Lee-Ruff, E., 1245
Leigh, W.J., 1136
Leong, W.K., 1327
Lessard, J., 687, 1225, 1648
Lewis, A.R., 1984
Lewis, F.D., 595
Leznoff, C.C., 138
Li, D., 281
Li, L., 1424
Li, X.P., 1626
Li, Z., 138
Limbach, H.-H., 943
Lin, H., 1471
Lin, R., 387
Lipkowski, J., 1163
Liu, M.T.H., 540
Liu, R., 525
Long, Y., 1671
López, E.R., 299
Lord, S.J., 1249
Lounila, J., 1788
Lu, J., 232
Lucas, D., 1648
Lucy, C.A., 281
Lugo, L., 299
Lukas, A., 1108
Ma, J., 752
Ma, K., 291
Macdonald, P.M., 1899
MacInnis, J.A., 340, 1994
Maekawa, H., 258
Magnion, D., 1655
Mahramanlıoğlu, M., 1208
Marangoni, D.G., 227, 340, 1241, 1994
Marder, T.B., 199, 205
Martell, A.E., 614
Marzilli, L.G., 1973
Maskill, H., 530
Massarweh, G., 2059
Matsumoto, M., 1638
May, L.J., 1797
Mazzola, E.P., 1941
McBreen, J., 738
McClelland, R.A., 978, 2069
McClung, R.E.D., 1728
McComb, M.E., 1716, 1752
McDonald, R., 1931
McGarvey, B.R., 502
McGovern, M., 1678
McKerrow, A., 903
McLean, R.J.C., 409
McLean, S., 1922
McMahon, J.B., 1941
Meany, J.E., 1108
Ménard, H., 1225, 1594
Meng, Q., 1528
Merica, S.G., 1281
Metivaud, V., 332
Meyer, C., 122
Meyers, C.Y., 960
Millar, R.W., 647
Miller, A.M., 595
Min, J.-S., 659
Mirifico, M.V., 511
Mischne, M.P., 237
Mislankar, A.G., 1262
Mitchell, S.L., 1405
Mizerski, T., 922
Mizuno, H., 1066
Mobinikhaledi, A., 178
Modro, A.M., 890
Modro, T.A., 890
Mohammadi-Ziarani, G., 223
Mondal, A.B., 451
Mondieig, D., 332
Moore, A.N.J., 681
Moore, S.J., 1973
Moorthy, J.N., 1356
Morales-Ríos, M.S., 130
Morin, F.G., 1892
Morris, R.H., 1899
Mortier, J., 98
Motekaitis, R.J., 614
Mugnier, Y., 1648
Muir, K.W., 155
Munro, A.P., 550
Murthy, K.S.K., 216
Musson, S.P., 1617
Nakajima, J., 1066
Nakashima, T.T., 1728
Natividad-Preyra, R., 113
Nelson, B.R., 1295
Nelson, J.H., 1973
Neverov, A.A., 1005
Newcomb, M., 1123
Nguyen, D., 463
Nguyen, M.T., 817
Nguyen, Q.T., 1671
Ni, Y., 387
Nilsson, J., 990
Nishiyama, T., 258

© 1999 NRC Canada

Nunes, M., 1050
O'Brien, S.E., 28
Okamoto, Y., 738
Okano, L.T., 1356
Okuyama, T., 577
Olah, G.A., 525
Oleschuk, R.D., 1716
Oliveira, C.M.S., 1050
Oliveira, J.A.B.P., 401
Oonk, H.A.J., 332
Orvig, C., 2033
Otín, S., 2046
Oumar-Mahamat, H., 1577
Ovans, R., 1356
Ozin, G.A., 2001
Paal, K., 271
Paddock, R.L., 1249
Paine, S.W., 459
Palepu, R., 340, 1994
Palopoli, C., 57, 1492
Pan, Y., 291
Pankratov, A.N., 2053
Peñéñory, A.B., 676
Peeling, J., 1887
Peng, Z.H., 1394
Penner, G.H., 1813
Percival, P.W., 326
Perez, L., 1508
Perreault, H., 319, 1716, 1752
Persaud, A.T., 409
Persy, G., 605
Pettitt, B.A., 1834
Pezacki, J.P., 1230
Phillips, O.A., 216
Pialoux, A., 1384
Pierro, A., 1218
Ping, Z., 1671
Plunian, B., 98
Pocker, Y., 1108
Pojarlieff, I.G., 849
Pollack, R.M., 634
Polozov, A.M., 1274
Pomeroy, R.K., 1327
Popelier, P.L.A., 28
Popik, V.V., 459, 806
Posakony, J.J., 182
Potvin, P.G., 1310
Power, W.P., 1951
Prakash, O., 1191
Prakash, S.G.K., 525
Pratt, R.C., 182
Puddephatt, R.J., 155
Pulkkinen, A., 1788
Qi, Y., 1444
Qin, H., 481
Qin, Z., 155
Quail, J.W., 1295
Rabbitt, L.C., 639
Rajabalee, F., 332
Raju, N.P., 1424
Ramnauth, J., 1245
Rampey, M.E., 94
Rankin, K.N., 1599
Rappoport, Z., 584, 719
Raspoet, G., 817
Rasul, G., 525
Ratcliffe, C.I., 1911
Rathore, R., 913
Ratnani, R., 1262
Rauk, A., 74
Reber, C., 16
Reese, R.S., 1077
Rego, G.S., 313
Reis, R., 1336
Ren, X., 387
Rettig, S.J., 182, 425, 434, 439, 1821, 2033
Reynolds, W.F., 1922, 1941
Richard, J.P., 922
Ridd, J.H., 647
Rieck, T., 1697
Ripmeester, J.A., 313
Rishavy, M.A., 967
Rizzotto, M., 57
Robertson, B.E., 1295
Robinson, B.H., 842
Rochon, F.D., 2059
Roe, D.C., 205
Rojas-Lima, S., 2025
Rosenberg, L., 1931
Rossi, R.A., 676
Roy, L.E., 1214, 1465
Rozental, E., 537
Ruest, L., 12
Rutenburg, I., 695
Sabbah, R., 249, 1508
Sadki, S., 1349
Sage, M.L., 1775
Sala, L.F., 57, 1492
Salas-Peregrin, J.M., 57
Santaballa, J.A., 997
Santana-Marques, M.G.O., 401
Santillan, R., 2025
Saunders, W.H., 810
Sauriol, F., 1057
Scacchi, G., 1177
Schaad, L.J., 875
Schlaf, M., 1899
Schmeisser, J.M., 1136
Schowen, K.B., 781
Schowen, R.L., 781, 943
Schröder, D., 774
Schurko, R.W., 1973
Schüth, J., 326
Schutte, R., 1626
Schwarz, H., 774
Schwieger, W., 495
Seltzer, S., 557
Setyawati, I.A., 2033
Sham, S., 1782
Sharma, V., 1191
Sharp, T.L., 1465, 1537, 1589
Shchavlev, A.E., 2053
Shi, Y., 868
Shimizu, G.H.K., 313
Shoemaker, J.A.W., 1856
Shojania, S., 1716
Shustov, G.V., 74, 540
Sierraalta, A., 1521
Signorella, S., 57, 1492
Sikorska, E., 472
Sikorski, M., 472
Silverman, D.N., 726
Silvestru, A., 356
Simon, P., 1349
Simon, Y., 1177
Sinbandhit, S., 98
Skov, K.A., 182, 1821
Ślebocka-Tilk, H., 1577
Smirnov, S.N., 943
Smith-Palmer, T., 227
Snieckus, V., 868
Solá, M., 1476
Soldi, V., 1050
Soliven, M., 1697
Song, J., 1009
Sorensen, P.E., 978
Sott, R.S., 990
Spencer, P., 391, 523
Steel, C., 1097
Steenken, S., 2069
Steer, R.P., 472
Stern, G.A., 1734
Stevefelt, J., 518
Steytler, D.C., 842
Still, I.W.J., 113
Stirling, C.J.M., 1105
St-Martin, D., 12
Storr, A., 425, 434
Streitweiser, A., 654
Studer-Martinez, S.L., 94
Su, X., 1471
Suárez-Castillo, O.R., 130
Summers, D.A., 425
Sun, H., 1471
Sun, Yizhen, 614
Sun, Yujun, 677
Sung, K., 459

© 1999 NRC Canada

Svartman, E.L., 511
Swarts, J.C., 378
Syvitski, R.T., 1761
Tachikawa, H., 1419
Taconnet, S., 1177
Takagi, H.D., 1498, 1638
Takagi, T., 416
Talami, S., 1105
Tan, J., 781
Tanase, T., 1492
Tang, A., 291
Tantirungrotechai, Y., 1946
Tanwar, M.P., 1191
Taylor, N.J., 199, 205, 1249
Tee, O.S., 950
Terrier, F., 639
Teruel, H., 1521
Thompson, G.R., 1626
Thompson, M., 1678
Thompson, R.C., 425
Tian, J., 781
Tidwell, T.T., 525, 802, 806
Tomioka, H., 1066
Toner, A.J., 2095
Torrent, M., 1476
Toste, F.D., 113
Toullec, J., 760
Touzelin, B., 1384
Toy, P.H., 1123
Tracey, A.S., 2088
Trifonov, L.S., 1514
Trotter, J., 425, 434, 439
Trudell, M.B., 1009
Tu, C., 726
Tuck, D.G., 502
Tunçay, M., 1208
Tuppurainen, K., 1788
Turner, C.D., 463
Turujman, S.A., 1941
Ulstrup, J., 1085
Um, I.-H., 659
Underhill, R.S., 281
Valliant, J.F., 146
van Lier, J., 138
Van-Thanh, N., 122
Van Verth, J.E., 810
Vashchenko, A.V., 416
Vasini, E.J., 511
Vasquez, P.C., 308
Vaultier, M., 98
Velasco, I., 2046
Velleca, F., 1218
Verdier, P., 243
Vigroux, A., 1148
Viola, L., 860
Vogels, C.M., 1196, 1249
Vyprachticky, D., 738
Wadsworth, T.L., 1009
Wagner-Brennan, J.M., 595
Walker, N.M., 2095
Walker, R.A., 227
Walsh, J.M., 391, 523
Waltz, W.L., 37
Wan, P., 868
Wang, D.Z., 654
Wang, J., 232
Wang, S., 1424
Wang, Y., 367
Wang, Z.Y., 1444
Warkentin, J., 1340
Wasylishen, R.E., 1962, 1973
Watanuki, K., 258
Wayner, D.D.M., 681
Weil, J.A., 1295
Welch, M.J., 614
Wellwood, H.L., 1196
Wentzell, P.D., 391, 523
Werstiuk, N.H., 752
Westaway, K.C., 879
Westcott, S.A., 199, 205, 1196, 1249
Westmore, J.B., 1734
Wichlacz, M., 1514
Wiesenthal, A., 1057
Wilkinson, F., 472
Williams, A.R., 94
Williams, D.L.H., 550
Williams, I.H., 830
Williot, F., 1648
Wirz, J., 605
Withers, S.G., 1
Wojtyk, J., 903
Wu, G., 1782
Xu, F.-P., 1009
Xu, W., 1899
Yamada, Y., 1419
Yamamoto, H., 1728
Yamataka, H., 577
Yang, H., 1671
Yang, J., 356
Yang, X.Q., 738
Yao, X., 634
Yatsimirsky, A.K., 1005
Ye, H.-F., 2015
Yeo, L., 2105
Yeung, K.K.-C., 281
Young, V.G., Jr., 733
Yu, A., 667
Zaworotko, M.J., 1196, 1249, 1436
Zhang, D., 1869
Zhang, Q., 232
Zhang, Y., 1424
Zhao, B.-p., 868
Zhao, G., 1471
Zhao, X., 291
Zheng, J.-B., 1009
Zhou, Z., 1471
Zhu, S., 1471
Zhuo, K., 232
Ziegler, T., 1476
Zimpel, Z., 1295
Zinczuk, J., 237
Zong, H., 387
Zunic, V., 1356

© 1999 NRC Canada

Canadian Journal of Chemistry

Revue canadienne de chimie

Contents
Volume 77, 1999

Sommaire
Volume 77, 1999

January / Janvier

ARTICLES

Stephen G. Withers 1998 Hoffmann La Roche Award Lecture
Understanding and exploiting glycosidases **1**

Luc Ruest, Carl Berthelette, Marco Dodier, Laurence Dubé, and David St-Martin Ryanoids and related compounds. Isolation and characterization of four minor ryanoids from the plant *Ryania speciosa* Vahl: 8,9-didehydroryanodine, 10-*O*-acetylryanodol, 3-*O*-benzoylryanodol, and a first natural 4-deoxyryanoid: 4-deoxy-8_{ax}-hydroxy-10-*O*-methyl-10-epiryanodine (4-deoxyester A) **12**

Pierre D. Harvey and Christian Reber Distortions in square-planar palladium(II) halides: a nonempirical molecular orbital model study **16**

Germán Cavigliasso and Delano P. Chong Accurate density-functional calculation of core-electron binding energies with a scaled polarized triple-zeta basis set. VI: Extension to boron-containing molecules. **24**

Sean E. O'Brien and Paul L.A. Popelier Quantum molecular similarity. Part 2: The relation between properties in BCP space and bond length **28**

H. Golchoubian, W.L. Waltz, and J.W. Quail Synthesis, structure, and reactivity of macrocyclic heterobimetallic complexes of (Co, Cu), (Co, Ni), (Co, Zn), (Zn, Cu), (Zn, Ni) combinations **37**

Verónica Daier, Sandra Signorella, Marcela Rizzotto, María Inés Frascaroli, Claudia Palopoli, Carlos Brondino, Juan Manuel Salas-Peregrin, and Luis F. Sala Kinetics and mechanism of the reduction of Cr^{VI} to Cr^{III} by D-ribose and 2-deoxy-D-ribose **57**

Stephen A. Decker and Mariusz Klobukowski The energy barrier for CO migration in $Mn_2(CO)_6(H_2PCH_2PH_2)_2$: a PM3(tm) study **65**

Gennady V. Shustov and Arvi Rauk Dioxirane oxidation of nitrosoamines. An ab initio study **74**

R.F.W. Bader Can there be more than a single definition of an atom in a molecule? **86**

April J. Angel, Anne E. Finefrock, Kristen L. French, Douglas R. Hurst, Angela R. Williams, Mary E. Rampey, Shannon L. Studer-Martinez, and Charles F. Beam Preparation of *N*-aryl-4-oxo-4*H*-1-benzothiopyran-2-acetamides from trilithiated acetoacetanilides and lithiated methyl thiosalicylate **94**

Jacques Mortier, Michel Vaultier, Barbara Plunian et Sourisak Sinbandhit Réactions d'addition conjuguée d'organolithiens aux acides carboxyliques α,β-insaturés **98**

Ian W.J. Still, Rosanne Natividad-Preyra, and F. Dean Toste A versatile synthetic route to 1,5-dithiocins from *o*-mercapto aromatic aldehydes **113**

Alpha O. Diallo, Claude Meyer, and Nguyen Van-Thanh The molecular complexes of deoxycholic acid and cholesterol with CH_3COOD studied by infrared spectroscopy **122**

Martha S. Morales-Ríos, Oscar R. Suárez-Castillo, Celina Alvarez-Cisneros, and Pedro Joseph-Nathan ^{13}C NMR and crystallographic evidence of push–pull effects in furoindolic β-enamino esters **130**

Zhaopeng Li, Johan van Lier, and Clifford C. Leznoff Heterocyclic aromatic amide protecting groups for aryl and phthalocyaninesulfonic acids **138**

Russell A. Bell, Kieran C. Dickson, and John F. Valliant The total synthesis of a technetium chelate – tamoxifen complex **146**

© 1999 NRC Canada

COMMUNICATION

Zengquan Qin, Hilary A. Jenkins, Simon J. Coles, Kenneth W. Muir,and Richard J. Puddephatt **155**
Self-assembly of one-dimensional polymers by coordination and hydrogen bonding in palladium(II) complexes

IUPAC Recommendations / IUPAC recommendation **iii**

Instructions to Authors / Recommendations aux auteurs **I-1**

Notes for authors of papers presenting the results of X-ray crystal structure analyses / Recommandations aux auteurs d'articles décrivant a détermination de structures par diffraction des rayons Xcristallines **v**

Author Index / Index des auteurs **AI-1**

February / Février

ARTICLES

Alex G. Fallis 1998 Alfred Bader Award Lecture **159**
Tangents and targets: The synthetic highway from natural products to medicine

Charles R. Clark, Allan G. Blackman, M. Ross Grimmett, and Akbar Mobinikhaledi C(2)-H isotopic exchange in coordinated imidazoles revisited. The case of the $[Co(NH_3)_5ImH]^{3+}$ ion **178**

Jeffrey J. Posakony, Russell C. Pratt, Steven J. Rettig, Brian R. James, and Kirsten A. Skov Porphyrins incorporating heterocyclic *N*-oxides: (oxidopyridyl)porphyrins, porphyrin-*N*-oxides, and a tirapazamine–porphyrin conjugate **182**

Stephen A. Westcott, Nicholas J. Taylor, and Todd B. Marder Reactions of $(\eta^5\text{-}C_9H_7)Rh(\eta^2\text{-}C_2H_4)_2$ with quinones: molecular structure of $[(\eta^5\text{-}C_9H_7)Rh(2,3,5,6\text{-}C_6O_2(CH_3)_4)]$ **199**

Stephen A. Westcott, Ashok K. Kakkar, Nicholas J. Taylor, D. Christopher Roe, and Todd B. Marder Synthesis, structure, and solution dynamics of indenyl rhodium complexes containing bulky phosphine ligands: molecular structures of $(\eta^5\text{-}1\text{-}CH_3\text{-}C_9H_6)Rh(\eta^2\text{-}C_2H_4)(PCy_3)$ (Cy = cyclohexyl) and $(\eta^5\text{-}1\text{-}CH_3\text{-}C_9H_6)Rh(dcpe)$ (dcpe = $Cy_2PCH_2CH_2PCy_2$) **205**

Oludotun A. Phillips, K.S. Keshava Murthy, Charles Y. Fiakpui, and Edward E. Knaus Synthesis of 5-phenyl-10-methyl-7*H*- pyrimido[4,5-*f*][1,2,4]triazolo[4,3-*a*][1,4]diazepine and its evaluation as an anticonvulsant agent **216**

Robert Chênevert, Ghodsi Mohammadi-Ziarani, Dave Caron, and Mohammed Dasser Chemoenzymatic enantioselective synthesis of (–)-enterolactone **223**

Richard A. Walker, D. Gerrard Marangoni, and Truis Smith-Palmer A capillary electrophoretic determination of the kinetics of tetradecanedisulfate hydrolysis **227**

Jianji Wang, Kelei Zhuo, Qiufen Zhang, and Jinsuo Lu Thermodynamics of the interaction of HCl with D-xylose in water at 278.15–318.15 K **232**

Mirta P. Mischne, Silvia N. Huber, and Juan Zinczuk Photochemical reaction of β-ionone derivatives in the presence of oxygen. A convenient synthesis of substituted 1,2,4-trioxanes **237**

Komla Oscar Awitor, Laurent Bernard, Olivier Bonnin, Bernard Coupat, Jean Paul Fournier et Philippe Verdier Préparation du chlorure mercureux et mesure de sa pression de vapeur **243**

Raphaël Sabbah et Safi Ider Energétique des liaisons inter- et intramoléculaires dans les trois acides carboxypyridiniques (acides picolinique, nicotinique et isonicotinique) **249**

Tomihiro Nishiyama, Hideaki Kameyama, Hideki Maekawa, and Kouhei Watanuki Ether synthesis using trifluoromethanesulfonic anhydride or triflates under mild reaction conditions **258**

Catherine Barré, Sophie Carret, Michel Guerro, Philippe Le Grel, and Michèle Baudy-Floc'h α-Halogenohydrazides: useful starting material for the synthesis of hydrazinoazapeptides and azauracils **263**

Ronald Kluger, Krisztina Paal, and J. Gordon Adamson An ether-linked tetrafunctional acylating reagent and its cross-linking reactions with hemoglobin **271**

Author Index / Index des auteurs **AI-1**

© 1999 NRC Canada

March / Mars

ARTICLES

Charles A. Lucy, Ken K.-C. Yeung, Shilin Fu, Dongmei Li, Tracey L. Henselwood, and Royale S. Underhill 1998 W.A.E. McBryde Medal Lecture
Searching for the Holy Grail in analytical separations **281**

Zhongfang Chen, Keqin Ma, Yinming Pan, Xuezhuang Zhao, and Auchin Tang Theoretical studies of heterofullerenes $C_{68}X_2$ (X = N, B) **291**

J. García, M.J. Comuñas, L. Lugo, E.R. López, and J. Fernández Excess molar volumes of liquid 1-bromoalkane + alkane mixtures. Nitta–Chao characterization of the bromine–bromine and bromine–methylene interactions in binary 1-bromoalkane + alkane mixtures **299**

Alfons L. Baumstark, Franci Kovac, and Pedro C. Vasquez Oxidation of secondary alcohols and ethers by dimethyldioxirane **308**

George K.H. Shimizu, Gary D. Enright, Gabriela S. Rego, and John A. Ripmeester One-dimensional ribbons of solvated Ag sulfonates **313**

Daniel D. Asres and Hélène Perreault Preparation, isolation, and characterization of permethylated galactosides and fucosides **319**

Paul W. Percival, Brenda Addison-Jones, Jean-Claude Brodovitch, Khashayar Ghandi, and Joachim Schüth Free radicals formed by H(Mu) addition to pyrene **326**

Valérie Metivaud, Fazil Rajabalee, Harry A.J. Oonk, Denise Mondieig, and Yvette Haget Complete determination of the solid (RI)–liquid equilibria of four consecutive *n*-alkane ternary systems in the range $C_{14}H_{30}$–$C_{21}H_{44}$ using only binary data **332**

Judith A. MacInnis, Greg D. Boucher, R. Palepu, and D. Gerrard Marangoni The properties of a family of two-headed surfactant systems: the 4-alkyl-3-sulfosuccinates 2. Surface properties of alkyl sulfosuccinate micelles **340**

Elena Junquera, Valentin G. Baonza, and Emilio Aicart Energetics of the encapsulation of *o*-, *m*-, and *p*-hydroxybenzoic acids by β-cyclodextrin and its methylated and hydroxypropylated derivatives in aqueous solution **348**

John E. Drake, Robert J. Drake, Anca Silvestru, and Jincai Yang Tetraorganodichalcogenoimidodiphosphinato derivatives of dimethyltellurium(IV) compounds. Crystal structures of $Me_2Te[(SPPh_2)_2N]_2$, $Me_2TeCl[(SPPh_2)_2N]$, $Me_2TeI[(SPPh_2)_2N]$, and $Me_2TeCl[(OPPh_2)(SPPh_2)N]$ **356**

Youliang Wang and John R. Gunn Computational study on small water clusters using a semiempirical valence bond approach **367**

W.C. (Ina) du Plessis, Johannes J.C. Erasmus, Gert J. Lamprecht, Jeanet Conradie, T. Stanley Cameron, Manuel A.S. Aquino, and Jannie C. Swarts Cyclic voltammetry of ferrocene-containing β-diketones as a tool to obtain group electronegativities. The structure of 3-ferrocenoyl-1,1,1-trifluoro-2-hydroxyprop-2-ene **378**

Xiaoling Ren, Ruisen Lin, Yaming Ni, and Hanxing Zong Apparent molar volumes of glycine, L-alanine, and L-serine in water + ethanol mixtures at 298.15 K **387**

Peter D. Wentzell, Darren T. Andrews, Jennifer M. Walsh, Jean M. Cooley, and Paige Spencer Estimation of hydrocarbon types in light gas oils and diesel fuels by ultraviolet absorption spectroscopy and multivariate calibration **391**

M. Teresa S.R. Gomes, Cristina M.F. Barros, M. Graça O. Santana-Marques, and João A.B.P. Oliveira The adsorption of carbon dioxide by tertiary alkanolamines **401**

Author Index / Index des auteurs **AI-1**

April / Avril

ARTICLES

Anthony Treveidi Persaud, Diane Beauchemin, Heather Edith Jamieson, and Robert J.C. McLean Partial leaching as an aid to slurry nebulization for the analysis of soils by ICP-MS with flow injection and mixed-gas plasmas **409**

© 1999 NRC Canada

Andrei V. Afonin, Alexander V. Vashchenko, Tatsuya Takagi, Atsuomi Kimura, and Hideaki Fujiwara Specific intramolecular interactions C—H···N in heteroaryl vinyl ethers and heteroaryl vinyl sulfides studied by ^{1}H, ^{13}C, and ^{15}N NMR spectroscopies and by ab initio calculations on molecular structures as well as on nuclear shieldings **416**

Steven J. Rettig, Alan Storr, David A. Summers, Robert C. Thompson, and James Trotter Iron(II) 2-methylimidazolate and copper(II) 1,2,4-triazolate complexes: systems exhibiting long-range ferromagnetic ordering at low temperatures **425**

Steven J. Rettig, Alan Storr, and James Trotter The methylgallium-2-carboxylatobenzimidazolato hexamer, $[MeGa{\cdot}C_8H_4N_2O_2]_6{\cdot}C_6H_6{\cdot}(Me_2C_6H_4)_2$; synthesis and X-ray crystal structure **434**

Johann Grünefeld, Wolfgang Kliegel, Steven J. Rettig, and James Trotter Reaction of diphenylborinic acid with pyridinium and phosphonium bisacyl methylides. Crystal and molecular structures of resulting *B,N*- and *B,P*-betaines **439**

Anup Kumar Bhattacharya, Anath Bondhu Mondal, Anadi C. Dash, G.S. Brahma, and Rupendranath Banerjee Kinetics of oxidation of hydrogen peroxide and ascorbic acid by a tribridged manganese(IV,IV) dimer in feebly acidic media **451**

J. Andraos, Y. Chiang, S.J. Eustace, A.J. Kresge, S.W. Paine, V.V. Popik, and K. Sung Solvent isotope effect on the hydroxide-ion-catalyzed hydration of ketenes in aqueous solution **459**

Herbert L. Holland, Carl D. Turner, Peter R. Andreana, and Doan Nguyen Biotransformation of organic sulfides. Part 12. Conversion of heterocyclic sulfides to chiral sulfoxides by *Helminthosporium* sp. NRRL 4671 and *Mortierella isabellina* ATCC 42613 **463**

M. Sikorski, E. Sikorska, F. Wilkinson, and R.P. Steer Studies of the photophysics and spectroscopy of alloxazine and related compounds in solution and in the solid state **472**

Huiping Qin and T. Bruce Grindley Determination of the configuration of ribitol in the C-polysaccharide of *Streptococcus pneumoniae* using a synthetic approach **481**

Yining Huang, Zhimei Jiang, and Wilhelm Schwieger A structural investigation of the singly layered silicates, silinaite and makatite, by vibrational spectroscopy **495**

Martyn A Brown, Jesus A. Castro, Bruce R. McGarvey, and Dennis G. Tuck A complex of gallium with a Schiff base – bis(orthoquinone) ligand **502**

Esther Lea Svartman, José Alberto Caram, María Virginia Mirífico, and Enrique Julio Vasini Electrochemistry of 1,2,5-thiadiazole 1,1-dioxide derivatives with 3,4 substituents presenting separated, connected, and fused π-systems **511**

Jörgen Stevefelt Calculation of atomic recombination in a decaying high-temperature hydrogen gas column **518**

ADDITIONS AND CORRECTIONS/AJOUTS ET CORRECTIONS

Peter D. Wentzell, Darren T. Andrews, Jennifer M. Walsh, Jean M. Cooley, and Paige Spencer Additions and corrections: Estimation of hydrocarbon types in light gas oils and diesel fuels by ultraviolet absorption spectroscopy and multivariate calibration **523**

Obituary / Nécrologie **v**

Author Index / Index des auteurs **AI-1**

May-June / Mai-Juin

This issue is dedicated to Professor A. Jerry Kresge
Ce tirage est dédié au Professeur A. Jerry Kresge

ARTICLES

G.K. Surya Prakash, Golam Rasul, George A. Olah, Ronghua Liu, and Thomas T. Tidwell Preparation, ^{1}H and ^{13}C NMR, and ab initio/IGLO study of mono-*O*-protonated deltic acid and theoretical investigation of di-, tri-, and tetra-*O*-protonated deltic acids **525**

Juan Crugeiras and Howard Maskill The 4,4′-dimethoxytrityl carbenium ion by ionization of 4,4′-dimethoxytrityl alcohol in acetonitrile – aqueous perchloric and nitric acids containing electrolytes: kinetics, equilibria, and ion-pair formation **530**

© 1999 NRC Canada

Esther Rozental, Carmela Azran, Harold Basch, and Shmaryahu Hoz Strain in bicyclobutane: on the interpretation of quantitative data **537**

Gennady V. Shustov, Michael T.H. Liu, and K.N. Houk Facile formation of azines from reactions of singlet methylene and dimethylcarbene with precursor diazirines: theoretical explorations **540**

Andrew P. Munro and D. Lyn H. Williams Synthesis and kinetics of decomposition of some novel *S*-nitrosothiols **550**

Michael S. Finnin and Stanley Seltzer The secondary α-deuterium isotope effect at the site of the enzyme-catalyzed *cis-trans* isomerization of maleylacetone. Mechanistic implications **557**

John Andraos The problem of distinguishability of rate constants in the two-step consecutive sequence $A \rightarrow B \rightarrow C$ **565**

Tadashi Okuyama and Hiroshi Yamataka A theoretical study on the reactivity of vinyl iodonium ions **577**

Claude F. Bernasconi, Rodney J. Ketner, Xin Chen, and Zvi Rappoport Detection and kinetic characterization of S_NV intermediates. Reactions of thiomethoxybenzylidene Meldrum's acid with thiolate ions, alkoxide ions, OH^-, and water in aqueous DMSO **584**

Frederick D. Lewis, Jill M. Wagner-Brennan, and Alan M. Miller Formation and behavior of intramolecular *N*-(styrylalkyl)aniline exciplexes **595**

Marco Capponi, Ivo G. Gut, Bruno Hellrung, Gaby Persy, and Jakob Wirz Ketonization equilibria of phenol in aqueous solution **605**

Ramunas J. Motekaitis, Yizhen Sun, Arthur E. Martell, and Michael J. Welch Synthesis, characterization, and Cu(II) solution chemistry of dioxotetraazamacrocycles **614**

Flavia Martins da Silva, Adriana Kniaseff Gomes, and Joel Jones, Jr. Organic reaction in water. Part 2: Michael addition in water without phase transfer agents **624**

Annika Karlsson, Anders Broo, and Per Ahlberg Regioselective protonation of ferrocene in superacid and formation of a C—H—Fe bond. An experimental and theoretical study of the structure and dynamics of the ferrocenonium ion **628**

Xudong Yao and Ralph M. Pollack Electronic effects on enol acidity and keto–enol equilibrium constants for ring-substituted 2-tetralones **634**

Michael R. Crampton, Lynsey C. Rabbitt, and François Terrier Electrophilic aromatic substitution in substituted anilines; kinetics of the reaction with 4,6-dinitrobenzofuroxan **639**

Robert P. Claridge, Ross W. Millar, and John H. Ridd ^{15}N nuclear polarization in the reactions of diallyl ether with nitrogen dioxide **647**

Daniel Ze-Rong Wang and Andrew Streitwieser Aggregation and ion pair acidity in THF: lithium and cesium enolates of α-phenylcyclohexanone **654**

Ik-Hwan Um, Ji-Sook Min, and Hye-Won Lee Structure–reactivity correlations in the reaction of 2,4-dinitrophenyl X-substituted benzoates with alicyclic secondary amines **659**

Yujun Sun, Michael Fenster, Annie Yu, Richard M. Berry, and Dimitris S. Argyropoulos The effect of metal ions on the reaction of hydrogen peroxide with Kraft lignin model compounds **667**

Gabriela S. Foray, Alicia B. Peñéñory, and Roberto A. Rossi Reactivity of aminyl radicals in radical nucleophilic substitution reactions with diphenylphosphide anion **676**

Andrew N.J. Moore and Danial D.M. Wayner Redox switching of carbohydrate binding to ferrocene boronic acid **681**

Elisa Soazara Chan-Shing, Denys Boucher, and Jean Lessard The electrochemical reduction of α-nitrocumene in a protic and basic medium on large surface area (porous) electrodes: electronation–protonation or electrocatalytic hydrogenation? **687**

Irina Rutenburg and Gerald W. Koeppl Classical variational rate theory portraits of the dynamical stereochemistry of the $F + H_2 \rightarrow FH + H$ reaction **695**

Robin A. Cox Styrene hydration and stilbene isomerization in strong acid media. An excess acidity analysis **709**

Joseph Frey and Zvi Rappoport Keto $\rightleftarrows$ enol equilibria for and oxidative cyclization to benzofurans of 2,2-ditipyl-1-R-ethenols. Comparison with dimesityl analogs **719**

J. Nicole Earnhardt, Chingkuang Tu, and David N. Silverman Intermolecular proton transfer in catalysis by carbonic anhydrase V **726**

© 1999 NRC Canada

Maurice M. Kreevoy and Victor G. Young, Jr. Geometric isotope effects in crystalline sodium hydrogen bis(4-nitrophenoxide) dihydrate **733**

H.S. Lee, X.Q. Yang, J. McBreen, D. Vyprachticky, and Y. Okamoto New chloride anion receptors: trifluoromethyl sulfonylated polyamines **738**

Robert Eliason Acid-catalyzed decomposition of diazodiphenylmethane in dimethylsulfoxide **744**

Nick Henry Werstiuk and Jiangong Ma An ab initio study on the magnetic susceptibility and magnetically induced current density distribution of the bicyclo[3.2.1]octa-3,6-dien-2-yl anion **752**

Sadjia Bennour and Jean Toullec General acid-catalyzed addition of methanol to (*E*)-*N*-benzylideneanilines **760**

Mark Brönstrup, Detlef Schröder, and Helmut Schwarz Oxidative dealkylation of aromatic amines by "bare" FeO^+ in the gas phase **774**

Jiaher Tian, Jue Tan, K. Barbara Schowen, and Richard L. Schowen The role of the medium in solvent isotope effects on serine protease action **781**

Lorenzo Brancaleon, Darryl Brousmiche, and Linda J. Johnston Photoinduced electron transfer chemistry of 2,3-dicyanonaphthalene **787**

Sarah E. Barber, Kathryn E.S. Dean, and Anthony J. Kirby A mechanism for efficient proton-transfer catalysis. Intramolecular general acid catalysis of the hydrolysis of 1-arylethyl ethers of salicylic acid **792**

Annette D. Allen and Thomas T. Tidwell Ring opening of cyclobutene-1,2-dione and 3-trimethylsilylcyclobutene-1,2-dione. Dimerization/decarbonylation of a bisketene to a ketenylbutenolide **802**

Jennifer Carter, Michael H. Fenwick, Wen-wei Huang, Vladimir V. Popik, and Thomas T. Tidwell Addition of the nitroxyl radical TEMPO to 1-naphthylketene: formation of an unusual adduct **806**

James E. Van Verth and William H. Saunders, Jr. Identity-reaction proton transfers from oxygen acids yielding localized vs. delocalized conjugate bases. An ab initio study **810**

Minh Tho Nguyen and Greet Raspoet The hydration mechanism of ketene: 15 years later **817**

Ian H. Williams and Paul A. Austin Theoretical simulation of Brønsted correlations for proton transfer and methyl transfer: the significance of the Brønsted coefficient β **830**

Duncan C. Hone, Brian H. Robinson, David C. Steytler, Roger W. Glyde, and John A. Cleverley Acid–base chemistry in high-performance lubricating oils **842**

Iva B. Blagoeva, Anthony J. Kirby, Asen H. Koedjikov, and Ivan G. Pojarlieff Multiple changes in rate-determining step in the acid and base catalyzed cyclizations of ethyl *N*-(*p*-nitrophenyl)hydantoates caused by methyl substitution **849**

Luis Viola and Rita H. de Rossi Effect of cyclodextrin on elimination reactions **860**

Maike Fischer, Yijian Shi, Bao-ping Zhao, Victor Snieckus, and Peter Wan Contrasting behaviour in the photosolvolysis of 1- and 2-hydroxy-9-fluorenols in aqueous solution **868**

L.J. Schaad, Laimutis Bytautas, and K.N. Houk Ab initio test of the usefulness of the Redlich–Teller product rule in computing kinetic isotope effects **875**

Kenneth Charles Westaway and W. Jiang Isotope effects in nucleophilic substitution reactions XI. The effect of ion-pairing, substituents, and the solvent on S_N2 transition states **879**

Agnes M. Modro and Tom A. Modro The phosphoryl and the carbonyl group as hydrogen bond acceptors **890**

Clifford A. Bunton, Houshang J. Foroudian, Nicholas D. Gillitt, and Anurag Kumar Reactions of aryl sulfides and phosphorus(V) esters of thiols with acidic hydrogen peroxide **895**

James Wojtyk, Andrew McKerrow, Peter Kazmaier, and Erwin Buncel Quantitative investigations of the aggregation behaviour of hydrophobic anilino squaraine dyes through UV/vis spectroscopy and dynamic light scattering **903**

Rajendra Rathore and Jay K. Kochi Vicinal–diaryl interactions in stilbenoid hydrocarbons as observed in the through-space charge delocalization of their cation radicals **913**

Tina L. Amyes, Tadeusz Mizerski, and John P. Richard How does organic structure determine organic reactivity? The effect of *ortho*-dimethyl groups on the nucleophilic substitution and alkene-forming elimination reactions of ring-substituted cumyl derivatives **922**

© 1999 NRC Canada

J. Peter Guthrie The hydration of ketene and carbon dioxide: an examination of the kinetics in terms of No Barrier Theory **934**

Sergei N. Smirnov, Hans Benedict, Nikolai S. Golubev, Gleb S. Denisov, Maurice M. Kreevoy, Richard L. Schowen, and Hans-Heinrich Limbach Exploring zero-point energies and hydrogen bond geometries along proton transfer pathways by low-temperature NMR **943**

Oswald S. Tee and Michael J. Boyd Aminolysis of naphthyl acetates catalyzed by cyclodextrins **950**

Yuqing Hou and Cal Y. Meyers The surprising formation of structurally distorted *ap*-9-(*o-tert*-butylphenyl)-9-methylthiofluorene and its facile homolysis into *sp*-9-(*o-tert*-butylphenyl)-3-methylthiofluorene and *sp*-9-(*o-tert*-butylphenyl)fluorene **960**

Mark A. Rishavy and W.W. Cleland ^{13}C, ^{15}N, and ^{18}O equilibrium isotope effects and fractionation factors **967**

Karen M. Engell, Robert A. McClelland, and Poul E. Sørensen The decomposition of methyl hemiacetals of benzaldehyde in aqueous solution: a study of the effect of aromatic substitution **978**

Jonas Nilsson, Kerstin S. Broo, Richard S. Sott, and Lars Baltzer Versatility of helix–loop–helix catalysts — cooperative $HisH^+$–His sites that span both helices **990**

X.L. Armesto, M. Canle L., V. García, and J.A. Santaballa Solvent isotope effects in the oxidation of dipeptides by aqueous chlorine **997**

Ayla Khan, Alexei A. Neverov, Anatoly K. Yatsimirsky, and R.S. Brown Strong Zn^{2+} and Co^{2+} catalysis of the methanolysis of acetyl imidazole and acetyl pyrazole **1005**

Weiguo Cao, Ihsan Erden, Richard H. Grow, James R. Keeffe, Jiangao Song, Mary B. Trudell, Teri L. Wadsworth, Fu-Pei Xu, and Ji-Bin Zheng Reactivity in acid-catalyzed carbon–carbon heterolysis **1009**

Wendy J. Dixon and Frank Hibbert Formation of a cyclic tetrahedral intermediate by the addition of water to 2-methyl-4*H*-3,1-benzoxazine followed by ring opening to 2-aminobenzyl acetate and 2-acetylaminobenzyl alcohol; pH-dependence of rate of reaction and product ratio **1035**

Wlodzimierz Galezowski, Iwona Grzeskowiak, and Arnold Jarczewski Kinetic study of the reactions of various types of C-acids with amine bases in acetonitrile. An unusual effect of common BH^+ cation on the rate constants **1042**

Eduardo Humeres, Valdir Soldi, Marilene Klug, Mauricéa Nunes, Célia M.S. Oliveira, and Patrick J. Barrie Hydrolysis and aminolysis of alkyl xanthate esters and cellulose analogues **1050**

John T. Edward, Francis L. Chubb, Denis F.R. Gilson, Rosemary C. Hynes, Françoise Sauriol, and Alain Wiesenthal Cage peroxides having planar bridgehead nitrogen atoms **1057**

Hideo Tomioka, Junichi Nakajima, Hidehiko Mizuno, Eiji Iiba, and Katsuyuki Hirai Spectroscopic studies on effects of triptycyl group on structures and reactivities of triplet arylcarbenes **1066**

R. Scott Reese and Marye Anne Fox Spectral and cyclic voltammetric characterization of self-assembled monolayers on gold of pyrene end-labeled oligonucleotide duplexes **1077**

A.M. Kuznetsov and Jens Ulstrup Proton and hydrogen atom tunnelling in hydrolytic and redox enzyme catalysis **1085**

Ernest Grunwald and Colin Steel About environmental isomers and their existence in liquid water **1097**

Stefano Talami and Charles J.M. Stirling A new silicon-mediated nitrogen to oxygen rearrangement **1105**

A. Esposito, A. Lukas, J.E. Meany, and Y. Pocker The reversible enolization and hydration of pyruvate: possible roles of keto, enol, and hydrated pyruvate in lactate dehydrogenase catalysis **1108**

Dennis N. Kevill and Malcolm J. D'Souza Correlation of the rates of solvolysis of phenyl chlorothionoformate and phenyl chlorodithioformate **1118**

Martin Newcomb, Seung-Yong Choi, and Patrick H. Toy Picosecond radical kinetics. Rate constants for ring openings of 2-aryl-substituted cyclopropylcarbinyl radicals **1123**

William J. Leigh, Rabah Boukherroub, Christine J. Bradaric, Christine C. Cserti, and Jennifer M. Schmeisser Steady state and time-resolved spectroscopic studies of the photochemistry of 1-arylsilacyclobutanes and the chemistry of 1-arylsilenes **1136**

Latifa Chahoua, Alain Vigroux, Yvonne Chiang, and James C. Fishbein Formation and nucleophilic capture of *N*-nitrosiminium ions **1148**

Dedication / Dédicace **iii**

© 1999 NRC Canada

Author Index / Index des auteurs **AI-1**

July / Juillet

ARTICLES

Jacek Lipkowski 1998 Alcan Award Lecture **1163**
Surface electrochemistry — surface science with a joy stick

S. Taconnet, Y. Simon, G. Scacchi et F. Baronnet Étude expérimentale et modélisation des réactions d'oxydation du néopentane et de l'isopentane **1177**

Om Prakash, Vijay Sharma, and Madan P. Tanwar Hypervalent iodine oxidation of α-substituted 2,4-dihydroxyacetophenones: synthesis of novel *o*-iodophenoxy ethers via rearrangement of iodonium ylides **1191**

Christopher M. Vogels, Heather L. Wellwood, Kumar Biradha, Michael J. Zaworotko, and Stephen A. Westcott Reactions of aminoboron compounds with palladium and platinum complexes **1196**

S. Göktürk, M. Mahramanlıoğlu, and M. Tunçay Surface tension studies of lauryl sulfobetaine – β-cyclodextrin and dodecyltrimethylammonium bromide – β-cyclodextrin inclusion complexes in aqueous solution **1208**

Kristin A. Fletcher, Carmen E. Hernández, Lindsay E. Roy, Karen S. Coym, and William E. Acree, Jr. Solubility of diphenyl sulfone in organic nonelectrolyte solvents. Comparison of observed versus predicted values based upon the general solvation model **1214**

Giuseppina Castronuovo, Vittorio Elia, Anna Pierro, and Filomena Velleca Chiral recognition in solution. Interactions of α-amino acids in concentrated aqueous solutions of urea or ethanol **1218**

Pierre Dabo, André Cyr, Jean Lessard, Louis Brossard, and Hugues Ménard Electrocatalytic hydrogenation of 4-phenoxyphenol on active powders highly dispersed in a reticulated vitreous carbon electrode **1225**

John Paul Pezacki Normal acid/base behaviour in proton transfer reactions to alkoxy substituted carbenes: estimates for intrinsic barriers to reaction and pK_a values **1230**

Brent E. Hawrylak and D. Gerrard Marangoni A 2-D NMR investigation of the micellar solubilization site in ionic micellar solutions **1241**

Jailall Ramnauth and Edward Lee-Ruff Photocycloelimination of α, α-dichlorocyclobutanones **1245**

Sarah J. Lord, Noah A. Epstein, Robert L. Paddock, Christopher M. Vogels, Tracy L. Hennigar, Michael J. Zaworotko, Nicholas J. Taylor, William R. Driedzic, Tom L. Broderick, and Stephen A. Westcott Synthesis, characterization, and biological relevance of hydroxypyrone and hydroxypyridinone complexes of molybdenum **1249**

John E. Drake, Layla N. Khasrou, Anil G. Mislankar, and Raju Ratnani Dimethyltellurium(IV) derivatives with mixed 1,1-dithio ligands. Crystal structures of $Me_2Te[S_2CNMe_2][S_2COEt]$ and $Me_2Te[S_2CNEt_2][S_2COMe]$ **1262**

Alexandre M. Polozov, Sheldon E. Cremer, and Phillip E. Fanwick Stereospecific thionation of 2-ethoxy-1,2-oxaphosphorinane 2-oxide and its derivatives with Lawesson's reagent **1274**

Simona G. Merica, Wojceich Jędral, Susan Lait, Peter Keech, and Nigel J. Bunce Electrochemical reduction and oxidation of DDT **1281**

D. Kumar Apparent molar volume of some ω-amino acids in aqueous electrolyte systems **1288**

K.C. Brown, B.R. Nelson, J.W. Quail, B.E. Robertson, J.A. Weil, and Z. Zimpel The structure and some molecular properties of acetone-picrylhydrazone **1295**

Ashraf A. El-Bindary, Adel Z. El-Sonbati, and Hanan M. Kera Thermodynamics of substituted pyrazolone. V: Potentiometric and conductometric studies of complexes of some transition metals with 4-(4-acetophenyl)hydrazono-3-methyl-2-pyrazolin-5-one **1305**

ADDITIONS AND CORRECTIONS / AJOUTS ET CORRECTIONS

Pierre G. Potvin Modeling complex solution equilibria. II. Systems involving ligand substitutions and uncertainties in equilibrium constants derived from formation constants **1310**

Author Index / Index des auteurs **AI-1**

© 1999 NRC Canada

August / Août

ARTICLES

Neil S. Cameron, Muriel K. Corbierre, and Adi Eisenberg 1998 E.W.R. Steacie Award Lecture **1311**
Asymmetric amphiphilic block copolymers in solution: a morphological wonderland

Faming Jiang, Kumar Biradha, Weng Kee Leong, Roland K. Pomeroy, and Michael J. Zaworotko **1327**
Dicarbonylcyclopentadienyliridium, $(\eta\text{-}C_5H_5)Ir(CO)_2$, as a ligand

Ayhan S. Demir, Zuhal Gercek, Nese Duygu, A. Cigdem Igdir, and Omer Reis Butenolide annelation using a manganese(III) oxidation. A synthesis of chromolaenin (Laevigatin) **1336**

Alex. D. Bain, P. Hazendonk, and P. Couture A reinterpretation of the substituent effect on the amide barrier. An experimental and theoretical study **1340**

S. Sadki, J.F. Fauvarque, M.T. Descarsin et P. Simon Électrosynthèse de films de polyparaphénylène déposés sur carbones **1349**

L.T. Okano, R. Ovans, V. Zunic, J.N. Moorthy, and C. Bohne Effect of cyclodextrin complexation on the photochemistry of the lignin model α-guaiacoxyacetoveratrone **1356**

Alexandre D. Konstantinov, Andrea N. Johnston, and Nigel J. Bunce Successive photocyanation of highly chlorinated aromatic compounds **1366**

Jun-ichi Ishiyama and Yuan L. Chow A novel photorearrangement of 1,3-diketonatoborinate: a photoinduced intramolecular alkylation on a conjugated carbonyl system **1374**

André Pialoux et Bernard Touzelin Étude du système U-Sr-O par diffraction X à haute température **1384**

Zhenghong Peng NMR conformational analysis on cyclic decapeptide template molecule **1394**

Kwang-Soon Choi, Kih-Soo Joe, Steven L. Mitchell, Candace J. Everall, and Keith R. Betty Determination of trace silicon in zirconium matrices and steels by inductively coupled plasma – atomic emission spectrometry **1405**

Yves Ducharme and Kimberly A. Harrison A versatile approach to the synthesis of oligonucleotide analogs containing neutral 5′-thioformacetal internucleoside linkages **1410**

Hiroto Tachikawa, Yoshihisa Yamada, and Tetsuji Iyama Mechanism of silylene extrusion reaction in cyclic polysilane via triplet energy surface: a direct MO dynamics study **1419**

Yousheng Zhang, Steven R. Breeze, Suning Wang, John E. Greedan, N.P. Raju, and Lijuan Li Polynuclear Co(II) and Cu(II) complexes of tetraacetylethane: $Cu^{II}_2(dpa)_2(tae)(O_2CCF_3)_2$, $\{[Cu^{II}_2(dpa)_2(tae)(4,4'\text{-bipy})](O_2CCF_3)_2\}_n$, and $[Co^{II}_2(dpa)_4(tae)](O_2CCH_3)_2(H_2O)_2$, dpa = 2,2′-dipyridylamine, tae = tetraacetylethane dianion **1424**

Eberhard Kiehlmann, Kumar Biradha, Konstantin V. Domasevitch, and Michael J. Zaworotko Crystal structures of dihydroquercetin 3-acetate and dihydroquercetin 3,3′,4′,7-tetraacetate: hydrogen bonding in 5-hydroxyflavanones **1436**

Timothy P. Bender, Yu Qi, Pierre Desjardins, and Zhi Yuan Wang Dendritic aryl imides containing the tetrahydro[5]helicene unit: synthesis, characterization, electrochemical behavior, and comparison with a linear oligoimide analogue **1444**

IUPAC Recommendations / Recommandations de I'UICPA **iii**

Author Index / Index des auteurs **AI-1**

September / Septembre

ARTICLES

Diethard K. Böhme 1998 J.C. Polanyi Award Lecture **1453**
Fullerene ions in the gas phase: chemistry as a function of charge state

Carmen E. Hernández, Karina M. De Fina, Lindsay E. Roy, Tina L. Sharp, and William E. Acree, Jr. **1465**
Solubility of phenanthrene in organic nonelectrolyte solvents. Comparison of observed versus predicted values based upon Mobile Order theory

© 1999 NRC Canada

Hongwei Sun, Zhifen Zhou, Huakuan Lin, Guanghua Zhao, Shourong Zhu, Xuncheng Su, and Yunti Chen Kinetic and equilibrium studies of the acid dissociation of the cobalt(II) complexes of *N*,*N*′-dialkyl-1,10-phenanthroline-2,9-dimathanamine ligands **1471**

Maricel Torrent, Liqun Deng, Miquel Duran, Miquel Solà, and Tom Ziegler Mechanisms for the formation of epoxide and chlorine-containing products in the oxidation of ethylene by chromyl chloride: a density functional study **1476**

Sandra Signorella, Claudia Palopoli, Alejandro Frutos, Graciela Escandar, Tomoaki Tanase, and Luis F. Sala 3-Deoxy-D-erythro-hexos-2-ulose bis(thiosemicarbazone) copper(II) chelate. Studies in solution and in the solid state **1492**

Nobuyoshi Koshino, Yoshio Kuchiyama, Shigenobu Funahashi, and Hideo D. Takagi Electron self-exchange, oxidation, and reduction reactions of bis(2,9-dimethyl-4,7-diphenyl-1,10-phenanthroline)copper(II/I) and bis(6,6′-dimethyl-2,′-bipyridine)copper(II/I) couples in acetonitrile: gated ET for the reduction, oxidation, and self-exchange processes **1498**

Raphaël Sabbah et Laurence Perez Étude thermodynamique des acides phtalique, isophtalique et téréphtalique **1508**

William A. Ayer, Monika Wichlacz, and Latchezar S. Trifonov Annotinine revisited. A new pentacyclo[7.3.3.$0^{1,13}$.$0^{2,12}$.$0^{5,13}$]pentadecane ester and other products derived from annotinine **1514**

H. Teruel and A. Sierraalta New aspects on the reactivity of $MoO_2(S_2CNEt_2)_2$ with Me_3SiX. A peculiar *trans* effect control **1521**

A. Jerry Kresge and Qingshui Meng Carboxylic acid amide enols: keto–enol/enolate interconversion of *N*-methylindoline-2-one and its 2-thione and 2-selone analogs in aqueous solution **1528**

Karina M. De Fina, Tina L. Sharp, and William E. Acree, Jr. Solubility of acenaphthene in organic nonelectrolyte solvents. Comparison of observed versus predicted values based upon Mobile Order theory **1537**

Christiane Ferradini et Jean-Paul Jay-Gerin La radiolyse de l'eau et des solutions aqueuses : historique et actualité **1542**

IUPAC Recommendations / Recommandations de I'UICPA **iii**

Author Index / Index des auteurs **AI-1**

October / Octobre

ARTICLES

H. Oumar-Mahamat, H. Ślebocka-Tilk, and R.S. Brown Long chain β-aminoethanols as micellar catalysts for the hydrolysis of diphenyl-*p*-nitrophenyl phosphate. The observation of an unusual enhancement of catalysis in the presence of added polyols **1577**

Karina M. De Fina, Tina L. Sharp, and William E. Acree, Jr. Solubility of biphenyl in organic nonelectrolyte solvents. Comparison of observed versus predicted values based upon Mobile Order theory **1589**

Chakib Ameziane Hassani et Hugues Ménard Étude de l'adsorption des hydrocarbures aromatiques polycycliques sur l'hydroxyde d'aluminium par chromatographie liquide à haute pression **1594**

Kathryn N. Rankin, W. David Chandler, and Keith E. Johnson Thermodynamic calculations for reactions involving hydrogen halide polymers, ions, and Lewis acid adducts. 4. The temperature dependence of some reactions of HF and HCl **1599**

F.J. Carmona, F.J. Arroyo, I. García de la Fuente, J.A. González, and J.C. Cobos Excess molar volumes of methanol or ethanol + *n*-polyethers at 298.15 K **1608**

Kulwinder K. Flora, Monika A. Dabrowski, Sean P. Musson, and John D. Brennan The effect of preparation and aging conditions on the internal environment of sol-gel derived materials as probed by 7-azaindole and pyranine fluorescence **1617**

Robert Schutte, Gordon R. Thompson, Kingsley K. Donkor, M. John M. Duke, Roger Cowles, Xiu Ping Li, and Byron Kratochvil Estimation of particle size distribution in Athabasca oil sands by indirect instrumental neutron activation analysis **1626**

© 1999 NRC Canada

Mitsuru Matsumoto, Makoto Itoh, Shigenobu Funahashi, and Hideo D. Takagi Electron transfer reactions of bis(1,4,7-trithiacyclononane)palladium(III/II), -platinum(III/II), and -gold(III/II) complexes in aqueous solution and in acetonitrile **1638**

F. Williot, M. Bernard, D. Lucas, Y. Mugnier, and J. Lessard Addition of cyclopentadiene derivatives on aromatic aldehydes or nitrosobenzene initiated by electrochemical reduction **1648**

Dino Mangion and Donald R. Arnold The photochemistry of 4-halobenzonitriles and 4-haloanisoles with 1,1-diphenylethene in methanol. Homolytic cleavage versus electron-transfer pathways **1655**

Hu Yang, Zhenghua Ping, Yingcai Long, and Quang Trong Nguyen Improved hydrophobic zeolites to fill silicone membranes for ethyl acetate extraction from water by pervaporation **1671**

Mark E. McGovern and Michael Thompson Thiol functionalization of surfaces for biosensor development **1678**

B.N. Achar and P.K. Jayasree New "molecular metals" based on symmetrically tetrasubstituted copper phthalocyanine complexes **1690**

IUPAC Recommendations / Recommandations de I'UICPA **iii**

Author Index / Index des auteurs **AI-1**

November / Novembre

This issue is dedicated to Professor Theodore P. Schaefer
Ce tirage est dédié au Professeur Theodore P. Schaefer

Ludger Ernst, Thomas Rieck, and Mark Soliven Preferred conformation and barriers to internal rotation of *ortho*-disubstituted cyclopropylbenzenes **1697**

Peter J. Heard, Alex D. Bain, and Paul Hazendonk Stereochemical rearrangements in tricarbonylrhenium(I) halide complexes of the nonracemic chiral ligand 2-[(4*R*,5*R*)-dimethyl-1,3-dioxan-2-yl]pyridine (L): a dynamic NMR study **1707**

S. Shojania, M.E. McComb, R.D. Oleschuk, H. Perreault, H.D. Gesser, and A. Chow Qualitative analysis of complex mixtures of VOCs using the inside needle capillary adsorption trap **1716**

R.E.D. McClung, T.T. Nakashima, H. Yamamoto, and G. Kotovych Determination of proton exchange rates in aqueous solution using TOCSY **1728**

Gary A. Stern and John B. Westmore Geometrical isomerism and ^{19}F NMR spectroscopy of octahedral perfluoroethyl- and perfluoropropyl-substituted β-diketonates and monothio-β-diketonates of rhodium(III) **1734**

Serge Lacelle Time-reversal in NMR of solids **1745**

Mark E. McComb, Lynda J. Donald, and Hélène Perreault Electrospray ionization mass spectrometry and on-line capillary zone electrophoresis – mass spectrometry for the characterization of citrate synthase **1752**

Raymond T. Syvitski and E. Elliott Burnell NMR and molecular structure of partially oriented mono and *para* methyl- and chlorobenzenes dissolved in nematic liquid crystals **1761**

Christopher D. Daub, Bryan R. Henry, Martin L. Sage, and Henrik G. Kjaergaard Modelling and calculation of dipole moment functions for XH bonds **1775**

Simon Sham and Gang Wu Zinc-67 NMR study of tetrahedral and octahedral zinc sites with symmetrical oxygen, nitrogen, and sulfur ligands **1782**

Juhani Lounila, Yrjö Hiltunen, Kari Tuppurainen, Anja Pulkkinen, and Reino Laatikainen Solvent dependence of rotational energetics and formyl-proton long-range spin–spin coupling behavior of 2,6-dichloro- and 2,6-dinitrobenzaldehydes using dipolar couplings and temperature dependence of long-range couplings **1788**

Alaa S. Abd-El-Aziz, Andrea L. Edel, Leslie J. May, Karen M. Epp, and Harold M. Hutton Controlled molecular design of ether- and ester-bridged norbornenes and their ring-opening metathesis polymerizations **1797**

Alex. D. Bain On combination lines in the NMR spectra of strongly coupled spin systems **1810**

Glenn H. Penner, Y.C. Phillis Chang, and H. Michelle Grandin A solid state NMR and molecular orbital study of hydroxylammonium chloride **1813**

© 1999 NRC Canada

Ian R. Baird, Steven J. Rettig, Brian R. James, and Kirsten A. Skov Synthesis and X-ray structural characterization of the ruthenium β-diketonato complexes: $Ru(hfac)_3$, *cis*-$Ru(hfac)_2(MeCN)_2$, and *cis*-$Ru(hfac)(acac)(MeCN)_2$ **1821**

Brian Pettitt and Werner Danchura Symmetry in double-diffusive convection **1834**

Pamela S. Bromberg, Kathleen M. Gough, and Ian M.C. Dixon Collagen remodeling in the extracellular matrix of the cardiomyopathic Syrian hamster heart as assessed by FTIR attenuated total reflectance spectroscopy **1843**

James A.W. Shoemaker and J. Stephen Hartman Chelated fluoroboron cations. I. Synthesis and NMR studies involving the tertiary-amine ligands *N*,*N*,*N*′,*N*′-tetramethylethylenediamine and *N*,*N*,*N*′,*N*″,*N*″-pentamethyldiethylenetriamine **1856**

Dingliang Zhang, Markus Heubes, Gerhard Hägele, and Friedhelm Aubke A ^{19}F nuclear magnetic resonance study of the conjugate Brönsted–Lewis superacid $HSO_3F–SbF_5$. Part 1 **1869**

Richard Buist, Scott Kroeker, and James Peeling Temperature dependence of the creatine kinase reaction measured in rat brain in vivo by ^{31}P NMR saturation transfer **1887**

Dharamdat Christendat, Ian S. Butler, Denis F.R. Gilson, and Frederick G. Morin Solid-state nuclear magnetic resonance studies of triphenylsilyl-, triphenyltin-, and triphenyllead(pentacarbonyl)manganese(I) complexes **1892**

Glenn A. Facey, Tina P. Fong, Dmitry Gusev, Peter M. Macdonald, Robert H. Morris, Marcel Schlaf, and Wei Xu Probing the motion of the η^2-dideuterium ligand by solution and solid-state ^2H NMR spectroscopy **1899**

G.W. Buchanan, M. Gerzain, and C.I. Ratcliffe Symmetry, disorder, and dynamics in solid crown ether complexes: ^2H NMR studies of 15-crown-5·NaI, 15-crown-5·$NaClO_4$, and 21-crown-7·KI **1911**

William F. Reynolds, Stewart McLean, Helen Jacobs, and Wayne W. Harding Assignment of ^1H and ^{13}C spectra for polyprenol-12, a molecule with severe ^1H and ^{13}C spectral crowding, with the aid of high-resolution, ^{13}C-detected, $^{13}C–^1H$ shift correlation spectra **1922**

Dawn M. Friesen, Robert McDonald, and Lisa Rosenberg Tris{(diphenylphosphino)dimethylsilyl}methane: a sterically hindered tripod **1931**

Eugene P. Mazzola, Sandra J. Bell, Saleh A. Turujman, Julie N. Barrows, John E. Bailey, Jr., Joseph B. McMahon, Tania K. Germann, and William F. Reynolds Nuclear magnetic resonance investigations of azo-hydrazone, acid–base equilibria of FD&C Yellow No. 5 (tartrazine) **1941**

A.D. Buckingham and Y. Tantirungrotechai The second dielectric virial coefficient of the dipolar Gay–Berne fluid **1946**

Michael J.T. Ditty and William P. Power ^{31}P chemical shielding as a function of bond angle: phosphorus chemical shielding surface of phosphinoborane $R_2PBR'_2$ **1951**

Scott Kroeker and Roderick E. Wasylishen A multinuclear magnetic resonance study of crystalline tripotassium tetracyanocuprate **1962**

Robert W. Schurko, Roderick E. Wasylishen, Scott J. Moore, Luigi G. Marzilli, and John H. Nelson Solid-state phosphorus-31 NMR study of phosphine- and phosphite-substituted cobaloximes **1973**

Colin A. Fyfe, Andrew R. Lewis, and Jean-Michel Chézeau A comparison of NMR distance determinations in the solid state by cross polarization, REDOR, and TEDOR techniques **1984**

Judith A. MacInnis, R. Palepu, and D. Gerrard Marangoni A nuclear magnetic resonance investigation of the micellar properties of a series of sodium cyclohexylalkanoates **1994**

Dedication / Dédicace **iii**

Author Index / Index des auteurs **AI-1**

December / Décembre

ARTICLES

Geoffrey A. Ozin 1999 Pure or Applied Inorganic Chemistry Award Lecture Curves in chemistry: supramolecular materials taking shape **2001**

Marie-Hélène Baron, Sabine Halut-Desportes, Hai-Fen Ye, Jack Huet, and Edith Favre Spectroscopic conformational study of PMS 952, a specific imidazoline ligand. Experimental results **2015**

Victor Barba, Cecilia Hernández, Susana Rojas-Lima, Norberto Farfán, and Rosa Santillan Preparation of *N*-aryl-substituted spiro-β-lactams via Staudinger cycloaddition **2025**

© 1999 NRC Canada

Ika A. Setyawati, Steven J. Rettig, and Chris Orvig Cationic iron(III) complex with a hexadentate N_2,N'_2,O_2-aminopyridylphenolate ligand **2033**

Yoshikato Koga Fluctuations in aqueous methanol, ethanol, and propan-1-ol: amplitude and wavelength of fluctuation **2039**

Carmen Jarne, Manuela Artal, José Muñoz Embid, Inmaculada Velasco, and Santos Otín Temperature and pressure dependence of the volumetric properties of binary mixtures containing polyhaloalkanes **2046**

Alexei N. Pankratov and Andrew E. Shchavlev Semiempirical quantum chemical PM3 computations and evaluations of redox potentials, basicities, and dipole moments of the diphenylamine series as analytical reagents **2053**

Fernande D. Rochon and Gassan Massarweh Reactions of monovalent ions with a versatile building block $[Cr(phen)(C_2O_4)_2]^-$. Molecular and crystal structures of $NaCr(phen)(C_2O_4)_2\cdot 3H_2O$, $KCr(phen)(C_2O_4)_2\cdot DMF\cdot 0.5H_2O$, $4\text{-}NH_3py[Cr(phen)(C_2O_4)_2]\cdot 2H_2O$, $N\text{-}(n\text{-butyl})_4[Cr(phen)(C_2O_4)_2]$, and $PPh_4[Cr(phen)(C_2O_4)_2]$ **2059**

Frances L. Cozens, V.M. Kanagasabapathy, Robert A. McClelland, and Steen Steenken Lifetimes and UV-visible absorption spectra of benzyl, phenethyl, and cumyl carbocations and corresponding vinyl cations. A laser flash photolysis study **2069**

S.C. Jakeway and U.J. Krull Consideration of end effects of DNA hybridization in selection of fluorescent dyes for development of optical biosensors **2083**

Sudeep Bhattacharyya, Raymond J. Batchelor, Frederick W.B. Einstein, and Alan S. Tracey Crystal structure and solution studies of the product of the reaction of β-mercaptoethanol with vanadate **2088**

Simon J. Coles, Michael B. Hursthouse, David G. Kelly, Andrew J. Toner, and Neil M. Walker Schiff base insertion in titanium alkyls; reduction of imine functions by benzyl addition **2095**

Rémi Valéro, Bernard Durand, Jean-Louis Guth et Thierry Chopin Influence des ions fluorure et de la silice amorphe sur la solubilité des gels de zircone et caractérisation des fluoro-complexes de zirconium en milieu moyennement acide **2099**

Lily Yeo and Kenneth D.M. Harris Temperature-dependent structural properties of a solid urea inclusion compound containing chiral guest molecules: 2-bromotetradecane/urea **2105**

Author Index / Index des auteurs **AI-1**

Contents for volume 77 / Sommaire pour volume 77 **C-1**

© 1999 NRC Canada